Material Forming

The 26th International ESAFORM Conference on Material Forming – ESAFORM 2023 – held in Kraków, Poland, April 19-21, 2023

Edited by
Lukasz Madej
Mateusz Sitko
Konrad Perzynski

MRF

Material Forming
ESAFORM 2023

The 26th International ESAFORM Conference on Material Forming – ESAFORM 2023 – held in Kraków, Poland, April 19-21, 2023

Editors
Lukasz Madej
Mateusz Sitko
Konrad Perzynski

Peer review statement

All papers published in this volume of "Materials Research Proceedings" have been peer reviewed. The process of peer review was initiated and overseen by the above proceedings editors. All reviews were conducted by expert referees in accordance to Materials Research Forum LLC high standards.

Copyright © 2023 by authors

Content from this work may be used under the terms of the Creative Commons Attribution 3.0 license. Any further distribution of this work must maintain attribution to the author(s) and the title of the work, journal citation and DOI.

Published under License by **Materials Research Forum LLC**
Millersville, PA 17551, USA

Published as part of the proceedings series
Materials Research Proceedings
Volume 28 (2023)

ISSN 2474-3941 (Print)
ISSN 2474-395X (Online)

ISBN 978-1-64490-246-2 (Print)
ISBN 978-1-64490-247-9 (eBook)

This book contains information obtained from authentic and highly regarded sources. Reasonable efforts have been made to publish reliable data and information, but the author and publisher cannot assume responsibility for the validity of all materials or the consequences of their use. The authors and publishers have attempted to trace the copyright holders of all material reproduced in this publication and apologize to copyright holders if permission to publish in this form has not been obtained. If any copyright material has not been acknowledged please write and let us know so we may rectify in any future reprint.

Distributed worldwide by

Materials Research Forum LLC
105 Springdale Lane
Millersville, PA 17551
USA
https://www.mrforum.com

Manufactured in the United State of America
10 9 8 7 6 5 4 3 2 1

Table of Contents

Preface
Committees

Additive manufacturing

Design and evaluation of liquid channel cross sections fabricated via metal fused filament fabrication
BACIKOGLU Mehmet Canberk, YAMAN Ulas 3

Modeling the shape of additive manufactured parts
BRUNI Carlo, CICCARELLI Daniele, PIERALISI Massimiliano, MANCIA Tommaso 13

Resources and manufacturing technology evaluation of hybrid additive metal laminated tooling for forming
DARDAEI JOGHAN Hamed, HAHN Marlon, AGBOOLA Ololade, TEKKAYA A. Erman 21

Prediction of surface topography change during chain of selective laser melting and burnishing
TEIMOURI Reza, SKOCZYPIEC Sebastian, GRABOWSKI Marcin..... 31

Development and processability of AISI S2 tool steel by laser powder bed fusion
SAGGIONETTO Enrico, FILIPPI Elena, DEDRY Olivier, TCHUINDJANG Jérôme T., MERTENS Anne..... 41

Experimental analysis of cold sprayed precursors for closed-cells aluminum foams
VISCUSI Antonio, PERNA Alessia Serena, ASTARITA Antonello, BORRELLI Domenico, CARAVIELLO Antonio, SICIGNANO Nicola, CARRINO Luigi 49

A machine learning approach for adhesion forecasting of cold-sprayed coatings on polymer-based substrates
PERNA Alessia Serena, CARRINO Luigi, CITARELLA Alessia Auriemma, De MARCO Fabiola, Di BIASI Luigi, TORTORA Genoveffa, VISCUSI Antonio 57

Process-dependent material characteristics of dmls-manufactured specimens
ZETTEL Dominic, BREITKOPF Piotr, NICOLAY Pascal, WILLMANN Roland..... 65

Development of a new method utilizing semi-solid aluminum wires for extrusion based additive manufacturing
NEZIC Nikola, SPETH Marco, ROUVEN RIEDMÜLLER Kim, LIEWALD Mathias 75

In-situ consolidation of additively manufactured continuous fiber reinforced material: Technical approach and results
OBERLERCHER Hannes, LAUX Marius, HEIM Rosmarie, BERNDT Alexander, AMANCIO-FILHO Sergio T., RIEMELMOSER Franz O. 85

Characterisation of the shape memory effect of PET polymer by FFF 3D printing
ERMOLAI Vasile, SOVER Alexandru, LANG Anette..... 93

In process monitoring of geometrical characteristics in laser metal deposition: A comparative study
LATTE Marco, GUERRA Maria Grazia, MAZZARISI Marco, ANGELASTRO Andrea, CAMPANELLI Sabina Luisa, GALANTUCCI Luigi Maria 101

Optical absorption and conduction of copper carbon nanotube composite for additive manufacturing
AYUB Hasan, KHAN Lehar Asip, MCCARTHY Eanna, AHAD Inam Ul, SREENILAYAM Sithara P., FLEISCHER Karsten, BRABAZON Dermot 111

Influence of process parameters and head orientation on bead geometry for coaxial wire laser additive manufacturing
ROCH Clément, TOURNIER Christophe, LAVERNHE Sylvain 119

Additive manufacturing of cermet produced by laser powder bed fusion using alternative Ni binder
PAPY Kevin, BORBELY Andras, SOVA Alexey, FAVRE Julien, BERTRAND Philippe, STAERCK Jean-Marc 129

Fused filament fabrication: Numerical adhesion modeling suitable for semicrystalline polymers
BENARBIA Adel, SOBOTKA Vincent, BOYARD Nicolas, ROUA Christophe 139

Application of the plane-strain-compression-test to determine the local mechanical properties of LPBF-manufactured 316l components
JENSCH Felix, BUHL Johannes, LAUE Robert, HÄRTEL Sebastian 149

Determination of welding heat source parameters for fem simulation based on temperature history and real bead shape
SZYNDLER Joanna, SCHMIDT Alexander, HÄRTEL Sebastian 159

Generating STL for forming trabecular bone structure in additive manufacturing using cell dynamics modeling
ROCHA Adones A., THIRÉ Rossana M.S.M., ARAUJO Anna-Carla 169

Analysis of additively manufactured anisotropic microstructures through crystal plasticity frameworks
BULUT Orhun, GÜNAY Enes, FENERCIOĞLU Tevfik Ozan, YALÇINKAYA Tuncay 179

2D FE modeling of the thermal history of the heat affected zone in AlSi10Mg LPBF
DELAHAYE Jocelyn, HABRAKEN Anne, MERTENS Anne 189

Semi-finished powder of aluminum matrix composite for a direct energy deposition additive manufacturing
JEDYNAK Angelika, ERTUGRUL Gökhan, NEUMANN Andreas, PIPPIG Robert, HÄRTEL Sebastian 199

Rapid tooling development for low volume injection molding of cosmetic compacts
VELLA Andrea, ROCHMAN Arif, VELLA Pierre 207

Composites forming processes

Modeling of 3D fluid-structure-interaction during in-situ hybridization of double-curved fiber-metal-laminates
POPPE Christian, KRUSE Moritz, KÄRGER Luise 219

Modelling the forming of tailored fibre placement preforms: A tetrahedral part with final orthotropic orientations
SIMON Jessy, HAMILA Nahiene, BINÉTRUY Christophe, COMAS-CARDONA Sébastien 231

Proposing a virtual simulation method to predict the shape-fidelity of 3D-knitted-textiles using knit-meshes and geometric invariants
DIETRICH Franz 239

Feasibility study of compression molding for large reinforcement structures in the commercial vehicle sector
LÜCKENKÖTTER Julian, LEIMBACH Jan-Patrick, STALLMEISTER Tim, MARTEN Thorsten, TRÖSTER Thomas 249

Compaction behaviour of magnesium alloy-based fibre metal laminates at varying forming parameters
LIU Zheng, SIMONETTO Enrico, GHIOTTI Andrea, BRUSCHI Stefania 259

Experimental setup and method for the characterization of ply-ply adhesion for fiber-reinforced thermoplastics in melt
PIERIK Rens, ROUWMAAT Thijs, GROUVE Wouter, WIJSKAMP Sebastiaan, AKKERMAN Remko 267

XCT-based microscale analysis of structure and deformability of abdominal wall meshes
SOETE Jeroen, MAES Arne, ROJAS Camilo, KYOSEV Yordan, SCHMIDT Ann-Malin, LOMOV Stepan V., MISEREZ Marc, KERCKHOFS Greet, WEVERS Martine 277

A unit-cell mesoscale modelling of biaxial non-crimp-fabric based on a hyperelastic approach
ZHENG Ruochen, SCHÄFER Bastian, PLATZER Auriane, COLMARS Julien, NAOUAR Naim, BOISSE Philippe 285

In-plane deformation measurements for validation of composite forming simulations
BRANDS Dennis, VAN KAMMEN Kevin M., WIJSKAMP Sebastiaan, GROUVE Wouter J.B., AKKERMAN Remko 293

Manufacturing of hybrid thermoplastic-thermoset fiber reinforced composite and metallization by cold spray technique
PARMAR Hetal, RUBINO Felice, POZA Pedro, CARLONE Pierpaolo 305

Thermo-chemical modeling and simulation of glass/elium® acrylic thermoplastic resin composites
DENIS Yvan, SIDDIG Nihad, GUITTON Raphael, LE BOT Philippe, DE FONGALLAND Antoine, LECOINTE Damien 313

Gate design algorithm to maximize the fiber orientation effectiveness in thermoplastic injection-molded components
PERIN Mattia, BERTI Guido A., LEE Taeyong, QUAGLIATO Luca 321

Investigation of the compaction behavior of uni- and bidirectional non-crimp fabrics
SCHÄFER Bastian, ZHENG Ruochen, BOISSE Philippe, KÄRGER Luise 331

Forming of textile fabrics with additively assembled protective elements on the human body
KYOSEV Yordan, MÜNKS Dominik 339

Process and structural simulation for the development of a pressure vessel through filament winding technology
BIANCHI Iacopo, FORCELLESE Archimede, GALLIANI Francesco, GRECO Luciano, MIGNANELLI Chiara, TREVISAN Giulio 347

Modeling multiaxial stress states in forming simulation of woven fabrics
KÄRGER Luise, SCHÄFER Florian, WERNER Henrik O. 357

Automated programming for the robotic layup process
GAMBARDELLA Antonio, ESPERTO Vitantonio, TUCCI Fausto, CARLONE Pierpaolo 367

Experimental study of woven fabrics forming defects
SHANWAN Anwar, GHANAMEH Mohamas-Fathi, BIJU Aditya, HIVET Gilles 375

Surrogate model of the thermoforming of fiber reinforced thermoplastics
MIDDELHOFF Jan, UJVARI Csenger, HÜRKAMP André, DRÖDER Klaus 385

Investigation on the pultrusion of thermoplastic preimpregnated polypropylene-glass tapes
TUCCI Fausto, RUBINO Felice, ESPERTO Vitantonio, PASQUINO Germana, CARLONE Pierpaolo 393

Crush core forming: An innovative technology to manufacture structural sandwich parts with variable thickness
SORRENTINO Luca, BELLINI Costanzo, PARODO Gianluca, RUBINO Felice 399

An Inverse method for determining fabric permeability in vacuum assisted resin infusion for composite parts forming
VOSNIAKOS George-Christopher, DIMAKOPOULOS Panagiotis J., VASILEIOU Anastasia 407

Extrusion and drawing

Phenomena of tool adhesion at elevated temperature in V-groove friction test of AA7075
FUNAZUKA Tatsuya, DOHDA Kuniaki, KINOSHITA Mizuki, SUZUKI Shiro 419

Effects of cold-drawing and low-temperature annealing on the sensing properties of NiTi alloys
LI Yongji, LIN Jianping, XIAO Yao, MIN Junying 429

Electron backscatter diffraction (EBSD) as a tool for analysis of metal flow in aluminum extrusion
PIRES Michael V., MADURA Jacek, MISIOLEK Wojciech Z., LEŚNIAK Dariusz, ZASADZIŃSKI Józef, JURCZAK Henryk 437

Chevron cracking during full forward impact extrusion of aluminum alloy EN AW 7075 in dependence of heat treatment condition and tribological system
MÜLLER Martina, SCHWARK Niklas, WEISER Ingo F., HERRIG Tim, BERGS Thomas ... 445

Effects of disc milling and indirect extrusion processing on mechanical properties of aluminum-graphene-composites with commercial GNPs
NEGENDANK Maik, GANCHULUUN Enkhtaivan, JAIN Nishant, MÜLLER Sören 455

Yield stress and work hardening behavior of extruded AA6082 profiles under different homogenization and extrusion conditions
WILLIAMS William M., SANDNES Lise, MA Jun, TRONVOLL Sigmund Arntsønn, WELO Torgeir 467

Experimental analysis and modeling of the recrystallization behaviour of a AA6060 extruded profile
NEGOZIO Marco, DONATI Lorenzo, PELACCIA Riccardo, REGGIANI Barbara, DI DONATO Sara 477

Process simulation of friction extrusion of aluminum alloys
DIYOKE George, RATH Lars, CHAFLE Rupesh, BEN KHALIFA Noomane, KLUSEMANN Benjamin 487

Numerical study on cold extrusion of gears varying the extrusion shoulder geometry
DELIKTAS Tahsin, LIEWALD Mathias 495

Investigations into the processing and texture of Pr-substituted NdFeB magnets produced by extrusion
RÜDIGER Alexander, GALL Sven, MÜLLER Sören 505

Friction extrusion processing of aluminum powders: Microstructure homogeneity and mechanical properties
CHAN Chang Yin-Cheng, RATH Lars, SUHUDDIN Uceu F. H., KLUSEMANN Benjamin . 515

Progression of plastic die deformation during copper extrusion
LECHNER Stefan, MÜLLER Sören 523

Investigation on the topological optimization of cooling channels for extrusion dies
PELACCIA Riccardo, REGGIANI Barbara, NEGOZIO Marco, DI DONATO Sara, DONATI Lorenzo 533

Investigation of the skin contamination predictability by means of QForm UK extrusion code
KNIAZKIN Ivan, PELACCIA Riccardo, NEGOZIO Marco, DI DONATO Sara, DONATI Lorenzo, REGGIANI Barbara, BIBA Nikolay, REZVYKH Ruslan, KULAKOV Ivan 543

Crystal plasticity finite element analysis of linear and non-linear extrusion processes
ŞIMŞEK Ülke, MIYAMOTO Hiroyuki, YALÇINKAYA Tuncay 553

Critical comparison of different techniques for producing profiled wires
KWIECIEŃ Marcin, MUSZKA Krzysztof, MAJTA Janusz 563

Forging and rolling

Design of a forging process to individually examine thermal, mechanical and tribological stress in the tool surface zone
BEHRENS Bernd-Arno, MÜLLER Felix, LORENZ Uwe 573

Hot die forging with nitrided and thermally stabilized DLC coated tools
SIEGMUND Martin, KIPP Christian, PEDDINGHAUS Julius, BRUNOTTE Kai, BRÄUER Günter, BEHRENS Bernd-Arno 583

Investigation of the joining zone formation of impact extruded hybrid components by varied forming sequence and partial cooling
PIWEK Armin, PEDDINGHAUS Julius, UHE Johanna, BRUNOTTE Kai, BEHRENS Bernd-Arno 591

Advanced automatic pass schedule design for hot rolling by coupling reinforcement learning with a fast rolling model
IDZIK Christian, GERLACH Jannik, BAILLY David, HIRT Gerhard 601

Beneficial effect of stress superposition on damage reduction in trimming processes
WEIß Alexander, FELDE Alexander, LIEWALD Mathias, ZERFAß Helmut 611

Determination of recrystallisation phenomenon in type 316 stainless steel VIM-VAR ingots during cogging operations
PAQUETTE Arthur, LANGLOIS Laurent, VIOLATOS Ioannis, RAHIMI Salaheddin, DUMONT Christian, BIGOT Régis 621

Study of forming defects and failure occurrence in the radial-axial rolling of super duplex stainless steel rings
MURILLO-MARRODÁN Alberto, GARCÍA GIL Eduardo, FERNANDEZ-GAMBOA Unai, CONDE Aintzane, LOZARES Jokin 629

Detailed study of tube hot rolling process by means of FEM
GARCÍA GIL Eduardo, DURÁN Gorka Llamazares, CONDE Aintzane, MURILLO-MARRODÁN Alberto, ATUTXA Jon Barco 639

Parametric identification on a dynamic behavior model for a forging machine
DURAND Camille, SONG Heyu, BIGOT Régis 649

An analytical approach for modelling incremental disk rolling process
ACAR Sadik Sefa, DINÇER Mehmet Şamil, OZCATALBAS Mustafa 657

Evolution of microstructure during hot incremental disk rolling of a nickel-based super-alloy
DINÇER Mehmet Şamil, OZCATALBAS Mustafa, ACAR Sadik Sefa, MUSIC Omer, ŞIMŞIR Caner 667

Effect of near beta-transus forging parameters on the mechanical and microstructural properties of Ti-6Al-4V – Application to hammer forging
AGIRRE Julen, ERICE Borja, ARRESE Peio, OTEGI Nagore, GALDOS Lander 675

Benchmarking mean-field models available in commercial FE software in application to two-blow forging of IN718 alloy
RESHETOV Aleksey, BYLYA Olga 683

Formability of metallic materials

Total strain on the outer surface of steel sheets in air bending
POKKA Aki-Petteri, KESTI Vili, KAIJALAINEN Antti 695

Prediction of forming limit diagram of automotive sheet metals using a new necking criterion
PHAM Quoc Tuan, ISLAM Md Shafiqul, SIGVANT Mats, CARO Perez Lluis 705

Anisotropic deformation behavior during cup drawing at room temperature of a ZX10 magnesium alloy sheet
HAMA Takayuki, HIGUCHI Koichi, NAKATA Yuto 711

Modelling failure of joining zones during forming of hybrid parts
WESTER Hendrik, STOCKBURGER Eugen, PEDDINGHAUS Simon, UHE Johanna, BEHRENS Bernd-Arno 717

Influence of process parameters and process set-up on damage evolution during stretch drawing of u-shaped profiles
MÜLLER Martina, WEISER Ingo Felix, HERRIG Tim, BERGS Thomas 727

Improved failure characterisation of high-strength steel using a butterfly test rig with rotation control
STOCKBURGER Eugen, WESTER Hendrik, JEGATHEESWARAN Vithusaan, DYKIERT Matthäus, BEHRENS Bernd-Arno 737

Investigation of the influence of loading direction after pre-forming on the formability and mechanical properties of DP600
NORZ Roman, VALENCIA Fabuer R., VITZTHUM Simon, UNGUREANU Bogdan, GERKE Steffen, BRÜNIG Michael, VOLK Wolfram 747

Heat assisted V-bending characteristics of high strength S700MC steel
GÖRTAN Mehmet Okan, CAGIRANKAYA Fatih, OZSOY Oguz 755

A stress-based proposal for wrinkling criterion of clamped surfaces
BORBÉLY Richárd, KÖLÜS Martin L., BÉRES Gábor J. 761

Evaluation of hot and warm forming of age-hardenable aluminium alloys into manufacturing of automotive safety critical parts
MYROLD Benedikte, JENSRUD Ola, HOLMESTAD Jon 771

Nonlinear stress path experiment using mild steel sheet for validation of material model
TAKADA Yusuke, KUWABARA Toshihiko 779

Damage prediction in roll forming of the high strength aluminum alloy AA7075
SUCKOW Timon, GROCHE Peter 787

Multi-scale modeling of the effect of crystallographic texture
REVIL-BAUDARD Benoit, CAZACU Oana 799

Experimental identification of uncoupled ductile damage models and application in flow forming of IN718
VURAL Hande, ERDOGAN Can, KARAKAŞ Aptullah, FENERCIOGLU Tevfik Ozan, YALÇINKAYA Tuncay 807

Deformation analysis of ZnMgAl coated steel sheet using digital image correlation (DIC) system
LISIECKA - GRACA Paulina, MUSZKA Krzysztof, KWIECIEŃ Marcin, DZIURDZIA Jakub 817

Hybrid SPD process of aluminium 6060 for microforming
PRESZ Wojciech, JASIŃSKI Cezary, MORAWIŃSKI Łukasz, ORŁOWSKA Marta 825

Influence of intercritical annealing temperature on formability and mechanical properties of medium-manganese-steel in press hardening
TILLY Karl Johann, PLUM Tobias, BAILLY David, HIRT Gerhard 833

Specific behavior of high-manganese steels in the context of temperature increase during dynamic deformation
JABŁOŃSKA Magdalena B., GRONOSTAJSKI Zbigniew, TKOCZ Marek, JASIAK Katarzyna, KOWALCZYK Karolina, SKWARSKI Mateusz, KOSTKA Michał 839

Effect of prestrain on mechanical behavior of aluminum alloys
VINCZE Gabriela, BUTUC Marilena C., WEN Wei, YÁNEZ Jesús, LOPES Diogo 847

Determination of the forming limit curve of locally annealed aluminum blanks
PICCININNI Antonio, LATTANZI Attilio, ROSSI Marco, PALUMBO Gianfranco 855

Friction and wear in metal forming

Galling-free fine blanking of titanium plates by carbon-supersaturated tool steel punch
AIZAWA Tatsuhiko, FUCHIWAKI Kenji, DOHDA Kuniaki 869

The influence of Particle Hardness on Wear in Sheet Metal Forming
ARINBJARNAR Úlfar, KNOLL Maximilian, MOGHADAM Marcel, NIELSEN Chris Valentin 879

Surface topography effects on galling of hot dip galvanized sheet metal
VENEMA Jenny, CHEZAN Toni, KORVER Frank 891

Influence of increased die surface roughness on the product quality in rotary swaging
FENERCIOĞLU Tevfik Ozan, SARIYARLIOĞLU Eren Can, ADIGÜZEL Erdem, ŞIMŞEK Ahmet Kürşat, KOLTAN Umut Kağan, YALÇINKAYA Tuncay 899

Design of a new simulative tribotest for warm forming applications having high contact pressure and surface enlargement
GALDOS Lander, AGIRRE Julen, ARANBURU Elixabet 909

Incremental and sheet metal forming

Numerical investigation on the deep drawing of sheet metals with an additively applied coating
MÄRZ Raphaela, HAFENECKER Jan, BARTELS Dominic, SCHMIDT Michael, MERKLEIN Marion 919

Numerical and experimental investigation of a backward extrusion process for forming geared components from coil
LEICHT Miriam, HENNEBERG Johannes, MERKLEIN Marion 929

Hot stamping of ultra-thin stainless steel for microchannels
GUO Nan, ZHANG Xianglu, HOU Zeran, YANG Daijun, MING Pingwen, MIN Junying 937

Approaches for load path design for stretch forming based on part surface geometry
REITMAIER Lisa-Marie, BAILLY David, HIRT Gerhard 943

Modifying mechanical properties of sheet metal materials by work hardening mechanisms induced by selective embossing
HEINZELMANN Pascal, BRIESENICK David, LIEWALD Mathias 951

Influence of surface pressure and tool materials on contact heating of aluminum
TRÂN Ricardo, PSYK Verena, WINTER Sven, KRÄUSEL Verena 959

Low-cost tooling concept for customized tube bending by the use of additive manufacturing
TRONVOLL Sigmund A., TREFFEN Helena, MA Jun, WELO Torgeir 969

Experimental investigation of the fluid-structure interaction during deep drawing of fiber metal laminates in the in-situ hybridization process
KRUSE Moritz, BEN KHALIFA Noomane 977

Modification of the surface integrity of powder metallurgically produced S390 via deep rolling
HERRMANN Peter, HERRIG Tim, BERGS Thomas 987

Electrically-assisted deep drawing of 5754 aluminium alloy sheet
DOBRAS Daniel, ZIMNIAK Zbigniew, ZWIERZCHOWSKI Maciej 997

Effect of shear angle in shearing on stretch flangeability of ultra-high strength steel sheets
YAGITA Ryo, KIMURA Shunsuke, ABE Yohei 1007

Effect of reduction ratio in flow forming process on microstructure and mechanical properties of a 6082 Al alloy
MUTLU Mehmet, ÖZSOY Atasan, FENERCIOĞLU Tevfik Ozan, KARAKAŞ Aptullah, BAYDOĞAN Murat 1015

Flow forming and recrystallization behaviour of CuZn30 alloy
MUTLU Mehmet, KARAKAŞ Aptullah, KUŞDEMIR Hakan, KOLTAN Umut Kağan, YALÇINKAYA Tuncay 1021

Mechanical and microstructural properties of AISI 4140 after flow-forming process
YAZGAN Elif, MUTLU Mehmet, AYDIN Güneş, KARAKAS Aptullah, FENERCIOGLU Tevfik Ozan, BAYDOGAN Murat 1029

Simulation of incremental sheet metal forming for making U-channel in two light-weight alloys
BHUSHAN Bharat, RAMKUMAR Janakarajan, DIXIT Uday Shanker 1037

Flange wrinkling in incremental shape rolling
ESSA Abdelrahman, ABEYRATHNA Buddhika, ROLFE Bernard, WEISS Matthias 1047

Innovative joining by forming technologies

Clinching with divided punch to prevent critical neck thicknesses
FALK Tobias, KROPP Thomas, DROSSEL Welf-Guntram 1059

An ANN based approach for the friction stir welding process intrinsic uncertainty
QUARTO Mariangela, BOCCHI Sara, GIARDINI Claudio, D'URSO Gianluca 1067

Modelling of the weld seam in the forming simulation of friction stir welded tailored blanks
BACHMANN Maximilian, RIEDMÜLLER Kim, LIEWALD Mathias, MERTEN Mathias .. 1075

Comparative investigation of partial cooling methods for induction heating of hybrid bulk components for hot forming
INCE Caner-Veli, KATZ Fabian RAATZ Annika 1083

FSW process mechanics and resulting properties for dissimilar Al-Ti T-joints
RANA Harikrishna, BUFFA Gianluca, FRATINI Livan 1091

Influence of process parameters on mechanical properties of lamination stacks produced by interlocking
MARTIN Daniel Michael, KUBIK Christian, KRÜGER Martin, GROCHE Peter 1101

Versatile self-piercing riveting with a tumbling superimposed punch
WITUSCHEK Simon, ELBEL Leonie, LECHNER Michael 1111

Lionel fourment ms on optimization and inverse analysis in forming

On the comparison of heterogeneous mechanical tests for sheet metal characterization
GONÇALVES Mafalda, OLIVEIRA Miguel Guimarães, THUILLIER Sandrine, ANDRADE-CAMPOS António..... 1121

On the inverse identification of sheet metal mechanical behaviour using a heterogeneous Arcan virtual experiment
HENRIQUES Joao, ANDRADE-CAMPOS António, XAVIER José..... 1131

On the constraints and consistency in implicit constitutive modelling using ANNs and indirect training
LOURENÇO Rúben, CUETO Elías, GEORGIEVA Pétia, ANDRADE-CAMPOS António.. 1143

Forming process optimisation for variable geometries by machine learning – Convergence analysis and assessment
ZIMMERLING Clemens, KÄRGER Luise 1155

Identification of the large strain flow curve of high strength steel via the torsion test and FEMU
VANCRAEYNEST Niels, COOREMAN Steven, COPPIETERS Sam 1167

Investigating the suitability of using a single heat transfer coefficient in metal casting simulation: An inverse approach
VASILEIOU Anastasia, VOSNIAKOS George-Christopher, PANTELIS Dimitrios I. 1175

Sensitivity analysis of the of the square cup stamping process using a polynomial chaos expansion
PEREIRA André F. G., MARQUES Armando E., OLIVEIRA Marta C., PRATES Pedro A. 1183

Coupling machine learning and synthetic image DIC-based techniques for the calibration of elastoplastic constitutive models
PRATES Pedro A., HENRIQUES Joan D. F., PINTO Jose, BASTOS Nelson, ANDRADE-CAMPOS Antonio..... 1193

A hybrid VFM-FEMU approach to calibrate 3D anisotropic plasticity models for sheet metal forming
ROSSI Marco, LATTANZI Attilio, AMODIO Dario 1203

Machining and cutting

Manufacturing of graded grinding wheels for flute grinding
DENKENA Berend, BERGMANN Benjamin, RAFFALT Daniel 1213

Modeling of surface hardening in burnishing process
TEIMOURI Reza, GRABOWSKI Marcin, SKOCZYPIEC Sebastian 1223

Orthogonal cutting with additively manufactured grooving inserts made from HS6-5-3-8 high-speed steel
KELLIGER Tobias, MEURER Markus, BERGS Thomas 1235

Machining of PAM green Y-TZP: Influence of build and in-plane directions on cutting forces and surface topography
SPITAELS Laurent, RIVIÈRE-LORPHÈVRE Edouard, MARTIC Grégory, JUSTE Enrique, DUCOBU François 1245

Analysis of Ti-6Al-4V micro-milling resulting surface roughness for osteointegration enhancement
CAPPELLINI Cristian, MALANDRUCCOLO Alessio, KIEM Sonja, ABENI Andrea 1255

Comparison of cutting tool wear classification performance with artificial intelligence techniques
COLANTONIO Lorenzo, EQUETER Lucas, DEHOMBREUX Pierre, DUCOBU François 1265

Hardware implementation of Monte Carlo and RSM method for the optimization of cutting force during turning of NiTi shape memory alloy
KOWALCZYK Małgorzata 1275

Investigation of surface finish and chip morphology in cryogenic machining biomedical grade polyetheretherketone
SAJJA Nikhil Teja, BERTOLINI Rachele, GHIOTTI Andrea, BRUSCHI Stefania 1285

Cutting force in peripheral milling of cold work tool steel
TAMURA Shoichi, MATSUMURA Takashi 1295

Evaluation of the surface integrity characteristics of internal threads machined on lead-free brass alloy
ZOGHIPOUR Nima, TORAMAN Yaren, KARA Koray, BAS Kaan Can, KAYNAK Yusuf 1303

Analytical method for determining cutting forces during orthogonal turning of C45 steel
ŚLUSARCZYK Łukasz, FRANCZYK Emilia 1313

Novel methodology for burr extension estimation on machined SLM surfaces
GINESTRA Paola, QUARTO Mariangela, ABENI Andrea, ATTANASIO Aldo, CERETTI Elisabetta, D'URSO Gianluca, GIARDINI Claudio 1323

On the impact of tool material and lubrication in ball end milling of ceramic foams
ROTELLA Giovanna, SANGUEDOLCE Michela, SAFFIOTI Maria Rosaria, TESTA Flaviano, UMBRELLO Domenico, FILICE Luigino 1331

Superfinishing processes applied on the biomedical implants surface to improve their performance
SAFFIOTI Maria R., ROTELLA Giovanna, UMBRELLO Domenico 1341

Evolution of contact lengths during the turning of treated Ti64 β
WAGNER Vincent, DESSEIN Gilles 1347

Investigation of machining performance of lead-free brass materials forged in different conditions after cooling with liquid nitrogen
ATAY Gokhan, ZOGHIPOUR Nima, KAYNAK Yusuf 1357

Material behaviour modelling

Process-informed material model selection
CONDE Mariana, COPPIETERS Sam, ANDRADE-CAMPOS António 1369

Simple multiaxial tests to assess dynamic ductility of 17-4PH
MANCINI Edoardo, CORTIS Gabriele, CORTESE Luca, UTZERI Mattia, SASSO Marco.. 1379

Nonlinear elastic stress triaxiality dependent constitutive model for fibre-reinforced polymer composites
OBID Štefan, HALILOVIČ Miroslav, STARMAN Bojan 1387

Calibration of thermo-viscoplastic constitutive model under biaxial loadings: A Feasibility Study
WANG Zhihao, GUINES Dominique, LEOTOING Lionel 1397

Extension of the modified Mohr-Coulomb fracture model by a strain rate and temperature dependence
VASQUEZ RAMIREZ Dominyka, WESTER Hendrik, ROSENBUSCH Daniel, BEHRENS Bernd-Arno 1407

Optimizing crystal plasticity model parameters via machine learning-based optimization algorithms
JUAN Rongfei, BINH Nguyen Xuan, LIU Wenqi, LIAN Junhe 1417

Correlation between porosity level and elastic modulus in a foamed hiped Ti alloy
GUGLIELMI Pasquale, CASTELLANO Anna, CUSANNO Angela, PALUMBO Gianfranco 1427

Micro-mechanical study of damage evolution in isotropic metallic materials
KNAAK Karl, REVIL-BAUDARD Benoit, CAZACU Oana 1435

Micromechanical modeling of failure in dual phase steels
AYDINER Ilbilge Umay, TATLI Berkehan, YALÇINKAYA Tuncay 1443

Local and nonlocal strain gradient approaches for size-dependent plastic deformation
ÜNSAL İzzet Erkin, GÜNAY Enes, YALÇINKAYA Tuncay 1453

Suitability evaluation of pre-formed cruciform sample without thickness reduction for high strain values in the center of the specimen under different strains paths
MITUKIEWICZ Grzegorz, LEOTOING Lionel, WANG Guan, GUINES Dominique, GOSZCZAK Jarosław, BATORY Damian 1463

Examination of intrinsic and extrinsic size effect in thin specimens through crystal plasticity frameworks
GÜNAY Enes, BULUT Orhun, YALÇINKAYA Tuncay 1471

Considering the stiffness of the forming tools in the numerical analysis of the ironing process
OLIVEIRA Marta C., NETO Diogo M., ALVES José L., MENEZES Luís F. 1481

ESAFORM 2021 cup drawing benchmark of an Al alloy: Critical follow up analysis of its potentials
OLIVEIRA Marta C., CAZACU Oana, REVIL BAUDARD Benoit, NETO Diogo M., FROHN SÖRENSEN Peter, MA Jun, LIU Wencheng, CRUZ Daniel J., SANTOS Abel D., VAN BAEL Albert, GHIABAKLOO Hadi, HABRAKEN Anne M. 1491

Combined material model to predict flow curves of cold forging raw materials having high strain hardening exponent
ZEREN Doğuş, KOCATÜRK Fatih, TOPARLI M. Burak 1503

Modelling of yield point phenomenon in bake-hardening grade steel
DESHMANE Nachiket S., PERDAHCIOGLU Semih E., VAN DEN BOOGAARD Ton 1511

Digital twin development for the sensitivity analysis of near solidus forming process
MUHAMMAD Sajjad, GORKA Plata, JOKIN Lozares, JOSEBA Mendiguren 1521

Finite element model for micro-stamping titanium bipolar plate
KHADEMI Maziar, ZHANG Peng Neo, PEREIRA Michael, SREENIVAS Achuth, WEISS Matthias 1531

New and advanced numerical strategies for material forming

Advanced CFD investigations of electromagnetic stirring of molten steel in continuous caster tundish
ZIELIŃSKA Monika, YANG Hongliang, MADEJ Łukasz, MALINOWSKI Łukasz 1543

Evaluation of data transfer influence in coupled monte carlo finite element model on microstructure evolution predictions
WERMIŃSKI Mariusz, PERZYŃSKI Konrad, SITKO Mateusz, MADEJ Łukasz 1551

Evaluation of data transfer methods efficiency in the random cellular automata model of dynamic recrystallisation
PAWLIKOWSKI Kacper, SITKO Mateusz, CZARNECKI Michał, MADEJ Łukasz 1549

Visual quality prediction of plastic product based on thermographic images
LE GOFF Ronan, MARCHAL Nils, AGAZZI Alban 1565

Estimation of rolling process variation by usage of a Monte-Carlo method
WEINER Max, RENZING Christoph, SCHMIDTCHEN Matthias, PRAHL Ulrich 1575

Influence of mesh in modelling of flow forming process
KRISHNAMURTHY Bhaskaran, SHITIKOV Andrei A., BLACKWELL Paul, BYLYA Olga 1583

Phase field modeling of ductile fracture and application in metal forming
WASEEM Sarim, ERDOGAN Can, YALÇINKAYA Tuncay 1593

A phase-field numerical framework to study ductile damage to fracture transition: An application to material forming processes
PINO MUÑOZ Daniel, BOUCHARD Pierre-Olivier, ELDAHSHAN Hazem, ALVES José, PERCHAT Etienne 1603

A meshless numerical solution of thermo-mechanics of hot-rolled steel bars on a cooling bed
VUGA Gašper, MAVRIČ Boštjan, HANOGLU Umut, ŠARLER Božidar 1611

Physics-informed machine learning in the determination of effective thermomechanical properties
SOYARSLAN Celal, PRADAS Marc 1621

Through process stochastic model of hot strip rolling
SZELIGA Danuta, CZYŻEWSKA Natalia, KUSIAK Jan, OPROCHA Piotr, PIETRZYK Maciej, PRZYBYŁOWICZ Paweł 1631

Non-conventional processes

Design of a user-friendly human machine interface for jet electrochemical machining
DAMM Philipp, MEICHSNER Gunnar, LEREZ Christoph, HACKERT-OSCHÄTZCHEN Matthias 1643

Digital twin for the determination of process input variables for electrochemical precision machining according to DIN SPEC 91399
THIELECKE Alexander, MEICHSNER Gunnar, HACKERT-OSCHÄTZCHEN Matthias ... 1653

Influence of material properties on near dry-EDM process: The discussion of research for titanium grade 2 and Inconel 625 alloy
ŻYRA Agnieszka, SKOCZYPIEC Sebastian, BOGUCKI Rafał 1663

Development of a method for performance characterisation of PEMEC process considering electrolyte temperature in case of hybrid polishing of 316L steel
KRZAK Daniel, ROY Florian, SALVATORE Ferdinando, GIDON Antoine, GUERIN Stéphane, RECH Joël 1673

Unconventional method for recycling CFRPs by using a milling process
BOCCARUSSO Luca, DE FAZIO Dario, DURANTE Massimo, FORMISANO Antonio, LANGELLA Antonio 1683

Consolidation behaviour of particle reinforced aluminium-matrix powders with up to 50 vol.% SiCp
SPETH Marco, RIEDMÜLLER Kim Rouven, LIEWALD Mathias 1689

A numerical approach to optimize the toolpath strategy for polymers forming
FORMISANO Antonio, DURANTE Massimo, BOCCARUSSO Luca, MEMOLA CAPECE Fabrizio 1697

Surface topography investigation during nanosecond pulsed laser engraving of SAE304 stainless steel
NIKOLIDAKIS Evangelos, KARMIRIS-OBRATAŃSKI Panagiotis, PAPAZOGLOU Emmanouil-Lazaros, KARKALOS E. Nikolaos, MARKOPOULOS P. Angelos, ANTONIADIS Aristomenis 1703

A numerical procedure to test the effects of the main variables in the submerged arc welding process
CONTE Romina, RODRÌGUEZ IZQUIERDO David, GAGLIARDI Francesco, AMBROGIO Giuseppina, FILICE Luigino 1711

The sound insulation capacity of some panels made of polymeric materials manufactured by 3D printing
HRIȚUC Adelina, DODUN Oana, MIHALACHE Andrei M., SLĂTINEANU Laurențiu, NAGÎȚ Gheorghe 1719

Machining of hybrid structures produced through cold spray technology: A preliminary study
PERNA Alessia Serena, VISCUSI Antonio, ASTARITA Antonello, BOCCARUSSO Luca, CARRINO Luigi, DURANTE Massimo 1729

Process characteristics of constrained friction processing of AM50 magnesium alloy
DE CASTRO Camila C., SHEN Junjun, DOS SANTOS Jorge F., KLUSEMANN Benjamin 1739

Analysis of the relationship between the properties of selected materials and the parameters of the EDD process
TRAJER Marcin, CZESZKIEWICZ Adrian, MACHNO Magdalena 1747

Modeling electrochemical machining based on effective parameters
WAIMANN Johanna, VAN DER VELDEN Tim, SCHMIDT Annika, RITZERT Stephan, REESE Stefanie 1759

Coefficient of friction of cemented carbides machined by sinking EDM
PETERSEN Timm, KÜPPER Ugur, HERRIG Tim, BERGS Thomas..... 1765

Effects of ultrasonic burnishing on the surface quality of corrosion-resistant tool steel using a hard-carbon-coated burnishing tool
HUUKI Juha, ULLAH Rizwan, FANGNON Eric 1775

Influences in deep hole sinking (EDM, ECM) that make it difficult to analyze the process status
SCHULZE Hans-Peter, HERZIG Mathias, KRÖNING Oliver 1781

Out-of-autoclave molding of carbon fiber composites pipes with interlaminar carbon nanotubes
BELLISARIO Denise, IORIO Leandro, PROIETTI Alice, QUADRINI Fabrizio, SANTO Loredana..... 1789

Polymer processing and thermomechanical properties

Two-step PM forging for precise fabrication of carbon fiber reinforced engineering plastic gears
AIZAWA Tatsuhiko, MIYATA Tomohiro, ENDO Kiyoyuki..... 1799

Exploring sheath-core yarns technology to optimise bio-composite performances
QUEREILHAC Delphine, FEMERY Jules, MOREL Guillaume, KORYCKI Adrian, DE LUYCKER Emmanuel, OUAGNE Pierre, CHABERT France 1809

Effect of energy director thickness on thermal diffusion and joint quality during ultrasonic welding of CF/PEEK composites
KORYCKI Adrian, CARASSUS Fabrice, GARNIER Christian, CHABERT France, DJILALI Toufik 1819

Laser transmission welding of PEKK: Influence of material properties and process parameters on the weld strength
MATUS AGUIRRE Marcela, GARNIER Christian, GILBLAS Rémi, COSSON Benoît, AKUÉ André, SCHMIDT Fabrice, CHABERT France 1829

Influence of roughness in ultrasonic welding of carbon fiber/PEEK composites
CARASSUS Fabrice, KORYCKI Adrian, GARNIER Christian, CHABERT France, YAHIAOUI Malik, DJILALI Toufik 1841

Insights on the use of PVB nanocomposites as energy directors in ultrasonic welding of epoxy composites
CILENTO Fabrizia, PALMIERI Barbara, SORRENTINO Luigi, GIORDANO Michele, MARTONE Alfonso 1851

Effect of compression during post-treatment to improve the mechanical strength of printed carbon fiber/ PEKK composites
COMBETTES Julien, ABADIE Amandine, FAZZINI Marina, BORLENGHI Andrea, BOSSHARD Jonas, GARNIER Christian, DESSEIN Gilles, CHABERT France 1861

Viscoelastic characterization of reformable epoxy vitrimers composites
PALMIERI Barbara, CILENTO Fabrizia, MARTONE Alfonso, GIORDANO Michele, AMENDOLA Eugenio 1871

Thermal and mechanical properties of Fdmed biocomposites in polylactic acid and food flour waste
PAPA Ilaria, LANGELLA Antonio, NAPOLITANO Francesco, RUSSO Pietro 1879

Characterization of the biaxial response of a thermoplastic ABS Sheet using DIC-instrumented bubble inflation technique
VAREDI Rasoul, BUFFEL Bart, DESPLENTERE Frederik 1887

Experimental measurement of CF/PEKK tapes heating behavior in the laser assisted automated fiber placement process
LE LOUËT Violaine, LE REUN Adrien, SOBOTKA Vincent, LE CORRE Steven 1897

Polymer-tool friction coefficient in temperature for thermoforming numerical simulation
CAUBET Benoit, LÉONARDI Frederic, AMAND Sylvain 1907

A local power law versus a well-identified viscosity curve over a large shear rate range in thermorheology of polymers
LIN Qiao, ALLANIC Nadine, MOUSSEAU Pierre, BEREAUX Yves, GIRAULT Manuel, DETERRE Rémi 1917

Sustainability on material forming

Energy and resource-efficient forming of gas cylinders by friction-spinning
DAHMS Frederik, HOMBERG Werner 1929

Technological and sustainability implications of wet and dry turning of Ti6Al4V EBM parts
COZZOLINO Ersilia, FRANCHITTI Stefania, BORRELLI Rosario, PIROZZI Carmine, ASTARITA Antonello 1939

Energy measurements and LCA of remanufactured automotive steel sheets
FARIOLI Daniele, FABRIZIO Matteo, KAYA Ertuğrul, MUSSI Valerio, STRANO Matteo 1947

Analysis of temperature effect on strength and microstructure in friction induced recycling process (FIRP)
BORGERT Thomas, HOMBERG Werner..... 1957

Sustainable tool technology: Wood-based forming tools
GEUEKE Michael, STEINHEIMER Rainer, LUTZ Maximilian, ENGEL Bernd..... 1967

Microstructure analysis of hybrid aluminum parts from recycled EN AW-6082 and EN AW-7075 chips
URSINUS Jonathan, KOCH Alexander, BRUNOTTE Kai, WALTHER Frank, BEHRENS Bernd-Arno 1977

Multi-criteria decision model of sustainable industrial production: A case study on 3D printed carbon PA
ANDREOZZI Marina, GENTILI Serena, MANCIA Tommaso, SIMONCINI Michela, VITA Alessio 1987

Characterization of friction stir consolidated recycled billet by uniaxial compression tests with miniaturized cylindrical specimen
LATIF Abdul, INGARAO Giuseppe, FRATINI Livan, HETZ Peter, MERKLEIN Marion ... 1997

Innovative self-learning disturbance compensation for straightening processes
BATHELT Lukas, DJAKOW Eugen, HENKE Christian, TRÄCHTLER Ansgar..... 2005

Biodegradable polymers for cosmetic packaging: A technical and life cycle perspective
MIFSUD Sarah, REFALO Paul, ROCHMAN Arif..... 2015

Property-controlled forming

Analysis of tool heating in cold forging using thin-film sensors
GRÖTZINGER Karl C.1, SCHOTT Anna, REKOWSKI Martin, EHRBRECHT Bernd, HEHN Thorsten, GERASIMOV Dmitry, LIEWALD Mathias 2027

Cryogenic reverse flow forming of AISI 304L
ARIAN Bahman, HOMBERG Werner, ROZO VASQUEZ Julian, WALTHER Frank, KERSTING Lukas, TRÄCHTLER Ansgar 2037

Control strategy for angular gradations by means of the flow forming process
KERSTING Lukas, ARIAN Bahman, ROZO VASQUEZ Julian, TRÄCHTLER Ansgar, HOMBERG Werner, WALTHER Frank 2049

Optimizing the microstructure in open-die forgings using reinforcement learning
REINISCH Niklas, BAILLY David, HIRT Gerhard 2061

Monitoring of fluctuating material properties for optimizing sheet-metal forming processes: a systematic literature review
ORTJOHANN Lucia, BECKER Marco, NIEMIETZ Philipp, BERGS Thomas 2071

Conception of a multivariable product property control for punch-hole-rolling
SPIES Daniel, MOLITOR Dirk Alexander, DAMON James, KNOLL Maximilian, DIETRICH Stefan, SCHULZE Volker, GROCHE Peter 2081

Experimental analysis on the influence of freeform bending on Barkhausen noise for steel tubes
MAIER Daniel, SCANDOLA Lorenzo, WERNER Matthias, STEBNER Sophie, ISMAIL Ahmed, LOHMANN Boris, MÜNSTERMANN Sebastian, VOLK Wolfram, LECHNER Philipp 2091

Fine blanking of pre-hardened high manganese steel to investigate the sheared surface hardening and part quality
SCHWEINSHAUPT Frank, VOIGTS Herman, HERRIG Tim, BERGS Thomas 2101

Modeling and control of tribological properties for subsequent forming process in skin-pass rolling
LI Xinyang, SCHULTE Christopher, ZHU Runyu, ABEL Dirk, HIRT Gerhard 2115

Keyword index
About the editors

Preface

Proceedings of the 26th International ESAFORM Conference on Material Forming (ESAFORM 2023)

The 26th International ESAFORM Conference 2023 was held in the historic city of Kraków, Poland, between 19-21 April 2023 at AGH University of Science and Technology.

ESAFORM is an association with the mission to stimulate applied and fundamental research in the broad field of material forming. Its annual conference, the International ESAFORM Conference on Material Forming, is used to achieve one of the main goals of ESAFORM: to spread scientific and technological information related to material forming within academia and industry. The most important idea of this event is to bring together researchers in the field to encourage discussion, collaboration and interchange of ideas.

ESAFORM 2023 was hosted by AGH University of Science and Technology. AGH is a modern state university that develops partner collaborations with colleges and universities in Poland, Europe, and all over the world. AGH is one of Poland's best technical universities, with approx. 18,000 students at 16 Faculties (various engineering faculties, science, sociology, business and management). AGH University widely collaborates with international scientific and industrial partners.

The ESAFORM 2023 was attended by more than 300 participants from 27 countries. During the event, approx. 240 presentations were delivered across sixteen organized mini-symposia focused on a broad spectrum of forming-related topics.

The proceedings present papers from MS01: Additive Manufacturing, MS02: Composites Forming Processes, MS03: Extrusion and Drawing, MS04: Forging and Rolling, MS05: Formability of Metallic Materials, MS06: Friction and Wear in Metal Forming, MS07: Incremental and Sheet Metal Forming, MS08: Innovative Joining by Forming Technologies, MS09: Lionel Fourment MS on Optimization and Inverse Analysis in Forming, MS10: Machining and Cutting, MS11: Material Behaviour Modelling, MS12: New and Advanced Numerical Strategies for Material Forming, MS13: Non-Conventional Processes, MS14: Polymer Processing and Thermomechanical Properties, MS15: Sustainability on Material Forming, MS16: Property-Controlled Forming.

The ESAFORM 2023 was organized under the patronage of the Dean of the Faculty of Industrial Computer Science and Modelling of the AGH University, the Mayor of the City of Kraków and the Minister of Science and Education in Poland. The conference was also co-financed from the state budget under the programme of the Minister of Education and Science called Excellent Science and by many supporting companies.

Committees

Esaform 2023 Chair

Lukasz Madej
AGH University of Science
and Technology, Poland

Organizing committee

Konrad Perzynski
AGH University of Science
and Technology, Poland

Mateusz Sitko
AGH University of Science
and Technology, Poland

Anna Smyk
Secretariat of the Conference
AGH University of Science
and Technology, Poland

Scientific committee

Prof. Alexander Brosius, Technische Universität Dresden, Germany
Prof. Anne-Marie Habraken, University of Liège, Belgium
Dr. Anne Mertens, University of Liège, Belgium
Prof. Antonello Astarita, University of Naples Federico II, Italy
Prof. António Gil Andrade-Campos, University of Aveiro, Portugal
Prof. Barbara Reggiani, University of Modena and Reggio Emilia, Italy
Prof. Beatriz Silva, University of Lisbon, Portugal
Dr. Benjamin Klusemann, Leuphana Universität Lüneburg, Germany
Prof. Bernd-Arno Behrens, University of Hannover, Germany
Prof. Carpoforo Vallellano, Universidad de Sevilla, Spain
Prof. Celal Soyarslan, University of Twente, Netherlands
Dr. Cédric Courbon, École nationale d'ingénieurs de Saint-Étienne, France
Dr. Chris Valentin Nielsen, Technical University of Denmark, Denmark
Dr. Christian Grandfils, University of Liège, Belgium
Dr. Daniel Cooper, University of Michigan, USA
Dr. Denise Bellisario, University of Rome Tor Vergata, Italy
Prof. Dermot Brabazon, Dublin City University, Ireland
Prof. Domenico Umbrello, University della Calabria, Italy
Prof. Dorel Banabic, Universitatea Tehnică din Cluj-Napoca, Romania
Dr. Gabriela Vincze, University of Aveiro, Portugal
Prof. Gianluca Buffa, University of Palermo, Italy
Prof. Giuseppe Ingarao, Università degli Studi di Palermo, Italy
Prof. Giusy Ambrogio, Università della Calabria, Italy
Dr. Guenael Germain, Arts et Métiers ParisTech, France
Dr. Hans-Peter Schulze, Leukhardt Schaltanlagen Systemtechnik GmbH, Magdeburg,Germany
Prof. Hinnerk Hagenah, Friedrich-Alexander-Universität Erlangen-Nürnberg, Germany
Dr. Holger Aretz, Hydro Aluminium Rolled Products GmbH Bonn Germany
Prof. Halilovič Miroslav, University of Ljubljana, Slovenia
Dr. Javad Hazrati, University of Twente, Netherlands
Prof. Katia Mocellin, MINES ParisTech, France
Prof. Laurentiu Slatineau, Gheorghe Asachi Technical University of Iasi, Romania

Dr. Lander Galdos, Mondragon University, Spain
Dr. Lionel Leotoing, INSA Rennes, France
Prof. Loredana Santo, University of Rome, Italy
Prof. Lorenzo Donati, Uniersity of Bologna, Italy
Prof. Lukasz Madej, AGH University of Science and Technology, Poland
Dr. Malte Stonis, IPH Hannover, Germany
Prof. Marc Bernacki, Mines Paristech, France
Dr. Margareta Coteata, Gheorghe Asachi Technical University of Iasi, Romania
Dr. Marilena Butuc, University of Aveiro, Portugal
Prof. Marion Merklein, Friedrich-Alexander-Universität Erlangen-Nürnberg, Germany
Prof. Markus Bambach, ETH, Zürich, Switzerland
Prof. Massimo Durante, University of Naples Federico II, Naples, Italy
Prof. Matteo Strano, Politecnico di Milano, Italy
Prof. Mihaela Banu, University of Michigan, USA
prof. Nooman Ben Khalifa, Leuphana University Lüneburg, Germany
Prof. Pedro J. Arrazola, Mondragon University, Spain
Prof. Peter Groche, Technischen Universität Darmstadt, Germany
Prof. Pierpaolo Carlone, University of Salerno, Italy
Prof. Rosa Di Lorenzo, Università degli Studi di Palermo, Italy
Prof. Sam Coppieters, KU Leuven, Belgium
Dr Sandra Raquel de Sousa Monteiro, University of Coimbra, Portugal
Prof. Sandrine Thuillier, Université Bretagne Sud, France
Prof. Semih Perdahcioglu, University of Twente, Netherlands
Dr Soeren Müller, Technische Universität Berlin, Germany
Dr. Sumsun Naher, University of London, UK
Prof. Takashi Matsumura, Tokyo Denki University, Japan
Prof. Torgeir Welo, Norges teknisk-naturvitenskapelige Universitet, Norway
Prof. Toshihiko Kuwabara, Tokyo University of Agriculture and Technology, Japan
Dr. Vincent Sobotka, University of Nantes, France
Prof. Wolfram Volk, Technische Universität München, Germany

Esaform Board of Directors

Prof. Livan FRATINI, President, University of Palermo, Italy
Prof. Robertt VALENTE, Vice-President, University of Aveiro, Portugal
Dr. Katia MOCELLIN, Treasurer, Ecole des Mines de Paris, France
Prof. Hinnerk HAGENAH, Secretary, Friedrich-Alexander University, Erlangen-Nuremberg, Germany
Prof. Sandrine THUILLIER, Deputy-Secretary, University of South Brittany, France
Prof. Ton van den BOOGAARD, Past-President, University of Twente, The Netherlands
Prof. Markus BAMBACH, ETH Zürich, Switzerland
Prof. Dorel BANABIC, Technical University of Cluj-Napoca, Romania
Prof. Dermot BRABAZON, Dublin City University, Ireland
Prof. Pierpaolo CARLONE, University of Salerno, Italy
Dr. France CHABERT, University of Toulouse, France
Prof. Joost DUFLOU, Catholic University of Leuven, Belgium
Prof. Junhe LIAN, University of Aalto, Finland
Prof. Anne-Marie HABRAKEN, University of Liège, Belgium
Prof. Benjamin KLUSEMANN, Leuphana University of Lüneburg, Germany
Prof. Lukasz MADEJ, AGH University of Science and Technology, Krakow, Poland
Dr. Gary MENARY, Queen's University of Belfast, UK
Dr. Sumsun NAHER, City University of London, UK
Prof. Marta OLIVEIRA, University of Coimbra, Portugal
Dr. Verena PSYK, Fraunhofer Institute for Machine Tools and Forming Technology, Germany
Dr. Domenico UMBRELLO, University of Calabria, Italy
Dr. Gabriela VINCZE, University of Aveiro, Portugal

Additive manufacturing

Design and evaluation of liquid channel cross sections fabricated via metal fused filament fabrication

BACIKOGLU Mehmet Canberk[1,2,a *] and YAMAN Ulas[1,b]

[1]Middle East Technical University, 06800, Ankara, Turkey

[2]Radar and Electronic Warfare Systems, ASELSAN, 06830, Ankara, Turkey

[a]cbacikoglu@aselsan.com.tr, [b]uyaman@metu.edu.tr

Keywords: Metal Fused Filament Fabrication, Interior Liquid Channel, Supportless Manufacturing, Material Characterization, Quality Control

Abstract. Metal Fused Filament Fabrication is an Additive Manufacturing method of manufacturing metal parts by using filaments composed of metal powders encased in plastic binders. It is advantageous for manufacturing parts with complex geometries using a wide range of materials, including stainless steel, copper, tool steel, nickel alloys, and titanium. When support structures are not required, complex parts with interior cavities can be produced using this method. In this study, interior channel cross sections for cold plates, the main elements in cooling high-power electronic units, are designed and fabricated without the use of support structures. Specimens are made of 17-4 PH stainless steel and copper using the method with two different systems. Straight and angled interior channels are fabricated separately to investigate the characteristics of supportless manufacturing and observe the sagging or warping effects on the liquid channel faces. Surface roughness and Coordinate Measuring Machine measurements are performed for parts to check if the quality requirements are fulfilled in terms of shrinkage and assembly. Density is determined for parts using the Archimedes method and compared with the porosity results obtained from Scanning Electron Microscope.

Introduction

Additive manufacturing (AM) [1] is a method that can be used to manufacture complex parts with a novel approach. Since AM has more freedom than conventional manufacturing processes it participates more in the industry day by day. With AM, most of the limitations in traditional machining can be eliminated, pushing the limits of design, creativity, and effectiveness in manufacturing. Furthermore, rapidity and affordability are other critical properties of AM that would create an innovative path for cutting-edge technologies and products.

Polymer-based materials and metal powders constitute two major branches in AM when raw materials are considered. According to the desired material and function of the parts, several AM methods can be used. Fused Filament Fabrication (FFF) is one of the most popular AM methods that extrudes material through a nozzle and constructs a part layer by layer. On the other hand, Selective Laser Melting (SLM) [2] is a process that various type of materials in powder form are distributed over a dynamic table and melted by a high-power laser to bond metal powders to each other layer-by-layer according to the 3D geometric model of the desired part. In SLM, parts can be manufactured with aluminum alloy powders, steel powders such as maraging steel, stainless steel, etc., and titanium alloys. These materials can be selected according to the application area, i.e., structural requirements, corrosion levels, thermal properties, etc. [3].

Manufacturing parts with interior channels is challenging due to the design and production criteria. By using traditional methods such as conventional welding, brazing, and friction stir welding (FSW), structures with interior channels can be produced in a limited manner. With the help of recent advancement in AM, especially in SLM, manufacturing limitations have been

Content from this work may be used under the terms of the Creative Commons Attribution 3.0 license. Any further distribution of this work must maintain attribution to the author(s) and the title of the work, journal citation and DOI. Published under license by Materials Research Forum LLC.

decreased. Complicated, cost-effective, and functional parts can be produced as end use artifacts [4]. Manufacturing of these parts with multi-staged conventional methods reduces freedom in design. SLM can produce structures that have voids inside due to the advantageous properties of the process itself [5]. More functional and effective parts with interior channels can be obtained with parameter optimization of AM machinery [6].

As mentioned, the SLM method is highly preferable for metal part production in AM. But a newly developed process called Metal Fused Filament Fabrication (M-FFF) is an alternative approach for metal part production. Developments and studies about this alternative show that M-FFF has great potential in metal production. For example, in the study of Henry et al. [7], 17-4 PH Stainless Steel (SS) is printed via the Atomic Diffusion Additive Manufacturing (ADAM) method on a Markforged Metal X 3D printer. It is shown that the material response is sensitive to extrusion paths and porosity is measured as 3.3% with scanning electron microscopy. Rodriguez et al. [8] manufactured parts with copper using the same 3D printer. The relative density of pure copper is found to be lower than 95%, which is worse than the other two AM technologies, SLM and Electron Beam Melting (EBM). Lower electrical conductivity, yield, and tensile strength are measured in the parts compared to the parts manufactured with SLM. Galati and Minetola characterized the same process [9]. Dimensions of the green parts and the sintered parts were evaluated. Relative density was around 90% for the sintered parts, which was far lower than the published values. Finishing operations must be performed to obtain desired surface finish and accuracy.

Design and Fabrication of Parts

Test parts are designed and manufactured using the M-FFF method to perform preliminary tests and measurements. Design and fabrication steps are explained in this section.

Design.

Parameters such as material, channel type and size, cooling path, and fin location can be optimized and adjusted to increase the thermal performance of a part used in thermal applications. Cross-section of the channel affects the thermal performance of the cold plate proportionally according to its heat transfer area. Since support structures printed inside the part cannot be removed after fabrication, interior channels must be printed without support structures to obtain the desired flow. To produce desired channel geometry, the design process must be performed according to the overhang angle criterion of the selected material.

Copper is used for manufacturing with the M-FFF method, which has advantageous thermal properties for thermal applications. Since pure copper's overhang angle requirement is 50º, angles larger than 50º are chosen for supportless manufacturing of channels. As stated before, the thermal performance of different types of channel cross-sections is one of the key points. Four different channel cross-sections are designed to control the quality of the test parts. 50º of overhang angle is considered during the design of these cross sections. In the first cross-section, droplet alike cross section (CS1) is designed, which is a typical shape for supportless manufacturing. A bigger flow area is formed in the second cross-section (CS2), which is like a triangle. In the third one, a column is constituted in the middle of the cross-section (CS3) to increase the heat transfer area. In the fourth cross section (CS4), two fin structures are added throughout the channel path. Essential dimensions of cross sections are remarked in Fig. 1. Specified cross sections have different perimeters of 12.9 mm, 15.7 mm, 20.7 mm, and 23.2 mm, respectively, which will directly affect the heat transfer area of the interior channel.

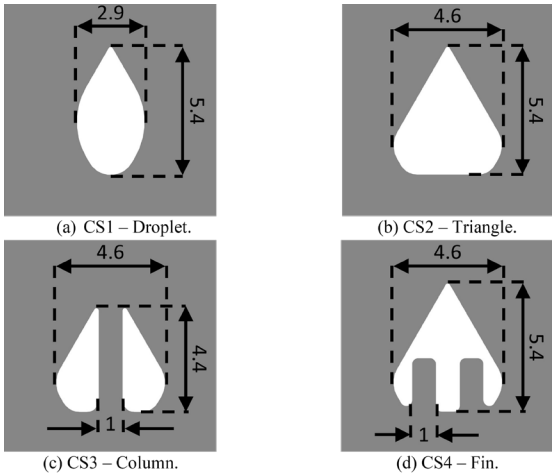

Fig. 1. Dimensions of the cross sections in mm.

Two kinds of testing parts are designed to observe the manufacturability of the cross-sections. In the first testing part (Fig. 2a), the aim is to monitor the quality of the cross-section, supportless manufacturing results, and uniformity of sintered part over a straight channel. In the second part, the same parameters are utilized for the angled channels in Fig. 2b. Also, a cylinder part is designed with 10 mm in diameter and 10 mm in height to determine the density and porosity parameters of copper.

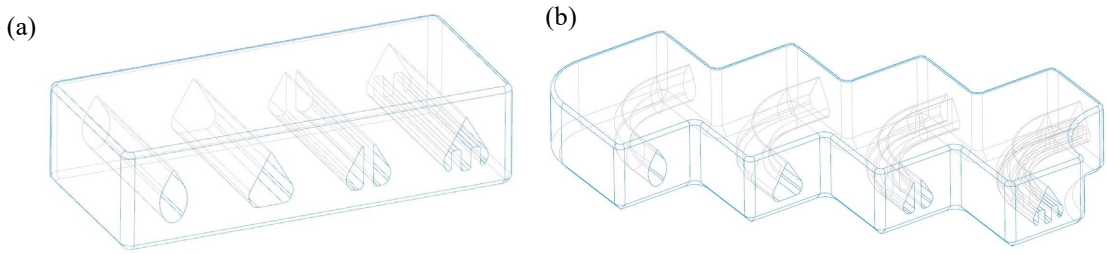

Fig. 2. Wire frames of the straight and angled test parts: (a) straight channels, (b) angled channels.

Outer regions of the parts don't include sharp corners like channel cross sections. Radii are created to eliminate sharp corners and residual stress that shows up during sintering, and to conserve the part's uniformity. In the M-FFF systems, the desired part is manufactured larger than the desired part considering shrinkage due to binder material in filaments. Printing simulation of straight and angled test parts made of copper are demonstrated in Fig. 3. Part details related to printing are noted in Table 1.

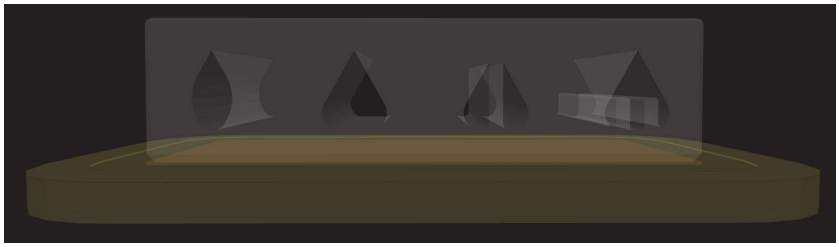

Fig. 3. Support control and layer view in the CAM software. Yellow is raft, orange is ceramic release and white is the part.

Table 1. Properties of the test parts as stated in the CAM software of the M-FFF system.

Test parts	*Straight*	*Angled*	*Cylinder*
Printed dimensions [mm]	46.4x20.9x11.9	66.2x66.2x11.9	Ø11.6x11.9
Final part dimensions [mm]	40x18x10	57x57x10	Ø10x10
Print time [hour]	7.2	13.2	2.5
Wash time [hour]	12.5	31	20
Dry time [hour]	4	4	4
Printed part mass [g]	89.6	178.2	16.3
Final part mass [g]	53.7	111	6.5
Number of wall layers	4	4	4

Fabrication.

Straight and angled interior channels are fabricated separately to investigate the characteristics of supportless manufacturing and observe the pouring or warping effects on the liquid channel faces. The fabrication process is performed using The Metal X 3D printer of Markforged. The Metal X Printer uses the ADAM method, which has a build volume of 300x220x180 mm. The printer has two nozzles, for metal material extrusion and ceramic support release material extrusion. The Metal X printer has two resolution options, 50 and 200 μm. After printing desired parts, green parts, which include both plastic and metal materials inside, are acquired Fig. 4. Green parts are subjected to a washing process to remove binders and clean parts, which results in obtaining brown parts. Then the sintering process is employed on brown parts to remove all plastic and binder materials and bond metal powders together. To obtain uniform shrinkage and prevent warping during sintering, the part is printed on a raft material, the same material as the desired part. A thin layer of ceramic powder between the green part and the raft helps to separate the parts.

Fig. 4. Green state of the manufactured straight and angled test parts.

While printing the test parts, 200 μm resolution is used. Test parts are made of 17-4 PH SS and copper. Since only 17-4 PH SS was initially available in producing company, a straight test part is manufactured with 17-4 PH SS (Fig. 5) to control the convenience of support generation on the CAM software. Then, the straight and angled (Fig. 6) test parts are produced with copper. Also, the cylinder part used in some characterization tests is shown in Fig. 7.

Fig. 5. Straight test part made of 17-4 PH SS.

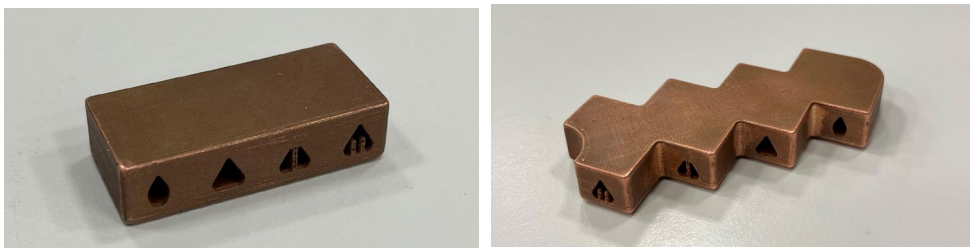

Fig. 6. Straight and angled test parts made of copper.

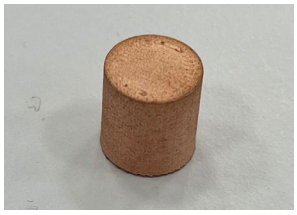

Fig. 7. Cylinder test part made of copper.

Material Characterization and Quality Control

Before material characterization and quality control tests, the test parts are inspected visually. High surface roughness at the bottom face of the test parts is observed due to the ceramic layer between the raft and the metal part. Some defects on the column structure of CS3 and the fin structure of CS4 are observed. Interior faces of the straight and angled test parts are less rougher than the internal faces of the channels manufactured with the SLM method. Measured masses of the test parts and the mass values calculated in the CAD software are stated in Table 2.

Coordinate Measuring Machine (CMM).

Dimensions of the straight and the angled test parts are measured with the Delta Slant gantry type CMM. Mainly, outer dimensions of the test parts are measured with the CMM, such as width, length, and height. For CS1 and CS2, channel height and width are measured with CMM as appropriately as possible. For CS3 and CS4, the CMM probe couldn't touch the faces of the interior channel since the probe diameter is 0.8 mm and the probe is bent while touching the interior faces. In addition, because of the deterioration of the column and the fin structures of CS3 and CS4, the risk of breaking the probe is increased. Thus, a microscope and a digital caliper are used for the measurement of these dimensions.

Table 2. Masses of the test parts.

Test part	Material	Mass in CAD [g]	Actual mass [g]	Difference
Straight	17-4 PH SS	48.9	43.0	-12.1%
Straight	Copper	53.7	54.3	+1.1%
Angled	Copper	111	112.8	+1.6%
Cylinder	Copper	6.5	6.7	+3.1%

Outer dimensions of the test parts are shown in Table 3. When the results are elaborated, it is seen that 17-4 PH SS part has more deviation than the copper counterparts in x- and y-axis, which are length and width, respectively. But in z-axis, 17-4 PH SS has a better result. Similar deviations are observed when the outer dimensions of the copper test parts are compared. For all outer dimensions in all axes of the three test parts, actual dimensions are greater than the CAD models, and much higher tolerances are obtained than the traditional manufacturing methods.

Table 3. Outer dimensions of the test parts.

	Part	*Straight*	*Straight*	*Angled*
	Material	17-4 PH SS	Copper	Copper
Width [mm]	**CAD dimension**	18	18	57
	Actual dimension	18.43	18.14	57.16
	Deviation	0.43	0.14	0.16
Length [mm]	**CAD dimension**	40	40	57
	Actual dimension	40.57	40.27	57.11
	Deviation	0.57	0.27	0.11
Height [mm]	**CAD dimension**	10	10	10
	Actual dimension	10.09	10.29	10.24
	Deviation	0.09	0.29	0.24

The results of the essential dimensions of channel cross-sections are shown in Table 4. Similar results are obtained when the straight and the angled copper test parts are compared. Dimensions for the channel height are less than the nominal dimensions. Fin thicknesses are mostly greater than the nominal dimensions, but there are some deteriorations in the fin thicknesses of both structures. These deteriorations affected average fin thickness negatively. 0.82 mm and 1.32 mm of fin thicknesses are observed when the lower and the upper limits are considered, which can be originated from spoilt extrusion, pouring, and uncontrolled shrinkage, as seen in Fig. 8.

CMM measurements of the cylinder test parts are shown in Table 5. The height of the cylinder is measured to be more than the nominal dimension. The actual diameter of the cylinder is 9.9 mm, with a 0.1 mm deviation from the designed value, which is acceptable when compared with the traditional machining methods.

Surface roughness.

Surface roughness is a surface property that determines the surface quality of a part. Summation of deviations in the normal vector of surface expresses surface roughness. Surface roughness affects the appropriateness of assembly, friction, and wear on the surface. Ra value indicates an arithmetic average of height deviation from the mean profile of the surface, and Rz value indicates the distance between the upper and lower points on the surface that is investigated. Surface roughness of the test parts is measured by the Mitutoyo Surftest SJ-400 device. Ra and Rz values are measured for upper surface, side surface, and bottom surface of the test parts and are indicated in Table 6.

Table 4. Dimensions of the channel cross sections.

	Part	*Straight*	*Angled*
	Material	Copper	Copper
CS1 Height [mm]	**CAD dimension**	5.5	5.5
	Actual dimension	5.34	5.35
	Deviation	-0.16	-0.15
CS2 Height [mm]	**CAD dimension**	5.5	5.5
	Actual dimension	5.36	5.33
	Deviation	-0.14	-0.17
CS3 Height [mm]	**CAD dimension**	4.63	4.63
	Actual dimension	4.18	4.11
	Deviation	-0.45	-0.52
CS3 Fin Thickness [mm]	**CAD dimension**	1.0	1.0
	Actual dimension	1.25	1.07
	Deviation	0.25	0.07
CS4 Height [mm]	**CAD dimension**	5.5	5.5
	Actual dimension	5.36	5.37
	Deviation	-0.14	-0.13
CS4 Fin Thickness [mm]	**CAD dimension**	1.0	1.0
	Actual dimension	0.99	1.05
	Deviation	-0.01	0.05

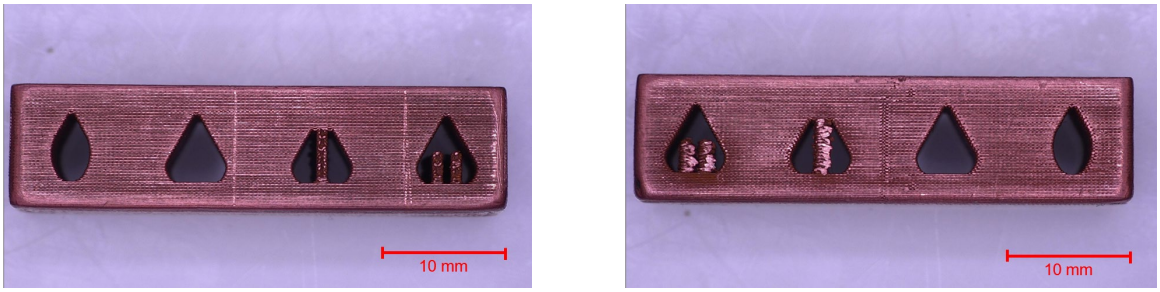

a) front view b) back view

Fig. 8. Deteriorations on the fin structures of CS3 and CS4 of the straight test parts.

Table 5. Dimensions of the cylinder test part.

	Part	*Cylinder*
	Material	Copper
Diameter [mm]	**CAD dimension**	10.0
	Actual dimension	9.9
	Deviation	-0.1
Height [mm]	**CAD dimension**	10.0
	Actual dimension	10.34
	Deviation	0.34

Table 6. Surface roughness of the test parts.

		Top Surface		Side Surface		Bottom Surface	
Part	**Material**	**Ra [µm]**	**Rz [µm]**	**Ra [µm]**	**Rz [µm]**	**Ra [µm]**	**Rz [µm]**
Straight	Copper	1.95	12.01	6.07	31.65	26.02	105.3
Angled	Copper	1.33	8.3	12.33	51.5	32.79	129.2

As seen from Ra and Rz values of the straight and the angled copper test parts, results are similar to each other. When surfaces are compared, the best surface quality is obtained on the upper surface, which is close to the surface roughness values of machined parts. Regarding the side surface, Ra and Rz values are fairly average and increased compared to the upper surface since the staircase effect is more perceivable. But on the bottom surface, surface roughness is increased significantly due to the ceramic layer residuals. Due to the sintering of the part, ceramic layer becomes more powdery and spoils the quality of the bottom surface of the final part.

Archimedes method.

Undesired porosity throughout the parts decreases the strength of the material and can cause crack propagation after force is applied. Also, density must be specified for the unknown materials to calculate other material properties and obtain the mass. To gain insight into the porosity and density of parts, Archimedes method, a measurement procedure to determine the density of parts, is applied for copper cylinder test parts. This method is based on measuring the test part's weight in air and water where the part is fully submerged. This difference gives the buoyancy force, which equals the weight of the displaced fluid. Since the part is completely submerged and the volume is the same for both cases, the ratio of the density of the test part and the density of the fluid equals to the ratio of the weight of the test part and the weight of the displaced fluid. As built parts are used, which means no machining or grinding operation is applied on the cylinder specimens. Density is evaluated according to the ISO 3369 test standard. Archimedes method is performed by using Precis XB 220A device at 24ºC ambient temperature. Measured densities of copper specimens are calculated via Eq. 1; where m_a is the mass of test piece determined by weighing in air, m_w is the mass of test part in liquid, and ρ_w is the density of distilled water at 24ºC ambient temperature which equals to 0.9973 g/cm^3 as specified in the standard. After the specimens are laid on the attachment in the water side of the device, no significant air bubbles are observed on the outer surfaces of them.

$$\rho = \left(\frac{m_a}{m_a - m_w}\right)\rho_w \quad (1)$$

After measuring the masses of the test parts in air and water, respectively, density values are obtained. The average density value for the test parts is found as 8.6462 g/cm3 where the standard deviation is 0.0383. Relative density is calculated as 96.50%, where Markforged specifies it as 98% in the datasheet for copper used on the 3D printer. That means copper specimens have 3.50% porosity inside on average. Defects in the part, such as open pores or closed pores infilled with air or bubbles, can be the main reason for the difference in relative density, which increases the porosity level of the parts.

Scanning Electron Microscope (SEM) Analysis.

SEM is used to analyze the porosity of the copper parts after sectioning. Manufactured copper cylinder parts are used for sectioning; specimens are machined by a lathe and ground with 800-grit sandpaper to obtain a surface as smooth as possible. Then, the Phenom XL G2 SEM is used to observe sections of the parts in a detailed manner. Randomly distributed voids are detected during screening. Although grinding marks are observed, porous structures are obtained as separable throughout the section. There is no significant distribution of voids on the sectioned

surface according to the occurrence in some specific areas, such as around the peripheral or close to the center. Screening images show that voids are distributed randomly around the sectioned surface. Some images obtained with the SEM are demonstrated in Fig. 9. Images are subjected to image processing on ImageJ software to perform porosity analysis. 3.92% of porosity is obtained, close to the result obtained in the Archimedes method. Average area of the pores is 18.08 μm^2, which corresponds to an average diameter of 4.8 μm.

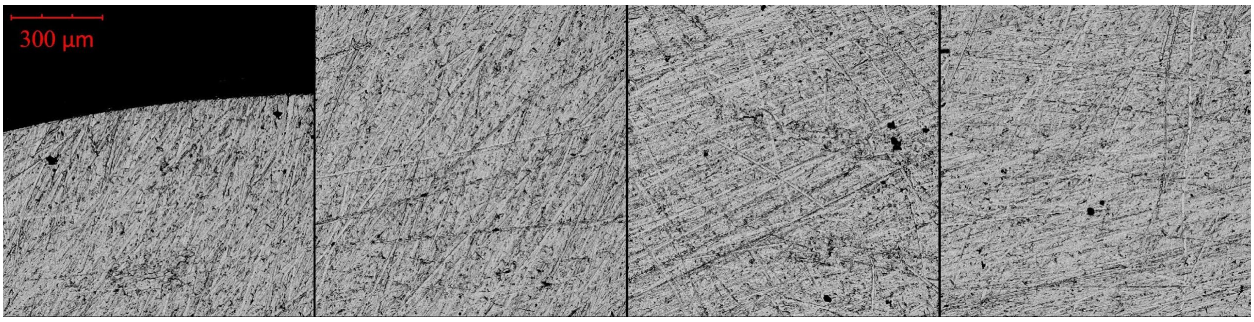

Fig. 9. Some SEM images of the cylinder test parts.

X-Ray Scanning.

X-ray imaging is performed to investigate the interior quality of the channel sections by taking images of the parts. X-ray inspection is done by using the Nordson Dage Quadra 7 instrument with an X-ray power of 160 kV. Details of the channel sections are illustrated in Fig. 10. Since the test parts subjected to X-ray scans are made of copper, details of the channel sections are obtained coarsely in observation because of the high density of copper. As a result of changing the areas of the cross sections, a blurry view around the channel occurs. The column structure of CS3 and the fin structure of CS4 is observed more precisely due to the constant and straight sections.

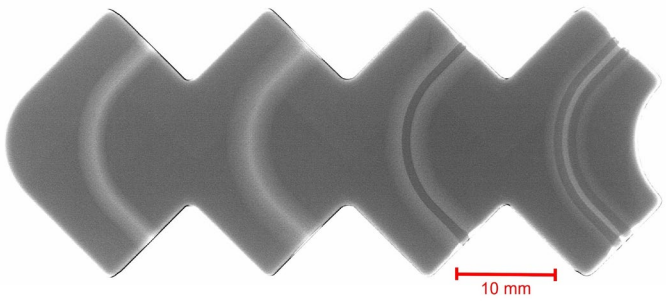

Fig. 10. X-ray inspection of the angled test part.

Summary

In this study, manufactured test parts using the M-FFF method are subjected to preliminary material characterization and quality control tests such as measurement of *surface roughness*, determination of dimensional accuracy with the *CMM*, scanning of parts with the *X-ray* device, calculation of the density with the *Archimedes method* and determination of porosity within the part with the *SEM analysis*. According to the CMM results, dimensions of the test parts are mostly greater than the nominal dimensions. For overall dimensions of the channel sections, mostly smaller dimensions are measured. Surface roughness results are significantly satisfying for upper and side surfaces compared to the SLM method. Thus, the M-FFF method can be used for the parts

that include liquid paths in terms of pressure drop. The result of X-ray scan shows that a device with more powerful X-ray source must be used to obtain images with finer details. Obtained results of density and porosity are lower than the datasheet results, which means that the manufactured parts must be qualified in terms of strength and leakage according to the application area. Despite these, the M-FFF method can be used for fast prototyping due to its speed, price, and modularity. As future works, process parameters and product range may be improved for the M-FFF method.

Acknowledgement
This work was supported in part by Middle East Technical University under the project contract ADEP-302-2022-11183.

References

[1] W.E. Frazier, Metal additive manufacturing: a review, J. Mater. Eng. Perform. 23 (2014) 1917-1928. https://doi.org/10.1007/s11665-014-0958-z
[2] W.J. Sames, F.A. List, S. Pannala, R.R. Dehoff, S.S. Babu, The metallurgy and processing science of metal additive manufacturing, Int. Mater. Rev. 61 (2016) 315-360. https://doi.org/10.1080/09506608.2015.1116649
[3] J. Armen, H.A. Bruck, Improving contact resistance in metal–ceramic heat exchangers running liquid metal by additive manufacturing and ceramic tubes with electroplated films, Int. J. Adv. Manuf. Technol. 113 (2021) 2101-2119. https://doi.org/10.1007/s00170-021-06813-0
[4] R.P.P. da Silva, M. V. V. Mortean, K.V. de Paiva, L.E. Beckedorff, J.L.G. Oliveira, F.G. Brandão, A.S. Monteiro, C.S. Carvalho, H.R. Oliveira, D.G. Borges, V.L. Chastinet, Thermal and hydrodynamic analysis of a compact heat exchanger produced by additive manufacturing, Appl. Therm. Eng. 193 (2021) 116973. https://doi.org/10.1016/j.applthermaleng.2021.116973
[5] Z. Gobetz, A. Rowen, C. Dickman, K. Meinert, R. Martukanitz, Utilization of Additive Manufacturing for Aerospace Heat Exchangers, Pennsylvania State University State College United States, (2016).
[6] D. Bacellar, V. Aute, Z. Huang, R. Radermacher, Design optimization and validation of high-performance heat exchangers using approximation assisted optimization and additive manufacturing, Sci. Technol. Built Environm. 23 (2017) 896-911. https://doi.org/10.1080/23744731.2017.1333877
[7] T.C. Henry, M.A. Morales, D.P. Cole, C.M. Shumeyko, J. C. Riddick, Mechanical behavior of 17-4 PH stainless steel processed by atomic diffusion additive manufacturing, Int. J. Adv. Manuf. Technol. 114 (2021) 2103–2114. https://doi.org/10.1007/s00170-021-06785-1
[8] J. Rodriguez, J.I. Vicente, J.C. Ezeiza, A. Zuriarrain, P.J. Arrazola, X. Badiola, E. Dominguez, D. Soler, Mechanical and electrical properties of additively manufactured copper. In IOP Conference Series: Mater. Sci. Eng. 1193 (2021) 012034. https://doi.org/10.1088/1757-899X/1193/1/012034
[9] M. Galati, P. Minetola, Analysis of density, roughness, and accuracy of the atomic diffusion additive manufacturing (ADAM) process for metal parts, Materials 12 (2019) 4122. https://doi.org/10.3390/ma12244122

Modeling the shape of additive manufactured parts

BRUNI Carlo[a *], CICCARELLI Daniele[b], PIERALISI Massimiliano[c] and MANCIA Tommaso[d]

DIISM Università Politecnica delle Marche, via Brecce Bianche 60131 Ancona, ITALY

[a]c.bruni@univpm.it, [b]d.ciccarelli@univpm.it, [c]m.pieralisi@univpm.it, [d]t.mancia@univpm.it

Keywords: FDM, Modeling, Additive Manufacturing

Abstract. The additive manufactured parts can be made by the use of suitable layer thicknesses of the polymer in order to respect the requirements of a refined geometry and of a surface appearance of the physical object that should be as similar as possible to the original CAD model. An other important variable is the digital datum that can represent a key variable of the realization procedure. The methodology proposed and followed in the present investigation got the objective to get a physical model, through the information obtained by a 3D scanning device, taking into consideration not only the digital treatment but also the building direction to guide the FDM layer deposition in order to realize the required surface appearance. The profiles of the specimen in the digital environment were compared to each other before realizing. The physical object obtained after digital treatment was similar to the one obtained by the original CAD.

Introduction

The prototyping is very useful in the initial phases of the project in order to verify some important features of the object to be definitively realized. In particular those related to the concept, geometrical and ergonomic characteristics. Sometimes such prototypes in particular for polymers got also properties very similar to those obtained by other technologies. For example injection molding widely used in fields when too much resistance values are not required.

The quality of the manufactured component is a function of the technology utilized and, in the sector of the additive manufacturing, on the type of technique among FDM, SLA, polyjet, etc. In particular the layer thickness and the deposition strategy, also represented by the building direction, are the main variables of the manufacturing process.

In addition the digital information for model realization represents an other variable affecting the process. In general the information to the 3D PRINTER is given by the Computer Aided Design and the geometrical information translated into some working formats like those based on the Standard Triangulation Language initially applied on STereoLithography some tens of years ago. Such formats are used by some researchers [1] and by the authors in previous works [2]. But, the input information can be also supplied to the management software of the machine unit using directly control nodes of the realized elements such as curves, surfaces, solids and composition of them [3]. The problem is represented by the amount of information sent into the machine software to generate the control instructions. That means time consumption and queues in processing digital data with related errors in loading and redundant instruction generation.

For this reason the STL represents a simplification in terms of digital information due to the approximation of the surface of the object to be realized with a surface characterized by an elevated number of triangles connected to each other by their vertices or nodes. The solid appearance of the digital object is represented by the versus of surface normal of each triangle. The external versus means a solid object while the internal versus a cavity or hole. Under these conditions the file format and the approximation to the original digital geometry play a key role in the precision of the input file in terms of geometry and then on the physical object respect of requirements [2-4]. Of course smoother and more accurate is the surface of the object better the STL approximation

Content from this work may be used under the terms of the Creative Commons Attribution 3.0 license. Any further distribution of this work must maintain attribution to the author(s) and the title of the work, journal citation and DOI. Published under license by Materials Research Forum LLC.

is. The improvement can be in general obtained managing the approximation tolerance in terms of the distance between the surface of the triangle to the original surface of the object and/or in terms of the number of triangles of the approximating surface.

The problem is represented by the description of the approximating surface when the geometry is detected by some 3D SCANNERS or similar techniques by which is possible to acquire the entire surface of the physical object or part of that. The technique of acquisition naturally determines the quality of the digital information with some musts represented by reduced setup and detection times. Normally but not always the acquired information is represented by a cloud of nodes that can be translated in the different available formats [5]. STL is one of them able to represent with a generally low amount of storing memory the acquired surface of the physical object. Such technique is very useful when some digital archives need to be realized about already existing geometries or when the realized geometry needs to be compared with original one in the computer aided environment [6,7]. Such procedure is very useful when simple geometries are detected while still represents a newness for those geometries characterized by complicated structural elements such as double curvature surfaces [6]. In particular when they are connected with planar ones. When using the described tools some computing phases need to be performed before comparing the detected with the original ones. The level of computing must be of course as high as high is the building performance of the RP machine used [8]. In particular the building strategy represents the key variable to tune other than the layer thickness in order to get a physical model respecting given geometrical requirements.

Considering that a methodology is proposed in order to evaluate the building direction variable in obtaining a FDM physical object, starting from the digital data acquired by a 3D SCANNER on photopolymerized physical model, as similar as possible to that given by the same technique when using original information. A compact FDM machine was used for the purpose with a digital input supplied with the STL format. The digital model was treated in order to increase the quality of the geometry up to the one of the original STL. It was observed that different digital treats are required when different building directions are considered.

Methodology, Digital Treatments and Experiments

Methodology.

The present investigation aims at proposing and applying a methodology to manage the digital data points given by a 3D scanning of an high quality complex surface made in a UV photopolymer shown in Fig.1. In order to use those as input for realizing a physical object with a surface as similar as possible to the one of the original. The acquired geometry was refined in its surface and in the connection between the complex part of that and the planar one. This acting on lines and surface elements and on the number and typology of triangles composing the approximating STL. The main variable of the investigation is represented by the building direction when reproducing by FDM the digital models with and without treatments. The methodology is reported in Fig. 2.

Digital treatments.

The data cloud obtained by the 3D scanner using LED-CMOS systems in order to get the shape of the physical object were computed by CAD in different ways, some of them reported in a previous research of the authors [2] in order to solve the problem of the connection between the complex part of the component represented by the dome and the planar part of that represented by the basis. Fig. 3 shows the particulars of the photopolymer model acquired as digital information. The digital treat was made considering a planar basis of 5.5 mm in order to include the defective scanned zone of the component and then rebuilding completely the basis with a thickness of 5.2 mm. After that the digital model was treated in the STL format improving the number of triangles approximating the CAD surface and applying some smoothing sequences using the Materialise software.

Fig. 1. Photopolymer model utilized to get the digital information by 3D SCANNING.

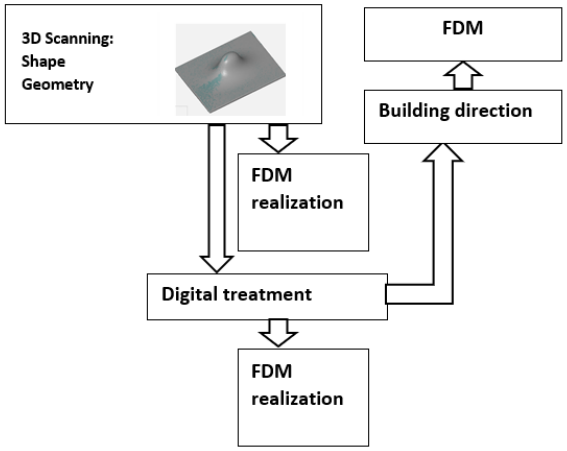

Fig. 2. Methodology.

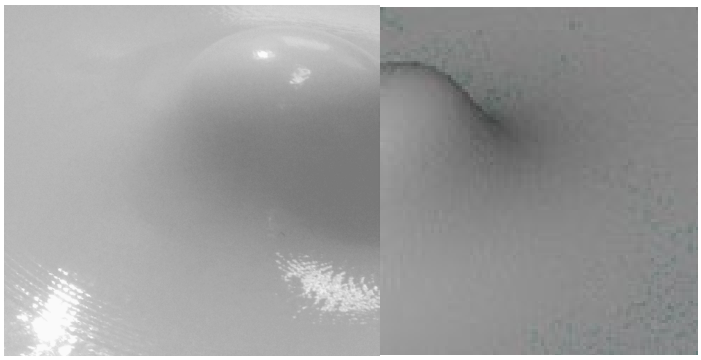

a) b)

Fig. 3. Particulars of the physical photopolymer (a) model and of the STL (b) obtained by the scanning device.

CAD profiles of the shape.

The profiles captured on the original shape in the CAD environment were reported by two equations.

The equation of the profile of the original CAD model in the longest direction:

$$y = -8E\text{-}07x^6 + 6E\text{-}05x^5 - 0.0012x^4 - 0.0091x^3 + 0.4423x^2 - 0.8688x + 0.549 \quad (1)$$

and the equation of the profile in the shortest direction:

$$y = 2E\text{-}08x^6 - 4E\text{-}06x^5 + 0.0002x^4 - 0.003x^3 - 0.0234x^2 + 0.0015x + 24.554 \quad (2)$$

where y represents the axis along the height of the dome and x the one on the basis in the longest and in the shortest directions respectively.

All of the digital models were realized by FDM after the comparison of the original CAD profiles with STL like shown in Table 1.

Table 1. CAD and STL main profiles.

CAD	STL
Original profiles by Eq. (1) and Eq. (2).	Profiles given by CAD. Profiles given before digital treatment. Profiles given after final digital treatment.

Realization of the physical objects.

The manufactured components were realized by a FDM compact machine taking into consideration the building direction. In one specimen the building direction was parallel to dome axis of the model while in the other the building direction was perpendicular. A 0.2 mm thickness layer was used with a filament in PLA material and a temperature of the extruder between 215 and 220°C selected. The scanning velocity of the extruder was 100 mm/s during working and 150 mm/s in idle movements. The comparison among the different physical models realized was made taking into consideration the CAD information, that without and with digital treatment along different building directions.

Results and Discussion

Digital treatments.

They were made in terms of the rebuilding of some reference nodes, lines and surfaces with related control points normally in the critical connections between the complex part of the model and the less complicated part represented by the planar basis. Such problem was already reported by the authors in a previous work of some of them [2]. Those are zones in which the building in the CAD environment requires the due attention and the digital data obtained by the scanning devices need to be always verified in order to be sure that the connections be always ensured. The lack means continuity solutions in the surface of the digital and subsequently of the physical models over those typical of scanning devices [8] and of the 3D printers [9].

Some of these problems may be corrected directly acting on the control points as described preserving the cloud points of the complex part when possible. The STL should be a subsequent way to simplify the problem by considering a surface alone able to approximate the whole mathematical elements of the model prior and after the treatments. The connection problems sometimes evidenced their effects in the physical realized models directly and in those realized by digital information obtained by the scanner. In Fig. 3a) the light waviness at basis of the photopolymerized model is evidenced and captured by the 3D scanning and sometimes amplified depending on the acquisition time, on the device and on some diffusive modes of the LED based light used by the SCANNER (fig. 3b). In Figs. 4a) and 4b) the comparison between 3D scanned STL after basis rebuilding and original STL is reported. After triangle refinement and smoothing the comparison can be observed in figs. 5a) and 5b). The improvement of the surface of the digital model was made using the Materialise software by which a further discretization of the triangulation representing the approximation to the cloud surface detected by the scanning device is made. In that way the dome surface is better described and the connection with the rebuilt plane improved.

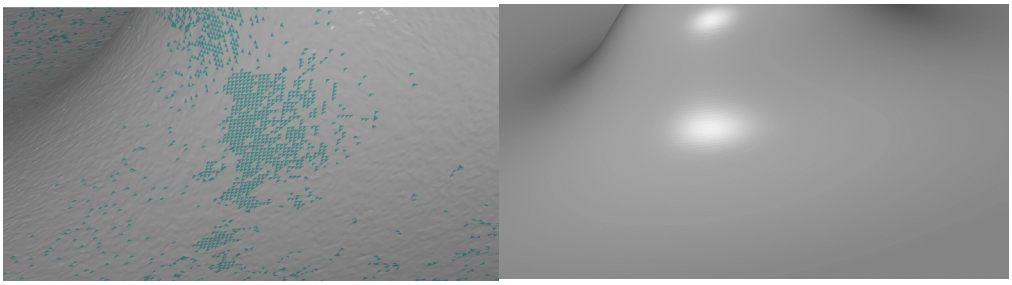

a) b)

Fig. 4. STL 3D scanned surface (a) and the STL obtained directly by the original CAD (b).

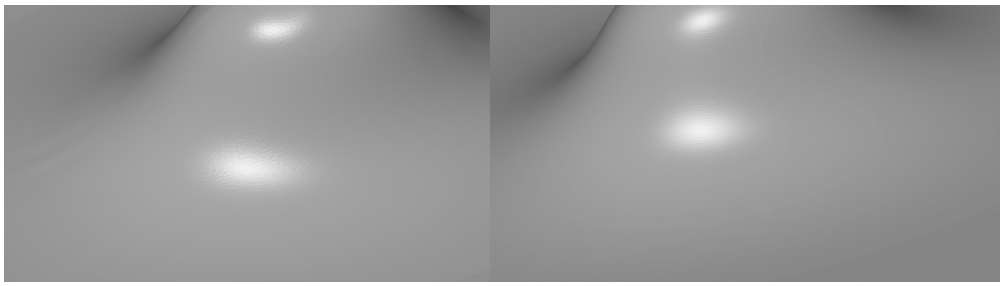

a) b)

Fig. 5. STL 3D scanned surface after digital treatments (a) and STL obtained directly by the original CAD (b).

Profiling.

The different profiles were computed in the CAD environment supported by image analysis techniques and then compared. The equations of the two semi-profiles are reported in the previous paragraph.

The comparison between the STL profile obtained directly by the CAD original model, the profile plot of points of the original CAD model and the STL obtained by the digital rebuilt model is made in the Fig. 6. An excellent approximation to the original profile is obtained in the STL standard.

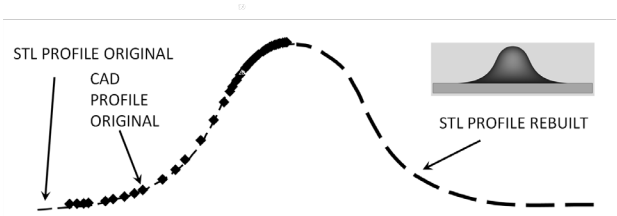

Fig. 6. Comparison between different profiles obtained along one direction of the object: CAD, STL and STL after digital rebuilding.

Realization of the FDM physical objects.

In Fig. 7 the comparison between the FDM models realized directly by the original CAD and that generated by the scanning device with the building direction parallel to the dome axis is shown. The problem at the basis is clearly observed. When the building direction is perpendicular to the dome axis the FDM produces its best performance and then the continuity solutions appear evidenced and the difference highlighted as in Fig. 8. In both the cases the waviness detected by the 3D SCANNER is copied on the FDM model reporting not only the original information of the

model geometry but also that of the physical photopolymer model from which the digital data were initially acquired. The connection problem to the basis due to the difficulty to catch at the same time the complex part of the model and plan part exists in that phase.

In Fig. 9 the FDM physical objects were realized from digital information detected by the 3D SCANNER after some reported treatments in order to allow the connection between the dome and the planar surface. By such operation the planar level is improved and the connection rebuilt. Such improvement appears able to describe the physical model when the building direction is parallel to the dome axis. But some continuity solutions still persist when the building direction perpendicular to the dome axis is applied as can be seen in Fig. 10. It means that the configuration perpendicular to the building axis requires further digital treatments in order to get a geometry as similar as possible to the one obtained when the original CAD is considered. Further corrections of the geometrical elements, the increase in the triangulation density as well as the smoothing of the STL surface permit the increase in the quality of the surface appearance of the FDM physical object like shown in Fig. 11. In other words the profiles of Fig. 6 are correctly reproduced on the realized models. In this way the FDM physical object appears similar to the surface of the original FDM without the need to plan a machining phases.

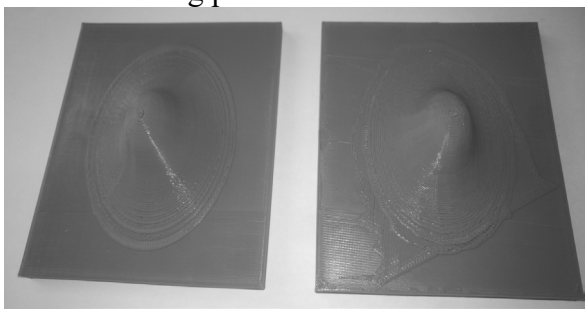

a) b)

Fig. 7. Comparison between FDM physical object realized by the CAD original data (a) and that directly obtained by the 3D scanning device information (b) with building direction parallel to the dome axis.

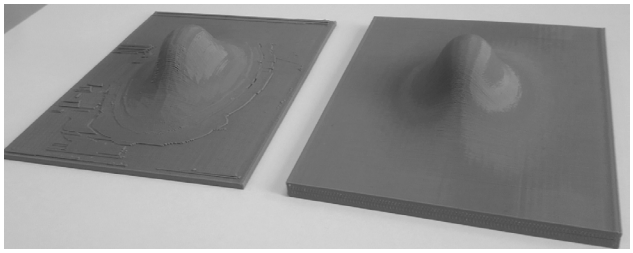

a) b)

Fig. 8. Comparison between the physical object obtained by the digital data directly given by the 3D scanning device (a) and model made by FDM considering the original CAD data (b) with building direction perpendicular to the dome axis.

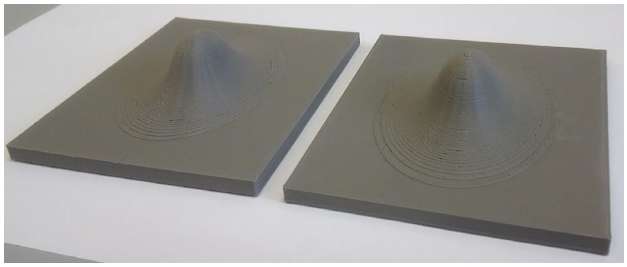

a) b)

Fig. 9. Comparison between the FDM model obtained after digital treatments (a) and that given by the original CAD (b) with the building direction parallel to the dome axis.

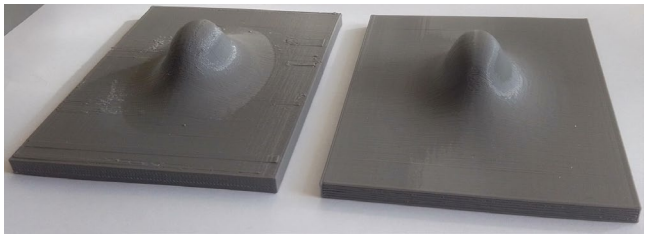

a) b)

Fig. 10. Comparison between the FDM model obtained after the digital treatment (a) and that given by the original CAD (b) with the building direction perpendicular to the dome axis.

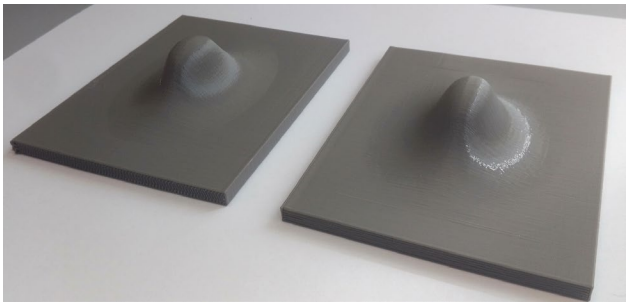

a) b)

Fig. 11. Comparison between the FDM model obtained after further digital treatment (a) and that given by the original CAD (b) with the building direction perpendicular to the dome axis.

The results can be reported in terms of the dome height. In particular the realized FDM object obtained by the 3D SCANNING device with the building direction perpendicular to that gives an height of 20.52 mm with a thickness basis of 2.63 mm. The rebuilt model without the final digital treatment is about 23.68 mm while the one obtained after is about 23.6 mm. The original data get a FDM model with a dome height of about 23.79 mm.

Such results are very useful in particular when these methodologies, as already reported by other authors [10,11], need to be applied in a manufacturing system.

Summary

The investigation aims at defining the best profile shape of the STL model under given conditions taking the dome reference from a 3D SCANNED one and by applying different digital treatments in the computer aided environment in order to get a physical result as similar as possible to that obtained by the original CAD information. In the realization of the FDM models the building direction variable is considered.

First of all the basis of the STL model was rebuilt and the connection with dome properly managed. But such digital treatment was able only to permit the realization of a FDM physical model with a building direction parallel to the dome axis. With a further treatment consisting mainly in a heavy refinement of the triangles approximating the cloud points a smoother surface of the dome than before was obtained. The final treatment got a profile very close to the STL of the original CAD model as shown by the comparison of them and to the original CAD information described by two equations obtained through the longest and shortest sides of the model.

Finally, the comparison between the two main FDM physical models, in particular the one obtained directly by the original CAD and the other one given after the digital treatment of 3D scanned data allows to state that they are similar to each other. Under the conditions of the present investigation when treating polymers the building direction represents the key variable for the obtaining physical surfaces respecting requirements. To do that many digital treatments are required.

References

[1] W. Zha, S. Anand, Geometric approaches to input file modification for part quality improvement in additive manufacturing. J. Manuf. Proc. 20 (2015) 465-477. https://doi.org/10.1016/J.JMAPRO.2015.06.021

[2] C. Bruni, T. Mancia, L. Greco, M. Pieralisi, Additive Manufacturing using UV Polymerization of Complex Surfaces Generated by Two Main B-Splines. Procedia Manuf. 47 (2020) 1078-1083. https://doi.org/10.1016/j.promfg.2020.04.352

[3] Y. Song, Z. Yang, Y. Liu, J. Deng, Function representation based slicer for 3D printing, Comput Aided Geom D 62 (2018) 276-293. https://doi.org/10.1016/j.cagd.2018.03.012

[4] A. Manadhachary, Y. Ravi Kumar, L. Krishnanand, Improve the accuracy, surface smoothing and material adaptation in STL file for RP medical models, J. Manuf. Process. 21 (2016) 46-55. https://doi.org/10.1016/j.jmapro.2015.11.006

[5] Q. Qi, P.J. Scott, X. Jiang, Status, comparison, and future of the representations of additive manufacturing data, Computer-Aided Design 111 (2019) 44-64. https://doi.org/10.1016/j.cad.2019.02.004

[6] C. Bruni, L. Greco, T. Mancia, M. Pieralisi, 24th International Conference on Material Forming (ESAFORM 2021) Integrating layer by layer manufacturing for the realization of polymer complex geometries with scanning devices: re-building by digital data.

[7] N. Decker, Y. Wang, Q. Huang, Efficiently registering scan point clouds of 3D printed parts for shape accuracy assessment and modeling, J. Manuf. Syst. 56 (2020) 587-597. https://doi.org/10.1016/j.jmsy.2020.04.001

[8] F. Dickin, S. Pollard, G. Adams, Mapping and correcting the distortion of 3D structured light scanners. Precis. Eng. 72 (2021) 543–555. https://doi.org/10.1016/j.precisioneng.2021.06.001

[9] K. Wi, V. Suresh, K. Wang, B. Li , H. Qin, Quantifying quality of 3D printed clay objects using a 3D structured light scanning system, Additive Manufacturing 32 (2020) 100987. https://doi.org/10.1016/j.addma.2019.100987

[10] S. Yin, Y. Ren, Y. Guo, J. Zhu, S. Yang, S. Ye, Development and calibration of an integrated 3D scanning system for high-accuracy large-scale metrology, Measurement 54 (2014) 65-76.

[11] X. Chen, G. Liu, Z. Chen, Y. Li, C. Luo, B. Luo, X. Zhang, Automatic detection system with 3D scanning and robot technology fordetecting surface dimension of the track slabs, Automat. Constr. 142 (2022) 104525.

Resources and manufacturing technology evaluation of hybrid additive metal laminated tooling for forming

DARDAEI JOGHAN Hamed[1,a *], HAHN Marlon[1,b], AGBOOLA Ololade[1,c] and TEKKAYA A. Erman[1,d]

[1] Institute of Forming Technology and Lightweight Components, TU Dortmund University, Baroper Str. 303, Dortmund 44227, Germany

[a]hamed.dardaei@iul.tu-dortmund.de, [b]marlon.hahn@iul.tu-dortmund.de, [c]ololade.agboola@tu-dortmund.de, [d]erman.tekkaya@iul.tu-dortmund.de

Keywords: Sheet Metal Lamination, Laser Metal Deposition, Deep Drawing Tools

Abstract. The rough surface finish caused by the stair step effect is the major drawback in the application of sheet metal laminates in rapid tooling. The application of laser metal deposition (LMD) and subsequent post-processing (milling, ball burnishing, and laser polishing) to reduce the stair-step effect in hybrid additive metal laminated forming tools was recently presented. In the present study, the energy consumption and manufacturing time of the hybrid process are compared with the conventional (milling plus hardening by heat treatment) as well as with full LMD and milled components. The hybrid process requires significantly less energy and manufacturing time compared to the LMD components. Since the surface hardness is sufficient for tooling in the hybrid process, no additional hardening is required, also resulting in a shorter manufacturing time and lower energy relative to the conventional method (depending on the part mass, a minimum of 29% is faster). The optimal sheet laminate combination based on the economic criteria for the tool with a radius of 6 mm is presented.

Nomenclature

Symbol	Unit	Description	Symbol	Unit	Description
E	MJ	Energy consumption	C_L	mm	Cutting length
a	mm	Length of square part	X	-	Mass ratio of final part to the initial
d	mm	Diameter of cylindrical hole	T	s	Process time
c	-	Ratio of thickness to length	ρ	kg/mm^3	Density
t	mm	Sheet thickness	SEC	MJ/kg	Specific energy
n	-	Number of sheet layers	Q	mm^3/min	Material removal rate
m	kg	Mass of part	f	mm/min	Feed rate
a_e	mm	Radial depth of cut	P_L	W	Laser power
V	mm^3	Volume of stair step	a_p	mm	Axial depth of cut

Introduction

Metal sheet lamination or layer laminate manufacturing (LLM) as a rapid tooling method was patented for show molds in 1942 by Hart F.V [1]. For several years, different industries, especially the automotive industry, showed high-interest beginning in the 1980s [2]. However, the main drawback of the LLM method is the segregated surface, named the stair step effect, due to the stacking of sheets with different thicknesses to build a defined radius or angle. There are various methods for reducing the stair step effect in forming tools made of sheet metal laminates. The state of research in this area (use of a flexible intermediate layer [3], chamfering the corner of the laminae [4], machining of the laminae [5], ball burnishing [6], brazing or soft soldering [7]) is

Content from this work may be used under the terms of the Creative Commons Attribution 3.0 license. Any further distribution of this work must maintain attribution to the author(s) and the title of the work, journal citation and DOI. Published under license by Materials Research Forum LLC.

already summarized [8]. In [8], the stair step effect was reduced using laser metal deposition (LMD). Based on the DIN EN ISO/ASTM 529000 [9], direct energy deposition (DED) is a subcategory of the additive manufacturing (AM) process in which concentrated energy is applied to the filling material. LMD is also a DED process in which a laser is used as an energy source and metal powder as the filling material. The main advantage of the application of LMD is that the manufactured tool does not require an additional hardening process. The local heating of the surface during LMD, compared to heating the entire part for hardening in conventional manufacturing, can result in significant energy savings. In [8], three post-processing processes (milling, ball burnishing, and laser polishing) have been explored to produce an improved surface. By milling, the extra material is machined from the deposited surface. In ball burnishing, the surface roughness is improved by plastic deformation. Laser polishing involves re-melting the surface with a laser (without additional powder) to improve the roughness. It is shown that the post-processing by ball burnishing can improve the tool's hardness; however, the best surface roughness is achieved by milling.

In the following, the economic aspect of the introduced hybrid additive laminated tooling concept is compared with the conventional method (milling followed by hardening) and with the fully deposited part by LMD, which is milled afterward to improve the surface roughness. In addition, an approach to identify the optimum sheet combination is provided.

Procedure and Methodic

Sheet lamination offers the possibility of combining different sheet thicknesses. As shown in Fig. 1, the number of possible sheet combinations with three sheet thicknesses 0.5, 1, and 2 mm increases exponentially with increasing radius. The selection of the proper combination is a multi-objective optimization depending on the required tool strength, energy consumption, cost, and placement of functional elements, e.g., sensors, heating, or cooling channels. This study will lower the number of possibilities based on energy consumption and manufacturing time.

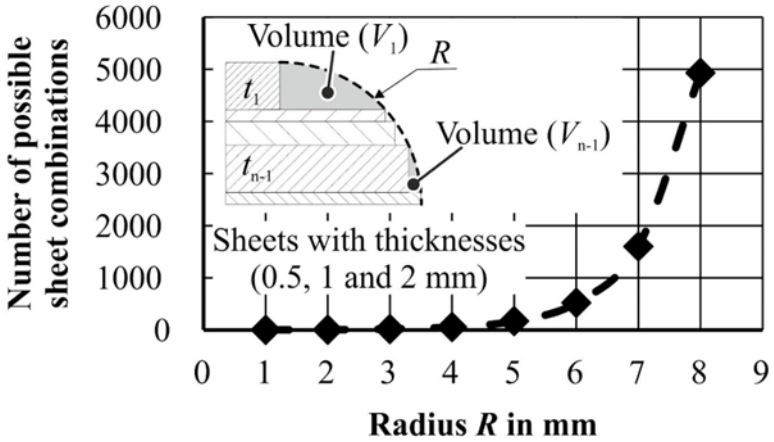

Fig. 1. Number of the possible sheet combinations for different radii with 0.5, 1, and 2 mm sheet thicknesses.

For systematic evaluation, it is necessary to define the process route of each method. As shown in Fig. 2, the hybrid additive laminated tooling starts with manufacturing the sheets. The sheets are laser-cut in different thicknesses and stacked based on the proper order. Next, the stair step areas (volumes) are filled with LMD, followed by post-processing.

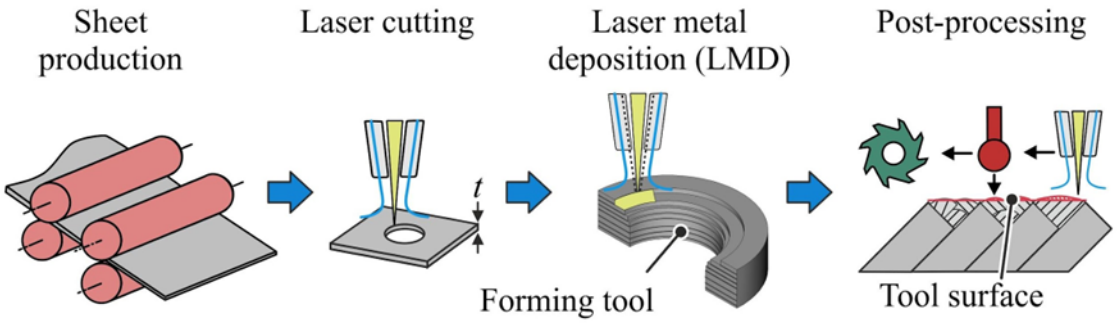

Fig. 2. Process route of hybrid additive laminated tooling.

For the calculation of the total energy consumption of hybrid additive laminated tooling (E_T^H) as shown in Eq. 1**,** the energy of sheet production (E_S), cutting energy by laser (E_C), required energy for the production of powder (E_P), and deposition (E_D) during LMD, and finally, the energy consumption during post-processing (E_{PP}) are considered.

$$E_T^H = E_S + E_C + E_P + E_D + E_{PP} \quad (1)$$

For the energy consumption of the conventional method (E_T^C), only the production energy for bulk material (E_B), milling (E_M), and hardening (E_H) are studied, as seen in Eq. 2:

$$E_T^C = E_B + E_M + E_H \quad (2)$$

To calculate the energy consumption of a fully deposited part by LMD with milling (E_T^{LMD}) as post-processing, the powder production (E_P), deposition (E_D), and milling (E_M) energies are taken into account (see Eq. 3).

$$E_T^{LMD} = E_P + E_D + E_M \quad (3)$$

For the estimation of the production time (T) for each process (hybrid, conventional, and fully LMD), the manufacturing time of the sheet, bulk material, and powder production are not considered.

Hybrid additive laminated tooling.

Since the manufacturing energy and time for a systematic evaluation strongly depend on the part geometry, it is assumed that an academic square part with length a and with a cylindrical hole with diameter d has to be manufactured (Fig. 3a). The ratio c is defined as the thickness of the part as a fraction of the length. In the hybrid process, it is assumed that the part is made from n sheets with a constant thickness t (Fig. 3b). The same geometry is used for the calculations for the conventional and fully LMD parts.

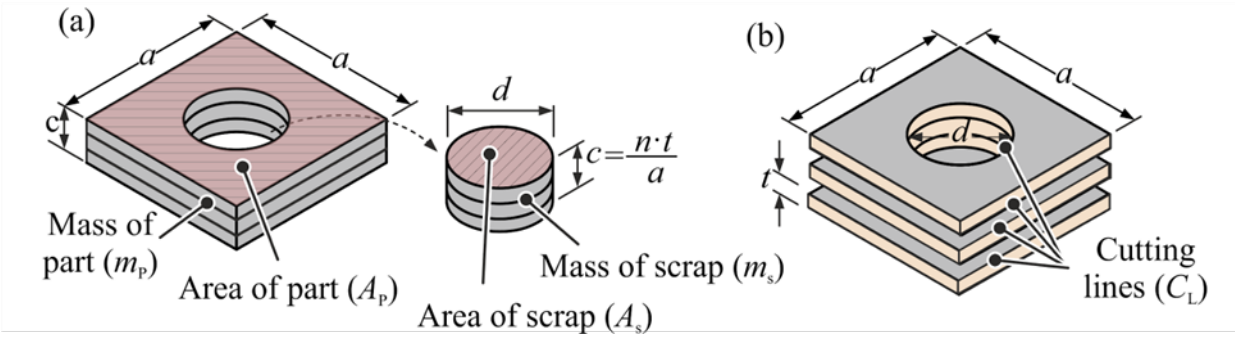

Fig. 3. (a) Assumed geometry for calculations (b) cutting length (C_L).

The mass ratio (X) is defined as the mass of the final part (m_P) to the mass of the initial state ($m_P + m_s$) as shown in Eq. 4. By taking into account that all the used sheets have an equal density (ρ), the mass ratio (X) can be defined as a ratio of final part surface (A_P) to the total initial surface ($A_P + A_s$), as illustrated in Fig. 3a. It yields the relation of the length of the square (a) and hole diameter (d) as provided in Eq. 4.

$$X = \frac{m_P}{m_P+m_S} = \frac{A_P}{A_P+A_S} = 1 - \frac{\pi d^2}{4a^2} \Rightarrow d = a \cdot \sqrt{\frac{4(1-X)}{\pi}} \tag{4}$$

Considering volume constancy, the length of the square (a) can be determined as:

$$c \cdot a^3 = \frac{m_P}{X \cdot \rho} \Rightarrow a = \sqrt[3]{\frac{c \cdot m_P}{X \cdot \rho}} \tag{5}$$

For the determination of the energy required for laser cutting, it is required to compute the cutting length (C_L) of sheets (Fig. 3b). The cutting length (C_L) is the sum of the perimeter of the square and the hole as provided in Eq. 6. Replacing the Eq. 4 and 5 in the Eq. 6 yields the cutting length (C_L) as a function of the material yield ratio (X), density, sheet thickness, and final part mass:

$$C_L = (4a + \pi d)n \; n = \frac{ca}{t} \Rightarrow \; (4a + \pi d)\frac{c.a}{t} = \frac{1}{4t}\left(\frac{c \cdot m_P}{X \cdot \rho}\right)^{\frac{2}{3}} \cdot \left(\sqrt{4\pi(1-X)} + 4\right) \tag{6}$$

The cutting length is calculated for three sheet thicknesses (Fig. 4a). It is concluded that the thinner the sheet thickness, the higher the cutting length for the same final part mass. For calculating the energy required for the laser cutting, the cutting information of the laser machine, model TC1005 from the company Trumpf, is used. Three steel sheets with a thickness of 0.5, 1.0, and 2.0 mm are used for the calculations. The feed rate for cutting the sheets with thicknesses 0.5, 1.0, and 2.0 mm are 9, 8, and 5 m/min, respectively. A laser power of 1700 W is required for cutting 0.5 and 1.0 mm sheets and 1200 W for 2 mm sheets. The total energy consumption of the machine for laser cutting the 0.5 and 1.0 mm sheets equals 42 kWh and 38 kWh for 2 mm sheets [10]. The cutting time can be calculated based on the cutting length (C_L) and feed rate during cutting. Afterward, the total energy consumption for laser cutting (E_C) can be calculated for different steel sheet thicknesses, as shown in Fig. 4b, assuming the density of steel (ρ) is 7900 kg/m^3. It can be seen that for the same final part mass, the thicker sheet thickness requires lower energy for cutting.

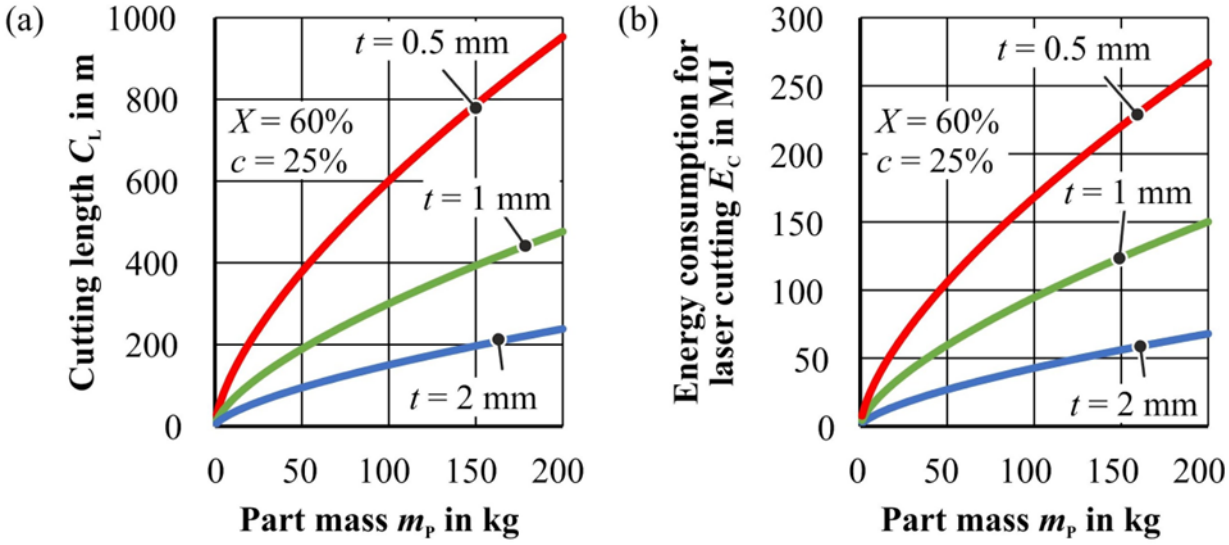

Fig. 4. (a) Cutting length, C_L (b) cutting energy with TC1005 machine.

Based on [11], the production of a 1 kg sheet requires 19.37 MJ of energy. Therefore, the required energy for sheet production (E_S) is equal to 19.37 [MJ/kg] · ($m_P + m_s$). The energy required for the production of the powder differs depending on the production method. According to [12], for producing the powder by gas atomization, 24.48 MJ/kg of energy is needed. In the hybrid method, it is assumed that the mass of the sum of the stair step volumes ($m_{Step} = \rho \cdot \sum_{i=1}^{n-1} V_i$), see Fig. 1, is 1% of scrap mass (m_S), i.e. the required powder by laser metal deposition (LMD) is 1% of m_S. The required powder energy production (E_P) for hybrid additive laminated tooling is $E_P = 0.2448$ [MJ/kg] · m_S. The deposition energy consumption with Lasertec 65 3D machine from the company DMG MORI as reported by [13], is 76.11 MJ/kg. By considering 1% of the scrap mass, the deposition energy for the hybrid method is $E_D = 76.11$ [MJ/kg]· ($0.01 m_S$) or $E_D = 0.7611$ [MJ/kg] · m_S.

Since only the sheet thickness of 1 mm will be considered in the rest of the calculations, it is assumed that the track distance during the post-processing is 1 mm and that for ball burnishing and laser polishing, the tool moves through the whole cutting length (C_L). The essential energy required for ball burnishing is considered based on the Ecoroll hydraulic aggregator HGP6.5, which is $E_{Ep.}^{B} = 3\,kW$. For laser polishing, the laser power during the polishing is considered as essential energy consumption ($E_{Ep.}$), where $E_{Ep.}^{L} = 1000$ W. The energy required for post-processing for the hybrid method (E_P^H) by ball burnishing and laser polishing is $E_P^H = T_P^H \cdot E_{Ep.}$, where T_P^H is the post-processing time. To compute the energy required for milling, the specific energy of finishing (SEC_F) from [14] is used, i.e. $SEC_F = 5.79$ MJ/kg. It is assumed that 20% of the deposited material (1% of m_S) needs to be milled. Therefore, the required energy is:

$$E_{PP}^{Hybrid} = 0.2 \cdot 0.01 \cdot m_S \cdot SEC_{Finishing} = 0.01158\,[MJ/kg] \cdot m_S \quad (7)$$

To determine the milling time, the radial depth of cut (a_e) and axial depth of cut (a_P) need to be defined to calculate the material removal rate $Q = f \cdot a_P \cdot a_e$ where f is the feed rate of the cutting tool. Therefore, the milling time is calculated as $T_M^H = \frac{Q_F^H}{0.01 \cdot m_S}$.

Conventional method.

For the production of bulk materials per kg, according to [15], 17.73 MJ of energy is required. This value is used to calculate the total energy required for producing bulk material in the conventional method:

$$E_{Bulk} = 17.73\ [MJ/kg] \cdot (m_P + m_s) = \frac{17.73}{X} \cdot m_P \quad (8)$$

The milling process is divided into two steps: rough milling and finishing. The specific energy (SEC_R) for rough milling is 0.848 MJ/kg [14]. The 99% of the scrap mass must be rough-milled, and the rest should be machined by finishing. The total energy and production time for the milling of the conventional method are calculated as shown in Eq. 9:

$$E_M^C = \left(0.99 \cdot SEC_R + 0.01 \cdot SEC_F\right) \cdot m_s = 0.8974 \left[\frac{MJ}{kg}\right] \cdot m_s \; and \; T_M^C = \frac{Q_F^H}{0.01 \cdot m_s} + \frac{Q_R^H}{0.99 \cdot m_s} \quad (9)$$

The energy consumption of the hardening process is significantly dependent on the type of hardening and furnace type. In this study, the furnace N120/85 HA from the company Nabertherm with an energy consumption of 13.6 kWh, is used for the calculations. It is assumed that the part will be quenched at 850 °C. According to [16], the required time for heating a part with a thickness of 80 mm is one hour. Considering the thickness of 80 mm and the thickness-to-length ratio (c) of 25% (see Fig. 2a), the length of the square (a) is calculated to be 320 mm. For steel, the corresponding weight will be approximately 64.7 kg. Considering the hour of homogenizing time, the required energy and time are evaluated as shown in Eq.10. Here, it is considered that during the homogenizing, the furnace works with 50% of its maximum power. It is noted that 1 kWh equals 3.6 MJ.

$$E_H^C = \frac{\left(13.6 + \frac{13.6}{2}\right) kWh}{64.7\ kg} \cdot 3.6 \frac{MJ}{kWh} \cdot m_{P.} = 1.14 \cdot m_P \; and \; T_H^C = \frac{2\ h}{64.7\ kg} \cdot m_P = 0.031 \cdot m_P \quad (10)$$

Fully deposited part (LMD plus milling).

For calculating the energy consumption of fully LMD parts followed by milling, the extra powder is required to be considered. This powder is waste material discharged during the positioning of the nozzle. This value is assumed as 20% of the final part mass. With this, the energy consumption for the powder production for the fully LMD part and the required energy during the deposition are:

$$E_P^{LMD} = 24.48 \left[\frac{MJ}{kg}\right] \cdot (0.2 \cdot m_P) = 4.896 \left[\frac{MJ}{kg}\right] \cdot m_P \; and \; E_D^{LMD} = 76.11 \left[\frac{MJ}{kg}\right] \cdot m_P \quad (11)$$

Considering the 1% of the part mass that needs to be milled, the required energy and time for the conventional method are:

$$E_M^{LMD} = 0.01 \cdot SEC_F \cdot m_{P.} = 0.0579 \left[\frac{MJ}{kg}\right] \cdot m_P \; and \; T_M^{LMD} = \frac{Q_F^{LMD}}{0.01 \cdot m_P} = \frac{\rho \cdot f \cdot a_p \cdot a_e}{0.01 \cdot m_P} \quad (12)$$

Results and Discussion

The energy consumption and manufacturing times are calculated based on the equations provided in the previous section and considering the following process parameters for the different processes in Table 1.

Table 1. Process parameters for milling, laser polishing, and ball burnishing.

Process	Laser polishing	Ball burnishing	Milling	
			Rough	Finishing
Feed rate f in [mm/min]	1000	900	600	200
Laser power P_L in [W]	1000	-	-	-
Radial depth of cut a_e in [mm]	-	-	25	25
Axial depth of cut a_p in [mm]	-	-	2	0.25

The total energy consumption for all three processes is shown in Fig. 5. It shows that the fully deposited method (LMD plus milling) has a very high energy consumption compared to the hybrid and conventional methods. It can be seen that there is no significant difference between the hybrid and the conventional method. Also, there is no significant difference between the different post-processing methods since the post-processing portion of the total energy consumption of the hybrid method is insignificant.

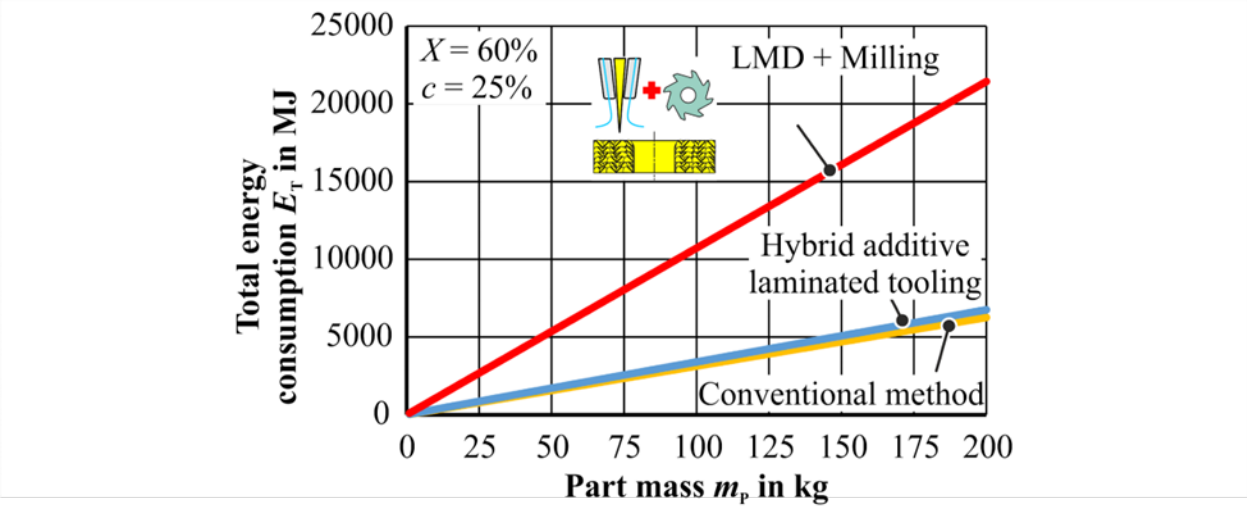

Fig. 5. Comparison of total energy consumption between hybrid, conventional, and fully LMD with the milling method.

The calculated manufacturing time for all three processes in Fig. 6a shows that fully deposited parts require a very high manufacturing time compared to the hybrid and conventional methods. The conventional method has a higher manufacturing time, even without considering the part transportation for hardening, than the hybrid method, as shown in Fig. 6b.
Between the different post-processing methods, the milling shows a shorter time; however, the difference between ball burnishing and laser polishing is insignificant. Since the processing time highly depends on feed rate, track distance, and tool diameter, the order of post-processing would be different. It should also be considered that the advantage of using laser polishing as post-processing is saving the cost of new tools and programming time. Also, laser polishing is a contactless process, so there is no tool wear. Finally, the focal distance of the laser allows the treatment of limited access areas. However, as mentioned, the main drawback is the reduction of the hardness of the treated surface [8].

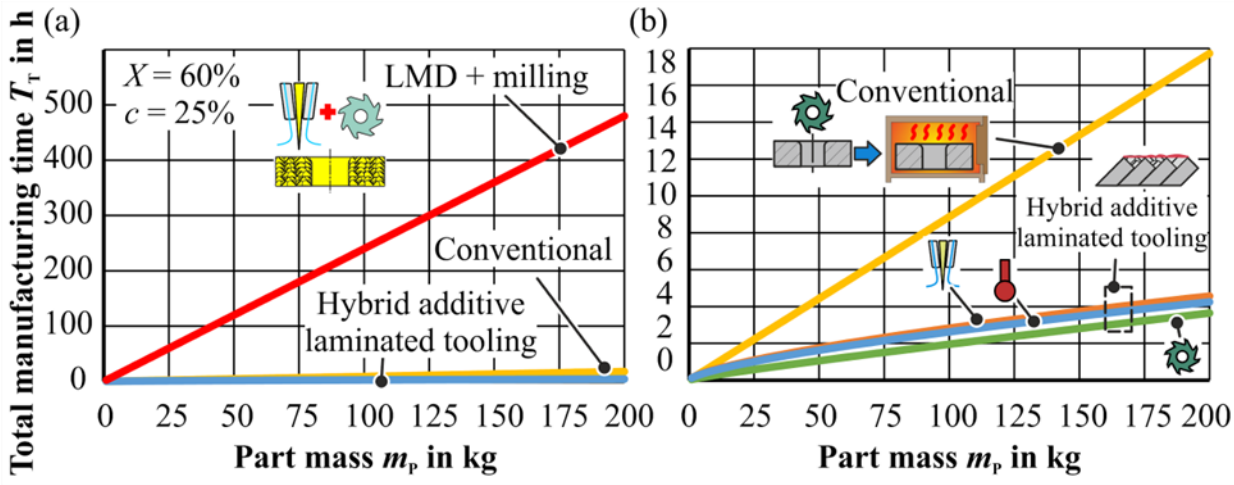

Fig. 6. Total manufacturing time (a) with LMD plus milling (b) without LMD plus milling.

As shown in Fig. 1, a high number of possible sheet combinations exist for each radius. Considering the same mechanical performance for all combinations, i.e. the tool strength is the same for all combinations, the number of sheet combinations can be limited by considering the energy, cost, and manufacturing time issues. For optimizing the sheet combinations, the following criteria are considered:

- The normalized laser cutting time (T_C^N),
- the normalized energy of production of metal powder and deposition energy ($E_P^N + E_{LMD}^N$),
- the normalized energy required for the laser cutting (E_C^N).

These factors (time and energy consumption) are desired to be kept as low as possible. For instance, for a radius of 6 mm, the energy and time are individually calculated and evaluated for all 520 combinations with different sheet thickness arrangements based on the mentioned criteria. The results are plotted in Fig. 7. It can be seen that the break-even point is around 0.33 for all criteria. Considering this value, the number of sheet combinations is reduced from 520 to 24.

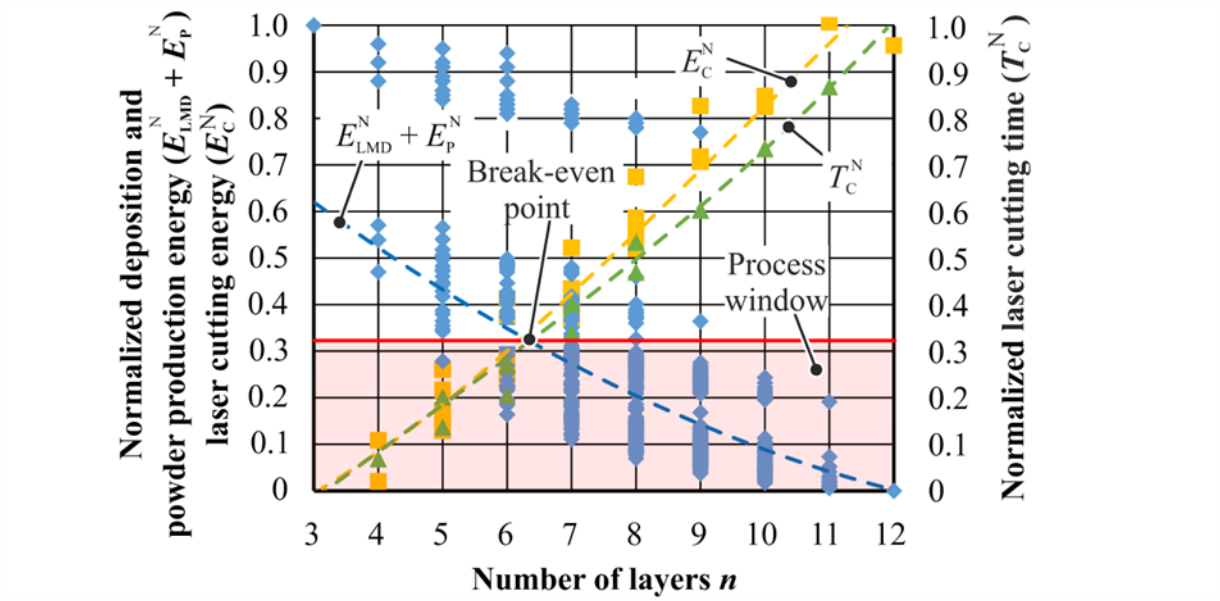

Fig. 7. Determination of break-even point for tool radius of 6 mm.

Summary

A systematic energy and manufacturing time evaluation of the introduced hybrid additive laminated tool manufacturing is provided. The results are compared with the conventional process route (milling followed by hardening) and also with a fully deposited part using laser metal deposition followed by milling as a post-processing method. The results show that the hybrid method is much more economical and faster than the fully deposited method and is comparable with the conventional method. However, the hybrid method is more suitable due to its ability to produce complex shapes in a shorter time. The production time depends considerably on the part geometry, but in this case the hybrid process is at least 29% (depending on the mass) faster than the conventional process. Laser polishing between the three post-processing methods provides an acceptable surface roughness without additional tooling costs and programming challenges compared to milling and ball burnishing but with lesser hardness (around 9% less as deposited). Since sheet lamination theoretically offers a high number of sheet combinations, the economic evaluation reduces the number of suitable sheet combinations for more effective manufacturing.

Acknowledgment

This result is part of the project titled "Reducing the stair step effect for dies manufactured by layer-laminated manufacturing by additive and formative post-processing," funded by the DFG (German Research Foundation) with project number 426515407. The authors are greatly thankful for the financial support. The authors also acknowledge Mr. Niklass Resse and Neshanth Paskaran for their support in part of the calculations.

References

[1] F.V. Hart, Mold and mold making method, U.S. patent: 2274060 A, priority date: 31.10.1938 (2274060)

[2] T. Nakagawa, K. Suzuki, A Low Cost Blanking Tool with Bainite Steel Sheet Laminated. In: J.M. Alexander (Ed.), Proceedings of the Twenty-First International Machine Tool Design and Research Conference, Macmillan Education UK, London, 1981, pp. 129-138. https://doi.org/10.1007/978-1-349-05861-7_18

[3] M. Kleiner, R. Krux, Entwicklung eines Verfahrens zur schnellen Herstellung von Tief- und Streckziehwerkzeugen aus Blechlamellen für die Prototypen- und Kleinserienfertigung (Rapid

Tooling), Forschung für die Praxis // Stahl-Zentrum Düsseldorf P 384 (2001), Verl. und Vertriebsges. mbH.
[4] W.R. Weaver, Process for the manufacture of laminated tooling, U.S. patent: 5031483 A, priority date: 06.10.1989
[5] D.F. Walczyk, D.E. Hardt, A New Rapid Tooling Method for Sheet Metal Forming Dies. In: R.P. Chartoff, A.J. Lightman, J.A. Schenk et al. (Eds.), Fifth International Conference on Rapid Prototyping, Dayton, Ohio, USA, 1994, pp, 275-289.
[6] L. Hiegemann, C. Agarwal, C. Weddeling, A.E. Tekkaya, Reducing the stair step effect of layer manufactured surfaces by ball burnishing, In: 19th ESAFORM, Springer Berlin Heidelberg, 2016, 190002-1-190002-6 https://doi.org/10.1063/1.4963612
[7] T. Himmer, T. Nakagawa, M. Anzai, Lamination of metal sheets, Comput. Ind. 39 (1999) 27-33. https://doi.org/10.1016/S0166-3615(98)00122-5
[8] H. Dardaei Joghan, M. Hahn, J.T. Sehrt, A.E. Tekkaya, Hybrid additive manufacturing of metal laminated forming tools, CIRP Annals 71 (2022) 225-228. https://doi.org/10.1016/j.cirp.2022.03.018
[9] DIN 52900: DIN EN ISO/ASTM 52900 (2021). Fundamentals and vocabulary. Beuth Verlag GmbH, Berlin
[10] TRUMPF GmbH + Co.: Datensammlung: TLC 1005 mit TLF 1800t, 2400t, 3000t, 3800t. TRUMPF GmbH + Co.:30–31
[11] F.E.K. Sato, T. Nakata, Energy Consumption Analysis for Vehicle Production through a Material Flow Approach, Energies 13 (2020) 2396. https://doi.org/10.3390/en13092396
[12] A.J. Yule, J.J. Dunkley, Atomization of Melts: For powder production and spray deposition, Clarendon, 1994
[13] A. Wippermann, T.G. Gutowski, B. Denkena, M.-A. Dittrich, Y. Wessarges, Electrical energy and material efficiency analysis of machining, additive and hybrid manufacturing, J. Clean. Product. 251 (2020) 119731. https://doi.org/10.1016/j.jclepro.2019.119731
[14] G. Zhao, Y.B. Guo, P. Zhu, Y. Zhao, Energy Consumption Characteristics and Influence on Surface Quality in Milling, Procedia CIRP 71 (2018) 111-115. https://doi.org/10.1016/j.procir.2018.05.081
[15] A. Guminski, T. Hübner, E. Rouyrre, S. von Roon, M. Schimmel, C. Achtelik, J.-M. Rhiemeier, U. Fahl, I. Bailey, Energiewende in der Industrie Potenziale und Wechselwirkungen mit dem Energiesektor, 2019
[16] D. Liedtke, H.-W. Zoch, G. Spur, Wärmebehandlung von Stählen. In: Zoch H-W, Spur G (eds) Handbuch Wärmebehandeln und Beschichten. Carl Hanser Verlag GmbH & Co. KG, München, 2019, pp. 335-501

Prediction of surface topography change during chain of selective laser melting and burnishing

TEIMOURI Reza[1,a *], SKOCZYPIEC Sebastian[1,b] and GRABOWSKI Marcin[1,c]

[1] Chair of Production Engineering, Department of Mechanical Engineering, Cracow University of Technology, Krakow, Poland

[a]reza.teimouri@pk.edu.pl, [b]sebastain.skoczypiec@pk.edu.pl, [c]marcin.grabowski@pk.edu.pl

Keywords: Surface Roughness, Selective Laser Melting, Burnishing, Simulation

Abstract. The present study developed theoretical models for simulation of surface topography and roughness of parts produced by the selective laser melting (SLM) process and their evolution after burnishing as post-treatment. The simulation algorithm has been integrated by combining principles of selective laser melting process, i.e., formation of the melt pool and kinematic of motion, followed by mechanic of burnishing through Z-map approach. To verify the simulation results, 316L stainless steel was 3D printed and then burnished under different burnishing depth. 3D surface profile and surface roughness of as-printed material and those post-processed by surface burnishing (SB) were measured through microscopic examination and surface roughness measurement, respectively. The results obtained through comparison of confirmatory experiments and simulation model affirmed that the proposed approach is accurate enough to predict the surface topography and roughness of as-printed and post-treated samples.

Introduction

Among various approaches for additive manufacturing (AM) of metallic material, selective laser melting (SLM) was significantly attractive to researchers and industries because of its ability to produce parts with complex geometries. However, due to the layer-upon-layer nature of production, the SLM suffers from a poor surface finish.

The post processing of AM samples by surface burnishing (SB) has some advantages over other mechanical surface treatment process. Compared to material-removal process [1-3], the burnishing causes surface sever plastic deformation and results in modification of surface and subsurface layers in terms of hardness, compressive residual stress and microstructure refining. On the other hand, compared to non-material removal process [4-6], burnishing results in superior surface finish. It has been reported that the surface finish of burnished samples can reach optical scale under optimum processing conditions [7]. On the other hand, further advantages of burnishing over the other non-material removal processes is its independency of complicated infrastructures such as ultrasonic apparatus or pneumatic units. The process can be implemented by a simple lathe or milling machine.

Recently, researchers have attracted it for the post-processing of metallic and non-metallic materials produced by AM. Rotella et al. [8] used ball burnishing for the post-processing of stainless steel GP1 produced by SLM. Sunny et al. [9] used interlayer roller burnishing as sequential to SLM to reduce the tensile residual stress of each built layer before addition of next one. Raaj et al. [10] applied SB for post-processing of Inconel 718 manufactured by electron beam additive manufacturing. Brujin et al. [11] stated that the SB is a suitable process for processing polymeric (fused filament fabricated) material produced by 3D printing. They stated that unlike to material removal-based surface finishing, burnishing doesn't change the chemical composition of samples because the temperature rise is limited.

The additive manufacturing chain that includes the SLM and post-processing must be designed and then optimized to a certain level to obtain the desired surface finish. In order to do so, the

Content from this work may be used under the terms of the Creative Commons Attribution 3.0 license. Any further distribution of this work must maintain attribution to the author(s) and the title of the work, journal citation and DOI. Published under license by Materials Research Forum LLC.

Materials Research Proceedings 28 (2023) 31-40 https://doi.org/10.21741/9781644902479-4

developing an integrated simulation model which can predict the final surface finish in short period of the time will be more vital. Thus, in the present work, novel physics-based theoretical simulations are proposed to predict the surface roughness evolution of parts produced by SLM and post-processed by the surface burnishing process. Accordingly, the present work aims to simulate the 3D surface topography and roughness of parts made by SLM and then modified by the burnishing process.

Theoretical Simulation

The topography of the surface in the SLM process is generated through the formation of the solidified melt pool and duplication using kinematic motion. Thus, the shape of melt pool during the printing process must be modelled in the first step. Heat input from the laser power source is calculated using a point moving heat source solution that is successfully used for the SLM process [12]. The point moving heat source solution was derived from a general convection-diffusion equation, which can be expressed as:

$$\begin{cases} T - T_0 = \dfrac{P\eta}{4\pi kR}\exp\left(\dfrac{-V_L(R_T + y)}{2\kappa}\right) \\ \kappa = \dfrac{k}{\rho c} \\ R_T = \sqrt{x^2 + y^2 + z^2} \end{cases} \tag{1}$$

where T is the localized temperature, P is the laser power, η is the coefficient that determines how much of the laser heat source is absorbed by powder; κ is thermal diffusivity, R_T is the distance from the heat source location, V_L is the scan velocity during the printing process that is in y direction; k is the heat conduction coefficient, and ρ is the material density. Fig. 1a represents a schematic illustration of the cross section of melt pool and its geometrical characteristics of the SLM process. It is created by the distribution of temperature induced by moving laser heat sources. The cross-section of the melt pool in xz plane (as shown in Fig. 1a) determines the formation of a surface generation of the SLM process. During the printing process, the maximum melt pool depth can be calculated by substituting the melt temperature in Eq. 5 at the location of $x=0$, $y=0$ as shown in Fig. 1. Accordingly, the molten pool depth (d) is the absolute root of the following equation:

$$\begin{cases} \Delta d + \exp(\Theta d) = 0 \\ \Delta = 2\pi k\left(\dfrac{T_m - T_0}{P\eta}\right) \\ \Theta = \dfrac{V_L}{2\kappa} \end{cases} \tag{2}$$

where T_m is the melting temperature.

According to the reports of several researchers, the profile of the melt pool cross-section is a paraboloid [13]. Accordingly, the equation of cross section profile, the consumed powder bandwidth (W_0) and melt pool width (W) (as shown in Fig. 1b) are calculated by Eq. 3:

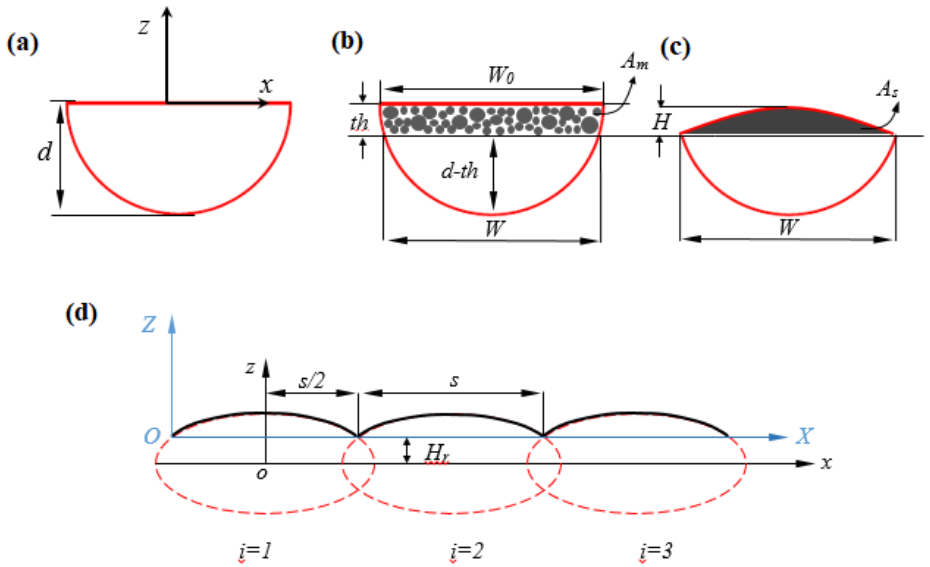

Fig. 1. (a) formation of cross section of melt pool (b) powder band width (c) solidified melt pool and formation of hump (d) generation of surface topography.

$$\begin{cases} z = x^2 - d \\ W_0 = 2\sqrt{d} \\ W = 2\sqrt{d - th} \end{cases} \tag{3}$$

where *th* is the layer thickness.

Once the melt pool is solidified, as a result of surface tension, a hump is formed on the upper side of the melt pool, as shown in Fig. 1c. Liu et al. [13] stated that the profile of the hump is a portion of an ellipse.

In order to calculate the maximum height of the hump area (that is usually called melt pool height), the mass conservation law is utilized. Accordingly, it is assumed that the mass of the region bounded by powder during melting is equal to the mass of the hump region after solidification. Hence, it can be said that the area of the region bounded by powder (i.e., A_m as shown in Fig. 1c) is equal to the hump area (i.e., A_s as demonstrated in Fig. 1e). Therefore, it can be written:

$$H = \frac{4}{W\pi}\left[Wth + 2\int_{\frac{W}{2}}^{\frac{W_0}{2}}\left(x^2 - d\right)dx\right] \tag{4}$$

By printing through a longitudinal direction, the melt pool with a fixed cross-section is lengthened to a predefined length. But, in the lateral direction, the cross sections of melt pools interact based on the hatch spacing value (s). Therefore, only a part of the ellipse contribution in the generation of surface topography, as shown in Fig. 1d. Accordingly, the surface generation equation can be:

$$Z = \left(\frac{2H}{W}\right)\left\{\sqrt{W^2 - \left[X - (i-1)s\right]^2} - \sqrt{W^2 - \left(\frac{s}{2}\right)^2}\right\} \qquad (i-1)s < X < is \qquad i = 1, 2, \ldots N \tag{5}$$

The obtained 3D surface profile of the material after SLM is named H (X, Y, Z).

In order to model the evolution of SLM surface topography after burnishing, Z-map approach is being utilized that transforms the cloud of points from tool coordinate system to workpiece coordinate system through series of transformation matrix. Here the initial surface topography is the H (X, Y, Z) which is obtained for 3D printed material; this matrix will be updated by applying the Z-map transformative model [14]. According to the principle of Z-map model, different

reference frames on the roller, burnishing tool, machine tool, and workpiece were defined and presented in Fig. 3. Here the reference coordinate system O_W-$X_WY_WZ_W$ that is called the workpiece coordinate system. During the burnishing process, the O_W-$X_WY_WZ_W$ is fixed on the workpiece. The O_M-$X_MY_MZ_M$ is called machine coordinate system. Its origin is connected to the machine spindle. It has translational movement with respect to workpiece coordinate system (as shown in fig. 3a-3c). The tool coordinate system, O_M-$X_MY_MZ_M$ has similar origins to the machine coordinate system (Fig. 3b). It is transformed into a machine coordinate system through a rotational movement. The local coordinate system that is located on the roller is shown by O_K-$X_KY_KZ_K$. Depending to the number of rollers distributed on the circumference of the tool (as shown in Fig. 3d), the O_K-$X_KY_KZ_K$ is transformed to the tool coordinate system by a rotation considering the angle between each roller. Accordingly, the main formulation that transforms an individual point on the roller to workpiece coordinate system is:

$$\begin{bmatrix} X_P^W \\ Y_P^W \\ Z_P^W \\ 1 \end{bmatrix} = \begin{bmatrix} \cos\Phi_k & -\sin\Phi_k & 0 & 0 \\ \sin\Phi_k & \cos\Phi_k & 0 & 0 \\ 0 & 0 & 1 & 0 \\ 0 & 0 & 0 & 1 \end{bmatrix} \begin{bmatrix} \cos\omega t & \sin\omega t & 0 & 0 \\ -\sin\omega t & \cos\omega t & 0 & 0 \\ 0 & 0 & 1 & 0 \\ 0 & 0 & 0 & 1 \end{bmatrix} \begin{bmatrix} 0 & 0 & 0 & V_f t \\ 0 & 0 & 0 & 0 \\ 0 & 0 & 1 & R \\ 0 & 0 & 0 & 1 \end{bmatrix} \begin{bmatrix} X_P^K \\ Y_P^K \\ Z_P^K \\ 1 \end{bmatrix} \tag{6}$$

where Φ_k is angle between the k-th roller and tool axes that is function of initial phase and number of roller which can be calculated by Eq. 7. ω is the annular velocity that is $\omega = 2\pi N/60$. Also, V_f is the feed velocity.

$$\Phi_k = \frac{\Phi_0 + 2\pi(k-1)}{N_R} \tag{7}$$

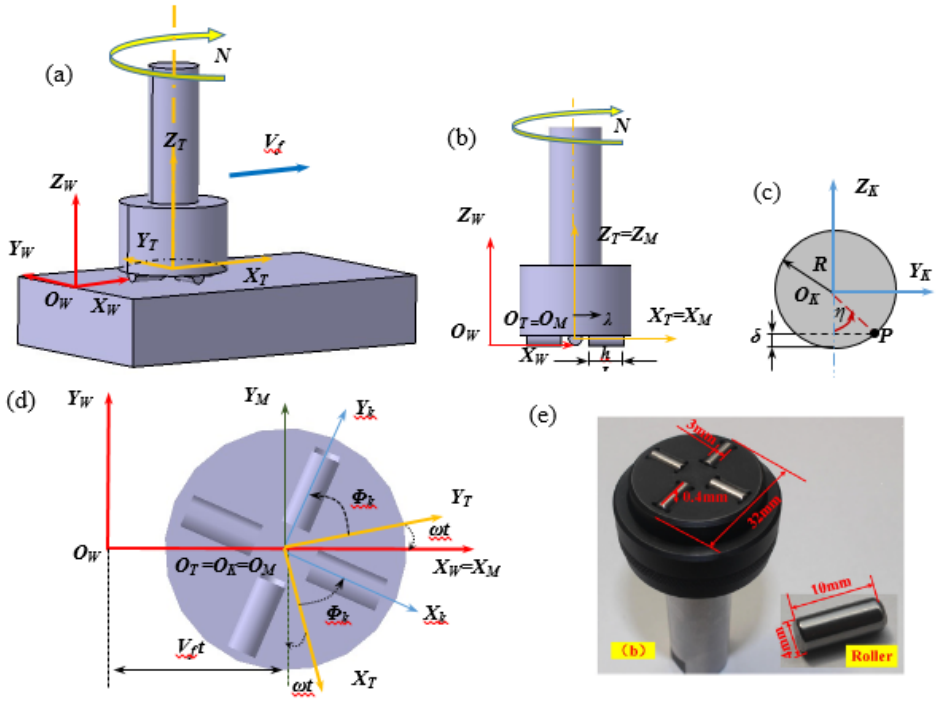

Fig. 2. (a) A schematic illustration of multi-roller rotary burnishing for flat surface including workpiece and tool coordinate systems (b) tool coordinate system (c) coordinate of an arbitrary point P on the roller with radius of r (d) trajectory of an obituary pint of P on different coordinate system i.e. roller, tool, machine and workpiece (e) real rotary burnishing tool with multi-roller.

In order to implement the algorithm, following steps need to be taken into consideration:
a) Initializing the burnishing process: burnishing parameters including the feed velocity (V_f), roller number (N_R), roller radius (R), depth of penetration (δ), and spindle speed (N) are set.
b) Discretization of workpiece surface: here, a slice of the workpiece with length of feed per revolution in X_W direction and width of $2R$ equal to the diameter of the burnishing tool in Y_W direction is considered. Here, the Z-map model of the workpiece with $m*n$ grids is established. The length and width of each grid are selected based on the gridding of the 3D printed surface in such a way that the hatch spacing is divided to 50 elements. Thus, the Δx equals $s/50$. Also, the width of each grid is selected as long as its length, i.e., $\Delta y=\Delta x$. Therefore, the selected region in X_W direction must be divided to:

$$\begin{cases} n_x = \dfrac{f}{\Delta x} \\ n_y = \dfrac{2R}{\Delta y} \end{cases} \tag{8}$$

c) Setting up the time increments: By identifying the processing length equal to f, it can be inferred that the process ends when this length is swept with burnishing tool. Therefore, the processing time can be obtained by dividing the burnishing feed rate i.e., f, by linear velocity i.e., V_f. Accordingly, the time increment (Δt) for processing the mesh length (Δx) with the same linear velocity is obtained by using the following formula:

$$\begin{cases} t = \dfrac{f}{V_f} = \dfrac{V_f \big/ N}{V_f} = \dfrac{1}{N} \\ \Delta t = \dfrac{\Delta x}{V_f} = \dfrac{1}{n_x N} \end{cases} \tag{9}$$

d) Discretization of the roller: Here it must be taken into consideration that the projection length of the roller element must be within the size of the workpiece's grid region. In other words, within each time increment, only one grid point of the workpiece is swept over by the discretized point of roller. In order to discretize the tool, couple considerations must be taken into account: (i) dividing the depth of penetration in different layers: based on the simulation's accuracy, the depth of penetration in axial direction (i.e. direction of Z_K) is divided into other parts and then the depth of each layer is δ_i (i=1, 2, …, n_i) will be $d\delta=\delta/n_i$; (ii) for each δ_i, there is a secant that causes variation of spreading angle. Their values can be calculated using the following equation:

$$\begin{cases} \eta_i = \cos^{-1}\left(\dfrac{R-\delta_i}{R}\right) \\ \delta_i = \dfrac{\delta_{\max}}{n_i} \end{cases} \tag{10}$$

Each layer must also be discretized based on dividing its corresponding spreading angle. Accordingly, the η_i is divided into n_j parts. Thus, each angular increment is calculated by:

$$\eta_{ij} = \frac{2\eta_i}{n_j} \quad j = 1,2,..,n_j \tag{11}$$

The value of n_j can be calculated arbitrary or based on interconnection with workpiece gridding using following equation:

$$\begin{cases} n_j = \dfrac{2\rho_i}{\Delta x} \qquad \rho_i = R\cos\eta_i \\ \eta_{ij} = \dfrac{2\eta_i}{n_j} \end{cases} \tag{12}$$

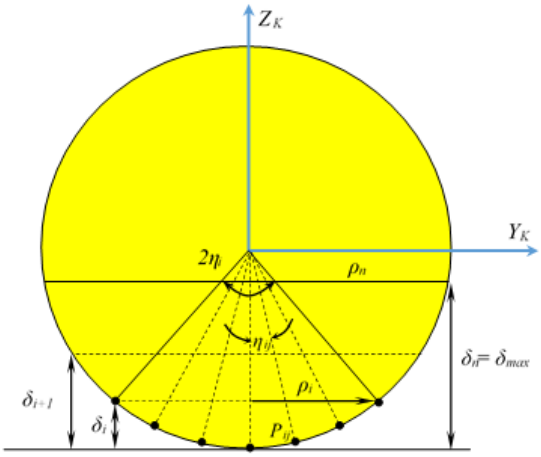

Fig. 3. Discretization of the roller in the contact region to check if the burnishing tool is within workpiece region.

Where Δx is the length of each grid in workpiece. Once the η_{ij} is determined, the position of each point in the roller coordinate system can be identified:

$$\begin{bmatrix} X^K_{P_{ij}} \\ Y^K_{P_{ij}} \\ Z^K_{P_{ij}} \end{bmatrix} = \begin{bmatrix} R \\ r\sin\eta_{ij} \\ -r\cos\eta_{ij} \end{bmatrix} \tag{13}$$

For the time t, the coordinate of the transformed point of the roller from the local coordinate system to the workpiece coordinate system i.e. (X^W_P, Y^W_P) is checked with the X_{max} and Y_{max} in H matrix. This point is accepted if the transformed point is within the workpiece range.

e) Checking the coincidence: For each transformed point (X^W_P, Y^W_P), a coincidence limit compared to workpiece gridding points i.e. H (X, Y) is defined where the distance between the points is less than ε. In other words, if the distance of (X^W_P, Y^W_P) and H (X, Y) is less than ε, the coincidence condition is met. In the present work, the coincidence limit has been set to ε=0.01µm.

f) Checking the engagement: For the coincident points, the values of $Z_P{}^W$ are compared with the Z in H matrix. If the $Z_P{}^W$ is less than Z, in the H matrix, the Z is replaced by $Z_P{}^W$; otherwise, the Z is kept.

g) 3D surface topography: When the process is finished (i.e., t=t_{max}), the updated workpiece matrix determines the final surface topography.

Experiments

In the present investigation, the stainless steel 316 L blocks with dimensions of 70 mm in length, 30 mm in width, and 10 mm in thickness were built by laser powder bed fusion process. An EOS M280 3D printer machine with 1100 nm wavelength discontinuous Yb-fibre laser was used to manufacture samples. The volumetric energy density for fabrication was set on 100 J/mm^3.The samples were printed based on optimized standard EOS parameters with 195W laser power, 1083 mm/s scan speed, 90 µm hatch spacing, and 20 µm layer thickness. As-built samples were detached from a substrate using wire electrical discharge machining.

A multi-roller rotary burnishing process was utilized for post-processing as-printed samples. The commercial burnishing tool model SPF20-S20 manufactured by SUNGINO cooperation comprises four rollers made of hardened steel. The length and diameter of rollers are 10 mm and 4 mm, respectively. During each revolution of the tool, a width of 20 mm can be burnished by this

tool. Thus, its more efficient in the vibration of flat surfaces compared to a single roller (or ball) burnishing tool. Fig. 4 demonstrates the experimental setup.

The main characteristic that needs to be measured in the present study is surface topography and roughness. In order to do so, a 3D surface roughness machine, namely TylorHobson was utilized. Measurements were carried out in a 1 mm^2 squared area.

The experiment was planned for confirmation of the developed model. For the SLM process mentioned in section 3.1, the sample was built based on the standard EOS parameter used for 3D printing of stainless steel 316. Then, the obtained surface topography and roughness of until material were compared with the predicted values.

For the burnishing process, from our preliminary experiments and the developed model, it was found that the main burnishing factor that has the greatest influence on the surface roughness evolution of the SLM sample is the burnishing depth. Thus, in the present study, the burnishing experiments for processing as-built material were carried out by variation of burnishing depth at 0.05 mm and 0.075 mm and 0.1 mm, while the spindle speed and linear velocity were kept constant at 800 RPM and 200 mm/min.

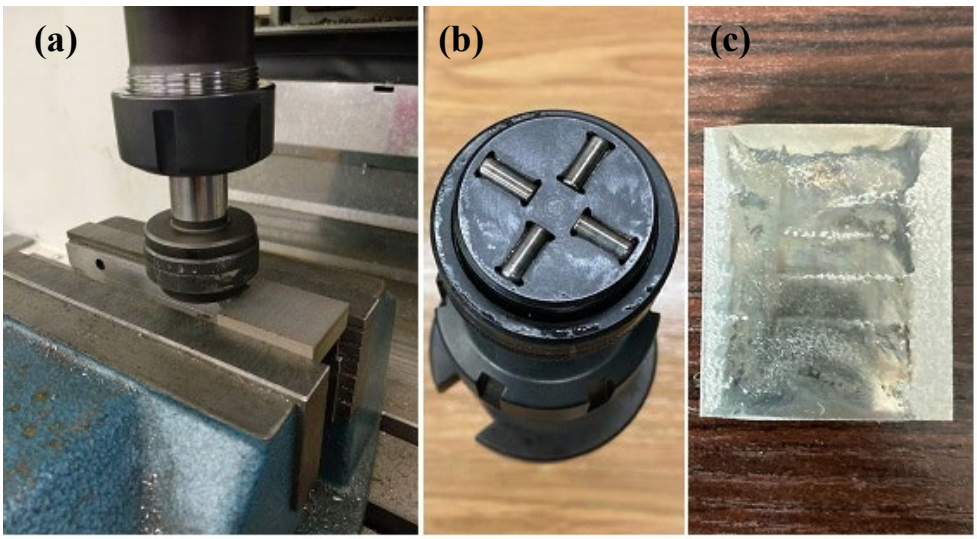

Fig. 4. (a) Burnishing experimental setup (b) multi-roller burnishing tool (c) burnished sample.

Results and Discussion

Fig. 5 illustrates the comparison between the measured and predicted surface roughness (Ra) of different samples. According to the presented results, it is seen that they are in good agreement in general; it indicates that the developed evolutionary simulation is reliable. It is seen that the maximum distance from the peak and valley (Rt) for as-built material measured through surface roughness is 12.303, while the predicted value is 12.276 µm. Moreover, the arithmetic surface roughness (Ra) value for the SLMed sample measured by the experiment was 6.62 µm, while the simulated value is 7.10 µm. For the burnished sample with depth of 0.05mm, the surface peaks are flattened due to plastic deformation. The Rt value was measured at 6.595 µm while the predicted one was at 7.353 µm. Fig. 5 illustrates that the arithmetic surface roughness values which were obtained through experiments and simulation are 2.65 µm and 3.23 µm, respectively. Moreover, for the samples processed by 0.075 mm and 0.1 mm burnishing depth, the measured values of Rt are 4.943 and 2.818, respectively. The Rt values obtained by the simulation model for the same processing conditions are 4.852 and 2.45, respectively. Also, the arithmetic surface roughness value which was measured by experiments are 1.11 µm and 0.288 µm, respectively. On the other

hand, the predicted values of Ra, which the simulation model calculated, are 1.31 µm and 0.355 µm, respectively.

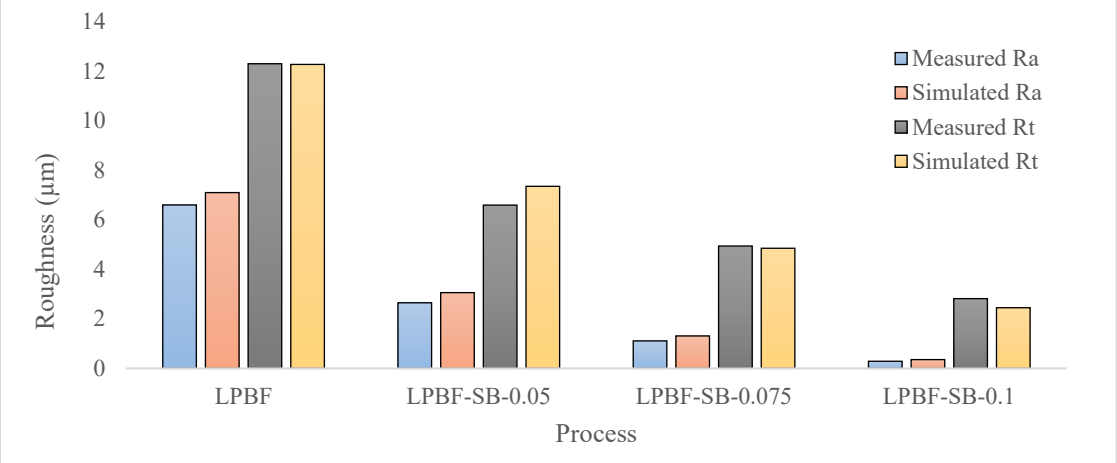

Fig. 5. Comparison between measured and predicted values of Ra and Rt under different conditions.

Fig. 6 shows that there are consistencies between the measured and predicted surface topography of the samples. In all the samples its seen that sinusoidal behaviour exist in one direction and the variation of surface peaks and valleys are following same trends while the burnishing depth increases.

Summary

The obtained results can be summarized as follows:

- The surface roughness of SLMed sample fabricated at EOS standard setting were in close agreement with those derived from the simulation model. The prediction error for calculating the Ra and Rt were about 7.5% and 2%, respectively.
- It was found that the prediction error of the surface roughness increases as burnishing is applied as a sequential process. Also, the error values increase by increasing the burnishing depth. However, the maximum prediction error in the worst case is 18.8% for Ra and 12.8% for Rt. This difference can be attributed to fracture of agglomerated partially fused particles because of high degree of plastic deformation resulting in big scratches on the surface of burnished sample during experiment; which hasn't been included in the model.

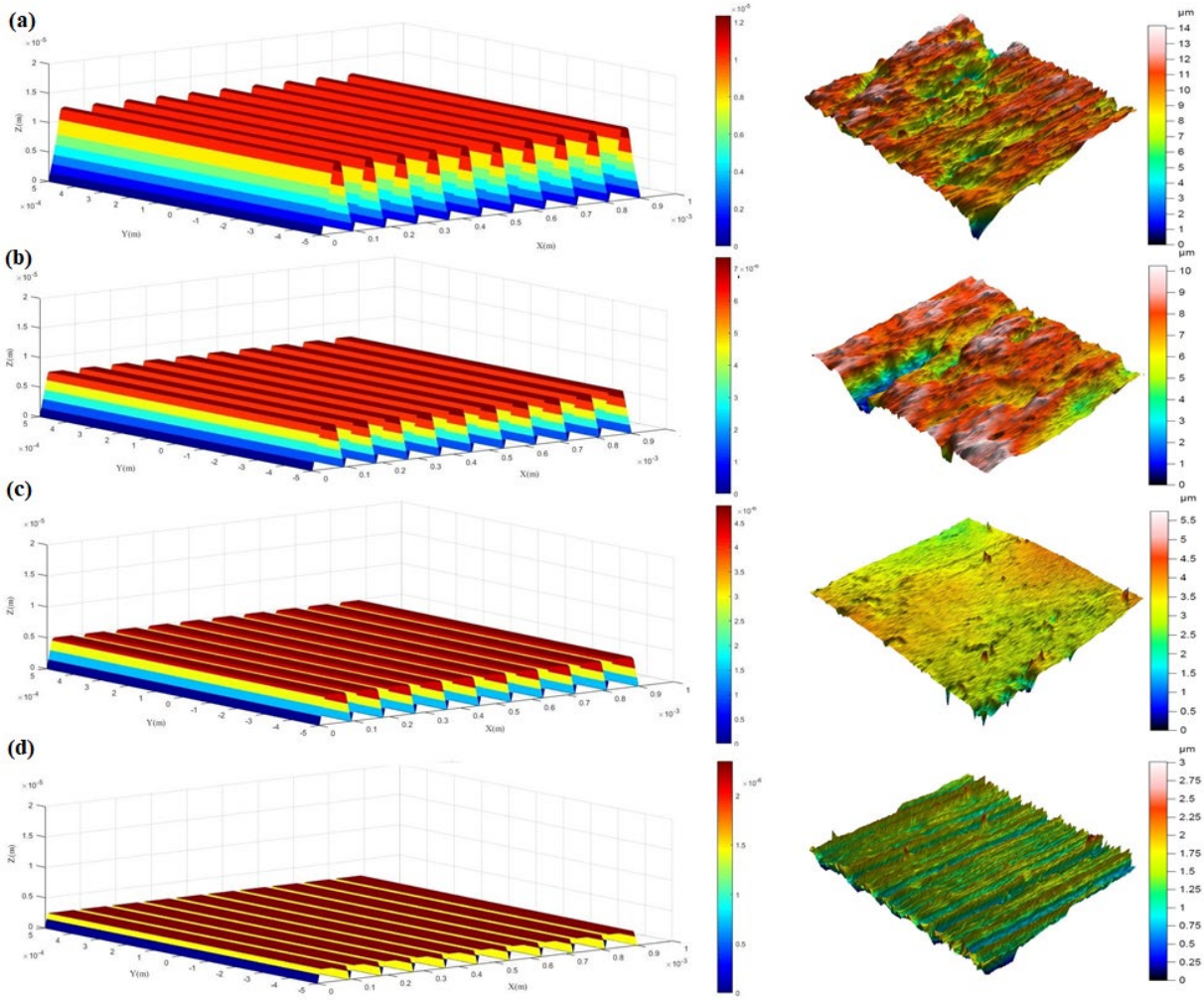

Fig. 6. Comparison of measured and simulated 3D surface topography (a) As-built (b) burnishing depth of 0.05 mm (c) burnishing depth of 0.075 mm (d) burnishing depth of 0.1 mm.

References

[1] J. Bedmar, N. Abu-ward, S. García-Rodríguez, B. Torres, J. Rams, Influence of the surface state on the corrosion behaviour of the 316 L stainless steel manufactured by laser powder bed fusion, Corros. Sci. 207 (2022) 110550. https://doi.org/10.1016/j.corsci.2022.110550

[2] L. Chen, B. Richter, X. Zhang, K.B. Bertsch, D.J. Thoma, F.E. Pfefferkorn, Effect of laser polishing on the microstructure and mechanical properties of stainless steel 316L fabricated by laser powder bed fusion, Mater. Sci. Eng. A 802 (2021) 140579. https://doi.org/10.1016/j.msea.2020.140579

[3] S. Bagehorn, J. Wehr, H.J. Maier, Application of mechanical surface finishing processes for roughness reduction and fatigue improvement of additively manufactured Ti-6Al-4V parts, Int. J. Fatigue 102 (2017) 135-142. https://doi.org/10.1016/j.ijfatigue.2017.05.008

[4] H. Zhang, R. Chiang, H. Qin, Z. Ren, X. Hou, D. Lin, G.L. Doll, V.K. Vasudevan, Y. Dong, C. Ye, The effects of ultrasonic nanocrystal surface modification on the fatigue performance of 3D-printed Ti64, Int. J. Fatigue 103 (2017) 136-146. https://doi.org/10.1016/j.ijfatigue.2017.05.019

[5] H. Soyama, Y. Okura, The use of various peening methods to improve the fatigue strength of titanium alloy Ti6Al4V manufactured by electron beam melting, AIMS Mater. Sci. 5 (2018) 1000-1015. https://doi.org/10.3934/matersci.2018.5.1000

[6] H. Soyama, C. Kuji, Improving effects of cavitation peening, using a pulsed laser or a cavitating jet, and shot peening on the fatigue properties of additively manufactured titanium alloy Ti6Al4V, Surf. Coat. Tech. (2022) 129047. https://doi.org/10.1016/j.surfcoat.2022.129047
[7] X.L. Yuan, Y.W. Sun, L.S. Gao, S.L. Jiang, Effect of roller burnishing process parameters on the surface roughness and microhardness for TA2 alloy, Int. J. Adv. Manuf. Technol. 85 (2016) 1373-1383. https://doi.org/10.1007/s00170-015-8031-0
[8] G. Rotella, L. Filice, F. Micari, Improving surface integrity of additively manufactured GP1 stainless steel by roller burnishing, CIRP Annals, 69 (2020) 513-516.
[9] S. Sunny, R. Mathews, H. Yu, A. Malik, Effects of microstructure and inherent stress on residual stress induced during powder bed fusion with roller burnishing, Int. J. Mech. Sci. 219 (2022) 107092. https://doi.org/10.1016/j.ijmecsci.2022.107092
[10] R.K. Raaj, P.V. Anirudh, C. Karunakaran, C. Kannan, A. Jahagirdar, S. Joshi, A.S.S. Balan, Exploring grinding and burnishing as surface post-treatment options for electron beam additive manufactured Alloy 718, Surf. Coat. Tech. 397 (2020) 126063. https://doi.org/10.1016/j.surfcoat.2020.126063
[11] A.C. de Bruijn, G. Gómez-Gras, M.A. Pérez, On the effect upon the surface finish and mechanical performance of ball burnishing process on fused filament fabricated parts, Additive Manufacturing 46 (2021) 102133. https://doi.org/10.1016/j.addma.2021.102133
[12] J. Ning, E. Mirkoohi, Y. Dong, D.E. Sievers, H. Garmestani, S.Y. Liang, Analytical modeling of 3D temperature distribution in selective laser melting of Ti-6Al-4V considering part boundary conditions, J. Manuf. Process. 44 (2019) 319-326. https://doi.org/10.1016/j.jmapro.2019.06.013
[13] B. Liu, G. Fang, L. Lei, An analytical model for rapid predicting molten pool geometry of selective laser melting (SLM), Appl. Math. Model. 92 (2021) 505-524. https://doi.org/10.1016/j.apm.2020.11.027
[14] H.Q. Chen, Q.H. Wang, Modelling and simulation of surface topography machined by peripheral milling considering tool radial runout and axial drift, Proceedings of the Institution of Mechanical Engineers, Part B: Journal of Engineering Manufacture 233 (2019) 2227-2240. https://doi.org/10.1177/0954405419838384

Materials Research Proceedings 28 (2023) 41-48 https://doi.org/10.21741/9781644902479-5

Development and processability of AISI S2 tool steel by laser powder bed fusion

SAGGIONETTO Enrico[1,a *], FILIPPI Elena[1,b], DEDRY Olivier [1,c], TCHUINDJANG Jérôme T.[1,d] and MERTENS Anne[1,e]

[1]Metallic Materials Science (MMS), Aerospace and Mechanical Engineering Dpt., University of Liège, Belgium

[a]enrico.saggionetto@uliege.be, [b]elena.filippi@student.uliege.be, [c]olivier.dedry@uliege.be, [d]j.tchuindjang@uliege.be, [e]anne.mertens@uliege.be

Keywords: Additive Manufacturing, Laser Powder Bed Fusion, Tool Steel, Process Map

Abstract. Nowadays, the advantages of Laser Powder Bed Fusion (LPBF) technology attract both industry and researchers. Indeed, it is possible to build up complex geometrical parts with higher mechanical properties than those obtained by conventional methods. However, LPBF involves complex phenomena due to the high heating and cooling rates that lead to out-of-equilibrium conditions. For this reason, few metal alloys are easily processable up to now. Nevertheless, research on new steels by LPBF has been growing in recent years, in particular, regarding the development of tool steels. This work thus focuses on the development of the tool steel AISI S2 by LPBF. The process map has been investigated by varying the laser power from 100 to 250 W and the scan speed from 400 to 2000 mm/s. By combining surface analysis by means of profilometer observations, density measurements by pycnometry, defects characterization and quantification and investigations on the melt pool morphology, the best process window is selected to have fully dense, defect-free parts. Furthermore, this study allows to have comprehensive insights on the effect of the parameters on the type of defects generated during the manufacturing.

Introduction

Among Additive Manufacturing (AM) technologies, Laser Powder Bed Fusion (LPBF) is a suitable technique to create near net-shape parts starting from powders. The advantage is to achieve complex parts in terms of geometry, avoiding difficult manufacturing processes. Moreover, the final mechanical properties of parts by LPBF can be higher than those obtained by conventional methods [1].

LPBF process involves complex physical phenomena, such as absorption and transmission of laser energy, rapid melting and solidification of material, microstructure evolution flow in a molten pool and material evaporation [2]. These complex phenomena may result in defects such as gas porosities, lack of fusion areas, cracks, spatters, key-hole porosities and balling [2-5]. Despite the problems and complexity faced during the process, the manufacturing of new alloys by LPBF has been growing over the recent years. Research is focusing on microstructural aspects, to gain comprehensive insights of the effect of the out-of-equilibrium conditions during melting and solidification on the final parts, both in terms of quality and mechanical properties. Significant attention has been given to the evaluation of the melt pool formed during the process [6-10], as it is crucial for understanding the processability and the type of defects generated.

Nowadays, one limitation of the LPBF process lies in the choice of raw material. Indeed, LPBF implies the use of metallic powder usually obtained by Gas Atomization (GA), a process that is difficult to control [11], especially for certain type of alloys. Therefore, few metal powders are easily available in the market (316L, Maraging Steels, Al, Ni and Ti alloys). LPBF manufacturing of other alloys has proved challenging and therefore there is a shortage of supply and demand for the less common raw material on the market.

Content from this work may be used under the terms of the Creative Commons Attribution 3.0 license. Any further distribution of this work must maintain attribution to the author(s) and the title of the work, journal citation and DOI. Published under license by Materials Research Forum LLC.

In particular, tool steels are difficult to process by LPBF, due to their complex chemical composition and poor weldability [12]. Indeed, their high carbon content (up to 1.5 wt. %) promotes the formation of martensite, which leads to crack formation within the printed part under the effect of residual stresses due to rapid cooling. The influence of increased carbon content on LPBF processability has been investigated more deeply in recent studies [12-15]. However, other recent works already showed the possibility to manufacture low alloy steels (~ 0.5 C wt. %) [6,16-21]. The present study thus aims to provide the basis for understanding the processability of low alloy tool steel grade AISI S2. The process map for this steel is developed exploring different sets of parameters. In particular, the volumetric energy density has been used to investigate the effect of different parameters on the types of defects generated and to select the process window for fully dense and defect-free parts.

Materials and Methods

Commercial gas atomized powders AISI S2 Tool Steel (0.49 C, 1.2 Si, 0.6 Mo, 0.6 Mn, Fe bal., wt. %) were used as raw material, provided by Sandvik Osprey LTD. The powder is in a spherical shape with a mean size of 31 µm, as revealed by SEM observations (Fig. 1). The bulk density of powders (ρ_{bulk} = 7.8 g/cm^3) was measured by means of a gas pycnometer AccuPyc II Serie 1345.

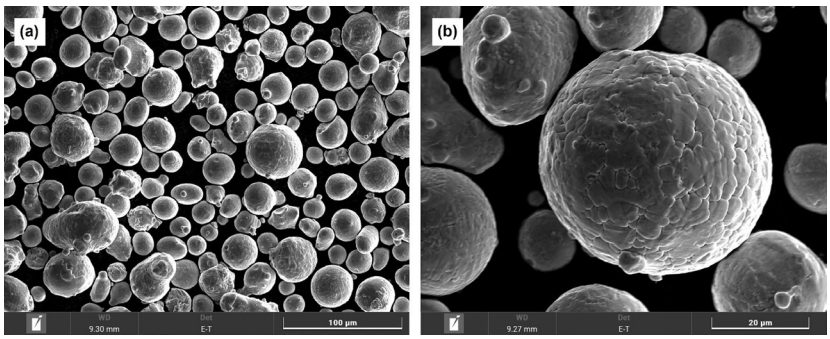

Fig. 1. SEM micrographs of (a) AISI S2 powders and (b) zoom on a particle with spherical morphology.

Starting from the powders, 20 cubes of 10x10x10 mm^3 were produced with an Aconity MIDI LPBF machine under Argon atmosphere. Different power (P) and scan velocity (v_s) were used (Table 1). P is considered as low (100 W), moderate (150 W), medium (200 W) and high (250 W). v_s is considered as low (400 - 800 mm/s), medium (800 - 1250 mm/s) and high (1250 - 2000 mm/s). A laser spot size of 80 µm with a gaussian distribution, a layer thickness (t) of 30 µm and a hatch spacing (h) of 80 µm were used for all samples. The scanning strategy implied a rotation of 90° for each layer, with no contouring. No substrate preheating was applied. Fully printed samples showed good dimensional tolerances (Fig. 2a), according to the desired initial geometrical features. Samples 1-2-3-6-11 were stopped during the manufacturing process due to evident surface defects that affect the quality of the subsequent layers (Fig. 2b-c-d). These samples were not considered for subsequent density measurements and profilometer analysis.

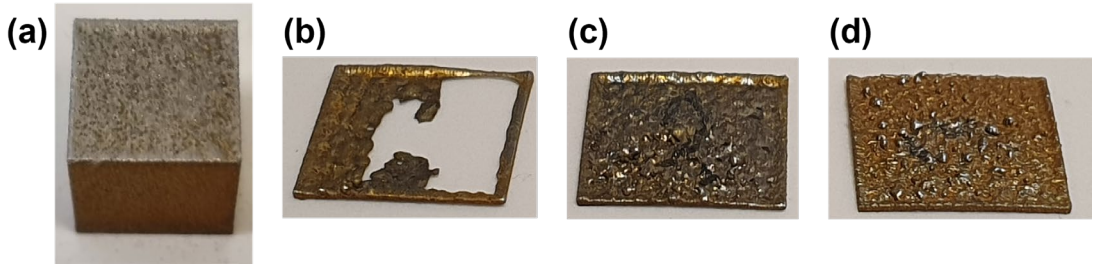

Fig. 2. Examples of (a) a fully printed and (b), (c), (d) interrupted samples.

The volumetric energy density (E_d) was used to correlate the results observed with the processing parameters (Eq. 1).

$$E_d = \frac{P}{t*h*v_s} \quad (1)$$

Table 1. Processing parameters and volumetric energy density for each sample.

Sample	P [W]	v_s [mm/s]	E_d [J/mm^3]
1	100	400	104
2	100	600	69
3	100	800	52
4	100	1000	42
5	100	1200	35
6	150	500	125
7	150	750	83
8	150	1000	63
9	150	1250	50
10	150	1500	42
11	200	500	167
12	200	750	111
13	200	1000	83
14	200	1500	56
15	200	2000	42
16	250	500	208
17	250	750	139
18	250	1000	104
19	250	1500	69
20	250	2000	52

After production, the density of each sample (ρ) was measured through a gas pycnometer and the relative density was calculated using the bulk density of powders, according to Eq. 2.

$$\%\, Density = \frac{\rho}{\rho_{bulk}} * 100 \quad (2)$$

The surface of the as-built samples was checked using an Alicona Infinite Focus G5 optical profilometer for roughness analysis. All the as-built samples were cut by Electro Discharge Machining perpendicularly to the laser scan direction of the last layer to obtain the cross section. After cutting, samples were hot mounted with an electrically conductive bakelite, then ground and polished down to 1 μm. Defects within the cross sections were analyzed through an optical microscope Olympus BX60 and quantify through Olympus Stream Analysis Software. Nital 3% was used to etch the cross sections.

Results

According to Eq. 2, all samples show a density above 96.5 %. A good correlation is observed between the density value and the fraction of internal porosity obtained by image analysis (Fig. 3a). In image analysis, all kinds of defects are considered. Small gas porosities are detected in all samples. Key-hole porosities at the bottom of melt pools are observed in samples produced with high E_d (Fig. 3b). Large spatters containing a porosity are detected in samples with low v_s (Fig.

3c). Cracks perpendicular to the building direction, initiated from the edge are detected in a few samples, without any specific correlation with processing parameters (Fig. 3d). Lack of fusion defects are visible in samples with low E_d (Fig. 3e).

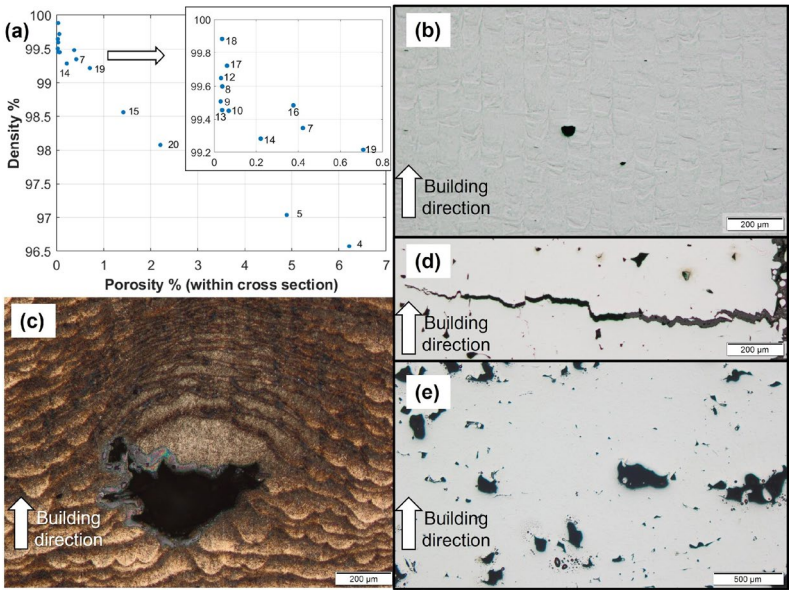

Fig. 3. (a) Correlation between density and porosity, (b) key-hole porosity, (c) entrapped porosity within large spatter, (d) crack perpendicular to the building direction initiated from sample edge and (e) lack of fusion defects.

Fig. 4 shows the most representative overviews of the sample's cross sections together with the corresponding zoom on top area. Nital etching allows to observe the features of the tracks within the sample and to distinguish the brighter top layer. The melt pool morphology is clearly visible. Increasing E_d (from left to right in Fig. 4) leads to a change in the type of defects due to a different melt pool morphology.

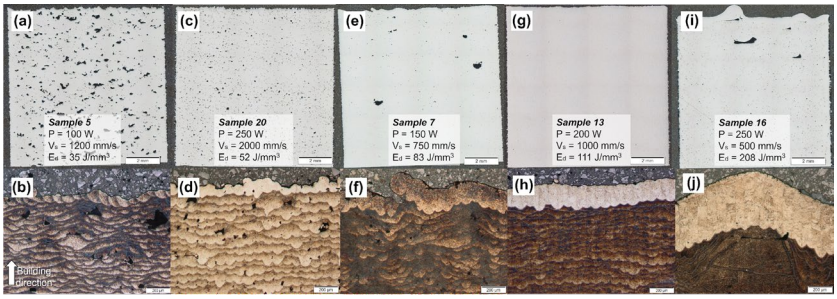

Fig. 4. (a), (c), (e), (g), (i) Cross section overviews and (b), (d), (f), (h), (j) zoom on tracks and top layer after etching with Nital.

Profilometer observations reveal different features of the surface roughness. The surface aspect depends on the quality of the scan tracks generated by the laser passage. The scan tracks generated with low E_d as result of low P (Fig. 5a) are more irregular than those obtained with high P (Fig. 5b). With intermediate value of E_d, P and v_s, the surface appears more regular, with only small spatters (Fig. 5c). On the contrary, high E_d and P and low v_s lead to an irregular surface despite the good overlapping of the scan tracks (Fig. 5e). In general, low v_s results in an irregular surface (Fig. 5d).

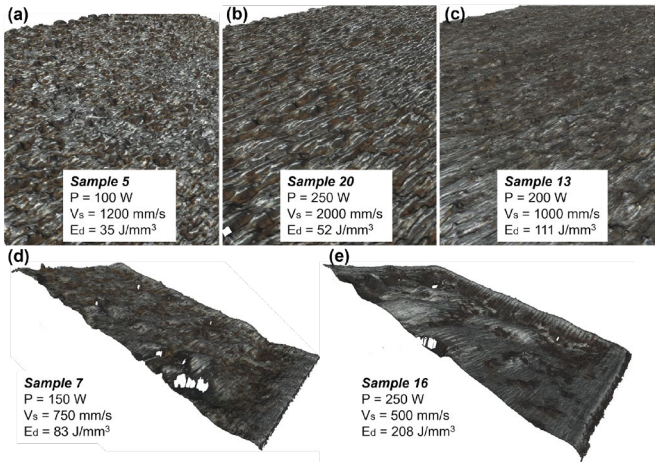

Fig. 5. Profilometer observations of the top surface after printing.

Discussion

The first approach in the LPBF of a new alloy consists in searching the best parameters to achieve fully dense and defect-free samples. Process maps are commonly used for this purpose. Although the primary aim is to obtain the best parts, investigations of defects generated using different parameters can provide good insights of both the alloy studied and the pure functioning of the LPBF process.

In this work, the effects of the two variable parameters (P and v_s) are investigated together with the variation in E_d (Eq. 1). All samples are compared in terms of density, amount and type of defects, tracks overlapping, melt pool morphology and surface quality. Particular attention is given to the quality of the top surface and the morphology of the melt pool within the top layer. Indeed, they can provide useful indications of the defects that may form in a hypothetical subsequent layer and thus understand the phenomena that have occurred in the layers below.

The use of low/moderate P (100 - 150W) and low v_s (400 - 800 mm/s) (samples 1, 2, 3, 6 and 7) does not allow for fully printed samples. The printing was stopped, excepted for sample 7. Despite the wide range of E_d (52 - 125 J/mm^3), the low P could not generate sufficient liquid phase for the powders to bond together, resulting in poor densification [3]. The metallurgical bond between layers is also compromised, leading to the possible material tear out (Fig. 2b), as also occurred in the top layer of sample 7 (Fig. 4f). Moreover, the low v_s causes an unstable melt pool generating big spatters (Fig. 2c-d) [22] that are not re-melted by the subsequent passage of the laser. If spatters are larger than the layer thickness, the spreadability of a new layer of powders is impeded, causing gaps and compromising the metallurgical layers bond [4]. Large pores (~ 400 µm) are found for instance in sample 7, that are located inside a big spatter (Fig. 3c). As the process advances, the presence of poorly printed layers leads to an irregular surface (Fig. 5d), affecting the printing of the subsequent layers.

With similar P (100 - 150 W) but higher v_s (1000 - 1250 mm/s) (sample 4 and 5), low E_d values (~ 40 J/mm^3) generate a shallow melt pool (Fig. 4b) [6]. As consequence, the metallurgical bond between two subsequent layers is compromised, causing the presence of lack of fusion areas (Fig. 4a-b) [5] that leads to low density (Fig. 3a). In this case, the poor metallurgical bond is caused by balling phenomena [3], visible in the top surface (Fig. 5a) where the tracks are clearly discontinuous. The increase in v_s is thus seen to avoid the generation of large spatters. This is easily understood since the higher v_s allows a faster cooling of the melt pool, and decreases the possibility of melted droplets being splashed out of the melt pool [22].

Low E_d values (~ 54 J/mm^3) resulting from higher P (200-250 W) and high v_s (1500-2000 mm/s) (samples 14, 15, 19, 20), leads to similar observations. Indeed, balling phenomena also occur, bringing about a low density (Fig. 3a) due to lack of fusion areas (Fig. 4c-d). However, this effect

is more restrained than observed at lower P. Indeed, the parts density is higher and the internal porosity are lower (Fig. 3a). In the present case, the higher P allows a better melting of the powders, leading to a better overlapping of the tracks as visible in the top layer (Fig. 5b). Furthermore, the melt pool height increases (Fig. 4d), allowing a better metallurgical bond with the previous layer. Therefore, the little increase of E_d (from 40 to 54 J/mm^3) results in a better processability, but the level of defects remains still high (Fig. 3a and 4c).

The combination of a moderate/medium P (150-200 W) and a medium v_s (750-1200 mm/s) (E_d = 50 - 111 J/mm^3) allows to achieve fully dense and defect-free parts (sample 08, 09, 10, 12 and 13). Indeed, this combination of parameters generate an ideal melt pool (Fig. 4h), regular and homogeneous within the cross section. The tracks have a proper overlap, which affects positively the density of the samples (Fig. 3a) and the spreadablilty of the subsequent powder layer. Indeed, no defects are found (Fig. 4g). Only small gas porosities are observed, which does not adversely affect the quality of the final part. Small spatters are visible in the top surface (Fig. 5c), but these can be easily re-melted by the subsequent laser passage. This range of parameters and especially the combination 200 W / 750-1000 mm/s (Ed ~ 97 J/mm^3) is thus considered as optimum for the realization of AISI S2 steel parts manufactured by LPBF.

Finally, high P (250 W) and low v_s (500-1000 mm/s) lead to a high E_d (104-208 J/mm^3) (sample 11, 16, 17 and 18). The deep melt pool (Fig. 4j) allows a good overlap of the tracks (Fig. 5e), resulting in high density above 99,5% (Fig. 3a). Despite this, the high E_d causes an instability of the melt pool, that is clearly irregular within the cross section (Fig. 4j). Indeed, increasing the melt pool depth also increases the possibility of gas entrapment, resulting in higher porosity. The large porosity detected (Fig. 4i) may be formed due to denudation process of powders around the melt pool due to the high E_d [2]. Key-hole defects (Fig. 3b) are also observed, formed due to the high E_d that causes metal evaporation and generate a recoil pressure towards the melt pool bottom [23]. Furthermore, the combination of low v_s and high E_d increases spattering [4], in terms of number and size of spatters. As a result, the spreadability of the subsequent layer of powders is compromised. The final part exhibits many surface irregularities, as shown by profilometer observations (Fig. 5e) and in the top layer of the cross section (Fig. 4i).

Based on the above explanations, it can be assumed that the “not processed” window (Fig. 6) results in an insufficient E_d to generate an adequate melt pool. Extensive balling and lack of fusion areas are expected due to the low P (100 - 150 W) and the high v_s (1500 - 2000 mm/s).

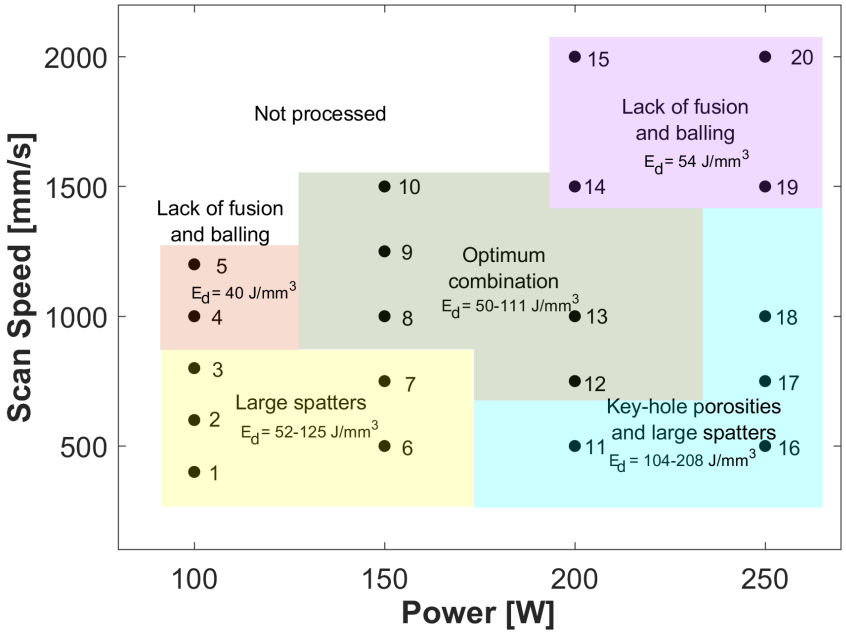

Fig. 6. Process map for AISI S2 tool steel by Laser Powder Bed Fusion.

Summary

The processability of the tool steel AISI S2 has been investigated and a process map has been built considering surface morphology, density measurements, defects characterization and quantification, tracks overlapping and melt pool morphology. The main outcomes can be summarized as follows:

- Medium v_s (750 - 1000 mm/s) and P (200 W) (Ed ~ 97 J/mm^3) allow to achieve fully dense and defect-free parts;
- High v_s (1000 - 2000 mm/s) and low E_d (35 - 69 J/mm^3) cause lack of fusion and balling, regardless of the P applied;
- Low v_s (400 - 1000 mm/s) and mostly high E_d (69 - 208 J/mm^3) cause large spatters and key-hole porosities, regardless of the P applied;

This work establishes a reference for further investigations of LPBF S2 tool steels. Furthermore, it lays the ground for the development by LPBF of new steels based on the modification of the S2 tool steel or similar grades.

Acknowledgments

This work was supported by the FNRS (Fonds National de la Recherche Scientifique of Belgium, PDR number 35298295). The authors acknowledge Sylvie Salieri for the samples preparation.

References

[1] S. Gorsse, C. Hutchinson, M. Gouné, R. Banerjee, Additive manufacturing of metals: a brief review of the characteristic microstructures and properties of steels, Ti-6Al-4V and high-entropy alloys, Sci. Technol. Adv. Mater. 18 (2017) 584-610. https://doi.org/10.1080/14686996.2017.1361305

[2] B. Zhang, Y. Li, Q. Bai, Defect Formation Mechanisms in Selective Laser Melting: A Review, Chinese J. Mech. Eng. English Ed. 30 (2017) 515-527. https://doi.org/10.1007/s10033-017-0121-5

[3] S. Chowdhury, N. Yadaiah, C. Prakash, S. Ramakrishna, S. Dixit, L.R. Gupta, D. Buddhi, Laser powder bed fusion: a state-of-the-art review of the technology, materials, properties & defects, and numerical modelling, J. Mater. Res. Technol. 20 (2022) 2109 -2172. https://doi.org/10.1016/j.jmrt.2022.07.121

[4] D. Wang, S. Wu, S. Mai, Y. Yang, Y. Liu, C. Song, Mechanisms and characteristics of spatter generation in SLM processing and its effect on the properties, Mater. Des. 117 (2017) 121 -130. https://doi.org/10.1016/j.matdes.2016.12.060

[5] J. Platl, H. Leitner, C. Turk, A.G. Demir, B. Previtali, R. Schnitzer, Defects in a Laser Powder Bed Fused Tool Steel, Adv. Eng. Mater. 23 (2021) 1-11. https://doi.org/10.1002/adem.202000833.

[6] M. A. Ryder, C.J. Montgomery, M.J. Brand, J.S. Carpenter, P.E. Jones, A.G. Spangenberger, D.A. Lados, Melt Pool and Heat Treatment Optimization for the Fabrication of High-Strength and High-Toughness Additively Manufactured 4340 Steel, J. Mater. Eng. Perform. 30 (2021) 5426-5440. https://doi.org/10.1007/s11665-021-05836-8

[7] V. Gunenthiram, P. Peyre, M. Schneider, M. Dal, F. Coste, R. Fabbro, Analysis of laser -melt pool -powder bed interaction during the selective laser melting of a stainless steel, J. Laser Appl. 29 (2017) 022303. https://doi.org/10.2351/1.4983259

[8] Q. Chen, Y. Zhao, S. Strayer, Y. Zhao, K. Aoyagi, Y. Koizumi, A. Chiba, W. Xiong, A.C. To, Elucidating the effect of preheating temperature on melt pool morphology variation in Inconel 718 laser powder bed fusion via simulation and experiment, Addit. Manuf. 37 (2021) 101642. https://doi.org/10.1016/j.addma.2020.101642

[9] Y. He, M. Zhong, N. Jones, J. Beuth, B. Webler, The Columnar-to-Equiaxed Transition in Melt Pools During Laser Powder Bed Fusion of M2 Steel, Metall. Mater. Trans. A Phys. Metall. Mater. Sci. 52 (2021) 4206-4221. https://doi.org/10.1007/s11661-021-06380-9

[10] R. Cunningham, C. Zhao, N. Parab, C. Kantzos, J. Pauza, K. Fezzaa, T. Sun, A.D. Rollett, Keyhole threshold and morphology in laser melting revealed by ultrahigh-speed x-ray imaging, Science (80-.) 363 (2019) 849 -852. https://doi.org/10.1126/science.aav4687
[11] A. L. Strauch, V. Uhlewinkel, M. Steinbacher, F. Großwendt, A. Röttger, A.B. Chehreh, F. Walther, R. Fechte-Heinen, Comparison of the processability and influence on the microstructure of different starting powder blends for laser powder bed fusion of a Fe3.5 Si1.5 C alloy, Metals 11 (2021) 1107. https://doi.org/10.3390/met11071107
[12] J. Saewe, N. Carstensen, P. Kürnsteiner, E.A. Jägle, J.H. Schleifenbaum, Influence of increased carbon content on the processability of high-speed steel HS6-5-3-8 by laser powder bed fusion, Addit. Manuf. 46 (2021) 102125. https://doi.org/10.1016/j.addma.2021.102125
[13] W. Hearn, E. Hryha, Effect of Carbon Content on the Processability of Fe-C Alloys Produced by Laser Based Powder Bed Fusion, Front. Mater. 8 (2022) 1-10. https://doi.org/10.3389/fmats.2021.800021
[14] M.A. Taha, A.F. Yousef, K.A. Gany, H.A. Sabour, On selective laser melting of ultra high carbon steel: Effect of scan speed and post heat treatment, Materwiss. Werksttech. 43 (2012) 913-923. https://doi.org/10.1002/mawe.201200030
[15] J. Kunz, M.L. Köhler, S. Herzog, A. Kaletsch, C. Broeckmann, Influence of an Increasing Alloying Content on the Microstructure of a High-Speed Steel in the Laser-Powder Bed Fusion Process, Steel Res. Int. 92 (2021), https://doi.org/10.1002/srin.202100438
[16] X. Kang, S. Dong, H. Wang, S. Yan, X. Liu, H. Ren, Effect of thermal cycle on microstructure evolution and mechanical properties of selective laser melted low-alloy steel, Materials 12 (2019) 1-15. https://doi.org/10.3390/ma12213625
[17] J.J.S. Dilip, G.D.J. Ram, T.L. Starr, B. Stucker, Selective laser melting of HY100 steel: Process parameters, microstructure and mechanical properties, Addit. Manuf. 13 (2017) 49-60. https://doi.org/10.1016/j.addma.2016.11.003
[18] W. Hearn, K. Lindgren, J. Persson, E. Hryha, In situ tempering of martensite during laser powder bed fusion of Fe-0.45C steel, Materialia 23 (2022) 101459. https://doi.org/10.1016/j.mtla.2022.101459
[19] W. Wang, S. Kelly, A Metallurgical Evaluation of the Powder-Bed Laser Additive Manufactured 4140 Steel Material, JOM 68 (2016) 869 -875. https://doi.org/10.1007/s11837-015-1804-y
[20] J. Damon, R. Koch, D. Kaiser, G. Graf, S. Dietrich, V. Schulze, Process development and impact of intrinsic heat treatment on the mechanical performance of selective laser melted AISI 4140, Addit. Manuf. 28 (2019) 275-284. https://doi.org/10.1016/j.addma.2019.05.012
[21] E. Jelis, M.R. Hespos, N.M. Ravindra, Process Evaluation of AISI 4340 Steel Manufactured by Laser Powder Bed Fusion, J. Mater. Eng. Perform. 27 (2018) 63-71. https://doi.org/10.1007/s11665-017-2989-8
[22] H. Zheng, H. Li, L. Lang, S. Gong, Y. Ge, Effects of scan speed on vapor plume behavior and spatter generation in laser powder bed fusion additive manufacturing, J. Manuf. Process. 36 (2018) 60 -67. https://doi.org/10.1016/j.jmapro.2018.09.011
[23] Y. Huang et al., Keyhole fluctuation and pore formation mechanisms during laser powder bed fusion additive manufacturing, Nat. Commun. 13 (2022) 1 -11. https://doi.org/10.1038/s41467-022-28694-x

Materials Research Proceedings 28 (2023) 49-56 https://doi.org/10.21741/9781644902479-6

Experimental analysis of cold sprayed precursors for closed-cells aluminum foams

VISCUSI Antonio[1,a *], PERNA Alessia Serena[1,b], ASTARITA Antonello[1,c], BORRELLI Domenico[2,d], CARAVIELLO Antonio[2,e], SICIGNANO Nicola[2,f] and CARRINO Luigi[1,g]

[1]Department of Chemical, Materials and Production Engineering, University of Naples "Federico II", P.le Tecchio 80, 80125 Naples, Italy

[2]Sòphia High Tech S.r.l., Via Malatesta 30 A, 80049 Somma Vesuviana (NA), Italy

[a]antonio.viscusi@unina.it, [b]alessiaserena.perna@unina.it, [c]antonello.astarita@unina.it, [d]domenico.borrelli@sophiahightech.com, [e]antonio.caraviello@sophiahightech.com, [f]nicola.sicignano@sophiahightech.com, [g]luigi.carrino@unina.it

Keywords: Cold Spray, Metal Foams, Precursors, 3D-Printing, Experimental Analysis

Abstract. Metal foams are a relatively new class of materials with many interesting combinations of physical and mechanical properties. Among them, the closed-cells aluminum foams are the most interesting for structural applications in the aerospace industry. There exist different methods to produce metal foams. An innovative manufacturing technique was developed in this study, proving the possibility to produce closed-cells aluminum foams through the cold spray additive manufacturing technology (CS). In particular, two different sets of samples were produced by varying the cold spray process parameters aiming at: i) studying the advantages and the issues of cold spray for manufacturing precursors for metal foams; ii) analyzing the correlation among the CS printing strategy and parameters, the foaming process and the physical and the morphological characteristics of the resulting foams; iii) finally, finding appropriate conditions to form closed-cells aluminum foams via CS.

Introduction

It is a matter of fact that, in the aerospace industry, the main trend at the design stage is currently directed toward the wider employment of lightweight materials, due to obvious environmental and economic reasons [1]. In this scenario, the closed-cells metal foams are rapidly emerging as a new class of advanced materials with very low specific weight and novel physical, mechanical, thermal, electrical and acoustic properties due to their cellular structure consisting of solid metal containing a large volume fraction of gas-filled pores [2].

Metal foams of different metals are available, such as: aluminum, nickel, magnesium, lead, zinc, copper, bronze, titanium, steel and even gold [3]. The more used in structural applications are aluminum foams that are characterized by low density coupled with high energy absorption capacity, high specific stiffness and reduced thermal and electrical conductivity; these materials can be used as core for sandwich structures, internal anti-buckling reinforcement for thin walled structures and so on [4,5].

The closed-cells aluminum foams can be manufactured through several methods [6]. The gas-releasing particle decomposition in semi-solids process, which is known as powder compact melting technique (PCMT), starts from a compacted powders mixture of aluminum alloy and a blowing agent in form of fine particles, obtaining the so-called foamable solid precursor [7]. Heating the precursor to a little above the melting temperature of the alloy leads the compacted metal matrix in a semi-liquid viscous state; the foaming agent decomposes and releases hydrogen,

Content from this work may be used under the terms of the Creative Commons Attribution 3.0 license. Any further distribution of this work must maintain attribution to the author(s) and the title of the work, journal citation and DOI. Published under license by Materials Research Forum LLC.

which blows bubbles in the soft alloy. Under these conditions, the released gas forces the melting precursor material to expand, modelling a highly porous structure.

In order to ensure satisfactory foaming results, appropriately starting powders have to be chosen [8]. The most suitable materials for foaming are pure aluminum or cast alloys (e.g. AlSi10Mg and AlSi12) coupled with titanium hydride (TiH_2), which is the foaming agent. Several other foaming parameters, which have to be suitably controlled, influence the final foam quality. The most important are powder mixing composition, particles dimensions and shape, distribution of blowing agent within the metal matrix, compaction pressure, time and temperature of foaming and heating rates [9].

Based on the mechanisms ruling PCMT, an innovative manufacturing technology was developed by the authors in this study, proving the possibility to produce closed-cells aluminum foams through the cold spray additive manufacturing technology. The problems encountering when using the traditional PCMT-based manufacturing processes for foams can be overcome through cold spray [10].

CS is a significantly greener, low-temperature, non-combustion, and scalable alternative process with an extraordinary potential. The bonding concept in CS is based on kinetic rather than thermal energy. During CS, feedstock powder particles (5-50 μm) accelerated to supersonic velocities (300-1200 m/s) by preheated compressed gas passing through a convergent-divergent nozzle, undergo severe plastic deformation upon impact and bond to the substrate [11]. CS, as a "cold" technique, can be used to process thermally sensitive materials [12,13], like the powder-based solid precursors for metal foams. The key idea is spraying the powder mixture on a metallic substrate and then carry out the foaming process in order to obtain the final foamed component. The shape of the precursor can be ruled by using a complex shaped substrate or by imposing a complex trajectory at the cold spray gun.

In line with this topic and with the scope to explore in details the developed manufacturing process, two different sets of samples were produced by varying the cold spray process parameters aiming at: i) studying the advantages and the issues of cold spray for manufacturing precursors for metal foams; ii) analyzing the correlation among the CS printing strategy and parameters, the foaming process and the physical and the morphological characteristics of the resulting foams; iii) finally, finding appropriate conditions to form closed-cells aluminum foams via CS.

For this scope, AlSi10Mg fine powders were mixed with titanium hydride particles to form the powder mixture precursors. Then, the low-pressure cold spray facility was used for the powder deposition by using different CS printing parameters; hence, the foaming process was carried out. SEM observations of the cross-sections of both the precursors and the resulting foams were carried out, pointing out the effectiveness of the process and the critical issues to be faced when cold spraying precursors for metal foams.

Materials and Methods

Micron sized powders of aluminum alloy AlSi10Mg and titanium hydride TiH_2, provided by LPW South Europe and Dymet, respectively, were used in this experimentation. The particle mean size of AlSi10Mg powder is 25 μm, while the mean diameter of TiH_2 particles is 10 μm.

The powder mixture was obtained through the sound assisted fluidization bed processes; the use of fluidization makes it possible to handle and process large quantities of powders, so obtaining a mixing to the scale of the primary particles [14]. The fluidization and mixing tests of these cohesive fine powders were performed by the experimental apparatus schematically reported in Fig. 1. It consists of a metallic fluidization column equipped with a porous plate gas distributor to maximize the uniformity of the gas flow rate entering the column. The acoustic field is introduced inside the column through a sound wave guide located at the top of the column. Pure dry nitrogen from a compressed tank is used as fluidizing gas. All the tests were carried out at room temperature and ambient pressure conditions. Both the preliminary fluidization/mixing tests and the

preparation of the final AlSi10Mg-TiH_2 mixtures to be used to produce the metal foam precursors were performed in this experimental apparatus.

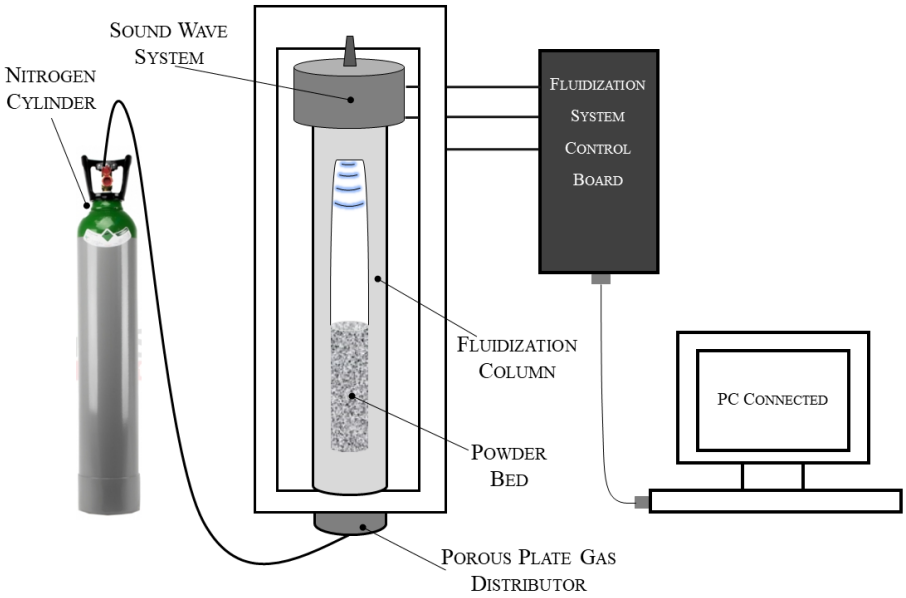

Fig. 1. Sound assisted fluidization bed process apparatus.

A mixture with a 2.5 wt.% of TiH_2 was prepared. The following fluidization process parameters were used based on preliminary fluidization/mixing tests: i) gas flow rate: 70 l/min; ii) acoustic field: 80 dB-150 Hz; fluidization time: 30 min. The SEM picture (Fig. 2) shows the effective mixing achieved with the blowing agent particles homogeneously dispersed within aluminum alloy powder.

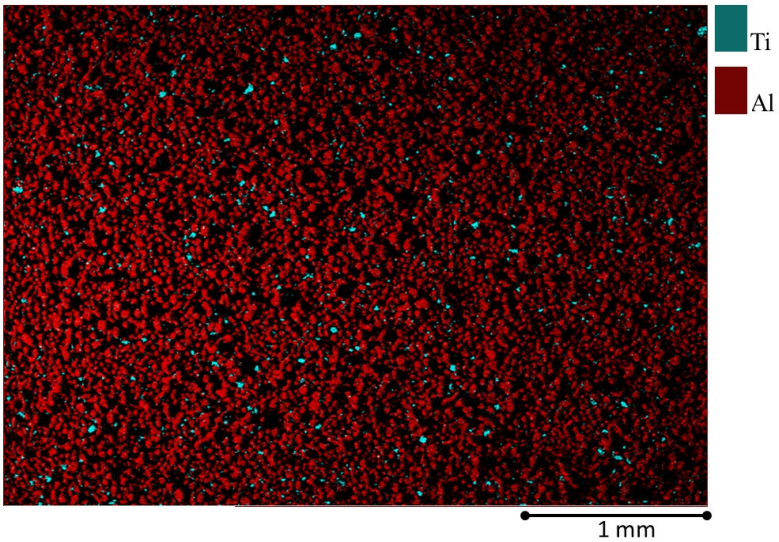

Fig. 2. SEM picture showing AlSi10Mg-TiH_2 mixture achieved through sound assisted fluidization bed process (2.5 wt.% of TiH_2, nominally).

The low-pressure cold spray facility was used for spraying the powder mixture constituting the foamable precursors. The spraying parameters such as fluid temperature and fluid pressure, stand-off distance (the distance between the substrate and the nozzle) and horizontal speed nozzle across the substrate were chosen after a preliminary experimental campaign that is not discussed in this paper for the sake of brevity. Two different sets of samples were produced by varying the cold

spray process parameters, in agreement to what reported in Table 1. The first raw of Table 1 reports the CS process parameters (CS_L) used to obtain less compact precursors characterized by internal microporosities that should promote the bubbles growth and the formation of lightweight materials. The second raw reports the CS process parameters (CS_H) used to manufacture more compacted precursors.

Table 1. Deposition process main parameters.

	Gas used	Gas temperature [°C]	Gas pressure [bar]	Stand-off distance (SoD) [mm]	Speed nozzle [mm/s]
CS_L	Air	400	6	30	1.0
CS_H	Air	600	7	5	1.0

The mixture was sprayed on a C40 thin steel plate producing a 30x40 nominal plane shape. One single pass was imposed to the spray gun, in agreement with the strategy shown in Fig. 3a. Macrographs of the foamable solid precursors manufactured via cold spray under CS_L and CS_H process conditions are shown in Fig. 3b and Fig. 3c, respectively.

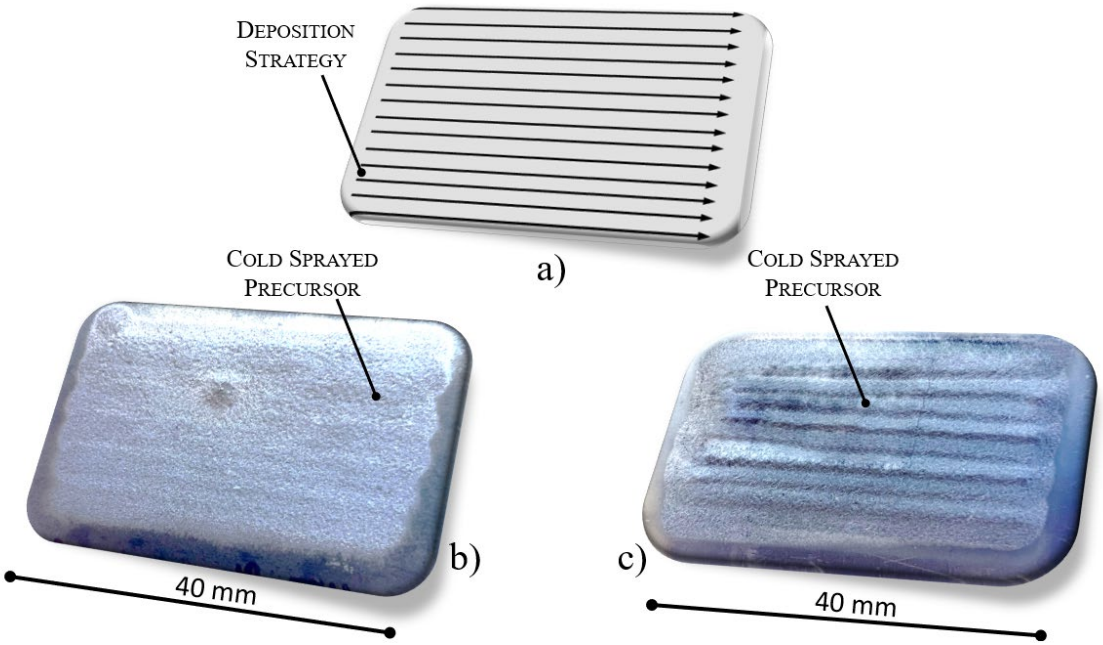

Fig. 3. a) Cold spray deposition strategy; b) macrograph of foamable solid precursor produced with CS_L process parameters; c) macrograph of foamable solid precursor produced with CS_H process parameters.

All the precursors made via cold spray were inserted within a preheated furnace set at a temperature of 660°C for the foaming process. The time needed for expansion was estimated in the range of 4-6 minutes; afterwards each sample has been taken out from the furnace and cooled at room temperature.

The cold sprayed precursors (obtained via CS_L and CS_H process parameters) before foaming as well as those resulting from the foaming process were cut for the cross-section observations. Hence, all the specimens were mounted and prepared according to the international ASTM standards for metallographic analyses through SEM microscopy. The blowing agent distribution after the cold spray deposition was analyzed, the shape of the cell and the expansion of the foam

were examined for the foamed samples. EDS inspections were also carried out with the scope to analyze the phenomena resulting from the foaming process, highlighting the critical issues of the manufacturing technology, for leading optimized process conditions.

Results and Discussion

The results from the SEM observations of the cross-sections of the cold sprayed precursors before foaming obtained by using CS_L and CS_H process parameters are reported in Fig. 4 and Fig. 5, respectively.

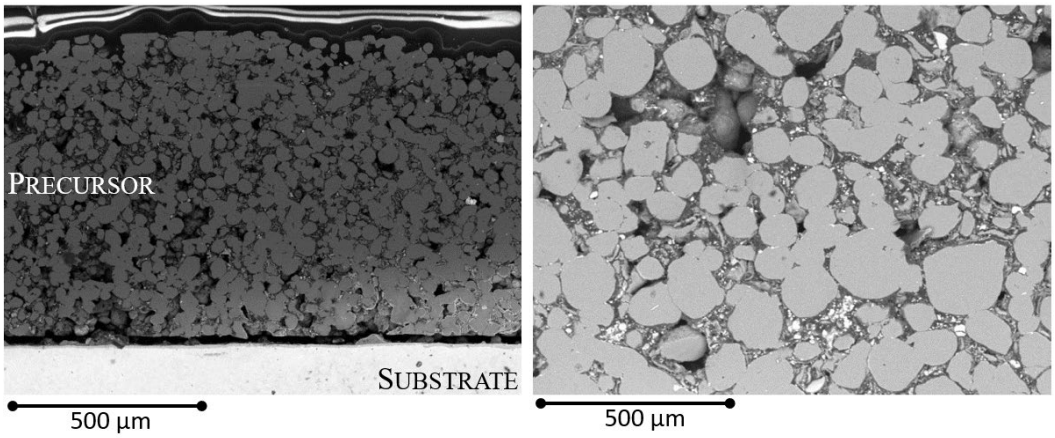

Fig. 4. SEM observations of the cross-sections of the cold sprayed precursors before foaming obtained by using CS_L process parameters at a) 150x, b) 500x.

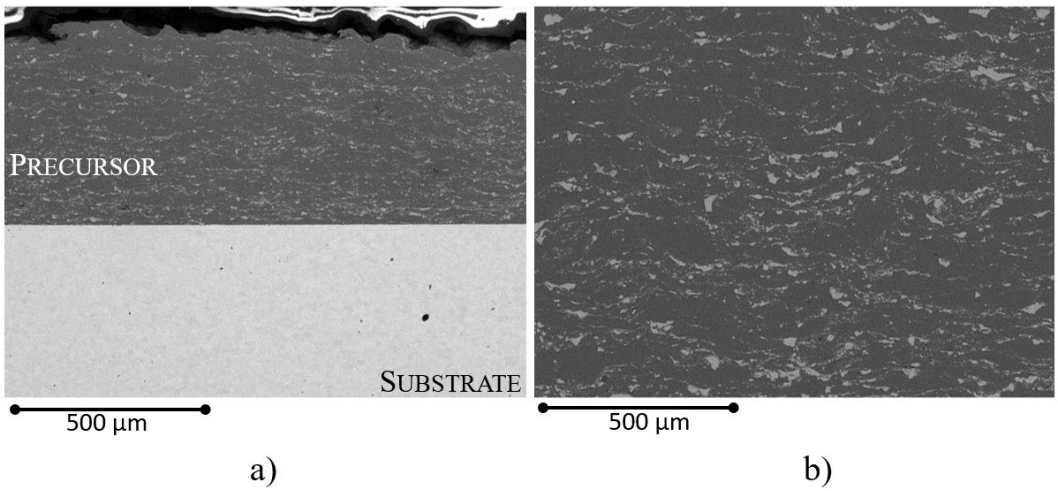

Fig. 5. SEM observations of the cross-sections of the cold sprayed precursors before foaming obtained by using CS_H process parameters at a) 150x, b) 500x.

From Fig. 4a the thickness of the specimen was estimated to be equal to about 800 µm. Moreover, voids and microporosities are well visible with the particles that are not completely deformed during the impact. This is clearer by looking the picture in Fig. 4b at 500x magnification. The white particles are the fragile TiH_2 powders that keep entrapped among aluminum particles, forming cluster and agglomerations homogeneously dispersed within the metal powders.

The cold sprayed precursors obtained by using CS_H process parameters are denser and more compact, as expected from literature [15], the particles deformed and flattened, and the coating thickness reduced at about 500 µm, due to particles compactness (Fig. 5a). The higher magnification picture in Fig. 5b shows a precursor appearing quite dense and free of porosity, with

the foaming agent particles (the lighter zones in the figure) homogeneously dispersed within the aluminum-silicon matrix. In fact, as proved in literature [16,17], the cold spray technology can create metal matrix composite depositions by mixing fragile materials with ductile material particles that deform and promote the coating formation and grow-up. Moreover, a stratification of TiH_2 particles, related to technology employed, can be identified.

Anyway, in both the examined cases, EDS analyses confirmed a weight percentage of TiH_2 within the coatings equal to 2.5±0.5 wt. %., proving the capability of CS to deposit the AlSi10Mg-TiH_2 mixture of precursor.

Fig. 6 shows the micrographs of the cross-sections of the aluminum foams obtained starting from the above-described precursors.

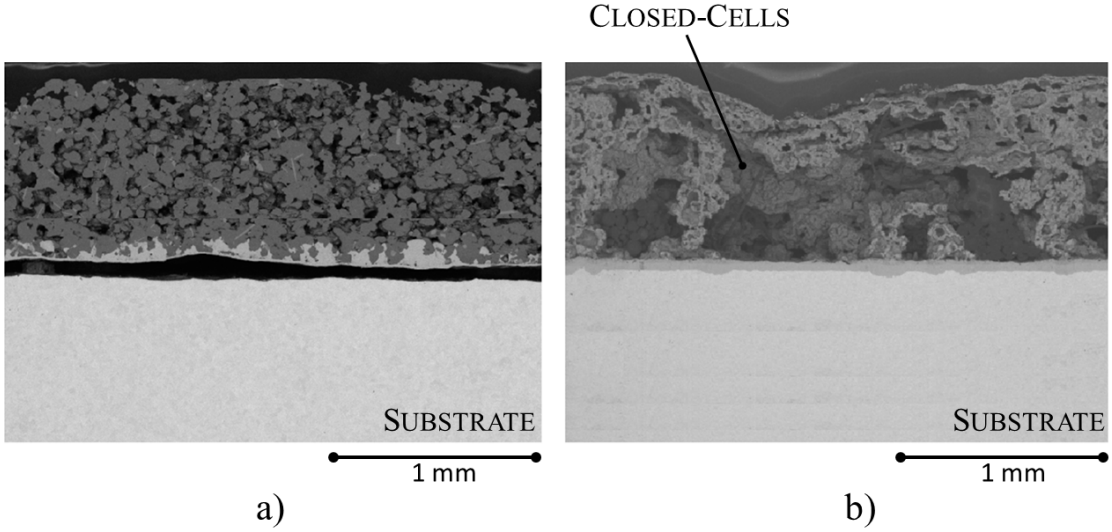

Fig. 6. Micrographs of the cross-sections of aluminum foams produced starting from precursors obtained by using: a) CS_L process parameters; b) CS_H process parameters.

It can be seen from Fig. 6a that no foaming occurs when the precursor is not quite compacted, and the CS process parameters are not properly set. In this case, the foaming agent was not capable of expanding the thick and so-already existing porous structure. The possible reason is that the oxygen entering within the porous material oxides completely the metal matrix that cannot expand and form the bubbles under the force of hydrogen released by TiH_2 dissociation mechanism. On the contrary, it can be seen from Fig. 6b that the material expands when the precursor is denser and well compacted, leading to a foam relative density [3] equal to 0.35, with the foam percentage porosity of 65%. Under these conditions, the aluminum matrix melts, and the foaming agents blows to form the closed-cells aluminum foams.

Summary

Based on the experimental results presented and discussed in the previous sections, the following conclusions could be drawn:

- The cold spray technology seems to be an effective technique to produce precursors for closed-cells aluminum foams.
- The sound assisted fluidization bad processes can be used to mix effectively micron size AlSi10Mg and TiH_2 particles forming the precursor, under the following process parameters: i) gas flow rate: 70 l/min; ii) acoustic field: 80 dB-150 Hz; fluidization time: 30 min.
- An existing porous structure for the precursor does not enhance the foaming process and the bubble formation.

- The CS process parameters need to be properly set (appropriate process parameters were found here: gas temperature: 600°C, gas pressure: 7 bar, SoD: 5 mm) to produce dense, compact and free of porosity metallic precursors, which are the characteristics to be ensured for a successful foaming.

References

[1] G. Sun, D. Chen, G. Zhu, Q. Li, Lightweight hybrid materials and structures for energy absorption: A state-of-the-art review and outlook, Thin-Walled Struct. 172 (2022) 108760. https://doi.org/10.1016/j.tws.2021.108760

[2] J. Banhart, Metal Foams: Production and Stability, Adv. Eng. Mater. 8 (2006) 781-794. https://doi.org/10.1002/adem.200600071

[3] J. Banhart, Manufacture, characterisation and application of cellular metals and metal foams, Prog. Mater. Sci. 46 (2001) 559–632. https://doi.org/10.1016/S0079-6425(00)00002-5

[4] L. Peroni, M. Avalle, M. Peroni, The mechanical behaviour of aluminium foam structures in different loading conditions, Int. J. Impact Eng. 35 (2008) 644-658. https://doi.org/10.1016/j.ijimpeng.2007.02.007

[5] J. Baumeister, J. Banhart, M. Weber, Aluminium foams for transport industry, Mater. Des. 18 (1997) 217-220. https://doi.org/10.1016/S0261-3069(97)00050-2

[6] J. Kahani Khabushan, S. Bazzaz Bonabi, F. Moghaddasi Aghbagh, A. Kahani Khabushan, A study of fabricating and compressive properties of cellular Al–Si (355.0) foam using TiH2, Mater. Des. 55 (2014) 792–797. https://doi.org/10.1016/j.matdes.2013.10.022

[7] J. Banhart, Aluminium foams for lighter vehicles, Int. J. Veh. Des. 37 (2005) 114-125. https://doi.org/10.1504/IJVD.2005.006640

[8] A. Viscusi, M. Durante, A. Formisano, An Experimental–Numerical Analysis of Innovative Aluminum Foam-Based Sandwich Constructions Under Compression Loads, Lect. Notes Mech. Eng. (2022) 131-150. https://doi.org/10.1007/978-3-030-82627-7_8

[9] A. Formisano, M. Durante, A. Viscusi, L. Carrino, Mechanical behavior and collapse mechanisms of innovative aluminum foam-based sandwich panels under three-point bending, Int. J. Adv. Manuf. Technol. 112 (2021) 1631-1639. https://doi.org/10.1007/S00170-020-06564-4/FIGURES/8

[10] C. Ensarioglu, A. Bakirci, H. Koluk, M. Cemal Cakir, C. Ensarioglu, A. Bakirci, M.C. Cakir, H. Koluk, Metal Foams and Their Applications in Aerospace Components, Sustainable Aviation. Springer, Cham. (2022) 27-63. https://doi.org/10.1007/978-3-030-91873-6_2

[11] A.S. Perna, A. Viscusi, R.D. Gatta, A. Astarita, Cold spraying on polymer-based composites: Understanding the single-particle adhesion, Surf. Coatings Technol. 447 (2022) 128837. https://doi.org/10.1016/j.surfcoat.2022.128837

[12] A.S. Perna, A. Viscusi, R.D. Gatta, A. Astarita, Integrating 3D printing of polymer matrix composites and metal additive layer manufacturing: surface metallization of 3D printed composite panels through cold spray deposition of aluminium particles, Int. J. Mater. Form. 15 (2022). https://doi.org/10.1007/s12289-022-01665-9

[13] A. Viscusi, R. Della Gatta, F. Delloro, I. Papa, A.S. Perna, A. Astarita, A novel manufacturing route for integrated 3D-printed composites and cold-sprayed metallic layer, Mater. Manuf. Process. 37 (2022) 568-581. https://doi.org/10.1080/10426914.2021.1942908.

[14] P. Ammendola, R. Chirone, F. Raganati, Fluidization of binary mixtures of nanoparticles under the effect of acoustic fields, Adv. Powder Technol. 22 (2011) 174-183. https://doi.org/10.1016/J.APT.2010.10.002

[15] A. Viscusi, M. Bruno, L. Esposito, G. Testa, An experimental/numerical study of bonding mechanism in cold spray technology for metals, Int. J. Adv. Manuf. Technol. 110 (2020) 2787-2800. https://doi.org/10.1007/s00170-020-06060-9

[16] A.S. Perna, A. Viscusi, A. Astarita, L. Boccarusso, L. Carrino, M. Durante, R. Sansone,

Manufacturing of a Metal Matrix Composite Coating on a Polymer Matrix Composite Through Cold Gas Dynamic Spray Technique, J. Mater. Eng. Perform. (2019). https://doi.org/10.1007/s11665-019-03914-6

[17] A.S. Perna, A. Viscusi, A. Astarita, L. Boccarusso, L. Carrino, M. Durante, R. Sansone, Manufacturing of a Metal Matrix Composite Coating on a Polymer Matrix Composite Through Cold Gas Dynamic Spray Technique, J. Mater. Eng. Perform. 28 (2019) 3211-3219. https://doi.org/10.1007/s11665-019-03914-6

Materials Research Proceedings 28 (2023) 57-64 https://doi.org/10.21741/9781644902479-7

A machine learning approach for adhesion forecasting of cold-sprayed coatings on polymer-based substrates

PERNA Alessia Serena[1,a], CARRINO Luigi[1,b], CITARELLA Alessia Auriemma[2,c], De MARCO Fabiola[2,d *], Di BIASI Luigi[2,e], TORTORA Genoveffa[2,f] and VISCUSI Antonio[1,g]

[1]Department of Chemical, Materials and Production Engineering, University of Naples Federico II, Piazzale V. Tecchio 80, 80125 Napoli, Italy

[2]Department of Computer Science, University of Salerno, Fisciano, SA, Italy

[a]alessiaserena.perna@unina.it; [b]luigi.carrino@unina.it; [c]aauriemmacitarella@unisa.it; [d]fdemarco@unisa.it; [e]ldibiasi@unisa.it; [f]tortora@unisa.it; [g]antonio.viscusi@unina.it

Keywords: Machine Learning, Cold Spray, Composites, Neural Networks, Thermal Spray

Abstract. Cold spray is a novel production technology for creating metallic layers on various materials. Using a pressurized gas travelling at supersonic speeds, the metallic particles are accelerated and impact the target surface obtaining adhesion through mechanical interlocking between the powders and the substrate. This method is especially well suited for coating thermosensitive materials like composites since it only requires a little amount of heat, as the powders remain in a solid state. The quality and comprehension of this manufacturing process can be greatly improved by using machine learning techniques. In order to evaluate the characteristics of the particle's deformation upon collision, the goal of this work is to forecast it using machine learning approaches. The parameters chosen as an input for the model were related to 3 macro-categories: process parameters, powder parameters and substrate parameters. As regards the output parameters, flattening and penetration were chosen as they are the main characteristics of the coating on which homogeneity and adhesion depend. In order to obtain reliable results, a mix of data FEM and experimental data were used to train the neural network. The model was then tested on a dataset of experimental data.

Introduction

The drive to reduce weight and manufacturing costs has raised the demand for polymeric materials dramatically in recent years. Thermosetting polymers, in particular, have become widely employed in a variety of industries, including aerospace, since they may be used as matrix for fibre-reinforced composite materials. However, as environmental concerns become more generally acknowledged, the use of thermosets is severely limited since they cannot be reused or recycled once the curing process is complete. High-performance thermoplastic materials, such as PEEK or ABS, are gaining popularity because of their high toughness, high melting temperature, and 100% recyclable nature.

Nonetheless, several applications remain out of reach because of these materials' poor surface qualities, such as poor wear and scratch resistance and low electrical conductivity. As a result, surface metallization may be the best option for combining the benefits of metals with thermoplastic polymers. However, when using the most common metallisation procedures, the melting temperature of the metallic materials to be sprayed must be reached, modifying its original properties and causing thermal distortions in the substrate.

Cold Gas Dynamic Spray, which uses kinetic energy and involves temperatures well below the melting point of the metallic particles, can be an adequate alternative for improving the surface properties of polymers [1].

Content from this work may be used under the terms of the Creative Commons Attribution 3.0 license. Any further distribution of this work must maintain attribution to the author(s) and the title of the work, journal citation and DOI. Published under license by Materials Research Forum LLC.

This approach is based on the high-speed impact of solid-state metallic particles; no chemical reactions are required, and deposition is made possible in large part by mechanical interlocking between the particles and the substrate [2].

Although this technology has been widely explored and employed on metal substrates, the underlying physics when the substrate is a polymer is yet unclear [3]. Because the final coating characteristics (such as powder deformation or penetration depth, which are closely related to coating adhesion) depend on a variety of factors, including the properties of the metallic powder and the polymeric substrates, as well as the spraying parameters set for the process, it is currently impossible to accurately predict how the metallic particles will behave when they impact on various substrates.

For this reason, several computer models have been developed recently to mimic the Cold Spray process' operational parameters and predict how a particle would behave when it comes in touch with a substrate [4-6]. The coating process utilized on polymers and composites, however, has only been the subject of a small number of publications published so far. A physical model that could precisely depict the processes that occurred when metallic particles were deposited on non-metallic substrates, however, was not practical to develop. In order to validate those models, it would be necessary to gather hundreds of testing scenarios and outcomes utilizing top-of-the-line tools (including sensors and high-speed cameras).

In this scenario, machine learning might potentially reduce the number of required experimental trials. As machine learning (ML) solutions are typically considered "black boxes," in order to have accurate forecasts, it is necessary to feed the model with accurate and numerous data. For this reason, training the model with a mix of experimental data, which are accurate but often scarce and fragmented, and computational data obtained from Finite Element models (FEM), which do not suffer from the issues of experimental data but are less accurate, could be a good solution to obtain accurate predictions of the coating characteristics.

With knowledge of the process parameters, particles and substrate characteristics, a machine-learning approach is used to forecast the deformation and flattening of the metallic particles after deposition.

Using low-pressure equipment, 30% of the data from the training set and the entire test set were collected experimentally, employing SEM analyses to determine the flattening and penetration depth.

The remaining test dataset was produced by performing a FE simulation of copper, aluminium, steel and particles collision upon PEEK and ABS-based polymeric substrates. Three best Machine Learning models have been selected: Linear regression, Gaussian process regression and Neural networks. In order to provide a methodological approach for future studies, a comparison of the results obtained with a dataset entirely composed of data obtained from the FE model and of the results obtained with the dataset composed of a mix of experimental and FEM data is proposed.

Materials and Methodologies

Input and output parameters**.**

The input parameters for the employed strategies fall into three macro-categories: impact velocity, which includes all the other process parameters such as temperature and pressure; *powder parameters* (Yp), which represent the yield strength of the powder material and *parameters of the substrate* (Ys), i.e. the yield strength of the substrate material, which also takes into account the presence of the fibres since these, if positioned appropriately under a layer of matrix at least comparable to the size of the powders, only stiffen the substrate, thereby causing a variation of the yield strength. The considered output parameters are the *penetration depth* of the particle and the *flattening*. The definition and evaluation of both parameters is furtherly illustrated in the following sections.

Dataset.

As highlighted in the introduction, the datasets employed were constructed employing both FEM and experimental data. In particular, the first training dataset is composed of 30% experimental data and 70% FEM data (mixed data), while the second dataset contains only FEM data. The test dataset for both suggested models is fully made up of experimental data.

CS experimental input data generation.

The substrate selected for the deposition was Polyether-ether-ketone (PEEK) and Acrylonitrile butadiene styrene (ABS), both unreinforced and reinforced with long carbon fibres.

The copper, aluminium and steel spherical powders were provided by LPW South Europe. Low-pressure cold spray equipment (DYCOMET) was used to conduct the aforementioned depositions.

Air was used as the carrier gas since earlier research found no discernible changes when other carrier gases were used [7–9]. The samples were positioned on a platform, and the spraying gun was installed on a robot (HIGH-Z S-400/T-CNC-Technik) and operated remotely while operating perpendicular to the substrates. The process parameters employed and the characteristics of the powders employed for the experiments are highlighted in Table 1.

Table 1. Characteristics of the powders and process parameters employed for the CS experiments.

Particle parameters	***Copper***	***Aluminium***	***Steel***
Mean radius [μm]	20	18	23
Yield strength (Yp) [GPa]	0.033	0.18	0.29
Process parameters			
Inlet Gas temperature [°C]	100 - 400	100 - 400	100 - 400
Standoff distance [mm]	10 - 4	10 - 4	10 - 4
Inlet gas pressure [MPa]	0.5 - 0.6	0.5 - 0.6	0.5 - 0.6
Gun traverse speed [mm s^{-1}]	7.5	7.5	7.5

For the purpose of measuring the flattening of the powders, the top surface of the coating was examined. The mean radius of the particles after the collision with the substrate (r) was measured using Image J software to calculate the percentage of particle flattening, defined as $r/r_0\ [\%] = \frac{(r-r0)}{r0}100$, where r_0 is the mean radius of the particle before the impact. The flattening values taken into account are the average flattening values calculated on three separate 500x500 micron micrographs that were examined. In order to evaluate the radius before and after the impact, SEM micrographs were analyzed through the Image J software, as portrayed in Fig.1.

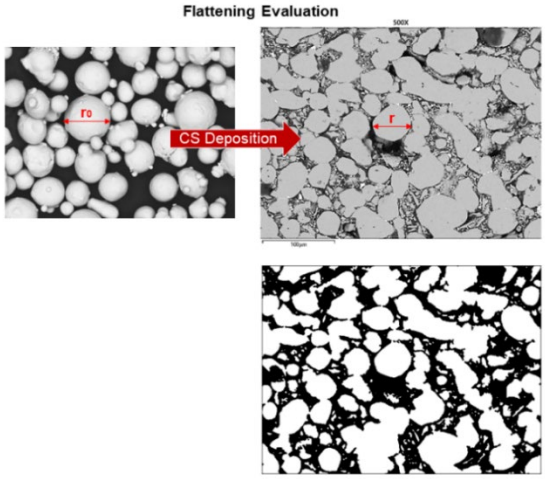

Fig. 1. Evaluation of the particles' mean radius before (r_0) and after the deposition (r).

To measure the penetration depth, the specimens were cut perpendicular`r to the top surface to inspect the cross-section and evaluate the height of the particle upon the impact [Hs0]. The penetration depth was defined as $Hs\,[\%] = \frac{(Hs_0 - Hs)}{Hs}\,100$. The specimen cross section was analysed in order to evaluate the height of the particle after the impact, SEM microscopy was employed as shown in Fig 2.

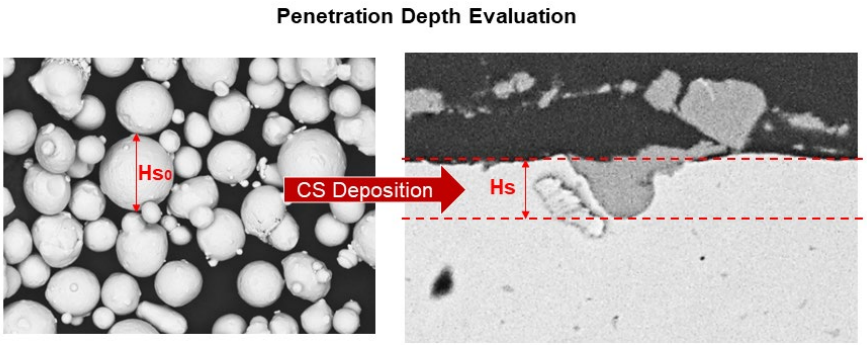

Fig. 2. Evaluation of the particles' mean height before (Hs_0) and after the deposition (Hs).

FEM input data generation.

A Lagrangian reference frame, which is frequently utilized in literature to represent high-velocity impact with minimal computing expense, was employed to model both the particle and the substrate. Using a 2D-axisymmetric model and an explicit dynamic analysis that took into account adiabatic heating effects, it was possible to simulate a spherical particle hitting perpendicular to a substrate that is at least five times bigger than the particle. This particle-to-substrate size ratio was determined by assuming that the elastic waves reflected from the boundaries did not reach the interface upon impact.

In keeping with the average particle size of the powder utilized for the experimental tests, a particle diameter of 20 microns was used for the simulation. The features of the substrate and the particles have been identified via earlier experiments using the supplies on hand at the testing site.

The Johnson-Cook model for plastic materials was used to model the behaviour of both the particle and the substrate's materials, and one of the ABAQUS software's algorithms—the surface-to-surface penalty contact algorithm—was used to model the interaction between the substrate and the impacting particle. The impact simulations were performed for each material combination (copper, aluminium, 316L steel, on PEEK and ABS) by varying the particle's speed between 50 m/s and 350 m/s with an increasing step of 30 m/s. The model generated 50 different values for the particle's penetration and flattening ratio depending on the input parameters.

ML Approaches and Performance Evaluation

We used three machine learning approaches: Linear regression (LR) Gaussian process regression (GPR) and Neural networks (NNs). LR is a simple method for determining a linear relationship between variables. This relationship illustrates the functional connection between the independent and dependent variables for a specific dataset. Consequently, LR models the unknown or dependent variable and the known or independent variable as a linear equation [10].

GPR is a nonparametric Bayesian method used for regression [11]. It performs well on small datasets and it infers a probability distribution model over all acceptable data-fitting functions. The neural network employed is a function-fitting neural network with three layers which is trained on the whole dataset. It can generalize an input-output relationship after training the data.

In order to evaluate the performance of the ML approaches, we calculated the Root-mean-square error (RMSE) [11], the R-Squared [12], the Mean Squared Error (MSE) [13] and Mean Average Error (MAE) [14].

RMSE is the square root of the squared mean error and is an outlier-sensitive metric.

R-squared is a linear regression model goodness-of-fit metric which represents the proportion of the variance in the dependent variable explained by the independent variables. R-squared measures the strength of the association between the model and the dependent variable.

The MSE indicates the mean squared discrepancy between the observed data values and the estimated data values.

MAE represents the distance between the predicted value and the measured value. When the values of these metrics are low, the model is more accurate.

Results and Discussion

In this section, the experimental results on the FEM dataset and the mixed dataset (FEM and experimental data) will be shown and discussed. Below are the best findings from each experiment.

Experiments with FEM-based dataset.

Observing the output by training the model with FEM data, it was possible to assess that the best models on the test set for penetration and flattening prediction were the forecast obtained with the GPR method (see Fig.3 and Fig.4). More specifically, the GPR model shows improved the penetration values and a decline in flattening performance. To comprehend this decline in flattening model evaluation metrics, further studies need to be conducted.

Penetration depth prediction (GPR)	
RMSE	1.45
R-Squared	0.73
MSE	2.1026
MAE	0.7654
Prediction Speed	~2200obs\sec

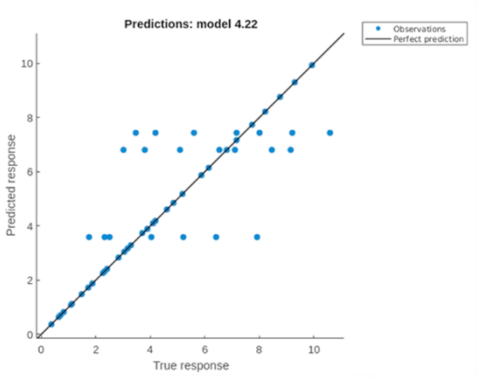

Fig. 3. Performance for the penetration depth prediction for FEM data.

Flattening prediction (GPR)	
RMSE	4.7387
R-Squared	0.34
MSE	22.451
MAE	2.0051
Prediction Speed	~1900obs\sec

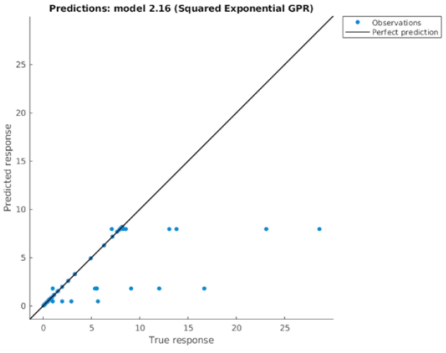

Fig. 4. Performance for the flattening prediction for FEM data.

Since the error values are quite small, we may conclude that the FEM models are capable of approximating the experimental data fairly correctly. In this context, machine learning can be an excellent tool for accelerating finite element analyses, which require a high computing cost. For this reason, machine learning may be used to simplify the models without losing information or to perform predictions on additional combinations of materials without the need to run additional simulations.

Experiments with dataset MIX.

The top models for the penetration on the test set are NN and LR for the flattening prediction, according to training the model with mixed data, as we can see in Fig. 5 and Fig. 6.

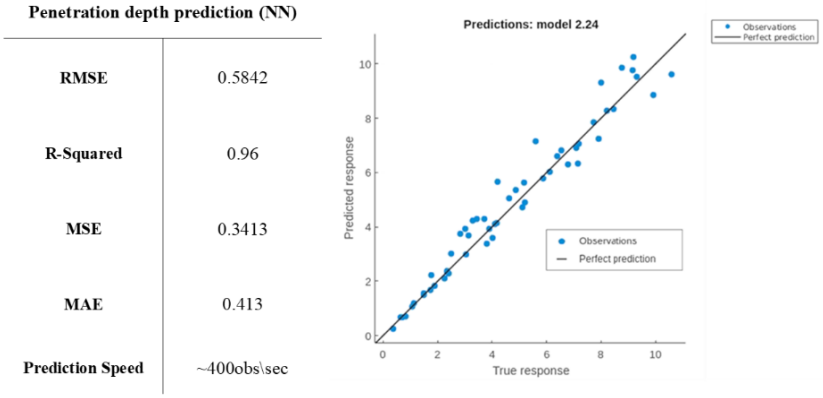

Penetration depth prediction (NN)	
RMSE	0.5842
R-Squared	0.96
MSE	0.3413
MAE	0.413
Prediction Speed	~400obs\sec

Fig. 5. Performance for the penetration depth prediction for mixed data.

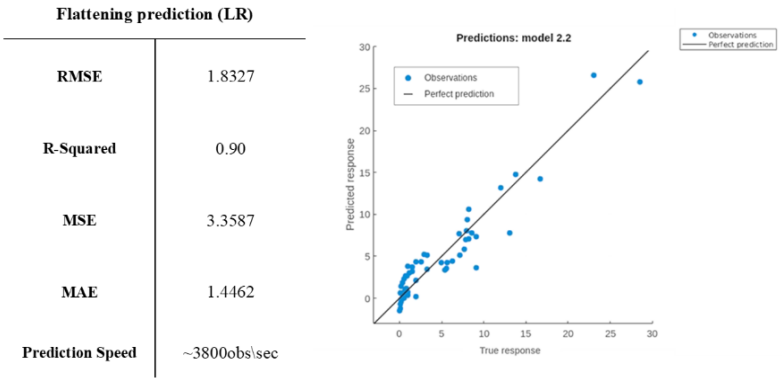

Flattening prediction (LR)	
RMSE	1.8327
R-Squared	0.90
MSE	3.3587
MAE	1.4462
Prediction Speed	~3800obs\sec

Fig. 6. Performance for the flattening prediction for mixed data.

It is possible to observe that by integrating the training set with experimental data, the prediction error may be furtherly lowered. In fact, by including 30% of experimental data in the training dataset, it is possible to obtain more accurate models.

Future investigations are required in order to assess the optimal value of the ratio between the experimental data and the FEM data in the training set, in terms of the accuracy of the prediction and the resources employed to create the dataset. In Fig. 7, we depicted the comparison of performance for penetration and flattening. For penetration, the best results, except for R-Squared, are achieved when the models is trained with mixed data. A similar behaviour is also evident when we consider the flattening output parameter.

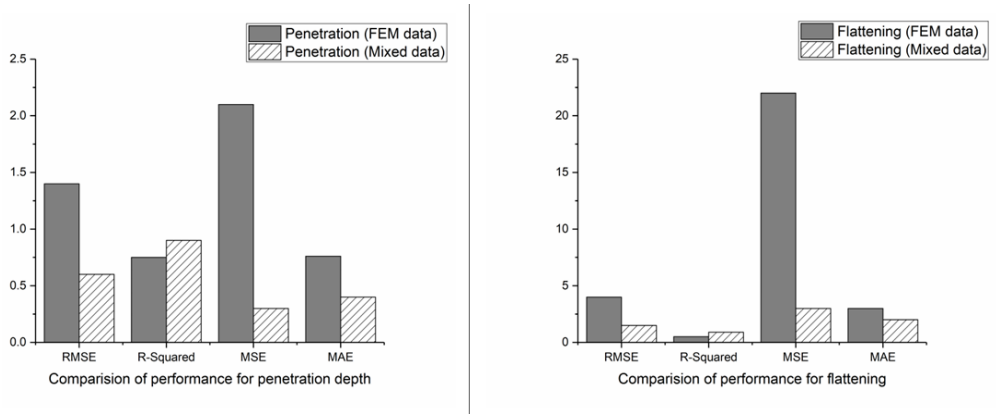

Fig. 7. Performance for penetration and flattening prediction for FEM and mixed data.

Summary

This study provides an overview of how machine learning techniques can be used to more accurately predict particular coating features, such penetration and flattening, in order to increase process efficiency. To be more precise, two sets of data, FEM data and mixed data (experimental and FEM data), were used to test various models, and the best ones—the GPR, LR, and NN—were selected.

The performed experiments show that the models get more accurate as the amount of data available increases. In particular, models fit the data better when trained on the mixed dataset. By providing a preliminary examination of the contribution of the parameters influencing the coating deposition, the use of machine learning appears to contribute to the optimization of the Cold Spray process. Future research can assist expand the dataset required to train the models and forecast the ideal combinations of parameters which will enhance the coating process.

References

[1] V.K. Champagne, The Cold Spray Materials Deposition Process. Fundamentals and Applications, Woodhead Publishing Series in Metals and Surface Engineering, 2007. https://doi.org/10.1533/9781845693787.1

[2] R.C.C. Dykhuizen, M.F.F. Smith, Gas Dynamic Principles of Cold Spray, J. Therm. Spray Techn. 7 (1998) 205-212. https://doi.org/10.1361/105996398770350945

[3] R. della Gatta, A.S. Perna, A. Viscusi, G. Pasquino, A. Astarita, Cold spray deposition of metallic coatings on polymers: a review, J. Mater. Sci. (2021). https://doi.org/10.1007/s10853-021-06561-2

[4] K.-H. Leitz, M. O'sullivan, A. Plankensteiner, T. Lichtenegger, S. Pirker, H. Kestler, L.S. Sigl, CFDEM modelling of particle heating and acceleration in cold spraying Cold Spraying-Technology Principle and Challenges, n.d. Available online: https://www-plansee-com.azureedge.net/fileadmin/user_upload/Plansee_Seminar/PDFs/CFDEM_modelling_of_particle_heating_and_acceleration_in_cold_spraying.pdf. (accessed 31 January 2023). doi:10.1016/j.ijrmhm.2018.02.003

[5] F. Rubino, A. Astarita, P. Carlone, Thermo-mechanical finite element modeling of the laser treatment of titanium cold-sprayed coatings, Coatings 8 (2018) 219. https://doi.org/10.3390/coatings8060219

[6] W.Y. Li, W. Gao, Some aspects on 3D numerical modeling of high velocity impact of particles in cold spraying by explicit finite element analysis, Appl. Surf. Sci. 255 (2009) 7878-7892. https://doi.org/10.1016/j.apsusc.2009.04.135

[7] R. della Gatta, A. Viscusi, A.S. Perna, A. Caraviello, A. Astarita, Feasibility of steel powder deposition on composites through cold spray, Mater. Manuf. Process. 36 (2021). https://doi.org/10.1080/10426914.2020.1832693

[8] A.S. Perna, A. Viscusi, A. Astarita, L. Boccarusso, L. Carrino, M. Durante, R. Sansone, Manufacturing of a Metal Matrix Composite Coating on a Polymer Matrix Composite Through Cold Gas Dynamic Spray Technique, J. Mater. Eng. Perform. 28 (2019) 3211-3219. https://doi.org/10.1007/s11665-019-03914-6
[9] A.S. Perna, A. Viscusi, A. Astarita, L. Boccarusso, A. Caraviello, L. Carrino, M. Durante, R. Sansone, Experimental study of functionalized polymer matrix composite with multi-material metal coatings produced by means of cold spray technology, Key Eng. Mater. 816 (2019) 267-272. https://doi.org/10.4028/www.scientific.net/KEM.813.267
[10] S. Ray, A Quick Review of Machine Learning Algorithms, 2019 International Conference on Machine Learning, Big Data, Cloud and Parallel Computing (COMITCon) (2019) 35-39.
[11] C.E. Rasmussen, Gaussian Processes in machine learning, Lecture Notes in Computer Science (Including Subseries Lecture Notes in Artificial Intelligence and Lecture Notes in Bioinformatics) 3176 (2004) 63-71. https://doi.org/10.1007/978-3-540-28650-9_4/COVER
[12] J. Nevitt, G.R. Hancock, Improving the Root Mean Square Error of Approximation for Nonnormal Conditions in Structural Equation Modeling, J. Exp. Educ. 68 (2010) 251-268. https://doi.org/10.1080/00220970009600095
[13] G.I. Webb, C. Sammut, C. Perlich, T. Horváth, S. Wrobel, K.B. Korb, W.S. Noble, C. Leslie, M.G. Lagoudakis, N. Quadrianto, W.L. Buntine, N. Quadrianto, W.L. Buntine, L. Getoor, G. Namata, L. Getoor, X.J.J. Han, J.-A. Ting, S. Vijayakumar, S. Schaal, L. de Raedt, Encyclopedia of Machine Learning, Encyclopedia of Machine Learning. (2010) 613-624. https://doi.org/10.1007/978-0-387-30164-8_488
[14] J. Fürnkranz, P.K. Chan, S. Craw, C. Sammut, W. Uther, A. Ratnaparkhi, X. Jin, J. Han, Y. Yang, K. Morik, M. Dorigo, M. Birattari, T. Stützle, P. Brazdil, R. Vilalta, C. Giraud-Carrier, C. Soares, J. Rissanen, R.A. Baxter, I. Bruha, R.A. Baxter, G.I. Webb, L. Torgo, A. Banerjee, H. Shan, S. Ray, P. Tadepalli, Y. Shoham, R. Powers, Y. Shoham, R. Powers, G.I. Webb, S. Ray, S. Scott, H. Blockeel, L. De Raedt, Mean Absolute Error, Encyclopedia of Machine Learning. (2011) 652-652. https://doi.org/10.1007/978-0-387-30164-8_525

Materials Research Proceedings 28 (2023) 65-74 https://doi.org/10.21741/9781644902479-8

Process-dependent material characteristics of DMLS-manufactured specimens

ZETTEL Dominic[1,2,a *], BREITKOPF Piotr[2,b], NICOLAY Pascal[1,c] and WILLMANN Roland[1,d]

[1]Carinthia University of Applied Sciences (CUAS), research group AMAViS[2] and CiSMAT Europastraße 4, 9524 Villach, Austria

[2]Université de Technologie de Compiègne (UTC), Laboratoire Roberval FR3272, CS 60319 60203 Compiègne Cedex, France

[a]d.zettel@cuas.at, [b]piotr.breitkopf@utc.fr, [c]p.nicolay@cuas.at, [d]r.willmann@cuas.at

Keywords: Direct Metal Laser Sintering, Strengthal, Thermal Conductivity, Microstructure

Abstract. Direct metal laser sintering is a 3D-printing technology involving a multitude of physical phenomena requiring the fine-tuning of multiple parameters (e.g., laser power, layer thickness) to achieve satisfying fabrication results [1]. Modifying each of these parameters can significantly influence the resulting material characteristics of the fabricated parts [2]. This work investigates the impact of the modification of the process parameters on the material characteristics of hardened aluminum specimens. A design of experiments was used to fabricate 85 aluminum specimens using 17 printing parameter sets. The specimens' dimensional accuracy, surface roughness, hardness, density, porosity, and thermal conductivity were investigated. Standardized, as well as self-designed test setups were used for this purpose. Furthermore, porosity measurements and microstructural investigations were performed using scanning electron microscopy and reflected light microscopy.

Introduction

Direct metal laser sintering (DMLS) is a well-known manufacturing technique that fabricates metallic structures following the layer-by-layer deposition principle. The metallic powder is selectively melted by a high-energy laser beam, following instructions from a 3D-CAD model (STL format). The solidification of tiny melt pools generated along the laser tracks create strong bonds between the different layers [3].

Due to the high process complexity of DMLS, every alloy requires tailor-made printing parameters ("standard parameter sets") to achieve maximum part density. Each parameter (e.g., hatch distance) can indeed influence one or several of the involved physical phenomena during printing (e.g., powder bed formation, fluid dynamics of the molten pool, solidification, residual stresses, heat absorption), resulting in strongly differing micro- and mesostructures [4]. It is also possible to modify these parameters to adjust the material characteristics of the fabricated structures (e.g., porosity). Furthermore, this can achieve parts with specific material characteristics (e.g., mechanical strength, thermal conductivity, damping capacity). However, to adjust the properties as desired, it is necessary to study all the involved phenomena, their mutual influence and their impact on the solidified micro- and mesostructure.

In this paper, we present the results of our work aimed at determining the influence of the main DMLS process parameters on the material properties of manufactured parts. We followed a design of experiments (DoE) methodology, and fabricated 85 specimens with 17 different sets of printing parameters (5 specimens per parameter set). The material characteristics (dimensional accuracy,

Content from this work may be used under the terms of the Creative Commons Attribution 3.0 license. Any further distribution of this work must maintain attribution to the author(s) and the title of the work, journal citation and DOI. Published under license by Materials Research Forum LLC.

surface roughness, hardness, density, porosity, and thermal conductivity) were then investigated using professional and self-designed tools.

Method and Material

The process regarding the development, fabrication, and characterization of aluminum specimens with different material characteristics is schematically shown in Fig. 1.

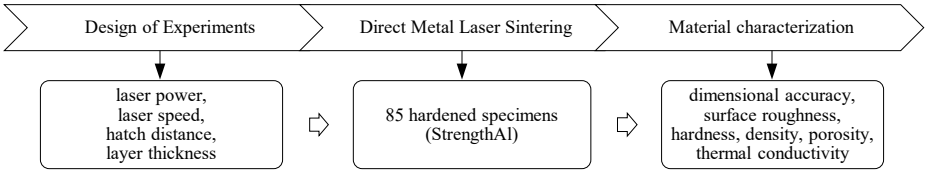

Fig. 1. Process for investigating the material characteristics of aluminium specimens fabricated with different printing parameter sets.

Design of Experiments. A DoE was performed, using the following variable parameters: laser power (P) [W], laser speed (v) [mm/s], hatch distance (h) [mm], and layer thickness (t) [mm]. The full factorial design (4 factors, 2 levels) results in 16 experiments with different energy densities (E) [J/mm³] given by:

$$E = \frac{P}{v \cdot h \cdot t} \quad (1)$$

To detect non-linear dependencies between factors, we added the "center point" experiment corresponding to the average values of parameters.

The specimens had the shape of rectangular solids (12*12*75 mm³), directly attached to the build platform without a support structure. Each printing parameter set from the DoE (17) was used five times. We, therefore, fabricated 85 specimens in total. The powder material is "StrengthAl" from the company m4p GmbH, a hardenable high-strength aluminum alloy consisting of Aluminum (main alloying element), Magnesium, Silicon, Scandium, Titanium, Zirconium, Manganese, and Chrome [5].

Direct Metal Laser Sintering. The fabrication of the specimens was executed with an EOS M290 printing system with a build volume of 250*250*325 mm³ and a 400 W Yb-fiber laser (spot size 100µm). A ceramic blade (hard recoating) was used for the powder recoating, and Argon as an inert gas. The platform temperature was set to 180°C. The exposure sequence of the specimens was directed against the gas flow to keep the concentration of impurities as low as possible. The "stripes" exposure pattern was used (stripe width 7 mm), and the rotation angle was set to 67°.

The specimens were hardened afterward (precipitation hardening – 6 hours, 350°C, slow cooling in the air). Machining (milling, turning) was then performed on the specimens to achieve proper test geometries.

Material characterization. One set of specimens (17 different printing parameter sets) was used for microstructural investigations and porosity measurements via scanning electron microscopy (SEM) (JSM-IT500 – JEOL) and reflected light microscopy (RLM) (Axio Imager.M2m – Zeiss). The specimens were embedded in cold embedding resin (CEM 1000 Blue Pulver) with subsequent grinding and polishing operations (Silicon Carbide paper – grain size P1200, diamond suspension – grain size 3 µm, Silicone Dioxide suspension – grain size 0.05µm). The metallographic specimens were then further treated with a Keller-Wilcox etchant.

The four remaining sets of specimens (4x17 specimens) were used to investigate the specimens' dimensional accuracy, surface roughness, hardness, density, porosity, and thermal conductivity. All tests were performed at room temperature (20°C).

Material Characteristics

Dimensional accuracy.

The dimensional inspection of the specimens (as-build) was executed using an outside micrometer (Micromar 40 ER – Mahr) with a resolution of 0.001mm. Both side lengths of the quadratic specimens were measured ten times (20 measurements per specimen). The dimensions as a function of the applied energy density are shown in Fig. 2.

There is quite a large dispersion in the measurement results (the standard deviation is high, for a given energy density, but there is also significant variability depending on the energy density: 11.906 – 12.433 mm). This phenomenon is at least partly due to the increase in the size of the melt pools when the energy density increases. Bigger melt pools also tend to aggregate more particles on the edges of the test specimens. It can be seen, however, that specimens fabricated with the same energy density but with different printing parameter sets (e.g., 112.23 J/mm³) show differences regarding their dimensions (red circles vs. black crosses).

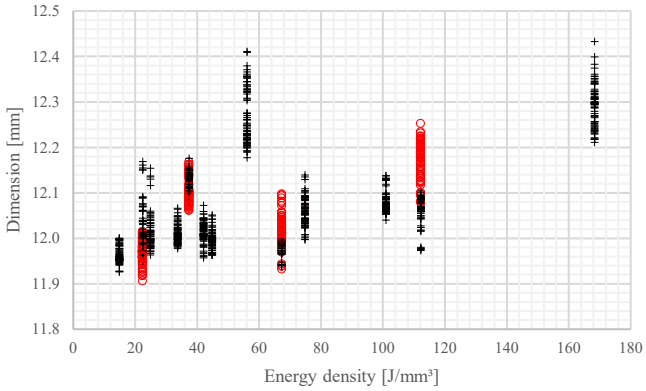

Fig. 2. Dimensional accuracy of printed specimens as a function of the applied energy density.

Surface roughness.

The surface roughness of the specimens (as-build) was measured using a perthometer (MarSurf GD25 – Mahr). Each side of every specimen was measured twice (8 measurements per specimen). The arithmetic average roughness (R_a), the average peak-to-valley profile roughness (R_z), and the maximum peak-to-valley profile height (R_{max}) as a function of the applied energy density are shown in Fig. 3.

The graph shows a correlation between the applied energy density and the surface roughness. The surface roughness slowly increases with the applied energy density, partly due to the increase of the size in the melt pools. Indeed, more particles adhere on the edges of bigger melt pools, which results in rougher surfaces. However, the energy density partly explains the observations. Specimens fabricated with the same energy density but with different printing parameter sets (e.g., 112.23 J/mm³) may not have the same surface roughness (red vs. black).

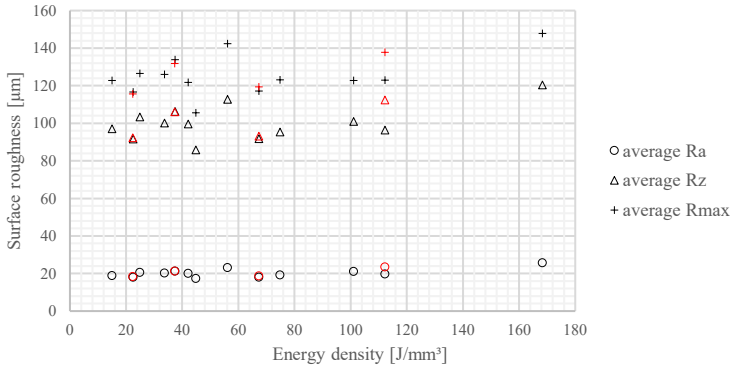

Fig. 3. Surface roughness of printed specimen as a function of the applied energy density.

Hardness.

The hardness testing of the specimens (milled) was performed using a universal hardness testing machine (ZHU 187.5 – ZwickRoell). Here, the Vickers hardness (HV) was measured using a diamond pyramid with an angle of 136° and a test force of 98.07 N. Each side of every specimen was measured twice (8 measurements per specimen). The HV as a function of the applied energy density is shown in Fig. 4.

The range of variation of the measurement results is extensive (46.2 – 163.1HV). The results show that the hardness increases to a certain energy (~70J/mm³). It then decreases again. This phenomenon is a consequence of the different printing parameter sets (different energy inputs) in combination with the subsequent hardening process. In the case of DMLS parts, hardening ("solution heat treatment") already occurs during the fabrication process when the melt pools quickly cool down. The second annealing step, called "aging treatment" still has to be performed afterward. Therefore, the solution heat treatment varies due to the different energy inputs of the printing parameter sets. Besides, specimens fabricated at lower energy densities show a more significant standard deviation in the measurement results than those fabricated at higher energy densities due to differences in the resulting porosity. The probability of hitting a (hidden) pore with the indenter is much higher in a porous material than in a more homogeneous one (the porosity increases when the energy density decreases, as shown later in this paper). It can also be seen that specimens fabricated with the same energy density but with different printing parameter sets (e.g., 112.23 J/mm³) show differences regarding their hardness (red circles vs. black crosses).

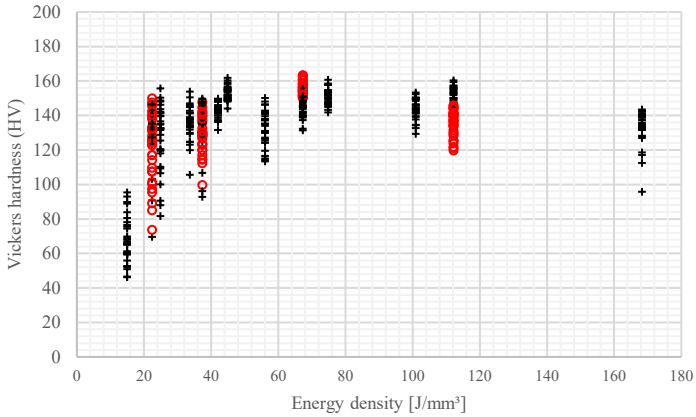

Fig. 4. Vickers hardness of printed specimens as a function of the applied energy density.

Density. The density (ρ) [g/cm³] of the specimens (milled) was determined according to:

$$\rho = \frac{m}{V} \quad (2)$$

where m [g] is the mass, and V [cm³] is the volume of the specimens. The specimens' weight was measured using a high-precision scale (AG204 DeltaRange - Mettler Toledo) with a resolution of 0.0001g. The specimens' volume was calculated using the dimensional inspection's measured volume. The density as a function of the applied energy density is shown in Fig. 5.

The range of variation of the measurement results is wide (2.21 - 2.65 g/cm³). The density significantly increases up to an energy density of about 30 J/mm³ and stays more or less constant above this point. There are no significant differences between specimens fabricated with the same energy density but different printing parameter sets (e.g., 22.45 J/mm³, red circles vs. black crosses).

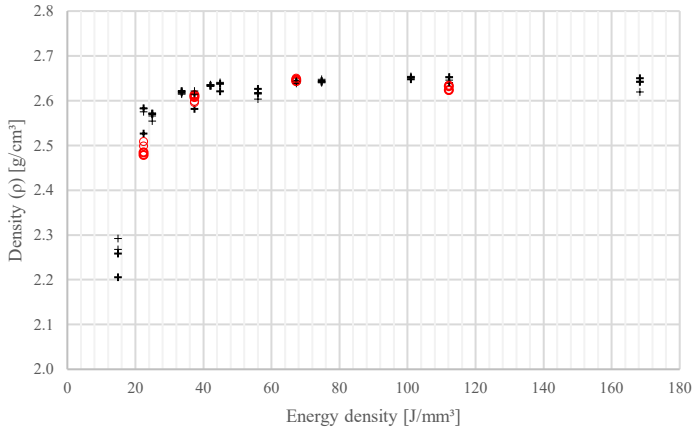

Fig. 5. Density of printed specimens as a function of the applied energy density.

Porosity and microstructure.

The porosity (pore size and pore size distribution) of the 17 metallographic specimens was measured using RLM and image processing software (ZEN core – Zeiss). The average total pore area in percent as a function of the applied energy density is shown in Fig. 6.

The range of variation of the measurement results is large (0.04 – 21.16%). The porosity significantly decreases for an energy density below 30 J/mm³. It stabilizes around 30 J/mm³ before slightly increasing for higher energy densities (>110 J/mm³). Specimens fabricated with the same energy density but with different printing parameter sets (e.g., 22.45 J/mm³) show differences regarding the average total pore area (red circles vs. black crosses).

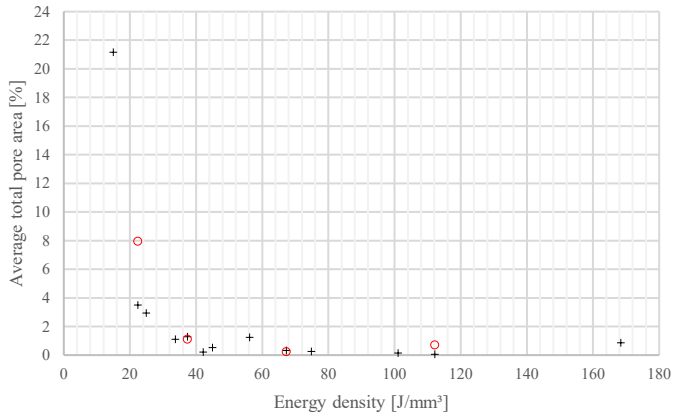

Fig. 6. Average total pore area of specimens as a function of the applied energy density.

The structure of the 17 metallographic specimens was further investigated using RLM and SEM. In this paper, we compare two specimens, the one with the lowest porosity (0.04%), and the one with the highest porosity (21.16%).

At first, the metallographic specimens (polished, not etched) were investigated using RLM, as shown in Fig. 7. Here, the different porosities are noticeable (Fig. 7, A vs. Fig. 7, B). A closer look at the porous structure (Fig. 7, B) shows that the pores are homogeneously distributed throughout the entire geometry. Due to irregular cooling rates (which depend on the build height and geometry of the printed part), DMLS parts can have an inhomogeneous microstructure with anisotropic material characteristics [6]. In our case however, the build height did not appear to influence the pore size and pore size distribution.

The metallographic specimens (polished, not etched) were further investigated using SEM, as shown in Fig. 8. Here, a magnification of 50 was used. The pictures clearly show the differences between the specimens regarding porosity. In the image of the porous structure (Fig. 8, B), fine powder particles that were not melted during the print job are still visible. There are significant differences in the size and shape of the pores. Also, note that the build direction cannot be detected from the pictures.

The metallographic specimens were etched to investigate them via RLM further, as shown in Fig. 9. Now, the typical laser beam tracks due to the layer-wise manufacturing principle of DMLS are visible. Fine powder particles are again apparent in Fig. 9, B. Splashes or inclusions could not be detected.

In addition, Energy Dispersive X-ray Spectroscopy (EDX) was used to investigate the distribution of alloy elements in three different specimens (porosities: 0.23%, 1.11%, and 21.16%). The results show that Aluminum (the main alloy element) and Magnesium are homogeneously distributed, also around pores. The remaining alloy elements (Silicon, Scandium, Titanium, Zirconium, Manganese, and Chrome) could not be detected due to the detection limit of the EDX apparatus (0.2% by mass) (JSM-IT500 – JEOL).

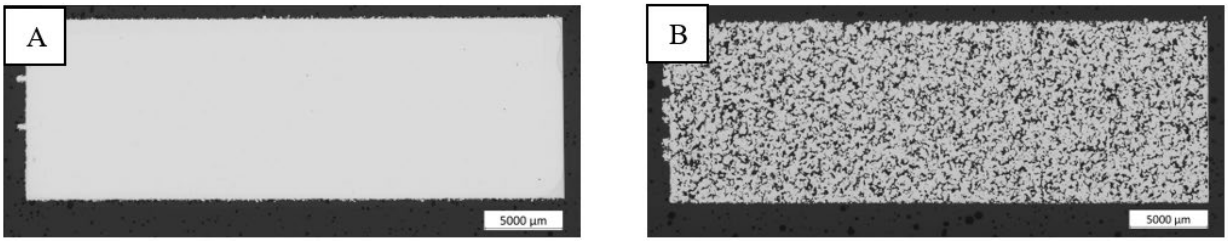

Fig. 7. RLM images of metallographic specimens showing different porosities (polished, not etched). A: dense structure fabricated with 112.23 J/mm³. B: porous structure fabricated with 14.96 J/mm³.

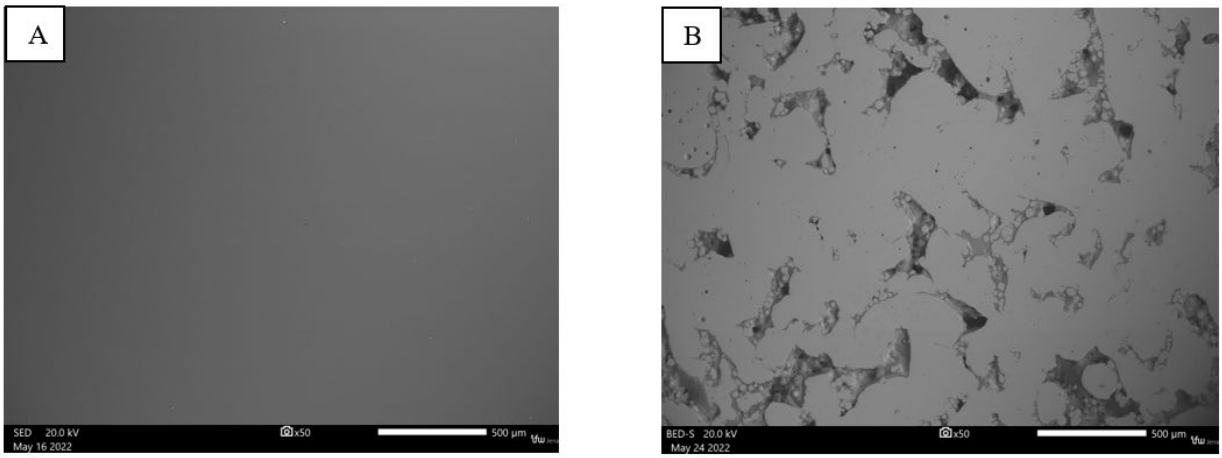

Fig. 8. SEM images of metallographic specimens showing different porosities (polished, not etched, magnification 50x). A: dense structure fabricated with 112.23 J/mm³. B: porous structure fabricated with 14.96 J/mm³.

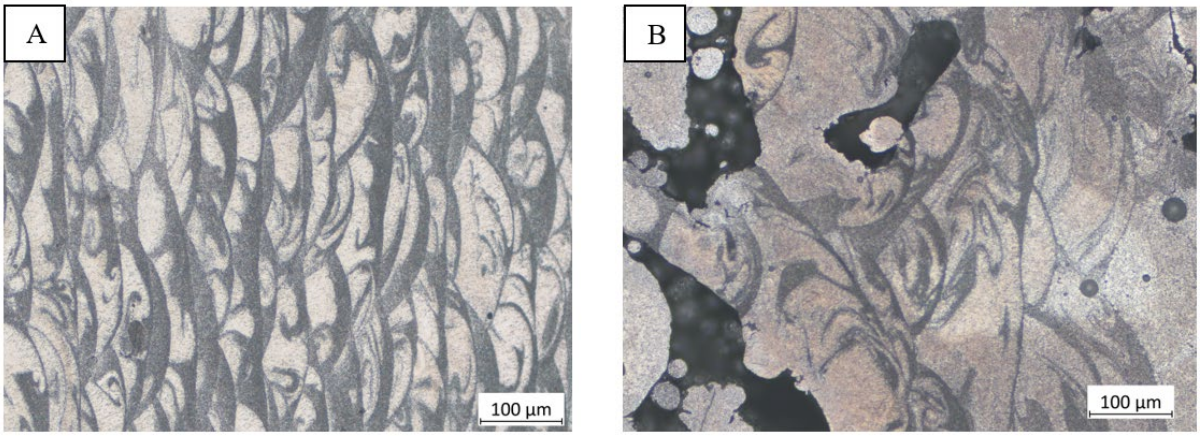

Fig. 9. RLM images of metallographic specimens showing different porosities (polished and etched). A: dense structure fabricated with 112.23 J/mm³. B: porous structure fabricated with 14.96 J/mm³.

Thermal conductivity. The specimens' thermal conductivity was measured using a self-designed test setup consisting of a hot plate (50°C) and a cold plate (0°C). On both plates, flux sensors are installed to measure the heat flux. PT1000 sensors are attached to each side of the specimens to measure the temperature gradient, as illustrated in Fig. 10.

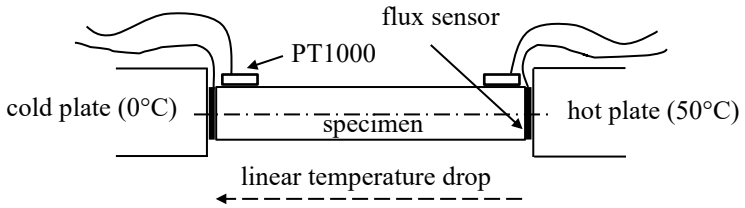

Fig. 10. Schematics of the self-designed test set-up used to measure the thermal conductivity of the fabricated samples.

The sensors are connected to an Arduino board, and digital tabletop multimeters are connected to a computer. The measured values are then used to calculate the thermal conductivity (λ) [W/mK] in Matlab (MathWorks) using:

$$\lambda = \frac{\phi \cdot x}{\Delta T \cdot A} \tag{3}$$

The heat flow (Φ) is obtained by:

$$\phi = \frac{Q}{t} \tag{4}$$

where (Q) [J] is the heat flux, t [s] is the time, x [m] is the length of the specimen, ΔT [K] is the temperature gradient between the two PT1000 sensors, and A [m^2] is the surface area of the specimen extremities in direct contact with the flux sensors.

We verified the validity of the measurements using a series of reference measurements using a known material with a thermal conductivity of 180 W/mK. All measurement results were located between 189.5 W/mK (5,3%) and 95.6 W/mK (4.4%). The average value for all 20 measurements was 179.02 W/mK.

Every printed specimen was measured five times. The measurement time was 180s. Fig. 11 and 12 show the thermal conductivity as a function of the applied energy density and the porosity.

Fig. 11 shows a wide range of variations in the measurement results (48.78-112.39 W/mK), probably due to substantial porosity variations between the different specimens, as shown in Fig. 12.

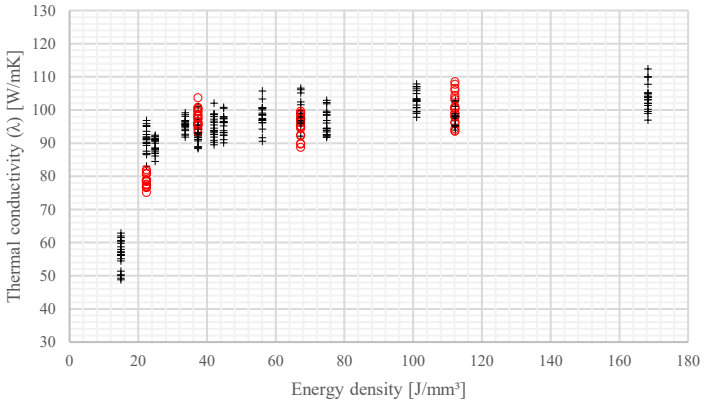

Fig. 11. Thermal conductivity of printed specimens as a function of the applied energy density.

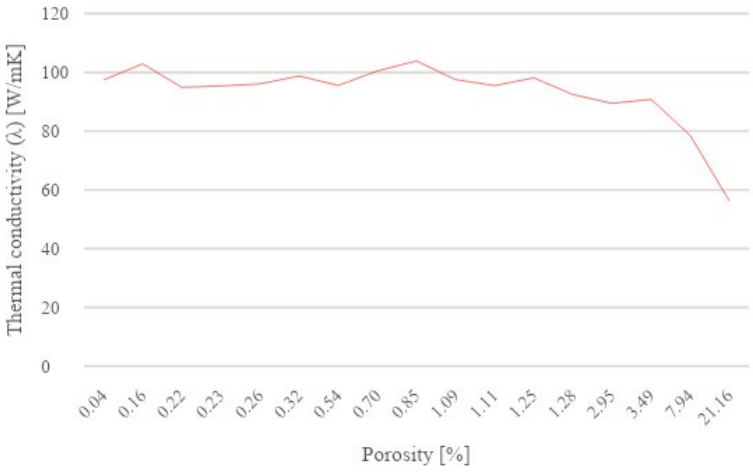

Fig. 12. Thermal conductivity of printed specimens as a function of the porosity.

Summary

An EOS M290 printing system was used to fabricate 85 aluminum specimens (StrengthAl) with 17 printing parameter sets, following a DoE approach (5x17 specimens). The modified printing parameters are the laser power (P) [W], laser speed (v) [mm/s], hatch distance (h) [mm], and layer thickness (t) [mm]. The specimens were then hardened (precipitation hardening) for 6 hours at 350°C with slow cooling in air. The specimens' dimensional accuracy, surface roughness, hardness, density, porosity, and thermal conductivity were then measured using professional tools and a self-designed test setup. Microstructural investigations were also performed using RLM and SEM.

The results show that changes in the process parameters (P, v, h, t) strongly affect the material characteristics, and while some variations follow visible trends, the energy density alone does not fully explain them. The hardening process also has an influence. Further work is required to better understand the physical mechanisms active during the formation and solidification of the melt pool.

Acknowledgement

This work was conducted in the frame of research cooperation between the research group Additive Manufacturing in Agile Virtual Systems for Product Design and Production Process Design (AMAViS^2), the Carinthia Institute for Smart Materials (CiSMAT), and the Laboratoire ROBERVAL of the Université de Technologie de Compiègne (UTC). AMAViS^2 and CiSMAT belong to the Carinthia University of Applied Sciences (CUAS). The work was mainly funded by AMAViS^2.

References

[1] J. Oliveira, A. LaLonde, J. Ma, Processing parameters in laser powder bed fusion metal additive manufacturing, Mat. & Design 193 (2020) 1-12.
[2] B.S. Rao, T.B. Rao, Effect of process parameters on powder bed fusion maraging steel 300: a review, Lasers Manuf. Mater. 9 (2022) 338-375. https://doi.org/10.1007/s40516-022-00182-6
[3] M.N. Jahangir, M.A.H. Mamun, M.P. Sealy, A review of additive manufacturing, AIP Conf. Proc. 1980 (2018), https://aip.scitation.org/doi/abs/10.1063/1.5044305
[4] T. Moges, G. Ameta, P. Witherell, A review of model inaccuracy and parameter uncertainty in laser powder bed fusion models and simulations, J. Manuf. Sci. Eng. 141 (2019) 1-14. https://doi.org/10.1115/1.4042789

[5] m4p material solutions GmbH, "www.metals4printing.com," 2022. Available: https://www.metals4printing.com/wp-content/uploads/datasheets/eng/Al-Base/m4p_Datasheet StrengthAl_EN.pdf. (accessed 02 May 2022).
[6] Z. Çağatay Öter, Anisotropic Mechanical Behavior of Direct Metal Laser Sintering (DMLS) Parts 3rd International Porous and Powder Materials Symposium (2017), Turkey.

Materials Research Proceedings 28 (2023) 75-84 https://doi.org/10.21741/9781644902479-9

Development of a new method utilizing semi-solid aluminum wires for extrusion based additive manufacturing

NEZIC Nikola[1,a *], SPETH Marco[1,b], ROUVEN RIEDMÜLLER Kim[1,c] and LIEWALD Mathias[1,d]

[1] Institute for Metal Forming Technology (IFU), University of Stuttgart, Holzgartenstraße 17, 70174 Stuttgart, Germany

[a]nikola.nezic@ifu.uni-stuttgart.de, [b]marco.speth@ifu.uni-stuttgart.de, [c]kim.riedmueller@ifu.uni-stuttgart.de, [d]mathias.liewald@ifu.uni-stuttgart.de

Keywords: Wire-Feed Additive Manufacturing, AlSi7Mg, Semi-Solid Processing

Abstract. In the field of additive manufacturing (AM) technologies, the development of metal-based extrusion processes constitutes a significant industrial trend in the recent years. Respective processes are differentiated into powder bed, powder-fed and wire-fed depending on the used feedstock. Among those, powder-fed AM represents the most widely used approach, despite its physical limitations leading to intense thermal gradients and an uncontrollable defective microstructure of produced parts. In this context, extrusion-based AM using a wire semi-finished product in the semi-solid state offers a novel alternative for the direct processing of metallic alloys, avoiding the limitations mentioned. For this reason, a new method for consecutive extrusion of semi-solid AlSiMg aluminum wires has been developed at the Institute for Metal Forming (IFU, Stuttgart, Germany), particularly investigating the influence of the material´s microstructure on the process result. By modifying microstructure via heat treatment, a specific modification of the rheological material behavior can be achieved in terms of a pronounced shear-thinning characteristic, thus systematically affecting extrusion and deposition. First, an experimental setup for continuously extruding semi-sold aluminum wires was realized. Subsequently, experimental investigations were carried out on the extrusion of aluminum wires prepared via the strain induced melt activated (SIMA) process as well as untreated aluminum wires, using a conductively heated printhead concept. The objective was to determine process parameters necessary for successful extrusion and deposition of the modified aluminum material as well as the final proof of concept regarding a specific transformation of the material´s microstructure during the extrusion process.

Introduction

Additive manufacturing (AM) represents one of the most rapidly advancing manufacturing technologies in recent decades and has a particular importance for various industrial sectors, for example in the field of product design, automotive engineering as well as aerospace and bio-medical technology [1,2]. In this context, especially AM of metals has become substantial for producing industries. The AM processes applied here are categorized according to the raw material and the energy source used. In terms of the raw material, a distinction is made between powder bed, powder-fed and wire-fed processes. The energy sources used to melt the raw material as rapidly as possible include electron beam, laser or electric arc [3]. However, such AM processes still suffer from a wide variety of technological disadvantages. Due to the high energy input during the production of metallic AM parts, for example, complex thermal gradients can occur in the workpiece's volumes, leading to defects such as porosity, lack of fusion, part distortion, cracks and delamination [4]. In addition, especially powder bed-based melting or sintering methods entail high production costs and a long process duration [5].

Against this background, recent studies in the field of Additive Manufacturing (AM) focus on the development of a wire fed semi-solid AM process route. Wire as feedstock offers some significant

Content from this work may be used under the terms of the Creative Commons Attribution 3.0 license. Any further distribution of this work must maintain attribution to the author(s) and the title of the work, journal citation and DOI. Published under license by Materials Research Forum LLC.

advantages based on the simpler process set up and higher deposition rate in contrast to powder resulting in a shorter process duration on the one hand and overall reduced equipment and production costs on the other hand [6]. The general process methodology based on wire as a feedstock involves heating the material into semi-solid state inside of the print head as well as a subsequent deposition in layers onto a print bed, similar to conventional fused deposition modeling (FDM) with plastics. Thereby, the direct processing of metallic alloys in the semi-solid state can be achieved through the specific control of the microstructure present in the material and therefore the resulting rheological behavior. The pronounced shear-thinning characteristic of semi-solid metals with a globular microstructure enabling the production of three-dimensional structures due to a low viscosity during extrusion and a dimensional stability of the deposited material [7].

Initial investigations in the field of semi-solid AM have been done in respect to the processing of low melting lead alloys, showing the general feasibility of this approach [8,9,10]. In the following, the semi-solid extrusion of magnesium alloy wires on a modified FDM-printer was discussed by Lima et al. [11]. Here, focus was put on the transformation of the feedstock material into the required globular microstructure within the print head. For aluminum alloys, first investigations using a conductively heated print head and an Al4018 welding wire were carried out by Herhold [12]. However, due to high friction as well as an inappropriate temperature distribution inside the print head, no satisfying results were obtained. Sharma et al [13] applied a modified print head design utilizing induction heating to temper an iron core and through conductive heat transport thereby the actual aluminum wire that is passed internally. This approach resulted in a steady state extrusion of a four-layer rectangular test piece made of Al5356 wire. Englert et al. [14] adapted the aforementioned inductive heating approach by equipping an extrusion nozzle with a modified induction coil. In the process, though, no cross-section reduction of the wire in the printhead has been implemented, and only continuous heating was realized. In this way, an Al4018 wire could be heated directly within the nozzle to subsequently produce cubic shaped parts. In both cases, however, interactions between the induced magnetic field and the print bed, the deposited part and other components of the machine assembly occurred.

In order to improve the semi-solid wire-fed AM process of aluminum alloys, a deeper understanding of the material behavior during the process is needed. Current state of the art focused on inductive heating of the wire, thereby successful extrusion could be investigated. However, due to the induced electro-magnetic field, interactions with the layered specimen as well as the machine parts could be observed. Additionally, in semi-solid forming normally a solidification pressure is needed, to produce a defect-free microstructure, which is difficult to apply with an inductive heating coil. In this paper the evaluation of viable process parameters for semi-solid additive manufacturing utilizing aluminum wire and a conductive heated print head design is presented, to eliminate the mentioned negative effects of the inductive heating approach. Thereby, an implementation of the specific transformation of the material´s microstructure into the extrusion process itself and the conductive heating design can reduce the overall process complexity, allowing a low-cost production approach.

Material and Methods

Raw material. When additive manufacturing is performed with semi-solid metal wires, particular attention must be paid to the liquid phase content of the material structure, as this crucially influences the continuous extrusion process. Here, low liquid phase contents result into increased extrusion forces and possible clogging of the nozzle, whereas high liquid phase contents enhance the formation of droplets at the nozzle opening. The formation or presence of droplets during extrusion has been referred to as an undesirable factor by several authors [8,12,13] resulting in a reduced accuracy of the manufactured parts. Due to the strong correlation between the processing temperature or rather the liquid phase content associated therewith and the resulting material´s

flow behavior, selection of a suitable aluminum alloy is a key issue. In this regard, suitable metal alloys for semi-solid metal forming processes usually offer following properties:

1. Solidification range (ΔT), defined as the temperature range between solidus and liquidus temperature, should found as extended as possible. Here, a range between 20 and 130 °C is recommended. [15]
2. Temperature sensitivity of solid phase content (−dφs/dT), which indicates the change in solid phase content per temperature unit for a specific alloy composition, should not exceed 0.015 [16]. Thus, in general a 1.5 % change in solid phase content of the melt is permissible for every 1 °C change in temperature. [15]
3. Processing temperature specifies the temperature interval in which the required solid phase content of 0,4-0,7 for the respective semi-solid processing procedure is present. [17]
4. Globular microstructure leads to shear-thinning material behavior and is therefore a mandatory requirement for semi-solid forming processes. [18]

Based on the alloy-specific requirements described above, an Al4018 welding wire from Drahtwerk Elisental W. Erdmann GmbH & Co. [19] has been chosen as raw material for the investigations presented in this paper. Table 1 shows the chemical composition of the material used, according to Drahtwerk Elisental W. Erdmann GmbH & Co. [19] and its thermophysical properties in accordance to the above-mentioned selection criteria.

Table 1. Chemical composition of Al4018 welding wire in wt.% [19] and its thermophysical properties [20].

Si	Fe	Cu	Mn	Mg	Zn	Ti	Al
7,19	0,14	0,00	0,00	0,6	0,00	0,02	Base
ΔT = 65 °C			−dφs/dT = 0.004			processing temperature = 565-595°C	

Fig. 1a) shows the microstructure of the wire material used, which is characterized by an enclosed silicon phase (dark) in an α-Al phase (bright). This cold worked microstructure is transformed to the necessary globular microstructure in the aluminum welding wire through heating into the semi-solid state as a sub step of the strain induced melt activated (SIMA) process [21]. In the present case of processing given Al4018 wire, a cross-section reduction of 44 % was performed in the last drawing stage, which means that the threshold value of 30% specified by Loué and Suéry [22] has been exceeded and a sufficiently high cold forming ratio with regard to optimal SIMA process requirements is reached. For heat treatment a convection oven was used to heat up the sample to a temperature of 575°C for a period of 15 minutes. In general, thixoforming operations require a solid phase content of 0,4-0,7 [17]. Therefore, within the corresponding temperature range for the present alloy (approximately 565-595°C), isothermal holding at 575°C has been chosen [20]. After heat treatment the aluminum filament was quenched in water. Fig.1b) illustrates the resulting microstructure, consisting of globular α-Al grains embedded in eutectic phase (intergranular) and eutectic phase enclosed within solid grains (intragranular).

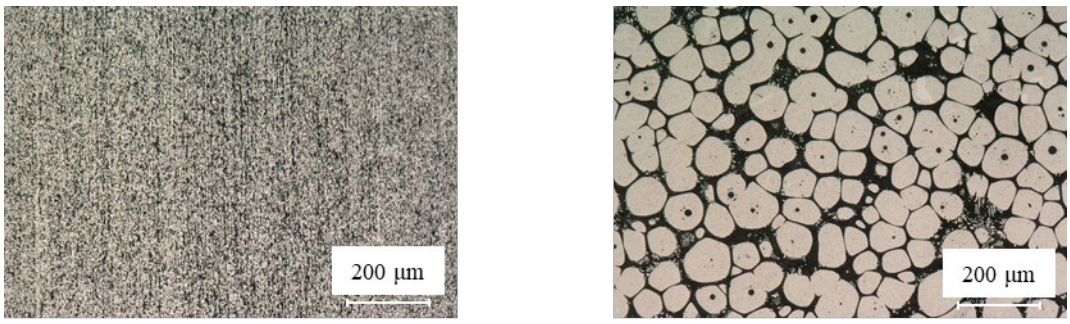

Fig. 1. Microstructure of the utilized Al4018 welding wire as is a) and after heat treatment b).

As an evaluation criterion to determine suitability of the generated microstructure for semi-solid additive manufacturing, grain size and grain shape were calculated using the image analysis software Fiji. Perfect globular grains feature a shape factor of unity. In general, a globular microstructure that is suitable for semi-solid forming is considered to feature a shape factor between 0.6 and 1 and a grain size smaller than 100 µm [23]. Compared directly, the microstructure produced in the filament material by heat treatment with the chosen parameter combination has an average grain size of 71 µm and a shape factor of 0.75 and is therefore within the stated limits. The heat-treated welding wire with a globular microstructure is utilized for extrusion and deposition studies in the course of semi-solid additive manufacturing.

Additive manufacturing setup. A prototype 3D-printer equipped with wire-feed and conduction heating devices was developed and built up for the present study. This AM setup consists of custom as well as commercially available components. Fig. 2 shows the setup used on the left and a schematic illustration of the printhead cross section on the right.

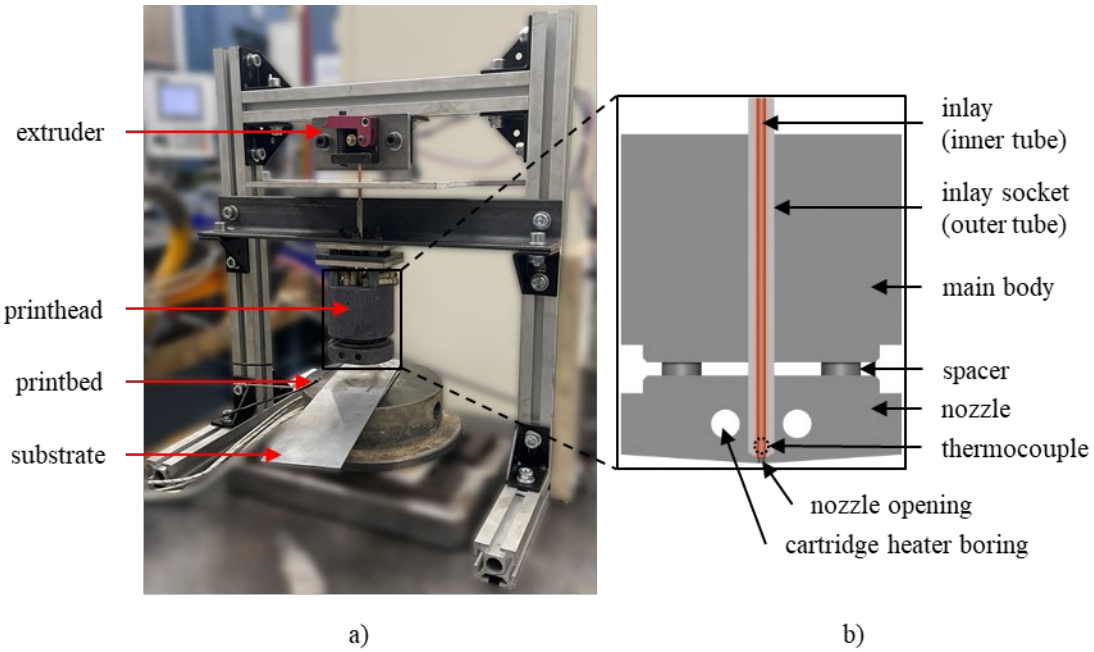

Fig. 2. Photograph of the additive manufacturing setup used a) and CAD rendering of the printhead cross section b).

The general design of the printhead includes a modular setup consisting of a main body and a nozzle separated by spacers. These spacers, between nozzle and main body, allow for thermal

decoupling of these components from each other through the resulting air gap whereby a large temperature gradient as well as separate heating of the two components can be realized. The guidance inside the printhead has been designed with an exchangeable inlay, allowing guide sleeves from different materials and with different diameters to be investigated. A conventional pinch roller extruder, which is usually applied for FDM with plastics, is used for wire feeding. The extruder is driven by a stepper motor, whose speed and thus the wire feed rate is controlled through the open source software *Estlcam*. For tempering the nozzle, conventional cylindrical cartridge heaters with an electrical power of 200 watts are inserted in appropriately prepared mounting holes. Control of the heating cartridges and thus of the temperature distribution within the nozzle is performed via a control unit. Thereby, current nozzle temperature can be measured by means of a thermocouple (Type J) integrated into the printhead and connected to the control unit.
For extrusion objectives, the aluminum wire having a diameter of 2 mm and a section length of 1 m is first supplied to the pinch roller extruder. After leaving the extruder, the Inlay guides the wire until its heating into semi-solid state inside the nozzle and its subsequent extrusion through the nozzle opening. For the final deposition of the semi-solid aluminum, a heated print bed is used on which an additional 2 mm thick aluminum sheet is placed serving as a substrate. The relative movement of the substrate to the print head is performed manually. Entire extrusion and deposition of the semi-solid aluminum wire takes place without inert gas atmosphere.

Experimental procedure. The aim of the investigations presented in this paper was to produce primitive samples with a simple geometry using the principle of semi-solid AM to demonstrate the fundamental feasibility of the project at hand. These samples should feature a homogeneous microstructure without defects and metallurgical joint between the layers. For this purpose, the extrudability of the heat-treated welding wires having a globular material structure was first investigated using the AM setup described above. During these investigations, numerous process parameters were changed according to Table 2 in order to initially demonstrate feasibility of the semi-solid AM process and afterwards to determine its ideal parameter combinations.

Table 2. Parameter variation extrusion trials.

Experimental parameter			
Wire material	heat-treated (575°C, 15 min)		
Material of Inlay	stainless steel	copper	brass
Inner diameter of Inlay [mm]	Ø 2,1		Ø 2,4
Nozzle temperature [°C]	565-630 (gradual increase in 5°C steps starting with 565°C)		
Main body temperature [°C]	540		560

Due to the modular concept of the printhead, especially the influence of different materials and variations of the inner diameter of the inlay on the extrusion process could be investigated during the experiments. Here, copper, brass and stainless steel with internal diameters of 2.1 mm and 2.4 mm were analyzed. The inlay socket was made from stainless steel in all tests conducted and provided secure seating for the inlay inside the printhead as well as its reinforcement due to low wall thickness. Regarding the temperature distribution in the printhead, a constant main body temperature was maintained in all tests, while the nozzle was heated in 5°C increments, starting at 565°C. The starting temperature of 565°C at the nozzle corresponds to the required processing temperature range for the considered aluminum alloy in the semi-solid state, which is between

565°C – 595°C. The feed rate was set to 1 mm/s, corresponding to an approximate deposition rate of 3,1 mm^3/s, in all experiments carried out. The quality of the final extrusion samples was evaluated on the basis of the external appearance and microstructural analysis. For this purpose, a digital light microscope with a maximum magnification of 5000x was used. The preparation of the samples involved mechanical sanding and polishing followed by etching of the sections with 5 % NaOH solution for 60 s. Finally, a transfer of the ideal process parameters found, was performed to the processing of untreated welding wire. The objective behind this approach was the implementation of the necessary microstructural transformation into the extrusion itself and therefore eliminate the additional step of heat treatment.

Results and Discussion

Based on the experimental results obtained, the influence of, on the one hand, the design of the guidance (inlay) and, on the other hand, the printhead temperature control on the extrusion quality were evaluated. With regard to the guidance, the tests performed showed extrusion of the aluminum wire with an inner diameter of 2.1 mm rather than 2,4 mm. This is due to the fact that the bigger inner diameter results in a larger air gap between the tube wall and the wire having a diameter of 2 mm, leading to a significantly lower heat transfer. Actually, no melting and thus no extrusion of the aluminum welding wire was observed with the inlay variant having a diameter of 2.4 mm. Because of this, further investigations on the guidance material were only carried out using the inner diameter of 2.1 mm.

In the examinations on suitable materials for the guidance, stainless steel, copper and brass were investigated in combination with the temperature settings for nozzle and main body listed in Table 2. When combining brass as material for the inlay and a nozzle temperature of 590°C, as well as both main body temperatures listed in Table 2, continuous extrusion could be achieved. However, a more detailed analysis of the nozzle cross-section after the performed tests revealed the positioning of the melting zone located near the contact area between aluminum wire and extrusion shoulder, the entire brass inlay had been disintegrated (see Fig. 3). This disintegration of the brass guidance can be attributed to diffusion of alloying elements into the semi-solid aluminum in combination with subsequent mechanical abrasion. Therefore, a brass inlay is not suitable for the semi-solid AM process in terms of a reliable process control.

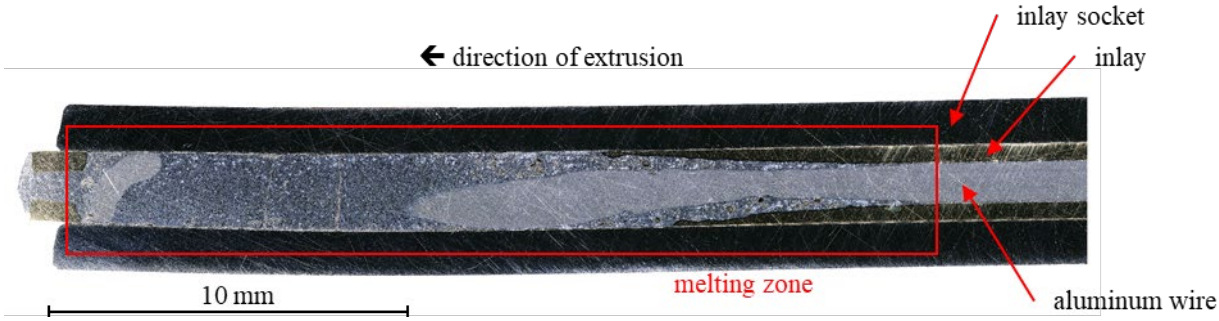

Fig. 3. Cross section of the inlay (brass) and inlay socket (stainless steel) with melted aluminum.

For stainless steel and copper as inlay materials, melting of the aluminum wire could be observed for a nozzle temperature of 590°C due to the formation of droplets at the nozzle opening, but no further extrusion. This can be attributed to the friction between the guidance and the semi-solid aluminum alloy itself, which prevented extrusion. However, by increasing the nozzle temperature up to 615°C in the case of stainless steel and 625°C for copper and simultaneously turning off active heating of the printhead main body, extrusion of the semi-solid aluminum gets feasible. The applied heating strategy relocated the melting zone closer to the extrusion shoulder and also decreased its dimensions. As a result, this led to reduced friction between guidance and wire, thus enabling extrusion.

The above described methodology for the extrusion of heat-treated wire also led to successful extrusion of untreated aluminum wires. Regarding this, Fig. 4 shows respective cross-sections of nozzles with a) stainless steel and b) copper as guiding material. The stainless-steel inlay reveals a gradual melting and simultaneous transformation of the untreated aluminum wire over a length of ~4,9 mm. The copper inlay, on the other hand, shows a significantly shorter melting and transformation zone, which is exclusively present at the immediate extrusion shoulder and nozzle opening. During the extrusion tests, the significantly larger melting zone within the stainless-steel inlay implied higher friction between the semi-solid aluminum and the guidance causing an increased force demand for the extrusion process in comparison to the copper inlay. Furthermore, when using the stainless-steel inlay, a nozzle temperature reduced by 10°C compared to the copper inlay had to be used in order to restrict the formation of the melting zone. Without reducing the nozzle temperature applied in the case of the steel inlay, no extrusion has been achieved using the extruder applied in the present study, since the required feeding force clearly exceeded the available capacities of the stepper motor. Even with an adapted temperature profile, steady-state extrusion was only present to a certain degree while using the stainless-steel inlay, as the force provided by the extruder was partially insufficient due to stick and slip effects and stagnation of the wire feed occurred. For the copper inlay, the forces required during the process to extrude the semi-solid aluminum did never exceed the extruder's capacity due to the already explained comparatively small melting zone (see Fig. 4).

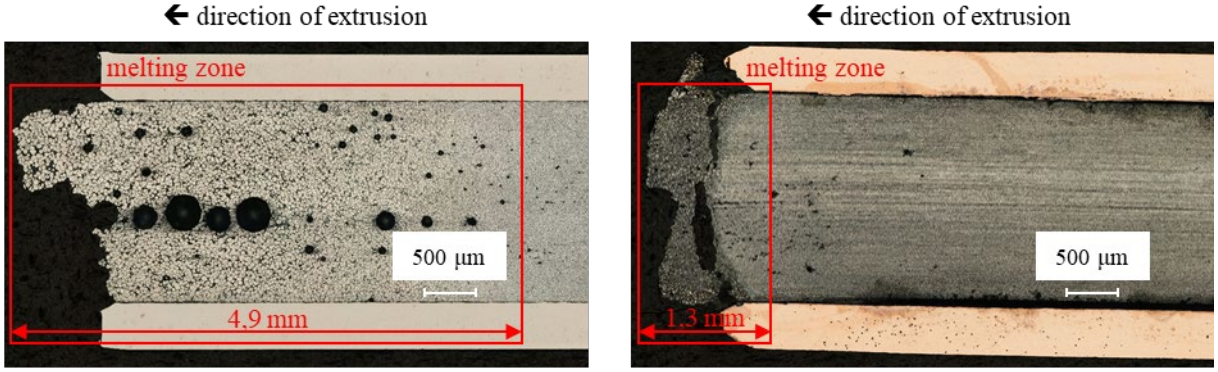

Fig. 4. Nozzle cross section with stainless steel a) and copper inlay b).

Table 3 shows the parameter combinations determined in the course of the extrusion studies providing a suitable operating window for steady state extrusion of aluminum welding wires.

Table 3. Best parameter combinations for extrusion and deposition.

Material Inlay 1	Inner diameter Inlay 1 [mm]	Temperatur nozzle [°C]	Temperature main body [°C]	Wire material
stainless steel	2,1	615	not heated	heat-treated, untreated
copper	2,1	625	not heated	heat-treated, untreated

Fig. 5 presents the resulting microstructure of fully extruded samples from untreated welding wires. In both cases, it can be seen that a complete transformed microstructure consisting of globular α-Al-grains embedded in an eutectic matrix is present. The smaller average grain size in the sample extruded with the copper inlay is attributed to the shorter holding time of the material in the semi-solid state caused by the reduced melting zone. This fact also contributes to the

considerably finer porosity, since the coalescence occurring in the semi-solid state with advancing holding time leads to coarsening of pores. Both of the presented grain sizes are sufficiently small for semi-solid extrusion however the smaller grain size produced through extrusion with the copper inlay is generally considered a beneficial factor and has a positive effect on the extrudability of the semi-solid aluminum.

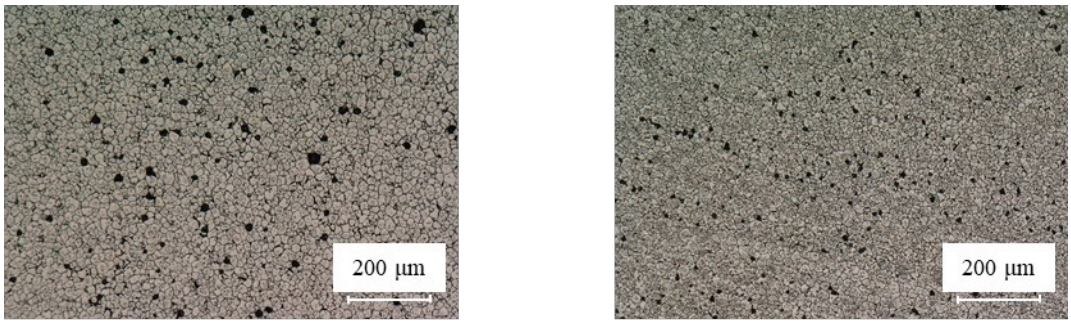

Fig. 5. Microstructure of extruded untreated aluminum wires with a) stainless-steel and b) copper inlay.

The manufacturing of a basic specimen took place using an untreated aluminum welding wire with the copper inlay as well as the corresponding process parameters listed in Table 3. Fig. 6a) shows the sample after extrusion and deposition of the semi-solid aluminum using the ideal process parameter combination. During the trials, a heated print bed with temperatures between 550-600°C was needed in order to achieve a good bonding of the layers. This can be attributed to the semi-solid state of both the already deposited and the just extruded aluminum, that enables an interface-free bonding of the two layers shown in Fig. 6b). The porosity described above is also found in the extruded specimen and can be classified as a defect in the material indicated by intergranular pores.

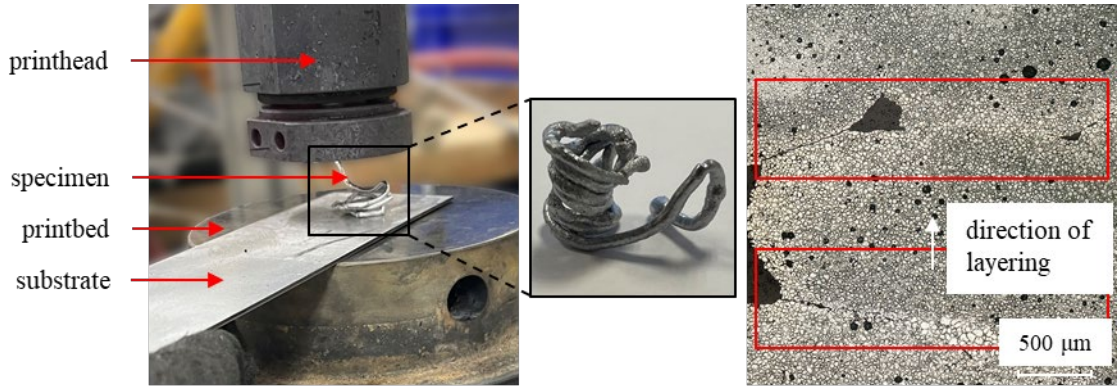

Fig. 6. Experimental procedure and specimen manufactured a), microstructural analysis of the specimen b).

Summary

In the present study, a novel manufacturing method has been presented enabling semi-solid additive manufacturing of aluminum wire utilizing a conductively heated printhead design. This also involved the fabrication of basic specimens by using a heated print bed as well as a manually moved aluminum substrate (6000 series) with a deposition rate of up to 3.1 mm^3/s. Thereby the required microstructural transformation of the untreated aluminum wire took place during heating inside the printhead, eliminating the need for an additional heat treatment. In the course of the experimental evaluation, three different inlay materials as well as variations of the inner diameter were tested. For 2.4 mm as an inner diameter no melting or extrusion could be observed due to an

excessive air gap and therefore poor heat transfer between guidance and aluminum wire. With brass as guidance, disintegration of the inlay material occurred in the melting zone, while stainless steel led to stagnant extrusion caused by a large melting zone resulting in high friction along with stick-and-slip effects. Copper with an inner diameter of 2.1 mm was found to be the most suitable choice and consequently has been applied for the fabrication of simple specimens featuring a partial interface-free bonding of consecutive layers. However, the extruded material also exhibited defects in form of porosity.

In future studies, a dedicated machine setup will be developed, which enables a controlled movement of the print bed in x-, y- and z-direction at a pre-defined speed. In addition, a reworked printhead concept including a heat sink will be implemented in the system in order to be able to influence the dimensions of the melting zone.

References

[1] O. Abdulhameed, A.Al-Ahmari, W. Ameen, S.H. Mian, Additive manufacturing Challenges, trends, and applications, Adv. Mech. Eng. 11 (2019) 1-27. https://doi.org/10.1177/1687814018822880

[2] W. Gao, Y. Zhamg, D. Ramanujan, K. Ramani, Y. Chen, C.B. Wiliams, C.C.L. Wang, Y.C. Shin, S. Zhang, P.D. Zavatieri, The status, challenges, and future of additive manufacturing in engineering, Comput. Des. 69 (2015) 65-89. https://doi.org/10.1016/J.CAD.2015.04.001

[3] W.E. Frazier, Metal Additive Manufacturing: A Review, J. Mater. Eng. Perform. 23 (2014) 1917-1928. https://doi.org/10.1007/s11665-014-0958-z

[4] K. Monroy, J. Delgado, J. Ciurana, Study of the pore formation on CoCrMo alloys by selective laser melting manufacturing process, Procedia Eng. 63 (2013) 361-369. https://doi.org/10.1016/J.PROENG.2013.08.227

[5] C.B. Williams, J.K. Cochran, D.W. Rosen, Additive manufacturing of metallic cellular materials via three-dimensional printing Example parts of designed mesostructure, Int. J. Adv. Manuf. Technol. 53 (2011) 231-239. https://doi.org/10.1007/s00170-010-2812-2

[6] B. Baufeld, E. Brandl, O. Van Der Biest, Wire based additive layer manufacturing: Comparison of microstructure and mechanical properties of Ti–6Al–4V components fabricated by laser-beam deposition and shaped metal deposition, J. Mater. Process. Technol. 211 (2011) 1146-1158. https://doi.org/10.1016/J.JMATPROTEC.2011.01.018

[7] W. Chen, L. Thornley, H.G. Coe, S.J. Tonneslan, J.J. Vericella, C. Zhu, E.B. Duoss, R.M. Hunt, M.J. Wight, D. Apelian, A.J. Pascall, J.D. Kuntz, C.M. Spadaccini, Direct metal writing: Controlling the rheology through microstructure, Appl. Phys. Lett. 110 (2017). https://doi.org/10.1063/1.4977555

[8] S. Finke, F.K. Feenstra, Solid freeform fabrication by extrusion and deposition of semi-solid alloys, J. Mater. Sci. 37 (2002) 3101–3106. https://doi.org/10.1023/A:1016137723481

[9] P.F. Mendez, Joining metals using semi-solid slurries, Master Thesis, Massachusetts Institute of Technology, 1992.

[10] C.S. Rice, Solid freeform fabrication using semi-solid processing, Master Thesis, Massachusetts Institute of Technology, 1995.

[11] D.D. Lima, K.N. Campo, S.T. Button, R. Caram, 3D thixo-printing: A novel approach for additive manufacturing of biodegradable Mg-Zn alloys, Mater. Des. 196 (2020) 109161. https://doi.org/10.1016/j.matdes.2020.109161

[12] L. Herhold, Modeling and validations of control parameters for material extrusion-based additive manufacturing of thixotropic aluminum alloys, PhD Thesis, University of Lousiville, 2018. https://doi.org/10.18297/etd/3055

[13] G.K. Sharma, P. Pant, P.K. Jain, P.K. Kankar, P. Tandon, Analysis of novel induction heating extruder for additive manufacturing using aluminum filament, J. Eng. Manuf. 235 (2021) 1961-1970. https://doi.org/10.1177/09544054211014451

[14] L. Englert, A. Klumpp, A. Ausländer, V. Schulze, S. Dietrich, Semi-solid wire-feed additive manufacturing of AlSi7Mg by direct induction heating, Addit. Manuf. Lett. 3 (2022) 100067. https://doi.org/10.1016/J.ADDLET.2022.100067
[15] Y.D. Li, D. Apelian, B. Xing, Y. Ma, Y. Hao, Commercial AM60 alloy for semisolid processing: Alloy optimization and thermodynamic analysis, Trans. Nonferrous Met. Soc. China (2010) 1572–1578. https://doi.org/10.1016/S1003-6326(09)60341-1
[16] Y.Q. Liu, A. Das, Z. Fan, Thermodynamic predictions of Mg-Al-M (M = Zn, Mn, Si) alloy compositions amenable to semisolid metal processing, Mater. Sci. Technol. 20 (2004) 35-41. https://doi.org/10.1179/026708304225011973
[17] G. Hirt et al, Thixoforming-Ein Verfahren mit Zukunft, Neuere Ent wicklungen in der Massivumformung, Fellbach b. 1995.
[18] H.V. Atkinson, Modelling the semisolid processing of metallic alloys, Prog. Mater. Sci. 50 (2005) 341-412. https://doi.org/10.1016/j.pmatsci.2004.04.003
[19] Information on https://www.elisental.de/de/
[20] Y. Birol, A357 thixoforming feedstock produced by cooling slope casting, J. Mater. Process. Technol. 186 (2007) 94–101. https://doi.org/10.1016/j.jmatprotec.2006.12.021
[21] K.P. Young, C.P. Kyonka, J.A. Courtois: US Patent 4,415,374. (1983)
[22] W.R. Loué, M. Suéry, Microstructural evolution during partial remelting of AlSi7Mg alloys, Mater. Sci. Eng. A 203 (1995) 1-13. https://doi.org/10.1016/0921-5093(95)09861-5
[23] A. Jabbari, K. Abrinia, A metal additive manufacturing method : semi-solid metal extrusion and deposition, J. Adv. Manuf. Technol. 94 (2018) 3819-3828. https://doi.org/10.1007/s00170-017-1058-7

Materials Research Proceedings 28 (2023) 85-92 https://doi.org/10.21741/9781644902479-10

In-situ consolidation of additively manufactured continuous fiber reinforced material: Technical approach and results

OBERLERCHER Hannes[1,2,a *], LAUX Marius[2,b], HEIM Rosmarie[3,c], BERNDT Alexander[2,d], AMANCIO-FILHO Sergio T.[1,e] and RIEMELMOSER Franz O.[2,f]

[1]TU Graz, Institute of Material Science, Joining and Forming, BMK Endowed Professorship for Aviation, Kopernikusgasse 24/I, 8010 Graz, Austria

[2]ADMiRE Research Center - Additive Manufacturing, Intelligent Robotics, Sensors and Engineering, School of Engineering and IT, Carinthia University of Applied Sciences, Europastrasse 4, 9524 Villach, Austria

[a]h.oberlercher@fh-kaernten.at, [b]m.laux@fh-kaernten.at, [c]r.heim@fh-kaernten.at, [d]a.berndt@fh-kaernten.at, [e]sergio.amancio@tugraz.at, [f]f.riemelmoser@fh-kaernten.at

Keywords: Additive Manufacturing, Continuous Reinforced Fiber, Deconsolidation, Consolidation Processes, Composite Material, Mechanical Properties

Abstract. Additive manufacturing (AM) of continuous fiber reinforced composites (CFC) is becoming increasingly important in the field of lightweight construction. The major advantage lies particular in the automated manufacturing process and in the production of complex geometries. Most work was done with traditional fusion filament fabrication (FFF) and the lack of separate consolidation units. AM CFCs produced in this manner have shown increased consolidation-related volumetric flaws -i.e. deconsolidation defects decreasing mechanical performance. The presence of deconsolidation defects, normally indicates either poor process parameters selection or inadequate in situ consolidation. Recently, there were several efforts in modifying the FFF of CFCs to minimize deconsolidation defects through in situ thermo-mechanical pressing. However, there are only limited fundamental knowledge on the in situ thermo-mechanical consolidation of FFF-CFCs. The present paper analyses the stated problem and proposes ways to decrease deconsolidation in FFF CF-PA6 laminates. For this purpose, we used a self-developed FFF 3D Printer coupled with a thermo-mechanical pressing unit. The influence of extrusion-, consolidation temperature, printing speed and in situ consolidation pressure on laminate microstructure and flexural strength was investigated. A comparison with FFF laminates printed in a common 3D printer was performed. The controlled 3D printing consolidation process leads to a homogeneous distribution of fibers in the matrix material and to an improvement of the material parameters of the reinforcing composite.

Introduction

Due to the efforts to increase efficiency, minimize costs and reduce emissions, many branches of industry are undergoing radical changes. Lightweight engineering through 3D printing provides measures towards these goals, as it allows several effects to be achieved at the same time: a) Lightweight engineering saves emissions in transport industry. b) In combination with 3D printing, it makes it possible to produce complex lightweight components economically in a resource-saving manner. c) Due to its flexibility and automation possibilities, 3D printing can be used particularly well in the field of structural element design. When high-performance materials such as composites are used, it becomes interesting for the automotive and aerospace industries. 3D printing is increasingly recognized as a technical solution in these areas and will significantly change the way complex, ultra-lightweight components are manufactured.

Content from this work may be used under the terms of the Creative Commons Attribution 3.0 license. Any further distribution of this work must maintain attribution to the author(s) and the title of the work, journal citation and DOI. Published under license by Materials Research Forum LLC.

The company Markforged (MF) was a pioneer in industrial use of AM CFC and produces components with considerable complexity. The mechanical properties of materials produced with this technology are lower than those of conventionally produced fiber composite components, such as those produced with automated tape laying or cast polymer molding technology. One of the reasons for the weakening properties is the high void content in the laminate caused by a poor choice of printing process parameters and resulting an inhomogeneous distribution of fibers in the matrix material [1,2]. An insufficient utilization of the reinforcing fibers is the result and can lead to premature failure of the component. In a preliminary investigation, the influence of consolidation in 3D printing of CFC was shown. It has been found that increasing the contact pressure on the molten filament can lead to a reduction in voids in the laminate and an improvement in mechanical properties [3-6].

Increased consolidation is not feasible with standard 3D printing technology of fiber composites. What would be required is a time-delayed additional consolidation in the range of the crystallinity temperature of the matrix material. This is the aim of the present work, which describes a technology for in-situ consolidation.

For this purpose, a self-developed consolidation printer (CP) and the MF technology were used. The following approach is considered: Specimens of the used material are printed with the CP technology under controlled conditions at the crystallinity temperature and compared with the test specimens of the MF technology. Material tests and microstructure analyses are carried out and compared with each other. By preparing microsections of the specimens, a closer look inside the structure of the material is obtained which defines the basis for further understanding in terms of its homogeneity.

Materials and methods

Parameters on the behavior of the matrix material as a function of time and temperature are not part of the manufacturer's specifications. For this purpose, preliminary tests had to be carried out, which are necessary for a controlled thermal consolidation of the material. The preliminary examination of the filament, the technical approach of the MF printer and CP, the test specimens and the defined process parameters are documented below.

Filament material.

The thermoplastic prepreg used in this study was a 1K roving of continuous carbon fiber, which was pre-impregnated with a nylon matrix (CF-PA6) [7]. The CF-PA6 filament has a diameter of about 0.389 [mm] and a fiber volume fraction f of 35.0 ± 0.1%. This value is in accordance with results reported by other authors, such as He et al. [8]. After a differential scanning calorimetry (DSC) analysis the glass transition temperature, crystallinity temperature and the melting temperature of the CF-PA6 prepreg material as well the PA6 matrix material of MF without reinforced fibers was determined (see Table 1).

Table 1. Results of DSC measurement.

Material	Glass transition temperature [C°]	Crystallinity temperature [C°]	Melting temperature [C°]
CF-PA6	66	169	225
PA6	54	163	242

CFC 3D printer.

To analyze the conventional consolidation strategy of 3D-printed CFC, the mechanical technology as well as the software of a Mark-two printer of MF was used. The mechanical construction of the MF printer has been reported by the manufacturer and in many papers [9-11]. For a consistent printing quality, some adjustments are made according to the manufacturer: The distance between the nozzle tip and the printer has to be set with a shim leveling to 0.127 [mm] by a constant nozzle temperature to 250 [°C]. A new continuous fiber filament role with a low moisture content was used for printing the test samples. To ensure a good hold of the printed pattern on the print bed, an adhesive glue, recommended by the manufacturer, was applied on the print bed. The default parameters of MF at the slicer software Eiger are used as printing condition for the CFC CF-PA6 material print.

Consolidation printer.

For a detailed consolidation study a consolidation test bench was developed and constructed. All technical functions for continuous fiber 3D printing are similar to MF. The printing bed is moving in x-, and y-axis direction and the printer head is moving in z-axis direction with a trapezoidal Tr8 x 1.5 [mm] thread. The filament feeder, cutter, hotend and nozzle are MF components. With this technical setup, the process and the printing quality of MF can be reproduced. In order to implement the influence of the consolidation, an in situ thermomechanical consolidation roller is installed after the nozzle tip. There is no mechanical coupling installed between the nozzle and the consolidation unit. Therefore, the fiber can only be deposited in x-direction and no curved paths are possible with this setup. Each path must be deposited individually to obtain the part width of the three-point bending specimen (see Fig. 2 CP Specimen).

With a load cell (HBM PW4M), the current consolidation pressure in the printing process was measured. The diameter of the consolidation roll is 26 [mm] and is tempered with a 12 [V] 30 [W] cartridge heater. The rotation of the consolidation roller is transmitted to the CFC filament by the contact pressure. The distance between printing nozzle and the consolidation role is adjustable and is in this study about [mm]. The consolidation roll is on the same level as the nozzle tip and applies a contact force about 5 [N] to the filament.

The printer was prepared with an open controller board from GT2560 Ref A+ and can be operated with an open-source slicer software. Various process parameters such as speed, temperature and the layer height can be changed additionally. These parameters were controlled with the Repetier-Host software (Hot-World GmbH & Co. KG). The G-code for the specimen geometry is developed independently in-house and imported into the control system of Repetier-Host. The schematic process of the consolidation test bench is shown in Fig. 1.

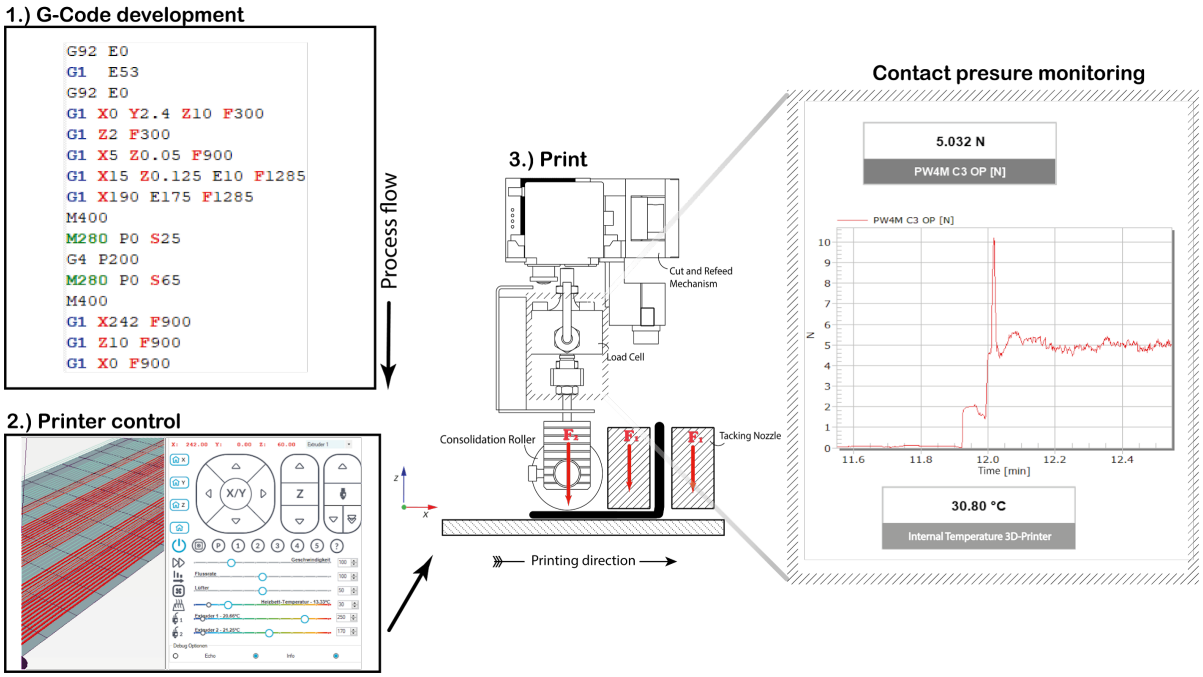

Fig. 1. Schematic process of the consolidation test bench.

Specimen geometry and mechanical testing.

The material tests were carried out using three-point bending tests. The dimensions are 60 x 15 x 2 [mm] (length x width x thickness) following the testing standards ISO 14125 with a line offset of approx. 0.9 [mm]. The pure PA6 coating and CFC loops at the reversal points produced by the MF printing process are removed. The printing strategy as well as the printing composition of the MF and the CP specimen is shown in Fig. 2. Each specimen consists of 14 layers, with 15 lines per layer. The layer height, printing speed and nozzle temperature for both printers were chosen of the default settings of MF and is listed in Table 2. The consolidation force on the CP samples is about 5 [N] for each line, while simultaneously maintaining the matrix material at its crystallinity temperature of 170 [°C] (see Table 1). In order to obtain reliable results of the mechanical tests, eight test samples are produced per series.

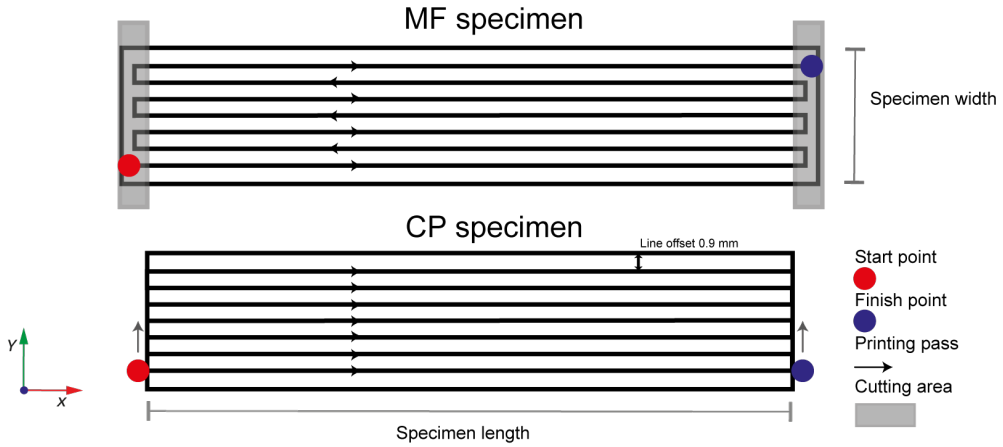

Fig. 2. Print path in a layer of MF and CP.

The three-point bending tests were conducted on a universal testing machine Z020 (Zwick/Roell). The manufacturer's software testXpert II was used on the testing machine to initialize the test parameters and record the test data.

Process parameters and data analysis.

The process parameters of the CP printer were controlled and measured with the Repetier-Host software and are listed in Table 2. The control of the process parameters of the MF system was realized with the Eiger software and contains the standard parameters of MF (see Table 2).

Table 2. Printing conditions.

Variation	Fiber-orientation	Nozzle height [mm]	Consolidation force roller [N]	Printing-speed [mm/s]	Nozzle tip temp. [C°]	Consolidation roller temp. [C°]	Printing bed [C°]	Internal temperature 3D-printer [C°]
CP	0°	0.127	5	15	250	170	30	30
MF		0.127	-	15	250	-	-	30

An HBM QuantumX MX1615 interface was used for data acquisition of consolidation pressure and chamber temperature of the CP printer. The visualization and data storage were implemented with the software catmanEasy. To ensure the correctness of the measured data, a reference measurement was made using a high-resolution balance.

Microstructural analysis.

The binocular microscope Axio Lab.A1 with a 5X and 20X magnification (Zeiss, Oberkochen) was used to observe the fiber distribution as well as the void content of the test specimens. The images were taken with a 2.0 MP Pixel-Fox digital camera (Dietermann & Heuser Solution, Greifenstein-Beilstein) and processed with the manufacturers image measuring software.

Results

In order to be able to assess the quality of the laminate, detailed information is required on the micro- and macrostructure as well as the respective mechanical properties of the laminate. For this purpose, the following investigations were carried out.

Cross-sectional observation.

Typical examples of cross-sectional microscopy images of the MF and CP specimens in the direction perpendicular to the fiber are shown in Fig. 3.

The 3D printed laminates of MF (see Fig. 3a), show a lot of micro and macro voids in the laminate. Larger voids have a size of approximately 200 [µm]. Individual layers with insufficient intimate contact are to be recognized in the observation. Layers in the laminate have a height of approximately 600 [µm] and indicate a deconsolidation mechanism in the printing process. Further, horizontal cracks indicate a delamination. The fibers show a good distribution in the matrix material.

On the right side on Fig. 3 the laminate of the CP test bench specimen is shown. This laminate has hardly any micro and macro voids. Individual layers are partially marked with larger matrix areas (see Fig. 3b yellow circle). A reduction in deconsolidation is shown in the region of the joining zone of each layer. The layer heights are significantly lower compared to the MF samples and are about 270 [µm] (see Fig. 3b).

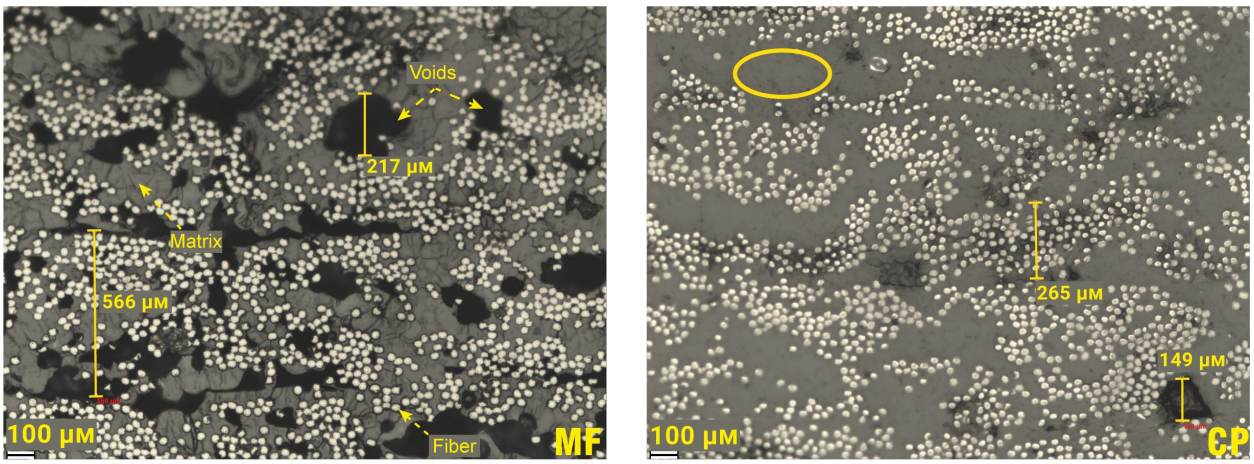

a) b)

Fig. 3. Microscopy images of a cross-section perpendicular to the fiber direction with a 20X magnification of a) MF and b) CP laminate with 14 layers.

Fig. 4 shows the laminates of MF and CP in 5X magnification. An expected high number of voids and delamination in the MF composite can be seen (see Fig. 4a). CP has a uniform mesostructure with a low proportion of voids (see Fig. 4b).

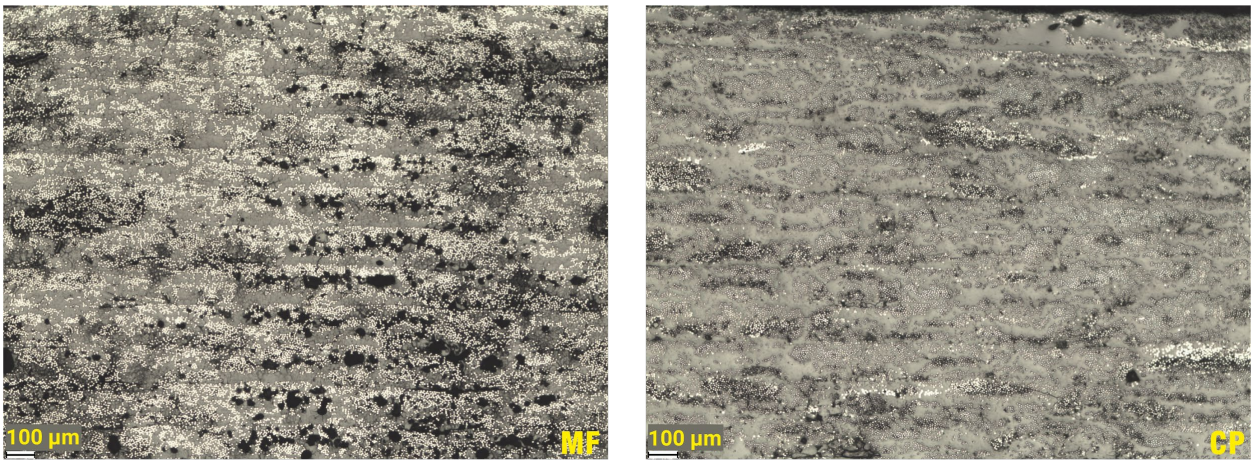

a) b)

Fig. 4: Microscopy images of a cross-section perpendicular to the fiber direction with a 5X magnification of a) MF and b) CP laminate with 14 layers.

Bending test results.

Fig. 5 shows the bending strength a) and the bending modulus b) of unidirectional CFC specimens printed using MF and CP, respectively. The average values of bending strength and bending modulus are 38.9 ± 3.2 [GPa] and 518.1 ± 42 [MPa] for MF specimens, and 39.2 ± 3.9 [GPa] and 610.9 ± 32 [MPa] for CP specimens, respectively. The CP specimens show an 15% improvement in bending strength and about 1% improvement in bending modulus.

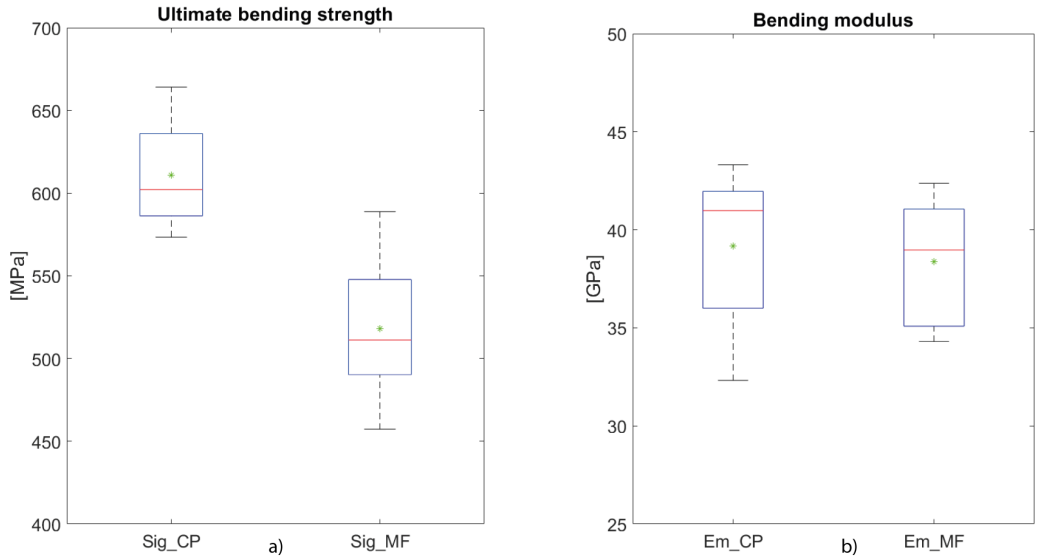

Fig. 5. Comparison of ultimate bending strength a) and bending modulus b) of the MF and CP technology.

Summary

In this study, a technical approach of a time-delayed thermal-mechanical consolidation of 3D printed CFC was investigated firstly. After a DSC analysis of the CF-PA6 material the glass transition temperature, crystallinity temperature and the melting temperature was determined. The CP test bench had the same technical approach as the MF printer, except for an additional in-situ thermo-mechanical consolidation unit. In the printing process, a force of 5 [N] was applied on the filament at a temperature close to the crystallinity temperature of the matrix material. In order to analyze the effects of in-situ consolidation in terms of microstructure and mechanical properties, a comparison was made with the printed test samples of MF technology.

The adopted process of in-situ consolidation has shown an improvement of the mechanical properties and the microstructure (15% for the bending strength and 1% for the bending modulus). In addition, the reduction of the void content was found in the CP composites in comparison to the MF composites. In summary, the MF laminates show clear signs of deconsolidation, while the CP composites are much more homogeneous.

In a next study, the influence of in-situ consolidation on the voids in the laminate and on the distribution of the fiber matrix will be analyzed. For this purpose, a traditional 2k full factorial design of experiment (DoE) will be used to investigate the different influences of the process parameters and microstructure of the 3D printed CFC laminate.

References

[1] F. Henninger, L. Ye, K. Friedrich, Deconsolidation behaviour of glass fibrepolyamide 12 composite sheet material during post-processing, Plastics rubber and composites processing and applications 27(6) (1998) 287-292

[2] T. Guglhör, Experimentelle und modellhafte Betrachtung des Konsolidierungsprozesses von carbonfaserverstärktem Polyamid-6, PhD Thesis, Universität Augsburg 2017.

[3] H. Oberlercher, R. Heim, M. Laux, A. Berndt, C. Becker, S. Traglia Amancio-Filho, F. Riemelmoser, Additive manufacturing of continuous carbon fiber reinforcedpolyamide 6: The effect of process parameters on the microstructure and mechanical properties, Structural Integrity Procedia 34 (2021) 111-120. https://doi.org/10.1016/j.prostr.2021.12.017

[4] M. Ueda, S. Kishimoto, M. Yamawaki, R. Matsuzaki, A. Todoroki, Y. Hirano, A.L. Duigou, 3D compaction printing of a continuous carbon fiber reinforced thermoplastic, Composites Part

A: Applied Science and Manufacturing 137 (2020) 105985. https://doi.org/10.1016/j.compositesa.2020.105985
[5] J. Zhang, Z. Zhou, F. Zhang, Y. Tan, Y. Tu, B. Yang, Performance of 3D-Printed Continuous-Carbon-Fiber-Reinforced Plastics with Pressure, Materials 13 (2020) 471. https://doi.org/10.3390/ma13020471
[6] G. Struzziero, M. Barbezat, A. Skordos, Consolidation of continuous fibre reinforced composites in additive processes: A review, Additive Manuf. 48 (2021) 102458. https://doi.org/10.1016/j.addma.2021.102458
[7] Markforged, Material Datasheet Composites, 2021. Available online: https://static.markforged.com/downloads/composites-data-sheet.pdf (accessed on 30 January 2023).
[8] Q. He, H. Wang, K. Fu, L. Ye, 3D printed continuous CF/PA6 composites: Effect of microscopic voids on mechanical performance, Elsevier, Compos. Sci. Technol. 191 (2020) 108077. https://doi.org/10.1016/j.compscitech.2020.108077
[9] Markforged, Product Specifications Mark Two, 2020. Available online: https://s3.amazonaws.com/mf.product.doc.images/Datasheets/Translations/DE/Markforged_Mark_Two_Printer_Datasheet_DE.pdf (accessed on 30 January 2023).
[10] M. Caminero, J. Chacon, I. Garcia-Moreno, J. Reverte, Interlaminar bonding performance of 3D printed continuous fibre reinforced thermoplastic composites using fused deposition modelling, Polym. Test. 68 (2018) 415-423. https://doi.org/10.1016/j.polymertesting.2018.04.038
[11] M. Mohammadizadeh, A. Lmeri, I. Fidan, M. Elkelany, 3D printed fiber reinforced polymer composites - Structural analysis, Composites Part B: Engineering 175 (2019) 107112. https://doi.org/10.1016/j.compositesb.2019.107112

Materials Research Proceedings 28 (2023) 93-100 https://doi.org/10.21741/9781644902479-11

Characterisation of the shape memory effect of PET polymer by FFF 3D printing

ERMOLAI Vasile[1,a *], SOVER Alexandru[1,b] and LANG Anette[1,c]

[1]Ansbach University of Applied Science, Faculty of Technology, Residenz str. 8, Ansbach, 91522, Germany

[a]vasile.ermolai@hs-anshach.de, [b]a.sover@hs-ansbach.de, [c]anette.lang@hs-ansbach.de

Keywords: Shape Memory Effect, Shape Recovery, PET, Fused Filament Fabrication

Abstract. In recent years the interest in finding new shape memory polymers has increased. Withal, fewer studies approached the use of regular materials such as polyethene terephthalate (PET), a widely available material. The research investigated the shape memory characteristics of regular PET 3D printed samples in two testing cycles. The recovery temperature was determined through dynamical mechanical, followed by tensile testing and heat treatment of the specimens. The results show PET has good shape memory properties, recording a slight increase in shape recovery during the second testing cycle without affecting the sample integrity. The thermal analysis of the recovered material shows that heat treatment time or/and temperature need to be improved to stabilise the PET material structure.

Introduction

Fused Filament Fabrication (FFF) is an extrusion-based additive manufacturing technology that uses filament shape thermoplastic materials as a feedstock. The material is heated until it reaches a viscous state and deposits layer-wise to build parts [1].

FFF disposes of a large variety of materials, including regular (polylactic acid), engineering grade (e.g., polycarbonate), or even high-performance polymers (e.g., polyether ether ketone) [2,3]. The technology is used for many applications, such as conceptual models, functional prototypes, tools and fixtures, replacement parts, biomedical applications, and others [4].

The design and production of a Shape Memory System (SMS) is another application of FFF. They are referred to as 4D printing because of their shape-changing behaviour over a period of time. These SMSs are compliant mechanisms that achieve motion based on a stimulus, in this case, shape change. This can be thermal, electromagnetic, light or pH-based and others [5-6].

The SMS is characterised by one or more shape-changing sequences and depends on the number of constituents. This way, the SMS can be divided into single, double, triple and multiple material mechanisms [5-7]. Regardless of the number of constituents, the working principle of polymeric SMS was classified into three mechanisms. The first is the dual-state mechanism. Here the permanent shape is memorised by the strong links of the polymeric chains (i.e., covalent bonds) and the temporary shape is maintained by the weak links (e.g., chain entanglements). The second is the dual-component mechanism. This one uses a more rigid component to "remember" the permanent shape and a softer one for the temporary shape. The third is the partial transition mechanism which uses a mixture of materials to provide the transition phases [8-10].

The shape memory properties are evaluated through the Fixity ratio (R_f) and Recovery ratio (R_r). Those are used to determine the Shape Memory Index (SMI) of the SMS [5-7] as follows:

$$R_f = \frac{\varepsilon_u}{\varepsilon_m} \quad (1)$$

$$R_r = \frac{\varepsilon_m - \varepsilon_p}{\varepsilon_m} \quad (2)$$

Content from this work may be used under the terms of the Creative Commons Attribution 3.0 license. Any further distribution of this work must maintain attribution to the author(s) and the title of the work, journal citation and DOI. Published under license by Materials Research Forum LLC.

$$SMI = R_f \times R_r \quad (3)$$

where ε_m is the specimen's elongation at 100%, ε_u is the elongation after release, and ε_p is the elongation after recovery.

For heat-sensitive SMSs, the permanent shape results after the part's manufacturing (i.e., after printing). Then the part is heated (at a temperature T_1 above the glass transition temperature) and deformed to a temporary shape. Then the permanent shape is recovered by heating the part at the same temperature, T_1 [5-7].

Polyethene terephthalate (PET) is a semicrystalline thermoplastic material and is characterised by both amorphous (i.e., transparent) and crystalline (i.e., opaque) phases [11,12]. It is widely used in the food industry for food and liquid containers [13,14] and as feedstock for additive manufacturing technologies such as FFF as a new or recycled material [15,16].

This work focused on evaluating the shape memory effect of specimens made of regular, neat PET. The sample deformation was made at room temperature in two testing cycles compared to the standard testing procedure. Shape memory specimens' cold deformation is documented in the literature [10,16,17]. The results show PET shape recovery is possible even after two cold deformation cycles.

Materials and Methods

The chosen material was a natural PET filament from BasicFil. This was printed as samples (i.e., type 5 of ASTM 638-14) using an Ultimaker 3 printer. Before printing, the material was dried in an oven at 65°C for four hours. The manufacturing instructions were generated using Cura 5.2.1 slicing tool using the main parameters described in Table 1.

Table 1. Printing process parameters.

1	Nozzle diameter (mm)	0.4	13	Print speed (mm/s)	30
2	Layer thickness (mm)	0.15	14	Travel speed (mm/s)	250
3	Extrusion width (mm)	0.4	15	Retraction distance (mm)	7
4	Number of walls	4	16	Retraction speed (mm/s)	35
5	Wall ordering	Outside to inside	17	Combing mode	Not in skin
6	Z seam position	Back left	18	Avoid printed at travel	Yes
7	Top/bottom layers	11	19	Z hop height (mm)	1.6
8	Top/bottom pattern	Lines	20	Regular fan speed (%)	15
9	Lines direction (°)	45/135	21	Maximum fan speed (%)	30
10	Extrusion temp. (°C)	245	22	Brim distance (mm)	0.1
11	Bed temp. (°C)	70	23	Brim width (mm)	3
12	Initial layer speed (mm/s)	15	24	Enclosure	Yes

The printing speed was controlled independently by each constructive element of the sample (e.g., walls, solid fill). The first layer and the brim were printed at a lover speed (i.e., 15 mm/s) to increase the adhesion with the build plate. To avoid the samples' deformation outside the gauge length, the walls closing was positioned in the samples' back left side (Fig. 1). This prevents closing contours from being placed by the slicing tool in the specimens' gauge or transition zones. Compared to the ASTM 638-14 standard specifications, the sample's thickness was increased to obtain an equal number of bottom and top layers. This way, the resulting thickness is 3.3 mm.

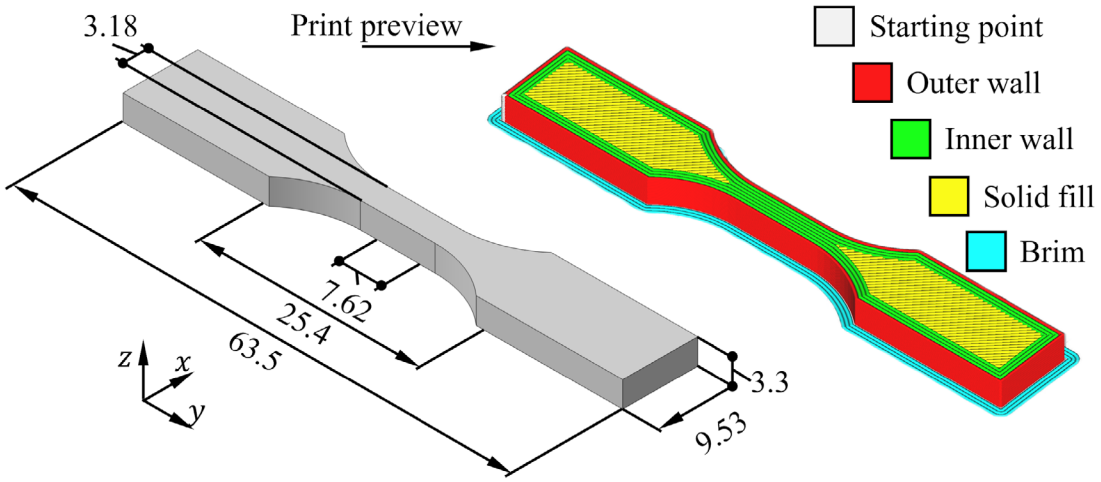

Fig. 1. CAD and printed specimen configuration.

The shape memory properties were determined by using the following steps:

1. Measurement of specimens' gauge length after marking;
2. Deformation at cold with 1 mm/min up to ε_m, the100% elongation;
3. Sample holding between clamping system for 5 minutes at ε_m;
4. Measurement of ε_u, the elongation after the release;
5. Heat treatment of the specimens in an oven at temperature T_1 for 5 minutes;
6. Measurement of ε_p, the recovery length.

The above-described steps were repeated for a second testing cycle, in which the new gouge length was the ε_p from the previous cycle. The testing cycles were performed with five replicates using an Instron 4411 universal testing machine with a load cell ok 5 kN. At the moment of testing, the laboratory had a temperature of 21°C and 52% moisture.

The heat treatment temperature T1 was established through dynamic mechanical analysis using TA instruments DMA 2980 equipment. Furthermore, to better understand PET's shape memory behaviour, musters of specimens' gauge zone at ε_u and ε_p were thermally analysed using Differential Scanning Calorimetry (DSC). An additional set of samples was prepared for the DSC measurements. The used equipment was a DSC 3+ from Mettler Toledo.

Results and Discussion

A dynamic mechanical analysis of the PET material was done to determine the recovery temperature for the shape memory characterisation. The test was performed in the multi-frequency method using a single cantilever bending at a frequency of 1 Hz. The temperature scans were performed at 2°C/min starting from 0 to 151.4°C when the material lost its properties. The glass transition temperature, T_g, occurs in a range, not on a single point or value. Based on the storage modulus onset, the T_g is at 76.22°C. It is the temperature at which this blend of PET starts to lose its mechanical properties. According to the loss modulus, the upper limit of the T_g range is 81.90°C. Usually, for shape memory polymers, the upper limit of the T_g is given by the tan δ modulus [10], because it is higher than the others. For the chosen blend of PET, the resulting tan δ modulus T_g value lies between the previously mentioned temperatures. All three diagrams are presented in Fig. 2. Based on these findings, a heat treatment temperature of 80°C was considered optimum for sample shape recovery.

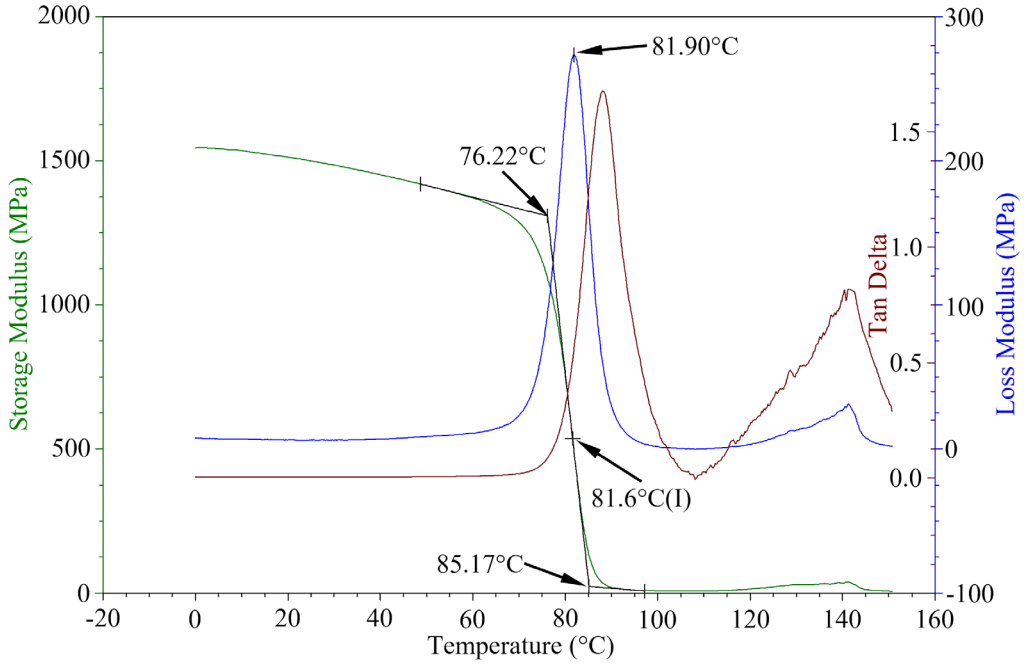

Fig. 2. Dynamical mechanical analysis of the chosen PET material.

All tested samples recorded similar deformation and shape recovery. In the first deformation-shape recovery cycle, the specimens presented a necking at the level of the gauge (see Fig. 3b). After the heat treatment at 80°C for 5 minutes, they partially recovered their shape (see Fig. 3c). Withal, in the second deformation-shape recovery cycle, the PET samples showed better shape memory effect compared to the previous one (see Fig. 3c and 3e).

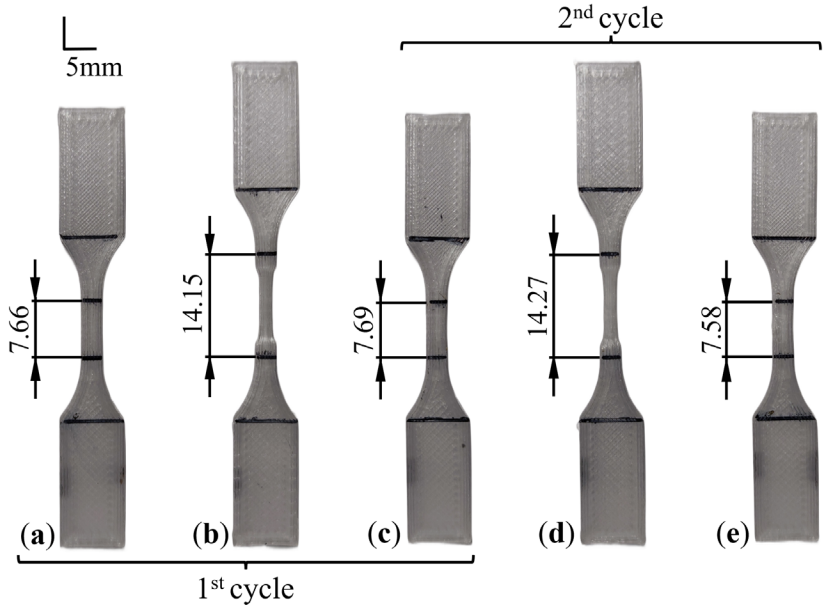

Fig. 3. Example of the PET samples at each step of the testing plan, with (a) initial, (b) first deformation, (c) first shape recovery, (d) second deformation, and (e) second shape recovery.

The fixity ratio, Rf, calculates the capacity of a material to memorise a shape by dividing ε_u at ε_m (Eq. 1). As presented in Fig. 4, the printed PET showed a good Rf in both of the testing cycles.

The samples recorded a slight increase in the second cycle compared to the first; the average fixity ratio is approximately 95%.

The recovery ratio, Rr, provides information regarding the materials' capability to recover their original shape when heated at temperature T_1. In the Fig. 4 plot, it is shown that in the first cycle, the PET samples showed an average recovery of 99.27%, and in the second cycle, it slightly increased to 100.19%. An example of the recovered parts is shown in Fig. 3.

The shape memory index gives information regarding materials' shape memory properties based on the previously presented ratios. Fig. 4 shows that PET samples averaged an SMI of 94.45% in the first testing cycle. The same samples gave an SMI average of 96.62% by performing a second set of trials. The resulting plot for each sample is presented in Fig. 4.

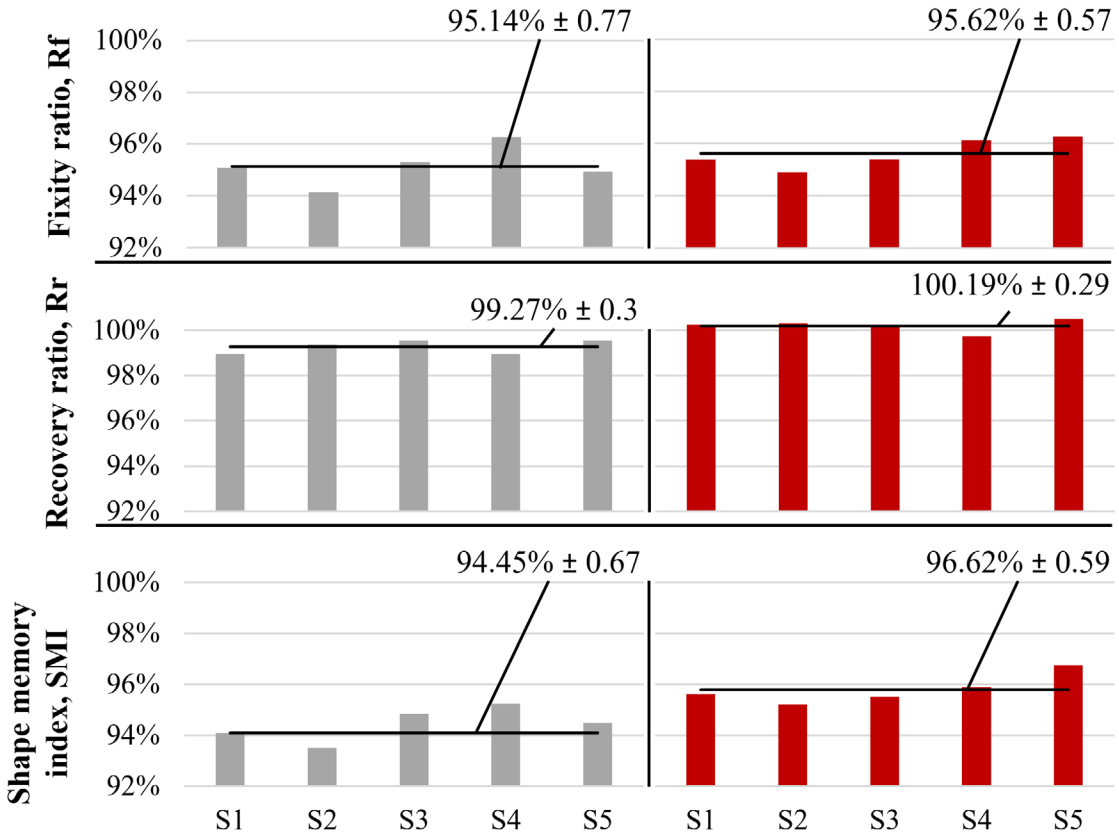

Fig. 4. Fixity ratio, recovery ratio and shape memory index of the tested samples.

To obtain more information regarding the shape memory properties increase in the second cycle, the stress-displacement plots of samples were analysed. Choosing the displacement instead of strain gives a more objective view as the specimens were elongated unevenly (see Fig. 5). At the first elongation, the samples showed similar peaks of the maximums stress with an average of 44.96±0.68 MPa and average stress at yield (at ε_m) of 28.33±0.28 MPa, in the second deformation cycle gave average maximum stress of 38.84±0.54 MPa and a 27.43±0.5 MPa yield average. By analysing the plots (see Fig. 5), it can be observed that the highest difference between the two cycles is at the maximum peak. For the rest of the tests, the results were comparable. As the samples are stretched, they follow the same pattern. First, a decrease of the load between 1 and 1.5 mm of displacement as the sample is necking. Then a slight but constant increase of the strength at yield.

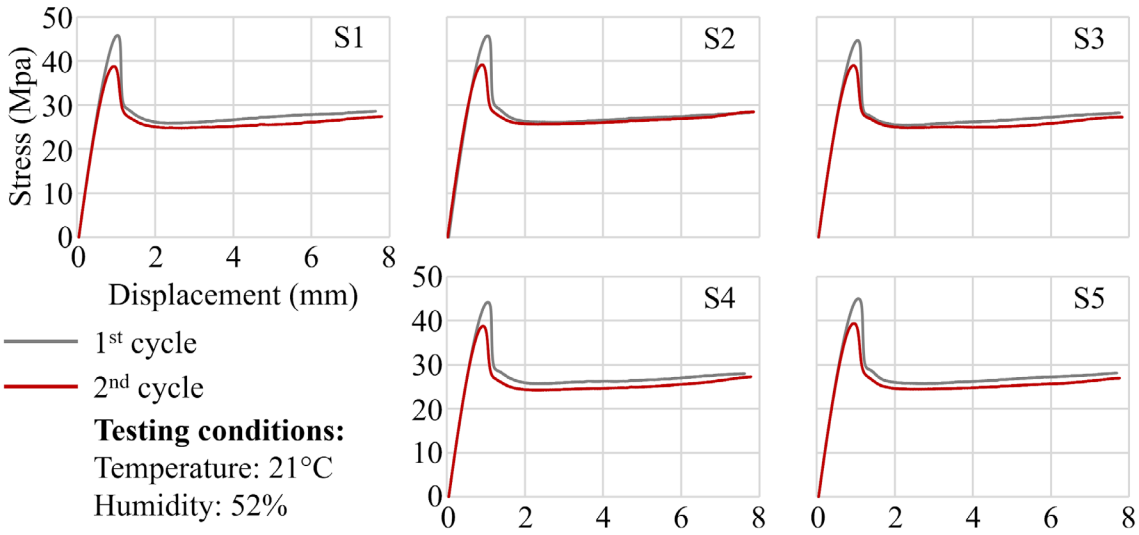

Fig. 5. Stress-displacement diagrams of the tested samples.

As the samples were elongated during the tensile test, the material situated in the gauge zone started to change its appearance from clear-transparent to an opaque white colour. This means that by stretching the sample, a change in crystallinity occurs in the material structure, from an initial amorphous to a semicrystalline state (Fig. 3). To find more information about the material behaviour, several DSC analyses were done on musters taken from the gauge zone. All studies were done by heating the material with 5 K/min from 20 to 100°C.

The first analysis was performed on a sample elongated at 100% (Fig. 3b). The result is presented in Fig. 6. It can be observed that between 40 and 60°C, the stretched material is taking energy, receiving a heat amount of 1.49 J/g. Because the material is deformed, it tends to regain its normal shape and consumes energy.

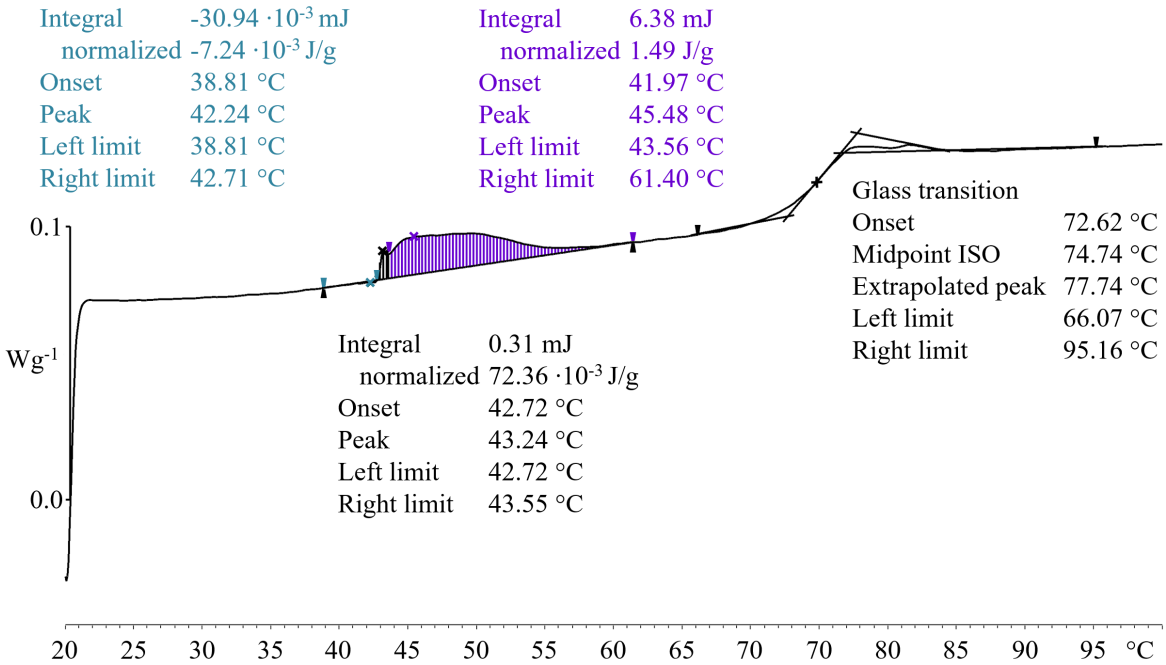

Fig. 6. DSC diagram of a first cycle elongated sample.

For the samples, after the first shape recovery, the DSC curves show that the heat-treated material is also absorbing energy between the 34 and 63°C range (see Fig. 7). However, the amount of energy required is less compared to the elongated materials. The material absorbed 0.72 J/g for the first sample, respectively 0.53 J/g for the second.

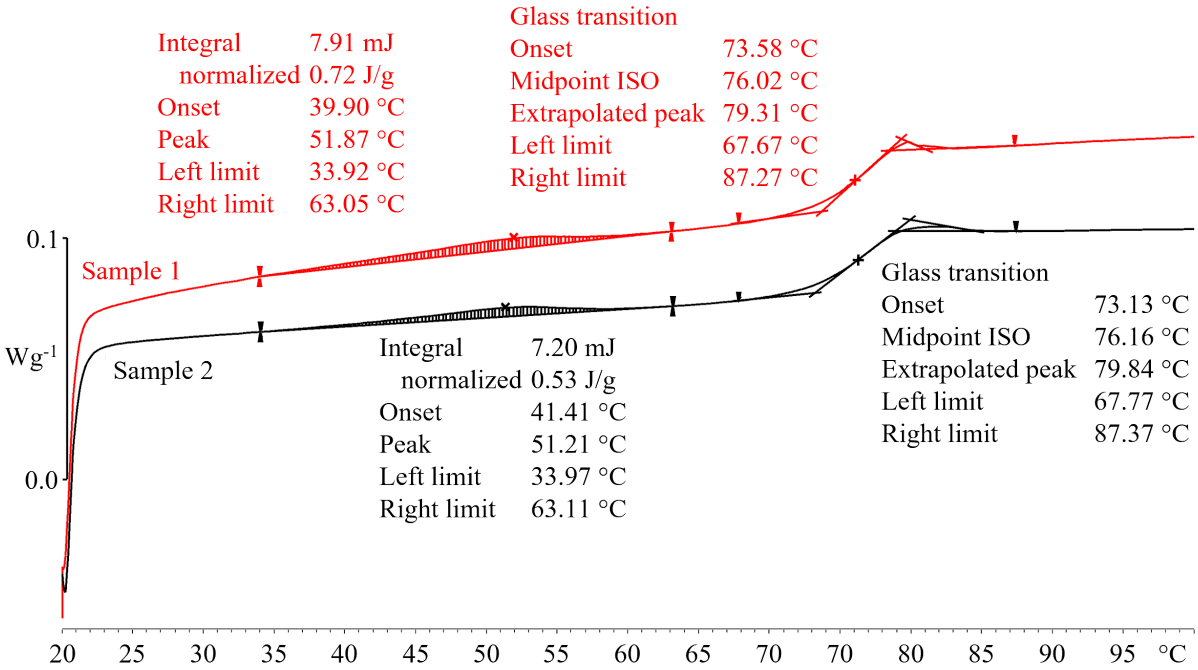

Fig. 7. DSC diagram of shape recovered samples.

Thermoplastics are characterised by covalent bonds of the polymeric chains and weaker bonds resulting from the chains' entanglements [11]. When stretched, the capacity of the chains to align with the load direction before breaking gives the maximum elongation. During the heat treatment, the polymeric chains tend to recover their natural state and reform the chains' entanglement. The DSC analysis of the heat-treated PET (Fig. 7) shows that the material required additional energy from the system. This suggests that an insufficient temperature or/and recovery time during the heat treatment possibly affected the polymeric chains' entanglement reformation. This aspect correlates with the decrease of the average maximum stress of ≈6 MPa during the tensile testing (Fig. 5). Further investigations are required for the structure of the elongated and heat-treated material to understand the PET shape memory properties better.

Summary

PET is a common thermoplastic material widely used in the food industry due to its good mechanical properties and processability. However, its shape memory properties were not thoroughly evaluated.

This study focused on evaluating the shape memory properties of PET 3D printed samples in two deformation-shape recovery cycles. Even if the samples' deformation was performed at cold, they obtained an average shape fixity of ≈95 in both testing cycles. On the other hand, the PET recovered its initial shape on an average of ≈99% testing cycle, respectively ≈100% in the second.

DSC analyses of the material heat-treated after elongation suggests that recovery temperature or/and time were not chosen accordingly to allow polymeric chains to entangle enough.

Further investigations are needed to better understand and control the PET material shape recovery during heat treatment.

References

[1] S. Singh, G. Singh, C. Prakash, S. Rama-Krishna, Current status and future directions of fused filament fabrication, J. Manuf. Process. 55 (2020) 288-306. https://doi.org/10.1016/j.jmapro.2020.04.049
[2] S. Kumar, R. Singh, T. Singh, A. Batish, Fused filament fabrication: A comprehensive review, J. Thermoplast. Compos. Mater. 36 (2020) 794-814. https://doi.org/10.1177/0892705720970629
[3] D. Popescu, A. Zapciu, C. Amza, F. Baciu, R. Marinescu, FDM process parameters influence the mechanical properties of polymer specimens: A review, Polym. Test. 69 (2018) 157-66. https://doi.org/10.1016/j.polymertesting.2018.05.020
[4] S. Hasanov, S. Alkunte, M. Rajeshirke, A. Gupta, O. Huseynov, I. Fidan, F. Alifui-Segbaya, A. Rennie, Review on Additive Manufacturing of Multi-Material Parts: Progress and Challenges, J. Manuf. Mater. Process. 6 (2022). https://doi.org/10.3390/jmmp6010004
[5] S. Valvez, P.N.B. Reis, L. Susmel, F. Berto, Fused Filament Fabrication-4D-Printed Shape Memory Polymers: A Review, Polym. 13 (2021) 701. https://doi.org/10.3390/polym13050701
[6] M. Rafiee, R.D. Farahani, D. Therriault, Multi-Material 3D and 4D Printing: A Survey, Adv. Sci. 7 (2020) 1902307. https://doi.org/10.1002/advs.201902307
[6] J. Carrell, G. Gruss, E. Gomez, Four-dimensional printing using fused-deposition modeling: a review, Rapid Prototyp. J. 26 (2020) 855-69. https://doi.org/10.1108/RPJ-12-2018-0305
[7] G. Scalet, Two-Way and Multiple-Way Shape Memory Polymers for Soft Robotics: An Overview, Actuators 9 (2020). https://doi.org/10.3390/act9010010
[8] J. Hu, Y. Zhu, H. Huang, J. Lu, Recent advances in shape–memory polymers: Structure, mechanism, functionality, modeling and applications, Prog. Polym. Sci. 37 (2012) 1720-1763. https://doi.org/10.1016/j.progpolymsci.2012.06.001
[9] M.C. Biswas, S. Chakraborty, A. Bhattachar-Jee, Z. Mohammed, 4D Printing of Shape Memory Materials for Textiles: Mechanism, Mathematical Modeling, and Challenges, Adv. Funct. Mater. 31 (2021) 2100257. https://doi.org/10.1002/adfm.202100257
[10] P.A. Quiñonez, L. Ugarte-Sanchez, D. Bermudez, P. Chinolla, R. Dueck, T.J. Cavender-Word, D.A Roberson, Design of Shape Memory Thermoplastic Material Systems for FDM-Type Additive Manufacturing, Materials 14 (2021) 4254. https://doi.org/10.3390/ma14154254
[11] G.W. Ehrenstein, Structure of Polymeric Materials, In: Polymeric materials, Hanser, Ohio, 2001, pp. 61-141. https://doi.org/10.3139/9783446434134.004
[12] A. Bartolotta, G. Di Marco, F. Farsaci, M. Lanza, M. Pieruccini, DSC and DMTA study of annealed cold-drawn PET: a three-phase model interpretation, Polym. 44 (2003) 5771-5777. https://doi.org/10.1016/S0032-3861(03)00589-5
[13] R. Nisticò, Polyethylene terephthalate (PET) in the packaging industry, Polym. Test. 90 (2020) 106707. https://doi.org/10.1016/j.polymertesting.2020.106707
[14] P. Benyathiar, P. Kumar, G. Carpenter, J. Brace, D.K. Mishra, Polyethylene Terephthalate (PET) Bottle-to-Bottle Recycling for the Beverage Industry: A Review, Polym. 14 (2022) 2366. https://doi.org/10.3390/polym14122366
[15] D. Fico, D. Rizzo, R. Casciaro R, C. Esposito Corcione, A Review of Polymer-Based Materials for Fused Filament Fabrication (FFF): Focus on Sustainability and Recycled Materials, Polym. 14 (2022) 465. https://doi.org/10.3390/polym14030465
[16] B. Pricop, Ș.D. Sava, N.M. Lohan, L.G. Bujoreanu, DMA Investigation of the Factors Influencing the Glass Transition in 3D Printed Specimens of Shape Memory Recycled PET, Polym. 14 (2022) 2248. https://doi.org/10.3390/polym14112248
[17] V. Ermolai, A. Sover, G. Nagîț, A.I. Irimia, 2022, Shape recovery properties of PET-based 3D printed samples, presented at Innovative Manufacturing Engineering & Energy (IManEE), Iași, 17-19 November.

Materials Research Proceedings 28 (2023) 101-110 https://doi.org/10.21741/9781644902479-12

In process monitoring of geometrical characteristics in laser metal deposition: A comparative study

LATTE Marco[1,a *], GUERRA Maria Grazia[1,b], MAZZARISI Marco[1,c], ANGELASTRO Andrea[1,d], CAMPANELLI Sabina Luisa[1,e] and GALANTUCCI Luigi Maria [1,f]

[1]Dept. of Mechanics, Mathematics and Management, Politecnico di Bari, Via Orabona 4 - 70125 Bari, Italy

[a]marco.latte@poliba.it, [b]mariagrazia.guerra@poliba.it, [c]marco.mazzarisi@poliba.it, [d]andrea.angelastro@poliba.it [e]sabinaluisa.campanelli@poliba.it, [f]luigimaria.galantucci@poliba.it

Keywords: Laser Metal Deposition, Process Monitoring, Image Processing, Laser Line

Abstract. Although it is experiencing a wide diffusion, there are still several limits to the use of additive manufacturing (AM) for the fabrication of metal components. This includes low productivity, poor dimensional accuracy and uncertainty about the mechanical properties of the final parts. The main cause of these undesirable effects lies in the intrinsic complexity of the metal AM processes, such as Laser Metal Deposition (LMD). Accurate monitoring of the process and optimization of the process parameters are therefore of fundamental importance to ensure the overall quality of the product. Nowadays, several optical methods are under development for the monitoring of geometric characteristics and their correlation with specific process parameters, such as the standoff distance. This paper presents a comparative study between two optical in-process monitoring methods performed on AISI 316L multilayer samples produced by the LMD process. The first is a laser line section method based on a laser diode mounted on the deposition head, while the second method uses a high-resolution CMOS camera placed on the horizontal plane with a front view of the sample. In both cases, ad-hoc image processing algorithms were used to process the data, reconstruct the morphology of the component, and extract geometrical information. Results were then validated using an offline scanning system and micrographic analyses. Both proposed systems allowed the monitoring of the deposition quality using appropriate Key Performance Indicators (KPIs). The study showed a good capability of the prototype systems to detect deposition defects due to undesired variations of the process conditions and to monitor the standoff distance.

Introduction

Despite the widespread adoption of additive manufacturing (AM), there are still several limitations to the use of some technologies for the fabrication of metal components. Laser Metal Deposition (LMD) is an AM technique implemented in several industrial sectors thanks to its several advantages. Although it is still characterized by poor dimensional accuracy, mainly due to variable thermal cycling, localized heat accumulation, irregular powder flow, etc. [1]. In-situ monitoring and process control can be used for avoiding unpredictable build failures and minimizing the time and cost of post-process characterization procedures [2].

The monitoring of the LMD process is carried out in different fields: monitoring of the thermal field for the high temperatures developed by the laser during the process [3], monitoring of the powder flow [4] and monitoring of geometrical parameters of the produced component [5]. Among the several outputs that need to be monitored and controlled to ensure the quality of the process/component, standoff distance and layer height are very important. In fact, a wrong standoff distance can lead to height deviations from the ideal building path [6].

Content from this work may be used under the terms of the Creative Commons Attribution 3.0 license. Any further distribution of this work must maintain attribution to the author(s) and the title of the work, journal citation and DOI. Published under license by Materials Research Forum LLC.

Nowadays, several optical methods are under development for the monitoring of geometric characteristics and their correlation with specific process parameters. These methods are based mainly on the use of CCD/CMOS camera, laser scanners and structured light scanners.

The CCD/CMOS cameras are widely used, as they are flexible and easy to implement. These systems can be used to monitor the melt pool geometry, its temperature, and the layer height during the process. Although, these method are not particularly suited for the evaluation of complex freeform geometries and they have been mostly applied to simple geometries such as thin walls [7]. In some monitoring system setups, the CCD/CMOS cameras are mounted on the deposition head. Toyserkani and Khajepour [8] studied a closed-loop control system for LMD process, based on a CCD or CMOS camera. A pattern recognition algorithm returned the tracks height and the angle of solid/liquid interface in real-time and the PID controller used these feedbacks to modify the laser pulse energy in order to improve the output. Hsu et al. [9] proposed a vision-based inspection system made up of three digital cameras for measuring the cladding height in the Direct Energy Deposition (DED) process. After the calibration of the system, an image-processing technique is employed to isolate the laser nozzle and the melt pool in the captured images. The height of the coating is then calculated using the distance between the nozzle tip and the center of the melt pool.

On the other hand, laser scan systems are also implemented in various works in the literature. This technique is based on the triangulation principle and, mounting the equipment on the deposition head, a three-dimensional representation of the built component can be obtained [10]. With respect to the CCD/CMOS cameras, this monitoring technique is usually more expensive and require additional movements of the deposition head during scanning. Nevertheless, the monitoring of complex geometries is less difficult to perform. In [11], Rodriguez-Araujo et al. used a scanning system based on a CMOS camera coupled to a laser line mounted to the laser head to acquire the 2D profiles of the deposited layers. Cao et al. [12] used a commercial laser displacement sensor to study the surface topography detection of 24CrNiMo alloy steel produced by direct laser deposition. Arejita et al. [13] presented a closed-loop control algorithm that dynamically controlled the melt pool size, deposition speed and standoff distance combining data from a laser line profiler and a NIT Tachyon 1024 micro-core MWIR camera.

Structured light 3D imaging systems project coded patterns into the object rather than a single line and utilize a coding approach to calculate the depth of each observed point. The precision of the measurements strongly depends on the calibration of the equipment according to the measured volume, but an acceptable accuracy can also be obtained by basic equipment [7]. Some authors have used a 3D scanner to monitor the part geometry [14]. Garmendia et al. [15] have integrated a structured light-based scanner into a DED system in order to obtain a complete reconstruction of the manufactured geometry, making possible to monitor the product quality while it is being built, avoiding any suspension of the production process or offline measurement.

Due to the high cost of the components, the complexity of the additional movements required for 3D scanning and the harsh environment in which the systems are operating, laser line scanners and structured light 3D imaging have become popular only in recent years [7].

Regarding the investigated geometries, in the literature, most studies deal with the monitoring of monolayers or thin walls component [16,17], while few studies focus on the geometric monitoring of massive and multilayer components made by LMD [18,19].

This work presents a comparative study between two optical in-process monitoring methods performed on AISI 316L massive multilayer samples produced by the LMD process. The first is a laser line section method (LL) based on a laser diode mounted on the deposition head, while the second method uses a high-resolution CMOS camera (FC from now on) placed on the horizontal plane with a front view of the sample. In both cases, ad-hoc image processing algorithms were used to process the data, reconstruct the morphology of the component, and extract geometrical

information. Results were then validated through an offline scanning system and micrographic analyses.

Material and Methods

The monitoring systems compared in this work were a laser line scanner and a high-resolution camera (Fig. 1(a)). The first system comprised a laser line diode with λ=532 nm and 5 mW of power as light source and an industrial CMOS camera (IDS UI148xSE-C) as receiver equipped with a 12.5 mm lens. These two components were assembled on an aluminum support structure properly designed to make the system configuration flexible according to the sample geometry. This system was configured as a layer wise system and it requires an additional movement of the deposition head after the completion of each layer. Data were acquired in a video format with a framerate of 8 frame/sec, while the scan speed was set to 200 mm/min (equal to the deposition speed). In this way the resolution, meant as the distance between two adjacent points on each single profile, was on the order of 0.06 mm, while the resolution along the scan axis was on the order of 0.4 mm depending on the camera frame rate and scan speed.

The second monitoring system consisted of a high-resolution camera, DSLR CANON EOS 760D equipped with a 50 mm lens focused on its minimum distance. The camera was placed on the horizontal plane with the lens oriented to get the sample length (Fig. 1(a)).

With the aim to compare the above-described systems, two samples (sample A and B in Fig. 1(b)) were fabricated by means of a LMD system, with the same material, geometry, and process parameters.

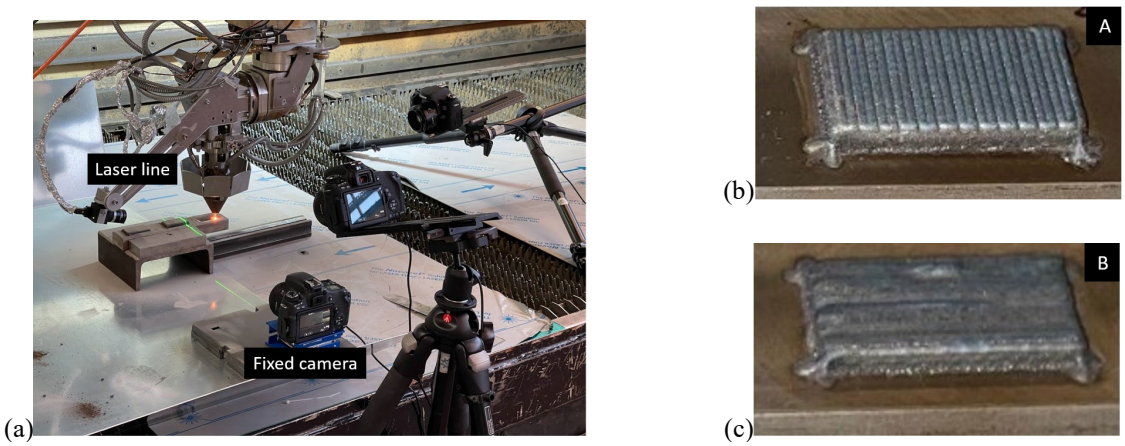

Fig. 1. (a) LMD with the monitoring systems (laser line on the left and fixed camera on the bottom), (b) sample A and (c) sample B.

The LMD system was a prototypal machine composed of a 3 kW CO_2 laser source and a pneumatic powder supply system. The AISI 316L stainless steel powders were carried by the gas to the 3-way multijet nozzle that conveyed them into the melt pool. Helium with a flow rate of 5 lpm was used as carrier gas, while with a flow rate of 11 lpm was used as shielding gas. The spot diameter was equal to 2 mm. The substrates (with a thickness of 25 mm) were also made of AISI 316L stainless steel. The samples were multilayer massive blocks (10 layers) with dimensions of 25 x 50 mm^2. These components were realized by adopting a bidirectional hatch strategy with a 90° rotation of the deposition direction at each layer and consequent modification of the deposition starting point. A 30% overlap between adjacent tracks was used. The sample A was realized in standard operating conditions, while during the fabrication of the sample B, defects were induced: laser shutdown at layer 3, powder flow suspension at layer 5, and deposition speed variations (50% and 150%) at layer 7.

Materials Research Proceedings 28 (2023) 101-110 https://doi.org/10.21741/9781644902479-12

Both methods followed a similar workflow, as shown in Fig. 2. The laser line scanner (LL), after the frame extraction and image processing (conducted by using an ad-hoc MATLAB algorithm), provided a detailed 3D point cloud of each sample layer. The latter was analyzed by GOM Inspect software for the computation of specific process indexes in order to check their suitability for process anomalies and defect detection. On the other hand, after the frame extraction and image processing, the high-resolution fixed camera (FC) provided a 2D single profile of the sample which was a local description of the geometry of the sample (the track facing the camera).

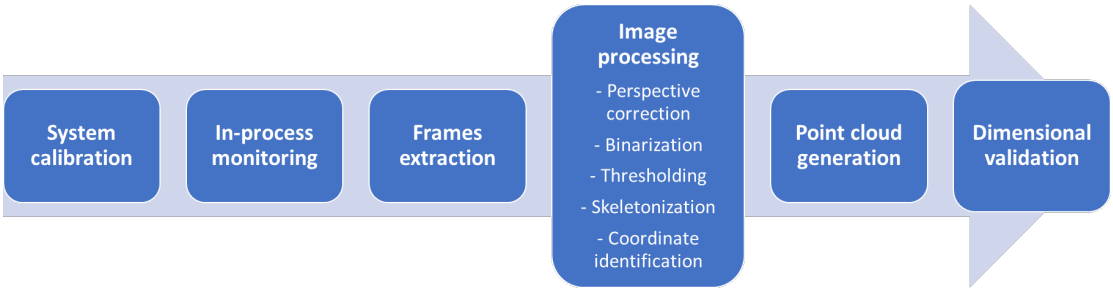

Fig. 2. Process monitoring workflow.

The collected data from both monitoring systems were then analyzed considering geometrical parameters. The average layer height was evaluated as the average distance of each layer point with respect to the base plate. The min-max layer height range and standard deviation were also considered.

The actual standoff distance was calculated as the difference between the design height of the tool center point (i.e., the tip of the nozzle) with respect to the base plate and the average height of the deposited layers, measured with the monitoring methods described above. In this way, it was evaluated the actual distance of the nozzle from the deposition plane and it was compared with the design (theoretical) standoff distance (*SOD_T*), which was set at 12 mm for this kind of nozzle. As can be seen from Fig. 3(a), the FC analysis of the different parameters can be done in-process. On the contrary, the LL analysis is performed at the end of the deposition of each layer. Fig. 3(b) shows one of the frames processed with this last method.

(a) 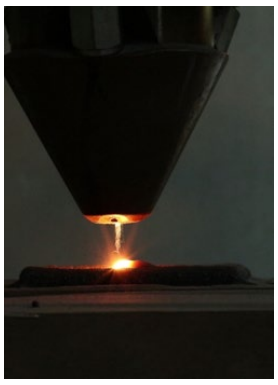 (b) 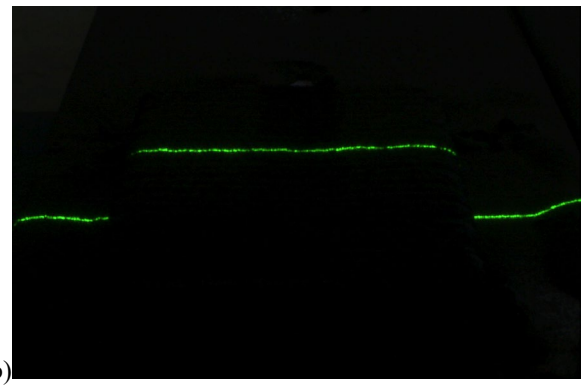

Fig. 3. (a) Frame analyzed by the FC system and (b) by LL system.

The validation procedure of the considered monitoring methods was carried out with an offline 3D scanning system (HandySCAN 3D by Creaform) with known accuracy used for the reconstruction and measurement of the external surface of the entire samples. Additionally, the samples were trimmed, polished and chemically etched, in order to perform a micrographic analysis (Hirox MXB-10C) for estimating the height value of each deposited layer.

Results and Discussion

The point clouds collected for each layer by the LL system were analyzed by means of the GOM Inspect software and, as first check, a colored map was extracted showing the height of each point with respect to the base plate (see Fig. 4). As it is possible to observe, the colored maps well described the layer surface, highlighting the differences between sample A and B with the detection of the areas affected by the induced defects. More in details, at layer 3 the laser shutdown produced a lack in the deposited material, which can be seen from the missing traces on the layer surface. At layer 5, the interruption of the powder flow had a similar effect on the part morphology. It is worth highlighting also how at layer 5 there is still a propagation of the defect induced at layer 3. Finally, at layer 7 the variation of the deposition speed induced a huge protrusion. It was not possible to perform the same analysis by the high-resolution camera due to the different nature of the two monitoring systems.

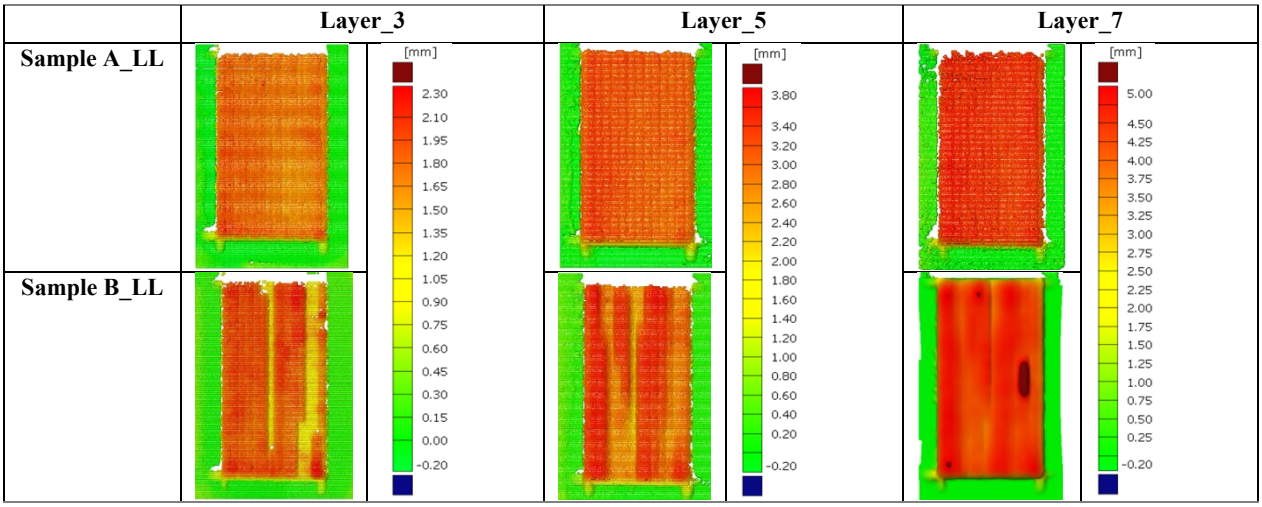

Fig. 4. Colored map showing the layer surface at layer 3, 5 and 7.

After the analysis of the entire layer surface made on the LL point clouds, the cumulative average height and the average layer height for each layer were evaluated for both LL and FC systems. The min-max height range and standard deviation were also computed in order to examine the variability within the entire layer surface for the LL and along the single profile for the FC. As shown in the Fig. 5(a), referring to the sample A, both systems enabled the effective monitoring of the cumulative average height (*H_avg*), showing a quite good convergence. This is because the layer surface was fairly homogeneous, without significant irregularities and defects, in accordance with the micrographic data and scan performed by the HandySCAN 3D. As reported in Fig. 5(b), the layer height values evaluated for each deposited layer (*Delta_H*) were quite similar with maximum differences on the order of 0.15 mm. It was also noted that the standoff distance (*SOD*) tends to decrease with the increase of the layer number. Slight reductions in standoff distance usually leads to a variation in the laser power density and powder flow distribution, deviating from the optimal conditions [4]. As a result, the amount of caught powder and the layer height decreases [20].

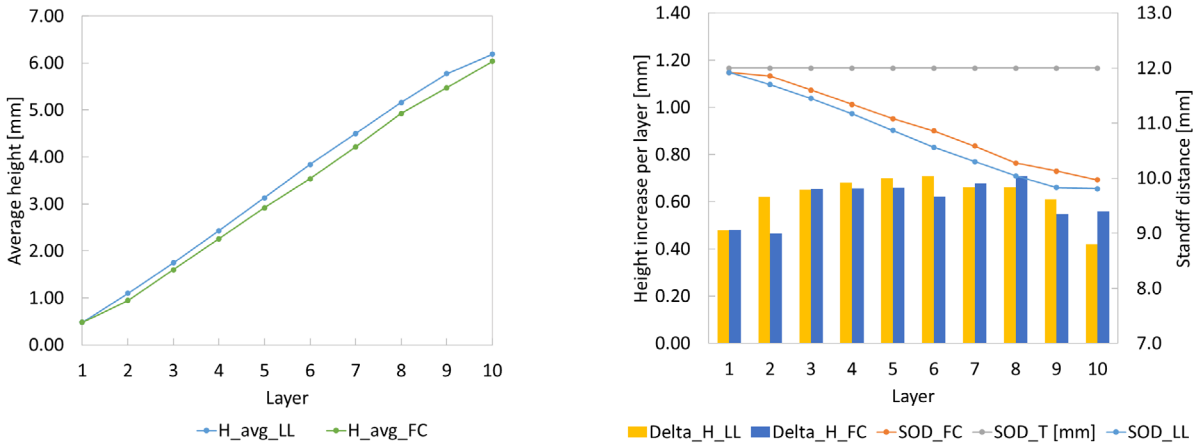

(a) (b)

Fig. 5. (a) Cumulative average height and (b) average layer height evaluated for each layer of the sample A.

The same evaluations were carried out on sample B. In this case, as can be observed from the graph (see Fig. 6), the deposition of ten layers was not possible as for sample A, due to the critical reduction of the standoff distance at layer 7 (layer growth higher than expected). The abrupt standoff distance reduction is to be avoided because it can cause equipment problems due to close interaction between nozzle and component. Considering the cumulative average height (see Fig. 6(a)) and the layer height (see Fig. 6(b)), there was still a convergence of results, with a significant difference registered at layer 5 where, from the colored map reported in Fig. 4, defects due to the powder flow interruption and the propagation of defect induced at layer 3 can be observed.

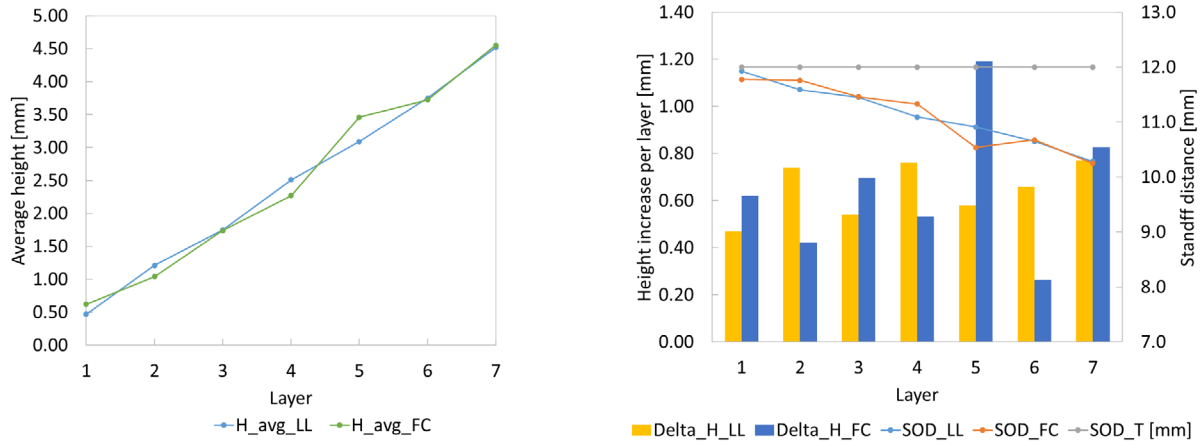

(a) (b)

Fig. 6. (a) Cumulative average height and (b) average layer height evaluated for each layer of sample B.

More generally, due to the 2D nature of the data coming from the FC, only the upper profile of the part facing the camera can be evaluated. This means that every process anomaly causing lack of materials within the layer, not affecting the first trace, is undetectable by this monitoring system (layer 5). On the other hand, when defects cause protrusions (anomalous material accumulation) within the deposited layer, even if these are not located along the side facing the camera, the FC technique is capable of detecting the irregularity (layer 7). Considering the layer 3, quite a good

convergence was found between LL and FC even in the presence of lack of material due to the laser interruption. Although, the area affected by the defect has a small extension with respect to the entire layer surface (see the colored map in Fig. 4), and it had a little influence on the average height value.

The standoff distance was also almost convergent with a more significant deviation registered at layer 5, for the above-mentioned reasons. Thus, both systems enabled the effective monitoring of the individual layer height and cumulative average height of the component, as well as the evaluation of the standoff distance for sample A and, to some extent, also in the presence of induced defects (sample B).

Although, from a monitoring point of view, the average layer height did not clearly indicate the onset of defects observed on sample B. For this reason, besides the average value, the min-max layer height range (*Range*) and standard deviation (*Std_Dev*) were also considered for the defect detection. In this case, considering first the LL system, there was an increase of these two indicators at layer 3, propagating at layer 4, a subsequent increase at layer 5 and another increase at layer 7 in correspondence of the last induced defect (see Fig. 7(a)).

Considering the FC system (Fig. 7(b)), in this case the range and the standard deviation were less sensitive to the induced defects except for the layer 7. The FC system indeed is capable of identifying, apart from the track facing the camera, only protrusions and accumulation of material exceeding the height of the visible track, see Fig. 3(a). Defects in the form of lack of material are not identified by this method.

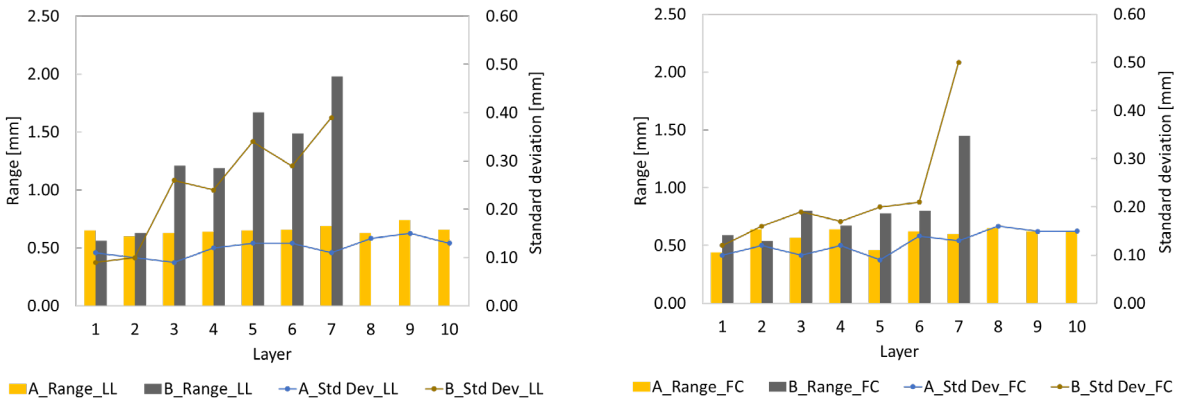

(a) (b)

Fig. 7. (a) Monitoring of the min-max layer height range and standard deviation performed by the LL method and (b) performed by the FC method.

Finally, the validation of the monitoring results was carried out considering the 3D reconstruction and the micrographic analysis of sample A. In the first method, the validation was conducted on the sample A. With this aim, a 3D comparison between the point cloud of the layer 10 obtained with the LL and the mesh obtained with the HandySCAN arm was carried out (see Fig. 8(a)). The estimated absolute average deviation was on the order of 0.055 mm, with maximum values approaching 0.2 mm. These deviations could be caused by unmolten residual powder that remains on the sample after the last layer deposition and which the process gas is unable to move away from the sample. This thin film of powder could slightly alter the in process scanning with LL.

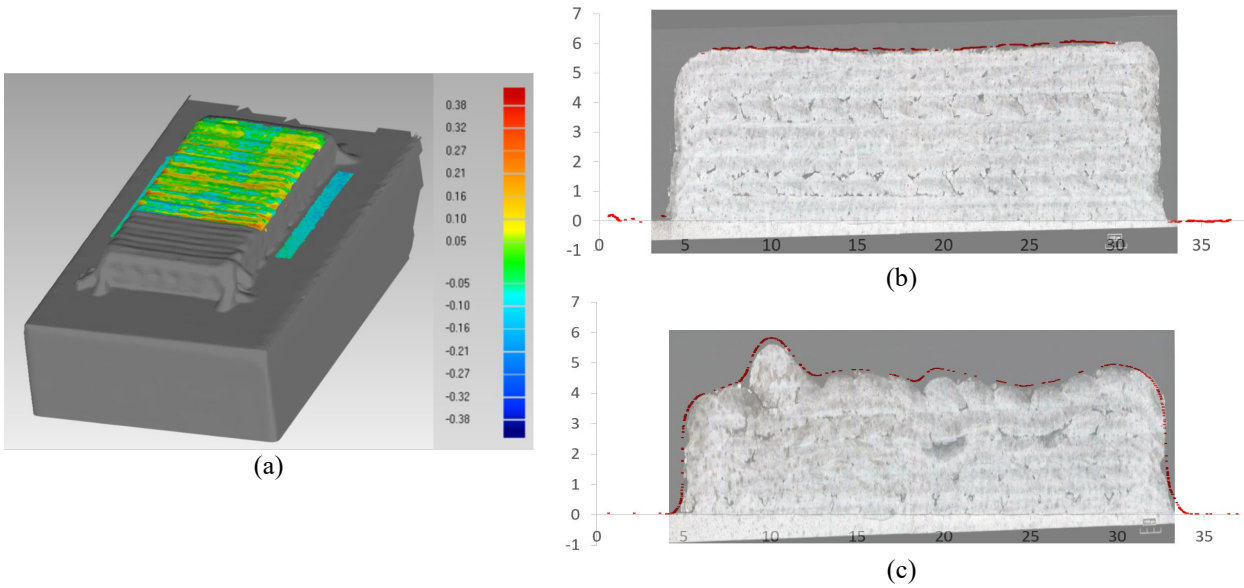

Fig. 8. (a) Comparison between the point cloud of the layer 10 obtained by the LL technique and the mesh obtained by the HandySCAN arm for sample A; (b) comparison between macrography and profile obtained by the LL method for sample A and (c) sample B.

The second method for the validation was a micrographic analysis. From Fig. 8(b) it is possible to observe a good correspondence between the transversal profile extracted from the LL system and the cross-section achieved by the micrographic analysis. Using this method, it was possible to evaluate the cumulative average height as well as each average layer height on the sample section. Micrographic analysis of sample B was also performed and compared with the profile extracted from a corresponding section (Fig. 8(c)).

Results for sample A are then reported in Fig. 9. The maximum deviation found with respect to metallography, for both techniques, was 0.13 mm.

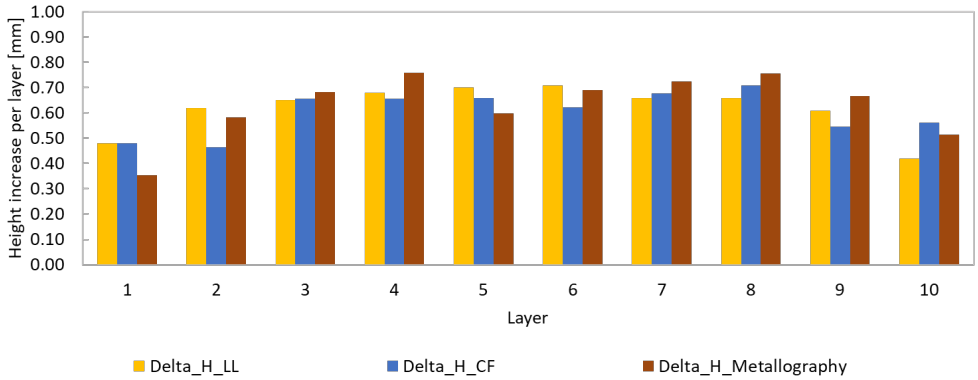

Fig. 9. Comparison of layers average heights as determined using each of the methods.

Summary

A comparative study between two optical in-process monitoring methods performed on AISI 316L multilayer samples produced by the LMD process has been presented. The first was a laser line section (LL) method based on a laser diode mounted on the deposition head, while the second method used a high-resolution CMOS camera placed on the horizontal plane (FC) with a front view of the sample. The systems enabled the effective monitoring of the average height of deposited layers and of the standoff distance. These also allowed the monitoring of the deposition

quality by means of appropriate KPIs as the min-max layer height range and standard deviation. The conducted analysis has shown remarkable results:

- The LL system was capable of evaluating the entire layer surface. At first, the 3D comparison tool allowed the detection of all the induced process defects in both forms, lack of material (layer 3 and 5) and material accumulation (layer 7). It was also possible to assess the average layer height, the min-max range and the standard deviation of the height values recorded at each layer, allowing a rapid detection of process defects.
- The FC system was capable to retrieve a single profile of the side facing the camera, which was almost sufficient to describe the layer geometry for the sample A (without induced defects), but it became ineffective when tested on sample B for the detection of defects in the form of lack of material.
- Regarding the standoff distance evaluation, the FC method offer the possibility to measure it directly via image analysis (nozzle – part distance), while the LL method allows only an indirect computation through the calculation of the height of the part.
- Both methods are threshold dependent in the image analysis, especially the FC when it is used in-process due to continuous variation of environmental light conditions. The use of illuminators is than recommended, in both closed and open chamber applications.
- Another important criterion for comparing the LL and FC methods is the capability to work in-process. In this case the FC method has advantages because it can work in-process and it does not require an additional movement of the deposition head to measure the layer surface. In this way, it can evaluate both the layer height and the standoff distance and it can generate an alert when the measured values exceed selected safety thresholds. On the other hand, the FC method appears to be more suitable for single track monitoring and generally simple geometries, while LL is more suitable for complex geometries requiring multi track and multilayer strategies.

Acknowledgements
This research work was undertaken in the context of the project PON ―R&I 2014 - 2020 ARS01_00906 ―Soluzioni Innovative per la qualità e la sostenibilità dei processi di ADDitive manufacturing.

References
[1] F. Kaji, H. Nguyen-Huu, A. Budhwani, J.A. Narayanan, M. Zimny, E. Toyserkani, A deep-learning-based in-situ surface anomaly detection methodology for laser directed energy deposition via powder feeding, J. Manuf. Process. 81 (2022) 624-637. https://doi.org/10.1016/j.jmapro.2022.06.046
[2] L. Yi, A. Shokrani, R. Bertolini, U. Mutilba, M.G. Guerra, E.G. Loukaides, P. Woizeschke, Optical sensor-based process monitoring in additive manufacturing, Procedia CIRP 115 (2022) 107-112. https://doi.org/10.1016/j.procir.2022.10.058
[3] M. Mazzarisi, A. Angelastro, M. Latte, T. Colucci, F. Palano, S.L. Campanelli, Thermal monitoring of laser metal deposition strategies using infrared thermography, J. Manuf. Process. 85 (2023) 594-611. https://doi.org/10.1016/j.jmapro.2022.11.067
[4] M. Mazzarisi, V. Errico, A. Angelastro, S.L. Campanelli, Influence of standoff distance and laser defocusing distance on direct laser metal deposition of a nickel-based superalloy, Int. J. Adv. Manuf. Technol. 120 (2022) 2407-2428. https://doi.org/10.1007/s00170-022-08945-3
[5] M.G. Guerra, V. Errico, A. Fusco, F. Lavecchia, S.L. Campanelli, L.M. Galantucci, High resolution-optical tomography for in-process layerwise monitoring of a laser-powder bed fusion technology, Additive Manufacturing 55 (2022) 102850. https://doi.org/10.1016/j.addma.2022.102850

[6] H. Borovkov, A.G. de la Yedra, X. Zurutuza, X. Angulo, P. Alvarez, J.C. Pereira, F. Cortes, In-Line Height Measurement Technique for Directed Energy Deposition Processes, JMMP 5 (2021) 85. https://doi.org/10.3390/jmmp5030085
[7] I. Garmendia, J. Leunda, J. Pujana, A. Lamikiz, In-process height control during laser metal deposition based on structured light 3D scanning, Procedia CIRP 68 (2018) 375-380. https://doi.org/10.1016/j.procir.2017.12.098
[8] E. Toyserkani, A. Khajepour, A mechatronics approach to laser powder deposition process, Mechatronics. 16 (2006) 631–641. https://doi.org/10.1016/j.mechatronics.2006.05.002.
[9] H.-W. Hsu, Y.-L. Lo, M.-H. Lee, Vision-based inspection system for cladding height measurement in Direct Energy Deposition (DED), Additive Manufacturing 27 (2019) 372-378. https://doi.org/10.1016/j.addma.2019.03.017
[10] S. Donadello, M. Motta, A.G. Demir, B. Previtali, Coaxial laser triangulation for height monitoring in laser metal deposition, Procedia CIRP 74 (2018) 144-148. https://doi.org/10.1016/j.procir.2018.08.066
[11] J. Rodriguez-Araujo, J.J. Rodriguez-Andina, ROS-based 3D on-line monitoring of LMD robotized cells, in: 2015 IEEE 13th International Conference on Industrial Informatics (INDIN), IEEE, Cambridge, United Kingdom, 2015, pp. 308–313. https://doi.org/10.1109/INDIN.2015.7281752
[12] L. Cao, S. Chen, M. Wei, Q. Guo, J. Liang, C. Liu, M. Wang, Study of surface topography detection and analysis methods of direct laser deposition 24CrNiMo alloy steel, Optics & Laser Technology 135 (2021) 106661. https://doi.org/10.1016/j.optlastec.2020.106661
[13] B. Arejita, I. Garmendia, J.F. Isaza, A. Zuloaga, Dynamic control for LMD processes using sensor fusion and edge computing, Procedia CIRP 111 (2022) 308-312. https://doi.org/10.1016/j.procir.2022.08.026
[14] I. Garmendia, J. Pujana, A. Lamikiz, J. Flores, M. Madarieta, Development of an Intra-Layer Adaptive Toolpath Generation Control Procedure in the Laser Metal Wire Deposition Process, Materials 12 (2019) 352. https://doi.org/10.3390/ma12030352
[15] I. Garmendia, J. Flores, M. Madarieta, A. Lamikiz, L.G. Uriarte, C. Soriano, Geometrical control of DED processes based on 3D scanning applied to the manufacture of complex parts, Procedia CIRP 94 (2020) 425–429. https://doi.org/10.1016/j.procir.2020.09.158
[16] M. Borish, B.K. Post, A. Roschli, P.C. Chesser, L.J. Love, K.T. Gaul, Defect Identification and Mitigation Via Visual Inspection in Large-Scale Additive Manufacturing, JOM 71 (2019) 893-899. https://doi.org/10.1007/s11837-018-3220-6
[17] J. Ye, N. Alam, A. Vargas-Uscategui, M. Patel, A. Bab-Hadiashar, R. Hoseinnezhad, I. Cole, In situ monitoring of build height during powder-based laser metal deposition, Int. J. Adv. Manuf. Technol. 122 (2022) 3739-3750. https://doi.org/10.1007/s00170-022-10145-y
[18] P. Xu, X. Yao, L. Chen, C. Zhao, K. Liu, S.K. Moon, G. Bi, In-process adaptive dimension correction strategy for laser aided additive manufacturing using laser line scanning, J. Mater. Process. Technol. 303 (2022) 117544. https://doi.org/10.1016/j.jmatprotec.2022.117544
[19] I. Garmendia, J. Pujana, A. Lamikiz, M. Madarieta, J. Leunda, Structured light-based height control for laser metal deposition, J. Manuf. Process. 42 (2019) 20-27. https://doi.org/10.1016/j.jmapro.2019.04.018
[20] H. Tan, W. Shang, F. Zhang, A.T. Clare, X. Lin, J. Chen, W. Huang, Process mechanisms based on powder flow spatial distribution in direct metal deposition, J. Mater. Process. Technol. 254 (2018) 361–372. https://doi.org/10.1016/j.jmatprotec.2017.11.026

Materials Research Proceedings 28 (2023) 111-118 https://doi.org/10.21741/9781644902479-13

Optical absorption and conduction of copper carbon nanotube composite for additive manufacturing

AYUB Hasan[1,a *], KHAN Lehar Asip[1,b], MCCARTHY Eanna[1,c], AHAD Inam Ul[1,d], SREENILAYAM Sithara P.[1,e], FLEISCHER Karsten[1,f] and BRABAZON Dermot[1,g]

[1]I-Form Advanced Manufacturing Research Centre, School of Mechanical and Manufacturing Engineering, Dublin City University, Dublin, Ireland

[a]hasan.ayub@dcu.ie, [b]leharasip.khan@dcu.ie, [c]eanna.mccarthy@dcu.ie, [d]inamUl.ahad@dcu.ie, [e]sithara.sreenilayam@dcu.ie, [f]karsten.fleischer@dcu.ie, [g]dermot.brabazon@dcu.ie

Keywords: Optical Absorption, Carbon Nanotube, Laser Sintering, Thermal-Electrical Expansion, Additive Manufacturing

Abstract. The applications of nanotechnology are growing widely as nanoscale structures provide unique properties such as high surface area unique plasmonic response and excellent conductivity that can be utilized for a wide range of applications. Optical absorption expansion of copper using carbon nanotube composite is one of the applications of nanotechnology for additive manufacturing of metals, particularly copper. Cu-CNTs mixtures at different percentage concentrations will be prepared via Resodyn, an acoustic mixer machine. Pure copper powder will be used with a spherical powder shape. The evaluation of the samples will be performed via spectroscopy to determine the reflection and thermal absorption of the light by the Cu-CNTs composition. The enhancement in the thermal absorption of Cu powder via additions of CNTs leads to the improvement in the bonding of particles by absorbing laser power. Due to the lower thermal expansion coefficient, sintering is possible at lower laser powers < 40%.

Introduction

Copper is one the unique metals having ductility and exceptional electrical and thermal conductivities of $58x10^6$ S/m and 400 W/m.K [1-3] Therefore, many engineering applications are possible due to these properties such as heat exchangers and heat sinks, thermal energy storage systems, etc., [4,5]. Moreover, heat transfer is further enhanced by making some geometrical changes by making fins, extended structures, and porous structures[6]. Metal Additive manufacturing (AM) has made it possible to manufacture complex structures with high accuracy and less material loss. Therefore, several complex components are being manufactured using different metals [7,8]. Despite having favorable properties, copper has the disadvantage of having high reflectivity which makes it difficult to manufacture using AM techniques such as L-BPF. The reflectivity of the copper can be reduced by increasing the absorption of the copper powder.

Considerable work is noted in the literature on additive manufacturing of copper powder. Lykov et.al [9] performed the additive manufacturing of pure copper powder using selective laser melting with a laser power of 200W. They manufactured cuboidal shape geometries and measured the maximum achieved relative densities. A maximum of 88% relative density was reported at 200W of the laser power. Jadhav et.al [10] also used pure copper to produce parts with a laser power of 300W. In their work lower relative densities were achieved due to insufficient diffusion of heat within the copper particles. Due to very high thermal conductivity, the heat was dissipated instantly from the melt pool. The issue of the lower laser power was addressed in numerous studies using high laser power up to 1kW which resulted in 96% relative densities of manufactured parts. However high laser power resulted in significant reflectivity due to that damage to the optical mirror [11–13]. In solution to this problem, the green and blue lasers were also by various authors

Content from this work may be used under the terms of the Creative Commons Attribution 3.0 license. Any further distribution of this work must maintain attribution to the author(s) and the title of the work, journal citation and DOI. Published under license by Materials Research Forum LLC.

[14]. The remedy to address this problem is either by playing with laser parameters such as laser power and scan speed etc. or by modifying the absorption rate of the copper powder.

In the present work, Cu-CNTs powder mixture with CNTs having percentage concentrations in the range of 0.1%-0.3% CNTs was prepared using a Resodyn, an acoustic mixer machine. The cold isostatic hydraulic pressing method was used to fabricate the copper pellets. The copper powder was used with a spherical shape[15]. The evaluation of the samples was performed via spectroscopy to determine the reflection and absorption of the light by the Cu-CNTs composition. The enhancement in the thermal absorption of Cu powder via additions of CNTs leads to the improvement in the bonding of particles by absorbing laser power. Due to the lower thermal expansion coefficient, sintering is possible at lower laser powers < 40%.

Material and Methods

The experimental setup for the laser sintering of carbon nanotubes composite mixed copper powder consisted of Resodyn, an acoustic mixer machine to mix Cu-CNTs in different concentrations. Cu-CNTs pellets were produced via compaction by using Autotouch 40Ton Hydraulic Press. Sintering was performed via fiber laser (I.P.G) having a wavelength of 1064nm and 200W power in a custom made sintering rig capable of maintaining an inert environment to avoid any oxidization and contamination.

The copper powder and CNTs were mixed using Resodyn, an acoustic mixer machine, and compacted using the hydraulic press. The effects of mixing ratios on the quality of samples are investigated experimentally. From Sigma Aldrich, a copper powder with spherical-shaped powder particles was used. Different weight percentage ratios of CNTs were added to achieve higher laser absorption and less reflection. In mixing and compaction, CNTs weight percentage was the operating parameter. To get the same size pellets compaction parameters were the same for all sets of experiments. During the compaction process, a die with a diameter of 20mm is used, which results for each sample, the diameter remains constant.

The Cu-CNTs composite spectroscopy was performed with Perkin Elmer Spectrum Two FTIR a well-known and easy-to-use equipment for spectroscopy.

Table 1. Physical properties of Copper and CNTs.

Product Form	Particle Size	Purity (%)	Melting/Boiling (C)	Density (kg/m^3)
Powder (spheroidal)	10-25 μm	98%	1083.4/2567	8960
Carbon nanotube (Multiwalled)	10-20 nm	95%	3652-3697	2200

Compaction of Cu-CNTs.

The present work demonstrates cold isostatic pressing using hydraulic press technology of Cu-CNTs mixtures. Spherical-shaped copper powder is received from Sigma-Aldrich with a purity of 98% having a particle size of 10-25 μm and multiwalled carbon nanotubes are received from Cheap Tubes with a purity of 95% and length of 10-30 μm. Further technical and physical properties of copper powders and carbon nanotubes are listed in Table 1. Cold isostatic hydraulic pressing is a well known method for powder compaction. The compaction process is illustrated in Fig. 1, where the compressive force is applied by moving the piston from the bottom of the compaction die. 20mm diameter Cu-CNTs pellets were produced using this die. The compaction pressure for each pellet was 793 MPa and the compaction holding time was 10 mins.

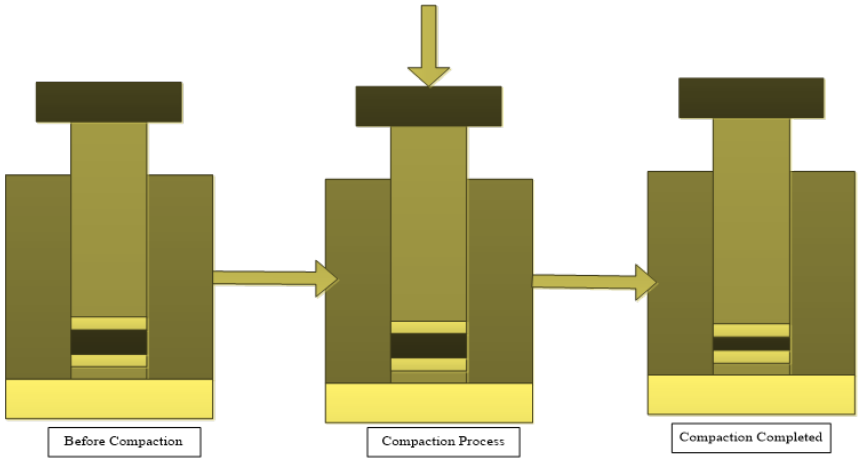

Fig. 1. The Schematic Diagram of Autotouch Hydraulic press compaction process.

Laser sintering.

The laser sintering of the Cu-CNTs composite pellets was carried in controlled temperature and air pressure, using a specially designed laser sintering rig shown in Fig. 2. The laser sintering rig contains two Calex PMU21 USB infrared temperature sensors to record the sintering temperature, UVFS Broadband Precision Window, -B Coated from Thorlabs to allow the laser beam to the sample and Argon gas connection to avoid oxidation and contamination during laser sintering. Fiber laser from IPG of 200W is used for laser sintering having wavelength of 1064nm. The laser sintering parameters are shown in Table 2. The laser spot size is fixed at 5µm.

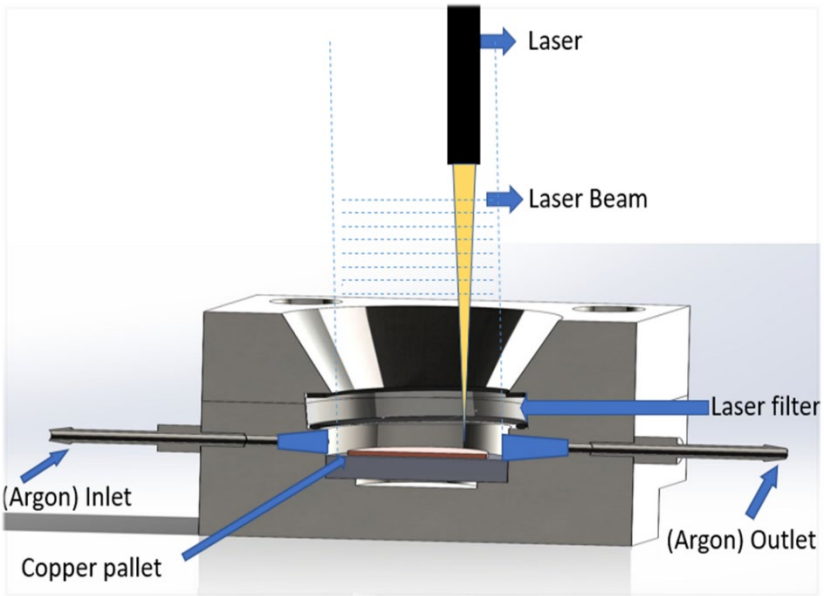

Fig. 2. Schematic of laser sintering setup demonstrating the passage for laser beam, argon inlet. Outlet, laser filter and copper pellet in the inert environment.

Table 2. Laser sintering parameters of sintering which include the laser power, laser spot size, and laser scan speed.

Power Percentage (%)	**Spot size** (μm)	**Scan Speed** (mm/s)
15	5	5
20	5	5
20	5	2
25	5	2
40	5	1
40	5	1
40	5	1
40	5	1
40	5	1

Results and Discussion

Spectroscopy of Cu-CNTs Composition.

Before performing the spectroscopy on Cu-CNTs samples, the reflectance of the pure copper pellet was measured and compared with the broadband mirror.

Fig. 3 presented the reflectance of pure copper where the reflectance of the copper pellet was measured laser wavelength of up to 1070 nm. The reflection and absorption of the Cu-CNTs and the pure copper are shown in Fig. 4. From the spectroscopy of the pure copper powder, it is observed that reflection is 100% at 1064 nm of wavelength. This high reflection of copper powder causes difficulties in laser sintering at low laser power and the reflection of the laser beam can damage the laser source. The addition of multiwalled CNTs reduces the reflection of the copper and increases the laser absorption. From Fig. 4 it can be analysed that the reflection of the Cu-CNTs gradually decreases with the increase of CNTs. The addition of 2% (mass) of CNTs reduced copper powder reflection at 1064 nm of wavelength by 8% compared to the pure powder.

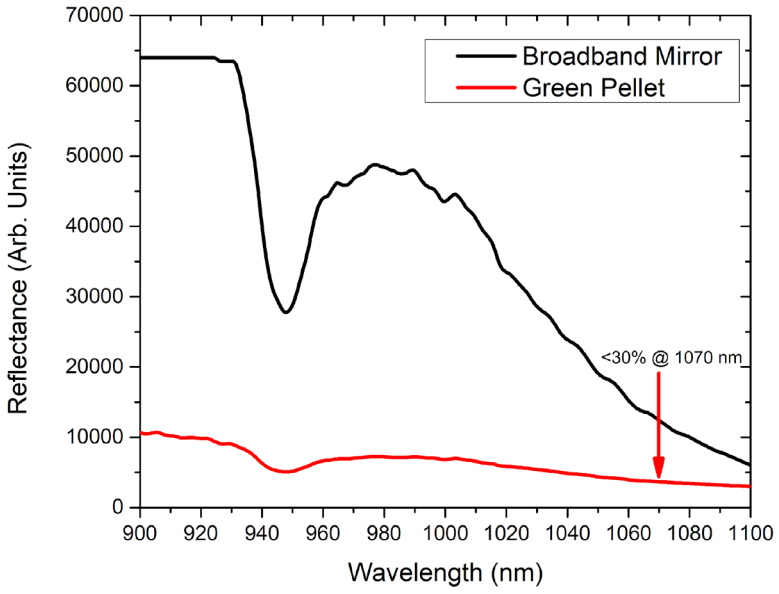

Fig. 3. Comparison of the spectroscopy results of green pellet and broadband mirror.

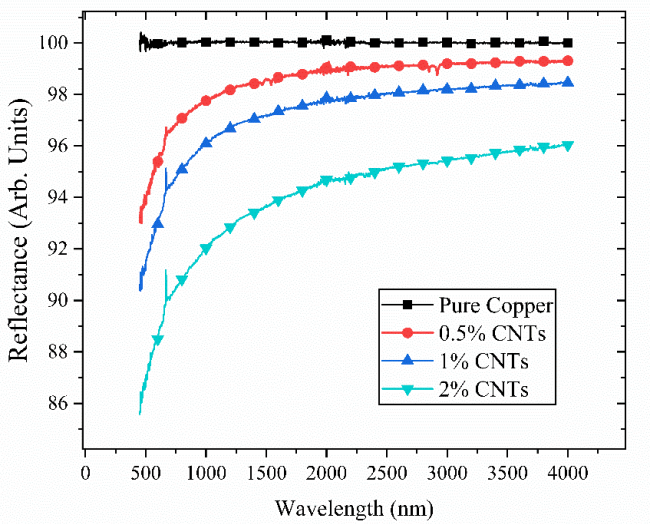

Fig. 4. The results for the reflectance of pure copper powder and Cu-CNTs powder with 0.5%-2% CNTs by mass percentage.

Laser sintering of Cu-CNTs Composition.

The pure copper compacted pellet was first laser sintered in the specially designed laser sintering rig shown in Fig. 2. The pure copper powder compacted pellet was first sintered to adjust the laser parameters. Fig. 5(a) shows the laser sintered pure copper pellet in the laser sintering rig with an Argon gas environment to prevent contamination and oxidation. Fig. 5 (b) shows the laser sintered pure copper pellet in an open atmosphere environment which clearly shows the contamination and oxidation. The laser parameter for pure copper sintering is shown in the Table 2. Fig. 6 (a), (b), (c), and (d) present the maximum pellet temperature for different scan speeds and laser power percentages. Fig. 6 (a) indicates that increasing the power percentage up to 40% and lowering the scan speed of the laser from 5 mm/s to 1 mm/s resulted in the pellet temperature being up to 570°C. Similarly, Fig. 6 (b),(c), and (d) present the temperature rise as a function of laser power and scanning speed for the Cu-CNTs powder containing 0.5%-1.5% of the CNTs. The same sintering parameters were used for the copper pellet having CNTs. Cu-CNTs pellet having 0.5% (mass%) of CNTs achieved the maximum temperature of 594 °C while with 1% and 1.5%, CNTs raised the pellet temperature up to 618°C and 657°C. Comparing to pure copper, with 1.5% CNTs 13% higher temperature was achieved which shows better absorption of the laser beam power into copper pellets.

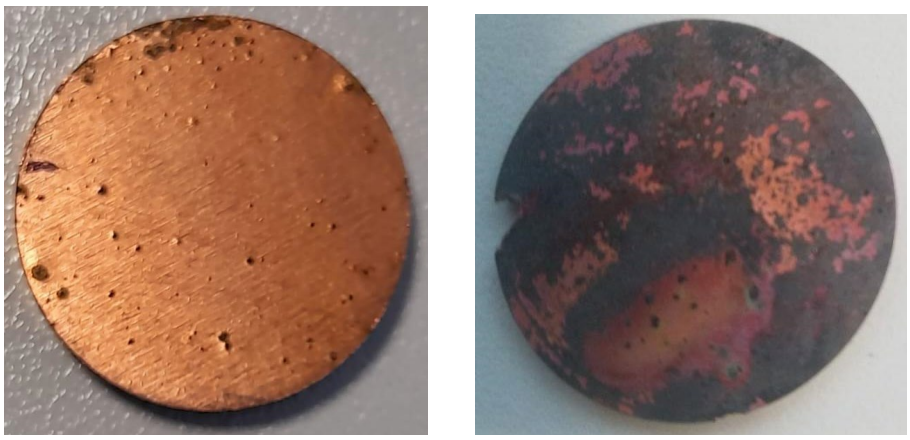

(a) (b)

Fig. 5. (a) Laser sintered pure copper pellet in sintering rig (b) laser sintering of copper pellet in open atmosphere environment.

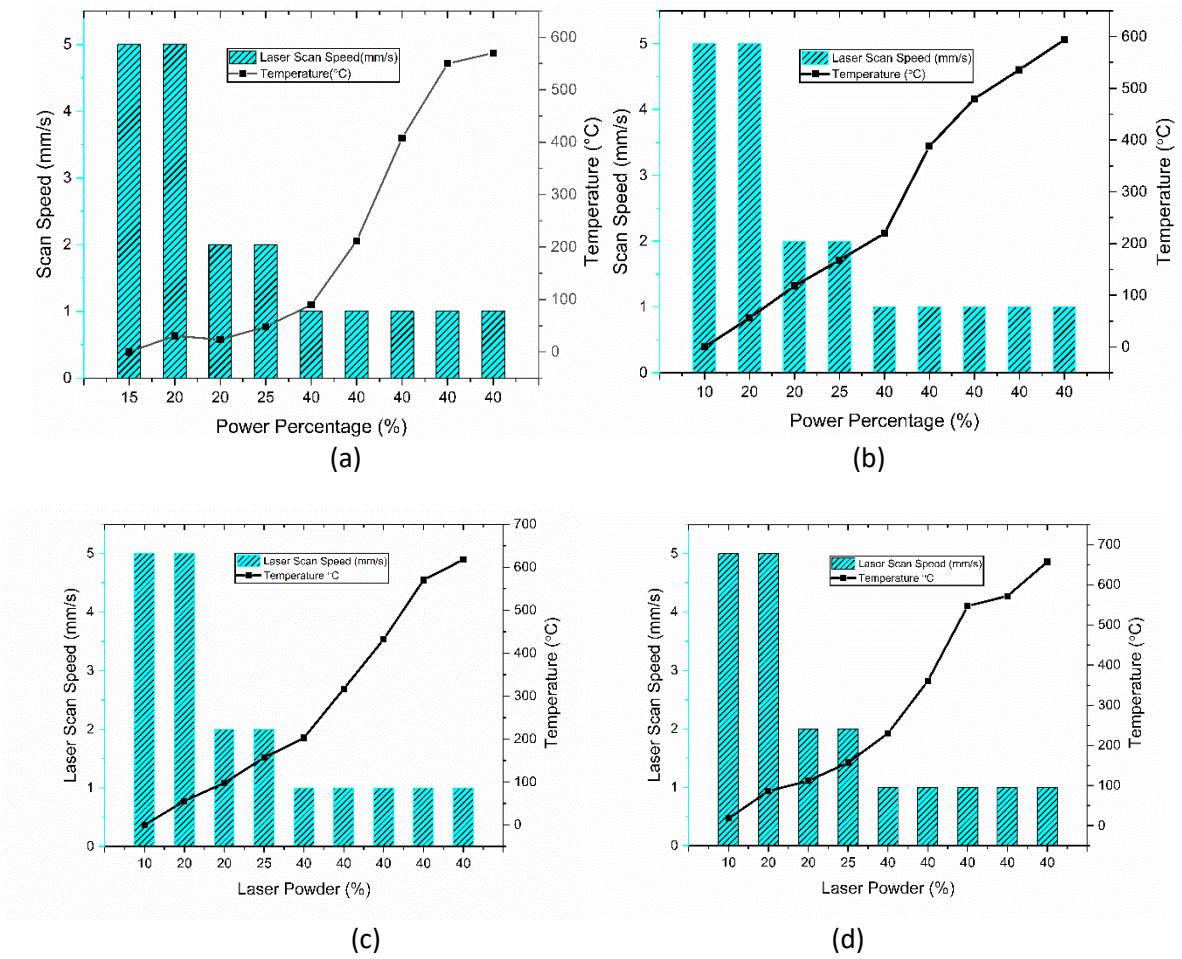

Fig. 6. The sintering temperature of pellet as a function of laser power percentage and laser scan speed (a) Pure copper powder (b) 0.5% CNTs mixed copper composite (c) 1% CNTs mixed copper composite (d) 1.5% CNTs mixed copper composite.

Microstructure of laser sintered pellets.

Cu-CNTs compacted laser sintered samples have mechanical properties that are determined by the microstructure distribution. The microstructure of the laser sintered pellets were analysed using Zeiss EVO LS-15 SEM. Fig. 7 shows the SEM images of laser sintered pellets without using polishing. Fig. 7 (a) shows the microstructure of the laser sintered pure copper pellet. The higher reflection of pure copper causes the loss of mechanical bonding of the powder particles leaving small pores on the surface. The addition of 0.5% of CNTs in the copper powder increased the bonding of the powder particles. Fig. 7 (b) shows the overlapping of the powder particles. In Fig. 7 (c), the addition of CNTs 1% of copper resulted in good consolidation of the particles and increases small pores on the surface comparing 0.5% of CNTs. The increase of CNTs percentage of 1.5% in copper resulted in high density in the pellet. Fig. 7 (d) shows the melted particles due to heat expansion in the pellet. The higher persistence of CNTs in the copper caused coarse particles on the surface of the pellet.

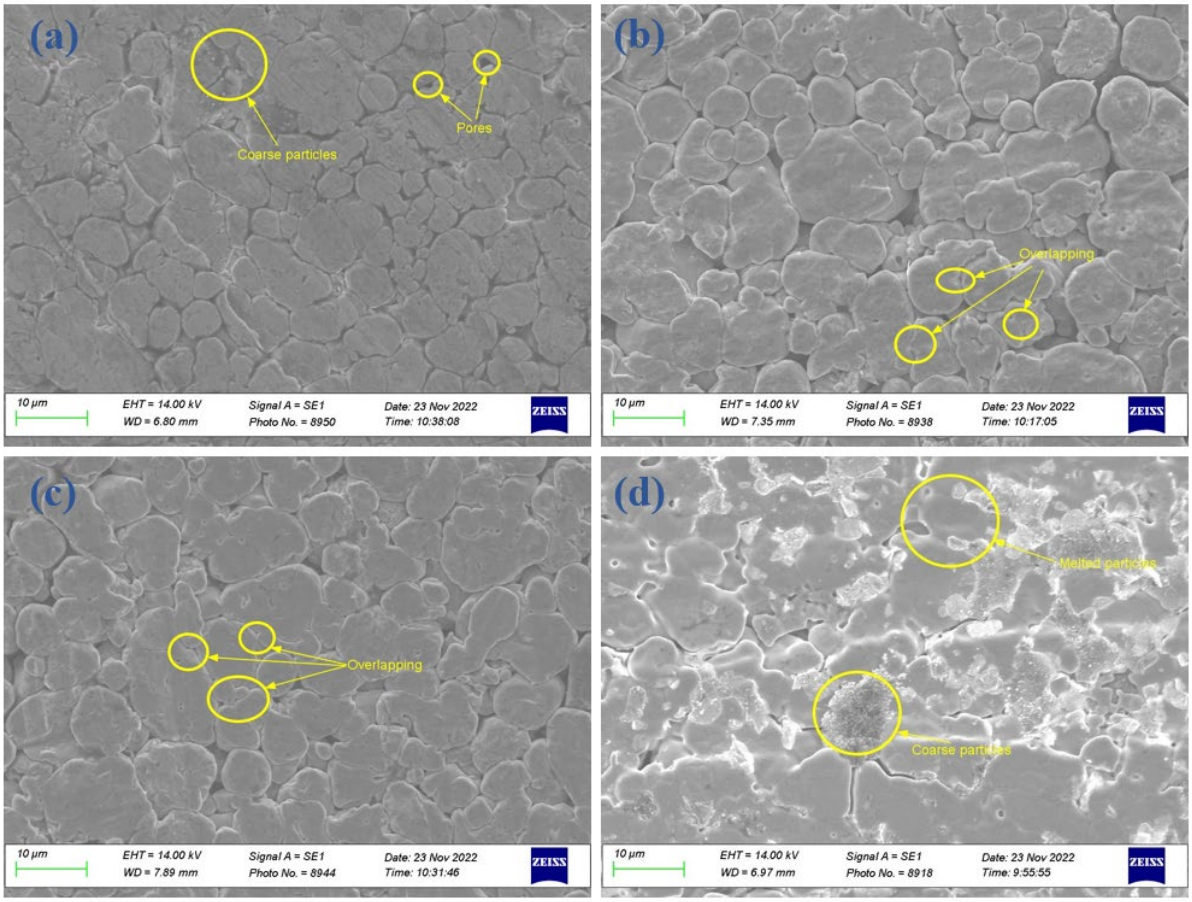

Fig. 7. SEM image of laser sintered samples (a) Pure copper pellet (b) 0.5% Cu-CNTs (c) 1% Cu-CNTs (d) 1.5% Cu-CNTs.

Summary

In this paper, the copper powder absorption was modified by adding different percentages of carbon nanotubes (CNTs). CNTs were added up to 1.5% to increase the laser power absorption ability of the copper powder. Spectroscopy was performed and results revealed that the reflectance of the copper powder by the addition of CNTs was decreased by 8%. Lesser contamination and oxidization were observed by using a specially designed laser sintering rig. The temperature of the pellet during sintering was controlled by adjusting the laser operating parameters. Improved consolidation of powder particles was observed by using a sintering rig as compared to the laser sintering in the open atmosphere environment.

Acknowledgment

This work is supported in part by a research grant from Sci-ence Foundation Ireland (SFI) under Grant Numbers 16/RC/3872, 19/US-C2C/3579, and is co-funded under the European Regional Development Fund.

References

[1] P. Roy, A.D. Bolshakov, Temperature-controlled switching of plasmonic response in gallium core-shell nanoparticles, J. Phys. D. Appl. Phys. 53 (2020) 465303. https://doi.org/10.1088/1361-6463/abaae2

[2] S. Durairaj, B. Sidhureddy, J. Cirone, A. Chen, Nanomaterials-based electrochemical sensors for in vitro and in vivo analyses of neurotransmitters, Appl. Sci. 8 (2018) 1504. https://doi.org/10.3390/app8091504

[3] S.P. Sreenilayam, I.U. Ahad, V. Nicolosi, V. Acinas Garzon, D. Brabazon, Advanced materials

of printed wearables for physiological parameter monitoring, Mater. Today 32 (2020) 147-177. https://doi.org/10.1016/j.mattod.2019.08.005
[4] A. Syafiuddin, M.A. Fulazzaky, S. Salmiati, A.B.H. Kueh, M. Fulazzaky, M.R. Salim, Silver nanoparticles adsorption by the synthetic and natural adsorbent materials: an exclusive review, Nanotechnol. Environ. Eng. 5 (2020) 1-18. https://doi.org/10.1007/s41204-019-0065-3
[5] L.J. Gibson, G. Editor, Cellular Solids 2003 (2021) 270-274.
[6] W. Tianquing, S.L. Poh, M. John, S. Chen-Nan, L.A Beng, Pool Boiling Heat Transfer Enhancement with Porous Fin Arrays Manufactured by Selective Laser Melting, Conference: 2019 18th IEEE Intersociety Conference on Thermal and Thermomechanical Phenomena in Electronic Systems (ITherm), Las Vegas, NV, USA, 2019, pp. 1107-1114, doi: 10.1109/ITHERM.2019.8757295.
[7] C.Y. Yap, C.K.Chua, Z.L. Dong, Z.H. Liu, D.Q. Zhang, L.E. Loh,S.L. Sing, Review of selective laser melting: Materials and applications, Appl. Phys. Rev. 2 (2015) 041101. https://doi.org/10.1063/1.4935926
[8] R. Neugebauer, B. Mller, M. Gebauer, T. Tppel, Additive manufacturing boosts efficiency of heat transfer components, Assem. Autom. 31 (2011) 344-347. https://doi.org/10.1108/01445151111172925
[9] P.A. Lykov, E.V. Safonov, A.M. Akhmedianov, Selective laser melting of copper, Mater. Sci. Forum 843 (2016) 284-288. https://doi.org/10.4028/www.scientific.net/MSF.843.284
[10] S.D. Jadhav, S. Dadbakhsh, L. Goossens, J.P. Kruth, J. Van Humbeeck, K. Vanmeensel, Influence of selective laser melting process parameters on texture evolution in pure copper, J. Mater. Process. Technol. 270 (2019) 47-58. https://doi.org/10.1016/j.jmatprotec.2019.02.022
[11] M. Colopi, L. Caprio, A.G. Demir, B. Previtali, Selective laser melting of pure Cu with a 1 kW single mode fiber laser, Procedia CIRP 74 (2018) 59-63. https://doi.org/10.1016/j.procir.2018.08.030
[12] T.T. Ikeshoji, K. Nakamura, M. Yonehara, K. Imai, H. Kyogoku, Selective Laser Melting of Pure Copper, JOM 70 (2018) 396-400. https://doi.org/10.1007/s11837-017-2695-x
[13] M. Colopi, A.G. Demir, L. Caprio, B. Previtali, Limits and solutions in processing pure Cu via selective laser melting using a high-power single-mode fiber laser, Int. J. Adv. Manuf. Technol. 104 (2019) 2473-2486. https://doi.org/10.1007/s00170-019-04015-3
[14] D. Heußen, Green Light for New 3D Printing Process. Available online: https://www.ilt.fraunhofer.de/en/press/press-releases/press-release-2017/press-release-2017-08-30.html (accessed 31 January 2023).
[15] H. Ayub, L.A. Khan, E. McCarthy, I.U. Ahad, K. Fleischer, D. Brabazon, Investigating the morphology, hardness, and porosity of copper filters produced via Hydraulic Pressing, J. Mater. Res. Technol. 19 (2022) 208-219. https://doi.org/10.1016/j.jmrt.2022.05.012

Materials Research Proceedings 28 (2023) 119-127 https://doi.org/10.21741/9781644902479-14

Influence of process parameters and head orientation on bead geometry for coaxial wire laser additive manufacturing

ROCH Clément[1,a *], TOURNIER Christophe[1,b] and LAVERNHE Sylvain[1,c]

[1] Université Paris-Saclay, ENS Paris-Saclay, LURPA, 91190, Gif-sur-Yvette, France

[a]clement.roch@ens-paris-saclay.fr, [b]christophe.tournier@ens-paris-saclay.fr, [c]sylvain.lavernhe@ens-paris-saclay.fr

Keywords: Additive Manufacturing, Laser Wire, Bead Geometry

Abstract. Among Directed Energy Deposition (DED) processes for metallic materials, Wire Laser Additive Manufacturing (WLAM), distinguishes itself by the use of a laser beam to melt a metallic wire and produce beads. Successive depositions of overlapping beads generate volumes to obtain parts. Thus, controlling bead geometries is essential for the additive manufacturing process. Several research works have studied these geometries and the influence of the main manufacturing parameters on their dimensions, but few investigated the effect of feeding direction or wire angle. Moreover, all studies on wire angle were carried out with lateral feeding and a constant laser orientation. This paper focuses on the influence of the deposition head orientation for a coaxial wire feed with 3 laser beams on bead geometries. An experimental campaign is conducted with different orientations relatively to a horizontal substrate and the external profiles are measured using optical instruments in order to extract the average profiles and characteristic dimensions. Results indicate an influence of the head rotation around its axis and lateral tilt on the height, width, and asymmetry of the beads.

Introduction

Metal additive manufacturing represents a major challenge for the development of new production strategies. Several processes are already in use, with either powder or wire as feedstock material. The use of wire results in simpler installations by reducing the constraints linked to powder handling, while producing solid parts with large volumes, as observed in Wire Arc Additive Manufacturing (WAAM). Wire Laser Additive Manufacturing (WLAM) is also based on a metallic wire, but with a laser beam as energy supply. Several configurations can be found in this category, depending on different technological choices or additional elements. For example, hot-wire limits the laser power required for manufacturing [1]. Differences are also possible in terms of material and power input, as the wire can be supplied along a different axis as the laser beam or along the same one, resulting in a coaxial configuration. This technology can be achieved by the use of multiple laser beams [2] or a ring beam [3].

Because of the wide variety of experimental devices and possible use cases, each installation requires the set-up of manufacturing recipes, often in an empirical manner by conducting several experiments. The usual approach consists in manufacturing single beads to define the initial process parameters, then in the study of overlapping beads to obtain surfaces, and finally in the study of layers, for single-bead walls or massive parts. Two profiles can be identified to describe single bead geometry: the external profile, also called reinforcement, and the internal profile, called penetration (Fig. 1). Rather than describing the complete geometries, specific dimensions are often used to characterize beads, as seen in figure 1 with width W, height H, contact angle θ_c and penetration P. Other typical dimensions not shown in the figure are the cross-section area A, which is considered as the additional area relatively to the initial part, and the dilution ratio, defined by the ratio between the area of the bead penetrating the substrate and the total area.

Content from this work may be used under the terms of the Creative Commons Attribution 3.0 license. Any further distribution of this work must maintain attribution to the author(s) and the title of the work, journal citation and DOI. Published under license by Materials Research Forum LLC.

The existing literature proposes several models to describe the reinforcement profiles, including elliptical [4,5], sinusoidal [6] or polynomial models of degree 2 [7,8] or 4 [9]. A comparative study by Ding et al [10] highlights that most of these models present a satisfactory representation of the beads, while Xiong et al [11] establish that the optimal model is linked to the ratio between wire feed speed and travel speed. Most studies focus on relations between bead dimensions and the main process parameters: laser power, wire feed speed and travel speed, showing that width and height can vary independently. Abioye et al [12] and Medrano-Tellez [13] establish that the link between power and wire feed speed is essential to guarantee stability, with two main process defects: dripping when power is too high compared to wire speed and stubbing when it is too low.

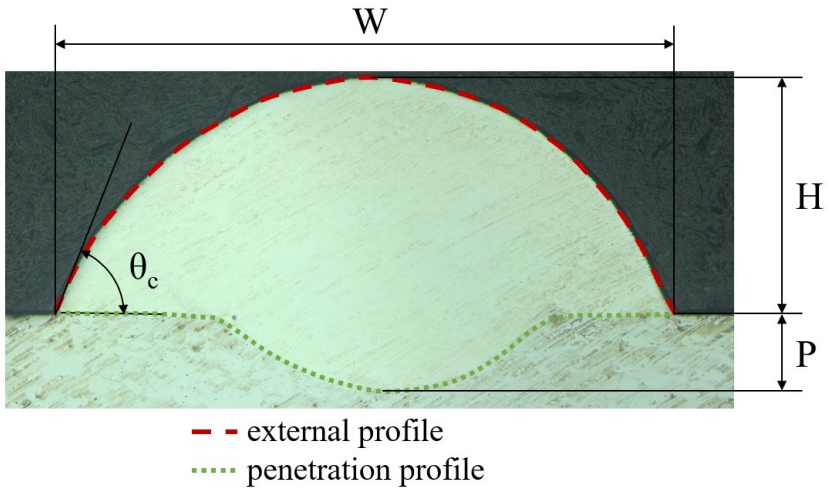

Fig. 1. Cross section of a bead with its dimensions.

One study focuses on feeding direction and found that it influences the appearance of the beads, with front feeding resulting in smoother beads [14]. For lateral configurations, where both laser beam and wire have different axes, the angle between wire and substrate also influences the produced geometries. However, the deposition head considered in this study uses three laser beams distributed around the wire to obtain a coaxial configuration. No articles investigating the influence of orientation and inclination on bead geometry for coaxial heads were found in the available literature. Most papers for coaxial technologies focus exclusively on wire feed speed, travel speed and laser power, with an occasional mention of the distance between the beams intersection point and the workpiece [15]. However, head orientation relatively to the travel direction can vary during manufacturing. In addition, variations in head tilt relatively to the substrate can be used to gain collision-free access to specific areas of the workpiece, or to manage gravity.

Therefore this study focuses on whether the tilt and orientation angles of a 3-beam coaxial head to the substrate have an effect on produced external bead geometries. This paper presents the experimental setup and process conditions before describing the method used to identify the effect of both head tilt and rotation. The obtained results are then presented and discussed before concluding.

Experimental Setup

The additive manufacturing cell (Fig. 2) is based on laser-wire technology, implemented by a Coaxworks head carried on a ABB IRB4600 robot and using an Ytterbium fibre laser power source with a maximum power of 4 kW. The feedstock is a 1.2 mm diameter IN718 wire and the parts are produced on S235 JR steel substrates which are 80mm long, 40mm wide and 10mm thick. A Xiris weld monitoring camera is attached to the head, enabling process monitoring. In addition,

the head's optics are protected by a flow of compressed air to expel smoke and spatters, and the weld pool is protected from oxidation by a flow of Argon at a pressure of 2 bars.

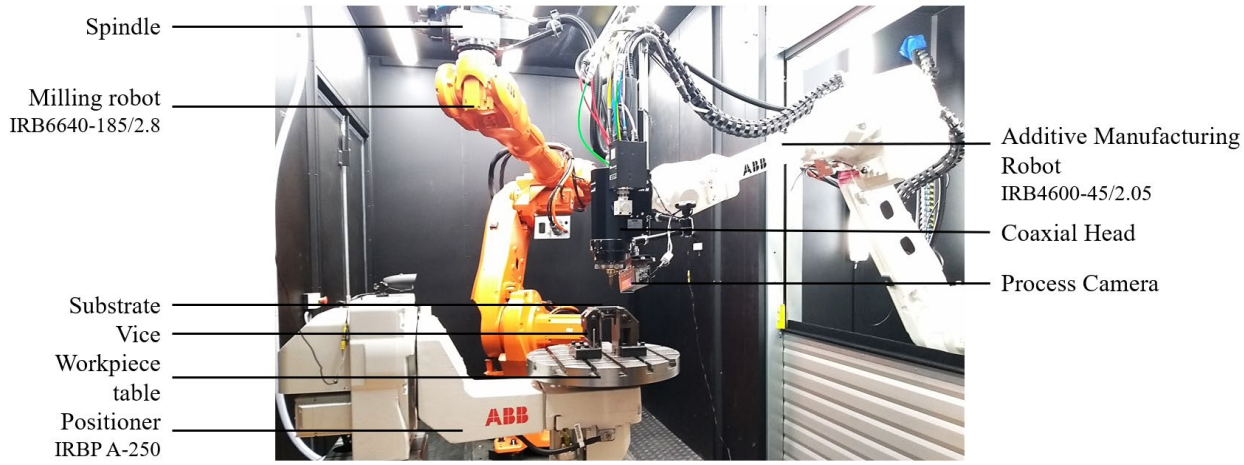

Fig. 2. Overview of the WLAM setup.

The head divides the initial beam into three laser beams, equally placed around the vertical axis of the head (z-axis) at 90, 150 and 30° angles to the x-axis respectively for beams 1, 2 and 3, and with an angle of 17.5° to z. In standard production configuration, the head is oriented so that its z-axis follows gravity.

Initial tests established a process window depending on three usual parameters (power, wire feed speed and travel speed) regarding both stubbing and dripping defects. In addition, two additional phenomena were observed. At low laser power and low wire speed, lack of fusion appears (Fig. 3a), where the energy is sufficient to melt the wire, but not the substrate, resulting in a bead without adherence. This phenomenon was already observed by Medrano Tellez [13], who characterizes it by a head speed too high for the power. In contrast, with low travel speed and high wire feed speed while keeping sufficient laser power to melt it, a wider and higher melt pool than other beads is obtained. Its behaviour is close to that of a liquid (Fig. 3b), similar to what can be observed in WAAM.

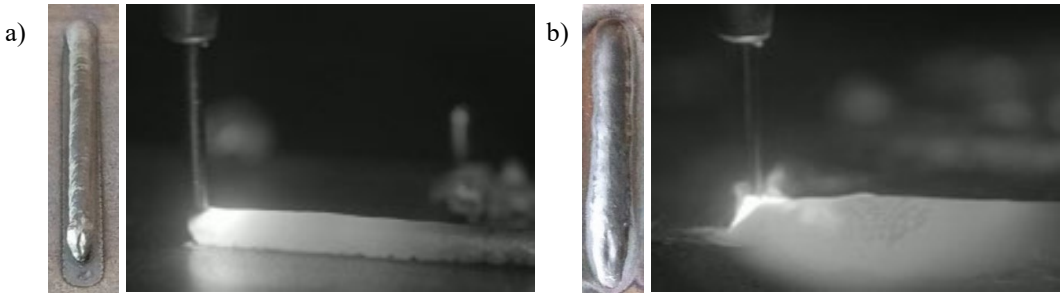

Fig. 3. Beads and process views for two defects: lack of fusion on the left and liquid behaviour on the right.

Method

According to the process window, an operating point with a travel speed of 1 m/min, a wire speed of 2 m/min and a power of 2.2 kW is used for all experiments. These parameters were determined with a working distance of 2 mm, which means that the intersection point of the three laser beams is 2 mm below the substrate surface. The dotted red segments on figure 4 stand for the axes of the

three laser beams, the continuous red segment for the head axis, and the black outline for the laser spot boundaries.

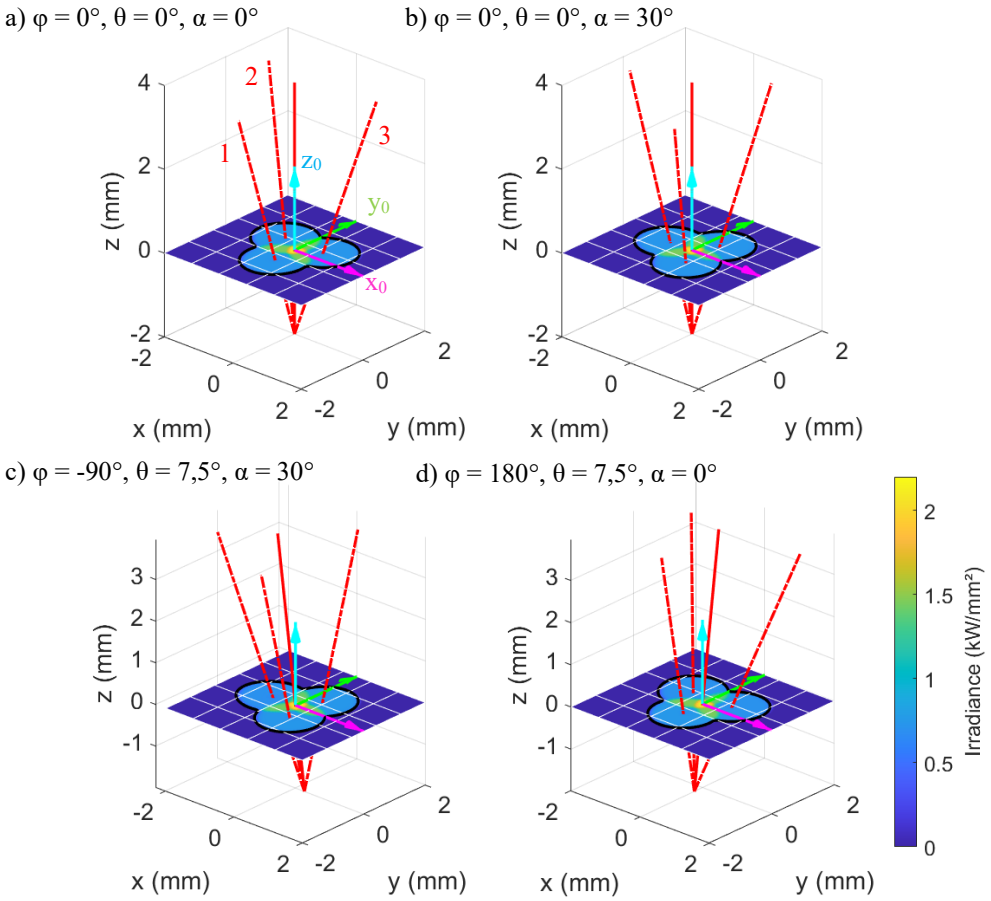

Fig. 4. Power density and laser spot limit for different head orientations.

During manufacturing the substrates remain fixed and the head travels along the x_0 axis of the substrate in the positive direction, with different orientations. To describe the head orientation, an intrinsic Euler formalism is used, corresponding to a rotation of angle φ (precession) about z_0, corresponding to the tilting direction, followed by a rotation of angle θ, called tilt, about x' and finally a rotation of angle ψ about z''. The angle $\alpha = \psi + \varphi$ will be used and referred to as head rotation, as it approximates the total rotation of the head around its axis when θ is small (0.2° deviation for θ = 7.5°). The limits of these angles are fixed by technological constraints (cable management and laser safety), with α constrained in the interval [-70°;70°] and θ inferior to 8°. For the experiments θ varies on two levels between 0 and 7.5°, φ on 8 levels between 180 and 135°, and α on 5 levels between -60 and 60°. Only the value φ = 0° is considered for θ = 0°. Therefore 45 tests were carried out, with four 60 mm beads deposited on each substrate, spaced 8 mm apart with a waiting time of around 1 minute to reduce the possible effects of thermal accumulation. Preliminary tests established that geometries of beads produced under these conditions are independent of manufacturing order. The produced parts were measured using an optical 3D measurement system over an area of 3.6 mm by 3.6 mm in the bead centre. The deposition direction x_0 was identified before subdividing the y_0 axis into 1000 intervals between -2 and 2 mm, resulting in a local height distribution for each value of y, corresponding to the variations in height inside the measurement window. The mean value and the standard deviation σ of the z values according to y were determined, leading to a statistical bead profile over the entire

measured area. Under the assumption of a Gaussian distribution of the values, a 95% confidence interval can be considered as ±1.96 σ. Using this mean profile, the parameters H, W and A were determined with their confidence intervals. A new value A_r is added, which represents the ratio between the area on the right of the bead (corresponding to positive values of y) to the total area, with the middle of the base serving as centre. This value is only determined for the mean profile and expresses if the bead is tilted to one side, serving as an indicator for asymmetry.

Results and Discussion

Among the 5 beads produced with θ = 0° and varying α, the angles α = -60° and α = -30° present stubbing, contrarily to the other beads which have a smooth appearance (Fig. 5). For α = -60°, the measurement area is not located in the centre but close to the start when stubbing is not as apparent. The dimensions as functions of the angle α are displayed on Fig. 6. The confidence interval for α = -30° is much larger than for the other values, while it does not appear for α = -60° after the measurement zone shift.

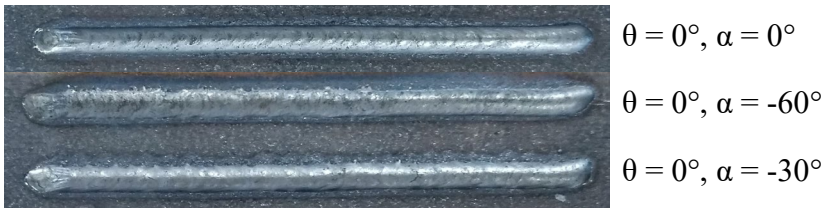

Fig. 5. Beads with or without stubbing (welding direction from right to left).

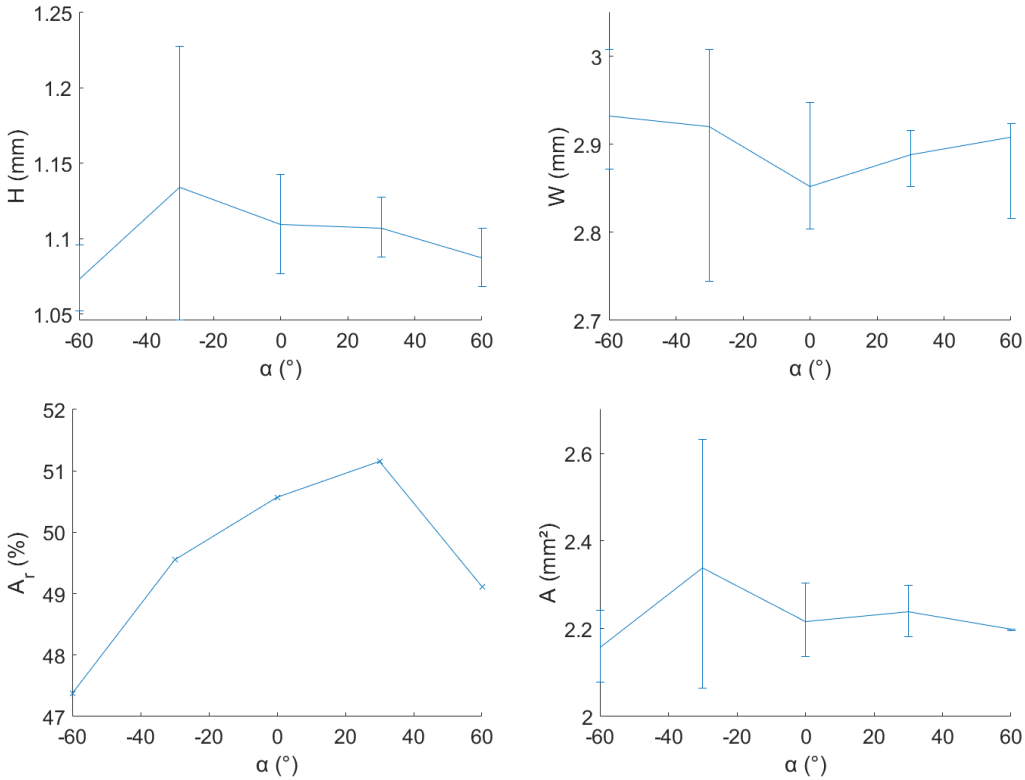

Fig. 6. Variations in bead dimensions for different head rotations.

These results do not show a significant evolution of the dimensions depending of the head rotation, except for A_r. This variation limited to around 4% of bead area indicates that the rotation without head tilt may introduce a slight asymmetry in bead profiles. It is notable that the configuration corresponding to an almost even ratio between left and right is achieved with α = -

Materials Research Proceedings 28 (2023) 119-127 https://doi.org/10.21741/9781644902479-14

30°, which places the beam number 3 on the front and the other two on the back, resulting in a symmetrical distribution on both sides of the melt pool (Fig. 4). Moreover, more matter is displaced to the right when beam 3 is placed on the side where y is positive, and more on the left when on the y negative side.

Some configurations with θ = 7.5° lead to dripping at the start of the bead, where a drop of material remains on the wire before being deposited, leading to a shifted start of the bead (Fig. 7). The rest of these beads is stable, which would rather indicate a defect in the starting parameters, particularly the duration between wire positioning and laser start. The variations in dimensions as a function of φ for different values of α are plotted in figure 8, and the dripping conditions do not lead to a wider interval, except for φ = -135°, α = -30°.

Fig. 7. Beads with dripping at the start.

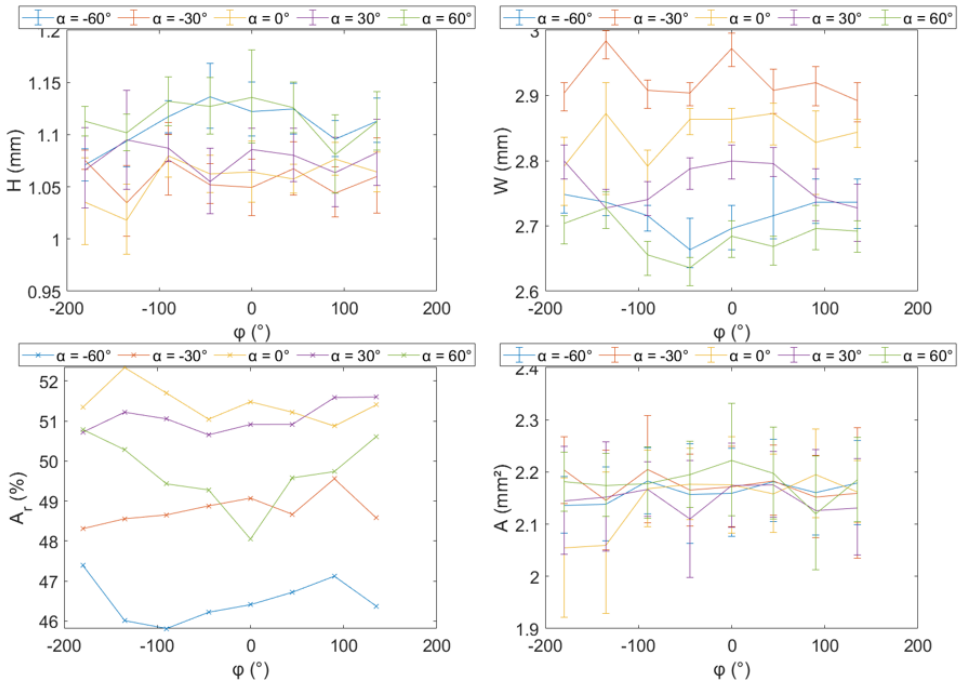

Fig. 8. Variations in bead dimensions for θ = 7.5°.

No significant variations in bead area can be observed, as the differences between mean values are inferior to the confidence intervals. This was expected as the ratio of wire feed speed to travel speed remains constant. Changes can be observed for the width and height, but they remain small (around 10%) and seem to be more related to head rotation than to the tilting direction. To help in the geometry comparison, 5 profiles are selected and displayed on Fig. 9.

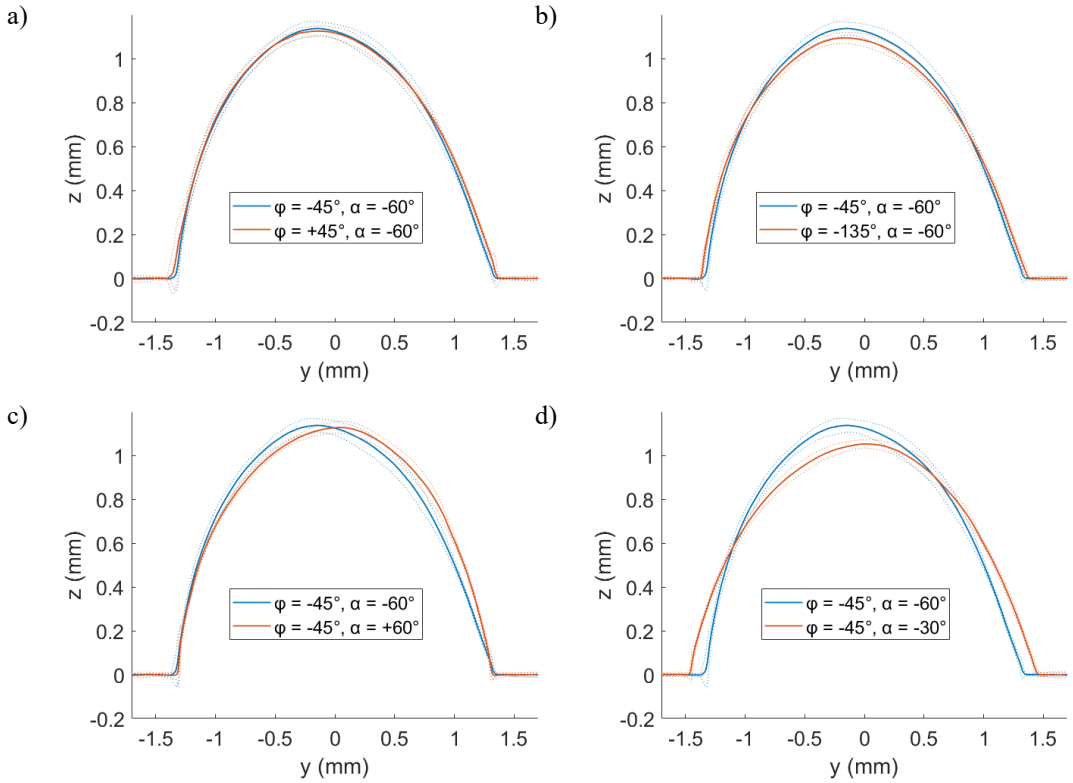

Fig. 9. Comparison of selected bead profiles for θ = 7.5°.

The width seems to depend little on the tilting direction, but more on the head rotation when the head is tilted (Fig. 8), whereas it does not seem to vary without tilt. Indeed, the widths for α = 60° are always smaller than those obtained for α = 0°, in turn smaller than for α = -30°. Fig. 9d compares beads and illustrates the width variation. The maximum width is then obtained for α = -30°, which corresponds to the only configuration tested where one laser beam is at the front of the wire and two beams are at the back (Fig. 10). The effects of head rotation on the ratio between area on the right and total area are observed again, and Fig. 9c shows the asymmetry in the full profile between two orientations.

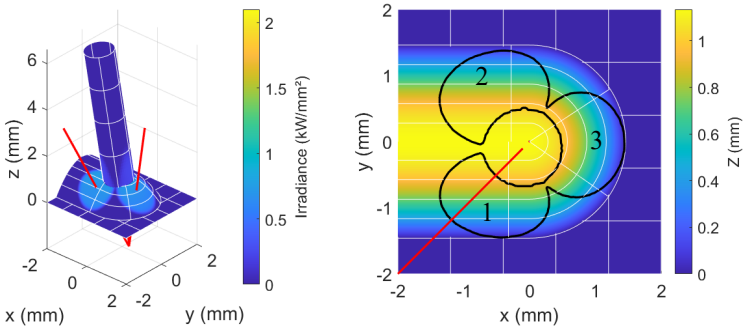

Fig. 10. Laser spot on a nominal bead model with θ = 7.5°, φ = -45° and α = -30°, 3D view on the left and top view on the right.

In contrast to the two previous quantities, bead height depends on the tilting direction. Indeed, variations due to the angle φ are greater than those observed by varying the angle α, but only for α = 60 or -60°. The height of the beads therefore depends on both tilting direction and head rotation. To ease the analysis, the head axis and laser spots are plotted in Fig. 11 for all the configurations of Fig. 9.

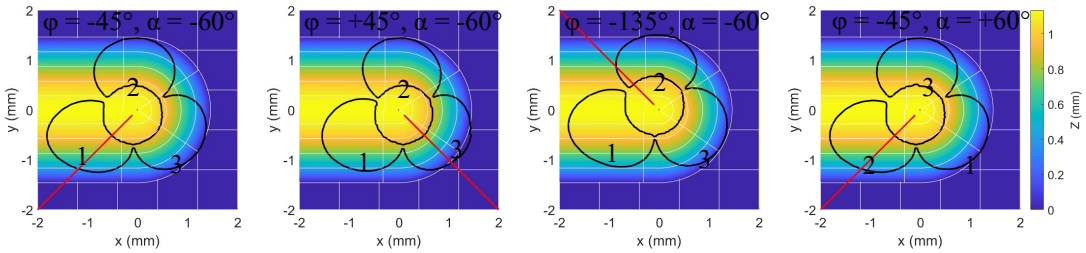

Fig. 11. Comparison of the different configuration of Fig. 9.

For the following discussion two terms are introduced: the front/back tilt to describe the angle around the y axis, and the lateral tilt to describe the angle around x. Thus, between φ = 45 and +45° lateral tilt does not vary, while the head is tilted either towards the front (φ = +45°) or the back (φ = 45°) of the melt pool. Fig. 9a shows that this variation from front to back tilting does not affect bead profile significantly. Fig. 9b highlights that change in lateral tilt leads to change in height without affecting width. Maximum height is obtained by tilting the head to the left side, where two beams are located. Indeed, as seen in figure 11, both α = 60 and -60° correspond to configurations where one laser is aligned with the y axis and on the right side (y positive). However, the configuration α = 0° also corresponds to a beam aligned with the y axis, but no link between α and H is observed for this value. When α = 0°, beam number 1 is aligned with y and located to the left of the profile, while for α = 60° it is beam 3 on the right side and beam 2 on the right side for α = -60°. The observed variations may also be influenced by defects in the power distribution between the beams, or defects in wire positioning. Further studies would allow to quantify their effects on the presented results.

Summary

In this paper the influence of orientation parameters on single beads external geometries was investigated. The beads were measured to extract mean profiles with their associated confidence intervals, allowing to obtain dimensions for the different tested angles. Results showed that head rotation mainly influences the width and asymmetry of the beads, with symmetrical and wide beads obtained when one beam is placed at the front and two beams at the back. For configurations with one beam on one side of the melt pool and the other two on the opposite side, the height of the bead depends on the lateral tilt of the head. No influence of front or back tilting was observed in this study.

The measured variations for a tilt angle up to 7.5° are around 10% of nominal values. A higher tilt angle could amplify these effects but achieving it on this setup would require using the 2-axis positioner, changing gravity direction relatively to the part. This study focused on external geometries without studying the penetration. However, a change in power density can lead to variations in bead-substrate interactions. Further analysis of dilution and penetration are part of the perspectives of this work.

Acknowledgement

We thank Adel Abbas for his help in measuring the manufactured beads.

References

[1] Z. Nie, G. Wang, J.D. McGuffin-Cawley, B. Narayanan, S. Zhang, D. Schwam, M. Kottman, Y. Rong, Experimental study and modeling of H13 steel deposition using laser hot-wire additive manufacturing, J. Mater. Process. Technol. 235 (2016) 171-186. https://doi.org/10.1016/j.jmatprotec.2016.04.006

[2] F. Du, J. Zhu, X. Ding, Q. Zhang, H. Ma, J. Yang, H. Cao, Z. Ling, G. Wang, X. Duan, S. Fan, Dimensional characteristics of Ti-6Al-4V thin-walled parts prepared by wire-based multi-laser

additive manufacturing in vacuum, Rapid Prototyp. J. 25 (2019) 849-856. https://doi.org/10.1108/RPJ-08-2018-0207
[3] A. Ayed, G. Bras, H. Bernard, P. Michaud, Y. Balcaen, J. Alexis, Study of Arc-wire and Laser-wire processes for the realization of Ti-6Al-4V alloy parts, MATEC Web of Conferences 321 2020. https://doi.org/10.1051/matecconf/202032103002
[4] W. Aiyiti, W. Zhao, B. Lu, Y. Tang, Investigation of the overlapping parameters of MPAW-based rapid prototyping, Rapid Prototyp. J. 12 (2006) 165-172. https://doi.org/10.1108/13552540610670744
[5] A. Sharma, N. Arora, B. Mishra, Mathematical Model of Bead Profile in High Deposition Welds, J. Mater. Process. Technol. 220 (2015) 65-75. https://doi.org/10.1016/j.jmatprotec.2015.01.009
[6] Y. Cao, S. Zhu, X. Liang, W. Wang, Overlapping model of beads and curve fitting of bead section for rapid manufacturing by robotic MAG welding process, Robot. Comput.-Integr. Manuf. 27 (2011) 641-645. https://doi.org/10.1016/j.rcim.2010.11.002
[7] G.H. Kim, S.I. Kang, S.B. Lee, Study on the estimate of weld bead shape and the compensation of welding parameters by considering weld defects in horizontal fillet welding, International Conference on Knowledge-Based Intelligent Electronic Systems, 2000, pp. 212-216. doi:10.1109/KES.1999.820157
[8] S. Suryakumar, K.P. Karunakaran, A. Bernard, U. Chandrasekhar, R. Nadella, D. Sharma, Weld bead modeling and process optimization in Hybrid Layered Manufacturing, Computer-Aided Des. 43 (2011) 331-344. https://doi.org/10.1016/j.cad.2011.01.006
[9] M. Kumar, S.S. Kumar, A. Sharma, Bi-polynomial fourth-order weld bead model for improved material utilization and accuracy in wire-arc additive manufacturing: A case of transverse twin-wire welding, Adv. Industr. Manuf. Eng. 2 (2021) 100049. https://doi.org/10.1016/j.aime.2021.100049
[10] D. Ding, Z. Pan, D. Cuiuri, H. Li, A multi-bead overlapping model for robotic wire and arc additive manufacturing (WAAM), Robot. Comput.-Integr. Manuf. 31 (2015) 101-110. https://doi.org/10.1016/j.rcim.2014.08.008
[11] J. Xiong, G. Zhang, H. Gao, L. Wu, Modeling of bead section profile and overlapping beads with experimental validation for robotic GMAW-based rapid manufacturing, Robot. Comput.-Integr. Manuf. 29 (2013) 417-423. https://doi.org/10.1016/j.rcim.2012.09.011
[12] T.E. Abioye, J. Folkes, A.T. Clare, A parametric study of Inconel 625 wire laser deposition, J. Mater. Process. Technol. 213 (2013) 2145-2151. https://doi.org/10.1016/j.jmatprotec.2013.06.007
[13] A.G. Medrano-Tellez, Fiber laser metal deposition with wire: parameters study and temperature control, PhD Thesis, University of Nottingham, 2010.
[14] S.H. Mok, G. Bi, J. Folkes, I. Pashby, Deposition of Ti-6Al-4V using a high power diode laser and wire, Part I: Investigation on the process characteristics, Surf. Coat. Technol. 202 (2008) 3933-3939. https://doi.org/10.1016/j.surfcoat.2008.02.008
[15] S. Ocylok, M. Leichnitza, S. Thieme, S. Nowotny, Investigations on laser metal deposition of stainless steel 316Lwith coaxial wire feeding, 9th International Conference on Photonic Technologies (LANE 2016), 2016.

Materials Research Proceedings 28 (2023) 129-138 https://doi.org/10.21741/9781644902479-15

Additive manufacturing of cermet produced by laser powder bed fusion using alternative Ni binder

PAPY Kevin[1,a *], BORBELY Andras[2,b], SOVA Alexey[1,c], FAVRE Julien[2,d], BERTRAND Philippe[1,e] and STAERCK Jean-Marc[3,f]

[1]University of Lyon, Ecole Centrale de Lyon - ENISE, LTDS, CNRS UMR 5513, 58 rue Jean Parot, 42023 Saint-Etienne, France

[2]Mines Saint-Etienne, Univ Lyon, CNRS, UMR 5307 LGF, Centre SMS, F - 42023 Saint-Etienne France

[3]Technogenia, Saint-Jorioz, France

[a]kevin.papy@ec-lyon.fr, [b]borbely@emse.fr, [c]aleksey.sova@enise.fr, [d]julien.favre@emse.fr, [e]philippe.bertrand@enise.fr, [f]jean-marc.staerck@technogenia.com

Keywords: Cermet, Tungsten Carbide, Laser Powder Bed Fusion, Hot Isostatic Pressing, Microstructure, Hardness

Abstract. Cermets are composite materials made of a ceramic reinforcement and a metal matrix, generally cobalt as binder, with mass content from 6 to 20 wt.%. Cermets are produced by conventional sintering process and are known for their high hardness, low friction coefficient, high wear resistance, and high melting temperature. Laser Powder Bed Fusion (L-PBF) is an additive manufacturing technology widely applied for direct fabrication of functional metallic parts with complex geometry such as internal channels or lattices structures. Considering several studies, production of cermets by L-PBF process is challenging. Recent publications have demonstrated the feasibility to produce WC-Co parts by L-PBF combined with Hot Isostatic Pressure (HIP) heat-treatment. HIP process is sometimes additionally performed as post-treatment to remove defects. HIP is performed at high temperatures and isostatic pressures in a furnace [1]. In this study, following an experimental design a parametric optimization was conducted in order to maximize the mass density of WC-17Ni. Process parameters were compared to those used for WC-17Co parts from recent study [2]. To improve the printed specimen integrity, the as-built samples were heat-treated. As-built and HIP samples were analyzed and compared in terms of mass density, microstructure, crystallographic phases, and macro hardness.

Introduction

Laser power bed fusion (L-PBF) is an Additive Manufacturing (AM) process employed for the production of complex functional parts using metal powder as feedstock material. The powder material is spread on the build platform by the scraper and compacted by the roller. Laser beam is controlled by the scanner on the XY plane, and the platform is moved in the Z direction. Then a new powder layer is deposited, and the process is repeated until the complete part is built. The final properties of the built parts, such as roughness, porosity, cracking propensity, and mechanical properties, depend on process parameters, such as laser power P (W), scanning speed Vs (mm/s), hatching distance Hd (µm) and layer thickness l (µm) [3-8]. These factors are important because re-melting depends on the amount of the volume energy density VED (J/mm^3) absorbed during the process [9], which is defined by the following equation:

$$VED = \frac{P}{Vs \times Hd \times l} \quad (1)$$

Content from this work may be used under the terms of the Creative Commons Attribution 3.0 license. Any further distribution of this work must maintain attribution to the author(s) and the title of the work, journal citation and DOI. Published under license by Materials Research Forum LLC.

Results in this study will only be reported in *VED* and expressed in J/mm^3. Cermets are composites material made of a hard refractory carbide embedded in a ductile metal binder matrix, usually cobalt matrix. The choice of transition metal such as Co, Fe or Ni, has been done based on their good wettability and solubility of W and C and based on their good mechanical properties. Cermets, also known as Hardmetals are extensively utilized for manufacturing of cutting tools and are classically manufactured by powder sintering [10–14]. Considering several studies, it can be concluded that L-PBF manufacturing of WC-Co parts remains challenging [15–17]. Studies show that preheating of the building plate to a high temperature is a key factor to allow the manufacturing of solid samples with reduced porosity [18]. Recently, the manufacturing of complex-shaped WC-Co parts were also demonstrated in without preheating plate [2]. Even with internal porosity and short cracks could be eliminated by post HIP treatment [19–23]. However, for developments in the field of hard metals, many studies have been conducted to find alternative materials to replace cobalt due to environmental issues related to its production. Therefore, new alternative binders are considered, especially Ni and Fe-alloys. In this study, nickel was chosen instead of cobalt. Nowadays, only a few studies based on the use of nickel as alternative binder could be found in the literature. Gu D. et al. [24–26] present different results using a mix of pure nickel and pure tungsten powder, with a particle size of 45 µm and 2.5 µm respectively. Tungsten carbide is formed by adding free carbon with a particle size of 30 µm, to obtain a tungsten carbide nickel powder with a ratio of 85wt.% W, 10wt.% Ni and 5wt.% C. First test was conducted on L- PBF process using a CO_2 laser. The following suitable parameters were chosen, a laser power of 1200W, a layer thickness of 100µm, a hatching distance of 150µm and a scan speed in the range from 800 mm/s to 1200 mm/s. Volume energy density of 83 J/mm^3 allowed to manufacture W-Ni-C by L-PBF. The samples showed a good densification level of 96,3% and the microhardness of the block-shaped WC formed at a laser scan speed of 800mm/s was 1619.7 $HV_{0.1}$, which increased to a maximum value of 1870.9 $HV_{0.1}$ by increasing the scan speed at 1000 mm/s. Different phases were observed such as the hexagonal WC and the cubic Ni_2W_4C (M_6C) phase [24,25].

Present article focuses on the AM of parts using Ni as alternative binder. First, the possibility to produce L-PBF parts was evaluated by determining the optimal process parameters. In a second step the benefits of HIP post heat treatment process will be evaluated to eliminate residual porosity and cracks. Finally, the microstructure, crystallographic phases and macro hardness will be analyzed. To compare the mechanical properties, manufacturing WC-Ni by L-PBF, was compared with sintered-HIP conventionally prepared WC-Co.

Material and Methods

Characterization of the powder.

Commercially available powder of agglomerated-sintered WC-17Ni, manufactured by spray drying by Oerlikon Metco® was used in this study. The powder was initially developed for thermal spray applications such as HVOF and HVAF. The granulometry distribution was measured using an Occhio 500XY nano particle analyzer (Occhio SA, Liège, Belgium). The particle size distribution is between 15 and 53 µm. SEM images of the particles are shown in Fig. 1. The particles have a spherical morphology. The average size of the WC grains (dark grey) is in the 1-2µm range. The carbide grains are uniformly distributed in the nickel matrix (light grey). Inductively coupled plasma mass spectrometry (ICP-MS) analysis indicates that the chemical composition of binder content was close the range stated by the supplier (C: 4.7 – 5.5, Ni: 14.5 – 19.5). In particular the measured nickel and carbon content was 20.1 wt.% and 5.1 wt.% correspondingly. X-ray diffraction was carried out on initial powder to determine the different phases. The XRD pattern shows only the WC and Ni phases in the initial powder (Fig. 1 d).

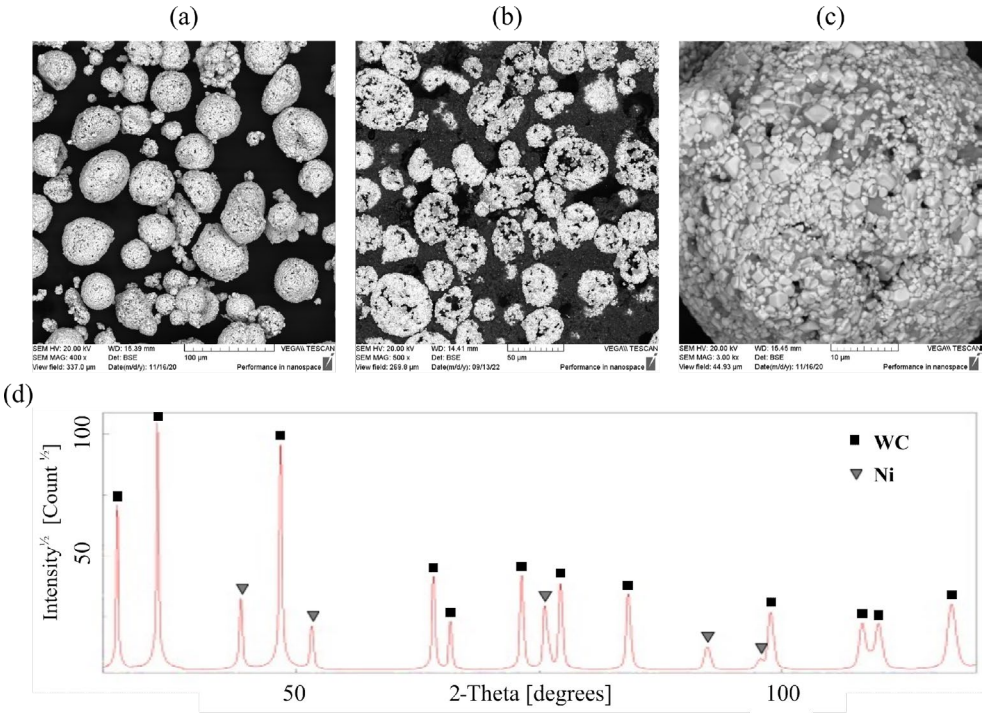

Fig. 1. SEM images of the WC-17Ni particles at different magnification (a) overview at x400, (b) cross section of particles, (c) overview at x3000 and (d) XRD pattern of WC-17Ni powder.

L-PBF and characterization equipment.

Pro X 200 DMP equipment supplied by 3D Systems® was used. The volume of the working chamber where the parts were manufactured was 140 × 140 × 125 mm^3. The L- BF machine was equipped with a 400 W fiber laser having a wavelength of 1070 nm. To prevent oxidation the working chamber was filled with nitrogen during manufacturing. Cube-shaped samples with dimensions of 10 × 10 × 10 mm^3 manufactured using L-PBF were used for post-treatment in order to reduce porosity. Samples was subjected to capsule-free HIP, which is a cycle applied during industrial processes. HIP was performed at 1450 °C with a furnace maintained at a pressure of 40 MPa for 5h. The relative density of the manufactured parts was determined by image analysis of microscope images using ImageJ [27]. The microstructure and elemental distribution were analyzed using a Zeiss Supra 55VP v2 SEM and EBSD maps were also recorded. X-ray diffraction (XRD) was employed for phase analysis using an X'PertPro MPD diffractometer with CuKα radiation. Phase quantities were obtained from Rietveld analysis performed with the MAUD software [28]. Vickers hardness (HV) was determined by applying a load of 30 kg for 10 s to all samples. Palmqvist toughness was determined by crack propagation measurement after indentation test [29].

Results and Discussion

Optimization of process parameters.

In this study, the possibility to produce cermet by L-PBF without preheated plate and the optimal process parameters will be determined. L-PBF process parameters were determined following a designed experimental optimization (DEO). Two different step was realized, first, single tracks were deposited with a powder layer thickness of 30 µm with different laser power and scan speed. Single tracks width was measured in order to determine the hatching distance.

Table 1. Ranges of L-PBF manufacturing parameters applied in the experiments.

Layer thickness [µm]	30
Laser power [W]	160 - 200 - 250
Scan speed [mm/s]	50 - 100 -150 -200 -250 -400
Hatching distance [µm]	80 - 280
Volume Energy Density [J/mm3]	160 - 650
Scan strategy	Rt - Hexagone

Then, 3D objects with simple geometries (cubes and parallelepipeds) were manufactured. The principal purpose of these experiments was to determine the parameters enabling the production of materials with the lowest amount of porosity and cracks. Table 1 summarizes the parameter ranges tested in the DEO. For manufacturing the cubes, two different scanning strategies were used, a hexagon (H) strategy, which reduces the residual stresses in the workpiece and allow creating large surfaces and a classical round trip (Rt) strategy with 90° rotation between each layer. The evolution of the porosity for WC-Ni sample is shown in Fig. 2. For a power of 160W, the porosity was the highest. Many of the cubes were not printed in full height and manufacturing was cancelled during the process. Following these observations, several parameters were set as non-optimal for this powder and parameter ranges were modified. In particular the width of VED window was decreased to 180 J/mm^3 - 300 J/mm^3 for 200W and 250W respectively. At the first stage for a VED of 200 J/mm^3 and for 300 J/mm^3, cubes with a hexagonal scanning strategy were manufactured but, the porosity was high due to inappropriate hatching distance.

For the Rt scanning strategy, samples had the lowest porosity rate of 1.06% and 0.84% for 200W and 250W respectively. Hexagonal scanning strategy shows a minimum porosity of 1.20% at 208 J/mm^3. For the lowest VED of 180 J/mm^3 porosity was the highest but it could be decreased by increasing the VED value.

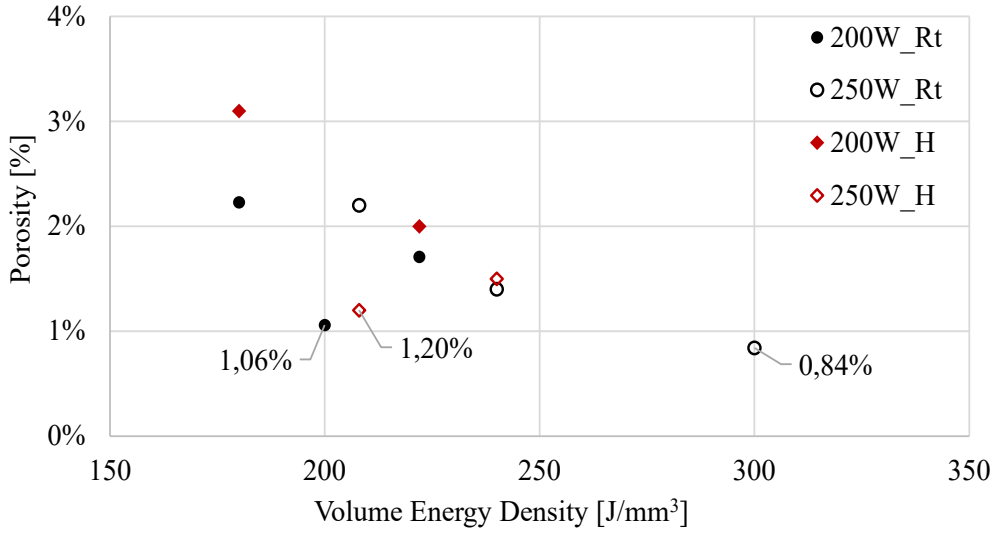

Fig. 2. Sample porosity vs. VED for round trip and hexagonal scanning strategies.

The microstructures of fabricated samples are shown in Fig. 3. Cracks are present in all samples. The smallest number of cracks is observed in the samples manufactured at VED 208 J/mm^3 and 300 J/mm^3 with a hexagonal and round-trip scan strategy respectively. During the fabrication of the samples with larger scanning surface the round-trip strategy presents some difficulties with

several defects. This problem was solved using optimized parameters at 208 J/mm^3 with hexagonal scanning strategy.

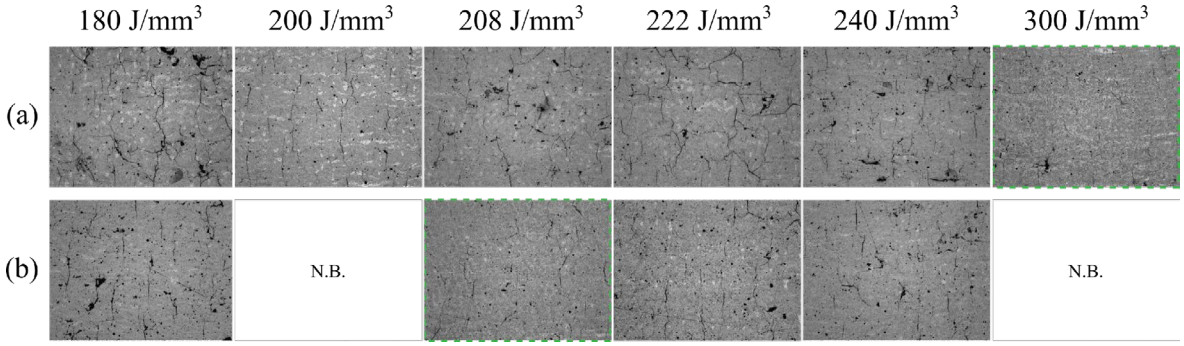

N.B. = No built

Fig. 3. SEM images of samples manufactured via (a) the round trip and (b) the hexagonal scanning strategy.

The material optimization stage determined parameters to achieve minimum porosity levels of 1.2% for WC-17Ni. In order to solve the remaining porosity problems, HIP post treatment is applied on the as-built samples (Fig. 4). HIP significantly modified integrity, microstructure and crystallographic phases. In particular, porosities and cracks were no longer visible in the images because high temperature and the external pressure promote material diffusion, allowing for pore and crack closure. According to image analysis, the relative density of the as-built samples was 98.80%, whereas of the samples after HIP post-treatment was 99.99% (Fig. 4 b).

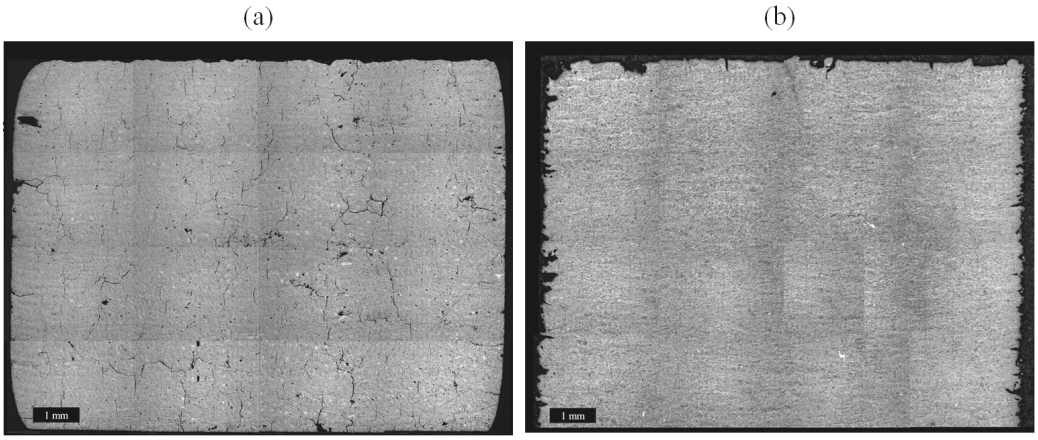

Fig. 4. Cross-section images of (a) as-built and (b) HIP-treated samples.

Microstructure and mechanical characterization.

The results of the XRD analysis performed on the as-built and HIP samples are shown in Fig. 5. The diffractograms show several phases. The most intense peaks correspond to WC.

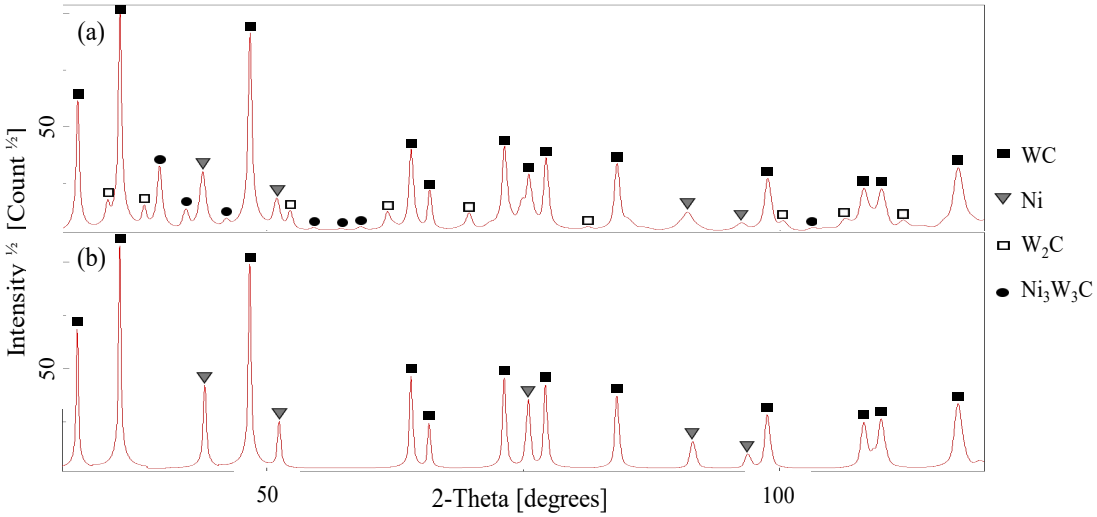

Fig. 5. XRD patterns of (a) the as-built and (b) HIP-treated samples.

At the same time the initial WC carbide has partially diffused in matrix and formed the complex phases such as W_2C carbide and the Ni_3W_3C ternary phase (M_6C). Also, the Ni matrix phase is present in the XRD pattern of the as-built sample. The XRD patterns of the HIP samples are presented on Fig. 5 b. A significant phase transformation is observed for the sample after HIP treatment. In particular, the W_2C carbide and M_6C phase have disappeared. The W-C phase diagram established by Okamoto in 2008 [30], allows to explain the disappearance of the W_2C phase. A temperature of 1450°C during HIP treatment allows the binder dissolution, then slowly cooled to room temperature, which leads to the disappearance of the W_2C phase.

EBSD analysis was performed on different samples to see the distribution of the different phases and to determine the carbide grain size. A 0.2µm step size was used and grains orientation was colored according to the inverse pole figures. No preferential orientation was observed for the samples. An indexing rate of 40% and 85% is obtained for as-built and HIP sample respectively (in Fig. 6 noise reduction was applied). The indexing rate is very low for the as-built sample (Fig. 6a), due to the presence of nano-sized grains making phase detection more difficult. A very large part of the map is non-indexed (black area), the other phases are detected but are present in very small fractions. In the as-built sample the most abundant phases are the WC phase (blue: 32.60 vol.%) and the W_2C phase (green: 9.26 vol.%). The other phases are present in area fractions lower than 1%. The phase distribution map shows a homogeneous distribution of the WC and Ni phases with a respective volume fraction of 72% and 13% for the HIPed sample. Dissolution of the smallest carbide grains is observed. The smallest equivalent WC grain size is 0.23 µm and 0.71µm for as-built and HIP sample respectively. The average grain size increases for the WC grains, from 0.60 µm to 1.58 µm for the HIP sample. The EBSD shows no preferred orientation of the WC grains in the as-built or HIP-treated material. However, a heterogeneous size distribution of WC grains is observed in both cases with zones of small and large grains (Fig. 6c and 6d). Further analysis is required to determine the preferential arrangement of the grains in the single track.

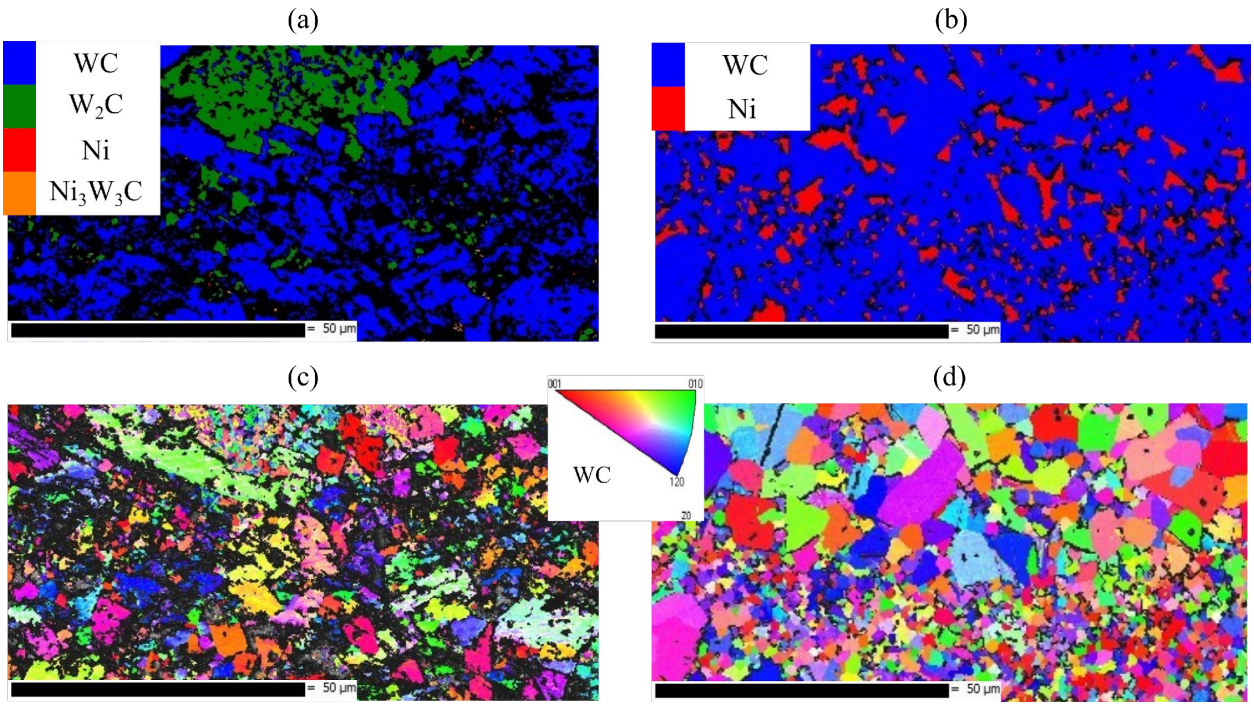

Fig. 6. EBSD grain mapping of WC-Ni (a) As-built and (b) HIP-treated sample and corresponding EBSD orientation map of WC-Ni (c) As-built and (d) HIP-treated.

Macrohardness tests were performed on the as-built and HIP-treated samples. Three measurements were performed per sample according to the standard methods at 30 kg. To reinforce the density obtained by images analysis results, the density variation of the samples is also measured by pycnometer. Results of mechanical tests are shown in Table 2.

Table 2. Characteristic values of the different WC-Ni samples.

Echantillon	Densité [g/cm^3]	HV_{30}	Tenacité Palmqvist [N.mm^{-1}]
As-built	13,94 ± 0,04	992 ± 54	1255 ± 589
HIP	14,15 ± 0,03	966 ± 21	0

Material cracking was observed near the corners of the indent for the as-built sample, which indicated high material brittleness (Fig. 7 a-b). The mean value obtained for the as-built samples was 992 HV_{30}, with a mean Palmqvist value of 1255 N.mm^{-1}. The hardness of the HIP-treated (966 HV_{30}) samples was slightly lower than that of the as-built samples. No material cracking is observed, likely due to elimination of the fragile W_2C phase (Fig. 7 c-d). Some dark points are observed on the optical image of the HIP sample, but these points do not correspond to porosities but to marks due to polishing process.

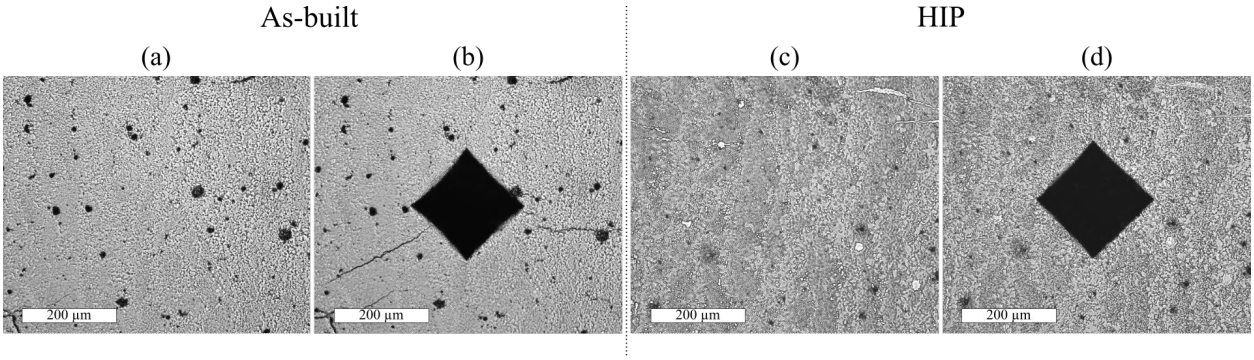

Fig. 7. Optical microscopy images of the WC-Ni samples before and after indentation tests; (a-b) as-built and (c-d) HIP-treated samples.

Summary

The manufacture of WC-17Ni parts using L-PBF was found to be feasible despite the presence of porosities and cracks. Samples with the lowest porosity fraction (1.2%) and highest integrity were obtained using a volume energy density of 208 J/mm^3. The as-built samples contained the brittle W_2C phase and some small-scale pores and cracks. The sample microstructure, relative density, and hardness were significantly improved through HIP post-treatment, resulting in close-to-zero porosity and no cracks. HIP allowed the complete dissolution of the undesirable brittle W_2C and M_6C phases. Initial phase present in the powder is observed in the sample after the HIP process. The macrohardness of the L-PBF-manufactured WC- 17Ni parts are comparable to the values obtained for the sintered WC-Co samples, with a hardness value around 1000 HV_{30}. The feasibility of L-PBF additive manufacturing to generate dense cermet samples using alternative binder as nickel was successfully assessed (Fig. 8).

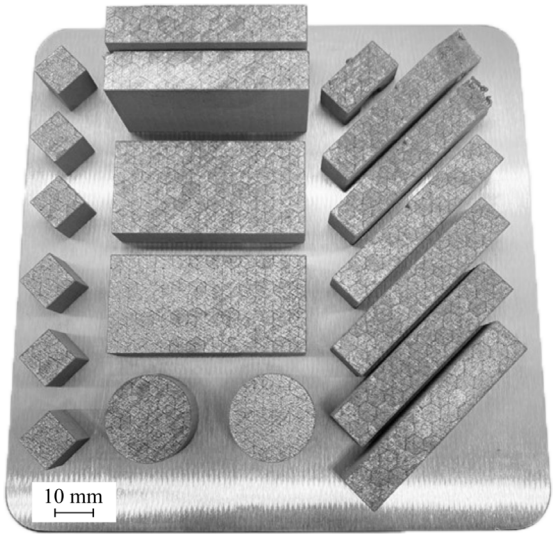

Fig. 8. L-PBF built plateform with samples manufactured from WC-17wt.% Ni powder.

References

[1] H.V. Atkinson, S. Davies, Fundamental aspects of hot isostatic pressing: An overview, Metall. Mater. Trans.: Physical Metallurgy and Materials Science 31A (2000) 2981-3000. https://doi.org/10.1007/s11661-000-0078-2

[2] K. Papy, S. Jean-Marc, S. Alexey, B. Andras, Additive Manufacturing feasibility of WC-17Co cermet parts by Laser Powder Bed Fusion, Procedia CIRP 111 (2022) 153-157. https://doi.org/10.1016/j.procir.2022.08.049

[3] E. Herderick, Additive manufacturing of metals: A review, Materials Science and Technology Conference and Exhibition 2011, MS and T'11 2 (2011) 1413–1425.
[4] N. Li, S. Huang, G. Zhang, R. Qin, W. Liu, H. Xiong, G. Shi, J. Blackburn, Progress in additive manufacturing on new materials: A review, J. Mater. Sci. Technol. 35 (2019) 242-269. https://doi.org/10.1016/j.jmst.2018.09.002
[5] B. Zhang, Y. Li, Q. Bai, Defect Formation Mechanisms in Selective Laser Melting: A Review, Chinese Journal of Mechanical Engineering (English Edition) 30 (2017) 515-527. https://doi.org/10.1007/s10033-017-0121-5
[6] S. Vock, B. Klöden, A. Kirchner, T. Weißgärber, B. Kieback, Powders for powder bed fusion: a review, Progress in Additive Manufacturing 4 (2019) 383-397. https://doi.org/10.1007/s40964-019-00078-6
[7] I. Gibson, B. Stucker, D. Rosen, Additive Manufacturing Technologies 3D Printing, Rapid Prototyping, and Direct Digital Manufacturing, Second Ed., Springer, New York, 2019. https://doi.org/10.1007/978-1-4939-2113-3
[8] C.Y. Yap, C.K. Chua, Z.L. Dong, Z.H. Liu, D.Q. Zhang, L.E. Loh, S.L. Sing, Review of selective laser melting: Materials and applications, Appl. Phys. Rev. 2 (2015) 041101. https://doi.org/10.1063/1.4935926
[9] L.N. Carter, M.M. Attallah, R.C. Reed, Laser Powder Bed Fabrication of Nickel-Base Superalloys: Influence of Parameters; Characterisation, Quantification and Mitigation of Cracking, 2012.
[10] C. Chen, Z. Guo, S. Li, Y. Xiao, B. Chai, J. Liu, Microstructure and properties of WC-17Co cermets prepared using different processing routes, Ceram. Int. 45 (2019) 9203-9210. https://doi.org/10.1016/j.ceramint.2019.01.265
[11] Z. Roulon, J.M. Missiaen, S. Lay, Carbide grain growth in cemented carbides sintered with alternative binders, Int. J. Refract. Metal. Hard Mater. 86 (2020) 105088. https://doi.org/10.1016/j.ijrmhm.2019.105088
[12] H.M. Ortner, P. Ettmayer, H. Kolaska, I. Smid, The history of the technological progress of hardmetals?, Int. J. Refract. Metals Hard Mater. 49 (2015) 3-8. https://doi.org/10.1016/j.ijrmhm.2014.04.016
[13] R.T. Faria, M.F. Rodrigues, I. de Andrade Esquef, H. Vargas, M. Filgueira, On the thermal characterization of a HPHT sintered WC-15% wt Co hardmetal alloy, Int. J. Refract. Metals Hard Mater. 23 (2005) 115-118. https://doi.org/10.1016/j.ijrmhm.2004.11.007
[14] A.S. Kurlov, A.A. Rempel', Effect of sintering temperature on the phase composition and microhardness of WC-8 wt % Co cemented carbide, Inorganic Materials 43 (2007) 602-607. https://doi.org/10.1134/S002016850706009X
[15] C.M. Fernandes, A.M.R. Senos, Cemented carbide phase diagrams: A review, Int. J. Refract. Metals Hard Mater. 29 (2011) 405–418. https://doi.org/10.1016/j.ijrmhm.2011.02.004
[16] A. Aramian, S.M.J. Razavi, Z. Sadeghian, F. Berto, A review of additive manufacturing of cermets, Addit. Manuf. 33 (2020) 101130. https://doi.org/10.1016/j.addma.2020.101130
[17] Y. Yang, C. Zhang, D. Wang, L. Nie, D. Wellmann, Y. Tian, Additive manufacturing of WC-Co hardmetals: a review, Int. J. Adv. Manuf. Technol. 108 (2020) 1653-1673. https://doi.org/10.1007/s00170-020-05389-5
[18] T. Schwanekamp, Parameter study on laser beam melting of WC- Co at 800°C pre-heating temperature, ICAT Proceedings of 7th International Conference on Additive Technologies, no. October, pp. 78-84, 2019.
[19] D. Bricín, M. Ackermann, Z. Jansa, D. Kubátová, A. Kříž, Z. Špirit, J. Šafka, Development of the structure of cemented carbides during their processing by slm and hip, Metals 10 (2020) 1-17. https://doi.org/10.3390/met10111477

[20] J. Chen, M. Huang, Z.Z. Fang, M. Koopman, W. Liu, X. Deng, Z. Zhao, S. Chen, S. Wu, J. Liu, W. Qi, Z. Wang, Microstructure analysis of high-density WC-Co composite prepared by one step selective laser melting, Int. J. Refract. Metals Hard Mater. 84 (2019) 104980. https://doi.org/10.1016/j.ijrmhm.2019.104980
[21] T. Schwanekamp, M. Reuber, Additive manufacutring of application optimized tungsten carbide precision tools, 6 th International Conference on Additive Technologies, January 2016, pp. 100–114, 2016. https://doi.org/10.1016/S0925-8388(03)00637-6
[22] T. Schwanekamp, Thermal Post-Treatment of Additively Manufactured WC-Co Processed by Laser Powder Bed Fusion, 2019.
[23] E. Uhlmann, A. Bergmann, W. Gridin, Investigation on Additive Manufacturing of Tungsten Carbide-cobalt by Selective Laser Melting, Procedia CIRP 35 (2015) 8-15. https://doi.org/10.1016/j.procir.2015.08.060
[24] D. Gu, W. Meiners, Microstructure characteristics and formation mechanisms of in situ WC cemented carbide based hardmetals prepared by Selective Laser Melting, Mater. Sci. Eng. A 527 (2010) 7585-7592. https://doi.org/10.1016/j.msea.2010.08.075
[25] D. Gu, Q. Jia, Novel crystal growth of in situ WC in selective laser-melted W - C - Ni ternary system, Journal of the American Ceramic Society 97 (2014) 684-687. https://doi.org/10.1111/jace.12828.
[26] D. Gu, In Situ WC-Cemented Carbide-Based Hardmetals by Selective Laser Melting (SLM) Additive Manufacturing (AM): Microstructure Characteristics and Formation Mechanisms, in Laser Additive Manufacturing of High-Performance Materials, Springer Berlin Heidelberg, 2015, pp. 151–173. https://doi.org/10.1007/978-3-662-46089-4_5
[27] Information on https://imagej.nih.gov/ij/ (accessed on 07 December 2022)
[28] Information on http://maud.radiographema.eu/ (accessed on 07 December 2022)
[29] “Hardmetals - Palmqvist toughness test - ISO28079.” 2009.
[30] H. Okamoto, C-W (Carbon-Tungsten), J. Phase Equilibria Diffus. 29 (2008) 543-544. https://doi.org/10.1007/s11669-008-9396-7

Materials Research Proceedings 28 (2023) 139-148 https://doi.org/10.21741/9781644902479-16

Fused filament fabrication: Numerical adhesion modeling suitable for semicrystalline polymers

BENARBIA Adel[1,2,a *], SOBOTKA Vincent[1,b], BOYARD Nicolas[1,c] and ROUA Christophe[2,d]

[1]Nantes Université, CNRS, LTEN, UMR 6607, F-44000 Nantes, France

[2]Cogit Composites company, 9117 rue des Vignerons 18390 Saint-Germain-du-Puy, France

[a]adel.benarbia@univ-nantes.fr, [b]vincent.sobotka@univ-nantes.fr, [c]nicolas.boyard@univ-nantes.fr, [d]christophe.roua@cogit-composites.com

Keywords: Fused Filament Fabrication (FFF), Heat Transfer, Adhesion, Interfacial Bonding, Crystallization, Phase Transformation, Semicrystalline Polymer, Numerical Simulation

Abstract. Numerous studies have been conducted to improve the adhesion quality at the interface between the filaments which remains one of the weak points in the FFF process. The interfacial adhesion of printed parts has already been investigated by several authors for amorphous polymers. However, for semicrystalline polymers, the influence of crystallization on adhesion kinetics as well as the description of partial melting at interfaces between filaments are not well taken into account in the models describing FFF process. The purpose of this work consists of proposing a predictive multiphysics model that enables the prediction of the adhesion degree for semi-crystalline polymers during FFF process. The coupling of a crystallization and melting model allows the estimation of the crystalline degree evolution at the interface. The use of a recent model predicting the molecular mobility as a function of temperature and crystallization makes it possible to estimate the degree of healing in anisothermal conditions. Finally, a parametric study is performed in order to propose process window improving the adhesion quality.

Introduction

In recent years, additive manufacturing has been the subject of many studies, regardless of the type of technology. The Fused Filament Fabrication (FFF) process being the most widespread, a great deal of attention has been paid to it. It is one of the affordable additive manufacturing technologies with a simple technology and a fast manufacturing speed. Nevertheless, one of the notable limitations of the FFF process is the decrease of the mechanical properties, compared to conventional processes like injection molding. These mechanical properties are low in the direction normal to the interfaces, resulting in high anisotropic properties [1]. The decrease in mechanical properties is related to the presence of porosities and the low interfacial strength between filaments. A lot of researches have been performed to improve the quality of the parts manufactured with this process [1,2].

Adhesion in the FFF process takes place in several steps. First, the material melted by the nozzle is deposited on the previous filament, intimate contact occurs and interfaces develop with the other filaments. This phenomenon called coalescence is strongly controlled by the rheological behavior of the material and the surface tension but also external pressures such as nozzle crushing. When coalescence begins, the healing process starts with the diffusion of polymer chains through the interfaces in order to create a real molecular bond with the others filaments [3].

Coalescence and healing are only possible if the chains present at the interfaces have sufficient molecular mobility [4]. Molecular mobility is governed by the thermodynamic state of the polymers, for the amorphous phase, mobility is restricted below the glass transition [5]. Finally, in

Content from this work may be used under the terms of the Creative Commons Attribution 3.0 license. Any further distribution of this work must maintain attribution to the author(s) and the title of the work, journal citation and DOI. Published under license by Materials Research Forum LLC.

the case of semicrystalline polymers, crystallization may limit the adhesion phenomenon. These mechanisms are therefore strongly dependent on the rheological behavior evolving with the temperature and the crystalline degree of the polymer [6].

Studies were conducted to predict the thermal history of the FFF process and its influence on interfacial adhesion. A large majority of the studies consider the heat transfer at the interface assuming a homogeneous temperature within the thickness of the filament [3,7]. But some studies have proposed thermal modeling at the filament scale in order to estimate more precisely the interface temperature [2]. From these works, numerical Finite Element Method (FEM) models were developed and showed good agreement with experimental tests in the case of amorphous polymers.

However, for semicrystalline polymers, even if some works take into account the influence of crystallization and melting enthalpies o heat transfer, none of them realize a real link with the adhesion physics [8]. The only studies that propose to predict the healing degree as a function of crystalline degree assume that adhesion stops abruptly at the beginning of crystallization [9]. In spite of this approximation the authors obtained consistent results with the experimental. Nevertheless, several studies showed that despite the presence of crystals, for low crystallinity degree, the adhesion mechanism can continue because the amorphous phase still has a certain level of mobility [10,11]. In recent years, a promising time-temperature-crystallization-superposition (TTCS) model has been studied in order to predict the evolution of molecular mobility as a function of temperature and crystallinity and could allow a better understanding of adhesion with semicrystalline polymer [10,12].

Multiphysics Modeling of FFF Process

In this work, heat transfers, phase transformations and adhesion physics are implemented in a coupled multiphysics model. The model does not represent the rheology of the deposited filament. Assuming an instantaneous flow, a non-deformable oblong section will be taken to build the model. The simulation is performed in a single computational step where the use of boolean conditions allows the model to evolve in order to represent the successive filaments deposition. This allows a strong coupling between heat transfers and phase transformations.

The numerical resolution was performed on a 2D model simulated by FEM on COMSOL® software. In agreement with the work of [2], we develop a dimensionless modelling with the simplifying hypothesis that the thermal exchanges occur mainly in the plane orthogonal to the deposition direction. A comparison between 2D and 3D models validated this assumption. The deposition is simulated by the domain activation method and the boundary conditions change according to the deposition steps.

Heat transfer and phase transformation are computed on the whole domain. At each calculation step, the healing degree is evaluated on filaments interfaces in order to predict their evolution over time as a function of temperature and crystalline degree.

The driving mechanisms of coalescence are more difficult to quantify and can make the simulation complex. Indeed, some authors agree that the phenomenon is driven only by viscous effects and surface tension [2,13]. While others describe a strong influence of the printing nozzle pressure on the filament geometry [3].

Based on these studies, our model will consider an oblong geometry with a constant and homogeneous section without defects. The oblong geometry allows to take into account the porosities present between the filaments. The fillet size will be based on micrographic observations of a printed part. An 8 filament high wall was simulated in one step. The model being adaptive, it is possible to simulate a wall of several filaments wide as shown Fig. 1.

Heat transfer.

The thermal model is represented in Fig. 1. In the domain, we solve the energy equation coupled with crystallization and melting. The source term present in the energy equation term depends on ΔH the crystallization and melting enthalpies and α the crystalline degree. In order to represent the effects of the heating nozzle, the initial temperature of each new filament is considered uniform and set to T_{NOZZLE} to represent the extrusion set point. The bottom surface of the first filament is fixed at the temperature T_{BED} throughout the simulation process in order to represent the printing plate setting. Heat transfer between the environment and the deposited filaments are considered only convective. It is considered a constant chamber temperature $T_{Chamber}$ throughout the deposit. The boundary conditions are re-evaluated at each deposit thanks to boolean variables in order to make the model evolve with the deposit. Thermal contact resistances (TCR) were applied between the filaments to represent contact imperfection [2].

The characterizations of thermal conductivity k, heat capacity Cp and density ρ were performed on PAEK (Polyaryletherketone). The thermal property measurements were performed above the glass transition in the semi-crystalline solid state taking into account the influence of temperature. We will consider a linear variation of the thermal properties with temperature and will realize the simplifying assumption that the values are identical whatever the crystalline degree.

Model parameters such as layer thickness, printing speed, nozzle temperature are chosen as representative of real process [14].

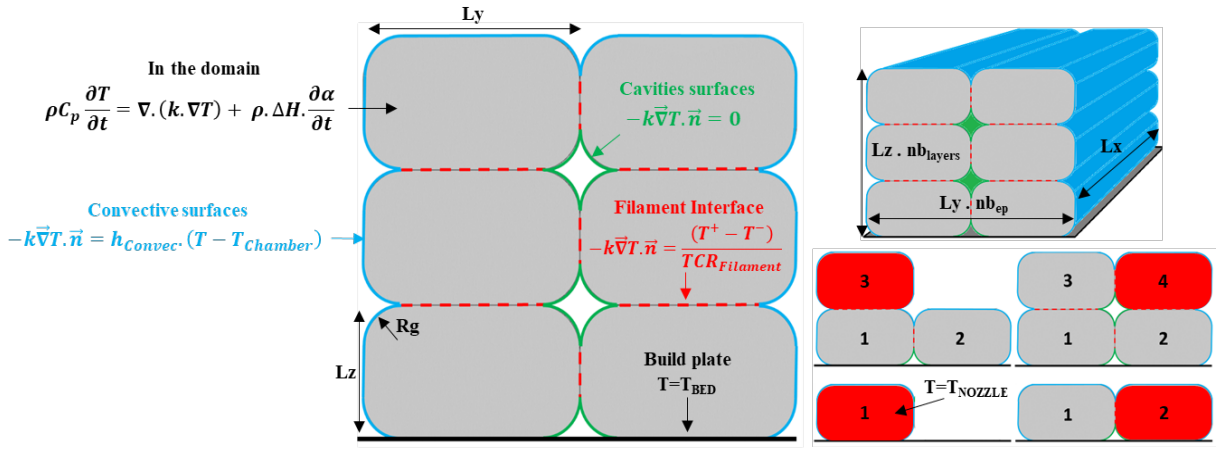

Fig. 1. Schematic representation of the case study.

Phase transformation: Crystallization/melting.

In order to predict the evolution of the crystalline degree as a function of the thermal history, a phase change model including crystallization and melting was added to the model.

Given the high heating rates of the interface during deposition, we will consider that the material undergoes a simple melting without simultaneous melting and recrystallization [15]. It is therefore possible to model the two mechanisms separately by considering a transition temperature $T_{Transition}$ at 300°C.

- Crystallization kinetics

In the case of the FFF process, crystallization generally takes place in non-isothermal conditions. In order to model the formation and growth of crystals we chose the Nakamura model Eq. (1) which is the most widely used in the literature [16].

Materials Research Proceedings 28 (2023) 139-148 https://doi.org/10.21741/9781644902479-16

$$\frac{d\alpha}{dt} = K_{NAK}(T).G(\alpha) \quad , \qquad with\ G(\alpha) = n\,(1-\alpha)[-\ln(1-\alpha)]^{1-\frac{1}{n}} \tag{1}$$

where α is the relative crystalline degree, $K_{NAK}(T)$ the Nakamura kinetics coefficient calculated by $K_{NAK}(T) = K_{AVRAMI}(T)^{1/n}$ obtained in isothermal conditions and n the Avrami index [17].

Furthermore, in the FFF process, when the previously crystallized filament is heated due to the new deposit, it is possible that at low interfacial temperatures the polymer is partially melted. The kinetics of crystallization from a partially melted state is not well explored and no model is available in the literature. We will therefore assume that during a recrystallization from a partial melt, the kinetics is not impacted and therefore the polymer behaves as if it had simply stopped the crystallization. As our PAEK has too high crystallization kinetics to be characterized by differential scanning calorimetry (DSC), a test campaign was performed on fast scanning calorimeter (FSC) to estimate the thermal dependency of the isothermal Avrami coefficients $K_{AVRAMI}(T)$ over the large temperature range [160°C – 300°C].

- Melting kinetics

The melting kinetics has been further explored in the case of thermoplastic polymers. It has been shown that the thermo-kinetic models available in the literature taking into account the heating rate only allow to represent a restricted range of rates [8]. Moreover, these models cannot predict the interruption of melting during isotherm or cooling.

In several works, authors made the assumption that the melting behavior depends only on the temperature by considering an instantaneous mechanism independent of the heating rate over a certain range [18]. In this study, we also have chosen this approach by taking a statistical distribution model of the crystalline lamellae thickness which is temperature dependent Eq. (2).

$$\alpha = \alpha_{max}.Melting(T) \tag{2}$$

Melting function was estimate by temperature integration of the melting peak measured on DSC and weighting α_{max} in order to represent the melting under conditions of incomplete crystallization, case where $\alpha_{max} < 1$.

Implementation of the melting and crystallization models in the same simulation model allows to predict the melting zone and time available for the interfacial healing. For example, it can be seen in Fig. 2 that the interface melted during the deposition because of the heat provided by the hot filament.

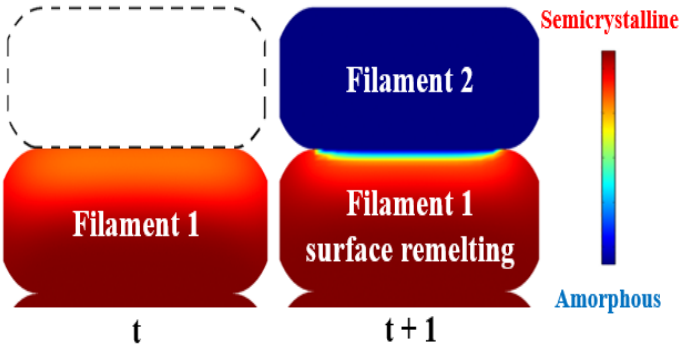

Fig. 2. Remelting of the filament surface after a second hot filament deposition.

Healing coupled with crystallization degree.

Prediction of healing at interfaces was also added in the modelling taking into account the coupling of an anisothermal healing model and a time-temperature-crystallization-superposition model

- Healing model.

In order to represent the adhesion kinetics in the anisothermal case, we proposed to use the empirical model largely defined in Eq. (3).

$$D_{Healing}(t) = \sqrt[4]{\int_0^t \frac{dt}{t_{welding}}} \tag{3}$$

where $D_{Healing}$ is the healing degree and $t_{welding}$ the experimental measured welding times to achieve complete welding of an interface under isothermal conditions.

Several authors showed that in the case of several thermoplastics, the welding times can be considered as equal to the molecule reptation times $t_{reptation}$ [19] with a good agreement with the experiment. In order to simplify the numerical solution, an integrative form was proposed by [2]. Taking into account the assumption that the relaxation times are equal to welding time, we obtain Eq. (4) with Δt the calculation step, and t the simulation time step.

$$[D_{Healing}]_{t+1} = \left(\frac{\Delta t}{t_{reptation}} + [D_{Healing}]_t^4\right)^{\frac{1}{4}} \tag{4}$$

- Time / Temperature / Crystallization Superposition (TTCS).

In order to represent the evolution of the molecular mobility during the process, it is necessary to know the relaxation time of the polymer according to its local environment. To our knowledge, no study takes into account the crystalline degree in its adhesion model. Indeed, while the evolution of molecular mobility as a function of temperature is well known with the time-temperature-superposition TTS, few studies focus on the influence of the presence of crystals on polymer diffusion.

But recently, some studies have converged to present a time-temperature-crystallization-superposition TTCS principle Eq. (5) based on experimental approaches [12].

Materials Research Proceedings 28 (2023) 139-148 https://doi.org/10.21741/9781644902479-16

$$\tau(T,\alpha) = \underbrace{a_t(T_{REF},\alpha_0,T)}_{\textbf{Thermal shift factor}} . \underbrace{a_\xi(T_{REF},\alpha_0,\alpha)}_{\textbf{Cristalline shift factor}} . \underbrace{\tau(T_{REF},\alpha_0)}_{\textbf{Reference time}} \quad (5)$$

where T_{REF} and α_0 are respectively the temperature and crystalline degree reference and τ the reptation time.

The model proposes a shift of rheological properties similar to thermal shift but with the crystalline degree. The postulated TTCS is very promising and has shown its consistency on several polymers. Moreover, several previous studies have shown that the evolution of rheological properties is proportional to the volume of crystallites and not to the shape or size of crystals [20]. These observations suggest that they can be applied to all types of crystallization. Moreover, the principle of TTCS allows to correctly represent the state of molecular mobility in cases of isothermal and anisothermal crystallization. Its general validity must be evaluated in order to apply it widely to all polymer families. Nevertheless, being the only model available in the literature, we will use it to predict the evolution of the mobility depending on the temperature and the crystalline degree. The thermal shift factors were fitted using the Williams-Landel-Ferry equation (WLF) [21] and the crystalline shift factors using a power law as proposed by defined [10] in Eq. (6).

$$\ln[a_t(T_{REF},\alpha_0,T)] = \frac{-C1(T-T_{REF})}{C2+(T-T_{REF})} \qquad and \qquad a_\xi(T_{REF},\alpha_0,\alpha) = 10^{B1.\alpha^{B2}} \quad (6)$$

where C1, C2, B1 and B2 are fitting coefficients.

Rheological measurements were carried out in our laboratory between 360°C and 400°C under nitrogen in the amorphous state in order to estimate the thermal shift factor. The model coefficients of the crystallinity shift factor are taken from the literature [10].

As previously explained, by integrating all these models in the same study, the multiphysics model is able to predict the evolution of reptation time as a function of temperature and crystalline degree in anisothermal condition. In order to explain the model, we have calculated the evolution of the relaxation time for several constant cooling rates. The results are shown in Fig. 3.

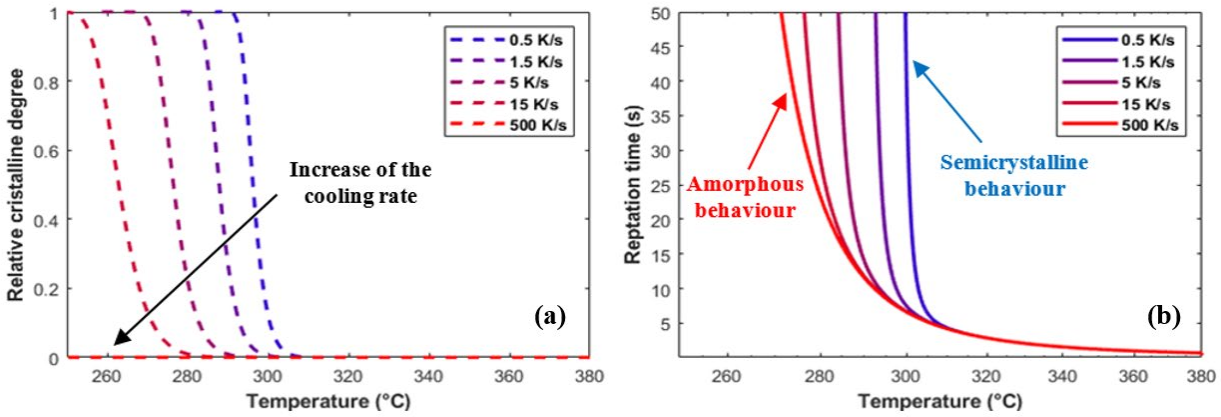

Fig. 3. (a) Relative crystalline degree and (b) the reptation time evolution under different cooling rate.

Fig. 3B represents the evolution of the creep time as a function of temperature and crystalline degree Fig. 3A. We notice that at high speed, the polymer remains amorphous during the cooling and the material follows the TTS law. But when the speed decreases and the material crystallizes, the reptation time increases quickly from the first moment of crystallization.

Results and Discussion

As said previously, a wall of 8 filaments high and 1 filament wide is simulated. All results are evaluated in the middle of the interface between the 5th and 6th layer so the results will begin at 32s. The simulations carried out from the multiphysics model allow to estimate the evolution of the crystallinity rate and the degree of healing according to the thermal history at the interface.

Simulations were performed with the TTCS model and with the TTC model in order to show the importance of taking into account the crystallization on the adhesion. Both cases were simulated with the same parameters except that the crystalline shift factor was numerically fixed at 1 to model the TTS.

With the conditions used in the simulation, it can be seen in Fig. 4, that the 5th filament crystallizes rapidly during cooling. During the next deposition, the heat generated by the upper filament partially melts the interface. The difference in the evolution of the degree of healing between the TTCS and TTS models describes the low molecular mobility of the chains due to the presence of crystals at the interface. Indeed, the final degree of healing is divided by 10.

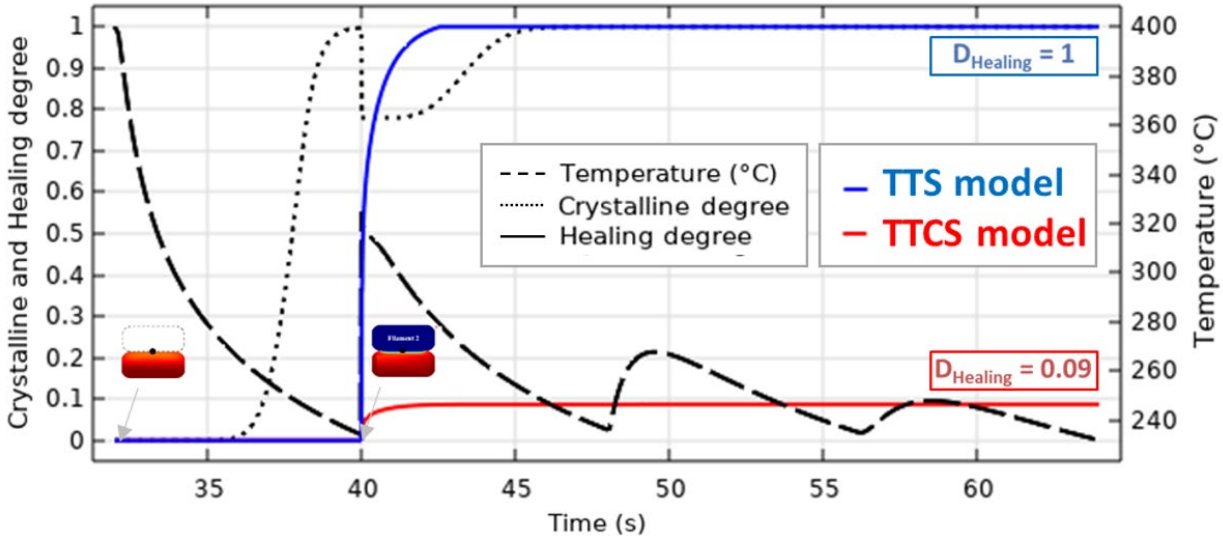

Fig. 4. Evolution of computed temperature, crystalline and healing degree with TTS and TTCS model.

To show the influence of the thermal environment on the adhesion degree, we varied the chamber and bed temperatures between 150°C and 270°C as shown Fig. 5. It is first noticed for temperatures lower than 200°C, *i.e.* where the cooling is fast, that the filament crystallizes completely before the next deposition. In these cases, only melting can allow a noticeable decrease of crystalline degree and thus a better adhesion. Because during deposition the interface temperature is not high enough to allow a total fusion, the healing degree are very low (<0.09). At high temperatures, the crystals are not yet formed at the time of deposition (T≥250°C) therefore a better healing degree is obtained.

This numerical study allows to estimate the process range in order to obtain a correct interface with a complete crystallization at the end of printing. Other parameters such as nozzle temperature, printing speed, number of beads per layer, deposit order can be tested to evaluate their influence on crystallization and adhesion.

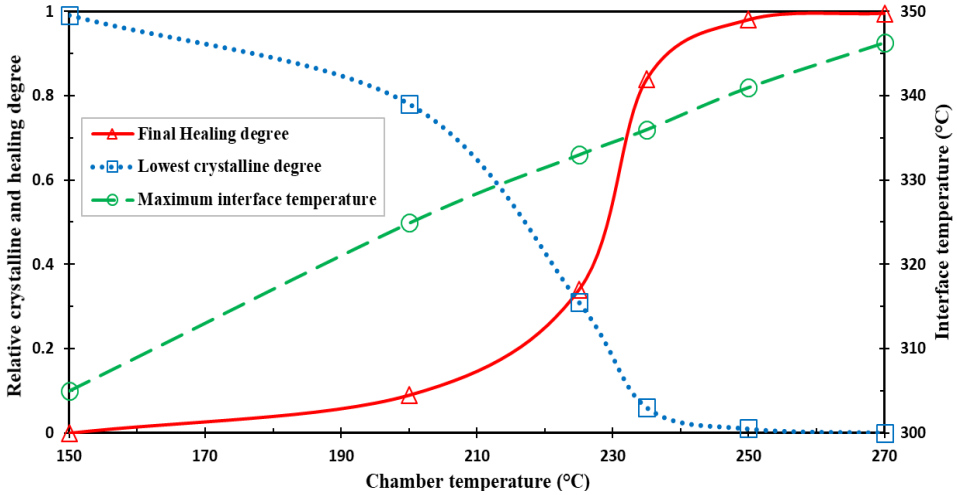

Fig. 5. Evolution of computed maximum interfacial temperature, lowest crystalline degree and final healing degree reaches after deposition as function of chamber temperature.

Summary

A multiphysics model was developed to represent the thermal history, crystalline and adhesion degree evolution at the filament scale in the FFF process. Modeling development allowed to calculate the evolution of the crystalline degree on the whole domain and in particular at the interfaces. Indeed, the model describes crystalline degree remaining after the melting generated by the deposit and the time before recrystallization. A brief parametric analysis demonstrates the non-negligible influence on the crystalline evolution on interfacial adhesion. In fact, it is shown that complete healing is only possible if the crystalline degree is close to zero. This model allows us to understand the influence of many printing parameters on adhesion and therefore to propose groups of parameters in order to improve the printing quality.

In order to confirm that the model correctly predicts the evolution of the crystalline degree as well as the effective adhesion degree of the printed part, an experimental study will have to be carried out and the adhesion values confronted with mechanical tests. Moreover, a next study will aim to model more finely the melting kinetics as well as the recrystallization kinetics through an experimental campaign.

References

[1] D. Popescu, A. Zapciu, C. Amza, F. Baciu, R. Marinescu, FDM process parameters influence over the mechanical properties of polymer specimens: A review, Polymer Test. 69 (2018) 157–66. https://doi.org/10.1016/j.polymertesting.2018.05.020

[2] A. Lepoivre, N. Boyard, A. Levy, V. Sobotka, Heat Transfer and Adhesion Study for the FFF, Additive Manufacturing Process. Procedia Manuf. 47 (2020) 948-955. https://doi.org/10.1016/j.promfg.2020.04.291

[3] D. Xu, Y. Zhang, F. Pigeonneau, Thermal analysis of the fused filament fabrication printing process: Experimental and numerical investigations, Int. J. Mater. Form. 14 (2021) 763-776. https://doi.org/10.1007/s12289-020-01591-8

[4] E. Barocio, B. Brenken, A. Favaloro, R.B. Pipes, Interlayer fusion bonding of semi-crystalline polymer composites in extrusion deposition additive manufacturing, Compos. Sci. Technol. 230 (2022) 109334. https://doi.org/10.1016/j.compscitech.2022.109334

[5] De Gennes. Reptation of a Polymer Chain in the Presence of Fixed Obstacles 1971:8.

[6] C.-T. Lo, F.C. Laabs, B. Narasimhan, Interfacial adhesion mechanisms in incompatible semicrystalline polymer systems, J. Polym. Sci. B Polym. Phys. 42 (2004) 2667-2679. https://doi.org/10.1002/polb.20148

[7] S.F. Costa, F.M. Duarte, J.A. Covas, Estimation of filament temperature and adhesion development in fused deposition techniques, J. Mater. Process. Technol. 245 (2017) 167-179. https://doi.org/10.1016/j.jmatprotec.2017.02.026

[8] A. Greco, A. Maffezzoli, Statistical and kinetic approaches for linear low-density polyethylene melting modeling, J. Appl. Polym. Sci. 89 (2003) 289-295. https://doi.org/10.1002/app.12079

[9] E. Barocio, B. Brenken, A. Favaloro, M. Ramirez, J. Ramirez, R.B. Pipes, Prediction of the Degree of Bonding in the Extrusion Deposition Additive Manufacturing Process of Semi-Crystalline Polymer Composites n.d.:11.

[10] C. Carotenuto, L. Grassia, L.P. Paduano, M. Minale, Non-Isothermal Crystallization Kinetics of an Ethylene-Vinyl-Acetate. II. Time-Temperature-Crystallinity-Superposition, Polym. Eng. Sci. 59 (2019) 2550-2556. https://doi.org/10.1002/pen.25242

[11] Minale M, Carotenuto C, Paduano LP, Grassia L. Nonisothermal Crystallization Kinetics of an Ethylene-Vinyl-Acetate: I Calorimetry Versus Rheology. Polymer Engineering & Science 59 (2019) 2557–63. https://doi.org/10.1002/pen.25248

[12] R. Pantani, V. Speranza, G. Titomanlio, Evolution of iPP Relaxation Spectrum during Crystallization, Macromol. Theor. Simul. 23 (2014) 300-306. https://doi.org/10.1002/mats.201300147

[13] S. Bakrani Balani, F. Chabert, V. Nassiet, A. Cantarel, Influence of printing parameters on the stability of deposited beads in fused filament fabrication of poly(lactic) acid. Additive Manuf. 25 (2019) 112–121. https://doi.org/10.1016/j.addma.2018.10.012
[14] A.R. Zanjanijam, I. Major, J.G. Lyons, U. Lafont, D.M. Devine, Fused Filament Fabrication of PEEK: A Review of Process-Structure-Property Relationships, Polym. 12 (2020) 1665. https://doi.org/10.3390/polym12081665
[15] T. Baumard, E.E. Rassy, N. Boyard, S.L. Corre, J.L. Bailleul, J. Bikard, et al. Caractérisation des cinétiques de cristallisation du poly(éther éther cétone) (PEEK) par mesure de la chaleur spécifique en calorimétrie différentielle à balayage rapide Congrès Français de Thermique SFT 2022, May 2022, Valenciennes, France. hal-03761852.
[16] K. Nakamura, T. Watanabe, K. Katayama, T. Amano, Some aspects of nonisothermal crystallization of polymers. I. Relationship between crystallization temperature, crystallinity, and cooling conditions, J. Appl. Polym. Sci. 16 (1972) 1077-1091. https://doi.org/10.1002/app.1972.070160503
[17] M. Avrami, Granulation, Phase Change, and Microstructure Kinetics of Phase Change. III, J. Chem. Phys. 9 (1941) 177–184. https://doi.org/10.1063/1.1750872
[18] C. Nicodeau. Continuous welding modeling of thermoplastic matrix composites. Engineering Sciences [physics]. Arts et Métiers ParisTech, 2005. English. NNT: 2005ENAM0018. pastel-00001506
[19] R.P. Wool, Polymer interfaces: Structure and strength, 1995.
[20] G. Lamberti, G.W.M. Peters, G. Titomanlio, Crystallinity and Linear Rheological Properties of Polymers, Int. Polym. Process. 22 (2007) 303-310. https://doi.org/10.3139/217.2006
[21] M.L. Williams, R.F. Landel, J.D. Ferry, The Temperature Dependence of Relaxation Mechanisms in Amorphous Polymers and Other Glass-forming Liquids, J. Am. Chem. Soc. 77 (1955) 3701–3707. https://doi.org/10.1021/ja01619a008

Materials Research Proceedings 28 (2023) 149-158 https://doi.org/10.21741/9781644902479-17

Application of the plane-strain-compression-test to determine the local mechanical properties of LPBF-manufactured 316l components

JENSCH Felix[1,a *], BUHL Johannes[1,b], LAUE Robert[2,c] and HÄRTEL Sebastian[1,d]

[1]Chair of Hybrid Manufacturing (FHF), Brandenburg University of Technology, 03046 Cottbus, Germany

[2]Professorship Virtual Production Engineering, Chemnitz University of Technology, 09126 Chemnitz, Germany

[a]felix.jensch@b-tu.de, [b]johannes.buhl@b-tu.de, [c]robert.laue@mb.tu-chemnitz.de, [d]haertel@b-tu.de

Keywords: LPBF-Process, Local Properties, Plane-Strain-Compression-Test

Abstract. In the Laser Powder Bed Fusion (LPBF) process for metal components, a CAD file is sliced into layers with a thickness of 20-80 micrometers and the component is built up layer by layer. For this purpose, a metal powder layer is applied in each case and melted locally. This process is repeated until the geometry is completely established. The mechanical properties of the manufactured part are controlled by the cooling rate. It is currently not considered in the design of LPBF components, that the printed part has a varying heat flow into the surrounding powder and into the support plate depending on its slenderness. As a result of the different temperature histories, different microstructures with correspondingly different mechanical properties are formed in the untreated state (as-built). These differences must be considered in the component design. In this work, walls of various thicknesses were produced from 316L stainless-steel alloy using the LPBF process. The walls could be used to create plane-strain-compression-test specimens of various heights and orientations. The tests were performed according to Graf et al. [1] and the flow curve was calculated from the force-displacement curve while taking friction into account. Following that, tensile strength, Young's modulus, yield strength, and yield stress were determined inversely. A clear dependence of the mechanical parameters on the degree of slimness was discovered, which was confirmed by microscopic examinations. To summarize, the plane-strain-compression-test is a quick and reliable method for determining the local variation of mechanical properties.

Introduction

Since its development in the 1980s, additive manufacturing has gained in importance from year to year [2]. This results from the large variety of shapes that layer-by-layer construction makes possible. Thus, it is possible to manufacture topology-optimized components where material is only provided along the load paths [3]. Consequently, fewer resources are consumed for such components and the degree of lightweight design is maximized [4]. However, the optimized structure is often very complex and can only be manufactured with a great deal of effort or not at all using conventional manufacturing processes, such as milling or turning [5]. Additive manufacturing processes such as selective laser melting (SLM) are increasingly being used to produce complex shape-optimized geometries [6].

In most cases, the topology-optimized geometry consists of thin structures that converge at the connection points and thus lead to material accumulations. Since thicker component areas cool more slowly than narrow ones, different cooling rates develop in the different component areas [7]. In addition to the grain size, the cooling rate of the material determines the composition of the

Content from this work may be used under the terms of the Creative Commons Attribution 3.0 license. Any further distribution of this work must maintain attribution to the author(s) and the title of the work, journal citation and DOI. Published under license by Materials Research Forum LLC.

microstructure. For example, in steels, martensitic, bainitic, ferritic, pearlitic and austenitic structures can develop [8]. In narrow areas, the cooling rate is higher, which is why a predominantly fine-grained martensitic or bainitic microstructure with an increased tensile strength develops [9]. In thicker areas, the cooling rate is lower, especially in the center of the cross-section, resulting in a coarser-grained softer ferritic or pearlitic microstructure with a lower tensile strength [10]. Furthermore, with an increased cooling rate, the average grain size decreases, which leads to strengthening by grain refinement [11]. Thus, depending on the cross-sectional area, a locally varying property profile develops over the component [12].

For complex components, empirical determination of the phase fractions and the resulting properties is only possible with a great deal of effort. Therefore, these are calculated by means of simulations. Zhang et al. determined the phase composition for Ti-6Al-4V by implementing a phenomenological phase transformation model into conventional simulation methods for additive manufacturing [13]. Another phenomenological microstructure model to determine the phase composition for Ti-6Al-4V was proposed by Nitzler et al. [14]. However, simulations of the L-PBF process to determine the phase composition take a lot of time and have no direct impact on the optimization of the part geometry.

In order to consider the properties resulting from the LPBF process during topology optimization, it is necessary to consider them in advance. This results in new challenges in the modeling of the anisotropic material behavior, the development of robust optimization algorithms and the integration of the process simulation into the structural optimization [15]. Considering the self-weight of the intermediate structure, the process-dependent loads, and the material properties dependent on the process time, Wang et al. provide an approach for a corresponding topology optimization [16]. Another possibility to consider process-dependent material properties is the description of geometry-dependent local material properties. A first step for this is the determination of the phase composition and its coupling with the mechanical properties depending on the slenderness of the manufactured structure.

The plane-strain-compression-test is an efficient test method for calculating the flow curve up to large plastic strains. It is based on the theoretical principles of the work of Nádai [17] and Orowan [18] and converted into a practical test for determining mechanical properties by Watts et al. [19] and Sellars et al. [20]. In this experiment, two opposing punches locally compress a strip-shaped sheet specimen. To avoid stress concentrations and consequently an early specimen failure due to fracture, the use of punches with rounded edges is recommended [21]. However, this increases the friction component, which must be eliminated by calculation to improve the quality of the results. In addition to friction, shearing, i.e. the deformation of material volume to the side of the punch, also has an influence on the measured force [22]. The ratio of punch width to specimen height influences both the friction component and the shear component. The larger this ratio is, the larger the friction component becomes and the smaller the shear component becomes [23]. The aim of the work is to efficiently obtain local flow stress differences in additively manufactured components using the plane-strain-compression-test, which is first investigated on small LPBF manufactured cuboids.

Materials and Methods

Specimen manufacturing.

The plane-strain-compression-specimens of 316L powder from m4p material solutions GmbH were produced with an EOS M290 from EOS GmbH. A laser power of approx. 200 W, a scanning speed of approx. 900 mm/s, a vector distance of 0.1 mm and a layer thickness of 0.04 mm were used. The laser was focused to a diameter of about 0.08 mm and the LPBF-process took place under argon atmosphere. Three narrow walls with a cross-section of 30 mm x 13 mm and a thickness of 1 mm, 1.5 mm, 2 mm and 3 mm were produced in each case in upright (0°) and horizontal (90°) orientation. These already have the final dimensions of the plane-strain-

compression-specimens and are used under as-printed conditions. Furthermore, three blocks each with the dimensions 30 mm x 13 mm x 25 mm were printed in upright and horizontal position. A plane-strain-compression-specimen with a thickness of 1 mm, 1.5 mm, 2 mm and 3 mm was eroded from each of these blocks by the wire EDM machine MAKINO U6 from Makino GmbH. (Fig. 1).

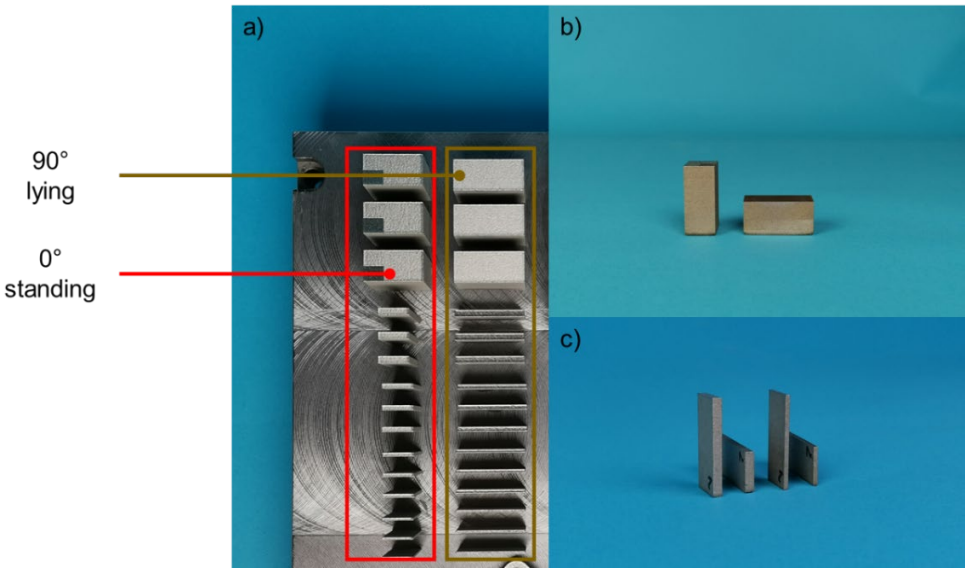

Fig. 1. Printed parts for the plane-strain-compression-test a) on the build plate, b) as blocks for wire EDM and c) as walls.

Plane-strain-compression-test.

The produced specimens were tested in a compression test on a Galdabini Quasar 50 universal testing machine with a maximum test load of 50 kN using 2.7 mm wide punches (Fig. 2). The tests took place under room temperature and with a quasi-static strain rate of $\dot{\varphi} = 0.01\ s^{-1}$ to avoid influences due to microstructural changes of the material.

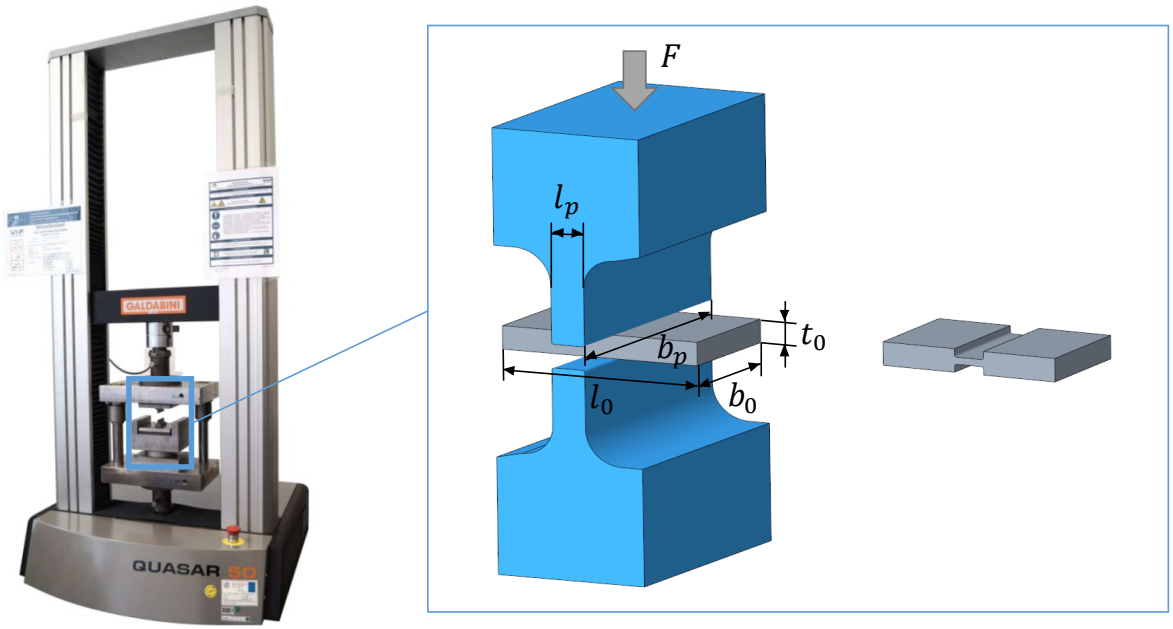

Fig. 2: Universal testing machine GALDABINI QUASAR 50 kN and the schematic structure of the plane-strain-compression-test.

During the test, raw data for applied force F and the distance Δt traveled by the punch. To determine the flow curve, the stress σ_{k_f} was calculated according to equation 1 and the corrected equivalent plastic strain φ according to equation 2 [24, 25].

$$\sigma_{k_f} = \frac{\sqrt{3}}{2} \cdot \frac{F}{A_v} \tag{1}$$

$$\varphi = \left| \frac{2}{\sqrt{3}} \cdot \ln\left(\frac{t_0}{(t_0 - \Delta t)}\right) \right| - \varepsilon_{el} \tag{2}$$

A_v is the product of the punch width l_p and the actual width of the specimen, t_0 the original thickness of the specimen and Δt the distance traveled by the punch. The plastic strain results from the difference between the total strain and the strain ε_{el} until the yield stress is reached. Since this is a comparative study, plastic flow was assumed for all specimens from an elongation of 0.02%.

Microstructure analysis.

Dynamic image analysis according to ISO 13322-2 using the CAMSIZER X2 particle analyzer from Microtrach Retsch GmbH resulted in percentiles D10 = 20 µm, D50 = 32 µm and D90 = 46 µm. The chemical composition of the powder was determined using the BRUKER TIGER S8 fluorescence spectrometer from Bruker Corporation.

To evaluate the microstructure, the specimens were cut perpendicular to the axis of motion of the punches and embedded in an electrically conductive resin. The specimens were then surface ground with 240-1200 µm grit sandpaper, polished with a diamond suspension, and final polished with a < 0.05 µm silica solution. Samples were etched for 12 s and at a temperature of 60°C in V2A acid solution (100 ml water, 100 ml hydrochloric acid and 10 ml nitric acid) and subsequently analyzed using Thermo Fisher Scientific Inc.'s Phenom XL Generation 2 desktop SEM. Both BSD detector analysis and EDX analysis were performed. For EDX analysis, three areas were examined in each sample, from which the mean value was determined.

Results and Discussion

Chemical composition.

Since the very high temperature of over 2800°C [26] for a short time can lead to the evaporation of individual elements and thus influence the mechanical properties, an EDX analysis was performed on all samples over an area of approximately 0.2 mm² (Table 1). From the measurements it can be seen that some of the main elements are lost during the LPBF process and therefore the proportion of minor elements increases from 0.1% to up to 2.7 %. In correlation with Fuerschbach et al., this burnup occurs particularly for the elements iron and nickel, with the manganese content also decreasing slightly [27]. In contrast, the molybdenum content increases by approx. 1 wt.% and the silicon content by 0.1 wt.%. The measured values are in a similar range for all samples regardless of the orientation and the manufactured geometry, so that it can be assumed that the determined flow curves do not vary decisively due to the chemical composition.

Materials Research Proceedings 28 (2023) 149-158 https://doi.org/10.21741/9781644902479-17

Table 1. Chemical composition [wt.%] of the used 316L powder.

Alloy element	**Fe**	**Cr**	**Ni**	**Mo**	**Mn**	**Si**	**other**
Powder	67.7	17.5	11.3	1.6	1.2	0.6	0.1
Block 1 0° 3 mm	65.9	17.3	10.4	2.6	0.9	0.7	2.2
Block 1 0° 1.5 mm	66.3	17.5	10.7	2.5	1.0	0.8	1.2
Block 4 90° 3 mm	66.0	17.3	10.3	2.6	0.9	0.7	2.2
Block 4 90° 1.5 mm	65.4	17.2	10.5	2.7	0.9	0.7	2.6
Wall 0° 3 mm	66.3	17.4	10.5	2.7	0.9	0.7	1.5
Wall 0° 1.5 mm	65.9	17.5	10.8	2.5	1.0	0.7	1.6
Wall 90° 3 mm	65.7	17.4	10.4	2.6	0.9	0.7	2.3
Wall 90° 1.5 mm	65.5	17.3	10.2	2.6	1.0	0.7	2.7

Microstructure analysis.

Fig. 3 a) shows the microstructure of the specimens prepared in different orientations and initial geometries. To compare the grain sizes, three large grains were marked in each image. It can be seen that the grains in the samples eroded from the blocks are larger than those of the walls. The line intersection method was used to determine the average grain size, which was 27.0 µm for "Block 1 0°," 19.5 µm for "Block 4 90°," and 18.5 µm for "Wall 0°." Due to insufficient etching, the average grain size of "Wall 90°" could not be determined. A smaller grain size leads to an increased yield strength and improved ductility as a result of grain refinement strengthening [28].

Furthermore, it can be seen in Fig. 3 a) that the microstructure and grains of specimens fabricated in 0° orientation are stretched in the build direction and perpendicular to the compression direction, respectively. This results in anisotropy, with specimens fabricated in 0° orientation having lower tensile strength than those fabricated in 90° orientation [29]. Relative to the same specimen cross-section, the specimens printed in 90° orientation exhibit a more spherical grain structure regarding the x-y-plane. The direction of grain growth is influenced by the heat flux, which flows through the component to a large extent in the opposite direction of construction [30]. Therefore, the grains of the components produced by the LPBF method exhibit elongation in the build direction (Fig. 3 b)).

In all fabricated specimens, a cellular substructure is formed, with the dark core elements demarcated by light edge regions (Fig. 4). According to Prashanth et al. and Zhong et al., this substructure is formed by a local enrichment of heavy elements, such as molybdenum, due to a high solidification rate and associated effects of constitutional undercooling [31, 32]. In addition, the shell areas of the cells have a high dislocation density and thus increase the mechanical properties of the printed samples [33]. Due to the layered structure, the cells pass through several heating phases, which reduces the solidification rate, especially in areas far from the surface [30]. Therefore, larger cells are found on the surface.

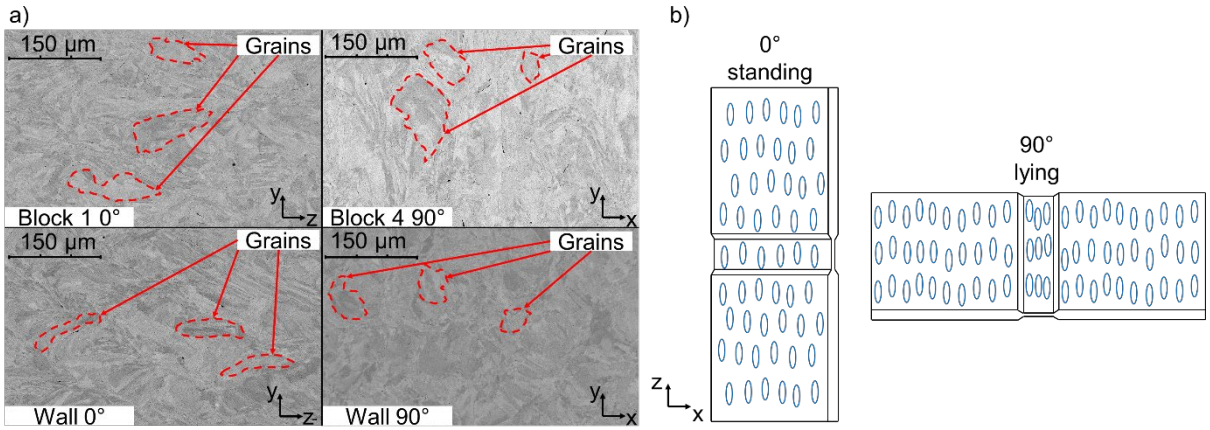

Fig. 3. Detected texture and grain sizes within SEM investigation of the a) Block 1 0°, Block 4 90°, wall 0° and 90° at a thickness of 3mm and b) stretching of the grains depending on the orientation of the printed samples.

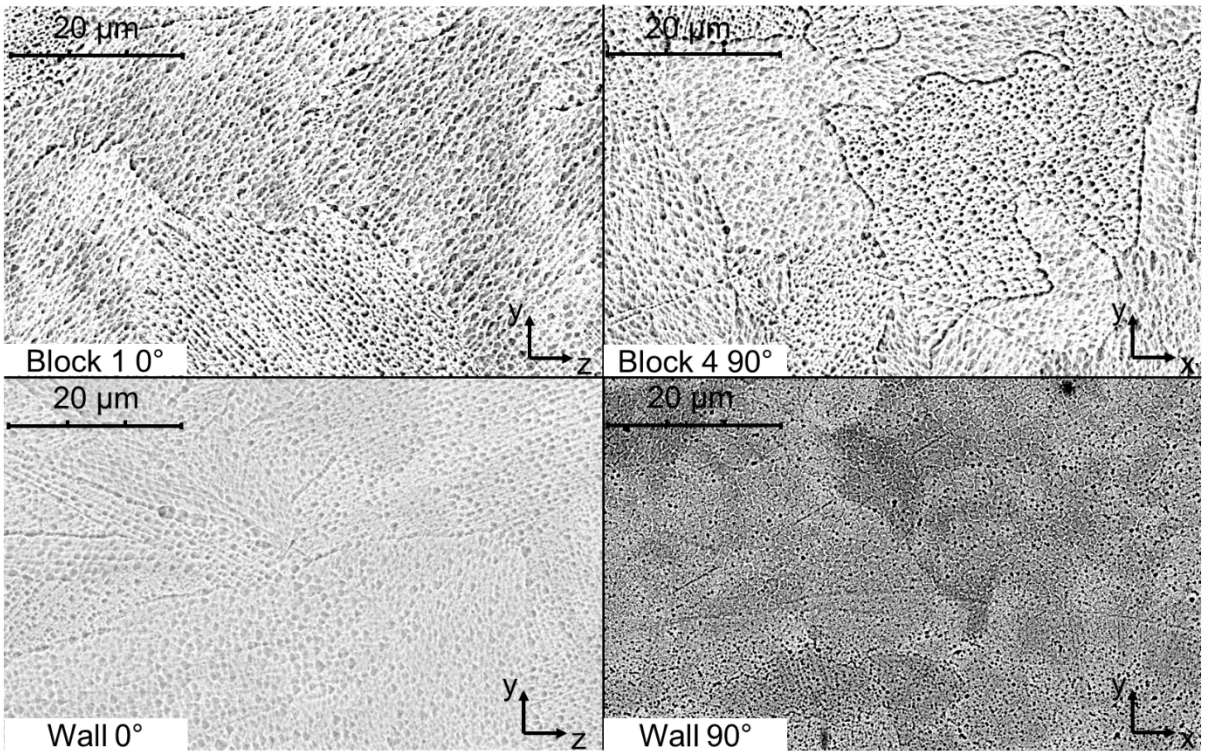

Fig. 4. Cellular substructure within SEM investigation of the a) Block 1 0°, b) Block 4 90°, c) wall 0° and d) wall 90° at a thickness of 3 mm.

Flow curves.

Finally, the qualitative difference in mechanical properties between thin and thick LPBF-manufactured specimens is shown. For this purpose, the repeatability of the compression tests is first presented using three flat compression specimens of equal thicknesses each made from three blocks in 0° orientation (Fig. 5 a)) and 90° orientation (Fig. 5 b)). In the figure, the influence of friction and shear due to the different ratio of punch width (constant) and specimen thickness (1.0, 1.5, 2, 3 mm) can be seen. The scatter increases with decreasing specimen thickness, so that the result for 1.0 mm is not included in the evaluation.

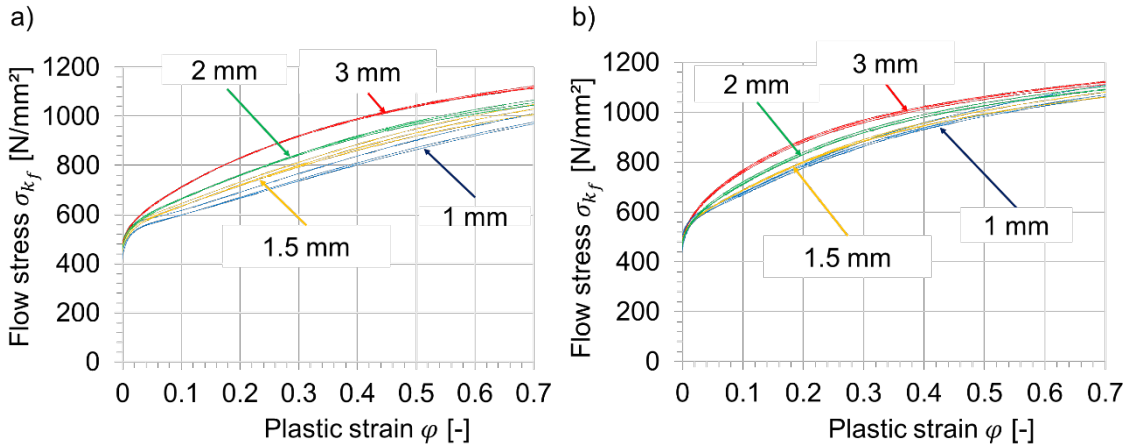

Fig. 5. Flow curves for specimens of thicknesses 1 mm, 1.5 mm, 2 mm and 3 mm taken respectively from blocks printed in a) 0° orientation and b) 90° orientation.

Fig. 6 shows the results for the directly printed walls, where the orientation again gives a clear difference in strength. However, as with the samples from the blocks, the same clear trend can be seen. In order to be able to make qualitative statements regarding the strength change due to the material properties exclusively on the basis of tests, the same specimen thickness from the block is compared with the printed specimen in the following.

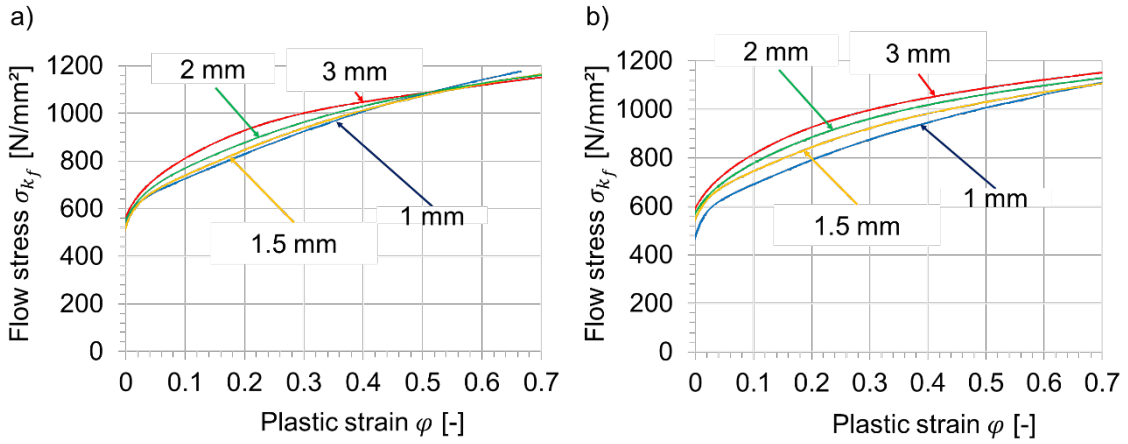

Fig. 6: Flow curves for as-printed plane-strain-compression-specimens at an orientation of the blocks of a) 0° and b) 90°.

Fig. 7 shows the flow curves for specimens with a thickness of 1.5 mm (a)) and 3 mm (b)) up to a plastic strain of 0.7. Both specimen thicknesses show higher flow stresses of the printed walls than the specimens of the same thickness from the blocks. The qualitative progression of the flow curves shows small differences, which are, however, not related to the material condition, but are rather seen in the test setup, or the specimen preparation.

The specimen printed in 0° orientation (block, 1mm) shows a lower slope than the specimen printed in 90° orientation up to a corrected plastic strain of approx. 0.25. From this value, the curves converge again up to the corrected equivalent plastic strain of 0.7. In contrast, the 1mm thick walls diverge from a plastic deformation of 0.2. It should be mentioned again that the grain growth of the specimen printed in 0° orientation was perpendicular to the punch width b_p and in 90° orientation parallel to the punch width b_p (Fig. 3 b)).

In the flow curves determined in the plane-strain-compression-test, this behaviour agrees only for the 1.5 mm thick walls. The flow curves of the 3 mm thick specimens from the block initially

show minor differences and finally meet at a yield stress of approx. 1110 N/mm². Thus, the analysis of the yield stress as a function of the compression direction or orientation in the build space leads to the result that no clear correlation can be identified. This result is confirmed in particular by the 3 mm thick walls.

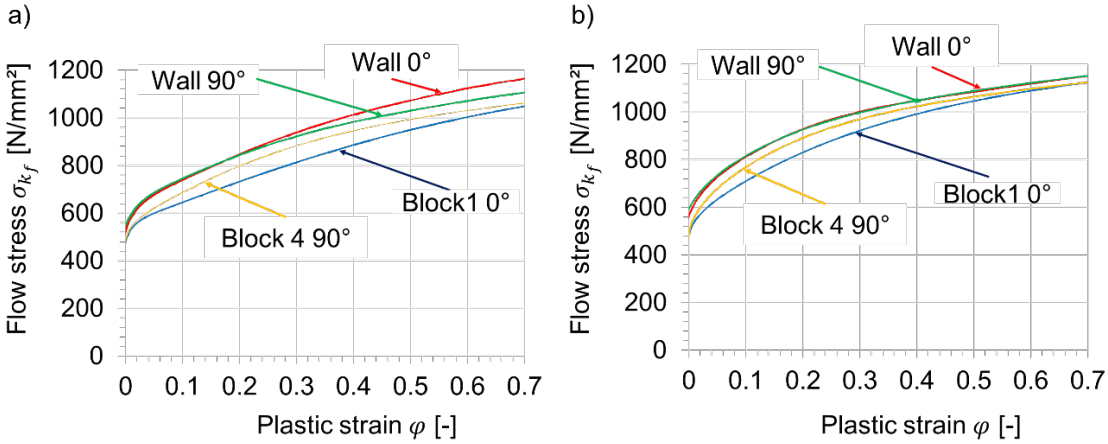

Fig. 7. Calculated flow curves for plane-strain-compression-specimens with a thickness of a) 1.5 mm and b) 3 mm.

Summary

In this work, the mechanical properties of different specimen geometries produced by the LPBF method were investigated in the plane strain compression test. The work shows that different mechanical properties can occur in components depending on the geometry. This results in a locally varying property profile for geometries with high complexity, which are usually produced by the LPBF method. Based on the research, the following conclusions can be drawn:

- The chemical composition of different LPBF specimen geometries is not significantly different.
- The grains are elongated along the build direction (for a specimen orientation of 0° perpendicular to the punch width and for a specimen orientation of 90° parallel to the punch width) and are larger for thick structures than for thin structures.
- The flow stress is significantly dependent on the component thickness and the orientation in the build space. The thinner the sample is printed, the higher the yield stress becomes compared to strips of the same thickness made from blocks. The influence of the orientation in the build space could not be clearly correlated.
- In areas close to the surface, a more pronounced cellular substructure develops due to a higher solidification rate, which also positively influences the mechanical performance.
- The plane-strain-compression-test is an effective test method to quickly obtain flow curves even from thin additive manufactured specimens. Thus, it is possible to estimate the effects of the local microstructure on the flow curve.

An industrial application is the consideration of these manufacturing-specific properties in the topology and structure optimization of components. However, further investigations are necessary for the practical application of the results in optimization programs. Accordingly, further geometries are to be considered in future investigations. In addition, a more detailed investigation of the phase composition and the resulting mechanical properties as a function of the manufacturing geometry is necessary.

References

[1] M. Graf, S. Fritsch, B. Awiszus, Determination of Forming Behaviour of EN AW-6060 by Different Testing Methods under Cold Bulk Forming Conditions, Procedia Manuf. 47 (2020) 1512-1519. https://doi.org/10.1016/j.promfg.2020.04.339

[2] M. Korpela, N. Riikonen, H. Piili, A. Salminen, O. Nyrhilä, Additive Manufacturing - Past, Present, and the Future, In: Collan, M., Michelsen, KE. (eds) Technical, Economic and Societal Effects of Manufacturing 4.0. Palgrave Macmillan, Cham., 2020, pp 17-41 https://doi.org/10.1007/978-3-030-46103-4_2
[3] J. Liu, A.T. Gaynor, S. Chen, Z. Kang, K. Suresh, A. Takezawa, L. Li, J. Kato, J. Tang, C.C.L. Wang, L Cheng, X. Liang, A.C. To, Current and future trends in topology optimization for additive manufacturing, Structural and Multidisciplinary Optimization 57 (2018) 2457-2483. https://doi.org/10.1007/s00158-018-1994-3
[4] H. Monteiro, G. Carmona-Aparicio, I. Lei, M. Despeisse, Energy and material efficiency strategies enabled by metal additive manufacturing - A review for the aeronautic and aerospace sectors, Energy Reports 8 (2021) 298-305. https://doi.org/10.1016/j.egyr.2022.01.035
[5] C. Van Sice, J. Faludi, Comparing Environmental Impacts of Metal Additive Manufacturing to Conventional Manufacturing, International Conference on Engineering Design, Proceedings of the Design Society 1 (2021) 671-680. https://doi.org/10.1017/pds.2021.67
[6] J. Holoch, S. Lenhardt, S. Revfi, A. Albers, Design of Selective Laser Melting (SLM) Structures: Consideration of Different Material Properties in Multiple Surface Layers Resulting from the Manufacturing in a Topology Optimization, Algorithms 15 (2022) 99. https://doi.org/10.3390/a15030099
[7] B. Brown, W. Everhart, J. Dinardo, Characterization of bulk to thin wall mechanical response transition in powder bed AM, Rapid Prototyping Journal 22 (2016) 801-809. https://doi.org/10.1108/RPJ-10-2015-0146
[8] S. Astafurov, E. Astafurova, Phase Composition of Austenitic Stainless Steels in Additive Manufacturing: A Review, Metals 11 (2021) 1052. https://doi.org/10.3390/met11071052
[9] J. Zhu, H. Zhou, C. Wang, L. Zhou, S. Yuan, W. Zhang, A review of topology optimization for additive manufacturing: Status and challanges, Chinese Journal of Aeronautics 34 (2021) 91-110. https://doi.org/10.1016/j.cja.2020.09.020
[10] M. Ragavendran, M. Vasudevan, Laser and hybrid laser welding of type 316L(N) austenitic stainless steel plates, Mater. Manuf. Process. 35 (2020) 922-934. https://doi.org/10.1080/10426914.2020.1745231
[11] M. Ma, Z. Wang, X. Zeng, A comparison on metallurgical behaviors of 316L stainless steel by selective laser melting and laser cladding deposition, Mater. Sci. Eng. A 685 (2017) 265-273. https://doi.org/10.1016/j.msea.2016.12.112
[12] T. Maity, N. Chawake, J. T. Kim, J. Eckert, K. G. Prashanth, Anisotropy in local microstructure - Does it affect the tensile properties of the SLM samples?, Manuf. Lett. 15 (2018) 33-37. https://doi.org/10.1016/j.mfglet.2018.02.012
[13] Q. Zhang, J. Xie, Z. Gao, T. London, D. Griffiths, V. Oancea, A metallurgical phase transformation framework applied to SLM additive manufacturing processes, Mater. Design 166 (2019) 107618. https://doi.org/10.1016/j.matdes.2019.107618
[14] J. Nitzler, C. Meier, K. W. Müller, W. A. Wall, N. E. Hodge, A novel physics-based and data supported microstructure model for part-scale simulation of laser powder bed fusion of Ti-6Al-4V, Advance Modelling and Simulation in Engineering Sciences 8 (2021) 16. https://doi.org/10.1186/s40323-021-00201-9
[15] P. Zhang, J. Liu, A. C. To, Role of anisotropic properties on topology optimization of additive manufactured load bearing structures, Scripta Mater. 135 (2017) 148-152. https://doi.org/10.1016/j.scriptamat.2016.10.021
[16] W. Wang, D. Munro, C. C. L. Wang, F. van Keulen, J. Wu, Space-time topology optimization for additive manufacturing, Struct. Multidisc. Optim. 61 (2020) 1-18. https://doi.org/10.1007/s00158-019-02420-6

[17] A. Nádai, „Plasticity: A Mechanics of the Plastic State of Matter, Nature 131 (1933). https://doi.org/10.1038/131383c0
[18] E. Orowan, The Calculation of Roll Pressure in Hot and Cold Flat Rolling, Procee. of the Insti. of Mech. Eng. 150(1) (1943) 140-167. doi:10.1243/PIME_PROC_1943_150_025_02
[19] A. B. Watts, H. Ford, An experimental investigation of the yielding of strip between smooth dies, Procee. of the Insti. of Mech. Eng. 167(1b) (1953) 448-464. doi:10.1177/002034835316701b28
[20] C. M. Sellars, G. J. Davies, Hot Working and Forming Processes, Proceedings of an International Conference on Hot Working and Forming Processes, Metals Soc., 1980.
[21] N. Becker, Weiterentwicklung von Verfahren zur Aufnahme von Fließkurven im Bereich hoher Umformgrade, Springer Berlin, Heidelberg, Stuttgart, 1994. https://doi.org/10.1007/978-3-662-10890-1
[22] P. Frey, Umformtechnische Strukturierung metallischer Einleger im Folgeverbund für mediendichte Kunststoff-Metall-Hybridbauteile, PhD Thesis, Friedrich-Alexander-Universität Erlangen-Nürnberg (FAU), 2021.
[23] N. Becker, K. Pöhlandt, K. Lange, Improvement of the Plane-Strain Compression Test for Determining Flow Curves, CIRP Annals 38(1) (1989) 227-230. https://doi.org/10.1016/S0007-8506(07)62691-2
[24] M.S. Mohebbi, A. Akbarzadeh, Y.-O. Yoon, S.-K. Kim, Flow stress analysis of ultrafine grained AA 1050 by plane strain compression test, Mater. Sci. Eng. A 593 (2014) 136-144. https://doi.org/10.1016/j.msea.2013.11.027
[25] A.P. Carvalho, L.M. Reis, R.P. Pinheiro, P.H.R. Pereira, T.G. Langdon,
R.B. Figueiredo, Using Plane Strain Compression Test to Evaluate the Mechanical Behavior of Magnesium Processed by HPT, Metals 12 (2022) 125. https://doi.org/10.3390/met12010125
[26] F. Yan, W. Xiong, E. Faierson, G.B. Olson, Characterization of nano-scale oxides in austenitic stainless steel processed by powder bed fusion, Scripta Mater. 155 (2018) 104-108. https://doi.org/10.1016/j.scriptamat.2018.06.011
[27] P.W. Fuerschbach, J.T. Norris, X. He, T. DebRoy, Understanding Metal Vaporization from Laser Welding, Sandia National Laboratories, Albuquerque, 2003.
[28] B. AlMangour, D. Grzesiak, J.-M. Yang, Rapid fabrication of bulk-form TiB2/316L stainless steel nanocomposites with novel reinforcement architecture and improved performance by selective laser melting, J. Alloy. Compd 680 (2016) 480-493. https://doi.org/10.1016/j.jallcom.2016.04.156
[29] A. Fedorenko, B. Fedulov, Y. Kuzminova, S. Evlashin, O. Staroverov, M. Tretyakov, E. Lomakin, I. Akhatov, Anisotropy of Mechanical Properties and Residual Stress in Additively Manufactured 316L Specimens, Materials 14 (2021) 7176. https://doi.org/10.3390/ma14237176
[30] A. Röttger, J. Boes, W. Theisen, M. Thiele, C. Esen, A. Edelmann, R. Hellmann, Microstructure and mechanical properties of 316L austenitic stainless steel produced by different SLM devices, Int. J. Adv. Manuf. Technol. 108 (2020) 769-783. https://doi.org/10.1007/s00170-020-05371-1
[31] K. Prashanth, J. Eckert, Formation of metastable cellular microstructures in selective laser melted alloys, J. Alloy. Compd. 707 (2017) 27-34. https://doi.org/10.1016/j.jallcom.2016.12.209
[32] Y. Zhong, L. Liu, S. Wikman, D. Cui, Z. Shen, Intergranular cellular segregation network structure strengthening 316L stainless steel prepared by selective laser melting, J. Nuc. Mater. 470 (2016) 170-178. https://doi.org/10.1016/j.jnucmat.2015.12.034
[33] A.J. Birnbaum, J.C. Steuben, E.J. Barrick, A.P. Iliopoulos, J.G. Michopoulos, Intrinsic strain aging, Σ3 boundaries, and origins of cellular substructure in additively manufactured 316L, Additive Manuf. 29 (2019) 100784. https://doi.org/10.1016/j.addma.2019.100784

Materials Research Proceedings 28 (2023) 159-168 https://doi.org/10.21741/9781644902479-18

Determination of welding heat source parameters for fem simulation based on temperature history and real bead shape

SZYNDLER Joanna[1,a] *, SCHMIDT Alexander[1,b] and HÄRTEL Sebastian[1,c]

[1]Chair of Hybrid Manufacturing, Brandenburg University of Technology, Cottbus, Germany

[a] Joanna.Szyndler@b-tu.de, [b] Alexander.Schmidt@b-tu.de, [c] Sebastian.Haertel@b-tu.de

Keywords: Finite Element Method (FEM), Wire Arc Additive Manufacturing (WAAM), Calibration Procedure, Goldak's Heat Source Parameters

Abstract. To improve process understanding and increase the numerical prediction quality of a wire arc additive manufacturing (WAAM) process, this paper focuses on determining the parameters of a numerical model that reproduces an experimental setup of a welding process, with particular attention given to the actual shape of the weld bead. The dimensions of the heat source (HS) model in a welding process are determined based on experimentally measured weld pool sizes as well as temperature history at selected points below and adjacent to a weld seam. The whole experimental setup is accurately reproduced within the Simufact.Welding software and an optimization procedure is applied to obtain the best possible agreement between experimental and numerical results. A validated numerical model with reliable parameters for two heat sources is later used to predict and observe material behavior during the WAAM process of more complex parts.

Introduction

The wire arc additive manufacturing process is becoming increasingly popular in many engineering industries due to its high deposition rate, low costs, nearly nonlimited build size, and near-net shape manufacturing of complex geometries. It enables the production of structurally efficient and free-formed shapes in a shorter time as compared to other AM processes. Moreover, varied materials can be applied together to obtain functionally graded materials [1,2]. The main advantage of WAAM is its ability to manufacture high-quality parts with strong structural and mechanical properties. All these and other advantages of the WAAM process are the reason for many research works focused on its applicability in aerospace, automotive, biomedical, or marine industries [3-7]. Most of the focus is concentrated on the microstructure and mechanical properties of the manufactured parts [8], controlling deposition shape [9], and analysis of the residual stress or distortions [10,11].

WAAM is executed by depositing subsequent layers of molten metal on top of each other until the expected geometry is created. Welding metals is a process that includes heating and cooling cycles, which strongly influences chemical-metallurgical reactions in liquid metal, phase transformations, grain growth, and therefore final material mechanical properties [12]. To better understand the mechanisms taking place during WAAM and to minimize the costs of experimental investigations at the same time, a simulation approach is eagerly applied, where not only finite element models [11,13-17], but also neural networks [16,18,19] or mathematical [20], recursive models [21] are increasingly used. However, to accurately simulate the final properties of the part obtained by the WAAM process, a realistic heat source shape and distribution is necessary [22].

Thus, to improve the understanding of the material behavior during a WAAM process, this work aims to determine the parameters of a numerical model that reproduces the welding process, with particular attention given to the actual shape of the weld bead. In this study, the dimensions of Goldak's heat source [23] model in a welding process are determined based on experimentally

Content from this work may be used under the terms of the Creative Commons Attribution 3.0 license. Any further distribution of this work must maintain attribution to the author(s) and the title of the work, journal citation and DOI. Published under license by Materials Research Forum LLC.

measured weld pool sizes as well as temperature history at selected points below and adjacent to a weld seam.

Experimental Procedure

The welding experiments have been conducted with an Arc 605 WAAM system of GEFERTEC GmbH (Berlin, Germany). As welding material, AWS A5.18 with a wire diameter of Ø = 1.2 mm was chosen. The chemical composition of the welding material is stated in Table 1. To conduct the temperature measurement a DMC Plus measuring amplifier of HBM (Darmstadt, Germany) was used.

Table 1. Chemical composition of AWS A5.18 % weight.

C	Mn	Si	Cu	Fe
0.06 - 0.13	1.4 - 1.6	0.7 - 1.0	≤ 0.3	Rest

To ensure the reproducibility of the experiments and reproduce a real WAAM process concerning the thermal characteristics as far as possible a device was constructed as shown in Fig. 1a. All the parts are made of AISI 1045, which is considered to be sufficiently comparable to the AWS A5.18 and thus a real WAAM component of AWS A5.18 concerning the thermal characteristics. Since the measurement of the melt pool temperature is not possible during the welding, the temperature measurement took place at four relevant points near the welding seam via type K thermocouples. To improve the response time of the thermocouples, the thermocouples were spot-welded at the indicated positions. In detail, the temperature was measured at the upper substrate surface near the welding seam (TC 1), at the lower substrate surface directly below the welding seam (TC 2), and at two points within the base plate at different distances to the welding surface (TC 4 and TC 5), as seen in Fig. 1b.

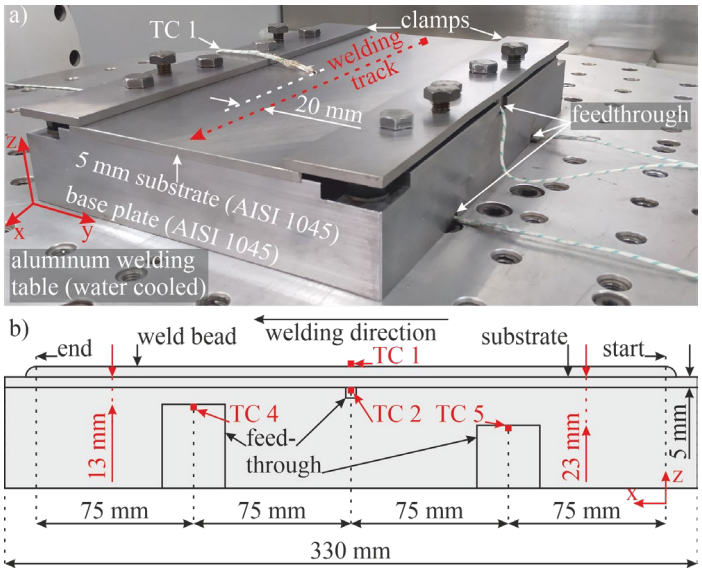

Fig. 1. Experimental setup for welding experiments with temperature measurement a) macroscopic image and b) cross-sectional sketch indicating positions of the thermocouples.

Since the melt pool characteristic is not stable when starting the welding process and thus not representative for the weld bead, the temperature measurement took place at least 75 mm after the starting of the welding process to ensure a quasi-static process state (Fig. 1b). With the device it is possible to perform welding experiments with and without preheating the substrate. The preheating of the substrate and the device enables the reproduction of the welding process of a real component in higher detail. In this case, preheating was not applied and thus the starting temperature of the

substrate was room temperature. Other relevant welding parameters are shown in Table 2. Subsequent scanning electron microscope (SEM) analyses of the welding seam were conducted with a Phenom XL G2 of ThermoFisher Scientific (Waltham, USA).

Table 2. Welding process parameter.

Welding mode [-]	CMT-process frequency [Hz]	Process gas [-]	Gas flow rate [l/min]	Current [A]	Voltage [V]	Feedstock velocity [mm/min]	Axis speed [mm/min]
Cold metal transfer (CMT)	3	Ar18CO$_2$	15	144	14.6	4,000	400

Results and Discussion

Temperature history plots show the highest recorded value (712°C) directly under the weld seam at the location of TC 2. The second highest temperature is noted by TC 1 – 180°C – on the top surface of the substrate. Thermocouples 4 and 5 record ca. 100 and 50°C as maximum values of observed temperatures (Fig. 2). Although TC 1 and TC 2 are in the same cross-section, the peaks of the respective temperature plots are temporally shifted to each other. TC 2 temperature plot represents the heat transfer from the electric arc, which is a moving HS, into the material by conduction. TC 2 temperature rises within a few seconds when the electric arc is passing the cross section above TC 2 and is falling shortly after the electric arc passed the relevant cross-section. TC 1 temperature history represents the heat transfer from the welding seam to TC 1 through the substrate by heat conduction. Thus, as long as the welding seam (TC 2) has a significantly higher temperature it acts as a stationary heat source regarding TC 1. Since TC 1 is 20 mm away from the welding seam and heat transfer by conduction takes time, the peak of TC 1 is delayed compared to TC 2.

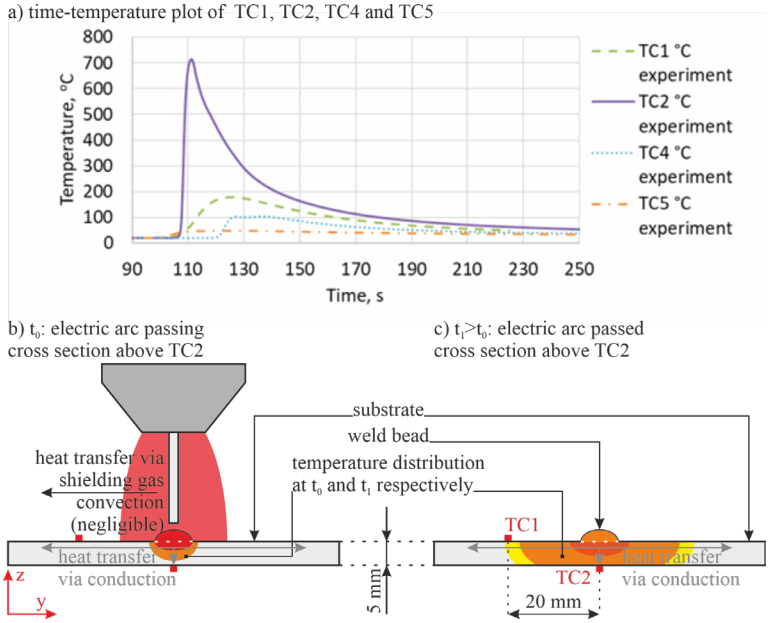

Fig. 2. a) Temperature history recorded by four thermocouples during the welding process of a single weld seam, b) schematic sketch of welding process at t_0 and c) schematic sketch of welding process at $t_1 > t_0$.

As is presented in Fig. 3a, SEM analyses are made in two locations: first at the cross-section in the middle of the weld seam (V1); second at the cross-section in the longitudinal direction at the end of the weld seam (V2). Fig. 2b shows that the depth of the fully melted zone of the base material

reaches ~1.41 mm during the welding process. A mixture of liquid and austenite phases existed till the ~1.9 mm level during the welding process. Lastly, the heat-affected zone reached a depth of ~3.5 mm. The longitudinal cross-section V2 enabled the estimation of the amount of material that overflows in the front and rear direction (Fig. 3c), which enabled the prediction of the initial values of the front and rear lengths of Goldak's heat source model. It is also visible there that the depth of the melted zone is not constant in a vertical direction and varies along the weld seam, which might be a result of the cold metal transfer mode.

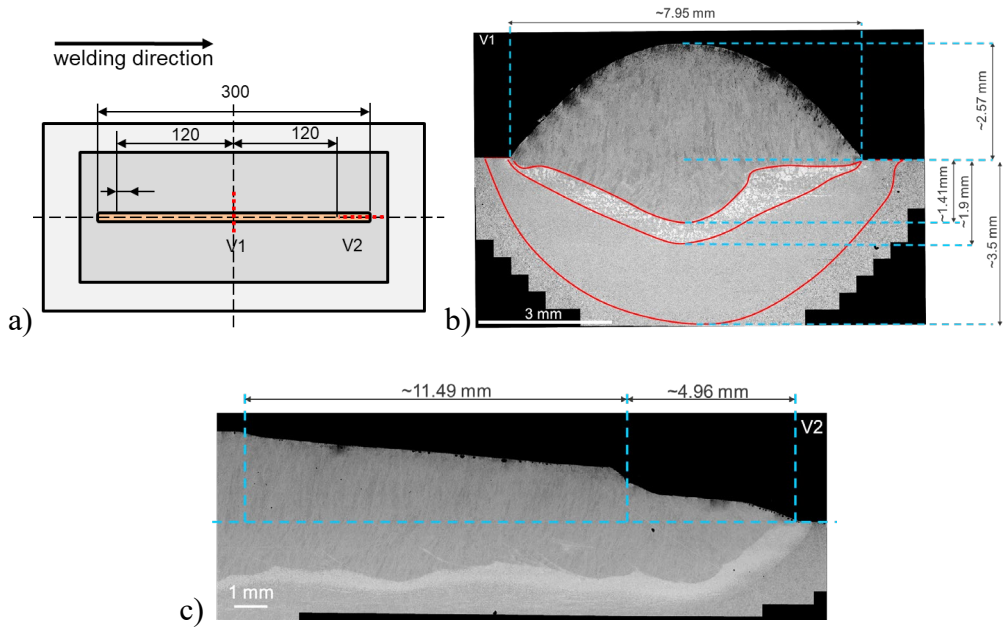

Fig. 3. a) Locations of the SEM analyses; b) in the middle of the seam, c) at the end of the seam in the longitudinal direction.

Numerical Simulation

To reproduce the experimental setup in a digital form, the Simufact.Welding 2021.1 software (Hexagon, Stockholm) is used, where a ground plate, substrate plate, and holding clamps are also included in the FE model (Fig 4a). To minimize the influence of the geometry of the weld seam on the quality of obtained results, a cross-section from metallography (Fig. 3b) was applied to represent the expected shape of the welding seam (Fig 4b).

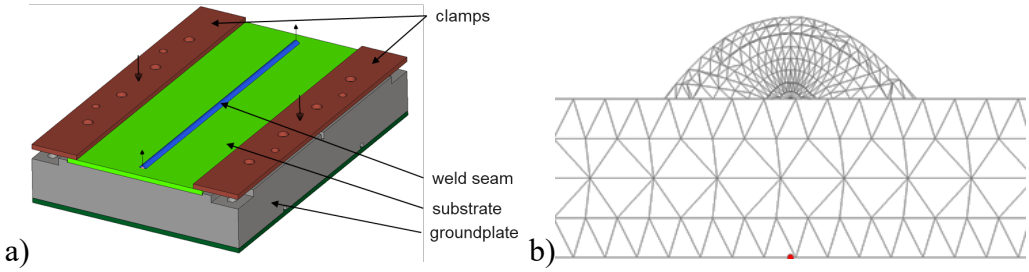

Fig. 4. FE model developed in Simufact. Welding software: a) full setup, b) cross-section of the weld seam.

Material properties of the AISI 1045 steel substrate, such as density and thermal capacity are taken from the literature [24, 25] (Fig. 5a, b), whereas thermal conductivity was measured with Linseis LFA 1000 Laser Flash test machine (Linseis Messgeräte GmbH, Selb, Germany) (Fig. 5c). Material properties of the AWS A5.18 wire are taken from the Simufact.Welding 2021.1 material database.

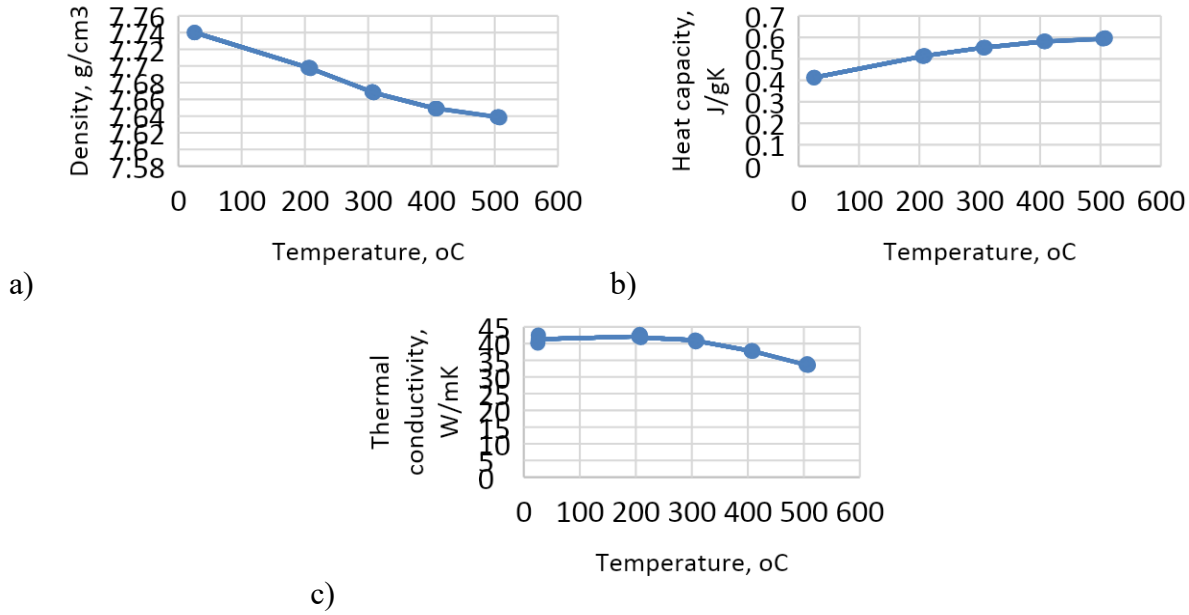

Fig. 5. Material properties of AISI 1045 as a function of temperature: a) density [24], b) heat capacity [25], c) thermal conductivity measured by Authors.

The convective heat transfer parameter h_{plate} in the function of temperature for a substrate (Fig. 6b), is calculated based on classical heat transfer equations characteristic for natural convection that is present over a flat surface facing up:

$$\beta = \frac{1}{T_f} \tag{1}$$

$$T_f = \frac{(T_s + T_\infty)}{2} \tag{2}$$

$$L_c = A_s/p \tag{3}$$

$$Ra_L = \frac{g\beta(T_s - T_\infty){L_c}^3}{v^2} Pr \tag{4}$$

$$Nu = 0.54{Ra_L}^{\frac{1}{4}} \tag{5}$$

$$h_{plate} = \frac{k}{L_c} Nu \tag{6}$$

where: A_s is the top surface area of the plate, p – circumference of the plate, Pr – Prandtl number (at T_f), Nu- Nusselt number, Ra_L - Rayleigh number, v – kinematic viscosity (at T_f), L_c - characteristic length, T_f - film temperature, k – thermal conductivity (at T_f).

The weld seam is treated as a horizontally placed cylinder, for which the natural convection parameter $h_{cylinder}$ is presented in Fig. 6a and calculated with the following equations:

$$Nu = \left\{ 0.6 + \frac{0.387{Ra_D}^{\frac{1}{6}}}{\left[1 + \left(\frac{0.559}{Pr}\right)^{\frac{9}{16}}\right]^{\frac{8}{27}}} \right\}^2 \tag{7}$$

$$h_{cylinder} = \frac{k}{D} Nu \tag{8}$$

Properties of air at atmospheric pressure such as: kinematic viscosity v, thermal conductivity k and Prandtl number Pr are described as functions of temperature with following equations:

$$v = -0.000000000000001080028067777848\ T^3 + 0.000000000078431258717711 2\ T^2 + \\ + 0.0000009317235889175 73\ T + 0.0000131184421229409 \quad (9)$$

$$k = 0.000000000004641045635296 73\ T^3 - 0.000000025220464123877 6\ T^2 + \\ + 0.0000756242633211078\ T + 0.0236352337830901 \quad (10)$$

$$Pr = 0.000000000000000000025041212039251900\ T^6 - 0.000000000000000020791991918815 7\ T^5 + \\ + 0.000000000000067316897714983\ T^4 - 0.000000001097177506888 35\ T^3 + \\ +0.000000941818163402441\ T^2 - 0.000346614970760939\ T + 0.737371365505794 \quad (11)$$

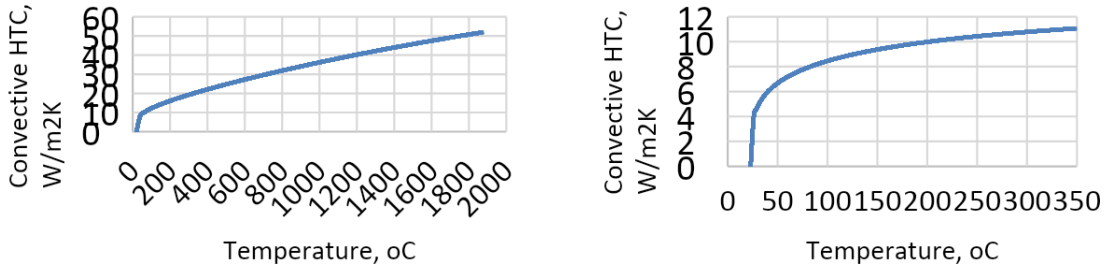

a) b)

Fig. 6. Convective heat transfer coefficient as a function of the temperature of the a) weld seam, and b) substrate to air.

A single seam is welded digitally with the same speed (6.66667 mm/s), voltage (14.6 V), and current (144 A) as welding parameters applied during the real experiment. The air temperature and initial temperature of the wire are set to 23°C, the initial temperature of all plates is set to 21.5°C, and arc efficiency is assumed to be 80%.

Goldak's heat source model [23] was used to describe the volumetric heat flux density distribution, where a_f, a_r, b, d are parameters related to the shape characteristic of the welding arc (Fig. 7). Values of the front (4.96 mm) and rear (11.49 mm) length of the heat source one, are read from the microscopic analysis presented in Fig. 3c. Values of the width and depth parameters are established based on optimization procedure applied to obtain a similar picture of the melted zone between the simulation and experiment. During this procedure, an advantage of applying two heat sources was used [26], which enabled to improve results in terms of temperature history recorded during the real test, especially on the top surface of the substrate. A targeted adjustment of the parameters for both HSs was done at the same time, to compare the calculated shape of the fusion zone and temperature history to the experimental data shown in Fig. 2 and 3b. The final values of the obtained parameters of both heat sources are gathered in Table 3.

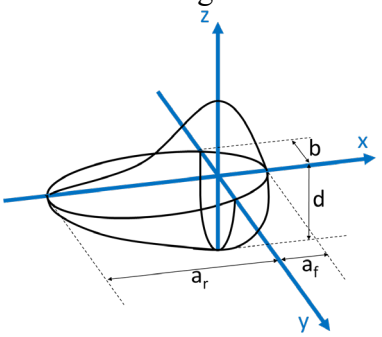

Fig. 7. Goldak's double ellipsoid heat source model; a_f – front length, a_r – rear length, b - width, d – depth.

Table 3. Obtained Goldak's heat source parameters.

	a_f [mm]	a_r [mm]	b [mm]	d [mm]
HS 1	4.96	11.49	3	2
HS 2	0.1	0.1	0.3	0.3

Validation of the Numerical Simulation Results

The simulation results with 2 heat sources show a particularly good agreement with the available experimental data. The geometry and size of the melted zone visible directly below the weld seam agree well with the microscopic results (Fig. 8). Based on the phase diagram characteristic of AISI 1045 steel, the fully liquid phase is assumed to occur above 1525°C, a mixture of liquid and austenitic phases is observed at temperatures of 1425-1525°C, and only the austenitic phase is present at 770-1425°C. These temperature ranges are used to determine the calculated geometry of the melt zone during FE simulation. As shown in Fig. 8, the fully liquid phase can be seen to a depth of ~1.46 mm, austenite + liquid to ~1.7 mm, and the pure austenite phase to ~4 mm. In contrast, if only one heat source is used, neither the geometry nor the size of the melt zone visible directly below the weld seam is realistically calculated, as a comparison of Fig. 8b with Fig. 8c shows. Moreover, the calculated Root Mean Square Error (RMSE) (see Fig. 9) between measured and simulated temperature history (for using HS1 and HS2 together) at selected points equals 6.25, 44.6, 7.07, and 3.91°C at TC 1, TC 2, TC 4, and TC 5, respectively. Such well prepared and validated the numerical model with dependable Goldak's heat source parameters can be later used to predict and observe material behavior during the WAAM process of much more complex parts.

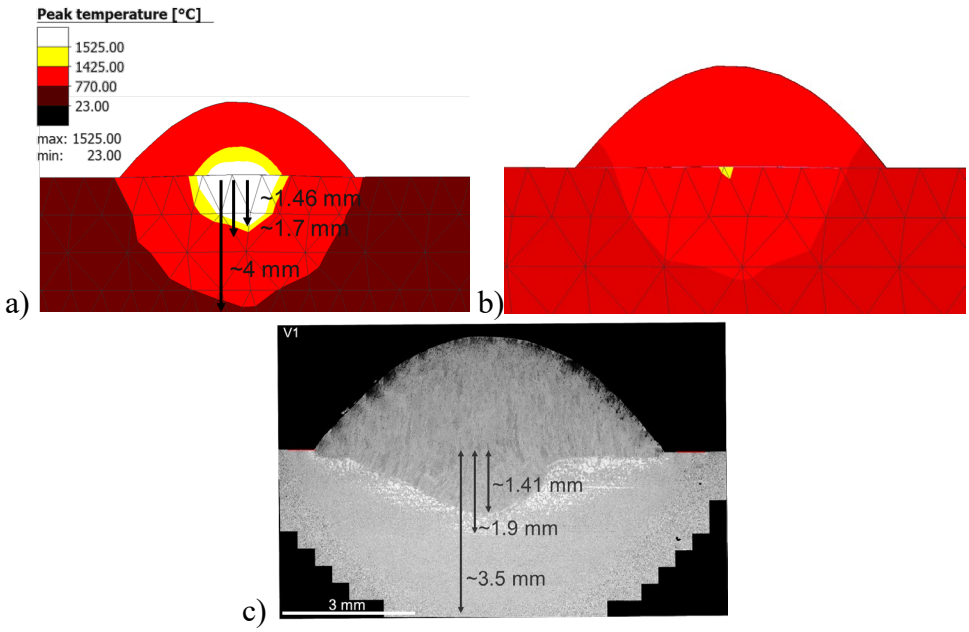

Fig. 8. Peak temperature distribution in the middle of the weld seam according to the simulation with a) 2 HSs; b) 1 HS; b)c) SEM-image of the weld seam indicating the temperature distribution during the welding process.

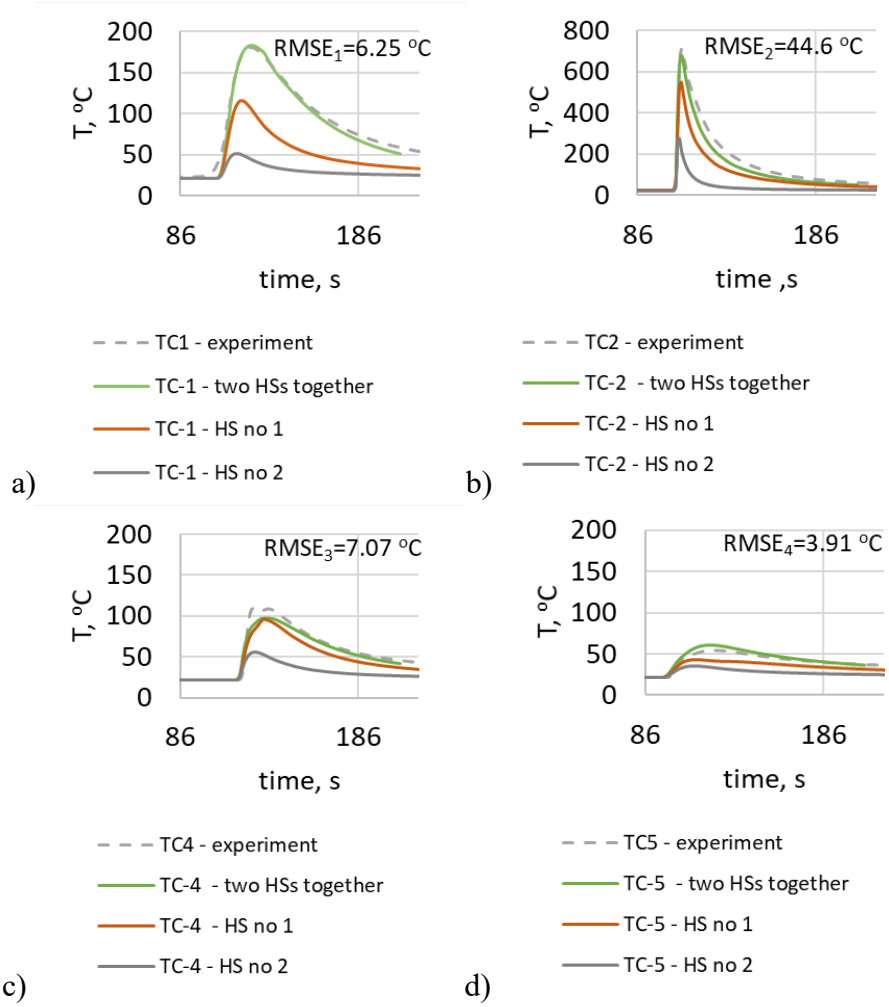

Fig. 9. Comparison between experimental (dotted lines) and numerical results (continuous lines) in terms of recorded temperature history in selected points: a) TC1, b) TC2, c) TC4, d) TC5.

For investigation purposes, also single HS models were calculated when only 1 Goldak's heat source was applied to weld a seam. Obtained results in form of temperature-time plots are presented in Fig. 9. As is noticeable, the application of the 2 HS model enables to obtain reliable temperature history at different locations of the base plate. Especially the prediction of temperature history on the top surface of the substrate is improved in comparison to the single HS model.

Summary

In this investigation, the parameters of Goldak's heat source model are determined based on experimentally measured weld pool sizes as well as temperature history at selected points below and adjacent to a weld seam. A single 300 mm long seam of AWS A5.18 wire is welded onto an AISI 1045 base plate. Four thermocouples are measuring temperature history: first on the top surface next to the weld seam, second directly under the weld seam, and two more thermocouples are placed under the base plate on two diverse levels. A microscopic analysis of the weld seam cut in the middle of its length gives information about the expected heat zone size and is also a hint for dimensions of the Goldak's HS. The whole experimental setup is accurately reproduced within the Simufact.Welding 2021.1 software and an optimization procedure is applied to obtain the best possible agreement between experimental and numerical results. In this case, a two-heat source model gives the most accurate results, where not only a melted zone of the material is accurately

predicted but also temperature history under the substrate, under the weld seam, and on the top surface of the substrate are very close to reality.

Acknowledgments
The IGF-project 21219 BG of the European Research Association for Sheet Metal Working (EFB e.V.) is funded by the German Federation of Industrial Research Associations (AiF) within the framework of the Industrial Collective Research (IGF) program by the Federal Ministry of Economic Affairs and Climate Action based on a decision by the German Bundestag.
The Authors would like to thank the EFB and the members of the industrial consortium for supporting the research activities.

References
[1] S.I. Evans, J. Wang, J. Qin, Y. He, P. Shepherd, J. Ding, A review of WAAM for steel construction – Manufacturing, material and geometric properties, design, and future directions, Structures 44 (2022) 1506-1522. https://doi.org/10.1016/j.istruc.2022.08.084
[2] S. Singh, S.K. Sharma, D.W. Rathod, A review on process planning strategies and challenges of WAAM, Materials Today: Proceedings, 47, 19 (2021) 6564-6575.
[3] V. Madhavadas, D. Srivastava, U. Chadha, S.A. Raj, M.T.H. Sultan, F.S. Shahar, A.U.M. Shah, A review on metal additive manufacturing for intricately shaped aerospace components, CIRP J. Manuf. Sci. Technol. 39 (2022) 18-36. https://doi.org/10.1016/j.cirpj.2022.07.005
[4] J. Ye, P. Kyvelou, F. Gilardi, H. Lu, M. Gilbert, L. Gardner, An end-to-end framework for the additive manufacture of optimized tubular structures, IEEE Access, 9 (2021) 165476-165489. https://doi.org/10.1109/ACCESS.2021.3132797
[5] X. Zuo, W. Zhang, Y. Chen, J.P. Oliveira, Z. Zeng, Y. Li, Z. Luo, S. Ao, Wire-based directed energy deposition of NiTiTa shape memory alloys: Microstructure, phase transformation, electrochemistry, X-ray visibility and mechanical properties, Additive Manuf. 59 (2022) 103115. https://doi.org/10.1016/j.addma.2022.103115
[6] M. Vishnukumar, R. Pramod, A.R. Kannan, Wire arc additive manufacturing for repairing aluminium structures in marine applications, Mater. Lett. 299 (2021) 130112. https://doi.org/10.1016/j.matlet.2021.130112
[7] T. Feucht, J. Lange, B. Waldschmitt, A.K. Schudlich, M. Klein, M. Oechsner, Welding process for the additive manufacturing of cantilevered components with the WAAM, Adv. Join. Process. 125 (2020) 67-78.
[8] F. Wang, S. Williams, P. Colegrove, A.A. Antonysamy, Microstructure and mechanical properties of wire and arc additive manufactured Ti-6Al-4V, Metall. Mater. Trans. A 44 (2013) 968-977. https://doi.org/10.1007/s11661-012-1444-6
[9] J. Xiong, G. Zhang, Forming appearance analysis in multi-layer single pass GMAW-based additive manufacturing, Int. J. Adv. Manuf. Technol. 80 (2015) 1767-1766. https://doi.org/10.1007/s00170-015-7112-4
[10] P.J. Ding, J. Mehnen, S. Ganguly, P.M.A. Sequeira, F. Wang, S. Williams, Thermo-mechanical analysis of wire and arc additive manufacturing process on large multi-layer parts, Comput. Mater. Sci. 50 (2011) 3315-3322. https://doi.org/10.1016/j.commatsci.2011.06.023
[11] X. Zhou, H. Zhang, G. Wang, X. Bai, Three-dimensional numerical simulation of arc and metal transport in arc welding based additive manufacturing, Int. J. Heat Mass Transfer 103 (2016) 521-537. https://doi.org/10.1016/j.ijheatmasstransfer.2016.06.084
[12] A.S. Azar, S.K. As, O.M. Akselsen, Determination of welding heat source parameters from actual bead shape, Comput. Mater. Sci. 54 (2012) 176-182. https://doi.org/10.1016/j.commatsci.2011.10.025

[13] Z. Hu, X. Qin, T. Shao, Welding thermal simulation and metallurgical characteristics analysis in WAAM for 5CrNiMo hot forging die remanufacturing, Procedia Eng. 207 (2017) 2203-2208. https://doi.org/10.1016/j.proeng.2017.10.982
[14] C.T.J. Panicker, K.R. Surya, V. Senthilkumar, Novel process parameter-based approach for reducing residual stresses in WAAM, Materials Today: Proceedings 59 (2022) 1119-1126. https://doi.org/10.1016/j.matpr.2022.03.025
[15] N.P. Gokhale, P. Kala, Thermal analysis of TIG-WAAM based metal deposition process using finite element method, Materials Today: Proceedings 44 (2021) 453-459.
[16] Y. Ling, J. Ni, J. Antonissen, H.B. Hamouda, J.V. Voorde, M.A. Wahab, Numerical prediction of microstructure and hardness for low carbon steel wire Arc additive manufacturing components, Simul. Model. Pract. Th. 122 (2023) 102664. https://doi.org/10.1016/j.simpat.2022.102664
[17] V. Gornyakov, Y. Sun, J. Ding, S. Williams, Modelling and optimizing hybrid process of wire arc additive manufacturing and high-pressure rolling, Mater. Design 223 (2022) 111121. https://doi.org/10.1016/j.matdes.2022.111121
[18] S. Bose, A. Biswas, Y. Tiwari, M. Mukherjee, S.S. Roy, Artificial neural Network-based approaches for Bi-directional modelling of robotic wire arc additive manufacturing, Materials Today: Proceedings 62 (2022) 6507-6513. https://doi.org/10.1016/j.matpr.2022.04.331
[19] Y. Wang, X. Xu, Z. Zhao, W. Deng, J. Han, L. Bai, X. Liang, J. Yao, Coordinated monitoring and control method of deposited layer width and reinforcement in WAAM process, J. Manuf. Process. 71 (2021) 306-316. https://doi.org/10.1016/j.jmapro.2021.09.033
[20] W.C. Ke, J.P. Oliveira, B.Q. Cong, S.S. Ao, Z.W. Qi, B. Peng, Z. Zeng, Multi-layer deposition mechanism in ultra high-frequency pulsed wire arc additive manufacturing (WAAM) of NiTi shape memory alloys, Additive Manuf. 50 (2022) 102513. https://doi.org/10.1016/j.addma.2021.102513
[21] C. Chen, H. He, J. Zhou, G. Lian, X. Huang, M. Feng, A profile transformation based recursive multi-bead overlapping model for robotic wire and arc additive manufacturing (WAAM), J. Manuf. Process. 84 (2022) 886-901. https://doi.org/10.1016/j.jmapro.2022.10.042
[22] J.A. Goldak, M. Akhlaghi, Computational Welding Mechanics, Springer, US, 2005.
[23] J. Goldak, A.P. Chakravarti, M. Bibby, A new finite element model for welding heat sources, Metall. Trans. B 15 (1984) 299-305. https://doi.org/10.1007/BF02667333
[24] M. Hojny, M. Glowacki, Numerical Modelling of Steel Deformation at Extra-High Temperatures, in P. Miidla (ed.), Numerical Modelling, IntechOpen, London, 2012. https://doi.org/10.5772/36562.
[25] A. Martinovs, S. Polukoshko, E. Zaicevs, R. Revalds, Laser Hardening Process Optimizations Using FEM, Engineering for Rural Development, 2020, pp. 1500-1508. https://doi.org/10.22616/ERDev2020.19.TF372
[26] H.M. Aarbogh, M. Hamide, H.G. Fjaer, A. Mo, M. Bellet, Experimental validation of finite element codes for welding deformations, J. Mater. Process. Technol. 210 (2010) 1681-1689. https://doi.org/10.1016/j.jmatprotec.2010.05.014

Materials Research Proceedings 28 (2023) 169-178 https://doi.org/10.21741/9781644902479-19

Generating STL for forming trabecular bone structure in additive manufacturing using cell dynamics modeling

ROCHA Adones A.[1,a *],THIRÉ Rossana M.S.M.[1,2,b] and ARAUJO Anna-Carla[2,c]

[1]Alberto Luiz Coimbra Institute for Graduate Studies and Research in Engineering/Metallurgical and Material Engineering Program (PEMM/COPPE), Federal University of Rio de Janeiro, Brazil

[2]Institut Clément Ader, Université de Toulouse, CNRS/INSA/ISAE/Mines Albi/UPS, France

[a]adones.rocha@coppe.ufrj.br, [b]rossana@metalmat.ufrj.br, [c]araujo@insa-toulouse.fr

Keywords: Additive Manufacturing, FFF, Biopolymers, STL Generation, Trabecular Bone

Abstract. There are two types of structures in bone with different densities: cortical bone, a denser region, and trabecular bone, a porous part. Poly(lactic acid) - PLA, a biopolymer widely used in additive manufacturing (AM), can be applied for fabricate products for medical and dental applications since it is biodegradable and biocompatible to several mammalian cell lines. This article proposes a methodology for generating STL to produce by AM a structure with geometry similar to that of trabecular bone using a mathematical model that describes the population dynamics of bone cells. Bone density values obtained by solving the differential equations model with finite differences are used to develop a mesh surface. This surface is converted into a binarized mesh using a binary algorithm and, finally, the STL file is obtained by applying the multidimensional arrays tool from Matlab® software. The produced file is analyzed by BoneJ® using the same procedure currently applied for bone tomography to obtain some geometry parameters as trabecular thickness, trabecular separation, bone fraction and connectivity; and the degree of anisotropy. 3D Printed samples were successfully produced by Fused Filament Fabrication (FFF) using PLA filament. It was noticed that the produced structure is similar to the morphology of the trabecular part of the femoral head, comparing the different strategies of obtain STL and real bone tomography.

Introduction

Bone architecture can be classified as cortical or trabecular. Cortical bone is made up of a compact region of mineralized material, while trabecular bone has structures known as trabeculae, which are highly porous [1]. Bone is a mineralized conjunctive tissue that exhibits four types of cells: osteoblasts, osteocytes, osteoclasts, and bone lining cells [2]. Bone composition is given by 50-70% of inorganic material (hydroxyapatite), 20-40% of organic material (collagen I), and 5-10% of water and other materials, such as lipids and fibrillin [3].

The trabecular region of the bone is the most affected by fractures and is the area where bone weakening can happen with different carcinomas and pathologies. However, more facts need to be clarified about the characteristics of this tissue region, as well as the strategies to reproduce it aiming as a replacing bone tissue (bone tissue engineering) and technical-academic studies (orthopedic surgeries).

It is noticed many techniques to reproduce the trabecular bone structure as capture and image processing using computed tomography that stands out as a gold standard [4]. This process is relatively high cost and it need for real experiments, so the use of mathematical models as Wolff and Roux laws is an alternative to obtain this architecture as a digital image. These mathematical approaches describe the architecture of trabeculae as responses to mechanical stimuli [4]. Recent

Content from this work may be used under the terms of the Creative Commons Attribution 3.0 license. Any further distribution of this work must maintain attribution to the author(s) and the title of the work, journal citation and DOI. Published under license by Materials Research Forum LLC.

progress has shown that this approach can be considered outdated since bone architecture can be related to cell effects [4] and bone cell remodeling [5].

A mathematical model developed by Komarova et al. [1] describes the dynamics of bone cells population, in view osteoclasts and osteoblasts in a basic multicellular unit. The authors explain the effect of local regulatory factors on cell production rates, employing a power law approximation. A system of differential equations is defined for variations in cell population (osteoblasts and osteoclasts) and bone mass. This model has been used in recent years in several studies to describe different phenomena and bone pathologies. Ayati et al. [6] adapted the mathematical modeling of Komarova et al. [1] to study the healthy cell population and those with tumor cells. In this paper, the cell diffusion and bone density were evaluated, with cell and bone density are described in one dimension. Valério et al. [7] investigated using the model to the anomalous (tumor) and healthy growth of the bone mass, considering disturbances in the origin, and applying the method of finite differences in two dimensions. Peyroteo et al. [8] studied the application of the finite element method to solve the remodeling equations and analyze the results in conditions of healthy bone and osteoporosis.

The work of Fernández-Cervantez et al. [9] applying the space-time adaptations of Ayati et al. [6] proposes to solve the system of differential equations using Euler's method for the temporal part and the finite difference method for the spatial part, to obtain a porous piece with a structure like the trabecular bone. Then, the authors used the 3D printing binder jetting technique to obtain printed pieces. The authors found patterns and profiles similar to those of trabecular bone morphology by assessing the image produced with the patterns of real trabecular bone.

In the image processing analysis of the trabecular bone structure, some parameters are important as defined by McGregor et al. [10]: Trabecular Thickness, Trabecular Separation, Bone Volume Fraction, Degree of Anisotropy and Connectivity. These parameters can be analyzed to mimic the trabecular structure, knowing that the study of Trabecular Thickness and Trabecular Separation dispersion in a certain range of values is important, since real bone does not have isotropic trabecular thickness and separation [11]. These characteristics of bone morphology may be key factors for tissue compatibility and regeneration when applied to tissue engineering scaffolds.

Filament Fusion Fabrication (FFF) is a simple 3D printing technique and relatively cheap when compared to other techniques that have greater precision [12]. In this technique, it is possible to obtain, with a 0.2 mm nozzle, structures that simulate a corresponding trabecular thickness of 0.2 mm. Most of the bones in the human body have thin trabecular, however, the femoral head bone has an average trabecular thickness of 0.19 mm, being the thickest documented [10]. Therefore, these structures have the potential to be printed by FFF, despite the relatively low accuracy of the technique compared to more robust AM techniques. Obtaining files that can be read by 3D printer software is essential for the operation of the technique, such as STL files that describe the surface with triangulation [12]. The present work seeks to apply the mathematical model proposed for cellular remodeling to obtain a STL that mimics the bone trabecular structure, for so it is analyzed the different bone parameters in comparison with real bone of femoral head in pieces printed by FFF.

Modeling the Bone Dynamics

Bone is a mineralized conjunctive tissue that exhibits four types of cells: osteoblasts, osteocytes, osteoclasts, and bone lining cells. This tissue performs important functions in the body, such as locomotion, support, and protection of soft tissues, calcium and phosphate storage, and bone marrow shelter. Despite its immobile appearance, bone is a highly dynamic organ. Bone material is continuously reabsorbed by osteoclasts and “rebuilt” by osteoblasts [8].

The model of bone remodeling proposed by Komarova et al. [1] takes into account that both osteoclasts and osteoblasts can produce local factors capable of activating or inhibiting themselves, or activating or inhibiting another cell type, i.e., signaling respectively autocrine and paracrine

factors. A simplified hypothesis considers that autocrine and paracrine factors only regulate the production rate of osteoclasts and osteoblasts and their removal rates are proportional to the current number of corresponding cells. Some growth factors were neglected, such as the action of the nuclear factor kappa β ligand-receptor activator (RANKL) and insulin (IGF) that can promote osteoclasts and osteoblasts survival. These assumptions reduced the number of parameters helping its implementation.

Equations (1) and (2) present the Komarova model describing the dynamics of cell populations for bone remodeling along the time (t). The main variables of the model are: number of cells of osteoclasts (C), number of cells of osteoblasts (B) and bone mass (ρ).

$$\frac{dC(t)}{dt} = \alpha_1 C(t)^{g11} B(t)^{g21} - \beta_1 C(t) \quad (1)$$

$$\frac{dB(t)}{dt} = \alpha_2 C(t)^{g12} B(t)^{g22} - \beta_2 B(t) \quad (2)$$

The constants α_i and β_i are called as cell production and removal activities, respectively, and $g_{i,j}$ represents the efficacy of autocrine or paracrine factors derived from osteoclasts (index 1) or osteoblasts (index 2).

Komarova model also propose Eq. 3 to calculate the bone mass $\rho\ (t)$ as a function of the cell population in steady state ($t \rightarrow \infty$), the constants are k_i that corresponds to the normalized activity of bone resorption (index C) and formation (index B). The term inside the parentheses in Eq. 3 corresponds to the number of cells that actively resorb or form bone, and the variables $\underline{C}$ and $\underline{B}$ indicate the values of number of cells in steady-state.

$$\frac{d\rho(t)}{dt} = -k_C(t) max\left(0, C(t) - \underline{C}\right) + -k_B(t) max\left(0, B(t) - \underline{B}\right) \quad (3)$$

To obtain estimates of the initial parameters, Komarova *et al*. used experimental data obtained from the histomorphometry analysis of bone sections [1].

A second model is proposed by Ayati et al. [6], an extended mathematical model adding a diffusion cells term (D_i), that it is multiply by the Laplacian of cell number, obtaining a field with cell population. The spatial distribution of C(t), B(t) and $\rho(t)$ is calculated using Eq. 4, 5 and 6, where u = (x, y, z). A numerical finite difference method can be used to solve this system.

$$\frac{\partial C(u,t)}{\partial t} = D_C \nabla^2 C(u,t) + \alpha_1 C(u,t)^{g11} B(u,t)^{g21} - \beta_1 C(u,t) \quad (4)$$

$$\frac{\partial B(u,t)}{\partial t} = D_B \nabla^2 B(u,t) + \alpha_2 C(u,t)^{g12} B(u,t)^{g22} - \beta_2 B(u,t) \quad (5)$$

$$\frac{\partial \rho(u,t)}{\partial t} = -k_1(u,t) max\left(0, C(u,t) - \underline{C}\right) + k_2 max\left((u,t) - \underline{B}\right) \quad (6)$$

Methodology for STL Surface using Cells Models

Two strategies (S1) and (S2) were developed in this article to produce the three-dimensional surfaces based on the presented models. The same cubic envelop was used for both strategies wherein bone and porous regions were produced, so a Basic Multicellular Unit, BMU. The first strategy used a 2D methodology for each layer and the second one calculated the regions in all envelop. The surfaces were transformed in STL file format for allowing 3D printing. The application of Matlab's tool *stlwrite* was used to export the surface volume produced with the two strategies.

Strategy 1 (S1).

This strategy is based on solving differential equations in two dimensions and applying the *isosurface* tool. Bone density values obtained by solving the differential equations model with finite differences are used to develop a mesh surface. This surface is converted into a binarized mesh using a binary algorithm and, finally, the STL file is obtained by applying the multidimensional arrays tool from Matlab® software. Strategy 2 (S2) solves the differential

equations in three dimensions, and with the obtained three-dimensional matrix, an *isosurface* similar to the one produced in S1 is created.

For two dimensions (x and y), applying finite differences in Eq. (4) and (5), Eq. (7) and (8) represents the model used for this strategy:

$$\frac{C_{i,j}^{(n+1)} - C_{i,j}^{(n)}}{\Delta t} = \frac{k_{i,j}C_{i+1,j}^{(n)} - 2C_{i,j}^{(n)} + C_{i-1,j}^{(n)}}{\Delta x^2}(D_c) + \frac{k_{i,j}C_{i,j+1}^{(n)} - 2C_{i,j}^{(n)} + C_{i,j-1}^{(n)}}{\Delta y^2}(D_c) + \alpha_1 C(u,t)^{g11} B(u,t)^{g21} - \beta_1 C(u,t), \quad (7)$$

$$\frac{B_{i,j}^{(n+1)} - B_{i,j}^{(n)}}{\Delta t} = \frac{k_{i,j}B_{i+1,j}^{(n)} - 2B_{i,j}^{(n)} + B_{i-1,j}^{(n)}}{\Delta x^2}(D_c) + \frac{k_{i,j}B_{i,j+1}^{(n)} - 2B_{i,j}^{(n)} + B_{i,j-1}^{(n)}}{\Delta y^2}(D_c) + \alpha_2 C(u,t)^{g12} B(u,t)^{g22} - \beta_2 B(u,t). \quad (8)$$

These meshes at different times can be "stacked" using the *Marching cubes algorithm* (*isosurface* tool from Matlab®) to obtain a three-dimensional surface. Using these meshes in Eq. 6, also a mesh is produced for bone mass. This strategy, called here as Strategy 1, would correspond to cell migration in the z direction that would continuously produce an extracellular matrix.

Strategy 2.

A second approach to obtaining an STL that mimics bone structure from bone remodeling would be to simply solve Eq. 5-7 in three dimensions applying finite differences. Strategy 2 (S2) obtained a three-dimensional matrix, an *isosurface* similar to the one produced in S1 is obtained with the Eqs. 9 and 10 for the population of osteoclasts (C) and osteoblasts (B).

$$\frac{C_{i,j,k}^{(n+1)} - C_{i,j,k}^{(n)}}{\Delta t} = \frac{k_{i,j}C_{i+1,j,k}^{(n)} - 2C_{i,j,k}^{(n)} + C_{i-1,j,k}^{(n)}}{\Delta x^2}(D_c) + \frac{k_{i,j}C_{i,j+1,k}^{(n)} - 2C_{i,j}^{(n)} + C_{i,j-1,k}^{(n)}}{\Delta y^2}(D_c) + \frac{k_{i,j}C_{i,j,k+1}^{(n)} - 2C_{i,j,k}^{(n)} + C_{i,j,k-1}^{(n)}}{\Delta z^2}(D_c) + \alpha_1 C(u,t)^{g11} B(u,t)^{g21} - \beta_1 C(u,t), \quad (9)$$

$$\frac{B_{i,j}^{(n+1)} - B_{i,j}^{(n)}}{\Delta t} = \frac{k_{i,j}B_{i+1,j,k}^{(n)} - 2B_{i,j,k}^{(n)} + B_{i-1,j,k}^{(n)}}{\Delta x^2}(D_B) + \frac{k_{i,j}B_{i,j+1,k}^{(n)} - 2B_{i,j}^{(n)} + B_{i,j-1,k}^{(n)}}{\Delta y^2}(D_B) + \frac{k_{i,j}B_{i,j,k+1}^{(n)} - 2B_{i,j,k}^{(n)} + B_{i,j,k-1}^{(n)}}{\Delta z^2}(D_B) + \alpha_2 C(u,t)^{g12} B(u,t)^{g22} - \beta_2 B(u,t). \quad (10)$$

Numerical Application

Parameters for bone dynamic model.

Table 1 shows the parameter values used in this article based in Ayati et al. [6]. The $g11$ value is different in a single cycle event, in this case is equal to 0.5 and for oscillatory changes the $g11$ value is equal to 1.1.

Table 1. Summary of parameters used in the model.

Parameters	Description	Value
α_1	Production rate of osteoclasts	3 [day^{-1}]
α_2	Production rate of osteoblasts	4 [day^{-1}]
β_1	Apoptosis rate of osteoclasts	0,2 [day^{-1}]
β_2	Apoptosis rate of osteoblasts	0,02 [day^{-1}]
k_C	Rate of bone's resorption	0,45% [day^{-1}]
k_B	Rate of bone's formation	0,0448% [day^{-1}]
D_C	Diffusion coefficient of osteoclasts	1x10^{-6} [bone mass mm^{-1}]
D_B	Diffusion coefficient of osteoblasts	1x10^{-6} [bone mass mm^{-1}]
$\underline{C}$	Cell population of osteoclasts in steady-state	1.06 [cell mm^{-1}]
$\underline{B}$	Cell population of osteoblasts in steady-state	212.13 [cell mm^{-1}]
$g11$	Autocrine signaling factor of osteoclasts	0.5 [single] 1.1 [osc.] [dimensionless]
$g21$	Paracrine signaling factor of osteoclasts	-0.5 [dimensionless]
$g22$	Autocrine signaling factor of osteoblasts	0.0 [dimensionless]
$g12$	Paracrine signaling factor of osteoblasts	1.0 [dimensionless]

Temporal Part Analysis - Single Remodeling Cycle. A separate function was created in auxiliary file to solve the Ordinary Differential Equations using adaptative Runge-Kutta method (ode45) in 150 days (t in days). The results are shown in Fig. (1).

Fig. 1a and 1b show that the addition of 10 active osteoclast cells led to a consequent increase in the number of osteoblasts, and consequently, the stabilization of the number of osteoclasts returns to a steady state.

Fig. 1c represents the evolution on percentage of bone mass: according to the role of the cells has an initial drop, related to the consumption performed by osteoclasts, and slow reformulation, related to the increase in the number of active osteoblastic cells.

Temporal Part Resolution - Periodic Remodeling Cycles. The literature points out that the change of osteoclasts parameters can be used to obtain the periodic cycles of remodeling. Komarova et al. [1] investigated the influence of each parameter on the stability and type of steady state obtained: the authors show the protagonist of the autocrine factor of osteoclasts (g_{11}); also, others authors point the same argument [14,15]. Low g_{11} values reproduced only one remodeling cycle, while values greater than 1.1 lead to a dynamic remodeling with oscillations with increasingly higher amplitudes. These results were therefore obtained in Figs. 1d, 1e, and 1f, below, where a progressive variation in cell number and mass is evident. Therefore, changing the model constants to obtain a non-stationary response applying the adaptative Runge-Kutta's method analogously can be seen in Fig. 1d, 1e and 1f.

The initial value problem for this ODE system can exemplify the bone remodeling mechanism. However, the bone mass distribution is only for a single BMU. Ayati et al. [6], Valério et al. [7] and Fernández-Cervantez et al. [9] solved the presented model by adding a diffusive term for cell population and bone mass shown in Eqs. 6-9.

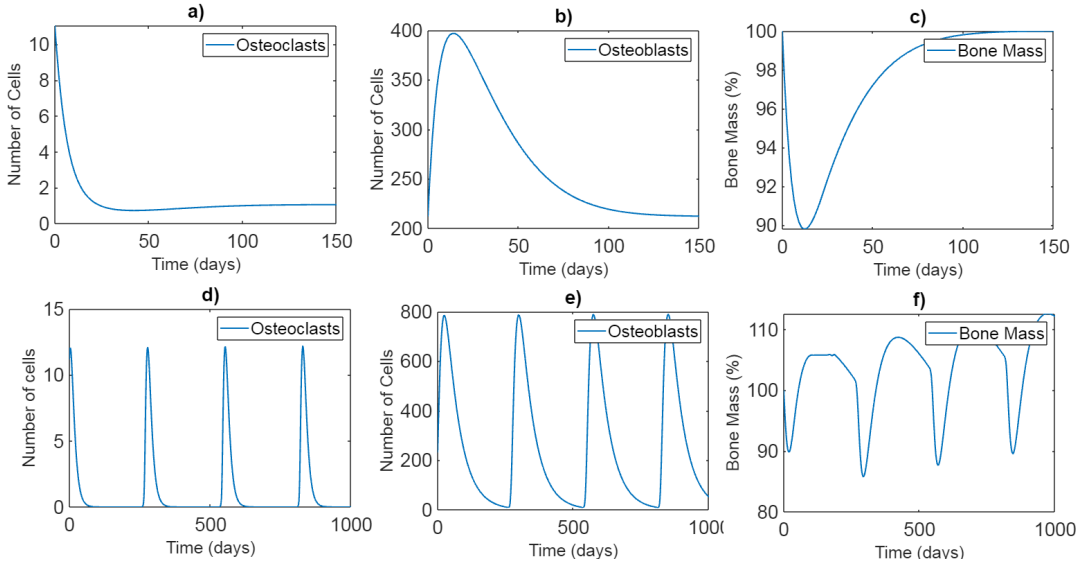

Fig. 1. Response to a bone remodeling cycle with the respective cellular behavior of osteoclasts (a), osteoblasts (b), and bone mass variation (c) and to periodic bone remodeling cycles with the respective cellular behavior of osteoclasts (d), osteoblasts (e), and bone mass variation (f).

Different BMUs were evaluated at each point of a given mesh or solid block. The approach of Valério et al. [7,9] and Fernandez-Cervantez et al. [9] were replicated below, in the respective Strategies 1 and 2. While in Strategy 1 the cell distribution is solved in x and y, in Strategy 2 it is solved in x, y and z. In order to obtain a three-dimensional block with the structure of trabecular bone, in the first form, therefore, it was necessary to apply the Multidimensional Matrices technique and the application of the *isosurface* tool after binarizing the data of each mesh x and y. In the second strategy, the matrix obtained already had orientations in three dimensions, which allowed the direct application of the *isosurface* tool, and binarizing the volume.

Resolution Space Part - Strategy 1.

The addition of a diffusive term to the bone cell remodeling model proposed by Ayati et al. [6] allowed the assessment of cell population distribution and bone mass. Therefore, the non-trivial steady-state conditions obtained in the temporal resolution (previous item) are defined for the temporal part of the model. The diffusive part is solved using finite differences, as follows. By defining a remodeling time in a series of meshes with different initial conditions the parameters are defined for a time of 150 days. Fig. 2 shows the distribution grids for the final time of 150 days for cell populations and bone mass. In this figure we can see the distribution of cells in different areas, that is, where there are osteoclasts there is less population of osteoblasts, Figs. 2a and 2b. Also, denser regions could be seen in Fig. 2c areas with presence of osteoblasts, and less dense regions could be seen in populated osteoclasts areas. A loop was used in this case, with dt = 0.01 days.

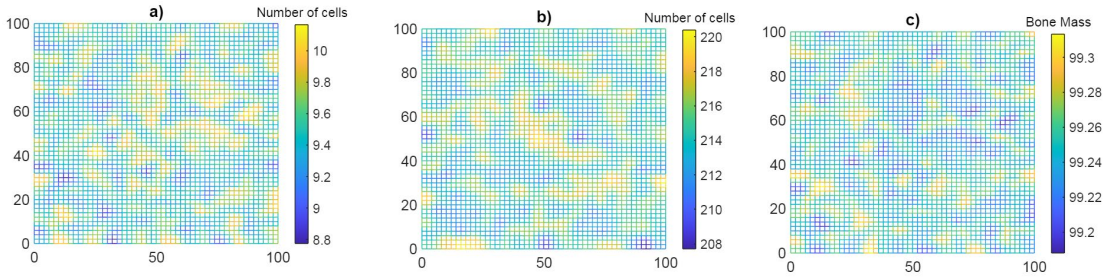

Fig. 2. Distribution of the cell population of osteoclasts (a), osteoblasts (b) and bone mass (c) with S1.

Resolution Spatial Part - Strategy 2.

Strategy 2 only proposes solving for x, y, and z dimensions and plotting an isosurface from the volumetric data produced at t = 150. It assumes the same conditions as Strategy 2: a series of meshes with different initial conditions (different amounts of cells).

The distributions of cell populations and bone mass can be obtained as shown in Fig. 3. This figure shows the three-dimensional distribution of cells and bone mass. As consideration of *isosurfaces* produced: the marching cubes algorithm connects areas with the same value (defined as *isovalue*). For this, the data was binarized (a 3D Matrix of zeros and ones) to produce the isosurface in Fig. 3c. The *stlwrite* algorithm in Matlab was applied in order to export the STL files.

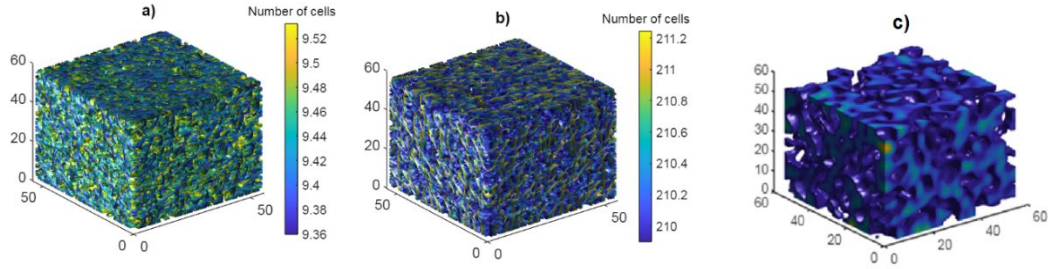

Fig. 3. Distribution of the cell population of osteoclasts (a), osteoblasts (b) and bone distribution (c) generated by Strategy 2 (dimensionless) in 150 days.

Analysis of 3D Printed Pieces

Experimental Setup.

The pieces were printed using the 3D Printer by FFF Dual Extruder N2 (Raise3D, Tesla, USA) for S1 and the Ultimaker 2+ for S2 (Ultimaker, Netherlands). The printing conditions were: nozzle temperature of 220°C, layer height of 0.15 mm, bed temperature of 60°C and printing speed of 5 mm/s (S1) and 60 mm/s (S2). The pieces were analyzed by microtomography using the equipment Easytom 130 (RX solutions, France) in Institut Clément Ader to obtain the microCT images.

Microtomography analyses.

The application of microtomography (microCT) of the printed pieces allowed the complete geometry of the manufactured workpieces. Fig. 4 shows the microCT images of the S1 (Fig. 4a), S2 (Fig. 4b) and of real bone (femoral head (FH) gently provided by the National Institute of Technology (INT-Brazil), Fig. 4c).

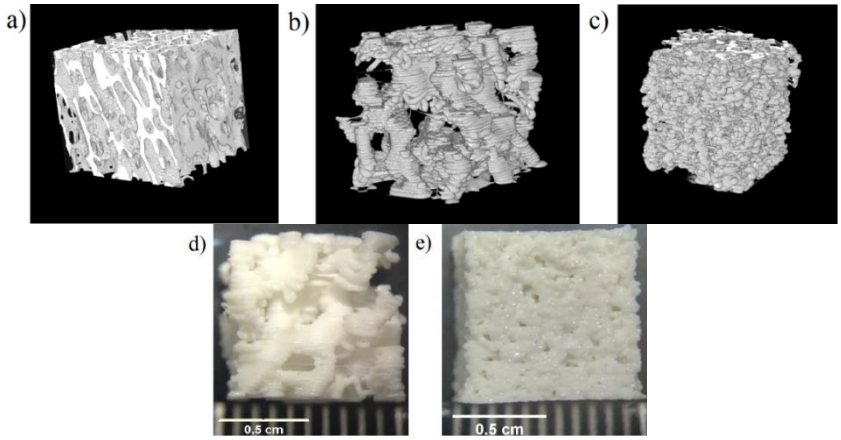

Fig. 4. MicroCT images obtained of the printed pieces with the different strategies: a) femoral head bone, b) S1, c) S2; the macrographs of the printed pieces: d) S1 and e) S2 obtained with magnifying glass (scale in cm).

The Bone J (ImageJ software plugin) was used in these analysis to obtain the parameters: trabecular thickness (TbTh, usually a mean value of thickness of the trabecula), trabecular separation (TbSp, the mean distance between the trabecula, it is similar to pore size), bone volume fraction (BV/TV, the fraction of material in the sample), degree of anisotropy (DA, it estimates how geometrically non-isotropic is the bone fraction), and connectivity (Conn, it gives an estimate of the number of connected trabeculae in the image) [11], [13].

The procedure to analyze the microCT images obtain were using the following image processing: no local means, unsharp mask, cropping image, binarize (Huang's method) and then use Bone J tool in the binarized images. For comparison, the microtomography of the femoral head (FH) bone also was characterized using the tool BoneJ. The choose of this kind of bone was because the parameters evaluated that could be printed by FFF was of this type of trabecular bone [10]. It is visible that pore size (TbSp) in S1 is greater than in real bone (FH). Some isotropy in z axes could be seen in Fig. 4a (FH). The morphology in S2 is closer of real bone, but the layers of 3D printing FFF technique misleading the accuracy.

Table 2. Bone parameters obtained with BoneJ of microCT images.

Strategy	TbTh (mm)	TbSp (mm)	BV/TV	DA	Conn.
S1	0.89±0.299	2.001±1.180	0.402	0.564	457.25
S2	0.418±0.165	0.946±0.432	0.323	0.657	2663
FH	0.213±0.072	0.552±0.217	0.2940	0.688	617

The real bone data, trabecular femoral head bone, is near that observed in the literature [10] as seen in Table 2. However, the comparison of the strategies shows that median values are greater than real bone. Peyroteo et al. [8] with the same mathematical model implemented an algorithm for density that could assess more precise thickness and separation between struts. Also, the distribution in the histogram in Fig. 5 can provide that the profile in the distribution of TbTh and TbSp in FH and S2 were closer. As seen in Fig. 5, the profile of distribution of TbTh and TbSp is closer than S1, and S1 has greater TbTh and TbSp. It is interesting to notice that DA in S2 is near of the real bone. Nevertheless, S1 seems different than the others probably because of the methodology of this strategy, a bone mesh growing in time and not on space.

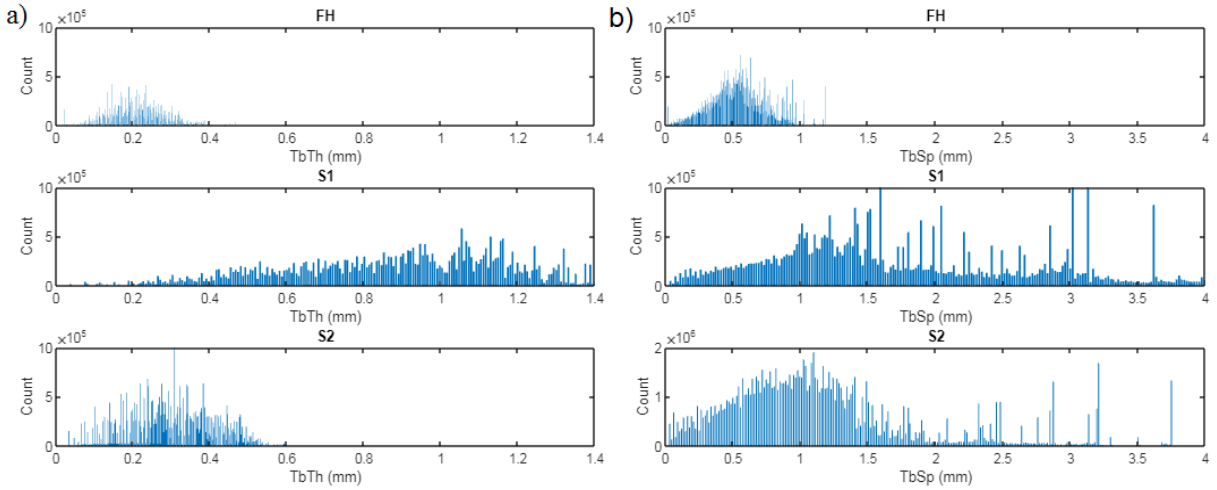

Fig. 5. Histograms for TbTh (a) and TbSp (b) for the different strategies and the femoral head bone.

Some modifications can be made in the algorithm proposed in methodology to reproduce exact profiles and morphological parameters, modifying some parameters in mathematical model and

printing conditions. But it is interesting to notice that porosity and pore size (related to TbSp parameter) greater than in real bone morphology it is necessary to provide angiogenesis [3] and permeability of nutrients in damage tissue [16, 17]. Future works can search the biological response in these printed pieces geometries, in comparison with the gold standard [17] of architecture scaffolds in Bone Tissue Engineering.

Summary

This work reproduced the structure of trabecular bone using the mathematical model of cell dynamics. Pieces with trabecular architecture were successfully printed by FFF technique, a cheaper AM kind of 3D printer. It was possible to evaluate the most influential parameters of the human bone and compare real bone parameters and printed pieces via micro-computed tomography. Comparing morphologies S1 and S2, the average TbTh in S1 is double of S2. S2 was similar to FH in terms of the TbTh and TbSp about the profile distribution, although high variability in S2. DA, an important parameter for the angiogenesis, was closer in S2 than in S1 compared with FH. Therefore, the results here presented suggest that S2 can be applied to future works along with the optimization of the mathematical model and the printing parameters.

Acknowledges

The authors are grateful to Dra. Cristiane Evelise Ribeiro da Silva, researcher in INT – National Institute of Technology (Rio de Janeiro – Brazil), for gently providing the microtomography of the femoral head. Part of this work was produced during the mobility of Rossana Thiré as a Visiting Professor financed by INSA Toulouse in October 2023.

References

[1] S.V. Komarova, R.J. Smith, S.J. Dixon, S.M. Sims, L.M. Wahl, Mathematical model predicts a critical role for osteoclast autocrine regulation in the control of bone remodeling, Bone. 33 (2003) 206-215. https://doi.org/10.1016/S8756-3282(03)00157-1

[2] R. Florencio-Silva, G.R. da S. Sasso, E. Sasso-Cerri, M.J. Simões, P.S. Cerri, Biology of Bone Tissue: Structure, Function, and Factors That Influence Bone Cells, Biomed. Res. Int. 2015 (2015) 1-17. https://doi.org/10.1155/2015/421746

[3] M.N. Collins, G. Ren, K. Young, S. Pina, R.L. Reis, J.M. Oliveira, Scaffold Fabrication Technologies and Structure/Function Properties in Bone Tissue Engineering, Adv. Funct. Mater. 31 (2021) 2010609. https://doi.org/10.1002/adfm.202010609

[4] Z. Wood, L. Lynn, J.T. Nguyen, M.A. Black, M. Patel, M.M. Barak, Are we crying Wolff? 3D printed replicas of trabecular bone structure demonstrate higher stiffness and strength during off-axis loading, Bone. 127 (2019) 635-645. https://doi.org/10.1016/j.bone.2019.08.002

[5] C. Boyle, I.Y. Kim, Three-dimensional micro-level computational study of Wolff's law via trabecular bone remodeling in the human proximal femur using design space topology optimization, J Biomech. 44 (2011) 935-942. https://doi.org/10.1016/j.jbiomech.2010.11.029

[6] B.P. Ayati, C.M. Edwards, G.F. Webb, J.P. Wikswo, A mathematical model of bone remodeling dynamics for normal bone cell populations and myeloma bone disease, Biol. Direct. 5 (2010) 1-17. https://doi.org/10.1186/1745-6150-5-28

[7] D. Valério, J. Neto, S. Vinga, Variable order 3D models of bone remodelling, Bulletin of the Polish Academy of Sciences: Technical Sciences. 67 (2019) 501-508. https://doi.org/10.24425/bpasts.2019.129649

[8] M.M.A. Peyroteo, J. Belinha, L.M.J.S. Dinis, R.M.N. Jorge, Bone remodeling: an improved spatiotemporal mathematical model, Arch. Appl. Mech. 90 (2020) 635-649. https://doi.org/10.1007/s00419-019-01631-z

[9] I. Fernández-Cervantes, M.A. Morales, R. Agustín-Serrano, M. Cardenas-García, P.V. Pérez-Luna, B.L. Arroyo-Reyes, A. Maldonado-García, Polylactic acid/sodium alginate/hydroxyapatite composite scaffolds with trabecular tissue morphology designed by a bone remodeling model

using 3D printing, J. Mater. Sci. 54 (2019) 9478-9496. https://doi.org/10.1007/s10853-019-03537-1
[10] M. McGregor, S. Patel, S. McLachlin, Mihaela Vlasea, Architectural bone parameters and the relationship to titanium lattice design for powder bed fusion additive manufacturing, Addit. Manuf. 47 (2021) 102273. https://doi.org/10.1016/j.addma.2021.102273
[11] L. Steiner, A. Synek, D.H. Pahr, Comparison of different microCT-based morphology assessment tools using human trabecular bone, Bone Rep. 12 (2020) 100261. https://doi.org/10.1016/j.bonr.2020.100261
[12] S.C. Ligon, R. Liska, J. Stampfl, M. Gurr, R. Mülhaupt, Polymers for 3D Printing and Customized Additive Manufacturing, Chem. Rev. 117 (2017) 10212-10290. https://doi.org/10.1021/acs.chemrev.7b00074
[13] J.F. Charles, A.O. Aliprantis, Osteoclasts: More than “bone eaters,” Trends Mol. Med. 20 (2014) 449-459. https://doi.org/10.1016/j.molmed.2014.06.001
[14] R. Detsch, A.R. Boccaccini, The role of osteoclasts in bone tissue engineering, J. Tissue Eng. Regen. Med. 9 (2015) 1133–1149. https://doi.org/10.1002/term.1851
[15] R. Domander, A.A. Felder, M. Doube, BoneJ2 - refactoring established research software, Wellcome Open Res. 6 (2021) 37. https://doi.org/10.12688/wellcomeopenres.16619.2
[16] B.N. Teixeira, P. Aprile, R.H. Mendonça, D.J. Kelly, R.M. da S.M. Thiré, Evaluation of bone marrow stem cell response to PLA scaffolds manufactured by 3D printing and coated with polydopamine and type I collagen, J. Biomed. Mater. Res. B Appl. Biomater. 107 (2019) 37-49. https://doi.org/10.1002/jbm.b.34093
[17] H.B. Pan, Z.Y. Li, W.M. Lam, J.C. Wong, B.W. Darvell, K.D.K. Luk, W.W. Lu, Solubility of strontium-substituted apatite by solid titration, Acta Biomater. 5 (2009) 1678-1685. https://doi.org/10.1016/j.actbio.2008.11.032

Materials Research Proceedings 28 (2023) 179-188 https://doi.org/10.21741/9781644902479-20

Analysis of additively manufactured anisotropic microstructures through crystal plasticity frameworks

BULUT Orhun[1,a], GÜNAY Enes[1,b] , FENERCIOĞLU Tevfik Ozan[2,c] and YALÇINKAYA Tuncay[1,d *]

[1]Department of Aerospace Engineering, Middle East Technical University, Ankara 06800, Türkiye

[2]Repkon Machine and Tool Industry and Trade Inc., 34980 Sile, Istanbul, Türkiye

[a]orhun.bulut@metu.edu.tr, [b]enes.gunay@metu.edu.tr, [c]ozan.fenercioglu@repkon.com.tr, [d]yalcinka@metu.edu.tr

Keywords: Crystal Plasticity, Size Effect, Additive Manufacturing

Abstract. In additive manufacturing processes, the resulting products might have highly anisotropic granular morphologies due to the complex thermal history. The most commonly observed morphology is columnar structure. The resulting morphology of grains is accompanied by the orientation alignment leading to plastic anisotropy. It has been shown in a recent study through local crystal plasticity calculations that the morphology evolution does not influence the mechanical behavior without considering the texture evolution [1]. However, the local frameworks do not consider the effect of the grain size which could be complicated due to high aspect ratio of the grains. This study aims to investigate the influence of the developed anisotropic grain structure on the macroscopic response through both local and non-local crystal plasticity frameworks to address the capacity of these models in capturing the realistic response. An additional subroutine is implemented (see [2]) into the crystal plasticity frameworks to obtain the slip resistance values at each material point based on grain geometries and misorientations. This allows the size dependent yielding of the crystals.

Introduction

Additively manufactured (AM) metallic alloy parts offer many benefits. The usage of additive manufacturing technology to create complex products has shown significant promise (see e.g. [3-6]). Through empirical studies over almost three decades, developments in additive manufacturing techniques have made them utilized in many industrial areas such as aerospace, automotive, construction. In these last decades, AM technology has become an important manufacturing methodology rather than a prototype production method. However, its application for manufacturing critical components is restricted by the inherent uncertainty associated with qualities, which frequently results from the variability in the manufacturing process itself (see e.g. [7]).

Some of the recent AM methods are based on melting and solidification of metallic powders during the process. Different kinds of microstructures can be resulted due to the complex thermal history of these processes which involve high temperature gradients and also high heating-cooling rates. This thermal history is highly dependent on the process parameters such as scanning strategy, hatch spacing, scan velocity. The high cooling rate in the complex heat transfer course during the AM processes results in the directional growth of grains. The thermal history influences not only the grain structure but also the grain orientation substantially (see [8]). Grain growth occurs along the direction of the highest temperature gradient where the solidification develops (see e.g. [9,10]). As a result, the final microstructures of AM products are observed to have anisotropic morphologies and consequent textures (see e.g. [11-13]). When additively made products are

Content from this work may be used under the terms of the Creative Commons Attribution 3.0 license. Any further distribution of this work must maintain attribution to the author(s) and the title of the work, journal citation and DOI. Published under license by Materials Research Forum LLC.

examined, it becomes clear that crystal orientation alignment frequently occurs concurrently with the development of columnar grain structure (see e.g. [14-16]). Also, a common defect in AM products is their porous microstructure (see e.g. [17,18]). However, porosity is not examined in this study in order to solely focus on the grain and orientation alignment.

Additively manufactured parts show altered microstructures and mechanical properties with respect to the process parameters. Therefore, analyzing microstructures has importance for not only estimating their characteristics but also for adjusting the process parameters to achieve desirable mechanical properties.

In a previous study, the mechanical properties of microstructures consisting of elongated grain morphology are investigated through a rate dependent local crystal plasticity finite element framework (see [1]). In this paper, different crystal plasticity mechanisms are employed through different ABAQUS UMAT subroutines. First, simulations are conducted with only the local crystal plasticity framework. Then, a lower-order strain gradient crystal plasticity is implemented where, the impact of intrinsic size effects is addressed. A higher-order strain gradient formulation could also have been used as in [19,20] through a UEL, however it is omitted in the current study. A lower-order approach can be a good starting point for comparing different crystal plasticity mechanisms.

Along with the implementation of lower-order strain gradient crystal plasticity, a different mechanism is also studied to recalculate the initial slip resistance of each material point as in [2]. With this method, the slip resistance of each slip system for every material point is calculated considering grain orientations and the distance of points to grain boundaries.

The structure of this work is as follows. Firstly, the crystal plasticity frameworks used in the finite element simulations are described. Then, the method for determining model parameters and producing polycrystalline representative volume elements (RVEs) is provided. Orientation restrictions on the grains to obtain a more realistic grain alignment are given. Finally, the outcomes of crystal plasticity finite element method (CPFEM) simulations are shown and thoroughly explained for the three methods used.

Crystal Plasticity Frameworks

In the current study, first, a local finite strain rate-dependent crystal plasticity framework (see [21]) is adapted for the analyses of microstructures (see [22,23] for example applications of this framework). In this framework, the deformation gradient $\boldsymbol{F}$ is multiplicatively decomposed into elastic part $\boldsymbol{F}^e$ and plastic part $\boldsymbol{F}^p$**.** Plastic velocity gradient can be obtained by integrating the plastic slip rates $\dot{\gamma}$ overall slip systems as

$$\mathbf{L}^{\mathrm{p}}=\dot{\mathbf{F}}^{\mathrm{p}}\mathbf{F}^{\mathrm{p}-1}=\sum_{\alpha=1}^{\mathrm{N}}\dot{\gamma}^{\alpha}\,(\mathbf{m}^{\alpha}\otimes\mathbf{n}^{\alpha}) \tag{1}$$

where α defines the slip system. $\boldsymbol{m}^{\boldsymbol{\alpha}}$ and $\boldsymbol{n}^{\boldsymbol{\alpha}}$ are the slip direction and slip normal of the slip system respectively. In this work, an aluminum alloy is analyzed with all 12 slip systems of the face-centered cubic (FCC) crystal. All slip systems are active at all times, since a rate-dependent model is used. The slip rate of the slip systems $\dot{\gamma}^{\alpha}$ is governed by the power law

$$\dot{\gamma}^{\alpha}=\dot{\gamma}_0=\left|\frac{\tau^{\alpha}}{g^{\alpha}}\right|^{n} sign(\tau^{\alpha}) \tag{2}$$

where $\dot{\gamma}_0$ is the reference slip rate, τ^{α} is the resolved shear stress, g^{α} is the slip resistance and n is the rate sensitivity exponent. The slip resistance consists of statistically stored dislocations (SSDs) and geometrically necessary dislocations (GNDs) parts.

$$g^{\alpha} = \sqrt{{g_{ssd}^{\alpha}}^{2} + {g_{gnd}^{\alpha}}^{2}} \tag{3}$$

For local crystal plasticity simulations, only the hardening from SSDs is considered, which is described by the following relation,

$$\dot{g}_{ssd}^{\alpha} = \sum_{\beta=1}^{N} h^{\alpha\beta} \left|\dot{\gamma}^{\beta}\right| \tag{4}$$

where N represents the number of total slip systems and latent hardening is $h^{\alpha\beta} = q^{\alpha\beta} h^{\alpha\alpha}$, where $q^{\alpha\beta}$ is the latent hardening coefficient. Peirce and Asaro's (sech) self-hardening law is used for the self-hardening,

$$h^{\alpha\alpha} = h_0 \left|\frac{h_0 \gamma}{g_s - g_0}\right|, \tag{5}$$

where h_0 is the initial hardening modulus, g_0 is the initial slip resistance and g_s is the saturation slip resistance. The implementation of a lower-order strain gradient framework into the crystal plasticity subroutine enables the inclusion of additional hardening as a result of GNDs. This implementation allows an intrinsic length scale parameter to be defined and the size effects to be captured [24].

$$g_{gnd}^{\alpha} = g_0 \sqrt{l \eta_{gnd}^{\alpha}} \tag{6}$$

where $l = \frac{\alpha_T^2 \mu_s^2 b}{g_0^2}$ is the length scale parameter, α_T is the Taylor coefficient, μ_s is the shear modulus and b is the length of Burger's vector. Density of GNDs on a slip system α is defined as,

$$\eta_{gnd}^{\alpha} = \left|\mathbf{n}^{\alpha} \times \sum_{\beta=1}^{N} \mathbf{m}^{\alpha} \mathbf{m}^{\beta} \nabla \gamma^{\beta} \times \mathbf{n}^{\beta}\right| \tag{7}$$

Numerical Analysis

All the crystal plasticity simulations are conducted with the commercial finite element analysis software ABAQUS using brick (C3D8) elements. The material used in all finite element method (FEM) simulations is AA6016 in T4 condition. The hardening parameters are fitted in a previous study (see [1]). The hardening parameters are taken as initial hardening modulus $h_0 = 190\ MPa$, saturation slip resistance $g_s = 95\ MPa$ and initial slip resistance $g_0 = 47 MPa$. Cubic elastic coefficients for aluminum sheet are used as $C_{11} = 108.2\ GPa$, $C_{12} = 61.3\ GPa$, and $C_{44} = 28.5\ GPa$ [25]. Reference slip rate $\dot{\gamma}_0$ is taken as $10^{-3}\ s^{-1}$ and rate sensitivity parameter n is taken as 20. A strong latent hardening is assumed for aluminum and q is taken as 1.4. To observe the strain gradient effects clearly, the length scale parameter is taken as 500 μm in non-local strain gradient CPFEM simulations.

The user subroutine code (UMAT) based on [21] is modified to recalculate the initial slip resistance g_0. This modification will be referred as geometry-dependent slip resistance subroutine in the consecutive sections. With this subroutine, initial slip resistance is calculated by the distance of material points to grain boundaries and grain orientations. This theory aims to simulate the influence of dislocation piling up at grain boundaries. The details can be found in [2]. The aim of this method is to examine size effects based on Hall-Petch relation. Initial slip resistance is calculated as,

$$g_0^\alpha = \tau_0 + \frac{K\left(1-m^{\alpha'}\right)^c}{\sqrt{L^\alpha}} \quad (8)$$

τ_0 is taken as the critically resolved shear stress of a theoretically infinite crystal which is considered as zero. This value is taken as close to zero, which is 0.05 MPa. L^α is the distance of a material point to grain boundaries in the slip direction. K and c are empirical coefficients taken as 0.414 and 0.134. Their values are obtained by fitting the stress-strain curve of 300 grain RVE with 47 MPa initial slip resistance. $m^{\alpha'}$ is the Luster-Morris parameter for each slip system and is found from the misorientations of grains as $m^{\alpha'} = \left(\frac{\boldsymbol{m}_A^\alpha . \boldsymbol{m}_B^\alpha}{|\boldsymbol{m}_A^\alpha||\boldsymbol{m}_B^\alpha|}\right)\left(\frac{\boldsymbol{n}_A^\alpha . \boldsymbol{n}_B^\alpha}{|\boldsymbol{n}_A^\alpha||\boldsymbol{n}_B^\alpha|}\right)$ where $\boldsymbol{m}^\alpha$ and $\boldsymbol{n}^\alpha$ are slip direction and slip normal respectively. Subscripts A and B correspond grains A and B respectively.

Polycrystalline RVEs with 300 grains are generated through Voronoi Tessellation (see [26]). Each morphology represents different grain elongation levels and is named as Equiaxed, Needle1, Needle2, Needle3 in consecutive parts of the paper. Grain aspect ratios are (1,1,1), (0.5,1,0.5), (0.25,1,0.25) and (0.1,1,0.1) for Equiaxed, Needle1, Needle2, Needle3 respectively. Grain morphologies can be seen in Fig. 1.

10% displacement is given to RVEs as the loading condition with $10^{-3}\ s^{-1}$ strain rate. Boundary conditions are applied such that all surfaces are kept straight and it is ensured that the stress triaxiality value stays constant at 0.33 during the loading (see e.g. [27]).

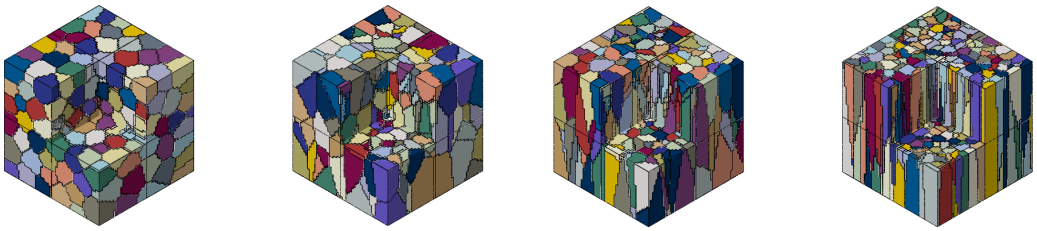

Fig. 1. Polycrystal RVE morphologies, from left to right: Equiaxed, Needle1, Needle2, Needle3.

Initially, all the RVEs are simulated at the same set of random orientations with the aforementioned crystal plasticity mechanisms separately. Following ZYX Euler convention, different orientation angle restrictions are assigned to corresponding RVEs. Crystals are tilted around the building direction (Y-axis) by restricting the X and Z rotations while the Y rotation is kept at zero. For restricted cases, [-90 +90], [-30 +30], [-10 +10] restricted intervals are assigned to Needle1, Needle2, Needle3 respectively. No restriction is applied for random orientation cases.

Numerical Results

Firstly, only the effects of grain morphologies are compared. All RVEs are assigned grains with the same set of random crystal orientations. A series of crystal plasticity finite element analyses using the three aforementioned mechanisms (i.e. local, strain-gradient, and geometry-dependent initial slip resistance subroutine in the local framework) are performed on every morphology by applying 10% strain in building-direction (Y axis) and the normal direction (Z axis) separately.

When there are no orientation restrictions on the grains (i.e., each one is randomly oriented), all three methods give very similar stress vs. strain responses. In Fig. 2a and Fig 2b, the results under the non-local crystal plasticity and geometry-dependent initial slip resistance modification are shown. Due to the presence of additional slip resistance from GND densities in the framework, higher amount of hardening with respect to the local framework is observed. However, beyond that, isotropic response is obtained for randomly oriented RVEs with all three methods.

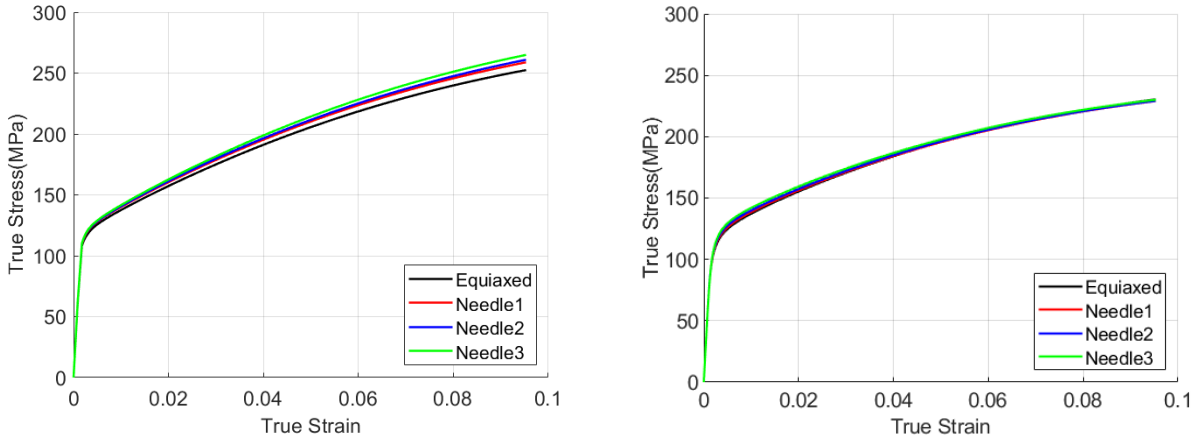

a) Non-local, building direction *b) Modified , building direction*

Fig. 2. Stress vs. Strain response of RVE finite element simulations with randomly oriented grains using different frameworks.

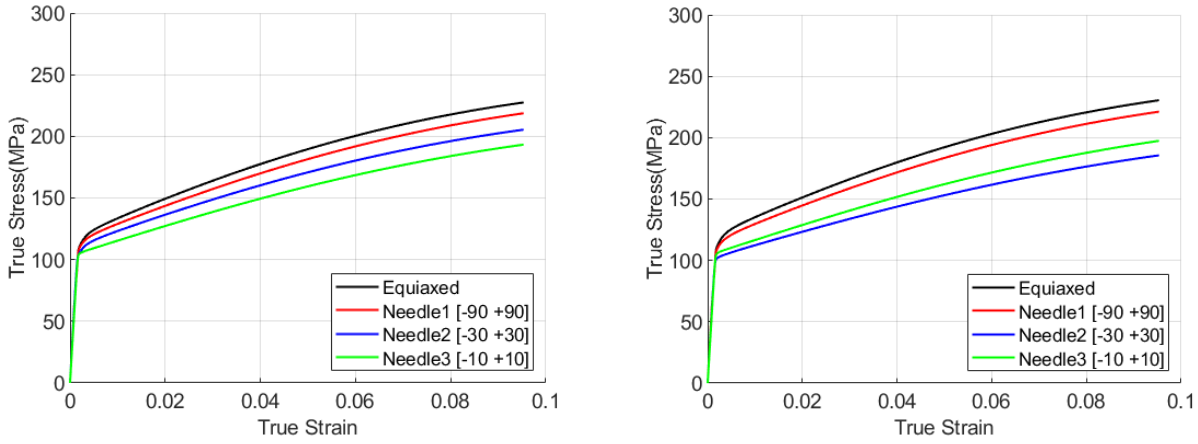

a) Building direction *b) Normal direction*

Fig. 3. Stress vs. Strain response of RVE finite element simulations with restricted crystal orientations using local framework with loading in building and normal directions.

To examine the results in a more realistic case, the crystal orientations of the grains have been increasingly aligned with the loading direction as the aspect ratio increases. The orientations of equiaxed grain morphology have been kept unrestricted. The rotations of crystals in X and Z axes have been restricted to previously mentioned intervals of Euler angles and the results are presented in Fig. 3. When the grains become more aligned, misorientations start to diminish gradually. Analyses in local framework have shown that, rather than the morphology, orientation has more impact on the mechanical response. A more anisotropic response is obtained for Needle2 case with [-30 +30] restriction compared to Needle1 and Equiaxed when the responses are compared in building and normal direction loading cases. However, the extreme case RVE with Needle3 morphology and [-10 +10] angle restriction does not show significant anisotropic response. This is because the misorientations between the grains are so small that it behaves as if there is a crystal symmetry between the grains.

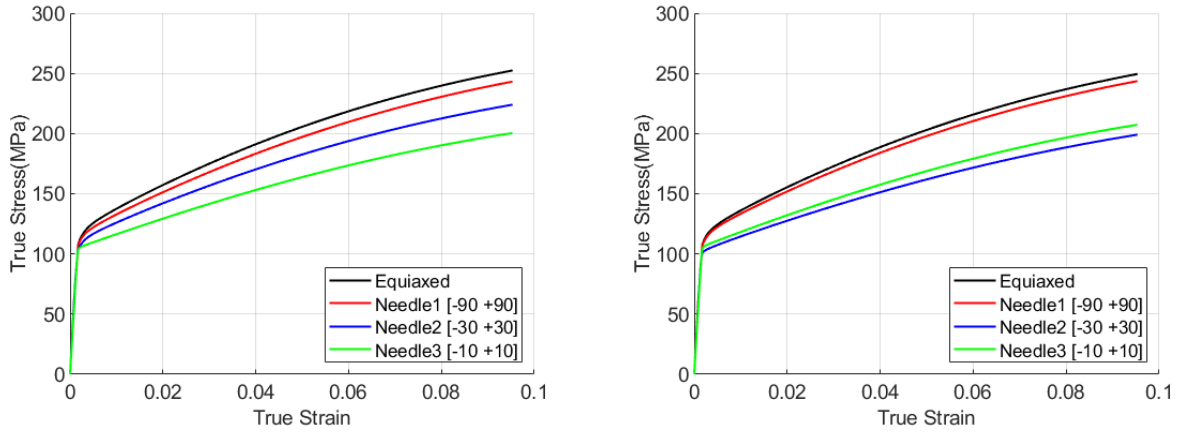

a) Building direction *b) Normal direction*

Fig. 4. Stress vs. Strain response of RVE finite element simulations with restricted crystal orientations using non-local framework with loading in building and normal directions.

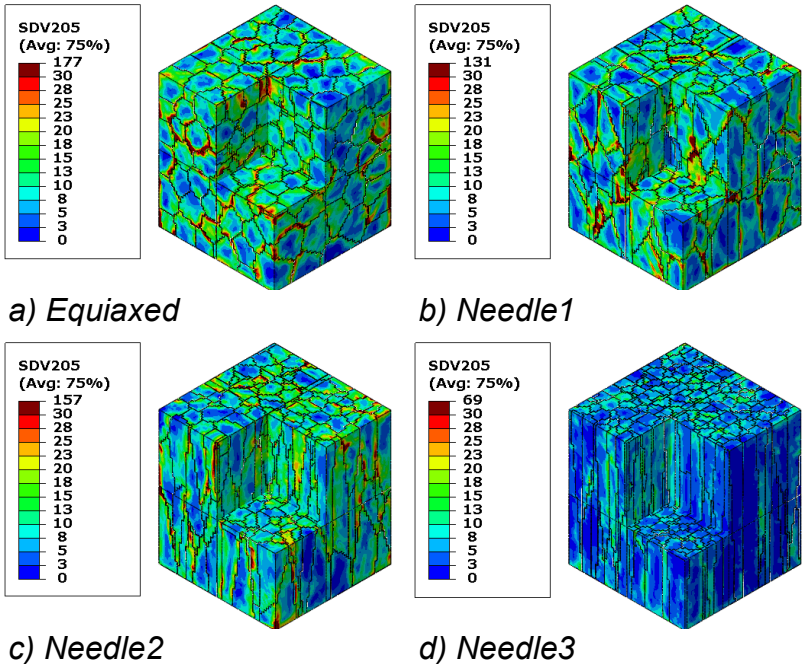

Fig. 5. Distribution of GND densities [1/mm] in RVEs from strain gradient framework simulations after loading in building direction with restricted orientations.

Fig. 4 shows the results of the same simulations through the strain gradient crystal plasticity framework. Needle2 shows highly anisotropic behavior compared to other morphologies similar to local framework. General trend of decrease in stress results stays same as the orientations become more restricted. However, there is an increased gap between the stress response of RVEs. This is a result of reduced misalignment between the grains causing GND densities to exist in smaller quantities. This can be seen in Fig. 5 as well, where the distributions of GND densities of all morphologies are shown. GNDs are most prominent at the grain boundaries. As the grains become more oriented in a particular direction (in this case, the building direction), the density of GNDs and their contribution to hardening begin to decrease.

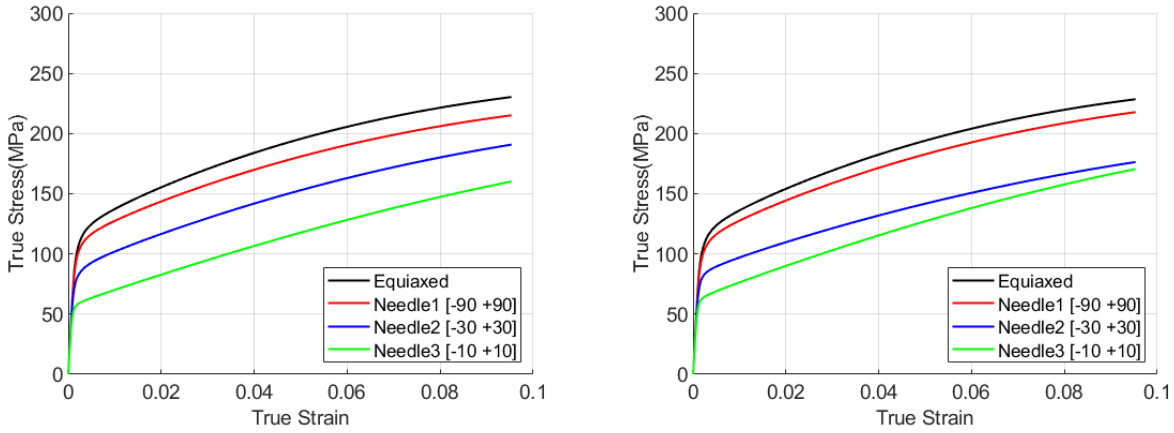

a) Building direction *b) Normal direction*

Fig. 6. Stress vs. Strain response of RVE finite element simulations with restricted crystal orientations using modified after loading in building and normal directions.

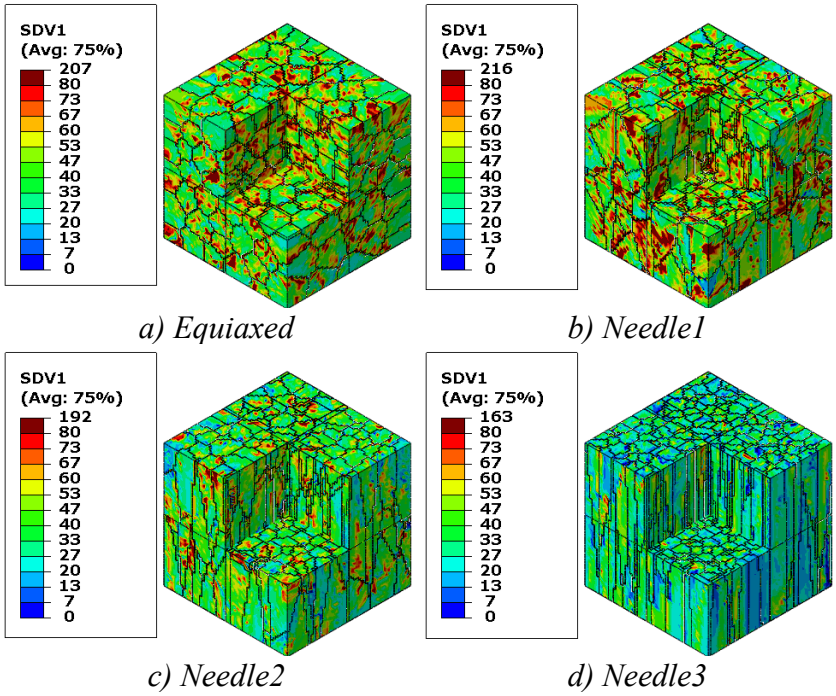

a) Equiaxed *b) Needle1*

c) Needle2 *d) Needle3*

Fig. 7. Distribution of the modified initial slip resistance g_0 in RVEs with restricted orientations.

The stress vs. strain results of simulations using the geometry-dependent initial slip resistance calculation subroutine are shown in Fig. 6. The most important factor here is that both of the previous methods do not affect the yielding point of the material significantly. This is because the initial slip resistance of the material is taken as constant. However, when the influence of morphology and orientation on the initial slip resistance is taken into account, overall yielding points of the RVEs also differ. As the grain orientations become more aligned, the yield stress of the RVE decreases as a result. In Fig 6b, it can be seen that stress values of Needle2 and Needle3 become closer when they are loaded in normal direction as opposed to building direction. This is a result of modifying the initial slip resistance. In both previously examined methods (i.e. local and non-local cases), Needle3 shows a higher stress response for normal direction loading. However, modifying the g_0 decreases the yield point so much that the stress value of Needle3

becomes lower than that of Needle2 at the end of displacement. This is a different result compared to ones obtained with other frameworks, since Needle2 shows the weakest response in normal direction in both local and non-local methods. Similar in other methods, anisotropic behavior is the strongest in Needle2.

The distribution of initial slip resistance calculated from the grain geometries and orientations are shown in Fig. 7. The randomly oriented Equiaxed morphology and the [-90 +90] restricted Needle1 morphology shows a similar distribution. This is also seen in Fig. 7 from their yield stress distributions being similar. On the other hand, when the misorientation between grains decreases in Needle2 and Needle3, there are fewer points with high initial slip resistance.

Summary

In this paper, anisotropic granular morphologies which developed in additive manufacturing techniques are examined with different crystal plasticity frameworks. Grains are elongated step by step for different RVEs.

Firstly, only the effect of morphology is examined with different crystal plasticity frameworks. It has been observed that when the strain gradient framework is taken into account, morphology without providing the proper texture does not significantly change the outcomes as in the prior study [1]. However, using a non-local model has benefits in terms of locating the GND density accumulations, especially at the grain boundaries. The influence of texture on GND densities is discussed and results have proven that lower-order SGCP can be a useful framework for the recognition of dislocation pile-ups in additive manufacturing products.

Different stress responses are obtained for different loading directions when grain orientations are restricted. Even though the lower-order SGCP framework contributes to hardening and makes stress responses stronger, it does not change the general trend observed in the previous study. In Needle1's case, a large range of possible orientations does not yield an anisotropic response regardless of the framework used in simulations. Needle2, on the other hand, shows a highly anisotropic response from the results with all frameworks since orientation restrictions on the grains is much narrower compared to Needle1. While Needle3 is assigned with most narrow orientation restrictions, the material shows less anisotropic behavior than Needle2. This is a result of building and normal directions lying on the symmetry axes of FCC crystal. Heavily aligning all grains with the loading direction causes the material to act similar to a single crystal specimen since grain misorientations become small. Without a modification of the initial slip resistance of grains, Needle3 displays a stronger response compared to Needle2 in normal direction. However, by modifying its initial slip resistance based on grain geometries and orientations, the yield stress of Needle3 is predicted to be lower than all other morphologies in normal direction.

References

[1] S.S. Acar, O. Bulut, T. Yalçinkaya, Crystal plasticity modeling of additively manufactured metallic microstructures, Procedia Struct. Integrity 35 (2022) 219-227. https://doi.org/10.1016/j.prostr.2021.12.068

[2] D. Agius, A. Kareer, A. Al Mamun, C. Truman, D.M. Collins, M. Mostafavi, D. Knowles, A crystal plasticity model that accounts for grain size effects and slip system interactions on the deformation of austenitic stainless steels, Int. J. Plast. 152 (2022) 103249. https://doi.org/10.1016/j.ijplas.2022.103249

[3] F. Singer, D. Deisenroth, D. Hymas, M. Ohadi, Additively manufactured copper components and composite structures for thermal management applications, in: 2017 16th IEEE Intersociety Conference on Thermal and Thermomechanical Phenomena in Electronic Systems (ITherm), IEEE, 2017: pp. 174-183. https://doi.org/10.1109/ITHERM.2017.7992469

[4] M. Lowther, S. Louth, A. Davey, A. Hussain, P. Ginestra, L. Carter, N. Eisenstein, L. Grover, S. Cox, Clinical, industrial, and research perspectives on powder bed fusion additively

manufactured metal implants, Addit. Manuf. 28 (2019) 565-584. https://doi.org/10.1016/j.addma.2019.05.033
[5] B. Blakey-Milner, P. Gradl, G. Snedden, M. Brooks, J. Pitot, E. Lopez, M. Leary, F. Berto, A. du Plessis, Metal additive manufacturing in aerospace: A review, Mater. Des. 209 (2021) 110008. https://doi.org/10.1016/j.matdes.2021.110008
[6] A. Uriondo, M. Esperon-Miguez, S. Perinpanayagam, The present and future of additive manufacturing in the aerospace sector: A review of important aspects, Proc. Inst. Mech. Eng., Part G: J. Aerosp. Eng. 229 (2015) 2132-2147. https://doi.org/10.1177/095441001456879
[7] J.C. Najmon, S. Raeisi, A. Tovar, Review of additive manufacturing technologies and applications in the aerospace industry, Additive Manufacturing for the Aerospace Industry. (2019) 7-31. https://doi.org/10.1016/B978-0-12-814062-8.00002-9
[8] T.F. van Nuland, J. van Dommelen, M.G. Geers, Microstructural modeling of anisotropic plasticity in large scale additively manufactured 316L stainless steel, Mech. Mater. 153 (2021) 103664. https://doi.org/10.1016/j.mechmat.2020.103664
[9] Z. Wang, K. Guan, M. Gao, X. Li, X. Chen, X. Zeng, The microstructure and mechanical properties of deposited-IN718 by selective laser melting, J. Alloys Compd. 513 (2012) 518-523. https://doi.org/10.1016/j.jallcom.2011.10.107
[10] E.W. Hovig, A.S. Azar, F. Grytten, K. Sørby, E. Andreassen, Determination of anisotropic mechanical properties for materials processed by laser powder bed fusion, Adv. Mater. Sci. Eng. 2018 (2018). https://doi.org/10.1155/2018/7650303
[11] E. Yasa, J. Deckers, J.-P. Kruth, The investigation of the influence of laser re-melting on density, surface quality and microstructure of selective laser melting parts, Rapid Prototyping J. 17 (2011) 312-327. https://doi.org/10.1108/13552541111156450
[12] C. Qiu, N.J. Adkins, M.M. Attallah, Microstructure and tensile properties of selectively laser-melted and of HIPed laser-melted Ti–6Al–4V, Mater. Sci. Eng. A 578 (2013) 230-239. https://doi.org/10.1016/j.msea.2013.04.099
[13] B. Song, X. Zhao, S. Li, C. Han, Q. Wei, S. Wen, J. Liu, Y. Shi, Differences in microstructure and properties between selective laser melting and traditional manufacturing for fabrication of metal parts: A review, Front. Mech. Eng. 10 (2015) 111-125. https://doi.org/10.1007/s11465-015-0341-2
[14] A. Charmi, R. Falkenberg, L. Ávila, G. Mohr, K. Sommer, A. Ulbricht, M. Sprengel, R.S. Neumann, B. Skrotzki, A. Evans, Mechanical anisotropy of additively manufactured stainless steel 316L: An experimental and numerical study, Mater. Sci. Eng. A 799 (2021) 140154. https://doi.org/10.1016/j.msea.2020.140154
[15] A.A. Antonysamy, J. Meyer, P. Prangnell, Effect of build geometry on the β-grain structure and texture in additive manufacture of Ti6Al4V by selective electron beam melting, Mater. Charact. 84 (2013) 153-168. https://doi.org/10.1016/j.matchar.2013.07.012
[16] K. Hara, K. Itoh, M. Kamiya, H. Fujiwara, K. Okamoto, T. Hashimoto, Alignment of crystallites in obliquely deposited cobalt films, Jpn. J. Appl. Phys. 33 (1994) 3448. https://doi.org/10.1143/JJAP.33.3448
[17] K. Moussaoui, W. Rubio, M. Mousseigne, T. Sultan, F. Rezai, Effects of Selective Laser Melting additive manufacturing parameters of Inconel 718 on porosity, microstructure and mechanical properties, Mater. Sci. Eng. A 735 (2018) 182-190. https://doi.org/10.1016/j.msea.2018.08.037
[18] B. Zhang, S. Liu, Y.C. Shin, In-Process monitoring of porosity during laser additive manufacturing process, Addit. Manuf. 28 (2019) 497-505. https://doi.org/10.1016/j.addma.2019.05.030

[19] T. Yalçinkaya, Strain gradient crystal plasticity: Thermodynamics and implementation, in: G. Z. Voyiadjis (Eds.), Handbook of Nonlocal Continuum Mechanics for Materials and Structures, Springer, London/Berlin, 2017, pp.1001-1033.
[20] T. Yalçinkaya, İ. Özdemir, İ. Tarik Tandoğan, Misorientation and grain boundary orientation dependent grain boundary response in polycrystalline plasticity, Computational Mechanics. 67 (2021) 937-954. https://doi.org/10.1007/s00466-021-01972-z
[21] Y. Huang, A user-material subroutine incorporating single crystal plasticity in the ABAQUS finite element program, Mech. Report 178 (1991).
[22] O. Bulut, S. S. Acar, T. Yalçinkaya, The influence of thickness/grain size ratio in microforming through crystal plasticity, Procedia Struct. Integrity 35 (2022) 228-236. https://doi.org/10.1016/j.prostr.2021.12.069
[23] T. Yalçinkaya, B. Tatli, I.E. Ünsal, I.U. Aydiner, Crack Initiation and Propagation in Dual-phase Steels Through Crystal Plasticity and Cohesive Zone Frameworks, Proce. Struct. Integrity 42 (2022) 1651-1659.
[24] C. S. Han, H. Gao, Y. Huang, W. D. Nix, Mechanism-based strain gradient crystal plasticity—I, Theory, J. Mech. Phys. Solids 53 (2005) 1188-1203. https://doi.org/10.1016/j.jmps.2004.08.008
[25] E. Nakamachi, C. Xie, H. Morimoto, K. Morita, N. Yokoyama, Formability assessment of FCC aluminum alloy sheet by using elastic crystalline viscoplastic finite element analysis, Int. J. Plast. 18 (2002) 617-632. https://doi.org/10.1016/S0749-6419(01)00052-3
[26] R. Quey, P. Dawson, F. Barbe, Large-scale 3D random polycrystals for the finite element method: Generation, meshing and remeshing, Comput. Methods Appl. Mech. Eng. 200 (2011) 1729-1745. https://doi.org/10.1016/j.cma.2011.01.002
[27] T. Yalçinkaya, S.O. Çakmak, C. Tekoğlu, A crystal plasticity based finite element framework for RVE calculations of two-phase materials: Void nucleation in dual-phase steels, Finite Elem. Anal. Des. 187 (2021) 103510. https://doi.org/10.1016/j.finel.2020.103510

Materials Research Proceedings 28 (2023) 189-198 https://doi.org/10.21741/9781644902479-21

2D FE modeling of the thermal history of the heat affected zone in AlSi10Mg LPBF

DELAHAYE Jocelyn[1,a], HABRAKEN Anne M.[2,b] and MERTENS Anne[1,c *]

[1]University of Liège, Faculty of Applied Sciences, Aerospace and Mechanics Department, Metallic Materials Science, Quartier Polytech 1, Allée de la Découverte 13A, B-4000 Liège, Belgium

[2]University of Liège, Faculty of Applied Sciences, ArGEnCo Department, Materials and Solid Mechanics, Quartier Polytech 1, Allée de la Découverte 13A, B-4000 Liège, Belgium

[a]jocelyn.delahaye@uliege.be, [b]anne.habraken@uliege.be, [c]anne.mertens@uliege.be

Keywords: Aluminium Alloys, LPBF, Thermal History, Microstructure, Modeling

Abstract. As an easily processable Al alloy, AlSi10Mg manufactured by Laser Powder Bed Fusion (LPBF) has received a lot of attention so far. However, it is well known that microstructural heterogeneities at the scale of the melt pool – in particular the weaker Heat Affected Zone whose microstructure evolves during the deposition of the next layer – exert a strong detrimental effect on the ductility of AlSi10Mg LPBF. In this work, a 2D Finite Element (FE) model is developed in order to tackle this issue and help in guiding the optimisation of LPBF process parameters. The model is calibrated using experimental measurements of the melt pool height. Furthermore, to allow for the efficient simulation of 5 successive layers, a remeshing procedure is implemented. No heat accumulation is observed during the deposition of these 5 layers. The thermal history of the HAZ can thus be studied with a thermal model for one layer.

Introduction

The Laser Powder Bed Fusion (LPBF) of Al alloys has been the subject of extensive work for almost a decade, dating back to the pioneering work of Thijs et al. [1] and Olakanmi et al. [2]. Among the wide variety of available Al alloys, the hypoeutectic AlSi10Mg alloy has received a particular attention in view of its good castability and weldability, its high melt fluidity and low shrinkage upon solidification [3-5]. However, microstructural heterogeneities at the scale of the melt pool remain a matter of concern, by compromising the ductility of AlSi10Mg LPBF components [6,7]. Indeed, the Heat Affected Zone (HAZ) whose microstructure evolves during the deposition of the subsequent layer has been shown to play an essential role in the tensile fracture of AlSi10Mg LPBF. The Si eutectic precipitates that are originally finely distributed in a cellular structure, tend to coarsen and globularize under the influence of the heat input associated to the deposition of next layer, as can be seen in Fig. 1. As a result, the fine cellular structure is broken, thus creating a weaker zone for damage initiation [6]. The microstructural homogeneity and the ductility of AlSi10Mg LPBF components may be restored to some extent by thermal or thermo-mechanical post-treatments but this improvement in ductility is achieved at the cost of a loss in strength [7-9]. As an alternative to post-treatments, optimisation of the processing parameters with the aim of minimizing the thickness of the HAZ appears as a viable option [10]. Physically based and validated Finite Element (FE) models are essential tools in that respect.

In this work, a 2D FE model is developed in order to tackle this issue and help in guiding the optimisation of LPBF process parameters. Two different calibration procedures were tested i.e. using experimental measurements of (1) the cell size or of (2) the melt pool height. Furthermore, to allow for the efficient simulation of 5 successive layers, a remeshing procedure is implemented.

Content from this work may be used under the terms of the Creative Commons Attribution 3.0 license. Any further distribution of this work must maintain attribution to the author(s) and the title of the work, journal citation and DOI. Published under license by Materials Research Forum LLC.

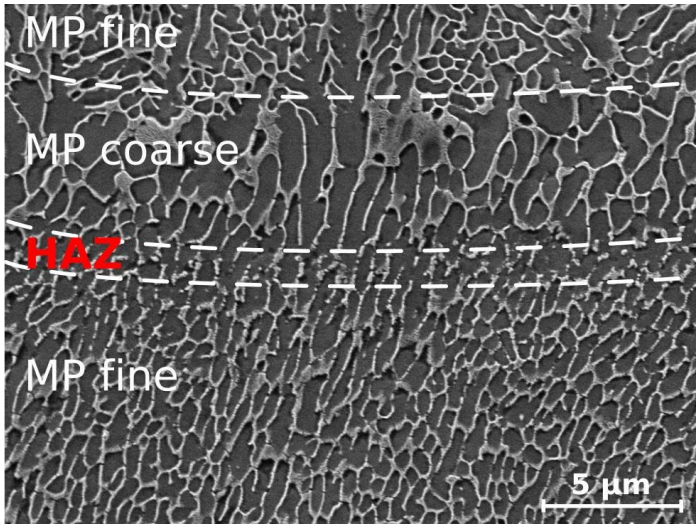

Fig. 1. SEM micrograph showing the fine cellular microstructure at the core of the melt pool (MP fine), the coarser cellular structure at the outskirts of the melt pool (MP coarse) and the Heat Affected Zone (HAZ) where the cellular structure of the fine eutectic Si precipitates is broken and globularized.

Materials and Methods

Sample fabrication.

In order to obtain experimental data for the calibration and validation of the FE model, two sets of AlSi10Mg LPBF samples, named as set A and set B, were fabricated under very distinct processing conditions. Samples of set A were processed using a MTT SLM 250 machine. The building parameters were as follow: a laser power of 175W, a scan speed of 195 mm/s, a powder layer thickness of 60 µm and a pre-heating temperature of 200°C. Samples of set B were fabricated using an EOS SLM equipment and the following processing parameters: a laser power of 370W, a scan speed of 1300 mm/s and a powder layer thickness of 40 µm without pre-heating i.e. considering a building platform temperature of 35°C. Both sets of samples were fabricated in the vertical direction. The processing parameters of set A were chosen to enhance the thickness of the HAZ, as opposed to the processing parameters of set B. More details may be found in [6,8,10].

Characterization.

Samples for microstructural characterization were ground and polished following standard practices and then etched using Keller's reagent (95 vol.% distilled water, 2.5 vol.% HNO_3, 1.5 vol.% HCl and 1 vol.% HF). Scanning electron microscopy was carried out using a Philips XL30 microscope. Image analysis was performed using the ImageJ software to determine the Al Cells size in the MP fine, MP coarse and HAZ (Fig. 1). The melt pool height was only measured on the last deposited layer, since the melt pool of the previous layers are overlapped due to the systematic re-melting of the underlying layer during the deposition of each new layer.

Finite Element model.

A 2D thermal finite element model of the LPBF process has been developed as follows. The temperature evolution in the part is given by the non-linear equation for an isotropic material:

$$\nabla . k\nabla T + Q = \rho c_p \frac{\partial T}{\partial t} \quad (1)$$

where ∇ is the gradient operator; k is the thermal conductivity, Q the power generated in the part, ρ the density, c_p the heat capacity and t the time. The enthalpy of fusion and vaporization are included in the heat capacity that is thus defined as an apparent heat capacity.

The boundary condition at the free surface for the heat exchange is defined as:

$$-k\nabla T.n = q_{laser} - h(T - T_{amb}) - \mathcal{E}\sigma\left(T^4 - {T_{amb}}^4\right) \quad (2)$$

where n is a unit vector normal to the surface; T_{amb}, the ambient temperature, h, the convection coefficient (taken as 20 W/m^{2}K); σ, the Stefan-Boltzmann's constant (5.67×10^{-8} W/m^{2}K^4), $\mathcal{E}$, the emissivity and q_{laser} the laser heat source. The laser is modeled by a Gaussian heat source:

$$q_{laser} = \frac{2AP}{\pi R^2} exp\left(\frac{2r^2}{R^2}\right) \quad (3)$$

where P is the laser power (i.e. 175 W or 370 W); R, the laser beam radius (40 µm); A, the laser absorbed energy; r, the radial distance from the beam centre.

The thermophysical properties are considered temperature dependent. These properties are obtained from [11] for the base plate made from aluminium alloy 2024, and from [8] for the AlSi10Mg powder bed and consolidated part. The laser absorbed energy A is chosen as a tuning parameter of the 2D FE model and is obtained through calibration based on experimental observations. In this study, two different calibration procedures have been tested: (1) based on experimental measurements of the cell size and (2) based on experimental measurements of the melt pool height. The academic finite element code LAGAMINE is used. It is developed since 1984 at the University of Liege [12-15]. To switch between the desactivated elements, the unfused powder, to the bulk material and vary the bulk properties, element birth and death technique is employed. The mesh of the system and boundary conditions are summarized in Fig. 2.

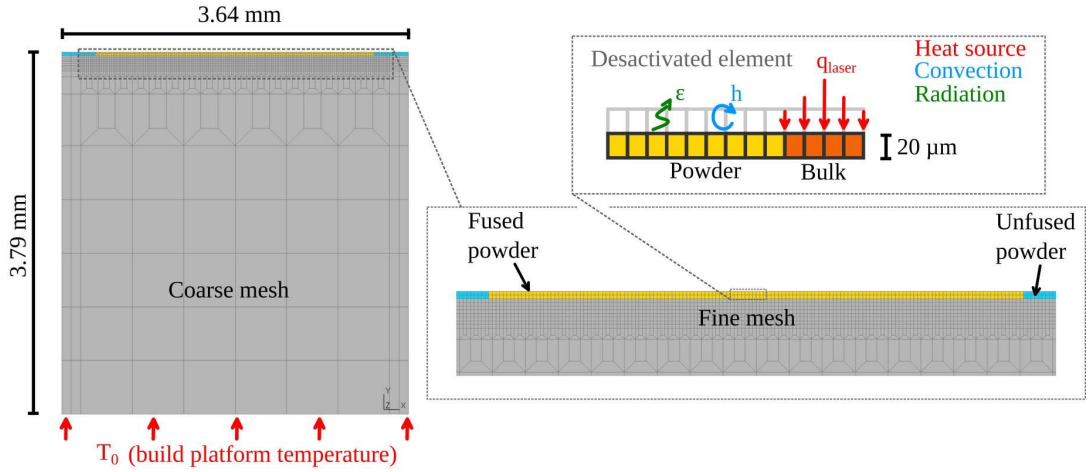

Fig. 2. Finite element domain with the boundary conditions: laser heat source, heat loss by convection, radiation, and build platform temperature. Desactivated elements are illustrated to highlight the birth and death technique.

The dimensions of the studied domain are 3.79 mm in height and 3.64 mm in width, that is large enough for the melt pool to reach a thermal steady state and to reproduce the heat drain effect of the build platform and previous solidified layers. The domain is discretized with 2D quadrilateral elements. Furthermore, the domain is divided in two zones: a fine meshed zone of size ranging from 40 µm to 2.5 µm where the laser is applied, fine enough to capture the steep thermal gradient, and a coarse zone below to save in number of elements and computation time.

In particular, a 2D multilayer simulation of the LPBF process was performed in this work, in order to investigate the effect of the number of fused layers on heat accumulation and thus on the thermal history of LPBF AlSi10Mg components. To reduce the computational costs of this

Materials Research Proceedings 28 (2023) 189-198 https://doi.org/10.21741/9781644902479-21

multilayer model, that can be high even in 2D, a remeshing strategy has been developed in order to keep the number of node constant independently of the number of layers under consideration. It consists in picking the temperature field at the end of the simulation for the first layer and set this temperature as an initial nodal condition for the second layer. This operation is then repeated for the third layer and so forth… As shown in Fig. 3, the change in powder bed height with the number of fused layers is incorporated in the coarse part of the mesh while the fine part remains the same. This approach allows to perform multilayer simulations while keeping the computation time reasonable.

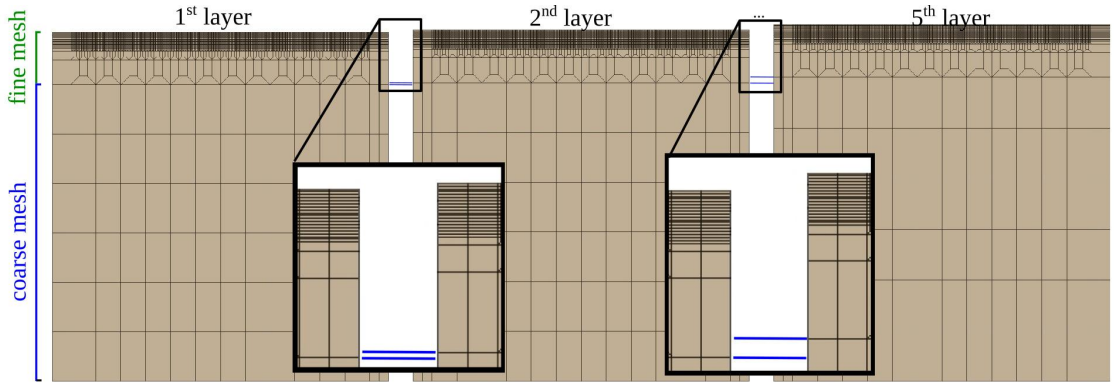

Fig. 3. Meshed domains for the first, second and fifth layer. The number of elements remain constant between the domains. The fine mesh part are the same between the domains while the coarse part changes.

Results and Discussion

Sensitivity to the mesh size.

Convergency was tested based on the size of the fine mesh zone ranging from 40 µm to 5 µm in Fig. 4. Based on the analysis of the line profile in Fig. 4(b) extracted from the temperature maps of Fig. 4(a), mesh convergency is shown. A mesh size of 10 µm offers a good compromise between accuracy and computation time. This is also demonstrated when analyzing the melt pool area with the laser beam travel time in Fig. 4(c). We should notice that it takes 1.8 ms for the melt pool to reach a steady state where its size no longer changes. Therefore, the size of the model is large enough to study the thermal history in the heat affected zone.

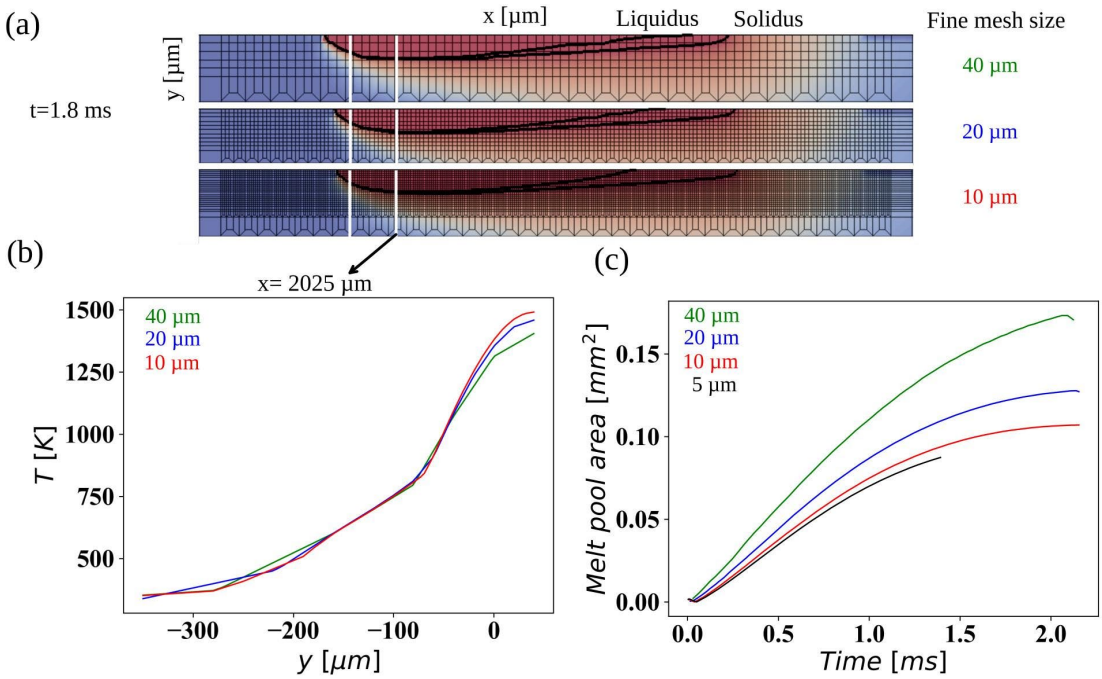

Fig. 4. (a) Temperature map of the melt pool taken at t=1.8 ms for different mesh refinements. (b) Corresponding temperature line profile at x = 2025 µm position and (c) melt pool area with the laser beam travel time.

Model calibration.

The results of the calibration of the 2D thermal model under the processing parameters of set B are shown in Fig. 5(a) for the calibration based on the melt pool height and in Fig. 5(b) for the calibration based on the cell size that can be computed from the cooling rates extracted at the liquidus isotherm line [6,8,10,16]. Fig. 5 shows a remarkable result in that the 2D FE model can only be calibrated against the melt pool height. Indeed, the cell size values computed from the FE model are systematically larger than the experimental values. This is a marked difference to previous reports concerning analytical model as e.g. Rosenthal's model [6,10,16] for which calibration based on cell size may be preferred in view of its greater flexibility as cell size may be measured at any location within the sample contrarily to the melt pool height that is only accessible in the last deposited layer.

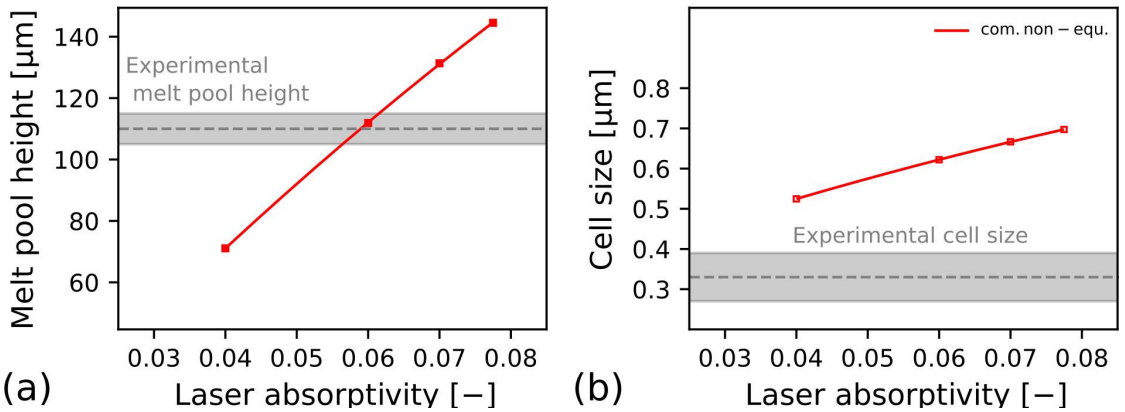

Fig. 5. (a) Melt pool height and (b) cell size calibration for the 2D thermal FE model.

This observation can be understood considering that the cell size is computed from the cooling rate that depends in turn on the thermal gradient. The heat flux transmitted by conduction in the part is also proportional to the thermal gradient. However, in the present 2D FE model, the heat flux is not evacuated through a surface but through a line. In this case, fewer paths are available for these fluxes. Therefore, the 2D model systematically experiences a lower thermal gradient compared to a 3D model. The 2D FE model will thus always overestimate the cell size.

The effect of the number of fused layers for samples of set B is studied by analyzing the thermal history of three points of interest (POIs) in Fig. 6. These POIs are located in such a way that their respective spacings correspond to 2 times the powder bed thickness, i.e. 40 µm. In this way, the thermal history can be compared between the fused layers. As can be seen in Fig. 6, the thermal history of POI1 exhibits five peaks corresponding to the five fused layers. The first peak corresponds to the maximum temperature experienced during the direct application of the heat flux of the laser. In view of the location of the three POIs, the maximum temperature of POI2 is then reached during the fusion of the third layer while the maximum temperature of POI3 is reached for the fifth layer. When comparing the temperature of the first peak for the three POIs, it can be seen that they have the same value around 2700K. In a similar way, the second and the third peaks of POI1 and POI2 match each other with values around 1750K and 1350K, respectively. The good match between the peaks for the three POIs indicates that they is no rise in temperature as the successive layers are fused. Furthermore, this observation is confirmed qualitatively by looking at the temperature distribution around the melt pool in Fig. 6(b-c). Indeed, the temperature distribution and the melt pool size obtained for the first layer (Fig. 6(b)) and for the fifth layer (Fig. 6(c)) are very similar. The cold area at the right-hand side of Fig. 6(c) corresponds to unfused powder.

This observation that the heat accumulation remains negligible during the deposition of five successive layers can be explained by considering both the thermophysical properties of AlSi10Mg and the processing conditions. Indeed, LPBF AlSi10Mg exhibits a high thermal conductivity with values ranging between 110 and 130 $W*m^{-1}*K^{-1}$ [8]. These values are much higher than those reported for LPBF Ti6Al4V (5-34 $W*m^{-1}*K^{-1}$)[17] or stainless steel 316L (14-34 $W*m^{-1}*K^{-1}$) [18] for which heat accumulation is observed. The high thermal conductivity of LPBF AlSi10Mg thus allows the rapid evacuation of heat from the melt pool and its vicinity towards the top surface of the part where it can be dissipated first through radiation just after the laser is switched off and later through convection. Moreover, the high laser scan speed (1300 mm/s) combined with a medium laser power (370W) used for the processing of set B samples result in relatively low heat input when compared to the processing parameters of [17] and [18], which also contributes to the negligible heat accumulation.

Microstructural observation of the HAZ dimensions along the whole sample height brings further confirmation of the above finding. Indeed, the HAZ has been found to exhibit a constant width throughout [8], thus also suggesting that the average temperature in the part remains constant. This result implies that the thermal history of the HAZ in LPBF AlSi10Mg processed under relatively low heat input is independent of the number of fused layers, and that it can be studied using one layer FE thermal model.

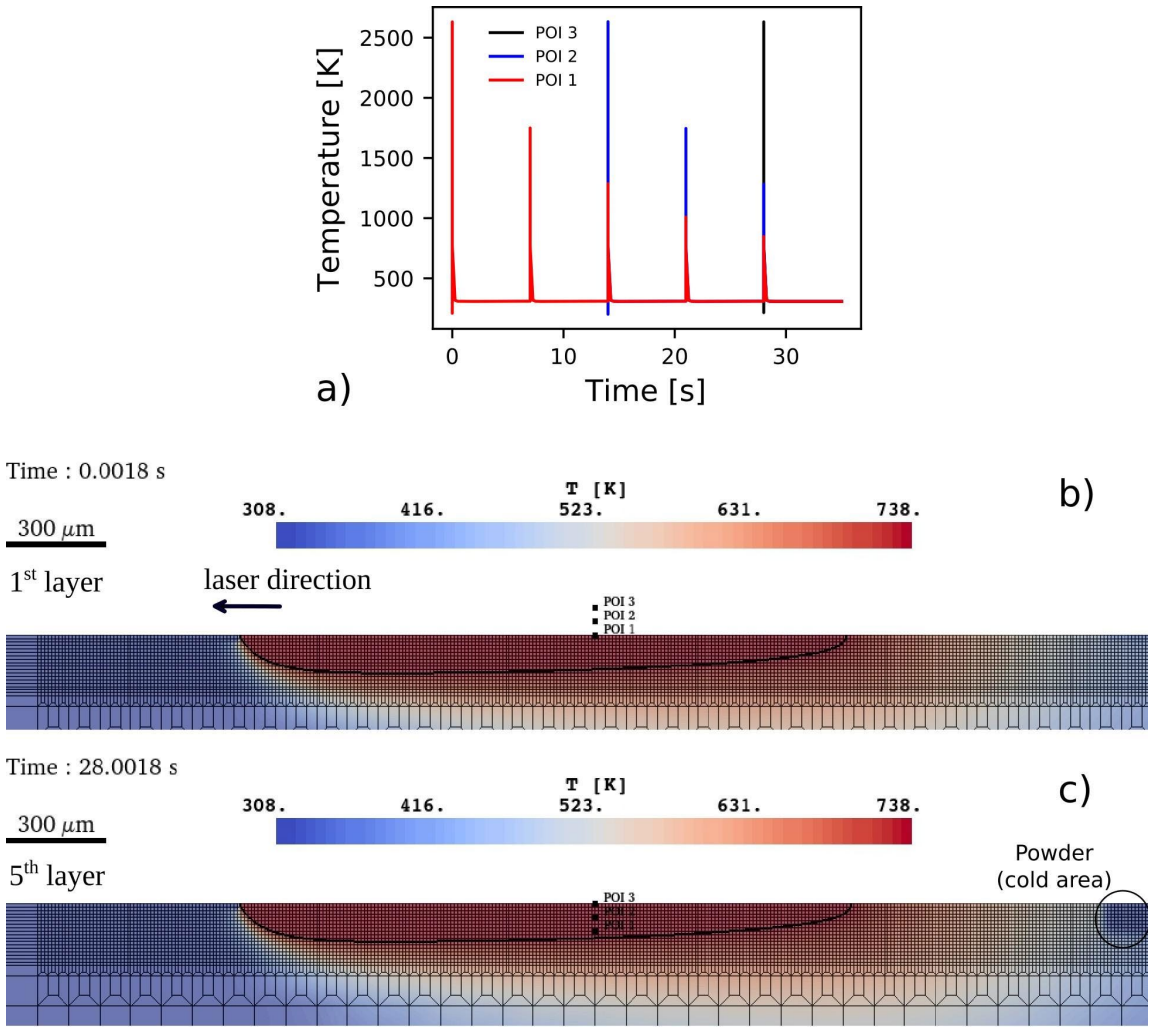

Fig. 6. (a) Thermal history of three POIs; temperature maps (b) for the first layer and (c) for the fifth layer.

The influence of the processing parameters on the thermal history of the HAZ is studied by comparing the result of FE simulations for the two sets of processing parameters A ("Sirris", with a relatively low laser power of 175W, a slow scan speed of 195 mm/s and build platform temperature of 200°C resulting in a relatively high heat input) and B ("Anyshape", with a laser power of 370W, a high laser scan speed of 1300 mm/s and build platform temperature of 35°C resulting in a relatively low heat input). These two parameters sets have been selected as (1) they are far enough from each other to expect different thermal histories and (2) the corresponding microstructures have been characterized in details [8].

The thermal histories in the HAZ for the two sets of processing parameters are plotted in Fig. 7(a). For set B (Anyshape), a peak of temperature is observed at 650K lasting for 1.5 ms. For set A (Sirris), on the contrary, the peak is wider, lasting over 2.5 ms. In the latter case, the end of the peak is not clearly visible as the temperature of the peak does not fall back to 473K, that is the build platform temperature, within the frame of the simulation.

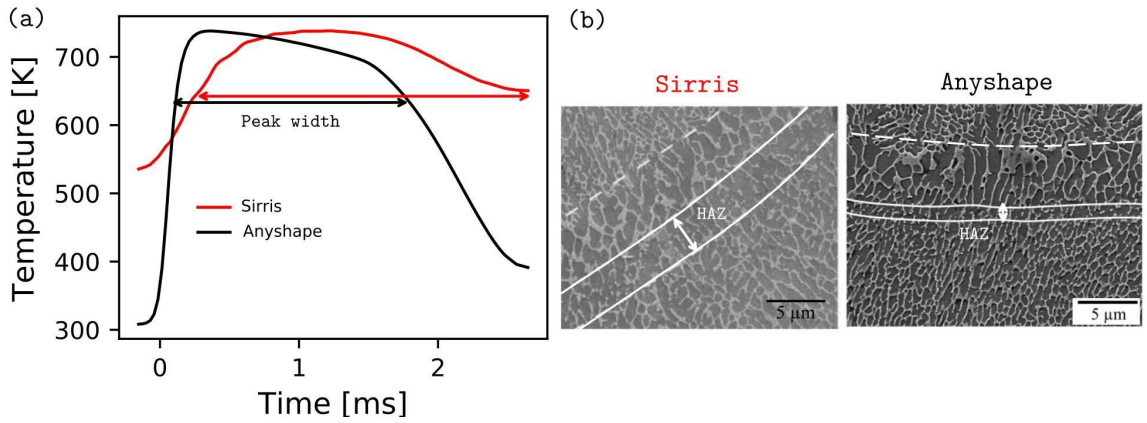

Fig. 7. (a) Thermal history of the HAZ and (b) corresponding SEM micrographs for set A (Sirris, average HAZ size: 5 µm) and set B (Anyshape, average HAZ size: 1.3 µm).

The difference observed between the duration of the peaks of temperature for the two different sets of processing parameters can first be explained in terms of the input energy. This energy is equal to A921 $J.m^{-1}$ for set A (Sirris) while it is A284 $J.m^{-1}$ for set B (Anyshape) (here, the A coefficient stands for the laser absorptivity). The excess energy injected under the processing parameters of set A takes longer to be evacuated from the part, giving way to a large temperature peak. Moreover, the build platform temperature also plays a role: a higher build platform temperature (set A) leads to smaller thermal gradient and consequently to a decrease in heat conduction, which again tends to increase the width of the peak. These observations are in agreement with the experimental HAZ size shown in Fig. 7(b). The results from the FE simulations are thus consistent with the experimental observations.

Summary

A 2D FE model for the thermal history of LPBF of AlSi10Mg is developed and calibrated using experimental measurements of the melt pool height. In order to allow for the efficient simulation of the deposition of five successive layers, without incurring excessive computational cost, a remeshing procedure is implemented by keeping a constant number of nodes independently of the number of fused layers. The results from the multilayer FE simulations highlight that no heat accumulation is observed in LPBF AlSi10Mg under processing conditions corresponding to relatively low heat input. In this case, the thermal history of the HAZ is independent of the number of fused layers, and it can be studied using a thermal FE model for one single layer. Indeed, the influence of two different sets of processing parameters on the thickness of the HAZ is correctly predicted by single layer FE simulations.

Acknowledgements

The authors wish to acknowledge the financial support of the European Fund for Regional Development and the Walloon Region under convention FEDER “Iawatha” and of the Walinnov Longlife AM project, convention n°1810016, funded by the Service Public de Wallonie - Economie Emploi Recherche (SPW-EER). As Research Director of FRS-FNRS, A.M. Habraken acknowledges the support of this institution. The authors are also grateful to the CAREM of the University of Liège, for providing access to SEM facilities, and to Mr O. Rigo (Sirris) and Dr S. Michotte (AnyShape), for their help with samples fabrication.

References

[1] L. Thijs, K. Kempen, J.P. Kruth, J. van Humbeeck, Fine-structured aluminium products with controllable texture by selective laser melting of pre-alloyed AlSi10Mg, Acta Mater. 61 (2013) 1809-1819. https://doi.org/10.1016/j.actamat.2012.11.052
[2] E.O. Olakanmi, R.F. Cochrane, K.W. Dalgarno, A review on selective laser sintering/melting (SLS/SLM) of aluminium alloy powders: Processing, microstructure, and properties, Prog. Mater. Sci. 74 (2015) 401-477. https://doi.org/10.1016/j.pmatsci.2015.03.002
[3] A. Mertens, J. Delahaye, J. Lecomte-Beckers, Fusion-based additive manufacturing for processing aluminium alloys: state-of-the-art and challenges, Adv. Eng. Mater. 19 (2017) 1700003. https://doi.org/10.1002/adem.201700003
[4] ASM International (Hrsg.): ASM Handbook Volume 2: Properties and Selection: Nonferrous Alloys and Special-Purpose Materials, ASM International, 2004
[5] L. Roger, Fundamentals of aluminium metallurgy Production, processing and applications, Woodhead Publishing in materials: CRC Press, 2011.
[6] J. Delahaye, J.T. Tchuindjang, J. Lecomte-Beckers, O. Rigo, A.M. Habraken, A. Mertens, Influence of Si precipitates on fracture mechanisms of AlSi10Mg parts processed by Selective Laser Melting, Acta Mater. 175 (2019) 160-170. https://doi.org/10.1016/j.actamat.2019.06.013
[7] L. Zhao, J.G. Santos Macias, L. Ding, H. Idrissi, A. Simar, Damage mechanisms in selective laser melting AlSi10Mg under as-built and different post-treatment conditions, Mater. Sci. Eng. A 764 (2019) 138210. https://doi.org/10.1016/j.msea.2019.138210
[8] J. Delahaye, How to feed and validate a phase-field model predicting the evaluation of microstructures and properties in AlSi10Mg processed by Laser Powder Bed Fusion, PhD Thesis, University of Liège (Belgium), 2022. https://hdl.handle.net/2268/293324
[9] L. Zhao, L. Song, J.G. Santos Macías, Y. Zhu, M. Huang, A. Simar, Z. Li, Review on the correlation between microstructure and mechanical performance for laser powder bed fusion AlSi10Mg, Addit. Manuf. 56 (2022) 102914. https://doi.org/10.1016/j.addma.2022.102914
[10] A. Mertens, J. Delahaye, O. Dedry, B. Vertruyen, J.T. Tchuindjang, A.M. Habraken, Microstructure and properties of SLM AlSi10Mg: Understanding the influence of the local thermal history, Procedia Manuf. 47 (2020) 1089-1095. https://doi.org/10.1016/j.promfg.2020.04.121
[11] K.C. Mills, Recommended values of thermophysical properties for selected commercial alloys, Woodhead, Cambridge, 2002
[12] S. Cescotto, R. Charlier: Frictional contact finite elements based on mixed variational principles. Int. J. Numer. Methods Eng, 36 (1993) 1681-1701. https://doi.org/10.1002/nme.1620361005
[13] R. T. Jardin, V. Tuninetti, J. T. Tchuindjang, N. Hashemi, R. Carrus, A. Mertens, A. M. Habraken, Sensitivity analysis inthemodeling of a high-speed, steel, thin wall produced by directed energy deposition. Metals 10(11) (2020) 1554. https://doi.org/10.3390/met10111554
[14] S. Fetni, T. Maurizi Enrici, T. Niccolini, H. S. Tran, O. Dedry, L. Duchêne, A. Mertens, A. M. Habraken, Thermal model for the directed energy deposition of composite coatings of 316L stainless steel enriched with tungsten carbides, Materials & Design 204 (2021) 109661, https://doi.org/10.1016/j.matdes.2021.109661
[15] MSM & GEG (ULiege), 2022. Lagamine software [WWW Document]. Univ. Liege. URL http://www.lagamine.uliege.be/dokuwiki/doku.php (Accessed 4.12.22).
[16] M. Tang, P.C. Pistorius, S. Narra, J.L. Beuth, Rapid solidification: selective laser melting of AlSi10Mg, JOM 67 (2016) 960-966. https://doi.org/10.1007/s11837-015-1763-3
[17] I. Roberts, C.J. Wang, R. Esterlein, M. Stanford, D.J. Mynors, A three-dimensional finite element analysis of the temperature field during laser melting of metal powders in additive layer manufacturing, Int. J. Mach. Tools Manuf. 49 (2009) 916-923. https://doi.org/10.1016/j.ijmachtools.2009.07.004

[18] Y. Liu, J. Zhang, Z. Pang, Numerical and experimental investigation into the subsequent thermal cycling during selective laser melting of multi-layer 316L stainless steel, Opt. Laser Technol. 98 (2018) 23-32. https://doi.org/10.1016/j.optlastec.2017.07.034

Materials Research Proceedings 28 (2023) 199-206 https://doi.org/10.21741/9781644902479-22

Semi-finished powder of aluminum matrix composite for a direct energy deposition additive manufacturing

JEDYNAK Angelika[1,a *], ERTUGRUL Gökhan[1,b], NEUMANN Andreas[1,c], PIPPIG Robert[2,d] and HÄRTEL Sebastian[1,e]

[1]Chair of Hybrid Manufacturing, Brandenburg University of Technology, Cottbus, Germany
[2]CMMC GmbH, Chemnitz, Germany

[a]Angelika.Jedynak@b-tu.de, [b]Gökhan.Ertugrul@b-tu.de, [c]Andreas.Neumann@b-tu.de, [d]robert.pippig@cmmc-engineering.com, [e]Sebastian.Haertel@b-tu.de

Keywords: Aluminum-Matrix Composites (AMCs), Direct-Vacuum-Casting (DVC), Direct Energy Deposition (DED), Additive Manufacturing (AM)

Abstract. Aluminum-Matrix Composites (AMCs) are particle-reinforced aluminum matrix composites that are well-established in high-performance lightweight components in the automotive and aerospace industries. So far, the use of AMC materials has been limited to components manufactured using casting technology (e.g. brake discs). The adaption of AMC materials in Additive Manufacturing (AM) processes, such as powder feedstock for Direct Energy Deposition (DED), is dependent on the availability of the corresponding semi-finished product. An approach for the production of such a semi-finished product is presented in the current work. This study presents, how powder as semi-finished product for the DED processes, is produced from cast ingots manufactured by Direct-Vacuum-Casting (DVC). The novel DVC process allows a SiC_P particle content of up to 35%, whereas conventional AMC casting processes can only achieve a fully embedded SiC_P particle content of up to 20%. Particular attention is paid to ensuring that the SiC_P particles remain completely embedded in the aluminum matrix after the semi-finished product has been produced. However, there is currently not an extensive literature existing on semi-finished products from AMC materials in AM processes. Therefore, in these investigations, ultrasonic atomization technology was used to produce of AMC powder with an average size of 80 µm as a feedstock material. The microstructure analysis of this powder demonstrated the presence of primary SiC_P particles with non-optimal distribution. Nevertheless, the AMC powder was used in the subsequent DED process studies. It was possible to develop the fundamentals for the deposition processing of AMC powder. As demonstrated by microscope techniques, secondary SiC_P particles were precipitated in an aluminum matrix with complete embedding during deposition, pointing the way forward to develop AMC powders as semi-finished products in AM processes.

Introduction

Aluminum matrix composites (AMCs) are composed of two material systems situated in one material. The aluminum alloy represents a matrix that utilizes low density and corrosion resistance. Ceramics are a possible reinforcement component of the hardness and wear resistance. Due to this unique combination of properties, AMCs are pertinent in various industrial sectors, such as the automotive and aerospace industries [1]. Conventionally, solid or liquid processing routes are available to produce AMC parts, such as sintering, stir casting, and squeeze casting [2]. These processes enable the production of AMC parts with completely embedment and an even distribution of ceramic particles in the matrix. The performance of AMC parts can be further enhanced by increasing the fraction of ceramic particles in the matrix. Therefore, the novel casting processes as Direct-Vacuum-Casting (DVC) allow a SiC_P particle content of up to 35%, whereas

Content from this work may be used under the terms of the Creative Commons Attribution 3.0 license. Any further distribution of this work must maintain attribution to the author(s) and the title of the work, journal citation and DOI. Published under license by Materials Research Forum LLC.

conventional AMC casting processes can only achieve a fully embedded SiC_P particle content of up to 20% [3]. However, the disadvantages of conventional processes are high tooling costs, limited component geometry, and size. Therefore, AM technologies are currently being developed, enabling the production of AMC components without the tooling and lead-time required in conventional processes [4].

The processing of AMCs using AM is still in the initial stage due to the lack of technologies to produce feedstock materials, especially AMC powders. The appropriate morphology, size, and chemical composition of AMC powders are crucial for the AM technologies, such as Laser Powder Bed Fusion (L-PBF) or Direct Energy Deposition (DED), to obtain fully dense components. Also, the uniform distribution of the reinforcement phase within/around the alloy powder particles is significant to achieve the desired mechanical performance of AMC components. The available methods to fabricate AMC powders are ball milling [5] or gas atomization [6]. During the ball milling, AMC powders arise mechanically by the collides of powder particles. The powders produced by this method exhibit, e.g. less sphericity and a mismatch between the reinforcement and the matrix. The more desirable approach to fabricating AMC powders is gas atomization, where the initial material is melted in a crucible and then sprayed by high-pressurized gas jets. This method ensures the production of spherical AMC powders with a uniform distribution of ceramic particles in the matrix. However, a prerequisite to fabricating such powders is a sufficiently long homogenization (by separately added ceramic particles) during melting to avoid segregation. Therefore, using a previously homogenized AMC material, e.g. by a novel DVC, could reduce the processing time of powder production and ensure good powder properties.

The current work presents an approach to the production of AMC powder. An AlSi9Mg aluminum alloy reinforced with 20 vol% SiC_P particles (SiC_P /AlSi9Mg) was considered. The initial material SiC_P /AlSi9Mg was manufactured by DVC and then atomized into SiC_P /AlSi9Mg powder using a novel ultrasonic atomization (UA) technology. In subsequent DED process studies, it was possible to develop the fundamentals for the deposition processing of SiC_P /AlSi9Mg powder. The microstructure evolution of SiC_P /AlSi9Mg powder and as-deposited SiC_P /AlSi9Mg material were investigated using different microscope techniques to determine the presence of SiC_P particles and their embedment behavior in the matrix.

Material and methods

Initial material.

AlSi9Mg aluminum alloy reinforced with 20 vol% SiC_P particles (SiC_P /AlSi9Mg) manufactured by the DVC process [3] was used in this work. The average size of SiC_P was 9.3 µm (=F600). The chemical composition of the aluminum matrix AlSi9Mg is listed in Table 1.

Table 1. Chemical composition of AlSi9Mg alloy in [wt.%] according to the EN AC-43300.

Si	Mg	Fe	Cu	Mn	Zn	Ti	Pb	Al	Others
9.0 - 10.0	0.25 – 0.45	<0.19	<0.05	<0.1	<0.07	<0.15	<0.03	Balance	0.1

Powder fabrication.

The SiC_P /AlSi9Mg powder was produced in the company 3DLab on the ATOLab+ machine using UA technology. In this method, the feed rods are gradually melted by the welding arc, creating a melt pool on the vibrating platform. The droplets are separated from the melt pool by ultrasonic vibrations and discharged by the inert gas flow. During the discharging stage, the formed droplets are solidified leading to the production of powder particles. The atomization process of investigated material was carried out in an atmosphere of pure argon (>99.998%) with a flow rate of 15 – 20 $Lmin^{-1}$. A significant process parameter was the vibration frequency of 35 kHz, the

amplitude of 80%, and the arc current of 130 A. Finally, the atomized SiC_P /AlSi9Mg powder was sieved with a mesh size of 100 µm.

Specimen manufacturing.

DED is performed with a laser metal deposition (LMD) system, Lunovu e-LMD. The LMD system consists of a 2.5 kW solid state laser power source, a coaxial nozzle corresponding powder feed unit, a 5-axis kinematics and a scanner (see Fig. 1). Laser wavelength and spot diameter are 960 – 1080 nm and 1.6 mm, respectively. Argon is used as a shielding gas with a 12 $Lmin^{-1}$ flow rate to avoid the atmospheric contamination. The nozzle uses a 3 $Lmin^{-1}$ powder gas flow rate to carry the powder to the melt pool. Substrate – nozzle distance is 13 mm to focus the laser and powder, simultaneously. The rotation of substrate is chosen between 5 – 10° angle to prevent the reflection (see Fig. 1b).

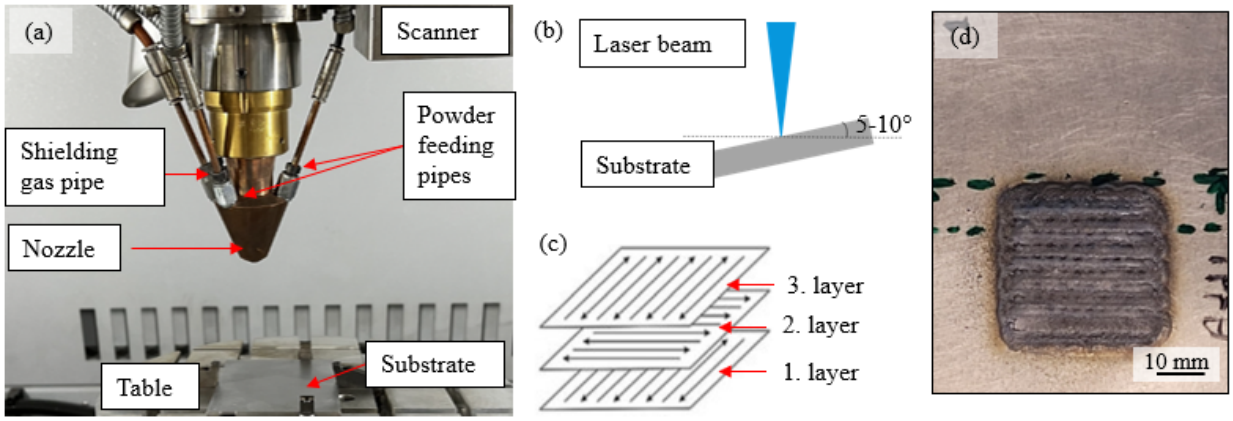

Fig. 1. (a) LMD system components, (b) demonstration of the rotation of substrate and (c) deposition strategy of the additively manufactured part.

The cuboid (length 30 mm, width 30 mm, high 2 mm) was deposited with a bidirectional scanning strategy (with a rotation of 90° to the scanning direction) (see Fig. 1c). The process parameters for the deposition of this part are listed in the Table 2. The distance between parallel track lines was defined as the hatch distance and was approximately 1.7 mm. The number of layers was 6. The overview of the additively deposited part is presented in Fig. 1d.

Table 2. Parameter setup for the manufacturing of the cuboid by DED process.

Laser Power, [W]	Scan Speed, [mms^{-1}]	Powder feed rate, [$gmin^{-1}$]
1750 (1. Layer) 1800 (Upper Layers)	500	1.3

Powder analysis.

To investigate the morphology (=sphericity) and distribution size of powder particles, scanning electron microscope (SEM) (Phenom XL, Thermofisher Scientific), equipped with a Secondary Electron (SE) detector was used. The imaged powder particles were analyzed with the integrated software ParticleMetric in the SEM to determine the distribution size and sphericity, represented as aspect ratio. The aspect ratio is an index for sphericity, where an aspect ratio of 1 equates to ideal powder sphericity. Approximately, one hundred powder particles were analysed.

For the microstructure analysis, the powder particles were ground using silicon carbide grinding papers with 1200 grit size and oxide polished (0.05 µm silica solution, Struers OP-S Suspension) using a vibratory polishing machine. The Digital Microscope (DM) VHX-7000 (Keyence Deutschland GmbH) was used to investigate the presence, size, morphology, and embedment behaviour of particles in the matrix of powder particles. The size of the particles was measured

with the integrated software in the DM on approximately 25 particles. The chemical composition of particles was measured by SEM using the energy-dispersive X-ray spectrometer (EDX) to determine their type.

Analysis of as-deposited specimen.

To investigate the porosity and microstructure of the as-deposited specimen, the cuboid was sectioned lengthwise to the deposited direction. The sectioned sample of this cuboid was then ground on silicon carbide grinding papers with grit sizes from 240 to 2500, polished using three steps diamond suspension (6 µm, 3 µm and 1 µm), and oxide polished (0.05 µm silica solution, Struers OP-S Suspension). The determination of porosity was carried out using the integrated software in the DM. The microstructure analysis of the as-deposited specimen was carried out in the same way as in the case of powder.

Results and discussion

Initial material.

SEM image of initial microstructure of as-cast SiC_P /AlSi9Mg is presented in Fig. 2. This microstructure exhibited a uniform distribution of SiC_P (primary) particles in the aluminum-based matrix.

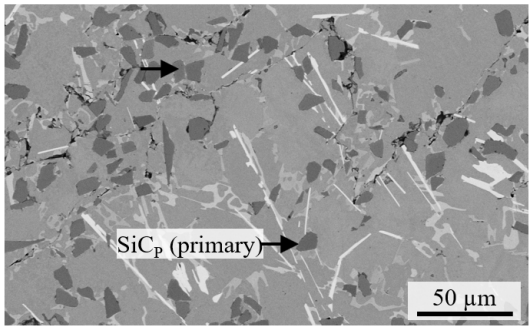

Fig. 2. SEM BSE image of initial microstructure of as-cast SiCP /AlSi9Mg.

Powder analysis.

SEM SE image of powder particles of SiC_P/AlSi9Mg is shown in Fig. 3 a. The powder particles were spherical and free of satellite particles. The size distribution and the aspect ratio (=sphericity) of powder particles in cumulative frequency are depicted in Fig. 3 b,c. The results have shown that the average size (d50) of powder particles was 80 µm. The particle size distribution (between d10 and d90) ranged between 63 µm and 92 µm that was suitable for DED process. The powder particles exhibited very good sphericity, only 10 % of all particles had an aspect ratio below 0.98 (d10) (see Fig. 3 c).

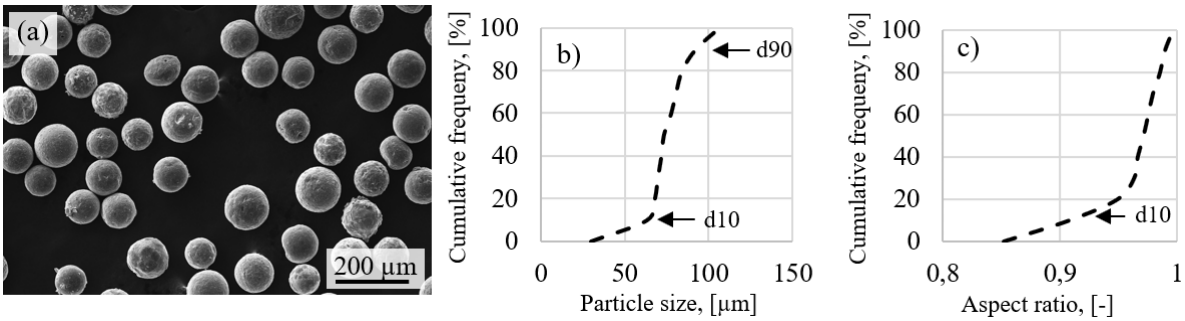

Fig. 3. (a) SEM SE image, (b) particle size distributions and (c) aspect ratio of SiCP /AlSi9Mg powder.

DM images of powder particles of SiC_P /AlSi9Mg in cross-sections are presented in Fig. 4. The powder particles exhibited three predominant types of particles. Their chemical composition was locally determined using EDX analysis (see Table 3), indicating the presence of SiC_P (primary), Al-Si-C and Al-C particles.

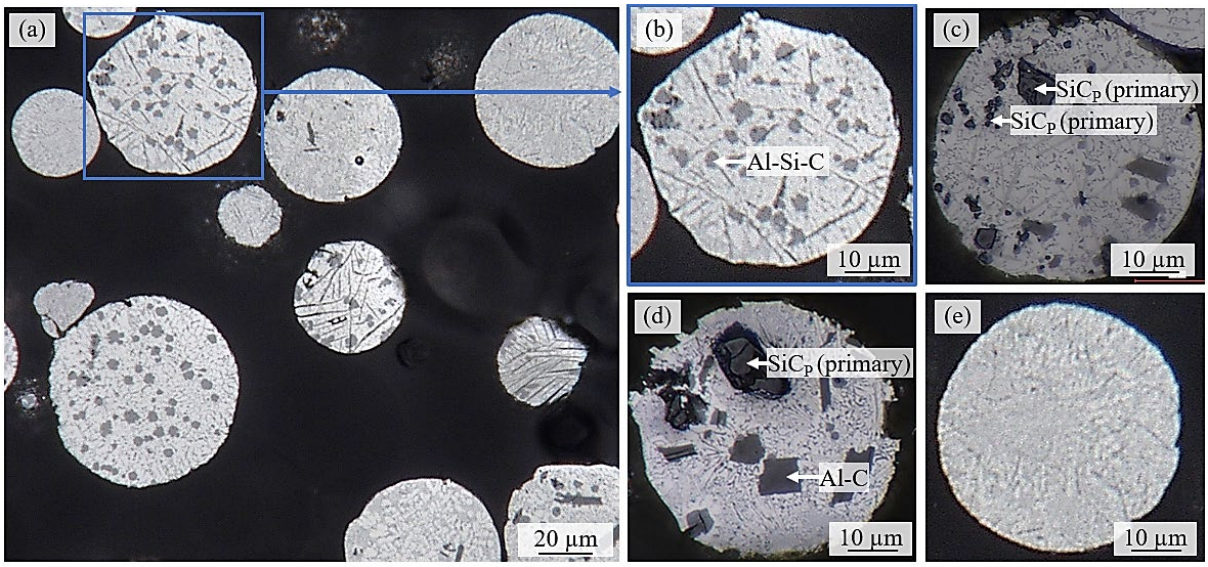

Fig. 4. DM images of particles of SiCP /AlSi9Mg powder in cross-section.

The similar morphology of the detected SiC_P particles in the powder particles, such as in the initial material, suggests that these particles exhibited resistance during welding arc melting (atomization process) and were transferred into the powder without re-melting. Therefore, the SiC_P in powder particles were determined as primary. However, their average size decreased from 9.2 µm (as-cast) to 4.5 µm (powder), which indicates their partial dissolution. Some primary SiC_P particles had internal cracks due to high thermal stress during the rapid solidification of droplets into powder particles. Furthermore, voids were formed at the interface between these SiC_P particles and the aluminum-based matrix, indicating the non-optimal embedment of these SiC_P particles in the matrix. The presence of primary SiC_P particles was not determined in every particle, indicating their non-uniform distribution in powder particles. The Al-Si-C particles were formed by the reaction of molten aluminum alloy and SiC_P particles [7,8]. The average size of these particles was 8.5 µm. Al-C particles were formed by the similar reaction, depending on the different local temperature and composition [7]. The low oxygen content in these particles indicates their reaction with oxide layer Al2O3 on the surface of initial material [9]. Moreover, some powder particles were formed without any precipitated particles.

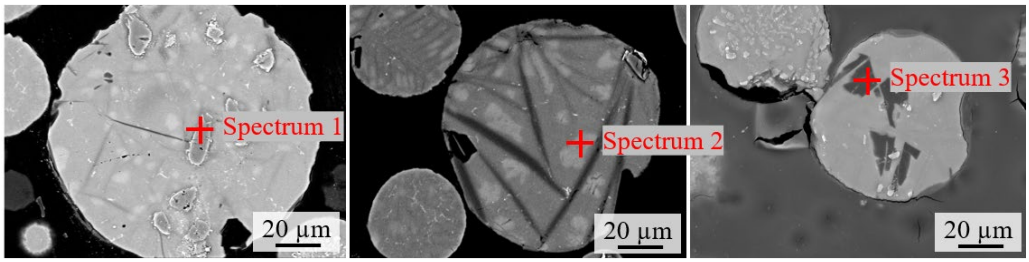

Fig. 5. SEM BSE images of particles of SiCP /AlSi9Mg powder in cross-section.

Table 3. Chemical composition (at.%) of phases in the microstructure of SiCP /AlSi9Mg powder.

Spectrum	C	Al	Si	O
Spectrum 1: SiC_P (primary)	49.5	1.5	49.0	--
Spectrum 2: Al-Si-C	37.8	17.0	45.2	--
Spectrum 3: Al-C	79.4	12.3	2.8	5.5

Analysis of as-deposited specimen.

The internal porosity of the as-deposited cuboid is 6.0%, and the pore size ranges between 5 µm to 120 µm. The formation of such high porosity in the as-deposited samples indicates the contamination issues as the result of moisture uptake in aluminum powders [10] or oxygen trapped in SiC_P particles powders processed by atomization process. Nevertheless, the as-deposited SiC_P /AlSi9Mg material was used for the analysis to investigate the presence, morphology and chemical composition of SiC_P particles and their embedment behavior in the matrix.

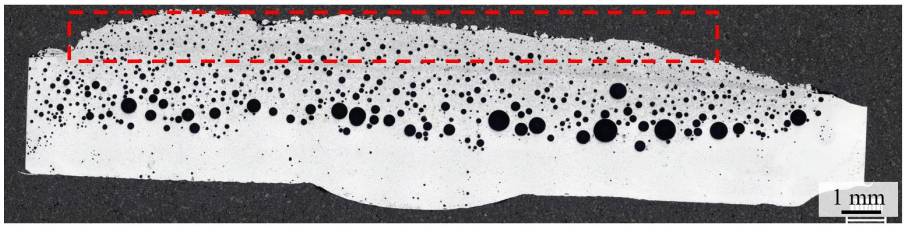

Fig. 6. DM image of the as-deposited cuboid from SiCP /AlSi9Mg in the longitudinal section.

The microstructure of as-deposited cuboid consisted of uniformly distributed and well-embedded particles in the aluminum alloy matrix. The microstructure from different areas within this part was found to have similar characteristics (see Fig. 7). However, the size of particles was finer at the bottom of the part (Fig. 7 c) as compared to the top/center and edge (Fig. 7 a,b).

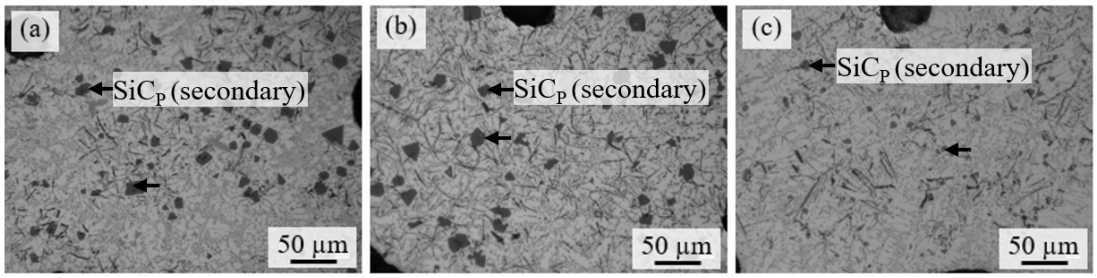

Fig. 7. DM images of microstructure of as-deposited cuboid from SiCP /AlSi9Mg: (a) at the edge, (b) at the top/centre and (c) at the bottom/centre.

The microstructure of as-deposited cuboid exhibited two predominant types of particles. Their chemical composition was locally determined using EDX analysis (see Table 4), indicating the presence of SiC_P and needle-like Al-Si-C particles (see Fig. 8). The size of the SiC_P was between 22 and 26 µm at the top of the part and 13 µm at the bottom. The shape of these particles was almost angular. Compared to SiC_P (primary) in powder particles, the SiC_P particles in the as-deposited part exhibited a different morphology (larger size and almost angular shape) and were uniformly distributed. That indicates the formation of these SiC_P particles during deposition via mechanism of complete dissolution of powder structure (e.g. primary SiC_P) and their precipitation. Therefore, the SiC_P in powder particles were determined as secondary. The in-situ formation of

SiC_P is thermodynamically possible and can result from the reaction of e.g. Al-C with Si in the melt [7]. In addition, needle-like Al-Si-C particles were formed and uniformly distributed in the microstructure of the as-deposited part. The oxygen content in these particles indicates their reaction with oxide layer Al2O3 on the surface of powder particles [9].

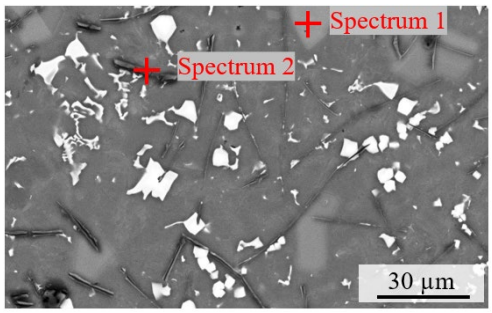

Fig. 8. SEM BSE image of as-deposited cuboid from SiCP /AlSi9Mg (top/centre).

Table 4. Chemical composition (at.%) of the measured spectrums in the microstructure of as-deposited cuboid from SiCP /AlSi9Mg (top/centre).

Spectrum	C	Al	Si	O
Spectrum 1: SiC_P (secondary)	36.1	1.8	60.3	--
Spectrum 2: Al-Si-C	9.6	53.2	9.2	28.0

Conclusions and outlook

In this work, SiC_P /AlSi9Mg powder was produced via ultrasonic atomization technology from the SiC_P /AlSi9Mg manufactured by the DVC process. The produced SiC_P /AlSi9Mg powder was then processed in the DED process. The investigations of the SiC_P /AlSi9Mg powder and as-deposited SiC_P /AlSi9Mg material with the focus on the microstructure analysis were carried out. The following conclusions can be drawn:

- The SiC_P /AlSi9Mg powder exhibited a particle size distribution between 63 µm and 92 µm and high sphericity, indicating its suitability for the processing with the DED process.
- In the microstructure of SiC_P /AlSi9Mg powder, three predominant particles: SiC_P (primary), Al-Si-C and Al-C were determined. The primary SiC_P particles were not uniformly distributed in powder particles and their embedment in the matrix was non-optimal.
- The porosity of the as-deposited sample from the SiC_P /AlSi9Mg powder was 6.0%, indicating moisture uptake in aluminum powders or oxygen trapped in SiC_P particles powders processed by atomization process. Nevertheless, the as-deposited part was used to study the evolution of the microstructure during deposition.
- In the microstructure of the as-deposited SiC_P /AlSi9Mg material, two predominant particles were determined: SiC_P and needle-like Al-Si-C. The different morphology (shape, size) of these SiC_P particles compared to the primary SiC_P particles (whether in powder or initial material) suggested their formation via the mechanism of dissolution and precipitation (as secondary SiC_P). The distribution of secondary SiC_P was uniform in the as-deposited material with the well-embedding.

Future work will focus on reducing porosity in the DED-processed SiC_P/AlSi9Mg material. Therefore, it is necessary to realize measures, such as drying the powder before the AM process, increasing the control of the gas atmosphere during the atomization process, or ensuring appropriate conditions for powder storage are needed to avoid of powder contamination.

References

[1] P. Garg, A. Jamwal, D. Kumar, K.K. Sadasivuni, C.M. Hussain, P. Gupta, Advance research progresses in aluminium matrix composites: Manufacturing & applications, J. Mater. Res. Technol. 8 (2019) 4924–4939. https://doi.org/10.1016/j.jmrt.2019.06.028

[2] V. Chak, H. Chattopadhyay, T.L. Dora, A review on fabrication methods, reinforcements and mechanical properties of aluminum matrix composites, J. Manuf. Process. 56 (2020) 1059–1074. https://doi.org/10.1016/j.jmapro.2020.05.042

[3] Graf Mea. New casting process for the production of AMCs with high volume content of einforced particle phase, Proceedings 5th IMTC 2021.

[4] A. Bandyopadhyay, B. Heer, Additive manufacturing of multi-material structures, Mater. Sci. Eng. R: Reports 129 (2018) 1–16. https://doi.org/10.1016/j.mser.2018.04.001

[5] X. Xi, B. Chen, C. Tan, X. Song, J. Feng, Microstructure and mechanical properties of SiC reinforced AlSi10Mg composites fabricated by laser metal deposition, J. Manuf. Process. 58 (2020) 763–774. https://doi.org/10.1016/j.jmapro.2020.08.073

[6] X.P. Li, G. Ji, Z. Chen, A. Addad, Y. Wu, H.W. Wang, J. Vleugels, J. Van Humbeeck, J.P. Kruth, Selective laser melting of nano-TiB2 decorated AlSi10Mg alloy with high fracture strength and ductility, Acta Mater. 129 (2017) 183–193. https://doi.org/10.1016/j.actamat.2017.02.062

[7] J. Chen, R. Zhang, B.S. Amirkhiz, H. Gu, Synthesis of In Situ SiC/Graphite/Al Hybrid Composite Coating by Laser Direct Energy Deposition, Metall. Mater. Trans. A 53 (2022) 484–502. https://doi.org/10.1007/s11661-021-06508-x

[8] R. Anandkumar, A. Almeida, R. Colaço, R. Vilar, V. Ocelik, J.Th.M. De Hosson, Microstructure and wear studies of laser clad Al-Si/SiC(p) composite coatings, Surf. Coat. Technol. 201 (2007) 9497–9505. https://doi.org/10.1016/j.surfcoat.2007.04.003

[9] A. Riquelme, P. Rodrigo, M.D. Escalera-Rodríguez, J. Rams, Corrosion Resistance of Al/SiC Laser Cladding Coatings on AA6082, Coat. 10 (2020) 673. https://doi.org/10.3390/coatings10070673

[10] C. Weingarten, D. Buchbinder, N. Pirch, W. Meiners, K. Wissenbach, R. Poprawe, Formation and reduction of hydrogen porosity during selective laser melting of AlSi10Mg, J. Mater. Process. Technol. 221 (2015) 112–120. https://doi.org/10.1016/j.jmatprotec.2015.02.013

Materials Research Proceedings 28 (2023) 207-216 https://doi.org/10.21741/9781644902479-23

Rapid tooling development for low volume injection molding of cosmetic compacts

VELLA Andrea[1,a], ROCHMAN Arif[1,b *] and VELLA Pierre[1,c]

[1]Department of Industrial and Manufacturing Engineering, University of Malta, Msida, MALTA

[a]andrea.vella.11@um.edu.mt, [b]arif.rochman@um.edu.mt, [c]pierre.vella@um.edu.mt

Keywords: Additive Manufacturing, 3D Printing, Rapid Tooling, Rapid Prototyping, Injection Molding

Abstract. This study aimed to explore the capability of different additive manufacturing (AM) or 3D printing technologies to rapidly manufacture mold inserts for injection molding as well as to evaluate the performance of the printed mold inserts and the quality of the injection molded parts. Fused filament fabrication (FFF), stereolithography (SLA), and multi-jet fusion (MJF) 3D printing technologies were used to produce the mold inserts, whereas a cosmetic compact base was selected as the case study part. The results obtained show that it is possible to use the mentioned technologies to manufacture tool inserts for rapid prototyping or low volume production of cosmetic compact bases using injection molding. When using the FFF mold inserts, the cosmetic compact bases produced were not of the best quality and surface finish but still acceptable for prototyping purposes only. The vertically printed SLA mold inserts as well as the MJF mold inserts produced cosmetic compact bases with no flashes and the best surface finish. The MJF mold inserts had excellent thermal properties so that apart from HDPE, a higher melting temperature ABS was also successfully molded. Also using the MJF mold inserts, the highest production number of 80 cosmetic compact bases of a good quality could be achieved.

Introduction

Rapid Tooling (RT) is a rapid production of tools or molds using additive manufacturing (AM) also as known as 3D printing technology, which were introduced a couple of decades ago [1]. Additive manufacturing is a layer-by-layer process using only one machine, which is capable of joining materials to manufacture a desired three-dimensional object. This technology is the opposite of traditional manufacturing, where an object is carved by removing the unwanted extra material [2]. In other words, rapid tooling is the use of AM technologies to produce tools, molds, or dyes, in order to produce parts using a subsequent manufacturing technique such as injection molding to produce parts or prototypes instead of using an AM technology directly, which may take longer and cost more if a certain quantity is required [3-5]. Although the process and technology used for rapid tooling is the same as the ones used in AM, the purpose is different. Using rapidly and additively manufactured tools/molds, the final products or prototypes are expected to be better since the parts can be molded from the desired molding material and fully dense.

RT could save time and money in the injection molding industry since the designer can analyze the performance of the AM tool and confirm that the tool has met its objectives before starting the long and expensive process of manufacturing the conventional tool steel mold. This will save a company months of work and tens of thousands of euros [6,7]. On the other hand, if a rapid tool will be used for the actual production of finished parts and not only to produce several prototypes to test the tool and its expectations, then surface finish will also be an issue and a very good quality product is expected [8]. In rapid manufacturing/rapid prototyping process, surface finish is not that of an issue since these technologies have a free form nature [1].

Content from this work may be used under the terms of the Creative Commons Attribution 3.0 license. Any further distribution of this work must maintain attribution to the author(s) and the title of the work, journal citation and DOI. Published under license by Materials Research Forum LLC.

RT can be divided in two categories, namely direct and indirect tooling. These two categories are further divided into other two categories which are soft tooling and hard tooling [10]. Hard tooling is used when high production runs are required. Normally for hard tooling tool, steels are applied using metal AM technologies such as, laser beam powder bed fusion process (LB-PBF). On the contrary, soft tooling is mostly used for a few runs. Therefore, this process could make use of thermoplastic materials, epoxy resins, and low melting temperature metallic alloys using AM technologies such as fused filament fabrication (FFF) and stereolithography apparatus (SLA).

This study aimed to explore the capability of different AM or 3D printing technologies to rapidly manufacture soft tools for injection molding as well as to evaluate the performance of the 3D printed soft tools and the quality of the injection molded parts.

Materials and Methods

Case Study Part.

A small Terra cosmetic compact of Toly Product Ltd. Malta was selected as the case study which consists of a lid and base. For this study, only the base was considered, as can be seen in Fig. 1, which is mass produced from a mixture of acrylonitrile butadiene styrene (ABS) and styrene acrylonitrile (SAN) polymers. The injection mold used in the actual mass production process had two sliders, one at the front and another at the back. The back section has sliding cores to form holes on each side of the cosmetic base to accommodate two metal pins, which are used as a hinge to allow the user to open and close the lid of the cosmetic compact. At the front side of the base, a protruded bump is formed using another slider which is used as a snap-fit join to lock or release the lid, Fig. 1a. The part was injected from the center on the bottom side, using a 2-cavity hot runner mold. The injection point can be easily observed on the center bottom of the original part, while the four ejector pins are located in the well sections of the part, as can be seen in Fig. 1b.

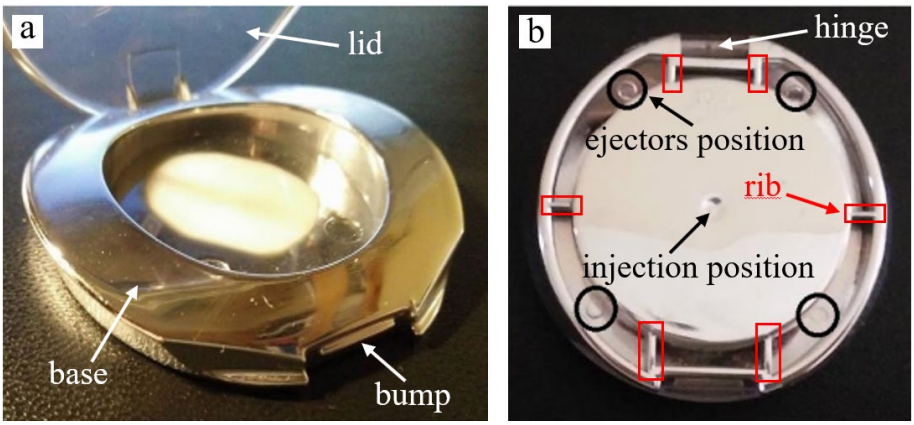

Fig. 1. Small Terra cosmetic compact top view (a) and its base's bottom view (b).

Part Design Simplification.

The design of the cosmetic base required slight simplifications so that the cosmetic bases could be produced without the above-mentioned sliders using a cold runner mold instead of the hot runner mold as in the actual mass production. The holes for the hinge metal pins and the snap-fit bump to lock the lid both of which are formed by the sliders were eliminated. On the bottom side, the base had six ribs in its recess to give the part extra rigidity and strength. Two of these ribs, one on each side, were eliminated to decrease part complexity and also at the same time to give space for ejector pins. The remaining four ribs which are close to the hinge and snap-fit areas are slightly thickened since they were considered to be weak so that it was not ideal for the tooling/mold inserts which are to be manufactured using additive manufacturing. The last necessary simplification was

to alter the parting line, which also determines the design of the core and cavity inserts as well as the position of the gate, as can be seen in Fig. 2.

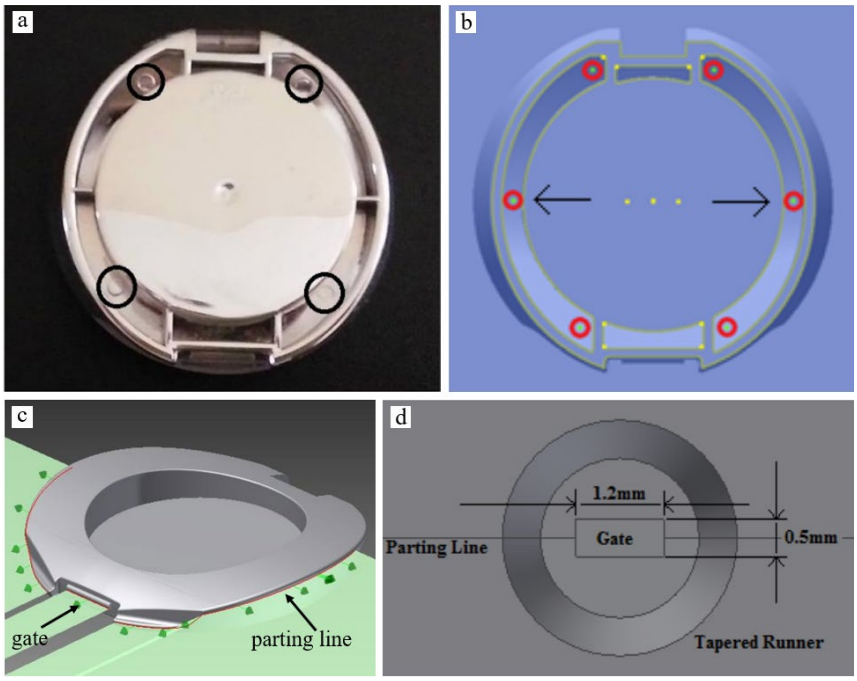

Fig. 2. Ejector pins position on old (a) and new (b) part design; new parting line and gate position (c,d).

Mold Design and Manufacture.

The mold designed for this study was a 2-plate, 2-cavity cold runner mold, without sliders as previously explained. The mold design started from a complete mold base including the mounting and cavity plates, locating ring, riser/spacer block, the locating sleeves, ejector pins, ejector retainer plate and support plate, etc. The cavity plates from both injection and ejection sides have a pocket for a metal insert on which two pockets on each side were machined to accommodate the 3D printed or additively manufactured (AM) mold inserts, as shown in Fig. 3.

Other mold components or features such as runner system, gate type and size, ejection forces including the number and position of the ejector pins, cooling time including the cooling channels were calculated or designed according to guidelines given in Kazmer [11] and Menges et al. [12], although they are for conventional mold design. However, since the aim of this study is not to achieve high production rates and the shortest of cooling or cycle time as well as the printed mold inserts are manufactured from polymer materials with a low heat conductivity, these calculations were not given a great deal of importance. They serve mainly as starting points of the mold design and to ensure that the deviation in the injection molding process including the molding results comes from the 3D printed mold inserts.

In deciding the gate type, the type of runner system, the desired method of de-gating, the allowable level of shear rates through the gate, the resulting flow that is desired as well as the material used in injection molding were all considered. A tab gate is usually used for a simple cold runner type characterized with a manual de-gating, moderate melt shear rates and radial flow. These characteristics were all desirable for this study, and thus, a tab gate, with dimensions as shown in Fig. 2, was designed. The shear rates and the pressure drop at the gate as well as the gate freeze time were also calculated according to Kazmer [11].

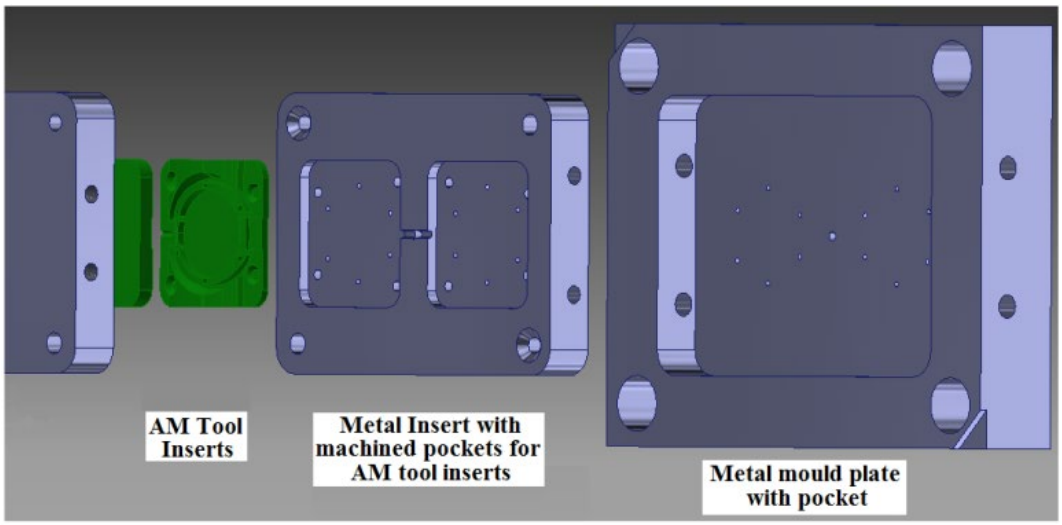

Fig. 3. Metal mold plate, metal insert, and 3D printed (AM) mold insert of the ejection side.

Although the cooling system and its efficiency is of great importance, it was kept simple not to compromise and complicate the machining of the channels. The cooling channels layout in the metal inserts can be seen in Fig. 4. Each cavity had its own U-shaped cooling line. The cooling channels were 46 mm apart on the ejection side and just 27 mm apart on the injection side as shown in Fig. 4a-b. On the ejection side, the cooling channels could not have been machined closer due to the ejector pin holes, while on the injection side there are no such restrictions, the cooling lines were made closer for increased efficiency, higher cooling and thermal dissipation rates. The flow direction of the coolant with a temperature of 19˚C, is indicated by the arrows in both Fig. 4a-b.

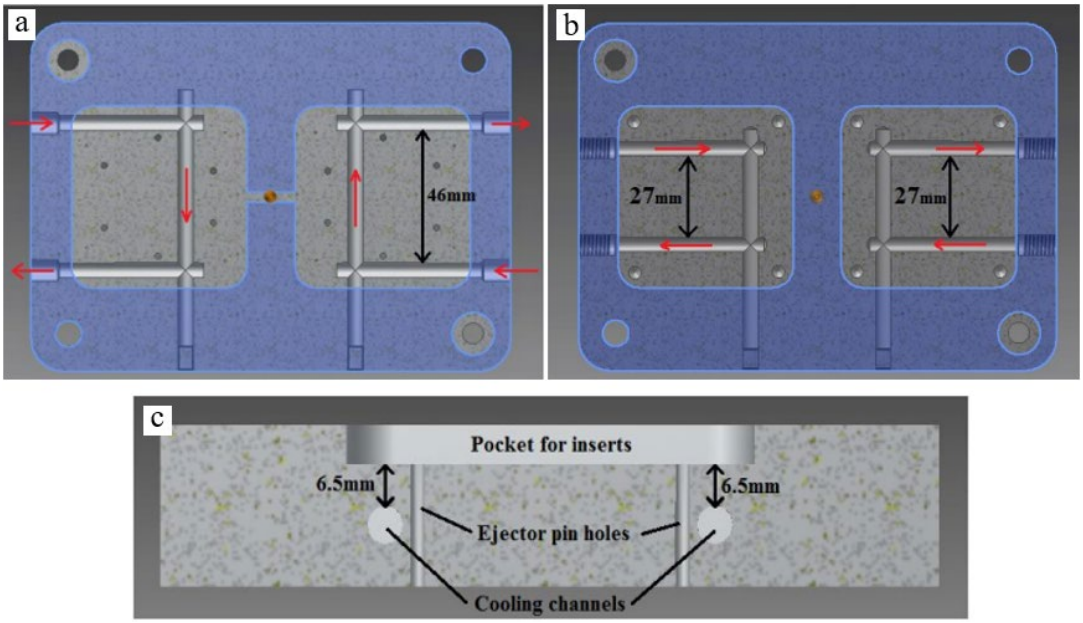

Fig. 4. Cooling channel layout on ejection (a) and injection side (b) of the mold as well as the cross-sectional view of ejection side (c).

In this study, three polymer additive manufacturing or 3D printing technologies were used to print the mold inserts, namely fused filament fabrication (FFF), stereolithography (SLA), and multi-jet fusion (MJF). Two desktop FFF 3D printers (Up Plus 2 and Zortrax M200) were used to manufacture the mold inserts using acrylonitrile butadiene styrene (ABS). ABS was selected based on its overall good properties for mold inserts such as good heat resistance, relatively high heat deflection temperatures, hardness, and toughness. For SLA technology, the mold inserts were printed with Formlabs Form 1+ printer using its standard resin and with Viper Si2 printer using its Accura Xtreme resin. Regarding the MJF technology, ProJet 3500 together with VisiJet M3-X material was used to build the mold inserts.

Fig. 5 shows an example for a mold insert that was manufactured using the FFF 3D printer Zortrax M200 before and after the removal of support material, and Fig. 6a shows another example for SLA mold inserts manufactured using Viper Si2. Fig. 6b and Fig. 6c show the final mold setup from the ejection and injection side which has two pockets and, on each of which, 3D printed mold inserts can be mounted, in this case two different FFF mold inserts 3D printed using UP Plus 2 printer.

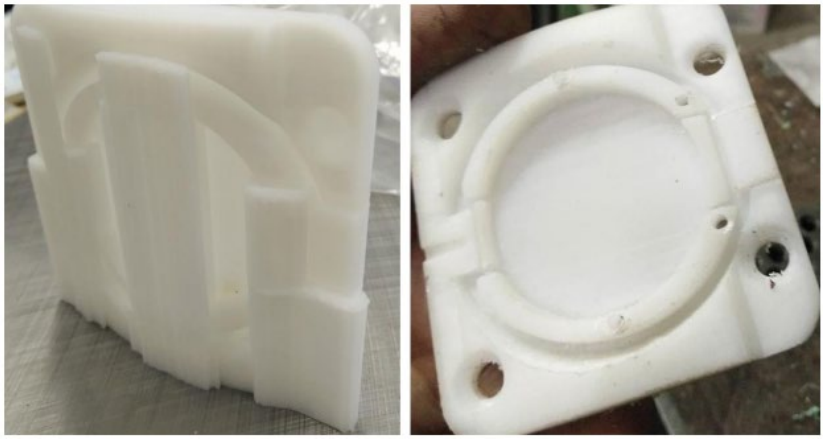

Fig. 5. An example for mold inserts FFF 3D printed on the Zortrax M200 before and after the removal of support material.

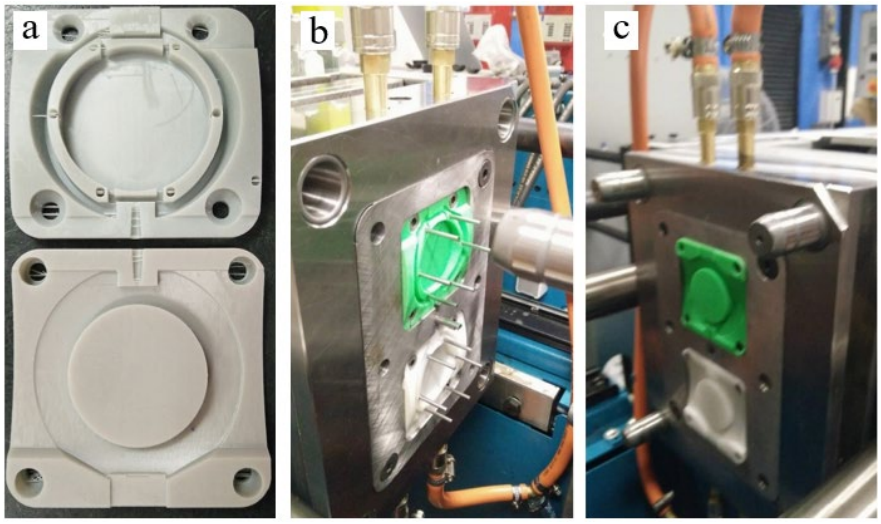

Fig. 6. SLA 3D mold inserts manufactured using Viper Si2 (a), ejection side (b) and injection side (c) of the 2-cavity mold with two different FFF mold inserts 3D printed using UP Plus 2.

Injection Molding Experiments.

The experiments were carried out on Boy 22E injection molding machine. Considering the fact that the mold inserts are printed from polymer materials, the selection of the molding materials was based mainly on a low processing temperature range. For the main injection molding experiments, high density polyethylene, HDPE HMA 016 from ExxonMobil Chemical, was used to produce the cosmetic compacts with the main processing parameters as shown in Table 1. Apart from HDPE, molding experiments using acrylonitrile butadiene styrene (ABS) were conducted to test the mold inserts printed using high temperature materials.

Table 1. Injection molding parameters for HDPE.

Temperature		Injection			Holding		Cooling
Melt	**Mold**	**Pressure**	**Speed**	**Time**	**Pressure**	**Time**	**Time**
165°C	19°C	800 bar	15 cm³/s	1.5 sec	342 bar	3.5 sec	35 sec

Results

Mold Inserts Temperature and Cooling Time.

Using an infrared camera, the temperature of the mold inserts as well as the parts upon mold opening can be observed as can be seen in Fig. 7 (left). The temperature of the parts and the cavity of the mold inserts was around 100˚C. Thus, after ejection of the part, further cooling of the mold inserts is required before closing them again to start a new molding cycle. In the case of Zortax mold inserts, further cooling time (open mold) of 240 s was required, which resulted in a total cycle time of 280 seconds including the injection time, the holding time, cooling time (with the mold closed) and the further cooling time with the mold open. Although the temperature of the mold inserts increased after each molding cycle, the desired mold temperature could be reached approximately at the same time as can be seen in Fig. 7 (right).

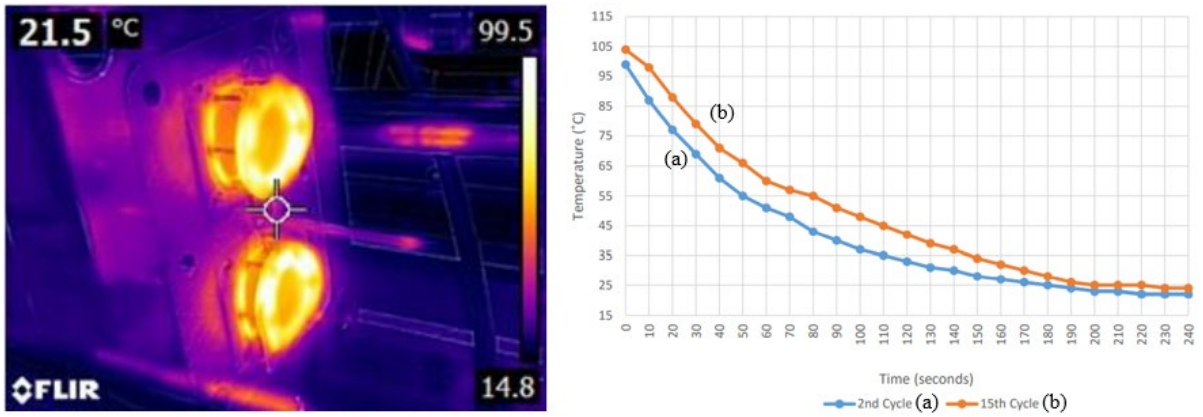

Fig. 7. IR thermal image of part (left) and parts' temperature decrease during further cooling after the mold is opened (right).

Evaluation of Molding Process and Molded Parts Quality.

Using the FFF printed mold inserts, several molding problems occurred especially during demolding e.g. puncturing of the parts by the ejector pins as the parts tended to stick onto the cavity surface of the mold inserts due to the relatively rough surface of the mold inserts as well as some flashes formed on the molded parts. This was solved by further decreasing the part temperature before demolding, the application of mold release agent, and the reduction of the ejection speed. Even though the mold inserts were printed with 100% infill, certain areas had voids, which collapsed slightly inwards during the first molding cycles. This was replicated on the molded parts. Overall, the cosmetic compacts were not of the best quality and surface finish but they are acceptable to produce prototypes with molding quality and from the desired molding material.

In contrast to the desktop FFF printed mold inserts, the quality and surface finish of the mold inserts printed with SLA Viper Si2 using Accura Extreme were excellent. However, the inserts printed horizontally showed steps on the top curved surfaces of the mold inserts which were replicated on the molded parts and also caused a formation of small and thin flashes, as shown in Fig. 8.

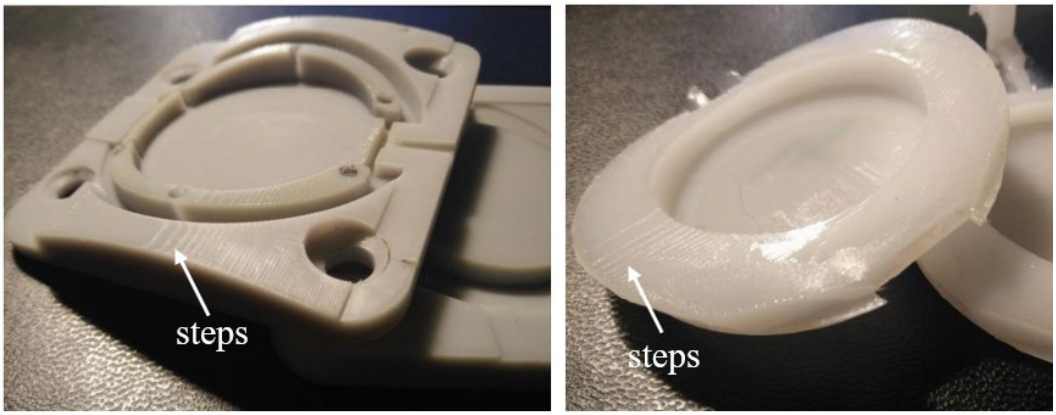

Fig. 8. Viper Si2 SLA horizontally printed inserts using Accua Extreme (left) and the molded cosmetic compact base (right).

The problems related to the above step and flash formation was eliminated by printing the mold inserts vertically. A finer surface finish of the curved sections of the mold inserts could also be achieved. This resulted in very few flashes only after the 15th molding cycle, while all front features of the molded parts were clearly replicated. A total of 27 molding cycles were carried out with a relatively good quality of the produced cosmetic compact bases, as can be seen in Fig. 9a.

Similar to FFF mold inserts, the tab gates of the SLA mold inserts lasted only a couple of molding cycles before breaking off. However, the strength and hardness of these SLA inserts were better compared to the FFF inserts. The rest of the mold features sustained the heat and pressure from the injected melt. The protruding sections of the mold inserts including the core on the injections side turned brownish in color as can be observed in Fig. 9b.

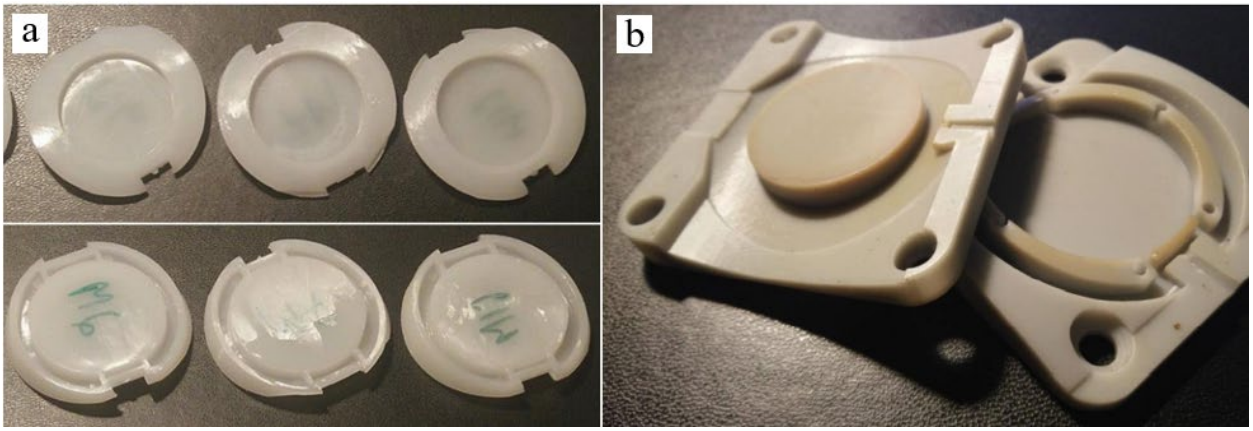

Fig. 9. Molded cosmetic compact bases (left) and used SLA mold inserts vertically printed using Viper Si2 and Accua Extreme resin (right).

The MJF mold inserts manufactured on a PolyJet 3500 printer using VisiJet M3-X material had excellent thermal properties. These inserts should be capable of withstanding temperatures up to 350˚C after annealing. Therefore, apart from molding using HDPE, ABS, which has a much higher processing temperature of around 200˚C, was also successfully used to mold a few parts at the end of the experiments using these mold inserts. No part puncturing occurred in the entire molding experiments and no flashes were formed up to the first 22 molding cycles. The parts produced show the best surface finish compared to ones molded using other mold inserts, Fig. 10.

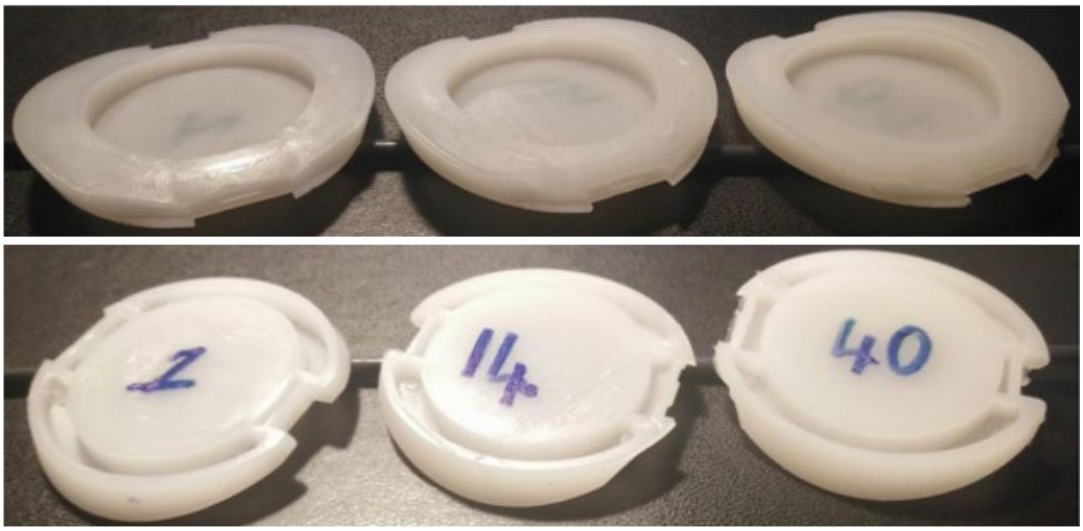

Fig. 10. Cosmetic compact bases top and bottom view molded using MJF mold inserts.

Fig. 11. MJF mold inserts with cracks after 40 molding cycles using HDPE and other 6 successful molding cycles using ABS as the molding material.

The MJF inserts performed excellently and, in contrast to other mold inserts additively manufactured using FFF and SLA 3D printers, the gate of the MJF mold inserts was not broken. The only drawback was that these inserts were discovered to be quite brittle and after a considerable amount of number of cycles, they cracked as shown in Fig. 11. These cracks initiated from weak areas such as the mounting holes. Other points of crack initiation were the ejector pin holes. These cracks kept propagating and getting bigger in size and depth, and after 40 molding cycles using HDPE and other 6 successful molding cycles using ABS. Despite the cracks, parts could be still injected but slight flashes were formed through the cracks formed.

Summary

Although there were some molding problems in the first runs when using the FFF mold inserts and the cosmetic compact bases produced were not of the best quality and surface finish, these could be substantially improved in the next runs. When using the vertically printed SLA mold inserts as well as the MJF mold inserts, the results obtained were excellent since no flashes were formed in the first few molding cycles and a good surface finish was also achieved. The MJF mold inserts had very good thermal properties so that apart from HDPE, ABS was also successfully molded which is the main material for the actual mass production of the cosmetic compact bases. The SLA inserts were considerably less thermal resistant, but a total of 27 molding cycles were easily accomplished producing 54 good cosmetic compact bases. The maximum production number of 80 cosmetic compact bases could be achieved using the MJF mold inserts. This proved that, using advanced materials available today, some of the AM technologies which are normally used for rapid prototyping, rapid manufacturing, and soft indirect rapid tooling applications, can also, easily be used, in hard direct tooling. This saves time and resources, which could give companies a competitive advantage, since development and manufacturing time are substantially reduced.

Acknowledgement

This project was carried out in a close collaboration with industrial partners and the authors wish to acknowledge their helpful support given especially by Mr. James Attard Kingswell from Toly Products Ltd. Malta as well as Mr. Maurice Campbell, Mr Joseph Borg and Mr. Matthew Spiteri from Methode Electronics Malta Ltd.

References

[1] G.N. Levy, R. Schindel, J.P. Kruth, Rapid Manufacturing and Rapid Tooling with Layer Manufacturing (LM) Technologies, State of the Art and Future Perspectives, CIRP Annals – Manuf. Technol. 52 (2003) 589-609. https://doi.org/10.1016/S0007-8506(07)60206-6

[2] S. Mellor, L. Hao, D. Zhang, Additive manufacturing: A framework for implementation, Int. J. Prod. Economics 149 (2014) 194-201. https://doi.org/10.1016/j.ijpe.2013.07.008

[3] P.D. Hilton, P.F. Jacobs, Rapid Tooling Technologies and Industrial Applications, Marcel Dekker, New York, 2000.

[4] S.O. Onuh, Y.Y. Yusuf, Rapid Prototyping Technology: Applications and Benefits for Rapid Product Development, J. Intell. Manuf. 10 (1999) 301-311. https://doi.org/10.1023/A:1008956126775

[5] R. Noorani, Rapid Prototyping: Principles and Applications: Hoboken, N.J Wiley, 2005

[6] J. Pomager. (2015, 2nd November 2015). 3D-Printed Injection Moulding: The Future of Rapid Prototyping? [Online]. Available: https://www.meddeviceonline.com/doc/3d-printed-injection-molding-the-future-of-rapid-prototyping-0001 (accessed: 30 January 2023).

[7] L. Zonder, N. Sella. (2014, 4th November 2015). Stratasys - Persision Prototyping: The Role of 3D Printed Molds in the Injection Molding Industry. [Online]. Available: http://www.stratasys.com/resources/~/media/B828788EF394436DB11BEB5209B2D22C.pdf (accessed: 30 January 2023).

[8] A. Gebhardt, Understanding Additive Manufacturing: Rapid Prototyping Rapid Tooling Rapid Manufacturing: Hanser Publishers, Munich, 2011. https://doi.org/10.3139/9783446431621.fm

[9] C.K. Chua, K.H. Hong, S.L. Ho, Rapid tooling technology. Part 1. A comparative study, Int. J. Adv. Manuf. Technol. 15 (2013) 604-608. https://doi.org/10.1007/s001700050108

[10] C.K. Chua, K.F. Leong, C.S. Lim, Rapid Prototyping Principles and Applications Third Edidtion: World Scientific Pub Co Inc, 2010. https://doi.org/10.1142/6665

[11] D.O. Kazmer, Injection Mold Design Engineering: Hanser Publishers, Munich, 2007. https://doi.org/10.3139/9783446434196.fm

[12] G. Menges, W. Michaeli, P. Mohren, How to Make Injection Molds vol. Third Edition: Hanser Publishers, Munich, 2001. https://doi.org/10.3139/9783446401808.fm

Composites forming processes

Materials Research Proceedings 28 (2023) 219-230 https://doi.org/10.21741/9781644902479-24

Modeling of 3D fluid-structure-interaction during in-situ hybridization of double-curved fiber-metal-laminates

POPPE Christian[1,3,a], KRUSE Moritz[2,b] and KÄRGER Luise[1,c *]

[1]Karlsruhe Institute of Technology (KIT), Institute for Vehicle System Technology (FAST), Institute Division Lightweight Design, Germany

[2]Institute for Production Technology and Systems, Leuphana University of Luneburg, Germany

[3] Simutence GmbH, Germany

[a]christian.poppe@partner.kit.edu, [b]moritz.kruse@leuphana.de, [c] luise.kaerger@kit.edu

Keywords: Composites, Process Simulation, Infiltration, Deep Drawing, FML, FSI, FEA

Abstract. Fiber-metal-laminates (FML) provide excellent fatigue behavior, damage-tolerant properties, and inherent corrosion resistance. A 2017-developed single-step process that combines deep-drawing with simultaneous infiltration (in-situ-hybridization) yields promising results. However, Fluid-Structure-Interaction (FSI) between the hybrid stack and the fluid pressure complicated the defect-free processing of double-curved parts. In this work, a Finite Element (FE) simulation approach for modeling the in-situ hybridization of FMLs is expanded to incorporate a both-sided (strong) FSI, aiming to facilitate apriori virtual support for process- and part development. Using Terzaghi's effective stress formulation, the proposed framework can predict metal sheet buckling and resin accumulation resulting from local fluid pressure during infiltration of the textile interlayers on part level. Different conditions are simulated, outlining the high relevance of considering strong FSI during process simulation. The part-level results are compared with experimental findings. Modeling challenges are discussed, along with suggested future enhancements of the simulation approach.

Introduction

The aerospace industry has driven the processing and application of Fiber Metal Laminate (FML) in recent decades [1,2]. Combining the best features of metals and composite materials, FML provides excellent fatigue behavior, damage-tolerant properties, inherent corrosion resistance, and good fire resistance [3,4]. Product examples are GLARE (Glass-Fiber Reinforced Aluminum Laminates) or ARALL (Aramid-Reinforced Aluminum Laminates). Beyond flat structures, defect-free manufacturing of three-dimensional curved FMLs with a high degree of automation still proves difficult and is extensively investigated in the literature [1,5, 6]. Despite experimental trials, several numerical models with varying focus and scale have been proposed and validated, enabling a prediction of potential wrinkling, fracture, or strains with metal sheets or fibers [6–10]. A strong FSI during in-situ hybridization has not been modeled so far. The classical manufacturing process using an autoclave is time-consuming, expensive, and the achievable geometric complexity of the components is very low [11]. In this regard, Mennecart et al. [12] suggested and developed, among others [13,14], an alternative manufacturing process by combining deep drawing with thermoplastic resin transfer molding, called hybrid liquid composite molding (HyLCM).

A schematic illustration of the principal process steps is given in Fig. 1. The stack is positioned between a matching punch and a die. The stack is clamped during the whole process using circumferential blank holders. In the first step, the hybrid stack is only slightly deformed, temporarily sealing the outer rim. Subsequently, reactive resin is centrally injected through a hole in the lower metal layer while deep drawing proceeds. The fluid pressure can bend the metal top

Content from this work may be used under the terms of the Creative Commons Attribution 3.0 license. Any further distribution of this work must maintain attribution to the author(s) and the title of the work, journal citation and DOI. Published under license by Materials Research Forum LLC.

layer during injection, as illustrated in Fig. 1. During the last 20% of the tool stroke, the resin is forced outward and infiltrates the core GF layers. The heated molds enforce isothermal curing.

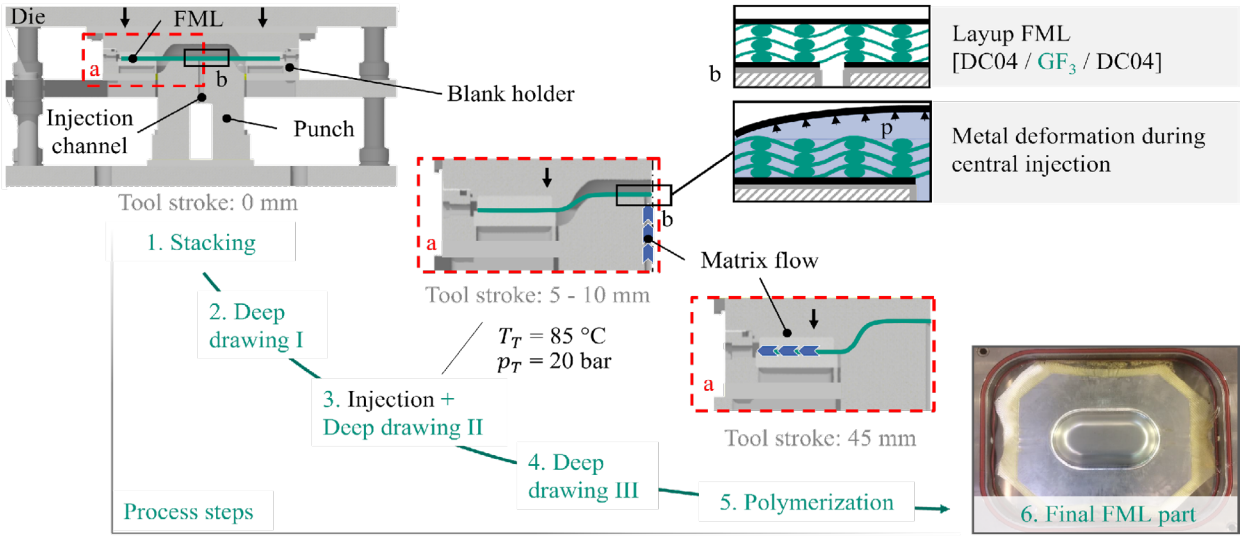

*Fig. SEQ Figure * ARABIC 1. Visualization of the combined deep-drawing and LCM process (HY-LCM) from Stacking (1.) to intermediate injection (3.) and final polymerization*

Objective

In a previous work [10], the authors presented a macroscopic process simulation model for the outlined process, which allows modeling the deep drawing of the FML stack, including transverse compression of the textile core layers and the simultaneously arising fluid progression. The deep-drawing model was verified with close-to-process trials. However, the presented model only incorporated a weak Fluid-Structure-Interaction (FSI). Local deformation was considered during fluid progression, but fluid pressure-related deformation was neglected.

As experiments and available literature show that an accurate prediction of potential defects requires modeling a strong FSI, this paper aims to implement and investigate a both-sided coupling between FML material deformation and fluid progression.

Exemplary Processing Results

Process trials are conducted at Leuphana University Lüneburg (Germany) with different parameter settings combining two DC04 metal sheets (1 mm) with six core layers made from a glass twill fabric (280 g/m^2, INTERGLAS 92125 FK800) [15]. A thermoplastic matrix (Arkema Elium® 150), with an initial viscosity of 100 mPas, mixed with 2.5 % hardener, is injected.

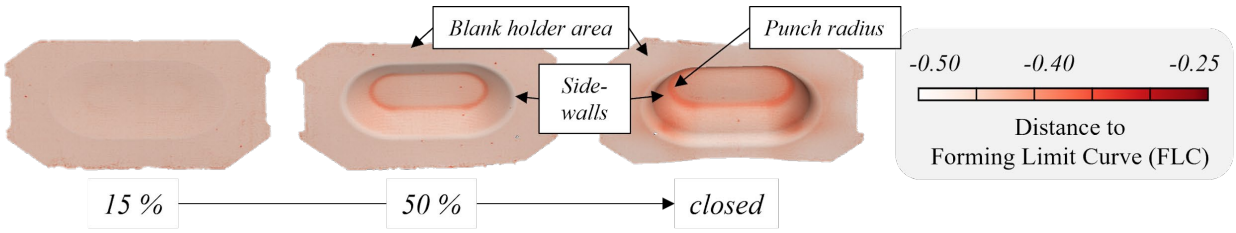

Fig. 2. Shaping and distance to the Forming Limit Curve, data obtained with GOM ARGUS measurements.

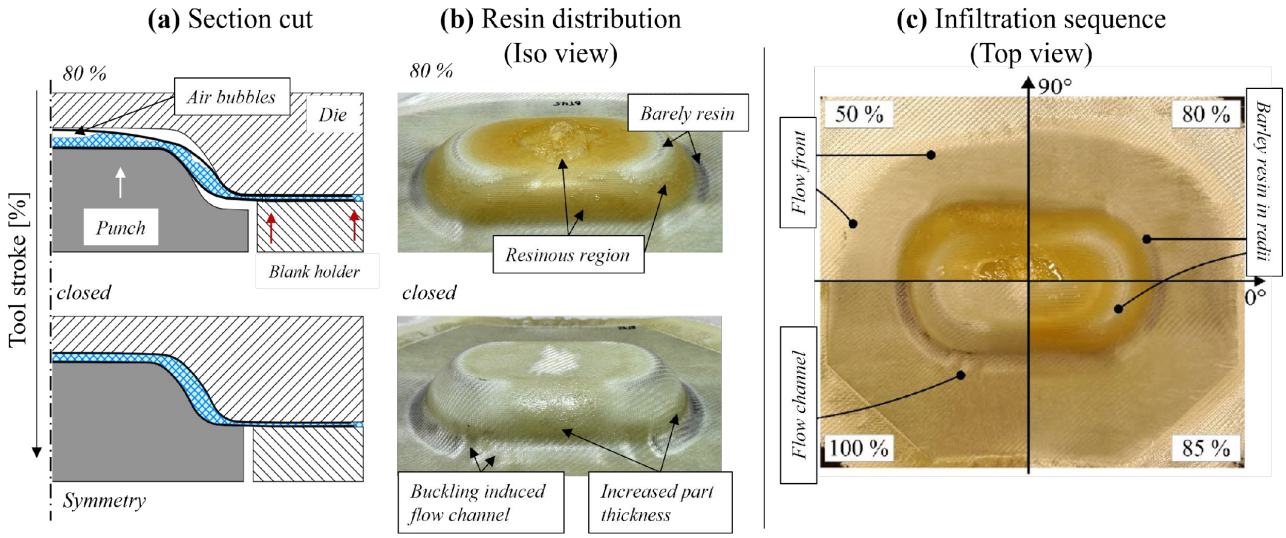

Fig. 3. Visualization of the FSI during FML processing; (a) Schematic section cut; (b) Photos illustrating the resin distribution; (c) Infiltration sequence and observed effects.

Fig. 2 summarizes a shaping of a part during the tool stroke and the distance to the Forming Limit Curve (FLC). The distance to the FLC indicates forming margin before failure. During dry forming trials, the FML stack is deep-drawn without buckling, as no additional fluid pressure is present, and other parameters are adjusted suitably. This changes when injecting the reactive resin. Driven by the fluid pressure between the metal sheets, bending of the metal sheet is observed close to the injection port and later towards the side walls of the geometry.

These observations are schematically illustrated in more detail in Fig. 3 (a,b). The resin first accumulates between the metal sheets, especially near the inlet and the side walls. The blank holder seals this region and prevents fluid-induced deformation in the flange area. Fig. 3 (b,c) shows that the fluid is forced through the flange during subsequent tool closure. Fluid is pushed out of the bottom area and other regions where high compressive stress is induced by the deep drawing of the metal, such as the punch radius or the side walls. These exemplary results illustrate the high relevance of strong FSI modeling for reliable virtual product- and process design for in-situ hybridized FMLs.

Process Simulation Model

This work's applied process simulation model originates from WCM modeling [16, 17], which has been expanded and verified to account for hybrid FML forming and weak FSI [10]. A schematical overview of the macroscopic FE-based simulation framework is given in Fig. 4.

Two fully-coupled submodels provide the core part of the model to describe the intra-ply behavior of the textiles (a). The FE-based draping submodel captures the macroscopic deformation mechanism, such as membrane, bending, or compaction behavior. A superimposed FE/CV-based fluid submodel describes the fluid progression and pressure field using Darcy's law for porous media flow. This approach implies that the fluid is modeled homogenized and purely liquid regions cannot be modeled discretely. Both submodels are formulated three-dimensionally, enabling a local prediction of fiber orientation, FVC, and modeling of squeeze flow as well as infiltration in the thickness direction. Despite that, the framework comprises a material model for the metal sheets, see Fig. 4b, and an interface model which describes the dry and infiltrated contact behavior during processing (cf. Fig. 4c).

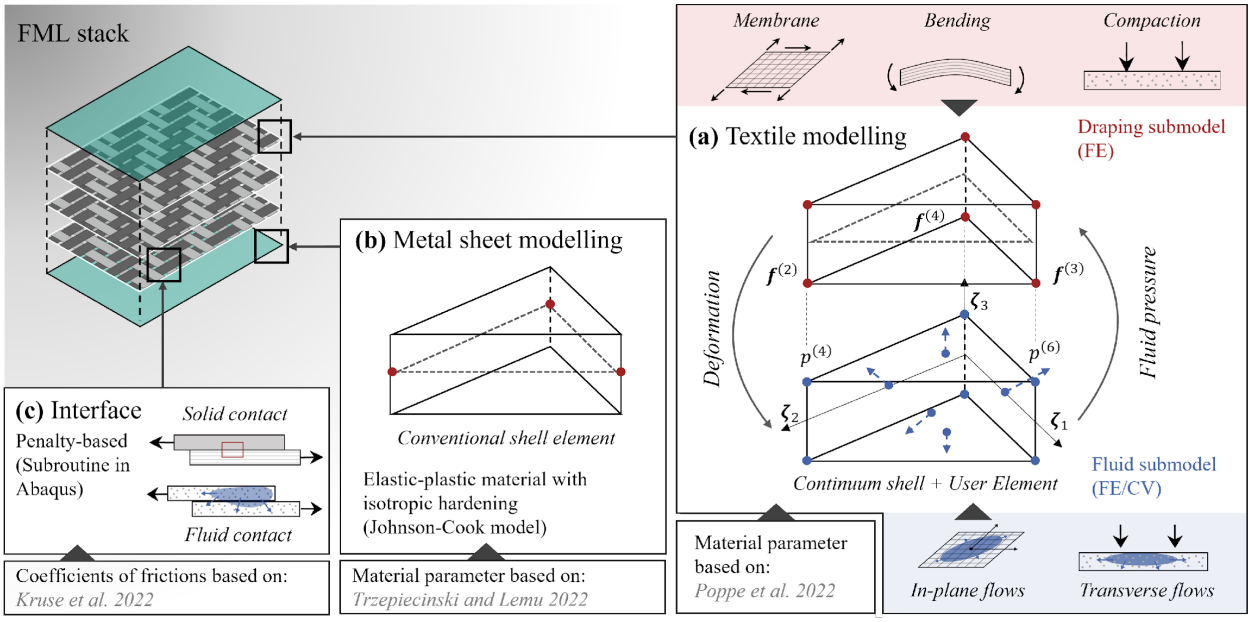

Fig. 4. Process simulation modelling framework in ABAQUS, clustered according to interface, metal sheet and textile modelling.

Draping submodel.

The relevant deformation modes of the glass fiber textile are in-plane shearing (membrane), out-of-plane bending, and compaction. They are implemented through a superimposed reduced-integrated continuum shell (SC6R) and a hyper-elastic material formulation (St. Venant-Kirchhoff material) in a thickness direction within a user element, see Fig. 4a. This approach neglects the required decoupling between the membrane and bending behavior [16]. In the case of the FML modeling, an overestimated bending stiffness can be accepted as the bending stiffness of the stack is dominated by the metal sheets. For a description of transverse compaction modeling, including identified material parameters, the reader is referred to our last year's contribution [10].

The hypervisco-elastic in-plane *membrane model* [18] has not been explicitly characterized for the here applied glass fiber textile. Yet, its prediction on the here-applied geometry has been compared to a membrane model designed for the used material [19]. A pre-study showed comparable fiber orientation, which is reasonable as the geometry is relatively simple and does not induce defects or shear looking. The former model was chosen as it proved more robust in combination with active strong FSI.

A transverse shear stiffness of $\kappa_{GF,11}, \kappa_{GF,22} = 1.0$ N/mm² is used to adapt the *out-of-plane bending* stiffness within the continuum shell. Based on these parameters and the underlining

Materials Research Proceedings 28 (2023) 219-230 https://doi.org/10.21741/9781644902479-24

membrane model, the model overestimates the textile's bending stiffness by approximately 100. However, compared to the bending stiffness supplied by the metal sheets, the bending stiffness of the textile is negligible.

Fluid submodel.

Darcy's law, in combination with mass conservation, is applied in a transient explicit formulation and is embedded in the superimposed user element (cf. Fig. 4a) to solve the pressure field and model flow front progression [17]

$$\int_{V_k} \rho C_{hyd}\, \dot{p}\; dv = \frac{\boldsymbol{K}(\phi)}{\eta \cdot \varphi} \int_{V_k} \mathrm{div}(\mathrm{grad}(p) - \rho g)\, dv \tag{1}$$

Using Eq. 1, a transient single-phase flow based on an explicit time integration scheme can be modeled. Here, $K(\phi)$ is the permeability tensor as a function of the current FVC ϕ. The viscosity is given by η, and $\varphi = 1 - \phi$ is the porosity.

The in-plane permeability values are given by

$$K_{11}(\phi) = 0.009 \cdot e^{-11.3 \cdot \phi}, K_{22}(\phi) = 0.004 \cdot e^{-11.8 \cdot \phi}, K_{33}(\phi) = 0.01 \frac{K_1(\phi) + K_2(\phi)}{2}, \tag{2}$$

and the permeability in the thickness direction, which has not been measured for the material yet, is estimated using a downscaling factor of 100 based on the results of a comparable material [20]. This estimation in the thickness direction is not a critical assumption as the fluid is contained between the sheets, and pressure-relevant flows are in-plane.

Based on the pressure field within the saturated domain, fluid progression is implemented using the flows across every element surface at the flow front in combination with element-based saturation values. The saturation values are updated in every increment, and saturated elements are added to the transient domain governed by Eq. 1.

Strong FSI.

To this point, a one-sided (weak) FSI is presented in the model as the deformation drives the pressure field and fluid progression in the textile. Terzaghi's effective stress, according to MacMinn et al. [21], is implemented to consider the fluid pressure and drag forces acting on the porous medium. As Eq. 3 shows, this yields two new nodal force terms that add up with the material reaction forces.

$$\hat{\boldsymbol{f}}_{\mathrm{R}}^{\mathrm{Node}} = \hat{\boldsymbol{f}}_{\mathrm{R}}^{\mathrm{Mat}} + \hat{\boldsymbol{f}}_{\mathrm{R}}^{\mathrm{p}} + \hat{\boldsymbol{f}}_{\mathrm{R}}^{\mathrm{d}} \quad \text{with } \hat{\boldsymbol{f}}_{\mathrm{R}}^{\mathrm{p}} = -\det(\boldsymbol{J})\, p \boldsymbol{I} \quad \text{and} \quad \hat{\boldsymbol{f}}_{\mathrm{R}}^{\mathrm{d}} = \det(\boldsymbol{J})\, \varphi \boldsymbol{N}\, \mathrm{grad}(p) \tag{3}$$

The first one represents the reaction forces $\hat{\boldsymbol{f}}_{\mathrm{R}}^{\mathrm{p}}$ caused by the fluid pressure within the skeleton structure of the deformable porous medium, and the second one representing the fluid drag $\hat{\boldsymbol{f}}_{\mathrm{R}}^{\mathrm{d}}$ between flow and fabric. In Eq. 3, $\boldsymbol{I}$ is the second-order unit tensor, and $\boldsymbol{N}$ represents the element shape function. Using the permeability values in Eq. 2, the method can be applied to the glass woven fabric without further adjustments. This formulation has been validated in [22].

Metal sheet.

The model comprises an elastic-plastic material model with isotropic hardening based on the built-in Johnson-Cook model for the metal sheets using conventional shell elements with a constant thickness (cf. Fig. 4) parameterized by Trzepiecinski and Lemu [23] for the same material. A comparison between experiments and the simulation on a single metal sheet yields a good agreement of the obtained reaction forces and deformations [10].

Interface. Contact behavior between ply and tool interfaces is modeled using penalty-based contact algorithms in ABAQUS/explicit, cf. Fig. 4. In the case of dry friction (solid contact), coulomb friction is modeled using coefficients of friction (CoF) that have been identified by Kruse et al. [24] ($\mu_{Tool,Metal}$ = 0.2, $\mu_{Tool,Textile}$= 0.253, $\mu_{Textile,Textile}$= = 0.334). Due to the metal sheet, high contact stresses of 2000 N/mm^2 are necessary to prevent excessive contact penetration. A damping of 1 N/s mm is used to reduce contact oscillations. In case of an infiltrated contact, hydrodynamic friction is used in combination with maximal tangential contact stress of $\tau_{t,max} = 1 \cdot 10^{-4}$ N/mm². Arising contact slips of several millimeters prevented the proper usage of cohesive zones during draping.

Small-Scale Application

Before part-level application, the outlined simulation approach is applied to a small slice of the final geometry to investigate the impact of infiltration during a processing sequence, see Fig. 5 (a,b). Similar to the physical process (cf. Fig. 1), an initial dry deep drawing phase is followed by a central injection phase within further punch movement, see Fig. 5c. Afterward, the partly pre-infiltrated stack is draped into the final shape without additional injection.

The tools are modeled as rigid surfaces, and displacement boundary conditions drive the blank holder and the punch. The stack is modeled as outlined above. The three textile core layers are homogenized into a single instance with an initial thickness of 1.2 mm. A constant pressure of 5 bar is applied to the inlet nodes between 0.5 and 4 seconds. Each metal sheet has an initial thickness of 0.5 mm. The tool geometry is derived from a deep-drawing configuration, resulting in a non-constant cavity in the closed state. A velocity of 100 mPas is assumed.

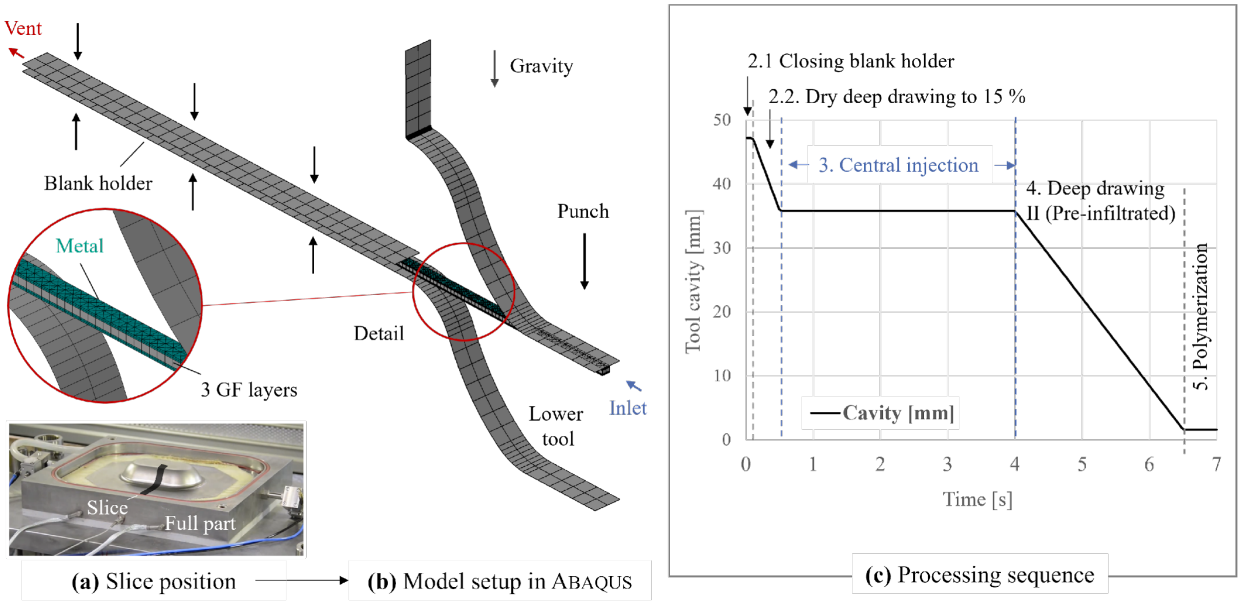

Fig. 5. Small scale demonstrator: (a) Slice position; (b) Setup and (c) Processing sequence.

To assess the impact of fluid progression along with strong FSI during processing, Fig. 6a comprises results for a dry deep-drawing reference. It shows that during a solely dry forming, the fabric layers are squeezed between the metal sheets, leading to significant compaction in the thickness direction below the blank holder and on the radii (cf. Fig. 6a). As deep-drawing of the metal sheets induces substantial in-plane strains, the textile layers are also compressed in the not

directly contacted side-wall region, recall Fig. 2. Consequently, the cavity is not entirely occupied by the FML laminate after the tool has closed completely.

Considering the injection and resulting FSI between fluid pressure and FML stack, see Fig. 6b, allows for predicting the above-made experimental observations. Injection leads to a severe increase in stack thickness towards the inlet. During the pre-infiltrated deep-drawing face (4.), the resin is forced through the side wall regions and eventually the blank holder. The fluid pressure prevents comparable high FVCs during processing and enforces a more homogeneous distribution. In this regard, the average FVC for the dry setup is predicted at 51.3 %, compared to only 40 % in the case of strong FSI consideration.

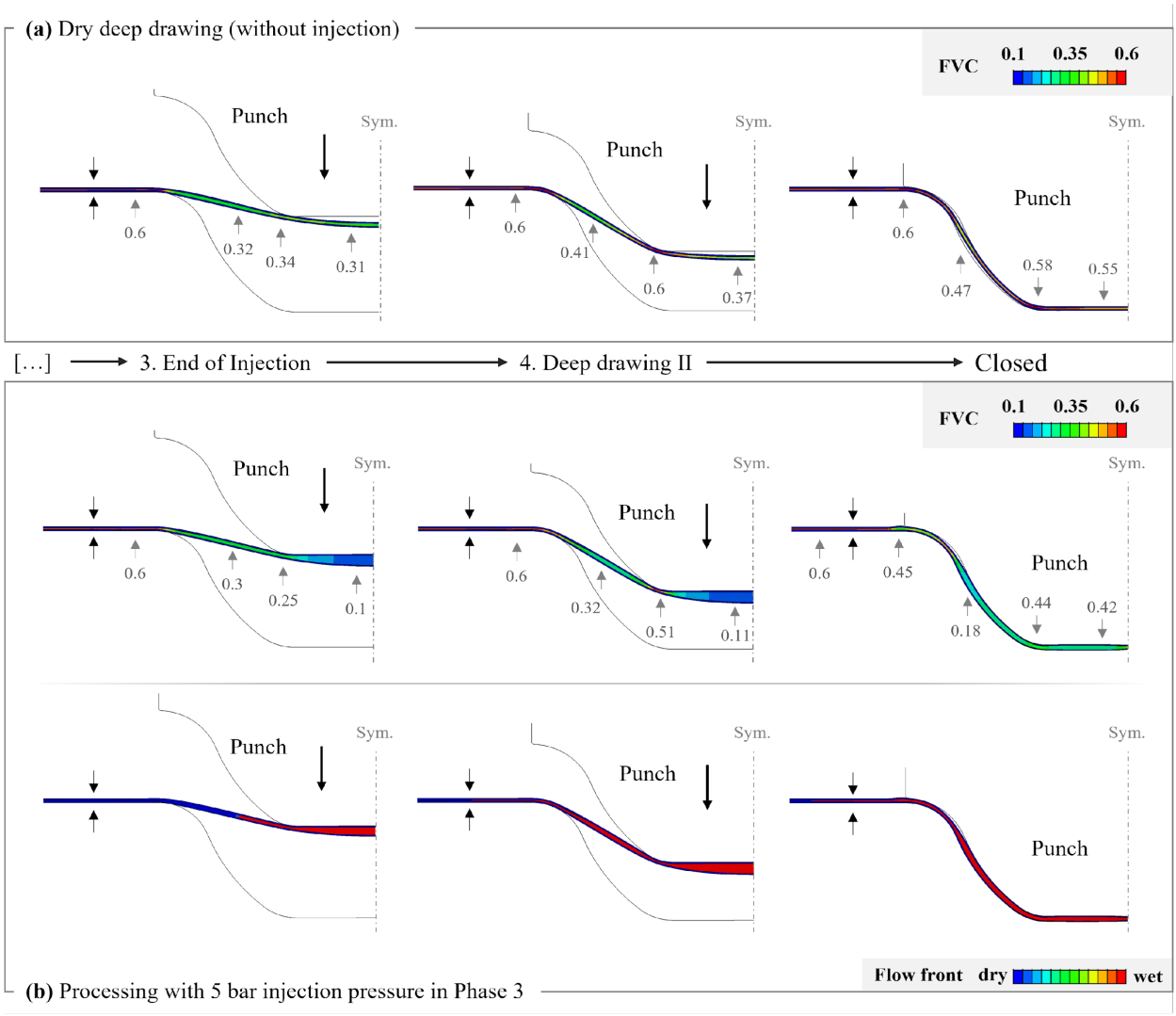

Fig. 6. Small demonstrator results: (a) Dry conditions; (b) Conditions according to Fig. 5 (c).

Part-scale Application

Finally, the outlined model is deployed on part level using the same geometry as for the physical process illustrated in Fig. 1. The modeling setup, comprising the FML stack, punch, lower tool, and blank holder, is shown in Fig. 7. Model settings are identical to the small-scale simulation trials, yet the simulation starts with a pre-saturated area, not matching the exact processing sequence, see Fig. 7b.

This adaption was necessary to reduce the required computational effort. The nonlinearity of implemented, interacting physical effects and the substantial stiffness differences between the fabric layers and the metal sheet requires a relatively small stable time increment during time integration in ABAQUS/explicit. A fluid amount of 100 ml is prescribed for the model (100 mPas). The outlined setup is simulated with both configurations to assess the impact of a one-sided (weak) and a both-sided (strong) FSI. The comparison of predicted punch reaction forces in Fig. 7 shows that significant differences only arise within the last 30% of the tool stroke when the available space of the metal sheets to evade the fluid pressure reduces to the cavity.

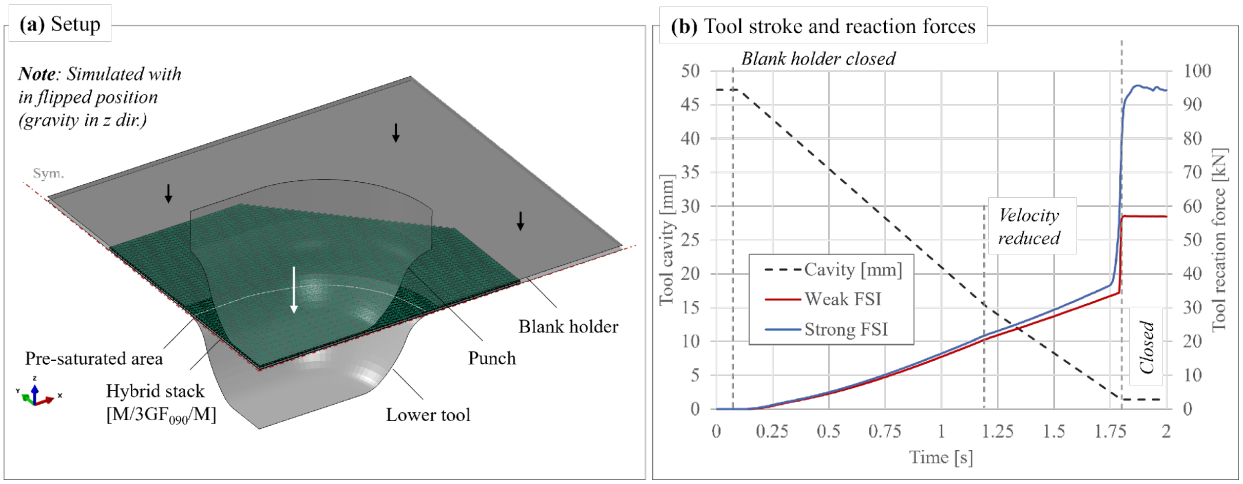

Fig. 7. Process simulation on part level; (a) Setup and (b) Tool stroke and obtained reaction forces during partly pre-infiltrated conditions using weak or strong FSI settings.

In contrast, significant differences arise early during processing when comparing the spatial distribution of the flow front, see Fig. 8, and the resulting FVC (cf. Fig. 9). Due to the local increase in the part thickness, less fluid is pushed toward the circumferential blank holder region. As a result, the flow front progression is overpredicted by the weak FSI approach.

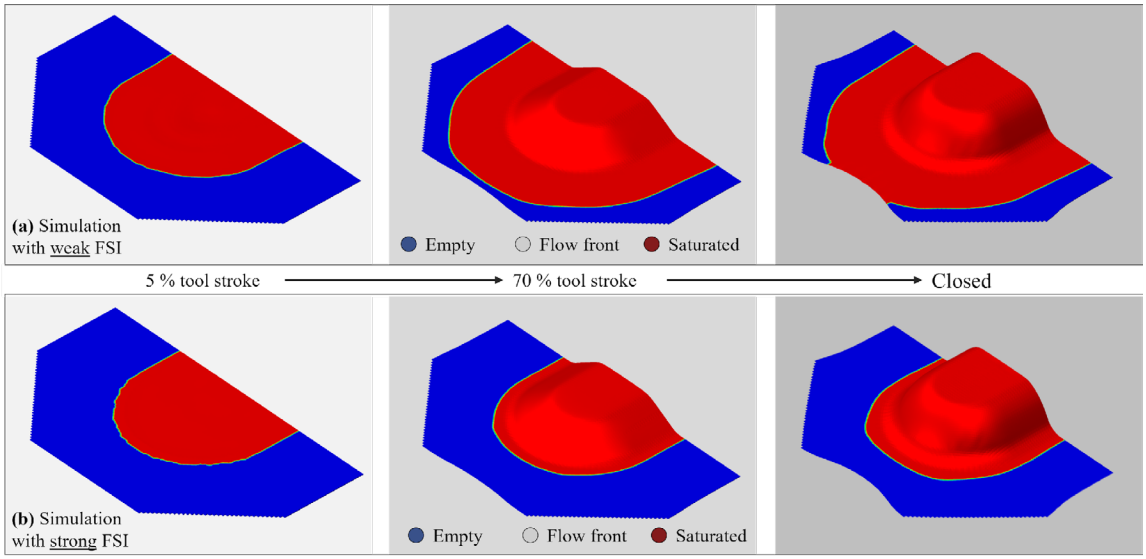

Fig. 8. Impact of FSI on flow front progression: (a) One-sided (weak) FSI, fluid pressure is not considered; (b) Both-sided (strong) FSI, fluid pressure leads to material deformation.

Fig. 9 summarizes the resulting FVC distribution and thickness for different regions of the geometry during 25, 70, and 100 % of the tool stroke. Regarding FSI consideration, comparable interactions to the small-scale demonstrator are present. As before, the compaction of the fabric results in increased part thickness in regions not directly contacted by the tool surfaces. This applies to both configurations.

Moreover, strong FSI increases the local stack thickness significantly as the fluid pressure beads the metal layers surrounding the fabric stack. Consequently, severe differences are predicted already at 25 % during processing. These differences reduce towards the end of the tool stroke as the FML stack is squeezed into the cavity, yet the average FVC for the weak FSI configuration is still 4% higher (55.8 % weak, 51.8 % strong).

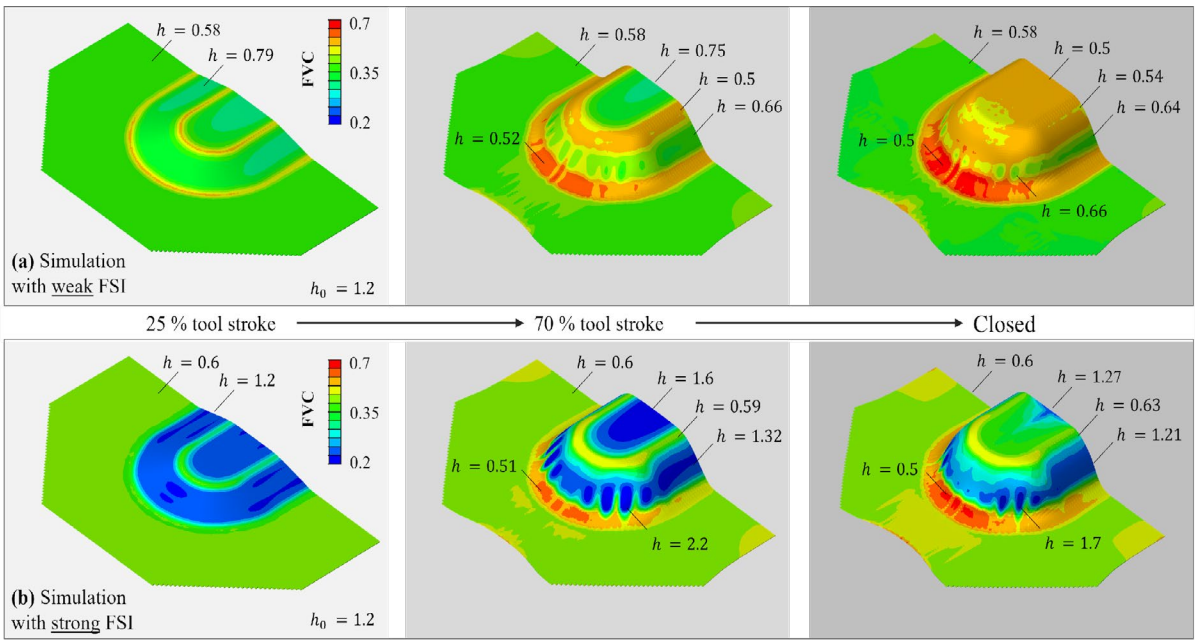

Fig. 9. Impact of FSI on FVC and part thickness (h) during partly pre-infiltrated forming.

Comparison with experiments.

Comparing the strong FSI results outlined in Fig. 8b and Fig. 9b with the above-introduced experimental observations, see Fig. 3, it becomes apparent that several effects can be predicted correctly. Although the single-phase-based modeling approach cannot predict pure resin areas, it can give a good prediction of where fluid accumulates during forming and in the final state. Moreover, fully-coupled interaction modeling between fluid, fabric, and metal sheets allows for predicting the onset of buckling of the metal sheets in the corners of the dome geometry. This buckling leads to flow channels similar to experimental observations, reducing the area's local FVC.

Summary

A fully-coupled macroscopic process simulation model for modeling producing in-situ hybridized, double-curved FML is presented. Experimental observations in the literature and on the here investigated FML process indicate a strong interaction between fluid pressure and forming of the FML stack. Reported defects such as buckling of the metal sheets, dry spots, or resin accumulations in corners could not be comprehensively numerically predicted so far, which hinders process- and part development.

Using an FE-based simulation approach combined with a control volume-based fluid progression model, the arising FSI can be considered directly via additional nodal reaction forces at the element nodes. Simulation trials on a slice of the actual geometry comparing a solely dry configuration with one that matches the processing sequence, including central injection, underline the importance of considering strong FSI in process simulation. Simulations on the part level confirm these observations and show that the simulation approach can predict the experimentally identified effects, such as resin accumulation and metal sheet buckling.

Outlook

For now, a relatively small time increment of 1E-07 is necessary to stabilize the simulation, resulting in substantial computation times on the part level. An improved interface modeling technique and stable time increment algorithm are assumed to improve the model's performance. Beyond that, a two-phase flow model would allow for predicting air entrapments and resin-rich regions. However, a two-phase model presumably requires a non-monlytic approach by coupling a proper-fluid solver with the proposed draping submodel. Heat transfer and resin kinetics should also be implemented into the proposed framework to increase prediction accuracy and support process parameter identification.

Acknowledgments

The authors would like to thank the German Research Foundation (DFG) for funding the projects BE 5196/4-1 and BE 5196/4-2. Moreover, the authors would like to thank the German Federal Ministry of Education and Research (BMBF) for the funding of the project" HyWet" (03INT614AC) as part of the Transatlantic Cluster for Lightweighting (TraCLight), for which some presented numerical methods were developed. This work is also part of the Young Investigator Group (YIG)" Tailored Composite Materials for Lightweight Vehicles", gratefully funded by the Vector Stiftung.

References

[1] Z. Ding, H. Wang, J. Luo, N. Li, A review on forming technologies of fibre metal laminates, Int. J. Lightweight Mater. Manuf. 4 (2021) 110-126. https://doi.org/10.1016/j.ijlmm.2020.06.006
[2] S. Krishnakumar, Fiber Metal Laminates – The Synthesis of Metals and Composites, Mater. Manuf. Process. 9 (1994) 295-354. https://doi.org/10.1080/10426919408934905
[3] A. Asundi, A.Y. Choi, Fiber metal laminates: an advanced material for future aircraft, J. Mater. Process. Technol. 63 (1997) 384-394. https://doi.org/10.1016/S0924-0136(96)02652-0

[4] M.R. Sadeghi, A.A.A. Jeddi, S. Shaikhzadeh Najar, Theoretical and ezperimental analysis of bending rigidity of plain and twill woven fabrics, J. Text. Inst. 108 (2017) 1700. http://doi.org/10.1080/00405000.2017.1280760
[5] T. Sinmazçelik, E. Avcu, M.Ö. Bora, O. Çoban, A review: Fibre metal laminates, background, bonding types and applied test methods, Mater. Design 32 (2011) 3671-3685. https://doi.org/10.1016/j.matdes.2011.03.011
[6] M. Smolnicki, G. Lesiuk, S. Duda, A.M.P. de Jesus, A Review on Finite-Element Simulation of Fibre Metal Laminates, Arch. Computat. Methods Eng. 1 (2022). https://doi.org/10.1007/s11831-022-09814-8
[7] H. Blala, L. Lang, S. Khan, S. Alexandrov, Experimental and numerical investigation of fiber metal laminate forming behavior using a variable blank holder force Prod. Eng. Res. Devel. 14 (2020) 509. https://doi.org/10.1007/s11740-020-00974-9
[8] H. Blala, L. Lang, L. Li, S. Alexandrov, Deep drawing of fiber metal laminates using an innovative material design and manufacturing process, Compos. Communic. 23 (2021) 100590. https://doi.org/10.1016/j.coco.2020.100590
[9] L. Li, L. Lang, B. Hamza, Q. Zhang, Effect of hydroforming process on the formability of fiber metal laminates using semi-cured preparation, Int. J. Adv. Manuf. Technol. 107 (2020) 3909–3920. https://doi.org/10.1007/s00170-020-05281-2
[10] C.T. Poppe, H.O. Werner, M. Kruse, H. Chen, N. Ben Khalifa, F. Henning, L. Kärger, Towards 3D Process Simulation for In Situ Hybridization of Fiber-Metal-Laminates (FML), Key Eng. Mat.926 (2022) 1399-1412. https://doi.org/10.4028/p-cr2tco
[11] J. Sinke, Manufacturing of GLARE Parts and Structures, Appl. Compos. Mater. 10 (2003) 293–305. https://doi.org/10.1023/A:1025589230710
[12] T. Mennecart, S. Gies, N. Ben Khalifa, A.E. Tekkaya, Analysis of the Influence of Fibers on the Formability of Metal Blanks in Manufacturing Processes for Fiber Metal Laminates, J. Manuf. Mater. Process. 3 (2019) 2. https://doi.org/10.3390/jmmp3010002
[13] B.-A. Behrens, S. Hübner, N. Grbic, M. Micke-Camuz, T. Wehrhane, A. Neumann, Forming and Joining of Carbon-Fiber-Reinforced Thermoplastics and Sheet Metal in One Step, Procedia Eng. 183 (2017) 227-232.
[14] Y. Lu, Y. Li, Y. Zhang, L. Dong, Manufacture of Al/CF/PEEK curved beams by hot stamping forming process, Mater. Manuf. Process. 1 (2022) 1597-1609. https://doi.org/10.1080/10426914.2022.2032140
[15] M. Gerdes, Experimental mold filling analysis and investigation of the forming behavior during deep drawing of fiber-metal laminates in the in-situ hybridization process, Master Thesis, Lueneburg, 2022.
[16] P. Boisse, R. Akkerman, P. Carlone, L. Kärger, S.V. Lomov, J.A. Sherwood, Advances in composite forming through 25 years of ESAFORM, Int. J. Mater. Form. 15(3) (2022). https://doi.org/10.1007/s12289-022-01682-8
[17] C.T. Poppe, C. Krauß, F. Albrecht, L. Kärger, A 3D process simulation model for wet compression moulding, Compos. Part A: Appl. Sci. Manuf. 145 (2021) 106379. https://doi.org/10.1016/j.compositesa.2021.106379
[18] C.T. Poppe, D. Dörr, F. Henning, L. Kärger, Experimental and numerical investigation of the shear behaviour of infiltrated woven fabrics Compos. Part A: Appl. Sci. Manuf. 114 (2018) 327-337. https://doi.org/10.1016/j.compositesa.2018.08.018
[19] F. Schäfer, H.O. Werner, F. Henning, L. Kärger, Compos. Part A: Appl. Sci. Manuf. 165 (2022) 107323. https://doi.org/10.1016/j.compositesa.2022.107323
[20] C.T. Poppe, Process simulation of wet compression moulding for continuous fibre-reinforced polymers, KIT Scientific Publishing, Karlsruhe, 2022.

[21] C.W. MacMinn, E.R. Dufresne, J.S. Wettlaufer, Large deformations of a soft porous material, Phys. Rev. Appl. 5 (2016) 044020. https://doi.org/10.1103/PhysRevApplied.5.044020
[22] C.T. Poppe, F. Albrecht, C. Krauß, L. Kärger, Towards numerical prediction of flow-induced fiber displacements during wet compression molding (WCM), Paper presented at ESAFORM 2021. 24th International Conference on Material Forming, Liège, Belgique, 2021. https://doi: 10.25518/esaform21.1938
[23] T. Trzepiecinski, H. Lemu, Effect of Computational Parameters on Springback Prediction by Numerical Simulation, Metals 7 (2017) 380. https://doi.org/10.3390/met7090380
[24] M. Kruse, H.O. Werner, H. Chen, T. Mennecart, W.V. Liebig, K.A. Weidenmann, N. Ben Khalifa, Investigation of the friction behavior between dry/infiltrated glass fiber fabric and metal sheet during deep drawing of fiber metal laminates, Prod. Eng. Res. Devel. 17 (2022) 37-46. https://doi.org/10.1007/s11740-022-01141-y

Materials Research Proceedings 28 (2023) 231-238 https://doi.org/10.21741/9781644902479-25

Modelling the forming of tailored fibre placement preforms: A tetrahedral part with final orthotropic orientations

SIMON Jessy[1,2,a *], HAMILA Nahiene[1,b], BINÉTRUY Christophe[2,c] and COMAS-CARDONA Sébastien[2,d]

[1]IRDL, UMR CNRS 6027, ENI Brest, F-29200, Brest, France

[2]Nantes Université, Ecole Centrale Nantes, CNRS, GeM, UMR 6183, Nantes, F-44000, France

[a]jessy.simon@enib.fr, [b]nahiene.hamila@enib.fr, [c]Christophe.Binetruy@ec-nantes.fr, [d]sebastien.comas@ec-nantes.fr

Keywords: Tailored Fibre Placement, Forming, Finite Element, Orthotropic Design

Abstract. Forming of conventional reinforcements to manufacture 3D fibre-reinforced composite parts with complex geometries is limited by the architecture of the reinforcement made of initially straight fibres. On the opposite preforms obtained by Tailored Fibre Placement (TFP) are made of curvilinear fibre tows maintained on a backing material through stitching. In theory, the degree of freedom offered by TFP allows to form doubly-curved parts from preforms whose designs are determined from the desired final fibre orientations. In practice, it requires numerical tools to determine the design of the flat TFP preforms from the desired 3D parts, known as flattening. However, flattening is a virtual process which cannot be validated directly. Besides, the behavior of TFP preforms during forming has never been studied. Consequently, developing a numerical model to predict the formability of TFP preforms was considered as of first importance. Moreover, numerical forming can be required in a flattening algorithm [1]. Based on the Finite Element Method, a TFP preform is modelled at the fibre tows scale using 2-node beam elements. The stitching yarn, which ensures the cohesion of the layers, is modelled implicitly using an embedded element approach. The backing material is removed. A full-scale simulation of forming is experimentally validated. A tetrahedral shape, which corresponds to a corner bracket, is used to demonstrate the potential of TFP preform forming. An orthotropic design of the final part is achieved without defects using a simple forming device, which represents important progress in the field [2].

Introduction

Forming of conventional reinforcements to manufacture 3D fibre-reinforced composite parts with complex geometries is inherently limited by the architecture of the reinforcement made of initially straight fibres. As opposed to regular fabrics, fibrous reinforcements made by Tailored Fibre Placement (TFP) are made of curvilinear fibre tows maintained on a backing material through stitching. In theory, the degree of freedom offered by TFP allows to form doubly-curved parts from preforms whose designs are determined from the desired final fibre orientations. The flattening step which consists in determining the flat pattern from the desired final part is virtual and can only be computed numerically for complex parts. However, developing such a numerical tool would require prior knowledge of the behavior of a TFP preform during forming (or unforming). Therefore, it is of primary importance to investigate the forming behavior of TFP preforms before focusing on the flattening step. Moreover, Sun et al. [1] shows the option to use a forming numerical tool as a step of the flattening operation to determine the reverse trajectory to be imposed to the final configuration in case of double diaphragm forming. This is why this work focused on developing a numerical tool to model the behavior of TFP preforms during forming.

Content from this work may be used under the terms of the Creative Commons Attribution 3.0 license. Any further distribution of this work must maintain attribution to the author(s) and the title of the work, journal citation and DOI. Published under license by Materials Research Forum LLC.

Previous work on TFP investigated the advantages of aligning fibres with the principal stress directions in 2D parts [3-5]. For instance, the stress concentration in notched plate can be removed by using curvilinear path circumventing geometric discontinuities [6-9]. The work by Uhlig et al. [10] compared the strength of TFP and Non-Crimp Fabrics (NCF) open-hole laminates using cyclic and tensile tests and showed similar performances. Examples of work focusing on the manufacturing of 3D shapes using TFP is quite limited. Takezawa et al. [11] manufactured a car hood from two distinct layers with optimal orientations based on Gaussian curvatures considerations. Rihaczek et al. [12] determined optimized flat pattern to form a stool by bending. This work follows a double objective. The first one is to demonstrate the ability of manufacturing 3D orthotropic parts from specifically designed flat TFP preforms which cannot be achieved by forming conventional textiles and will therefore represent a major improvement in the field of fibrous reinforcement forming. The second one is to propose a first efficient model to simulate the forming of TFP preforms. Validation of the proposed modelling strategy is addressed by experimental and numerical forming on a tetrahedral shape. This shape has a highly double curvature and corresponds to a corner bracket widely used to design composite structures. The forming of conventional reinforcements on this shape has been largely studied [13,14] and showed the complexity of manufacturing such a shape without defect.

This paper is organized as follow. The second section describes the experimental work on TFP preform forming on a tetrahedral shape with quantitative measurements. The next section introduces the finite element modelling strategy. Finally, the last section presents the results of the forming simulation and its comparison with the experimental forming.

Experimental Forming on a Tetrahedral Shape

TFP preform architecture.

A TFP preform is built from a continuous fibre tow deposited on a flat backing material along curvilinear trajectories and maintained in place through a zig-zag stitching pattern as illustrated in Fig. 1. The thickness of the preform is achieved through stacking of several layers. When manufacturing a TFP preform, the stitch length, width and tension can be varied. Depending on the layout pattern, intra-layer and inter-layer overstitching create additional bonding between the fibre tows in a layer and between layers. The numerous interactions between the different components of a TFP preform, namely, the backing material, the fibre tows and the stitching yarn, inherently make its realistic modelling difficult. Moreover, depending on the nature of the backing material, the formability of the TFP preform can be limited. When using a thermoforming process, a non-woven polymer film which will add polymer in the final part is a good choice. However, in this work the forming experiment are carried-out at ambient temperature. Since the cohesion conferred by the stitching yarn between the layers was deemed sufficient, the backing material was removed prior to forming.

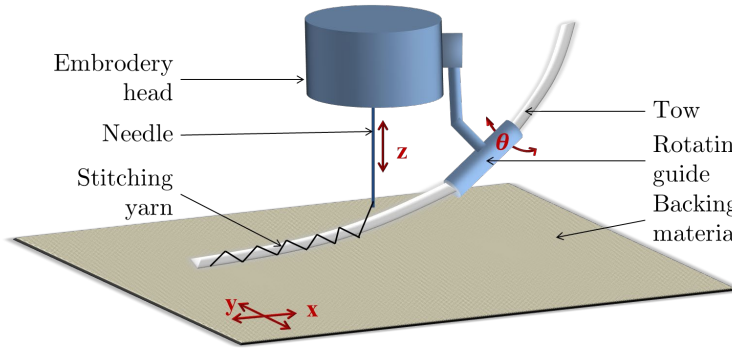

Fig. 1. TFP principle [2].

Material and manufacturing of the TFP preforms.

The TFP preforms where manufactured at IRT Jules Verne using the TFP ZSK © CMCW 0200-900D-2500 embroidery machine. A PolyVinyl Alcohol (PVA) water soluble film was used as backing material and removed by washing. Then, the TFP preform were dried in an oven at a temperature of 60◦C. The 2690 tex PET/E-glass continuous tow (from P-D-Glasseiden GMBH,

Oschatz, Germany) was stitched onto the PVA film (Gunold® Solvy film 80, Stecker) using a 24 tex PET stitching yarn (Serafil fine, Amman). The stitching length and width were set to 2.5 mm and the stitching tension to 5 10^{-2} N.

TFP preform design.

The objective is to obtain an orthotropic configuration in the final tetrahedral part. In practice, the determination of the flat pattern from the desired final configuration, namely, the flattening step, would require a numerical tool for complex geometries [1]. However, for the case of a tetrahedral shape, the flat pattern was determined analytically based on the assumption of the fibre tows inextensibility. Fig. 2 (a) shows the desired configuration of a 2-layer TFP preform. On each face of the tetrahedral shape, a 0/90° orientation is achieved. Since fibre tows are aligned with the three edges which converge through the vertex of the tetrahedron, their length must be conserved in the flat configuration. These constraints are satisfied with an angle of 120° between the edges in the flat configuration Fig. 2 (b). Therefore the fibre tows have initially an angle of 120° between the two layers on each face. During the forming step, a uniform in-plane shear deformation characterized by an angle of 30° is expected. Fig. 3 shows the flat pattern with is split into two layers. It should be noticed that several combinations of 2-layer lead to this flat pattern. As it will be highlighted at the end of this section, it was noticed to late that the chosen one was not optimal.

Forming device.

The forming device shown in Fig. 4 is composed of a tetrahedral punch mounted on the cross head of a universal testing machine (AGXplus by Shimadzu). Two transparent square plates (550 mm × 550 mm × 10 mm) made of poly(methyl methacrylate) are used as blank-holder. One plate is fixed within a metallic frame and the other lies directly onto the preform and only applies its self-weight. A pin system prevents the movable plate of the blank holder from moving in the plane. The tetrahedral part of the punch is 120 mm high and on top of a 20 mm thick base. The stroke punch stroke is 140 mm with a speed of 15 mm/min.

Quantitative measurements.

Optical measurements were carried out to compare the results with the forming simulations presented the last section using a camera positioned along the displacement axis of the punch which takes a picture every 2~mm. This setup allows visualizing the 2D displacement field orthogonal to the punch displacement. Moreover, at the end of the experiment, a picture of one face of the punch was taken to measure the inter-layer angle. Red-ink markers were drawn on the TFP preform in order to compute the 2D displacement field and a python script based on the open-source image-processing library OpenCV was used to track the position of these markers. This 2D displacement field allows extracting the preform contour for comparison with the simulation results in the last section.

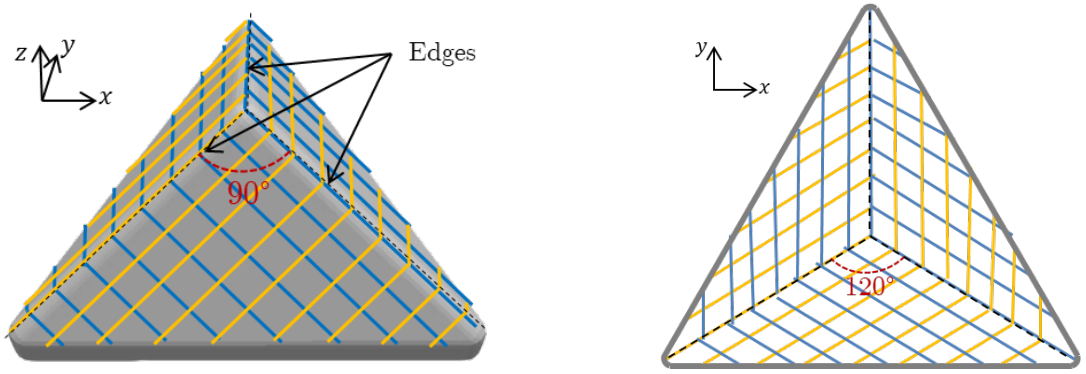

(a) (b)

Fig. 2. Desired orthotropic configuration (a) and analytically determined flat pattern (b).

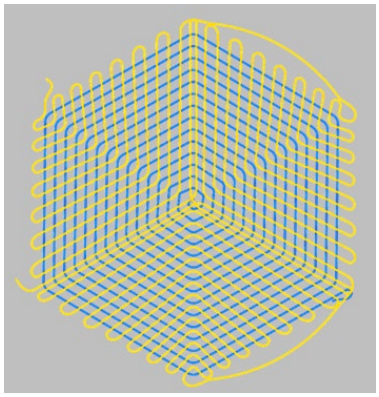

Fig. 3. TFP preform flat design (with reduced number of fibre tows for visibility).

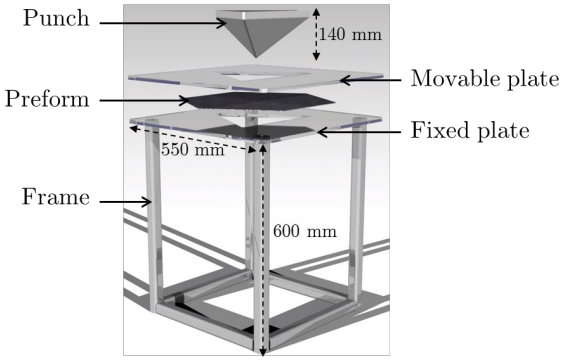

Fig. 4. Forming device.

Results.

The final configuration of the forming process as well as the force-displacement curve is shown in Fig. 5. No apparent defects such as wrinkles or fibre tow slippage were noticed. The force-displacement curve shows a first phase with a slow increase until 120 mm before increasing rapidly once contact with the thick base (120-140 mm) is established. Therefore, the minimal blank-holder used was sufficient to obtain a final configuration free of defects. Concerning the final inter-layer orientation, from the picture taken on one face, the trajectory of the fibre tows was extracted manually by drawing curves using Inkscape and saved as a svg file for post-processing. Then a python script extracted the curves representing each fibre tow and the angle at the intersection of two fibre tows was computed. Fig. 6 (a) shows the extracted trajectories and while Fig. 6 (b) presents a nice distribution of the inter-layer angle around 90°. Considering a normal distribution of the angles, a mean angle of 90.72◦ with a standard deviation of 4.31◦ is obtained. However, it must be noticed that due to the choice of the layers to obtain the flat TFP pattern, the fibre tows are parallel along the symmetry line of the faces. Another choice for the layer layout which eliminates this orientation defect was noticed too late.

(a)

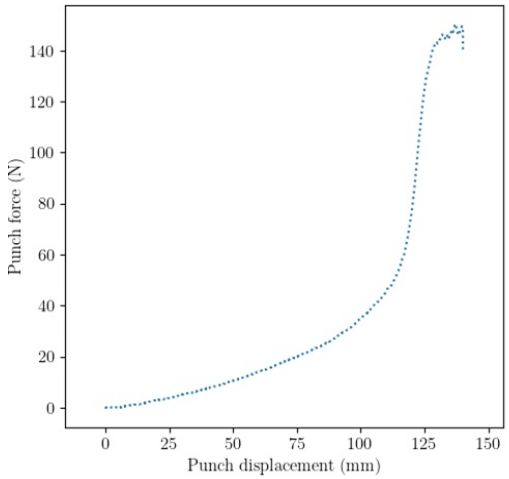

(b)

Fig. 5. Final configuration of the forming process (a), force-displacement curve (b).

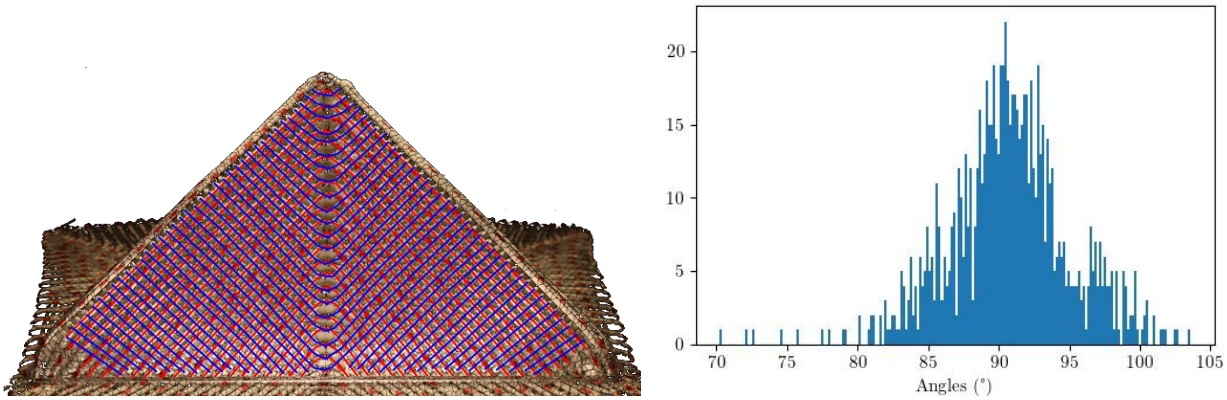

(a) (b)

Fig. 6. Manually extracted trajectories of the fibre tows on a face (a), inter-layer angle distribution on this face computed at fibre tows intersections.

Finite Element Model of a TFP Preform

Modelling strategy.

The model developed to simulate the forming of a TFP preform without backing material is based on the finite element method. Since the backing material is removed prior forming in this work or in a melted state when a thermoforming process is used, its contribution is neglected. To take into account the flexibility offered by the TFP technology in the preform design, it was chosen to use a semi-discrete approach where the preform is modelled at the scale of the fibre tows.

Hypothesis.

In this model, the fibre tows are considered to be quasi-inextensible. Although the backing material is removed prior forming, the stitching yarn is assumed to ensure the cohesion between the layers thanks to inter-layer overstitching.

Fibre tows.

The fibre tows are modelled as a continuum medium using 2-node shear-flexible beam element. The initial formulation of this type of element can be found in [15-17]. Since fibre tows cannot be considered as a perfect continuum medium, the section moduli, which relate the cross-section forces and moments to its deformation and curvatures, are considered to be independent. A high value of the tensile modulus ensures a weak enforcement of the quasi-inextensibility constraint.

Stitching yarn.

The stitching yarn is the component of a TFP preform whose contribution is the most difficult to take into account. To avoid burdensome computations implied by a realistic modelling of the stitching yarn and its interactions with the fibre tows, it is modelled implicitly as an embedded constraint between crossing fibre tows of adjacent layers. In other words, the stitching yarn is assumed to act as a perfect bond between fibre tows of adjacent layers which intersect. The embedding constraint principle is illustrated in Fig. 7 where two fibre tows intersect. To apply this constraint a node is required at the intersection between the elements of the lower fibre tow and those of the upper fibre tow. On the kinematic side, the displacement of this node is computed as function of the displacements of the lower beam element it is embedded in (host element). As a consequence, forces which are computed at this embedded node are transferred on the nodes of the host beam element. To take into account the resistance to rotation between crossing fibre tows, a linear torsional spring is added at each intersection. The vertical offset between the two crossing fibre tows in Fig. 7 is only for visibility purpose.

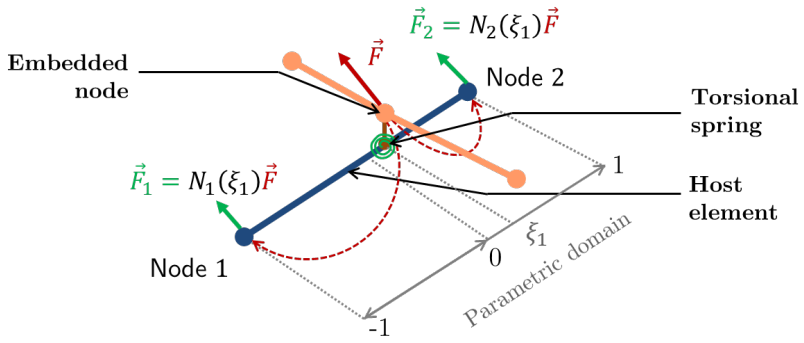

Fig. 7. Embedding constraint principle: Transfer of forces from an embedded node to the nodes of its host element.

TFP preform model.

Therefore, in this work, a 2-layer TFP preform without backing material is considered where the fibre tows are modelled explicitly using 2-node shear flexible elements and the stitching yarn is modelled implicitly through an embedding constraint where the fibre tows of adjacent layers intersect each other. The resistance to in-plane shear is taken into account through a linear torsional spring at these intersections.

Numerical Forming on a Tetrahedral Shape

Material parameters.

The model requires six independent material parameters for the beam elements corresponding to the six independent deformation modes (one for tension/compression, 2 for transverse shears, 2 for flexions and one for torsion). An additional parameter is required for the resistance to rotation between crossing fibre tows. No characterization of these material parameters was carried-out and their estimation is given in Table. 1.

Table. 1 Values of the material parameters for the beam elements and the torsional springs.

Modulus	**Tensile**	**Transverse shear 1**	**Transverse shear 2**	**Flexion 1**	**Flexion 2**	**Torsion**	**Torsional spring**
Value	1400	700	700	1	0.1	1	1
Unit	kN	kN	kN	kN mm²	kN mm²	kN mm²	N mm

Finite element solver.

A research code based on an explicit scheme is used to simulate the forming process with a time step of 10^{-4}s. The contact interactions between the TFP preform and the tools, namely, the tetrahedral punch and the blank-holders are solved using a forward increment Lagrangian multipliers method.

Finite element model.

The first layer is composed of beam elements of 2.5 mm. The second layer is meshed with the same element size but nodes additional nodes are required at intersections with the elements of the first layer. These additional nodes are embedded in the corresponding host elements of the first layer. The total number of beam elements is 22190 and the simulation runs in 12 h using four cores of an Intel(R) Core(TM) i7-8750H CPU 2.20 GHz processor. A friction coefficient of 0.2 between the fibre tows and the forming tools was chosen for simplicity even though it might be different since the blank-holders are made of different polymers. A displacement of 140 mm is imposed to the punch. Concerning the blank-holder, the fixed part is clamped and the movable part can only move along the punch axis as in the experiment. Rigid surfaces are used to model the tools.

Results.

A comparison between the experiment and the simulation is shown in Fig. 8 (a). In this figure, the contours of the preform in the experiment and in the simulation are superposed on the left part and shows good agreement. In Fig. 8 (b), the inter-layer angle field on one face of the punch is displayed. The colormap shows a distribution of the inter-layer angle around 90° as expected, except along the line of symmetry of the face as explained in the experimental section.

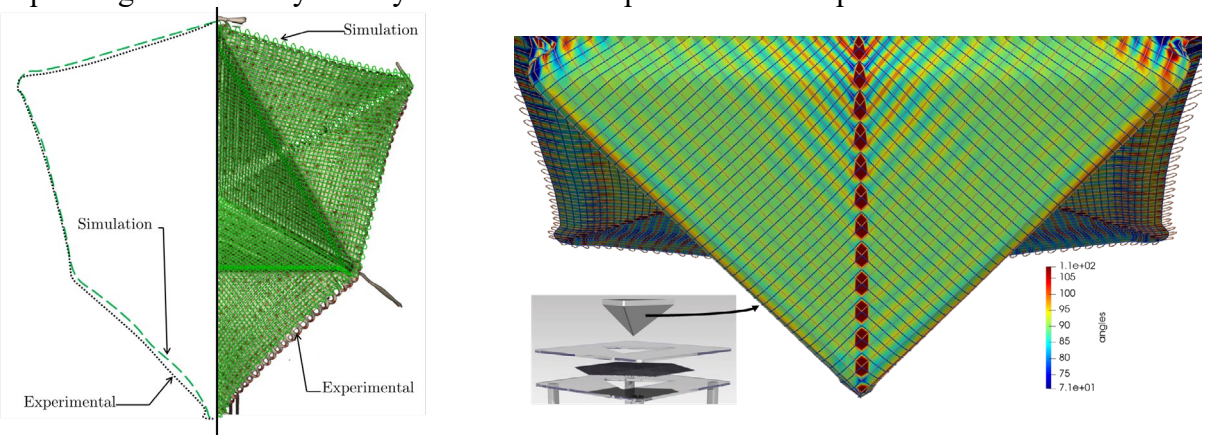

(a) (b)

Fig. 8. Superposition of the preform contour in the experiment and simulation (a), inter-layer angle field on a face of the punch (b).

Summary

This work demonstrates the ability to form a 2-layer TFP preform on a doubly-curved part with a final orthotropic configuration. Only a minimal blank-holder setup was needed to form the preform without defects. The orthotropic orientation in the final configuration shows great improvement compared to forming of regular fibrous reinforcements. The design of the flat TFP pattern was obtained analytically by considering the inextensibility of the fibre tows. A first finite element model was proposed to simulate the forming of TFP preform without backing material. Based on a semi-discrete approach, the fibre tows are modelled explicitly using 2-node shear-flexible beam elements while the stitching yarn is modelled implicitly using an embedding constraint. It assumes the stitching yarn to act as a perfect bond between crossing fibre tows of adjacent layers. Additional linear torsional spring take into account the resistance to in-plane shear of the reinforcement.

In future work, the development of a numerical tool to determine the flat pattern of more complex parts is of interest. Besides, a model which takes into account the backing material is currently developed.

References

[1] X. Sun, J. P. -H. Belnoue, W.-T. Wang, B. C. Kim, S. R. Hallett, “Un-forming” fibre-steered preforms: Towards fast and reliable production of complex composites parts, Composi. Sci. Technol. 216 (2021) 109060. https://doi.org /10.1016/j.compscitech.2021.109060

[2] J. Simon, N. Hamila, C. Binetruy, S. Comas-Cardona, B. Masseteau, Design and numerical modelling strategy to form Tailored Fibre Placement preforms: Application to the tetrahedral part with orthotropic final configuration, Compos. Part A: Appl. Sci. Manuf. 158 (2022) 106952. https://doi.org /10.1016/j.compositesa.2022.106952

[3] A. Spickenheuer, M. Schulz, K. Gliesche, G. Heinrich, Using tailored fibre placement technology for stress adapted design of composite structures, Plastics, Rubber and Composites 37 (2008) 227-232. https://doi.org/10.1179/174328908X309448

[4] K. Uhlig, A. Spickenheuer, L. Bittrich, G. Heinrich, Development of a Highly Stressed Bladed Rotor Made of a CFRP Using the Tailored Fiber Placement Technology, Mech. Compos. Mater. 49 (2013) 201-210. https://doi.org/10.1007/s11029-013-9336-4
[5] K. Katagiri, S. Honda, S. Nakaya, T. Kimura, S. Yamaguchi, H. Sonomura, T. Ozaki, S. Kawakita, M. Takemura, K. Sasaki, Tensile strength of CFRP with curvilinearly arranged carbon fiber along the principal stress direction fabricated by the electrodeposition resin molding, Compos. Part A: Appl. Sci. Manuf. 143 (2021) 106271. https://doi.org/10.1016/j.compositesa.2021.106271
[6] P.J. Crothers, K. Drechsler, D. Feltin, I. Herszberg, T. Kruckenberg, Tailored fibre placement to minimise stress concentrations, Compos. Part A: Appl. Sci. Manuf. 28 (1997) 619-625. https://doi.org/10.1016/S1359-835X(97)00022-5
[7] K. Gliesche, Application of the tailored fibre placement (TFP) process for a local reinforcement on an “open-hole” tension plate from carbon/epoxy laminates, Compos. Sci. Technol. 63 (2003) 81-88. https://doi.org/10.1016/S0266-3538(02)00178-1
[8] E.G. Koricho, A. Khomenko, T. Fristedt, M. Haq, Innovative tailored fiber placement technique for enhanced damage resistance in notched composite laminate, Compos. Struct. 120 (2015) 378-385. https://doi.org/10.1016/j.compstruct.2014.10.016
[9] H. M. El-Dessouky, M. N. Saleh, M. Gautam, G. Han, R. J. Scaife, P. Potluri, Tailored fibre placement of commingled carbon-thermoplastic fibres for notch-insensitive composites, Compos. Struct. 214 (2019) 348-358. https://doi.org/10.1016/j.compstruct.2019.02.043
[10] K. Uhlig, A. Spickenheuer, K.Gliesche, I. Karb, Strength of CFRP open hole laminates made from NCF, TFP and braided preforms under cyclic tensile loading, Plastics, Rubber and Composites 39 (2010) 247-255. https://doi.org/10.1179/174328910X12647080902772
[11] M. Takezawa, Y. Otoguro, K. Matsuo, T. Shibutani, A. Sakurai, T. Maekawa, Fabrication of doubly-curved CFRP shell structures with control over fiber directions, Comput.-Aided Design. 136 (2021) 103028. https://doi.org/10.1016/j.cad.2021.103028
[12] G. Rihaczek, M. Klammer, O. Başnak, J. Petrš, B. Grisin, H. Dahy, S. Carosella, P. Middendorf, Curved Foldable Tailored Fiber Reinforcements for Moldless Customized Bio-Composite Structures. Proof of Concept: Biomimetic NFRP Stools, Polymers 12 (2020). https://doi.org/10.3390/polym12092000
[13] S. Allaoui, P. Boisse, S. Chatel, N. Hamila, G. Hivet, D. Soulat, E. Vidal-Salle, Experimental and numerical analyses of textile reinforcement forming of a tetrahedral shape, Compos. Part A: Appl. Sci. Manuf. 42) (2011) 612-622. https://doi.org/10.1016/j.compositesa.2011.02.001
[14] P. Ouagne, D. Soulat, J. Moothoo, E. Capelle, S. Gueret, Complex shape forming of a flax woven fabric; analysis of the tow buckling and misalignment defect, Composites Part A: Applied Science and Manufacturing. 51 (2013) 1-10. https://doi.org/10.1016/j.compositesa.2013.03.017
[15] M. Géradin, A. Cardona, Flexible Multibody Dynamics: A Finite Element Approach. Wiley-Blackwell, New York, 2001.
[16] M. Ritto-Corrêa, D. Camotim, On the differentiation of the Rodrigues formula and its significance for the vector-like parameterization of Reissner-Simo beam theory: Differentiation of Rodrigues formula, Int. J. Numer. Meth. Eng. 55) (2002) 1005-1032. https://doi.org/10.1002/nme.532
[17] A. Ibrahimbegović, F. Frey, I. Kožar, Computational aspects of vector-like parametrization of three-dimensional finite rotations, Int. J. Numer. Meth. Eng. 38 (1995) 3653-3673. https://doi.org/10.1002/nme.1620382107

Materials Research Proceedings 28 (2023) 239-248 https://doi.org/10.21741/9781644902479-26

Proposing a virtual simulation method to predict the shape-fidelity of 3D-knitted-textiles using knit-meshes and geometric invariants

DIETRICH Franz[1,a*]

[1]Franz Dietrich, Behlertstraße 42C, 14467 Potsdam Germany

[a]mail@franz-dietrich.com

Keywords: Flat-Knitting, CBS, Simulation, On-Demand, FEM

Abstract. Though the level of machine digitization in flatbed-knitting (FBK) today is high, the design and development of knittable data sets are still currently very time-consuming, digital simulations methods are calculation expensive and insufficient in terms of accuracy of fit and technical properties. Knitting process retrofitting activities are executed mostly manually by an operator on the basis of the operator´s experience. This circumstance makes it more difficult to use the diverse potential for flexibility and on-demand purposes in future-networked-production for lightweight constructions for Automotive, Aerospace and aviation or Medical-Products. New easy-to-learn, intuitive, calculation inexpensive digital augmented workflows for the planning of knitted objects with complex 3D-shapes are needed. With regard to the requirements of composite forming, the aspects of wrinkling, slip and permeability are of particular importance. However, flatbed-knitted fabrics are subject to different requirements in some cases, which implies different questions from those posed by research in the area woven textile composites. In order to address a few of the questions raised by previous research on textile composites, this paper covers some of the current research topics in the field of 3D-knitted flatbed-knitting fabrics and shows references as well as potentials to already researched problem fields of textile reinforced composites. In doing so, the author strongly refers to the topics of the summarizing publication "Advances in composite forming through 25 years of ESAFORM" by P. Boisse et al. [1].

Introduction

To give a first impression of the current possibilities and concepts in the development of three-dimensional shaped flatbed-knitted textiles, a brief summary of current geometry-based approaches follows. The approaches presented currently show their greatest potential at the level of purely plastic-shape reproduction. Special consideration of material parameters to extend the product properties of the planned object are given little attention here. However, the presented methods could be suitable to derive FEM-calculable models on macro-scale level. A standardization towards certain restricted geometric variables is emerging. Most noticeable is the representation of a knittable geometry in quad and partial triangle meshes (Fig. 1).

The formation of these types is described in the following. Furthermore, technical knitted fabrics with different property zones in particular are currently a major focus of the author’s work. The mutually influencing material and stitch properties generally lead to results that are difficult to predict in the initial development stages. In the field of today's "craft / non-simulation-based" planning and individualization of 3D-knitted-technical-textiles, these property zones play a major role. On the one hand, mesh ratios are used to influence the plastic-shape and, on the other hand, to design zones with references to external forces. Different mesh-loop ratios often result from technical knitting/binding variations for loop formation. These are also not considered in depth here. In Yordan Kyosev's publication from 2019 entitled "Topology-Based Modelling of Textile Structures and Their Joint Assemblies", these are considered in more detail. Specifically, starting on page 100 of the aforementioned publication, the framework for FEM calibrations at the meso-scale level is described.

Content from this work may be used under the terms of the Creative Commons Attribution 3.0 license. Any further distribution of this work must maintain attribution to the author(s) and the title of the work, journal citation and DOI. Published under license by Materials Research Forum LLC.

Depending on the yarn properties at the micro-scale level, for example, the stitch height in combination with the pre-tensioning by yarn feeders has an influence on the strength of the knitted fabric under pressure and tension on macro-scale or product-scale level. The product scale level can be seen as the sum of all parameters acting on the entire textile-product. In order to be able to represent property changes at this level, additional geometry-based calculation models are required in addition to all the other levels mentioned above. Therefore, at the end of this paper, the author presents a new approach with reference to the mentioned influences of the stitch ratio on product-scale level.

In addition to the basic principles introduced below for the development of geometric standards, the author considers the field of research (varying ratios) to be one of high priority for technical design using digital simulations.

As illustrated, different stitch ratios have a major influence on the technical properties, shape contours and surface finish of 3D knitted technical textiles. The basic technical possibilities for influencing shape and thus important design criteria for three-dimensional technical textiles are, in addition to the stitch ratios: Darts and Notches, short- and Long-Rows with decreases and increases. In all these areas, elastic yarns and yarns with different properties can have a strong influence on the prospective shape. Knitted fabrics also have a highly indiscreet structure. This reality assumption makes it difficult to calculate distortions or other plastic and material property changes using FEM methods. Taken together, this forms a complex set of requirements for future tools for digital simulation, especially with regard to industrial use.

FEM-Simulations

Y. Kyosev sums up this challenge in textile technology in general as follows: during the modelling with FEM, the real system (…) has to be idealized first in order to achieve a somewhat simplified physical system. This first step is the building of the physical model, where certain assumptions have to be made [2].

To address the problem of abstracting real complexity in the field of flatbed-knitting, the author proposes the reduction of complexity in the form using of discrete Knit-Meshes. These digital Knit-Meshes in the form of stitch-ratio-proportion quad-meshes and partly triangulated quads can be used for dynamic-FEM calculation. Similar to the digital simulation of woven surfaces, the properties on the three levels: micro-, meso-, and macro-scale level give important parameters for the calculation. For the calculation method proposed in the paper, the author follows Y. Kyosev's statement: "The macro scale is the most important for the applications. It deals with the mechanical behaviour of the structure as a continuum membrane or plate with known properties" [ibid.]. Furthermore, Kyosev describes that there are several methods to obtain the properties at the macro-scale level, which are mostly derived on the specifications of the meso-scale. Most often, various mechanical tests with material samples are used [ibid.].

Despite the necessary connection of the different property levels described by Kyosev, the author devotes himself for the time being only to the macro level. This serves to set up a digital simulation model for deriving the internal forces at different stitch ratios within a knitted fabric.

In addition to the references to the field of textile composites outlined in the further text, the large medical technology companies and their customers in particular would have great advantages from further process innovations in the digital design of flat-knitted products. Since the author's previous focus has been on consumer products and medical devices, the demonstrator of the paper for the purpose of illustrating the process, in dealing with varying ratios, will be a bandage.

By using 3D CAD data from 3D scans and FEM calculation methods, the processes in the individualization of bandages could be further simplified in the future. In particular, specific body parts with high concave and convex plasticity (e.g., popliteal fossa, crook of the arm, kneecap) can

benefit from the use of scan data and semi-automatic data set optimization. Prosthetic applications would also be conceivable with reference to textile composites.

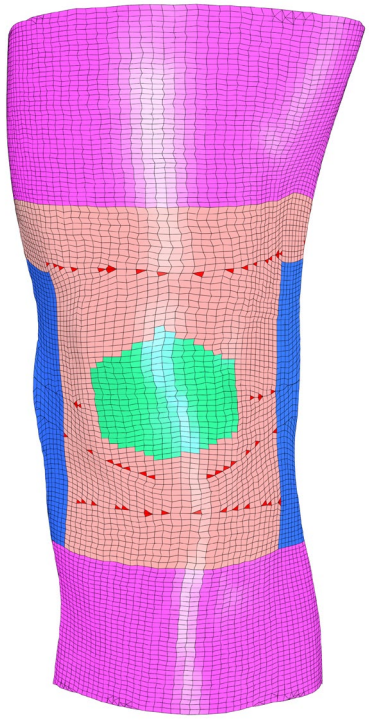

Fig. 1. Function zoned and topography optimized knit mesh.

Knit-Meshes

Several methods are currently known for creating knittable mesh topologies. K. Wu et al. describe in their publication "Wearable 3D Machine Knitting: Automatic Generation of Shaped Knit Sheets to Cover Real-World Objects," 2021, the following approach. The first step is to convert the cut mesh into a quad-dominant mesh where there are only triangles, quadrilaterals, and pentagons exist and all faces have the same size and the and have the same ratio between the edge lengths of course and wale [3].

Furthermore, they describe that the directions of course and wale are already determined during a surface cutting procedure. In two referenced earlier works, previous developments are introduced. Herein they also describe, on one hand, a vektorfield-oriented anisotropic remeshing pipeline and, on the other hand, the use of a local anisotropic parameterization method in conjunction with an extraction approach to generate an anisotropic quad-dominant mesh with relatively few triangles and pentagons [ibid.]. Through this form/step of categorization and modularization, they achieve an anisotropic quad-dominant mesh. In particular, this geometric property supports a later good calculability in the form of FEM calculations.

G. Nader et al. described another, partly similar, process in their 2021 published Work “KnitKit: A flexible system for machine knitting of customizable textiles”. The construction of the knit mesh starts here with a parameterization which generates orthogonal stripes with equal distances. It is followed by a remeshing step, which generates an adequate quad-dominant Knit-Mesh. The edges of this mesh are consistently aligned with the knitting direction and are divided into two groups: course-edges and wale-edges [4].

To create the wale and course contours/curves, they use a unit vectorfield-based analysis of the surface of an input mesh at each node/vertex. At each vertex of the input triangular mesh, they start by computing $\vec{v}$c as the rotation of $\vec{v}$w by π /2 in the respective local tangent plane. From

this cross-field ($\vec{v}c$; $\vec{v}w$) there is an orthogonal, equally spaced stripe pattern computed using Knoppel et al.'s [2015] method [ibid.]. In another concept, first published in 2019 by Mariana Popescu, a graph-theoretic foundation is set. Basically, a 3D geometry, Mesh or NURBS-Surfaces, is needed. A gauge edge and a knit-end-edge are marked with curves or surface edges. Between two more "left-side" & "right-side" bounding edges, an intermediate frequency curve (tween curve) or contouring curve series is created. These are subsequently subdivided in weft-direction in the height dimension of the planned stitch-ratio [5]. To create the warp lines of the knitting pattern, the vertices must be connected by edges. Resulting Edges describe the directions of the knitting pattern and represent the weft and warp directions of the knitting pattern. In the stitch creation step, only "weft" edges are added. Before the edges are added, for each vertex a set of potential connection points is defined. Two sets of at least four closest vertices on the adjacent contours are added to a list for the later Wire Frame-Mesh. If the four nearest points fall on the same coordinate, the knit-mesh will show a decrease or an increase. Through these superposed points the ends of a warp-line-segment will build a common end-point. This constructs a triangle as shown in red in Figure 1. This symbolizes a decrease or increase within the resulting mesh.

In a thesis published in 2020, Max Eschenbach summarizes various approaches, but especially M. Popescu's graph-based computational basis of knit meshes and knittable paths in a compendium. Part of his work is the publication of Cockatoo, which is a prototypical open-source software toolkit for generating (3d) knitting patterns from NURBS surface and mesh geometry [6].

Due to the comprehensibility of the latter approaches, the same categorization/modularization is applied in the further process. It is assumed that both the computability by kinematic-FEM-Computation and the basic structure of the mesh by quad-dominance and decrease/increase-triangles are well suited for the evaluation and simulation processes presented in the following.

The basic design features of an FEM-compliant geometric calculation basis are derived from the general remarks on textile FEM calculation by L. Girdauskaite et al. and interpreted for the present focal field of technical flat knitting. Girdauskaite et al. describe the basic method in an article summarizing on textile physical tests [7].

The crossing points of weft and warp lines represent the joints for a kinematic FEM calculation explained later. Between the crossing points, constructed lines behave like rods with constant or limited flexible length. This flexibility allows a later consideration of constituent material properties. However, these are not yet considered in the present paper. An outlined concept for linking the macro-scale-knit-meshes with the meso-scale-binding-variants is touched upon under headline Experimental measurement.

The purpose of the presented process is the evaluation of form-giving cut features and the subsequent fit optimization by means of additionally entered different stitch ratios. However, as described, an accurate distribution of forces at the macro level requires further linkage with property models at the meso-scale level. These will be considered in further studies.

Simulation Differences for Woven Textiles

At this point, the research results presented so far will serve as a comparison between digital simulation of woven and knitted textiles. Due to the technical characteristics of the structure and the machine binding logic of both textile-production-methods (Knit & Woven Fabric), fundamental differences arise. These differences create very different geometric assumptions at the macro- and meso-scale levels for calculating shear and other material properties such as the effects of stress and strain on the textile.

Measuring Textile Composites, Knitted & Woven Materials

Analysis and modelling of the deformation behaviour of fabrics, textile composites and prepregs can be performed more or less at one or more of three scales: (1) microscopic, (2) mesoscopic, and (3) macroscopic. In terms of scale, simulations of flat-knitted three-dimensional textiles are

Materials Research Proceedings 28 (2023) 239-248 https://doi.org/10.21741/9781644902479-26

currently mostly subjected to macroscopic analyses of the behaviour of the entire mesh shell/geometry (continuum membrane; Kyosev:2019), similar to the summary publication mentioned above regarding woven textiles by P. Boisse et al [8]. Since simulation methods at the macro level for three-dimensional flat knitting have so far been little standardized and are often very application-specific, (1), (2) and (3) are currently usually considered separately or a link is neglected.

Another complicating factor is that there are no generally valid calculation concepts for the shear behaviour of the individual stitch loops, taking into account different ratios, or the many different combinations for stitch loop/mesh formation and various knitting techniques (e.g., plating, weft insertion). Compared to woven fabric, the complexity of derivation increases here. This is because a stitch loop has multidirectional intersections and connections, as shown below.

Experimental Measurement

Experimental measurement for woven materials relates in part to the derivation of different shear angles. P. Boisse et al. describe essentially two different methods. One is the picture frame test and the other is the bias extension test [ibid]. Whether these two test methods are usable for the three-dimensional flatbed- knitting has to be evaluated in experiments. Furthermore, the researchers state earlier in 2017 that two relationships are required to analyse the results of an in-plane shear test [9]. A kinematic relationship that relates the in-plane shear angle to the extension of the Sample. For flatbed-knitting, the second dependence might be different and a third is required. For example, instead of shear angles, the focus of a question could be directions vectors related to truss centres resulting from the construction properties for stitch/mesh-loops at the meso-scale level. A mesh loop on the meso-scale level is described by a quad cell (polygon) in the digital model on the macro-scale plane. The centre of a truss can be related to one another cell-truss-centre. Changes in the positions of any node i in certain directions $\overrightarrow{vn}$ can be analysed. The resulting direction vectors can be used to optimize an FEM-based deformation analysis. The forces applied in warping experiments would then be expressed in "flow directions" within the knitted fabric. The third dependency can be achieved through investigations at the micro-scale level. Here we are concerned with the forces acting within the mesh loop elements at the yarn level. These can be represented in global coordinates by the relationships between the internal nodal forces and nodal displacements [10] within the truss:

$$F = Ku \tag{1}$$

Analyses could take the form of deviation measurements in applied 2D samples. This form of quality determination and analysis of visual warpage behaviour is today part of the craft practice in the development of three-dimensional knitted fabrics (for e.g.: car seats.). Color-coded zones or knitted-in measuring points could be detected and assigned with the aid of invariant moments (e.g.: Hu moments). This enables a point or area-accurate comparison between textile at rest and distortion.

Digital Augmented Experimental Measurement

Another possibility arises from taking 4D scans. With the help of the evaluation of different recording frames, the exact distortion behaviour in motion could be investigated. In the author's experience, point cloud data is also very well suited for machine learning-based analyses of the behaviour of specific clusters.

Colours, patterns or point-groups can be used as invariant moments or invariant geometries. Knitted-in position-sensors would also be conceivable.

DIC, Invariant Moment & Geometries (3D-Scan)

The described procedures have similarities to the digital image correlation (DIC) which was described by Boisse et al. The DIC method is divided into a two-dimensional & a photogrammetric three-dimensional analysis method for pattern recognition.

The mentioned Hu-moments are rather used for shape recognition of geometries as a whole with closed contours. It hereby forms an important foundation in AI-assisted shape recognition. Based on the briefly described different approaches of image and geometry analysis, further methods can be designed which can be adapted for flat-knitting-/ and woven-textile-/ -based-composites. The experimental and digital augmented measurements and evaluations of deviations or errors will be important here in the future in order to achieve further simulation concepts for adequate computation.

Reengineering 3D-Scans and Remeshing

To obtain a computable mesh shell of a 3D scan or a 3D model, e.g., of a knee, the approaches presented above (Knit-Meshes) are partially applicable. Behind each of the approaches is the assumption that certain geometric properties are given. Therefore, the approaches can be described as application-specific. A generalistic approach for the construction of knit meshes is currently not known to the author. Therefore, each approach has advantages and disadvantages when applied to an arbitrary geometry. The author uses a workaround of proprietary software processes and commercial applications. These are described briefly below to provide a summary at the end of the paper with respect to the process foci described above (slip, wrinkling and permeability) in the development of textile-composite materials.

Knitting Technicians Best Praxis

The concepts presented for knit mesh creation have, as mentioned, in part very application-specific advantages & disadvantages. The author considers the lack of possibility to influence the position of darts or gores & notches to be the biggest disadvantage. In practice, these are used by knitting technicians in addition to changing the stitch ratio in order to influence the shape and material properties. The author therefore focuses on the removal and insertion of material quantities in certain cut sections with excess material or excessive stretch. Cut material-areas are adjusted at the edges and provided with the triangular shapes described above (increase/decrease) Afterwards the mesh is joined at row transitions. This is followed by the calculation of the internal warpage behaviour by means of kinematic calculation (Fig. 2).

In order to ensure a quantitative evaluation of the results, a geometric invariant is used. In addition to the visually observable effects, this gives another possibility to evaluate the shape accuracy after given adjustments.

Knit Mesh Preparation

A feature of the commercial NURBS modelling software Rhinoceros 3D is used to create the quad mesh. The integrated quad mesh tool allows a homogeneous quad recalculation of given NURBS or polygon geometries. The generated quad geometry is relatively uniform and quad-dominated. The ratio deviations from the actual mesh ratio are readjusted by dynamic relaxation. Here, as shown below, all segments dS are equated and relaxed in the knit-mesh ratio.

Dynamic Relaxation

The dynamic relaxation method is based on discretizing the continuum under consideration by lumping the mass at nodes and defining the relationship between nodes in terms of stiffness. An iterative process is followed by simulating a pseudo-dynamic process in time, with each iteration based on an update of the geometry [11]. Considering Newton's second law of motion in the x direction at the i^{th} node at time t:

$$R_{ix}\,(t) = M_i\,A_{ix}\,(t) \tag{1}$$

The forces generated by the expansion of each edge segment led to a realignment of the whole mesh due to the internal references of the discrete structure.

According to the principle of equilibrium of forces, the relationship between the residuals and the geometry can be determined:

$$R_{ix}(t + \Delta t) = P_{ix}\,(t + \Delta t) + \sum \frac{T_m\,(t+\Delta t)}{l_m\,(t+\Delta)} \times \left(x_j(t + \Delta t) - x_i(t + \Delta t)\right) \tag{2}$$

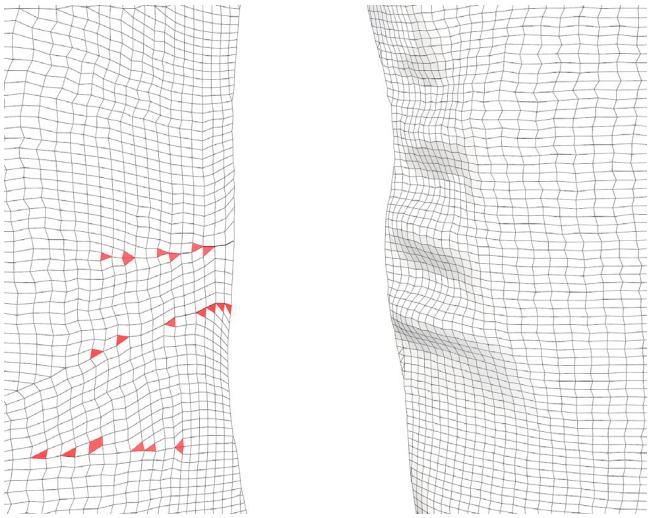

The sum must cover the forces in all the connections between the node and other nodes. By repeating the use of the relationship between the residuals and the geometry, and the relationship between the geometry and the residual, the pseudo-dynamic process is simulated. Residuals $T_m(t), R_i(t)$are computed until the structure is in static equilibrium [ibid.].

Reducing Wrinkles

Fig. 2 shows the comparison of a relaxed mesh-shell to an author-edited mesh-shell. The wrinkles that appeared after the material was relaxed into a uniform knittable mesh-ratio were achieved by removing material and changing the mesh proportions in certain areas. This process is described below.

FEM – Calculation

To simulate the shape accuracy of a knitted fabric, taking into account the knitted fabric weave and stitch ratios, three main laws can be required for the modelling of mechanical systems – kinematic, constitutive (material) and equilibrium [12].

Only kinematic equations were used to calculate the following patterns. Since textile kinematics assumes that relationships between the movement of individual nodes in a mechanical system consisting of nodes and connecting edges lead to internal deformations, a readability of a deformation due to external and internal force influences in the knit mesh can be assumed. The algorithms used are based on the basic algorithm of the kinematic model. All points $\vec{x}$ on a doubly curved geometry surface can be parametrically represented with surface coordinates u_i:

$$\vec{x} = \vec{x}\,(u_1, u_2) \tag{3}$$

The elementary length dS of a surface segment, between two closely spaced points/nodes (i, j) is given by the initial prepared Knit-Mesh and its constituent uniform mesh ratios. The stitch ratios

correspond to the selected stitch ratios of a knitted fabric. In this case, an initial stitch ratio of 1.47 mm width and 1.1 mm height was chosen. For faster simulation calculation, the stitch ratio was multiplied by a factor of two (2.94 mm x 2.2 mm). The lower number of nodes (i, j) and edges speeds up the calculation.

$$dS^2 = G_{ij} du_j du_i \tag{4}$$

An angular threshold is used to define the possible shear inside each triangular face of the triangulated simulation quad-meshes. This threshold value is basically present. It is represented by the given initial angle of the triangular legs of each face. This determination thus represents a part of the Stiffness matrix, where K is the stiffness matrix of the system, u is the vector with the nodal displacements and F represents the external forces.

$$K \cdot u = F \tag{5}$$

In addition, internal forces act. The external forces pull the Knit-Mesh against a given avatar, which acts as a collision object. While the internal forces are generated by the one recurrence of the inner triangles edges(diagonals). These represent a simplified truss. This form does not give exact results, but serves as a necessary variable for the computational model. The virtual external work is due to the external forces described and can be represented by Eq. 1.

The equilibrium state is reached when the nodal displacement u_i = is less than 0.01mm/s for given forces δW_i.

The material constitutive parameters were disregarded for the time being, since a large number of experimental measurements are necessary for this. T. Pusch sums up that: due to the strong anisotropy of continuous fibre fabrics, the material properties depend on the type of loading. This requires a high level of testing for a complete experimental analysis. In general, the directional properties can be investigated in tension, compression, bending, and shear tests by experimental measurements on knitted material specimens fabricated for survey purposes [13]. Yarn elongation and/or stretching are considered to be neglected for the time being in the descriptions of deformation shown. Truss and Quad-Edges behave roughly stiffly.

Geometric Invariants

In a digital simulated polygonal representation of a knitted fabric (zoned Knit-Mesh, Fig. 1), geometric invariants are required in order to draw conclusions about the shape reproduction of knitted fabric (shape-fidelity) due to compressive, tensile and relaxation stress. In this case, invariance can be related to physical reality. However, this requires a high level of testing for a complete experimental analysis as mentioned above. Invariance describes a property that remains unchanged after operations or transformations of a certain kind have been applied to objects. The author hypothesizes that on the one hand distance deviations between the simulated knit geometry and a 3D-Scan-avatar-model may be suitable for a) predicting shape-fidelity from given deviations and b) enabling optimized parameter sets for repeated FEM simulation. On the other hand, area deviations in the quad faces and length deviations of the warp-/ and weft-, truss-lines or of the edges of the faces could be used to evaluate strongly overstretched areas. The method proposed extends the previous experimental measurements and proposes a purely digital computational model for virtual simulation. In further research, this digital data can be enriched with real measurement data to obtain a material property (micro-/ & meso-scale) database. This database may then be used to inform future simulations of knitted fabric. Furthermore, it may serve as training data for machine learning algorithms.

Used Geometric Invariants

To evaluate the kinematically calculated distortions resulting a) from the cutting treatment and b) from altered mesh ratios, a distance deviation between the 3D scan and the approximated knitted mesh structure is used as a geometric invariant for quantifiable quality determination.

Distance-Map

In order to display the deviations of the generated knitted fabric quantitatively, a point cloud of the 3D scan is compared with the calculated knitted topography. For this purpose, a tool for distance analysis of geometry and point clouds in the Rhinoceros 3D software is used. Four different additionally applied mesh ratios were calculated. The deviations and *Input-zones* are shown in Table 1.

Table 1. List of deviation und ratio variants.

Deviations	Example 1	Example 2	Example 3	Example 4
Mean	0.3021334 mm	0.2793425	0.2868251	0.2223705
Standard	0.8120128 mm	0.7525181	0.7775481	0.5867296
Average	0.02830526 mm	0.02766336	0.02774314	0.02790652
Max.	14.86173 mm	9.210369	8.264878	4.742685
Mesh Ratio Zone (mm)	Equal (grey) Course 1,47 Wale 1,1	Equal: 1,47/1,1 Red: 1,47/0,8	Equal: 1,47/1,1 blue: 0,8/0,8	Equal: 1,47/1,1 Red: 1,47/0,8 blue: 0,8/0,8 green: 0,6/0,8
Ratio Plot				

Summary

At the beginning, the special requirements and challenges for working with woven-based composites were outlined. These can be found in: wrinkling, permeability and slippage.

From the author's point of view, the basic assumptions for calculation and analysis models behave somewhat differently. This is mainly related to the more complex material-internal force relationships. Nevertheless, the surveying apparatuses can be used to analyse the material behaviour under other implications. These were listed under the heading "Experimental Measurement" and "digital augmented experimental measurement".

References

[1] P. Boisse, G. Akkerman, P. Carlone, L. Kärger, S.V. Lomov, J.A. Sherwood, Advances in composite forming through 25 years of ESAFORM, in: Int. J. Material Forming, Springer-Verlag Fr. SAS, part of Springer Nature (2022) 30. https://doi.org/10.1007/s12289-022-01682-8

[2] Y. Kyosev, The finite element method (FEM) and its application to textile technology, in: V. Dieter, Simulation in textile technology, Woodhead Publishing Ltd., Oxford, 2012, pp. 172-222. https://www.doi.org/10.1533/9780857097088
[3] K. Wu, M. Tarini, C. Yuksel, J. McCann. X. Gao, Wearable 3D Machine Knitting: Automatic Generation of Shaped Knit Sheets to Cover Real-World Objects, IEEE Trans Vis Comput Graph IEEE T VIS COMPUT GR 28 9 (2022) 3180-3192. https://www.doi.org/10.1109/TVCG.2021.3056101
[4] G. Nader, Y.H. Quek, P.Z. Chia, O. Weeger, S. Yeung, KnitKit: A flexible system for machine knitting of customizable textiles - Supplemental Document, ACM Trans. Graph. 40, 4, Article 64 (2021). https://doi.org/10.1145/3450626.3459790
[5] M.A. Popescu, KnitCrete: Stay-in-place knitted formworks for complex concrete structures, ETH-Dissertation, Serie: ETH-Dissertation, Nr.26063 (2019). https://www.research-collection.ethz.ch
[6] M. Eschenbach, Cockatoo (2020). https://github.com/fstwn/cockatoo [acs: 02.01.2023]
[7] L. Girdauskaite, G. Haasemann, S. Krzywinski, Modellierung und Simulation, in: C. Cherif, Textile Werkstoffe für den Leichtbau, Springer-Verlag Berlin, Heidelberg, 2011, pp. 573-663. https://doi.org/10.1007/978-3-642-17992-1
[8] P. Boisse, G. Akkerman, P. Carlone, L. Kärger, S.V. Lomov, J.A. Sherwood, Advances in composite forming through 25 years of ESAFORM, in: Int. J. Mater. Form. Springer-Verlag Fr. SAS, part of Springer Nature (2022) 30. https://doi.org/10.1007/s12289-022-01682-8
[9] P. Boisse, N. Hamila, E. Guzman-Maldonado, Angela Madeo, G. Hivet, F. Dell'Isola, The bias-extension test for the analysis of in-plane shear properties of textile composite reinforcements and prepregs: a review, Int. J. Mater. Form. 10 (2017) 473-492. https://hal.archives-ouvertes.fr/hal-01313827
[10] Y. Kyosev, Topology-Based Modeling of Textile Structures and Their Joint Assemblies: Principles, Algorithms and Limitations, Springer Nature Switzerland, Cham, Switzerland, 2019. https://doi.org/10.1007/978-3-030-02541-0
[11] W.J. Lewis, Tension Structures: Form and Behavoir, Thomas Telford Publishing, London, 2003. 978-0-7277-3236-1 (ISBN)
[2] Y. Kyosev, The finite element method (FEM) and its application to textile technology, in: V. Dieter, Simulation in textile technology, Woodhead Publishing Ltd., Oxford, 2012, pp. 178. https://www.doi.org/10.1533/9780857097088
[13] T. Pusch, Textilphysikalische Prüfungen, in: C. Cherif, Textile Werkstoffe für den Leichtbau, Springer-Verlag Berlin, Heidelberg, 2011, pp. 509-572. https://doi.org/10.1007/978-3-642-17992-1

Materials Research Proceedings 28 (2023) 249-258 https://doi.org/10.21741/9781644902479-27

Feasibility study of compression molding for large reinforcement structures in the commercial vehicle sector

LÜCKENKÖTTER Julian[1,a *], LEIMBACH Jan-Patrick[2,b], STALLMEISTER Tim[1,c], MARTEN Thorsten[1,d] and TRÖSTER Thomas[1,e]

[1]Paderborn University, Chair of Automotive Lightweight Design, Warburger Str. 100, 33098 Paderborn, Germany

[2]LIA GmbH, Hohenloher Weg 16, 33102 Paderborn, Germany

[a]julian.lueckenkoetter@upb.de, [b]jan.leimbach@lia-group.de, [c]tim.stallmeister@upb.de, [d]thorsten.marten@upb.de, [e]thomas.troester@upb.de

Keywords: Compression Molding, Fiber Content, Process Development, Lightweight Design

Abstract. Due to an increasing volume of shipments, there is a significant need for more delivery vehicles. One approach to reduce the associated increase in carbon dioxide (CO_2) emissions is a new light weight design approach involving the substitution of conventional materials with glass fiber mat-reinforced thermoplastics (GMT) based on polypropylene (PP). The application of GMT by compression molding is a widely used process in the automotive industry. However, application in the commercial vehicle sector requires much larger dimensions, making it necessary to clarify whether the manufacturing process and material are suitable for semi-structural applications on this scale. To find this out, two replacement geometries are abstracted in this study and manufactured by varying the main manufacturing parameters. The feasibility can be demonstrated by recording and analyzing the resulting process variables and measuring the formed fiber distribution. At the end of the paper, recommendations are given for the production of GMT structures on the scale of commercial vehicles.

Introduction

Background.

Current studies on the development of parcel services clearly show that national and international shipment volumes have risen sharply in recent years and continue to rise further. While 2.4 billion shipments were delivered in Germany in 2011, the total increased to 4.5 billion in 2021. Compared with the previous year 2020, this represents an increase of 11.2 %. By 2026, the volume of shipments is forecast to reach around 5.7 billion [1]. To cope with the growing volume of shipments, significantly more delivery vehicles will be needed. In addition to high investments, the increasing volume of traffic also leads to greater strain on the infrastructure in inner-city traffic. This in turn results in longer idle times for all road users and increased emissions of greenhouse gases, which are crucial to climate change. For this reason, it is a necessary consequence to reduce the emission of climate-damaging combustion gases such as CO_2.

Two thirds of the vehicle fleet of parcel services consists of light commercial vehicles. These include commercial vehicles with a gross vehicle weight of up to 7.5 tons [2]. Current floor assemblies for box bodies of these light commercial vehicles consist of numerous individual parts, which entails many manufacturing and assembly steps. This is not only time-consuming but also cost-intensive. Furthermore, the lightweight potential of such bodies is limited and therefore requires a new and systemic development approach.

Content from this work may be used under the terms of the Creative Commons Attribution 3.0 license. Any further distribution of this work must maintain attribution to the author(s) and the title of the work, journal citation and DOI. Published under license by Materials Research Forum LLC.

Project approach.

In this project, a process is to be developed that allows the modular subdivision of the loading floor for light commercial vehicles. For this purpose, an integral design with materials not commonly used for this area will be applied. By reducing the vehicle weight, the mass-dependent driving resistances correlating with CO_2 emissions can be minimized and the assembly effort for the floor structure can be kept to a minimum [3]. On the other hand, the lower unladen weight of the vehicle means that more parcels can be moved with a single vehicle, so that in total fewer delivery vehicles need to be used to cope with the increasing volume of parcels (cf. Fig. 1a).

Within the scope of the project, the floor modules will be manufactured from GMT, which is processed by compression molding (cf. Fig. 1b). The PP based material offers excellent weight specific mechanical properties, outstanding cost efficiency and a high degree of design freedom. The advantages over thermosets are based on shorter process times, almost unlimited recyclability and higher toughness [4-6]. Compression molding is well established and has been used in the automotive industry for many years. The heated GMT cuttings are pressed into cavities at forming pressures of up to 200 bar, so that complex structural components can be produced via flow movements of the material [4, 5]. Furthermore, due to the higher fiber length compared to fiber-reinforced granules in injection molding, higher mechanical strengths can be generated [6].

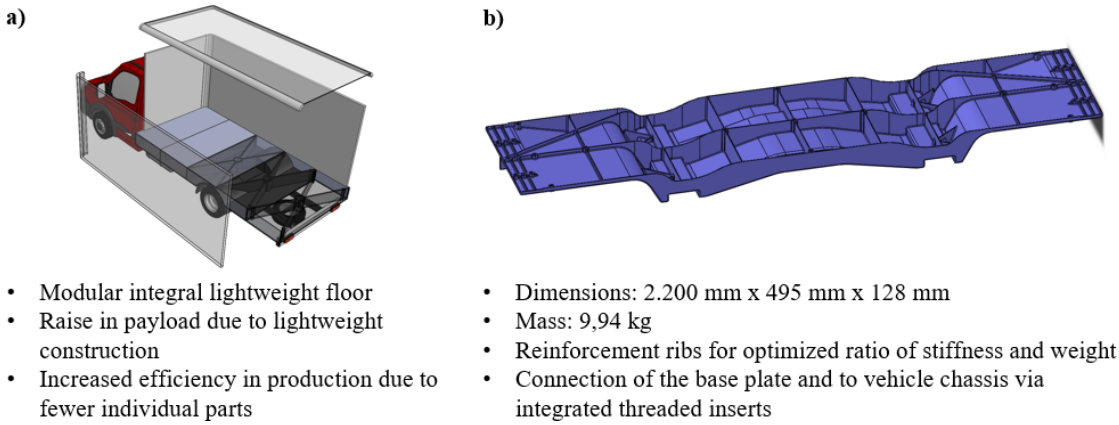

Fig. 1. a) Illustration of a commercial vehicle up to 3.5 t with box body and the associated project goals b) Design model of the floor module based on GMT.

Fig. 1b) shows the current design status of the topology-optimized CAD model of the floor module. The opposing requirements for stiffness and minimum weight can be met via reinforcement ribs. By stringing together eight modules, the entire store floor of the delivery vehicle is represented. A base plate can be mounted using threaded inserts integrated in the compression molding process. On the underside, the modules can be connected to the different geometries of the vehicle manufacturers underbodies.

Experimental Approach

To validate the process concept, it is necessary to investigate whether compression molding of GMT is suitable for the large dimensions of commercial vehicle sector in terms of mold filling and homogeneous fiber distribution. As shown in [4], the filling of the cavity in the course of the material flow movement can lead to accumulation of glass fibers in some places and thus to voids in other places of the component. These phenomena correlate with the final mechanical properties of the component. Rubio et. al. [5] found that the simpler the geometry, the more homogeneous the resulting properties are. Pöhler [7] investigated the fiber content of compression molded reinforcement ribs with a length of 90 mm as a function of the geometric design parameters. With a nominal fiber content of about 52 %, the fiber content in the rib tip was reduced up to 30 %. For

a compromise between lightweight construction and homogeneous cavity filling, Pöhler defined a demolding angle of 1.0 °, a minimum rib width of 3.0 mm and an insertion radius of 6.0 mm [7].

Rib geometry.

Since no comparable work is available for rib lengths greater than 90 mm, two different rib lengths are considered in this study and need to be investigated. As the final geometry of the floor module had not yet been determined at the time the tests were carried out, the rib lengths 87 mm and 200 mm were selected in order to be able to analyze a clear influence of the rib lengths. The rib length L, which is more than twice as long, is compensated by an increased demolding angle α and width W at the uppermost point. The minimum rib thickness is identical. Since a modular compression molding tool is used, other main dimensions of the rib are identical (cf. Fig. 2 a-b) and Fig. 3 a-c). A list of all different parameters is given in Table 1.

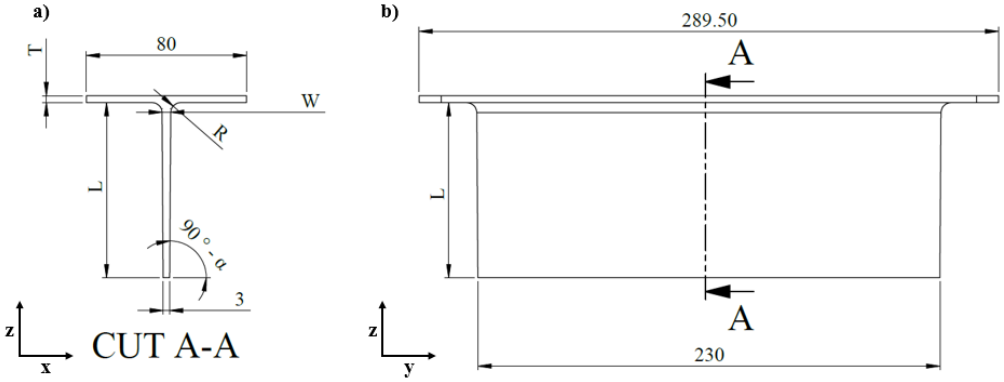

Fig. 2. Dimension of investigated ribs with a) cut view and b) longitudinal view.

Table 1. Parameters of "Rib 87 mm" and "Rib 200 mm".

Parameter	**Rib 87 mm**	**Rib 200 mm**
Rib length L	87 mm	200.0 mm
Insertion radius R	5.0 mm	6.0 mm
Rib width top W	4.3 mm	9.8 mm
Demolding angle α	0.4 °	1.0 °
Flange thickness T	Depending on material insert and mold filling (1.7 mm – 11.5 mm)	

Process technology.

The used compression molding tool can hold various cavities due to the pocket in the lower mold plate. Temperature regulation up to 95°C is enabled via a water-based temperature control unit. A cutout of the same size as the face of the cavity is provided in the upper mold plate, so that sealing of the process via vertical flash faces is possible (cf. Fig. 3 a).

Holes for piezoelectric pressure sensors are recessed at various positions within the cavities so that the resulting pressure in the cavity can be measured. In the cavity for the shorter rib length, holes are also provided for temperature sensors at the same position on the opposite cavity wall. In both cavities, two temperature sensors are positioned at the lowest point parallel to the direction of material flow in order to be able to measure the temperature of the melt shortly before the mold is completely filled (cf. Fig. 3 b-c).

As in Stallmeister et. al. [8], piezoelectric load cells are used to record the resulting press force and a draw-wire sensor is used to detect the press stroke. The data from the pressure sensors, the load cells and the draw-wire sensor are recorded simultaneously, so that no time offset has to be considered in the analysis.

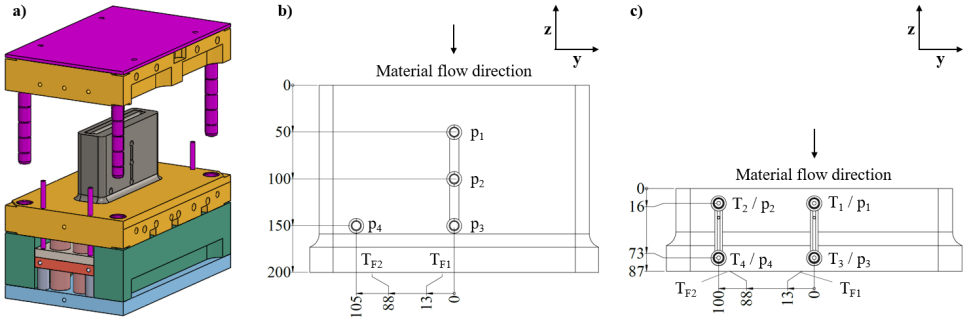

Fig. 3. a) Compression molding tool and b) – c) cavities with the respective geometric positions of the sensors.

Materials.

A widely used PP-based GMT with a fiber mass fraction of 52 % from Mitsubishi Chemicals Advanced Materials (MCAM) is used for the majority of the tests. According to the manufacturer, the material has good flow properties, a very homogeneous fiber distribution and is applied for semi-structural applications. A GMT with 33% fiber mass fraction from MCAM is used to analyze the flow behavior as a function of the fiber content. The main properties can be found in Table 2.

Table 2. Material properties of the GMT used according to MCAM.

Material properties	**GMT PP-GF52**	**GMT PP-GF33**
Thickness (laminate)	4.8 mm	5.4 mm
Density (laminate)	1.34 g/cm³	1.12 g/cm³
Density (molded)	1.40 g/cm³	1.16 g/cm³
Tensile strength	145 MPa	70 MPa
Tensile modulus	8600 MPa	4600 MPa
Melting point	165°C	166°C

Process sequence.

GMT cuttings with the dimensions of 260 mm x 50 mm are used for specimen production. To achieve a defined mass for the specific trial, smaller sheets are added until the desired weight is reached. Fig. 4 a-d) shows the following process steps.

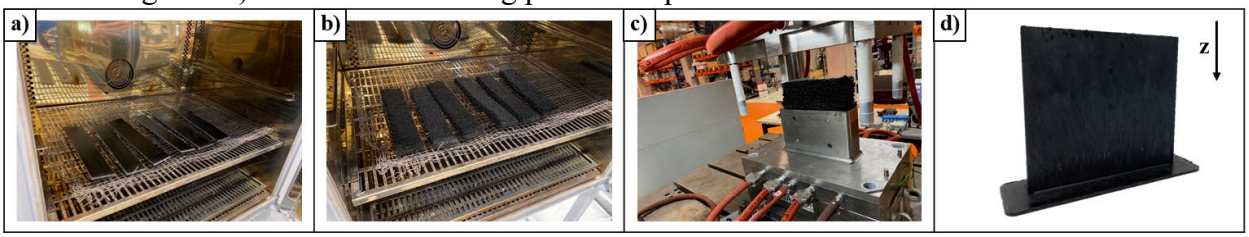

Fig. 4. Process sequence: a) GMT in furnace, b) heated GMT, c) GMT stack on cavity, d) manufactured rib.

The cuttings are placed next to each other in a 250°C convection oven and are heated for 10 minutes (cf. Fig. 4 a-b) Before transfer to the compression molding tool, the sheets are stacked in the oven to minimize temperature loss to the ambient air. After the GMT stack is centered on the cavity, the press stroke of a hydraulic forming press with a maximum press force of 50 tons is immediately actuated to form the rib (cf. Fig. 4 c-d). Closing speed of the press is about 30 mm / sec. The press force F is calibrated based on the desired forming pressure p, which is calculated from the press force F and the projected area of the cavity A_{cav}, before the test (cf. Eq. 1).

Forming pressure p is maintained for a time s of approx. 60 seconds. After completion of the pressing process, the rib is ejected via the ejector unit of the tool.

$$p = \frac{F}{A_{cav}} \tag{1}$$

Process Parameters.

In order to obtain various information on mold filling and fiber distribution in the ribs, applied forming pressures (100, 150 and 200 bar), mass of the inserted material (approx. 450-650 g) and temperature of the cavity (25°C and 90°C) for GMT PP-GF52 are systematically varied. The cavity temperatures 25°C and 90°C are marked T_{25} and T_{90} in the following. The investigations are mainly concentrated on the 200 mm long rib type and are occasionally carried out for the 87 mm long rib type (approx. 350 g – 400 g of GMT). Furthermore, the influence of a reduced fiber mass fraction (33 %) is investigated for defined test points. Each test point is performed at least twice.

Analysis methods.

To evaluate the quality of the ribs, the complete shape was visually inspected. In this context, it is useful to determine the resulting flange thickness by measuring the local thickness in at least three places and then calculating an average value. Furthermore, the resulting pressures in the cavity are analyzed as a function of the geometric position in the cavity. By means of the temperature measurements within the tool, it is possible to estimate the flowability of the GMT melt.

In order to gain an insight into the resulting fiber contents and distributions, X-rays of the ribs and point density measurements as a function of cavity depth are performed. While 2D X-ray is very well suited for the detection of fiber accumulations and voids, density measurement allows a quantitative and time-saving measurement of the resulting fiber content, since a determination of fiber content via ashing method according to DIN ISO 1172 [9] is too time-consuming for the large number of samples (up to 120 specimens). PP has a density of approx. 0.9 g/cm³ and E-glass fibers of approximately 2.6 g/cm³ [4]. Considering the specification for the pressed laminate, fiber accumulation or voids can be classified numerically (cf. Table 2). This is done by measuring the mass of the sample in ambient air (m_{GMT}) and under complete coverage with a known fluid (m_F). The difference between the masses is the mass of the displaced fluid. By dividing with the known density of the fluid ρ_F (in this case ethanol), the volume of the displaced fluid and thus the volume of the specimen V_{GMT} can be determined. Afterwards, the density ρ_{GMT} of the body can be calculated (cf. Eq. 2) [10].

$$\rho_{GMT} = \frac{m_{GMT}}{V_{GMT}} = \frac{m_{GMT}}{\frac{m_{GMT} - m_F}{\rho_F}} = \frac{m_{GMT} * \rho_F}{m_{GMT} - m_F} \tag{2}$$

Results

Mold filling.

In the following, only the results for complete shaped ribs with a length of 200 mm and the material PP-GF52 are considered, since mold filling for the 87 mm long rib is already state of the art. The heated GMT stack has an approximate temperature of 200°C before insertion, which was determined in advance with an infrared camera. At a forming pressure of 100 bar and a low cavity temperature (T_{25}), the mold filling can be improved with increased GMT mass (450-660 g), but a complete mold formation is not possible (cf. Fig. 5 a-c). Instead, the resulting flange thickness grows with increasing material input (up to 8.2 mm). If the temperature of the cavity is increased (T_{90}), complete mold formation is already possible from an inserted mass of 450 g. For this material input, the resulting flange thickness is reduced from approx. 3.2 mm (T_{25}) to 2.0 mm (T_{90}).

At a forming pressure of 150 bar, mold formation is possible from a GMT mass of 490 g (T_{25}). A positive influence on mold formation can be observed due to the lower flange thickness (2.1 mm

at 450 g GMT mass). Once again, complete mold formation is possible with a mass of 450 g when the cavity is heated up (T_{90}).

If the forming pressure is increased to 200 bar, complete ribs are possible in some cases from a mass of 450 g (T_{25}). Reliable mold filling can also be achieved starting from a mass of approx. 490 g (cf. Fig. 5 d). Variations between individual test points may be due to different transfer times and resulting temperature losses.

Basically, it can be stated that mold tempering is very advantageous for complete mold formation. It is also advisable to increase the forming pressure and the insertion mass. However, it must be considered that the increased GMT mass can lead to an undesirably high wall thickness in real components.

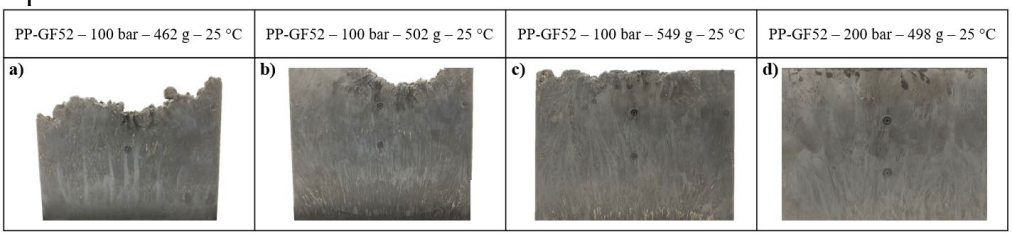

Fig. 5. Mold filling of the 200 mm long rib for selected process parameter combinations a) – d).

Process Monitoring.

Fig. 6 shows the recorded process parameters for the rib geometry with a length of 200 mm produced from GMT PP-GF52. The calculated forming pressure p, the measured values of cavity pressure p_1 – p_4 and the temperature T_{F1} – T_{F2} in the base of the rib as a function of time t are presented for two different combinations of process parameters (cf. Fig. 6 a-b). Since the calculated forming pressure p is proportional to the press force F, the force is not shown separately (cf. Eq. 1). Furthermore, the recorded press stroke changes only minimally as soon as the maximum press pressure has been applied, so this is also not shown. The process start is defined as soon as the measured force rises.

Forming pressure.

In both diagrams it is visible that forming pressure drops minimally after a steep start. Subsequently, the desired forming pressure level is reached with a reduced gradient. This phenomenon is due to the fact that the stacked GMT layers are initially compressed and start to enter the cavity since the mentioned threshold value is reached. After a compression time of at least 60 seconds, the process is terminated.

Cavity pressure.

With a small time offset, which is based on the distance between the insertion radius and the 1st pressure sensor, the cavity pressure at sensor p_1 increases with a similar slope. It is noticeable that the maximum pressure in the cavity is clearly below the calculated forming pressure. Furthermore, it is visible that the pressure p_1 does not remain constant and decreases over time. The qualitative trend of the sensors p_2 - p_4 corresponds essentially to the described trend of p_1. However, there is a premature pressure drop with increasing cavity depth (p_2, p_3/p_4) and nearness to the outer wall (p_4). This effect will be due to the thermal shrinkage of the GMT, as the material thickness decreases with increasing cavity depth, allowing the heat to dissipate faster. Furthermore, the heat can be dissipated even better at the outer edges of the cavity, so that full pressure drop occurs first at sensor p_4 (cf. Fig. 6 a-b).

Furthermore, a fundamental difference can be observed in the characteristics of the cavity pressures for different process parameters. While the cavity pressures p_1-p_4 at a forming pressure of 150 bar for a high cavity temperature (T_{90}) start almost simultaneously and reach a common maximum (cf. Fig. 6 a), a clear time offset in the pressure rise and a difference in the respective maxima can be seen at a pressure of 100 bar and a low cavity temperature (T_{25}). In addition, the

cavity pressures are maintained for a significantly shorter time and are significantly lower in relation to the calculated pressure (cf. Fig. 6 b).

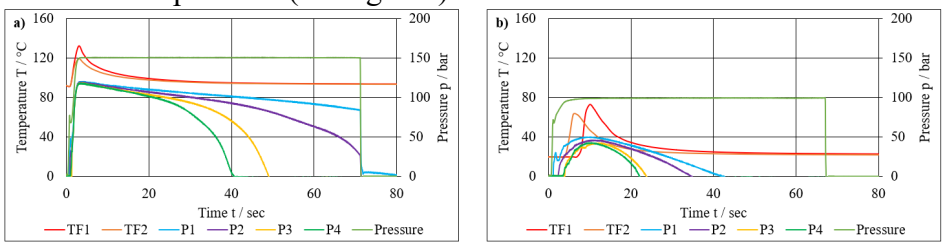

Fig. 6. Process diagrams with parameter combinations a) 150 bar, 649 g, T_{90} and b) 100 bar, 662 g, T_{25}.

Temperatures.

Examination of the resulting temperature in the base of the rib at two positions provides information about the temperature of the melt - and thus the flowability of the GMT - and about the geometric characteristics of the flow front. In the case of Fig. 6 a) both sensors reach their maximum almost simultaneously. However, the temperature at the sensor with the smaller wall distance is about 10 K lower. Compared to the set cavity temperature, there is an offset of 30-40 K. In comparison with other forming pressures and GMT masses, no significant differences can be observed.

In the second example (cf. Fig. 6 b), the maxima of the temperature sensors occur with a time offset. Here, the melt seems to first hit the sensor in the outer areas of the cavity wall. Compared to T_{25}-cavity wall, the maximum temperature offset is 40-50 K. At a maximum of 70°C, the temperature of the material is significantly below the melting temperature of the material, so that a clearly poorer flowability can be concluded.

For temperature sensors T1-T4, which are aligned orthogonally to the press direction of the 87 mm long rib, temperature offset of the GMT is even lower to the prevailing temperature in the tool (cf. Fig. 3 c). If the cavity is not heated, the maximum measured temperature is 40°C. If the cavity is heated to 90°C, the temperature of GMT is 100°C. It can be concluded from this that the outermost layer of material solidifies immediately on the cavity wall and the molding is driven from inside the structure.

Further analysis of cavity pressure.

As can be seen in Fig. 6, the measured cavity pressure sometimes differs significantly from the calculated forming pressure p. Insufficient pressure within the cavity can result in the GMT not being properly compacted. As a consequence, air pockets and fiber accumulations could result, since the pressure is not high enough to push fibers all the way to the bottom. In order to investigate this in more detail, the maximum ratio of the acting pressure ratio $p_{r,max}$ was determined for all test points for the pressure sensor p_1 (cf. Eq. 1 and 3).

$$p_{r,max} = \frac{p_{1,max}}{p_{max}} \tag{3}$$

Fig. 7 below shows this ratio as a function of inserted GMT mass, rib length, glass fiber content and cavity temperature for both rib types. Low values for a 200 mm long rib for a cavity temperature of 25°C (cf. Fig. 7 a) are due to insufficient mold filling. It can be observed that the ratio can be increased up to 0.75 when the forming pressure and GMT mass are increased. A further increase is possible with a tempered cavity, but the maximum is at a value of about 0.85 (cf. Fig. 8 b). The above-mentioned ratios can be achieved with a reduced fiber content (PP 33) even with significantly lower GMT masses (cf. Fig. 7 a-b).

Much less mass is required for the mold filling of the 87 mm long rib. Specimens prepared show that ratios of up to 92 % can be achieved even at low forming pressures and when using

GMT PP-GF52 (PP 52). At cavity temperature of 90°C and use of GMT PP-GF33 (PP 33), even a ratio of 1.0 is possible (cf. Fig 7 a-b).

From the results, it is concluded that the moldability of GMT is more advantageous with lower fiber content and shorter ribs. This is justified by the lower flow resistance due to reduced fiber content and shorter material flow paths. The impact of a reduced pressure ratio on the mechanical properties must be determined by separate investigations.

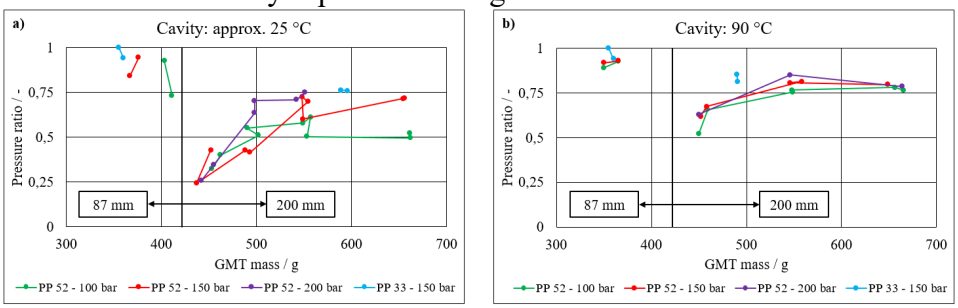

Fig. 7. Maximum pressure ratio of sensor p_1 as a function of process parameters for a) cavity temperature of approx. 25°C and b) cavity temperature of 90°C.

Qualitative fiber distribution.

A low pressure ratio could mean that a homogeneous fiber distribution might not be present for a rib length of 200 mm. To investigate this in more detail, the results of the X-ray images of the ribs are presented and analyzed below.

When analyzing the X-ray images of the 200 mm long ribs (cf. Fig. 8 a-e), it is noticeable that for the most part there is a very homogeneous fiber distribution. Only at a forming pressure of 150 bar and a low material loading of 488 g there are larger voids (cf. Fig 8 a). Smaller voids in the base of the ribs cannot be completely eliminated for PP-GF52 by increasing forming pressure, GMT mass and cavity temperature (cf. Fig. 8 b-c). In comparison, there appear to be fewer voids for a PP-GF33 (cf. Fig. 8 d). Increasing the temperature to 90 °C almost completely eliminates them (cf. Fig. 8 e).

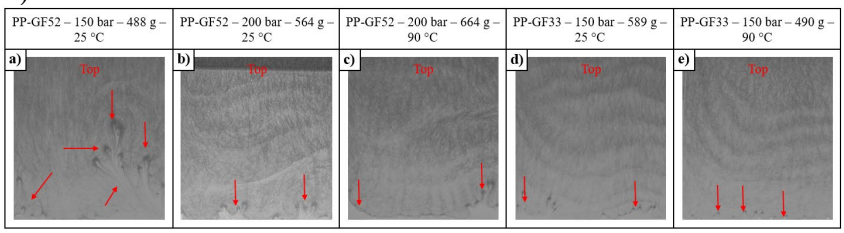

Fig. 8. X-rays of the ribs with a length of 200 mm for different parameter combinations a)-e). The full height (200 mm) and approx. half of the width (145 mm) are shown starting from the cavity wall.

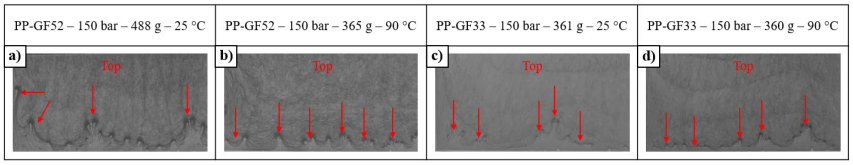

Fig. 9. X-rays of the ribs with a length of 87 mm for different parameter combinations a)-d). The full height (87 mm) and approx. 75% of the width (217 mm) are shown starting from the cavity wall.

In relation to the total rib length, the voids are significantly more pronounced in the 87 mm ribs (cf. Fig. 9 a-d). For PP-GF52, minimization is possible by increasing the cavity temperature

(cf. Fig. 9 a-b). For PP-GF33, the voids are again smaller, but complete elimination is not possible by tempering the cavity (cf. Fig. 9 c-d).

Quantitative fiber distribution.

To determine the density, the ribs are divided into rectangular test pieces. For ribs with a length of 200 mm, the test pieces have a size of 20 mm x 20 mm and for ribs with a length of 87 mm a size of 10 mm (parallel to flow direction) x 20 mm. For comparison, an average value is calculated for each height row (cf. Fig 10 a-b).

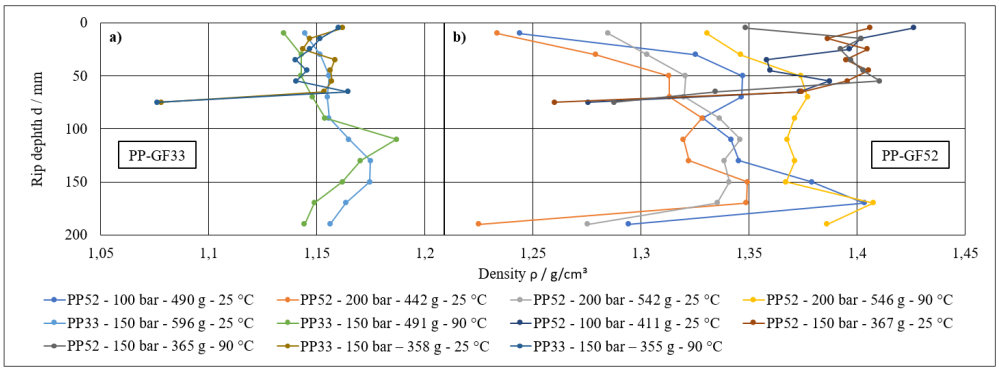

Fig. 10. Density measurements for both rib types with materials a) PP-GF33 and b) PP-GF52.

For rib length 200 mm, it is noticeable that the density, despite decreasing cavity pressure, rises continuously with increasing rib depth. When using PP-GF52, the density is many times below the value from the data sheet for the starting material. It is possible that the prevailing pressure is not sufficient to cause enough compression for the large wall thicknesses. A lack of glass fibers is unlikely at this point (cf. Fig. 10 b). For PP-GF33, the density is more homogeneous, with a tendency to increase as well (cf. Fig. 10 a).

In the deepest row, the density for PP-GF52 is significantly lower than in the penultimate row for many ribs. This will be due to the voids detected in the X-ray image. In contrast, for a high forming pressure and a tempered cavity, almost no drop is observed and the density value corresponds to the data plot for molded GMT. Obviously, an increased forming pressure, a sufficient amount of GMT and a tempered cavity leads to a satisfying compression and fiber distribution in the material (cf. Fig. 10 b).

For the 87 mm long rib, the value for compressed GMT from the data sheet is achieved (almost) for all specimens in the first row. With decreasing rib depth, this remains relatively constant and decreases again more strongly in the last row. In this application, a strong decrease is also observed for PP-GF32 (cf. Fig. 10 a-b). Basically, the findings made correlate well with the X-ray images and the certain pressure ratios. Voids occur only in the lowest areas and are more pronounced in the geometry of an 87 mm long rib. This can be answered by the low demolding angle. Furthermore, the increased pressure ratios for the GF-PP33 and the 87 mm long rib result in improved compression. This can be compensated for a 200 mm long rib by a high forming pressure and tempering of the cavity. A sufficient amount of GMT is also essential.

Summary

In the research project, floor modules for delivery vehicles should be produced from GMT using the compression molding process. Due to the dimensions prevailing in the commercial vehicle sector and a topology optimization carried out, reinforcing ribs up to a length of 200 mm may be required to meet the mechanical requirements. This goes beyond the previous state of the art, so that it was necessary in this study to abstract two substitute geometries of the floor module and to

test the process for its suitability for this application scenario by varying the most significant process parameters (e.g. forming pressure, mass, temperature of cavity, fiber content).

By analyzing the mold filling, the resulting process parameters (e.g. resulting pressures and temperatures in the cavity) and methods for qualitative and quantitative determination of the fiber distribution, a basic feasibility for the application in the commercial vehicle sector can be demonstrated. To prevent voids without any fibers, it must be ensured that the demolding angle of the cavity is greater than or equal to 1 °, sufficient amount of GMT is used (≥ 450 g), high forming pressure (≥ 150 bar) is applied and that the tool is heated (≥ 90 °C).

The knowledge gained will be used for further design of the floor module. Nevertheless, further mechanical tests will have to be carried out to confirm the study carried out. Moreover, a process simulation with the 3DTimon software will be validated on the basis of the recorded measurement data. This is to be used in the final stage to predict the manufacturing process of the whole floor module.

Acknowledgement
The research project is funded by the German Federal Ministry for Economic Affairs and Climate Action as part of "Technologietransfer-Programm Leichtbau". Thanks are due to all project members not mentioned by name. Special thanks go to Dr. Manel Ellouz of Bielefeld University of Applied Sciences for her support in the preparation and discussion of the X-ray images.

References
[1] KE-CONSULT Kurte&Esser GbR, KEP-Studie 2022 - Analyse des Marktes in Deutschland, Cologne, 2022.
[2] KE-CONSULT Kurte & Esser GbR, BIEK Kompendium Teil 2, 2018.
[3] B. Klein, T. Gänsicke, Leichtbau-Konstruktion. Dimensionierung, Strukturen, Werkstoffe und Gestaltung, eleventh ed., Springer Vieweg, Wiesbaden, 2018. https://doi.org/10.1007/978-3-658-26846-6
[4] AVK – Industrievereinigung Verstärkte Kunststoffe e. V., Handbuch Faserverbundkunststoffe / Composites, fourth ed., Springer Vieweg, Wiesbaden, 2014. https://doi.org/10.1007/978-3-658-02755-1
[5] A. Rubio, P. Eguizabal, M.A. Mendizabal and J.F. Liceaga, Influence of the processing parameters on glass mat reinforced thermoplastic (GMT) stamping, Compos. Manuf. 3 (1992) 47-52. https://doi.org/10.1016/0956-7143(92)90183-U
[6] J.L. Thomason, The influence of fibre length and concentration on the properties of glass fibre reinforced polypropylene: 5. Injection moulded long and short fibre PP, Compos. Part A 33 (2002) 1641-1652. https://doi.org/10.1016/S1359-835X(02)00179-3
[7] S. Pöhler, Konzeptionierung und Auslegung eines Vorderachsträgers in hybrider Leichtbauweise im C-Segment, Shaker-Verlag, Düren, 2021. ISBN: 9783844082104
[8] T. Stallmeister, T. Tröster, In-Mold-Assembly of Hybrid Bending Structures by Compression Molding. Key Eng. Mater. 926 (2022) 1457-1467. https://doi.org/10.4028/p-5fxp53
[9] DIN EN ISO 1172:1998-12, Prepregs, Formmassen und Laminate; Bestimmung des Textilglas- und Mineralfüllstoffgehalts, Beuth Verlag GmbH, Berlin, 1998.
[10] Information on http://www.tomchemie.de/Mathe/3.1.3/3.1.3.htm (accessed 31 January 2023).

Materials Research Proceedings 28 (2023) 259-266 https://doi.org/10.21741/9781644902479-28

Compaction behaviour of magnesium alloy-based fibre metal laminates at varying forming parameters

LIU Zheng[1,a *], SIMONETTO Enrico[1,b], GHIOTTI Andrea[1,c] and BRUSCHI Stefania[1,d]

[1]Department of Industrial Engineering, University of Padova, Via Venezia 1, 35131 Padova, Italy

[a]zheng.liu@studenti.unipd.it, [b]enrico.simonetto.1@unipd.it, [c]andrea.ghiotti@unipd.it, [d]stefania.bruschi@unipd.it

Keywords: Fibre Metal Laminates, Magnesium Alloy, Forming, Compaction Behaviour

Abstract. This research presents a methodology for the compaction characterization of thermoplastic prepregs with a twill weaving style under a range of parameters typical of the thermoforming process applied to magnesium alloy-based fibre metal laminates (FMLs). The compaction tests were conducted making use of a plate-to-plate mode testing setup. The through-thickness and transverse width of the prepregs were evaluated on the FML specimen cross-section at varying compaction force and temperature. Significant deformations were observed at the lowest compaction force above the prepreg polymer melting point, whereas a further increase in the compaction force led to gradually smaller through-thickness and in-plane deformations. Additionally, a higher decrease in thickness and increase in width of the prepregs were detected at higher temperatures.

Introduction

Nowadays, the aerospace and automotive industries are facing more and more environmental and economic challenges to manufacture parts that have to meet the requested high standards. In particular, the energy efficiency in transportation can be enhanced by reducing the weight of their structures. FMLs, as a hybrid material system interlacing metallic and fibre-reinforced polymer (FRP) sheets (hereafter called prepreg), show high potentials for that thanks to the high strength-to-weight ratio they offer, combined with good fatigue and impact [1] performances.

The manufacturing of the FML components usually involves the forming of the metal and prepreg sheets into the designed shape individually, followed by the bonding of the two parts with adhesives [2,3]. However, this process chain necessitates a long time and use of several dies, which, overall, increase the manufacturing costs. On the contrary, thermoforming, as a single step forming technique, facilitates the manufacturing process since the forming and bonding of the metal and FRP sheets are carried out simultaneously at elevated temperature.

It is worth underlining that, being the FML a hybrid system, the inhomogeneity in the metal and prepreg characteristics exacerbates the challenges of quality control during both the manufacturing step and subsequent in-service life of the formed component [4]. Therefore, a more comprehensive understanding of the metal and FRP sheets deformation mechanisms during forming becomes mandatory, also in the view of improving the FML formability. Among the deformation mechanisms arising during forming, the transverse flow of the prepreg significantly affects the performances of the formed component, especially in case of parts having a doubly-curved shape and high thickness [5]. During deformation, the prepreg transverse flow may be induced by an uneven distribution of the normal pressure at the bending areas, where the polymer matrix is squeezed outwards transversely. As a result, a change in the fibre volume fraction is also obtained [6].

The FML part thickness variation during the fabrication process significantly depends on the part geometrical features. In the stamping process of hat-shaped parts, a reduction of the thickness

Content from this work may be used under the terms of the Creative Commons Attribution 3.0 license. Any further distribution of this work must maintain attribution to the author(s) and the title of the work, journal citation and DOI. Published under license by Materials Research Forum LLC.

was observed at the radii at the bottom as a consequence of high compaction forces [7]. Under a uniform normal pressure, the polymer matrix is squeezed transversely from the high-pressure region toward adjacent areas facing a lower load. Similar results were also presented in the [8] when stamping cup-shaped components: material accumulation was found in the bottom and side walls adjacent to the radii areas.

Another potential driver behind the thickness variation of FML parts is the structure of the fibres within the prepregs. For uniaxially oriented, namely unidirectional (UD), prepregs, since the fibre can migrate with the resin along the transverse direction, only the matrix is squeezed along the longitudinal direction due to the inextensibility of the fibres [9]. While for the cross-plied UD or woven fabrics, even if the transverse behaviour can be limited to some extent due to the pin-joint structure [5], the influence of a normal pressure gradient on the nonuniform distribution of thickness cannot be neglected.

The polymer matrix of the prepregs used in existing FMLs is either thermosetting or thermoplastic. Thermosetting polymers, such as the epoxy resin, have been widely used, such as the FMLs named GLARE [10]. However, their forming cycle is quite long due to the time needed for the thermosetting polymer curing process [11]. On the other hand, thermoplastic polymers represent an alternative solution thanks to some benefits such as good recyclability, outstanding toughness, and shorter forming time [12]. The thermoforming process applied to FMLs with thermoplastic resin-based prepregs has to be carried out at temperatures higher than the melting limit of the thermoplastic resin. Due to the high mobility and flow characteristics of the polymer matrix at elevated temperatures, its thickness dynamically varies at varying process parameters. After forming consolidation takes place, during which the molten polymer matrix transfers into a solid state by cooling down below its glass transition point. The compaction behaviour of cross-plied UD carbon fibre reinforced thermoplastic tapes (CF/PPS and CF/PEEK) at different temperatures and normal pressures was investigated in [13]. Above their melting points, the thermoplastic polymers exhibit dramatic deformations, with higher in-plane deformations and gradually smaller through-thickness displacements as the temperature rises.

To gain a comprehensive understanding of the deformation mechanisms arising during the thermoforming process applied to magnesium alloy-based FMLs with a PA6 thermoplastic polymer matrix, the compaction behaviour of the prepregs was experimentally investigated at varying thermoforming parameters.

Materials and Methods

Materials.

The FMLs investigated in this study are made of two layers of AZ31B magnesium alloy sheets (thickness 0.5 mm) as skins and one layer of glass fibre-reinforced PA6 consolidated prepreg (Tepex® 102-RG600 (2)/47% Type B, thickness 1 mm) as core. The mechanical characteristics of the magnesium alloy sheets and prepregs in the as-received condition were determined by carrying out standard tensile tests (ISO-6892) on a 50 kN MTS™ 322 hydraulic dynamometer, see Table 1. The main material data of the prepregs are presented in Table 2.

Table 1. Mechanical properties of the AZ31B sheets and prepregs.

AZ31B sheets		**Prepregs**	
Elastic Modulus	45 GPa	Tensile modulus	18 GPa
Yield Strength	158±2 MPa	Tensile strength	380±5 MPa
Tensile Strength	248±4 MPa	Strain at break	2.3%
Shear Modulus	16.7 GPa	Flexural Modulus	16 GPa
Poisson's Ratio	0.35	Flexural Strength	300 ±5 MPa

Table 2. Main characteristics of the prepregs.

Layup	**Value**		**Unit**
	Longitudinal	**Transversal**	
Fibre	E-Glass		
Weaving style	Twill 2/2		
Area weight (dry fabric)	600		g/m²
Yarn count	1200		tex
Yarn density	2.5	2.5	1/cm
Weight rate	50	50	%
Fibre content	47		Vol-%
Thickness per layer	0.5		mm
Laminate density	1.8		g/cm³

Compaction tests.

To assess how the prepregs behave during the thermoforming process, compaction tests with the above-mentioned material system were conducted on the testing apparatus shown in Fig. 1 (a). The prepreg is positioned in the centre of the AZ31B sheets, as shown in the sketch of Fig. 1(b). The width of the AZ31B sheets (40 mm) is twice that of the prepreg (20 mm), which facilitates the observation of the change in the width of the prepreg. The tests were performed on the MTS™ 322 hydraulic dynamometer equipped with the MTS™ 651 environmental chamber for heating up the specimen to the testing temperature. To achieve a uniform temperature distribution, the apparatus is heated up for 1 hour before assembling the specimen. Afterwards, the metal sheets and prepreg stacked according to the sketch of Fig. 1 (b) are placed on the lower punch for 5 minutes to assure they reached the target temperature (*Tt*). The force *F* is applied to the specimen in a controlled way when the upper and lower punches touch both the surfaces of the FML specimen, in a plate-to plate configuration. The normal pressure *p* can be calculated from Eq. (1), where *A* is the contact area of the prepreg with the metal sheets.

$$p = \frac{F}{A} \tag{1}$$

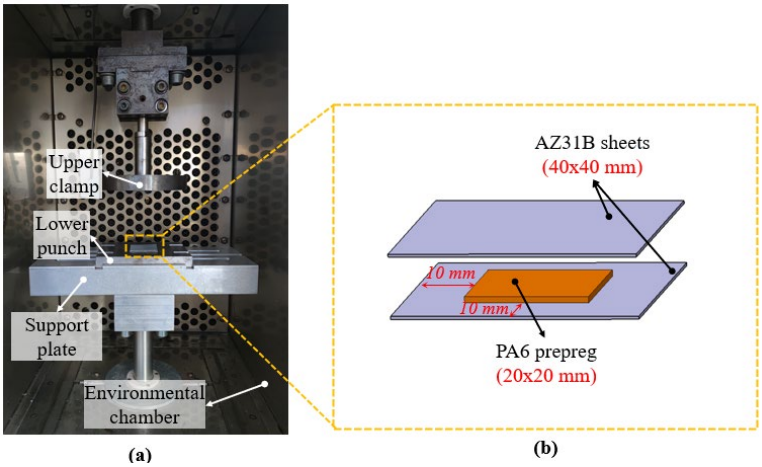

Fig. 1. Compaction tests: (a) testing apparatus, and (b) sketch of the employed FML sample.

Three levels of testing temperatures were selected to assess the effect of temperature on the compaction behaviour of the prepregs, namely 215°C, 235°C, and 255°C. Among them, 235°C and 255°C are both above the PA6 melting temperature, which is 220°C, while the 215°C testing temperature was selected to have a comprehensive evaluation of the prepreg compaction behaviour both below and above the melting point of the polymer matrix. To investigate how the FMLs behave differently under various levels of compaction force, the compaction tests were carried out at each testing temperature applying different forces, namely 40 N, 120 N, 200 N, 600 N,1000 N, and 2000 N, which is equivalent to the normal pressure varying from 0.1 MPa to 5 MPa. To be consistent with a typical thermoforming cycle, a ramp-dwell loading method was used as shown in Fig. 2: the force rises at 10 N/s to the target force (*Ft*) in the ramp period, followed by its holding in the dwell period for 240 s, after which the specimen is left to cool down to room temperature (*Tr*) still with the force applied to finish the consolidation process. For each testing condition, three tests were performed to assure the repeatability of the results.

The tested specimens were saw cut along the A-A and B-B planes as shown in Fig. 3 (a), and then these two cross-sections were polished. The through-thickness and transverse width of the prepreg within the FML were measured by making use of a microscope.

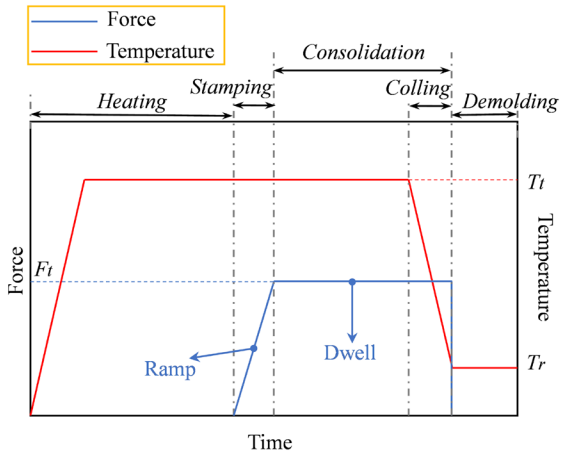

Fig. 2. Experimental procedure of the compaction tests.

Results and Discussion

Thickness variation.

After the consolidation process at different forces and temperatures, the thickness of the prepregs was measured on the cross-sections shown in Fig. 3. Fig.4 reports the normalized thickness t/t_0 versus the compaction force F for the three levels of testing temperature. Overall, the measured thickness changes dramatically at temperatures below and above the melting point of the PA6 polymer matrix. At 215°C, the thickness reduction is very limited, regardless of the compaction force, as the solid state of the polymer matrix at this temperature imparts thermally stable properties to the prepreg, resulting in an almost elastic response [11]. When testing above the PA6 melting point, the polymer matrix viscous response induces a more obvious decreasing thickness at increasing loading. For both the testing temperatures above the PA6 melting point, the prepreg thickness decreased dramatically when the applied compaction force was lower than around 600 N, then it remained stable at increasing compaction force.

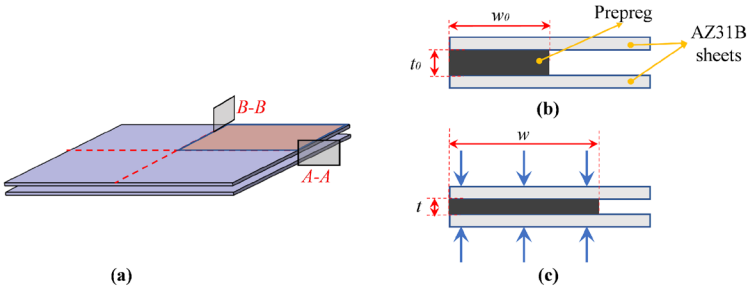

Fig. 3. Scheme of the prepreg thickness measurement method: (a) selection of the cross-sections, (b) before and (c) after consolidation.

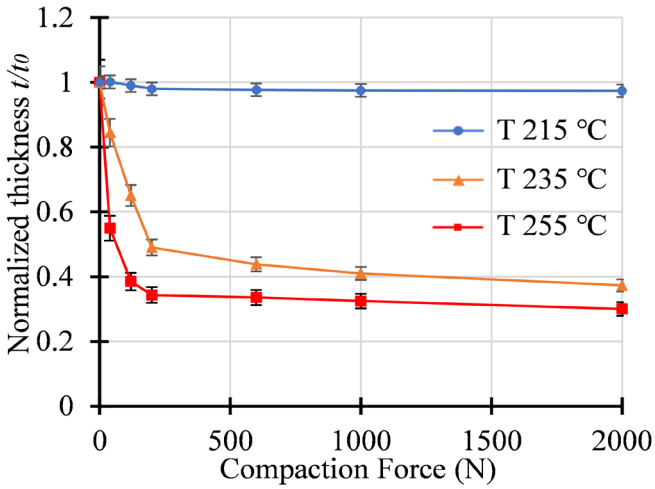

Fig. 4. Normalized thickness of the prepregs at varying compaction force.

Fig. 5 shows the morphology of the FMLs in the cross-section when tested at 235°C under 40 N, 600 N, and 2000 N compaction forces. When a compaction force of 40 N is applied, the warp and weft fibres within layer 1 and layer 2 are separated by the polymer matrix present in a high amount between them. At increasing compaction force, the gap between the warp and weft fibres becomes narrow as more polymer matrix together with some fibres is squeezed towards the adjacent areas; the warp fibres within layer 1 touch the weft fibres within layer 2 when the compaction is 600 N, which is shown by the neglectable gap between them in Fig. 5 (b). Fig. 6

shows the micrograph of the edge of the FML at 600 N compaction force. The concurrent pattern of squeezing flow, also known as shear flow (namely the resin pushes the fibres transversely), and bleeding flow (namely the resin bleeds out without shifting the fibres) enables the high compressibility of the prepregs. At the same time, the undulation of the weft yarns is gradually flattened at increasing compaction force, inducing a more uniform distribution of the warp fibres between these two plies of weft fibres. As more warp fibres in the middle area along the thickness direction are squeezed out, the gap between the two plies of weft fibres becomes narrower. When there are not enough warp fibres separating these two plies of weft fibres, two plies of weft fibres with the same orientation meet each other thus acting as an individual ply with a larger thickness as shown in Fig. 5 (c), which is relevant to 2000 N compaction force. Due to the PA6 lower viscosity at 255°C than at 235°C, the higher flow and mobility of the polymer matrix facilitate the squeezing flow of the resin together with the fibres from the centre to the edge areas, which causes a further reduction of the prepreg thickness for the same loading conditions.

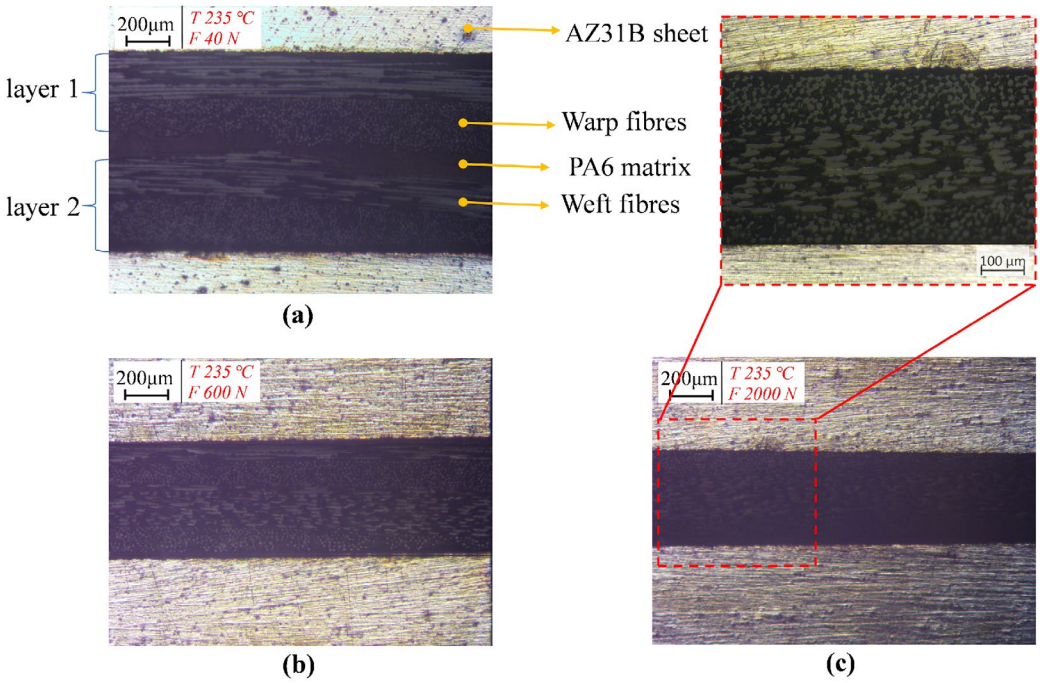

Fig. 5. Morphology of the FMLs on the cross-section tested at 235°C under (a) 40 N, (b) 600 N, and (c) 2000 N compaction force.

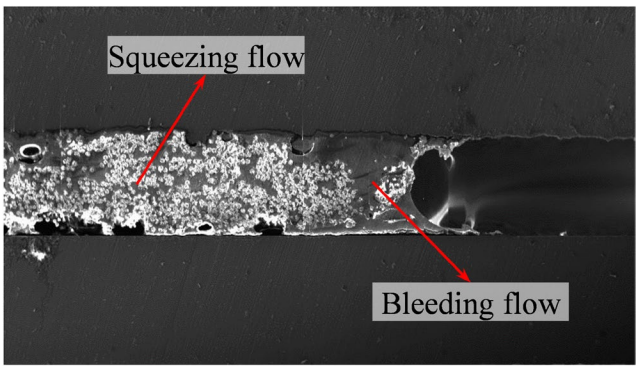

Fig. 6. SEM image of the edge of the FML at 235 °C under 600 N compaction force.

Width increase.

The compaction force promotes a redistribution of the fibres and matrix via a transverse squeezing that influences the prepreg width. Fig. 7 shows the normalized width *w/w0* versus the compaction force *F* for the three levels of testing temperature. As expected, like the through-thickness compaction behaviour, no changes in the prepreg width can be observed at 215°C testing temperature, regardless of the applied compaction force. When the testing temperatures are above the PA6 melting point, the normalized width increases at increasing compaction force, but for values lower than 600 N, whereas, for higher compaction force values the normalized width reaches a steady state. The transverse widening observed in experiments was shown to grow in tandem with the increase in temperature. As a result of its lower viscosity at these temperatures, the molten polymer matrix is able to transfer the load to the fibres, which permits an increased motion of the polymer matrix and fibres.

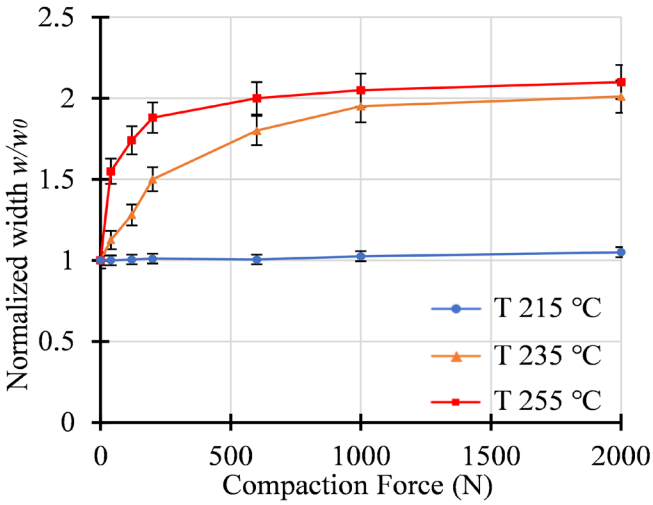

Fig. 7. Normalized width of the prepregs at varying compaction force.

Summary

In this research, the compaction behaviour of thermoplastic prepregs with a twill weaving style under a range of parameters typical of the thermoforming process applied to magnesium alloy-based FMLs was investigated. By conducting compaction tests, the through-thickness and transverse width of the prepregs within the tested FMLs at different loading conditions were measured and compared. The main findings can be summarized as follows:

- When testing below the melting point of the polymer matrix, the prepregs exhibit no significant variations in the thickness and width. Above the melting point of the polymer matrix, a dramatic decrease in the thickness and an increase in the width of the prepregs were observed.
- Most of the compaction occurred when the compaction force was below 600 N, above which a compaction limit was reached with just slight variations in the prepreg thickness and width.
- Moreover, the lower viscosity of the polymer matrix at higher temperatures allows for a greater compaction.

The results of this experimental research of this study are the basis for the analytical modelling of the compaction behaviour of the PA6-based prepregs with a twill 2/2 weaving style at elevated temperatures, which will be further implemented into FEM to predict the thickness distribution of thermoformed FMLs with doubly-curved shapes.

References

[1] X. Zhang, Q. Ma, Y. Dai, F. Hu, G. Liu, Z. Xu, G. Wei, T. Xu, Q. Zeng, W. Xie, Effects of surface treatments and bonding types on the interfacial behavior of fiber metal laminate based on magnesium alloy, Appl. Surf. Sci. 427 (2018) 897-906. https://doi.org/10.1016/j.apsusc.2017.09.024

[2] H.O. Werner, D. Dörr, F. Henning, L. Kärger, Numerical modeling of a hybrid forming process for three-dimensionally curved fiber-metal laminates, AIP Conference Proceedings 2113 (2019) 020019. https://doi.org/10.1063/1.5112524

[3] C.T. Poppe, H.O. Werner, M. Kruse, H. Chen, N.B. Khalifa, F. Henning, L. Kärger, Towards 3D Process Simulation for In Situ Hybridization of Fiber-Metal-Laminates (FML), Key Eng. Mater. 926 (2022) 1399-1412. https://doi.org/10.4028/p-cr2tco

[4] H. Chen, S. Li, J. Wang, A. Ding, A focused review on the thermo-stamping process and simulation progresses of continuous fibre reinforced thermoplastic composites, Compos. B Eng. 224 (2021) 109196. https://doi.org/10.1016/j.compositesb.2021.109196

[5] Z. Ding, H. Wang, J. Luo, N. Li, A review on forming technologies of fibre metal laminates, Int. J. Lightweight Mater. Manuf. 4 (2021) 110-126. https://doi.org/10.1016/j.ijlmm.2020.06.006

[6] J.P.-H. Belnoue, O.J. Nixon-Pearson, D. Ivanov, S.R. Hallett, A novel hyper-viscoelastic model for consolidation of toughened prepregs under processing conditions, Mech. Mater. 97 (2016) 118-134. https://doi.org/10.1016/j.mechmat.2016.02.019

[7] A. Ghiotti, S. Bruschi, M. Kain, L. Lizzul, E. Simonetto, G. Tosellob, Simultaneous bonding and forming of Mg fibre metal laminates at high temperature. J. Manuf. Process. 72 (2021) 105-114. https://doi.org/10.1016/j.jmapro.2021.10.017

[8] T. Heggemann, W. Homberg, Deep drawing of fibre metal laminates for automotive lightweight structures, Compos. Struct. 216 (2019) 53-57. https://doi.org/10.1016/j.compstruct.2019.02.047

[9] J.A. Barnes, F.N. Cogswell, Transverse flow processes in continuous fibre reinforced thermoplastic composites, Compos. 20 (1989) 38-42. https://doi.org/10.1016/0010-4361(89)90680-0

[10] R. Alderliesten, On the development of hybrid material concepts for aircraft structures, Recent Pat. Eng. 3 (2009) 25-38. https://doi.org/10.2174/187221209787259893

[11] T. Sinmazcelik, E. Avcu, M.O. Bora, O. Coban, A review: fibre metal laminates, background, bonding types and applied test methods, Mater. Des. 32 (2011) 3671-3686. https://doi.org/10.1016/j.matdes.2011.03.011

[12] Y. Yang, R. Boom, R. Irion, D.-J. v. Heerden, P. Kuiper, H. de Wit, Recycling of composite materials, Chem. Eng. Process 51 (2012) 53-68. https://doi.org/10.1016/j.cep.2011.09.007

[13] J.P.-H. Belnoue, M.A. Valverde, M. Onoufriou, X. Sun, D.S. Ivanov, S.R. Hallett, On the physical relevance of power law-based equations to describe the compaction behaviour of resin infused fibrous materials, Int. J. Mech. Sci, 199 (2021) 106425. https://doi.org/10.1016/j.ijmecsci.2021.106425

Materials Research Proceedings 28 (2023) 267-276 https://doi.org/10.21741/9781644902479-29

Experimental setup and method for the characterization of ply-ply adhesion for fiber-reinforced thermoplastics in melt

PIERIK Rens[1,2,a*], ROUWMAAT Thijs[1,2], GROUVE Wouter[1], WIJSKAMP Sebastiaan[2] and AKKERMAN Remko[1,2]

[1]Faculty of Engineering Technology, Chair of Production Technology, University of Twente, Drienerlolaan 5, Enschede, 7522 NB, the Netherlands

[2]ThermoPlastic composites Research Center (TPRC), Palatijn 15, Enschede, 7521 PN, the Netherlands

[a]e.r.pierik@utwente.nl

Keywords: Hot Press Forming, Thermoplastic Matrix Composites (TPC), Ply-Ply Adhesion

Abstract. Process simulation software for hot press forming is a vital tool for the development of complex continuous fiber-reinforced thermoplastic parts for structural applications. The simulation tools need to be accurate to truly facilitate the design stage, which in turn requires accurate material characterizations and constitutive models. The material forming behavior is composed of different deformation mechanisms, one of which is the separation of adjacent plies or delamination. Currently, the resistance against delamination or ply-ply adhesion is modeled as a constant tensile stress that needs to be overcome, the value of which is based on an educated guess. To date, no standard exists to characterize this material property for thermoplastic matrix composites (TPC) in melt. Hence, we discuss and evaluate several methods to measure ply-ply adhesion of TPCs. The most promising approach, a so-called probe test, was further pursued and a setup was designed and manufactured for the use in a rheometer. Subsequently, we measured the required normal force to separate two C/LM-PAEK tapes in melt. Repeated tests on the same specimen resulted in an increasing adhesive peak force, which we relate to a change in the amount and distribution of the matrix material at the ply's surface. The peak force increased also with increasing compression time and pressure. We found a reasonable correlation of the average measured peak force with the values currently assumed in simulation software.

Introduction

Hot press forming is an attractive technology to manufacture small to medium-sized parts from continuous fiber reinforced thermoplastic blanks through remelting and reshaping. The process is rapid, cost-effective, and automatable. Complex parts can be produced with tailored lay-ups based on unidirectional (UD) fiber reinforced tapes using automated fiber placement (AFP) or automated tape laying (ATL) processes [1]. Moreover, thermoplastic matrix composite (TPC) parts can be welded to create large structural components [2]. However, the development of a proper production line becomes increasingly difficult with more complex parts and materials, as defects like forming-induced wrinkles could occur.

The development stage of a new part is facilitated by process simulation software that provide design engineers the tools for virtual design iterations and, with that, reduce trial-and-error costs [3,4]. The predictions of these simulations need to be accurate, especially on defect generation, to truly enable first-time-right defect-free manufacturing. In turn, accurate predictions require accurate material characterization and constitutive modeling to properly describe the material behavior during forming. Hence, different deformation mechanisms that occur during forming are

Content from this work may be used under the terms of the Creative Commons Attribution 3.0 license. Any further distribution of this work must maintain attribution to the author(s) and the title of the work, journal citation and DOI. Published under license by Materials Research Forum LLC.

commonly considered, which can then be characterized and modeled separately to capture the material's forming behavior.

One of the considered deformation mechanisms is delamination [5], which describes the separation of adjacent plies during the hot forming process. The resistance against delamination, or the ply-ply adhesion, is currently often described as a constant tensile stress based on an educated guess [3] or as a certain adhesion stiffness [6]. Moreover, the adhesive tension (normal direction) as used in numerical simulations indirectly affects the friction between adjacent plies (tangential direction) through the use of a penalty method that models the normal pressure in the ply-ply contact [5]. In our recent work [7,8], we investigated the ply-ply friction response to improve the constitutive friction modeling, for which the coupling with ply-ply adhesion of TPC in melt needs to be investigated in more detail as well. A standard to characterize the ply-ply adhesion for TPC in melt is to the best of our knowledge not defined.

The study of Mulye et al. [9] seems to be the only one that dealt with characterizing the ply-ply adhesion of TPCs in melt. These authors used a DMA with only the molten matrix material to measure the polymer melt strength as function of the debonding rate, which was subsequently used in a forming simulation for a fiber-reinforced PA-66 part to improve the prediction of local discontinuous plies (patches). Although the prediction of the patch's position and orientation improved, characterization of only the matrix material itself could result in an overestimation of the ply-ply adhesion, especially for plies with high fiber volume fractions. Contrary, the fibers were included in studies on the characterization of ply-ply adhesion of thermoset composites [e.g. 10-13], using different methods.

Given the above, this research aims to develop a setup and method to measure the required normal force to separate TPC tapes in melt for the characterization of ply-ply adhesion.

Background

The mechanisms and factors influencing ply-ply adhesion of TPCs will be presented in this section together with a brief description of some experimental methods to measure adhesion.

Ply-ply adhesion.

The creation of a bond between two molten TPC plies that are brought into contact develops through two mechanisms [14,15]. First, intimate contact or sufficient wetting needs to be established, meaning that the polymer chains of both surfaces are in close physical contact. Secondly, at locations with intimate contact, the polymer chains interdiffuse over the interface to form an entangled network, a process referred to as healing.

The formation of intimate contact is hindered due to the asperities on the ply's surface. Hence, the degree of intimate contact can be enhanced by applying a normal pressure. A lower viscosity of the polymer also promotes intimate contact formation. Thus, the time required for intimate contact depends on the applied pressure and polymer viscosity. The presence of fibers at the surface leads to local dry fiber-fiber contacts, which do not contribute to the formation of a strong bond. Therefore, Çelik et al. [16] proposed an effective intimate contact, considering only the intimate contact of matrix-rich areas in a study on contact development of UD C/PEKK tapes with AFP. Squeeze flow and percolation of matrix material increase the effective intimate contact.

The healing process starts once the polymer surfaces are locally in intimate contact. The polymer chains diffuse and form entanglements across the interface, leading to a fully entangled network comparable to the one in the bulk. The time required to establish this state depends on the polymer dynamics, for which generally de Gennes' theory of reptation is used [17]. A typical time in this theory is the reptation time, which denotes the required time for a certain polymer chain to escape from its initial configuration and, with that, form new entanglements with neighboring chains. According to Wool et al. [14], the strength of an interface grows through interdiffusion with time to the power ¼ and a fully entangled structure is achieved at a timescale comparable to

the reptation time, which is probably in the order of less than a second for the polymer melt considered here [18].

The timescales involved in ply-ply bonding of TPCs are, however, not so straightforward, as experimental studies found hundreds of seconds for healing [15,19] or intimate contact formation [20]. Polymer degradation, reducing the chain mobility, could have affected the healing process in the study of Avenet et al. [15], while the relatively long timespan for intimate contact formation found by Levy et al. [20] is probably due to the low consolidation pressure applied (1.34 kPa).

Adhesion test setups.

Adhesion was frequently characterized for thermoset composites for a variety of purposes as well as for the performance of (pressure-sensitive) adhesives. An overview of the different methods found in literature is visualized in Fig. 1 [21,22]. Crossley et al. [22] designed a setup to peel prepreg tape off a surface (Fig. 1a). A comparable test method is the T-peel test (ASTM D1876) [23], the fixed arm peel test [23], and the floating roller peel test (ASTM D3167), as visualized in Fig. 1b-d, respectively. For all four tests, the adhesion is quantified by gradually peeling surfaces from each other. Other techniques for adhesion characterization are the probe [10,12] and loop test (ASTM D6195), schematically illustrated in Fig. 1e and 1f, respectively. An interface is created by bringing the surfaces into contact and the formed adhesion can subsequently be measured by pulling. The probe and loop test are based on a more direct separation of the surfaces in normal direction, though the loop test actually features a combination of peeling and pulling.

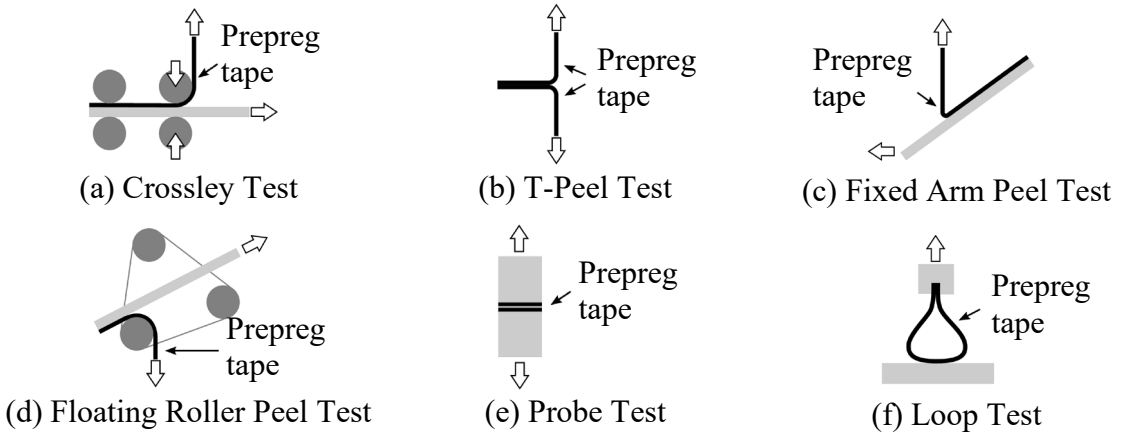

Fig. 1. Schematic illustration of several testing methods to measure adhesion [21,22].

Design of the Test Setup

A brief concept evaluation will be presented first followed by the final design of the test setup.

Concept evaluation.

From the four peel methods (Fig. 1a-d), we expect that the T-peel test (Fig. 1b) would suit the best for the use with TPCs, as it avoids the use of moving or rolling parts and the specimen can be pre-consolidated to form the ply-ply bond, closely resembling the situation in actual hot press forming. Contrary, the formed contact with the loop test (Fig. 1f) is not predefined and the stiffness and geometry of the loop will affect the measurement. The probe test will be more robust regarding contact formation and probably results in a more straightforward separation by pulling compared to the loop test.

Preliminary experiments were conducted with both the T-peel and probe method to determine the best suitable approach. During testing with the T-peel method, unwanted movement of the specimen due to slight misalignments and/or the convective heat flow in the oven resulted in variations in the pull force. Further, this measured force is a combination of adhesive failure and

bending of the specimen. Contrary, the pull force measured with the probe test can directly be used to calculate an apparent tensile stress for adhesive failure, as considered in simulation software for hot press forming. The probe tests was also slightly easier regarding specimen mounting and test cycle time. However, we observed slippage of the specimen in the clamps during the probe tests and specimens tended to bend in the force direction. These effects need to be minimized to reduce variations and to obtain a pure ply-ply adhesion measurement. All in all, the probe test was found the most promising.

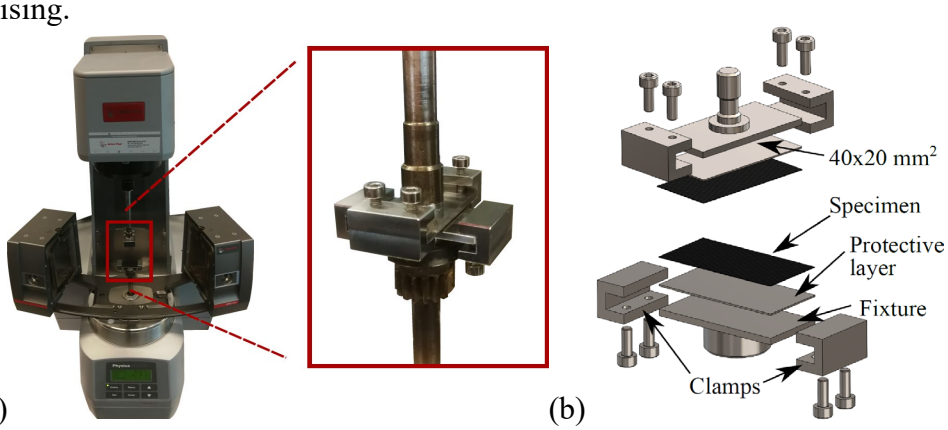

Fig. 2. Test setup mounted in an Anton Paar MCR501 rheometer (a) and (b) exploded view of the test setup with top and bottom fixture featuring direct connections for the rheometer.

Setup design.

The probe test fixture as used for the preliminary tests was further developed. The final setup mounted in an Anton Paar MCR 501 rheometer is shown in Fig. 2a. An exploded view of the designed setup, consisting of a top and bottom fixture out of stainless steel with direct connections for the rheometer is shown in Fig. 2b. The clamps at either side of the fixtures can be used to fix the TPC tapes. The usable surface area of each fixture is 40x20 mm^2, resulting in an overlap area of 20x20 mm^2 in case of a 0°/90° interface. Protective layers out of steel, measuring 40x20x1 mm^3, were used to shield the fixture from the molten polymer and served as a backing material for the TPC tape (see Fig. 2b), as will be discussed in the next section.

Experimental Work

Materials.

The composite material used in this research consisted of a unidirectional (UD) carbon-fiber reinforcement with a pre-impregnated LM-PAEK thermoplastic matrix. The tape, known as TC1225 C/LM-PAEK, was manufactured by Toray Advanced Composites. The melting temperature equals 305°C, according to the manufacturer.

Specimen preparation.

The tape material was supplied in 12 inch rolls, from which 39x18 mm^2 strips were cut with the fibers in the longitudinal direction. The strip width was chosen slightly smaller than the width of the fixture to ensure that the whole specimen was supported. The matrix material at the ends of the strips was removed using a blow torch to improve the clamping of the specimen in the setup. Next, a co-consolidation step was used to bond a strip to the protective metal plate. A bond between the metal plate and the tape material stronger than the ply-ply adhesion avoids parasitic bending of the specimen during testing, i.e. the metal served as a rigid backing material. Strips were placed on the protective layers in an oven at a temperature of 330°C under a slight pressure (around 50 kPa) for 10 minutes. The specimens were dried overnight before testing.

Test procedure.

Two co-consolidated strips were clamped in the top and bottom fixture of the test setup (see Fig. 2b) to form a test specimen. The fixtures were then mounted in an Anton Paar MCR501 rheometer and the oven was set to the test temperature T_t. A nitrogen flow was applied to avoid degradation during testing. A schematic illustration of the experimental procedure is shown in Fig. 3. The tapes at the top and bottom fixture were brought into contact with a controlled compression force F_c, resulting a normal pressure p, for a compression time t_c. After t_c, the force was put to zero for a short period of time t_x to ensure a force reading equal to zero at the start of the measurement. Subsequently, a constant upward displacement rate $\dot{\lambda}$ was applied to the top fixture to separate the plies, yielding a peak force F_{max}, as illustrated in Fig. 3. Besides the force, the time t and displacement λ were logged as well with a sampling frequency of 200 Hz. The measured data was smoothed with a Gaussian filter with a 50 points window to suppress the high-frequency scattering.

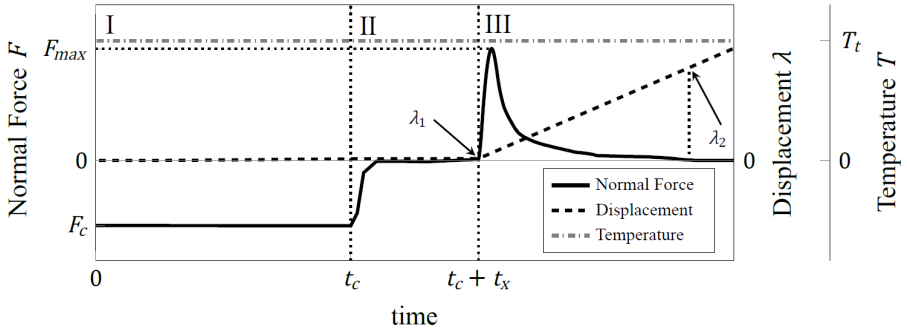

Fig. 3. Experimental procedure used to measure ply-ply adhesion.

Experiments.

All tests were performed at a temperature of 340°C and a displacement rate of 0.05 mm/s. In a first series of experiments, the effect of repeated testing of the same specimen on the peak force was investigated. Repeated tests on the same specimens, under different conditions, greatly reduces the experimental time required for a full characterization of the ply-ply adhesion. A normal pressure of 15 kPa was applied for 120 s followed by separation of the plies, which was repeated for ten times and performed for three specimens.

In a second series of tests, we investigated the effect of the compression phase on the subsequent ply-ply adhesion force by varying the compression time and pressure as listed in Table 1. The measurements were conducted in triplicate and a fresh specimen was used for each test. The longer compression times marked with an asterisk were only measured with a pressure of 15 kPa.

*Table 1. Test matrix for the second series of tests to investigate the effect of the compression phase. Compression times marked with * were tested only with a pressure of 15 kPa.*

Parameter	Input	Unit
T	340	°C
$\dot{\lambda}$	0.05	mm/s
p	3, 15, 31	kPa
t_c	10, 30, 60, 120*, 240*, 480*	s

Microscopy.

The ply's surface in the contact area was analyzed using a Keyence VHX-7000 digital microscope before and after testing to investigate whether the test invoked changes in the surface morphology of the tape. Micrographs were made from tapes in pristine state and after being measured for 3 and 12 times.

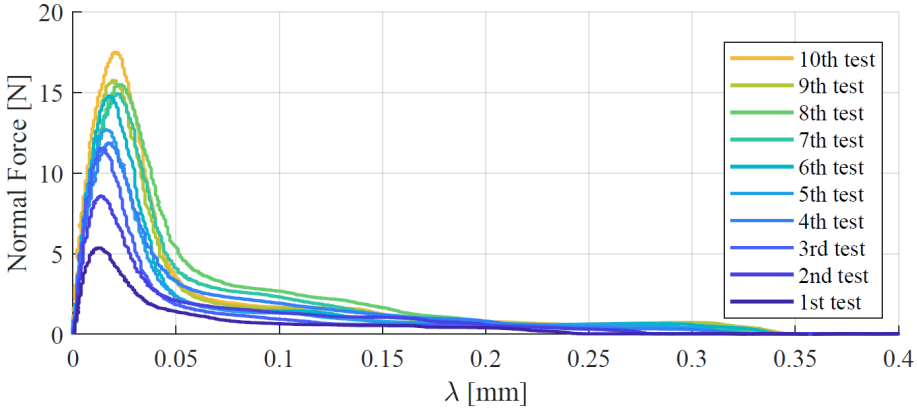

Fig. 4. Normal force versus displacement curves for a single specimen measured ten times with a compression phase (time of 120 s and pressure of 15 kPa) between each run.

Results

The normal force-displacement curves of a specimen tested repeatedly for 10 times are shown in Fig. 4. A clear peak adhesion can be observed followed by a gradual decrease in force towards zero at full separation around 0.3 mm. The peak force F_{max} gradually increases with increasing number of repetitions. The average trend of F_{max} over three specimens as function of the number of tests is shown in Fig. 5a. The error bars denote the standard deviation, indicating a large spread between the specimens. The increase in F_{max} with succeeding tests is further visualized in Fig. 5b, in which F_{max} is normalized with the first measured peak force for each of the three specimens.

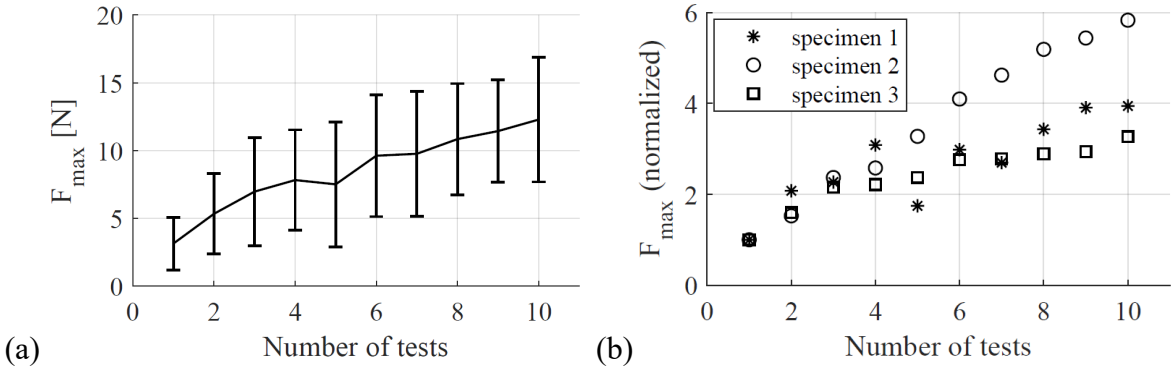

Fig. 5. Average peak force with number of repetitions (a) with the error bars denoting the standard deviation over three specimens and (b) normalized peak force with repetitions for each of the thee specimens measured.

The effect of the compression phase on the measured peak force is shown in Fig. 6a and 6b through varying the compression time and applied pressure, respectively. A longer compression time or higher pressure resulted in a higher F_{max}. Within the chosen experimental window, the peak force continued to grow without showing a sign of an asymptotic value. Even for the tests conducted with an extended compression time at a pressure of 15 kPa (see Fig. 6a), a limiting value for the peak force was not reached.

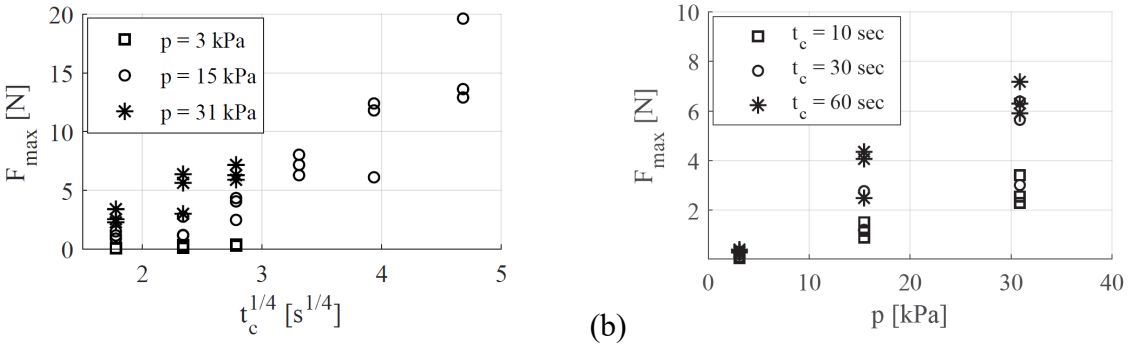

Fig. 6. Effect of the compression phase on the measured normal peak force through (a) the compression time and (b) the applied pressure.

Micrographs of the surfaces of the plies before and after testing are visualized in Fig. 7. The pristine state, shown in Fig 7a, clearly shows the fiber direction with matrix material distributed over the whole surface, shown by the lighter shade areas in the micrograph. The matrix material tended to form clutters in the contact area on the ply's surface after three repeated adhesion tests, as visualized in Fig. 7b. We observed a partition on the ply's surface, as highlighted in the micrograph by the red line, with contact (left) and non-contact (right). With more repetitions, the clutters formed into larger patches of matrix material, as visualized in the micrograph of a ply's surface tested for 12 times (see Fig. 7c). Note that the micrographs only show a small part at the boundary of the ply-ply contact, though the observations outlined above a more general and apply to the whole contact area.

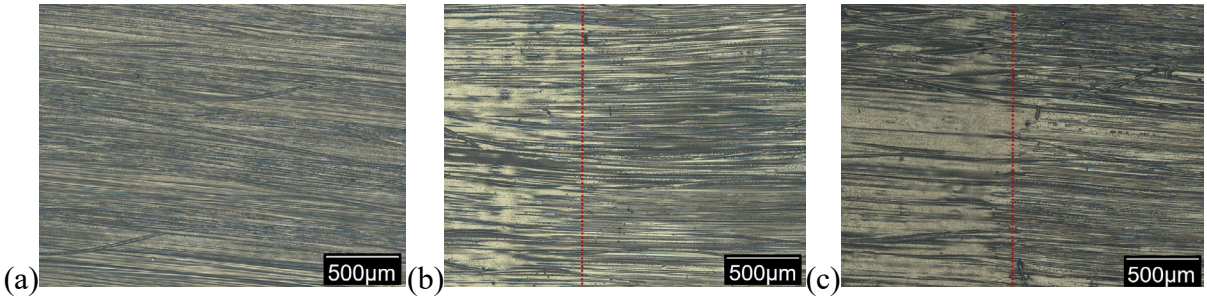

Fig. 7. Micrographs of the ply's surface (a) in pristine state and after tested for (b) 3 times and (c) 12 times. The red line approximately corresponds to the border between contact (left) and non-contact (right). The matrix material is visible by the lighter shade color.

Discussion

Repeated tests.

The peak force increased with the number of repetitions on the same specimen (see Fig. 5), meaning that reconsolidation of a specimen in the setup affects the subsequent ply-ply adhesion. The change in adhesion after repeated reconsolidation suggests to measure a specimen only once, consequently increasing the experimental time required for a full characterization of the ply-ply adhesion. More importantly, this reconsolidation effect disputes the representativity of the initial consolidation to simulate the actual ply-ply bond during hot press forming. Based on the experimental observations and the micrographs of the ply's surface as shown in Fig. 7, we believe that the force increase relates to a change in the amount and distribution of the matrix material in the contact area after repeated testing. The formation of clutters and larger patches of matrix material may be due to polymer strings between the top and bottom ply. These polymer strings tend to pull matrix material towards the ply's surface during a ply-ply adhesion test. Once a polymer string fails, the polymer settles in clutters on the ply's surface. With more repetitions, more matrix material gathers at the surface, forming larger agglomerates and increasing the

subsequent peak adhesive force. A change in the matrix material itself through degradation was found less probable to explain the increase in ply-ply adhesion based on control tests without nitrogen and DSC measurements.

Besides the increase in adhesion with repeated testing, quite a large spread was obtained on the measured peak force F_{max} as indicated by the error bars in Fig. 5a. This variation could be attributed to local variations in the fiber volume fraction at the ply's surface, leading to different effective intimate contacts between the specimens. Preliminary tests with an additional layer of matrix material in the ply-ply interface substantiated this idea of a change in effective intimate contact, as we measured a lower spread in F_{max} (not shown here).

Effect of the compression phase.

In the second series of tests, the effect of the compression phase on the measured peak force was investigated using fresh specimens for each test (see Fig. 6). The peak force increased with increasing compression time and pressure, as expected from literature. A higher pressure enhances the formation of effective intimate contact, resulting in a higher adhesion [15,16]. The timespan at which we observed an increase in ply-ply adhesion is also comparable to findings in earlier research on TPCs [15,19,20]. It remains unclear which mechanism, either intimate contact formation or healing, dominates this behavior. A ¼ power relation between force and time seems to appear at longer compression times, suggesting a healing process, though more experiments are required to validate this trend.

An apparent tensile stress σ_{max} can be computed through dividing the measured peak force by the total surface area of 18x18 mm^2, which can be used in process simulation software to describe the ply-ply adhesion. The maximum apparent tension values for different compression times and pressures are listed in Table 2, which are of the same order of magnitude as considered elsewhere. For example, Haanappel [5] estimated an adhesive tensile stress of 100 kPa for forming simulations with C/PEEK using the software package AniForm [4]. Recently, the tensile stress was lowered in an update on AniForm based on advancing insight. Lastly, Mulye et al. [9] found an average tensile stress of 6.2 kPa in their research on a thermoplastic composite with a PA-66 matrix.

The compression phase in the ply-ply adhesion tests was necessary to create a bond between the two ply's surfaces that were brought into contact. Ideally, the created ply-ply bond mimics the one present in pre-consolidated blanks or in layups produced with AFP or ATL to properly simulate the actual hot press forming process. However, the exact time and pressure that should be used for the compression phase remains unclear. Future research could be to investigate which values for the compression time and pressure should be used to mimic a certain process or the use of pre-consolidated specimens could be considered.

Table 2. Maximum apparent tensile stress σ_{max} in ply-ply adhesion for different compression times t_c and pressures p computed from the measured peak force and the surface area.

σ_{max} [kPa]		t_c [s]					
		10	30	60	120	240	480
p [kPa]	3	0.3	0.7	1.1	-	-	-
	15	3.7	5.3	11.2	22.1	31.2	47.5
	31	8.5	15.5	19.9	-	-	-

Summary

A setup was designed and manufactured to measure the required normal force to separate two plies, or the ply-ply adhesion, of thermoplastic matrix composites (TPC) in melt. The design is based on a so-called probe test, as used in adhesion tests for thermoset composites, and can be mounted in a rheometer. TPC tapes were brought into contact for a certain compression time under

a controlled pressure, after which the formed bond was separated with a constant upward displacement rate while measuring the normal force. Repeated adhesion tests on a single specimen with a compression phase between each run resulted in an increase of the normal peak force, implying that a fresh specimen needs to be used for proper ply-ply adhesion characterization. The increase in force was attributed to the formation of clutters and patches of matrix material in the contact area on the ply's surface, increasing the peak force after each adhesion test.

Increasing the compression time and applied pressure resulted in an increase of the peak force. A higher pressure is expected to increase the formation of intimate contact, consequently increasing the ply-ply adhesion. The compression time could affect the peak force through both the formation of intimate contact and the healing process. The latter mechanism might prevail as the force versus time curve seems to follow the typical ¼ power law relation, though the data is not conclusive enough on this aspect. Future work is to determine suitable parameters for the compression phase to mimic the ply-ply bond as formed in pre-consolidated blanks or after the AFP or ATL process.

Acknowledgements
This work was performed as part of the MaterialenNL research program under project number 17880, which is financed by the Dutch Research Council (NWO). The authors also gratefully acknowledge the financial and technical support from the industrial and academic members of the ThermoPlastic composites Research Center (TPRC).

Data availability
The supplementary data for this conference article is available in the 4TU.ResearchData repository under DOI: 10.4121/21805422.

References
[1] T.K. Slange, Rapid Manufacturing of Tailored Thermoplastic Composites by Automated Lay-up and Stamp Forming, Ph.D. thesis, University of Twente, Enschede, The Netherlands, 2019.
[2] Y.M. Buser, G. Bieleman, W.J.B. Grouve, S. Wijskamp, R. Akkerman, Characterization of orthotropic electrical conductivity of unidirectional C/PAEK thermoplastic composites, in: 20th European Conference on Composite Materials, Lausanne, Switzerland: ECCM, 2022.
[3] S.P. Haanappel, R.H.W. Ten Thije, U. Sachs, B. Rietman, R. Akkerman, Formability analyses of uni-directional and textile reinforced thermoplastics, Compos. Part A 56 (2014) 80-92. https://doi.org/10.1016/j.compositesa.2013.09.009
[4] AniForm, Virtual Forming, Information on http://www.aniform.com. (accessed 31 January 2023).
[5] S.P. Haanappel, Forming of UD Fibre Reinforced Thermoplastics, PhD Thesis, University of Twente, Enschede, The Netherlands, 2013.
[6] D. Dörr, M. Faisst, T. Joppich, C. Poppe, F. Henning, L. Kärger, Modelling approach for anisotropic inter-ply slippage in finite element forming simulation of thermoplastic UD-tapes, in: 21th International Conference on Material Forming, Palermo, Italy: ESAFORM, 2018, 020005.
[7] E.R. Pierik, W.J.B. Grouve, S. Wijskamp, R. Akkerman, On the origin of start-up effects in ply-ply friction for UD fiber-reinforced thermoplastics in melt, in: 24th International Conference on Material Forming, Liège, Belgium: ESAFORM, 2021, 3695.
[8] E.R. Pierik, W.J.B. Grouve, S. Wijskamp, R. Akkerman, Prediction of the peak and steady-state ply-ply friction response for UD C/PAEK tapes, Compos. Part A 163 (2022) 107185. https://doi.org/10.1016/j.compositesa.2022.107185
[9] P.D. Mulye, J. Hemmer, L. Morançay, C. Binetruy, A. Leygue, S. Comas-Cardona, P. Pichon, D. Guillon, Numerical modeling of interply adhesion in composite forming of viscous discontinuous thermoplastic prepregs, Compos. Part B 191 (2020) 107953. https://doi.org/10.1016/j.compositesb.2020.107953

[10] D. Budelmann, H. Detampel, C. Schmidt, D. Meiners, Interaction of process parameters and material properties with regard to prepreg tack in automated lay-up and draping processes, Compos. Part A 117 (2019) 308-316. https://doi.org/10.1016/j.compositesa.2018.12.001
[11] K.J. Ahn, J.C. Seferis, T. Pelton, M. Wilhelm, Analysis and characterization of prepreg tack, Polym. Compos. 13 (1992) 197-206. https://doi.org/10.1002/pc.750130308
[12] O. Dubois, J.-B. Le Cam, A. Béakou, Experimental analysis of prepreg tack, Exp. Mech. 50 (2010) 599-606. https://doi.org/10.1007/s11340-009-9236-7
[13] A. Endruweit, G.Y.H. Choong, S. Ghose, B.A. Johnson, D.R. Younkin, N.A. Warrior, D.S.A. De Focatiis, Characterisation of tack for uni-directional prepreg tape employing a continuous application-and-peel test method, Compos. Part A 114 (2018) 295-306. https://doi.org/10.1016/j.compositesa.2018.08.027
[14] R.P. Wool, B.-L. Yuan, O.J. McGarel, Welding of polymer interfaces, Polym. Eng. Sci. 29 (1989) 1340-1367.
[15] J. Avenet, A. Levy, J.-L. Bailleul, S. Le Corre, J. Delmas, Adhesion of high performance thermoplastic composites: development of a bench and procedure for kinetics identification, Compos. Part A 138 (2020) 106054. https://doi.org/10.1016/j.compositesa.2020.106054
[16] O. Çelik, D. Peeters, C. Dransfeld, J. Teuwen, Intimate contact development during laser assisted fiber placement: microstructure and effect of process parameters, Compos. Part A 134 (2020) 105888. https://doi.org/10.1016/j.compositesa.2020.105888
[17] P.G. de Gennes, Reptation of a polymer chain in the presence of fixed obstacles, J. Chem. Phys. 55 (1971) 572-579. 10.1063/1.1675789
[18] F.N. Cogswell, Thermoplastic Aromatic Polymer Composites, Butterworth-Heinemann, Oxford, United Kingdom, 1992. ISBN: 978-0-7506-1086-5
[19] F. Yang, R. Pitchumani, Healing of thermoplastic polymers at an interface under nonisothermal conditions, Macromolecules 35 (2002) 3213-24. https://doi.org/10.1021/ma010858o
[20] A. Levy, D. Heider, J. Tierney, J.W. Gillespie, Inter-layer thermal contact resistance evolution with the degree of intimate contact in the processing of thermoplastic composite laminates, J. Compos. Mater. 48 (2013) 491-503. https://doi.org/10.1177/0021998313476318
[21] D. Budelmann, C. Schmidt, D. Meiners, Prepreg tack: a review of mechanisms, measurement, and manufacturing implication, Polym. Compos. 41 (2020) 3440-3458. https://doi.org/10.1002/pc.25642
[22] R.J. Crossley, P.J. Schubel, N.A. Warrior, The experimental characterization of prepreg tack, in: 17th Inter. Conference on Composite Materials, Edinburgh, United Kingdom: ICCM, 2009.
[23] D.R. Moore, J.G. Williams, A protocol for determination of the adhesive fracture toughness of flexible laminates by peel testing: fixed arm and T-peel methods, ESIS protocol, 2010.

Materials Research Proceedings 28 (2023) 277-284 https://doi.org/10.21741/9781644902479-30

XCT-based microscale analysis of structure and deformability of abdominal wall meshes

SOETE Jeroen[1,a *], MAES Arne[1,2,3,b], ROJAS Camilo[1,c], KYOSEV Yordan[4,d], SCHMIDT Ann-Malin[4,e], LOMOV Stepan V.[1,f], MISEREZ Marc[5,g], KERCKHOFS Greet[1,2,3,6,h] and WEVERS Martine[1,i]

[1] Dept of Materials Engineering, KU Leuven, Leuven, Belgium

[2] Biomechanics lab, Institute of Mechanics, Materials and Civil Engineering, UCLouvain, Louvain-la-Neuve, Belgium

[3] Pole of Morphology, Institute of Experimental and Clinical Research, UCLouvain, Brussels, Belgium

[4] Institut für Textilmaschinen und Textile Hochleistungswerkstofftechnik, TU Dresden, Dresden, Germany

[5] Dept. of Abdominal Surgery, University Hospital Gasthuisberg, Leuven, Belgium

[6] Prometheus, Division for Skeletal Tissue Engineering, KU Leuven, Leuven, Belgium

[a]jeroen.soete@kuleuven.be, [b]arne.maes@kuleuven.be, [c]camilo.rojas@kuleuven.be, [d]yordan.kyosev@tu-dresden.de, [e]ann-malin.schmidt@tu-dresden.de, [f]stepan.lomov@kuleuven.be, [g]marc.miserez@kuleuven.be, [h]greet.kerckhofs@uclouvain.be, [i]martine.wevers@kuleuven.be

Keywords: XCT, Knitted Textiles, Synthetic Meshes, Abdominal Wall Hernia Repair

Abstract. Abdominal wall hernia repair mostly involves the implantation of a synthetic mesh material. The link between the mesh microstructure, mechanical behaviour and clinical outcome is still not fully understood, complicating the selection of a suitable patient-specific mesh. Here, we created a parametric 3D model of a synthetic mesh based on X-ray microfocus computed tomography (XCT) images. The model was implemented in a *TexMind* Warp Knitting Editor software and then exported for finite element model (FEM) analysis. This model allows better understanding of the mechanical behaviour of the mesh and identifying the influence of single structural parameters that are essential for the design of the mesh. We also used the XCT-based filament paths to directly build a FEM, representing all 3D structural details of the as-produced product. Whilst the mechanical analysis of the mesh is feasible, important difficulties are identified, related to the initial relaxed mesh contacts configuration and necessity of the mesh pretension in experiments and calculations.

Introduction

An abdominal hernia is a medical condition in which an internal organ partially protrudes through the surrounding structures, i.e. the musculofascial layers of the abdominal wall. There is a lifetime risk for inguinal hernia of about 27% for men and 3% for women. Consequently, abdominal wall hernia repair is among the most frequently performed surgeries, and it is mostly performed on adults younger than 65 years old [1]. Hernia repair involves in most cases the implantation of a synthetic mesh material to substantially reduce the rate of hernia recurrence [2,3]. Nowadays, a wide range of mesh types is available for the surgeon to choose from in terms of polymer type (degradable or not), fibre structure (mono- vs. multifilament), textile structure (woven vs. knitted), strength, stiffness, elasticity, pore size, weight per area, etc. [4]. Depending on the manufacturing process, synthetic meshes can be divided in woven, non-woven or knitted (weft or warp).

Content from this work may be used under the terms of the Creative Commons Attribution 3.0 license. Any further distribution of this work must maintain attribution to the author(s) and the title of the work, journal citation and DOI. Published under license by Materials Research Forum LLC.

Nowadays, however, most commercially available meshes are fabricated by warp-knitting since it allows to achieve the desired mesh properties, both structurally and biomechanically [5].

Clinical outcome and postoperative quality of life are strongly influenced by the structural and biomechanical properties of the mesh, [6]. Biomechanically, the mesh should ideally behave in a similar manner to the native tissues of the abdominal wall, whilst being able to withstand the *in vivo* mechanical loads, as internal abdominal pressure can reach values up to 20 kPa [7]. Current mesh designs generally can withstand the high forces within the abdominal wall, but often have anisotropic characteristics concerning elasticity. In that case, mesh positioning should conform to the elasticity of the abdominal wall. However, many of the biomechanical tests used in vitro for the mechanical characterization of synthetic meshes currently still lead to inconsistent and non-robust results. Only scarce information is available on the biomechanical behaviour of the meshes after implantation, which if present strongly relates to the biocompatibility of the material and consequent tissue ingrowth. There is, hence, a need for better understanding of the structural changes during loading and the in vivo effects on mechanical properties of the meshes to be able to improve their design.

State-of-the Art of Warp-Knitted Meshes Modelling and Mechanical Characterisation

The warp knitting technology provides a unique possibility to produce structures, which satisfy all technical requirements for hernia repair [8, 9]. Especially the mesh type fabrics produced by fine mono-filaments have excellent seam slippage characteristics – the longer chains of loops remains stable during deformation [10]. At the same time knitted meshes provide a reduced contact area with a foreign body, hence decreasing the risk for granuloma bridging and providing sufficient open space for tissue ingrowth [11].

The mechanical response of surgical warp-knitted meshes is studied in [12-15]. The mesh biaxial tension and shear mechanical response is studied experimentally in these papers (including *in-vivo* measurements). In [16] the mechanical response of the mesh represented as a membrane is modelled, which advances this work towards a model of a warp-knitted loops in a mesh structure. These developments are included in a general "landscape" of geometrical and mechanical models of warp-knitted fabrics [17-20]. The available geometrical models create an idealized 3D sketch of the fabrics, which does not represent the relaxed state of the material and has to be refined using mechanical modelling with finite element method (FEM).

X-ray Microfocus Computed Tomography (XCT) provides the opportunity for direct observation and modelling of the 3D geometry of textiles [21], including knitted fabrics [22] in a relaxed or loaded state. In the present paper we compare parametric FEMs of a warp-knitted surgical mesh created using the *TexMind* software [20] and a "digital twin" of the real mesh, with an XCT-based FEM. These fine-tuned parametric models would allow optimization of the surgical mesh in future work.

Developments of the XCT-based geometrical models and simulation of their mechanical behaviour is well-aligned with similar studies of the composite reinforcements under forming [23].

Materials

A DynaMesh®-CICAT Visible mesh (FEG Texiltechnik, Aachen, Germany) was used in this study. This mesh is designed for the extraperitoneal repair of primary ventral (umbilical, epigastric) and incisional hernias [24]. This anisotropic large pore surgical mesh is a monofilament (+/- 100 μm) polyvinylidene fluoride (PVDF, grade SOLEF 1008 of Solvay Solexis) mesh with black orientation strips (Fig. 1a) that act as guides in the correct positioning of the implant during surgery, for conforming to the elasticity of the abdominal wall. Moreover, the black orientation filaments, are impregnated with iron oxide for allowing MRI visibility of the mesh. The PVDF filaments provide good biocompatibility, as they induce less granuloma formation and are less affected by degradation and embrittlement when compared to their polypropylene-based

counterparts [25, 26]. The warp-knitting pattern used in this mesh is the key to tear propagation resistance and provides the desired high porosity of the mesh.

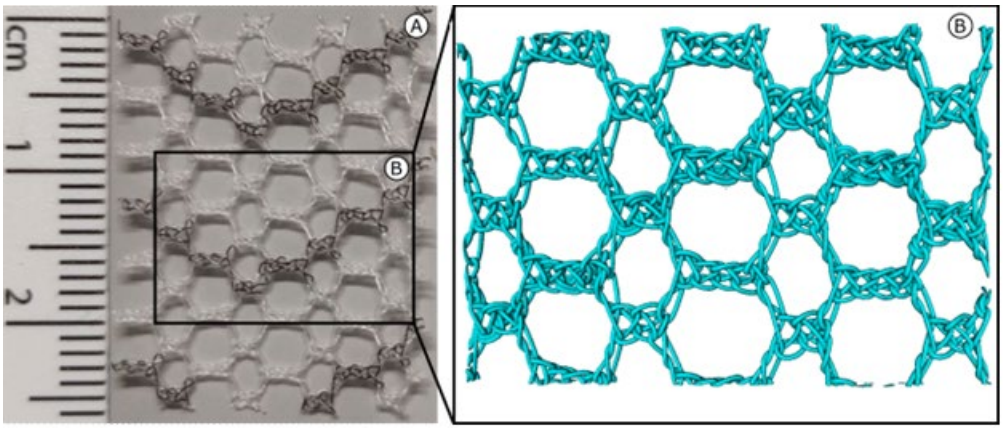

Fig. 1. The surgical mesh DynaMesh®-CICAT: (a) a photo; (b) XCT 3D rendering.

XCT Registration and Analysis of the Mesh 3D Image

A 2 cm by 2.5 cm piece of the DynaMesh®-CICAT surgical mesh was placed in between two half-cylinder Styrofoam parts to keep the fabric straight, while preserving a relaxed state. The assembly was slid into a polysulfone (PSU) sample holder and mounted on the rotation stage of a Bruker SkyScan 1172 scanner, equipped with a closed Hamamatsu 100 kV/10 W microfocus X-ray tube, and a 12-bit detector of 4000 × 2700 pixels. The acquisition parameters are listed below (Table 1). Cross-sectional imaging reconstruction was performed by applying a filter back-projection algorithm in the BRUKER SkyScan software NRecon, with a post-alignment filter to optimize the center of rotation value and a median filter to improve the signal to noise ratio.

Table 1. XCT acquisition parameters.

Tube Voltage [kV]	37	Detector Rows	1332
Tube vCurrent [µA]	234	Detector Columns	2000
Tube Power [W]	8,7	Exposure timing (ms)	215
Hardware filter	None	Voxel size (µm)	8,94
Rotation step [deg]	0,4	Frame Averaging	3
Sector scan [deg]	180	Random movement	ON
Detector binning	2x2		

XCT-based 3D voxelized structures are not suitable as input for mechanical modelling as the voxels create stepped surfaces, which result in an unrealistic and erroneous mechanical behavior in the modelling. Therefore, the aim was to perform a finite element meshing of each individual filament in the surgical mesh structure, extracted using the Avizo XFiber module (Fig. 1b), allowing to obtain smooth filament surfaces.

Transformation of the XCT Dataset Into a FE Model

The transformation of the XCT dataset into a parametric FEM started with the processing of the filament segment nodes and points, by visual inspection of the location and interpenetrations. The original points that represent each filament segment are replaced with interpolated points, with an inter-point distance of 178 µm. This distance allows representing the filament segment without

over-constraining the spline or losing information. The distance is controlled by the smaller radius of curvature, where more points are needed.

With the new equidistant points, a spline is created that serves as the base for a path pultrusion, allowing the creation of each individual yarn. It is possible that for some tight curvature radii, a spline can be created, but a pultrusion of the specified fibre diameter will not provide realistic results, as it generates self-penetrating fibres. Here, having the equidistant points comes in handy, as it is possible to manually edit the points in question and reduce the curvature radius.

To reduce the required computational resources, a general element size of 100 µm was used in the model. One fibre had a high curvature, forcing to reduce the element size to 20 µm, to avoid negative volumes (Fig. 2a, inset). The boundary conditions were set for biaxial tension (Fig. 2b).

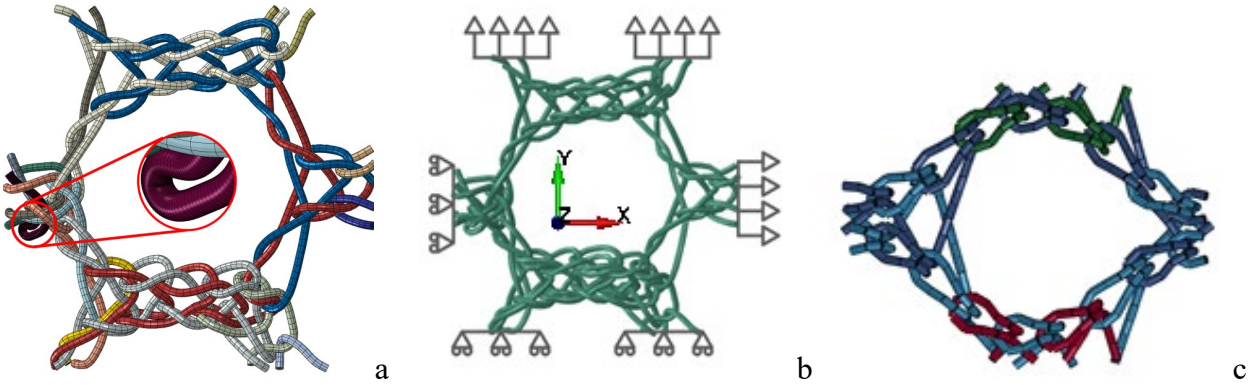

Fig. 2. FE models based on the XCT image, Abaqus (a), with boundary conditions for biaxial tension (b), and exported from TexMind for LS Dyna (c).

Parametrical Modelling of the Warp Knitted Structures

Fig. 3 shows the knitting pattern and the idealised geometrical model of the warp-knitted mesh. Depending on the run-in settings on the machine (derived yarn length per 480 loops) and the bending stiffness of the monofilament yarns the loops will be formed with different geometry. A more stiff filament, at sufficiently large yarn length, forms wider loops, while lower yarn length per loop, and material with lower bending rigidity, forms narrow loops. The yarn length per loop influences the possibility for slippage of the yarn during deformation, and in this way wider and larger loops will result in a larger initial elongation and a lower elasticity modulus.

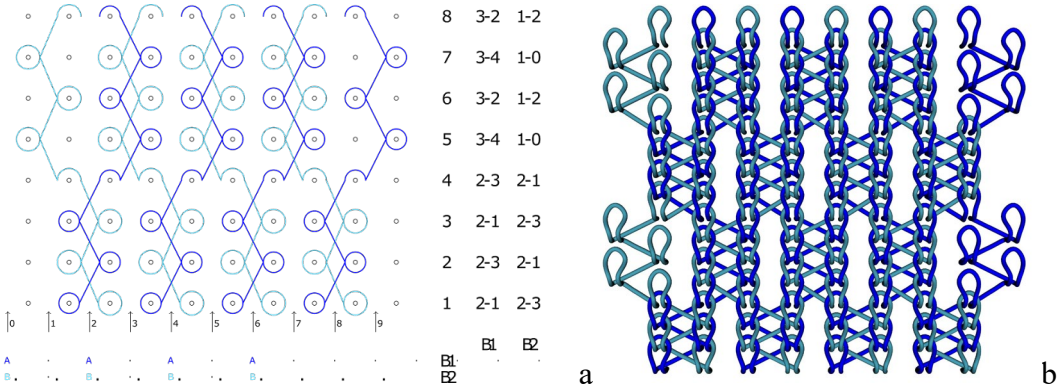

Fig. 3. Pattern of common warp knitted fabrics for production of hernia mesh, lapping and threading notation (a), idealised geometrical model (b), by TexMind Warp Knitting Editor [20].

The idealized geometrical model can be refined by adjusting the loop centre position in the horizontal direction, based on the sum of the horizontal projections of the resulting forces of all

yarns during the knitting process, the flexibility or stiffness coefficient and a scaling factor [19]. Fig. 4 represents the reconstructed FE geometry of one unit cell of the investigated mesh structure, compared with the parametrically modelled one. From the XCT image the yarns can be well-recognized. The loops move not only around the horizontal axis, but they rotate as well under the influence of the yarn tension. Such a rotation of the knitted cells is not implemented yet in the parametrical model, but this can be an extension of the model in the future, in a similar way as the correction of the horizontal loop centre position.

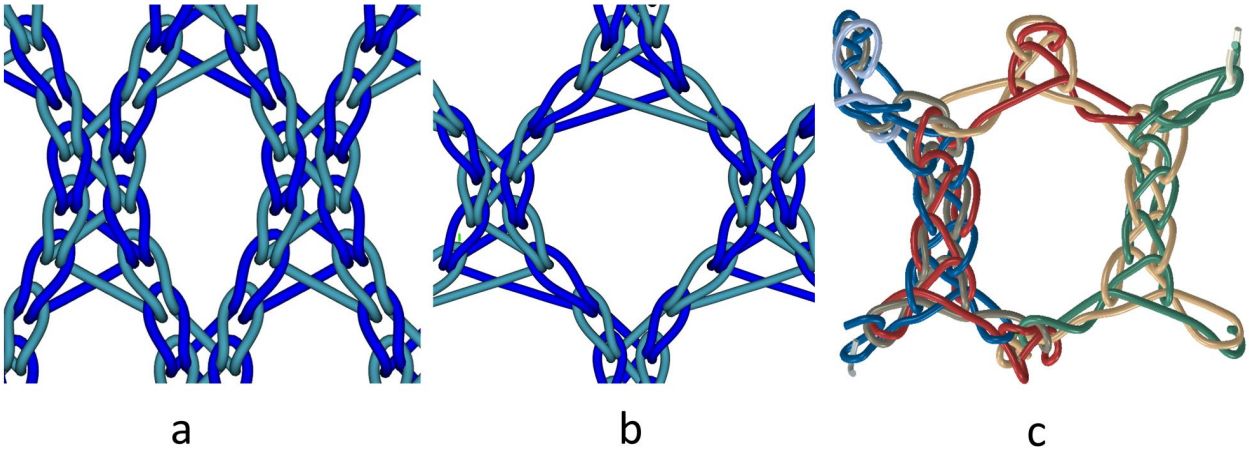

Fig. 4. Comparison of the parametrically modelled structure, two different machine gauges (a,b) with the one obtained by XCT analysis (c).

The parametric modelling of the warp knitted structure is performed without information about the available yarn length per loop. Two figures with different machine gauge (spacing between the needles) and level of side deformation are visualised at Fig. 4a and 4b and they still have different configurations than the reconstructed geometry Fig.4c. The reconstructed geometry shows longer loops in the transition areas between the single linear elements, which can be achieved as well with larger run-in for these steps on computer-controlled machines. For the proper modelling in such case an iterative process with variation of the loop length per each loop and comparison of the simulated and extracted geometry is required, but its implementation is a complex procedure.

The modelled warp knitted fabrics store the coordinates of the single yarns in the memory and as files with lists of 3D coordinates. During the application of explicit FEM software for the modelling process, the element length influences the integration time step. In order to keep all elements with equal length, the curves of the yarn paths are fitted with cubic splines, and then starting from the first node of each yarn, the next node for export for FEM is located from the yarn path so, that the element length remains constant to the value, specified by the user (0.25 mm in this case). The computed nodal coordinates are saved as a text file for LS-Dyna or Abaqus, with the required format as nodes, and then elements between these are placed by interpolation. The complete process is implemented as C++ library, using The Visualization Toolkit (VTK) for visualisation and processing. The model exported in LS Dyna is shown in Fig. 2c.

Modelling of the Biaxial Tension of the Mesh

Biaxial tension on X and Y directions with the equal displacements U_0 on the two axes was applied in LS Dyna to the FE model, exported from *TexMind* and in Abaqus for the XCT-based model. Fig. 5 shows the calculated displacement – force diagrams. The initial regions with low resistance are corresponding to the regime of unbending of the filaments and transition of the loops to the locked condition. In XCT-based model, Fig. 5a, this region exhibits certain resistance to loading, albeit low. For the loading in X direction this low stiffness behavior continues till the end of the

calculation. The inset in Fig. 5b shows details of this region for *TexMind* model. The jumps and negative force values correspond to the resolving of contacts caused by the sliding of the yarns. The forces in this region in this model should be taken as zero. After the loops are locked, the resistance is given by the elongation of the yarns.

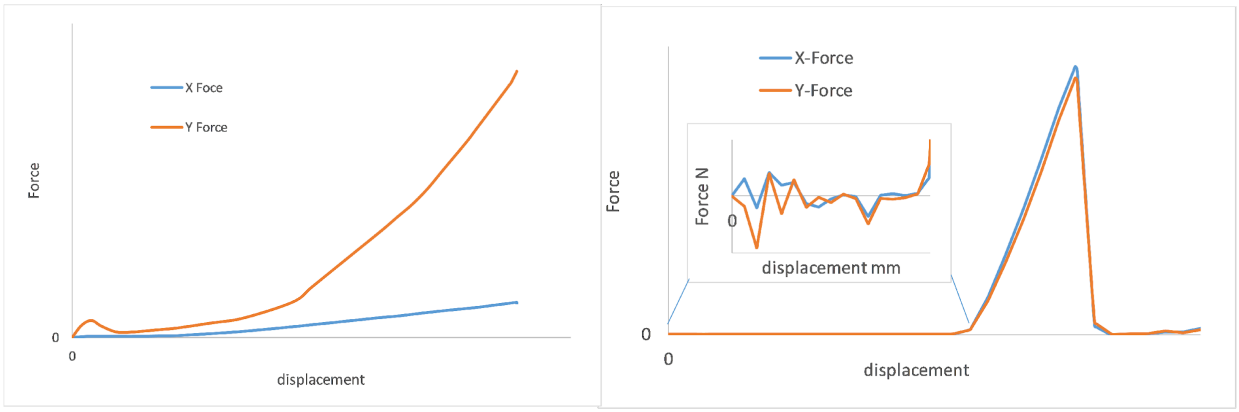

Fig. 5. Biaxial tension diagrams, calculated for the XCT-based digital twin in Abaqus (a) and for the idealised model in LS Dyna (b).

The graphs in Fig. 5 are plotted without specification of the absolute values of force and displacement, because in the present calculations FE convergence problems have forced us to use quite arbitrary values for the filaments and contact properties, based on the FE convergence requirements rather than on the physics. However, the present results allow making certain observations, which highlight difficulties in achieving true-to-life calculations.

The transition-to-locking regime depends very much on the fabric conditions and pre-tension (not accounted for in the calculations). This most probably explains the fact that in *TexMind* calculations, the force is the same in both directions: *TexMind* model operates with ideal distances between the filaments in the loop contacts. In the XCT-based model apparently the fabric is looser in X than in Y direction, which also corresponds to the behavior described by the manufacturer (dyna-mesh.com) The pre-tension will be “the must” for the experimental measurements and for the future modelling, as it allows stabilization of the initial tension conditions.

Summary

We have created geometrical and mechanical models for warp-knitted abdominal wall meshes. The models are built as “digital twins” with the help of 3D imaging with XCT, and using design of 3D mesh structures with *TexMind* software. XCT represents exact knitting pattern, so should theoretically result in the most accurate simulations. *TexMind* possesses the ability to virtually tweak the knitting pattern and, in that way, to optimize the pattern in terms of mechanical behavior. As such, we would able to optimize current mesh designs, or even come up with new mesh patterns that more closely resemble the mechanical behaviour of native fascia tissue.

We developed a methodology of 3D image acquisition of surgical abdominal meshes with XCT and methods and routines for creation of FE models for the real meshes on micro-level. The analysis of the mechanical behavior of a complex mesh under biaxial tension is feasible, whilst important difficulties are identified for development of true-to-life finite elements modelling. In future work, the limitations of the present study will be tackled to obtain models of the larger part of the mesh (as in Fig. 1b), a more precise reproduction of the knitting pattern and an experimental validation of the mechanical properties.

Acknowledgements

The FWO large infrastructure I013518N project is acknowledged for their financial support of the X-ray infrastructure and the KU Leuven XCT Core facility is acknowledged for the 3D image acquisition and quantitative post-processing tools (https://xct.kuleuven.be/).

References

[1] C. Towsend, Chapter 13: Surgery in the geriatric patient, in Sabiston Textbook of Surgery: The Biological Basis of Modern Surgical Practice, Elsevier, 2022.

[2] N.A. Henriksen, A. Montgomery, R. Kaufmann, F. Berrevoet, B. East, J. Fischer, W. Hope, D. Klassen, R. Lorenz, Y. Renard, M.A. Garcia Urena, M.P. Simons, Guidelines for treatment of umbilical and epigastric hernias from the European Hernia Society and Americas Hernia Society, British Journal of Surgery 107 (2020) 171-190. https://doi.org/10.1002/bjs.11489

[3] M.P.Simons, M. Smietanski, H.J. Bonjer, R. Bittner, M. Miserez, T.J. Aufenacker, R.J. Fitzgibbons, P.K. Chowbey, H.M. Tran, R. Sani, F. Berrevoet, J. Bingener, T. Bisgaard, K. Bury, G. Campanelli, D.C. Chen, J. Conze, D. Cuccurullo, A.C. de Beaux, H.H. Eker, R.H. Fortelny, J.F. Gillion, B.J. van den Heuvel, W.W. Hope, L.N. Jorgensen, U. Klinge, F. Köckerling, J.F. Kukleta, I. Konate, A.L. Liem, D. Lomanto, M.J.A. Loos, M. Lopez-Cano, M.C. Misra, A. Montgomery, S. Morales-Conde, F.E. Muysoms, H. Niebuhr, P. Nordin, M. Pawlak, G.H. van Ramshorst, W.M.J. Reinpold, D.L. Sanders, N. Schouten, S. Smedberg, R.K.J. Simmermacher, S. Tumtavitikul, N. van Veenendaal, D. Weyhe, A.R. Wijsmuller, The HerniaSurge Group, International guidelines for groin hernia management, Hernia 22 (2018) 1-165. https://doi.org/10.1007/s10029-017-1668-x

[4] D. Le, C.W. Deveney, N.L. Reaven, S.E. Funk, K.J. McGaughey, R.G. Martindale, Mesh choice in ventral hernia repair: so many choices, so little time, The American J. Surg. 205 (2013) 602-607. https://doi.org/10.1016/j.amjsurg.2013.01.026

[5] L. Miao, F. Wang, L. Wang, T. Zou, G. Brochu, R. Guidoin, Physical Characteristics of Medical Textile Prostheses Designed for Hernia Repair: A Comprehensive Analysis of Select Commercial Devices, Materials 8 (2015) 8148-8168 https://doi.org/10.3390/ma8125453

[6] N. Sanbhal, L. Miao, R. Xu, A. Khatri, L. Wang, Physical structure and mechanical properties of knitted hernia mesh materials: A review, J. Industr. Text. 48 (2017) 333-360. https://doi.org/10.1177/1528083717690613

[7] W.S. Cobb, J.M. Burns, K.W. Kercher, B.D. Matthews, H. James Norton, B. Todd Heniford, Normal Intraabdominal Pressure in Healthy Adults, J. Surgic. Res. 129 (2005) 231-235. https://doi.org/10.1016/j.jss.2005.06.015

[8] K. Baylón, P. Rodríguez-Camarillo, A. Elías-Zúñiga, J.A. Díaz-Elizondo, R. Gilkerson, K. Lozano, Past, present and future of surgical meshes: A review, Membranes 7 (2017) 47. https://doi.org/10.3390%2Fmembranes7030047

[9] X. Zhang, P. Ma, Application of knitting structure textiles in medical areas, Autex Res. J. 18 (2018) 181–191. https://doi.org/10.1515/aut-2017-0019

[10] Y. Kyosev, Warp Knitted Fabrics Construction, Milton: CRC Press LLC, 325, 2019

[11] L.-M. Zhu, P. Schuster, U. Klinge, Mesh implants: an overview of crucial mesh parameters, World journal of gastrointestinal surgery 7 (2015) 226. https://doi.org/10.4240%2Fwjgs.v7.i10.226

[12] B. Hernández-Gascón, E. Peña, G. Pascual, M. Rodríguez, J.M. Bellón, B. Calvo, Long-term anisotropic mechanical response of surgical meshes used to repair abdominal wall defects, J. Mech. Behav. Biomed. Mater. 5 (2012) 257-271. https://doi.org/10.1016/j.jmbbm.2011.09.005

[13] M.S. Yeoman, D. Reddy, H.C. Bowles, D. Bezuidenhout, P. Zilla, and T. Franz, A constitutive model for the warp-weft coupled non-linear behavior of knitted biomedical textiles, Biomaterials 31 (2010) 8484-8493. https://doi.org/10.1016/j.biomaterials.2010.07.033

[14] E. Pena, B. Hernandez-Gascon, and B. Calvo, Human abdomen: Mechanical modeling and clinical applications. Biomechanics of Living Organs: Hyperelastic Constitutive Laws for Finite Element Modeling, ed. Y. Payan and J. Ohayon, 2017, pp. 267-285.
[15] A. Tomaszewska, D. Reznikov, Combined numerical and experimental approach to determine numerical model of abdominal scaffold, Comput. Methods Biomech. Biomed. Engin. 25 (2022) 1235-1248. https://doi.org/10.1080/10255842.2021.2005788
[16] B. Hernandez-Gascon, N. Espes, E. Pena, G. Pascual, J.M. Bellon, B. Calvo, Computational framework to model and design surgical meshes for hernia repair, Comput. Methods Biomech. Biomed. Engin. 17 (2014) 1071-1085. https://doi.org/10.1080/10255842.2012.736967
[17] Y. Kyosev, Topology-Based Modeling of Textile Structures and Their Joint Assemblies: Principles, Algorithms and Limitations, Springer eBook Collection. Cham: Springer International Publishing, 238, 2019
[18] S. Sha, A. Geng, Y. Gao, B. Li, X. Jiang, H. Tao, L. Luo, X. Yuan, H. Ke et al., Review on the 3-D simulation for weft knitted fabric, J. Engin. Fibers Fabrics 16 (2021) 15589250211012528.
[19] H. Liu, Y. Kyosev, G. Jiang, Yarn level simulation of warp-knitted clothing elements – first results and challen ges, Communic. Develop. Assembl. Text. Products 3 (2022) 115-126. https://doi.org/10.25367/cdatp.2022.3.
[20] Y. Kyosev, TexMind Warp Knitting Editor 3D, TexMind UG: Heidenau, 2022.
[21] N. Naouar, D. Vasiukov, C.H. Park, S.V. Lomov, P. Boisse, Meso-FE modelling of textile composites and X-ray tomography, J. Mater. Sci. 55 (2020) 16969-16989. https://doi.org/10.1007/s10853-020-05225-x
[22] Harjkova, G., M. Barburski, S.V. Lomov, O. Kononova, and I. Verpoest, Weft knitted loop geometry measured with X-ray micro-computer tomography. Textile Research Journal, 2014. 84: pp. 500-512.
[23] P. Boisse, R. Akkerman, P. Carlone, L. Karger, S.V. Lomov, J. Sherwood, Advances in composite forming through 25 years of ESAFORM, Int. J. Mater. Forming 15 (2022) 39. http://doi.org/10.1007/s12289-022-01682-8
[24] DynaMesh. Tailored Implants Made of PVDF. 2022 [cited 2022 14/11/2022]; Information on: https://en.dyna-mesh.com/company-gb/.
[25] H. Wang, B. Klosterhalfen, A. Müllen, T. Otto, A. Dievernich, S. Jockenhövel, Degradation resistance of PVDF mesh in vivo in comparison to PP mesh, J. Mech. Behav. Biomed. Mater. 119 (2021) 104490. https://doi.org/10.1016/j.jmbbm.2021.104490
[26] C.D. Klink, K. Junge, M. Binnebösel, H.P. Alizai, J. Otto, U.P. Neumann, U. Klinge, Comparison of Long-Term Biocompability of PVDF and PP Meshes, J. Invest. Surgery 24 (2011) 292-299. https://doi.org/10.3109/08941939.2011.589883

Materials Research Proceedings 28 (2023) 285-292 https://doi.org/10.21741/9781644902479-31

A unit-cell mesoscale modelling of biaxial non-crimp-fabric based on a hyperelastic approach

ZHENG Ruochen[1,a *], SCHÄFER Bastian[2,b], PLATZER Auriane[1,c], COLMARS Julien[1,d], NAOUAR Naim[1,e] and BOISSE Philippe[1,f]

[1]Univ Lyon, INSA-Lyon, CNRS UMR5259, LaMCoS, F-69621, France

[2]Karlsruhe Institute of Technology (KIT), Institute of Vehicle System Technology (FAST), Karlsruhe, Germany

[a]ruochen.zheng@insa-lyon.fr, [b]bastian.schaefer@kit.edu, [c]auriane.platzer@insa-lyon.fr, [d]juline.colmars@insa-lyon.fr, [e]naim.naouar@insa-lyon.fr, [f]philippe.boisse@insa-lyon.fr

Keywords: Biaxial NCF, Hyperelastic, Meso-Scale Model, Unit Cell

Abstract. Understanding the mechanical properties of carbon fiber reinforcements is necessary for the simulation of forming processes. A unit-cell mesoscopic model provides a tool to implement virtual material characterizations which can be served as an input for macroscopic modelling, avoiding complex experimental tests and significantly reducing calculation time. Meanwhile, the occurrence of some local defects during the forming process, such as the gapping, would be easier to be detected through a mesoscopic approach. In this research, a novel mesoscale model for biaxial non-crimp fabric is developed based on the geometry measured from the results of X-ray tomography. A hyperelastic constitutive law is applied to the fiber yarns which are considered as a continuous medium. One type of unit-cell model is chosen and validated through a comparison with experimental tests and its in-plane shear behavior is studied.

Introduction

Biaxial non-crimp fabric (Bi-NCF) is increasingly used nowadays due to its higher lightweight potential and lower cost of manufacturing in various areas such as aeronautics and automotive [1]. Unlike a woven fabric, its fiber yarns in both directions are straight without any undulations and each of them is bound with a stitching loop along a specific direction that can be adapted to a desired formability [2]. Different stitching patterns strongly effect the final mechanical properties and drapability of the Bi-NCF [3,4]. Some optical observation methods were carried out by many researchers in order to better understand the internal geometry of NCFs, which is a critical step for the mesoscopic modelling [5,6].

In the literature, macroscopic approaches are commonly used to predict the forming behavior of fibrous reinforcements [7-10]. However, such an approach may encounter difficulties when predicting some local defects, such as the gapping which occurs when the two adjacent yarns move away from each other and leave an empty zone without fibers. These gapping defects are often detected through a numerical result of the in-plane transverse strain at this macroscale [7,11]. Furthermore, yarn-yarn and also stitch-yarn slippage, which usually occur in non-crimp-fabrics, is hard to be seen via a macroscopic continuum approach. An alternative is using microscopic approaches, where each filament of the fiber yarn is modelled by beam or solid elements. This micro-model is realistic but complex and time-consuming. Therefore, mesoscopic approaches are much more used on the Biaxial-NCF or even UD-NCF [12,13].

Mesoscopic modelling considers each fibrous yarn as a solid medium and the surrounding stitches are modelled by finite beam or bar elements. The contact behavior between the stitches and yarns are considered as well. Therefore, the local deformation of NCFs, such as the yarn's compression, the slippage between yarns and stitches, as well as the development of gap, is visible

Content from this work may be used under the terms of the Creative Commons Attribution 3.0 license. Any further distribution of this work must maintain attribution to the author(s) and the title of the work, journal citation and DOI. Published under license by Materials Research Forum LLC.

at this scale. This work aims to develop and introduce a unit cell mesoscopic model in commercial software Abaqus, on which virtual material characterization can be conducted and different stitching pattern can be analyzed.

Unit Cell Mesoscopic Model

In this research, a $0^{\circ}/90^{\circ}$ carbon fiber biaxial NCF with a polyester tricot stitching is selected. The two layers are bound together during the production process with loop formation in the warp direction. The fiber yarns in the warp direction which are characterized with a "Z" stitching pattern are shown in Fig. 1a, and the weft fiber yarns are shown in Fig. 1b. Its areal weight is 600 g/m^2.

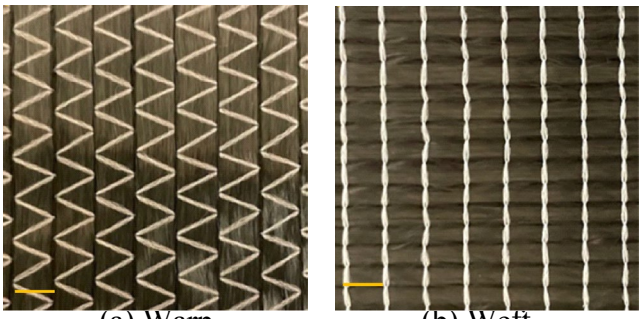

(a) Warp (b) Weft

Fig. 1. carbon biaxial non-crimp fabric architecture.

In order to better understand its internal geometry, an X-ray tomography was firstly carried out, as shown in Fig. 2a. Several geometrical parameters, such as the width and thickness of weft and warp fiber yarns, the knitting position (where the stitch passes through the two layers of fiber yarns), the initial gap between fiber yarns, were measured to serve as input for the mesoscopic model.

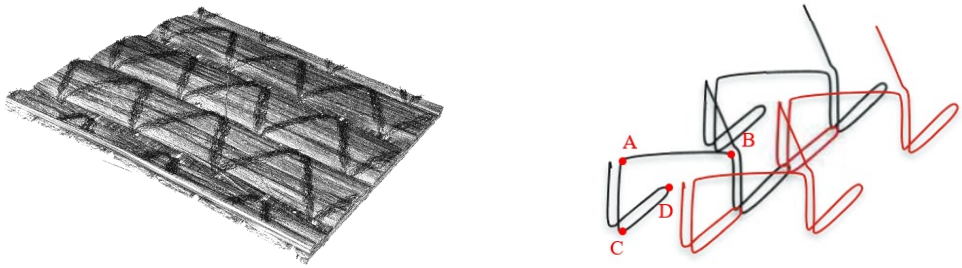

(a) (b)

Fig. 2. Geometry of NCF (a) X-ray tomography (b) tricot stitching pattern schema [24].

The cross-section shape of the fiber yarns was assumed to be circular, flat, elliptic or biconvex in several researches [14-16]. In this study, the yarn's section was built as a half elliptical shape and the yarn is considered to be straight as an ideal initial configuration. The tricot stitch pattern is shown in Fig. 2b. It is complex to observe the stitch geometry since some of stitch yarns are hidden between the fiber yarns. Researchers use tracer fiber techniques to extract the stitching path [6] and define mathematical equations to describe these explicitly [17]. For an example of stitching loop shown in Fig. 2b, the A, B, C and D points are the knitting position where the stitch yarn goes through the two layers of fiber yarn. Their locations can be confirmed from tomography results. From A to B and C to D, two elliptical equations are respectively used to describe the stitch yarn to wrap around the weft and wrap yarn. From A to C is a straight line to describe the piercing stitch. Through repeating these steps, the whole stitching pattern can be generated. After assembling the fiber yarns and stitches, a simulation of the shrinkage of the stitch is carried out in order to tighten the initial loose structure and realize the interaction between the yarn systems [18].

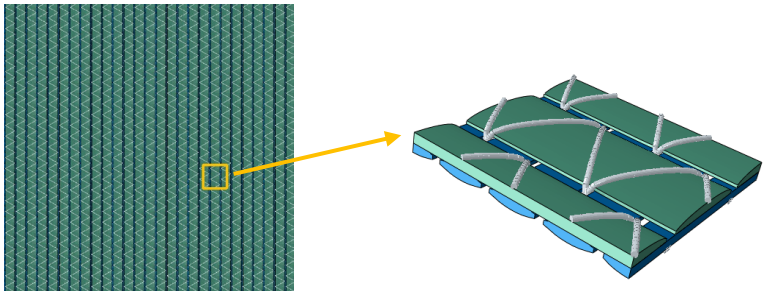

Fig. 3. Modeling of biaxial NCF.

One selected type of unit cell model is shown in Fig. 3. It has the smallest size to contain at least one entire stitching loop and is able to represent the entire mechanical properties of the NCF. A half yarn position is chosen as this model's boundary rather than the gap position because it will not break the stitching loop connection (which is point D in Fig. 2b). Otherwise the separation of stitches may happen which requires additional boundary conditions.

Boundary Conditions and Periodicities

It is assumed that the biaxial NCF is a periodic medium if the internal slippage is neglected and in order to guarantee this periodicity, appropriate kinematic boundary conditions need to be imposed on the unit cell so that it can represent the mechanical property of entire fabric [19]. The displacement field $\underline{\varphi}(\underline{X})$ of the structure can be split into two parts, as shown in Fig. 4: the macroscopic displacement field $\underline{\varphi_m}(\underline{X})$ which is known since it is the input of the simulation and the periodic local displacement $\underline{w}(\underline{X})$ which is unknown [20,21].

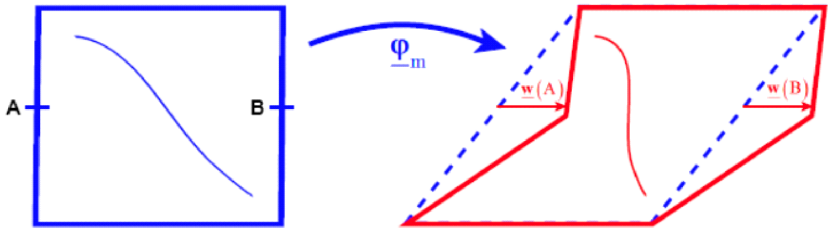

Fig. 4. Initial and deformed periodic structure, displacement field.

This can be expressed as:

$$\underline{\varphi}(\underline{X}) = \underline{\varphi_m}(\underline{X}) + \underline{w}(\underline{X}) \tag{1}$$

To ensure the periodicities, it is necessary to make sure that the local displacements of two opposite sides $\underline{X^+}$ and $\underline{X^-}$ are equal

$$\underline{w}(\underline{X^+}) = \underline{w}(\underline{X^-}) \tag{2}$$

Then the boundary conditions can be obtained as:

$$\underline{\varphi}(\underline{X^+}) - \underline{\varphi}(\underline{X^-}) = \underline{\varphi_m}(\underline{X^+}) - \underline{\varphi_m}(\underline{X^-}) \tag{3}$$

Materials Research Proceedings 28 (2023) 285-292 https://doi.org/10.21741/9781644902479-31

Mechanical Behavior of the Fiber Yarn and Stitch

In this study, the polyester stitch was modelled by two-node beam elements and was considered as a linear elastic material. A traction test was carried out to measure its tensile stiffness. A hyperelastic constitutive law which had been proposed by A. Charmetant [22] was used for the carbon fiber yarn.

Hyperelastic constitutive law.

The fiber yarn is specific as it contains thousands of filaments of carbon fibers, giving it high tensile stiffness and relatively low shear stiffness. From the cross-sectional images at the microscopic scale, the two-point covariance, which represents the probability that two points separated by a distance x to belong to the same phase of the fiber, looks similar along the width and thickness of each fiber yarn [20]. Thus, it can be assumed that the spatial distribution of these filaments inside the yarn is isotropic and the fiber yarn is considered to be transverse isotropy. Four deformation modes are used to describe the fiber yarn's behavior, which are the elongation along the fiber direction, the compaction of the cross section, the transverse shear (distortion of the cross section), and the longitudinal shear along the fiber direction, as shown in Fig. 5.

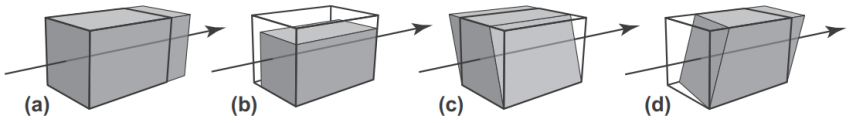

Fig. 5. Four deformation modes of fiber yarn (a) elongation (b) compaction of cross section (c) transverse shear (d) longitudinal shear.

Thus, the deformation gradient tensor, $\underline{F}$, which allows the transformation of fiber yarn from its initial position $\underline{X}$ to its deformed position $\underline{x}$, can be split into four matrixes associated with these four deformation modes.

$$\left[\underline{F}\right] = \left[\underline{\underline{F_{elong}}}\right] \vdots \left[\underline{\underline{F_{comp}}}\right] \vdots \left[\underline{\underline{F_{dist}}}\right] \vdots \left[\underline{\underline{F_{sh}}}\right] \tag{4}$$

The hyperelastic equation defines the material's elastic strain energy potential based on the strain state. Four physically based invariants I_{elong}, I_{comp}, I_{dist}, I_{sh} are defined as a function of the classical invariants I_1 to I_5 of the right Cauchy Green strain tensor $\underline{\underline{C}}$ and then used to describe these different deformation modes.

These classical invariants are expressed as:

$$I_1 = trace(\underline{\underline{C}}),\ I_2 = \frac{1}{2}(trace\left(\underline{\underline{C}}\right)^2 - trace(\underline{\underline{C}}^2)), I_3 = det(\underline{\underline{C}})$$

$$I_4 = \underline{\underline{C}} : \underline{\underline{M}}, \qquad I_5 = \underline{\underline{C}}^2 : \underline{\underline{M}} \tag{5}$$

where $\underline{\underline{M}}$ is a structural tensor defined by a unit vector of preferred direction $\underline{M}$, i.e. the fiber direction:

$$\underline{\underline{M}} = \underline{M} \otimes \underline{M} \tag{6}$$

The four physically based invariants are introduced in [22] and expressed as:

$$I_{elong} = \frac{1}{2} ln\, ln\, I_4\,,\; I_{comp} = \frac{1}{4} ln\, ln\, (\frac{I_3}{I_4})\,,\; I_{dist} = \frac{1}{2} ln\, ln\, (\frac{I_1 I_4 - I_5}{2\sqrt{I_3 I_4}} + \sqrt{(\frac{I_1 I_4 - I_5}{2\sqrt{I_3 I_4}})^2 - 1})\,,\; I_{sh} = \sqrt{\frac{I_5}{I_4{}^2} - 1} \quad (7)$$

Then, the deformation energy is assumed to be the sum of the energies of these four deformation modes:

$$w(\underline{\underline{F}}) = w_{elong}(I_{elong}) + w_{comp}(I_{comp}) + w_{dist}(I_{dist}) + w_{sh}(I_{sh}) \quad (8)$$

The second Piola-Kirchhoff stress tensor is defined as

$$\underline{\underline{S}} = 2\frac{\partial w}{\partial \underline{\underline{C}}} = 2(\frac{\partial w_{elong}}{\partial I_{elong}}\frac{\partial I_{elong}}{\partial \underline{\underline{C}}} + \frac{\partial w_{comp}}{\partial I_{comp}}\frac{\partial I_{comp}}{\partial \underline{\underline{C}}} + \frac{\partial w_{dist}}{\partial I_{dist}}\frac{\partial I_{dist}}{\partial \underline{\underline{C}}} + \frac{\partial w_{sh}}{\partial I_{sh}}\frac{\partial I_{sh}}{\partial \underline{\underline{C}}}) \quad (9)$$

Experimental tensile tests and compaction tests on woven fabric and single fiber yarn were carried out in several previous researches [22,25]. Since the studied Bi-NCF is also made of carbon fibers, the same material parameters are temporarily used and are shown in Table 1.

Table 1. Parameters of the constitutive model for the yarn.

Deformation mode	Strain energy function	Material parameters
Elongation	$w_{elong}(I_{elong}) = \frac{1}{2} K_{elong} {I_{elong}}^2$	K_{elong}=108500 N
Compaction	$w_{comp}(I_{comp}) = \lvert K_{comp} {I_{comp}}^p \quad 0 \;\; if\; I_{comp} > 0$	K_{comp}=1.25 Mpa $P = 1.84$
Transverse shear	$w_{dist}(I_{dist}) = \frac{1}{2} K_{dist} {I_{dist}}^2$	K_{dist}=0.6Mpa
Longitudinal shear	$w_{sh}(I_{sh}) = \frac{1}{2} K_{sh} {I_{sh}}^2$	K_{sh}=2Mpa

Numerical Study

The virtual tests such as the elongation tests or compaction tests can be done on the unit cell model. In this study, an in-plane shear simulation was carried out to validate this unit cell model through comparing the deformed geometry and the shear force with the experimental results, after assuming that the shear deformation is uniformly distributed. Fig. 6a shows the in-plane shear deformation schema. The nodes at the bottom corner were fixed and the nodes at the top corner were stretched. The unit cell length was 10 mm, and the displacement of the stretched nodes was set up as 5 mm. The deformed configuration of this unit cell is shown in Fig. 6b. During the shear deformation, it can be seen that one segment of stitch is always stretched and another one is compressed. The fiber yarns are also compressed by the tightened stitches. In order to validate the deformed geometry, the yarn's width as well as the gap are measured. They all show a good agreement with the experiments.

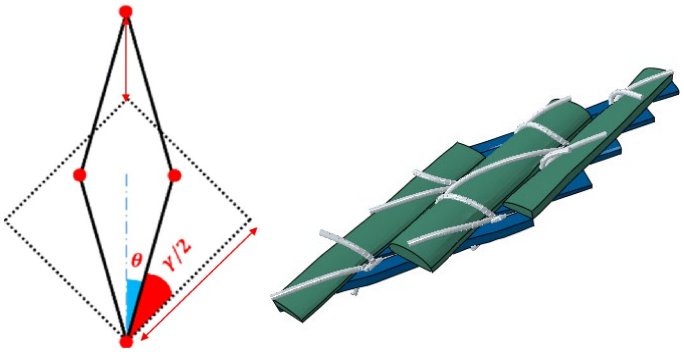

(a) (b)

Fig. 6. (a) Schema of an in-plane shear deformation [26] (b) Deformed unit cell model.

The shear angle during this deformation can be expressed as:

$$\gamma = \frac{\pi}{2} - 2\theta = \frac{\pi}{2} - 2(\frac{\sqrt{2}L+D}{2L}) \quad (10)$$

where L is the unit cell length and D is the displacement.

In order to compare with the experimental results, the reaction force F which is measured at the fixed nodes is normalized by the frame length [23]:

$$F_{nor} = \frac{F \cdot L}{\sqrt{2}L+D} / L \quad (11)$$

The simulation results of normalized shear force and shear angle are shown in Fig. 7, showing a good agreement with the experimental results.

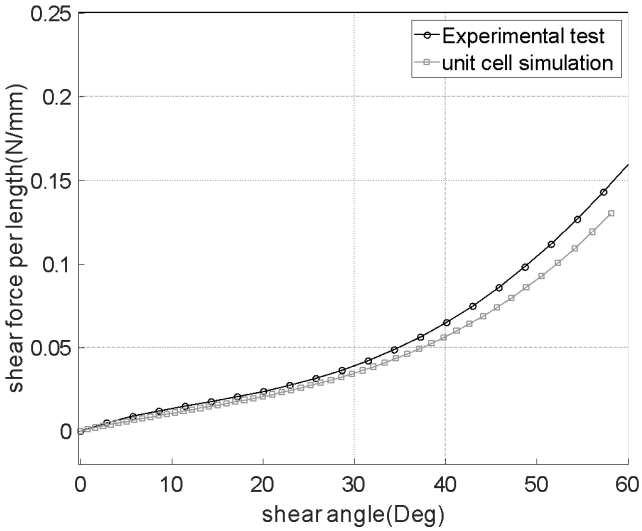

Fig. 7. Shear force normalized vs. shear angle.

Summary

A unit cell mesoscopic finite element model with explicitly described geometry of fiber yarns and stitches is proposed in this study. This model is validated through an in-plane shear simulation, where the shear force and the deformed geometry are in good agreements with experimental results. It shows that this model is able to conduct virtual material characterization and significantly reduce the necessary amount of experimental tests. Furthermore, the geometry of stitches and yarn's section can be easily adjusted which allows for the analysis of different stitching patterns, with the opportunity to develop tailored NCFs with optimized deformation behavior for specific applications.

The hyperelastic constitutive law that is applied on carbon fiber yarns in this study does not consider the bending behavior which is necessary when conducting forming simulation and analyzing gapping defect. The generalized continua approach is needed to be developed and implemented in the future work.

Acknowledgement

This work is funded by the French National Research Agency (ANR) and the Deutsche Forschungsgemeinschaft (DFG, German Research Foundation) in the collaborative project "Composite forming simulation for non-crimp fabrics based on generalized continuum approaches".

References

[1] P. Middendorf, C. Metzner, Aerospace applications of non-crimp fabric composites, in: Stepan V. Lomov (Eds.), Non-Crimp Fabric Composites, Woodhead Publishing (2011) 441-449. https://doi.org/10.1533/9780857092533.4.441

[2] A. Schnabel, T. Gries, Production of non-crimp fabrics for composites, in: Stepan V. Lomov (Eds.), Non-Crimp Fabric Composites, Woodhead Publishing (2011) 3-41. https://doi.org/10.1533/9780857092533.1.3

[3] S. Bel, P. Boisse, F. Dumont, Analyses of the Deformation Mechanisms of Non-Crimp Fabric Composite Reinforcements during Preforming, Appl. Compos. Mater. 19 (2012) 513-528. https://doi.org/10.1007/s10443-011-9207-x

[4] H. Krieger, T. Gries, S. E. Stapleton, Shear and drape behavior of non-crimp fabrics based on stitching geometry, Int. J. Mater. Form. 11 (2018) 593-605. https://doi.org/10.1007/s12289-017-1368-1

[5] H. Yin, Q. Li, L. Iannucci, Meso-scale Finite Element (FE) modelling of biaxial carbon fibre non-crimp-fabric (NCF) based composites under uniaxial tension and in-plane shear, Compos. Struct. 290 (2022) 115538. https://doi.org/10.1016/j.compstruct.2022.115538

[6] W. Wu, W. Li, Parametric modeling based on the real geometry of glass fiber unidirectional non-crimp fabric, Text. Res. J. 89 (2019) 3949-3959. https://doi.org/10.1177/0040517518824846

[7] J. Schirmaier, D. Dörr, F. Henning, and L. Kärger, A macroscopic approach to simulate the forming behaviour of stitched unidirectional non-crimp fabrics (UD-NCF), Compos. Part A 102 (2017) 322-335. http://dx.doi.org/10.1016/j.compositesa.2017.08.009

[8] B. Chen, J. Colmars, N. Naouar, N, P. Boisse, P, A hypoelastic stress resultant shell approach for simulations of textile composite reinforcement forming. Compos. Part A Appl. Sci. Manuf. 149 (2021) 106558. https://doi.org/10.1016/J.COMPOSITESA.2021.106558

[9] L. Kärger, S. Galkin, E. Kunze, M. Gude, B. Schäfer, Prediction of forming effects in UD-NCF by macroscopic forming simulation - Capabilities and limitations. Paper presented at ESAFORM 2021, 24th International Conference on Material Forming, Liège, Belgique. https://doi.org/10.25518/esaform21.355

[10] P. Boisse, N. Hamila, E. Vidal-Sallé, F. Dumont, Simulation of wrinkling during textile composite reinforcement forming. Influence of tensile, in-plane shear and bending stiffnesses, Compos. Sci. Technol. 71 (2011) 683-692. https://doi.org/10.1016/j.compscitech.2011.01.011

[11] S. Galkin, E. Kunze, L. Kärger, R. Böhm, M. Gude, Experimental and Numerical Determination of the Local Fiber Volume Content of Unidirectional Non-Crimp Fabrics with Forming Effects, J. Compos. Sci. 3 (2019) 19. https://doi.org/10.3390/jcs3010019

[12] G. Creech, A. K. Pickett, Meso-modelling of Non-Crimp Fabric composites for coupled drape and failure analysis. J. Mater. Sci. 41 (2006) 6725-6736. https://doi.org/ 10.1007/s10853-006-0213-6

[13] L. Li, Y. Zhao, H. Vuong, Y. Chen, J. Yang, Y. Duan, In-plane shear investigation of biaxial carbon non-crimp fabrics with experimental tests and finite element modeling, Mater. Des. 63 (2014) 757-765. https://doi.org/10.1016/j.matdes.2014.07.007

[14] S.V. Lomov, G. Huysmans, Y. Luo, R.S. Parnas, A. Prodromou, I. Verpoest, F.R. Phelan, Textile composites: modelling strategies, Compos. Part A 32 (2001) 1379-1394. https://doi.org/10.1016/S1359-835X(01)00038-0

[15] J. Whitcomb, X. Tang, Effective Moduli of Woven Composites, J. Compos. Mater. 35 (2001) 2127-2144. http://doi.org/10.1177/002199801772661380

[16] D. Goyal, X. Tang, J. Whitcomb, A. D. Kelkar, Effect of various parameters on effective engineering properties of 2 × 2 braided composites. Mech. Compos. Mater. Struct. 12 (2005) 113-128. https://doi.org/10.1080/15376490490493998

[17] S.V. Lomov, E.B. Belov, T. Bischoff, S.B. Ghosh, T. Truong Chi, I. Verpoest, Carbon composites based on multiaxial multiply stitched preforms. Part 1. Geometry of the preform, Compos. Part A 33 (2002) 1171-1183. https://doi.org/10.1016/S1359-835X(02)00090-8
[18] M. Q. Pham, E. Wendt, E. Häntzsche, T. Gereke, C. Cherif, Numerical modeling of the mechanical behavior of textile structures on the meso-scale for forming process simulations of composite 3D preforms, Engin. Reports 4 (2022) 12348. https://doi.org/10.1002/eng2.12348
[19] C. Miehe, J. Dettmar, A framework for micro-macro transitions in periodic particle aggregates of granular materials, Comput. Methods Appl. Mech. Engin. 193 (2004) 225-256. https://doi.org/10.1016/j.cma.2003.10.004
[20] P. Badel, E. Vidal-Sallé, E. Maire, P. Boisse, Simulation and tomography analysis of textile composite reinforcement deformation at the mesoscopic scale, Compos. Sci. Technol. 68 (2008) 2433-2440. https://doi.org/10.1016/j.compscitech.2008.04.038
[21] P. Badel, E. Vidal-Sallé, P. Boisse, Computational determination of in-plane shear mechanical behaviour of textile composite reinforcements, Computat. Mater. Sci. 40 (2007) 439-448. https://doi.org/10.1016/j.commatsci.2007.01.022
[22] A. Charmetant, E. Vidal-Sallé, P. Boisse, Hyperelastic modelling for mesoscopic analyses of composite reinforcements, Compos. Sci. Technol. 71 (2011) 1623-1631. https://doi.org/10.1016/j.compscitech.2011.07.004
[23] J. Cao, R. Akkerman, P. Boisse, J. Chen, H.S. Cheng, E.F. de Graaf, J.L. Gorczyca, P. Harrison, G. Hivet, J. Launay, W. Lee, L. Liu, S.V. Lomov, A. Long, E. de Luycker, F. Morestin, J. Padvoiskis, X.Q. Peng, J. Sherwood, Tz. Stoilova, X.M. Tao, I. Verpoest, A. Willems, J. Wiggers, T.X. Yu, B. Zhu, Characterization of mechanical behavior of woven fabrics: Experimental methods and benchmark results, Compos. Part A Appl. Sci. Manuf. 39 (2008) 1037-1053. https://doi.org/10.1016/j.compositesa.2008.02.016
[24] Q. Steer, J. Colmars, P. Boisse, Modeling of tricot stitch non crimp fabric in forming simulations, AIP Conference Proceedings 2113 (2019) 020004.https://doi.org/10.1063/1.5112509
[25] A. Iwata, T. Inoue, N. Naouar, P. Boisse, S. V. Lomov, Coupled meso-macro simulation of woven fabric local deformation during draping, Compos. Part A 118 (2019) 267-280. https://doi.org/10.1016/j.compositesa.2019.01.004
[26] A. Habboush, N. Sanbhal, H. Shao, J. Jiang, N. Chen, Characterization and Analysis of In-Plane Shear Behavior of Glass Warp-Knitted Non-Crimp Fabrics Based on Picture Frame Method, Materials 11 (2018) 1550. https://doi.org/10.3390/ma11091550

Materials Research Proceedings 28 (2023) 293-304 https://doi.org/10.21741/9781644902479-32

In-plane deformation measurements for validation of composite forming simulations

BRANDS Dennis[1,2,a,*], VAN KAMMEN Kevin M.[1,b], WIJSKAMP Sebastiaan[2,c], GROUVE Wouter J.B.[1,d] and AKKERMAN Remko[1,2,e]

[1]Faculty of Engineering Technology, Chair of Production Technology, University of Twente, Enschede, the Netherlands

[2]ThermoPlastic composites Research Center (TPRC), Enschede, the Netherlands

[a]d.brands@utwente.nl, [b]k.m.vankammen@student.utwente.nl, [c]sebastiaan.wijskamp@tprc.nl, [d]w.j.b.grouve@utwente.nl, [e]r.akkerman@utwente.nl

Keywords: Composite Forming, Thermoplastic, Unidirectional, Carbon Fiber, Photogrammetry, Validation

Abstract. Validation of composites forming simulations is essential to improve simulation predictions. Detailed validation requires reliable and well-controlled forming processes with precise methods for comparison to simulation results. This study presents some preliminary results from press forming experiments with cross-ply laminates shaped over a dome geometry. The material studied is a unidirectional carbon-fiber reinforced thermoplastic composite. The forming experiments were combined with a deformation measurement technique based on photogrammetry to measure the in-plane deformation on the surface of the laminate after forming. The obtained full-field deformation measurements allow for a direct and quantitative comparison with simulations. The accuracy and precision of the methodology are discussed in detail. The combination of a versatile forming experiment and a detailed analysis method as presented in this article could enable a more precise validation of composite forming simulations.

Introduction

The development of composite forming simulation models based on finite elements has already resulted in various commercial implementations to date. [1] These high-fidelity design tools can be used to address challenges in the complex relation between part design, process design and the occurrence of defects through the prediction of deformation and stress during processing. In this way, virtual design iterations using simulations allow engineers to mitigate some of the risks associated with production delays, unforeseen costs and wasted material.

However, like any model, composite forming simulations will have inherent limitations in terms of accuracy and precision. Moreover, because simulations are generally an ideal representation of reality, they cannot always account for material variability or uncertainties in boundary conditions. The prediction of wrinkling is a particular challenge in composites forming, because these defects can be relatively small compared to the overall geometry and the physical buckling phenomenon underlying this defect is sensitive to the aforementioned variabilities and uncertainties. Therefore, validation efforts are required to evaluate the limitations of current simulation models. Knowing the discrepancies properly can serve as a basis for future improvements to composites forming simulations.

This article follows up a previous publication [2] where a dome was used to study wrinkling with changing laminate geometry and layup on a simple generic toolset. Wrinkles were observed more easily by not closing the press fully and careful choice of the boundary conditions allowed the material behavior to dominate over handling influences in the result. Those results already taught a lot about the material's limitation in forming. However, for validation, the wrinkling can

Content from this work may be used under the terms of the Creative Commons Attribution 3.0 license. Any further distribution of this work must maintain attribution to the author(s) and the title of the work, journal citation and DOI. Published under license by Materials Research Forum LLC.

mainly be used as a qualitative measure, limiting the accuracy due to subjective interpretation. Wrinkling quantification may be possible through measurement of the laminate surface and an appropriate wrinkling metric, such as local curvature as featured in the work of Dörr et al. [3] Nevertheless, a quantitative comparison of wrinkles may still be complicated due to the variability in exact shape, size and location of individual wrinkles and folds. Hence, despite wrinkling being the predominant defect of interest, it only allows for an indirect way to validate many of the complex inputs (e.g. material models) to the simulation.

In a related field of study, sheet metal forming, a well-established technique to validate simulations is the measurement of the deformations. Hence, professionalized and automated implementations of such systems, for example the ARGUS system by GOM Metrology [4], could serve as a source of inspiration to further develop high-end techniques applicable to composites forming. For metal forming, typically, a polka-dot pattern with a 1-5 mm resolution is applied to the blank using direct printing or chemical etching. The deformed pattern after forming is digitized using photogrammetry and used to calculate major strain, minor strain and thickness reduction. These quantities may be compared against simulations directly or related to forming defects through a forming limit diagram.

In composites forming the main deformation of interest is arguably the reorientation of the fiber direction(s), or the related shear angle [5]. Limited extensibility in fiber direction will have a pronounced effect on the overall deformation, resulting in dominant shear behavior and local thickening rather than thinning. The fiber directions may be tracked intuitively using drawn lines [6], a tracer in the fabric [7,8] or directly from the materials' inherent pattern [9,10]. However, full field strain measurements, using photogrammetry for example, provide a more complete picture of the local deformations. Haanappel et al. [11] have applied photogrammetry on a dot pattern to measure the deformation from stamp forming thermoplastic composites, allowing correlation of the measured shear strains on the top surface with simulation results. Sachs et al. [12] extended this technique by applying a pattern on both sides of the laminate to measure the relative movement of the outer plies through the thickness direction, used to validate ply-ply slip and friction in the simulations. Kunze et al. [13] showed that photogrammetry can even be applied on internal plies of a layup through CT measurements and a pattern applied with a special paint for good x-ray contrast.

This article presents a study where the versatile dome forming experiment is combined with a deformation measurement technique based on photogrammetry. The resulting measured deformation fields enable a quantified means to directly validate the in-plane material behavior in composite forming simulation models. By varying the blank dimensions and layup, the dome experiment allows for a wide range of deformations, highlighting the influence of the various underlying deformation mechanisms. However, in this study the layup will be limited to cross-ply, because of the pronounced role in-plane shear deformation has during forming and the direct link with wrinkling defects through the other dominant deformation mechanism, namely bending.

On a historical side note, there is a striking resemblance between the study described in this article and the work by Martin et al. [14] published 30 years ago. However, the capabilities of modern day computer simulations require a more detailed and quantified look into the local deformations, making this topic ever more relevant today.

Method

In preparation for the forming experiments, flat laminates were prepared from Toray TC1225 and Solvay APC materials, both are unidirectional carbon fiber reinforced thermoplastic composite tapes typically applied in the aerospace industry. Some datasheet characteristics on these materials are collected in Table 1.

Materials Research Proceedings 28 (2023) 293-304 https://doi.org/10.21741/9781644902479-32

Table 1. Material characteristics, from datasheet [15,16].

	Toray TC1225	Solvay APC
Fiber	T700	AS4D
Fiber areal weight [g/m2]	145	145
Fiber volume fraction [%]	59	59
Matrix	LM-PAEK	PEKK-FC
Resin content by weight [%]	34	34
Glass transition temperature [°C]	147	159
Melting temperature [°C]	305	337
Consolidated ply thickness [mm]	0.14	0.14

Laminates were press consolidated from loosely stacked plies inside a picture frame mold, with multiple laminates separated by caul sheets and release agents applied to all tooling surfaces. Solvay APC was consolidated at 375°C, 10 bar for 15 minutes and Toray TC1225 at 365°C, 10 bar for 20 minutes. Finally, blanks were cut to final dimension using a water cooled diamond saw. Blanks were dried at 120°C overnight and press formed the same day. The test matrix for the forming experiments is comprised of different layups and blank dimensions according to Table 2.

Table 2. Test matrix with number of formed blanks for combinations of width and layup. The same test matrix was used for both materials.

		$[0/90]_{2s}$	$[45/-45]_{2s}$	$[90/0]_{2s}$	$[0/90]_{4s}$
Width	40 mm	2			2
	80 mm	2			2
	110 mm	2			2
	140 mm	4	2	2	2

# Plies	8	16
Length	295 mm	380 mm
Thickness	≈ 1.1 mm	≈ 2.2 mm
Tool gap	3.1 mm	4.2 mm

Prior to forming, a dot pattern was applied in a rectangular grid to all blanks, see Fig. 2a. Dots are spaced 5 mm apart with a 1.7 mm diameter and the grid is aligned with both fiber directions in the layup. The pattern is painted onto the laminate using a heat resistant silver spray paint and a mask in the form of a sticker. This mask was cut using a CNC-plotter and applied to the laminate using transfer tape to prevent deformation.

Press forming was conducted on the 200 ton Pinette Emidecau Industries press at TPRC, in which the same procedure was applied as previous research [2]. Steel tooling was used having a square base and a hemisphere dome shaped cavity, with dimensions according to Fig. 1. The 8-ply laminates use a 1.1 mm nominal cavity, where it is 2.2 mm for all 16-ply laminates. The tool temperature was 220°C for all experiments.

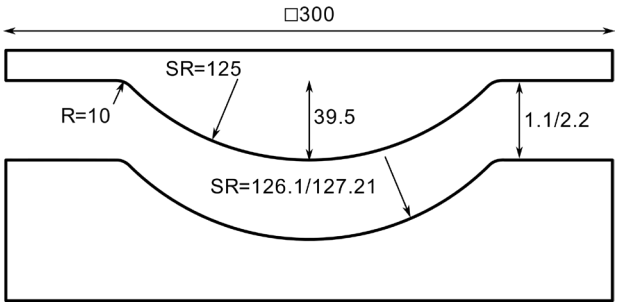

Fig. 1. Hemisphere tool set illustration with dimensions in millimeters. A single male punch is used in combination with two female dies for specific nominal cavity sizes.

The forming process cycle consists of suspending the blank in a shuttle frame, equal to the previous study [2], with the dot pattern facing downwards towards the female die tooling. The blank was then heated to 365°C for Toray TC1225 or 375°C for Solvay APC inside an infrared oven, before a quick automatic transfer places it between the press tooling, which close to form the part. The velocity of the tool is approximately 100 mm/s initially and switches to 20 mm/s when the tools are spaced 10 mm apart. No consolidation pressure was applied, instead a fixed tool gap was used according to Table 2.

The deformation measurement method and calculation is similar to the study of Haanappel et al. [11], which utilizes photogrammetry to digitize the dot pattern on formed parts. First, the part is photographed in a dedicated photography set-up with adequate lighting, a remote control turntable, a surface with reference marks and polarizing light filters to cancel out unwanted specular reflections. A Sony DSC-RX100M3 digital camera was used with a small aperture (f/8) and a low iso-number (200) for a large depth of field and high picture quality. Each part was photographed from 16 equidistant angles around the part, at a fixed elevation. An example photo is shown in Fig. 2b.

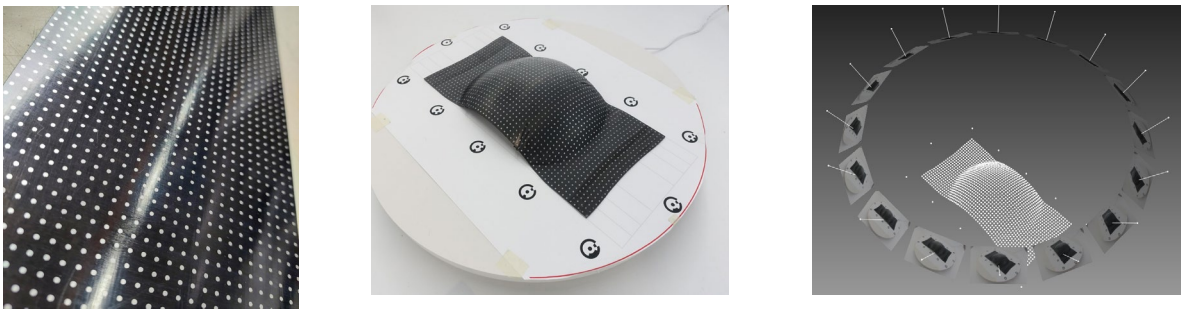

(a) (b) (c)

Fig. 2. (a) Dot pattern on undeformed laminate (b) Formed Solvay APC $[0/90]_{2s}$ 140 mm wide part in photography setup (c) Digitized dot pattern in the PhotoModeler [17] software with camera positions for individual photos.

These photos were subsequently analyzed in the photogrammetry software PhotoModeler [17] First, all visible dots are marked for each photo. Then, the software optimizes for the camera orientation and parameters to determine the locations of each dot in 3D space, including a confidence region. A reference length is used to scale the point cloud to real world length units. An example of a final PhotoModeler project state is shown in Fig. 2c. The undeformed configuration was not analyzed with photogrammetry, but assumed to match the design of the paint mask pattern. Finally, points are sorted to have corresponding node locations and meshed with a triangular element topology that is the same for both configurations.

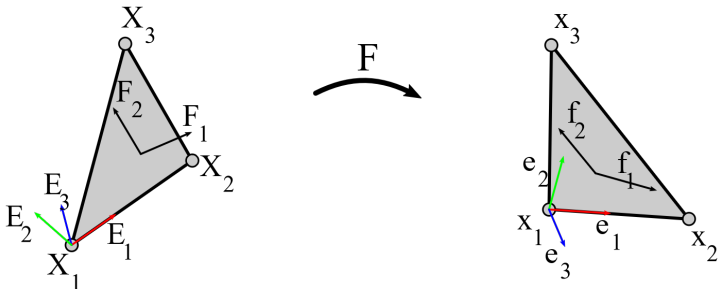

Fig. 3. Vector definitions in initial (left) and deformed (right) configurations.

The deformation can now be calculated for each triangular element by comparing the deformed configuration with the initial configuration, see Fig. 3. Elements in the initial configuration are defined by three nodes in 3D space (X_1, X_2, X_3), linear shape functions, two fiber directions (F_1, F_2) and a local coordinate system. The deformed configuration is similar, but has unknown fiber directions still. The deformation gradient tensor $\boldsymbol{F}$ is readily calculated from the shape functions [18] based on the 2D nodal coordinates in their respective local coordinate systems.

The deformation gradient tensor maps the fiber directions to the deformed configuration using

$$f_1 = \boldsymbol{F} \cdot F_1 \quad \text{and} \quad f_2 = \boldsymbol{F} \cdot F_2 \,. \tag{1}$$

And, based on the difference in fiber directions between configurations, the shear angle is calculated using

$$\gamma = \cos^{-1}(f_1 \cdot f_2) - \cos^{-1}(F_1 \cdot F_2), \tag{2}$$

based on unit fiber directions. Although only a single fiber direction is present on the outer ply, it is assumed that the second fiber direction on the ply below behaves according to the same deformation gradient. The latter term in equation 2, the initial fiber angle, is 90° for all laminates considered in this article. Next, the Green-Lagrange strain can be calculated from the deformation gradient according to

$$\boldsymbol{E} = {}^{1}/_{2}\,(\boldsymbol{F}^T \cdot \boldsymbol{F} - \boldsymbol{I})\,, \tag{3}$$

where $\boldsymbol{I}$ is the second order identity tensor. Standard tensor coordinate transformation rules are applied to align it with the first fiber direction. Finally, results calculated for each element are averaged component wise in the nodes for continuity arguments.

Results

Only six parts in Solvay APC material were analyzed for in-plane deformation due to an identified issue, which will be addressed in the discussion section. Pictures for each of the formed parts are nevertheless included in the digital dataset that is published alongside this article.

Fig. 4 shows the obtained results for a Solvay APC $[0/90]_{2s}$ dome with a width of 140 mm. Three components of the Green-Lagrange strain show that the majority of the deformation occurs in shear (xy-component). Most shear deformation is located in the four corners, near the base of the hemisphere, with a 10-13° shear angle at maximum. The shear deformation is not exactly symmetric over the vertical axis because the laminate was not centered over the dome geometry.

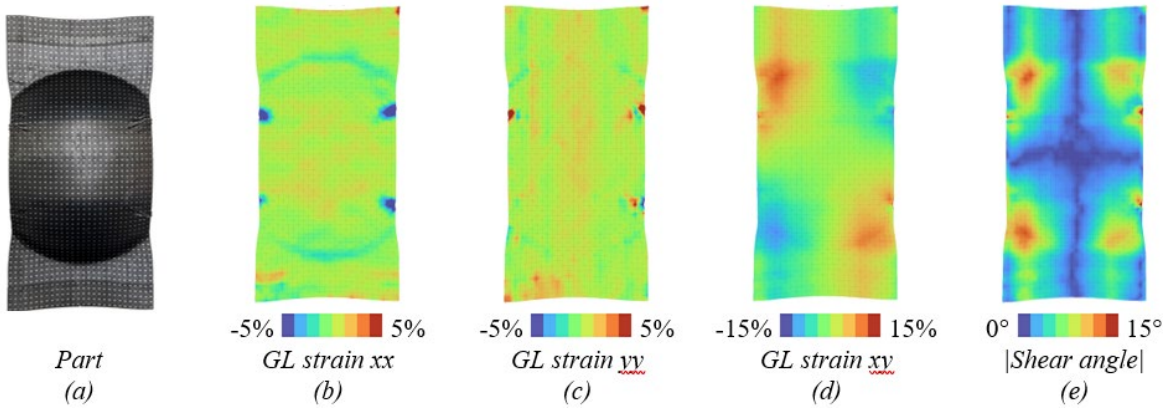

Fig. 4. Deformation results for a Solvay APC $[0/90]_{2s}$ dome 140 mm wide. The xx-direction is based on the local fiber direction, originally in length direction of the laminate.

Four distinct areas with significant compressive normal strain in xx-direction (fiber direction) are observed, which correspond with the locations of the wrinkles on the formed part. In the vicinity of a wrinkle the material is concentrated, bringing points closer together, therefore showing a compressive strain. The transverse strain (yy-component) has a band of positive strain values running in length direction over the dome, which could be related to transverse flow deformation. Near the wrinkles the distorted elements result in local high and low values for the transverse strain.

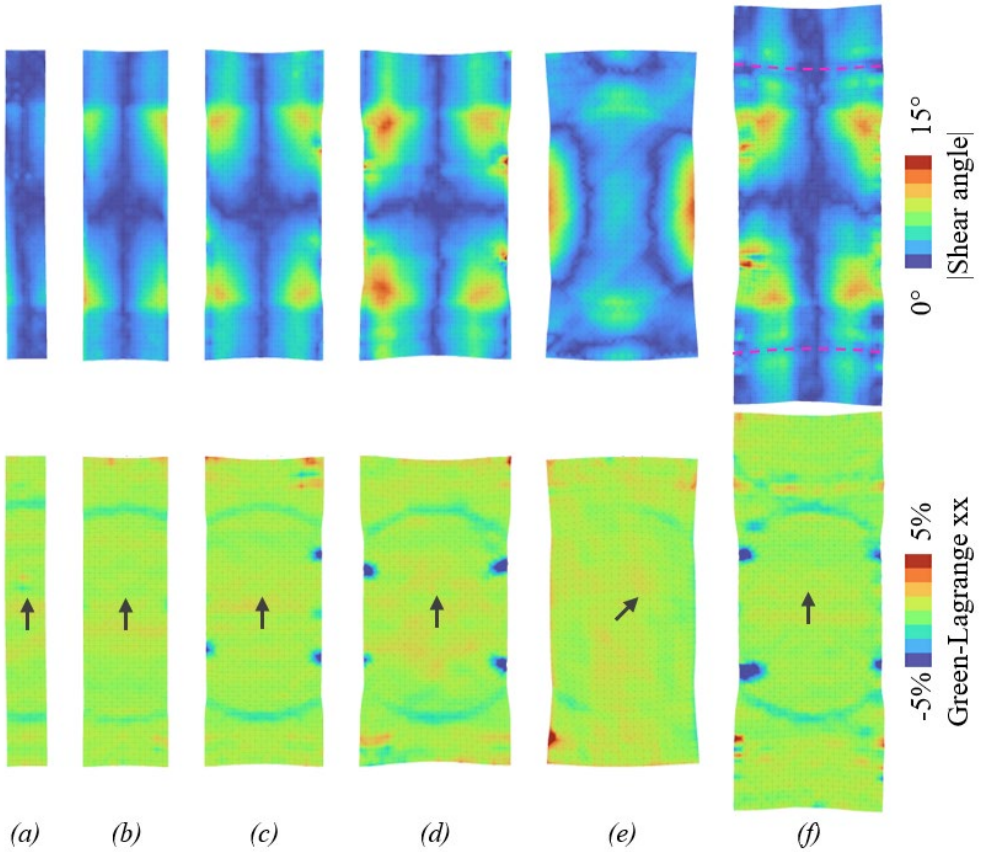

Fig. 5. Results for six domes from Solvay APC. Above: Absolute shear angle. Below: Strain in fiber direction (approximately indicated using an arrow). (a) $[0/90]_{2s}$ 40mm (b) $[0/90]_{2s}$ 80mm (c) $[0/90]_{2s}$ 110mm (d) $[0/90]_{2s}$ 140mm (e) $[45/-45]_{2s}$ 140mm (f) $[0/90]_{4s}$ 140mm.

Fig. 5 shows the most relevant results for each of the six parts analyzed. Subfigures (a)-(d) show parts with the same $[0/90]_{2s}$ layup and a varying width. It is observed that the shear deformation increases with width and the deformation is propagated more from the base of the dome towards the edge of the laminate. However, for the 110 mm and 140 mm wide parts the shear deformation is close to zero on the far left and right edge below the dome, indicating a sudden drop in in-plane deformation. This finding corresponds with the observations for the Green-Lagrange xx results in Fig. 5a-d, where wrinkling is indicated for widths of 110 and 140 mm by compressive strain. The results obtained for these parts thereby illustrate the interrelation between in-plane deformations, in particular the presence of local wrinkling, and the resulting decrease in shear deformation elsewhere in the part.

The part with a $[45/-45]_{2s}$ layup in Fig. 5e shows a completely different shear deformation pattern and no compressive strain in fiber direction. Indeed, no wrinkling was observed on this part. Therefore, this is possibly an interesting validation case for simulations due to the reduced influence of bending whilst still introducing large shear deformation.

The part with a $[0/90]_{4s}$ layup in Fig. 5f has the same typical shear deformation pattern in the four corners as the 8-ply variant, however, less shear deformation is propagated from the base of the hemisphere to the part edge, which may be related to the longer laminate length. Also, some deformation is concentrated around the two PI-tapes that were used to handle the molten laminate throughout the press forming process, indicated with magenta lines in Fig. 5f. This means that the influence of the tape cannot be neglected for this forming process, possibly due to adhesion and friction with the laminate, or an effect on the local laminate temperature.

Discussion

Because of the goal to use these deformation measurements for accurate validation of forming simulations, the discussion in this article focusses on the several aspects concerning the accuracy and precision of the methodology and its results.

Fig. 6 shows the element values for absolute shear angle. The element value is an intermediate result in the calculation, right before the nodal averaging is applied to obtain Fig. 5. For some parts, a pattern of lines is observed in these element value, possibly indicating an accuracy issue. Interestingly, this pattern cancels out during the nodal averaging step in the calculation, hence they are not observed in Fig. 5. Moreover, it seems that not all parts suffer equally from this artifact, meaning it is an inconsistent error in a fixed methodology.

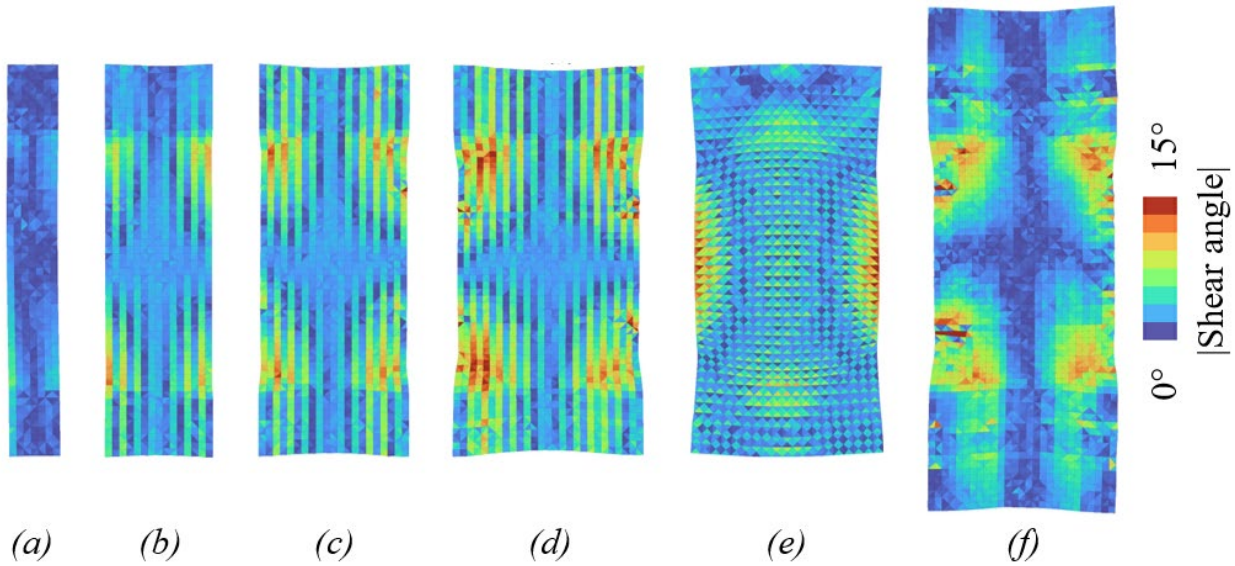

Fig. 6. Element values of the absolute shear angle. Subfigures a-f correspond with Fig. 5, in which the nodal values are plotted.

The cause for the observed element value artifacts was found in the application method of the dotted pattern onto the undeformed laminates. Fig. 7 shows a zoomed photo of an undeformed laminate, where alternating rows of dots are shifted horizontally. The same issue was found for the pattern in the paint mask sticker. Possibly, the scanning strategy of the plotter introduced this relatively repeatable error. The shift was quantified to be approximately 0.2 mm from a leftover sticker.

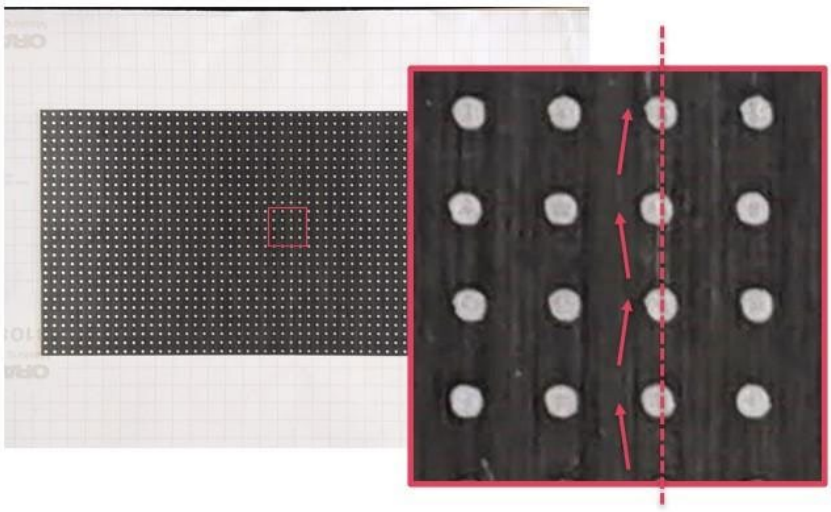

Fig. 7. Zoomed area of an undeformed laminate. A distortion is observed in the dot pattern where every other row has a horizontal shift.

Due to the repetitive nature of the error, a correction was attempted by manually assigning a 0.2 mm displacement to every other row of nodes in the undeformed configuration. This technique allows to resolve the striped patterns in the element values observed in Fig. 6c and 6d. The parts in Fig. 6a and 6f don't seem to have any issues, therefore not requiring any correction. Finally, parts in Fig. 6b and 6e have an inhomogeneous error and correction only works successfully for some areas. The effect on the nodal values is mostly zero, since alternating plus and minus contributions are averaged to zero in central node locations. However, non-zero contributions

remain in the nodal values on the edges of the part. The magnitude of which can be understood geometrically from the angle formed by the distortion and the grid size, through $\Delta\gamma = \left(\frac{0.2}{5}\right) \approx 2.3°$. Hence, it may be concluded that the inaccurate placement of the pattern resulted in a significant loss of accuracy for the nodal values on the edge of the part. Moreover, because the error can be inhomogeneous and inconsistent between parts, it is impossible to truly correct for.

The precision of the photogrammetry technique used to measure the locations of the dots in the deformed configuration will inevitably lead to a precision for the in-plane deformations measured. The PhotoModeler software [17] output includes precision values on the x-, y- and z-coordinates for each node, specified as one standard deviation for a normal distribution. This probability can be propagated using Monte Carlo simulation to assess its influence on the nodal values for each of the in-plane deformation results.

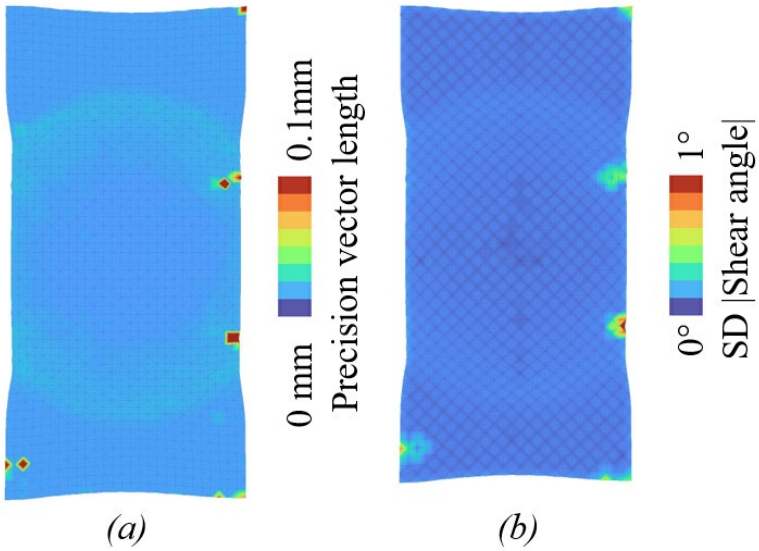

Fig. 8. Solvay APC $[0/90]_{2s}$ 140mm wide. (a) Euclidean length of the precision vector (standard deviations on x- y- and z-positions) (b) Standard deviation on the nodal absolute shear angle, obtained using Monte Carlo simulation from the precision on node positions.

An example is shown in Fig. 8 for the 140 mm wide $[0/90]_{2s}$ part in Solvay APC. The precision on the nodal positions, resulting from the photogrammetry analysis, is shown in Fig. 8a. It is observed that the majority of points was determined with a standard deviation of about 0.015mm on its 3D position, with a few outliers. Subsequently, a thousand meshes in the deformed configuration were sampled, with each node position based on individual normal distributions in x-, y- and z-direction. The resulting in-plane deformation values are approximately normally distributed with a standard deviation indicative of the precision, see Fig. 8b. Instinctively, a large precision vector results in higher standard deviation on the deformation in the surrounding area. Besides a few outliers, the majority of points has a standard deviation less than 0.15° on the absolute shear angle and 0.15% on each of the Green Lagrange strain components. Naturally, these values will be affected by the details of the photogrammetry implementation and are therefore specific to this study.

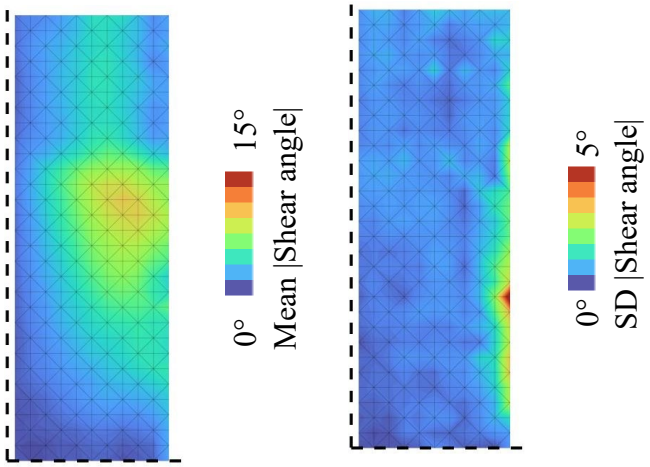

Fig. 9. Nodal results from quadrant averaging for Solvay APC [0/90]2s 110 mm wide. Dashed lines indicate symmetry planes. Results plotted on undeformed geometry. (a) Mean value (b) Standard deviation.

Process variability is another important aspect to consider in validation studies. Although not directly obtained from the analyzed parts in this study, the expected symmetry in the forming results may be used to estimate this variability. Fig. 9 shows an example were the symmetries were used to average the absolute shear angle over each of the four quadrants. In this way, a more reliable mean deformation was obtained to compare against simulations. The spread is indicated by the standard deviation, which is higher than the precision achieved with the photogrammetry method. Nevertheless, it is recommended for future studies to analyze repetitive experiments to account for inherent process variability.

Summary

This article presented results from a forming study on cross-ply laminates from unidirectional thermoplastic composite material combined with measurements of the in-plane deformations. This proposed combination of methodologies is able to provide high-resolution strain and shear angle data, allowing a quantitative validation of composite forming simulations. It is particularly suited to investigate the delicate balance between the in-plane shear and bending (wrinkling) mechanisms that dominate the forming of cross-ply layups, which can be influenced experimentally by changing the width and layup of the laminate formed over the dome geometry.

Validating and improving forming simulations requires the most accurate and precise knowledge of the real-world process as possible. To this extent, the accuracy and precision of the deformation measurement technique have been discussed. An accuracy concern was raised related to the undeformed dot pattern in the current study, which affected the nodal results on edges of a part. However, this mistake can easily be overcome in the future. Furthermore, propagation of the precision in photogrammetry towards the in-plane deformation results using Monte Carlo simulation showed that, in this study, a standard deviation of 0.15° on the shear angle and 0.15% on the Green Lagrange strain values were achieved. As such, the repeatability of experiments may be the bottleneck to obtain reliable data for validating composite forming simulations accurately.

Data Availability

The dataset in this study is available in the 4TU.ResearchData repository under DOI: 10.4121/21688493

Acknowledgments

This work is part of the research program "MaterialenNL" with project number 17880, which is (partly) financed by the Dutch Research Council (NWO). The authors also gratefully acknowledge the financial and technical support from the industrial and academic members of the ThermoPlastic composites Research Center (TPRC).

References

[1] D. Dörr, W. Brymerski, S. Ropers, D. Leutz, T. Joppich, L. Kärger, F. Henning, A Benchmark Study of Finite Element Codes for Forming Simulation of Thermoplastic UD-Tapes, Procedia CIRP 66 (2017) 101–106. https://doi.org/10.1016/j.procir.2017.03.223

[2] D. Brands, L.G.Genova, E.R. Pierik, W.J.B. Grouve, S. Wijskamp, R. Akkerman, Formability Experiments for Unidirectional Thermoplastic Composites, Key Eng. Mater. 926 (2022) 1358–1371. https://doi.org/10.4028/p-x3g086

[3] D. Dörr, T. Joppich, F. Schirmaier, T. Mosthaf, L. Kärger, F. Henning, A method for validation of finite element forming simulation on basis of a pointwise comparison of distance and curvature, AIP Conf Proc 2016, 1769. https://doi.org/10.1063/1.4963567

[4] GOM Metrology, ARGUS: Optical forming analysis 2022. https://www.gom.com/en/products/3d-testing/argus (accessed December 7, 2022).

[5] A.C. Long, Composites forming technology, Woodhead Publishing Limited, 2007.

[6] P. de Luca, P. Lefébure, A.K. Pickett, Numerical and experimental investigation of some press forming parameters of two fibre reinforced thermoplastics: APC2-AS4 and PEI-CETEX, Compos. Part A Appl. Sci. Manuf. 29 (1998) 101–110. https://doi.org/10.1016/S1359-835X(97)00060-2

[7] C. Qian, R. Weare, C. Pasco, N. Kourra, A. Attridge, M. Williams, K. Kendall, Numerical and experimental studies of multi-ply woven carbon fibre prepreg forming process, Procedia Manuf. 47 (2020) 93–99. https://doi.org/10.1016/j.promfg.2020.04.142

[8] R.H.W. Thije, R. Akkerman, A multi-layer triangular membrane finite element for the forming simulation of laminated composites, Compos. Part A 40 (2009) 739–753. https://doi.org/10.1016/j.compositesa.2009.03.004

[9] Z. Wang, J. Luo, Z. Gong, Q. Luo, Q. Li, G. Sun, On correlation of stamping process with fiber angle variation and structural performance of thermoplastic composites, Compos. Part B Eng. 247 (2022) 110270. https://doi.org/10.1016/j.compositesb.2022.110270

[10] G. D'Emilia, A. Gaspari, E. Natale, Stamopoulos AG, Di Ilio A. Experimental and numerical analysis of the defects induced by the thermoforming process on woven textile thermoplastic composites. Eng. Fail. Anal. 135 (2022) 106093. https://doi.org/10.1016/j.engfailanal.2022.106093

[11] S.P. Haanappel, R.H.W. Thije, U. Sachs, B. Rietman, R. Akkerman, Formability analyses of uni-directional and textile reinforced thermoplastics, Compos. Part A 56 (2014) 80–92. https://doi.org/10.1016/j.compositesa.2013.09.009

[12] U. Sachs, S.P. Haanappel, B. Rietman, R. Ten Thije, R. Akkerman, Formability of fiber-reinforced thermoplastics in hot press forming process based on friction properties, Key Eng. Mater. 554-557 (2013) 501–506. https://doi.org/10.4028/www.scientific.net/KEM.554-557.501

[13] E. Kunze, B. Schwarz, T. Weber, M. Müller, R. Böhm, M. Gude, Forming Analysis of Internal Plies of Multi-Layer Unidirectional Textile Preforms using Projectional Radiography, Procedia Manuf. 47 (2020) 17–23. https://doi.org/10.1016/j.promfg.2020.04.110

[14] T.A. Martin, D. Bhattacharyya, R.B. Pipes, Deformation characteristics and formability of fibre-reinforced thermoplastic sheets, Compos. Manuf. 3 (1992) 165–172. https://doi.org/10.1016/0956-7143(92)90079-A
[15] Solvay. Solvay APC product datasheet 2021.
[16] Toray Cetex ® TC1225 product datasheet 2021.
[17] PhotoModeler Technologies. PhotoModeler Premium 2022. https://www.photomodeler.com/
[18] O.C. Zienkiewicz, R.L. Taylor, D.D. Fox, The Finite Element Method for Solid and Structural Mechanics, Seventh ed. Elsevier Ltd., 2014

Materials Research Proceedings 28 (2023) 305-312 https://doi.org/10.21741/9781644902479-33

Manufacturing of hybrid thermoplastic-thermoset fiber reinforced composite and metallization by cold spray technique

PARMAR Hetal[1,a*], RUBINO Felice[2,b], POZA Pedro[2,c] and CARLONE Pierpaolo[1,d]

[1]Department of Industrial Engineering, University of Salerno, Italy

[2] Department of Chemical, Energy and Mechanical Technology, University of Rey Juan Carlos, Italy

[a*]hparmar@unisa.it; [b]felice.rubino@urjc.es, [c]pedro.poza@urjc.es, [d]pcarlone@unisa.it

Keywords: Polymer Matrix Composites, Cocuring, Resin Infusion, Metallization, Cold Spray

Abstract. Polymer and polymer matrix composites (PMCs) have found applications in aerospace sector. Thermosets (TS) possess higher corrosion resistance, shape retention and durability. Thermoplastics (TP) are easier for remolding in comparison to the former. Surface metallization is one of the recently applied trends for electrical and thermal properties improvement. In different metallization methods, primary restrain is the thermoset surface degradation, whereas thermoplastics have been found to be favorable for metallization. The presented article is part of continuous study aiming the cocuring of thermoset-thermoplastic resin with fibrous reinforcement. The composite manufacturing stage consisted of resin infusion (RI) process route for realizing the composite. Main objective of this stage was the through thickness and linear direction impregnation of thermoset to ensure the sound composite comprising contact between thermoplastic layer as well as fiber reinforcement. Fiber reinforcement combined with the resin infusion auxiliary materials were placed over the thermoplastic material prior to the vacuum bagging stage. Catalyzed thermoset resin impregnation in the vacuum bagged preform was conducted under the cocuring cycle. The composite panel was subsequently metallized via low-pressure cold spraying technique. The coating formation was analyzed with process parameters variation. Qualitatively, coating formation on such hybrid composite substrate was observed. However, the substrate manufacturing was found to have influence on the coating quality. Adhesion pull-off test displayed detachment zone directly in the coating substrate interphase. Presence of voids and less thermoset resin was noticed in the case of coating attempts varying process parameters such as traverse speed and standoff distance. Higher adhesion was noted with lowest selected 1 mm/s traverse speed and 10 mm standoff distance.

Introduction

Recent industrial sectors advances are aided by advanced materials and manufacturing technique development in order to ensure improved performance [1-7]. Specifically, in the aerospace sector, there has been an increase in the usage of polymer and PMCs to exploit the weight reduction as well as the high strength to weight ratio advantages. Reduced electrical and thermal conductivity are main limitations for the polymeric and PMC materials system, which have been addressed by using various techniques. Metallization is one amongst them, with primary focus on electroless plating, chemical vapor deposition (CVD), physical vapor deposition (PVD), which depicts their inherent process drawbacks [8]. Besides that, thermal spray processes suffers from substrate surface deterioration in high temperature conditions as well as high temperature induced flames [9]. On the other hand, since cold spray is the low processing temperature method, it is feasible to metallize polymer and PMCs [10,11]. Literature suggests adapting low pressure cold spraying

Content from this work may be used under the terms of the Creative Commons Attribution 3.0 license. Any further distribution of this work must maintain attribution to the author(s) and the title of the work, journal citation and DOI. Published under license by Materials Research Forum LLC.

(LPCS) process for metallizing thermoplastic polymer substrate [12-14]. Major investigations comprised of deposition attempts of Al [8], Ti [15], Sn [16], Cu [13] and also formation of interlayers [13]. The focus of the cold spray (CS) study was in determining processing parameters influence on coating performance for the substrate materials such polymers and glass fiber reinforced polymer (GFRP), carbon fiber reinforced polymer (CFRP), and carbon fiber-polyetheretherketone (CF-PEEK) reinforced PMCs [17,18]. Conversely for the thermoset based composites, easier metallization is not feasible owing to the challenges including erosion of brittle matrix, fiber breakage, and exposure of fibers [19]. Che et al. attempted Al high pressure cold spraying (HPCS) study for CFRP substrate yielding substrate removal and fiber breakage [20]. In case of Cu deposition on thermoset epoxy substrate, presence of erosion and reduction in deposition efficiency (DE) was observed [12]. Several diverse strategies have been applied for mitigating the issues arising in thermoset metallization.

The "co-curing" strategy was described in literature in which placement of thermoplastic coupling layer over the thermoset substrate are subjected to the cure together to manufacture a hybrid composite [21]. During co-curing, diffusion of thermoset precursors in the thermoplastic species is intended to provide a reaction induced phase separation and interphase. The resultant heterogeneous morphology can exhibit the TP and TS mechanical interlocking [22]. Some investigations applied this approach for welding the TP and TS surfaces. The employed welding processes ranged from resistance welding, induction welding to ultrasonic welding [21,23,24].

Under the resin infusion process, the presented work contains a co-curing concept for manufacturing of thermoset-thermoplastic composite and LPCS process for metallization. The investigation is concentrated on realizing the co-cured hybrid composite and studying the effect of the CS process parameters variation on the coating quality. For manufacturing purposes, resin infusion process has been employed. A microstructural analysis was followed by the CS campaign. Adhesion between the coating and the substrate being important criteria, was assessed by the adhesion peel-off test. The article includes findings of this campaign and discussion based on it.

Materials and Methods

The material selection for the presented work was conducted focusing on advanced aerospace applications point of view. A high Tg (217°C) temperature amorphous thermoplastic PEI (ULTEM 1000) film was used with the resin infusion stack to form TS-TP composite. The high-density aerospace application grade RTM6 epoxy resin was selected for realizing a thermoset resin infused composites.

Vacuum assisted resin infusion (VARI) from the out of autoclave (OoA) manufacturing route was employed for the composite manufacturing. The RTM6 epoxy resin flow in the reinforcement was induced under VARI action (Fig. 1 a). Progressing flow front towards the spiral outlet is visible in the image. Placement of PEI layer bellow CF reinforcing layers and auxiliary materials is followed by vacuum bagging operation of the preform maintaining the vacuum inside the vacuum bag cavity. Two stage curing cycle was opted for facilitating the co-curing of the TS-TP inside the CF reinforcement. The designated curing temperature 180°C was considered for the Epoxy resin curing stage (also evidenced in literature for PEI-Epoxy interphase generation). As a primary stage, resin and mould preheating and beginning of resin infusion was initiated at 90°C temperature. Total two hours of dwell time was dedicated at the 180°C curing temperature with the intermediate hold at 160°C temperature.

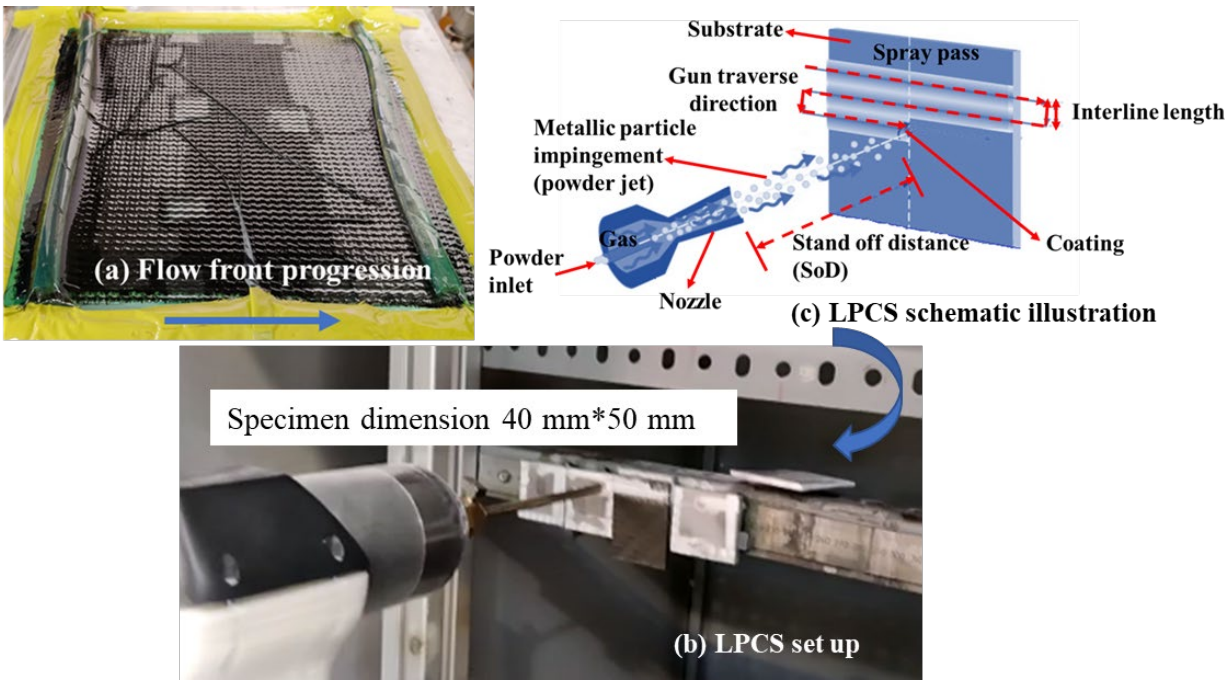

Fig. 1. (a) Resin infusion set-up for hybrid composite manufacturing consisting of 8 CF layers (b) LPCS metallization set-up (c) LPCS process schematic with general process parameters illustration.

The experimental scheme of process parameters for the LPCS of the manufactured composite panels is indicated in the Table 1. Fig. 1 (c) depicts illustrative view on the cold spraying process and highlights the relative process parameters while the actual set-up is included in Fig. 1(b). Processing parameters namely, traverse speed and stand-off distance (SoD) were varied while keeping constant interline length 3 mm and air flow 383 L/m. Al plus Al_2O_3 (min 1%) powder was utilized for the composite surface metallization. The cold spray gas temperature and chamber pressure were maintained constant at 360°C and 6 bar for each variation respectively. The total approximate spray duration to coat the composite sample (40*50*3) was 106 s. The manufactured reference case and metallized composite panels were subjected to the microstructural analysis by the optical microscopy (OM). Prior to the OM observation, the samples were subjected to the metallographic specimen preparation according to the standard prescribed procedure. The samples were cut by the abrasive disc cutter and polished with the abrasive rough paper grades and fine polished subsequently.

Table 1. Cold spraying processing parameters conditions.

Sample identification code	Gun Traverse Speed (mm/s)	SoD (mm)	Interline length (mm)
CS05	1	10	3
CS06	2	10	
CS07	1	30	
CS08	2	30	
CS12	2	20	

Adhesion peel-off test was conducted for determining the adhesion strength of the coated composite specimens. During the peel-off test, the Araldite (industrial grade) adhesive was applied over the sample surface and the test stub (dolly) with 10 mm diameter. Required force for the

complete debonding of the specimen and the stub was recorded for each combination. The failure surface observation of coated and uncoated surfaces was undertaken to understand the mode of failure and adhesion behavior of the coating-composite.

Results and Discussions

Analysis of manufactured hybrid composites.

In the primary stage of manufacturing a direct resin infusion step is conducted as opposed to the hybrid interlayer method [25] where hot pressing action is necessary. The presence of distribution media aided in the uniform distribution of the epoxy resin through the fiber bundles. The uniform pressure distribution due to the vacuum bagging operation resulted in the close contact between three interacting constituents beyond the preheating temperature of 90°C. The resin viscosity was decreased upon the preheating operation prior to the RI step. This step facilities reduction in the voids as well as smooth flow of the RTM6 through the spiral inlet and beginning with the linear flow front movement plus the transversal flow of the rein through reinforcing stack. A close contact between the PEI thermoplastic layer and the reinforcement stack being infused with the thermoset resin is established under vacuum. The flow front movement in all associated trials were found to be linear. The visual inspection of coated hybrid composite panel in the cross-sectional view indicated close contact of coating with the substrate. Fig. 2 (a) presents the coated hybrid panel which is further elaborated in Fig. 2 (b) and (c). The in-plane and through thickness percolation of the RTM6 Epoxy resin through the fiber tows during the RI process is highlighted in the Fig. 2 (b). A clear distinguishing presence of both the PEI and RTM6 resin was detected in the OM images acquired after the etching operation. In the micrograph Fig. 2, light-orange areas are highlighted as the PEI film and dark-orange areas corresponded to the RTM6 infused in the reinforcing fiber tows. Light areas are fibers and metallic particles. The empty spaces between the fiber tows, the inter-tow regions are filled with majorly RTM6 in the remaining substrate.

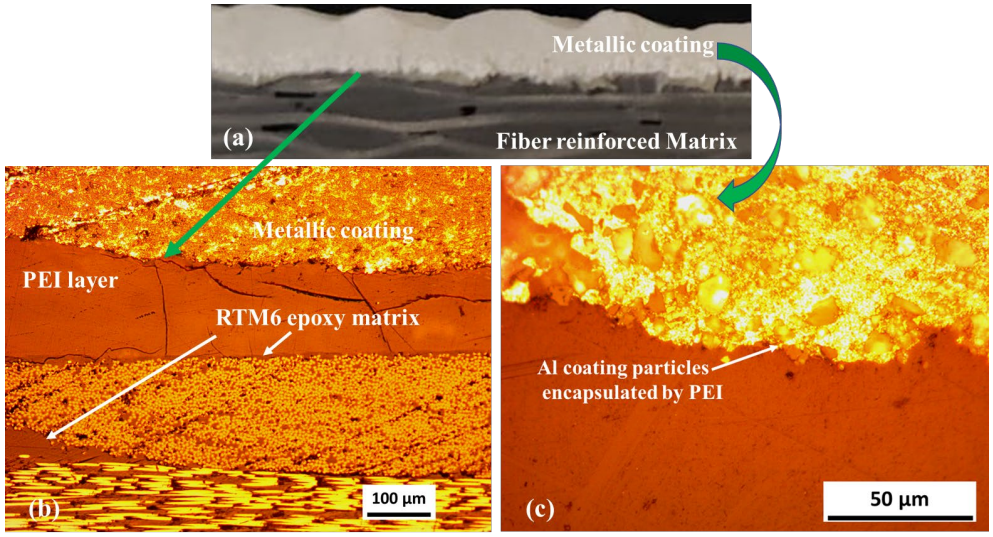

Fig. 2. The cross-sectional optical micrograph after the resin infusion depicting (a) hybrid composite panel cross sectional view (b) Presence of Epoxy resin in the inter-tow region and PEI-RTM6 close contact, magnification 10x. (c) PEI-coating region, magnification 50x.

The main area of interest is the interphase created at the top surface where PEI and Epoxy are said to have been experienced inter-diffusion in the curing stage. The dwell time of the 2 h was sufficient for cocuring of PEI-RTM6 constituents upon inter-diffusion.

Analysis of metallized hybrid composites.

The cold spray process parameters variation and its influence on the hybrid composite coating was assessed. The experiments were conducted at constant N_2 gas temperature and chamber pressure. The interline length after a preliminary campaign was determined to be 3 mm for each trial for covering the entire available surface area. The spray gun was facing the substrate side with PEI layer adhered to the composite substrate. Al (plus Al_2O_3) Coating was formed in each process parameters variation indicating the suitability of the gas temperature of 360°C for the PEI polymer softening. As indicated in Fig.2 (c), the softened PEI formed a close contact with imparting Al particles, also some amount of particle-particle bonding can be expected. The high velocity impact (also including the variation in the traverse speed and SoD) resulted in the adherent coating as confirmed in the visible inspection. The Fig. 3 left side images are representative sample top coating surface.

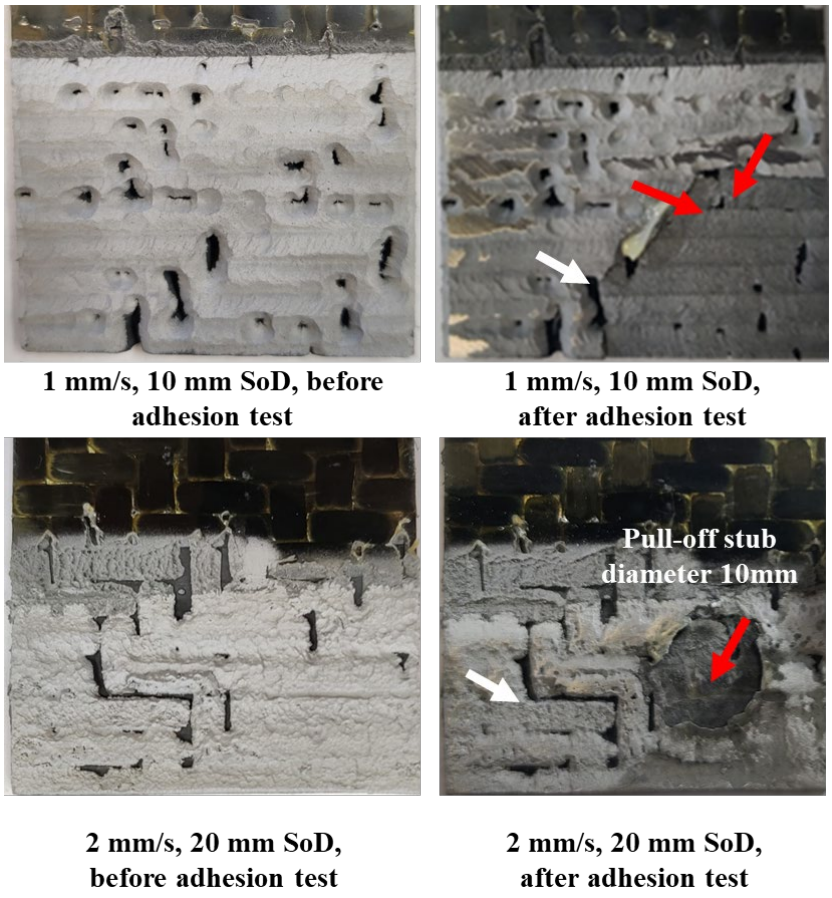

Fig. 3. LPCS panels with processing parameters variation and subsequent adhesion pull-off test coupons. The images contain top surface view to highlight the coating pattern and positioning of defects.

Visible voids extending from the coating through the TP layer and eventual up to the fiber reinforcing material was created in process of cold spraying. The formed coating top surface carried the impression of the fiber tows intertwined in the substrate reinforcing layers, where the voids appeared only in the inter-tow cites. Such occurrences are highlighted by means of the white arrows. The primary reason can be the substrate condition, which is favorable for the substrate excessive softening and cracking in the substrate while the particle impact impinges the coating particles into the substrate surface. Such abrupt occurrences are noted between the consecutive

passes and is the combined result of the manufacturing and coating processes. Overall, the coating thickness in the range of 0.3 mm to 1.5 mm was achieved. In comparison, lower traverse speed 1 mm/s in combination with SoD 10 and 30 mm achieved improvement in the coating thickness as compared to the cases with faster traverse speed of 2 mm/s. The possible reason for such attribute can be the greater exposure of the spray gun over the allocated surface locations of the substrate. Also, another process parameter SoD plays important role, where the intermediate 20 mm value with the higher traverse speed yielded thinner and less adherent coating on the substrate surface. Increase in the SoD generally promotes scattering of the impinging coating particles in the spray path and loss of coating material or loose bonding. Similarly, a faster nozzle speed can be insufficient for the bonding of the metallic particles with the available softened TP surface. Thirdly, as previously mentioned, the effect of the overall substrate manufacturing condition i.e., voids in the panel, voids between the TP layer and the fiber reinforcement, non-uniform contact between the TP and TS constituents, can affect the coating quality. In the opportune condition of optimum balance between the manufacturing and spraying condition, uniform and more adherent coating can be realized.

Adhesion test.

The adhesion pull-off tests were undertaken for the coated samples with different coating conditions. Referring to the Fig. 3 top left side image, the topography of the coating top surface was not flat. The pull off test necessitates a stronger attachment between the flat coating surface and the pull off stub (dolly) prior to the test. The coated samples were hence roughly grinded on the 320-mesh abrasive paper and were subjected to the application of the adhesive on the dolly and substrate surface. The circular impression of the stub was remained on the coated substrate post failure (highlighted with red arrows in Fig. 3). A complete detachment of the stub from the glued substrate surface and presence of any mode of failure i.e., adhesive or mixed mode was considered as the success of the test.

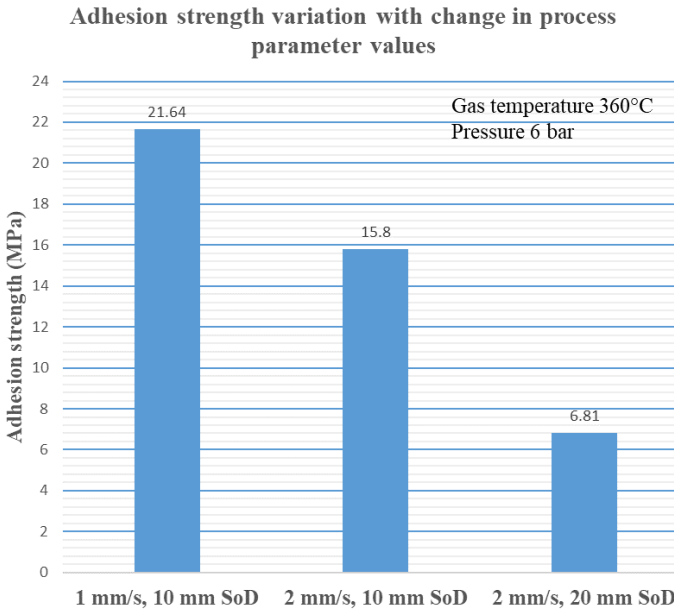

Fig. 4. obtained adhesion strength trend corresponding to the various cold spray conditions.

The obtained adhesion strength values for each condition of processing parameters are reported in the Fig. 4. Fracture surface observation (Fig. 3) indicated the presence of adhesive mode of failure, where certain portion of coating was detached from the substrate. Some loosely bonded Al particles are visible around this impression.

The inferior coating condition of 2 mm/s, 20 mm SoD also yielded a void and crack passing through the substrate in the circular impression. This again can be linked to the combination of manufacturing condition and spraying parameters influence. There is also a trend of reduction in adhesion strength with faster traverse speed, which in combination with SoD changes derives loosely bonded coatings with the substrate. The case of lowest SoD on the other hand provides a direct exposure of coating particle stream avoiding the particle scattering and less availability of the contact area surface in each time interval. These worked as the favorable working conditions for the interlocking of the impinging metallic particle in the softened PEI matrix. The designated

Tg for PEI is 220°C, and the provided gas temperature of 360°C can also in a way induce the substrate heating. This could be the primary condition for each of these coatings to be formed on the RI manufactured composite panels. The reinforcing fiber and encompassing RTM6 resin was well adhered to the PEI top layer, since the failure images show few cases of the substrate damage and fiber pluck out. Further research on the remaining CS condition is underway for determining the adhesion behavior of the coatings.

Summary

Hybrid thermoset-thermoplastic composite manufacturing was feasible by implementing resin infusion route. The manufacturing condition affected the coating deposition. In the cold spraying of PEI-CF- RTM6 epoxy composites, a clear influence of processing parameters traverser speed and SoD was found. Highest adhesion strength was obtained with lower values of traverse speed and SoD. Increase in SoD resulted in weaker bonding. Microstructural observations exhibited particle -particle bonding and coating particle encapsulation by means of PEI softened matrix during CS.

References

[1] P. Boisse, R. Akkerman, P. Carlone, L. Kärger, S. V. Lomov, J.A. Sherwood, Advances in composite forming through 25 years of ESAFORM, Int. J. Mater. Form. 15 (2022) 39. https://doi.org/10.1007/s12289-022-01682-8

[2] R.M.F. Paulo, F. Rubino, R.A.F. Valente, F. Teixeira-Dias, P. Carlone, Modelling of friction stir welding and its influence on the structural behaviour of aluminium stiffened panels, Thin-Walled Struct. 157 (2020) 107128. https://doi.org/10.1016/j.tws.2020.107128

[3] F. Rubino, M. Pisaturo, A. Senatore, P. Carlone, T.S. Sudarshan, Tribological Characterization of SiC and B4C Manufactured by Plasma Pressure Compaction, J. Mater. Eng. Perform. 26 (2017) 5648-5659. https://doi.org/10.1007/s11665-017-3016-9

[4] F. Rubino, P. Poza, G. Pasquino, P. Carlone, Thermal spray processes in concentrating solar power technology, Metals 11 (2021) 1-30. https://doi.org/10.3390/met11091377

[5] H. Parmar, T. Khan, F. Tucci, R. Umer, P. Carlone, Advanced robotics and additive manufacturing of composites: towards a new era in Industry 4.0, Mater. Manuf. Process. 37 (2021) 483-517. https://doi.org/10.1080/10426914.2020.1866195

[6] F. Tucci, P. Carlone, A.T. Silvestri, H. Parmar, A. Astarita, Dissimilar friction stir lap welding of AA2198-AA6082: Process analysis and joint characterization, CIRP J. Manuf. Sci. Technol. 35 (2021) 753-764. https://doi.org/10.1016/j.cirpj.2021.09.007

[7] F. Tucci, R. Bezerra, F. Rubino, P. Carlone, Multiphase flow simulation in injection pultrusion with variable properties, Mater. Manuf. Process. 35 (2020) 152-162. https://doi.org/10.1080/10426914.2020.1711928

[8] M.R. Rokni, P. Feng, C.A. Widener, S.R. Nutt, Depositing Al-Based Metallic Coatings onto Polymer Substrates by Cold Spray, J. Therm. Spray Technol. 28 (2019) 1699-1708. https://doi.org/10.1007/s11666-019-00911-y

[9] X.L. Zhou, A.F. Chen, J.C. Liu, X.K. Wu, J.S. Zhang, Preparation of metallic coatings on polymer matrix composites by cold spray, Surf. Coatings Technol. 206 (2011) 132-136. https://doi.org/10.1016/j.surfcoat.2011.07.005

[10] M. Grujicic, C.L. Zhao, W.S. DeRosset, D. Helfritch, Adiabatic shear instability based mechanism for particles/substrate bonding in the cold-gas dynamic-spray process, Mater. Des. 25 (2004) 681-688. https://doi.org/10.1016/j.matdes.2004.03.008

[11] H. Parmar, F. Tucci, P. Carlone, T.S. Sudarshan, Metallisation of polymers and polymer matrix composites by cold spray: state of the art and research perspectives, Int. Mater. Rev. 67 (2021) 1-25. https://doi.org/10.1080/09506608.2021.1954805

[12] A. Ganesan, M. Yamada, M. Fukumoto, Cold spray coating deposition mechanism on the thermoplastic and thermosetting polymer substrates, J. Therm. Spray Technol. 22 (2013) 1275-1282. https://doi.org/10.1007/s11666-013-9984-x
[13] A. Ganesan, J. Affi, M. Yamada, M. Fukumoto, Bonding behavior studies of cold sprayed copper coating on the PVC polymer substrate, Surf. Coatings Technol. 207 (2012) 262-269. https://doi.org/10.1016/j.surfcoat.2012.06.086
[14] A. Małachowska, M. Winnicki, M. Stachowicz, M. Korzeniowski, Metallisation of polycarbonates using a low pressure cold spray method, Surf. Eng. 34 (2018) 251-258. https://doi.org/10.1080/02670844.2016.1277843
[15] M. Gardon, A. Latorre, M. Torrell, S. Dosta, J. Fernández, J.M. Guilemany, Cold gas spray titanium coatings onto a biocompatible polymer, Mater. Lett. 106 (2013) 97-99. https://doi.org/10.1016/j.matlet.2013.04.115
[16] H. Che, X. Chu, P. Vo, S. Yue, Metallization of Various Polymers by Cold Spray, J. Therm. Spray Technol. 27 (2018) 169-178. https://doi.org/10.1007/s11666-017-0663-1
[17] V. Gillet, E. Aubignat, S. Costil, B. Courant, C. Langlade, P. Casari, W. Knapp, M.P. Planche, Development of low pressure cold sprayed copper coatings on carbon fiber reinforced polymer (CFRP), Surf. Coatings Technol. 364 (2019) 306-316. https://doi.org/10.1016/j.surfcoat.2019.01.011
[18] F. Rubino, F. Tucci, V. Esperto, A.S. Perna, A. Astarita, P. Carlone, A. Squillace, Metallization of Fiber Reinforced Composite by Surface Functionalization and Cold Spray Deposition, Procedia Manuf. 47 (2020) 1084-1088. https://doi.org/10.1016/j.promfg.2020.04.353
[19] J. Affi, H. Okazaki, M. Yamada, M. Fukumoto, Fabrication of aluminum coating onto CFRP substrate by cold spray, Mater. Trans. 52 (2011) 1759-1763. https://doi.org/10.2320/matertrans.T-M2011807
[20] H. Che, P. Vo, S. Yue, Metallization of carbon fibre reinforced polymers by cold spray, Surf. Coatings Technol. 313 (2017) 236-247. https://doi.org/10.1016/j.surfcoat.2017.01.083
[21] E. Tsiangou, S. Teixeira de Freitas, I. Fernandez Villegas, R. Benedictus, Investigation on energy director-less ultrasonic welding of polyetherimide (PEI)- to epoxy-based composites, Compos. Part B Eng. 173 (2019) 107014. https://doi.org/10.1016/j.compositesb.2019.107014
[22] B. Lestriez, J.P. Chapel, J.F. Gérard, Gradient interphase between reactive epoxy and glassy thermoplastic from dissolution process, reaction kinetics, and phase separation thermodynamics, Macromolecules 34 (2001) 1204-1213. https://doi.org/10.1021/ma0012189
[23] C. Brauner, S. Nakouzi, L. Zweifel, J. Tresch, co-curing behaviour of thermoset composites with a thermoplastic boundary layer for welding purposes, Adv. Comp. Lett. (2020). https://doi.org/10.1177/2633366X20902777
[24] F. Lionetto, M.N. Morillas, S. Pappadà, G. Buccoliero, I. Fernandez Villegas, A. Maffezzoli, Hybrid welding of carbon-fiber reinforced epoxy based composites, Compos. Part A Appl. Sci. Manuf. 104 (2018) 32-40. https://doi.org/10.1016/j.compositesa.2017.10.021
[25] H. Parmar, A. Gambardella, A.S. Perna, A. Viscusi, R. Della Gatta, F. Tucci, A. Astarita, P. Carlone, Manufacturing and metallization of hybrid thermoplastic-thermoset matrix composites, ESAFORM 2021. (2021). https://doi.org/10.25518/esaform21.2727

Materials Research Proceedings 28 (2023) 313-320 https://doi.org/10.21741/9781644902479-34

Thermo-chemical modeling and simulation of glass/elium® acrylic thermoplastic resin composites

DENIS Yvan[1,a *], SIDDIG Nihad[1,b], GUITTON Raphael[1,c], LE BOT Philippe[1,d], DE FONGALLAND Antoine[1,e] and LECOINTE Damien[1,f]

[1] Nantes Université, IRT Jules Verne, F-4400 Nantes, France

[a]yvan.denis@irt-jules-verne.fr, [b]nihad.siddig@irt-jules-verne.fr, [c]raphael.guitton@irt-jules-verne.fr, [d]philippe.lebot@irt-jules-verne.fr, [e]antoine.de-fontgalland@irt-jules-verne.fr, [f]damien.lecointe@irt-jules-verne.fr

Keywords: Composites Materials, Polymerization Kinetics, Infusion Simulation, Reactive Resin

Abstract. The recyclability limitations of wind blades significantly reduce their environmental benefit as a green energy source. Therefore, the use of new and sustainable materials is crucial. The Zero wastE Blade ReseArch project (ZEBRA), led by the French technical research center IRT Jules Verne, is looking to accelerate the industry transition to circular economy by designing and manufacturing the first 100% recyclable wind blades using the thermoplastic resin Elium®, developed by Arkema, with a consortium regrouping: LM Wind Power, Arkema, CANOE, Owens Corning, ENGIE and Suez. In this work, the polymerization kinetics of the reactive thermoplastic resin Elium® was characterized through isothermal and dynamic Differential Scanning Calorimetry (DSC) tests. The experimental curves are fitted to two different models from the literature; then the model parameters are identified and used as input to simulations. One model is selected and evaluated using a PAM-RTM© simulation for pure resin and the infusion of Owens Corning glass/Elium® composites [1]. The numerical results are compared with experimental data collected from Vacuum-assisted resin infusion (VARI) tests with the help of a robust monitoring system [2]. Then the model is used to predict the flow and polymerization behavior for thick and more complex parts.

Introduction

The main objective of the ZEBRA project is to reduce the economic cost and environmental impact of wind turbine blades by studying the possibility to accelerate the wind market's transition to a circular economy. From a strategic consortium, an establishment made to bring together the entire value chain: from materials development to wind turbine blade recycling, manufacturing, operation, and dismantling was made. The roles in the project consortium are demonstrated in Fig. 1(b). The ZEBRA project, led by the IRT Jules Verne, brings together industrial players and research centers and aims to demonstrate the technical, economic and environmental feasibility of thermoplastic wind turbine blades with an eco-design approach to facilitate recycling. The project, launched for 42 months, has an overall budget of 18.5 million euros.

To make wind blades sustainable and recyclable, different stages are necessary, from eco-design to recycling passing by manufacturing. This paper mainly focuses on the reactive thermoplastic resin Elium® which replaces the conventional thermoset resin generally used. Vacuum-assisted resin infusion (VARI) processes [8] are generally used to make large or complex parts. Indeed, VARI is well known as a low-cost and straightforward composite manufacturing method, even if a large quantity of consumable material is used and wasted. Although the VARI process allows the manufacture of large and complex geometries, it is also sensitive to many factors.

Content from this work may be used under the terms of the Creative Commons Attribution 3.0 license. Any further distribution of this work must maintain attribution to the author(s) and the title of the work, journal citation and DOI. Published under license by Materials Research Forum LLC.

(a)

(b)

Fig. 1. Zebra project: (a) the first 100% recyclable wind blade manufactured by LM wind power, (b) ZEBRA project and the role of the consortium partners.

First, the manufacturing conditions, particularly the atmosphere around the manufacturing set-up, which is not always controlled, especially for very large parts. The study presented here shows that the Elium® resin is very sensitive to the boundary and initial conditions of the process, notably in terms of temperature. Stacking defects, ply misalignments or geometrical difficulties will also cause high variability in the process control. Good management of the tooling and the consumables used (flow medium, vacuum bag, etc.) will also have an essential influence on good infusion. The operator efficiency can also lead to variations in the quality of the infusion. Mastering the infusion process depends on identifying the main risks associated with the different induced variabilities. Most of these variations can be identified in situ by a robust process control monitoring system. However, depending on the complexity and size of the part being manufactured, in situ monitoring can be complex and expensive. The numerical simulation tool is therefore valuable for anticipating possible challenges on the first hand, but also to propose appropriate infusion strategies leading to an optimal part quality. It is well known that the simulation of the composite transformation process requires a complete ecosystem, both numerical and physical. A complex multiphysics coupling is therefore necessary and needs to be fed by measured experimental data. Furthermore, the simulation will operate within a specific set of process conditions. Therefore, several results will be presented depending on different initial conditions, especially in temperature. As the simulation is complex, the work in this article will mainly focus on the polymerization kinetics of the Elium® resin used in this project. For a good description of the kinetics, both dynamic and isothermal tests are necessary to describe this very sensitive resin behavior correctly. The study is presented through three parts; first an experimental approach to validate the modeling of a thin

plate in the filling and polymerization phases. Second, the model is used to predict the process behavior for thick plates, the paper is concluded with some discussion and perspectives.

Experimental Set-Up and Observations

To study the whole infusion process, an experimental approach with increasing complexity is followed, along with using a robust monitoring system to observe the behavior of the resin, its temperature evolution, and its degree of polymerization over time. First on simple and thin plates, then on thicker and more complex parts. Focus on the thermal evolution and therefore, closely related to the polymerization will be explained here. To have access to the desired data, a complete monitoring bench was set up with several instruments such as thermocouples [13], heat flow sensors, dielectric sensors [11], optical fibers [12], profilometers, standard and infrared cameras for front-flow monitoring. The idea is to take benefits of each method and synchronize them to a unique monitoring system. All these data, in addition to revealing quantitative information about the infusion process, also allow a better understanding of the flow and resin transformation mechanisms.

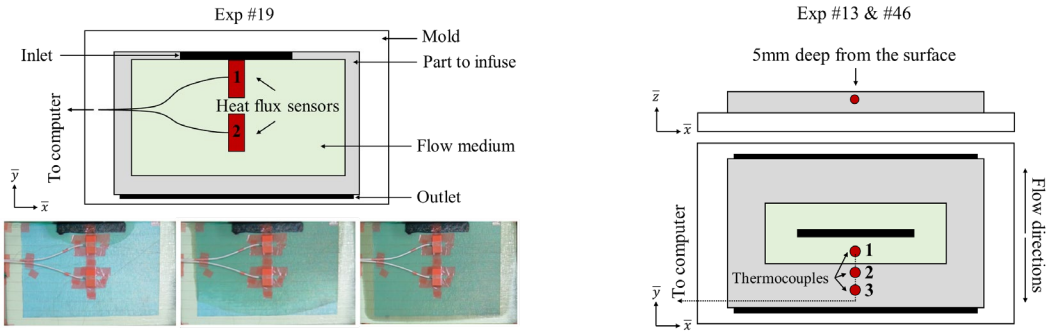

Fig. 2. Experimental set up: (a) infusion #19 using heat flux sensors, (b) infusion #13 and infusion #46 using thermocouples.

Many experiments led to a good understanding of the resin and of the process. In this work, only three of them are shown and are described in the Table 1 below.

Table 1. Experimental conditions of infusion 13, 46 and 19.

Parameter	#Exp13	#Exp46	#Exp19
Initial resin temperature [°C]	24.8	19.6	19.5
Peak temperature [°C]	≈ 65	60-78	≈ 40
Time to peak	2h56	3h52	4h10
Thickness of the plate [mm]	25	25	≈ 4.7

Experiments #13 and #46 are also described in Fig. 2(b). They are infused under the same setup, stacking, and boundary conditions. Only the initial resin temperature was different. The idea was to check its influence on the process. Indeed, an important data for mastering the resin Elium® is the thermal behavior for both filling and polymerization phases. To observe it, several experiments were done by using thermocouples (Fig. 2(b)). The acquired data, such as described in Fig.3(a), are then used to monitor the infusion but also to compare experimental data to numerical simulation. Also, using heat flux sensors as described in Fig. 2(a) gives information about the

polymerization time and behavior. Fig. 3(b) shows the behavior of the heat flux in two different places. A post-treatment of these data leads to an estimation of the polymerization degree during the process.

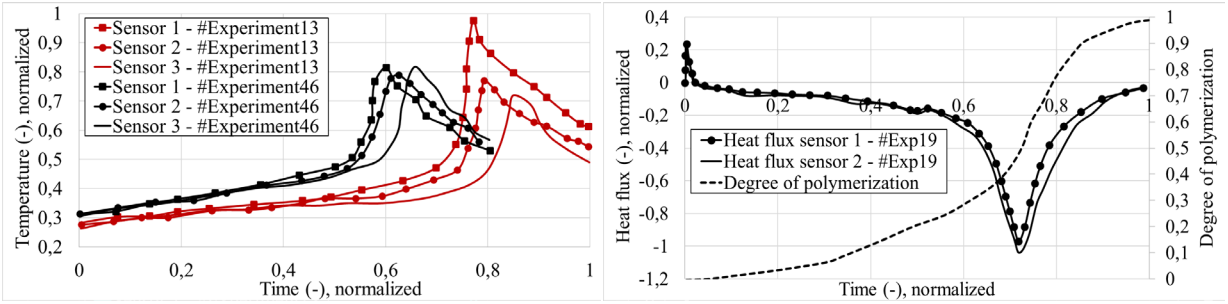

(a) (b)

Fig. 3. Experimental observations: (a) temperature evolution during both filling and polymerization phases, (b) heat flow measured during filling and polymerization phases and the interpreted degree of polymerization.

In Fig. 3(a) it is possible to see that during the filling phase (0 to 0.4 units of time), the thermal behavior is mainly isotherm. On the contrary, after that step, the temperature rate quickly increases, and the behavior becomes mainly dynamic. It is also shown that the resin is very sensitive to its initial temperature but also very sensitive to its own reaction. It is therefore necessary to model both the isothermal and dynamic behavior (respectively Fig. 4(b) & Fig. 4(a)). Both DSC tests are then necessary, and the results are shown on Fig. 4.

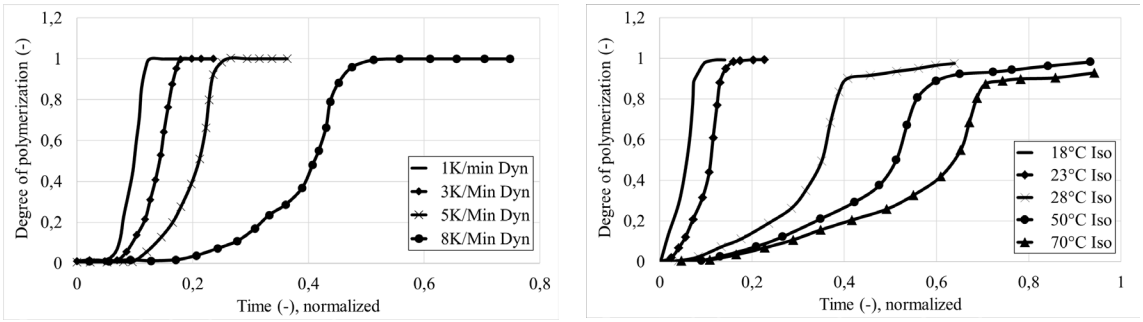

(a) (b)

Fig. 4. Interpreted DSC scans of the resin: (a) dynamic kinetics, (b) isothermal kinetics.

The specific behavior of the resin and its sensitivity have a direct impact on the appearance of defects and geometrical distortions or internal stresses, which can occur even from the beginning of the process. To manage such difficulties, a multiphysics model and a numerical workflow, considering both isothermal and dynamic description of the polymerization kinetics during the whole process is necessary.

Modeling and Infusion Simulations

Several approaches exist in the literature [1, 3-7, 9, 14] to numerically model the behavior of the polymerization kinetics of the Elium® resin. Some of the previous studies follow a physico-chemical theory [3, 6, 7, 9] which leads to a subtil and detailed description of the mechanism during the polymerization. These models are often quite complex and require a lot of work to integrate and validate them into a simulation software. Moreover, for a manufacturing process simulation, staying at a larger scale without going into chemical details is enough. A macroscopical

approach is then enough to be able to reach the polymerization and thermal behavior of the resin during the filling and curing phases. From the literature two mathematical models seem to be adapted to model the resin kinetics [4, 5].
First, the polynomial form of Bailleul [5], coupled with an Arrhenius law (Eq. 1).

$$\frac{d\alpha}{dt} = A_0 e^{-\frac{E_0}{RT}} \sum_{i=0}^{7} a_i \alpha^i \quad (1)$$

This one is easy to identify but stay very sensitive since a polynomial form of degree 7 is used. Eq. 2 represents the second model which is a semi-empirical Arrhenius type autocatalytic model, adapted for the Elium® resin by the work of Han et al [1].

$$\frac{d\alpha}{dt} = A_1 e^{-\frac{E_1}{RT}}(1-\alpha)^{n_1} + A_2 e^{-\frac{E_2}{RT}}(\alpha_{max}-\alpha)^{n_2}\alpha^{m_2} \quad (2)$$

However, most of the works in those papers do not identify the kinetics for both the isothermal and the dynamic scans. Indeed, it is often difficult to satisfy a good fitting for both approaches. Nevertheless, as said earlier and considering the sensitivity of the Elium® resin, it is proposed here to assume some modeling error (while remaining within the experimental tolerance) which gives some flexibility in parameter fitting and identification to fit both isothermal and dynamic DSC curves. An inverse optimization method leads to the identification of the model parameters. Fig. 5 shows the results of the fitting for the two models. As can be seen, the Bailleul model does not fit properly for high temperature rate. It was then decided to only implement the identified Han model into PAM-RTM©. However, to ensure that PAM-RTM© solver compiles and computes the models correctly, a comparison of the numerical results from an in-house solver using the open-source library FreeFem++ [10] was made.

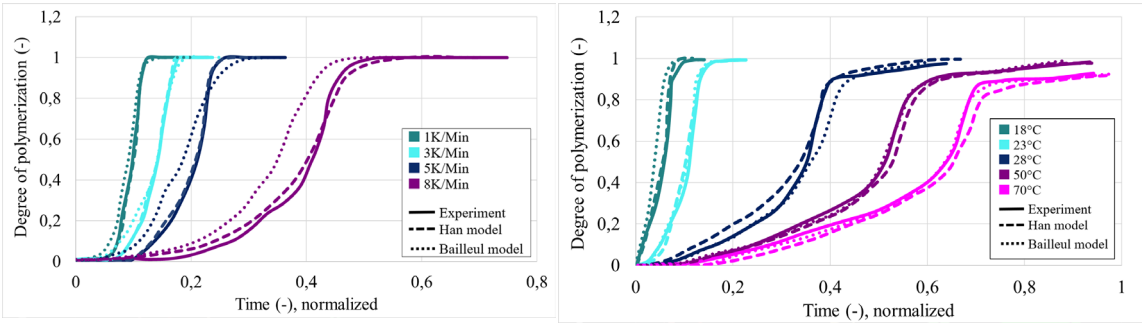

Fig. 5. Fitted model for the DSC approach: (a) dynamic behavior, (b) isothermal behavior.

Before comparing the thermal and chemical behavior of the resin, a correlation test simulation on the filling phase is also proposed in Fig. 6 for experiment #19. Indeed, many other parameters will influence the polymerization of the resin, such as the thickness of the part, the material defects like the preferential channels, gaps or overlaps, the influence of the flow medium, etc. Filling tests were carried out on thin plates first. Virtual sensors were also introduced into the PAM-RTM© infusion simulation software. It was experimentally found that the wetting effect at the flow front location could be neglected at first [8] for thin plates. A camera and infrared camera system were used to follow the flow front experimentally and the comparison with the simulation is shown in Fig. 6. It can be observed that the simulation gives a good flow result for this simple case. The value Δt on the figure represents the difference between the experimental and the numerical filling time for each step. At the beginning, there is a little delay between both approaches. It can be easily explained because of the fast track just under the inlet in the experimental set-up, which is not considered in the simulation.

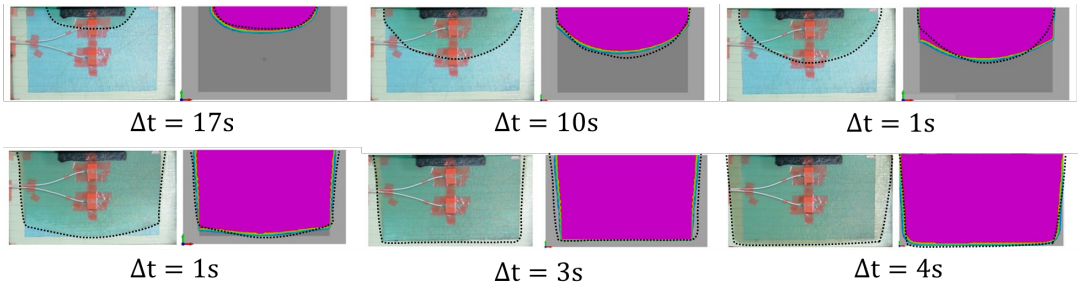

Fig. 6. Flow front comparison between experiment #19 and simulation on PAM-RTM©.

More local measurements were also made using the flow sensors to reach the thermal behavior of the resin and then deduce the degree of polymerization. It was useful to compare with the simulation and validate the model by confronting it with manufacturing cases.

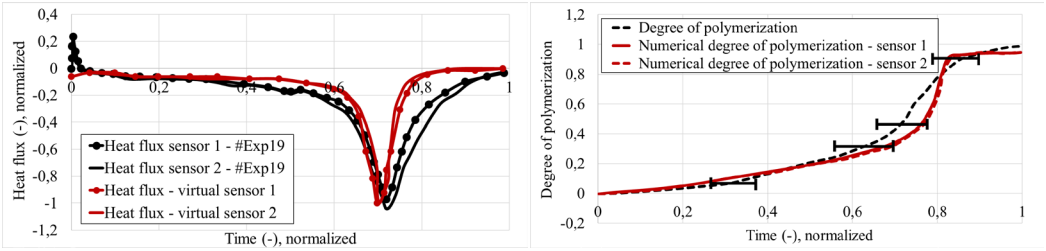

Fig. 7. Comparison between numerical and experimental data of experiment #19: (a) heat flow sensors, (b) extrapolated vs numerical degree of polymerization.

However, in Fig. 7(b) there is still a strong experimental variability in the polymerization phase. In the same way, the discrepancies between the experimental and simulated results shown in Fig. 7(a) also introduce some limitations either for the numerical model or experimental variabilities. The gaps between the flow measurements and the simulation approach (Fig. 7(a)) can be explained by different assumptions:

- Numerical initial conditions do not exactly match the initial measured temperature and thus affect the simulation results.
- Numerical boundary conditions do not represent the real forming process: considering the tooling thermal behavior, process artifacts (blanks, flow medium, ...), and convection around the part and mold.
- The use of a perfect numerical description of the material (perfect stacking, perfect permeability, no sensor intrusiveness, ...), which does not correspond to reality. Variations may therefore apply.

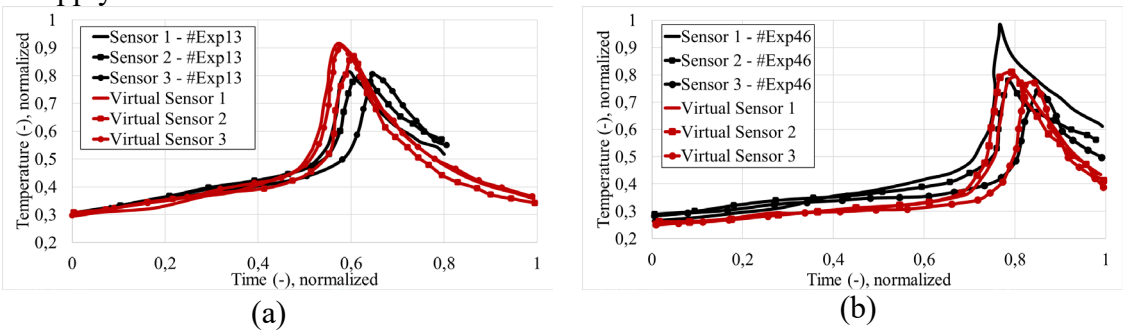

Fig. 8. Comparison of temperature between numerical and experimental approaches: (a) experiment #13, (b) experiment #46.

To check some of these assumptions, the simulation of experiment #13 and experiment #46 was made by applying different initial resin temperatures (Table. 1). Results can be seen in the Fig. 8. It can be seen that the model properly considers the variation of the initial resin temperature, which has a major impact on the peak time.

It is now shown that the infusion process using the Elium® resin is very sensitive to the initial condition, other simulations were made considering the boundary conditions. To do that, simulations on a 25 mm thick plate were carried out to predict the filling and polymerization behaviors for thick parts taking into account the influence of the tools on the thermal behavior.

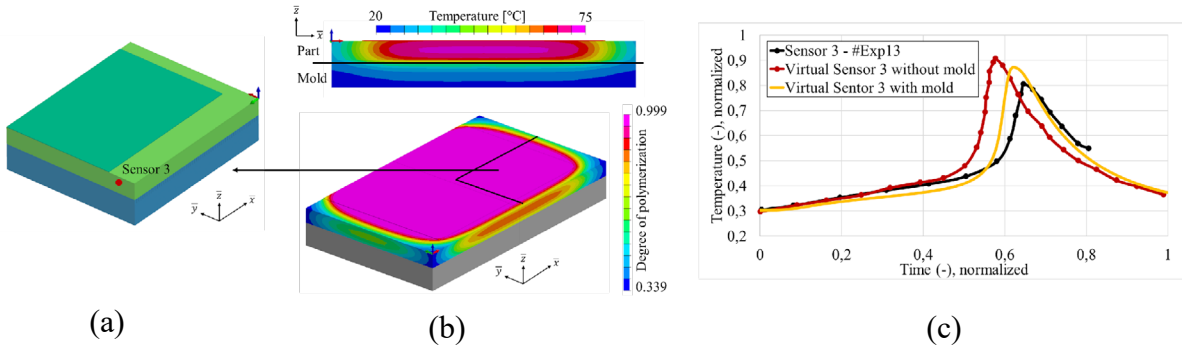

(a) (b) (c)

Fig. 9. Influence of the set up on the thermal and kinetics behavior: (a) 25mm thick plate modeling using PAM-RTM© (Quarter of the part using symmetry of the problem), (b) temperature and polymerization field during the curing phase, (c) temperature behavior over time considering the mold.

To illustrate the influence of the boundary conditions on this process, Fig. 9 shows that the mold can have a considerable impact on the thermal behavior and then the polymerization of the resin if the part is thick (Fig. 9(b)). On Fig. 9(c), the management of the boundary condition (through the thermal conductance with the mold or the convection with the air) led to a better mastering of the simulation. Further investigations are under work to check the influence of these mechanisms on the final distortion of the part.

Summary

The work presented in this paper presents a simulation approach to the filling and polymerization phase of the Elium® resin using the commercial PAM-RTM© tool from ESI group. It is first shown that the polymerization model must take into account both the isothermal behavior and the dynamic behaviors of the chemical reaction. Consequently, a larger range of error in the modeling is made but by comparing with the experimental values, a good consistency on the simulated results is still possible. In fact, because of a robust and advanced monitoring system, it can be noticed that the behavior of the Elium® resin is very sensitive to its environment - boundary and initial conditions - and that the simulation allows having quite good predictions. It will also allow, in future works, to propose reliable predicted infusion strategies adapted to the studied case.

Acknowledgement

This study is a part of the ZEBRA project led by IRT Jules Verne (French Institute of Research and Technology in Advanced Manufacturing). The authors wish to thank the industrial partners of this project: LM Wind Power, Arkema, Owens Corning, ENGIE, Suez and CANOE, and the Research Institute in Civil and Mechanical Engineering (GeM), Ecole Centrale de Nantes, Nantes University.

References

[1] N. Han, I. Baran, JSM. Zanjani, O. Yuksel, L. An, R. Akkerman, Experimental and computational analysis of the polymerization overheating in thick glass/Elium® acrylic thermoplastic resin composites, Compos. Part B: Eng. 202 (2020) 108430. https://doi.org/10.1016/j.compositesb.2020.108430

[2] P. le Bot, G. Lebreton, N. Siddig, P. Couarraze, O. Fouché, C. Sébastien, A. de Fongalland, F. Cara, P. Gérard, Anomaly detection during thermoplastic composite infusion: Monitoring strategy through thermal sensors, in Key Engineering Materials, Achievements and Trends in Material Forming 926 (2022) 1423-1436.

[3] SF. Gayot, C. Bailly, T. Pardoen, P. Gérard, F. Van Loock, Processing maps based on polymerization modelling of thick methacrylic laminates, Mater. Des. 196 (2020) 109-170. https://doi.org/10.1016/j.matdes.2020.109170

[4] J. Avenet, A. Levy, JL. Bailleul, S. Le Corre, J. Delmas, Adhesion of high performance thermoplastic composites: Development of a bench and procedure for kinetics identification, Compos. Part A: Appl. Sci. Manuf. 138 (2020) 106054. https://doi.org/10.1016/j.compositesa.2020.106054

[5] N. Boyard, J.L. Bailleul, M.H. Boutaous, Experimental determination and modeling of transformation kinetics, Heat Transfer in Polymer Composite Materials: Forming Processes (2016) 77-119. http://doi.org/10.1002/9781119116288.ch3

[6] T. Srinivas, S. Sivakumar, S.K. Gupta, D.N. Saraf, Free radical polymerizations associated with the trommsdorff effect under semibatch reactor conditions. II: Experimental responses to step changes in temperature, Polym. Eng. Sci. 36 (1996) 311-321. https://doi.org/10.1002/pen.10418

[7] R.G.W. Norrish, E.F. Brookman, The mechanism of polymerization reactions. I. The polymerization of styrene and methyl methacrylate, Proceedings of the Royal Society of London. Series A, Math. Phys. Sci. 171.945 (1939) 147-171.

[8] W. Li, J. Krehl, J.W. Gillespie jr, D. Heider, M. Endrulat, K. Hochrein, M.G. Dunham, C.J. Dubois, Process and performance evaluation of the vacuum-assisted process, J. Compos. Mater. 38 (2004) 1803-1814. http://doi.org/10.1177/0021998304044769

[9] F. Cara, B. Taillet, P. Gérard, Preliminary study of curing kinetics and mechanical characterization of reactive thermoplastic resins with new calorimetric cell mounted on DMA, AIP Conference Proceedings 2113 (2019) 130011. https://doi.org/10.1063/1.5112671

[10] F. Hecht, New development in FreeFem++, J. Numeric. Math. 20 (2012) 251-266. https://doi.org/10.1515/jnum-2012-0013

[11] P. Carlone, F. Rubino, V. Paradiso, F. Tucci, Multi scale modeling and online monitoring of resin flow through dual scale textiles in liquid composite molding process, Int. J. Adv. Manuf. Tehnol. 96 (2018) 2215-2230. https://doi.org/10.1007/s00170-018-1703-9

[12] S. Konstantopoulos, E. Fauster, R. Schlediewski, Monitoring the production of FRP composites: a review of in-line sensing methods, Express Polym. Letter. 8 (2014) 823-840. http://doi.org/10.3144/expresspolymlett.2014.84

[13] G. Tuncol, M. Danisman, A. Kaygar, EM. Sozer, Constraints on monitoring resin flow in the resin transfer molding (RTM) by using thermocouple sensors, Compos. Part A. 38 (2018) 1363-1386. http://doi.org/10.1016/j.compositesa.2006.10.009

[14] P. Carlone, D. Aleksendrić, Soft computing in the design and manufacturing of composite materials, Woodhead publishing (2015) ISBN 9781782421795.

Materials Research Proceedings 28 (2023) 321-330 https://doi.org/10.21741/9781644902479-35

Gate design algorithm to maximize the fiber orientation effectiveness in thermoplastic injection-molded components

PERIN Mattia[1,a], BERTI Guido A.[1,b], LEE Taeyong[2,3,c] and QUAGLIATO Luca[2,3,d *]

[1]Department of Management and Engineering, University of Padua, 36100, Vicenza, Italy

[2]Division of Mechanical and Biomedical Engineering, Ewha Womans University, Seoul 03760, Republic of Korea

[3]Division of Mechanical and Biomedical Engineering, Graduate Program in System Health Science and Engineering, Ewha Womans University, Seoul 03760, Republic of Korea

[a] mattia.perin@phd.unipd.it, [b] guido.berti@unipd.it, [c] tlee@ewha.ac.kr, [d] lucaq@ewha.ac.kr

Keywords: Injection Molding, Fibers Reinforced Composite (FRC), Injection Gate Location, Fiber Orientation, Machine Learning

Abstract. This research presents an automatic algorithm, implemented in a Visual Basic Architecture (VBA), for the optimization of the gate location in thermoplastic injection molding of short fibers reinforced composite materials. The algorithm receives, as input, the geometry of the component and, according to the user's choice, defines the injection points grid, and relevant versors, on a pre-constructed mesh, automatically runs the finite volume method (FVM) simulation and exports the fiber orientation tensor (FOT) on each node of the mesh. The nodal coordinate of the part and the relevant FOT are then used as the training dataset for a Gradient Boosting (GB) algorithm for the full correlation between injection gate locations and the resulting fiber orientation distribution (FOD), allowing to define the injection gate configuration better suited to maximize the effectiveness of the reinforcement fibers. By coupling the trained GB algorithm with a finite element method (FEM) simulation it was confirmed that the developed algorithm can predict the influence of the gate location on the FOD and the resulting mechanical performances, improving the stiffness between 3.8% and 32.6%, on simple and complex geometries alike.

Introduction

In recent years, the injection molding process has been growing in both importance and utilization thanks to the development of innovative polymers and reinforcements [1, 2]. This is especially the case in the automotive industry, where lightweight design [3] and recyclability [4] are becoming ever-growing focus points for research and development. Although injection molding is considered a fairly well-established manufacturing process, several independent parameters must be properly set to achieve a high quality of the molded parts, especially in terms of minimizing warpage, shrinkage, and weld-lines on the critical region of the component [5-7]. Besides, the recent trend is to incorporate woven composite into an injection-molded thermoplastic matrix to achieve recyclability while enhancing the mechanical properties of the molded part [8].

For the case of short fibers-reinforced thermoplastic polymers (SFRTP) the fiber orientation is influenced by both the component geometry and the injection gates configuration. As it is well known from various recent contributions, fiber orientation is responsible for static, fatigue, and fracture properties of SFRTP [9, 10]. In addition, as demonstrated for both short glass fibers (SGF) and short carbon fibers (SCF), the interaction between polymer matrix and fibers reinforcement plays a pivotal role in controlling the notch sensitivity [11, 12]. Accordingly, controlling and optimizing the fiber orientation in injection molded components becomes of paramount importance to maximize the effectiveness of the reinforcement.

Content from this work may be used under the terms of the Creative Commons Attribution 3.0 license. Any further distribution of this work must maintain attribution to the author(s) and the title of the work, journal citation and DOI. Published under license by Materials Research Forum LLC.

For SFRTP, the fiber orientation distribution (FOD) is influenced by both the injection gates and the geometry of the component, and in a lesser manner by the applied processing conditions. The component geometry varies from case to case and is not easy to generalize. For this reason, recent contributions dealing with the optimization of injection-molded components focused on controlling the global thickness distribution and inserting local rib networks to limit the warpage [13, 14]. On the other hand, injection gate (IG) design has also attracted the interest of researchers over the years, and various modeling technics have been applied to achieve greater optimization considering different criteria, as hereafter summarized.

Zhai et al. [15, 16] developed a recursive approach and a sequential linear programming algorithm to identify the IG locations, allowing for a balanced filling on injection-molded parts. The optimization criterion is based on a uniform distribution of the clamping force during the filling phase and was validated on a U-shape part. Li et al. [17] developed a black-box algorithm for the optimization of the IG considering the injection pressure, warpage, residual stress, and weld lines as optimization criteria. Similarly, Moayyedian and Mamedov [18] proposed a multi-objective optimization approach to defining the combination of process parameters and IG locations, allowing for a reduction of the molding defects, such as shrinkage, warpage, and short shot. More recently, Moayyedian and Mamedov [19] also proposed a methodology for the reduction of the same molding defects but based on an artificial neural network and Taguchi techniques, showing a relatively low margin error, quantified in 15%, and attributed to uncontrollable process variability. Besides, the only contribution dealing with fiber orientation optimization for the SFRTP focuses on the IM process parameters, thus the IG location was considered a constant in the analysis [20]. Other recent contributions proposed case studies investigating the effect of different IG configurations, and process parameters, on the filling time and quality of the molded component [21-23]. However, being these highly customized approaches, they can hardly be extended to different geometries and, most of all, they are all based on unfilled thermoplastic polymers. Accordingly, a general and customizable design approach for the gate location in the case of SFRTP seems to be missing in the literature,

To this aim, this research presents an algorithm able to automatically set up a user-defined number of injection molding FVM simulations, implemented in Autodesk Moldflow Insight 2023, run them, and export the fiber orientation tensor (FOT) on one or more control volumes defined by the user. The coordinates IG points, relevant versors, and the average fiber orientation tensor in the control volumes of interest are used to train and validate a machine learning (ML) model, based on the Gradient Boosting (GB) algorithm.

The proposed algorithm can suggest the best IG location allowing for the maximization of the FOD along one or more regions of interests and directions, with assigned priorities, resulting in customized stiffness enhancement. The maximization is carried out considering the load path, thus the directions along which the reaction forces are maximum, because of the applied displacements. The procedure has been developed and tested considering three geometries with an increasing level of feature complexity by mapping the FOD and relevant mechanical properties from the FVM simulation onto the FEM simulation, implemented in Abaqus 2020. The application of the IG optimization procedure allowed improving the component's stiffness between 3.8% and 32.6%, showing the effectiveness and the generality of the proposed algorithm.

Materials and Methods

This chapter is subdivided into three sections. The first deals with the proposed VBA algorithm for the automatic definition of the injection gate grid and the export of the FOD from each one of the FVM simulations. The first section also includes some details of the implemented machine learning model, based on the Gradient Boosting (GB) algorithm. The second section briefly describes the material properties of the employed polyamide-6 reinforced with 20% of short carbon fibers (PA6-20CF) and the relevant calibration into the FVM simulation. Finally, the third section

explains the mapping procedure for the transfer of the FOD, and relevant mechanical properties, from the FVM to the FEM simulation, for the evaluation of the stress distribution on the considered components as a consequence of the applied displacements.

Gate Location Optimization Algorithm

The IG location optimization algorithm is composed of four steps, as summarized in Fig. 1. All the steps are implemented in VBA programming, except for the ML-GB model of step#4, implemented in Python 3.11 and coupled with the scikit-learn 1.1.1 and SciPy 1.7.1 open-source libraries. In the algorithm, step#1 is devoted to the definition of the IG candidates on the selected model geometry that can be defined by the user on a predetermined grid or manually deployed. Step#2 receives the matrix with the IG candidates, and their relevant versors, to assure a perpendicularity onto the geometry and prepares the input files for the FVM simulation, comprehensive of all IG configurations to be tested.

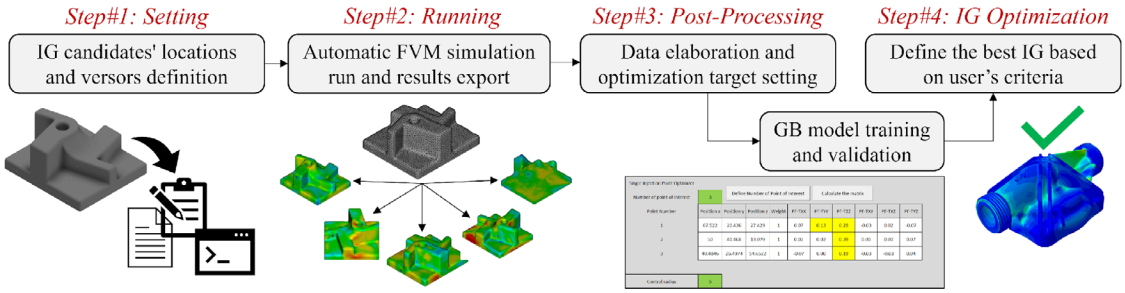

Fig. 1. Working flow for the injection gate (IG) optimization algorithm.

After the completion of all FVM simulations setup in step#2, step#3 creates a single result dataset file including i) coordinates of the IG point, ii) coordinates of all the nodes of the mesh (same for each simulation), and iii) results of the FOT (6 components) for each node. During step#3, the user is required to input the locations of interest and the relevant direction, or directions, along which the FOD should be oriented. To this aim, FEM simulations have been utilized to identify the regions of interest on the considered parts and, within those regions, the directions along which the stress components are maximum. Thus, by aligning the fibers along these directions, their effectiveness can be improved, allowing for an improvement in stiffness.

Before reaching step#4, the dataset constructed in step#3 is utilized to train and validate the prediction part of the architecture, based on the GB algorithm. 80% of the database is utilized for training purposes, whereas the remaining 20% is dedicated to validation. During the training, a k-fold validation, with k=5, is employed to assure accuracy and the absence of overfitting. If both conditions are satisfied, the user is presented with the location of the IG allowing for the maximization of the FOD in the locations of interest.

At this point, two important clarifications must be made. First, if the user is not satisfied with the accuracy of the prediction carried out by the GB model, the procedure can be upgraded by setting a finer grid for the IG location candidates in step#1, where only the new FVM simulations must be run and then integrated with those of the previous phase. Second, the proposed methodology considers only a single injection gate. Future studies are going to be focused on the direction of multiple IG optimization for better applicability in industrial applications.

Material Properties and FVM Simulation Setting

For the setting of the FVM simulations, the material properties relevant for the PA6-20CF material, as calibrated in previous works of one of the authors [9, 10, 12], have been employed. For their calibration into the FVM simulation, necessary for the subsequent mapping onto the FEM mesh,

the Ramberg-Osgood constitutive model, Eq. 1, has been employed and coupled with an anisotropic Hill'48 yield function, Eq. 2. The α and β parameters are calculated according to the FOT, for each element of the mesh as in Eq. 3, referring to the region of the model where it is maximum. In Eq. 3, λ_I represents the first eigenvalue of the fiber orientation tensor on each element of the mesh, whereas α_m, β_m and $\lambda_{m,I}$, are the reference values for the considered material, and are calculated during the material properties calibration. Fig. 2 shows the experimental engineering stress-strain curves for the considered PA6-20CF material (Fig. 2a), the comparison between experimental and constitutive modeling load-displacement curves (Fig. 2b), and model constants and reference values for the Ramberg-Osgood and anisotropic Hill'48 models (Fig. 2c).

$$\sigma = E^{1/n}\left(K\right)^{(n-1)/n}\left(\varepsilon_{p,eff}\right)^{1/n} \tag{1}$$

$$\sigma_{eff} = \sqrt{\frac{\left(\alpha\sigma_{11}-\beta\sigma_{22}\right)^2+\left(\beta\sigma_{22}-\beta\sigma_{33}\right)^2+\left(\beta\sigma_{33}-\alpha\sigma_{11}\right)^2+6\left[\left(\sigma_{12}\right)^2+\left(\sigma_{23}\right)^2+\left(\sigma_{31}\right)^2\right]}{2}} \tag{2}$$

$$\alpha\left(\lambda_I\right)=\theta+\left[\frac{\left(\alpha_m-\theta\right)}{\left(\lambda_{m,I}-1/2\right)}\right]\left(\lambda_I-1/2\right) \quad , \quad \beta\left(\lambda_I\right)=\theta+\left[\frac{\left(\beta_m-\theta\right)}{\left(\lambda_{m,I}-1/2\right)}\right]\left(\lambda_I-1/2\right) \tag{3}$$

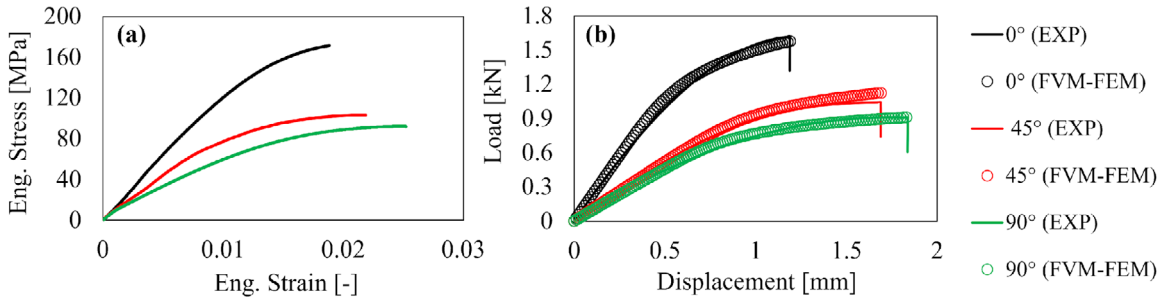

(c)

Parameter	Definition	Value
K	Strength coefficient	80.6 MPa
n	Hardening exponent	10.16
E_m	Polymer matrix elastic modulus	4.25 GPa
E_f	Fiber elastic modulus	105.6 GPa

Parameter	Definition	Value
α_m	Weight factor for the fiber direction	2.125
β_m	Weight factor for the direction normal to the fibers	1.214
$\lambda_{m,I}$	First eigenvalue of the fiber orientation matrix (strong fibers alignment region)	0.85

Fig. 2. (a) Materials properties and (b) comparison between experimental and constitutive modeling results of load-displacement curves for 0°, 45°, and 90° directions. (c) Model constants for the Ramberg-Osgood model and anisotropic Hill'48 yield function.

As concerns the mesh for the FVM simulation, the same mesh strategy, 3mm side 3D tetrahedral elements, has been employed and verified through mesh sensitivity analysis. In terms of injection molding process parameters, to avoid any bias, the same mold temperature, molten material temperature (at the nozzle), and cooling temperature of 285°C, 85°C, and 25°C, have been employed in all simulations. Regarding the injection time, it has been kept automatically controlled during the simulation, to avoid short-shot, whereas the post-pressure has been set at 80% of the injection pressure, for a total of 20s.

FVM-FEM Mapping and Tested Components

To test the improvement of the FOD with respect to the applied displacements, a mapping procedure to account for the FOD-dependent material properties in the structural FEM simulation has been employed. The structural FEM simulation has been implemented in ABAQUS 2020. The procedure is summarized in Fig. 3 and is based on the Ramberg-Osgood and anisotropic Hill'48 formulations presented in the previous section whereas the mapping is carried out by Autodesk Helius 2023.

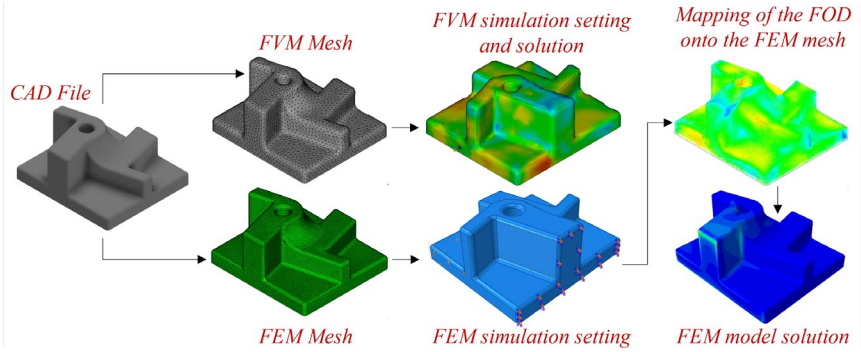

Fig. 3. Main steps in the mapping procedure for the consideration of the fiber orientation of the FVM simulation into a FEM structural simulation environment.

For each element of the FVM mesh, a corresponding set of elements in the FEM mesh is located based on their relevant position in the GCS, the same for both simulations. According to the FOT of each element of the FVM simulation, a specific set of mechanical properties is mapped onto the FEM simulation mesh. This procedure has been successfully applied and validated in other works of one of the corresponding author [9, 10, 12]. To test the IG design algorithm, three components have been considered, as shown in Fig. 4. The three parts have an increasing level of complexity and have all been subjected to a tensile displacement of 5 mm.

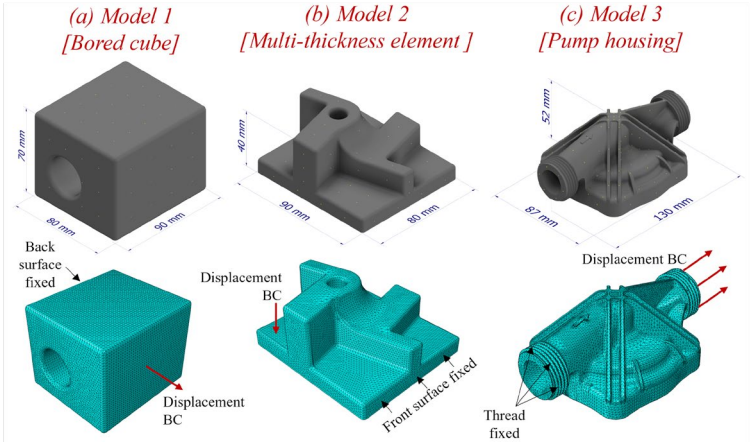

Fig. 4. Mechanical parts use for the validation of the IG location design algorithm. (a) Bored cube, (b) Multi-thickness element on a square base, and (c) Pump housing.

The three geometries of Fig. 4 have been all meshed with C3D10I tetrahedron elements, thanks to their good compatibility with those of the FVM simulation, whereas a quadratic integration scheme has been employed to allow for a better description of the deformation behavior between the edges and within the elements. The total number of elements for the three models is 306,165 (Fig. 4a), 243,183 (Fig. 4b), and 211,149 (Fig. 4c), respectively. The FEM simulations have been implemented in the ABAQUS/Standard environment, considering a static-implicit solution

technique. Finally, the simulation time has been divided into 100 steps for easier export and comparison of the results among the simulation cases of the same part.

Results and Discussion

To validate the IG location optimization algorithm, the procedure summarized in Fig. 1 has been applied to the three components of Fig. 4. The results, and relevant considerations, are reported in this chapter of the paper.

The initial step, prior to the application of the IG design algorithm, is the identification of the regions of the model subjected to high stress, or stress concentration, due to the displacement boundary conditions, or specific geometrical features. Accordingly, three FEM simulations considering only elastic material properties equal to E = 14GPa and ν = 0.37, representative of a sort of 0° direction for the PA6-20CF material, have been implemented. The results, reported in Fig. 5, allowed identifying two regions of interest for Model 1, four for Model 2, and three for Model 3, respectively. In Fig. 5, the normalized stress components (-1, +1 range) on the regions of interest are reported and are utilized as a reference for the directions along which to maximize the FOD. Rather than a quantitative estimation, the aim of this preliminary phase is the definition of the regions of the model where to focus on the optimization of the effectiveness of the FOD.

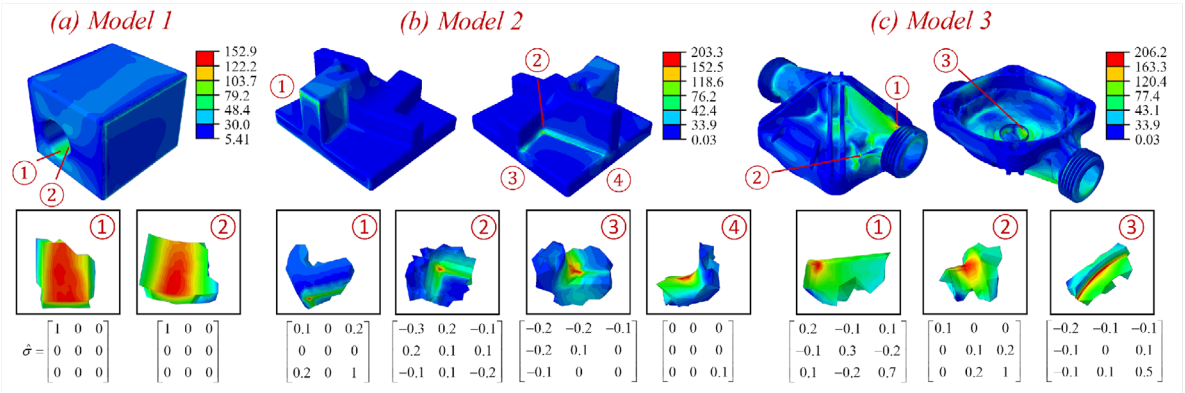

Fig. 5. Identification of the regions of interest from isotropic properties FEM for (a) Bored cube, (b) Multi-thickness element on square base, and (c) Pump housing models.

As defined in Fig. 1, the algorithm requires the definition of a mesh grid and the list of the IG candidates, with relevant versors, to assure perpendicularity with the geometry. For the three models of Fig. 4, 80, 70, and 140 IG candidate locations have been randomly assigned on an automatically generated 3 mm mesh grid in the relevant FVM simulations. The results, in terms of stress components ($\sigma_{x,y,z}$) for the best and worst IG locations, among the tested candidates, for the three tested components, are reported in Fig. 6a, 6b, and 6c, respectively.

The stress components of Fig. 6 are the average values relevant to a control volume of R = 5 mm around the element with the peak stress. As expected, a lower fibers alignment along the directions of loading (load path) results in a lower stress component along the same direction, a fact caused by a lower stiffness of the material. Since all simulations have been set up considering a displacement boundary condition, the reaction force is calculated according to the material properties, Fig. 2a. Thus, the higher the alignment of FOD with the reaction force direction, caused by the applied displacement boundary condition [9, 10], the higher the resulting stress.

This fact is clear when analyzing the difference between the best and worst IG configurations, for all three components reported in Fig. 6. For instance, in Model 1, due to the proximity of the two regions of interest, the average improvement is around +30%. For more complex parts, such as Model 2, the improvement is represented by a reduction of the compressive stresses, which has also a positive effect on the performances of the component due to the low compressive strength

of fibers reinforced materials. In general, the IG design algorithm gives priority to the regions identified by a high normalized value, as shown in Fig. 5. On the other hand, in some conditions, the optimization may result in a higher improvement of the effectiveness of the reinforcement in a region of the model which is not the main priority. This is clearly visible from the results of Fig. 6c, where region ③ shows a higher stiffness improvement than region ②, although the latter has the highest priority according to the normalized stress presented in Fig. 5c.

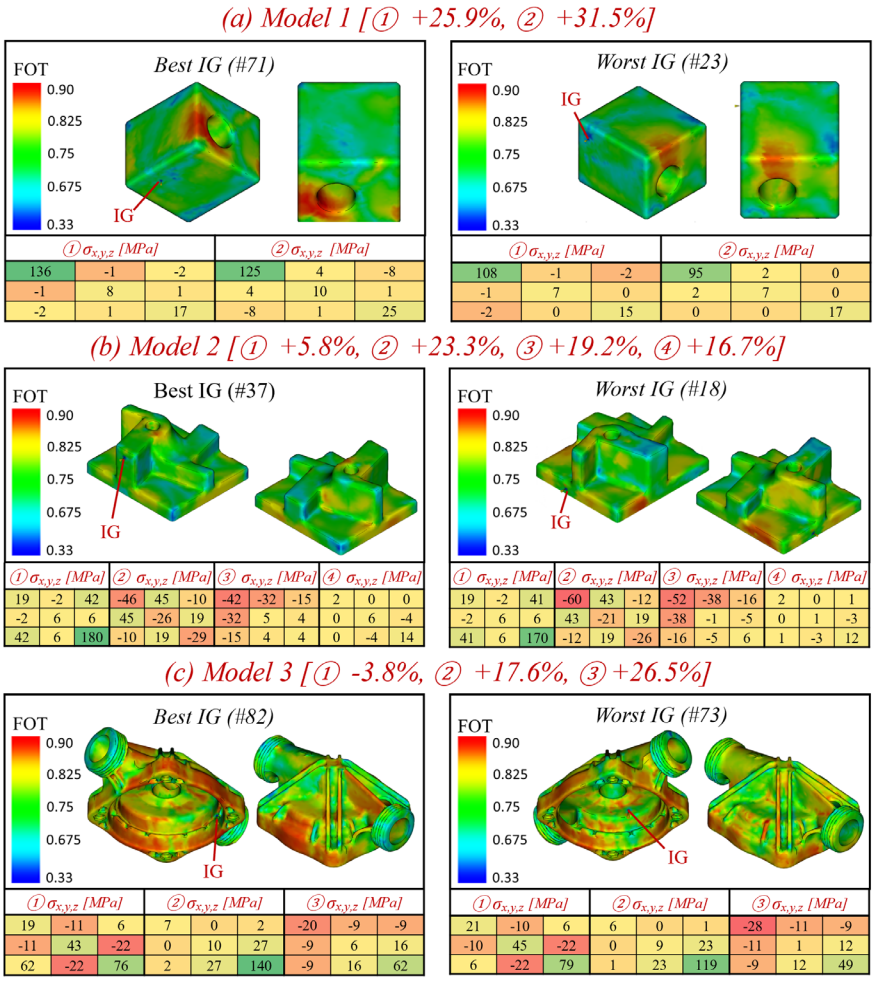

Fig. 6. FOT distribution (FVM simulation) and stress components (FEM simulation) for the best and worst IG locations for (a) Model 1, (b) Model 2, and (c) Model 3.

From a general perspective, it is interesting to highlight that, according to the results presented in Fig. 6, for all three models and even before the final optimization stage, implemented through the ML-GB algorithm, the average improvement in terms of FOD is clear and quantified in 28.7%, 16.3%, and 13.4% for the three investigated components. The almost two times higher stiffness improvement estimated for the bored cube part is related to the relative simplicity of the geometry, which makes it easier for the IG optimization algorithm to identify the best IG location.

In order to achieve full optimization for the IG location, the FOD resulting from the FVM simulations of each of the three components have been utilized for training and validation for the ML-GB algorithm. The average deviations between true and predicted values for the FOD for the components have been calculated at 5.6%, 4.8%, and 3.5% for the training datasets, and 5.2%,

4.8%, and 3.4%, for the validation datasets, respectively. These deviations are the average ones relevant for the 5-fold validations and show the quality of the prediction and the absence of bias.

By employing the trained GB model, further improvements on the FOD could be achieved, as reported in Fig. 7. For the case of Model 1, due to the low complexity of the geometry, the FVM simulation-based analysis was sufficient in identifying a fairly good IG location, thus the stiffness improvement provided by the application of the GB algorithm is minimal. However, for both Model 2 and Model 3, the application of the trained GB model allowed identifying a better IG location, not previously included in the FVM simulation database, which achieved a further improvement of the effectiveness of the fibers reinforcement. For Model 2 the average stiffness improvement, with respect to the results of Fig. 6, is quantified in 4.6%, whereas for Model 3 is it quantified in 3.3%.

(a) Model 1 [① +2.2%, ② +0.8%]

After Gradient Boosting Optimization					
① $\sigma_{x,y,z}$ [MPa]			② $\sigma_{x,y,z}$ [MPa]		
139	-2	2	126	2	0
-2	9	1	2	10	1
2	1	15	0	1	20
Before Gradient Boosting Optimization					
136	-1	-2	125	4	-8
-1	8	1	4	10	1
-2	1	17	-8	1	25

(c) Model 3 [① +7.9%, ② +2.1%, ③ +0%]

After Gradient Boosting Optimization								
① $\sigma_{x,y,z}$ [MPa]			② $\sigma_{x,y,z}$ [MPa]			③ $\sigma_{x,y,z}$ [MPa]		
21	-12	7	7	0	2	-19	-10	-11
-12	46	-24	0	10	27	-10	5	15
7	-24	82	2	27	143	-11	15	62
Before Gradient Boosting Optimization								
19	-11	6	7	0	2	-20	-9	-9
-11	43	-22	0	10	27	-9	6	16
62	-22	76	2	27	140	-9	16	62

(b) Model 2 [① +5%, ② +8.7%, ③ +4.8%, ④ +0%]

After Gradient Boosting Optimization											
① $\sigma_{x,y,z}$ [MPa]			② $\sigma_{x,y,z}$ [MPa]			③ $\sigma_{x,y,z}$ [MPa]			④ $\sigma_{x,y,z}$ [MPa]		
22	-2	43	-42	43	-11	-40	-37	-15	2	0	1
-2	4	1	43	-24	22	-37	1	-4	0	6	-4
43	1	189	-11	22	-34	-15	-4	6	1	-4	14
BeforeGradient Boosting Optimization											
19	-2	42	-46	45	-10	-42	-32	-15	2	0	0
-2	6	6	45	-26	19	-32	5	4	0	6	-4
42	6	180	-10	19	-29	-15	4	4	0	-4	14

Fig. 7. Stress components for the best IG locations before and after the GB-IG optimization for (a) Model 1, (b) Model 2, and (c) Model 3

Summary

The research presented in this paper detailed a highly customizable algorithm for the optimization of the injection gate location in the thermoplastic injection molding process for the maximization of the effectiveness of the fibers reinforcement in SFRC. The IG prediction algorithm proved to be able to achieve a concurrent optimization of the FOD in various regions of interest while prioritizing those with the highest stress distribution. Being implemented on freeware SW, the proposed algorithm can be implemented directly to various components, from low to high complexity, allowing for higher exploitation of the potentials of SFRC. On the other hand, as also previously mentioned, more research work should be oriented on extending the proposed methodology to multi-gate injection molding, to allow for the application to bigger geometries where a single IG is not sufficient. In addition to that, the influence of the injection molding process parameters on the FOD is going to be accounted for as well, to allow for a more comprehensive and realistic prediction and optimization of the IG locations.

Acknowledgments

This research was supported by the BK21 FOUR (Fostering Outstanding Universities for Research) funded by the Ministry of Education (MOE, Korea) and National Research Foundation of Korea (NRF-5199990614253).

References

[1] T. Ishikawa, K. Amaoka, Y. Masubuchi, T. Yamamoto, A. Yamanaka, M. Arai, J. Takahashi, Overview of automotive structural composites technology developments in Japan, Compos. Sci. Technol. 155 (2018) 221-246. http://doi.org/10.1016/j.compscitech.2017.09.015

[2] P. Boisse, R. Akkerman, P. Carlone, L. Kärger, S.V. Lomov, J.A. Sherwood, Advances in composite forming through 25 years of ESAFORM, Int. J. Mater. Forming 15 (2022) 39. https://doi.org/10.1007/s12289-022-01682-8

[3] L. Quagliato, C. Jang, N. Kim, Manufacturing process and mechanical properties characterization for steel skin – Carbon fiber reinforced polymer core laminate structures, Compos. Struct. 209 (2019) 1-12. http://doi.org/10.1016/j.compstruct.2018.10.078

[4] T. Evens, G.-J. Bex, M. Yigit, J. De Keyzer, F. Desplentere, A. Van Bael, The influence of mechanical recycling on properties in injection molding of fiber-reinforced polypropylene, Int. Polym. Process. 34 (2019) 398-407. http://doi.org/10.3139/217.3770

[5] N.Y. Zhao, J.Y. Lian, P.F. Wang, Z.B. Xu, Recent progress in minimizing the warpage and shrinkage deformations by the optimization of process parameters in plastic injection molding: a review, Int. J. Adv. Manuf. Technol. 120 (2022) 85-101. http://doi.org/10.1007/s00170-022-08859-0

[6] S. Kitayama, S. Hashimoto, M. Takano, Y. Yamazaki, Y. Kubo, S. Aiba, Multi-objective optimization for minimizing weldline and cycle time using variable injection velocity and variable pressure profile in plastic injection molding, Int. J. Adv. Manuf. Technol. 107 (2020) 3351-3361. http://doi.org/10.1007/s00170-020-05235-8

[7] E.I. Kurkin, O.E. Lukyanov, V.O. Chertykovtseva, O.U. Espinosa Barcenas, Molding gate optimization for weld line location away from structures loaded area, J. Phys.: Conference Series 1925 (2021) 012056. http://doi.org/10.1088/1742-6596/1925/1/012056

[8] E. Jeong, Y. Kim, S. Hong, K. Yoon, S. Lee, Innovative Injection Molding Process for the Fabrication of Woven Fabric Reinforced Thermoplastic Composites, Polym. 14 (2022). http://doi.org/10.3390/polym14081577

[9] L. Quagliato, Y. Kim, J.H. Fonseca, D. Han, S. Yun, H. Lee, N. Park, H. Lee, N. Kim, The influence of fiber orientation and geometry-induced strain concentration on the fatigue life of short carbon fibers reinforced polyamide-6, Mater. Des. 190 (2020) 108569. http://doi.org/10.1016/j.matdes.2020.108569

[10] L. Quagliato, J. Lee, J.H. Fonseca, D. Han, H. Lee, N. Kim, Influences of stress triaxiality and local fiber orientation on the failure strain for injection-molded carbon fiber reinforced polyamide-6, Eng. Fract. Mech. 250 (2021) 107784. http://doi.org/10.1016/j.engfracmech.2021.107784

[11] M. Ricotta, M. Sorgato, M. Zappalorto, Tensile and compressive quasi-static behaviour of 40% short glass fibre - PPS reinforced composites with and without geometrical variations, Theor. Appl. Fract. Mec. 114 (2021) 102990. http://doi.org/10.1016/j.tafmec.2021.102990

[12] L. Quagliato, M. Ricotta, M. Zappalorto, S.C. Ryu, N. Kim, Notch effect in 20% short carbon fibre-PA reinforced composites under quasi-static tensile loads, Theor. Appl. Fract. Mec. 122 (2022) 103649. http://doi.org/10.1016/j.tafmec.2022.103649

[13] J.H. Fonseca, G. Han, L. Quagliato, Y. Kim, J. Choi, T. Keum, S. Kim, D.S. Han, N. Kim, H. Lee, Design and numerical evaluation of recycled-carbon-fiber-reinforced polymer/metal hybrid engine cradle concepts, Int. J. Mech. Sci. 163 (2019) 105115. http://doi.org/10.1016/j.ijmecsci.2019.105115

[14] J.H. Fonseca, L. Quagliato, S. Yun, D. Han, N. Kim, H. Lee, Preliminary design of an injection-molded recycled-carbon fiber–reinforced plastic/metal hybrid automotive structure via

combined optimization techniques, Struct. Multidiscip. O. 64 (2021) 2773-2788. http://doi.org/10.1007/s00158-021-02988-y
[15] M. Zhai, Y. Lam, C. Au, Gate location optimization scheme for plastic injection molding, e-Polymers 9 (2009). https://doi.org/10.1515/epoly.2009.9.1.1515
[16] M. Zhai, Y. Xie, A study of gate location optimization of plastic injection molding using sequential linear programming, Int. J. Adv. Manuf. Technol. 49 (2009) 97-103. http://doi.org/10.1007/s00170-009-2376-1
[17] Z. Li, X. Wang, A Black Box Method for Gate Location Optimization in Plastic Injection Molding, Adv. Polym. Technol. 32 (2013) 793-808. http://doi.org/10.1002/adv.21322
[18] M. Moayyedian, A. Mamedov, Multi-objective optimization of injection molding process for determination of feasible moldability index, Procedia CIRP 84 (2019) 769-773. https://doi.org/10.1016/j.procir.2019.04.213
[19] M. Moayyedian, A. Dinc, A. Mamedov, Optimization of Injection-Molding Process for Thin-Walled Polypropylene Part Using Artificial Neural Network and Taguchi Techniques, Polym. 13 (2021) 4158. https://doi.org/10.3390/polym13234158
[20] K. Li, S.-L. Yan, W.-F. Pan, G. Zhao, Optimization of fiber-orientation distribution in fiber-reinforced composite injection molding by Taguchi, back propagation neural network, and genetic algorithm–particle swarm optimization, Adv. Mech. Eng. 9 (2017) 168781401771922. http://doi.org/10.1177/1687814017719221
[21] M. Huszar, F. Belblidia, H.M. Davies, C. Arnold, D. Bould, J. Sienz, Sustainable injection moulding: The impact of materials selection and gate location on part warpage and injection pressure, Sustainable Mater. Technol. 5 (2015) 1-8. http://doi.org/10.1016/j.susmat.2015.07.001
[22] M.S. Shreyas, L.G. Sannamani, Optimum Gate Location in Injection Mold of Nasal Foreign Body Removal Cover, Int. J. Eng. Res. Technol. 9 (2020) 1-5. http://doi.org/10.17577/IJERTV9IS050010
[23] K. Yang, L. Tang, P. Wu, H. Yi, Research on Optimization of Injection Molding Process Parameters of Automobile Plastic Front-End Frame, Adv. Mater. Sci. Eng. 2022 (2022) 1-18. http://doi.org/10.1155/2022/5955725

Materials Research Proceedings 28 (2023) 331-338 https://doi.org/10.21741/9781644902479-36

Investigation of the compaction behavior of uni- and bidirectional non-crimp fabrics

SCHÄFER Bastian[1,a *], ZHENG Ruochen[2], BOISSE Philippe[2] and KÄRGER Luise[1]

[1]Karlsruhe Institute of Technology (KIT), Institute of Vehicle System Technology (FAST), Karlsruhe, Germany

[2]Université de Lyon, LaMCoS CNRS, INSA-Lyon, F-69621, France

[a]bastian.schaefer@kit.edu, [b]ruochen.zheng@insa-lyon.fr, [c]philippe.boisse@nsa-lyon.fr, [d]luise.karger@kit.edu

Keywords: Fabrics/Textiles, Experimental Characterization, UD-NCF, Biax-NCF

Abstract. The through-thickness compaction behavior of engineering textiles significantly influences the resulting component properties during liquid composite molding processes (LCM). It determines the final fiber volume content and thus the necessary press force, the permeability as well as the final mechanical properties. In the present work, the behavior of a uni- and bidirectional carbon fiber non-crimp fabric (UD- & Biax-NCF) with the same fiber type and areal density of fibers in the respective main reinforcement directions is tested in a punch-to-plate setup. Thereby, the influence of the relative fiber orientation at the interfaces of a layup as well as the number of plies is investigated. A combined influence of roving nesting and superposition of stitching patterns is observed. This results in a common influence of decreasing resistance to compaction for higher numbers of layers, while the relative orientation of the interfaces in a layup is only significant for the Biax-NCF.

Introduction

Non-crimp fabrics (NCFs) have straight fibers compared to woven fabrics with undulated fibers and therefore provide a higher lightweight potential. The resulting component properties during liquid composite molding processes are significantly influenced by the through-thickness compaction behavior. It determines the final fiber volume content (fvc) and thus the necessary press force, the permeability as well as the resulting mechanical properties [1]. The compaction behavior of woven fabrics as well as biaxial NCFs (Biax-NCF) has been investigated more extensively [2-8], compared to unidirectional NCFs (UD-NCF) [9-11].

A typically measured thickness or fvc vs pressure diagram for engineering textiles has two distinct regions: the first region is dominated by a low compression resistance due to the low bending stiffness of crimped fibers and closing of initial gaps between the fibers; in the second region the fibers come into contact with each other and the resistance to compression is more dominated by an increasing number of high Hertzian contact forces [12]. The compaction behavior is largely determined by the architecture of the textile, the type of fiber and the areal density [4, 5, 10]. Textiles with a higher areal density tend to have a smaller resistance to compaction because they have more yarns in a roving and usually a more rounded shape of fiber bundles [4, 7, 13] Additional factors influencing the compaction of multi-ply stacks are the number of layers and layup sequence [7]. Increasing the number of plies in a layup reduces the resistance to compaction, due to rovings of different layers sliding into gaps at the inhomogeneous interfaces. This effect is called nesting and usually more pronounced for woven fabrics compared to NCFs [14]. For NCFs, the compaction behavior is also influenced by the superposition of the stitching patterns and tension in the stitching during production [7, 10, 14].

Content from this work may be used under the terms of the Creative Commons Attribution 3.0 license. Any further distribution of this work must maintain attribution to the author(s) and the title of the work, journal citation and DOI. Published under license by Materials Research Forum LLC.

In a recent benchmark by Yong et al. [8] two glass-fiber fabrics (woven and Biax-NCF) were investigated at over 20 institutes in dry and wet conditions in order to investigate the conformity of compaction test results. Thereby, no distinct influence could be attributed to the size of the specimen, shape of the testing device or weight determination method. However, three main sources for variability were identified: thickness measurement method, machine compliance and specimen saturation in wet compression tests. However, a correction of the machine compliance as described by Sousa et al. [15] led to a good agreement between different institutions.

The compaction behavior of textiles is strongly dependent on the individual properties of the fabric and care must be taken when conducting the experiments to obtain compliant results. In this work, the behavior of a uni- and bidirectional carbon fiber NCF with the same fiber type and areal density of fibers in the respective main reinforcement directions is tested, based on the principles for the measuring method outlined in [15]. Thereby, the influence of the relative fiber orientation at the interfaces of a layup as well as the number of plies is investigated.

Experimental Procedure

Materials.

In this study, a unidirectional (UD300) and bidirectional (MD600) non-crimp fabric both without binder are used. The fabrics are manufactured by Zoltek and produced from the same PX35-50K continuous carbon (CF) fiber heavy tows. Both fabrics are stitched together with a 76 dtex PES yarn in a Tricot pattern. The UD-NCF consists of a single layer of aligned CF tows with thin glass fibers (GF) on the back for improved handleability and the MD-NCF of two layers in a 0°/90° orientation. Both fabrics have a similar number of CFs with about 300 g/m^2 in their respective main reinforcing directions. The most relevant characteristics of the NCFs used in this study are listed in Table 1.

Table 1. Characteristics of the investigated NCFs.

	Stitching length	*Tow width*		*Areal density*			
		0°	*90°*	*Total*	*0°*	*90°*	*stitching*
Unit	[mm]	[mm]	[mm]	[g/m^2]	[g/m^2]	[g/m^2]	[g/m^2]
UD300	3.6	5.0	-	328.86	309.86	9.7 (GF)	9.3
MD600	2.6	5.0	2.5	602.24	301.53	292.52	8.19

Punch-to-plate compaction tests.

The compaction behavior is investigated with a simple punch-to-plate setup mounted on a universal testing machine with a 50 kN load cell, cf. Fig. 1 a). Undeformed stacks of two, four, six or eight plies with a size of 200 x 200 mm^2 are compacted with a 150 x 160 mm^2 punch at a constant speed of 1 mm/min. Each measurement is repeated four times with a new stack of material for each test. Additionally, three different layups for each material are investigated with relative orientations of $\Delta\Theta = 0°, 45° \; or \; 90°$ between the CFs at the interfaces of each ply in a stack, cf. Fig. 1 b). In the UD-NCF layups, the front side (f) of the fabric with a zigzag pattern is facing up for each ply. This is the same for the Biax-NCF in layups with a relative interface orientation of $\Delta\Theta = 45°$ or 90°, while every second ply is flipped over with its back side (b) facing up for $\Delta\Theta = 0°$. The fabrics were stacked randomly to represent the typical case of an automated stacking process.

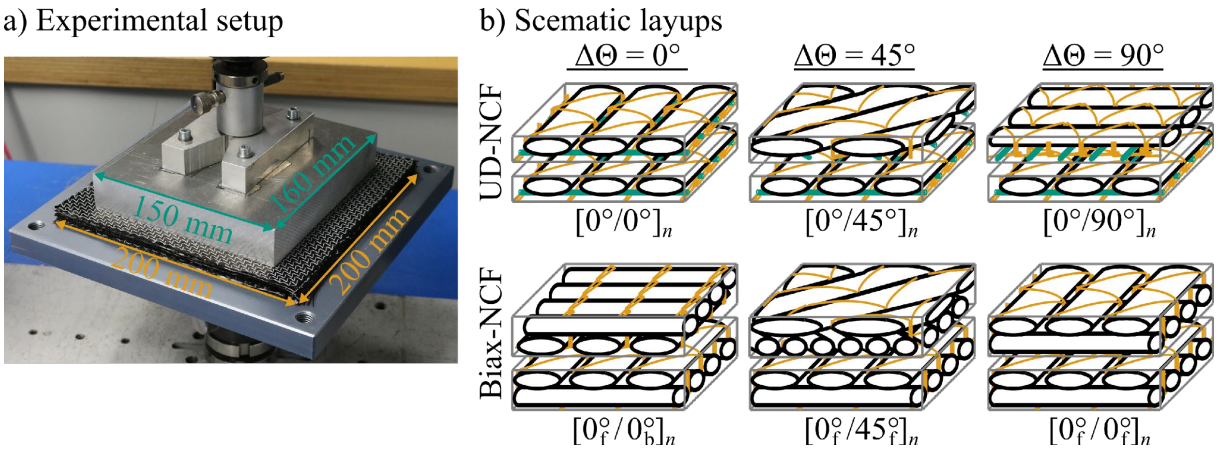

Fig. 1. a) Experimental punch-to-plate compaction test setup; b) Schematic lay-ups of the investigated combinations for different relative fibre orientations at the interfaces with the PES stitching of the NCFs in orange and the GF in green.

The fabric stacks of n_L-plies are compacted to a remaining thickness t_{rem} equivalent to a theoretical fiber volume content Φ of 65 %, cf. Fig. 2 a), according to

$$\Phi = \frac{m_A \cdot n_L}{\rho_{CF} \cdot t_{rem}} = \frac{(m_{total} - m_{stitching} - m_{GF}) \cdot n_L}{\rho_{CF} \cdot t_{rem}}, \quad (1)$$

where $\rho_{CF} = 0.00181\ g/mm^3$ is the density of the utilized CFs and m_A is the areal density of the CFs in the stack, which is approximated by subtracting the weight of the stitching $m_{stitching}$ and GFs m_{GF} from the total measured areal density m_{total}.

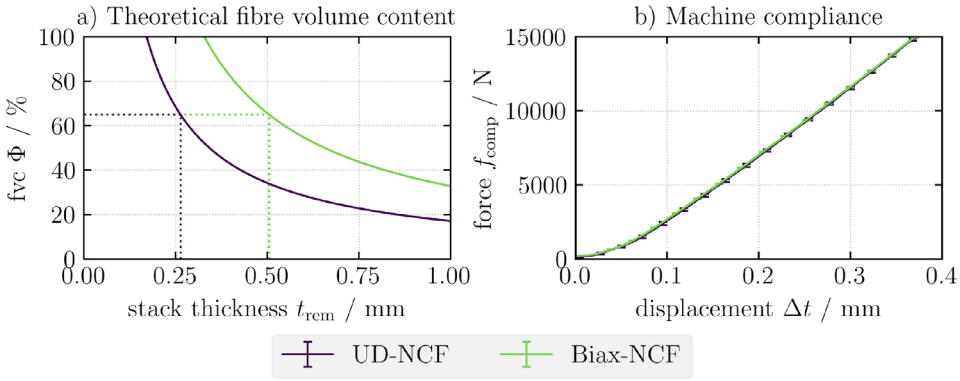

Fig. 2. a) Theoretical fibre volume content for a single layer ($\mathbf{n_L = 1}$) according to Eq. 1; b) Machine compliance curve during the loading stage.

Machine compliance adjustment.

Based on the results of the recent benchmark conducted by Yong et al. [8], machine compliance has a significant influence on the measured thickness during compaction tests. Therefore, the machine compliance was measured based on the method outlined by Sousa et al. [15]. Without a fabric, the top and bottom plates are brought into contact with each other ($\Delta t = 0$) and further pressed together with a prescribed speed of 1 mm/min. The machine force is measured as a

function of the cross-head displacement, cf. Fig. 2 b). The results were used to correct the true remaining stack thickness t_{rem} of each trial according to

$$t_{rem} = t_{meas} - \Delta t(f_{comp}), \tag{2}$$

where t_{meas} is the measured thickness according to the cross-head displacement reading and $\Delta t(f_{comp})$ is the thickness correction depending on the compaction force. The slight non-linearity of the curves indicates a small instability in the testing setup caused by non-controlled elements in the testing fixtures used (e.g. un-parallelism of the plates, internal friction, different materials). However, a good agreement is found between the compliance curve measured prior to testing of the UD- and Biax-NCF.

Results and Discussion

Influence of machine compliance.

In order to highlight the importance of adjusting the results for machine compliance, especially for varying numbers of layers n_{L}, Fig. 3 shows the results of the UD-NCF for the $[0°/0°]_n$-layups with ($[0°/0°]_n$) and without ($[0°/0°]_n^{\mathrm{raw}}$) machine compliance adjustment. Especially for high fiber volume contents, Φ is linear in n_{L} but very sensitive to small changes in the individual ply thickness, cf. Eq. 1. Since the compaction forces for all configurations are of the same order of magnitude, the thickness correction Δt results in larger deviations for the final fvc for fewer layers. This results in a deviation of $\Delta\Phi = 8 - 15\%$ from the targeted final fvc of $\Phi^{\mathrm{target}} = 65\%$. The maximum forces reduce due to the averaging over the smallest common resulting stack thickness t_{rem} among all trials after adjustment according to Eq. 2. Most importantly, however, the position of the curves changes in relation to each other. While an increase in the resistance to compaction is observed for the raw data, a decrease is observed after taking the machine compliance into account.

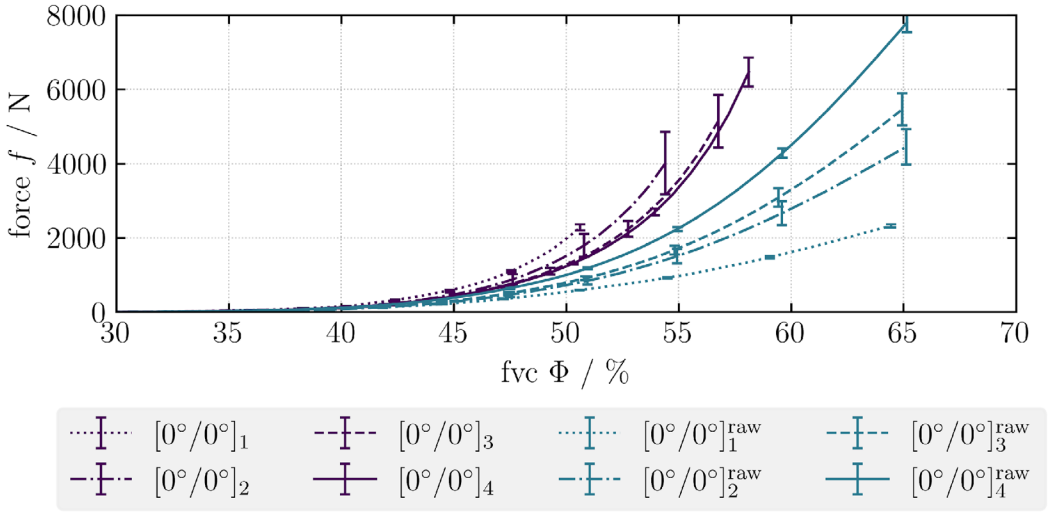

Fig. 3. Influence of the machine compliance adjustment on the results for UD-NCF with a $\boldsymbol{[0°/0°]_n}$*-layup.*

Influence of the number of layers n_L.

The resulting forces over fiber volume content for different $\Delta\Theta$ are presented in Fig. 4. All compaction curves show the well-known non-linear shape with progressively increasing forces [2]. For Biax-NCF the resistance to compaction decreases for an increasing number of layers independent of the layup sequence due to nesting of the layers. This observation is more

pronounced for a $\Delta\Theta$ of 0° or 90°. The offset of 45° decreases the area of superimposed stitching seams compared to continuously stacked layups [7]. This also results in a smaller scatter in the experimental results for $\Delta\theta = 45°$. Since the layers were stacked randomly, it is possible for stitching patterns for a $\Delta\Theta$ of 0° or 90° to coincide between the layers causing an increased resistance to compaction for some of the trials as shown by Korkiakoski et al. [10]. The decrease in resistance to compaction seems to diminish as the number of layers increase, indicating a threshold for even higher n_L. In literature, this threshold is reached at about 10-15 layers for many textiles [2, 3, 6].

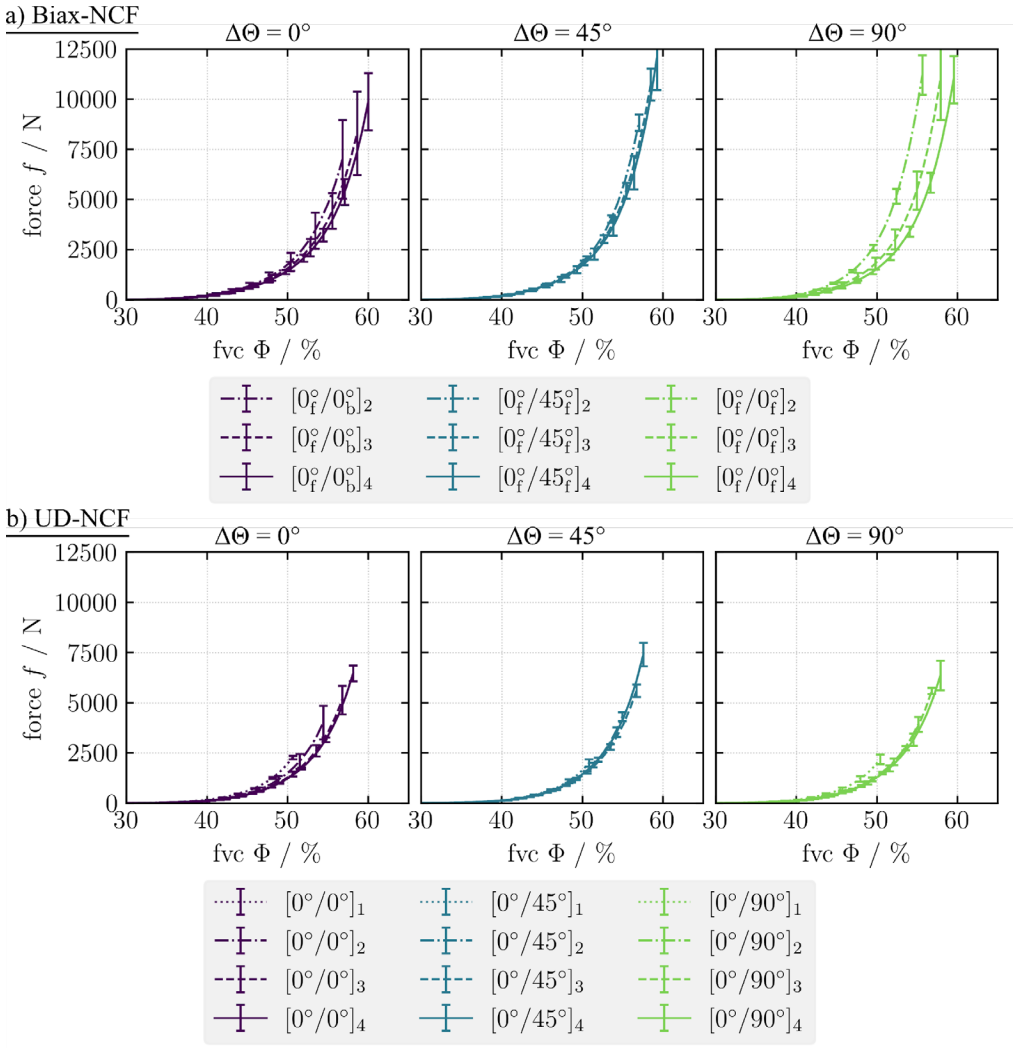

Fig. 4. Compaction test results for different relative interface orientations Θ | a) Biax-NCF; b) UD-NCF.

A similar trend is observed for the UD-NCF, but mainly for an increase of n_L from two to four, cf. Fig. 4 b). A further increase of the number of layers only slightly affects the compaction response with strongly overlapping experimental scatter. Presumably, the GF on the back of the UD-NCF prevent such a strong nesting effect as for Biax-NCF. For $\Delta\Theta = 45°$ the results for $n_L = 8$ is even lower compared to $n_L = 6$ and all curves in general are closer to each other just like for the Biax-NCF. This further indicates a noticeable influence of the superimposed stitching. The threshold for the influence of n_L for the UD-NCF seems to be nearly reached for 8 layers, indicated by a very small decrease in the compaction resistance for more than six layers.

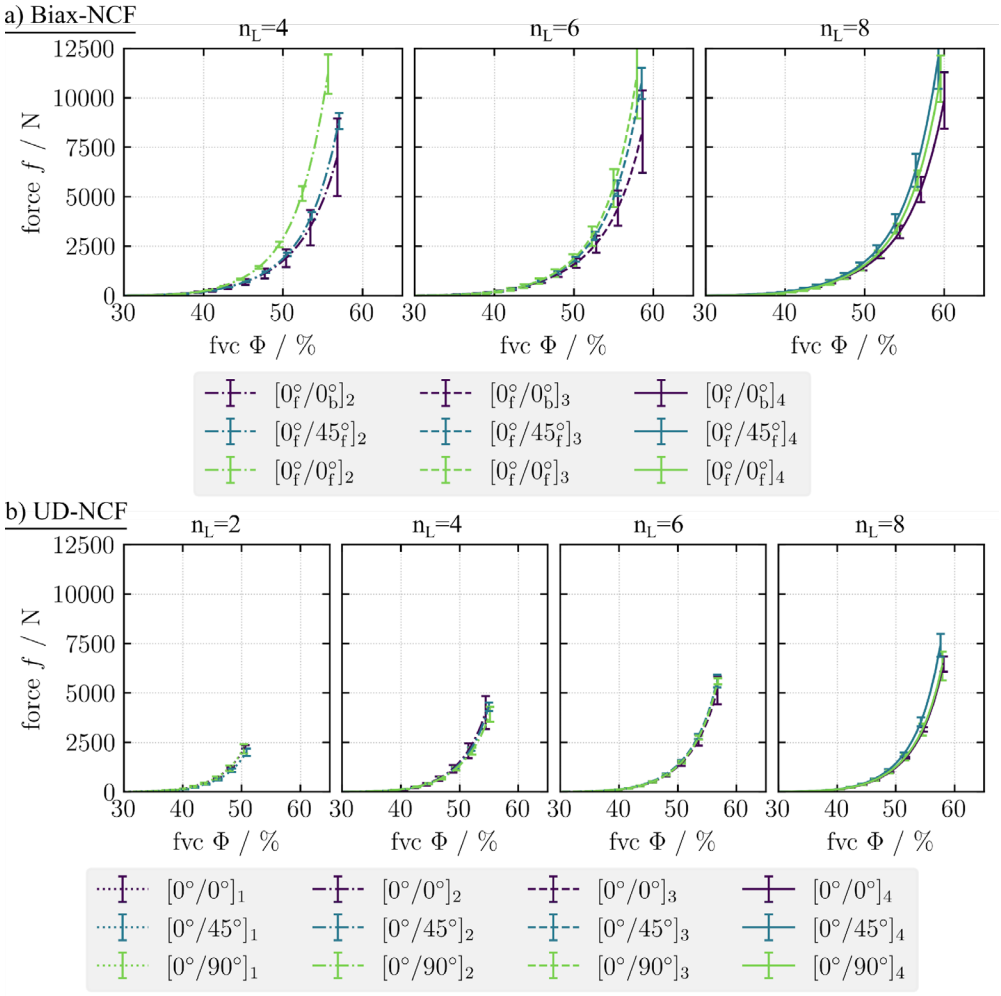

Fig. 5. Compaction test results for different number of layers $\mathbf{n_L}$ | a) Biax-NCF; b) UD-NCF.

Influence of the relative interface orientation $\Delta\Theta$.

To make it easier to assess the influence of the relative interface orientations, the results are shown again in Fig. 5 depending on the number of layers n_L. For Biax-NCF the $[0^\circ_\mathrm{f}/0^\circ_\mathrm{b}]_n$-layup requires the smallest compaction force to achieve a targeted fvc independent of n_L, cf. Fig. 5 a). This reinforces the assumption that the influence of the number of layers is caused by a combination of nesting of rovings as well as the influence of superimposed stitching patterns. For the $[0^\circ_\mathrm{f}/0^\circ_\mathrm{f}]_n$-layups, mainly superposition of stitching causes a decreasing resistance to compaction for larger stacks, while for the $[0^\circ_\mathrm{f}/0^\circ_\mathrm{b}]_n$-layups the effect is amplified by a stronger possibility for nesting of the rovings. In contrast, the compaction behavior of UD-NCF is barely influenced by the relative layer orientation and very similar for the respective number of layers, cf. Fig. 5 b).

Summary

In this work, a study on the compaction behavior of UD- and Biax-NCF for different layup-types and relative fiber orientations at the interfaces is presented. First, the relevance of considering the machine compliance was emphasized, especially in order to study the behavior for different numbers of layers. Comparing the UD- and Biax-NCF to each other, some similarities can be observed. With an increasing number of layers, the resistance to compaction for both materials decreases independent of relative interface orientation. This effect is weakest for $\Delta\Theta = 45°$,

indicating a combined influence of roving nesting and superposition of the stitching patterns. The stiffness decrease is smaller for the UD-NCF, which is presumably due to the glass fibers preventing pronounced nesting. For both fabrics, the influence of n_{L} is diminishing, indicating a threshold for these effects. However, more experiments with even more layers are necessary for both materials to identify the exact threshold. An influence of the relative interface orientation is only distinctly observed for Biax-NCF. Turning over every second layer in a $[0_{\mathrm{f}}^{\circ}/0_{\mathrm{b}}^{\circ}]_n$-layup reduces the required forces for a targeted fvc, which can be used to reduce required pressing forces [16].

The results of this study allow a better understanding of the two investigated non-crimp fabrics and could be used to parametrize an analytical or simulation model to design molding processes. Therefore, the compaction behavior for different velocities as well as very high and low numbers of layers should be addressed in further studies.

Acknowledgments
The authors would like to thank the Deutsche Forschungsgemeinschaft (DFG, German Research Foundation) and the French National Research Agency (ANR) for funding the collaborative project "Composite forming simulation for non-crimp fabrics based on generalized continuum approaches" (project number 431354059), which the presented work is carried out for. The work is also part of the Young Investigator Group (YIG) "Tailored Composite Materials for Lightweight Vehicles", generously funded by the Vector Stiftung.

References
[1] C.T. Poppe, C. Krauß, F. Albrecht, L. Kärger, A 3D process simulation model for wet compression moulding, Compos. Part A: Appl. Sci. Manuf. 50 (2021) 106379. https://doi.org/10.1016/j.compositesa.2021.106379
[2] F. Robitaille, R. Gauvin, Compaction of textile reinforcements for composites manufacturing. I: Review of experimental results, Polym. Compos. 19 (1998) 198-216. https://doi.org/10.1002/pc.10091
[3] B. Chen, E.J. Lang, T.-W. Chou, Experimental and theoretical studies of fabric compaction behavior in resin transfer molding, Mater. Sci. Eng. A317 (2001) 188-196. https://doi.org/10.1016/S0921-5093(01)01175-3
[4] S.V. Lomov, M. Barburski, T. Stoilova, I. Verpoest, R. Akkerman, R. Loendersloot, Ten Thije, R. H. W., Carbon composites based on multiaxial multiply stitched preforms. Part 3: Biaxial tension, picture frame and compression tests of the preforms, Compos. Part A: Appl. Sci. Manuf. 36 (2005) 1188-1206. https://doi.org/10.1016/j.compositesa.2005.01.015
[5] J. Yang, J. Xiao, J. Zeng, D. Jiang, C. Peng, Compaction Behavior and Part Thickness Variation in Vacuum Infusion Molding Process, Appl. Compos. Mater. 19 (2012) 443-458. https://doi.org/10.1007/s10443-011-9217-8
[6] L. Li, Y. Zhao, J. Yang, J. Zhang, Y. Duan, An experimental investigation of compaction behavior of carbon non-crimp fabrics for liquid composite molding, J. Mater. Sci. 50 (2015) 2960-2972. https://doi.org/10.1007/s10853-015-8860-0
[7] T. Grieser, P. Mitschang, Investigation of the compaction behavior of carbon fiber NCF for continuous preforming processes, Polym. Compos. 38 (2017) 2609-2625. https://doi.org/10.1002/pc.23854
[8] A.X.H. Yong, A. Aktas, D. May, A. Endruweit, S.V. Lomov, S. Advani, P. Hubert, S.G. Abaimov, D. Abliz, I. Akhatov, M.A. Ali, S. Allaoui, T. Allen, D.C. Berg, S. Bickerton, B. Caglar, P. Causse, A. Chiminelli, S. Comas-Cardona, M. Danzi, J. Dittmann, C. Dransfeld, P. Ermanni, E. Fauster, A. George, J. Gillibert, Q. Govignon, R. Graupner, V. Grishaev, A. Guilloux, M.A. Kabachi, A. Keller, K. Kind, D. Large, M. Laspalas, O.V. Lebedev, M. Lizaranzu, A.C. Long, C. López, K. Masania, V. Michaud, P. Middendorf, P. Mitschang, S. van Oosterom, R. Schubnel, N.

Sharp, P. Sousa, F. Trochu, R. Umer, J. Valette, J.H. Wang, Experimental characterisation of textile compaction response: A benchmark exercise, Compos. Part A: Appl. Sci. Manuf. 142 (2020) 106243. https://doi.org/10.1016/j.compositesa.2020.106243
[9] A. Hammami, B.R. Gebart, Analysis of the vacuum infusion molding process, Polym. Compos. 21 (2000) 28-40. https://doi.org/10.1002/pc.10162
[10] S. Korkiakoski, M. Haavisto, M. Rostami Barouei, O. Saarela, Experimental compaction characterization of unidirectional stitched non-crimp fabrics in the vacuum infusion process, Polym. Compos. 37 (2016) 2692-2704. https://doi.org/10.1002/pc.23464
[11] D. Droste, L. Krishnappa, S. Bornemann, J.-H. Ohlendorf, M.G. Vargas Gleason, A.S. Herrmann, W. Lang, Investigation of the compaction behaviour of a quasi-unidirectional non-crimp fabric during the vacuum infusion process, J. Compos. Mater. 56 (2022) 2509-2524. https://doi.org/10.1177/00219983221092011
[12] P. Boisse, R. Akkerman, P. Carlone, L. Kärger, S.V. Lomov, J.A. Sherwood, Advances in composite forming through 25 years of ESAFORM, Int. J. Mater. Form. 15 (2022) 99. https://doi.org/10.1007/s12289-022-01682-8
[13] J. Yang, J. Xiao, J. Zeng, D. Jiang, C. Peng, Compaction Behavior and Part Thickness Variation in Vacuum Infusion Molding Process, Appl. Compos. Mater. 19 (2012) 443-458. https://doi.org/10.1007/s10443-011-9217-8
[14] S.V. Lomov, I. Verpoest, T. Peeters, D. Roose, M. Zako, Nesting in textile laminates: geometrical modelling of the laminate, Compos. Sci. Technol. 63 (2003) 993-1007. https://doi.org/10.1016/S0266-3538(02)00318-4
[15] P. Sousa, S.V. Lomov, J. Ivens, Methodology of dry and wet compressibility measurement, Compos. Part A: Appl. Sci. Manuf. 128 (2020) 105672. https://doi.org/10.1016/j.compositesa.2019.105672
[16] F. Behnisch, V. Lichtner, F. Henning, P. Rosenberg, Development of a Reactive Polyurethane Foam System for the Direct Sandwich Composite Molding (D-SCM) Process, J. Compos. Sci. 5 (2021) 104. https://doi.org/10.3390/jcs5040104

Materials Research Proceedings 28 (2023) 339-345 https://doi.org/10.21741/9781644902479-37

Forming of textile fabrics with additively assembled protective elements on the human body

KYOSEV Yordan[1,a *] and MÜNKS Dominik[1,b]

[1] Chair of Development and Assembly of Textile Products, Institute of Textile Machinery and High Performance Material Technology (ITM), TU Dresden, Dresden, Germany

[a] yordan.kyosev@tu-dresden.de, [b] dominik.muenks@tu-dresden.de

Keywords: Draping, Forming, Textile Structure, Additive Manufacturing, Textile, Rigid-Soft-Structures, Reinforcements

Abstract. Stab protective clothing is used in a wide range of applications, including military and police applications, but is also becoming increasingly important for civilian users. A relatively new way of manufacturing personal protective equipment is additive manufacturing. This makes it possible to produce new types of stab protection geometries by applying polymer layers to textiles. Such composite structures represent a mechanical system of rigid bodies with constraints, especially with large continuous protective surfaces. As a result, the wearing comfort is limited. This paper presents two methods for numerically simulating the forming of reinforced textiles with solid polymer elements over the body as part of the development and optimization process of such garments.

Introduction

Stab protection clothing is getting more important for both military and civil users, as the statistics of the national polices of several countries shows. The fact that in countries such as the UK or Germany more than 40,000 attacks with a knife or other sharp object are reported each year [1, 2] is an argument that wearing stab protective clothing is essential for various professions. There are several investigation the possibilities of improvement of the stab resistance of textile structures, based on the using non-woven fabrics [3], or triaxial textiles [4]. The properties of the fabrics are important and normally fabrics with very high density and high seam slippage resistance are required [5]. Analytical methods for investigation of the stab resistance for woven fabrics is reported in [6]. Other researchers use combination of different fiber types and found that the use of wool fibers in combinations with aramid significantly increases the stab resistance of the woven structure [7]. In the latest decade the additive manufacturing provides new possibilities for integration of protective elements in the textiles, as both laser sintering [8] and fused filament disposition of polymers [9] are applied for such applications and demonstrate that can satisfy the norms. The placement of additional solid elements increases the stab protection especially against needles and other small elements, but with the increasing of the size of these elements, can again gets negative effect in the reduction of the wear comfort of the protective clothing. This work presents a method for numerical simulation of the forming of reinforced textiles with solid polymer elements over the body as part of the development and optimization process of such clothing.

Problem Description

Safety textile products for stab protection have often additional elements, who have to stop the sharp elements and avoid the interpenetration on the human body [10]. In order to ensure some freedom of the motion, it is essential to have smaller protective plates on the areas of the body, where more motion happens or where the radius of the curvature is lower (Fig.1), and larger plates on the more statical areas and such those with lower curvature, in order to keep the protection rate higher.

Content from this work may be used under the terms of the Creative Commons Attribution 3.0 license. Any further distribution of this work must maintain attribution to the author(s) and the title of the work, journal citation and DOI. Published under license by Materials Research Forum LLC.

Fig. 1. Curvature areas on the human body, hier viusalised as Gaus curvature.

The protective elements can be produced with different form and integrated on the textile structure using additive manufacturing. Fig. 2 demonstrates one possible form of such protecting elements, which can be printed over knitted structure.

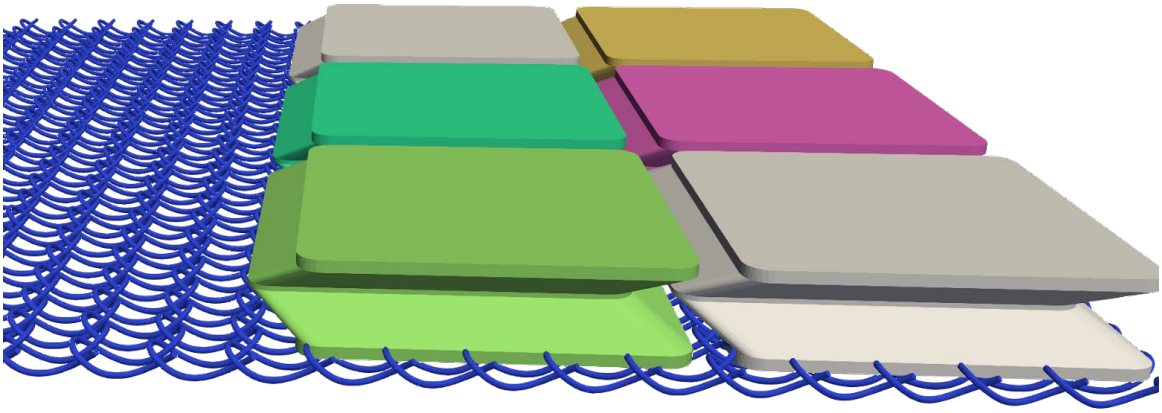

Fig. 2. Schematic illustration of a possible protective elements applied to a knitted fabric.

After determining and testing the required thickness and suitable material for the panels [9], the main task for the developer of protective clothing with such elements is the placement of the protective elements in a way, which provides the best function – in this case stab protection and the best wear comfort. In order to provide best function, elements the plates are prepared with a form which allow that they incline in each other (Fig. 3).

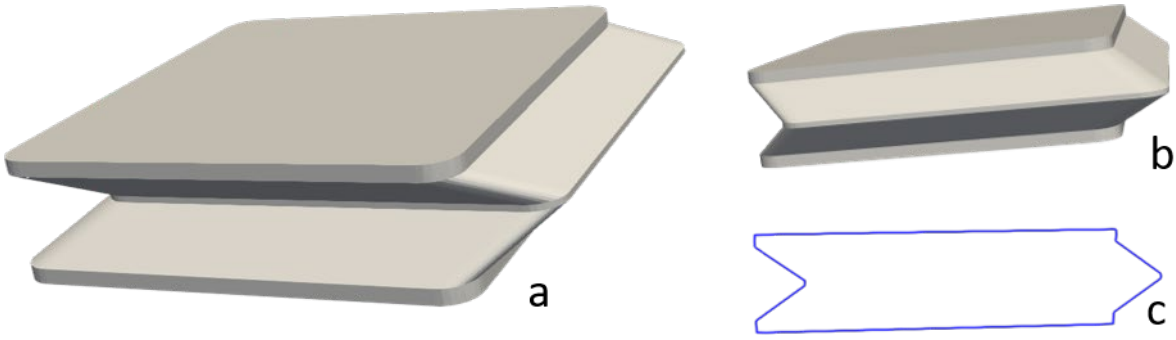

Fig. 3. Element of the protective structure a) and b) side view c) cross-section.

The convex triangle element on the two sides can incline in the concave negative elements on the other sides of the next plates and in this way to provide dense structure (Fig. 4a). Such structure retain small flexibility and allow some limited bending over curvatures which depends on the distance between the plates (Fig. 4b and 4c).

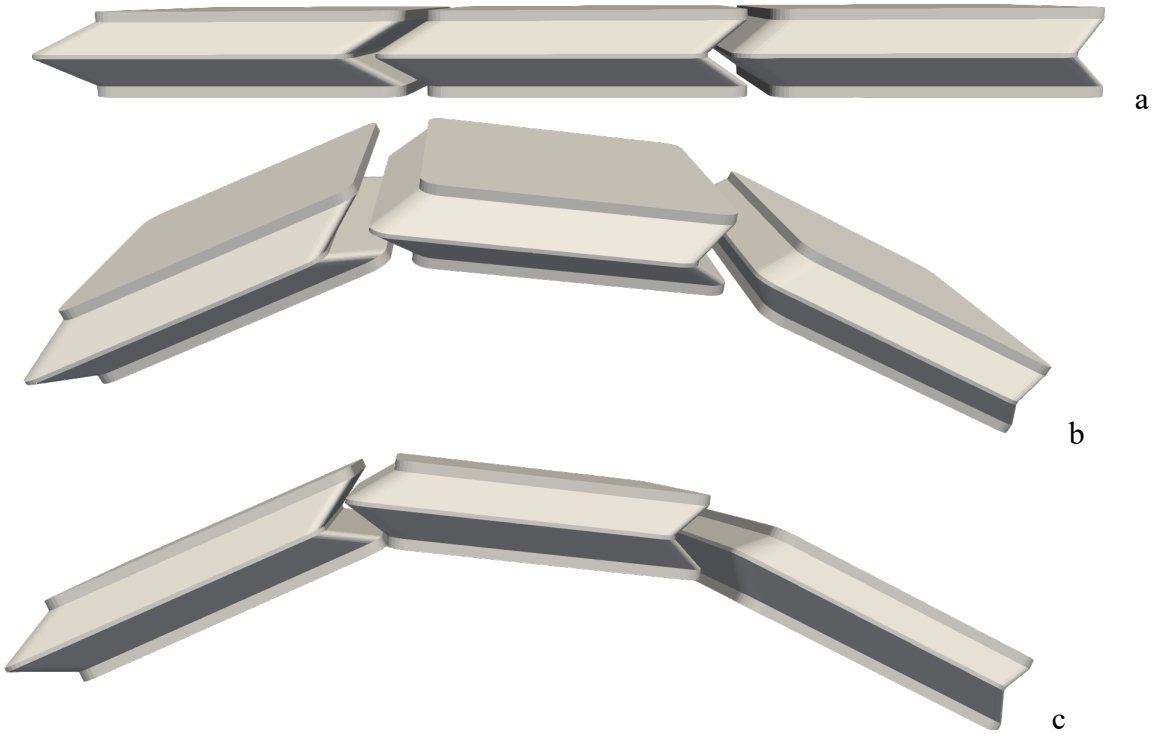

Fig. 4. Set of additive manifactured elements a) in horizontal direction b) bent with larger distance between the plates c) bent with smaller distance beween the plates.

The principal question is with which algorithms, software or method the forming over the body of such composite structure (basis textile and plates) can be simulated in order the optimal parameters for the geometry of the plates, the distance between these, the elasticity of the textile and the final pattern construction can be optimized. The common clothing CAD software can perform well draping simulation on the body, but consider all accessories as buttons in the best case as connected to the textile, but ignore their contact detection. The classical FEM software would require complex mezzo-scale level simulation of the structure, connected with the plates, but such one requires large simulation times and is not really suitable for engineering development process at the current time.

Proposed Procedure

The classical methods from the last 25 years in the area of composites forming are reported very detailed in [21]. The commonly used and reported there shell and solid shell methods could be extended for simulation of the current case of soft materials with integrated plates, but as in the current case the properties of the structure are dominated by rigid bodies, the authors decided to use another technique. The basis textile structures can be generated as 3D geometry using different software packages. Wisetex is very powerful for creation of woven fabrics [11], TexMind Weft [12] and Warp Knitting Editors [13] provide 3D geometry for the corresponding structures [14, 15]. In the current case the weft knitted structure is generated parametrically with the TexMind Weft Knitting Software and exported as STL file. 3D protective elements can be created with

Autodesk Fusion 360 and also saved as an STL file. The human body can be obtained by 3D or 4D scanning, but for the testing of the procedure is generated with MakeHuman [16].

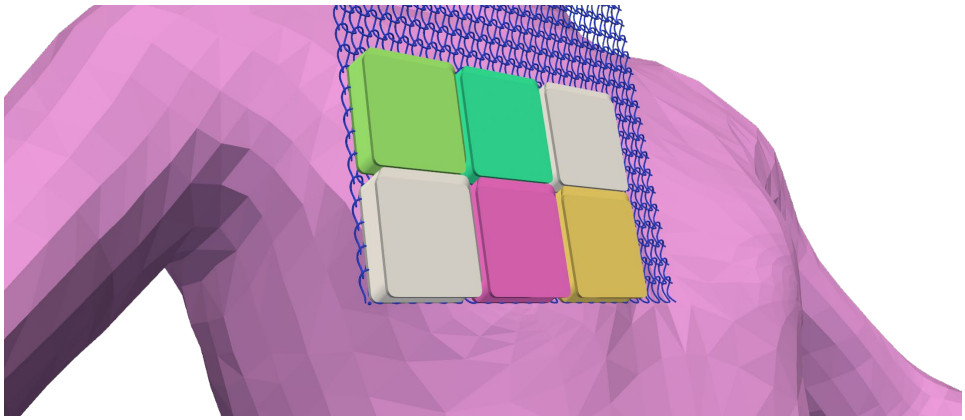

Fig. 5. Task describtion – protective elements, placed over elastic textile have to be formed to suit the human body.

For the simulation with large number of contacts and complex geometries with rigid bodies with constraints the impulse based methods are reported to provide very good performance and simplicity of the code [17, 18]. In the current case the implementation of BulletPhysics [19], especially its Python port is applied [20]. The Library allow import of the geometries as contact shapes from STL files, setting friction coefficients and all required dynamic effect. For the simulation the physical system is simplified and the complete textile layer, which provides the connection between the plates is replaced by a constrains between the plates. As suitable replacement of the complete knitted structure (Fig. 6a) two point-to-point constrains between the plates are applied (Fig. 6b).

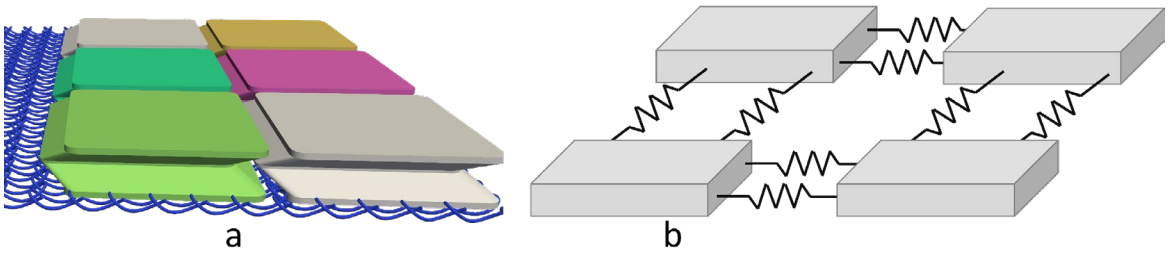

Fig. 6. Modelling of the elasticity of the knitted structure as paired springs (connecting links).

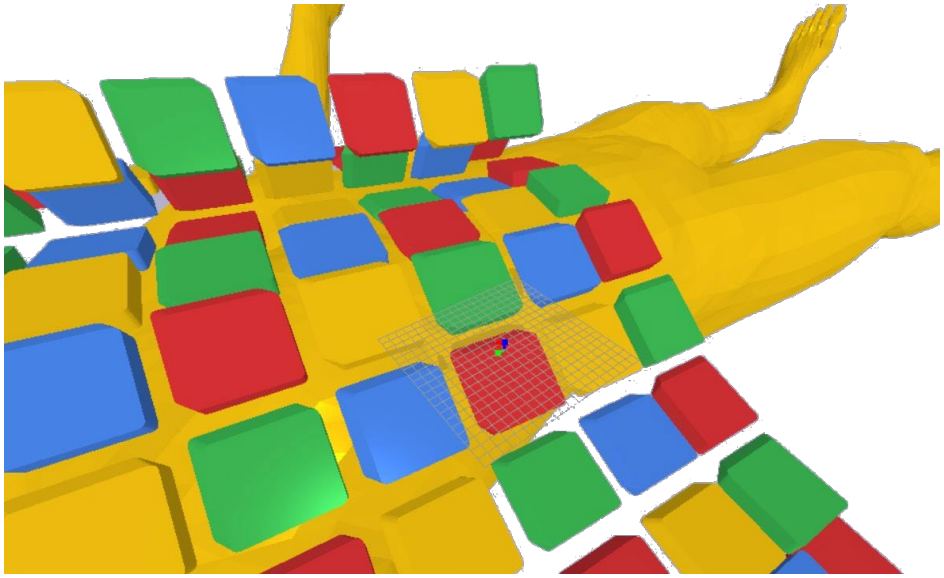

Fig. 7. Modelling of the elasticity of the knitted structure as paired springs (connecting links).

The paired two connection between each plate actually leaded to very stiff structure (Fig. 7), where the rows moves completely as a rigid type and does not allow single plates to move over the human body as it is the case if the distance between the plates is larger.

In a second trial the two pairs are replaced by only one per connection between the plates (Fig. 8a). In this way the single elements have more freedom to more around the body, as it is the case if they are produced with additive manufacturing over flexible textile structure. The starting simulation step is visualization in Figure 8b, where the plates are starting to move down to the body based on the applied acceleration.

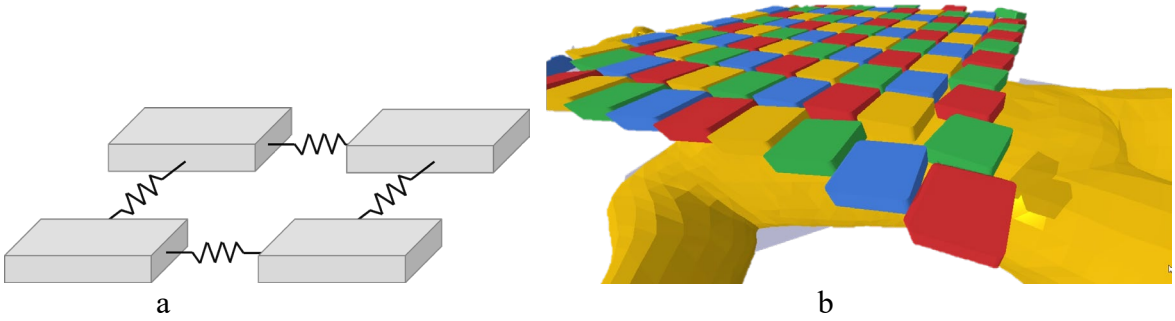

Fig. 8. a) Mechanical model of the plates, where each one is connected to the next with only one constrain b) view from the beginning of the simulation process.

After adjustment of the limits of the constraints (limitation of the maximal force) the model was able to run and simulate the process, where the initially printed elements over the flat textile will deform over the human body (Fig. 9). The principle was proven and seems that can be a basis for refinement for complex simulations, but it has shown as well several open problems, which becomes not solved until the finalization of this text. One of these is that for the proper contact simulation of the elements with concave geometry does not work properly with the simplified using of boundary box of the element and requires special treatment, forcing using the algorithms for concave triangular meshes. Applying this algorithms for the form (Fig. 3) at lower distance between the plates leads to sticking of the elements and completely limiting their flexibility. Another parameter is the limit of the maximal force in the constraints between the plates. It has

the physical meaning similar to the stiffness of the connection. For low values the solver needs very long time to converge the structure and satisfy the constraints. Using high level of the maximal force the plates leads to unnatural configurations in case the plates contacts together.

Fig. 9. Example of simulation state of the structure over the body.

Summary

Novel structures for stab protection can be produced using additive manufacturing, depositing polymer layers over textiles. Such composite structure represent mechanical system of rigid body with constraints. For the analysis and optimization of such structures, and especially the forming process when the clothing is wearied, in the current case impulse based solver is applied and two models are tested. The more natural replacement of the textile background trough two constrains parallel between each two plates leads to rigid structure and was not able to be formed over the human body with the current simulation trials. Probably more careful adjustment of the simulation parameters could give the better results. A model with only one constrain as connection between each two plates demonstrated ability to be used for forming simulation, but remains sensible regarding all model parameters. Although all difficulties and sensibilities, the models were computed on a normal home use computer with Intel 7 processor with 2,6 GHz and 16 GB RAM for few seconds, which is promising for integration in engineering software after refinement of the model and parameters.

Acknowledgments

The IGF research project 21622 BR of the Forschungsvereinigung Forschungskuratorium Textil e. V. is funded through the AiF within the program for supporting the „Industriellen Gemeinschaftsforschung (IGF)“ from funds of the Federal Ministry for Economic Affairs and Climate Action on the basis of a decision by the German Bundestag.

References

[1] G. Allen, M. Harding, Knife crime statistics https://commonslibrary.parliament.uk/research-briefings/sn04304/ (accessed 25 Oct 2021)

[2] Bundeskriminalamt 2021 Lagebilder - Bundeslagebild Gewalt gegen Polizeivollzugsbeamtinnen und Polizeivollzugsbeamte 2020: Bundeslagebild 2020 https://www.bka.de/SharedDocs/Downloads/DE/Publikationen/JahresberichteUndLagebilder/GewaltGegenPVB/GewaltGegenPVBBundeslagebild2020.html (accessed 26 December 2022)

[3] L. Bao, S. Sato, H. Morioka, S. Soma, Improving Stab-resistant Textile Materials with a Non-woven Fabric Structure, J. Text. Engin. 62 (2016) 37–42. https://doi.org/10.4188/jte.62.37
[4] M. El Messiry, E. Eltahan, Stab resistance of triaxial woven fabrics for soft body armor, J. Industr. Text. 45 (2016) 1062–1082. https://doi.org/10.1177/1528083714551441
[5] P. Reiners, Y. Kyosev, M. Aurich, Influence of seam slippage on the stab resistance of woven structuresfor membranes, VI International Conference on Textile Composites andInflatable Structures STRUCTURALMEMBRANES 2015 (2015), Ed. Oñate, K.-U.Bletzinger, B. Kröplin, pp. 477–83.
[6] S.M. Hejazi, N. Kadivar, A. Sajjadi, Analytical assessment of woven fabrics under vertical stabbing - The role of protective clothing, Forensic Sci. Int. 259 (2016) 224–33. https://doi.org/10.1016/j.forsciint.2015.12.036
[7] P. Reiners, Y. Kyosev, L. Schacher, D. Adolphe, K. Küster, Experimental investigation of the influence of wool structures on the stab resistance of woven body armor panels, Text. Res. J. 86 (2016) 685–695. https://doi.org/10.1177/0040517515596934
[8] A.S. Koohestani, A. Bashari, Advanced bulletproof and stab- and spike-resistant textiles, in: Advances in Functional and Protective Textiles, The Textile Institute Book Series, Elsevier, 2020, pp. 261–289. http://doi.org/10.1016/B978-0-12-820257-9.00012-6
[9] D. Ahrendt, E.J.I. Massot, S. Krzywinski, J. Krzywinski, Hybrid material designs by the example of additive manufacturing for novel customized stab protective clothing, Light Weight Armour Group for Defense and Security (2019) 286–294.
[10] P. Fenne, Protection against knives and other weapons, in: Textiles for Protection, Elsevier, 2005, pp. 648–677. http://doi.org/10.1533/9781845690977.3.648
[11] S. Lomov, WiseTex—A Virtual Textile Composites Software Advanced Weaving Technology, Ed. Y. Kyosev and F. Boussu, (Cham: Springer International Publishing) 2022, pp. 293–318
[12] Y. Kyosev, Weft Knitting Editor 3D (TexMind), 2022
[13] Y. Kyosev, Warp Knitting Editor 3D (TexMind), 2022
[14] Y. Kyosev, Warp Knitted Fabrics Construction (Milton: CRC Press LLC), 2019
[15] Y. Kyosev, Topology-Based Modeling of Textile Structures and Their Joint Assemblies: Principles, Algorithms and Limitations (Springer eBook Collection), (Cham: Springer International Publishing), 2019
[16] Make Human Software, www.makehuman.org, (accessed 26 December 2022)
[17] B. Mirtich, J. Canny, Impulse-based simulation of rigid bodies, Proceedings of the 1995 symposium on Interactive 3D graphics - SI3D ‘95 the 1995 symposium (Monterey, California, United States, 09.04.1995 - 12.04.1995), Ed. M. Zyda, New York, USA: ACM Press, 1995, 181
[18] J. Bender, Impulse-based dynamic simulation in linear time, Comp. Anim. Virtual Worlds 18 (2007) 225–233. https://doi.org/10.1002/cav.179
[19] E. Coumans, Bullet physics simulation, ACM SIGGRAPH 2015 Courses SIGGRAPH ‘15: Special Interest Group on Computer Graphics and Interactive Techniques Conference, Los Angeles California, 09.08.2015-13.08.2015, New York, NY, USA: ACM, 2015, p. 1
[20] E. Coumans, Y. Bai, 2016-2021 PyBullet, a Python module for physics simulation for games, robotics and machine learning. Information on https://pybullet.org/wordpress/.
[21] P. Boisse, R. Akkerman, P. Carlone, L. Kärger, S.V. Lomov, J.A. Sherwood, Advances in composite forming through 25 years of ESAFORM, Int. J. Mater. Form. 15 (2022) 39. https://doi.org/10.1007/s12289-022-01682-8

Materials Research Proceedings 28 (2023) 347-556 https://doi.org/10.21741/9781644902478-38

Process and structural simulation for the development of a pressure vessel through filament winding technology

BIANCHI Iacopo[1,a *], FORCELLESE Archimede[1,b], GALLIANI Francesco[2,c], GRECO Luciano[1,d], MIGNANELLI Chiara[1,e] and TREVISAN Giulio[2,f]

[1]Università Politecnica delle Marche, Via Brecce Bianche 12, 60131 Ancona, Italy

[2]COMEC INNOVATIVE S.R.L., Via Papa Leone XIII 40, 66100 Chieti, Italy

[a]i.bianchi@pm.univpm.it, [b]a.forcellese@staff.univpm.it, [c]galliani.francesco@comecinnovative.it, [d]l.greco@pm.univpm.it, [e]c.mignanelli@pm.univpm.it, [f]trevisan.giulio@comecinnovative.it l

Keywords: Filament Winding, CFRP, Pressure Vessel, FEM Simulation

Abstract. Recently, Università Politecnica delle Marche and COMEC Innovative srl are involved in the research project "Smart Tow Winding" funded by MIUR (Ministry of Education, University and Research), concerning the development of an innovative process for the realization of a pressure vessel through Filament Winding (FW) technology. In this context, a design procedure for type IV composite pressure vessel is proposed. To design the component, the dedicated simulation software CADWIND was used to virtually generate the pressure vessel through the definition of the desired geometry, the type of prepreg, the number of layers and the bandwidth. The generated file was imported in the FEM simulation software Siemens NX with the aim of evaluating the structural resistance under an internal pressure of 70 MPa. Different external configurations of mandrels and stratification were tested in order to optimize the geometry of the vessel and the resistance to weight ratio. A high performance and low weight vessel configuration was finally identified.

Introduction

In recent years, the market for lightweight structural components has constantly increased and it has triggered the use of high performance composite materials such as Carbon Fiber Reinforced Polymers (CFRPs). These components find applications in several sectors such as sport equipment, energy production, and biomedical. Moreover, they are particularly suitable for road and aerospace transport applications. In fact, the weight saving achieved by means of high specific mechanical properties composites can result in a reduction in fuel use and, consequently, lower service life costs and environmental impacts [1-3]. Despite significant effort in automation [4], at present, carbon fiber parts production strongly relies on manual operations and it is therefore time consuming and expensive. For this reason, to achieve a sustainable development of composite materials and innovative transport systems, it is crucial to improve manufacturing systems automation and production speed [5].

In this context, MIUR (Ministry of Education, University and Research) is funding the research project titled "Smart Tow Winding" concerning the development of an innovative process for the fabrication of a pressure vessel through Filament Winding (FW) technology involving the Marche Polytechnic University and COMEC Innovative srl.

In this regard, the development of the technology of Smart Tow Winding constitutes an innovation in the corporate sector as it allows to combine an innovative material, such as composite, with an automated production process. This technology is an automated version of the conventional filament winding (FW) process, which is a widely practiced technique for high performance composite structures, such as pressure vessels, fuel tanks, pipes, and rocket motor

Content from this work may be used under the terms of the Creative Commons Attribution 3.0 license. Any further distribution of this work must maintain attribution to the author(s) and the title of the work, journal citation and DOI. Published under license by Materials Research Forum LLC.

cases. FW allows the production of composite parts by winding composite filaments over a rotating mandrel. The winding angle of the filament can be modified depending of the expected loads on the components, maximizing the mechanical resistance along the most stressed directions. In this way it is possible to satisfy the stringent structural requirements of the aerospace and transport industries.

Smart tow winding can be used for the construction of fuel storage tanks, containing from combustible gases to natural gases, which nowadays are an excellent solution to reduce CO_2 emissions. The traditional structure of tanks, used for on-board storage of gaseous fuel under pressure, present a central cylindrical body and two dome-shaped external caps; this is due to the fact that spheres incur the lowest membrane stress on their walls compared to any other shape [6,7]. These pressure tanks can be realized in metals, composite materials or obtained as a combination of these materials. In particular, five different types of vessels are defined [8]: Type I, II, III, IV, V. Type I is fully made by metal material, while Type II consist in an inner metal liner supporting 55% of the internal pressure load, reinforced with composite hoop wraps. Type III, is similar to Type II with an inner metal liner, externally covered by a composite reinforcement supporting up to 80% of the pressure load. For what concern Type IV, it is made externally of composite material and presents an inner liner made of plastic material, which does not support the load, but contains the gas and works as a mandrel for the Filament Winding process. The last typology, Type V, it is fully made by composite material, without internal liner.

Generally, gas used in industrial applications is stored inside cylindrical Type I tanks, since they are the least expensive, but the heaviest. Type II tanks, on the other hand, are commonly used at high pressures for stationary applications: they are lighter than Type I tanks, but at the same time more expensive. For uses where high lightness must be guaranteed, Type III, IV, and V tanks are used, in which the composite material is generally reinforced by means of glass, aramid, or carbon fibers [9].

Specifically, Type IV and V ones are the lightest ones at all, as they do not have metal liners; however, they are the most expensive due to the use of composite material.

With regard to the winding patterns with which these tanks can be made, they vary, depending on the geometry of the tank, the manufacturing process, the fiber arrangement, the precision of the machine, and the cost. Since filament-wound composite pressure vessels are more inclined to failure in domed sections, the shape of the dome and the winding of the fibers are important for the structural integrity of the vessel [10].

The high number of parameters related to pressure vessel production (e.g. number, percentage coverage and orientation of layers, filament path, raw materials, internal liner..) makes the design process complicated and time consuming. For this reason, a rapid and easy to apply design procedure for filament wound parts is required.

Hence, in the context of advanced composite manufacturing processes and simulations [11], this work focuses on the design and optimization of a type IV pressure vessel since it is a promising alternative in various applications (i.e. energy and transport) were low weight and high performances are required. After preliminary considerations with structural theories (netting theory, isotensoid vessel), virtual models were created by means of a FW dedicated software that allowed to define all the parameters of several possible composite layers. An iterative procedure with a FEA software was then used to optimize the structure parameters considering typical working loads (70 MPa internal pressure) and constraints.

Materials and Methods

In the present work, a preliminary design of a Type IV pressure vessel was investigated. The tank under pressure is characterized by a 380 mm diameter in the central cylindrical zone and a total length of about 540 mm. An internal thermoplastic liner, in high-density polyethylene (HDPE), is used as mandrel during the filament winding process. For the composite material used for the external winding, a towpreg composed by a thermosetting polymer matrix reinforced with carbon fibers, was chosen. The internal service pressure and burst pressure values were defined equal to 70 and 105 MPa, respectively, with a safety factor of 1.5, according to the suitable values in several transport applications [12]. Details about the material parameters according to their datasheet are reported in Table 1. The mechanical properties of the composite material were calculated considering the general "rule of mixture" and a fiber weight fraction equal to 68%.

Table 1. Mechanical properties of matrix, carbon fibers and composite material.

Material parameters	Unit	Values
Carbon fibers (Toray T700)		
Tensile strength	MPa	4900
Young modulus	GPa	230
Elongation at break	%	2.1
Density	g/cm³	1.8
Volume fraction	%	56.3
Epoxy resin		
Tensile strength	MPa	73
Young modulus	GPa	3.7
Elongation at break	%	9
Density	g/cm³	1.1
Volume fraction	%	43.7
Composite		
Tensile strength (longitudinal)	MPa	2790
Tensile strength (transversal)	MPa	~73
Young modulus (longitudinal)	GPa	131.1
Young modulus (transversal)	GPa	8.3
Density	g/cm³	1.6

To design the pressure vessel, an iterative procedure was followed (Fig. 1). Input geometric parameters were used to define the dome profile through a spreadsheet, while the design parameters, such as carbon fiber mechanical properties, service pressure and safety factor, were used to lead the netting analysis. The obtained results were implemented in CADWIND simulation software to virtually generate the pressure vessel through the definition of the desired geometry, the type of prepreg, the number of layers and the bandwidth. Then, the generated file was imported in the FEM simulation software Siemens NX with the aim of evaluating the structural resistance under the internal service and burst pressure values of 70 and 105 MPa. If the results obtained satisfy the safety structural requirements, the stratification analyzed can be considered as an acceptable design from the mechanical requirements perspective; otherwise, the study should continue identifying a new stratification that improves criticalities arising from the previous one. Moreover, other than the structural requirements, the weight of the structure was evaluated during

each design iteration in order to identify the alternative that fulfils safety conditions and presents the lightest weight possible among the considered laminations.

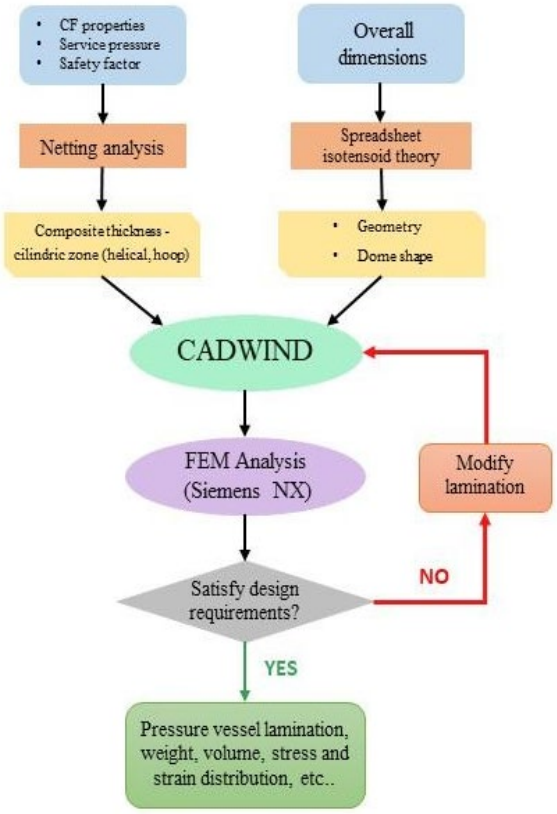

Fig. 1. Iterative design procedures applied for the definition of the optimal pressure vessel.

Netting analysis.

The netting analysis is a method that can be used to preliminarily estimate the thickness of helical and hoop layers of a composite tank that allow it to withstand the working loading conditions. The analysis considers that the pressure load is only supported by carbon fibers and the epoxy resin does not give any structural contribution. According to Mariotte theory, the internal pressure yields to two main stress components along the circumferential and axial directions. The first one is supported by helicoidal windings, while the second by hoop windings. For this reason, many tubular structures or tanks are produced using both low values of winding angles (helicoidal windings) and values near to 90° (hoop windings). Therefore, this theory allows to calculate the thickness of the fiber layers considering any combination of two different values of winding angles to obtain the tank laminate structure [13].

Spreadsheet isotensoid theory.

In order to guarantee high structural strength of the pressure vessel, the definition of the external geometry of the domes is fundamental since it is the most complex zone of the component. To generate the tridimensional geometry, a meridian curve was realized and then was rotated around a central axis. Referring to the European patent of isotensoid tanks obtained by filament winding process [14], this curve was defined by points through a spreadsheet in which input data of cylindrical zone diameter and length and opening end's diameter were inserted. The output

information of this step was the meridian curve, which was than exported to a file compatible with the filament winding dedicated software CADWIND.

Filament Winding process simulation.

The simulation of filament winding process was performed using CADWIND software, which can simulate the winding process, based on a physical model, and calculate the fiber path and winding pattern (Fig. 2) [15]. After importing the geometry of the mandrel, composite laminates were created using different process parameters, which are listed in Table 2.

This allows to create a file to be imported in FEA software that reports information about the model mesh, and laminate stratification, orientation and thickness. With this model, the wound filament is considered perfectly straight and possible undulation and degradation of the composite mechanical properties are not considered [16].

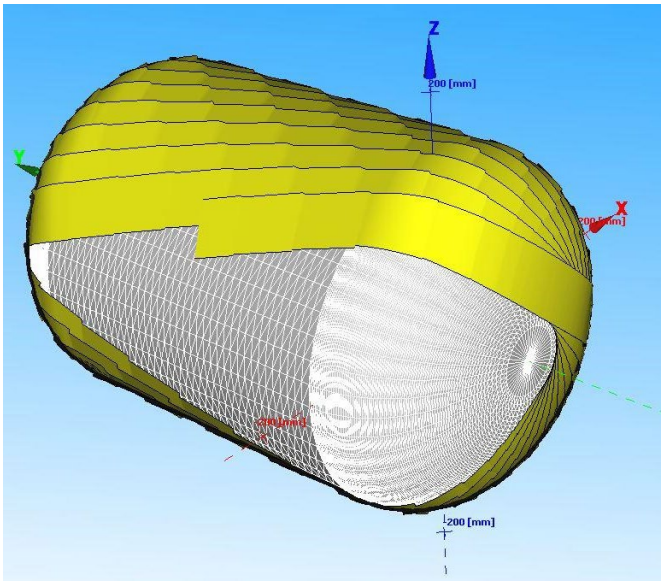

Fig. 2. Simulation of filament winding process performed using CADWIND software.

A friction factor equal to 0.3 was considered for the composite prepreg in the process simulation. The “Turning zone” represent the zone in which the filament orientation starts to change the winding angle in order to come back and wind the opposite mandrel side and the “Coverage” represents percentage of filament coverage on the mandrel. The associated values are defined to obtain a symmetric component avoiding a high overlap of the wound material that implicates a thickness increase. The material parameters are listed in Table 3.

Different external configurations of mandrels and stratification were tested in order to optimize the geometry of the vessel and the resistance to weight ratio.

An accurate choice of layering requires many considerations such as identifying the number of composite layers to deposit and defining the winding angle of each layer. The latter is fundamental, as the more the angle is reduced, the greater is tank’s area covered. The choice of the winding angle also influences the mechanical resistance of the component: if it is about 90°, the resistance to tangential stresses increases, while material layers with low values of winding angle better withstand axial stresses.

Table 2. Laminate parameters.

Laminaton	**Winding angle [°]**	**Turning zone front to**	**Turning zone back from**	**Coverage [%]**
1	10	20	105	102.1
2	15	14	111	133.3
3	20	8	117	107.0
4	25	5	120	102.1
5	30	7	118	130.1
6	35	5	120	122.8
7	40	6	119	147.1
8	45	9	116	153.6
9	50	12	113	150.2
10	55	15	110	140.3
11	60	17	108	120.7
12	65	27	98	123.8
13	70	30	95	188.2
14	75	35	90	155.5
15	80	41	84	162.2
16	85	40	85	184.7

Table 3. Material parameters.

TEX value (single roving) [g/km]	Bandwidth (single roving) [mm]	Fiber density [g/cm3]	Fiber volume fraction [%]	Fiber mass fraction [%]	Matrix density [g/cm3]	Resulting ply thickness [mm]
1000	6	1.8	56.5	68	1.1	0.16

Moreover, it is necessary to deposit some hoop layers after a defined number of helicoidal layers both to compact the underlying layers and to remove any resin's excess.

Once identified the layering to analyze, the FEM file created is imported on the software used to conduct FEM analysis.

Structural simulation of the pressure vessel.

In order to simulate the performances of the composite pressure vessel, the software Siemens NX was used, with the FEA NX Nastran solver. To this purpose, the file created in CADWIND was imported in NX to analyze the selected laminate. The model was imported as constituted by 2D shell elements with a defined laminate structure. The linear-elastic material mechanical properties were defined, and a structural linear simulation was carried out. The preliminary structural simulations of the pressure vessel conducted considering two fixed constraints on the most external frames, at the end of the domes.

Results and Discussions

Thickness distribution on pressure vessel.

The netting theory was used to evaluate the thickness distribution on layers with both hoop (~90°) and helical (variable θ) winding angles. The angle θ was continuously varied from 0° to 90°, and the resulting laminate thickness was registered. It was observed that by increasing the value of θ, the required thickness of helical layers increases while the number of hoop layers decreases.

For θ values between 54° and 55°, if constant internal pressure is considered, the total thickness value of the pressure vessel is minimized.

The resulting minimum total thickness of carbon fibers is about 10.18 mm, which is divided in 3.84 mm for helicoidal layers and 6.34 mm for hoop layers. Considering that netting theory evaluates only the fibers contribution and that fiber volume fraction is about 56.3%, the minimum thickness of total composite laminate is about 18.08 mm.

Pressure vessel model definition.

Based on pressure vessel dimensions, as described in section *Spreadsheet isotensoid theory*, a meridian curve that represents the external domes profile was obtained. The medium thickness of each layer depends on both the towpreg characteristics and the coverage percentage. In fact, in order to guarantee a good covering of the mandrel, the towpreg tends to overlap itself involving a greater coverage percentage than 100% on each layer. So, this confirm that the medium thickness of each layer which approximately various from 0.2 mm to 0.3 mm depends on the coverage percentage.

Considering these values and the results obtained by netting theory, to ensure that the tank operates safely at least 70 - 80 layers of towpreg are required. According to this information, the first layering tested was $[85_6/10_4/15_4/20_4/85_6/30_4/35_4/45_4/85_6]$.

Table 4. Maximum stress and strain values of each reference layer.

Winding angle	**Maximum stress**		**Maximum strain**	
	Internal pressure 70 MPa	*Internal pressure 105 MPa*	*Internal pressure 70 MPa*	*Internal pressure 105 MPa*
85°	993 MPa	1500 MPa	0.004	0.006
10°	1290 MPa	2333 MPa	0.004	0.026
15°	899 MPa	1350 MPa	0.022	0.022
20°	788 MPa	1200 MPa	0.006	0.014
85°	990 MPa	1482 MPa	0.007	0.009
30°	720 MPa	1116 MPa	0.006	0.009
35°	800 MPa	1170 MPa	0.006	0.008
45°	820 MPa	1265 MPa	0.005	0.006
85°	992 MPa	1485 MPa	0.005	0.006

FEM simulations.

The mentioned layering was tested using both a service pressure of 70 MPa and a burst pressure of 105 MPa to analyze the pressure vessel structural response under bursting conditions. This laminate was characterized by 84 plies, a weight of 21 kg and a thickness of the cylindric zone of about 20 mm. To observe the resulting stress and strain values of the pressure vessel, the results obtained were analyzed considering a reference ply for each winding angle used in the laminate. Table 4 shows the maximum values of stress and strain along the fibers direction evaluated in each reference layers, imposing the different pressure values of 70 MPa and 105 MPa.

(a)

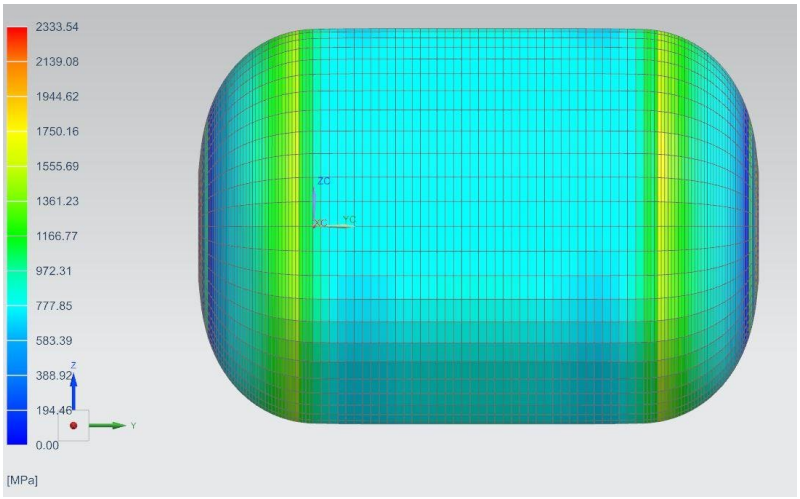

(b)

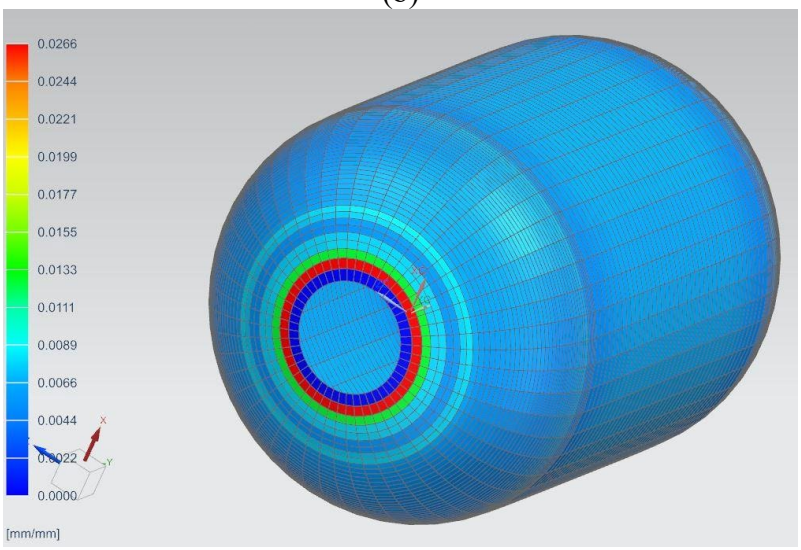

Fig. 3. (a) Strain and (b) stress distributions on the ply with 10° winding angle for the 105 MPa test.

Fig. 3 shows the strain and stress distributions on the ply with 10° winding angle obtained by CADWIND software simulations. As far as the stress values is concerned, Fig. 3b shows that the pressure vessel is in safe conditions also when internal burst pressure is applied; although there are some areas that are more stressed than others, they fall within the set limit values of 2500 MPa. For what concerns the strain values resulting from the service pressure analysis (Fig. 3a), the tank is generally in safe condition with the exception of the ends of external domes where the reached strain values are greater than the limit value of 0.007. As expected, it is noticed that stress and strain values resulting from the test performed using burst pressure (105 MPa) are greater than those obtained using the internal service pressure (70 MPa).

Summary

This study addressed the procedure used for the preliminary design and the structural analysis of a Type IV pressure vessel. The focus was both on the definition of external domes geometry and on the composite material used for the winding which confers the structural strength to the tank. The identified laminate sequence is chosen using CADWIND, a software which is dedicated to

filament winding processes. Then it was analysed to verify its structural behaviour through Siemens NX FEA software. The main results are summarized below:

- According to netting analysis, the minimum value of total composite laminate thickness is about 18.08 mm. Considering the thickness of the cylindric zone, the netting theory provides results that are similar to those of the FEM simulations. However, more complex approaches are needed for the domes of the vessels.
- Using a spreadsheet and knowing pressure vessel's dimensions, the external domes isotensoid geometry was defined.
- Netting analysis combined with CADWIND allowed to determine the minimum number of layers to introduce on the layering, which is about 70 - 80 layers.
- The used laminate sequence is characterized by 84 plyes, a weight of 21 kg and a thickness of the cylindric zone of about 20 mm.
- The FEM analysis shows that the tank tested using an internal pressure of 70 MPa is in safe conditions in terms of stress and strain except for some criticalities on the ends of the external domes.
- Instead, the tank tested using an internal pressure of 105 MPa is in safe conditions in terms of stress only: strain values are higher than the limit on almost all layers analyzed.

This study can be considered as a starting point to optimize the layering through an iterative process. In this way it is possible to obtain a pressure vessel which is in safe conditions also considering strain values. Moreover, the procedure here presented can be used as a reference point for the design of filament wound components with different mandrel geometry. Future works could focus on a further optimization of the composite lamination by means of localized reinforcement (i.e. composite patches) that provides increased strength in the highest stress regions while reducing the number of laminate layers and the overall part weight. The FEM results will be validated by means of pressure test to determine the quality of the lamination and the proposed design procedure.

Acknowledgement
This research was supported by the Italian Ministry of University and Research (MUR, Ministero dell'Università e della Ricerca) within the National Operational Programme on Research and Innovation 2014-2022 (Programma Operativo Nazionale "Ricerca e Innovazione" 2014-2020 (PON "R&I" 2014-2020) - area di specializzazione "Fabbrica Intelligente") project "SMART TOW WINDING Nuove soluzioni ad elevata automazione per l'impregnazione e avvolgimento di Tow" (CUP: B19C20000340005, ARS01_00871).

References
[1] I. Bianchi, S. Gentili, L. Greco, M. Simoncini, Effect of graphene oxide reinforcement on the flexural behavior of an epoxy resin, Procedia CIRP 112 (2022) 602-606. https://doi.org/10.1016/J.PROCIR.2022.09.057
[2] A. Forcellese, T. Mancia, M. Simoncini, S. Gentili, M. Marconi, A. Vita, A. Nardinocchi, V. Castorani, Comparative life cycle assessment of carbon fiber reinforced composite components for automotive industry, ESAFORM 2021 - 24th Int. Conf. Mater. Form. (2021). https://doi.org/10.25518/ESAFORM21.2542
[3] A. Forcellese, T. Mancia, A.C. Russo, M. Simoncini, A. Vita, Robotic automated fiber placement of carbon fiber towpregs, Mater. Manuf. Process. 37 (2021) 539-547. https://doi.org/10.1080/10426914.2021.1885706
[4] F. Henning, L. Kärger, D. Dörr, F.J. Schirmaier, J. Seuffert, A. Bernath, Fast processing and continuous simulation of automotive structural composite components, Compos. Sci. Technol. 171 (2019) 261-279. https://doi.org/10.1016/j.compscitech.2018.12.007

[5] A. Vita, V. Castorani, M. Germani, M. Marconi, Comparative life cycle assessment and cost analysis of autoclave and pressure bag molding for producing CFRP components, Int. J. Adv. Manuf. Technol. 105 (2019) 1967-1982. https://doi.org/10.1007/s00170-019-04384-9
[6] R.C. Hibbeler, Mechanics of materials, Pearson Prentice Hall, 2011.
[7] F. Daghia, E. Baranger, D.T. Tran, P. Pichon, A hierarchy of models for the design of composite pressure vessels, Compos. Struct. 235 (2020) 111809. https://doi.org/10.1016/j.compstruct.2019.111809
[8] C.P. Fowler, A.C. Orifici, C.H. Wang, A review of toroidal composite pressure vessel optimisation and damage tolerant design for high pressure gaseous fuel storage, Int. J. Hydrogen Energy. 41 (2016) 22067-22089. https://doi.org/10.1016/J.IJHYDENE.2016.10.039
[9] H. Barthélémy, Hydrogen storage - Industrial prospectives, Int. J. Hydrogen Energy. 37 (2012) 17364-17372. https://doi.org/10.1016/J.IJHYDENE.2012.04.121
[10] H.S. Roh, T.Q. Hua, R.K. Ahluwalia, Optimization of carbon fiber usage in Type 4 hydrogen storage tanks for fuel cell automobiles, Int. J. Hydrogen Energy. 38 (2013) 12795-12802. https://doi.org/10.1016/J.IJHYDENE.2013.07.016
[11] P. Boisse, R. Akkerman, P. Carlone, L. Kärger, · Stepan, V. Lomov, J.A. Sherwood, Advances in composite forming through 25 years of ESAFORM, Int. J. Mater. Form. 1 (2022). https://doi.org/10.1007/s12289-022-01682-8
[12] E. Lainé, J.C. Dupré, J.C. Grandidier, M. Cruz, Instrumented tests on composite pressure vessels (type IV) under internal water pressure, Int. J. Hydrogen Energy 46 (2021) 1334-1346. https://doi.org/10.1016/J.IJHYDENE.2020.09.160
[13] G. Verchery, The netting analysis as a limit case of the laminated structure, Mater. Sci. (2013)
[14] J.C. Murphy, Filament-wound isotensoid pressure vessels having geodesic domes, European Patent EP0714753A2 (1995).
[15] C. Laval, CADWIND 2006 - 20 years of filament winding experience, Reinf. Plast. 50 (2006) 34-37. https://doi.org/10.1016/S0034-3617(06)70913-4
[16] C. Shen, X. Han, Damage and failure analysis of filament wound composite structure considering fibre crossover and undulation, Adv. Compos. Lett. 27 (2018) 55-70. https://doi.org/10.1177/096369351802700202

Materials Research Proceedings 28 (2023) 357-366 https://doi.org/10.21741/9781644902479-39

Modeling multiaxial stress states in forming simulation of woven fabrics

KÄRGER Luise[1,a *], SCHÄFER Florian[1,b] and WERNER Henrik O.[1,2,c]

[1] Karlsruhe Institute of Technology (KIT), Institute of Vehicle System Technology, Institute Division Lightweight Design, Karlsruhe, Germany

[2] Karlsruhe Institute of Technology (KIT), Institute of Applied Materials, Institute Division Material Sciences, Karlsruhe, Germany

[a]luise.kaerger@kit.edu, [b] florian.schaefer93@t-online.de, [c] henrik.werner@kit.edu

Keywords: Hyperelastic, Invariant-Based, Constitutive Modeling, Multiaxial Coupling

Abstract. During the forming of woven fabrics, different multiaxial stress states can occur, depending on the given process conditions and the complex deformation mechanisms of the interwoven structure of the textile. Particularly under constrained forming conditions, induced e.g. by blank holders or by adjacent metal layers in fiber-metal-laminate (FML) forming, the multiaxial stress states may include in-plane compression. A hyperelastic, invariant-based constitutive model has been proposed in previous work to consider such biaxial and normal-shear coupling for both positive and also negative strains. In the present work, this constitutive model is applied to forming simulation at component scale to investigate the significance of individual coupling aspects for the prediction of the forming behavior under different multiaxial stress states. For that purpose, FMLs and pure fabric laminates are formed to a tetrahedron geometry. In a comparative simulation study, the individual strain couplings of the invariant-based material model are differently activated or suppressed. The simulation results reveal that biaxial coupling has a significant effect on the draping behavior, if the draping is partially constrained. In contrast, the coupling effects are much smaller for free draping conditions.

Introduction

In the past two decades, a large number of material models have been developed to describe the forming behavior of textile materials at meso and macro scale [1,2]. However, only macroscale models are suitable for forming simulation at component level [3] and enable virtual validation and optimization of forming processes [4,5]. Since textiles are prone to large shear, non-orthogonal material models are required [6-8]. This can be realized by hypoelastic or hyperelastic material modeling. Hypoelastic approaches [9-11] describe stress rates as direct functions of strain rates, depending on the stiffness. At each timestep, stress increments can be calculated directly from strain increments, which makes hypoelastic approaches convenient for implementation in nonlinear finite element approaches. For sufficient accuracy, however, they require sufficiently small timesteps. The advantage of hyperelastic approaches [12-14] is the integral representation of the stress-strain relationship, which enables timestep-independent solutions. The stress-strain relation is based on the strain energy density and their differentiation with respect to strain measures.

For woven fabrics that exhibit pronounced orthotropy with two preferred directions, the strain energy potential can be easily decomposed into distinct strain energy components, depending on different invariants of the deformation state [15-17]. The invariant-based energy formulation has the additional advantage of being independent of the choice of the basis reference system. Since experimental studies have shown interdependencies between distinct strain components, hyperelastic models with invariant-coupling, e.g., biaxial-tension [18] and tension-shear coupling

Content from this work may be used under the terms of the Creative Commons Attribution 3.0 license. Any further distribution of this work must maintain attribution to the author(s) and the title of the work, journal citation and DOI. Published under license by Materials Research Forum LLC.

[19], have been proposed. A recent review on modelling coupling mechanisms in woven fabrics, with particular focus on invariant-based constitutive modeling is given in [20].

In the context of fiber-metal-laminate (FML) forming, Schäfer et al. [21] have introduced an invariant-based model, which considers both biaxial and normal-shear coupling, but not just for positive strains (i.e. tension), but also for negative strains. The additional consideration of compressive strains in biaxial and normal-shear coupling becomes necessary, if wrinkling is suppressed during forming, e.g. due to adjacent metal layers as in FML forming, but also due to blank holders or grippers [21]. Under such constrained condition in thickness direction, the bending and wrinkling behavior becomes insignificant compared to the complexly interacting components of the membrane behavior, namely shear, tension and compression [22,23].

In the present work, the invariant-based constitutive model presented by Schäfer et al. [21] is used to evaluate the significance of different strain couplings in forming simulation at component scale. For that purpose, the invariants that control the couplings in the different components of the strain energy densities are activated or suppressed in different combinations. Additionally, the effects are compared for strongly constrained forming of FML and less constrained forming of a pure fabric laminate. First, the material [21] is summarized with the most essential equations to indicate the interactions that are considered in the strain energy density components. Subsequently, the numerical test case, a tetrahedron geometry, and the applied materials are introduced. Finally, the forming simulation results are presented and discussed in terms of the coupling aspects and their significance on the forming results for varying forming conditions.

Hyperelastic Multiaxially Coupled Invariant-Based Constitutive Model

The hyperelastic invariant-based model, examined in this work for multiaxial coupling effects, was originally proposed and verified in our previous work [21]. For the sake of brevity, only the most important equations of the model are presented in the following. For more details, the reader is kindly referred to [21]. The invariant-based model was implemented in a user subroutine VUMAT for forming simulation in ABAQUS/EXPLICIT. Membrane and bending behavior are modeled in a decoupled way by superimposed finite membrane elements M3D3 and finite shell elements S3R. The membrane elements use the new VUMAT, while the shell elements use a bending idealization with section integration and deactivated membrane properties.

The basic assumption of the membrane model is the additive decomposition of the total strain energy density

$$W_{tot} = W_{TC}(I_4, I_8) + W_{S,TC}(I_{10}, I_4, I_8) \tag{1}$$

into a tension-compression component $W_{TC}(I_4, I_8)$ and a tension-compression-dependent shear component $W_{S,TC}(I_{10}, I_4, I_8)$. The components are based on invariants I_i of the right Cauchy-Green (RCG) tensor to be independent of the choice of the coordinate system.

Tension-compression coupling.

The tension-compression-dependent strain energy density component W_{TC} is composed of two components $W_{M,a}$ and $W_{N,b}$ according to the two fiber directions a and b, where the indices M and N represent tension (T) or compression (C). The composition depends on the current strain state:

$$W_{TC}(I_4, I_8) = W_{M,a}(I_4, I_8) + W_{N,b}(I_4, I_8) \tag{2}$$

with $M = T$ for $I_4 > 1$; $M = C$ for $I_4 \leq 1$; $N = T$ for $I_8 > 1$; and $N = C$ for $I_8 \leq 1$ [21]. The invariants I_4 and I_8 are the quadratic stretches in fiber directions a and b, respectively.

For tension, the strain energy densities are

$$W_{T,a}(I_4, I_8) = \widehat{W}_{T,a}(I_4) \cdot k_{TC,a}(I_8) \quad and \quad W_{T,b}(I_4, I_8) = \widehat{W}_{T,b}(I_8) \cdot k_{TC,b}(I_4) \tag{3}$$

with the uniaxial strain energy densities

$$\widehat{W}_{T,a} = a_a\left(\sqrt{I_4} - 1\right)^3 + b_a\left(\sqrt{I_4} - 1\right)^2; \quad \widehat{W}_{T,b} = a_b\left(\sqrt{I_8} - 1\right)^3 + b_b\left(\sqrt{I_8} - 1\right)^2 \tag{4}$$

where a_i and b_i are material parameters to be determined by unidirectional tensile tests. In Eq. (3), the influence of transverse strains is considered by the fiber-fiber-interaction factors

$$k_{TC,a}(I_8) = exp\ exp\ \left(c_a\left(\sqrt{I_8}-1\right)\right) + p_{min,a}\ \left(1 - exp\ exp\ \left(c_a\left(\sqrt{I_8}-1\right)\right)\right) \quad (5)$$

$$k_{TC,b}(I_4) = exp\ exp\ \left(c_b\left(\sqrt{I_4}-1\right)\right) + p_{min,b}\ \left(1 - exp\ exp\ \left(c_b\left(\sqrt{I_8}-1\right)\right)\right) \quad (6)$$

taking values greater than 1 for transverse tension and values between 0 and 1 for transverse compression. The tension-compression parameter $p_{min,i}$ is introduced to limit the influence of the transverse strains on the tensile strain energy density, which is particular important in the case of negative transverse strains [21]. $p_{min,i}$ can take values between 0 (complete strain energy reduction due to compression is possible) and 1 (no influence). In this work, $p_{min,i}$ is set to 0.75 for negative and positive transverse strains. Primarily, the biaxial coupling coefficient c_i provides a strictly monotonous increase or decrease of the strain energy density for positive or negative transverse strains, respectively. It can be determined by biaxial tension tests.

Compression is typically not considered in composite forming simulation, since the textile material can easily buckle and wrinkling can occur. However, under constrained conditions, e.g. by blank holders or adjacent metal layers, wrinkling is suppressed and the resulting multiaxial stress states may include in-plane compression. In this case, a linear stress-strain relation and no strain components coupling is assumed, leading to the compressive strain energy densities

$$W_{C,a}(I_4) = d_a\left(\sqrt{I_4}-1\right)^2 \qquad and \qquad W_{C,b}(I_8) = d_b\left(\sqrt{I_8}-1\right)^2 \quad (7)$$

where d_i are material parameters that are proportional to the compressive [21]. To date, there is no test setup available for a reliable characterization of the compressive stiffness, since the fabrics are prone to buckling. Therefore, the compression stiffness is assumed according to numerical parameter studies performed by Werner et al. [23].

Normal-shear coupling.

Shear is a prevalent deformation mechanism in woven fabrics, and thus, crucial for material modeling. According to the mesoscopic nature of the interwoven fiber bundles, pure shear can be divided in three zones with very low, medium and high shear stiffness. To capture this steadily increasing shear stiffness, a polynomial of third order is assumed for the stress-strain relation, which leads to the shear strain energy density

$$W_S(I_{10}) = \frac{1}{2}s_1 I_{10}^2 + \frac{1}{3}s_2 I_{10}^3 + \frac{1}{4}s_3 I_{10}^4 \quad (8)$$

where the shear invariant I_{10} represents the shear angle, and material parameters s_i can be determined by pure shear tests [21]. The shear strain energy density is increased for superimposed fiber tension and decreased for superimposed fiber compression. In the case of positive fiber strains, additional strain energy densities

$$W_{ST,a}(I_{10}, I_4) = \frac{1}{3}\ I_{10}^3\ s_{T,a}\ (I_4 - 1)^2\ ; \quad W_{ST,b}(I_{10}, I_8) = \frac{1}{3}\ I_{10}^3\ s_{T,b}\ (I_8 - 1)^2 \quad (9)$$

are added, where $s_{T,i}$ are material parameters that can be determined by combined tension-shear tests [21]. In the case of negative fiber strains, the shear strain energy densities (8) and possibly (9) are multiplied by exponential reduction factors

$$k_{SC,a}(I_4) = exp\ exp\left(s_{C,a}(I_4 - 1)^3\right); \qquad k_{SC,b}(I_8) = exp\ exp\left(s_{C,b}(I_8 - 1)^3\right) \quad (10)$$

with the compression-shear parameter $s_{C,a}$ to achieve a smooth asymptotic reduction of the shear strain energy density [21]. Thus, $k_{SC,i}$ can take values less or equal to 1, but always greater than zero.

Total strain energy density.

Combining the tension strain energy density (3) and the compression strain energy (7) with the shear strain energy density (8), influenced by fiber tension (9) or fiber compression (10), yields:

$$W_{\mathrm{tot}} = \begin{cases} W_{\mathrm{T,a}} + W_{\mathrm{T,b}} + W_{\mathrm{S}} + W_{\mathrm{ST,a}} + W_{\mathrm{ST,a}} & \text{for} \quad I_4 > 1 \text{ and } I_8 > 1 \\ W_{\mathrm{T,a}} + W_{\mathrm{C,b}} + \left(W_{\mathrm{S}} + W_{\mathrm{ST,a}}\right) \cdot \ k_{\mathrm{SC,b}} & \text{for} \quad I_4 > 1 \text{ and } I_8 \leq 1 \\ W_{\mathrm{C,a}} + W_{\mathrm{T,b}} + \left(W_{\mathrm{S}} + W_{\mathrm{ST,b}}\right) \cdot \ k_{\mathrm{SC,a}} & \text{for} \quad I_4 \leq 1 \text{ and } I_8 > 1 \\ W_{\mathrm{C,a}} + W_{\mathrm{C,b}} + W_{\mathrm{S}} \cdot \ k_{\mathrm{SC,a}} \cdot \ k_{\mathrm{SC,b}} & \text{for} \quad I_4 \leq 1 \text{ and } I_8 \leq 1 \end{cases} \tag{11}$$

Fig. 1 depicts total strain energy surfaces for selected shear angles I_{10}.

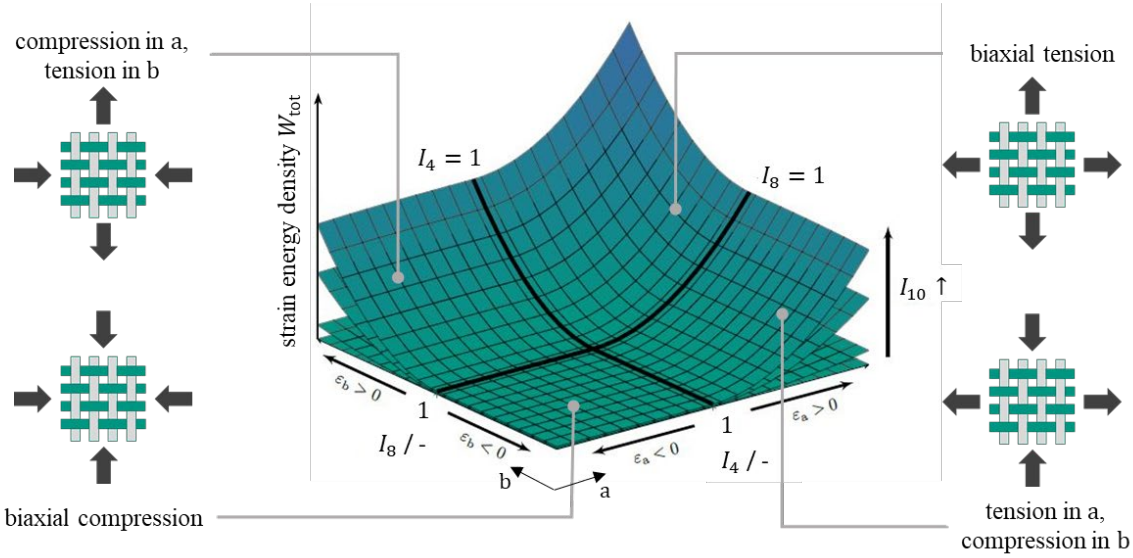

Fig. 1. Qualitative representation of the total strain energy density W_{tot} for selected shear angles I_{10} and with dependence on the invariants I_4 and I_8. The bold lines $I_4 = 1$ and $I_8 = 1$ represent superposition of uniaxial load in fiber directions b and a, respectively, with shear I_{10} [21].

Model verification.

The prediction capability of the new multiaxially-coupled invariant-based constitutive model was verified by means of tensile and bias-extension tests [21], partly with comparison to experimental results. The simulation results of these verification tests at coupon level revealed that the new model is capable to capture transverse coupling effects, i.e. transverse stresses in the case of constrained loading and, vice versa, transverse strains in the case of free loading [21]. This is in contrast to the ABAQUS built-in FABRIC model, which is not able to predict transverse effects. In Fig. 2, the effect of differently activated coupling mechanisms is illustrated at the example of a simple uniaxial tensile test, where the resulting transverse strain component ε_{22} is compared to experimental results from Cherouat and Bourouchaki [24]. The results in Fig. 2 and particularly in Fig. 2 (b) confirm that the biaxial normal strain coupling is responsible for correctly predicting the deformed fabric shape [21], which is clearly concave in transverse direction, as observed in experiments [24].

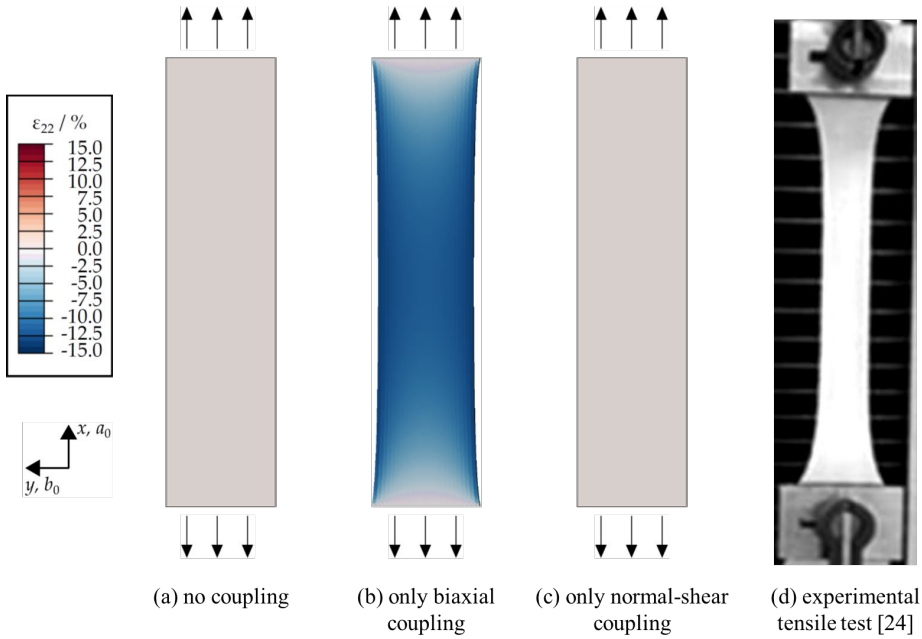

Fig. 2. Transverse strain component ε_{22} in a uniaxial tensile test for differently activated couplings [21].

Parametric Study on Individual Multiaxial Couplings and their Effects on Forming Results

To investigate the significance of the different tension-compression and normal-shear interactions, the proposed constitutive model is applied to forming simulation at component scale. Furthermore, forming simulation of a fiber-metal laminate (FML) is compared to forming simulation of a pure fabric to analyze the effect of different forming constraints on the multiaxial interactions.

Numerical test case and materials.

A 280 x 280 mm FML with three woven fabric layers and two metallic cover layers is formed into a tetrahedron shape, following the work of Yao et al. [19]. For comparison, three fabric layers without metal blanks are formed into the same geometry. In both cases, a blank holder pressure of 2 MPa is applied to prevent wrinkling. The inter-ply behavior between the rigid-body tools, the metal sheets and the fabric plies is modelled as COULOMB friction with the same friction parameters as used in [21]. The model setup including dimensions and boundary conditions is given in Fig. 3.

The metal material is steel DC04 and is assumed to behave elastic-plastic, as characterized experimentally and modelled by Werner et al [22,23].The fabric material is a plain weave fabric according to the industrial TWINTEX® TPP60N22P-060 with comingled glass/PP fibers, used and characterized by Komeili et al. [25]. The material behavior of the woven fabric is assumed nonlinear elastic according to the equations given in Section 2. The material parameters of the nonlinear models for steel and woven fabric are all the same as in our previous work [21], partly taken from the mentioned literature [22,23,25] and partly assumed. Failure and damage are not considered, neither in the metal sheets nor in the woven fabric.

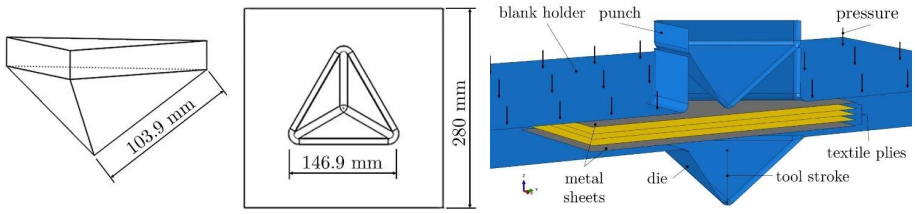

Fig. 3. Tetrahedron geometry: Dimensions and half FE-model of tool and FML.

Materials Research Proceedings 28 (2023) 357-366 https://doi.org/10.21741/9781644902479-39

It needs to be noted that the forming simulation example is a purely numerical test case to expose the effect of different interactions. Some of the material parameters are assumed, the blank holder pressure is comparatively high to avoid wrinkling and the forming simulation is conducted up to a rather large tool stroke with strains reaching values beyond failure or yielding. Nevertheless, the test case is chosen and suited to illustrate the importance of the distinct multiaxial coupling aspects for stronger and weaker forming constraints.

Results for FML forming.

Fig. 4 shows the distribution of the resulting shear angle γ_{12} for the deformed FML, where the Fabric material model available in Abaqus (Fig. 4a) is compared to four different configurations of the new hyperelastic material model with differently activated strain couplings.

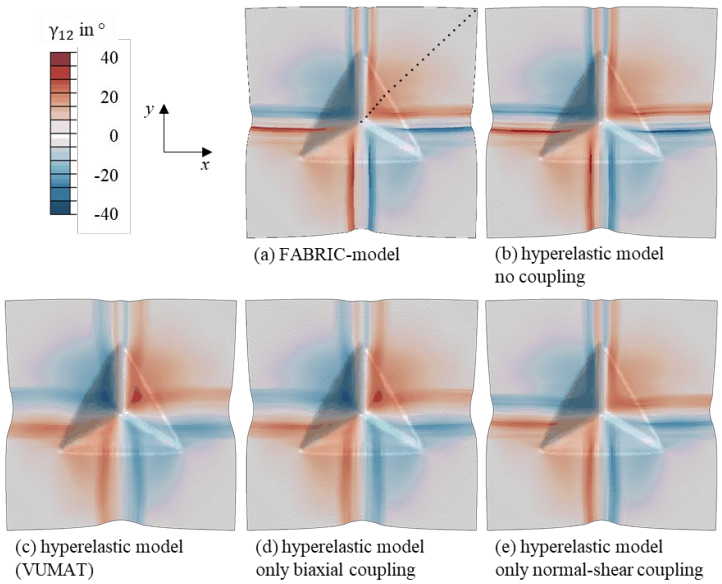

Fig. 4. Shear angles γ_{12} within the inner fabric layers of an FML with two metal blanks, formed into a tetrahedron geometry: Comparison of (a) the FABRIC material model and (b to e) four different configurations of the new hyperelastic material model with differently activated strain couplings.

The results reveal that the *normal-shear coupling* (Fig. 4e) has only marginal effect on the forming results, since the shear angle distribution is comparable to the *FABRIC model* (Fig. 4a) and the *hyperelastic model without coupling* (Fig. 4b). In contrast, the *fully coupled hyperelastic model* (Fig. 4c) and the model with *biaxial normal coupling* (Fig. 4d) lead to considerably higher shear angles. The same conclusion can be drawn from Fig. 5, where the shear angle is plotted along the dotted line in Fig. 4a and is compared for all five configurations. An explanation for the strong influence of *biaxial normal coupling* is the presence of high normal stresses due to the encasing metal layers that hinder formation of wrinkles and promote deformation in shear. Interestingly, just a minor effect of normal-shear coupling can be observed by the green *only normal-shear coupling* curve in Fig. 5. It is located just slightly below the gray *no-coupling* curve, because the higher tensile strains partly impede shear deformation. The same is observed for the *fully coupled VUMAT* model, which is slightly below the *only biaxial coupling* curve that neglects normal-shear coupling.

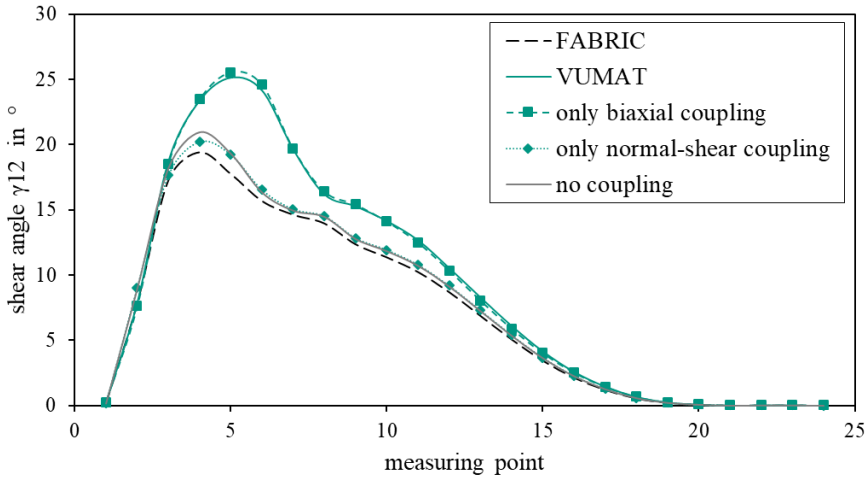

Fig. 5: Shear angle γ_{12} within the formed inner fabric layers of an FML along the dotted line in Fig. 4a: Comparison of the FABRIC material model and four different configurations of the new hyperelastic material model.

Results for pure fabric forming.

To investigate the relevance of biaxial and normal-shear coupling for weakened forming constraints, forming simulations are performed for three fabric layers without metal blanks. Furthermore, the friction coefficient between fabric and tool is smaller than the friction coefficient between fabric and metal sheet, which further reduces the resistance against deformation in the fabric. These modifications are implemented to facilitate shear deformation and material draw-in, and thus, to reduce normal stresses in fiber direction.

The resulting shear angles γ_{12} of the deformed three fabric layers are depicted in Fig. 6. Again, the ABAQUS/EXPLICIT built-in FABRIC model (Fig. 6a) is compared to four configurations of the new hyperelastic material model with differently activated strain couplings. As Fig. 6 reveals, the influence of interacting strain components on the resulting shear deformation is much smaller than in the more strongly constrained FML forming case. This conclusion is again confirmed by Fig. 7, where the shear angle is plotted along the dotted line in Fig. 6a. Again, the results of the fully coupled hyperelastic model (Fig. 6c) and the biaxial normal coupling (Fig. 6d) are close together and are above the results of the other configurations, but the difference between the curves is much smaller than for the constrained forming results shown in Fig. 5. Overall, the shear deformation is, as expected, larger than in the case of FML forming with metal blanks, which results from reduced friction, smaller normal strains and less coupling effects.

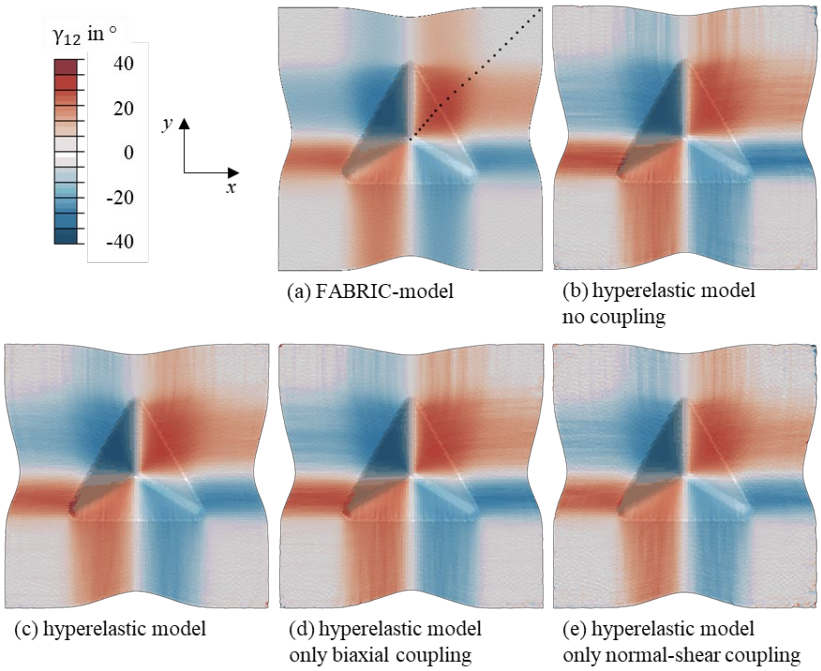

Fig. 6. Shear angle γ_{12} within a pure woven fabric with three fabric layers, formed into a tetrahedron geometry without metal blanks: Comparison of (a) the FABRIC material model and (b to e) four different configurations of the new hyperelastic material model with differently activated strain couplings.

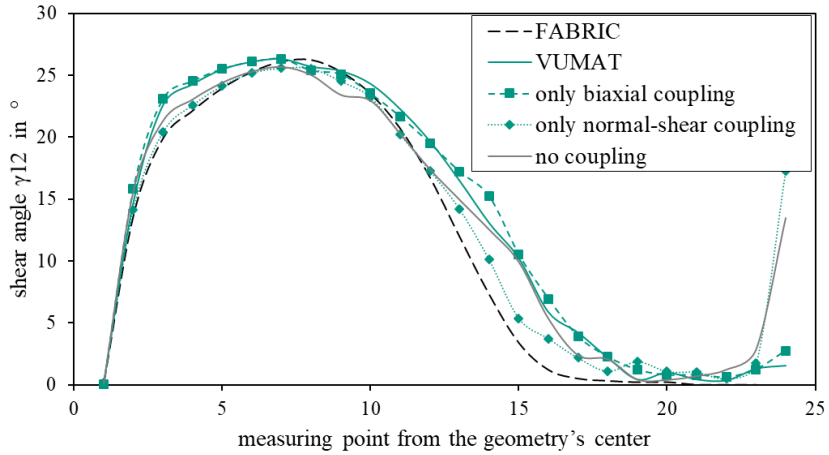

Fig. 7. Shear angle γ_{12} along the dotted line in Fig. 6a within the formed pure woven fabric: Comparison of the FABRIC material model and four different configurations of the new hyperelastic material model.

Summary

Forming simulation at component scale was performed to evaluate the significance of individual coupling effects in constitutive modeling of the fabric plies. For this purpose, a previously proposed invariant-based constitutive model, which includes biaxial and normal-shear coupling for positive and negative strains, was examined at the example of forming simulation to a tetrahedron. To compare the influence of strong and weak forming constraints on the multiaxial coupling effects, a fiber-metal laminate (FML) and a pure fabric laminate were formed to the tetrahedron geometry. Based on the simulation results, it could be shown that biaxial coupling has a significant effect on the forming results, if forming is constrained by adjacent metal layers. In the case of free or almost free draping conditions, this coupling effect is much smaller.

Nevertheless, blank holder forces also cause forming constraints that can partially prevent wrinkling and promote the importance of biaxial strain coupling. The results also revealed that biaxial coupling has a larger influence on the forming results than normal-shear coupling.

Acknowledgement
The support by the German Research Foundation (DFG) for the project HyRTM on FML manufacturing (no. 269244876, HE 6154/4-2) and for the project AMECOMP on textile forming simulation (no. 431354059, KA 4224/6-1) is gratefully acknowledged.

References

[1] P. Bussetta, N. Correia, Numerical forming of continuous fibre reinforced composite material: A review. Composites Part A: Appl. Sci. Manuf. 113 (2018) 12-31. https://doi.org/10.1016/j.compositesa.2018.07.010

[2] P. Boisse, R. Akkerman, P. Carlone, L. Kärger, S.V. Lomov, J.A. Sherwood, Advances in composite forming through 25 years of ESAFORM, Int. J. Mater. Form. 15 (2022) 39. https://doi.org/10.1007/s12289-022-01682-8

[3] L. Kärger, S. Galkin, D. Dörr, C. Poppe, Capabilities of Macroscopic Forming Simulation for Large-Scale Forming Processes of Dry and Impregnated Textiles. Procedia Manuf. 47 (2020) 140-147. https://doi.org/10.1016/j.promfg.2020.04.155

[4] S. Chen, L.T. Harper, A. Endruweit, N.A. Warrior, Formability optimisation of fabric preforms by controlling material draw-in through in-plane constraints. Composites Part A 76 (2015) 10-19. https://doi.org/10.1016/j.compositesa.2015.05.006

[5] L. Kärger, S. Galkin, C. Zimmerling, D. Dörr, J. Linden, A. Oeckerath, K. Wolf: Forming optimisation embedded in a CAE chain to assess the structural performance of composite components. Compo. Struct. 192 (2018) 143-152. https://doi.org/10.1016/j.compstruct.2018.02.041

[6] P. Xue, X. Peng, J. Cao, A non-orthogonal constitutive model for characterizing woven composites, Composites Part A: Appl. Sci. Manuf. 34 (2003) 183-193. https://doi.org/10.1016/S1359-835X(02)00052-0

[7] W. Lee, J. Cao, P. Badel, P. Boisse, Non-orthogonal constitutive model for woven composites incorporating tensile effect on shear behavior, Int. J. Mater. Form. 1 (2008) 891-894. https://doi.org/10.1007/s12289-008-0239-1

[8] P. Badel, E. Vidal-Sallé, P. Boisse, Large deformation analysis of fibrous materials using rate constitutive equations. Comput. Struct. 86 (2008) 1164-1175. https://doi.org/10.1016/j.compstruc.2008.01.009

[9] M.A. Khan, T. Mabrouki, E. Vidal-Sallé, P. Boisse, Numerical and experimental analyses of woven composite reinforcement forming using a hypoelastic behaviour. Application to the double dome benchmark. J. Mater. Process. Technol. 210 (2010) 378-388.

[10] F.J. Schirmaier, D. Dörr, F. Henning, L. Kärger, A macroscopic approach to simulate the forming behaviour of stitched unidirectional non-crimp fabrics. Compos. A 102 (2017) 322-335. http://dx.doi.org/10.1016/j.compositesa.2017.08.009

[11] B. Chen, J. Colmars, N. Naouar, P. Boisse, A hypoelastic stress resultant shell approach for simulations of textile composite reinforcement forming. Composites Part A: Appl. Sci. Manuf. 149 (2021) 106558. https://doi.org/10.1016/j.compositesa.2021.106558

[12] A. Charmetant, J.G. Orliac, E. Vidal-Sallé, P. Boisse, Hyperelastic model for large deformation analyses of 3D interlock composite preforms. Compos. Sci. Technol. 72 (2012) 1352-1360. https://doi.org/10.1016/j.compscitech.2012.05.006

[13] D. Dörr, F. Henning, L. Kärger, Nonlinear hyperviscoelastic modelling of intra-ply deformation behaviour in finite element forming simulation of continuously fibre-reinforced

thermoplastics, Compos. A 109 (2018) 585-596. https://doi.org/10.1016/j.compositesa.2018.03.037
[14] V. N. Khiêm, H. Krieger, M. Itskov, T. Gries, S. E. Stapleton, An averaging based hyperelastic modeling and experimental analysis of non-crimp fabrics. Int J of Solids and Structures 154 (2018) 43-54. https://doi.org/10.1016/j.ijsolstr.2016.12.018
[15] Y. Aimène, E. Vidal-Salle, B. Hagège, F. Sidoroff, P. Boisse, A Hyperelastic Approach for Composite Reinforcement Large Deformation Analysis, Journal of Composite Materials 44 (1) (2010) 5-26. https://doi.org//10.1177/0021998309345348
[16] X. Peng, Z. Guo, T. Du, W.-R. Yu, A simple anisotropic hyperelastic constitutive model for textile fabrics with application to forming simulation, Composites Part B: Engineering 52 (2013) 275-281. https://doi.org/10.1016/j.compositesb.2013.04.014
[17] C. Poppe, D. Dörr, F. Henning, L. Kärger: Experimental and numerical investigation of the shear behaviour of infiltrated woven fabrics, Composites Part A 114 (2018) 327-337. https://doi.org/10.1016/j.compositesa.2018.08.018
[18] Y. Yao, X. Huang, X. Peng, P. Liu, G. Youkun, An anisotropic hyperelastic constitutive model for plain weave fabric considering biaxial tension coupling, Text. Res. J. 89 (2019) 434-444. https://doi.org/10.1177/0040517517748495
[19] Y. Yao, X. Peng, Y. Gong, Influence of tension-shear coupling on draping of plain weave fabrics, J. Mat. Sci. 54 (8) (2019) 6310-6322. https://doi.org/10.1007/s10853-019-03334-w
[20] H.O. Werner, F. Schäfer, F. Henning, L. Kärger, Material Modelling of Fabric Deformation in Forming Simulation of Fiber-Metal Laminates - A Review on Modelling Fabric Coupling Mechanisms, ESAFORM (2021) 2056, Liège, Belgique. https://doi.org/10.25518/esaform21.2056
[21] F. Schäfer, H.O. Werner, F. Henning, L. Kärger, A Hyperelastic Material Model considering Biaxial Coupling of Tension-Compression and Shear for the Forming Simulation of Woven Fabrics, Compos. A: in press (2022) 107323. https://doi.org/10.1016/j.compositesa.2022.107323
[22] H.O. Werner, D. Dörr, F. Henning, L. Kärger, Numerical modeling of a hybrid forming process for three-dimensionally curved fiber-metal laminates, AIP Conference Proceedings 2113 (2019) 020019. https://doi.org/10.1063/1.5112524
[23] H.O. Werner, C. Poppe, F. Henning, L. Kärger, Material Modeling in Forming Simulation of Three-Dimensional Fiber-Metal-Laminates - A Parametric Study, Procedia Manuf. 47 (2020) 154-161. https://doi.org/10.1016/j.promfg.2020.04.160
[24] A. Cherouat, H. Bourouchaki, Numerical Tools for Composite Woven Fabric Preforming, Adv. Mat. Sci. Eng. 2013 (2013) 709495. https://doi.org/10.1155/2013/709495
[25] M. Komeili, Multi-Scale Characterization and Modeling of Shear-Tension Interaction in Woven Fabrics for Composite Forming and Structural Applications, Dissertation, The University of British Columbia, Okanagan, 2014. https://dx.doi.org/10.14288/1.0074335

Materials Research Proceedings 28 (2023) 367-374 https://doi.org/10.21741/9781644902479-40

Automated programming for the robotic layup process

GAMBARDELLA Antonio[1, a], ESPERTO Vitantonio[1, b], TUCCI Fausto[1, c] and CARLONE Pierpaolo[1, d]

[1]Department of Industrial Engineering, University of Salerno, Italy

[a]angambardella@unisa.it, [b]vesperto@unisa.it, [c]ftucci@unisa.it, [d]pcarlone@unisa.it

Keywords: Robotic Layup, Automated Layup, Prepreg, Fiber Placement, Industrial Robot

Abstract. Hand layup is still appreciated in modern industry for processing composite materials. Since is a manual process, reaching a standardization is impossible and this limits the applicability of this process. AFP and ATP offer a good level of automation and standardization, but both these processes are effective on simple-shaped surfaces. The conventional manufacturing processes have been increasing their level in automation thanks to the implementation of tooling machines and software that are able to automatically generate routes and tasks for manufacturing of a desired component. The goal of this research project is to take a step forward in the evolution of CAE software for tasks and routes management of the robotic layup process. In this paper a script implemented with MATLAB is described. The implemented script can automatically generate movements for robotic layup given a desired mold: starting from a user-given surface, the surface can be divided into sub-surfaces, and the software can automatically generate paths for each part of the surface according to the manual techniques studied by professional laminators.

Introduction

Advantages properties of fiber reinforced polymers (FRPs) have promoted their wide usage in several applicative sectors, ranging from aerospace, automotive, through to naval and construction industries [1] to improve the performance and reduce the weight of their components [1–14]. Advanced FRPs are multi-phase materials made of continuous reinforcing fibers, oriented in one or more specific direction, embedded within a polymeric matrix.

Nevertheless, despite of high specific strength and stiffness, corrosion resistance, and design flexibility, FRPs are affected by some drawbacks limiting their further application. As a multi-phase material, FRPs have an anisotropic behavior dependent on reinforcements' orientation [6]. This leads to excellent performance under longitudinal loading, but scarce (matrix dependent) behavior in case of transverse loading. In most lightweight composites, matrix is constituted by polymeric materials, both thermosetting or thermoplastic resins, whose main roles are to keep together the fibers, transfer and distribute loads, and protect them from the atmospheric agents. To improve the material properties and reduce anisotropic behavior, the most used strategy is to lay the fibers plies in different directions [15].

Hand layup has been the earliest manufacturing technique used for shaping composite products [16]. Also classified as a no-industrial process, this technique offers the advantage of low-cost suitability for the production of small batches. But as a manual process, the hand layup carries all the problems lead by the operator actions. From a quality point of view, this means that it is impossible to reach a standardization of all the pieces produced [4]. To improve the repeatability and reduce the human intervention, other manufacturing processes have been developed such as, among others, liquid composite molding, pultrusion, filament winding. Through the years, most of the manufacturing processes to fabricate fiber-reinforced composite products are based on conventional techniques such as the autoclave. But the demand for automation is rapidly increasing in the industry in order to achieve lower costs, repeatability, and reduction in material scraps [5].

Content from this work may be used under the terms of the Creative Commons Attribution 3.0 license. Any further distribution of this work must maintain attribution to the author(s) and the title of the work, journal citation and DOI. Published under license by Materials Research Forum LLC.

Recently, the application of automated manufacturing to composite layup led to the development of an innovative process, namely robotic composite layup [5], based on the replacement of human operations by one or more opportunely programmed and eventually collaborative robots [17].

During past few decades, advancements in automated composites manufacturing processes such as, automated fiber placement (AFP) and automated tape placement (ATP) (or other commonly known name of automated tape layup, ATL) technologies have revolutionized the fabrication of aerospace components. Major aircraft manufacturers have been utilizing automated techniques for many years now in their production lines to rapidly manufacture their flagship aircrafts such as Boeing 787 and Airbus A350 XBW, containing more than 50% composite parts by weight [7], [8]. Compared to other aerospace manufacturing techniques e.g., resin transfer molding (RTM), AFP and ATP systems are the most advanced and commercially used automated machines for large-scale aerostructures manufacturing. In terms of functionality, both AFP and ATP systems are very similar even though both methods use different approaches to fabricate specific components using resin pre-impregnated fabrics (commonly known as prepregs) [9]. One of the major differences between the two processes is that the AFP machine places multiple narrow pre-impregnated fiber tows whereas the ATP machine lays up larger and wider unidirectional tapes [9], [10]. Instead of conventional robots, both AFP and ATP use machine tool-based processes that can significantly reduce the cost of composite parts, especially large components, main wing structure, ribs, fixed trailing edge, nacelle structure, spoilers, flaps, ailerons, and tail cones [5]. Despite the benefits in terms of automation and reduced human involvement, these two processes are expensive: they are effective only for large parts with low to medium geometric complexity and have been implemented in those industrial fields capable of justifying high capital and operating costs. AFP/ATL are therefore technically and economically incompatible with the production of small to medium-sized components or complex-shaped parts, or with production volumes that cannot justify the usage of such expensive systems. In such situations, manual processes are needed leading to variability in part quality depending on the experience of each operator [18]. In this context, the robotic layup process has been developed to offer a high level of automation and standardization, reducing human involvement while at the same time offering the ability to process even complex shapes. Many efforts have been made in recent years to improve robotic processes and make them free from the actions of operators. Most of the knowledge about prepreg layup has been developed from the personal experience of professional laminators, who have implemented and collected strategies and techniques over the years to improve the layup process and reduce time and defects. Transferring this knowledge to a robotic process requires the constant attention of a professional laminator when coding robotic movements. The goal of this research project has been to implement a code capable of automatically handling the laying of a complex shaped surface. Another constraint that was considered during this study is to plan the entire layup of the mold surface using only one properly equipped robotic arm and clamp system. As demonstrated in previous work, processing the layup with two or three collaborative robots can certainly provide more accurate robotic handling as well as can promote the success of the process, but all this make the process complex and economically disadvantageous.

The implemented algorithm is able to handle a set of strategies and techniques on different mold geometries. The experience of professional laminators was translated to be used with a robotic arm equipped with a specific end-effector.

Materials and methods

In order to collect and organize the techniques implemented by professional laminators, CAE software has been used to implement an algorithm to manage the surfaces of each mold analyzed and manage layup strategies. The software used has been MATLAB. "Gmsh," an open-source CAE software widely used for FEM analysis, has been used for mesh generation.

Complex-shaped molds have been used during testing to make the experimental campaign as generalizable as possible. The three molds used for the test campaign have been designed to be a workbench for the implemented algorithm. They have different shapes and require different layering strategies. They include planes with different inclinations, curved parts, fillets, and spherical parts. Moreover, they also include concave and convex parts that require specific steps to be processed.

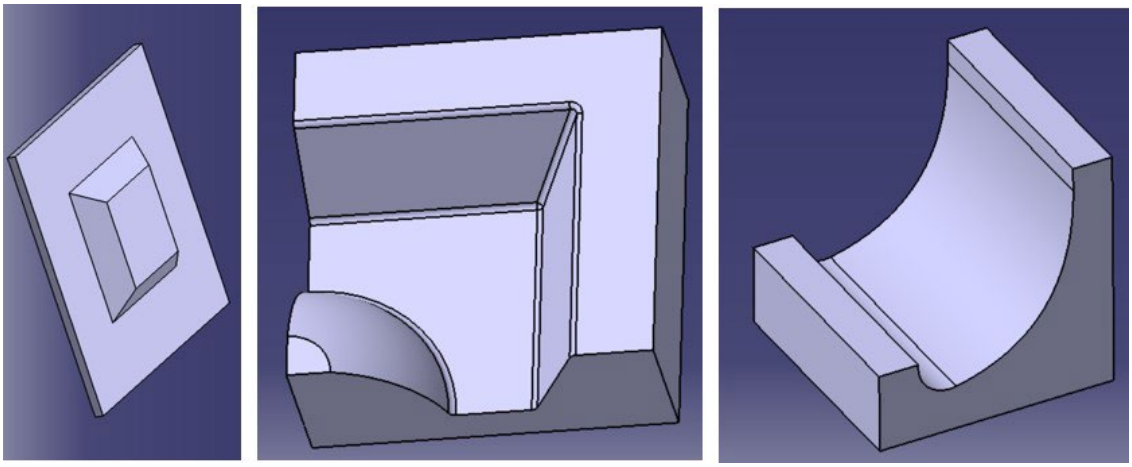

Fig. 1. The molds used as workbench

As a collaborative robotic, a Comau Smart SiX 6 has been used, which is a robotic arm with 6 degrees of freedom (DOF). All the simulations are performed in MATLAB environment and the robotic process is simulated thank to Robotics System Toolbox add-on. The information regards the robot is included in the URDF model which uses the XML standard to describe a robot which includes kinematic and dynamic behavior, visual representation, and collision model.

For this test, the end-effector used is composed of three terminals: cylindrical roller for flat surfaces, a profiled roller for fittings and small radius curvatures, and a punch for consolidating prepreg in corners and tight parts. The cad models of the end-effector and the mold have been made with CATIA V5 CAD software, loaded into MATLAB environment, and then the end-effector linked to the robotic arm model and mold placed in desired position inside the virtual working area of the robot.

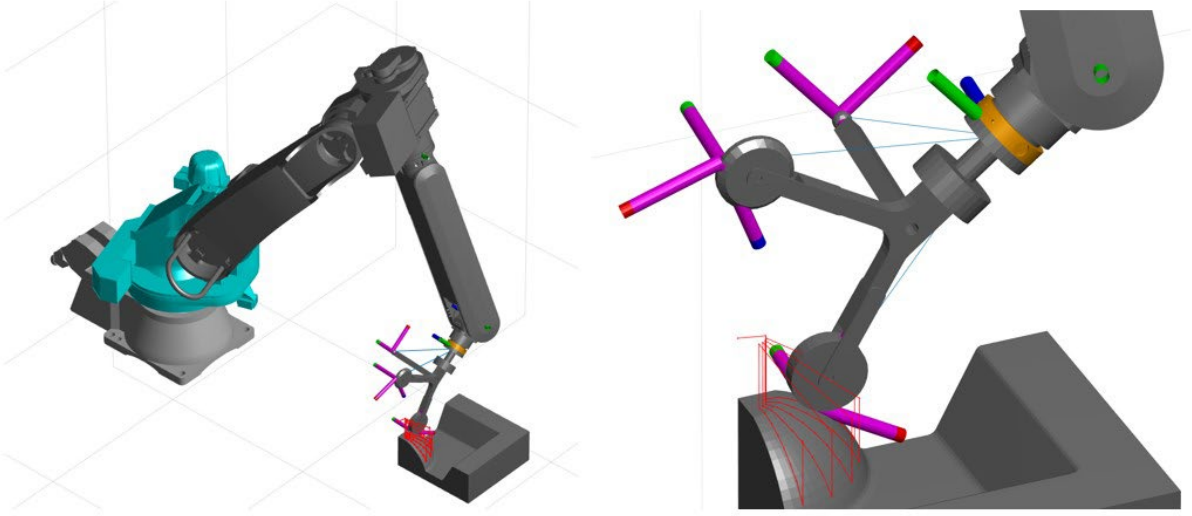

Fig. 2.The robot, the end effector, and a mold imported in MATLAB environment

The implemented algorithm is able to recognize the different parts of the surfaces of a mold and apply the correct strategies for the layup phase.

The process begins with loading the mesh of the mold surface. Triangles have been chosen for the elementary entities of the mesh. The mesh includes information about the coordinates of the points and how they are connected together to form the triangles. Cleaning the surface from unnecessary points is the first step: the mold mesh also includes sides that are not required for layup. The sides of triangles were used to identify the normal vector of each elementary surface: the vector product of two sides gives a vector directed to the normal of the plane identified by the triangle. By placing this vector in the center of the triangle and considering only its modulus, the normal vector of the triangle has been obtained. The normal vectors are then used to identify the sub-surfaces that compose the mold surface. An algorithm has been implemented that can analyze the orientation of the normals and group triangles with the same orientation in space and collect them into an array. At this point, the mesh, mesh nodes, and triangles are ready to be used in the next step, where paths are defined according to the strategies of experienced laminators.

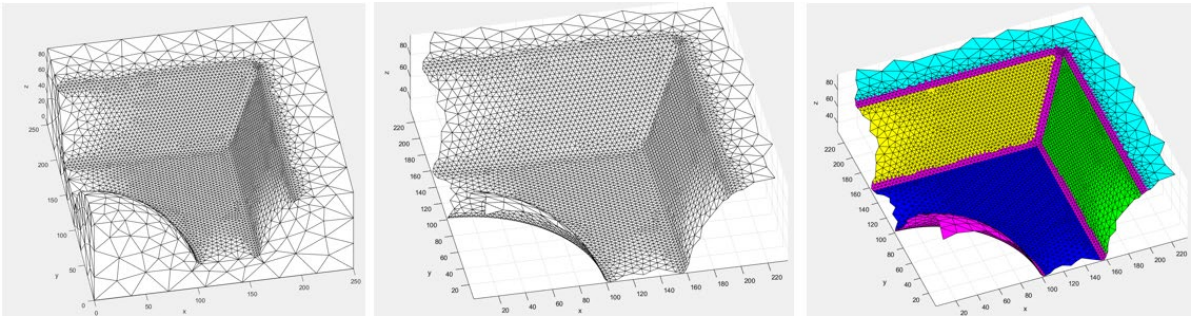

Fig. 3. The mesh of a used mold (left); the same mesh cleared of elements not to be processed (center); the mesh divided into sub-surfaces (right)

The strategies have been translated into routes and tasks to be performed in a specific situation. Starting from a literature review, the approaches used during the experimental trials have been collected. Following the most common scenarios are listed with the approaches used in previous works.

The main human techniques have been listed in the work of M. Elkington et al. “Hand layup: understanding the manual process” [19]. Eight different techniques used in different scenarios are described in this paper: one handed guiding; two handed guiding; manual folding; hoop shearing; double-tension shearing; tension-secured shearing; tension and sticking; mold interaction shearing. Some of these techniques involve both of the operator's hands. But in most cases, careful selection of a prepreg clamp system or choice of starting point can enable the robot to replicate the same pressure applied by the operator.

An important aspect is the definition of the boundaries of each sub-surface. These boundaries are defined by the user with a manual selection of points. In this way, it is possible to define how the parts of the surface are connected to each other and their relative inclination.

Another challenge is the choosing the areas of the sub-surfaces to process first. The friction between mold and prepreg is very high (and even higher between two consecutive layers). For this reason, starting layup from the correct part of the surface is crucial to the good result of the process. For example, if the surface to be treated has a concave shape, starting with the upper parts of the mold with the idea of then moving to the lower areas may lead to insufficient prepreg to cover the lower part, resulting in bridging defects (Fig. 4A).

The same could happen with an edge that joins two or three sub-surfaces with different inclinations. In these areas, depending on the order of the processed surfaces, two different

Materials Research Proceedings 28 (2023) 367-374 https://doi.org/10.21741/9781644902479-40

scenarios could occur: an excess of material, which could lead to wrinkling; or a deficiency of material, which could lead to bridging [20].

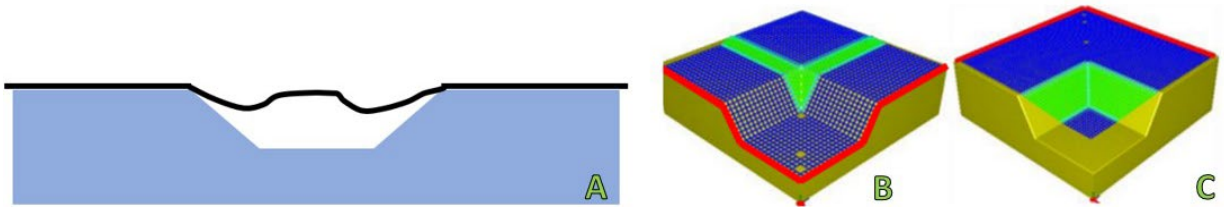

Fig. 4. On the left (A), an incorrect choice of starting point that led to the bridging defect; on the right, a mold processed in two ways: in the first (B), the process began by consolidating the lower part (red lines); the second (C) began by consolidating the upper part. The green areas represent the portions of prepreg where the defect occurs.

The Fig. 4B and Fig. 4C show that different starting positions lead to the two situations mentioned. In case shown in Fig. 4B, the layup has started consolidating the lower part and then moving to the upper part: the green part represents the area where there is excess material, which led to wrinkles. In case shown in Fig. 4C, the layup has started from the upper part: the green part is not enough to cover the remaining area, which led to a bridging defect.

To avoid the problems mentioned above, the algorithm is able to study the shape of the surfaces and whether there are any concave or convex parts. If so, the software implements routes starting from the bottom of the concavity or the top of the convexity: the layup will then begin by laying the material starting from the proper sub-surface. In this way, the amount of prepreg will be sufficient to cover that part of the surface avoiding defects such as bridging.

Several cases are included in the algorithm that are based on the experience gained during previous work and the experience of professional laminators. The algorithm is able to understand the inclination or curvature of sub-surfaces. For each subsurface, the shape of the surrounding parts is detected. Through the analysis of the normal vectors of the triangles and the coordinates of their centers and nodes, it is possible to understand whether a subsurface is located, for example, at the bottom of a concave mold. In this way, it is possible to determine the most appropriate sub-surface to start layup.

After sticking the first subsurface, the algorithm is programmed to start consolidating the nearest fittings, and routes are designed starting from these edges. Moreover, processing a subsurface requires gradual movement. For this reason, each part of the surface is processed in steps: movement along the entire length of the subsurface is avoided and steps are chosen according to the extension of the surface and the size of the tool used.

Results and discussion

The implemented algorithm can process the given mesh elements and generate specific routes based on the experience of professional laminators. From the experiences gained in the works mentioned, starting on the proper side of the mold surface is critical to achieving a good layup. For the given molds, the algorithm proposed the following sub-surface sequence (Fig. 5).

In mold "a," the algorithm chose to start from the top and then move down toward the base of the mold. The reason for this choice is that the elements of the other sub-surfaces gradually go down without a subsequent ascent. In mold "b," which is probably the most complex, the algorithm chose to start at the bottom of the mold, then consolidate the neighboring fillets, and then work its way up. In this case, the chosen part represents the bottom of a cavity. Therefore, in order to have enough material to cover the other parts, the streaking action of the end effector on the prepreg must start from that surface. In the "c" mold, on the other hand, there are two planes at different heights joined by a concave surface. In this case, the best solution would be to start from one of

the two planes by gradually moving upward. The algorithm chose to start from the higher plane because this choice is shared with other cases contained within it. In all these cases, pre-shearing prepregs can reduce the occurrence of defects. After consolidating each subsurface, the algorithm generates instructions to consolidate neighboring fittings before moving further. The solutions shown are just a proposal derived from a series of cases included in the implemented algorithm. Of course, the end user can control these sequences by clicking on the mesh elements: after rejecting the proposed solution, the software asks the user to select the sub-surface where they want the layup to begin.

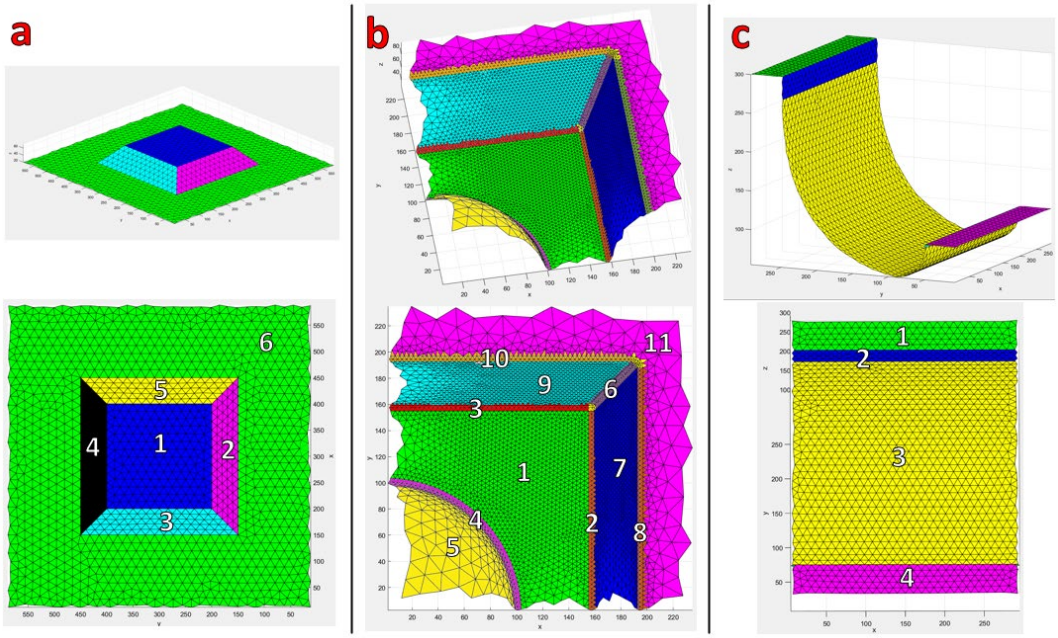

Fig. 5.The meshes of the molds in which the order of layups for each mold is indicated.

It is also possible to introduce new cases to increase the range of different recognized scenarios.

Summary

The implemented algorithm makes possible the automatic handling of mold meshes in order to design their layup. Since automatic actions have been implemented, the design time for an assigned mold to be processed is reduced: trajectory calculations are automatically performed by the software, which also generates the correct positioning of tangent, normal, and binormal vectors. The proper management of these angles prevents the occurrence of unwanted collisions during layup. The operator who now sees a routing solution offered for the end effector is still required to perform a check, thus a simulation of the process. But the time to calculate the positions of the mentioned vectors has still been reduced.

This results in faster reconfiguration and adaptability of the used resources, i.e., the robotic cell, and also reduces its actual utilization time.

Clearly, the end user is free to reprogram the layup to his liking.

References

[1] M. Alberto, Introduction of Fibre-Reinforced Polymers − Polymers and Composites: Concepts, Properties and Processes, Fiber Reinforced Polymers - The Technology Applied for Concrete Repair (2013) 3-40. https://doi.org/10.5772/54629.

[2] P. Carlone, F. Rubino, V. Paradiso, and F. Tucci, Multi-scale modeling and online monitoring of resin flow through dual-scale textiles in liquid composite molding processes, International Journal of Advanced Manufacturing Technology, 96 (2018) 2215-2230. https://doi.org/10.1007/s00170-018-1703-9.
[3] F. Rubino et al., Metallization of fiber reinforced composite by surface functionalization and cold spray deposition, Procedia Manuf, 47 (2020) 1084-1088. https://doi.org/10.1016/j.promfg.2020.04.353.
[4] A. T. Bhatt, P. P. Gohil, and V. Chaudhary, Primary Manufacturing Processes for Fiber Reinforced Composites: History, Development & Future Research Trends, IOP Conf Ser Mater Sci Eng, 330(1) (2018), https://doi.org/10.1088/1757-899X/330/1/012107.
[5] C. Grant, Automated processes for composite aircraft structure, Industrial Robot 33 (2006) 117-121. https://doi.org/10.1108/01439910610651428.
[6] H. Parmar, T. Khan, F. Tucci, R. Umer, and P. Carlone, Advanced Robotics and Additive Manufacturing of Composites : Towards a New Era in Industry 4.0, Materials and Manufacturing Processes 37 (2022) 483-517. https://doi.org/10.1080/10426914.2020.1866195
[7] D. Gan, J. S. Dai, J. Dias, R. Umer, and L. Seneviratne, Singularity-free workspace aimed optimal design of a 2T2R parallel mechanism for automated fiber placement, J Mech Robot 7 (2015) 1-9. https://doi.org/10.1115/1.4029957.
[8] K. Kozaczuk, Automated Fiber Placement Systems Overview, Transactions of the Institute of Aviation, 245 (2016) 52-59. https://doi.org/10.5604/05096669.1226355.
[9] J. Sloan, ATL & AFP: Defining the megatrends in composite aerostructures, https://www.compositesworld.com/articles/atl-and-afp-defining-the-megatrends-in-composite-aerostructures, (accessed 31 January 2023).
[10] P. Debout, H. Chanal, and E. Duc, Tool path smoothing of a redundant machine: Application to Automated Fiber Placement, Computer-Aided Design 43 (2011) 122-132. https://doi.org/10.1016/j.cad.2010.09.011.
[11] M. Elkington, D. Bloom, C. Ward, A. Chatzimichali, and K. Potter, Hand layup: understanding the manual process, Advanced Manufacturing: Polymer and Composites Science 1 (2015) 138-151 https://doi.org/10.1080/20550340.2015.1114801.
[12] S. Chiaverini, B. Siciliano, and O. Egeland, Review of the Damped Least-Squares Inverse Kinematics with Experiments on an Industrial Robot Manipulator, IEEE Transactions on Control Systems Technology 2 (1994) 123-134. https://doi.org/10.1109/87.294335.
[13] F. Tucci, R. Bezerra, F. Rubino, and P. Carlone, Multiphase flow simulation in injection pultrusion with variable properties, Materials and Manufacturing Processes 35 (2020) 152-162. https://doi.org/10.1080/10426914.2020.1711928.
[14] P. Boisse, R. Akkerman, P. Carlone, L. Kärger, S. V. Lomov, and J. A. Sherwood, Advances in composite forming through 25 years of ESAFORM, International Journal of Material Forming 15 (2022). https://doi.org/10.1007/s12289-022-01682-8.
[15] V. Esperto, A. Gambardella, G. Pasquino, F. Tucci, M. Durante, and P. Carlone, Modeling and simulation of the robotic layup of fibrous preforms for liquid composite molding in ESAFORM 2021 - 24th International Conference on Material Forming (2021). https://doi.org/10.25518/esaform21.475.
[16] M. Raji, H. Abdellaoui, H. Essabir, C. A. Kakou, R. Bouhfid, and A. El Kacem Qaiss, Prediction of the cyclic durability of woven-hybrid composites (2018). https://doi.org/10.1016/B978-0-08-102290-0.00003-9.
[17] B. Wang, The Future of Manufacturing: A New Perspective, Engineering 4 (2018) 722-728. https://doi.org/10.1016/j.eng.2018.07.020.
[18] A. Gambardella, V. Esperto, F. Tucci, and P. Carlone, Defects Reduction in the Robotic Layup Process, Key Eng Mater 926 (2022) 1437–1444. https://doi.org/10.4028/p-7v9349.

[19] M. Elkington, D. Bloom, C. Ward, A. Chatzimichali, and K. Potter, Hand layup: understanding the manual process, Advanced Manufacturing: Polymer and Composites Science 1 (2015) 138-151. https://doi.org/10.1080/20550340.2015.1114801.
[20] M. Elkington, C. Ward, A. Chatzimichali, K. Potter, Preshearing: The Evolution of Manual Layup, ECCM16 – 16th European Conference on Composite Materials (2014).

Materials Research Proceedings 28 (2023) 375-384 https://doi.org/10.21741/9781644902479-41

Experimental study of woven fabrics forming defects

SHANWAN Anwar[1,a *], GHANAMEH Mohamas-Fathi[1,b], BIJU Aditya[1,c] and HIVET Gilles[1,d]

[1]Laboratory of Mechanics, Orléans University, 8 rue Léonard de Vinci, 45072 Orléans, France

[a]anwar.shanwan@univ-orleans.fr, [b]mohamad-fathi.ghanameh@univ-orleans.fr, [c]adityabiju99@gmail.com, [d]gilles.hivet@univ-orleans.fr

Keywords: Mesoscopic Defects, Buckles, Gapping, In-Plane Pull-Out, Woven Fabric

Abstract. The manufacturing of composite materials can be ensured by several industrial processes, like Liquid Composite Molding (LCM). This technology is used to produce composite parts with complex geometries because it provides a very good compromise in terms of repeatability, production rates and cost. During the forming phase of an LCM process, a fabric can be formed by highly double curved punch geometries where it could be submitted to several deformations and mechanical stresses that lead to the appearance of different types of defects: buckles, gapping, in-plane pull-out, etc. In order to understand their phenomenology, different types of defects were generated inside samples of glass and carbon fabrics so as to understand their mechanisms of appearance. This work focuses on the phenomenology of appearance of forming defects and the definition of experimental parameters allowing the generation of calibrated defects, such as buckles and gapping, inside samples of glass and carbon woven fabrics. The definition of these parameters allows the manufacturing of composite parts with calibrated defects, which in turn helps to define the influence of these defects on the mechanical behavior of composites materials.

Introduction

Composite materials are broadly used in several industrial fields, thanks to their excellent mechanical properties. They are usually used to substitute metallic alloys due to their higher strength, lower weight and improved service life. Numerous manufacturing processes of composite materials are known in the industry [1] where the choice of a specific process depends on various criteria. The Liquid Composite Molding (LCM) process is among the most interesting processes to produce composite parts with complex geometries. In addition, this process is appropriated for the forming of fiber-reinforced polymeric composites due to its economic advantages and the capacity to produce high performance parts [2]. An LCM process has two main phases: the forming of a fabric and the injection of a liquid resin inside the formed fabric. Many research have focalized on the forming phase overall the past years [3,4] because during this phase, the fabric is subjected to several stresses that induce various deformation mechanisms such as stretching and compression, in-plane and out-of-plane bending, and shearing [5,6]. These mechanisms often lead to the appearance of several forming defects at the macroscopic scale (wrinkles) [7] and the mesoscopic scale (buckles, in-plane pull-out, and gapping) [8,9].

Content from this work may be used under the terms of the Creative Commons Attribution 3.0 license. Any further distribution of this work must maintain attribution to the author(s) and the title of the work, journal citation and DOI. Published under license by Materials Research Forum LLC.

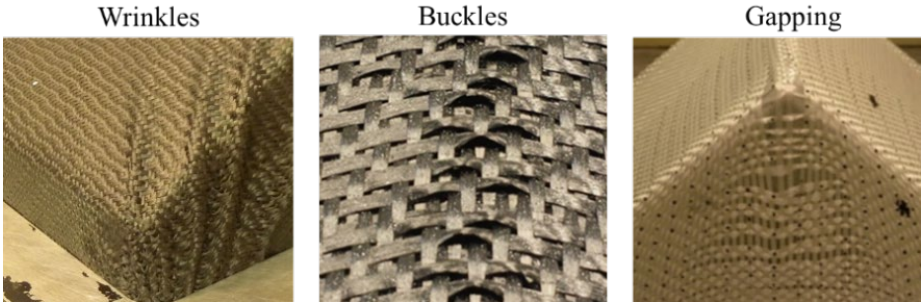

Fig. 1. Forming defects of different types [9].

The appearance of forming defects leads to a local heterogeneity of the preformed fabric and might impact the mechanical properties of the final composite parts. Hence, the understanding of the mechanisms of appearance of the defects seems to be crucial to avoid them or at least to reduce their magnitude. Wrinkles defects were widely studied in various studies [7,10,11]. Shanwan et al. [12] have proposed several experimental strategies to reduce their appearance or sometimes even completely avoid them. As for the mesoscopic defects, they are still not completely understood. In an interesting field of investigation, C. Tephany et al. [13] developed an experimental bench to study the buckle defects during a complex forming of a flax woven fabric. They used Digital Images Correlation (DIC) technique to accurately measure the buckle's height. Allaoui et al. [14] studied the effect of the inter-ply sliding on the buckle's appearance during the forming of woven fabrics on a prismatic tool. Capelle et al. [15] designed a specific blank holder system in order to optimize the preforming process parameters during complex geometry forming. To continue these investigations, Cruanes et al. [16] have focused on the impact of buckle defects on the mechanical properties of composite materials, specifically on the fatigue behavior. Their results showed that the orientation of buckles with respect to the tow's paths can highly reduce the mechanical performance of the composite parts. M.M. Salem et al. [17] investigated the influence of the cohesion of different woven fabrics on the reduction or prevention of the appearance of sliding defects of some vegetal and synthetic fabrics. On the other hand, Labanieh et al. [18] held an experimental and analytical research to study the mechanisms of appearance of gapping defects during the preforming of a woven carbon fabric by a hemispheric shape. Their results have demonstrated the strong effect of shear stresses and yarn tension on the appearance of gapping.
Further investigations of buckles and gapping defects were carried out by Shanwan et al. [9,19] to understand and analyze these defects in depth. In order to acheive this goal, they developed a new experimental and polyvalent machine which makes it possible to produce different types of calibrated defects within samples of woven fabrics. Due to this machine, it is possible to ensure two main goals: the first one is to understand the mechanisms and criteria of appearance of forming defects while the second goal aims to produce composite parts from fabric samples containing calibrated defects, generated by the machine, of different types and amplitudes. The produced composite samples could be tested and compared with composite samples without defects. Due to this machine, the defects are generated under the same experimental parameters and the same boundary conditions that could be found during the forming phase of an LCM process. In this work, we present a new analysis of buckles, in-plane pull-out, and gapping defects, which is more developed than the one described in [9,19] where the experimental analysis was only focalized on gaping and buckles defects without referring to the in-plane pull-out. In addition, this study has experimentally approved the assumption of the previous studies [9,19] (i.e. the concomitance between the gaping and the buckles defects).

Material and Experimental Procedure

Two types of fabrics were used for this study: the first one is a balanced plain weave glass fabric (taffetas), produced by Chomarat Company and denoted G-WEAVE 600P. This fabric has an areal weight of 600 g/m^2 ± 5% and a thickness of 0.55 mm. The yarn width is 3 mm and the average spacing between two yarns is 1 mm. The yarn count is 600 Tex for both the warp and the weft directions. The second fabric is a 2.5D interlock carbon fabric, denoted G1151®, produced by Hexcel company. It has a surface weight of 630 g/m² and a unit cell of 6 warp yarns and 15 weft yarns, distributed on three levels. The tested samples are cut as a plus (+) form of 300x300 mm^2 with a usable central area of 100x100 mm^2, as shown in Fig. 3 and Fig. 4.

The machine used in this work is equipped with four brushless AC servo motors. Each motor commands one machine axis individually, either by a force command, or by a displacement command with different speeds. Each axis is also equipped with a displacement sensor, a force sensor and two position sensors to define the beginning and the end of its stroke. In order to record the experimental parameters during the experiments, a special LabVIEW program was developed to command the machine and to ensure the acquisition of different parameters, such as the tensile forces, the speed and the position of each axis. The bench is also equipped with a digital camera and an interferometer (Gocator 3100) placed above the sample during the test. The interferometer is a three-dimensional Digital Image Correlation (DIC) system that progressively measures the height of buckles during the experiments. The acquisitions of the camera and the interferometer are adjustable to be asynchronized in order to have two information sources about the sample evolution. Fig. 2 shows an example of such acquisitions whereas Fig. 3 illustrates a sample on the bench, where the lower longitudinal and the two transverse sides of the sample are clamped by a defined and adjustable compression. However, few tows from the upper longitudinal side are completely clamped by a tight fixation and pulled at a constant speed up to a defined displacement (in-plane pull-out in the direction of the yellow arrow in Fig. 3). This displacement simulates the same movement of the tows in contact with the punch during the forming phase of an LCM process. During the experiments, the forces and the displacements of each axis are continuously recorded by a LabVIEW program and synchronized with a simultaneous acquisition of images of the interferometer and the camera.

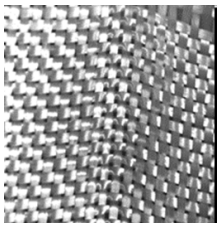

By camera

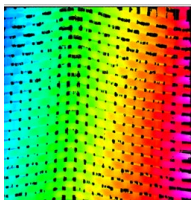

By interferometer

Fig. 2. Acquisitions mode.

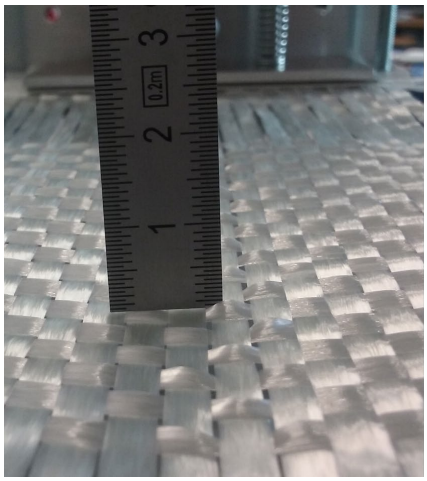

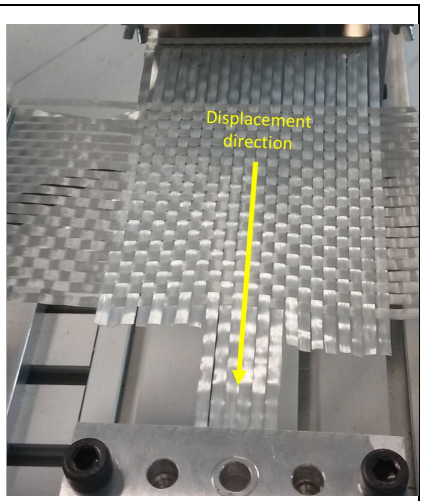

Fig. 3. Placement of a sample on the machine.

Results and Discussion

The results of this section confirm a previous expectation that we assumed during the studies [9] and [19] about the concomitance between buckles and gapping defects. In addition, this study presents a detailed investigation to better understand the interactions between the displacement of the longitudinal yarns and the deformation of the transverse yarns and its influence on the possible appearance of buckles and gaping defects. These investigations are explained by means of Fig. 4 and Fig. 5. As shown by Fig. 5, the displacement of the pulled longitudinal yarns leads to a displacement of the transverse yarns due to the friction between the two networks of the fabric yarns. Subsequently, an in-plane bending of the transverse yarns takes place in the useful area of the sample, whereas the parts of the same yarns, which are clamped between the transverse jaws, do not rotate because of the static friction between the metal and the yarns. When the traction force, transmitted to the transverse yarns, overcomes the static friction between the metallic jaws and the fabric, the transverse yarns between the jaws rotate and continue their an in-plane bending.

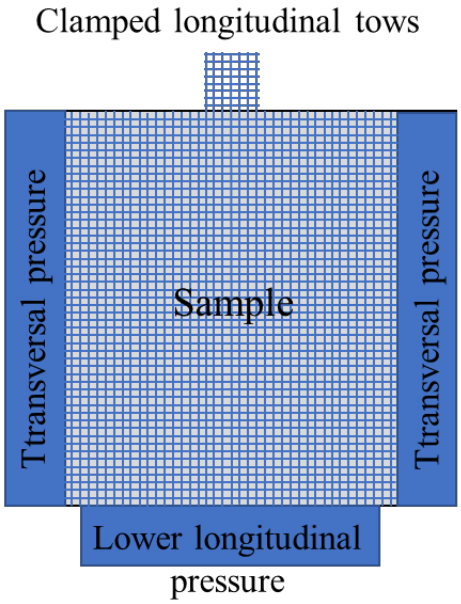

Fig. 4. Form of the prepared samples before the experiments.

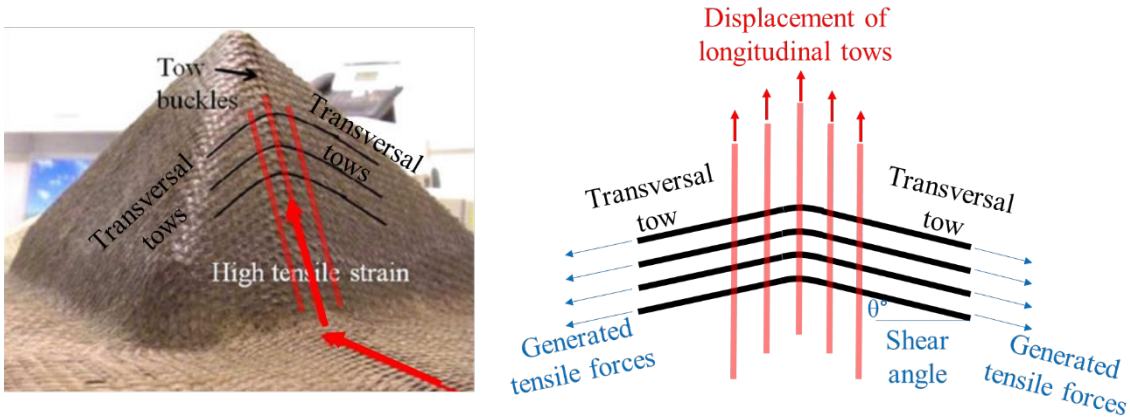

Fig. 5. Phenomenology of appearance of the forming defects [9].

Depending on the bending stiffness of the yarns, the in-plane bending continues until a defined shear angle where it stops and becomes an out-of-plane bending of the transverse yarns. It is at this moment that the buckle defects appear. Then, the amplitude of buckles increases until the end of the first phase which ends at the peak of the curve force/displacement, as shown in Fig. 6. At this moment, the traction force applied on the yarns overcomes the static friction between the fabrics yarns (cohesion) where a relative sliding of the longitudinal yarns takes place with respect to the transverse ones. This moment announces the beginning of the second phase (in-plane pull-out). Depending on the homogeneity of the transverse pressure, applied on the transverse yarns, and/or the regularity of the sample thickness, the displacement of the longitudinal yarns provokes either a simple pull-out of these yarns from the fabric or a displacement of some transverse yarns with the pulled longitudinal ones with respect to the other transverse yarns. In this last case, we observe the formation of some gaps inside the sample which lead to the appearance of weave pattern heterogeneity defects, sometimes called decohesion or even gapping defects. The second phase is also characterized by many oscillations due to a stick-slip phenomenon. Finally, the third phase of the curve starts at the beginning of the loss of contact between the lower part of the sample and the metallic jaws that clamp it. This phase continues until the sample is no longer held between the jaws.

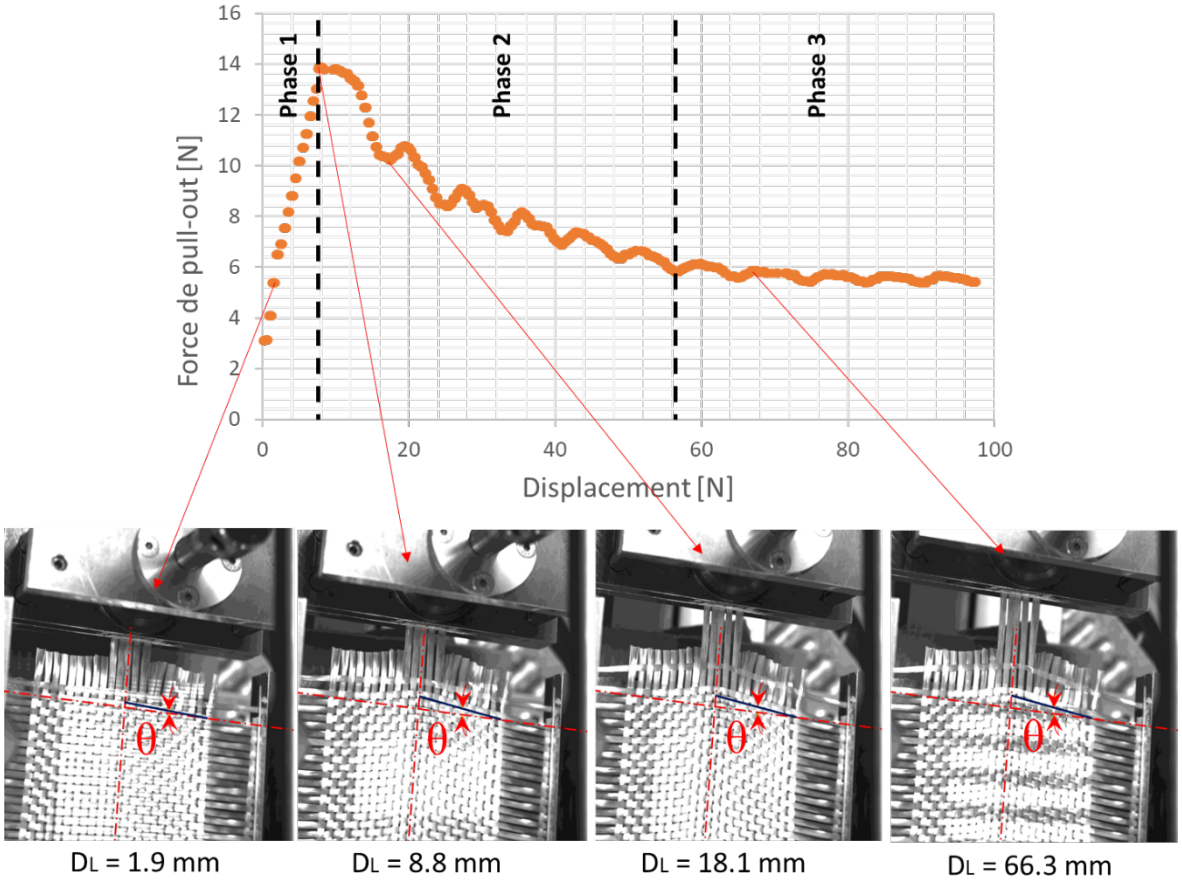

Fig. 6. Different phases of preforming defects appearance.

The above-mentioned phenomenology was verified by a measurement of displacements of the transverse yarns, directly executed on the recorded images (Fig. 6), by means of the ImageJ software. The measurements showed that the shear angle θ° increases during the phase 1, up to 13°, then it remains constant during the other two phases. The measured values are presented in

Table 1, where D_L and D_T respectively refer to the displacement of the longitudinal and the transverse yarns.

Table 1. Relationship between the yarn's displacements and the shear angle.

Phase 1			Phase 2	Phase 3
$D_L = 0$	$D_L = 1.9\ mm$	$D_L = 8.8\ mm$	$D_L = 18.8\ mm$	$D_L = 66.3\ mm$
$D_T = 0$	$D_T = 2.1mm$	$D_T = 5.2mm$	$D_T = 5.2mm$	$D_T = 5.2mm$
$\theta° = 0°$	$\theta° = 8.6°$	$\theta° = 13°$	$\theta° = 13°$	$\theta_s = 13°$

Next, the appearance of defects was investigated on two types of fabrics, as a function of four experimental parameters: the number of the pulled tows, the transverse compression, the longitudinal compression, and the speed of displacement of the pulled longitudinal yarns. Each parameter was tested at three different values with a repeatability of three experiments per value while the other parameters were fixed for each tested parameter. In total, 36 experiences were carried-out for each type of fabric (4 parameters * 3 values * 3 repeatability). Fig. 7 shows an example of one set of such experiments, carried-out on a cross glass fabric sample, where the transverse pressure was set at 0.05, 0.10, and 0.15 bars whereas the other experimental parameters were fixed as follows: The lower longitudinal pressure = 0.05 bar, The speed of displacement = 1 mm/sec, and the number of pulled tows = 7. The choice of these parameters was selected as those of a forming process.

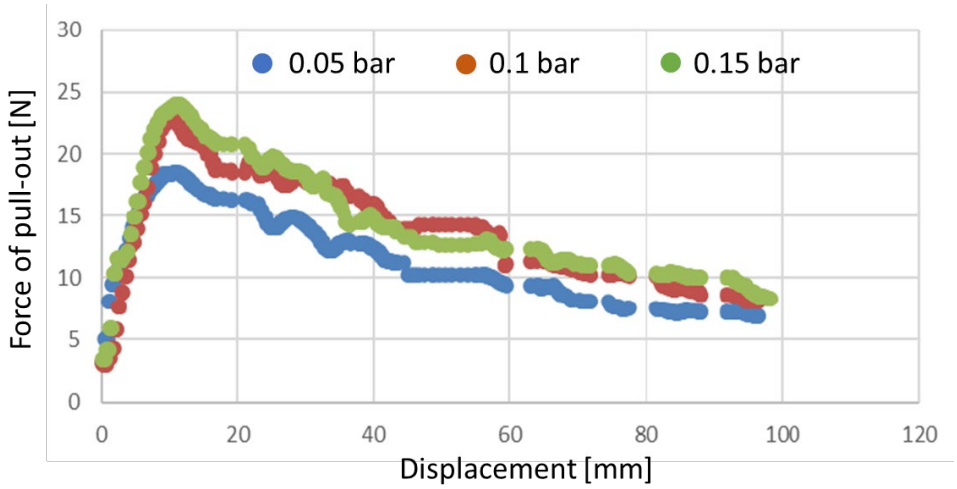

Fig. 7. Evolution of the pull-out force of the upper longitudinal yarns with the displacement.

As shown by these curves, an increase of the transverse pressure leads to an increase in the pull-out force of the longitudinal yarns. This increase is very logical as the traction force should overcome the friction between the fabric and the blank holder which increases with the normal pressure according to the Coulomb's law of friction. The tests presented by these curves corresponded to the appearance of buckles and gapping defects, with respect to the above-mentioned parameters. Fig. 8 shows an example of buckles and gapping appearance.

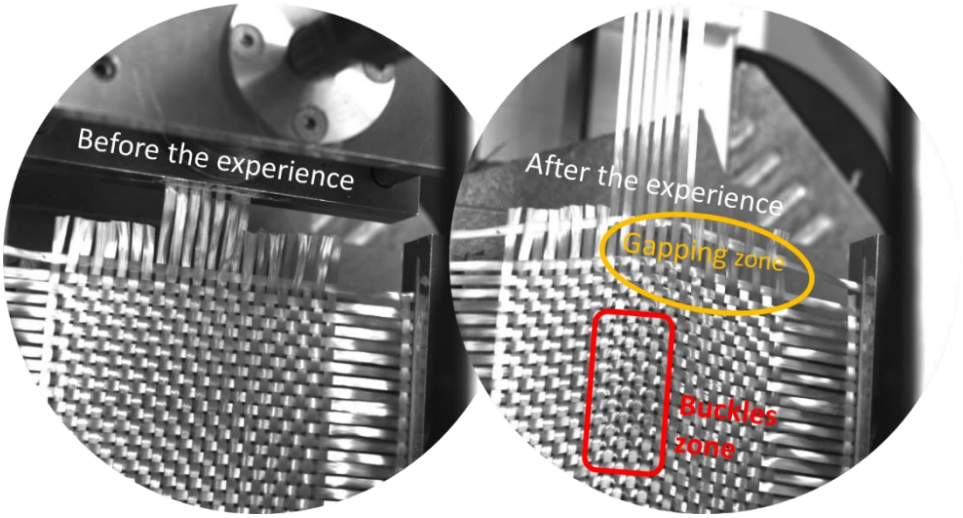

Fig. 8. Appearance of buckles and gapping defects on samples of glass fabric.

The Table 2 presents the group of experiments that studies the influence of the transverse pressure evolution on the defect's appearance. The experiments were repeated for three numbers of the pulled tows (3, 5, and 7) whereas the other experimental parameters were kept constant as follows: the longitudinal pressure = 0.05 bar, and the speed of displacement = 1 mm/sec. Thus, the Table 2 contain 9 series of experiences. In this table the symbol (✓) refers to the appearance of the defects whereas the symbol (x) indicates to a non-appearance of defects. Many deep analyses could be done but at this stage of the study we focalized on the definition of the experimental parameters allowing the appearance of forming defects and the comparison between the influence of these parameters on the defect's appearance for two types of fabrics.

Table 2. Experiments parameters allowing the appearance of buckles and gapping in glass fabric samples.

Number of tows	Transverse Pressure (P_T)	Buckles	Gapping
3	0.05 bar	x	x
	0.1 bar	✓	x
	0.15 bar	✓	x
5	0.05 bar	✓	x
	0.1 bar	✓	x
	0.15 bar	✓	x
7	0.05 bar	✓	✓
	0.1 bar	✓	✓
	0.15 bar	✓	✓

For the other experimental parameters, the influence of their evolution on the forming process was also tested. The Fig. 9 shows, for example, whether the velocity of pull-out has an influence on the pull-out force. The curves show a decrease in the pull-out force if the velocity increases and

the ratio of the force reduction is almost proportional to the ratio of increase in the velocity. This result needs a deeper analysis with other effects that should be considered, like the dynamic effect, the variability related to the heterogeneous behavior the fibrous structures.

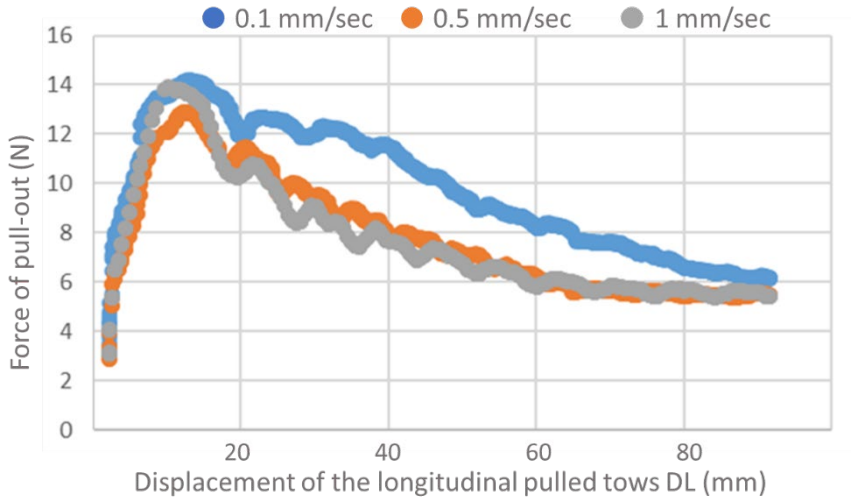

Fig. 9. Influence of the pull-out velocity on the pull-out force evolution.

Finally, when applying the same experimental parameters, that allowed the appearance of buckles and gapping defects in the case of glass fabric samples, on samples of the interlock carbon fabric G1151, it was possible to generate buckles defects only, without any appearance of gapping. Consequently, it can be concluded that the appearance of preforming defects is not only related to the experimental parameters, but also to the cohesion of the fabric as well as the boundary conditions during the process. This conclusion was indeed confirmed by the experiences presented in Fig. 10 that shows two examples of forming experiments on carbon and glass fabrics where both tests were executed under the same following conditions which are as follows: width of the pulled tows = 25±2 mm, displacement speed = 1 mm/sec, transverse pressure = 0.15 bar, and the longitudinal pressure = 0.05 bar.

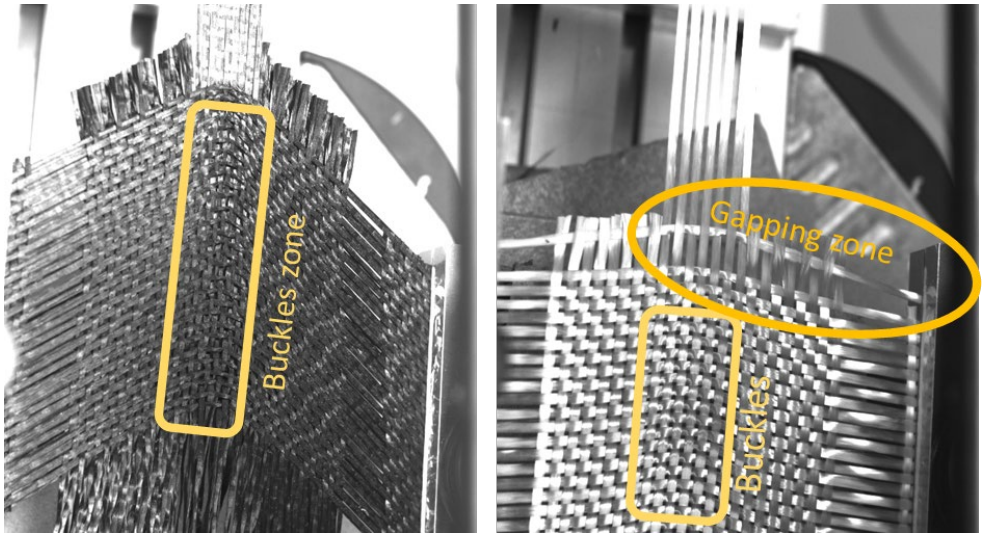

Fig. 10. Generated defects on glass and carbon fabrics.

Summary

This research contributed to the understanding of preforming defects and their mechanisms of appearance. It has been demonstrated that buckles, gapping and/or pull-out defects could not be separated even if it is sometimes possible to generate this or that defect. These defects are always concomitant and the appearance of one or both of them depends on the experimental parameters, the boundary conditions and the cohesion of the tested fabric.

References

[1] Y. Li, Y. Xiao, L. Yu, K. Ji, D. Li, A review on the tooling technologies for composites manufacturing of aerospace structures: materials, structures and processes, Compos. Part A: Appl. Sci. Manuf. 154 (2022) 106762. https://doi.org/10.1016/j.compositesa.2021.106762

[2] S. Konstantopoulos, C. Hueber, I. Antoniadis, J. Summerscales, R. Schledjewski, Liquid composite molding reproducibility in real-world production of fiber reinforced polymeric composites: a review of challenges and solutions, Adv. Manuf. Polym. Compos. Sci. 5 (2019) 85-99. https://doi.org/10.1080/20550340.2019.1635778

[3] P. Boisse, R. Akkerman, P. Carlone, L. Kärger, S.V. Lomov, J.A. Sherwood, Advances in composite forming through 25 years of ESAFORM, Int. J. Mater. Form. 15 (2022) 39. https://doi.org/10.1007/s12289-022-01682-8

[4] B. Liang, P. Boisse, A review of numerical analyses and experimental characterization methods for forming of textile reinforcements, Chin. J. Aeronaut. 34 (2021) 143-163. https://doi.org/10.1016/j.cja.2020.09.027

[5] R. Bai, B. Chen, J. Colmars, P. Boisse, Physics-based evaluation of the drapability of textile composite reinforcements, Compos. Part B Eng. 242 (2022) 110089. https://doi.org/10.1016/j.compositesb.2022.110089

[6] F. Nosrat Nezami, T. Gereke, C. Cherif, Analyses of interaction mechanisms during forming of multilayer carbon woven fabrics for composite applications, Compos. Part Appl. Sci. Manuf. 84 (2016) 406-416. https://doi.org/10.1016/j.compositesa.2016.02.023

[7] P. Boisse, J. Huang, E. G-Maldonado, Analysis and Modeling of Wrinkling in Composite Forming, J. Compos. Sci. 5 (2021) 3. https://doi.org/10.3390/jcs5030081

[8] R. Azzouz, S. Allaoui, R. Moulart, Composite preforming defects: a review and a classification, Int. J. Mater. Form. 14 (2021) 1259-1278. https://doi.org/10.1007/s12289-021-01643-7

[9] A. Shanwan, S. Allaoui, J. Gillibert, G. Hivet, Development of an experimental approach to study preforming mesoscopic defects of woven fabrics, 24th International Conference on Material Forming, Liège, Belgium, Apr. 2021. https://doi.org/10.25518/esaform21.1580

[10] S. Chen, O. P.L. McGregor, L.T. Harper, A. Endruweit, N.A. Warrior, Defect formation during preforming of a bi-axial non-crimp fabric with a pillar stitch pattern, Compos. Part A : Appl. Sci. Manuf. 91 (2016) 156-167. https://doi.org/10.1016/j.compositesa.2016.09.016

[11] P. Boisse, N. Hamila, A. Madeo, Modelling the development of defects during composite reinforcements and prepreg forming, Philos. Transact. A Math. Phys. Eng. Sci. 374 (2016) 20150269. https://doi.org/10.1098/rsta.2015.0269

[12] A. Shanwan, S. Allaoui, Different experimental ways to minimize the preforming defects of multi-layered interlock dry fabric, Int. J. Mater. Form. 12 (2019) 69-78. https://doi.org/10.1007/s12289-018-1407-6

[13] C. Tephany, J. Gillibert, P. Ouagne, G. Hivet, S. Allaoui, D. Soulat, Development of an experimental bench to reproduce the tow buckling defect appearing during the complex shape forming of structural flax based woven composite reinforcements, Compos. Part Appl. Sci. Manuf. 81 (2016) 22-33. https://doi.org/10.1016/j.compositesa.2015.10.011

[14] S. Allaoui, C. Cellard, G. Hivet, Effect of inter-ply sliding on the quality of multilayer interlock dry fabric preforms, Compos. Part Appl. Sci. Manuf. 68 (2015) 336-345. https://doi.org/10.1016/j.compositesa.2014.10.017

[15] E. Capelle, P. Ouagne, D. Soulat, D. Duriatti, Complex shape forming of flax woven fabrics: Design of specific blank-holder shapes to prevent defects, Compos. Part B Eng. 62 (2014) 29-36. https://doi.org/10.1016/j.compositesb.2014.02.007
[16] C. Cruanes, A. Shanwan, S. Méo, S. Allaoui, M-P. Deffarges, F. Lacroix, G. Hivet, Effect of mesoscopic out-of-plane defect on the fatigue behavior of a GFRP, Mech. Mater. 117 (2018) 214-224. https://doi.org/10.1016/j.mechmat.2017.11.008
[17] M.M. Salem, E. De Luycker, K. Delbe, M. Fazzini, P. Ouagne, Experimental investigation of vegetal and synthetic fabrics cohesion in order to prevent the tow sliding defect via frictional and pull-out test, Compos. Part Appl. Sci. Manuf. 139 (2020) 106083. https://doi.org/10.1016/j.compositesa.2020.106083
[18] A.R. Labanieh, C. Garnier, P. Ouagne, O. Dalverny, D. Soulat, Intra-ply yarn sliding defect in hemisphere preforming of a woven preform, Compos. Part Appl. Sci. Manuf. 107 (2018) 432-446. https://doi.org/10.1016/j.compositesa.2018.01.018
[19] A. Shanwan, S. Allaoui, J. Gillibert, G. Hivet, Development and Implementation of an Experimental Machine to Study Woven Fabric Preforming Defects, Exp. Tech. 46 (2022) 299-316. https://doi.org/10.1007/s40799-021-00483-z

Materials Research Proceedings 28 (2023) 385-392 https://doi.org/10.21741/9781644902479-42

Surrogate model of the thermoforming of fiber reinforced thermoplastics

MIDDELHOFF Jan[1,a *], UJVARI Csenger[1,b], HÜRKAMP André[1,c] and DRÖDER Klaus[1,d]

[1]Technische Universität Braunschweig, Institute of Machine Tools and Production Technology, Langer Kamp 19b, 38106 Braunschweig, Germany

[a]j.middelhoff@tu-braunschweig.de, [b]c.ujvari@tu-braunschweig.de, [c]a.huerkamp@tu-braunschweig.de, [d]k.droeder@tu-braunschweig.de

Keywords: Thermoforming, Composite Forming, Machine Learning, Artificial Neural Networks, Surrogate Modelling

Abstract. In the thermoforming process shearing of fiber reinforced thermoplastics (FRTP) leads to wrinkle formation and is therefore one of the most critical deformation mechanism. The target value to predict wrinkle formation is the shear angle which is considered in this paper. To predict the shear angle distribution during the thermoforming of FRTPs a Convolutional Neural Network (CNN) is used. The approach is based on the consideration of the principal curvature characteristics, resulting in the reduction of any complex geometry to planar, parabolic, elliptical, semi-spherical and hyperbolic areas. In similar research, CNNs are trained for each specific geometry. In this work, the CNN refers to a database of the mentioned curvature characteristics. In theory, all forming geometries can be created from these, which is why the CNN is enabled to predict the forming result of any complex geometry. In this paper, the benchmark geometry of a double dome is selected as the validation geometry and the error in the prediction of the shear angle is compared with the results of numerical forming simulations performed.

Introduction

Due to their high mechanical properties combined with low densities, FRTPs offer a high potential for lightweight design applications. The production of flat components made of FRTP is often realised by the thermoforming process, which represents a high potential for large-scale production [1]. Thermoforming usually involves heating fiber reinforced thermoplastic sheets (organo sheets) above the melting temperature of the matrix to enable draping of the fibers in the melt-viscous matrix during the forming process.

The draping behaviour is mainly determined by the in-plane shear property of the organo sheet. Furthermore, the different deformation modes transverse compression, out-of-plane bending and in-plane tension are important variables which influence the formability of the material and thus the forming result [2]. Accordingly, multiple defects such as wrinkling or fiber fracture can occur due to excessive shear stresses or tensile stresses [2]. The defects are mainly reduced by the selection of suitable process parameters, which increases the component quality. In addition to adjusted process parameters, additional technical supporting structures such as clamping systems or blank holders can be used to reduce the formation of wrinkles through the application of in-plane tensile stresses [3]. Due to the different influences of process parameters and additional supporting structures on the occurrence of defects, large cavity depths, sharp geometric transitions and three-dimensional space corners are difficult to produce and object complexity is limited [4]. A possible process adjustment for an increase in part quality for complex cavities is the implementation of stepwise forming with segmented stamps [5]. Due to this innovative tool concept, the parameter space of the process is increased. However, in order to avoid inefficient and expensive experiments, numerical investigations were implemented in order to examine

Content from this work may be used under the terms of the Creative Commons Attribution 3.0 license. Any further distribution of this work must maintain attribution to the author(s) and the title of the work, journal citation and DOI. Published under license by Materials Research Forum LLC.

optimal segmentation and sequencing strategies for selected cavities. The numerical modelling of FRTPs even on the most common used macro-scale is timesensitive due to the complex material behaviour, thus surrogate models are useful for further time savings in the prediction of suitable segmentation and sequencing strategies. These types of Machine Learning (ML) architectures are already able to model the forming behaviour of different geometries as well as different process conditions [6]. These approaches will be addressed in this paper and extended with the approach explained in the following chapter. The presented investigations are the basis for further work on the implementation of the ML-based prediction of segmentation and sequencing strategies for increasing the prediction quality of shear stresses.

Curvature Analysis Approach

The goal of this research is to link a shear angle as the target variable with curvature values derived from the geometry of the cavity. The implementation of different basic geometries as a database enables a deep learning architecture the prediction of shear angles for all possible geometries.

The target value is the shear angle, which represents an important parameter for the prediction of local wrinkling, while the input value is given by the curvature of an examined complex cavity. This approach was derived from Coutadin et al. and developed further [7]. In this previous research, an existing tool geometry is imported as an STL file and the curvatures of the cavity are calculated. In the areas that exceed a previously defined critical curvature value, a segmentation cut is applied. Sequencing is further performed through a genetic optimisation algorithm. In the work of Zimmerling et al. [8], the topology of the test geometry is imported into the convolutional neural network as greyscale images as well as the output of the shear angle. The approach presented in this paper differs from [7] by reducing the data set for the CNN to the 5 most frequently occurring curvature characteristics. This avoids the necessity of a continuous implementation of new test geometries, since the description of all forms of complex geometries is possible using the five main forms of curvature. The methodology behind the approach is illustrated in Fig. 1.

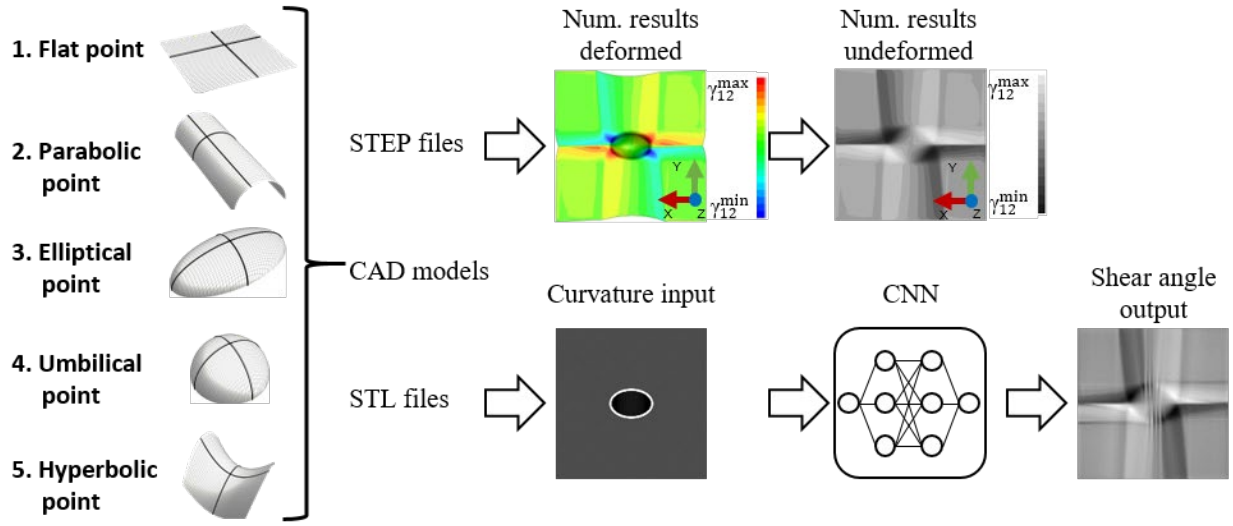

Fig. 1. Workflow of the curvature analysis approach.

The five relevant curvature characteristics are shown on the left. Out of these, the first four curvatures shown in Fig. 1 are considered in this paper. All curvatures are dependent on the two principal curvature components κ_1 and κ_2. If $\kappa_1 = \kappa_2 = 0$, a flat point results. Accordingly, a planar surface is defined by this point. A parabolic point exists if the product of the two curvatures is $\kappa_1 \cdot \kappa_2 = 0$, with $\kappa_1 + \kappa_2 \neq 0$. An elliptical point is defined by $\kappa_1 \cdot \kappa_2 > 0$. A special type of the elliptic point exists for $\kappa_1 = \kappa_2$. This is referred to as the umbilical point, which results in a hemispherical geometry. The case of a hyperbolic point, considered in further work, occurs if $\kappa_1 \cdot \kappa_2 < 0$. [9]

Parameterized CAD models were developed from the curvature components illustrated and a large number of geometry variants were created. From these, STL files were derived, which are used for the curvature calculation. In this work, the mean curvature H (see Eq. 1) is applied, which represents the arithmetic mean of the two principal curvatures.

$$H := \frac{1}{2}(\kappa_1 + \kappa_2) \tag{1}$$

Numerical models are built for the individual surface curvatures in order to create an FEM database for the surrogate model. The models represent the pure curvature types, therefore no boundary effects occur in the output of the shear angle. Therefore, the resulting shearing effects exclusively result from the curvature types.

The calculated curvature values are then combined with results on the shear angle of the simulations. As a result, the curvature values are assigned with the shear angle distribution for the material used and provides the surrogate model with a training data set. The coupling enables the surrogate model to predict complex geometries not previously trained, since the local geometric characteristics of the cavity can be reduced to the previously trained curvature characteristics.

Parametrization

For the creation of the CAD models, the parameterization of the ellipse and the paraboloid visualized in Fig. 2 is chosen. The outer dimensions of the die, which also equal the main dimensions of the organosheet, were left constant. For the ellipse, variants were created in the intervals shown for the radii R_{ye} and R_{xe} with a step size of 1 mm for the database. With the same step size, variants with variable radius R_{xp} and variable depth were created for the models of the paraboloid. For the visualisation of the occurring curvature characteristics of the geometries as well as for the representation of the simulation results in the undeformed sheet, greyscale images are used based on Zimmerling et al. [8]. The geometry variants created are further transferred as a step file to the automated numerical model generation in the software LS-Dyna.

Ellipse	Symbol	Parameter	Interval
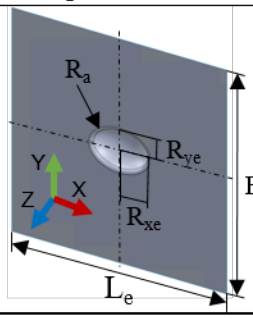	L_e	Length die ellipse	235 mm
	B_e	Width die ellipse	235 mm
	R_{ye}	Radius y-direction ellipse	20...50 mm
	R_{xe}	Radius x-direction ellipse	30…60 mm
	R_a	Outer Radius	4 mm
Paraboloid	**Symbol**	**Parameter**	**Interval**
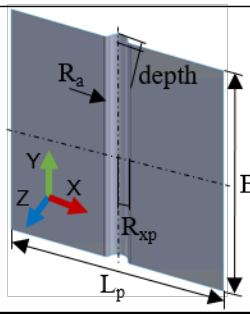	L_p	Length die paraboloid	235 mm
	B_p	Width die paraboloid	235 mm
	R_{xp}	Radius x-direction paraboloid	10…50 mm
	R_a	Outer Radius	4 mm
	depth	Depth paraboloid	10…60 mm

Fig. 2. Parametrisation of elliptical and parabolic models with the parameter-range for generation of the training dataset.

Numerical Model

In the FEM software tool LS-Dyna, an isothermal forming simulation is set up consisting of punch, die and sheet. The blank is a glass fiber reinforced organo sheet with polyamide 6 matrix (Tepex dynalite 102RG600(4)/47%). The fabric is an E-Glass roved in twill 2/2 style with 47% fiber content and a total thickness of 2 mm. In the forming simulation, the temperature is chosen marginally above the matrix melting temperature, which is around 220°C for polyamide 6. Punch and die are modelled as rigid bodies, while the organo sheet is described by the material card MAT_249_REINFORCED_THERMOPLASTIC [10]. Within this material card, the fibers are described as an anisotropic-hyperelastic material and the matrix as elasto-plastic. The material card has been calibrated and validated in previous work using tensile and bias extension tests. A disadvantage of the material card is the lack of options for implementing bending stiffnesses. For numerical models using shell elements, the stiffness is unrealistically high, due to the fact that in classical approaches such as the Kirchhoff theory, the bending stiffness is given by the tensile stiffness and thickness while slippage between fibers leading to lower bending stiffness is not considered [11]. Therefore, the bending behaviour is adjusted through the position and number of integration points to the neutral axis of the sheet [12]. The friction between the individual contact pairs was investigated using a friction test setup. From these investigations, values for the friction coefficients above the matrix melting temperature at 230°C are obtained and used.

As a result of the simulation, the shear angle is given, which is projected onto the mesh of the initial sheet. Therefore the element-size was set to 2 mm, resulting in a mesh with 117x117 elements. This is exported together with the element IDs and the coordinates of the nodal points in order to couple the shear angles with the curvatures of the cavity in the subsequent step.

Design of the Artificial Neural Network

In this research, CNNs, which are a kind of feed-forward network, are used because they are specially designed for spatially structured data such as the grey-scale mesh resulting from the previous chapter [8]. The basic structure of a CNN consists of an input, several convolutional and pooling layers and the output. The activity of each neuron is determined by stepwise comparison with smaller convolutional matrices (kernels) moved over the input. In the process, each kernel extracts different features from the input data, allowing the individual activated neurons of deeper layers to abstract only local sections of the entire input data and creating what is called a "feature map". In deeper layers, the data is further compressed, which enables the detection of more complex features. Subsequently, compressed data is decoded in the decoder by transposed convolutional layers. [13]

The CNN presented in this paper is built using the deep learning framework PyTorch and the library fastai. A total of 87 variants of ellipses, 31 paraboloids and 10 planar surfaces were taken as the dataset, which was split randomly into 90% training data and 10% validation data. The training data set was divided into 16 batches and a total of 300 epochs were trained. First, the elliptical variants were trained for 200 epochs, followed by the parabolic and planar surface variants. The batch normalisation implemented in PyTorch counteracts an internal covariate shift and ensures a high learning rate in the network [14]. In a subsequent step, we tested variants of each geometry with out-of test range parameters and two previously unseen double-dome geometries with the CNN in order to investigate the prediction quality of this curvature approach.

Results and Discussion

Fig. 3 shows the results of the training geometries of a flat surface (plate), the parabolic and the elliptical geometries. In addition to the listed geometries, the curvatures serving as input for the CNN and the results of the FEM simulations are presented as comparative images. The simulation results are visualised on the undeformed blank and display the shear angle distribution as a greyscale image. The representation of the curvatures and the FEM simulations each represent normalised values within fixed limits to ensure comparability. Furthermore, three result values of the prediction are shown. The root mean square error (RMSE) along with the minimum and maximum shear angle differences $\left|\Delta\gamma_{12}^{min}\right|$ and $|\Delta\gamma_{12}^{max}|$ of the prediction compared to the FEM results. The shear angle differences are calculated by subtracting the shear angle obtained from the numerical model from the predicted shear angle.

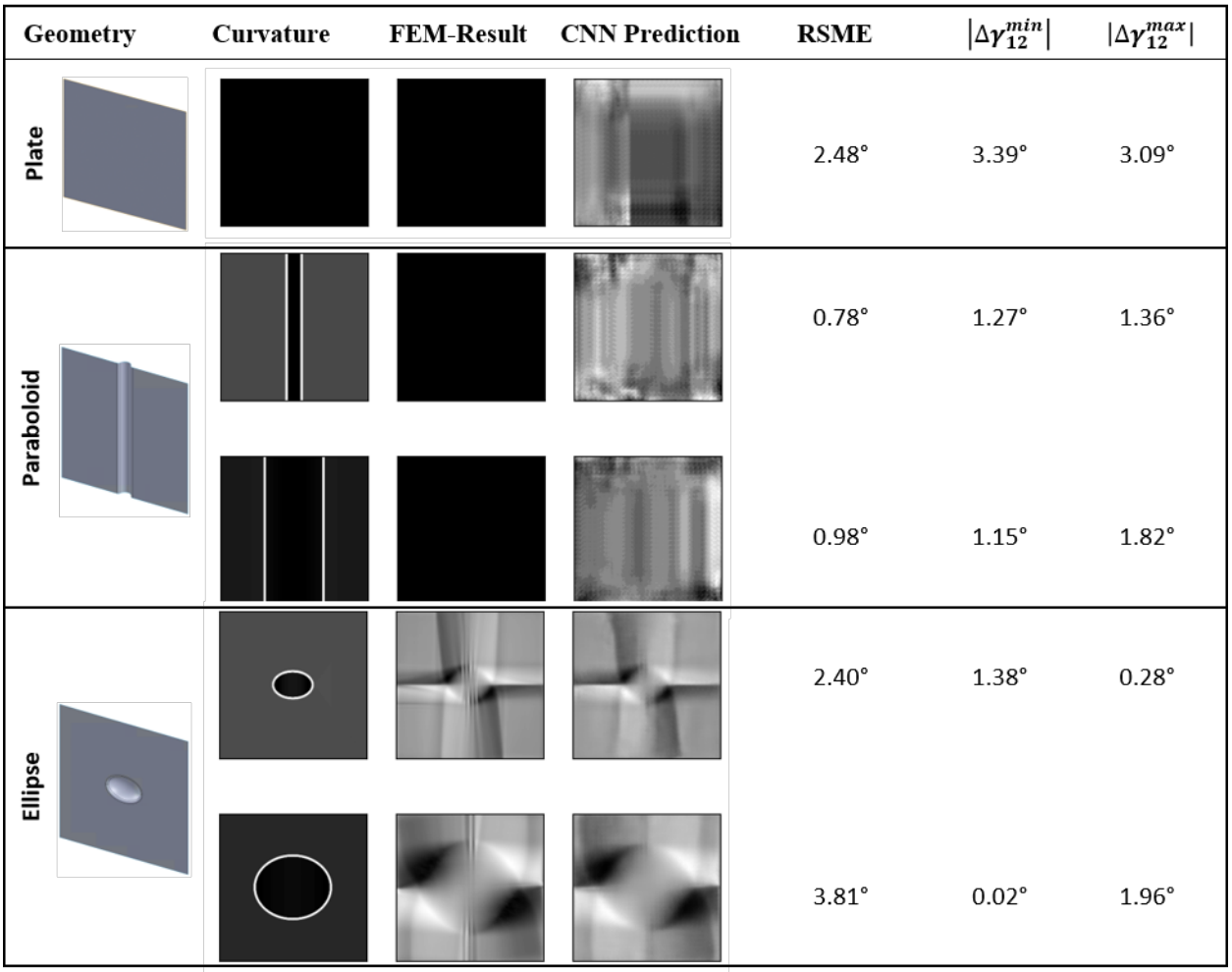

Fig. 3. Visualisation of the test geometries, their curvatures and the results for the shear angle from the FEM-Model and from the CNN Prediction.

For ellipse and paraboloid, the smallest (top) and the largest (bottom) parameter combination are shown, which were examined during testing, but not part of the training data. The comparison of the result images and values shows a high agreement between simulation and prediction of the CNN. Here, the percentage error values for the plate are 4.33 %, while the error for the parabolic validation geometries is below 2 %. The error of the ellipse can also be described as low with 4.19 % for the smallest parameter combination (top image ellipse in Fig. 3) and 6.65 % for the largest combination, so that a reliable prediction of the shear angle can be achieved through the curvature images with a very small data set.

As a final validation, a complex geometry of a double dome, which was not part of any previously used dataset, was examined with the CNN. Two configurations were chosen as examples, which are visualised in Fig. 4. The double dome is composed of the two trained curvature variants of the ellipse and the paraboloid. The network was presented with both a double dome with identical ellipses (bottom) and a double dome with elliptical areas of different sizes (top).

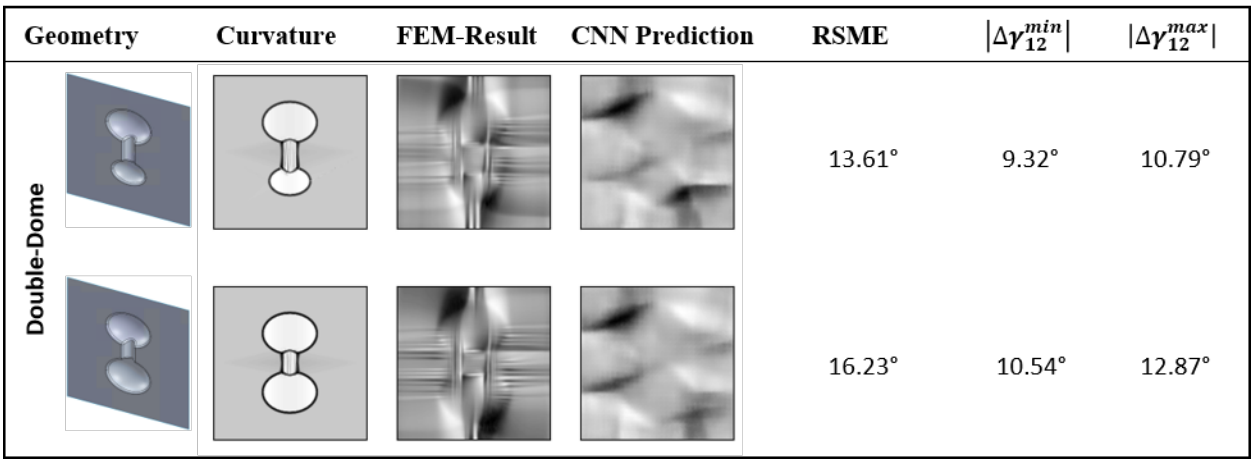

Fig. 4. Visualisation of Double-Dome Geometry, its curvatures and the results for the shear angle from the FEM-Model and from the CNN Prediction.

As shown in the result values, the RSME of the double-dome geometry with elliptical areas of different sizes is lower than the RSME of the double-dome geometry with two ellipses of the same size. Nevertheless, both errors are larger than the test errors of the elliptical, parabolic and planar geometries, with a percentage deviation of over 20 %. This is particularly visible in the transition between the elliptical and parabolic sub-area, which is not reliably predicted by the CNN. One reason for this may be the hyperbolic course in the transition, so that in further work the fifth curvature variant of hyperbolic geometries should be implemented for a more accurate result.

Summary

In the thermoforming process for manufacturing flat components from thermoplastic fiber composites, one of the main deformation mechanisms is shear deformation. As a result of high shear angles in the composite, wrinkles occur during the forming process. Predicting the shear angle as a parameter for localisation of upcoming wrinkles is therefore of central importance, hence the reliable prediction of this parameter was carried out in this paper by means of a Convolutional Neural Network. The results of numerical forming simulations provided the basis for the data. The training of the network was done by using only the occurring curvatures to predict the forming result of unseen, complex geometries (double dome) on the basis of the shear angle with a currently increased error in the range of 23 % to 28 %. In further work, the remaining curvature of a hyperbolic structure will be added to the database and further adjustments to the CNN will be applied. This should ensure in future that the neural network can reduce all complex geometries to the 5 curvature characteristics and thus provide a reliable prediction with a lower error for the selected target variable.

Acknowledgements

The IGF-Project “Material-specific thermoforming through controlled mould elements” of the European Research Association for Sheet Metal Working (EFB e.V.) was funded by the Federal Ministry of Economics and Energy (BMWi) under the funding number 20677BG of the German Federation of Industrial Research Associations (AiF) on the basis of a decision by the German Bundestag. The authors are thankful for this financial support.

References

[1] C. Hopmann, M. Walter, Einführung in die Kunststoffverarbeitung, Carl Hanser Verlag GmbH & Co. KG, 2015.
[2] R. Azzouz, S. Allaoui, R. Moulart, Composite preforming defects: a review and a classification, Int. J. Mater. Form. 14 (2021) 1259-1278. https://doi.org/10.1007/s12289-021-01643-7

[3] U. Breuer, M. Neitzel, V. Ketzer, R. Reinicke, Deep drawing of fabric-reinforced thermoplastics: Wrinkle formation and their reduction, Polym. Compos. 17 (1996) 643-647. https://doi.org/10.1002/pc.10655
[4] K. Dröder, Prozesstechnologie zur Herstellung von FVK-Metall-Hybriden, Springer Berlin Heidelberg, Berlin, Heidelberg, 2020.
[5] J. Middelhoff, A. Hürkamp, K. Dröder, Numerical Modelling of a Demonstrator to Investigate Geometric Parameter Influences on the Thermoforming of Fiber-Reinforced Thermoplastics, Proceedings of the 20th European Conference on Composite Materials, ECCM20, Lausanne, Switzerland, 2022
[6] C. Zimmerling, D. Dörr, F. Henning, L. Karger, A meta-model based approach for rapid formability estimation of continuous fibre reinforced components, AIP Conference Proceedings, Volume 1960(1), 2018, pp. 020042. https://doi.org/10.1063/1.5034843
[7] S. Coutandin, Prozessstrategien für das automatisierte Preforming von bebinderten textilen Halbzeugen mit einem segmentierten Werkzeugsystem, Dissertation, Shaker Verlag
[8] C. Zimmerling, D. Trippe, B. Fengler, L. Karger, An approach for rapid prediction of textile draping results for variable composite component geometries using deep neural networks. In: Proceedings of the 22nd International ESAFORM Conference on Material Forming: ESAFORM 2019, AIP Publishing, 2019, pp. 20007 https://doi.org/10.1063/1.5112512
[9] W. Kühnel, Differentialgeometrie: Kurven - Flächen - Mannigfaltigkeiten, 5., aktualisierte Auflage, Springer eBook Collection. Vieweg+Teubner, Wiesbaden, 2010
[10] A. Hürkamp, R. Lorenz, T. Ossowski, B.-A. Behrens, K. Dröder, Simulation-based digital twin for the manufacturing of thermoplastic composites, Procedia CIRP 100 (2021) 1-6. https://doi.org/10.1016/j.procir.2021.05.001
[11] P. Boisse, R. Akkerman, P. Carlone, L. Kärger, S.L. Lomov, J.A. Sherwood, Advances in composite forming through 25 years of ESAFORM, Int. J. Mater. Form. 15 (2022). https://doi.org/10.1007/s12289-022-01682-8
[12] M. Grubenmann, J. Heingärtner, P. Hora, D. Bassan, Influence of temperature on in-plane and out-of-plane mechanical behaviour of GFRP composite. J. Phys.: Conf. Ser. 1063 (2018) 12146. https://doi.org/10.1088/1742-6596/1063/1/012146
[13] S. Kollmannsberger, D. D'Angella, M. Jokeit, L. Hermann, Deep Learning in Computational Mechanics: An Introductory Course (Studies in Computational Intelligence, 977), Springer International Publishing, Cham, 2021
[14] S. Ioffe, C. Szegedy, Batch Normalization: Accelerating Deep Network Training by Reducing Internal Covariate Shift, In: International Conference on machine learning, 2015 pp. 448-456. https://doi.org/10.48550/arXiv.1502.03167

Materials Research Proceedings 28 (2023) 393-398 https://doi.org/10.21741/9781644902479-43

Investigation on the pultrusion of thermoplastic preimpregnated polypropylene-glass tapes

TUCCI Fausto[1,a *], RUBINO Felice[2,b], ESPERTO Vitantonio[1,c], PASQUINO Germana[3,d] and CARLONE Pierpaolo[1,e]

[1]Department of Industrial Engineering, University of Salerno, 132 Via Giovanni Paolo II, 84084, Fisciano (SA), Italy

[2]Department of Civil and Mechanical Engineering, University of Cassino and Southern Lazio, Folcara, 03043, Cassino (FR), Italy

[3]Universitas Mercatorum, 10 Piazza Mattei, 00186, Rome (RM), Italy

[a]ftucci@unisa.it, [b]frubino@unisa.it, [c]vesperto@unisa.it, [d]germana.pasquino@unimercatorum.it [e]pcarlone@unisa.it

Keywords: Pultrusion, Thermoplastic, Polypropylene, Prepregs, Tapes

Abstract. Pultrusion processes have been widely used and developed to produce composite profiles in fiber-reinforced thermoset. Recently industry and research community are investigating the adoption of thermoplastic polymers in the production of pultruded components exhibiting structural stability at higher temperatures and improved sustainability. Aiming to study the thermoplastic pultrusion process and how the process parameters settings affect the composite profiles produced, a laboratory-scale pultrusion line has been designed and produced. The pultrusion die is fed by polypropylene pre-impregnated tapes reinforced by unidirectional continuous glass fibers. It consists of a tapered converging cavity heated by electrical plates governed by PID controllers and a straight cooling die. This work aims to study the feasibility of the process, the consolidation of the tapes, and the interactions between the processed materials and the cavity walls by using embedded traveling thermocouples and load cells. The experimental test presented in this paper highlights that the preimpregnated tapes processed have been well-consolidated with the parameters adopted and the pultruded profile presents good quality at a visual inspection of the external surfaces and cross-section, indicating a good melting and hardening of the polypropylene matrix. The interactions between the processed materials and the die walls are evaluated by means of a cross-analysis of thermal and load data.

Introduction

Pultrusion is a widely consolidated process for the manufacturing of constant cross-section profiles in continuous fibers reinforced thermoset [1]. The success of this process is related to several factors: i) the high tensile properties due to the orientation and the volume fraction of the reinforcement; ii) the continuous nature of the process, which in turn guarantee high productivity, repeatability, and automation; iii) the low energy and human intervention required; iv) low or null waste of raw materials [2,3]. Due to their properties, pultruded profiles are widely employed in many industrial or civil sectors [4,5]. Traditionally, thermoset systems have been preferred for their low viscosity and their easy manufacturability. Nevertheless, generally, thermosets presents several drawbacks if compared to thermoplastics, namely lower in-service temperature, lower mechanical properties, production of dangerous volatile compounds due to the polymerization during the manufacturing or process related defects and distortions [6,7]. Moreover, the thermoplastic polymers can be remelted and re-used, promoting a more sustainable production [8].

Of course, the adoption of a different matrix system requires a different pultrusion line, equipped with features designed to process thermoplastics. The major difference stands in the

Content from this work may be used under the terms of the Creative Commons Attribution 3.0 license. Any further distribution of this work must maintain attribution to the author(s) and the title of the work, journal citation and DOI. Published under license by Materials Research Forum LLC.

presence of a heating die and a successive cooling die. The former is responsible for the matrix melting and flowing; the latter give place to the matrix cooling and hardening [9]. In the thermoplastic pultrusion the reinforcement impregnation can be done either online or offline. In the first case, the polymeric system is heated up, in order to minimize the viscosity and injected through the advancing fibers within the heating die. The offline impregnation is based on the usage of preimpregnated tissues or tapes [10]. The pultrusion of preimpregnated tapes guarantees a better distribution of the matrix and the absence of dry zones, but it requires longer crossing time to ensure the tapes consolidation in a unique composite profile, and therefore, a lower processing speed. In the case of pultrusion of preimpregnated tapes, the heating die presents a highly sloped tapered chamber, converging to the final cross-section shape. Such slope constrains the advancing tapes and determines an increase in the pressure, which in turn confers the shape of the profile, promotes the transversal flow of the melted matrix and consolidates the tapes. The cooling die presents a straight cavity with the shape of the final cross-section which holds the materials in their positions while the matrix is hardening [11,12].

Therefore, the main factors affecting the thermoplastic pultrusion are the heating ramp, determining the thermoplastic softening and melting, the transversal compression, determining the transversal flow of the polymer and the compaction of the tapes, and the cooling ramp, hardening the thermoplastic. The main challenges in the monitoring of the process and the measurement of the variables of interest in pultrusion are related to the fact that all the transitions and shaping phases are included into a closed non-transparent die. The method of the traveling thermocouple is the most commonly adopted to collect the internal temperature data [7]. It is carried out by connecting a thermocouple to the advancing materials at the die entrance and measure the temperature during the time necessary to cross the pultrusion die. The data collected in the time domain can be transferred to the position domain since the velocity of the process is constant and known and it corresponds to the pulling speed. The evaluation of the pressure can be achieved by means of pressure sensors [13], nevertheless these sensors cannot be fixed easily in a pultrusion die without altering its geometry. Moreover, the measurement achieved is representative of the localized pressure at the sensor location, while the pressure in a tapered cavity exhibits a marked variability along with the die [14]. More pieces of information on the advancing materials transitions and on their interaction with the die cavity, can be indirectly inferred from the measurement of the pulling force, since it strictly depends on the nature of the interaction between processed materials and the die cavity walls [15].

This study aims to analyze the pultrusion of tapes in glass fiber reinforced polypropylene pultruded in a laboratory scale line. The internal temperature and the pulling force data have been analyzed to detect, describe, and quantify the main behaviors occurring along with the pultrusion die.

Materials and Methods

The pultrusion line adopted in the present experimental activity consists of a 300 mm heating die followed by a 300 mm cooling die. The line adopted is illustrated in Fig. 1a.

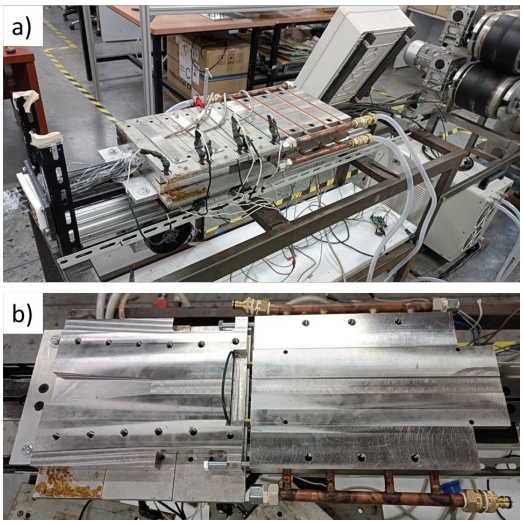

Fig. 1. a) Thermoplastic pultrusion setup; b) view of the disassembled lower sides of the heating die and cooling die.

In the thermoplastic pultrusion setup shown in Fig. 1a, the advancing direction is oriented from the left towards the right. The preimpregnated tapes approach the pultrusion line presents from the heating die side, where three couple of electric platens are provide heating energy to the system. The platens' powers are governed by three PID controllers, receiving the feedback signals from three sensors fixed on each of the upper side platens. The cooling die is mechanically fixed downstream the heating die. The cooling system is based on water circulation through a copper pipes grid embedded within milled cavities. The water cooling and circulation is governed by an industrial chiller, with temperature setpoint of 13°C. Fig. 1b shows the internal cavities of the disassembled lower sides. The heating die presents a tapered converging zone to favor the tapes entrance and to compact them, followed by a straight cavity with constant cross-section. The tapered zone has a length of 160 mm. The cavity of the cooling die is straight with constant rectangular cross-section 25 mm wide and 4 mm thick.

This setup has been used to pultrude preimpregnated tapes provided by CompTape BV (Delft, Netherlands) in glass roving reinforced polypropylene. Each tape has dimensions of 6.35 mm in width and 0.6 mm in thickness and contains the 60% in volume of reinforcement. The tapes have been arranged in 6 layers of 4 tapes per layer. With this arrangement, 24 preimpregnated tapes have been pultruded, to achieve a profile with a fiber volume fraction of 55%. Considering the polypropylene matrix, a temperature of 200°C has been set for the platens. The dies have been mounted on supports free to slide on a longitudinal guide. At the limit of the guide a compressive button load cell is fixed to measure the pulling force (Fig. 2b). The pulling system, consisting of counter-rotating caterpillars, moves the tapes at a velocity of 170 mm/min.

The internal temperature of the advancing tapes within the pultrusion dies has been measured using the traveling thermocouple method: Once the process is stationary (the pulling force are stable), the bulb of a wire thermocouple is connected to one of the tapes, in such a way to have the bulb between the third and the fourth layer and at the middle of the pultruded width. The aim is to measure the temperature of a point as close as possible to the barycenter of the cross-section. The wire must be as thin as possible to have a low invasive measure. In this case, the two wires for the two conductor alloys of the k-type thermocouple (chromel-alumel) have diameter of 0.2 mm. Once the bulb crosses the entire length of the two dies, the wires have been cut.

During pultrusion, the load cell measures the overall force resisting to the pulling. Such force is related to the interactions arising at the contact between dies' walls and pultruded materials. The

local interaction between die and advancing materials has been evaluated cutting the tapes at the heating die inlet and analyzing the unloading curve, as described in [16].

The collection of the data acquired by the load cell and the thermocouple has been managed using an Arduino board equipped with signals' amplifiers (Fig 2a) and connected to a computer.

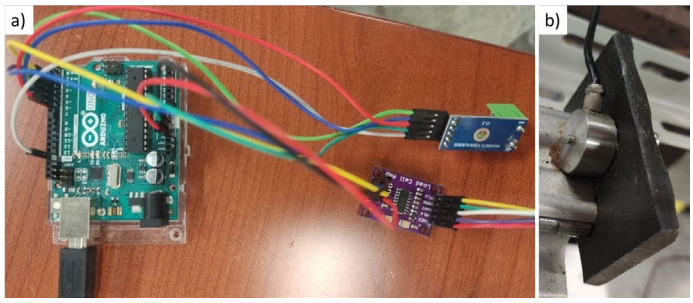

Fig. 2. a) Data collection management board equipped with signals' amplifiers; b) compressive button load cell fixed at the guide limit.

Results and Discussion

The described setup for thermoplastic tapes pultrusion has produced well compacted and continuous pultruded composites.

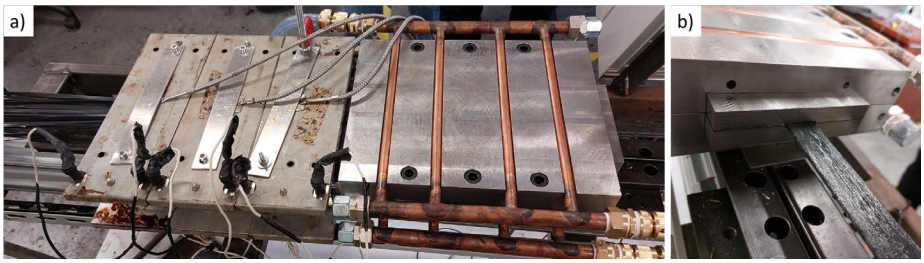

Fig. 3. a) Pultrusion setup while processing glass-polypropylene tapes; b) obtained pultruded profile.

Fig. 3a shows the pultrusion dies during the process. It is worth noting the tapes approaching to the heating die inlet. Each tape is separated with each other, and all of them are converging driven by the shape of the heating die cavity. At the cooling die outlet, the pultruded profile appears continuous and compacted, as demonstrated in the close up in Fig. 3b.

The internal temperature of the pultruded materials acquired by the traveling thermocouple and the load discharge curve measured by the load cell is reported in Fig. 4.

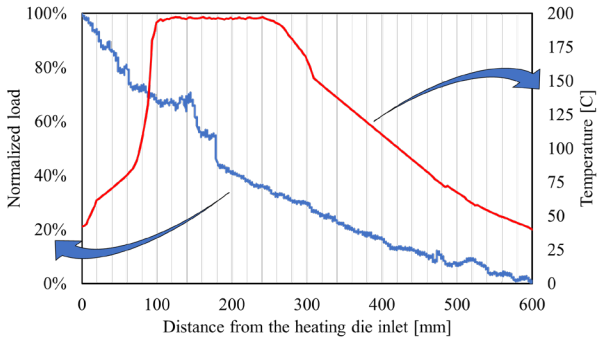

Fig. 4. Total load discharge curve and internal temperature of the advancing materials along with the heating and the cooling dies.

The tapes reach the heating die entrance with a temperature slightly superior to the environmental conditions, due to the diffusion in the air of the heat from the heating die. The temperature increase is slight along with the initial 80 mm. Indeed, at the heating die entrance, the cavity is wider, and the tapes are not in direct contact with each other and with the die. After this point the compaction and compression of the tapes driven by the converging walls determines a sharp increase in the temperature, which reaches approximately 195°C. This temperature is kept constant until 250 mm of distance from the heating die inlet. Even if the cooling die starts from 300 mm from the inlet, the heat dissipation of the cooling fluid affects also the temperature of the final portion of the heating die. The transition effects are visible in a continuous decrease in the slope of the temperature curve until the end of the heating die. Along with the last 300 mm, the heat dissipation gives place to a linear decrease in the temperature.

The polypropylene transitions are driven by the temperature and affect the interaction with the dies' walls. The earliest 150 mm are characterized by an irregular decrease of the total load with large fluctuations. Indeed, in this zone, the tapes are not compressed against the die walls. The contact is furthermore irregular if compared to the stationary process because of the absence of the pretension due to the cut of the tapes. The tape compaction can be recognized by the drop in load between 140 mm and 160 mm of distance from the die inlet. The melting temperature is reached and overcome starting from 100 mm from the heating die inlet. The effects of melting and rheological evolution of polypropylene can be observed clearly between 160 mm and 180 mm by a marked drop in the resisting load. Drops in the cumulated load indicate peaks in the local force. Indeed the thermoplastic passes from a solid state to a gel state, characterized by an adhesive local interaction typical of the high viscosity fluids, and finally reaches the melt state. The low viscosity reached by the polypropylene after 180 mm from the die inlet gives place to a lubricant effect promoting the sliding of the materials. The main resistance between 180 mm and 350 mm from the heating die inlet is related to the viscous drag. The linear decrease in the total load curve indicates a constant resistant force along with this zone. The polypropylene solidifies again in the last 250 mm from the inlet. The transition to a solid compact composite determines a solid friction interaction between the die walls and the pultruded profile surface. This interaction can be recognized by the fluctuations visible from 350 mm from the heating die inlet and becoming larger in the last 150 mm of the die.

Summary

This work presents an experimental setup for the pultrusion of glass/polypropylene preimpregnated tapes. The measurement of the internal temperature evidenced that the polypropylene melts in the heating die, where it is compacted and shaped. The heat dissipation in the cooling die gives place to a fast solidification of the matrix. The compaction of the tapes gives place to the most prominent local loads peaks, while the melted polypropylene acts as a lubricant, promoting a regular and smooth sliding of the advancing taps.

Acknowledgement

Authors gratefully acknowledge CompTape BV (Delft, Netherlands) for its precious support in the choice of materials and for the tapes supply.

References

[1] P. Boisse, R. Akkerman, P. Carlone, L. Kärger, S. V. Lomov, J.A. Sherwood, Advances in composite forming through 25 years of ESAFORM, Int. J. Mater. Form. 15 (2022). https://doi.org/10.1007/s12289-022-01682-8

[2] L. Nickels, The future of pultrusion, Reinf. Plast. 63 (2019) 132-135. https://doi.org/10.1016/j.repl.2019.01.003

[3] A.M. Fairuz, S.M. Sapuan, E.S. Zainudin, C.N.A. Jaafar, Polymer composite manufacturing using a pultrusion process: A review, Am. J. Appl. Sci. 11 (2014) 1798-1810. https://doi.org/10.3844/ajassp.2014.1798.1810
[4] A. Vedernikov, A. Safonov, F. Tucci, P. Carlone, I. Akhatov, Pultruded materials and structures: A review, J. Compos. Mater. 54 (2020) 4081-4117. https://doi.org/10.1177/0021998320922894
[5] P. Zhou, C. Li, Y. Bai, S. Dong, G. Xian, A. Vedernikov, I. Akhatov, A. Safonov, Q. Yue, Durability study on the interlaminar shear behavior of glass-fibre reinforced polypropylene (GFRPP) bars for marine applications, Constr. Build. Mater. 349 (2022) 128694. https://doi.org/10.1016/j.conbuildmat.2022.128694
[6] A. Vedernikov, A. Safonov, F. Tucci, P. Carlone, I. Akhatov, Modeling Spring-In of L-Shaped Structural Profiles Pultruded at Different Pulling Speeds, Polym. 13 (2021). https://doi.org/10.3390/polym13162748
[7] A. Vedernikov, F. Tucci, P. Carlone, S. Gusev, S. Konev, D. Firsov, I. Akhatov, A. Safonov, Effects of pulling speed on structural performance of L-shaped pultruded profiles, Compos. Struct. 255 (2021) 112967. https://doi.org/10.1016/j.compstruct.2020.112967
[8] R. Bernatas, S. Dagreou, A. Despax-Ferreres, A. Barasinski, Recycling of fiber reinforced composites with a focus on thermoplastic composites, Clean. Eng. Technol. 5 (2021) 100272. https://doi.org/10.1016/j.clet.2021.100272
[9] K. Minchenkov, A. Vedernikov, Y. Kuzminova, S. Gusev, A. Sulimov, A. Gulyaev, A. Kreslavskaya, I. Prosyanoy, G. Xian, I. Akhatov, A. Safonov, Effects of the quality of pre-consolidated materials on the mechanical properties and morphology of thermoplastic pultruded flat laminates, Compos. Commun. 35 (2022) 101281. https://doi.org/10.1016/j.coco.2022.101281
[10] P. Simacek, S.G. Advani, Simulating tape resin infiltration during thermoset pultrusion process, Compos. Part A Appl. Sci. Manuf. 72 (2015) 115-126. https://doi.org/10.1016/j.compositesa.2015.01.020
[11] K. Minchenkov, A. Vedernikov, A. Safonov, I. Akhatov, Thermoplastic pultrusion: A review, Polym. 13 (2021) 1-36. https://doi.org/10.3390/polym13020180
[12] A. Vedernikov, K. Minchenkov, S. Gusev, A. Sulimov, P. Zhou, C. Li, G. Xian, I. Akhatov, A. Safonov, Effects of the Pre-Consolidated Materials Manufacturing Method on the Mechanical Properties of Pultruded Thermoplastic Composites, Polym. 14 (2022) 1-15. https://doi.org/10.3390/polym14112246
[13] F. Tucci, R. Bezerra, F. Rubino, P. Carlone, Multiphase flow simulation in injection pultrusion with variable properties, Mater. Manuf. Process. 35 (2020) 152-162. https://doi.org/10.1080/10426914.2020.1711928
[14] S.S. Rahatekar, J.A. Roux, Numerical simulation of pressure variation and resin flow in injection pultrusion, J. Compos. Mater. 37 (2003) 1067-1082. https://doi.org/10.1177/0021998303037012005
[15] A.A. Safonov, P. Carlone, I. Akhatov, Mathematical simulation of pultrusion processes: A review, Compos. Struct. 184 (2018) 153-177. https://doi.org/10.1016/j.compstruct.2017.09.093
[16] F. Tucci, D. Larrea-Wachtendorff, G. Ferrari, P. Carlone, Pulling force analysis in injection pultrusion of glass/epoxy composites, Mater. Manuf. Process. 00 (2022) 1-12. https://doi.org/10.1080/10426914.2022.2049296

Materials Research Proceedings 28 (2023) 399-406 https://doi.org/10.21741/9781644902479-44

Crush core forming: An innovative technology to manufacture structural sandwich parts with variable thickness

SORRENTINO Luca[1,a], BELLINI Costanzo[1,b], PARODO Gianluca[2,c] and RUBINO Felice[1,d *]

[1]Department of Civil and Mechanical Engineering, University of Cassino and Southern Lazio, Cassino, Italy

[2]Department of Industrial Engineering, University of Salerno, Via Giovanni Paolo II, 132, 84084 Fisciano, Italy

[a]luca.sorrentino@unicas.it, [b]c.bellini@unicas.it, [c]gparodo@unisa.it, [d]rubino.felic@gmail.com

Keywords: Crush Core Forming, Sandwich Structures, Variable Thickness, Composite Materials

Abstract. Sandwich structures, constituted in honeycomb core and skin in composite material, are usually employed to produce parts having a constant thickness or simple shape. Indeed, sandwich components with complex shapes, curvature or varying thickness are costly to manufacture due to the preliminary machining operations required on the core prior the molding process. A novel approach to manufacture complex sandwich structures, knows as Crush Core Forming (CCF) process, consisting in press-forming simultaneously the core material and the skins into the shape is under study. Such a method is potentially able to increase the production rate and lowering the overall costs. The present work aims to develop an experimental route to produce sandwich panels by means of CCF process and build a FE model of the forming process and validate it against the experimental studies. Experimental study was conducted to derive the fundamental parameters and properties for core and skins to be added in the FEM model of the CCF process. After, the numerical model was implemented to simulate the forming of the core and skins. Finally, a laboratory scale sandwich part was produced to validate the model outputs and assessing the reliability of the proposed approach.

Introduction

Composite sandwich structures offer opportunities of lightweight design and sustainable mobility thanks to their high strength-to-weight ratio, especially bending and torsional stiffness. Sandwich panels are currently employed in several fields, from aeronautics, to automotive and marine transportation [1]. Examples of application include aircraft interior, car body panel, boat hulls [2]. Sandwich panels usually are produced by means of autoclave processes bonding the composite skins with the core under the action of pressure and heat, however in the last years new pre-pregs, which can be processed by out-of-autoclave (OoA) techniques and can be cured under vacuum condition and with conventional ovens, have been commercialized [2,3]. Moving from the autoclave manufacturing toward OoA processes allows to significant cost saving and faster production routes without sacrificing the performances of the components [4–7]. Despite these progresses, composite sandwiches are commonly produced only in simple shape and have constant thickness.

For the manufacturing of more complex shape structural panels, the core is generally obtained through machining operations, while the bonding and curing of the skins are made as subsequent steps [8]. Recently, the use of additive processes allows to realize core with high strength-to-weight ratio and with more complex shapes known as lattice structures [9,10]. However, the low production rate does not allow the development of such technology for series products.

Content from this work may be used under the terms of the Creative Commons Attribution 3.0 license. Any further distribution of this work must maintain attribution to the author(s) and the title of the work, journal citation and DOI. Published under license by Materials Research Forum LLC.

Recently, in high-volume production application, such as lightweight automotive interiors, a reduction in production time is required to manufacture sandwich structures compatible with market demands. For this purpose, first studies on core crushing are present in scientific literature [11,12]. Forming behavior of curved sandwich plates differ from that observed in monolithic sheet material and in composite panels due to the presence of the core material, which affects the overall deformation of the sandwich plate and the occurrence of surface defects [12]. During the manufacturing core and skins are subject to complex load and multi-axial deformations, including in-plane tension/compression and shear and out-of-plane bending [12].

Typical issues observed during the forming process are surface waviness, local buckling, fracture of the skins as well as crushing of the core structure, and they were ascribed as the main factors limiting the formability of thin sandwich panels [11–15]. Optimization of the core design, so that it can provide sufficient resistance against skin buckling and core cell collapsing, demonstrated to be able to mitigate these defects and, therefore, plastic forming method could be used to produce complex shaped panels from flat sandwich plates [12]. In this context, development of numerical simulation techniques for the sandwich forming process able to predict the forming behaviors of core and skins and the forming-induced defects would be helpful. In very recent works, Cai et al. [12] and Chen et al. [11] proposed finite element models and analytical models to determine the main failure factors in plastic forming of curved sandwich panels. The first authors investigated the multi-point forming of sandwich structures having polyurethane egg-box-like core and aluminum face sheets. They observed that the limits in formability are mainly related to occurrence of wrinkling or dimpling on the face sheets, while the core cell fracture has lower influence [12]. The other authors developed a multiscale model of the sandwich structure having composite skins and honeycomb cellular core. The results indicate that the formability of sandwiches with complex curvature is due to the local crushing of the core. In the authors' best knowledge, besides these few contributions no other works dealing with numerical simulation or experimental approach are available for the published literature, especially in the case of composite skinned sandwiches for structural applications. Moreover, there are no studies that investigate not only the plastic forming process of the core but also the efficacy of the bonding between skins/core and the resin cure of the skins in a one-shot forming process of structural parts. In the present manuscript a novel approach to manufacture complex sandwich structures, knows as Crush Core Forming (CCF) process, consisting in press-forming of both core and skins in a one-shot operation, is under study. Such a method is potentially able to increase the production rate and lowering the overall costs. The present work aims to develop an experimental route to produce sandwich panels by means of CCF process and build a FE model of the forming process and validate it against the experimental studies. In fact, compression tests were performed on the honeycomb core to estimate the deformability and the densification of the core material under the action of the forming load, while the composite skins were subjected to bias extension and cantilever test to assess their formability. These properties were used as input data for the FEM model developed to simulate the forming of the core and skins and estimate the occurrence of forming-induced defects. A laboratory scale sandwich part was produced to validate the model outputs and assessing the reliability of the proposed approach.

Materials and Methods

Fig. 1 shows the case study designed for the investigation of the CCF process. For the forming process, a press system was used with heated plates up to 250°C with dimensions 400x400 mm^2. EP121-68-40 fiberglass prepreg impregnated with 40% epoxy resin from Gurit Ltd was used as face sheets for the sandwich panels. It is a prepreg with 8H satin texture and a resin cure temperature of 120°C. The skins were produced with 2 plies layered with rolling direction in the direction of the long side of the panel.

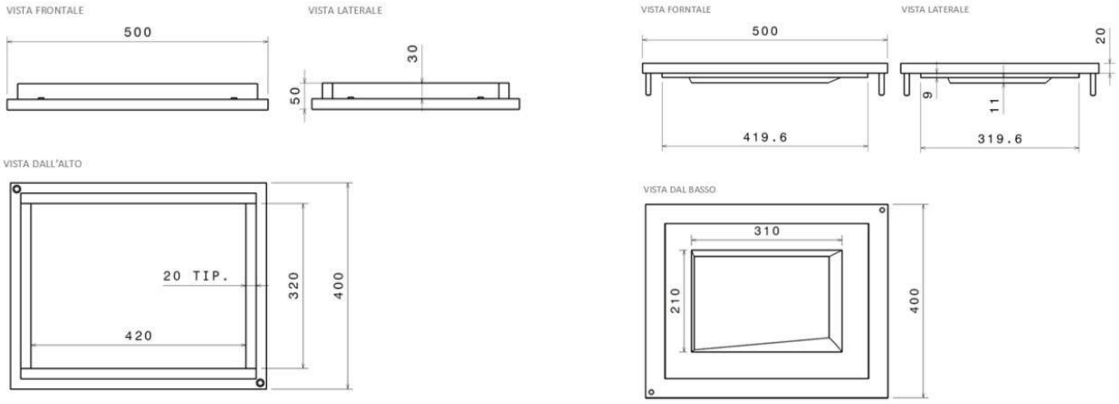

a) b)

Fig. 1. Scheme of the upper half mold (a) and lower half-mold (b) for the case study considered (dimensions in mm).

The hexagonal cell honeycomb HRH10-3.2-48 from Hexcel HexWeb was adopted as core. It is a core in Nomex that has cell dimensions of 3.2 mm, height of 19 mm and a density of 48 kg / m^3. The characterization of the core was conducted according to ASTM C365 along the thickness of the core, both at room temperature and at the prepreg cure temperature of 120°C. The compression tests were conducted with three replicas for each test temperature (see Fig. 2).

a) b)

Fig. 2. Compression test of the core: a) During test; b) at the end of the test.

The formability of prepreg skin was assessed by bias extension test (Fig. 3) and by cantilever testing, respectively for the in-plane shear behavior and the out-of-plane bending behavior. The specimens for the bias extension test are 50 mm x 200 mm in dimension and were tested at testing speed of 50 mm/min. Three replications were considered for the test. ASTM D1388 standard was adopted for the cantilever test, which recommends specimens with size of 10x100 mm^2 and an overhang length of 50 mm. Five replications were considered.

Materials Research Proceedings 28 (2023) 399-406 https://doi.org/10.21741/9781644902479-44

Fig. 3. Bias extension test per EP121-68-40.

Once the single parts of the sandwich have been characterized, the CCF process was conducted. The optimal process parameters were determined by the trial-and-error method, evaluating the goodness of the adhesion between skin and core through ultrasonic non-destructive testing. The process parameters, which resulted in free-defects sandwich panels, are: 100 kN closing force, molds temperature of 120°C, holding time of 90 min. The temperature trend on the mold was measured by using J-type thermocouples placed inside the mold as shown in Fig. 4. Once the cure of the skins was completed, the mold was opened, and the component extracted.

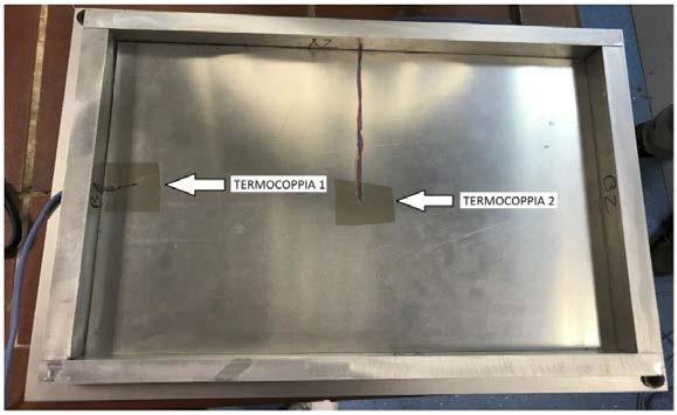

Fig. 4. Locations of the thermocouples on the surface of upper half-mold.

The numerical analysis was conducted by adding the properties of the materials, derived from the experimental characterization in the PAM-FORM software developed by Esi Group. For the present case study, brick-type and shell elements were considered for the core and skins, respectively (see Fig. 5 and 6). Specifically, for the skins and tools Belitschko-Tsai type 4-node square elements were used, while Flanagan-Belytschko type 8-node elements were used for the core. The tools were modeled as rigid bodies, while the mechanical behavior of the core and skins was implemented in the software as a point list.

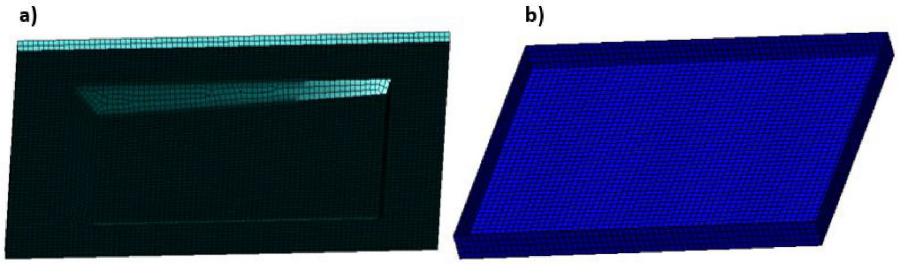

Fig. 5. CAD tools in PAM-FORM environment: a) upper mold; b) lower mold.

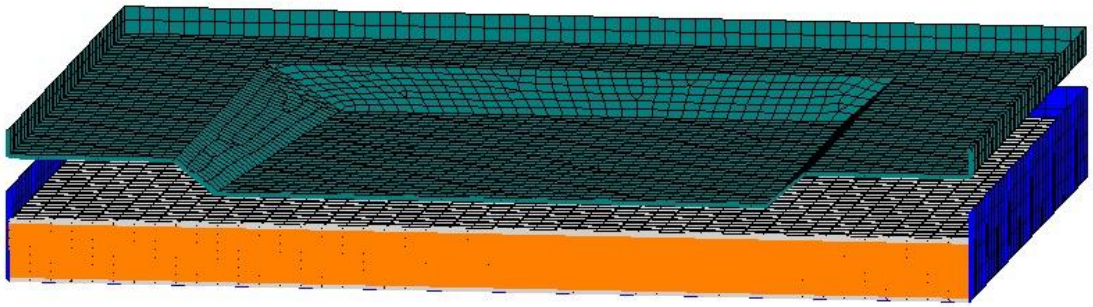

Fig. 6. Section view of CCF process developed for the case study in PAM-FORM environment.

Results and Discussion

In this section the results from the experimental characterization and numerical analysis of CCF process are reported and discussed

Compression test.

Fig. 7 report the force/displacement curves acquired during the compression tests on the three specimens and the photos of core before and after the test. By analyzing the curves, it is possible to observe a first peak of mechanical resistance of about 2100 N, after which there is a collapse of the load and a plateau up to an overall displacement of 14 mm of the upper plate. In this stage of the test, the failure of the core cells occurred, which, once completed, led to a new increase in measured load. Therefore, the investigated core is compressible up to a thickness of about 5 mm, lower than that necessary for the realization of the case study of the present work. Tests conducted at 120°C showed the same results, but with about 30% lower initial stiffness and strength.

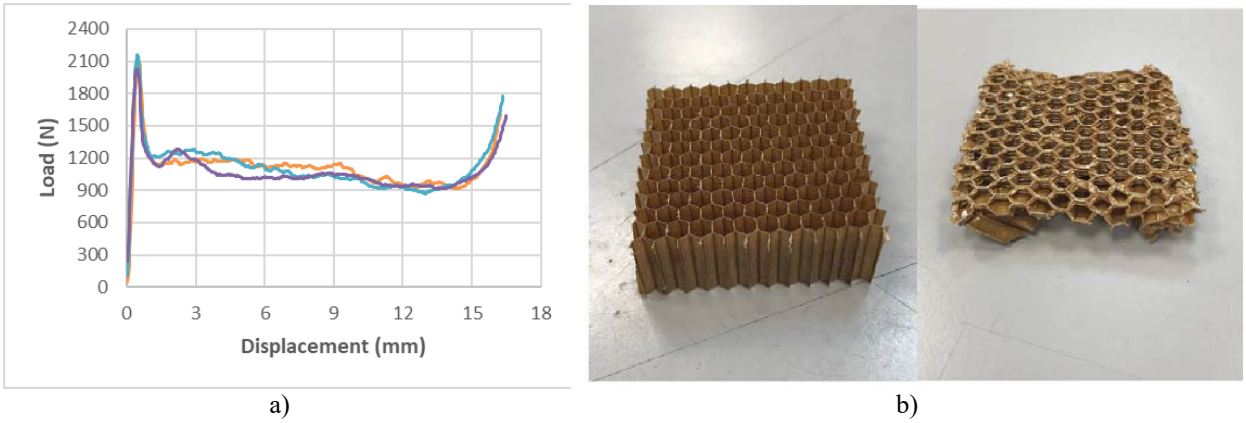

a) b)

Fig. 7. Compression test results on the core material: a) Load-displacement curves; b) specimen image before and after the compression tests.

Cantilever test.

The results from the cantilever tests on prepreg laminates are shown in Fig. 8. From these it is possible to observe that the flexural stiffness of the prepreg EP121-68-40 at room temperature varies between 22 and 28 kPa. In the case of tests conducted at the forming temperature, the flexural stiffness has lower values between 17 and 18 kPa. In the latter case, the tests showed a greater repeatability of the measurement with a limited scattering.

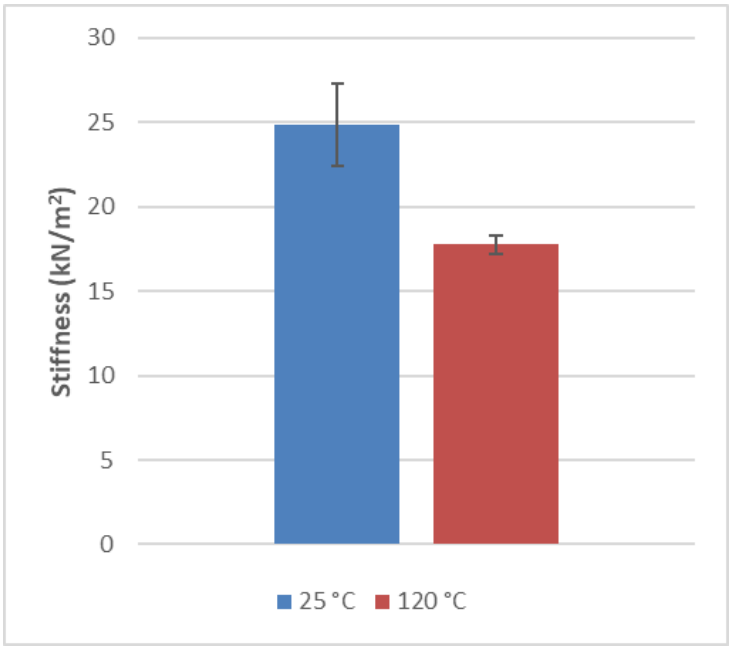

Fig. 8. Prepreg stiffness derived from cantilever test.

Bias extension test.

The results from the bias extension test are shown in Fig. 9. The load-displacement curves showed an exponential trend, with a significant increase in load after a displacement of approximately 15 mm. These curves were normalized with respect to the size of the specimen, then the average curve was extrapolated and used as input into the PAM-FORM calculation code.

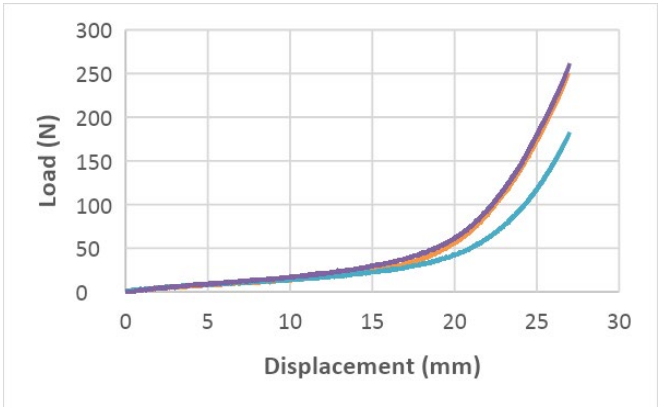

a)

b)

Fig. 9. Results from bias extension test on the EP121-68-40 prepreg: a) load vs displacement curves; b) images of the prepreg specimens during the test.

CCF process: comparison between experimental and numerical outcomes.

Measurement of temperature by using thermocouples during the forming process and the ultrasonic control on the formed part confirmed soundness of the manufactured sandwiches, confirmed by the good adhesion between core and skins after the forming.

From visual analysis it can be observed that the variation of orientation of the fabric is located near the vertices of the cavity, or where there is a greater variation of the normal of the piece surface (Fig. 10). By analyzing the simulated panel, it is possible to assess that the software was able to predict with good accuracy the formability and directional variation of the reinforcement of the skin with the presence of wrinkles near the vertices of the pocket.

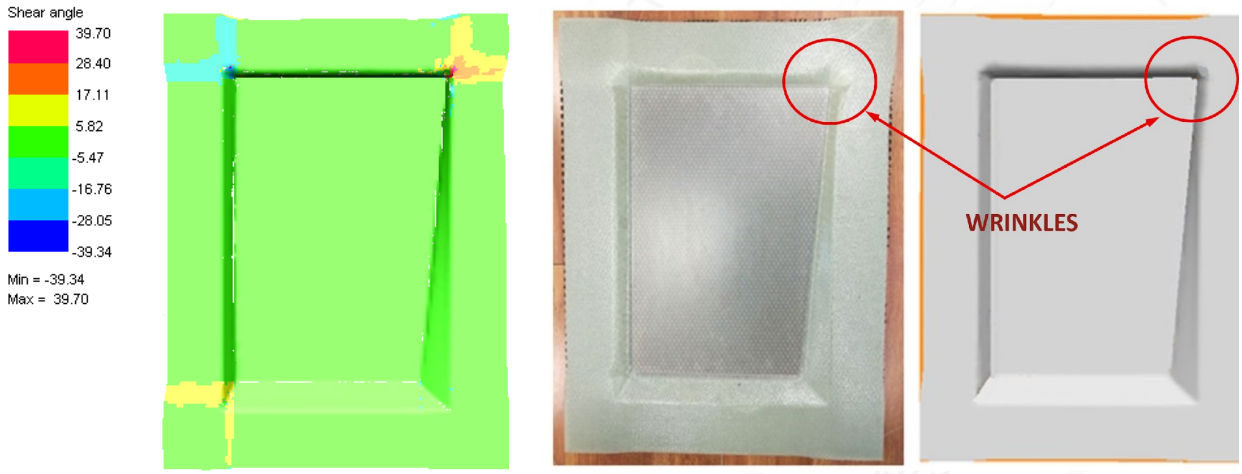

a) b)

Fig. 10. Sandwich panel manufactured by CCF process: a) numerical shear angle; b) comparison between experimental and numerical results.

Summary

In the present work, an innovative approach to produce structural sandwich structures, known Crush Core Forming (CCF), has been investigated. This process allowed to form simultaneously the core and the skin in a single forming step to produce structural sandwich panels with complex shapes, reducing time and manufacturing costs. First, the mechanical behavior of the core and the skins has been obtained through compression tests, bias extension tests and cantilever tests. Subsequently, the results of the tests conducted on the prepreg cure temperature of 120°C were added as input in the PAM-FORM simulation environment. A case study has been realized through CCF process, showing the reliability of the proposed approach, while the outcomes proved the model's capability to predict the plastic deformation of the core and relative angular variation of the skin sheets with the formation of wrinkles near the vertices of the cavity.

References

[1] F. Rubino, A. Nisticò, F. Tucci, P. Carlone, Marine Application of Fiber Reinforced Composites: A Review, J. Mar. Sci. Eng. 8 (2020) 26. https://doi.org/10.3390/jmse8010026

[2] J. Kratz, P. Hubert, Processing out-of-autoclave honeycomb structures: Internal core pressure measurements, Compos Part A Appl. Sci. Manuf. 42 (2011) 1060-1065. https://doi.org/10.1016/j.compositesa.2011.04.009

[3] P. Boisse, R. Akkerman, P. Carlone, L. Kärger, S. v. Lomov, J.A. Sherwood, Advances in composite forming through 25 years of ESAFORM, Int. J. Mater. Forming 15 (2022) 39. https://doi.org/10.1007/s12289-022-01682-8

[4] F. Rubino, V. Paradiso, P. Carlone, Flow monitoring of microwave pre-heated resin in LCM processes, in: AIP Conf Proc, 2017: pp. 030017. https://doi.org/10.1063/1.5008004

[5] F. Rubino, F. Tucci, V. Esperto, P. Carlone, Filling Time Reduction in Liquid Composite Molding Processes, J. Compos. Sci. 6 (2022) 222. https://doi.org/10.3390/jcs6080222
[6] P. Carlone, F. Rubino, V. Paradiso, F. Tucci, Multi-scale modeling and online monitoring of resin flow through dual-scale textiles in liquid composite molding processes, Int. J. Adv. Manuf. Technol. 96 (2018) 2215-2230. https://doi.org/10.1007/s00170-018-1703-9
[7] F. Rubino, V. Esperto, F. Tucci, P. Carlone, Flow enhancement in liquid composite molding processes by online microwave resin preheating, Polym. Eng. Sci. 60 (2020) 2377-2389. https://doi.org/10.1002/pen.25477
[8] M. Jaafar, H. Makich, M. Nouari, A new criterion to evaluate the machined surface quality of the Nomex® honeycomb materials, J. Manuf. Process. 69 (2021) 567-582. https://doi.org/10.1016/j.jmapro.2021.07.062
[9] C. Bellini, R. Borrelli, V. Di Cocco, S. Franchitti, F. Iacoviello, L. Sorrentino, Titanium lattice structures manufactured by EBM process: Effect of skin material on bending characteristics, Eng. Fract. Mech. 260 (2022) 108180. https://doi.org/https://doi.org/10.1016/j.engfracmech.2021.108180
[10] C. Bellini, R. Borrelli, V. Di Cocco, S. Franchitti, F. Iacoviello, L. Sorrentino, Bending properties of titanium lattice structures produced by electron beam melting process, Fatigue & Fracture of Engineering Materials & Structures 44 (2021) 1961-1970. https://doi.org/https://doi.org/10.1111/ffe.13468
[11] S. Chen, O.P.L. McGregor, A. Endruweit, L.T. Harper, N.A. Warrior, Simulation of the forming process for curved composite sandwich panels, Int. J. Mater. Forming 13 (2020) 967-980. https://doi.org/10.1007/s12289-019-01520-4
[12] Z.-Y. Cai, X. Zhang, X.-B. Liang, Multi-point forming of sandwich panels with egg-box-like cores and failure behaviors in forming process: Analytical models, numerical and experimental investigations, Mater. Des. 160 (2018) 1029–1041. https://doi.org/10.1016/j.matdes.2018.10.037
[13] C.C. Besse, D. Mohr, Plasticity of formable all-metal sandwich sheets: Virtual experiments and constitutive modeling, Int. J. Solids. Struct. 49 (2012) 2863-2880. https://doi.org/10.1016/j.ijsolstr.2012.04.032
[14] K.P. Jackson, J.M. Allwood, M. Landert, Incremental forming of sandwich panels, J. Mater. Process. Technol. 204 (2008) 290-303. https://doi.org/10.1016/j.jmatprotec.2007.11.117
[15] H. Nassar, M. Albakri, H. Pan, M. Khraisheh, On the gas pressure forming of aluminium foam sandwich panels: Experiments and numerical simulations, CIRP Annals. 61 (2012) 243-246. https://doi.org/10.1016/j.cirp.2012.03.116

Materials Research Proceedings 28 (2023) 407-416 https://doi.org/10.21741/9781644902479-45

An Inverse method for determining fabric permeability in vacuum assisted resin infusion for composite parts forming

VOSNIAKOS George-Christopher[1,a *], DIMAKOPOULOS Panagiotis J.[1,b] and VASILEIOU Anastasia[2,c]

[1]National Technical University of Athens, School of Mechanical Engineering, Manufacturing Technology Laboratory, Heroon Politehniou 9, 15773 Athens, Greece

[2]The University of Manchester, Department of Mechanical, Aerospace & Civil Engineering, Dalton Nuclear Institute, Oxford Rd, Manchester M13 9PL, United Kingdom

[a]vosniak@central.ntua.gr, [b]pjdimako@gmail.com, [c]anastasia.vasileiou@manchester.ac.uk

Keywords: Composite Materials, Resin Infusion, Permeability, Genetic Algorithms

Abstract. Vacuum Assisted Resin Infusion (VARI) method employs a mould on top of which a number of fabric pieces are laid up and impregnated by resin drawn through vacuum. Simulation of VARI depends on the determination of fabric permeability. In this work, permeability value is selected from a set of discrete values by a genetic algorithm. An impregnation simulation model is run on Comsol^{TM} to compute the flow front propagation inside the fabric. The genetic algorithm compares the evolution (propagation) of the impregnation front, in a space and time dimension, with the corresponding result of one single actual impregnation experiment, obtained by machine vision. A simple part suffices for this experiment assuming homogenous fabric porosity. The computational cost of the method is low, making it superior to experimental determination of permeability on expensive custom-made devices.

Introduction

Industrial production of large batches of laminate, e.g. carbon or glass fibre, composite parts, of small to medium size and complex geometry is mostly conducted exploiting Resin Transfer Molding (RTM) using a heated mold pair arrangement. The resin along with the catalyst (hardener) is then injected into the mold through the inlet ports. After hardening, the part is separated from the mold. RTM imparts good dimensional accuracy and good surface quality to both sides of the part. Vacuum Assisted Resin Infusion (VARI) is a comparatively low-cost method that is able to produce small to large parts, its main characteristics being similar to those of RTM. However, instead of the metal top surface of the RTM mold, an elastic membrane is used. Moreover, VARI uses vacuum to draw the resin into the mold displacing the air it encounters and flowing towards the vacuum port(s). The mold is in contact with only one surface of the fabric, the other surface being of inferior surface finish.

Permeability of the fabric is an extremely important factor in VARI as it is directly related to the completion of the impregnation. Experimental and computational / numerical simulation methods or a combination have been used to determine it.

Experimental determination of permeability is based on monitoring the propagation of resin front by exploiting different sensors, such as pressure sensors [2], images of the evolution of the front through the fabric [3], custom designed dielectric sensors [4], optical fibers woven into the preformed material [5]. Both saturated and unsaturated flow tracking was reported in some of these works. Based on experimental data, neural networks have also been trained to predict permeability from input parameters (fabric type, porosity, input pressure) [6,7].

To calculate permeability numerical models based on the Stokes / Darcy equations are experimentally validated. The models express macro-scale phenomena using standard software

Content from this work may be used under the terms of the Creative Commons Attribution 3.0 license. Any further distribution of this work must maintain attribution to the author(s) and the title of the work, journal citation and DOI. Published under license by Materials Research Forum LLC.

such as Comsol™ [8] or 2D schemes based on voxels or boundary elements [9,10]. Models at micro-scale [11] are inevitably of limited size. In macro-scale modeling the way in which the fabric is modeled is pivotal, e.g. using permeable and non-permeable yarns [12], incorporating stochastic fabric diversity [13].

Since the permeability of a fabric is not known a priori to use the corresponding value in the numerical model, several simulations are performed until the results match the experimental ones either following brute force [8,13] or within an optimization loop [14]. Another approach reported computes bulk permeability and saturation rate at mesoscale and introduces them to the macroscale simulation validated against experimental measurement in a 1D infusion test [15].

In a very comprehensive review on composite forming, benchmarking work on 1D and 2D permeability measurement is reviewed being expected to lead to a pertinent ISO standard [16]. However, it is also recognized that shear and compaction of preforms does alter permeability locally, which undermines to some extent the generality of the benchmarking concept.

In the present work, determination of the fabric permeability value is based on the comparison of experimental results and the numerical prediction of the propagation of the flow front, iteratively through a genetic algorithm. The difference of the two fronts at consecutive moments yields the evaluation of the corresponding permeability value tested. Due to its stochastic nature the approach is efficient requiring only one experiment on a simple shape recorded on camera.

The next section describes the numerical modeling of the VARI process. Next is the description of the experiment providing the reference of the front evolution and in the next section the genetic algorithm that determines the optimal permeability for the specific fabric. Then, conclusions and suggestion of future work are drawn up.

Experimental Recording of Flow Front Evolution

A single VARI experiment suffices to provide a reference for the evolution of the flow front for comparison with the predicted evolution by the numerical simulation subsequently.

The specimen consists of two-ply glass fiber fabric measuring 200 X 75 mm with a nominal thickness of 0.02 mm per ply, plain weaving and weighing 25 gr / m^2. An appropriate peel ply was used with 0.15 mm thickness, a flow medium (mesh) with 1.2 mm thickness, a bottom bag (perforated) with 65 MPa strength and a vacuum bag (SBF 130B) with strength 45 MPa and thickness 0.075 mm. Entry and exit tubing had a diameter of 10 mm.

The resin was a 2-part Alphapoxy™ HX-3 by Vivacity Engineering. Its viscosity at 25ºC is 325-375 mPa.s. Usage time at 25ºC is 45-60 min, full hardness being achieved after 24 hr. The mold was an aluminium plate of 1 mm thickness stiffened by ribs, see Fig. 1(a).

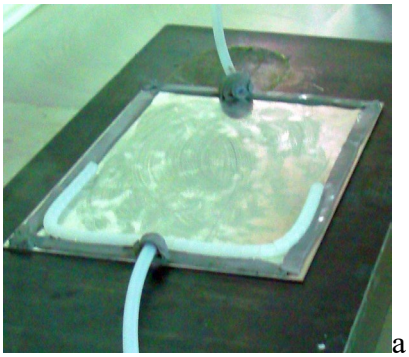
a

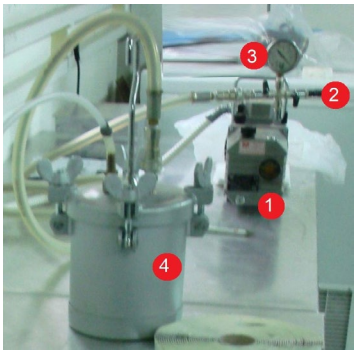

b

Fig. 1. Experimental layout (a) mold with fabric, vacuum bag and in/out pipes (b) vacuum pump (1), regulating valves (2), manometer (3), resin trap (4).

Special sealing tape is employed to secure the vacuum bag on the mold. A two stage vacuum pump (DVP™ RC.8D) is used with nominal pressure is 0.01 mbar and flow rate: 10.2 – 9.5 m^3/hr. A manometer of range – to -1 bar was used to measure the actual vacuum pressure achieved and a

system of hand-regulated valves is used for controlling the vacuum circuit, which also comprises a downstream resin trapping vessel. The equipment is shown in Fig. 1(b).

The resin-saturated fabric is visibly darker than the unsaturated part, therefore the flow front is clearly delineated, see Fig. 2(a). In order to record the evolution of the front a 12 Mpixel CCD camera was used and 22 snapshots were taken at 1 sec intervals until the resin front reached the end of the fabric. Six tracks were defined about the axis of symmetry of the fabric parallel to it and the intersection points of the flow front with these tracks were recorded at each snapshot, see points A – F in Fig. 2(b). Their distance along flow direction (x axis) from the starting edge of the fabric was measured in pixels and scaled to mm. Thus, the mean distance of the six points defining each flow front was calculated representing a 'linearized' flow front,

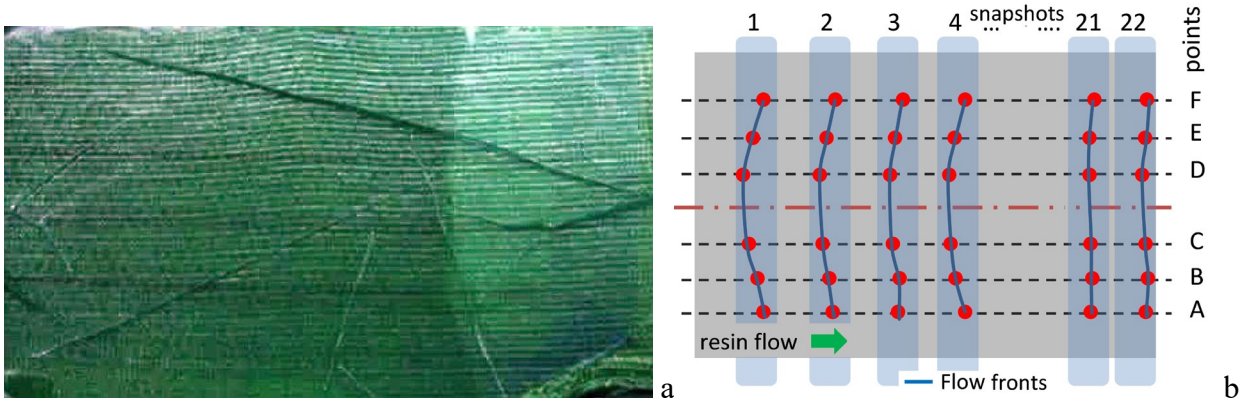

Fig. 2. Resin flow front (a) snapshot during the experiment (b) designated snapshots and points.

Numerical Simulation of VARI

Darcy's law governing one dimensional flow through porous media is expressed as:

$$v = \frac{k}{\mu}\frac{\partial^2 p}{\partial x^2} \tag{1}$$

v: resin velocity (m/s), k: fabric permeability (m^2), μ: resin viscosity (Pa·s), p: pressure (Pa).

Fabric filaments are bundled into tows which leave gaps between them as they are intertwined. These are visible as they are of the order of magnitude of mm (inter-tow gaps). Within a bundle gaps exist of 2-3 orders of magnitude smaller than those (intra-tow gaps). Resin flow between filaments of a bundle is modelled by a sink term describing resin flow around the gap. A corresponding expression for mass continuity is:

$$\nabla v = -S \tag{2}$$

where S is the sink term, its negative sign denoting that resin flow is reduced in the regions of non-saturated intra-tow gaps because it is absorbed by them.

Combining Darcy's law and continuity equation [28]:

$$v = -\frac{k}{\mu}\nabla(p) \tag{3}$$

$$\frac{\partial(\rho\varphi)}{\partial t} + \nabla(v\rho) = 0 \tag{4}$$

where φ is fabric porosity. Finally, using the sink term and assuming incompressible resin:

$$\varphi \frac{\partial S}{\partial t} - \nabla\left(\frac{k}{\mu}\nabla(p)\right) = 0 \quad (5)$$

As the viscosity ratio of resin to air is quite high (10^4-10^6) zero pressure drop is assumed in the unsaturated section of the part and thus equal pressure on the flow front and the exit. Function S is defined to ensure smooth transition from a saturated to an unsaturated region [8]:

$$S(p) = \frac{2}{\pi}(ap) \rightarrow \frac{\partial S}{\partial t} = \frac{\partial S}{\partial p}\frac{\partial p}{\partial t} = \left(\frac{2}{\pi}\frac{\alpha}{1+(\alpha p)^2}\right)\frac{\partial p}{\partial t} \quad (6)$$

where $\partial S/\partial p$: moisture capacity and α: form factor [1/Pa] determining the length corresponding to phase change. [8].

The point at which the resin changes phase is determined by comparing the pressure resulting from Eq. 6 to the characteristic pressure at the flow front: $p > p_c a$. Normally, p_c = 1000 Pa [8].

The model was set up on Comsol™ concerning a fabric shaped as a parallelogram with resin flowing from one narrow end to the opposite along x direction, see Fig. 3(a).

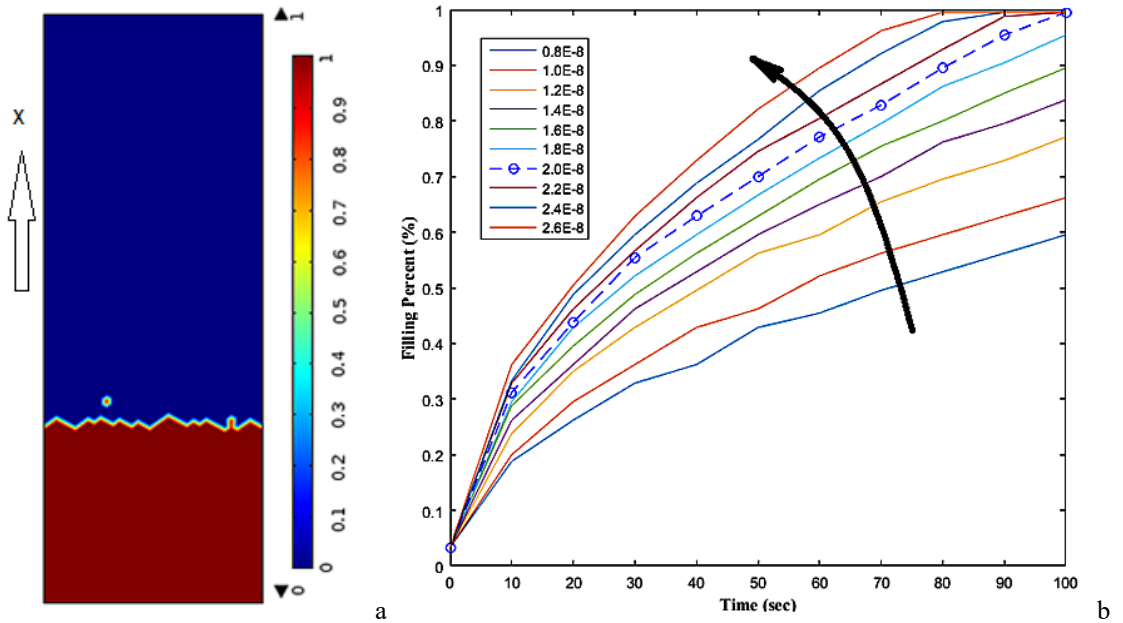

Fig. 3. Simulation of resin infusion (a) flow front snapshot for t=30 sec, permeability 3.2e^{-12} m^2 and quadric fine mesh (b) evolution of filling percentage for different fabric permeability values.

The resin's change of viscosity with time was not modelled since it was considered fairly small (for AIRSTONE 710EL Epoxy Resin and 713H Hardener which is equivalent to the system used in the experiment, viscosity is reported by the manufacturer to be 150-200 mPa.s within the first 30 min, whereas impregnation time was a small fraction of 30 min in this case. Note that the fabric was modelled at single scale, i.e. ignoring the intra-tow gaps, which is knowingly a simplification at the same time allowing faster computation compared to dual scale modelling.

It is possible to record the flow front along a few lines parallel to the flow direction, interpolating between these points to draw up the complete flow front line, see Fig. 3(a). In addition, the filling percentage is used as a termination criterion for the simulation as calculated using the Derived Values>Average>line_Average method in COMSOL™. Fig. 3(b) shows the variation of filling percentage with time for various permeability values. It is clear that the higher the permeability, the earlier the filling ends, even before the front touches the fabric's right edge.

The density of the mesh can be set by the user as Extra Fine, Fine and Normal. In addition the discretization type of elements can be selected from the set: linear, quadratic, cubic, quatric, quintic, sextic and septic. Selection of different combinations impacts not only the accuracy of the flow front solution but also the actual position of the mesh nodes in the domain studies and hence the distance of the predicted flow front from the experimentally determined one. In particular, different combinations were tried for a simulation run for two layered GFRP fabrics at 0.8 bar vacuum and permeability 8.94 X 10^{-10} m^2. Concentrating on the experimental flow front position corresponding to the first snapshot recorded, which is located 10.52 mm downstream the entry baseline, Table 1 clearly shows superiority of combination Linear – Fine.

Table 1. Difference in predicted distance of the flow front from the baseline.

Density	**Extra Fine**		**Fine**		**Normal**	
Discretisation	Distance (mm)	Rel.error (%)	Distance (mm)	Rel,error (%)	Distance (mm)	Rel.error (%)
Linear	3,97	-62%	**10,53**	**0%**	12,96	23%
Quadratic	1,69	-84%	4,8	-54%	5,9	4,6
Cubic	2,74	-74%	6,85	-35%	8,43	2,07

Repeated execution of the simulation with different input values for permeability is implemented by corresponding calls from within a Matlab™ program by exploiting the Livelink™ application. Results are also transferred in the same way, in this case the flow front vector depicting its position at a predefined number of time points. Such repeated calls and passing back of the results are needed by the Genetic Algorithm described next.

Permeability Determination by Genetic Algorithm

The optimum value of permeability is the one that yields minimum deviation between the experimentally determined evolution of the flow front and the evolution predicted by the simulation model. This is determined by a Genetic Algorithm (GA) that uses the simulation model in order to evaluate the potential permeability solutions, see Fig. 4. The GA is based on the one reported on in [17].

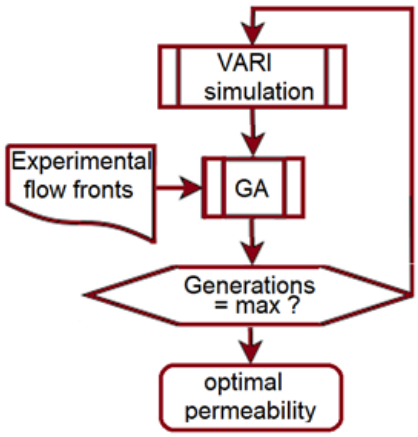

Fig. 4. Evolutionary determination of permeability overview.

The chromosome consists of an integer index to a set of 1000 permeability values spanning a user-defined range, in this case 3 X 10^{-9} to 9 X 10^{-10} (m^2). Thus the integer representation is decoded into a real representation.

The evaluation functions used is the Root Mean Square (RMS) of the difference of the x coordinate of the experimental (x_{e_i}) and the corresponding simulated (x_{s_i}) flow front considering all snapshots (T):

$$f_{eval} = \sqrt{\frac{\sum_{i=0}^{i=T}(x_{e_i} - x_{s_i})^2}{T}} \quad (7)$$

Note that the simulated flow front is by model construction a vertical line, whereas the experimental flow front can be considered as a circular arc with large radius that passes from the six 6 recorded points per snapshot, see Fig. 1(b). Thus, the experimental flow front is replaced by a vertical line passing from the mean x coordinate of these six points. The value of f_{eval} can be considered as a metric for the mean distance between the two flow fronts, measured and simulated one, over all snapshots considered. Normally all 22 snapshots taken should be taken into account, but it is up to the user to exclude any 'outlier' snapshots.

Since the chromosome is just one integer variable crossover operator would not keep any genes of the parent but the offspring would be an entirely new chromosome, which is exactly what mutation operator does in this case. Thus, crossover operator was abolished and only mutation was applied, indeed with a high probability of 40%. Elitism was constrained to 10%. Population consisted of 10 individuals and the initial population resulted from a random selection of 10 out of the 1000 permeability indices.

In order to validate the approach, the genetic algorithm was run first using instead of experimental flow front data the ones obtained by running the simulation model with a known permeability value, namely 3.7 X 10^{-9} m^2. In order to save computational cost only 10 snapshots were considered and the results are shown in Table 2. The cost was 0.554473 mm, which is deemed small enough to be accepted and the permeability determined was 3.71 X 10^{-9} m^2. The non-zero cost and associate small difference in predicted permeability is due to the discretization, i.e. the element nodes being inevitably some small distance apart from the actual flow front which is determined in the continuous domain rather than the discretized one.

Table 2. Difference between target and predicted flow fronts for the validation run.

snapshot number	1	2	3	4	5	6	7	8	9	10
time (sec)	0	2	4	6	8	10	12	14	16	18
target (mm)	9,55166	60,62378	85,18519	104,2885	119,29825	134,308	144,83431	158,8694	169,3957	178,9474
predicted (mm)	9,55165	60,62378	85,18518	104,2885	120,2729	134,308	146,39376	158,8694	169,3957	178,9474
relative error (%)	0,000001	0	0	0	-0,008170	0	-0,010767	0	0	0

The GA was then run with the actual experimental flow front evolution values for 500 generations. The evolution of the cost with the number of generations is shown in Fig. 5. The optimum permeability determined is 8.71 X 10^{-10} corresponding to a cost of 8435 μm.

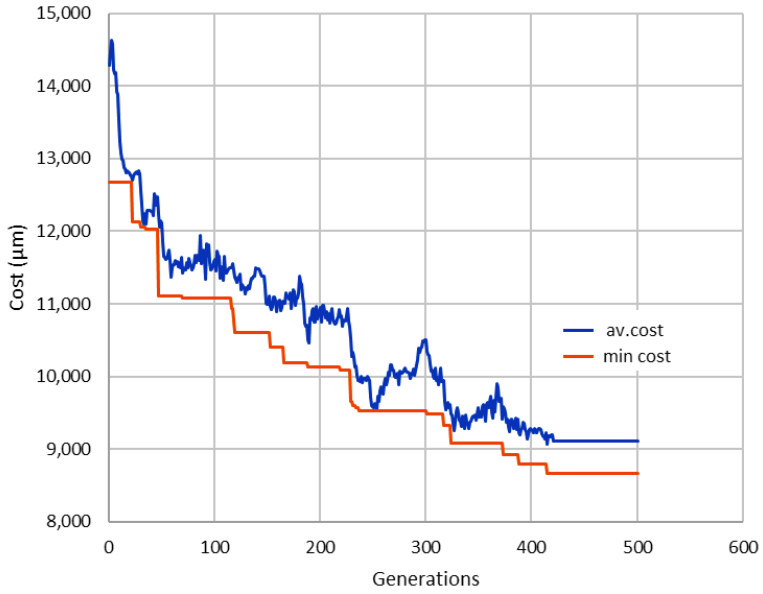

Fig. 5. Evolution of average and best (minimum cost) solution for the experiment conducted.

Characteristic snapshots of the experimental and the simulated flow front are shown in Fig. 6.

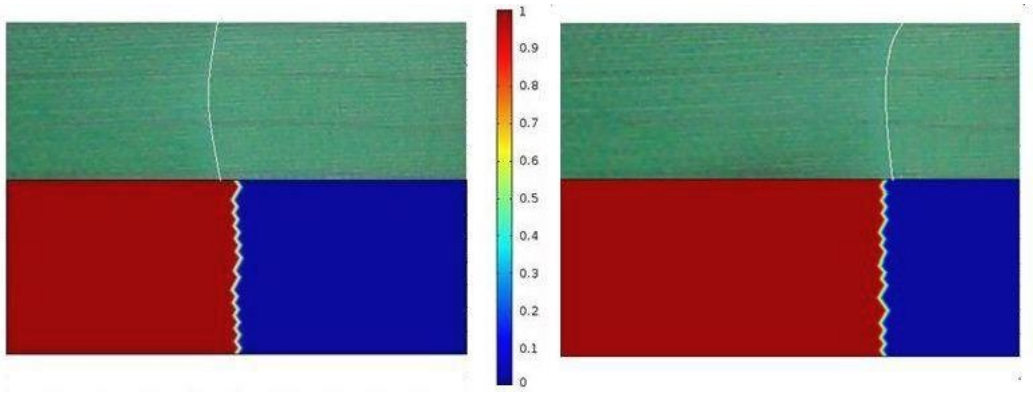

Fig. 6. Experimental (up) / simulated (down) flow front at 6 sec (left) and 12 sec (right).

A comparison between experimental and optimally predicted by the simulation flow front evolution in terms of their mean distance from the baseline is shown in Table 3 for a set of 11 snapshots for the 2-ply fabric. Furthermore, analogous experiments increasing the number of fabric plies to 3 and 4 was performed and the flow front evolution was measured as in the 2-ply experiment. The GA was run for these cases, too, resulting in lower overall permeability as well as higher impregnation time, namely 3,59 x 10^{-10} m^2 and 51 sec respectively for 3 plies and 1,07 x 10^{-10} m^2 and 117 sec respectively for 4 plies. This decrease in permeability with the increase of number of plies is reasonable and has also been reported in literature, e.g. [19]. The comparison between experimental and optimally predicted flow front evolution for the 3 ply fabric is also provided in Table 3.

Table 3. Difference between measured and predicted flow fronts for 2 and 3 ply cases.

plies	snapshot number	1	2	3	4	5	6	7	8	9	10	11
2	time (sec)	0	2	4	6	8	10	12	14	16	18	20
	target (mm)	10,5	42,5	72,5	97	114	134	146,5	159	172,5	185	192,5
	predicted (mm)	10,53	60,62	83,24	102,73	120,27	133,33	144,83	156,92	167,45	177,97	186,94
	relative error (%)	-0,29	-42,64	-14,81	-5,91	-5,50	0,50	1,14	1,31	2,93	3,80	2,89
3	time (sec)	0	5	10	15	20	25	30	35	40	45	50
	target (mm)	2,5	34	61,5	85,5	108,5	130	146,7	165	176	187,5	197
	predicted (mm)	2,74	59,99	82,97	102,18	117,83	132,81	144,81	156,59	168,6	180,02	189,62
	relative error (%)	-9,60	-76,44	-34,91	-19,51	-8,60	-2,16	1,29	5,10	4,20	3,99	3,75

Given that the simulation model is at single scale, i.e. approximate compared to a dual scale approach, the results are promising, namely the deviation of the experimentally determined and simulated flow fronts is mostly acceptable except for the snapshots corresponding to the first 20% of the experiment duration. The latter may, in addition to this simplification, be attributed to the effect of the vacuum bag compressing the fabric non-homogeneously, as also noted in [18].

On an Intel® Core™ i7-5500U computer 800 generations were run in about 80 min. The simulation run takes about 20 sec. Thus, an exhaustive search of 1000 permeability values would take by comparison 330 min.

Summary

The method advocated for determining permeability of fibre reinforced fabrics relies on simulation with a flow front evolution reference determined by a simple experiment on a simple fabric shape. By comparison, dedicated devices for determining permeability purely experimentally make use of special sensors and are expensive to make or acquire. Nevertheless, benchmarking has led to an ISO standard (ISO/DIS 4410). As far as this is still under development, visual tracking of the flow front coupled with numerical simulation in an optimisation loop may be a worthwhile addition to the sensor-based methods. In fact, there is plenty of scope in this direction since research on permeability evaluation in Liquid Composite Moulding (LCM) processes is an ongoing topic of research and of particular significance in process simulation [16].

The genetic algorithm as a tool for optimization coupled with a set of discrete values of permeability proved efficient, although it was, by definition, impossible to validate the result against experimentally measured permeability. Yet, the trend of permeability decreasing with increasing number of fabric pieces was clear and in accordance with results reported in literature.

The number and position of points to be considered on the flow front in the experimental setting and their simulation counterparts does influence the predicted permeability. This is connected to the fact that, for reasons of lowering computational cost, the fabric is modelled as single scale, i.e. ignoring the intra-tow gaps, that would otherwise have provided more accurate flow front shape. This is clearly an issue for further improvement.

The formulation of the genetic algorithm would most probably benefit from a binary representation of the integer indices to permeability. It is suggested that in the same range of values

a finer step could be applied in this way and also that crossover operator could be meaningfully introduced in which case the number of generations to reach the optimum permeability would be slashed by at least one order of magnitude. This is the next step in further work, which will also allow inclusion of the type and density of finite element discretisation in the chromosome as two extra variables to be optimized. The chromosome could also be augmented by the critical pressure for phase change of the resin as a variable to be optimized, which has been taken as constant from literature (1000 Pa).

References

[1] A. Hindersmann, Confusion about infusion: An overview of infusion processes, Compos. Part A: Appl. Sci. Manuf. 126 (2019) 105583. https://doi.org/10.1016/j.compositesa.2019.105583

[2] C. Di Fratta, F. Klunker, P. Ermanni, Innovative approach to track flow front in LCM processes through pressure sensors in line quality control, 11th Intern. Conf. on Flow Processing in Composite Materials (FPCM 11), 2012, pp. 204-211.

[3] N. Vernet, E. Ruiz, S. Advani, J.B. Alms, M. Aubert, M. Barburski, B. Barari, J.M. Beraud, D.C. Berg, N. Correia, M. Danzi, T. Delaviere, M. Dickert, C. Di Fratta, A. Endruweit, P. Ermanni, G. Francucci, J.A. Gracia, A. George, C. Hahn, F. Klunker, S.V. Lomov, A. Long, B. Louis, J. Maldonado, R. Meier, V. Michaud, H. Perrin, K. Pillai, E. Rodriguez, F. Trochu, S. Verheyden, M. Wietgrefe, W. Xiong, S. Zaremba, G. Ziegmann, Experimental determination of the permeability of engineering textiles: Benchmark II, Compos. Part A: Appl. Sci. Manuf. 61 (2014) 172-184. https://doi.org/10.1016/j.compositesa.2014.02.010

[4] P. Carlone, G.S. Palazzo, Unsaturated and saturated flow front tracking in liquid composite molding processes using dielectric sensors, Appl. Compos. Mater. 22 (2015) 543-557. http://doi.org/10.1007/s10443-014-9422-3

[5] V. Antonucci, M. Esposito, M.R. Ricciardi, M. Raffone, M. Zarrelli, M. Giordano, Permeability characterization of stitched carbon fiber preforms by fiber optic sensors, Express Polym. Lett. 5 (2011) 1075–1084. http://doi.org/10.3144/expresspolymlett.2011.105

[6] S. Konstantopoulos, C. Hueber, E. Mühlbachler, R. Schledjewski, Identification of the effect of typical curvatures encountered in RTM parts on localized permeability of fibrous preforms, Adv. Manuf. Polym. Compos. Sci. 2 (2016) 57-66. https://doi.org/10.1080/20550340.2016.1229829

[7] H. Golestanian, M. Poursina, Neural Network Analysis Application To Permeability Determination of Fiberglass and Carbon Preforms, Chinese J. Polym. Sci. 27 (2009) 22-229.

[8] F. Klunker, S. Aranda, W. Surjoseputro, W. Wu, G. Ziegmann, C. Elsenhans, H. Behnke, Modelling the resin infusion process, Part I: Flow modelling and numerical investigation for constant geometries, Zeitschrift Kunststofftechnik/J. Plast. Technol. 7 (2011) 178-201.

[9] B. Verleye, S. Lomov, A. Long, D. Roose, C.C. Wong, Permeability of Textile Reinforcements : Efficient Prediction and Validation, Polymer. (2007) 2-3.

[10] X. Zeng, A. Endruweit, L.P. Brown, A.C. Long, Numerical prediction of in-plane permeability for multilayer woven fabrics with manufacture-induced deformation, Compos. Part A Appl. Sci. Manuf. 77 (2015) 266–274. https://doi.org/10.1016/j.compositesa.2015.03.027

[11] J.P. Dunkers, F.R. Phelan, C.G. Zimba, K.M. Flynn, D.P. Sanders, R.C. Peterson, R.S. Parnas, X. Li, J.G. Fujimoto, The prediction of permeability for an epoxy/E-glass composite using optical coherence tomographic images, Polym. Compos. 22 (2001) 803-814. http://doi.org/10.1002/pc.10582

[12] M. Griebel, M. Klitz, Homogenization and Numerical Simulation of Flow in Geometries with Textile Microstructures, SIAM Multiscale Model. Simul. 8 (2010) 1439-1460. http://dx.doi.org/10.1137/09077059X

[13] F. Zhang, B. Cosson, S. Comas-Cardona, C. Binetruy, Efficient stochastic simulation approach for RTM process with random fibrous permeability, Compos. Sci. Technol. 71 (2011) 1478-1485. https://doi.org/10.1016/j.compscitech.2011.06.006
[14] G. Morren, H. Sol, B. Verleye, S.V. Lomov, Permeability Identification of a Reference Specimen Using an Inverse Method, 2007 SEM Annu. Conf. Expo., 2007, 8.
[15] P. Carlone, F. Rubino, V. Paradiso, F. Tucci, Multi-scale modeling and online monitoring of resin flow through dual-scale textiles in liquid composite molding processes, Int J. Adv. Manuf. Techn. 96 (2018) 2215-2230. https://doi.org/10.1007/s00170-018-1703-9
[16] P. Boisse, R. Akkerman, P. Carlone, L. Kärger, S.V. Lomov, J.A. Sherwood, Advances in composite forming through 25 years of ESAFORM. Int. J. Mater. Form. 15 (2022) 1-30. http://doi.org/10.1007/s12289-022-01682-8
[17] A.N. Vasileiou, G.-C. Vosniakos, D.I. Pantelis, Determination of local heat transfer coefficients in precision castings by genetic optimisation aided by numerical simulation, Proc. Inst. Mech. Eng., Part C: J. Mech. Eng. Sci. 229 (2015) 735-750. https://doi.org/10.1177/0954406214539468
[18] L. Joubaud, F. Trochu, J. Le Corvec, Analysis of resin flow under flexible cover in Vacuum Assisted Resin Infusion (VARI), J. Adv. Mater. 37 (2005) 3-10.
[19] P. Mitschang, M. Glawe, D. Kreutz, G. Rieber, D. Becker, Influence of textile parameters on the through-the-thickness permeability of woven textiles, Proc. 11th Intern. Conf. on Flow Processing in Composite Materials (FPCM 11), 2012, 37-45.

Extrusion and drawing

Materials Research Proceedings 28 (2023) 419-428 https://doi.org/10.21741/9781644902479-46

Phenomena of tool adhesion at elevated temperature in V-groove friction test of AA7075

FUNAZUKA Tatsuya[1,a *], DOHDA Kuniaki[2,b], KINOSHITA Mizuki[3,c] and SUZUKI Shiro[3,d]

[1]Faculty of Engineering, Toyama University, Toyama, Japan

[2]Department of Mechanical Engineering, Northwestern University, Illinois, USA

[3]Graduate School of Science and Engineering for Education, Toyama University, Toyama, Japan

[a]funazuka@eng.u-toyama.ac.jp, [b]dohda.kuni@northwestern.edu, [c]m2171212@ems.u-toyama.ac.jp, [d]suzuki.shirou@finetec.co.jp

Keywords: Hot Extrusion, 7075 Aluminum Alloy, Tribology in Manufacturing

Abstract. 7000 series aluminum alloys are high-strength alloys used in various lightweight products in the transportation equipment and aerospace industries. AA7075 extrusions are expected to find further applications in multiple fields, including aircraft parts, automotive parts, and sporting goods. However, the high deformation resistance and surface cracking defects caused by tool galling and adhesion have resulted in extremely low productivity. In this study, the V-groove compression test was proposed as a method to determine the coefficient of friction in hot metal forming. Using AA7075 as the experimental material, what did the V-groove compression test at various temperatures to compare the results with calibration curves created from the numerical analysis and observe the growth of adhesion.

Introduction

The advantages of 7000 series aluminum alloys are high strength, excellent corrosion resistance, and good electrical and thermal conductivity. Thus, these are used in various products to reduce weight in transportation equipment and aerospace applications [1]. In producing aluminum alloys by hot extrusion, the billet is passed through an opening die and pressed to shape. A cross-sectional shape with a surface finish can be obtained in a single deformation. Hot extrusion is widely used in the production of aluminum alloys because of its high productivity and extrusion yield [2]. However, AA7075 has the lowest extrusion productivity due to cracks that develop on the extrudate surface during hot extrusion, especially under high speed and high-temperature conditions, and due to adhesion to the tool. This cracking defect is known as tearing. In addition, AA7075 is one of the least deformable aluminum alloys and has high flow stress, which significantly limits the extrusion speed from 0.8 to 2.0 m/min. In our previous research, we reported that tearing was caused by low-melting intermetallic compounds containing magnesium (Mg) and zinc (Zn) [3]. It reported that the intermetallic compound with a low melting point locally melted due to the heat generated by the forming process.

The crack propagates due to the strong tensile stress applied to the product at the forming part during extrusion. As a method to suppress tearing defects that occur during the hot extrusion of 7000-series aluminum alloys, a coating on the die bearing section is proposed to reduce friction between the billet and tool interface [4]. Three coatings, AlCrN, TiAlN, and Diamond-like Carbon (DLC), were applied. The hot forward-backward extrusion friction test measured their friction coefficients, a friction test simulating plastic working at high temperatures. The friction coefficients from the friction tests and the occurrence of tearing when various die coatings were used showed that tearing was reduced for the low-friction AlCrN at high temperatures. It reported

Content from this work may be used under the terms of the Creative Commons Attribution 3.0 license. Any further distribution of this work must maintain attribution to the author(s) and the title of the work, journal citation and DOI. Published under license by Materials Research Forum LLC.

that this was due to the improvement of material flowability, and homogenization of tensile stress imparted to the product by low friction in the forming section. Therefore, it is necessary to investigate the extrusion tribology that contributes to tool adhesion and material fluidity to suppress tearing.

Friction tests for plastic forming can be classified into three types: basic friction tests such as pin-on-disk tests, friction tests simulating plastic forming, and friction tests using actual workpieces. The basic friction test is a simple way to obtain the coefficient of friction. Still, it does not apply to plastic forming because it does not involve a deformation process involving an increase in surface area. In particular, the surface area expansion ratio becomes extremely large when extrusion or forging is assumed. Friction tests using actual machines are only possible on those machines, making it challenging to obtain general-purpose results. Therefore, conducting friction tests that simulate extrusion and forging is necessary. The most common friction test that simulates extrusion and forging is the ring compression test. However, the compression ratio of this test is only about 50 percent and a friction test that allows a larger surface area expansion ratio is needed. In addition, reports of friction tests simulating hot extrusion and hot forging include the two-cylinder crossed friction test by Kalin et al. [5-7] and the Warm and Hot Upsetting Sliding Test (WHUST) by Dubar et al. [8-10] as examples of hot friction tests. Although these have been reported, there are few examples of friction tests simulating hot extrusion and hot forging. The hot forward-backward extrusion friction test conducted by the authors is also a friction test that simulates plastic forming. Still, it can only identify the friction coefficient for the entire process and is not suitable for measuring friction phenomena that change in complex ways during forming [4].

Zhang et al. proposed the T-shape compression test (TSCT), which can evaluate friction in complex extrusion and compression deformations and achieve a high surface area enlargement of more than 50% [11]. From the stimulation of the TSCT, Fereshteh-Saniee et al. conducted friction tests on AZ31 and AZ80 alloys in this test for hot plastic working of magnesium alloys. They reported that the experimental and simulation results agreed [12]. In addition, TSCT and ring compression tests were conducted to evaluate the friction of Dry, MoS2, and CASP during hot working. And it was reported that the experimental and simulation results agreed and that MoS2 was highly influential in lubricating the alloy during hot working based on the calibration curve created from the simulation. In addition, the friction coefficient of TSCT is higher than that of the ring compression test due to the difference in surface area expansion. These reports indicate that TSCT is effective as a basic friction test for micro- to macro-scale, cold- and hot-forging.

In this study, a hot V-groove friction test is proposed as a friction test that simulates hot extrusion and forging regarding the TSCT. In the hot V-groove friction test, a cylindrical test piece is compressed using a V-groove tool. The friction coefficient is identified from the aspect ratio of the compressed product since either longitudinal extrusion or transverse compression is the preferred deformation because of friction. The characteristics of this test are that it combines both extrusion and compression deformation, has a high surface area expansion ratio of more than 50 percent, and is a two-dimensional deformation in which the circle is collapsed. The dimensions and compression ratio can be easily changed. In this research, tool dimensions and the mechanism of adhesion under different temperatures and compaction amounts are investigated as part of the development of the V-groove friction test. By using AA7075 as the test material and varying the temperature and stroke amount, this study aims to examine the effect of working temperature on the process of adhesion growth during hot forming.

Experimental Method

The AA7075 shown in Table 1 was used in this study. The test pieces were turned to a diameter of 7.0 mm and a length of 70 mm. These dimensions were chosen because the size should be at least 10 times larger than the diameter so that deformation in the depth direction can be ignored.

Fig. 1 shows the 100-ton vertical hydraulic press used in this experiment. The press has a furnace in the forming section to provide a hot test environment. A data logger from the hydraulic system and a displacement transducer read the test force and stroke rate.

Table 1. Chemical composition of AA7075 (mass%).

Alloy	Si	Fe	Cu	Mn	Mg	Cr	Zn	Zr	Ti	Al
AA7075	0.08	0.21	1.78	0.05	2.46	0.19	5.61	-	0.01	Bal.

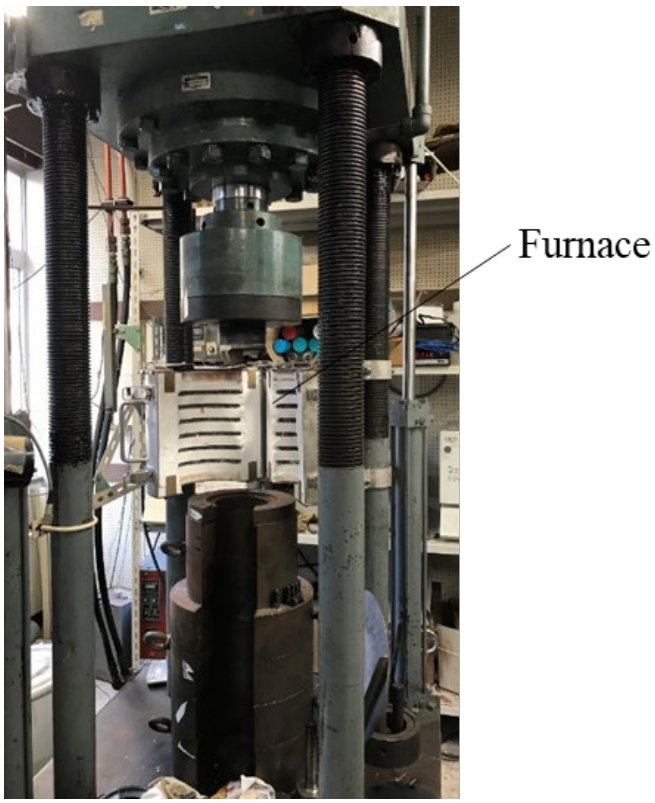

Fig. 1. 100-ton vertical hydraulic press machine.

Table 2 shows the conditions of the hot V-groove friction test and the numerical analysis conditions. Fig. 2 shows a schematic diagram of the V-groove friction test AISI H13 (HRC48) nitrided tool used as the tool material. The numerical analysis software used was DEFORM-3D by Yamanaka Eng Co., Ltd. The groove angles were 15° and 30°, and the groove corner radius R was 1.0 mm and 3.0 mm, referring to the study by Zhang et al. to examine the tool geometry for the hot V-groove friction test [11]. The groove depth was set to 10 mm. The punch stroke is set to 0.1 mm/s with a stroke volume of 4.5 mm. The temperatures of the billet and testing machine were 400°C and 500°C.

The Hot V-groove friction test numerical analysis was performed for shear friction coefficients $m = 0.1, 0.2, ...,1.0$. The shear friction model was used as the friction model. The material data was used from previous authors' AA7075 research [4]. Friction changes the height (H) and width (W)

of the test piece after the V-groove friction test. When friction is low, extrusion becomes dominant, and the height of the test piece increases.

On the other hand, when friction is high, compression becomes dominant, and the width of the test piece grows. Calibration curves were created from the sample's aspect ratio (H/W) after forming at each friction coefficient. The friction coefficients were identified by comparison with the aspect ratio of the model after the experiment. Experiments were conducted three times each for reproducibility.

The amount of elemental deposition on the V-groove tool surface was measured by Electron Probe Micro Analyzer (EPMA, JEOL) to confirm the deposition growth process. Fig. 3 shows the schematic diagram of the measurement points.

Table 2. V-groove friction test and numerical analysis conditions.

Testing conditions		
Billet material		AA7075
Tool material		AISI H13
Billet shape	[mm]	φ7.0×70
Punch speed *V*	[mm/s]	0.1
Punch stroke	[mm]	4.5
Billet temperature *T*	[°C]	400, 500
Groove depth	[mm]	10
Groove angle	[°]	15, 30
Corner radius R	[mm]	1.0, 3.0
Lubrication		No-lubricant
Tool surface treatment		Nitriding
Numerical analysis conditions		
Simulation soft		DEFORM-3D
Numerical analysis method		Lagrangian method
Billet material		AA7075
Tool material		AISI H13
Number of elements		100,000
Heat transfer coefficient	[Nmm/sec°C]	11
Friction model		Share friction model
Share friction coefficient *m*	[-]	0.1, 0.2, . . . 1.0

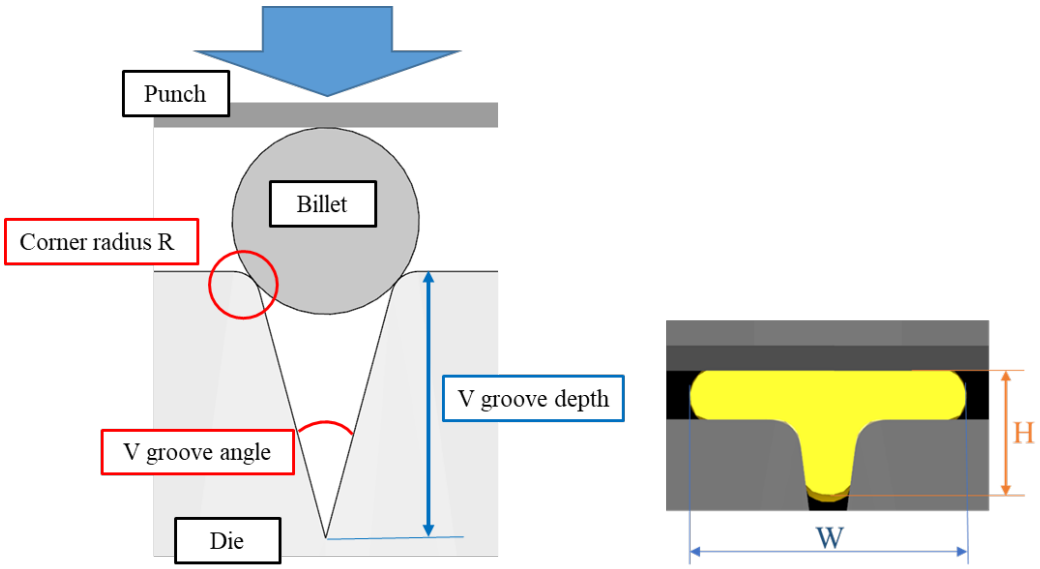

Fig. 2. Schematic view of V groove compression test (left) and shape of the test piece after the test (right (H: hight, W: width)).

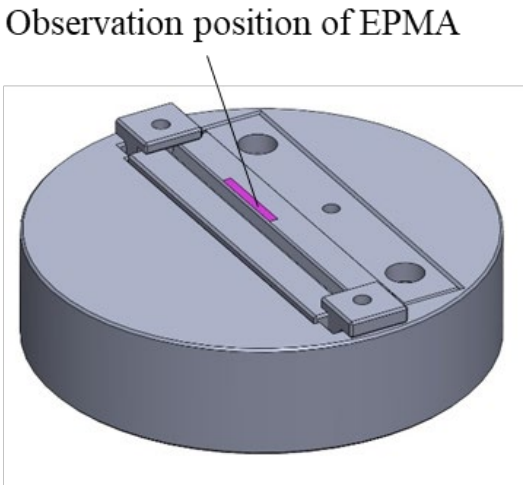

Fig. 3. Schematic of tool for V-groove compression test and EPMA observation position.

Experimental Results

Fig. 4 shows the calibration curves for each tool condition generated from the numerical analysis. The friction coefficient cannot be determined for the R1, 15° condition because the shear friction coefficient does not determine the magnitude of the aspect ratio. Under the R3, 15° condition, a right ascending calibration curve was observed, but the aspect ratio increased and decreased under low friction, indicating that an accurate friction coefficient may not be obtained. In the R3, 30° condition, the shear friction coefficients of m = 0.9 and 1.0 could not analyze, and a calibration curve could not be generated. Based on these results, the basic V-groove shape of the die for the V-groove compression test was determined to have an R radius of 1 mm and a V-groove angle of 30°.

Fig. 5 shows the V-groove compression test conducted at a test temperature of 400°C. As a result, H/W was 0.526, and the coefficient of friction was m = 0.9.

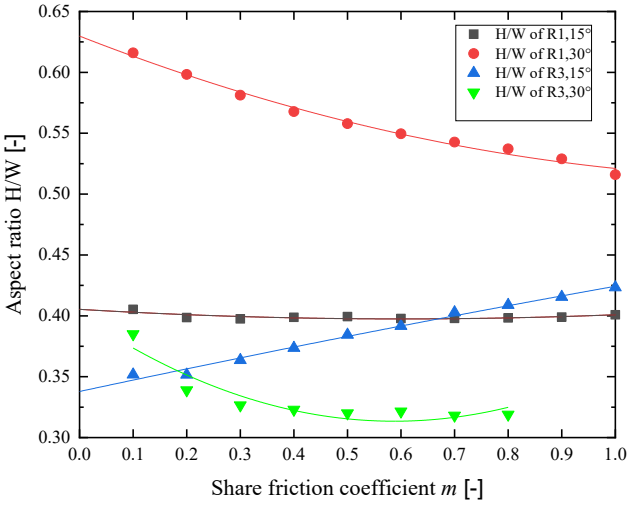

Fig. 4. V-groove compression test calibration curves for each tool condition (Simulation soft: DEFORM-3D, Temperature: 400°C, punch speed: 0.1 mm/s).

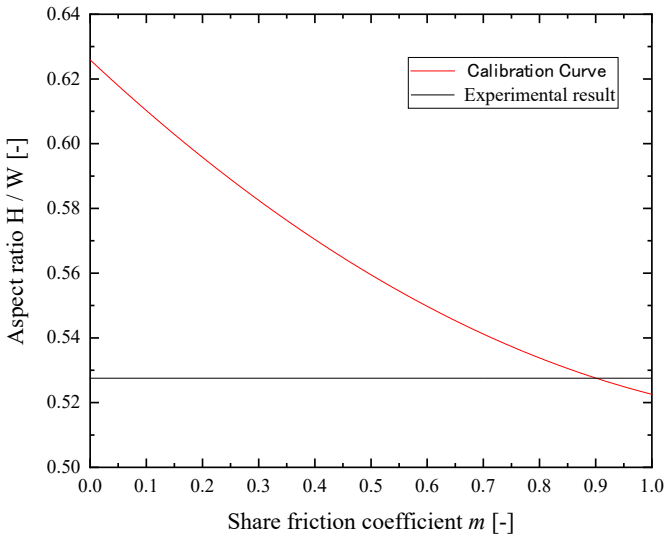

Fig. 5. Calibration curves and experimental aspect ratios (test temperature: 400°C, punch speed: 0.1 mm/s).

Fig. 6 shows an numerical analysis (m=0.9) and experimental force-punch stroke diagram for the V-groove friction test at a test temperature of 400°C. The experimental and numerical force curves were similar. The maximum force was 176.0 kN in the numerical analysis and 176.9 kN in the experiment. Fig. 7 compares the material flow between the experimental and numerical results. At the corner radius R, the material flow is divided into extrusion in the direction of punch travel and compression in the vertical movement of the extrusion. From the sample dimensions after the test shown in Fig. 7 and the calibration curve shown in Fig. 4, it can assume that material flow in

the direction of extrusion is dominant when friction is low, and material flow in the direction of compression is dominant when friction is high.

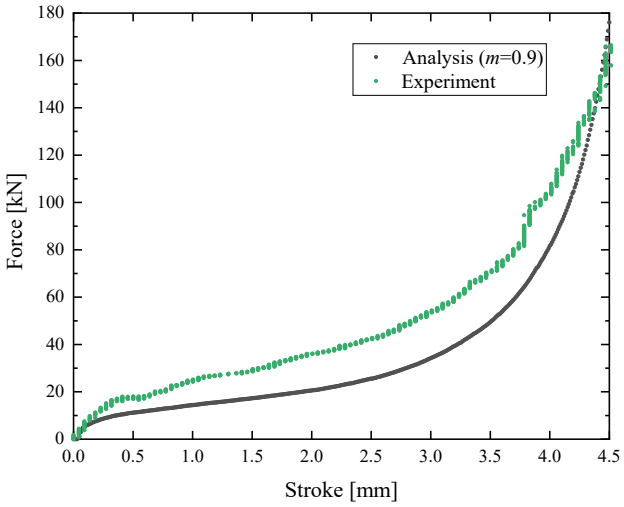

Fig. 6. Force-stroke curves for V-groove compression test and numerical analysis (test temperature: 400°C, punch speed: 0.1 mm/s).

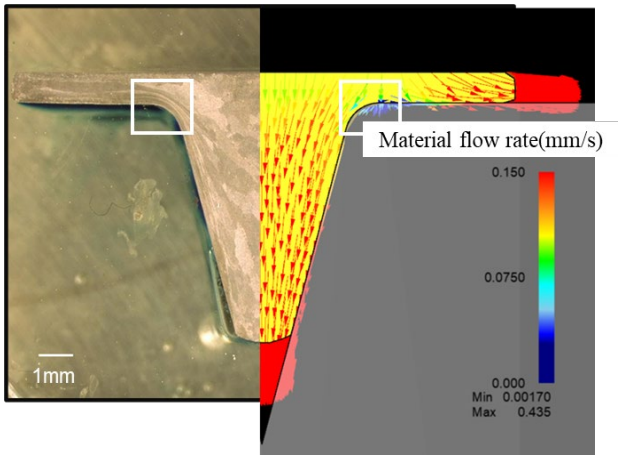

Fig. 7. Comparison of experimental and numerical material flow (test temperature: 400°C, punch speed: 0.1 mm/s).

Based on the experimental and numerical results of the V-groove compression test at 400°C, this test was validated as a friction test simulating hot extrusion and forging. Friction and adhesion between the die and aluminum on the tool surface are assumed to be significant causes of tearing defects on the product surface and burning on the tool at high temperatures and high forging speeds, which is a friction problem in extrusion and forging. Therefore, we conducted a V-groove compression test at 500°C and compared the results with those at 400°C to evaluate friction and adhesion to the tool as a function of temperature.

Fig. 8 shows the experimental results of the V-groove compression test at 500°C and the calibration curve. H/W from the experiment was 0.538, and the coefficient of friction was m = 1.0. The results of a previous hot forward-backward extrusion friction test at 500°C between a nitrided tool and AA7075 conducted by the authors also showed m=1.0, which is the same result as in the present study [4].

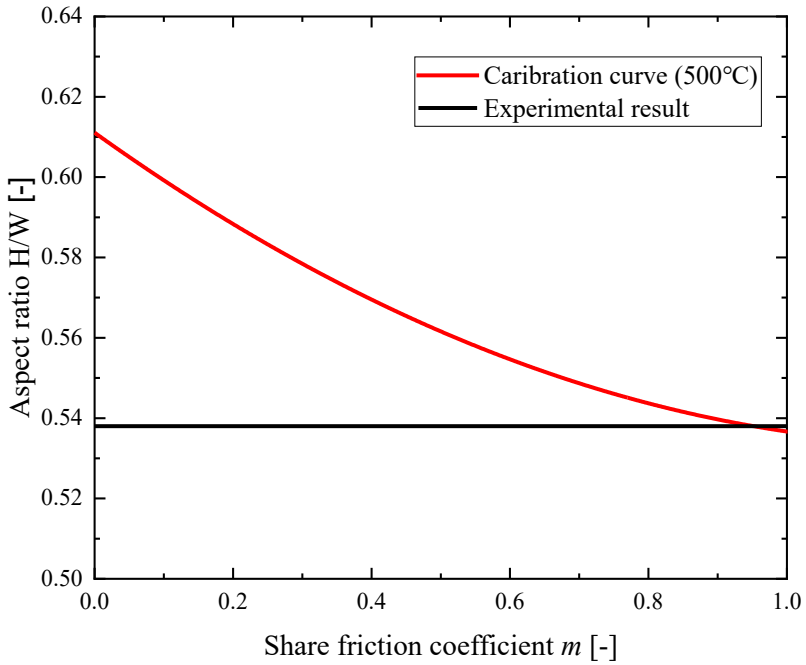

Fig. 8. Calibration curves and experimental aspect ratios (test temperature: 500°C, punch speed: 0.1 mm/s).

Fig. 9 shows the adsorption of alloying elements and oxygen (O) on the tool in the V-groove compression test at 400°C and 500°C. Before the test, aluminum (Al) was removed with sodium hydroxide solution and then analyzed by EPMA. The results of the EPMA analysis show that the adsorption of the alloying elements increased with increasing temperature in the Mg case. The strong O reaction on the entire tool surface at 500°C indicates that the tool surface is strongly oxidized, while the responses of Cu and Zn are small at 400°C and strong at 500°C, respectively. Previous studies by the authors have confirmed that magnesium oxide (MgO) is deposited by O on the tool surface and oxidized at high temperatures during the hot extrusion of AA6063 and Mg contained in the alloying elements [13]. At 400°C, the reaction of O is also vital in the Mg range, suggesting that MgO is formed.

On the other hand, at 500°C, the entire tool is uniformly oxidized, and the extent of Mg deposition is considered to have increased. The V-groove friction test also showed the same tendency, with Mg firmly adhering at the R part where the high surface pressure is applied, and from the quaternary state diagram of the Al-Zn-Mg-Cu alloy, Al+ $Al_2Mg_3Zn_3$+ $Al_5Cu_2Mg_2$ at 400°C or higher [14]. Since the composition of AA7075 in this study contains 1.6% Cu, $Al_2Mg_3Zn_3$ melts at temperatures above 480°C, and $Al_5Cu_2Mg_2$ melts at temperatures above 500°C. The Cu and Zn have not adhered at 400°C on the tool.

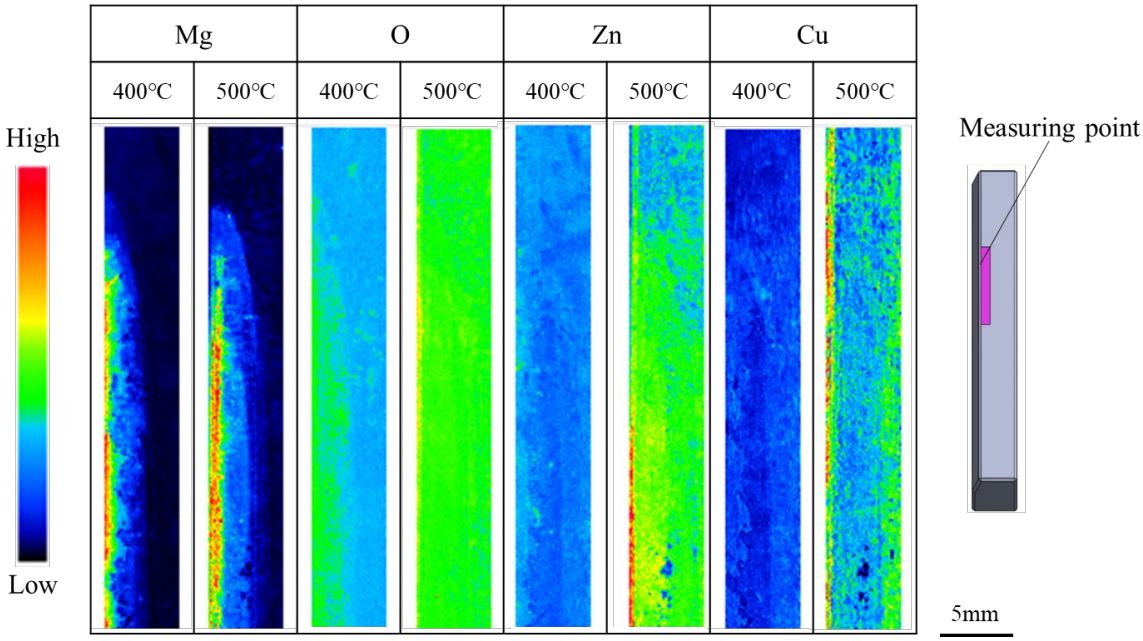

Fig. 9. Elemental analysis of tool surface after V-groove compression test (test temperature: 400, 500°C, punch speed: 0.1 mm/s).

Summary

In this study, the hot V-groove friction test is proposed as a friction test simulating extrusion and forging, measuring the coefficient of friction at various temperatures, and evaluating the adhesion to the tool surface. The hot V-groove friction test is practical as a friction test that simulates plastic forming at high temperatures because it achieves a high surface area expansion ratio. In addition, it was possible to reproduce the adhesion process of the tool surface during extrusion. The results obtained are listed below.

- The tool geometry was optimally affected by friction when the corner radius of the groove R was 1.0 mm, and the groove angle was 30°.
- From the calibration curve obtained from the numerical analysis, the shear friction coefficient *m* of AA7075 at 400°C was 0.9, and at 500°C, the shear friction coefficient *m* was 1.0.
- The EPMA evaluation of tool surface adhesion at 400°C and 500°C showed that the extent of Mg adhesion increased with increasing temperature, and the oxidation of the tool surface became stronger; Cu and Zn adhesion became more active at 500°C due to melting of intermetallic compounds.

Future research will include investigating the effects of surface pressure, heat generation, and tool surface adhesion using analysis and investigating the impact of tool surface treatment on tribological properties by applying die coating, tool surface texturing, and V-groove compression testing.

References

[1] W.Z. Misiolek, Metalworking: Bulk-forming, In: ASM Handbook, 10th edn. S.L. Semiatin, Ed. Almere (the Netherlands), ASM International, 2005, pp. 522-527.

[2] P.K. Saha, Aluminum Extrusion Technology, Almere (the Netherlands), ASM International, 2000. https://doi.org/10.31399/asm.tb.aet.9781627083362

[3] S. Ngernbamrung, T. Funazuka, N. Takatsuji, S. Murakami, K. Dohda, Tearing mechanism of high-strength 7000 series aluminum alloy in hot extrusion, J. Jpn. Inst. Light. Met. 68 (2018) 660-666. https://doi.org/10.2464/jilm.68.660

[4] T. Funazuka, K. Dohda, N. Takatsuji, C. Hu, N. Sukunthakan, Effect of die coating on surface crack depth of hot extruded 7075 aluminum alloy, Friction (2022) 1-13. https://doi.org/10.1007/s40544-022-0649-y
[5] J. Jerina, M. Kalin, Initiation and evolution of the aluminium-alloy transfer on hot-work tool steel at temperatures from 20C to 500C, Wear 319 (2014) 234-244. https://doi.org/10.1016/j.wear.2014.07.021
[6] J. Jerina, M. Kalin, Aluminium-alloy transfer to a CrN coating and a hot-work tool steel at room and elevated temperatures, Wear 340 (2015) 82-89. https://doi.org/10.1016/j.wear.2015.07.005
[7] M. Kalin, J. Jerina, The effect of temperature and sliding distance on coated (CrN, TiAlN) and uncoated nitrided hot-work tool steels against an aluminum alloy, Wear 330 (2015) 371-379. https://doi.org/10.1016/j.wear.2015.01.007
[8] E. Vidal-Sallé, M. Dubar, J.C. Boyer, L. Dubar, Fem numerical simulation of the warm and hot upsetting sliding test, Int. J. Mater. Form. 3 (2010) 315-318. https://doi.org/10.1007/s12289-010-0770-8
[9] A. Dubois, M. Dubar, L. Dubar, Warm and hot upsetting sliding test: Tribology of metal processes at high temperature, Procedia Eng. 81 (2014) 1964-1969. https://doi.org/10.1016/j.proeng.2014.10.265
[10] A. Dubois, M. Dubar, C. Debras, K. Hermange, C. Nivot, C. Courtois, New environmentally friendly coatings for hot forging tools, Surf. Coat. Technol. 344 (2018) 342-352. https://doi.org/10.1016/j.surfcoat.2018.03.055
[11] Q. Zhang, E. Felder, S. Bruschi, Evaluation of friction condition in cold forging by using T-shape compression test, J. Mater. Process. Technol. 209 (2009) 5720-5729. https://doi.org/10.1016/j.jmatprotec.2009.06.002
[12] F. Fereshteh-Saniee, H. Badnava, S.M. Pezeshki-Najafabadi, Application of T-shape friction test for AZ31 and AZ80 magnesium alloys at elevated temperatures, Mater. Des. 32 (2011) 3221-3230. https://doi.org/10.1016/j.matdes.2011.02.042
[13] T. Funazuka, N. Takatsuji, T. Tsuchiya, S. Oda, Pick-up defect mechanism in hot extrusion of Al-Mg-Si series alloy, J. Jpn. Inst. Light. Met. 70 (2020) 415-421. https://doi.org/10.2464/jilm.70.415
[14] H. Watanabe, On the Al-Side Phase Diagram of the Quarternary System Al-Zn-Mg-Cu, J. Jpn. Inst. Light. Met. 23 (1959) 596-600. https://doi.org/10.2320/jinstmet1952.23.10_596

Materials Research Proceedings 28 (2023) 429-436 https://doi.org/10.21741/9781644902479-47

Effects of cold-drawing and low-temperature annealing on the sensing properties of NiTi alloys

LI Yongji[1,a], LIN Jianping[1,2,b*], XIAO Yao[1,3,c] and MIN Junying[1,2,d]

[1]School of Mechanical Engineering, Tongji University, Shanghai, 201804, China

[2]Shanghai Key Laboratory for A&D of Metallic Functional Material, Tongji University, Shanghai 200092, China

[3]Institute for Advanced Study, Tongji University, Shanghai, 200092, China

[a]yongji@tongji.edu.cn, [b]jplin58@tongji.edu.cn, [c]xiaoy10@tongji.edu.cn, [d]junying.min@tongji.edu.cn

Keywords: NiTi Alloys, Cold-Drawing, Low-Temperature Annealing, Sensing Properties

Abstract. As an intelligent material, NiTi alloy exhibits shape memory effect and superelasticity. Its electrical resistance varies with deformation, thus making NiTi alloy a potential sensing material. Linearity and sensitivity are the two principal characteristics of sensors. Linearity reveals the deviation of the actual resistance-strain response from an ideal straight line and sensitivity is the change in input required to generate a unit change in output. Though conventional polycrystalline NiTi alloys possess high sensitivity and large strain range, the non-linear resistance-strain responses were not negligible thus hindering their sensing application. It was found that cold-drawing combing with low-temperature annealing had affected the linearity, while the influence rules were not clear. The electrical resistance of the fabricated NiTi alloy wires with various areal reductions were measured during stretching, and the results shown that the cold-drawn and annealed NiTi alloys exhibited better linearity though with decreased sensitivity. This investigation provides foundation for subsequent research on improving or tailoring the sensing properties of NiTi alloys.

Introduction

Shape memory alloys (SMAs), particularly NiTi alloys are special class of smart or intelligent materials gaining remarkable attention[1]. NiTi alloys possess the outstanding properties of shape-memory effect, superelasticity, high damping capacity as well as excellent wear resistance[2]. And they have been extensively applied in automotive, aerospace, mini actuators and micro-eletromechanical systems (MEMS).

Electric resistance is an important physical property of SMAs and it have been used to investigate the martensitic transformation, orientation, aging and plastic deformations[3]. Several researchers have noticed that changes in deformation are coupled to changes in electrical resistance of superelastic NiTi wires[4–6]. This relationship is of great importance because it makes NiTi a potential perception material, thus could further enrich its intelligent performance. Linearity and sensitivity are the two principal characteristics of sensors. The linearity is characterized by the non-linearity error, which is the maximum deviation of the change in the resistance from a specified straight line applied to the measured data points. The sensitivity is the ratio of change in the resistance to the strain. However, conventional polycrystalline shows a severer non-linear resistance-strain response, which hinders its sensing application.

The functional properties of NiTi are structure-sensitive, so they are possible to be improved by some process through creating well-developed structures. Lin et al. [7] fabricated three polycrystalline NiTi samples with different grain sizes from 35 nm to 110 nm and one crystalline-amorphous NiTi nanocomposite sample. They found that grain refinement and partial

Content from this work may be used under the terms of the Creative Commons Attribution 3.0 license. Any further distribution of this work must maintain attribution to the author(s) and the title of the work, journal citation and DOI. Published under license by Materials Research Forum LLC.

amorphization can significantly improve the linearity of stress-strain response. Hua et al.[8] produced NiTi crystalline-amorphous nanocomposite by cold rolling with low-temperature annealing, which demonstrates near-linear superelasticity under stress of 2.3 GPa. Inspired by these strategies for improving its mechanical properties, we consider it practicable to change the electrical behaviors of NiTi by introducing amorphous structure. According to the preliminary results, it was found that cold-drawing combing with low-temperature annealing had affected the electrical behavior of NiTi alloy wires, while the influence rules were not clear.

The present work aims to investigate the effects of cold-drawing and low-temperature annealing on the sensing properties of NiTi alloy wires.

Materials and Experiments

Commercial superelastic NiTi wires with an initial diameter of 0.3 mm were purchased from PEIERTECH Incorporation (Jiangsu, China). The as-received nanocrystalline NiTi alloy wire was solution treated at 800 ℃ for 60 min in a muffle furnace and subsequently quenched by water.

Then the solution-treated samples were cold-drawn to thinner wires by continuous multi-pass processes using diamond dies without intermediate annealing. The die was lubricated with MoS_2 and the drawing speed was 300 mm/min. Due to the significant work hardening and cracking, it is difficult to lead the wires to pass through the die. And mechanical grinding is not applicable to make the wire end to a thinner diameter. Instead, a corrosion solution of HF: HNO_3: H_2O=1:5:20 by volume ratio was used to reduce the diameter of the wire end. According to the initial wire diameter of each drawing pass, the corrosion time varied from 5 min to 30 min. The summarized cold-drawing parameters including corrosion time, die diameter, pass or total areal reduction were listed in Table 1.

Table 1. Cold-drawing parameters of the NiTi wires.

Drawing Pass	Wire Diameter	Corrosion Time	Die Diameter	Pass Areal Reduction	Total Areal Reduction
1	0.3 mm	30 min	0.25 mm	30.6 %	30.6 %
2	0.25 mm	20 min	0.2 mm	36.0 %	55.6 %
3	0.2 mm	15 min	0.17 mm	27.8 %	67.9 %
4	0.17 mm	12 min	0.15 mm	22.1 %	75.0 %
5	0.15 mm	10 min	0.13 mm	24.9 %	81.2 %
6	0.13 mm	8 min	0.11 mm	28.4 %	86.6 %
7	0.11 mm	5 min	0.1 mm	17.4 %	88.9 %

The cold-drawn wires with final diameters of 0.2 mm, 0.15 mm, 0.1 mm (area reduction were 55.6 %, 75.0 %, 88.9 %, respectively) were then annealed at 300 ℃ for 60 min. As shown in Fig. 1, the tensile tests were executed on an MTS E44 testing machine with a loading and unloading rate of 5 mm/min at room temperature. The specimen elongation was measured via the crosshead travel monitor with resolution of 0.04 μm. The gauge length of the specimen was about 50 mm and the maximum elongation was 3 % with a strain rate of about $1.7 \times 10^{-3}\ /s$. The variations of electrical resistance were synchronously measured by a high precision multi-meter (GDM-8342, Good Will Instrument) with an accuracy of 0.1 %. The end of thin wire was clamped by three-jaw metal collet, and the electric cables of the multimeter were fixed on the collet by screws. For ensuring the NiTi wires insulate from the tensile machine, the collets were connected to the grip

holders with insulated handles. Both the crosshead travel distance and the measured electrical resistance were transferred to PC for further processing.

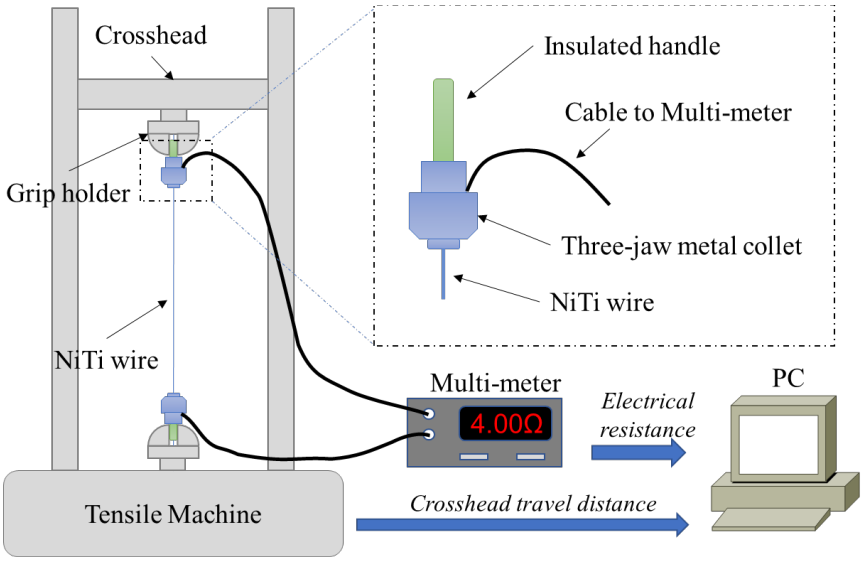

Fig. 1. Schematic diagram of the electrical resistance measurement.

Based on the measured data of electrical resistance and crosshead travel distance, the change ratio of resistance-strain curve is achieved. Through the least-squares method, the fitting line is achieved based on the experimental data. The calculation schematic of linearity and sensitivity is shown in Fig. 2. The sensitivity is defined as the slope of the fitting line, which is a unitless value. The linearity is characterized by the non-linearity error (NLE), which is calculated by Eq. 1.

$$NLE = \frac{\Delta_{max}}{Y_{max}} \times 100\% \, . \tag{1}$$

where Δ_{max} is the largest difference between the experimental data and the fitting line and Y_{max} is the largest change ratio of resistance.

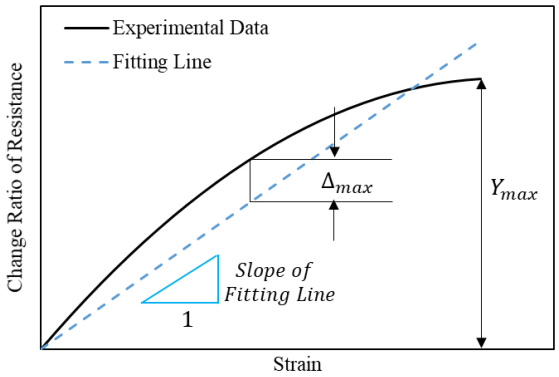

Fig. 2. Schematic diagram of the calculation of linearity and sensitivity.

According to the resistance formula (Eq. 2a and Eq. 2b), the electrical resistance is determined by two factors: the electrical resistivity (ρ) and size factor (L/S).

$$R_0 = \rho_0 * L_0/S_0 \, . \tag{2a}$$

$$R_\varepsilon = \rho_\varepsilon * L_\varepsilon / S_\varepsilon \,. \tag{2b}$$

where R is the measured resistance, ρ is the electrical resistivity, L is the length of the wire and S denotes the cross-sectional area of the specimen. The subscript 0 and ε stands for initial undeformed state and deformed state with a strain of ε, respectively.

From the constant volume assumption (Eq. 3a) [9] and the strain formula (Eq. 3b), the relative change ratio of electrical resistivity is inferred as Eq. 4.

$$L_\varepsilon * S_\varepsilon = L_0 * S_0 \,. \tag{3a}$$

$$L_\varepsilon = L_0 * (1 + \varepsilon) \,. \tag{3b}$$

$$\frac{detdet\,(\rho_\varepsilon)}{\rho_0} = \frac{\rho_\varepsilon - \rho_0}{\rho_0} = \frac{R_\varepsilon * {L_0}^2}{R_0 * {L_\varepsilon}^2} - 1 = \frac{R_\varepsilon - R_0 * (1+\varepsilon)^2}{R_0 * (1+\varepsilon)^2} \,. \tag{4}$$

Then assuming that the resistivity is constant, the relative change ratio of size factor is inferred as Eq. 5.

$$\frac{detdet\,(L_\varepsilon / S_\varepsilon)}{\frac{L_0}{S_0}} = \frac{L_\varepsilon/S_\varepsilon - \frac{L_0}{S_0}}{\frac{L_0}{S_0}} = (1+\varepsilon)^2 - 1 \approx 2\varepsilon \,. \tag{5}$$

To clarify the crystal structural change by cold-drawing and low-temperature annealing, Micro X-ray diffractometry (Micro-XRD) was carried out on Bruker D8 Advance using Cu-Kα radiation operated at 30 kV, 150 mA and a scanning speed of 4 °/min. A 2θ angle range from 5 ° to 85 ° was selected.

Results and Discussions

As shown in Fig. 3, the initial electrical resistivity exhibits a large variability in different NiTi alloy wires. The as-received NiTi alloy material possesses an initial electrical resistivity of 0.9 $\mu\Omega \cdot m$, which is higher by two orders of magnitude than common metal such as copper, aluminum. The resistivity of the cold-drawn NiTi (CD) increases significantly with the areal reduction. For the low-temperature annealed NiTi wires (CD+LTA), their resistivities maintain the same variation trend with the areal reduction but they decrease comparing with their cold-drawn counterparts. Notably, the electrical resistivities of the annealed NiTi wires with different areal reduction remain above that of the as-received.

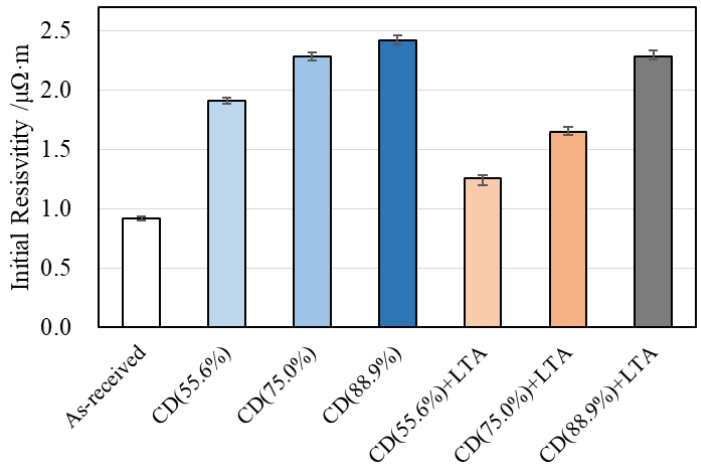

Fig. 3. The initial electrical resistivity of the NiTi alloy wires.

Materials Research Proceedings 28 (2023) 429-436 https://doi.org/10.21741/9781644902479-47

Fig. 4(a) displays resistance change ratio as a function of strain obtained during stretching of the as-received NiTi alloy wire and six tailored materials. The sensitivity and the non-linearity errors are summarized in Table 2. By comparing with the as-received sample, the cold-drawn and annealed NiTi wires demonstrates nearly linear resistance vs. strain relationship though with decreased sensitivity. With similar properties of linearity, the low-temperature annealed NiTi wires exhibited higher sensitivity than the cold-drawn ones.

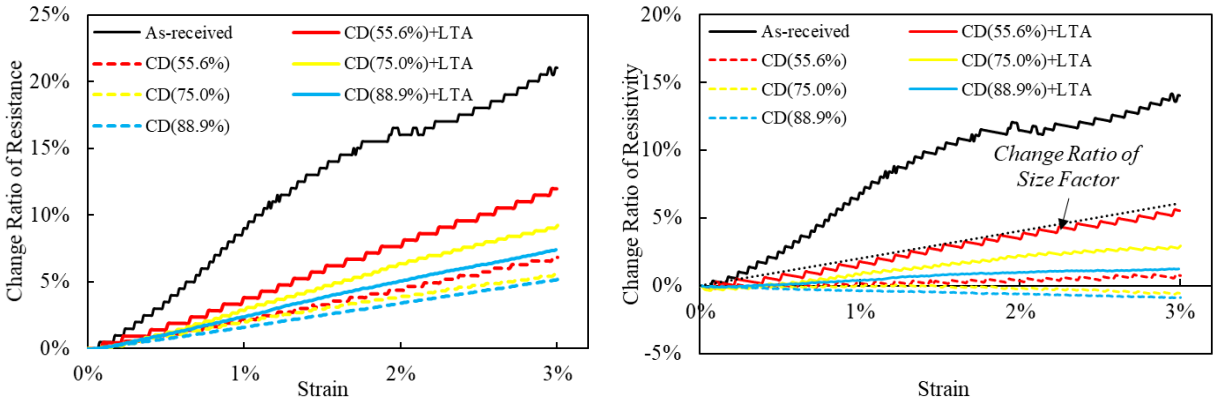

Fig. 4. (a) The resistance change ratio vs. strain curves and (b) the resistivity change ratio vs. strain curves of different NiTi alloy wires.

Table 2. Sensing sensitivities and non-linearity errors of different NiTi alloy wires.

Sample	Sensitivity	Non-Linearity Error
As-received	7.00	10.68 %
CD(55.6 %)	2.29	3.77 %
CD(75.0 %)	1.84	4.84 %
CD(88.9 %)	1.72	2.17 %
CD(55.6 %)+LTA	3.99	5.07 %
CD(75.0 %)+LTA	3.15	3.35 %
CD(88.9 %)+LTA	2.48	2.64 %

The factors of resistance variation were decoupled to the resistivity and the size factor. According to Eq. 5, the change ratio of size factor is only determined by strain and the slope is about 2. The resistivity change ratio vs. strain curves of different NiTi wires are shown in Fig. 4(b), in which the curve of size factor change ratio also added. For the as-received sample, the resistivity change ratio displays severe nonlinearity as well as a bigger slope than the size factor. The linearities of the tailored material are much better than the as-received one though the slopes are smaller. The slopes decrease with the areal reduction both for the cold-drawn and the annealed NiTi wires, while the latter ones are better than the former ones. Worth noting is that the resistivity change ratio becomes negative for the cold-drawn NiTi with 75.0 % or 88.9 % areal reduction and this issue will be discussed later.

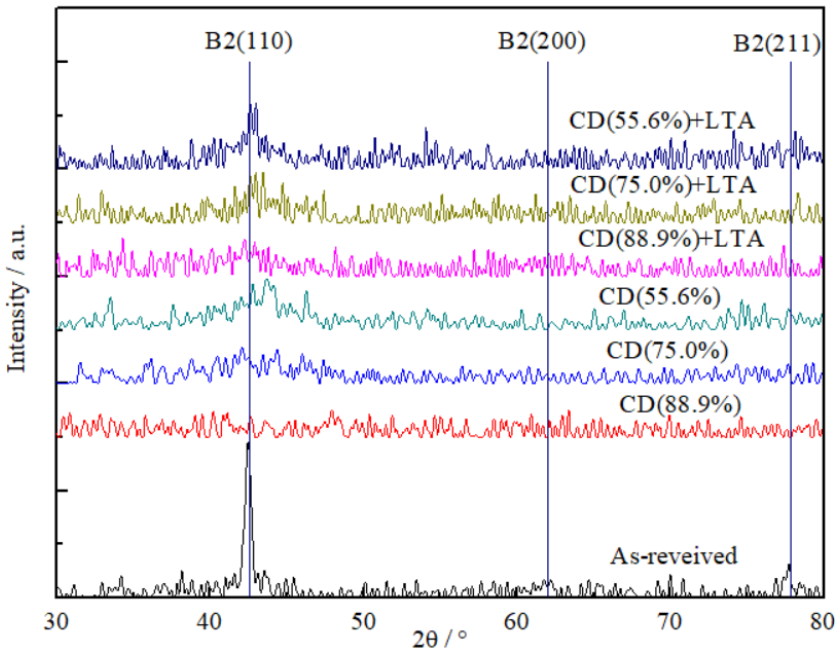

Fig. 5. Micro-XRD patterns of the as-received NiTi wire and six tailored ones.

Fig. 5 gives the Micro-XRD patterns of the different NiTi alloy wires. The Micro-XRD patterns of as-received wire shows that it is comprised of austenite phase (B2). There are marked drops in the intensity of the austenite peak for all of the cold-drawn wires and the low-temperature annealed wires. With the increasing of areal reduction, the intensities of the austenite peaks of both two kind of materials decrease, which illustrates that amorphization is intensified. The peak intensity of the annealed NiTi is higher than the cold-drawn one with the same areal reduction, which indicates that recrystallization of the austenite occurs to a certain extent in the low-temperature annealing processes.

According to the initial electrical resistivities and the Micro-XRD patterns, it suggests that cold-drawing leaded to amorphization of NiTi alloy and the amorphous phase rise with the increasing of areal reduction. In the subsequent low-temperature annealing, amorphous phase is subjected to recrystallization. For the as-received nanocrystalline NiTi material, elastic deformation appeared first in the stretching process and the stress-induced austenite-to-martensite transformation occurred when the strain exceeded about 1.5 %. The non-linear resistance-strain response is directly relevant to the stress-induced phase transformation. Ahadi and Sun [10] carried out in-situ tensile X-ray diffraction experiments for investigating the structure evolution during stress-induced transformation. NiTi alloy with a low B2 peak exhibited a continuous and smooth peak shift from B2 peak to B19'(Martensite) peak, while NiTi alloy with a higher peak displayer a sudden appearance of B19' peak. For the cold-drawn and the annealed NiTi wires, the containing amorphous phase suppresses the austenite-to-martensite transformation resulting in a continuous and smooth transformation, thus leading a more linear resistance-strain response.

Considering the negative slope of resistivity-strain response of the cold-drawn with great areal reduction (75.0 %, 88.9 %), it is assumed that the resistivity of pure amorphous phase is negative correlation with deformation. The amorphous phase is unstable and it can be subjected to crystallization under the stress [11]. The resistivity decreases in the crystallization process as the resistivity of crystal is lower than that of amorphous. Thus, there is a competitive relationship between crystalline and amorphous, which haves opposite effect on electrical resistivity of the deformed NiTi material. For CD 75.0 % and CD 88.9 %, the amount of amorphous is higher than other samples, so the amorphous phase plays a major role in resistivity variation resulting in a

negative slope. The changing sensitivity, i.e., the slopes of the resistance vs. strain curves, is attributed to the differences of amorphous phase content.

Summary

In this study, the effects of cold-drawing and subsequent low-temperature annealing on the sensing properties of NiTi alloy wires were investigated. The cold-drawn and annealed NiTi alloys exhibited better linearity though with smaller sensitivity. The greater areal reduction caused a better linearity. Combing with the initial electrical resistivities and the XRD patterns, it is inferred that amorphous phase is generated in NiTi alloy due to cold-drawing and low-temperature annealing. The amorphous phase suppresses martensitic transformation of the crystalline phase and consequently contributed to the improvement of linearity in the resistance-strain response.

Cold-drawing combining with low-temperature annealing is a practicable approach to regulate the sensing properties of NiTi alloys. For further investigations, the quantitative relationships between microstructures and sensing properties should be appealed.

Acknowledgments

This work was financially supported by National Natural Science Foundation of China (Grant No. 52075390).

References

[1] M. Sobczyk, S. Wiesenhütter, J.R. Noennig, T. Wallmersperger, Smart materials in architecture for actuator and sensor applications: A review, J. Intell. Mater. Syst. Struct. 33 (2022) 379-399. https://doi.org/10.1177/1045389X211027954

[2] N. Gangil, A.N. Siddiquee, S. Maheshwari, Towards applications, processing and advancements in shape memory alloy and its composites, J. Manuf. Process. 59 (2020) 205-222. https://doi.org/10.1016/j.jmapro.2020.09.048

[3] Y. Chen, O. Tyc, L. Kadeřávek, O. Molnárová, L. Heller, P. Šittner, Temperature and microstructure dependence of localized tensile deformation of superelastic NiTi wires, Mater. Des. 174 (2019) 107797. https://doi.org/10.1016/j.matdes.2019.107797

[4] S. Sławski, M. Kciuk, W. Klein, Change in Electrical Resistance of SMA (NiTi) Wires during Cyclic Stretching, Sensors 22 (2022) 3584. https://doi.org/10.3390/s22093584

[5] N. Michaelis, F. Welsch, S.-M. Kirsch, S. Seelecke, A. Schütze, Resistance monitoring of shape memory material stabilization during elastocaloric training, Smart Mater. Struct. 28 (2019) 105046. https://doi.org/10.1088/1361-665X/ab3d62

[6] A. Gurley, T.R. Lambert, D. Beale, R. Broughton, Dual measurement self-sensing technique of NiTi actuators for use in robust control, Smart Mater. Struct. 26 (2017) 105050. https://doi.org/10.1088/1361-665X/aa8b42

[7] H. Lin, P. Hua, Q. Sun, Effects of grain size and partial amorphization on elastocaloric cooling performance of nanostructured NiTi, Scripta Mater. 209 (2022) 114371. https://doi.org/10.1016/j.scriptamat.2021.114371

[8] P. Hua, M. Xia, Y. Onuki, Q. Sun, Nanocomposite NiTi shape memory alloy with high strength and fatigue resistance, Nat. Nanotechnol. 16 (2021) 409-413. https://doi.org/10.1038/s41565-020-00837-5

[9] M. Barati, S.A. Chirani, M. Kadkhodaei, L. Saint-Sulpice, S. Calloch, On the origin of residual strain in shape memory alloys: experimental investigation on evolutions in the microstructure of CuAlBe during complex thermomechanical loadings, Smart Mater. Struct. 26 (2017) 25024. https://doi.org/10.1088/1361-665X/aa5745

[10] A. Ahadi, Q. Sun, Stress-induced nanoscale phase transition in superelastic NiTi by in situ X-ray diffraction, Acta Mater. 90 (2015) 272–281. https://doi.org/10.1016/j.actamat.2015.02.024

[11] Y. Zhang, S. Jiang, M. Wang, Atomistic investigation on superelasticity of NiTi shape memory alloy with complex microstructures based on molecular dynamics simulation, Int. J. Plast. 125 (2020) 27-51. https://doi.org/10.1016/j.ijplas.2019.09.001

Materials Research Proceedings 28 (2023) 437-444 https://doi.org/10.21741/9781644902479-48

Electron backscatter diffraction (EBSD) as a tool for analysis of metal flow in aluminum extrusion

PIRES Michael V.[1,a *], MADURA Jacek[2,b], MISIOLEK Wojciech Z.[1,c]
LEŚNIAK Dariusz[2,d], ZASADZIŃSKI Józef[2,e] and JURCZAK Henryk[3,f]

[1]Loewy Institute, Lehigh University, Bethlehem, PA, USA

[2]AGH University of Science and Technology, Krakow, Poland

[3]Albatros Aluminium, Wałcz, Poland

[a]mvp217@lehigh.edu, [b]madura@agh.edu.pl, [c]wzm2@lehigh.edu, [d]dlesniak@agh.edu.pl, [e]zas@agh.edu.pl, [f]h.jurczak@albatros-aluminium.com

Keywords: EBSD Technique, Porthole Dies, Aluminum Extrusion

Abstract. Electron backscatter diffraction was used to analyze the crystallographic texture within extruded AA6005 hollow profiles, allowing for the analysis of metal flow through various extrusion porthole die designs of different metal deformation conditions. Control of metal flow through a die design is necessary to meet industry demands for faster-running dies, tighter tolerances, thinner walls, and reduced extrusion loads. A standard die was compared with an innovative die design that doubled the extrusion exit speed. Analysis of metal flow was performed to provide additional insight into the uniformity of the metal flow, especially near the extrusion welds. Finite element method simulations were performed to predict the die exit temperature and plastic strain distributions. Local texture varied across the core and surface regions of the tube wall but remained consistent between both extrudates. A peripheral coarse grain structure was found within both extrudates, due to their elevated exit die temperatures.

Introduction

The purpose of this work is to develop a quality control tool, which can analyze the homogeneity of an extrudate's microstructure and local crystallographic texture for an innovative porthole die design that allows for the minimization of the resistance to deformation. This translates into increasing the efficiency of the extrusion production process in the area of forming limit diagrams. A die design that ensures optimal metal flow translates into an increase in the flow rate in the connection with the load capacity of the press. An optimal die design also provides a reduction in the extrusion force, which is beneficial from the point of view of energy balance and die strength [1]. For these reasons, testing is required to determine the dies' effectiveness. Finite element method (FEM) numerical simulations as well as metallurgical characterization techniques may be utilized to predict and determine part properties. In this study, a standard porthole die design was compared to a new innovative porthole die design with increased extrusion exit speed in an attempt to increase production during the extrusion process. FEM numerical calculations were performed using QForm UK Extrusion software. The extrusion model is based on the Lagrange-Eulerian approach, which included coupled simulations of the material flow and die deflection during the process [2]. The approach uses a proprietary material model of a deformed aluminum alloy developed based on a high-temperature compression test on a Gleeble 3800 metallurgical process simulator. Simulations of different variants of dies were carried out under identical process parameters, including heating the billet to 480°C. FEM numerical calculations were performed to predict both the exit temperature and plastic strain distribution throughout the extrudate cross sections but still requires validation through experimental data.

Content from this work may be used under the terms of the Creative Commons Attribution 3.0 license. Any further distribution of this work must maintain attribution to the author(s) and the title of the work, journal citation and DOI. Published under license by Materials Research Forum LLC.

Materials Research Proceedings 28 (2023) 437-444 https://doi.org/10.21741/9781644902479-48

Electron Backscatter Diffraction (EBSD) was utilized as the experimental method of choice to characterize the localized microstructural texture and average grain size within the resultant extrudates, as a result of their deformation conditions. Election backscatter diffraction, or backscatter Kikuchi diffraction, is a scanning electron microscope (SEM) based technique that can be used to determine local microstructural texture, generally associated with the crystallographic orientation of individual grains within a material. This allows for microstructure reconstruction and detailed characterization of the microstructural properties of a material [3]. EBSD utilizes automated Kikuchi pattern indexing software to determine the orientation of multiple grains at once, making it a fast and accurate method for generating large quantities of data. Indexing of patterns involves the identification of individual (Kikuchi) bands based on the presence or absence of specific crystallographic poles (zone axes) as well as bandwidth [4, 5]. It is important to define the notation of the extrudate axes to better describe the areas of interest for the EBSD analysis, which is shown in Fig. 1, below.

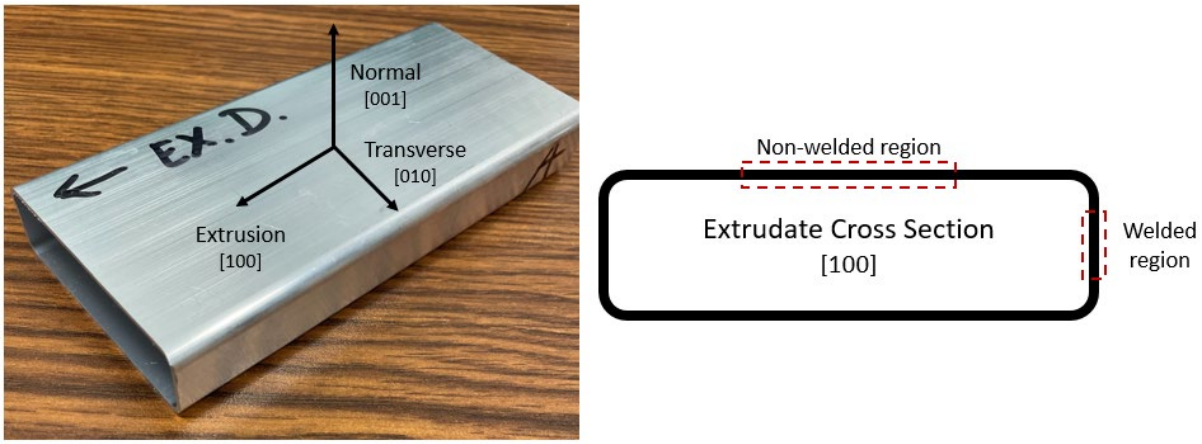

Fig. 1. Example of extrudate direction notation and regions of interest.

It is expected to obtain a homogenous microstructure within the extrudate as a result of die design, and therefore, altering deformation conditions. EBSD, as a proposed modern tool for metal flow analysis, will help to indirectly verify these results and the FEM predictions of exit temperature and plastic strain distribution.

Experimental Procedure

The samples analyzed in this study were thin-walled extrudates from 7-inch AA6005 billets extruded on 17 MN hydraulic press. Two profiles, A and D, were developed and extruded at the same temperature within different two-cavity dies consisting of similar web designs. Thus, the localization of transverse welds was the same. Profile A consisted of a conventional die with a maximum extrusion exit speed of 24 m/min and a specified maximum ram load of 15.36 MN. Profile D consisted of a new die with an innovative design ensuring an almost doubled increase in the extrusion exit speed of 42 m/min. The construction ensured a reduced plastic flow resistance, which was indicated by a lower maximum extrusion load of 14.88 MN. Both extrudates were cooled on the press run-out table under forced air. The maximum extrusion speed was determined for each of the dies in industrial trials while maintaining the required product surface quality. The measurement of the extrudate extrusion exit speed corresponded to the puller speed on the runout table. This was measured by sensors and using press software. The maximum speed was determined by the force capabilities of the press with simultaneous control of the temperature and the quality of the extrudates surface.

Improved process parameters were the result of using an extrusion die with larger ports, increasing the volume of metal flow by 45%. Thin webs were also used to ensure an even metal flow to the welding chambers. Equal filling of the bearing took place using a special port with a dedicated geometry. The new die design was developed based on FEM numerical simulations of the extrusion process. In the extrusion process design for the hollow sections of aluminum alloys, the exact conditions required to occur on the bearing surface must be determined. This can be obtained by numerical analysis, which includes parameters such as plastic strain and temperature distributions [6]. The developed extrusion process ensured a slight die deflection but yielded a high dimensional accuracy of extrudates. Both numerical simulations and physical measurements confirmed this. The deflection in the core and bearings was the result of numerical simulations, which is an elastic deformation that translates into the geometric accuracy of extrudates. Physical measurements were carried out after the experiment, which confirmed no evidence of plastic deformation of the tooling.

To prepare for experimental characterization, the extrudates were sectioned using a Struers Accutom-50 high-speed abrasive cutoff blade and mounted in epoxy resin, set in a vacuum to remove air bubbles, and left to cure overnight. Samples were metallographically prepared to a 0.25 μm finish with diamond media on a Buehler AutoMet250 automatic polishing unit before a 0.05 μm finish with colloidal silica on a vibratory polisher. Samples were cleaned in an ultrasound bath with ethanol and airdried using high heat. Silver paint was applied to the surface of the sample and left to dry for a minimum of 12 hours to prevent the buildup of current on the sample surface within the electron microscope.

Electron backscatter diffraction (EBSD) was performed in an FEI SCIOS Focused Ion-Beam (FIB) unit. Data was generated using EDAX TEAM software and analyzed with TSL OIM v8 software. EBSD maps were rebuilt using NPAR and further cleaned to achieve higher accurate confidence indexing (CI > 0.2) throughout the area of interest. An accelerating voltage of 10 kV was used in combination with a current of 6.4 nA during image collection. Maps were taken with a maximum sampling grid of 1024 x 800 pixels, individually modified to reduce both the scan area and total collection time. Maps were generated using a step size between 3-4 μm, consisting of hexagonal pixels. The EBSD camera was optimized using an *Ultra-Fast* setting to acquire a maximum of 170 frames per second (fps) under the listed conditions.

Numerical Investigation

FEM numerical simulations of the exit temperature and plastic strain distributions were performed for both extrudates A & D. The areas of interest highlighted within a black box, shown in both Fig. 2 and 3, for both the *non-welded* and *welded* regions correspond to the fields of view discussed later in the *Results & Discussion* section, shown as EBSD maps in Fig. 4. The exit temperature simulations, shown in Fig. 2, exhibited a variation of 10 °C throughout the entire cross-section, but was consistent across the full wall thickness at any given point, within a single degree. Comparing both profiles, A & D, a maximum exit temperature of 550°C was recorded near the center of the *non-welded* regions, steadily decreasing to a minimum temperature of 540°C as the cross-sectional corners were approached. In respect to the *welded* regions, profiles A & D were again consistent amongst each other, but with opposing results at either side of the extrudate. For the purpose of this study, the area of interest was focused on the right side of the extrudate cross-section, with a recorded exit temperature of 550°C.

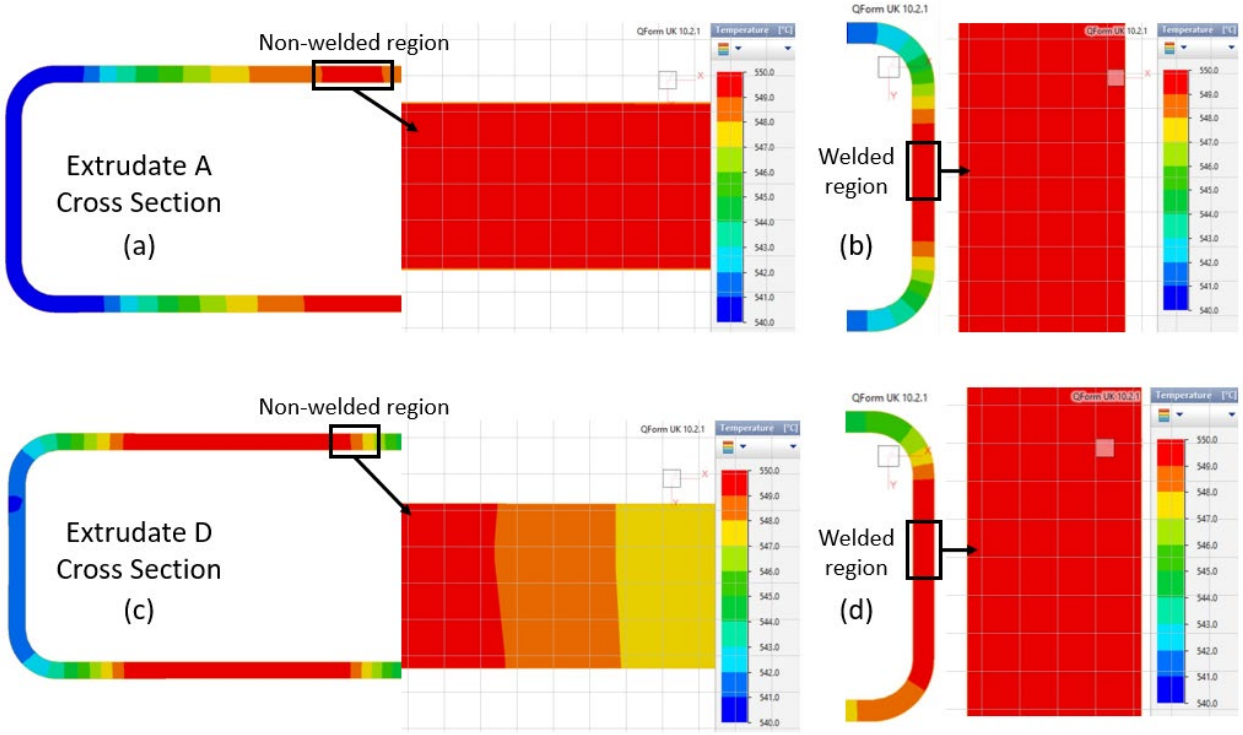

Fig. 2. FEM simulation of Exit Temperature for both Extrudate A (a, b) and Extrudate D (c, d).

The plastic strain simulations, shown in Fig. 3, exhibited a consistent strain gradient throughout the entire die other than at the center of both *welded* regions, including both sides of each extrudate. A minimum plastic strain, corresponding to the light blue color, was recorded at the center of the wall thickness where the least deformation is expected to occur. A gradient was recorded on either side of the wall thickness as the surface was approached, where the extrudate and die are in contact and the most deformation is expected to occur. The only discrepancy in the strain gradient occurred within the *welded* regions, where the localization of the longitudinal weld is believed to exist. Overall, the outer surface of the extrudate experienced a larger plastic strain compared to that of the inner surface, which was more apparent within the *welded* regions than within the *non-welded* regions. Upon closer inspection, a more balanced strain distribution across the wall thickness was revealed for profile A in the *non-welded* region, whereas a more balanced distribution was revealed for profile D in the *welded* region.

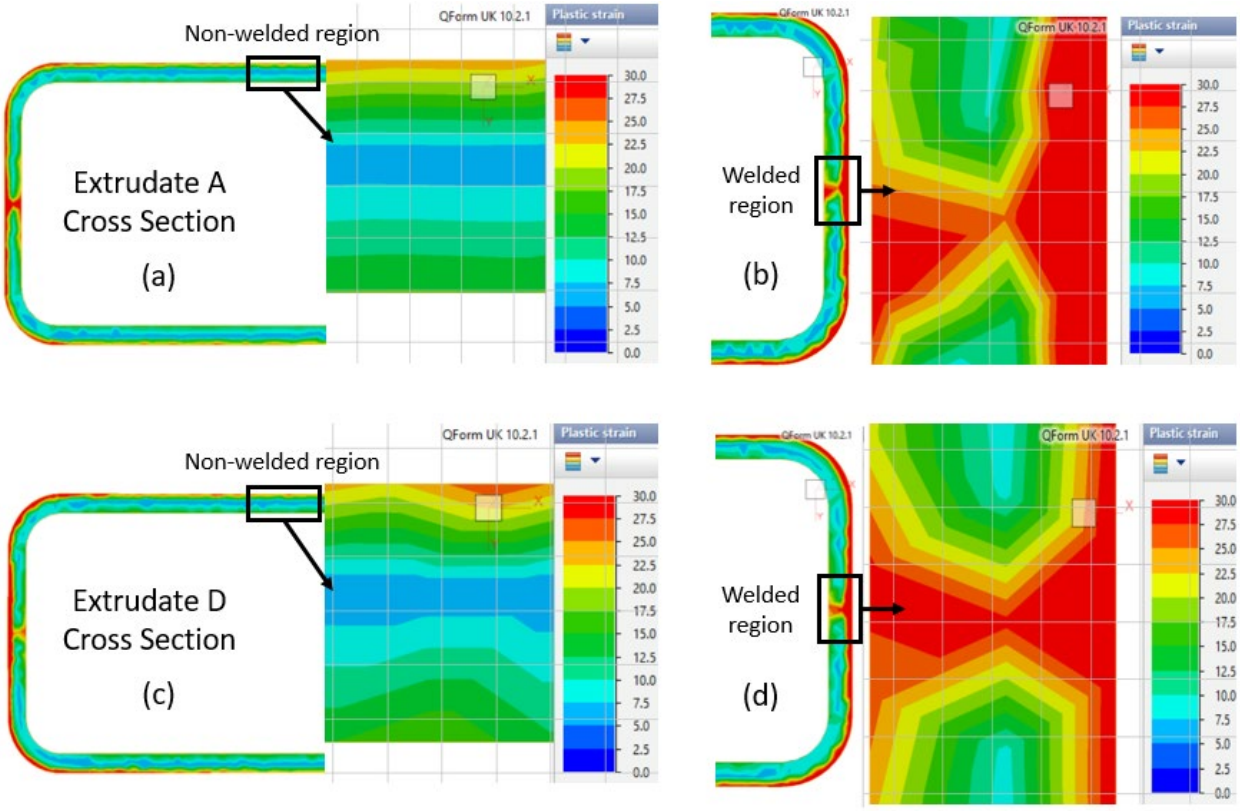

Fig. 3. FEM simulation of Plastic Strain for both Extrudate A (a, b) and Extrudate D (c, d).

Results and Discussion

Election backscatter diffraction was utilized to measure the microstructural texture and grain size of hot extruded AA6005 billets. A few considerations were made to generate accurate indexed patterns. As aluminum is a beam-sensitive material, a low accelerating voltage/beam current was necessary to reduce beam damage during mapping, which led to a loss in collection time and pattern quality. In addition, low magnification (80-100x) imaging was necessary to generate large enough fields of view for the regions of interest within the extruded samples. Below a magnification of ~250x, distortion of the image can occur due to a large focal plane when tilted at 70° for the EBSD technique. Using a low magnification can also make smaller grains difficult for the software to distinguish. A step (pixel) size of 3-4 µm was used to balance between pattern quality and collection time. The EDAX TEAM software incorporates Neighbor Pattern Averaging and Re-indexing (NPAR), which was used for post-process map rebuilding, greatly improving the accuracy of results and quality of the images presented in this study [7, 8].

Samples A and D were analyzed. EBSD maps of their areas of interest were generated, shown in Fig. 4. Throughout each field of view for both samples, the center of the extrudate exhibited a strong [001] texture corresponding to the color red/orange, whereas the surfaces in contact with the die transitioned into a [101] texture corresponding to the color green. In addition, a weak [111] texture corresponding to the color blue was recorded throughout the extrudate, but in larger amounts near the extrudate surface. The localized microstructure can be seen to vary from extrudate core to its surfaces due to different strain and friction conditions of the die. This result was to be expected and validated the plastic strain gradients recorded in the FEM simulations in Fig. 3.

Comparing the *non-welded* regions (Fig. 4a & 4c) the overall texture profile remained the same, but a decrease in average grain size from 95.6 µm to 83.7 µm occurred as the extrusion exit speed doubled. Within the *welded* regions (Fig. 4b & 4d) there was a drastic increase in average grain size from 66.5 µm to 82.8 µm. This increase in average size was likely a result of abnormal grain

growth, occurring near the outer surface within extrudate D. It is necessary to state that microstructural imperfections are known to occur during hot extrusion of aluminum alloys, such as in this case, a peripheral coarse grain (PCG) structure. This was more evident within the *non-welded* regions, but existed for both profiles A & D. Eivani et. al. concluded that elevated temperatures above 500°C during extrusion could cause PCG to form [9]. The presence of a PCG structure within both profiles may validate the FEM simulations in Fig. 2, which recorded exit temperatures entirely above 540°C. Van Geertruyden et. al. concluded that PCG is likely the result of delayed recrystallization, forming within a few seconds after exiting the die at elevated temperatures. He also found that a lack of recrystallization-inhibiting elements, such as Cr, increased the depth of PCG within the AA6xxx extrudate [10]. The low alloying content of these AA6005 extrudates while also undergoing air-cooling suggested the presence of PCG was likely to occur.

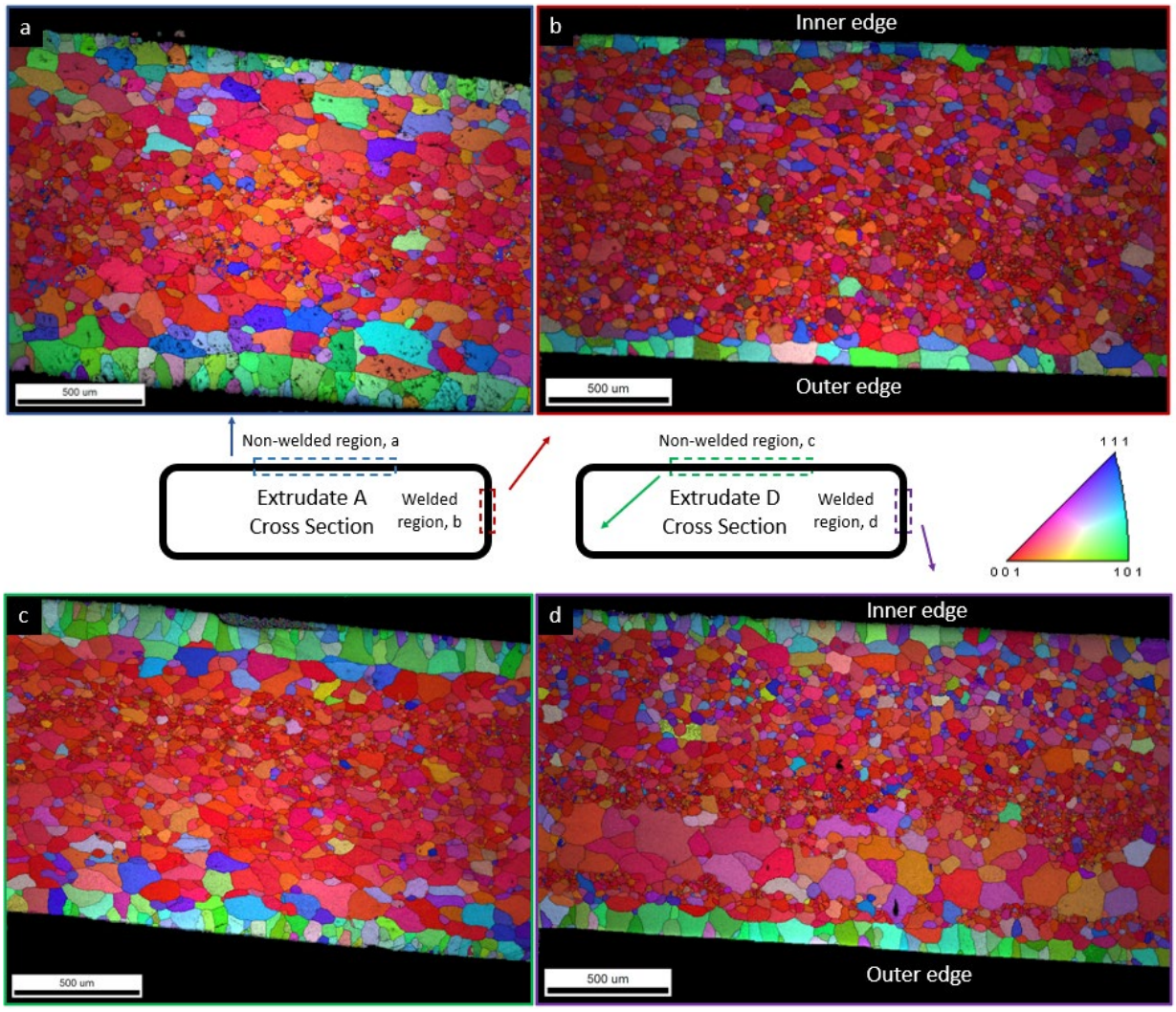

Fig. 4. EBSD crystallographic orientation maps of Extrudate A (a, b) and Extrudate D (c, d).

Inverse pole figures (IPFs) were generated for each region of interest corresponding to the extrusion [100], transverse [010], and normal [001] directions. These figures represent binary black-and-white intensity maps that relate to the area of points (in this case, grains) bound to a specific crystallographic direction. A higher intensity of dark area correlates to a stronger texture for any given plane. Fig. 5, shows the majority of grains were orientated towards both the <100>

and <110> family of planes along the extrusion [100] direction for both *non-welded and welded* regions between both extrudates. While along the transverse [010] direction, there was a weak or randomized texture as the intensity of points was spread homogeneously between the IPFs. Comparing each family of planes between all four areas of interest exhibited a consistent texture profile, implying that increasing the extrusion exit speed had little to no effect on the result of microstructural orientation.

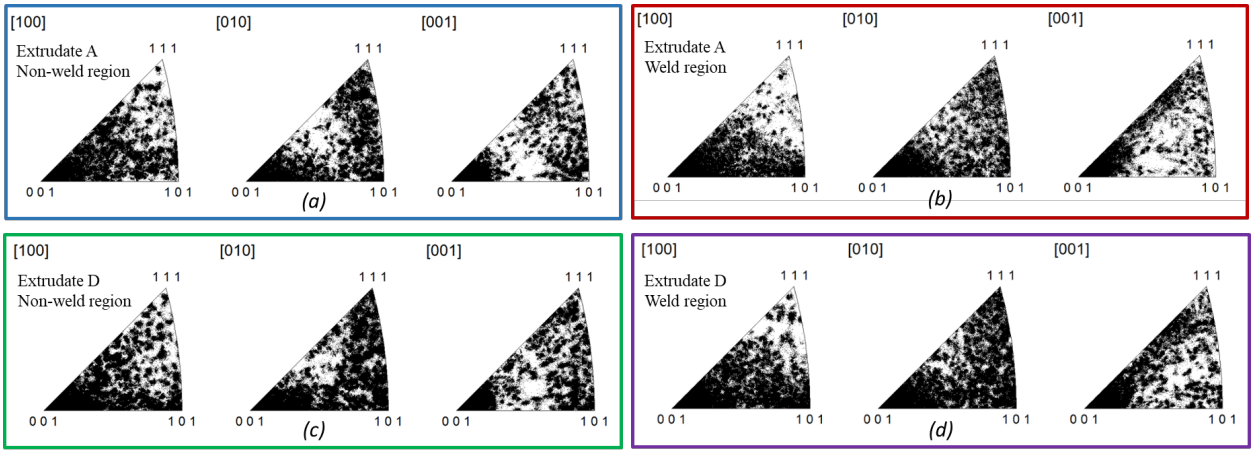

Fig. 5. Inverse pole figures for both Extrudate A (a, b) and Extrudate D (c, d).

Summary

Electron backscatter diffraction was utilized as a characterization method to analyze the localized microstructural texture, grain size, and metal flow of hot extruded AA6005 hollow profiles and to verify FEM predictions of exit temperature and plastic strain distribution. The average grain size decreased from 95.6 µm to 83.7 µm within the *non-welded* region and increased from 66.5 µm to 82.8 µm as the extrusion exit speed doubled. The increased grain size within the *welded* region was likely due to abnormal grain growth, but its cause was yet to be confirmed in this study. Similar die exit temperatures >500°C were recorded for both extrudates using the FEM simulations. Literature has shown this may have likely contributed to the PCG structure found throughout both extrudates. Local crystallographic texture varied across the core to surface, but remained consistent between both extrudates, with a strong [100] texture within the core regions, transitioning into a [101] texture along the surfaces. The varied texture from core to surface validated the plastic strain FEM simulations, which predicted the presence of strain gradients across the wall thickness.

The consistent texture profile between both extrudates implied that an increase in exit speed had no significant effect on the resultant microstructural orientation. But, without a clear difference in exit temperature between both profiles, an assumption cannot be made if it has any effect on the resultant texture. Overall, EBSD proved to be sensitive to local deformation conditions, detecting differences between the core and surfaces of the extrudate and can be used for the analysis of extrudate quality.

References

[1] Sheppard, Extrusion of Aluminum Alloys, Kluwer Academic Publishers, Norwell. T., 1999. http://dx.doi.org/10.1007/978-1-4757-3001-2

[2] N. Biba, S. Stebunov, A. Lishny, The Model for Coupled Simulation of Thin Profile Extrusion, Key Eng. Mater. 504 (2012) 505-510. https://doi.org/10.4028/www.scientific.net/KEM.504-506.505

[3] W. Van Geertruyden, S. Claves, W.Z. Misiolek, Electron Backscatter Diffraction Analysis of Microstructural Evolution in Hot-Deformed 6xxx Series Aluminum Alloys, Metall. Mater. Trans. A. 33 (2002) 693-700. https://doi.org/10.1007/s11661-002-0132-3

[4] K. Rajan, Representations of Texture in Orientation Space, in: A.J. Schwartz, M. Kumar, B. L. Adams, D.P. Field (Eds.), Electron Backscatter Diffraction in Materials Science. New York: Springer, 2, 2009, pp. 31-38. https://doi.org/10.1007/978-1-4757-3205-4_3

[5] K. Rajan, Fundamentals of Automated EBSD, in: A.J. Schwartz, M. Kumar, B.L. Adams, D.P. Field (Eds.), Electron Backscatter Diffraction in Materials Science. New York: Springer, 2, 2009, pp. 51-64. https://doi.org/10.1007/978-1-4757-3205-4_5

[6] J. Zasadzinski, A. Rekas, W. Libura, D. Lesniak, Numerical Analysis of Aluminum Alloys Extrusion Through Porthole Dies, Key Eng. Mater. 424 (2010) 105-111. https://doi/org/10.4028/www.scientific.net/KEM.424.105

[7] P.P. Camus, S.I. Wright, M.M. Nowell, R. de Kloe, Scientific Analysis of NPAR Processing of EBSD Results for Beam-Sensitive Materials, Microscop. Microanal. 23 (2017) 1836-1837. https://doi.org/10.1017/S1431927617009849

[8] S.I. Wright, M.M. Nowell, S.P. Lindeman, P.P. Camus, M. De Graef, M.A. Jackson, Introduction and comparison of new EBSD post-processing methodologies, Ultramicroscopy 159 (2015) 81-94. https://doi.org/10.1016/j.ultramic.2015.08.001

[9] A.R. Eivani, J. Zhou, J. Duszczyk, Mechanism of the formation of peripheral coarse grain structure in hot extrusion of Al-4.5Zn-1Mg, Philos. Mag. 96 (2016) 1188-1196. https://doi.org/10.1080/14786435.2016.1157637

[10] W.H. Van Geertruyden, H.M. Browne, W.Z. Misiolek, P.T. Wang, Evolution of surface recrystallization during indirect extrusion of 6xxx aluminum alloys, Metall. Mater. Trans. A 36 (2005) 1049-1056. https://doi.org/10.1007/s11661-005-0298-6

Materials Research Proceedings 28 (2023) 445-454 https://doi.org/10.21741/9781644902479-49

Chevron cracking during full forward impact extrusion of aluminum alloy EN AW 7075 in dependence of heat treatment condition and tribological system

MÜLLER Martina[1,a], SCHWARK Niklas[1,b*], WEISER Ingo F.[1,c], HERRIG Tim[1] and BERGS Thomas[1,2,d]

[1]Laboratory for Machine Tools and Production Engineering (WZL) of RWTH Aachen University, Campus-Boulevard 30, 52074 Aachen, Germany

[2]Fraunhofer Institute for Production Technology IPT, Steinbachstr. 17, 52074 Aachen, Germany

[a]martina.mueller@wzl.rwth-aachen.de, [b]N.Schwark@wzl.rwth-aachen.de, [c]I.Weiser@wzl.rwth-aachen.de, [d]t.bergs@wzl.rwth-aachen.de

Keywords: Aluminum, Full Forward Impact Extrusion, Chevron Cracking, Heat Treatment

Abstract. In addition to the growing demand for energy efficiency, the current and future legal emission limits in the transport sector lead to an increasing demand for weight-reduced components. By substituting conventional materials with weight-reduced components, such as the aluminum alloy EN AW 7075 (AlZn5.5MgCu), emissions during vehicle service life can be reduced. Chevron cracks, also called internal cracks, can be caused by a variety of reasons during cold extrusion processes and pose a great, non-visible challenge for product quality [1]. However, the cause effect relations between the heat treatment condition and the tribological system in regard to damage development have not yet been sufficiently analyzed. In order to examine these relations, the first forming step of a ball pivot was investigated using full forward impact extrusion. Experiments with different tribological systems were investigated by varying lubricant and die treatment with regard to friction and wear reduction. In addition, the effect of the workpiece formability on crack formation was examined by comparing the T6 and soft annealed state of EN AW 7075 as workpiece materials. During this study, the microstructure of both conditions was investigated to highlight differences. A validated FE process simulation using the simulation software Forge NxT 3.2 accompanied the process in order to evaluate the stress state during the full forward impact extrusion process and its relation to the occurrence of chevron crack formation. In the experiments conducted during this study, chevron cracking occurred during full forward impact extrusion of EN AW 7075 in state T6, while in soft annealed condition none appeared. Unlike the heat treatment condition, the tribological system had no impact on the occurrence of chevron cracking but on the severity of the cracks.

Introduction

The cold impact extrusion (CIE) process is an established, resource saving manufacturing process. CIE plays an important role in the cost-effective production of complex and ready-to-install components that are produced in large quantities. There is a large spectrum of possible component geometries that can be produced by CIE. Those are used in a wide range of applications, especially in the automotive industry [2]. Due to a growing demand for the CIE of high-strength products with lightweight properties, especially the production of parts using higher priced, lightweight materials like aluminum alloys becomes increasingly attractive. In many cases, the process limits of forming technologies, which are primarily determined by the material formability [3], are already exploited to their maximum. Exceeding the material formability limit can result in workpiece defects. These defects occur as surface or internal cracks, also called chevron cracks or

Content from this work may be used under the terms of the Creative Commons Attribution 3.0 license. Any further distribution of this work must maintain attribution to the author(s) and the title of the work, journal citation and DOI. Published under license by Materials Research Forum LLC.

Materials Research Proceedings 28 (2023) 445-454 https://doi.org/10.21741/9781644902479-49

central bursting. While surface cracks can be easily and quickly detected, as they can be seen by visual inspection, chevron cracks pose a much greater challenge for product quality [1]. Thus, the topic of chevron cracking has been part of many studies in recent years, and a variety of reasons was presented for the occurrence of these defects during the extrusion process. McVeigh and Liu showed that low friction between workpiece and tool leads to the increased occurrence of chevron cracking since the hydrodynamic stress increases with decreased friction [4]. In addition, unsuitable material hardening behavior [4], hard, brittle microstructural phases or non-metallic inclusions [3], as well as unsuitable or improper heat treatments of the workpieces [5] can lead to an increased occurrence of chevron cracks. As follows from McAllen et al. [6], different geometrical properties of the reduction die, for example larger shoulder angles, can also cause defects in form of surface and chevron cracks. However, the correlation between the tribological system (TS) and the occurrence of chevron cracks has not yet been sufficiently analyzed.

Consequently, the aim of this work is to investigate this correlation by determining the material behavior of aluminum alloy EN AW 7075 during full forward impact extrusion (FFIE), which is a process variant of CIE, in order to avoid chevron cracking. FFIE experiments with two different heat treatment conditions (T6 and soft annealed), three different lubricants and three different reduction die treatments were performed and subsequently analyzed in order to investigate the cause effect relations between these parameters and the occurrence of chevron cracking. All experiments were repeated three times to increase statistical value. The experiments were performed using a full factorial design.

Methods, Machines and Materials

Workpiece, tool material and experimental setup.

The experiments were conducted using full forward impact extrusion. The tools for the full forward impact extrusion, which consist of a punch, reduction die and shaft die, are shown in Fig. 1 (b). As tool material, high speed steel HS 6-5-2C (material number 1.3334) as well as the carbon steel G52 (no AISI equivalent) were used and hardened to 62 HRC. The reduction dies were provided with a shoulder opening angle of $\alpha = 45°$, had an initial diameter of $d_a = 31.4$ mm and a taper diameter of $d_{i1} = 20.6$ mm, see Fig. 1 (b). In order to prevent the sample from clinging to the inner wall of the die after taper, a heel was provided to increase the diameter to $d_{i2} = 20.7$ mm.

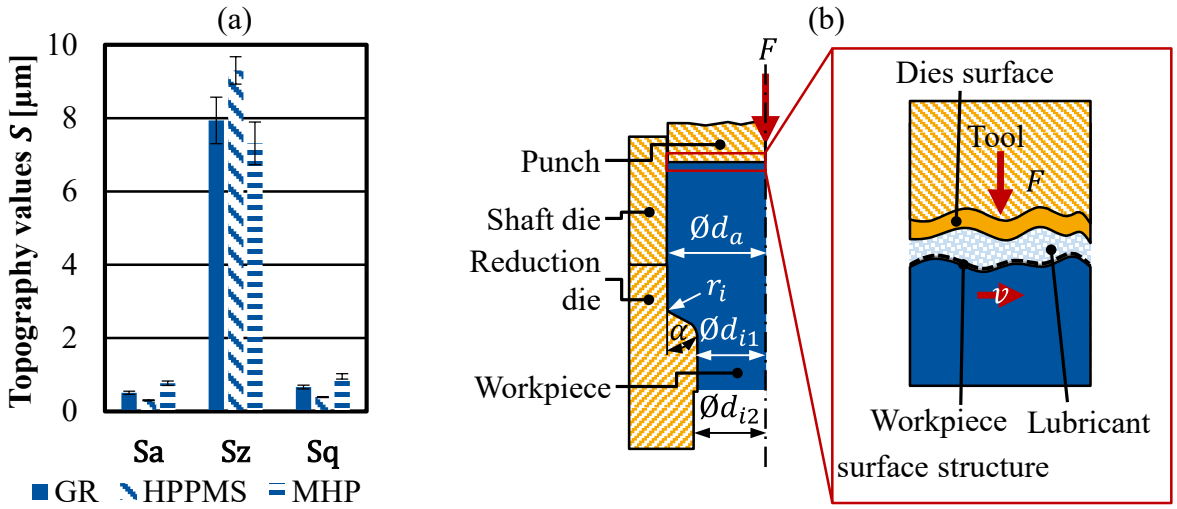

Fig. 1. Topography values of the dies according to ISO 25178 (a) and schematic illustration of the used tools (b).

The reduction die surfaces were finished by means of three different treatments. The first die was provided with a CrAlN-MoSx coating using high power pulsed magnetron sputtering (HPPMS) and were subsequently polished (Rz = 1 µm). The second die was processed by machine hammer peening (MHP) in order to increase wear resistance due to residual compressive stresses and to form lubricant pockets at the same time. The last die was ground (GR) after the manufacturing process. After treatment, the surface roughness was measured according to DIN EN ISO 25178 using a combined roughness and contour measurement system Hommel Etamic nanoscan 855 by Jenoptik AG. The results of these measurements are shown in Fig. 1 (a).

The experiments were carried out using the Schuler AG hydraulic press HPX-400. The press has a maximum pressing force of F_{max} = 4000 kN and was adjusted to a constant velocity of v = 12 mm/s. The punch path was kept constant at s = 12 mm. The results were partly evaluated using statistical methods of Design of Experiments (DoE), including main effects calculation. For DoE, adjustable parameters, also called factors, and their settings are determined, while the other process parameters remain constant. During the experiments, all combinations between the settings of the adjustable parameters are tested [8]. As adjustable parameters, die treatment (A) and lubricant (B) were chosen.

As workpiece material, the aluminum alloy EN AW 7075 was used, which is a widely used material for cold forming processes [7]. It is a hardenable wrought alloy, which provides high to highest static strength properties [6]. In order to transfer the material from the T6 condition to the soft annealed condition, the material was heat treated, see Fig. 2 (a). As can be seen in Fig. 2 (b-c), the texture was reshaped and showed a finer appearance in the soft annealed state. Before and after the treatment, microsections were etched using nitric acid n_{HNO_3}, hydrochloric acid n_{HCl}, hydrofluoric acid n_{HF} and water n_{H_2O}. Before the experiments were conducted, all workpieces were turned, ground and then shot-peened with aluminum granulate to improve lubricant bonding.

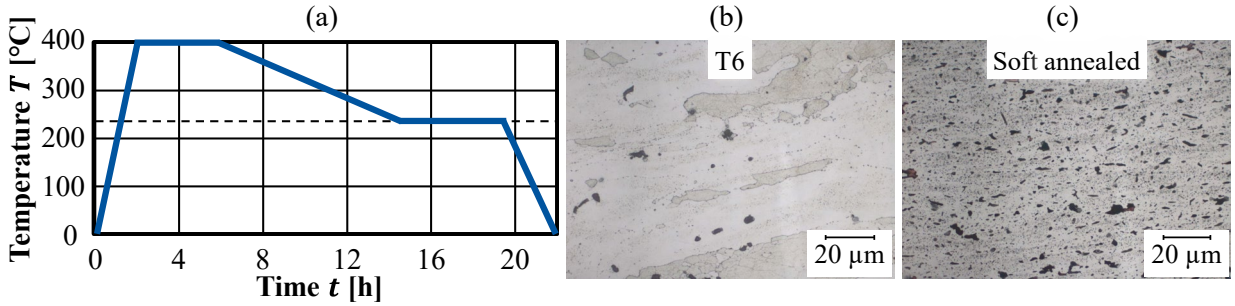

Fig. 2. Time table of heat treatment (a) and microsections of heat treatment condition T6 (b) and soft annealed (c).

Three different dry lubricants were applied on the workpieces. The application was carried out according to the recommendations of the lubricant manufacturer. The first lubricant (S1) was a water-soluble, low-dust lubricant for dry or wet treatment of aluminum workpieces prior to forming. It is used as an alternative to zinc stearate powder and wax systems. The lubricant was dissolved in distilled water with a solid content of 20 g/l and afterwards applied on the workpieces using a lubricant bath. The second lubricant (S2) was an aqueous polymer dispersion with a solid content of 20.5%, which forms a transparent, non-slip film and was applied on the workpieces using a lubricant bath with a 35% concentration. The third lubricant (S3) was an aqueous suspension of solid lubricants with a solid content of 26%. It was applied using a lubricant bath with a 45% concentration.

Numerical setup.

The experiments were accompanied by a finite elements (FE) simulation model using Forge NxT 3.2. The workpiece was modelled as an elasto-plastic, deformable volume. The punch and die were assumed to be rigid, non-deformable bodies. To reduce the required computing power and the calculation time, only one twelfth of the rotationally symmetrical components was implemented, see Fig. 3 (a). In post processing, these components were combined in order to analyze the complete workpiece. The velocity of the punch v as well as the punch path s were set to $v = 12$ mm/s and $s = 12$ mm to reflect the conditions of the experiments. For modelling the friction, a coupled friction model as a combination of Tresca's and Coulomb's friction models was used, see Fig. 3 (b).

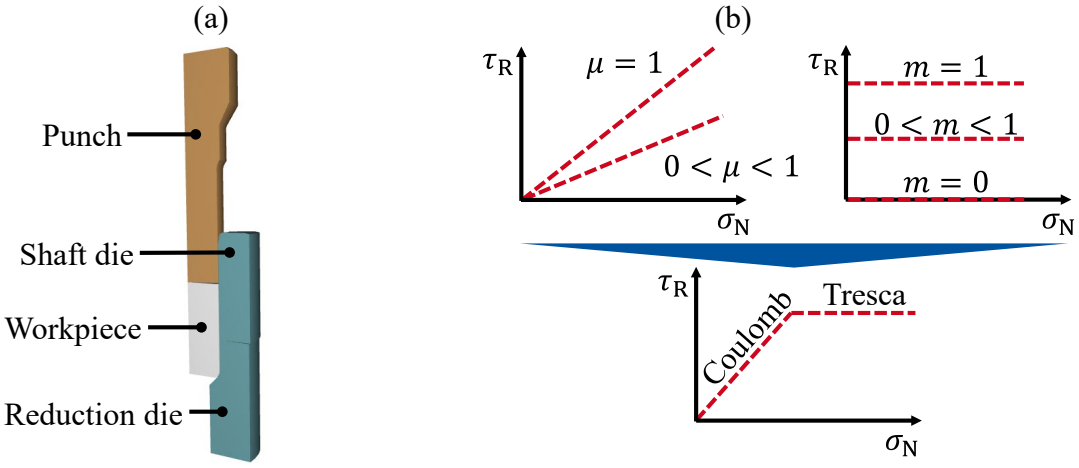

Fig. 3. Image of simulation model (a) and used friction model (b).

In order to represent various tribological conditions during forming, different coefficients of friction μ and friction factors m were used during the simulations. These are listed in Table 1.

Table 1. Coefficients of friction μ and friction factors m of implemented frictions laws.

Description	**Coefficients of friction μ / friction factors m**
Low friction	0.02 / 0.05
High friction	0.2 / 0.4

The meshing was carried out with the triangulation method, in which the geometry of the components was simulated using triangular facets. In order to reduce the calculation complexity on the one hand and to lower the error level on the other hand, a convergence analysis was carried out. Starting from a coarse mesh, the elements were reduced in size until the results of the simulation (punch force, stress distribution) converged. The mesh determined by the convergence analysis defined the edge length to a minimum mesh size of l_{min} = 0.02 mm.

Experimental and Numerical Results

Experimental results.

The diagram in Fig. 4 (a) displays the punch force-time-graphs of the first stroke of the different test pairings. Comparing the graphs reveals a similar course of each test pairing. At first, the punch force F increased quadratically until a linear progression was established, which continued until the maximum punch force F_{max} was achieved. With the exception of the TS that is induced by

HPPMS and S1, the gradient of the punch force-time-graphs reached a continuous, decreasing negative value after reaching the maximum punch force F_{max} and before the end of the FFIE process where the punch force F dropped to F = 0 kN. However, in the course of the TS consisting of HPPMS and S1, the gradient of the punch force-time-graph underwent a change of sign after reaching the maximum punch force F_{max}. The punch force F increased to a local maximum before the end of the FFIE process. The drop in the force curve can be explained by sudden stress relief after the occurrence of a chevron crack. Besides the similar course of each punch force-time-graph, different maximum punch forces F_{max} were achieved in each experiment. The highest punch force F_{max} = 751 kN was achieved by using S3 and the HPPMS treated die. The use of the HPPMS treated die and S1 required the lowest punch force F_{min} = 619 kN. The punch force F did not increase or decrease systematically with increasing stroke number. Thus, wear effects that occurred during this study can supposedly be neglected.

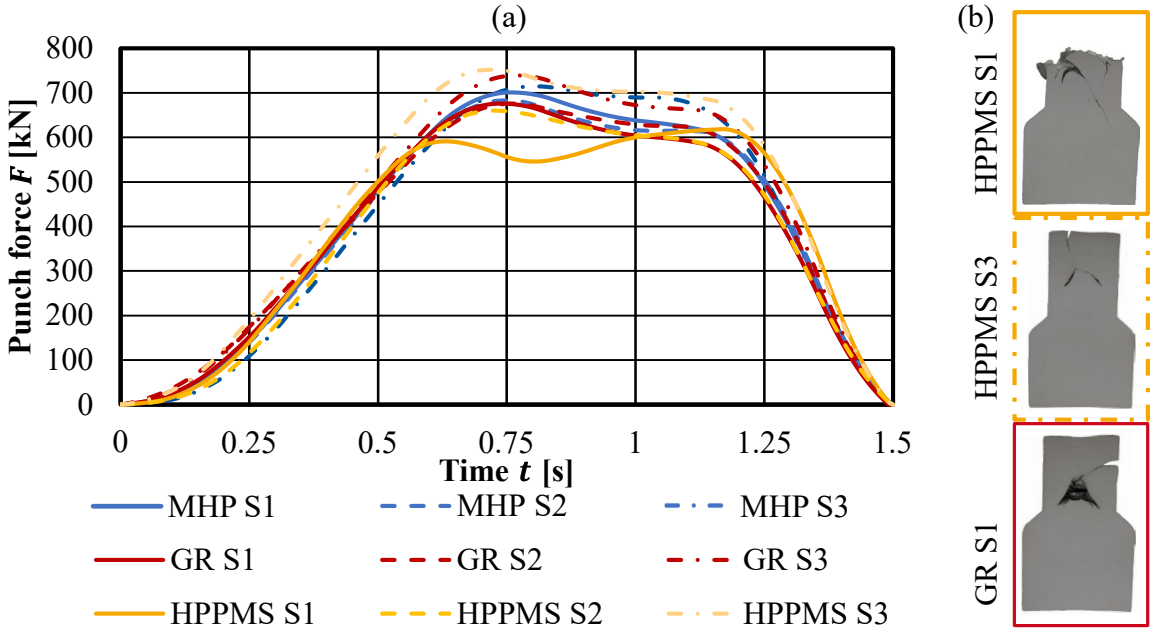

Fig. 4. Punch force-time-diagram of first stroke using different tribological systems and heat treatment condition T6 (a) and severity of chevron cracking depending on friction (b).

As can be seen in Fig. 4 (b), the severity of the chevron cracking varied regarding the TS. A dependency of chevron cracking and punch force can be postulated since the characteristics of the chevron cracks became more distinctive with lower punch force F, as the hydrostatic stress in the center of the workpiece was reduced with lower friction [5], although there were exceptions from this rule. The GR treated specimen had less critical chevron cracks during this study. In the lubricated state, the punch forces were lower than under dry conditions. While using S3, a MHP surface finish in the lubricated state decreased the punch force compared to a HPPMS surface finish. This can be explained by the formation of lubricant pockets, which lead to reduced friction behavior. Although with S1 and S2, this effect was reversed. On this account, hydrodynamic and hydrostatic effects could occur, which decreased friction and therefore the punch force. On the contrary, the very homogenous surface of the HPPMS process seemed not to grant hydrodynamic effects. As a result, the lubricant effect E_B was lower when using HPPMS-finished surfaces.

Table 2 summarizes the results of the evaluation using DoE. All the effects shown were calculated with the ground die (A- setting) and no lubrication (B- setting) as a reference. HPPMS or MHP were used as the A+ setting, and S1, S2 or S3 as the B+ setting. For each effect calculation,

all possible combinations of the *plus* and *minus* settings of A and B were considered. The effects of all combinations of the parameter settings A and B were calculated in comparison to the reference state. The effect of each factor was calculated as the difference between the average maximum force F_{max} in the experiments when the factor had the *plus* setting and the average maximum force F_{max} when the factor had the *minus* setting. As an example, the effect E_A was calculated by

$$E_A = \frac{F_{max,A+,B+} + F_{max,A+,B-}}{2} - \frac{F_{max,A-,B+} + F_{max,A-,B-}}{2} \quad (1)$$

For the calculation of effect E_{AB}, the setting of AB is given by the multiplication of the settings of factors A and B. So, for the combination of settings A- and B- or A+ and B+, the AB+ setting would be assumed, whereas for A+ and B- or A- and B+, AB- would be assumed. The effects in dependency of the *plus* or *minus* setting of the other factor were calculated as follows:

$$E_{A(B\overset{+}{-})} = E_A \overset{+}{-} E_{AB}. \quad (2)$$

As the force for the forming process does not significantly change between the experiments, the effects can be mostly explained by increased or decreased friction behavior. Regarding the main effects, the results indicate that the use of lubricants had a positive effect E_A on the maximum punch force F_{max} independently of the die treatment. The MHP treated die, on the other hand, showed a negative effect E_B on the maximum punch force F_{max}, while the HPPMS treated die had a positive effect E_B on the maximum punch force F_{max}. Considering the main effects E, the HPPMS treated die showed a positive effect $E_{A(B-)}$ on the maximum punch force F_{max} when dry pressing. The MHP treated die had the opposite effect $E_{A(B-)}$ and showed a negative effect on the maximum punch force F_{max}.

Table 2. DoE effects maximum punch force F_{max} of die treatment (A) and lubricant (B).

Effect E	HPPMS			MHP		
	SS1	SS2	SS3	SS1	SS2	SS3
E_A [kN]	-98.17	-85.65	-62.81	66.61	54.60	47.70
E_B [kN]	-307.92	-268.07	-205.89	-405.65	-390.34	-357.89
$E_{A(B-)}$ [kN]	-148.01	-148.01	-148.01	114.50	114.50	114.50
$E_{A(B+)}$ [kN]	-48.33	-23.28	22.39	18.72	-5.31	-19.10
$E_{B(A-)}$ [kN]	-357.76	-330.43	-291.09	-357.76	-330.43	-291.09
$E_{B(A+)}$ [kN]	-258.07	-205.70	-120.69	-453.54	-450.25	-424.69

Fig. 5 compares the punch force-time-graphs using workpiece material in T6 and soft annealed heat treatment conditions with the ground die and lubricant S1. The test pairing was chosen for further analysis due to its average damage value regarding the severity of chevron cracks. By comparing the two courses, it can be seen that the maximum punch force F was significantly lower when in soft annealed than in T6 condition. Furthermore, the punch force-time-graph of the soft annealed heat treatment condition showed no drop in punch force F but a nearly linear progression after reaching the maximum punch force F_{max}. Moreover, the gradient of the punch force-time-graph for the soft annealed condition was smaller compared to the T6 condition during the rise and

fall of the punch force F during of the process. Using the soft annealed condition, no chevron cracks emerged during pressing. The workpiece was free of defects.

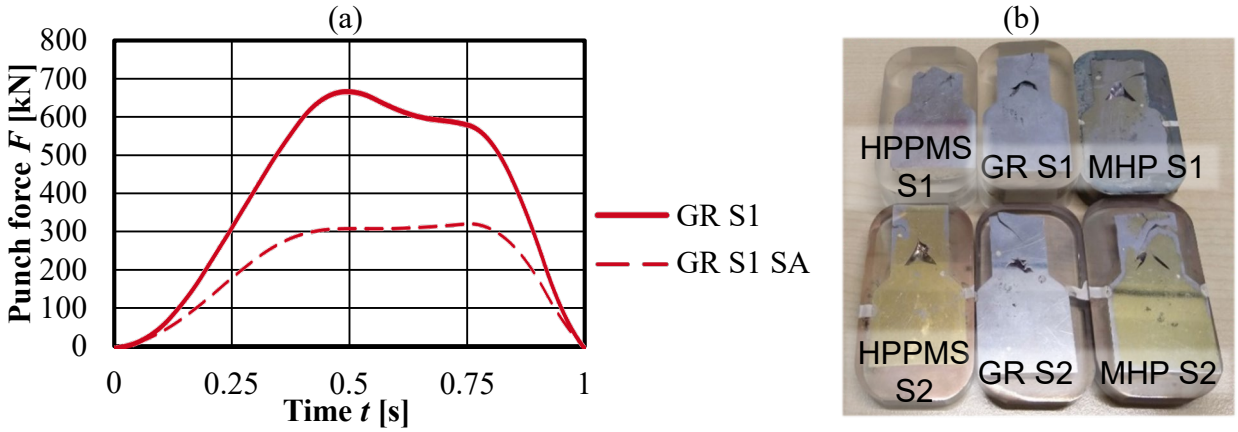

Fig. 5. Punch force-time-diagram of first stroke soft annealed and heat treatment condition T6 (a) and typical chevron crack formation during the experiments (b).

Numerical results.

In order to validate the simulation model, the punch force during FFIE and the geometry of the finished workpiece were compared to the simulation results. Fig. 6 (a) shows this comparison. The simulation was conducted using only the Hensel Spittel parameters [10] of EN AW 7075 in the soft annealed state, as the parameters for the heat treatment condition T6 were not available during this study. Regarding the punch force, the experimental data were comparable to the simulation data using low friction conditions. Both the experimental data and the simulation with low friction conditions reached a similar maximum punch force of about 300 kN. The maximum punch force during the experiments was about 8% higher than the punch force in the low friction simulation. The simulation model with low friction conditions shared a very similar gradient with the experimental data at the beginning of the FFIE process. The key difference was the negative force gradient at the end of the process, which decreased slower in the experimental data, which was the result of the reduced punch velocity at the end of the experiments. Furthermore, the lode parameter as well as triaxiality were investigated in order to evaluate the workpiece damage [9]. The triaxiality η is defined as

$$\eta = \frac{\sqrt{2}\cdot(\sigma_1+\sigma_2+\sigma_3)}{3\cdot\sqrt{(\sigma_1-\sigma_2)^2+(\sigma_1-\sigma_3)^2+(\sigma_2-\sigma_3)^2}} \tag{3}$$

where σ_1, σ_2 and σ_3 are the principal stresses [10]. The Lode parameter $\underline{\theta}$ is described by

$$\underline{\theta} = 1 - \frac{2}{\pi}\cdot arccos\,(\xi) \tag{4}$$

where ξ is the normalized third deviatoric stress invariant [11]. Using the lode parameter, areas of tensile and compressive stress can be identified in a simulation model. Fig. 6 (b) shows that most chevron cracks during the experiments occurred in the areas where areas with high compressive stresses met areas with high tensile stresses. The stress tensor in material flow direction in the center of the peg was characterized by large compressive stress values, while the surrounding area was characterized by large tensile stresses. The tensile stress values on the inside of the peg increased during the process, and lead to material failure in this area, which resulted in the occurrence of a chevron crack. Afterwards, tensile stress values continued to grow until another

chevron crack occured. Chevron cracks and cracks that started at the surface of the peg mostly seemed to grow alongside the areas where tensile and compressive stresses met.

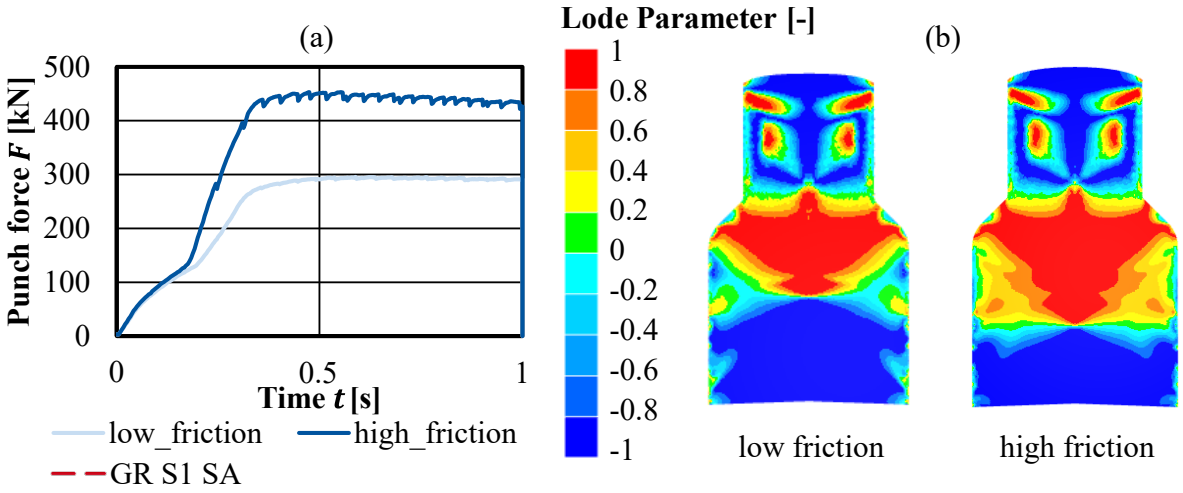

Fig. 6. Punch force over time during simulation (a) and Lode parameter during forming (b).

In Fig. 7 (a), the triaxiality at the end of the forming process is shown. Using both low and high friction conditions, tensile stress could be found near the surface of the peg, while the center was largely influenced by compressive stress. In the center of the extruded shoulder, which coincides with the area where most chevron cracks occurred, sheer stress was dominating and the highest von Mises stress values occurred. Right above this zone, the von Mises stress values decreased significantly, which lead to material failure in this specific area.

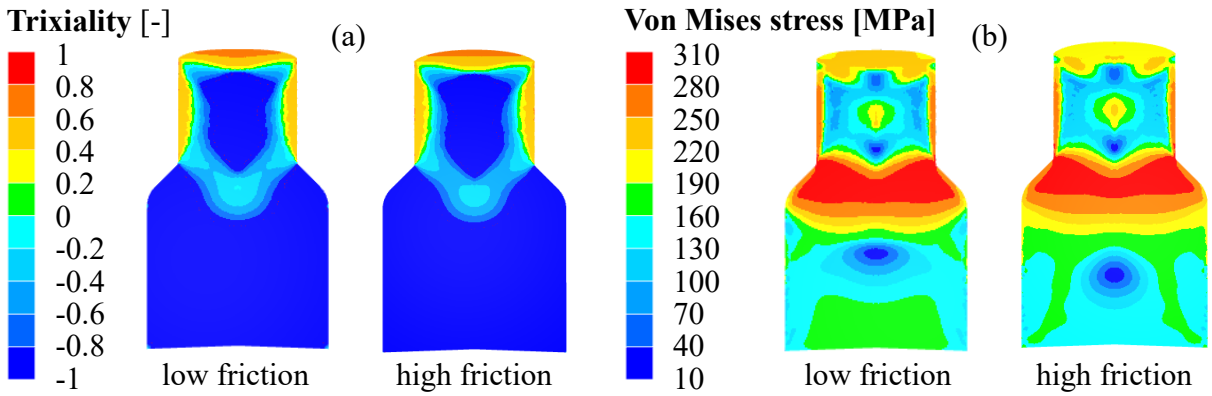

Fig. 7. Triaxiality during forming (a) and von Mises stress during forming (b).

Regarding the simulation of chevron cracks during the FFIE process, simulations in Forge were carried out using the normalized Latham-Cockcroft damage criterion, which is the most commonly used damage criterion in cold forming [12] and has already been proven to be suitable for the analysis of chevron cracks in cold extrusion processes [13]. For cold forming, a critical damage parameter of 0.5 is suggested. No chevron cracks occurred in the experiments that use the process parameters presented in this paper while using specimen in the soft annealed state, which was confirmed by the simulation results. Nevertheless, in order to investigate the growing process of chevron cracks during the forming simulation without changing the material behavior of EN AW 7075, the critical damage parameter was set to 0.2. In this theoretical case, the formation of chevron cracks started early during the FFIE process in the center of the reduction shoulder. Throughout the crack growth, the area between the crack itself and the lateral surface of the

workpiece showed an increased value for the Latham-Cockcroft damage criterion when compared to the rest of the specimen. Once the first chevron crack reached a certain width, another chevron crack occurred in the same area that the first one occurred in. During the experiments, multiple chevron cracks only appeared in a few specimen. On the other hand, the chevron cracks grew larger than in the simulation model, which can be explained by the different heat treatment condition. Furthermore, the resulting damage parameter was largely influenced by the friction conditions used during the simulation. By using high friction parameters, the occurrence of chevron cracks during the FFIE process was significantly reduced, which confirms the experimental results. It should be noted that, unlike in the experiments, the occurrence of chevron cracks during the simulations did not affect the punch force-time-diagram.

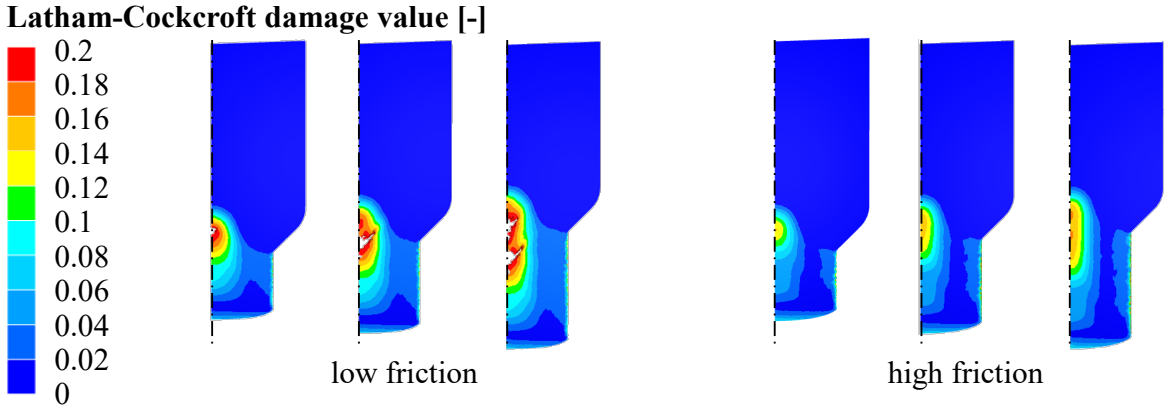

Fig. 8. Latham-Cockcroft damage value during FFIE simulation.

Summary

Within the present study, extensive analyses were carried out to investigate the cause-effect relations between heat treatment condition, damage development and tribological system. For this purpose, FFIE experiments were executed with workpieces made of the aluminum alloy EN AW 7075 in the different heat treatment conditions T6 and soft annealed as well as different tribological systems. The key findings of this study are as follows:

- A dependency between friction and chevron crack characteristics was shown. With increasing maximum punch force $\boldsymbol{F_{max}}$ and thus with increasing friction, the chevron crack characteristics that occurred in heat treatment condition T6 became less distinctive. These findings were also confirmed by the numerical investigations of this study.
- It was shown that the punch force-time-graph at the occurrence of chevron cracks had a different characteristic than that of defect-free components. All courses showed a drop in punch force $\boldsymbol{F}$ in form of a buckling after reaching the maximum force $\boldsymbol{F_{max}}$. This buckling did not occur in other experiments without chevron cracks with the same tool geometry and experimental parameters [13]. The buckling of the curve became increasingly apparent as the chevron cracks became more distinctive and is considered as a result from the sudden stress relief due to bursting of the material.
- The simulation model with low friction showed a mostly similar force curve to the experimental data using the soft annealed state of EN AW 7075. Simulations showed that chevron cracks occur in the areas where high tensile and high compressive stresses met.

Acknowledgment
This work was funded by the Deutsche Forschungsgemeinschaft (DFG, German Research Foundation) – Projektnummer 460819047 (TriboLub).

References
[1] H. Haghighat, A. Parghazeh, An investigation into the effect of strain hardening on the central bursting defects in rod extrusion process, Int. J. Adv. Manuf. Technol. 93 (2017) 1127-1137. https://doi.org/10.1007/s00170-017-0577-6
[2] Volz, H., Kaltmassivumformung: Präzision in Serie, Available online: https://www.massivumformung.de/fileadmin/user_upload/6_Presse_und_Medien/Veroeffentlichungen/Extra-Info/Kaltmassivumformung_Druckversion_12-10-04.pdf. 2017 (accessed 18 November 2022).
[3] C. Buse, Potenziale und Grenzen der Schallemissionsanalyse zur Online-Prozessüberwachung in der Kaltmassivumformung von Stahlwerkstoffen, PhD Thesis, Univ. Hannover, 2017.
[4] C. McVeigh, W.K. Liu, Prediction of central bursting during axisymmetric cold extrusion of a metal alloy containing particles. Int. J. Solid. Struct. 43 (2006) 3088-3105. https://doi.org/10.1016/j.ijsolstr.2005.05.019
[5] G. Dieter, K. Howard, S.L. Semiatin, Handbook of workability and process design, ASM International, 2003.
[6] P. McAllen, P. Phelan, Ductile Fracture by Central Bursts in Drawn 2011 Aluminium Wire, Int. J. Fract. 135 (2005) 19–33. https://doi.org/10.1007/s10704-005-3470-5
[7] B.A. Behrens, S. Hübner, H. Vogt, O. Golovko, S. Behrens, F. Nürnberger, Mechanical properties and formability of EN AW-7075 in cold forming processes, IOP Conf. Ser.: Mater. Sci. Eng. 967 (2020). https://doi.org/10.1088/1757-899X/967/1/012017
[8] J. Antony, Design of Experiments for Engineers and Scientists, Elsevier insights, Elsevier, Amsterdam, 2014. https://doi.org/10.1016/B978-0-08-099417-8.00010-9
[9] A. Hensel, Th. Spittel, Kraft- und Arbeitsbedarf bildsamer Formgebungsverfahren. VEB Deutscher Verlag für Grundstoffindustrie, Leipzig, 1978.
[10] M. Basaran, Stress State Dependent Damage Modeling with a Focus on the Lode Angle Influence, Diss. RWTH Aachen, Shaker, Aachen, 2011.
[11] Y. Bai, T. Wierzbicki, A new model of metal plasticity and fracture with pressure and Lode dependence, Int. J. Plast. 24 (2008) 1071-1096. https://doi.org/10.1016/j.ijplas.2007.09.004
[12] S. Stebunov, A. Vlasov, N. Biba, Prediction of fracture in cold forging with modified Cockcroft-Latham criterion, Procedia Manuf. 15 (2018) 519-526. https://doi.org/10.1016/j.promfg.2018.07.264
[13] J. Choi, H. Lee, Y. Im, A study on chevron crack formation and evolution in a cold extrusion, J. Mech. Sci. Technol. 24 (2010) 1885-1890. https://doi.org/10.1007/s12206-010-0605-z
[14] M. Müller, R. Hild, D. Trauth, T. Bergs, Investigation of different tribological systems during full forward impact extrusion of aluminum alloy EN AW 6082, Industr. Lubric. Tribol. 72 (2019) 709-712. https://doi.org/10.1108/ILT-08-2019-0316

Materials Research Proceedings 28 (2023) 455-466 https://doi.org/10.21741/9781644902479-50

Effects of disc milling and indirect extrusion processing on mechanical properties of aluminum-graphene-composites with commercial GNPs

NEGENDANK Maik[1,a *], GANCHULUUN Enkhtaivan[1,b], JAIN Nishant[2,c] and MÜLLER Sören[1,d]

[1]Extrusion Research and Development Center of TU Berlin, Gustav-Meyer-Allee 25, 13355 Berlin, Germany

[2]Chair of Advanced Ceramic Materials, TU Berlin, Hardenbergstr. 40, 10623 Berlin, Germany

[a]maik.negendank@strangpressen.berlin, [b]taiwanaa_91@yahoo.com, [c]nishant.jain@tu-berlin.de, [d]soeren.mueller@tu-berlin.de

Keywords: Aluminum, Graphene, Composites, Al/GNP Composites, Disc Milling, Extrusion, Mechanical Properties

Abstract. In this study aluminum-graphene-composites were manufactured applying a powder metallurgical approach. After graphene exfoliation and mechanical mixing, powders were disc milled, compacted and extruded into round rods. Two different sources of commercial graphene nano platelets (GNP) (by 1. Sigma Aldrich (SA) and 2. Alfa Aesar (AA)) were investigated with the main difference being their specific surface area. One subject of the study was to investigate the effect of disc milling processing on the mechanical properties of Al/GNP composites. Results indicated that micro hardness as well tensile yield strength (TYS) and ultimate tensile strength (UTS) were not improved significantly or only slightly when SA-GNPs and a disc milling duration of 1min were applied. Varying the extrusion ratio from R=9:1 to R=14:1 and R=31:1 as well as applying conic or flat face dies for extrusion did not have a significant effect on the mechanical properties. But when disc milling duration is extended to 5min, significantly increased micro hardness (up to 30%), TYS (up to 17%) and UTS (up to 26%) were observed. Application of AA-GNPs as a second source of commercial GNPs also resulted in significantly increased micro hardness (up to 49%), increased TYS (up to 16%) and UTS (up to 27%) when disc milling of 5min is conducted in the powder processing stage. SEM analysis indicated that after 5min disc milling aluminum particles were deformed from spherical into a plate-like shape. Additionally, GNP exfoliation and its dispersion in the Al matrix seemed to be improved by the longer milling duration and could be a reason for the enhanced strengthening effect of GNPs.

Introduction

Graphene is a 2-dimensional carbon-based material ideally consisting of planar carbon monolayers, where carbon is sp^2-hybridized. It was first synthesized successfully in 2004 [1]. Due to exceptional high intrinsic strength and elastic modulus [2] monolayer graphene is highly attractive to be applied as strengthening additive for composite materials such as aluminum-graphene-composites. But due to high van der Vaals forces, graphene layers tend to agglomerate which is detrimental to the mechanical composite properties [3]. Thus, graphene exfoliation and its homogeneous dispersion in the matrix material are key for achieving a high strengthening effect. Furthermore, the formation of carbides can be a reason for decreasing strength and ductility [4]. The current study investigates a processing approach of graphene sonication (for exfoliation), disc milling, cold compaction and indirect extrusion to manufacture aluminum-graphene-nanoplatelet(GNP)-composites. In a prior study, aluminum and graphene powders were mixed mechanically only, then compacted and extruded. This approach did not lead to significant

Content from this work may be used under the terms of the Creative Commons Attribution 3.0 license. Any further distribution of this work must maintain attribution to the author(s) and the title of the work, journal citation and DOI. Published under license by Materials Research Forum LLC.

strengthening. The main reason for that was assumed to be GNP agglomeration, as GNPs were found to be aligned in relatively thick layers around aluminum particles, especially for high GNP contents [5]. Thus, for the current study disc milling was added to the process chain. Disc milling is a method usually applied to reduce the size of particles through compression, shearing and friction forces. Thus, with disc milling a high amount of energy can be introduced into the powder mixture, aiming to decrease the GNP agglomeration around aluminum particles and improve GNP dispersion. Furthermore, in this study two different commercial graphene sources were applied and the resulting mechanical properties of the Al/GNP composites are compared.

Materials and Methods

In this study Al/GNP composites were prepared via a powder metallurgical route. Same pure (99.7%) aluminum powder as in a previous publication [5] was applied as matrix material. Aluminum with mean particle size of 49µm was provided by TLS Technik GmbH & Co. Spezialpulver KG, Germany. In the first part of this research the effects of GNP-content, extrusion ratio, die angle and milling duration on micro hardness and tensile properties were investigated exemplarily. In order to study the general relationships between processing parameters and the material properties for each condition one rod was extruded. Micro hardness was tested on one rod cross section extracted from the middle length of each rod, three samples were cut from the middle to end region of the rod and tested in tensile tests. For the first part of the study GNPs provided by Sigma Aldrich were applied. All extrusion experiments were carried out on a small scale 0.5MN extrusion press with a container of 30mm diameter at Extrusion R&D Center TU Berlin. Billets were prepared by first GNP exfoliation through sonication (Branson Sonifier 450) in ethanol for 10min. The GNP/ethanol solution was then added to aluminum powder in an Eirich intensive mixer and batches with GNP-contents of (0.25%), 0.5% and 1.0% were prepared. Mechanical mixing was performed for 360s at 1800rpm. Subsequently powders were dried in a vacuum furnace for 16h at T=50°C. Powder mixtures were then disc milled applying the milling tools given in Fig. 1 rotating at 1000rpm for 1min and exemplarily for 5min. Milling batch size was 100g, respectively. Due to significant heat generation overall milling duration of 5min was split into 5 steps of 1min each with cooling breaks of a couple minutes in between. The weight of the tools (2 rings and 1 disc) rotating within the milling die was 9.2kg (Fig. 1). Milled powders were then sieved with mesh size of 172µm and subsequently cold compacted with 200MPa into solid discs for better specimen handling. Compacts were then extruded at 300°C in indirect extrusion mode applying different extrusion ratios of R=9:1, R=14:1 and R=31:1. Additionally, two different die angles ($2\langle$=180° flat face die and a conic die with $2\langle$=130°) were applied for selected samples to investigate its effect on the composites' properties, exemplarily.

In the second part of the investigation an alternative graphene source, provided by Alfa Aesar, was applied. The Alfa Aesar (AA)-GNPs especially featured a significantly higher specific surface area of 529m^2/g than the Sigma Aldrich GNPs (108m^2/g). In order to characterize their qualities both graphene sources were investigated by Raman spectroscopy. The effect of AA-GNP content as well as the effect of powder mixing or mixing with additional disc milling for 5min on the mechanical properties was studied. Extrusion of the 5min disc milled material with AA-GNPs was carried out applying the conic die ($2\langle$=130°) with diameter 8.0mm (R=14:1). Effects of extrusion ratio, milling duration and die angle variation were not investigated for AA-GNPs.

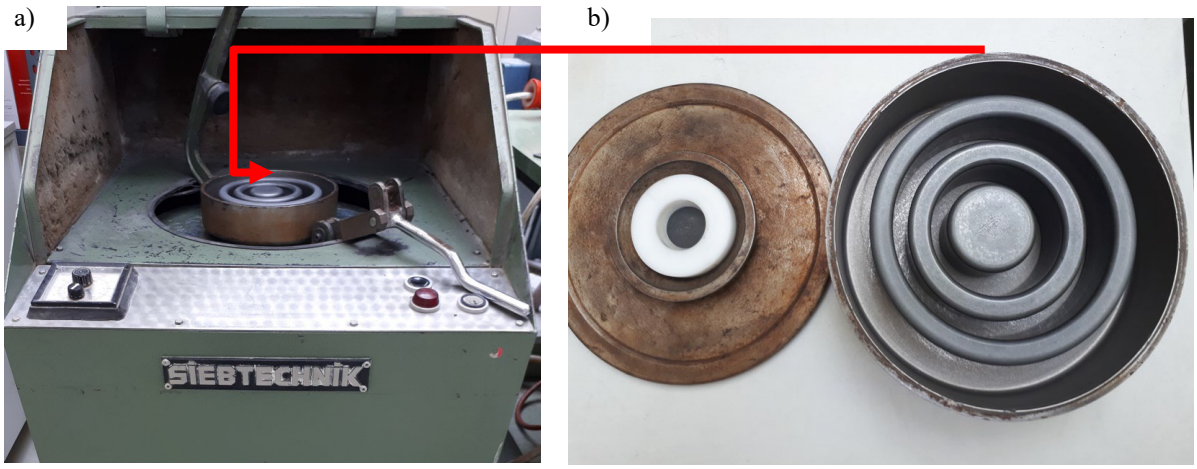

Fig. 1. a) Disc mill b) milling die with two milling rings and one disc.

Results and Discussion

Powder characterization.

In a first step the initial powders were investigated via SEM in as received condition. Results are displayed in Fig. 2. The pure aluminum powder is given in Fig. 2a. The powder predominantly is of spherical shape with varying size between 5µm and 70µm. Mean particle size was 47µm. Fig. 2b presents the GNPs provided by Sigma Aldrich. These GNPs were mostly found attached to each other and had a very flat shape with sharp edges. In contrast, the GNPs provided by Alfa Aesar consisted more of spheric particles with very fine platelets on their surface (Fig. 2c).

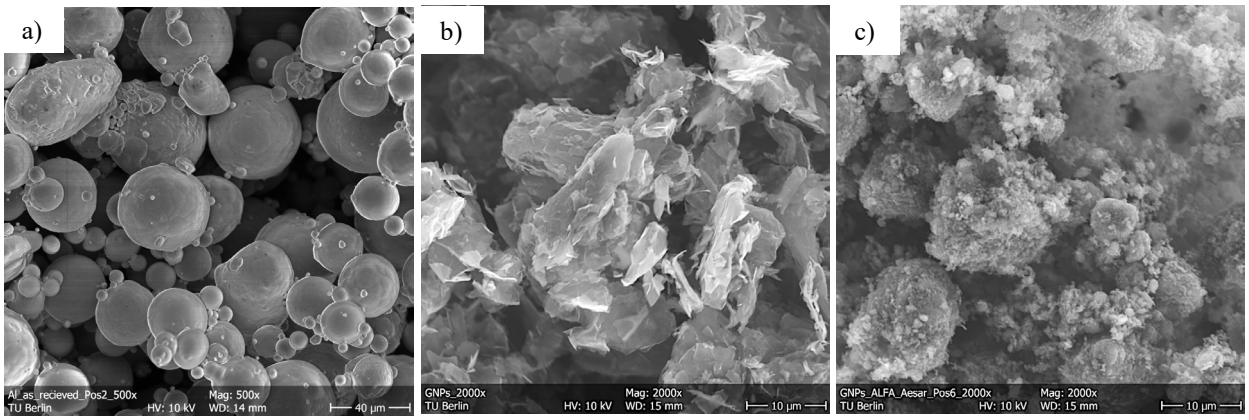

Fig. 2. SEM images of as received a) pure Al powder (99.7%), b) Sigma Aldrich (SA)-GNPs c) Alfa Aesar (AA)-GNPs.

In order to investigate the effect of each powder processing step on morphology and GNP dispersion, the composite powders with GNP content of 1% were selected exemplarily. SEM images are given in Fig. 3. Al-particles remained their initial spherical shape after mechanical mixing for 6min at 1800rpm as shown in Fig. 3a. SA-GNPs seemed to be relatively well distributed in the powder as no larger agglomerates were found. Although, often a few GNPs were stacked on top of each other. After 1min of disc milling first effects of the high energy input due to the milling process can be noticed (Fig. 3b). The surface of aluminum particles became rougher and their shape mostly was not as ideally spheric as in the initial state. After 5min of disc milling, due to the high impact energy through friction and shearing in the mill, aluminum particles were found to be deformed into plates with a rough surface (Fig. 3c). The results after 5min of disc milling seemed

to be comparable to the deformation of aluminum powder after 1h of ball milling presented in [6]. Thus, applying disc milling instead of ball milling could be an option to produce composites since milling time and thus cost could be reduced significantly.

After mixing, the AA-GNPs were found to be attached to Al-particles in form of small chunks as indicated in Fig. 3d. But after disc milling for 5min they were found in a very thin, flat shape and reduced in size (Fig. 3e). Hence, it can be concluded that the high energy input throughout the disc milling process had a positive effect on the dispersion of AA-GNPs in the composite powder.

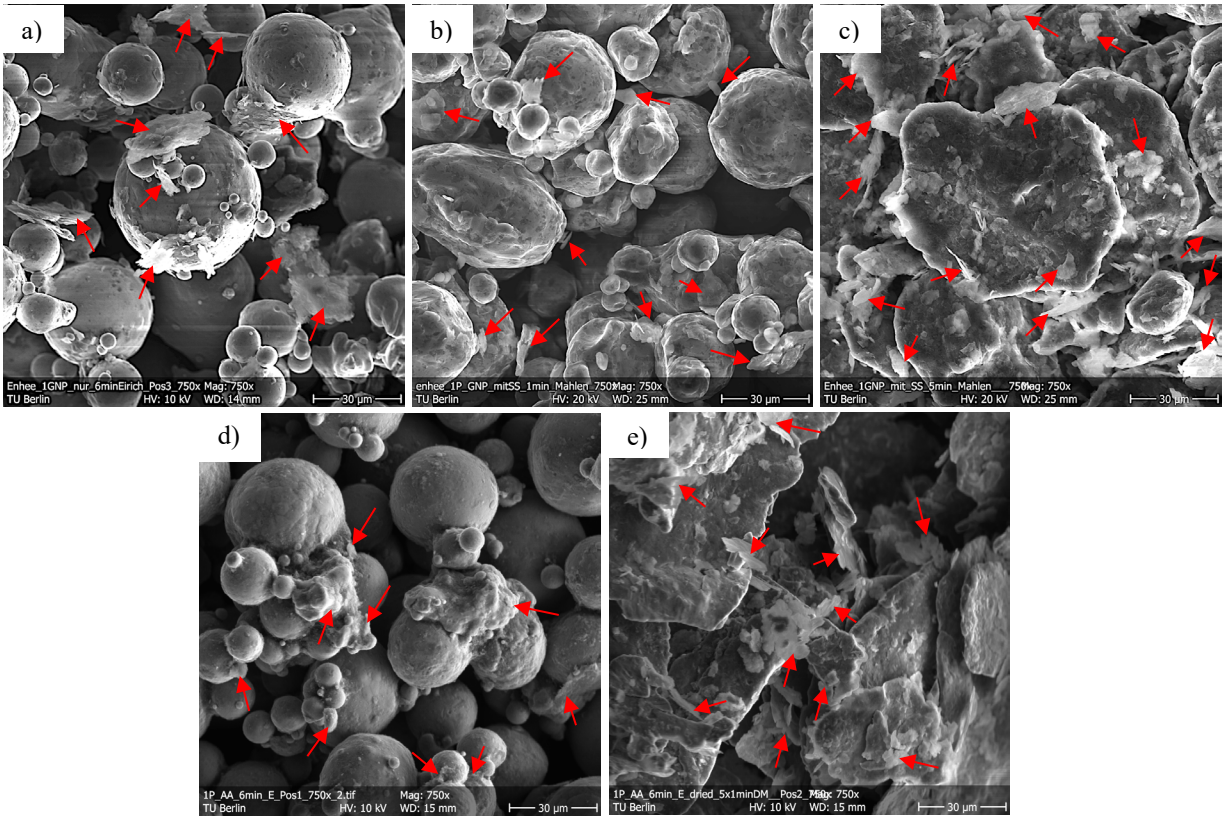

Fig. 3. SEM images of composite powders a) 1% SA-GNP after mechanical mixing, GNPs exemplarily indicated with arrows b) 1% SA-GNP after 1min disc milling c) 1% SA-GNP after 5x1min disc milling d) 1% AA-GNP after 6min of mechanical mixing e) 1% AA-GNP after 5x1min disc milling.

Raman spectroscopy is a fast, nondestructive method with high-resolution that can be applied for the characterization of e.g. lattice structure of carbon-based materials and thus provides information on the morphology and quality of GNPs [7]. The Raman spectra of the applied two different commercial GNPs are given in Fig. 4a and Fig. 4b. In both spectra the presence of the three prominent peaks namely D-band at ~1325cm^{-1}, G-band at ~1565cm^{-1} as well as 2D band at ~1650cm^{-1} were observed. The G-band corresponds to intrinsic in-plane C-C vibration modes of graphene and is characteristic for carbon-based compounds [8]. The D-band relates to the magnitude of defects or disorder in the crystal structure of graphene [9]. The 2D-band is related to number of graphene layers in the GNPs [10]. The defect density of GNPs can be predicted with the intensity ratios of D-band and G-band (I_D/I_G) and the number of graphene layers in the GNPs with the ratio of 2D-band to G-band (I_{2D}/I_G) [11].

Hence, the presence of both, G band as well as 2D band on the specific wavelength positions and the fact that the 2D intensity is much lower than the G-band (I_{2D}/I_G) leads to the conclusion that both GNP sources can be characterized as multilayer graphene. Furthermore, the ratio of I_D/I_G

leads to the conclusion that both GNPs contain defects and are disordered at least to some extent. By comparing the two GNP sources it can be stated that the AA-GNPs seem to be of better quality since the I_D/I_G ratio as a measure for defects and disorder is lower (Table 1). Additionally, the I_{2D}/I_G-ratio is higher for AA-GNP, which indicates that it consists of a fewer number of layers [10, 11]. Thus, both quality criteria were found to be in favor of the AA-GNPs.

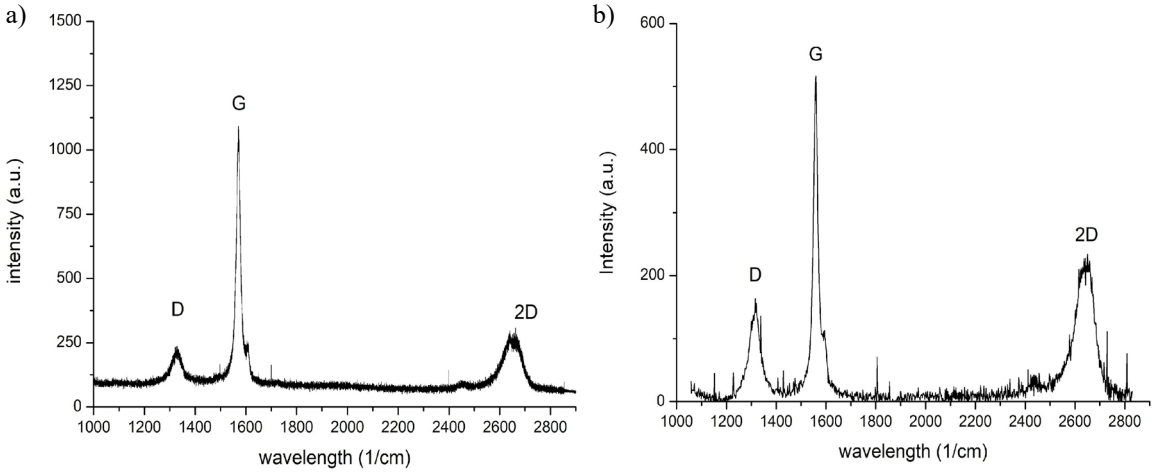

Fig. 4. Raman spectra for a) Sigma Aldrich GNPs GNPs b) Alfa Aesar GNPs.

Table 1. Results of Raman spectroscopy on both graphene sources.

	Sigma Aldrich (SA) GNPs		**Alfa Aesar (AA) GNPs**	
Peak	wavelength [1/cm]	Intensity [a.u.]	wavelength [1/cm]	Intensity [a.u.]
D band	1329	223	1317	159
G band	1571	1090	1560	515
2D band	2652	279	2649	258
I_D/I_G		0.80		0.62
I_{2D}/I_G		0.26		0.50

Characterization of mechanical properties.

Mechanical properties of the Al/GNP composites were characterized in terms of micro hardness and tensile testing properties in dependence of graphene content and relevant process parameters. The basic assumption for the effect of GNP-addition to the aluminum matrix material would be that if no agglomerates are formed, the mechanical properties of the composite should increase because of graphene's excellent mechanical properties.

Table 2a and Fig. 5a summarize the results of micro hardness testing on extruded composites with respect to the three SA-GNP contents (0%, 0.5% and 1.0%) as well as for the three different extrusion ratios (R=9:1, R=14:1 and R=31:1) when disc milling was conducted for 1min.

It can be noticed that the addition of SA-GNPs to pure aluminum did not lead to significantly increased hardness values. The only slight increase was observed for the 0.5%-SA-GNP-composite extruded at R=14:1. In that case hardness improved from 37.7 HV to 39.7HV (+5%). But a further increase of GNP content to 1.0% SA-GNPs resulted in a hardness of 37.3HV and thus, basically was the same as for pure aluminum. The effect of the extrusion ratio on micro hardness was limited as well but slightly more significant compared to the effect of SA-GNP content. For pure aluminum

the effect was insignificant. But for SA-GNP contents of 0.5% and 1.0% an increasing tendency of micro hardness with increasing extrusion ratio could be observed (Fig. 5a). The highest effect was found for the 0.5% SA-GNP composites by extruding with R=14:1 instead of R=9:1. By that hardness was increased from 35.7HV to 39.7HV (+11%). In case of the 1.0% SA-GNP composites hardness increased by 7% when extruding with R=31:1 instead of R=9:1.

Table 2b presents the effect of extrusion die angle (2〈) on micro hardness. For pure aluminum hardness increased by 5% from 37.7HV to 39.5HV when a flat face die (2〈=180°) is applied instead of a conic one with 2〈=130°. For the composite material with 0.5% SA-GNPs the opposite effect was found as hardness decreased by 8% when the flat face die was applied instead of the conic one. For the 1% composite there was no effect at all. Hence, a clear systematic effect of the die angle on micro hardness was not observed.

Table 2c and Fig. 5b represent the hardness values of SA-GNP-composites after t_{DM}=1min of disc milling and after 5min (5x1min). Hardness of pure aluminum increased by 5% from 37.7HV to 39.5HV after 5min. As the Al-particles are deformed into plates at the longer milling duration (Fig. 3c & Fig. 3e), strain hardening is assumed to be the main reason for the increased hardness. In case of the 1% SA-composite the increase in micro hardness was 30% as it increased from 35.3HV after 1min to 45.7HV after 5min. This was the first and only real significant effect in all the micro hardness testing of SA-GNP containing composites. Hence, as presented in Fig. 3c the longer milling duration seemed to have improved exfoliation of SA-GNPs and maybe even decreased their size leading to a better SA-GNPs dispersion in the composite. Through its improved dispersion the graphene was more effective in increasing the micro hardness of the composite.

Table 2. Micro hardness of extruded composites containing SA-GNPs a) effect of extrusion ratio R and GNP content b) effect of die angle for R=14:1 after 1min disc milling c) effect of disc milling duration at R=14:1.

a) GNP content	R	HV0.5
0%	9:1	36.8±0.4
0.5%	9:1	35.7±0.4
1.0%	9:1	35.8±0.6
0%	14:1	37.7±0.6
0.5%	14:1	39.7±0.2
1.0%	14:1	37.3±0.4
0%	31:1	37.7±1.3
0.5%	31:1	38.1±0.2
1.0%	31:1	38.3±0.3

b) GNP content	die angle 2α [°]	HV0.5
0%	130	37.7±0.6
0%	180	39.5±0.6
0.5%	130	39.7±0.2
0.5%	180	36.4±0.2
1.0%	130	37.3±0.4
1.0%	180	37.3±0.6

c) GNP content	t_{DM}	HV0.5
0%	1min	37.7±0.6
0%	5min	39.5±0.6
1.0%	1min	35.3±0.5
1.0%	5min	45.7±1.6

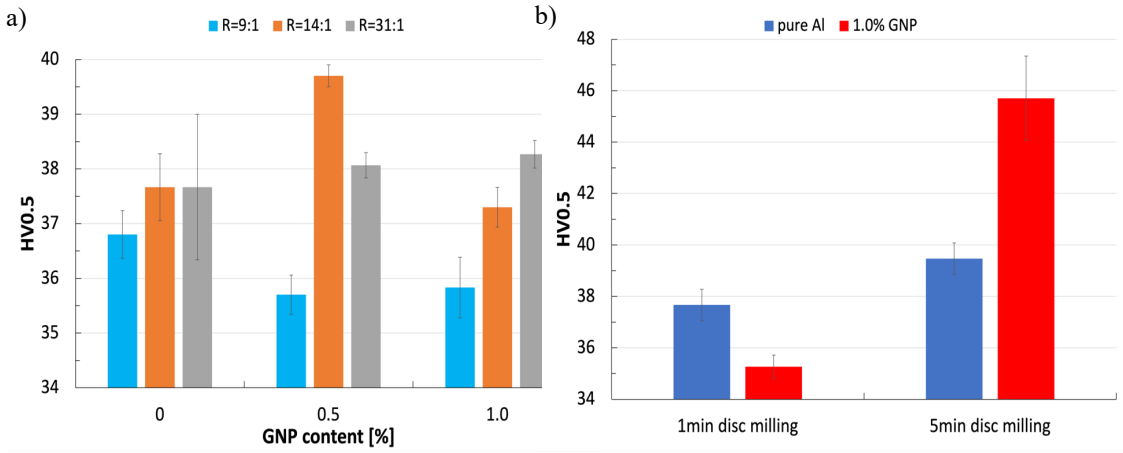

Fig. 5. Micro hardness of extruded composites containing SA-GNPs, a) processed via 6min mechanical mixing and 1min disc milling, extrusion at R=14:1 with conic die (2α=130°) b) effect of disc milling duration, applying R=14:1 and 2α=130° for extrusion.

Similar to the data representation of micro hardness, the results of tensile testing on the extruded SA-GNP composites are given in Table 3 and visualized in Fig. 6.

As observed before for the micro hardness, the tensile yield strength (TYS) did not change drastically with SA-GNP content nor with extrusion ratio. Values between 85MPa and 92MPa were measured for all composites that included disc milling for only 1min. The same can be stated for the ultimate tensile strength (UTS) since values varied between 110MPa and 116MPa. Even for the fracture strain no significant effect of the GNP content was measured. Values were between 25% and 29%. As can be noticed in Table 3b the effect of extrusion die angle (flat vs. conic) also did not have a relevant effect on the tensile properties of 1min disc milled SA-GNP composites.

Lastly, the effect of disc milling duration was investigated in tensile testing. Results are given in Table 3c and Fig. 6. In case of pure aluminum, a longer milling duration led to a reduction in TYS from 94MPa to 84MPa (-10%) while an increase in UTS from 116MPa to 126MPa (+9%) was observed. A reduction of TYS seemed to be very surprising since longer milling duration should lead to higher amount of deformation (generation of dislocations) in the Al-matrix and thus a work hardening effect. Hence, these experiments will be repeated in the future to figure out if that finding was a real effect that could maybe be related to softening by recovery or recrystallization due to significant heat generation during the milling process. For the 1.0%-SA-GNP composites an extension of milling duration resulted in increasing TYS from 81MPa to 95MPa (+17%) as well as increasing UTS from 112MPa to 141MPa (+26%). The fact that composite strengths increased could be related with improved SA-GNP dispersion in the composite (Fig. 3c) and hence a more effective strengthening effect of the graphene.

Table 3. a) Tensile test results for composites containing SA-GNPs, processed via 6min mechanical mixing and 1min disc milling, extrusion with conic die (2α=130°) b) Effect of die angle for R=14:1 after 1min disc milling c) effect of disc milling duration (t_{DM}).

a)

GNP content	R	TYS [MPa]	UTS [MPa]	ε_{frac} [%]
0%	9:1	92±2	114±2	29±1
0.5%	9:1	85±2	110±2	28±1
1.0%	9:1	87±2	111±1	25±3
0%	14:1	94±2	116±1	28±2
0.5%	14:1	90±2	114±6	25±4
1.0%	14:1	90±2	116±2	27±1

b)

GNP content	die angle 2α	TYS [MPa]	UTS [MPa]	ε_{frac} [%]
0.5%	180°	87±3	113±2	32±3
0.5%	130°	90±2	114±6	25±4
1.0%	180°	89±2	115±2	22±8
1.0%	130°	90±2	116±2	27±1

c)

GNP content	t_{DM}	TYS [MPa]	UTS [MPa]	ε_{frac} [%]
0%	1min	94±2	116±1	28±1
0%	5min	84±2	126±1	29±4
1.0%	1min	81±1	112±1	23±1
1.0%	5min	95±1	141±1	17±3

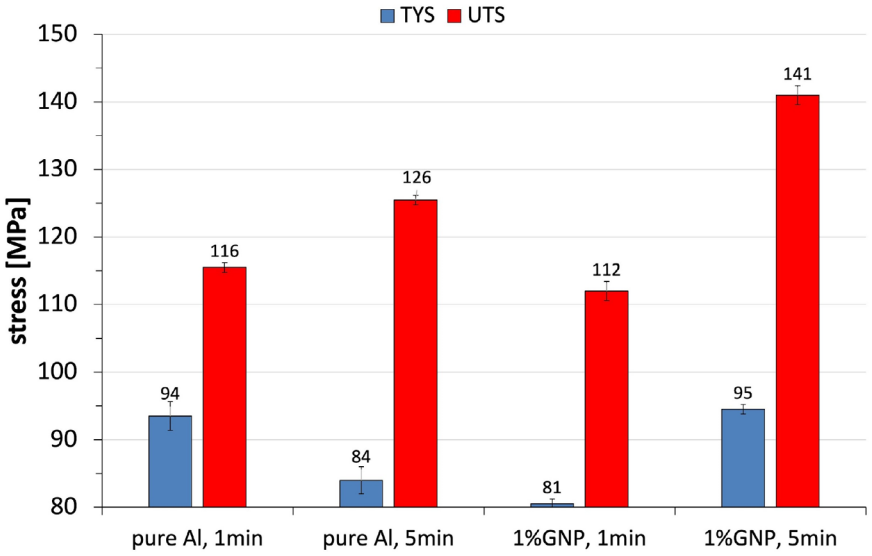

Fig. 6. Effect of disc milling duration on TYS and UTS of pure aluminum and 1%-SA-GNP composite rod materials.

When the strengths values of pure Al are compared to those of the 1% SA-GNP composite produced with same milling duration, it has to be noted that the addition of 1% GNP decreased TYS from 94MPa to 81MPa (-14%) after 1min of disc milling. UTS remained about constant and fracture strain decreased from 28% to 23%. Microstructural analysis with SEM will be carried out on the extruded rod material soon in order to investigate if maybe GNP agglomerations have formed locally for the relatively high graphene content of 1% and if those could be the reason for the detrimental YS. However, after a milling duration of 5min the addition of 1% SA-GNPs resulted in increased TYS from 84MPa to 95MPa (+13%) and UTS from 126MPa to 141MPa (+12%). Again, this could be due to improved GNP dispersion in the aluminum matrix after the longer milling duration and thus, an improved strengthening effect of graphene.

Since the results for SA-GNP composites were not as good as expected an alternative graphene source produced by Alfa Aesar (AA) was applied for the second part of the study. The effects of increasing AA-GNP content on micro hardness and tensile properties were investigated, after

applying powder processing via mechanical mixing only on the one hand and additional 5min disc milling on the other hand.

Fig. 7a presents the effect of AA-GNP content on micro hardness. In case of extruded composites produced from powders that were mechanically mixed only, increasing the AA-GNP content did not affect micro hardness as it remained about constant around 35HV. But powder processing via 5min of disc milling step, significantly increased hardness of extruded rods from 36HV to 43HV (+20%) in case of the 0.25% AA-GNP composite. The addition of a higher AA-GNP content of 1.0% increased micro hardness even further to 54HV, which means an increase of 49%. However, hardness decreased to values comparable to pure Al when AA-GNP content was 0.5%. This result could not yet be explained. If upcoming microstructure analysis with SEM should not show significant GNP agglomeration these tests will be repeated for verification.

In Fig. 7b the results of TYS and UTS are presented in dependence of GNP content and powder processing approach. Very similar to the prior micro hardness findings, composites where powders were processed via only mechanical mixing prior to extrusion, the TYS and UTS values did not change significantly with increasing AA-GNP content. TYS remained about constant in the range between 76MPa and 82MPa. UTS values varied only slightly between 105MPa to 113MPa. Fig. 7c presents the results of the measured fracture strains. For the composites no effect was observed when AA-GNP additions of 0.25% and 0.5% were applied as fracture strain remained about constant at 28%. But increasing AA-GNP content to 1.0% resulted in significant reduction to a fracture strain of 18%. As a reason for that decrease the formation of GNP agglomerates is assumed.

When the effect of AA-GNP content is studied for the approach including the 5min disc milling step, it can be noted that TYS increased from 79MPa (pure Al) to 92MPa (+16%) for the 0.25% composite. The UTS also increased from 112MPa to 142MPa (+27%). The increase in composite strength is supposed to be based on the improved AA-GNP dispersion that was noticed in Fig. 3e. Fracture strain of 5min disc milled samples were found to decrease with increasing AA-GNP content it was found to be reduced from 32% (pure Al) to 21% for 0.25% AA-GNP and to 26% for 0.5% AA-GNP. As previously noticed for micro hardness values, the material with an AA-GNP content of 0.5% also featured a low TYS of only 77MPa and a UTS of only 112MPa, which is comparable to pure aluminum. This value marks a significant drop when being compared to the 0.25% AA-GNP composite (92MPa). This again is a reason to repeat the tests for this condition. Unfortunately, the samples with the highest AA-GNP content of 1.0% could not be characterized by tensile testing since the extruded rod featured significantly cracking and it was impossible to manufacture samples for tensile testing. Hence, this condition will also be part of upcoming investigations again.

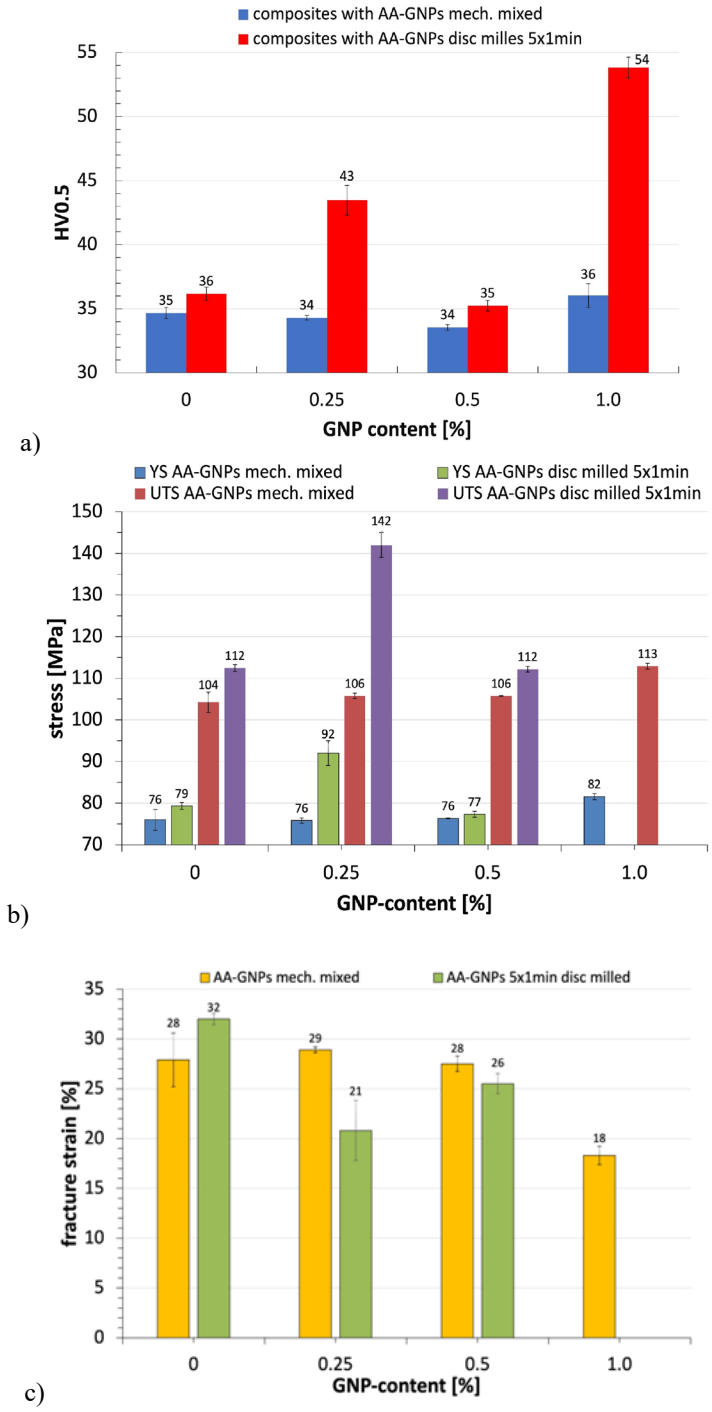

Fig. 7. Mechanical properties of extruded Al/GNP composite rods with different contents of AA-GNPs and initial powder processing via mechanical mixing only vs. additional 5min disc milling a) micro hardness b) TYS and UTS c) fracture strain.

Finally, when initial powder processing via mechanical mixing only is compared to the approach that featured the 5min disc milling, increased strength values were observed. For pure aluminum the increase in TYS was very low from 76MPa (mixed) to 79MPa (5min disc milled) and UTS from 104MPa to 112MPa (+8%). However, for the 0.25% AA-GNP composite 5min disc milling increased TYS from 76MPa to 92MPa (+21%) and UTS from 106MPa (mixed) to 142MPa (+34%). As previously assumed, the main reasons for increased strengthening are strain hardening of aluminum through plastic deformation during disc milling as well improved dispersion of GNPs in the aluminum matrix and thus an enhanced strengthening effect of the graphene additive.

Summary

The present study applied two different commercial graphene sources to investigate the disc milling process as a step in the powder metallurgical production chain for the manufacture of Al/GNP composites and the effects of process parameters on the mechanical properties. From the results the following conclusions can be drawn:

- When 1min of disc milling is applied, the addition of up to 1.0% of SA-GNPs did not significantly affect the mechanical properties of composites.
- Additionally, the application of either flat face die (2⟨=180°) or conic die with 2⟨=130°, as well as variation of extrusion ratio from 9:1, 14:1 and 31:1 did not have a significant effect on the mechanical composite properties.
- However, increasing the disc milling duration to 5min led to plate-like shaped Al-particles, a better exfoliation and dispersion of SA-GNPs and thus to increased micro hardness of up to 30%, increased TYS up to 17% and UTS up to 26%.
- Composites containing AA-GNPs improved in micro hardness by up to 49% (for 1% AA-GNPs) compared to pure Al, increased in TYS by up to 16% (for 0.25% AA-GNPs) and in UTS by up to 27% (0.25% AA-GNPs) when powders were disc milled for 5min.

References

[1] K.S. Novoselov, A.K. Geim, S.V. Morozov, D. Jiang, Y. Zhang, S.V. Dubonos, I.V. Grigorieva, A.A. Firsov, Electric field effect in atomically thin carbon films, Science 306 (2004) 666–669. /https://doi.org/10.1126/science.1102896

[2] C. Lee, X. Wei, J.W. Kysar, J. Hone, Measurement of the Elastic Properties and Intrinsic Strength of Monolayer Graphene, Science 321 (2008) 385–388. https://doi.org/10.1126/science.1157996

[3] F. Chen, N. Gupta, R.K. Behera, P.K. Rohatgi, Graphene-Reinforced Aluminum Matrix Composites: A Review of Synthesis Methods and Properties, The Journal of The Minerals, Metals & Materials Society (TMS) 70 (2018) 837-845. https://doi.org/10.1007/s11837-018-2810-7

[4] S.F. Bartolucci, J. Paras, M.A. Rafiee, J. Rafiee, S. Lee, D. Kapoor, N. Koratkar, Graphene-aluminum nanocomposites, Mater. Sci. Eng. A 528 (2011) 7933-7937. https://doi.org/10.1016/j.msea.2011.07.043

[5] M. Negendank, H.R. Faezi, O. Ovsianytskyi, O. Goerke, A. Gurlo, S. Mueller, Extrusion and characterization of aluminum/graphene composites, 24th International Conference on Material Forming (online), 2021. https://doi.org/10.25518/esaform21.3714

[6] F. Rikhtegar, S.G. Shabestari, H. Saghafian, The homogenizing of carbon nanotube dispersion in aluminium matrix nanocomposite using flake powder metallurgy and ball milling methods, Powder Technol. 280 (2015) 26-34. https://doi.org/10.1016/j.powtec.2015.04.047

[7] J.B. Wu, M.L. Lin, X. Cong, H.N. Liu, P.H. Tan, Raman spectroscopy of graphene-based materials and its applications in related devices, Chem. Soc. Rev. 47 (2018) 1822-1873. https://doi.org/10.1039/c6cs00915h

[8] B. Sahoo, J. Paul, Solid state processed Al-1100 alloy/MWCNT surface nanocomposites, Materialia 2 (2018) 196-207. https://doi.org/10.1016/j.mtla.2018.08.003

[9] B. Sahoo, S.D. Girhe, J. Paul, Influence of process parameters and temperature on the solid state fabrication of multilayered graphene-aluminium surface nanocomposites, J. Manuf. Process. 34 (2018) 486-494. https://doi.org/10.1016/j.jmapro.2018.06.042

[10] A. Sharma, V.M. Sharma, J. Paul, Fabrication of bulk aluminum-graphene nanocomposite through friction stir alloying. J. Compos. Mater. 54 (2020) 45-60. https://doi.org/10.1177/0021998319859427

[11] B. Sahoo, R. Kumar, J. Joseph, A. Sharma, J. Paul, Preparation of aluminium 6063-graphite surface composites by an electrical resistance heat assisted pressing technique, Surf. Coat. Technol. 309 (2017) 563-572. https://doi.org/10.1016/j.surfcoat.2016.12.011

Materials Research Proceedings 28 (2023) 467-476 https://doi.org/10.21741/9781644902479-51

Yield stress and work hardening behavior of extruded AA6082 profiles under different homogenization and extrusion conditions

WILLIAMS William M.[1,a], SANDNES Lise[1,b], MA Jun[1,c], TRONVOLL Sigmund Arntsønn[1,d] and WELO Torgeir[1,e *]

[1]Norwegian University of Science and Technology (NTNU), Department of Mechanical and Industrial Engineering, Richard Birkelands vei 2B, Trondheim, Norway

[a]william.m.williams@ntnu.no, [b]lise.sandnes@ntnu.no, [c]jun.ma@ntnu.no, [d]sigmund.tronvoll@ntnu.no, [e]torgeir.welo@ntnu.no

Keywords: Aluminum Extrusion, Thermo-Mechanical History, Work Hardening

Abstract. The mechanical properties of extruded AlMgSi alloys are affected by the applied thermo-mechanical parameters employed during the entire production process. In the following, the effect of different extrusion speeds and homogenization conditions paired with either air or water quenching, is examined on four different sets of rectangular hollow AA6082-T4 profiles. These profiles were fabricated and extruded under industrial conditions and selected cross sections of each profile were examined by optical microscopy to determine the microstructure and level of recrystallization. Uniaxial tension testing was used to explore the effect of homogenization conditions and extrusion cooling rate on mechanical properties. Tensile tests showed that the water-quenched extrusions had a higher yield and ultimate strength compared to air-quenched extrusions. Moreover, samples that had a recrystallized microstructure typically showed a larger standard deviation of mechanical properties, which may lead to product quality and consistency issues for metal forming operations. Overall, the present work provides a more in-depth understanding of how the selected thermo-mechanical parameters affect the resulting properties of such profiles. This can further contribute to expanding the potential for effective accommodation of extrusion parameters for zero-defect products.

Introduction

Aluminum alloys, such as the AlMgSi alloys, are commonly used for structural applications in the form of extruded products as they allow for customizing cross sectional geometry with efficient use of material. This allows the profile geometry to be tailored for the specific application area, and the production process tailored to the geometry [1]. The resulting mechanical properties of such aluminum profiles are affected by the entire production process, including the alloy chemical composition and the applied thermo-mechanical history, from casting to final product [2]. As industry pushes towards the goals of reducing climate impact, increasing process adaptability and product customization, deeper understanding of the interactions of different manufacturing process-steps is required to fully utilize the favorable properties of aluminum extrusions.

Stretch bending of aluminum profiles is a commonly used forming method for producing lightweight products [3]. However, a variety of challenges are related to such forming processes particularly for industrial applications; e.g., springback, tool wear, and geometric defects [4]. In order to improve the fabrication process and the prediction of the material response during stretch bending, there is a need for an accurate model of the work hardening behavior. Moreover, an accurate model is critical for predicting geometric recovery such as springback after forming, allowing for adaptive processes which can compensate for this behavior. Recently, Ma et al. [5], have shown that an accurate prediction of the forces during forming is possible provided the material hardening behavior is known. With this information, tool wear can be modeled and maintenance schedules can be developed. Moreover, Ma and Welo [6] have recently used

Content from this work may be used under the terms of the Creative Commons Attribution 3.0 license. Any further distribution of this work must maintain attribution to the author(s) and the title of the work, journal citation and DOI. Published under license by Materials Research Forum LLC.

analytical methods to assess the springback problem for aluminum profiles. In their work, they have shown how springback calculation can become quite complex for complicated bend geometries with variable stress states along the profile length. In their analysis, the stress state is a function of position along a cross section with stress gradients developing through transition zones and becoming stable in a uniform bending zones. When the forming process reaches the point where the entire material cross section is in the plastic state, the stress gradient will decrease as the flow stress curve approaches the saturation stress of the model [6]. Thus, once a specific part geometry is considered and the material hardening behavior is properly modeled, Ma and Welo's method can be applied in combination with finite element methods to predict springback and final part geometry of stretch bended aluminum extrusions.

Using process and property models which can account for the thermo-mechanical history to determine production parameters can allow for optimization of material and energy use by more holistic design methods. Furu et al. [7] propose a modeling framework which connects several independent models of separate process steps together. Thus, optimization of certain AlMgSi alloys, such as AA6082, by simulation is now possible with respect to several key factors such as properties and cost. Accurate prediction of dispersoid development during homogenization is critical to prediction of material structure, properties, and thus responses to later process steps with models by Dons et al. [8] and Dons [9] predicting these material characteristics. For example, the strength of AA6xxx alloys is affected by dispersoid size and density as it can determine the precipitation development during both natural (NA) and artificial aging (AA) as shown by Myhr et al. [10, 11]. This framework can also account for work hardening effects due to dislocation strengthening from pre-strain as shown by Granum et al. [12], and it is possible that this modeling family can be expanded to more accurately predict the hardening behavior of AlMgSi alloys.

However, the deformation experienced during extrusion also lead to further effects on properties. Schikorra et al. [13] divided extruded material into shear intensive zones (SIZs) or a main deformation zone (MDZ), with the higher strain and strain rates of the SIZ leading to higher potential for dynamic recrystallization during extrusion. Per Zhang et al. [14], during dynamic recrystallization grain size is a function of temperature and strain rate, and Schikorra et al. argued that this is a result of a critical strain value being reached, while Van Geertruyden et al. [15] suggests that it is based on deformation energy stored in the material from the extrusion process. Both the previous works are focused on PCG surface layers, but work by Wang et al. [16] shows that internal weld seams behave similarly. Extrusion bridge designs which increased strain also increased recrystallization of an AA6082-type alloy, consistent with the work on PCG surface layers. Similarly, work by Birol [17] shows that by increasing the number density of dispersoids (by increasing Cr and Zr) recrystallization was reduced along weld seams of extruded 6082 tubes.

The effects of homogenization parameters on dispersoid density are not limited to recrystallization, as dispersoid density effects the response of 6xxx series aluminums to aging. Work by Rakhmonov et al. [18] explains how a higher density of smaller dispersoids then resulted in an increase in β'' particles after AA, and thus improved strength. The developed as a result of alloying elements still present in solid solution, rather than in non-strengthening dispersoids. This understanding is in line with the reduction in quench sensitivity with NA found by Strobel et al. [19] in a study focused on high dispersoid density 6xxx series alloy. Alternatively, it was shown by Frodal et al. [20] that lower cooling rate decreases yield strength, due to an increase in the size of precipitate free zones around dispersoids and grain boundaries in multiple T6 aged 6xxx series alloys.

In short, variations in early extrusion production steps, such as homogenization treatment, cooling after extrusion and ageing conditions, may change the material response to downstream processes like subsequent forming operations. This work seeks to provide an example data set for the process modeling community where critical details of the material history and process

parameters are known, the mechanical properties measured, and potential impacts on downstream processes considered. The current work will show how process steps, which change the microstructure of extruded profiles, result in changes to the mechanical behavior of the material. As a result, this work will present data necessary for the process and property modeling community to move forward.

Methods

Homogenization and Extrusion.

Four sets of AA6082.26 profiles were extruded at Benteler Automotive Raufoss AS, employing differing homogenization and extrusion parameters, as listed in Table 1. and shown schematically in Fig. 1. All profiles are extruded from a single log with the composition measured at casting, as listed in Table 2. Sample sets are labeled based on their homogenization parameters and extrusion speed (either S or L) and the quenching fluid after extrusion (either A or W). Billets were homogenized for either 2.25 hours at 530°C (samples S) or for 12 hours at 590°C (samples L) before extrusion. The profiles used for this study are taken from four extrusions, with 2 prior extrusions used to ensure that all equipment was at stable operating temperature and providing stable operation conditions. Prior to extrusion, billets are heated to 470°C and then extruded at either 7 m/min (samples S) or 10 m/min (samples L). After extrusion, either forced air quenching (samples A) was applied over 40 meters after extrusion exit or water spray quenching (samples W) over 10 meters, with all extrusions reaching a temperature near 65°C after these processes. All extrusions had an extrusion ratio of 55, and the profile nominal cross-section dimensions are 60 × 40 mm with a wall thickness of 3 mm. A schematic of the profile cross section is shown in Fig. 2. Note that the extruded profiles under four sets of parameter combinations are labeled individually as SA, LA, SW, and LW.

Table 1. Homogenization and extrusion parameters for materials used for this study, all extrusions are AA6082.26.

Extrusion	1	2	3	4
Homogenization Temp [°C]	530	590	530	590
Homogenization Time [hours]	2.25	12	2.25	12
Extrusion Speed [m/min]	7	10	7	10
Quenching Fluid	Air	Air	Water	Water
Sample Label	SA	LA	SW	LW

Table 2. Composition of AA6082.26 extrusions used for this study.

Al	B	Ni	Cr	Cu	Fe	Si	Mg	Mn	Ti	V	Zn	Zr
97.5	0.004	0.002	0.145	0.0025	0.151	0.921	0.628	0.5155	0.0215	0.0145	0.0435	0.001

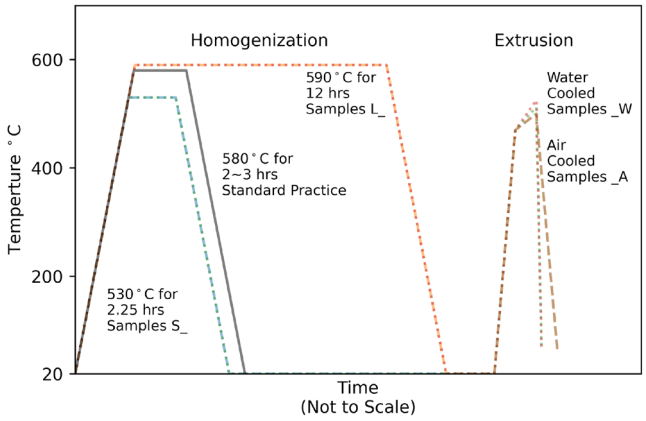

Fig. 1. Schematic of homogenization and extrusion temperatures over time with specific parameters varied for this study shown (dashed lines, also given in Table 1), in comparison to industry standard process parameters [21] shown with the solid line.

Microscopy.

Optical microscopy (OM) was done to characterize the level of recrystallization. OM imaging was done on corner sections of the extrusion cross section, with the extrusion direction normal to the image plane using a Zeiss Axio Vert Inverted Light Microscope with a 5x lens. Fig. 2 shows the image plane position and orientation with respect to the extrusion direction. OM surfaces were polished to 1 µm and anodized at room temperature in Baker's reagent (10 ml HBF_4 (48%) + 400 ml distilled water) for 90 seconds before imaging. OM images have a resolution of 0.685 µm/px, with image stitching used to show the full cross sections.

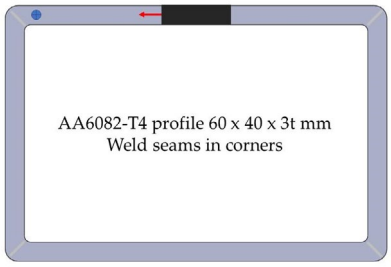

(a) Hollow Rectangular Profile Cross Section

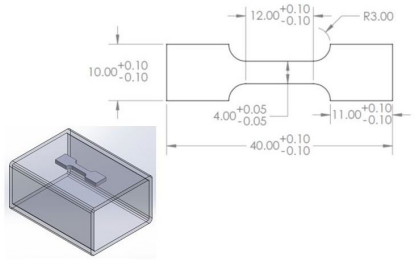

(b) Mechanical Test Sample Dimensions and Position

Fig. 2. Cross section of rectangular hollow extrusions (a) and location of samples within cross section with dimensions of uniaxial tension samples (b). The blue arrow in (a) indicates the surface normal of the OM images of extrusion cross sections.

Tensile Tests.

Subsize tensile test samples were machined from the profiles with a so-called dogbone geometry, having a nominal cross-section of 3 x 4 mm and a gauge length of 12 mm. The position of the samples with respect to profile geometry is according to the schematic shown in Fig. 2. In order to determine possible variation, 3 samples along the same flange of a profile were used for testing. Uniaxial tension tests of the samples were done with an initial nominal strain rate of 0.001 1/s using an Instron ElectroPuls E10000 servo-electric load frame. Digital image correlation (DIC) [22] *in-situ* measurement of material deformation was used with Correlated Solutions VIC-Snap 8 and VIC-2D 7 software. Strain measurement was done using virtual extensometers within the

DIC data set. The engineering strain is used for determining uniform elongation, ultimate tensile strength (UTS), and an offset strength (OFS) at 0.002. This offset is chosen for ease of comparison to the Voce initial stress value explained below. The true plastic strain is calculated, with the elastic strain component removed using a Young's modulus of 70 GPa [23]. As AA6082 shows soft knee yielding and determining individual moduli per sample is highly sensitive to experimental setup and selection of data points, the single reference value was used for all samples. A Voce-type hardening model (Eq. 1) is then fit to the material behavior up to 20% plastic strains, ϵ^p, as given by:

$$\sigma_{True} = K + Q * \left(1 - e^{(-b\epsilon^p)}\right) \quad (1)$$

where σ_{True} is true flow stress, K is the initial stress value, Q is the saturation stress value, and b is the hardening exponent.

The plastic anisotropy ratio, r, is calculated at ϵ^p = 5% in the loading direction and is thus r_0, not to be confused with normal and planer anisotropies $\underline{R}$ and ΔR respectively. The calculation uses the nearest measured longitudinal plastic strain to ϵ^p = 5% and the corresponding measured lateral plastic strain. From these measured strains, the thickness plastic strain is calculated assuming incompressibility. 5% plastic strain was chosen as a representative point considering the range of plastic strains experienced during stretch bending [24].

Results

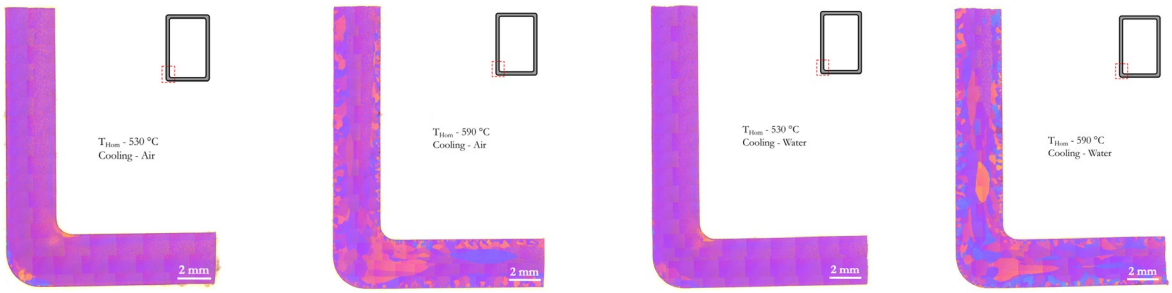

(a) Extrusion SA (b) Extrusion LA (c) Extrusion SW (d) Extrusion LW

Fig. 3. Optical microscopy imaging of the cross sections of AA6082.26 with variable extrusion histories as given in Table 1. Extrusion direction is out of the image plane.

Microstructure.

OM images of the cross sections are presented in Fig. 3, and show a fibrous grain structure is present in some part of all extrusions, with a peripheral coarse grain (PCG) layer in both the LA and LW extrusions. There is PCG growth in the corners of SA and SW, though it does not extend through the profile thickness along the weld seams. Note that the depths of the PCG layer for the LA extrusion are not symmetric on the inner and outer surfaces of the profile. The level of recrystallization in the LW cross section resulted in a thicker PCG layer in comparison to the LA extrusion. The difference in the recrystallization behavior between the T_{Hom}=530°C (S) and T_{Hom}=590°C (L) extrusion pairs is consistent with expectations based on dispersoid density after their respective homogenization parameters. Differences in recrystallization between extrusion pairs based on cooling method are still noticeable in Fig. 3, though less significant. As stated above, a fibrous-grained core is still present in both LA and LW samples. For the LA and LW cross sections, there is also recrystallization of the core within the profile corner with a PCG layer consisting of grains that are smaller than the recrystallized core. So, a PCG layer covers both the interior and exterior surfaces of the L extrusion profiles over 2 "core" areas with a fibrous core in the central areas of the webs and flanges and a recrystallized core in the corners.

Materials Research Proceedings 28 (2023) 467-476 https://doi.org/10.21741/9781644902479-51

Mechanical Properties.

The experimental flow stresses (σ_{True} vs plastic true strain ϵ^p) sorted by extrusion are shown in Fig. 4 with the curves ending at UTS. As expected and shown in Fig. 4, the material response varied based on both homogenization and cooling parameters. Water quenched extrusions; i.e., those with a higher cooling rate, showed a higher initial flow stress as reflected in both the stress-strain, $\sigma_{True} - \epsilon^p$, curves of Fig. 4 and the Voce initial strength K shown in Fig. 5 (d). The average OFS of the water-quenched extrusions (162.2 MPa and 152.1 MPa, for extrusions SW and LW respectively), as shown in Fig. 6 (a), is higher than the air-quenched extrusions (137.7 MPa and 139.3 MPa for extrusions SA and LA respectively). This difference is not dramatic, but with a variance ratio (between group variance/within group variance) of 17.34 it is greater than the difference between samples from the same extrusion. UTS showed a more significant difference between the water-quenched samples (258.6 MPa and 248.5 MPa for extrusions SW and LW respectively) and air-quenched samples (221.2 MPa and 232.8 MPa for extrusions SA and LA respectively), as shown in Fig. 6 (a). The UTS variance ratio is 46.14, which reflects a stronger relationship between an extrusion's thermo-mechanical history and UTS compared to OFS. This trend is also reflected in the saturation stress Q of the Voce model, shown in Fig. 5 (b).

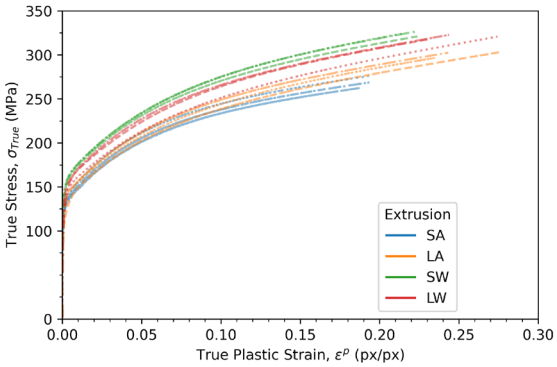

*Fig. SEQ Figure * ARABIC 4. Experimental true stress vs plastic true strain of AA6082.26 with varied thermo-mechanical histories as explained and labelled in Table 1.*

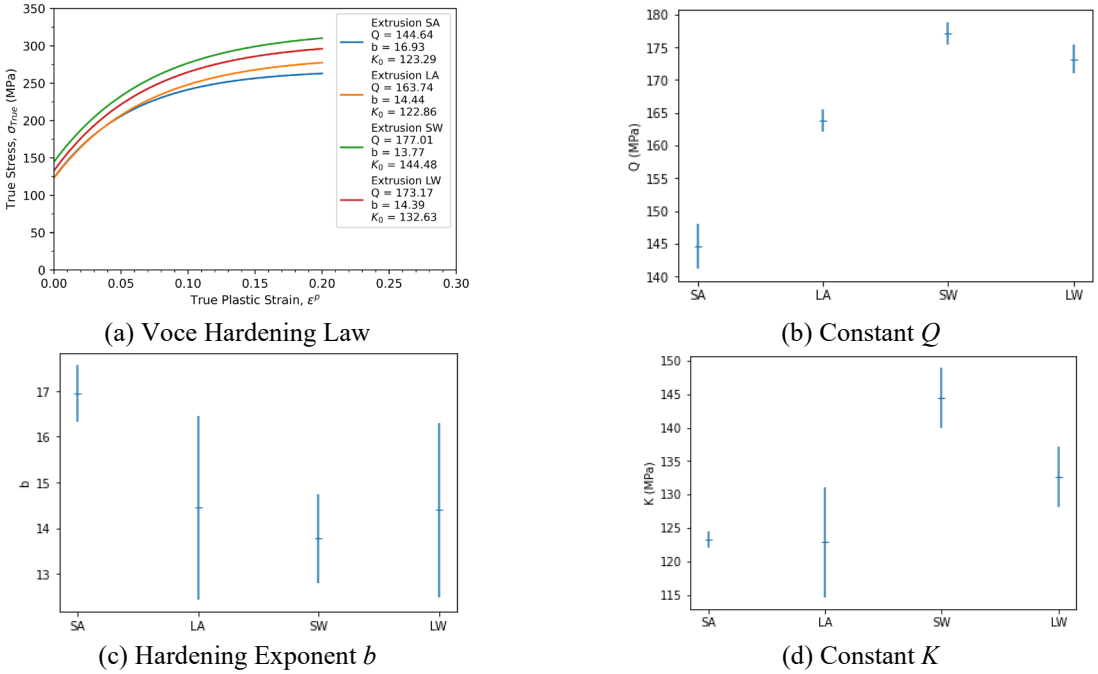

(a) Voce Hardening Law (b) Constant Q

(c) Hardening Exponent b (d) Constant K

Fig. 5. Fit of a Voce like hardening law to experimental true stress vs plastic true strain data of AA6082.26 with varied thermo-mechanical histories as given in Table 1. The Voce like hardening law is plotted for each extrusion in (a) using the constant Q (b), hardening exponent b (c), and constant K (d).

In contrast to strength, the ductility of the samples is better sorted by homogenization parameters than by cooling rate. The uniform elongation, as shown in Fig. 6 (b), is higher for both L sample sets, but the standard deviation (SD) is larger. In contrast, the level of consistency in both UTS and flow stress curves shown in Fig. 4 for both S extrusions is notable. It is important to observe that this trend is however not reflected in the strain to failure, in comparison to uniform elongation. The SW extrusion had similar failure strains as that of the L samples, implying significant elongation after UTS.

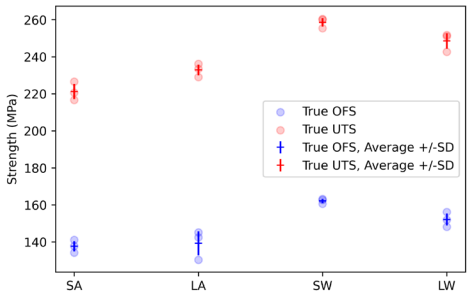

(a) Ultimate Strength (UTS) and 0.002 Offset Strength (OFS)

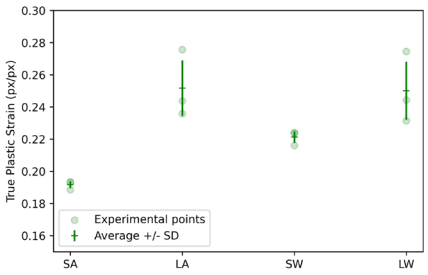

(b) Uniform Elongation

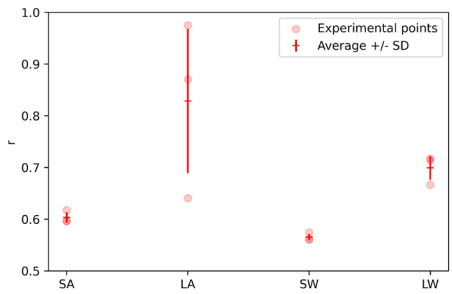

(c) Plastic Ratio *r*

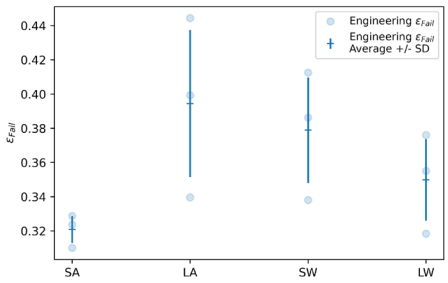

(d) Engineering Strain at Failure

Fig. 6. Mechanical properties of AA6082.26 T4 with variable extrusion histories as given in Table 1. Ultimate Tensile strength (UTS) and 0.002 offset strength (OFS) are shown in (a), uniform elongation in (b), plastic ratio r at 5% plastic strain in (c), and engineering failure strain in (d).

Discussion

As shown in the results section higher extrusion speeds in combination with homogenization parameters, and thus a lower number density of dispersoids, increases the recrystallization in AA6082 extrusions. On thin wall profiles, such as hollow rectangular extrusions, this can result in a significant portion of the cross section being PCG or recrystallized. This difference in material microstructure changes mechanical behavior, especially initial yielding, plastic deformation, and work hardening, due to the influence of grain size and texture on these properties.

Considering the recrystallization of the L extrusions, primarily within the different portions of a cross section, recall the work of Schikorra *et al*. [13]. Their framework is helpful to understand the differences between the PCG around the surface of the L cross sections, the fibrous core, and the coarser recrystallized grains in the corners as shown in Fig. 3. The higher recrystallization in combination with the higher extrusion speeds of the L samples is consistent with understandings presented above in [14], [15]. However, these results suggest that the material making up the corners does not fit cleanly within either SIZ or MDZ categories. Also, material which is within the same category of SIZ on the internal and external surfaces are not similar thicknesses, which is consistent with the different deformation histories of each. Thus, further work is needed to investigate the material flow path within this particular toolset to clarify the link between

deformation history and recrystallization. Based on Wang et al. [16], it is reasonable that the higher strain experienced by the material from the MDZ in the corners is resulting in the coarser grain growth. It also explains why there is also recrystallization in the S cross section corners, while the majority of the cross section retains a fibrous microstructure. In short, the PCG layer recrystallization is driven by strain history as part of the SIZ of the extruded material which is consistent around all surfaces. In the corners, a recrystallized core from the MDZ develops as a result of a longer flow path than the fibrous core. Thus it is also possible that the material making up the corners does not fit within either SIZ or MDZ categories.

As stated in the results section above, the mechanical characteristics of the profiles have a stronger relationship to the extrusion cooling rate than the homogenization parameters. However, it is clear from both the literature and differences between the SW and LW extrusions that the homogenization parameters have an effect. This work examines NA AA6082, and as such β' particles develop at nucleation points (which are often dispersoids [19]). Alloying elements which would have developed into β'' particles during AA remain in solid solution, strengthening the material. While Frodal et al. [20] was of AA rather than NA 6xxx series, it is consistent with this understanding of the results. The SW samples had higher UTS and OFS than LW samples, as well as higher average Voce constants Q and K as shown in Fig. 6 (a), Fig. 5 (b) and (d) respectively.

It is also interesting to note from these figures that both recrystallized extrusions LA and LW had higher uniform elongations and r at 5% ϵ^p, likely due to the recrystallized grain structure within these extrusions. Both characteristics suggest the LA and LW extrusions would have better formability, as r approaching 1 implies more isotropy and higher uniform elongations imply a larger allowable strain range for forming before localization. However, for both of these characteristics, the SD of the tested samples are larger than for the S samples (and in the case of r for LA, larger than the LW samples) which suggests possible production consistency issues. While these characteristics might imply better forming performance, recrystallized profiles tend to have an "orange peel" like surface texture which may cause issues for parts and profiles that must meet surface quality requirements for either paint or appearance for surfaces visible to the end user. It is also important to note that while the mechanical properties of initial flow stress and UTS of the LW samples were higher than both SA and LA samples, the SW extrusions are the best performing for applications where maximum mechanical strength is needed based on the extrusions tested.

Summary

Four sets of AA6082.26 rectangular hollow profiles are produced using industrial equipment and methods, using differing homogenization and extrusion parameters. Both microstructural characteristics and mechanical properties of the extruded profiles were examined. The influences of thermo-mechanical history on the property of extruded profiles were discussed. The main conclusions are summarized as follows:

- Extrusions with longer time and higher temperature homogenization resulted in higher levels of uniform elongation and more isotropic plastic deformation regardless of extrusion cooling rate.
- Higher extrusion cooling rates led to higher strengths overall (both ultimate and offset strengths), with this effect being larger in extrusions with shorter homogenization time.
- The hardening behavior of the material up to 20% plastic strain can be represented regardless of homogenization or extrusion parameters using a Voce like hardening law for the flow stress behavior.
- Extrusions with longer time and higher temperature homogenization showed higher standard deviations across a number of mechanical parameters, including hardening exponent b, plastic ratio r, and uniform elongation.

Based on these results, the extrusion cooling rate is more critical to control than recrystallization with respect to mechanical characteristics. For process modeling, homogenization effects on

ductility due to microstructural composition and the effect of extrusion cooling rate on strength are the primary effects of each process which then interact to result in the hardening behavior. Further work can proceed along two lines, either via investigation of the material or investigation of the subsequent forming process. Investigation of the material would involve TEM imaging and measurement of dispersoid size and density, as well as β' precipitate development during natural aging. Work proceeding along the forming process would show the impact of these property variations on dimensional accuracy of formed parts.

Acknowledgments
This work was funded by the Research Council of Norway project AdaptAl - Adaptive Control of Aluminum Manufacturing (project number: 314054), and supported by the NTNU Aluminum Product Innovation Center (NAPIC).

References
[1] D.H. Ko, B.H. Kang, D.C. Ko, B.M. Kim, Improvement of mechanical properties of Al6061 extrudate by die cooling with N2 gas during hot extrusion, J. Mech. Sci. Technol. 27 (2013) 153-161. https://doi.org/10.1007/s12206-012-1213-x
[2] S.K. Fjeldbo, Y. Li, K. Marthinsen, T. Furu, Through-process sensitivity analysis on the effect of process variables on strength in extruded Al-Mg-Si alloys, J. Mater. Process. Technol. 212 (2012) 171-180. https://doi.org/10.1016/j.jmatprotec.2011.08.020
[3] J. Cao, M. Banu, Opportunities and challenges in metal forming for lightweighting: Review and future work, J. Manuf. Sci. Eng. Trans. ASME 142 (2020) 1-24. https://doi.org/10.1115/1.4047732
[4] A.E. Tekkaya, P.O. Bouchard, S. Bruschi, C.C. Tasan, Damage in metal forming, CIRP Ann. 69 (2020) 600-623. https://doi.org/10.1016/j.cirp.2020.05.005
[5] J. Ma, T. Welo, G. Ringen, Efficient Prediction of Real-Time Forming Forces in Flexible Stretch Bending, Esaform 2021, no. April, 2021. https://doi.org/10.25518/esaform21.4040
[6] J. Ma, T. Welo, Analytical springback assessment in flexible stretch bending of complex shapes, Int. J. Mach. Tools Manuf. 160 (2021). https://doi.org/10.1016/j.ijmachtools.2020.103653
[7] T. Furu, R. Østhus, J. Søreide, O.R. Myhr, A Novel Methodology for Optimization of Properties, Costs and Sustainability of Aluminium Extrusions, Mater. Sci. Forum 877 (2016) 625-632. https://doi.org/10.4028/www.scientific.net/MSF.877.625
[8] A.L. Dons, E.K. Jensen, Y. Langsrud, E. Trømborg, S. Brusethaug, The alstruc microstructure solidification model for industrial aluminum alloys, Metall. Mater. Trans. A Phys. Metall. Mater. Sci. 30 (1999) 2135-2146. https://doi.org/10.1007/s11661-999-0025-9
[9] A.L. Dons, The Alstruc homogenization model for industrial aluminum alloys, J. Light Met. 1 (2001) 133-149. https://doi.org/10.1016/S1471-5317(01)00007-4
[10] O.R. Myhr, Ø. Grong, K.O. Pedersen, A combined precipitation, yield strength, and work hardening model for Al-Mg-Si alloys, Metall. Mater. Trans. A Phys. Metall. Mater. Sci. 41 (2010) 2276-2289. https://doi.org/10.1007/s11661-010-0258-7
[11] O.R. Myhr, Ø. Grong, C. Schäfer, An Extended Age-Hardening Model for Al-Mg-Si Alloys Incorporating the Room-Temperature Storage and Cold Deformation Process Stages, Metall. Mater. Trans. A Phys. Metall. Mater. Sci. 46 (2015) 6018-6039. https://doi.org/10.1007/s11661-015-3175-y
[12] H. Granum, O.R. Myhr, T. Børvik, O.S. Hopperstad, Effect of pre-stretching on the mechanical behaviour of three artificially aged 6xxx series aluminium alloys, Mater. Today Commun. 27 (2021). https://doi.org/10.1016/j.mtcomm.2021.102408
[13] M. Schikorra, L. Donati, L. Tomesani, A.E. Tekkaya, Microstructure analysis of aluminum extrusion: Grain size distribution in AA6060, AA6082 and AA7075 alloys, J. Mech. Sci. Technol. 21 (2007) 1445-1451. https://doi.org/10.1007/BF03177357

[14] C. Zhang, C. Wang, R. Guo, G. Zhao, L. Chen, W. Sun, X. Wang, Investigation of dynamic recrystallization and modeling of microstructure evolution of an Al-Mg-Si aluminum alloy during high-temperature deformation, J. Alloys Compd. 773 (2019) 59-70. https://doi.org/10.1016/j.jallcom.2018.09.263
[15] W.H. Van Geertruyden, H.M. Browne, W.Z. Misiolek, P.T. Wang, Evolution of surface recrystallization during indirect extrusion of 6xxx aluminum alloys, Metall. Mater. Trans. A Phys. Metall. Mater. Sci. 36 (2005) 1049-1056. https://doi.org/10.1007/s11661-005-0298-6
[16] Y. Wang, A. Zang, Y. Mahmoodkhani, M. Wells, W. Poole, N. Parson, The Effect of Bridge Geometry on Microstructure and Texture Evolution During Porthole Die Extrusion of an Al–Mg–Si–Mn–Cr Alloy, Metall. Mater. Trans. A Phys. Metall. Mater. Sci. 52 (2021) 3503-3516. https://doi.org/10.1007/s11661-021-06322-5
[17] Y. Birol, Effect of Cr and Zr on the grain structure of extruded en AW 6082 alloy, Met. Mater. Int. 20 (2014) 727-732. https://doi.org/10.1007/s12540-014-4018-x
[18] J. Rakhmonov, K. Liu, P. Rometsch, N. Parson, X.G. Chen, Effects of Al(MnFe)Si dispersoids with different sizes and number densities on microstructure and ambient/elevated-temperature mechanical properties of extruded Al–Mg–Si AA6082 alloys with varying Mn content, J. Alloys Compd. 861 (2021) 157937. https://doi.org/10.1016/j.jallcom.2020.157937
[19] K. Strobel, M.A. Easton, M.D.H. Lay, P.A. Rometsch, S. Zhu, L. Sweet, N.C. Parson, A.J. Hill, Quench Sensitivity in a Dispersoid-Containing Al-Mg-Si Alloy, Metall. Mater. Trans. A Phys. Metall. Mater. Sci. 50 (2019) 1957–1969. https://doi.org/10.1007/s11661-019-05130-2
[20] B.H. Frodal, E. Christiansen, O.R. Myhr, O.S. Hopperstad, The role of quench rate on the plastic flow and fracture of three aluminium alloys with different grain structure and texture, Int. J. Eng. Sci. 150 (2020) 7491. https://doi.org/10.1016/j.ijengsci.2020.103257
[21] O. Reiso, Extrusion of AlMgSi alloys, Mater. Forum 28 (2004) 32-46.
[22] H. Schreier, J.-J. Orteu, M.A. Sutton, Image Correlation for Shape, Motion and Deformation Measurements, Boston, MA: Springer US, 2009.
[23] HYDRO, Technical datasheet - Extruded products Alloy EN AW - 6082 [AlSi1MgMn], Hydro, 2019, 3-5.
[24] T. Welo, J. Ma, J. Blindheim, T. Ha, G. Ringen, Flexible 3D stretch bending of aluminium alloy profiles: An experimental and numerical study, Procedia Manuf. 50 (2020) 37-44. https://doi.org/10.1016/j.promfg.2020.08.008

Materials Research Proceedings 28 (2023) 477-486 https://doi.org/10.21741/9781644902479-52

Experimental analysis and modeling of the recrystallization behaviour of a AA6060 extruded profile

NEGOZIO Marco[1,a *], DONATI Lorenzo[1,b], PELACCIA Riccardo[2,c], REGGIANI Barbara[2,d] and DI DONATO Sara[1,e]

[1]DIN Department of Industrial Engineering – University of Bologna, Viale Risorgimento 2, 40136, Bologna, Italy

[2]DISMI Department of Sciences and Methods for Engineering, University of Modena and Reggio Emilia, Via Amendola 2, 42122, Reggio Emilia, Italy

[a]marco.negozio2@unibo.it, [b]l.donati@unibo.it, [c]riccardo.pelaccia@unimore.it, [d]barbara.reggiani@unimore.it, [e]sara.didonato2@unibo.it

Keywords: Recrystallization, Aluminum Alloy, Extrusion, FEM, Microstructure, 6XXX

Abstract. The microstructure of Al-Mg-Si alloys is gaining nowadays an increasing industrial interest because it influences the strength, crash, corrosion and esthetic properties of the extruded profiles. In order to investigate and predict the recrystallization behaviour in the extrusion of 6XXX aluminum alloys, experimental and numerical activities are still needed. In this work, the extrusion of an industrial-scale AA6060 aluminum alloy hollow profile was carried out. An innovative recrystallization model was developed and optimized by comparing the microstructural data experimentally acquired with the outputs of the simulation performed using the Finite Element commercial code Qform Extrusion. A good correlation between numerical prediction and experimental data was found, thus proving the reliability of the proposed AA6060 recrystallization model.

Introduction

The microstructure of 6XXX aluminum alloy extruded profiles is of primary interest for extrusion companies since it affects the product performances [1,2]. To date, the relationship between process parameters and grain structure evolution is not fully understood due to the high number of factors that affects the final microstructure of the profile. For this reason, the scientific community is pooling efforts to investigate the recrystallization of aluminum alloys during the extrusion process. Moreover, in order to control the final microstructure at a die design stage without performing expensive experimental trial and errors, it is mandatory the development of reliable models for the recrystallization prediction to be implemented into FE (Finite Element) codes.

In Fig. 1, a typical microstructural evolution during the extrusion of 6XXX aluminum alloys is shown. Two different types of structures can be detected. In the fibrous structure (Fig. 1b,d), grains are deeply elongated and they are characterized by a length (the dimension along the extrusion direction) several times greater than the width and thickness. Instead, in the recrystallized structure (Fig. 1c,e), grains have a spherical equiaxed shape (Fig. 1a) so that they can be characterized by a single average grain diameter. The fully recrystallized state is always detectable in the billet material as consequence of the casting phase and further homogenization process. Immediately after the die exit, the profile always shows a fibrous microstructure (immediate profile quenching) due to the strain field applied during the extrusion process. If the profile is not immediately quenched and its temperature remains higher than the alloy recrystallization temperature for a sufficient amount of time, the structure may recrystallize (fully or partially Fig. 1c,e). If the energy stored in the material during the deformation process is lower than a certain critical level, the microstructure of the profile still remains fibrous (Fig. 1d).

Content from this work may be used under the terms of the Creative Commons Attribution 3.0 license. Any further distribution of this work must maintain attribution to the author(s) and the title of the work, journal citation and DOI. Published under license by Materials Research Forum LLC.

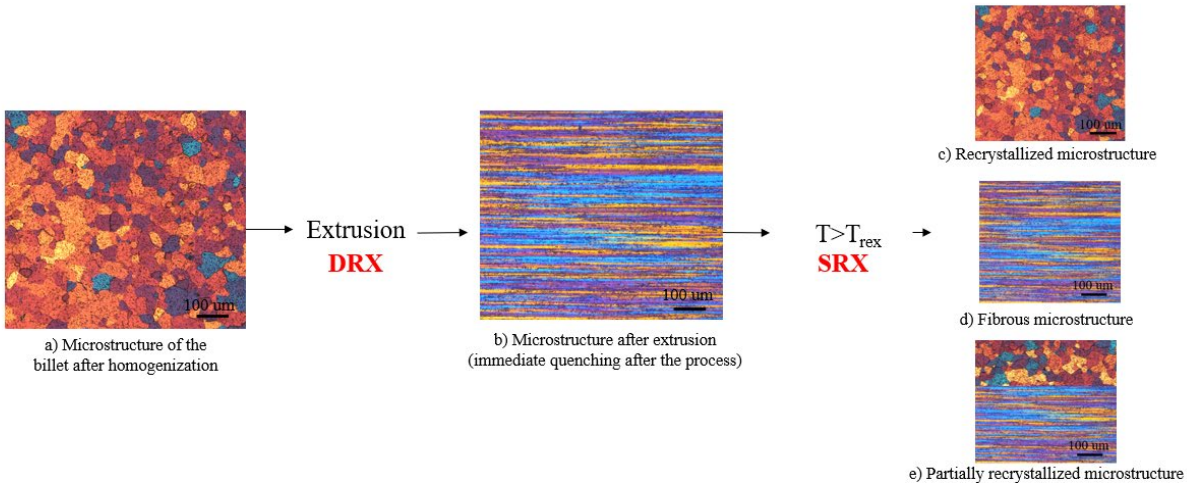

Fig. 1. schematization of the microstructure evolution during the extrusion process of a 6XXX aluminum alloy.

During and after the extrusion of 6XXX aluminum alloys, two main recrystallization mechanisms can be distinguished: the first, called dynamic recrystallization (DRX), occurs while the material is deforming [3]. This phenomenon is related to the material strain field and involves, for low stacking fault materials (LSFE), nucleation and grain growth or, for high stacking fault materials (HSFE as aluminum alloys), other different behaviours that are still under debate in the research community.

The second main recrystallization mechanism is the static recrystallization (SRX), which occurs after the hot deformation and causes the rearrangement of the microstructure through nucleation and growth [4]. Several studies have been made to investigate the SRX in the hot deformation processes of aluminum alloys also using finite element model simulations [5-7]. However, many of these works were performed using laboratory-scale or simple-profile extrusions as experimental campaigns. Moreover, none of the investigated models has been extensively tested on extrusions of industrial-scale cases or on complex geometry profiles, thus limiting the strain and strain rate fields for the modeling validation.

In this work, an industrial-scale extrusion of AA6060 aluminum alloy hollow profile was investigated. Numerical activities involving Finite Element (FE) simulation of the extrusion were performed with the commercial Qform Extrusion code. Moreover, an innovative recrystallization model was developed, comparing the achieved results with the microstructural data experimentally collected for the industrial-scale profile. The final aim of this work was to propose a reliable model able to accurately predict the microstructural behaviour in the hot extrusion of AA6060 aluminum alloy profiles.

Experimental Procedure

The geometry of the profile under investigation is reported in Fig. 2. It was produced by the Profilati SpA plant of Medicina (Italy). The production batch involved the extrusion of 17 billets and the data about profile exit temperature and extrusion load were acquired during the whole process and used to validate the numerical simulation results. The analyzed sample comes from the extrusion of the seventh billet in order to have steady-state conditions in the tool-die set.

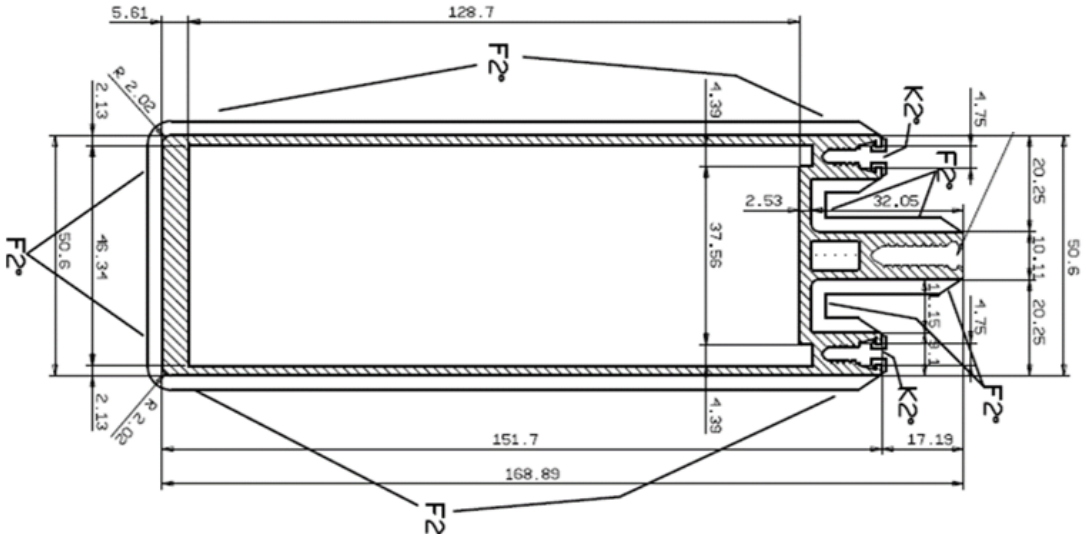

Fig. 2. Geometry of the extruded profile.

In Table 1, the extrusion process and the geometry parameters of billet and tools are reported.

Table 1. Process parameters and geometry tolerances.

Process parameters and geometry tolerances	**Profile**
Aluminum alloy	AA6060
Extrusion ratio	27
Ram speed [mm/s]	8
Container temperature [°C]	430
Billet temperature [°C]	480
Die temperature [°C]	510
Ram acceleration time [s]	5
Billet length [mm]	950
Billet diameter [mm]	203
Container diameter [mm]	211
Billet Rest length [mm]	44

The microstructure of the profile is reported in Fig. 3b-g. The investigated samples were grinded, polished and etched with electrolytical etching. The images of the etched samples were acquired by using polarized light microscopy Zeiss AXIO and the measurement of the average grain dimension was carried out according to the ASTM-E112 regulation. The images of Fig. 3 clearly show a fully recrystallized microstructure, within an average dimension range of 45 μm to 110 μm. The analysed samples were taken at the middle length of the extrusion profile, corresponding to a ram stroke of 475 mm. From the entire cross-section of the profile, six zones were selected (Fig. 3b-g). From each zone, 10 random points were extracted and, in each of these, the dimensions of the statically recrystallized diameter were measured. Half of these grain sizes were used for the model calibration and the other half for the validation. During the calibration, these values were used to find the material constants of the recrystallization model while, during the validation, the values were used to assess the accuracy of the model predictions.

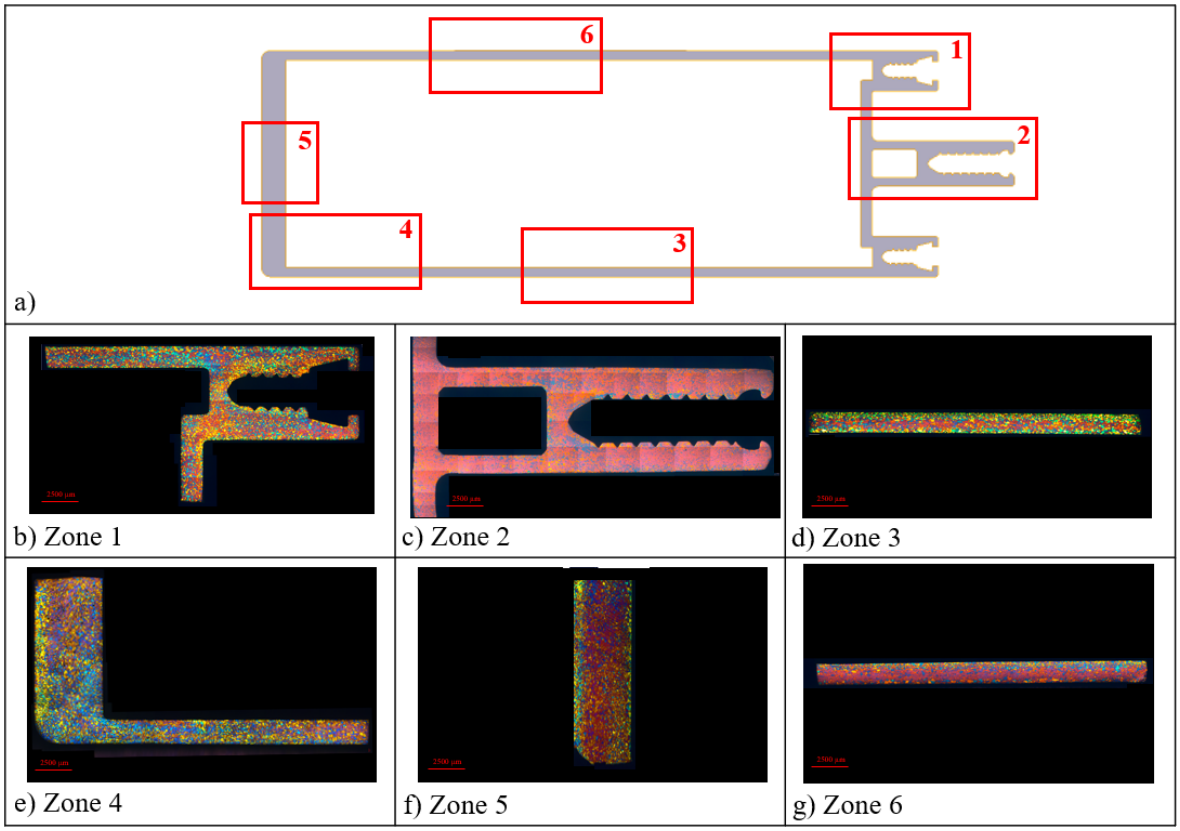

Fig. 3. Microstructure of the investigated AA6060 profile.

Modeling

The static recrystallization kinetic was modeled according to [8]: the average diameter of the static recrystallized grain D_{rex} was calculated as following:

$$D_{rex} = X_{rex} * N^{-1/3} \quad (1)$$

where N is the nucleation density and X_{rex} is the fraction of recrystallized material. The X_{rex} value was considered equal to 1 since the acquired images show a completely recrystallized microstructure. In order to determine N, different nucleation contributions must be considered [8]:

$$N = N_{PSN} + N_{GB} + N_C \quad (2)$$

where N_{PSN} is the nucleation occurred from deformation zones around particles larger than a critical size. It is often the main nucleation mechanism in 6XXX aluminum alloys which contains large undeformable particles, and involves the growth of nuclei in turbulent deformation zones with random orientations. N_{GB} is the nucleation from old grain boundaries and N_C is the nucleation from retained cube grains which survived the applied deformation. These three contributions can be calculated as following [8]:

$$N_{PSN} = C_{PSN}\, exp\left(\frac{-A_{PSN}}{(Pd-Pz)}\right) \quad (3)$$

$$N_{GB} = C_{GB}\, \delta\, A(\varepsilon)\, S_{GB} \quad (4)$$

$$N_C = C_C\, \delta\, A(\varepsilon)\, S_C \quad (5)$$

where C_{PSN}, A_{PSN}, C_{GB} and C_C are the material constants which need to be calculated in order to optimize the model for the investigated AA6060 aluminum alloy. Pd is the Stored Energy, driving force for recrystallization which act in the form of dislocation substructures and concentrations of vacancies [9]. Pz is the Zener Drag Pressure, retarding force for recrystallization which depends on the dispersoids size and density and alloying elements in solid solution [10].

$$Pd = \frac{Gb^2}{10}\left[\rho i(1 - ln(10b\rho i^{0,5})) + \frac{2\theta}{b\delta} * \left(1 + ln\ ln\ \left(\frac{\theta c}{\theta}\right)\right)\right] \quad (6)$$

where G is the material shear modulus (2.05x10^{10} Pa), b the Burgers vector (2.86x10^{-10} m), ρi the dislocation density, δ the subgrain size, θ the misorientation angle and Θc the misorientation angle limit (15°). The dislocation density ρi and the misorientation angle θ were calculated according to [9] as a function of the strain rate $\dot{\varepsilon}$, the temperature T and the strain ε (Fig. 4a,b).

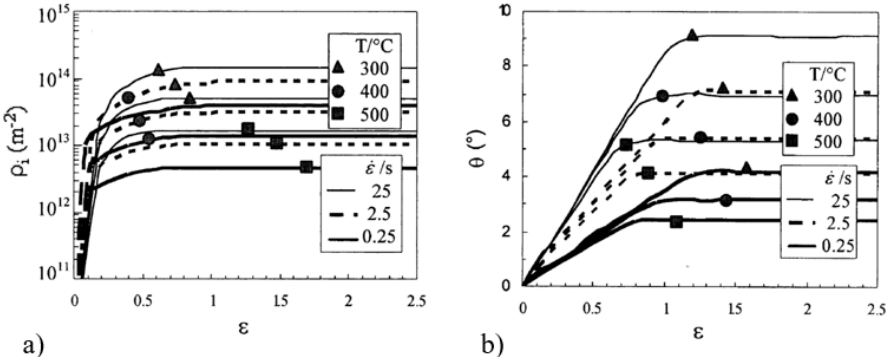

Fig. 4. a) Dislocation density [9], b) Misorientation angle [9].

The subgrain size and the Zener-Hollomon parameter were calculated according to [11]:

$$\frac{1}{\delta} = C\ (lnZ)^n \quad (7)$$

$$Z = \dot{\varepsilon}\ exp\ \left(\frac{Q}{RT}\right) \quad (8)$$

where C=3.36x10^{-9} m^{-1}, n=5.577, Q is the activation energy of the AA6060 (161000 J/mol*K [12]), R is the universal gas constant (8.341 J/mol) and $\dot{\varepsilon}$ is the maximum strain rate for each point of material flow during the extrusion deformation path.
$A(\varepsilon)$ is the grain boundary area per volume at a given strain and S_{GB}, which can be assumed as S_{GB}=S_C=S [13], is the number of subgrain larger than a critical subgrain size δ^*, calculated as followed:

$$\delta^* = \frac{4\gamma}{Pd - Pz} \quad (9)$$

According to what reported in literature [8], $A(\varepsilon)$ was modelled as:

$$A(\varepsilon) = \frac{1}{D_0}[(exp\ exp\ (\varepsilon)\ + exp\ exp\ (-\varepsilon)\ + 1)] \quad (10)$$

where D_0 represents the average grain size in the billet material after the homogenization process. According to the work of [10], the Zener Drag pressure is calculated as following:

$$Pz = \frac{3 * f * \gamma}{4 * r} \quad (11)$$

where f and r are the fraction area and the mean size of the dispersoids, respectively, and γ is the grain boundary energy (0.3 J/m^2 [13]). As an approximation, values of f and r were taken from the work of [14], where the distribution of dispersoids were analysed in different AA6060 aluminum alloys (f= 0.013%, r= 125 nm).

Numerical Investigation

The simulation of the analysed extrusion process was performed using Qform Extrusion, a commercial ALE (Arbitrarian Lagrangian Eulerian) FE code. The constitutive model used for the description of the AA6060 flow stress was proposed by Hensel-Spittel [15]. According to the proposed equation (Eq. 12), the material flow stress $\underline{\sigma}$ depends on the contribution of strain $\underline{\varepsilon}$, strain rate $\underline{\dot{\varepsilon}}$ and temperature T:

$$\underline{\sigma} = A \cdot e^{m_1 T} \cdot \underline{\varepsilon}^{-m_2} \cdot \underline{\dot{\varepsilon}}^{-m_3} \cdot e^{\frac{m_4}{\underline{\varepsilon}}} \cdot (1+\underline{\varepsilon})^{m_5 T} \cdot e^{m_7 \underline{\varepsilon}} \cdot \underline{\dot{\varepsilon}}^{m_8 T} \cdot T^{m_9} \quad (12)$$

The values of the Hensel-Spittel constants ($m1$-$m9$) used for the simulation of the AA6060 aluminum alloy, reported in Table 2, were taken from the Qform material database.

Table 2. Hensel-Spittel and for the AA6060 aluminum alloy.

Parameters	AA6060
A	280 [MPa]
m1	-0.00461 [K^{-1}]
m2	-0.16636
m3	0.12
m4	-0.02056
m5	0.00036 [K^{-1}]
m7	0
m8	0 [K^{-1}]
m9	0

The friction conditions between workpiece and tools were also taken from the software database according to the default values optimized for extrusion (Table 3). The values of the material properties used in the simulation are reported in Table 4.

Table 3. Friction conditions.

Surface	Friction condition
Billet-Container	Sticking condition
Billet-Ram	Sticking condition
Billet-Die	Sticking condition
Bearings	Levanov model (m = 0.3, n = 1.25)

Table 4. Material parameters for the AA6060 aluminum alloy.

Material Properties	AA6060
Density [Kg/m3]	2690
Specific heat [J/kg K]	900
Thermal conductivity [W/m K]	200
Thermal expansivity [m/K]	2.34*10-5
Young's modulus [GPa]	68.9
Poisson's ratio	0.33

In order to validate the results of the simulation, the values of the numerical extrusion load and profile exit temperature were compared to the experimental ones. With regard to the extrusion load, the experimental peak value was found at 23.4 MN while the numerical one at 23.3 MN. Consequently, the numerical error in the extrusion load prediction was under the 1%. Moreover, the experimental exit temperature of the profile (recorded by using a pyrometer fixed at the exit of the die) was found at 557°C while the numerical one at 562°C, with a prediction error close to the 1%. As a result, the average error in the extrusion load and temperature prediction was found below the 1%, thus proving the reliability of the simulation.

Results and Discussion

The material constants of the recrystallization model were obtained by applying the Levenberg-Marquardt non-linear regression algorithm [16], implemented in Matlab®, using as input data the "calibration set" of points in which the grain size was experimentally calculated. For each considered point, the values of temperature, strain and maximum strain rate were calculated by the simulation using Qform software. A different set of points ("validation set") were used to validate the results of the numerical microstructure prediction.

Considering the trend of eq. 10, since this equation was investigated in rolling processes which typically have stain values considerably lower than 10 [8], it has been noticed that for values of strain higher than 10 (Fig. 5a), typical of industrial-scale extrusions, the formula returned unreasonably high values of $A(\varepsilon)$ and, consequently, of N_{GB} and N. For this reason, $A(\varepsilon)$ has been calculated according to eq. 13, limiting the growth of the parameter to a maximum value (Fig. 5b):

$$A(\varepsilon) = \frac{1}{D_0}\left[p_1 - p_2\, e^{p_3\, \varepsilon^{p_4}}\right] \tag{13}$$

where p_1, p_2, p_3, p_4 are material constants. These values were added to the other material constants and optimized using the Levenberg-Marquardt algorithm mentioned above.

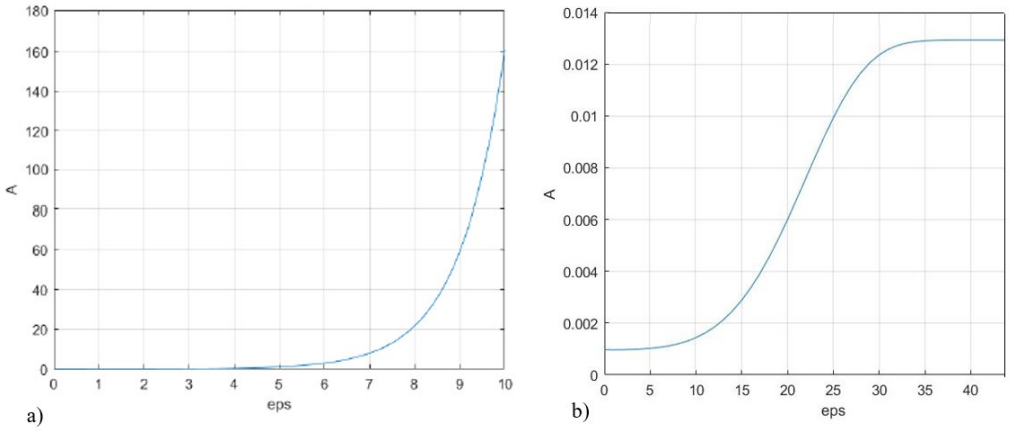

Fig. 5. a) A(ε) calculated according to Eq. (10), b) schematization of A(ε) calculated according to Eq. 13.

The outputs of the non-linear regression method are summarized in Tab. 5. After acquired these values, the model was implemented into Qform Extrusion and used to calculate the average grain size of the extruded profile.

In Fig. 6, the numerical simulation of the grain size after the complete SRX is reported. Red and blue areas correspond to the part of the profile in which the grain size have higher and lower dimensions, respectively. The numerical range of grain size dimension resulted between 52 μm and 96 μm.

Table 5. Recrystallization model material constants AA6060.

Material constants	**AA6060**
C_{PSN}	5.00021 e^{13}
A_{PSN}	872954
C_{GB}	0.0002145
C_C	0.0002145
p_1	1.9
p_2	1.06
p_3	1 e^{-7}
p_4	6

Fig. 6. Numerical average grain size of the investigated extruded profile.

In Fig. 7, the comparison between experimental and numerical grain size calculated in the "validation set" of points is reported. In details, the x-axis represents the diameter of grains experimentally measured while the y-axis represents the numerical predicted dimensions. Consequently, if the numerical measure perfectly matches the experimental one, the point is expected to be exactly on the 45° green line.

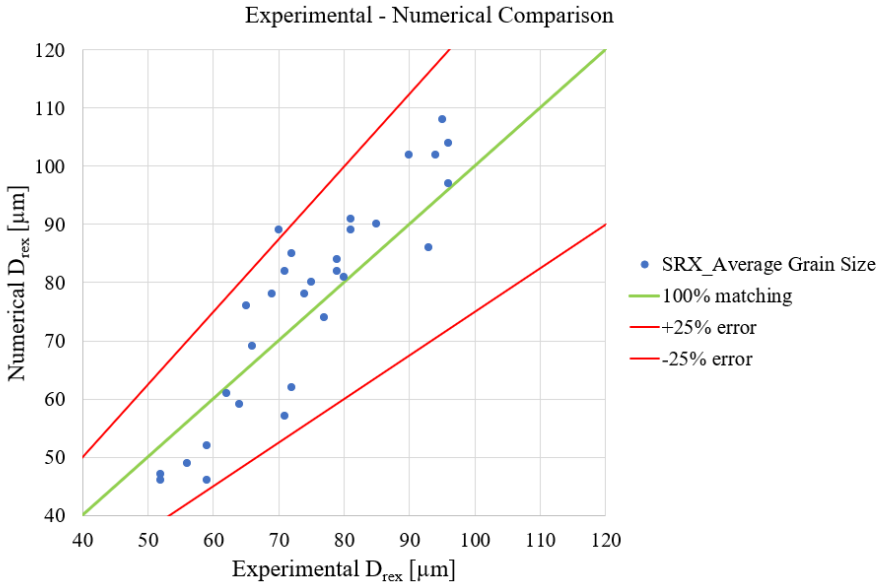

Fig. 7. Comparison between experimental and numerical grain size.

In order to facilitate the understanding of the prediction accuracy, two additional red lines were reported corresponding to a ± 25% of error. Since the high number of both process and

metallurgical factors affecting the final grain size, the industrial complexity of the analysed extruded geometries and the approximations deriving from the selected measurement methodology for the experimental analysis of the grain dimension, the range of ± 25% of error, also used by Donati L. et al. in [11] for the analysis of a laboratory-scale extruded profile, should be considered as a range of excellent prediction accuracy. As can be seen in Fig. 10, over the 95% of the blue dots fall within the red lines, thus proving the accuracy of the developed recrystallization model.

Summary

In the present work, the development of the recrystallization model of the AA6060 aluminum alloy was carried out together with the FE simulation using Qform Extrusion code. The microstructural analysis of the profile was performed and the collected data were used for the validation of the proposed model. The main outcomes of this work can be summarized as following:

- An innovative static recrystallization model was developed and optimized using the data experimentally acquired from the investigate AA6060 extruded profile.
- The prediction error of the average grain size in over the 95% of the analysed points remain below the ± 25% thus proving the good experimental-numerical agreement and the reliability of the proposed model. Further investigations are still needed to investigate the model accuracy in different AA6060 extruded profiles.

References

[1] L. Donati, B. Reggiani, R. Pelaccia, M. Negozio, S. Di Donato, Advancements in extrusion and drawing: a review of the contributes by the ESAFORM community, Int. J. Mater. Form. 15 (2022). https://doi.org/10.1007/s12289-022-01664-w

[2] C. Zhang, C. Wang, Q. Zhang, G. Zhao, G.L. Chen, Influence of extrusion parameters on microstructure, texture, and second-phase particles in an Al-Mg-Si alloy, J. Mater. Process. Technol. 270 (2019) 323-334. https://doi.org/10.1016/j.jmatprotec.2019.03.014

[3] C. Zhang, C. Wang, R. Guo, G. Zhao, L. Chen, W. Sun, X. Wang, Investigation of dynamic recrystallization and modeling of microstructure evolution of an Al-Mg-Si aluminum alloy during high-temperature deformation, J. Alloy. Compd. 773 (2018) 59-70. https://doi.org/10.1016/j.jallcom.2018.09.263

[4] T. Zhang, L. Li, S. Lu, L. Zhengfang, P. Chen, G. Hai, Static recrystallization kinetics and microstructure evolution of 7055 aluminum alloy, Metall. Res. Technol. 116 (2019) 120. https://doi.org/10.1051/metal/2018046

[5] T. Furu, R. Østhus, N. Telioui, R. Aagård, M. Bru, O.R. Myhr, Modeling the Effect of Mn on Extrudability, Mechanical Properties and Grain Structure of AA6082 Alloys, Proceedings of the Eleventh International Aluminum Extrusion Technology Seminar ET 2016, Chicago 3-6, 1 (2016) 567-590.

[6] A.R. Eivani, H.R. Jafarian, J. Zhou, Simulation of peripheral coarse grain structure during hot extrusion of AA7020 aluminum alloy, J. Manuf. Process. 57 (2020) 881-892. https://doi.org/10.1016/j.jmapro.2020.07.011

[7] Z. Peng, T. Sheppard, Prediction of Static Recrystallisation after Extrusion of Shaped Aluminium Sections, Mater. Sci. Forum 467–470 (2004) 407-420. https://doi.org/10.4028/www.scientific.net/msf.467-470.407.

[8] H.E. Vatne, T. Furu, R. Orsund, E. Nes, Modelling recrystallization after hot deformation of aluminum, Acta Mater. 11 (1996) 4463-4473. https://doi.org/10.1016/1359-6454(96)00078-X

[9] C.M. Sellars, Q. Zhu, Microstructural modelling of aluminium alloys during thermomechanical processing, Mater. Sci. Eng. A 280 (2000) 1-7. https://doi.org/10.1016/S0921-5093(99)00648-6

[10] F.J. Humphreys, M. Hatherly, Recrystallization and related annealing phenomena, Second edition, Elsevier, Oxford, UK, 2004.

[11] L. Donati, A. Segatori, M. El Mehtedi, L. Tomesani, Grain evolution analysis and experimental validation in the extrusion of 6XXX alloys by use of a lagrangian FE code, Int. J. Plast. 46 (2013) 70-81. https://doi.org/10.1016/j.ijplas.2012.11.008
[12] M. Cheng, Effect of preheating condition on strength of AA6060 Aluminium Alloy for extrusion. Diss. Auckland University of Technology, 2010.
[13] C.O. Paulsen, Recrystallization Behaviour in Extruded Profile of Non-Dispersoid Containing Al-Mg-Si Alloys, PhD Thesis, Department of Materials Science and Engineering NTNU-Trondheim, Materials Science and Engineering, 2015.
[14] Q. Xiaoming, N. Parson, X. Grant Chen, Effect of post-homogenisation cooling rate and Mn addition on Mg2Si precipitation and hot workability of AA6060 alloys, Canadian Metallurgical Quarterly 59 (2020) 189-200. https://doi.org/10.1080/00084433.2020.1719332
[15] A. Hensel, T. Spittel, Kraft und Arbeitsbedarf bildsamer Formgeburgsverfahren, 1. Auflage, Leipzig: VEB Deutscher Verlag fur Grundstoffindustrie, 1978.
[16] P.E. Gill, W. Murray, Algorithms for the Solution of the Nonlinear Least-Squares Problem, SIAM J. Numeric. Analys. 15 (1978) 977-992. https://doi.org/10.1137/0715063

Materials Research Proceedings 28 (2023) 487-494 https://doi.org/10.21741/9781644902479-53

Process simulation of friction extrusion of aluminum alloys

DIYOKE George[1,a *], RATH Lars[1,b], CHAFLE Rupesh[1,c], BEN KHALIFA Noomane[2,3,d] and KLUSEMANN Benjamin[1,3,e]

[1]Solid State Materials Processing, Institute of Material Mechanics, Helmholtz-Zentrum Hereon, Max-Planck-Straße 1, 21502 Geesthacht, Germany

[2]Institute of Material and Process Design, Helmholtz-Zentrum Hereon, Max-Planck-Straße 1, 21502 Geesthacht, Germany

[3]Institute for Production Technology and Systems, Leuphana University Lüneburg, Universitätsallee 1, 21335 Lüneburg, Germany

[a]george.diyoke@hereon.de, [b]lars.rath@hereon.de, [c]rupesh.chafle@hereon.de, [d]noomane.ben_kalifa@leuphana.de, [e]benjamin.klausemann@leuphana.de

Keywords: Finite Element Method, Process Simulation, Solid-State Materials Processing, Friction Extrusion, Aluminium Alloy

Abstract. The friction extrusion (FE) process is a solid-state material processing technique in which a translating extrusion die is pressed against a billet/feedstock material in a rotating extrusion container to produce an extruded rod or wire. A key aspect of FE is the generation of severe plastic deformation and frictional heat due to the relative rotation, leading to an improved microstructure. Numerical simulations of FE are highly complex due to contact between the tool and the workpiece, and the interplay between thermo-mechanical conditions and the present severe plastic deformation. In the present work, a three-dimensional finite element model is developed to study the material flow behavior for different extrusion ratios for a 60° die angle during friction extrusion. The developed model is numerically validated against experimental data. The spatial temperature and strain distributions illustrate the effect of extrusion ratio on the deformation characteristics of the extruded aluminum alloys, thereby assisting in understanding the material flow behavior.

Introduction

Extrusion is a solid state forming process in which a metal feedstock is forced through an orifice or die opening in order to obtain a reduction in diameter and increase in length of the feedstock. In direct extrusion, the extruded metal is forced to flow in the direction of applied force, while in indirect extrusion, the metal flows in the opposite direction. The friction extrusion (FE) process is a relatively novel approach compared to conventional extrusion because of the added rotational motion. This process was developed and patented in 1993 by The Welding Institute, UK [1]. An illustration of the indirect FE setup and mechanism of operation are shown in Fig. 1.

Content from this work may be used under the terms of the Creative Commons Attribution 3.0 license. Any further distribution of this work must maintain attribution to the author(s) and the title of the work, journal citation and DOI. Published under license by Materials Research Forum LLC.

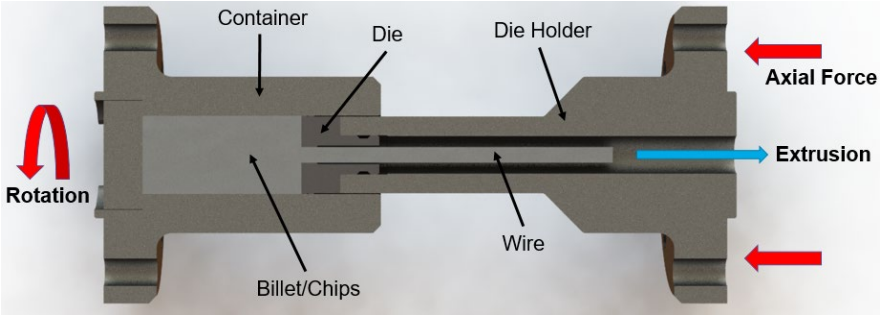

Fig. 1. Schematic of friction extrusion setup. The figure is reprinted from [2], under the terms of the Creative Commons Attribution 4.0 license (https://creativecommons.org/licenses/by/4.0).

FE involves relatively high pressure and relative rotation to force the metallic feedstock in the container through the die, resulting in a fully consolidated extrudate. As a result, reshaping billets into rods, tubes, and wires is possible through FE. Based on the process features, FE is capable of meeting the increasing demand of producing materials with improved mechanical properties [3] for application in automobile and aircraft industries. FE also provides a suitable alternative for material processing thus lower force and energy are required since more heat is generated via friction and rotation as compared to conventional extrusion where preheating the feedstock before extrusion is necessary in order to minimize the force required for extrusion.

The quality of the extrudate has been associated with a number of factors. In FE experiments, the extreme changes observed in processing characteristics and microstructural evolution have been attributed in particular to the friction condition [4], where the friction condition controls the introduced strain and thermal evolution [2,4]. For instance, Peng et al. [5] ascribed the formation of hot cracks during extrusion to the material flow governed by the temperature gradient across the wire diameter. Furthermore, the work from Yu et al. [6] showed that the die angle has a significant influence on the material flow, where the die surface geometry affects the frictional heating at the contact region. Therefore, it is of interest to study the influence of variable extrusion ratios on the material flow behavior.

A fundamental understanding of the mechanism of heat generation and related material flow during a friction-based process is of high significance because it can minimize the number of trials and therefore cost of experiments. Numerical models can help significantly in this regard, where a suitable description of the friction conditions is essential for processes like FE to achieve correct simulation predictions. Often, a constant friction value with a suitable friction law is used in numerical calculations, especially in friction-based processes performed using finite element method (FEM). The commonly adopted friction models in FEM are shear and Coulomb friction models. Shear friction models with constant friction factor have been applied in FE [7], friction stir welding (FSW) [8,9] and refill friction stir spot welding (refill FSSW) [10], whereas the Coulomb friction model is less frequently applied [11]. One example includes the application of a temperature-dependent friction coefficient in a simulation of refill FSSW [12]. Furthermore, to model the material response during thermo-mechanical processing, a constitutive model is also necessary, which accounts for the thermal and mechanical effects. One of the simplest models in this regard is the Arrhenius constitutive model, which is widely employed to describe the relationship between flow stress, strain rate and temperature at elevated temperatures in metallic materials [13].

In the present model, the effect of extrusion ratio on the process and thermo-mechanical conditions is studied. The process parameters used are deduced from a force-controlled FE experiment. The description of the experimental setup, the numerical method and the simulation inputs are presented in the following section.

Experimental Setup and Finite Element Method

The FE process is performed on the FE100 (Bond Technologies, IN, USA), a dedicated friction extrusion machine. The tooling setup consists of a rotating 42CrMo4 steel container with charged AA2024 billet and an X40CrMoV5-1 die, featuring a 60° die angle and 10 mm die bore sizes as shown in Fig. 2(a). The experiment is conducted only for the 10 mm die bore with one billet, serving as validation data for the numerical simulation. The experiment is performed force-controlled, where a constant extrusion force of 300 kN and spindle rotation of 90 rpm are applied. The temperature was recorded via a K-type thermocouple at two-thirds of the die radius within the die, located 18 mm from the die face, as shown in Fig. 2(a). In experiment, the feedstock material in the as-cast condition is machined to have a based cylindrical shape of 50 mm length and 49.50 mm diameter, with a chamfer of 60° angle and 5 mm height at the edge, see also Fig. 3(a). The billet is locked against rotation towards the container. For initiating FE, a program step with higher rotation and lower force (300 rpm, 50 kN) is used to ensure defined contact between the die and feedstock to avoid torque overload.

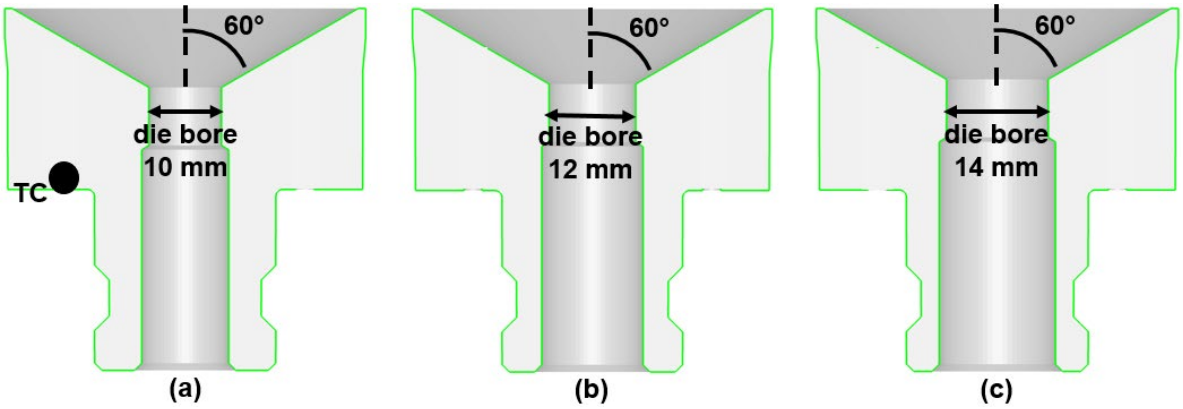

Fig. 2. Schematic extrusion die showing angle, including the location of the thermocouple (TC). Variable die bores are investigated, leading to different extrusion ratios: (a) ER = 25.0, (b) ER = 17.36, and (c) ER = 12.25.

The numerical model is set up in DEFORM 3D. The rotating extrusion container and the translating extrusion die, Fig. 3(b), are modeled as rigid and meshed with approximately 20,000 elements each to account for thermal conduction. The workpiece is modeled as rigid-viscoplastic material, where an adaptive mesh with approximately 50,000 elements with variable size is applied to resolve the thermo-mechanical properties at the contact region with the die as depicted in Fig. 3(c).

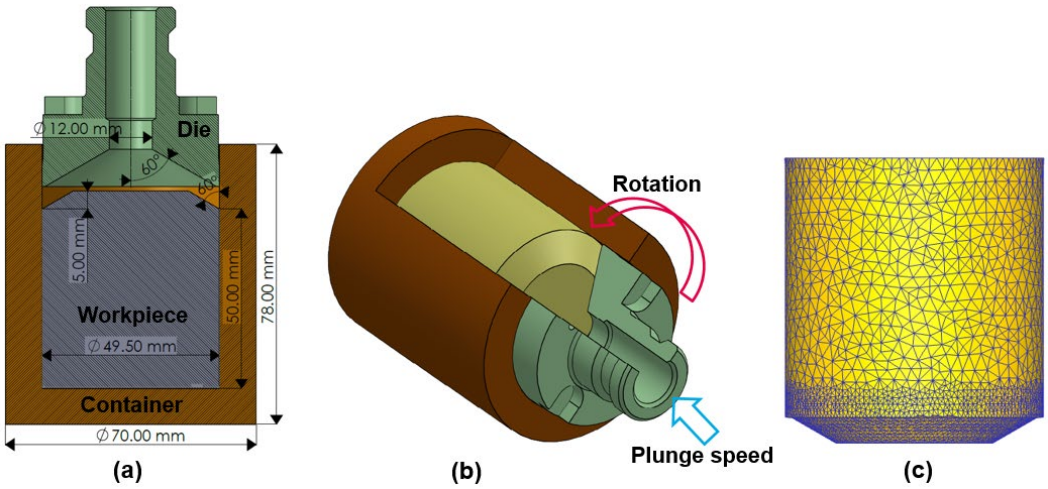

Fig. 3. Process model geometry: (a) Simulation set up and object dimensions; (b) Operational mechanism of FE and; (c) Workpiece showing adaptive mesh and a 60° angle at the edge to improve initial contact conditions.

The Arrhenius equation, relating strain rate, flow stress and deformation temperature, is applied to capture the material behavior during FE [14]. Based on a hyperbolic sine function, the Arrhenius equation can be written as:

$$\underline{\dot{\varepsilon}} = A[sinh\ sinh\ (\alpha\sigma)\ ]^n exp\left(-\frac{Q}{RT}\right) \quad (1)$$

where $\underline{\dot{\varepsilon}}$ is the strain rate, Q is the activation energy due to thermal deformation, n is the stress exponent, A and α are material constants, R is the gas constant, T represents the temperature and σ the initial flow stress. Flow stress data of AA2024 alloy are deduced from a hot compression test conducted at deformation temperatures between 200°C and 500°C under strain rates of 0.001-10 s^{-1} [15, 16]. The following parameters are used: $A = 1.96 \cdot 10^8$ s^{-1}, $\alpha = 0.016 MPa^{-1}$, $n = 4.27$ and $Q = 148$ kJ mol^{-1}. Non-isothermal process conditions are applied for all objects with reference temperature at 20 °C. Other values used in this simulation to relate different thermal interactions between the objects are: 0.02 N s^{-1} mm^{-1} C^{-1} for convection between tools and environment, and 11 N s^{-1} mm^{-1} C^{-1} for conduction between workpiece and tools as recommended for DEFORM 3D forming operations.

After several investigations on the two friction models, i.e. shear and Coulomb, a significant better agreement between experiment and simulation was obtained by modelling the mechanical interaction between the translating die and the rotating container with the workpiece via a Coulomb friction model, where a temperature-dependent friction coefficient μ is used [12], see Table 1.

Table 1. Friction coefficient as function of temperature [12].

Friction coefficient	0.5	0.36	0.3	0.26	0.2	0.1	0.08
Temperature (°C)	20	160	200	300	400	500	600

Although the experiment is performed force-controlled, due to numerical stability reasons, the simulation is performed displacement- or velocity-controlled, respectively. The die speed applied in the simulation is deduced from the die velocity during the FE experiments with the FE100 as shown in Fig. 4, and a rotational speed of 90 rpm is applied on the die.

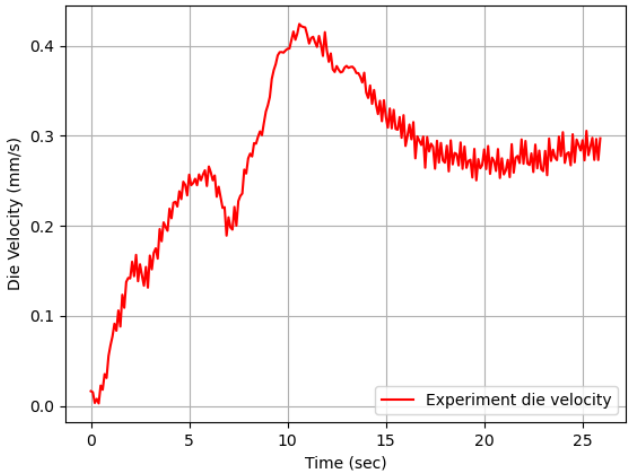

Fig. 4. Experimental die velocity obtained from the force-controlled experiment for ER 25.0 with FE100, which is used as simulation input.

Results and Discussion

As shown in Fig. 5, the results of the velocity-controlled simulation are in good agreement with the force-controlled experiment for both force and thermal history. During the deformation, the rapid increase in force and temperature at the onset of the process is related to the initial "cold" state of the workpiece, i.e. deformation resistance, and filling of the die angle cavity before extrusion. After the initial ramp-up, the process force shows a quasi-steady state due to sufficient material softening achieved.

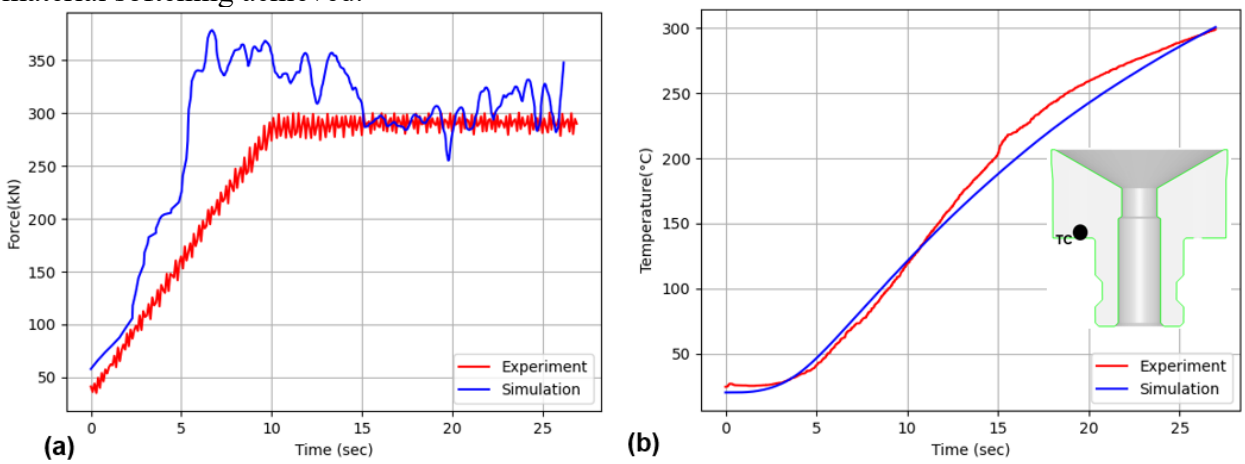

Fig. 5. Comparison between experimental and simulation results for (a) process force and (b) thermal history for ER 25.0.

The generated heat is directly related to the temperature; therefore, material softening depends on the contact condition and mechanical interaction between the workpiece and the extrusion die. Fig. 5 shows the calculated spatial temperature distribution at the interface between the workpiece and extrusion die. The maximum temperature is obtained at the contact layer to the die as shown in Fig. 6, because of the direct interaction between the rotating workpiece and translating extrusion die. The maximum temperature decreases with decreasing extrusion ratio viz, 551°C, 525°C, and 511°C, see Fig. 6(a), (b) and (c), respectively. This effect is attributed to less frictional heat with decreasing extrusion ratio, which is consistent with the findings of Baffari et al. [7] for a 90° die.

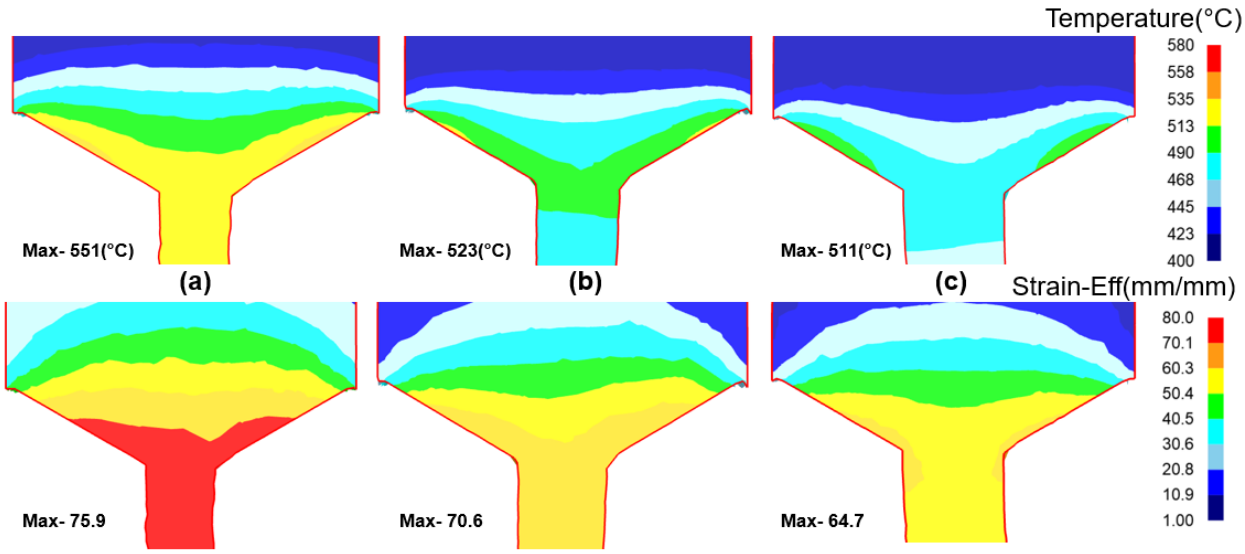

Fig. 6. Spatial temperature and strain distribution results for different extrusion ratios: (a) ER 25.0, (b) ER 17.36 and, (c) ER 12.25.

Next to the temperature, the resulting material deformation plays a crucial role in terms of the resulting microstructure and quality of the extrudate. Fig. 6 depicts that strain values close to the die orifice are higher compared to the rest of the workpiece. This is due to the edge of the die orifice, which induces severe plastic deformation on the workpiece during processing. Consequently, higher extrusion ratios induce more severe plastic deformation leading even to maximum strain values of 75. It is evident that the strain distribution is less homogeneous with decreasing extrusion ratio; see Fig. 6.

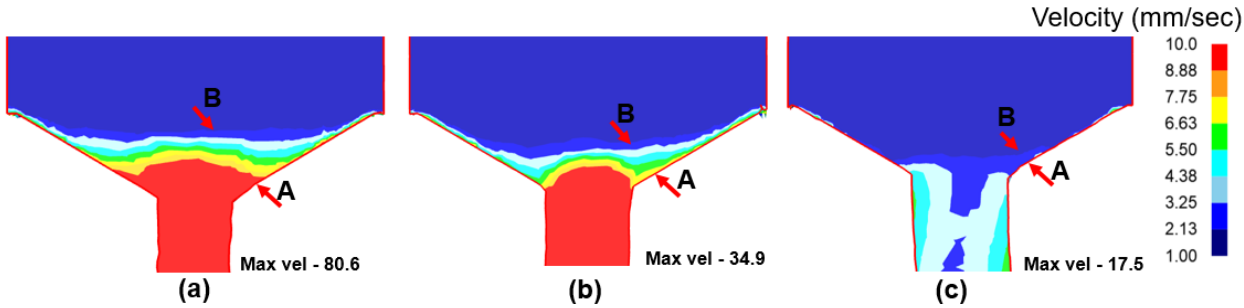

Fig. 7. Material flow velocity for different extrusion ratios: (a) 25.0, (b) 17.36 and (c) 12.25.

In FE, the mechanical interaction between the die and workpiece leads to thermo-mechanical conditions as described above, which are strongly influenced by the transition between the container and die, in particular, the die orifice. A homogeneous material flow is assumed to occur due to homogeneous deformation and, in this regard, better mechanical properties. As illustrated in Fig. 7, a higher probability of homogeneous material flow is observed at high extrusion ratios. The origin of the homogeneous material flow for high extrusion ratios can be traced to more severe plastic deformation induced. As depicted in Fig. 7, the velocity distribution region marked by points (A) and (B) decreases as the extrusion ratio decreases. The non-homogeneous material flow for the low extrusion ratio in Fig. 7(c) is attributed to less deformation due to sliding tendencies between the workpiece and the die.

Summary

The process simulation of the friction extrusion (FE) process accurately predicts the force and thermal history occurring in the force-driven FE experiment. The following conclusions are drawn:

- The maximum temperature is predicted at the contact region between the die and the workpiece for all cases due to direct mechanical interaction.
- Die geometry has a profound effect on the resultant thermo-mechanical conditions.
- A higher extrusion ratio leads to more uniformly distributed and higher values of maximum strain due to increased severe plastic deformation.
- At high extrusion ratios, the material flow is more homogeneous, and therefore a superior properties of the extruded rod could be anticipated.

Funding

This project has received funding from the European Research Council (ERC) under the European Union's Horizon 2020 research and innovation program (grant agreement No 101001567)

Data Availability

The data related to this research is available online (https://doi.org/10.5281/zenodo.7399955)

References

[1] E. Nicholas, W. Thomas and S. Jones, U.S. Patent (5): 262-123 (1993)
[2] L. Rath, U.F.H. Suhuddin, B. Klusemann, Comparison of Friction Extrusion Processing From Bulk and Chips of Aluminum-Copper Alloys, Key Eng. Mater. 926 (2022) 471-480. https://doi.org/10.4028/p-vw04z5
[3] S. Whalen, M. Olszta, M. Reza-E-Rabby, T. Roosendaal, T. Wang, D. Herling, B.S. Taysom, S. Suffield, N. Overman, High speed manufacturing of aluminum alloy 7075 tubing by Shear Assisted Processing and Extrusion (ShAPE), J. Manuf. Process, 71 (2021) 699-710. https://doi.org/10.1016/j.jmapro.2021.10.003
[4] R.M. Halak, L. Rath, U.F.H. Suhuddin, J.F. dos Santos, B. Klusemann, Changes in processing characteristics and microstructural evolution during friction extrusion of aluminum, Int. J. Mater. Form. 15 (2022) 24. https://doi.org/10.1007/s12289-022-01670-y
[5] Z. Peng, T. Sheppard, Study of surface cracking during extrusion of aluminum alloy AA 2014, Mater. Sci. Technol. 20 (2004) 1179-1191. https://doi.org/10.1179/026708304225022016
[6] H. Yu, S.P Hyuk, S.Y Bong Die angle dependency of microstructural inhomogeneity in an indirect-extruded AZ31 magnesium alloy, J. Mater. Process. Technol. 224 (2015) 181-188. https://doi.org/10.1016/j.jmatprotec.2015.05.003
[7] D. Baffari, G. Buffa, L. Fratini, A numerical model for Wire integrity prediction in Friction Stir Extrusion of magnesium alloys, J. Manuf. Process. 247 (2019) 1-10. https://doi.org/10.1016/j.jmatprotec.2017.04.007
[8] R. Jain, S. Pal, S. Singh, Thermo-mechanical Simulation of Friction Stir Welding Process Using Lagrangian Method, Simul. Des. Manuf. (2018) 103–146. https://doi.org/10.1007/978-981-10-8518-5_4
[9] G. Buffa, J. Hua, R. Shivpuri, L. Fratini, A continuum based FEM model for friction stir welding model development, Mater. Sci. Eng. A 419 (2006) 389-396. https://doi.org/10.1016/j.msea.2005.09.040
[10] S.H. Raza, T. Mittnacht, G. Diyoke, D. Schneider, B. Nestler, B. Klusemann, Modeling of temperature- and strain-driven intermetallic compound evolution in an Al–Mg system via a multiphase-field approach with application to refill friction stir spot welding, J. Mech. Phys. Solid. 169 (2022) 105059. https://doi.org/10.1016/j.jmps.2022.105059
[11] M. Iordache, C. Badulescu, D. Iacomi, E. Nitu, C. Ciuca, Numerical Simulation of the Friction Stir Welding Process Using Coupled Eulerian Lagrangian Method, IOP Conference Series: Mater. Sci. Eng. 145 (2016) 022017. https://doi.org/10.1088/1757-899X/145/2/022017

[12] V.S.R. Janga, M. Awang, M.F. Yamin, U.F.H. Suhuddin, B. Klusemann, J.F. dos Santos, Experimental and Numerical Analysis of Refill Friction Stir Spot Welding of Thin AA7075-T6 Sheets, Mater. 14 (2021) 23. https://doi.org/10.3390/ma14237485
[13] T. Sheppard, A. Jackson, Constitutive equations for use in prediction of flow stress during extrusion of aluminum alloys, Mater. Sci. Technol. 13 (1997) 203-209. https://doi.org/10.1179/mst.1997.13.3.203
[14] M.O. Bodunrin, Flow stress prediction using hyperbolic-sine Arrhenius constants optimised by simple generalised reduced gradient refinement, J. Mater. Res. Technol. 9 (2020) 2376-2386. https://doi.org/10.1016/j.jmrt.2019.12.070
[15] S.B Bhimavarapu, A. Maheshwari, D. Bhargava, S. Narayan, Compressive deformation behavior of Al 2024 alloy using 2D and 4D processing maps, J. Mater. Sci. 46 (2011) 3191-3199. https://doi.org/10.1007/s10853-010-5203-z
[16] R. Jain, S. Pal, S. Singh, Numerical modeling methodologies for friction stir welding process, in: Computational Methods and Production Engineering: Research and Development, Elsevier, 2017, pp. 125-169. https://doi.org/10.1016/B978-0-85709-481-0.00005-7

Materials Research Proceedings 28 (2023) 495-504 https://doi.org/10.21741/9781644902479-54

Numerical study on cold extrusion of gears varying the extrusion shoulder geometry

DELIKTAS Tahsin[1,a *], LIEWALD Mathias[1,b]

[1]Institute for Metal Forming Technology, University of Stuttgart, Holzgartenstraße 17, 70174 Stuttgart, Germany

[a]tahsin.deliktas@ifu.uni-stuttgart.de, [b]mathias.liewald@ifu.uni-stuttgart.de

Keywords: Metal Forming, Cold Forging, Gears, Simulation, Production Technology

Abstract. Cold forging processes, such as cold extrusion and in particular the Samanta process, provide a considerable potential for improvement in gears production. The method behind the Samanta process is based on the principle of cold extrusion in stacks. After partial forming of a workpiece, another workpiece is inserted into the die in order to eject a completely formed gear in the direction of the punch movement. Although this operating principle offers great potential for high-volume production, the industrial relevance of this process is limited by disadvantages such as high tool loads, limited gear accuracy and deformations on both face ends of the gear wheel. In order to overcome the technological challenges associated with the Samanta process, the die geometry was adapted. In this case the die operating surface was modified in terms of an extended forming zone length combined with an undercut in the tooth cavities of the die. In this paper the numerical results for this novel process regarding the correlations between geometric die parameters and resulting process data, such as punch force, contact pressure and die filling, are presented. The spline-based tool was methodically varied between one linear and two square (concave, convex) designs and was numerically evaluated using Deform 3D™ software.

Introduction

As an integral part of the modern automotive and mechanical engineering industry, gears are used in a wide variety of drive systems. Due to the high demands placed on gears in terms of performance, operational reliability and smooth running, they are usually manufactured using machining processes [1,2]. Machining processes, especially for gear production, are time and material consuming. Due to the ecological disadvantages of machining processes, it is important to find better alternatives in the long term. Cold forming is an alternative with a high potential for substituting machining processes. Cold extrusion in particular offers the possibility of producing gears with high output and improved material utilisation. In addition, the gears benefit from process-related strain hardening and an uninterrupted fibre structure [3]. The most common process for cold extrusion of gears is the Samanta process, in which the blanks are pressed in stacks through a toothed die. In this process, the workpiece is partially formed, then the punch is retracted and a new workpiece is inserted into the die. By extruding the second workpiece, the partially formed and thus toothed workpiece is ejected downwards out of the die, enabling the manufacture of a fully toothed workpiece [4]. Due to the established die geometry in this process, there are some process-specific disadvantages, such as an extreme tool load, shape and dimensional deviations of the gearing and deformations on the face ends of the workpiece. To overcome these disadvantages, a new process based on the Samanta process was developed at the Institute for Metal Forming Technology in Stuttgart, Germany. The so-called Guided Material Flow (GMF) process differs from the Samantha process by means of a modified die operating surface. Main feature of this redesign is an extended extrusion shoulder and thus forming zone. This extended forming zone is hypothetically intended to distribute the required forming work over a longer stroke and therefore reduce the die load. An improved accuracy of the extruded gear is expected.

Content from this work may be used under the terms of the Creative Commons Attribution 3.0 license. Any further distribution of this work must maintain attribution to the author(s) and the title of the work, journal citation and DOI. Published under license by Materials Research Forum LLC.

Extending the extrusion shoulder increases the friction surface between the workpiece and the die. Hence, an undercut was added into the die cavity as a second feature in order to compensate the increase in friction surface.

Cold Extrusion of Gears

Samanta process.

The Samanta process is a special process in the field of cold extrusion which can be performed with full and hollow blanks. The special feature of the process is the characteristic process principle, which is shown schematically in Fig. 1a. Blank 1 is placed in the die and partially formed by means of the hollow punch and the mandrel in the first phase of the process. For the second phase, the hollow punch and the mandrel are retracted until blank 2 can be loaded. Due to the partial forming of blank 2, blank 1 is completely pressed through the toothed active surface of the die. Thus, the toothed workpiece is dropped out the die on its lower side, eliminating the need for an ejection process [4]. No ejection simplifies the tools, eliminates the risk of ejector marks and offers the potential for higher production output [5]. Using the Samanta process a gear accuracy with a tolerance class between 10 and 11 for helical and straight gears can be achieved. However, the automotive sector demands gear accuracies of IT 6 or better [6]. In addition, gears formed using the Samanta process exhibit typical features such as partial tooth underfilling (inflow area) on the bottom side and "crown-shaped" deformation on the top side of the gears (see Fig. 2b). Both of these areas necessitate material removal by machining, which reduces material utilisation of the process and also calls for additional production steps [7].

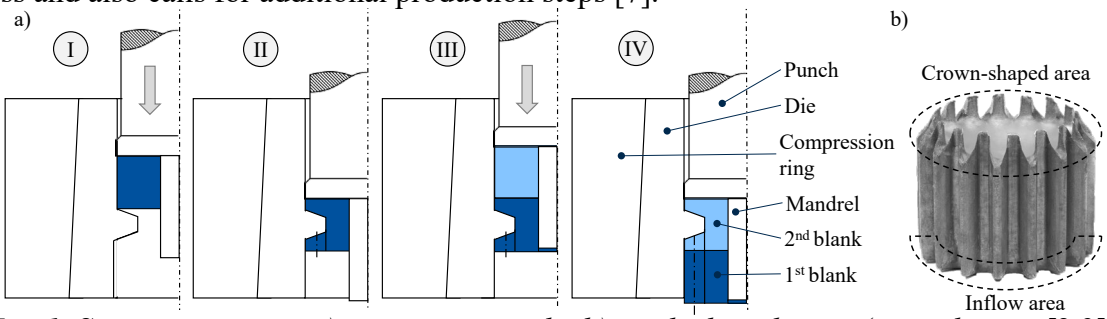

Fig. 1. Samanta process, a) process principle, b) toothed workpiece (according to [8,9]).

Guided Material Flow (GMF) process.

Based on the process principle of the Samanta process, a novel process for the cold forming of gears was developed at the Institute of Metal Forming Technology. The GMF process is a cold extrusion process for full and hollow blanks. It differs from the conventional Samanta process in the design of the operating die surface. Fig. 2a shows the sectional view of the tooth cavity in the GMF process and Fig. 2b a comparison of the die design between the two related processes.

Comparing both designs, two decisive features appear crucial: Characteristic 1 consists in the significantly extended length of extrusion shoulder and thus forming zone of the die. This has the effect of distributing the required forming work over a longer stroke, which on the one hand decreases the maximum punch force and on the other hand increases the friction surface between the die and the workpiece. In order to compensate the increased friction surface, the die cavity was modified by an undercut. Therefore, characteristic 2 consists of an undercut in the die cavity located at the area of the tip circle diameter of the toothing. This undercut highlighted with purple colour in Fig. **2**a serves to induce a contact separation between the die and the workpiece in the area of the tooth tip of the formed gear. Through this new design of the die active surface in the GMF process, the maximum punch force could be reduced by about 38% compared to a similar Samanta process [10]. Decreasing the maximum punch force leads to a reduction of elastic die deflection and thus to an improved accuracy of dimension and shape of the gearing as well as to a

reduction of tool wear. All geometric die parameters in the design of the die operating surface of the GMF process were determined based on practical experience in the field of cold forming within the scope of preliminary investigations. The complex die surface was designed by simulative evaluation and iterative adaptation of the individual contours (see Fig. 2) on different levels along process direction. Since the tooth cavity varies steadily in process direction, the material flow is controlled systematically, which finally led to the name of this novel process.

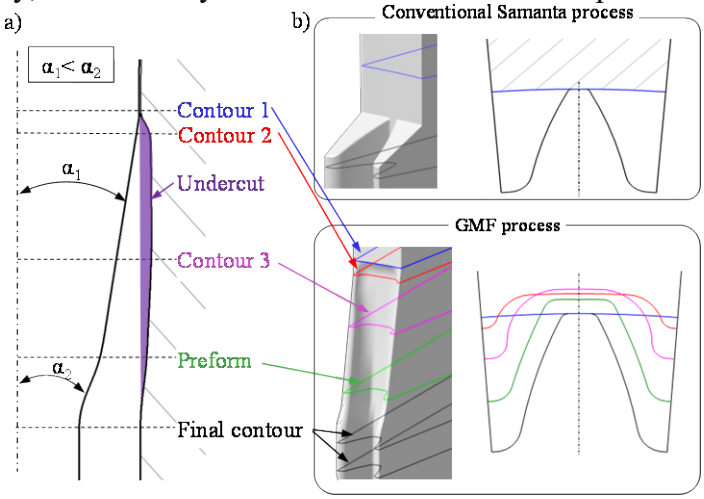

Fig. 2. GMF process, a) sectional view of die cavity, b) comparison of die design with Samanta process.

The initially designed die model was not suitable for the performance of comprehensive numerical investigations within the scope of a research project. The reason for this is the large number of geometric parameters and thus process influencing variables. Therefore, the number of geometric die parameters was significantly reduced in a new die model. Main objective of this simplification was performing a numerical analysis more effectively in order to identify relationships between geometrical die parameters and relevant process data in the GMF process. New design of the die used in the GMF process was achieved by means of splines and mathematical functions, as shown in Fig. 3. As boundary conditions for the adaptable design of the GMF die, the tip and root diameters of the involute toothing were selected. These two boundary conditions located at the respective ends of the forming zone enabled the geometrical profile of the extrusion shoulder to be implemented as a polynomial function *f(z)*. Corresponding polynomial function $f(z)=a_n\text{-}z^n+a_{n-1}\text{-}z^{n-1}+...a_1\text{-}z^1+a_0$ allows the variation of the geometric profile of the extrusion shoulder by changing the exponent.

This paper presents the numerical results for the linear and quadratic versions of the extrusion shoulder geometry in the GMF process. Aim of the numerical investigations was to determine the effect of different extrusion shoulder geometries on relevant process data during cold extrusion of gears in the GMF process. For this purpose, the toothing to be formed was kept fixed and the shape and length of the extrusion shoulder were varied for each version. The variation of the linear extrusion shoulder version was based solely on the forming zone length, since in this case the extrusion shoulder angle results from the gear data. In the case of the quadratic extrusion shoulder, there are two types - convex and concave. They differ in terms of the sign of the coefficient for the highest order of polynomial in the polynomial function. In the evaluation of the simulation, the geometric modification of the quadratic polynomial function is based on the angle α at the vertex of the parabola (see Fig. **3**).

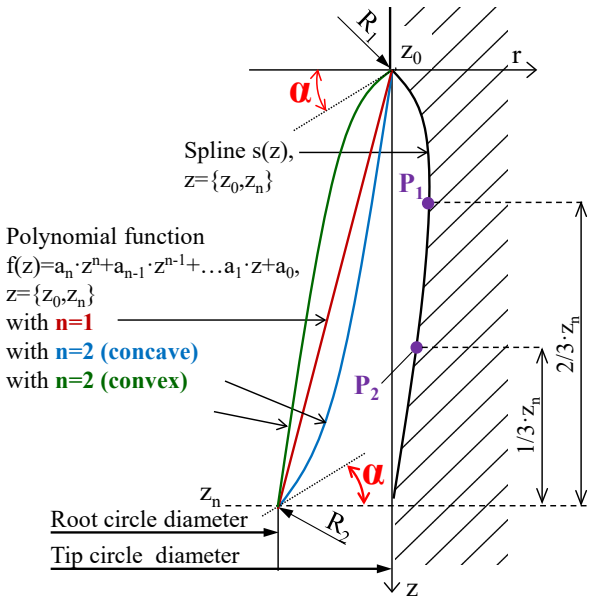

Fig. 3. Sectional view of re-designed die cavity in the GMF process with variation of extrusion shoulder profile.

The undercut in the area of the tip circle diameter of the gearing was designed with a spline as a guide curve. This spline was approached by four points as boundary conditions. The first point was at the beginning (z_0), the second at the very end of the forming zone (z_n) and thus also define the starting and end points of the spline. Two further points are located at 1/3 and 2/3 of the forming zone's length. The radial position of the two points along the spline was defined in relation to the tip diameter of the teeth. Point P_1 was defined 0.1 mm and the point P_2 0.3 mm larger than the tip diameter of the toothing.

Numerical Investigations

The numerical investigations were intended to determine any effects of geometric changes on the die operating surface in the GMF process and on significant process parameters. Analysis was performed by variation of design of the extrusion shoulder and numerical computation of the punch force, the contact pressure on the die and the die filling. By adjusting the coefficients of the polynomial function within most suitable intervals, a methodical evaluation could be conducted. Through numerical preliminary investigations, suitable range of intervals for the polynomial coefficients were determined for the very first practical trials. The geometric profile of the undercut was not varied in this FE analysis.

Simulation setup.

Fig. 4a shows the general setup of the simulation model in software Deform 3D™. All simulations within the numerical analysis were conducted according to this depicted simulation setup. In order to perform a DOE study based on 3D models, a corresponding simulation had to be set up for each process variation. Here, only the die models were replaced. Punch and die in simulation were implemented as rigid objects. The hollow workpiece segment of 4,615 ° (half tooth) has a height of 25 mm was defined as a plastic object made of material 16MnCr5. Workpieces were modelled with 80,000 mesh elements and simulatively deformed at room temperature at a punch speed of constant 40 mm/s. The friction in the simulation was defined as shear friction with a friction factor of 0.12 [11]. All dies were designed for extrusion of the same gear geometry. The simulated gear has involute teeth with a modulus *m* of 1 mm and a number of teeth *z* of 39. Dimensions of gear and utilized simulation data are listed in Fig. 4b. In the DOE, the extrusion shoulder geometry was varied between a linear and two quadratic (concave, convex)

geometries. Also, the length of the extrusion shoulder and therefore the forming zone length as well as the tangent angle α at the apex of the quadratic extrusion shoulder were varied between 30°, 50° and 70° within predefined intervals.

a)

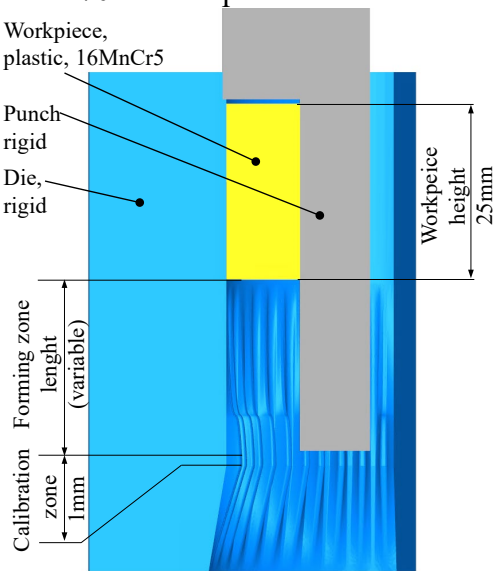

b)

Gear dimensions	
Tooth geometry	Involute
Nr. of teeth	39
Module m	1.00 mm
Tooth height	2.17 mm
Tooth width	1.57 mm
Tip circle diameter	41,00 mm
Root circle diameter	36.67 mm

Simulation parameters	
Software	DEFORM 3D
Mesh workpiece	80,000
Temperature	20 °C
Friction	shear, 0.12
Punch speed	40 mm/s
Simulation type	Lagrangian incremental
Solver	SPOOLES

Fig. 4. Simulation, a) Setup in Deform 3D™, b) Gear dimensions and simulation parameters.

Results and Discussion

This chapter presents the numerical results for geometrically varying extrusion shoulder versions in the GMF process in relation to relevant process parameters. Relevant process parameters in cold extrusion do include the punch force, the contact pressure onto the die active surface and the die filling of the toothing. A comparison with the conventional Samanta process for forming the same gear (see Fig. 4b) also was performed.

Linear design for extrusion shoulder in GMF process.

As shown in previous publication [10], the highest contact pressure onto the die surface is located in the area of the extrusion shoulder and thus at the root circle diameter of the formed toothing.

Fig. 5 shows the numerical results for the DOE study with a linear extrusion shoulder. The red dashed line in the diagram represents the numerical reference results obtained from simulation of the conventional Samanta process with an equivalent simulation setup. Based on preliminary numerical investigations, the forming zone length was varied between 2 mm and 13 mm for analysis objectives. Beyond this interval, no complete die filling or increased process forces were detected using the linear extrusion shoulder in the GMF process for forming this gear. The results in Fig. 5 indicate that the die in GMF process having a linear extrusion shoulder design in every case is exposed to lower loads compared to the conventional Samanta process. The conventional Samanta process requires a maximum punch force of 430 kN, and, in contrast, the linear design of die in GMF process requires 415 kN (2mm length of forming zone) with a decreasing tendency as the forming zone length increases. This shows that when extending the forming zone length from 2 mm to 9 mm, the maximum punch force can be reduced from 415 kN down to 270 kN. In case of lengths of forming zones beyond 9 mm, the peak punch force converges to this measured value. Also, underfilling in the tooth tip occurs at a forming zone length of 13 mm. Comparing the results with the conventional Samanta process reveals that with the linear design of die in the GMF process for forming this gear, a punch force reduction of approx. 38 % can be achieved. In addition, it can be observed that the contact pressure in the die also decreases as the forming zone length increases. Thus, the maximum contact pressure decreases from 2,920 MPa (length of forming zone equals 2mm) to a value of 2,150 MPa (length of forming zone equals 12 mm). Compared to the

conventional Samanta process, a reduction in die contact pressure from 3,000 MPa to 2,150 MPa also was achieved, which equals a drop by approx. 28 %.

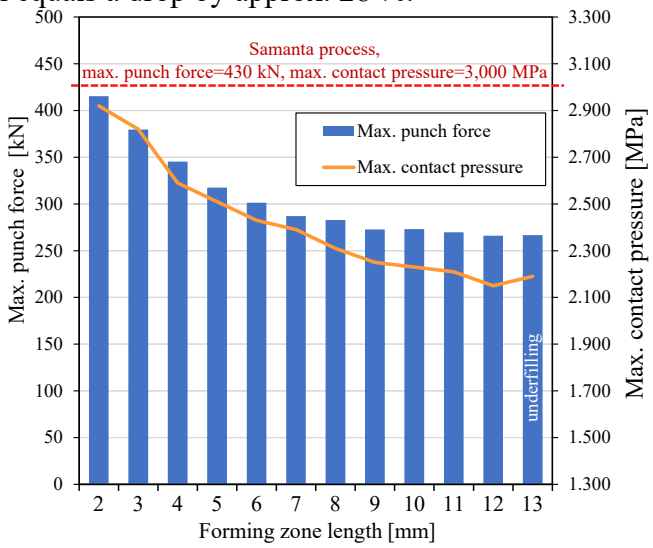

Fig. 5. Numerical results for linear extrusion shoulder geometry in GMF process.

Quadratic design of extrusion shoulder in GMF process.

In this chapter, the numerical results for a concave and a convex extrusion shoulder design being used for the GMF process are presented. The geometry of the extrusion shoulder with a quadratic polynomial function was varied based on the angle α. Here, the numerical investigation was performed at three different angles α - 30°, 50° and 70° (as shown in Fig. 3). In addition, the forming zone length was varied between 15 mm and 40 mm by 5 mm increments.

Concave extrusion shoulder design.

The chart in Fig. 6 summarizes the numerical results of the GMF process with a concave extrusion shoulder at an angle α of 30° and 50°. For the concave design with a tangent angle α of 30° (see Fig. 6a), obviously, the maximum punch force appears independent from the length of forming zone. Also, a maximum punch force of approx. 280 kN was determined. Thus, almost the same punch force reduction can be achieved with this process as with the linear extrusion shoulder design. Furthermore, the maximum contact pressure with this concave extrusion shoulder (α=30°) was observed at the same level as in the conventional Samanta process. Fig. 6 b shows the numerical results for the GMF process with concave extrusion shoulder design having an angle α of 50°. By increasing the tangent angle α at the vertex of the parabola from 30° to 50°, the level of the maximum punch force decreases marginally. Also, analogous to Fig. 6a no dependence was found between the forming zone length and the maximum punch force when using an angle of 50° at the concave extrusion shoulder. In this figure the maximum punch force consistently remains at a level of approx. 268 kN. It was found also, that the maximum contact pressure in this process was calculated as high as in the conventional Samanta process. As the forming zone length increases, underfilling of the toothing occurs, starting at a forming zone length of 20 mm. Such underfilling was also found in the process variant with a tangent angle α of 70°, regardless of the forming zone length. This underfilling was always found in the area of the tooth tip, since the corresponding extrusion shoulder design achieved insufficient material displacement in radial outward direction.

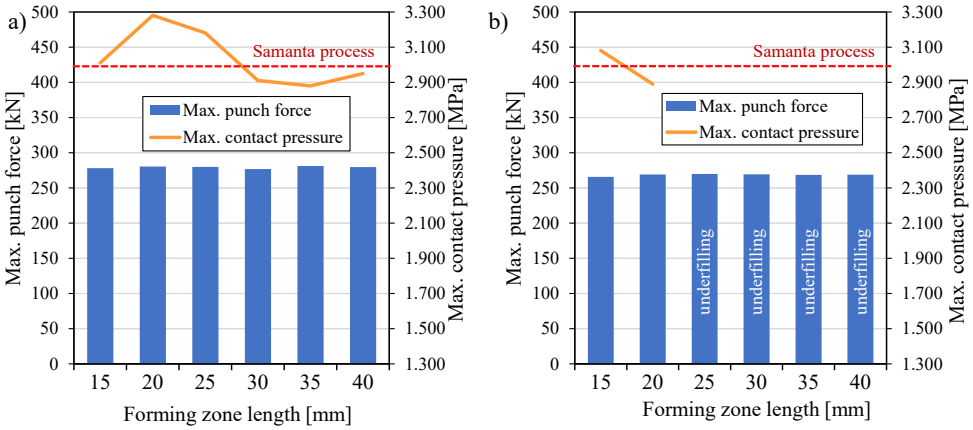

Fig. 6. Numerical results for concave extrusion shoulder geometry in GMF process, a) α=30°, b) α=50°.

Convex extrusion shoulder design.

The diagrams in Fig. 7 summarise the results of the convex extrusion shoulder in the GMF process with tangent angle α at 30°, 50° and 70°. Fig. 7a illustrates the results of the convex process version with angle α at 30°, indicating a significant reduction of the maximum contact pressure compared to the conventional Samanta process. The contact pressure of this extrusion shoulder design seems to correlate inversely with the maximum punch force. While the maximum punch force may reach a local maximum at a forming zone length of 25 mm, a local minimum of the maximum contact pressure appears here. In addition, the maximum punch force for this convex extrusion shoulder design appear remarkably lower than in the conventional Samanta process, irrespective of the forming zone length. However, even the lowest value of the maximum punch force in this process variant is higher than the lowest in the process variants having a concave design. Furthermore, underfilling also occurs at the toothing tip starting at a forming zone length of 35 mm.

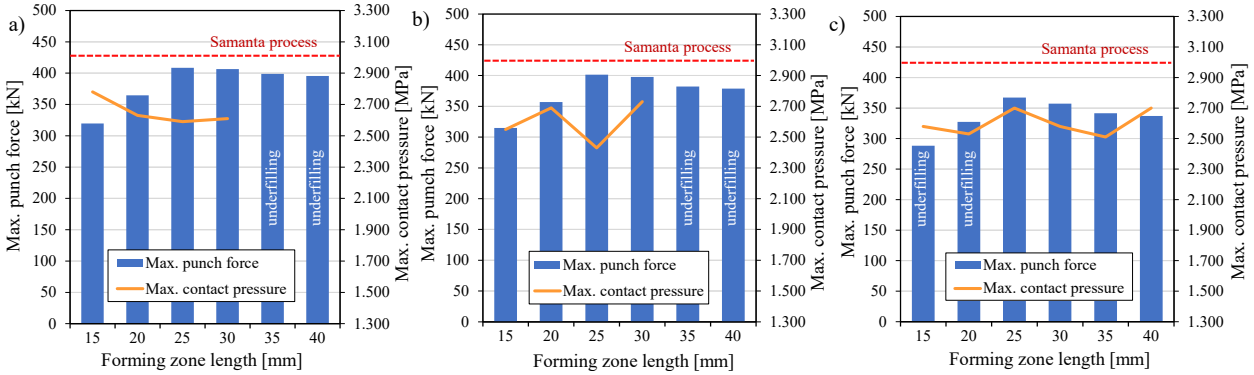

Fig. 7. Numerical results for convex extrusion shoulder geometry in GMF process, a) α=30°, b) α=50°, c) α=70°.

Fig. 7b shows the numerical results for the convex extrusion shoulder design in the GMF process with an angle α of 50°. The results are almost identical to the results for the convex version with a tangent angle of 30°. One difference however is observed: the maximum contact pressure does not show a clear correlation with the maximum punch force. Fig. 7c shows the numerical results of the convex extrusion shoulder in the GMF process having an angle α of 70°. By increasing the tangent angle α up to 70°, an underfilling of the tooth tip already occurs at a forming zone length of 15 mm. This underfilling also occurs at a forming zone length of 20 mm. A further increase of

the forming zone length results into complete die filling. Increasing the angle to 70° also leads to a general reduction in the maximum punch force for the convex extrusion shoulder variant. In addition, a local maximum of the maximum punch force at a forming zone length of 25 mm was observed. Maximum contact pressure was calculated at a level of 2,500 to 2,700 MPa and therefore was found lower than the maximum contact pressure occurring in the Samanta process. Hence, the maximum contact pressure appears nearly independent from the tangent angle α for the convex extrusion shoulder design in the GMF process.

Analysis of material flow.

An analysis of the material flow in Fig. 8 shows that the geometric shape of the extrusion shoulder has a significant influence on the material flow. Blue dots in that figure indicate contact areas between workpiece and die.

Linear extrusion shoulder design.

The linear extrusion shoulder design as depicted in Fig. 8a results into a steady increase of the friction surface between workpiece and die during the process. Friction surface at the tooth flanks increases only slightly when increasing the forming zone length, resulting into a reduction of the maximum punch force due to the forming work distribution. In Fig. 8b a difference in flow velocity of the material in the cavity and at the centre of the blank can be detected. The difference of about 5 m/s consists at a horizontal level on the blank. Due to this fact, there is a temporary reduction of the tooth height during the process. Here, the reduction of the tooth height is hindered by any effects of friction between the workpiece and the die in the area of the tooth flank. When enlarging the forming zone length, the axial material flow near the centre of the blank dominates, which evidently reduces the tooth height and finally results in underfilling of the toothing.

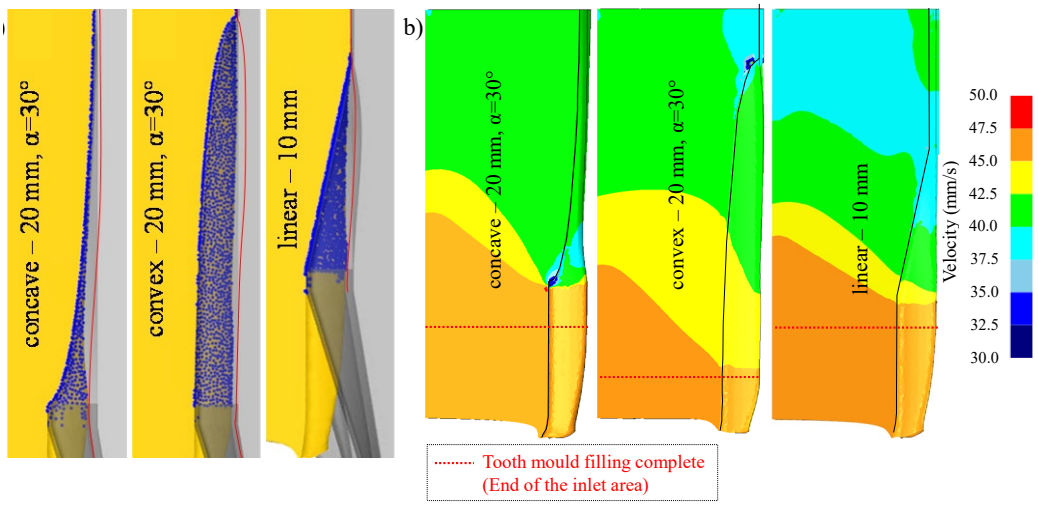

Fig. 8. GMF process at steady condition, a) contact area, b) material flow velocity.

Concave extrusion shoulder design.

Due to its shape, the concave extrusion shoulder design leads to a radial displacement of the material into the tooth cavity mainly at the lower end of the extrusion shoulder. This means that the effect of the undercut is barely noticeable and that the friction surface between workpiece and die in the area of the tooth flanks becomes minimal. Therefore, the friction surface and thus also the maximum punch force appear almost independent of the forming zone length. In the upper area of the concave extrusion shoulder, the low angle of the extrusion shoulder leads to a very slight deformation of the teeth. The material flows in an axial as well as radially inward direction, which causes the instantaneous workpiece in the toothing area to become temporarily smaller than the original blank diameter (blank diameter equals tip diameter). The temporary reduction of the tooth height results from the different flow resistances in the process along process direction, which

results into different flow velocities on the inner and outer diameter of the workpiece. In Fig. 8b, the maximum difference in flow velocities in process direction is observed around 10 mm/s. The low friction surface between the workpiece and the die in the area of the tooth flank favours the reduction of the tooth height, as the accumulated material can flow unhindered into the centre of the blank. As the forming zone length increases and the angle α increases, the reduction of the tooth height dominates, resulting into underfilling of the toothing.

Convex extrusion shoulder design.

In the convex shoulder design, depicted in Fig. 8, the main part of the tooth forming occurs in the upper area of the extrusion shoulder. As a result, the material in the upper area of the extrusion shoulder increases marginally in diameter compared to the original blank diameter. This means, the cavity is filled with material at the start of the process and the friction surface between the die and the workpiece increases rapidly. Due to the gradual tapering of the cavity in process direction, the die cavity was completely filled towards the end of the stroke. However, at mid-height of the extrusion shoulder, it can be observed that the material flows in a radially inward direction, causing the tooth height to temporarily decrease. Reason for this is also the differing flow velocity of the workpiece material in process direction. Enlarged friction surface between workpiece and die in the area of the tooth flank hinders the reduction of the tooth height, since the accumulated material is held in the die by the friction forces and the die tapering. Therefore, the tooth height reduction is less prominent in this process. When using the convex extrusion shoulder designs at 30° and 50°, a complete die filling was not achieved as the forming zone length increases. The more the forming zone length increases, the more material flows in the radially inward direction and thus the tooth height decrease seems to dominate. The reduced volume of workpiece material in the cavity cannot be compensated by tapering the tooth cavity to a complete die filling. In case of the process with a tangent angle of 70°, a complete die filling could not be achieved at small forming zone lengths. The reason for this is the big tangent angle in the upper area of the die shoulder. This steep design in the upper part of the forming zone results into a low radial displacement of workpiece material. Less material is thus displaced into the cavity at the start of the process. Moreover, the shortened forming zone length prevents any further displacement of material volume into the cavity. The material in this process variant is not formed sufficiently towards the cavity into the toothing area, which is why the axial material flow dominates here. As a result, despite the taper of the cavity in process direction, the die is not completely filled. An extension of the forming zone length results into complete die filling, as more material can be formed into the cavity through a longer path of the extrusion shoulder.

Summary

In this paper, the newly invented GMF process was numerically investigated under variation of the extrusion shoulder design. The extrusion shoulder design was modelled internally by linear as well as quadratic polynomial functional splines. Using this model, a three-dimensional simulation was performed to form the required gearing shape, whereby the geometric parameters of the extrusion shoulder were varied. In this way, the model of die was modified in the simulation between the two extrusion shoulder types (linear, quadratic), the forming zone length and the tangent angle α at the vertex of the quadratic polynomial function. As a result, the influence of these parameters on the maximum punch force, the maximum contact pressure acting internally in the die and the die filling of the gearing could be determined. In summary, it can be stated that a significant reduction of the maximum punch force can be achieved when using the new GMF process compared to the conventional Samanta process. In the case of a linear extrusion shoulder design, a steady decrease in the maximum punch force was observed when enlarging the forming zone length from 2 mm up to 12 mm. Overall, a reduction of the maximum punch force by approx. 38% was achieved compared to the conventional Samanta process. For the concave extrusion shoulder design, it was found that the maximum punch force remains almost independent of the

forming zone length. A reduction in the maximum punch force equal to that of the linear extrusion shoulder design was also achieved here. Maximum contact pressure was calculated at the same level as with the conventional Samanta process. With the convex variant, only a slight reduction in force and contact pressure was observed. Authors as next will focus on progressive optimisation of the die´s active surface, since a reduction of the maximum punch force by somewhat 50% was detected compared to a corresponding Samanta process design. The numerical results have also shown that the different extrusion shoulder geometries lead to different flow velocities of the material in the cavity and near the centre of the blank. This effect strongly influences the underfilling of the tooth at the lower end of the gear. Although the linear and concave shoulder designs show extremely low process forces, the inlet area was found extended in these variants compared to the concave shoulder design. This in fact results into a higher loadable gear height when applying the convex shoulder design, so, more effort will be put on further numerical investigations to assess the tooth underfilling in the inlet area. Therefore, future developments will consider the loadable gear height in order to analyse the grade of material utilisation in these processes.

References

[1] A. Schwager, M. Kammerer, K. Siegert, A. Felde, E. Körner, V. Szentmihalyi, Cold Forming of Helically Internal Toothed Wheels, in: New Developments in Forging Technology, 2003, pp. 489-503.

[2] C. Kiener, Kaltfließpressen von gerad- und schrägverzahnten Zahnrädern, Friedrich-Alexander-Universität Erlangen-Nürnberg, 2020.

[3] K. Lange, M. Kammerer, Fließpressen. Springer-Verlag Berlin Heidelberg, 2008. https://doi.org/10.1007/978-3-540-30910-9

[4] S. Samanta, M. Ypsilanti, Verfahren und Einrichtung zum Herstellen von Zahnrädern, Schutzrecht DE 25 33 670, 1975.

[5] W. Koll, W. König, Kaltfließpressen von Bauteilen mit Verzahnungen, in Präzisionsumformtechnik, Springer Berlin Heidelberg, 1990, pp. 193-213. https://doi.org/10.1007/978-3-642-95606-5_48

[6] T. Bausch, Innovative Zahnradfertigung-Verfahren, Maschinen und Werkzeuge zur kostengünstigen Herstellung von Stirnrädern mit hoher Qualität, 5. Auflage. Renningen: Expert Verlag, 2015.

[7] M. Merklein, C. Kiener, Researching of commonalities and differences in cold forging of spur and helical gears, Prod. Eng. 13 (2019) 391-397. https://doi.org/10.1007/s11740-019-00887-2

[8] M. Merklein, C. Kiener, R. Neher, Influence of tribological conditions on cold forging of gears, Prod. Eng. 12 (2018) 367-375. https://doi.org/10.1007/s11740-017-0785-9

[9] C. Kiener, K. Andreas, M. Merklein, Basic Numerical Analysis of a ‘ Samanta ’ Based Forward Extrusion Process, Adv. Mater. Res. 1140 (2016) 27-34. https://doi.org/10.4028/www.scientific.net/AMR.1140.27

[10] M. Liewald, T. Deliktas, Cold extrusion of spur and helical gears using a Guided Material Flow Process (Modified Samanta Process), in *52*nd ICFG Plenary Meeting, 2019.

[11] R. Velu, M.R. Cecil, Quantifying Interfacial Friction in Cold Forming using Forward Rod Backward Cup Extrusion Test, J. Inst. Eng. Ser. C 93 (2012) 157-161. https://doi.org/10.1007/s40032-012-0018-0

Materials Research Proceedings 28 (2023) 505-514 https://doi.org/10.21741/9781644902479-55

Investigations into the processing and texture of Pr-substituted NdFeB magnets produced by extrusion

RÜDIGER Alexander[1,a *], GALL Sven[2,b] and MÜLLER Sören[1,c]

[1]Extrusion Research & Development Center, Technische Universität Berlin, Gustav-Meyer-Allee 25, 13355 Berlin, Germany

[2]INGWERK GmbH, Rohrdamm 88, 13629 Berlin

[a]a.ruediger@tu-berlin.de, [b]sven.gall@ingwerk.com, [c]soeren.mueller@tu-berlin.de

Keywords: Pr/NdFeB, Anisotropic Magnets, Extrusion, Hot Deformation

Abstract. Crystallographically and magnetically textured but dimensionally limited NdFeB permanent magnets produced by hot deforming processes such as die-upsetting and back-extrusion have been extensively researched in the past [1]. In order to investigate the possibility of producing longer magnets which can subsequently be cut to the required length, the extrusion of permanent magnets was investigated as a further hot deformation process. For this purpose, the process control with regard to the tools used as well as the process parameters were modified from the common forming processes for extrusion. Therefore, a praseodymium-substituted NdFeB powder was encapsulated in steel and extruded by varying the extrusion ratio (9.9:1 & 13.9), the billet insert temperature (800°C & 850°C) and the extrusion speed (0.6 - 10.5 mm/s). In addition, the glass lubrication system was changed during the experiments. Since the resulting magnetic properties for hot deformation depend on the produced anisotropy, texture analyses were also carried out in the first step by means of X-ray diffraction on the cross-sections of the produced strands. For the parameter variation, strands could be realized with the applied concept. However, cracks were found in the magnetic material for all tests. Based on the texture analyses, anisotropy could be generated in the magnet material for all strands.

Introduction

Permanent magnets based on NdFeB are widely used in further areas due to their excellent magnetic properties in the form of high energy product $(BH)_{max}$. For anisotropic magnets, this is based on an alignment of the hard magnetic $Nd_2Fe_{14}B$ phase during the manufacturing process. In addition to the sintering route, in which a magnetic field must be applied during the manufacturing process for alignment, anisotropy can also be achieved by hot deformation (Figure 1). The advantage of this is that no magnetic field is required [1]. In order to improve the coercivity of sintered magnets, neodymium is often substituted in parts with dysprosium in many alloys. However, this is characterized by low availability and a high price. As a further substitution variant, it is possible to add praseodymium to the powder alloys without strongly affecting the magnetic properties. The lower purchase price compared to neodymium plays a decisive role in this case [2-4]. Another approach to improve the coercivity is to keep the grain size of the magnets as small as possible [5,6]. Due to the production method of the powder for the hot- deformation processes, these are especially distinguished for this purpose.

Here, the magnetic powders for further processing are produced by the melt-spinning process. In this, the molten starting material is applied to a wheel at high rotational speeds. The material spun off undergoes very rapid cooling and grain sizes in the sub-µm range are achieved. In the final powder, the grains are present in the platelet-shaped particles without crystallographic preferred orientation. Die-upsetting and back-extrusion are two forming processes that have already been intensively researched and applied in practice [1,7]. They can be used to produce

Content from this work may be used under the terms of the Creative Commons Attribution 3.0 license. Any further distribution of this work must maintain attribution to the author(s) and the title of the work, journal citation and DOI. Published under license by Materials Research Forum LLC.

block magnets or ring magnets with high magnetic properties. As already mentioned, these high magnetic properties are based on the formation of a suitable texture by hot-deforming. In the die-upsetting example, the powder is first hot compacted. This step is carried out in an argon atmosphere, since the powder tends to oxidize at the high operating temperatures. The pre-compacted blank is then hot-deformed. In this process, the formation of anisotropy is based on the fact that a liquid phase is formed at the grain boundaries and the grains undergo preferential grain growth in the a-axis direction of the tetragonal NdFeB unit cell. The grain growth is thereby fed by diffusion processes in the liquid phase [8-12]. Fig. 1 compares the manufacturing processes for sintered magnets and for the hot-deformed magnets (die-upsetting and back-extrusion) with the manufacturing approach studied in the experiments. In addition, the anisotropy achieved for the hot-deformed magnets is shown based on the C-axis orientation of the $Nd_2Fe_{14}B$ phases.

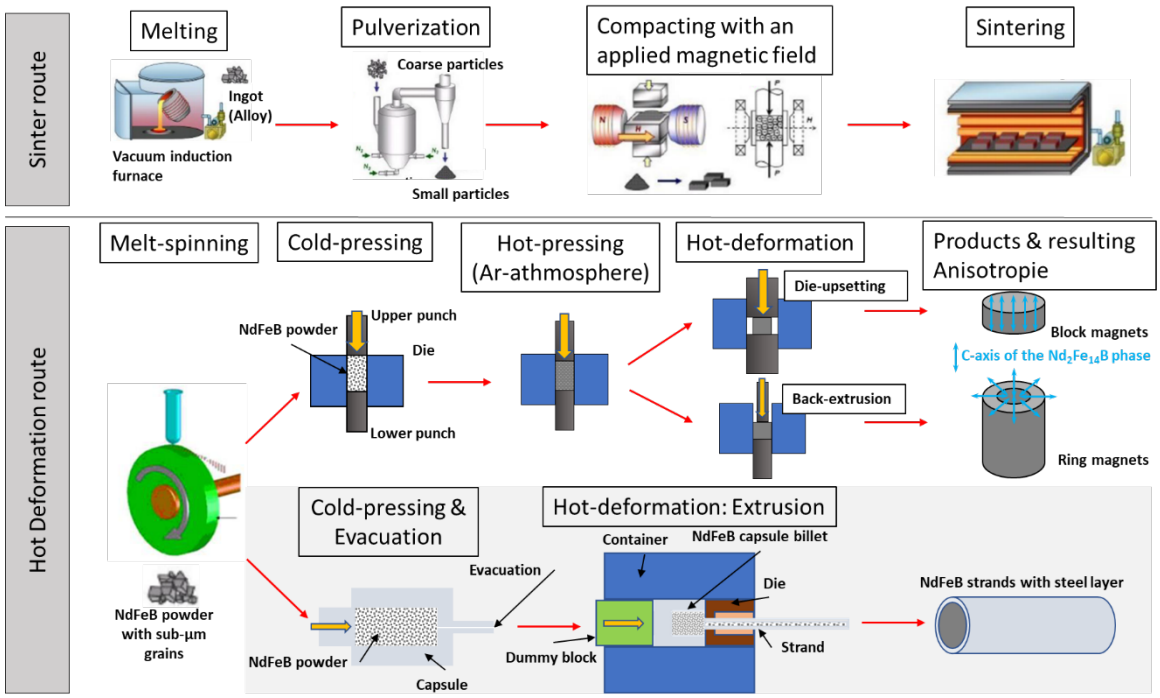

Fig. 1. Manufacturing processes of NdFeB magnets via sintering and hot-deformtion as well as the chosen investigation approach via extrusion [13].

The present investigations are intended to provide initial information on the conditions under which the extrusion of Pr/NdFeB is possible. For this purpose, in contrast to die-upsetting, the process control is adapted in such a way that pre-compaction at high temperatures is avoided and the powder is thus pressed directly. In order to obtain a first impression of the magnetic properties, texture measurements are carried out on the samples according to the correlation between these and the anisotropy achieved in the material.

Experimental Procedure

A Dy-free powder alloy with Nd substituted by Pr was used for the tests. The alloy composition is shown in Table 1. This was produced by the company Magnequench by means of the melt-spinning process for further processing by hot-deformation. Furthermore, Table 1 shows the particle size distribution of the powder used.

Table 1. Alloy composition and particle size distribution of the powder used.

element	Nd	Pr	Dy	B	Co	Ga	Fe
[ICP%]	7,80	22,60	0,00	0,88	3,90	0,49	64,33
Particel sizes by mesh & max. diameter	**>40 >425 µm**	**>60 >250µm**	**>100 >150µm**	**>200 >75µm**	**>325 >53µm**	**>375 >45µm**	**<375 <45µm**
[wt.%]	0,0	19,7	40,1	27,5	4,8	1,4	6,5

Direct extrusion was selected as the process for hot-deforming. For this, the set-up shown in Fig. 2 consisting of die (Hot work tool steel 1.2367) with ceramic ring insert (Al2O3), inlet ring (1.2367) with half die angle of α = 60°, glass pad, evacuated capsule billet with applied glass lubrication (slurry) and dummy block (1.2367) in a container with a diameter of 85 mm was used. The extrusions were carried out on the 8 MN extrusion press of the Extrusion Research & Development Center (TU Berlin).

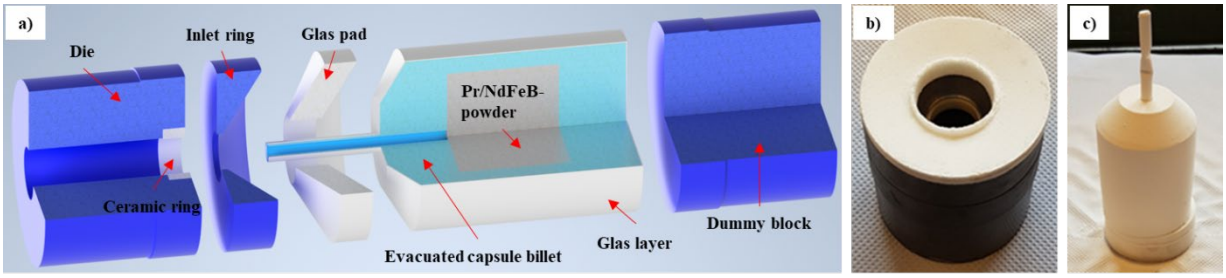

Fig. 2. a) Illustration of the experimental setup; b) Assembly of die, ceramic ring, inlet ring and glass pad; c) evacuated capsule billet with glass layer.

The powder was extruded in the encapsulated and evacuated form shown above, since the powder tends to oxidize at the forming temperatures applied. Accordingly, a capsule was first manufactured from mild steel (1.0577) with an outer diameter of 80 mm and a wall thickness of 8 mm, and then filled with the powder. In order to increase the output, the powder was also cold pre-compacted before evacuation. Furthermore, a two-part glass-based lubrication system, consisting of a glass pad and a glass layer sprayed onto the billet, was used for the extrusions. The purpose of this is to minimize friction and provide thermal insulation against the tools (container, die with ceramic ring, inlet ring and dummy block). The operating temperature of the mentioned tools was set to 500°C for the experiments. In the direct extrusion process used, the NdFeB billet together with the capsule material is pressed through the die by the dummy block and tapered to form a strand. Here, the inlet ring serves to improve the material flow into the deformation zone. The final cross-sectional geometry of the strand is determined by the ceramic ring, which represents the bearing channel of the die. In the best case, this remains intact throughout the entire extrusion.

For the tests, the billet operating temperatures, the diameter of the bearing channel, the ram speed and the type of glass lubrication system (Reimbold & Strick Handels- und EntwicklungsGmbH) used were varied (Table 2).

Table 2. Used experimental parameters.

	Billet operating temperature [°C]	Diameter oft he bearing channel [mm]	Extrusion ratio [-]	Ram speed [mm/s]	Glass lubrication system with application temperature range
#1	800	27	9,9:1	8,8	Pad: RS2745 0,1-0,4 (780 °C -1140 °C) Slurry: RS2745/10,063 (780 °C -1140 °C)
#2	800	22,8	13,9:1	10,5	as in #1
#3	850	22,8	13,9:1	8,7	as in #1
#4	850	22,8	13,9:1	6,8	as in #1
#5	850	22,8	13,9:1	4,8	Pad: NP7595 0,1-0,4 (620 °C -1000 °C) Slurry: GO12649 (620 °C -1000 °C)
#6	850	22,8	13,9:1	0,6	as in #5

For the qualitative investigations of the extruded strands, visual inspections of the strands were carried out on the one hand, and metallographic analyses in the form of X-ray diffraction (XRD) were performed on strand cross-sections to show the obtained textures on the other hand. When preparing the samples for XRD analyses, they were first grounded with a grit size of 4000 and then polished with diamond suspensions at 6 µm, 3 µm and 1 µm levels. The texture measurements were performed on the polished cross-sections of the strands in the center and in the edge region of the magnetic material. The measurements were carried out at the Department of Metallic Materials at the TU Berlin on a diffractometer from the Huber company using a location-sensitive detector OED 50 M from M. Braun GmbH. These involved monochromatic Co-Kα radiation (λ = 0.17887 nm), an accelerating voltage of 40 kV, a current of 25 mA, and a collimator with a diameter of 1 mm, and the crystal orientations {004}, {310}, {313}, {410}, {411}, and {006} were measured. For the measurements, the samples were rotated azimuthally (φ) in 5° steps from 0° to 355° and repeated for tilt angle steps (Ψ) of 5° ranging from 0° to 55°. The program MTEX was used to determine the orientation distribution functions (ODF) and create the pole figures.

Results and Discussion

Fig. 3 shows the resulting strands of the test extrusions. It can be seen that for all test parameters, strands could be extruded which also contain magnetic material. In addition, Table 3 summarizes the extrusion forces measured during the tests as a function of the stepwise parameter adjustments. The total force to be applied by the extrusion press is the sum of the die force and the friction force. The forces are determined by load cells which are coupled to the container for the friction force and to the die for the die force. In the case of the used container (diameter of 85 mm), the total force is also restricted to 6.5 MN in order to avoid exceeding the critical yield stresses of the used tools.

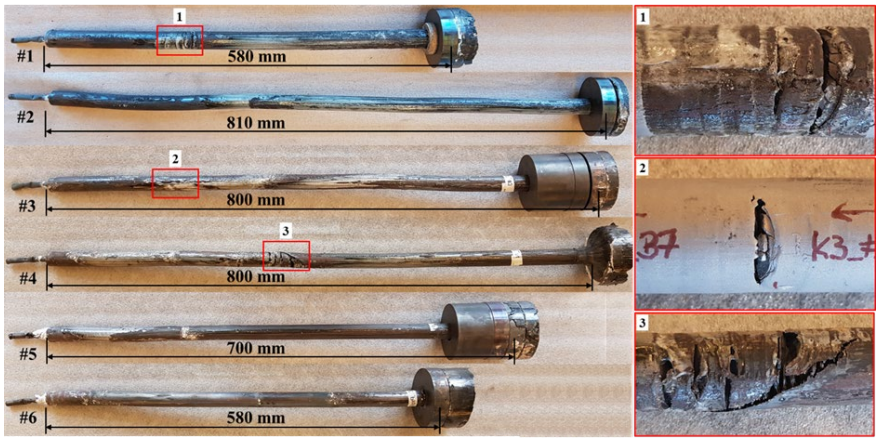

Fig. 3. Strands of tests No. 1 to No. 6 (left); 1-3) Pressing defects.

Table 3. Measured extrusion forces as function of the stepwise parameter adjustments.

	#1	#2	#3	#4	#5	#6
Parameter adjustments		Increased extrusion ratio Increase Ram Speed	Increased billet Temperatur Decreased Ram speed	Decreased Ram speed	Changed Glass lubrication system Decrease Ram speed	Decrease Ram speed
Die Force [MN]	4,1	4,9	4,8	5,1	4,4	4,0
Friction Force [MN]	1,0	1,3	1,5	1,2	0,4	0,3
Total force [MN]	5,1	6,2	6,3	6,3	4,8	4,3

For test No. 1, the required die force and the friction force between billet and container were measured to be 4.1 MN and 1.0 MN, respectively. By increasing the ram speed and decreasing the bearing channel diameter, the die force increased as expected to 4.9 MN. The friction force was measured at 1.3 MN, resulting in a total force of 6.2 MN to be provided by the extrusion press. This results in very high stresses for the ram and the used tools. To counteract these, the billet operating temperature was increased and the extrusion speed reduced for test No. 3. However, despite the adjustments, 4.8 MN and 1.5 MN were measured for the die and friction forces, respectively. It can be assumed that the adjustment of the extrusion speed is not sufficient to achieve sufficiently high differences in the mean logarithmic forming speeds which can be calculated according to the formula [14]:

$$\underline{\dot{\varphi}_g} = \frac{(V-1)\cdot 2\cdot tan\alpha}{D_0 \cdot D_S} \quad (1)$$

Here V is the extrusion ratio, α is the die angle, D_o is the container diameter and D_s is the strand diameter. The determined small reduction from 7.5 1/s to 6.3 1/s could therefore not be sufficient to achieve a relevant reduction in the flow stresses of the material. For test No. 4, the ram speed was further reduced. Here, too, no relevant deviations from the values of test No. 2 could be observed with 5.1 MN and 1.2 MN. This could equally be attributed to a still slight reduction of the mean logarithmic forming speed to 4.9 1/s. In addition, it could be considered for the tests that manual loading oft he billet can lead to delays in the extrusion process.

This means that even short time differences can lead to strong cooling of the billet due to the high temperature gradient between the container and the billet, which can also lead to an increase in the flow stresses in the deformation zone. In order to further reduce the forces, a new lubrication system suitable for use at lower temperatures was used for tests No. 5 and No. 6. At the same time, the ram speed was further reduced for test No. 5. As a result, the die and friction forces were significantly reduced to values of 4.4 MN and 0.4 MN, respectively. The reduction in the friction force, which is measured by load cells attached to the container, can thus be attributed to the reduced friction between container and billet surface. The lower die force can also be explained by a reduction in friction. In this case it is due to the reduced friction between the billet and die, since the measured values for the forming force are recorded via load cells on the die, i.e. decoupled from the friction force. The improved material flow at the die, i.e. facilitated by the more suitable lubrication system, also improves the formability. For test No. 6, a further reduction in the ram speed also resulted in lower values for the die and friction forces of 4.0 MN and 0.3 MN in the steady-state of extrusion. In contrast to the previous tests, however, this billet could not be extruded completely, which resulted in an increase in the total force to a maximum acceptable value of 6.5 MN for the test setup, above which forming was no longer achieved with the corresponding extrusion force. In this case, it can be assumed that the set low ram speed during the extrusion results in excessive cooling of the billet and thus freezing of the billet. Figure 3 also

Materials Research Proceedings 28 (2023) 505-514 https://doi.org/10.21741/9781644902479-55

shows the strand lengths obtained. For tests No. 1 to No. 5, the theoretical lengths calculated via the volume consistency (approx. 600 mm for ER. 9.9:1; approx. 800 mm for ER. 13.9:1) could be achieved, whereby the deviating strand length for test No. 5 is due to a shortened capsule cover of 10 mm. In accordance with the not completely extruded billet in test No. 6, a reduced strand length of 580 mm was realized here. Also extrusion defects for strands No. 1, No. 3 and No. 4 are shown in Figure 3. These are cracks in the shell material of the strand areas with magnetic core, which are perpendicular to the extrusion direction. The magnet material in these areas is also characterized by strong transverse cracks, in some cases also beyond the areas of the shell cracks (see Figure 3, detail view 2). Figure 4 shows the theoretical positions of the magnet material as well as the real cutting positions for removing the relevant magnet areas in the resulting strands for the two different extrusion ratios. The strand sections shown in Figure 5 were extracted according to these cutting positions. For reasons of equivalence with respect to strand No. 2, strands No. 3 and No. 4 are not shown.

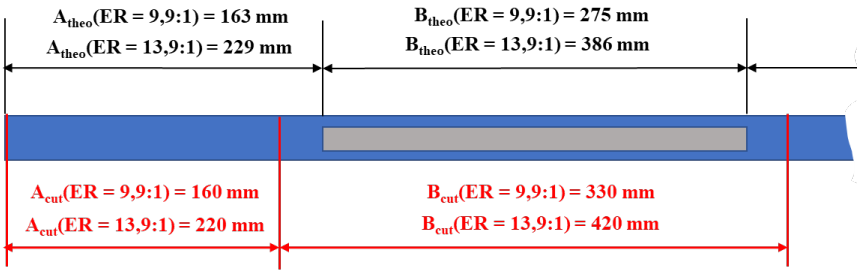

Fig. 4. Theoretical position of the magnetic material in the strand (black); removal positions for the magnetic material (red).

In addition, Fig. 5 shows the sections through the magnet-filled areas in order to compare them with the theoretical material flow.

While for the experiments No. 1 to No. 5 the section lengths of 330 mm and 420 mm given in Fig. 4 were observed due to the complete extrusion of the billets, only a section of 340 mm could be taken for experiment No. 6. The cross-sections also show that the magnetic material is present in different proportions over the length of the sections. Thus, for all tests, there is a pronounced back-end defect at the end of the section, in which the capsule bottom material flows forward in the middle of the strand and the magnetic material is therefore present in a ring shaped area in the cross-section. On the other hand, a variable area fraction of the magnetic material can also be seen in the areas without back-end defect, whereby this decreases over the extrusion. In the case of tests No. 5 and No. 6, it can be seen that magnetic material is already present in the strand before the theoretically determined position. In the case of test No. 5, it can be assumed that the shortened capsule cover is the cause of the displaced position of the magnet. In the case of test No. 6, it could be assumed that, due to the low extrusion speed, the flow stresses for the steel are higher than for the magnet material as a result of the rapid cooling of the billet. This would result in a pre-flow of the magnet material in the center of the strand. Furthermore, in Fig. 5, cracks can be seen in the magnet material along the entire strand length for all tests, not just in the defect areas shown in Fig. 4. On the one hand these could be explained by insufficient matching of the forming properties of the material composite and on the other hand by the difference in the thermal expansion coefficients of the two materials.

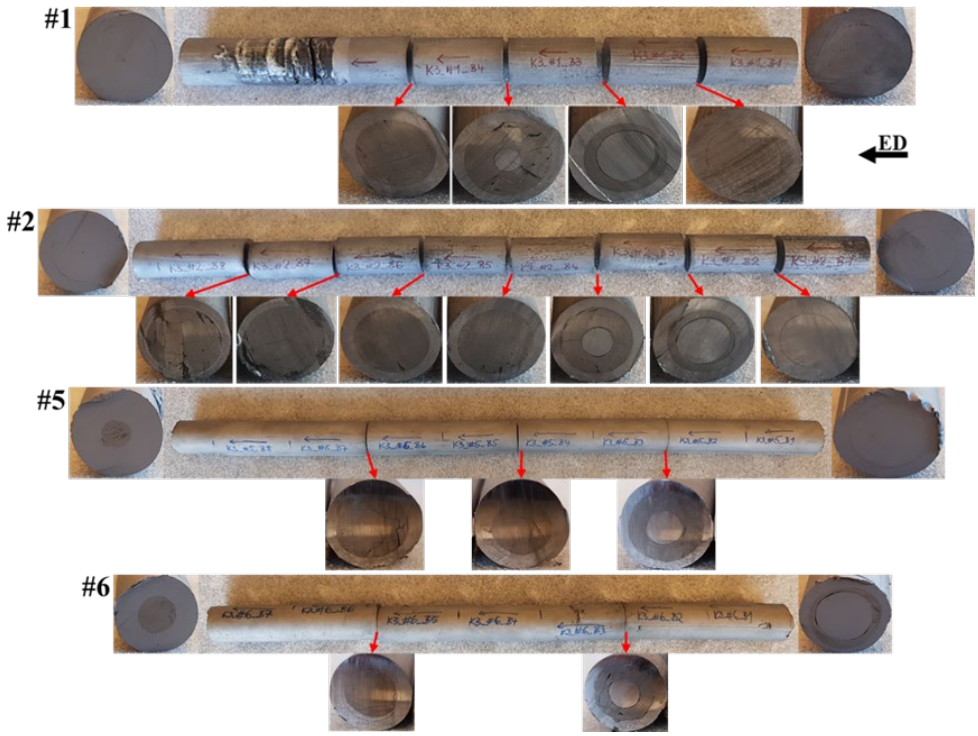

Fig. 5. Resulting strands and strand cross sections.

Fig. 6 shows the pole figures determined by XRD for selected tests at the edge and in the center of the magnetic material. For the investigations, sample cross-sections were considered in which the area fraction of the magnetic material was the largest. Since the pole figures for tests No. 2 to No. 5 do not show any decisive differences, these are represented for the edge by test No. 2 and for the center by test No. 3.

In general, an orientation of the lattice structure can be determined for all tests, both at the edge and in the center, in which the (002) planes are preferably perpendicular to the cross-sectional plane and rotated with respect to the extrusion direction. The (100) planes are primarily oriented in the cross-sectional plane or perpendicular to it. According to these orientations, the (110) planes are thus preferably rotated by 45° to the orientation of the (100) planes, as can be seen in Fig. 6. Furthermore, it can be seen that a certain proportion of the (001) planes are oriented horizontally in the cross-sectional planes, especially in the measuring positions at the edge. This indicates that an theoretically expected anisotropy is more pronounced in the center regions. In theory, the hot-deforming of Pr/NdFeB results in an anisotropy in which the (002) planes are perpendicular to the applied pressure direction. This can be seen in the die-upsetting and back-extrusion processes (Fig. 1). Consequently, in the process used here, a radial orientation of the c-axes of the tetragonal unit cell, corresponding to the anisotropy in back-extrusion magnets, would ideally be expected in the cross-sectional area of the strand.

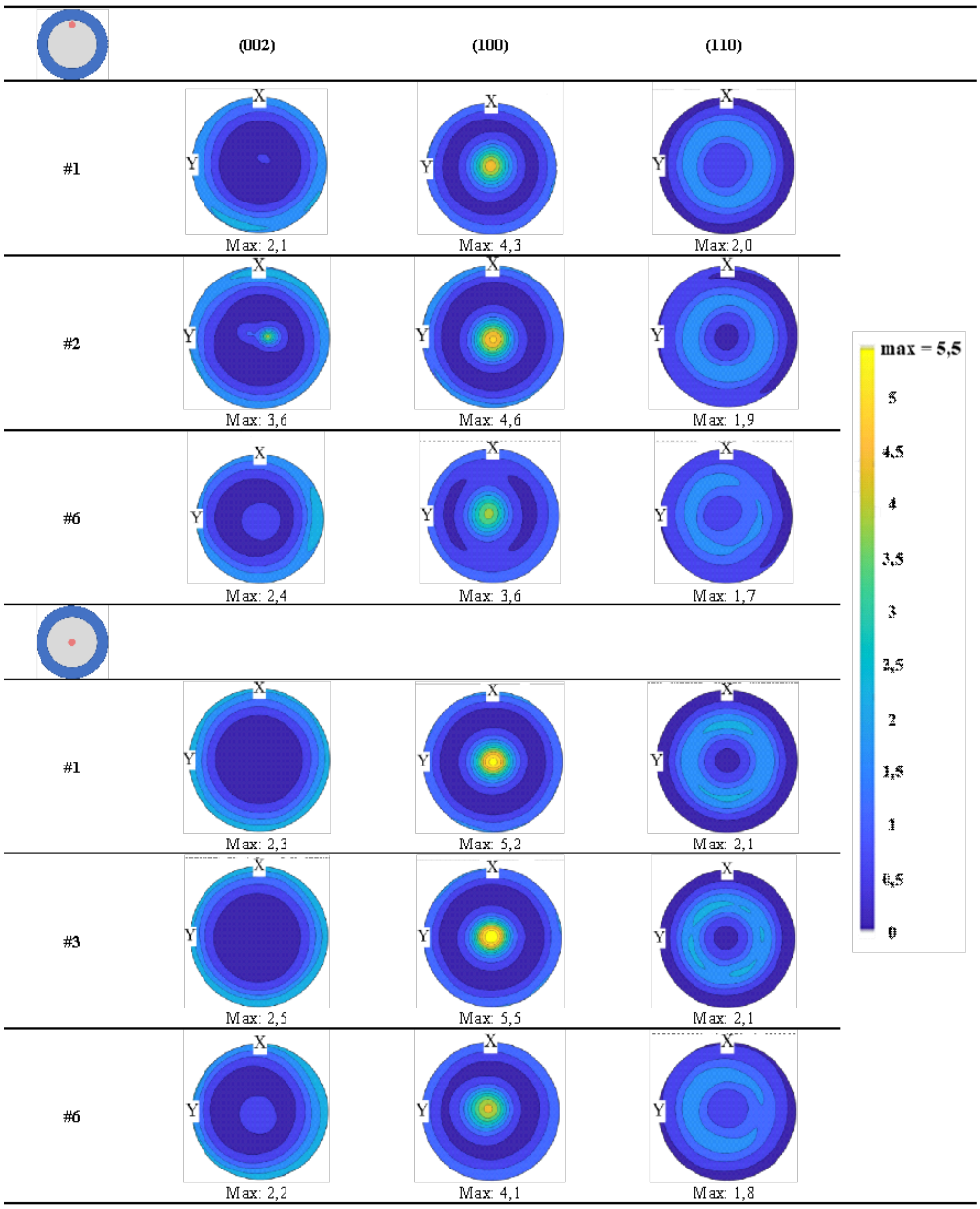

Fig. 6. Pole figures determined by XRD at the edges and in the center of the strands; the colored legend represents the intensity range of the displayed pole figures.

For the occurrence of the perpendicular to the extrusion direction orientated (002) planes in the edge region, it can be assumed that, due to too rapid cooling of the magnetic material, no sufficient rotation of the grains in the liquid phase required for hot deformation is possible at the extrusion speeds used because of the large temperature gradient between the container and the billet. Consequently, the temperatures in this area could drop too quickly into the temperature range of the solidifying temperature of the liquid phase. A similar argument can be made for test No. 6 in the center of the strand. Here, the possibly too slow pressing speed for the experimental setup could lead to a rapid cooling of the billet down to the center of the material and thus cause the observed superimposed anisotropy. Furthermore, it can be assumed that the not achieved radial anisotropy can be explained by insufficient shear of the material based on the possibly too low selected extrusion ratios. In general, it should be noted that for further tests to optimize the

anisotropy, the tools must be adapted with regard to realise a constant Temepratur in the billet over the entire extrusion.

Summary

With the selected test setup for direct extrusion of encapsulated magnetic powder, strands with magnetic material or at least partial strands (Test No. 6) could be processed for all parameters. A pronounced back-end defect was observed for all strands. For some strands, partial cracks of the strand shell and and in these areas strong cracks in the magnetic material perpendicular to the extrusion direction could be observed. In addition, the magnet material was riddled with finer cracks in all tests. In future, consideration can be given here to adapt the capsule material in order to better match the flow properties to the magnet material in the temperature range used.

Furthermore, a comparable texture was produced in the edge areas and the centers of the magnet material in all tests. In this, the c-axes of the Pr/NdFeB unit cell were preferably perpendicular and rotated with respect to the extrusion direction. Purely radial anisotropy of the magnet material could not be generated.

In summary, it can be assumed that the excessive temperature gradient between the tools and the magnetic billet led to an unfavorable cooling for the process. For further tests, it is useful to develop a concept that allows higher operating temperatures to be realized for the tools in order to counteract the decrease in Temperature of the magnetic material during extrusion. In addition, to enhance shear and thus anisotropy, an increase in the extrusion ratio may be considered.

References

[1] O. Gutfleisch, Controlling the properties of high energy density permanent magnetic materials by different processing routes, J. Phys. D: Appl. Phys. 33 (2000). https://doi.org/10.1088/0022-3727/33/17/201

[2] N.A. Dormidontov, A.G. Dormindontov, A.S. Lileev, A.V. Kamynin, A.A. Lukin, Effect of partial substitution of neodymium with praseodymium on the magnetic and process properties of sintered magnets of type NdFeB, Metal Sci. Heat Treat. 58 (2017) 608-613. https://doi.org/10.1007/s11041-017-0064-6

[3] S. Hirosawa, Y. Matsuura, H. Yamamoto, Magnetization and magnetic anisotropy of $R_2Fe_{14}B$ measured on single crystals, J. Appl. Phys. 59 (1986) 873-879. http://doi.org/10.1063/1.336611

[4] I. Poenarua, A. Lixandrua, S. Riegg, Ce and La as substitutes for Nd in $Nd_2Fe_{14}B$-based melt-spun alloys and hot-deformed magnets: a comparison of structural and magnetic properties, J. Magn. Magn Mater. 478 (2019) 198-205. https://doi.org/10.1016/j.jmmm.2019.01.095

[5] Y. Une, M. Sagawa, Enhancement of coercivity of Nd-Fe-B sintered magnets by grain size reduction, J. Japan Inst. Met. Mater. 76 (2012) 12-16.

[6] J. Liu, H. Sepehri-Amin, T. Ohkubo, Grain size dependence of coercivity of hot-deformed Nd–Fe–B anisotropic magnets, Acta Mater. 82 (2015) 336-343. https://doi.org/10.1016/j.actamat.2014.09.021

[7] L. Li, C.D. Graham, Mechanism of texture formation by hot deformation in rapidly quenched FeNdB, J. Appl. Phys. 67 (1990) 4756-4758. https://doi.org/10.1063/1.344776

[8] R.K. Mishra, E.G. Brewer, R.W. Lee, Grain growth and alignment in hot deformed Nd-Fe-B magnets, J. Appl. Phys. 63 (1988) 3528-3530. https://doi.org/10.1063/1.340731

[9] R. Shioi, H. Miyawaki, T. Morita, Orientation mechanism of hot-deformed anisotropic RE-Fe-B magnets, Denkiseiko 82 (2011) 31-37.

[10] R.K. Mishra, T.Y. Chu, L.K. Rabenberg, The development of the microstructure of die-upset Nd-Fe-B magnets, J. Magn. Magn. Mater. 84 (1990) 88-94. https://doi.org/10.1016/0304-8853(90)90168-P

[11] J. Liu, H. Sepehri-Amin, T. Ohkubo, Microstructure evolution of hotdeformed Nd-Fe-B anisotropic magnets, J. Appl. Phys. 115 (2014) 17A744. https://doi.org/10.1063/1.4867960

[12] R.K. Mishra, Microstructure of hot-pressed and die-upset NdFeB magnets, J. Appl. Phys. 62 (1987) 967-971.
[13] Information on http://www.shinetsu-rare-earth-magnet.jp/e/masspro/
[14] M. Bauser, G. Sauer, K. Siegert, Strangpressen, Aluminium-Verlag, Düsseldorf, 2 Edition, 2001

Materials Research Proceedings 28 (2023) 515-522 https://doi.org/10.21741/9781644902479-56

Friction extrusion processing of aluminum powders: Microstructure homogeneity and mechanical properties

CHAN Chang Yin-Cheng[1,a *], RATH Lars[1,b], SUHUDDIN Uceu F. H.[1,c] and KLUSEMANN Benjamin[1,2,d]

[1]Helmholtz-Zentrum Hereon, Institute of Materials Mechanics, Solid State Materials Processing, Max-Planck-Straße 1, 21502 Geesthacht, Germany

[2]Leuphana University Lüneburg, Institute for Production Technology and Systems, Universitätsallee 1, 21335 Lüneburg, Germany

[a]chang.chan@hereon.de, [b]lars.rath@hereon.de, [c]uceu.suhuddin@hereon.de, [d]benjamin.klusemann@hereon.de

Keywords: Friction Extrusion, Solid-State Processing, Aluminum, Powder Consolidation

Abstract. Friction extrusion (FE) is a solid-state process categorized as an energy-efficient process, utilizing the intrinsic friction-induced heat to plasticize and manufacture fully consolidated extrudate from various feedstocks, i.e. solid billet, chips and powder. Friction in the relative motion between the feedstock and the non-consumable die generates heat as well as imposes severe plastic deformation; this combination enables dynamic recrystallization and refinement of the microstructure. This study demonstrates the feasibility of directly extruding aluminum alloy powder into fully consolidated wire in a single step process. The extrudate is free of noticeable defects and shows predominantly homogeneous microstructure along the cross-section of the wire. The powder evolution upon passing through the die orifice was investigated in terms of morphology and microstructure. Additionally, the mechanical properties of the extrudate, i.e. microhardness and ultimate tensile strength, were compared to solid billets of AA7075 in different temper states and shows adequate mechanical properties without possible post-heat treatments.

Introduction

Friction extrusion (FE) process, developed and patented by Thomas et al. [1] in 1993, is used to extrude diverse materials, i.e. aluminum [2], magnesium [3] and copper [4] alloys. FE, schematically shown in Fig. 1, differs primarily from classical extrusion in the relative rotational motion, utilizing the well-established concept from friction stir welding (FSW). Friction occurs at the interface of the feedstock and the die, which introduces shear deformation and elevated temperature, resulting in the initiation of recrystallization and grain refinement. Three essential control factors in FE, i.e. axial force, rotational speed and die geometry, determine the extrudate properties and geometry, which have been extensively studied in the literature for different materials. The effect of the rotational speed and extrusion force was investigated and the rotational speed as the critical process parameter determined [5,6]. The die geometry not only defines extrudate shape but also affects the material flow prior to extrusion. Darshell et al. [7] and Halak et al. [8] discussed the influence of different die profiles and angles, respectively.

The FE from powder feedstock has attracted particular interest in the past few years, as it demonstrates the ability to extrude rod and tube directly from powder precursor [9,10] and led to better mechanical properties, such as ductility and electrical conductivity, compared to conventional analogous processing techniques [11]. Additionally, friction consolidation (FC) process that can be viewed as the FE without a die orifice, revealed the formation of the supersaturated solid solution of the immiscible alloy, which initiates the potential to achieve novel

Content from this work may be used under the terms of the Creative Commons Attribution 3.0 license. Any further distribution of this work must maintain attribution to the author(s) and the title of the work, journal citation and DOI. Published under license by Materials Research Forum LLC.

properties [12]. Strain and strain rate prior to FE are the decisive factors of the extrudate properties and have been studied using marker materials in solid billet feedstock [13]. In contrast to a solid billet feedstock, additional consolidation is necessary for powder FE. Furthermore, the influence of powder flow ability on strain and strain rate needs to be considered. Despite the numerous advantages of using powder as feedstock in FE and the possibility of accomplishing novel properties, the material flow of powder in front of the die is still rarely studied.

To understand the consolidation and deformation of the powder feedstock during FE, the present study analyzes the powder evolution within the residual feedstock, in particular of the powder shape alteration and the elimination of powder boundaries. In addition, the microstructure and properties of the extrudate are studied.

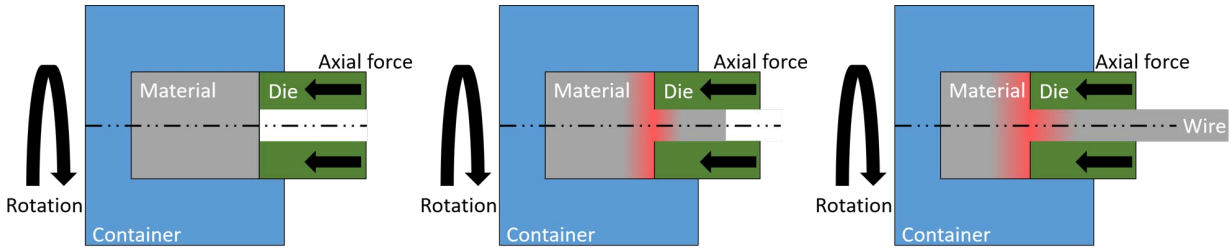

Fig. 1. Illustration of the FE process, including two machine parts, container and die.

Materials and Methods

Aluminum gas-atomized 7075 powder with a particle size smaller than 106 µm, stored in dry air, was used in this study. The dedicated friction extrusion machine FE100 manufactured by Bond Technologies was used. The machine allows forces up to 1000 kN, torques of 3500 Nm and rotational speeds of 1000 rpm. Along with high-speed data acquisition, FE100 enables the exploration of broad parameter combinations. The two essential tooling parts, shown in Fig. 1, namely a rotating powder container machined from 4140 steel with an inner diameter of 50 mm and a hydraulically driven extrusion die with a flat face from H13 steel with a 10 mm die orifice, were applied in the current study, which resulted in an extrusion ratio of 25. The temperature was recorded via type-K thermocouple embedded 1 mm from the extrusion die surface at a radius of 16.5 mm. The powders of ~ 150 g were filled in the powder container with a 0.6 mm AA7075 plate placed on top and pre-compacted with 100 kN to prevent powder spill before extrusion. The initial stage of the process applied a rotational speed of 300 rpm with 55 kN to establish complete contact between the extrusion die and the material. After the extrusion die advanced for 1 mm, the transition to the force-controlled friction extrusion process was conducted via a 10 s ramp. The constant 100 kN force with the powder container constantly rotating at 200 rpm were denoted as the process parameter in this study.

After extrusion, the extruded wire and the residual feedstock were sectioned transversely and longitudinally to the extrusion direction, respectively, and prepared following standardized metallography procedures. The microstructure of the wires was subjected to an additional electrolytic etching with Barker's solution at 20 V for 80 s and inspected with a Leica DMi8 optical microscope. In contrast, the microstructure of residual feedstock was analyzed by an FEI Quanta 650 field-emission scanning electron microscope (SEM) equipped with EDAX Apollo X energy dispersive X-ray spectroscopy (EDX). Furthermore, microhardness was tested with an EMCO-TEST Durascan 70 G5 with a load of 0.2 kg and ultimate tensile strength (UTS) was measured by an Imprintec i3D BVR according to DIN SPEC 4864. The mechanical properties of the extruded wire were compared with the as-received AA7075-T651 bar material and the annealed sample by heat treating the sample at 404 °C for 150 minutes followed by oven cooling.

Results and Discussion

The microstructure overview in the cross-section of the extrudate, processed at 100 kN and 200 rpm, is shown in Fig. 2. No noticeable defects and a fine-grained microstructure were observed in the core of the wire, indicating the powder is fully consolidated after FE. Grains, with grain size smaller than 10 µm, are predominantly present through the full cross-section of the wire, while at the periphery, larger grains up to 50 µm and defects can be noticed. The reasons might refer to the extensive residual heat in the die bearing promoting grain growth and the relative rotating motion between the extrudate and the die.

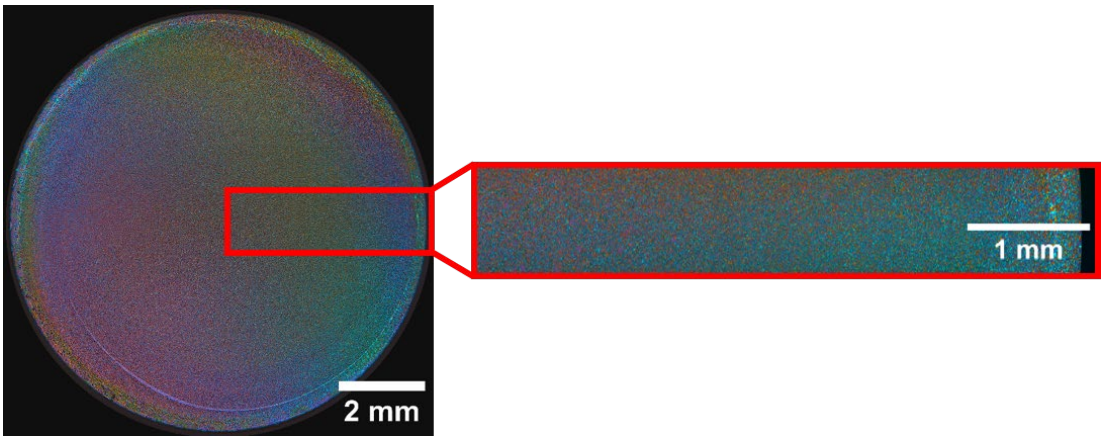

Fig. 2. Micrograph of etched cross-section of the wire extruded at 100 kN, 200 rpm, including enlarged section at the position highlighted by the red frame.

The powder evolution analysis is conducted on the residual feedstock after FE. The overview geometry of the specimen can be seen in Fig. 3(a). The left up and down corners of the specimen were fractured. Spherical raw powders, Fig. 3(b), have been found within the fracture area, indicating that the pre-compaction stage has not affected the powder in these regions prior to FE. Several positions at the center of the residual feedstock have been subjected to SEM for a powder evolution study. Fig. 3(c-g) reveals the evolution of powder during the FE process. High porosity has been identified as highlighted by white circles in Fig. 3(c) in form of void volume between as well as pores within individual powders, which is regarded as the starting condition of the powder after pre-compaction. The morphology of the powder alters gradually by approaching the die orifice and accompanies by the pores removal due to the extrusion force combined with the rising temperature and completed in Fig. 3(d). In Fig. 3(e), approximately 6 mm advanced entering the die orifice, the powders have been elongated in the extrusion direction, indicating the mechanical effect of the tooling has contributed to the FE. The powder boundaries begin to fade, suggesting the merge of the powder is potentially under the diffusion route with a much lower temperature, maximum 503 °C according to temperature measurement, compared to the conventional sintering temperature (580 – 620 °C) for AA7xxx alloys [14]. In Fig. 3(f), the large amount of powder boundaries vanishes and suggests that the powder consolidation nearly finished prior to entering the die orifice and material flow onwards can be considered similar to FE from a solid billet feedstock. However, the different strengths and the flow ability among the pre-compacted powder, solid billet or chips have a tremendous impact on the initial heat generation and the heat dissipation,

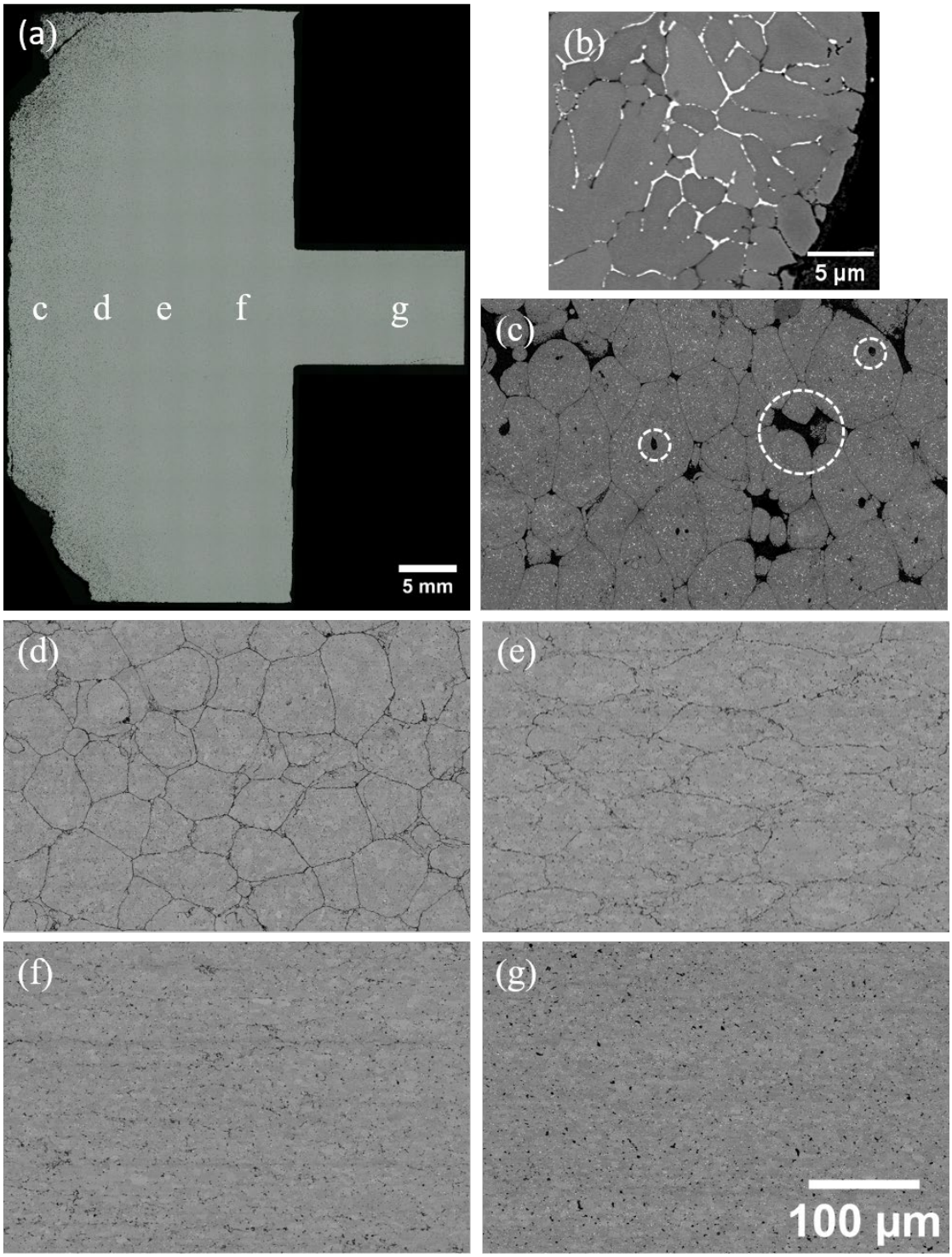

Fig. 3. Overview of residual feedstock (a), base powder (b) and powder evolution in the center from the left of the specimen (c) to the extrudate (g).

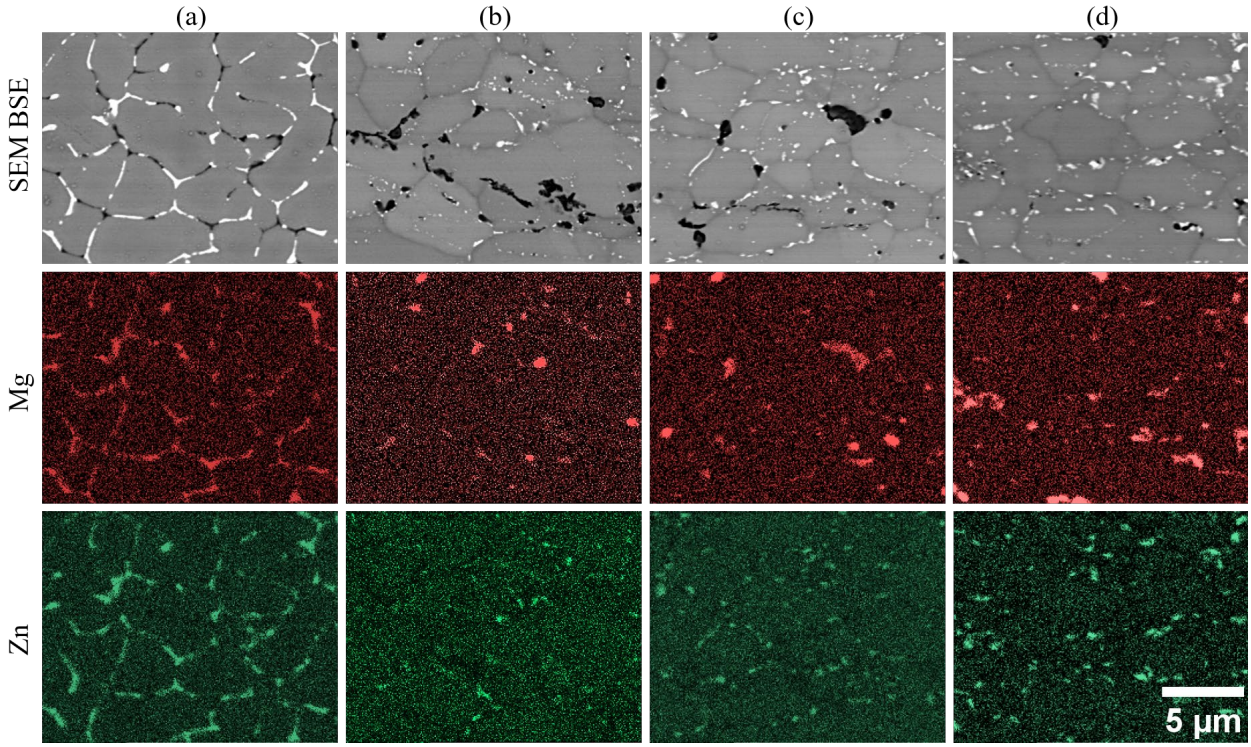

Fig. 4. SEM backscatter images from base powder (a) and different distance to the die orifice, i.e. 6 mm (b) and 4 mm (c) advanced and 10 mm (d) retreated, and the corresponding EDX mapping of Mg and Zn.

which hinder the direct implantation of the strain and strain rate found in the literature for solid billet as well as chips feedstock into the powder [13, 15]. After passing through the die orifice, the microstructure of the extrudate transforms into the final microstructure as shown at the position of 10 mm, Fig. 3(g), after the die orifice. No powder boundary has been found, indicating the powder is fully consolidated after the FE and further confirming the previous finding in Fig. 2.

In the aluminum alloy AA7075, two major alloying elements, magnesium and zinc, form the $MgZn_2$ phase at the grain boundary, which is observed in all the SEM images as white particles. Therefore, the residual feedstock is subjected to EDX to disclose and complement the powder evolution in the FE before entering the extrusion orifice. The EDX mapping of the Mg and Zn as well as the corresponding SEM backscatter images are shown in Fig. 4(a-d). In the base powder, Fig. 4(a), most of the $MgZn_2$ phases are larger and located at the grain boundary, which is the typical behavior of this phase in AA7075. The discontinuity observed in the EDX mapping can be explained by the re-melting of solid particles [16]. Approaching the extrusion die, the $MgZn_2$ phases are fragmented into smaller particles under shear and longitudinal deformation or diffuse into the grains as reported that FE can form a forced supersaturated solid solution [12]. By comparing the different grain orientations in the raw powder, Fig. 3(b), and near the extrusion die, Fig. 4(b-d), the transformation of the randomly distributed grains aligned in the extrusion direction can be observed, indicating the effect of the deformation. In Fig. 4(b), the capture position is adjacent to the powder boundary, where the $MgZn_2$ phases are rarely found, which corresponds to the observation of the unprocessed base powder. The reason could be that the rapid solidification rate of gas-atomized powder impedes the diffusion behavior of alloying elements on the powder surface [16]. Since the melting point of $MgZn_2$ phases is much below the processing temperature of FE, the incipient melting of existing phases may occur before the die orifice and could explain

the smaller defects observed in Fig. 4(c). However, the huge defects may be due to the isolated pores that typically find in powder metallurgy materials [17]. It needs to be mentioned that the grain size observed in the SEM images is also below 10 µm and comparable to the base powder.

The microhardness was evaluated over the cross-section for a part in the middle of the extrudate, see Fig. 5(a). The FE extrudate shows a relatively homogeneous hardness, 115.6 HV, except for the outer ring with slightly larger grains. At the lower part of the mapping, one region with significantly lower microhardness is supposed to be a defect, as observed at the periphery of the cross-section in Fig. 2. By comparing the extrudate to AA7075 alloys in different temper states, T6 and O, Fig. 5(b), the hardness is 67 % of AA7075-T6 and 80 % higher than the annealed state. AA7075 is a precipitate hardenable alloy, and T6 temper is the peak artificial aging. Therefore, the lower hardness after high temperature exposure during FE (maximum measured temperature of 503 °C) is expected due to the dissolution of strengthening precipitates.

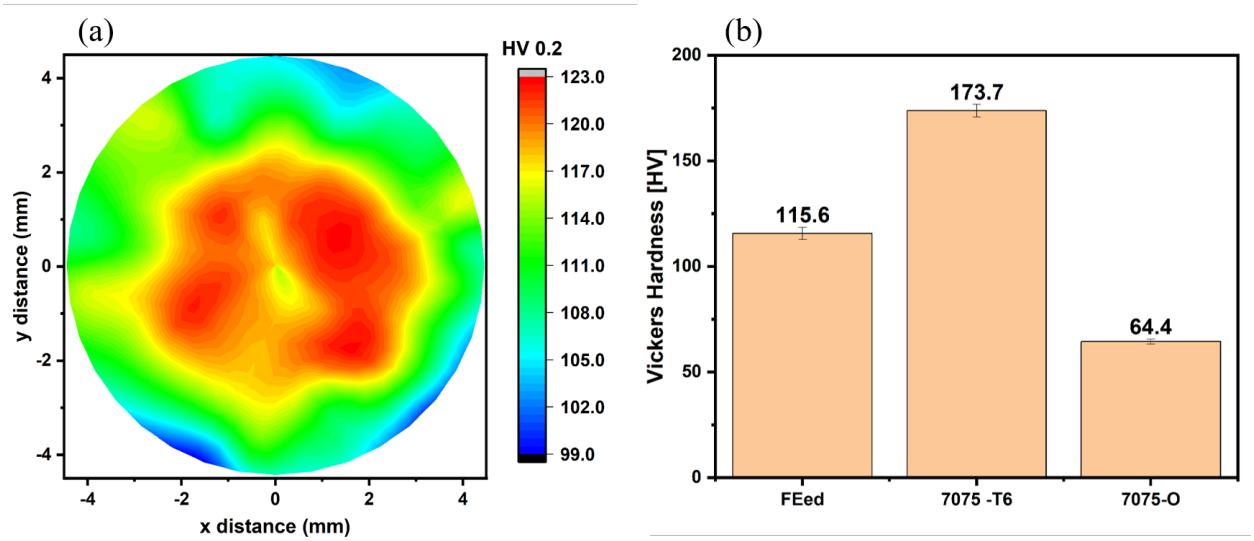

Fig. 5. Microhardness mapping of the cross-section for the extrudate (a) and comparison to the base material in different temper states.

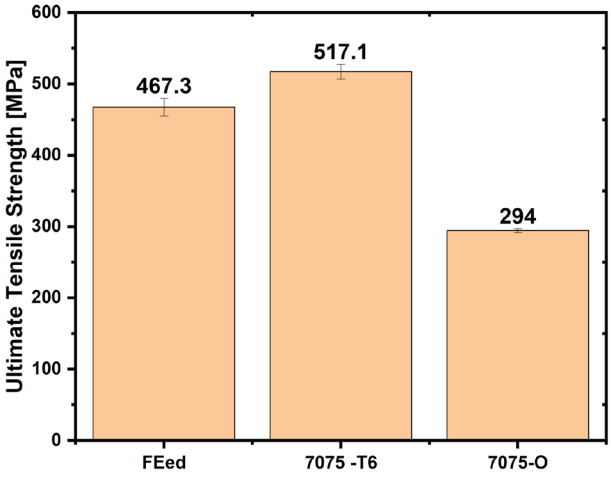

Fig. 6. Ultimate tensile strength for the extrudate and comparison to the base material in different temper states.

The UTS of the FE extrudate as well as for AA7075-T6 and AA7075-O is shown in Fig. 6. The extrudate UTS is 467.3 MPa, which shares the same trend as the microhardness, with 90 % of the T6 state and 59 % more than the annealed state. The recrystallization and the grain refinement enabled the improvement of the mechanical properties; however, the precipitate strengthening effect dictated the mechanical properties of 7075 alloys, and the further increase of UTS after artificial aging has been proven [18]. The UTS value is comparable to the FE from AA7075 solid billet feedstock [8, 18], indicating full consolidation of the powder during FE.

Summary

In the present study, friction extrusion based on powder material was investigated in terms of extrudate microstructure as well as powder evolution in front of the extrusion orifice. The fully consolidated wire was successfully extruded directly from the powder feedstock. Additionally, the mechanical properties of the final extrudate were analyzed. The main findings are summarized as follows:

- Fully consolidated wire with predominantly homogeneously distributed fine grains and no noticeable defects in the core is successfully extruded from powder feedstock without a complex powder metallurgy procedure. Larger grains and defects are observed at the periphery of the wire; hence, a cooling system has been planned to introduce to prevent the grain coarsening issue.
- The combination of pressure and elevated temperature leads to extensive porosity removal within the powder feedstock, followed by the elongation of powder particles in the extrusion direction as well as the elimination of powder boundaries finally forming the consolidated extrudate.
- Adequate mechanical properties without post-heat treatment, comparable results to extrusion from solid billet feedstock, and the potential to improve the properties by applying artificial aging are achieved and demonstrated.

Funding

This project has received funding from the European Research Council (ERC) under the European Union's Horizon 2020 research and innovation programme (grant agreement No 101001567).

Data Availability

The data related to this research will be made available online.

References

[1] W.M. Thomas, E.D. Nicholas and S.B. Jones, U.S. Patent 5,262,123. (1993).

[2] W. Tang, A.P. Reynolds, Production of wire via friction extrusion of aluminum alloy machining chips, J. Mater. Process. Technol. 210 (2010) 2231-2237. https://doi.org/10.1016/j.jmatprotec.2010.08.010

[3] G. Buffa, D. Campanella, L. Fratini, F. Micari, AZ31 magnesium alloy recycling through friction stir extrusion process, Int. J. Mater. Form. 9 (2016) 613-618. https://doi.org/10.1007/s12289-015-1247-6

[4] X. Li, N. Overman, T. Roosendaal, M. Olszta, C. Zhou, H. Wnag, T. Perry, J. Schroth, G. Grant, Microstructure and Mechanical Properties of Pure Copper Wire Produced by Shear Assisted Processing and Extrusion, JOM 71 (2019) 4799-4805. https://doi.org/10.1007/s11837-019-03752-w

[5] M.A. Ansari, R.A. Behnagh, M. Narvan, E.S. Naeini, M.K.B. Givi, H. Ding, Optimization of Friction Stir Extrusion (FSE) Parameters Through Taguchi Technique, Trans. Indian Inst. Met. 69 (2016) 1351-1357.

[6] D. Baffari, A.P.Reynolds, X. Li, L. Fratini, Influence of processing parameters and initial temper on Friction Stir Extrusion of 2050 aluminum alloy, J. Manuf. Process. 28 (2017) 319-325. https://doi.org/10.1016/j.jmapro.2017.06.013
[7] J.T. Darsell, N.R. Overman, V.V. Joshi, S.A. Whalen, S.N. Mathaudhu, Shear Assisted Processing and Extrusion (ShAPE™) of AZ91E Flake: A Study of Tooling Features and Processing Effects, J. Mater. Eng. Perform. 27 (2018) 4150-4161. https://doi.org/10.1007/s11665-018-3509-1
[8] R.M. Halak, L. Rath, U.F.H.R. Suhuddin, J.F. dos Santos, B. Klusemann, Changes in processing characteristics and microstructural evolution during friction extrusion of aluminum, Int. J. Mater. Form. 15 (2022) 24. https://doi.org/10.1007/s12289-022-01670-y
[9] S. Whalen, M. Olszta, C. Roach, J. Darsell, D. Graff, M. Reza-E-Rabby, T. Roosendaal, W. Daye, T. Pelletiers, S. Mathaudhu, N. Overman, High ductility aluminum alloy made from powder by friction extrusion, Materialia 6 (2019) 100260. https://doi.org/10.1016/j.mtla.2019.100260
[10] X. Li, T. Wang, X. Ma, N. Overman, S. Whalen, D. Herling, K. Kappagantula, Manufacture aluminum alloy tube from powder with a single-step extrusion via ShAPE, J. Manuf. Process. 80 (2022) 108-115. https://doi.org/10.1016/j.jmapro.2022.05.060
[11] X. Li, C. Zhou, N. Overman, X. Ma, N. Canfield, K. Kappagantula, J. Schroth, G. Grant, Copper carbon composite wire with a uniform carbon dispersion made by friction extrusion, J. Manuf. Process. 65 (2021) 397-406. https://doi.org/10.1016/j.jmapro.2021.03.055
[12] M. Komarasamy, X. Li, S.A. Whalen, X. Ma, N. Canfield, M.J. Olszta, T. Varga, A.L. Schemer-Kohrn, A. Yu, N.R. Overman, S.N. Mathaudhu, G.J. Grant, Microstructural evolution in Cu–Nb processed via friction consolidation, J. Mater. Sci. 56 (2021) 12864-12880. https://doi.org/10.1007/s10853-021-06093-9
[13] X. Li, M. Reza-E-Rabby, A. Guzman, G. Grant, S. Mathaudhu, M. Hinton, A. Reynolds, Strain and strain rate in friction extrusion, J. Mater. Res. Technol. 22 (2022) 882-893. https://doi.org/10.1016/j.jmrt.2022.07.116
[14] G.B. Schaffer, S.H. Huo, On development of sintered 7xxx series aluminium alloys, Powder Metall. 42 (1999) 219-226. https://doi.org/10.1179/003258999665558
[15] D. Baffari, G. Buffa, D. Campanella, L. Fratini, A.P. Reynolds, Process mechanics in Friction Stir Extrusion of magnesium alloys chips through experiments and numerical simulation, J. Manuf. Process. 29 (2017) 41-49. https://doi.org/10.1016/j.jmapro.2017.07.010
[16] M.R. Rokni, C.A. Widener, G.A. Crawford, Microstructural evolution of 7075 Al gas atomized powder and high-pressure cold sprayed deposition, Surf. Coat. Technol. 251 (2014) 254-263. https://doi.org/10.1016/j.surfcoat.2014.04.035
[17] A. Hadrboletz, B. Weiss, Fatigue behaviour of iron based sintered material: a review, Int. Mater. Rev. 42 (1997) 1-44. https://doi.org/10.1179/imr.1997.42.1.1
[18] R. Kalsar, X. Ma, J. Darsell, D. Zhang, K. Kappagantula, D.R. Herling, V.V. Joshi, Microstructure evolution, enhanced aging kinetics, and mechanical properties of AA7075 alloy after friction extrusion, Mater. Sci. Eng. A. 823 (2022) 142575. https://doi.org/10.1016/j.msea.2021.142575

Materials Research Proceedings 28 (2023) 523-532 https://doi.org/10.21741/9781644902479-57

Progression of plastic die deformation during copper extrusion

LECHNER Stefan[1,a *] and MÜLLER Sören[1,b]

[1]Extrusion Research & Development Center, Technische Universität Berlin, Gustav-Meyer-Allee 25, 13355 Berlin, Germany

[a]stefan.lechner@strangpressen.berlin, [b]soeren.mueller@tu-berlin.de

Keywords: Copper Extrusion, Plastic Die Deformation, 3D Scanning, Numerical Analysis

Abstract. In copper extrusion, the dies are continuously subjected to high thermo-mechanical stress. This results in elastic and plastic die deformation as well as extensive wear. To estimate the strain of possible hard phase surface modifications during service, knowledge of the deformation behavior of the extrusion dies is required. Therefore, the plastic deformation of dies made of four different tool materials was investigated in the present study. The applied tool materials were hot-work tool steel 1.2367, special hot-work tool steel CS1, nickel-based alloy 2.4668 (Alloy 718) and cobalt-based alloy 2.4775 (Stellite 1). 3D scans of the dies were created, both in the initial state and after each of three extrusion cycles, utilizing structured-light scanning. The extrusion trials were carried out using an 8MN extrusion press configured for direct extrusion and billets made of commercially pure copper Cu-DHP (CW024A). By evaluation of the 3D scans, the progression of plastic die deformation was determined in dependence on the tool material. Finally, the results were compared to corresponding numerical investigations on die deformation.

Introduction

In the product portfolio of copper extrusion plants, semi-finished products such as rods and tubes represent one of the largest items. The processing temperatures of copper-based alloys are usually in the range of 600-1050°C, which is why the extrusion tools are subjected to high thermo-mechanical stresses [1]. This results in elastic and plastic die deformation as well as extensive wear [2]. In order to counteract plastic tool deformation, high-temperature nickel- and cobalt-based alloys are used as tool materials in addition to the widely used hot-work tool steels [3]. One possible approach to reduce adhesive and abrasive wear is the application of hard phase surface modifications like coatings or diffusion layers [4]. These can offer good resistance to abrasion and adhesion due to their great hardness and possibly high chemical inertness [5]. However, some of these surface modifications also exhibit quite brittle deformation behavior, which entails the risk of cracking or ablation when the substrate is overly deformed.

To estimate the strain of the surface modifications during service, knowledge of the deformation behavior of the dies is required. For this purpose, tool deformation was investigated in a previous study by means of FEM-based numerical analyses [6]. In the present study, the extrusion dies were 3D scanned to determine the actual die deformation and to compare it with the results of the simulations. One die each made of the tool materials hot-work tool steel 1.2367, special hot-work tool steel CS1, nickel-based alloy 2.4668 (Alloy 718) and cobalt-based alloy 2.4775 (Stellite 1) was 3D scanned in the initial state and after each of three extrusion cycles using structured-light scanning. Evaluating the 3D scans, the progression of plastic die deformation was determined in dependence on the tool material. In conclusion, the experimental results were compared with those of the numerical investigations.

Content from this work may be used under the terms of the Creative Commons Attribution 3.0 license. Any further distribution of this work must maintain attribution to the author(s) and the title of the work, journal citation and DOI. Published under license by Materials Research Forum LLC.

Experimental Procedure

In order to investigate the plastic deformation behavior of dies during copper extrusion, a die was designed according to literature [1] and four pieces were manufactured using different tool materials. A CAD-model of the die design is given in Fig. 1. The applied tool materials were hot-work tool steel 1.2367, special hot-work tool steel CS1, nickel-based alloy 2.4668 (Alloy 718) and cobalt-based alloy 2.4775 (Stellite 1). Due to the low toughness of the cobalt-based alloy and the resulting high risk of cracking, an insert (Ø60 x 20 mm) was shrink fit into a holder made of 1.2367. Furthermore, all dies were equipped with a thermocouple to measure the profile exit temperature. Billets were prepared from copper alloy CW024A (Cu-DHP) and extrusion trials were carried out on the 8MN extrusion press of the Extrusion Research & Development Center. The extrusion press was configured in direct extrusion setup and the extrusion forces were recorded with integrated load cells. The applied extrusion parameters as well as die and billet dimensions are listed in Table 1.

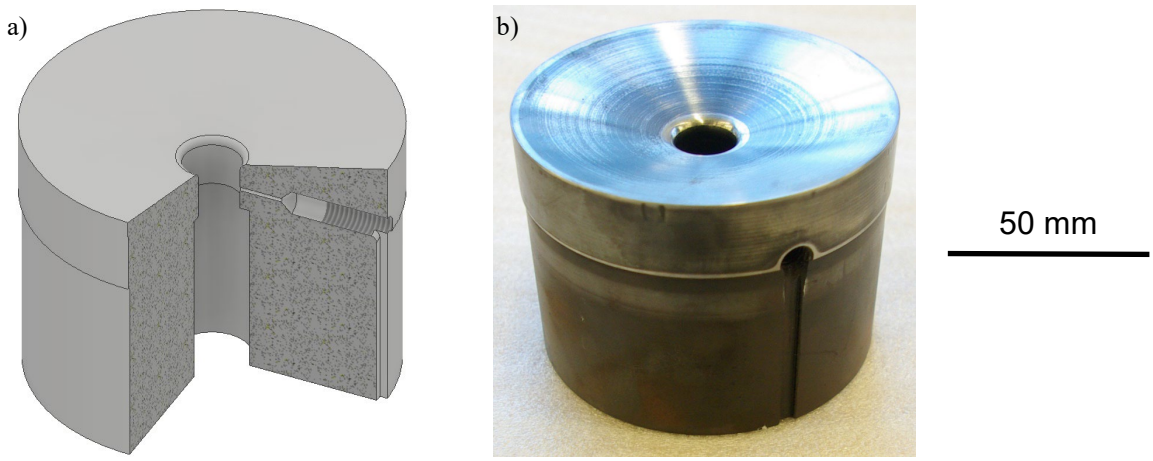

Fig. 1. Illustrations of the die geometry: a) CAD model and b) photograph.

Table 1. Die dimensions and extrusion parameters.

Semi die angle	Outer Diameter	Bearing channel diameter	Bearing channel length	Inlet radius
75°	95 mm	15 mm	10 mm	2 mm
Ram speed	Extrusion ratio	Billet temperature	Billet dimensions	Tool temperatures
20 mm/s	40.1 : 1	850 °C	Ø92 x 300 mm	500 °C

Structured-Light 3D Scanning.

The creation of virtual copies of the dies enables the study of the progression of plastic deformation and the comparison with numerical analyses. Therefore, the dies were scanned using an AICON smartSCAN-HE structured-light scanner. The test volume was 161 mm x 208 mm x 130 mm and with a test distance of 397 mm the resulting average distance between measuring points was 0.064 mm. To keep measurement time and data volume low, only the upper third of the dies, which contains the functional surface, was scanned (see Fig. 2, a). Each die was scanned in

the initial state to set a benchmark and after each of three extrusion cycles. Prior to each scan an anti-reflective coating was applied to the dies to avoid interfering reflections. The 3D scans generated surface meshes, which were imported in the software GOM Inspect 2019 for further analysis. In order to determine the plastic deformation of the dies after individual extrusion cycles, a scan of a die in its current state was superimposed on the scan of the initial state in each case (see Fig. 2, b). Using the local-best-fit function of the software and the thermocouple receptors as reference point, an accurate positioning of the two surface meshes was achieved. Subsequently, an area comparison was performed, in which the distance to the nearest point of the mesh in the current state is output for each point of the benchmark mesh (see Fig. 2, c).

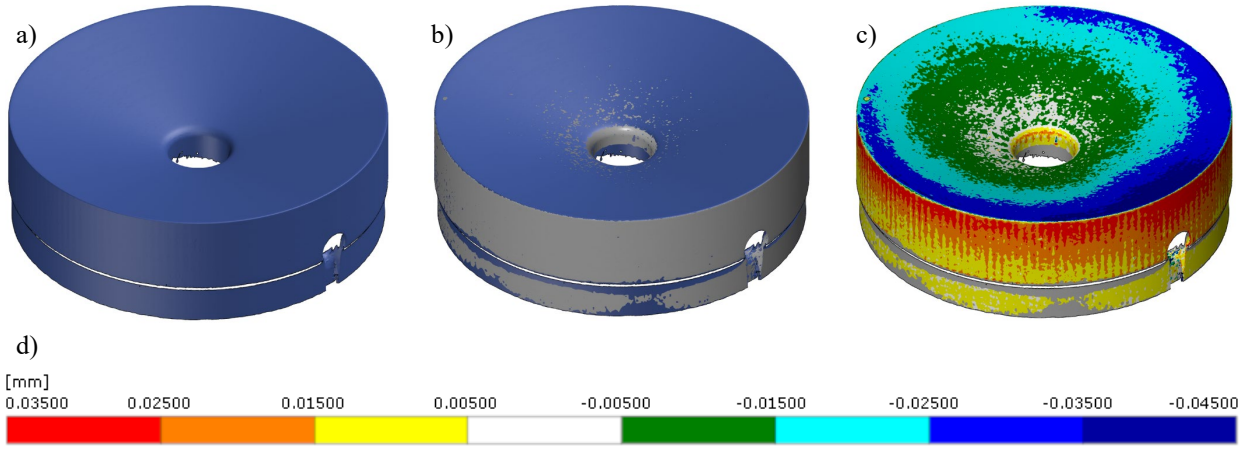

Fig. 2. Data processing sequence for the analysis of 3D scans: a) import of the generated surface mesh, b) superimposing two meshes from different states of the die, c) surface comparison of both meshes, and d) legend for surface comparisons.

Results and Discussion

Extrusion Trials and Structured-Light 3D Scanning.

As basis for the investigation of the progressive tool deformation, a reference scan was made of each of the four dies in their initial state. Subsequently, a total of twelve extrusion trials with consecutive 3D scans was carried out using the four dies made of different tool materials and performing three repetitions per die. On average, the maximum die force was 3.4MN and the highest temperature measured in the bearing channel was approximately 800 °C [6]. The results of surface comparisons of the die made of hot-work tool steel 1.2367 are presented in Fig. 3. Detail a) of Fig. 3 depicts the comparison between the benchmark scan and the state after the first extrusion cycle. Considering the lateral surface, an expansion of approx. 0.03 mm is observed. Since the dies were manufactured with an undersize of 0.25 mm with respect to the container bore, at least elastic expansion of the lateral surface is to be expected during the extrusion process. However, the measured expansion suggests that the yield strength of the material has been exceeded and plastic deformation has occurred. Corresponding to the radial expansion of the lateral surface, a significant lowering of the outer area of the conical face was observed (0.02-0.04 mm). This lowering diminishes towards the center of the die. Inlet radius and bearing channel also exhibit a plastic change in geometry. On average, a diameter reduction of approx. 0.02 mm and 0.01 mm is found at the radius and in the bearing channel, respectively. This deformation is due to an exceeding of the yield strength, considering the very high temperatures present in the bearing channel (superficially above 800°C). A more detailed discussion of the acting forces and resulting deformations is provided in a later section of this study by means of numerical investigations. The comparison between benchmark scan and the state after the second extrusion cycle is shown in

Fig. 3, b). No significant differences can be observed on the lateral surface compared to the state after the first extrusion cycle. There are two reasons for this. On the one hand, plastic deformation induces strain hardening at small strains, as is shown in Fig. 4. Thus, the stress required to cause further plastic deformation is higher than in the first extrusion cycle. However, since the process conditions and therefore the acting forces are approximately equivalent for all extrusion cycles, the stress present in the material is not sufficient to cause further plastic deformation. On the other hand, the deformation of the die in this area is geometrically limited by the inner diameter of the container bore. At the inlet radius and bearing channel, a slight diameter enlargement was measured. This does not correspond to the expected material behavior, since an increase in plastic deformation is to be expected due to the high temperatures and stresses. One possible explanation is the mechanical post-processing of the dies functional surfaces in preparation for the respective 3D scan. Due to the strong adhesion of copper to the die materials, it was necessary to remove adhering copper and lubricant residues (graphite-based) using fine sandpaper and polishing fleece. A slight removal of tool material could not be completely avoided. Following the third extrusion cycle, this phenomenon can also be observed on the lateral surface of the die (see Fig. 3, c). In the area of the bearing channel, in turn, a significant increase in plastic deformation and thus reduction of diameter was measured. This amounts to approx. 0.02-0.03 mm after three extrusion cycles.

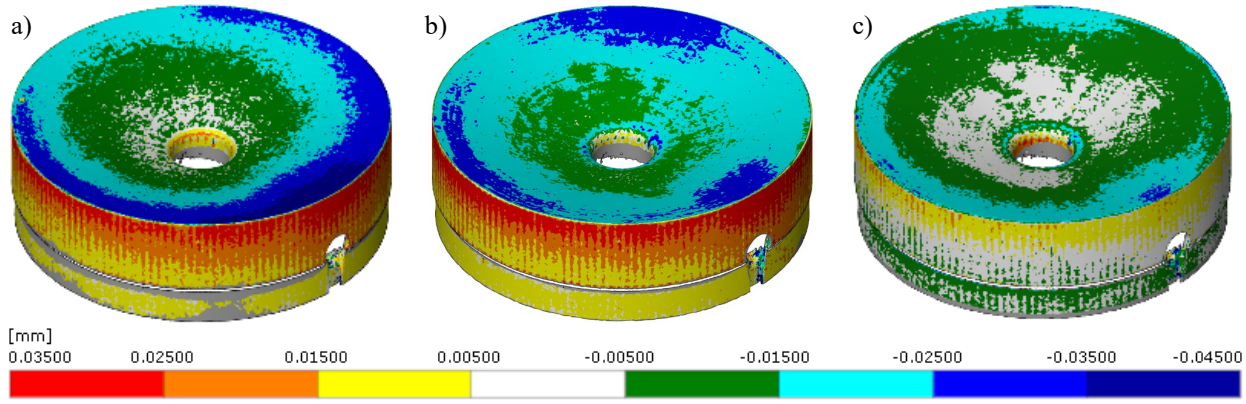

Fig. 3. Surface comparisons for the die made of hot-work tool steel 1.2367 in different states: a) after one, b) after two, and c) after three extrusion cycles.

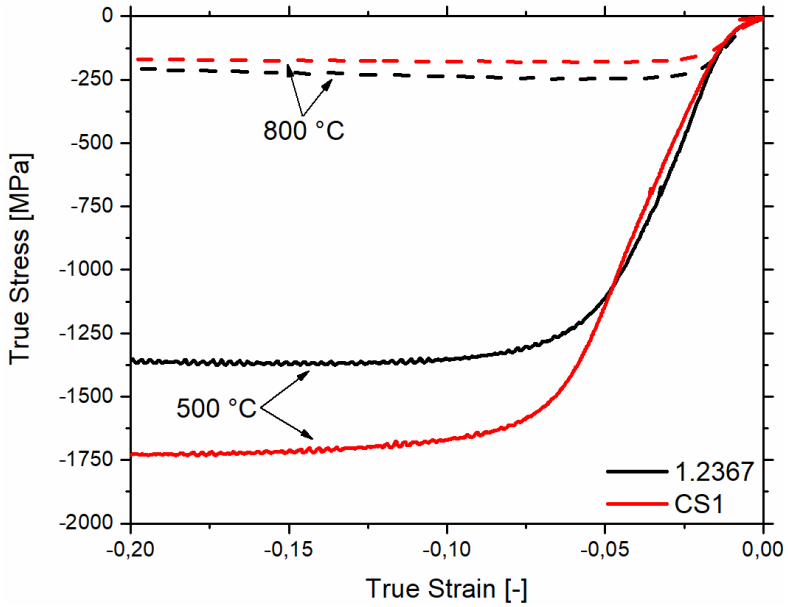

Fig. 4. True stress-true strain curves of hot-work tool steel 1.2367 and special hot-work tool steel CS1 at 500°C and 800°C, obtained by means of hot compression tests at a strain rate of 0.005 s^{-1} [6].

Compared to the hot-work tool steel 1.2367 shown so far, the lateral surface of the die made of special hot-work tool steel CS1 does not expand to any significant extent (see Fig. 5). This is due to the elevated hot strength of CS1 in the temperature range of 500-650°C (see Fig. 4). The slight decrease in lateral surface diameter can be explained, analogously to the die made of 1.2367, by the mechanical post-processing for cleaning the die. In the bearing channel, on the other hand, a strong increase in plastic deformation with the number of extrusion cycles is seen. As a result of the reduced hot strength at temperatures above 750°C, significantly greater deformation occurs in the vicinity of the inlet radius and bearing channel than with hot-work tool steel 1.2367. At the inlet radius, a mean lowering of 0.01-0.02 mm (1st cycle), 0.04 mm (2nd cycle) and 0.04-0.06 mm (3rd cycle) was observed. In the bearing channel, the diameter reduction after the first cycle is 0.01-0.02 mm on average with a local peak of 0.04 mm, followed by 0.02-0.04 mm (2nd cycle) and 0.05-0.06 mm (3rd cycle).

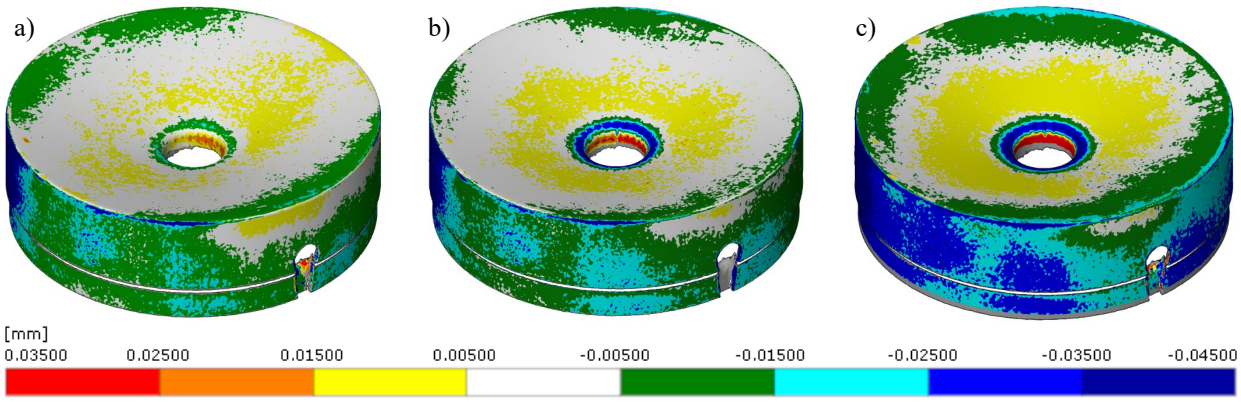

Fig. 5. Surface comparisons for the die made of special hot-work tool steel CS1 in different states: a) after one, b) after two, and c) after three extrusion cycles.

Materials Research Proceedings 28 (2023) 523-532 https://doi.org/10.21741/9781644902479-57

In contrast to the two hot-work tool steels investigated, the die made of the nickel-based alloy 2.4668 (Alloy 718) shows only very slight plastic deformation overall. As shown in Fig. 6, no remarkable increase in plastic deformation is observed over three extrusion cycles. The evaluation of the 3D scans showed only a diameter reduction of up to 0.02 mm in the bearing channel. At this point, the excellent high-temperature properties of the nickel-base alloy become apparent [7]. Due to almost invariant high-temperature strength up to temperatures of 700°C [6] and the work hardening occurring in the area of the inlet radius and bearing channel, the unchanged process conditions of the three extrusion cycles do not lead to any significant change in die geometry.

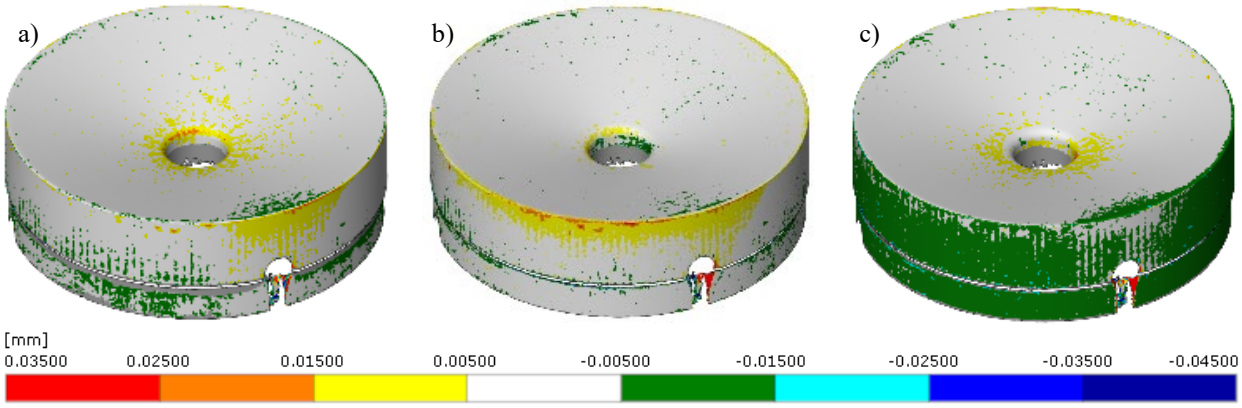

Fig. 6. Surface comparisons for the die made of nickel-based alloy 2.4668 in different states: a) after one, b) after two, and c) after three extrusion cycles.

The surface comparisons for the die made of cobalt-based alloy 2.4775 are shown in Fig. 7. With regard to the use of an insert in combination with a tool holder, there are some distinctive features to be considered when evaluating the 3D scans of this die. Since the shrink-fit of the insert was realized only by insertion and not by pressing, setting of the insert occurred during the first extrusion cycle. As the relative positioning of insert and tool holder no longer corresponds to the benchmark, the alignment of the surface meshes in the evaluation was carried out taking only the insert into account. Therefore, a strong displacement results for the tool holder, as can be seen in Fig. 7. The asymmetry of this displacement suggests that the insert was slightly tilted relative to the holder either in its initial state or after setting. For the insert a lowering of the conical face by 0.01 mm was detected in proximity to the tool holder. Furthermore, a large-area and uniform lifting of the area around the inlet radius by 0.01 mm, and a diameter reduction of the bearing channel by 0.01 mm were measured (see Fig. 7, a). These dimensional alterations remained unchanged over the course of the further extrusion cycles (see Fig. 7, b and c). Due to the excellent hot strength of the cobalt-based alloy [3], no measurable plastic deformation was expected in the material under the stresses and temperatures encountered. Rather, it is suspected that due to an inaccurately manufactured fit in the tool holder, the insert experienced a bending during setting, causing the outer area to lower and the area close to the center to raise.

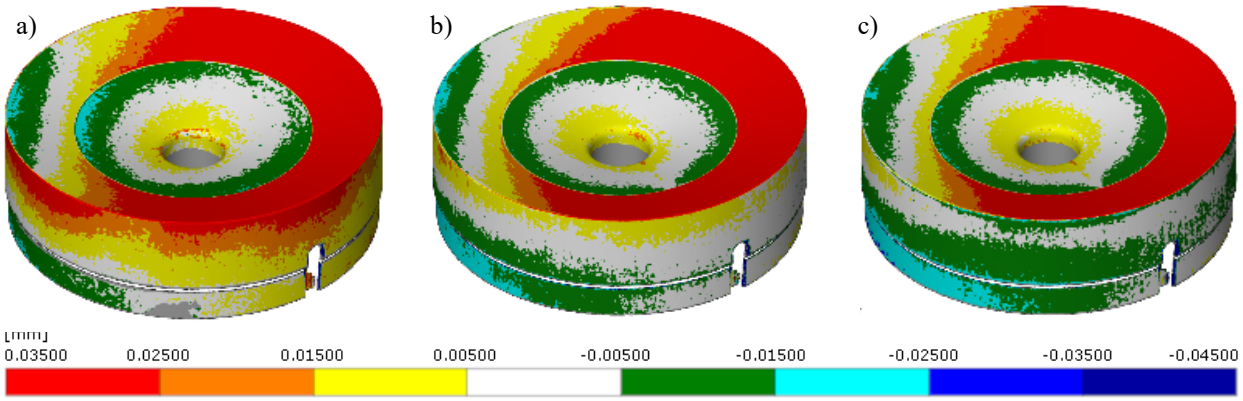

Fig. 7. Surface comparisons for the die made of cobalt-based alloy 2.4775 in different states: a) after one, b) after two, and c) after three extrusion cycles.

Comparison of Experimentally and Numerically Obtained Die Deformation Data.

In parallel to the extrusion trials, FE analyses were carried out in order to numerically model the die deformation. For this purpose, the FE-software DEFORM 2D was used and a rotationally symmetric model was built. The visco-plastic deformation behavior of copper was modeled using flow stress data gained by means of hot compression tests. In the first step of the FE analysis, which represents the extrusion process, the dies were modeled rigid. In the subsequently performed decoupled die stress analysis, elasto-plastic models were implemented to describe the material behavior of the different die materials. The identification of the required flow behavior of the tool and billet materials as well as model design and verification are described in detail in [6]. Since only very small deformations in the range of a few microns are predicted for the two tools made of 2.4668 and 2.4775, solely the two hot-work tool steels investigated will be discussed below. Fig. 8 and 9 illustrate the deformation of the dies estimated by the numerical analyses. The contour of the die in the initial state is represented by the green line and the deflection of the bulk material (magenta) has been scaled up by a factor of 10 for better visualization. The displacement after the third extrusion cycle is indicated by vectors. Fig. 8, b) and c) depict the total displacement at the edge between lateral surface and outer perimeter of the conical face. Analogous to the 3D scans of the extrusion dies, the simulation predicts a significantly pronounced plastic deformation of the hot work tool steel 1.2367 (0.017 mm) compared to CS1 (0.006 mm). While the value for 1.2367 is underestimated by about 40%, simulation and 3D scans match for CS1.

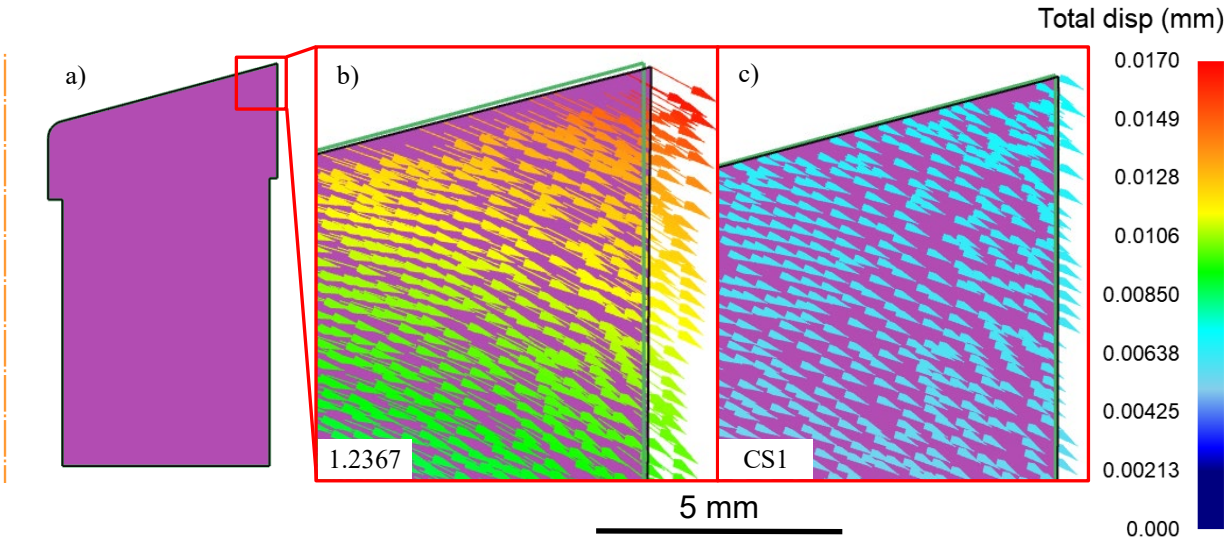

Fig. 8. a) 2D FE-Model of the extrusion die and estimated totals displacement at the lateral surface after three extrusion cycles for the use of b) hot-work tool steel 1.2367 and c) special hot-work tool steel CS1.

Fig. 9, b) and c) show the absolute displacement of the die material in proximity to the inlet radius and bearing channel. For hot-work tool steel 1.2367, the estimated lowering is approx. 0.02 mm. The diameter reduction of the bearing channel by 3 microns is negligible. This again reveals a considerable underestimation of deformation by the numerical model, since the measured diameter reduction was 0.02-0.03 mm. The same applies for CS1, which is estimated to have both a major lowering of the inlet radius (0.035 mm), and a noticeable diameter reduction of the bearing channel (0.016 mm). These values are again underestimated by up to 40% and 70%, respectively. One reason for the inaccuracy of the simulation is the underlying simplicity of the elasto-plastic material model chosen, since neither creep nor fatigue phenomena are taken into account.

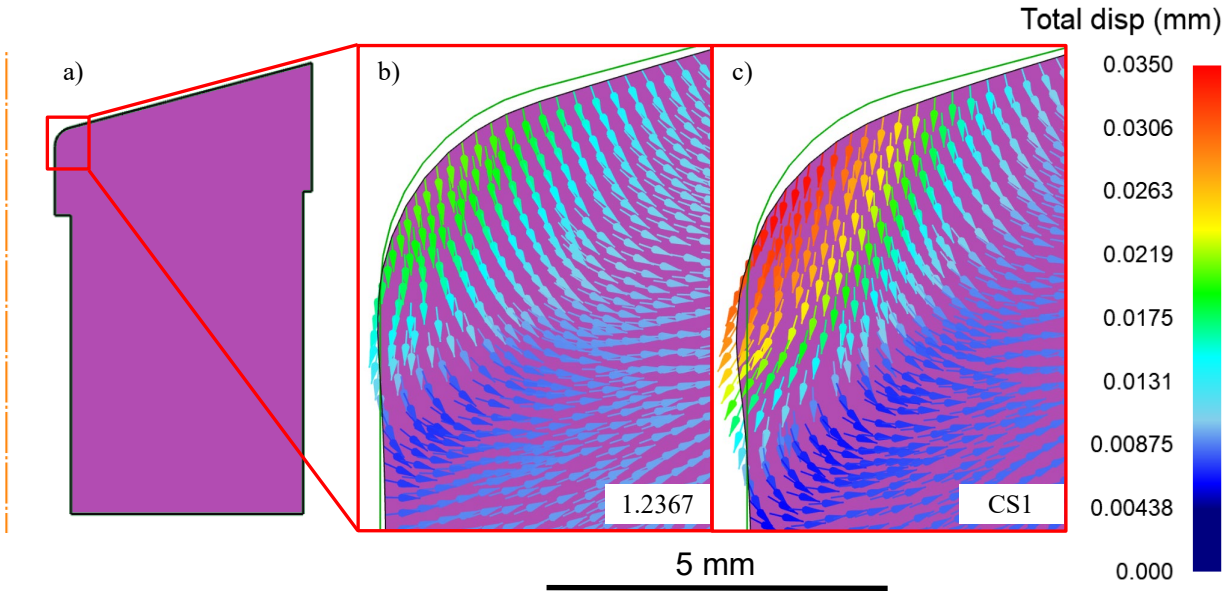

Fig. 9. a) FE-Model of the extrusion die and estimated totals displacement at the inlet radius after three extrusion cycles for the use of b) hot-work tool steel 1.2367 and c) special hot-work tool steel CS1.

The cause of the observed displacements are pressure differences in the extruded material. As illustrated in Fig. 10, the normal pressure acting on the die decreases from the conical face towards the bearing channel. Consequently, stress states are created in the die material which, if sufficiently intense, cause a plastic material displacement in extrusion direction and towards the die center. This effect is more pronounced for the special hot-work tool steel CS1, since its yield strength at temperatures above 750°C is lower than that of 1.2367 (see Fig. 4). At lower temperatures, strain-induced hardening would counteract the increasing plastic deformation as the yield strength shifts to higher stresses under repeated loading [8]. However, in the case of high temperatures, softening mechanisms take effect that counteract strain-induced hardening and prevent a significant increase in yield strength. Therefore, further plastic deformation occurs upon re-loading.

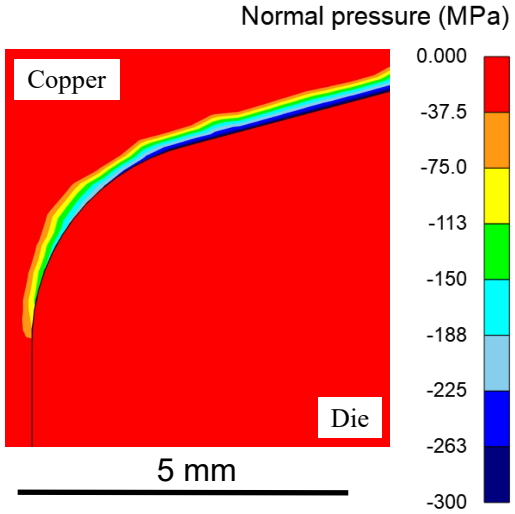

Fig. 10. Normal pressure acting on the die surface in proximity to the inlet radius.

Summary

For the purpose of studying the progression of plastic die deformation during copper extrusion, trials with dies made of four different tool materials were performed. Geometric measurement of the dies was conducted before and after each of three extrusion cycles using 3D structured-light scanning. The evaluation of the scans and the comparison with numerical investigations resulted in the following findings:

- Due to their limited hot strength in the temperature range above 600 °C, the hot-work tool steels investigated are subject to significant plastic deformation that progresses with the number of extrusion cycles.
- Both the nickel- and cobalt-based alloy exhibit very little plastic deformation, irrespective of the number of pressing cycles.
- The results of the numerical investigations indicate a very good agreement with the 3D scans. Both the direction of the displacement and the influence of the tool material can be reproduced accurately by the simulation. However, with the given material models, the absolute values of displacement are underestimated by the simulation.

References

[1] M. Bauser, G. Sauer, K. Siegert, Strangpressen: Aluminium Fachbuchreihe, Aluminium-Verlag, Düsseldorf, 2001.

[2] M. Schwartz, R. Ciocoiu, D. Gheorghe, I. Ciuca, Failures of AISI H21 die in copper hot extrusion, Mater. High Temp. 31 (2014) 95-101. https://doi.org/10.1179/1878641313Y.0000000001

[3] W. Kortman, Warmarbeitswerkstoffe für Strangpressmatrizen in der Buntmetallverarbeitung, in: H. Gers (Ed.), Strangpressen, Wiley-VCH Verlag, Weinheim, 2007, pp. 17-32. https://doi.org/10.1002/9783527610235.ch3

[4] B.A. Behrens, G. Bräuer, H. Paschke, M. Bistron, Reduction of wear at hot forging dies by using coating systems containing boron, Prod. Eng. Res. Devel. 5 (2011) 497-506. https://doi.org/10.1007/s11740-011-0308-z

[5] J. Lin, J.J. Moore, B. Mishra, M. Pinkas, W.D. Sproul, The structure and mechanical and tribological properties of TIBCN nanocomposite coatings, Acta Mater. 58 (2010) 1554-1564. https://doi.org/10.1016/j.actamat.2009.10.063

[6] S. Lechner, R. Nitschke, S. Müller, Numerical analysis of plastic die deformation during high temperature copper extrusion, ESAFORM 2021, 24th International Conference on Material Forming (2021), Liège, Belgique. https://doi.org:10.25518/esaform21.4785

[7] K. Müller, Fundamentals of Extrusion Technology, Giesel Verlag GmbH, Isernhagen, 2004.

[8] K. Lange, Umformtechnik - Handbuch für Industrie und Wissenschaft, Part 1: Grundlangen, second ed., Springer, Berlin, 1984.

Materials Research Proceedings 28 (2023) 533-542 https://doi.org/10.21741/9781644902479-58

Investigation on the topological optimization of cooling channels for extrusion dies

PELACCIA Riccardo[1,a *], REGGIANI Barbara[1,b], NEGOZIO Marco[2,c], DI DONATO Sara[2,d], DONATI Lorenzo[2,e]

[1]DISMI – Department of Science and Methods for Engineer, Viale G. Amendola 2, 42122, Reggio Emilia (RE), Italy

[2] DIN- Department of Industrial Engineering, University of Bologna, Viale Risorgimento 2, 40136, Bologna, Italy

[a]riccardo.pelaccia@unimore.it; [b]barbara.reggiani@unimore.it; [c]marco.negozio2@unibo.it; [d]sara.didonato2@unibo.it; [e]l.donati@unibo.it

Keywords: Topological Optimization, Cooling Channels, Liquid Nitrogen, Extrusion, Dies

Abstract. During the extrusion process, high temperatures are generated, due to friction and deformation works, potentially leading to profile and die defects. Among the suggested solutions aimed at controlling the thermal field of the process, the most accredited one involves the manufacturing of cooling channels at the mating face between the die and a third plate. Despite the proven efficiency of well-designed channels, the main drawback lies in the managing of the many variables involved that strongly affect the cooling efficiency and balancing. In this frame, aim of the work is to investigate the applicability of the topological optimization tool, proposed by COMSOL Multiphysics software, for the design of cooling channels in extrusion dies. To validate the tool, an industrial case study has been selected and results compared between not optimized and optimized cooling solutions.

Introduction

Temperatures developed during the hot extrusion of industrial aluminum profiles are frequently nearby critical thresholds that can be detrimental for the profile quality, the die lifetime and the overall productivity [1]. To face the issue, one of the most efficient solution lies in the flowing of liquid nitrogen in a channel milled and drilled in the mating surface between the die and a third plate, the backer, incorporated in the tooling set as support to limit the die deflections [2]. Even if the use of nitrogen nowadays represents a consolidated industrial practice due to its proved efficiency [3,4], the channel design still represents a challenge due to the many variables involved, strongly affecting the fluid-dynamic and thermal performances of the nitrogen flow [5]. To date, nitrogen cooling channels are still designed based on die makers experience and their effectiveness judged merely by observing the out coming profile, a practice motivated by the complexity and cost of a continuous experimental monitoring of cooling efficiency: a glossy surface states a good design, a matt one a poor design. However, the surface appearance is mostly related to the gaseous nitrogen flowing from the channel' outlets that creates an inert atmosphere around the profile reducing oxidation, rather than to the overall channel performances. Nevertheless, this drawback can be overcome by the adoption of reliable numerical models at the process and channel design stage able to return continuous maps, in space and time, of all the parameters required to properly judge the selected solution. In addition, the level of complexity force not only through numerical approaches, but also demands for automated, robust and comprehensive methodologies.

If many works have been reported on aluminum extrusion FE (Finite Element) modelling [6,7], stating the robustness and reliability of the approach, only recently Reggiani and Donati [8], and Pelaccia et al. [9,10] proposed a comprehensive numerical model for the prediction of the thermal

Content from this work may be used under the terms of the Creative Commons Attribution 3.0 license. Any further distribution of this work must maintain attribution to the author(s) and the title of the work, journal citation and DOI. Published under license by Materials Research Forum LLC.

gradient during the extrusion process with nitrogen cooling. In addition, very promising results have already been achieved, by the same authors, by integrating the comprehensive FE model in an optimization platform able to change the channel sections iteratively and automatically along the path [11]. However, the main limitation of the procedure lies in leaving the optimizer free to vary only the cross-sections point by point, but not the path. More challenging and ambitious is the topological optimization applied to cooling channels that allows to attain any path within the design space, instead of dealing with a predefined configuration.

Currently, topological optimization is widely used in many engineering applications at the concept level of a design process, including the optimization of cooling channels in injection molds [12] and stamping tools [13]. However, to the best of the authors knowledge, a free-shape topological optimization has never been applied for the design of cooling channels in extrusion dies, thus motivating the proposed work.

Therefore, in this context, an industrial case study previously investigated [10] has been selected to present and validate the approach. The process parameters and the experimental settings were selected as input for the subsequently numerical analysis. The original channel design, merely based on the die-maker expertise without the support of the simulation, was compared in terms of cooling efficiency with the new one designed using the numerical approach based on topological optimization.

Experimental Analysis

The Fig. 1 shows the tooling set composed by the mandrel, die and backer [10]. The mandrel with five portholes was designed to obtain the industrial hollow profile shown in Fig. 2a, while a planar cooling channel was manufactured in the backer surface in contact with the die (Fig. 1c).

a) b) c)

Fig. 1. The tooling set: a) mandrel; b) die; c) backer with the cooling channel [10].

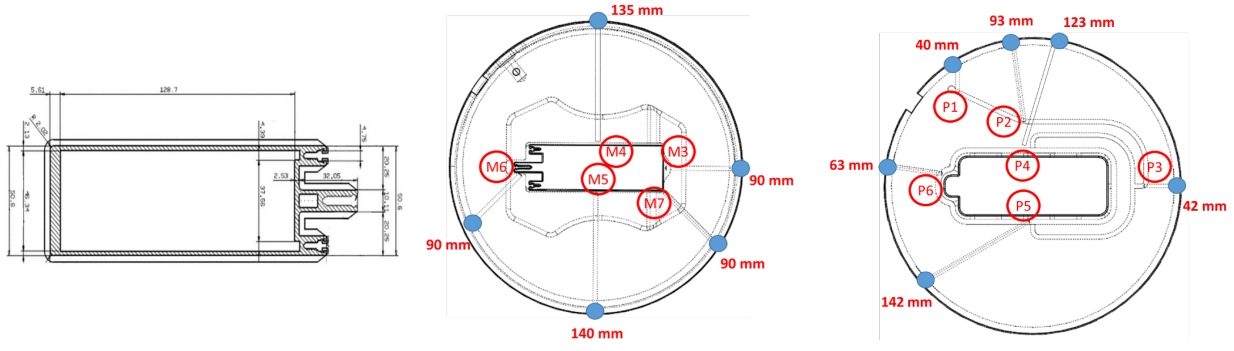

a) b) c)

Fig. 2. a) Profile drawing, b) thermocouple locations in the die, c) thermocouple locations in the backer; dimensions in millimetres report the acquired depths of the thermocouple holes [10].

Eleven thermocouples were positioned within the tooling set (Figs. 2b and 2c) in order to monitor the temperature field during the whole extrusion process. Five thermocouples were placed in the die around the bearings where the highest temperatures were generated (M7 was broken during the trials), six in the backer by following the nitrogen path with the aim to evaluate the cooling channel performances. The experimental campaign consisted in the extrusion of seventeen AA6060 billets in different conditions of extrusion speed and nitrogen flow rate. In detail, four different conditions were evaluated, excluding the first billet used to warm up the tooling set: the extrusion process without nitrogen cooling using the standard ram speed of 8 mm/s selected by the extruder (billets 2-4), the extrusion process with nitrogen valve opened at 40% maintaining the standard ram speed (billets 5-8), the extrusion process with nitrogen valve fully opened maintaining the standard ram speed (billets 9-12) and the extrusion process at increased ram speed of 50% (12 mm/s) by continuing to use the maximum nitrogen flow rate (billets 13-17). The thermal history of the tooling set recorded by the thermocouples is reported in Fig. 3. At first, it is worth nothing the temperature difference of about 200°C already in the uncooled condition between the cooling channel plane and the bearings, a trend that highlights the great distance between the cooling channel and the area where the highest amount of heat is developed. In the die, the thermal field showed a rapid rise in temperature in all thermocouples during the extrusion of each billet and a subsequent temperature decrease during the dwell time for the billet change. On the other hand, the heat exchange between the hot die and the less warm backer made more stable the temperatures in the backer, showing minimal differences between the extrusion phase and the billet phase change.

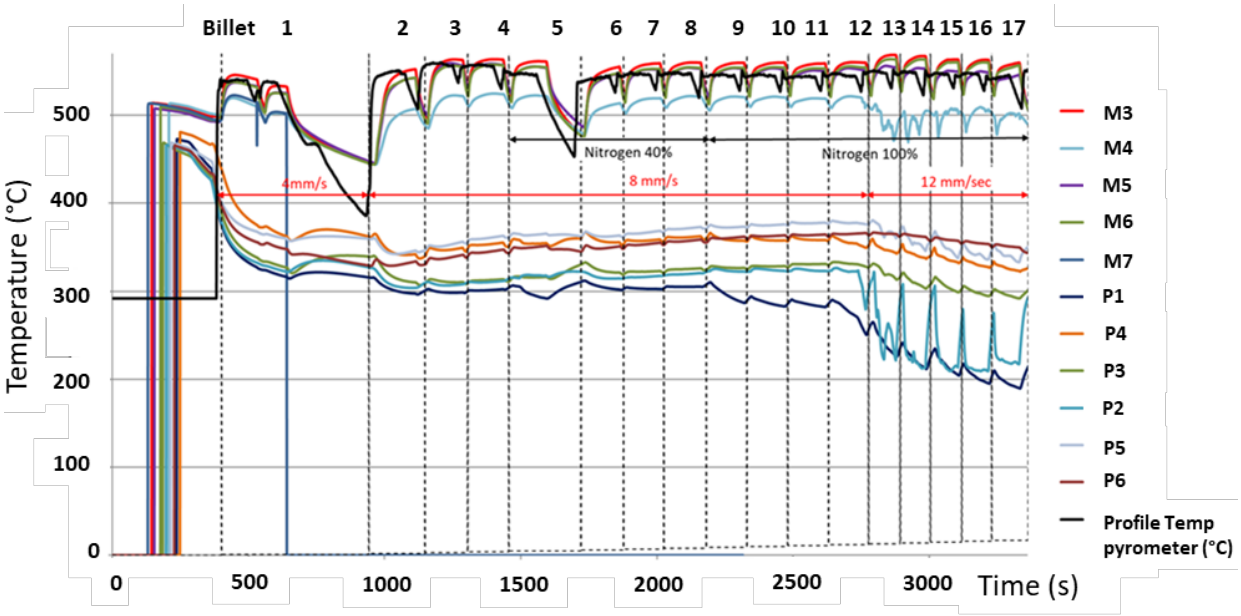

Fig. 3. Temperature history of the whole extrusion process [10].

By analyzing in detail the thermal history of the fourth billet (steady-state uncooled condition), it was detected the highest value of 565 °C in the bearings recorded by thermocouple M3, positioned closer to the short side of the profile without wings (Fig. 2b). Moreover, the thermocouples M6 and M5, positioned respectively near the wings and at the center of the lower side, acquired the same maximum temperature of 560 °C. The lowest temperature of 525°C was recorded by M4, located at the center of the upper side. In the backer, the lowest temperatures of 300°C and 311 °C were registered by the thermocouples P1 and P2 respectively, located along the initial portion of the cooling path. Thermocouples P3, P4, P5 and P6 were positioned in the die

and recorded temperatures of 313 °C, 355 °C, 360 °C and 345 °C, respectively. Notably, the higher radial distance of thermocouples P1-P3 than thermocouples P4-P6 from the profile exit was the cause of their temperature' differences.

Starting from the thermal field of the fourth extrusion, it is immediately clear the inefficiency of the cooling channel design since not significant change in temperatures was found both in the backer and in the die when the nitrogen valve was opened at 40% (billets 5-8). The same trend was obtained in the die from the ninth to the twelfth extrusion when the maximum nitrogen valve was used. Also during the last extrusion, after eight billets extruded with nitrogen cooling, the heat removal in the die had a limited effect visible only in the thermocouple M4 (from 525 °C of the uncooled condition to 505°C). When the nitrogen valve was opened at 40%, the combination of high-pressure drops induced by the channel design and the high thermal gradient between the nitrogen and the tooling set caused a formation of a large amount of gas nitrogen that congested the nitrogen flow within the channel (an increase of volume of 177 times occurs during the phase change). In addition, the selected channel design did not promote the gas purging, thus limiting the liquid nitrogen flow with a long transitory also when the nitrogen valve was fully opened (effective cooling only in P1 and P2 nearby the nitrogen inlet). Therefore, the experimental campaigns showed the limits of the selected channel design and confirmed the issues that can occur using a design approach based only on the experience. In the next paragraphs, after the validation of the numerical model of the extrusion process with nitrogen cooling, a first attempt of new design approach based on the topological optimization of the cooling channel is proposed and deeply assessed.

Numerical Model of Extrusion Process with Nitrogen Cooling

A full comprehensive numerical model of the extrusion process was implemented in the COMSOL Multiphysics code by modelling the extrusion process with a pure Eulerian approach. Therefore, the geometry of the material flow was in the already deformed configuration (Fig. 4a), the tooling set was merged into one solid tool to avoid the contact analysis, while the ram and the container, required only for a Lagrangian approach, were replaced by proper thermal and frictional boundary conditions. The cooling channel was replaced with a 1D cooling path that follows the middle line path of the real 3D channel and integrated within the 3D model of the tooling set (Fig. 4b). The numerical approach based on the 1D modelling of the nitrogen cooling was tested and validated in different previous works of the authors [8-11], proving the good accuracy of the achieved results at very reduced computational time if compared to the approach based on a full 3D model of the nitrogen flow. In this work, the accuracy of the numerical model was demonstrated by analyzing, in terms of temperature prediction, the experimental-numerical differences in both uncooled and cooled conditions.

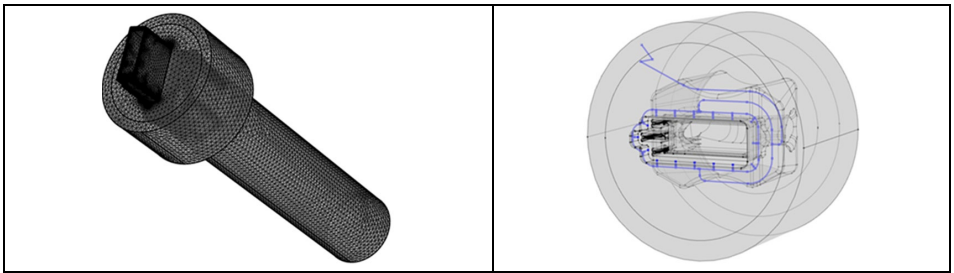

Fig. 4. The 3D model for the simulations: a) the billet and the die set, b) the tooling set combined with the 1D cooling channel.

Table 1. Process Parameters set in the comprehensive stationary simulations of the extrusion process.

Process Parameters	Billet 4	Billet 17
Billet Temperature	480 [°C]	480 [°C]
Die Temperature	520 [°C]	Starts from steady state uncooled simulation
Container Temperature	430 °C	Starts from steady state uncooled simulation
Ram Temperature	440 °C	Starts from steady state uncooled simulation
Temperature of backer surfaces in contact with press	280 °C	280°C
Ram Speed	8 [mm/s]	12 [mm/s]
Inlet Nitrogen Pressure		4.5 [bar]
Inlet Nitrogen Temperature		-196 [°C]

The numerical uncooled condition was compared with the fourth extrusion, while the stationary numerical analysis of the cooled condition was compared with the last extrusion where it was experimentally found a visible cooling effect in the tooling set. In Table 1 are reported the main parameters required to prepare the steady state 3D simulations of the extrusion process integrated with the 1D model of the cooling channel. About the nitrogen cooling, a model based on the Homogenous Flow approach [14] was implemented that allows to predict the pressure drops and the cooling channel inefficiency caused by the gas formation however avoiding the effective simulation of the phase change. Indeed, the physical properties of nitrogen (dynamic viscosity, density, heat transfer coefficient etc.) were replaced with expressions that depends on the nitrogen vapor title ω_g, not set constant but as a function of the heat exchange within the channel. The details about the model were presented and deeply discussed elsewhere [14]. Figure 5 shows the numerical comparison of the thermal field between the uncooled (billet 4) and the cooled (billet 17) conditions in the die and in the mandrel, specifically in the planes where the thermocouples were positioned. It is immediately clear that the simulation properly predicted the inefficiency of the cooling channel designed by the die maker: not significantly differences in temperature were obtained in the die, while the small cooling effect in the backer was localized at the entrance of the cooling channel nearby the thermocouples P1 and P2, confirming the experimental evidence.

In detail, Table 2 reports the experimental-numerical comparison in terms of thermocouple's temperature in the backer. Except for P2 and P4, the average numerical errors were below the 5%, thus confirming the accuracy of the implemented model and its capability to predict the cooling efficiency induced by the channel design and the nitrogen gas formation. In this way, the numerical testing of the cooling channel designed with the support of the topological optimization can be considered as trustworthy even in absence of an experimental testing.

Table 2. Thermocouple temperatures in the backer: Experimental vs Numerical results (Billet 4 and Billet 17).

	Thermocouples Temperature [°C]					
Billet 4	**P1**	**P2**	**P3**	**P4**	**P5**	**P6**
Experimental	300	311	313	355	360	345
Numerical	313	357	327	366	366	341
Err%	+4.3%	+14.8%	+4.5%	+3.1%	+1.7%	-1.2%
Billet 17	**P1**	**P2**	**P3**	**P4**	**P5**	**P6**
Experimental	196	219	296	326	340	350
HFM numerical	205	210	298	260	355	335
%Err	+4.6%	-4.1%	-1%	-20.4%	+4.4%	-4.3%

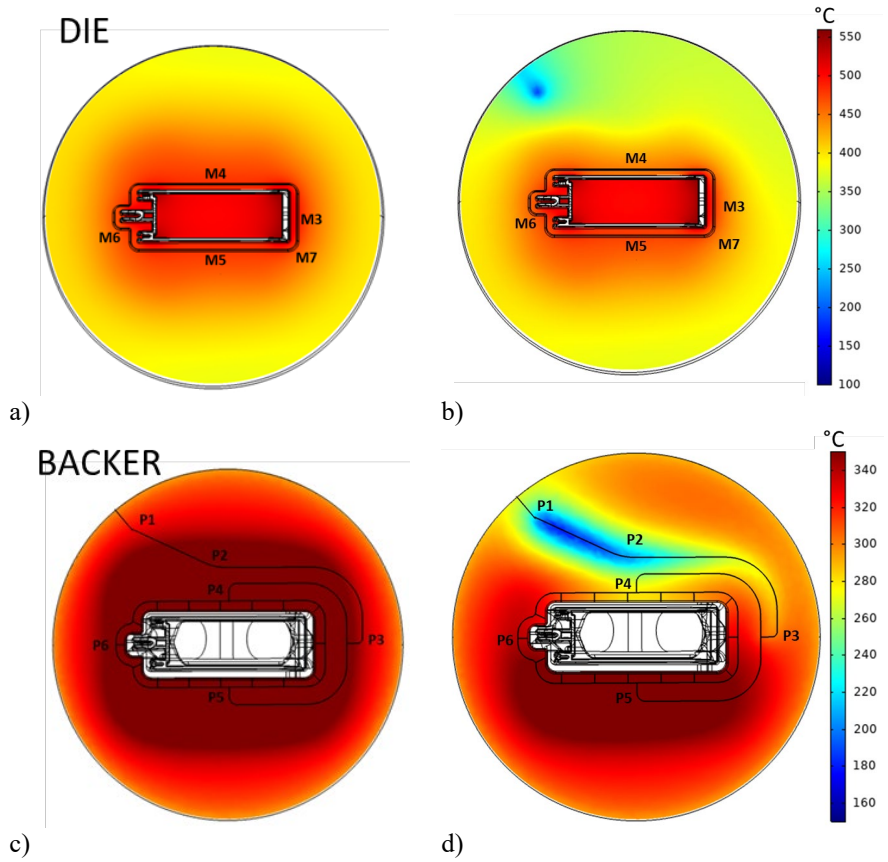

Fig. 5. Thermal maps in steady state condition: a) Uncooled Die (billet 4), b) Cooled Die (billet 17), c) Uncooled Backer, d) Cooled Backer.

Topological Optimization

For the topological optimization of the cooling channel, only the backer surface was modelled (Fig. 6a) allowing the tool to "virtually milled" it by the nitrogen flow in order to satisfy the selected objective functions. In the topological optimization approach based on the density method [15], the nitrogen flow was modelled using the Darcy flow model in order to treat the backer as a porous media with the porosity and the other physical properties controlled with penalization functions [15]. Following this approach, the elements of the mesh with the porosity equal to zero were considered as solid with the physical properties of the steel, while the elements with porosity equal to one were treated as liquid nitrogen. The density approach was controlled by the output material volume factor θ having the following expression:

$$\theta = \frac{(\tanh(\beta(\theta_f - \theta_\beta)) + \tanh(\beta\theta_\beta))}{(\tanh(\beta(\theta_f - \theta_\beta)) + \tanh(\beta\theta_\beta))} \quad (1)$$

where θ_f is the filtered material volume factor, β the slope and θ_β the projection point. When θ was equal to one the material was considered liquid; on the contrary, it was considered solid with a zero value. The slope and the projection point were calibrated to control the interpolation through intermediate values (set equal to 1 and 0.5, respectively). The interpolation was then constructed such that the physical governing equations of fluid flow were solved wherever the control variable was equal to one, while equations associated with the solid material were solved where the control variable was equal to zero. In details, the permeability, conductivity, density and specific heat capacity were expressed by the selected formulations [15]:

$$c = c_l + (1-\theta)^3 * (c_s - c_l) \quad (2)$$
$$k = k_s + (1-\theta) * (k_l - k_s) \quad (3)$$

$$\rho = \rho_s + (1-\theta) * (\rho_l - \rho_s) \quad (4)$$

$$c_p = c_{ps} + (1-\theta) * (c_{pl} - c_{ps}) \quad (5)$$

where the subscript l indicates the properties of the liquid nitrogen, while the subscript s the properties of the steel. The Fig. 6a shows the initial setting for the topological optimization: one nitrogen inlet was selected close to the original one, ten outlets were selected instead of the sixteen of the original design in order to reduce the excessive pressure drops. The number of outlets were selected as input; however, further investigations will be focused on the possibility to include the choice of outlets as objective function. Eleven temperature control points were used to implement an objective function related to the temperatures balance around the profile exits. The latter was imposed as the minimization of the standard deviation with respect to the temperature control value of 250°C combined to the minimization of the differences in temperature between the control points:

$$\Delta T_{min} = \sqrt{\frac{\Sigma_{i=1}^{n} (T_i - T_{ref})^2 + \Sigma_{i,j=1\, i\neq j}^{n} (T_i - T_j)^2}{n + \frac{n!}{2*(n-2)!}}} \quad (6)$$

The temperature reference of 250°C was selected reasonable to avoid thermal shocks in the tooling set as well as to guarantee an adequate cooling in the bearings located away from the cooling channel. A convective heat flux perpendicular to the backer plane was defined as boundary condition (heat transfer coefficient of 11000 W/m^{2}K at a temperature of 550°C) with the aim to replicate, in a simplified way, the heat exchange between the backer and the hot die. As constraints, a maximum θ_{avg} of 0.25 was imposed, to avoid an excessive volume of channels (not feasible from a technological point of view), together with maximum inlet pressure of 5 bars, the maximum available for the nitrogen plant used during the experimental trials. The optimization problem was solved using the Method of Moving Asymptotes (MMA) [15-16].

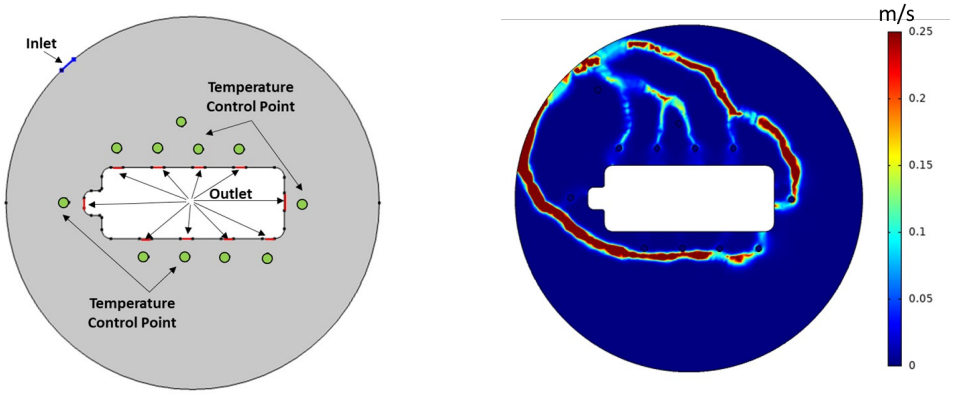

a) b)

Fig. 6. Topological optimization: a) Problem setting, b) Velocity field of the nitrogen within the channel.

The Fig. 6b shows the velocity profile of the nitrogen flow after 280 iterations of the optimizer (computational time of 10h). The results obtained from the topological optimization was then used to design the new cooling channel. Fig 7 presents the comparison between the old and the new design. The L-shaped channel, that connected the external nitrogen pipeline with the backer surface, was imposed fixed in order to analyze the difference in terms of cooling efficiency of the sole planar path. The topological optimization suggested to split the channel in three different paths instead of just one with a lot of ramifications as in the original design. A rectangular cross-section was selected since the channel is commonly milled: the width of 8 mm was suggested by the results of the topological optimization, the depth was set variable in order to guarantee an adequate

nitrogen flow rate also in locations far from the inlet (for longer route, higher hydraulic diameter to reduce the pressure drops).

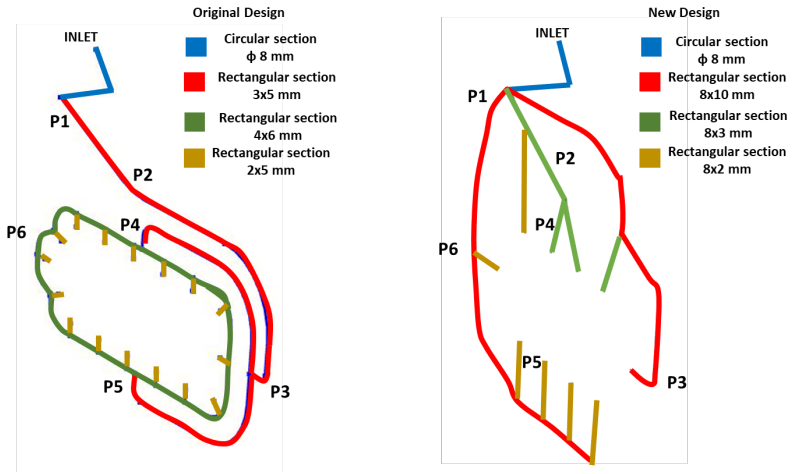

Fig. 7. The comparison between the old design and the new one.

Results and Discussion

The final step of the work was the testing of the new cooling channel design and the comparison with the old one in terms of cooling efficiency as predicted by the 3D model. The same process parameters and boundary conditions for the simulation of last extrusion were selected for both cooling channel designs (billet 17 in Fig. 3). In details, Fig. 8 evidences the differences in terms of cooling efficiency between the old design and the new one: a great cooling was achieved in the backer with the new design, highlighted by the large blue area around the profile exit, with a low cooling effect in the area near the right corner of the lower side, where the simulation properly predicted the gas formation. The great cooling effect obtained in the backer allowed to reduce the temperature around the bearings, detecting a minimum of 420°C in the thermocouple M4. The unbalance of the cooling in the backer caused the peak temperature difference of 45°C in the bearings (Table 4), thus suggesting the need for further investigation. Indeed, in this first optimization, the properties of the nitrogen within the Darcy fluid model were set constant and equal to those of liquid nitrogen, thus neglecting the effect of the phase change nearby the outlets of the longest cooling path. However, the achieved results clearly show the benefits of the proposed approach based on topological optimization of the cooling channel design, gaining a cooling efficiency significantly higher than that of the original design.

Table 3 Thermocouple temperatures in the Die: Old Design vs New Design (Billet 17).

Billet 17	Thermocouples Temperature [°C]				
	M3	**M4**	**M5**	**M6**	**M7**
Experimental Old Design	560	502	547	557	
Numerical Old Design	548	524	528	558	513
Numerical New Design	465	420	445	460	455

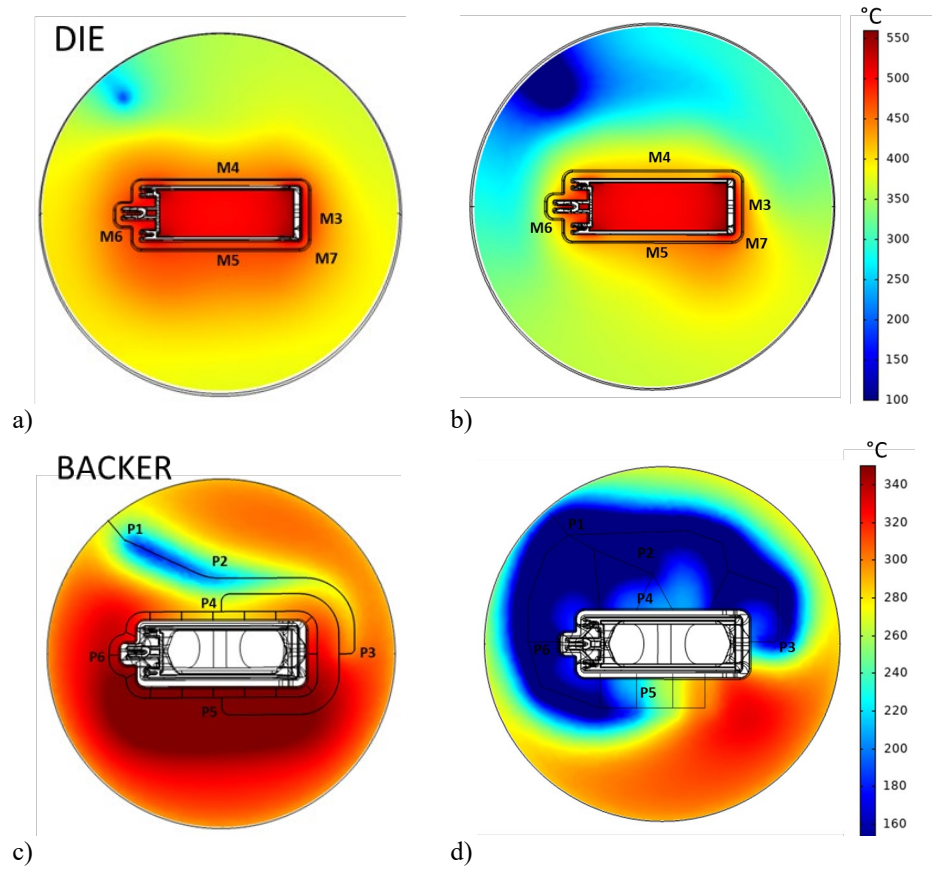

Fig. 8. Thermal map in steady state condition: a) Die Old Design, b) Die New Design, c) Backer Old Design, d) Backer New Design.

Summary

For the first time, an approach based on the topological optimization was implemented and tested for the design of the cooling channel in extrusion dies. The experimental campaign of the selected case study proved the limit of the design approach merely based on the experience without the support of numerical tools. The 1D model of the nitrogen cooling integrated with the 3D model of the extrusion process allowed to properly predict the cooling efficiency with an average experimental-numerical error of 6% in terms of temperatures, showing the poor performances of the original channel design. The new channel, designed on the basis of the topological optimization toolkit, guaranteed a great cooling in the backer and a significant decrease of temperature around the bearings (a maximum decrease of 104°C in the thermocouple M4). Further investigations will be focused on the integration of the nitrogen phase change in the topological analysis and on the testing of different objective functions in order to include, for example, technological constraints.

Acknowledgments

Project funded under the National Recovery and Resilience Plan (NRRP), Mission 04 Component 2 Investment 1.5 – NextGenerationEU, Call for tender n. 3277 dated 30/12/2021. Award Number: 0001052 dated 23/06/2022

References

[1] P.K. Saha, Aluminum extrusion technology, ASM International, Materials Park, OH, USA, 2000.

[2] L. Donati, et al, Effect of liquid nitrogen die cooling on extrusion process conditions, Key Eng. Mater. 491 (2012) 215-222. https://doi.org/10.4028/www.scientific.net/KEM.491.215

[3] P. Stratton, Raising productivity of aluminium extrusion with nitrogen, Int. Heat Treat. Surf. Eng. 2 (2008) 105-108. https://doi.org/10.1179/174951508X429221
[4] A.F. Ciuffini, et al., Surface Quality Improvement of AA6060 Aluminum Extruded Components through Liquid Nitrogen Mold Cooling, Metals 8(6) (2018) 409. https://doi.org/10.3390/met8060409
[5] A.J Norwood, et al., Analysis of cooling channels performance, Int. J. Comput. Integr. Manuf. 17(8) (2004) 669-678. https://doi.org/10.1080/0951192042000237528
[6] L. Donati, B. Reggiani, R. Pelaccia, M. Negozio, S. Di Donato, Advancements in extrusion and drawing: a review of the contributes by the ESAFORM community, Int. J. Mater. Form. 15 (2022) 41. https://doi.org/10.1007/s12289-022-01664-w
[7] N. Biba, et al., The Model for Coupled Simulation of Thin Profile Extrusion, Key Eng Mater 504-506 (2012) 505-510. https://doi.org/10.4028/www.scientific.net/KEM.504-506.505
[8] B. Reggiani, L. Donati, Prediction of liquid nitrogen die cooling effect on the extrusion process parameters by means of FE simulations and experimental validation, J. Manuf. Process 41 (2019) 231-241. https://doi.org/10.1016/j.jmapro.2019.04.002
[9] R. Pelaccia, M. Negozio, L. Donati, B. Reggiani, L. Tomesani, Extrusion of Light and Ultralight Alloys with Liquid Nitrogen Conformal Cooled Dies: Process Analysis and Simulation, J. Mater. Eng. Perform. 31 (2021) 1991-2001. https://doi.org/10.1007/s11665-021-06320-z
[10] R. Pelaccia, B. Reggiani, et al., Liquid nitrogen in the industrial practice of hot aluminium extrusion: experimental and numerical investigation, Int J Adv Manuf Technol. 119 (2022) 3141-3155. https://doi.org/10.1007/s00170-021-08422-3
[11] R. Pelaccia, M. Negozio, et al., Assessment of the Optimization Strategy for Nitrogen Cooling Channel Design in Extrusion Dies, Key Eng Mater. 926 (2022) 460-470. https://doi.org/10.4028/p-f7i0y2
[12] S. Kambampati, H.A. Kim, Level set topology optimization of cooling channels using the Darcy flow model, Struct. Multidisc. Optim. 61 (2020) 1345-1361. https://doi.org/10.1007/s00158-019-02482-6
[13] X. Zhao, M. Zhou, et al., Topology optimization of channel cooling structures considering thermomechanical behavior, Struct Multidisc Optim 59 (2019) 613-632. https://doi.org/10.1007/s00158-018-2087-z
[14] R. Pelaccia, P. E. Santangelo, A Homogeneous Flow Model for nitrogen cooling in the aluminum-alloy extrusion process, Int. J. Heat Mass Transf. 195 (2022) 123202. https://doi.org/10.1016/j.ijheatmasstransfer.2022.123202
[15] X. Zhao, M. Zhou, et al., A “poor man’s approach” to topology optimization of cooling channels based on a Darcy flow model, Int. J. Heat Mass Transf. 116 (2018) 1108-1123. https://doi.org/10.1016/j.ijheatmasstransfer.2017.09.090
[16] K. Svanberg, The method of moving asymptotes: a new method for structural optimization, Int J Numer Methods Eng 24 (1987) 359-397 https://doi.org/10.1002/nme.1620240207

Materials Research Proceedings 28 (2023) 543-552 https://doi.org/10.21741/9781644902479-59

Investigation of the skin contamination predictability by means of QForm UK extrusion code

KNIAZKIN Ivan[1,a *], PELACCIA Riccardo[2,b], NEGOZIO Marco[3,c], DI DONATO Sara[3,d], DONATI Lorenzo[3,e], REGGIANI Barbara[2,f], BIBA Nikolay [1,g], REZVYKH Ruslan[1,h] and KULAKOV Ivan[1,i]

[1]Micas Simulation Ltd., 107 Oxford Road, Oxford, OX4 2ER, UK

[2]DISMI- Department of Sciences of Methods for Engineering, University of Modena and Reggio Emilia, Viale Amendola 2, 42124, Reggio Emilia, Italy

[3]DIN- Department of Industrial Engineering, University of Bologna, Viale Risorgimento 2, 40136, Bologna, Italy

[a]ivanknjazkin@gmail.com, [b]riccardo.pelaccia@unimore.it, [c]marco.negozio2@unibo.it, [d]sara.didonato2@unibo.it, [e]l.donati@unibo.it, [f]barbara.reggiani@unimore.it, [g]nick@qform3d.com, [h]info@qform3d.com, [i]kulakov@qform3d.com

Keywords: Skin Contamination, Back-End Defect, FEM, QForm Extrusion, ALE Approach

Abstract. The paper presents an innovative approach implemented in QForm UK Extrusion FEM software to analyse one of the core defects encountered in profile extrusion known as billet skin defect. The validation of the algorithm has been performed based on a number of experimental case studies taken from the literature [1,2]. Additionally, the sensitivity of the accuracy of the results to the variation in initial parameters has been analysed for both types of profile shapes: solid and hollow. Based on this, practical recommendations have been formalised for the successful industrial use of the presented algorithm.

Introduction

Aluminium profile extrusion is a process that allows the production of numerous cross-sectional shapes: from simple solid forms to complex hollow shapes. Since these shapes are used for the most highly developed industries, they are subjected to strict requirements regarding geometrical and performance properties. In addition, the modern extrusion process has to be designed to provide high productivity combined with minimal material waste.

One of the typical defects inevitably formed during the direct profile extrusion process is the so-called billet skin defect which is a type of back-end defect. In general, the most critical form of this defect arises during the end of the process cycle if the inlet opening in the tool is incorrectly designed or if the discard length of the billet is too short. Eventually, it causes the penetration of the contaminated content into the profile (Fig. 1).

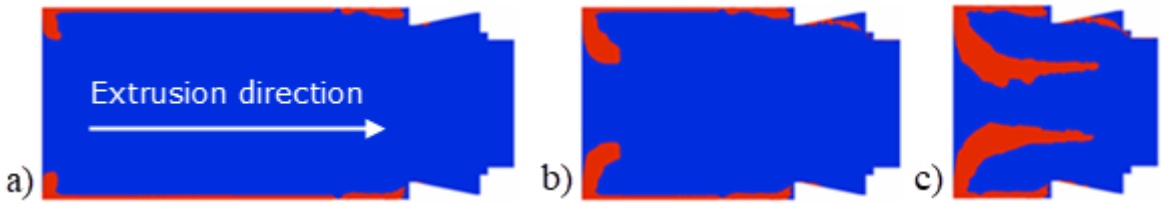

Fig. 1. Stages of extrusion: a) initial, b) intermediate, c) ending. Billet skin is marked by red.

Content from this work may be used under the terms of the Creative Commons Attribution 3.0 license. Any further distribution of this work must maintain attribution to the author(s) and the title of the work, journal citation and DOI. Published under license by Materials Research Forum LLC.

In turn, this results in surface defects and a loss of durability in the finished product [3]. In technical literature it's common to distinguish two types of billet skin flow [2,3]. Flow type 1, also called inward flow, occurs when defective material flows into the tool ports along dead metal zones formed between the container and inlet surface of the tool. Since the material involved in such flow forms the outer shape of the profile, this flow may only lead to surface defects. Whereas, flow type 2, also called forward flow, occurs when the skin layer accumulated at the corner between the container wall and the contact surface of the dummy block starts to flow into the tool ports, causing the appearance of the defective material inside the wall of the profile cross-section.

Skin contamination of the profiles is a potential reason for increasing scrap in the aluminium extrusion process. However, it can be avoided if a proper discard length is chosen to sheer off all the accumulated contaminated material from the skin. The complexity of the process mechanics forcibly invokes the need for a numerical tool to accurately predict the optimal discard length. Even though the impact of the discard length significantly affects the overall process efficiency, few papers have been published on this subject. To the best of authors knowledge, only two studies were performed to investigate the skin defect on profiles of industrial complexity [4,5] where both front-end and back-end defects are analysed using numerical simulation with the Arbitrary Lagrangian Eulerian (ALE) approach. In [6], a Lagrangian approach was used for the simulation of the extrusion process and the skin propagation was checked by tracing the array of points located at the distance of the thickness of contaminated layer. On the one hand, the use of a pure Lagrangian tool resulted in an increase of the prediction accuracy but, on the other hand, it led to a considerable rise in computational time of the simulation.

Unlike the other case studies listed above, this paper aims to find a way to predict the billet skin defect in extruded profile's by means of ALE numerical simulation using an innovative method implemented in QForm UK Extrusion which combines high accuracy in the prediction with low computational time of the simulation.

Description of the Method for Simulation of Billet Skin Propagation

There are two basic ways to describe the motion of deforming material commonly used in numerical simulation, i.e., Lagrangian and Eulerian. Principal differences, limitations and other details of these approaches and their combinations are discussed in [7]. The method used in this paper for billet skin tracking involves points tracing over the Lagrangian-Eulerian mesh environment where points move based on the velocity solution achieved at every step of extrusion simulation of the entire billet.

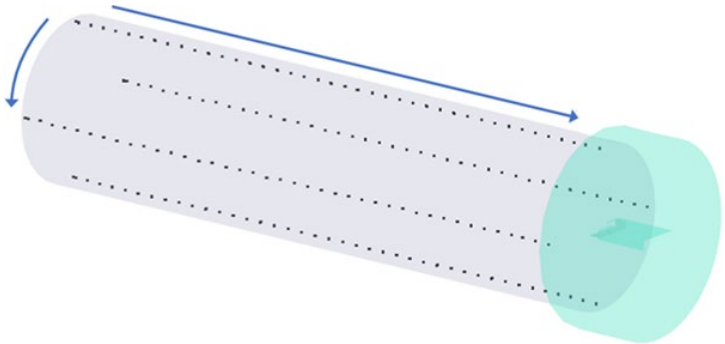

Fig. 2. Initial position of tracking points: 4 lines, 40 points per line.

The settings available as inputs for such kind of analysis are skin thickness, number of lines and number of points per line. Skin thickness value defines the points' radial offset from the upset billet's outer surface. The number of lines is the parameter that determines the number of sectors of the circle so that the points are created along the borders of these sectors. For example, if the number of lines is 2, then there are only two sectors 2x180° with lines located opposite each other,

if the number of lines is 4, then there are four sectors 4x90° (Fig. 2), etc. Additionally, there is a special continuous solid object built based on the specified points. Therefore, there are three different ways to plot the results of such kind of tracing, i.e., array of points, deformed continuous object and billet skin distribution presented in the same way as all the standard typical fields for FEM packages (Fig. 3). This kind of simulation is optional and performed in the post-processor by the implementation of a standard subroutine.

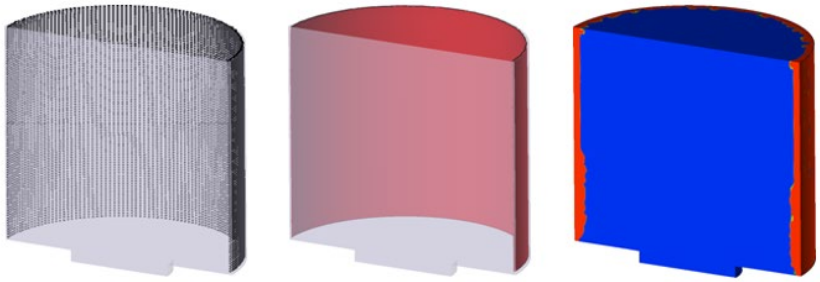

Fig. 3. Types of billet skin representation: array of points (left), continuous solid object (middle), field (right).

Description of the Case Studies

Solid profile.

The authors of the work [1] prepared the special billet with the core material of AA 6063 alloy and skin material of AA 3003 alloy. These materials have similar flow stress levels at high temperatures but react differently to the etching process, therefore billet skin propagation could be clearly recognised on the cross-cuts.

Table 1. Technological and geometrical parameters of the project.

Parameter	Value
Alloy	AA 6063
Extrusion ratio	5.5
Container temperature [°C]	Variable: 20, 500
Billet temperature [°C]	450
Tool temperature [°C]	450
Lubrication	Variable: with and without
Extrusion velocity [mm/s]	19
Billet length [mm]	91
Billet diameter [mm]	91
Container diameter [mm]	94
Ram stroke [mm]	69.5
Billet skin thickness [mm]	1

In this case study, the 40 mm bar was extruded through a flat die under different friction and temperature conditions. There were three experiments carried out, i.e., extrusion without lubricant with a cold container (room temperature), extrusion with a hot container (500°C) without lubrication, and extrusion using a hot container with a lubricated ram. This allowed the authors to obtain different results of metal flow patterns at the contact surfaces between the billet and tools, which eventually affected the shape of the contaminated layer. Process parameters and geometrical detail are listed in Table 1.

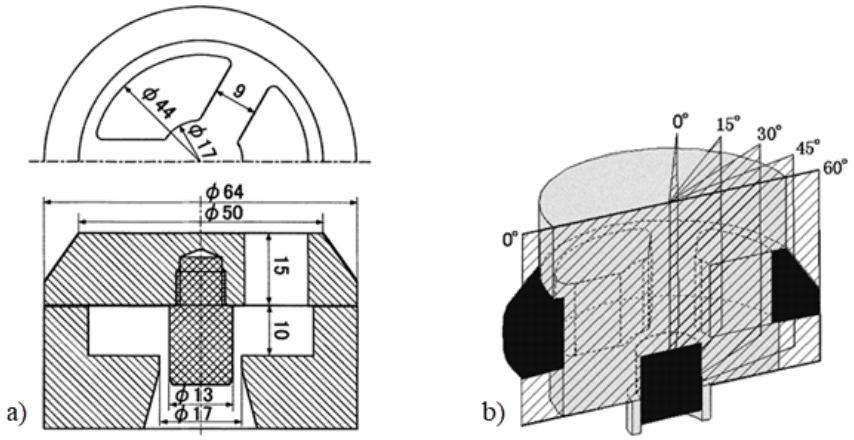

Fig. 4. Geometrical details of the second case study: a) tool scheme; b) cross-cut planes analysed in experiment (right).

Hollow profile.

In this case [2], AA 1100 alloy was used as a core material and AA 1050 as a billet skin material. Similar to the first presented case, the etching characteristics of the alloys differed, allowing qualitative identification of the billet skin propagation. For this purpose, the authors have designed a porthole tool with sixfold symmetry (Fig. 4a). The investigation was divided into two significant steps: analysis of the evolution of billet skin shape at different ram strokes for the case where no lubrication was used, and analysis of billet skin pattern depending on different friction conditions on ram and container. For both cases, the results of billet skin propagation were analysed for five different planes (Fig. 4b). Technological parameters and critical dimensions of the project are listed in Table 2. The authors of the work also performed tests using colloidal graphite lubrication but this part of the experiment isn't considered in the current paper.

According to the presented data, several simulations were done using a coupled thermomechanical task for the material flow domain and tools (Fig. 5).

Table 2. Technological and geometrical parameters of the project.

Parameter	**Value**
Alloy	AA 1100
Extrusion ratio	20.9
Container temperature [°C]	400
Billet temperature [°C]	400
Die temperature [°C]	400
Lubrication	Variable: no lubricant, boron nitride
Extrusion velocity [mm/s]	0.017
Billet length [mm]	50
Billet diameter [mm]	49.5
Container diameter [mm]	50
Ram stroke	Variable: from 35 to 46
Billet skin thickness [mm]	0.5

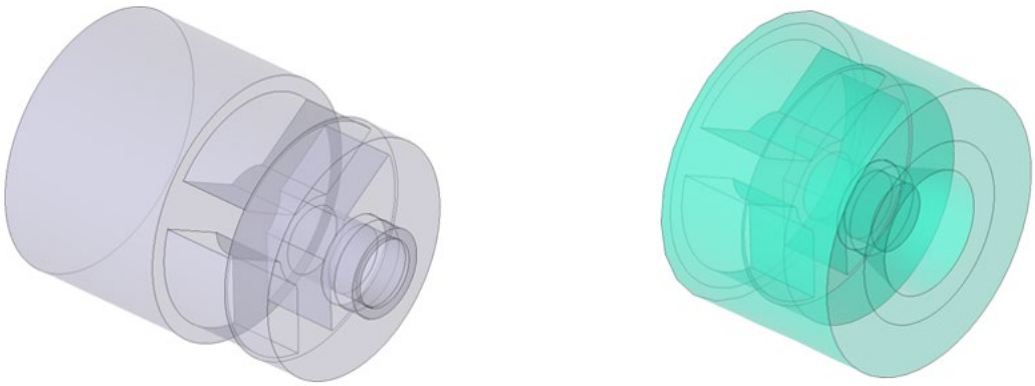

Fig. 5. Geometrical representation of the second case study: material flow domain (left) and porthole tool (right).

Description of the Models Used in the Simulation

Coupled task.

Material flow and temperature are simulated, taking into account the deformation of the tool and the temperature distribution in it. This means that tool deformation influences the material flow, while the tool distortion itself depends on the material's contact pressure. Similarly, temperature evolution in billet material is defined not only by heat generation due to plastic deformation and friction but also by heat exchange with the tool. Such a coupled solution is obtained through several iterations combined with automated remeshing of the flow domain. The heat flux between the billet and tooling set is specified by Newton-Richmann law in the following form:

$$q_n = \alpha(T_1 - T_2) \tag{1}$$

where α - heat transfer coefficient (by default equal to 30000 W/m^2K in QForm UK Extrusion), which takes into account the number of coefficients of heat transfer between the workpiece and lubrication and between lubrication and the tool, T_1 is the billet temperature, T_2 is the tool temperature.

Table 3. Hensel-Spittel parameters for AA 6063 and AA 1100.

Parameter	Solid design	Hollow design
A [MPa]	250.7	265
m_1 [K^{-1}]	-0.000498	-0.00458
m_2	0.126346	-0.12712
m_3	0.135122	0.12
m_4	-0.0052884	-0.0161
m_5 [K^{-1}]	-1.06775x10^{-6}	0.00026
m_7	0.00005655	0
m_8 [K^{-1}]	2.53717 x10^{-8}	0
m_9	0	0

Flow stress.

Hensel-Spittel equation (2) defines the dependence of the flow stress (σ_s) on the strain (ε), strain-rate ($\dot{\varepsilon}$), and temperature ($\boldsymbol{T}$) were used to describe flow curves for the billet material used in both considered projects. Table 3 contains values of the coefficients used in the simulation.

$$\sigma_s = A \cdot e^{m_1 T} \cdot T^{m_9} \cdot \varepsilon^{m_2} \cdot e^{\frac{m_4}{\varepsilon}} \cdot (1+\varepsilon)^{m_5 T} \cdot \varepsilon^{m_7 \varepsilon} \cdot \dot{\varepsilon}^{m_3} \cdot \dot{\varepsilon}^{m_8 T} \quad (2)$$

Friction.

Levanov friction law was used to describe friction between aluminium and steel. This friction model is a generalisation of the Coulomb and Siebel friction laws. When the normal contact pressure is low (typical for the bearing area), Levanov's shear stress is close to Coulomb's. When the normal contact pressure is high (which is typical for the rest of the billet usrface), Levanov's shear stress is close to Siebel's shear stress. According to the Levanov friction model, the shear stress (τ) on the contacting surface of the workpiece depends on the friction factor ($\boldsymbol{m}$), flow stress ($\sigma_{\boldsymbol{s}}$) of the workpiece material, normal contact pressure ($\sigma_{\boldsymbol{n}}$), and Levanov coefficient ($\boldsymbol{n}$):

$$\tau = m \cdot \frac{\sigma_s}{\sqrt{3}} \cdot \left(1 - e^{-n \cdot \frac{\sigma_n}{\sigma_s}}\right) \quad (3)$$

In QForm UK Extrusion the default value of Levanov coefficient that was used for all simulations is equal to 1.25.

Mesh.

To investigate the impact of initial mesh size, two different mesh variations were created for both hollow and solid profile designs, where an increased adaptation coefficient in the container area was used to make the mesh finer. The visual and quantitative differences between the initial and adapted mesh can be seen in Fig. 6 and Table 4, respectively.

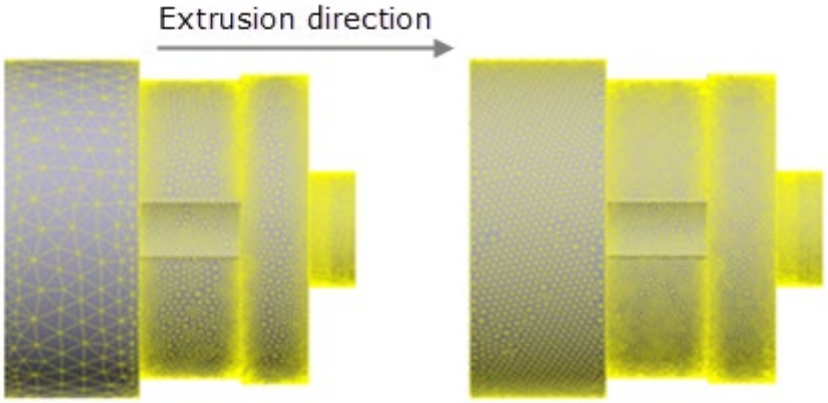

Fig. 6. Initial (left) and adapted (right) mesh for hollow profile.

It's been observed that for the proposed approach mesh density influenced the smoothness of the resulting skin shape but didn't significantly affect the qualitative picture of its propagation. Therefore, further analysis is presented for the cases with mesh generated with the default settings.

Table 4. Mesh properties.

	Initial mesh	**Adapted mesh**
Nodes, #	145586	174961
Surface elements, #	70958	91570
Volume elements, #	786554	931870

Results and Discussion

Solid profile.

The simulation of the extrusion process was performed using standard hot AA 1100 alloy available in the QForm material database. The total computational time for the simulation resulted in 2 hours. For the cases where no lubrication was used in actual experiments, the friction properties were selected according to the default extrusion settings, i.e., Levanov friction law with the friction factor equal to 1. For the experiment where lubrication was used, the friction factor (m) was assumed to be equal to 0.5 in simulation to evaluate the sensitivity of this parameter on the final result.

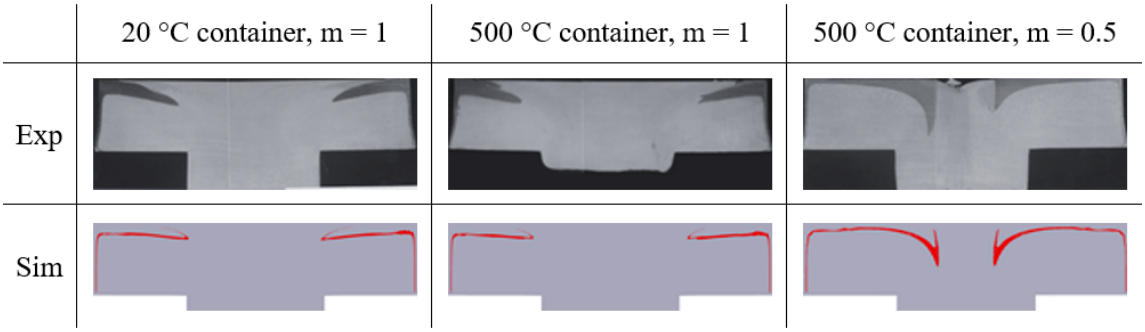

Fig. 7. Comparison of billet skin propagation in experiments with the solid profile.

As it can be clearly seen from Fig. 7, simulation has fully matched the experimental results. It's worth mentioning that the difference in container temperature (20°C vs 500°C) had no significant effect on the results of billet skin flow. Which is quite logical in this case since the design configuration is simple and difference in temperature doesn't affect the general behaviour of the flow pattern.

Nevertheless, the change in friction conditions on the ram surface led to a significant change in the billet skin shape. In this case, the use of lubricant worsened the flow pattern of billet skin since the contaminated material is located closer to the bearing exit of the tool.

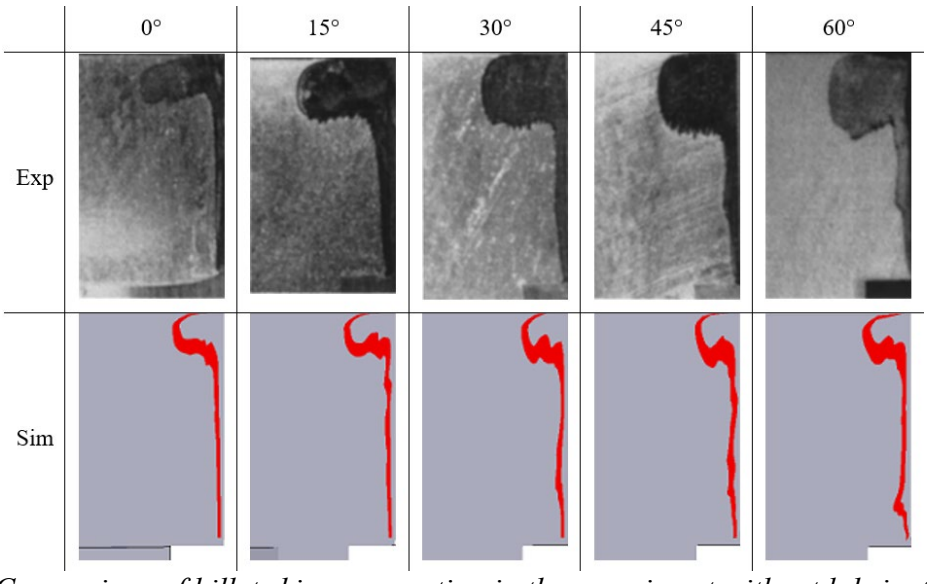

Fig. 8. Comparison of billet skin propagation in the experiment without lubrication and simulation for 35 mm ram stroke.

It can also be seen that the experimental result in the case of the lubricated contact surface of the ram is remarkably asymmetrical. It could be caused by different production factors such as inaccurate container alignment, an asymmetrical upsetting of the billet in the container, etc. In a simulation the asymmetry is also possible but mostly due to the difference in the mesh. In general, such kind of asymmetry can be minimised or even eliminated by making the mesh finer or by the use of symmetry planes.

Hollow profile.

In this case, the simulation was performed with standard extrusion AA 6063 alloy from the QForm material database. The total computational time for the simulation resulted in 3 hours and 30 minutes. As mentioned before, the first step of algorithm verification was to assess the evolution of billet skin shape at different ram strokes. For all the experiments where no lubrication was used, the friction conditions were set in accordance with the default extrusion friction available in the QForm database mentioned before.

Fig. 8 presents the results of the first test where the process was stopped at 35 mm ram stroke. It can be seen that the most intensive propagation of the contaminated layer is achieved on the cross-cut located in the middle of the port (60°). The area of billet skin decreases as you move away from this section reaching its minimum on the cross-cut plane (0°) placed right in the middle of the mandrel web (separation element of the tool). Simulation shows a similar trend of billet skin propagation qualitatively matching experimental results. For both practical and simulation results the origination of inward flow can be seen in sections 45° and 60°.

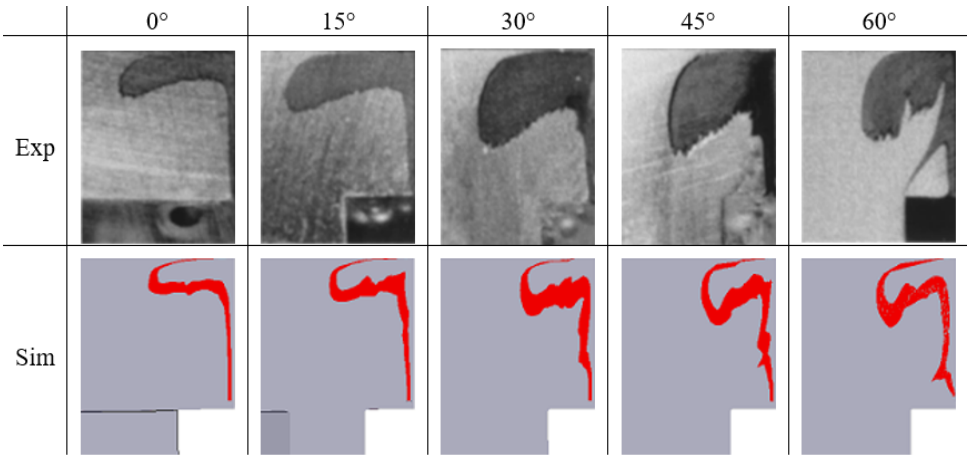

Fig. 9. Comparison of billet skin propagation in the experiment without lubrication and simulation for 41 mm ram stroke.

Fig. 9 compares the results of the same test but with the ram stroke equal to 41 mm. In this case, the inward flow is clearly defined for section 60°, which determines the intensive metal flow from the regions close to the container surface. Whereas the flow in section 0° that crosses the middle of the web has no sign of inward flow and billet skin propagates radially along the ram surface. For this stage of the process (41 mm ram stroke) simulation shows qualitatively the same result obtained in the practical experiment, which indirectly confirms the general correctness of the initial parameters used in the simulation. Slight deviations in inward flow might be caused by the sensitivity of this kind of back-end defect to the mesh size, specifics of the tracing algorithm or billet skin visualisation in the software.

In a similar way, Fig. 10 presents the results of the final moment of the extrusion process of the billet for the ram stroke equal to 46 mm. At this stage contaminated material flows into the ports for the sections 30°, 45° and 60°.

Another part of the investigation in this experiment was assessing the impact of lubrication on the flow pattern of billet skin. To simulate this influence, the friction factor was assumed to be equal to 0.9 on the contact surfaces of the ram and container. In this case, simulation matched the experimental result quite well (Fig. 11) with a minor deviation that adjustment of the friction factor

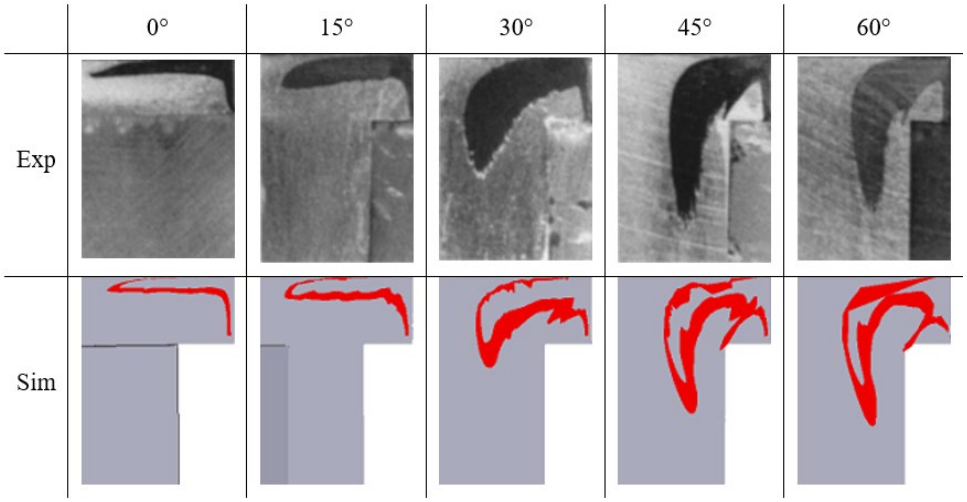

Fig. 10. Comparison of billet skin propagation in experiment without lubrication and simulation for 46 mm ram stroke.

can eliminate. In this case, if compared with the process that was carried out without lubrication for a similar ram stroke, it can be clearly seen that the volume of contaminated material approaching the ports is less, which indicates the positive influence of lubrication on billet skin propagation in contrast to the result obtained for the solid profile. However, it should be noted that containers of direct extrusion of aluminium profiles are generally not lubricated in industrial conditions.

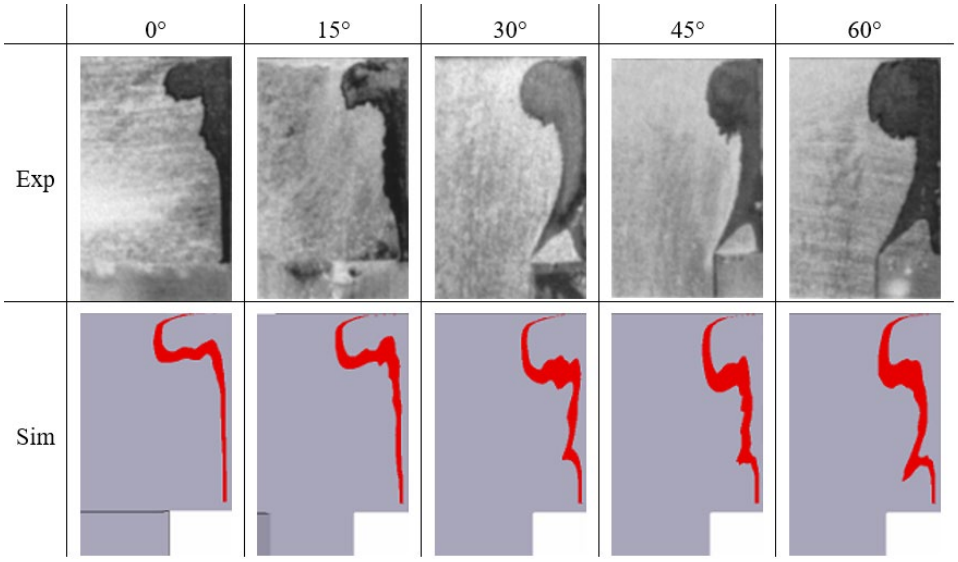

Fig. 11. Comparison of billet skin propagation in experiment with BN lubrication and simulation for 39 mm ram stroke.

Summary

In the present work, the innovative method of billet skin prediction implemented in QForm UK Extrusion was used and verified based on two experimental studies. It's worth noting that from a practical point of view, the results obtained in cases where no lubrication was used have a higher

value, since most industrial extrusion trials are performed without any lubrication of the container, ensuring the adhesion of billet aluminium to tool steel. The qualitative comparison was carried out for solid and hollow profiles extruded with different friction conditions. Parameters affecting the accuracy of this method have been varied to define the sensitivity of the applied approach.

As a summary, the presented research allows us to draw the following key findings:

- A good numerical-experimental matching was achieved on the skin contamination behaviour with and without lubrication.
- The total computational time for the two simulations (2 hours for the solid profile, 3 hours, and 30 min for the hollow profile) proved to be several times lower than the computational time reported in [6] without causing a decrease in the prediction accuracy. PC with Intel Core i9-9940X (14 cores, 4.20 GHz max. frequency) was used to obtain simulation results.
- Friction is a crucial parameter affecting the propagation of the contaminated layer.
- Default friction settings recommended for simulation in QForm UK Extrusion provided high accuracy of the results for experiments carried out without lubrication.
- Lubrication can lead to both positive and negative effects on the propagation of the contaminated layer.
- Even a significant change in container temperature has a minor effect on the flow pattern of billet skin in case of extrusion of simple solid bars.

References

[1] Y.T. Kim, K. Ikeda, Flow behaviour of the billet surface layer in porthole die extrusion of aluminum, Metall. Mater. Trans. A 31 (2000) 1635-1643. https://doi.org/10.1007/s11661-000-0173-4

[2] T. Ishikawa, H. Sano, Y. Yoshida, N. Yukawa, J. Sakamoto, Y. Tozawa, Effect of Extrusion Conditions on Metal Flow and Microstructures of Aluminum Alloys. CIRP Annals 55(1) (2006) 275-278. https://doi.org/10.1016/S0007-8506(07)60415-6

[3] H.S. Valberg, M. Lefstad, A.L. de Moraes Costa, On the mechanism of formation of back-end defects in the extrusion process, Procedia Manuf. 47 (2020) 245-252. https://doi.org/10.1016/j.promfg.2020.04.207

[4] S. Lou, Y. Wang, C. Liu, S. Lu, C. Su, Analysis and Prediction of the Billet Butt and Transverse Weld in the Continuous Extrusion Process of a Hollow Aluminum Profile, J. Mater. Eng. Perform. 26 (2017) 4121- 4130. https://doi.org/10.1007/s11665-017-2771-y

[5] M. Negozio, R. Pelaccia, L. Donati, B. Reggiani, L. Tomesani, T. Pinter, FEM Validation of front end and back end defects evolution in AA6063 and AA6082 aluminum alloys profiles, Procedia Manuf. 47 (2020) 202-208. https://doi.org/10.1016/j.promfg.2020.04.178

[6] M. Negozio, R. Pelaccia, L. Donati, B. Reggiani, FEM Analysis of the Skin Contamination Behavior in the Extrusion of a AA6082 Profile, Key Eng. Mater. 926 (2022) 452-459. https://doi.org/10.4028/p-y37nm3

[7] I. Kniazkin, Prediction of Underfilling Defect in Aluminium Profile Extrusion Based on ALE Simulation, Key Eng. Mater. 926 (2022) 537-544. https://doi.org/10.4028/p-42gaq6

Materials Research Proceedings 28 (2023) 553-562 https://doi.org/10.21741/9781644902479-60

Crystal plasticity finite element analysis of linear and non-linear extrusion processes

ŞIMŞEK Ülke[1,a], MIYAMOTO Hiroyuki[2,b] and YALÇINKAYA Tuncay[1,c *]

[1]Department of Aerospace Engineering, Middle East Technical University, Ankara, 06800, Türkiye

[2] Department of Mechanical Engineering, Doshisha University, Kyoto, 610-0321, Japan

[a]ulke.simsek@metu.edu.tr, [b]hmiyamot@mail.doshisha.ac.jp, [c]yalcinka@metu.edu.tr

Keywords: Crystal Plasticity, Twist Extrusion, Severe Plastic Deformation

Abstract. Severe plastic deformation (SPD) induced by conventional forming processes such as extrusion has a significant effect on texture evolution and strength of metals. Conventional twist extrusion (TE) process can be used to produce ultra-fine grained (UFG) structures without introducing any significant change in the overall dimensions of the sample. However, the commercialization for industrial usage has been limited because of production efficiency and non-uniform distribution of grain refinements. In order to overcome these difficulties a new process called nonlinear twist extrusion (NLTE) has been introduced recently where TE mold channel is modified to restrain strain reversal and rigid body rotation of the workpiece. Prediction of the texture evolution in these processes is crucial for mold design and process parameters. In this work, the texture evolution during NLTE and TE processes are investigated through crystal plasticity finite element method. Single copper crystal which has a billet form is fully extruded through the TE and NLTE mold models separately. In addition to spatial stress and strain evolution investigations, the orientation differences and texture evolution of extruded billets are examined for two different initial orientations of single copper crystal. Moreover, the deformation histories at different locations of the sample are analyzed with crystal plasticity finite element method (CPFEM) to compare the performance of both techniques.

Introduction

Severe Plastic Deformation (SPD) is an efficient manufacturing technique to produce ultrafine-grained (UFG) structures with high densities of lattice defects. In recent years, SPD methods have been popular with their capability for refining the grain size of materials to sub-micrometer and nanometer scales [1]. The strength and resistance to the plastic flow of polycrystalline materials depend on the grain size. Usually, UFG materials have several advantages compared to coarse-grained counterparts with their high strength and other superior properties, including potential use in super-plastic forming operations at elevated temperatures [2]. Various early reports describe interesting results from different SPD techniques to produce UFG structured materials. Equal channel angular pressing (ECAP) (see e.g. [3]), high-pressure torsion (HPT) (see e.g. [4]), accumulated roll bonding (ARB) (see e.g. [5]), multi-directional forging (MDF) (see e.g. [6]), and twist extrusion (TE) (see e.g. [7]) can be listed as the most popular SPD processes. All these methods have certain advantages and disadvantages compared to each other. ECAP process has some operational difficulties and produces excessive waste compared to the other SPD processes. A potential problem in HPT processing is the strain which varies across the disk specimen. Besides, HPT and ECAP processes do not apply to large bulk materials. ARB process also suffers in-homogeneity of strain distribution, and it requires multi-passes. The grain refinement ability of MDF is lower than all other SPD processes, and grain size reduction is not homogenous through the center of the sample. TE process has in-homogenous distribution characteristics, and strain

Content from this work may be used under the terms of the Creative Commons Attribution 3.0 license. Any further distribution of this work must maintain attribution to the author(s) and the title of the work, journal citation and DOI. Published under license by Materials Research Forum LLC.

distribution increases from the center to the periphery. It also requires multi-passes to increase the homogeneous distribution of grains through the workpiece.

In SPD processing, UFG formation is facilitated in deformation routes that involve high dislocation accumulation, and strain reversal or redundant strain reduces the rate of the dislocation accumulations and hence retard the UFG formation. Therefore, the non-linear twist extrusion (NLTE) technique has recently been developed by the authors (see [8]) based on TE, aiming to avoid strain reversal and rigid body rotation, which retard the UFG formation. Numerical analysis of the NLTE process shows the advantages of this process in terms of punching force and deformation distribution.

The numerical modeling of texture evolution during SPD techniques is crucial for understanding the grain refinement mechanisms. The results can be used for optimizing the process and mold parameters for SPD methodology. Nowadays, the crystal plasticity finite element method (CPFEM) is an effective tool for simulating texture evolution during SPD. In recent years, CPFEM simulations of some SPD methods have been performed in various studies. For example, the capability of the CPFE approach in predicting texture formed during ECAP and deformation heterogeneity of single crystal materials were examined (see e.g. [9]). The deformation history and texture evolution during TE were investigated (see e.g. [10]). Crystallographic texture evolution in simple shear extrusion (SSE) process was compared with experimental results (see e.g. [11]). Coupling of FEM flow and crystal plasticity simulations were conducted during the helical extrusion process (see e.g. [12]).

In this study, a single copper crystal with a billet form is fully extruded through the TE and NLTE mold models separately. In addition to spatial stress and strain evolution investigations, the orientation differences and texture evolution of extruded billets are examined for two different initial orientations of single copper crystal, i.e. (<111>and<100>) using crystal plasticity finite element technique. Moreover, the deformation histories at different locations of the sample are analyzed to compare the performance of both methods.

Finite Element Models

Fig. 1 shows the Abaqus finite element models of the twist extrusion processes. In the LTE process, a billet is pressed through a die with two straight channels separated by a section with helical geometry. Apart from being continually rotated in the helical part of the die, a cross-section of the billet normal to the extrusion axis stays unchanged during its translational movement. The mold model of LTE and punch are considered rigid bodies in CPFEM simulations. Encastre boundary conditions (u1=u2=u3=R1=R2=R3=0) were applied through mold geometry from its rigid body reference point (center of mass). Velocity boundary conditions (2 mm/s) were applied through punch rigid body reference point (center of mass). Similarly, the model forNLTE is also presented in Fig. 1.

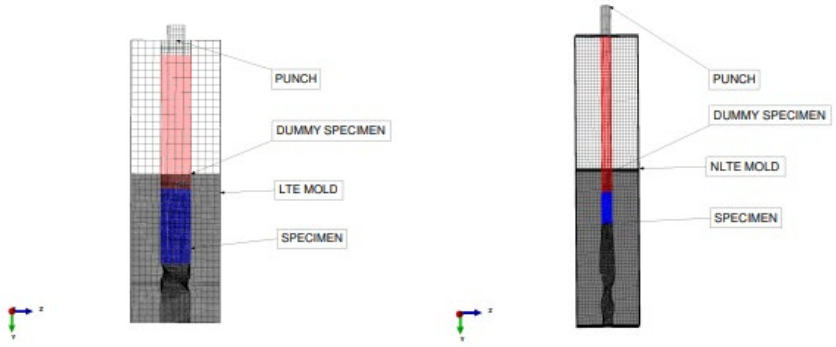

Fig. 1. LTE (left) and NLTE (right) processes FEM model.

Table 1. FEM model mesh parameters of simulated LTE and NLTE processes.

Model	Element Type	Element Family	Number of Elements
LTE Mold	Implicit-Tetrahedral-C3D4-Rigid	3D Stress	33777765
LTE Punch	Implicit-Hexahedral-C3D8R	3D Stress	925
LTE Specimen	Implicit-Hexahedral-C3D8R	3D Stress	159989
NLTE Mold	Implicit-Tetrahedral-C3D4-Rigid	3D Stress	419316
NLTE Punch	Implicit-Hexahedral-C3D8R	3D Stress	1679
NLTE Specimen	Implicit-Hexahedral-C3D8R	3D Stress	48750

The significant difference from LTE is that the billet is extruded, keeping rotation around the longitudinal axis so that the strain reversal is avoided. The mold model of NLTE and punch are considered rigid bodies. Boundary conditions are applied to the model same as in LTE simulations. Single copper crystal specimens are modeled with square and cylindrical shapes for LTE and NLTE, respectively. The square specimen dimensions were 20mm × 20mm × 50mm, and the dimensions of the cylindrical specimen were 20mm r = 10mm×30mm. Mesh properties of SPD models are presented in Table 1.

Crystal Plasticity Constitutive Model

This study utilizes a modified version of a crystal plasticity framework implemented as a UMAT (user-defined material model) subroutine [13]. In the classical crystal plasticity theory, the deformation gradient tensor **F** is multiplicatively decomposed into an elastic component $\boldsymbol{F^e}$ and a plastic component $\boldsymbol{F^P}$ [14] according to

$$\boldsymbol{F = F^e F^p} \tag{1}$$

According to Schmidt's Law, the resolved shear stress (τ^α) on a slip system is the leading cause of dislocation slip [15], which can be calculated by,

$$\tau^\alpha = \boldsymbol{\sigma}: \mathbf{s}^{*\boldsymbol{\alpha}} \otimes \mathbf{m}^{*\boldsymbol{\alpha}} \tag{2}$$

In Eq. 2, $\boldsymbol{\sigma}$ is the Cauchy stress tensor is projected on the slip systems where $\mathbf{m}^{*\boldsymbol{\alpha}}$ and $\mathbf{s}^{*\boldsymbol{\alpha}}$ are the slip direction and normal to slip plane in the current configuration, and α represents the slip system number. $\mathbf{m}^{\boldsymbol{\alpha}}$ and $\mathbf{s}^{\boldsymbol{\alpha}}$ are in the reference configuration,

$$\mathbf{s}^{*\boldsymbol{\alpha}} = \mathbf{F}^{\mathbf{e}}\mathbf{s}^{\boldsymbol{\alpha}} \tag{3}$$

$$\mathbf{m}^{*\boldsymbol{\alpha}} = \mathbf{m}^{\boldsymbol{\alpha}}\mathbf{F}^{\mathbf{e-1}} \tag{4}$$

The plastic velocity gradient, $\mathbf{L^P}$ is calculated by,

$$\dot{\mathbf{F}}^{\mathbf{p}}\mathbf{F}^{\mathbf{p-1}} = \mathbf{L}^{\mathbf{P}} = \sum_{n=1}^{\alpha} \dot{\gamma}^\alpha \mathbf{s}^{\boldsymbol{\alpha}} \otimes \mathbf{m}^{\boldsymbol{\alpha}} \tag{5}$$

The power law type rate-dependent formulation, which relates the slip rate on each slip system to the resolved shear stress τ^α and the slip resistance g^α is given in Eq. 6

$$\dot{\gamma}^\alpha = \dot{\gamma}_0 \text{sign}(\tau^\alpha) \left| \frac{\boldsymbol{\tau^\alpha}}{\mathbf{g}^{\boldsymbol{\alpha}}} \right|^{\mathbf{n}} \tag{6}$$

where $\dot{\gamma}_0$ is the reference shear strain rate, and n is the rate sensitivity parameter. The slip resistance g^{α} is calculated considering the latent hardening as presented below. The hardening moduli $h^{\alpha\beta}$ gives the rate of strain hardening on slip system α due to slip system β. The occurrence of self and latent hardening is phenomenologically described by Eq. 8, with q representing latent hardening matrix.

$$\dot{g}^{\alpha} = \sum_{k=1}^{12} h^{\alpha\beta} \left|\dot{\gamma}^{\beta}\right| \tag{7}$$

$$h^{\alpha\beta} = q^{\alpha\beta} h^{\alpha\alpha}(\gamma) \tag{8}$$

Pierce, Asaro, and Needleman [16] have used a simple form for the self-hardening moduli,

$$h_{\alpha\alpha}=h(\gamma)=h_0 \operatorname{sech}^2 \left|\frac{h_0\gamma}{g_s-g_0}\right| \tag{9}$$

where h_0 is the initial hardening modulus, g_s is the stage I stress, and γ is the Taylor cumulative shear strain on all slip systems in Eq. 10.

$$\gamma = \sum_{\alpha} \int_0^t |\dot{\gamma}^{\alpha}| dt \tag{10}$$

In the literature, there is a lot of inconsistent experimental data for single-crystal copper tension tests. Therefore, pure copper polycrystalline stress-strain data under tensile tests are used to calibrate single-crystal copper mechanical properties through homogenization. Symmetric boundary conditions are applied to representative volume element (RVE) cube composed of 500 hundred randomly oriented grains. RVE cube is illustrated in Fig. 2. Data and homogenization curve are illustrated in Fig. 3. The Parameters of a single copper crystal are given in Table 2.

Fig. 2. 500 grained calibration cube model for homogenization.

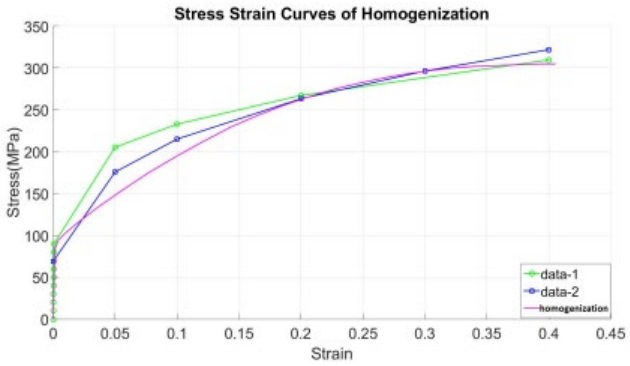

Fig. 3. Homogenization curve vs. data [17].

Table 2. Single crystal copper UMAT material model parameters.

Model	C_{11}	C_{12}	C_{44}	g_0	g_s	h_0	$\dot{\gamma}_0$	n	q
UMAT	168000	121400	75400	25	115	120	0.001	17	1.4

CPFEM Simulation Results

Finite element simulations of LTE and NLTE processes are performed for initially <100> and <111> oriented single copper specimens. The simulations illustrate an initial quadratic increase of the load in LTE and NLTE processes when the specimen head enters the twist zone. After the sudden increase, the slope of the curve starts to decrease, and the punch force slightly increases throughout both processes. The required punch force is less than the LTE process for the NLTE process (Fig.4). This is one of the prominent advantages of NLTE. Black curves show the initially <111> oriented single copper crystal results, and green curves show the initially <100> oriented single copper crystal simulation results. In the LTE process, initially <100> oriented single copper crystal faces with more punch force compared to initially <111> oriented single copper crystal. On the contrary, in the NLTE process, initially <111> oriented single copper crystal needs more punch force throughout the process. Since the cross-section areas are different for both cases, punch pressures are compared for a better presentation. However, the punch forces are dependent on the frictional coefficient. In these calculations, the friction coefficient is set to be low (less than 0.01) due to the convergence problems of implicit solver in contact non- linearities and frictional discontinuities. If the fiction coefficient increases, the punch forces will also increase for both processes. The sharp increase in the LTE case is due to the sudden change in the cross-section, which does not exist in the proposed smoother non-linear process.

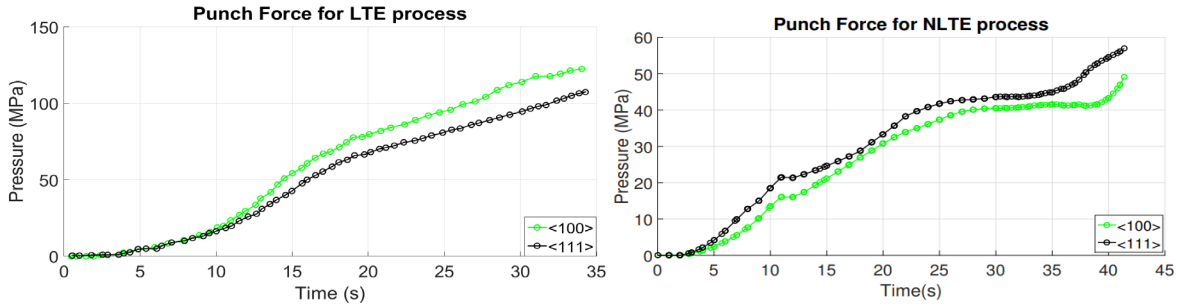

Fig. 4. LTE and NLTE processes punch forces according to the single-crystal copper initial orientation.

Von Mises stress contours are illustrated in Fig. 5 and Fig.6 for LTE and NLTE processes for initially <100> oriented single copper crystal, respectively. The stress values show an increase from the specimen center to the periphery, and maximum stresses can be observed at the edge of the surfaces. In the LTE process, stress evolution is more heterogeneous, and higher stress values are obtained in periphery regions. On the contrary, in the NLTE process, the stress distribution is more homogenous, and high-stress values are inspected in the periphery region and throughout the single copper specimen.

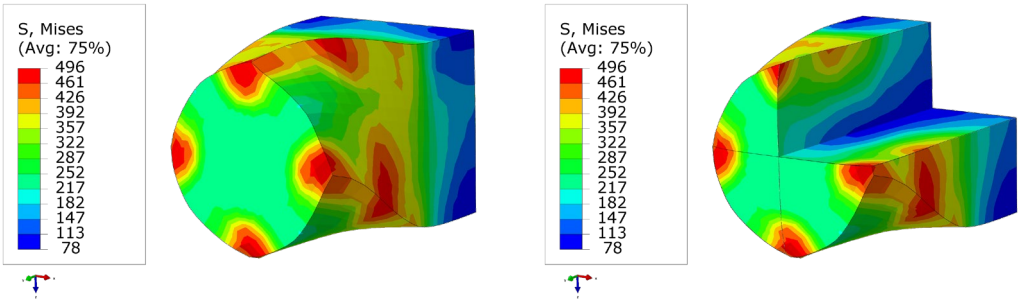

Fig. 5. Von Mises stress (MPa) results of <100> oriented copper single crystal after one pass of LTE (left) with section view (right).

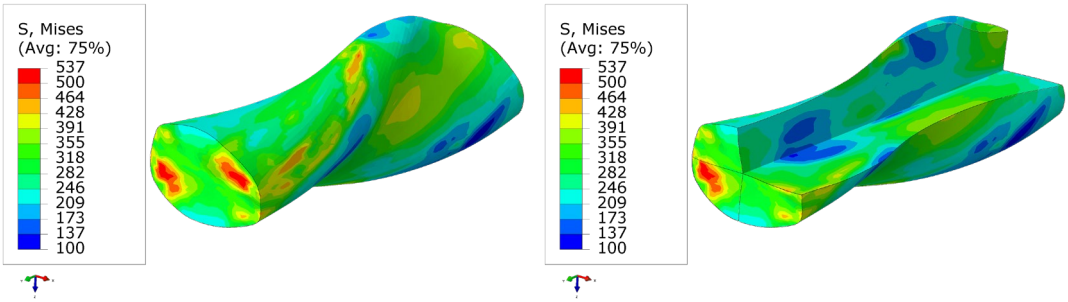

Fig. 6. Von Mises stress (MPa) results of <100> oriented copper single crystal after one pass of NLTE (left) with section view (right).

Fig. 7 and Fig.8 show the equivalent plastic strain distribution in LTE and NLTE processes, for initially <111> oriented single copper crystal, respectively. In the LTE process, a smaller magnitude of equivalent plastic strain evolves around the specimen center, and there is a gradual increase from the center to the surface of the specimen for both initial conditions. Distinctively, in the NLTE process, equivalent plastic strain evolves uniformly. Equivalent plastic strain distributions are more homogenous in the center when compared to the periphery region. Single copper crystal is subjected to much more plastic equivalent strain during the NLTE process. To show the deformation characteristics of LTE and NLTE processes, two typical elements of workpieces were chosen at the center and the periphery sections of the specimen distinctively. The selected elements are highlighted in Fig. 9.

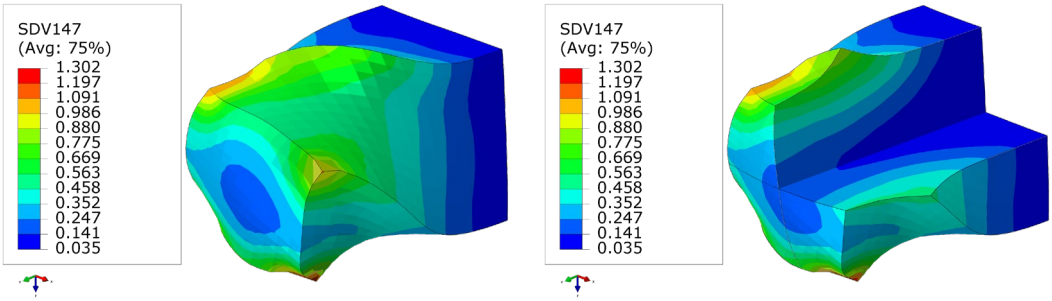

Fig. 7. Plastic equivalent strain results of <111> oriented copper single crystal after one pass of LTE process (left) with their section view (right).

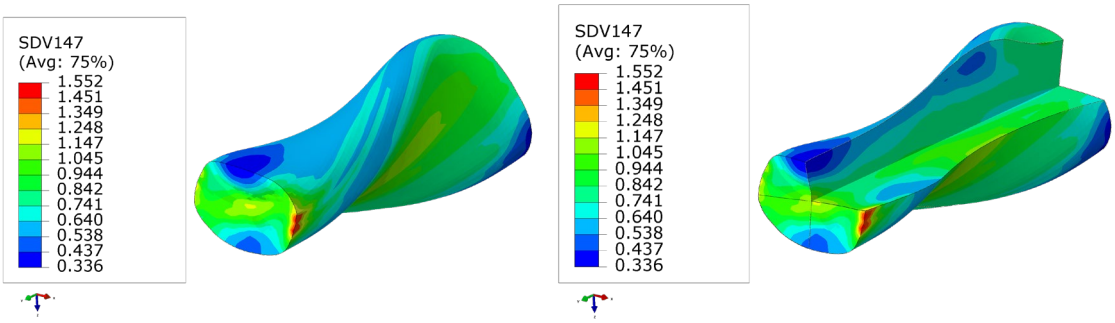

Fig. 8. Plastic equivalent strain results of <111> oriented copper single crystal after one pass of NLTE process (left) with their section view (right).

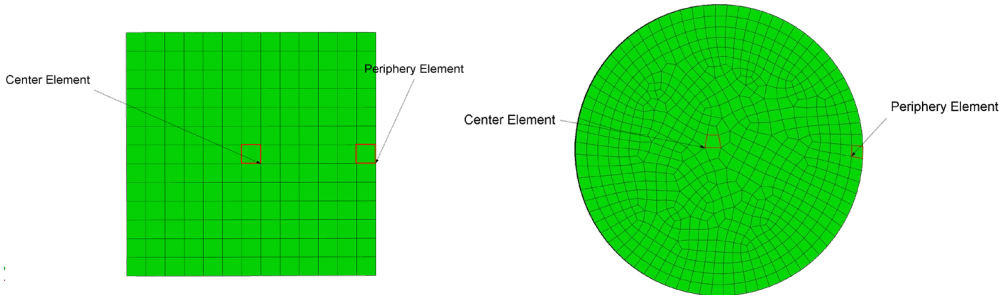

Fig. 9. Investigated elements with their local coordinates at the center and the middle for LTE process (left) and the NLTE process (right).

Certain texture components of face-centered cubic (FCC) materials assist in understanding the final texture of a single copper crystal after deformation. Table 3 pole figures show the main texture components of FCC materials: Copper, Brass, Goss, and S orientations. It gives information about mechanical behaviors and physical and chemical properties of materials and is associated with the performance in their production and investigation in engineering applications. Hence, an accurate understanding of deformation mechanisms and precise control of texture evolution becomes a requirement for developing new materials [18].

Materials Research Proceedings 28 (2023) 553-562 https://doi.org/10.21741/9781644902479-60

Table 3. Texture components and pole figures for face centered cubic (FCC) materials according to [111], [110] and [100] plane respectively [19].

Components Name	Directions	Bunge Euler Angles (ZXZ)	Pole Figures of Components [111] [110] [100]
Cube	[001]<100>	0º 0º 0º	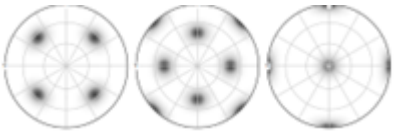
Goss	[011]<100>	0º 45º 0º	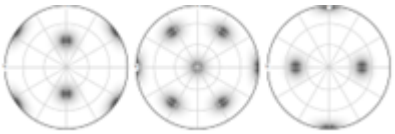
Brass	[0-11]<211>	35º 45º 0º	
Copper	[-211]<111>	90º 35º 45º	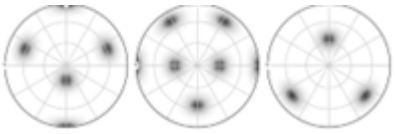
S	[111]<110>	60º 32º 65º	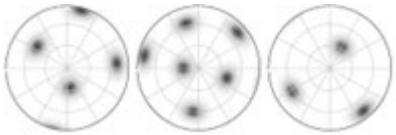

FCC materials with high or medium stacking fault energy (SFE) grains tend to rotate toward the copper-type textures with increasing deformation, and dislocation slip has been recognized as the dominant deformation mechanism during the whole deformation stage. SFE plays an essential role in determining the dominant mechanisms of plastic deformation. In metals with high SFE (e.g., aluminum and copper), slip is the dominant deformation mode, and the rolling texture is composed of copper, brass, and S texture components. In materials with low SFE, the copper-oriented grains cluster at the prior deformation stage. However, with increasing loading, these grains rotate to the brass-type textures, and the latter dominates in the final textures' at large deformations. The rolling texture in these metals is known as alloy-type texture and is composed of a strong brass component and a minor Goss orientation [20]. After the first pass of LTE and NLTE processes, results for the center and periphery elements are illustrated in Fig.10, respectively. The initial orientation distributions significantly change by the processes for one pass. The distribution of the orientations in pole figures after the LTE and NLTE processes resemble the main orientation pole figures of copper and s textures orientation distributions. Thus, the pole figures of NLTE and LTE processes show that the elements of the single copper specimen face shear deformation during both processes, and their dominant deformation is dislocation slip. Moreover, after one pass, the center and periphery elements' orientation distributions are very close in the NLTE process compared to the LTE process.

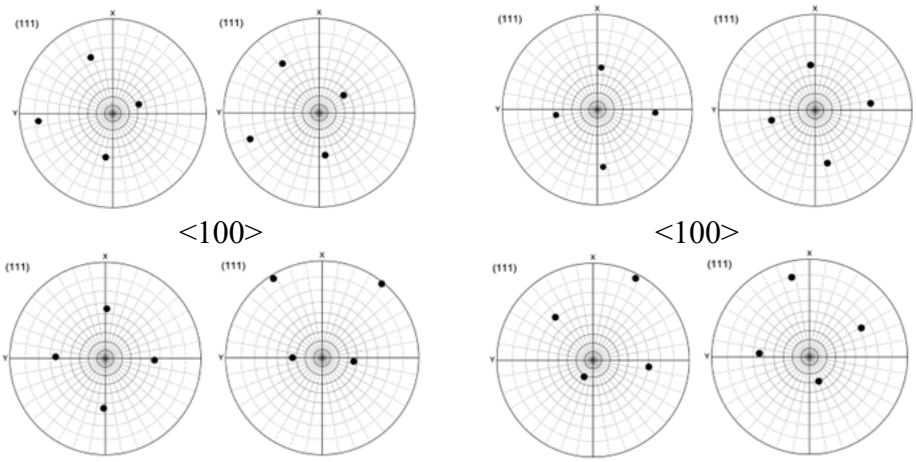

Fig. 10. Pole figures of center (left) and periphery (right) elements of single crystal copper specimen after LTE process according to the initial orientations (<100> and <111>) (Left) and pole figures of center (left) and periphery (right) elements of single crystal copper specimen after NLTE process according to the initial orientations (<100> and <111>) (Right).

Summary

In this study, simulations of a single copper crystal workpiece extrusion through both LTE and NLTE processes were performed for two different initial orientations of workpieces. In this way, a detailed comparative grain refinement performance by using crystal plasticity finite element analysis was addressed. The initial result reveals that the NLTE process has advantages in terms of punching force and deformation distribution. While the LTE process induces strain evolution, increasing from center element to periphery elements, more homogenous plastic strain distribution is examined in the NLTE process. In addition, the orientation distribution of the NLTE process is more homogenous when compared to the LTE process. The SPD analyses were performed under low friction coefficient and backpressure due to the convergence problems of implicit CPFEM UMAT code. For that reason, a more comprehensive analysis will be performed with explicit VUMAT code, and the results will be compared to experimental results as a next step.

References

[1] R.Z. Valiev, R.K. Islamgaliev, Bulk nan-structured material forms severe plastic deformation, Prog. Mater. Sci. 45 (2000) 103-189.

[2] P.Z Alexander, L.G Langdon, Using high-pressure torsion for metal processing: fundamentals and applications, Progr. Mater. Sci. 53 (2008) 893-979. https://doi.org/10.1016/j.pmatsci.2008.03.002

[3] A. Nassef, S. Samy, W.H. El Garaihy, Enhancement of mechanical properties for QAl-Mg-Si alloy using equal channel angular pressing, World Acad. Sci. Eng. Technol. 9 (2015) 131-136.

[4] M. Murashkin, I. Sabirov, D. Prosvirnin, I. Ovid'ko, V. Terentiev, R. Valiev, S. Dobatkin, Fatigue behavior of an ultrafine-grained al-mg-si alloy processed by high-pressure torsion, Metals 5 (2015) 578-590. https://doi.org/10.3390/met5020578

[5] Y. Saito, H. Utsunomiya, N. Tsuji, T. Sakai, Novel ultra-high straining process for bulk materials development of the accumulative roll-bonding (arb) process, Acta Metall. 47 (1999) 579-583. https://doi.org/10.1016/S1359-6454(98)00365-6

[6] A. Heczel, F. Akbaripanah, M.A. Salevati, R. Mahmudi, A. Vida, J. Gubicza, A comparative study on the microstructural evolution in am60 alloy processed by ECAP and MDF, J. Alloy. Compd. 763 (2018) 629-637. https://doi.org/10.1016/j.jallcom.2018.06.002

[7] Y. Beygelzimer, R. Kulagin, Y. Estrin, L.S. Toth, H.S. Kim, M.I. Latypov, Twist extrusion as a potent tool for obtaining advanced engineering materials: A review, Adv. Eng. Mater. 19 (2017) 1- 24. https://doi.org/10.1002/adem.201600873
[8] T. Yalçınkaya, Ü. Şimşek, H. Miyamoto, M. Yuasa, Numerical Analysis of a New Nonlinear Twist Extrusion Process, Metals 9 (2019) 1-15. https://doi.org/10.3390/met9050513
[9] S.R. Kalidindi, B.R. Donohue, S. Li, Modeling texture evolution in equal channel angular extrusion using crystal plasticity finite element models, Int. J. Plast. 25 (2009) 768-779. http://doi.org/10.1016/j.ijplas.2008.06.008
[10] M.I. Latypov, M. Lee, Y. Beygelzimer, D. Prilepo, Y. Gusar, H.S. Kim, Modeling and characterization of texture evolution in twist extrusion, Met. Mat. Soc. 1 (2015) 1-13.
[11] H. Sheikh, R.Ebrahimi, Modeling the effect of backpressure on dislocation cell structure during simple shear extrusion, UFGSNM 17 (2017) 1-9.
[12] Z. Xu, C. Zhang, K. Wang, K. Zhang, G. Zhao, L. Chen, Crystal plasticity prediction of texture evolution during helical extrusion process of aluminium alloys under three-dimensional deformation path, J. Alloy. Compd. 830 (2020) 1-16. https://doi.org/10.1016/j.jallcom.2020.154598
[13] Y. Huang, User-material subroutine incorporating single crystal plasticity in the ABAQUS finite element program, Mech. Report 178 (1991).
[14] T. Yalçınkaya, W. Brekelmans, M. Geers, BCC single crystal plasticity modelling and its experimental identification, Modell. Simul. Mater. Sci. Eng. 16 (2008) 1-16. https://doi.org/10.1088/0965-0393/16/8/085007
[15] E.B.W. Schmid, Plasticity of crystals with special reference to metals, Hughes &Co, London, 1950.
[16] D. Peirce, R.J. Asoro, A. Needleman, Material rate dependence and localized deformation in crystalline solids, Acta Metall. 31 (1983) 1951-1976. https://doi.org/10.1016/0001-6160(83)90014-7
[17] N. Fang, A new quantitative sensitivity analysis of the flow stress of 18 engineering materials in machining, J. Eng. Mater. Technol. 127 (2005) 192-196. https://doi.org/10.1115/1.1857935
[18] H. Yan, X. Zhao, N. Jia, Y. Zheng, T. He, Influence of Shear banding on the formation of brass-type textures in polycrystalline fcc Metals with Low Stacking Fault Energy, J. Mater. Sci. Technol. 30 (2014) 408-416. http://doi.org/10.1016/j.jmst.2013.11.010
[19] D. Raabe, F. Roters, Using texture components in crystal plasticity finite element simulations, Int. J. Plast. 20 (2004) 339-361. https://doi.org/10.1016/S0749-6419(03)00092-5
[20] L.A.I. Kestens, H. Pirgazi, Texture formation in metal alloys with cubic crystal structures, Mater. Sci. Technol. 32 (2016) 1303-1315. https://doi.org/10.1080/02670836.2016.1231746

Materials Research Proceedings 28 (2023) 563-570 https://doi.org/10.21741/9781644902479-61

Critical comparison of different techniques for producing profiled wires

KWIECIEŃ Marcin[1,a,*], MUSZKA Krzysztof[1,b] and MAJTA Janusz[1,c]

[1]AGH University of Science and Technology, Faculty of Metals Engineering and Industrial Computer Science, Al. A. Mickiewicza 30, 30-059, Krakow, Poland

[a]mkwiecie@agh.edu.pl, [b]muszka@agh.edu.pl, [c]majta@agh.edu.pl

Keywords: Metal Forming, Surface Quality, Wire Drawing Process

Abstract. Profiled wires manufactured by the drawing and rolling processes are widely used for production of industrial screens used in the particles separation processes. The main goals in the production processes of such screens are to obtain increased durability and surface quality due to its demanding working environment i.e. high abrasive wear and aggressive condition. The present studies were focused on the analysis of the effects of applied wire drawing and rolling processes on the mechanical properties and surface quality of the produced profile wires. The differences in the schedules of the metal forming processes as well as in the deformation inhomogeneities in the drawn products were analysed. As a result of the applied deformation methods, different surface quality and mechanical properties were obtained. The rolling process has been shown to provide better surface quality and a lower YS/TS ratio, which is critical for further deformations such as the bending process of round industrial screens. The investigations were preformed using austenitic stainless steel.

Introduction

Changes in the mechanical properties of the metallic materials are one of the main effects of plastic deformation processes. They become particularly important in drawing and rolling processes of the profiled wires where the effects of inhomogeneity of plastic deformation play a crucial role [1]. Controlling of the mechanical property distribution at the cross-section, especially in the case of profiled wires, creates new opportunities in the applications of such products. However, this requires a good knowledge of the relationships occurring between strain or strain rate and individual mechanical properties [2-4]. The development of such relationships is a part of the thermo-mechanical description of deformation process like drawing or rolling. Those can be considered as a crucial aspect in the case of multi-step deformation. The possibility of prediction of the level of yield stress (YS), tensile strength (TS) and the so-called yield ratio (YS/TS) [5] for the individual deformation steps have to be taken into account in the development of the metal forming processes [5-6]. Therefore, the main aim of the present work is to critically assess the effects of drawing and rolling on the mechanical properties, especially yield ratio, as well as the quality of precise profiled wires (Ra) aimed for filtration screens [7,8].

Experimental Procedure

In the present study AISI 304L austenite stainless steel was used in order to determine the differences in the mechanical as well as the microstructural behaviour of the material using different deformation process routes i.e. drawing and rolling processes. The chemical composition of the tested steel grade is presented in Table 1.

Content from this work may be used under the terms of the Creative Commons Attribution 3.0 license. Any further distribution of this work must maintain attribution to the author(s) and the title of the work, journal citation and DOI. Published under license by Materials Research Forum LLC.

Table 1. Chemical composition of the tested steel [wt. %].

Material	C	Mn	Si	S	P	Cr	Ni	N
AISI 304L	0.02	1.54	0.37	0.006	0.035	18.16	8.10	0.075

The tests were focused on the analysis of the influence of the deformation method i.e. wire drawing and rolling processes, on the mechanical properties as well as the microstructure development. Additionally, both analysed effects cause changes in the surface quality, which is very important in the case of the profile wires due to their application [8]. Schematic presentation of the process is shown in the Fig. 1. The final shapes and dimensions of the wires were similar. The dimensions of the profiled wires are presented in Table 2.

Table 2. Dimensions of the final thin profile wire.

Shape	Initial wire rod diam. [mm]	A [mm]	B [mm]	α [°]	
28Sb	3.55/3.43	2.20	4.50	23	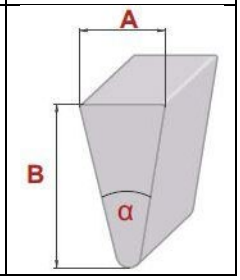

The rolling process was performed in three steps while the drawing process was conducted as four step process. In the case of rolling, the first step was performed on a duo rolling mill with flat rolls, followed by profile rolls. In the case of drawing, the first step involved flattening the wire rod in a two-roll drawing machine, while the second and third deformation passes were carried out using profiled roller dies - the so-called Turks head [9]. The samples after the rolling and drawing processes were tested for mechanical properties in tensile tests on the Zwick Z250 tensile machine with a strain rate of $0.1s^{-1}$. Roughness of the surfaces was measured using optical profilometer VykoNT9800/9300 from Veeco. The roughness was measured in three to five places in order to obtain average values.

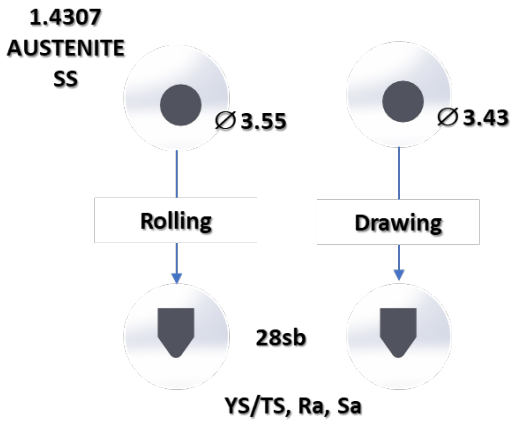

Fig. 1. Schematic presentation of forming schedule.

The microstructural changes were analysed using optical ZEISS Axio Imager M1m microscope. The microstructure analysis was performed in the initial wire rods and after last step of deformation, both in the drawn and rolled specimens.

Results and Discussion

The results of testing the mechanical properties of profiled wires obtained in the rolling and drawing processes are presented in Table 3. The profile wire was rolled from the initial diameter of 3.55 mm while the wire drawing process was conducted using initial wire diameter of 3.43 mm. The differences in diameters were caused by the conditions of the industrial process, where different diameters of wire rods were used in the rolling and drawing processes. The final mechanical properties of the finished products were measured to obtain the YS/TS ratio, since good formability is required for further bending of rounded filter screens. In both cases an increase of the mechanical properties was observed. The obtained results indicate that in the rolling process the YS/TS ratio was 91%, while in the drawing process it was 96%. These results clearly show that after the rolling process, the further stages of the screen manufacturing process (resistant spot welding and bending), especially in the case of cylindrical screens, will run more efficiently. In the case of drawn profile wires intended for further deformation (bending), an annealing process may be necessary to improve the ductility of more hardened materials.

Table 3. Mechanical properties of the AISI 304L stainless steel after rolling and drawing process.

Deformation Method	**Profile**	**YS** [MPa]	**TS** [MPa]	**YS/TS** [%]
Rolling	ϕ3.55 [mm]	637.0	863.8	73.75
	28sb	1313.1	1441.8	91.08
Drawing	ϕ3.43 [mm]	623.5	805.3	77.43
	28sb	1346.4	1399.9	96.18

The deformed wires were analysed both in terms of shape evaluation and microstructure development. Based on the analysis of the shape accuracy and macrostructure obtained from each stage of the drawing process (shown in Fig. 2), it can be observed that the plastic flow of the material, forced by the process conditions, gives the correct shape of the corners of the profile wires.

Fig. 2. Analysis of the shape of drawn profile wires after each stage of deformation.

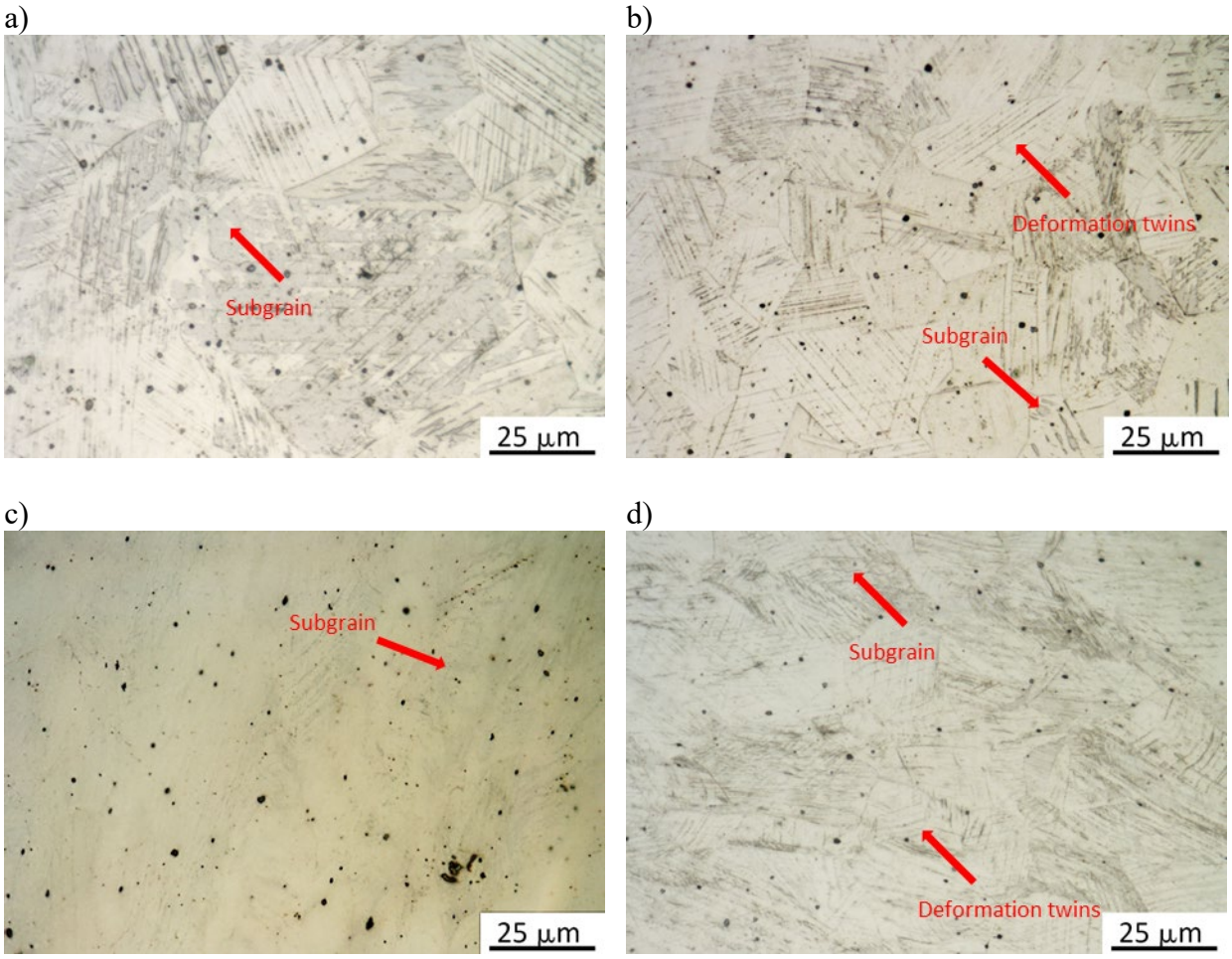

Fig. 3. Microstructures of the AISI 304L Austenitic Stainless Steel at the initial stage, in the centre -a) and close to the surface -b); profile wires after drawing process in the centre-c) and top surface of profile wired -d).

The initial material was characterized by equiaxial austenite grains with visible annealing twins. It was also observed that structural effects related to the martensitic transformation occurred (Fig. 3a, b). In the microstructures of the materials after drawing process it can be seen that the effect of the deformation caused forming the deformation twins (Fig. 3c). There are also visible areas where the deformation was initiated in two planes of slip (or twinning). However, no shear bands which are crossing grain boundaries can be observed. In the case of the near-surface areas of the layers, the microstructure of the deformed material indicates a more significant deformation, which can be estimated on the basis of a stronger deformation of grains and a larger amount of subgrains in the microstructure (Fig. 3d). Also, it can be seen that formation of the microstructure of the so-called lenticular structure, indicating a high degree of deformation of the material (about 80 %).

Materials Research Proceedings 28 (2023) 563-570 https://doi.org/10.21741/9781644902479-61

Fig. 4. Shape analysis of the rolled profile wires after each step of deformation.

The deformation degree during rolling process is significantly larger in each step of rolling due to higher reduction. The final shape, without deviations can be obtained in 3 step process (Fig. 4).

The microstructure of the initial wire rod is characterized by a high degree of homogeneity of austenitic structure (Fig 5a,b). In the microstructures of the material after rolling process, a slight degree of grain refinement can be observed, mainly in the central zone of the profile wire (Fig 5c). Final microstructure after rolling process in the top surface area of the profile wire can be characterized by high refinement of the grains without additional microstructural effects such as twinning or slip planes (Fig 5d).

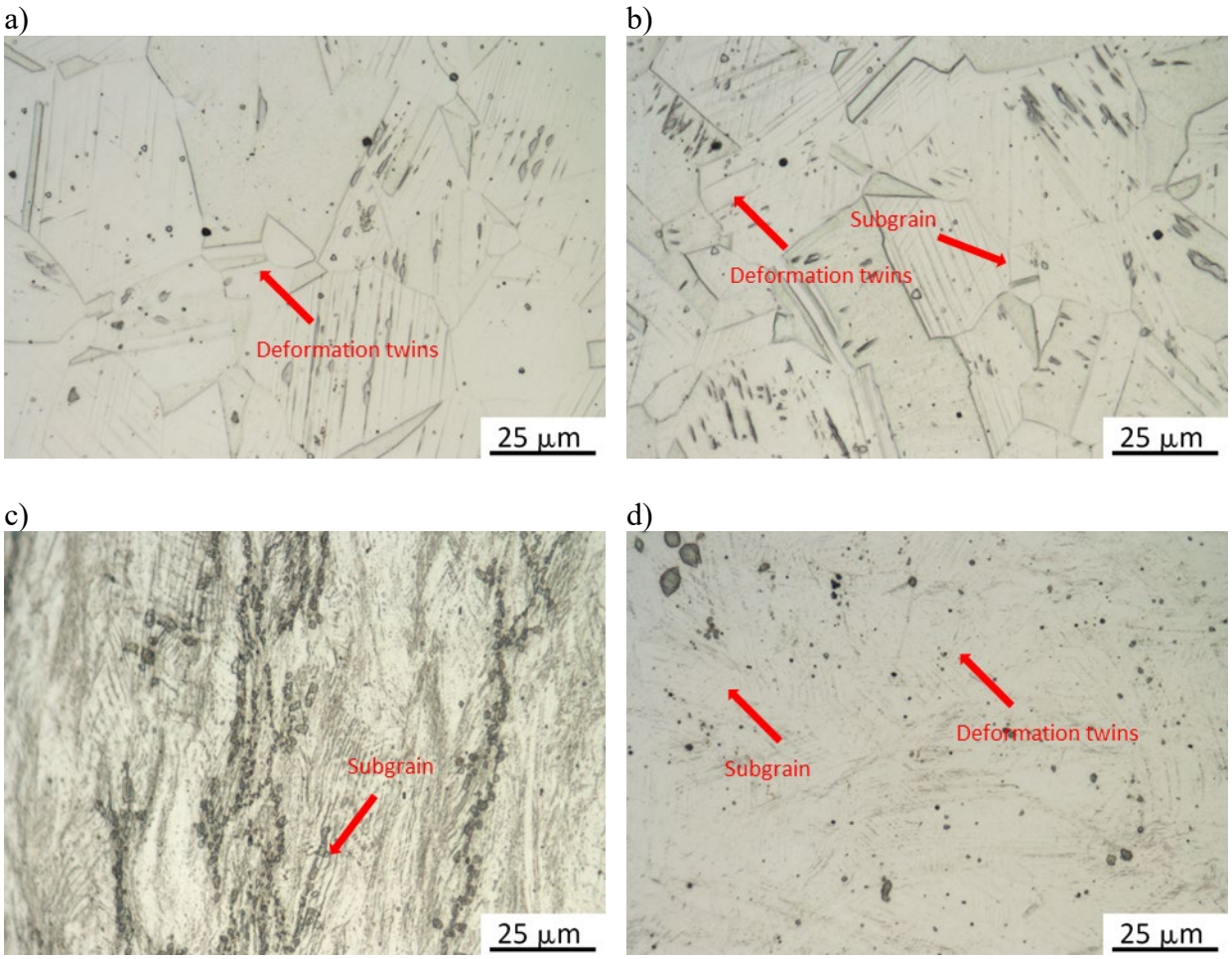

Fig. 5. Structure development of the AISI 304L Austenitic Stainless Steel at the initial stage, in the centre -a) and close to the surface -b); profile wires after rolling process in the centre-c) and top surface of profile wire -d).

According to customers' requirements the profiled wires used for industrial filtration screens must meet the requirements regarding the roughness of the surface, especially in the screens used in the offshore applications. The initial roughness Ra of the wire rod aimed for the rolling process was equal to 0.17 µm and in the case of wire rod aimed for the drawing process it was equal to 0.18 µm. After rolling Ra decreases to about 0.16 µm while after drawing process Ra increased to 0.25 µm. Such high increase was caused most likely by the low quality of die surface and the mechanical (stress and strain) state obtained in the drawing process. The obtained results suggest that the rolling process is more suitable for the profiles tested in the present study (28sb). All of the results of the roughness measurement are presented in Table 4.

Table 4. Surface roughness of the profile wires produced by two different metal forming processes.

Deformation Method	**Profile**	**Ra_{avg} [µm]**	**Sa_{avg} [µm]**
Rolling	ϕ3.43 [mm]	0.17±0,03	0.33±0,05
	Profile wire	0.16±0,01	0.51±0,04
Drawing	ϕ3.55 [mm]	0.18±0,03	0.34±0,03
	Profile wire	0.25±0,02	0.78±0,11

Summary

In the presented research results, the influence of two different metal forming processes on the surface quality, mechanical properties and microstructure of the produced profile wires was analysed. Based on the conducted research, it can be concluded that:
As expected, the applied metal forming process has a significant impact on the surface quality of finished products. Nevertheless, the presented studies have shown that in the current production conditions, the rolling process allows to obtain a lower, required surface roughness, mainly due to the mechanical state (state of deformation and state of stress) occurring during deformation. It should be expected that with sufficiently high surface quality of the tools used and changes in the deformation schedules (e.g. thanks to the use of the so-called smoothing threads - skin pass), these relationships may change. Such research will be the focus of further studies.

Acknowledgements

The support from the National Centre for Research and Development, Poland through the grant NCBiR POIR.01.01.01-00-0961/19.

References

[1] T.S. Cao, C. Vachey, P. Montmitonnet, P.-O. Bouchard, Comparison of reduction ability between multi-stage cold drawing and rolling of stainless steel wire - Experimental and numerical investigations of damage, J. Mater. Process. Technol. 217 (2015) 30-47. https://doi.org/10.1016/j.jmatprotec.2014.10.020
[2] M. Okayasu, D. Ishida, Effect of microstructural characteristics on mechanical properties of austenitic, ferritic, and γ-α duplex stainless steels, Metall. Mater. Trans. A Phys. Metall. Mater. Sci. 50 (2019) 1380-1388. https://doi.org/10.1007/s11661-018-5083-4
[3] K. Yoshida, Technological trend and problem in wire drawing of various super fine wires, J. Jpn. Soc. Technol. Plast. 41-470 (2000) 194-198.
[4] K. Yoshida, T. Shinohara, Growth and disappearance of flaws on wire surface in wiredrawing, Wire J. Int. (2004) 52-57.
[5] S.F.P.M Obers, J.J. Overal, W.J. Wong, C.L. Walters, The effect of the yield to tensile strength ratio on stress/strain concentrations around holes in high-strength steels, Mar. Struct. 84 (2022) 103205. https://doi.org/10.1016/j.marstruc.2022.103205
[6] F.C. Magalhães, A.E.M. Pertence, H.B. Campos, M.T.P. Aguilar, P.R. Cetlin, Defects in axisymmetrically drawn bars caused by longitudinal superficial imperfections in the initial material, J. Mater. Process. Technol. 212 (2012) 237-248. https://doi.org/10.1016/j.jmatprotec.2011.09.009
[7] T. Shinohara, K. Yoshida, Deformation analysis of surface flaws in stainless steel wire drawing J. Mater. Process. Technol. 162-163 (2005) 579-584. https://doi.org/10.1016/j.jmatprotec.2005.02.125
[8] T.S. Cao, C. Vachey, P. Montmitonnet, P.-O. Bouchard, Comparison of reduction ability between multi-stage cold drawing and rolling of stainless steel wire - Experimental and numerical

investigations of damage, J. Mater. Process. Technol. 217 (2015) 30-47. https://doi.org/10.1016/j.jmatprotec.2014.10.020
[9] J. Araki, H. Suzuki, Studies on wire drawing through Turks head rolls, Eng, 24 (1975) 81-114.

Forging and rolling

Materials Research Proceedings 28 (2023) 573-582 https://doi.org/10.21741/9781644902479-62

Design of a forging process to individually examine thermal, mechanical and tribological stress in the tool surface zone

BEHRENS Bernd-Arno[1,a], MÜLLER Felix[1,b] and LORENZ Uwe[1,c *]

[1]Institute of Forming Technology and Machines, Leibniz University Hanover, Germany

[a]behrens@ifum.uni-hannover.de; [b]f.mueller@ifum.uni-hannover.de;
[c]ulorenz@ifum.uni-hannover.de

Keywords: Forging Die, Tool Design, Numerical Investigation, Temperature Monitoring, Online Measurement

Abstract. The surface layer of hot forging tools undergoes local microstructural changes due to high thermo-mechanical and tribological loads. Tools made of hot working steel are usually pre-heated and experience extreme heating and cooling during each forging cycle, affecting their local wear behaviour significantly. Therefore, the analysis of these tool surface layers in die forging and their effect on wear behaviour is of great importance. The microstructural changes in the tool surface layer mainly depend on thermal loads, which are highly influenced by the tool cooling system. A process and a suitable tool system are developed to vary the thermal and mechanical loads on the tool surface layer and fundamentally examine the resulting microstructural changes.

Introduction

Tools in hot forging are exposed to high process related loads and stresses, for which a distinction can be made between thermal, mechanical, tribological and chemical loads. Thermal loads result from thermal expansion due to the increased base tool temperature. Additional thermal loads come from the frequent alternations between the rapid heating of the tool surface area during forming and the rapid cooling due to the relatively cold base material underneath. This is further increased by the cooling of the tools. The mechanical loads result from the forces on the tool during forging. Combined with the relative movement between the tool and the deforming work piece, these lead to tribological stress [1]. All of these loads can cause permanent damage to the tool surface area and ultimately lead to tool failure. The main reason for tool failure is predominantly the wear of the contours [2]. The loss of strength of the material in the tool surface layer is caused by the thermal loads and results in wear. During forging, peak temperatures in the thermally highly stressed tool areas exceed the tempering temperature of the tool material, thus softening the tool surface layer [3].

During forging the heated work piece is placed in the engraving, forged, taken out of the engraving, and subsequently cooled through convection and radiation by spraying the coolant and lubricant into the engraving. The temperature rises to its peak value during contact of the up to 1250 °C hot work piece and the tool with heat being transferred from the first into the latter. Following the forming process, there is a considerable drop of temperature in the engraving surface. The tool starts cooling with the warm work piece still in the die. Due to thermal conduction, the heat flows into the colder base material below the heated zone and thus reduces the contact temperature in the surface. After removing the work piece, the temperature of the engraving surface drops due to radiation and convection. Finally, the cooling lubricant is sprayed into the engraving which cools the tools below base temperature and thus exposes them to additional thermal stress. A considerable amount of heat is extracted from the tool by evaporation of the lubricant. As a result of the spraying process, the temperature in the tool surface area drops below the base tool temperature. Afterwards, the temperature of the engraving surface once again reaches the set base tool temperature and the next work cycle begins (Fig. 1, left) [4]. The base

Content from this work may be used under the terms of the Creative Commons Attribution 3.0 license. Any further distribution of this work must maintain attribution to the author(s) and the title of the work, journal citation and DOI. Published under license by Materials Research Forum LLC.

tool temperature can mainly be adjusted by the billet temperature, the amount coolant applied, the overall length of a forging cycles and the tool pre-heating.

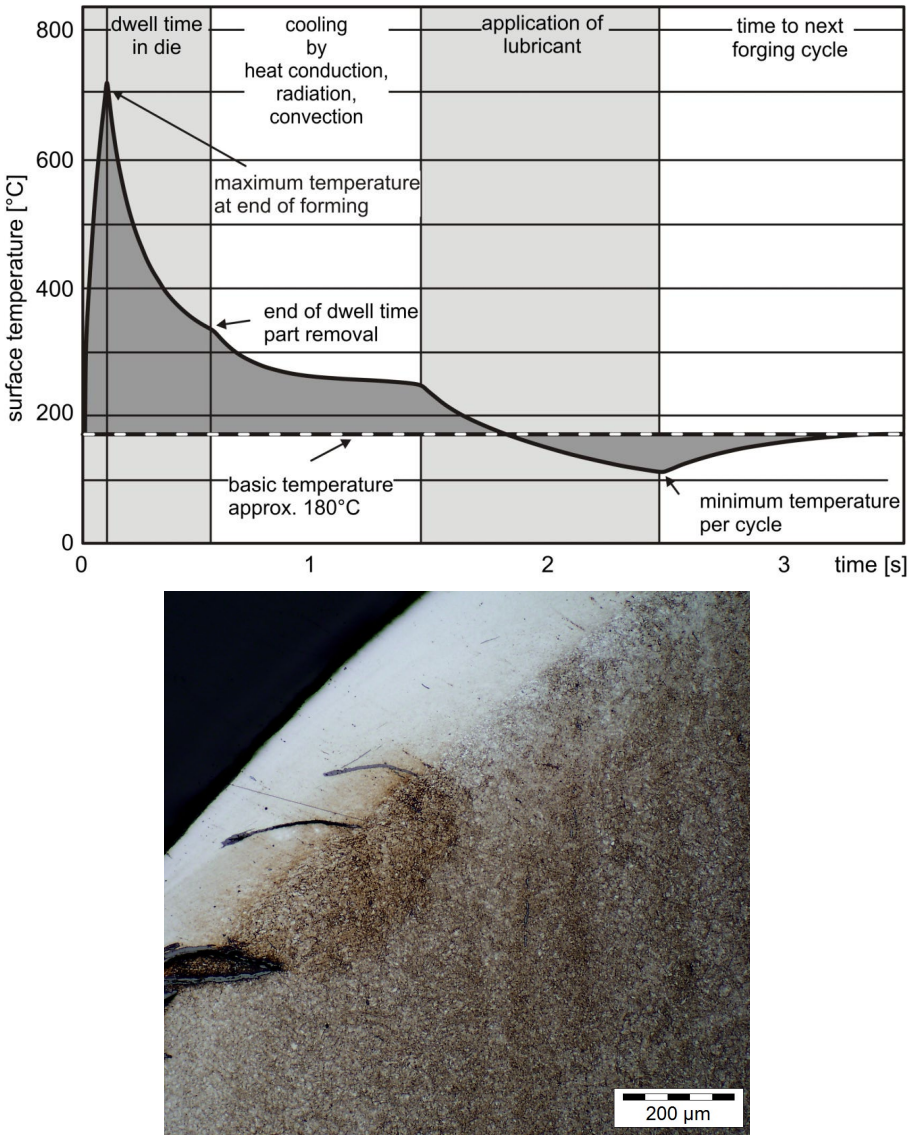

Fig. 1. Tool surface temperature during forging [4] and a tool surface layer with a white, rehardened zone.

The peak temperature in the tool surface area during a forging cycle depends mostly on the temperature of the work piece and the base tool temperature. The great differences between the work piece and base tool temperature lead to a high temperature increase in the tool surface layer during each forging cycle [4]. In metallographic analysis, rehardened tool surface layers often appear as white layers (Fig. 1, right). They form when the tool surface area is exposed to high temperature gradients exceeding the austenite start temperature in combination with cooling above the critical speed [5]. The effects of rehardened zones on the tool wear is controversially discussed in literature. Rehardened zones are often seen as component damage [6]. Some studies compare the rehardening of the tool surface layer as a heat treatment that strengthens the tool surface area [7] and refer to the potential of the special wear resistance when exposed to abrasive stress [8]. Due to engraving areas with convex radii being predominantly at risk of wear, structural changes in these tool edge areas have a decisive influence on the wear behaviour.

Separation of Lubricant and Cooling

To analyse the tool surface layer behaviour under different thermal conditions during forging, the tool cooling needs to be varied. In industrial forging, the lubrication is usually carried by the coolant. When applying a conventional water-graphite suspension to the tool surface area, the heat is dissipated by the evaporation of the water from the thermally sprayed tool areas and the friction conditions on the tool surface are improved by the remaining graphite. Since the cooling lubricant for the spray unit is usually premixed to ensure stable operation, a targeted control of the cooling by specifying a certain amount of water per area and time is not possible.

In order to enable targeted control of the cooling process, the cooling lubrication process has to be separated according to its functions into two independent processes, cooling and lubrication. Therefore, the cooling is carried out by an air-water mixture, which is applied to the tool surface via a spraying system by Gerlieva. The control unit of the supply system can be used to specifically regulate air-water spray parameters such as pressure and duration. The regulation of the spray parameters is to take place in such a way that different base tool temperatures are achieved. Next, the lubrication process is designed. Due to the functional separation of cooling and lubrication, the possibility of conventional lubrication, e.g. by means of a water-graphite suspension, is no longer applicable. For lubrication, the technology of electrostatic powder application is used with powdered boron nitride as the lubricant. Studies have shown that this type of lubricant application can significantly reduce tool wear [9]. Lubrication is applied by a powder coating system by ITW / GEMA Oberflächentechnik. Due to the functional separation of cooling and lubrication, the application is carried out in two stages. Cooling is stage I and lubrication stage II. The lubrication process is controlled by regulating the applied voltage potential, as well as the disperse duration and pressure.

Material Characterization

Steels of different strength are formed to determine the influence of the mechanical load on the tool surface layer. The yield strength of the materials have a direct influence on the mechanical stress on the tool, which in turn influences the transformation behaviour of the material in the tool surface layer. The AFP (Precipitation hardening ferritic-pearlitic) steel 38MnVS6 is selected due to its high-alloy content (Table 1). Because of this, comparatively high flow stresses at high temperatures and thus high mechanical loads on the tools during hot forming when compared to the low alloyed steel C45 are expected. The last mentioned steel is also picked for this study to represent a common forging steel with the option of heat treatment.

Table 1. Chemical composition of the materials under consideration according to the manufacturer's specifications (wt. %).

	C	Si	Mn	P	Cr	Mo	V	N
38MnVS6	0.34 – 0.41	0.15 – 0.80	1.20 – 1.60	0.025	< 0.3	< 0.08	0.08 – 0.2	0.01 – 0.02
C45	0.45	0.25	0.65	-	-	0.020 – 0.035	-	-
X37CrMoV5-1	0.41	0.97	0.32		4.77	1.30	0.46	

For a realistic numerical representation of the mechanical material behaviour of the steels, flow curves of both forging steels are needed at different strain rates and temperatures to calculate the loads on the tool during forging. Flow-curves are recorded through uni-axial cylinder compression tests, which are carried out at constant deformation rates of 0.1, 10 and 50 s^{-1} at process-relevant temperatures of 700°C, 1,000°C and 1,200°C. Tests are performed in the forming simulator

Gleeble 3800 GTC by DSi. The sample temperature is set by using controlled conductive heating controlled by type K thermocouples. To ensure statistical validation, at least three test repetitions are carried out. Based on the force-displacement curves obtained, the effective flow stress k_f is determined as a function of the equivalent plastic strain ϕ, the rate of deformation $\dot{\phi}$ and the forming temperature T. After the experiments, the flow curves are fitted and extrapolated using the Hensel-Spittel 1 model [10] for 38MnVs6 following methods already presented in detail in [11]:

$$k_f = A \cdot \varphi^{m_1} \cdot \dot{\varphi}^{m_2} \cdot \varphi^{-m_3/T} \cdot e^{m_4/\varphi} \quad (1)$$

A = 2550, m1 = - 0.0028, m2 = - 0.076, m3 = 0.1 and m4= - 0.03

For C45 the GMT Model [15] was applied:

$$k_f = c_1 e^{c_2 T} \cdot \varphi^{n_1+Tn_2} \cdot e^{\frac{l_1 T+l_2}{\varphi}} \cdot \dot{\varphi}^{m_1 T+m_2} \quad (2)$$

C_1 = 3600, C_2 = - 0.038, n_1 = 0.000044, n_2 = - 0.05, l_1 = - 0.00003, l_2 = - 0.0006, m_1 = - 0.00009 and m_2 = - 0.02

The resulting flow curves are displayed in Fig. 2. The thicker drawn lines represent the mean experimentally measured flow curve, while the thinner lines represent the corresponding calculated curve from the fitted extrapolation model. As displayed, the flow resistance of 38MnVs6 steel is 10-20% higher, depending on the forming conditions. In the higher temperature range, a more pronounced strengthening of 38MnVs6 as a function of the strain rate is noticeable.

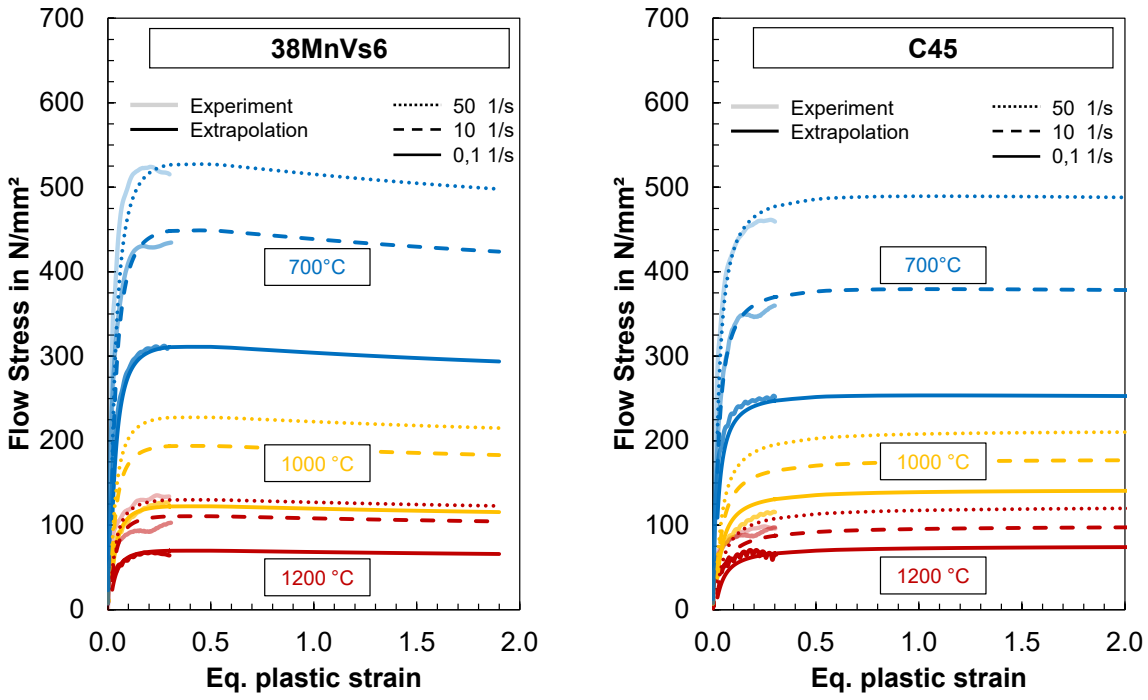

(a) (b)

Fig. 2. Recorded and extrapolated flow curves for the steels 38MnVs6 (a) and C45 (b).

Additionally, in order to be able to assess in the context of a numerical load study whether the tool can withstand the mechanical load during forging, the yield strength of the used tool steel

X37CrMoV5-1 (case hardness: 48+2 HRC) is also determined using uni-axial compression tests carried out with the Gleeble 3800 GTC forming simulatior at temperatures of up to 800°C. The yield strength $R_{p0,2}$ of the tool steel X37CrMoV5-1 is noted in Table 2 for different temperatures and determined according to the method presented in [13]. It becomes clear that a high strength is maintained at a temperature of up to 400°C. Stepping up to a temperature of 800°C, which can be reached in the tool surface layer [4], shows a strong decrease in the tool yield strength. Especially at this temperature, the expected risk of plastic deformation increases based on the measured yield strengths.

Table 2. Recorded yield strength $R_{p0,2}$ of X37CrMoV5-1 at process relevant temperatures.

	20 °C	**200 °C**	**400 °C**	**800 °C**
X37CrMoV5-1	1888 MPa	1703 MPa	1512 MPa	409 MPa

Tool Design

A rotationally symmetrical tool system, which experiences high thermal loads in the surface area during forging, is selected for easy adjustment of the thermal loads. The dies are to be made of hot working tool steel X37CrMoV5-1 (case hardened to 48+2 HRC). The geometry of the upper die has engravings, where locally different loads occur during forging (Fig. 3, left). In previous research results, it was shown that these tools display the essential structural changes and the associated wear due to abrasion and plastic deformation, which mainly occurs on the convex tool radius. Besides high surface pressures, a high thermal load is to be expected at these points due to the relatively long time of contact and the deep penetration of the tool into the work piece. To characterize the cooling behaviour, the tool temperature during forging is analysed. The temperature development of the near-surface edge areas is recorded by using thermocouples (TC) inserted into the tool. The recording takes place continuously over the entire forging process during the heating and cooling phases. Encapsulated Type K thermocouple with a 1.5 mm diameter are selected for which 1.6 mm diameter holes are integrated into the tools. The TC wiring is to exit the tools to the sides (Fig. 3, right). Thermal paste is used to increase the heat transfer and decrease reaction time between the tool and the TC.

Numerical Investigation of the Die Load

In order to enable a realistic prediction of the die load, an FE model of the forging process is set up using the FE application *simufact.forming 16*. Due to the complex tool geometry with six channels for the TC, a complete 3D model is necessary to theoretically derive a sink load in each channel (Fig. 3, right).

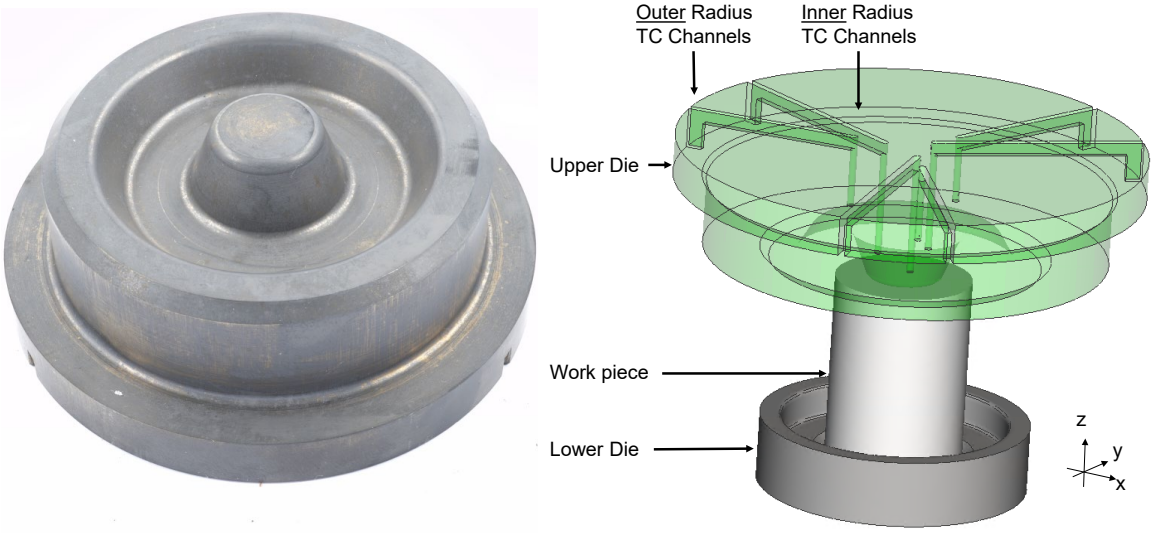

Fig. 3. Upper forging die (left) and CAD-view of the 3D-FE calculation model showing the Initial design of the upper die with channels for thermocouples (right).

For this purpose, the upper die is modelled fully thermo-mechanically coupled, while the lower die is set as an analytically rigid body. To reliably assess the tool stability, the most extreme parameter set is mapped in the process model, at which the highest thermo-mechanical load is expected. These are at a base tool temperature of 400°C, a work piece temperature of 1200°C, a friction factor of m = 0.6 and the material data set of the steel 38MnVs6. With these parameters, the stationary state during series forging is represented in the FE simulation. For a later evaluation of the temperature-time history, the return stroke and the subsequent cooling phase are taken into account in addition to the actual forming step. The influence of the spray cooling is taken into account by applying corresponding heat transfer coefficients, which were previously determined experimentally in [11].

To evaluate the numerical results regarding the thermo-mechanical loading, a sectional plane of the tool with the TC channels closest to the surface is shown in this study. In the following illustrations, the TC channels are also highlighted with a black or white outline for better visibility.

Fig. 4 shows the calculated temperature distribution at the end of the forming process before the removal of the part and spray cooling for the mentioned parameter set. This shows that a peak temperature of approximately 900 °C is reached in the mandrel radius of the die engraving. Based on this, a re-hardening of the tool surface layer can be expected after cooling. Furthermore, the heat-affected zone does not reach the tips of the channels during the forming process, which can be seen as advantageous for the structural die stability. However, this circumstance prevents the measurement from being able to resolve the direct surface heating caused by the work piece contact.

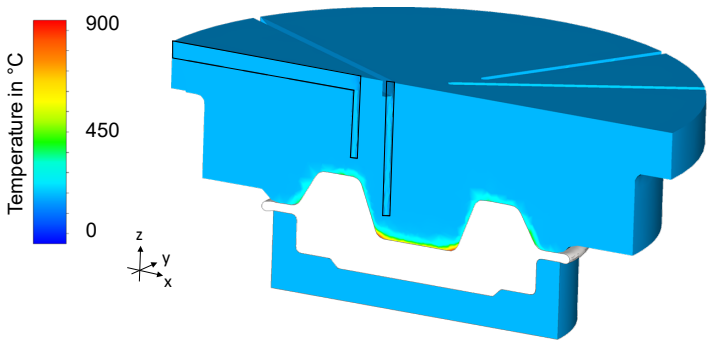

Fig. 4. Temperature distribution in the upper die at the end of forming.

For the evaluation of a possible crack risk, the common main normal stress hypothesis according to Rankine is applied, which can be used as a first assessment criterion for brittle fracture materials, such as the hardened tool steel used here [14]. In order to make crack-critical areas directly visible, only the 1st principal stress (tensile stresses) exceeding the experimentally determined yield strength at 400 °C is visualised in Fig. 5.

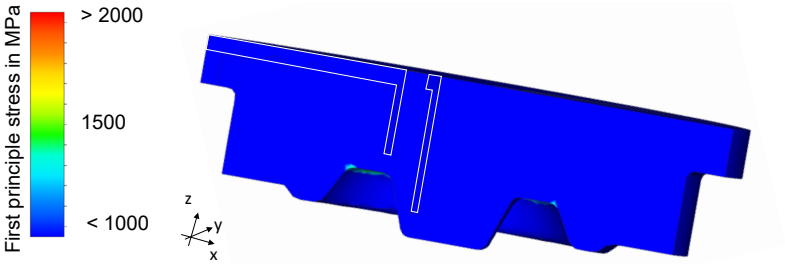

Fig. 5. First principle stress distribution on the upper die limited to the critical value range.

This allows for a clear assessment, that the areas around the TC channels are not under significant tensile load and thus uncritical with regard to a possible risk of cracking. Only in the area of the inner radii of the engraving slight cracking can be expected, which is also known from previous studies with this die geometry [7].

For the estimation of plastic deformation, the yield criterion according to von Mises is applied to compare the flow stress in the die with the experimentally determined values for the yield strength. It must be taken into account that the die load increases exponentially towards the end of the forming process. Thus, the von Mises comparative stress at three different stages of the forming stroke, characterised by the respective burr thickness subsequently measurable on the component, is shown in the following Fig. 6.

These different stroke lengths in respect to the burr thickness are chosen starting from the stroke at which a complete filling (burr thickness = 2.4 mm, Fig. 6, a) is achieved. Fig. 6, c) clearly shows that a critical condition is reached, when a burr thickness of 1.6 mm is formed, as the equivalent stress in the centre of the die exceeds the experimentally determined yield point at 400°C. In relation to the TC channels, an unwanted deformation of the channel walls would most likely occur at this stage of forming as well. Reducing the forming stroke length results in a reduction of the burr thickness to 2.0 mm (Fig. 6, b), with the burr being less strongly formed radially. By reducing the forming stroke, the loads on the tool decrease, as less material has to be displaced into the decreasing burr gap. At this stroke setting the von Mises stress does not exceed the given yield strength so there is a significantly reduced risk of deformation. Keeping in mind that the chosen

process parameters for this stability estimation represent the most extreme case, for further forging experiments, this forming stroke length will be used for experimental forging tests.

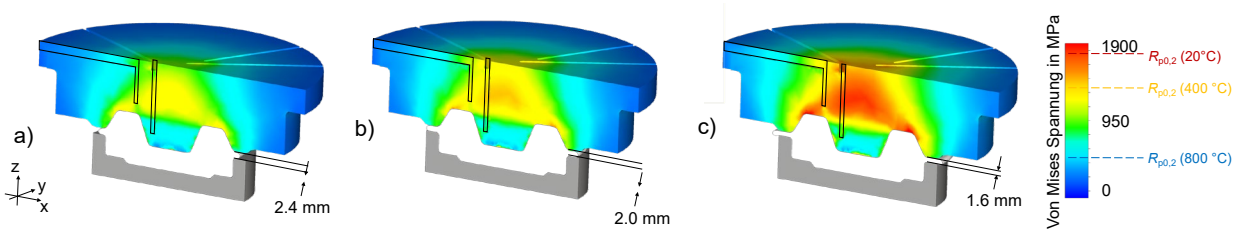

Fig. 6. Distribution of von Mises stress in the die at different stroke lengths.

Regarding the general die design, however, it became clear that the outer radius TC channel tips are located directly in a mechanical loaded area. This implies that the heath thermocouples used in the process are also subjected to mechanical stress. Since these cannot be represented and analysed within the framework of the FE analysis, it can be concluded from the results shown that damage to the measuring tip might not be completely ruled out. There is therefore a risk that no valid data can be recorded in the process without any recognisable signs of damage being visible from the outside resulting in invalid data. Furthermore, the simulation shows that the position of the TC channels is not close enough to the surface zone to record its heating phase. With this application, the temperature measurement can however be used to reliably validate the base tool temperature in the mandrel area. With regard to these two findings, it is concluded that the outer TC channels offer no added value and can therefore be assessed as an unnecessary risk. These channels are therefore removed in the following design update and the demonstration tools are manufactured accordingly (Fig. 7).

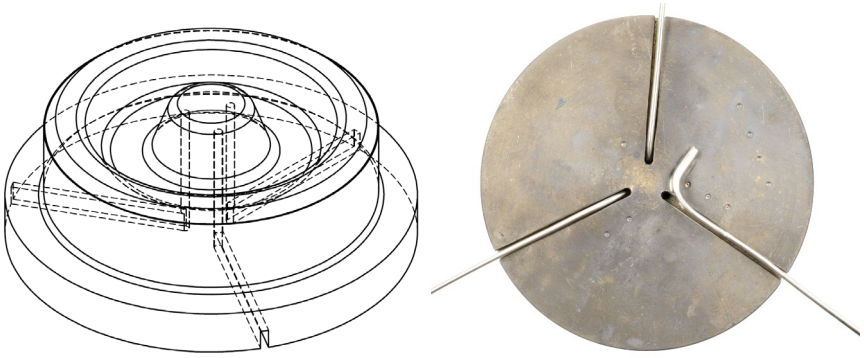

Fig. 7. Updated die Design for thermally loaded tool with channels for three mantled thermocouples.

A tool equipped with TC is then stressed in forging tests. The tool is pre-heated to 200°C. Cylindrical work pieces made of steel C45 are used with a diameter of 30 mm and a height of 40 mm. The billets are heated to 1200°C and forged with a forging cycle time of 8 s. Between each forging cycle, boron nitride powder is applied for lubrication and water is sprayed for cooling. Fig. 8 shows the comparison of the measured temperature curve with the numerically determined one during a forging cycle for a tool base temperature of 200°C. Here a characteristic deviation is recognizable, as the temperatures in the simulation are evaluated directly on the bottom of the channel wall, while in reality there is an additional heat transition from the channel wall to the mantle thermocouple. This reduces the measurement dynamics that can be achieved in reality and consequently shifts the measured temperature curve to lower and time-delayed values. In practice,

this deviation has no relevant influence on the validity of the die stress simulation carried out. In fact, the example of an excerpt from the recorded temperature-time curve shows that it was possible to achieve highly reproducible process execution.

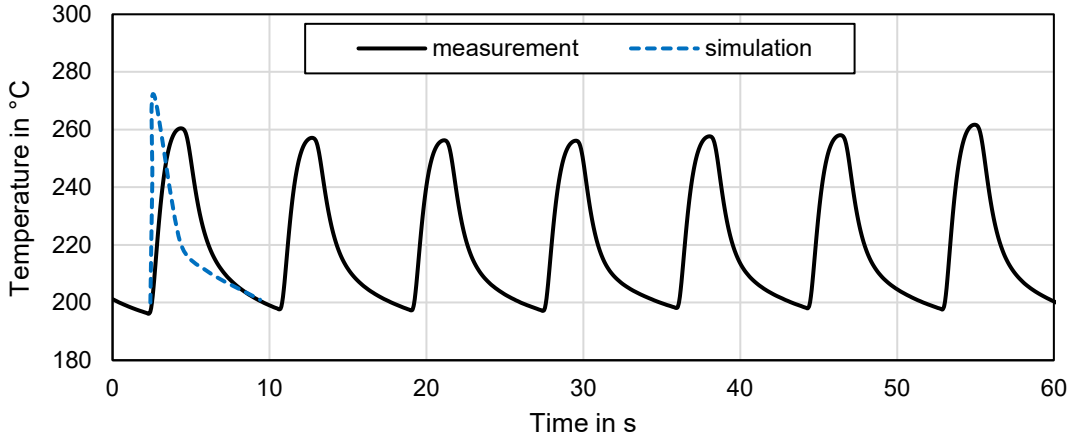

Fig. 8. Temperature measurement at the tool mandrel.

Summary

The main objective was to develop a process to investigate microstructural changes in the surface zones of hot forging dies under varying cooling conditions, as well as varying tribological and mechanical loads. A primarily thermally loaded tool system was investigated and equipped with multiple internal TC at predetermined positions for better regulation of the tool temperature. To ensure structural stability of the tool system, the thermo-mechanical loads on the die were calculated using a FE-model. The mechanical stresses on the dies will be altered by varying the forging steels of different flow resistance. The necessary material data regarding the mechanical behaviour was obtained by uniaxial compression tests using the forming simulator Gleeble 3800 GTC. To investigate the influence of thermal and tribological loading on the microstructure in the surface zone, cooling and lubrication strategies were developed, achieving different stationary die temperatures. Here, the separation of lubrication and cooling functions replaced the conventional lubrication with a water-graphite suspension by using boron nitride powder for lubrication and a water-air-combination for cooling. With these methods, temperature measurements at a short distance from the surface can be carried out and monitored during forging. During forging tests it was shown that for a base temperature of 200°C the peak temperature values after each forging cycle are consistently ranging around 260°C. Taking into account the aforementioned dynamic losses of the thermocouple measurement, this corresponds to an actual measured value of approximately 270°C at the selected measuring point.

Acknowledgements

The presented investigations are carried out within the project ID 349885770 “Influence of cooling of forging dies on the process-related microstructural changes in the surface zone and their effect on wear behaviour” of the German Research Foundation (DFG). We are thankful for the assistance provided.

References

[1] R. Seidel, H. Luig, Friction and wear processes in hot die forging, in: H. Berns et al., New Mat. Processes Experiences for Tooling, CH-Andelfingen, MAT SEARCH, 1992, pp.467-480.
[2] K. Lange, L. Cser, M. Geiger, Tool life and tool quality in bulk metal forming, CIRP Ann. Manuf. Technol. 41 (1992) 667-675. https://doi.org/10.1016/S0007-8506(07)63253-3

[3] S. Joshy, K.R. Jayadevan, A. Ramesh, Influence of in-service thermal softening on wear and plastic deformation in remanufactured hot forging dies, Eng. Res. Express 1 (2019) 025024. https://doi.org/10.1088/2631-8695/ab504f
[4] W. Stute-Schlamme, Konstruktion und thermomechanisches Verhalten rotationssymmetrischer Schmiedegesenke, Dissertation, Universität Hannover, 1981
[5] B.J. Griffiths, D.C. Furze, Tribological advantages of white layers produced by machining, ASME Trans., J. Trib. 109 (1987) 338-342. https://doi.org/10.1115/1.3261363
[6] Y.Y. Yang, H.S. Fang, W.G. Huang, A study on wear resistance of the white layer, Tribol. Int. 29 (1996) 425-428. https://doi.org/10.1016/0301-679X(95)00099-P
[7] B.-A. Behrens, J. Puppa, U. Lorenz, Development of an intelligent hot-working steel to increase the tool wear resistance, The 11th TOOLING 2019 conference & exhibition, 2019
[8] L. Xu, S. Clough, P. Howard, D. StJohn, Laboratory assessment of the effect of white layers on wear resistance for digger teeth, 1995
[9] J. Puppa, B.-A. Behrens, Optimization of cooling and lubrication for nitrided and ceramic-coated hot forging dies, Appl. Mech. Mater. 794 (2015) 97-104. https://doi.org/10.4028/www.scientific.net/AMM.794.97
[10] A. Hensel, T. Spittel, Kraft- und Arbeitsbedarf bildsamer Formgebungsverfahren, Verlag Grundstoffindustrie, 1978
[11] B.-A. Behrens, J. Gibmeier, C. Kock, Investigations on Residual Stresses within Hot-Bulk-Formed Components Using Process Simulation and the Contour Method, Metals 11 (2021) 566. https://doi.org/10.3390/met11040566
[12] Gesellschaft für metallurgische Technologie- und Softwareentwicklung mbH, „MatILDa,“ [Online]. Available: https://www.gmt-stahl.de/en/matilda-2/. (accessed on 08 January.2020)
[13] I.Y. Malik, U. Lorenz, B.-A. Behrens, Microstructure and wear behaviour of high alloyed hot-work tool steels 1.2343 and 1.2367 under thermo-mechanical loading. Proc. IOP Conf. Ser. Mater. Sci. Eng. 629 (2019) 012011. https://doi.org/10.1088/1757-899X/629/1/012011
[14] W. Rankine, On the stability of loose earth. Philos. Trans. Royal Soc. London 147 (1857) 9-27. https://doi.org/10.1098/rstl.1857.0003

Materials Research Proceedings 28 (2023) 583-590 https://doi.org/10.21741/9781644902479-63

Hot die forging with nitrided and thermally stabilized DLC coated tools

SIEGMUND Martin[1,a *], KIPP Christian[2,b], PEDDINGHAUS Julius[1,c], BRUNOTTE Kai[1,d], BRÄUER Günter[2,e] and BEHRENS Bernd-Arno[1,f]

[1]Institute of Forming Technology and Machines, Leibniz Universität Hannover, An der Universität 2, 30823 Garbsen, Germany

[2]Institute for Surface Technology, Technische Universität Braunschweig, Bienroder Weg 54 E, 38108 Braunschweig, Germany

[a]siegmund@ifum.uni-hannover.de, [b]chrkipp@tu-braunschweig.de, [c]peddinghaus@ifum.uni-hannover.de, [d]brunotte@ifum.uni-hannover.de, [e]guenter.braeuer@ist.fraunhofer.de, [f]behrens@ifum.uni-hannover.de

Keywords: Hot Die Forging, Wear, Nitriding, Coating, Tool Life, Diamond-Like Carbon

Abstract. Hot forging dies are subjected to high loads, which can lead to early tool failures. Abrasive wear, plastic deformation and thermal softening of the surface layer can be counteracted in particular by a high surface hardness. Thermochemical diffusion treatments and coatings are established as wear protection measures. DLC coatings, which feature excellent frictional properties and high hardness, are commonly applied on cold forging tools. However, the low coating adhesion to steel and the thermal stability of the diamond bond limit the current range of application. In this study, DLC coatings are applied in metallic treatment atmospheres with the aim of increasing the diamond bond's temperature resistance. Furthermore, the influence of weak and intense nitriding to coating adhesion is investigated to reduce coating delamination. A pre-selection of modified DLC coatings for hot forging dies was carried out on the basis of hardness and scratch tests. The most promising tungsten DLC coating was tested in serial forging tests. Based on tool contour comparisons before and after forging, the potential as a wear protection measure for hot forging dies was determined. Tool wear was reduced by up to 29 % after 100 forging cycles with the tungsten DLC coating compared to the nitrided reference.

Introduction

Hot die forging is an economical process for the production of dynamically loaded high strength components in large quantities. About 15 % of the economic efficiency of forging processes is determined by tooling and setup costs [1]. An increased tool life can reduce these costs, enabling the forging industry to compete on an international market.

The primary limiting factor for the lifetime of hot forging dies is wear, which results from the high mechanical, thermal, tribological and chemical process-related loads. Abrasive wear describes the loss of material from the surface of a solid component caused by the contact and relative movement of an opposing object. In addition, these superimposed loads can cause plastic deformation and cracking [2]. The surface layer of the forging dies softens in contact with the hot blanks, which promotes abrasive wear and plastic deformation [3]. The use of cooling lubricants reduces the thermal tool load. However, the resulting cyclic temperature change leads to tensile and compressive stress changes in the tool surface layer, which can cause the formation of thermomechanical crack networks [4].

Common wear protection measures for hot forging dies aim to increase the hardness of the surface layer, to counteract abrasion, plastic deformation and thermal softening. Therefore, thermomechanical diffusion treatments such as nitriding are established processes. Diffusion of

Content from this work may be used under the terms of the Creative Commons Attribution 3.0 license. Any further distribution of this work must maintain attribution to the author(s) and the title of the work, journal citation and DOI. Published under license by Materials Research Forum LLC.

the nitrogen into the tool surface layer results in the formation of a nitrided zone. It consists of a compound layer and a diffusion zone. The compound layer is a complete conversion of the steel surface in iron nitrides. In the diffusion zone nitride precipitations are formed. Coatings can be applied to further increase hardness and thus wear resistance. Duplex treatments are commonly used, i.e. the coating is applied on nitrided surfaces. Nitriding counteracts early coating cracking, which is associated with softer surface layers below the coating (also known as "egg shall" effect) [5].

In cold forming processes, diamond-like carbon coatings are used for wear protection of forging dies [6]. The amorphous hydrogen-containing layers exhibit stochastically distributed networks of carbon and hydrogen. Both sp^2- and sp^3-hybridized forms of carbon are simultaneously present [7]. The first form describes the graphite bond and is known for its excellent friction properties. In sp^3-hybridized form (diamond bond), the carbon atoms are arranged as a tetrahedron, resulting in a high hardness of 1500 – 3500 HV [8]. A major disadvantage of DLC coatings is their low adhesion to steel, which leads to an early coating delamination. This is related to an inappropriate residual stress condition due to the application process [9]. Li et al investigated the influence of the sp^3/sp^2-ratio on DLC coating adhesion. They determined that an increased sp^3 content increases the hardness, but also reduces the toughness and thereby the adhesion of the coating [10]. Another promising approach to increase coating adhesion is prior plasma nitriding, which results in a less precipitous hardness gradient [11]. Due to the diamond bond's low thermal stability, the field of applications of DLC coatings is limited, i.e. decomposition in air occurs at approximately 700°C and under loads earlier. According to Behrens et al, temperature resistance can be increased by metallic elements in the treatment atmosphere. This has been proven in particular for the element's chromium and tungsten [12].

In this study, modified treatment atmospheres for DLC coatings containing the previously mentioned and other metallic elements are investigated with the aim of delaying or shifting the coating decomposition to higher temperatures. Furthermore, a suitable nitriding to increase the adhesion of the coating is to be determined. This is intended to enable the coatings to withstand the loads from hot die forging (up to 1200°C, currently up to 700°C).

Methods

First, the procedure for specimen and tool fabrication is explained. Furthermore, the surface layer modifications are described. Appropriate coating characterization methods are used to determine the most promising DLC coating which is applied to hot forging dies. The DLC coated tools and nitrided references are used in serial forging tests. Wear behavior is investigated by high-resolution images, contour comparisons and metallographic analysis.

Specimen and tool fabrication.

All specimens (ø35 mm x 4 mm) and tools were made of hot work tool steel AISI H11 and quenched and tempered to a hardness of 48 ± 2 HRC. Prior to nitriding, the surface was blasted with glass beads and cleaned.

Surface modification.

The surface modification includes nitriding and DLC coating of specimens and tools. A pre-selection of suitable DLC coating systems for hot forging dies is determined on the basis of microhardness tests and scratch tests.

Nitriding.

Two different nitriding processes were applied to the specimens (co. Rübig Anlagentechnik, type PN 100/150). Both nitriding treatments were carried out at a temperature of 520°C and for a duration of 16 h. The pulse-pause ratio was 100 µs (pulse) to 500 µs (pause). A pressure of 300 Pa was adjusted in the treatment chamber. As a significant difference, the nitrogen content in the treatment atmosphere was varied (10 % and 80 % N_2), the other part of the atmosphere was hydrogen.

DLC-Coating.

In total, three metal-containing DLC coating systems were applied to previously nitrided specimens (10 % and 80 % N_2) with the aim of increasing temperature resistance. The DLC coatings were applied on a PACVD coating system. Niobium (40 %) and tungsten (30 %) were used as atmosphere modifying elements (Nb40 and W30), due to the high potential already identified in previous studies [12]. In addition, a combined DLC coating system containing the elements niobium (20 %) and chromium (20 %) was investigated (Nb20Cr20).

Layer characterization.

To determine the influence of the metallic elements in the treatment atmosphere on wear-reducing properties, such as high hardness, microhardness measurements according to Vickers were carried out. These were performed according to DIN EN ISO 6507 with a microhardness tester (co. Qness, type Q10A+). The hardness of the DLC coating was measured three times for each specimen and the standard deviation was determined. Furthermore, the Lc2 value was determined three times for each specimen after tempering the specimen at 600°C in scratch tests according to DIN EN ISO 20502 (co. Rtec Instruments, type SMT-5000), which describes the delamination of coatings.

Serial Forging Tests.

For characterization of the application behavior and qualification of DLC coated hot forging dies, serial forging tests were carried out on an eccentric press (co. Eumuco, type SP30d). A fully automated blank feeding system, forged part removal and spray cooling provide reproducible process conditions (Fig. 1, left). The blanks were made of the steel AISI 4140 with the dimensions ø30 x 40 mm. An inductive push-through heating system was used to heat the blanks. In one series of experiments, the blanks were heated to 1200°C and in another to 900°C. Between the forging cycles, a graphite-containing lubricant (co. Carl Bechem, type Berulit 906 HP) was applied in a ratio of 1:10 mixed with water. The forging dies were preheated to a temperature of 180°C.

In the serial forging tests, a highly tribological loaded forging die geometry was investigated, which is characterized by long material flow distances (Fig. 1, right). The forging dies were loaded up to 100 (900°C) and 1500 forging cycles (1200°C). Based on the layer characterization, the most promising coating DLC (W30) was applied to the previously quenched, tempered and nitrided (10 % and 80 % N_2) tool surfaces. In addition to the coated hot forging dies, quenched and tempered (unnitrided) as well as nitrided (10 % and 80 % N_2) reference tools were investigated.

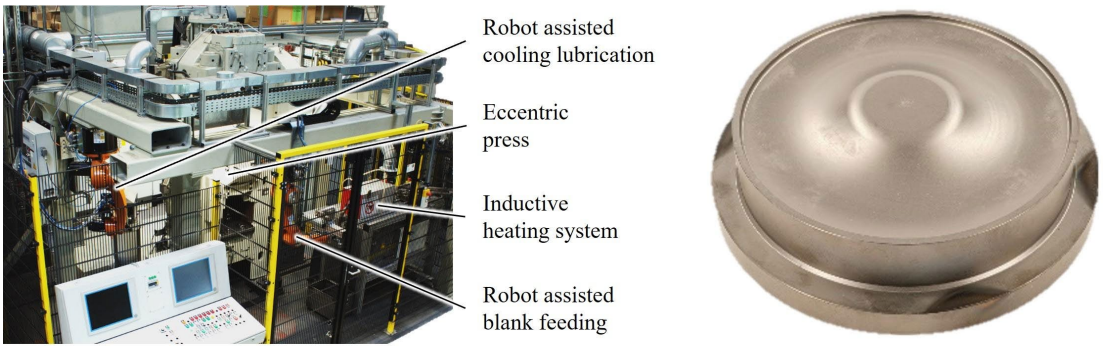

Fig. 1. Fully automated serial forging process (left) and high tribological loaded hot forging die (right).

Wear analysis.

The performance and wear progress were characterized in dependence of the forging cycles. For this purpose, high-resolution images of the wear-critical central elevated area were obtained (cf. Fig. 4) using a 3D profilometer (co. Keyence, type VR- 3200). Based on these images, an

initial wear analysis was carried out. Additional images were taken of non-critical wear areas, which were used to reference the tool contours before and after forging (cf. Fig. 5). The area between the profiles represents the planimetric wear which was determined according to DIN 50320. Six contour measurements were defined for each tool. Due to the focus depth, the area of analysis was limited to ±14 mm from the tool center. All specimens were metallographically prepared and etched with Nital to examine the microstructure and surface layer through light microscopy (co. Zeiss, type LEO 1530).

Results and Discussion

First, the characterization of the nitrided and DLC coated surface layers (microhardness measurements and scratch tests) is presented. Afterwards, the high-resolution images, contour comparisons and metallographic analyses of the forging dies are discussed.

Nitriding. Both determined hardness depth profiles for the nitriding processes 10 % and 80 % N_2 are shown in Fig. 2 (left). At a high nitrogen content of 80 %, a maximum hardness of approximately 1310 HV 0.005 was determined. In comparison, the hardness depth profile of the 10 % N_2 nitriding shows a maximum hardness of approximately 1170 HV 0.005. As a result of the increased nitrogen content, the precipitation behavior of nitrides is affected, leading to these differences. In addition, the diffusion of the nitrogen deeper into the material was enabled. This results in an approximately two times higher nitriding depth. A comparable hardness gradient can be seen for both nitriding processes, which can be explained by the identical treatment time and temperature. Furthermore, an increased nitrogen content results in additional diffusion processes, which leads to a homogeneous nitrogen distribution. Consequently, two nitriding processes with different characteristics are available for the subsequent application of the DLC coatings in order to investigate the influence on the coating adhesion.

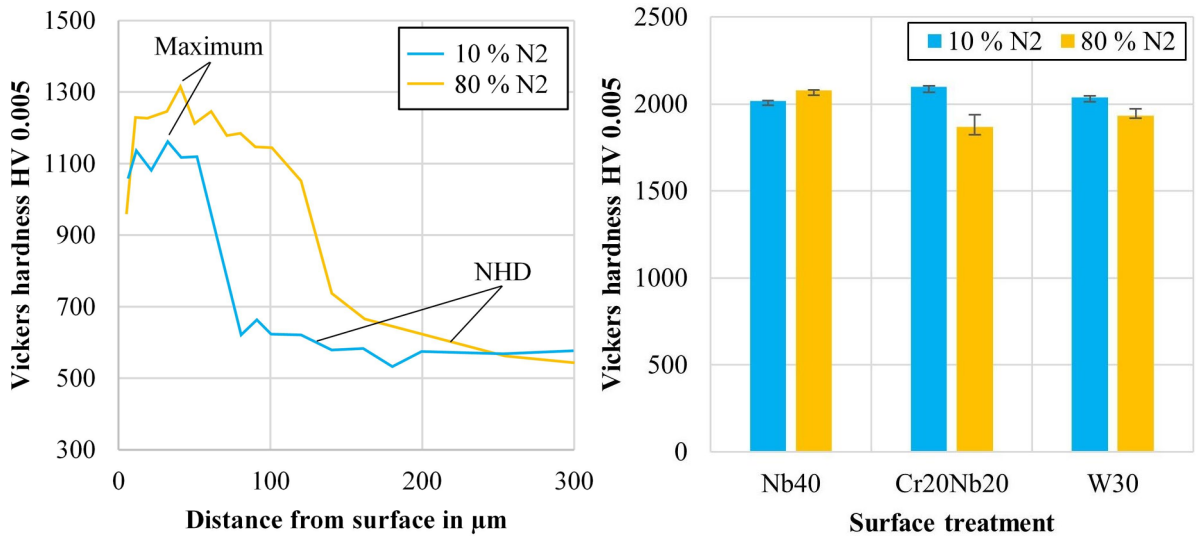

Fig. 2. Hardness depth profiles of the nitriding variants with a nitrogen content of 10 % and 80 % N_2 (left) and microhardness measurement on differently modified DLC coated specimens (right).

DLC Coating.

Cross-section microhardness tests were performed on the modified DLC coating systems Nb40, Cr20Nb20 and W30. The results are shown in Fig. 2 (right). It can be seen that the three DLC coating systems have a comparable hardness of approximately 2000 HV 0.005. Thus, for all variants, increased wear protection can be assumed compared to uncoated nitrided tools, if the DLC coatings withstand the thermal loads of hot die forging. Considering that the determined

hardness is comparable to conventional DLC coatings [8], no negative influence of the modified treatment atmosphere can be observed.

Scratch tests were carried out to determine the most appropriate modified DLC coating system for hot die forging, and the results are shown in Fig. 3. The results show that the DLC coating system Nb40 is prone to early coating delamination at a temperature of 600°C (which approximately represents the maximum temperature of thermally loaded regions on hot forging dies). This behavior can be improved through the addition of the element chromium. The DLC coating system Cr20Nb20 features two to three times higher resistance to coating delamination. By combining DLC (W30) with 10 % N_2 nitriding, the highest coating resistance was observed. Therefore, DLC (W30) can be assumed to have the highest resistance to the loads associated with hot forging processes.

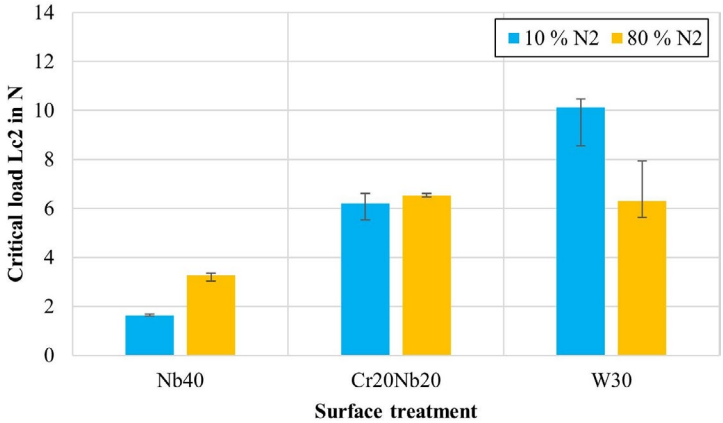

Fig. 3. Characterization of coating delamination at 600 °C of different metallic DLC coatings.

Wear analysis.

After the serial forging tests were carried out on the differently treated forging dies, high-resolution images were analyzed for the qualitative characterization of the wear behavior. The results after 1500 forging cycles are shown in Fig. 4. Maximum abrasive wear is present on the central elevated area radius of the quenched and tempered reference tool. In particular, the grooves in the direction of material flow are a characteristic feature of abrasion and a high tribological load. Due to the low hardness and significant thermal softening, this result was to be expected. Fine and coarse thermomechanical crack networks have formed in the middle of the central elevated area and near the radius. Intensively nitrided tools show an increased crack sensitivity compared to the 10 % N_2 variants. The DLC (W30) coated tools show finer crack networks than the nitrided reference tools and slightly reduced wear, therefore a coating removal can be assumed. This particularly affects the 10 % N_2 coated tool, since a lower hardness below the coating promotes cracking.

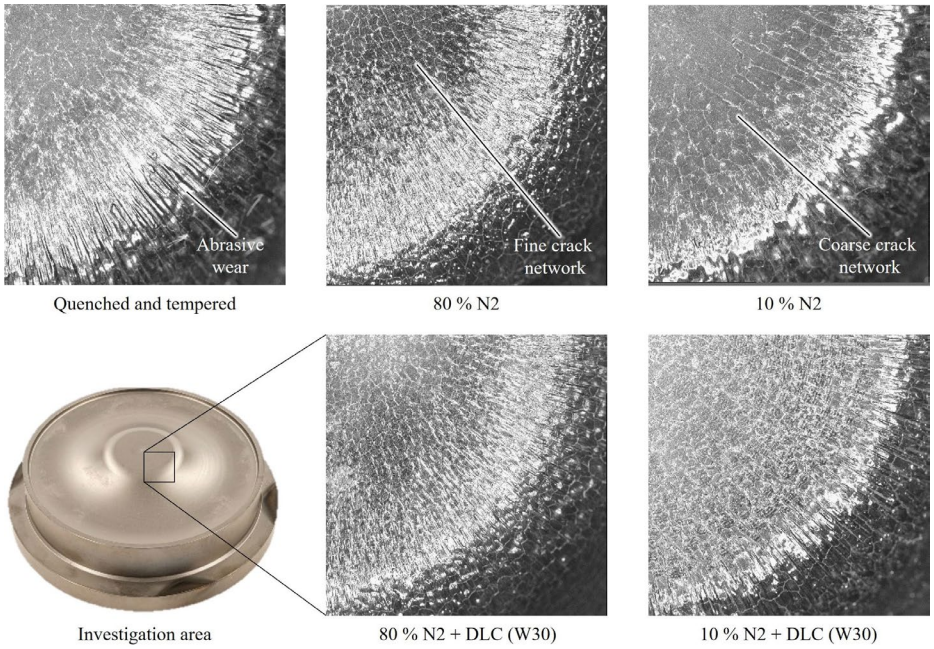

Fig. 4. High-resolution images of the differently treated hot forging dies after 1500 forging cycles.

Contour Measurement.

The profile comparisons (Fig. 5, right) show a negative geometry deviation, which means abrasion is the main wear mechanism. Since no positive deviations are detectable, plastic deformation and adhesive wear either did not occur, or were superimposed by abrasion. Compared to the 10 % N_2 nitrided reference tool, a wear reduction of approximately 23 % was measured for the DLC coated forging die after 1500 forging cycles (Fig. 5, left). This correlation cannot be determined for the 80 % N_2 nitrided and DLC coated variant. A possible explanation is the almost two times higher layer adhesion, which can be observed from the results of the scratch tests (Fig. 3). After 100 forging cycles, the DLC coated forging dies exhibit less material removal than the nitrided reference dies. Abrasive wear was reduced by approximately 28 % with the DLC coated 80 % N_2 variant. In general, the lowest planimetric wear was observed after 1500 forging cycles for the uncoated 80 % N_2 nitrided tool.

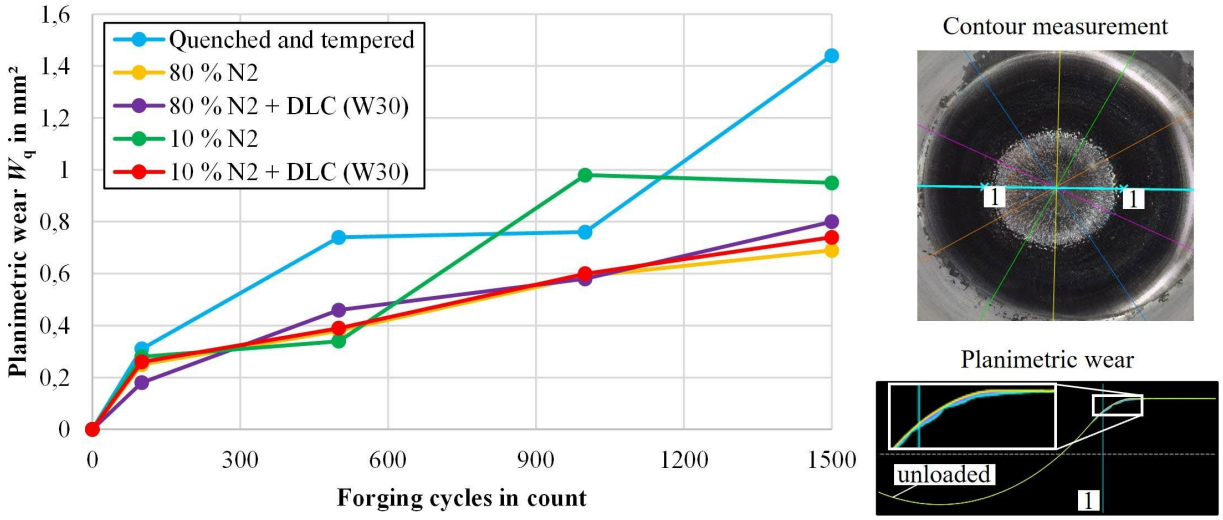

Fig. 5. Contour comparisons in dependence of the forging cycles of the differently treated forging dies.

Metallography.

Metallographic cross-sections (Fig. 6) of the DLC coated tools were prepared and analyzed after reaching 100 forging cycles (900°C) or 1500 (1200°C). At a blank temperature of 1200°C and after 1500 forging cycles, significant cracks are detectable in the surface layer. Crack initiation was promoted by the hard surface as a result of nitriding. In the light gray zone, the surface layer has been thermally softened and the nitriding zone below is visible. The 10 % N_2 nitrided forging die with DLC coating no longer shows a coating after 1500 forging cycles at a blank temperature of 1200°C. Considering the contour comparisons (Fig. 5), the DLC coating seems to be present up to 500 forging cycles. Similarly, no DLC coating was observed on the 80 % N_2 nitrided tool after 1500 forging cycles. Additional serial forging tests at 900 °C were carried out with 100 forging cycles to confirm the increased thermal stability of the DLC (W30) coatings. Fig. 6 shows the results of the metallographic analysis and for both nitrided DLC coated variants (10 % and 80 % N_2) a thin white layer is visible, which is assumed to represent the DLC coating. The thick layer beneath it, is probably the compound layer. Similar to the serial forging tests at 1200°C, a maximum wear reduction of 29 % was found (80 % N_2).

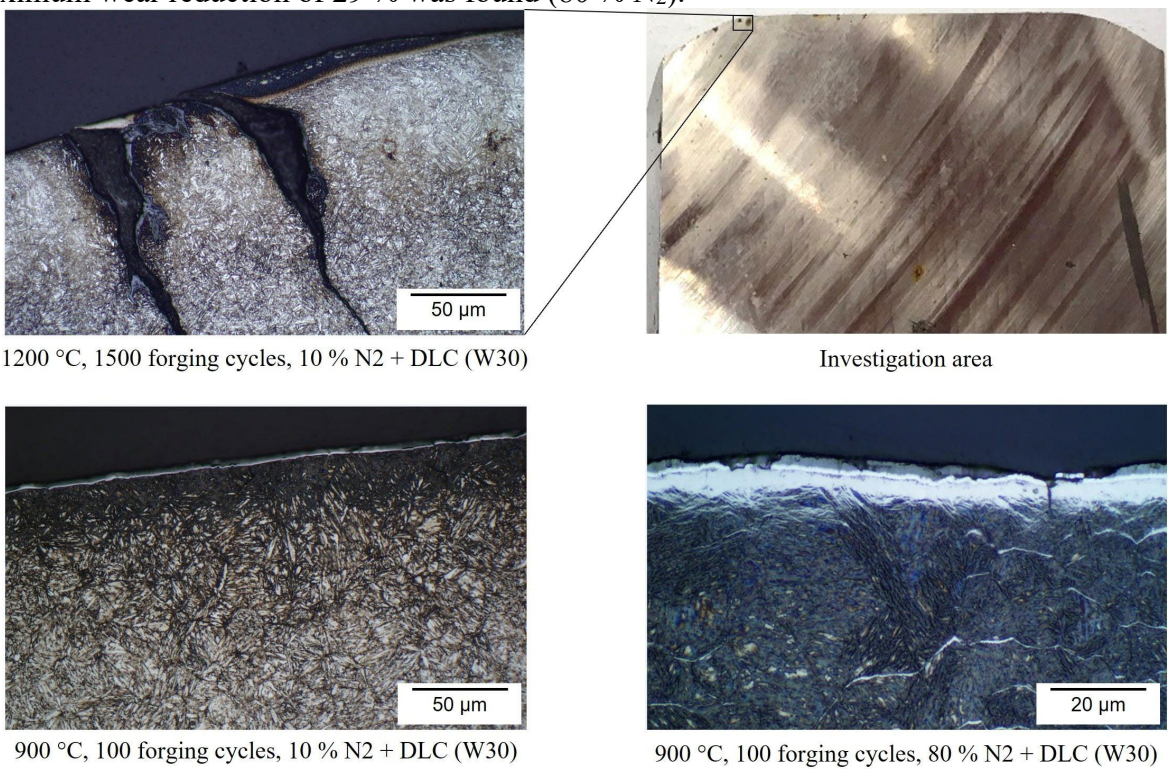

Fig. 6. Metallographic analyses of the forging dies subjected to different loads and treatments.

Summary

To qualify metallic modified DLC coating systems as wear protection measures for hot forging tools, Nb40, Cr20Nb20 and W30 were applied to differently nitrided (10 % and 80 % N_2) specimens. Vickers hardness tests did not indicate any reduction of wear reducing properties such as high hardness through the modification. Scratch tests showed the highest resistance to coating delamination at a temperature of 600°C for the DLC (W30) coating (10 % N_2). Serial forging tests were carried out using a high tribological loaded forging die with blanks heated up to 900°C and 1200°C. After 1500 forging cycles, high-resolution images showed slightly lower wear and increased crack sensitivity for the DLC coated tools compared to the nitrided references. Based on contour comparisons, it was found that the DLC coated tool with 10 % N_2 nitriding had approximately 23 % less planimetric wear than the nitrided reference tool after 1500 forging

cycles. A possible explanation is the increased layer adhesion, which was determined in the scratch tests. After 100 forging cycles and a blank temperature of 1200°C, a reduction in planimetric wear was observed for all DLC coated tools, which amounted to up to 28 %. Metallographic analysis showed no DLC coatings after 1500 forging cycles. Verification of higher temperature stability than conventional DLC coatings (700°C) was obtained through metallographic analysis of forging dies loaded with blanks heated to 900°C. Thin white layers are visible on these metallographic cross-sections, which are associated with an intact DLC coating.

Further destructive metallographic analyses are planned in the future to determine more precisely the layer degradation of the DLC coatings at a blank temperature of 1200°C. In addition, primary thermal loaded hot forging dies with modified DLC coatings are investigated to increase the range of applications.

Acknowledgment
The results presented were obtained in the research project “Investigations on the application of metal containing DLC-coatings as wear protection systems for forging dies” financed under project number 283898001 by the German Research Foundation (DFG). The authors would like to thank the German Research Foundation for the financial support.

References

[1] A. Mahdi Abd, Estimation of Wear Depth as an Approach to Predict Tool Service Life in Cold Forming Process, DJES 12 (2020) 13–34. https://doi.org/10.24237/djes.2019.12202
[2] F. Klocke, Manufacturing Processes 4: Forming, Springer Berlin Heidelberg, Berlin, Heidelberg, 2013.
[3] H. Paschke, A. Nienhaus, K. Brunotte, T. Petersen, M. Siegmund, L. Lippold, M. Weber, M. Mejauschek, P. Landgraf, G. Braeuer, B.-A. Behrens, T. Lampke, Adapted diffusion processes for effective forging dies, in: Proceedings of the 21st International ESAFORM Conference on Material Forming, 2018, pp. 40016.
[4] H. Paschke, T. Yilkiran, L. Lippold, K. Brunotte, M. Weber, G. Braeuer, B.-A. Behrens, Adapted surface properties of hot forging tools using plasma technology for an effective wear reduction, Wear 330-331 (2015) 429–438. https://doi.org/10.1016/j.wear.2015.02.009
[5] J. Smolik, Hard Protective Layers on Forging Dies - Development and Applications, Coatings 11 (2021) 376. https://doi.org/10.3390/coatings11040376
[6] A. Wank, G. Reisel, B. Wielage, Behavior of DLC coatings in lubricant free cold massive forming of aluminum, Surf. Coat. Technol. 201 (2006) 822-827. https://doi.org/10.1016/j.surfcoat.2005.12.043
[7] R. Paul, S.N. Das, S. Dalui, R.N. Gayen, R.K. Roy, R. Bhar, A.K. Pal, Synthesis of DLC films with different sp 2 /sp 3 ratios and their hydrophobic behaviour, J. Phys. D: Appl. Phys. 41 (2008) 55309.
[8] I. Gotman, E.Y. Gutmanas, G. Hunter, 1.8 Wear-Resistant Ceramic Films and Coatings, in: Comprehensive Biomaterials II, Elsevier, 2017, pp. 165-203.
[9] S. Delfani-Abbariki, A. Abdollah-zadeh, S.M.M. Hadavi, M. Abedi, S.M.R. Derakhshandeh, Enhancing the adhesion of diamond-like carbon films to steel substrates using silicon-containing interlayers, Surf. Coat. Technol. 350 (2018) 74-83. https://doi.org/10.1016/j.surfcoat.2018.06.055
[10] C. Li, L. Huang, J. Yuan, Effect of sp3 Content on Adhesion and Tribological Properties of Non-Hydrogenated DLC Films, Materials 13 (2020) 1911. https://doi.org/10.3390/ma13081911
[11] C. Kipp, P. Kaestner, G. Braeuer, T. Lampke, Influence of Plasma-Nitriding on the Adhesion of DLC Films, in: TANGER Ltd, 2022, pp. 449-456.
[12] A. Krause, M. Stonis, B.-A. Behrens, Diamond-Like Carbon as a Wear-Protection Layer for Semi-Hot Forging, Schmiede Journal 1 (2013) 40-43.

Materials Research Proceedings 28 (2023) 591-600 https://doi.org/10.21741/9781644902479-64

Investigation of the joining zone formation of impact extruded hybrid components by varied forming sequence and partial cooling

PIWEK Armin[1,a *], PEDDINGHAUS Julius[1,b], UHE Johanna[1,c], BRUNOTTE Kai[1,d] and BEHRENS Bernd-Arno[1,e]

[1]Leibniz University Hannover, Institute of Forming Technology and Forming Machines, An der Universität 2, 30823 Garbsen, Germany

[a]piwek@ifum.uni-hannover.de, [b]peddinghaus@ifum.uni-hannover.de, [c]uhe@ifum.uni-hannover.de, [d]brunotte@ifum.uni-hannover.de, [e]behrens@ifum.uni-hannover.de

Keywords: Friction Welding, Hot Forging, Tailored Forming, Joining Zone, Partial Cooling

Abstract. Hybrid material concepts enable the combination of beneficial properties of different materials to extend the limited potential of monolithic components. When it comes to steel and aluminium, a wear-resistant and a lightweight metal are combined to produce a weight-reduced high-performance component with load-adapted areas. A method to create hybrid gear shafts is a novel approach called Tailored Forming. The process chain consists of joining e. g. by friction welding and subsequent impact extrusion under elevated temperature. Before forming, an axial temperature gradient is set in the serial arranged semi-finished products to adjust the different yield stresses of the dissimilar materials through induction heating of the steel part. The subsequent forming is intended to positively influence the joining zone thermo-mechanically and geometrically. However, prior work indicated a limitation of the influence on the joining zone in forward rod extrusion. Therefore, approaches are being researched that enable a stronger formation of the joining zone geometry to influence the resulting bond qualities through surface enlargement. A forward rod extrusion process of friction welded hybrid semi-finished products made of 20MnCr5 (AISI 5120H) combined with EN AW-6082 (AA6082) was carried out experimentally. Complementary to prior investigations, in which mainly the aluminium section was reduced through the die angle followed by the steel, the forming sequence of the materials was reversed to increase the joining zone surface with variation of the forming path. Additionally, a cooling of the aluminium side was realized through an immersion cooling to adjust maximum temperature gradients and further equalize the different yield stresses. Hardness tests, metallographic and SEM images of cross-sections were taken to evaluate the bond quality with regard to the temperature influence, joining zone formation, occurring defects and the resulting intermetallic compound (IMC). Impact extrusion with initially steel formed followed by aluminium resulted in a spherical formation of the joining zone and consequently in greater surface area, but also lead to partial defects in the IMC. The partial cooling of the aluminium allowed higher temperature gradients to be set, thus reducing defects through improved material flow in the joining zone.

Introduction

An effective use of resources is becoming more crucial to deal with rising energy prices as well as increased environmental responsibilities. Monolithic components have their material-specific restrictions, thus new concepts and production techniques must be created to meet the rising standards. Monolithic materials cannot always meet the ever-more-complex and occasionally conflicting criteria put on lightweight constructions. One option to address these demands for lightweight concepts and attain a required load-adapted functionality is through hybrid components, which utilize different materials. In the case of steel and aluminium, the positive mechanical properties are combined to produce a high-performance component with low weight.

Content from this work may be used under the terms of the Creative Commons Attribution 3.0 license. Any further distribution of this work must maintain attribution to the author(s) and the title of the work, journal citation and DOI. Published under license by Materials Research Forum LLC.

Using the example of a hybrid gear shaft, aluminium can serve as a structural element, while steel is used in a power transmitting area [1].

State of the Art

Within sheet metal forming, especially for the automotive industry, application-adapted hybrid semi-finished products called tailored blanks have been widely used since their development by ThyssenKrupp in 1983 [2]. Due to the local adaptations such as a local variation of the sheet thickness or sheet material, the components are optimised for a subsequent forming process or the end application [3]. This concept can also be applied to bulk metal forming. Contrary to compound forging of hybrid materials, where the joining is realised by forming [4-6], the hybrid semi-finished products are first pre-joined and then further processed by forming in order to positively influence the joining zone. The combination of joining and forming has been addressed by some studies for similar and dissimilar material pairings. For instance hot forging of cladded work pieces consisting of two different steel alloys using upsetting tests was investigated numerically and experimentally by Wang et al with regard to material distribution and the effect of friction [7]. Furthermore, in the studies by Foydl et al, an extrusion process was developed, in which aluminium profiles were reinforced by steel wires. For further processing into connecting rods, the components were cut to size and used as semi-finished products for a die forging process [8]. Basic research into joining by friction welding and subsequent upsetting of solid hybrid components made of copper and aluminium or steel and copper was carried out by Domblesky et al. The results obtained from upsetting indicate a good workability of hybrid materials [9].

Based on the concept of the studies mentioned, the new approach called Tailored Forming enables a production of load-adapted high-performance components by forming pre-joined hybrid semi-finished products. The process chain can differ in terms of joining processes used such as friction welding, lateral angular co-extrusion (LACE) or cladding and subsequent forming processes such as impact extrusion or die forging [10].

The joining zone of the two hybrid materials is usually the weakest area, where the failure of the component occurs. Therefore, the basic motivation is the enhancement of the weak point through suitable measures such as reducing tensile stresses and thus defects by a pressure superimposition [11-13], an adjustment of the yield stresses by a viable heating strategy [14] or improvement of the stress state by an inversed forming sequence [15]. The last two aspects mentioned have a direct influence on the shape of the joining zone, which results in an increase of bond strength and quality through surface enlargement [15] and influencing IMCs, which in general are characterised by their brittleness. The creation of a sufficiently sound bond is the setting of the lowest possible IMC thickness, which should not exceed a certain thickness. According to Herbst et al. sufficiently narrow IMC thicknesses smaller than 1 µm indicate high bond strengths, while for thicknesses greater than 1 µm, the strength decreases significantly [16]. A sufficiently sound bound can be achieved through a subsequent forming operation. During the impact extrusion of serially arranged hybrid semi-finished products, it is crucial that the yield stress differences between the two materials are as small as possible. In this way, a high local degree of forming can be achieved and influence can be exerted on the joining zone geometry. If the yield stress difference between steel and aluminium is too high, the local deformation is not sufficient and the different materials flow one after the other into the extrusion shoulder with only a parallel displacement of the interface. In previous work [17], the influence on the joining zone properties after friction welding and impact extrusion under elevated temperatures of steel-aluminium billets was investigated. In various forming processes such as backwards cup (full forward) extrusion or hollow forward extrusion, it was possible to geometrically influence the joining zone so that larger joining zone surfaces were created. In the case of forward rod extrusion, however, the joining zone did not change and remained flat, almost as it was after friction welding (see Fig. 1). Since in forward rod extrusion no additional compressive stress is initiated by forming tools as in the other

processes investigated, the axial temperature gradient is particularly important in the case in order to set the previously mentioned local deformations resulting in a spherical shape of the joining zone [17]. Due to this, a larger temperature gradient must be set in order to further equalise the yield stresses and also to influence the joining zone geometry. This is possible e. g. by actively cooling the aluminium.

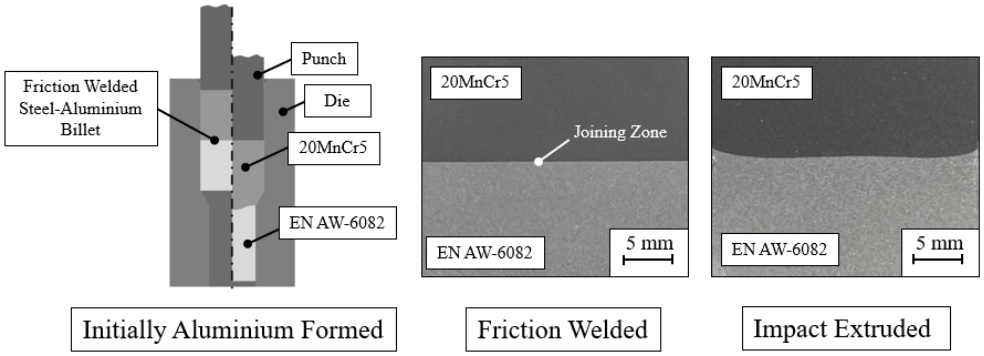

Fig. 1. Joining zone after friction welding and forward rod extrusion.

According to Gumm an increased flow rate of the centre material is observed if the harder metal undergoes the forming process first. In case the softer material is pressed through the die first, lower pressures in the forming zone and a formation of cavities in in the joining zone of compound forged components is observed [15]. Therefore, the sequence of materials is another crucial factor to further enhance the joining zone geometry through an improved stress state in the forming zone. Another aspect to reduce unwanted tensile stresses is the application of a pressure superimposition. Particularly in cold extrusion of hybrid materials, fractures occur inside the component due to differing yield stresses, which can be significantly reduced by this measure with the similar effect of the selection of material sequence [11-13]. However, this does not have any influence on the surface enlargement [17], but is required to ensure the reduction of defects.

Deriving from the state of the art, a pressure-superimposed forward rod extrusion with partial aluminium-side cooling is carried out within the scope of this study by means of Tailored Forming. Furthermore, contrary to the previous work, the material sequence is inverted so that the steel is formed first followed by the softer aluminium. In order to reproduce the formation of the joining zone and the resulting surface enlargement, the forming path is varied. The two heating strategies (without vs. with cooling) are compared with regard to the joining zone formation. The process changes enable an improvement of the mentioned joining zone characteristics. The friction welded and impact extruded steel-aluminium bonds are evaluated by means of metallographic images and hardness tests. Furthermore, the resulting IMC is characterised by SEM images and EDX analyses. The process changes enable an improvement of the joining zone characteristics.

Tailored Forming for the Production of a Hybrid Transmission Shaft

The process chain of Tailored Forming (see Fig. 2) first includes friction welding of the hybrid material pair consisting of steel (soft-annealed 20MnCr5) and aluminium (EN AW-6082 T6 condition) in a serial arrangement. Then the joined semi-finished products are formed in a forward rod extrusion process with prior inductive heating, which in the context of this study takes place both with and without immersion cooling. This is followed by machining to produce the final component, which is characterised by a load-adapted material distribution. The process chain of Tailored Forming has already been used in earlier work to create customised, hybrid machine parts in serial and coaxial arrangements like axial bearing washers or bevel gears [10].

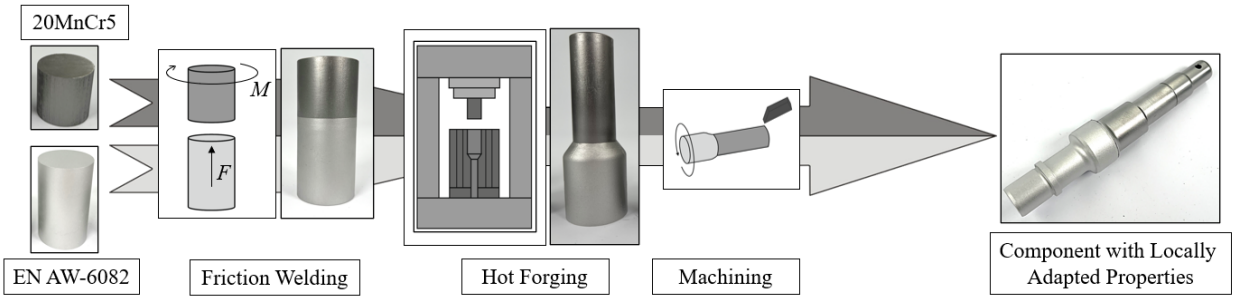

Fig. 2. Process chain of Tailored Forming for a hybrid shaft with reversed forming sequence.

Rotatory Friction Welding

Before joining, the welding surfaces of both semi-finished products made of 20MnCr5 and EN AW-6082 are first machined and cleaned with ethanol to remove irregularities and impurities. After preparation, the materials are immediately joined on the KUKA Genius Plus friction welding machine with the experimental set-up and parameters shown in Fig. 3.

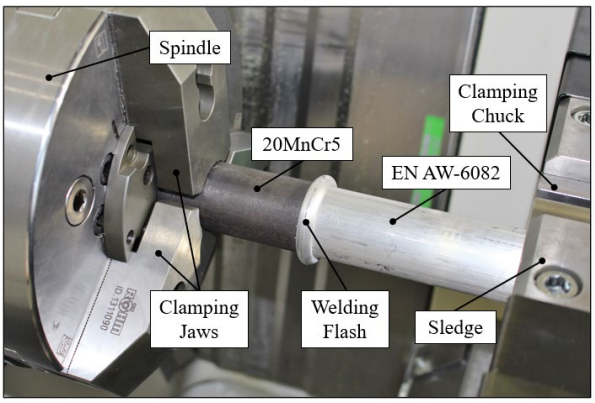

a)

Parameter	Value
Billet Diameter D	40 mm
Rotation speed n	1500 rpm
Relative Friction Path s_R	4 mm
Friction Pressure p_F	120 MPa
Upsetting Pressure p_U	200 MPa
Upsetting Time t_U	2 s

b)

Fig. 3. Rotatory friction welding: a) experimental set-up, b) investigated parameters.

The parameters were chosen according to the previous work [18] and are designed to prevent unnecessary shortening and to set low temperatures in order to keep the emerging intermetallic phase as small as possible. The steel rotates at a speed of n = 1500 rpm on the spindle side, while on the sledge side the aluminium is rubbed against it with a relative friction path of s_R = 4 mm at a friction pressure of p_F = 120 MPa. After completion of the friction phase, the upsetting phase takes place with an upsetting pressure of p_U = 200 MPa and an upsetting time of t_U = 2 s. The resulting welding flash consists of aluminium as only this material is plastically deformed in the process due to its lower strength compared to steel. After the process, the welding flash is removed by machining and the specimens are shortened to a length of 105 mm (42 mm steel, 63 mm aluminium) for the subsequent impact extrusion process.

Inductive Heating and Immersion Cooling

With the help of an induction coil, the friction-welded hybrid component is heated partially to equalise the significantly different yield stresses of steel and aluminium before the forming process. In order to achieve a favorable flow behavior, an inhomogeneous temperature distribution in the hybrid semi-finished product is necessary. According to simulations and material data, the yield stresses at steel temperatures of 900°C or higher and aluminium temperatures of 20°C are approximately the same level [14]. Due to the time required to heat up and process the component in combination with the thermal conduction during this time, it is not technically possible to reach this ideal equalisation for the forming process. The aim is therefore to achieve the largest possible

temperature gradient between the two materials. To investigate the influence of the temperature gradient on the material flow, the heating is carried out with and without partial cooling of the aluminium side before forming. During the heating phase, the steel side is in the induction coil, which consists of six rectangular windings. The magnetic field is generated by a 40 kW mid-frequency generator (TRUMPF TruHeat MF 3040) with a frequency range between 5 - 30 kHz. The edge of the aluminium part is at the same level as the lowest coil winding and is cooled by the surrounding water when used with immersion cooling (see Fig. 4).

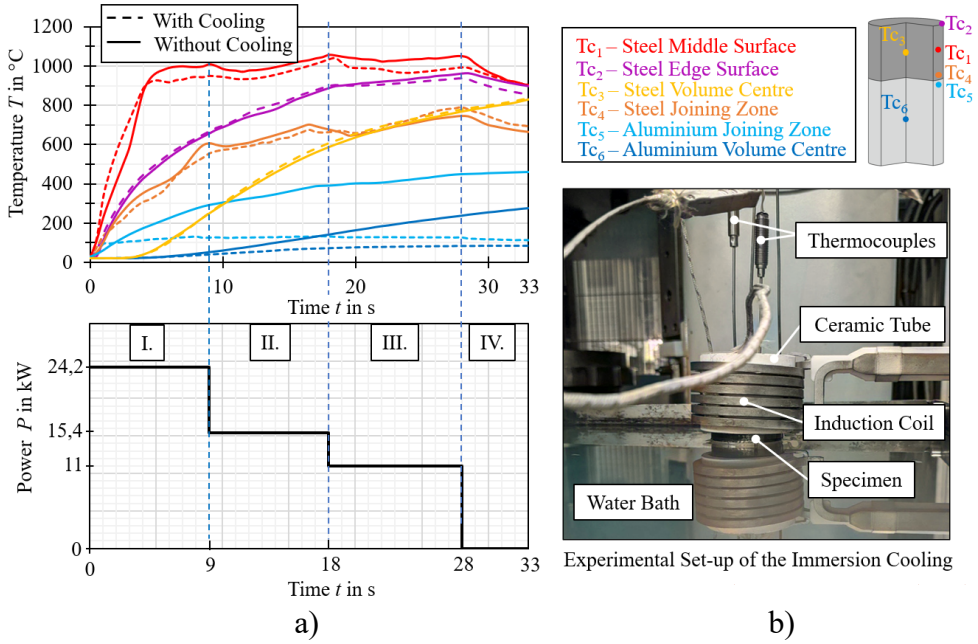

Fig. 4. Partial heating: a) measured temperatures during induction heating with and without immersion cooling, b) positions of the thermocouples (Tc) and experimental set-up.

The temperature curves shown in Fig. 4 were determined during induction heating without subsequent forming using six thermocouples Type K. Induction heating takes place in segments I to III, where the power is continuously reduced in each stage to counteract overheating close to the surface. After a total of 28 s, the induction heating is finished and the sample is moved out of the coil by a pneumatic cylinder in segment IV so that an automated robot gripper can transfer the sample into the tool with a transfer time of approx. 5 s. By using the immersion cooling, significantly lower temperatures of 84°C instead of 237°C without cooling (Tc_6) are set in the aluminium part of the sample, while the steel temperatures at $t = 28$ s remain the same for both heating strategies reaching nearly 800°C (Tc_3). When comparing the material centres (Tc_3 and Tc_6), a temperature gradient of 694 K can be set with the help of cooling, while only 532 K are achieved without cooling. This corresponds to an increase of approx. 30.5%. An estimated yield stress of about 250 MPa for steel and about 140 MPa (uncooled) and 175 MPa (cooled) for the aluminium is set for strain rate of $\dot{\varphi} = 10$ 1/s and $\varphi = 0.4$.

Impact Extrusion

The forward rod extrusion of the specimens was carried out on a Lasco SPR 500 screw press and took place immediately after the transfer from the induction heating in the tooling system seen in Fig. 5a). To reduce tensile stresses inside the component, a counterpressure $p_{Counter}$ = 160 MPa was generated by four gas springs, which are connected to the counter punch via a transverse beam. The process is designed in such a way that the counterpressure acts on the component shortly before the joining zone passes the extrusion shoulder.

To observe the influence of the forming process on the geometric shape of the joining zone, the immersion depth of the punch was varied in a range of 8 mm with a step width of 2 mm. The relative forming path *s* (see Fig. 5 b)) describes the distance of the joining zone beyond the lower extrusion shoulder. In the case of a negative value for *s*, the joining zone has not passed the lowest point of the impact extrusion shoulder.

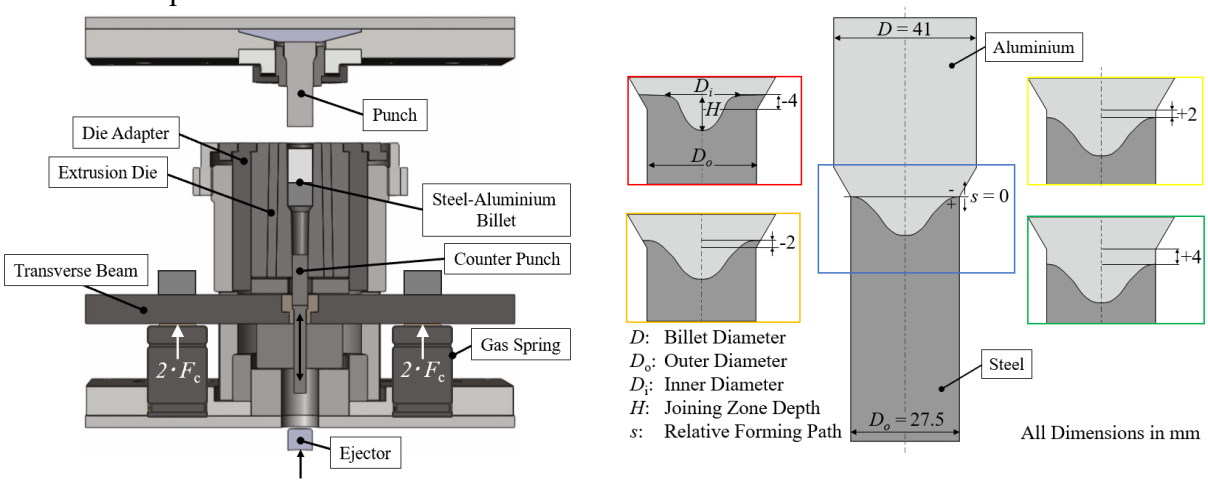

a) b)

Fig. 5. a) Tooling system for forward rod extrusion [19], b) Formation of the joining zone geometry after impact extrusion depending on the relative forming path s.

After forming, the samples were quenched in a water bath. To avoid thermal cracking, first the aluminium was quenched for 1 s, then the steel for 5 s and again the aluminium for 5 s, before the entire specimen was completely immersed for another 20 s. The samples were then cross-sectioned to measure the inner and outer diameter such as the depth of the joining zone to calculate the surface enlargement. The joining zone has a paraboloid geometry, which is why the modified surface area A_{JZ} was calculated approx. using the following equation:

$$A_{Jz} = \frac{\pi \cdot (\frac{D_i}{2})}{6 \cdot H^2} \left[\left(\left(\frac{D_i}{2}\right)^2 + 4 \cdot H \right)^{\frac{3}{2}} - \left(\frac{D_i}{2}\right)^3 \right] + \frac{\pi}{4}(D_o^2 - Di^2) \quad (1)$$

At a relative forming path *s* = -4 mm, the joining zone has not yet fully passed through the impact extrusion shoulder, which is why the paraboloid geometry is not found over the entire cross-section. Therefore, the unformed circular ring (D_o - D_i) was taken into account in the calculations. Samples with *s* = +4 were further prepared metallographically. Light microscopic and SEM images as well as EDX analyses were performed using a field emission scanning electron microscope Supra VP 55 to evaluate the cooling effect and the forming sequence on the joining zone geometry and quality as well as the emerging IMC.

Results and Discussion

The joining zone depth *H*, which contributes significantly to the surface enlargement, increases with higher relative forming paths *s* and reaches its maximum for *s* = +4 (see Fig. 6). In this case

a joining zone surface of $A_{JZ} = 1010.11$ mm^2 is obtained which corresponds to a surface enlargement of approx. 70% compared to the unaffected, flat joining zone after friction welding or with initially aluminium formed. The measured and calculated values for each variation are shown in Table 2. As the joining zone is passing through the extrusion shoulder, steel forms a funnel, dragging the materially bonded aluminium along with it. The material is drawn more strongly into the centre due to the locally varying forming speed and forms the funnel shape in the absence of subsequent material flow. With increased relative forming path *s*, the effect mentioned becomes stronger, which is why the shape of the joining zone between steel and aluminium is characterised by a steadily increasing joining zone depth *H*.

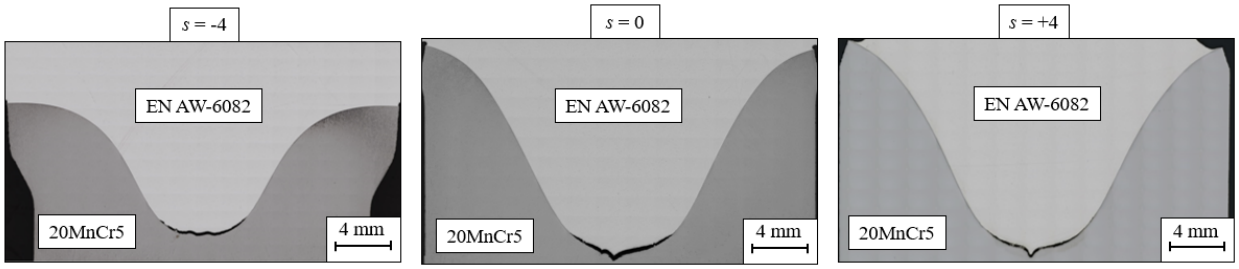

Fig. 6. Exemplary images of the joining zone formation for s = [-4, 0, +4].

Table 1. Comparison of the surface enlargement depending on relative forming path s.

Initially Formed Material	Relative Forming Path *s* [mm]	Inner Diameter D_i [mm]	Outer Diameter D_o [mm]	Joining Zone Depth *H* [mm]	Joining Zone Surface A_{JZ} [mm^2]	Surface Enlargement [%]
Aluminium	4	27.5	27.5	0	593.96	0
Steel	-4	21.8	27.5	9.5	803.44	35.2
Steel	-2	27.5	27.5	12.35	943.67	58.88
Steel	0	27.5	27.5	12.9	968.58	63.07
Steel	2	27.5	27.5	13.3	986.92	66.16
Steel	4	27.5	27.5	13.8	1010.11	70.06

The occurring defect in the centre of the specimen is caused by the funnel formation, which usually occurs in monolithic semi-finished products due to a lack of subsequent material flow at the end of the forming process [20]. A locally weak bond in the centre of the joined materials before forming is pre-existent, due to low relative friction speeds in the friction welding process. Combined with an increased forming speed in the centre and differing yield stresses, a detachment of the two materials is very likely. The defect can mostly be avoided if the extrusion takes place with high friction between the extrusion die and the specimen [21]. In this regard the use of a counterpressure can set the required stress state [11-13]. Since the gap was nevertheless observed during the tests carried out, it can be assumed that the set of a counterpressure $p_{Counter} = 160$ MPa is not sufficient to completely compensate the tensile stresses acting in the joining zone.

The greater temperature gradient caused by the immersion cooling (see Fig. 4) provides a better equalisation of the yield stresses, thus a lower deformation resistance ratio and therefore a less pronounced paraboloid shape. Furthermore, the constriction of the aluminium is largely prevented (see Fig. 7) so that, unlike the sample without cooling, no gap extends over the entire circumference of the component surface near the joining zone. Due to the improved material flow, the central defect is also slightly reduced from 132 µm to 53 µm, but cannot be completely prevented. The influence of the partial cooling is also reflected in the measured hardness (HV0.1),

which show an average increase of 12 HV from 61 HV without cooling to 73 HV with cooling for the aluminium. The hardnesses in the steel are subject to relatively large deviations, but also increased slightly on average by 8 HV from 283 HV to 291 HV.

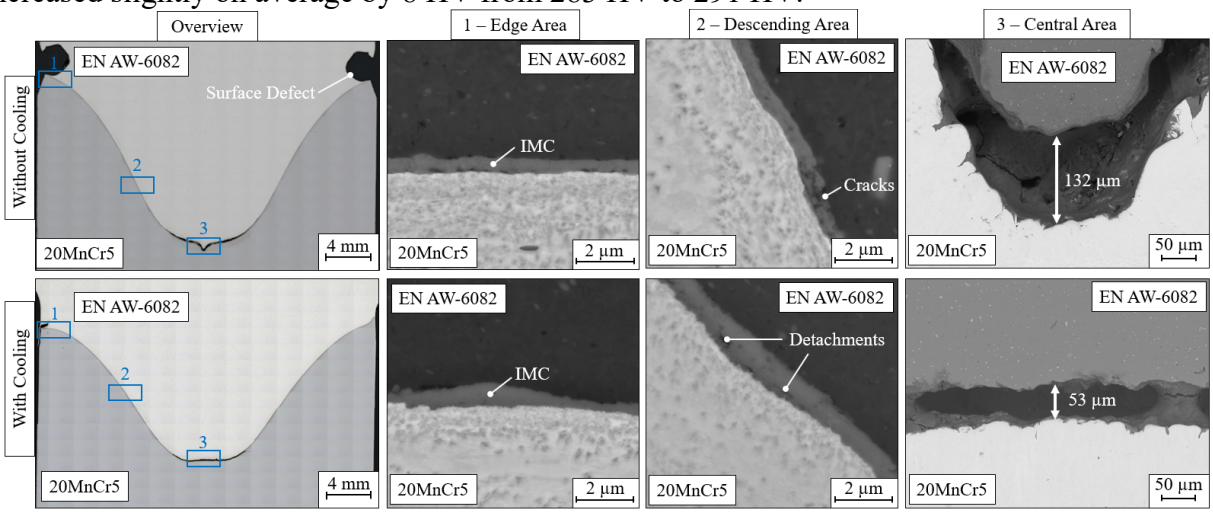

Fig. 7. Metallographic and SEM images of the joining zone (s = +4 mm) without and with cooling with a counter pressure of $p_{Counter}$ = 160 MPa.

Regardless of the used heating strategy, the formed IMCs have been influenced by the surface enlargement leading to a relatively homogenous structure. The thickness in the edge area as well as in the descending area is varying between 0.6 to 0.8µm. Near the central area, the brittle IMCs are destructed after forming due to the detachment between the two materials. The IMC thicknesses in the edge area are approx. in the same size range compared to the thicknesses in the central area, which is why no thinning of the IMC can be certainly observed due to the surface enlargement. However, since the IMC does not exceed the critical thickness of 1 µm [16] combined with the increase in surface area compared to a flat joining zone, a potential improvement of the bond strength can be assumed.

As expected, the chemical composition in the joining zone was not influenced by the cooling. An EDX line scan of the specimen without cooling at a forming path of s = +4 mm (see Fig. 8) is exemplary shown in Fig. 8. A diffusion and hence a deposition of manganese and silicon into the area of the joining zone with a concentration of up to 5 wt.% is seen, indicating the existing IMC.

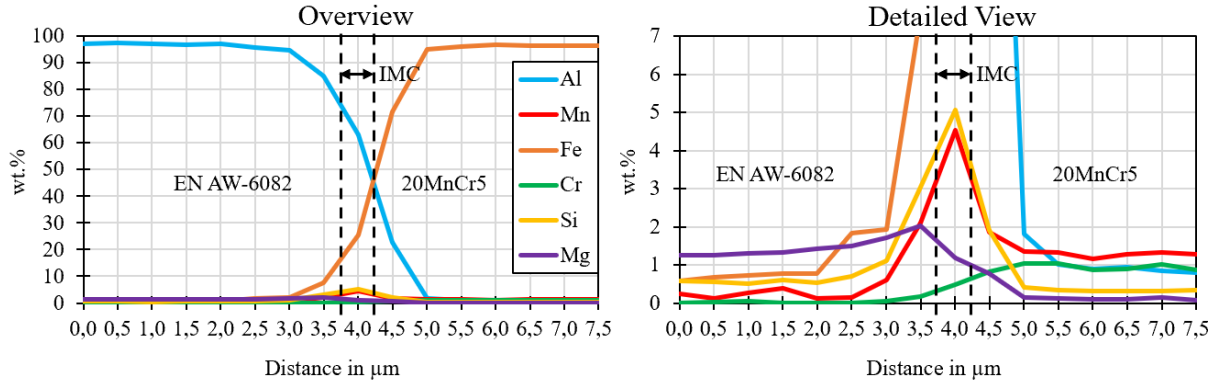

Fig. 8. EDX analysis of the descending area for a specimen without cooling (s = +4 mm).

Summary
In this study, a forward rod extrusion process was used which, based on preliminary work, focused on the forming sequence and the use of partial cooling for the aluminium side. The variation of the forming path showed a material flow-related increase of the surface enlargement of up to 70%. Furthermore, the complete passing of the joining zone through the impact extrusion shoulder resulted in defects near the surface as well as on the interior, which could be reduced with the help of the improved material flow through immersion cooling. A homogenous formation of the IMC is ensured in the enlarged areas. Partial detachments or cracking of the IMC was observed regardless of cooling in the areas with increased surface area, especially in the centre at the highest material flow rates. For future work, the counter pressure should be increased further in order to compensate the tensile stresses that occur for a defect-free bond. Furthermore, mechanical tests should be carried out to prove that the enlarged surface also improves the bond strength of the joining zone. To investigate the possible adjustable maximum temperature gradients, selecting other cooling strategies such as air-spray cooling should be considered.

Acknowledgments
The results presented in this paper were obtained within sub-project B03 of the Collaborative Research Centre 1153 “Process chain to produce hybrid high performance components with Tailored Forming” funded by the Deutsche Forschungsgemeinschaft (DFG, German Research Foundation) - SFB 1153 TP B03 - 252662854. The authors thank the DFG for the financial support of this project and also the Institute of Materials Science for the SEM/EDX investigations.

References
[1] S. Rosenthal, F. Maaß, M. Kamaliev, M. Hahn, S. Gies, A. E. Tekkaya, Lightweight in Automotive Components by Forming Technology, Automot. Innov. 3 (2020) 195-209. https://doi.org/10.1007/s42154-020-00103-3
[2] ThyssenKrupp Steel AG, ThyssenKrupp Tailored Blanks bring steel to the right place, compact 26(2) (2007) 32-33.
[3] M. Merklein, M. Johannes, M. Lechner, A. Kuppert, A review on tailored blanks - Production, applications and evaluation, J. Mater. Process. Technol. 214 (2014) 151-164. https://doi.org/10.1016/j.jmatprotec.2013.08.015
[4] P. Groche, S. Wohletz, A. Erbe, A. Altin, Effect of the primary heat treatment on the bond formation in cold welding of aluminum and steel, J. Mater. Process. Technol. 214 (2014) 2040-2048. https://doi.org/10.1016/j.jmatprotec.2013.12.021
[5] P. Groche, S. Wohletz, M. Brenneis, C. Pabst, F. Resch, Joining by forming - A review on joint mechanisms, applications and future trends, J. Mater. Process. Technol. 214 (2013) 1972-1994. https://doi.org/10.1016/j.jmatprotec.2013.12.022
[6] S. Wohletz, P. Groche, Temperature Influence on Bond Formation in Multi-material Joining by Forging, Procedia Eng. 81 (2014) 2000-2005. https://doi.org/10.1016/j.proeng.2014.10.271
[7] J. Wang, L. Langlois, M. Rafiq, R. Bigot, H. Lu, Study of the hot forging of weld cladded work pieces using upsetting tests, J. Mater. Process. Technol. 214 (2014) 365-379. https://doi.org/10.1016/j.jmatprotec.2013.09.009
[8] A. Foydl, I. Pfeiffer, M. Kammler, D. Pietzka, T. Matthias, A. Jager, A.E. Tekkaya, B.-A. Behrens, Manufacturing of Steel-Reinforced Aluminum Products by Combining Hot Extrusion and Closed-Die Forging, Key Eng. Mater. 504-506 (2012) 481-486. https://doi.org/10.4028/www.scientific.net/KEM.504-506.481
[9] J. Domblesky, F. Kraft, B. Druecke, B. Sims, Welded preforms for forging, J. Mater. Process. Technol. 171 (2006) 141-149. https://doi.org/10.1016/j.jmatprotec.2005.06.066

[10] B.-A. Behrens, J. Uhe, I. Ross, J. Ursinus, T. Matthias, S. Bährisch, Tailored Forming of hybrid bulk metal components, Int. J. Mater. Form. 15 (2022) 42. https://doi.org/10.1007/s12289-022-01681-9
[11] D.-C. Ko, B.-M. Kim, The prediction of central burst defects in extrusion and wire drawing, J. Mater. Process. Technol. 102 (2000) 19-24. https://doi.org/10.1016/S0924-0136(99)00461-6
[12] H. Hoche, A. Balser, M. Oechsner, A. Franceschi, P. Groche, Enhancement of the residual stresses of cold full-forward extruded parts by application of an active counter punch, Materialwissenschaft und Werkstofftechnik 50 (2019) 669-681. https://doi.org/10.1002/mawe.201900050
[13] C. Soyarslan, A.E. Tekkaya, Prevention of Internal Cracks in Forward Extrusion by Means of Counter Pressure: A Numerical Treatise, Steel Res. Int. 80 (2009) 671-679. https://doi.org/10.2374/SRI08SP170
[14] C. Büdenbender, I. Ross, H. Wester, A. Zaitsev, B.-A. Behrens, Numerical Investigation of an Extruded Shaft for High Temperature Applications Manufactured by Tailored Forming, in: Production at the leading edge of technology. Lecture Notes in Production Engineering, Springer, Berlin, Heidelberg, 2021, pp. 182-192. https://doi.org/10.1007/978-3-662-62138-7_19
[15] P. Gumm, Kombination von Umformung und Kaltpreßschweißen beim Fließpressen und Rohrziehen (Dissertation), VDI Verlag GmbH, Technische Hochschule Braunschweig, 1964.
[16] S. Herbst, H.J. Maier, F. Nürnberger, Strategies for the Heat Treatment of Steel-Aluminium Hybrid Components, HTM J. Heat Treat. Mater. 73 (2018) 268-282. https://doi.org/10.3139/105.110368
[17] A. Piwek, J. Uhe, J. Peddinghaus, I. Ross, B.-A. Behrens, Comparison of the joining zone development of hybrid semi-finished products after different extrusion processes, 31st International Conference on Metallurgy and Materials, Orea Congress Hotel Brno, Czech Republic, EU, May 18 - 19, 2022. https://doi.org/10.37904/metal.2022.4398
[18] B.-A. Behrens, D. Duran, T. Matthias, I. Ross: Enhancement of the interface friction welded steel-aluminium joints, Prod. Eng. Res. Devel. (2021) 169-176. https://doi.org/10.1007/s11740-020-00994-5
[19] B.-A. Behrens, R. Goldstein D. Duran, Role of Thermal Processing in Tailored Forming Technology for Manufacturing Multi-Material Components, Heat Treat 2017: Proceedings of the 29th ASM Heat Treating Society Conference, October 24-26, Columbus, Ohio, USA, 2017
[20] H.S. Valberg, M. Lefstad, A.L. de Moraes Costa, On the Mechanism of Formation of Back-End Defects in the Extrusion Process, Procedia Manuf. 47 (2020) 245-252. https://doi.org/10.1016/j.promfg.2020.04.207
[21] I. Balasundar, T. Raghu, Investigations on the extrusion defect - Axial hole or funnel, Mater. Des. 31 (2010) 2994-3001. https://doi.org/10.1016/j.matdes.2010.01.027

Materials Research Proceedings 28 (2023) 601-610 https://doi.org/10.21741/9781644902479-65

Advanced automatic pass schedule design for hot rolling by coupling reinforcement learning with a fast rolling model

IDZIK Christian[1,a *], GERLACH Jannik[1,b], BAILLY David[1,c] and HIRT Gerhard[1,d]

[1]Institute of Metal Forming (IBF), RWTH Aachen University, Aachen, Germany

[a]christian.idzik@ibf.rwth-aachen.de, [b]jannik.gerlach@ibf.rwth-aachen.de,
[c]david.bailly@ibf.rwth-aachen.de, [d]gerhard.hirt@ibf.rwth-aachen.de

Keywords: Hot Rolling, Reinforcement Learning, Multi-Objective Optimization

Abstract. Rolling is a well-established forming process for producing finished or semi-finished products in various industries. Although highly automated, most rolling processes are designed manually by experts based on their knowledge, highly specialized heuristics and analytical process models or numerical simulations. This manual design approach does not lead to an optimization accounting for multiple objectives. Previous work [1] has shown the potential of coupling reinforcement learning (RL) with fast analytical rolling models (FRM) to optimize hot rolling processes. However, the designed pass schedules do not robustly reach the desired final height within typical industrial tolerances. Therefore, in this paper the existing approach of coupling RL with an FRM is extended by dynamically ranges for height reductions. This extension guarantees that the target height is always reached exactly. In addition to the height reduction, the RL algorithm can determine the inter-pass time, initial slab temperature and rolling velocity. For the optimization, an objective function, called reward function, considering all relevant optimization objectives such as the final grain size and energy consumption, was developed. An exemplary training was performed for a defined starting (140 mm) and final height (25 mm). The resulting, automatically designed pass schedules reach the target height and fulfill all defined optimization objective including the required average austenite grain size.

Introduction

Hot rolling of flat products is a widely-used metalworking process, in which the material is heated above its recrystallization temperature and then passed through an arrangement of rolls to reduce its thickness. It is typically used for processing cast slabs or ingots into heavy plates or sheets with the desired geometry and material properties for various industries such as the automotive and construction industry. In fact, a large proportion of all steel (> 90%) and aluminum (> 60%) products are rolled at some point during their manufacture, as Allwood et al. [2] pointed out.

With an annual global crude steel production of over 1,900 million tons in 2021 [3], it is clear that even small process improvements such as energy savings are of significant importance. It is therefore logical to further optimize the process parameters in hot rolling e.g. the height reduction, so that desired product properties, such as final geometry, grain size and corresponding mechanical properties, are achieved more efficiently thus minimizing the energy consumption.

The product properties are determined by the initial material state, material properties like flow stress, heat transfer, microstructure evolution as well as the process parameters of each pass. These include height reduction, rolling velocity and inter-pass time among others. The challenge lies in the fact that (hot) rolling consists of several subsequent and coupled passes with the process parameters summarized in one overarching pass schedule. These dependencies result in a change of properties during each pass, therefore indirectly influencing every subsequent pass.

Due to the complex interactions between the process parameters, the material properties as well as the processing constraints, the design and optimization of the pass schedule represents a complex multi-objective optimization problem. Despite great progress, detailed finite element

Content from this work may be used under the terms of the Creative Commons Attribution 3.0 license. Any further distribution of this work must maintain attribution to the author(s) and the title of the work, journal citation and DOI. Published under license by Materials Research Forum LLC.

simulations as well as the use of classical optimization algorithms or specialized heuristics for process design are time consuming and hence not yet applicable for process optimization in the industrial context. Therefore, process design is often only based on experience of long-time rolling mill operators or fast process models. Previous work by Scheiderer et al. [1] showed that coupling RL with a FRM is very promising. RL is applied, since after a successful training process it is capable of solving given problems, e.g. to identify strategies in terms of a pass schedule, within seconds. During the training process, the learning part of the RL algorithm, which is called agent, learns through goal oriented interaction with a virtual process environment. Within the presented work, the required data for the RL-agent is provided by the FRM. However, the final height is not robustly reached within typical industrial tolerances.

To tackle this challenge, this paper presents a workflow to ensure that the final target height is always reached exactly within the tolerance. After a brief overview of the current pass schedule design approaches and the application of RL for process optimization, the coupled approach is shown and explained. The focus lies on the newly developed reward function and workflow for robust attainment of the target height. Finally, an exemplary training is presented and discussed.

Pass schedule Design and Optimization

Various approaches to design and optimize pass schedules exist, the first objective of which is always to guarantee the attainment of a target height. Known approaches to distribute the height reduction to several passes are, for example, to set the height reduction per pass to the maximum permitted by the rolling mill limitations [4] or to aim for a uniform distribution of the rolling forces between the individual passes [5]. These approaches are usually used to design a first version of a pass schedule, which is then further optimized.

As, Özgur et al. [6] pointed out in an extensive literature review, these pass schedules are mostly designed based on expert knowledge, analytical rolling models, finite element (FE) simulations and heuristics, and are therefore rarely optimized for several objectives simultaneously. These different approaches are often specialized for specific use cases, which makes a comparison or transferability almost impossible. A similar conclusion was reached by Pandey et al. [7] after their literature review demonstrating that, despite numerous methods, expertise is always needed.

In recent years, evolutionary algorithms have been increasingly used to design and optimize pass schedules, as shown by the work of Wu et al. [8] and Hernandez et al. [9]. However, these algorithms do not learn relationships between process parameters and target variables, thus a separate design process has to be performed for each pass schedule. With the usage of RL in contrast, knowledge can be (partially) transferred to other pass schedules.

Fast Rolling Models

Fast rolling models (FRM) are able to calculate rolling forces and microstructure development for complete rolling processes within a few seconds. For this purpose, they usually consist of simplified, analytical models using semi-empirical equations to describe the material behavior. Numerous fast rolling models with different emphases can be found in the literature.

Beynon and Sellars [10] present a rolling model called SLIMMER, which is able to describe the microstructure evolution and predict the rolling force and torque during hot rolling. Inspired by their work, Lohmar et al. [11] extended a similar model to include height resolution within the workpiece and considered the influence of shear during deformation. In addition to these classical approaches, data-driven methods have also been increasingly used in recent years to model the hot rolling process, for example by Shen et al. [12] to predict rolling forces.

Reinforcement Learning for Process Optimization

Reinforcement Learning (RL) is a branch of Machine Learning, which attempts to imitate natural learning behavior through reward and punishment. It consists of an iterative learning approach, in which it learns by mapping states to actions while trying to maximize a numerical reward [13].

In recent years, RL applications sprung up across the manufacturing field with exponential publication growth year by year as Li et al. [14] stated. The authors analyzed 264 different publications between 2013 and October 2022 and found, that optimizing energy consumption as well as costs and reducing reliance on expert knowledge as the main objectives of these applications. Esteso et al [15] came to similar conclusions and add that the great majority of RL applications in production technology utilize simplified (virtual) environments with discrete action spaces. Panzer and Bender [16] also conducted a literature review and conclude that in numerous applications RL outperforms previously used heuristics or algorithms. However, they are still not yet applied in real production.

There are already several successful applications of RL for the optimization of forming processes, such as in open die forging [17] and wire hot rolling [18]. Reinisch et al. [17] coupled a process model with a RL algorithm to design and optimize pass schedules for open-die forging in terms of final ingot geometry, press force and process duration. The designed pass schedules led to executable forging processes. Moreover, Gamal et al. [18] demonstrated that RL in combination with process data identifies model parameters and thus improve model predictions for bar and wire hot rolling processes. For hot rolling, Scheiderer et al [1] published a RL approach, which can design pass schedules considering several optimization objectives. The authors used a database of simulation data to train the RL algorithm. However, the target height could not be exactly achieved, which in any case is necessary for industrial application. Therefore, in this paper, based on this previous work, the coupling is extended to such an extent that the target height is always reached exactly. For this purpose, the previously statically defined limits of the height reduction are dynamically adjusted so that they prevent the target height from being undershot.

Advanced Coupling of RL with FRM

In this chapter, the advanced coupling between a FRM and a RL algorithm is presented. Fig. 1 schematically shows the structure of the coupled approach. The approach consists of an RL agent, representing the learning part, an environment, representing the problem and a set of selectable actions within defined ranges. At each discrete time step, the RL agent perceives the current state of the environment and performs actions, which result in changes of the environment. In this concrete use case, the RL agent chooses the process parameters of the next pass based on the current slab geometry and temperature. These process parameters lead to a change of the geometry and the temperature of the slab and therefore the state of the material. These changes are calculated by the FRM based on the chosen parameters, the previous material state and the material properties such as the flow stress. The RL agent designs the pass schedule pass by pass, thus feedback can be given to the agent directly after each pass

Based on the FRM results, a numerical reward is calculated evaluating the quality of the chosen process parameters (actions). It can be either positive or negative, representing a reward or a punishment, respectively. The reward as well as the current state are passed to the RL agent, which stores the information. Based on all stored information, neural networks aim to learn relationships between the previous states, the process parameters, the resulting new state and the reward.

The goal lies in identifying a sequence of process parameters (pass schedule), which result in a maximized reward. The described steps are repeated until the desired goal, here the target height, is reached. As soon as this is the case, the pass schedule design is completed, an iteration is finished and the material state is reset to the initial state. Afterwards, another iteration of the training process is performed. The training is carried out until the designed pass schedule converges. This means that the pass schedule does not really change from iteration to iteration.

Each further iteration provides the RL algorithm with new information and therefore helps improving the choice of process parameters in further iterations. To guarantee continuous improvement of the designed process, the chosen reward function is of essential importance. Here,

it e.g. tracks and rewards, whether the final grain size matches the desired one, or punishes the exceeding of the maximum rolling force of the rolling mill.

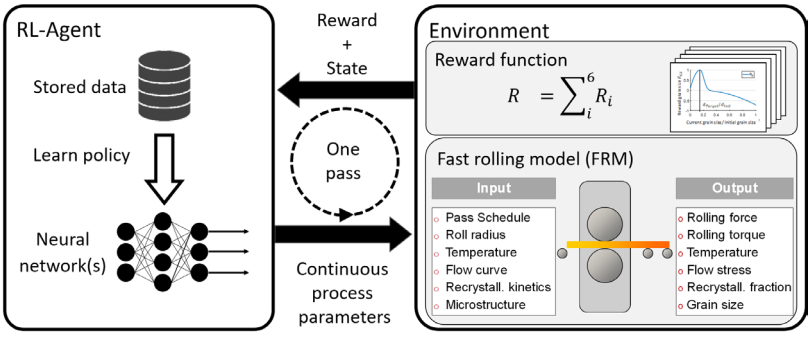

Fig. 1. Schematic depiction of the coupling of the RL algorithm with the FRM.

As previously mentioned, the pass schedule design is performed pass by pass. Hence, it follows that the reward is also calculated directly after each pass instead of only receiving feedback after a complete pass schedule. However, the RL algorithm can only process a single numerical value to evaluate all defined optimization objectives. Thus, each objective first has to be evaluated separately, before being summarized to one numerical value. Table **1** lists all considered optimization objectives.

Table 1. Overview of the optimization objectives.

Optimization objective	**Goals**
Grain size R_d	Final average austenite grain size after rolling
Force/torque R_F / R_T	No exceeding of the rolling mill limits (80% of max optimal)
Energy consumption R_E	Minimization of the energy consumption
Process time R_{time}	Minimization of the process duration
Height reduction R_{deltaH}	Minimization of total number of passes

In this paper, the reward R for each pass is composed as a weighted sum of six components R_i as shown in Eq. 1. The prioritization here lies in achieving a desired grain size as it corresponds to mechanical properties. Therefore, this reward component is provided with a higher weighting than the others. An evaluation of the height is not necessary as the target height is always achieved exactly by dynamic adjustment of the height reduction, which will be described later.

$$R = \sum_i^6 w_i \cdot R_i = 3 \cdot R_d + R_F + R_T + R_E + R_{time} + R_{deltaH} \quad (1)$$

For the definition of the individual reward components R_i, continuous functions were chosen, which scale between -1 and 1 to ensure no prioritization only by function design. To prevent the accumulation of positive rewards by simply adding a large number of passes, most reward components are defined negatively. Selected reward functions for individual objectives are described in more detail below.

During optimization, some goals are to be exactly reached ($R_d/R_F/R_T$), while others are to be minimized (R_E/R_{time}) or maximized (R_{deltaH}). Fig. **2** (left) shows the reward for the rolling force (R_F). The definition for the rolling torque (R_T) is equivalent to the one for the force. In both cases, it is important not to exceed the rolling mill limits while still using enough of the available supplies. Therefore, the reward increases up to an optimal working point (F_{opt}) sitting at 80% of the

maximum rolling mill force. This ensures that unintentional exceeding of the rolling stand limits is prevented even if process deviations or material fluctuations occur. If the defined operating point is exceeded, the reward decreases and reaches a penalty of -1 at the maximum rolling mill force.

Fig. 2 (right) shows the reward for the austenite grain size (R_d). The punishment increases the further the current grain size deviates from the desired target grain size (d_{Target}). Once the grain size lies within the desired tolerance, the reward (R_d) becomes positive.

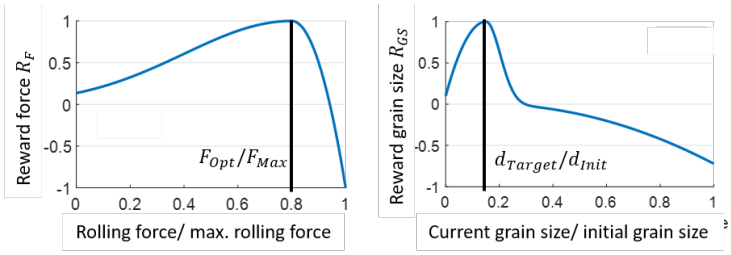

Fig. 2. Reward functions for rolling force (left) and grain size (right).

For components requiring the minimization or maximization of a given process parameter, parabolas as shown in Fig. 3 on the left for energy consumption (R_E) and on the right for height reduction (R_{deltaH}) are used. These reward components are only defined between 0 and -1 so that the agent is forced to minimize the punishment. The energy consumption is calculated considering the rolling torque, rolling speed, roll radius and the process duration for each pass.

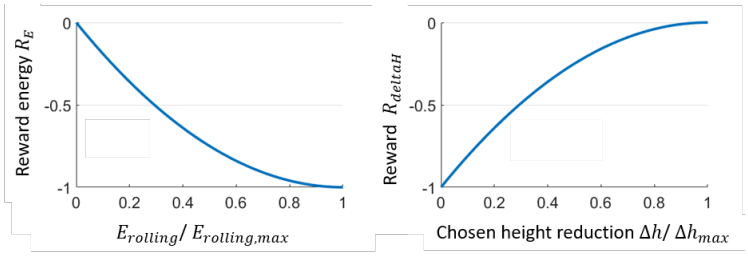

Fig. 3. Reward functions for energy consumption (left) and for height reduction (right).

In addition to the aspects described so far, the advanced coupled approach also has to ensure that the final height is exactly reached. Seeming to be particularly easy using human knowledge in process design, this has proven to be difficult for the RL algorithm in the past. In the work of Scheiderer et al. [1], the limits defined for the height reduction were the same absolute values for each pass. Therefore, the RL agent had to learn how to reach the target height, which did not always turn out to be successful. As soon as the maximum possible height reduction Δh was greater than the remaining difference between the initial height h_0 of the current pass and the target height h_{Target}, there was a risk that the pass schedule leads to heights below the target height. To prevent this, dynamic adjustments of the height reduction limits $[\Delta h_{min}, \Delta h_{max}]$ are implemented.

For the maximum permissible height reduction (Δh_{max}), two process-technological limits need to be respected. On the one hand, there is a maximum possible height reduction ensuring that no damage like cracking occurs. This limit ($\Delta h_{max,1}$) is material-dependent and typically lies at around 40 % of the initial height h_0 of the regarded pass. On the other hand, the bite condition during rolling has be taken into account. Depending on the friction coefficient μ and the roll radius r, it defines the maximum possible height reduction ($\Delta h_{max,2}$), for which the material is still drawn into the roll gap. However, since there are uncertainties regarding the friction coefficient, here, 85 % of the possible maximum height reduction is used. This ensures rollable pass. The

Materials Research Proceedings 28 (2023) 601-610 https://doi.org/10.21741/9781644902479-65

corresponding developed method is shown in Fig. 4. Based on the two calculated maximum possible height reductions ($\Delta h_{max,1}, \Delta h_{max,2}$), the smaller one is selected, so that both limitations are always fulfilled. In the next step, it is checked whether the chosen height reduction is larger than the remaining height difference between the current height and the target height h_{Target}. If so, the maximum permissible height reduction Δh_{max} is lowered to this difference.

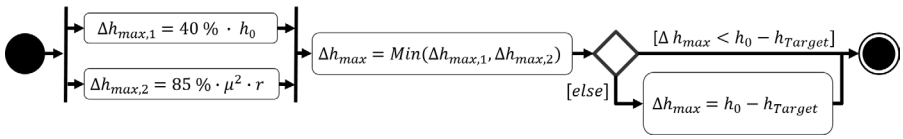

Fig. 4. Calculation of maximum height reduction Δh_{max} to guarantee reaching the desired final height.

Regarding the minimum height reduction (Δh_{min}), there are no fixed limits. Small height reductions are principally allowed, see Fig. 5. However, they usually lead to longer process times, which are punished by the reward function as shown in Eq. 1.

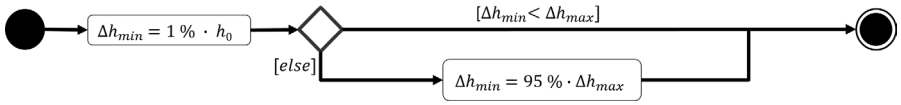

Fig. 5. Calculation of minimum height reduction Δh_{min} to guarantee reaching the desired final height.

Results: Training for Designing and Optimizing a Pass Schedule

The above described approach was used to design a pass schedule for reversing hot rolling of a S355 steel slab with an initial height of 140 mm to a target height of 25 mm on the universal rolling mill Bühler VRW-400 at the Institute of Metal Forming (IBF). Furthermore, the optimization aimed to reach a final grain size ($d_{Target} = 30\ \mu m$). The rolling mill limits were set to a force ($F_{max} = 4\ MN$) and torque ($F_{max} = 65\ kNm$), while energy consumption and process time were to be minimized. During the training, the RL agent was able to vary the process parameters within the limits shown in Table 2.

For the results shown in the following, an established RL algorithm, the Deep Deterministic Policy Gradient (DDPG) [19] was used. This algorithm uses two neural networks, allowing it to solve problems with continuous action spaces. One network estimates the cumulative long-term reward based on the current state and the chosen actions. The second network tries to learn a suitable strategy based on the reward estimation.

For the coupling with RL, an already existing fast rolling model is used, which was developed and validated at IBF by Lohmar et al [11]. It consists of several modules allowing the prediction of deformation, temperature and austenite grain size evolution as well as rolling forces and torques.

Table 2: Ranges of the RL agent's selectable process parameters.

Process parameter	**Limits**	
	Minimal	Maximum
Height reduction Δh	Δh_{min}	$\Delta h_{max}(\mu = 0.3, r = 205\ mm)$
Initial temperature	1000 [°C]	1200 [°C]
Inter-pass time	5 [s]	30 [s]
Rolling velocity	100 [mm/s]	500 [mm/s]

The presented training was carried out with 20,000 iterations, which corresponds to 20,000 calculated pass schedules. This equals about 24 hours of calculation time (CPU: Intel Xeon E3-1270). Fig. 6 shows the height evolution in black and the grain size evolution in red for the first and the final designed pass schedules. It is evident that the number of passes (from 18 to 8 passes) and the process time have been reduced and that the target grain size has been reached. Furthermore, both pass schedules reach the desired target height, regardless of the training progress. This is ensured by the dynamic adjustment described in Fig. 4 and Fig. 5.

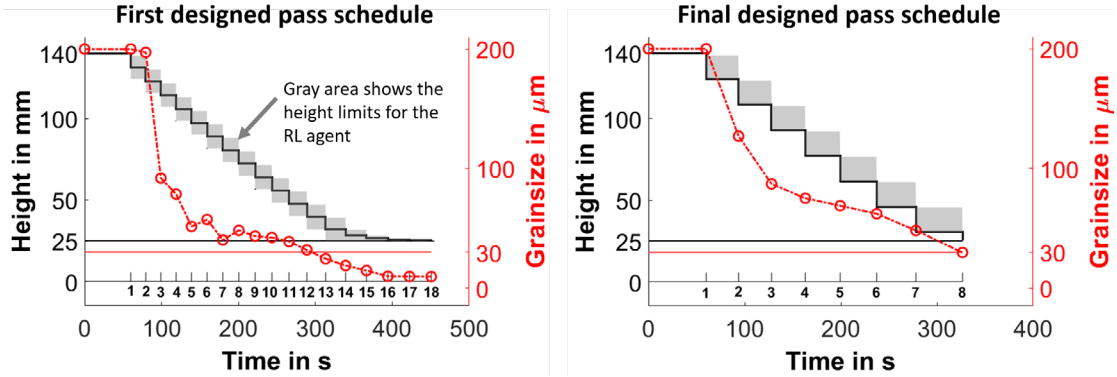

Fig. 6. The first (left) and the final (right) designed pass schedule after 20,000 iterations by the RL agent.

For comparison, Table 3 shows two pass schedules, one designed using static limits for Δh and one designed by the presented extended approach. In both cases, the same optimization objectives and boundary conditions were used. Both lead to similar results, e.g. final grain size.

Table 3. Comparison of the final designed pass schedule with static Δh limits and with the new dynamic approach.

Pass Number	**Height after each pass in [mm]**	
	Static Δh	Dynamic Δh
1	124.32	124.32
2	108.64	108.64
3	92.64	92.95
4	77.27	77.27
5	61.59	61.59
6	46.22	45.91
7	33.31	30.54
8	24.88	25.00

Although the difference between the two pass schedules appears to be negligible, it is of great importance since an undershooting of the final height is irreversible and leads to unsaleable products. The comparison demonstrates that the presented approach successfully supports the RL agent in identifying strategies, which lead to saleable products.

In addition to the resulting pass schedules, taking a closer look at the training progress is of interest, too. Therefore, the results achieved using the dynamic Δh are shown in more detail. Fig. **7** shows the evolution of the total reward R_{total} of the complete pass schedule in blue and the deviation ΔGS between the final average grain size and the target one in red during training. The evolution of the total reward over the iterations clearly shows that the reward increases the most within the first 1,000 iterations. Afterwards, it increases only slightly until it reaches a constant level at about 2,500 iterations.

A similar pattern can also be found for the deviation of the final grain size from the target one (ΔGS). The initial deviation of about 20 µm is significantly reduced in the first 1,000 iterations, so that the deviation at 2,500 iterations lies at only a few µm. Subsequently, the desired grain size is reached. The results show that the training is clearly converging towards a total reward of about -10, at which the target grain size is reached. Comparing the evolutions of the total reward and the deviation from the target grain size, it is noticeable that both correlate well, especially at the beginning and up to about 1,000 iterations. This strongly indicates that at the beginning the RL agent is trying to achieve the target grain size as soon as possible. This results from the prioritization of this component in the reward function. This indicates that weighting of individual components in the overarching reward function can be used to successfully focus on certain optimization objectives while still achieving all other desired objectives.

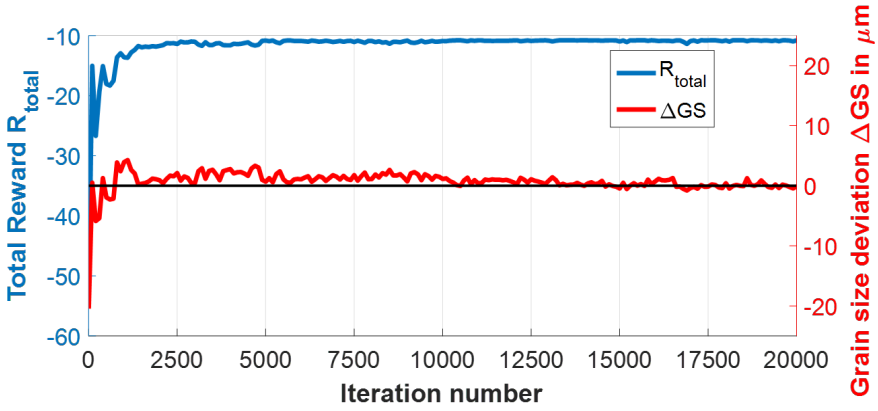

Fig. 7. Evolution of the total reward in blue and the deviation of the average grain size from the target grain size (30 µm) ΔGS in red.

Fig. 8 shows the evolution of the energy consumption as well as the total number of passes of the designed pass schedules during the training. It is noticeable that the energy consumption initially increases significantly, peaks at around 500 iterations at 0.14 GJ and then continuously decreases until it reaches a constant level at about 5,000 iterations with a value of 0.12 GJ.

Another example for the well-defined prioritization in the reward function is the evolution of the number of passes in the pass schedules laid out. The aim was to favor height reductions that are as large as possible so that the required number of passes is as low as possible. A small number of passes usually results in a shorter process time and thus higher efficiency. Here, the number of passes per pass schedule strives very quickly from 18 to the minimum possible number of eight.

In addition to the values shown here, the analysis of the resulting rolling forces and torques showed that the maximum rolling mill limitations were retained at all times during the training. Moreover, the final height is exactly reached by using the dynamic adjustment of the height

reduction presented in this work, it can be stated that rollable pass schedules have been laid out successfully after only a few thousand iterations. Moreover, the dynamic adjustment of the height reduction accelerated the training progress significantly compared to the previous work [1].

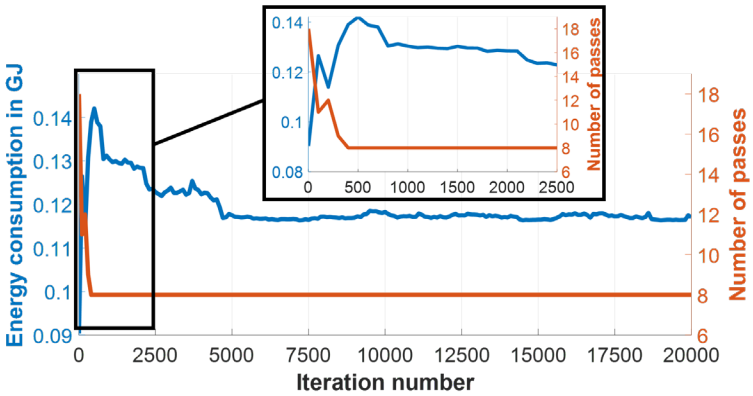

Fig. 8: Evolution of the energy consumption in blue and of the total number of passes in orange of the designed pass schedules during the training.

Summary

The results show that the coupling of RL with an FRM can successfully learn the complex interactions between process parameters, material behavior and the final properties such as the final austenite grain size. The approach does not require explicit knowledge or procedure and can automatically design pass schedules for multiple optimization objectives based on a reward function. The presented extension, the dynamic adjustment of the height reduction, ensures that the target height is always hit exactly. It guarantees automatically designed pass schedule that lead to saleable products. Furthermore, compared to the results of previous work, learning could rather be accelerated. Additionally, the further objectives, especially the target grain size, were successfully achieved. Following next, the designed pass schedules are to be experimentally validated, while the knowledge of the trained RL agents will be transferred to design further pass schedules with varying starting and final geometries.

Acknowledgement

Funded by the Deutsche Forschungsgemeinschaft (DFG, German Research Foundation) under Germany´s Excellence Strategy – EXC-2023 Internet of Production – 390621612.

References

[1] C. Scheiderer, T. Thun, C. Idzik, A.F. Posada-Moreno, A. Krämer, J. Lohmar, G. Hirt, T. Meisen, Simulation-as-a-Service for Reinforcement Learning Applications by Example of Heavy Plate Rolling Processes, Procedia Manuf. 51 (2020) 897-903. https://doi.org/10.1016/j.promfg.2020.10.126

[2] J.M. Allwood, J.M. Cullen, M.A. Carruth, Sustainable materials. With both eyes open ; [future buildings, vehicles, products and equipment - made efficiently and made with less new material]. UIT Cambridge, Cambridge, 2012

[3] World Steel Association, 2022 World Steel in Figures. World crude steel production 1950 to 2021. https://worldsteel.org/steel-topics/statistics/world-steel-in-figures-2022/

[4] D.S. Svietlichnyj, M. Pietrzyk, On-Line Model for Control of Hot Plate Rolling. In: Beynon JH (Hrsg) 3rd International Conference on Modelling of Metal Rolling Processes. IOM Communications, London, S (1999) 62-71

[5] M. Schmidtchen, R. Kawalla, Fast Numerical Simulation of Symmetric Flat Rolling Processes for Inhomogeneous Materials Using a Layer Model − Part I. Basic Theory, Steel Res. Int. 87 (2016) 1065-1081. https://doi.org/10.1002/srin.201600047

[6] A. Özgür, Y. Uygun, M.-T. Hütt, A review of planning and scheduling methods for hot rolling mills in steel production, Comput. Ind. Eng. 151 (2021) 106606. https://doi.org/10.1016/j.cie.2020.106606
[7] V. Pandey, P.S. Rao, S. Singh, M. Pandey, A Calculation Procedure and Optimization for Pass Scheduling in Rolling Process. A Review, J. Mater. Sci. Mech. Eng. 5 (2018) 126-130
[8] S. Wu, X. Zhou, J. Ren, G. Cao, Z. Liu, N. Shi, Optimal design of hot rolling process for C-Mn steel by combining industrial data-driven model and multi-objective optimization algorithm. J. Iron Steel Res. Int. 25 (2018) 700–705. https://doi.org/10.1007/s42243-018-0101-8
[9] C.A. Hernández Carreón, J.E. Mancilla Tolama, G. Castilla Valdez, I. Hernández González, Multi-Objective Optimization of the Hot Rolling Scheduling of Steel Using a Genetic Algorithm. MRS Adv. 4 (2019) 3373-3380. https://doi.org/10.1557/adv.2019.436
[10] J.H. Beynon, C.M. Sellars, Modelling Microstructure and Its Effects during Multipass Hot Rolling. Iron Steel Inst. Jap. 32 (1992) 359–367. https://doi.org/10.2355/isijinternational.32.359
[11] J. Lohmar, S. Seuren, M. Bambach, G. Hirt, Design and Application of an Advanced Fast Rolling Model with Through Thickness Resolution for Heavy Plate Rolling. In: J. Guzzoni, M. Manning (Hrsg) 2nd International Conference on Ingot Casting Rolling Forging, ICRF 2014
[12] S. Shen, D. Guye, X. Ma, S. Yue, N. Armanfard, Multistep networks for roll force prediction in hot strip rolling mill, Machine Learning with Applications 7 (2022) 100245. https://doi.org/10.1016/j.mlwa.2021.100245
[13] R.S. Sutton, A. Barto, Reinforcement learning. An introduction. Adaptive computation and machine learning, The MIT Press, Cambridge, MA, London, 2018
[14] C. Li, P. Zheng, Y. Yin, B. Wang, L .Wang, Deep Reinforcement Learning in Smart Manufacturing: A Review and Prospects, CIRP J. Manuf. Sci. Technol. 40 (2022) 75-101. https://doi.org/10.1016/j.cirpj.2022.11.003
[15] A. Esteso, D. Peidro, J. Mula, M. Díaz-Madroñero, Reinforcement learning applied to production planning and control, Int. J. Prod. Res. (2022) 1-18. https://doi.org/10.1080/00207543.2022.2104180
[16] M. Panzer, B. Bender, Deep reinforcement learning in production systems: a systematic literature review, Int. J. Prod. Res. 60 (2022) 4316-4341. https://doi.org/10.1080/00207543.2021.1973138
[17] N. Reinisch, F. Rudolph, S. Günther, D. Bailly, G. Hirt, Successful Pass Schedule Design in Open-Die Forging Using Double Deep Q-Learning, Processes 9 (2021) 1084. https://doi.org/10.3390/pr9071084
[18] O. Gamal, M.I.P. Mohamed, C.G. Patel, H. Roth, Data-Driven Model-Free Intelligent Roll Gap Control of Bar and Wire Hot Rolling Process Using Reinforcement Learning, IJMERR 10 (2021) 349–356. https://doi.org/10.18178/ijmerr.10.7.349-356
[19] D. Silver, G. Lever, N. Heess, T. Degris, D. Wierstra, M. Riedmiller, Deterministic Policy Gradient Algorithms, Proceedings of the 31 st International Conference on Machine Learning, 32. Aufl, Beijing, China, 2014, 387-395

Materials Research Proceedings 28 (2023) 611-620 https://doi.org/10.21741/9781644902479-66

Beneficial effect of stress superposition on damage reduction in trimming processes

WEIß Alexander[1,a *], FELDE Alexander[1,b], LIEWALD Mathias[1,c] and ZERFAß Helmut[2,d]

[1]University of Stuttgart, Institute for Metal Forming Technology (IFU), Germany

[2]Bilstein & Siekermann GmbH + Co.KG, Germany

[a]alexander.weiss@ifu.uni-stuttgart.de, [b]alexander.felde@ifu.uni-stuttgart.de, [c]mathias.liewald@ifu.uni-stuttgart.de, [d]h.zerfass@bsh-vs.com

Keywords: Stress Superposition, Trimming, Damage Reduction, Crack Formation

Abstract. Trimming processes are frequently used for the manufacturing of fastener heads and similar parts with high precision requirements for specific regions of the part. Compared to conventional cold forging processes, the desired geometry can be achieved with significantly lower forces. However, trimming of sharp-edged geometries often leads to a highly inhomogeneous material flow and stress state in the workpiece, resulting in crack formation at such edges. To address this shortcoming, superposition of compressive stresses can be used to reduce the damage in the trimming process significantly. In this paper, the beneficial effect of stress superposition on damage reduction in a trimming process of a splined part is presented. By means of a numerical investigation using the FE-software DEFORM 3D, the impact of compressive stress superposition on the damage respectively crack formation at the edges of a splined part was investigated. Afterwards, trimming dies were manufactured and experimental investigations with three different trimming die geometries and different preform geometries were conducted to manufacture the splined parts. The edges of the splined parts were then characterized with a digital microscope and compared to the numerical results.

Introduction and State of the Art

Cold forging is widely used due to its advantages regarding production of high-volume parts, the work hardening of the material due to the deformation and the possibility to obtain near net shape parts right after the forming process. Furthermore, high surface qualities and very low tolerances with regard to dimensional accuracy of the pressed components can be achieved [1]. Trimming processes are often used to trim scrap material from hot forged parts [2]. But trimming processes are also used e.g. for the manufacturing of complex, sharp-edged geometries with high accuracy requirements for which a conventional cold forging process would not lead to a sufficient filling of the die cavity [3]. One example of such a combined process is the production of fasteners. In particular, in the production of screws with hexagonal head and flange, the shape of the hexagonal head is trimmed while the trimmed material forms the flange in the simultaneous upsetting process. Afterwards, the flange is trimmed with a circular shaped tool. Hence, there are two different categories of trimming processes:

- Category A: Trimming processes in which the produced flange is relatively thin and gets sheared off directly at the initial trimming contour by the knock out pin while the punch is still in its end position (e.g. hexagonal screws without flange). [4]
- Category B: Trimming processes in which the produced flange is relatively thick and remains at the part (e.g. hexagonal screws with flange). Here, the flange is usually trimmed with a circular trimming punch in a following forming stage. [3]

Content from this work may be used under the terms of the Creative Commons Attribution 3.0 license. Any further distribution of this work must maintain attribution to the author(s) and the title of the work, journal citation and DOI. Published under license by Materials Research Forum LLC.

Regarding trimming processes of category A, there are several scientific investigations. In [5], the trimming process of a fastener with a hexagonal head has been investigated numerically while the study was mainly focused on the tool load. It was found that the stopping distance has a major impact on the tool load but also affects the load of the knock out pin which is used to shear off the flange. In [6], a numerical investigation using 2D- and 3D-simulations was conducted to determine the impact of different trimming die geometries on the effective stress within the trimming die. Specifically, the corner geometry, land width, petal angle and rake angle were varied and beneficial values were obtained for these four parameters regarding screw sizes M6 and M20.

In [7], a trimming process of a fastener with a hexagonal head was investigated numerically using seven different damage models. Afterwards, the numerical results were compared to cracks that actually occurred on the sheared off chip of a real pressed part. Main objective of this study was the exact numerical modeling of the crack formation in the sheared off chip, whereby Cockcroft-Latham-Oh damage model was the most accurate model to reproduce those diagonal cracks numerically. Further investigations of the same authors show similar results [8].

In [9], the influence of different geometrical parameters on the target geometry of a fastener with a hexagonal head without flange was investigated. Three geometric phenomena were observed with respect to the target geometry – a roll-over at the top of the fastener head, an underfilling and a burr formation in the lower area of the head. The radius at the cutting edge was found to be the most significant parameter for these geometric deviations. A relatively new study from 2021 comprises an investigation on the die-service life of trimming dies for bolts with hexagonal head [10]. In this study, various combinations of geometric parameters of the trimming dies were investigated and the dies were used until failure due to, for example, broken cutting edges. Cutting edge radius and cutting width were found as the most significant parameters for die-service life.

Regarding trimming processes of category B and especially crack formation in such processes, the authors proposed the topic "Process limits in trimming of non-circular and asymmetrical geometries" as a study in the German Cold Forging Group (GCFG) in 2020 [3]. The aim of this study was a deeper knowledge of damage development during trimming of sharp-edged workpieces. For this purpose, a numerical parameter study was carried out based on a real part geometry of a hexagonal screw with flange. The impact of the workpiece preform geometry and tool geometry on the damage development in the workpiece was investigated. Normalized Cockcroft & Latham criterion was used for damage calculation. Among other things, an approach to superimpose compressive stresses was investigated. This approach showed promising numerical results in terms of damage reduction at the edges of the hexagonal screw. However, the results were not validated with an experimental investigation resulting in the initiation of this present study with the aim of proofing the beneficial effect of stress superposition on damage reduction in trimming processes.

Superposition of compressive stresses for an increased formability is also used in other applications, such as fine blanking [11]. In addition, there are also approaches to use stress superposition in lateral extrusion of brittle materials [12,13] and hollow lateral extrusion [14]. A more in-depth investigation of the connection between the stress state and the pore size in the microstructure as well as the resulting damage was carried out by [15]. Besides an improved formability, there are also investigations on the influence of stress superposition on residual stresses within the workpiece [16].

Material and Methods

The numerical investigations were performed with the FE-software DEFORM. Since the non-alloyed carbon steel EN 1.0214 is a common material for fasteners, this material was chosen for the numerical investigations. The used flow curves for the numerical investigation are depicted in

Materials Research Proceedings 28 (2023) 611-620 https://doi.org/10.21741/9781644902479-66

Fig. 1 and comprise data for two different strain rates (20 s^{-1} and 1 s^{-1}) and four different temperatures ranging from 20°C up to 300°C.

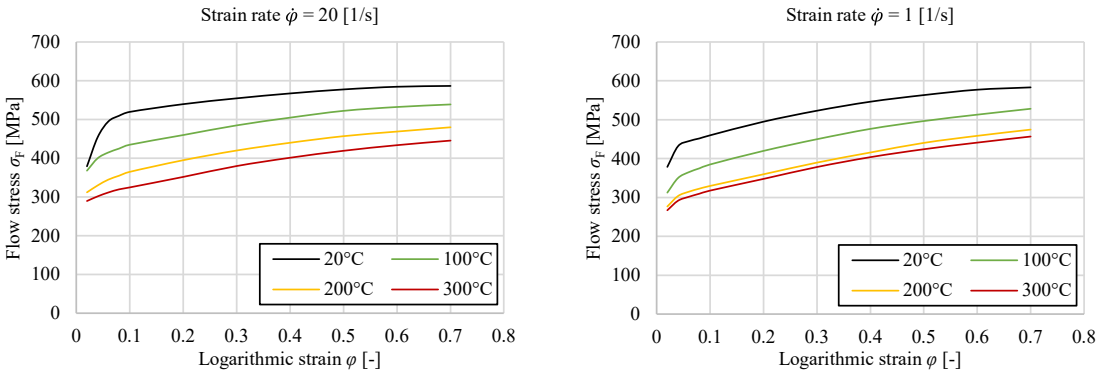

Fig. 1. Flow curves of the non-alloyed carbon steel EN 1.0214.

In order to proof the beneficial effect of stress superposition on damage reduction in trimming processes, a demonstrator geometry with a high susceptibility to crack formation during a conventional trimming process was chosen. In the previous GCFG-study, a screw with a trimmed hexagonal head was investigated (Fig. 2a) [3]. In coordination with the project partner, a gear-shaped geometry with a number of teeth of z_{spline} = 8 and a module of m_{spline} = 2 mm was selected for the present study as a demonstrator geometry (Fig. 2b). The large difference between the tip diameter and root diameter should most likely result in crack formation during conventional trimming. The shaft side of the demonstrator geometry was selected analogously to the hexagonal screw considered in the first study [3] which is based on a real process (Fig. 2c). In this way, it was possible to use the transfer system of the horizontal press without any modifications and the same process sequence. Just a modified trimming die had to be produced.

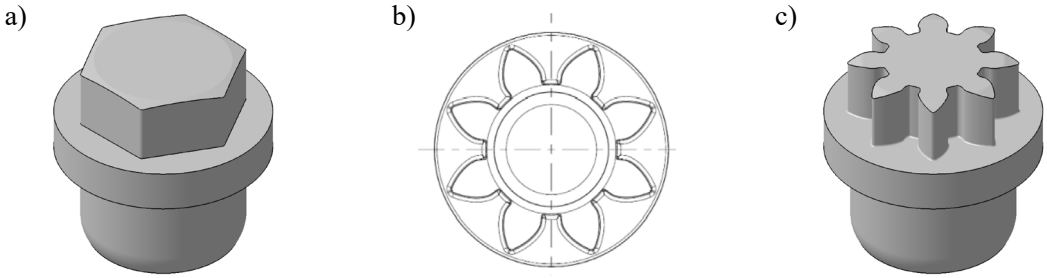

Fig. 2. a) Standard geometry with trimmed hexagonal shape [3], b) defined splined shape for the present study and c) modified geometry with trimmed splined shape.

For the numerical investigation, a multi-stage forming process has been developed in DEFORM comprising upsetting and heading as 2D-simulations, a 2D-3D-conversion and the trimming process as a 3D-simulation. The trimming process of the flange was not carried out, due to the fact that the damage at the edges can already be determined during the trimming process of the spline. Fig. 3 shows the developed multi-stage forming process for the numerical investigation in DEFORM. Since a high variety of different tool geometries was investigated, the workpiece was modelled as an ideal-plastic object whereas the tools were rigid objects. This approach has already been proven beneficial in the first study [3].

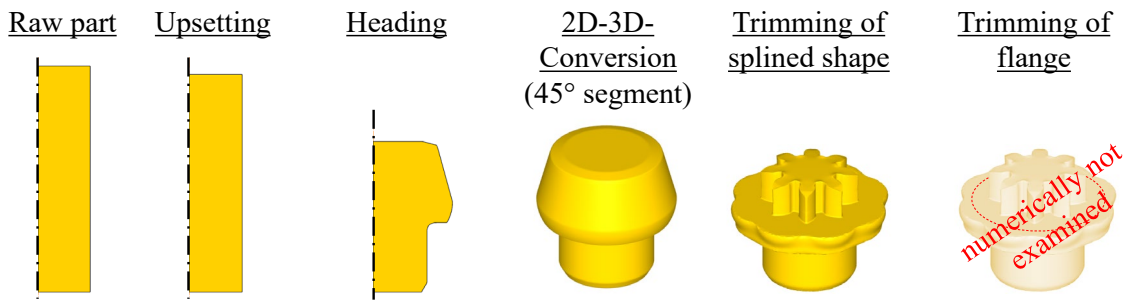

Fig. 3. Developed multi-stage forming process for the numerical investigation in DEFORM.

In the numerical investigation, shear friction model was used with a constant friction coefficient of $m = 0.1$. Furthermore, the velocity of the punch was set to 10 mm/s in each stage. For the upsetting and the heading process the number of elements for the FEM mesh was chosen to 2,500 elements with a minimum element edge length of 0.1 mm. Regarding the relatively simple geometries during upsetting and heading, this element edge length provides sufficient accuracy for the representation of the small radii. The raw part has a diameter of 19.7 mm and a length of 37.3 mm. After the upsetting process, the diameter is 20.75 mm and the length 33.62 mm. The initial preform angle of the conical shape in the heading stage is 16.5°. The preform angle was also varied to 25° since the tools were already available; a further increased value was not investigated based on the findings in [3] (the preform would need a very high radial dimension to meet the required height, and the amount of displaced material would increase disproportionately). The upsetting process is followed by an 2D-3D-conversion. Here, a 45° segment was investigated since this is the angle for simulate one complete tooth (Fig. 3 shows the 360° model for better overview). To decrease calculation time, also half of a tooth could be investigated. However, the relevant area of the tooth (the tooth tip) is directly in the symmetry plane which can influence the calculated workpiece properties. Therefore, one complete tooth was investigated. The hexagonal screw on which the demonstrator geometry is based on, has a wrench size of 19 mm to get an overall idea of the part size depicted in Fig. 2a. In the case of the demonstrator geometry of this study, the tip diameter is 21.6 mm and the root diameter is 12.6 mm.

The model of the 3D-simulation of the trimming process is shown in Fig. 4a. A 45° segment was investigated. This segment was modelled with a FEM mesh consisting of 180,000 elements. Mesh windows were used to obtain an accurate numerical result in the relevant area of the trimming zone. The smallest element size was 0.06 mm. Fig. 4b shows the stop-criterion of the process (flange height of 5.4 mm). The calculated workpiece geometry is depicted in Fig. 4c.

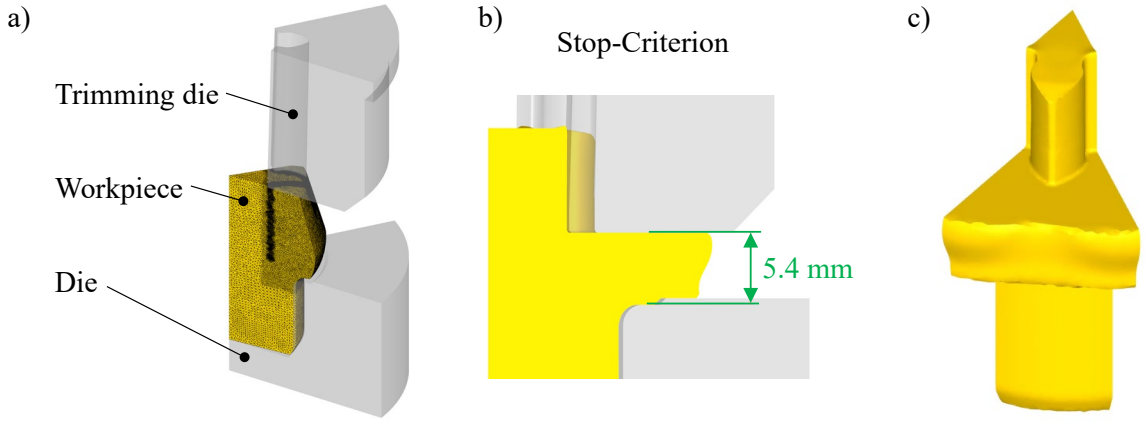

Fig. 4. a) Simulation setup, b) final height of the flange as a stop criterion and c) calculated workpiece geometry.

Materials Research Proceedings 28 (2023) 611-620 https://doi.org/10.21741/9781644902479-66

Regarding the stress superposition, five different trimming dies were used initially. Fig. 5 shows the dies considered for the numerical investigation. The reference die is designed like a conventional trimming die with a cutting edge radius of 0.25 mm. All other dies have the same cutting edge radius. Variant V1 features an indentation of 0.25 mm relative to the face of the die, which is applied close to the contour as an offset at a distance of 0.5 mm. Variant V1b is based on variant V1, but has an increased offset geometry distance of 1.0 mm (with regard to the tooth tip without the tooth root). Variant V2 features an annular indentation of 0.25 mm with a radial offset relative to the tip diameter of 0.5 mm. Variant V3 is designed to apply a compressive stress only in the local area of the tooth tip. For this purpose, the entire surrounding area is designed as a indentation. The offset of V3 was also selected to 0.5 mm, like V1 and V2.

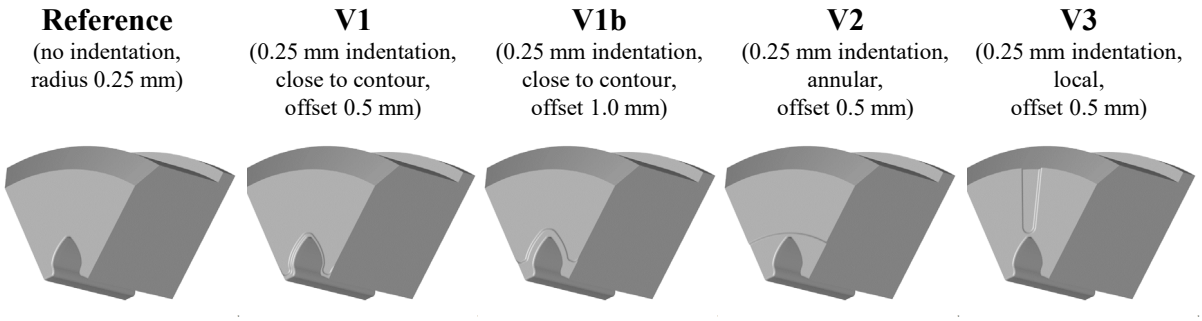

Fig. 5. Initially used trimming dies for the numerical investigation.

The experimental investigations were carried out on a mechanical press. In preparation, the series process for the production of a hexagonal screw with flange shown in Fig. 6 was equipped on the horizontal multi-stage press. Afterwards, the parts were pressed using the splined dies and the parts with cracks were analyzed using a Keyence digital microscope VHX-5000. Finally, the critical damage value was determined by comparing the numerically determined damage distribution with the measured crack height.

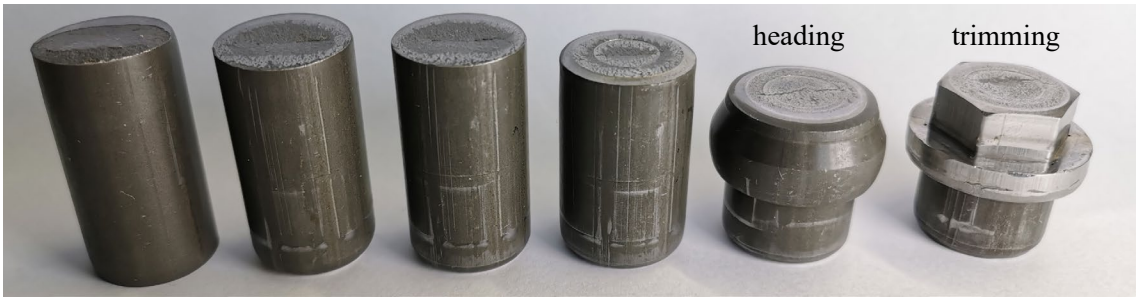

Fig. 6. Multi-stage process for production of a hexagonal screw with flange.

Results and Discussion

At first, the numerical results are evaluated. The geometry and the respective distribution of damage with Normalized Cockcroft & Latham damage model is shown in Fig. 7. The modified die geometry is well visible on the top side of the flanges. Regarding the determined damage values, also the maximum damage value for each variant is listed. As expected, the highest damage values occur at the tooth tip of the splined geometry. The reference die leads to the highest value of $D_{max,ref} = 5.41$. For all other variants the damage value is reduced due to the superposition of radial compressive stress. This can be explained by the additional redirection of the material flow at the transition of the indentation, which leads to an additional radial force. Owing to the highly inhomogeneous material flow caused by the large differences between tip and root diameter, the

modified variants have a different impact on the damage values. Variant V2 leads to the most homogeneous material flow due to the annular indentation and, as a result, provides the smallest damage value of $D_{max,V2} = 2.94$. With regard to the forces, there are only minor differences between all variants with 525 kN to 575 kN (Fig. 7). This can be explained with the only slightly varying volume differences of the indentations. Without an experimental test, the damage value only indicates the potential area of possible damage, but must always be validated with an experimental test. Therefore, it cannot be determined solely from the numerical results whether a crack will occur or not.

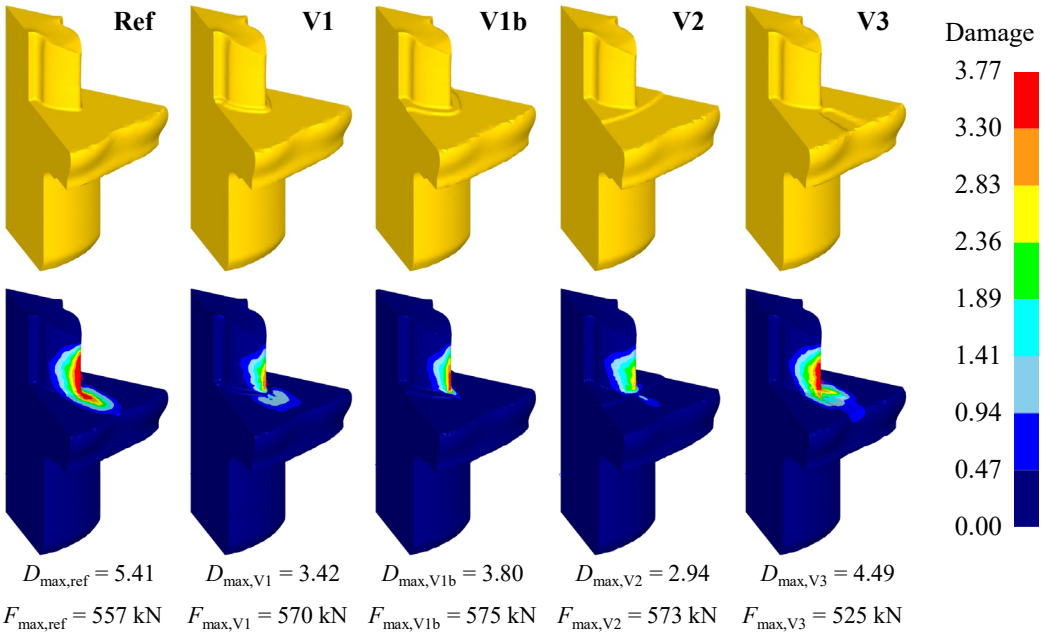

Fig. 7. Calculated geometries and respective distribution of damage with Normalized Cockcroft & Latham.

Due to the smallest numerically determined damage values, variant V2 was selected for the experimental investigations. The manufactured die with the splined contour replaced the hexagonal die in the process sequence depicted in Fig. 6. Initially, several parts were pressed with the conventional machine setting. Fig. 8 a shows the reference trimming die for the spline shaped parts. A pressed part is depicted in Fig. 8b. The crack formation at the sharp edges of the tooth tips is clearly visible. A detailed view of one tooth is shown in Fig. 8c. Thus, it can be concluded that the selected demonstrator geometry has a high vulnerability to crack formation with respect to conventional trimming processes.

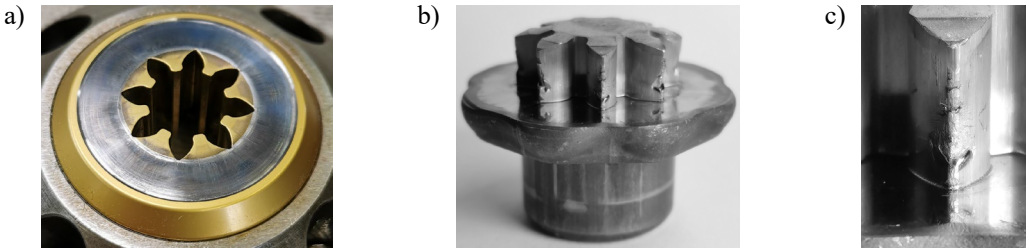

Fig. 8. a) Trimming die without indentation (reference), b) pressed part with cracks and c) detail of tooth tip.

Subsequently, the experimental investigation with the trimming die with an annular indentation of 0.25 mm was conducted. The pressed parts showed also cracks at the sharp edges of the tooth tips (Fig. 9b and Fig. 9c). At first, the initiation position of the cracks looked quite similar compared to the variant without compressive stress superposition. Therefore, also a comparison of Fig. 8c and Fig. 9c doesn't show much difference. But in fact the initiation position of the cracks was slightly lower which is made clear in Fig. 11 later.

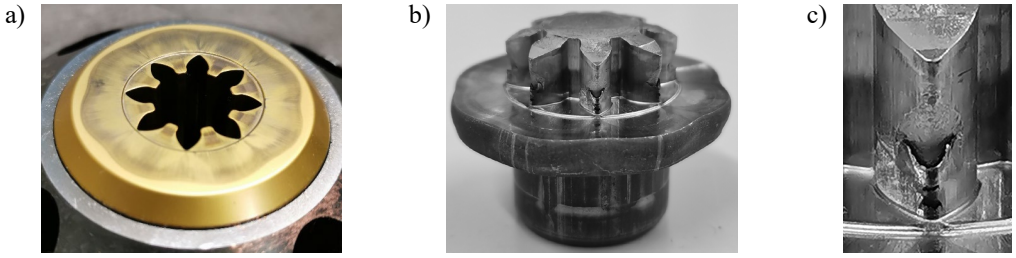

Fig. 9. a) Trimming die with annular indentation of 0.25 mm, b) pressed part with cracks and c) detail of tooth tip.

In a further investigation, the indentation was increased from 0.25 mm to 1.0 mm (Fig. 10a). As a result, there is a larger deflection of the material and, thus, higher induced compressive stresses occur. With this adjustment it was possible to press parts without any cracks. One exemplary part is shown in Fig. 10b with a detailed view in Fig. 10c.

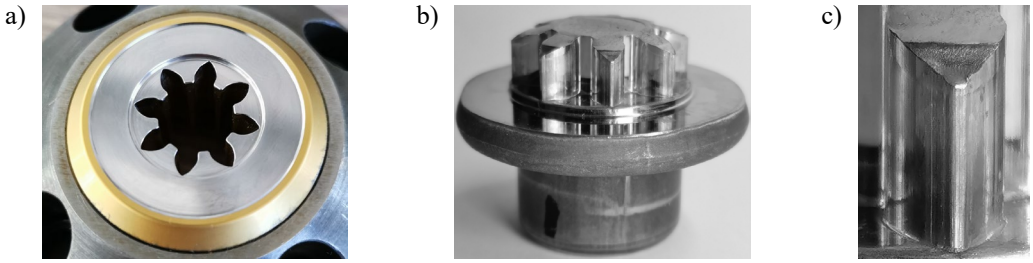

Fig. 10. a) Trimming die with annular indentation of 1.0 mm, b) pressed part without cracks and c) detail of tooth tip.

Besides those different die geometries, also the preform angle was varied in the experimental investigation using the trimming die with a 0.25 mm deep indentation. For comparison of the experimental results with the numerically determined damage values over 400 teeth were characterized using the Keyence digital microscope VHX-5000. In particular, the total trimming height h from the top edge to the flange, the trimming height s from the crack initiation to the flange and the difference between those two heights - the trimming height without crack a - were measured.

Fig. 11 shows the measured heights for characterization of crack initiation as well as the impact of the investigated variants with respect to the indentation and the preform angle on the trimming length without crack a. Furthermore, the number of measurements is indicated, since at some parts the very sharp edges were deformed due to the impact in the container after the forming process. Without a compressive stress superposition, an average trimming height without crack of $a = 1.02$ mm was determined. With a compressive stress superposition by the indentation of 0.25 mm, a 35 % higher value of $a = 1.38$ mm could be achieved for the same preform. The preform which was used initially in the numerical investigation comprising an angle of 16.5° has only a slight impact on the height a. Here, the average value is 1.33 mm. Regarding the variant with 1 mm indentation, no cracks occurred on any of the pressed parts. The height a therefore

always corresponded to the total trimming height h, with an average value of h = 5.22 mm. The maximum value of the total trimming height for one part with a very low end position of the trimming die was h = 5.80 mm.

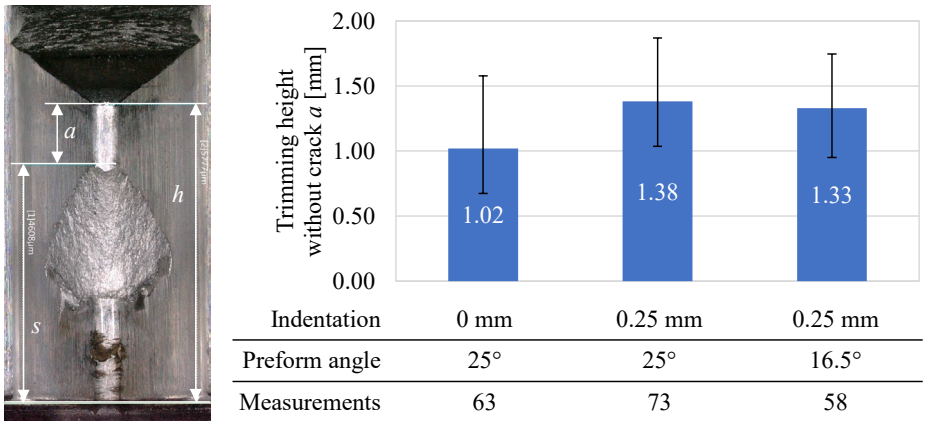

Fig. 11: Measured heights for characterization of crack initiation and impact of the investigated variants on the trimming length without crack a.

To compare the numerical and experimental results, the additional preform with an angle of 25° and the additional trimming die geometry with an indentation of 1 mm were first added in the numerical investigations and further simulations were carried out. Based on the average trimming height without crack *a*, the critical damage value was then identified for the reference die and the die with an indentation of 0.25 mm as well as for the preform angles 25° and 16.5°. Using this procedure, an average critical damage value of 0.93 was identified. The preform angle has no major impact and the penetration depth has no impact on the critical damage value. Fig. 12a shows the comparison of an edge of a pressed part (no indentation, preform angle 16.5°) and the numerically calculated damage distribution. The color scale is formatted in such a way that the critical damage value represents the transition from orange to red color (red circle).

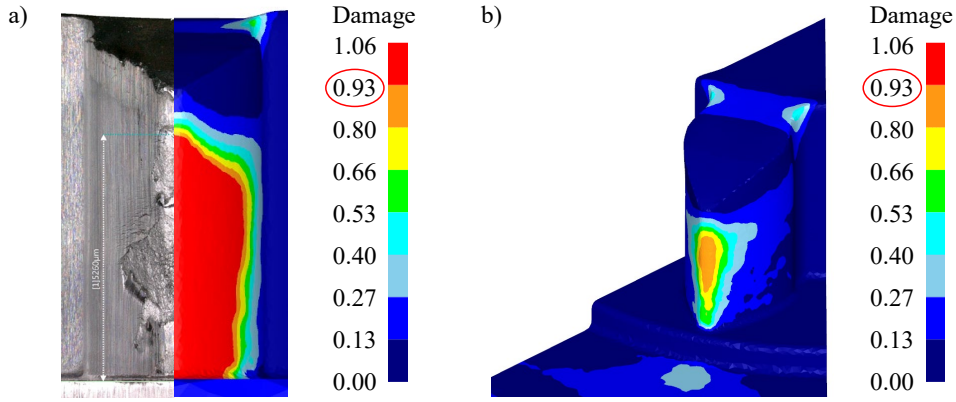

Fig. 1. a) Comparison of an edge of a pressed part (no indentation, preform angle 16.5°) and the numerically calculated damage distribution and b) calculated damage distribution of the variant with an indentation of 1 mm.

According to the damage distribution illustrated, the crack initiation height can be estimated quite accurate with ± 0.1 mm in height for all investigated variants. However, there is a difference in the shape of the cracks on the real part and the area with damage values higher than 0.93, which is probably due to the lack of element deletion. Using element deletion would in particular affect adjacent elements, which could lead to a more realistic representation of the shape of the crack.

The analysis of the variant with an indentation of 1 mm in Fig. 12b demonstrates, that the calculated damage values are lower than the critical damage value of 0.93. Since no cracks occurred during the experimental investigations with this trimming tool, it can be concluded that the numerical model can represent the crack initiation behavior realistically. In summary, compressive stress superposition can be used to improve trimming processes of parts which are vulnerable to crack formation.

Summary

In this contribution, a numerical study with a subsequent experimental investigation regarding superposition of compressive stresses in trimming processes of bulk forming parts has been conducted. At first, a gear-shaped demonstrator geometry which is vulnerable for crack formation during a conventional trimming process was defined. Afterwards, different trimming die geometries for stress superposition were investigated and their impact on the damage development in the workpiece was evaluated. Based on the numerical results, the trimming die which leads to the lowest damage values in the workpiece was selected and manufactured for the subsequent experimental investigation.

In the experimental investigations, different trimming die geometries and preform geometries were conducted to manufacture the splined parts. Besides the initially investigated trimming die geometries, also an additional geometry was investigated comprising an indentation of 1.0 mm for stress superposition. The edges of the splined parts were then characterized with the Keyence digital microscope VHX-5000 and compared to the numerical results for identification of the critical damage value. It was found that a minor compressive stress superposition (indentation of 0.25 mm) leads to slightly reduced damage values in the workpiece compared to a conventional die without compressive stress superposition. Using a further increased compressive stress superposition (indentation of 1 mm), it was even possible to press components without crack formation entirely.

In summary, it was shown that the superposition of compressive stresses is a useful method for improving trimming processes of parts that are vulnerable to crack formation. Since damage is very specific in terms of material and geometry, it is not possible to directly transfer the determined critical damage value to completely different geometries or materials. Experimental validation is always required to investigate on damage development. However, the developed simulation model can be used as a comprehensive basis for the investigation of similar splined geometries and other materials in the future. The method of compressive stress superposition in trimming processes can be transferred to other parts for which no trimming process could be applied so far, thus the existing process limits of trimming processes can be improved significantly.

Acknowledgements

The research project “Investigation of local stress superposition during trimming of asymmetric geometries” was funded by the German Cold Forging Group (GCFG) as a study (no. 47) based on the decision of all members of the GCFG. The authors would like to thank the German Cold Forging Group for the financial support. Furthermore, the authors would like to thank the project partners Bilstein & Siekermann GmbH + Co. KG, prosimalys GmbH and Arnold Umformtechnik GmbH & Co. KG for the collaboration within the project.

References

[1] K. Lange, M. Kammerer, K. Pöhlandt, J. Schöck, 2008, Fließpressen - Wirtschaftliche Fertigung metallischer Präzisionswerkstücke, Springer-Verlag Berlin Heidelberg, ISBN: 9783540309093.

[2] E. Doege, B.-A. Behrens, Handbuch Umformtechnik. Grundlagen, Technologien, Maschinen, 2010. https://doi.org/10.1007/978-3-662-43891-6

[3] M. Liewald, A. Weiß, A. Felde, Prozessgrenzen beim Angraten unrunder und asymmetrischer Geometrien, Final report of GCFG-study, German Cold Forging Group, 2021.
[4] C. MacCormack, Finite Element Analysis & Die Profile Optimisation for a Cold Forging Process, PhD Thesis, University of Dublin, Trinity College, Ireland, 2000.
[5] C. MacCormack, J. Monaghan, Failure analysis of cold forging dies using FEA, J. Mater. Process. Technol. 117 (2001) 209–215. https://doi.org/10.1016/S0924-0136(01)01139-6
[6] C. MacCormack, J. Monaghan, A finite element analysis of cold-forging dies using two- and three-dimensional models, J. Mater. Process. Technol. 118 (2001) 286–292. https://doi.org/10.1016/S0924-0136(01)00960-8
[7] J. Petruska, J. Borkovec, J. Hulka, R. Foret, Application of ductile fracture criteria to industrial cutting processes, Adv. Mater. Res. 264–265 (2011) 913–918. https://doi.org/10.4028/www.scientific.net/AMR.264-265.913
[8] J. Borkovec, J. Petruska, Evaluation of four fracture criteria in compressive loading conditions, Postępy w Inżynierii Mechanicznej (eng. Developments in Mechanical Engineering) 1 (2013) 19–28.
[9] S.C. Park, D.H. Lee, D.C. Ko, B.M. Kim, M.H. Kim, K.H. Lee, Integrated process design of Al6061 alloy bolts for fastening offshore platforms, J. Mech. Sci. Technol. 33 (2019) 3695–3707. https://doi.org/10.1007/s12206-019-0711-5
[10] F. Kocatürk, B. Tanrıkulu, S. Doğan, C. Kılıçaslan, S. Yurtdaş, U. İnce, Optimization of trimming process in cold forging of steel bolts by Taguchi method, Int. J. Pressure Vessel. Piping 194 (2021) 104503. https://doi.org/10.1016/j.ijpvp.2021.104503
[11] Schuler, Metal Forming Handbook, Springer-Verlag Berlin Heidelberg New York This, 1998, https://doi.org/10.1007/978-3-642-58857-0, ISBN: 3540611851
[12] A. Felde, S. Rudolf, M. Liewald, Enhancement of Process Limits in Cold Extrusion, New Developments in Forging Technology, 2009, pp. 293–309. ISBN: 9783883553757
[13] S. Rudolf, Beitrag zur Erweiterung der Verfahrensgrenzen des Quer-Fließpressens, Institute for Metal Forming Technology, University of Stuttgart, 2014. ISBN: 9783883554044
[14] J. Wälder, M. Liewald, Hollow Lateral Extrusion of Tubular Billets – Further Development of the Cold Forging Process, Appl. Mech. Mater. 794 (2015) 160–165. https://doi.org/10.4028/www.scientific.net/AMM.794.160
[15] O. Hering, A. Dunlap, A.E. Tekkaya, A. Aretz, A. Schwedt, Characterization of damage in forward rod extruded parts, Int. J. Mater. Form. 13 (2020) 1003–1014. https://doi.org/10.1007/s12289-019-01525-z
[16] A. Franceschi, J. Stahl, C. Kock, R. Selbmann, S. Ortmann-Ishkina, A, Jobst, M. Merklein, B. Kuhfuß, M. Bergmann, B.-A. Behrens, W. Volk, P. Groche, Strategies for residual stress adjustment in bulk metal forming, Arch. Appl. Mech. 91 (2021) 3557–3577. https://doi.org/10.1007/s00419-021-01903-7

Materials Research Proceedings 28 (2023) 621-628 https://doi.org/10.21741/9781644902479-67

Determination of recrystallisation phenomenon in type 316 stainless steel VIM-VAR ingots during cogging operations

PAQUETTE Arthur[1,a], LANGLOIS Laurent[2,b *], VIOLATOS Ioannis[1,c], RAHIMI Salaheddin[1,d], DUMONT Christian[3,e] and BIGOT Régis[2,f]

[1]Advanced Forming Research Center (AFRC), University of Strathclyde, 85 Inchinnan Drive, Inchinnan, Renfrewshire, PA4 9LJ, United Kingdom

[2]Arts et Métiers Institute of Technology, Université de Lorraine, ESAM Université, LCFC, 4 rue Augustin Fresnel, E-57070, France

[3]Aubert et Duval, Usine des Ancizes, Les Ancizes, 63770, France

[a]arthur.paquette@strath.ac.uk, [b]laurent.langlois@ensam.eu, [c]ioannis.violatos@strath.ac.uk, [d]salah.rahimi@strath.ac.uk, [e]christian.dumont@eramet.com, [f]regis.bigot@ensam.eu

Keywords: Cogging, Simulation, Recrystallisation, Stainless Steel, Ingot-To-Billet Conversion Process

Abstract. This study is focused on understanding the effects of key process parameters on the onset of recrystallisation of coarse, elongated, and dendritic grains of the as-cast microstructure during ingot-to-billet conversion, consisting of successive cogging, upsetting, and reheating operations, in type 316 austenitic stainless steel. The microstructural characteristics of the initial as-cast ingot (e.g., size, orientation and morphology of grains), and the complex thermo-mechanical path have significant impact on recrystallisation behaviours, which make the existing material models inefficient of precise microstructure prediction. These investigations aim at exploring the recrystallisation mechanisms and their dependency on the forging process parameters. Cogging trails were conducted on VIM-VAR stainless steel ingots and microstructural observations were made to identify the recrystallisation mechanisms. Finite element simulations coupled with constitutive material models were developed in parallel, to enable microstructurally informed prediction of the cogging process. Thus, static and discontinuous dynamic recrystallisations occur in succession after reaching a threshold level of deformation during cogging. Grain growth occurred in the statically recrystallised grains during reheating. The importance of the reheating and the associated static recrystallisation on the efficiency of the billet conversion process in terms of grain refinement is thus highlighted.

Introduction

The ingot-to-billet conversion process, consisting of hot forging operations of cogging and upsetting with intermediate reheating, is typically performed to generate a homogeneous and equiaxed grain microstructure from the initial as-cast's coarse, elongated, and dendritic structure. The different steps of the conversion route cause the occurrence of several metallurgical mechanisms, which lead to the evolution of microstructure. Continuous (CDRX) or Discontinuous (DDRX) dynamic recrystallisation are the main mechanisms of microstructure evolution, occurring during the hot forming operation. The plastic strain, strain rate and the temperature are the main thermomechanical parameters governing these mechanisms [1]. During intermediate reheating (i.e., between cogging/upsetting operations), static recrystallisation (SRX) can occur depending on the temperature and the accumulated strain energy in form of geometrically necessary dislocation density produced during the previous forming operations. Further, grain growth can also occur when the material is held at high temperatures for a long time, in particular, during heating and reheating processes.

Content from this work may be used under the terms of the Creative Commons Attribution 3.0 license. Any further distribution of this work must maintain attribution to the author(s) and the title of the work, journal citation and DOI. Published under license by Materials Research Forum LLC.

Materials Research Proceedings 28 (2023) 621-628 https://doi.org/10.21741/9781644902479-67

The occurrence of these mechanisms are well-known in the case of austenitic stainless steels with an initial fine and equiaxed grain structure [1]. With the aim of optimising a forging route, the grain size can be predicted by Finite Element (FE) simulation integrating materials models, like the JMAK model [2], or full field models with scale transition [3].
However, the microstructural characteristics of the initial as-cast ingot have a significant impact on recrystallisation behaviours, which make the existing material models inefficient of predicting microstructure evolutions to a reasonable accuracy. For instance, the crystallographic texture resulting from the oriented solidification of the material during its casting, confers to the material an anisotropic plastic behaviour as described for type 718 nickel alloy by [4].

The present work aims at understanding the recrystallisation mechanisms in the as-cast microstructure occurring during ingot-to-billet conversion process of type 316 stainless steel. These involve investigating the effect of heating and thermomechanical processing on the evolution microstructure in the as-cast material with a coarse, elongated and dendritic grain microstructure. For this purpose, cogging trials were carried out following a typical industrial forging route, including intermediate heating. A FE simulation of the process was also conducted in parallel to estimate the evolution of stress, strain and temperature throughout the whole process. The experimental details are presented in a first part, and the second part is devoted to the numerical modelling of the cogging process. Finally, experimental and numerical results are presented and discussed.

Experiments

The initial ingot was a cylinder with a diameter of 190mm and a length of 600 mm (Fig. 1a). It was manufactured through a consecutive vacuum induction melting (VIM) and vacuum arc re-melting (VAR) processes. The as-cast macrostructure, similar to that reported by Park et al. for nickel superalloys [5], consisted of coarse dendritic grains elongated according to the solidification direction, oriented at ≈ 60° upwards with respect to the axis of the ingot (Fig. 1b), except in the centre, where the grains had their long axis parallel to that of the ingot.

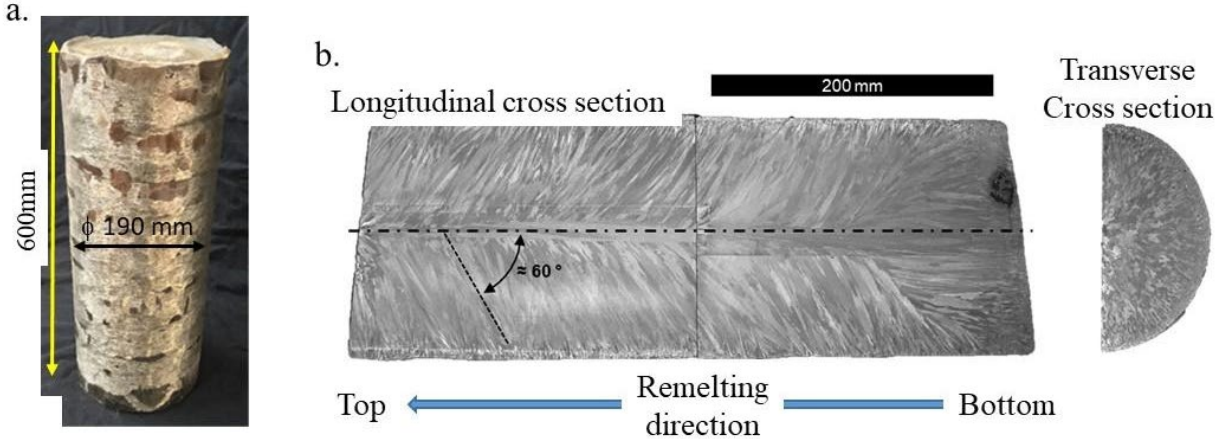

Fig. 1. Initial VIM/VAR melted type 316 austenitic stainless steel ingot, (a) a photograph of the ingot after being ground for the removal of surface scales, and (b) optical microscopy appearances of the longitudinal and transverse cross-sections of the ingot exhibiting the coarse, elongated, and dendritic grains, oriented at ≈ 60° to the axis of the billet.

The heating and cogging route is schematically depicted in Fig. 2. It consisted of three section-reduction stages of 20 %, 12 % and 12 % respectively, after an initial 12 h soaking at 1250°C, followed by two additional cogging stages of 20 % section-reduction after an intermediate 90 min reheating at 1250°C.

To investigate the effect of the different steps of the cogging route on the grain structure, and to highlight the occurrence of the different recrystallisation mechanisms, two ingots were forged. An ingot was subjected to the first three section-reduction stages before cooling to room temperature. The second was cogged according to the complete route presented in Fig 2, but the last two section-reduction stages were applied on its half-length only. Each section-reduction stage consisted of two successive cogging passes with an intermediate 90° rotation of the ingot (i.e., change of forging direction). Each cogging pass consisted of blows with an advancing feed of the ingot between two successive blows. The advancing feed of each stage and the target section dimensions are given in Table 1.

Table 1. Target section dimensions and feed of each stage (dimensions in mm).

Forging stage	1st	2nd	3rd	4th	5th
Target dimensions (mm²)	170 × 170	160 × 160	150 × 150	135 × 135	120 × 120
Feed (1st blow) (mm)	110	80	80	60	60
Feed (following blows) (mm)	60	30	30	30	30

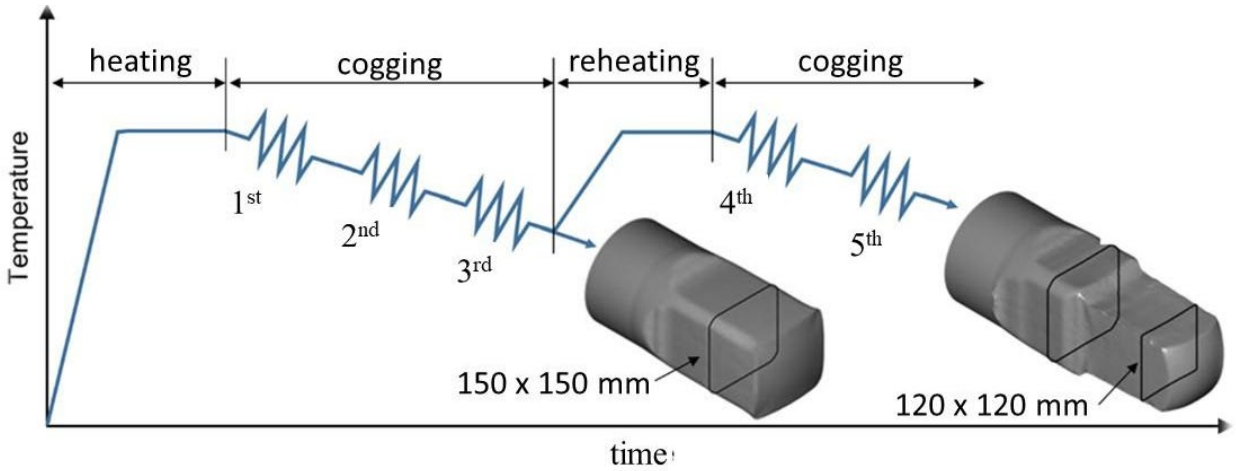

Fig. 2. Schematic illustration of the cogging route on the as-cast ingots.

The heating and reheating were performed in an electric furnace. The cogging operation were carried out using a LASCO® SPR-400 screw press. The ingots were initially coated with a refractory material to reduce oxidation during heat treatment and to limit heat losses during transfer from the furnace to the press. The ingots were handled by a six-axis robot equipped with a gripper (Fig. 3a and c), with unlockable compliances accommodating the axial and vertical deformation of the ingots during cogging blows. The anvils, whose main dimensions are given in Fig. 3b, were pre-heated to 450°C using embedded heating cartridges. Stoppers were placed between the upper and lower anvils to control the stroke.

After cogging, the ingots were optically scanned using a ATOS III Scan GOM® system. The ingots were then cut, ground and chemically etched to obtain optical macrographs from their longitudinal cross-sections. Smaller specimens were also machined out for further analyses at higher magnification by optical microscopy.

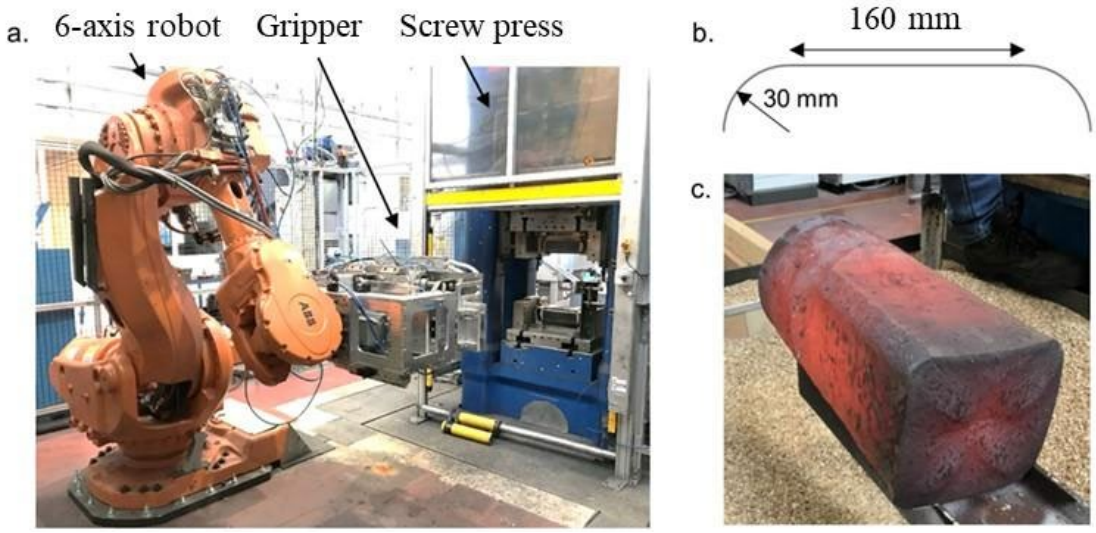

Fig. 3. (a) Experimental set-up, (b) the anvil profile, and (c) photographs of the ingot after the first three stages of the cogging operations.

Modelling and Simulation

The FE simulations were performed using the commercial Forge NxT 3.0® software to predict the evolution of temperature, plastic strain and strain rate within the ingot throughout the cogging route. A simplified Hensel-Spittel viscoplastic constitutive law was implemented into the FE model for the material's thermomechanical behaviour (Eq. 1). The material properties data for 316L were taken from the Forge® database.

$$\sigma = A \cdot e^{m_1 T} \cdot \varepsilon^{m_2} \cdot \dot{\varepsilon}^{m_3} \cdot e^{\frac{m_4}{\varepsilon}} \quad (1)$$

As shown by Paquette et al. [6], the anisotropy of the solidification induced textured microstructure was considered using the orthotropic Hill-48 criterion (Eq. 2). The constitutive law and the Hill criterion parameters are given in Table 2.

$$\sigma_0{}^2 = F \cdot (\sigma_{22} - \sigma_{33})^2 + G \cdot (\sigma_{11} - \sigma_{33})^2 + H \cdot (\sigma_{11} - \sigma_{22})^2 + 2L \cdot \sigma_{23}{}^2 + 2M \cdot \sigma_{13}{}^2 + 2N \cdot \sigma_{12}{}^2 \quad (2)$$

The Hill criterion was expressed in an anisotropic reference frame, assuming a grain orientation similar to that of the as-cast material (i.e., the solidification structure). In Eq. 2, the index 3 corresponds to the direction of solidification. The orientation of the anisotropic frame is symmetrically distributed around the axis of the ingot; hence the index 3 direction being orientated at 60° with respect to the axis of the ingot. The central zone of the ingot with the axially elongated grains was not taken into account.

Table 2. Hensel Spittel constitutive law parameters and orthotropic Hill-48 criterion parameters.

Hensel Spittel	A	m1	m2	m3	m4
	8905.34	-0.00383	0.01246	0.09912	-0.02413

Orthotropic Hill-48 criterion	F	G	H	L	M	N
	0.5	0.5	0.5	0.68	0.68	1.5

A Tresca limited Coulomb law ($\underline{m} = 0.4$, $\mu = 0.8$) was implemented to simulate the friction behaviour between the material and the anvil. The heat exchange rate between the ingot and the ambient medium was set to 10 $Wm^{-2}K^{-1}$, and to 10^4 $Wm^{-2}K^{-1}$ for the exchange with the anvils. The temperature of the anvil was set to 450 °C to make it similar to that of the experiments. According to the symmetries of the problem, the ingot was modelled by a quarter of the cylinder, with two planes of symmetry implemented (see Fig. 4). The ingot was meshed with tetrahedral elements with an average size of about 6.5 mm. The dies were considered as rigid bodies and their surfaces were meshed with triangular elements of 15 mm average size.

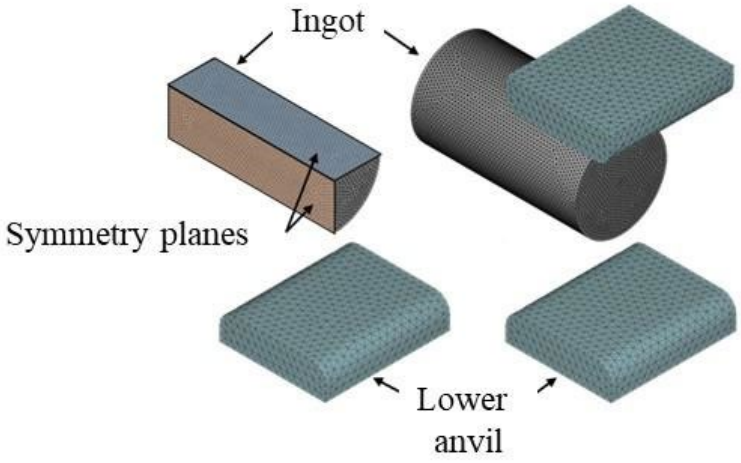

Fig. 4. Numerical model of the cogging operations.

A particular attention was paid to the temperature prediction, as it is one of the most influential thermomechanical parameters driving the recrystallisation mechanisms. The duration of each step of the cogging route, recorded during the trial, including the transfer from the furnace to the press, and the position of the ingot before each blow were therefore implemented in the simulation.

Results and Discussion

In Fig. 5, the 3D scan of the ingot after the first three stages of cogging and the simulated geometry obtained with both orthotropic and isotropic criteria are shown. It can be seen that the end of the ingot exhibited lobes along the diagonals. This feature was not captured by the FE simulation with the isotropic criterion implemented. On the other hand, the FE simulation with the anisotropic material model implemented allowed to predict the formation of these features, suggesting the important role of the anisotropy on the deformation behaviour of the as-cast material during the forging process. The geometrical discrepancy between the experimental and FE predicted geometries of the cogged ingot are highlighted by the circles in Fig. 5, and can partially be ascribed to the fact that the specific orientation of the grain at the centre of the ingot was not taken into account in the FE model.

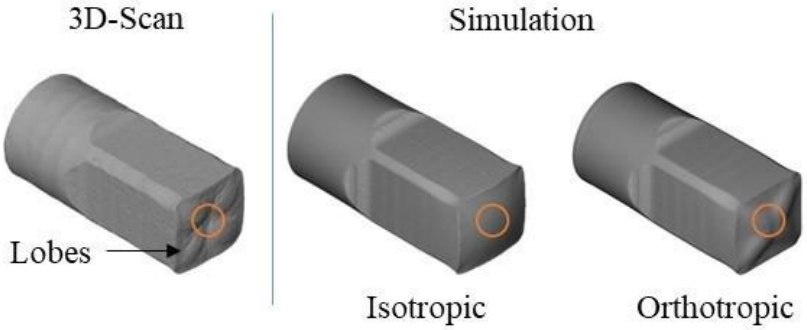

Fig. 5. Geometry of the ingot after the first three cogging stages; 3D scan after cogging trials, and FE simulated with isotropic and anisotropic material behaviours.

Fig. 6 presents macrographs of the two ingots. The macrograph of the first ingot (Fig. 6a) shows the macrostructure obtained at the end of the first three cogging stages, before the reheating. No obvious occurrence of recrystallisation can be seen from this macrograph.

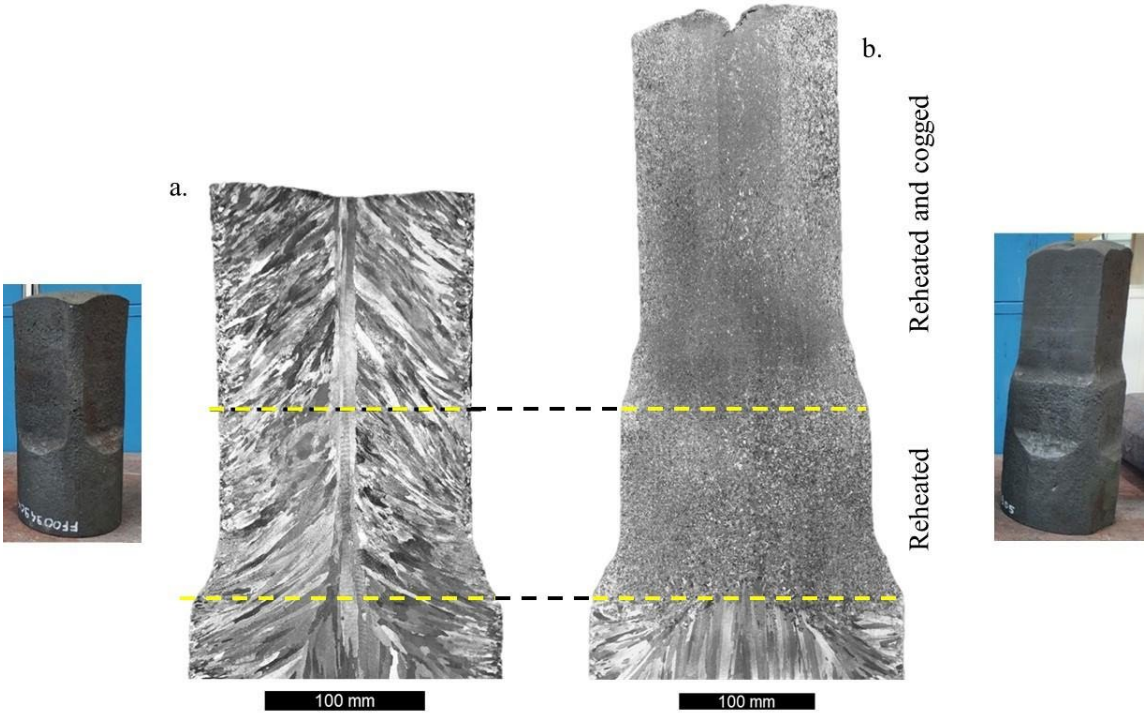

Fig. 6. Optical macrographs taken from the longitudinal cross-sections of the cogged ingots, (a) after the first three stages of cogging, and (b) following the complete cogging route plus reheating.

The macrograph of the second ingot can be split into two zones, (i) a reheated zone (RZ) which was re-heated after being cogged through the first three stages, and (ii) a reheated and cogged zone (RCZ) which was subjected to the complete cogging route. The onset of recrystallisation in both RZ and RCZ can clearly be seen in Fig. 6b. The difference in grain structure between the first ingot and the RZ is in the reheating, which has resulted in SRX of the material deformed during the first three cogging stages.

Analyses of higher magnification micrographs taken from different areas of these ingots were carried out to identify the recrystallisation mechanisms occurring during the cogging process (Fig. 7). Fig. 7a displays the microstructure in the cogged zone of the first ingot, where DDRX was observed at some boundaries of the parent microstructure. In the RZ of the second ingot, the recrystallised grains were large, but equiaxed. This confirms the occurrence of SRX, promoted by the deformation of the initial microstructure, induced by cogging. DDRX was very limited during the first cogging stages, and the plastic deformation was accommodated by strain hardening. SRX occurred during the reheating, and was followed by grain growth. In the RCZ, necklace type DDRX was observed. Such necklace-type DRX was previously reported in the literature for as-cast microstructures composed of large and elongated grains [6].

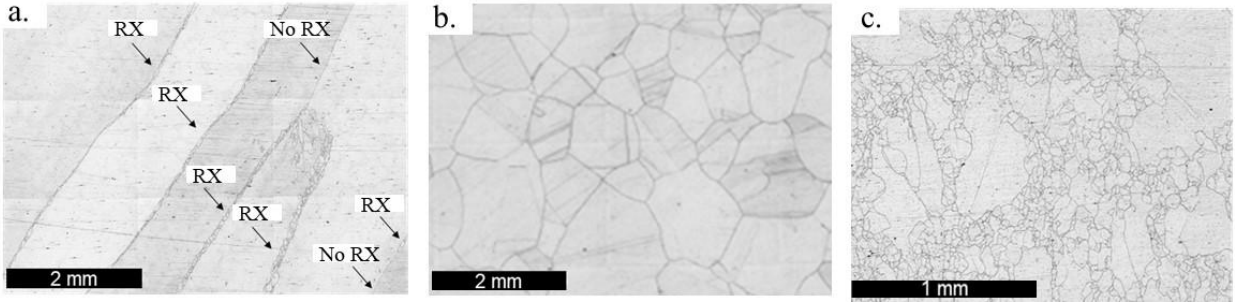

Fig. 7. Optical micrographs of the billets after cogging operations;(a) the cogged zone of the first ingot, (b) the reheated zone, and (c) the reheated and cogged zone of the second ingot.

Evolution of plastic strain and temperature during the first three cogging stages were estimated by FE simulation (Fig. 8). The maximum predicted strain was at the extremity of the ingot and was ascribed to the formation of the particular feature described in Fig. 5, as an edge effect. The final temperature at the core of the ingot was between 900 °C and 1000 °C, which are relatively low for DRX; and can explain the occurrence of strain hardening in the cogged zone of the first ingot.

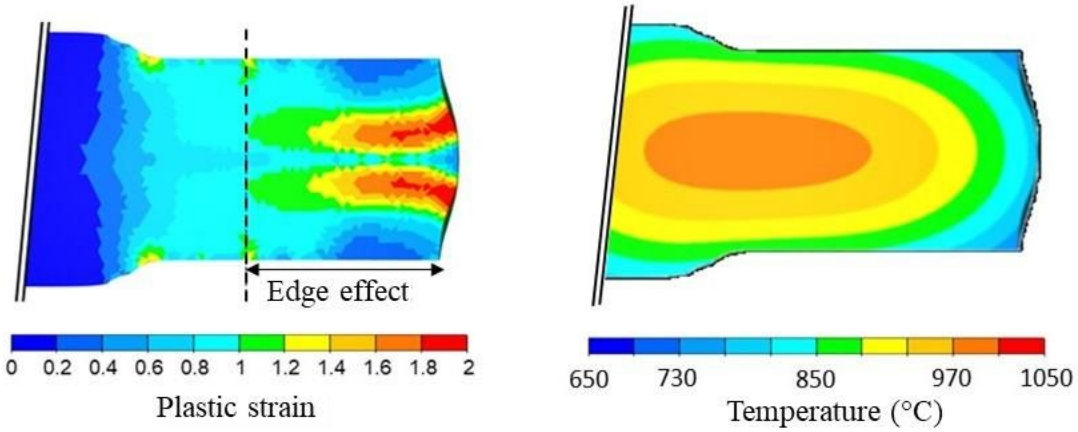

Fig. 8. Distributions of plastic strain and temperature predicted by FE simulations along the longitudinal cross-section of the ingot after the first three cogging stages.

Comparison of FE results and microstructures provided in Fig. 6 and Fig. 8, respectively, allowed to identify that SRX occurred during the reheating in the areas where the plastic strain obtained at the end of the first cogging stage was higher than the threshold value of ≈ 0.2.

The validity of the implemented anisotropic material model for equiaxed and recrystallised microstructure, such as that observed in the RZ, is questionable since the crystallographic texture of the microstructure issued from SRX was not characterised, and the parameters proposed by Paquette et al. [6] may not remain suitable. The last two cogging stages were therefore not simulated.

Summary

Cogging trials of VIM-VAR processed 316 type stainless steel ingots have been performed to investigate the recrystallisation mechanisms of an as-cast microstructure containing coarse, elongated, and dendritic grains. The cogging operations led to an insignificant amount of DDRX, localised to grain boundaries primarily. Otherwise, the cogging induced deformation led to strain

hardening during the initial stages of cogging, resulting in a significant level of static recrystallisation during the follow-up reheating. The latter led to new coarse, but equiaxed grains which then underwent DDRX during the following cogging stages (i.e., creating necklace structure). The efficiency of the SRX was a function of temperature gradient between the last cogging stage and the follow-up reheating. The large equiaxed grains after the reheating were most likely generated by normal grain growth, following the static recrystallisation. This must have been promoted by the higher temperature and the holding time of the reheating.

The strain hardening induced during the cogging process typically results from a competition between dislocations generation, their dynamic recovery, and the dynamic recrystallisation. The latter phenomena being favoured by a high temperature, as the lower the temperature at the end of the cogging stages the higher the strain hardening will become, and hence the more efficient the static recrystallisation during reheating. This study has shown the importance of temperature control and the role of static recrystallisation, as important parameters in optimising ingot-to-billet conversion processes.

Acknowledgement
The authors also would like to thank Alexandre Fendler for his technical contribution during the experiments. The authors express their thanks to ISEETECH for the provision of the VULCAIN Platform facilities.

References

[1] R.D. Doherty, D.A. Hughes, F.J. Humphreys, J.J. Jonas, D. Juul Jensen, M.E. Kassner, W.E. King, T.R. McNelley, H.J. McQueen, A.D. Rollett, Current issues in recrystallization: A review, Mater. Sci. Eng. A 238 (1997) 219-274. https://doi.org/10.1016/S0921-5093(97)00424-3

[2] M. Fanfoni, M. Tomellini, The Johnson-Mehl-Avrami-Kolmogorov model: a brief review, Nuovo Cimento della Societa Italiana di Fisica D – Condensed Matter, Atomic, Molecular and Chemical Physics, Biophysics. 20 (1998) 1171-1182. https://doi.org/ 10.1007/BF03185527

[3] D.A. Ruiz Sarrazola, L. Maire, C. Moussa, N. Bozzolo, D. Pino Munoz, M. Bernacki, Full field modelling of dynamic recrystallization in a CPFEM context – Application to 304L steel, Comput. Mater. Sci. 184 (2020) 109892. https://doi.org/10.1016/j.commatsci.2020.109892

[4] J. Terhaar, J. Poppenhäger, D. Bokelmann, H. Schafstall, K. Kelkar, Considering the solidification structure of VAR ingots in the numerical simulation of the cogging process, 7th International Symposium on Superalloy 718 and Derivatives (2010) 65-77. https://doi.org/10.1002/9781118495223.ch4

[5] N.K. Park, J.T. Yeom, J.H. Kim, X.X. Cui, Characteristics of VIM/VAR-Processed Alloy 718 Ingot and the Evolution of Microstructure During Cogging, in: Superalloys 718, 625, 706 and Various Derivatives, Presented at the Superalloys TMS (2005) 253-260. https://doi.org/10.7449/2005/Superalloys_2005_253_260

[6] A. Paquette, S. Rahimi, I. Violatos, L. Langlois, C. Dumont, J. Blaizot, M. Rosochowska, R. Bigot, On the evolution of microstructure and mechanical properties of type 316 austenitic stainless steel during ingot to billet conversion process, ESAFFORM2021 (2021), https://doi.org/10/25518/esaform21.929

Materials Research Proceedings 28 (2023) 629-637 https://doi.org/10.21741/9781644902479-68

Study of forming defects and failure occurrence in the radial-axial rolling of super duplex stainless steel rings

MURILLO-MARRODÁN Alberto[1,a *], GARCÍA GIL Eduardo[1,b], FERNANDEZ-GAMBOA Unai[1,c], CONDE Aintzane[1,d] and LOZARES Jokin[1,e]

[1] Department of Mechanics, Design and Industrial Management, University of Deusto, Avda Universidades 24, Bilbao 48007, Spain

[a]alberto.murillo@deusto.es, [b]e.garcia@deusto.es, [c]unai.gamboa@opendeusto.es, [d]aintzane.conde@deusto.es, [e]jokin.lozares@deusto.es

Keywords: Radial-Axial Ring Rolling, Super Duplex Stainless Steel, VDOE, Cracks, Fishtail

Abstract. Welding neck flanges are commonly manufactured by radial-axial ring rolling (RARR). The service conditions of these elements are very demanding (mechanical loads and corrosive environments). For this reason, materials such as super duplex stainless steel (SDSS) are used, which could present workability problems under certain process conditions. In this work, a study of forming defects and failure occurrence in the RARR of SDSS flanges has been proposed. Firstly, a finite element model of the industrial RARR process was developed and validated. Then, a multivariate factorial analysis based on a virtual design of experiments was performed to identify the determinant parameters of the process. The diameter of the mandrel was identified as the most determinant parameter. An increase in diameter reduces the probability of developing underfilling defects and the development of cracks in the flange neck. The mandrel radial speed has no significant effect on the cracking of underfill defects while reducing the rotational speed of the king-roll could improve the uniformity of the deformation distribution in the flange section.

Introduction

The oil and gas industry demands extreme operating conditions, often combining high pressures with highly corrosive environments. In pipelines, flanges of 25 %Cr super duplex stainless steels (SDSSs) are generally used, as they require high strength and corrosion resistance [1]. The UNS S32760, which is considered an SDSS, meets these requirements thanks to the mixture of both austenite and ferrite which leads to a material with excellent mechanical properties and corrosion resistance. In addition, it typically contains 25% Cr and 7% Ni-doped with a small amount of N, (0.3%) providing improved corrosion properties, and allowing its use in the marine environment [2]. However, cracks could be generated in welding neck flanges made of SDSS during hot forming and thus, its workability at high temperatures could be limited under certain conditions [3].

Weld-neck flange rings of high diameter are manufactured on ring rolling machines, by enlarging the diameter of ring blanks. In this hot forming process, first, the blanks are heated to the forging temperature. Then, the RARR machine reduces the wall thickness using the king-roll and mandrel. In addition, two axial rolls act simultaneously to decrease the height of the blanks [4]. In this hot forming process, one of the most problematic issues is controlling fishtail and underfilling defects [5]. The fishtail could be defined as an undesirable plastic deformation at the ring's upper surface, which leads to a geometrical defect as there is a lack of material in that region. Giorleo et al. [6] investigated the influence of the mandrel idle speed on the fishtail, keeping the king-roll rotation speed constant. Nevertheless, they concluded that the effect of mandrel idle speed on fishtail was not significant. Zhou et al. [7] identified that a higher king-roll rotational speed increases fishtail, given that deformation is concentrated in the surface area of the ring in

Content from this work may be used under the terms of the Creative Commons Attribution 3.0 license. Any further distribution of this work must maintain attribution to the author(s) and the title of the work, journal citation and DOI. Published under license by Materials Research Forum LLC.

the axial direction, as the diameter increase per revolution decreases. Allegri et al. [8] proposed a non-constant rotational speed of the main roller to keep the angular velocity of the ring constant. They conclude that maintaining a constant rotational speed in the ring could decrease fishtail dimension by 50%.

Regarding material damage and crack development, the ductility of SDSS decreases with lower temperature and higher strain rate, which facilitates the occurrence of plastic flow instabilities. The uneven uniformity of both strain and temperature in the ring section could lead to material failure [9]. Zhou et al. [10] highlighted the importance of uniform deformation and temperature distributions during RARR, given that they not only result in microstructure defects such as band structure and mixed crystals but also lead to internal cracks or even cause the interruption of the process. Meng et al. [11] analyzed the effect of geometries of king-roll and mandrel on material deformation uniformity. An increase in king-roll diameter was associated with better deformation uniformity, but caused workability problems due to the higher cooling rate, while mandrel geometry increase showed only positive effects on plastic deformation distribution.

In this work, a Virtual Design of Experiments (VDOE) has been proposed, using finite element method simulations of the RARR process to analyze the effect of selected process parameters on the development of cracks and forming defects on welding neck flanges made of S32760 SDSS.

Materials and Methods

Welding neck flanges made of S32760 SDSS were manufactured in an industrial RARR mill of the company ULMA Forging. Under investigated conditions, some of the flanges showed problems associated to crack development in the internal diameter (ID) surface of the neck region, and fishtail defects. Fig. 1 shows the FE model of the industrial RARR mill, and the cracks and fishtail defects identified in some RARR flanges.

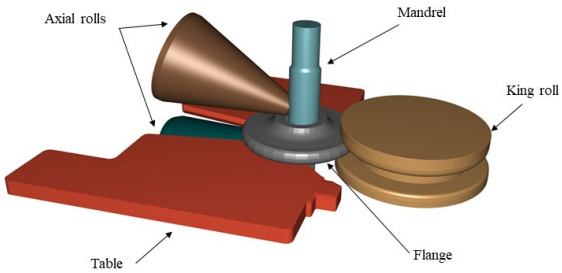

(a)

(b)

(c)

Fig. 1. (a) Fe model of the RARR mill of ULMA Forging, (b) cracks identified in the ID of the neck and (c) example of fishtail defect.

Materials Research Proceedings 28 (2023) 629-637 https://doi.org/10.21741/9781644902479-68

The software Forge NxT was used to simulate the RARR process. The finite element (FE) model counted with king-roll, both conical upper and lower rolls, mandrel, and the ring, whose geometry was generated from the prior state of the ring before the RARR (see Fig. 1a). The lateral guiding rolls were not included as the FE model has implemented the self-centering of the flange. All geometries were set up as rigid objects, while the flange material behavior was set as viscoplastic according to

$$\sigma = 28332 \cdot e^{-0.0051T} \cdot \varepsilon^{-0.1} \cdot \dot{\varepsilon}^{0.112} \cdot e^{\frac{-0.035}{\varepsilon}} \quad (1)$$

where σ is the flow stress (MPa), T is the temperature of the material (ºC), ε is the strain (-), and $\dot{\varepsilon}$ stands for strain rate (s^{-1}). The values of the material constants were obtained from a set of compression tests performed by Kang et al. [12]. The contact conditions with the elements were modeled using Coulomb limited to Tresca friction model [13], with friction coefficients of $\mu = 0.4$ and $m = 0.8$. Heat exchange between the flange and tools was modeled with a contact conductance HTC = 10.000 W/m^{2}K and free convection with ambient media was assumed. The mesh of the ring was structured into 48 parts with an element size of 20 mm, refined to 10 mm in the neck of the flange. The mesh of tools had an element size of 20 mm. All the kinematics of the model were set to the values used in the experiments performed in the RARR mill. First, in order to validate the model, axial and normal forces were adjusted to the values recorded from the mill, and the ring growth speed vs diameter was reproduced by the simulation. The geometry of the manufactured flange and dimensional tolerances in hot conditions are compared to the values obtained in the simulation in Fig. 2.

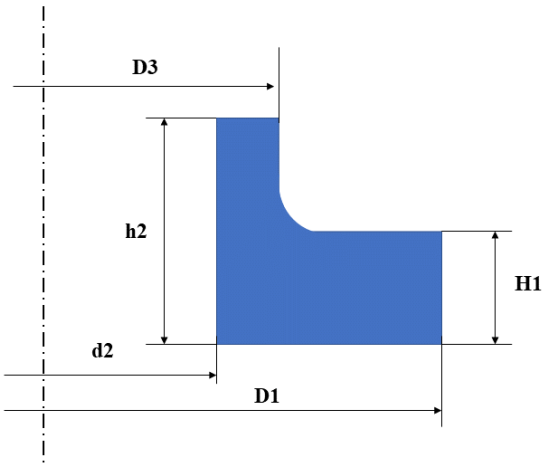

	Measure (mm)	Tolerance (mm)	Deviation (mm)	Error (%)
D1	1385.5	±10	-3.5	0.3
d2	1032.7	+14/-13	+4.2	0.4
D3	1102	+18/-9	-5.7	0.5
H1	113.1	+5 /-6	-0.9	0.8
h2	194.8	+16/-	+11.8	6.1

Fig. 2. Geometries of the flange in hot conditions compared to the simulated values.

The validated model was calculated using a king-roll rotational velocity of 25 rpm, a mandrel radial velocity of 3.03 mm/s, and a mandrel diameter of 170 mm. These were the selected variables to analyze their effect on the development of geometrical and crack defects. Then, a virtual design of experiments was carried out by simulating the RARR process. The conducted factorial analysis consisted of three levels and three factors. As a result, a total number of 27 simulations were carried out considering the conditions listed in Table 1.

Table 1. Factors and levels considered in the factorial analysis.

Factors	**Level 1**	**Level 2**	**Level 3**
King-roll angular velocity (KAV)	15 rpm	25 rpm	35 rpm
Mandrel radial velocity (MRV)	2.64 mm/s	3.03 mm/s	3.57 mm/s
Mandrel diameter (MD)	120 mm	170 mm	220 mm

The response variables selected to analyze the effect of the factors listed in Table 1 were the material ductile damage, fishtail defect, and uniformity of both strain and temperature in the flange section.

Damage. The simulation of damage in the RARR process has been considered by implementing the Latham&Cockroft ductile damage model. The damage in the material *D* is estimated according to

$$D = \int_{\varepsilon_0}^{\varepsilon_f} \frac{\sigma_1}{\sigma_{eq}} d\varepsilon \tag{2}$$

where σ_1 is the first principal stress, σ_{eq} Von Mises equivalent stress, ε_0 and ε_f the initial and final deformation, respectively. In order to compute the accumulated damage in each simulation, three sensors have been set in the neck of the flange to estimate the maximum damage value at the end of the RARR process, as illustrated in Fig. 3.

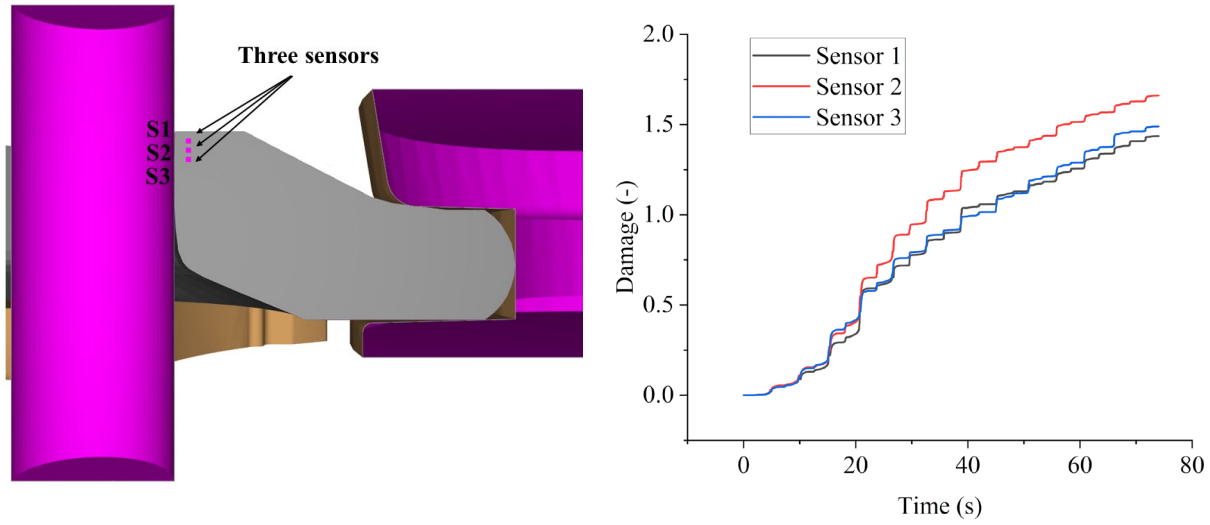

(a) **(b)**

Fig. 3. Sensors to compute the ductile damage on the neck of the flange during RARR (a) Initial position and (b) evolution of damage computation KAV = 15 rpm, MRV=2.64 mm/s and MD = 170 mm.

Fishtail. The fishtail defect can be appreciated in Fig. 1c. In order to measure and quantify the severity of this defect, the depth of the depression in the flange surface region has been measured in the simulation.

Uniformity of Plastic Strain (*SDP*) and Temperature (*SDT*). The uniformity of plastic strain and temperature in the section were analyzed through the calculation of the standard deviation according to

$$SDP = \sqrt{\sum_{i=1}^{N} (\varepsilon_i - \varepsilon_a)^2 / N}. \tag{3}$$

$$SDT = \sqrt{\sum_{i=1}^{N} (T_i - T_a)^2 / N} \quad (4)$$

Where N is the total number of analyzed points (12 in the neck of the flange), ε_i and T_i are the strain and temperature at a point, and ε_a and T_a stand for the average values of strain and temperature in the region analyzed. The position of these 12 sensors in the neck of the flange is provided in Fig. 4.

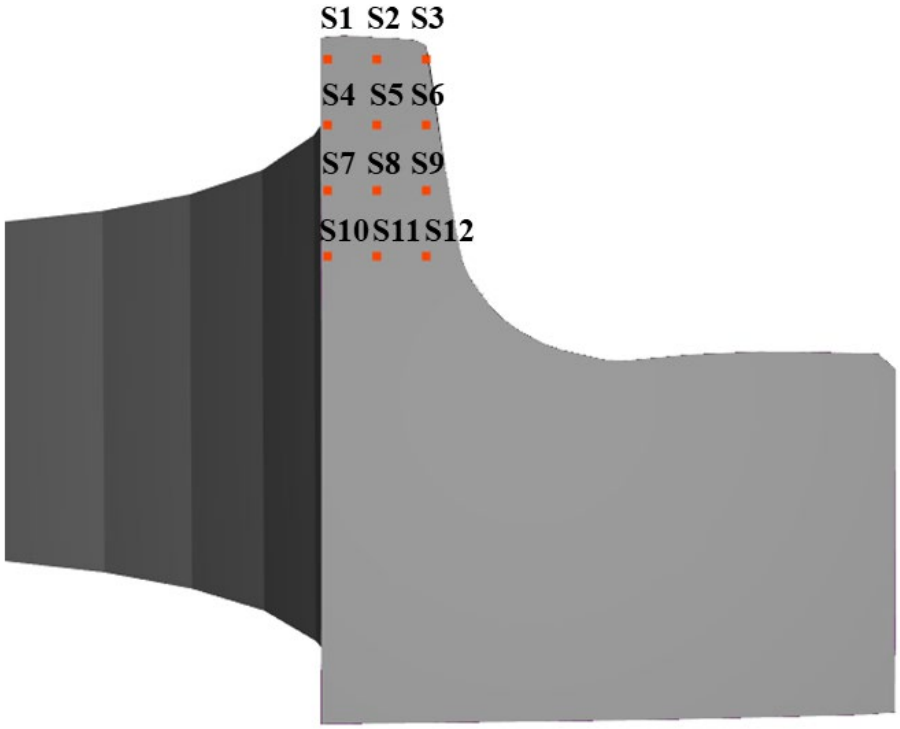

Fig. 4. Position of the 12 sensors in the neck of the flange to measure the uniformity of strain and temperature in the region where cracks are developed.

Results and Discussion

The results of the multivariate factorial analysis are provided. The Pareto chart with the standardized effects of each of the factors on the analyzed response variables is depicted in Fig. 5. In each of the charts, the factors are ordered from the highest to lowest standardized effect value.

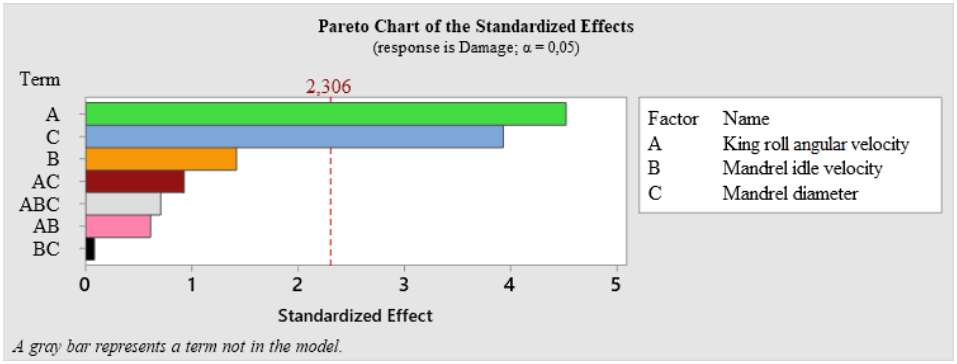

(a)

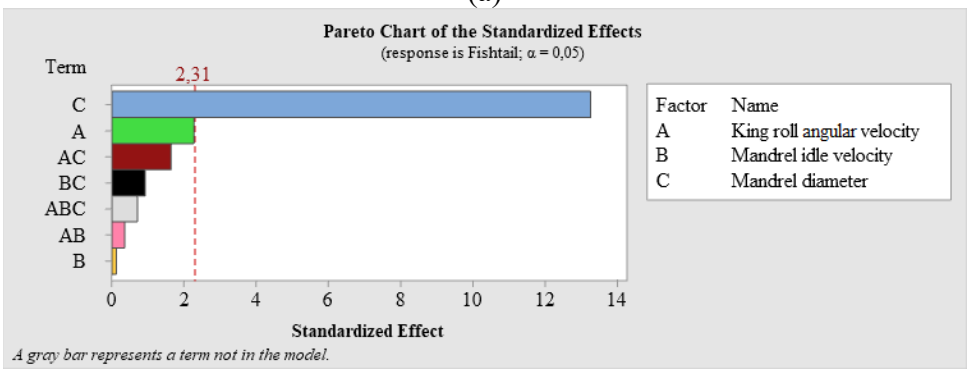

(b)

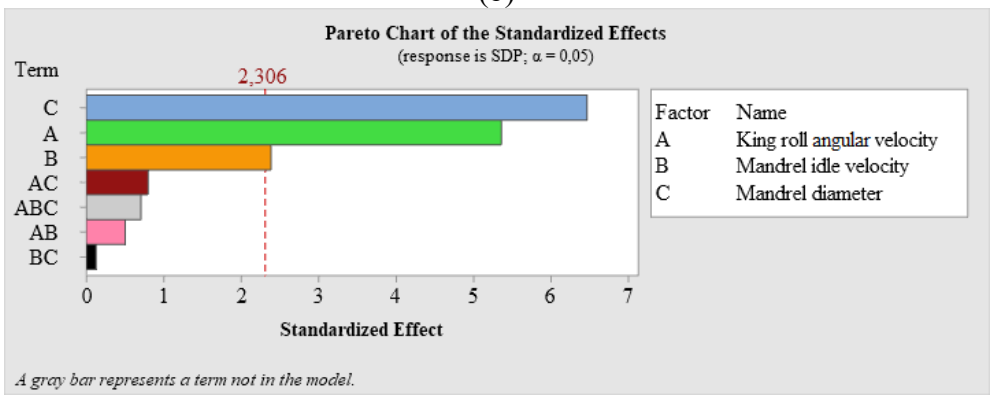

(c)

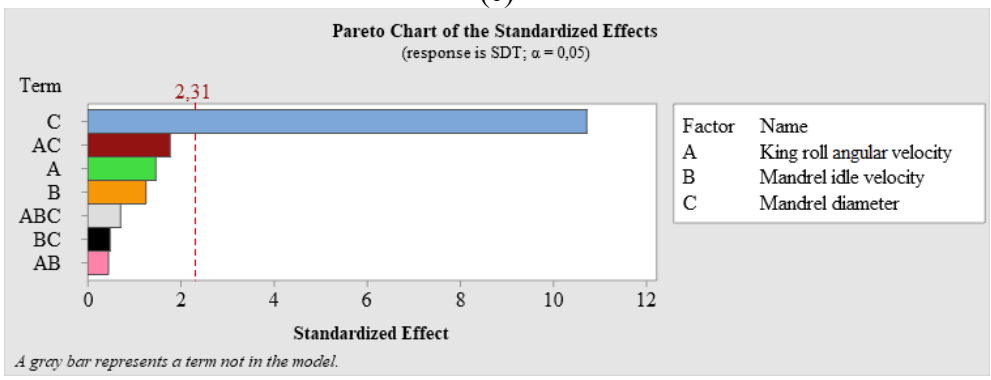

(d)

Fig. 5. Pareto chart of standardized effects of factors on (a) Damage, (b) Fishtail defect, (c) SDP, and (d) SDT.

The results shown in Fig. 5 put into evidence which factors contribute more to the variability in the response variables. Lenth's method was used to check which effects are significant (red dotted line). It is an objective method to test the effects of unreplicated factorial designs [14]. According to the results, KAV velocity shows a significant effect on Damage and uniformity of deformation. The MRV only provides a significant effect on the uniformity of deformation, but lower compared to the rest of the considered factors. Finally, the MD is the factor that shows a clear significant effect on all the considered response variables, namely, damage, fishtail, and uniformity in both, temperature and strain in the flange section. One interesting aspect to discuss is the interaction between the king-roll rotational speed and mandrel radial velocity, which has not shown any significant effect on the analyzed variables. In addition, the statistical significance of the model coefficients was determined by the P value. The P value less than 0.05 (95% confidence level) indicates that the model terms are significant [15]. After the revision of the results, it was confirmed the significance of the effects identified in the Pareto. Furthermore, the analysis of residuals confirmed that they were randomly distributed and had near-constant variance. Then, the main effects of the factors that showed significance in the previous analysis are presented in Fig. 6. No interaction between the analyzed factors has been identified.

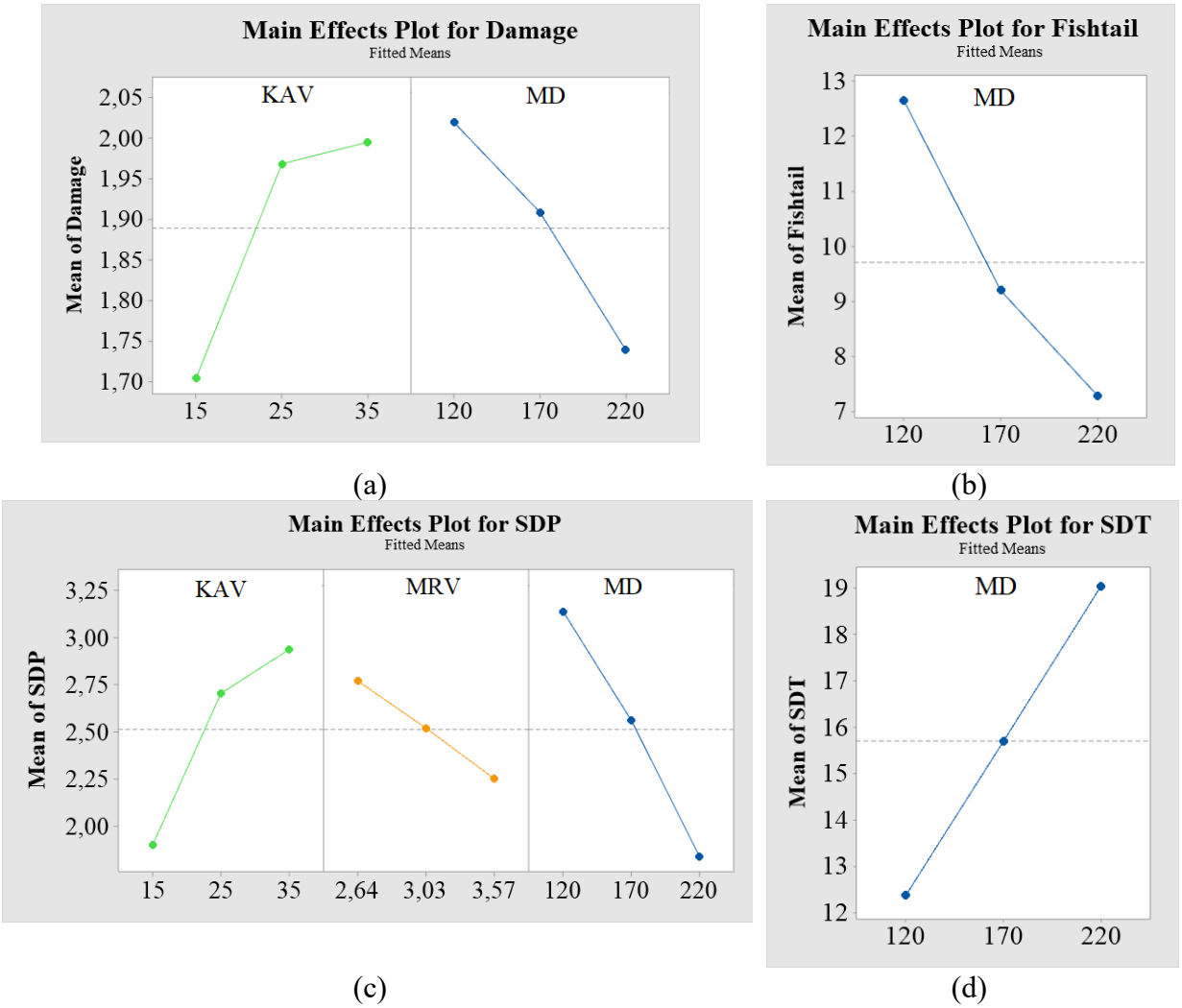

Fig. 6. Main effects of factors on (a) Damage, (b) Fishtail defect, (c) SDP, and (d) SDT.

According to the results of Fig. 6, the reduction in ductile damage in the neck of the flange could be achieved by reducing the KAV or increasing the MD. Regarding the fishtail defect, the MD shows a strong effect, reducing the fishtail the higher the MD. The uniformity of temperature in the neck of the flange depends on the effect of the MD, showing a higher deviation the higher the diameter of this element. In the case of uniformity of plastic strain, a decrease of KAV increases the uniformity, while an increase of the MRV or MD is associated with better uniformity of plastic deformation in the analyzed region of the flange.

From the analysis of the main effects, it is concluded that reducing the KAV presents a positive effect not only on the ductile damage but also on the fishtail defect and uniformity of plastic strain in the neck of the flange. However, the dimensions of the king-roll and flange should be considered given that material flow in the section of the flange depends on the combined effect of flange rotation, and mandrel and axial rolls displacement. A similar material flow could be obtained with higher KAV if the diameter of the king-roll or flange is reduced.

In the case of the MD, it is important to highlight that shows a significant effect on all the analyzed variables. However, the effect of the diameter of this tool on SDSS damage during the process or fishtail defect is not clear in the literature. A higher diameter is associated with lower values of fishtail, lower values of ductile damage, and better uniformity of plastic strain. The only drawback is a lower uniformity of temperature in the neck of the flange, which is expected given that the contact region with the ID of the flange is increased and there is a higher thermal exchange with the mandrel. A further thermo-mechanical study could provide insightful information about the impact of mandrel diameter on the stress state in the section of the flange and the material flow.

Summary

A study of forming defects and failure occurrence in the RARR of SDSS flanges has been proposed. First, a FE model of the RARR industrial process has been developed and validated. Then, some determinant process parameters, such as KAV, MRV, and MD, have been modified and simulated. The effect of modifying these process parameters on the development of cracks and fishtail defects has been assessed by means of a multivariate factorial analysis. From this study, the flowing conclusions have been drawn:

- The increase in mandrel diameter reduces underfilling defects and also the development of failures due to ductile damage in the ID of the flange neck. Nevertheless, it leads to an increase in forces in the early stages of the process. In addition, the higher contact area with the mandrel leads to a low temperature in the flange ID during the process, which could favor the precipitation of intermetallic phases that reduce SDSSs hot workability.
- The reduction of king-roll angular velocity hinders the development of cracks in the ID of the flange neck and improves the strain distribution on the flange section.
- The mandrel radial velocity doesn't show a significant effect on the development of cracks or fishtail defects. It only shows a slight effect on the strain distribution of the flange section, leading to better uniformity at higher values.

References

[1] A.P. Kölblinger, S.S.M. Tavares, C.A. Della Rovere, A.R. Pimenta, Failure analysis of a flange of superduplex stainless steel by preferential corrosion of ferrite phase, Eng. Fail. Anal. 134 (2022) 106098. https://doi.org/10.1016/j.engfailanal.2022.106098

[2] F. Khoshnaw, C. Marinescu, A. Sofronia, C. Munteanu, M. Marcu, L.E. Barbulescu, C. Ciobota, E.M. Cojocaru, S. Tanasescu, A. Paraschiv, Microstructural and thermoanalytical characterization of super duplex stainless steel - UNS S32760-F55, Mater. Today Commun. 28 (2021) 102644. https://doi.org/10.1016/j.mtcomm.2021.102644

[3] N. Serban, V.D. Cojocaru, M.L. Angelescu, D. Raducanu, I. Cinca, A.N. Vintila, et al, High temperature deformation behaviour of an industrial S32760/1.4501/F55 super duplex stainless steel (SDSS) alloy, Metall. Ital. 111 (2019) 41-48.
[4] Z.W. Wang, S.Q. Zeng, X.H. Yang, C. Cheng, The key technology and realization of virtual ring rolling, J. Mater. Process. Technol. 182 (2007) 374-381. https://doi.org/10.1016/j.jmatprotec.2006.08.020
[5] L. Liang, L. Guo, J. Yang, H. Zhang, Formation mechanism and control method of multiple geometric defects in conical-section profiled ring rolling, J. Mater. Process. Technol. 306 (2022) 117628. https://doi.org/10.1016/j.jmatprotec.2022.117628
[6] L. Giorleo, E. Ceretti, C. Giardini, Speed Idle Roll Law Optimization in a Ring Rolling Process, Key Eng. Mater. 651–653 (2015) 248-253. https://doi.org/10.4028/www.scientific.net/KEM.651-653.248
[7] J. Zhou, X.T. Gong, X.B. Yang, W.J. Xu, Effect of Drive Roll Rotation Speed on Ring Rolling Process, Adv. Mater. Res. 189-193 (2011) 2586–2592. https://doi.org/10.4028/www.scientific.net/AMR.189-193.2586
[8] G. Allegri, L. Giorleo, E. Ceretti, C. Giardini, Driver roll speed influence in Ring Rolling process, Procedia Eng. 207 (2017) 1230–1235. https://doi.org/10.1016/j.proeng.2017.10.875
[9] W. Shen, F. Wang, Z. Yang, C. Li, P. Lin, X. Zhu, Investigation of the Crack Initiation and Propagation in Super Duplex Stainless Steel During Hot Working, in: Z. Peng, J.-Y. Hwang, J.P. Downey, D. Gregurek, B. Zhao, O. Yücel et al. (Eds.) 11th International Symposium on High-Temperature Metallurgical Processing, Cham: Springer International Publishing, 2020, pp. 157-67. https://doi.org/10.1007/978-3-030-36540-0_15
[10] G. Zhou, L. Hua, J. Lan, D.S. Qian, FE analysis of coupled thermo-mechanical behaviors in radial–axial rolling of alloy steel large ring, Computat. Mater. Sci. 50 (2010) 65-76. https://doi.org/10.1016/j.commatsci.2010.07.008
[11] W. Meng, G. Zhao, Y. Guan, The Effects of Forming Parameters on Conical Ring Rolling Process, The Scientific World Jo. 2014 (2014) 235656. https://doi.org/10.1155/2014/235656
[12] J.H. Kang, S.J. Heo, J. Yoo, Y.C. Kwon Hot working characteristics of S32760 super duplex stainless steel, J. Mech. Sci. Technol. 33 (2019) 2633-2640. https://doi.org/10.1007/s12206-019-0511-y
[13] A. Murillo-Marrodan, E. Garcia, F. Cortes, A Study of Friction Model Performance in a Skew Rolling Process Numerical Simulation, Int. J. Simul. Modell. 17 (2018) 569-582. https://doi.org/10.2507/IJSIMM17(4)441
[14] K.Q. Ye, M. Hamada, Critical Values of the Lenth Method for Unreplicated Factorial Designs, J. Qual. Technol. 32 (2000) 57-66. https://doi.org/10.1080/00224065.2000.11979971
[15] G. Vairamani, T.S. Kumar, S. Malarvizhi, V. Balasubramanian, Application of response surface methodology to maximize tensile strength and minimize interface hardness of friction welded dissimilar joints of austenitic stainless steel and copper alloy, Trans. Nonferrous Metal. Society of China 23 (2013) 2250-2259. https://doi.org/10.1016/S1003-6326(13)62725-9

Materials Research Proceedings 28 (2023) 639-648 https://doi.org/10.21741/9781644902479-69

Detailed study of tube hot rolling process by means of FEM

GARCÍA GIL Eduardo[1,a *], DURÁN Gorka Llamazares[1,b], CONDE Aintzane[1,c], MURILLO-MARRODÁN Alberto [1,d] and ATUTXA Jon Barco [2,e]

[1]University of Deusto, Avda. Universidades 24. 48007 Bilbao, Spain

[2]Tubos Reunidos Group, Barrio de Sagarribai, s/n 01470 Amurrio, Álava, Spain

[a]e.garcia@deusto.es, [b]gorka.llamazares@opendeusto.es, [c]aintzane.conde@deusto.es, [d]alberto.murillo@deusto.es, [e]Jbarco@tubosreunidos.com

Keywords: Tube Rolling, Hot Forming, FEM Simulation

Abstract. In this paper seamless tubes hot manufacturing calibration rolling is studied by means of a finite element model, to improve product quality and process performance. Based on real data provided by an industrial partner, Tubos Reunidos Group, a finite element model of the process has been created and validated for the thermo-mechanical analysis of the process. The model has been used for the study of the wall thickness evolution and peripherical distribution during process, the eccentricity and the polygonization effects. Results show that the tube velocity in the process is one of the factors affecting wall thickness eccentricity, due to mass flow conservation. Regarding polygonization and eccentricity effect it has been found that both effects increase in the rolling stands with higher reduction ratio, and are corrected afterwards. These effects are mainly due to the ovality of the rolls. However, the effect the different sliding velocity along roll perimeter has implications in the local deformation of the material in contact with the roll, causing local compressive stress areas in addition to the predominant tension areas.

Introduction

The manufacturing of seamless pipes is a complex process in which high temperature, strain rates and forces are involved to achieve a high-quality product. Seamless pipes are used in severe environments applications, such us, refineries, transport of fluids under high pressures, oil drilling operations, etc. Usually, seamless tubes offer higher resistance and mechanical properties than welded pipes [1].

The manufacturing process of seamless tubes consists of three steps, piercing, elongation in mandrel mill and final rolling calibration. The three steps have influence on the quality and accuracy of the final product; however, in the last step the geometrical accuracy is given to product.

The efforts for improving the quality of the tubular products obtained with this process have been extended from the beginning of the process itself, as it can be seen in the research work of Vargas et al. [2]. However, the studies involving numerical models are more recent, mainly from the present century. In 2003, Bayoumi [3] developed a steady-state analytical model of the roll-pass geometry, which studied the effects of roll gap opening and the inter-stand velocity increase ratio in process parameters such as wall thickness, inter-stand tensions, roll load and rolling. The results showed that the interstand velocity increase ratio increased the inter-stand tension while the roll load remains almost unchanged. Carvalho et al. [4] modeled the process for the manufacture of seamless tubes both numerically and via hot torsion testing and predictions of final average ferrite grain sizes were given, with larger predictions for ferrite grains sizes, which were attributed to the assumptions made during the study.

The analytical models gave an interesting insight for the process; however, they were limited in terms of the accuracy of the results and the number of variables analyzed. Therefore, most of the recent works use the Finite Element Method, FEM, to simulate the process with a higher

Content from this work may be used under the terms of the Creative Commons Attribution 3.0 license. Any further distribution of this work must maintain attribution to the author(s) and the title of the work, journal citation and DOI. Published under license by Materials Research Forum LLC.

accuracy and broader studies. The calculation power increase of computers and the improvements of the commercial software, has boosted the complexity of calculations and the results obtained.

The high accuracy demanded by final pipe users respond to the need to thinner but homogenous walls, free form residual stresses and superficial defects. Dimensioning of the tubes is based on the thinnest and, consequently, weakest section. Thus geometrical non-homogeneities such us eccentricity and polygonization lead to an increase in weight of material [5]. Accordingly, important research efforts have been dedicated to improve the geometrical accuracy of the final product. In fact, these effects are not exclusive of this rolling mill, since they can be generated even in piercing phase [6], and elongation in mandrel mill [7].

During the rolling of the tube its diameter is reduced progressively, higher reductions are performed in the initial boxes while lighter reduction occur at the end. In the rolling stands with greater reductions, the rolls have an elliptical shape to prevent material from jamming, which leads to polygonization of the tube. A study devoted to reduce polygonization [8] concluded that interstand tension and the correct selection of initial diameter are key factor for reducing this effect. Jiang et al. [9] developed a high precision FE model for predicting the defect of inner polygon. The model allowed the identification of the peak stress at the roll root contact area while the stress of the roll gap contact area was smaller, leading to a distribution of six stress peaks. These works pointed out the difficulties faced to obtain a proper and accurate Finite Element Model: material behavior constitutive model, contact and friction boundary conditions, and heat transfer.

Another aspect of interest is related to the tube eccentricity. Jiang et al. [10,11], designed a set of eccentric rolls which induced a moment on the tube causing it to rotate around its axis while it advances through the mill. In [10] the tube rotation method is presented for a single pass of the tube rolling process and analyzed by means of FEM, showing an improvement in the evenness of thickness distribution. Afterwards, in [11] the theory of the rotation is analyzed along with a FEM that is validated with experimental results. The rolling forces, torque, energy consumption are evaluated, from a process point of view, and the thickness, temperature and stress of the tube are studied from a product point of view. This technology is applied to thick steel tubes in a recent contributions of the authors [12].

In this paper a FEM model of the hot tube Sizing Mill, SM, of AISI 1016 has been developed based and validated with industrial data with the aim of fully understand the factors affecting the final geometry of the tube at the end of the process: wall thickness, eccentricity, and polygonization. Thanks to the model the reasoning for their occurrence, and alternatives to reduce its relevance have been obtained. The model has been also modified to evaluate the effect of typical alterations occurring in plant in the real process: pre-existing eccentricity, tube temperature heterogeneity, or roll misalignment.

Experimental Setup

In this study the calibration rolling of AISI 1016 steel is studied. Material composition % in wt. is presented in Table 1.

Table 1. Chemical composition of the AISI 1016 steel.

C	Si	Mn	Ni	P	S	Cr	Mo	Al	Cu
0.12 - 0.17	max 0.3	0.3 - 0.6	max 0.25	max 0.035	max 0.035	max 0.2	max 0.05	max 0.01	max 0.3

The calibration consists of seven driven stands of three rolls each, as it can be seen in Fig. 1, which are equally distributed to reduce the tube diameter from 200.50 mm to 180.80 mm. The disposition of the rolls in each box is rotated 60º from one box to another, giving as result that the groove of the rolls in the preceding box is the border of the rolls in the next, as shown in Fig. 1.

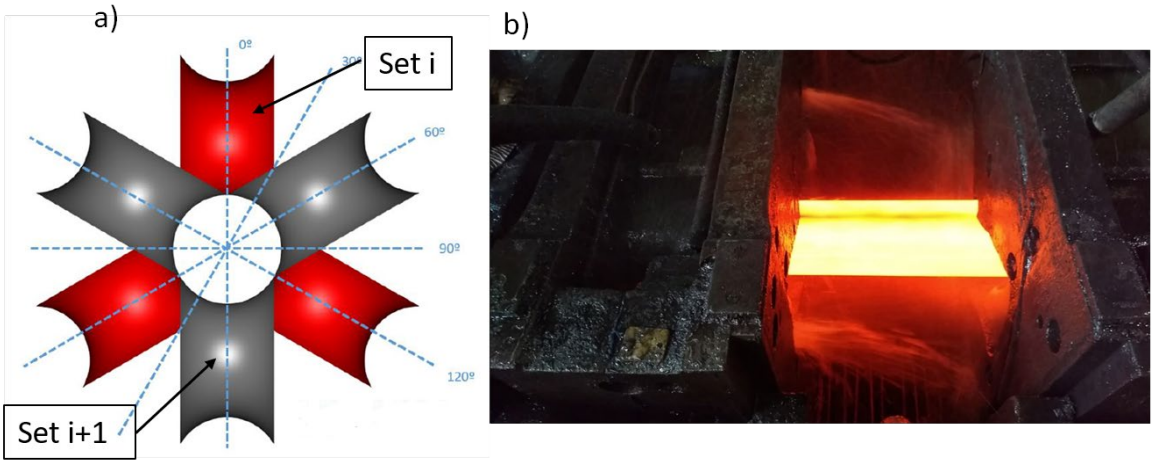

Fig. 1.a) Disposition of the rolls in the driven mill stand of two subsequent sets, where the rotation can be seen. B) Experimental image of the rolled tube passing between two driven stands.

Before entering rolling stands the material is reheated in a gas furnace to a temperature of 1020ºC. Then the material is pushed into the SM and is driven by the rolls thanks to friction. According to the measurements recorded by Tubos Reunidos Group on shop the advanced mean velocity of the tube is 1018.9 mm/s. Fig. 1 b) shows the tube passing between two boxes. By contrast, the tangential velocity of the rolls varies along the mill from 876.5 mm/s in the first stand to 1124 mm/s in the last two stands. Accordingly, for the analysis of the process it is important to notice that the usual contact between the roll and the tube is sliding contact.

During the rolling of the tube the mean power consumed by the electric motors was 24 kW, and the mean temperature of the billet between stands was 980.43ºC. After the process the final length of the tube was measured. Additionally, a tube was stopped in the middle of the process to measure its wall thickness between driven stands. For the thickness measurements, ten values have been acquired circumferentially equally distributed along tube perimeter using infrared IMS system. Results are used in section 4 for comparing experimental with numerical results.

Numerical Model

In this section the numerical model developed for the simulation of the SM is presented. The geometries of the different elements involving the mill were designed according to data provided by Tubos Reunidos Group separately using SolidWorks software and assembled together before being exported to Forge NxT®.

The model, Fig. 2, consists of seven rolling stands with 3 rolls in each stand, the tube or billet, a guide to lead the tube into the SM and a pusher used to feed the tube into the mill. For simplicity of the simulation, all tools were selected as non-deformable (rigid) objects with thermal properties and the billet (tube) was set as a deformable object with thermal properties. The tools where meshed with 2D triangular elements, while the billet was meshed with 3D tetrahedral P1+ linear elements with a bubble node, size factor of 0.7, volumic size factor of 2.2 and mesh size of 4 mm to achieve at least 3 elements on the tube initial thickness. The Hensel-Spittel constitutive law is chosen to model AISI 1016 behavior at different temperatures, strain, and strain rates. The materials coefficient were provided by the software and validated with the industrial partner [13]. The coefficients used are shown in Table 2.

Table 2. Hansel-Spittel coefficients for AISI 1016.

Coefficient	Value
A1	752.5394
m1	-0.00219
m2	-0.1523
m3	0.13792
m4	-0.0486

According to experimental data the initial temperature of the billet was set to 1020ºC, and that of the rolls to 50ºC. Heat transfer coefficient were set according to [14]. Regarding friction, based on [15] the viscoplastic or Norton law was selected for the contact between the rolls and the tube with a coefficient of 0.33, adjusted by curve fitting comparing experimental and numerical results, mainly velocity and power consumption.

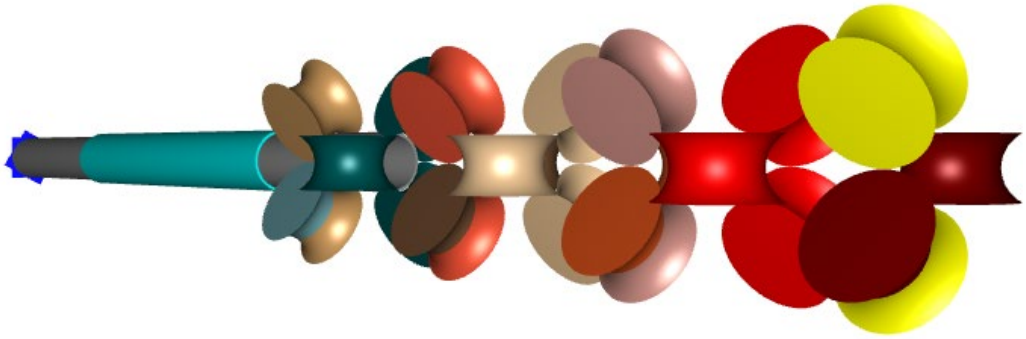

Fig. 2. Geometrical disposition of the model with the tube and the 7 driven stand rolls.

Results and Discussion

The results of the model are presented in this section along with the discussion of the main aspects obtained from the simulation.

For the validation of the numerical model the obtained results of power consumption, tube velocity evolution, temperature and tube thickness evolution and length increase are compared to experimental results. On the one hand the mean power obtained from the simulation is 28 kW, which is 16.7% higher than the experimental measurement, a result accurate enough result given the dispersion of experimental measurements done on-shop.

Billet velocity increases along the process from 968 to 1049 mm/s which agrees with the experimental measurements described in previous section.

The temperature evolution of the billet during the milling process is fairly constant both numerical and experimentally, being the difference of 4% between the experimental mean value (980.38ºC) and the numerical one (1016.51ºC).

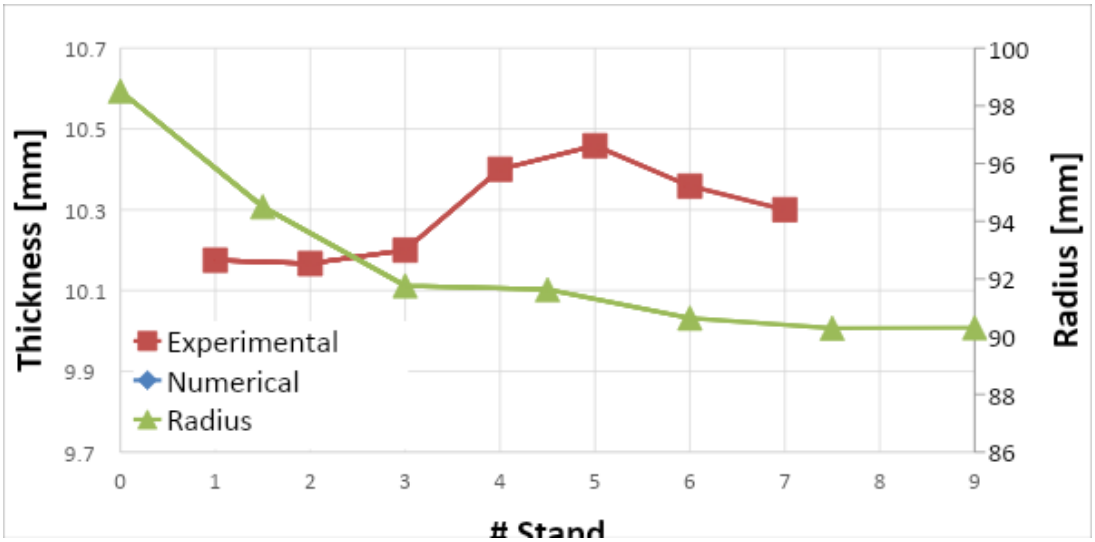

Fig. 3. Mean thickness evolution measured after each rolling stand. Experimental vs. Numerical.

Finally, the geometrical accuracy of the model is analyzed comparing the mean thickness evolution after each rolling stand. In Fig. 3 it can be seen that the agreement is good with a maximum deviation below 6%. Once the validity of the model has been justified, the model is used to study in detail eccentricity and polygonization effects during the process.

First the wall thickness increase is discussed. As in any plastic forming process, the volumetric flow rate must be kept constant during the rolling, (assuming that the density is constant). Accordingly, the diameter reduction must be accompanied with a length or/and thickness increase. In order to avoid the effect of thickness increase during the process, it would be necessary to adjust the billet velocity to keep the cross-section area constant while the diameter is reduced, for that the material velocity should be updated

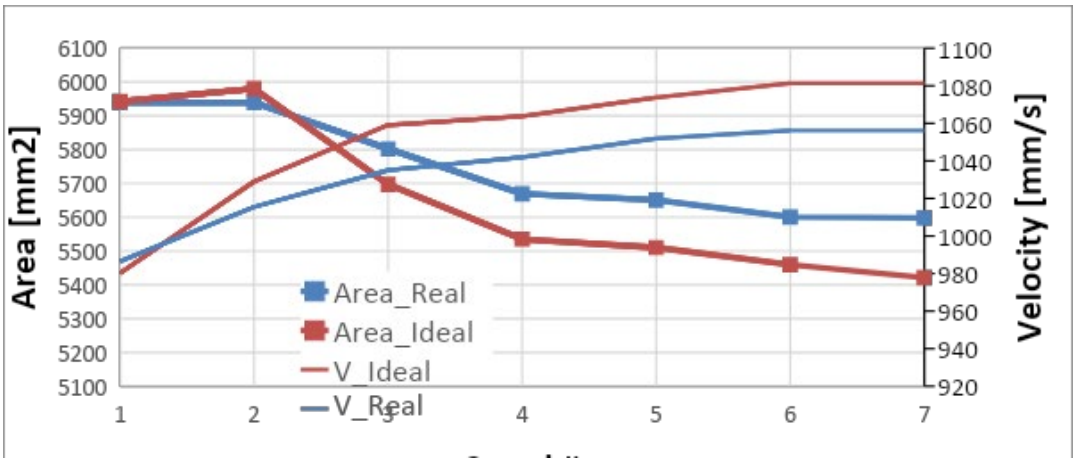

Fig. 4. Evolution of cross section area and tube velocity along the process. Real values are obtained from the model, and ideal values have been calculated to keep tube thickness constant.

From the model the real area after each rolling stand and the real velocity have acquired and they have been compared to the ideal area that would maintain the wall thickness constant, giving as a result the ideal velocity in each stand, that is, the velocity of the material that would make the wall thickness constant, results are shown in Fig. 4.

Results show that the velocity of the tube in the real process is lower than the ideal one, up to a 3% in the last stand. This analysis has not been found in literature, and it must be pointed out that the implementation of this solution in the industrial process would improve the quality of the product but a proper assessment of rolls velocity must be done to match the material flow given the effects of friction and sliding.

Fig. 5 shows the wall thickness evolution at different angles (0º, 30º, 60º, 90º, and 120º) (see Fig. 1)as well as the eccentricity evolution measured after each rolling step. Two interesting conclusions can be obtained from this graph.

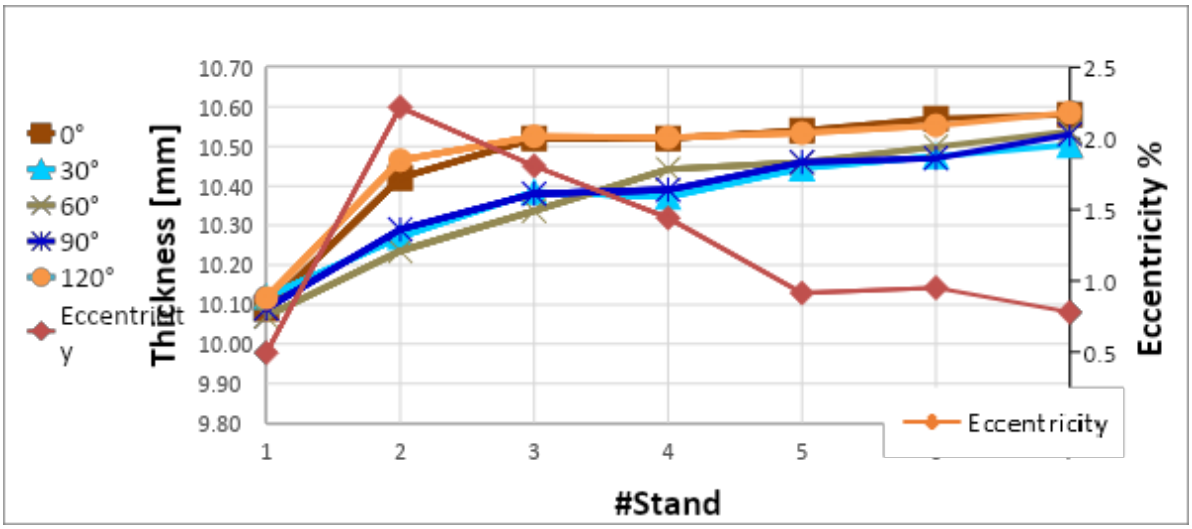

Fig. 5. Wall thickness evolution at different angles (0º, 30º, 60º, 90º, and 120º) and eccentricity evolution measured after each rolling stand.

On the one hand, it can be seen that the thickness evolution can be divided into 3 groups: group 1 involving 0º and 120º, group 2 with 30º and 90º, and 60º. The behavior of group 1 correspond to the planes that face the groove of the roll in the second stand, thus they experiment an important thickness increase. Group 2, instead, face the border of the roll at the second stand, leading to a smaller thickness increase. Finally, the plane at 60º is in the middle of the roll between the groove and the border. Looking at the eccentricity evolution it can be seen that it is at the stage of maximum difference between group 1 and group 2, that is in the second roll, that the eccentricity is higher. Then, as long as the lines trend to merge the eccentricity is reduced.

Thus, a clear relationship between the thickness evolution at circumferentially and the eccentricity is set. This difference is caused by the roll perimeter design, which is not circular but elliptical. It is also important to notice, that the biggest increase in eccentricity is generated in the rolls with the higher diameter reduction which are stands two and three, as shown in Fig. 3.

In order to fully understand the phenomena occurring at the contact between the rolls and the tube the sliding velocity and the longitudinal stresses of the tube are analyzed hereafter. Fig. 6 a) shows the relative velocity in the tube axial direction between the roll and the tube in the stand 3. There it can be seen that in the groove of the roll the material is moving faster than the roll, while in the corners of the roll it is the opposite: the tangential velocity of the roll is higher than the velocity of the tube. Fig. 6 b) shows the displacement of the material passing through the roll, where it is appreciated how the material is pushed forward in the area of the corner of the rolls, and it is retained in the groove of the roll, causing an undulated shape. This effect, which is due to the different diameter of the roll along its perimeter is enhanced by the roller's ovality. Moreover, it creates a stress-strain distribution which is depicted in Fig. 7 a) strain, and b) stress.

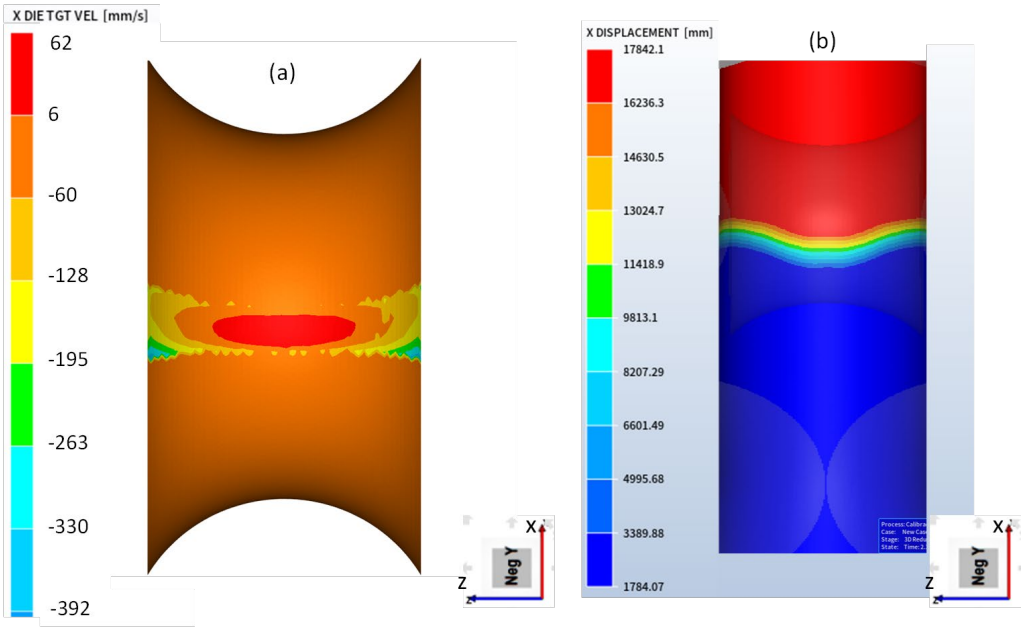

Fig. 6. a) Relative velocity between the roll and the tube in stand two. b) Tube material displacement at the pass of stand 3.

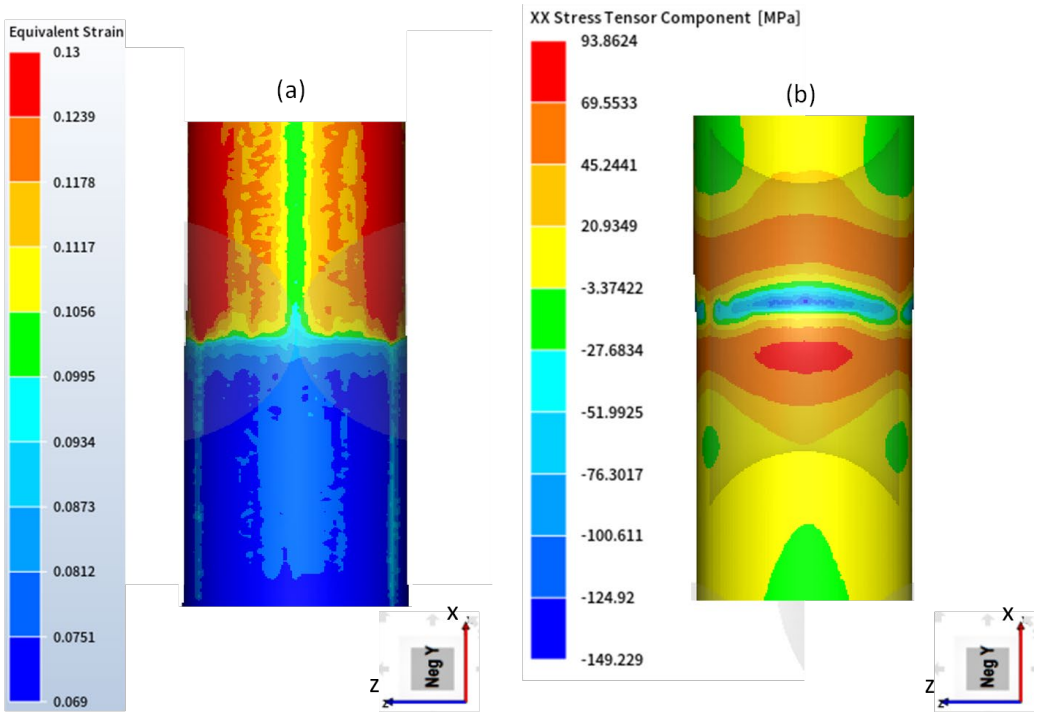

Fig. 7. a) Equivalent strain of tube material when passing through stand 3. b) Axial stress of the tube material in the surroundings of stand 3.

In Fig. 7 b) it can be seen that most of the tube is under tension stress (positive), which agrees with literature. However, in the contact region between the roll and the tube important compressive stresses are generated which are higher in the groove section and almost 0 in the corners of the roll. This finding has not been reported previously and is one of the reasons for the generation of eccentricity effect. The equivalent strain shown Fig. 7 a) confirms the difference in behavior between the central region in contact with the groove and the regions in contact with the border of

the roll. As above mentioned, the growing diameter of the roll along its wildness is responsible for this effect, and the ovality of roll's perimeter enhances the consequences.

Finally, the polygonization effect is addressed. It is related to the ovality of the rolls, which is high in the initial stands and reduced in the last ones. The evolution of this effect is shown in Fig. 8.

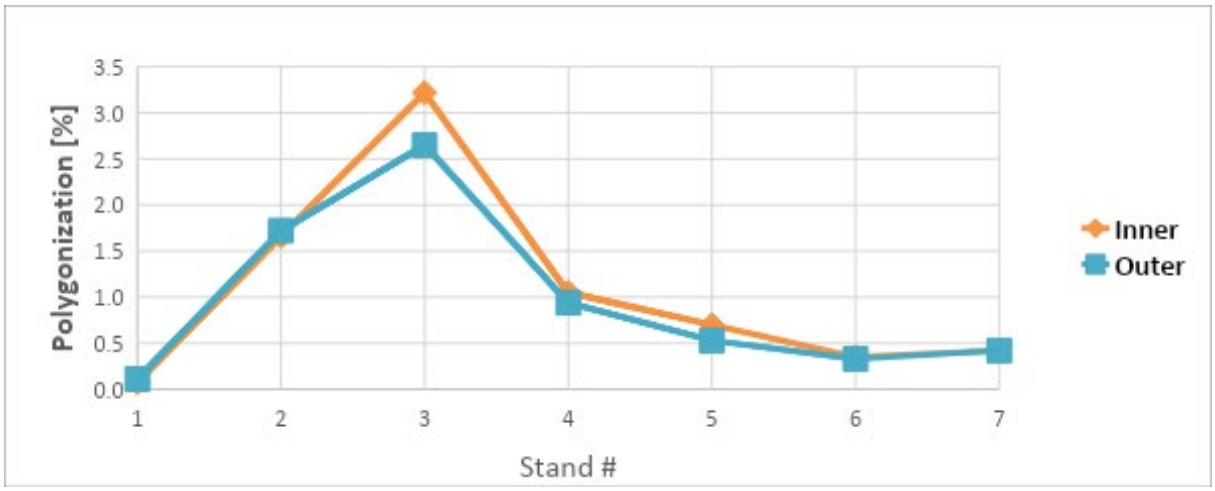

Fig. 8. Evolution of polygonization effect along the SM.

This effect increases from 0 at the beginning of the process to a maximum of 3.2% in stand number 3, where the maximum diameter reduction is done. Afterwards, the polygonization is reduced up below 0.5% at the end of the SM. This phenomenon is due to the ovality of the rolls, which flatten the tube passing over the groove of the roll. Since the ovality of the rolls decreases along the stands so does the ovality.

Finally, the radial deviation from the theoretical circular profile has been calculated in the cross section of the tube after each stand. Results are depicted in Fig. 9, the evolution of the radial deviation follows a sinusoidal trend with 3 positive peaks and 3 negative peaks, which represent the polygonization effect. These peaks are clearly relevant after stands 2 and 3, those with higher reduction and ovality, and consequently the higher polygonization of the tube in those positions. Then, in subsequent stands those peaks are flattened. This way it is illustrated how the tube profile is expanded in the corner of the roll ((positive and negative peaks) and flattened in the groove of the subsequent roll, due to the 60º rotated configuration is rotated 60º of the mill. This flattening effect of the rotated stands reduces progressively the big deviation created in stands 2 and 3, but the geometry is not fully corrected after stand 7.

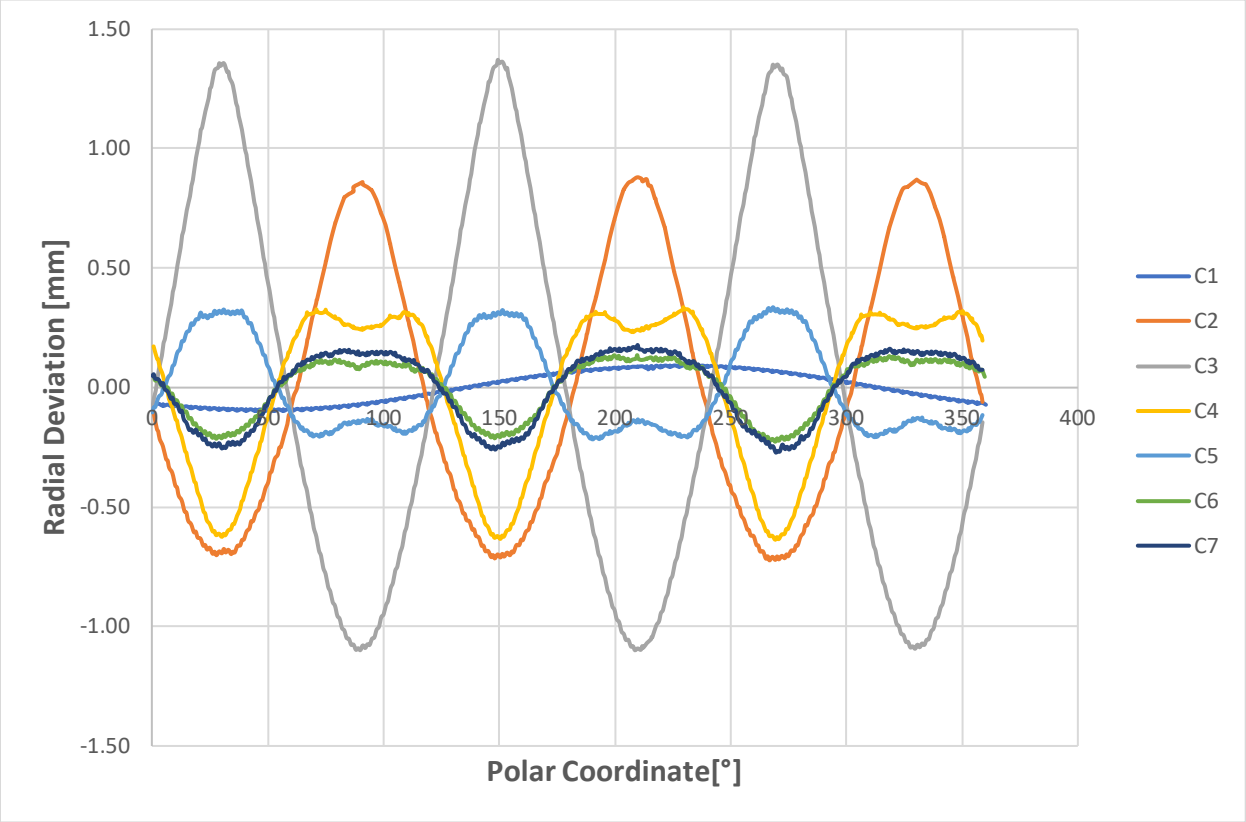

Fig. 9. Radial deviation of the tube along the periphery of the tube in each stand.

This polygonization is an undesired effect for tube produces and is due to the ovality of the roll's profile. Perfect circular rolls would strongly reduce this phenomenon; however, those type of roll profile could present limitations for material flow during rolling, according to actual experience.

Summary

In this paper the calibration rolling of seamless AISI 1016 tubes is deeply analyzed by means of a FEM validated thanks to experimental data provided by an industrial partner, Tubos Reunidos Group. From the work developed the following conclusions can be drawn:

- The effect of thickness increase is analyzed based on material flow. Results show that increasing tube velocity will help reducing this effect.
- The effects of eccentricity and ovality have been deeply assessed. Both effects increase between stands 2 and 3, and decrease progressively in the subsequent stands. The ovality of the rolls has been found to be the cause of both effects since it distorts the circularity of the tube.
- Process parameters such as relative velocity, material displacement, equivalent strain and axial tension are evaluated in the contact between the rolls and the material showing that the difference of tangential speeds along rolls perimeters leads to non-homogenous stress-strain states on tube material.

References

[1] V. Gopinathan, O. Pawelski, V.C. Venkatesh, Effect of cold and hot rolling and normalising on the structure and properties of welded joints, J. Mech. Work. Technol. 1 (1978) 361-370. https://doi.org/10.1016/0378-3804(78)90038-4

[2] J.M. Vargas, C. Pagliano, F. Medina, F. Muratori, F. Paganin, J. Paiuk, Process Optimization for the Manufacturing of Seamless Steel Tubes in a Continuous Mandrel Mill and a Stretch Reducing Mill, IFAC Proc. 22 (1989) 147-153. https://doi.org/10.1016/S1474-6670(17)53102-X
[3] L.S. Bayoumi, Analysis of flow and stresses in a tube stretch-reducing hot rolling schedule, Int. J. Mech. Sci. 45 (2003) 553–565. https://doi.org/10.1016/S0020-7403(03)00047-X
[4] R.N. Carvalho, M.A.C. Ferreira, D.B. Santos, R. Barbosa, Simulation of the Process of Hot Rolling of Seamless Tubes, Mater. Sci. Forum 539–543 (2007) 4602-4607. https://doi.org/10.4028/www.scientific.net/MSF.539-543.4602
[5] F. Foadian, A. Carradó, H. Palkowski, Precision tube production: Influencing the eccentricity and residual stresses by tilting and shifting, J. Mater. Process. Technol. 222 (2015) 155-162. https://doi.org/10.1016/j.jmatprotec.2015.03.008
[6] A. Murillo-Marrodán, E. García, J. Barco, F. Cortés, Analysis of Wall Thickness Eccentricity in the Rotary Tube Piercing Process Using a Strain Correlated FE Model, Metals 10 (2020) 1045. https://doi.org/10.3390/met10081045
[7] Z. Wei, C. Wu, A new analytical model to predict the profile and stress distribution of tube in three-roll continuous retained mandrel rolling, J. Mater. Process. Technol. 302 (2022) 117491. https://doi.org/10.1016/j.jmatprotec.2022.117491
[8] K. Stefański, W. Kubiński, Diminishment of internal polygonization of tubes in hot stretch-reducing mill, Metall. Foundry Eng. 36 (2010) 21. https://doi.org/10.7494/mafe.2010.36.1.21
[9] Y.-Z. Jiang, X.-J. Li, X.-P. Zhang, K.-F. He, G.-F. Bin, High Precision FE Modeling for Predicting Inner Polygon Defect of Hot Rolled Seamless Steel Tubes, KSCE J. Civ. Eng. 22 (2018) 4445–4453. https://doi.org/10.1007/s12205-018-1014-6
[10] Y. Jiang, H. Tang, Method for Improving Transverse Wall Thickness Precision of Seamless Steel Tube Based on Tube Rotation, J. Iron Steel Res. Int. 22 (2015) 924-930. https://doi.org/10.1016/S1006-706X(15)30091-1
[11] Y. Jiang, H. Tang, X. Zhang, Rotation mechanics and numerical simulation of hot rolling process under asymmetric rolls, Int. J. Mech. Sci. 151 (2019) 785-796. https://doi.org/10.1016/j.ijmecsci.2018.12.006
[12] J. Yong-zheng, Z. Sheng-shuo, F. Zhi-gang, Application of asymmetric roll pass for improving roundness of ultra-thick steel tubes, Int. J. Adv. Manuf. Technol. 119 (2022) 3571-3581. https://doi.org/10.1007/s00170-021-08456-7
[13] Tubos Reunidos Group n.d. https://www.tubosreunidosgroup.com/es/home (accessed December 8, 2022).
[14] R. Langbauer, G. Nunner, T. Zmek, J. Klarner, R. Prieler, C. Hochenauer, Investigation of the temperature distribution in seamless low-alloy steel pipes during the hot rolling process, Adv. Ind. Manuf. Eng. 2 (2021) 100038. https://doi.org/10.1016/j.aime.2021.100038
[15] A. Murillo-Marrodan, E. Garcia, F. Cortes, A Study of Friction Model Performance in a Skew Rolling Process Numerical Simulation, Int. J. Simul. Model. 17 (2018) 569-582. https://doi.org/10.2507/IJSIMM17(4)441

Materials Research Proceedings 28 (2023) 649-656 https://doi.org/10.21741/9781644902479-70

Parametric identification on a dynamic behavior model for a forging machine

DURAND Camille[1,a *], SONG Heyu[1,b] and BIGOT Régis[1,c]

[1]Arts et Metiers Institute of Technology, Université de Lorraine, LCFC, HESAM Université, F-57070 Metz, France

[a]camille.durand@ensam.eu, [b]heyu.song@ensam.eu, [c]regis.bigot@ensam.eu

Keywords: Target Function, Sensitivity Study, Optimization Methods, Dynamic Behavior Model, Screw Press

Abstract. Dynamic models using masses, dampers and springs have been developed to represent the behavior of energy piloted machines. These models were proven to estimate more accurately the required amount of energy to forge a part. But how to identify the parameters of the model to accurately represent the behavior of a specific machine? In this study, the case of a strike without billet on a screw press is investigated, different target functions are tested to identify the model parameters and a sensitivity study of the optimization is performed. Results are encouraging.

Introduction

For forging processes using energy limited machines, such as hammers or screw presses, it is difficult to accurately predict the amount of energy that the billet actually absorbs as plastic deformation. This is due to energy losses caused by the dynamic behavior of the machines. That is why some dynamic models of forging machines were developed: first, models with masses and springs for gravity drop hammer [1,2] and then models with dampers in parallel with springs [3, 4]. For these models, the parameters were theoretically identified based on machine specifications. But nowadays, with the development of high-speed cameras, stereo vision systems and sensors, further experimental investigations are possible on forging hammers. For example, impact velocity was measured on a counter blow hammer and thus kinetic energy was deduced to determine blow efficiency [5,6]. Moreover, Yoneyama [7] was able to monitor the load, the pressure, the friction and the contact temperature while upsetting steel billets on a gravity drop hammer. Different sensors technologies to monitor ram displacement and load were also compared in the case of a screw press [8]. And finally, a dynamic model consisting in a spring-mass-damper model, was experimentally determined for a forging hammer [9]. To identify the parameters of such an experimentally based model, numerical optimization methods are required. And to guaranty the unicity, the accuracy and the reliability of the identified parameters, the target function has to be well defined [10] and a sensitivity study can be performed.

In this study, the method developed in a previous work to determine a dynamic model based on experiments [9] will be applied on a screw press. Once the model determined, a parametric identification will be run with different targets functions and results will be analyzed. Based on the analysis, a target function is chosen and a sensitivity study is conducted to ensure a proper model determination.

The Production System and its Dynamic Model

The focus is set on the screw press of the Vulcain Platform in Metz (Fig. 1.a). It is a direct drive screw press SPR 400 from Lasco, with a maximal energy of 28.9kJ for a maximal speed of 680 mm/s. A specific toolholder is mounted on the press, that allows the monitoring of the forging load, thanks to a load sensor embedded in the lower die, and the monitoring of the ram

Content from this work may be used under the terms of the Creative Commons Attribution 3.0 license. Any further distribution of this work must maintain attribution to the author(s) and the title of the work, journal citation and DOI. Published under license by Materials Research Forum LLC.

displacement, thanks to three laser sensors attached to the lower die, in addition to the magnetic encoder of the press [11].

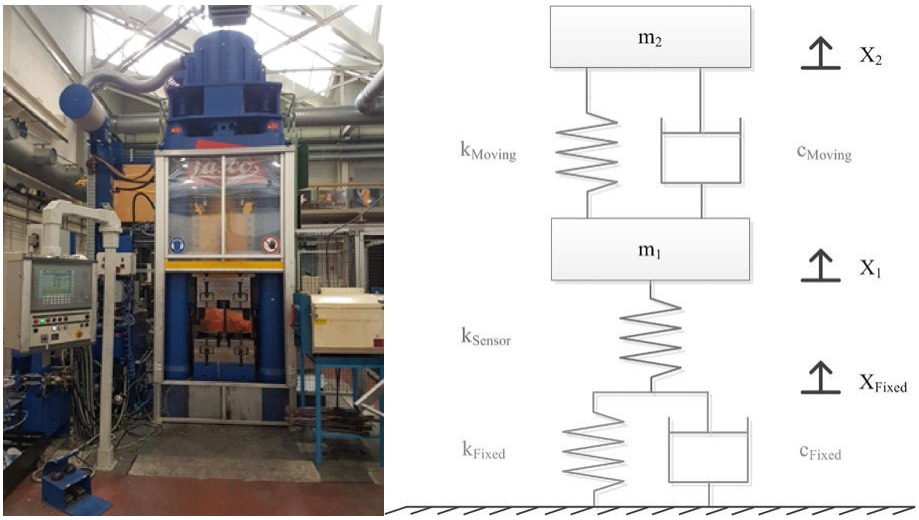

Fig. 1. a) the screw press b) the model of the screw press and its tool during a bare strike without billet.

An experimental campaign was launched to determine the dynamic model called the BIM model [9] of the screw press. Knowing the initial conditions and recording the load in function of the time for bare strikes (without billet), the model can be determined according to the method described in [9]. A Fast Fourier Transform (FFT) is performed on the load signal recorded during the strike (Fig. 2). As the impact duration is very short, it is not possible to have an analysis with a lot of frequency levels. Even though, two peaks are identified, thus a model with two degrees of freedom will be able to describe the dynamic behavior of the screw press (Fig. 1.b). The initial impact speed is known to be 365 mm/s. The load sensor is considered in the model thanks to the k_{sensor} spring and its value is set to $3.3997.10^{10}$ N/m as given by the supplier.

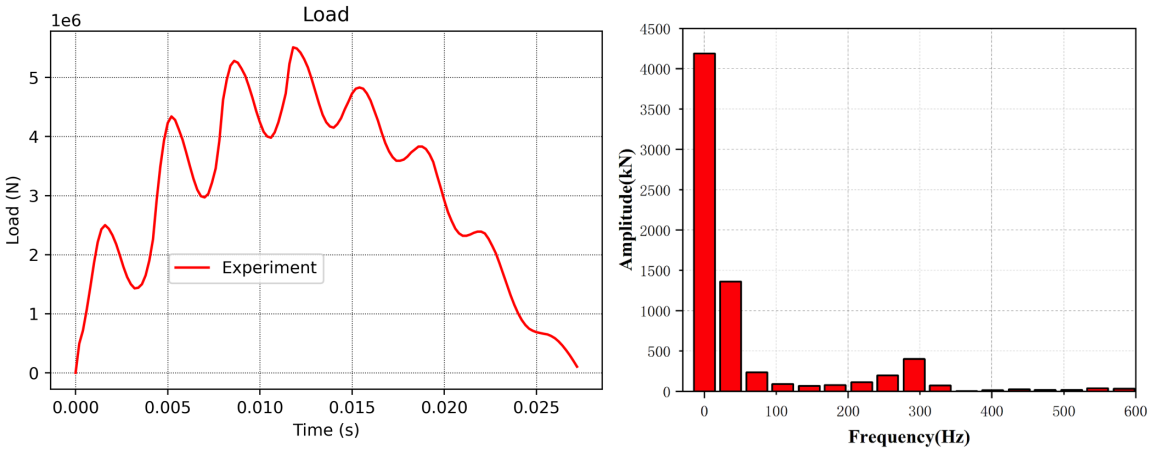

Fig. 2. a) the load signal measured by the sensor embedded in the lower die b) the FFT of the load.

Parametric Identification

Once the model defined, the parameters (m_1, m_2, k_{fixed}, k_{moving}, c_{fixed}, c_{moving}) have to be identified thanks to optimization algorithms. The optimizations were programed using Python. First, a target function was defined with a least square method only applied on the load in function of the time,

but in most of the cases the second vibration mode was lost. So, the FFT was also included in the target function. To ensure a good identification, three different target functions were analyzed using least squares (1) or gradient descent algorithms (2)(3) [10]:

$$CF1\ (load, FFT) = f \cdot \sum_{i=1}^{n} \frac{\left(load_i^{exp} - load_i^{sim}\right)^2}{\|load^{exp}\|^2} + (1-f) \cdot \sum_{1=1}^{m} \frac{\left(FFT_i^{exp} - FFT_i^{sim}\right)^2}{\|FFT^{exp}\|^2} \quad (1)$$

$$CF2\ (load, FFT) = f \cdot \sqrt{\sum_{i=1}^{n} \frac{\left(load_i^{exp} - load_i^{sim}\right)^2}{\|load^{exp}\|^2}} + (1-f) \cdot \sqrt{\sum_{1=1}^{m} \frac{\left(FFT_i^{exp} - FFT_i^{sim}\right)^2}{\|FFT^{exp}\|^2}} \quad (2)$$

$$CF3\ (load, FFT) = f \cdot \sqrt{\frac{1}{n}\sum_{i=1}^{n} \frac{\left(load_i^{exp} - load_i^{sim}\right)^2}{\|load^{exp}\|^2}} + (1-f) \cdot \sqrt{\frac{1}{m}\sum_{1=1}^{m} \frac{\left(FFT_i^{exp} - FFT_i^{sim}\right)^2}{\|FFT^{exp}\|^2}} \quad (3)$$

With $load^{exp}$ the load recorded by the sensor embedded in the lower die and FFT^{exp} the FFT deduced from that load signal.
And $load^{sim}$ the load obtained with the model and FFT^{sim} the FFT deduced from the modeled load.
With f a balance weight for the load and the spectrum, f was chosen equal to 0.5.

Results and Discussion

The load in function of the time, as well as the FFT, were plotted for the three different target functions and are compared to the experimental results (Fig. 3). For each function, the target value is also indicated. The three load curves obtained are significantly different, whereas the three FFT are very similar with the one coming from the experiments. Regarding the load curves, dephasing is observed in all curves as well as differences of amplitudes. As CF1 and CF2 have very closed definition (CF2 has just a square root more), results were expected to be similar, but this is not the case. The load curve for CF2 is singular compared to the ones for CF1 and CF3. For the experimental load curve, the load increase with important variations until reaching a peak, and after the load peak, the load decreases with smaller and smoother variations. CF1 and CF3 are following this trend, but this is not the case for CF2. This may be explained by the fact that the target functions may have found different local minimums.

Based on these results, the target function CF3 is chosen to perform a sensitivity analysis because it shows the best fit with the lowest target value.

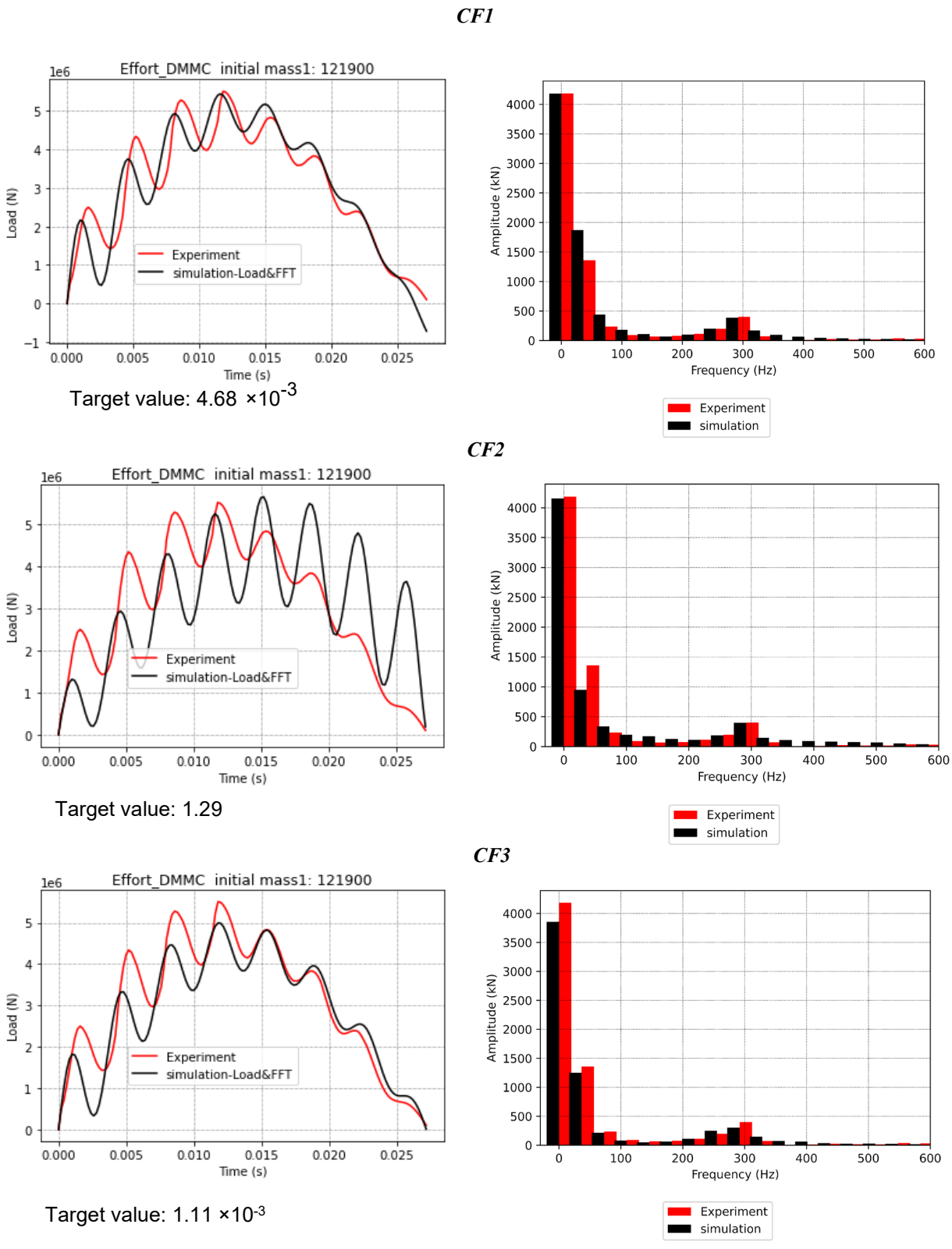

Fig. 3. a) comparison of experimental and simulated load signal for the 3 different target functions b) comparison of FFT on the experimental and simulated load signals for the 3 different target functions.

Sensitivity Analysis

To ensure the convergence of the algorithm to a minimum, a criterion on the target function variation is used and called *TolFun*. The minimization is stopped if, at the increment *i+1*, the equation is satisfied:

$$\frac{\left|CF3\ (load,FFT)_i - CF3\ (load,FFT)_{i+1}\right|}{\left|CF3\ (load,FFT)_i\right|} < TolFun \quad (4)$$

TolFun is obtained with a convergence study: the optimization is run with smaller and smaller values of *TolFun* and the identified parameters and target values of each *TolFun* values are compared (Table **1**). When the variation of these parameters is less than 1%, the *TolFun* value is considered to be adequate. There is no significant improvement of the target function or variation of identified parameters for *TolFun* values lower than 0.1. thus, *TolFun* will be set to 0.1.

Table 1. Target values and parameters values for different convergence criteria.

Convergence criterion	Fonction coût	m (kg)	c (N.s/m)	k (N/m)
1	1.5×10^{15}	3207	730117	2.07×10^{9}
1e-1	$\mathbf{1.1\times10^{-3}}$	**3192**	**360000**	$\mathbf{9.94\times10^{9}}$
1e-2	1.1×10^{-3}	3192	360000	9.94×10^{9}
1e-3	1.1×10^{-3}	3192	360000	9.94×10^{9}
1e-4	1.1×10^{-3}	3192	360000	9.94×10^{9}
1e-5	1.1×10^{-3}	3192	360000	9.94×10^{9}
1e-6	1.1×10^{-3}	3192	360000	9.94×10^{9}

Satisfying the equation (4) is not sufficient to ensure the convergence to a global minimum. The initial set of parameters can also have an impact on the solution find by the algorithm. The initial parameters are defined thanks to suppliers' documentations, when possible and a sensitivity study of the optimization on the initial parameters is conducted. For that, 50 new sets of initial parameters are generated by creating a +/- 10% perturbation according to a uniform law on the reference parameters. 46 optimizations are converging to the same target value with the same identified parameters, thus a global solution seems to be reached.

Then a sensitivity study of the optimization on the initial speed conditions is realized. 50 optimizations were run with 50 different values for the initial speed v_1 and v_2: the 50 different speed values were generated by creating a +/- 5% perturbation according to a uniform law on the reference speed values. Results are plotted (Fig. 4): 37 optimizations were converging to the same target value with 37 same sets of parameters identified.

The impact of the speed on the simulated load at k_{sensor} is also of interest. Thus, optimizations were run with +/-10% uncertainty error for the press input speed and the impact on the load was plotted (Fig. 5). Uncertainty error on the determination of the speed only affects the magnitude of the load with a relative deviation of 3.8%.

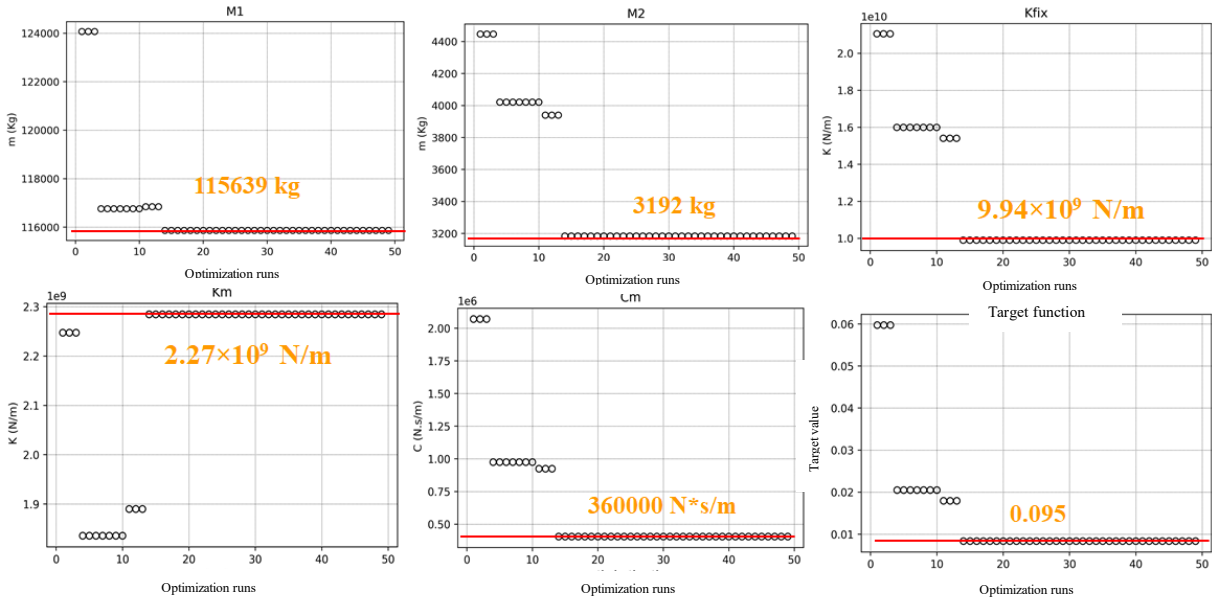

Fig. 4. Identified parameters values (m_1, m_2, K_{fixed}, K_{moving}, C_{moving}) and the target value for the 50 optimization runs with 5% uncertainties on the initial speed conditions.

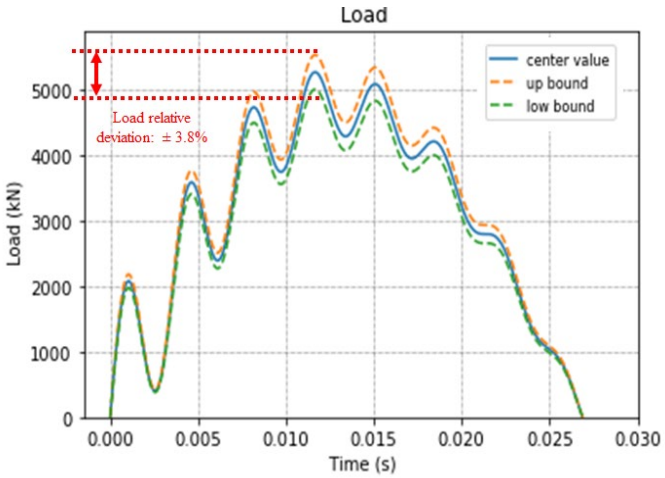

Fig. 5. Simulated load signal for the +/- 10% uncertainties on the initial speed conditions.

Finally, the impact of the parameters identification on the load simulated is also considered. For that, 10% uncertainty error was set for the identified parameters and the load response is plotted (Fig. 6). Uncertainty errors on the identified parameters induce a relative deviation of the load of 1.5% and affect both the load and the vibration mode.

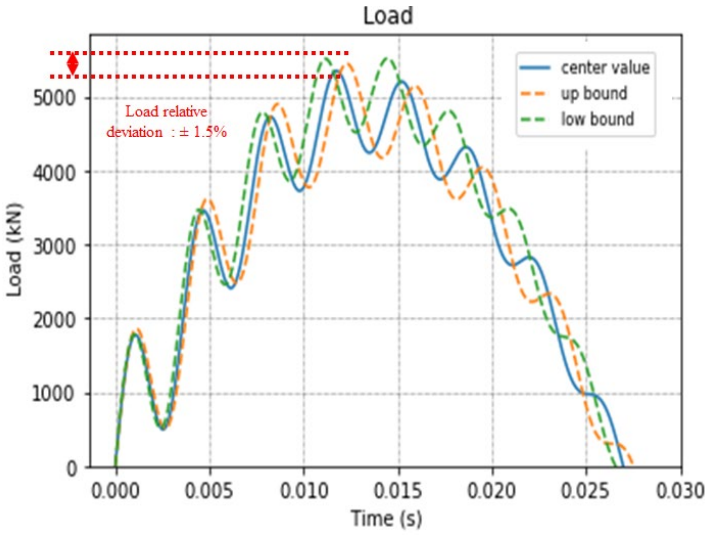

Fig. 6. Simulated load signal for the +/- 10 % uncertainties on the set of identified parameters.

Discussion

Concerning the parametrical identification, three different target functions were already tested and the one that seemed to be the best in terms of target values and load signal fitting was chosen. Despite these different tests, even more target functions could have been tested as well and the target function chosen could be different. The study can also be enlarged by testing different optimization algorithms to ensure that the global minimum is found. For instance, the target function integrates the load in function of the time and the FFT of that signal, but maybe the target function still can be improved by adding the ram displacement into consideration. Thus, the coefficient *f* of the target function could be revised, to give a different weight to each term.

Then, with the target function that was chosen, a sensitivity study of the algorithm on the initial set of parameters was conducted. The results converge; thus, it seems to indicate that a global minimum has been found. To ensure that fact, the study could be enlarged with a bigger perturbation on the initial set of parameters and with a higher number of optimizations.

The impact of the initial speed conditions on the parameters identified and the load simulated was considered. Concerning the parametric identification, results are converging, more than half of the sets of parameters identified are the same. Thus, the optimization is not significantly sensible to uncertainties on the ram speed. And the impact on the load simulated is lower than 4%, so it is negligible.

For the uncertainties on the identification of the set of parameters, it has an impact on the load's amplitude variation and on its dephasing. A relative deviation of 1.5% on the load amplitude was observed, thus remaining very low.

Summary

In this preliminary work on the parametric identification of a dynamic behavior model of a forging machine, one target function was chosen and a sensitivity study on the optimization was conducted. For the uncertainties ranges investigated, results are encouraging as they show a low sensitivity of the algorithm to perturbations on the initial conditions and on the initial set of parameters. But the study should be continued by testing other algorithms and larger ranges of uncertainties to ensure an accurate identification.

Furthermore, here the parametric identification is performed on a model of a press and its tools obtained thanks to bare strike, without billet. Thus, it could be interesting to validate the identified parameters on a case of a model integrating a blow on a billet.

Besides, the model presented here is valid for an entire production system including the press and its tools, but as several different tools can be installed on the same machine, it would be wise to dissociate the tools from the machine in such a dynamic model. And this would necessitate some changes in the target function's definition.

References

[1] S. Tobias, Survey of the development of Petro-Forge forming machines, Int. J. Mach. Tool. Des. Res. 25 (1985) 105-197.

[2] S. Vajpayee, M.M. Sadek, S.A. Tobias, The efficiency and clash load of impact forming machines to the second order of approximation, Int. J. Mach. Tool. Des. Res. 19 (1979) 237-252. https://doi.org/10.1016/0020- 357(79)90013-1

[3] S. Vajpayee, M.M. Sadek, Analytical study of forming efficiency as influenced by the process and the machine structure, Int. J. Prod. Res. 15 (1977) 203-218. https://doi.org/10.1080/00207547708943118

[4] V. Gregorian, M.M. Sadek, S.A. Tobias, Noise generated by a laboratory drop hammer and its interrelation with the structural dynamics and process parameters, Int. J. Mach. Tool. Des. Res. 16 (1976) 301-318. https://doi.org/10.1016/0020-7357(76)90040-8

[5] L. Galdos, E.S. de Argandoña, N. Herrero, M. Ongay, J. Adanez, M. Sanchez, The calibration of high energy-rate impact forging hammers by the copper-column upsetting method and high speed Camera measurements, Key Eng. Mater. 611–612 (2014) 173-177. https://doi.org/10.4028/www.scientific. net/KEM.611-612.173

[6] R. Chen, Z. Li, K. Zhong, X. Liu, Y. Wu, C. Wang, Y. Shi, A stereo-vision system for measuring the ram speed of steam hammers in an environment with a large field of view and strong vibrations, Sensors 19 (2019) 996. https://doi.org/10.3390/s19050996

[7] T. Yoneyama, Development of a friction sensor for hot forging, Int. J. Adv. Manuf. Technol. 90 (2017) 2251-2261. https://doi.org/10.1007/s00170-016-9539-7

[8] C. Durand, L. Freund, C. Baudouin, R. Bigot, J.D. Guérin, Comparison of different sensor technologies to monitor a forging process. 24th Int. Conf. on Material Forming ESAFORM (2021), Liège, Belgique, 2021. https://doi.org/10.25518/esaform21.1475

[9] J.F. Mull, C. Durand, C. Baudouin, R. Bigot, A new tailored solution to predict blow efficiency and energy consumption of hammer-forging machines, Int. J. Adv. Manuf. Technol. 111 (2020) 1941-1954. https://doi.org/10.1007/s00170-020-06237-2

[10] G. Venet, C. Baudouin, C. Pondaven, R. Bigot, T. Balan, Parameter identification of 42CrMo4 steel hot forging plastic flow behaviour using industrial upsetting presses and finite element simulations, Int. J. Mater. Forming 14 (2021) 929-945. https://doi.org/10.1007/s12289-020-01609-1

[11] C. Durand, R. Bigot, C. Baudouin, Contribution to the characterization of metal forming machines: application to screw presses, 17th Int. Conf. Met. Form. Met. Form. 2018, 16-19 Sept. 2018.

Materials Research Proceedings 28 (2023) 657-666 https://doi.org/10.21741/9781644902479-71

An analytical approach for modelling incremental disk rolling process

ACAR Sadik Sefa [1,3,a *], DINÇER Mehmet Şamil [2,3,b] and OZCATALBAS Mustafa[3,c]

[1]Department of Aerospace Engineering, Middle East Technical University, Ankara, Turkey

[2]Department of Metallurgical and Materials Engineering, Middle East Technical University, Ankara, Turkey

[3]Repkon Machine and Tool Industry and Trade Inc., Istanbul, Turkey

[a]sadik.acar@metu.edu.tr, [b]samil.dincer@metu.edu.tr, [c]mustafa.ozcatalbas@repkon.com.tr

Keywords: Incremental Forming, Disk Rolling, Velocity Field, Strain Rate Field, Analytical Model, Contact Zone, Deformation Field

Abstract. In the context of the current study, an analytical method is developed to determine the deformation field of the workpiece under the forming roller for an unconventional incremental radial disk rolling (IRDR) process. As the industrial forming machine is in the development phase, the machine and process design requires a preliminary assessment tool that is sensitive to process parameters and roller geometry. Establishing a parametric relationship between process parameters and induced deformation field enables designers to determine the parameters needed to obtain the target geometry and microstructure as well as the forming machine requirements. Instantaneous roller-workpiece interface, i.e. contact zone, and cross-sections that plastic flow occurs in between are calculated. The contact zone is spatially discretized to two-dimensional surface elements. The principle of volume conservation during plastic deformation is utilized to obtain velocity fields in three dimensions. Strain rate distributions are calculated by taking the gradient of the velocity fields in respective directions. Average values of strain at each cross-section are the accumulated plastic strain that is created by the multiple circumferential passes of the roller and computed numerically, accounting for different strain rates and contact times at each pass. Obtained contact zone geometries, deformation fields, and the effect of different process parameters are discussed. Results show that deformation occurs mainly in the circumferential direction and the tangential velocity of the roller in the circumferential direction has a more pronounced effect on the deformation than the radial advance of the roller per revolution.

Introduction

Having a firm grip on the deformation of the material is essential in a forming operation. Controlling the deformation allows for avoiding possible failures, defects, and undesired inhomogeneities and estimating other crucial forming phenomena such as residual stresses, springback, buckling, pile-up at the onset of forming zone, and diametral growth for cylindrical and disk-shaped products [1,2]. Also, the deformation has a significant effect on the microstructural evolution during the process which affects the mechanical performance of the final product [3]. Microstructural effects are important especially for the hot forming operations due to the recrystallization and grain growth which are usually dictated by narrow temperature, deformation, and time limitations [4]. Therefore, obtaining the desired microstructure depends on the degree of control the process designer can exert on the deformation of the material.

In the literature, mathematical models are often used to assess the deformation of the material in forming operations [5]. One of these methods is the upper-bound method which utilizes an energy functional that has to be minimized to obtain the correct kinematically admissible velocity

Content from this work may be used under the terms of the Creative Commons Attribution 3.0 license. Any further distribution of this work must maintain attribution to the author(s) and the title of the work, journal citation and DOI. Published under license by Materials Research Forum LLC.

field. Kinematic admissibility was derived from the incompressible volume principle [6]. Rolling applications combined the analytical methods with the finite element method for plane-strain rolling [7]. Analytical methods are used to provide the material property update to the finite element model [8]. The volumetric restrictions and plastic flow velocity field are often determined by different approaches based on the upper-bound method such as arc tangent velocity field and cosine velocity field methods [9,10]. The analytical methods are employed to optimize the process parameters of wire flat rolling [11]. The aim was mainly the determination of required rolling force and torque [12]. In extrusion problems, velocity fields had to be substantially modified according to the die geometry [13].

The incremental radial disk rolling (IRDR) process employs two forming rollers which are positioned reciprocally and pulled radially outward. Rollers form the rotating workpiece disk to a higher diameter and a lower thickness. One of the differences between conventional rolling processes and IRDR process is that the axis of roller rotation is either parallel to the axis of the roller feed (radial) or located on the radial-axial(thickness) plane for IRDR while the axis of roller rotation and axis of roller feed are generally perpendicular to each other in conventional rolling [14]. Another difference is that a relatively smaller portion of the workpiece material is subjected to plastic deformation at any instant during the IRDR process. Compared to conventional rolling processes, tube spinning is more similar to IRDR. Apart from the final workpiece shape, the difference distinguishing IRDR from tube spinning is that circumference of the roller path increases and the curvature of the material under the contact zone decreases as the roller moves away from the centre of the disk throughout the IRDR process. Therefore, ensuring the plastic flow stability and homogenous deformation during the IRDR process is much more difficult [15].

Previous studies investigated relatively simpler deformation states of conventional rolling processes. Developed models considered much simpler tool designs and contact zones as the current process requires a complex tool geometry. Also, deformation fields for the current rolling machine have never been researched before. This study focuses on developing parametrical velocity field, strain, and strain rate expressions accounting for any tool geometry, workpiece geometry, and process parameter set. The study aims to provide a preliminary assessment tool for the optimization of the process and the roller geometry for the IRDR process. An analytical method is developed and utilized to determine strain and strain rate distribution in the workpiece material under the forming roller. The forming machine is still in the development phase and optimization of the process requires the evaluation of an extensive number of combinations of process and roller parameters. Even though approaches involving the finite element method are useful, their computational cost is extremely high compared to the current method. Therefore, far fewer finite element method (FEM) simulations are needed in cooperation with the current method. A validation study of the current method with experiments and FEM is in progress. Also in future works, the deformation fields found by the current method will be employed to determine roller geometry and process parameter ranges satisfying the requirements derived from time, force, microstructure, and processing map limitations.

Theory

Roller geometry depends on four independent parameters: roller nose radius (R_n), roller radius (R_r), roller attack angle (α), and roller height (Δt) which is equal to the thickness reduction in this study. Roller geometry also includes smooth angle, smooth nose radius, length of the upper levelling, upper levelling draft angle and length of the lower levelling but they are not included in the calculations due to the limitations of the analytical method. Previous studies showed that the length of the upper levelling and the upper levelling draft angle parameters affect the material pile-up at the onset of feed direction and other parameters control mainly the springback and final surface quality [16]. These subjects are not in the context of the current study and can be neglected in the calculations. The general layout of the moving parts of the machine and the roller geometry

is shown in Fig. 1. Workpiece is attached to the mill which provides the rotational drive to the workpiece.

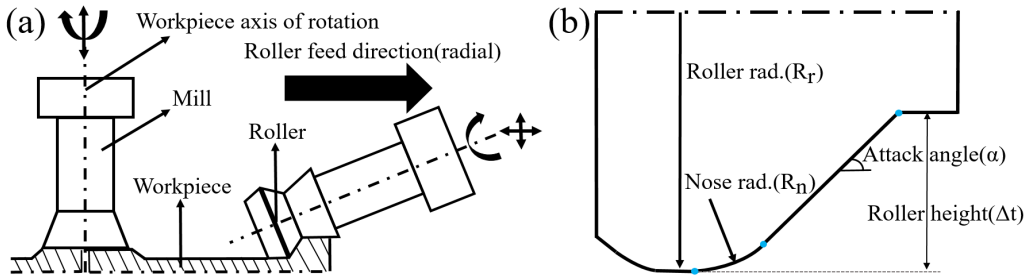

Fig. 1. (a)Layout and motion of roller, mill and workpiece, (b) roller geometry.

The roller is pulled radially outward as the workpiece turns and the roller idles around its axis of rotation. The roller bites the material and the contact zone develops. The area and shape of the contact zone depend on roller geometry, radial feed (f) and radial feed per revolution (pitch, p). Thickness reduction is assumed to be equal to roller height (Δt) to reduce the number of independent variables. The width of the contact zone is assumed to be parallel to the circumferential direction and the system is defined in the Cartesian coordinate system since the width of the contact zone is usually very short compared to the circumference of a near-circular roller path. The origin is defined at a location radially inward by pitch amount with respect to the bottom of the roller nose. The trials with CAD models showed that the contact zone can be represented by a region within seven points, four of which lie on the radial-axial(thickness) plane that the width(b) is zero. Eqs. 1 and 2 provide parametric expressions for radial and axial(thickness) distances between points.

$$L_1 = R_n \sin\alpha, \qquad L_2 = \frac{\Delta t - R_n(1 - \cos\alpha)}{\tan\alpha}, \qquad t_1 = R_n(1 - \cos\alpha), \qquad t_2 = \Delta t - R_n(1 - \cos\alpha) \tag{1}$$

$$t^* = R_r - R_n(1 - \cos\alpha) - \sqrt{\left(R_r - R_n(1 - \cos\alpha)\right)^2 - b_{mid}^2} \tag{2}$$

Broadwise locations of points P_5, P_6 and P_7 are expressed as b_{up}, b_{mid} and b_{low}, respectively. Fig. 2 illustrates point locations which are calculated with found distances. The three-dimensional geometry of the contact zone is obtained parametrically by utilizing cubic area interpolation between these points.

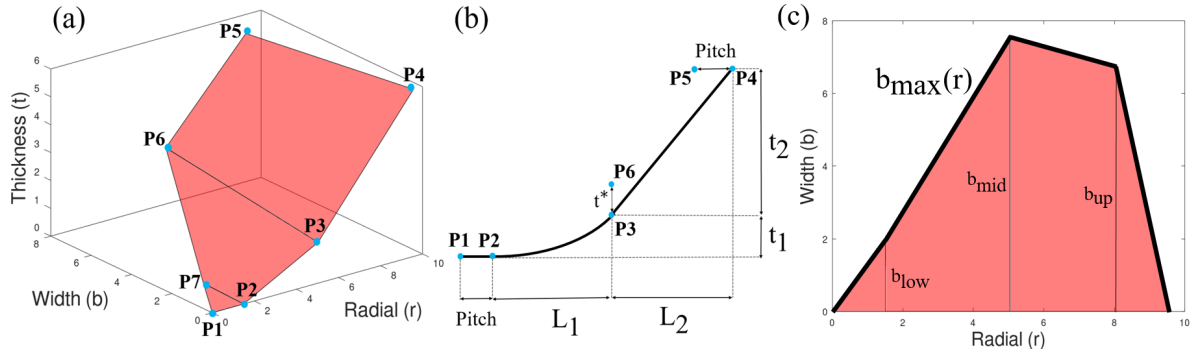

Fig. 2. (a)Points defining the contact zone, (b)Positions of points in radial(r)-axial(t) plane, (c)Maximum width as a function of radial location.

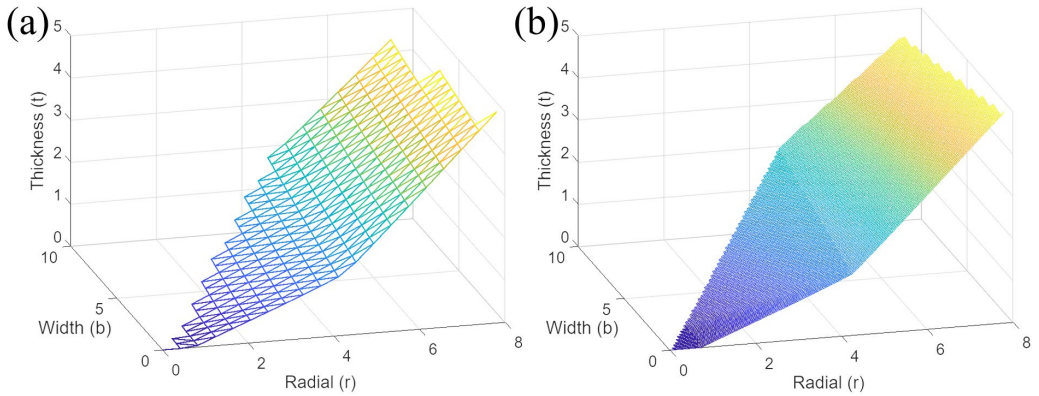

Fig. 3. Discretization of the contact zone with (a)450 and (b)13000 elements.

Interpolated area is spatially discretized into triangular surface elements using Delaunay Triangulation [17]. The centroidal location of each element is calculated and the developed analytical model is implemented on these centroids. Fig. 3 compares contact zones obtained by different mesh densities. The contact zone employing finer mesh which has 13000 surface elements, accurately captured the curvature of the nose region as well as the flatness of the lower levelling region below the nose. Also, the model with finer mesh achieved a more precise contact zone boundary representation.

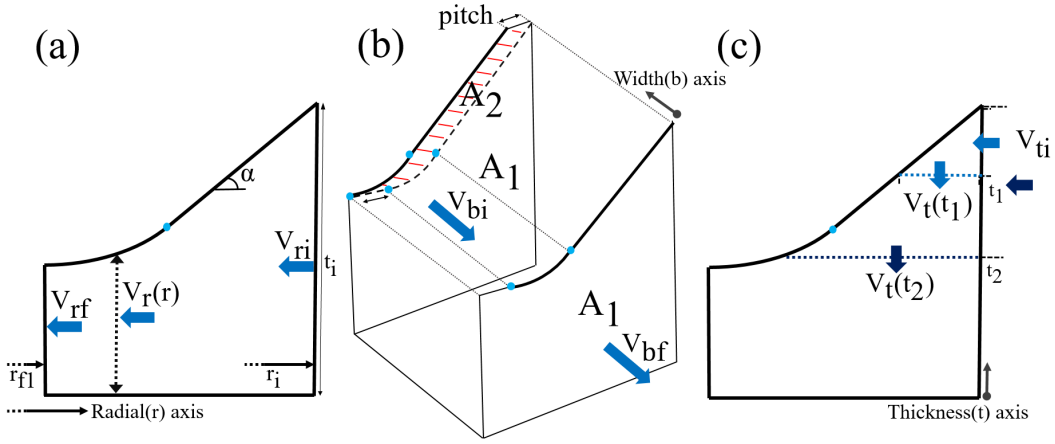

Fig. 4. Plastic flow directions and cross-sections in (a)radial, (b)width and (c)thickness axes.

Derivation of Velocity Field.

The material is assumed to undergo no elastic strain relaxation between circumferential passes since the induced plastic strain is expected to be much higher than the elastic strain. Strain rate calculations start with the derivation of analytic expressions for plastic flow velocities in three axes. Fig. 4 illustrates flow velocities and cross-sections that the flow travels in corresponding directions. Calculations rely on the assumption that plastic deformation induces no volume change. Flow in each direction is assumed to be independent of each other. The tangential velocity of the roller in the circumferential direction is much higher than that in the radial direction for process parameters tested in this study. Therefore the contribution of plastic flow in different directions to each other is negligible. This assumption should be improved in the future. Firstly, initial volumetric flow rates are calculated. Then, cross-sections normal to the flow are parametrically expressed for any location. The plastic velocity that the material has to have while travelling through a defined cross-section is obtained by employing the volume conservation principle. The velocity found is the average velocity of the material flowing below the corresponding point of the roller as the cross-section is dictated by the contact zone and the radial location of the roller, in

Materials Research Proceedings 28 (2023) 657-666 https://doi.org/10.21741/9781644902479-71

addition to process parameters. Finally, strain rate expressions are obtained by taking the gradient of the velocity field along the corresponding direction.

The radial plastic velocity field is illustrated in Fig. 4(a). For calculations, the radial axis is separated into two regions, the inclined region and nose region, divided by the upper end of the roller nose whose radial location (r^*) is formulated in Eq. 3 where r_i is the initial radius. For all calculations, subscript i and the term "initial" denote the initial properties just before entering the contact zone. Radial location of the bottom end of the nose (r_{f1}) is also given in Eq. 3.

$$r^* = r_i - \frac{\Delta t - R_n(1 - \cos\alpha)}{\tan\alpha} \quad \text{and} \quad r_{fl} = r^* - R_n \sin\alpha \tag{3}$$

Only the variation of thickness with radius is different for these two regions. Volume conservation in radial direction and radial flow velocity as a function of radius are expressed in Eq. 4 where feed (f) is the initial radial velocity and t_i is the initial thickness.

$$V_r(r)t(r)\, 2\pi\, r = f\, t_i\, 2\pi\, r_i \;\rightarrow\; V_r(r) = \frac{f\, r_i\, t_i}{r\, t(r)} \tag{4}$$

Variations of thickness with radial location and consequent radial flow velocities are formulated in Eqs. 5 and 6.

$$t(r) = t_i + \frac{r - r_i}{\tan\alpha} \quad \rightarrow \quad V_r(r) = \frac{f\, r_i\, t_i\, \tan\alpha}{r\,(t_i\, \tan\alpha + r - r_i)} \qquad \text{for} \quad r^* < r < r_i \tag{5}$$

$$t(r) = t_f + R_n - \sqrt{R_n^2 - (r - r_{fl})^2} \;\rightarrow\; V_r(r) = \frac{f\, r_i\, t_i}{r\,(t_f + R_n - \sqrt{R_n^2 - (r - r_{fl})^2})} \quad \text{for} \quad r_{fl} < r < r^* \tag{6}$$

Circumferential plastic flow is shown in Fig. 4(b). Material starts to flow under the roller when it encounters the furthest point of the contact zone in the width axis: b_{mid} which is broadwise location of P_6 shown in Fig. 2(a). The initial cross-section that plastic flow velocity passes has an area of A_1+A_2. As the flow continues under the contact zone, the cross-sectional area is assumed to be linearly decreased to A_1. A_2 is the projectional area of the contact zone on the radial-axial plane and equal to pitch times Δt. The expression found for A_1 is given in Eq. 7.

$$A_1 = t_f\,(R_n \sin\alpha + p) + \frac{t_i^2 - (t_f + R_n\,(1 - \cos\alpha))^2}{2\tan\alpha} + R_n^2\,(\sin\alpha\left(1 - \frac{\cos\alpha}{2}\right) - \frac{\alpha(\text{rad})}{2}) \tag{7}$$

Volume conservation in the width axis and resulting relation for circumferential velocity field expression are presented in Eqs. 8 and 9 where V_{bi} is the known initial tangential velocity in the circumferential direction. Variation of the cross-sectional area with broadwise location is obtained by the use of assumed linear area decrease between $b = b_{mid}$ *and* $b = 0$.

$$V_b(b)A(b) = V_{bi}\,(A_1 + A_2) \;\rightarrow\; V_b(b) = V_{bi}\,\frac{(A_1 + A_2)}{A(b)} \tag{8}$$

$$A(b) = A_1 + A_2\,\frac{b}{b_{mid}} \;\rightarrow\; V_b(b) = V_{bi}\, b_{mid}\,\frac{A_1 + A_2}{A_1\, b_{mid} + A_2\, b} \tag{9}$$

In radial and circumferential velocity field calculations, initial cross-sections were assumed to be constant and all cross-sections were parallel to each other. In contrast, for the axial velocity field, the initial cross-section has normal in the radial direction and it is assumed to be a function of thickness. Because, the material enters the contact zone in the radial direction and is pressed downward in the axial axis at any point on the roller, as demonstrated in Fig. 4(c). The expression for axial plastic velocity is formulized in Eq. 10.

$$V_t(t)\,(r_i - r)\,2\pi\,\frac{r_i + r}{2} = f\,(t_i - t)\,2\pi\, r_i \;\rightarrow\; V_t(t) = 2f\, r_i\,\frac{(t_i - t)}{(r_i - r)(r_i + r)} \tag{10}$$

Axial flow velocity as a function of axial location is presented in Eq. 11.

$$r = r_i - (t_i - t)\tan\alpha \;\rightarrow\; V_t(t) = \frac{2f\,r_i}{\tan\alpha\left(2\,r_i - (t_i - t)\tan\alpha\right)} \tag{11}$$

Strain Rate Distribution.

Strain rates are calculated by taking the gradient of the velocity field in respective directions. Eqs. 12 and 13 provide the radial strain rate expression which is the gradient of Eqs. 5 and 6 in the radial direction.

$$\dot{\varepsilon}_r = \frac{dV_r}{dr} = f\,r_i\,t_i\,\tan\alpha\,\frac{-t_i\,\tan\alpha - 2r + r_i}{r^2(t_i\,\tan\alpha + r - r_i)^2} \quad \text{for} \quad r^* < r < r_i \tag{12}$$

$$\dot{\varepsilon}_r = \frac{dV_r}{dr} = f\,r_i\,t_i\,\frac{-\sqrt{R_n^2 - (r - r_{fl})^2}\,(t_f + R_n) + R_n^2 - (r - r_{fl})^2 - r\,(r - r_{fl})}{r^2\sqrt{R_n^2 - (r - r_{fl})^2}\left(t_f + R_n - \sqrt{R_n^2 - (r - r_{fl})^2}\right)^2} \quad \text{for} \quad r_{fl} < r < r^* \tag{13}$$

Circumferential and axial strain rate relations are shown in Eqs. 14 and 15 which are gradients of velocity fields in circumferential (b) and axial (t) directions, see Eqs. 9 and 11, respectively.

$$\dot{\varepsilon}_b = \frac{dV_b}{db} = -V_{bi}\,b_{mid}\,\frac{A_2\,(A_1 + A_2)}{(A_1\,b_{mid} + A_2\,b)^2} \tag{14}$$

$$\dot{\varepsilon}_t = \frac{dV_t}{dt} = -\frac{2f\,r_i}{(2\,r_i - (t_i - t)\tan\alpha)^2} \tag{15}$$

Strain Distribution.

Strain at each element is considered as the cumulative plastic strain induced by circumferential passes of the roller. At each circumferential pass, the material is subjected to varying strain rates under the contact zone in three directions. As the strain rate distributions are found, strain increments ($\Delta\varepsilon_j$) at each pass and the sum of the strain increments (ε_j, accumulated strain) can be calculated according to Eq. 16 for each element. In the strain equation, j is the direction of the strain and strain rate, e is the domain of locations that the element presented at previous passes and Δt(e) is the duration of contact time for each location. b_{max} values are calculated by interpolation between b_{up}, b_{mid} and b_{low} at known previous radial locations as shown in Fig. 2(c).

$$\varepsilon_j = \sum_e \Delta\varepsilon_j\,(e) = \sum_e \Delta t(e)\,\dot{\varepsilon}_j(e) \quad \text{where} \quad \Delta t(e) = \frac{b_{max}(e)}{V_{bi}} \tag{16}$$

Results

The workpiece material and the process temperature does not affect the results of this study. Also, even though the developed method is capable of accounting for varying initial radii, all calculations in this study are done for only one value of initial radius which is 120 mm. It is found that the contact zone changes as the roller moves in the radial axis for low radii. As the roller further moves away from the centre, the contact zones at different radial locations become very similar. The employed initial radius is chosen to be obeying the second trend. Also, a mesh dependency study is carried out but it is not presented here to restrict the extent of the paper. Results for only the finer mesh are evaluated. Firstly, the effect of roller geometry on the contact zone is investigated. Four roller geometry (RG) parameter sets are created and tabulated in Table 1. Obtained contact zones are shown in Fig. 5. To preserve comparability, each contact zone was formed by the same process parameter set which is 0.3 mm/s feed rate(f) and 25 RPM spindle rate. A higher roller radius leads to a wider contact zone, comparing RG1 and RG2. Contact zones of RG1 and RG3

show the effects of nose radius and roller height. The inclined region constitutes a much higher portion of the contact zone than the nose region for the roller with a lower R_n and higher Δt. Also, increased roller height elongated the contact zone in the radial direction. Examining the contact zone of RG4, a low attack angle also causes a significant increase in the radial length of the contact zone.

Table 1. Dimensions of 4 different roller geometries (RG).

	Roller Radius, R_r [mm]	Nose Radius, R_n [mm]	Attack Angle, α [°]	Roller height, Δt [mm]
RG1	35	5	45	5
RG2	70	5	45	5
RG3	35	2.5	45	7.5
RG4	70	2.5	30	7.5

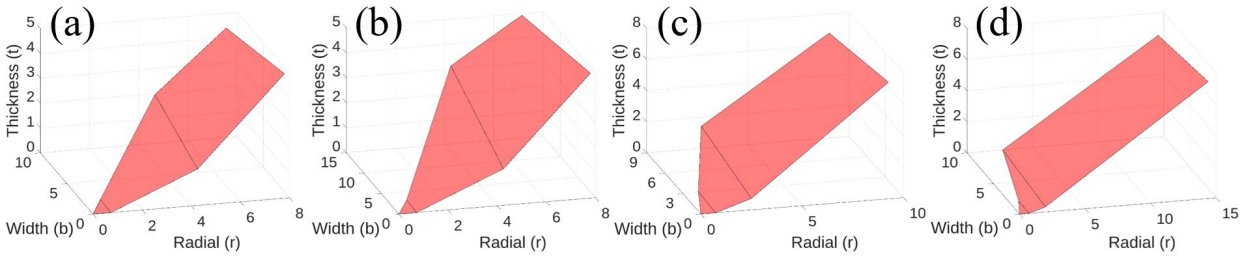

Fig. 5. Contact zones of (a) RG1, (b) RG2, (c) RG3 and (d) RG4 for w=25 RPM, f=0.3 mm/s.

For investigations on deformation distribution, only one roller geometry which is RG1, is employed so that the effect of process parameters could be examined clearly. The effect of roller geometry on the deformation will be studied in the future. Fig. 6 shows directional and the von Mises equivalent strain rate distributions. The radial strain rate ($\dot{\varepsilon}_r$) is equal to zero at the beginning of the radial axis for a pitch amount of length since that region is flat and induces no radial deformation. Then, the magnitude of the $\dot{\varepsilon}_r$ increases with r because the round profile of the nose region leads to higher cross-sectional area differences between different radial locations on the nose region. On the inclined region, the magnitude of $\dot{\varepsilon}_r$ linearly decreases with r due to the increasing thickness of the workpiece.

Circumferential strain rate ($\dot{\varepsilon}_b$) values are similar along the width axis. Magnitude of $\dot{\varepsilon}_b$ is much higher than strain rates in other directions which shows that material flows mainly in the width axis. Axial strain rate ($\dot{\varepsilon}_t$) is very small and almost constant along the contact zone. Along the radial axis on the b=0 plane, the equivalent von Mises strain rate is around 1.3 for the given process and roller parameters.

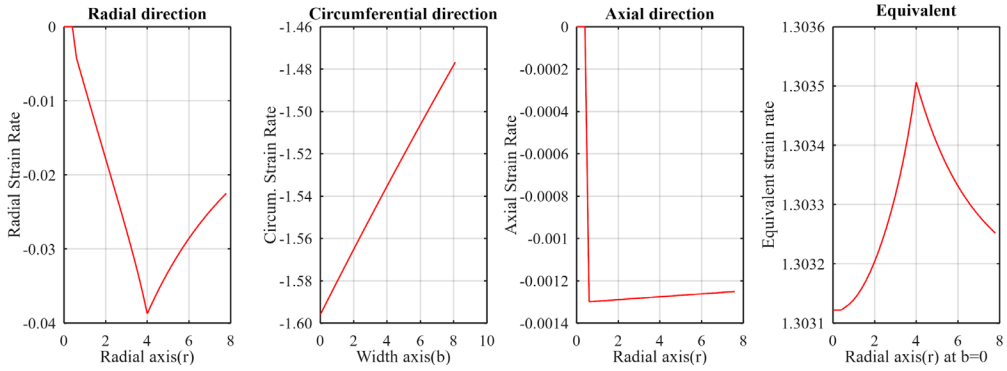

Fig. 6. Radial, circumferential, axial, and von Mises equivalent strain rate distributions for w=25 RPM, f=0.3 mm/s, $t_i = 15$ mm and roller geometry of RG1.

Materials Research Proceedings 28 (2023) 657-666 https://doi.org/10.21741/9781644902479-71

Variations of mean von Mises equivalent strain rate and strain with process parameters are shown in Fig. 7. In each plot, the effect of only one process parameter is tested and other parameters are kept constant. As shown previously, equivalent strain rate distribution is very uniform along the contact zone thus the mean value can represent the deformation behaviour accurately. For strain distribution, however, the mean value provides only a general perspective since strain value increases accumulatively as the circumferential passes form the material.

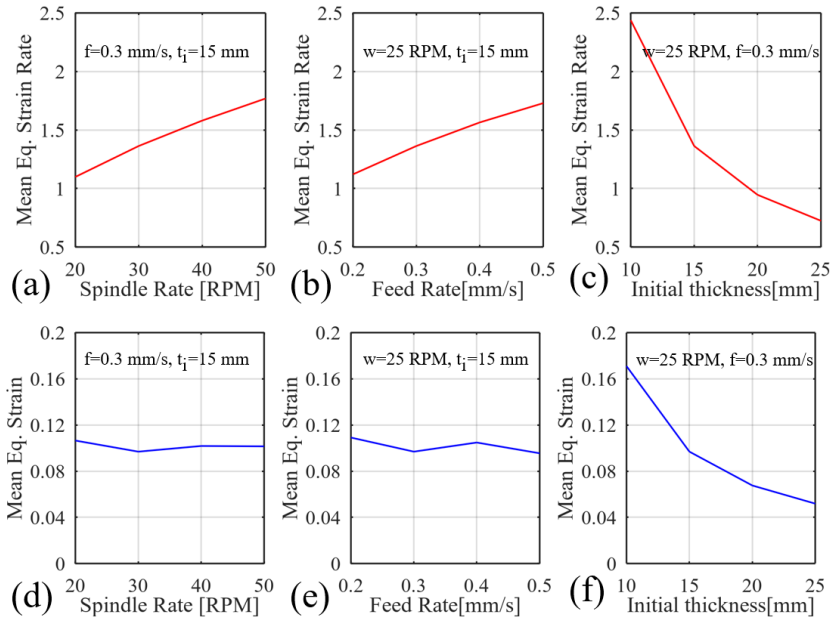

Fig. 7. Mean equivalent strain rate and strain for RG1 roller geometry and varying (a,d) spindle rates, (b,e) feed rates, (c,f) initial thicknesses.

Fig. 7(a) indicates an increase in spindle rate results in a higher mean equivalent strain rate while Fig. 7(d) clearly shows that obtained mean equivalent strains are similar. Positive proportionality between spindle rate and strain rate is due to the higher tangential velocity in the circumferential direction for increasing spindle rate. Even though an increased spindle rate leads to a smaller radial bite which is called pitch, the effect of tangential velocity appears to be higher and overcomes the negative effect of pitch decrease. As the tangential velocity increases, contact time per pass decreases. Consequently, similar mean equivalent strain values are obtained.

A very similar trend is observed for feed rate as shown in Fig. 7(b,e). The equivalent strain rate increases with increasing feed rate but the equivalent strain remains almost constant. As the feed rate is increased while the spindle rate is kept constant, the pitch increases and the tangential velocity does not change. Therefore, a higher equivalent strain rate is obtained for a higher feed rate. Thus the total number of circumferential passes is lower for higher pitch and cumulative strain is similar for different feed rate values. Having similar mean equivalent strain values for different sets of feed rate and spindle rate confirms that the calculated velocity fields are accurate.

Mean strain rate and strain are more sensitive to initial thickness than other parameters as shown in Fig. 7(c,f) For the constant thickness reduction, the proportional decrease in the cross-sectional area during forming is much higher for low initial thicknesses. For different initial thicknesses, the pitch is kept constant and the bite area is not modified. However, the ratio of the bite area to the rest of the circumferential cross-section decreases with increasing initial thickness, and consequently, the strain rate also decreases. For constant feed rate and spindle rate, the total number of passes and contact time per pass do not change. Thus, mean strain rate and strain follow the same trend.

Summary
An analytical method is developed to predict deformation fields for an incremental disk rolling process. Effects of process parameters and roller geometry on the contact zone and plastic deformation fields are examined.

Roller radius is proved to have a considerable effect on the circumferential width of the contact zone which is important for the circumferential plastic deformation. Radial deformation and radial length of the contact zone are mainly controlled by the roller height and the attack angle. Also, nose radius has an important effect on the radial plastic flow since the highest radial strain rate is calculated at the nose-inclined region interface.

The equivalent strain rate is proved to increase with increasing spindle rate due to the higher tangential velocity despite the shorter pitch. It shows that the tangential velocity is more influential on the deformation than the pitch. It can be said that the deformation can be controlled by adjusting the spindle rate without having to modify process time as the process time is controlled by only the feed rate. Increasing the feed rate also causes a higher strain rate but the underlying cause is the higher pitch which enables shorter process time. Therefore a compromise can be established between strain rate and process time by optimizing the process parameters provided that their effects are well understood as aimed by the current study. Strain rate affects recrystallization, failures, forces and related machine requirements as the process time affects grain growth, tool life and related machine requirements. This analytic method plays a key role in machine development as it provides insight into the connection between machine design, process parameters and induced deformation.

Acknowledgement
This work was supported by The Scientific and Technological Research Council of Türkiye, TÜBİTAK.

References
[1] L. Chevalier, Prediction of defects in metal forming: Application to wire drawing, J. Mater. Process. Technol. 32 (1992) 145-153. https://doi.org/10.1016/0924-0136(92)90171-n
[2] J.J. Lee, G.J. Park, Optimization of the structural and process parameters in the sheet metal forming process, J. Mech. Sci. Technol. 28 (2014) 605-619. https://doi.org/10.1007/s12206-013-1125-4
[3] Y.V.R.K. Prasad, T. Seshacharyulu, Modelling of hot deformation for microstructural control, Int. Mater. Rev. 43 (1998) 243-258. https://doi.org/10.1179/imr.1998.43.6.243
[4] X.-M. Chen, Y. C. Lin, M.-S Chen, H.-B. Li, D.-X. Wen, J.-L. Zhang, M. He, Microstructural evolution of a nickel-based superalloy during hot deformation, Mater. Des. 77 (2015) 41-49. https://doi.org/10.1016/j.matdes.2015.04.004
[5] Z. Wusatowski, Fundamentals of Rolling, Pergamon Press, Oxford, 1969
[6] S. Alexandrov, E. Lyamina, Y.R. Jeng, A general kinematically admissible velocity field for axisymmetric forging and its application to hollow disk forging, Int. J. Adv. Manuf. Technol. 88 (2017) 3113-3122. https://doi.org/10.1007/s00170-016-9018-1
[7] J. Zhang, Z. Cui, Prediction of velocity and deformation fields during multipass plate hot rolling by novel mixed analytical-numerical method, J. Iron Steel Res. Int. 18 (2011) 20-27.
[8] S. Serajzadeh, Y. Mahmoodkhani, A combined upper bound and finite element model for prediction of velocity and temperature fields during hot rolling process, Int. J. Mech. Sci. 50 (2008) 1423-1431. https://doi.org/10.1016/j.ijmecsci.2008.07.004
[9] S. Li, Z. Wang, Y. Guo, A novel analytical model for prediction of rolling force in hot strip rolling based on tangent velocity field and MY criterion, J. Manuf. Process. 47 (2019) 202-210. https://doi.org/10.1016/j.jmapro.2019.09.037.

[10] D.H. Zhang, Y.M. Liu, J. Sun, D.W. Zhao, A novel analytical approach to predict rolling force in hot strip finish rolling based on cosine velocity field and equal area criterion, Int. J. Adv. Manuf. Technol. 84 (2016) 843-850. https://doi.org/10.1007/s00170-015-7692-z
[11] S.P. Hamidpour, A. Parvizi, A.S. Nosrati, Upper bound analysis of wire flat rolling with experimental and FEM verifications, Meccanica 54 (2019) 2247-2261. https://doi.org/10.1007/s11012-019-01066-4
[12] H.L. Nascimento, Y. Shigak, S.C. Santos, A.Z. Hubinger, A study of the rolling load calculation models for flat cold rolling process, J. Comput. Meth. Eng. 2 (2016) 320-334.
[13] C.T. Chen, F.F. Ling, Upper-bound solutions to axisymmetric extrusion problems, Int. J. Mech. Sci. 10 (1968) 863-879. https://doi.org/10.1016/0020-7403(68)90090-8
[14] P. Agrawal, S. Aggarwal, N.Banthia, U.S. Singh, A. Kalia, A. Pesin, A comprehensive review on incremental deformation in rolling processes, J. Eng. Appl. Sci. 69 (2022). https://doi.org/10.1186/s44147-022-00072-w
[15] D. Marini, D. Cunningham, J. Corney, A Review of Flow Forming Processes and Mechanisms, Key Eng. Mater. 651-653 (2015) 750-758. https://doi.org/10.4028/www.scientific.net/kem.651-653.750
[16] A. Abedini, S. Rash-Ahmadi, A. Doniavi, Roughness optimization of flow-formed tubes using the Taguchi method, Int. J. Adv. Manuf. Technol. 72 (2014) 1009-1019. https://doi.org/10.1007/s00170-014-5732-8.
[17] S. Fortune, Voronoi Diagrams and Delaunay Triangulations, in: D.Z. Du, F. Hwang (Eds.), Computing in Euclidean Geometry, 1995, pp. 225-265.

Materials Research Proceedings 28 (2023) 667-674 https://doi.org/10.21741/9781644902479-72

Evolution of microstructure during hot incremental disk rolling of a nickel-based super-alloy

DINÇER Mehmet Şamil[1,2,a *], OZCATALBAS Mustafa[2,b], ACAR Sadik Sefa [1,2,c], MUSIC Omer[3,d] and ŞIMŞIR Caner[1,e]

[1]Middle East Technical University, Ankara 06800, Turkey

[2]Repkon Machine and Tool Industry and Trade Inc., Istanbul 34980, Turkey

[3]TED University, Ankara 06420, Turkey

[a]samil.dincer@metu.edu.tr, [b]mustafa.ozcatalbas@repkon.com.tr, [c]sadik.acar@metu.edu.tr, [d]omer.music@tedu.edu.tr, [e]csimsir@metu.edu.tr

Keywords: Hot Process, Recrystallization, FEM, JMAK

Abstract. In the aerospace industry, the turbine disk plays a crucial role. Controlling the average grain size during the hot forming of nickel-based superalloys such as Inconel 718 is critical for turbine disk production. Recrystallization is primarily responsible for evolution of microstructure during a hot forming process. In the current study, Finite Element Method (FEM) is employed to assess grain size evolution during an incremental disk rolling process. FEM simulations are used to obtain temperature, strain and strain rate distributions. Then, utilizing these deformation distributions, recrystallization and consequent average grain size distributions are calculated using Johnson-Mehl-Avrami-Kolmogorov (JMAK) equations. Simulations are conducted for different spindle rates of the workpiece. This process is sensitive to the temperature and meta-dynamic recrystallization. Results show that temperature increases with the spindle rate due to the inelastic heat generation. Also a higher grain size variation through thickness is obtained for the simulation with lower spindle rate since meta-dynamic recrystallization fraction is higher.

Introduction

A wide range of alloys have good mechanical properties at room temperature, however, only a few alloys can be used at elevated temperatures. The primary category of these alloys is Nickel-based superalloys. These properties are governed mostly by the microstructure [1]. The key to achieving good and uniform characteristics during the manufacturing process is being able to control the grain size. Most frequently used approach is to simulate the process using FEM. This provides an understanding of microstructure evolution of the material during the process and reduces the number of trials required for process development. The reason is that temperature, strain, and strain rate distributions are significant parameters affecting the grain size [2]. JMAK equations can calculate recrystallization fractions with these values [3].

At elevated temperatures, three different forms of recrystallization can occur. These are static, dynamic, and meta-dynamic [4]. Static recrystallization may occur if there is cold work in the material before heating. When the material is subjected to hot deformation, dynamic recrystallization takes place. A more accurate description of the occurrence of dynamic recrystallization is strain rate being greater than zero. Meta-Dynamic recrystallization is similar to static recrystallization, but it only occurs if the dynamic recrystallization fraction(X_{DRX}) is lower than 1 during the hot deformation process. Fig. 1 depicts the summary of the recrystallization phenomenon.

Content from this work may be used under the terms of the Creative Commons Attribution 3.0 license. Any further distribution of this work must maintain attribution to the author(s) and the title of the work, journal citation and DOI. Published under license by Materials Research Forum LLC.

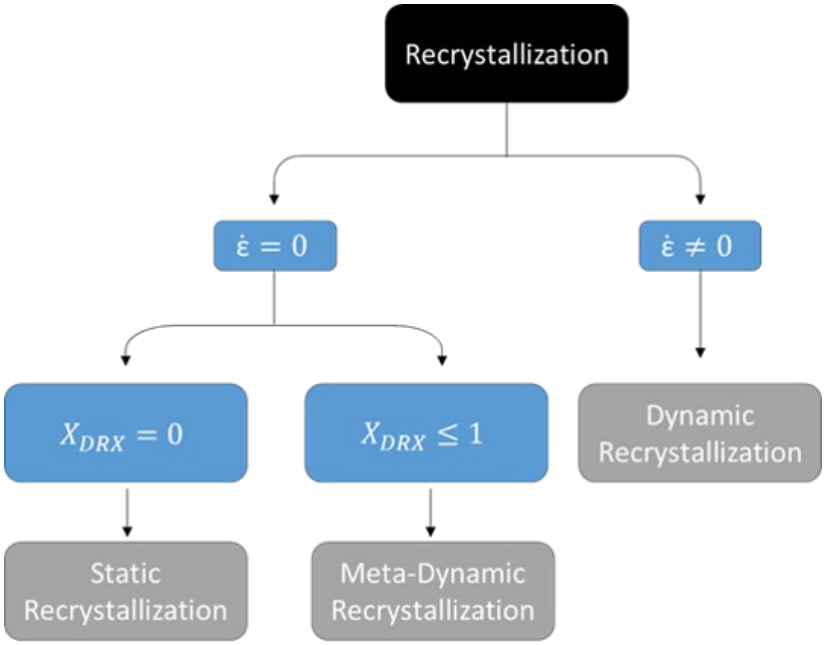

Fig. 1. Summary of Recrystallization.

All these calculations are covered by JMAK equations [3]. However, the majority of equations are empirical. Experiments have to be conducted to determine the material coefficients. To predict material parameters for recrystallization and grain growth, single and double compression tests have to be applied. Provided that the initial grain diameter is known, the single compression test is applied with different sets of constant strain rate and constant temperature. With these experimental results, dynamic recrystallization parameters can be obtained with the curve fitting method. To predict meta-dynamic recrystallization and grain growth parameters, a double compression test has to be applied with different combinations of strain rate, temperature, and waiting time between loadings [2]. These equations can be employed once the relationship between properties has been determined.

Dynamic recrystallization equations:

$$X_{DRX} = 1 - exp\left(A_1 \times \frac{\varepsilon(t) - A_3 \times {\varepsilon_c}^{A_2}}{\varepsilon_{0.5} - A_4 \times \varepsilon_c}\right) \quad (1)$$

$$\varepsilon_c = A_{crit} \times B_1 \times {d_0}^{B_2} \times \dot{\varepsilon}^{B_3} \times Z^{B_4} \times exp\left(\frac{Q_{B_5}}{R \times T}\right) \quad (2)$$

$$\varepsilon_{0.5} = C_1 \times {d_0}^{C_2} \times \dot{\varepsilon}^{C_3} \times Z^{C_4} \times exp\left(\frac{Q_{C_5}}{R \times T}\right) \quad (3)$$

$$D_{DRX\ Nuclei} = D_1 \times {d_0}^{D_2} \times \dot{\varepsilon}^{D_3} \times Z^{D_4} \times exp\left(\frac{Q_{D_5}}{R \times T}\right) \quad (4)$$

Meta-Dynamic recrystallization equation:

$$X_{MDRX} = 1 - exp\left(E_1 \times \left(\frac{t}{t_{0.5}}\right)^{E_2}\right) \quad (5)$$

$$t_{0.5} = F_1 \times \varepsilon^{F_2} \times {d_0}^{F_3} \times \dot{\varepsilon}^{F_4} \times Z^{F_5} \times exp\left(\frac{Q_{F_6}}{R \times T}\right) \quad (6)$$

$$D_{MDRX\ Nuclei} = G_1 \times {d_0}^{G_2} \times \dot{\varepsilon}^{G_3} \times Z^{G_4} \times exp\left(\frac{Q_{G_5}}{R \times T}\right) \quad (7)$$

Grain growth:

$${d_{grain\ growth}}^{H_1} = {d_0}^{H_2} + H_3 \times exp\ exp\left(\frac{Q}{R \times T}\right) \times t \quad (8)$$

Table 1. Parameters list.

Material coefficients	A_1-A_4	Dynamic recrystallization fraction
	B_1-B_5	Critical strain
	C_1-C_5	Half recrystallized volume fraction strain
	D_1-D_5	The average grain diameter of dynamically recrystallized fraction
	E_1-E_2	Meta-dynamic recrystallization fraction
	F_1-F_6	Half recrystallized volume fraction time
	G_1-G_5	The average grain diameter of meta-dynamic recrystallized fraction
	H_1-H_3	Grain growth
d_0		The initial average grain diameter
$\dot{\varepsilon}$		Strain rate
ε		Strain
Q		Activation Energy
R		Gas constant
T		Temperature
Z		Zener-Hollomon parameter
X_{DRX}		The fraction of dynamic recrystallization
$D_{DRX\ Nuclei}$		The average diameter of dynamic recrystallization
X_{MDRX}		The fraction of meta-dynamic recrystallization
$D_{MDRX\ Nuclei}$		The average diameter of meta-dynamic recrystallization
$d_{grain\ growth}$		The average grain diameter of grain growth

Recrystallization is governed by strain, strain rate, and temperature, as demonstrated by the preceding equations and Fig. 1. These equations are only applicable to isothermal conditions with a constant strain rate. However, the deformation in the hot incremental disk rolling process is not completely isothermal and the strain rate is not constant or uniform. Both strain rate and temperature are a function of time. To include that effect, these equations need to be updated with their differential form with respect to time [5]. However, assuming isothermal and constant strain rate condition is not a completely wrong assumption when the spindle rate is optimized accordingly as demonstrated in this study.

Modelling Approach

As the workpiece spins, four rollers deform the workpiece radially outward. As the thickness of the workpiece decreases, the outer diameter of the workpiece increases. Forge NxT commercial finite element software using implicit time integration scheme is used for the process simulations. These simulations consist of thermo-mechanical calculations. The Johnson-Cook plasticity material model is used to simulate the flow of bulk material in order to examine the history of temperature, strain, and strain rates. Ideally, process would be simulated as it is; however, this is not feasible due to large computational time. Instead, an angular segment of the disk is modelled

with boundary conditions applied at each side of the disk. These boundary conditions could be applied as cyclic symmetry boundary condition. However, this option is not available in the software at the moment. Instead, boundary conditions are applied as two planes which are adiabatic and allow for sliding of the nodes along the plane, but do not allow for node separation. Due to the numerical integration of the variables, the time step of the simulation has to be small for microstructure evaluation. To overcome this problem and reduce computational time, a comparison between angular segments of varying size and a full disk model was performed. This study showed that 1/8 angular segment of the disk produces similar results with full model. Results of the convergence study are not included here for brevity. As demonstrated in Fig. 2, the horizontal plane of the disk exhibits mirror symmetry. Thus, only top half of the disk can be used with symmetry boundary condition at the horizontal plane. The two boundary conditions applied through the planes do not fully reflect the nature of the process. Therefore, to minimize their effect on the results, only results for the middle of the angular segment are taken into consideration, as shown in Fig. 3 [6]. Rollers are assumed to be frictionless and do not rotate around their axes, the assumption being that the effect of friction can be neglected. Effect of friction and roller rotation will be examined separately in future studies. The temperature of the process atmosphere is controlled by a furnace. Heat transfer due to conduction between the rolles and the workpiece, radiation and convection with the environment are all included together. Value taken is: 50W/m^{2}K which is the average of the value widely available in the literature. The metallurgical part of the calculations is uncoupled with a thermo-mechanic solver. Outputs of the thermo-mechanical model are used to calculate the recrystallization and growth mechanism. Mechanical and thermal parameters of Inconel 718 are taken from JMatPro material property simulation software and the JMAK equations parameters are taken from Forge NxT Software.

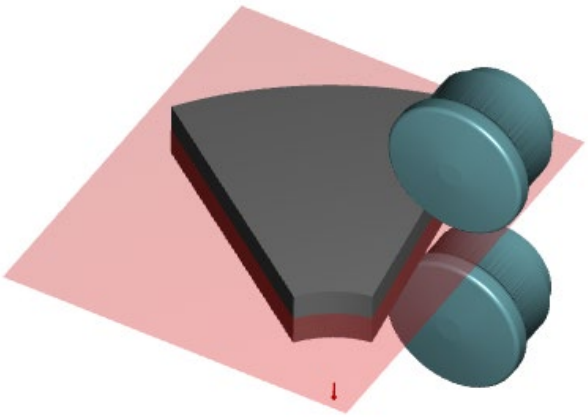

Fig. 2. The simulation model of an incremental disk rolling.

Results and Discussion

This section simulates and compares the effect of three distinct spindle rates (RPM of the workpiece). Fig. 3 illustrates the portion of the simulated part that is shown in the subsequent figures.

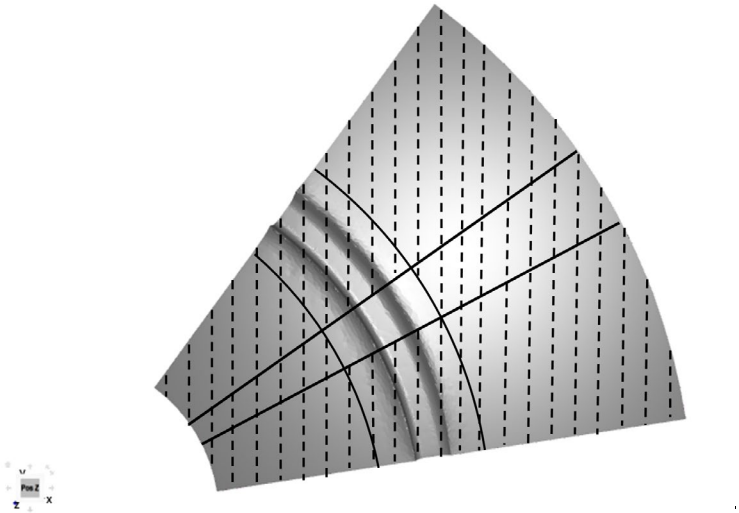

Fig. 3. Comparable area of the simulation model.

The results of simulations with three different spindle rates are evaluated. Temperature, equivalent strain, dynamic recrystallization, meta-dynamic crystallization, and average ASTM grain diameter are compared. The spindle rate has a significant effect on the temperature. The inelastic heat generation increases as the deformation rate increases. Temperature change is not found to be important unless it exceeds the range of the JMAK equation parameter. Despite grain growth being unaffected at the time scale of the first pass, it will be modified during the rest of the process. The other issue is that the temperature exceeds 1030°C for the fastest spindle rate case, as seen in Fig. 4(c). This temperature level is close to the upper limit of the JMAK equation parameter range for Inconel 718. These limits come from the processing map of Inconel 718. 1030°C is the most efficient temperature for the dynamic recrystallization range for forged Inconel 718 [7]. It was shown that the material starts to behave differently above this temperature [3]. The equivalent strain is also strongly affected by the spindle rate as it is an expected result due to the nature of the rolling process as shown the Fig. 5. Results show that equivalent strain values are very high even after the first pass for the high spindle rate case. The reason for having different equivalent strain values for the same thickness reduction is that the plastic flow in the circumferential direction increases when the spindle rate is increased. For high spindle rates, elements become elongated not only in the radial direction but also in the circumferential direction.

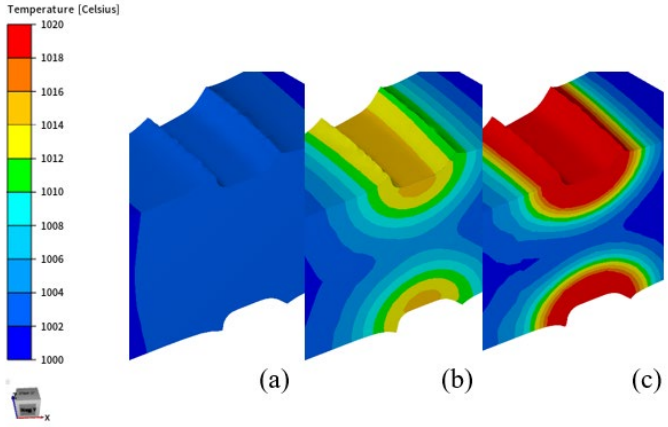

Fig. 4. (a) The lowest spindle rate, (b) medium spindle rate, (c) fastest spindle rate result of temperature distribution during the process.

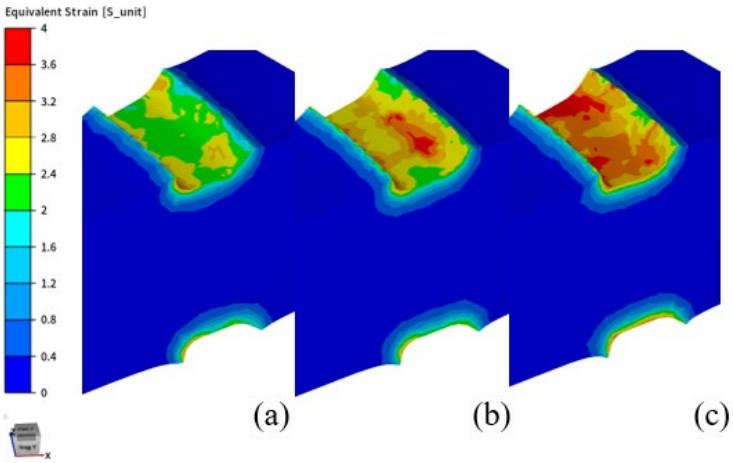

Fig. 5. (a) The lowest spindle rate, (b) medium spindle rate, (c) fastest spindle rate result of Equivalent strain distribution during the process.

Dynamic recrystallization occurs due to the deformation. Temperature, strain, and strain rate change over time. Therefore every parameter in Eq. 1 is affected even though the dynamic recrystallization equation contains no time parameter. The area of dynamic recrystallization fraction is almost constant throughout the first pass for different temperature and equivalent strain values, as shown in Fig. 6. When the deformation rate increase with the spindle rate, the critical strain (ε_c) value and half recrystallization fraction strain ($\varepsilon_{0.5}$) value increase. So the affected dynamic recrystallization zone stays the same.

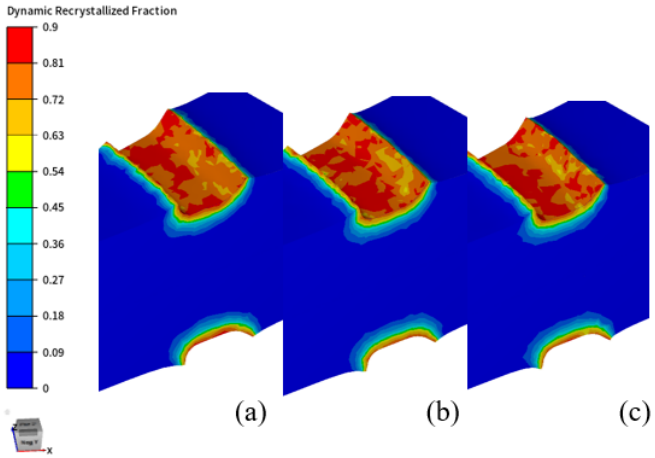

Fig. 6. (a) The lowest spindle rate, (b) medium spindle rate, (c) fastest spindle rate result of dynamic recrystallization distribution during the process.

The area of meta-dynamic recrystallization is affected by the spindle rate since changing the spindle rate modifies the time interval between two subsequent passes. The primary variable in meta-dynamic recrystallization is the time. When the spindle rate is low, meta-dynamic recrystallization can take place over a longer period of time, as shown in Fig. 7.

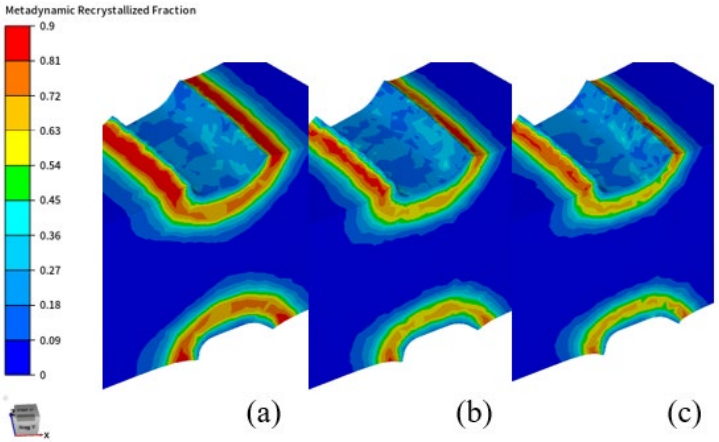

Fig. 7. (a) The lowest spindle rate, (b) medium spindle rate, (c) fastest spindle rate result of meta-dynamic recrystallization distribution during the process.

Fig. 8 illustrates the variation of the average grain diameter with the spindle rate. Recrystallization plays a substantial role in grain size reduction. Although the overall recrystallization zone is similar in all three simulations, the time between subsequent passes is high for low spindle rate. Therefore lower spindle rate leads to a higher variation of ASTM grain size through the thickness due to the meta-dynamic recrystallization.

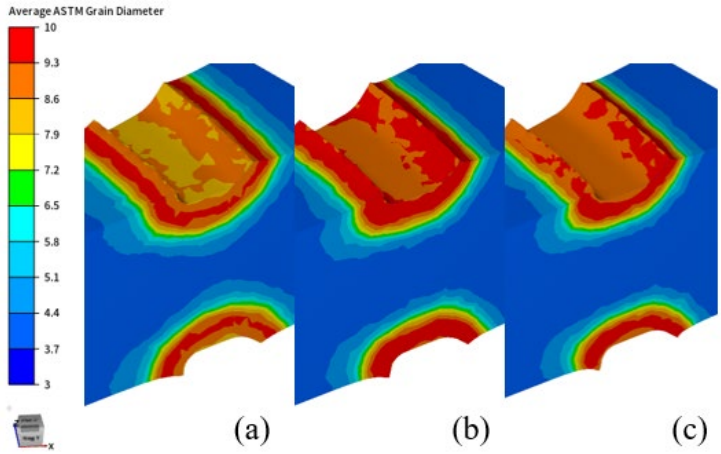

Fig. 8. (a) The lowest spindle rate, (b) medium spindle rate, (c) fastest spindle rate result of average ASTM grain diameter distribution during the process.

Summary

These results demonstrate the significance of the spindle rate as a process parameter in hot incremental disk rolling. The temperature increases dramatically at high spindle rates due to inelastic heat generation. The stability of the JMAK equations depends on the temperature. At the slowest spindle rate, temperature change is negligible. When the spindle rate increases, elongation in the circumferential direction becomes considerable. Effects of equivalent strain and temperature cannot be observed in the first circumferential pass for dynamic recrystallization. On the other hand, the area of meta-dynamic recrystallization is influenced by the spindle rate. The time between subsequent passes decreases when the spindle rate is increased. Therefore, the meta-dynamic recrystallization fraction decreases as the spindle rate increases. Forming with a lower spindle rate leads to a higher variation of ASTM grain size through the thickness. There was no linear dependence found between average ASTM grain size and spindle rate. The optimum spindle

rate is between the lowest and the medium spindle rate. The limiting factors of spindle rate range are temperature change which is important for JMAK equation stability and meta-dynamic recrystallization fraction which changes the variation ASTM grain size through the thickness.

Acknowledgment
This work was supported by The Scientific and Technological Research Council of Türkiye, TÜBİTAK.

References
[1] C.T. Sims, A history of superalloy metallurgy for Superalloy Metallurgists, Superalloys 1984 (Fifth International Symposium), 1984, 399-419. https://doi.org/10.7449/1984/Superalloys_1984
[2] G. Shen, S.L. Semiatin, R. Shivpuri, Modeling microstructural development during the forging of waspaloy, Metall. Mater. Trans. A 26 (1995) 1795–1803. https://doi.org/10.1007/bf02670767
[3] S.H. Mousavi Anijdan, M. Aghaie-Khafri, V. Joshaghani, Forging optimization and microstructural simulation of an Inconel 718 alloy used in turbine discs, J. Appl. Math. Phys. 05 (2017) 1658-1667. https://doi.org/10.4236/jamp.2017.59138
[4] C.M. Sellars, J.A. Whiteman, Recrystallization and grain growth in hot rolling, Metal Sci. 13 (1979) 187-194. https://doi.org/10.1179/msc.1979.13.3-4.187
[5] T. Matsui, H. Takizawa, H. Kikuchi, Numerical simulation of ring rolling process for ni-base articles, Superalloys 2004 (Tenth International Symposium), 2004. https://doi.org/10.7449/2004/Superalloys_2004_907_915
[6] O. Music, E.C. Sariyarlioglu, Mechanics of Tube Spinning: A Review, Int. J. Adv. Manuf. Technol. 123 (2022) 709-735. https://doi.org/10.1007/s00170-022-10175-6
[7] Y.V.R.K. Prasad, S. Sasidhara, K.P. Rao, Hot working guide: A compendium of processing maps. Materials Park, OH: ASM International, 1997.

Materials Research Proceedings 28 (2023) 675-682 https://doi.org/10.21741/9781644902479-73

Effect of near beta-transus forging parameters on the mechanical and microstructural properties of Ti-6Al-4V – Application to hammer forging

AGIRRE Julen[1,a *], ERICE Borja[1,2,b], ARRESE Peio[1,c], OTEGI Nagore[1,d] and GALDOS Lander[1,e]

[1]Mechanics and Industrial Production Department, Mondragon Unibertsitatea, Loramendi 4, 20500 Mondragon, Spain

[2]IKERBASQUE, Basque Foundation for Science, 48009 Bilbao, Spain

[a]jagirreb@mondragon.edu, [b]berice@mondragon.edu, [c]peio.arrese@alumni.mondragon.edu, [d]notegi@mondragon.edu, [e]lgaldos@mondragon.edu

Keywords: Hammer Forging, Hot Forging, Ti-6Al-4V, Thermomechanical Testing, Intermediate Rate Testing, Adiabatic Heating, Microstructure, Mechanical Properties

Abstract. Ti-6Al-4V is a widely employed material in the aerospace, power generation and bioengineering industries due to its low density, excellent corrosion resistance and outstanding mechanical properties. Hammer forging is one of the most utilized manufacturing processes to produce high-performance titanium components and it is known that the process parameters highly affect the microstructure, and thus, the mechanical properties of the manufactured parts. Ti-6Al-4V alloy has a temperature dependent dual structure and forging below or above the β-transus transition temperature (≈980ºC) highly influences the resultant microstructure. Due to the significant adiabatic heating in high-speed hammer forging processes the β-transus temperature can be exceeded during the process. Therefore, it is of vital importance to study the phase transformation limits and the resultant effects on the mechanical properties to establish the optimum processing window for the hammer forging of Ti-6Al-4V. In this work, the Direct-Impact Drop Hammer (DIDH), a purpose-built laboratory hammer with a maximum blow speed of 5 m/s is employed to perform intermediate strain rate (≈200 s^{-1}) uniaxial compression tests of Ti-6Al-4V at 900ºC, 940ºC, 980ºC, 1000ºC and 1020ºC. The flow behaviour of this titanium alloy is experimentally characterized under a wide range of hammer forging conditions, and the microstructure of the tested samples is analysed to study the influence of the adiabatic heating on the phase transformation of Ti-6Al-4V.

Introduction

Ti-6Al-4V has become one of the most employed titanium alloys in the aerospace and the biomedical sectors due to its outstanding mechanical properties and relatively low density. The high cost of this alloy is justified in demanding applications as it offers superior performance and good corrosion resistance even under extreme environments [1]. Ti-6Al-4V is a dual α-β structure titanium alloy, and a variety of resulting microstructures can be obtained depending on the processing route and posterior heat treatment employed to obtain the components [2,3]. The final microstructure highly influences the mechanical properties of the manufactured part; therefore, it is of vital importance to analyse the influence of temperature on the phase transformation of this titanium alloy to correctly define the process parameters

Hammer forging is one of the most employed manufacturing processes for Ti-6Al-4V components, as it is versatile and very cost-effective for large series production [4]. The forging temperature range for this titanium allow is however, narrow, and in general two forging strategies are differentiated in function of the processing temperature [1]. On the one hand,

Content from this work may be used under the terms of the Creative Commons Attribution 3.0 license. Any further distribution of this work must maintain attribution to the author(s) and the title of the work, journal citation and DOI. Published under license by Materials Research Forum LLC.

α-β forging, when forging is carried out below the β-transus temperature (≈980ºC); and on the other hand, β forging, if the forging temperature is above β-transus [5]. Due to the high adiabatic heating found in hammer forging attributed to the high strain rates reached in the process (≈200 s^{-1}), the temperature in some zones of the forged component can exceed the β-transus critical temperature [6]. This can result in undesired resulting microstructures, and hence, poor mechanical properties in the manufactured part.

Therefore, the narrow processing temperature range of Ti-6Al-4V and the complexity of hammer forging itself, makes essential the use of finite element (FE) numerical simulations to explore diverse forging strategies and determine optimised process parameters [4]. It is well-known however that the correctness of the simulation results is directly linked to the accuracy of input parameters and boundary conditions. The correct definition of the material behaviour under the process conditions is one of the most important input parameters, and experimental testing is generally needed for that purpose. Experimental data is employed to calibrate the material models that numerically represent critical aspects, such as the flow behaviour and the microstructural evolution of the material in function of the processing strategy.

Experimental material characterization at the intermediate strain rate range found typically in hammer forging processes (10^2-10^3 s^{-1}) is however challenging, and consequently, the flow behavior and phase transformation of Ti-6Al-4V under these conditions is rarely reported in the literature. The use of universal testing machines equipped with conventional load cells becomes extremely challenging for testing at this strain rate range since they often have a limited stroke velocity. If such velocity is not an issue, then inertia effects and wave propagation become more relevant making the load measurements more troublesome [7]. The most used equipment for dynamic testing is the well-known Split Hopkinson Pressure Bar (SHPB) system, but it also has certain limitations when it comes to testing at these strain rates [7]. As an alternative to the SHPB systems for intermediate strain rate testing, we developed an in-house designed and constructed laboratory facility: the Direct-Impact Drop Hammer (DIDH). In this work, this purpose built machine was employed for the experimental characterisation of Ti-6Al-4V under hammer forging conditions.

The Direct-Impact Drop Hammer (DIDH)

Considering the difficulties to perform intermediate strain rate tests employing universal hydraulic commercial testing devices and SHPB systems, an automatized in-house Automatic ThermoMechanical Tester (ATMT) was designed and constructed. This testing machine is capable of reproducing a wide range of hot and cold industrial metal forming conditions, from low strain rates (<1 s^{-1}) up to intermediate strain rates (>100 s^{-1}). This novel apparatus (Fig. 1a) was designed to be able to test diverse forming strategies, including intermediate heating cycles combined with different loading rate scenarios. The ATMT is composed of four main sections: a heating furnace (max. 1350ºC), an isothermal hydraulic press for low strain rate tests (<1 s^{-1} and max. 1350ºC), a cooling system, and the main novelty, the Direct-Impact Drop Hammer for intermediate strain rate testing. To reduce human errors as much as possible and increase the repeatability of the tests, the apparatus is fully automatized and the sample manipulation is carried out by an electro-pneumatic arm that is integrated in the machine.

Focusing on the DIDH, its mechanical module is comprised of a 92 kg hammer that is pushed by a high-pressure pneumatic cylinder propelling it towards the anvil, the fixed part of the system. The hammer can be set-up at different heights, which allows for impact velocities to range from 2.5 to 5 m/s and a maximum applicable deformation energy of 1.15 kJ. Regarding data acquisition, the anvil is instrumented with a piezoelectric force sensor allowing for direct force measurements. The kinematics of the tests are recorded with a high-speed camera (Fig. 1b) and post-processed by Digital Image Correlation (DIC). The suitability of the DIDH for the mechanical characterisation within this strain rate regime was successfully demonstrated [8]. Interestingly, this device

incorporates an optimized cooling system which is capable of quenching the tested sample in less than 1 s after the high-speed test takes place. This is of particular interest for the microstructural evolution characterisation of materials combining both high temperatures and intermediate strain rate tests.

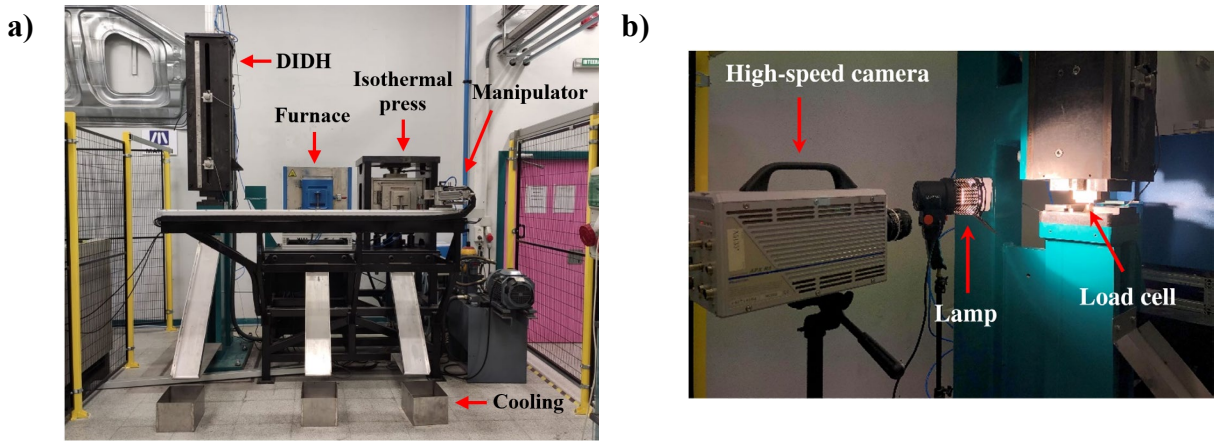

Fig. 1. a) The Automatic ThermoMechanical Tester (ATMT) and b) the data acquisition setup in the DIDH.

Experimental Procedure

In this work, the new DIDH was employed to characterise the flow behaviour of Ti-6Al-4V alloy under hammer forging conditions. Uniaxial compression tests were performed at 900 ºC, 940ºC, 980ºC, 1000ºC and 1020ºC using Ø16x24 mm cylindrical samples and they were air cooled after the compression. A deformation speed of 5 m/s was employed in all the cases, which means that a deformation energy of 1.15 kJ was applied to the samples. These were painted with the CONDAERO 313 glass coating to protect the surface from oxidation and reduce the friction between the sample and the tools.

To monitor the hammer kinematics, a Photron Fastcam-APX RS250K high-speed camera with appropriate illumination lamps was utilised. It was set up to record at 15,000 fps with a resolution of 256 x 512 px^2. The specimen length history $l[t]$ was obtained by DIC analysis from the displacement history of the hammer, which was calculated by post-processing the high speed camera images with the GOM Correlate software [9]. To obtain the force histories $F[t]$, a Kistler 9106A piezoelectric force sensor mounted directly on the anvil was employed in combination with a Tektronix TSD 2004B oscilloscope with an acquisition frequency of 300 kHz. As the displacement of the DIDH tests was recorded with a lower acquisition frequency, the displacement histories were linearly interpolated for the load cell time base.

The axial true stress (σ), true strain (ε) and true strain rate ($\dot{\varepsilon}$) were calculated by $\sigma = F[t]/A[t]$, $\varepsilon = \ln(h[t]/h_0)$, and $\dot{\varepsilon} = v[t]/h[t]$, respectively, where $F[t]$ is the force measured by the piezoelectric $\dot{\varepsilon}$rce sensor, h_0 is the initial sample height, $h[t]$ and $A[t]$ are the instantaneous height and cross-section area of the sample, respectively, and $v[t]$ is the instantaneous tool velocity, assuming [0] = 0 s^{-1}.

Results and Discussion

The same blow speed (5 m/s), and hence, the same deformation energy (1.15 kJ) was employed in all the tests, therefore, as the strength of the Ti-6Al-4V decreases with increasing the forming temperature, higher deformations were obtained at higher temperatures (
Fig. **2**). Final true strains of 0.63, 0.77, 1.01, 1.12 and 1.15 were reached in the tests performed at 900ºC, 940ºC 980ºC, 1000ºC and 1020ºC, respectively. Three repetitions were performed per condition showing very little deviation between them, with a mean stress deviation of 1.29 % in the worst case. This is mainly because the tests are performed automatically in the DIDH.

Fig. 2. Initial sample and samples tested in the DIDH at 900ºC, 940ºC, 980ºC, 1000ºC and 1020ºC (from left to right).

A friction factor (*m*) of 0.3 was estimated by inverse simulation taking into account the barrelling of the tested samples (Fig. 2). FORGE® simulation software was employed for that purpose. The estimated friction factor is in accordance with the friction reported by Zhu et al. [10] for Ti-6Al-4V alloy forgings using glass lubricant.

Force-displacement curves of the intermediate strain rate tests performed in the DIDH at 900ºC, 940 ºC, 980ºC, 1000ºC and 1020ºC are presented in Fig. 3. The high-speed blow of the DIDH lead to some oscillations in the force readings particularly at the beginning of the curves. However, these fade out to certain extent as tests progress leaving the piezoelectric load cell noise as the only source of the oscillations, and the material behavior is clearly identified.

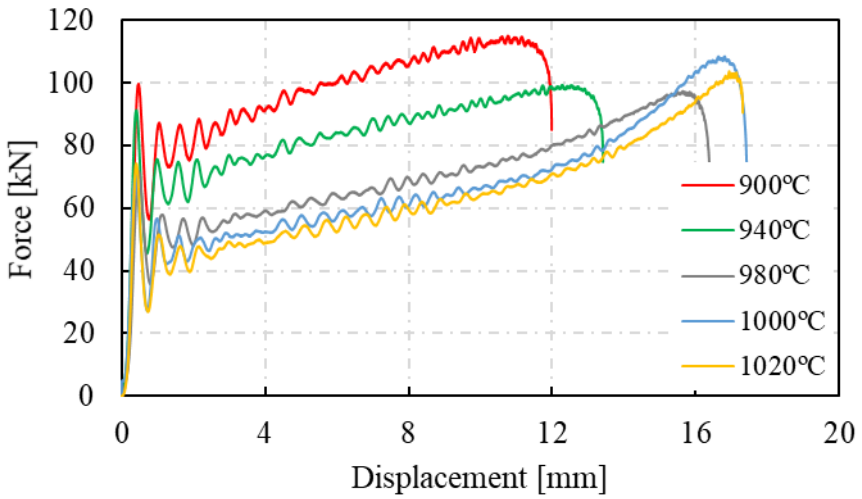

Fig. 3. Force-displacement curves of tests performed in the DIDH with a blow speed of 5 m/s at 900ºC, 940ºC, 980ºC, 1000ºC and 1020ºC.

The true stress-strain curves are shown in Fig. 4. A clear and coherent temperature dependency is observed in the results, with lower forces at higher temperatures. The softening observed in the curves can be attributed to the considerable adiabatic heating and low heat dissipation times found at these strain rates. No analytical adiabatic heating correction was applied to the flow curves

presented in Fig. 4. The true strain rate evolution is also presented in Fig. 5, in which the intermediate strain rates reached in the tests demonstrate that the DIDH is capable of testing at strain rates comparable to those found in industrial hammer forging operations. This results are of significant industrial and scientific relevance as few laboratory thermomechanical testers allow testing at both intermediate strain rates and high temperatures. Therefore, the study of the flow behavior of Ti-6Al-4V under hammer forging conditions is hardly reported in the literature.

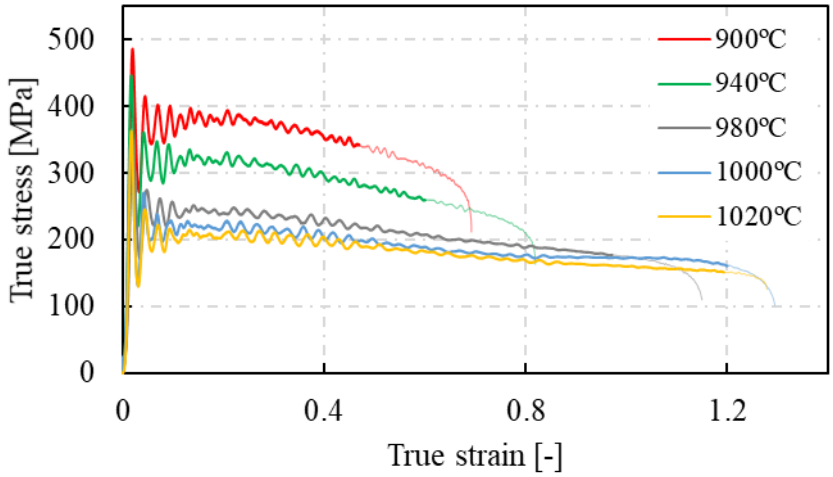

Fig. 4. True stress-true strain curves of Ti-6Al-4V tested in the DIDH at intermediate strain rates (≈200 s^{-1}).

A non-constant strain rate evolution is observed in Fig. 5, which occurs due to the nature of the DIDH tests. The hammer velocity starts decreasing once it gets into contact with the sample until it completely stops. Anyhow, due to the optimised sample dimension a relatively constant strain rate evolution is attained up to high strain levels, especially at higher temperatures. As a reference, thicker solid line are depicted in Fig. 4 and Fig. 5 until the strain rate dropped below 80 % of the initial strain rate value.

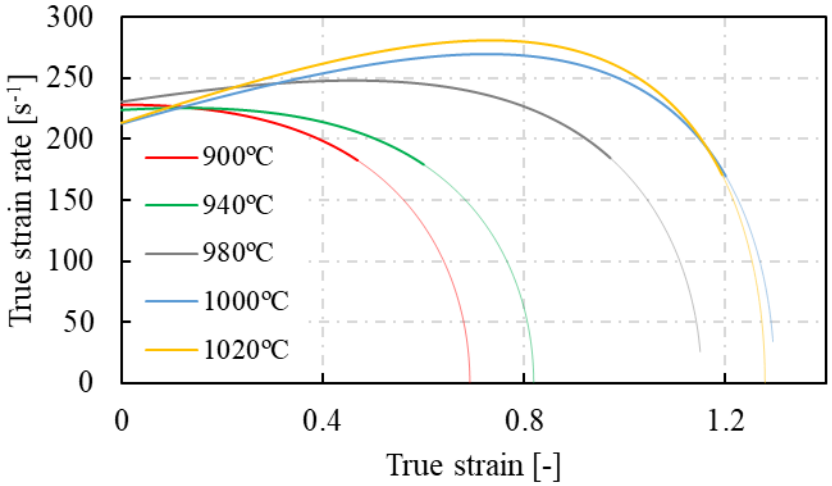

Fig. 5. True strain rate evolution of the DIDH tests at intermediate strain rates.

The effect of this strain rate drop in the flow curves is irrelevant, as the initial and the final strain rates are in the same order of magnitude. Mean strain rates attained up to this point for the

tests at 900ºC, 940ºC, 980ºC, 1000ºC and 1020ºC are 215 s^{-1}, 215 s^{-1}, 235 s^{-1}, 245 s^{-1} and 250 s^{-1}, respectively. At higher strain levels beyond the 80 % strain rate drop, the strain rate decreases considerably and the rate effect becomes more significant in the flow curves, with a sharp drop at the end of the curves (Fig. 5).

The strain rate dependency of Ti-6Al-4V is clearly observed in the comparison between the low strain rate (<10 s^{-1}) flow curves at 900ºC presented by Porntadawit et al. [11] and the intermediate strain rate (215 s^{-1}) flow curve obtained from the test in the DIDH at the same temperature (Fig. 6). A classical strain rate dependency is shown, with higher flow stresses at higher strain rates.

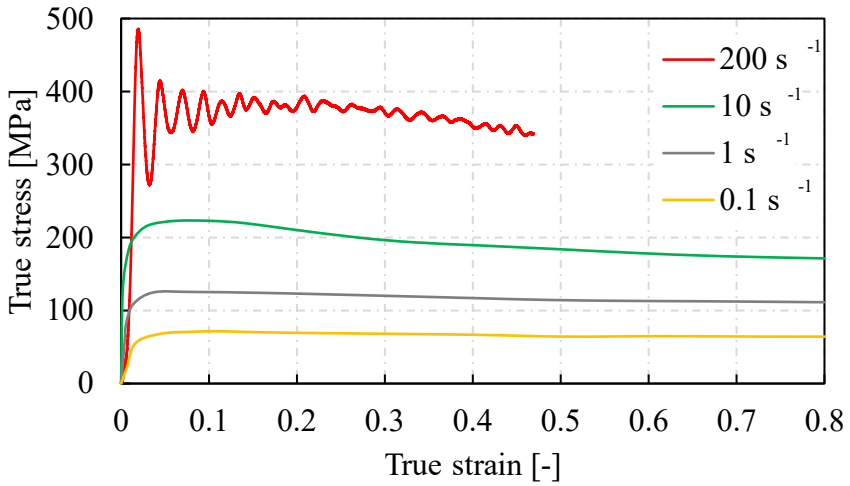

Fig. 6. Comparison between low strain rate (0.1 s^{-1}, 1 s^{-1} and 10 s^{-1}) flow curves of Ti-6Al-4V at 900 ºC extracted from [11] and the intermediate strain rate flow curve obtained from the DIDH test at the same temperature.

Once the tests were performed, the tested samples were cut from the cross-section to analyse the resulting microstructure (Fig. 7). Samples were prepared for microstructural analysis by conventional sanding and polishing procedures and they were etched with Kroll's reagent.

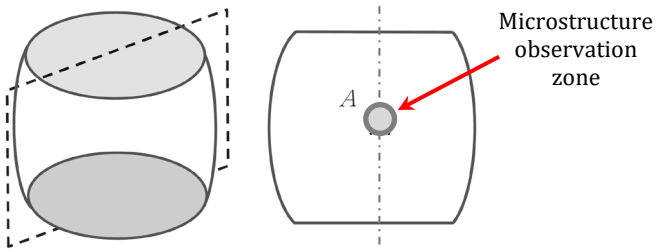

Fig. 7. Cutting plane of the tested samples to analyse the resulting microstructure.

Fig. 8 shows the micrographs of the samples tested in the DIDH at intermediate strain rates (≈200 s^{-1}) at temperatures of 900ºC, 940ºC, 980ºC, 1000ºC and 1020ºC. A clear bimodal microstructure composed of equiaxed α phase and lamellar α-β is found at the tests performed at 900ºC and 940ºC, with lower equiaxed α fractions with higher temperatures. Samples tested at 980ºC and 1000ºC, close to the β-transus transition temperature, show even lower equiaxed α fractions, and the sample tested at 1020ºC show a clear β microstructure.

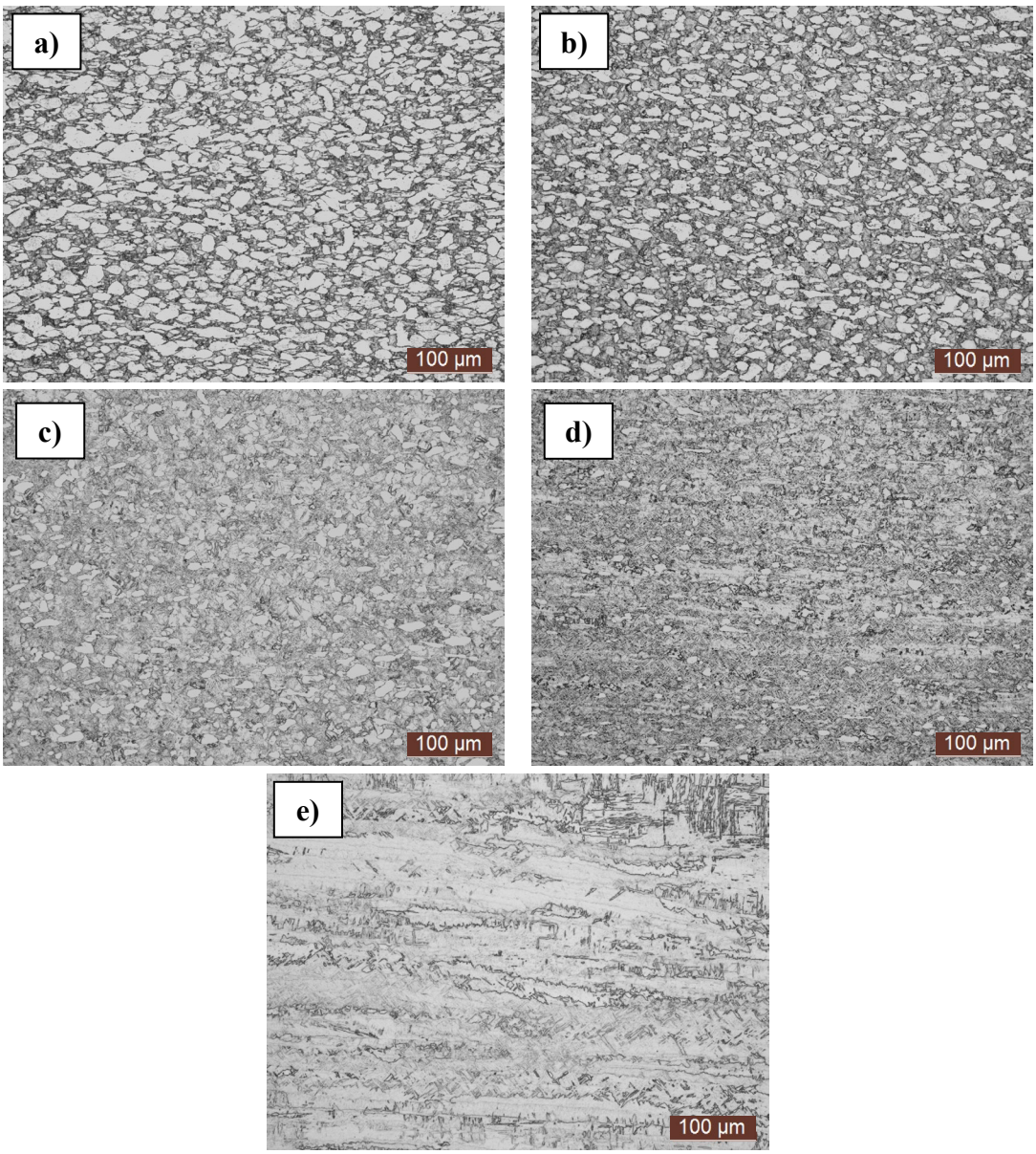

Fig. 8. Micrographs of the samples tested in the DIDH at intermediate strain rates at a) 900ºC, b) 940ºC, c) 980ºC, d) 1000ºC and e) 1020ºC.

Summary

The following conclusions were extracted from the present work:

- The purpose-built laboratory hammer, the Direct-Impact Drop Hammer (DIDH), is a suitable thermomechanical tester for testing under both intermediate strain rates and high temperatures. As the tests are performed automatically, the results show a great repeatability.
- The flow behaviour of Ti-6Al-4V was successfully characterised under a wide variety of hammer forging conditions. A clear temperature dependency was observed in the tests perform from 900ºC to 980ºC. This dependency decreased significantly in the tests performed from 980ºC to 1020ºC, close and beyond the β-transus transition temperature.
- A clear bimodal microstructure was found in the tests performed below the β-transus temperature, at 900ºC and 940ºC, with a lower equiaxed α phase fraction at higher temperatures. Even lower α fractions were observed at the tests performed at 980ºC and

1000ºC, close to the β-transus temperature, and only β-phase microstructure was observed in the tests performed at 1020ºC.

Acknowledgments
The authors would like to acknowledge the financial support of the Basque Government through the Hazitek projects OGFORGE, TIFORGE and DIGICUT. Special thanks to ULMA Forja S. Coop. and Fagor Arrasate S. Coop. for the financial and technical support. The authors would also like to thank the support of Transvalor, CEMEF MINES ParisTech and the Centre of Advanced Structural Analysis (CASA) at the Norwegian University of Science and Technology (NTNU).

References
[1] A. Mamedov, H. Ozturk, T. Makas, Investigation of Mechanical and Microstructural Properties of Ti-6Al-4V Alloy Depending on Hot Forging Process Parameters, Procedia Eng. 207 (2017) 2155-2160. https://doi.org/10.1016/j.proeng.2017.10.974
[2] Y. Okazaki, On the effects of hot forging and hot rolling on the microstructural development and mechanical response of a biocompatible Ti alloy, Materials 5 (2012) 1439-1461. https://doi.org/10.3390/ma5081439
[3] A. Alimov, I. Sizova, N. Biba, M. Bambach, Prediction of mechanical properties of Ti-6Al-4V forgings based on simulation of microstructure evolution, Procedia Manuf. 47 (2020) 1468-1475. https://doi.org/10.1016/j.promfg.2020.04.326
[4] T. Altan, G. Ngaile, G. Shen, Cold and Hot Forging: Fundamentals and Applications, ASM International, 2005. https://doi.org/10.1361/chff2005p001
[5] A. Astarita, A. Ducato, L. Fratini, V. Paradiso, F. Scherillo, A. Squillace, C. Testani, C. Velotti, Beta forging of Ti-6Al-4V: Microstructure evolution and mechanical properties. Key Eng. Mater. 554–557 (2013) 359-371. https://doi.org/10.4028/www.scientific.net/KEM.554-557.359
[6] S. Luo, J. Yao, J. Li, H. Du, H. Liu, F. Yu, Influence of forging velocity on temperature and phases of forged Ti-6Al-4V turbine blade, J. Mater. Res. Technol. 9 (2020) 12043-12051. https://doi.org/10.1016/j.jmrt.2020.08.106
[7] T. Bhujangrao, C. Froustey, E. Iriondo, F. Veiga, P. Darnis, F.G.Mata, Review of intermediate strain rate testing devices, Metals 10 (2020) 1-24. https://doi.org/10.3390/met10070894
[8] J. Agirre, B. Erice, D. Abedul, E. Saenz de Argandoña, N. Otegi, L. Galdos, A Laboratory-Scale Instrumented Forging Hammer as an Intermediate Strain Rate Testing Device, EPJ Web Conf 250 (2021) 01002. https://doi.org/10.1051/epjconf/202125001002
[9] GOM. Correlate 2019. Information on https://www.gom.com/
[10] Y. Zhu, W. Zeng, X. Ma, Q. Tai, Z. Li, X.Li, Determination of the friction factor of Ti-6Al-4V titanium alloy in hot forging by means of ring-compression test using FEM, Tribol. Int. 44 (2011) 2074-2080. https://doi.org/10.1016/j.triboint.2011.07.001
[11] J. Porntadawit, V. Uthaisangsuk, P. Choungthong, Modeling of flow curve at high temperature for a Ti-6Al-4V alloy, Adv. Mater. Res. 849 (2014) 195-199. https://doi.org/10.4028/www.scientific.net/AMR.849.195

Materials Research Proceedings 28 (2023) 683-692 https://doi.org/10.21741/9781644902479-74

Benchmarking mean-field models available in commercial FE software in application to two-blow forging of IN718 alloy

RESHETOV Aleksey[1,a *] and BYLYA Olga[1,b]

[1]University of Strathclyde, NMIS Advanced Forming Research Centre, 85 Inchinnan Drive, Inchinnan, PA4 9LJ, United Kingdom

[a]aleksey.reshetov@strath.ac.uk, [b]olga.bylya@strath.ac.uk

Keywords: Mean-Field Modelling, JMAK-Type Models, Full-Field Modelling, FEA, Multi-Step Industrial Forging

Abstract. This paper analyses the potential of standard mean-field models available in commercial FE software Deform®, Forge® and QForm® for a microstructural prediction during multistage forging process of Inconel 718 at conditions close to industrial ones. The special set of experimental trials including heating, forging, reheating and final forging were conducted on 5 MN hydraulic press with detailed measurements of temperature distributions, timings and forging parameters. The microstructure distribution was investigated after each stage of the process (optical and EBSD) and compared with the predictions obtained in three softwares. Standard and optional capabilities as well as limitations and challenges of the models were investigated, and some improvement ideas were proposed.

Introduction

Microstructural modelling, as well as appropriate calibration and application of available mean-field microstructure evolution models for industrial hot forging processes, remains a bottleneck [1,2]. It is getting even more complex when these models are applied for the real-life technological processes where material goes through number of forging and reheating stages. The goal of such complicated route is to get a final part with a required microstructure. Due to a large number of technological parameters involved in this process, troubleshooting and optimisation of the manufacturing route requires the capability of microstructure evolution models to predict final microstructure with some acceptable accuracy.

All the most popular commercial FE metal forming softwares, like Deform®, Forge® and QForm® have some in-built capabilities for microstructural modelling. The study presented in this paper carried out using Inconel 718 alloy. For this and similar to it nickel-based superalloys dominating mechanisms during hot forging, which are intended to be simulated, are Dynamic (DRX), Meta-Dynamic (MDRX) and Static (SRX) recrystallisation along with the static Grain Growth (GG). There also few other microstructural mechanisms which are not directly modelled in available in-built models, but which should however be kept in mind as they can affect the results: Recovery (RC), Twinning (TW) and Continues Recrystallisation (CRX). The question of their consideration will be briefly touched in the Results and Discussion section.

The microstructural models in-built into the three above mentioned metal forming softwares for DRX, MDRX, SRX and GG have quite similar mathematical structure (with minor variations in shape and coding realisation) and individual material library of default parameters. Three recrystallisation models belong to the so-called JMAK-type class of the models [3] and the grain-growth model is described with the classical model of P.A. Beck [4].

The limitations of the JMAK-type models are well known and analysed in many papers [1, 5-7]. They are not well fitted for the processes with the sharp changes in temperatures and strain rates. The set of material parameters is normally suitable for a fixed range of temperatures and

Content from this work may be used under the terms of the Creative Commons Attribution 3.0 license. Any further distribution of this work must maintain attribution to the author(s) and the title of the work, journal citation and DOI. Published under license by Materials Research Forum LLC.

strain rates which they are optimised for, etc. However, these models are the simplest, intuitively "physically" clear and available as in-built models in the commercial FE softwares.

The main goal of this benchmarking study was to work out some practical conclusions regarding application of standard models. The set of tests consisting of heating, forging, reheating and second blow forging was specially designed for this purpose. Accurate direct measurements of all possible process parameters was done for the fine tuning of FE models providing robust prediction of the thermo-mechanical histories of all points of the performs. All the data gathered was further used as input for the microstructural modelling. Separate analysis of microstructure at every stage provided an ability to decouple the models of recrystallisation and give additional information on the reason of the "wrong" behavior of the models.

The special attention was addressed to investigation of the areas of the forged billets where microstructure prediction was not accurate. The reasons of inaccurate prediction were analysed to suggest possible improvements of the models.

Methodology

Forging trials.

Two-blows forging route with reheating between the blows was employed to obtain experimental data for benchmarking microstructure evolution models (see Fig. 1). The standard double truncated cone (DTC) geometry with 50.8 mm initial height was used for the forging. The billets were machined from IN718 material with standard chemical composition. Forging trials of IN718 DTC geometry were carried out at the sub-solvus temperature of 990°C on 5 MN hydraulic press. The dies of the press were heated up to 600°C. The billets were reheated in the furnace back to 990°C between the blows. Taking into account non-isothermal conditions of the forging, relatively bulky billets, as well as multi-stage forging route, these trials mimic a real industrial forging conditions for this alloy. To track the microstructure evolution at the various stages of the forging route, three DTC-s were forged using following routes:

- DTC#1: 1st blow air cooling (AC)
- DTC#2: 1st blow reheating in furnace back to 990°C AC
- DTC#3: 1st blow reheating 2nd blow AC (full route)

A number of real-time process parameters was recorded during the forging trials. Such press readings as velocity of top ram, force and displacement were recorded as a function of a time. Along with that, temperature in 3 reference points was measured for each processed billet during all the forging route including initial heating and final air cooling. For this purpose 3 thermocouples were embedded into the each proceed billet: one thermocouple for the centre of the billet and two thermocouples were embedded on the 5mm distance from the top and bottom surface of the billet in the same way as it was shown in [2, 8]. The example of obtained thermocouples readings is shown in Fig. 2. The trial of each billet was video-recorded to define the exact time of each operation of the processing route. The shape of final geometry of forged parts was analysed using a 3D blue light-based metrology scanning system (by GOM ATOS TripleScan III).

Digital twin of the experiment. Digital twins of thermo-mechanical processing were created for each processed billet. By the term "digital twin" here is implied validated FE simulations which reproduce particular forging conditions, heating and cooling profiles, timings of operations, as well as peculiarities of metal flow for each forged billet. The FE models were created using several commercially available FE packages: DEFORM, QFORM and FORGE. Each of these software developers has its own mean-field microstructure evolution model for IN718 material, which was benchmarked in this work.

This phase of study is critically important because microstructure evolution models employ macroscopic process parameters, namely strain, temperature and strain rate obtained from FE

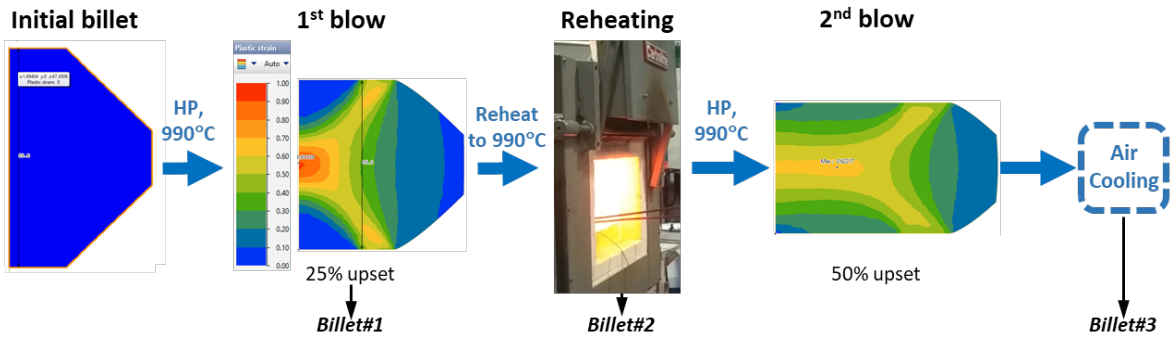

Fig. 1. Forging route used for two-blow forging trials of IN718 on hydraulic press.

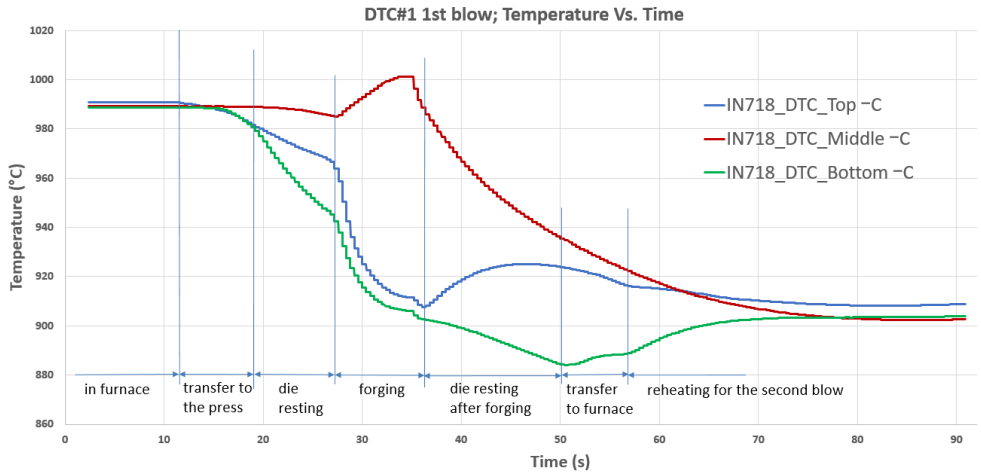

Fig. 2. Thermocouples readings for the DTC#2 (just the 1st blow and transfer back to furnace).

simulations. The settings in the FE models were adjusted in a way to reflect actual forging conditions. The calibration procedure consisted of following steps:

- Defining exact time of each operation using video-recordings and thermocouples' readings. The full list of simulated operations was: pre-heating, transfer to furnace, die resting before the 1st blow, 1st blow forging, die resting after the 1st blow, transfer back to the furnace, re-heating, transfer for the 2nd blow, die resting, 2nd blow forging, die resting, transfer for air cooling, air cooling.
- Adjusting heat-exchange coefficients in simulations in a way to repeat experimentally obtained profiles of temperature in reference points.
- Friction conditions were validated by superimposing images from GOM scan and those obtained in the simulations.
- Validating metal flow in the simulations using available experimental data. The final shapes and positions of the holes drilled for the thermocouples were used to validate the metal flow and strain values locally in the vicinity of the billets' dead-zones and central locations. Also force readings from the press were used to check the force prediction in simulations.

More detailed description of the procedure of creating digital twins is shown in earlier studies [2, 8].

The main calibration criteria for the simulations were temperature and strain fields, which have had to be similar to those obtained in the experiment and to be equal between FE simulations created in various FE packages. Fig. 3 demonstrates the comparison between the temperature fields and strain fields in all utilised FE packages for the billet after the first blow (Fig. 3*a*) and the second blow (Fig. 3*b*).

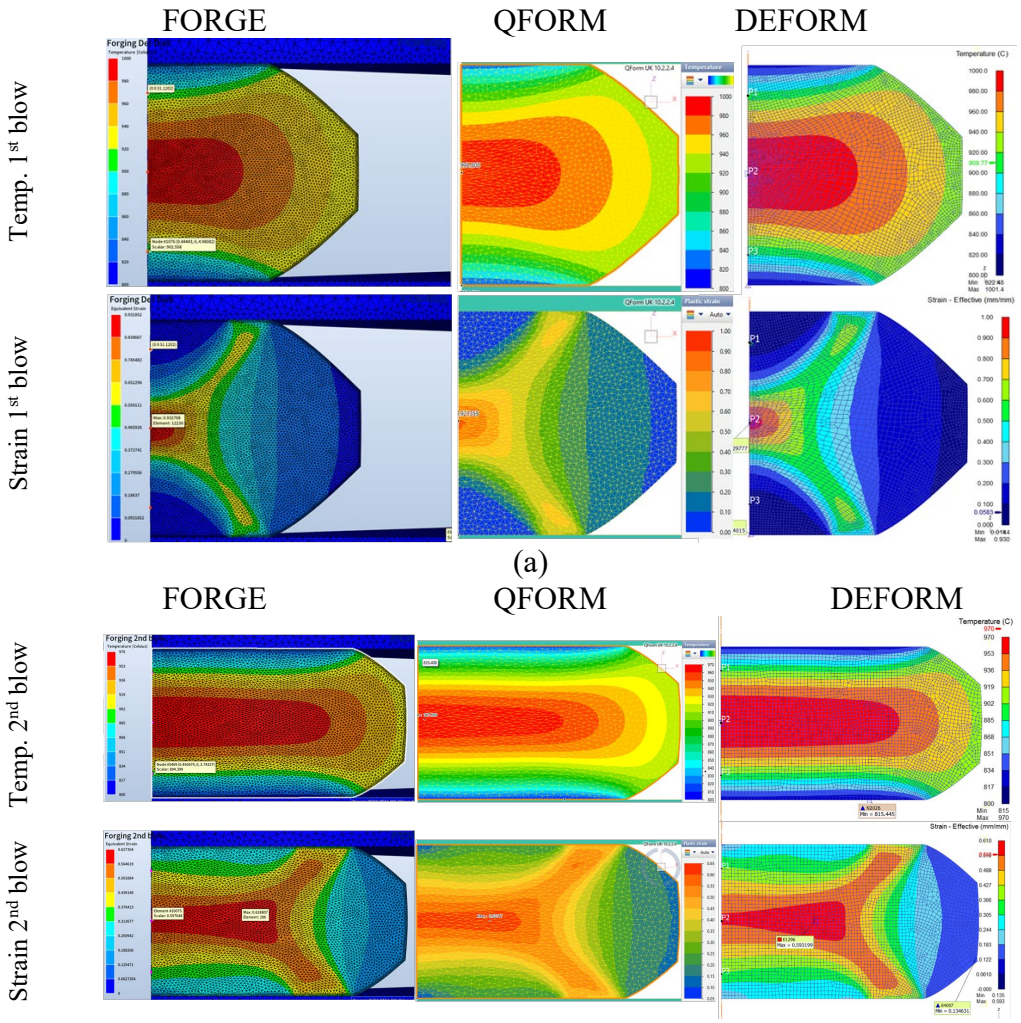

Fig. 3. Comparison between the temperature fields and strain fields in all utilised FE packages: (a) temperature and strain fields straight after the first blow; (b) temperature and strain fields straight after the second blow.

Methodology of microstructure study.

Processed double truncated cones were cut in half and prepared for optic microscopy and EBSD analysis. The boundaries of recristallised area in the billet's cross-sections were defined using optical microscopy with the accuracy 5%. EBSD maps were obtained in reference points of each forged billet, namely central area and area where recrystallisation was initiated.

Benchmarked mean-field microstructure evolution models.

Standard mean-field models available in commercial FEA software Deform®, Forge® and QForm® were used for microstructural prediction during multistage forging process. All the models were used "as is" with the default set of parameters for IN718 available in the material libraries of each software. For the detailed description of the models and values of the model parameters please refer to description of the models [9-11]. The initial grain size of the material was set to 17μm and temperature limit of 950°C was used for the initiation of microstructure evolution in all the models. All the microstructure evolution mechanisms available in the models were set as active: DRX, MDRX, SRX and static GG. It was also assumed that material was fully recovered (no retained strain) after the re-heating operation before the second blow.

Results and Discussion

The outputs of microstructure evolution models for total recrystallized volume fraction are compared with the experimental observations in Table 1 (for the scale from 0% to 100%) and Table 2 (for the scale from 0% to 5%). The scale used in Table 2 allows to compare the boundaries of the recrystallised area more precisely. Note that total RX volume fraction presented in the tables below shown as a summary of contribution from all three various types of recrystallisation: DRX, MDRX and SRX. According to [12, 13] all three mechanisms were in play during the selected processing route.

As it follows from the Table 1 and Table 2, none of the standard JMAK-type models embedded in the commercially available FEA software and used with the default settings have demonstrated accurate predictions. Though the boundaries of recrystallised area for DTC#1 was predicted by FORGE and QFORM models quite well (see the first row of Table 2), the volume fraction of the recrystallised material was predicted wrongly. It is assumed that this type of models should predict microstructure evolution for one single forging operation correctly on the condition that model is calibrated in proper way. Such a big disagreement with the experiment indicates that default settings of the models are not suitable for this case and model should be re-calibrated. In this particular case, large value of total RX vol% predicted by models is caused by overestimated MDRX vol%, while prediction of DRX is much closer to the experimental value of 26%.

Table 1. Comparison of microstructure evolution models outputs for RX vol% versus experiment in scale 0 to 100%.

Route	Total RX volume fraction in scale 0 to 100%			
	Experiment	DEFORM	FORGE	QFORM
DTC#1: 1st blow + AC	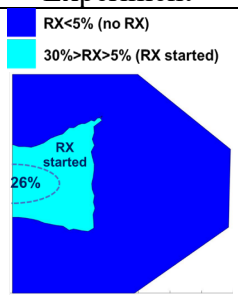	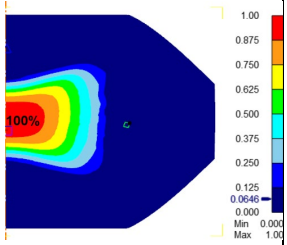	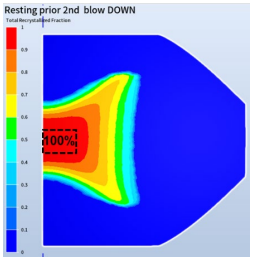	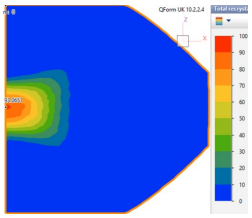
DTC#2: 1st blow + reheating + AC	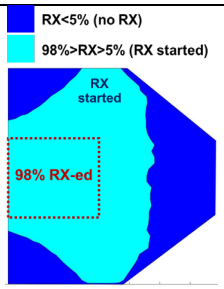	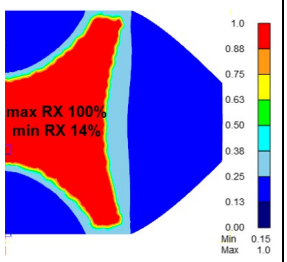	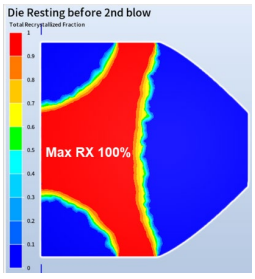	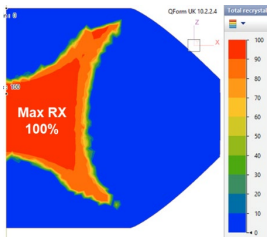
DTC#3: 1st blow + reheating + 2nd blow + AC	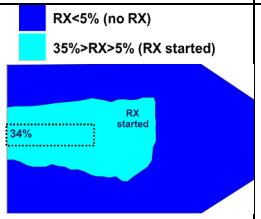	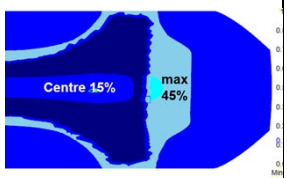	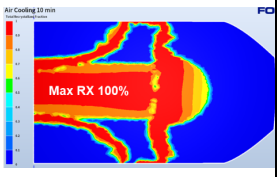	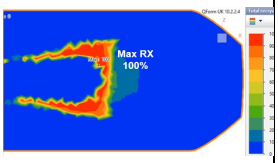

Table 2. Comparison of microstructure evolution models outputs for RX vol% versus experiment in scale 0 to 5%.

Route	Total RX volume fraction in scale 0 to 5% (for indicating onset of RX)			
	Experiment	DEFORM	FORGE	QFORM
DTC#1: 1st blow + AC	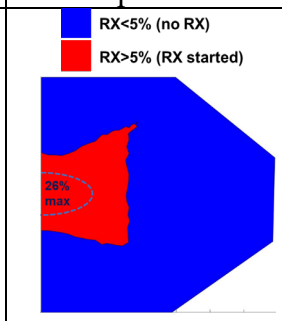	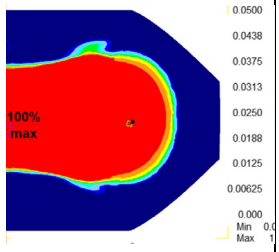	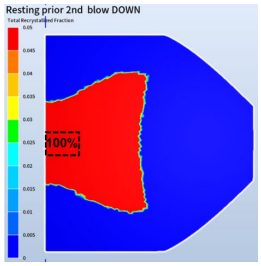	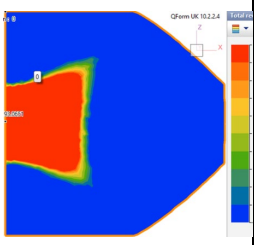
DTC#2: 1st blow + reheating + AC	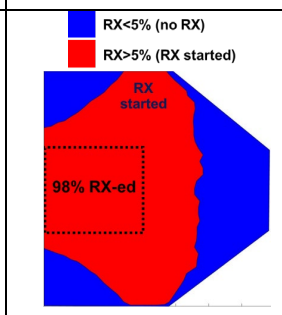	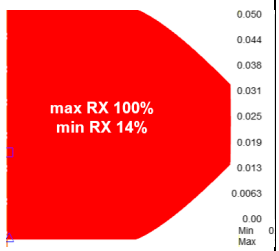	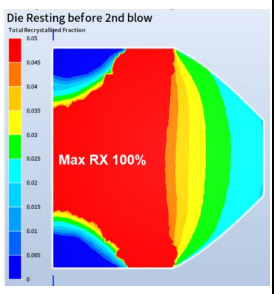	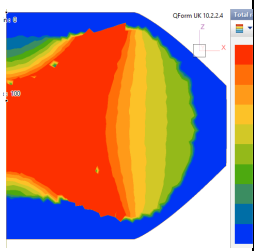
DTC#3: 1st blow + reheating + 2nd blow + AC	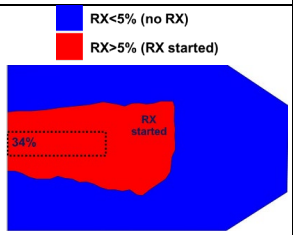	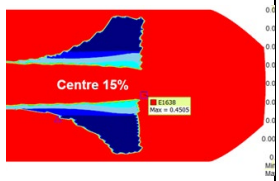	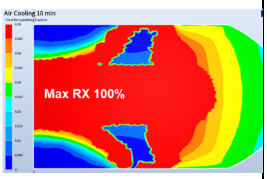	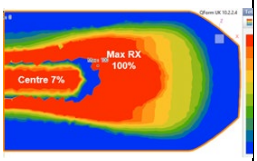

For the more complex processing routes used for DTC#2 and DTC#3 the prediction of the models became worse. For these more complicated cases the problem of transferring material and its properties between in-line manufacturing operations prevails.

It is important to note that all used standard JMAK-type models were de-coupled models. This fact limits their application for multiple-blows simulations as changes in the microstructural state are not connected with the model of the material (i.e. flow stress data) directly. To compensate this essential drawbacks and transfer key material parameters between the operations, the software developers use number of assumptions and patches [5]. However, even in their current de-coupled form these models can be improved significantly to make their prediction more accurate. Several reasons causing wrong predictions, as well as suggestions regarding model improvements are given below.

Temperature limits for activation various microstructure evolution mechanisms.

The value of temperature limit is important as it largely defines (together with accumulated plastic strain) recrystallised area and RX volume fraction. JMAK-type models implemented into FE softwares have single temperature limit for all microstructure evolution mechanisms and do not allow to set various temperature limit for DRX, SRX and MDRX separately. Probably it is not correct approach, because according to the experimental observations grain growth activation requires higher temperature threshold than nucleation process. Ideally temperature limits should

be set separately for each microstructure evolution mechanism as a function of temperature and some internal state variables which characterise microstructure state, e.g. dislocation density, grain size, etc. Also, it could be beneficial do not use "hard cut-off" by temperature with some particular temperature value, but have temperature limit as function of some process parameters instead, e.g. strain and strain rate. It will better fit "physics" of the recrystallisation, as bigger strain and strain rate results in bigger internal energy and, correspondently, requires lower temperature limit for the activation of RX mechanism.

The way of representing multiple rounds of recrystallisation by the model.

As it can be seen from the third row of Table 1 and Table 2, the prediction for the RX vol% after the second blow looking strange. The reason is that in all the benchmarked models the RX vol% during the second blow is overlapped with the RX vol% fields remained after the first blow. There is an assumption in the models that if RX vol% getting close to 100% during the recrystallisation, then all recrystallised fractions are reset back to 0% considering a fully non-recrystallised new microstructure obtained. This solution is inconvenient for representation of multiple rounds of RX, because it is not possible to distinguish between the fully recrystallised material during the previous operations and material which was never recrystallised, for example, dead-zones. It is also hard to distinguish RX during the second blow and compare it with experimentally defined RX-ed area after the second blow. It would be beneficial to reconsider the way of representation of RX vol% in such a way to make the previous rounds of recrystallisation visible to the user.

Transferring non-uniform microstructure to the re-heating operation.

As can be seen from Fig. 4 (a, b, c) DTC#1 has various types of non-uniform microstructure after the first blow. The microstructures differ by grain size, grain shapes and dislocation densities. These three types of microstructure later re-heated in the furnace for the second blow. During the re-heating SRX occurs. It is assumed that SRX will have different kinetics for all these 3 cases. The problem is that SRX models in their current form cannot take into account such peculiarities of microstructure. Current equations for SRX volume fraction and grain size have average grain size parameter in some power (material constant) [3-5], but it cannot be used to describe bimodal microstructure or partially recrystallised microstructure adequately. The possible solution of this problem within current architecture of the SRX model is utilising both average recrystallised and non-recrystallised grain sizes in the SRX model equations. Such modifications of the model was already tested by developers of FORGE FEA software [5].

Transferring accumulated plastic strain and microstructure to the second blow.

This problem is partially overlapped with the previous one as microstructures after the reheating operation can be also quite different, see Fig. (d, e, f), so it is assumed that it should influence kinetics of DRX during the second blow. This part of the problem could be partially sorted out in the similar manner as suggested above.

The second part of the problem is figuring out what ratio of the accumulated plastic strain should go for the second blow after the re-heating operation. Obviously material which was not SRX-ed in full and have remained strain will be DRX-ed in different way and its rheology also will be different. There is a patch to solve this problem in the FE softwares, namely, "retaining strain" which is calculated as inverse ratio to "RX total vol%":

$$\varepsilon_i = (1 - X_{rex})\varepsilon_{i-1} \quad (1)$$

Alternatively "retaining strain" can be calculated as a function of parameters which define recovery, e.g. time and temperature. This way is better as it covers the cases when SRX did not happen, but deformed grains were recovered during the re-heating operation.

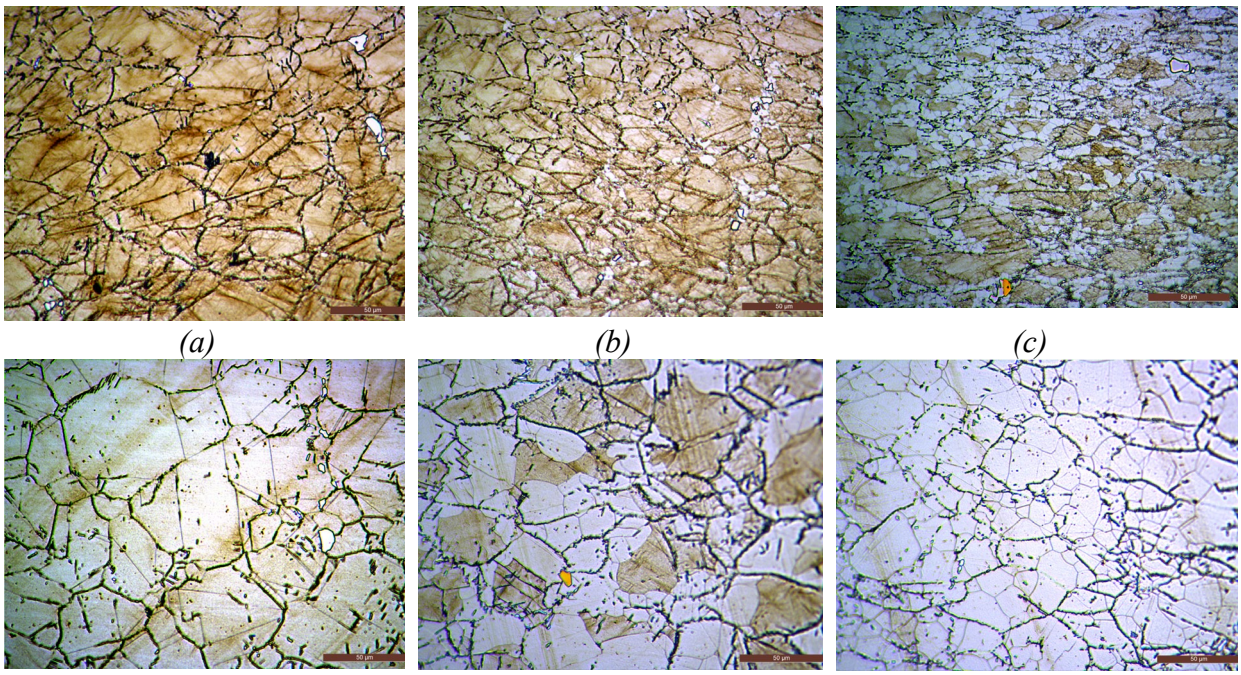

Fig. 4. Optic microscopy images obtained at some reference points of the processed billets: (a) DTC#1: non-recrystallised location with heavily-deformed initial grains; (b) DTC#1: necklace microstructure - location where DRX initiated; (c) DTC#1: heavily DRX-ed location in the centre of the billet; (d) DTC#2: location at the vicinity of bottom dead-zone where SRX was not started; (e) DTC#2: partially SRX-ed location; (f) DTC#2: fully SRX-ed location in the centre of the billet.

However, due to de-coupled nature of the investigated models, Eq. 1 influences only the critical strain needed for the following round of RX, but it is not coupled with the model of the material, i.e. flow stress data, so the metal flow on the second blow does not take into account changes in microstructure. The only solution here is employing coupled model where some microstructure parameters are coupled with the material model and flow stress data is recalculated on each step of simulation taking into account microstructure changes. To this end microstructure evolution model should be re-written in incremental form.

Taking into account contribution of other mechanisms of microstructure evolution.

Apart from DRX, MDRX, SRX and static GG described in the investigated models, there are also some microstructure evolution mechanisms which were not taken into account. Among them are recovery (RC), twinning (TW) and continues dynamic recrystallisation (CDRX). All listed mechanisms were also in play during the thermo-mechanical processing used for this study and they influenced average grain size of non-recrystallised grains as well as level of internal energy locked in the material. These mechanisms cannot be taken into account within the decoupled approach and can be described only by coupled models.

To sum up, there are number of ways for improving standard JMAK-type models in their current de-coupled state without changing their mathematical formulation. In brief, the proposed improvements include: setting temperature limits for each microstructure evolution mechanism; calculating retained strain (strain transferred to the next blow); better way of representing multiple rounds of RX; taking into account both average recrystallised and non-recrystallised grain sizes.

Each FEA package tested in this study has strong points in its own mean-field model which are useful for microstructure prediction during multi-pass forging processes. For instance, DEFORM Avrami model has inbuilt capability to use multiple sets of model parameters for various

temperatures and strain rates, which potentially allows to cover wide range of process parameters; it also uses retaining strain concept which allows to some extent compensate drawbacks of the de-coupled model. FORGE JMAK-model has possibility to use tabulated parameters, also software developers suggested the way of modelling heterogeneous microstructures during multi-pass processes [5]. QFORM JMAK-model also has inbuilt equation for calculating retaining strain and option for cyclic recrystallisation inbuilt in GUI, also due to convenient Lua programming the model can be easily modified by user. All these features listed above give user good possibilities to adjust the model in each software for the particular multi-stage forging processes.

Mean-field models in itself operate with some representative volume of the material and averaged characteristics of the process. This approach can work well if the representative volume is uniform. However, the problems arise when material is non-uniform, for instance in the case of partially recrystallised microstructure, or in the case when there are grains with big difference in properties in the same representative volume. Although it is challenging, these more complicated cases could also be described by mean-field approach providing that some new alternative equivalent parameters introduced into the model for representing current state of the microstructure.

Full-field modelling at the meso-scale level, e.g. by using DIGIMU (Transvalor) software, could be useful tool for getting better understanding of microstructure evolution in the cases when prediction of mean-filed models is not accurate, e.g. microstructures with non-uniform distribution of grains by size; or with non-uniform distribution of dislocation density (stored energy) among the grains. It can help to find out what new equivalent parameters could be introduced into the mean-field models to get robust prediction for these cases. Such alternative equivalent parameters potentially could be equivalent dislocation density, equivalent work of plastic deformation, equivalent grain sizes, aspect ratio of grains, etc.

Summary

1) All JMAK-type models considered in the paper have a big potential for predicting microstructure evolution during multiple-blow forging process. The peculiarities of this processes should be taken into account and models should be adjusted to it correspondingly. Developers of FEA packages improving their models continuously and microstructure evolution models embedded into DEFORME, FORGE and QFORM in their current state have plenty of opportunities for the adjustments and improving their predictions.
2) For the cases of bimodal microstructure or necklace microstructure where average grain size cannot represent the microstructure correctly, outputs of the model should be considered critically. For instance, to estimate the scatter in the results, upper and lower-bound methods can be used with two various average grain sizes.
3) Mean-field models should be calibrated for the particular (narrow) range of process parameters (strain rate and temperature range) as they cannot predict microstructure evolution within the wide range of process parameters correctly. In addition to this, model of the material, i.e. flow stress data, should be calibrated for the particular range of process parameters as well.
4) Coupled mean-field models are required for predicting microstructure evolution during multistage thermo-mechanical processing in more accurate way. It is implied that such type of models should have in the model of the material some parameter which characterises current state of the microstructure, for instance, dislocation density or work of plastic deformation. Full-field modelling using DIGIMU Transvalor software can be effective tool for getting better understanding of active microstructure evolution mechanisms in play and identification of parameters for coupled mean-field models.

References

[1] O. Bylya, A. Reshetov, N. Stefani, M. Rosochowska, P. Blackwell, Applicability of JMAK-type model for predicting microstructural evolution in nickel-based superalloys, Procedia Eng. 207 (2017) 1105-1110. https://doi.org/10.1016/j.proeng.2017.10.1067

[2] A. Reshetov, N. Stefani, O. Bylya, B. Krishnamurthy, P. Blackwell, Aspects of high strain rate industrial forging of Inconel 718, Superalloys 2020, Springer, Cham (2020) 461-470. https://doi.org/10.1007/978-3-030-51834-9_45

[3] W. Johnson, R. Mehl, Reaction kinetics in processes of nucleation and growth, T. Am. I. Min. Met. Eng. 135 (1939) 416–458.

[4] P.A. Beck, M.L. Holdsworth, P.R. Sperry, T. Metall. Soc. AIME 180 (1949) 163.

[5] N. Stefani, O. Bylya, A. Reshetov, P. Blackwell, On the applicability of JMAK-type models in predicting IN718 microstructural evolution, Comput. Meth. Mater. Sci. 17 (2017) 59-68.

[6] M. Irani, S. Lim, M. Joun, Experimental and numerical study on the temperature sensitivity of the dynamic rectystallization activation energy and strain rate exponent in the JMAK model, J. Mater. Res. Technol. 8 (2019) 1616–1627. https://doi.org/10.1016/j.jmrt.2018.11.007

[7] J. Zhang, C.W. Zheng, D.Z. Li, A Multi-phase Field Model for Static Recrystallization of Hot Deformed Austenite in a C-Mn Steel, Acta Metall. Sin. 31 (2018) 208–215, https://doi.org/10.1007/s40195-017-0595-2

[8] N. Stefani, Novel experiment methodology for investigation of recrystallization during industrial hot forging of Inconel 718, Eng. D Thesis, 2020.

[9] DEFORM^{TM}, 2014, DEFORM^{TM} V11.0.1 System Documentation, Reed Road Columbus, Ohio: Scientific Forming Technologies Corporation.

[10] Micas Simulation LTD, QFORM v8 FE package documentation: Description of Microstructure evolution model, Available at: http://www.qform3d.co.uk/db_files/17/123.pdf

[11] M. Teodorescu, P. Lasne, R. Logé, Modeling recrystallization for 3D multi-pass forming processes, Mater. Sci. Forum 558-559 (2007) 1201-1206. http://doi.org/10.4028/www.scientific.net/MSF.558-559.1201

[12] A. Nicolaÿ, G. Fiorucci, J.M. Franchet, J. Cormier, N. Bozzolo, Influence of strain rate on subsolvus dynamic and post-dynamic recrystallization kinetics of Inconel 718, Acta Mater. 174 (2019) 406-417. https://doi.org/10.1016/j.actamat.2019.05.061

[13] R.P. Guest, S. Tin, The dynamic and metadynamic recrystallization on IN718, Superalloys 718, 625, 706 and Derivatives 2005, TMS 2005, pp. 373-383. https://doi.org/10.7449/2005/Superalloys_2005_373_383

Formability of metallic materials

Materials Research Proceedings 28 (2023) 695-704 https://doi.org/10.21741/9781644902479-75

Total strain on the outer surface of steel sheets in air bending

POKKA Aki-Petteri[1,a *], KESTI Vili[2,b] and KAIJALAINEN Antti[1,c]

[1]University of Oulu, Materials and Mechanical Engineering, P.O. Box 4200, 90014 Oulu, Finland

[2]SSAB Europe, Rautaruukintie 115, 92101 Raahe, Finland

[a]aki-petteri.pokka@oulu.fi, [b]vili.kesti@ssab.com, [c]antti.kaijalainen@oulu.fi

Keywords: Air Bending, Steel, Digital Image Correlation, Strain Distribution, Total Strain, Bend Shape

Abstract. Air bending is a commonly used method for sheet-metal forming. However, several challenges exist around the bending behavior of materials with poor global formability, that are difficult to study using conventional bending test methods, and thus may not be fully understood. In this study, nine thermomechanically rolled steel grades with various strengths and ductility properties are bent using three different punch radii. The strain distributions on the outer surface are measured using Digital Image Correlation (DIC). The relationships between the strain distribution, peak strain, and total strain (area under the strain distribution curve) are determined. The total strain is observed to be independent from the peak strain and the shape of the strain distribution. The total strain is found to depend on the bend angle and sheet thickness. An analytical formula for approximating the total strain is derived. Potential for further approximations of the total strain, strain distribution and bend shape are discussed.

Introduction

Air bending is a commonly used forming method for sheet metals due to its flexibility, cost-effectiveness, and speed. A large range of bend angles can be achieved without tool changes just by controlling the punch displacement. The radius of the bent sheet is usually controlled by changing the punch radius. However, the shape of the bend is also dependent on the material properties. The distribution of strain and curvature on the outside bend surface can vary significantly depending on the work-hardening properties of the material. When bending materials with poor global formability (i.e., low work-hardening and uniform elongation), the inside radius of the bent sheet may decrease far below the punch radius, leading to high local strains and bend shapes that may be difficult to predict [1]. Various terms have been used referring to this phenomenon in previous studies: multi-breakage, gap formation, punch-sheet separation, punch detachment, punch-sheet-liftoff, loss of contact with the punch/sheet etc. [2-8]. The phenomenon has been known for a long time. However, research on the root of the phenomenon, i.e., the causes and effects of the strain distribution development in air bending, has been relatively scarce. Strain distributions in air bending have been studied by several authors [1,9-14], but not for a large selection of materials and punch radii, that would allow thorough analysis of the effects of certain tool parameters and material properties. Research in this area is therefore necessary.

In this paper, nine steel grades are bent in a 3-point bending setup using three different punch radii. The development of the strain distribution on the outer curvature is measured from each test using a Lavision Digital Image Correlation (DIC) system. The aim of the paper is to study the relationships between the strain distributions, peak strains, and total strains (area under the strain distribution curve).

Content from this work may be used under the terms of the Creative Commons Attribution 3.0 license. Any further distribution of this work must maintain attribution to the author(s) and the title of the work, journal citation and DOI. Published under license by Materials Research Forum LLC.

Experimental Procedure

Nine thermomechanically rolled steel grades are tested in this study. Table 1 provides the sheet thicknesses, tensile properties of the investigated materials, along with the typical minimum bend radii for corresponding grades, provided by a steel manufacturer. The tensile data was measured from ISO 6892 compliant tests, using dog-bone specimens with straight sections of 6 × 8 × 45 mm^3, and strain rates of 0.0025 1/s (to yield point) and 0.008 1/s (after yield point). Both longitudinal and transverse directions were tested, relative to the material's rolling direction. In terms of the direction of the major strains relative to the rolling direction, the longitudinal (0°) tensile test corresponds to the transverse (TD) bend test and the transverse (90°) tensile test corresponds to the longitudinal (RD) bend test.

Table 1. Sheet thicknesses (t) and mechanical properties of the tested materials. The yield strength (R_e), ultimate tensile strength (R_m), uniform elongation (A_g) and total elongation with 40 mm gage length (A_{40}) were measured from the performed tensile tests. The minimum bend radii to 90° bend angle (R_{min}) were provided by a steel manufacturer for corresponding grades.

Material	t [mm]	R_e [MPa]	R_m [MPa]	A_g [%]	A_{40} [%]	R_{min} (to 90°)
St355 (0°/90°)	5.94	438/480	496/502	16.4/15.4	32.7/31.2	0.3 t
St500 (0°/90°)	5.92	585/628	653/669	11.7/10.4	26.9/25.4	0.8 t
St700 (0°/90°)	6.04	785/818	864/907	6.0/4.5	18.2/15.2	1 t
St900_1 (0°/90°)	5.99	974/1024	1042/1142	3.2/2.2	13.4/8.2	3 t
St900_2 (0°/90°)	5.93	1034/1067	1130/1151	3.9/3.1	13.9/11.4	3.5 t
St1100_1 (0°/90°)	6.01	1132/1127	1161/1172	4.7/4.7	15.4/13.8	3.5 t
St1100_2 (0°/90°)	5.93	1098/1111	1253/1271	2.9/2.4	12.1/10.8	3 t / 4 t
St1500 (0°/90°)	5.68	1537/1500	1761/1780	3.4/3.1	10.6/9.4	6 t
St1700 (0°/90°)	6.09	1740/1680	1958/1975	2.7/2.7	9.6/9.0	6 t

The bending tests are conducted in both longitudinal (RD) and transverse (TD) orientations. In this paper, the longitudinal bend orientation (RD) refers to the bend axis being parallel to the rolling direction, and the transverse orientation (TD) refers to the bend axis being perpendicular to the rolling direction. The bend specimens were cut from the 6 mm thick sheets into rectangular strips with a width of 80 mm. The specimen width is small enough to prevent exceeding the force limit of the used Zwick 100 kN universal tensile test machine, while still ensuring plane strain conditions at the center of the bend.

The specimens were bent in room temperature using purpose-built bending tools, shown in Fig. 1a. Using the tensile test machine for the bend tests allows accurate measurements of the bending force and punch displacement. The punch displacement is then used for calculating the bend angle according to ISO 7438 [15]. The measured vertical force is used to adjust the punch displacement and bend angle calculations for the vertical elasticity of the setup (51.9 kN/mm).

The shape of the die (lower bend tool) is illustrated in Fig. 1b. The openings allow an unobstructed line-of-sight between the DIC cameras and the measured specimen surface. The die width, i.e., the distance between the centers of the two shoulders, is also adjustable with this tool. The shoulders rotate freely in their sockets. To minimize the effect of friction even further, a PTFE lubricant spray is applied to the shoulders before each test.

Fig. 2 shows a schematic representation of the bending geometry used in this paper. Three bending tool setups are used in this study, in order to achieve a large variety of strain distributions, and to observe their effects on the behavior of the materials. The parameters for each setup are presented in Table 2. In each setup, the specimens were bent until they either fractured or reached the bend angle of α_{end}. Two repeat tests were conducted for each combination of tool setup, material, and bend orientation. Therefore, a total number of 108 tests are included in this study.

A DIC system, Strainmaster by Lavision, was used in this study for measuring the deformations on the outer bend surface. The system was equipped with two monochrome CCD cameras with a resolution of 2456 × 2058 pixels. The captured images were processed in the DaVis 8.4 software, which uses an iterative least squares matching (LSM) algorithm for displacement and strain calculation. The DIC recording and processing parameters are presented in Table 3. After calculating the strain maps from each image of each test, the values of the major strain were extracted from three sections positioned at the center of the bend, as illustrated in Fig. 1c. The average of the peak values of the three sections were also calculated at each point in time, as well as the average total strain (Riemann sums) of the three sections.

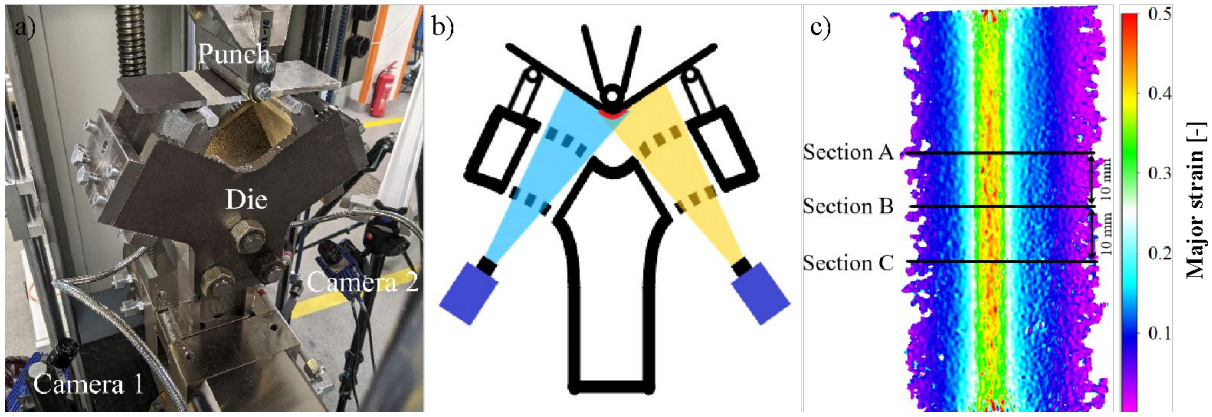

Fig. 1. a) The bending test setup, b) positioning of the DIC cameras, and c) sections A – C on a strain map of the St1100_1 (RD) at 90° bend angle, using a punch radius R_p = 2 t.

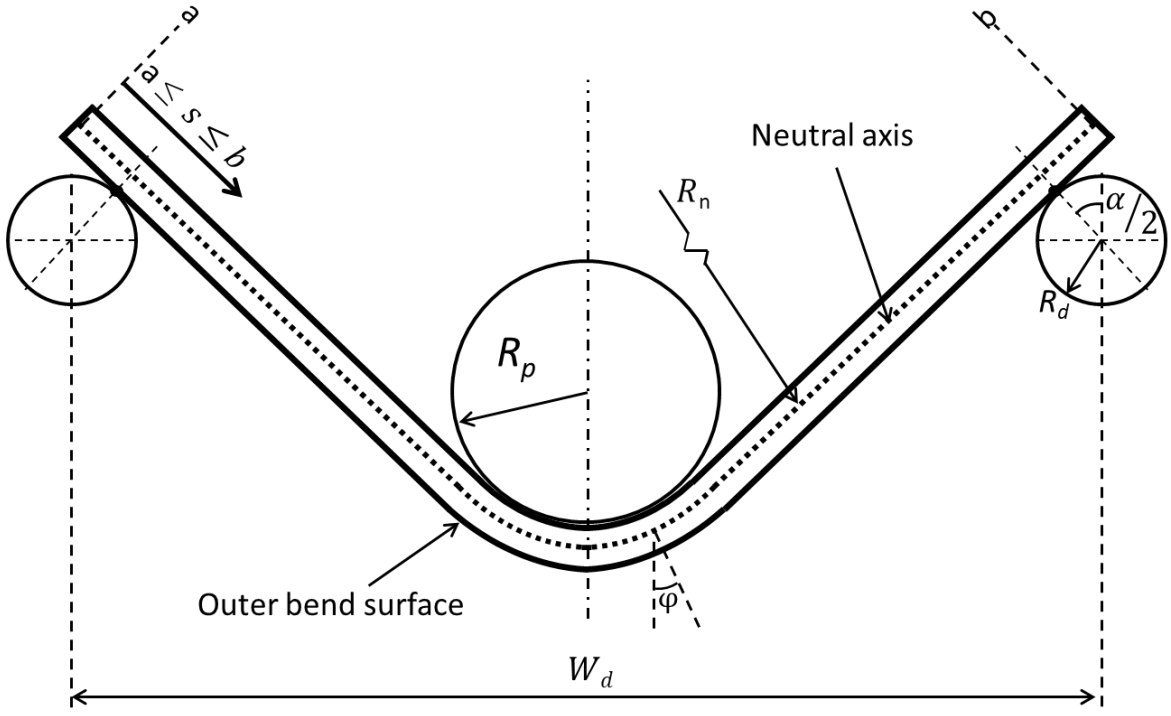

Fig. 2. The bending tool geometry and parameters involved in the analytical solution for the total strain $A_{\varepsilon b}$.

Table 2. Bending tool setup parameters: Punch radius (R_p), die width (W_d), radius of the die shoulders (R_d), vertical speed of the punch (V_p) and the final bend angle before unloading (α_{end}).

Tool setup	R_p	W_d [mm]	R_d [mm]	V_p [mm/s]	α_{end} [°]
1	4 mm ≈ 0.66 t	90	6	1	120
2	12 mm ≈ 2 t	90	6	1	100
3	24 mm ≈ 4 t	110	6	1	110

Table 3. Recording and processing parameters for the DIC system.

DIC system	Lavision Strainmaster (Stereo DIC)
Sensor and digitization	2456 × 2058, 12-bit
Lens, imaging distance	35 mm C-mount, 0.37 – 0.57 m
Imaging rate	2 Hz
Subset size	15x15 pixels
Step size	5 pixels
Strain window, smoothing method	5x5 data points, 2nd order polynomial fit
Virtual strain gage size	35 pixels
Image scale	21 – 30 pixels/mm
St.dev of principle strain	450 - 1700 microstrain
Interpolation, shape function, algorithms	6th order spline interpolation; affine shape function; LSM (iterative least squares matching) algorithm based on optical flow estimation

Before each test, a black-and-white speckle pattern was spray painted on the specimen surfaces to improve the DIC measurement reliability and to minimize glare. To minimize the effect of paint peeling on the measurements, the surfaces were cleaned with ethanol before painting and the tests were conducted as soon as possible after painting to prevent the paint from becoming excessively dry and brittle.

Results and Discussion

Fig. 3 shows the strain distributions of St700 in the RD direction measured at 30°, 60° and 90° bend angles and with three different punch radii. Fig. 3b illustrates the area under the strain distribution curve at 30°, i.e., the total strain $A_{\varepsilon b}$, as well as the peak strains ε_{b_max} at 30° and 90° angles. The distributions are similar for all three punches at 30° but as the bend angle increases, the effect of the punch radius on the strain distribution is clear. With the punch radius R_p = 0.66 t, the deformation increases mostly at the center, creating a narrow strain distribution with large peak strain at the center. In contrast, when using larger punches, as in Figs. 3b and 3c, the deformation is spread more evenly, creating a wider strain distribution with lower peak strains at the center. In fact, when using the largest punch (R_p = 4 t), the peak strain does not increase at all between 60° and 90° bend angles, as the deformation increases solely from the sides.

Fig. 4a presents the developments of the peak strain ε_{b_max} (average peak values of sections A, B and C) for St355 (TD) and St700 (RD) using three different punches. The peak strains develop almost identically in the first 15°, but after around 15 – 20° bend angle (0.05 – 0.10 peak strain) the effects of the punch radii and the material properties start to show. With the smallest punch radius (R_p = 0.66 t), the peak strain increases almost linearly between 30 – 90° bend angles for both materials, with only a slight stagnation in peak strain towards the end of the test. For R_p = 2 t, the stagnation of peak strain seems to start at around 30 – 40° bend angle, and for R_p = 4 t, around 15 – 20° bend angle.

The differences in material properties can also be seen in Fig. 4a. St355 produces lower peak strains than St700 with all three punches. This is due to the greater strain-hardening and ductility

of St355 compared to St700, indicated by their values of A_g and A_{40} in Table 1. In general, materials with greater work-hardening have greater resistance to strain localization, which leads to wider strain distributions and lower peak strains in bending.

Fig. 4b presents the developments of the total strain $A_{\varepsilon b}$ for St355 and St700. The total strain $A_{\varepsilon b}$ was calculated as the average of the Riemann sums of the strains in sections A, B and C shown in Fig. 1c. For clarification, the total strain $A_{\varepsilon b}$ represents the area under the strain distribution curve, as illustrated in Fig. 3b, and could also be described as the difference in length between the outer surface and the neutral axis. As can be seen in Figs. 4a and 4b, the total strain seems to grow at a similar, constant rate in all six tests, despite the differences in the peak strain development. The linear growth of the total strain continues until around 80°, after which some stagnation can be seen for all curves. It is assumed, that the apparent stagnation is mostly caused by loss of data at the later stages of the test, due to parts of the measured surface going beyond the field-of-view of the DIC cameras due to increased curvature. This can be seen in Figs. 3b and 3c, where the distributions at 90° angle are "cut off" at the edges, meaning that the increase of strain at the edges could not be fully measured. As the strain distribution is wider when using a larger punch, more data is lost at the edges with larger punches compared to smaller punches.

The peak strains and total strains from all tests at 50° and 80° angles are presented in Fig. 5. Despite the large number of tests and the variety in the peak strain values, no correlation between the total strain and peak strain or punch radius can be seen. At any given bend angle, the total bend strain value seems to be roughly constant, regardless of the peak strain or punch radius.

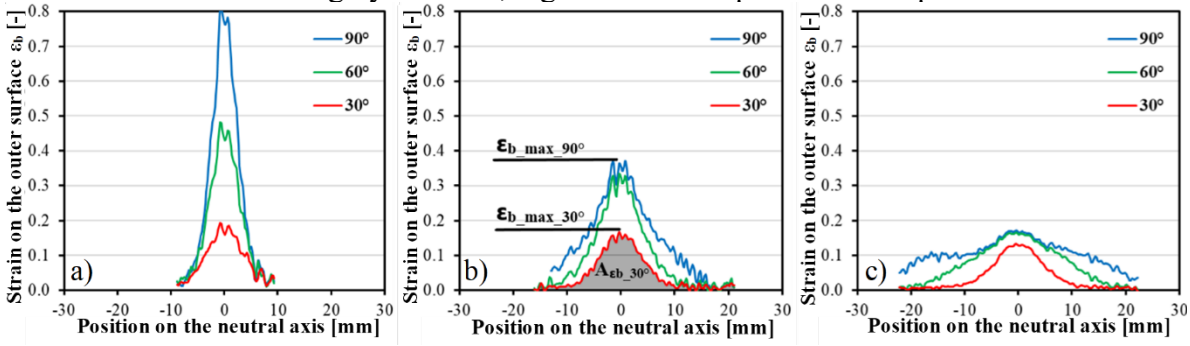

Fig. 3. Strain distributions at 30°, 60° and 90° bend angle, extracted from section B of St700 in the longitudinal direction (RD), using a punch radius of a) R_p = 0.66 t, b) R_p = 2 t and c) R_p = 4 t. The position on the neutral axis corresponds to a value of the arc coordinate s.

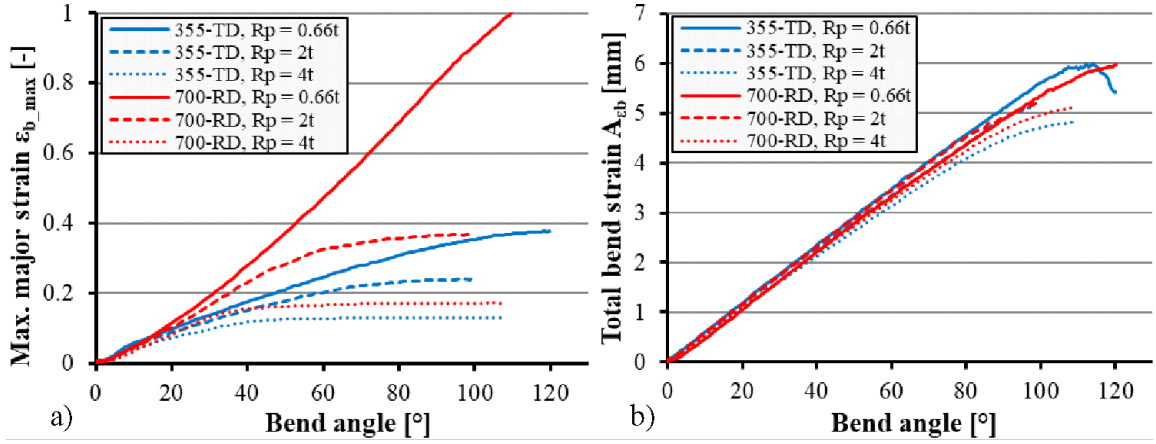

Fig. 4. Development of a) the peak strain and b) the total strain of St355 (TD) and St700 (RD), with punch radii of R_p = 0.66 t, R_p = 2 t, and R_p = 4 t.

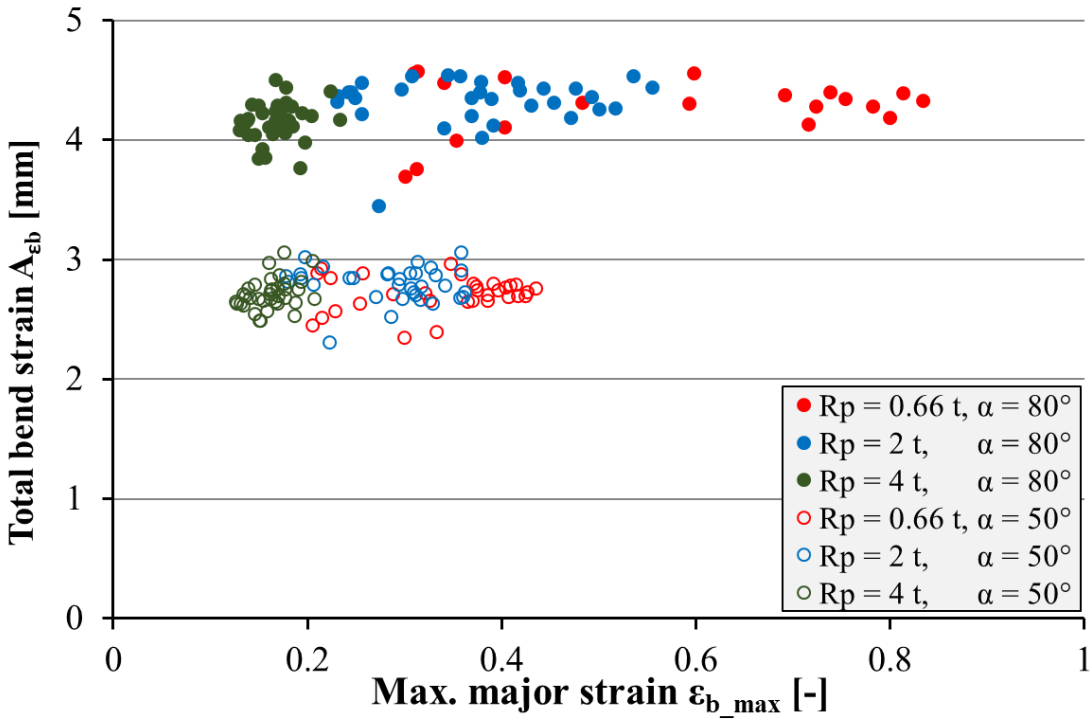

Fig. 5. Relationship between the total bend strain $A_{\varepsilon b}$ and the peak strain ε_{b_max}.

The total strain $A_{\varepsilon b}$ seems to be independent of the material properties, punch radius, the shape of the strain distribution or bend geometry. Assuming that the apparent stagnation after 80° is indeed caused by the limitations in the DIC field-of-view, the total strain seems to be a linear function of the bend angle. It should be possible to find an analytical solution for this relationship.

The parameters involved in this section are presented in Fig. 2. The bending angle α can be expressed as a sum of the rotation angles ϕ of the incremental arc lengths ds of the neutral axis, between the points a and b at the end of each flange, as follows:

$$\alpha = \int_a^b \frac{d\varphi(s)}{ds} ds \tag{1}$$

where s is an arc coordinate indicating the position on the neutral axis, and a and b are the end points of the neutral axis. The radius of the neutral axis R_n can also be expressed as

$$\frac{d\varphi}{ds} = \frac{1}{R_n}. \tag{2}$$

If the neutral axis is assumed to be positioned at the mid-thickness of the sheet, the strain on the outer surface ε_b can be given as

$$\varepsilon_b = \frac{t}{2R_n} \tag{3}$$

Combining Eq. 1, 2, and 3, the total strain on the outer bend surface (i.e., the strain distribution area) can be calculated as

$$A_{\varepsilon_b} = \int_a^b \varepsilon_b\,(s)\,ds = \int_a^b \frac{t}{2R_n}(s)\,ds = \frac{t}{2}\int_a^b \frac{1}{R_n}(s)\,ds = \frac{t}{2}\int_a^b \frac{d}{dS}\varphi\,(s)ds = \frac{\alpha t}{2} \tag{4}$$

The total strain $A_{\varepsilon b}$ seems to be a function of the bend angle and sheet thickness. If the total strain is constant for a given bend angle and sheet thickness, and all strain distributions in air bending are assumed to follow a known shape, e.g., a triangular function, the peak strain could be used to approximate the width of the strain distribution and the shape of the bent sheet. The approximate shape of the sheet could then be used for calculating the bend allowance and bend deduction, as well as approximating the effects of multi-breakage (loss of punch-sheet contact). Therefore, the peak strain ε_{b_max} at a given bend angle could be considered a decent stand-alone measure for the strain distribution. Furthermore, the effects of different material and tool parameters on the strain distribution development can then be investigated through simple linear regression, using the measured peak strain at a specific bend angle as the dependent variable.

In Fig. 6, the average total strains of all tests for each punch radius are plotted against the bend angle. The analytical total strain, calculated using Eq. 4, is included as a reference. Again, the total strain increases linearly for all punch radii until around 80°, after which a stagnation can be seen, presumably due to the limits of the DIC field-of-view (FOV). Although the analytical approximations are mostly within the standard deviation of the measured average values, the approximation seems to slightly underestimate the total strains. This could be due to the assumption of a fixed neutral axis in the analytical solution. If the neutral axis shifts towards the inside surface of the bend, the total strain on the outer surface will increase. For more precise analytical solutions and approximations in future works, the effects of the neutral axis shift could be considered.

Other factors that affect these measurements include the potential errors in the bend angle calculation, variation in sheet thickness and the loss of data due to fractures. If the ISO 7438 bend angle calculation overestimates the real bend angle, as was found by Cheong et al. [10], this would cause a downward bias to the measured $A_{\varepsilon b} - \alpha$ curves. However, the calculation of bend angle is hugely dependent on the tool geometry, so the previous findings may not necessarily apply for the geometry used in this study. Nevertheless, the calculation error of the bend angle introduces an additional unknown variable, and direct measurement of the bend angle would be preferable in future works.

As the total strain seems to be directly proportional to the sheet thickness, variations in sheet thickness will increase the scatter in the measured total strain. For more precise measurements and predictions, the sheet thickness variation should also be taken into account.

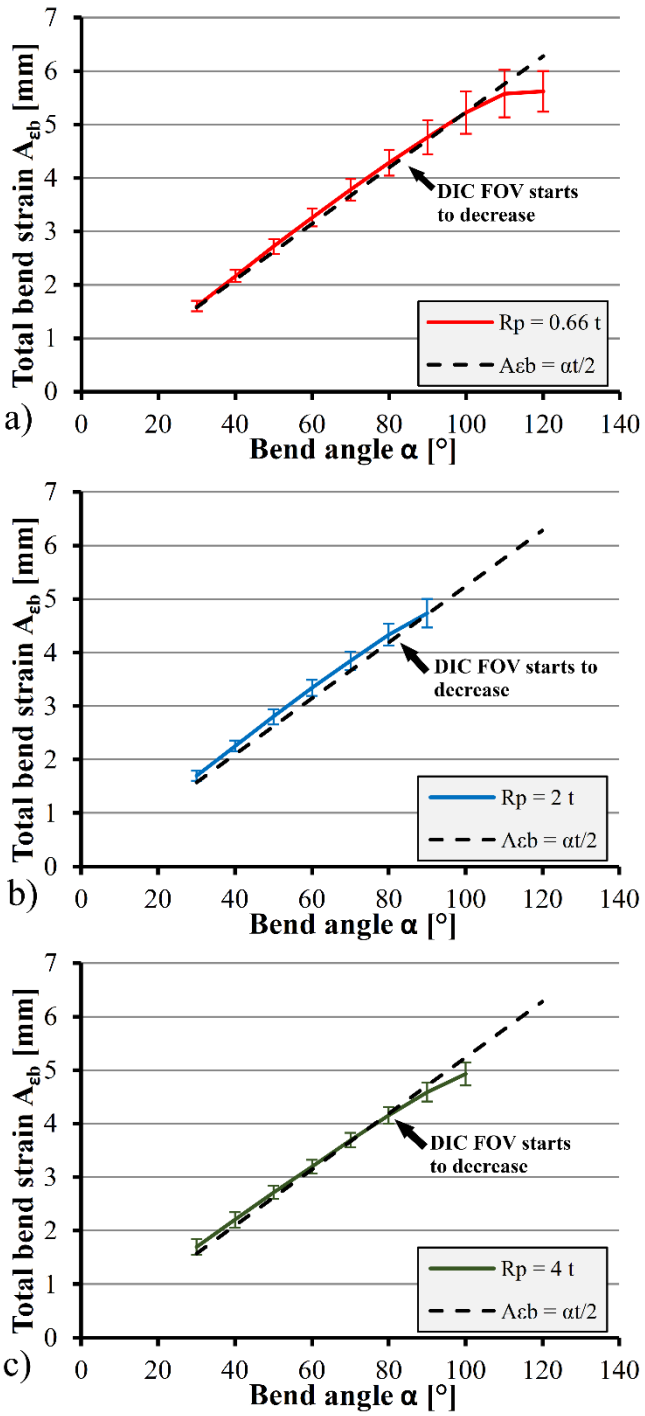

Fig. 6. Average total strain $A_{\varepsilon b}$, measured from bends with punch radius of a) R_p = 0.66 t, b) R_p = 2 t and c) R_p = 4 t. Analytical total strain is included as a reference, calculated as $A_{\varepsilon b} = \alpha t/2$, where t = 6 mm and α is the bend angle in radians.

Out of the 36 specimens tested with the punch radius R_p = 0.66 t, 16 fractured before 80° bend angle. For R_p = 2 t, four specimens fractured before 80°. As the tests were stopped at fracture, no data was gathered from these specimens after their fracture. Consequently, the sample size is decreased for the smaller punches and larger angles, meaning that the remaining specimens have more weight on the results. This increases the effect of random variation on the results, and could potentially introduce a bias, as only the specimens with the greatest ductility remain.

Part of the scatter and deviations in the total bend strain $A_{\varepsilon b}$, seen in Figs. 5 and 6 could be reduced if the DIC strain measurement setup and procedures were optimised for capturing the entire strain distribution. The setup and procedures used in this study were developed prioritizing the measurement of the peak strain, leading to increased noise and loss of data around the edges of the strain distributions. This could also be refined in future works.

Summary

The aim of this study was to characterize nine thermomechanically rolled steel grades with various strengths and ductility properties by means of their bendability properties using three different punch radii. The strain distributions on the outer curvature are measured throughout the test with a DIC system. The target was to understand and determine the relationships between the strain distribution, peak strain and total strain in air bending. The main observations and conclusions of the work can be summarized as follows:

- The strain distribution and peak strain had no measurable effect on the total strain on the outside surface. The total strain was found to grow at a similar rate throughout the test regardless of the punch radius or material properties.
- The total strain on the outside surface of the bend seems to be a function of the bend angle and sheet thickness. A decent approximation for the total strain was achieved with an analytical formula.
- The peak strain could be considered a decent stand-alone value for describing or approximating the strain distribution for a certain bend angle and sheet thickness. Possible use cases and benefits of such an approximation are discussed. These could include estimating the bend shape, multi-breakage, bend allowance and bend deduction, as well as allowing the use of simple linear regression for investigating the effects of certain material and tool parameters on the strain distribution development.

Acknowledgments

Financial assistance of the Business Finland, project FOSSA– Fossil-Free Steel Applications, is acknowledged.

References

[1] A.-P. Pokka, A.-M. Arola, A. Kaijalainen, V. Kesti, J. Larkiola, Strain distribution during air bending of ultra-high strength steels, ESAFORM 2021 (2021). https://doi.org/10.25518/esaform21.2509

[2] S.D. Benson, Press Brake Technology: A Guide to precision sheet metal bending, Society of Manufacturing Engineers, Dearborn, Michigan, 1997.

[3] V. Vorkov, R. Aerens, D. Vandepitte, J.R. Duflou, The Multi-Breakage Phenomenon in Air Bending Process, Key Eng. Mater. 611–612 (2014) 1047-1053. https://doi.org/10.4028/www.scientific.net/KEM.611-612.1047

[4] A. Väisänen, K. Mäntyjärvi, J.A. Karjalainen, Bendability of Ultra-High-Strength Steel, Key Eng. Mater. 410–411 (2009) 611-620. https://doi.org/10.4028/www.scientific.net/KEM.410-411.611

[5] J. Heikkala, A. Väisänen, Usability Testing of Ultra High-Strength Steels, Proc. ASME 2012 11th Biennial Conference on Engineering Systems Design and Analysis 4 (2012) 163-173. https://doi.org/10.1115/ESDA2012-82770

[6] V. Kesti, A. Kaijalainen, A. Väisänen, A. Järvenpää, A. Määttä, A.-M. Arola, K. Mäntyjärvi, R. Ruoppa, Bendability and Microstructure of direct quenched Optim® 960QC, Mater. Sci. Forum 783-786 (2014) 818-824. https://doi.org/10.4028/www.scientific.net/MSF.783-786.818

[7] A.-M. Arola, V. Kesti, R. Ruoppa, The effect of punch radius on the deformation of ultra-high strength steel in bending, Key Eng. Mater. 639 (2015) 139-146.

[8] L. Wagner, H. Schauer, H. Pauli, J. Hinterdorfer, Improved bendability characterization of UHSS sheets, IOP Conf. Ser. Mater. Sci. Eng. 651 (2019) 012019. https://doi.org/10.1088/1757-899X/651/1/012019
[9] M. Kaupper, M. Merklein, Bendability of advanced high strength steels - A new evaluation procedure, CIRP Ann. - Manuf. Technol. 62 (2013) 247-250. https://doi.org/10.1016/j.cirp.2013.03.049
[10] K. Cheong, K. Omer, C. Butcher, R. George, J. Dykeman, Evaluation of the VDA 238-100 Tight Radius Bending Test using Digital Image Correlation Strain Measurement, J. Phys. Conf. Ser. 896 (2017) 12075. https://doi.org/10.1088/1742-6596/896/1/012075
[11] A.-M. Arola, A. Kaijalainen, V. Kesti, A.-P. Pokka, J. Larkiola, Digital image correlation and optical strain measuring in bendability assessment of ultra-high strength structural steels, Procedia Manuf. 29 (2019) 398-405. https://doi.org/10.1016/j.promfg.2019.02.154
[12] S. Gothivarekar, S. Coppieters, A. Van de Velde, D. Debruyne, Advanced FE model validation of cold-forming process using DIC: Air bending of high strength steel, Int. J. Mater. Form. 13 (2020) 409-421. https://doi.org/10.1007/s12289-020-01536-1
[13] R. Ruoppa, R. Toppila, V. Kesti, A. Arola, Bendability tests for ultra-high-strength steels with optical strain analysis and prediction of bending force, Proc. METNET Seminar 2014 Moscow (2014) 68-78.
[14] C. Suppan, T. Hebesberger, A. Pichler, J. Rehrl, O. Kolednik, On the microstructure control of the bendability of advanced high strength steels, Mater. Sci. Eng. A 735 (2018) 89-98. https://doi.org/10.1016/j.msea.2018.07.080
[15] SFS-EN ISO 7438:2016: Metallic materials – Bend test.

Materials Research Proceedings 28 (2023) 705-710 https://doi.org/10.21741/9781644902479-76

Prediction of forming limit diagram of automotive sheet metals using a new necking criterion

PHAM Quoc Tuan [1,a *], ISLAM Md Shafiqul [1,b], SIGVANT Mats[1,2,c] and CARO Perez Lluis [3,d]

[1]Department of Mechanical Engineering, Blekinge Institute of Technology, Karlskrona 37141, Sweden

[2]Volvo Cars, Department 81110 Strategy & Concept, Olofström, Sweden

[3]RISE Research Institutes of Sweden, Component Manufacturing Unit, Olofström, Sweden

[a]quoc.tuan.pham@bth.se, [b]shafiqul.islam@bth.se, [c]mats.sigvant@bth.se, [d]lluis.perez.caro@ri.se

Keywords: Forming Limit Diagram, DP800, AA6016, MMFC2, MK Method

Abstract. A theoretical model for predicting the forming limit diagram of sheet metal, named MMFC2, was recently proposed by the authors based on the modified maximum force criterion (MMFC). This study examines the application of MMFC2 for two automotive sheets, DP800 and AA6016, which are widely used in making car body parts. Uniaxial tensile and bulge tests are conducted to calibrate constitutive equations for modeling the tested materials. The developed material models are employed into different frameworks such as MMFC, MMFC2, and Marciniak-Kuczynski (MK) models to forecast the forming limit curve (FLC) of the tested materials. Their predictions are validated by comparing with an experimental one obtained from a series of Nakajima tests. It is found that the derived results of MMFC2 are comparable to that of MK model and agreed reasonably with experimental data. Less computational time is the major advantage of MMFC2 against the MK model.

Introduction

The formability of sheet metal is commonly evaluated by using a forming limit diagram (FLD). In this concept, a graphical representation of the forming limit, the forming limit curve (FLC), is used to separate the safe forming region in the strain space. Different testing setup, such as the Nakajima and Marciniak tests, can be used to determine the FLC experimentally [1]. In order to reduce the cost of experimental methods, huge efforts have been made to predict the FLC theoretically.

Publications of Swift [2] and Hill [3] are considered the pioneering works for this task. Storen and Rice [4] presented an alternative theoretical approach for FLC prediction. In this approach, the bifurcation analysis of deformation velocity was coupled with the deformation theory to determine the initiation of localized necking. Based on observations of geometrical imperfection of the tested coupon, Marciniak and Kuczynski [5] introduced a numerical procedure for predicting the FLC. Later, Hora et al. [6] formulated a criterion (MMFC) for neck determination based on the strain path change at the onset of diffuse neck.

Previous studies published in the literature demonstrate that these theoretical models may provide good predictions for FLC of some particular materials. Reviewing studies pointed out that there is not exist a universal model that can be applied for any metallic sheets. Recently, the MMFC is attractive because of its validation, which can be done with the use of digital cameras and correlation techniques (DIC). However, the application of the MMFC is limited due to some numerical issues, as discussed in references [7,8]. Recently, the authors discussed the reliability of theoretical assumptions implied in the MMFC, which leads to an improved version named MMFC2 [9].

Content from this work may be used under the terms of the Creative Commons Attribution 3.0 license. Any further distribution of this work must maintain attribution to the author(s) and the title of the work, journal citation and DOI. Published under license by Materials Research Forum LLC.

This study presents comparisons between the applications of the original MMFC and the new version (MMFC2) for predicting the FLC of two automotive sheet metals, DP800 and AA6016. In addition, the predictions of MK model are also put into the comparison. Experimental FLC determined from the Nakajima tests are provided to discuss the reliability of these theoretical predictions.

The MMFC2 Model

Based on experimental observations of the strain path change beyond the diffuse neck, Hora et al. [6] introduced the condition for neck initiation as follows.

$$\frac{\partial \sigma_1}{\partial \varepsilon_1} + \frac{\partial \sigma_1}{\partial \beta}\frac{\partial \beta}{\partial \varepsilon_1} \geq \sigma_1 \tag{1}$$

In this equation, σ_1 and ε_1 denotes the principal major stress and the principal major strain, respectively; $\beta = \Delta\varepsilon_2/\Delta\varepsilon_1$ is the ratio between the minor and major strain increments. This equation results in an evolution of β, which is expressed as follows.

$$\Delta\beta = \frac{\sigma_1 - \frac{\partial \sigma_1}{\partial \varepsilon_1}}{\frac{\partial \sigma_1}{\partial \beta}}\Delta\varepsilon_1 \tag{2}$$

Hence, the strain localization is determined as soon as β approaches zero, indicating the plane-strain forming mode.

The condition is formulated based on the condition of maximum loading force observed during a uniaxial tensile test. In the MMFC, the strain path change is enforced to keep the maximum force unchanged. However, numerous experiments pointed out that the force drop may be up to 10% after the maximum for many automotive sheet metals [10]. Therefore, a scaling factor, ξ is proposed to slowdown the changing rate of β. Consequently, the evolution of β is updated as follows.

$$\Delta\beta = \xi\frac{\sigma_1 - \frac{\partial \sigma_1}{\partial \varepsilon_1}}{\frac{\partial \sigma_1}{\partial \beta}}\Delta\varepsilon_1 \tag{3}$$

In order to determine the value of ξ, a finite element simulation for uniaxial tensile test should be conducted to compare the simulated β evolution with the curve predicted by the MMFC for the uniaxial tension mode. In this study, a recommended value ($\xi = 0.5$) is adopted in the subsequent calculation without any further calibration.

For ductile materials, necking may occur before the fracture. Therefore, theoretical assumption of plane-strain forming mode at necking required in MMFC seems to overreach. An alternative condition for detecting the strain localization is presented as follows.

$$\left|\frac{d(\Delta\beta)}{d\underline{\varepsilon}}\right| \tag{4}$$

In other words, the localized neck is supposed to occur when the acceleration of strain path change reaches its minimum.

Calculation of the Forming Limit Curves

This study investigates two automotive sheet metals, i.e., DP800 and AA6016. The thickness of both materials is 1.2 mm. A series of Nakajima tests are conducted following the ISO 12004-2 standard to determine the experimental FLC for the examined materials. During these tests, the ARAMIS digital image correlation (DIC) system is used to monitor the strain field distribution on

the surface of the deformed specimens. The experimental FLC is calculated using the FLC built-in function in ARAMIS.

A proper material model is needed to calculate the theoretical FLC. For this purpose, constitutive models used to describe material's behavior under complex stress states were previously calibrated by Barlo et al. [11] and not be repeated here. The Swift hardening law [1] is adopted for DP800 whereas the Voce model [2] is applied for AA6016. Moreover, the Yld2000-2d yield function proposed by Barlat et al. [12] is applied to capture the yield surface of these tested materials. The formulations of these functions are expressed below.

$$\text{Swift}: H(\underline{\varepsilon}) = C(\varepsilon_0 + \underline{\varepsilon})^n \tag{5}$$

$$\text{Voce}: H(\underline{\varepsilon}) = S - a.exp(-b\underline{\varepsilon}) \tag{6}$$

$$\text{Yld2000-2d}: \underline{\sigma} = \left\{\frac{1}{2}\left(\left|X_1^{'} - X_2^{'}\right|^m + \left|2X_1^{''} + X_2^{''}\right|^m + \left|X_1^{''} + 2X_2^{''}\right|^m\right)\right\}^{1/m} \tag{7}$$

where C, ε_0, n, S, a, and b are hardening parameters; $X_{1,2}^{',''}$ are the principal values of two linearly transformed tensors which contain eight anisotropic parameters (α_1 – α_8) and the exponent parameter m. The calibrated parameters of each hardening law and yield function for the investigated materials are reported in Table 1 and Table 2, respectively.

Table 1. Hardening parameters of the tested materials.

Hardening law	Swift			Hardening law	Voce		
	C [MPa]	ε_0	n		S [MPa]	a [MPa]	b
DP800	1322.89	0.0012	0.165	AA6016	336.84	215.9	8.179

Table 2. Parameters of the Yld2000-2d function calibrated for the tested materials.

Yield function	α_1	α_2	α_3	α_4	α_5	α_6	α_7	α_8	m
DP800	0.9037	1.0270	1.0546	1.0055	1.0165	0.9367	0.9917	1.0306	6
AA6016	0.9633	0.9996	0.9438	1.0244	1.0134	0.9906	0.9683	1.1448	8

Fig. 1 depicts the calibrated hardening laws for both tested materials in comparison with the experimental data obtained from uniaxial tensile tests. Fig. 2 compares the predicted yield locus of these materials. These material models are employed in the framework of MMFC2 to predict their FLC. Moreover, the predictions of the original MMFC and MK models for the tested materials are also calculated for comparison purposes. A detailed description of these models can be found in Pham et al. [9].

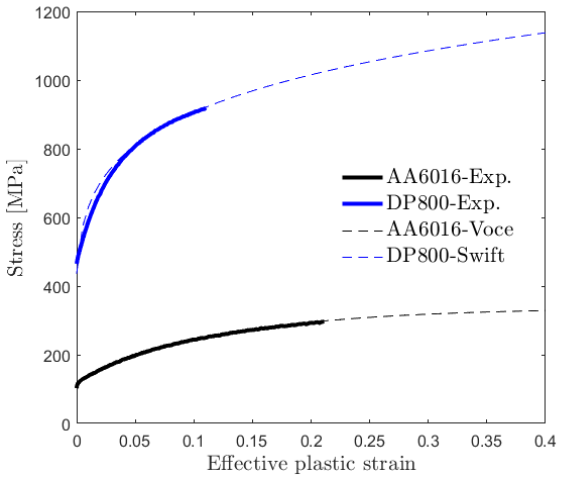

Fig. 1. Calibrated hardening law of the tested materials DP800 and AA6016.

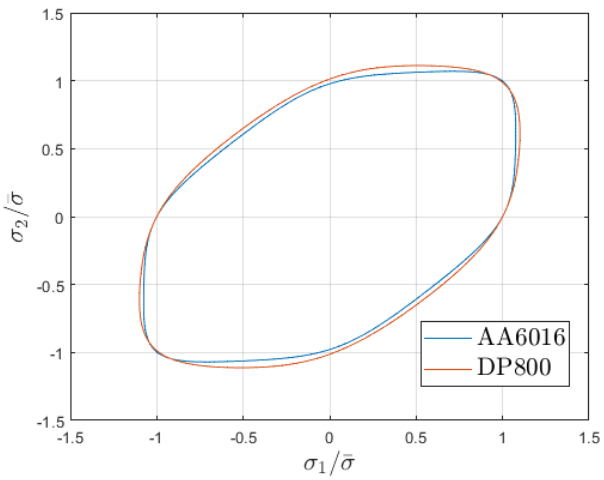

Fig. 2. Yield locus predicted by Yld2000-2d function for the tested materials.

Discussion

The predicted FLCs of DP800 and AA6016 sheets, based on different models, are compared with experimental data in Fig. 3 and Fig. 4, respectively. To simplify the comparison of the predicted and experimental FLCs, the experimental data were offset so the lowest forming limit point was moved to the plane strain region.

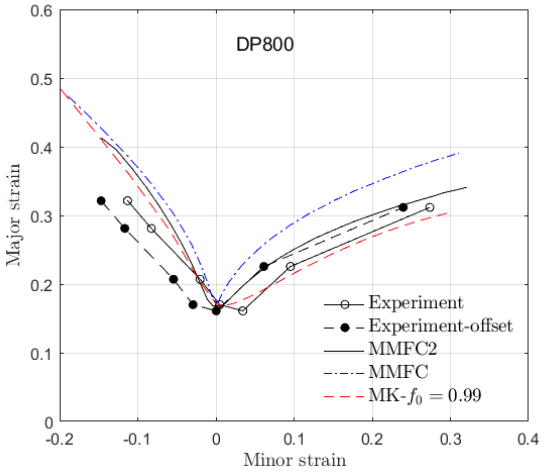

Fig. 3. Experimental and predicted FLCs of DP800.

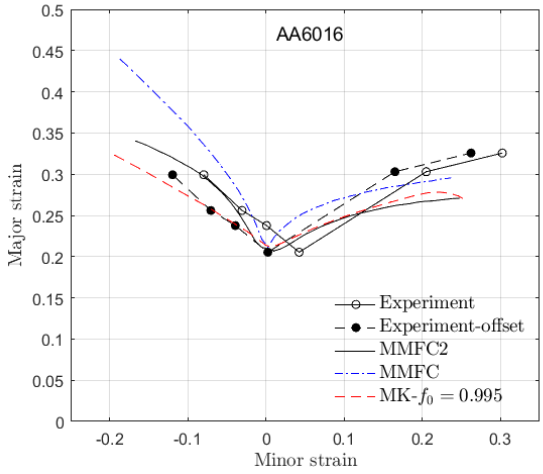

Fig. 4. Experimental and predicted FLCs of AA6016.

It can be seen in Fig. 3 that the MK model provides an excellent prediction of the experimental data of DP800, especially the region comprised between plane strain and biaxial tension. The MMFC model overestimates the experimental data, except for the plane strain point. Between uniaxial tension and plane strain regions, the MMFC2 agrees with MK model prediction, which is slightly higher than the experimental data. However, the results of MMFC2, in the right-side of the curve, lie in between these two other predictions.

In the case of AA6016 shown in Fig. 4, all theoretical models underestimate the experimental data in the biaxial tension regimes, probably due to the use of the Voce hardening law, which

shows a saturation stress in large strain ranges. In addition, the selected value of the exponent parameter, m influences the derived results, as discussed in [8]. Again, the MK model provides the best prediction for the left-side of the experimental curve. In contrast, the result of MMFC is significantly higher than the experiment. On the one hand, the MMFC2 presents an intermediate prediction for the left-side curve, whereas on the other hand, the result of this model for the right-side curve is close to that of the MK model.

The comparisons reveal that the prediction of the MK model is the most reliable among the considered theoretical models. The good performance of the MK model has been demonstrated in the literature for different materials subjected to different loading scenarios [13]. This study affirms the conclusion. The MMFC seems to overestimate the measured data of the tested materials. The MMFC2 improves the accuracy of the MMFC. Compared to the MK model, the MMFC2 derives comparable predictions for the FLC of the tested materials with an around five times faster computational time. The reason for the computational benefit of MMFC2 is due to its formulation, which does not require solving any system of non-linear equations as the MK model does. Details on the computational time of each theoretical model implemented in this study are reported in Table 3. According to this table, the computational efficiency of the MMFC2 seems negligible since the MK computational time is very good. However, the advantage gains more attractive when either a more complex material, such as, a distortional hardening model is adopted or a huge number of simulations is inquired, for example, in a data-driven application.

Table 3. Comparison between the computational time of theoretical models.

Theoretical model	MMFC	MMFC2	MK
Computational time (s)	20	25	120

Summary

This work aims to verify the potential of the newly proposed model MMFC2 for theoretically predicting the FLC of sheet metal. Two automotive sheets, DP800 and AA6016, were investigated by comparing the theoretical predictions of three different models, i.e., MMFC, MMFC2, and MK, with the experimental FLC obtained from Nakajima tests. The following conclusions can be made after this study.

- All theoretical models predict similar forming limits at the plane strain region, which are close to the experimental measurement.
- The MMFC model presents remarkably higher forming limits than the measured FLC.
- For both investigated materials, the predictions of the MMFC2 are comparable to those of MK model within a significant reduction of computational time.

Acknowledgement

The authors gratefully acknowledge the financial support from KK-stiftelsen (grant number 20200125) and VINNOVA in the Sustainable Production subprogram within Vehicle Strategic Research and Innovation (FFI) program (grant number 2020-02986).

References

[1] D. Banabic, Sheet Metal Forming Processes: Constitutive Modelling and Numerical Simulation, Springer Berlin, Heidelberg, 2010. https://doi.org/10.1007/978-3-540-88113-1

[2] H.W. Swift, Plastic instability under plane stress. J. Mech. Phys. Solid. 1 (1952) 1-18. https://doi.org/10.1016/0022-5096(52)90002-1

[3] R. Hill, On discontinuous plastic states, with special reference to localized necking in thin sheets, J. Mech. Phys. Solid. 1 (1952) 19-30. https://doi.org/10.1016/0022-5096(52)90003-3

[4] S. Storen, J. Rice, Localized necking in thin sheets, J. Mech. Phys. Solid. 23 (1975) 421-441. https://doi.org/10.1016/0022-5096(75)90004-6

[5] Z. Marciniak, K. Kuczynski, Limit strains in the processes of stretch-forming sheet metal. Int. J. Mech. Sci. 9 (1967) 609–620. https://doi.org/10.1016/0020-7403(67)90066-5
[6] P. Hora, L. Tong, B. Berisha, Modified maximum force criterion, a model for the theoretical prediction of forming limit curves, Int. J. Mat. Form. 6 (2013) 267-279. https://doi.org/10.1007/s12289-011-1084-1
[7] H. Aretz, Numerical restrictions of the modified maximum force criterion for prediction of forming limits in sheet metal forming, Model. Simu. Mater. Sci. Eng. 12 (2004) 677. https://doi.org/10.1088/0965-0393/12/4/009
[8] Q.T. Pham, B.H. Lee, K.C. Park, Y.S. Kim, Influence of the post-necking prediction of hardening law on the theoretical forming limit curve of aluminium sheets, Int. J. Mech. Sci. 140 (2018) 521-536. https://doi.org/10.1016/j.ijmecsci.2018.02.040
[9] Q.T. Pham, M.S. Islam, M. Sigvant, L.P. Caro, M.-G. Lee and Y.-S. Kim: submitted to International Journal of Solids and Structures (2022).
[10] N. Manopulo, P. Hora, P. Peters, M. Gorji, F. Barlat, An extended modified maximum force criterion for the prediction of localized necking under non-proportional loading, Int. J. Plast. 75 (2015) 189-203. http://doi.org/10.1016%2Fj.ijplas.2015.02.003
[11] A. Barlo, M. Sigvant, B. Endelt, On the Failure Prediction of Dual-Phase Steel and Aluminium Alloys Exposed to Combined Tension and Bending, IOP Conf. Ser.: Mater. Sci. Eng. 651 (2019) 012030. https://doi.org/10.1088/1757-899X/651/1/012030
[12] F. Barlat, J. Brem, J.W. Yoon, K. Chung, R. Dick, D. Lege, F. Pourboghrat, S.-H. Choi, E. Chu, Plane stress yield function for aluminum alloy sheets—part 1: theory, Int. J. Plast. 19 (2003) 1297-1319. https://doi.org/10.1016/S0749-6419(02)00019-0
[13] M.C. Butuc, G. Vincze, The performance of Marciniak – Kuczynski approach on prediction of plastic instability of metals subjected to complex loadings, Numisheet 2018, IOP Publishing, Journal of Physics: Conference Series 1063 (2018) 12061. http://doi.org/10.1088/1742-6596/1063/1/012061

Materials Research Proceedings 28 (2023) 711-716 https://doi.org/10.21741/9781644902479-77

Anisotropic deformation behavior during cup drawing at room temperature of a ZX10 magnesium alloy sheet

HAMA Takayuki[1,a *], HIGUCHI Koichi[1,b] and NAKATA Yuto[1,c]

[1]Graduate School of Energy Science, Kyoto University, Yoshida-honmachi, Sakyo-ku, Kyoto 606-8501, Japan

[a]hama@energy.kyoto-u.ac.jp, [b]koichi.higuchi.72a@gmail.com, [c]nakata.yuto.64r@st.kyoto-u.ac.jp

Keywords: Magnesium Alloy, Room-Temperature Cup Drawing, Twinning, Lankford Value, Thickness Strain

Abstract. Magnesium (Mg) alloy sheets have low density and high specific strength; thus, they are expected to facilitate weight reduction of structural components. However, because of the strong crystal anisotropy of the hexagonal structure and the strong basal texture observed in typical rolled Mg alloy sheets, their press formability at room temperature is low. To improve the room-temperature press formability, ZX series Mg alloy sheets that weakened the basal texture have recently been developed. The plastic deformation behavior of a rolled Mg-1.5mass%Zn-0.1mass%Ca (ZX10Mg) alloy sheet was studied in a previous study [7], and it was reported that the plastic deformation behavior showed strong in-plane anisotropy and differed notably from that of AZ series rolled Mg alloy sheets. In the present study, cylindrical cup drawing of a ZX10Mg alloy sheet was performed at room temperature and the drawability was examined in terms of cup height distributions, strain evolution, and texture evolution. The cup height differed significantly between the rolling and transverse directions. The thickness at the cup edge was the largest in the rolling direction and the smallest in the transverse direction. The magnitude relationship of the thickness correlated with the Lankford values under compression. The mechanism that yielded the difference in texture evolution was also discussed.

Introduction

Magnesium (Mg) alloy sheets have low density and high specific strength; thus, they are expected to facilitate weight reduction of structural components [1]. However, because of the strong crystal anisotropy of the hexagonal structure and the strong basal texture observed in typical rolled Mg alloy sheets, their press formability at room temperature is low [2,3]. To improve the press formability, ZX series Mg alloy sheets that weakened the basal texture have recently been developed. Chino et al. [4-6] conducted the room-temperature Erichsen cupping test of ZX series Mg alloy sheets and reported that their stretchability is superior to that of AZ series rolled Mg alloy sheets. Hama et al. [7] reported that the work-hardening behavior of a rolled Mg-1.5mass%Zn-0.1mass%Ca (ZX10Mg) alloy sheet shows strong in-plane anisotropy, which differs notably from those of typical AZ series rolled Mg alloy sheets. Nakata et al. [8] conducted room-temperature V-bending tests of a ZX10 Mg alloy sheet and studied the bendability in terms of activities of slip and twinning systems. It is expected that ZX series Mg alloy sheets exhibit not only better stretchability and bendability but also superior drawability, which is also one of the important properties for industrial applications. It is also presumed from the previous study that anisotropic deformation is exhibited during drawing because of the strong in-plane anisotropy of the work-hardening behavior. However, room-temperature drawability of ZX series Mg alloy sheets have not been studied yet.

In the present study, cylindrical cup drawing of a ZX10Mg alloy sheet was performed at room temperature and the drawability was discussed in terms of cup height and strain distributions.

Content from this work may be used under the terms of the Creative Commons Attribution 3.0 license. Any further distribution of this work must maintain attribution to the author(s) and the title of the work, journal citation and DOI. Published under license by Materials Research Forum LLC.

Texture evolution was also measured to discuss the correlation between the macroscopic and mesoscopic deformation behaviors.

Experimental Methods

A rolled ZX10 Mg alloy sheet with 1.0 mm thickness produced by Sumitomo Electric Industries, Ltd. [7] was used. Circular cup drawing tests were conducted at room temperature. The experimental procedures were the same as those reported in a literature [9]. A photograph of the experimental setup for cup drawing test is shown in Fig. 1. The diameters of punch and die cavity were 27.8 mm and 30 mm, respectively. The punch and die shoulder radii were 5.0 mm and 7.0 mm, respectively. The diameter of the circular specimen was 40 mm, which corresponds to the drawing ratio of 1.33. The distance between the die and the blank holder was set to 1.1 mm and kept unchanged during forming. A solid lubricant (Moly Paste, Sumico Lubricant Co.) was used for lubrication between the sheet and the dies. The punch was penetrated to a stroke of 16 mm with a punch speed of 5 mm/min.

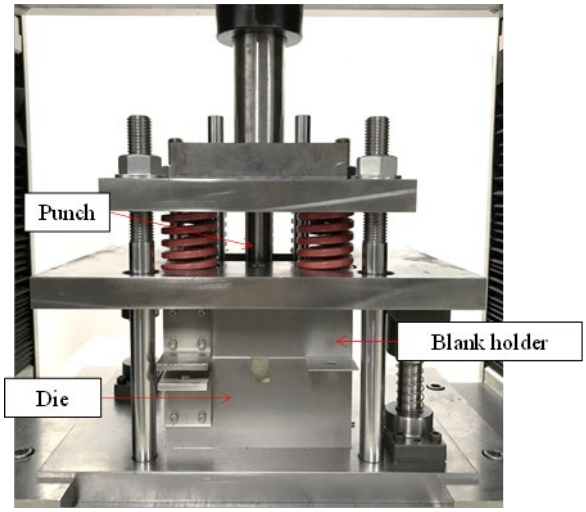

Fig. 1. Experimental setup for the cylindrical cup drawing.

Thickness and cup height of the products were measured using a micrometer and a two-dimensional laser displacement sensor (LJ-V7080, Keyence Co.), respectively. Electron backscattered diffraction (EBSD) measurements were conducted to measure the texture at some points. Fig. 2 shows the pole figure of the initial sample [7]. In the (0001) pole figure, strong peaks appeared in the vicinity of the normal direction (ND), but at the same time weak peaks appeared near the transverse direction (TD), showing that the basal texture is less pronounced than that of typical AZ series rolled Mg alloy sheets [10, 11].

Results and Discussion

Figs. 3 (a) and 3 (b) show the photograph of a drawn cup and the distributions of cup height in the circumferential direction at different punch strokes, respectively. In Fig. 3 (b), the vertical axis denotes the relative height in which the height at the rolling direction (RD) was set to zero in order to exclude the effect of the curvature at the cup bottom. Moreover, considering the symmetry of the deformation, only the results in the first quadrant is shown.

The cup height was larger in the TD than in the RD already at the stroke of 8 mm. The increasing trend is pronounced from the angle of 15° to 60°. The cup height increased with increasing the punch stroke. This trend was more pronounced in the vicinity of the angle of 60°, which eventually

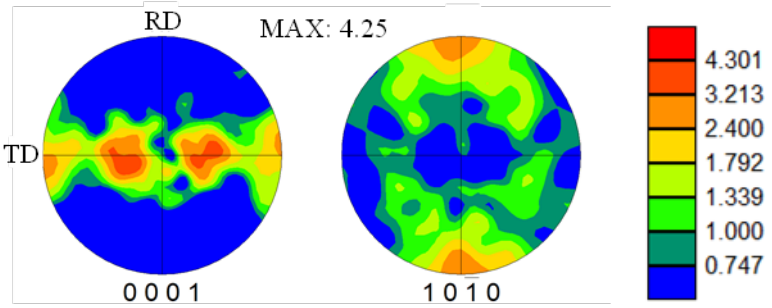

Fig. 2. Initial pole figures of the sample.

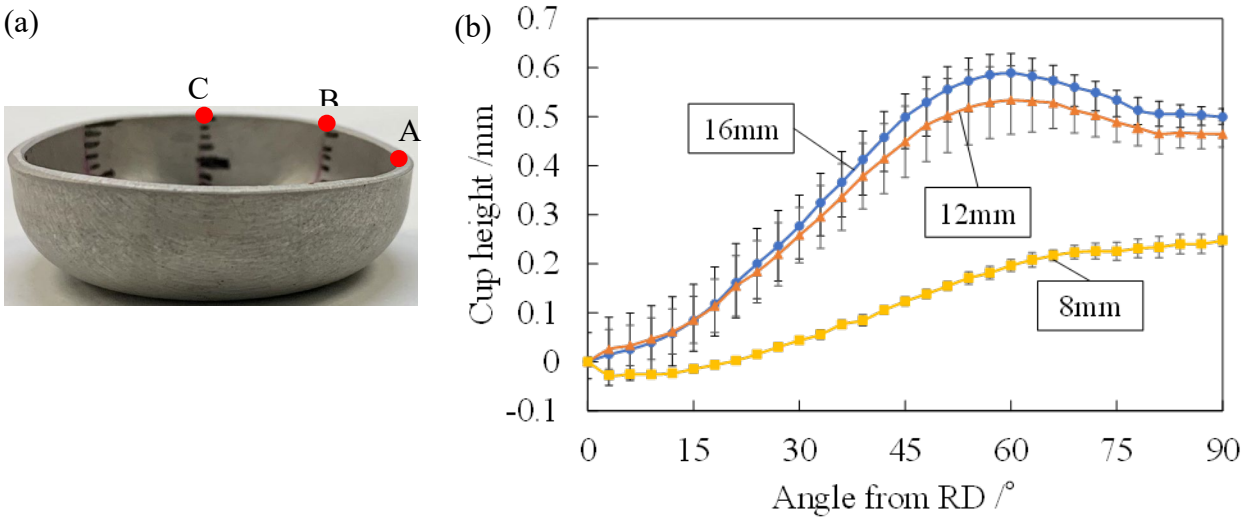

Fig. 3. Geometry of the drawn cup. (a) Photograph of a drawn cup, and (b) distribution of cup height.

resulted in earing formation in the vicinity of the angle of 60°. The tendency of the cup height distribution at the punch stroke of 16 mm remained almost unchanged from that of the punch stroke of 12 mm. It is noted that the cup heights differed largely between the RD and TD also in the final product.

Fig. 4 shows the evolution of thickness strain at the points near the sheet edge in the RD, diagonal direction (DD), and TD, i.e., points A, B, and C in Fig. 3 (a), respectively. The thickness strains increased largely from the punch stroke of 4 mm to 13 mm. The thickness strain was the largest in the RD and that of the DD was larger than that of the TD until the stroke of 13 mm. Thereafter, the thickness strains decreased because of ironing between the punch and the die. Eventually, the thickness strains at the RD and DD became almost the same.

Fig. 5 shows the pole figures measured at the points A and B of the drawn cup. Compared to the initial pole figure shown in Fig. 2, strong peaks near the ND did not appear at both points. In contrast, strong peaks appeared near the TD and RD at the points A and B, respectively. These results show that the texture evolution depended largely on the region.

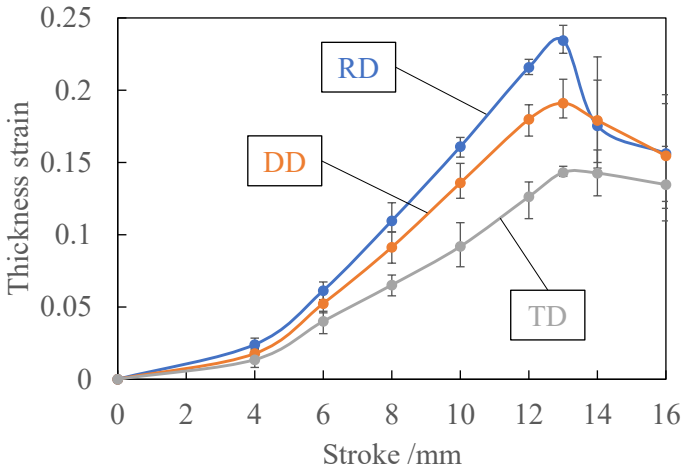

Fig. 4. Evolution of thickness strain at the sheet edge.

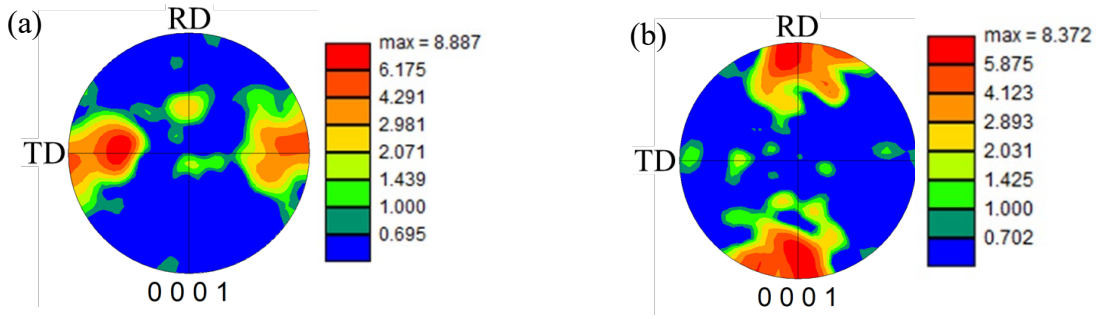

Fig. 5. (0001) pole figures measured at the points (a) A and (b) B.

Results and Discussion

Thickness distributions. The mechanism that the thickness strain was the largest in the RD and the smallest in the TD is discussed. Large thickening occurred at the sheet edge because the sheet edge was subjected to circumferential compression before the sheet edge was drawn into the die cavity. Specifically, during drawing, the regions near the sheet edge in the RD, DD, and TD are subjected to compression in the TD, DD, and RD, respectively. This indicates that thickness increase would be the largest in TD compression and the smallest in RD compression. It may be useful to consider the correlation with Lankford value to examine the difference in thickness increase depending on the direction. However, Lankford values of the Mg alloy sheet would be different between tension and compression because of the polar character of twinning [12]. Therefore, the Lankford values were measured under both tension and compression. In the compression test, comb-shaped dies were attached to the specimen to avoid occurrence of out-of-plane buckling. In both tension and compression tests, longitudinal and width strains were measured using a digital image correlation (DIC) method. In the DIC method, the software GOM Correlate Professional V8 (GOM) was used. Plastic strains were evaluated by subtracting elastic strains estimated using Young's modulus and Poisson ratio from the measured total strains.

Figs. 6 shows the evolution of Lankford values as a function of longitudinal strain. Under tension, the Lankford value was the largest in the RD at small strains, and that in the DD was larger than that of the TD. However, the Lankford values in the DD and TD tended to increase as the strain increased, while the Lankford value in the RD remained almost unchanged; thus, that of the DD became the largest at large strains. Under compression, the Lankford value in the RD was the largest, and that of the DD was larger than that of the TD. This trend remained unchanged in the

strain range tested in this work. Apparently, the magnitude relationship of the Lankford value differed between tension and compression. Moreover, the magnitude relationship of the Lankford value under compression at large strains is consistent with that of thickening on the drawn cup before the sheet was subjected to ironing. These results show that, for the ZX10 Mg alloy sheet, the thickness strain distribution should be evaluated not by the Lankford value under tension but by that of compression. Moreover, these results also suggest that the difference in the Lankford value between the RD and TD also yielded the notable difference in the cup height between the RD and the TD.

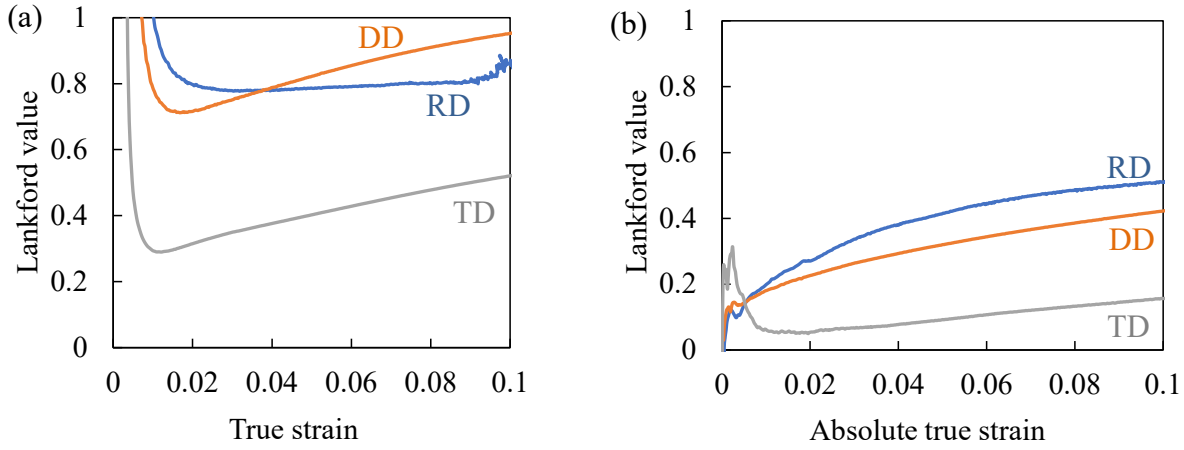

Fig. 6. Evolution of Lankford value under (a) tension and (b) compression.

Texture evolution. Next, the difference in texture evolution depending on the region is discussed. As discussed in a literature [7], under TD compression, twinning is active at the grains whose basal planes oriented near the ND, whereas it is not at the grains whose basal planes oriented near the TD. As a result, the peaks near the ND observed in the initial pole figure tend to disappear and strong peaks appear near the TD. This texture evolution is consistent with that observed at the point A which experienced TD compression

Similarly, under RD compression, twinning is easy to active at both grains whose basal planes oriented near the ND and the TD; thus, the peaks near the TD and ND observed in the initial pole figure disappeared and the peaks near the RD appeared [7]. This is also consistent with the result at the point B.

These results suggest that the texture evolution observed at the sheet edge was primarily governed by circumferential compression and, moreover, one of the reasons that the texture evolution differed depending on the region is the difference in the twinning activity.

Summary

Room-temperature cylindrical cup drawing of a ZX10Mg alloy sheet was conducted and the drawability was discussed. The results obtained in this study can be summarized as follows.

(1) The cup height started increasing largely after the punch stroke exceeded 8 mm. The maximum height appeared at 60° from the rolling direction. The cup height was larger in the transverse direction than in the rolling direction.

(2) The thickness at the cup edge was the largest in the rolling direction and the smallest in the transverse direction before the sheet was subjected to ironing. The magnitude relationship of the thickness correlated with the Lankford values under compression.

(3) The difference in twinning activity was one of the reasons that yielded the difference in the texture evolution depending on the direction.

Acknowledgements
The authors would like to thank Sumitomo Electric Industries, Ltd. for providing the ZX10 Mg alloy sheet used in this study. The authors gratefully acknowledge Mr. Sohei Uchida of TRI Osaka for his kind assistance in performing the EBSD measurements. This work was supported by Japan Society for the Promotion of Science JSPS, KAKENHI, grant number JP20H02480 and the AMADA Foundation (AF-2019004-A3).

References
[1] A.I. Taub, A.A. Luo, Advanced lightweight materials and manufacturing processes for automotive applications, MRS Bull. 40 (2015) 1045-1053. https://doi.org/10.1557/mrs.2015.268
[2] F.-K. Chen, T.-B. Huang, C.-K. Chang, Deep drawing of square cups with magnesium alloy AZ31 sheets, Int. J. Mach. Tools Manuf. 43 (2003) 1553-1559. https://doi.org/10.1016/S0890-6955(03)00198-6
[3] E. Doege, K. Dröder, Sheet metal forming of magnesium wrought alloys — formability and process technology, J. Mater. Process. Technol. 115 (2001) 14-19. https://doi.org/10.1016/S0924-0136(01)00760-9
[4] Y. Chino, X. Huang, K. Suzuki, M. Mabuchi, Enhancement of stretch formability at room temperature by addition of Ca in Mg-Zn alloy, Mater. Trans. 51 (2010) 818-821. http://doi.org/10.2320/matertrans.M2009385
[5] Y. Chino, T. Ueda, Y. Otomatsu, K. Sassa, X. Huang, K. Suzuki, M. Mabuchi, Effects of Ca on tensile properties and stretch formability at room temperature in Mg-Zn and Mg-Al alloys, Mater. Trans. 52 (2011) 1477-1482. http://doi.org/10.2320/matertrans.M2011048
[6] Y. Chino, K. Sassa, X. Huang, K. Suzuki, M. Mabuchi, Effects of Zinc concentration on the stretch formability at room temperature of the rolled Mg-Zn-Ca alloys, J. Japan Inst. Metals 75 (2011) 35-41. (in Japanese)
[7] T. Hama, K. Higuchi, H. Yoshida, Y. Jono, Work-hardening behavior of a ZX10 Magnesium alloy sheet under monotonic and reverse loadings, Key Eng. Mater. 926 (2022) 926-932. https://doi.org/10.4028/p-7bgcsj
[8] T. Nakata, T. Hama, K. Sugaya, S. Kamado, Understanding room-temperature deformation behavior in a dilute Mg-1.52Zn-0.09Ca (mass%) alloy sheet with weak basal texture, Mater. Sci. Eng. A 852 (2022) 143638. https://doi.org/10.1016/j.msea.2022.143638
[9] T. Hama, K. Hirano, R. Matsuura, Cylindrical cup drawing of a commercially pure titanium sheet: experiment and crystal plasticity finite-element simulation, Int. J. Mater. Form. 15 (2022) 8. https://doi.org/10.1007/s12289-022-01655-x
[10] T. Hama, Y. Tanaka, M. Uratani, H. Takuda, Deformation behavior upon two-step loading in a magnesium alloy sheet, Int. J. Plast. 82 (2016) 283-304.
[11] T. Hama, T. Suzuki, S. Hatakeyama, H. Fujimoto, H. Takuda, Role of twinning on the stress and strain behaviors during reverse loading in rolled magnesium alloy sheets, Mater. Sci. Eng. A 725 (2018) 8-18. http://doi.org/10.1016/j.msea.2018.03.124
[12] D Steglich, X. Tian, J. Bohlen, T. Kuwabara, Mechanical testing of thin sheet Magnesium alloys in biaxial tension and uniaxial compression, Exp. Mech. 54 (2014) 1247-1258. https://doi.org/10.1007/s11340-014-9892-0

Materials Research Proceedings 28 (2023) 717-726 https://doi.org/10.21741/9781644902479-78

Modelling failure of joining zones during forming of hybrid parts

WESTER Hendrik[1,a *], STOCKBURGER Eugen[1,b], PEDDINGHAUS Simon[1,c], UHE Johanna[1,d] and BEHRENS Bernd-Arno[1,e]

[1]Institute of Forming Technology and Machines (IFUM), Leibniz Universität Hannover, An der Universität 2, 30823 Garbsen, Germany

[a]wester@ifum.uni-hannover.de, [b]stockburger@ifum.uni-hannover.de, [c]peddinghaus@ifum.uni-hannover.de, [d]uhe@ifum.uni-hannover.de, [e]behrens@ifum.uni-hannover.de

Keywords: Pre-Joined Hybrid Semi-Finished Parts, Numerical Modelling, Cohesive Zones, Local Tensile Tests

Abstract. Combining diverse materials enables the use of the positive properties of the individual material in one component. Hybrid material combinations therefore offer great potential for meeting the increasing demand on highly loaded components. The use of hybrid pre-joined semi-finished products simplifies joining processes through the use of simple geometries. However, the use of pre-joined hybrid semi-finished products also results in new challenges for the following process chain. For example, the materials steel and aluminium may form brittle intermetallic phases in the joining zone, which can be damaged in the following forming process under the effect of thermo-mechanical loads and thus lead to a weak point in the final part. Due to their small thickness as well as their position in the component, the analysis of the joining zone is only possible by complex destructive testing methods. FE simulation therefore offers an efficient way to analyse the development of damage in the process design and to reduce damage by process modifications. Therefore, within this study a damage model based on cohesive zone elements is implemented in the FE software MSC Marc 2018 and calibrated using experimental local tensile tests performed under process relevant conditions.

Introduction

Given the constant shortage of energy as well as raw material resources and the associated costs, the conservation of resources in all areas is of great importance to society as a whole. The manufacturing industry in particular offers a wide range of potentials that extend across development, production and subsequent part usage. The resulting steadily increasing demands on components in terms of strength, functional integration and weight can no longer be met by monolithic materials. In this context, hybrid components show great potential, due to the possibility to locally use suitable materials at the right place. In recent years, composite forging has developed considerably for the production of hybrid components such as gear elements [1], whereby the semi-finished products are joined during the forging process. For example, hybrid bulk metal components such as connecting rods, wheel hubs and control arms are manufactured by Leiber Group GmbH & Co. KG, where the material composite is produced in particular by frictional and interlocking connection [2].

Groche et al. studied the influence of process variables on the welding of steel and aluminium by cold extrusion [3]. The billets' initial microstructural states, height ratio as well as the treatment of welding surfaces were investigated. They found that the precipitation hardened state of aluminium alloys are more suited for processing than the soft annealed state if the intention is to obtain a sound bonding behaviour with steel. An innovative manufacturing route for the production of hybrid components named Tailored Forming was developed using hybrid pre-joined semi-finished [4]. The material combination of steel and aluminium has great potential for industrial

Content from this work may be used under the terms of the Creative Commons Attribution 3.0 license. Any further distribution of this work must maintain attribution to the author(s) and the title of the work, journal citation and DOI. Published under license by Materials Research Forum LLC.

application in hybrid components. On the one hand, the high lightweight potential of aluminium alloys can be exploited. On the other hand, components that are subject to special requirements in terms of strength and load-bearing capacity can be made of steel. However, use of hybrid components also result in new challenges with regard to component design and the development as well as implementation of manufacturing processes. When using dissimilar metallic material combinations, the bonding zone in particular represents a critical point during forming and in the final component. Therefore, it requires special consideration. Previous investigations show that during impact extrusion critical tensile stresses occur within the joining zone which can lead to local rupture [5]. However, the joining zone within the process as well as in the final component can only be analysed at great expense and in destructive tests. Therefore, this work focuses on the experimental analysis of bonding strength of hybrid pre-joined semi-finished parts consisting of steel and aluminium taking into account process relevant temperatures. Based on the results a newly developed material model [6] for describing the damage development within the joining zone is calibrated and implemented in the commercial FE software MSC Marc.

Materials and Methods

Tailored Forming process chain.

The processing of pre-joined hybrid semi-finished products requires adapted process chains. In particular, the diverging material properties and the resulting requirements on the forming process must be taken into account for material combinations of different types, such as steel and aluminium. The Tailored Forming process chain for manufacturing a hybrid demonstrator shaft in the material combination 1.3505 (100Cr6) and 3.2315 (EN AW-6082) is shown schematically in Fig. 1 and described in detail in the following. The joining of the steel and aluminium is carried out by friction welding. Afterwards, the part is heated inductively. Previous studies have shown that temperature control is of particular importance for the forming of hybrid steel-aluminium semi-finished products. Therefore, an inhomogeneous temperature field is set via induction heating [7]. The aim is to heat the steel as much as possible and keep the aluminium as cold as possible, to match the flow stresses of both materials. After heating, forming is carried out by an impact extrusion process on a screw press (Lasco SPR 500). The process takes 0.12 s, whereby the diameter is reduced by 31.5 %. Finally, the part is finished by turning and a high-performance component is created.

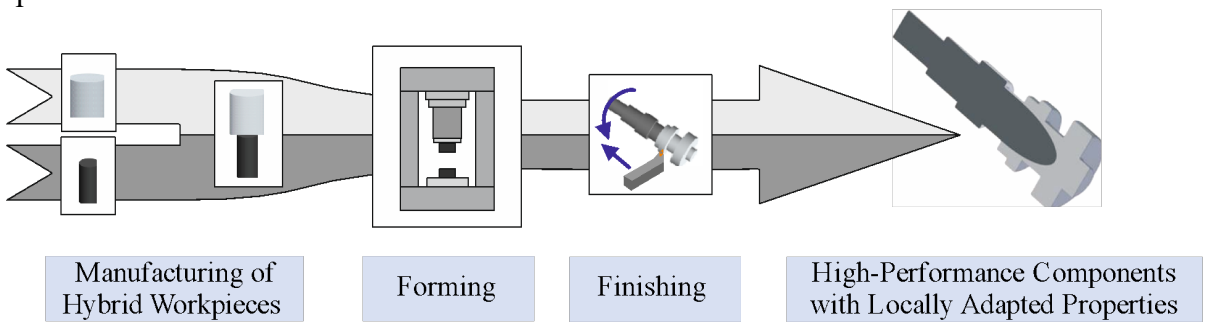

Fig. 1. Tailored Forming process chain for the production of hybrid shafts according to [8].

Thermo-mechanical material modelling.

In order to describe the material behaviour of the used aluminium EN AW-6082, flow curves are taken from previous work [5]. For the 100Cr6, flow curves from Simufact Forming 16.0 database are used to model the steel. A comparison of the used flow curves for different temperatures and a strain rate of 1 s^{-1} is given in Fig. 2. The comparison of the yield stresses of the materials clearly shows that inhomogeneous heating is required to adjust the yield stress levels. Comparable flow stress levels can be defined between 600°C and 1000°C in the case of 100Cr6 and between 20°C and 300°C in the case of the EN AW-6082. The temperature and strain rate

dependent flow curves were implemented in the FE software Simufact Forming 16 and MSC MARC Mentat 2018 for a simulation of the inductive heating and the impact extrusion.

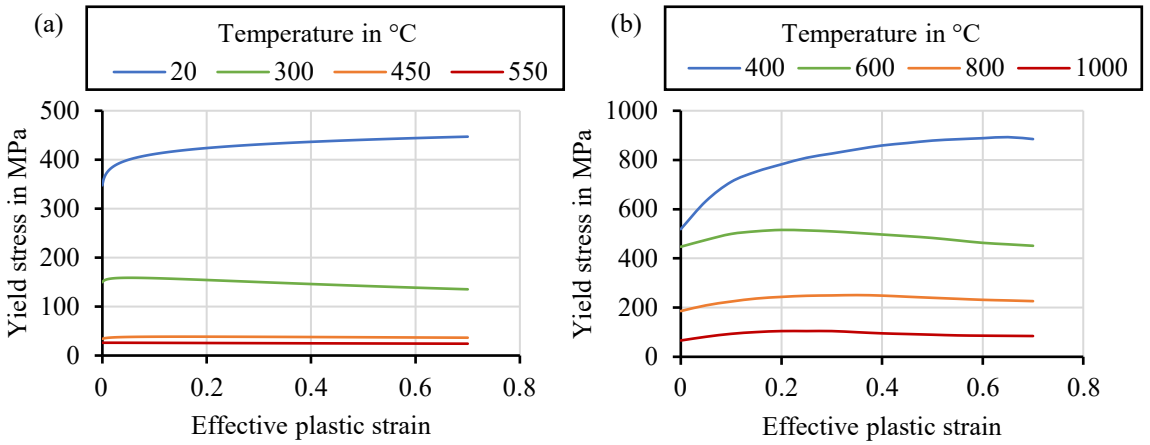

Fig. 2. Flow curves for various temperatures and a strain rate of 1 s^{-1} for EN AW-6082 (a) and 100Cr6 (b).

Analysis of local bonding strength.

The resulting local bonding strength after friction welding is investigated by local tensile tests (as shown in Fig. 3) using miniaturised sample geometries on the forming dilatometer DIL805A/D+T. The use of miniaturised samples with a thickness of 1 mm allows local analysis of bond strength as a function of the semi-finished product diameter. In order to physically map the critical thermo-mechanical stresses of the hybrid semi-finished products, which lead to failure of the joining zone, the tensile tests are carried out at various testing temperatures. The temperatures for tensile testing are determined based on numerically calculated temperatures in the joining zone during impact extrusion. The tensile tests are performed at a quasi-static strain rate of 0.001 s^{-1}.

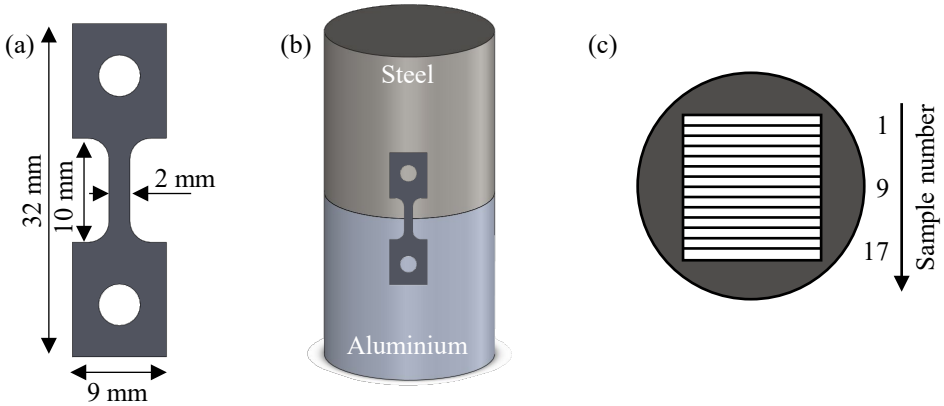

Fig. 3. Procedure for characterising the local bonding strength of joining zones: sample geometry (a) and sectional view (b) as well as top view (c) of the sample extraction area.

Numerical model of induction heating and impact extrusion.

Numerical simulation allows a realistic determination of temperature distribution during the impact extrusion process. To determine process relevant testing temperature for the tensile tests a numerical model representing induction heating as well as the forming process was first developed using the commercial FE software Simufact Forming 16. The model for induction heating consists of the hybrid billet placed within the induction coil. During heating, only the steel is heated

inductively, the aluminium is heated by thermal conduction. Between steel and aluminium an adhesive contact was defined and an intermetallic layer of 0.07 µm was assumed [9] with a thermal conductivity of 10 W/mK according to Nacke [10]. Boundary conditions like current, time and frequency were taken from experiments and set as input. Thermal material data was defined based on Simufact Forming 16 database. The relative permeability was determined by Behrens et al. using the method described in [7]. The calculated inhomogeneous temperature field after induction heating is transferred to the semi-finished product of the impact extrusion model. The elastic-plastic material behaviour of steel and aluminium parts is modelled as shown before. The impact extrusion tool system consists of a die and a punch, which are modelled as rigid heat conducting bodies with an initial temperature of 250 °C. Friction is modelled by the combined friction model consisting of the Tresca formulation with $m = 0.3$ and the Coulomb formulation with $\mu = 0.1$. The press kinematics were derived from experimental data of the used screw press and considered within the numerical model. However, the modelling of the joining zone requires cohesive zone elements. Since these are not available in Simufact Forming, another model of the extrusion process was created in the FE software MSC Marc 2018.

Damage modelling.

The brittle material behaviour of the joining zone is of particular importance in the forming of hybrid semi-finished products. However, the very low thickness of the intermetallic phase compared to the dimensions of the semi-finished products is challenging. Conventionally, the damage in thin layers is modelled by flat cohesive zone elements [11]. Their constitutive behaviour is described via traction separation laws, which take into account expansion under normal or shear loading. However, cohesive zone elements are flat and therefore cannot be used to describe the constitutive behaviour in bulk metal forming. In this context, Töller et al. developed a new concept for damage modelling of thin joining zones [6]. As shown in Fig. 4, the model combines the damage to cohesive zone elements described by traction separation behaviour with damage induced by severe membrane deformation such as stretching, which can occur during forming of hybrid semi-finished parts within the joining zone. Membrane deformation is considered using the Internal Thickness Extrapolation (InTEx) concept. This enables the use of cohesive zone elements for bulk forming simulation by consideration of a thickness within the element formulation. Tractions within the cohesive elements are calculated from resulting separations δ and stiffness k with a linear relationship. As proposed by Töller, a large but finite artificial stiffness k is introduced. The stiffness can be interpreted as a penalty parameter to model the brittle behaviour of thin intermetallic phases. Due to the use of effective tractions the tractions are reduced by local prevailing damage D. Thus, a local pre-damage as well as the damage by membrane deformation during forming process can be taken into account. A detailed description of the developed model can be found in [6]. To model the damage in joining zones of semi-finished hybrid parts during forming processes within the Tailored Forming process chain, the modelling concept was implemented in the cohesive element formulation of the commercial FE software MSC Marc 2018 using the user subroutine UCOHESIVE. This software was selected because, contrary to Simufact Forming, it supports the use of cohesive zone elements. The presented work deals with the development of a methodology determining the model parameters taking into account the thermo-mechanical process boundary conditions. The calibration of the model was done inversely by numerical simulation of the local tensile tests. The elastic-plastic material behaviour of steel and aluminium was described as shown before. The displacements are applied via the nodes on the end sample faces according to experimental tensile test. The isothermal test temperatures are imposed on all nodes of the model via a thermal boundary condition. The joining zone in the centre of the sample is modelled via cohesive zone elements. The failure time determined from the experimental force-displacement curves and the applied force are used as the target variables. Since the focus is on determining the value $t_{t,max}$ and only samples with a joining zone normal to the direction of

Materials Research Proceedings 28 (2023) 717-726 https://doi.org/10.21741/9781644902479-78

loading are analysed, the value for $t_{s,max}$ is specified analogously to the procedure in [6] via the ratio $t_{t,max}/t_{s,max}$ = 1.22. Damage due to membrane deformation is described via the Lemaitre damage model [12]. The parameters s = 1 and S = 0.34 for the description of the Lemaitre damage model are chosen accordingly to [6].

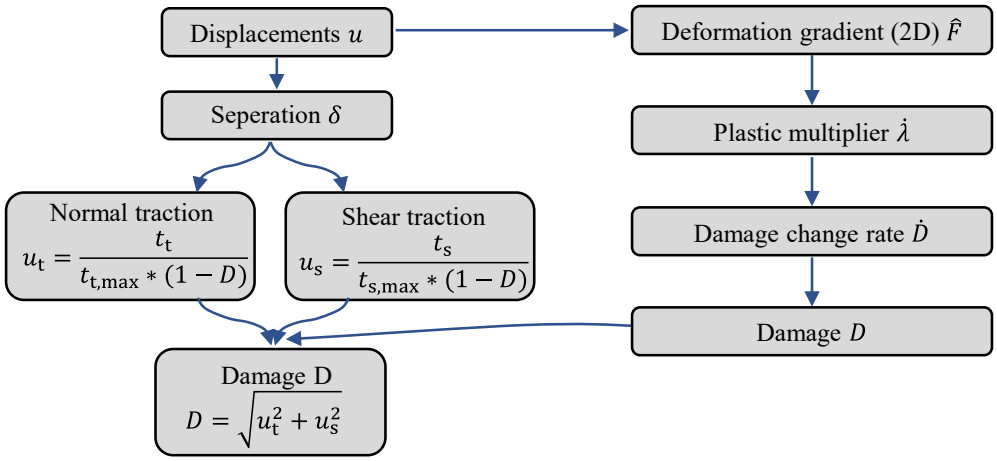

Fig. 4. Schematic representation of damage model for thin intermetallic phase.

Results

Numerical analysis of induction heating and impact extrusion.

As shown in Fig. 2, the flow curves of the materials differ significantly demonstrating the need for inhomogeneous heating to adjust the material flow properties for impact extrusion. According to the flow curves, the steel semi-finished product should be heated to 900°C and the aluminium semi-finished product to 300°C for homogenous material flow properties. The adjustability of the temperature field was investigated by experimental and numerical analyses of the inductive heating. The numerical simulation is used for the process analysis regarding the temperature development in order to define proper testing temperatures, as shown in Fig. 5 (a). Analogously to the experimental process, the semi-finished steel product is inductively heated for 25 s. A maximum temperature of 900°C is reached. During the transfer period of 5 s until the start of the impact extrusion, the maximum temperature drops to approx. 800°C due to heat transfer processes. The aluminium is heated only by heat conduction from the steel and reaches a maximum temperature of approx. 400°C after 30 s before forming. The maximum temperature of the joining zone is 420°C before the forming process starts. Due to the short forming process period of only 0.12 s, no significant temperature change is observed during forming, as shown in Fig. 5 (b). Fig. 5 (c) and (d) display the temperature distribution of the inhomogeneous heated semi-finished product after the transfer period from the induction heating and before the impact extrusion, both at the process time of 30 s. Based on this analysis, the bond strength of the joining zone is investigated in local tensile tests at the process relevant temperatures of 400°C and 450°C. The results of the tensile tests are used to determine the bond strength of the joint zone.

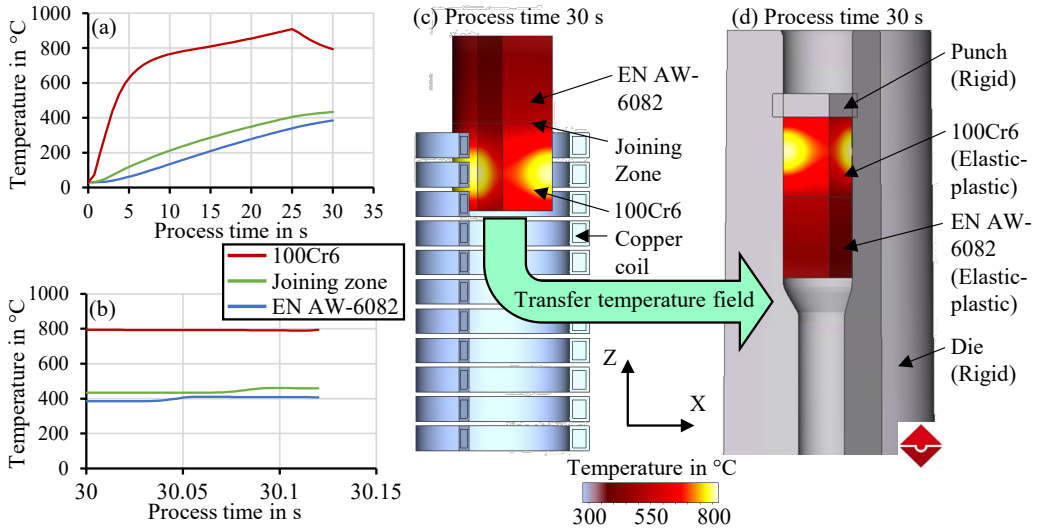

Fig. 5. Temperature development during induction heating (a) and impact extrusion (b) as well as coupled numerical process chain consisting of induction heating process (c) and impact extrusion (d).

Local bond strength and damage model calibration.

Fig. 6 shows the determined bond strengths as a function of temperature and the sample extraction area from the semi-finished product for a load normal to the joining zone. The sample extraction area can be found in Fig. 3 (c). Therefore, the bond strengths of samples with low and high numbers correspond to the edge area and the sample no. 9 to no. 11 to the bond strength in the centre of the friction-welded semi-finished product. For sample no. 10 no results could be determined at room temperature, because the samples failed directly.

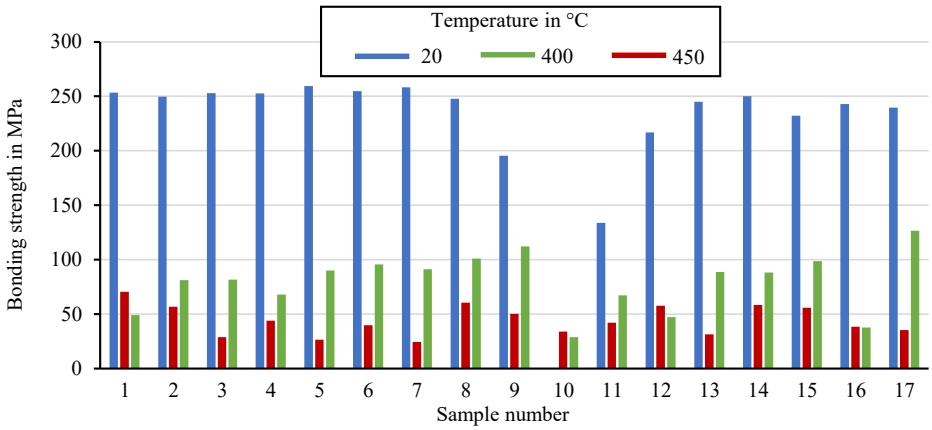

Fig. 6. Bond strength for normal loading depending on temperature and sample extraction area.

In particular, the tests at room temperature show a strong dependence on the removal position. Thus, the samples from the edge region exhibit a significantly higher bond strength than samples from the middle region. The tests also show a clear dependence on temperature. With increasing temperature, the bond strength decreases significantly. An optical analysis of the fracture surfaces showed a failure in the joining zone for all samples. Thus, at the process relevant temperatures compared to room temperature, even low tensile loads are critical with regard to a possible local failure of the joining zone and must be particularly taken into account in the process design.

As the stress-strain curve in Fig 7 (a) shows exemplarily for the sample 4 at 20°C, the samples from the edge region exhibit significant plastic deformation. An optical analysis of the samples shows a clear necking in the aluminium region and a failure of the monolithic material aluminium. Thus, the bond strength is greater than the tensile strength of the aluminium. Samples from the middle region like sample 9 in Fig 7 (b) show lower bond strengths and no pronounced plastic deformation. An optical analysis of the fracture zone shows failure in the joining zone without significant plastic deformation of the monolithic materials. The bond strength is thus below that of the weaker monolithic material aluminium and can be determined directly. The strong dependence of the bond strength is due to the process characteristics of friction welding. While high relative velocities prevail in the edge zone, which cause the oxide layer on the aluminium to break up and flow out, the relative velocity decreases toward the centre of the semi-finished product [13].

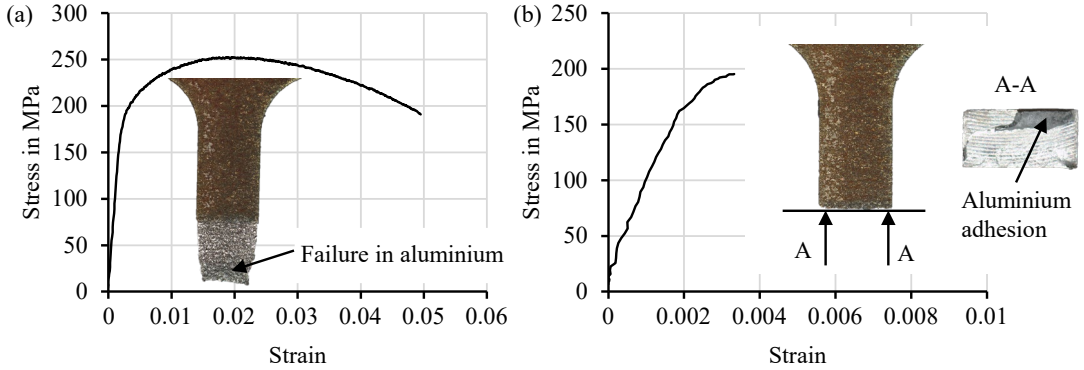

Fig. 7. Stress-strain curves and optical images after failure for sample 4 (a) and sample 9 (b) at 20°C.

For the determination of $t_{t,max}$ to calibrate the damage model, the performed tensile tests were mapped in the FE software MSC Marc 2018 with the corresponding experimental boundary conditions. A representation of the numerical model of the tensile test is given in Fig. 8. The temperature dependent values of $t_{t,max}$ were determined numerically iteratively by comparison with the experimental force-displacement curves and the time of failure. For the calibration, the sample no. 8 is used. This specimen exhibited the highest bond strength at failure in the joining zone without significant plastic deformation of the aluminium part. Thus, the calculated stress can be directly related to the bonding strength.

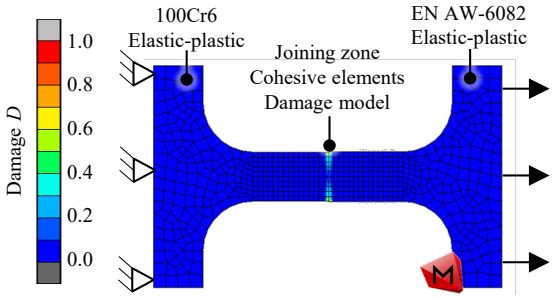

Fig. 8. Numerical model of tension test with joining zone modelled by means of cohesive elements.

A comparison of the force-displacement curves for the temperatures considered using the corresponding value for the damage parameter $t_{t,max}$ can be found in Fig. 9 (a) to (c). The

numerically inverse determined values can be found in Fig. 9 (d). The force-displacement curves agree well, so that the model and also the methodology can be considered validated. The force level at fracture is well predicted. However, there are small deviations regarding the length change at fracture between experiment and simulation. This is probably due to a slight plastic deformation of the specimens in the aluminium part, which is underestimated in the simulation. For a later application of the numerical representation of the impact extrusion process considering the damage of the joining zone, the local distribution of the maximal bond strength according to the findings of the local tensile tests has to be taken into account by defining local initial values for the pre-damage D and maximal bond strength $t_{t,max}$. For samples extracted at larger diameters of the semi-finished product, which show plastic deformation and failure of the aluminium, the achievable bond strength $t_{t,max}$ is increased by 25 % for later application. The decrease of the bonding strength with decreasing diameter towards the centre of the semi-finished product can be taken into account in the application by the damage parameter D as pre-damage, which is scaled according to the results in Fig. 6 taking into account the local position.

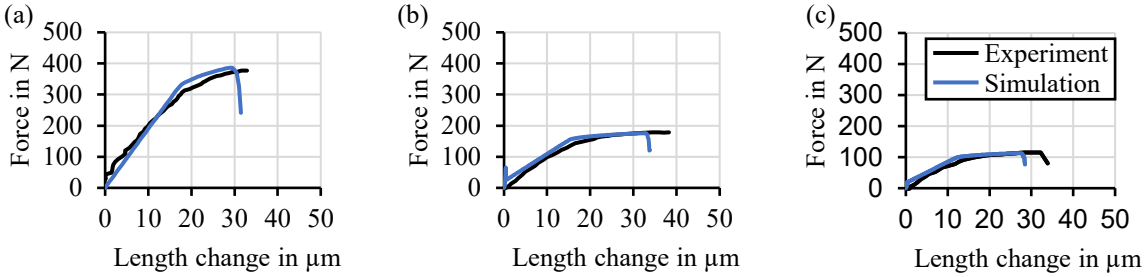

(d)

Temperature in °C	20 (RT)	400	450
Damage parameter $t_{t,max}$ in MPa	250	130	100

Fig. 9. Force-displacement curves from experiment and simulation at a temperature of 20°C (a), 400°C (b) and 450°C (c) for sample no. 8 as well as the determined temperature dependent damage parameter $t_{t,max}$ (d).

For a numerical analysis of the impact extrusion taking the joining zone into account, the process was also modelled in MSC Marc 2018. The boundary conditions were selected analogously to the described procedure for the tensile test simulations. As in the tensile tests, the joining zone itself is represented by cohesive zone elements. Since the damage model requires a three-dimensional mapping, a quarter model is used. The inhomogeneous temperature distribution is taken from the inductive heating in analogy to the procedure in Simufact Forming and imposed as initial temperature on the nodes in the Marc model. The extrapolation of temperature results from the nodes within the 2D space of the induction heating simulation (Simufact Forming) to the 3D space of the impact extrusion process model (MARC) is done via the radial relation $r = \sqrt{x^2 + x^2}$. The von Mises stress distribution after forming is shown in Fig. 10 (a). Due to heating, very low stresses are present, especially in the aluminium. In the steel part, higher stresses are present at the transition area to the aluminium. This is due to the physically induced inhomogeneous temperature distribution also in the steel component. As can be seen in Fig. 5, lower temperatures occur in the transition area of the steel due to heat conduction effects into the aluminium. This cannot be completely prevented even by adapted induction heating. Fig. 10 (b) shows the distribution of damage before and after forming. As can be seen, initial damage to the joining zone is already present before forming for small diameters in order to map the influence of the friction welding process on the local bond strength. After forming, damage can be seen in the

central area of the joining zone. This damage has already been observed by Behrens et al. for impact extrusion of the steel/aluminium combination 20MnCr5/EN AW-6082 pre-joined by laser welding, as shown in Fig. 10 (c) [14]. For this material combination, it was experimentally proven that an applied counterpressure prevents tearing of the joining zone by reducing the tensile stresses present. In subsequent investigations, other parameters of the damage model must therefore be further identified using the methodology described here and finally validated on the basis of experimental impact extrusion tests.

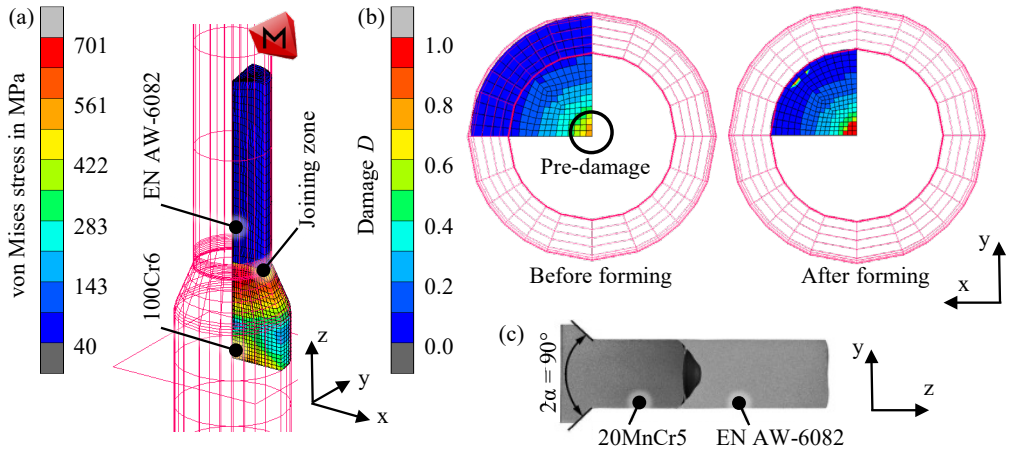

Fig. 10. von Mises stress after impact extrusion (a), damage within the joining zone before and after forming (b) as well as metallographic cross-section view of the component from [14] (c).

Summary

The scope of this work was the development of a methodology for the numerical inverse calibration of a damage model to describe the failure of a joining zone in hybrid pre-joined semi-finished products made of 100Cr6 and EN AW-6082. For this purpose, local tensile tests were performed at room temperature with miniature tensile samples taken from hybrid semi-finished products. To account for the effect of process relevant forming temperatures, the tests were also carried out at elevated temperatures. The test temperatures were defined based on numerical simulations of the inhomogeneous induction heating and the impact extrusion process. The results showed a strong influence of the sample extraction area and temperature on the achievable bond strength. The damage parameter $t_{t,max}$ was determined inversely by a numerical simulation of the performed tensile tests. The numerically calculated force-displacement curves showed good agreement with the experimental results.

An initial numerical simulation of the impact extrusion process shows that damage occurs in the joining zone. In further investigations, the other parameters of the model are calibrated by supplementary tensile tests with varying the angle between the loading direction and the joining zone of EN AW-6082 as well as 100Cr6 to improve the model quality. Finally, the model will be validated by means of experimental extrusion tests regarding the failure behaviour of the joining zone. The validated model will then be used to evaluate and design concepts such as a counterpressure concept in order to ensure damage-free production of hybrid components.

Acknowledgements

The results presented in this paper were obtained within the Collaborative Research Centre 1153 “Process chain to produce hybrid high-performance components by Tailored Forming” in the subproject C01. The authors would like to thank the German Research Foundation (Deutsche

Forschungsgemeinschaft, DFG, 252662854) for the financial and organisational support of this project. The authors would like to thank the subproject B03 for friction welding of hybrid semi-finished parts and the subproject C04 for support regarding the damage model.

References

[1] P. Wu, B. Wang, J. Lin, B. Zuo, Z. Li, J. Zhou, Investigation on metal flow and forming load of bi-metal gear hot forging process, Int. J. Adv. Manuf. Technol. 88 (2017) 2835-2847. https://doi.org/10.1007/s00170-016-8973-x

[2] R. Leiber, Hybridschmieden bringt den Leichtbau voran, Aluminium Praxis (2011) 7-8.

[3] P. Groche, S. Wohletz, A. Erbe, A. Altin, Effect of the primary heat treatment on the bond formation in cold welding of aluminum and steel by cold forging, J. Mat. Process. Technol. 214 (2014) 2040-2048. https://doi.org/10.1016/j.jmatprotec.2013.12.021

[4] B.-A. Behrens, J. Uhe, Introduction to tailored forming, Prod. Eng. Res. Devel. 15 (2021) 133-136. https://doi.org/10.1007/s11740-021-01022-w

[5] B.-A. Behrens, D. Duran, D., J. Uhe, T. Matthias, Numerical investigations on the influence of the weld surface and die geometry on the resulting tensile stresses in the joining zone during an extrusion process, 24th Int Conf Mat Form, Liège, Belgique (2021). https://doi.org/10.25518/esaform21.919

[6] F. Töller, S. Löhnert, P. Wriggers, Membrane mode enhanced cohesive zone element, Eng. Comp. 39 (2022) 722-743. https://doi.org/10.1108/EC-08-2020-0489

[7] B.-A. Behrens, H. Wester, S. Schäfer, C. Büdenbender, Modelling of an induction heating process and resulting material distribution of a hybrid semi-finished product after impact extrusion, 24th Int Conf Mat Form, Liège, Belgique (2021). https://doi.org/10.25518/esaform21.574

[8] R. Goldstein, B.-A. Behrens, D. Duran, Role of Thermal Processing in Tailored Forming Technology for Manufacturing Multi-Material Components, Heat Treat Conference (2017).

[9] S. Herbst, H. Aengeneyndt, M.J. Maier, F. Nürnberger, Microstructure and Mechanical Properties of Friction Welded Steel-Aluminum Hybrid Components after T6 Heat Treatment, Mater. Sci. Eng: A 696 (2017) 33-41. https://doi.org/10.1016/j.msea.2017.04.052

[10] B. Nacke, Ein Verfahren zur numerischen Simulation induktiver Erwärmungsprozesse und dessen technische Anwendung. Dissertation, Hannover (1987).

[11] G. Lélias, E. Paroissien, F. Lachaud, J. Morlier, Experimental characterization of cohesive zone models for thin adhesive layers loaded in mode I, mode II, and mixed-mode I/II by the use of a direct method, Int. J. Solid. Struct. 158 (2019) 90-115. https://doi.org/10.1016/j.ijsolstr.2018.09.005

[12] J. Besson, Continuum Models of Ductile Fracture: A Review, Int. J. Dam. Mech. 19 (2010) 3-52. https://doi.org/10.1177/1056789509103482

[13] S. D. Meshram, T. Mohandas, G. M. Reddy, Friction welding of dissimilar pure metals, J Mat Proc Tech 184 (2007) 330-337. https://doi.org/10.1016/j.jmatprotec.2006.11.123

[14] B.-A. Behrens, J. Uhe, F. Süer, D. Duran, T. Matthias, I. Ross, Fabrication of steel-aluminium parts by impact extrusion, Mater. Today: Proceedings 59 (2022) 220-226. https://doi.org/10.1016/j.matpr.2021.11.093

Materials Research Proceedings 28 (2023) 727-736 https://doi.org/10.21741/9781644902479-79

Influence of process parameters and process set-up on damage evolution during stretch drawing of u-shaped profiles

MÜLLER Martina[1,a *], WEISER Ingo Felix[1,b], HERRIG Tim[1,c] and BERGS Thomas[1,2,d]

[1]Laboratory for Machine Tools and Production Engineering WZL of RWTH Aachen University, Campus-Boulevard 30, 52074 Aachen, Germany

[2]Fraunhofer Institute for Production Technology IPT, Steinbachstr. 17, 52074 Aachen, Germany

[a]martina.mueller@wzl.rwth-aachen.de, [b]f.weiser@wzl.rwth-aachen.de, [c]t.herrig@wzl.rwth-aachen.de, [d]t.bergs@wzl.rwth-aachen.de

Keywords: Damage, Stretch Drawing, Dual Phase Steel

Abstract. The damage state in the form of voids and lattice defects of a sheet metal component has a substantial impact on the performance of a component in service regarding fatigue or crash behaviour. Therefore, managing the damage evolution during forming, especially the accumulation and distribution of damage, by targeted changes of the process parameters and set-up enables to improve component performance by influencing the stress-strain state [1]. The evolution of the stress-strain state during the forming process and along the process route represents the most significant factor influencing the resulting damage state. This paper focuses on the influence of the damage state of sheet metal components in order to improve the performance of a component regarding fatigue and crash behavior. Considering a variation of the process parameter (drawing die radius) and change in process set-up (singlestep, multistep, reverse stretch drawing) the damage accumulation and distribution within the component is analyzed using a calibrated LEMAITRE damage model. For the consideration of this paper, an u-shaped geometry of dual phase steel DP800, which is often found as an element in vehicle body construction, is used.

Introduction

The automotive sector is one of the main contributors to CO_2 emissions [1]. Due to the climate goals of the European Union to become a net zero greenhouse gas emitting economy by 2050 [2], it is necessary to rethink the approaches in this sector and to find a way to significantly reduce CO_2 emissions. One approach is lightweight design [3]. Lightweight design enables to reduce CO_2 emissions in every life cycle by means of resource efficiency.

Stretch drawing, often combined with deep drawing, is one of the most important processes for the production of three-dimensional sheet metal components and is used in particular in the manufacturing of vehicle bodies in the automotive sector [4]. Since 40% of the total mass is attributed to the vehicle body, stretch drawing is a lever for saving CO_2 by implementing lightweight design measures [5]. One possibility to introduce lightweight design measures in stretch drawing is to reduce the thickness of the sheet metal in order to save weight. In the automotive industry in particular, however, the components used have to meet stringent requirements in order to ensure the safety of passengers in the best possible way [6].

In the field of lightweight design, high-strength materials or topology optimization are currently used in order to save material and thus weight [7]. What is currently only insufficiently exploited are the possibilities offered by the control of ductile damage along the process chain and by ductile damage meaning *the formation, growth and coalescence of voids in the microstructure. These voids are formed in structural materials by decohesion at interfaces such as phase or grain*

Content from this work may be used under the terms of the Creative Commons Attribution 3.0 license. Any further distribution of this work must maintain attribution to the author(s) and the title of the work, journal citation and DOI. Published under license by Materials Research Forum LLC.

Materials Research Proceedings 28 (2023) 727-736 https://doi.org/10.21741/9781644902479-79

boundaries and inclusions, or by the formation of new surfaces within phases or inclusions. This damage causes degradation of the performance of the corresponding component [8]. Damage control then enables either the damage accumulation or the damage distribution to be adapted by adjusting the process parameters or process set-up in such a way that components achieve a higher performance in their subsequent application or can be designed lighter [9].

On the one hand, damage development is dependent on the strain state. However, ductile damage only occurs in combination with plastic strain. On the other hand, damage is dependent on the stress state. Li has thereby shown in the context of forming that it is not sufficient to use equivalent stress alone to model damage [10]. The three-dimensional stress state in the form of the VON MISES stress σ_{vm}, the lode parameter θ and the triaxiality η must be used (Eq. 1- 3). Whereby I_1 is the first invariant of the CAUCHY stress tensor σ and J_2 and J_3 are the second and third invariants of the deviatoric stress tensor s.

$$\sigma_{vM} = \sqrt{3J_2} \tag{1}$$

$$\eta = \frac{I_1}{\sigma_{vM}} \tag{2}$$

$$L = -\left(\frac{J_3}{\sigma_{vM}}\right)^3 \tag{3}$$

Lode parameter θ and triaxiality η are proven to have an influence on the damage and in particular also on the shape of the resulting voids. While the triaxiality η has a particular effect on the size of the voids, the lode parameter θ influences the geometry of the voids. Both parameters have in common, that they cannot be measured during stretch drawing [11]. Therefore numerical or analytical modelling is necessary.

Materials and Methods

Approach. In this paper the objective is to investigate the damage development in the form of damage accumulation and distribution. For this purpose, classical stretch drawing (SD, Fig. 1a)) with different drawing die radii r_{DR} as well as multistep stretch drawing (MSSD, Fig. 1b)) and reverse stretch drawing (RSD, Fig. 1c)) are considered. The aim is to generate the same geometry on different process routes in order to identify the influence of different load paths on damage development, so that in the future the damage development can be specifically adjusted in the form of accumulation and distribution in order to achieve a higher component performance. Due to the dependence of the damage on the stress and strain states, the load paths are first analyzed in terms of the time- and location-dependent states, which requires numerical modelling performed in this work. Afterwards the load paths are correlated with damage accumulation and distribution to disclose cause effect relations.

Stretch drawing, reverse stretch drawing and multi-step stretch drawing process. In the present work, the focus is on a u-shaped geometry from DP800 dual phase steel with a sheet thickness of $s = 1.5$ mm. The punch velocity v_p was set to $v_p = 15$ mm/s and the blank holder was position controlled due to different necessary blank holder forces to prevent the sheet metal from bypassing the drawing groove. The different processes are schematically depicted in Fig. 1.

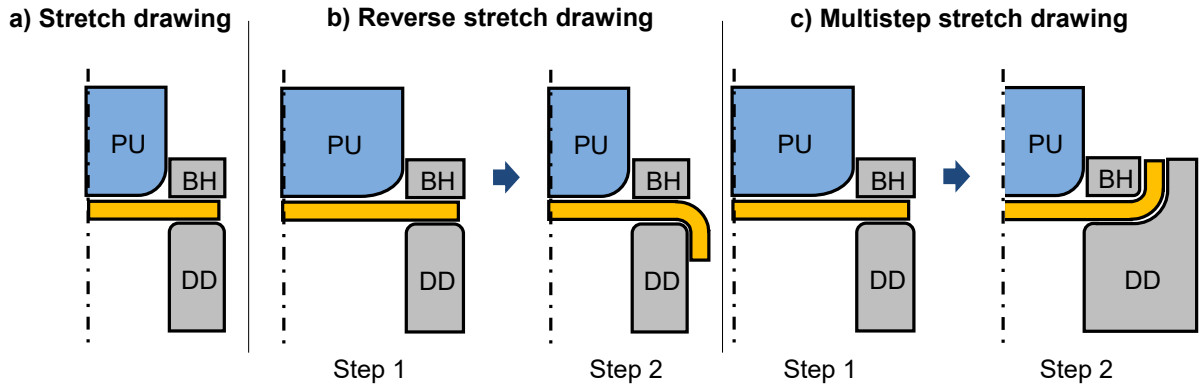

*Fig 1. SEQ Figure * ARABIC 1. Schematic illustration of a) stretch drawing, b) reverse stretch drawing and c) multistep stretch drawing.*

Process model. The SD, MSDD and RDD processes were modelled using Abaqus/explicit. To save computation time, the geometry was reduced to one quarter using symmetry. A general contact with a uniform COULOMB friction coefficient of $\mu = 0.05$ was applied to model the contact of the part, as identified in prior strip drawing tests. The parameters of the mesh as well as the types of the bodies can be seen in table 1. A LEMAITRE damage model was utilized in this paper which is based on the work of SPRAVE [12]. The model parameters of the calibrated material model are consistent with prior work [8]. The constitutive model was implemented as a VUMAT subroutine and was successfully used and validated in earlier work [13, 14].

The LEMAITRE damage model is based on the definition of the damage variable D. The parameter reflects the influence of voids and microcracks on the plastic behavior of the material [15]. The damage parameter D is defined as the ratio of the damage-free area increment ∂S and the area increment affected by damage ∂S_D (Eq. 4). As the damage grows the area increment affected by damage ∂S_D becomes greater. Thus the forces F respectively the stresses σ applied to the material are not distributed over the entire material cross section. Therefore the concept of effective stress $\tilde{\sigma}$ is introduced (Eq. 5) and used to estimate the response of the material to applied stress under consideration of damage evolution [16].

$$D = \frac{\partial S_D}{\partial S} \tag{4}$$

$$\tilde{\sigma} = \frac{\partial F}{\partial S - \partial S_D} = \frac{\sigma}{1-D} \tag{5}$$

Table 1. Parameter of the mesh and types of bodies for process model.

Name	**Mesh**	**Type of body**
Sheet	C3D8R	Solid deformable body
Punch, blank holder, die	R3D4	Discrete rigid

Reference process, reference position and area under investigation. As reference process the SD with a drawing die radius of $r_{DR} = 3$ mm is considered. The triaxiality η, lode parameter θ and damage parameter D analysis is performed at a point in the outer bend of the component (reference point (RP)), which is in principle the most sensitive area for performance in later applications. For the comparison of the die radii r_{DR}, a punch path s of $s = 25$ mm is used as reference position. This punch path s corresponds to the punch path shortly before the first component fails. For the comparison of the different process set-ups, the reference position of $s = 7.5$ mm is determined

accordingly. Due to material limitations, the process set-up only considers the area in which the components have the same geometry or have the same cup height as a functional measure of the geometry respectively.

Results

Influence of drawing die radius r_{DR} on load path and damage evolution. The damage distribution of the damage parameter D in dependence of the drawing die radius r_{DR} in the cross section of the components is shown in Fig. 2a), the course of triaxiality η and lode parameter θ in dependence of equivalent plastic strain φ_{pl} in Fig. 2b) and the course of damage parameter D in dependence of equivalent plastic strain φ_{pl} in Fig. 2c). Considering the course of the lode parameter θ as a function of the equivalent plastic strain φ_{pl} in Fig. 2b), the curves for the different die radii r_{DR} differ, in particular for the mean value ($\theta_{med.r_{DR=3}}$ =0.121, $\theta_{med.r_{DR=6}} = 0.118$, $\theta_{med.\,r_{DR=9}} = 0.116$). All curves initially start at a value of almost $\theta = 1$ and then drop and continue to progress in an oscillating manner. The course of $r_{DR} = 3$ mm, however, shows a steep peak before ending. The course of the triaxiality η, however, differs. The course of die radius r_{DR} = 3 mm of the triaxiality η has a higher value on average ($\eta_{med.r_{DR=3}} = 0.6$, $\eta_{med.r_{DR=6}} = 0.519$, $\eta_{med.r_{DR=9}} = 0.518$). Due to the non-steady shaped courses, a clear and explicit description of the courses is not possible respectively. However, what stands out concisely is the decreasing peak of $\eta_{r_{DR=3}}$ at the end. The different components also reach different equivalent plastic strains in the reference point at the reference position ($\varphi_{pl.\,r_{DR=3}} = 0.258$, $\varphi_{pl.\,r_{DR=6}} = 0.272$, $\varphi_{pl.\,r_{DR=9}} = 0.277$). The courses of the damage parameter D as a function of the equivalent plastic strain φ_{pl} in Fig. 2c) show a quadratic course with an offset with ascending drawing die radius r_{DR} for all three die radii r_{DR}. The difference in the die radius of r_{DR} = 3 mm is particularly pronounced. The damage parameter D is consistently higher for the same equivalent plastic strain φ_{pl} .

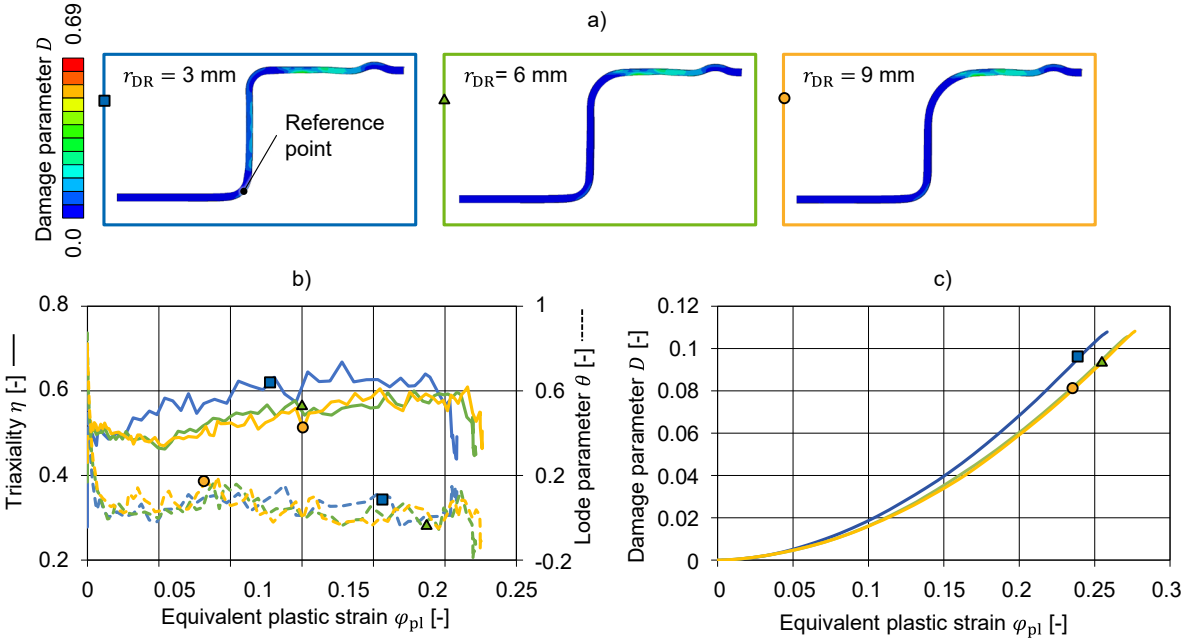

*Fig. 2. a) Damage parameter **D** distribution in cross section of components; b) course of triaxiality η and lode parameter Θ in dependence of equivalent plastic strain φ_{pl} at RP; c) course of damage parameter **D** in dependence of equivalent plastic strain φ_{pl} at RP considering different drawing die radii r_{ddr}.*

Fig. 3a) shows the course of VON MISES stress σ_{vm} in dependence of punch path s, Fig. 3b) shows the course of damage parameter D in dependence of punch path s, Fig. 3c) the damage distribution D in the cross section of the component with a drawing die radius r_{DR} = 3 mm and Fig. 3d) the course of damage parameter D in dependence of the distance x to the symmetry plane. The VON MISES stresses σ_{vm} of the individual curves all start at σ_{vm} = 0 MPa. A reverse square increase of all curves follows. With increasing die radius r_{DR}, however, a smaller gradient appears. After achieving the maximum and a slight decrease, all curves then decline to reach a quasi-stationary value to oscillate around. The drop occurs with increasing die radius r_{DR} at a later punch path s ($\sigma_{med.vM\ r_{DR}\,=\,3\ mm}$ = 806.51 MPa, $\sigma_{med.vM\ r_{DR}\,=\,3\ mm}$ = 826.98 MPa, $\sigma_{med.vM\ r_{DR}\,=\,3\ mm}$ = 832.58 MPa). The progression of the damage variable D as a function of the punch path s starts at s = 0 mm for all three curves until the first contact between blank holder and sheet and punch and sheet has been established. From a punch path of s = 2.2 mm, the curve of the die radius r_{DR} = 3 mm begins to increase, followed by the curve of the die radius r_{DR} = 6 mm and finally the curve of the die radius r_{DR} = 9 mm. Irrespective of the offset of the curves, the course of the three curves initially shows a quadratic increase, which changes to a steep linear increase and finally approaches a final value in a quadratic manner. At the reference position, the damage parameter D reaches a value of $D_{r_{DR}\,=3\ mm}$ = 0.108, $D_{r_{DR}\,=6\ mm}$ = 0.106 and $D_{r_{DR}\,=9\ mm}$ = 0.108. Considering the damage parameter D in dependence of the distance x to the symmetry plan, the three courses of the different die radii r_{DR} in the area of the wall have a nearly identical course. The same can be seen in the transition area and after the wall. In the area of the wall, in contrast, the three curves show a different course. There is a local maximum of the damage variable D with the smallest die radius r_{DR} = 3 mm. Equivalent to this is the maximum value of the damage parameter D in this area with decreasing die radius r_{DR}.

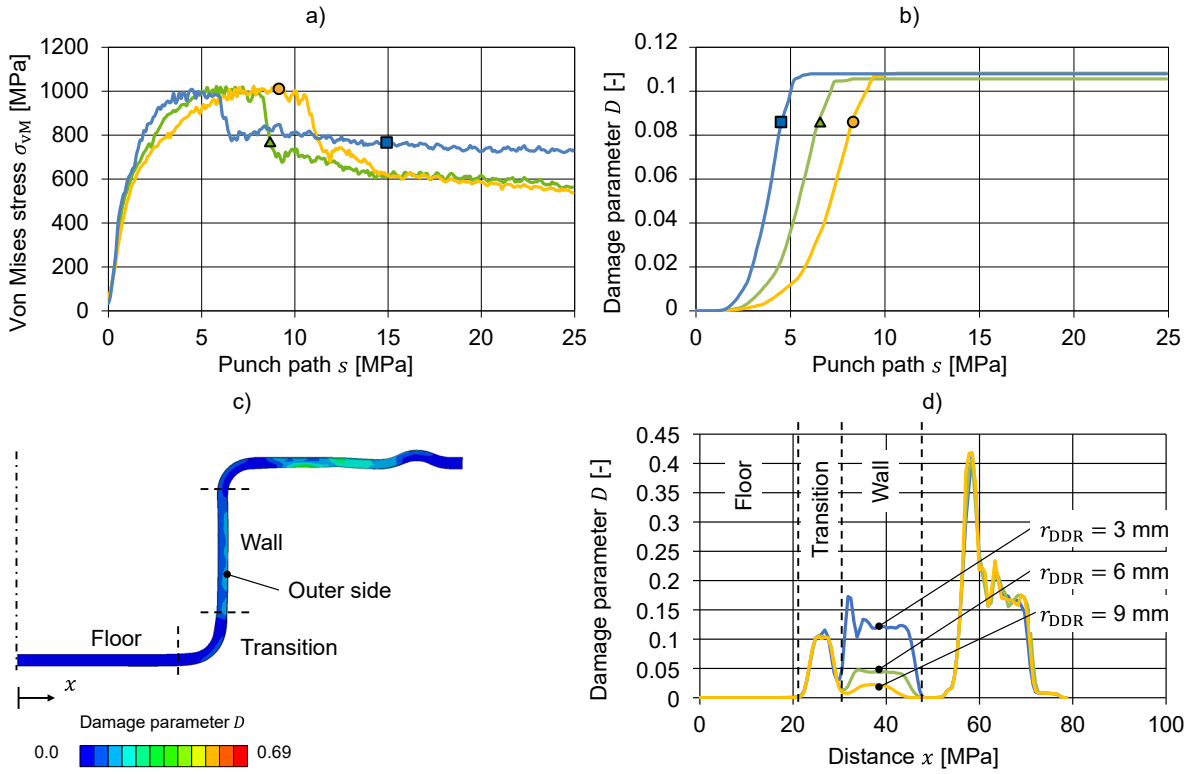

Fig. 3. a) Course of VON MISES stress σ_{vm} in dependence of punch path s at RP; b) course of damage parameter D in dependence of punch path s at RP; c) damage distribution D in cross section of component r_{DDR} = 3 mm; d) course of damage parameter D in dependence of distance x to symmetry plane considering different drawing die radii r_{ddr}.

Materials Research Proceedings 28 (2023) 727-736 https://doi.org/10.21741/9781644902479-79

Influence of process set-up on load path and damage evolution. The distribution of the damage parameter D in the cross section of the components from SD, MSSD and RSD are depicted in Fig. 4a). Considering the different heights of the cups shown in the figure, only the area up to the transition of the wall into the die radius r_{DR} was selected for the analysis of the results. This is a consequence of the fact that the maximum drawing depth was limited due to material constraints and the objective is to compare geometrically almost identical components. The courses of η_{SD}, θ_{SD} and D_{SD} are the same than in Fig. 2 since no damage respectively change of stress and strain state occurs in the reference position after a punch path of $s = 6$ mm. The damage distribution, however, differs.

The course of triaxiality η and lode parameter θ in dependence of equivalent plastic strain φ_{pl} are shown in Fig. 4b). The outer side of the outer bend, which is under consideration, experiences different equivalent plastic strains φ_{pl} to obtain the same geometry ($\varphi_{pl\,SD\,max.} = 0.26$, $\varphi_{pl\,MSSD\,max.} = 0.52$, $\varphi_{pl\,RSD\,max.} = 0.56$). The courses of the triaxiality η of MSSD and RSD show a similar behavior with mean values of $\eta_{med.MSDD} = 0.523$ and $\eta_{med.RDD} = 0.53$. Both courses start with a steep rise. After a quadratic drop, an almost linear curve follows, which drops at 0.34 and then rises again. Considering the lode parameter θ of MSDD, the course begins with a value of almost $\theta \approx 1$. The course then drops with a steep gradient into the negative range followed by an oscillating curve. This results in an average value of $\theta_{med.MSSD} = 0.21$. The course of the lode parameter θ of RSD starts similar to the course of MSDD. However, when the course drops with a steep gradient the curve remains in the positive range and starts to oscillate around a value of $\theta_{med.RSD} = 0.19$. The course of damage parameter D in dependence of equivalent plastic strain φ_{pl} considering different process set-ups is shown in Fig. 4c). The curves of MSSD and RSD depict a similar course. SD, however, has a slightly higher level of damage parameter D. The maximum value of damage parameter D obtained are $D_{MSSD} = 0.52$ and $D_{RSD} = 0.41$.

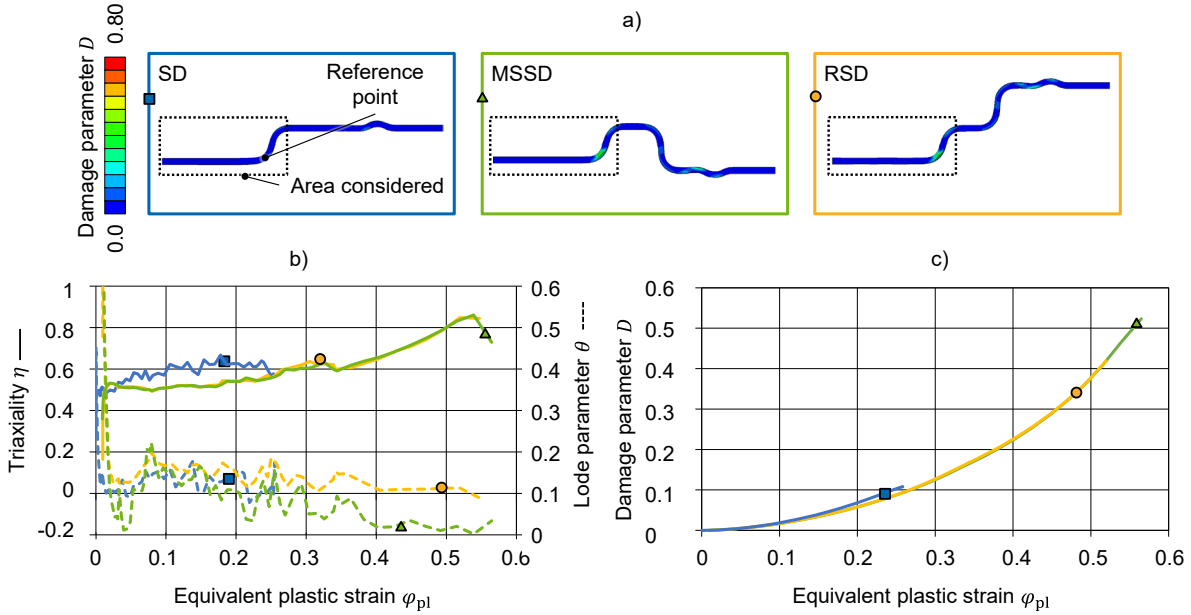

*Fig. 4. a) Damage parameter **D** distribution in cross section of components; b) course of triaxiality η and lode parameter Θ in dependence of equivalent plastic strain φ_{pl} at RP; c) course of damage parameter **D** in dependence of equivalent plastic strain φ_{pl} at RP considering different process set-ups.*

The course of VON MISES stress σ_{vm} in dependence of punch path s can be seen in Fig. 5a). The initial values of the RSD and MSSD processes differ. Since a U-profile is produced in the first step and is rotated 180° or is not rotated depending on the process route, the courses start differently. Despite the different start, both courses show a reverse square increase which is very similar. The mean values of VON MISES stress σ_{vm} obtained are $\sigma_{med.vM\ MSSD} = 882.52$ MPa and $\sigma_{med.vM\ RSD} = 852.58$ MPa. Fig. 5b) shows the course of damage parameter D in dependence of punch path s. The courses of MSSD and RSD depict a very similar quadratic course which start to elevate from a punch path s of $s = 3$ mm. The course of SD, on the other hand, shows a s-shaped course, which depicts a stronger elevation at $s = 3$ mm followed by a steady course of $D_{SD} = 0.108$. The Course of damage parameter D in dependence of distance x to symmetry plane considering different process set-ups can be seen in Fig. 5c). All three courses begin with a damage parameter $D = 0$. With the start of the transition from floor to wall, the damage parameter D increases for the first time in the courses. For MSSD and RSD, the curves show an initial quadratic rise, which changes to a linear rise with a very high gradient, and then fall off inversely. The course of SD shows a course with also a quadratic rise, but with a lower gradient as well as rise and descent shifted further to higher x values. Considering the wall of the three components, there is a small rise in damage parameter D for MSSD and RSD.

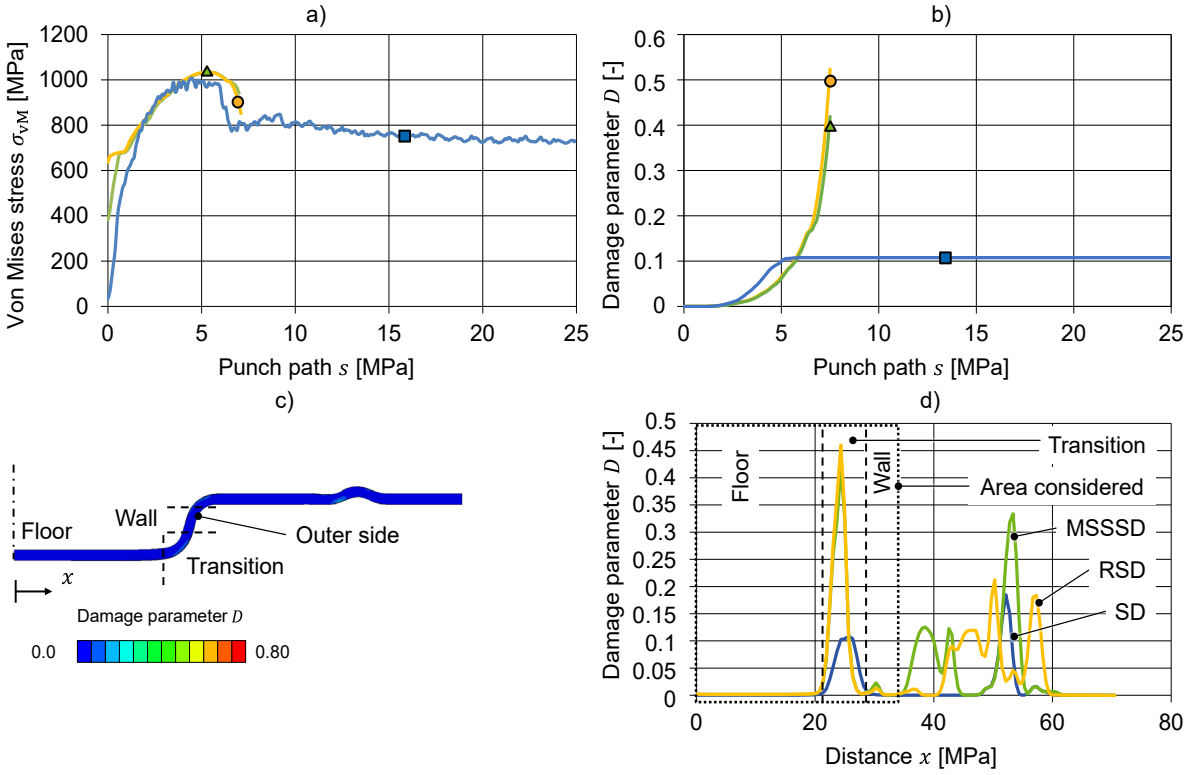

Fig. 5. a) Course of VON MISES stress σ_{vm} in dependence of punch path s at RP; b) course of damage parameter D in dependence of punch path s at RP; c) damage distribution D in cross section of component r_{DDR} = 3 mm; d) course of damage parameter D in dependence of distance x to symmetry plane mm considering different process set-ups.

Discussion

Change of die radii r_{DR}. The comparison of the load paths and the damage development at the reference point using different die radii r_{DR} shows a distinction, especially for $r_{DR} = 3$ mm. As early as from an equivalent plastic strain φ_{pl} of $\varphi_{pl} = 0.025$, a higher value of the triaxiality η

becomes apparent, which can be consulted moderately for the damage development. Analogously, the damage parameter D differs from the other two curves at the same point in strain. Due to the different equivalent strains φ_{pl} needed, however, all three achieve an almost identical damage parameter value D in the end. When observing the course of the damage parameter D as a function of the punch path s, a later onset of damage development with increasing die radius r_{DR} becomes apparent. It is concluded that this is due to the time dependent course of the bending radius of the sheet. With a smaller die radius r_{DR}, the final bending radius is reached sooner than with a higher die radius r_{DR}. Accordingly, the damage development begins at a later stage, since damage is always associated only with plastic deformation.

Considering the different equivalent plastic strains φ_{pl} at the reference point depending on the die radius r_{DR}, it is noticeable that although the bending radius is significantly smaller at $r_{DR} = 3$ mm, the equivalent plastic strain φ_{pl} is lower than with a greater die radius r_{DR}. It is assumed that the larger contact area of the sheet and the die with increasing die radius r_{DR} results in a larger frictional surface. This larger frictional surface leads to a higher flow resistance of the sheet, which results in higher punch forces. The higher punch forces required also result in higher stresses above the yield point at the reference point, which are reflected in a higher equivalent plastic strain φ_{pl}. With regard to the damage distribution in the component, it is assumed that the smaller die radius r_{DR} and the correspondingly smaller bending radius result in correspondingly higher damage parameter D in the wall of the component. This is brought into the context of greater predominant stresses in this area due to the smaller bending radius.

Change of process set-up. The course of triaxiality η of RSD and MSSD show a very similar course. The two courses differ only in the equivalent plastic strain φ_{pl} achieved. Similar to the observation of the different die radii r_{DR}, the necessary punch forces and the associated higher stresses at the reference point also seem to lead to more deformation being introduced into the area under consideration. A similar result can be seen in the course of the damage parameter D over the equivalent strain respective of the punch path s. The two curves do not differ in their characteristics, but in the final values obtained due to different equivalent strains φ_{pl}. However, severe thinning takes place in the reference position respectively the bend of the component.

Summary

A total of six different process routes for the production of a geometrically similar component were investigated. On the one hand, different drawing ring radii r_{DR} ($r_{DR} = \{3, 6, 9$ mm$\}$) and, on the other hand, different process set-ups (stretch drawing, multistep stretch drawing, reverse stretch drawing) were analyzed. The individual routes were compared with each other on the basis of their load paths and the associated damage development.

When comparing the die radii r_{DR}, a larger die radius r_{DR} at the selected reference point was found not to result in a lower damage parameter D. However, the damage development starts at a later stage with respect to the punch path s or the equivalent plastic strain φ_{pl}. Furthermore, the die radius r_{DR} was shown to have an influence on the damage distribution in the component. Particularly in the wall, a larger die radius r_{DR} resulted in less damage, which can be used for later applications to increase the performance of the component in respect of the use case. Considering the different process setups, the RSD and MSSD show very similar load paths despite different process routes, but differ in the equivalent plastic strain φ_{pl} and thus the values of the damage parameter D are different. The deformation at the reference point, however, is so severe that there is significant sheet thinning and a high damage parameter D. Due to this, the RDS and MSDD are not recommended as a suitable process route.

To complement the numerical analysis of the load paths and damage development, experimental investigations will be carried out. For this purpose, the process routes of the different die radii r_{DR} will be selected on the basis of the present results. The numerically determined load paths will then be correlated with the results regarding the damage development. Nevertheless, the present results have already enabled a pre-selection of possible process routes to be considered and the corresponding load paths to be determined.

Acknowledgements
This research was funded by Deutsche Forschungsgemeinschaft (DFG, German Research Foundation; Project number 278868966 – TRR 188; *Damage Controlled Forming Processes*). The authors would also like to thank A. Erman Tekkaya, Till Clausmeyer, Alexander Schowtjak and Jan Gerlach from the Institute of Forming Technology and Lightweight Components of TU Dortmund, sub-project S01 of TRR 188, for the usage of their implementation of the LEMAITRE damage model. Simulations were performed with computing resources granted by RWTH Aachen University under project rwth0907.

References
[1] Information on https://www.europarl.europa.eu
[2] Information on https://climate.ec.europa.eu
[3] H.J. Kim, C. McMillan, G.A. Keoleian, S.J. Skerlos, Greenhouse Gas Emissions Payback for Lightweighted Vehicles Using Aluminum and High-Strength Steel, J. Ind. Ecol. 14 (2010) 929-946. https://doi.org/10.1111/j.1530-9290.2010.00283.x
[4] F. Klocke, Manufacturing Processes: 4. Forming, Springer Berlin Heidelberg, Berlin, Heidelberg, 2013.
[5] N.P. Lutsey, Review of technical literature and trends related to automobile mass-reduction technology, University of California, Davis, 2010.
[6] Information on https://ec.europa.eu/commission/presscorner/detail/en/IP_22_4312
[7] J. Tschorn, D. Fuchs, T. Vietor, Potential impact of additive manufacturing and topology optimization inspired lightweight design on vehicle track performance, Int. J. Interact. Des. Manuf. (IJIDeM) 15 (2021) 499-508. https://doi.org/10.1007/s12008-021-00777-x
[8] M. Müller, I.F. Weiser, T. Herrig, T. Bergs, Numerical prediction of the influence of process parameters and process set-up on damage evolution during deep drawing of rectangular cups, International Conference on Accuracy in Forming Technology (ICAFT), 2022
[9] G. Hirt, E. Tekkaya, T. Clausmeyer, J. Lohmar, Potential and status of damage controlled forming processes, Prod. Eng. 14 (2020) 1-4. https://doi.org/10.1007/s11740-019-00948-6
[10] Y. Li, M. Luo, J. Gerlach, T. Wierzbicki, Prediction of shear-induced fracture in sheet metal forming, J. Mater. Process. Technol. 210 (2010) 1858-1869. http://doi.org/10.1016/j.jmatprotec.2010.06.021
[11] C.C. Roth, D.Mohr, Ductile fracture experience with locally proportional loading histories, Int. J. Plast. (2016) 328-354. https://doi.org/10.1016/J.IJPLAS.2015.08.004
[12] L. Sprave, A. Schowtjak, R. Meya, T. Clausmeyer, A.E. Tekkaya, A. Menzel, On mesh depend-encies in finite-element-based damage prediction: application to sheet metal bending, Prod. Eng. 14 (2020) 123-134. https://doi.org/10.1007/s11740-019-00937-9
[13] M. Nick, M. Müller, H. Voigts, I.F. Weiser, T. Herrig, T. Bergs, Effect of Friction Modelling on Damage Prediction in Deep Drawing Simulations of Rotationally Symmetric Cups, Defect and Diffusion Forum 414 (2022) 103-109. https://doi.org/10.4028/p-29o20d
[14] M. Nick, A. Feuerhack, T. Bergs, T. Clausmeyer, Numerical Investigation of Damage in Single-step, Two-step, and Reverse Deep Drawing of Rotationally Symmetric Cups from DP800 Dual Phase Steel, Procedia Manuf. 47 (2020) 636-642. https://doi.org/10.1016/j.promfg.2020.04.195

[15] J. Lian, Y. Feng, S. Münstermann, A modified Lamaitre Damage Model Phenomenologically Accounting for the Lode Angle 31 Effect on Ductile Fracture, Procedia Mater. Sci. 3 (2014) 1841-1847. https://doi.org/10.1016/j.mspro.2014.06.297
[16] T.S. Cao, Models for ductile damage and fracture prediction in cold bulk metal forming processes: a review, Int. J. Mater. Form. 10 (2017) 139-171. https://doi.org/10.1007/s12289-015-1262-7

Materials Research Proceedings 28 (2023) 737-746 https://doi.org/10.21741/9781644902479-80

Improved failure characterisation of high-strength steel using a butterfly test rig with rotation control

STOCKBURGER Eugen[1,a,*], WESTER Hendrik[1,b], JEGATHEESWARAN Vithusaan[1,c], DYKIERT Matthäus[1,d] and BEHRENS Bernd-Arno[1,e]

[1]Institute of Forming Technology and Machines (IFUM), Leibniz Universität Hannover, An der Universität 2, 30823 Garbsen, Germany

[a]stockburger@ifum.uni-hannover.de, [b]wester@ifum.uni-hannover.de, [c]jegatheeswaran@ifum.uni-hannover.de, [d]dykiert@ifum.uni-hannover.de, [e]behrens@ifum.uni-hannover.de

Keywords: CP800, Butterfly Specimen, Experimental-Numerical Procedure

Abstract. A forming limit diagram is the standard method to describe the forming capacity of sheet materials. It predicts failure due to necking by limiting major and minor strains. For failure due to fracture, the fracture forming limit diagram is used, but fracture caused by plastic deformation at a shear-dominated stress state cannot be predicted with a conventional fracture forming limit diagram. Therefore, stress-based failure models are used as an alternative. These models are describing the fracture of sheet materials based on the failure strain and the stress state. Material-specific parameters must be determined, but a standardised procedure for the calibration of stress-based failure models is currently not established. Most test procedures show non-constant stress paths and varying stress states in the crack initiation area, which leads to uncertainties and inaccuracies for modelling. Therefore, a new test methodology was invented at the IFUM: a prior presented butterfly test rig was extended to enable an online rotation to adapt the loading angle while testing. First, butterfly tests with CP800 were performed for three fixed loading conditions. The tests were modelled numerically with boundary conditions corresponding to the tests. Based on the numerical results, the stress state as well as failure strain were identified and the stress state deviations were calculated. Afterwards, the necessary angular displacements to compensate the stress state deviations for the adaptive test rig were iteratively determined with numerical simulations using an automatised Python script. Finally, the butterfly tests were performed experimentally with the determined adaptive loading angles to identify the specimen failure and compared to the simulations for validation.

Introduction

The forming limit diagram (FLD) defines the critical major and minor strains of a sheet metal, which lead to material failure if exceeded. The FLD is conventionally used to describe forming limits due to necking. Failure due to fracture can be described with the fracture forming limit diagram (FFLD). However, the FLD and the FFLD give an inadequate prediction of the failure for high-strength steel (HSS) sheets, since it is valid for linear strain paths and for the strain states between uniaxial tension and biaxial tension [1]. Modern forming processes and HSS sheets often show non-linear strain paths. Furthermore, failure due to fracture initiation caused by plastic deformation at a shear-dominated stress state cannot be predicted by the FLD or the FFLD [2]. As an alternative to the FFLD, failure models based on the stress state are used. Those failure models describe the failure of the sheet metal under consideration of the stress state by means of the stress-state-dependent equivalent plastic strain at failure ε_f, which allows statements in the case of non-linear strain paths and shear-dominated stress states. To describe the three-dimensional stress state,

Content from this work may be used under the terms of the Creative Commons Attribution 3.0 license. Any further distribution of this work must maintain attribution to the author(s) and the title of the work, journal citation and DOI. Published under license by Materials Research Forum LLC.

Materials Research Proceedings 28 (2023) 737-746 https://doi.org/10.21741/9781644902479-80

the stress triaxiality η and the normalised Lode angle θ are used. A common stress-based model is the Modified Mohr-Coulomb (MMC) failure model [3], which can be written as

$$\varepsilon_{f,MMC} = \left[c_1 \cdot \left(\eta + \frac{1}{3} \cdot sin\left(\frac{\theta\pi}{6}\right) \right) + c_2 \cdot \left(\sqrt{\frac{1+c_1^2}{3}} \cdot cos\left(\frac{\theta\pi}{6}\right) \right) \right]^{-\frac{1}{n}} \quad (1)$$

whereby c_1, c_2 and n are material-specific parameters. For the calibration of the failure models, failure characterisation experiments are performed, but a standardised procedure for testing and calibrating is currently not available. Used failure characterisation experiments mostly result in non-constant stress paths in the area of the specimen failure [4]. In Fig. 1 (A) common failure characterisation specimen such as the Miyauchi, holed tensile as well as waisted tensile specimen are shown and in Fig. 1 (B) the corresponding non-constant stress paths are visible from those specimens. Only the hydraulic bulge test leads to a constant stress path. In order to minimise the resulting uncertainties and inaccuracies of the failure characterisation for stress-based failure models, a new experimental-numerical testing methodology for an improved failure characterisation with constant stress paths is engineered and presented within the scope of this work.

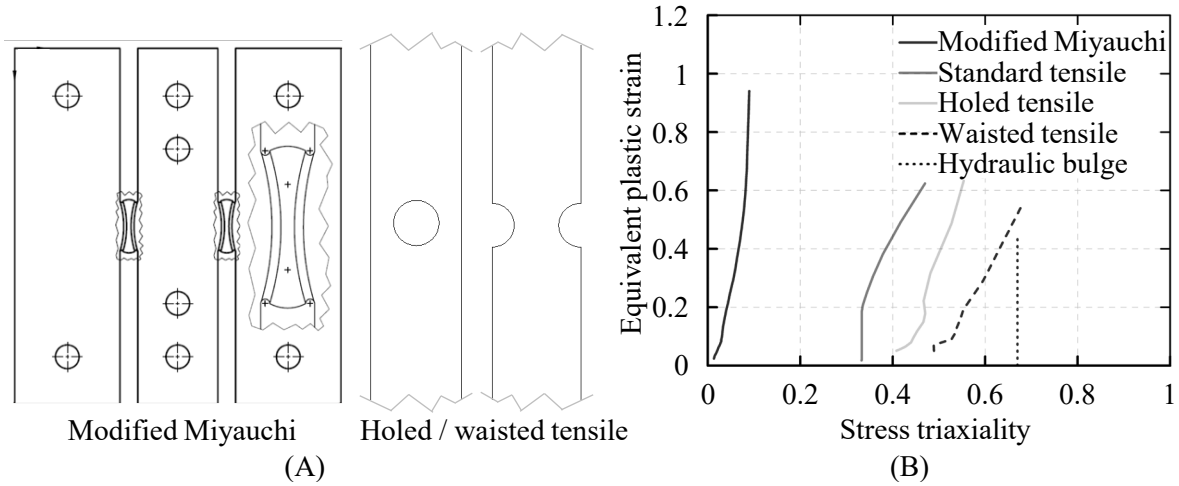

Fig. 1. Failure characterisation specimen and resulting non-constant stress paths based on the work from Behrens et al. [4].

New Experimental-Numerical Failure Characterisation Methodology

The module for the new adaptive test methodology is based on a prior developed test module shown by Stockburger et al. in [5]. In this test module, according to the test principle of Arcan et al. [6], a butterfly specimen can be tested under different orientations or loading angles α to the normal loading direction of the tensile testing machine, whereby different stress states can be achieved in the test area of the specimen. Using the butterfly specimen has the advantage compared to conventional failure characterisation specimen that the specimen failure is not initialised at the specimen edge, but in the centre of the specimen. Nevertheless, as for other specimen the stress paths of the butterfly specimens are not entirely constant. To estimate the characteristic stress state and the equivalent plastic strain at failure which is needed to calibrate models like the MMC failure model, the butterfly specimen must be numerically modelled considering boundary conditions from the experiments.

Materials Research Proceedings 28 (2023) 737-746 https://doi.org/10.21741/9781644902479-80

In order to solve the problem of non-constant stress paths in the experiment, a new adaptive test module was developed. Fig. 2 shows an illustration of the module for the new adaptive test methodology. The new test module consists of two separate specimen holders, which each have an outer ring gear and a recess for the butterfly specimen. Two mounting plates are used to attach the butterfly specimen to the specimen holder. The outer ring gears from the upper and lower specimen holders are each in contact with a worm shaft, while the upper and lower worm shafts are connected to two electric motors by two bevel gears. A rotational movement of the specimen holders is generated when the electric motors are activated and thus the current loading angle α can be changed by an adaptive loading angle α_{adap}. The rotation is regulated by a control device with a sensor, that determines the angular position. The entire test module is attached to a tensile testing machine by means of two connecting plates. Overall, the tensile testing machine is applying the load, which is transferred from the two separate specimen holders to the butterfly specimen. With the presented testing module, loading angles α are continuously adjustable during testing in order to obtain constant stress states.

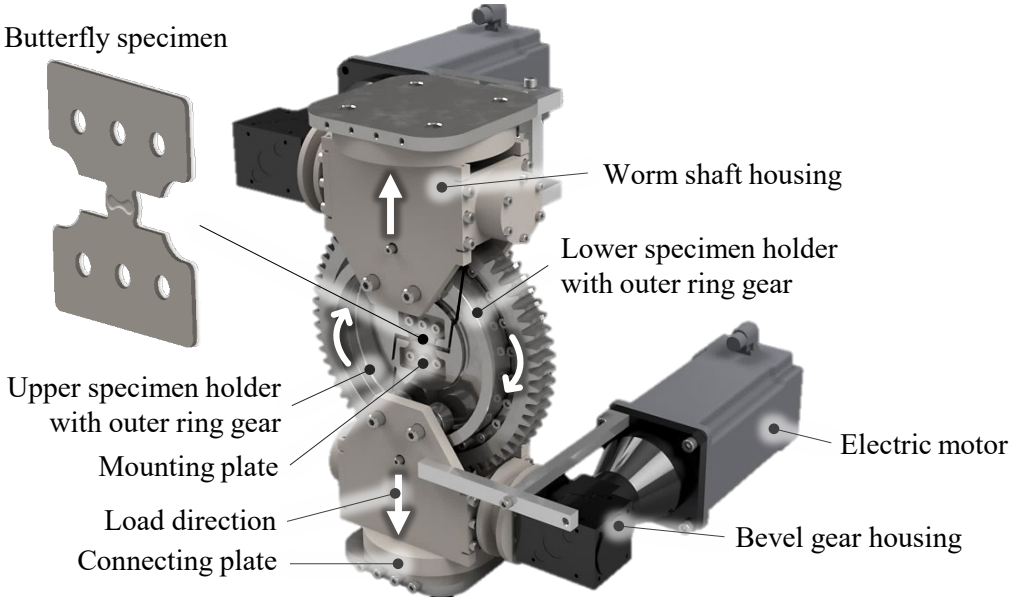

Fig. 2. Module for the new adaptive test method with butterfly specimen.

The design of the adaption loading angle α_{adap} is carried out iteratively with the aid of a numerical model of the test module. For this purpose, tests with a fixed loading condition α are first carried out experimentally and then mapped numerically. The experimental displacements up to specimen failure serve as boundary conditions for the simulation model, which is shown in Fig. 3 (A). Based on the results, the required adaption loading angle α_{adap} is now calculated numerically. For this purpose, the adaption loading angle α_{adap} is varied automatically within a sensitivity study using a Python script as shown in Fig 3 (B). First, a variation range of the adaption loading angle α_{adap} and the step size of it is specified. Consequently, a simulation is carried out iteratively for each adaption loading angle α_{adap} in the variation range. In order to determine the time of the angle adaption at which the simulations start, the stress triaxiality is taken as an indicator. The maximal deviation of the stress triaxiality was subjectively defined as 0.03. As soon as the equivalent plastic strain-stress triaxiality path showed a change higher than the maximal deviation, the iterative simulations for the adaption loading angle α_{adap} begin. Depending on the outcome, the procedure is repeated for further adaption. After the numerical design, experimental tests are performed using the numerically-iterative determined angle adaption. Those results are

used to identify the material failure under constant stress states and to verify the numerical procedure. Finally, the MMC failure model can be calibrated as well as compared for the fixed and the new adaptive test methodology.

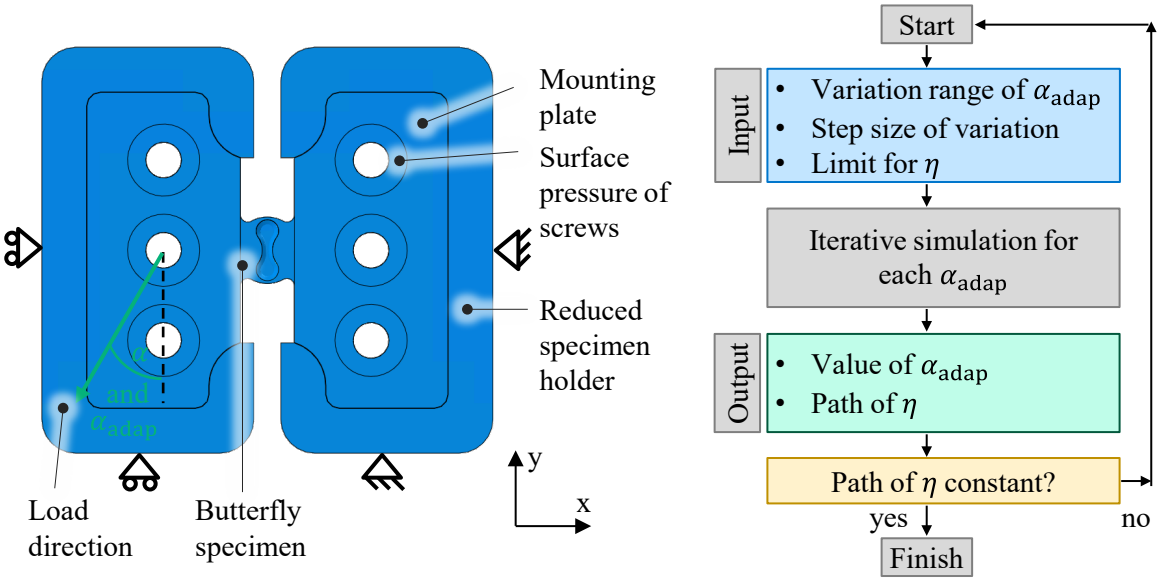

Fig. 3. Simulation model of the butterfly tests (A) and sequence plan of the Python script (B).

Application of the New Failure Characterisation Methodology

The new failure characterisation methodology was applied to the complex-phase HSS CR570Y780T-CP (CP800) from voestalpine Stahl GmbH. The outer contour of the specimen was cut by waterjet and the thickness reduction in the examination area of the specimen was carried out by milling. The new butterfly test module was installed in the tensile testing machine S100/ZD from DYNA-MESS Prüfsysteme GmbH. First, butterfly tests for the fixed configuration of the loading angles -3°, 28° and 74.5° were performed. For measuring the specimen displacement and estimation of fracture occurrence in the examination area, the optical measurement system Aramis from Carl Zeiss GOM Metrology GmbH was used. For each loading angle the tests were repeated three times. The testing temperature corresponded to room temperature and the testing speed was set to 0.05 mm/s.

Afterwards, the experiments with fixed loading conditions were numerically modelled to estimate the equivalent plastic strain at failure and the stress triaxiality as well as the normalised Lode angle paths. The FE models were generated in Abaqus/Standard for each loading angle with the corresponding displacements until failure in x- and y-direction from the experiments. The boundary conditions were extracted from the optical measurements using digital image correlation and directly applied to the specimen holder. The elastic behaviour of the material was described with a modulus of elasticity of 210 GPa and a Poisson's ratio of 0.3. The data required for modelling the plastic flow behaviour, such as flow curve and anisotropy parameters, are summarised in Table 1 and were previously published by Behrens et al. in [7]. The hardening behaviour was modelled by the Hockett-Sherby approach [8] and the anisotropy by the Hill48 yield function [9]. The Hockett-Sherby approach describes the flow stress k_f of the material as a function of the equivalent plastic strain ε and the four material parameters a, b, c as well as d. The specimen holder was geometrically reduced and modelled as rigid body with 210 GPa as elastic modulus and 0.3 as Poisson's ratio. A discretisation of the specimen was done with linear reduced-integrated hexahedral elements with hourglass control, referred to as C3D8R in Abaqus. The examination area of the specimens was meshed with an element edge length of 0.1 mm and the

thickness of the specimens by five elements. The surface pressures of the screws acting on the mounting plates were modelled with a surface pressure of 204 MPa, which results from the tightening torque of the screws.

Table 1. Parameters for the extrapolation approach and anisotropy function from [7].

	Equation		a in MPa	b in MPa	c	d
Hockett-Sherby	$k_f = a - (a - b) \cdot e^{c \cdot \varepsilon^d}$ (2)		4.96 E-05	502.5	0.823	0.170
	F	G	H	L	M	N
Hill'48	0.495	0.531	0.469	1.5	1.5	1.634

Further, the numerical models were evaluated with regard to the equivalent plastic strain, the stress triaxiality path and the normalised Lode angle path. The models were analysed on the surface of the investigation area. The equivalent plastic strain was plotted as a function of the triaxiality and of the normalised Lode angle. Based on these curves, the characteristic stress state was calculated by the area-weighted centroid. The equivalent plastic strain at failure and the characteristic stress state from the fixed configuration are later compared to the values of the adaptive tests.

Next, the design of the adaption loading angle α_{adap} was carried out. The procedure is shown in Fig. 4 exemplarily for the adaptions of the loading angle 28°. First, the course of the equivalent plastic strain-stress triaxiality curve for the fixed loading condition α was considered. Based on the illustrated curve, a value for the stress triaxiality was manually selected, at which the angular adaption begins. When selecting the limit value, care was taken to intervene early enough to correct the curve with regard to a more constant path. In Fig. 4 (A), the limit value is marked orange at a stress triaxiality of 0.135. Now the Python script was used to design the angle adaption. During pre-processing, only the displacement boundary conditions were automatised redefined by a subroutine to change the loading. With the changed input variables, the simulation was proceeded. In the example given, the adaption loading angle α_{adap} was varied between 5° and 6°. The corresponding influence of the angle adaption on the stress state is displayed in Fig. 4 (B). 6° was selected as the adaption loading angle α_{adap} and the limit for the stress triaxiality was set to 0.139. When choosing the values, care was taken again to ensure that the path remains as constant as possible.

Materials Research Proceedings 28 (2023) 737-746 https://doi.org/10.21741/9781644902479-80

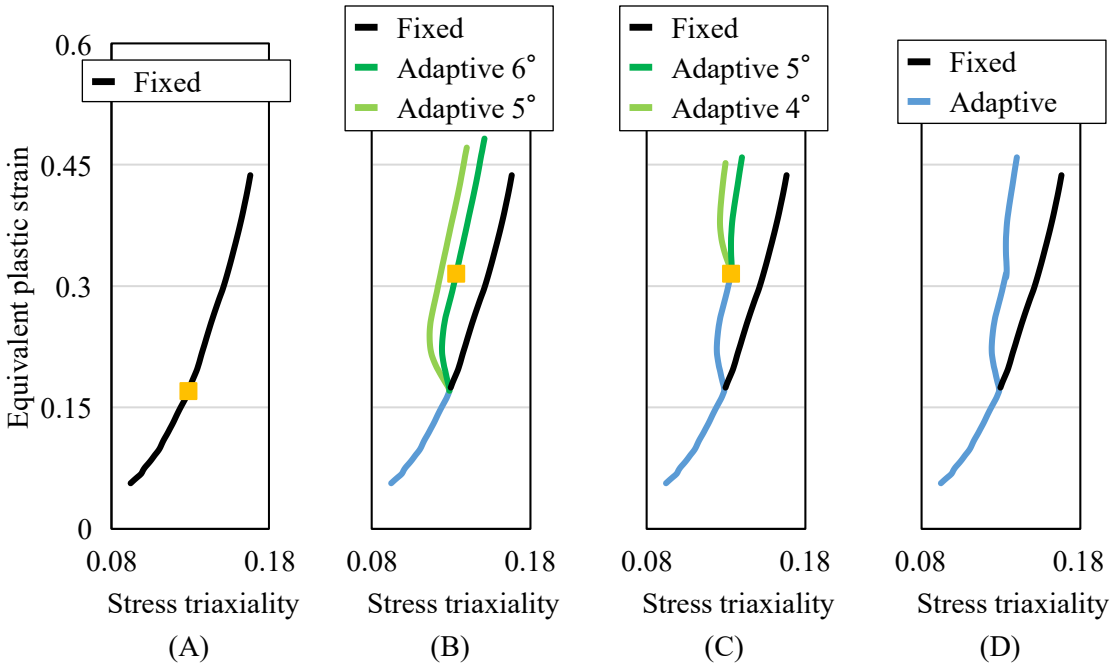

Fig. 4. Iterative design of the angular adaptions for the loading angle 28°.

In order to design the second angle adaption, a next adaption loading angle α_{adap} were chosen manually. Now the subroutine proceeded further in the same way as for the first angle adaption. Next, the adaption loading angle α_{adap} 4° and 5° were compared. The equivalent plastic strain-stress triaxiality paths after the second angle adaption are illustrated in Fig. 4 (C). With regard to a constant curve, the adaption loading angle α_{adap} of 5° was selected. Fig. 4 (D) compares the final equivalent plastic strain-stress triaxiality path of the designed adaptive test for a loading angle α of 28° with the path for a fixed loading condition α.

Additionally, butterfly experiments with the designed angular adaptions were carried out with the new butterfly test module for the three loading angles α -3°, 28° and 74.5°. Here, the limit values for the stress triaxialities served as boundary conditions with displacements in x- and y-direction. A comparison of the experimental and numerical force-displacement curves for the adaptive test methodology is shown in Fig. 5 (A). The comparison shows that the properties as well as boundary conditions used to describe the flow behaviour and the structure of the FE model represented the experimental tests sufficiently accurate and were therefore considered validated in this range. Based on the comparison, the models were considered suitable for the evaluation of the stress state. For increasing the loading angle, the force rises and the displacement until failure reduces.

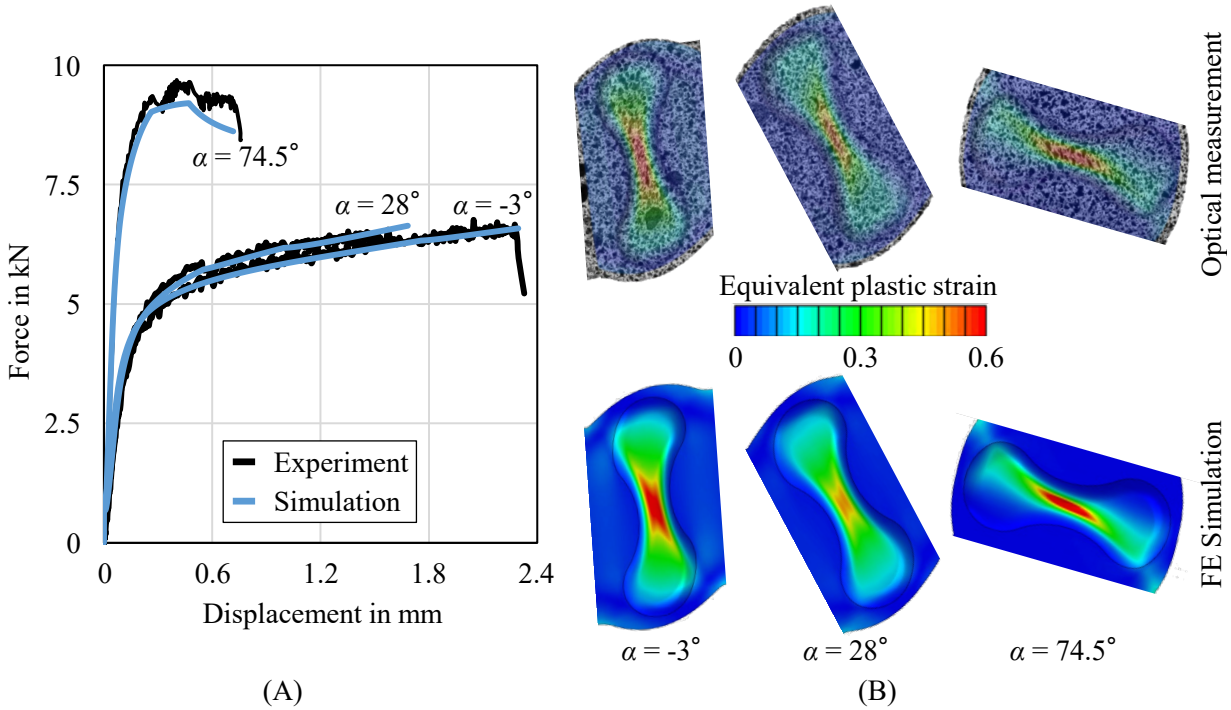

Fig. 5. Comparison of the experimental as well as numerical force-displacement curves (A) and equivalent plastic strain distribution of the butterfly specimen (B) for the adaptive test methodology.

Fig. 5 (B) illustrates the equivalent plastic strain distribution directly before failure of the butterfly tests with the adaptive test methodology. The deformation is accumulated in the centre of all three specimen for both, the experiments and the simulations. Comparing the optical measurement from the experiments and simulation results, the equivalent plastic strain distribution is very similar. In general, the equivalent plastic strain reduces from a loading angle of -3° to 28° and rises again for 74.5°. In the centre of the specimen, the equivalent plastic strain and the stress state were further evaluated.

Fig. 6 (A) illustrates the comparison of the numerically determined equivalent plastic strain-stress triaxiality paths at the location of fracture initiation. It shows that the angular adaptions in the adaptive tests compared to the tests with fixed loading condition α result in significantly more constant paths with regard to the equivalent plastic strain-stress triaxiality path. Further, it is evident in Fig. 6 (A) that higher equivalent plastic strains are achieved in the adaptive tests compared to the fixed tests. This is due to higher displacements until failure for the adaptive tests. This is also shown in the comparison of the characteristic stress states in Fig. 6 (B). Due to the more constant equivalent plastic strain-stress triaxiality path in the adaptive tests, smaller characteristic values are achieved than in the fixed tests. This is due to the fact that the area under the curves decreases because of the more constant stress path. As a result, the centre of gravity of the area shifts to smaller values and the characteristic values decrease. In the tests with a fixed loading condition α, the stress state change during the tests is large and non-constant stress paths are present.

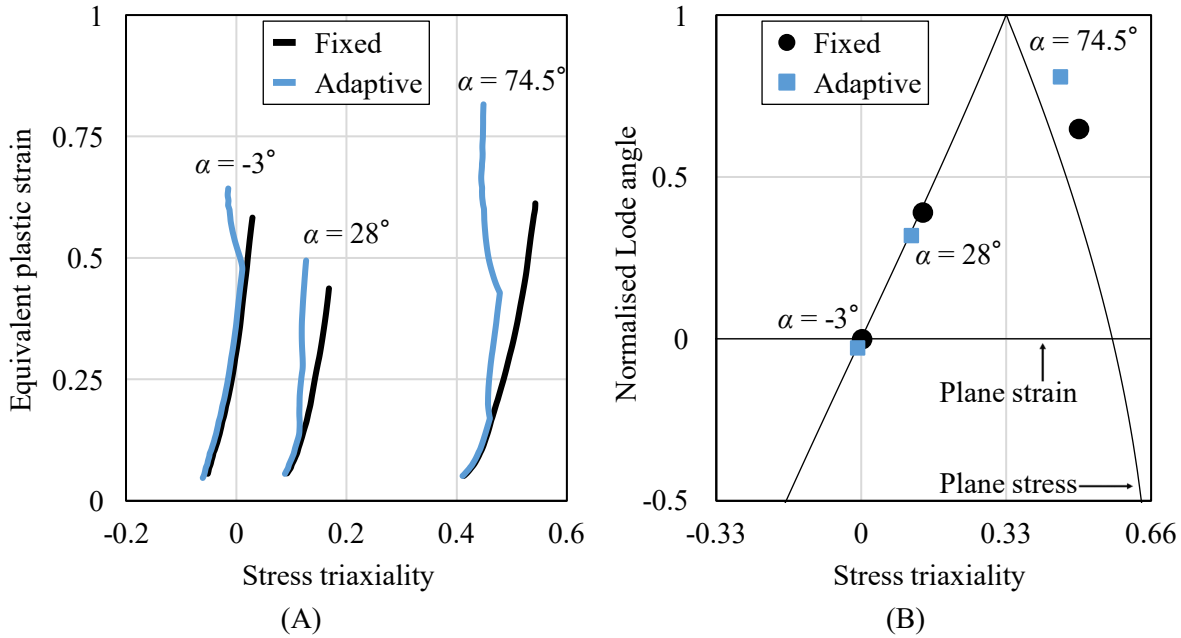

Fig. 6. Equivalent plastic strain-stress triaxiality paths (A) and characteristic stress states (B) for the fixed and adaptive test methodology.

A comparison of the calibrated MMC failure models for the test methodology with fixed loading condition α and for the new adaptive test methodology is presented in Fig. 7. The failure models are shown for plane stress in Fig. 7 (A) and plane strain state in Fig. 7 (B). The failure curves in the plane stress and plane strain state are of similar course for both methods. The major difference is the higher level of the failure curve achieved with the adaptive test methodology due to higher equivalent plastic strains of each test. A minor difference is that the failure curve from the fixed test methodology has a lower slope than the failure curve of the adaptive test methodology. Anyway, the higher accuracy of the failure model for the adaptive test methodology compared to the fixed test methodology needs to be proven by the simulation of forming processes, which is planned for future investigations.

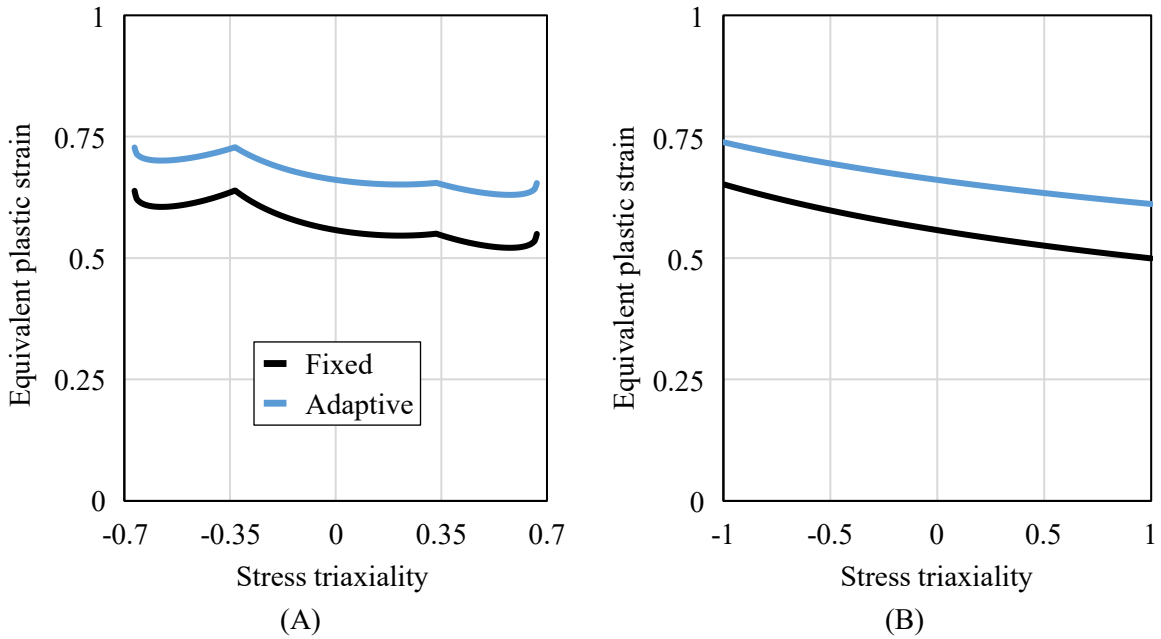

Fig. 7. Plane stress (A) and plane strain state (B) of the fitted MMC-model for the fixed and adaptive test methodology.

Summary

In this work a new experimental-numerical failure characterisation methodology is presented. Conventional failure characterisation tests show a non-constant stress path and therefore inaccuracies for modelling. Butterfly tests for the fixed loading conditions -3°, 28° and 74.5° were performed and numerically modelled. Based on the results for the stress path of the simulations, angle adaptions while testing were iteratively-numerical determined to correct the stress path into a constant path. Afterwards, butterfly experiments were performed using the estimated adaptive angles and compared to the simulations. Therefore, it was possible to achieve a more constant stress path and to minimise the change in the stress state at the location of fracture. Finally, MMC failure model were calibrated for both methodologies and compared to each other, which showed the influence of the new failure characterisation methodology.

In future investigations, more loading angles for the butterfly tests will be experimentally performed and numerically modelled to enhance the data for the failure model parametrisations. Further, it is planned to optimise the Python script to estimate the angle adaptions not subjectively anymore but automatically based on general criteria. Then, demonstrators in the style of a B-pillar as shown in [10] will be experimentally produced and the tests will be reproduced numerically using the MMC failure models from the fixed as well as adaptive test methodology. Based on the results, the failure prediction of the new adaptive test methodology will be evaluated regarding its potential for a higher accurate failure modelling.

Acknowledgements

The authors would like to thank the German Research Foundation (Deutsche Forschungsgemeinschaft, DFG) for the financial and organisational support of this project with the number 405334714. Furthermore, the authors would like to thank voestalpine Stahl GmbH for providing the material under investigation.

References

[1] Standard ISO 6892-1:2020-06, Metallic materials - Tensile testing – Part 1: Method of test at room temperature, Beuth Verlag GmbH, Berlin, Germany, 2020.

[2] Y. Li, M. Luo, J. Gerlach, T. Wierzbicki, Prediction of shear-induced fracture in sheet metal forming, J. Mat. Proc. Tech. 210 (2010) 1858-1869. https://doi.org/10.1016/j.jmatprotec.2010.06.021
[3] Y. Bai, T. Wierzbicki, A new model of metal plasticity and fracture with pressure and Lode dependence, Int. J. Plast. 24-6 (2008) 1071-1096. https://doi.org/10.1016/j.ijplas.2007.09.004
[4] B.-A. Behrens, A. Bouguecha, M. Vucetic, I. Peshekhodov, Characterisation of the quasi-static flow and fracture behaviour of dual-phase steel sheets in a wide range of plane stress states, Arch. Civil Mech. Eng. 12 (2012) 397-406. https://doi.org/10.1016/j.acme.2012.06.017
[5] E. Stockburger, H. Vogt, H. Wester, S. Hübner, B.-A. Behrens, Evaluating Material Failure of AHSS Using Acoustic Emission Analysis, Mat. Res. Proc. 25 (2023) 379-386. https://doi.org/10.21741/9781644902417-47
[6] M. Arcan, Z. Hashin, A. Voloshin, A method to produce uniform plane-stress states with applications to fiber-reinforced materials, Exp. Mech. 18 (1978) 141-146. https://doi.org/10.1007/BF02324146
[7] B.-A. Behrens, K. Brunotte, H. Wester, M. Dykiert, Fracture Characterisation by Butterfly-Tests and Damage Modelling of Advanced High Strength Steels, Key Eng. Mat. 883 (2021) 294-302. https://doi.org/10.4028/www.scientific.net/kem.883.294
[8] J.E. Hockett, O.D. Sherby, Large strain deformation of polycrystalline metals at low homologous temperatures, J. Mech. Phys. Solid. 23 (1975) 87-98. https://doi.org/10.1016/0022-5096(75)90018-6
[9] R.A Hill, Theory of the yielding and plastic flow of anisotropic metals, Proc. R. Soc. A 193 (1948) 281-297. https://doi.org/10.1098/rspa.1948.0045
[10] B.-A. Behrens, S. Jüttner, K. Brunotte, F. Özkaya, M. Wohner, E. Stockburger, Extension of the Conventional Press Hardening Process by Local Material Influence to Improve Joining Ability, Proc. Manuf. 47 (2020) 1345-1352. https://doi.org/10.1016/j.promfg.2020.04.258

Materials Research Proceedings 28 (2023) 747-754 https://doi.org/10.21741/9781644902479-81

Investigation of the influence of loading direction after pre-forming on the formability and mechanical properties of DP600

NORZ Roman[1,a *], VALENCIA Fabuer R.[2,b], VITZTHUM Simon[2,c], UNGUREANU Bogdan[2,d], GERKE Steffen[2,e], BRÜNIG Michael[2,f] and VOLK Wolfram[1,g]

[1]Chair of Metal Forming and Casting, Technical University of Munich, Walther-Meissner-Str. 4, 85748 Garching, Germany

[2]Universität der Bundeswehr, Institut für Mechanik und Statik, Werner-Heisenberg-Weg 39, Neubiberg, 85579 Germany

[a]roman.norz@utg.de, [b]fabuer.ramon@unibw.de, [c]simon.vitzthum@utg.de, [d]simon.vitzthum@utg.de, [e]steffen.gerke@unibw.de, [f]michael.bruenig@unibw.de, [g]wolfram.volk@utg.de

Keywords: Non-Proportional Load Paths, Cross-Loading, Onset of Yielding, Formability

Abstract. The material behaviour after non-proportional strain paths is subject of numerous current investigations. These investigations show that in addition to the stress state, a change in the direction of loading also has a significant influence on the material behaviour. In this work, the influence of non-proportional strain paths on the mechanical properties such as tensile strength, uniform strain, elongation at fracture and yield strength as well as the influence on formability is determined. For this purpose, a dual-phase steel CR330Y590-DP, with a thickness of 0.8 mm, is investigated in more detail. The material is pre-strained to different strain values and then further examined with Nakajima and tensile tests. The influence of the loading direction is determined by five different post-strain directions (0°, 22,5°, 45°, 67.5°and 90°) to the initial pre-strain direction. In addition to the method according to the standard, the yield strength is determined by a temperature-dependent determination method, which is based on the thermoelastic effect. This method has already been qualified for simple uniaxial tensile tests and a relation to the microstructural behaviour was proven. Thus, it provides valuable conclusions on the microstructural behavior for the tests performed within this study with a change in the loading direction.

Introduction

Non-proportional load paths are being investigated for several years. Many researchers focus on the effect on the mechanical properties by using tensile or shear tests but also on the formability using Nakajima experiments. One of the most looked at materials are dual-phase steels with different strengths. By using shear tests, Hérault et al. [1] analysed the influence of uniaxial pre-strain on the elasto-plastic behavior. To describe the material behavior using the Homogeneous Anisotropic Hardening model (HAH-model), experiments with a pre-forming level of at least $\varepsilon = 2\%$ are required due to the significant material behaviour evolution below that level. Larsson et al. [2] investigated the influence of pre-forming height and a change in loading direction on Docol 600DP and Docol 1200DP using tensile and shear tests with pre-formed material. The pre-forming height, as well as a change in loading direction not only influence the onset of yielding but also the formability in the tensile test experiments. A change in loading direction by 45° or 90° after a pre-forming of $\varepsilon = 10\%$ lead to a reduced formability. Liao et al. [3] used SEM, EBSD and TEM to investigate the microstructural effects of a proportional, pseudo cross and cross-loading in DP500, DP600 and DP800. For the experiments with a change in loading direction, yielding

Content from this work may be used under the terms of the Creative Commons Attribution 3.0 license. Any further distribution of this work must maintain attribution to the author(s) and the title of the work, journal citation and DOI. Published under license by Materials Research Forum LLC.

occurred at lower stress compared to the monotonic experiments. This effect is enhanced at higher pre-forming levels. The evolution of texture was found to be weak for all three DP-steels and cannot explain the effects on the mechanical properties. Nevertheless, the presence of a soft ferritic and a hard martensitic phase leads to a very inhomogeneous plastic deformation of the material. At the onset of yielding the soft and weakly strain hardened ferrite grains control the mechanical behaviour. For a DP800 the effect on the onset of yielding takes place already at very low strains of $\varepsilon = 1\%$ and increases as the pre-forming height reaches higher levels [4]. This effect was also captured by other researchers [5]. Yu and Shen [6] looked at various pre-forming states for a DP590. They investigated the influence of a uniaxial, plane-strain and equi-biaxial pre-forming state on the tensile test results. The pre-forming state also influences the mechanical properties. The Young's – modulus is reduced with increasing pre-forming height, where the equi-biaxial pre-forming state lead to the strongest decrease.

The aim of this study is to determine the influence of three different plane-strain pre-forming levels and three different post-loading directions on the mechanical properties using tensile tests. The influence of the pre-forming on the formability will be examined by standard Nakajima experiments. The experiments in this paper are conducted with a CR330Y590-DP (DP600) steel with an initial thickness of 0.8 mm.

Experimental Procedure

The pre-forming of the material took place on a hydraulic Dieffenbacher press in combination with a modified Marciniak-tool developed by Weinschenk and Volk [7]. To ensure a homogenous plane-strain pre-forming, the specimen geometry was adapted from prior investigations [8,9] and was optimized for the used DP600 steel. The change in loading direction is obtained by a rotation of the tensile test and Nakajima specimens. For the tensile tests, five tensile test samples can be manufactured from one single pre-formed specimen, while for the Nakajima experiments only one specimen can be extracted. All pre-forming specimens are cut out under 0° to the initial rolling direction, see Fig. 1.

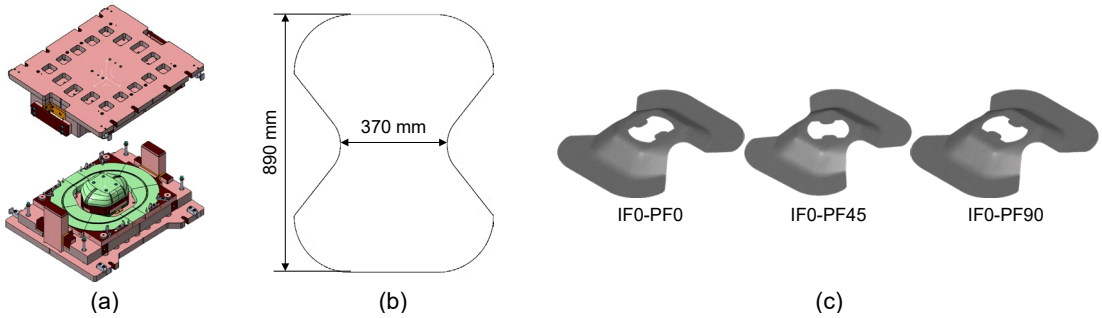

Fig. 1. (a) The used modified Marciniak tool, (b) Specimen geometry used for the plane-strain pre-forming. (s) Specimen extraction and nomenclature of the cut-out specimens.

For the tensile tests specimens according to DIN 50125 – geometry H with a width of 12.5 mm are used. The strain measurement is done by a laser extensometer with a gauge length of 50 mm and a constant strain rate of 0.001 1/s. To determine the onset of yielding, the temperature based method according to Vitzthum et al. [10] was employed. This method makes use of the thermo-elastic effect where the temperature decreases during the elastic deformation and increases during the plastic deformation. A closer description of the method can be found in [10].

The Nakajima experiments are carried out on a BUP1000 in combination with an Aramis 4M DIC system. The punch speed was set to 1 mm/s and a measuring frequency of the DIC-System of 10 Hz is applied. To minimize the friction between the punch and the specimen a PVC-pad with lubricant is used. To assess the onset of necking the Time Dependent Evaluation Method (TDEM)

proposed by Volk and Hora [11] is applied. Four different Nakajima specimens are tested, ranging from 30 mm for the uniaxial strain state to 235 mm for the biaxial strain state.

Experimental Results

The results of the experiments with the initial material show a low dependency of the loading direction on the stress-strain curves (Fig. 2) as well as the forming limit curves (Fig. 7). All investigated directions differ only marginally. This changes for the pre-formed experiments. The influence of a change in loading direction can clearly be seen. At a pre-forming level of $\varepsilon_{v.Mises}$ = 0.066 and $\varepsilon_{v.Mises}$ = 0.097 specimens with a change in loading direction of 45° show the lowest fracture strain, while the elastic-plastic transition is different for all specimens with a change in loading direction. This effect increases for higher pre-forming levels. At a pre-forming level of $\varepsilon_{v.Mises}$ = 0.121 the fracture elongation of the specimen with a change in loading direction is almost the same.

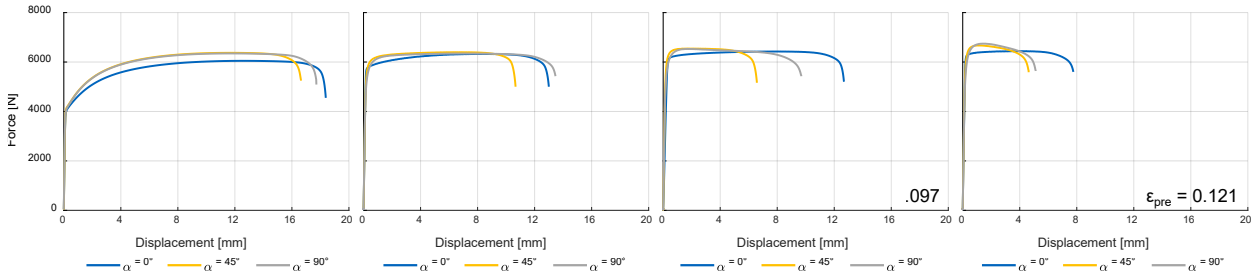

Fig. 2. Force-Displacement curves of the initial material and the three investigated pre-forming heights.

As many researchers have found a significant influence of the pre-forming and a change in loading direction on the elastic-plastic transition, the onset of yielding is further examined. To determine the onset of yielding, three different methods are employed. Next to the classic $R_{p0,2\%}$, depicted as $YS_{0.2\%}$ two temperature based methods are also applied. The temperature is measured throughout the experiment using a PT1000 thermometer, see Fig. 3 (a). The onset of yielding was then determined at the temperature minimum (YS_{Tmin}) and at zero plastic strain (YS_0). YS_0 is calculated by fitting two regression lines into the first derivative of the temperature signal, see Fig. 3 (b). One line is fitted into the elastic region where the temperature is decreasing while the other line is fitted into the area around the temperature minimum where the derivative is zero. The onset of yielding is then determined at the intersection of the two lines and via an angle bisector. A closer description of this method can be found in Vitzthum et al. [10].

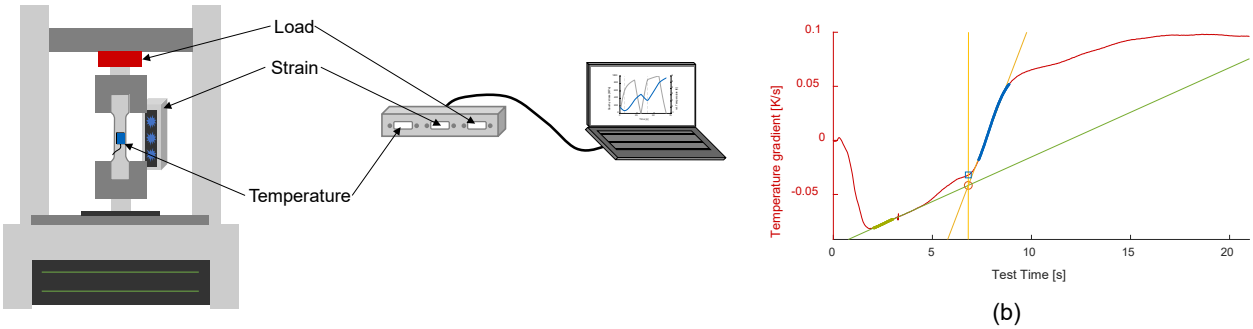

Fig. 3. (a) Experimental setup using the thermometer, (b) Determination of YS0 using the temperature derivative.

The onset of yielding is strongly dependent on a change in loading direction and the pre-forming level. The higher the pre-forming level, and when there is no change in loading direction, the closer the onset of yielding assessed by the three different methods is moving together. As soon as there is a change in loading direction, the temperature signal changes significantly. While specimens with no change in loading direction show a sharp temperature signal, almost like a V-shape, the specimens with a change in loading direction have a round temperature signal, almost like an U-shape, shown in Fig. 4.

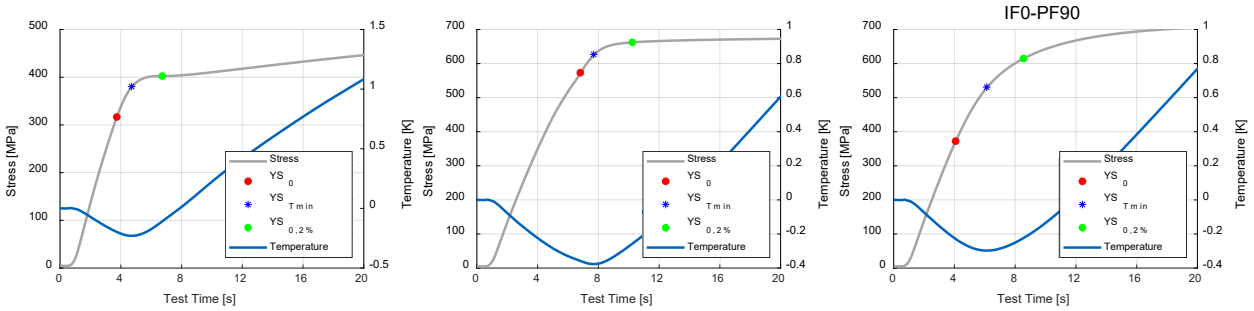

(c)

Fig. 4. (a) Onset of yielding for an initial specimen in 0° to the rolling direction, (b) Pre-formed specimen with no change in loading direction (IF0-PF0), (c) Pre-formed specimen with a change in loading direction by 90° (IF0-PF90).

Looking at all results for the different angles and pre-forming heights, it can be seen, that the onset of yielding for the $YS_{0.2\%}$ method is steadily increasing with increasing pre-forming level almost untouched by a change in loading direction, see Fig. 5 (a). The temperature-based results however, show a strong dependency on a change in loading direction as soon as a pre-forming took place, Fig. 5 (b) and (c). These results indicate that when a change in loading direction occurs after a pre-forming, some grains start to yield a lot earlier than others do. This leads to the smooth and round temperature signal. While the grains of specimens with no change in loading direction yield almost at the same time, leading to this sharp V-like shape. This effect is more substantial, the higher the pre-forming level is.

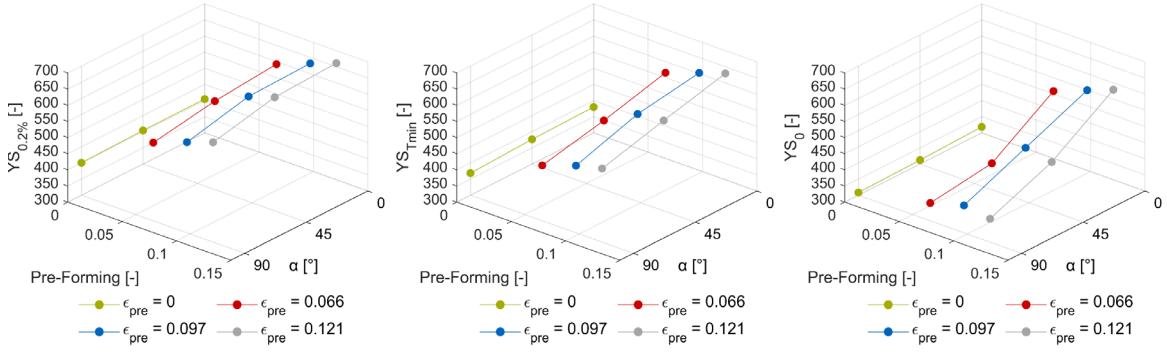

(a) (b) (c)

Fig. 5. Results for the $YS_{0.2\%}$ method (a), (b) for the temperature minimum and (c) for the YS0-method.

In the Nakajima experiments, for high pre-forming levels and a change in loading direction, shear failure is observed. When using the Time Dependent Evaluation Method (TDEM-method) a significant overestimation of the formability for such specimens is found, shown in Fig. **6** (b). The

evaluation of specimens with such a shear failure is performed by a modified TDEM-method, see Fig. 6 (a), which was already used in [8]. In Fig. 6, the two methods are shown for a 30 mm wide specimen with a change in loading direction of 45° (IF0-PF45) and a pre-forming level of ε_{pre} = 0.193.

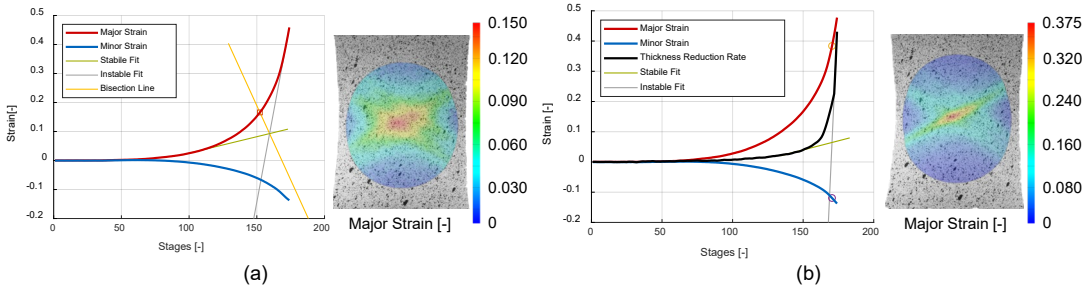

Fig. 6. (a) Method used in Volk et al. [8] for Shear-Failure, (b) Time Dependent Evaluation Method [11].

The higher the pre-forming level, the more a change in loading direction influences the formability, see Fig. **7**. For the pre-forming level with ε_{pre} = 0.151, the IF0-PF45 specimens show the lowest formability, this is different to the results for the HC340LAD [8]. The most severe influence was observed on the plane-strain post-forming and a change in loading direction by 90° (IF0-PF90) after a pre-forming of ε_{pre} = 0.193. Here, almost instant necking occurs.

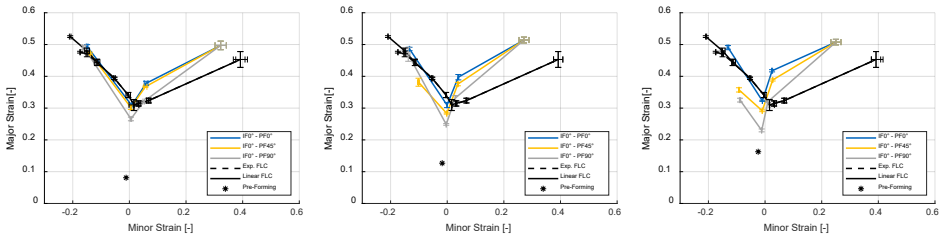

Fig. 7. (a) Forming Limit Curves for ε_{pre} = 0.097, (b) Forming Limit Curves for ε_{pre} = 0.151 (c) Forming Limit Curves for ε_{pre} = 0.193.

In comparison to the results for the micro-alloyed steel HC340LAD and the aluminium alloy AA6016-T4, the effect of a change in loading direction is somewhere in between. The HC340LAD showed a stronger dependency on the formability, see [8], while the AA6016-T4 showed almost no influence of a change in loading direction on the formability [12].

One reason for such a dependency on a change in loading direction might be the presence of voids. Asik et al. [13] found, that void growth and nucleation for a DP600 steel already takes place before the uniform elongation is reached. These voids primarily occur at inclusions and at the ferrite-martensite interface but also martensite cracking leads to the creation of voids. Due to the banded structure of the martensite inside the ferritic matrix, the damaged area is dependent on the loading direction. Gerstein et al. [14] investigated the voids after deformation of a DP600 using SEM – microscopy. Voids caused by plastic deformation have shown an elongated shape in the direction of loading. By using in-situ X-Ray microtomography Maire et al. [15] also found, that the biggest cavities in tensile test showed an elongated shape in the direction of loading. If the stress state has a higher triaxiality than that in the tensile test, the cavities are likely to become more isotropic. As the pre-forming state in this study is plane-strain, the voids might show that elongated appearance in the direction of the first loading step. This could explain the anisotropic

damage behaviour in the Nakajima experiments for specimens with a change in loading direction. In Fig. 8 the different fracture surfaces are shown. While the specimens with no change in loading direction (Fig. 8 a and d) show a ductile fracture with many small voids, the 30 mm wide specimens with a change in loading direction show almost a brittle fracture surface (Fig. 8 b and c). The number of voids is significantly reduced, compared to (Fig. 8 a). This can explain the reduced formability of the material as the ductility is reduced after a change in loading direction. For the plane-strain specimens with a width of 100 mm a different behaviour is observed. While the specimens with no change in loading direction (Fig. 8 d) show again a ductile fracture surface with many small voids, the specimens with a change in loading direction have considerably big voids caused by hard martensitic inclusions which can be seen in the big void in (Fig. 8 f). In between the vast voids, a shear behaviour is found where the big voids started to coalescence. The increased void growth and the coalescence of the voids could lead to the significant reduction in formability.

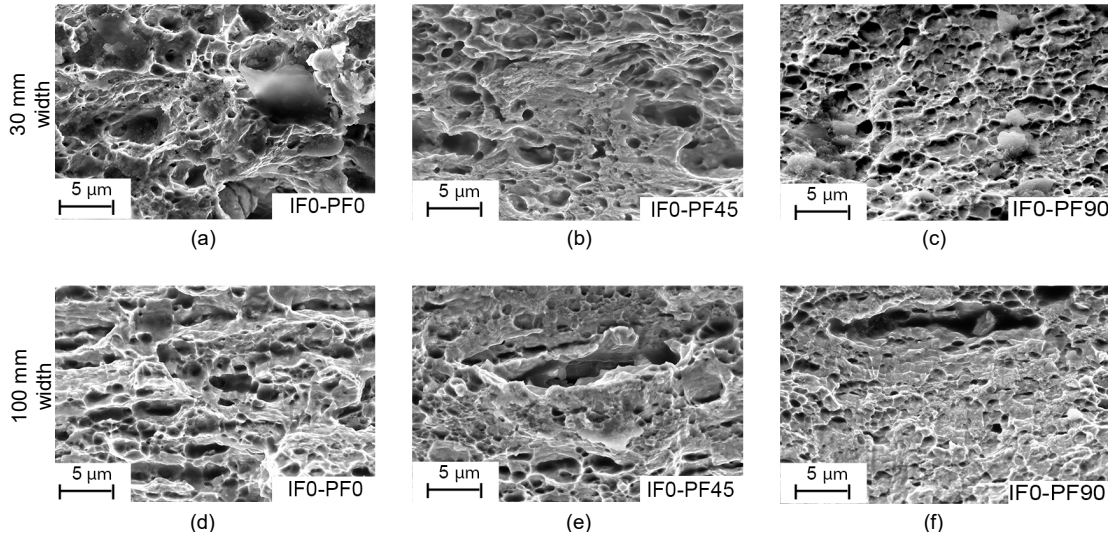

Fig. 8. SEM-images for two different specimen widths (30 mm and 100 mm) and the three investigated post-loading directions IF0-PF0 (a,d), IF0-PF45 (b,e) and IF0-PF90 (c,f) for the pre-forming height of ε_{pre} = 0.193.

Summary

In this paper, the influence of a plane-strain preforming at different levels as well as a change in loading direction has been investigated. By using tensile and Nakajima tests, the impact on the mechanical properties like yield strength and fracture elongation as well as the Forming Limit Curve has been quantified. It is found, that a change in loading direction strongly affects the onset of yielding in tensile test by using temperature-based methods. This effect is not captured by using the classical $YS_{0.2\%}$ method. This might be caused by the fact that some grain orientations start to yield earlier than others and therefore lead to a continuous increase in temperature and a U-shaped temperature signal. For specimens with no change in loading direction no such effect is observed. In fact, the two temperature-based methods, temperature minimum YS_{Tmin} and yield strength at zero strain $YS_{0,}$ are moving closer together. This indicates that the grains with different orientations almost yield at the same time, leading to a sharp elastic-plastic transition.

For the Nakajima experiments, a strong effect on the formability after a certain level of pre-forming is noticed. Especially on the left-hand side of the Forming Limit Curve, this influence was determined. As some of the specimens, mostly those with a significant loss of formability did not show a ductile necking failure but instead a shear failure, the Time Dependent Evaluation Method (TDEM-method) was not applicable. To determine the limit strains for those specimens, the same procedure as for the TDEM-method, but instead of the thickness reduction rate $\dot{\varphi}_3$ the Major Strain

is used to fit the two regression lines. This method showed better results in comparison to the TDEM-method, which overestimates the limit strains for shear failure specimens.

As voids caused by the pre-forming process might be the cause for this anisotropic behaviour, SEM-microscopy will be carried out with the pre-formed material in order to detect voids inside the material. In addition, the disposal of the voids is of interest as some researchers found that voids are aligned in certain directions.

Acknowledgements
The authors would like to thank the German Research Foundation (DFG) for their financial support under the grant numbers 455960756. Furthermore, the support of Wolfgang Saur (Institut für Werkstoffe des Bauwesens, Universität der Bundeswehr München) in performing the scanning electron micrographs is gratefully acknowledged.

References

[1] D. Hérault, S. Thuillier, S.-Y. Lee, P.-Y. Manach, F. Barlat, Calibration of a strain path change model for a dual phase steel, Int. J. Mech. Sci. 194 (2021) 106217. https://doi.org/10.1016/j.ijmecsci.2020.106217.

[2] R. Larsson, O. Björklund, L. Nilsson, K. Simonsson, A study of high strength steels undergoing non-linear strain paths—Experiments and modelling, J. Mater. Process. Technol. 211 (2011) 122-132. https://doi.org/10.1016/j.jmatprotec.2010.09.004

[3] J. Liao, J.A. Sousa, A.B. Lopes, X. Xue, F. Barlat, A.B. Pereira, Mechanical, microstructural behaviour and modelling of dual phase steels under complex deformation paths, Int. J. Plast. 93 (2017) 269-290. https://doi.org/10.1016/j.ijplas.2016.03.010

[4] V. Tarigopula, O.S. Hopperstad, M. Langseth, A.H. Clausen, Elastic-plastic behaviour of dual-phase, high-strength steel under strain-path changes, European Journal of Mechanics - A/Solids 27 (2008) 764-782. https://doi.org/10.1016/j.euromechsol.2008.01.002

[5] F. Barlat, G. Vincze, J.J. Grácio, M.-G. Lee, E.F. Rauch, C.N. Tomé, Enhancements of homogenous anisotropic hardening model and application to mild and dual-phase steels, Int. J. Plast. 58 (2014) 201-218. https://doi.org/10.1016/j.ijplas.2013.11.002

[6] H.Y. Yu, J.Y. Shen, Evolution of mechanical properties for a dual-phase steel subjected to different loading paths, Mater. Des. 63 (2014) 412-418. https://doi.org/10.1016/j.matdes.2014.06.003

[7] A. Weinschenk, W. Volk, FEA-based development of a new tool for systematic experimental validation of nonlinear strain paths and design of test specimens, Penang, Malaysia, Author(s), 2017, pp. 20009.

[8] W. Volk, R. Norz, M. Eder, H. Hoffmann, Influence of non-proportional load paths and change in loading direction on the failure mode of sheet metals, CIRP Annals 69 (2020) 273-276. https://doi.org/10.1016/j.cirp.2020.03.009

[9] R. Norz, S. Vitzthum, W. Volk, Failure behaviour of various pre-formed steel sheets with respect to the mechanical grain boundary properties, Int. J. Mater. Form. 15 (2022) 1215. https://doi.org/10.1007/s12289-022-01700-9

[10] S. Vitzthum, J. Rebelo Kornmeier, M. Hofmann, M. Gruber, E. Maawad, A.C. Batista, C. Hartmann, W. Volk, In-situ analysis of the thermoelastic effect and its relation to the onset of yielding of low carbon steel, Mater. Des. 219 (2022) 110753. https://doi.org/10.1016/j.matdes.2022.110753

[11] W. Volk, P. Hora, New algorithm for a robust user-independent evaluation of beginning instability for the experimental FLC determination, Int. J. Mater. Form. 4 (2011) 339-346. https://doi.org/10.1007/s12289-010-1012-9

[12] R. Norz, F.R. Valencia, S. Gerke, M. Brünig, W. Volk, Experiments on forming behaviour of the aluminium alloy AA6016, IOP Conf. Ser.: Mater. Sci. Eng. 1238 (2022) 12023. https://doi.org/10.1088/1757-899X/1238/1/012023
[13] E.E. Aşık, E.S. Perdahcıoğlu, A.H. van den Boogaard, Microscopic investigation of damage mechanisms and anisotropic evolution of damage in DP600, Mater. Sci. Eng. A 739 (2019) 348-356. https://doi.org/10.1016/j.msea.2018.10.018
[14] G. Gerstein, H.-B. Besserer, F. Nürnberger, L.A. Barrales-Mora, L.S. Shvindlerman, Y. Estrin, H.J. Maier, Formation and growth of voids in dual-phase steel at microscale and nanoscale levels, J. Mater. Sci. 52 (2017) 4234–4243. https://doi.org/10.1007/s10853-016-0678-x
[15] E. Maire, O. Bouaziz, M. Di Michiel, C. Verdu, Initiation and growth of damage in a dual-phase steel observed by X-ray microtomography, Acta Mater. 56 (2008) 4954-4964. https://doi.org/10.1016/j.actamat.2008.06.015

Materials Research Proceedings 28 (2023) 755-760 https://doi.org/10.21741/9781644902479-82

Heat assisted V-bending characteristics of high strength S700MC steel

GÖRTAN Mehmet Okan[1,a *], CAGIRANKAYA Fatih[2,b] and OZSOY Oguz[2,c]

[1]Hacettepe University, Mechanical Engineering Department, Ankara, Turkey

[2]TEKNOROT Steering & Suspension Parts, Düzce, Turkey

[a]okangortan@hacettepe.edu.tr, [b]fatih.cagirankaya@teknorot.com, [c]oguz.ozsoy@teknorot.com

Keywords: V-Bending, Springback, Mild Temperature Forming, High Strength Steel

Abstract. Increasingly stringent regulations force automotive manufacturers to reduce their product weights without compromising passenger safety. To overcome this problem, high strength steels are used that enable a higher payload capacity whilst reducing the plate thickness and overall weight. However, high strength steels are generally associated with lower formability and significantly greater springback compared to mild steels. In the current study, bendability characteristics of high strength S700MC steel in mild temperatures are investigated using V-bending tests. A temperature range between 25°C and 650°C is analysed. Springback characteristics as well as hardness distribution along the thickness direction in the bent area is investigated for several bent samples.

Introduction

Due to the stricter demands in terms of greenhouse gas emission regulations, automotive manufacturers are forced to use lightweight solutions in their design. Two major approaches have been developed in sheet metal forming industry to reduce the thickness and hence weight of parts without compromising the safety and toughness [1]. The first one is to replace conventional materials with their higher strength counterparts and so to be able to carry the same loads using less material. However, due to the limitations in ductility of advanced high strength steels (AHSS) and ultra-high strength steels (UHSS), this strategy can be only used in comparatively simple geometries such as bumper reinforcements, door beams or seat tracks, which can be cold-formed using multiple stage bending or roll-forming processes. The second strategy is the application of a press hardening process where austenitized steels are hot-formed in a press and quenched in the same die system. That way, martensitic microstructure is obtained, resulting in strengths that exceed 1500 MPa in the produced parts without major formability problems [2]. Nevertheless, press hardening process is significantly more energy demanding than conventional stamping or deep drawing processes. In best-case scenario, more than 69% of the energy related to forming is consumed during the heating and related operations in press hardening [3].

There are multiple studies about formability and especially about bendability of steels. Recent ones focus on advanced high strength steels. Majority of the articles investigate critical bending angle and fracture formation depending on the used steels microstructure and mechanical properties. Four different failure types are defined for bending of steels, namely waviness with a flattening on the outside, ductile cuts, fine cracks and instable cracks [4]. Furthermore, it is reported that fracture formation starts during bending before reaching the maximum force in the process [5]. Moreover, regardless of microstructure, bendability of steels improves as strain hardening increases and resistance against crack formation getting higher [6-8]. However, all these studies are conducted at room temperature.

To increase the energy efficiency of the forming operations and to be able to use high strength steels in the manufacturing of complex parts, it is intended to develop mild temperature forming

Content from this work may be used under the terms of the Creative Commons Attribution 3.0 license. Any further distribution of this work must maintain attribution to the author(s) and the title of the work, journal citation and DOI. Published under license by Materials Research Forum LLC.

strategies for conventional high strength steels. The idea behind the mild temperature forming is to shape steels at a temperature level below austenitizing region. That way a decrease in strength and increase in formability is expected. Hence, springback can be reduced. Moreover, since the temperatures are kept below austenitizing region, minimum change is foreseen in microstructure and mechanical properties after forming process is finished and parts are cooled to room temperature. In the current study, bending characteristics of high strength steel S700MC is investigated at mild temperatures ranging from 25°C to 650°C. Springback after bending is evaluated. Moreover, mechanical properties are characterized using hardness measurements.

Material and Methodology

A hot-rolled structural high-strength steel sheet S700MC made for cold forming with a thickness of 4 mm has been used in the study. Mechanical properties and chemical composition of the material are given in Table 1 and Table 2, respectively.

Table 1. Mechanical properties of S700MC steel.

Yield Strength	Tensile Strength	Elongation
792.2 MPa	941.2 MPa	13.2%

Table 2. Chemical composition of S700MC steel (in mass %).

C	Si	Mn	Ni	Mo	Fe
0.78	0.083	1.94	0.15	0.168	balance

Bending samples are prepared using shear-cutting with a length and width of 150 mm and 50 mm, respectively. Width of the samples coincides with the rolling direction of the steel sheets. V-bending test are conducted on those samples according to the ISO 7438:2020 standard. A bending die with an angle of 90° is prepared for this purpose. Since mild steels are usually bent with a r/t ratio of 1, the same ratio is used in the experiments. Die system is shown in Fig. 1.

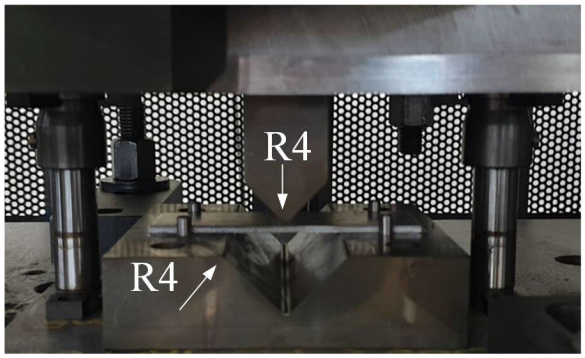

Fig. 1. V-bending die system.

Bending tests are conducted at room temperature and additionally at elevated temperatures ranging from 150°C to 650°C with increments of 100°C. Induction heating is used to heat the samples in bending region. Temperature of the samples are measured with a laser sensor during heating. A hydraulic press with a capacity of 400 tons is used for forming tests. Motion control mode is used and ram speed is set constant to 40 mm /sec. Dwell time at lower dead center is set to 2 seconds. All samples are cleaned with acetone prior to bending. No lubrication is used.

All bending tests are repeated at least three times. Springback on all samples are measured using mechanical angle gauge with a precision of 0.1°. Crack formation on outer side of the bent samples are investigated with optical microscopy and dye-penetrant testing.

All bent samples are cut in the middle section. The cross section is ground with sand papers between P400 and P2500 grit. Afterwards, surfaces are polished with 6 μm and 1 μm diamond solution. Prepared surfaces are etched with 4% Nital solution for approximately 10 seconds. Microstructure of the bent section is investigated using optical microscopy (Nikon Eclipse LV150).

Strain hardening behavior of the samples in the bending region along the thickness direction is characterized using Vickers hardness measurements according to ISO 6507-1 with a load of 500 g and dwell time of 15 seconds (Future-Tech FM-700e).

Results and Discussion

Outside section of samples bent at different temperatures are shown in Fig. 2. A clear crack formation is observed on samples formed at temperatures below 550°C. There are multiple reasons for the crack formation. At room temperature, ductility of the material is not sufficient to accomplish the bending. However, when the temperature is increased, material enters the blue brittleness region. Therefore, it becomes highly brittle and blue cracks are observed. Apparently, the investigated material exits the blue brittleness region at 550°C and crack free samples are generated at temperatures above that level.

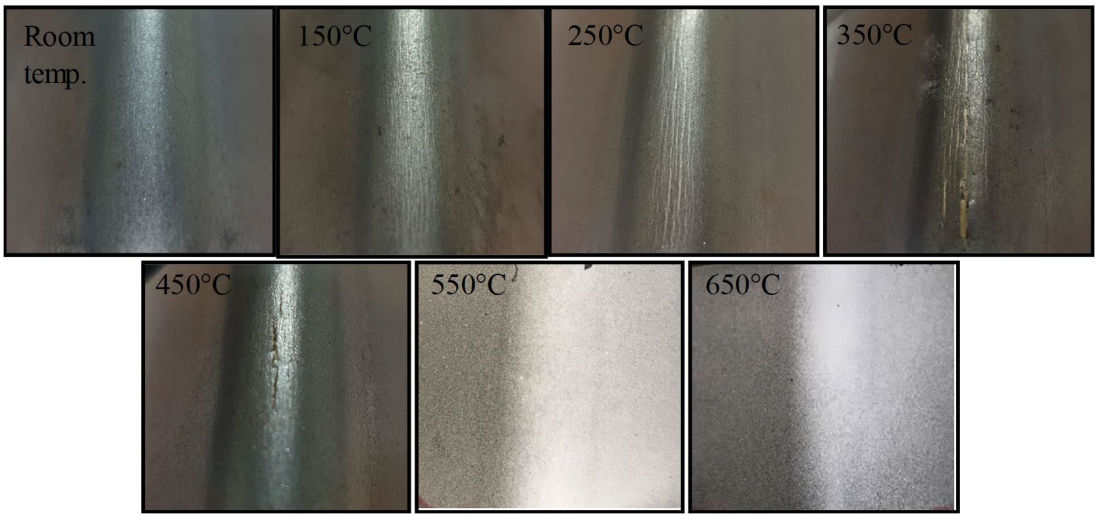

Fig. 2. Outside section of the bent samples at different temperatures.

Side view of the bent samples are shown in Fig. 3. Thanks to the low r/t ratio, springback value of sample bent at room temperature is comparatively low at 90.6°. At temperatures higher than 150°C, no springback is observed in the bent samples. In the die-design process, every bending angle above 90° is a challenge. Even though springback at room temperature of the investigated case is low, it necessitates a certain over-bending. Since there is no springback at elevated temperatures, it is seen as major advantage of mild temperature forming of S700MC steel.

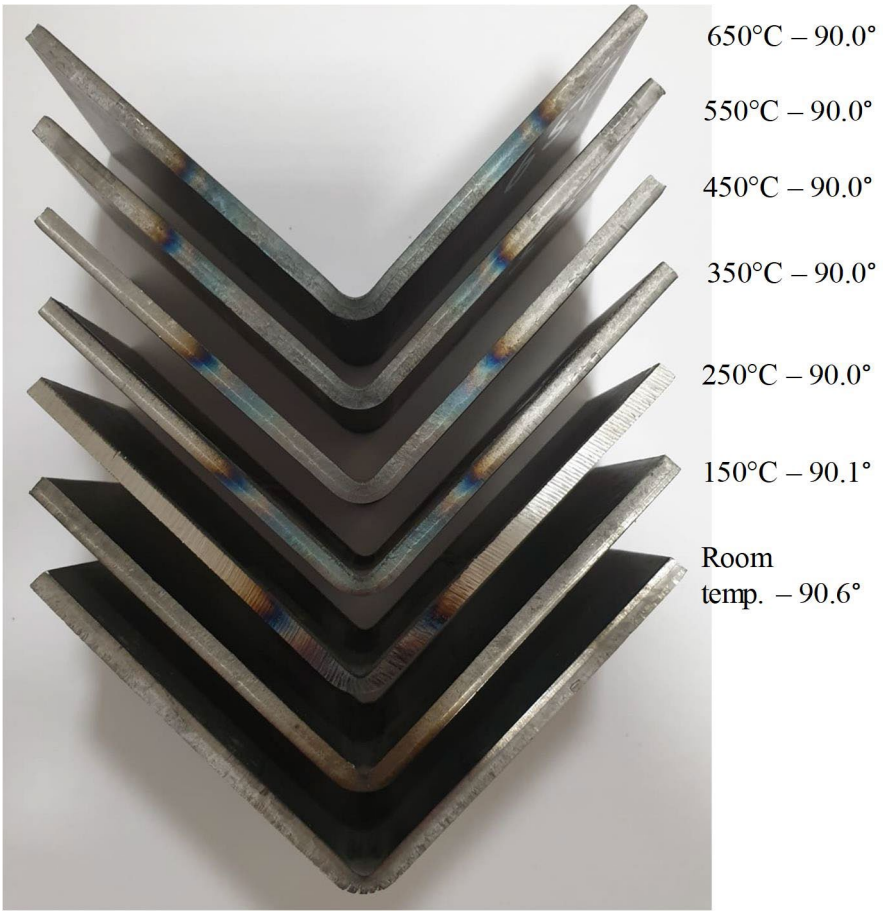

Fig. 3. Side view of bent samples at different temperatures.

Optical microscopy results are shown in Fig. 4. Initial microstructure of S700MC steel is predominantly in ferritic-pearlitic form. This structure remains the same after bending at all temperatures. Since all investigated temperatures were below A_1 level, austenitizing of the microstructure was not expected. Moreover, there isn't any significant change in the grain size. This is attributed to the fast heating and cooling of the material prior and after bending. During heating of steels below A_1 temperature, recovery and recrystallization is expected which yields in dislocation density drop and grain growth. However, both of those processes are time dependent. Thanks to rapid heating and cooling, recrystallization wasn't observed in the microstructure.

Optical microscopy investigations also reveal that there are buckling marks on the inside of samples bent at room temperature. Those marks may act as stress concentration points in repeated loading conditions and reduce fatigue life significantly. However, no sign of buckling is observed at samples bent at 550°C and 650°C. It is seen as an important advantage of forming at mild temperature for S700MC steel.

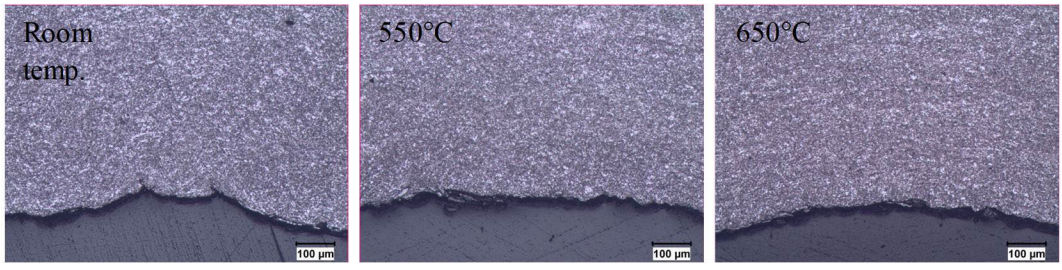

Fig. 4. Microstructure of bent samples.

An important aspect of mild temperature bending of high strength steels is the mechanical properties after forming. Steels formed at room temperature are expected to exhibit a certain amount of strain hardening. As a result, static strength of the parts increases. Strength change can be characterized using hardness measurements [9]. In the current study, Vickers hardness of bent samples along thickness direction in bent are is measured. Results are shown in Fig. 5.

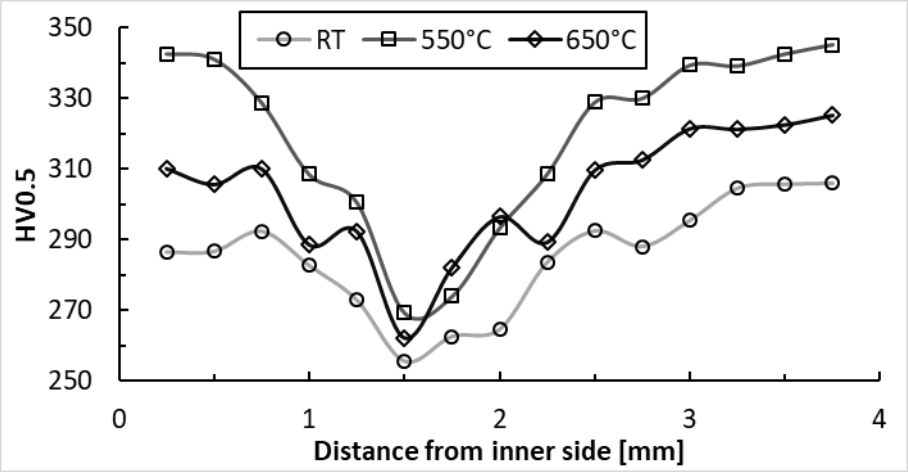

Fig. 5. Hardness distribution along thickness direction.

It is clear from Fig. 5 that the neutral axis of all investigated samples are shifted about 0.5 mm inwards. As we move away from the neutral axis both inwards and outwards, strength of the investigated steel increases due to strain hardening. Since strain value on the outside is higher due to neutral axis shift, hardness level on the outside is approximately 7% higher compared to inside section. When the bending temperature is increased to 550°C, a more significant strain hardening is observed in the bent area. Usually, if temperature of steels is increased, first recovery and later recrystallization is expected. As a result, decline in dislocation density and grain growth occurs. Therefore, strength of steels decrease. However, in the investigated case, a more significant strength increase is observed in samples bent at 550°C compared to the ones bent at room temperature. Underlying reason for that increase should be investigated more in detail using microstructural analysis.

When hardness distribution of the sample bent at 650°C is compared to the one bent at 550°C, a drop in hardness is observed which is less than 10%. All these investigations suggest a strain hardening in the investigated steel even at elevated temperatures.

Summary

In the current study, bending characteristics of hot-rolled structural high-strength steel sheet S700MC made for cold forming is investigated at mild temperatures. Studied temperatures are kept below austenitizing temperature to decrease the energy requirement of the bending operation while increasing the formability characteristics. Following conclusions are drawn:

- Increase in temperature enables better formability and reduced crack formation risk for S700MC steel.
- Crack formation on the outside of the samples formed at temperatures up to 450°C is observed which is due to the blue brittleness of the material in that region
- Reduced springback is observed as the bending temperature increases.
- A significant hardness increase is observed in the samples bent at 550°C and 650°C compared to the ones bent at room temperature.

- In the outer and inner region of all bent samples, an increase in hardness is observed which indicates a strain hardening despite the rise in temperatures.
- No grain growth is observed in the samples bent at elevated temperatures.

Acknowledgements
The conducted work was under a project funded under the SMART EUREKA CLUSTER on Advanced Manufacturing Program. Moreover, the authors thank the Turkish Research Council for financially supporting the project 9210025.

References

[1] S. Keeler, M. Kimchi, P.J. Mooney (Eds.), Advanced High-Strength Steels Application Guidelines Version 6.0, 2017.
[2] H. Karbasian, A.E. Tekkaya, A review on hot stamping, J. Mater. Process. Technol. 210 (2010) 2103-2118. https://doi.org/10.1016/j.jmatprotec.2010.07.019
[3] E. Meza-Garcia, A. Rautenstrauch, M. Braunig, V. Krausel, D. Landgrebe, Energetic evaluation of press hardening processes, Proc. Manuf. 33 (2019) 367-374. https://doi.org/10.1016/j.promfg.2019.04.045
[4] M. Kaupper, M. Merklein, Bendability of advanced high strength steels—A new evaluation procedure, CIRP Ann. - Manuf. Technol. 62 (2013) 247-250. http://doi.org/10.1016/j.cirp.2013.03.049
[5] A. Mishra, S. Thuillier, Investigation of the rupture in tension and bending of DP980 steel sheet, Int. J. Mech. Sci. 84 (2014) 171-181. http://doi.org/10.1016/j.ijmecsci.2014.04.023
[6] C. Suppan, T. Hebesberger, A. Pichler, J. Rehrl, A. Kolednik, On the microstructure control of the bendability of advanced high strength steels, Mater. Sci. Eng. A 735 (2018) 89-98. https://doi.org/10.1016/j.msea.2018.07.080
[7] D. Rèchea, T. Sturel, O. Bouaziz, A. Col, A.F. Gourgues-Lorenzon, Damage development in low alloy TRIP-aided steels during air-bending, Mater. Sci. Eng. A 528 (2011) 5241-5250. https://doi.org/10.1016/j.msea.2011.03.042
[8] K. Benedyk, A. Pichler, T. Kurz, O. Kolednik, Die Versagensmechanismen pressgehärteter und hochfester Stähle im Dreipunkt-Biegeversuch, BHM 159 (2014) 122-129. https://doi.org/10.1007/s00501-014-0237-1
[9] M.D. Taylor, K.S. Choi, X. Sun, D.K. Matlock, C.E. Packard, L. Xu, F. Barlat, Correlations between nanoindentation hardness and macroscopic mechanical properties in DP980 steels, Mater. Sci. Eng. A 597 (2014) 431-439. http://doi.org/10.1016/j.msea.2013.12.084

Materials Research Proceedings 28 (2023) 761-770 https://doi.org/10.21741/9781644902479-83

A stress-based proposal for wrinkling criterion of clamped surfaces

BORBÉLY Richárd[1,a], KÖLÜS Martin L.[1,b] and BÉRES Gábor J.[1,c] *

[1]John von Neumann University, GAMF Faculty of Engineering and Computer Science, Izsáki road 10. 6000, Kecskemét, Hungary

[a]borbely.richard@gmaf.uni-neumann.hu, [b]kolus.martin@gamf.uni-neumann.hu, [c]beres.gabor@gamf.uni-neumann.hu

Keywords: Wrinkling Limit, Clamped Surfaces, Stress-Based Diagram

Abstract. This study presents a possible stress-based limit theory regarding the wrinkling occurrence of clamped surfaces. There are several theorems that describe the buckling and/or the wrinkling phenomenon in different forms and conditions, but a general description, which would represent the limit state of wrinkling in sheet metal forming still does not exist according to the authors knowledge. This could be particularly important for the finite element simulations that are mostly used for process minoring purposes. However, some software work with body elements is suitable for the representation of wrinkles, users do not receive information about how close a process is to the wrinkling limit, or how it is affected by the input parameters. This is even less estimable if shell, or membrane elements are used in a finite element code. In this work, a purely analytical calculation for the wrinkling limit stress of clamped surfaces is carried out, i.e., when blank holder tool acts on the sheet. To take into consideration the effect of the normal pressure, Wang and Cao's proposal was used. After expressing the critical stress by its major and minor principal components using anisotropic yield criteria, a novel illustration method of the wrinkling limit has become available and is published in this article.

Introduction

During the manufacturing of complex sheet parts in the press shop, necking or facture and the geometrical defects (like wrinkling and springback) are the most frequent failure modes [1]. Necking or fracture and wrinkling take place during the forming process, however springback can be considered as a post-forming defect. Although the occurrence of necking and fracture are deeply studied and different limit theorems are already introduced with the aim of process monitoring, wrinkling is less researched. Or at least, an accepted wrinkling limit theory for general cases (e.g., when blank holder also works) is not yet available, with the use of which one can monitor how close a process is to the risk of wrinkling. In this study a proposal can be seen for the stress-based wrinkling limit determination of clamped surfaces, using the basis of Wang and Cao's theory [2,3].

Most of the studies that cover the limits of formability, where the failure of a component is considered under different stress conditions and then the material behavior is summarized into one diagram, are directed to the classical forming limit diagram (FLD). This tool is accepted for necking evaluation in general by the sheet forming society. The FLD indicates the limit of global formability from shearing up to biaxial failure [4,5], i.e., the failure risk in negative (compression) stress states is less discussed in detail. Nevertheless, remarkable improvements have been made in the past, both on the practical determination [6] and the theoretical description [7] of the FLD. To this article, the development of the stress-based forming limit diagram proposed by Stoughton and Zhu [8] has a special importance, which calculation method partially forms the basis of the stress components' calculations applied in this manuscript.

In the respect of compression generated failure modes, the wrinkling is particularly problematic on sheet workpieces that require aesthetic appearance. Besides, wrinkles formed in the first drawing step can cause unpleasant complications in a subsequent press forming operation, too.

Content from this work may be used under the terms of the Creative Commons Attribution 3.0 license. Any further distribution of this work must maintain attribution to the author(s) and the title of the work, journal citation and DOI. Published under license by Materials Research Forum LLC.

Some of the parameters affecting this phenomenon are the stress state, the initial work piece geometry and the blank holder force. The latter one was analytically described by Ju and Johnson in an energy-based model [9] and was later used for discussing the behavior of axisymmetric drawn parts by Agrawal et al. [10]. The biggest drawback of this model is that it only works for cylindrical geometry.

Wang and Cao's article [2] lighted up a different, but also energy-based theorem, in which they proposed the calculation of the deformation energy of a completely flat sheet and a buckled sheet to judge the critical wrinkling conditions. The main advantage of this model is that it does not depend directly on the geometry, thus it is useful to any component geometry. They defined both the critical wrinkling stress as well as the optimal blank holder pressure that need to eliminate wrinkling, using the equations of anisotropic plasticity, expanded for different stress states in [3].

It should be also noted that, although the definition of rupture is perhaps exact even now, the onset of wrinkling is still based on individual subjective judgement. It is therefore necessary to define a preliminary boundary condition that is considered as the criterion of wrinkling. For example, in Wang and Cao's work, the transition from semi-sinusoidal to completely sinusoidal characteristic of surface wrinkles was nominated to the analytical condition. However, Hutchinson and Neale [11] developed an exact, purely theoretical equation (not detailed here), which states that wrinkling occurs when the sum of the bending stress and the stress resultants from buckling and stretching is zero, it is still not yet implemented in practice.

In this study, a possible way for wrinkling risk calculation is presented to define a wrinkling limit diagram that can serve as an input boundary for the design of forming processes. We base our claims on previous experimental investigations and numerical simulations, which are only partially addressed here.

Description of the Wrinkling Behavior

The analytical calculation of wrinkling limit criterion was carried out based on the proposals of Wang and Cao [2,3]. In this methodology, the critical, equivalent wrinkling stress can be obtained by the strain energy difference of a perfectly flat sheet (E_0) and a buckled sheet (E_b), during a deformation process. If negative stress acts on the edge of the component, i.e., for example on the flange of a drawn workpiece, wrinkling can develop if the strain energy of buckling is the larger one. However, when blank holder is applied during a deep drawing process, the optimum of the external work of the blank holder (W) is exactly the same as the difference of the two mentioned energy terms:

$$W = E_0 - E_b \tag{1}$$

Assuming that the external work of the blank holder can be mathematically described in the knowledge of the normal force and the buckling deflection, as well as the normal force itself is a non-linear function of the buckled height (δ), the normal pressure can be expressed in the following form, according to [2]:

$$p = \frac{3(E_0 - E_b)}{4\delta L w} \tag{2}$$

This is the case of a simplified, rectangular flat blank, which has L length, w width and s thickness (see Fig. 1). Applying the deduction of the energy terms based on [2,3], in which Swift hardening law [12] and Hill48 anisotropic plastic potential [13] was used, each energy members can be obtained according to Eq. 3 and Eq. 4.

$$E_0 = \frac{1}{w} \iint \bar{\sigma}\, d\bar{\varepsilon}\, dV = \frac{KLs}{n+1} (\varepsilon_0 + c_1 \varepsilon_{1_0})^{n+1} \tag{3}$$

$$E_b = \frac{2Ks}{n+1}\left[\frac{c_2 s}{2} + (\varepsilon_0 + c_3)\left(\frac{1}{m^2\delta} + \frac{s}{2}\right)\right]^{n+1} \cdot \left[\frac{1}{m^2\delta} + \frac{s}{2}\right]^{-n} \cdot tan^{-1}(m\delta) \quad (4)$$

In these functions, K, ε_0 and n refer to the constants of the Swift hardening law, while c_1, c_2 and c_3 are material parameters considering the plastic anisotropy and the stress state. The frequency of the wave mode is given by m.

With combining Eq. 1-4, the optimal blank holder pressure can be obtained by a purely analytical formula, which contains practically understandable material parameters as well as the u_t edge displacement and the L length of the blank:

$$p = \frac{3Ks}{4(n+1)\delta}\left\{\left[\varepsilon_0 + c_1 ln\left(1 - \frac{2u_t}{L}\right)\right]^{n+1} - \frac{2}{L}\left[\frac{c_2 s}{2} + (\varepsilon_0 + c_3)\cdot\left(\frac{1}{m^2\delta} + \frac{s}{2}\right)\right]^{n+1} \cdot \left[\frac{1}{m^2\delta} + \frac{s}{2}\right]^{-n} \cdot tan^{-1}(m\delta)\right\} \quad (5)$$

It means that the critical edge displacement (or the critical, normalized edge displacement u_{tcr}/L) for a given component length has to be known to obtain the critical normal pressure, which needs to eliminate wrinkling. Wang and Cao defined this critical value at the transition point, where half sinusoid wave form changes to a complete sinusoid wave form. With performing the above analysis (Eq. 1-5) by continuously changing L lengths (L_1, L_2, ..., L_i), intersecting curves will be output, at which the transition points will determine the edge displacement dependent function of the critical normal pressure:

$$p_1\left(L_1, \frac{u_{tcr}}{L}\right) - p_2\left(L_2, \frac{u_{tcr}}{L}\right) = 0 \quad (6)$$

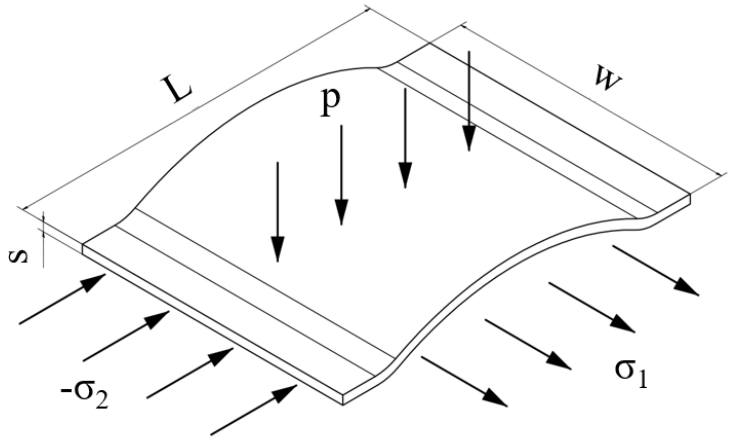

Fig. 1. A simplified, rectangular buckled sheet, affected by tension and compression stresses (the ut edge displacement is interpreted along the L direction).

Assuming that the equivalent plastic strain is direct function of the edge displacement and the stress state, it can be expressed from the associated flow rule that belongs to the Hill48 yield criterion, i.e.,

$$\varepsilon^{pl} = c_1 \cdot \ln\left(1 - \frac{2u_{tcr}}{L}\right) \quad (7)$$

In Eq. 7, c_1 parameter follows from the anisotropic criterion of yielding and embodies the effect of the stress state (α), too.

$$c_1 = \sqrt{\frac{1+r}{1+2r} \cdot \left(1 + \frac{r(1+\alpha)^2 + (\alpha+\alpha r-r)^2}{(1+r-\alpha r)^2}\right)} \tag{8}$$

The stress ratio is calculated as the ratio of the minor and the major principal stresses:

$$\alpha = -\frac{\sigma_2}{\sigma_1} \tag{9}$$

Now, the critical wrinkling stress can be considered as the equivalent stress, and it can be given in the function of the normal pressure. This fact also means that the critical pressure needs to eliminate wrinkling became known for any equivalent stress values that may be experienced in a deformable workpiece.

$$\sigma_{cr} = K\sqrt{\frac{1+r}{1+\alpha^2+r(1-\alpha)^2}}\left[\varepsilon_0 + c_1 \cdot ln\left(1 - \frac{2u_{tcr}}{L}\right)\right]^n \tag{10}$$

Proposal for the Wrinkling Limit Stress Diagram

For a given material, the hardening parameters (K, ε_0, n) and the average anisotropy coefficient (r) are constants in Eq. (10). Therefore, the slope of the σ_{cr}-p_{cr} curve only depends on the stress state. Fig. 2 shows an example for the calculated σ_{cr}-p_{cr} values of DC04 steel sheet, in which diagrams the equivalent stress is the same but the α stress ratio changes from -1/0.01 up to -1/1.0. The applied material parameters (K, ε_0, n and r) are listed slightly below in Table 1.

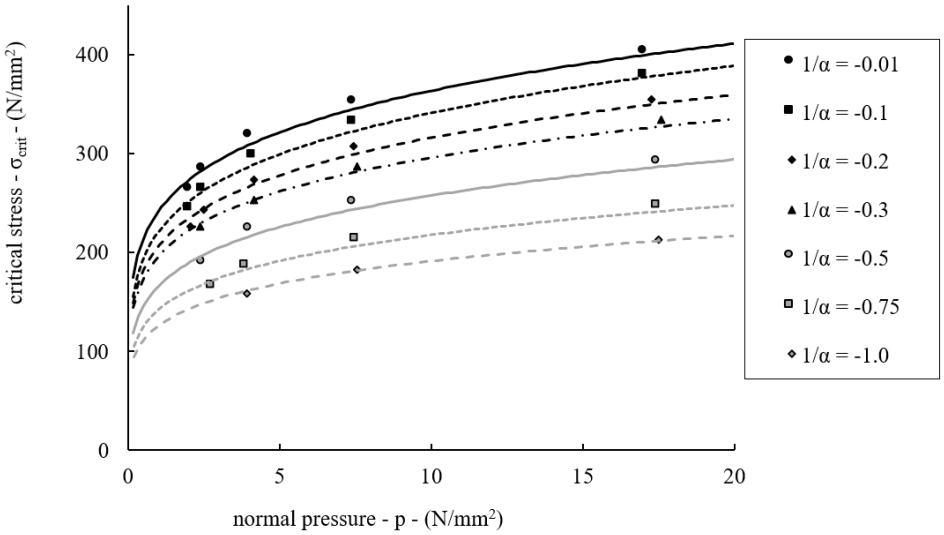

Fig. 2. The critical stress – critical pressure functions for different stress ratios.

Now it can be observed that α = -1/0.01 belongs to the nearly pure compression (the denominator cannot be zero) that exists on the outer sheet edge. With α = -1/1.00, the tension stress component is the same than the compression stress. At the surrounding regions of the inner edge of a drawn part, α = -1/0.20…+1/2.00 are typical values according to finite element simulations.

Considering the above phenomenon, the critical stress can therefore be determined for any blank holder pressure and for any stress ratio. Since the stress ratio is known for all coordinate points of a real workpiece in a finite element simulation, the risk of wrinkling can now be expressed as the function of the location coordinate. This does not only mean that the process monitoring can be achieved after implementing the curves of Fig. 2 into a finite element code (which is very time

consuming and complicated), but a clear and well-understandable limit diagram can also be created similar to the FLD. To do this, first, the stress ratio dependent relationship between the critical stress and the normal pressure should be determined analytically. Based on our experiences, it can be solved by simple power laws (Eq. 11), since the normal pressure is directly dependent on the amount of the plastic strain (see Eq. 3 – 5).

$$\sigma_{crit}(\alpha) = \gamma \cdot p^{\zeta} \tag{11}$$

In Eq. 11, the stress state dependent critical wrinkling stress is only expressed by two parameters. This model (continuous lines in Fig. 2) has relatively good agreement with the calculated points (dots in Fig. 2) in the practical range of the blank holder pressure. The regression coefficients of the power law curves are about $R^2 = 0.984…0.994$ for the different stress states.

Knowing the critical stress and the stress ratio, the associated, principal stress components can be calculated using an arbitrary yield criterion. Here we assume plain stress state, since the binder pressure is close to zero in practice ($\sim 2 \ldots 8\ \frac{N}{mm^2}$), thus it is much smaller than the tension (σ_1) and much higher than the compression ($-\sigma_2$) stresses (only exception is the outer edge where $\sigma_1 \approx 0$). Because Wang and Cao used the Hill48 quadratic yield function during the derivations of the energy terms, it is obvious to use it now, too. Although, there is not much difference in using other yield function, for example Yld89, as we shall see later.

Hill derived his suggestion for the yielding of anisotropic sheet metals on the basis of the von Mises yield criterion [1]. If the anisotropy axes coincide with the principal axes, the proposed model in plane stress state can be expressed in the following form:

$$2f(\boldsymbol{\sigma}) = H(\sigma_2 - \sigma_1)^2 + G\sigma_1^2 + F\sigma_2^2 = 1 \tag{12}$$

The relationship between the yield constants and the plastic strain ratios can be obtained by using the associated flow rule,

$$\frac{H}{G} = r_0;\ \frac{H}{F} = r_{90} \tag{13}$$

The yielding point at uniaxial loading ($\bar{\sigma} = \sigma_1\ and\ \sigma_2 = 0$) can be taken into account as

$$2f(\boldsymbol{\sigma}) = H\left(1 + \frac{1}{r_0}\right)\bar{\sigma}^2 \tag{14}$$

and hence the yield criterion can be defined through the plastic strain ratios:

$$\bar{\sigma}^2(r_0 + 1) = r_0(\sigma_2 - \sigma_1)^2 + \sigma_1^2 + \frac{r_0}{r_{90}}\sigma_2^2 \tag{15}$$

After some rearrangement and introducing α, we get

$$\bar{\sigma} = \sigma_1\sqrt{\left\{1 + \alpha^2\left[\frac{r_0(1+r_{90})}{r_{90}(1+r_0)}\right] - 2\alpha\frac{r_0}{1+r_0}\right\}} \tag{16}$$

Finally, the minor principal stress can be obtained by Eq. 9.

In the case of the Yld89 yield criterion, the determination of the principal stress components is originated from the equation of

$$f(\boldsymbol{\sigma}) = a|K_1 + K_2|^M + a|K_1 - K_2|^M + c|2K_2|^M = 2\bar{\sigma}^M \tag{17}$$

in which

$$K_1 = \frac{\sigma_1 + h\sigma_2}{2} \tag{18}$$

$$K_2 = \sqrt{\left(\frac{\sigma_1 - h\sigma_2}{2}\right)^2 + p^2\sigma_{12}^2} \tag{19}$$

If the coordinate system coincides with the principal directions, the shear stress and hence $p^2\sigma_{12}^2$ can be neglected, and the terms in brackets are simplified as follows:

$$K_1 + K_2 = \sigma_1$$

$$K_1 - K_2 = h\sigma_2 \tag{20}$$

Incorporating Eq. 20 into Eq. 17, the Yld89 yield theory will reduce to

$$f(\boldsymbol{\sigma}) = a|\sigma_1|^M + a|h\sigma_2|^M + c|\sigma_1 - h\sigma_2|^M = 2\bar{\sigma}^M \tag{21}$$

and the relationship between the major principal stress and the equivalent stress can be expressed using the stress ratio (α) again:

$$\sigma_1 \left\{\frac{1}{2}[a + a|h\alpha|^M + c|1 - h\alpha|^M]\right\}^{\frac{1}{M}} = \bar{\sigma} \tag{22}$$

The constants *a*, *c* and *h* can be determined from the strain ratios [14], while the minor principal stress component can be calculated from Eq. 10 again.

As a result of the derivations detailed above, the wrinkling criterion can be edited in the stress space analytically, which, like the FLD, provides a transparent method for process monitoring. As an example, the results obtained by the principal stresses' calculations for both the Hill48 and the Yld89 criteria can be seen in Fig. 3.

To this figure, the mechanical parameters of the applied DC04 sheet were characterized by tensile tests, and the necessary values are summarized in Table 1. (The data acquisition is not detailed here.)

Table 1. applied material parameters.

	K	ε_0	n	r_0	r_{90}
DC04	578	0.017	0.220	1.823	2.380

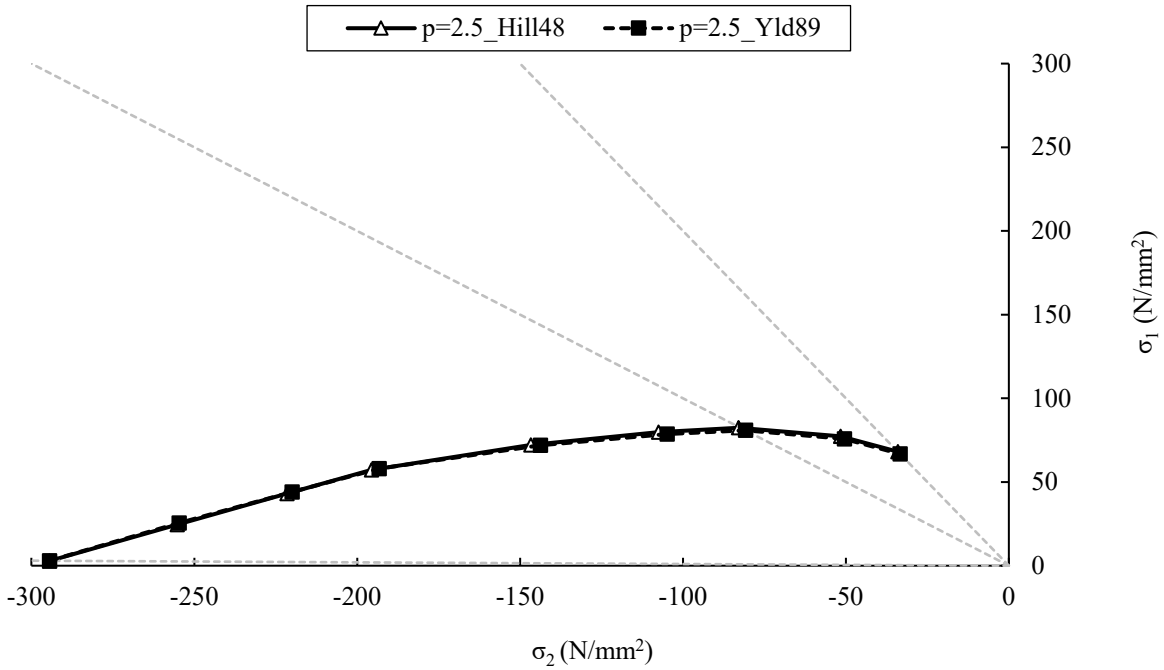

Fig. 3. Stress-based wrinkling limit curves calculated based on the Hill48 and the Yld89 yield criteria. The normal pressure value is 2.5 N/mm^2 for both cases.

It is worth mentioning that the calculated curves in Fig. 3 belong to $p = 2.5\ \frac{N}{mm^2}$ normal pressure. Since it was introduced that the wrinkling limit stress is the function of the blank holder pressure, the wrinkling limit diagram should be interpreted as a curve family, instead of one curve. With the shifting of the limit curve, both the effect of the stress state and the blank holder pressure can be visualized, as well as the limit values can be compared with numerical results. Fig. 4 shows the calculated limit curves of the DC04 sheet for three different blank holder pressures. In the graph, numerically obtained stress points from the outer edge of a drawn cup are also seen, just after the time step when wrinkles appear in the simulation at lower blank holder forces.

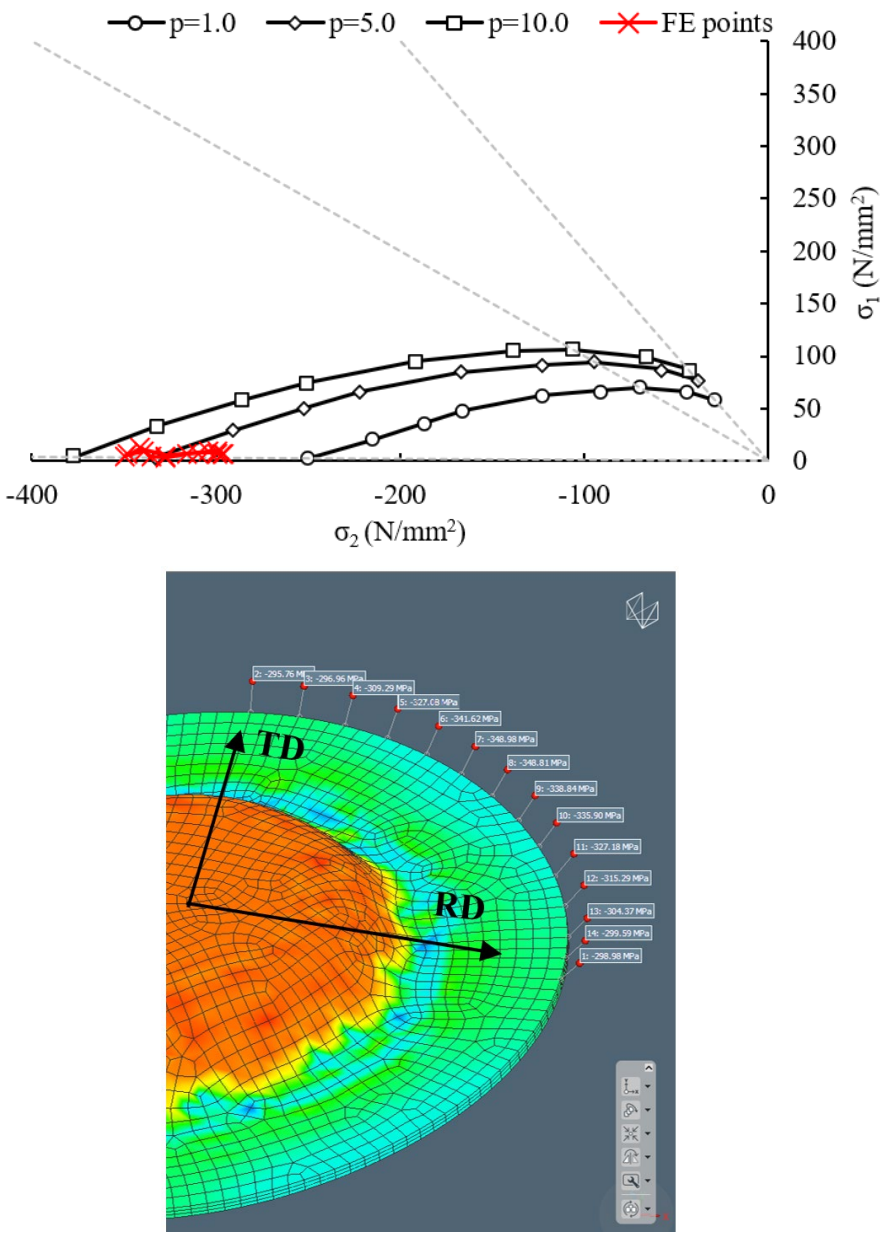

Fig. 4. Stress-based wrinkling limit curves for three different blank holder pressures and numerical points from a drawn part's flange. The pressure values are given in N/mm^2 in the graph, the applied blank holder pressure was 5 N/mm^2 in the simulation (no visible wrinkles).

The simulation was carried out in Simufact Forming 2021.1 software. The input material parameters are listed in Table 1, next to which Coulomb friction coefficient was used with the value of 0.12 on the die side and 0.20 on the punch side. The initial element size was 1.4 mm, and the sheet was discretized to three layers in the thickness direction that resulted in a total number of 6696 sheet mesh elements for a diameter Ø66 mm initial blank with 1 mm sheet thickness. The simulation results' validation was done by cup drawing tests supported by digital imagine correlation system, but a detailed insight to the measurements is not possible due to the limited content of the paper. The geometrical data of the tests are following. Punch diameter and radius: Ø33.0 mm and 5 mm; die diameter and radius: Ø35.4 mm and 5 mm (1.2 mm clearance). The applied blank holder pressure for the simulation results of Fig. 4 was 5 N/mm^2.

Consequently, it can be observed that the numerically obtained points form the outer perimeter of the flange are far above the limit curve of 1 N/mm^2 blank holder pressure, thus wrinkling is expected next to this value. At the same time, the stress points more or less fall below the limit curve of 5 N/mm^2, and wrinkles exist neither in the simulation, nor in the practice with this setting. Naturally, this analysis can be performed for any location point of a drawn part, although above α = 1/1.0 stress ratio, we do not think it make sense in terms of wrinkling.

It is also visible that the critical stress seems to be reached earlier at the inner region of the flange, since the decrease of the stress ratio causes the decrease of the compression stress, too. In this way authors recognize that this may lead to controversy and are currently working on the possible development of the theory.

Summary

With the calculation and then the allocation of the critical equivalent stress that causes wrinkling at a given blank holder pressure as indicated in this article, an easy-to-understand diagram was edited in the major and minor stresses' coordinate system. This diagram is logically consistent with the forming limit curve (either strain-, or stress-based), since it is also stress state dependent, but takes into consideration the blank holder pressure, too. Despite the simplifications during the calculations, the results that show the wrinkling risk at any specimen locations are comparable to the practical blank holder values. In addition, applying this criterion in a finite element code, the process monitoring from the perspective of wrinkling could become possible.

References

[1] D. Banabic, H.J. Bunge, K. Pöhlandt, A.E. Tekkaya, Formability of Metallic Materials, Springer-Verlag Berlin Heidelberg, 2000.

[2] X. Wang, J. Cao, An Analytical Prediction of Flange Wrinkling in Sheet Metal Forming, J. Manuf. Process. 2 (2000) 100-107. https://doi.org/10.1016/S1526-6125(00)70017-X

[3] J. Cao, X. Wang, An analytical model for plate wrinkling under tri-axial loading and its application, Int. J. Mech. Sci. 42 (2000) 617-633. https://doi.org/10.1016/S0020-7403(98)00138-6

[4] S. Keeler, W.A. Backofen, Trans. ASM 56 (1963) 25-48.

[5] G.M. Goodwin: Society of Automotive Engineers No. 680093 (1968) 380-387.

[6] M. Merklein, A. Kuppert, M. Geiger, Time dependent determination of forming limit diagrams, CIRP Annals – Manuf. Technol. 59 (2010) 295–298. https://doi.org/10.1016/j.cirp.2010.03.001

[7] D. Banabic, F. Barlat, O, Cazacu, T. Kuwabara, Advances in anisotropy and formability, Int. J. Mater. Form. 3 (2010) 165-189. https://doi.org/10.1007/s12289-010-0992-9

[8] T.B. Stoughton, X. Zhu, Review of theoretical models oft he strain-based FLD and their relevance to the stress-based FLD, Int. J. Plast. 20 (2004) 1463-1486. https://doi.org/10.1016/j.ijplas.2003.11.004

[9] T.X. Yu, W. Johnson, The buckling of annular plates in relation to the deep-drawing process, Int. J. Mech. Sci. 24, (1982) 175-188. https://doi.org/10.1016/0020-7403(82)90036-4

[10] A. Agrawal, N.V. Reddy, P.M. Dixit, Determination of optimum process parameters for wrinkle free products in deep drawing process, J. Mater. Process. Technol. 191 (2007) 51–54. http://doi.org/10.1016/j.jmatprotec.2007.03.050

[11] J.W. Hutchinson, K.W. Neale, Proceedings of Int. Symp. on Plastic Instability, Paris, France (1985) 1841–1914.

[12] H.W. Swift, Plastic instability under plane stress, J. Mech. Phys. Solid. 1 (1952) 1-18. https://doi.org/10.1016/0022-5096(52)90002-1

[13] R. Hill, A theory of the yielding and plastic flow of anisotropic metals, The hydrodynamics of non-Newtonian fluids I, Proceedings of the Royal Society of London. Series A, Mathematical and Physical Sciences 193 (1948) 281-297.
[14] F. Barlat, J. Lian, Plastic behavior and stretchability of sheet metals. Part I: A yield function for orthotropic sheets under plane stress conditions, Int. J. Plast. 5 (1989) 51-66. https://doi.org/10.1016/0749-6419(89)90019-3

Materials Research Proceedings 28 (2023) 771-778 https://doi.org/10.21741/9781644902479-84

Evaluation of hot and warm forming of age-hardenable aluminium alloys into manufacturing of automotive safety critical parts

MYROLD Benedikte[1,a *], JENSRUD Ola[1,b] and HOLMESTAD Jon[1,c]

[1]SINTEF Manufacturing, Box 163, 2831 Raufoss, Norway

[a]benedikte.myrold@sintef.no, [b]ola.jensrud@sintef.no, [c]Jon.Holmestad@sintef.no

Keywords: Hot and Warm Forming, Formability, Hardening of Aluminium Alloys

Abstract. Lightweight solutions will become increasingly necessary for the next generation of passenger cars. Applications of age-hardenable high strength aluminium material can be superior to traditional low strength alloys, especially if the processing of the parts itself is cost effective. Sheet forming of aluminium at elevated temperatures has been addressed in the current work. Warm forming directly after solution heat treatment can eliminate several process steps and reduce cycle time in the production of light weight load bearing car components. However, this is not straight forward as 6xxx alloys need minimum critical cooling rate to achieve the full potential of precipitation hardening. The technical forming methods must take this into the thermomechanical setup during the process steps of handling, lubrication, deformation, and final ageing. Elevated forming temperatures, more likely warm than hot show high formability of the alloys. Further, a short artificial ageing time demonstrate required strength and fatigue capacity in real components. Reduction of the deformation temperature to below 300°C is still favourable when lubrication for serial production is the issue. The modified thermomechanical method is appropriate for achieving accurate geometrical tolerances, uniform properties, and high productivity for aluminium automotive parts. The paper describes a feasibility study and method development for forming of sheet material of hardenable aluminium alloys at intermediate temperatures.

Introduction

Forming at elevated temperatures (>500°C) has been demonstrated earlier by reference [1] and [2] and showed advantages compared to traditional cold forming with respect to spring back, formability, and microstructural control. Forming of aluminium blanks is commonly carried out cold in soft annealed temper (O-temper), which provides very good and tight tolerances. Annealing for O-temper is time consuming and thus requires high energy consumption. Additionally, O-temper parts needs new heat treatment to reach T6 properties with challenges to keep tolerances and microstructure within expectations. Jensrud et al. developed a new profile shaping technique for manufacturing of automotive components in as quenched condition (W-temper). This gives a good formability and a reduction in processing time due to in-line heat treatment integrated with the mechanical operation [3]. This method is a measure of efficiency.

Content from this work may be used under the terms of the Creative Commons Attribution 3.0 license. Any further distribution of this work must maintain attribution to the author(s) and the title of the work, journal citation and DOI. Published under license by Materials Research Forum LLC.

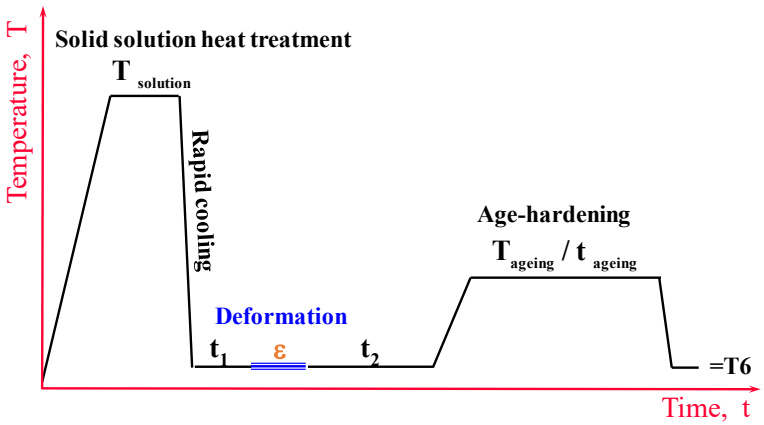

Fig. 1. The process route of forming in W-temper [5].

Forming prior to age hardening may also advantageously be carried out at elevated temperatures. Hot forming of aluminium has been widely explored and gives a further improved formability and productivity. A process with integrated forming and hardening has been proposed where the blank is simultaneously formed and quenched from solution heat treatment before artificial ageing [1,4]. This proved to be an effective process in terms of formability, efficiency, spring-back and properties. However, challenges with lubrication are encountered that results in sticking and thinning.

This research has been conducted in the framework of the above-mentioned work, except that hot forming is replaced by warm forming. Hot forming is defined as deformation at elevated temperatures below the recrystallization temperature [5]. This new proposal includes the integrated forming and quenching step with the alteration that the forming and final quenching happens as the material has reached an intermediate temperature of 200-300°C. Warm forming will provide a more controllable friction regime compared to hot forming and still obtains a low flow restriction and sufficient ductility. The deformation hardening mechanism combined with precipitation hardening is not well understood. The key mechanisms in age hardening of alloys deformed in W-temper are the interactions between dislocations, vacancies and formation of Guinier Preston (GP) zones, i.e. the first stage of precipitation hardening [6,7]. The contribution of each mechanism in age hardening after warm forming should be considered. As self-diffusion of dislocations increases with increasing temperatures, it would be reasonable to believe that the dislocations are annihilated during warm forming and therefore does not provide any strength contribution. However, whether the exposure time to high temperatures after forming are long enough for the dislocations to annihilate is not known.

In this paper, the quench sensitivity of relevant alloys has been carefully considered to obtain the required mechanical properties of load bearing automotive components. The limitations and latitude of the quenching step has been identified.

The sheet material evaluated is within AA6010 with a thickness of 5.3 mm. In this work it has been developed a process by a press quench tooling set-up integrated with heat treatment capability. The formability of the sheets is investigated by forming experiments performed in flat tool with subsequent testing of mechanical properties [8]. In this thermo-mechanical process, the solution heat treatment sequence of the material is a pre-process of the blank before the forming step with direct ageing from the press operation as the last step.

Materials Research Proceedings 28 (2023) 771-778 https://doi.org/10.21741/9781644902479-84

Method Development

The experimental setup requires proper control of time and temperature. During this method development, the cooling rate was measured with a thermo-logger that collected data with 0.1s intervals before the data was used for time control of the cooling. To select parameters for the forming trials, several experiments were designed and conducted at a laboratory scale. The experiments were intended to map cooling rate, quench sensitivity and resulting properties of the selected material. The cooling rates are so fast that it is difficult to manually stop the cooling or form at the correct temperatures during cooling. A manageable cooling rate had to be found that would not compromise the hardening of the material. Small sheet samples were cooled with different media; water, steel, compressed air, still air and insulated material. It was found that cooling the sheet between two steel plates gives a suitable cooling rate for the lab simulation of the process. The measured cooling rates for the different cooling media are listed in Table 1.

Table 1. Measured cooling rates for samples cooled from SHT in different cooling media.

Cooling medium	Cooling rate (°C/s)
Water	310
Closed steel	37
Open steel	18
Compressed air	10
Insulation	1.7

The selected cooling method still gives a high cooling rate so that manual handling of the sample during the experiments is difficult. To enable forming at elevated temperatures the cooling rate had to be slightly reduced to maintain temperature control when approaching the forming temperatures of 200-300°C, this can be achieved by cooling the samples in heated steel plates. A cooling tool was built as two steel plates with hinges and a handle that is heated in the oven to 100°C. After solution heat treatment, the samples are placed between the heated steel plates and cooled to the selected intermediate temperatures before being transported to the press for deformation and subsequent ageing. This process was validated by comparing the mechanical properties with a traditional process route shown in Table 2. The mechanical properties are not severely affected with the new proposed process route. Illustrations of the hot forming process route and the warm forming process route are shown in Fig. 2 and Fig. 3, respectively.

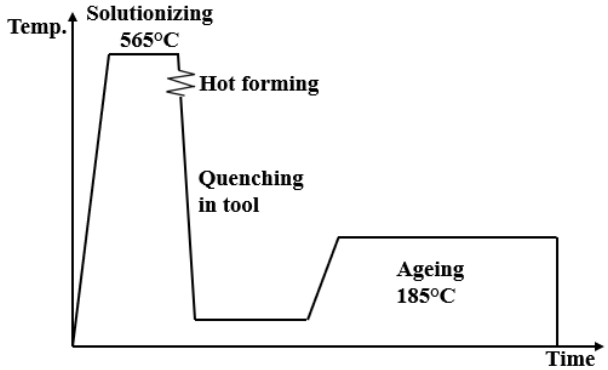

Fig. 2. Process route for hot forming.

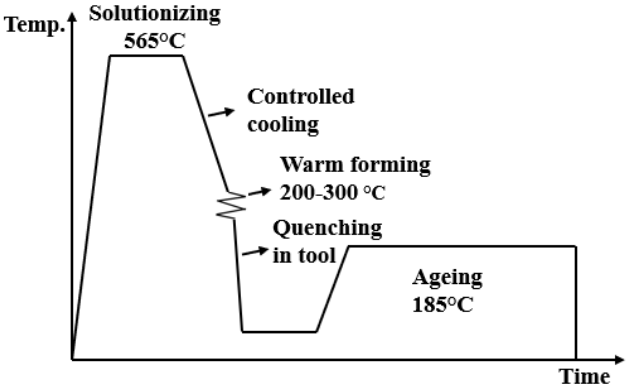

Fig. 3. Process route for warm forming.

Table 2. Comparison of mechanical properties after hot forming, warm forming and T6 condition with no deformation as reference.

	Yield strength (MPa)	Tensile strength (MPa)	Ag (%)	A (%)	Hardness HV10
Warm forming route	360	382	7.1	11.5	132
Hot forming route	354	373	7.9	13.9	130
Reference	364	382	7.5	12.6	135

At this point most process parameters have been selected and verified. The parameters for solution heat treatment, natural ageing and artificial ageing were selected based on the current industrial processes. Furthermore, the optimal forming temperature had to be found by investigation of all aspects of the material response to the process of forming at intermediate temperatures. The following experiments were conducted to find the influence on strength, ductility, anisotropy, and formability. After solution heat treatment, samples were cooled in a suitable manner and formed at 25°C (water quench), 100°C (between dies in the press), 200°C (cooling tool), 300°C (cooling tool) and 400°C (dies in the press). The samples were formed in a flat pressing tool by compression of 15% with a forming speed of 59 mm/s.

After solution heat treatment the different conditions were analysed by tensile testing, shear testing and tear testing. The presented results are the averages from 3 parallel samples with standard deviations represented by error bars.

Results and Discussion

The tensile test results from samples being formed at different temperatures are shown in Fig. 4 and Fig. 5. The results show stable tensile strength and significant variations in yield strength. The elongation does not seem to have been severely affected by the different cases. This indicates that there is no significant reduction in tensile strength due to an altered cooling sequence. The contributions of hardening mechanisms are complex, and it would require TEM investigations to identify the strengthening precipitates for each deformation temperature. As the forming temperatures are varying, the cooling sequences are also different. The precipitation mechanisms might differ for the different conditions. It is reasonable to assume that the distributions of precipitation and dislocations vary with temperature, which may explain the reduction in yield strength for the case of deformation at 200°C. However, for this alloy and the tested conditions the varying contribution of mechanisms do not seem to have diminished the final properties of the material.

Another possible explanation to the small variations in the final properties of the material after deformation at elevated temperatures might be the high cooling rate during forming. The temperatures of the material at the end of deformation are not known. The cooling rate between cold dies and with applied force is high, and there is a possibility the samples have reached room temperature before the deformation is finished. In that case, the same hardening mechanisms would apply for all cases. However, with a die speed of 59mm/s and a deformation of 15%, the deformation is finished after 0.01s. This is not enough time for the samples to reach room temperature before the deformation is complete. Although, if the material temperature would be low at the end of deformation, the same would apply in a forming operation of larger scale as the sheet thickness would be the equal and have the same temperature gradient as in these experiments.

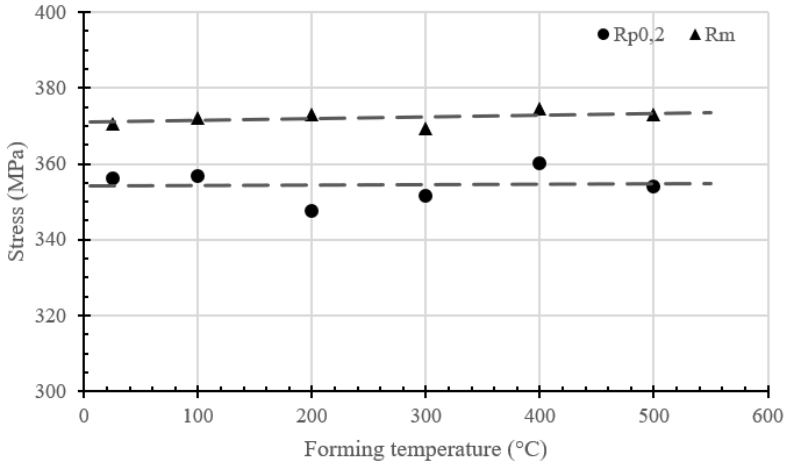

Fig. 4. Results from tensile tests of different forming conditions. Yield strength ($R_{p0,2}$) and tensile strength (R_m).

The elongation shown in Fig. 5 is not significantly affected by deformation temperature compared to cold forming. Ideally, the ductility should be improved at elevated forming temperatures, but it seems that hot forming is required for a slight increase in elongation. However, it is beneficial that severe reduction in elongation is not observed.

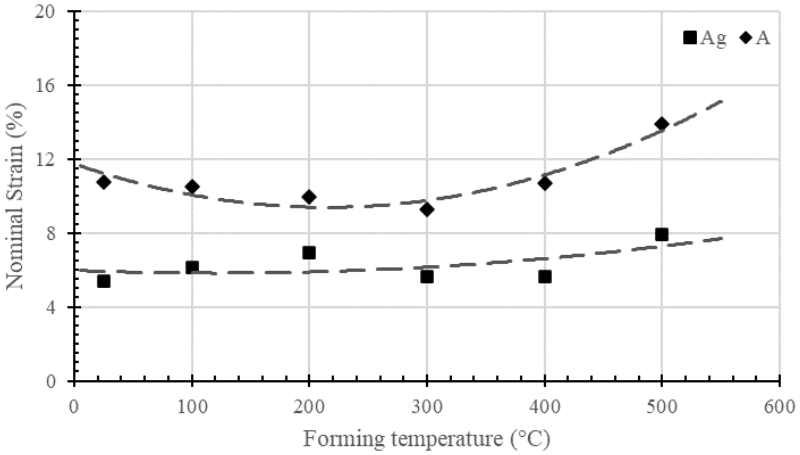

Fig. 5. Results from tensile tests of different forming conditions. Fracture elongation (A) and elongation at maximum force (Ag).

Shear testing were performed according to ASTM B831-05. A notched, rectangular specimen is subjected to a single shear force to failure in a fixture using a tensile test machine. The shear

strength is the maximum force required to fracture the sample. Three parallels were tested for each condition. The results from shear testing are shown in Fig. 6, i.e. the average shear strength with standard deviation for the different quenching and forming conditions. The shear test shows the fracture shear strength. Insignificant differences are observed for the shear strength of the different conditions. There is a large variation for the undeformed condition which was water quenched.

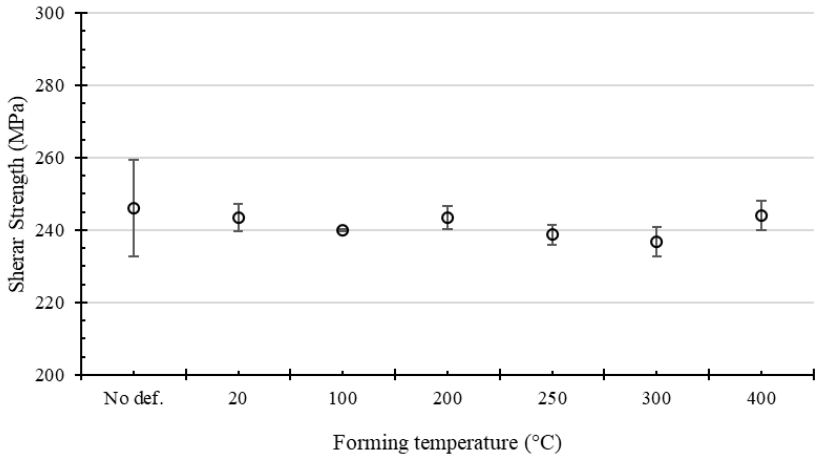

Fig. 6. Shear test results from samples deformed at different temperatures. Average shear strength with standard deviation.

Table 3. Results from shear tests.

Shear tests		
Forming temperature	**Cooling medium**	**Shear Strength (MPa)**
No def.	Water	246
20°C	Water	243
100°C	Cold dies	240
200°C	Cooling tool	243
250°C	Cooling tool	239
300°C	Cooling tool	237
400°C	Cold dies	244

Tear tests were performed according to ASTM B871-1 and involves a single edge notched specimen that is statically loaded through pin loading holes. The test is an indicator of toughness and provides a comparative measure of resistance to unstable fracture. The tear test shows the ability of a material to absorb plastic deformation and can reveal significant reduction in toughness. The tear strength shown in Fig. 7 is reduced for intermediate forming temperatures. The samples being water quenched and quenched in a cold tool have a higher tear strength than the samples being pre-cooled in the cooling tool. This indicates that the cooling rate affects the toughness of the material as the cooling rate is slower for the samples cooled in the cooling tool.

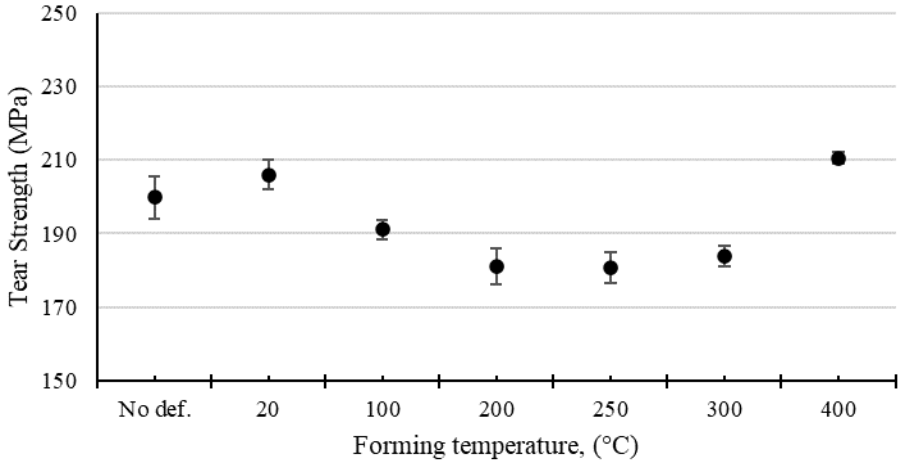

Fig. 7. Tear test results from samples formed at different temperatures. Average tear strength with standard deviation.

Table 4. Tear test results, average tear strength.

Tear tests		
Forming temperature	**Cooling medium**	**Tear Strength (MPa)**
No def.	Water	200
20°C	Water	206
100°C	Cold dies	191
200°C	Cooling tool	181
250°C	Cooling tool	181
300°C	Cooling tool	184
400°C	Cold dies	210

When comparing the tear test results with the tensile test results, the reduction in tear strength applies to the same conditions that show increased work hardening. Hence, the total performance of the material at all forming temperatures argue for a capable method and material. There are no test results that suggest that the proposed method inflict detrimental effects on the alloy properties. However, further testing of the method will be conducted, including hot tensile testing, microstructure investigations and additional alloys.

Summary

A method for warm forming of an AA6010 sheet material at intermediate temperatures have been developed. The proposed process route results in acceptable material properties in terms of strength, ductility, and toughness. The high strength material holds a potential of above 350 MPa in tensile strength, which is well above the common requirement for age hardenable aluminium alloys. In addition to satisfying material properties, the method enables sheet forming with good formability and extended possibilities in terms of lubrication.

Acknowledgement

The research has been carried out as a part of the Norwegian Research Council funded BIA-IPN project SUFICCS (Superior Fatigue Stressed Chassis Components). The project involves the following partners: Raufoss Technology AS, Hydro Aluminium AS, AP&T, SINTEF Manufacturing AS and SINTEF Industry. The experiments were carried out at SINTEF Manufacturing AS.

References

[1] R.P. Garrett, J. Lin, T.A. Dean, Solution Heat treatment and Cold Die Quenching in Forming AA 6xxx Sheet Components: Feasibility Study, Adv. Mater. Res. 6-8 (2005) 673-680. http://doi.org/10.4028/www.scientific.net/AMR.6-8.673

[2] O. Jensrud, K.E. Snilsberg, A. Kolbu, Conceptual testing of Press Form Hardening of High-Strength Aluminium Alloys, Aluminium Extr. Finish. (2016) 16-20.

[3] O. Jensrud, T. Høiland, A new advanced profile shaping technique for design and manufacturing of automotive components, The ExtruForm®, ET08 Orlando 13-16. May 2008, Proceedings of the ET08, Vol. 2 2008.

[4] B. Myrold, O. Jensrud, K.E. Snilsberg, The Influence of Quench Interruption and Direct Artificial Ageing on the Hardening Response in AA 6082 during Hot Deformation and In-Die Quenching, Metals 10 (2020) 935. https://doi.org/10.3390/met10070935

[5] ASM International, Metals Handbook, Vol. 14: Forming and Forging, 1988.

[6] O. Jensrud, K. Pedersen, Warm forming as an energy efficient process in manufacturing of high strength aluminium parts, Metall. Sci. Technol. 31 (2013).

[7] A. Latkowski, J. Grytiecki, M. Bronicki, Arch. Metal. 32 (1989) 313-325.

[8] K.E. Snilsberg, T. Welo, K.E. Moen, B. Holmedal, O. Jensrud, C. Koroschetz, A New Tribological System Test for Integrated Hot Forming and Die Quenching of Aluminium Alloy Sheets, ESAFORM Dublin, 2017.

Materials Research Proceedings 28 (2023) 779-786 https://doi.org/10.21741/9781644902479-85

Nonlinear stress path experiment using mild steel sheet for validation of material model

TAKADA Yusuke[1,a] and KUWABARA Toshihiko[1,b *]

[1]Tokyo Univ. Agriculture and Technology, 2-24-16 Nakacho, Koganei-shi, Tokyo 184-8588, Japan

[a]takada.no12@gmail.com, [b]kuwabara@cc.tuat.ac.jp

Keywords: Mechanical Test, Biaxial Stress, Mild Steel Sheet, Yield Function, Linear Stress Path, Nonlinear Stress Path, Contour of Plastic Work, Biaxial Tube Expansion Test

Abstract. A linear stress path (LSP) experiment was performed using uniaxial and biaxial tensile tests with a cold-rolled mild steel sheet (SPCD; nominal thickness: 0.8 mm) as the test material. In the LSP experiment, nine LSPs were applied to the specimens to measure the contours of plastic work and the directions of the plastic strain rates, β, for a plastic strain range of $0.002 \leq \varepsilon_0^{\mathrm{p}} \leq 0.234$. Then, the Yld2000-2d yield function (Barlat et al., 2003) was used to identify a material model that accurately reproduces the experimental data observed in the LSP experiment. Furthermore, a nonlinear stress path (NLSP) experiment was performed. The NLSP consists of two linear stress paths with σ_x: σ_y = 4:1 and 1:1, and a curved stress path connecting the LSPs. The measured work hardening behavior and β values were compared with those calculated using the Yld2000-2d yield function identified from the LSP experiment. It was found that the deformation behavior of the test sample predicted by the material model determined from the LSP experiment clearly shows some deviation from that observed for the NLSP experiment.

Introduction

One of the most influential factors that affect the accuracy of sheet metal forming simulations is a material model. In order to guarantee the accuracy of the forming simulation, it is necessary to guarantee the accuracy of the material model used for the analysis. Guaranteeing the accuracy of the material model means that the deformation behavior of the material in real forming operations should be reproduced by the material model.

To experimentally determine a material model, many linear stress paths (LSPs) are applied to the material using biaxial tensile tests with cruciform test pieces [1,2] and/or the biaxial tube expansion test (BTET) with tubular specimens, to which an axial force and an internal pressure are simultaneously applied [3]. However, the stress paths in real sheet metal forming processes are generally nonlinear. Therefore, verifying that the material model determined using an LSP experiment can reproduce the deformation behavior of the material under nonlinear stress paths (NLSPs) is crucial for establishing an accurate material model.

Many studies have investigated the deformation behavior of materials subjected to NLSPs. However, most of them measured the subsequent yield surface of the materials by first applying a specific plastic strain and then, after unloading, subsequent loading paths in loading directions different from the pretrain direction to the test sample [4-8]. Of note, such NLSP experiments have been utilized to verify the validity of distortional plasticity models [9-13]. There have been several studies that have used NLSPs without unloading to verify the accuracy of material models for test samples [14-17]. However, the plastic strain applied to the test samples in these studies are less than several percent.

Takada and Kuwabara [18] investigate the deformation behavior of a cold-rolled mild steel sheet for deep drawing (SPCD) subjected to LSPs and NLSPs. The deformation behavior of the test sample is precisely measured until specimen fracture. The objective of this study is to clarify

Content from this work may be used under the terms of the Creative Commons Attribution 3.0 license. Any further distribution of this work must maintain attribution to the author(s) and the title of the work, journal citation and DOI. Published under license by Materials Research Forum LLC.

whether the deformation behavior of a test sample under a NLSP can be reproduced using the material model determined from an LSP experiment. In this study the deviation of the NLSP from the LSP is much larger than that used in [18].

Experimental Method

The test material used in the present study was a 0.8-mm-thick mild steel sheet, SPCD, with deep drawing quality. The work hardening characteristics and *r*-values at 0°, 45°, and 90° (transverse direction, TD) with respect to the rolling direction (RD) are shown in Table 1. It is the same material as used in [18].

Table 1. Mechanical properties of test material (SPCD).

Tensile direction /°	$\sigma_{0.2}$ /MPa	$\varepsilon_{\mathrm{TS}}^{\mathrm{p}}$*	c** /MPa	n**	α**	r-value***
0	146	0.241	560	0.269	0.0030	1.91
45	158	0.227	586	0.267	0.0038	1.63
90	155	0.236	563	0.271	0.0038	2.25

* Logarithmic plastic strain giving the maximum tensile load.

** Approximated using $\sigma = c(\alpha + \varepsilon^{p})^{n}$ for ε^{p}= 0.002~$\varepsilon_{\mathrm{TS}}^{\mathrm{p}}$

***Measured at uniaxial nominal strain of ε_{N}=0.1

Two types of biaxial tensile test were performed to measure the plastic deformation behavior of the test material from initial yield to fracture. Fig. 1 (a) shows a schematic diagram of the cruciform specimen used for the biaxial tensile tests with the as-received sheet sample. The geometry of the specimen is that recommended in ISO 16842 [19]. The specimen arms were parallel to the RD and TD of the material. Each arm of the specimen had seven slits (length: 30 mm, width: 0.2 mm) at 3.75-mm intervals to remove the geometric constraint on the deformation of the 30 × 30 mm2 square gauge area. The slits were fabricated using laser cutting.

Fig. 1 (b) shows a schematic diagram of the tubular specimen used for the BTET. The specimens were fabricated by bending a sheet sample into a cylindrical shape and CO2 laser welding the sheet edges together to fabricate a tubular specimen with an inner diameter of 47.1 mm, a length of 230 mm, and a gauge length (distance between the grips of the testing machine) of 150 mm. Two types of tubular specimen were fabricated. For type I specimens, the RD was in the axial direction; for type II specimens, the RD was in the circumferential direction. Type I specimens were used for the tests with $\sigma_x \leq \sigma_y$ and type II specimens were used for the tests with $\sigma_x \geq \sigma_y$; the maximum principal stress direction was always taken to be the circumferential direction. Because the measurement results for the BTET include the effect of prestrain due to bending during the preparation of the circular tube test pieces, they were corrected using the data obtained from the cruciform test piece. For details, refer to [3].

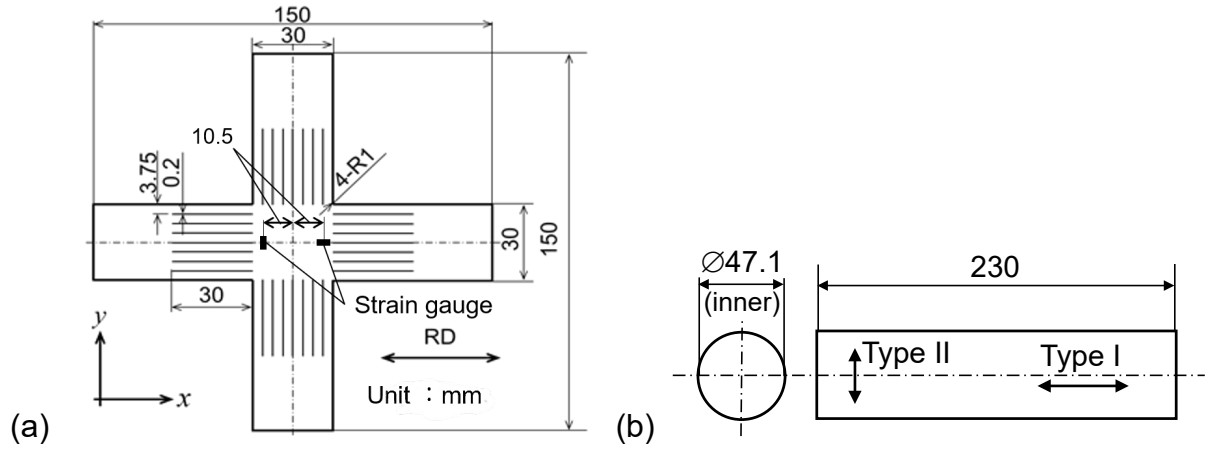

Fig. 1. Specimens used for biaxial tensile tests [19]. (a) Cruciform specimen and (b) tubular specimen. In (b), ↔ indicates the RD of the original sheet sample. The RD is taken in the axial direction for type I specimens and in the circumferential direction for type II specimens.

For details of the servo-controlled tension-internal pressure testing machine used in the experiment, see [3]. For details of the measurement method of the axial and circumferential strain components, ε_ϕ and ε_θ, the axial radius of curvature, R_ϕ, and the calculation method of the axial and circumferential stress components, σ_ϕ and σ_θ, see [20].

Linear Stress Path Experiment. For the LSP experiment, both cruciform and tubular specimens were subjected to seven LSPs, namely $\boldsymbol{\sigma_x}:\boldsymbol{\sigma_y}$ = 4:1, 2:1, 4:3, 1:1, 1:2, 3:4, and 1:4, where $\boldsymbol{\sigma_x}$ and $\boldsymbol{\sigma_y}$ are the true stress in the RD and TD, respectively. For $\boldsymbol{\sigma_x}:\boldsymbol{\sigma_y}$ =1:0 and 0:1, the uniaxial tensile test specimens standardized in JIS13B were used. The equivalent plastic strain rate was controlled to be approximately constant at $\mathbf{5 \times 10^{-4}\ s^{-1}}$.

Nonlinear Stress Path Experiment. Fig. 2 shows the NLSP applied to the test sample in the NLSP experiment. The NLSP was determined by assuming that the material deforms following the IH model based on the Yld2000-2d yield function [21] as determined in Fig. 3. The first stress path was the LSP with $\sigma_x:\sigma_y$ = 4:1. When $\varepsilon_0^{\mathrm{p}}$ reached 0.07, the stress path was changed to the second loading. $\varepsilon_0^{\mathrm{p}}$ gradually increased along the second loading. Then, when $\varepsilon_0^{\mathrm{p}}$ reached 0.09, the stress path followed the LSP with $\sigma_x:\sigma_y$ =1:1. The equivalent plastic strain rate was controlled to be approximately constant at $5 \times 10^{-4}\ \mathrm{s}^{-1}$. Two specimens, Exp.1 and Exp.2, were used for the NLSP experiment.

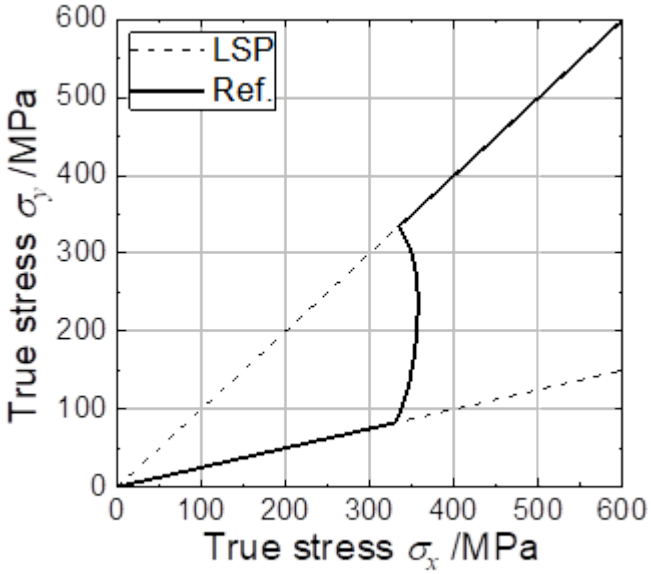

Fig. 2. Nonlinear stress path.

In the NLSP experiment, the evolution of $\varepsilon_x^{\mathrm{p}}(t)$ and $\varepsilon_y^{\mathrm{p}}(t)$ was approximated using a polynomial function for every stress path section between abrupt stress path change points, and the instantaneous value of β was calculated as $\tan^{-1}\{d\varepsilon_y^{\mathrm{p}}(t)/d\varepsilon_x^{\mathrm{p}}(t)\}$.

Experimental Results

The contours of plastic work in the stress space [22,23] were measured to identify appropriate material models for the test samples subjected to uniaxial and biaxial tension. With the true stress-logarithmic plastic strain curve measured for the RD used as reference data for work hardening, the plastic work per unit volume, $\boldsymbol{W_0}$, and uniaxial true stress, $\boldsymbol{\sigma_0}$, associated with particular values of $\boldsymbol{\varepsilon_0^{\mathrm{p}}}$ (referred to as the reference plastic strain hereafter) were determined. Next, from the biaxial and uniaxial stress-strain curves, the stress points that give the same plastic work as $\boldsymbol{W_0}$ were plotted in the principal stress space to determine the contour of plastic work associated with $\boldsymbol{\varepsilon_0^{\mathrm{p}}}$.

Fig. 3 shows the stress points that form work contours. Each stress point represents an average of two specimen data points; the difference between the two points was less than 1.4% of the flow stress for all data points. We measured up to $\boldsymbol{\varepsilon_0^{\mathrm{p}}} = 0.234$ for all LSPs. To quantitatively evaluate the shape change of the work contours with increasing $\boldsymbol{\varepsilon_0^{\mathrm{p}}}$, the nondimensional work contours were determined by dividing the value of the stress points that formed each work contour by the $\boldsymbol{\sigma_0}$ value belonging to the work contour. It was confirmed that the stress points along the stress paths of $\boldsymbol{\sigma_x}$: $\boldsymbol{\sigma_y}$ = 4:1, 2:1, 4:3, 1:1, and 3:4 do not fall on a single point with increasing $\boldsymbol{\varepsilon_0^{\mathrm{p}}}$; therefore, the test material exhibited differential hardening (DH). Fig. 3 also includes the yield loci calculated using the selected yield functions. The solid line is that based on the Yld2000-2d yield function, the exponent, $\boldsymbol{M}$, and parameters, $\boldsymbol{\alpha_1 - \alpha_6}$, of which were determined to approximate the shape of the work contour and the directions of the plastic strain rate, $\mathbf{D^p}$, for $\boldsymbol{\varepsilon_0^{\mathrm{p}}}$ =0.10. The evolution of the work contours with $\boldsymbol{\varepsilon_0^{\mathrm{p}}}$ is well reproduced by the DH model based on the Yld2000-2d yield function, as indicated by the red and black dotted lines for $\boldsymbol{\varepsilon_0^{\mathrm{p}}}$ =0.002 and 0.10, respectively.

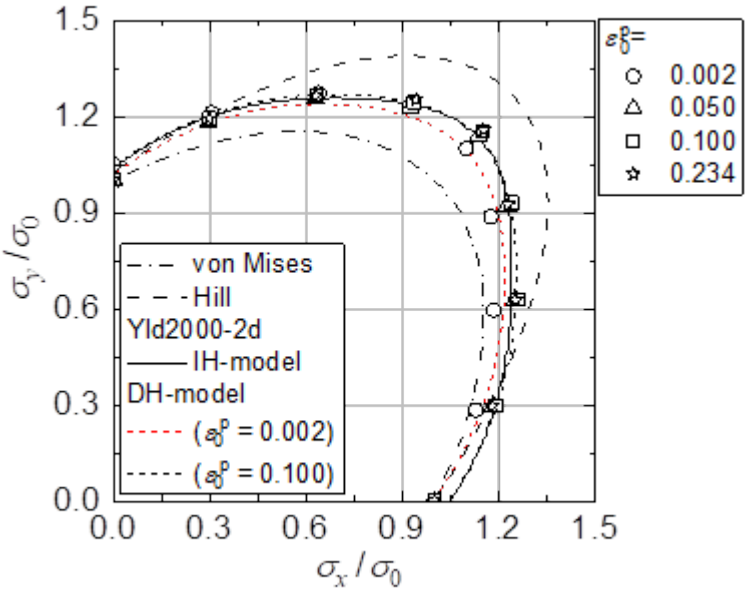

Fig. 3. Measured contours of plastic work normalized by σ_0 belonging to same group of work contours.

Fig. 4 compares the measured directions of $\mathrm{D^p}$, β, with those predicted using the selected yield functions. Again, the measured data are well reproduced by the Yld2000-2d yield function for all loading directions. Moreover, it is noteworthy that the experimental tendency for β to decrease for σ_x:σ_y = 4:3 and increase for σ_x:σ_y = 3:4 with increasing $\varepsilon_0^{\mathrm{p}}$ was well reproduced by the DH model.

In summary, the evolution of the contours of plastic work and the directions of the plastic strain rates with increasing $\varepsilon_0^{\mathrm{p}}$ measured in the LSP experiment are accurately reproduced by the DH model based on the Yld2000-2d yield function.

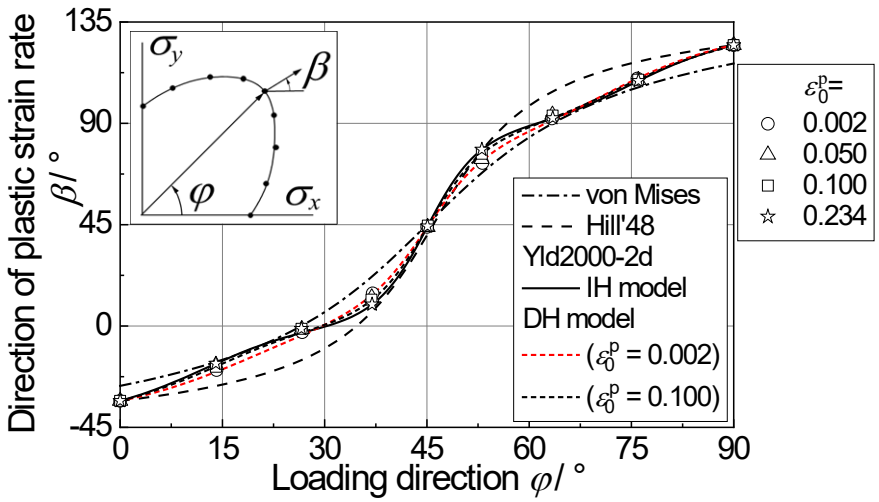

Fig. 4. Measured directions of plastic strain rates compared with those calculated using selected yield functions.

Fig. 5 shows the $\sigma_x - \varepsilon_x^{\mathrm{p}}$ and $\sigma_y - \varepsilon_y^{\mathrm{p}}$ curves observed for the NLSP shown in Fig. 2. Two specimens were used, and the reproducibility of the two tests was good. The small protrusion in the black line was caused by the change in σ_x along the second (curved) stress path.

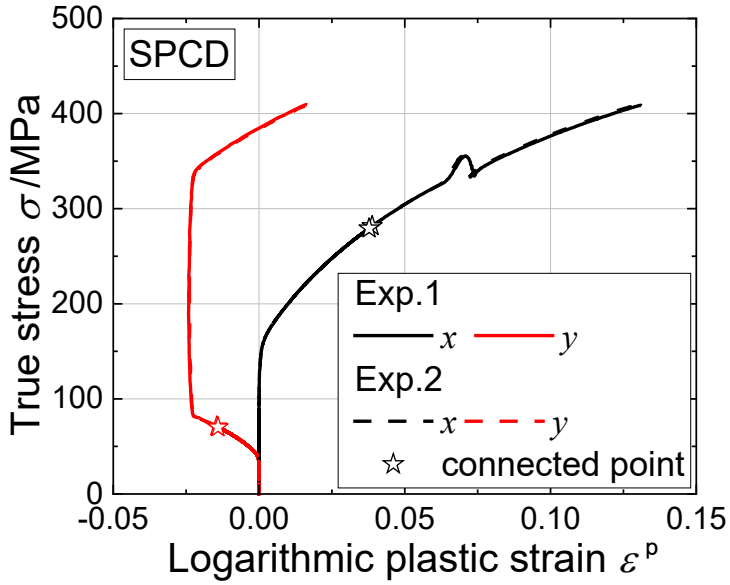

Fig. 5. $\sigma_x - \varepsilon_x^p$ and $\sigma_y - \varepsilon_y^p$ curves observed for the NLSP shown in Fig. 2. Those for the lower strain range than the star marks were measured using a cruciform specimen, and those for the higher strain range than the star marks were measured using the BTET.

Fig. 6 shows the variation of loading direction, φ, with increasing $\varepsilon_0^{\mathrm{p}}$ for the stress path shown in Fig. 2. The largest deviation of the experimental values from the prediction by the Yld2000-2d yield function with DH was $\Delta\varphi = 5.8°$ at $\varepsilon_0^{\mathrm{p}} = 0.08$.

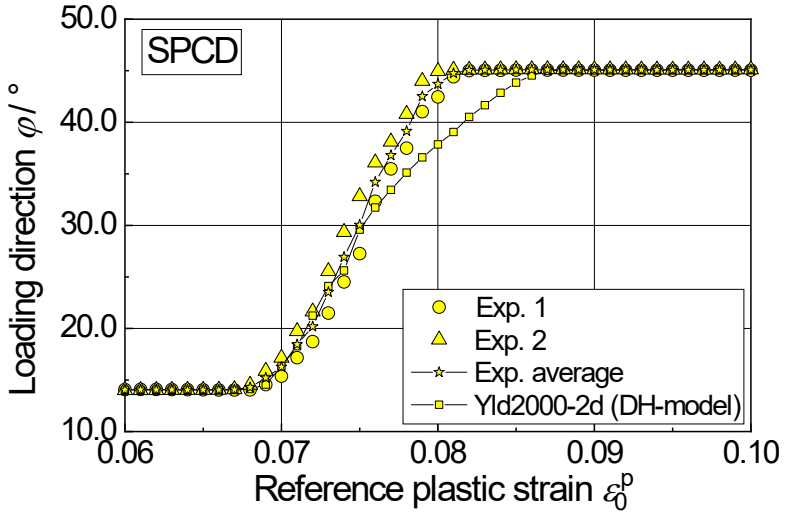

Fig. 6. Variation of loading direction, φ, with increasing ε_0^p for the stress path shown in Fig. 2.

Fig. 7 shows the change in the direction of plastic strain rate, β, with increasing ε_0^p for the stress path shown in Fig. 2. The largest deviation of the experimental values from the prediction by the Yld2000-2d yield function with DH was $\Delta\beta = 20.4°$ at $\varepsilon_0^p = 0.08$. It is noted that β reached 35° at $\varepsilon_0^p = 0.08$, and remained almost constant at $\beta = 35°$ for $\varepsilon_0^p \geq 0.08$; it was 9° lower than the prediction by the Yld2000-2d yield function. Considering that the stress state almost reached equibiaxial tension at $\varepsilon_0^p = 0.08$ in the experiment, this difference in β between the NLSP and LSP was possibly caused by the change in texture during the NLSP for $\varepsilon_0^p \leq 0.08$. Therefore, we can conclude that the deformation behavior predicted by the material model determined from the LSP experiment clearly shows some deviation from that observed for the NLSP experiment.

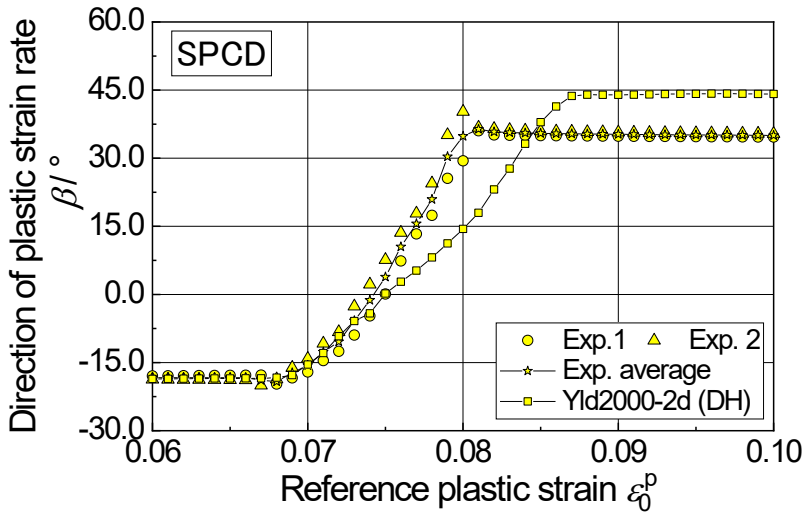

Fig. 7. Change in direction of plastic strain rate, β, with increasing ε_0^p for the stress path shown in Fig. 2.

Summary

The deformation behavior of a mild steel sheet was observed both for the LSPs and NLSP. A proper material model was determined from the LSP experiment using the Yld2000-2d yield

function. Moreover, a NLSP experiment was performed for the test sample, and the deformation behavior of the test sample during the NLSP experiment was precisely measured, and compared with that predicted using the Yld2000-2d yield function. It was found that the deformation behavior of the test sample predicted by the material model determined from the LSP experiment clearly shows some deviation from that observed for the NLSP experiment.

References

[1] T. Kuwabara, S. Ikeda, K. Kuroda, Measurement and analysis of differential work-hardening in cold-rolled steel sheet under biaxial tension, J. Mater. Process. Technol. 80-81 (1998) 517-523. https://doi.org/10.1016/S0924-0136(98)00155-1

[2] T. Kuwabara, A. Van Bael, E. Iizuka, Measurement and analysis of yield locus and work-hardening characteristics of steel sheets with different R-values, Acta Mater. 50 (2002) 3717-3729. https://doi.org/10.1016/S1359-6454(02)00184-2

[3] T. Kuwabara, F. Sugawara, Multiaxial tube expansion test method for measurement of sheet metal deformation behavior under biaxial tension for a large strain range. Int. J. Plast. 45 (2013) 103-118. http://doi.org/10.1016/j.ijplas.2012.12.003

[4] S.S. Hecker, Yield surfaces in prestrained aluminum and copper, Metal. Trans. 2 (1971) 2077-2086. https://doi.org/10.1007/BF02917534

[5] K. Ikegami, A historical perspective of experimental study on subsequent yield surfaces for metals (part 1), J. Soc. Mat. Sci., Jpn. 24 (1975) 491-504 (in Japanese) https://doi.org/10.2472/jsms.24.491

[6] K. Ikegami, A historical perspective of experimental study on subsequent yield surfaces for metals (part 2), J. Soc. Mat. Sci., Jpn., 24 (1975) 709-719 (in Japanese). https://doi.org/10.2472/jsms.24.709

[7] Y. Ohashi, K. Kawashima, T. Yokochi, Anisotropy due to plastic deformation of initially isotropic mild steel and its analytical formulation, J. Mech. Phys. Solid. 23 (1975) 277-294. https://doi.org/10.1016/0022-5096(75)90029-0

[8] E. Shiratori, K. Ikegami, K. Kaneko, The influence of the Bauschinger effect on the subsequent yield condition, Bull. JSME 16 (1973) 1482-1493. https://doi.org/10.1299/jsme1958.16.1482

[9] F. Barlat, S.Y. Yoon, S.Y. Lee, M.S. Wi, J.H. Kim, Distortional plasticity framework with application to advanced high strength steel, Int. J. Solids Struct. 202 (2020) 947-962. https://doi.org/10.1016/j.ijsolstr.2020.05.014

[10] J.J. Ha, M.-G. Lee, F. Barlat, Strain hardening response and modeling of EDDQ and DP780 steel sheet under non-linear strain path, Mech. Mater. 64 (2013) 11-26. http://dx.doi.org/10.1016/j.mechmat.2013.04.004

[11] H. Kim, F. Barlat, Y. Lee, S.B. Zaman, C.S. Lee, Y. Jeong, A crystal plasticity model for describing the anisotropic hardening behavior of steel sheets during strain-path changes, Int. J. Plast. 111 (2018) 85-106. https://doi.org/10.1016/j.ijplas.2018.07.010

[12] J. Qin, B. Holmedal, O.S. Hopperstad, A combined isotropic, kinematic and distortional hardening model for aluminum and steels under complex strain-path changes, Int. J. Plast. 101 (2018) 156-169. https://doi.org/10.1016/j.ijplas.2017.10.013

[13] M.S. Wi, S.Y. Lee, J.H. Kim, J.M. Kim, F. Barlat, Experimental and theoretical plasticity analyses of steel materials deformed under a nonlinear strain path, Int. J. Mech. Sci. 182 (2020) 105770. https://doi.org/10.1016/j.ijmecsci.2020.105770

[14] S.S. Hecker, Experimental Investigation of Corners in the Yield Surface, Acta Mech. 13 (1972) 69-86. https://doi.org/10.1007/BF01179659

[15] T. Kuwabara, M. Kuroda, V. Tvergaard, K. Nomura, Use of abrupt strain path change for determining subsequent yield surface: experimental study with metal sheets, Acta Mater. 48 (2000) 2071-2079. https://doi.org/10.1016/S1359-6454(00)00048-3

[16] K. Yoshida, T. Tsuchimoto, Plastic flow of thin-walled tubes under nonlinear tension-torsion loading paths and an improved pseudo-corner model, Int. J. Plast. 104 (2018) 214-229. https://doi.org/10.1016/j.ijplas.2018.02.013
[17] T. Hama, S. Yagi, K. Tatsukawa, Y. Maeda, Y. Maeda, H. Takuda, Evolution of plastic deformation behavior upon strain-path changes in an A6022-T4 Al alloy sheet, Int. J. Plast. 137 (2021) 102913. https://doi.org/10.1016/j.ijplas.2020.102913
[18] Y. Takada, T. Kuwabara, Nonlinear biaxial tensile stress path experiment without intermediate elastic unloading for validation of material model, Int. J. Solid. Struct. 257 (2022) 111777. https://doi.org/10.1016/j.ijsolstr.2022.111777
[19] ISO 16842: 2014 Metallic materials −Sheet and strip −Biaxial tensile testing method using a cruciform test piece.
[20] T. Hakoyama, T. Kuwabara, Effect of biaxial work hardening modeling for sheet metals on the accuracy of forming limit analyses using the Marciniak-Kuczynski approach, in: H. Altenbach, T. Matsuda, D. Okumura (Eds.), From Creep Damage Mechanics to Homogenization Methods, Springer, 2015, pp. 67-95. https://doi.org/10.1007/978-3-319-19440-0_4
[21] F. Barlat, J.C. Brem, J.W. Yoon, K. Chung, R.E. Dick, D.J. Lege, F. Pourboghrat, S.H. Choi, E. Chu, Plane stress yield function for aluminum alloy sheets-part 1: theory, Int. J. Plast. 19 (2003) 1297-1319. https://doi.org/10.1016/S0749-6419(02)00019-0
[22] R. Hill, J.W. Hutchinson, Differential hardening in sheet metal under biaxial loading: a theoretical framework, J. Appl. Mech. 59 (1992) S1-S9. https://doi.org/10.1115/1.2899489
[23] R. Hill, S.S. Hecker, M.G. Stout, An investigation of plastic flow and differential work hardening in orthotropic brass tubes under fluid pressure and axial load, Int. J. Solid. Struct. 31 (1994) 2999-3021. https://doi.org/10.1016/0020-7683(94)90065-5

Materials Research Proceedings 28 (2023) 787-798 https://doi.org/10.21741/9781644902479-86

Damage prediction in roll forming of the high strength aluminum alloy AA7075

SUCKOW Timon[1,a *] and GROCHE Peter[1,b]

[1]Institute for Production Engineering and Forming Machines, TU Darmstadt, Otto-Berndt-Str. 2, 64287 Darmstadt, Germany

[a]suckow@ptu.tu-darmstadt.de, [b]groche@ptu.tu-darmstadt.de

Keywords: Roll Forming, Aluminum, 7075, Material Failure, Damage, FEM

Abstract. The high-strength AA7075 alloy offers great potential for lightweight construction thanks to its high specific strength. However, high strength and low ductility are challenging for forming the material in the peak-aged T6-condition in terms of material failure and springback. Therefore, this alloy is usually formed in temperature-supported process routes, which poses major challenges for process design. For cold forming of the alloy in the T6-condition, a reliable prediction of material failure is required in terms of process design. Within this study, this is achieved by applying the modified Mohr-Coulomb (MMC) criterion and an increment based damage evolution rule to the FE-model. To validate the failure prediction and verify the general applicability to different profile geometries, two U-profiles and a V-profile are roll formed. Failure occurs during forming for all profile geometries and the experimental results show a good agreement with the failure prediction. The quality of the damage prediction strongly depends on the calibration for the MMC criterion and the setup of the FE-model, depending on the mesh size and the element type used.

Introduction

Recent developments show that roll forming of high-strength aluminum alloys has become a focus of research and development [1-3]. Roll forming is an economical process for the production of long profiles, particularly in mass production [4]. For commercial vehicles, the use of high-strength aluminum is possible for the side impact beam, A- and B-pillars and other impact-absorbing components. The versatile shaping potential in roll forming compared to die or swivel bending processes allow additional design freedom for the optimal design of the profiles [5]. Additionally, smaller bending radii can be achieved during roll forming, which contributes to an increase in design freedom [6,7].

However, high strength and low ductility of lightweight materials, such as the AA7075 alloy, are challenging for process design. This is expressed in large safety factors and compromises in terms of the target geometry of components, especially with regard to achievable bending radii and bending angles. Process design is of particular relevance in roll forming due to the three-dimensional forming, as various production-related defects can occur. In roll forming of high-strength materials, the occurrence of cracks in the outer fibre of the bending zone and a high springback are critical [8]. The occurrence of cracks is particularly critical for small ratios of the bending radius r to the sheet thickness s and for large bending angles. A plane strain state is present in the outer fibre of the bending zone where fracture occurs [9].

Damage Prediction. Accurate prediction of damage is necessary to improve process design. The modelling of damage in forming technology has been developed over the last decades and is used in the design of forming processes for the optimal utilisation of process windows and for the prediction of material failure [10]. Failure is the final stage of damage and appears in forming processes through intolerable and function-restricting cracks [11]. In general, the damage of metals can be described using uncoupled fracture criteria or coupled damage models [11]. In coupled

Content from this work may be used under the terms of the Creative Commons Attribution 3.0 license. Any further distribution of this work must maintain attribution to the author(s) and the title of the work, journal citation and DOI. Published under license by Materials Research Forum LLC.

damage models, the elastic and/or plastic material behaviour is linked to the evolution of damage. Due to the higher practicability, uncoupled fracture criteria are widespread in the field of metal forming [11]. Metals usually fail as the result of nucleation, growth and coalescence of microscopic voids within the metal structure during forming processes [12]. All three mechanisms are dependent on the stresses and strains during forming. Developments in modelling damage have shown that damage is dependent on the stress triaxiality η [12,13]. The stress triaxiality η is defined as the ratio of the hydrostatic stress σ_m to the equivalent stress $\bar{\sigma}$:

$$\eta = \frac{\sigma_m}{\bar{\sigma}} \tag{1}$$

where hydrostatic stress,

$$\sigma_m = \frac{\sigma_1+\sigma_2+\sigma_3}{3} \tag{2}$$

equivalent stress,

$$\bar{\sigma} = \sqrt{\frac{(\sigma_1-\sigma_2)^2+(\sigma_2-\sigma_3)^2+(\sigma_3-\sigma_1)^2}{2}} \tag{3}$$

and σ_1, σ_2 and σ_3 are the principal stresses. Another significant parameter for the extent of damage in three-dimensional stress states is the Lode angle parameter $\bar{\theta}$. This is relevant especially for small stress triaxialities and is employed for example in the modified Mohr-Coulomb (MMC) criterion by Bai and Wierzbicki [13] and the Lou-Huh criterion [12]. All stress directions (loading conditions) can be characterized by the parameters η and $\bar{\theta}$,.

MMC Criterion. The equivalent plastic strain at fracture $\bar{\varepsilon}_f$ depends on the stress triaxiality and the lode angle parameter in the MMC criterion [14]:

$$\bar{\varepsilon}_f = \left\{\frac{A}{c_2}[1-c_\eta(\eta-\eta_0)] \times \left[c_\theta^s + \frac{\sqrt{3}}{2-\sqrt{3}}(c_\theta^{ax}-c_\theta^s)\left(\sec\left(\frac{\bar{\theta}\pi}{6}\right)-1\right)\right]\left[\sqrt{\frac{1+c_1^2}{3}}\cos\left(\frac{\bar{\theta}\pi}{6}\right)+c_1\left(\eta+\frac{1}{3}\sin\left(\frac{\bar{\theta}\pi}{6}\right)\right)\right]\right\}^{-\frac{1}{n}} \tag{4}$$

Eight parameters (A, n, c_η, η_0, c_θ^s, c_θ^{ax}, c_1 and c_2) need to be found for the calibration of the MMC criterion, but only two have to be determined from fracture tests. An explanation of the parameters can be found in [14]. The effects of c_η and c_1 are similar in terms of stress triaxiality, which reduces Eq. 4 to:

$$\bar{\varepsilon}_f = \left\{\frac{A}{c_2}\left[c_\theta^s + \frac{\sqrt{3}}{2-\sqrt{3}}(c_\theta^{ax}-c_\theta^s)\left(\sec\left(\frac{\bar{\theta}\pi}{6}\right)-1\right)\right]\left[\sqrt{\frac{1+c_1^2}{3}}\cos\left(\frac{\bar{\theta}\pi}{6}\right)+c_1\left(\eta+\frac{1}{3}\sin\left(\frac{\bar{\theta}\pi}{6}\right)\right)\right]\right\}^{-\frac{1}{n}} \tag{5}$$

The parameters A and n are determined from the power hardening curve: $\bar{\sigma} = A\varepsilon^n$ [14]. The parameters c_1 and c_2 are determined from material tests up to material fracture, where the fracture strain $\bar{\varepsilon}_f$, stress triaxiality η and lode angle parameter $\bar{\theta}$ are determined numerically and/or experimentally. For accurate damage prediction, the tests should cover load paths that are close to the investigated forming process [11]. The parameters c_θ^{ax} and c_θ^s could be determined from careful plasticity tests and determination of the yield surface [14]. Potential simplifications are the assumption of c_θ^{ax}=1 and $c_\theta^s = 1$ or the determination of the values by the material tests up to

Materials Research Proceedings 28 (2023) 787-798 https://doi.org/10.21741/9781644902479-86

fracture [14]. The final function provides a three-dimensional fracture locus in the space of stress triaxiality and lode angle parameter. A relationship between the equivalent plastic strain $\bar{\varepsilon}_p$ during the forming process and the equivalent plastic strain at fracture $\bar{\varepsilon}_f = f(\eta, \bar{\theta})$ from the fracture locus provides the damage evolution rule, where material failure occurs when $D \geq 1$ [13]:

$$D(\bar{\varepsilon}_p) = \int_0^{\bar{\varepsilon}_p} \frac{d\bar{\varepsilon}_p}{f(\eta,\bar{\theta})} \tag{6}$$

Damage Prediction in Roll Forming. Wang et al. [15] provide an example for the application of damage models in roll forming with the application of the Oyane model. Shear stresses in the forming zone are responsible for material failure [15]. Furthermore, Wang et al. [15] hypothesize that roll forming seems to be a sheet forming process but is intrinsically a bulk forming process in terms of stress and strain state. Deole et al. [8] use the fracture criterion of Lou and Huh [16] for failure prediction. For calibration, additional bending tests are carried out to represent the plane strain state over the entire loading path [8]. In contrast to [15], the damage and final material failure are related to the plane strain tension state in the outer edge fibre in the bending radius [8]. In the work of Talebi et al. [9], fracture criteria (Rice-Tracey, Crockoft-Latham and Ayada) are used with two different approaches to calibrate the models. The basic approach is the calibration of the model with a uniaxial tensile test. In the extended calibration, with additional material tests, the failure prediction error is reduced from 88 % to 8 % [9]. Lee et al. [2] provide another study on fracture and damage modelling on the roll forming of a bumper beam made of the high-strength aluminum alloy AA7075-T6 using the GISSMO damage model. The summary of the previous approaches shows contradictory statements on the dominant failure-critical stress states and emphasizes the relevance of the calibration and application of fracture criteria and damage models in roll forming. All approaches have in common, that only one profile flower is investigated. Within this study, three different profile flowers are investigated. Due to the application-oriented research, an industrially widespread FE-solver (Marc Mentat) for roll forming is used for the numerical simulation, as well as for calibration of the MMC criterion. All tests for calibration of the MMC criterion are conducted on a universal testing machine. The aim of the study is to apply an easy-to-use fracture criterion in combination with a damage evolution rule on the one hand. On the other hand, a low experimental and numerical effort with a simultaneously accurate damage and failure prediction is strived for.

Results

Calibration of the MMC Criterion. To calibrate the MMC criterion for the peak-aged AA7075-T6 alloy, material tests up to fracture are performed on a Zwick Roell 100 universal testing machine for measuring the equivalent plastic strain at fracture $\bar{\varepsilon}_f$. Plastic strain is measured by optical strain measurement with the GOM Aramis system, after applying a stochastic pattern on the surface of the specimens. Three specimens were tested for each geometry. Before testing, the specimens were milled out of the sheet metal at a 90 ° angle to the rolling direction. Additionally, FE-simulations of the material tests are carried out for each geometry in Marc Mentat 2012 for determining the average values of the stress triaxiality η_{avg} and the lode angle parameter $\bar{\theta}_{avg}$ during plastic deformation. Within the material tests, different loading conditions in terms of stress triaxiality and lode angle parameter are applied. Fig. 1a shows the strain paths for different specimens and

the parameter set, obtained by the material tests and Fig. 1b shows the specimens for calibration of the MMC criterion.

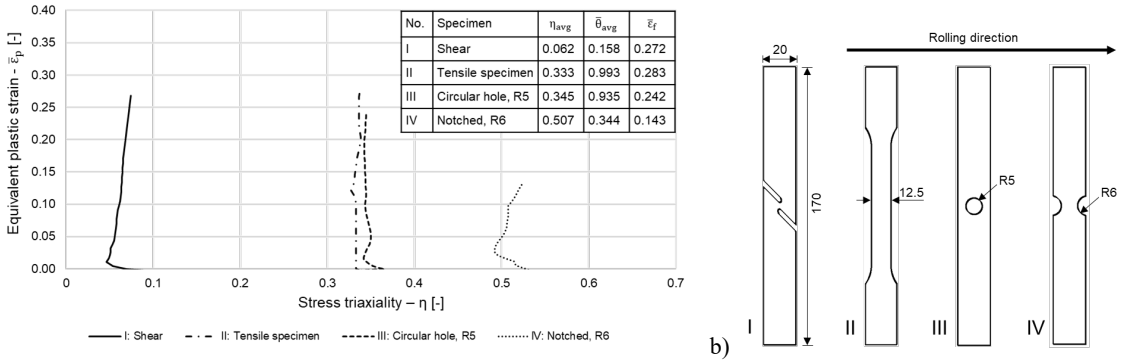

Fig. 1. a) Plastic strain $\boldsymbol{\varepsilon_f}$ and stress triaxiality $\boldsymbol{\eta}$ during the calibration experiments. b) Specimens for calibration of the MMC criterion: I: Shear; II: Tensile specimen; III: Circular hole, R5; IV: Notched, R6.

The set of parameters is the basis for calculating the constants of the MMC criterion. Since the lode angle parameter $\bar{\theta}$ is greater than zero for all specimens, c_θ^{ax} is set to 1, as recommended by Bai and Wierzbicki [14]. The remaining parameters c_1, c_2 and c_θ^s are determined by the nonlinear least-squares solver "lsqcurvefit" via Matlab:

$$\min_{(c_1,c_2,c_\theta^s)} (\Delta\bar{\varepsilon}_f)^2 = \min_{(c_1,c_2,c_\theta^s)} \left[\frac{1}{N}\sum_{i=1}^{N}\left(\bar{\varepsilon}_{f,i} - \hat{\bar{\varepsilon}}_{f,i}(c_1,c_2,c_\theta^s)\right)^2\right] \tag{7}$$

The values for $\bar{\varepsilon}_{f,i}$ are determined from the calibration tests, while $\hat{\bar{\varepsilon}}_{f,i}(c_1,c_2,c_\theta^s)$ are the function values of the optimized MMC criterion (Eq. 5). The parameters $n = 0.0862$ (hardening exponent) and $A = 784.96$ are obtained from the flow curve from uniaxial tensile tests. In addition, the tensile strength $R_m = 590$ MPa and yield strength $R_{p0,2} = 528$ MPa are determined in these tests. Fig. 2a shows the calibrated fracture locus in the $(\eta, \bar{\theta}, \bar{\varepsilon})$-space and Fig. 2b in the $(\eta, \bar{\varepsilon})$-space.

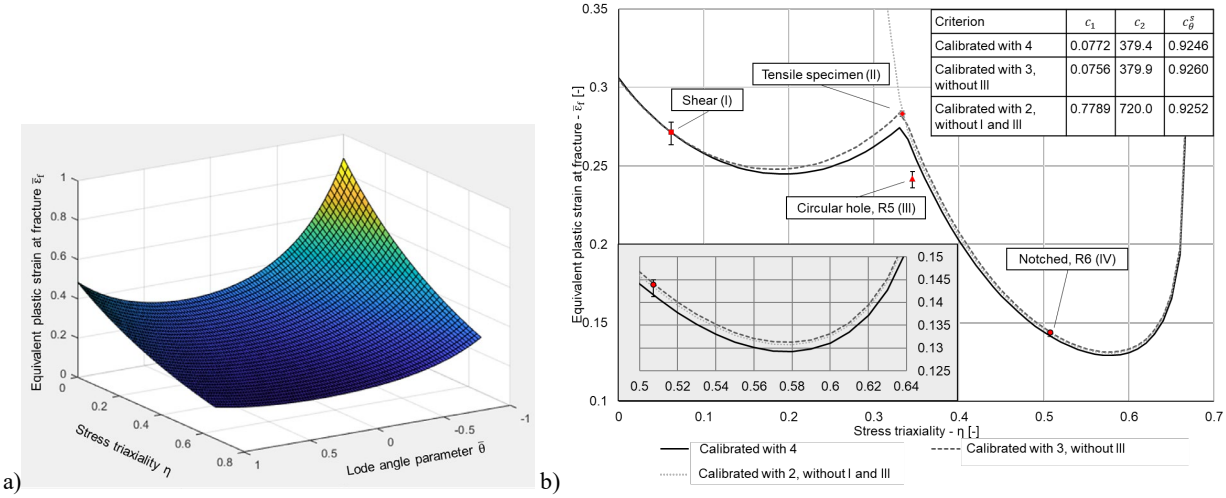

Fig. 2. Representation of the MMC fracture criterion. a) In the $(\boldsymbol{\eta}, \boldsymbol{\bar{\theta}}, \boldsymbol{\bar{\varepsilon}})$-space, calibrated with 4 specimens. b) In the $(\boldsymbol{\eta}, \boldsymbol{\bar{\varepsilon}})$-space for plane stress condition. Calibrated with 2, 3 and 4 specimens.

Materials Research Proceedings 28 (2023) 787-798 https://doi.org/10.21741/9781644902479-86

To investigate the influence of various specimen geometries on the shape of the fracture locus, the fracture locus is illustrated in $(\eta, \bar{\varepsilon})$-space, which is representative for plane stress condition. In plane stress condition, η and $\bar{\theta}$ are dependent on each other, as shown in Eq. 8:

$$\bar{\theta} = 1 - \frac{2}{\pi} \cdot \cos^{-1}\left(-\frac{27}{2}\eta\left(\eta^2 - \frac{1}{3}\right)\right) \tag{8}$$

The shape of the fracture locus is influenced by removing material tests for calibration of the fracture locus (Fig. 2b). Calibrating the fracture criterion with two, three, four or five specimens does not have a high impact on the shape of the fracture locus for stress triaxialities above $\eta = 0.\overline{3}$. During roll forming, bending stresses are expected to be dominant during forming. This would correspond to a stress triaxiality of $\eta = 0.577$. The max. relative error of the fracture locus in plane stress condition for the stress triaxiality of $\eta = 0.577$ is 1.1 % ($\bar{\varepsilon}_f = 0.0014$). For the stress triaxiality of $\eta = 0.\overline{3}$, the relative error is 3.3 % ($\bar{\varepsilon}_f = 0.009$). Less material tests for the calibration of the MMC criterion result in reduced experimental effort and thus in a more efficient calibration of the criterion. The effect of a reduced number of material tests on the damage prediction during roll forming is discussed within this study.

Experimental Setup. Within this study, three different profiles are investigated in order to apply different loading conditions in the bending zone, as shown in Fig. 3a. The profile flowers are presented in each case up to the stage where failure occurs. The difference between the U-profiles is the forming strategy (constant radius vs. constant length) and the flange length. The experiments were performed on two different roll forming machines. The U-profiles were formed on a VOEST P 450/4 roll forming machine and the V-profile on another conventional roll forming machine of the Deakin University, Australia. Feeding speed of the sheet was 1 m/min, the initial sheet length 1500 mm and no lubrication was used. Within the roll forming experiments, the cracks occurred in the bending radii for all profile flowers. Fig. 3b shows the experimental setup for roll forming of a U-Profile and the occurrence of cracks after the third pass.

a)

U-Profile - constant radius		
Interstation distance: 520 mm		
Roll diameter: 250 mm		
Initial sheet width: 170 mm		
Flange length: 42.5 mm		
Pass	Angle [°]	Radius [mm]
1	13	3
2	29	3
3	47	3

U-Profile - constant length		
Interstation distance: 520 mm		
Roll diameter: 250 mm		
Initial sheet width: 170 mm		
Flange length: 57.2 mm		
Pass	Angle [°]	Radius [mm]
1	15	17,004
2	30	8,049
3	45	5,096

V-Profile - constant length		
Interstation distance: 400 mm		
Roll diameter: 140 mm		
Initial sheet width: 75 mm		
Pass	Angle [°]	Radius [mm]
1	10	25,85
2	20	12,6
3	30	8,18
4	40	5,98
5	50	4,65
6	60	3,77

b)

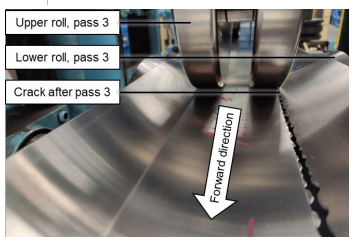

Fig. 3. Profile flowers, investigated within this study. Fracture occurred in the last pass for each profile within the roll forming experiments (marked red).b) Experimental setup and occurrence of cracks (U-Profile - constant radius).

FE Model. The aim of the FE model is to support the design of the roll forming process with regard to the final geometry and manufacturing-related defects such as material failure. By applying the MMC criterion in combination with a damage evolution rule in the FE model, a prediction of the damage and thus a determination of the process limits is possible. Accurate prediction of damage requires accurate prediction of local stresses and strains in the FE model. The setup of the FE model including material parameters and boundary conditions is shown in Fig. 4. Mesh size and element type are varied with regard to the conflict of objectives between a good prediction of the stresses and strains and the computation time. The variation of the mesh size is similar for all profiles. The mesh size in the bending zone is small, compared to the remaining part of the sheet. The flow curve is obtained from uniaxial tensile tests with a strain rate of 0.002 1/s.

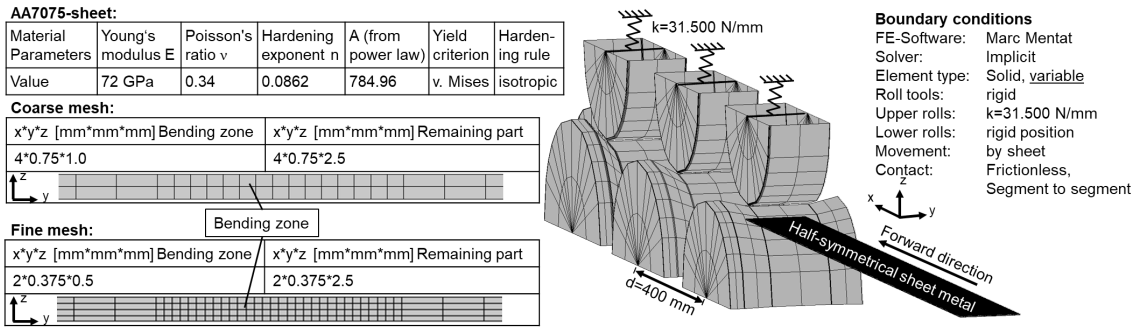

Fig. 4. Setup of the FE model based on the example of the U-profile (constant radius).

Damage Prediction. For damage prediction, the MMC-criterion is applied to the critical node in the FE-model, which is on the outer fibre of the bending zone. Fig. 5a shows the evaluation node for investigating the roll forming process and damage prediction within this study. For all profile flowers, the node is located at the point with the highest plastic strain in the failure-critical forming stage. The node is located in the steady-state area of the sheet at a length of 600 mm (half sheet length). Plastic deformation in the bending zone occurs primarily, when the sheet passes through the forming rolls (Fig. 5b). The stress exceeds the yield stress, which leads to a permanent plastic deformation.

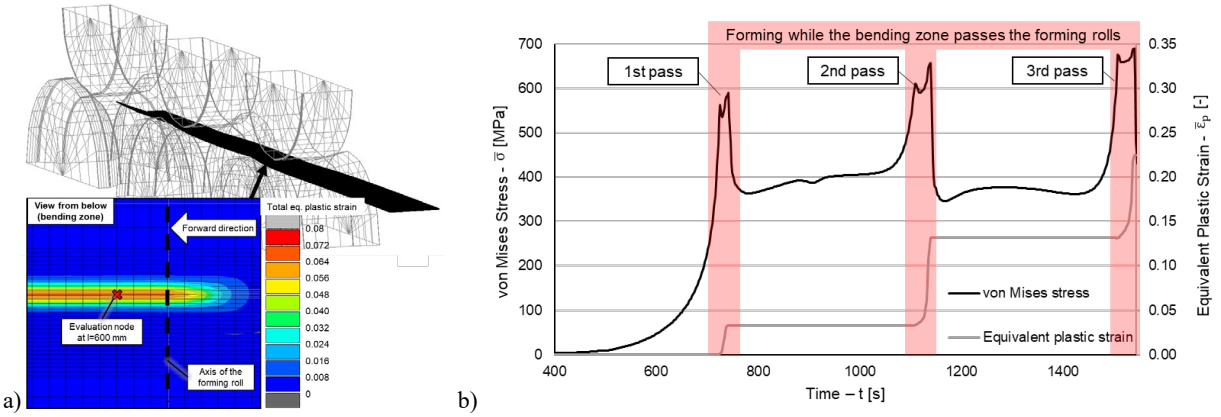

Fig. 5. a) Location of the evaluation node in the bending zone in the example of the U-profile (constant radius). b) Development of equivalent plastic strain and von Mises stress during the roll forming process.

For nonlinear loading paths, a nonlinear incremental rule must be applied for accurate prediction of damage, as proposed by Bai and Wierzbicki [13]. Within this study, the loading path is considered in the damage evolution rule by summing up the damage value for each increment in the FE-simulation, while considering the loading condition in terms of stress triaxiality and lode angle parameter. For an accurate prediction of damage, the time step for each increment should be small enough to represent the current stress- and strain state and thus the loading path during forming. In this study, one increment is evaluated every 2 mm in the forward direction of the sheet. Increasing the distance to 10 mm per increment leads to a relative error in damage prediction of up to 15 %, due to the inaccurate representation of the loading path. The incremental damage D_{inc} for each node and time increment in the FE-model is calculated by the following equation:

$$D_{inc,\ t} = \frac{\bar{\varepsilon}_{p,t} - \bar{\varepsilon}_{p,t-1}}{\frac{1}{2}\left(\bar{\varepsilon}_f(\eta,\bar{\theta})_t + \bar{\varepsilon}_f(\eta,\bar{\theta})_{t-1}\right)} \tag{9}$$

where $\bar{\varepsilon}_{p,t}$ is the equivalent plastic strain at the evaluated node in the FE-model and $\bar{\varepsilon}_f(\eta,\bar{\theta})_t$ is the equivalent strain at fracture, calculated by the loading condition $(\eta,\bar{\theta})$ of the evaluation node. The total Damage D is defined as the sum of the incremental damage D_{inc}, where n is the total number of increments up to the evaluated time t in the FE-model:

$$D = \sum_{t=1}^{n} D_{inc,t} \tag{10}$$

In the following section, the damage prediction is applied for different profile flowers, mesh and element types. Table 1 shows the naming scheme for the FE-models. Fig. 6 depicts the loading condition for the different profile flowers in order to analyze the differences between the different profile types. The stress states correspond to the plane-stress state and the calibration tests cover a large section of the load path, but the difference between the profile flowers is small. Furthermore, for all profile flowers, the non-linear loading paths follow a similar trend, with increasing stress triaxiality during bending in roll forming in each pass. At the beginning of the plastic deformation in each stage, the loading condition is between shear and uniaxial tension and develops towards stress states between plane strain tension and biaxial tension. An additional test for matching the biaxial tension would be helpful to cover all loading conditions, but is not possible with a universal testing machine.

Table 1. Naming scheme for the FE-models.

Profile	**Mesh**	**Element type**
U-cR: U - constant radius	**C**: coarse	**FI**: Fully integrated 8-node-Element (Type 7)
U-cL: U - constant length	**F**: fine	**RI**: 8-node Element with reduced integration / hourglass control (Type 117)
V: V-Profile		

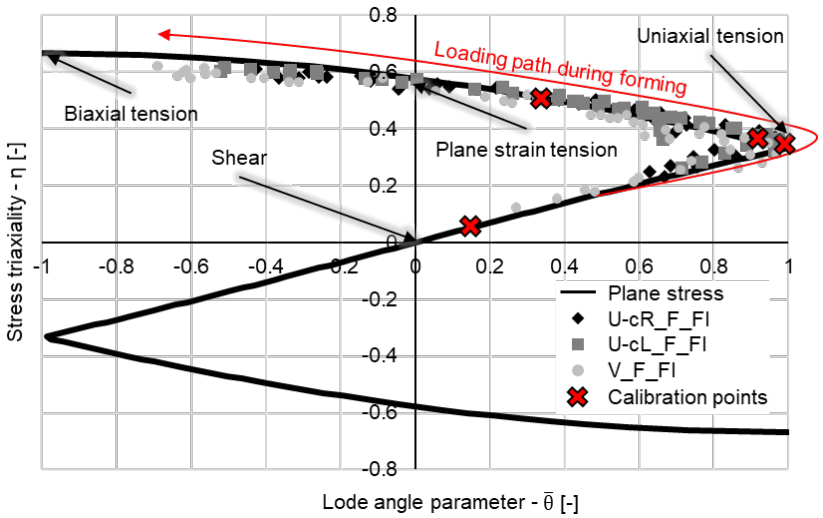

Fig. 6. Representation of the loading condition during plastic forming in the outer fibre of the bending zone for different profile flowers compared to the plane stress condition and the calibration tests.

After a short introduction to the typical stress states during roll forming, various parameters in the FE models are analyzed. The aim is an accurate and efficient prediction of the damage. Efficient means with low experimental and numerical effort. If it is not explicitly described, the prediction of the damage is based on the MMC criterion, based on four material tests. Table 2 and Fig. 7 show the results for different profile flowers, varying the element type and the mesh size in order to overcome the conflict of objectives. It is shown, that the damage is underestimated when the mesh is too coarse, which is fatal for a process design. The same tendency is shown for the reduced integrated elements. This is mainly due to the underestimated plastic strain and stress triaxiality. For the V-profile, the trend is reversed, although the differences are significantly smaller. Furthermore, this leads to a conservative process design and is therefore not too critical. In summary, the fully integrated elements with fine meshing provide the best results in terms of damage prediction. However, the computation time is high, particularly for the fine meshed simulations: 55.200 elements (153 h) instead of 10.800 elements (16 h) for the coarse mesh. The reduced integrated elements decrease the computation time by approx. 5 %. Finer meshing is not practicable due to the already high computing time.

*Table 2. Comparison of ductile fracture (experimental) and predicted damage (numerical) for different mesh and element types. Damage underestimated numerically: marked in red. *Fracture estimated in pass 5 already.*

Profile flower	**U-Profile (constant radius)**				**U-Profile (constant length)**				**V-Profile**			
Mesh	C		F		C		F		C		F	
El. Type	FI	RI	FI	RI	FI	RI	FI	RI	FI	RI	FI	RI
Ductile fracture (exp.)	3rd pass				3rd pass				6th pass			
Damage at pass of experimental fracture	1.08	0.96	1.52	1.42	0.91	0.75	1.01	0.99	1.16	1.19	1.03*	1.09

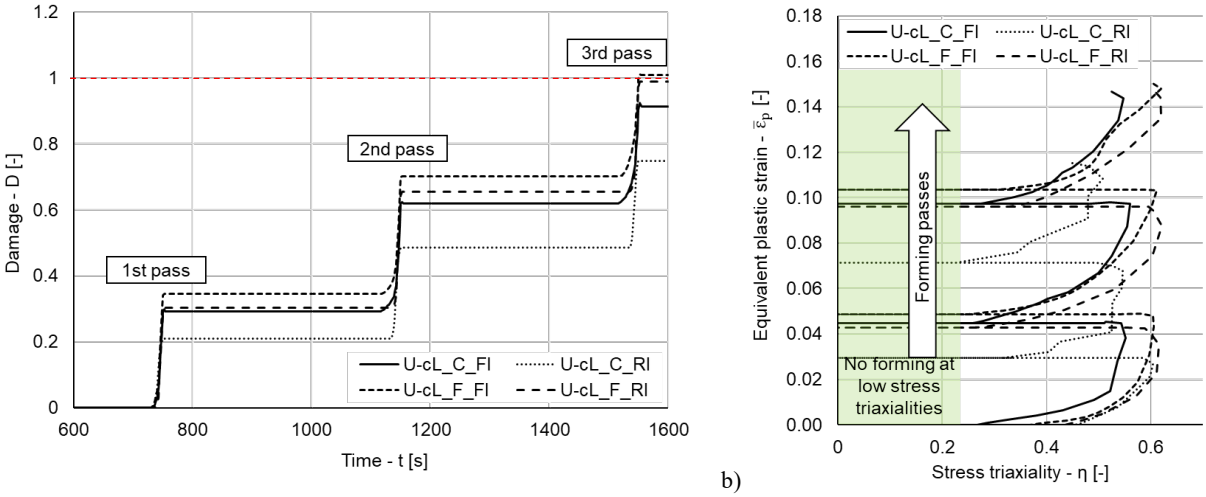

Fig. 7. Numerical prediction of damage (a) and loading paths (b) in the $(\boldsymbol{\eta}, \bar{\boldsymbol{\varepsilon}})$-space during roll forming of the U-Profile (constant length), for different mesh sizes and element types.

In Fig. 8, the different profile types are compared to each other in terms of damage prediction with the best-suited mesh and element type: fully integrated elements with a fine mesh. Damage prediction for the U-Profiles is accurate, while material failure for the V-Profile is predicted too early. Damage is 1.03 in pass 5 already, although there is no material failure experimentally until the 6th pass. This corresponds to an error in the damage prediction of at least 3 %.

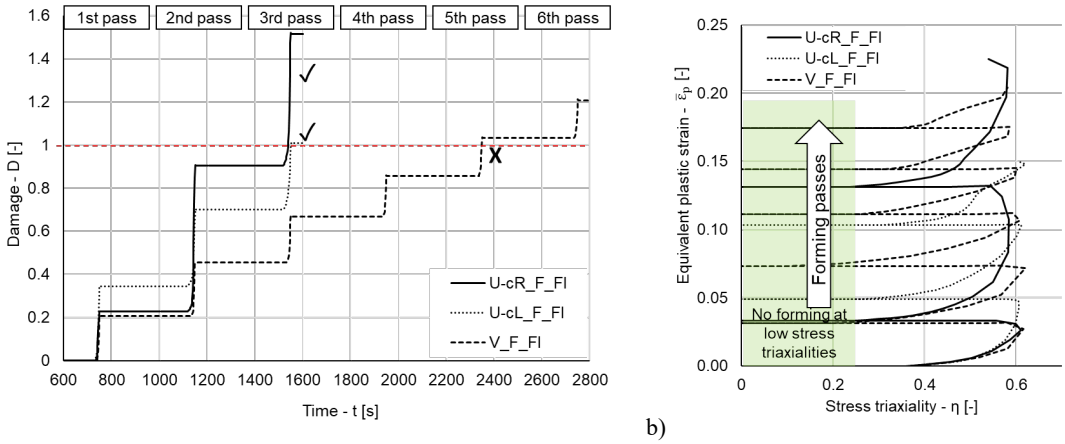

Fig. 8. Numerical prediction of damage (a) and loading paths (b) in the $(\boldsymbol{\eta}, \bar{\boldsymbol{\varepsilon}})$-space during roll forming for all profiles.

In the following section, the MMC criteria, calibrated with a varying number of material tests (Fig. 2b), are compared in terms of failure prediction. Table 3 and Fig. 9 show the results in relation to the number of material tests for calibration of the MMC criterion. Excluding material tests to calibrate the MMC criterion leads to a less accurate prediction of damage. In this case, the damage is underestimated. The reason is the insufficiently represented loading condition in the calibrated MMC criterion, which is replaced by model-based assumptions. The exclusion of a single sample (III: circular hole) leads to a small but decisive deviation in the damage prediction for the U-profile (constant length). The additional exclusion of the shear specimen (I), however, leads to a high deviation of the damage prediction of up to 16 %. This highlights the fact that not only the plane strain condition should be captured to calibrate the damage criterion, as further loading conditions, even $\eta < 0.33$, occur during roll forming.

*Table 3. Comparison of ductile fracture (experimental) and predicted damage (numerical) for different calibrations. Damage underestimated numerically: marked in red. *Fracture estimated in pass 5 already.*

Profile flower	**U-Profile (constant radius)**			**U-Profile (constant length)**			**V-Profile**		
Calibrated with X material tests	4	3	2	4	3	2	4	3	2
Damage at pass of experimental fracture	1.52	1.49	1.31	1.01	0.99	0.96	1.03*	1.01*	0.95

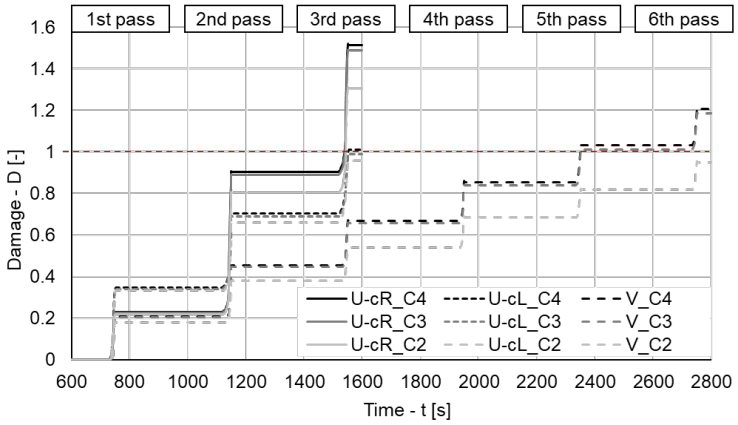

Fig. 9. Numerical prediction of damage for different calibrations of the MMC criterion.

Summary

The investigations have shown that roll forming of the high-strength aluminum alloy AA7075 in the peak-aged T6-condition is challenging, as material failure occurs in an early stage of the process. The application of the MMC criterion in combination with the used incremental damage evolution rule is suitable for predicting material failure during roll forming of the AA7075 alloy. This is even possible for a simple setup of the FE-model, with a von Mises yield criterion, an isotropic hardening rule and neglecting the friction. The roll forming process covers a wide range of loading conditions in terms of stress triaxiality η and Lode angle parameter $\bar{\theta}$, independent of the profile flower. The loading paths are not linear, as they include loading conditions from shear/uniaxial tension up to plane strain tension and biaxial tension, but the used incremental damage evolution rule was shown to be suitable for damage and failure prediction.

The calibration of the MMC criterion is based on material tests with optical strain measurement for determining fracture strain $\bar{\varepsilon}_f$ and FE-simulations for determining the stress triaxiality and the Lode angle parameter. The FE solver Marc Mentat proved to be suitable for performing the material tests and the roll forming simulation. For calibration of the MMC criterion it is recommended to use at least a tensile specimen, a notched specimen and a shear specimen. Otherwise, the loading conditions occurring during roll forming are only insufficiently represented in the MMC criterion. Adding a specimen with a circular hole leads to further improvement of damage prediction. Another result of the study is the recommendation of the element type and meshing that is best suited for predicting the damage. A prediction of the global material behavior, e.g. the forming force or springback is given with a coarse mesh [1]. However, for accurate prediction of damage, the prediction of local stresses and strains must also be accurate, but too fine meshing results in excessive computation time. Therefore, a meshing with four elements in thickness direction with fully integrated elements is recommended.

The inaccurate damage prediction for the V-profile may be due to the high non-linearity of the loading path compared to the other profile flowers. Given that the tests were carried out with one

material, further tests should be carried out with different materials to confirm the suitability of the MMC criterion in combination with the incremental damage evolution rule used.

Acknowledgement
The authors gratefully acknowledge financial support from the Hessen State Ministry for Higher Education, Research and the Arts- Initiative for the Development of Scientific and Economic Excellence (LOEWE) for the Project ALLEGRO (Subproject A1). In addition, the authors would like to thank the DAAD for funding the international exchange programme "Laser heat assisted roll forming of new high strength aluminium alloys" and the Institute for Frontier Materials at Deakin University for the support in conducting the roll forming tests (V-profile) within this project. Further thanks go to my colleague Dirk Molitor for programming the Matlab code.

References
[1] T. Suckow, P. Groche, Evaluation of Cold Roll Forming Strategies for the Production of a High-Strength Aluminum Hat Profile, Key Eng. Mater. 926 (2022) 690-699. https://doi.org/10.4028/p-y5090o
[2] S. Lee, J. Lee, J. Song, J. Park, S. Choi, W. Noh, G. Kim, Fracture simulation of cold roll forming process for aluminum 7075-T6 automotive bumper beam using GISSMO damage model, Procedia Manuf. 15 (2018) 751-758. https://doi.org/10.1016/j.promfg.2018.07.314
[3] T. Suckow, J. Schroeder, P. Groche, Roll forming of a high strength AA7075 aluminum tube, Product. Eng. 15 (2021) 573-586. https://doi.org/10.1007/s11740-021-01046-2
[4] K. Sweeney, U. Grunewald, The application of roll forming for automotive structural parts, J. Mater. Process. Technol. 132 (2003) 9-15. https://doi.org/10.1016/S0924-0136(02)00193-0
[5] O. Röcker, Untersuchungen zur Anwendung hoch- und höchstfester Stähle für walzprofilierte Fahrzeugstrukturkomponenten, PhD Thesis, Technische Universität Berlin, 2008.
[6] K. Mäntyjärvi, M. Merklein, J. Karjaleinen, UHS Steel Formability in Flexible Roll Forming, Key Eng. Mater. 410 (2009) 661-668. http://doi.org/10.4028/www.scientific.net/KEM.410-411.661
[7] O.M. Badr, B. Rolfe, P.D. Hodgson, M. Weiss, Forming of high strength titanium sheet at room temperature, Mater. Des. 66 (2015) 618-626. http://doi.org/10.1016/j.matdes.2014.03.008
[8] A.D. Deole, M.R. Barnett, M. Weiss, The numerical prediction of ductile fracture of martensitic steel in roll forming, Int. J. Solid. Struct. 144-145 (2018) 20-31. https://doi.org/10.1016/j.ijsolstr.2018.04.011
[9] H. Talebi-Ghadikolaee, H.M. Naeini, M.J. Mirnia, M.A. Mirnia, M.A. Mirzai, S. Alexandrov, M.S. Zeinali, Modeling of ductile damage evolution in roll forming of U-channel sections, J. Mater. Process. Technol. 283 (2020) 116690. http://doi.org/10.1016/j.jmatprotec.2020.116690
[10] T.S. Cao, Models for ductile damage and fracture prediction in cold bulk metal forming processes: a review, Int. J. Mater. Form. 10 (2017) 139-171. https://doi.org/10.1007/s12289-015-1262-7
[11] A.E. Tekkaya, O.-O. Bouchard, S. Bruschi, C.C. Tasan, Damage in metal forming, CIRP Annals. 69 (2020) 600-623. https://doi.org/10.1016/j.cirp.2020.05.005
[12] Y. Lou, S. Lim, K. Pack, New ductile fracture criterion for prediction of fracture forming limit diagrams of sheet metals, Int. J. Solid. Struct. 49 (2012) 3605-3615. https://doi.org/10.1016/j.ijsolstr.2012.02.016
[13] Y. Bai, T. Wierzbicki, A new model of metal plasticity and fracture with pressure and Lode dependence, Int. J. Plast. 24 (2008) 1071-1096. https://doi.org/10.1016/j.ijplas.2007.09.004
[14] Y. Bai, T. Wierzbicki, Application of extended Mohr-Coulomb criterion to ductile fracture, Int. J. Fract. 161 (2010) 1-20. https://doi.org/10.1007/s10704-009-9422-8

[15] H. Wang, Y. Yan, F. Jia, F. Han, Investigations of fracture on DP980 steel sheet in roll forming process, J. Manuf. Process. 22 (2016) 177-184. https://doi.org/10.1016/j.jmapro.2016.03.008
[16] Y. Lou, H. Huh, Prediction of ductile fracture for advanced high strength steel with a new criterion: Experiments and simulation, J. Mater. Process. Technol. 213 (2013) 1284-1302. https://doi.org/10.1016/j.jmatprotec.2013.03.001

Materials Research Proceedings 28 (2023) 799-806 https://doi.org/10.21741/9781644902479-87

Multi-scale modeling of the effect of crystallographic texture

REVIL-BAUDARD Benoit[1,a *] and CAZACU Oana[1,b]

[1]Department of Mechanical & Aerospace Engineering, University of Florida, REEF, Shalimar, USA

[a]revil@ufl.edu; [b]cazacu@reef.ufl.edu

Keywords: Crystallographic Texture, Polycrystalline Model, Macroscopic Plasticity, Metal Forming

Abstract. Among processes involving plastic deformation, sheet metal forming requires a most accurate description of plastic anisotropy. One of the main sources of mechanical anisotropy is crystallographic texture, which induces directionality in the macroscopic plastic properties of the polycrystalline metallic alloy sheets (e.g. anisotropy in yield stresses, Lankford coefficients). Recently, we develop a single-crystal yield criterion that satisfies the intrinsic symmetries of the constituent crystals and the condition of insensitivity to hydrostatic pressure [1]. Moreover, this single-crystal criterion is defined for any 3-D stress state. It was shown that the use of this single-crystal criterion for the description of the plastic behavior of the constituent crystals in conjunction with appropriate homogenization procedures leads to an improved prediction of the plastic anisotropy in macroscopic properties under uniaxial loading for polycrystalline aluminum alloys. In this paper, using this polycrystalline model, we simulate the deformation response of sheets of various crystallographic textures. Examples demonstrate the predictive capabilities of the model to describe the influence of the crystallographic texture on the macroscopic behavior and on the final shape of parts obtained using deep-drawing.

Introduction

Elastic/plastic constitutive models based on macroscopic orthotropic yield criteria are usually used to describe the mechanical behavior of metallic materials and leads to accurate predictions when applied to sheet forming operations (e.g. see [2]). Another approach is to use multi-scale models which explicitly account for the plastic response of the constituent at the grain scale as well as a statistical description of the texture of the material. Usually the grain-level behavior is modeled using a viscoplastic approach based on a power-type law or a rate-independent model based on the Schmid law or a regularized form of Schmid law (e.g. see [3–6]).

Recently, Cazacu, Revil, and Chandola [1] developed an analytical yield criterion for single-crystals. For any 3-D stress state, this yield function is continuous and differentiable and satisfies the symmetries requirements associated with the cubic lattice. Consequently, this yield criterion accounts for the specificities of the plastic flow of the crystal. For general loadings, four anisotropy coefficients are involved in this yield criterion. It was shown that the use of this single-crystal criterion for the description of the plastic behavior of the constituent crystals in conjunction with appropriate homogenization procedures leads to an improved prediction of the plastic anisotropy in macroscopic properties under uniaxial loading for polycrystalline aluminum alloys (see [7,8]).

While one ingredient of a multi-scale model is the constitutive model at the crystal scale level, another ingredient is the texture of the material. For aluminum alloys, the texture plays an important role and induce specific effects on forming properties, resulting in the formation of specific earing profile during cup deep drawing [9]. Depending on the rolling reduction and rolling temperature, the textures of rolled aluminum vary between the typical cube recrystallization texture and the typical rolled Aluminum texture. For a same aluminum alloy, changing the texture

Content from this work may be used under the terms of the Creative Commons Attribution 3.0 license. Any further distribution of this work must maintain attribution to the author(s) and the title of the work, journal citation and DOI. Published under license by Materials Research Forum LLC.

induce a change in the earing profile [10]. In this paper, using our polycrystalline model, we simulate the deformation response of sheets of various crystallographic textures.

Polycrystalline model based on Cazacu et al. [1] single-crystal law

In our model, the polycrystalline material is represented by a finite set of grains characterized by orientation and volume fraction to reproduce the material texture. Elastic deformations are modeled using Hooke's law for the type of symmetry shown by cubic crystals. The crystal plastic behavior is modeled using the Cazacu et al. single-crystal criterion [1], normality rule, and isotropic hardening described by a Swift-type law. The effective stress of the single-crystal is expressed in terms of cubic stress-invariants and relative to the Cartesian coordinate system $Ox_1x_2x_3$ associated with the crystal axes is given by:

$$\bar{\sigma}_{grain}=\frac{3}{\left(27-4cn_1^2\right)^{1/6}}\left\{\begin{array}{l}\left[\frac{1}{2}m_1\left(\sigma_{11}'^2+\sigma_{22}'^2+\sigma_{33}'^2\right)+m_2\left(\sigma_{12}'^2+\sigma_{13}'^2+\sigma_{23}'^2\right)\right]^3\\ -c\left[n_1\sigma_{11}'\sigma_{22}'\sigma_{33}'-n_3\left(\sigma_{33}'\sigma_{12}'^2+\sigma_{11}'\sigma_{23}'^2+\sigma_{22}'\sigma_{13}'^2\right)+2n_4\sigma_{12}'\sigma_{13}'\sigma_{23}'\right]^2\end{array}\right\}^{1/6} \quad (1)$$

where $\boldsymbol{\sigma}'$ denotes the Cauchy stress deviator, m_1, m_2, n_1, n_3, n_4 are anisotropy coefficients and c is a parameter that describes the relative importance of the second-order and third-order cubic stress-invariants on yielding. The plastic strain-rate of each crystal $\mathbf{d}^{\mathrm{p}}_{grain}$ is uniquely defined for any stress state and can be easily calculated as:

$$\mathbf{d}^{\mathrm{P}}=\dot{\lambda}\frac{\partial\bar{\sigma}_{grain}}{\partial\boldsymbol{\sigma}} \quad (2)$$

where $\dot{\lambda}$ is the plastic multiplier, and $\bar{\sigma}$ is given by Eq.1.

The multi-scale model using the single-crystal law (1) was implemented in a finite-element (FE) framework. In the FE calculations, the polycrystal behavior is obtained by considering 250 grains per element. It is considered that the total strain-rate of each grain belonging to a given element is equal to the overall strain-rate $\mathbf{D}$. At the time increment *(n)*, the stress in each grain is computed by solving the governing equations, namely:

$$\begin{aligned}&\mathbf{D}^{(\mathrm{n})}_{grain}=\left(\mathbf{R}^{(\mathrm{n})}\right)^T\mathbf{D}^{(\mathrm{n})}\mathbf{R}^{(\mathrm{n})}\\&\mathbf{D}^{(\mathrm{n})}_{grain}=\mathbf{D}^{\mathrm{e(n)}}_{grain}+\mathbf{D}^{\mathrm{p(n)}}_{grain}\\&\boldsymbol{\sigma}^{(n)}_{grain}=\boldsymbol{\sigma}^{(n-1)}_{grain}+\left(\mathrm{C}^{el}:\mathbf{D}^{\mathrm{e(n)}}_{grain}\right)\mathrm{dt}\\&\bar{\sigma}^{(n)}_{grain}-Y\left(\bar{\varepsilon}^{p\,(\mathrm{n})}_{grain}\right)\le 0\\&\mathbf{D}^{\mathrm{p(n)}}_{grain}=\dot{\lambda}_{grain}\frac{\partial\bar{\sigma}^{(n)}_{grain}}{\partial\sigma}\end{aligned} \quad (3)$$

where $\mathbf{D}^{(\mathrm{n})}_{grain}$, $\mathbf{D}^{\mathrm{p(n)}}_{grain}$ and $\mathbf{D}^{\mathrm{e(n)}}_{grain}$ are respectively the crystal's total strain-rate, the plastic and elastic strain-rate with C^{el} being the fourth-order elasticity tensor , $\boldsymbol{\sigma}^{(n-1)}_{grain}$ and $\boldsymbol{\sigma}^{(n)}_{grain}$ are the stress tensors at the beginning and end of the increment, respectively, while $\bar{\varepsilon}^{p\,(\mathrm{n})}_{grain}$ is the equivalent plastic strain in the given grain, $Y\left(\bar{\varepsilon}^{p\,(\mathrm{n})}_{grain}\right)$ is the hardening law, and $\dot{\lambda}_{grain}$ the plastic multiplier. The stress of the polycrystal at the end of the increment is given by:

$$\boldsymbol{\sigma}^{(n)}=\left(\sum_{\mathrm{i}}w_{\mathrm{i}}\mathbf{R}^{(\mathrm{n})}_{\mathrm{i}}\left(\boldsymbol{\sigma}^{(n)}_{grain}\right)_{\mathrm{i}}\left(\mathbf{R}^{(\mathrm{n})}_{\mathrm{i}}\right)^T\right)/\left(\sum_{\mathrm{i}}w_{\mathrm{i}}\right) \quad (4)$$

where $\left(\boldsymbol{\sigma}_{grain}^{(n)}\right)_i$ is the stress tensor of grain *i*, and $\mathbf{R}_i^{(n)}$ is the transformation matrix for passage from the crystal axes of grain *i* to the loading frame axes, while w_i is the weight of the grain *i*. To describe the macroscopic response of FCC polycrystals, the model given by Eq. 1-4 was implemented in the commercial FE solver Abaqus Standard (implicit solver, see Abaqus (2014)). A polycrystalline aggregate composed of N crystals was associated with each FE integration point. The set of governing equations are solved for each of the constituent crystals using a fully-implicit backward Euler method.

Influence of the Initial Texture of the Material on The Earing Profile for Aluminum Alloy

Hirsch [10] has shown that for an Al-Mg-Mn alloys, it is possible by changing the rolling reduction and rolling temperature to change the texture of the material from a typical cube recrystallization texture to a ß-fiber rolling texture. This change in texture components leads to a change in the earing profile during cup deep-drawing. For a typical recrystallized aluminum alloy, a four ear profile with a minimum height at 45° to the rolling direction (RD) is observed, while for a ß-fiber rolling texture, a four ear profile with maximum height at 45° to RD is obtained (see [9]).

The polycrystalline model described in the previous section was used to assess it capability to accurately describe the influence of the initial texture of the material on the earing profile. For this purpose, the coefficients involved in the yield criterion [1] are kept fixed (i.e. $m_1 = 0.36$, $m_2 = 0.18$, $n_1 = 0.21$, $n_1 = 0.11$ $n_4 = 0.08$ and $c = 1.227$) and only the initial texture of the material is changed to reflect different rolling conditions. Two generic textures were generated using the software MTex [11] and the experimental observations reported in [10]. The main components and their weights are summarized in Table 1.

Table 1. Texture components and their weights.

Cube recrystallized Texture					Rolling Texture				
Texture component	Euler Angles			weight	Texture component	Euler Angles			weight
	ϕ_1	ψ	ϕ_2			ϕ_1	ψ	ϕ_2	
Cube	0	0	0	55%	C	90	35	45	20%
R	63	31	60	25%	S	63	31	60	20%
Goss	70	45	0	10%	B	35	45	0	60%
P	45	15	10	5%					
Q	0	45	0	5%					

For the cube recrystallized texture material, the pole figures as well as the anisotropy in uniaxial yield stresses and r-values obtained with the polycrystalline model with the given set of parameters are plotted in Fig. 1. It is to be noted that the polycrsytalline model predicts a minimum r-value of 0.6 along the direction 45° from RD and two maxima which are located along RD and TD. Concerning the yield stresses, the maximum is predicted at 45° from RD at minima are along RD and TD.

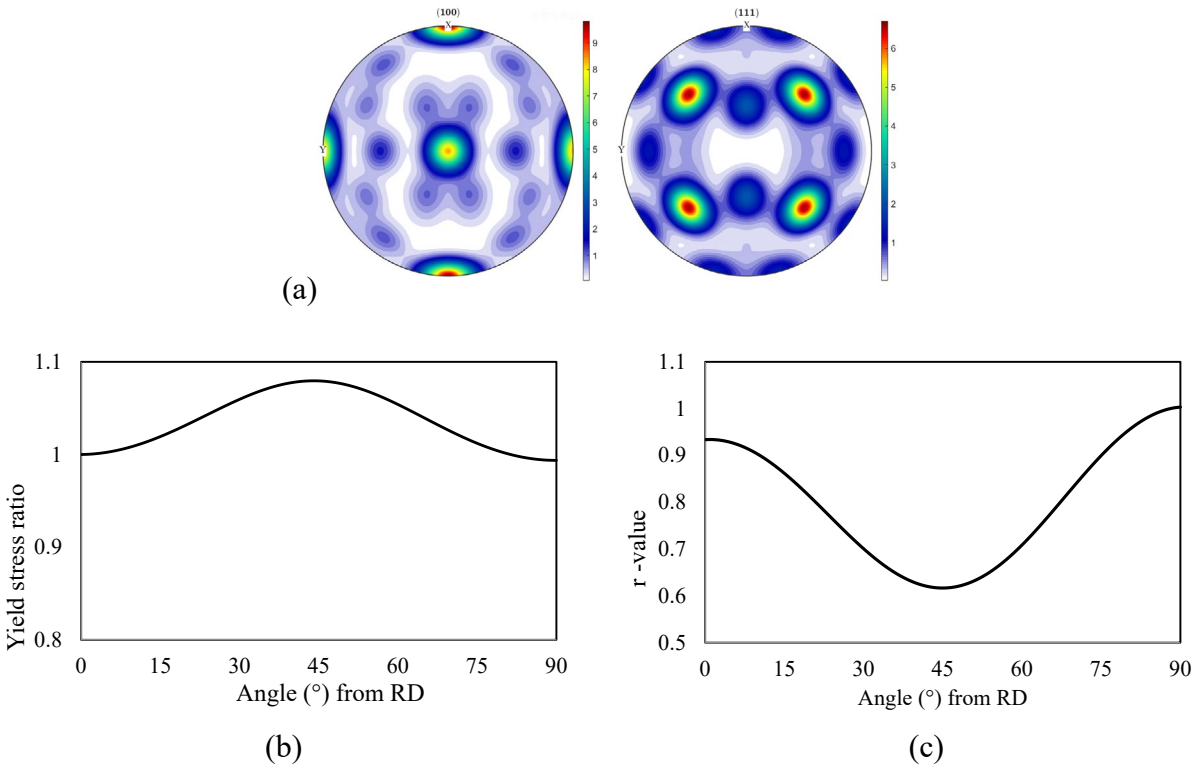

Fig. 1. Cube recrystallized material: (a) (100) and (111) pole figure; predictions of the anisotropy using the polycrystalline model based on the single-crystal law [1]: b) Uniaxial tensile flow stresses; (c) Lankford coefficients (r-values).

For the rolling texture material, the pole figures as well as the anisotropy in uniaxial yield stresses and r-values obtained with the polycrystalline model are shown in Fig. 2. Note that for a rolling texture, the polycrsytalline model predicts a maximum r-value along the direction ~ 45° from RD (r = 1.51), while the two minima are located along RD and TD.

Comparisons between the anisotropy predictions obtained with the polycrystalline model based on the single crystal yield criterion [1] with the same single crystal anisotropy coefficients show the influence of the initial texture of the material on its mechanical response. While for typical cube texture, it is predicted that the minimum r-value is obtained for a tensile test at an angle of 45 ° from RD, for a typical rolling texture, a maximum r-value is obtained for the same orientation. It is also worth noting that the amplitude of the r-value variation predicted also depends on the initial texture.

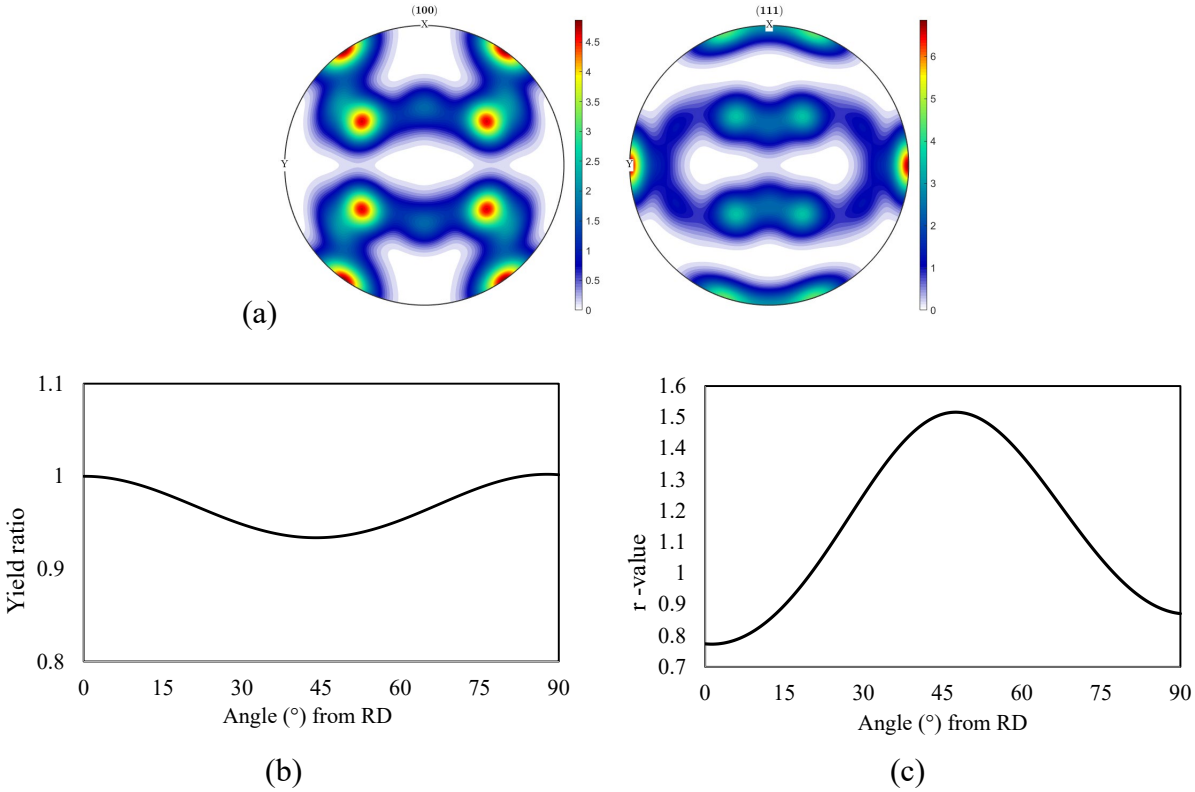

Fig. 2. Rolling texture material : (a) (100) and (111) pole figure; predictions of the anisotropy using the polycrystalline model based on the single-crystal law [1]: (b) Uniaxial tensile flow stresses; (c) Lankford coefficients (r-values).

The polycrystalline model based on the Cazacu et al. [1] single crystal criterion (see Eq.(1)) was applied to study the influence of the initial texture of the material on the forming of a cylindrical cup. A blank of thickness 1 mm and radius of 50 mm was drawn by a punch of radius 30 mm into a die of opening radius of 31.2 mm. The blank-holder force was of 40 kN. In all the FE simulations presented hereafter, a polycrystalline aggregate composed of 250 orientations representative of the overall texture of the material is associated with each FE integration point. In the FE simulations of the circular cup, a total of 10900 reduced integration elements (Abaqus C3D8R) was used to mesh a quarter of the blank, resulting in the consideration of 2 725 000 grains in the FE simulation. In terms of computational time, one simulation of the cup drawing process performed using 6 cores takes about 3h40 on a desktop computer (Intel Core i7-4770 / 16GB RAM).

For the cube recrystallized texture material, the predicted isocontours of the equivalent plastic strain of the fully drawn cup using the polycrystalline model is shown in Fig.3 along with the predicted earing profile. For this initial texture, it is predicted a 4 ears profile with the maximum height being obtained for RD and the minimum height being obtained at 45° from RD. For the rolling texture material, using the same anisotropy coefficients (i.e. $m_1 = 0.36$, $m_2 = 0.18$, $n_1 = 0.21$, $n_1 = 0.11$ $n_4 = 0.08$ and $c = 1.227$), the polycrystalline model based on the single crystal criterion [1] also predicts a four ears profile, but with the maximum height obtained for the 45° from RD direction and the minimum height obtained at RD and TD.

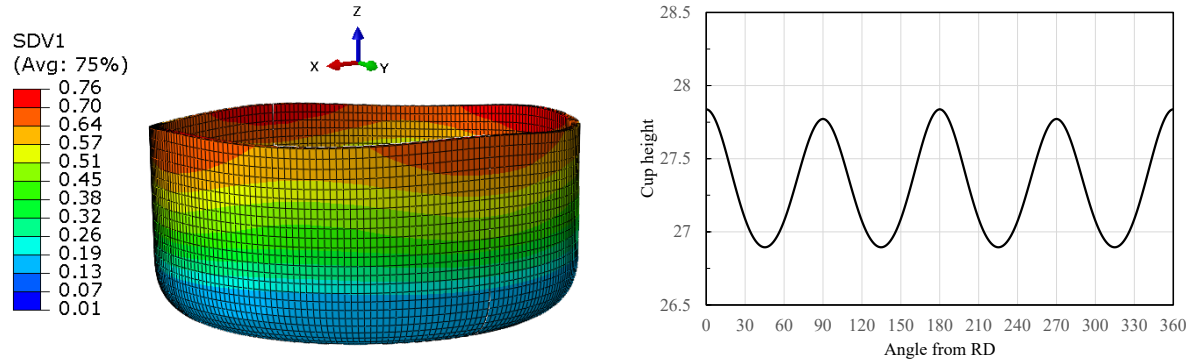

(a) (b)

Fig. 3. FE results obtained with the polycrystalline model based on the Cazacu et al. [1] single crystal criterion (with $m_1 = 0.36$, $m_2 = 0.18$, $n_1 = 0.21$, $n_1 = 0.11$ $n_4 = 0.08$ and $c = 1.227$) for an aluminium alloy with a cube recrystallized texture : (a) Isocontours of the equivalent plastic strain; (b) earing profile.

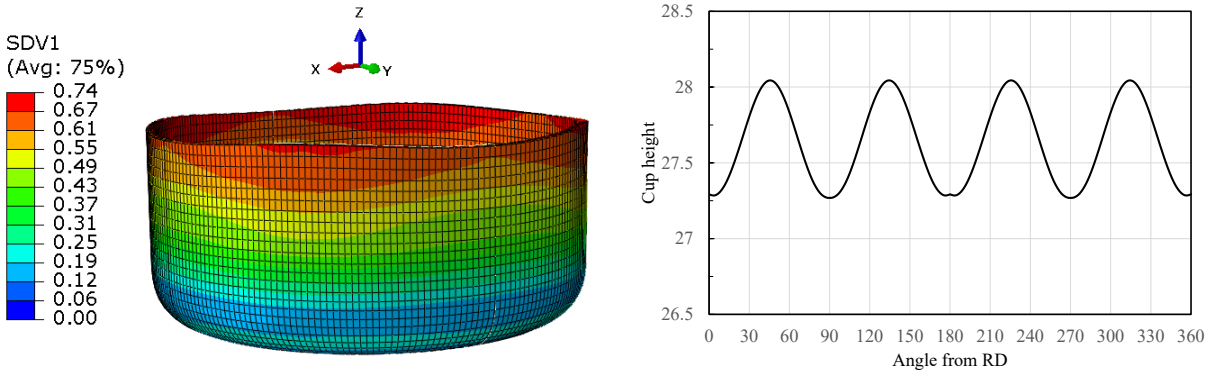

(a) (b)

Fig. 4. FE results obtained with the polycrystalline model based on the Cazacu et al. [1] single crystal criterion (with $m_1 = 0.36$, $m_2 = 0.18$, $n_1 = 0.21$, $n_1 = 0.11$ $n_4 = 0.08$ and $c = 1.227$) for an aluminium alloy with a rolling texture: (a) Isocontours of the equivalent plastic strain; (b) earing profile.

To further compare the predictions of the polycrystalline model for the two different materials, in Fig 5 are superposed the predictions of the earing profile and the punch load. It is worth recalling that in the simulations, only the initial texture was different, the material parameters and deep drawing process parameters (friction, type of elements, blankholder forces) being the same. It is to be noted that the polycrystalline model is able to capture the influence of the initial texture on the mechanical response of the material and furthermore on the earing profile obtained during cup deep-drawing. Furthermore, the trends seen experimentally in a Al-Mg-Mn alloy by [9] are also accurately predicted by the polycrystalline model, that is for a typical recrystallized aluminum alloy, a four ear profile with a minimum height at 45° to RD is predicted, while for a rolling texture, a four ear profile with the maximum height at 45° to RD is predicted, which is similar to experimental observations. Furthermore, the polycrystalline model predicts an slightly higher punch force for the material with a rolling texture than for the material with a cube recrystallized texture.

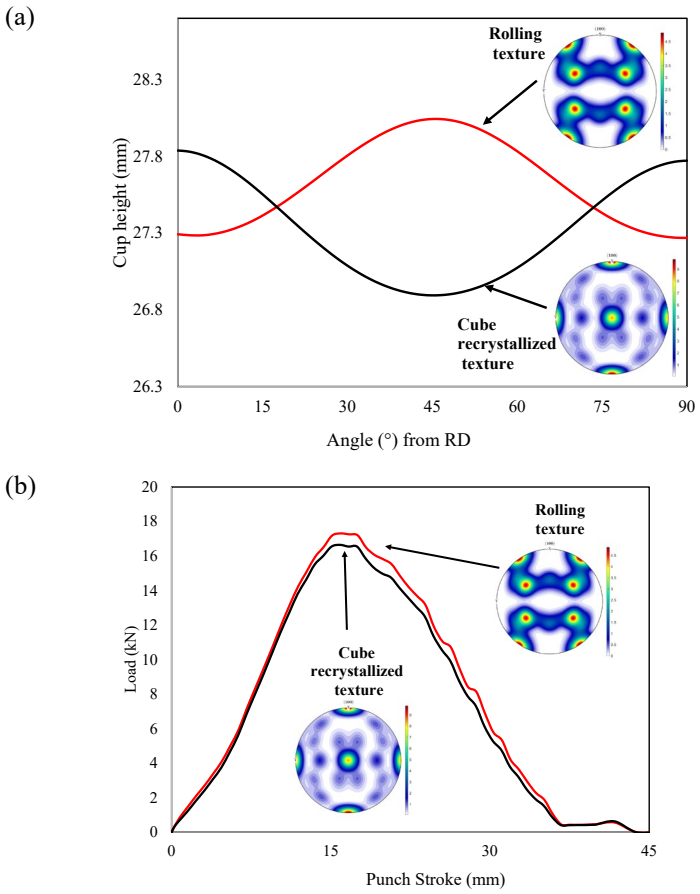

Fig. 5. Comparison of the predictions obtained with the polycrystalline model based on the Cazacu et al. [1] single crystal criterion (with $m_1 = 0.36$, $m_2 = 0.18$, $n_1 = 0.21$, $n_1 = 0.11$ $n_4 = 0.08$ and $c = 1.227$) for aluminium alloys with a cube recrystallized texture and a rolling texture, respectively: (a) earing profile; (b) forming force vs. punch stroke.

Summary

In this paper, we further illustrated the capabilities of the polycrystalline model [7] to predict the mechanical response of aluminum alloys in forming operations. Key in the formulation of this polycrystalline model is the use for the description of the plastic behavior at the crystal scale, the recent single-crystal yield criterion [1]. This cubic single-crystal yield criterion is defined for any stress state and involves the correct number of anisotropy coefficients required to satisfy the intrinsic symmetries of the cubic lattice and the condition of yielding insensitivity to hydrostatic pressure.

Using this polycrystalline model, simulation of the cup drawing process have been simulated for two aluminum alloy with different initial textures in order to investigate the influence of the initial texture on the shape of the formed part. The first material considered is characterized by a cube recrystallized texture. For this material, the polycrystalline model predicts a minimum r-value at 45° orientation and the maximum for TD. This in turn results in a predicted four ears profile with a minimum height at 45° to RD. Using the same set of material parameters, but changing the initial texture to a typical rolling texture, the polycrystalline model predict a completely different anisotropy for the material. For a rolling texture, it is predicted a minimum r-value for RD and TD while the maximum r-value is predicted for the 45° direction. Similarly, the polycrystalline model is also able to account for the influence of the initial texture on the final shape of the cup. For a rolling texture, a four ear profile with the maximum height at 45° to RD is predicted. These predictions are in agreement with experimental observations on Al alloys, i.e. the transition from

a cube recrystallized texture to a rolling texture induce a transition between an ear profile with the minimum height at 45° to an earing profile with the maximum height at 45°. Furthermore, the polycrystalline model predict a slightly higher punch force for the material with a rolling texture than a material with a cube recrystallized texture.

References

[1] O. Cazacu, B. Revil-Baudard, N. Chandola, A yield criterion for cubic single crystals, Int. J. Solid. Struct. 151 (2018) 9-19. https://doi.org/10.1016/j.ijsolstr.2017.04.006

[2] O. Cazacu, B. Revil-Baudard, Plasticity of Metallic Materials: Modeling and Applications to Forming, Elsevier, 2020.

[3] O. Cazacu, B. Revil-Baudard, N. Chandola, Plasticity-Damage Couplings: From Single Crystal to Polycrystalline Materials, Springer, 2019.

[4] N. Chandola, O. Cazacu, B. Revil-Baudard, Prediction of plastic anisotropy of textured polycrystalline sheets using a new single-crystal model, Comptes Rendus Mécanique 346 (2018) 756-769.

[5] E. Schmid, W. Boas, Plasticity of Crystals (Translation by F.A. Hughes & Co. Limited), Chapman & Hall Ltd, London, 1951.

[6] C.F. Elam, Distortion of metal crystals, Clarendon Press, 1935.

[7] B. Revil-Baudard, O. Cazacu, N. Chandola, Finite Element Analysis of AA 6016-T4 Sheet Metal Forming Operations Using a New Polycrystalline Model, Key Eng. Mater. 926 (2022) 1067–1074. http://doi.org/10.4028/p-3b1ez2

[8] A.M. Habraken, T.A. Aksen, J.L. Alves, R.L. Amaral, E. Betaieb, N. Chandola, L. Corallo, D.J. Cruz, L. Duchêne, Bernd Engel, E. Esener, M. Firat, P.Frohn-Sörensen, J. Galán-López, H. Ghiabakloo, L.A.I. Kestens, J. Lian, R. Lingam, W. Liu, J. Ma, L.F. Menezes, T. Nguyen-Minh, S.S. Miranda, D.M. Neto, A.F.G. Pereira, P.A. Prates, J. Reuter, B. Revil-Baudard, C. Rojas-Ulloa, B. Sener, F. Shen, A. Van Bael, P. Verleysen, F. Barlat, O. Cazacu, T. Kuwabara, A. Lopes, M.C. Oliveira, A.D. Santos, G. Vincze, Analysis of ESAFORM 2021 cup drawing benchmark of an Al alloy, critical factors for accuracy and efficiency of FE simulations, Int. J. Mater. Form. 15 (2022) 1–96. https://doi.org/10.1007/s12289-022-01672-w

[9] J. Hirsch, Texture and anisotropy in industrial applications of aluminium alloys, Arch. Metall. Mater. 50 (2005) 21-34.

[10] J. Hirsch, Texture evolution and earing in aluminium can sheet, Mater. Sci. Forum 495 (2005) 1565-1572. http://doi.org/10.4028/www.scientific.net/MSF.495-497.1565

[11] F. Bachmann, R. Hielscher, H. Schaeben, Texture analysis with MTEX–free and open source software toolbox, Solid state phen. 160 (2010) 63-68. https://doi.org/10.4028/www.scientific.net/SSP.160.63

[12] O. Cazacu, New yield criteria for isotropic and textured metallic materials, Int. J. Solid. Struct. 139–140 (2018) 200-210. https://doi.org/10.1016/j.ijsolstr.2018.01.036

Materials Research Proceedings 28 (2023) 807-816 https://doi.org/10.21741/9781644902479-88

Experimental identification of uncoupled ductile damage models and application in flow forming of IN718

VURAL Hande[1,a], ERDOGAN Can[1,b], KARAKAŞ Aptullah[2,c], FENERCIOGLU Tevfik Ozan[2,d] and YALÇINKAYA Tuncay[1,e *]

[1]Department of Aerospace Engineering, Middle East Technical University, 06800 Ankara, Turkey

[2]Repkon Machine and Tool Industry and Trade Inc., 34980 Şile, Istanbul, Turkey

[a]vural.hande@metu.edu.tr, [b]cane@metu.edu.tr, [c]aptullah.karakas@repkon.com.tr, [d]ozan.fenercioglu@repkon.com.tr, [e]yalcinka@metu.edu.tr

Keywords: Ductile Fracture, Fracture Locus, Flow Forming Process

Abstract. The aim of this study is to calibrate the parameters of the Johnson-Cook (JC) and modified Mohr-Coulomb (MMC) ductile failure models for Inconel 718 and predict the formability limit in the flow forming process using the aforementioned uncoupled damage models. Uniaxial tensile tests are performed on four different specimen geometries to cover a variety of stress states. A hybrid methodology combining finite element simulations and experimental findings is used to calibrate the JC and MMC damage models. The models are implemented in the finite element solver Abaqus using a user-defined subroutine. Results show that the calibrated models agree well with the experimental data in all tensile tests. In shear dominant loads, the MMC model is found to be more capable of showing accurate crack propagation. In flow forming simulations, a significant difference is observed between the JC and MMC models in the prediction of damage. Lode parameter-dependent damage models, such as the MMC, are found to be more suitable for the prediction forming limits in the flow forming process.

Introduction

Flow forming, or spinning, is an incremental metal forming process used to produce axisymmetric parts and it has been widely adopted in the automotive and defense industries (see e.g. [1]). The thickness of a tubular preform material is incrementally reduced by utilizing one or more rotating rollers. It has several benefits such as low scrap material, low cost due to simple tool processing, smooth surface quality, and high geometrical accuracy. The preform thickness can be reduced by up to 80 % throughout the process. Such high deformations under complex forces potentially lead to surface defects or complete rupture. As in many forming applications, it is crucial to identify the regions that are more susceptible to crack initiation or defects and to estimate the formability limits in flow forming.

In computational structural analysis, ductile fracture models have been widely adapted to describe the ductile failure of metallic materials. According to their relationship with constitutive equations, damage models employed in finite element (FE) simulations can be separated into coupled and uncoupled models. Coupled models in which the damage parameters and constitutive equations are coupled, and the stress is influenced by the damage evolution (e.g. [2-4]). Uncoupled models exclude the effect of damage evolution from constitutive relations. They are often referred to through a failure criterion, which consists of plastic strain, strain rate, stress state, and temperature (e. g. [5,6]). Uncoupled models are more common in engineering applications because of their simplicity in implementation and parameter calibration, despite coupled models providing more realistic failure predictions. It has been discussed that a ductile failure criterion depends only on stress triaxiality (T) could be insufficient for shear dominant ductile failures (see [7]). To

Content from this work may be used under the terms of the Creative Commons Attribution 3.0 license. Any further distribution of this work must maintain attribution to the author(s) and the title of the work, journal citation and DOI. Published under license by Materials Research Forum LLC.

overcome this problem, Lode angle parameter ($\bar{\theta}$), which is connected to the third deviatoric stress invariant, has been considered in more recent models (e.g. [8,9]).

In the literature, many attempts have been made to predict forming limits using damage models for incremental metal-forming processes (e.g. [10,11,12,13]). The MMC model is used in one of the authors' earlier studies for flow forming analyses to analyze forming limits and the influence of process parameters in failure. In [14], the MMC model for 6016-T6 aluminum alloy is adopted from the literature to examine the effect of the thickness reduction ratio and the involvement of different roller arrangements on the damage. The strain rate and temperature dependencies for the 4340-steel alloy were included in the plasticity and MMC models in [15], and the implications of process variables including feed rate, roller speed, and offset of the rollers on damage are studied.

The aim of this study is first to calibrate the damage model parameters for Inconel 718 (IN718) through a hybrid experimental-numerical approach. Tensile tests are carried out on four specimen geometries to cover various stress states. The DIC (digital image correlation) technique is used to extract accurate displacement-force values from the experiments. For this material, the plasticity model is constructed using experimental data and FE simulations. The MMC and JC damage models are adopted to model ductile damage. A good correlation between the FE results and the experimental data is achieved with the calibrated models. Then, the failure prediction capabilities of the calibrated damage models are investigated with the simulation of the flow forming process.

Methods

Materials and Tensile Tests.

Tensile tests are performed for IN718 alloy under quasi-static conditions. IN718 is nickel-based precipitation hardenable superalloy where gamma double prime (γ”) precipitations are nucleated after the aging treatment to have improved mechanical properties. IN718 has good fatigue and creep strength with high corrosion resistance, and it has been widely used in the hot sections of gas turbines engines such as turbine discs and blades. The chemical composition of the alloy is given in Table 1. For this material, 4 different specimens representing different stress-state conditions are manufactured. The geometries of the specimens are shown in Fig. 1. Specimens are named as smooth tension (ST), notch tension (NT10), plane-strain tension (PST) and in-plane shear (ISS). Specimens are prepared with a thickness of 3 mm. They are spray-painted in white and then patterned in black dots for displacement and strain measurements with the digital image correlation (DIC) method. MTS 100kN Tension-Torsion Fatigue/Static test machine and a high-speed camera are used to obtain the force and displacement data. Displacement-controlled tests are carried out with a strain rate of 1 mm/min. NCORR open-source 2D DIC software is used to process the images captured by the high-speed camera. Force data is obtained from the test machine while the displacements are extracted from the DIC analysis using a virtual extensometer at the center of the specimens spanning vertically with a gauge length of 40, 50, 8.1, and 28 mm for ST, NT10, PST and ISS specimens, respectively.

Table 1: Chemical composition of IN718 [wt.%].

Element	Ni	Nb	Mo	Ti	Al	Cr	Cu	Si	Fe	Mn	C
Content	54.35	4.96	2.77	0.95	0.56	18.59	0.04	0.32	16.68	0.28	0.5

Plasticity and Damage Models.

The constitutive behavior is governed by the classic J2 plasticity with isotropic hardening. The extended voce rule is used to define the hardening law, as

$$\sigma = \sigma_y + q_1\left(1-c_1 e^{-b_1 \bar{\varepsilon}_p}\right) + q_2\left(1-c_2 e^{-b_2 \bar{\varepsilon}_p}\right) \quad (1)$$

where σ_y is the yield stress of IN718 and $\bar{\varepsilon}_p$ is the equivalent plastic strain. q_i, c_i and b_i are material-specific constants.

Two different damage models are chosen to evaluate their applicability to flow forming simulation. The first of these models is the JC model, which is only stress triaxiality and equivalent plastic strain dependent. Due to its simplicity, it has been frequently used in many applications in the literature. In this study, the JC model is utilized independently of strain rate and temperature, as

$$\varepsilon_f(T) = \widehat{D}_1 + \widehat{D}_2 \exp(-\widehat{D}_3 T) \quad (2)$$

where, T is the stress triaxiality and ε_f is the plastic strain value at failure. $\widehat{D}_1$, $\widehat{D}_2$ and $\widehat{D}_3$ are calibration parameters for the JC model. The second model is the MMC model defined as

$$\varepsilon_f(T, \bar{\theta}) = \left\{ \begin{array}{l} \frac{A}{\widehat{C}_2}\left[\widehat{C}_3 + \frac{\sqrt{3}}{2-\sqrt{3}}\left(\widehat{C}_4 - \widehat{C}_3\right)\left(\sec\left(\frac{\bar{\theta}\pi}{6}\right) - 1\right)\right] \\ x\left[\sqrt{\frac{1+\widehat{C}_1^2}{3}} + \cos\left(\frac{\bar{\theta}\pi}{6}\right) + \widehat{C}_1\left(T + \frac{1}{3}\sin\left(\frac{\bar{\theta}\pi}{6}\right)\right)\right] \end{array} \right\}^{-\frac{1}{n}} \quad (3)$$

where, T is the stress triaxiality, $\bar{\theta}$ is the Lode angle parameter and ε_f is the plastic strain value at failure. A, n, $\widehat{C}_1$, $\widehat{C}_2$, $\widehat{C}_3$ and $\widehat{C}_4$ are calibration parameters for MMC model. Stress triaxiality and Lode angle parameter are formalized as

$$T = \frac{\sigma_m}{\sigma_{eq}} \text{ and } \bar{\theta} = 1 - \frac{6\theta}{\pi} = 1 - \cos^{-1}\left(\frac{J_3}{2\,\sigma_{eq}{}^3}\right) \quad (4)$$

where the mean stress is $\sigma_m = \frac{tr(\sigma)}{3} = \frac{\sigma_{11} + \sigma_{22} + \sigma_{33}}{3}$, σ_{eq} is the von-Mises equivalent stress and J_3 is defined as the third deviatoric stress invariants.

The damage accumulation rule is expressed with the following integral

$$D = \int_0^{\varepsilon_f} \frac{d\bar{\varepsilon}_p}{\varepsilon_f} \quad (5)$$

Initially, the material is assumed to be undamaged, D = 0, and when D reaches 1 and is interpreted as the material is completely failed.

FE Modelling.

Displacement controlled explicit FE simulations are conducted to calibrate and verify the plasticity and damage model parameters. The MMC model is implemented as a user-defined field subroutine (VUSDFLD) while the inbuilt JC damage model in Abaqus is used. The geometries and mesh of 4 different specimens are shown in Fig. 1. One-fourth of geometries are simulated for

ST, NT and PST utilizing the symmetry planes to reduce the computational cost. For the ISS, analysis is taken with the full model. 8-node linear brick elements (C3D8R) with reduced integration are used and element deletion is utilized to represent material failure. To have boundary conditions consistent with experiments, the parts held and pulled in the machine are modeled as rigid bodies while the section where DIC analysis is conducted is modeled as a deformable body.

Calibrated and validated damage models are then applied to the finite element model of the backward flow forming (FF) process using the dynamic explicit solver of Abaqus. The FE model and mesh are shown in Fig. 2. This model consists of a preform, a mandrel, and 3 rollers rotating and moving in the axial direction. The process is called the backward FF process because the material flows in the direction opposite to the axial movement of the rollers. Mandrel and rollers are modeled as rigid bodies while the preform tube is a deformable body. The rollers are placed around the mandrel with 120 degrees between them with a certain axial offset. This ensures that the thickness of the material is incrementally reduced and a thickness reduction ratio of 40% in total is applied. Both tangential and normal contact are featured in the model with a 0.05 friction coefficient for tangential contact. The preform tube is meshed using hexahedral elements with reduced integration (C3D8R) and enhanced hourglass control is used to prevent mesh distortion. There are 168000 elements in total, with 7 elements in the thickness direction.

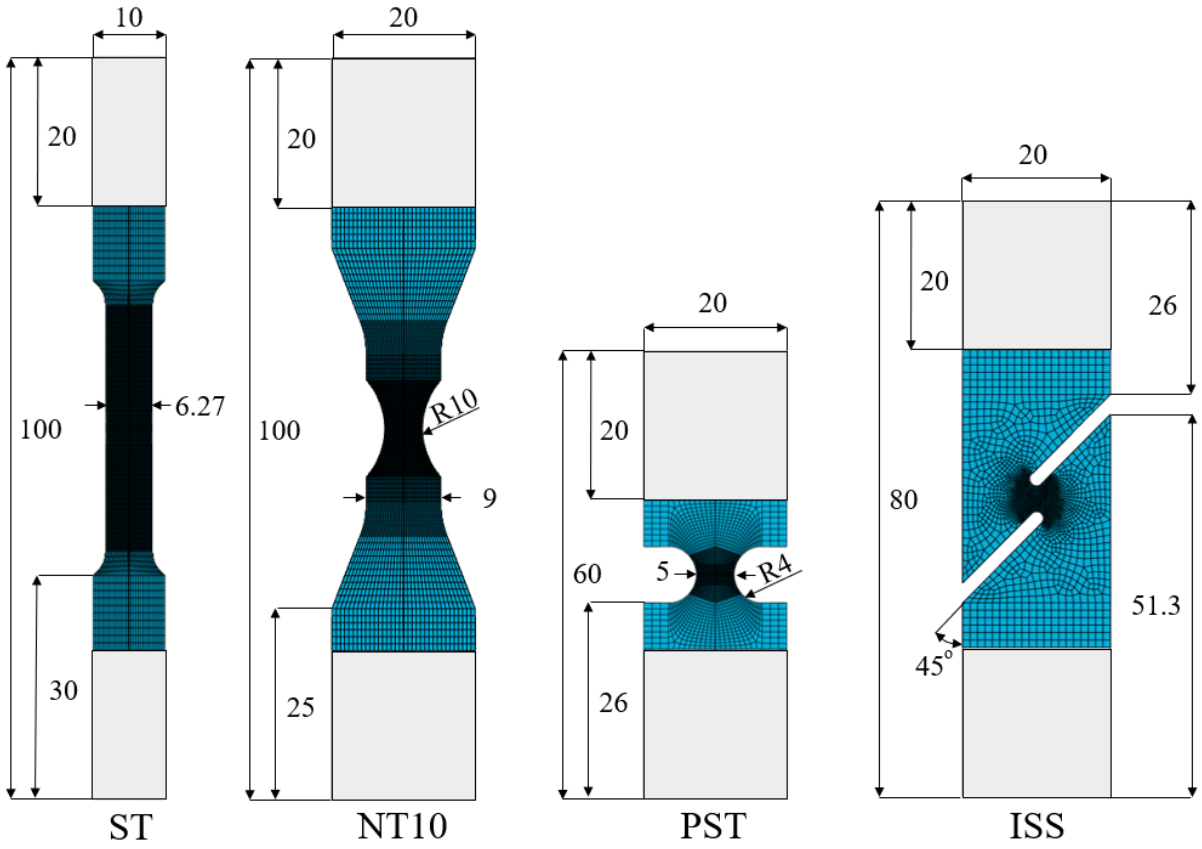

Fig. 1. Dimensions and finite element models of specimens.

Results and Discussion

Plasticity Model Calibration.

Since an uncoupled modeling approach is used in the current work, hardening parameters can be calibrated with the experimental data independently of the damage parameters. Using the force-displacement data obtained from the experiments, the true stress-strains curves are obtained using up to necking from the ST specimen. The hardening law parameters are then fitted using the MATLAB curve-fitting tool. The yield stress and material constants of the hardening laws are shown in Table 2. Density, Young's modulus and Poisson's ratio are taken as 8.22 g/cm^3, 200 GPa and 0.294, respectively.

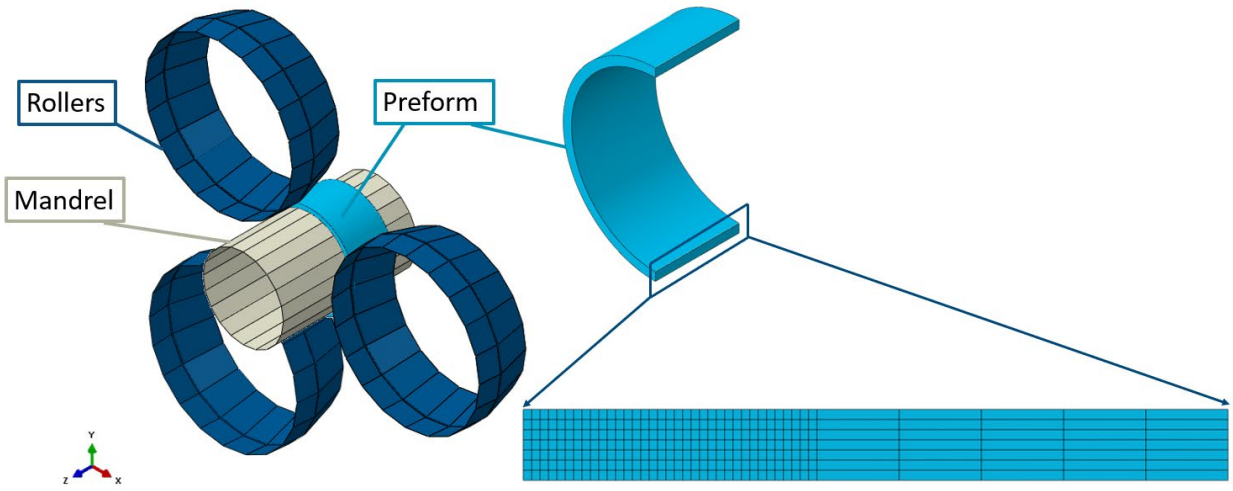

Fig. 2. Finite element model of flow forming process.

Table 2. Calibrated parameters of the hardening law.

σ_y [MPa]	q_1 [MPa]	c_1	b_1	q_2 [MPa]	c_2	b_2
789	499.6	0.1731	106.7	499.6	1.761	4.351

Damage Model calibration.

The MMC damage model parameters are calibrated using a hybrid experimental and numerical approach which has been applied and verified for a wide range of materials and experiments in the literature. In this approach, plastic strain averaged stress triaxiality and Lode angle parameter data are extracted from the FE simulations of the specimens up to the experimentally observed failure point. The place where sudden decreases in force-displacement curves is taken as the fracture initiation and the equivalent plastic strain value at this point is selected as failure strain. The failure strain, averaged T and $\bar{\theta}$ values are taken from the critical elements which have the highest equivalent plastic strain. In ST, NT10 and PST specimens, the critical elements are in the center of the specimens, while the critical points of the ISS are in the middle of the curved region in the gauge section. The failure strain, averaged T and $\bar{\theta}$ values are given in Table 3.

Materials Research Proceedings 28 (2023) 807-816 https://doi.org/10.21741/9781644902479-88

Table 3. Fracture strain, averaged T and $\bar{\theta}$ for all specimens.

Specimen	T_{ave}	$\bar{\theta}_{ave}$	ε_f
ST	0.4040	0.9614	0.6512
NT	0.4849	0.7650	0.5245
PST	0.5494	0.5882	0.4564
ISS	0.1205	0.1546	0.5069

Then, the calibration of the MMC and JC model parameters is simply done using the MATLAB curve fitting tool. Since there are 3 calibration parameters in the JC criterion, using ST, NT10, and PST specimens is sufficient for calibration. For the data given in Table 3, 5 calibration parameters are identified while $\hat{C}_4$ is taken as 1 for the MMC model. Firstly, $\hat{C}_3$ is assumed to be 1 and the other 4 parameters are fitted to the damage criterion. Then, $\hat{C}_3$ is included in the parameter fitting by keeping A as constant. The calibrated damage parameters are given in Table 4.

Table 4. Calibrated parameters of the MMC and JC damage models for IN718.

	$\hat{D}_1$	$\hat{D}_2$	$\hat{D}_3$			
JC	0.04	1.798	2.679			
	A [MPa]	n	$\hat{C}_1$	$\hat{C}_2$	$\hat{C}_3$	$\hat{C}_4$
MMC	1946	2.216	10.39	14420	4.517	1

Ductile Failure Simulations.

The results obtained from FE simulations with the calibrated damage models for 4 different specimens are shown in Fig. 3. Note that experiments are repeated 3 times for each geometry to check variation between specimens. Experimental results are shown with black dashed lines, while the orange and blue solid lines represent JC and MMC simulations, respectively. Due to the changes in manufacturing and micromechanical inhomogeneities, slight variations in failure strain are observed between tests. In the smooth tension test, the variation is found to be higher than normal. Nevertheless, the failure strain value is calibrated based on the average of multiple tests for each specimen geometry. It is clear that the models are able to capture the experimental force-displacement relation for all specimens. In ST, NT10 and PST simulations, JC and MMC models yield almost exactly the same response. However, for ISS specimen, although the failure points predictions are similar, the subsequent failure response is vastly different for the JC model.

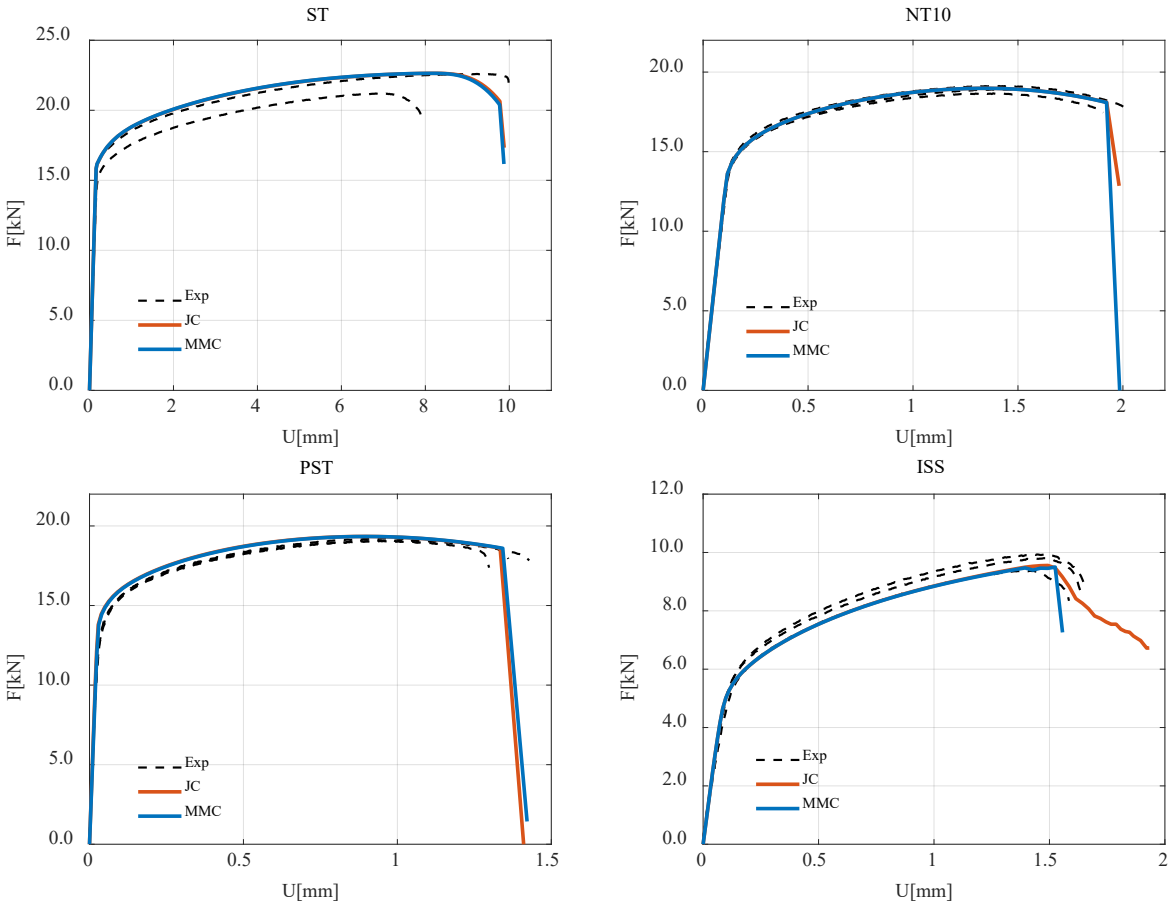

Fig. 3. Experimental comparison of JC and MMC damage models. Force vs. displacement curves for 4 tensile specimens.

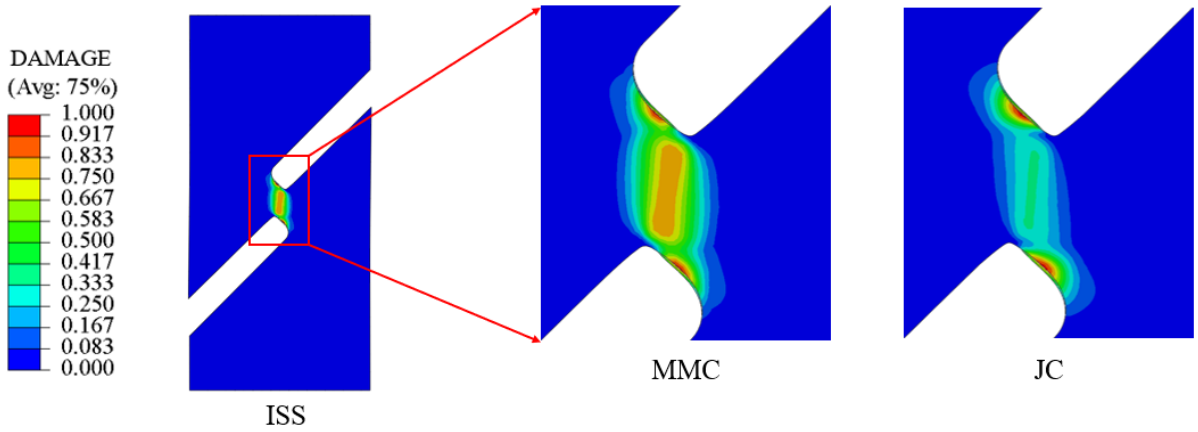

Fig. 4. Comparison JC and MMC damage distribution for ISS at the onset of failure.

In Fig. 4, the damage distributions at the onset of failure are plotted for the ISS specimen using the JC and MMC models. The JC model is known to be insufficient at predicting failure in shear dominant loads due to the lack of Lode parameter effect. One can see that in the gauge section, the JC model predicts lower damage values compared to the MMC model. This results in a gradual decrease of load for the JC model while the MMC model yields a sudden drop after the initiation of failure which is more compatible with the experimental observations.

Materials Research Proceedings 28 (2023) 807-816 https://doi.org/10.21741/9781644902479-88

Flow Forming Process Simulations.

The verified damage models are applied for the simulation of the flow forming process with two different preform geometries. Geometries differ by their thickness to inner diameter ratios. Preform 2 has double thickness to diameter ratio compared to Preform 1. Simulations are performed at the same feed rate, revolution speed, and the other geometrical parameters are kept constant. Simulation results are depicted in Fig. 5. The highest damage is predicted to be at the inner surfaces where the preform is in contact with the mandrel for both models. Due to the shear dominant nature of the process, the JC model gives significantly smaller damage accumulations compared to the MMC model. At 40% reduction, the damage exceeds 1 with the MMC model while it is much less than 1 for the JC model. With a higher thickness to diameter ratio, the damage is found to increase and spread over a larger area. It is normally expected that the crack would form on the outer surface of the flow formed specimen, which is not captured with the current models. However, referring to a previous study of the authors [15], a more realistic modeling approach with temperature dependent plasticity and damage models is important and would change the damage distribution.

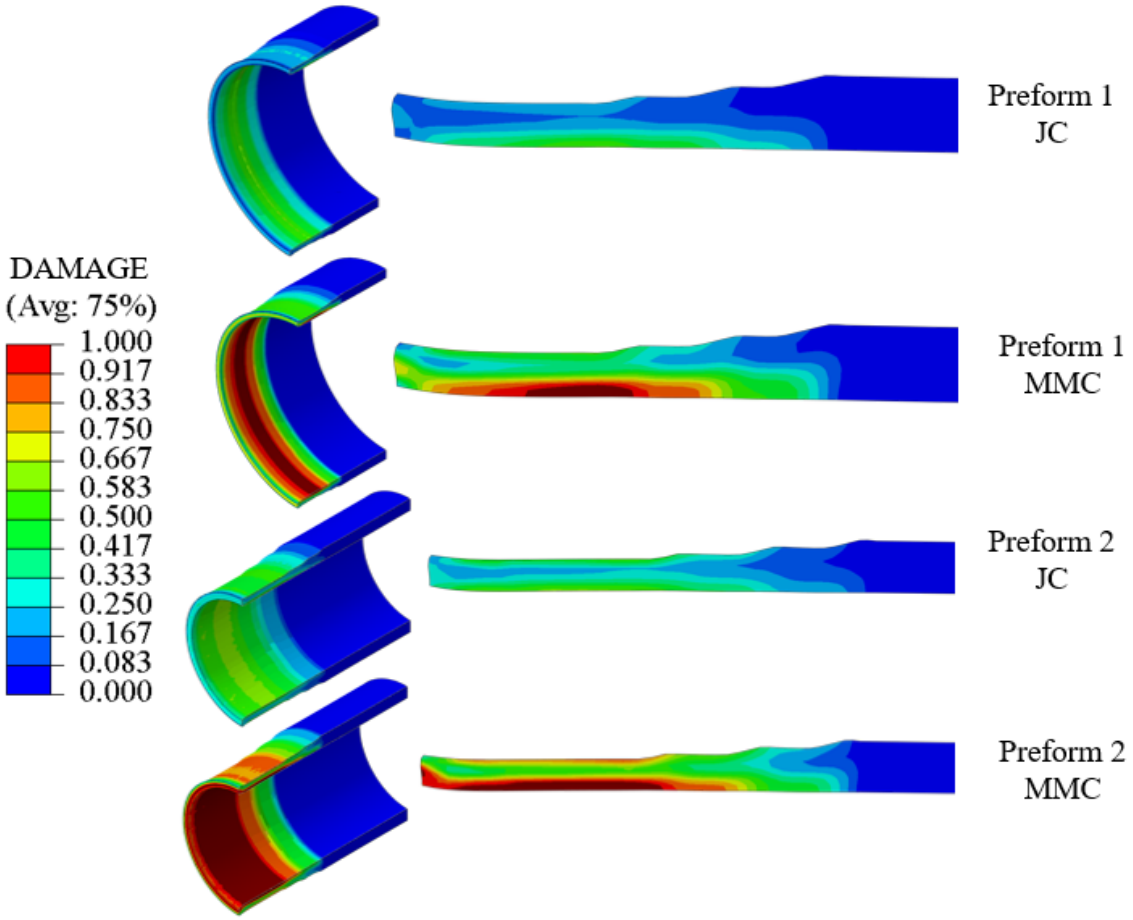

Fig. 5. Distribution of damage over the preform at 2 different geometries.

Summary
In this work, ductile failure model calibration is performed with experiments using four geometries for IN718 nickel alloy. Calibrated models are then verified through FE element analysis of the specimens and results are found to be in good agreement with experimental data. The MMC model is more capable of predicting experimental force-displacement curves in the shear dominant failure case. Furthermore, the two damage models are implemented in a flow forming simulation to discuss the differences in damage accumulation. Models show a disparity in the distribution of damage at two different preform geometries. It is concluded that the MMC failure criterion is a more appropriate choice for forming processes such as flow forming. It should be noted that the current FE model should be extended to include temperature and strain rate effects to accurately make an experimentally comparative study.

References
[1] A. Karakas, T.O. Fenercioğlu, T. Yalçinkaya, The influence of flow forming on the precipitation characteristics of Al2024 alloys, Mater. Lett. 299 (2021) 130066. https://doi.org/10.1016/j.matlet.2021.130066
[2] A.L. Gurson, Continuum theory of ductile rupture by void nucleation and growth: part I—yield criteria and flow rules for porous, J. Eng. Mater. Technol. 99 (1977) 2-15. https://doi.org/10.1115/1.3443401
[3] J. Lemaitre, Coupled elasto-plasticity and damage constitutive equations, Comput. Methods Appl. Mech. Eng. 51 (1985) 31-49. https://doi.org/10.1016/0045-7825(85)90026-X
[4] T. Yalçinkaya, C. Erdogan, I.T. Tandogan, A. Cocks, Formulation and implementation of a new porous plasticity model, Procedia Struct. Integr. 21 (2019) 46-51. https://doi.org/10.1016/j.prostr.2019.12.085
[5] G.R. Johnson, W.H. Cook, Fracture characteristics of three metals subjected to various strains, strain rates, temperatures and pressures, Eng. Fract. Mech. 21 (1985) 31-48. https://doi.org/10.1016/0013-7944(85)90052-9
[6] Y. Bai, T. Wierzbicki, A new model of metal plasticity and fracture with pressure and Lode dependence, Int. J. Plast. 24 (2008) 1071-1096. https://doi.org/10.1016/j.ijplas.2007.09.004
[7] T. Wierzbicki, Y. Bao, Y.W. Lee, Y. Bai, Calibration and evaluation of seven fracture models, Int. J. Mech. Sci. 47 (2005) 719-743. https://doi.org/10.1016/j.ijmecsci.2005.03.003
[8] Y. Bai, T. Wierzbicki, Application of extended mohr-coulomb criterion to ductile fracture. Int. J. Fract., 161 (2010) 1-20. https://doi.org/10.1007/s10704-009-9422-8
[9] D. Mohr, S.J. Marcadet, Micromechanically-motivated phenomenological Hosford-Coulomb model for predicting ductile fracture initiation at low stress triaxialities, Int. J. Solid Struct. 67-68 (2015) 40-55. https://doi.org/10.1016/j.ijsolstr.2015.02.024
[10] R. Li, Z. Zheng, M. Zhan, H. Zhang, Y. Lei, A comparative study of three forms of an uncoupled damage model as fracture judgment for thin-walled metal sheets, Thin-Walled Struct. 169 (2021) 108321. https://doi.org/10.1016/j.tws.2021.108321
[11] W. Xu, H. Wu, H. Ma, D. Shan, Damage evolution and ductile fracture prediction during tube spinning of titanium alloy, Int. J. Mech. Sci. 135 (2018) 226-239. https://doi.org/10.1016/j.ijmecsci.2017.11.024
[12] H. Wu, W. Xu, D. Shan, B.C. Jin, An extended gtn model for low stress triaxiality and application in spinning forming, J. Mater. Process. Technol. 263 (2019) 112-128. https://doi.org/10.1016/j.jmatprotec.2018.07.032
[13] A.K. Singh, A. Kumar, K.L. Narasimhan, R. Singh, Understanding the deformation and fracture mechanisms in backward flow-forming process of Ti-6Al-4V alloy via a shear modified

continuous damage model, J. Mater. Process. Technol. 292 (2021) 117060. https://doi.org/10.1016/j.jmatprotec.2021.117060
[14] H. Vural, C. Erdoğan, T.O. Fenercioğlu, T. Yalçinkaya, Ductile failure prediction during the flow forming process, Procedia Struct. Integr. 35 (2022) 25-33. https://doi.org/10.1016/j.prostr.2021.12.044
[15] C. Erdogan, H. Vural, T.O. Fenercioglu, T. Yalcinkaya, Effect of process parameters on ductile failure behavior of flow forming process, Procedia Struct. Integr. 42 (2022) 1643-1650. https://doi.org/10.1016/j.prostr.2022.12.207

Materials Research Proceedings 28 (2023) 817-824 https://doi.org/10.21741/9781644902479-89

Deformation analysis of ZnMgAl coated steel sheet using digital image correlation (DIC) system

LISIECKA-GRACA Paulina[1,a *], MUSZKA Krzysztof[1,b], KWIECIEŃ Marcin[1,c] and DZIURDZIA Jakub[2,d]

[1]AGH University of Science and Technology, Faculty of Metals Engineering and Industrial Computer Science, 30 Mickiewicza Av., 30-059, Krakow, Poland

[2]ArcelorMittal Tubular Products, 1 Ujastek St., 30-969, Kraków, Poland

[a]graca@agh.edu.pl, [b]muszka@agh.edu.pl, [c]mkwiecie@agh.edu.pl, [d]jakub.dziurdzia@arcelormittal.com

Keywords: Digital Image Correlation (DIC), ZnMgAl Coating, Tubular Products

Abstract. Protective metallic coatings may be applied to the finished tubes and pipes using the hot dip method or may be applied to cold rolled sheet that is then used in the roll forming process of tubes manufacturing. In the latter case applied coating must ensure the proper adhesion and lack of cracks during deformation. In this work, the main objective is to assess the plastic deformability of steel sheets covered with an advanced ZnMgAl coating. The assessment of the susceptibility of the ZnMgAl coatings to plastic deformation was carried out using three-point bending tests, supported by the digital image correlation technique. A standard bending test of a steel sheet with a ZnMgAl coating at different bending angles was also used. The comparison of the results of the tests carried out allowed for the formulation of conclusions for direct use in industrial practice.

Introduction

Optimization and control of the processes of industrial metal forming of steel products requires an understanding of the behavior of the charge material under deformation conditions similar to those, in which it will be formed. Pipes with open-joints are produced from steel sheet in the rolling process, so the accompanying deformations in the bending process are significant [1]. The steel sheet used in the production process should be characterized by good mechanical properties and formability. It should also be remembered that in a pipe manufactured using the open-joint method, the weakest point is the joint/weld. The protective coating can also be used to protect the weld. There are many types of protective coatings on the market today. Many of them are based on zinc. Galvanized steels produced by hot-dip galvanizing find many applications, e.g. in the construction and automotive industries [2-4]. By introducing aluminum and magnesium into a standard zinc coating, a ZnAlMg coating was obtained, which provides excellent corrosion and wear resistance [5]. One of them is the Zn Al3,5Mg3 (Trade name: Magnelis®) coating patented by ArcelorMittal. This coating is characterized by the great corrosion resistance and wide range of possible applications. Compared to standard Zn coatings, Magnelis provides similar level of corrosion resistance protection with much thinner layer of coating. So far, this coating has not been widely studied in terms of its ductility. The coated ZnAlMg steel plate can be used to the production process of the open-joint tubes. This however requires high cracking resistance both of the steel sheet and coating during the roll-forming process. Even a micro damage of the coating may lead to cracking in the most deformed areas and may be the cause of the deteriorations in the in-service corrosion resistance [5-7]. Thus, obtaining the information of the correlation between microstructure and mechanical properties during the roll forming of open-joint tube process is necessary. This knowledge will allow to improve the quality of the coating and to optimize the parameters of the deformation process. Therefore, the main purpose of the presented work was to

Content from this work may be used under the terms of the Creative Commons Attribution 3.0 license. Any further distribution of this work must maintain attribution to the author(s) and the title of the work, journal citation and DOI. Published under license by Materials Research Forum LLC.

assess the properties of ZnMgAl coated steel sheet used for the production of tubular products where it is subjected to the process of deformation by bending.

Materials

Three types of steel sheets were used in the tests. The base material was hot-rolled steel sheet, the chemical composition of which is shown in Table 1. The base material was E220 steel sheet with a ZnMgAl coating with a total thickness of 1.4 mm. The other two steel sheets of the S235 grade were taken as the reference material - one with a standard Zn coating and the other without this coating. The thickness of both sheets was 1.5 mm.

First, the quality of every coating was investigated using the Nova NanoSEM FEI scanning electron microscope (SEM). Additionally, the thickness and homogeneity of the surface was measured (Fig.1).

Table. 1. Based chemical composition of the steel sheet (% wt.).

Material	C	Mn	Si	P	S	Al	Cu	Sn
E220	0,049	0,20	0,004	0,023	0,015	0,032	0,021	0,002
S235JRH	0,15	0,12	0,030	0,020	0,025	0,01	0,55	-

Fig. 1a and b present the initial microstructure of the cross – section of specimen with standard Zn coating (as received). Analysis of the sheet steel with Zn coating showed good coating adherence to the base sheet. The mean thickness of the Zn coating was approximately 98 μm. During the microstructural analysis the cracks of the Zn coating were not observed.

A similar analysis was performed for the ZnMgAl-coated sample (Fig. 1c, d). In the case of the main research material, the measurement of the coating thickness showed that the ZnMgAl layer is smaller than in the case of the standard Zn layer and is about 38 - 40 μm. Its microstructural analysis showed good adhesive properties and cracks were also not visible.

Based on the microstructural analysis of steel sheets coated with Zn and ZnMgAl it can be concluded that the initial quality of both samples is sufficient for their use in the rolling process.

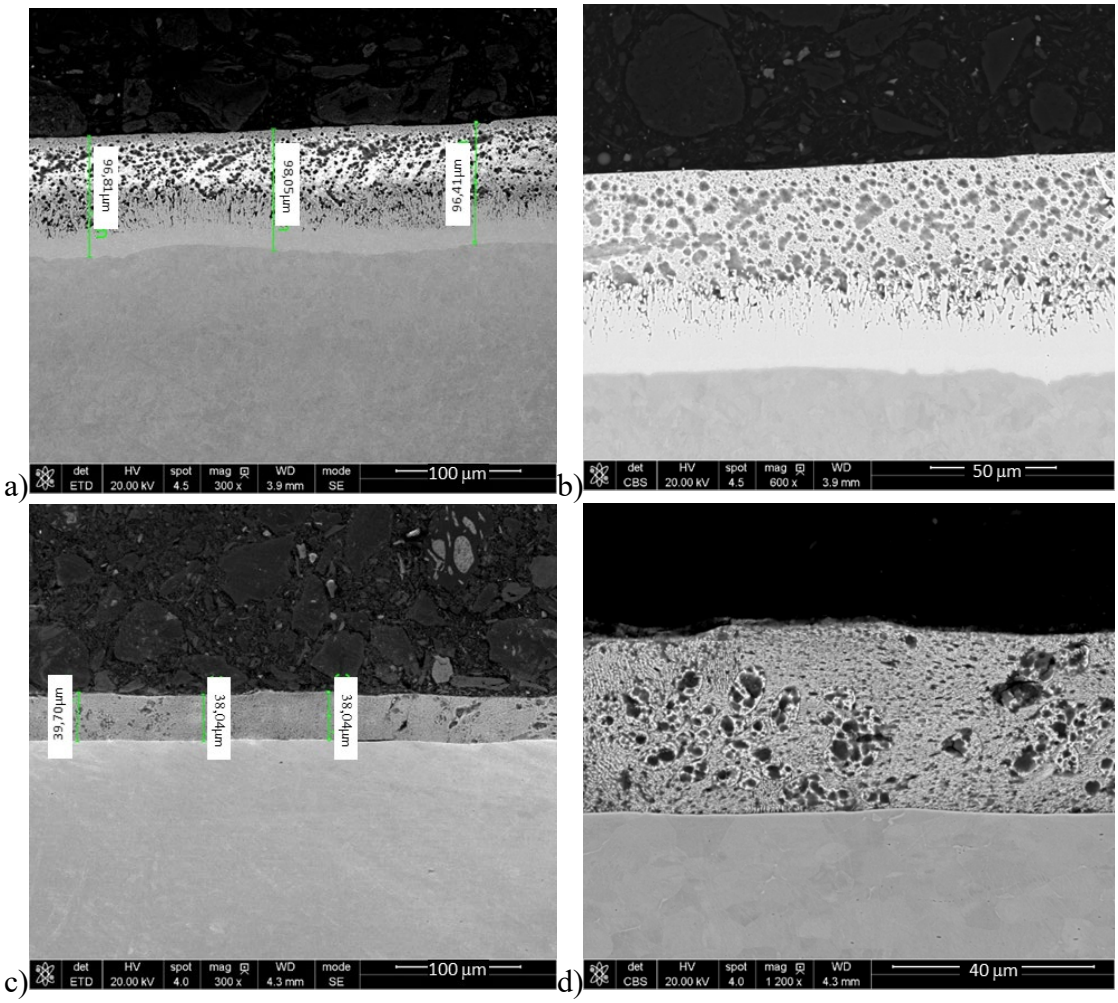

Fig. 1. The example of the cross – section of the steel sheet with standard Zn coating – a); b) and ZnMgAl coating – c); d).

Experimental Procedure

In order to obtain the data for the analysis of deformation susceptibility of steel sheet with ZnMgAl coating, the experimental procedure was divided into two steps. The first stage included the three-point bending test. The radius of the upper tool was equal 5 mm. In this part of work, the three different sheets were deformed: 1) base material (with no coating) 2) sheet with standard Zn coating, and 3) sheet with ZnMgAl coating. The experiments were performed at room temperature with the velocity of the bending load of 1mm/min. The experimental procedure was combined with Digital Image Correlation (DIC) analysis. The DIC system consist of high resolutions CCD 5mpx camera. In order to obtained the accreted results, the DIC analysis was made using two different lenses. In first case the whole surface of the samples were analyzed ale for this the lens of 2.8/50 was used. In the second case only most deformed area was analyzed. and for this measurement the stereo microscope was used as a lens. Postprocessing of the obtained images was made using Istra4D software. The second stage of the investigation was focused only on the steel sheet with ZnMgAl coating. In this stage, the bending test based on the ISO 7438:2016 standard was applied. The bending angle ranging between 90 and 180 deg was used. Similarly, like in the pervious test, the bending test was made at the room temperature, but the angle on the upper tool was equal 30 deg.

Results and Discussion

In the presented work, the DIC strain measurement was applied to analyze deformation of coated sheets subjected to the three-point bending test. During the test, DIC method was applied to track the strain distribution during the deformation process [8-9]. The upper tool displacement was kept the same for the all analyzed specimens. Results obtained for the one-time step before end of the deformation process with the stress–strain curve are presented in the Fig. 2. DIC strain distribution maps show typical strain accumulation for the three-point bending test localized in the lower part of the specimen. The highest strain accumulation was observed in the sample with standard zinc coating and the lowest value was obtained for the sample with ZnMgAl coating. In the case of sheet with zinc coating the additional strain concentration can be observed in the upper part of the specimen (under the upper tool), what suggests the possibility of the zinc coating crack occurrence in this area.

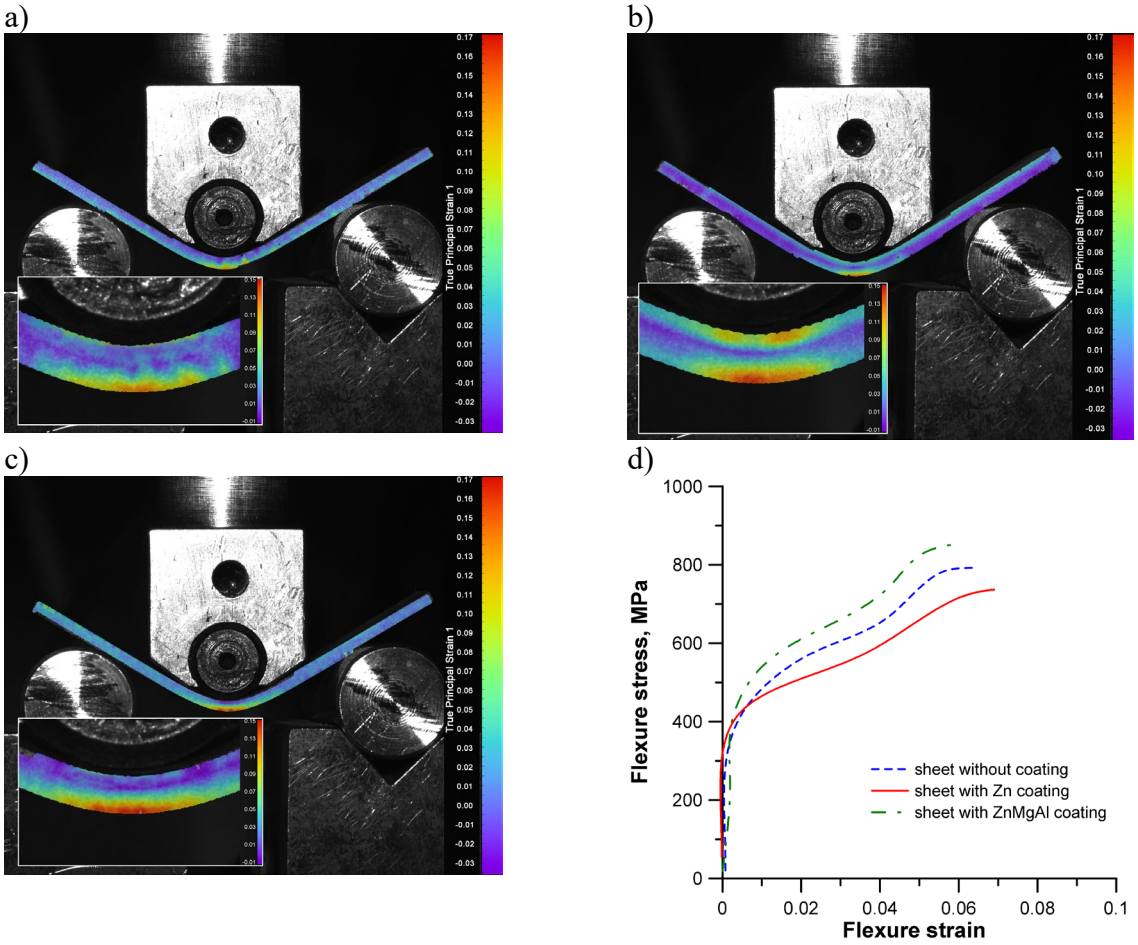

Fig. 2. The true principal strain distributions maps obtained in DIC analysis for sheet plate without the coating – a); with standard zinc coating – b); with ZnMgAl coating – c); and the stress – strain curve obtained in the three – point bending test using two type of the lenses.

The main aim to use the DIC analysis was the estimate the local deformation value on the sample thickness during the bending test in order to related these values with the coating deformation susceptibility in related to the open join tube production process.

Additionally, based on the obtained DIC results, it can be expected that on the sheet with the zinc coating the cracks will appear in the external and internal surfaces of the specimen. For the specimen without coating the cracking of the oxide scale also took place. For confirmation, all

specimens after the three-point bending test were analyzed using Zeiss optical microscope (Fig. 3). Observations were carried out on the outer and inner surfaces, where the accumulation of deformations was the greatest (Fig. 3a).

The obtained micrographs revealed the flaking of the oxide scale layer - especially on the internal surface of the specimen with no coating (Fig. 3b). In the case of the second specimen with zinc coating clear cracking both at external and internal surface was visible. A digital crack assessment was made and compared with patterns based on the PN-EN ISO 4628-4:2004(U) standard. It was found that the internal cracks can be assigned to the ASTM 4 group and external cracks to the ASTM 2 group. For the last analyzed specimen, with the ZnMgAl coating, no visible cracks were found at any of the analyzed surfaces (internal and external).

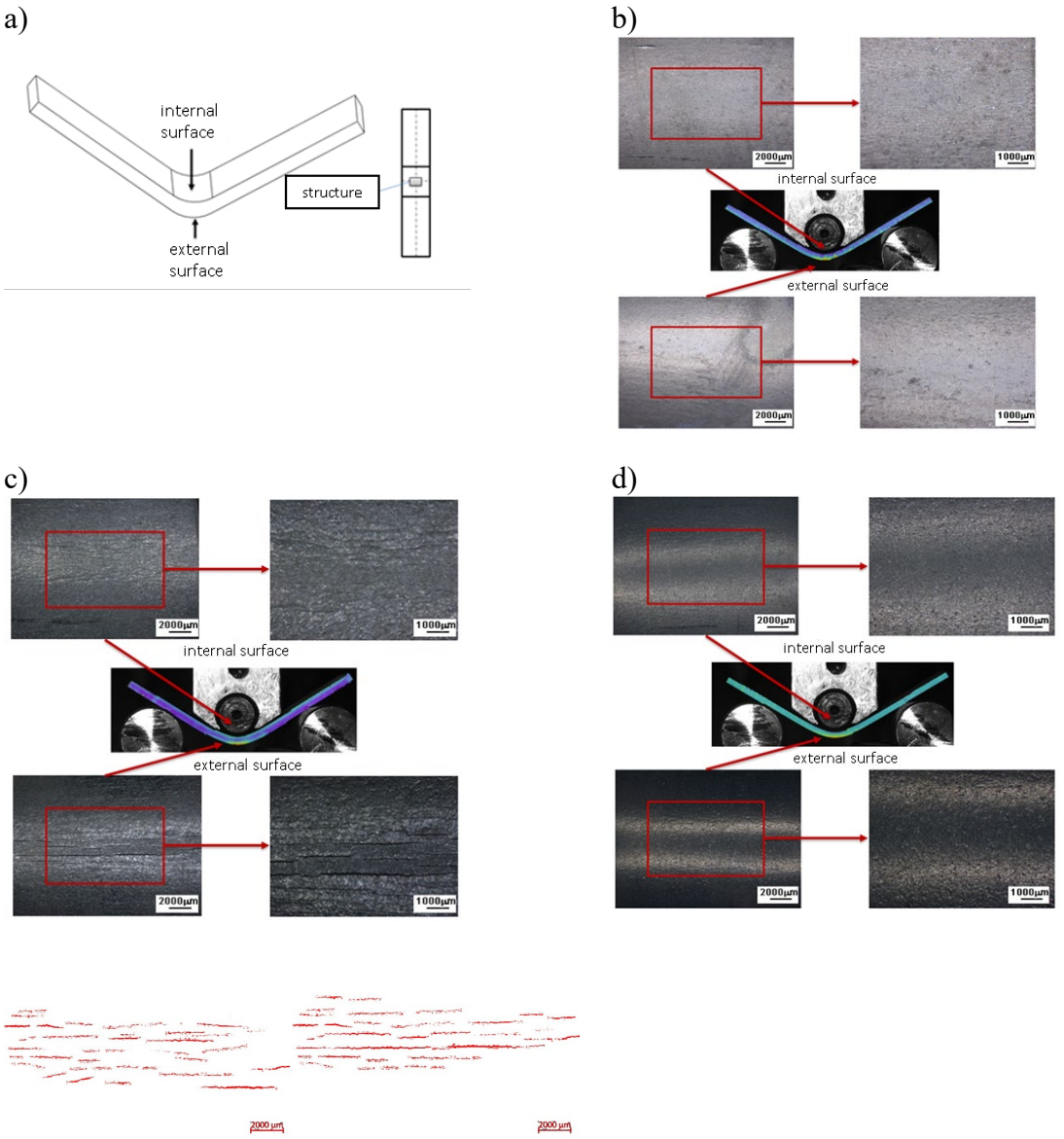

Fig. 3. Position of the optical microscope analysis of surface quality bending sample on the internal and external surface - a). Obtained results for the specimen without the coating - b); with standard zinc coating with comparison to the patterns from PN-EN ISO 4628-4:2004(U) standard - c) and with ZnMgAl coating - d).

Materials Research Proceedings 28 (2023) 817-824 https://doi.org/10.21741/9781644902479-89

The surface that was observed using DIC system was subjected to the scanning electron microscope observation using FEI Nova Nano SEM. For the analysis the specimen with zinc coating and ZnMgAl coating was used. Fig. 4 shows that in the case of the specimen with standard zinc coating the coating detachment and cracking (marker with the red arrows) can be observed. On the second analyzed specimen the any layer damage was not found.

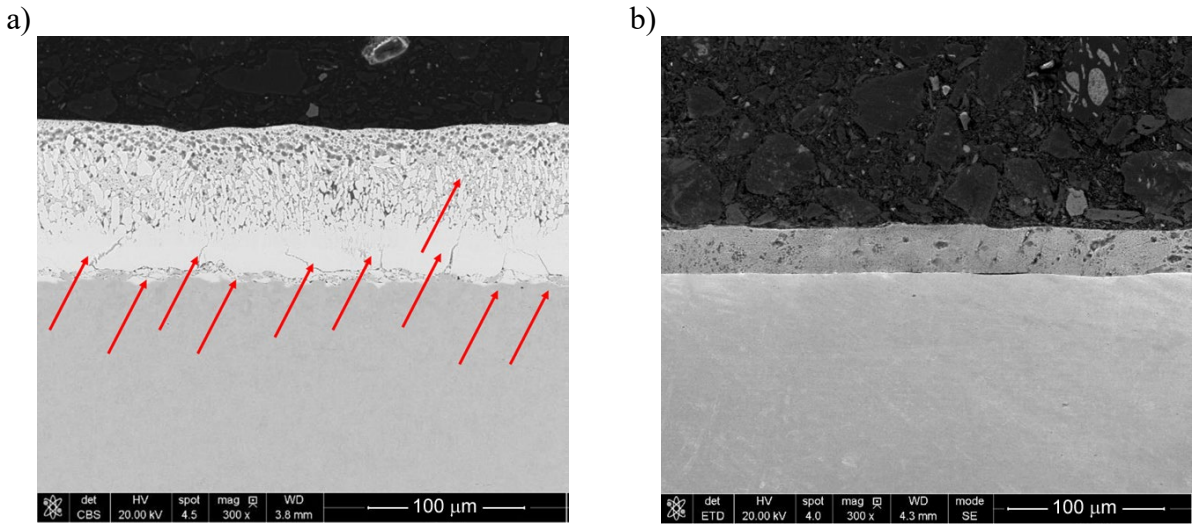

Fig. 4. The SEM image for specimen with Zn coating – a) and ZnMgAl coating – b).

The analysis of the three-point bending test results confirmed that the steel sheet with ZnMgAl coating is suitable to the deformation process.

Additionally, in order to design the roll-forming process, bending test is usually performed to check the springback angle and select the roll forming pass design. In the current study this test was also performed but its aim was more focused on the analysis of the ZnMgAl coating adhesion. The obtained results for the bending test with angle equal to 90deg are presented in the Fig. 5. Additional analysis performed after bending shows that, similarly to the previous test, the cracks were not visible either of the surface (internal and external).

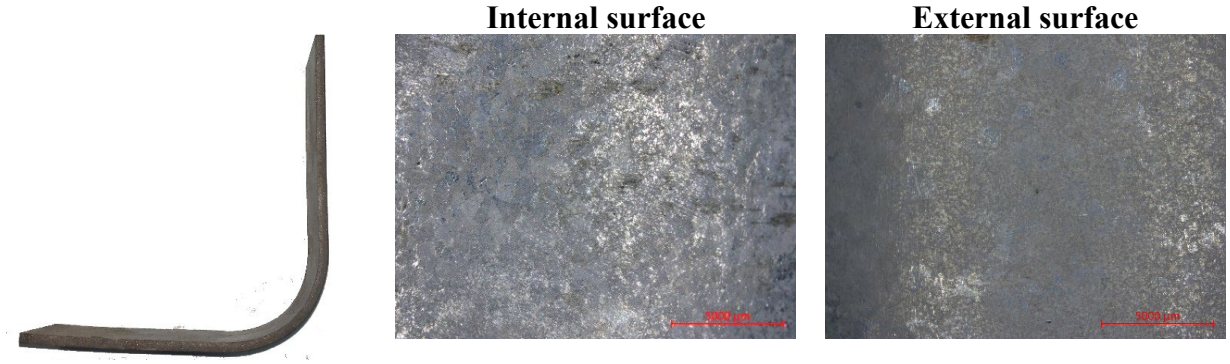

Fig. 5. The shape of the specimen after bending test with microstructure of internal and external surface.

Summary

The tests carried out and the analysis of their results allowed for the assessment of the suitability of the steel sheet with the ZnMgAl coating for the process of forming pipes with an open joint. For this purpose, a standard bend test and a three-point bend test combined with a digital image correlation system were used. In the case of the three-point bending test, the test results of a steel sheet without a protective coating and with a standard zinc coating were taken as the starting point. Based on the DIC analysis, areas of strain concentration were determined where the protective coating could crack. Both bending tests, i.e. standard and three-point bending, showed that the tested material with ZnMgAl coating can be successfully used in the pipe production process.
Based on the presented results, the following conclusions can be drawn:

- The microstructural analysis of the sheet steel with coating shows good adherence to the base steel for both analyzed coatings.
- In the case of the sheet plate without the coating strain distribution analysis showed the points localization at maximum strain value. Additional microstructure analysis showed that in this area the flaking of scale layer occurred.
- The DIC analysis of steel sheet with standard zinc coating showed the highest strain concentration both at internal and external surface. Microstructural analysis showed significant cracks. Based on the ISO standard was coating cracking was assigned to the ASTM 4 group for the internal surface and ASTM 2 group for the external surface.
- Based on the DIC analysis of the plate with ZnMgAl coating the strain concentration (beside standard strain localization characterized for the three-point bending test) was not observed. The microstructure analysis confirmed lack of the visible cracks on the surface.

Acknowledgements

The support from the National Centre for Research and Development, Poland through the grant no. POIR.01.01.01.00.0510/18 is greatly appreciated.

References

[1] P. H. Chan, K. Y. Tshai, M. Johnson, S. Li, The flexural properties of composite repaired pipeline: Numerical simulation and experimental validation, Compos. Struct. 133 (2015) 312-321. https://doi.org/10.1016/j.compstruct.2015.07.066
[2] A. Masoud, S. Bekir, K.J. Bart, P. Yutao, Cracking behavior and formability of Zn-Al-Mg coatings, Mater. Des. 212 (2021) 1-15. https://doi.org/10.1016/j.matdes.2021.110215
[3] S.M.A. Shibli, B.N. Meena, R. Remya, A review on recent approaches in the field of hot dip zinc galvanizing process, Surf. Coat. Technol. 262 (2015) 210-215. https://doi.org/10.1016/j.surfcoat.2014.12.054
[4] S.T. Vagge, V.S. Raja, R. Ganesh Narayanan, Effect of deformation on the electrochemical behavior of hot-dip galvanized steel sheets, Appl. Surf. Sci. 253 (2007) 8415-8421. https://doi.org/10.1016/j.apsusc.2007.04.045
[5] C. Yao, H. Lv, T. Zhu, W. Zheng, X. Yuan, W. Gao. Effect of Mg content on microstructure and corrosion behavior of hot dipped Zn-Al-Mg coatings, J. Alloy. Compd. 670 (2016) 239-248. https://doi.org/10.1016/j.jallcom.2016.02.026
[6] S. Thomas, N. Birbilis, M.S. Venkatraman, I.S. Coles, Self-repairing oxides to protect zinc: Review, discussion and prospects, Corros. Sci. 69 (2013) 11-22. https://doi.org/10.1016/j.corsci.2013.01.011
[7] B. Gao, S.W. Li, Y. Hao, G.F. Tu, L. Hu, S.H. Yin, The Corrosion Mechanism of Zn-5% Al-0.3% Mg Coating, Adv. Mat. Res. 189 (2011) 1284-1287. https://doi.org/10.4028/www.scientific.net/AMR.189-193.1284
[8] T.C. Chu, W.F. Ranson, M.A. Sutton, Applications of digital-image-correlation techniques to experimental mechanics, Exp. Mech. 25 (1985) 232. https://doi.org/10.1007/BF02325092.

[9] T. He, L. Liu, A. Makeev, B. Shonkwiler, Characterization of stress–strain behavior of composites using digital image correlation and finite element analysis, Compos. Struct. 140 (2016) 84. https://doi.org/10.1016/j.compstruct.2015.12.018

Materials Research Proceedings 28 (2023) 825-832 https://doi.org/10.21741/9781644902479-90

Hybrid SPD process of aluminium 6060 for microforming

PRESZ Wojciech[1,a *], JASIŃSKI Cezary[1,b], MORAWIŃSKI Łukasz[1,c] and ORŁOWSKA Marta[2,d]

[1]Warsaw University of Technology, Narbutta 85, 02-524 Warsaw, Poland

[2]Military University of Technology, gen. Sylwestra Kaliskiego 2, 00-908 Warsaw, Poland

[a]wojciech.presz@pw.edu.pl, [b]cezary.jasinski@pw.edu.pl, [c]lukasz.morawinski@pw.edu.pl, [d]marta.orlowska@wat.edu.pl

Keywords: UFG Metals, Aluminium 6060, Hybrid SPD, Microforming

Abstract. The increasing share and expansion of miniature devices requires the mastery of miniature parts production, including metal parts. In metal microforming, due to the conditions of mechanical similarity, the aim is to use materials with the smallest grain. Ultra-fine-grained metals (UFG) fulfill this requirement. These metals can be obtained, inter alia, in SPD processes such as ECAP. The work uses the extension of the SPD based on ECAP with additional metal forming operations necessary to obtain blanks for microforming in the form of a 0.2 mm foil. Three variants of the technological process were performed. This foil was then subjected to a micro-drawing operation aimed at determining the influence of the foil preparation process on the sheet metal microforming process flow.

Introduction

The miniaturization of devices [1], which has been progressing for several decades, imposes the miniaturization of the parts used for their production, which are largely produced by metal forming technology [2]. Reducing the dimensions to about one millimeter causes a change in the dominant physical phenomena. Difficulties in the accurate design of technological processes for miniature parts, combined with the growing demand for them, led to the separation of a relatively new branch of metal forming, which is microforming [3]. This is because of the natural granularity of the polycrystalline materials used [4] and the surface layer treated as an area with a certain thickness, mainly dependent on the structure of the material [5]. The share of both of these features increases as the product becomes smaller, the material of which can no longer be considered uniform throughout its volume. The proposed avoidance of many of the unfavorable scale effects is the concept of using ultrafine grain metals (UFG) [6-8]. Within the presented work, the field of interest was narrowed down to sheet metal microforming processes. As a method of obtaining ultra-fine grain, the ECAP process was adopted on the stand used in previous works [9]. The selected material for the tests is aluminium alloy 6060, which was chosen because of its high (in the group of aluminium alloys) strength properties.

The main purpose of the work was to develop a research method allowing for the assessment of the possibility of using this alloy with the UFG structure obtained by the ECAP method for sheet metal microforming processes. It should be noted that the UFG materials obtained from the ECAP process are in the form of rods that must undergo further deformations [10], so that the final effect is a foil with a UFG structure. The influence of the technological path of preparing foil with a thickness of 0.2 mm made of aluminium alloy 6060 on the possibility of sheet metal microforming was initially examined. The process of free micro-drawing was adopted as the verification process. It was chosen because of the simplicity of implementation, which favours further miniaturization and reduces the number of process parameters in research. Due to the

Content from this work may be used under the terms of the Creative Commons Attribution 3.0 license. Any further distribution of this work must maintain attribution to the author(s) and the title of the work, journal citation and DOI. Published under license by Materials Research Forum LLC.

Materials Research Proceedings 28 (2023) 825-832 https://doi.org/10.21741/9781644902479-90

difficult formability of the selected material discussed in the literature, it was decided to use heat treatments to improve this feature.

Material Preparation

The extended UFG metal fabrication process with the ECAP main operation was used in the work to prepare 0.2 mm thick 6060 aluminium foil. Three series of material in the form of foil, marked respectively with the symbols CG (material not subjected to ECAP), UFG F (material subjected to ECAP in the delivery condition) and UFG G (material supersaturated before ECAP) were punched with a 4 mm diameter punch. Then, the obtained discs were used to carry out the micro-drawing operation.

The hot-extruded bar PN EN 6060 ø50 was used as the initial material. The bar was divided into billets with dimensions of 8x8x45 mm by milling according to the scheme shown in Fig. 1a. Part of the billets were subjected to supersaturation (annealing for 2 hours at 525°C, cooling in water). These billets were used to prepare a series of UFG G material. Then, a two channel turns mtECAP (2x110°) was performed six times at 150°C. ECAP was performed for a batch of supersaturated material (UFG G) and as delivered (UFG F). The rods obtained in this way were subjected to free upsetting (Fig. 1b) at 150°C, obtaining plates with a thickness of 1 mm. Upsetting was carried out in three subsequent operations with a comparable increase in surface area (~2 times) to enable renewal of lubricating layer. In addition, identical upsetting was applied to the billets that were not subject to the ECAP. The diagram of the upsetting operation is shown in Fig. 1c. The obtained material was mainly subjected to natural ageing, however, the use of elevated temperature in the ECAP and upsetting operations meant that the material stayed in total for almost an hour at a temperature close to 150°C, which could initiate the processes related to artificial ageing.

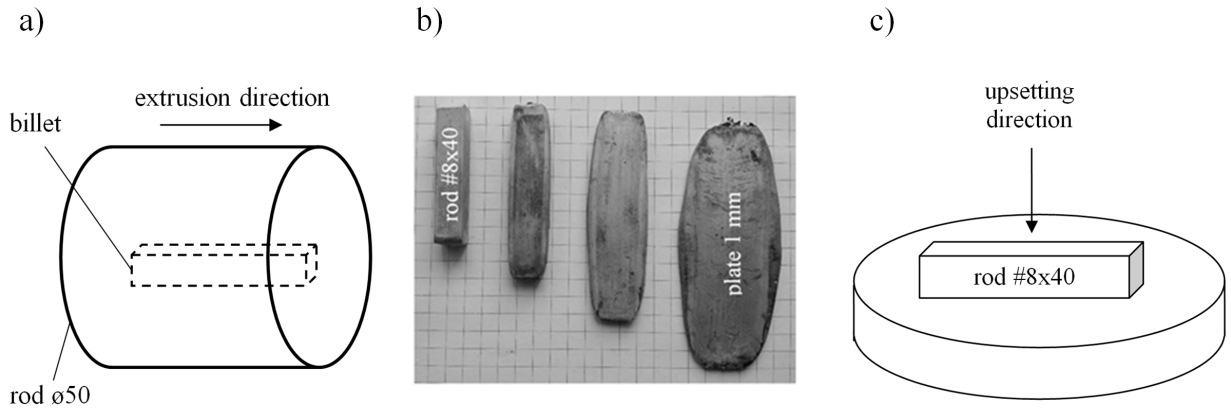

Fig. 1. Scheme of orientation of the taken billets in relation to the ø50 mm rod (a), the result of subsequent upsetting operations at a thickness of ≈ 5, 3 and 1 mm (b) and the scheme of upsetting operations (c).

In the next stage of the process, the obtained plates were cut into 6 mm wide strips, which were rolled to a thickness of 0.2 mm at room temperature to obtain a foil intended for microforming. The method of taking strips from plates are shown in Fig. 2. Full material preparation process is presented in Table 1.

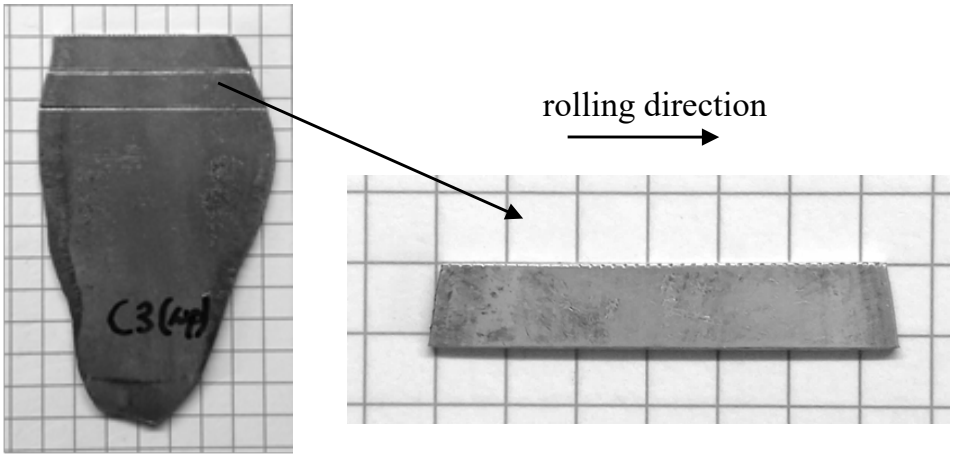

Fig. 2. Preparation of metal strips for the rolling process.

Table 1. Material preparation process (green color mean that operation was performed).

Operation	Cutting from ø50 rod	Supersaturation	mtECAP	Upsetting	Cutting	Rolling
Result	billet (#8x45 mm)	billet (#8x45 mm)	Rod (#8x40 mm)	Plate (1 mm thick)	Strip (6 mm wide)	Foil (0,2 mm thick)
CG						
UFG F						
UFG G						

Material Analysis

In order to verify the effect of supersaturation on the material properties after the ECAP, a uniaxial tensile test for specimen with 10 mm gauge length [9] was performed, in which the yield strength $R_{p0.2}$, tensile strength R_m and elongation A were determined. These parameters were determined for the material immediately after the ECAP process and after additional upsetting. Tensile test for a thin foil was not performed. Fig. 3 presents the obtained results and compares them with the parameters of the material as delivered.

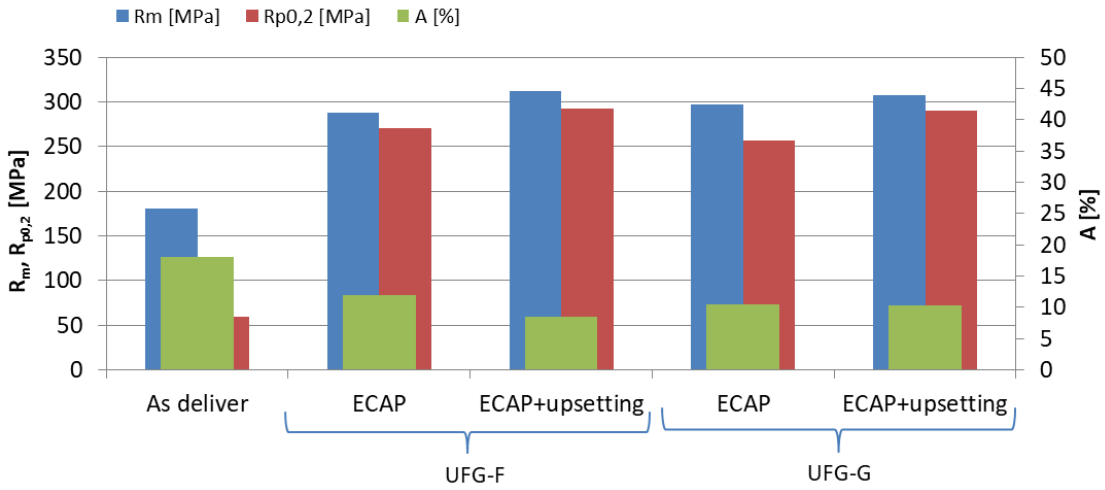

Fig. 3. Comparision of R_m, $R_{p0.2}$ and A for prepared series of material in two stages of the process.

Materials Research Proceedings 28 (2023) 825-832 https://doi.org/10.21741/9781644902479-90

The obtained 0.2 mm foils were subjected to EBSD structural analysis. Fig. 4 shows the corresponding grain size distribution for CG and UFG foil.

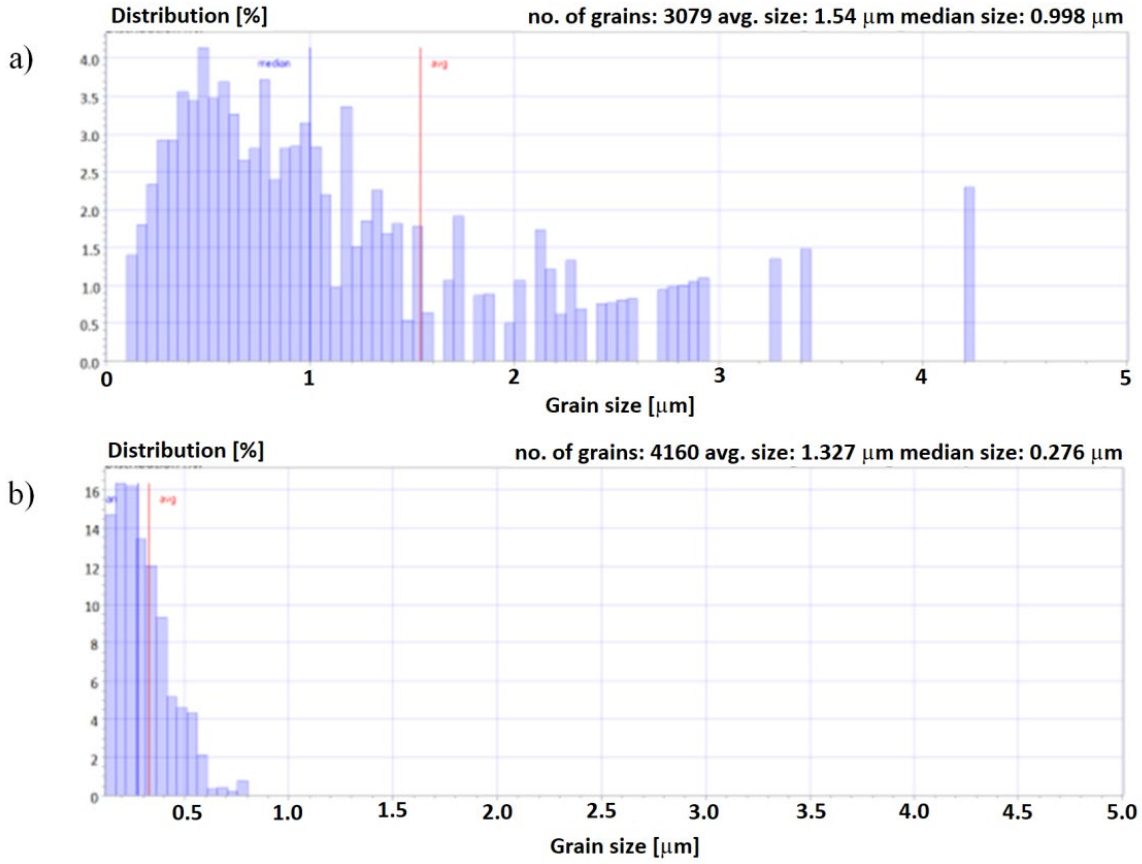

Fig. 4. Grain size distribution of 6060 aluminum foil for CG (a) and UFG-F (b) series.

Collected data indicate a noticeable effect of supersaturation on the properties of the obtained material, however, this effect is different immediately after ECAP and after additional upsetting. The supersaturated material (UFG-G series) shows higher strength and lower plasticity after ECAP compared to the UFG-F series, however, after additional upsetting, this relationship is reversed and the UFG-G series shows lower strength and higher plasticity. This phenomenon may be caused by the influence of increased tamperture occurring during upsetting, which may partially eliminate the strengthening effects. Finally, a positive effect of supersaturation on the formability of the obtained UFG plates was observed.

Structural analysis of foils intended for sheet metal microforming leads to the conclusion that the ECAP process unifies the structure of the material in the entire volume of the obtained foil. The foil made of the CG material is characterized by a much greater grain size variation, despite the fact that the large plastic deformation that took place during subsequent metal forming operations significantly fragmented the grains.

Formability Determination

Formability determination was performed by means of micro-drawing process. Carrying out the drawing process requires a preliminary operation, which is the preparation of the preform. In this case it was a disc with a diameter of 3.8 mm. A micro-blanking process with a blank holder, which in turn required preforms in the form of 10x7x0.2 mm strips. In this process, a precise micro-device placed on the testing machine table was used. The micro-device ensured precise positioning

of the tools. The micro-blanking operation was additionally used to analyze the technological variants of CG, UFG-F and UFG-G. The courses of forces were recorded (Fig. 6a), the cut strengths and the fill factors of the graph were determined (Table 2). To reduce the complexity of the tools, free micro-drawing was carried out in the system shown in Fig. 5a, consisting of the same device as for micro-blanking. For this kind of process the drawing ratio should be bigger than 0.55 [1] , and 0.58 was chosen.

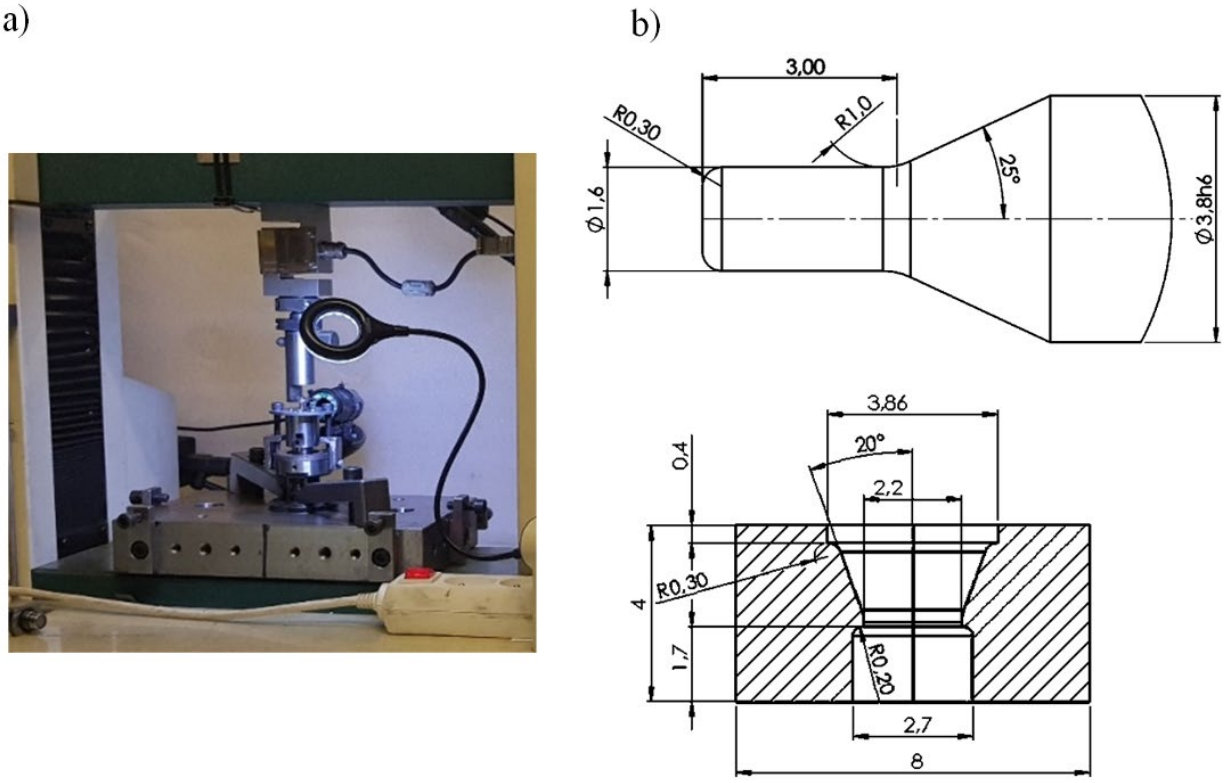

Fig. 5. Setup for micro-drawing (a) and dimensions of the tools used (b).

The dimensions of the tools are shown in Fig. 5b. Lubrication was applied with a lubricant based on MoS2 from the die side and light oil from the punch side. The coefficient of extrusion in the process was 0.54. The following description refers to the force recorded during the process (Fig. 6b).

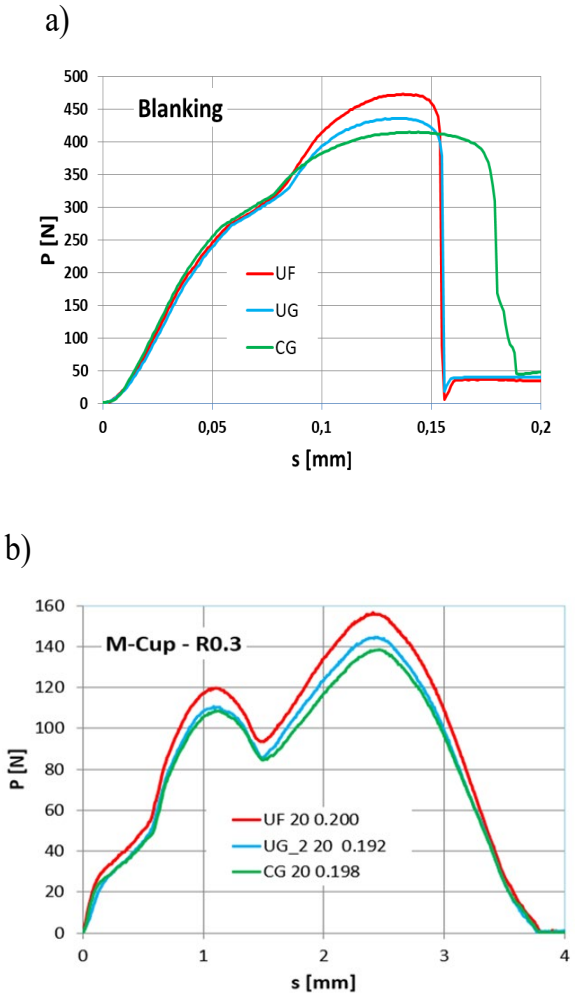

Fig. 6. Course of forces during micro-blanking (a) and micro-drawing (b) of 0.2 mm foil for three series of material.

The disk is placed in the cavity of the matrix (Fig. 5b) enabling its precise positioning. The precisely guided punch presses centrally on the foil, the force of the process increases to the value of the first maximum. After reaching it, the edge of the disc begins to be drawn into the die, sliding on its conical surface. As the punch moves, the force decreases and reaches a minimum value, after which it increases again due to the strengthening of the material and the thickening of the edge of the cup. When the strengthening and thickening of the material is no longer able to compensate for the decreasing perimeter of the edge, the force of the process decreases until its full completion. The threat here is the possible cracking of the bottom, which is the main phenomenon limiting the process.

Table 2. Cut strength R_t and graph fill factor λ for three series of 0.2 mm foil.

	CG	UF	UG
R_t [MPa]	168	185	181
λ	0,67	0,51	0,55

Despite the slightly higher cut strength determined for the material from the UFG-F series, the effect of supersaturation before the ECAP on the blanking process conditions was not observed. An increase in the micro-drawing process force was observed in the case of the UFG-F material. With regard to the CG and UFG-G materials, slight differences in the force course were observed, requiring further research. The shape and appearance of the cups surface (Fig. 7) as well as the size of the lugs indicating the presence of flat anisotropy in the assessment of the image from the light microscope do not indicate significant differences in individual material series.

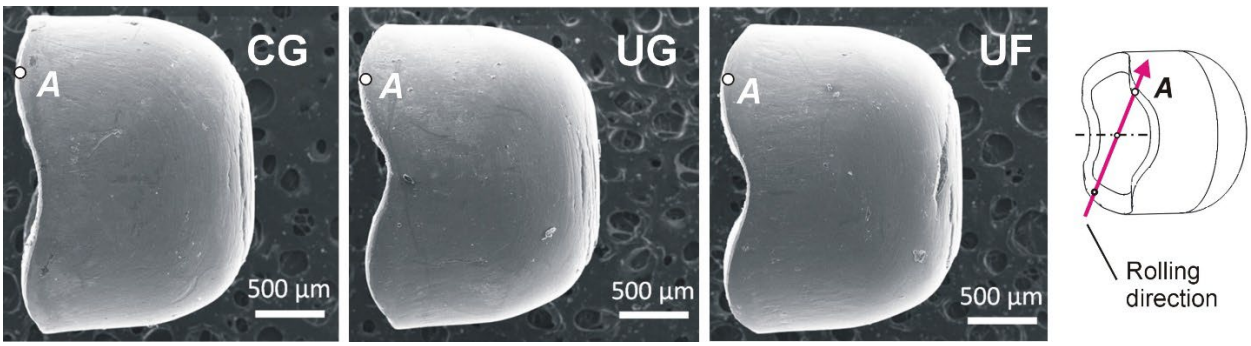

Fig. 7. SEM images of obtained micro cups for three series of material.

Summary

The presented paper proposes a research method for selection of process parameters enabling the use of UFG materials obtained by the ECAP method for use in sheet metal microforming. The applied ECAP has been enriched with the process of obtaining thin foils by initial multiple upsetting with the possibility of increasing the temperature and subsequent multiple rolling at room temperature. The obtained material in the form of a foil with a thickness of 0.2 mm made of aluminium alloy 6060 was then subjected to a micro-drawing operation recognized as a process determining the formability of the prepared materials in the conditions of sheet metal microforming. Necessary to prepare preforms for the micro-drawing process, the micro-blanking process was used to additionally compare the characteristics of foils from different series.

Based on the prepared research, it was found that the obtained material in the form of a foil is characterized by a uniform structure and is consistent throughout its volume without structural defects and cracks. The ECAP process plays a key role in unifying the structure throughout the volume of the foil. Its omission results in a significant decrease in the homogeneity of the material, despite the large deformations to which the material is subjected during upsetting and rolling, which causes significant grain refinement comparable to ECAP.

Despite the noticeable differences in strength properties occurring after the upsetting process for the supersaturated material and the material processed as delivered, no effect of supersaturation of the billets material before the ECAP process on formability was observed in the conditions of the sheet metal microforming.

Some differences in process flow for prepared materials was observed in micro-blanking and micro-drawing (Fig. 6), but for clearly distinguishes the formability there are planed extension of micro-drawing process in the next research.

References

[1] A.B. Frazier, R.O. Warrington, C. Friedrich, The Miniaturization Technologies: Past, Present, and Future, IEEE Trans Ind Electron. 42 (1995) 423-430. https://doi.org/10.1109/41.464603

[2] A. Jäger, S. Habr, K. Tesař, Twinning-detwinning assisted reversible plasticity in thin magnesium wires prepared by one-step direct extrusion, Mater. Des. 110 (2016) 895-902. http://doi.org/10.1016/j.matdes.2016.08.016

[3] M.W. Fu, W.L. Chan, A review on the state-of-the-art microforming technologies, Int. J. Adv. Manuf. Technol. 67 (2013) 2411–2437. https://doi.org/10.1007/s00170-012-4661-7
[4] Z. Jiang, J. Zhao, H. Lu, D. Wei, K. Manabe, X. Zhao, X. Zhang, Influences of temperature and grain size on the material deformability in microforming process, Int. J. Mater. Form. 10 (2017) 753–764. https://doi.org/10.1007/s12289-016-1317-4
[5] U. Engel, Tribology in microforming, Wear 260 (2006) 265-273. https://doi.org/10.1016/j.wear.2005.04.021
[6] W. Presz, A. Rosochowski, The influence of grain size on surface quality of microformed components, 9th Int. Conf. Mater. Form. ESAFORM 2006, Glas UK, 2006, pp. 587-590.
[7] W. Presz, Scale effect in design of the pre-stressed micro-dies for microforming., Comput. Meth. Mater. Sci. 16 (20160 1-8.
[8] W.J. Kim, S.J. Yoo, H.K. Kim, Superplastic microforming of Mg-9Al-1Zn alloy with ultrafine-grained microstructure, Scr. Mater. 59 (2008) 599-602.
[9] M. Ciemiorek, W. Chromiński, C. Jasiński, M. Lewandowska, Microstructural changes and formability of Al–Mg ultrafine-grained aluminum plates processed by multi-turn ECAP and upsetting, Mater. Sci. Eng. A. 831 (2022) 142202. https://doi.org/10.1016/j.msea.2021.142202
[10] M. Lipińska, L. Olejnik, M. Lewandowska, A new hybrid process to produce ultrafine grained aluminium plates, Mater. Sci. Eng. A 714 (2018) 105-116. https://doi.org/10.1016/j.msea.2017.12.096
[11] H. Tschaetsch, Metal Forming Practise, ISBN-10 3-540-33216-2, Springer Berlin Heidelberg New York, 2006, pp. 185-186.

Materials Research Proceedings 28 (2023) 833-838 https://doi.org/10.21741/9781644902479-91

Influence of intercritical annealing temperature on formability and mechanical properties of medium-manganese-steel in press hardening

TILLY Karl Johann[1,a *], PLUM Tobias[1,b], BAILLY David[1,c] and HIRT Gerhard[1,d]

[1] Institute of Metal Forming, RWTH Aachen University, Aachen, Germany

[a]karl.tilly@ibf.rwth-aachen.de, [b]tobias.plum@ibf.rwth-aachen.de,
[c]david.bailly@ibf.rwth-aachen.de, [d]gerhard.hirt@ibf.rwth-aachen.de

Keywords: Press Hardening, Medium Manganese Steel, Formability, Hot Stamping

Abstract. Ultra-high-strength-steel parts produced by press hardening are widely used in the automotive sector for lightweight construction and passenger safety applications. Medium-manganese-steels (MMnS) are currently investigated as an alternative to boron-manganese steels. Their favorable mechanical properties of high strength and high ductility after quenching are often based on rather complex heat treatment strategies resulting in a multiphase microstructure. One possible way such a microstructure can be obtained, is intercritical annealing and subsequent quenching during the press hardening process. For this processing route formability during hot stamping and final properties of the quenched material are dependent on the annealing temperature. For a successful part production, an annealing temperature that satisfies both, in-process properties, as well as final mechanical properties is mandatory. In this paper, the suitability of the intercritical annealing process route for press hardening of MMnS is investigated for a specific MMnS alloy. Formability in hot stamping conditions with respect to different annealing temperatures (range 700°C – 800°C) are examined by performing hot tensile tests, as well as experimental trials using a hot stamping tool. Final properties are analyzed by tensile tests. The formability during hot tensile tests and hot stamping show a strong positive correlation to the annealing temperature, while the values for uniform and ultimate elongation of the quenched material shows a strong negative correlation to the annealing temperature. The tensile strength of the quenched material shows a low sensitivity to the annealing temperature. No annealing temperature that satisfies both, in-process and final properties, could be found for the investigated MMnS alloy.

Introduction

Increasing demands for passenger safety and reduction of CO_2 emissions in the automotive sector led to the increased usage of high strength steels in autobody applications. The main advantage of advanced-high-strength-steels is the lightweight construction potential due to their mechanical properties.[1] Direct press hardening, consisting of the three steps austenitization, hot stamping and tool-quenching, is a widely used process to produce high strength autobody parts from sheet metals.[2] The commonly used manganese-boron steels such as 22MnB5 typically achieve tensile strengths of 1500 MPa und residual formabilities of minimum 5 % in the quenched state with fully martensitic microstructure [3]. In order to improve the performance of parts produced from manganese boron steels strategies such as tailored heating, or the usage of tailored materials such as tailor-welded blanks or cladded material have been investigated. The strategies of tailored processes or properties for press hardening of manganese-boron-steels mostly rely on reducing the strength of sections of the structural component in exchange for an improved ductility. Therefore the overall component performance, for example total energy absorption in a crash, can be

Content from this work may be used under the terms of the Creative Commons Attribution 3.0 license. Any further distribution of this work must maintain attribution to the author(s) and the title of the work, journal citation and DOI. Published under license by Materials Research Forum LLC.

Materials Research Proceedings 28 (2023) 833-838 https://doi.org/10.21741/9781644902479-91

improved. On the downside to the production process of parts with tailored properties is more complex as for example segmented tools or tailor welded blanks are necessary. [3,4]
As an alternative to the commonly used manganese-boron-steels, steels of the medium-manganese alloy class (MMnS) have been investigated, with the aim of providing a material with high strengths and simultaneously high ductility for press hardening processing. The favorable mechanical properties of MMnS are based on a fine-grained multi-phase microstructure after press hardening that consists of retained austenite and martensite. To achieve this microstructure, it is often necessary to employ multistep heat treatment procedures (for example Quench and Partitioning) before or after the hot stamping operation, wich leads to a more complex processing compared to manganese boron steels [5-9].
In this paper it will be investigated whether a single heat treatment of intercritical annealing is suitable for hot stamping processing of a specific MMnS alloy.

Investigated Alloy and Processing

For the investigations presented in this paper, 2 mm thick sheets of a medium manganese steel alloy were used. The chemical composition of the steel is shown in Tab. 1. The schematic temperature curve of the intercritical annealing and phase fractions before and after quenching are shown in Fig. 1. Before quenching, different fractions of austenite (γ) and primary martensite (α'_p) depend on the annealing temperature. After quenching, a phase transformation of the austenite to retained austenite (γ_r) and secondary martensite (α'_s) as shown is expected, while the primary martensite percentage is anticipated to be stable.

Table 1. Chemical composition (wt. %).

Fe	C	Mn	Si	Al	Cr	P	S	N
bal.	0.30	4.99	1.55	0.004	0.04	0.005	0.003	0.004

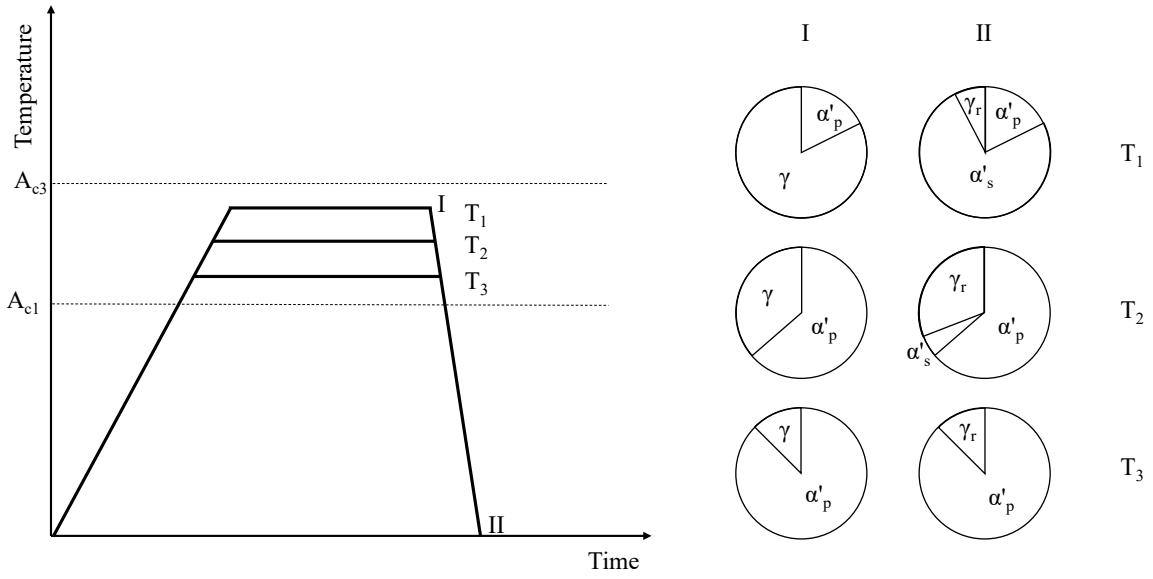

Fig. 1. Schematic illustration of phase fractions before and after quenching from different intercritical annealing temperatures.

Hot Tensile Tests

In order to verify the expected material behavior in terms of dependence of formability during hot stamping on the blank temperature during prior annealing, hot tensile tests were performed on a TA Instruments DIL805 dilatometer. The annealing temperature was varied in an interval of 700°C to 800°C. All specimens were inductively heated to the respective annealing temperature at a rate of 10 K/s. The soaking time was set to 5 min. After annealing, the specimens were quenched to 600°C and tensile tests were performed at a strain rate of 0.5 1/s. The uniform elongation is taken as an indicator of the materials formability with respect to the annealing temperature.

Fig. 2 shows the measured uniform elongation values at different annealing temperature. As expected, higher annealing temperatures, and therefore higher phase fractions of austenite, result in higher ductility. The highest uniform elongation could be found for an annealing temperature of 800°C (100 % austenite). It is notable that in a relatively small temperature interval from 720°C to 750°C the ductility of the material increases rapidly, indicating a switch between the materials behavior being dominated by the properties of the martensitic phase to being dominated by the properties of the austenitic phase.

A logistic function (Eq. 1) can be fitted to the data points to be able to approximate a continuous correlation between formability and annealing temperature. The formabilities of the single martensitic and austenitic phases are represented by the lower and upper limits of the curve.

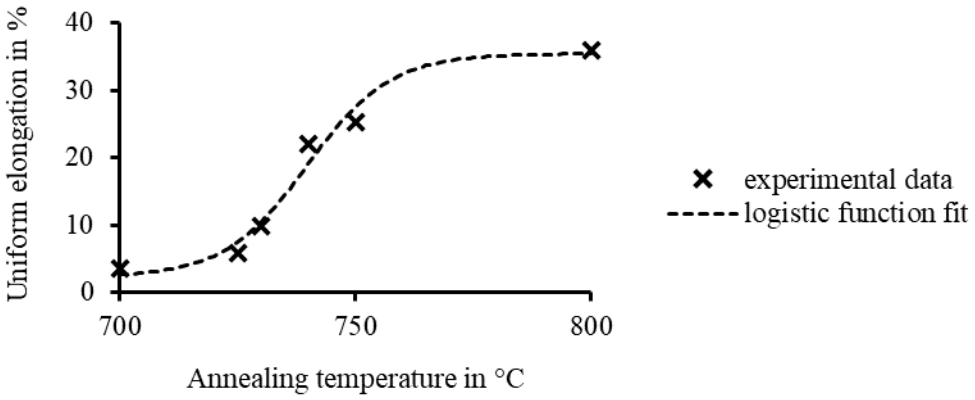

Fig. 2. Dependence of uniform elongation on the annealing temperature during hot tensile testing.

$$A_g = \frac{A_{g,max}}{1+e^{-k(T-T_0)}} \quad (1)$$

Hot Stamping Experiments

For further investigation of the material's formability at different annealing temperatures hot stamping experiments were performed on a single acting hydraulic deep drawing press using a hot stamping tool resembling a miniaturized b-pillar part. The tool does not have an active water-cooling system. However, as cycle times were larger than 10 minutes, the tool temperature can be assumed to be room temperature. Prior to annealing the blanks are spray-coated with boron nitride for friction reduction and basic scaling protection. The blanks were heated in a convection furnace for 7 minutes at different annealing temperatures (700°C, 730°C, 750°C, 800°C). After annealing the blanks were manually transferred to the pressing tool and formed with a constant tool speed of 35 mm/s (drawing depth of 25 mm). After forming the parts are quenched in the closed tool for 10 s.

Materials Research Proceedings 28 (2023) 833-838 https://doi.org/10.21741/9781644902479-91

Fig. 3 a) shows the dimensions of the hot stamped T-Shape profile. The notches at the bottom of the part are necessary for aligning the blank in the tool using two pilot rods. As can be seen in Fig. 3 b) only an annealing temperature of 800°C (fully austenitic microstructure) leads to a crack-free part. At annealing temperatures of 700°C, 730°C, and 750°C severe crack form at the upper part of the profile. With increasing annealing temperature additional cracks at the left and right shoulder part of the part start to appear. One possible explanation for cracks occurring at more locations with increasing annealing temperature is the increasing ductility of the material. At 700°C annealing temperature, the crack in the center part of the profile starts to form at very low drawing depths due to the poor ductility of the material. Therefore, almost all deformation for the rest of the drawing process takes place in the cracked region on the sheet. At higher annealing temperatures, the material is more ductile. The crack in the center appears at a higher drawing depth which leads to a more uniform thinning of the material which again leads to additional cracks forming.

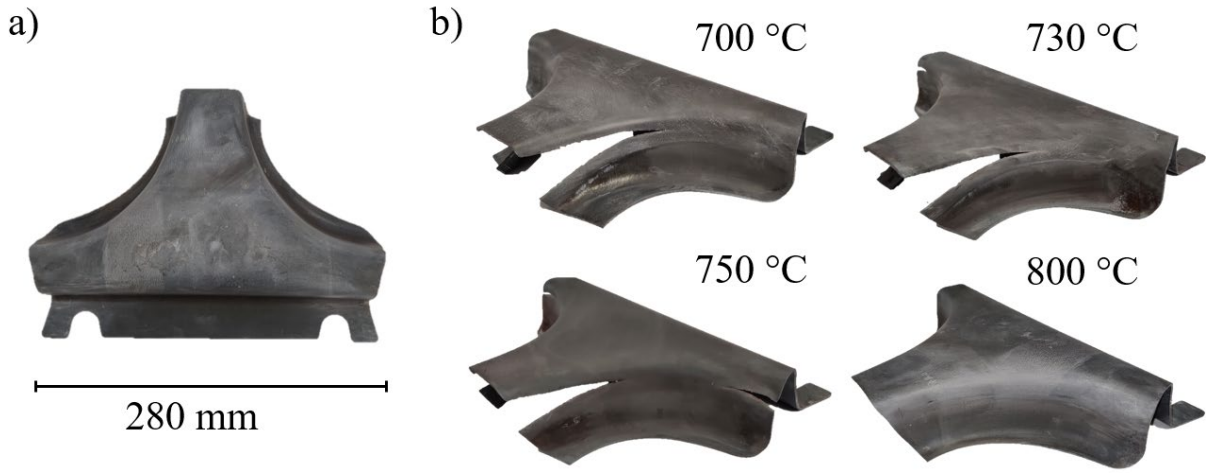

Fig. 3. a) Dimensions of T-shape profile. b) T-shape profiles processed with different annealing temperatures.

Material Properties of Quenched Specimens

In order to assess the mechanical properties of the quenched material with respect to the annealing temperature, further quenching experiments were conducted using the hot stamping tool. For each annealing temperature a rectangular sheet was heated according to the annealing of the T-shape profiles and quenched between the blank holder and the die of the hot stamping tool for 10s. Tensile test specimens were cut from the quenched sheets and quasi-static tensile tests were performed at room temperature. Table 2 shows the mechanical properties in the quenched state with respect to the different annealing temperatures.

Table 2. Mechanical properties in quenched state with respect to annealing temperature.

Annealing temperature [°C]	$R_{p0,2}$ [MPa]	R_m [MPa]	A_g [%]	A [%]
700	576	1250	21.0	21.2
730	420	1277	6.4	6.4
750	574	1263	2.4	2.4
800	877	1300	0.6	0.6

While yield strength and tensile strength only show a low sensitivity to the annealing temperature, uniform and total elongation show a strong dependence on the annealing temperature. An annealing temperature of 800°C results in a fully austenitic microstructure after annealing and a fully martensitic microstructure after quenching. This microstructure displays a very brittle behavior. With decreasing annealing temperature, and therefore higher phase fraction of retained austenite in the quenched state, the ductility of the material increases. At 730°C annealing temperature the ductility is comparable to standard manganese boron steels. At 700°C annealing temperature, the material displays very favorable mechanical properties in the quenched state.

Summary

This paper investigates the suitability of intercritical annealing and subsequent press hardening for processing high strength parts from medium manganese steel sheets. The choice of a specific annealing temperature influences phase fractions of austenite and martensite in the microstructure during hot stamping and after quenching. For different annealing temperatures formability was investigated by hot tensile tests and hot stamping experiments. Final mechanical properties were investigated by tensile tests. Hot tensile tests show an increasing formability with increasing annealing temperatures. In hot stamping experiments, part production without cracking was only possible for an annealing temperature of 800°C.

While yield strength and tensile strength in quenched material state show very low sensitivity to the annealing temperature, ductility increases heavily with decreasing annealing temperature. Mechanical properties of tensile strengths of 1250 MPa and total elongations of 21.2 % could be achieved at an annealing temperature of 700°C. While for both, in-process and final mechanical properties, an adequate annealing temperature could be found, no investigated annealing temperature satisfies both conditions, as a strong trade-off relationship between favorable final mechanical properties and formability during hot stamping was evident.

As a result, due to the identified trade-off relationship of the intercritical annealing route, it is not yet possible to achieve optimal processing conditions and final properties with the same annealing temperature. In this regard, further research has to be conducted in the processing of the investigated medium manganese steel alloy in press hardening.

Acknowledgement

Funded by the Deutsche Forschungsgemeinschaft (DFG, German Research Foundation) under Germany´s Excellence Strategy – EXC-2023 Internet of Production – 390621612.

References

[1] J.H. Schmitt, T. Iung, New developments of advanced high-strength steels for automotive applications, Comptes Rendus Physique 19 (2018) 641-656. https://doi.org/10.1016/j.crhy.2018.11.004

[2] H. Karbasian, A.E. Tekkaya, A review on hot stamping, J. Mater. Process. Technol. 210 (2010) 2103-2118. https://doi.org/10.1016/j.jmatprotec.2010.07.019
[3] D. Rosenstock, J. Banik,; S. Myslowicki, Hot stamping steel grades with increased tensile strength and ductility - MBW-K 1900, tribond 1200 and tribond 1400, IOP Conf. Ser.: Mater. Sci. Eng. 651 (2019) 012040. https://doi.org/10.1088/1757-899X/651/1/012040
[4] M. Merklein, M. Wieland, M. Lechner, S. Bruschi, A. Ghiotti, Hot stamping of boron steel sheets with tailored properties: A review, J. Mater. Process. Technol. 228 (2016) 11-24. https://doi.org/10.1016/j.jmatprotec.2015.09.023
[5] J. Speer, R. Rana, D. Matlock, A. Glover, G. Thomas, E. de Moor, Processing Variants in Medium-Mn Steels, Metals 9 (2019) 771. https://doi.org/10.3390/met9070771
[6] B. De Cooman, J. Speer, Quench and Partitioning Steel: a New AHSS Concept for Automotive Anit-Intrusion Applications, Steel Res. Int. 77 (2006) 634-640. https://doi.org/10.1002/srin.200606441
[7] C. Wang, W. Li, S. Han, L. Zhang, Y. Chang, W. Cao, H. Dong, Warm Stamping Technology of the Medium Manganese Steel, Steel Res. Int. 89 (2018) 1700360. https://doi.org/10.1002/srin.201700360
[8] Y.-K. Lee, J. Han, Current opinion in medium manganese steel, Mater. Sci. Technol. 31 (2015) 843-856. https://doi.org/10.1179/1743284714Y.0000000722
[9] C. Blankart, S. Wesselmecking, U. Krupp, Influence of Quenching and Partitioning Parameters on Phase Transformations and Mechanical Properties of Medium Manganese Steel for Press-Hardening Application, Metals 11 (2021) 1879. https://doi.org/10.3390/met11111879

Materials Research Proceedings 28 (2023) 839-846 https://doi.org/10.21741/9781644902479-92

Specific behavior of high-manganese steels in the context of temperature increase during dynamic deformation

JABŁOŃSKA Magdalena B.[1,a *], GRONOSTAJSKI Zbigniew[2,b], TKOCZ Marek[1,c], JASIAK Katarzyna[2,d], KOWALCZYK Karolina[1,e], SKWARSKI Mateusz[2,f] and KOSTKA Michał[1,g]

[1]Silesian University of Technology, Faculty of Materials Engineering, Krasińskiego 8, 40-019 Katowice, Poland

[2]Wrocław University of Technology, Faculty of Mechanical Engineering, Ignacego Łukasiewicza 5, 50-371 Wrocław, Poland

[a]magdalena.jablonska@polsl.pl, [b]zbigniew.gronostajski@pwr.edu.pl, [c]marek.tkocz@polsl.pl, [d]katarzyna.jasiak@pwr.edu.pl, [e]karolina.kowalczyk@polsl.pl, [f]mateusz.skwarski@pwr.edu.pl, [g]michkos976@student.polsl.pl

Keywords: High-Manganese Steel, TWIP, Dynamic Deformation, Microstructure, Temperature, Twinning

Abstract. In recent years, a development of AHSS steels for manufacturing parts for the automotive industry is the observed trend. The high-manganese steels with aluminium and silicon addition, exhibiting twinning induced plasticity (TWIP) effect, are one of the most interesting modern materials, due to their unique combination of both very good strength and great ductility. However, the material behaviour during plastic deformation depends not only on the chemical composition but also on deformation conditions, inter alia, strain rate and temperature. TWIP steels can be used for production of energy-absorbing parts, therefore it is very important to analyse their deformation behaviour at high strain rates. The paper presents the effect of deformation in quasi-static and dynamic conditions on the microstructure of an experimental TWIP steel. The experiments were performed on tensile testing machine and on the flywheel machine. The microstructure was analyzed by optical and scanning transmission electron microscopy. Thanks to the measurements during the quasi-static test and numerical simulations of both tensile tests, the temperature increase was determined in the sample region from which the sections for microstructural studies were taken. It was found that the temperature increase in dynamic conditions can affect the microstructure evolution in the investigated TWIP steel.

Introduction

The autobody components made of non-ferrous materials are nowadays more common than they used to be earlier, however, the most responsible parts in terms of passengers safety are still made of steel [1,2]. In recent years, considerable efforts have been focused on the development of high-manganese steels for the automotive industry. With the specific Mn, Al and Si content, these steels are characterized with the stacking fault energy (SFE) value in the range of ca. 20 to ca. 50 mJ/m^2 which favors twinning as a dominant deformation mechanism. This phenomenon was ultimately confirmed in many studies [2,3]. The concept of a steel with the so called twinning induced plasticity (TWIP) effect was proposed for the first time by Grassel and Fromayer [4]. During the analysis of steel with 15 and 25% of Mn content, the authors established that the unique combination of high mechanical properties and high ductility is determined by the mechanical twins formation in the austenitic grains [5]. The same authors proved that TWIP steel with an advantageous combination of mechanical and plastic properties should contain the amount of manganese within the range of 20% wt. to 30% wt., the aluminium content – from 3% wt. to 5%

Content from this work may be used under the terms of the Creative Commons Attribution 3.0 license. Any further distribution of this work must maintain attribution to the author(s) and the title of the work, journal citation and DOI. Published under license by Materials Research Forum LLC.

wt. and the carbon content not exceeding 0.6% wt. The TWIP steels are characterized by good work hardening, which is mostly the result of twinning, but also dynamic strain ageing (DSA). Moreover, these steels are extremely sensitive to the strain rate [6]. The studied carried out in [7] proved an influence of the strain rate on the ability to transfer dynamic loads by the TWIP steel, confirming an increase in the impact resistance under the influence of increasing strain rate. The dynamic deformation conditions favors the mechanical twins growth in TWIP steel [8, 9]. However, the high strain rate causes the rapid temperature increase in a deformed region. It was proved that temperature rise above 200°C in numerous MnAl steels causes the increase of the SFE value which promotes the dislocation slip and slows down the mechanical twins growth [10]. There's a limited information in the literature about the effect of heat generated during dynamic deformation on the TWIP steel microstructure evolution [11].

The aim of the study was to determine a temperature increase due to conversion of the deformation work into the heat in experimental TWIP steel samples subjected to tensile tests at two different conditions and to analyse how the heat generated affects the deformation mechanism in the investigated steel.

Research Methodology

The research was carried out on an experimental high-manganese steel with the chemical composition given in Table 1. The steel was smelted in a vacuum induction furnace and cast using the gravity casting technique. 120 mm long ingots with a cross-section of 20 x 40 mm were homogenized in an air furnace at 1200°C and then hot-rolled to a thickness of ca. 2 mm. After hot rolling, the steel was subjected to solution heat treatment (1100°C / 2 h / water quenching).

Table 1. The chemical composition of the investigated steel.

Element content, wt. %										
C	Mn	Al	V	P	S	Ce	La	Nd	N	Fe
0.42	21.10	2.55	0.002	<0.01	0.006	0.011	<0.005	<0.005	43ppm	bal.

The dog-bone samples with the dimensions given in Fig. 1a were cut-out of the obtained strips to perform the quasi-static tensile test (at the strain rate of 0.5 s^{-1} – Fig. 1b) on the Instron tensile testing machine and the dynamic one (at the strain rate of 1000 s^{-1} – Fig. 1c) on the flywheel machine. The latter method is described in [12]. The initial temperature of samples was ca. 20ºC. The temperature changes in the sample tested at the lower strain rate were recorded by FLIR T840 thermal imaging camera. Temperature measurement methodology during quasi-static tensile tests was presented in [13].

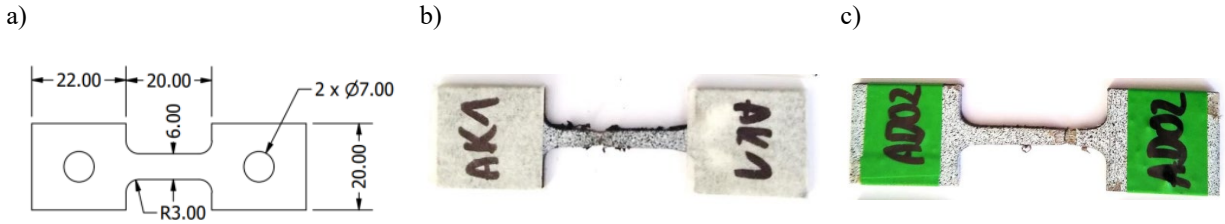

Fig. 1. The sample dimensions used in tensile tests (a) and samples after quasi-static (b) and dynamic (c) tensile tests.

The numerical modelling of quasi-static and dynamic tensile tests were performed in Forge NxT 3.2 – a commercial finite element method software dedicated for metal forming and heat

treatment simulations. To reduce the computation time, a geometric model of ⅛th of a sample was used (Fig. 2). The fine tetrahedral mesh was generated in the sample volume.

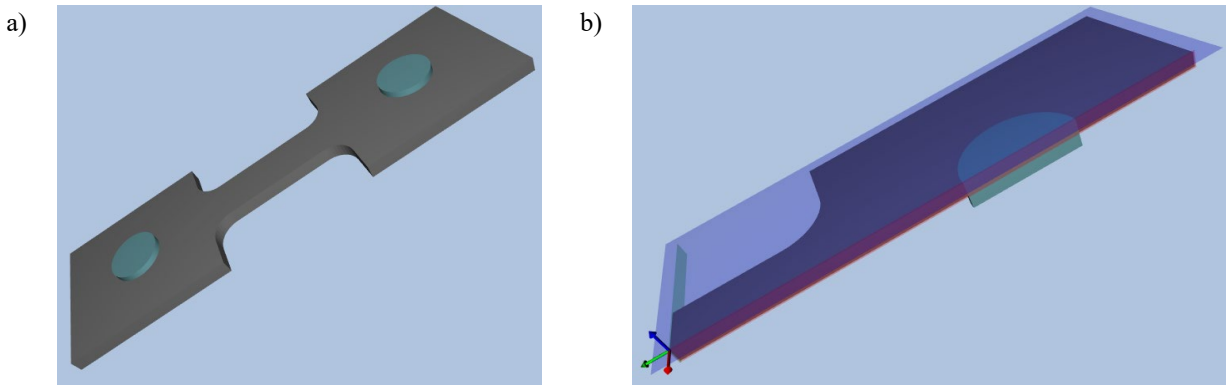

Fig. 2. The geometric model of a sample used in tensile tests with the gauge length of 10 mm, the width of 6 mm and the thickness of 1.4 mm (a) and symmetry planes utilized in simulations (b).

The flow stress of the investigated TWIP steel was defined with the equation:

$$\sigma_p = A \cdot \exp(m_1 T) \cdot (\varepsilon + \varepsilon_{b0})^{m_2} \quad (1)$$

where: T – temperature of the sample, ε – equivalent strain, A, m_1, m_2, ε_{b0} – coefficients of the Eq. 1.

The coefficients in Eq. 1 were calculated separately for each strain rate on the basis of the experimentally determined mechanical properties (such as the offset yield strength $R_{p0.2}$, the ultimate tensile strength R_m and the uniform elongation A_g), by means of Cold Rheology Generation Tool included in the Forge NxT 3.2 software, The Eq. 1 coefficient values as well as the mechanical properties obtained in experiments are collected in Table 2. The physical and thermal properties such as density (7400 kg/m^3), specific heat (500 J/kgK) and thermal conductivity (17 W/mK) were taken from [14]. Adiabatic conditions on the sample-die interface were assumed.

Table 2. Mechanical properties and coefficients of the flow stress function.

Strain rate [s^{-1}]	$R_{p0.2}$ [MPa]	R_m [MPa]	A_g [%]	A	m_1	m_2	ε_{b0}
0.5	245	523	54	1169.71	-0.0009	0.468808	0.0370259
1000	410	650	48	1397.58	-0,0009	0.467435	0.0753929

Microstructural observations were made on microsections parallel to the longitudinal sample axis, in the necked region, by means of the light microscope Olympus GX71 and scanning transmission electron microscope Hitachi HD-2300A. In order to reveal the microstructure, the material was etched in 6% Nital (94 ml of ethyl alcohol, 6 ml of HNO_3 acid).

Results and Discussion

To verify the correctness of the simulation results, calculated temperature distributions and the maximum temperature change in the sample deformed at 0.5 s^{-1} were compared to the corresponding experimental measurements (Fig. 3). It seems like quite good accuracy of

simulation results was obtained. In both cases the maximum temperature started to rise intensively on the onset of necking which was predicted in the simulation almost in the same moment as it happened in the experiment. The most notable difference is the necking location. In the real test it has occurred in the weakest cross-section of the gauge length while in the simulation – at the sample center. It is obvious that the numerical model definition has forced prediction of the necked region at the center of a sample. The other solution would be possible if some inconsistency or a flaw in the sample geometry, the finite element mesh, the material model or boundary conditions appeared or was there something like that defined on purpose.

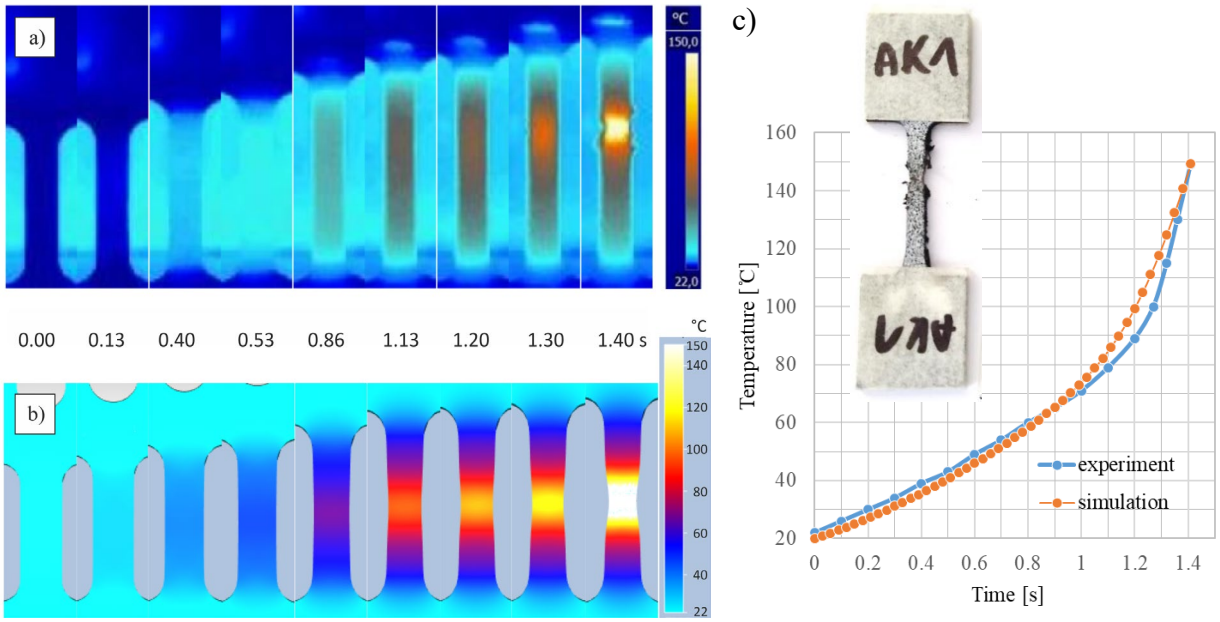

Fig. 3. Comparison of measured (a) and calculated (b) temperature distributions and the maximum temperature (c) in the sample tested at the strain rate of 0.5 s^{-1}.

The mechanical properties, presented in Table 2, as well as the corresponding flow curves (Fig. 4c) indicate that significantly higher stresses are required to deform of the investigated steel under dynamic loading. It is well reflected in the von Mises stress distributions presented in Figs. 4a and 4b. However it is worth to notice that the steel still exhibits the excellent uniform elongation (A_g) at very high strain rates. It is only slightly smaller than the elongation observed in the quasi-static conditions.

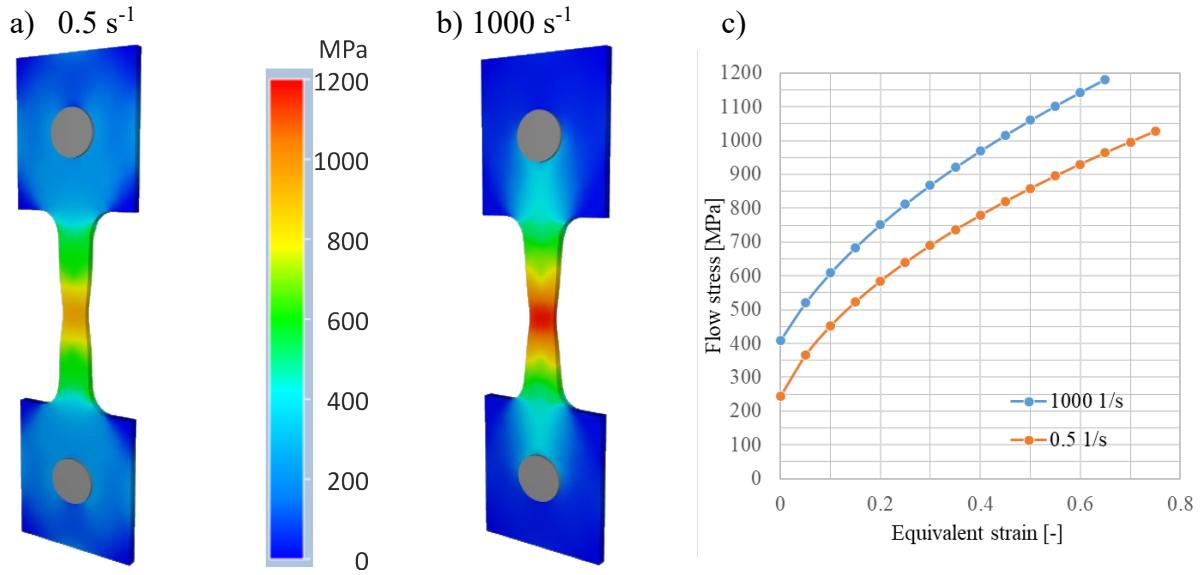

Fig. 4. Calculated von Mises stress distributions in the investigated TWIP steel samples subjected to (a) quasi-static and (b) dynamic tensile tests as well as a comparison of TWIP steel flow curves for the analysed strain rates (c).

A comparison of temperature changes in both selected deformation cases is presented in Fig. 5. As it was expected, the significantly higher flow stress of the investigated steel during deformation at the strain rate of 1000 s^{-1} caused more intensive temperature increase in the sample. According to the numerical simulation results, the temperature at the center after reaching equivalent strain of ca. 0.8 can exceed 200°C. Similar research results were presented in the work [11]. Such a deformation temperature in some MnAl steels increases stacking fault energy (SFE) and promotes dislocation slip.

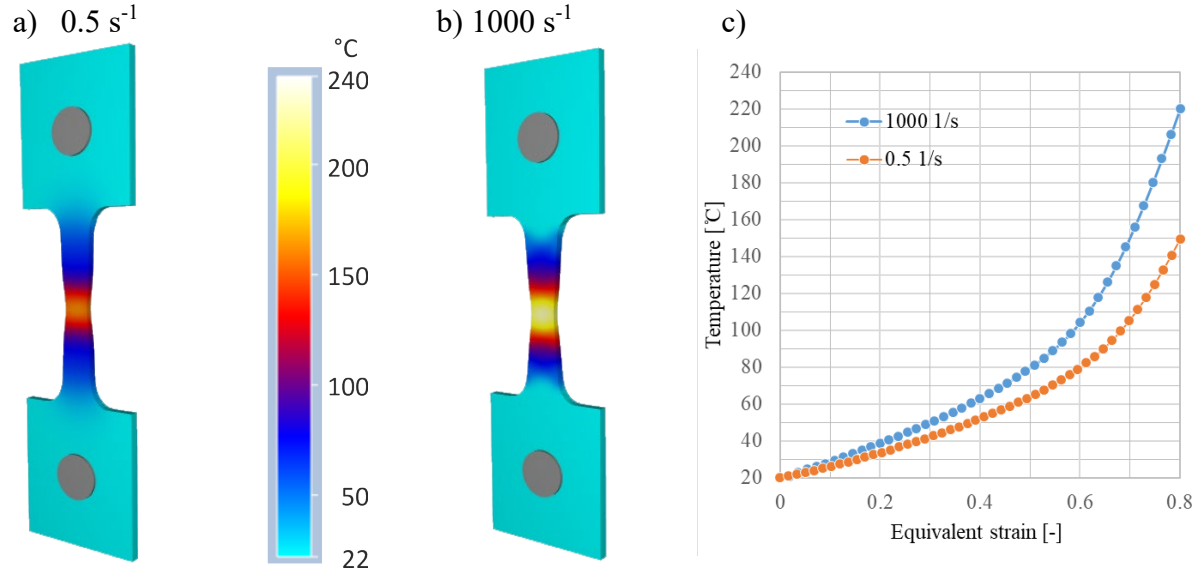

Fig. 5. Calculated temperature distributions in the investigated TWIP steel samples subjected to (a) quasi-static and (b) dynamic tensile tests as well as a comparison of the maximum temperature (c).

Materials Research Proceedings 28 (2023) 839-846 https://doi.org/10.21741/9781644902479-92

Microstructure Analysis

The microstructure of the studied steel at the initial state is fully austenitic (Fig. 6a). It is characterized by the presence of austenite grains with characteristic coherent annealing twins (Fig. 6b) and tangled dislocations observed near the grain boundaries (Fig. 6c).

After the tensile tests, effects of deformation are clearly visible in the microstructure. The austenite grains are elongated towards the tensile direction (Figs. 6 d,g). In the austenite matrix containing dislocations cells, the generation of mechanical twins occurs in the primary and secondary twinning system (Figs. 6 e,f). At the strain rate of 1000 s^{-1}, the generation of multi-twins as well as nano-twins is observed (Figs. 6 h,i). This leads to the activation of several slip and twinning systems. Moreover, the twin bundles can be observed. The interactions between twins take place and individual micro shear bands appear (Fig. 6h).

The development of micro shear bands results from the evolution of dislocation structure. This phenomenon can be associated with the intensive temperature increase calculated in the sample deformed at the strain rate of 1000°C. It could cause the increase of stacking fault energy and thus, possibly, the *rearrangement of the dislocation structure*.

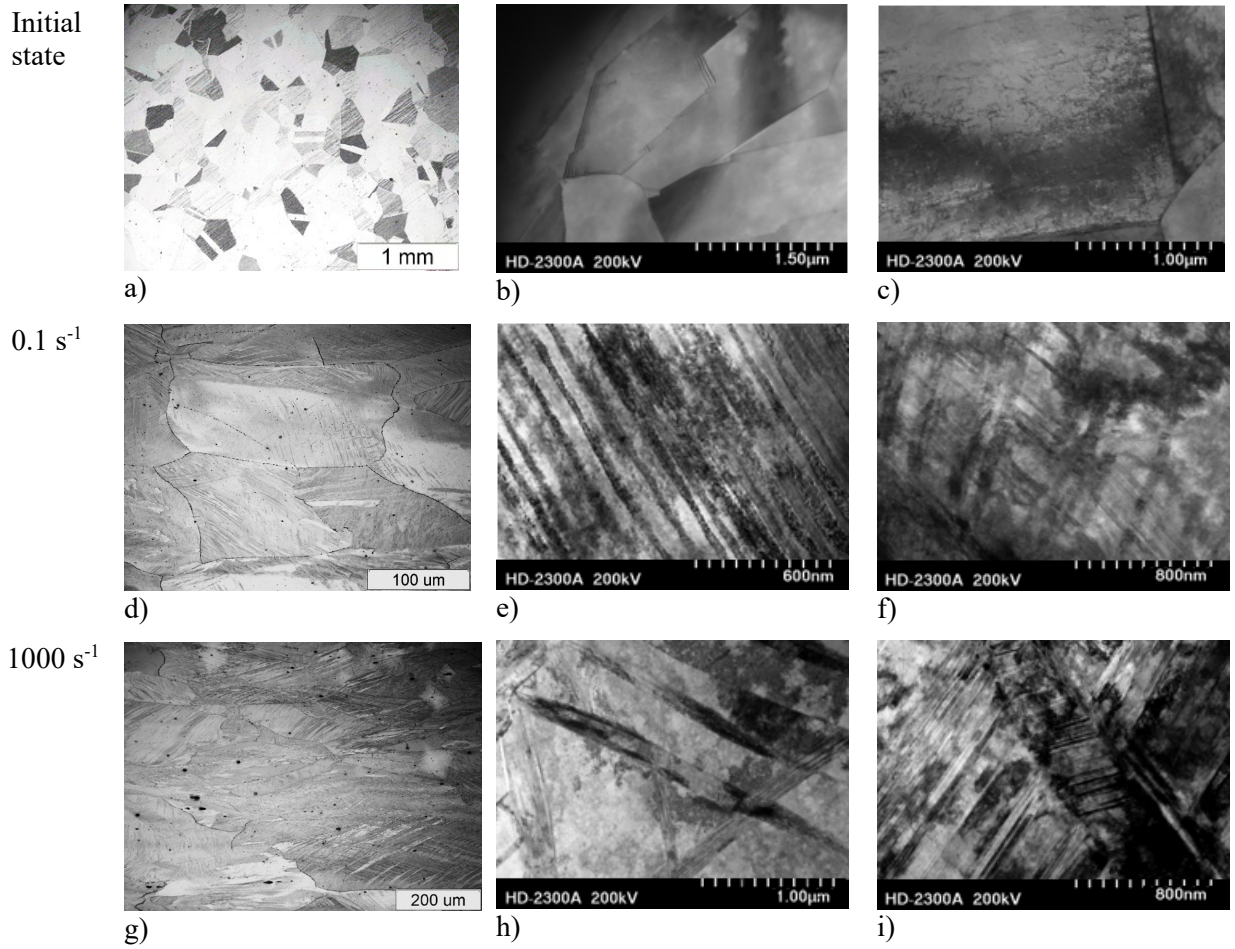

Fig. 6. The microstructure of the investigated steel in the initial state and after deformation at various strain rates; taken from the necked regions where the equivalent strain was ca. 0.8.

Summary

The experimental, high-manganese austenitic steel tested in this work can be classified as a material exhibiting TWIP effect. It was proved that it has good strength, comparable to the currently used steels for elements that increase the safety of vehicles, and very high elongation, even during deformation at very high strain rates. This unique features indicate that TWIP steels are excellent materials for the production of energy-absorbing parts that are designed to withstand severe deformation without fracture during a collision.

The convergence of experimental and simulation results was obtained for the test performed in the quasi-static conditions. This suggests that the prepared simulation model can provide correct results also for dynamic deformation conditions. The conducted numerical simulations made it possible to determine the temperature increase in the sample tested at high strain rate, which was not possible during the experiment.

During deformation at the strain rate of 0.1 s^{-1}, the temperature of the investigated steel reached over 150°C in the necked region of the tensile sample. In these conditions the mechanical twinning is a dominant deformation mechanism. However, at the strain rate of 1000 s^{-1}, the temperature noticeably exceeding 200°C was calculated in the region from which micro-sections for microstructural investigations were taken. The effects of microstructure evolution observed in the sample indicate that such a high temperature probably affected the stacking fault energy of the investigated steel as well as promoted the development of micro-bands and the rearrangement of dislocation structure.

Acknowledgments

The financial support of the National Science Centre, Poland, granted under the project UMO-2019/35/B/ST8/02184 “Effect of the heat generated during deformation at high strain rates on the structure and properties of high manganese steels with twinning as the dominant deformation mechanism”, is gratefully acknowledged.

References

[1] D. Frómeta, A. Lara, L. Grifé, T. Dieudonné, P. Dietsch, J. Rehrl, C. Suppan, D. Casellas, J. Calvo, Fracture resistance of advanced high-strength steel sheets for automotive applications, Metall. Mater. Trans. A: Phys. Metall. Mater. Sci. 52 (2021) 840-856. https://doi.org/10.1007/s11661-020-06119-y

[2] K.S Raghavan., A.S Sastri., M.J Marcinkowski., Nature of work-hardening behavior in Hadfields manganese steel, Trans. Metall. Soc. Aime 245 (1969) 1569-1575.

[3] L. Remy, Kinetics of fcc. deformation twinning and its relationship to stress-strain behaviour, Acta Metall. 26 (1978) 443–451. https://doi.org/10.1016/0001-6160(78)90170-0

[4] O. Grässel, G. Frommeyer, Effect of martensitic phase transformation and deformation twinning on mechanical properties of Fe-Mn-Si-Al steels, Mater. Sci. Technol. 14 (1998) 1213-1217. https://doi.org/10.1179/mst.1998.14.12.1213

[5] A. Kozłowska, K. Radwański, K. Matus, L. Samek, A. Grajcar, Mechanical stability of retained austenite in aluminum-containing medium-Mn steel deformed at different temperatures, Arch. Civil Mech. Eng. 21 (2021) 269-275. https://doi.org/10.1007/s43452-021-00177-8

[6] Y.F. Shen, N. Jia, R.D.K. Misra, L. Zuo, Softening behavior by excessive twinning and adiabatic heating at high strain rate in a Fe-20Mn-0.6C TWIP steel, Acta Mater. 103 (2016) 229-242. https://doi.org/10.1016/j.actamat.2015.09.061

[7] A. Śmiglewicz, M.B. Jabłońska, The effect of strain rate on the impact strength of the high-Mn steel, Metalurgia 54 (2015) 631-634. ISSN 0543-5846 UDC – UDK 669.74.15:539.55.375:531.76=111

[8] A. Śmiglewicz, W. Moćko, K. Rodak, I. Bednarczyk, M.B. Jabłońska, Study of dislocation substructures in high-Mn steels after dynamic deformation tests, Acta Phys. Polon. A 130 (2016) 942-945. https://doi.org/10.12693/APhysPolA.130.942
[9] H.K. Yang, Z.J. Zhang, F.Y. Dong, Q.Q. Duan, Z.F. Zhang, Strain rate effects on tensile deformation behaviors for Fe-22Mn-0.6C-(1.5Al) twinning-induced plasticity steel, Mater. Sci. Eng. A 607 (2014) 551–558. https://doi.org/10.1016/j.msea.2014.04.043
[10] V. Shterner, I.B. Timokhina, H. Beladi, On the work-hardening behaviour of a high manganese TWIP steel at different deformation temperatures, Mater. Sci. Eng. A 669 (2016) 437-446. https://doi.org/10.1016/j.msea.2016.05.104
[11] M.B. Jabłońska, Structure and properties of a high-manganese austenitic steel strengthened in the result of mechanical twinning in processes of dynamic deformation, Monograph, Silesian University of Technology Publisher, ISBN: 978-83-7880-363-8.
[12] Z. Gronostajski, A. Niechajowicz, R. Kuziak, J. Krawczyk, S. Polak, The effect of the strain rate on the stress-strain curve and microstructure of AHSS, J. Mater. Process. Technol. 242 (2017) 246-259. https://doi.org/10.1016/j.jmatprotec.2016.11.023
[13] M.B. Jabłońska, K. Jasiak, K. Kowalczyk, I. Bednarczyk, M. Skwarski, M. Tkocz, Z. Gronostajski, Deformation behaviour of high-manganese steel with addition of niobium under quasi-static tensile loading, Mater. Sci.-Poland 40 (2022) 1-11. https://doi.org/10.2478/msp-2022-0029
[14] V. Garcia-Garcia, Microstructural and mechanical analysis of double pass dissimilar welds of twinning induced plasticity steel to austenitic/duplex stainless steels, Int. J. Press. Vessel. Piping. 198 (2022) 104665. https://doi.org/10.1016/j.ijpvp.2022.104665

Materials Research Proceedings 28 (2023) 847-854 https://doi.org/10.21741/9781644902479-93

Effect of prestrain on mechanical behavior of aluminum alloys

VINCZE Gabriela[1,2,a *], BUTUC Marilena C.[1,2,b], WEN Wei[3,c], YÁNEZ Jesús[1,d] and LOPES Diogo[1,e]

[1]Centre of Mechanical Technology and Automation (TEMA), Department of Mechanical Engineering, University of Aveiro, 3810-193 Aveiro, Portugal

[2]LASI - Intelligent Systems Associate Laboratory, Portugal

[3]Department of Engineering, Lancaster University, Lancaster LA1 4YR, UK

[a]gvincze@ua.pt, [b]cbutuc@ua.pt, [c]w.wen2@lancaster.ac.uk, [d]jvallez@ua.pt, [e]diogoaflopes@ua.pt

Keywords: Aluminum Alloys, Mechanical Behavior, Asymmetric Rolling

Abstract. Sheet metal forming involves many times large plastic strain and strain path changes. It is well known that the plastic behavior of metals is strain path sensitive. In monotonic loading, the microstructure as well as the crystallographic texture evolve during deformation leading usually to a gradual material hardening that tends to saturate at large strains. Such evolution can be interrupted if a severe change of strain path occurs. The simplest way to change drastically the strain path is through reverse loading, namely, by loading the material in opposite direction to the previous one. In this case, the material behavior can show one or more characteristics, such as the Bauschinger effect, transient hardening, softening or hardening. This work investigated the effects of the prestrain on the mechanical response of the material subjected to reverse simple shear. The prestrain is produced by rolling, either symmetric or asymmetric, and different amounts of equivalent strain. Three routes of rolling are used, namely, symmetric, asymmetric continuous, and asymmetric reverse [1]. The Bauschinger effect slightly decreases with the prestrain increase for the initial material. After rolling, the Bauschinger effect is insensitive to the rolling route, and it is also insensitive to the amount of the rolling prestrain.

Introduction

Aluminum alloys are very good choices for many applications from the aerospace industry to packaging, due to their advantageous strength-to-weight ratio and their high recyclability without loss of their properties. However, the forming operation of aluminum alloys faces some challenges, due to the low formability at room temperature and high springback. The latter mainly due to the low stiffness compared with steels. It is also well known that a high influence on the mechanical behavior of aluminum alloys subject to plastic deformation is related to their texture. An easy way to change the texture of the material is by rolling. Moreover, asymmetric rolling allows the creation of different texture components by controlling the rolling route. Another important factor during forming operation is the strain path changes. An abrupt change in strain path can cause a Bauschinger effect, a transient behavior, permanent softening, or higher hardening rate compared to monotonic loading. The effects of strain path changes were extensively studied over the years by experimental and numerical methods [2-8]. Moreover, many researchers stated that the Bauschinger effect is associated with the amplitude of springback and is an indispensable parameter that should be considered for an accurate prediction of springback [9,10]. The aim of this study is to analyze the influence of the amount of prestrain in the Bauschinger parameter for a large range of values.

Content from this work may be used under the terms of the Creative Commons Attribution 3.0 license. Any further distribution of this work must maintain attribution to the author(s) and the title of the work, journal citation and DOI. Published under license by Materials Research Forum LLC.

Material and Experimental methods

Material.

The material used in this study is an aluminum-silicon-magnesium alloy AA6022-T4 with an initial thickness of 2 mm and chemical composition given in Table 1. The material has a strong cube texture typical for recrystallized aluminum sheets as can be seen in Fig. 1. A complete characterization of this material can be found in [1,11].

Table 1. Chemical composition of the material as-received wt. %.

Si	Fe	Cu	Mn	Mg	Cr	Zn	Ti	Others	Al
0.8-1.5	0.05-02	0.01-0.11	0.02-0.1	0.45-0.7	0.1	0.25	0.15	0.15	Balance

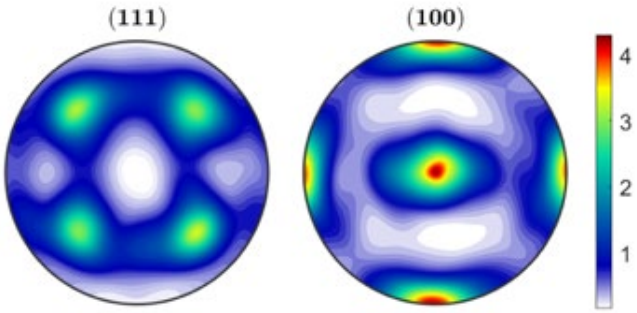

Fig. 1. Pole figures {111},{100} of the initial material.

Asymmetric rolling.

The in-house asymmetric rolling mill presented in Fig. 2 was used for rolling. The diameters of the rolls are 180 mm and the length is 300 mm. Detailed description of this mill can be found in [1]. The asymmetry was introduced by imposing different speeds for the upper and bottom rolls of the mill. For symmetric rolling, the angular speed of both rolls was 15 rpm. For asymmetric rolling, a ratio of 1.36 of the rolls' speeds was produced by the angular speeds of 15 rpm and 11 rpm.

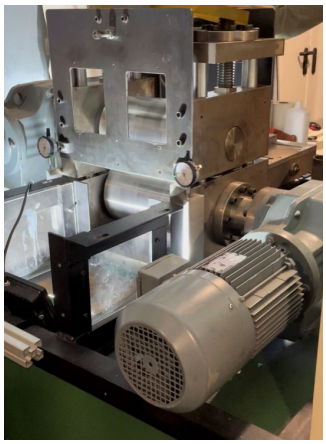

Fig. 2. Asymmetric rolling mill.

The total thickness reduction was 50%, and was obtained in 4 passes, with a thickness reduction of 15% per pass. Regarding asymmetric rolling, two types of strain paths were produced by the rotation of the sheet between two subsequent passes. Namely, (1) asymmetric continuous (ARC) when no rotation of the sheet occurred between two subsequent passes, and (2) asymmetric reverse

route (ARR) when rotation of 180º around the rolling direction (RD) occurred between two subsequent passes. The rolling route produces a forward or a reverse shear deformation in sheet thickness, corresponding to ARC and ARR respectively. An illustration of the rolling route is presented in Fig. 3.

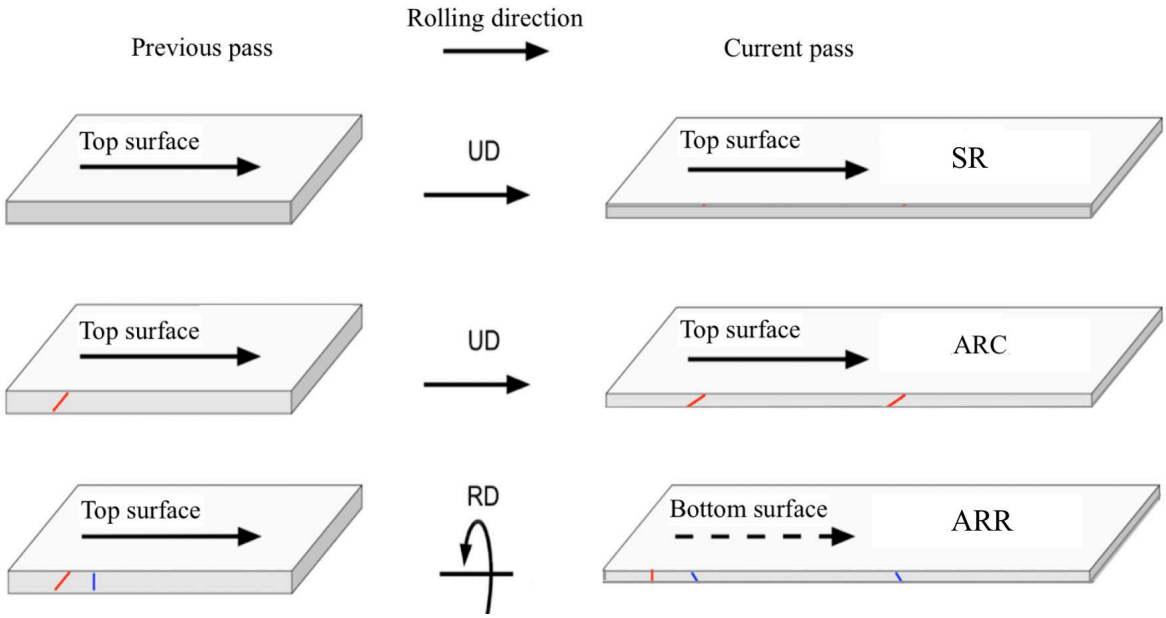

Fig. 3. Rolling routes: SR - symmetric rolling, ARC - asymmetric rolling continuous, ARR - asymmetric rolling reverse.

Simple shear test.

The study of the Bauschinger effect on sheet metals by tension-compression test is difficult due to the buckling that occurs during compression. Thus, to avoid buckling, an easy way is to promote reverse loading in simple shear tests. The as-received material was tested in simple shear and reverse loading at 10%, 20% and 30% shear prestrain. The rolled material was tested in reverse shear for a shear prestrain nearby 10%. The in-house simple shear device was used for these tests. The sample geometry is a rectangle with 34x13 [mm^2], corresponding to length and width, respectively. The thickness is variable according to the rolling. The shear deformation area is 34x3 [mm^2]. The strain measurements were made by Digital Image Correlation using the GOM system and the software ARAMIS 5M. The setup of the simple shear test can be seen in Fig. 4.

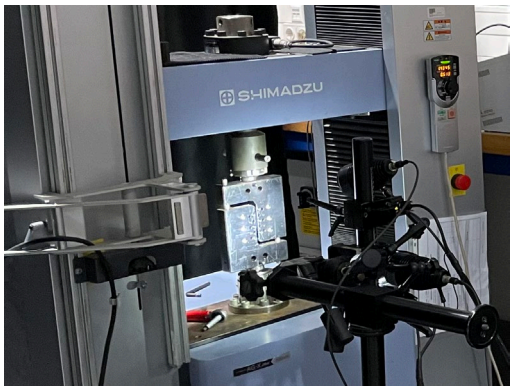

Fig. 4. Setup of the simple shear test.

Bauschinger Parameter

The Bauschinger coefficient was calculated as proposed by Hou et al. [12]

$$\beta = \frac{\tau_{p2}}{\tau_{p1}} \quad (1)$$

Where τ_{p1} and τ_{p2}, denoting the flow stress at the end of prestrain and the yield stress of reloading respectively, are schematically represented in Fig 5.

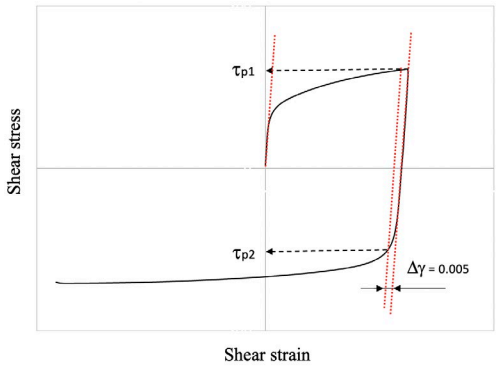

Fig. 5. Schematic representation of Bauschinger parameter calculation.

Thus, if β = 1, means that Bauschinger effect does not occur. If β decreases, means that the Bauschinger effect is more pronounced and opposite if β increases.

Results and Discussion

Initial material.

The initial material was tested in reverse shear for three amounts of prestrain, namely 10%, 20% and 30 % shear strain. The results are presented in Fig. 6 and are in agreement with data existing in the literature [3]. Namely, it can be noticed the existence of the Bauschinger effect, no plateau and a higher strain hardening that led to an overshooting of the monotonic shear stress-shear strain curve.

It can be observed from Fig. 7 that the Bauschinger coefficient increases with the increase of pre-strain amount for initial material, which means that the Bauschinger effect is reduced with the increase of pre-strain.

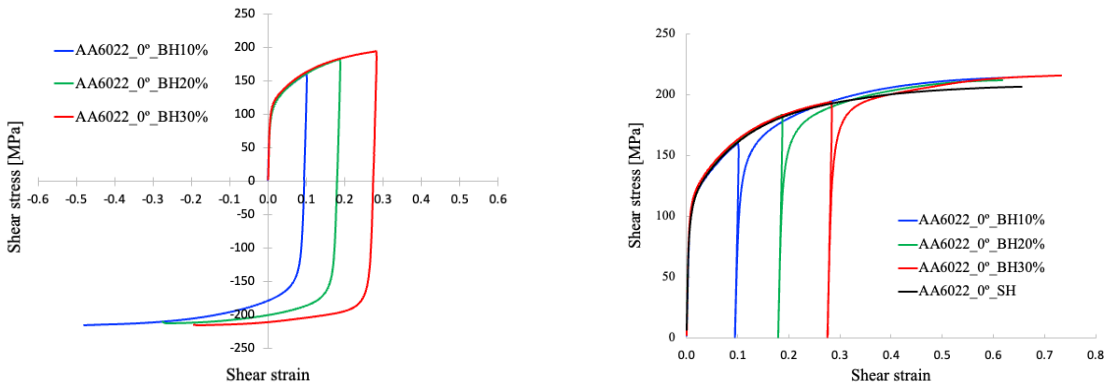

a) b)

Fig. 6. Simple shear and reverse shear of AA6022-T4: a) reverse shear; b) monotonic and revere shear transformed to the first quadrant.

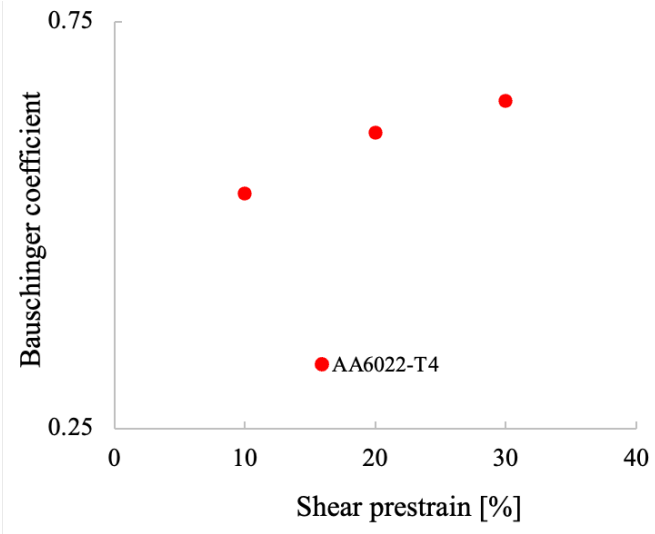

Fig. 7. Evolution of Bauschinger coefficient with the prestrain for material before rolling.

After rolling.

The shear stress-shear strain curves after each pass of rolling are presented in Fig. 8. It can be observed that after each pass the curves are superimposed which means that the material behavior is not affected by the rolling route. After rolling, the material has the same response as the initial material when submitted to reverse loading, showing the Bauschinger effect without plateau. It is worth to mention that the difference in the prestrain deformation is introduced by the difficulty in controlling the test when DIC is used. The Bauschinger coefficient seems to stabilize with the increase of prestrain as can be seen in Fig. 9, where the β is plotted versus equivalent strain corresponding to prestrain, and it is produced by shear or rolling + shear. The values after rolling are very close to the one obtained for the initial material after 30% prestrain. This trend is observed for all three routes. A very small difference in β between the rolling routes can be observed with the lowest value corresponding to ARC and the highest to ARR. The material processed by SR has the lowest variation of β between the rolling passes, only 2%, while for ARC and ARR this variation is about 5% and 4%, respectively. The saturation of the Bauschinger effect observed in figure 9 is related to the dislocation density. In theory, the short-term and long-term Bauschinger effects are caused by the dislocation in the pile-up that can travel backwards upon reversal loading. Their reverse motion is assisted by the back-stress, leading to a drop in the flow stress. Those dislocations also tend to recombine with other dislocations, leading to a lower dislocation hardening level. After a large accumulated strain, more dislocation will be pinned in the forest structures and thus become non-reversible, leading to a less significant Bauschinger effect.

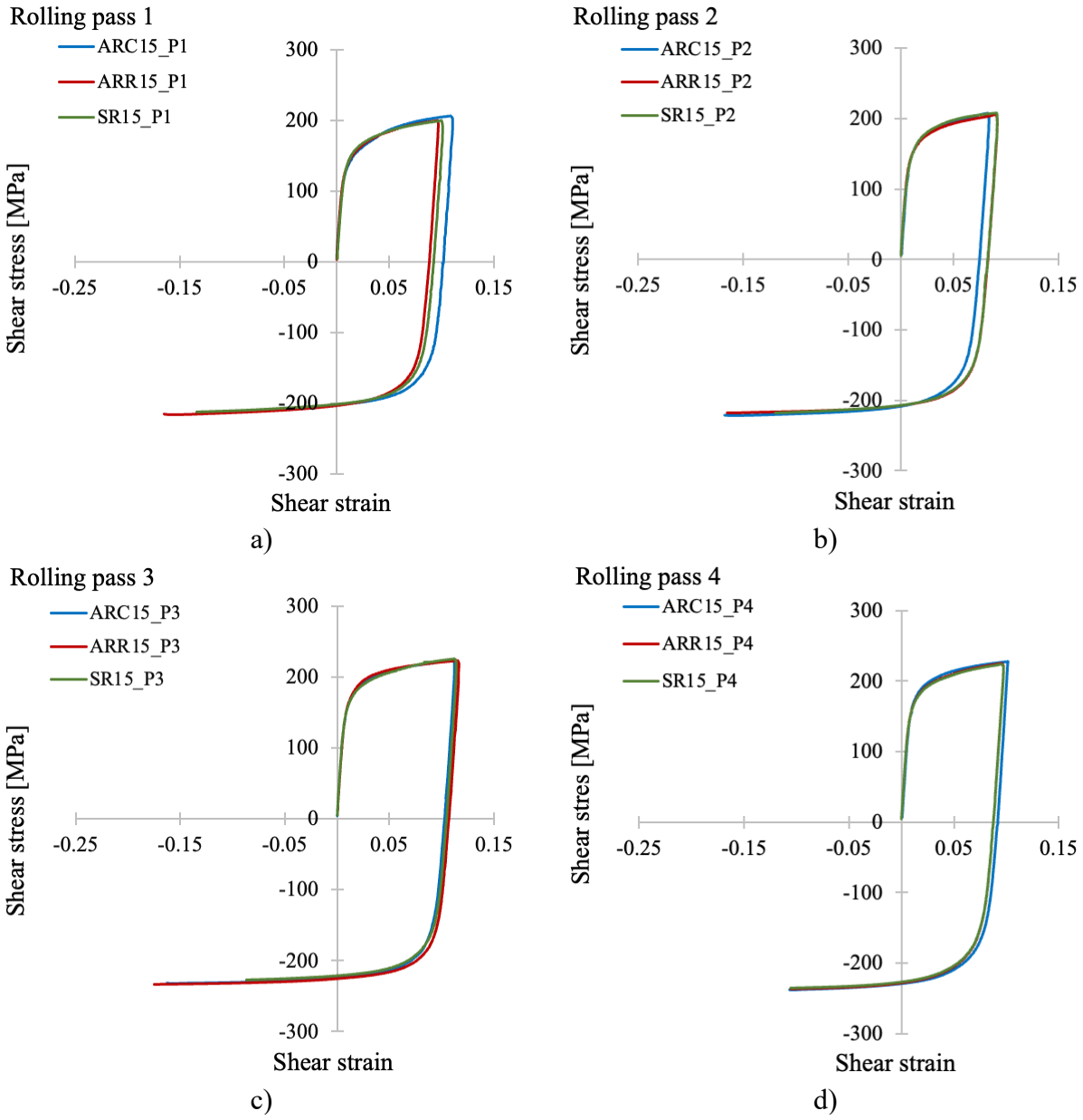

Fig. 8. Shear stress-shear strain after ARC, ARR and SR: a) pass 1; b) pass 2; c) pass 3 and d) pass 4.

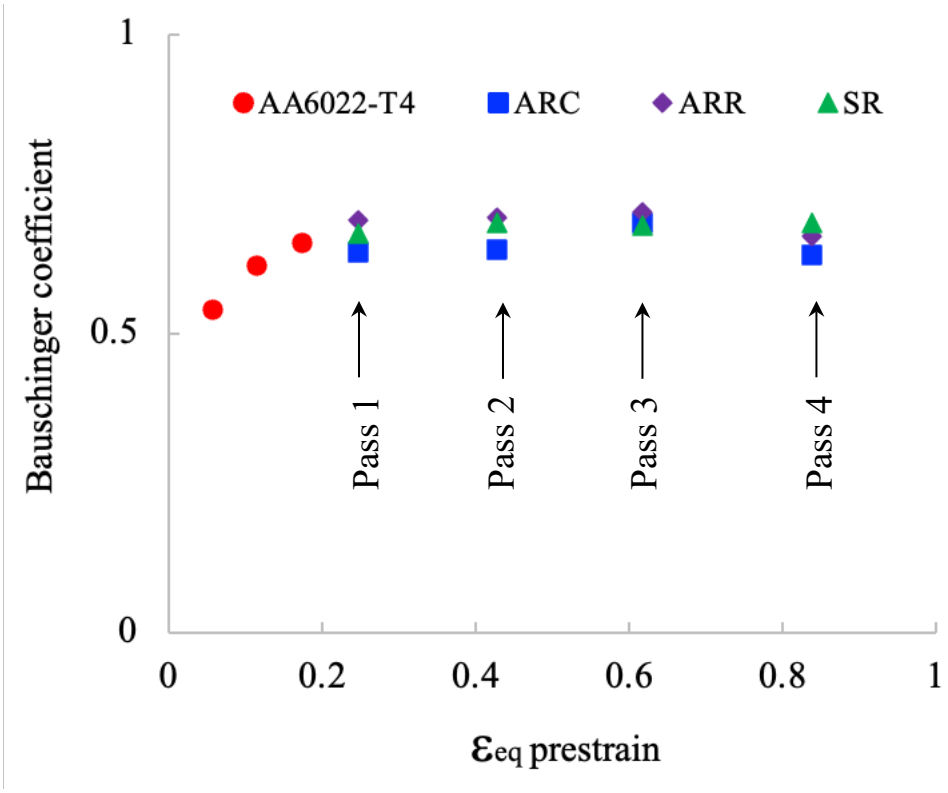

Fig. 9. Evolution of Bauschinger parameter with rolling pass.

Summary

The dependence of the Bauschinger effect on the prestrain quantity was investigated by reverse simple shear test. A large equivalent plastic prestrain was produced by three types of rolling, i.e. symmetric, asymmetric continuous, and asymmetric reverse, rolled in 4 passes. The Bauschinger effect seems to be almost insensitive to the rolling route. The results show an initial increase of the Bauschinger parameter with the increase of prestrain amount followed by a stabilization after approximately 20% equivalent prestrain. These results suggest that the contribution of the Bauschinger effect determined for low prestrain level can be used for the prediction of springback even for large plastic deformation. Nevertheless, it is worth mentioning that other sources of springback should be considered since recent results obtained in V-bending and U-bending tests for the material processed by the same conditions show that the springback after rolling increases.

Acknowledgments

This work was supported by the projects POCI-01-0145-FEDER-032362 (PTDC/EME-ESP/32362/2017) financed by the Operational Program for Competitiveness and Internationalization, in its FEDER/FNR component, and the Portuguese Foundation of Science and Technology (FCT), in its State Budget component (OE), UIDB/00481/2020 and UIDP/00481/2020 - FCT and CENTRO-01-0145-FEDER-022083 - Centro Portugal Regional Operational Program (Centro2020), under the PORTUGAL 2020 Partnership Agreement, through the European Regional Development Fund, and 2022.05783.PTDC financed exclusively by national funds through FCT, I.P. and composed only of one State Budget component (OE).

References

[1] G. Vincze, A.B. Pereira, D.A.F. Lopes, J.M.V. Yánez, M.C. Butuc, Study on Asymmetric Rolling Process Applied to Aluminum Alloy Sheets, Machines 10 (2022) 641. https://doi.org/10.3390/machines10080641

[2] G. Vincze, E.F. Rauch, J.J. Gracio, F. Barlat, A.B. Lopes, A comparison of the mechanical behaviour of an AA1050 and a low carbon steel deformed upon strain reversal, Acta Mater. 53 (2005) 1005-1013. https://doi.org/10.1016/j.actamat.2004.10.046

[3] E.F. Rauch, J.J. Gracio, F. Barlat, Work-hardening model for polycrystalline metals under strain reversal at large strains, Acta Mater. 55 (2007) 2939-2948. https://doi.org/10.1016/j.actamat.2007.01.003

[4] J-H. Schmitt, E.L. Shen, J.L. Raphanel, A parameter for measuring the magnitude of a change of strain path: validation and comparison with experiments on low carbon steel, Int. J. Plast. 10 (1994) 535-551. https://doi.org/10.1016/0749-6419(94)90013-2

[5] C. Teodosiu, Z. Hu, Z., Microstructure in the continuum modeling of plastic anisotropy, in: J.V. Cartensen, T. Leffers, T. Lorentzen, O.B. Pedersen, B.F. Sørensen, G. Winther (Eds.), Proceedings of the Risø International Symposium on Material Science: Modelling of Structure and Mechanics of Materials from Microscale to products, Roskilde, Denmark. Risø National Laboratory, 1998, pp. 149-168.

[6] J. Qin, B. Holmedal, O.S. Hopperstad, Experimental characterization and modeling of aluminum alloy AA3103 for complex single and double strain-path changes, Int. J. Plast. 101 (2018) 156-169. https://doi.org/10.1016/j.ijplas.2018.08.011

[7] M. Butuc, F. Barlat, J. Gracio, G. Vincze, A Theoretical Study of the Effect of the Double Strain Path Change on the Forming Limits of Metal Sheet, Key Eng. Mater. 554-557 (2013) 127-138. https://doi.org/10.4028/www.scientific.net/KEM.554-557.127.

[8] G. Vincze, F. Barlat, E.F. Rauch, C.N. Tome, M.C. Butuc, J.J. Grácio, Experiments and modeling of low carbon steel sheet subjected to double strain path changes, Metall. Mater Trans. A44 (2013) 4475-4479. https://doi.org/10.1007/s11661-013-1895-4

[9] M. Banu, M. Takamura, T. Hama, O. Naidim, C. Teodosiu, A. Makinouchi, Simulation of springback and wrinkling in stamping of a dual phase steel rail-shaped part, J. Mater. Process. Technol. 173 (2006) 178-184. https://doi.org/10.1016/j.jmatprotec.2005.11.023

[10] M.C. Oliveira, J.L. Alves, B.M. Chaparro, L.F. Menzes, Study on the influence of work-hardening modelling in springback prediction, Int. J. Plast. 23 (2007) 516-543. https://doi.org/10.1016/j.ijplas.2006.07.003

[11] G. Vincze, A. Lopes, M.C. Butuc, J. Vallez Yánez, D. Lopes, L. Holz, A. Graça, A.B. Pereira, Numerical and Experimental Analysis of the Anisotropy Evolution in Aluminium Alloys Processed by Asymmetric Rolling, European J. Computat. Mech. 31 (2022) 319-350. https://doi.org/10.13052/ejcm2642-2085.3131

[12] Y. Hou, M-G Lee, L. Jianping, M. Junying, Experimental characterization and modeling of complex anisotropic hardening in quenching and partitioning (Q&P) steel subject to biaxial non-proportional loadings, Int. J. Plast. 156 (2022) 156-169. https://doi.org/10.1016/j.ijplas.2022.103347

Materials Research Proceedings 28 (2023) 855-865 https://doi.org/10.21741/9781644902479-94

Determination of the forming limit curve of locally annealed aluminum blanks

PICCININNI Antonio[1,a *], LATTANZI Attilio[2,b], ROSSI Marco[2,c] and PALUMBO Gianfranco[1,d]

[1]Department of Mechanical Engineering, Mathematics & Management Engineering, Division of Production Technologies, Polytecnic University of Bari, via Orabona 4, 70125 Bari, Italy

[2]Department of Industrial Engineering and Mathematical Sciences, Università Politecnica delle Marche, via Brecce Bianche 12, 60131 Ancona, Italy

[a]antonio.piccininni@poliba.it, [b] a.lattanzi@staff.univpm.it, [c]m.rossi@staff.univpm.it, [d]gianfranco.palumbo@poliba.it

Keywords: Laser Heat Treatment, Aluminum Alloy, FEM, FLC, Bulge Test

Abstract. The research of innovative manufacturing routes to improve the complexity of structural Aluminum (Al) components and reduce the vehicles' weight remains an open question. The adoption of short-term heat treatments to obtain an optimized distribution of properties has shown great potential in enhancing the formability of Al alloys at room temperature. Such a complex approach needs the implementation of methodologies based on numerical simulations able to correctly simulate the forming process. Accordingly, the definition of a proper identification procedure to provide reliable constitutive parameters, possibly employing a limited number of tests, becomes crucial. In this work, we introduce a novel methodology for the evaluation of the Forming Limit Curve (FLC) of laser annealed AA5752-H32 sheet based on the material information from different heterogeneous tests carried out in specific tribological condition, i.e. in absence of friction. Therefore, we investigate an experimental procedure to simultaneously generate an equi-biaxial mechanical state over a wide range of annealing conditions by means of hydraulic bulge test. The results are integrated with full-field data from uniaxial tensile and plane strain tests to provide a testing protocol for the characterization of the failure behavior accounting for the different temperature/time conditions of the sheet metal.

Introduction

The continuous demand for greener and lighter transportations is moving the attention to the improvement of the design criteria, among which the choice of the material for the structural components plays a key role. At the same time, it is widely recognized that Aluminum (Al) alloys are ranked as an ideal candidate to match those requirements [1]. Nevertheless, excellent fire resistance (especially when dealing with the subway applications [2]) combined with high strength-to-weight ratio are partially counterbalanced by the poor formability at room temperature [3]. Several solutions have been investigated over the last decades to overcome such a limitation: the increase of the working temperature – i.e. the theoretical base of the forming operations in warm conditions – has shown great potentialities over a large variety of components [4,5]. A promising and innovative alternative to the warm forming principle is based on splitting the manufacturing process into two separate steps: during the first phase, the material properties are locally modified by means of a short-term heat treatment (for example, by means of a laser heating) so that the blank, once cooled down, can be stamped at room temperature. It has been demonstrated that the optimization of the distribution of the material properties is able to enhance the formability at room temperature [6,7].

Splitting the process into two separate sub-steps automatically implies the need of a robust and systematic approach to design both the steps, especially due to the large number of parameters

Content from this work may be used under the terms of the Creative Commons Attribution 3.0 license. Any further distribution of this work must maintain attribution to the author(s) and the title of the work, journal citation and DOI. Published under license by Materials Research Forum LLC.

involved in. Moreover, if the numerical approach is indicated as the most reliable methodology to design such a complex process, the proper characterization of the material behavior is a key aspect to be addressed to study in detail the mechanical response in the following forming operation.

While the effect of annealing on the constitutive behavior of the alloy can be investigated by considering, separately, samples of the same material treated at different grades, recently, the application of full-field measurements as the Digital Image Correlation (DIC) has allowed to disentangle the heterogeneous distribution of mechanical properties due to the local annealing [8, 18-20]. In this framework, dealing with heterogenous information makes possible to involve advanced calibration methods based on inverse problems. Generally, they are distinguished in numerical simulation-based methods, such as the Finite Element Model Updating (FEMU), and energy balance-based methods, namely the Virtual Fields Method (VFM) or the Equilibrium Gap Method (EGM) [11]. In the field of metal plasticity, inverse identification methods offer different strategies to produce an enriched calibrations even in the case of complex material models [23]: for instance, for the identification of the hardening behavior including post-necking data [13,14], or to characterize the anisotropic plasticity models [12,15,16] or the thermomechanical behavior of metals [17].

The present work investigates the stretching behavior of a locally laser-annealed AA5752-H32 sheet in a hydraulic bulge test. The aim is to provide heterogenous material data in the biaxial and equi-biaxial stretch conditions spanning over the whole annealing range, that can be coupled with an inverse approach as in [24], or to build a more comprehensive Forming Limit Curve. Different heating strategies have been preliminarily simulated by solving the thermal transient problem and the modification of the material properties have also been numerically predicted. The nodal peak temperatures, being strictly connected to the final level of annealing, were then transferred on the structural model, where the material behavior was modelled according to the hardening law that has been previously calibrated by the same authors [18]. The results, integrated with those coming from the plane strain [19] and from the drawing side, allow to provide a testing methodology to characterize the necking behavior at different material conditions using a limited number of tests.

Material and Methodology

Material.

Bulge tests were simulated considering locally modified AA5754 Al blanks, initially purchased in the H32 state, whose composition is reported in Table 1.

Table 1. Chemical composition of the investigated alloy.

	Al [%]	Cr [%]	Cu [%]	Fe [%]	Mg [%]	Mn [%]	Si [%]	Ti [%]	Zn [%]
AA5754-H32	Bal.	0.024	0.057	0.377	3.057	0.187	0.259	0.017	0.025

Annealing investigation.

The prediction of the material properties at the end of the local heating started from a preliminary characterization step based on the physical simulation of several annealing treatments exploiting the potentialities of the Gleeble system (model 3180). Dog-bone specimens (AA5754-H32) were subjected to a heat treatment composed of a preliminary heating step (rate around 900°C/s), holding at the test temperature and rapid cooling down to room temperature. Being the ends of the specimen clamped by cooled jaws, a parabolic distribution of temperatures occurs during the whole test (equivalent to simultaneously subjecting the same specimen to several heat treatments at the temperatures belonging to the parabolic distribution): hardness tests, carried out once the specimen cools down to room temperature, allowed to easily associate the modification of the material property to the temperature-time history. Hardness measurements were arranged in terms of the Ann variable variable according to Eq. 1: HV_{H32}, HV_{meas} and HV_{H111} refer to the

Materials Research Proceedings 28 (2023) 855-865 https://doi.org/10.21741/9781644902479-94

hardness of the material in the as-received conditions (H32), measured one and in the annealed state (H111), respectively.

$$Ann = \frac{HV_{H32} - HV_{meas}}{HV_{H32} - HV_{H111}} \tag{1}$$

The distribution of the defined variable, as well as its dependency with the peak temperature (T_{peak}), fitted by the sigmoid function, widely used in several applications [14], expressed in Eq. 2, where $\boldsymbol{T}^*$ and λ represents the curve's midpoint and growth rate (or steepness), respectively.

$$Ann = \frac{1}{1 + \exp\left[-\lambda \cdot \left(T^* - T_{peak}\right)\right]} \tag{2}$$

Although Eq. 2 offers a direct analytical description of the percentage of annealing due to the temperature distribution, it does not provide direct information about the different mechanical properties and, therefore, cannot be straightforwardly adopted in structural problems. In this sense, the authors proposed a constitutive model to predict the hardening behavior as function of the T_{peak}. By expressing the annealing level through the general variable T_{peak}, the corresponding flow curve can be predicted using the following logistic expression:

$$\sigma\left(\varepsilon_p, T_{peak}\right) = \sigma_{H111}\left(\varepsilon_p\right) + \frac{\sigma_{H32}\left(\varepsilon_p\right) - \sigma_{H111}\left(\varepsilon_p\right)}{1 + \exp\left\{-\left[\beta \tanh\left(\frac{\varepsilon_p}{\varepsilon_0}\right) + c_\beta\right]\left(T^* - T_{peak}\right)\right\}} \tag{3}$$

where ε_p is the accumulated plastic strain, the $\sigma_{H32}\left(\varepsilon_p\right)$ and $\sigma_{H111}\left(\varepsilon_p\right)$ indicates the flow curves of the material at H32 and fully-annealed (H111) conditions, respectively; β, ε_0, T^* and c_β are the material coefficients regulating the logistic expression. All the coefficients can be inversely calibrated by considering the flow stress curves at different annealing grades. Details about the calibration of the hardening model in Eq. 3 by using a hybrid numerical-experimental procedure on uniaxial tensile data can be found in [18].

Two-steps FE analysis of the heat-treatment and mechanical test.

The adopted approach started from the simulation of the laser heating by solving the thermal transient problem. The investigated heating strategies were based on: (i) a circular track described by the center of the laser spot (indicated by the red square in Fig. 1a) with a radius equal to 30 mm (labelled as AH, standing for *Annular Heating*) and (ii) a linear track, 40 mm long, at two different distances from the center of the blank (20 mm and 30 mm, respectively labelled as LT20 and LT30, where LT stands for *Linear Track*). The simulated strategies were designed to investigate the equi-biaxial stress state over different material conditions (the gradient of properties came from the local laser heating) within the same bulge test.

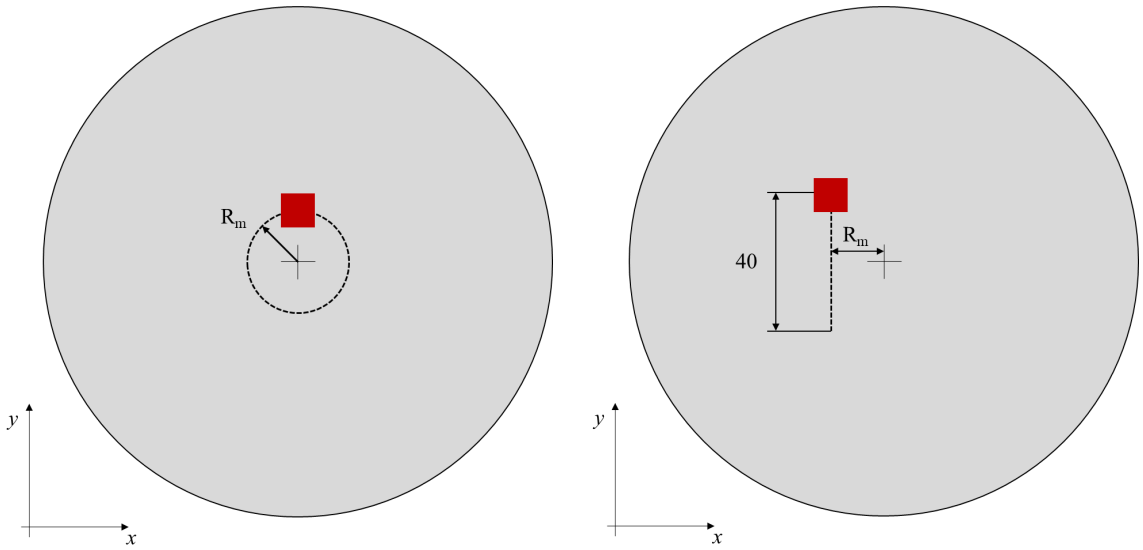

a) b)

Fig. 1. The investigated heating strategies: a) AH, b) LT. The diameter of the blank is 300 mm, while the gauge area has a diameter of 200 mm (corresponding to the die opening).

Laser heating strategies were simulated implementing a temperature feedback loop (DFLUX user subroutine), setting the heating temperature at 550°C and the feed rate at 5 mm/s. Results from the thermal simulations were processed by means of a Python script to numerically predict the final distribution of the variable *Ann* according to Eq. 2.

In this study, we consider the peak temperature T_{peak} as the common empirical variable to connect the predicted level of annealing with the hardening behavior. Thus, the computed T_{peak} from the transient-thermal analysis is used as input of the structural analysis through the constitutive model in Eq. 3. The forming bulge is replicated numerically by modelling the die as rigid body and the aluminum blank as continuum shell under the hypothesis of plane stress condition due to the small thickness of the sheet metal. Note that the constitutive equations were implemented in Abaqus/Standard® by means of a user material subroutine, employing the well-known Euler Backward integration algorithm for the reconstruction of stress from strain data. Other implicit or semi-implicit algorithms can be also used for the stress update as, for example, the one introduced in [22] for anisotropic plasticity problems.

In this work, we also assumed an isotropic plasticity behavior, while the hardening behavior of the AA5754 was described by using a modified version of the Voce's law, according to the previous experimental investigation reported in [18]:

$$\sigma(\varepsilon_p) = Y(1 + \varepsilon_p) - R\exp(-b\varepsilon_p). \quad (4)$$

All the material coefficients used in this numerical study, including the ones characterizing the logistic formulation in Eq. 3, are listed in Table 2.

Table 2. Material coefficient of the constitutive equation.

Modified Swift hardening law			
Material state	Y	R	b
As received (H32)	232.74	98.32	20.08
Fully annealed	213.36	148.53	26.99
Logistic hardening model			
β	c_β	T^*	ε_0
0.01095	0.01423	301.35	0.005

Results

Treatment strategies for the heterogeneous bulge test.

Results from the thermal simulations were initially analyzed in terms of maximum temperature distribution: Fig. 2 confirms that the heating temperature close to 550°C was reached and kept along the whole heat treatment in each of the investigated strategies.

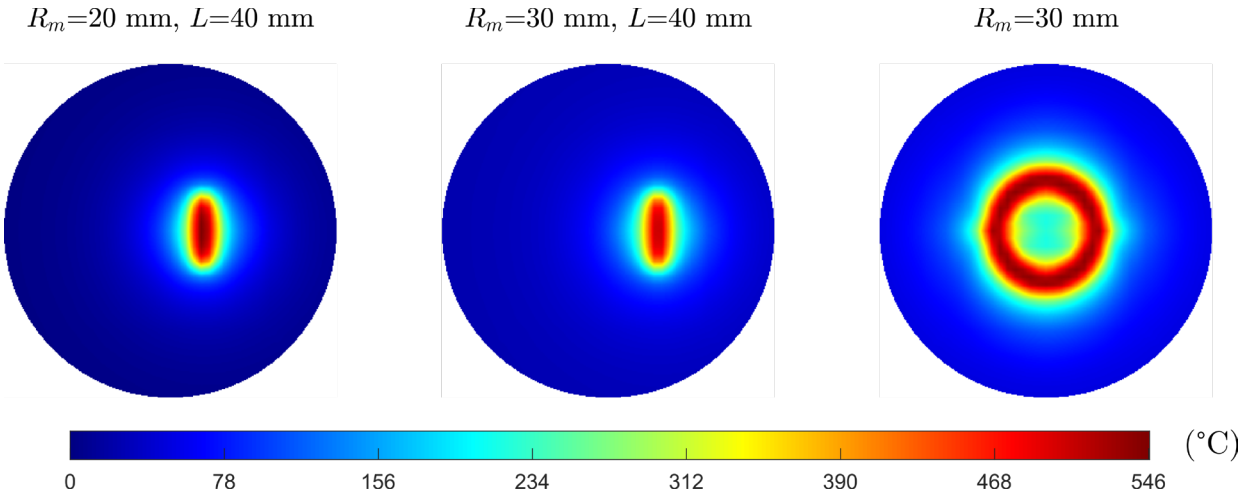

Fig. 2. Results from the transient-thermal analysis: distribution of the peak temperature T_{peak} for the three heat-treatment strategies.

The final distribution of properties, express in terms of the variable *Ann*, was compared among the three strategies along a radial path as shown in Fig. 3 (the *0* radial position corresponds to the center of the circular blank).

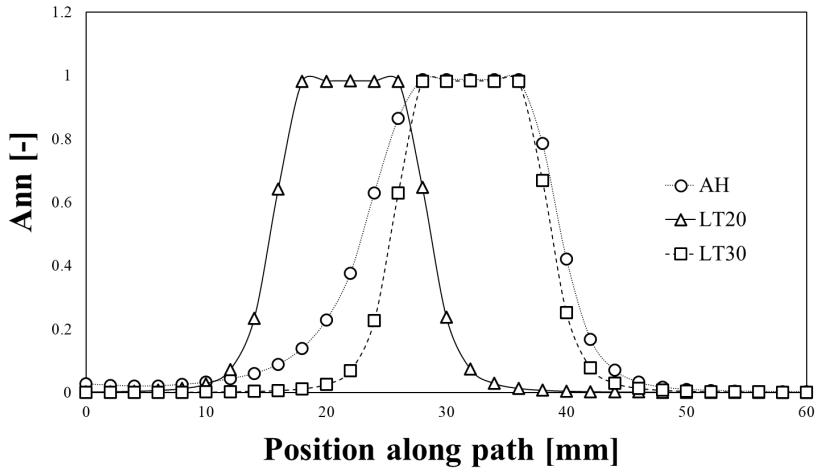

Fig. 3. Predicted distribution of the Ann variable along the radial

It can be observed that all the geometries show an almost complete annealing (*Ann* close to 1) in the region irradiated by the laser spot (around 10 mm wide in the radial direction). It can also be seen that the annular tracking (AH) modifies a slightly larger portion of the blank close to its center (the transition region is less steep if compared with the *Ann* distribution resulting from the LT30 strategy).

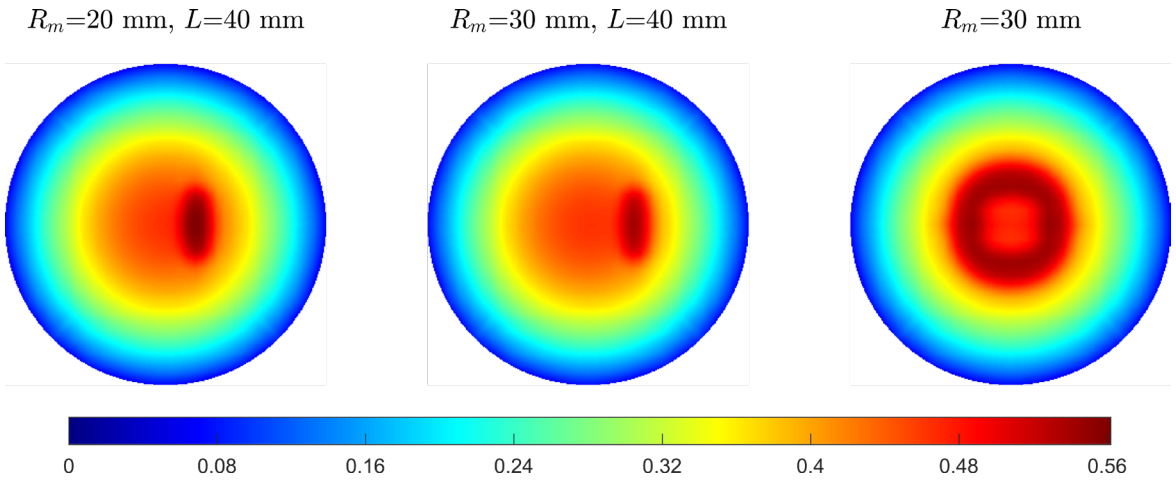

Fig. 4. Maps of accumulated equivalent plastic strain over the bulge test gauge area for the three heat-treatment strategies.

The design of a heterogenous test requires a quantitative method to classify the strain and stress distribution, that, for this study, must consider the annealing temperature and the amount of plastic deformation accumulated during the loading phase. Fig. 4 depicts the maximum plastic strain achieved in our simulated experiments. Note that we impose the same maximum forming pressure for each case study (4.4 MPa) to obtain comparable values of equivalent plastic strain $\bar{\varepsilon}_p$. In all the cases, the maximum $\bar{\varepsilon}_p$ obtained is around 0.56 and is located over the material points identified by the fully annealed condition, although they are quite far from the dome apex. It is worth noticing that, although we imposed the same target forming pressure to all the tests, obtaining similar values of maximum equivalent plastic strain, the macroscopic effect of the annealing treatment on the specimen can be observed on the maximum dome height, which is 60 mm for the LT strategy and 62 mm for the AH one.

To be consistent with previous studies aimed to quantify the heterogeneity of the mechanical states produced by unconventional mechanical test [19,25], the classification and comparison of the three strategies is carried out following two main visualization methods:

- The diagram of major and minor principal strains, also used to infer the FLC;
- The diagram of normalized stress (widely used in the case of anisotropic plasticity), where the stress state for each material point is reported on the yield surface.

It is worth noting that the following diagrams includes only datapoints where the $\bar{\varepsilon}_p > 2\%$: this because low values of plastic deformation – corresponding to low values of dome height – are strongly affected by uncertainties when measured with optical techniques as DIC.

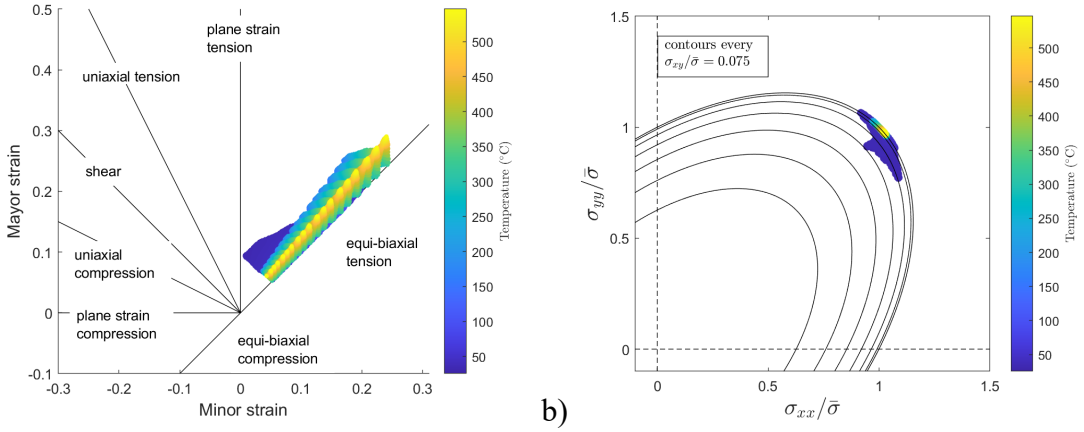

Fig. 5. Distribution of major and minor strains (a) and stress states on the normalized stress plane (b) produced by the bulge test on the specimen exposed to the linear treatment with R_m=20 mm and L=40 mm.

When looking at the results from the LT20, the forming limit diagram shown in Fig. 5a suggests that all the points close to the fully annealed state (yellow point) are characterized by a slope of the strain path slightly higher than that of the equi-biaxial state. On the other hand, material points characterized by lower level of annealing (peak temperature around 400°C) are closer to the bisector of the first quadrant. When moving far from the locally annealed zone, the strain path diverges from the equi-biaxial state more evidently.
The distance between the linear track and the center of the circular blank seems not to have an appreciable effect: in fact, when increasing the distance up to 30 mm, the evolution of the strain paths (Fig. 6a) resembles the distribution shown in Fig. 5a.

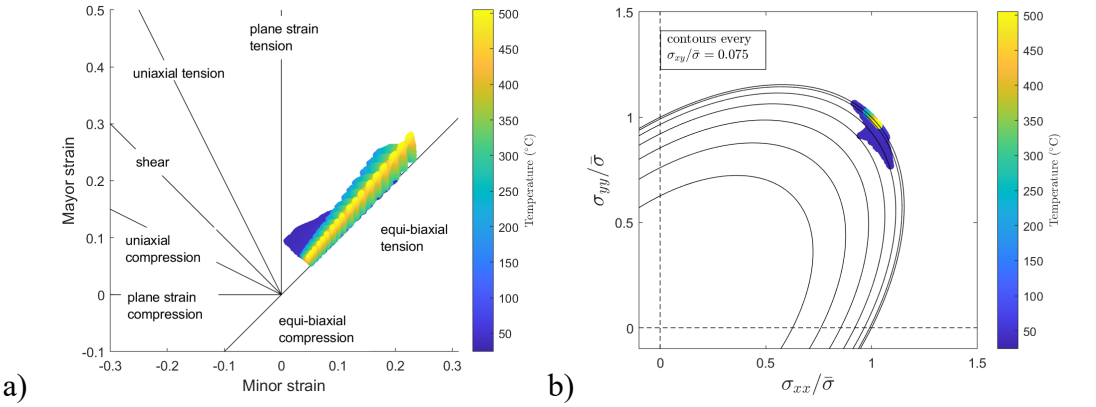

Fig. 6. Distribution of major and minor strains (a) and stress states on the normalized stress plane (b) produced by the bulge test on the specimen exposed to the linear treatment with R_m=30 mm and L=40 mm.

The evolution of the strain paths slightly changes when focusing the attention on the AH strategy. The scatter of the slope in the strain paths from the material point at the higher level of annealing is larger and a wider span of intermediate annealing conditions reaches the almost equi-biaxial state during the forming (Fig. 7, a and b).

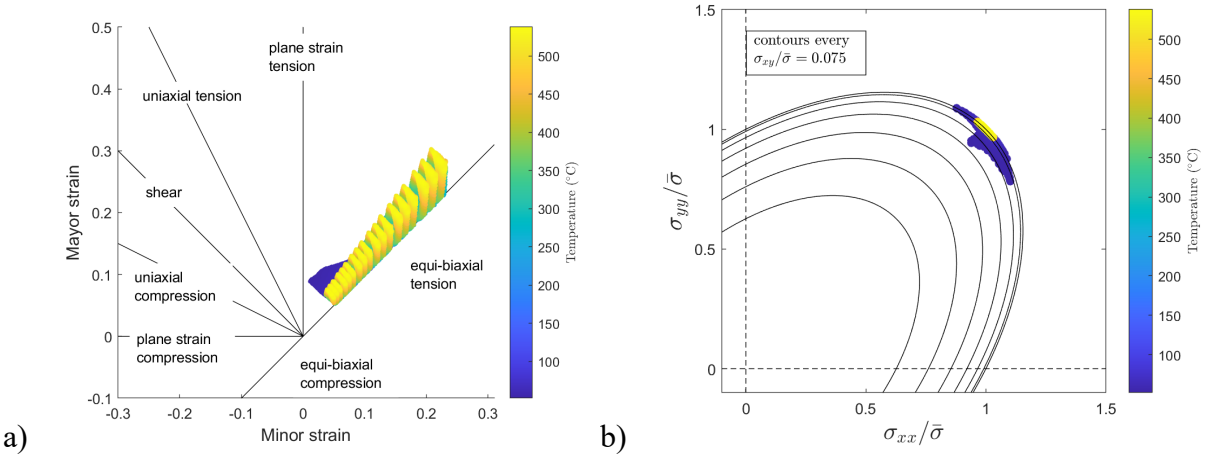

Fig. 7. Distribution of major and minor strains (a) and stress states on the normalized stress plane (b) produced by the bulge test on the specimen exposed to the circular treatment with R_m=30 mm.

The difference between the three investigated geometries are confirmed when looking at the strain paths from a radial path of nodes: for both the LT strategies, the points characterized by the fully annealed conditions, despite slightly diverging from the equi-biaxial state, reached a final strain condition higher than the other points characterized by intermediate levels of annealing (Fig. 8a and Fig. 8b).

On the other hand, when the AH strategy is taken into account, the final strain components (major and minor) are quite close regardless of the reached level of annealing.

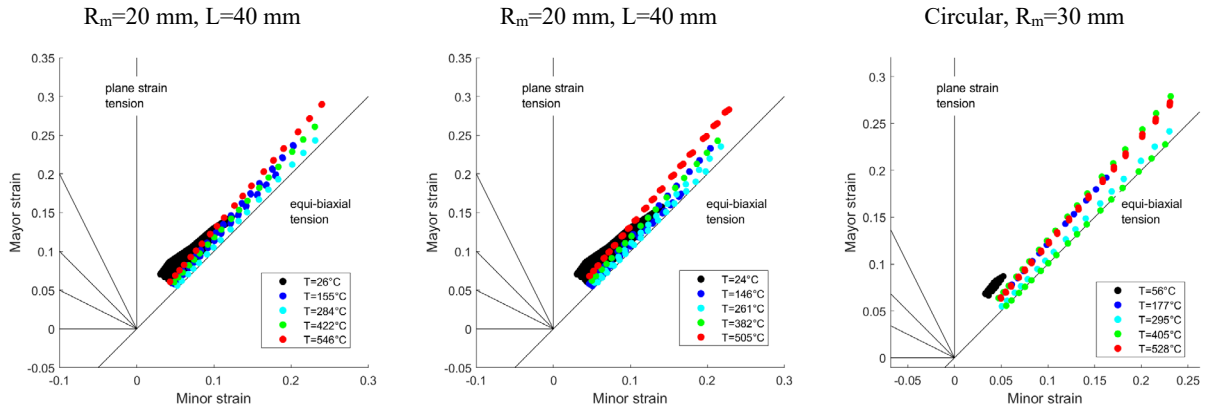

Fig. 8. Distribution of major and minor strains obtained by sampling measurement points along a horizontal path in the case of five annealing temperatures, for all the heat-treatment configurations.

FLC curve reconstruction from different heterogenous tests.

The strain path distributions from the locally annealed bulge tests, combined with the strain evolutions from the other two types of tests (tensile test and plane strain tests) allow to cover a wide portion of the forming limit diagrams. The onset of necking, particularly difficult to infer from the numerical simulation of the characterization tests (plane strain and bulge test) can be qualitatively drawn, embracing the limit conditions not only belonging to the material points in the fully annealed conditions but also some characterized by an intermediate level of annealing.

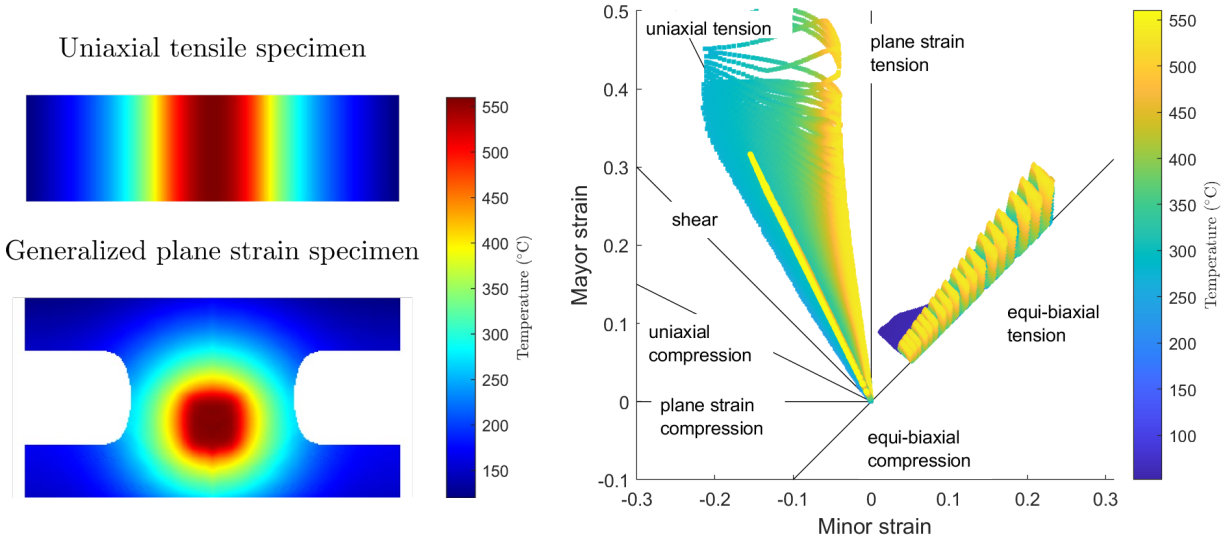

a) b)

Fig. 9. Integration of different heterogeneous tests with the bulge specimen exposed to circular heat-treatment: a) distribution of the peak temperature for the uniaxial and generalized plane strain specimens, b) combined FLC diagram including all full-field data.

Summary

The present work focuses the attention on the third characterization tests when considering a gradient of properties in a AA5754-H32 blank that has been locally annealed by means of laser heating. The simulation of the bulge test, in combination with the tensile and the plane strain tests, complete the set of characterization methodology to assess the strain behavior of a locally-modified blank. The three investigated laser heating, different in terms of extent of the annealed region (a single linear track against a circular path) seemed not to have a significant influence on the evolution of the slope of the strain paths from points both in annealed conditions and those characterized by an intermediate level of annealing. Nevertheless, when looking at the strain paths along the radial direction, the AH strategy led to a more uniform distribution of strains, since material points at different levels of annealing reached almost the same limit strain (major and minor components). The results from the numerical simulation of the bulge test, combined with those from the plane strain test and tensile tests allowed to cover a wide portion of the forming limit diagram. It must be highlighted that, at this stage, the numerical simulation does not provide direct information about the necking instability and failure behavior due to the absence of a proper modelling of plastic damage. Therefore, the FLD reconstruction here presented should be intended as an investigation about the domain of principal strains that can be achieved by the material points over the whole range of annealing. As a consequence, a qualitative indication of a forming limit diagram could only be drawn.

References

[1] A. Taub, E. De Moor, A. Luo, D.K. Matlock, J.G. Speer, U. Vaidya, Materials for Automotive Lightweighting, Annu. Rev. Mater. Res. 49 (2019) 327–59. https://doi.org/10.1146/annurev-matsci-070218-010134

[2] DIN EN 45545-2. Railway applications - Fire protection on railway vehicles - Part 2: Requirements for fire behaviour of materials and components 2016.

[3] S.S. Hecker, Formability of Aluminum Alloy Sheets, J. Eng. Mater. Technol. 97 (1975) 66-73. https://doi.org/10.1115/1.3443263

[4] G. Palumbo, A. Piccininni, Numerical-experimental investigations on the manufacturing of an aluminium bipolar plate for proton exchange membrane fuel cells by warm hydroforming, Int. J. Adv. Manuf. Technol. 69 (2013) 731–742. https://doi.org/10.1007/s00170-013-5047-1
[5] A. Piccininni, A. Lo Franco, G. Palumbo, Warm Forming Process for an AA5754 Train Window Panel, J. Manuf. Sci. Eng. 144 (2022) 1–12. https://doi.org/10.1115/1.4052583
[6] M. Geiger, M. Merklein, U. Vogt, Aluminum tailored heat treated blanks, Prod. Eng. 3 (2009) 401-410. https://doi.org/10.1007/s11740-009-0179-8
[7] A. Piccininni, G. Palumbo, Design and optimization of the local laser treatment to improve the formability of age hardenable aluminium alloys, Materials 13 (2020). https://doi.org/10.3390/ma13071576
[8] M. Rossi, A. Lattanzi, A. Piccininni, P. Guglielmi, G. Palumbo, Study of Tailor Heat Treated Blanks Using the Fourier-series-based VFM, Procedia Manuf. 47 (2020) 904-909. https://doi.org/10.1016/j.promfg.2020.04.278
[9] M.A. Sutton, J.J. Orteu, H.W. Schreier, Image Correlation for Shape, Motion and Deformation, Springer, 2009.
[10] F. Pierron, M. Grediac, The virtual fields method: Extracting constitutive mechanical parameters from full-field deformation measurements, Springer New York, NY, 2012. https://doi.org/10.1007/978-1-4614-1824-5
[11] S. Avril, M. Bonnet, A.S. Bretelle, M. Grédiac, F. Hild, P. Ienny, F. Latourte, D. Lemosse, S. Pagano, E. Pagnacco, F. Pierron, Overview of identification methods of mechanical parameters based on full-field measurements, Exp. Mech. 48 (2008) 381–402. https://doi.org/10.1007/s11340-008-9148-y
[12] D. Lecompte, S. Cooreman, S. Coppieters, J. Vantomme, H. Sol, D. Debruyne, Parameter identification for anisotropic plasticity model using digital image correlation, Eur. J. Comput. Mech. 18 (2009) 393–418. https://doi.org/10.3166/ejcm.18.393-418
[13] M. Grédiac, F. Pierron, Applying the Virtual Fields Method to the identification of elasto-plastic constitutive parameters, Int. J. Plast. 22 (2006) 602-627. https://doi.org/10.1016/j.ijplas.2005.04.007
[14] M. Rossi, A. Lattanzi, F. Barlat, A general linear method to evaluate the hardening behaviour of metals at large strain with full-field measurements, Strain 54 (2018) 12265. https://doi.org/10.1111/str.12265
[15] M. Rossi, F. Pierron, M. Štamborská, Application of the virtual fields method to large strain anisotropic plasticity, Int. J. Solid. Struct. 97–98 (2016) 322-335. https://doi.org/10.1016/j.ijsolstr.2016.07.015
[16] A. Lattanzi, F. Barlat, F. Pierron, A. Marek, M. Rossi, Inverse identification strategies for the characterization of transformation-based anisotropic plasticity models with the non-linear VFM, Int. J. Mech. Sci. 173 (2020) 105422. https://doi.org/10.1016/j.ijmecsci.2020.105422
[17] J.M.P. Martins, S. Thuillier, A. Andrade-Campos, Calibration of a modified Johnson-Cook model using the Virtual Fields Method and a heterogeneous thermo-mechanical tensile test, Int. J. Mech. Sci. 202–203 (2021) 106511. https://doi.org/10.1016/j.ijmecsci.2021.106511
[18] A. Lattanzi, A. Piccininni, P. Guglielmi, M. Rossi, G. Palumbo, A fast methodology for the accurate characterization and simulation of laser heat treated blanks, Int. J. Mech. Sci. 192 (2021) 106134. https://doi.org/10.1016/j.ijmecsci.2020.106134
[19] A. Piccininni, A. Lattanzi, M. Rossi, Investigation of the plane strain behaviour of a laser-heat treated aluminium alloy Key Engineering Material 926 (2022) 1030-1038. doi:10.4028/p-ic4qyv

[20] A. Piccininni, A. Lattanzi, M. Rossi, G. Palumbo, Investigation of The Anisotropic Behaviour of Laser Heat Treated Aluminium Blanks . Paper presented at ESAFORM 2021. 24th International Conference on Material Forming, Liège, Belgique. (2021). https://doi.org/10.25518/esaform21.4086
[21] F. Grytten, B. Holmedal, O.S. Hopperstad, T. Børvik, Evaluation of identification methods for YLD2004-18p, Int. J. Plast. 24 (2008) 2248-2277. https://doi.org/10.1016/j.ijplas.2007.11.005.
[22] M. Rossi, A. Lattanzi, L. Cortese, D. Amodio, An approximated computational method for fast stress reconstruction in large strain plasticity, Int. J. Numer. Meth. Eng. 121 (2020) 3048-3065. https://doi.org/10.1002/nme.6346
[23] M. Rossi, A. Lattanzi, L. Morichelli, J.M. Martins, S. Thuillier, A. Andrade-Campos, S. Coppieters, Testing methodologies for the calibration of advanced plasticity models for sheet metals: A review, Strain 58 (2022) e12426. https://doi.org/10.1111/str.12426
[24] M. Rossi, A. Lattanzi, F. Barlat, J.H. Kim, Inverse identification of large strain plasticity using the hydraulic bulge-test and full-field measurements, Int. J. Solid. Struct. 242 (2022) 111532. https://doi.org/10.1016/j.ijsolstr.2022.111532
[25] M.G. Oliveira, S. Thuillier, A. Andrade-Campos, Evaluation of heterogeneous mechanical tests for model calibration of sheet metals, J. Strain Anal. Eng. 57 (2021) 208-224. https://doi.org/10.1177/03093247211027061

Friction and wear in metal forming

Materials Research Proceedings 28 (2023) 869-878 https://doi.org/10.21741/9781644902479-95

Galling-free fine blanking of titanium plates by carbon-supersaturated tool steel punch

AIZAWA Tatsuhiko[1,a *], FUCHIWAKI Kenji[2,b] and DOHDA Kuniaki[3,c]

[1]Shibaura Institute of Technology, 3-15-10 Minami-Rokugo, Ota-City, Tokyo 144-0045, Japan

[2]Hatano Seimitsu Co, 183-7 Hirasawa, Hatano-City, Kanagawa 257-0015, Japan

[3]Northwestern University, Evanstone, IL 60268, USA

[a]taizawa@sic.shibaura-it.ac.jp, [b]kenji-fuchiwaki@hatanoseimitsu.co.jp, [c]dohda.kuni@northwestern.edu

Keywords: Forging, Fine Blanking, Galling Free, Titanium, Carbon-Supersaturation, Tool Steel Punch, High-Speed Steel Punch, In Situ Solid Lubrication

Abstract. The carbon supersaturated tool steel and high-speed steel punches were utilized to demonstrate that the titanium work materials were forged in high reduction of thickness and fine-blanked without adhesion of their fragments and deposition of their oxide debris particle. This galling free forging and fine blanking came from the in situ formation of the free carbon tribofilm only on the highly stressed interfaces between the punch/die and the titanium work. Under this in situ solid lubrication, the low frictional state was sustained to induce less bulging deformation of work during the forging process. The fine blanking of titanium plates advanced without adhesive wear and fractured regions on their sheared surface. The long life of tools was certified even in fine blanking of titanium and titanium alloy plates.

Introduction

Titanium and titanium alloys have been utilized as typical high strength, light-weight and bio-compatible structural materials in the aerospace industries [1], in the medical applications [2] and in the mechanical part-markets [3]. For manufacturing of those parts and members, various metal forming processes, such as forging, drawing and fine blanking, are utilized to shape their feedstock like bars, plates and billets into products. As reported in [4-5], those processes encountered severe wears by adhesion of fresh titanium fragments and by deposition of titanium oxide debris particles onto the punches and dies. In practical operations during forming the titanium alloy bar to its glass-frames, the cleansing and polishing steps must be included to eliminate the adhesive films and to clean up the debris particles between the successive forging steps under the limited reduction of thickness [4]. In addition, as studied in [5-7], the ceramic dies and their coatings and DLC (Diamond Like Carbon) coatings, were also subjected to highly frictional state with metal sticking during the deep drawing process and in the BOD (Ball-On-Disk) testing in dry, respectively. In particular, TiAlN, TiN and TiCN experienced extremely high friction and seizure against the pure titanium balls.

The pretreatment of SKD11 and AISI420 punches and dies by the low temperature plasma carburizing, played a significant role in dry and cold forging of the pure titanium and β-titanium alloy wires [8-9]. No galling or no adhesion wear occurred in those forging steps even in high reduction of thickness. As explained in detail [10], this anti-galling behavior in metal forming of titanium bars was attributed to in situ formation of free carbon tribofilms onto the highly stressed contact interface of punches and dies to the titanium works during forming process. In addition, this galling-free forging process was characterized by the low friction and low work-hardening even in higher reduction of thickness than 70% [11-12]. This pretreatment to punches and dies are

Content from this work may be used under the terms of the Creative Commons Attribution 3.0 license. Any further distribution of this work must maintain attribution to the author(s) and the title of the work, journal citation and DOI. Published under license by Materials Research Forum LLC.

attractive to the near-net shaping by forging steps in galling-free and to the fine-blanking with fully burnished surface.

In the present paper, the carbon supersaturated (CS-) tool steel and high-speed steel punches are prepared by the low temperature plasma carburizing. This CS-SKD11 punch and die is utilized to upset the pure titanium bar till the reduction of thickness reaches 70%. The loading - displacement curves are online monitored to describe the compressive and flattening deformation of titanium work. The homogeneous flattening deformation proves that the low frictional state is preserved during forging. The CS-YXR high-speed steel punch is also prepared for fine blanking the pure titanium plates. The normal YXR punch suffers from severe adhesion of titanium fresh surfaces even in a single shot. The punch edges and side surfaces are completely adhered and eroded by the titanium fragments. On the other hand, no galling occurs on the CS-YXR punch edge and side surfaces even after fine blanking the titanium plates repeatedly. This significant difference in galling behavior proves the effectiveness of carbon supersaturation to steel punches and dies for fine blanking the difficult-to-metal-forming work materials.

Methods and Materials

The plasma carburizing system for carbon supersaturation process is first explained with notes on the plasma processing setup and conditions with reference to the previous studies in the literature. The forging and fine blanking setups and systems are also stated with comments on the extension of laboratory-scale methods to the mass production in industries.

Carbon supersaturation process.

The plasma carburizing system was schematically illustrated in Fig. 1a. With reference to the previous studies in [13-14], the hollow cathode device was employed to increase the carbon-ion and CH-radical densities more than 3 x 10^{17} ions/m^3 and to deepen the carbon supersaturated layer thickness. It was estimated to be 40 μm in case of the plasma carburizing at 673 K for 14.4 ks by 70 Pa.

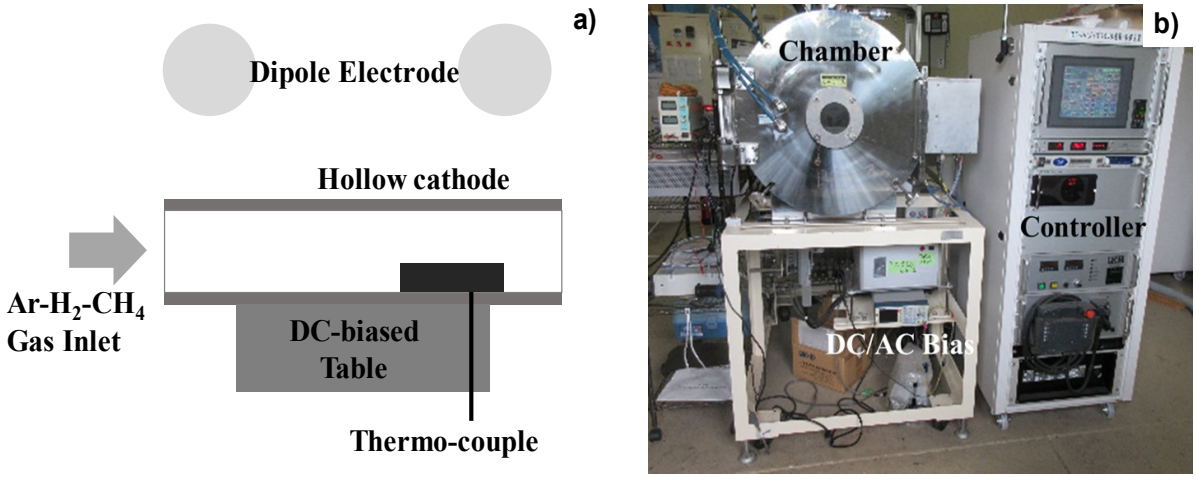

Fig. 1. Low temperature plasma carburizing system. a) Schematic view on the experimental setup, and b) overview on the whole system.

The dipole electrodes were utilized to ignite the RF (Radio-Frequency) plasma while the DC (Direct Current) plasma was also induced by applying the bias voltage to the bottom of hollow cathode. In the following experiments, the RF-voltage and the DC-bias were constant by +220 V and -400 V, respectively. After evacuation down to the base pressure of 0.01 Pa, the argon gas was introduced to a chamber in Fig. 1b at RT to clean the punch and die surfaces. After increasing the process temperature up to 673 K under the argon atmosphere, the hydrogen gas was

also introduced with the argon gas with the flow rate of 160 mL/min for argon and 20 mL/min, respectively. The total pressure was constant by 70 Pa. After presputtering by the DC-plasmas for 1.8 ks, the methane gas was introduced as a carbon source into argon and hydrogen mixture gas by the flow rate of 20 mL/min. At the specified duration of 14.4 ks, the specimen was cooled down in the chamber under the nitrogen atmosphere before evacuation down to atmospheric pressure. The processing temperature was in situ monitored by the thermocouple, which was embedded into the base plate below the hollow cathode device in Fig. 1a. The total pressure and each flow rate of argon, hydrogen and methane gasses were also measured for process control. The deviation of temperature and pressure in operation was ± 0.1 K and ± 0.05 Pa, respectively. After [8, 11-12], no iron and chromium carbides were synthesized in the plasma-carburized layer. The peak shift of α-ion to the lower 2θ angles in XRD analysis revealed that the α-lattices in the carburized SKD11 layer expanded by themselves through supersaturation of carbon solutes into steel substrates. The maximum surface roughness of punches at 5 mm away from their edge was 0. 35 μm before carburizing and 0.366 μm after carburizing. Hardness of SKD11 punch increased from 700 HV to 950 HV.

Forging process.

The CNC stamping system (ZEN-04; Hoden-Seimitsu, Co., Ltd., Kanagawa, Japan) was used for forging the pure titanium wire with the diameter of 1.0 mm in dry at the room temperature. The load to stroke curves were measured in every reduction of thickness by the load cell, which was embedded into the lower die in Fig. 2a. The overview of this stamping system was depicted in Fig. 2b. No lubricating oils and solid lubricants were utilized in the forging experiments. The punching speed was constant by 1 mm/s.

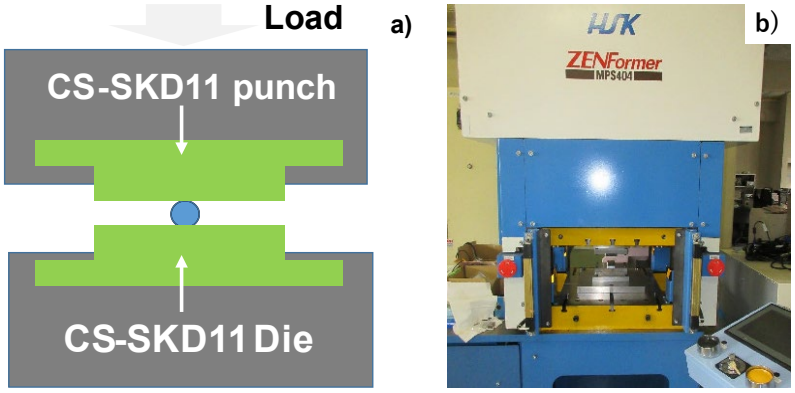

Fig. 2. CNC forging system. a) Schematic view on the forging experimental setup, and b) overview on the whole forging system.

Fine blanking process.

The pure titanium plate with the thickness of 2.0 mm, was blanked with narrow clearance of 4% at the room temperature as illustrated in Fig. 3a. The mechanical stamper (FB 160-FDE; Mori Steel Works Co., Ltd.; Saga, Japan), specially accommodated for fine-blanking process was used for this experiment as shown in Fig. 3b. The punching speed was 5 mm/s.

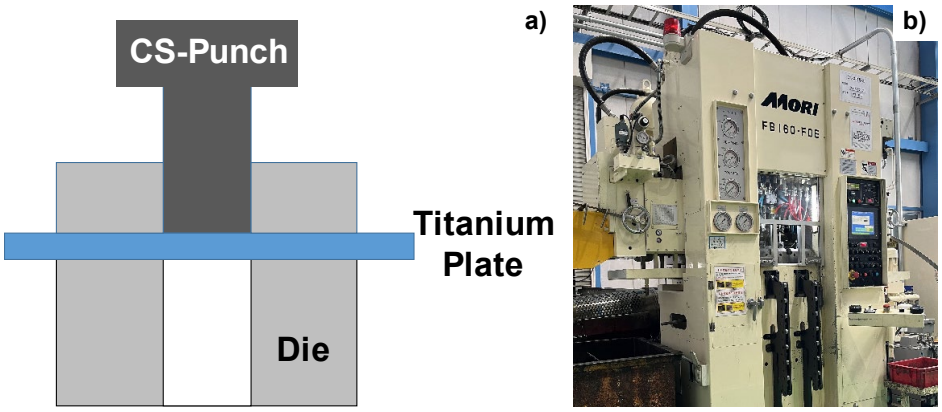

Fig. 3. Fine blanking system. a) Schematic view on the fine-blanking experimental setup, and b) overview on the whole system.

The maximum loading capacity was 1600 kN. The loading sequence for fine blanking was CNC-programmed. The punch with and without carbon-supersaturation were employed to describe the effect of carbon supersaturation on the galling behavior. Each punch was fixed into the punch holder, which was further set up into the upper die set. In the following experiments, FBH9-HMC with the viscosity of 101 m^2/s was utilized as a lubricating oil.

Work and tool materials.

Pure titanium wires and plates were respectively utilized as a work material for upsetting and fine blanking experiments. Their chemical composition consists of hydrogen by 0.0012 mass%, oxygen by 0.097 mass%, nitrogen by 0.007 mass%, iron by 0.042 mass%, carbon by 0.007 mass%, and titanium for balance. A tool steel type SKD11 (or AISI/SAE D3) was employed as a punch material for forging. A high-speed steel type YXR7 was used as a punch for fine blanking. Their chemical compositions were listed in Table 1.

Table 1. Chemical composition of SKD11 and YXR7 punch substrates.

Punch	C	Si	Mn	P	S	Cr	Mo	V	W	Fe
SKD11	1.44	0.3	0.35	0.27	0.06	11.1	0.8	0.2	---	in balance
YXR7	0.8	0.8	0.3	---	---	4.7	5.5	1.3	1.3	in balance

Characterization.

SEM (Scanning Electron Microscopy) - EDX (Energy Dispersive X-ray spectroscopy) was used for microstructure analysis and element mapping on the contact interface of forging and fine-blanking tools to the titanium work materials. Raman spectroscopy (JOEL, Co., Ltd.; Kanagwa, Japan) was also utilized to characterize the binding state of tribofilms.

Results

CNC-stamping was first utilized to describe the upsetting behavior of pure titanium bar with increasing the reduction of thickness. SEM-EDX and Raman spectroscopy were used to analyze the contact interface between the CS-SKD11 punch and the titanium work. Fine blanking system was also utilized to describe the difference of YXR7 punch surface with and without the carbon supersaturation to the fine-blanking punch.

Forging of pure titanium by CS-SKD11 punch.

The pure titanium bar with the diameter of 1.0 mm was upset to the specified reduction of thickness (r), using the CS-SKD11 punch and die. Figure 4 depicts the variation of contact interface width (Wi) with increasing r. When $r < 30\%$, Wi is less than the upset bar width (Wo); e.g., when $r = 20\%$, Wo = 1.15 mm and Wi = 0.70 mm. However, when $r > 50\%$, this Wi

Materials Research Proceedings 28 (2023) 869-878 https://doi.org/10.21741/9781644902479-95

approaches to Wo; e.g., when r = 50%, Wo = 1.7 mm and Wi = 1.5 mm. This reveals that the bulging deformation is suppressed with increasing r and the upset titanium bar homogeneously flattens with r.

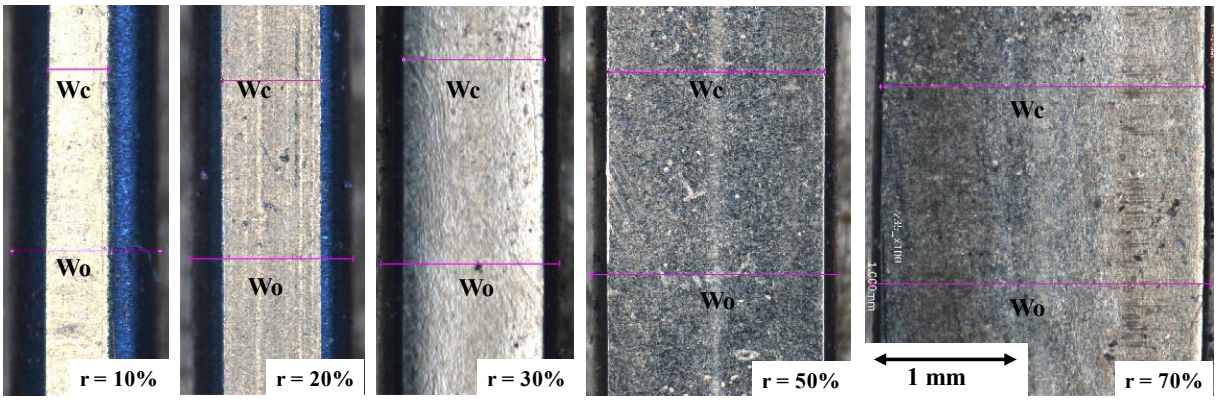

Fig. 4. Variation of the contact interface width at each reduction of thickness by r = 10%, 20%, 30%, 50% and 70% during the upsetting with the use of CS-SKD11 punch and die.

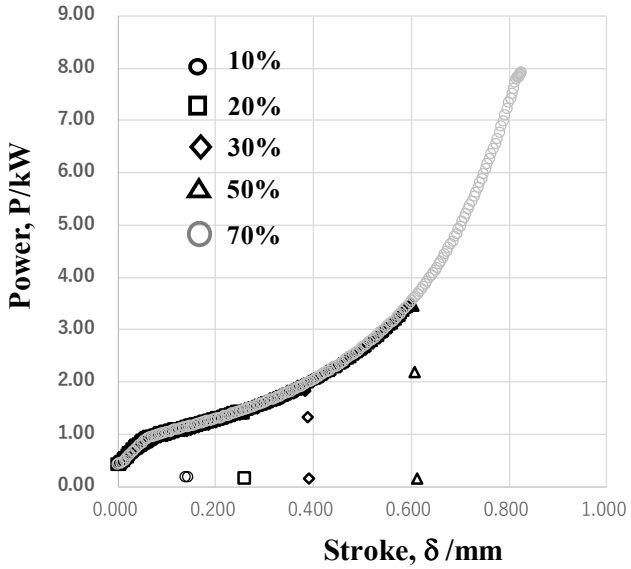

Fig. 5. The measured forging load to stroke relationship at each reduction of thickness for r = 10%, 20%, 30%, 50% and 70%, respectively.

After the empirical relationship between the friction coefficient (μ) and the bulging deformation ratio (= (Wo-Wi)/(2Wo)) in [15], μ is estimated to be 0.05 to 0.1. After the inverse analysis on the friction coefficient using the finite element simulation in [11], μ is estimated to be 0.05. Under this low friction on the interface between the CS-SKD11 punch and the pure titanium works, its thickness is homogeneously upset to r = 70%.

The in-situ measured forging load was plotted against the applied stroke at each reduction of thickness. As depicted in Fig. 5, every load-stroke curve at r = 10%, 20%, 30%, 50% and 70% is edited to one master load-stroke relationship. This implies that the pure titanium work homogeneously deforms with increasing the stroke, irrespective of the reduction of thickness. The forging load abrupt increases in the exponential manner with the stroke when r > 30%. This reveals that the true contact interface area expands by flattening behavior in Fig. 4.

The low friction on the contact interface as well as the homogeneous forging behavior proves that no galling occurs during this forging process with high reduction of thickness. Through the

precise analysis on the contact interface, the interfacial state is described after upsetting the pure titanium bars up to r = 70% in twenty shots.

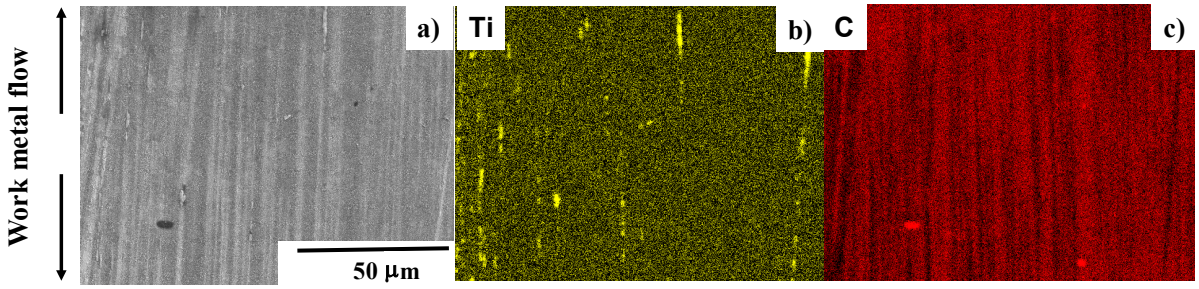

Fig. 6. SEM image and element mapping on the true contact interface between the CS-punch and the pure titanium work after continuously forging up to r = 70% in twenty shots.

As shown in Fig. 6a, many gray stripes are formed on the interface along the direction of work metal flow. Since the CS-punch surface was cleansed and polished before experiment, no surfactants and residuals were left on the punch and die surfaces. Hence, these stripes were in situ formed during the forging steps. SEM-EDX analysis was used to search for the element mapping in correspondence to these stripes among the main constituent elements of SKD11 such as iron and chromium, the titanium, the oxygen and the carbon. The iron and chromium maps were the same as before forging experiments; no correlations to SEM image in Fig. 6a were noticed. As shown in Fig. 6b, several thin titanium stripes were seen together with the oxygen mapping. There was no significant correlation to the SEM image. Figure 6c shows the carbon mapping on the interface; the gray stripes are carbon films, in situ formed onto the contact interface between the CS-SKD11 punch and the titanium work during the forging process.

This SEM-EDX analysis on the contact interface of CS-SKD11 punch to the titanium work proves that the in-situ formed free carbon tribofilm works as a solid lubricant medium on the true contact interface to lower the friction coefficient and to make homogeneous metal flow along the CS-punch interface. Nearly the same in situ solid lubrication was also observed on the contact interface between CS-die and the titanium work. These low frictional state of punch and die as well as the smooth work flow along their interfaces, characterizes the galling-free forging behavior when using the carbon supersaturated special tools.

To be noticed, no carbon maps in stripes in Fig. 6 were detected outside of the true contact area on the CS-punch and CS-die surfaces. That is, the applied stresses working on the true contact interface are necessary to in situ form the free carbon tribofilm. High compressive normal stress induces the diffusion of carbon solutes in the CS surface zones to the true contact interfaces of punch and die so that these free carbon agglomerates form the carbon tribofilm only on the contact interface.

Fine blanking of pure titanium by YXR punch.

In the fine blanking, the punch head is subjected to high normal stresses when punching out the work materials under the narrow clearance between the punch and die. The punch edge experiences the high shear stress transients and local metal flow change. The punch side surfaces are also subjected to shearing flow of work materials. Under these mechanical conditions with more severity than forging, the plastic distortion of work materials could result in galling damage on the XYR7 punches when fine-blanking the ductile and high-strength stainless steel and titanium plates.

In the present experiment, a bare YXR7 punch was used as a reference to describe the galling behavior when fine-blanking the pure titanium plate with the thickness of 2 mm in a single shot under the lubricating conditions. The CS-YXR7 was also utilized to demonstrate the role of carbon supersaturation in galling-free fine blanking.

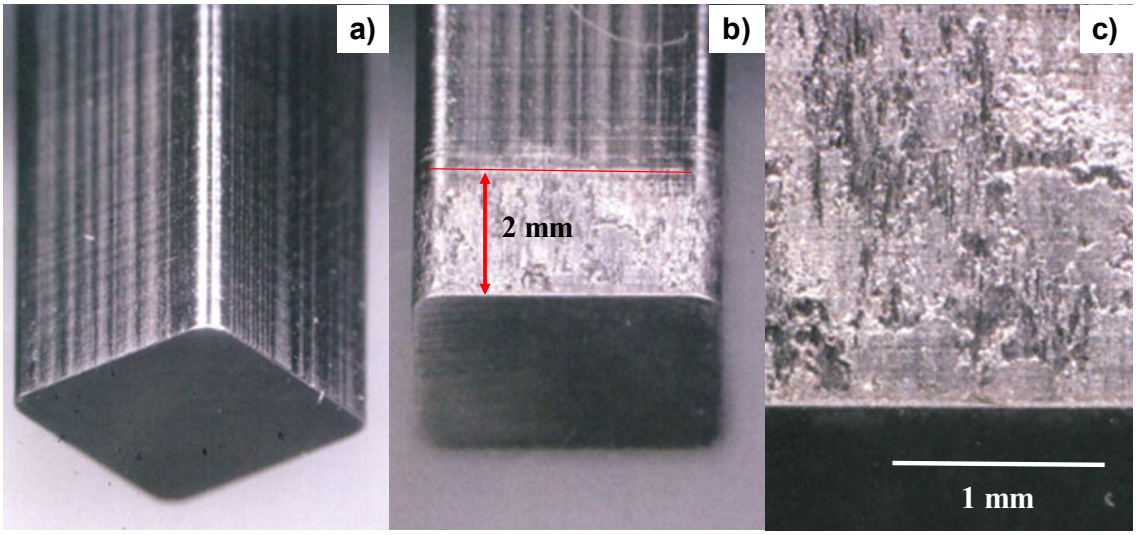

Fig. 7. YXR7 fine-blanking punch before and after fine blanking the pure titanium plate with the thickness of 2.0 mm in a single shot. a) YXR7 punch before fine blanking test, b) YXR7 punch after fine blanking test, and c) adhesion layer on the punch side surfaces.

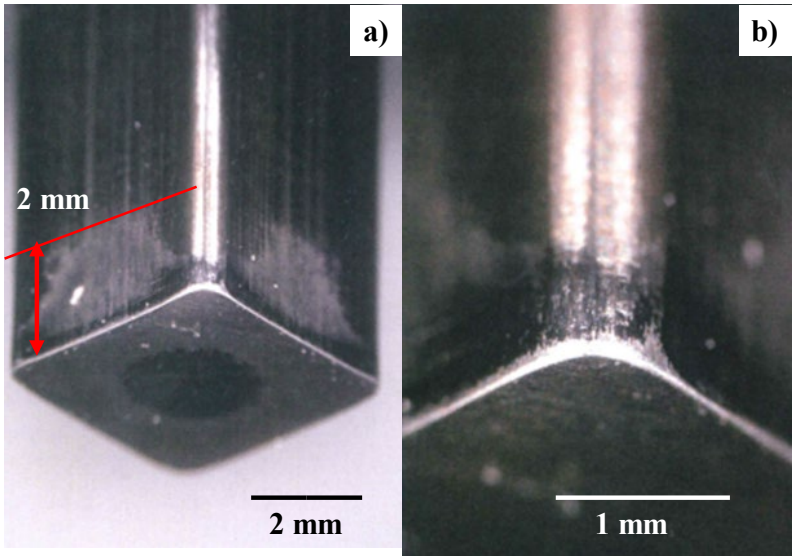

Fig. 8. CS-YXR7 punch after successively fine blanking the austenitic stainless steel AISI304 plates in three shots and the pure titanium plates in two shots. a) CS-YXR7 punch after fine blanking test, and b) punch surfaces around its edge and corner.

Fig. 7a and 7b compare the YXR7 punch surfaces before and after fine blanking the pure titanium plate with the thickness of 2.0 mm. No wears were seen both on the punch head after fine blanking in a single shot. However, its side surfaces with the length around 2 mm were almost covered by the fragments of titanium work. In particular, as seen in Fig. 7c, the titanium fragments adhered and eroded into the YXR7 punch., resulting in total failure of punch. This galling behavior proves that the fresh sheared titanium work is easy to adhere onto the punch side surfaces in the high normal and shear stress conditions under the narrow clearance.

Fine blanking of pure titanium by CS-YXR punch.

CS-YXR7 punch was used to make fine blanking the AISI316 plates with the thickness of 3 mm in three shots and then to punch out the pure titanium plate with the thickness of 2 mm in two shots. Fig. 8a shows the overview of CS-YXR7 after a series of fine blanking shots.

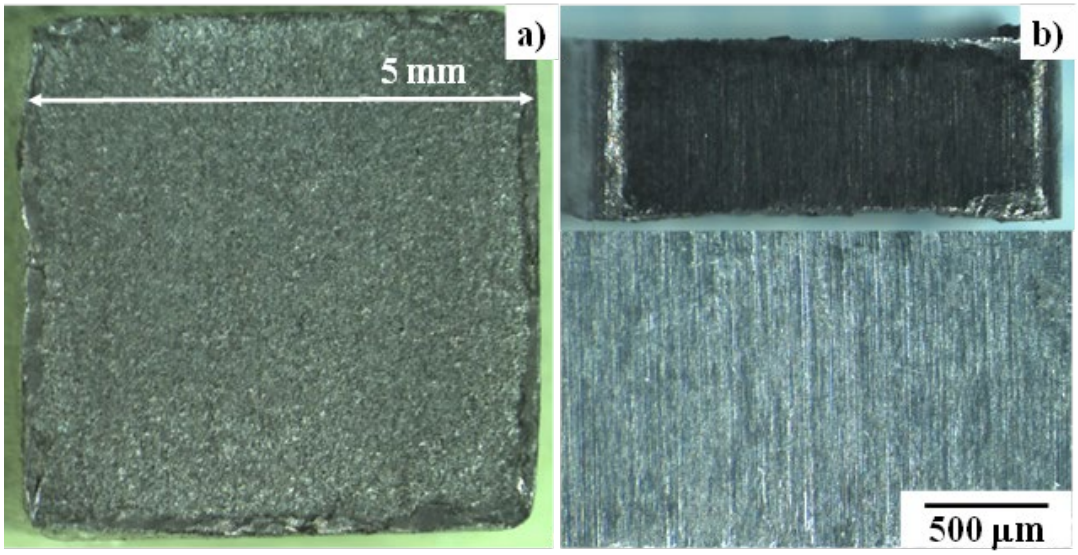

Fig. 9. The side and bottom surface of titanium blank, punched pout by the CS-YXR7 punch.

In contrast to the severe adhesion of titanium fragments onto the bare YXR7 punch in Fig. 8b and 8c, the CS-XYR7 punch is completely free from the galling of sheared titanium work even after punching the stainless steel and titanium plates in several times. This implies that in situ formed free carbon tribofilms are formed on the highly stressed contact surfaces of punch under the narrow clearance in the similar manner to the in situ solid lubrication as seen in Figure 6 when forging the pure titanium plate. Once the tribofilm is formed on the fine blanking punch, no adhesive wear of metal works occurs even with increasing the number of shots.

This galling-free behavior suggests that the quality of punched-out blank is expected to be improved by this fine blanking process. Fig. 9 depicts the top and side surfaces of punched-out titanium blank. No fractured regions are detected on every four side surface of blank. This proves that CS-YXR7 punch is suitable to high qualification in fine blanking of titanium plates to products.

Discussion

The flash temperature on the highly stressed contact interface between the punches/dies and the work materials was thought as a main process parameter to govern the galling heavier in forging [7, 16]. In fact, the oxidation wear of carbon-based coatings such as diamond and DLC (Diamond Like Carbon) in stamping and forging [17] suggested that the chemical galling had overwhelming influence on the abrasive wear of tool surfaces at hot spots. As compared in Figs. 7 and 8, the active metals such as pure titanium with chemical compatibility to various inorganic materials, induced the adhesive wear onto the steel tool surfaces at RT even under the lubricating conditions. This mechano-chemically adhesive galling under highly stressed condition, accompanied with erosion of titanium into the tools. Under the free carbon tribofilms, in-situ formed onto the carbon supersaturated SKD11 and YXR7 punches, this adhesive galling is completely suppressed to make forging and fine-blanking repeatedly without metallic sticking and seizure. This reveals that inactive tribofilm is needed to be free from the mechano-chemical adhesion galling.

As had been discussed in the dry tribological behavior of carbon-based coatings [6-7], the high friction coefficient, experienced in the TiN, TiCN, TiAlN and other ceramic coatings, much reduced in the silicon-bearing DLC and nano-laminated DLC coatings during the BOD testing. This implies that adhesive galling is effectively suppressed on the bound carbon surface of the amorphous carbon microstructure. In the present in-situ solid lubrication, the free carbon film with nearly the same Raman spectroscopy as the hydrogenated DLC (or a:C:H) works as an inactive buffer interface between the fresh titanium and the steel punch.

Let us consider the effect of carbon bound state on the frictional behavior. Although the SKD11 houses the iron and chromium carbides by heat treatment and the YXR7 has a low carbon content, severe galling occurs as seen in Fig. 7. The bound carbon in the carbides and the alloying carbon element have no capacity of in situ solid lubrication. The weakly bound carbon in the amorphous carbon film has a little capacity to reduce the friction under mild tribological conditions. The unbound carbon tribofilm has a significant capacity to be free from mechano-chemical adhesion wears in fine blanking. This difference in the bound state of carbons on the contact interface, directly reflects on the galling process of titanium works.

As keenly discussed in [10] and suggested in [18-19], the supersaturated carbon in the steel punches diffuses onto the contact interface to titanium work under high stress gradient, and, forms a free-carbon tribofilm. As seen in Figs. 4 and 8a, no tribofilms were formed outside of the true contact area. In case of forging process, the carbon stripes were formed as a thin tribofilm on the true contact interface of CS-SKD11 punch to titanium work. In case of fine blanking, the carbon film was also formed as a thin tribofilm on the contact interface of CS-YXR7 punch. Remember that high normal stress was applied onto the contact interface when forging the pure titanium wire, and that higher normal stress and high shear stress were combined and applied onto the contact interface when fine-blanking the pure titanium plate. This reveals that tribofilm thickness is dependent on the applied stress level during metal forming processes. To be noticed, the free-carbon tribofilm formed onto the YXR7 punch surface is so tough not to be delaminated even in high and combined stress conditions without galling. Owing to this in situ formation of tough tribofilm, the CS-YXR7 punch is also free from adhesive wearing even with increasing the number of shots as discussed in [20]. This carbon supersaturation into punch and die substrates are necessary to prolong the tool life without severe galling in the fine blanking of titanium plates.

As reported in [21-22], the abrasive and adhesive galling processes were effectively suppressed by the nanotexturing onto the punch side surface when punching out the electrical steel sheets. This was because the debris particles were ejected through the nanotextured grooves to the outside of punching process. This nanotexturing effect can be also accommodated to this fine blanking with the use of CS-steel punches. The titanium and titanium alloys parts with fully burnished surface can be near-net shaped by this fine blanking without significant galling and abrasive wear. The effect of galling-free fine blanking on the product quality and tool life is a next issue to advance this new type tooling for fine blanking.

Summary

The carbon supersaturation by the low temperature plasma carburizing is essential to protect the tool steel and high-speed tool steel punches and dies from adhesion wear during the forging and fine blanking of titanium and titanium alloy works. In particular, the free-carbon tribofilm, in situ formed on the YXR7 punch, minimizes the mechanical and chemical galling damages during the fine-blanking of titanium plates. Under the shearing stress transients in fine-blanking, this in situ solid lubrication plays a role to prevent the punch surfaces from severe galling. This tooling is available in the industries to continuously punch out the complex-shaped blanks of austenitic stainless steels, titanium and titanium alloys with fully burnished surfaces.

Acknowledgment

The authors would like to express their gratitude to S-I. Kurozumi (Nano-Film Coat, llc.) for his help in experiments.

References

[1] G.W. Kuhlman, Forging of titanium alloys, in: Metalworking: Bulk forming, Vol. 14 in ASM Handbook, 2005.

[2] M. Chandrasekaran, Forging of metals and alloys for biomedical applications, Ch. 10 in: Metals for biomedical devices, 2nd Ed. Woodhead Publishing, 2019, pp. 293-310.

[3] D.S. Fernández, B.P. Wynne, P. Crawforthc, K. Fox, M. Jackson, The effect of forging texture and machining parameters on the fatigue performance of titanium alloy disc components, Int. J. Fatigue 142 (2021) 105949. https://doi.org/10.1016/j.ijfatigue.2020.105949
[4] T. Kihara, Visualization of deforming process of titanium and titanium alloy using high speed camera, Proc. 2019-JSTP Conference 2019, pp. 41-42.
[5] S. Kataoka, M. Murakawa, T. Aizawa, H. Ike, Tribology of dry deep-drawing of various metal sheets wit use of ceramic tools, Surf. Coat. Technol. 178 (2004) 582-590. https://doi.org/10.1016/S0257-8972(03)00930-7
[6] K. Dohda K., T. Aizawa, Tribo-characterization of silicon doped and nano-structured DLC coatings by metal forming simulators, Manuf. Lett. 2 (2014) 82-85. https://doi.org/10.1016/j.mfglet.2014.03.001
[7] K. Dohda, M. Yamamoto, C. Hu, L. Dubar, K.F. Ehman, Galling phenomena in metal forming, Friction 9 (2020) 686-696. https://doi.org/10.1007/s40544-020-0430-z
[8] T. Aizawa, T. Yoshino, Y. Suzuki, T. Shiratori, Free-forging of pure titanium with high reduction of thickness by plasma carburized SKD11 dies, Materials 14 (2021) 2536. https://doi.org/10.3390/ma14102536
[9] T. Aizawa, T. Yoshino, Y. Suzuki, T. Shiratori, Anti-galling cold, dry forging of pure titanium by plasma-carburized AI-SI420J2 dies, Appl. Sci. 11 (2021) 595. https://doi.org/10.3390/app11020595
[10] T. Aizawa, T. Shiratori, In-situ solid lubrication in cold dry forging of titanium by isolated free carbon from carbon-supersaturated dies, J. Friction (2022) (in press).
[11] S. Ishiguro, T. Aizawa, T. Funazuka, T. Shiratori, Green forging of titanium and titanium alloys by using the carbon supersaturated SKD11 dies, Appl. Mech. 3 (2022) 724-739. https://doi.org/10.3390/applmech3030043
[12] T. Aizawa, T. Funazuka, T. Shiratori, Near-net forging of titanium and titanium alloys with low friction and low work hardening by using carbon-supersaturated SKD11 dies, Lubricants 10 (2022) 203. https://doi.org/10.3390/lubricants10090203
[13] T. Aizawa, Low temperature plasma nitriding of austenitic stainless steels, Ch. 3 in Stainless Steels and Alloys, IntechOpen, UK, London, 2019, pp. 31-50.
[14] D.M. Geobel, C. Becatti, I.G. Mikellides, A.L. Ortega, Plasma hollow cathodes, J. App. Phys.130 (2021) 050902. https://doi.org/10.1063/5.0051228
[15] J.J. Hong, W.C. Yeh, Application of response surface methodology to establish friction model of upset forging, Adv. Mech. Eng. 10 (2018) 1-9. https://doi.org/10.1177/1687814018766744
[16] K. Dohda, C. Boher, F. Rezai-Aria, N. Mahayotsanun, Tribology in metal forming at elevated temperatures, Friction 3 (2015) 1-27. https://doi.org/10.1007/s40544-015-0077-3
[17] S. Takeuchi, Treatise on the CVD diamond coatings, Ohm-Sha (2022).
[18] Y. Cao, F. Ernst, G.M. Michal, Colossal carbon supersaturation in austenitic stainless steels carburized at low temperature, Acta Mater. 51 (2003) 4171-4181. https://doi.org/10.1016/S1359-6454(03)00235-0
[19] R. Rementeria, J.D. Poplawsky, E. Urones-Garrote, R. D-Reyes, C. Garcia-Mateo, F.G. Caballero, Carbon supersaturation and clustering in bainitic ferrite at low temperature, Proc. 5th Int. Symp. Steel Science, Nov. 14, 2017, Kyoto, Japan, ISIJ (2017) 29-34.
[20] T. Aizawa, K. Fuchiwaki, Galling-free fine blanking of titanium plates using carbon supersaturated high-speed steel punch, J. Carbon Research (2023) (in press).
[21] T. Aizawa, T. Shiratori, Y. Kira, T. Inohara, Simultaneous nano-texturing onto a CVD-diamond coated piercing punch with femtosecond laser trimming, Appl. Sci. 10 (2020) 2674. https://doi.org/10.3390/app10082674
[22] T. Aizawa, T. Inohara, T. Yoshino, Y. Suzuki, T. Shiratori, Laser treatment of CVD diamond coated punch for ultra-fine piercing of metallic sheets, Ch. 4 in: Engineering Applications of Diamond, Intech Open, UK, London, 2021, pp. 43-65.

Materials Research Proceedings 28 (2023) 879-890 https://doi.org/10.21741/9781644902479-96

The influence of Particle Hardness on Wear in Sheet Metal Forming

ARINBJARNAR Úlfar[1,a *], KNOLL Maximilian[1,b], MOGHADAM Marcel[2,c] and NIELSEN Chris Valentin[1,d]

[1]Department of Civil and Mechanical Engineering, Technical University of Denmark, Produktionstorvet 425, 2800 Kongens Lyngby, Denmark

[2]FalCom A/S, Laustrupbjerg 7, 2750 Ballerup, Denmark

[a]ulari@dtu.dk, [b]maxkn@dtu.dk, [c]mmoghadam@falcom.net, [d]cvni@dtu.dk

Keywords: Tribological Testing, Particles, Contamination, Lubricant Additive

Abstract. Particles exist in any tribo-system, whether it is closed to the environment or not. These particles originate from various sources, for example: contaminants such as dust or fibres from the environment; wear debris from abrasive/adhesive wear; and particles that are intentionally included in lubricant formulations. The particles affect the tribo-system in which they occur, but it is not always clear how. In this work, three types of chemically inert particles of similar size but different hardness are mixed with an otherwise pure oil and tested tribologically. Three tribological testing methods, pin-on-disc, four-ball, and bending-under-tension, are used to investigate the effect of the particles on friction and wear under sheet metal forming conditions. The hardness of the particles had a large effect on wear development, but little to no effect on the coefficient of friction found by pin-on-disc testing. Including particles of any hardness helped the oil in which they were included resist variation in load, leading to less wear for higher loads compared to the pure oil.

Introduction

Various types of particles are endemic to tribological systems. Some particles are added to a tribo-system on purpose, while others enter the tribo-system accidentally or are unintentionally created through tribological or chemical mechanisms. There are essentially three sources by which the concentration of particles in a running tribo-systems increases over time. One of the sources are particles that are generated through tribological mechanisms such as adhesive or corrosive wear. These can be of different shapes and chemical compositions but would generally include some part of either the workpiece or tool. Another source is the environment, which can introduce particles of material such as dust or fibres from fabrics into the tribo-system. Lastly, depending on the lubricant formulation, the use and aging of the lubricant can lead to bacterial growth, which eventually forms bacterial cells [1]. These cells can be considered solid particles, but often help by improving the wear resistance of the lubricant rather than degrading it. These sources cause an increase in the concentration of particles in a tribo-system, with some particles already existing within the tribo-system, due to e.g., improper cleaning [2] or particles being included in the lubricant formulation.

The presence of particles in a tribo-system is often considered unwanted and has even been used as an indicator of mechanical systems undergoing severe wear [3]. Jiang and Wang [4] investigated the effect of wear particles of different sizes and concentration on wear in a locomotive engine. They applied a roller-on-roller test using a base-oil that included some concentration of particles collected from used oils and filters from running locomotive engines. Their result showed that the concentration of particles and the size of the particles are positively related to the amount of wear that occurs in the tribological test. The particles they used consisted mainly of iron and oxidation products, but also included some copper and aluminium. Abou El

Content from this work may be used under the terms of the Creative Commons Attribution 3.0 license. Any further distribution of this work must maintain attribution to the author(s) and the title of the work, journal citation and DOI. Published under license by Materials Research Forum LLC.

Naga and Salem [5] investigated how the presence of wear particles in a lubricating oil affected the degradation of the oil. They found that metallic particles can have a catalytic effect and speed up the oxidation of various chemicals in the lubricant composition. An increasing concentration of particles made this effect more pronounced, meaning that the effectiveness of the lubricant was degraded even more quickly. In their paper on the tribology in the wheel-rail contact of locomotives, Olofsson et al. [6] discussed the role that particles play in wear. The role is, independently of where the particles originate, essentially twofold. On one hand, the particles are free to move in a contact interface and therefore lead to three-body abrasive wear. Olofsson et al. note that the hardness of the particles in this case does not have a large effect on the wear rate, provided they are at least 20% harder than the surfaces in contact. This effect is the same as that used by other researchers investigating the use of solid particles in lubricant formulation. On the other hand, the particles can become embedded in a surface and initiate severe two-body abrasive wear.

Many researchers have investigated intentionally adding solid particles to a lubricant to improve the lubricant's tribological performance. Luo et al. [7] added alumina particles with an average size of 78 nm to an oil and found that the particles improved the friction reduction and wear resistance properties of the oil under four-ball and thrust-ring conditions at loads of 147 N and 200 N respectively. The particles they used are harder than the active test components, which had a hardness of between 44 - 66 HRC and were thought to promote rolling over sliding as well as forming a tribo-film that helps resist wear. Padgurskas et al. [8] used iron, copper, and cobalt particles to improve the friction and wear behaviour of a lubricant under four-ball test conditions. They included mixtures of the particles, which showed an even larger improvement in tribological performance compared to single particle lubricants, with the best mixture being equal concentrations of iron and copper. Li et al. [9] investigated the effect of wear particles in a lubricant used in a rolling process and found that the wear particles had an anti-wear and anti-friction effect, at least under the four-ball conditions applied in their work. However, the particle also affected the stability of the lubrication mechanism in a deleterious way, which lead to increased wear after some time. In other work [10], the efficacy of $CaCO_3$ particles of two sizes for improving tribological conditions was evaluated. The particles were added to a base oil, along with a surfactant to ensure proper dispersion, and then tested by applying pin-on-disc testing, four-ball testing, and bending-under-tension testing. The particles were found to drastically improve the tribological performance of the base oil, through what appeared to be physical mechanisms. Peng et al. [11] evaluated the wear resistance of a tribo-system that included SiO_2 particles of different sizes and found that as the size of the particle decreased, the wear resistance and friction reduction improved. At some point, the size of the particles exceeded some critical point and the wear amount, and friction, became higher than for the pure lubricant. An increased concentration of the particles emphasized this behaviour even more.

In summary, depending on the specific properties of particles, such as size and hardness, they can have different effects on the tribo-system in which they are added. Some property of particles in a tribological system means the difference between their acting as abrasives, causing wear, and their acting as ball-bearings to promote rolling over sliding, reducing wear. In this work, three types of particles are added to pure paraffin oil with the aim of investigating the effect of the particle hardness on their role in wear, with a focus on sheet metal forming. Therefore, $CaCO_3$ particles are used as they have been shown to be beneficial to tribo-systems, $BaSO_4$ particles as they are slightly harder than the $CaCO_3$ particles, and SiO_2 particles as they are much harder than the other particles.

Experimental Methods and Materials

Particles. Some of the properties of the particles used in this work, given in supplier datasheets, are shown in Table 1. The size of the particles is similar, with the SiO_2 particles being slightly

larger but in the same range. The hardness of the particles is given on the Mohs-scale which shows that the $CaCO_3$ particles are softest, the $BaSO_4$ being slightly harder and the SiO_2 particles being significantly harder. All particles used in this work had a nodular shape, i.e., almost spherical.

Table 1. Properties of particles used in this work.

Chemical formula	$CaCO_3$	$BaSO_4$	SiO_2
Commercial name	Polyplex 2	Portaryte® B 10	Silverbond M500
Particle size D10% [µm]	~ 0.4	0.8	2.2
Particle size D50% [µm]	2.0 - 2.6	2.6	5.0
Particle size D90% [µm]	~ 5.4	8.2	11.7
Hardness [Mohs]	3.0	3.5	7.0
Bulk density [g/cm^3]	0.8	1.7	0.42
Oil absorption [g/100ml]	17.4	10	23
Source	[12]	[13]	[14]

The lubricant mixtures tested in this work are derived from base mixtures that contain the specific particle, Ph. Eur. grade paraffin oil as the base oil, and Tween60 as surfactant to allow proper and homogeneous dispersion of the particles in the base oil. The base mixtures were prepared in a similar way, involving first dissolving the surfactant in the paraffin oil using a Dispermat CV3-Plus high-speed dissolver, followed by adding the particles and dispersing them using the same high-speed dissolver. The resulting base mixture was then diluted by adding more paraffin oil to arrive at a lubricant mixture of a fixed nominal concentration. The lubricant mixture was then agitated before use to ensure proper dispersal of the particles in the base oil. The nominal concentrations of single particle types tested in this work are 10 wt%, 20 wt% and 40 wt%. They were prepared using a scale that has a resolution of 10 mg, leading to the uncertainty of concentration being less than 1% of the nominal concentration.

Tribological Testing. Pin-on-disc testing involves placing a pin into contact with a rotating disc under some load, as shown in Fig. 1. Also shown in the figure is the specific testing machine used in this work, which is a standard *CSM Instruments Tribometer*. The tribometer has a built-in force transducer that measures friction load, allowing the device to calculate the friction coefficient based on the applied load. In this work the pin-on-disc test was performed according to DIN 50324:1992 for testing of friction. Two loads were applied, 1 N and 10 N, to investigate how the difference in load affects the tendency of the particles for being embedded in surfaces and affecting friction in that way. The disc component used in this testing is made from *Vanadis 4E*, a tool-steel from *Uddeholm* that has been ground and polished to a surface roughness of Ra = 0.06 µm after hardening to 62 HRC. The pin component consists of a ball-holder and a ball, which is made from EN 1.4301 steel, with a hardness of 25 HRC, grade G100 and diameter Ø6 mm. The amplitude of roughness of surfaces that were in contact was therefore much smaller than the particle size for all particle types. A fresh part of the discs and an unused ball were used in each test.

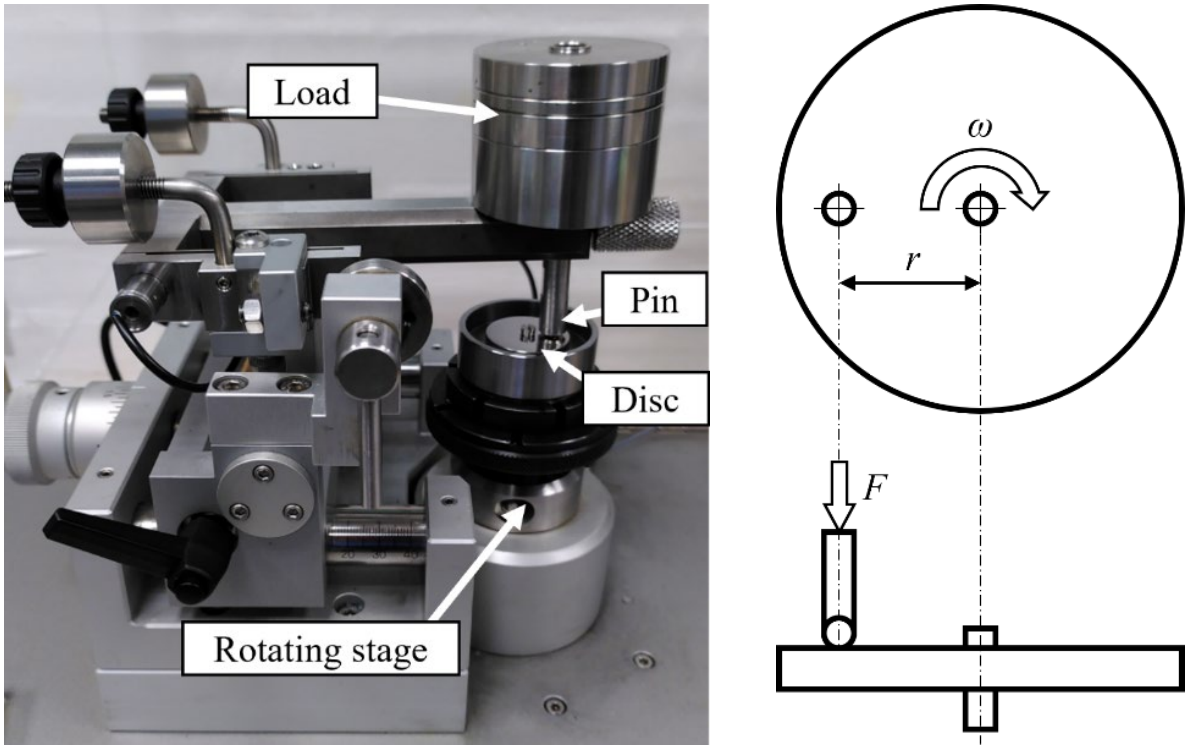

Fig. 1. (a) Standard CSM Tribometer with pin-on-disc configuration. (b) Principle of the pin-on-disc test.

Test parameters, besides applied load and track radius, were kept constant through all tests. The sliding speed was set to 50 mm/s, with the total sliding distance being 100 m. The track radii were in the range 8 mm – 14 mm with the rotational speed being adjusted based on the track radii so that the linear sliding speed was constant. The amount of lubricant-particle mixture used in each test, 7 ml – 10 ml, was enough to submerge the disc component to a depth of at least 5 mm. The approximate kinematic viscosity of the mixtures used in this work is on the order of 200 ± 100 cSt, so according to the Hersey-number of the system, the boundary lubrication mechanism is dominant. Each test condition, i.e., particle concentration and type of particle, was repeated three times to account for reproducibility.

Four-ball testing involves establishing sliding contact conditions between three balls that are fixed in place and one ball that rotates under some load, as shown in Fig. 2. Also shown in the figure is the testing machine used in this work, which was custom-built for the Technical University of Denmark. In this work, four-ball testing was performed as a wear test as defined in the ISO 20623:2018 standard, applying a load of 300 ± 5 N or condition C2. The test was performed over a period of 3,600 ± 1 seconds at a constant rotational speed of 1,420 ± 20 rpm. For each test, a fresh set of 100Cr6 chromium steel bearing balls of hardness 60 HRC - 66 HRC, Ø12.7 mm, and grade G20, were used as test balls. 10 ml of lubricant were used in each test, ensuring that the balls were covered to a depth of at least 5 mm. This test enables the determination of how the presence of particles of different hardness in the lubricant affects the wear resistance properties of the lubricant under boundary lubrication conditions. A further two load levels, 150 N and 450 N were applied for a 10 wt% concentration of particles to see how the load level affects the particle behaviour. Each test condition, i.e., particle concentration, type of particle and load level, was repeated three times to account for reproducibility.

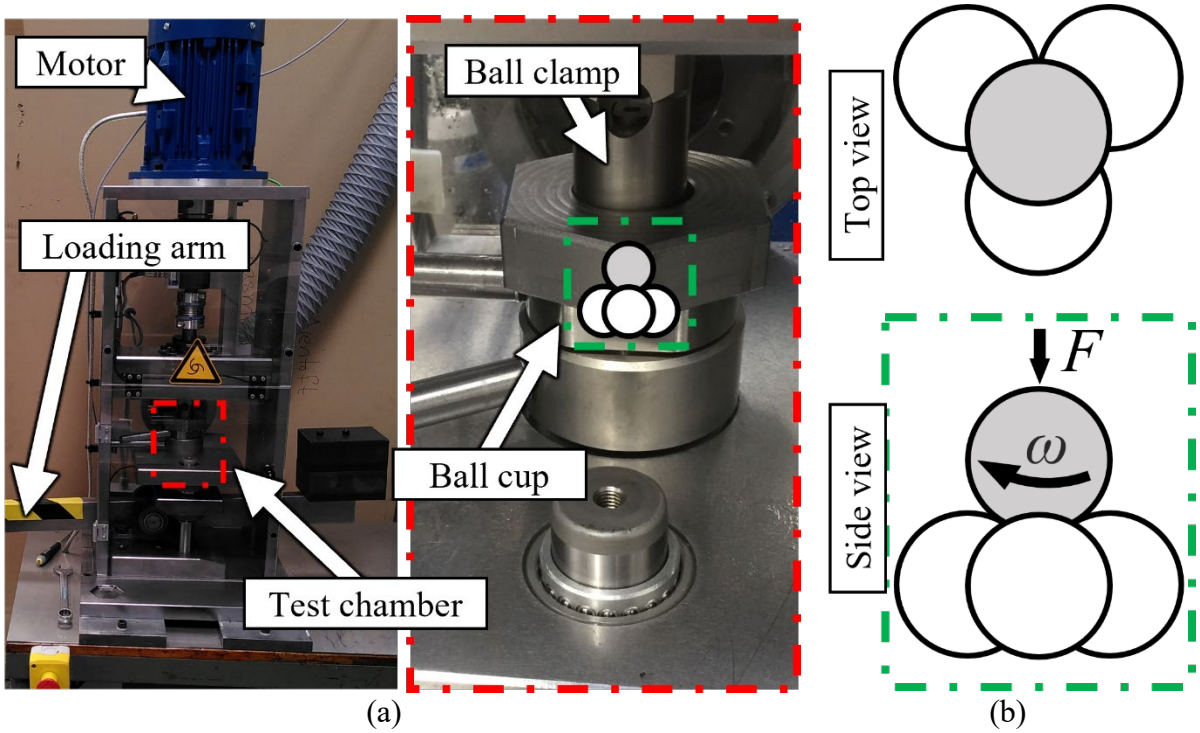

Fig. 2. (a) Four-ball testing machine including close-up of test chamber. (b) Principle of four-ball test.

Bending-under-tension testing was applied as a simulation of a deep drawing process to investigate how the different particles behave in a tribological system that is typically found in industrial sheet metal forming. The principle of the test revolves around bending a strip over a tool-pin under back-tension, as shown in Fig. 3. The difference between the back-tension force, F_b, and the drawing force, F_d, will then be due to the force required to deform the strip and friction. As the force required to deform the strip is nearly constant, then any increase in drawing force will be caused by an increase in friction in the tool-pin/strip interface. The nominal concentration of 20 wt% particles suspended in paraffin oil was applied here. The tool-pins were made from *Vanadis 4E* tool-steel hardened to 62 HRC and polished, while the strip was EN 1.4301 stainless steel with a 2B surface finish and a 30 mm x 1 mm cross-section. The edges of the strip are harder than the middle due to strain-hardening from roller cutting. A back-tension of 180 MPa ± 10 MPa was applied across 50 strokes, the sliding length of which was set to 30 mm. The sliding speed was 30 mm/s, with an idle time of 0.5 s between strokes which meant that the production rate was 40 strokes/min. Each test was repeated so that two data-sets exist for each test set-up.

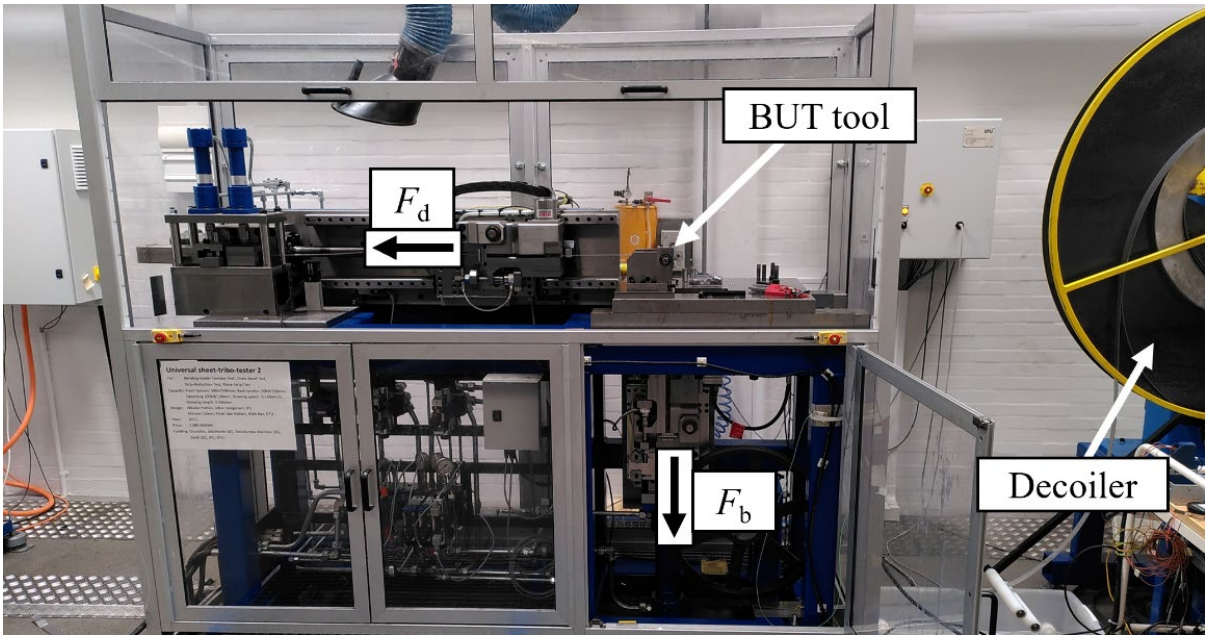

(a)

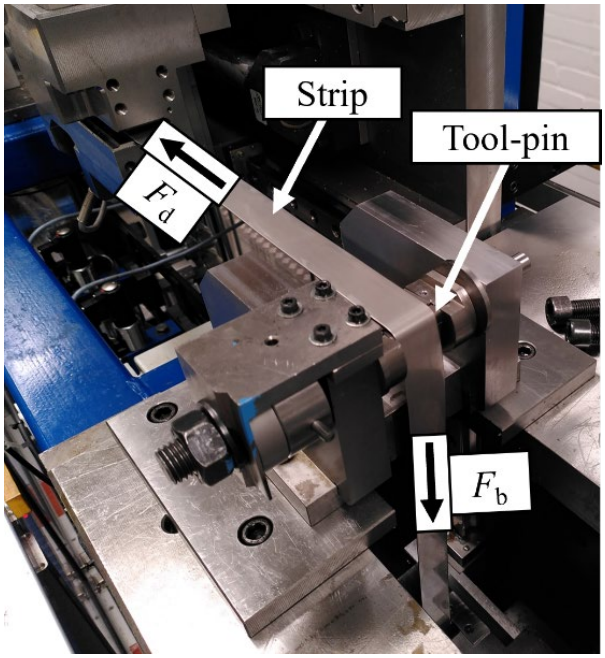

(b)

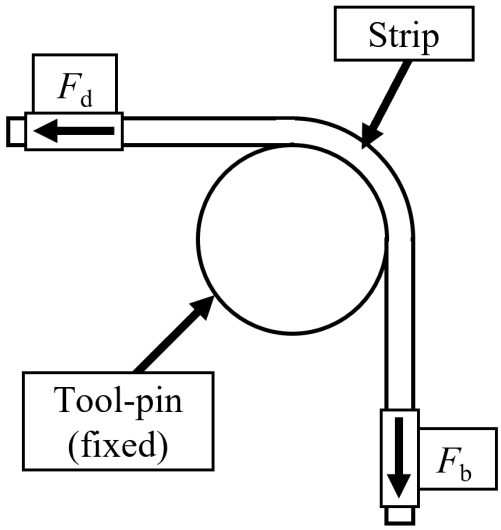

(c)

Fig. 3. Bending-under-tension (BUT) test shown by (a) an overview of the testing machine, (b) a close-up of the testing area, and (c) the principle of the test.

Optical Methods. An Olympus LEXT 4000 laser confocal microscope was used to capture images of wear scars on pin-on-disc discs, four-ball specimens and BUT tool-pins. Captured images were then processed in SPIP, an image processing software. Fig. 4(a) shows a typical disc after pin-on-disc testing, and the location of where images are taken of the wear scars on its surface. Fig. 4(b) shows a typical wear scar found in four-ball testing, along with where its parallel and perpendicular diameters are measured. Reported wear scar diameters are averaged between the two measurements. Fig. 4(c) shows the acquisition strategy employed for acquiring images of the surfaces of tool-pins used in BUT testing. The middle region of wear scars is imaged.

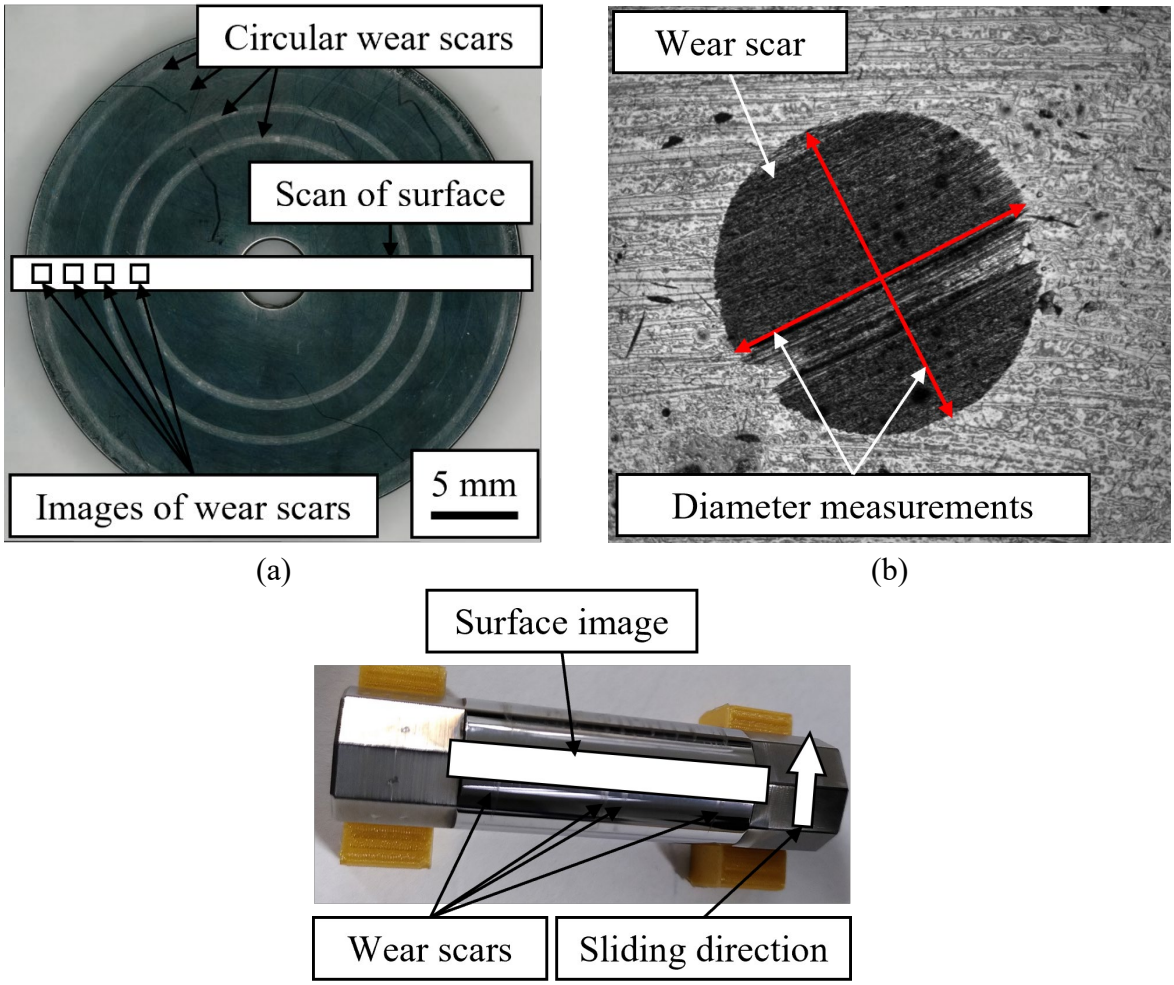

Fig. 4. Explanation of (a) acquisition of images of wear scars from pin-on-disc testing, (b) measuring of wear scars on four-ball specimens, and (c) acquisition of images of wear scars from tool-pin after bending-under-tension testing.

Results

Pin-On-Disc Testing. The influence of the particles on friction was estimated through pin-on-disc testing. The average friction coefficient is determined from the resulting friction profile, and all data-points from each test load are plotted together for comparison and shown in Fig. 5.

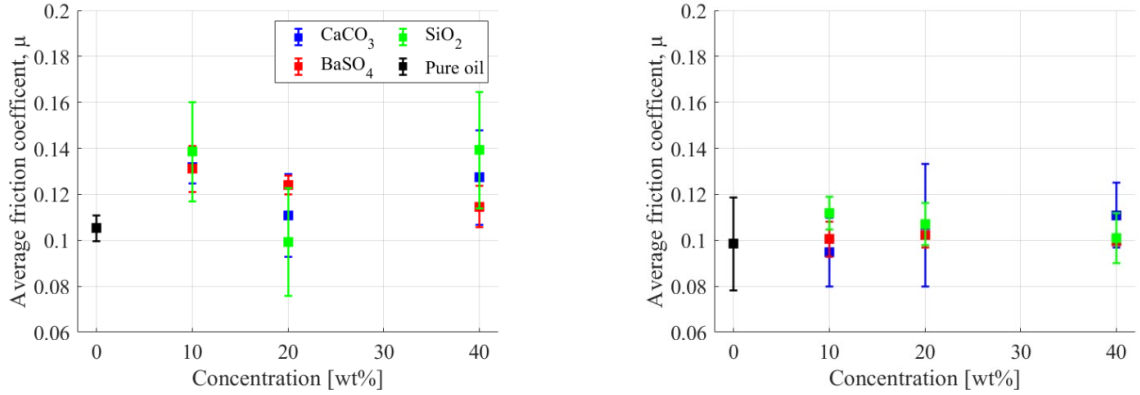

Fig. 5. Average friction coefficient found in pin-on-disc tests for (a) 1 N load and (b) 10 N load. Error bars denote standard deviation of data-set.

Materials Research Proceedings 28 (2023) 879-890 https://doi.org/10.21741/9781644902479-96

No influence by the particle type on friction could be found in the range of loads tested here. Further, compared to the pure oil, friction was not changed much by adding particles to the system. The wear scars that formed on the surface of the discs were, however, very different. Typical examples of the wear scars are shown in Table 2, where wear scar images were taken so that the centre of the disc was to the right of the wear scar. The wear scars from SiO_2 particles were clearly the most pronounced, the size of the wear scar increasing with the concentration of the particles. The $BaSO_4$ particles also showed severe wear scars compared to the pure oil, at least for higher concentrations, which showed very little wear. Applying $CaCO_3$ particles of a small concentration led to a reduction in the size of the wear scar. This effect was emphasized for increasing concentration of $CaCO_3$ to the point that no wear scar could be detected for 20 wt% and 40 wt% concentrations of $CaCO_3$. The applied load did not have much effect on the development of wear when particles were included, although it did increase wear in all cases.

Four-Ball Testing. Two sets of tests were performed using the four-ball configuration, varying either the concentration of particles in the mixture for a constant load, or varying the load for a constant concentration. The results of the former are shown in Fig. 6, whereas the latter is shown in Fig. 7. The wear scar diameter found in the four-ball tests clearly changed as function of particle concentration. For the SiO_2 particles, the wear scar diameter increased compared to the pure paraffin oil and then continued to increase for an increasing concentration of particles. The wear scar for the $BaSO_4$ particles of 10 wt% concentration was smaller than for the pure oil, but then increased with increasing concentration to a similar level as the pure oil. Wear scars found on balls used with $CaCO_3$ particles decreased in size compared to pure oil and were then stable for an increasing concentration of particles.

For changing loads, the behaviour was somewhat different. For the pure oil, as might be expected, the wear scar diameter increased with increasing load as there are no boundary additives included. Including particles prevented this increase, at least somewhat, reducing how much the wear scar diameter increased with increasing load. For a small load, the $CaCO_3$ and $BaSO_4$ particles showed a similar wear scar diameter as the pure paraffin oil. The wear scar diameter increased less with increasing load when these particles were included compared to the pure oil. This is similar to what Ji et al. [15] found for nano particles of $CaCO_3$ under four-ball test conditions in a range of loads using lithium grease as the base lubricant. They explained that for lower loads, the particles behaved based on the ball-bearing mechanism, but that as the load is increased and shearing of the surface becomes more likely, the surface energy of sheared surfaces causes a tribochemical reaction and leads to a boundary layer forming on the worn surface. The SiO_2 particles caused wear for small loads, but then prevented it from growing as the applied load is increased. This is likely due to the particles causing extreme wear in the beginning until the contact pressure is decreased enough that the particles could no longer penetrate the surface of the balls, and instead start to only act in a way that separates the surfaces.

Table 2. Typical wear scars found in pin-on-disc testing using the different particles.

Particle	None		$CaCO_3$		$BaSO_4$		SiO_2	
Load	1 N	10N	1 N	10 N	1 N	10 N	1 N	10 N
0 wt%	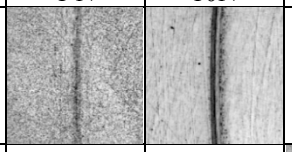		-	-	-	-	-	-
10 wt%	-	-	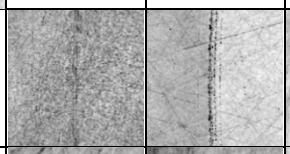					
20 wt%	-	-	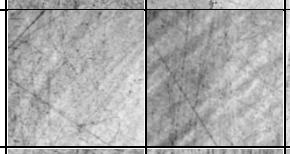					
40 wt%	-	-	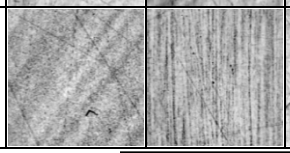					
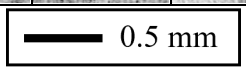 0.5 mm								

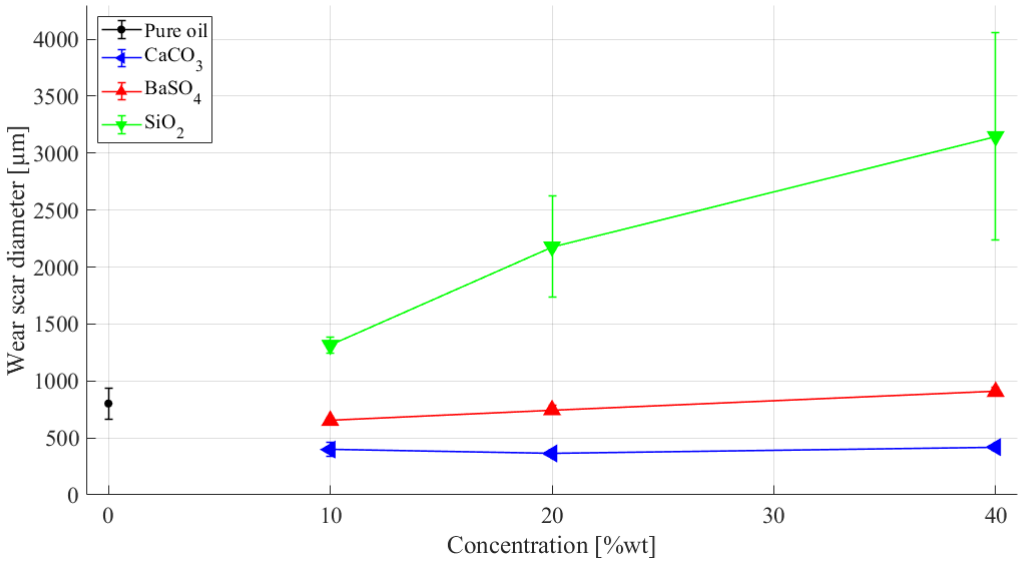

Fig. 6. Wear scar diameters from four-ball testing for different concentrations of particles for load of 300 N. Error bars are plus-minues one standard deviation of measured wear scar diameters.

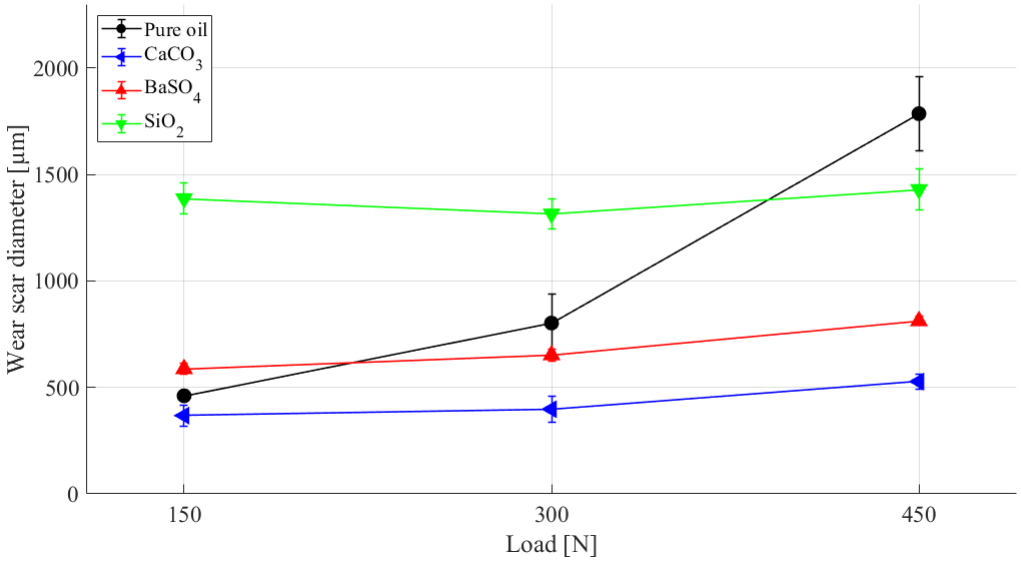

Fig. 7. Wear scar diameter from four-ball testing as a function of applied load for a constant 10 wt% particle concentration. Error bars are plus-minus one standard deviation of measured wear scar diameters.

Bending-Under-Tension Testing. Drawing force, F_d, profiles from BUT testing are shown in Fig. 8. The drawing force was influenced by the presence of particles and the particle type. For the pure oil (PO), pick-up quickly started to occur, leading to a steady increase in the drawing force until the end of the test. Including $BaSO_4$ particles showed a similar development of the force profile, although the force increased less. Including SiO_2 particles led to a quicker increase in force, indicating more severe conditions. The $CaCO_3$ particles showed only a small increase in force across the 1500 mm sliding length, indicating that they are beneficial to the wear resistance properties of the lubricant.

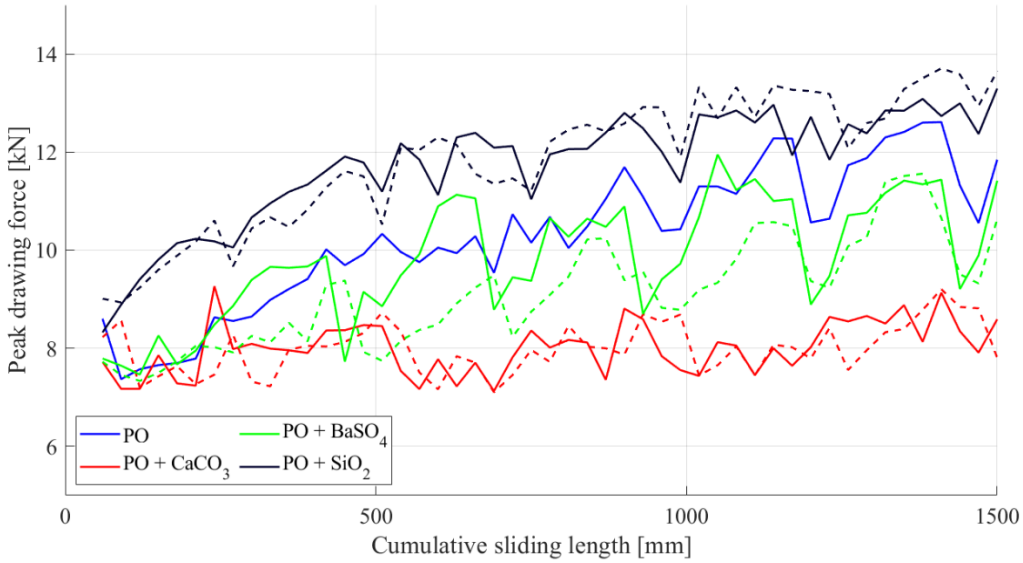

Fig. 8. Drawing force measured in BUT testing. Solid lines and dashed lines of the same colour are repetitions of the same test conditions. The concentration of particles was 20 wt%.

Images of the surfaces of selected tool-pins were captured and are shown in Table 3. The pure oil exhibited a high tendency for pick-up as can be seen on the surface of the tool-pin, which is consistent with the observations of the drawing force. The $CaCO_3$ particles prevented this and led to less wear on the tool-pin surface. The $BaSO_4$ particles helped in reducing wear, but the surface of the tool-pin ended up looking comparable to that of the pure oil. The SiO_2 particles clearly led to much more pick-up, potentially due to localised wear scars causing more favourable conditions for pick-up, or even heating up of the tool-pin near the surface.

Table 3. Surfaces of tool-pins used with different particles of 20 wt% concentration. The drawing direction is from bottom to top of figures. Solid profiles shown in Fig. 8 belong to the surfaces shown here.

Particles	Surface of tool-pins
None	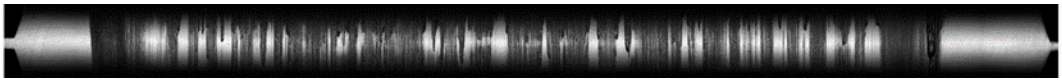
$CaCO_3$	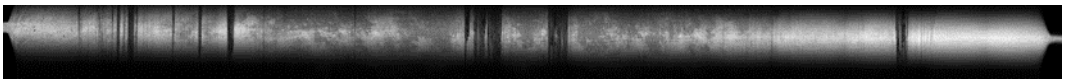
$BaSO_4$	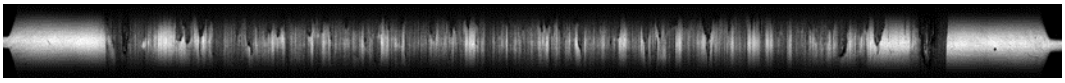
SiO_2	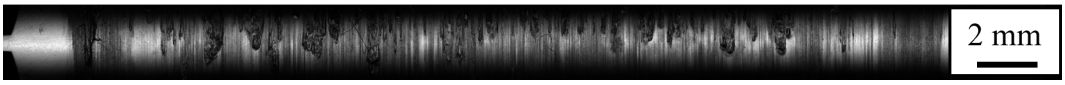

Summary

Including particles in a tribo-system, either accidentally or intentionally, has a large effect on the wear development of the tribo-system. The hardness of the particles is a clear factor in how the particles affect the tribo-system, with harder particles increasing wear and softer ones inhibiting it through surface separation without surface penetration. Based on the results of this work, the following conclusions are drawn:

- Inclusion of particles of any hardness, in the force and concentration range tested here, had little to no effect on the coefficient of friction measured in pin-on-disc testing.
- The hardness of particles included in a tribo-system has a large effect on the development of wear in the tribo-system. A higher particle hardness leads to more severe wear.
- Including any particles in a tribo-system makes the system more robust in the face of varying loads. For a pure paraffin oil, wear readily increases with increasing load, but including particles reduced this effect, in the range tested here.
- The particle hardness was important for tribo-systems that include sheet metal forming conditions. High hardness, such as for the SiO_2 particles, lead to increased abrasion and more wear. The $BaSO_4$ did not change conditions much compared to the pure oil, at least not in terms of wear. The $CaCO_3$ particles promoted rolling of the particles as surface penetration was not possible and reduced wear compared to the pure oil.

Acknowledgments

The authors would like to thank A.G. Garcia from the Department of Chemical and Biochemical Engineering at the Technical University of Denmark for help with formulating the lubricant mixtures. Furthermore, U. Arinbjarnar and C.V. Nielsen would like to thank the Danish Council for Independent Research, grant number DFF – 0136-00159A, for the funding of this investigation.

References

[1] B. Seidel, D. Meyer, Influence of artificial aging on the lubricating ability of water miscible metalworking fluids, Prod. Eng. 13 (2019) 425–435. https://doi.org/10.1007/s11740-019-00891-6
[2] M.R. Sari, A. Haiahem, L. Flamand, Effect of lubricant contamination on gear wear, Tribol. Lett. 27 (2007) 119-126. https://doi.org/10.1007/s11249-007-9215-z.
[3] T. Kjer, Wear rate and concentration of wear particles in lubricating oil, Wear 67 (1981) 217. https://doi.org/10.1016/0043-1648(81)90105-8
[4] Q.Y. Jiang, S.N. Wang, Abrasive wear of locomotive diesel engines and contaminant control, Tribol. Trans. 41 (1998) 605-609.
[5] H.H. Abou El Naga, A.E.M. Salem, Effect of worn metals on the oxidation of lubricating oils, Wear 96 (1984) 267-283. https://doi.org/10.1016/0043-1648(84)90041-3
[6] U. Olofsson, Y. Zhu, S. Abbasi, R. Lewis, S. Lewis, Tribology of the wheel-rail contact-aspects of wear, particle emission and adhesion, Vehicle System Dynamics 51 (2013) 1091-1120. https://doi.org/10.1080/00423114.2013.800215
[7] T. Luo, X. Wei, X. Huang, L. Huang, F. Yang, Tribological properties of Al2O3 nanoparticles as lubricating oil additives, Ceram. Int. 40 (2014) 7143-7149. https://doi.org/10.1016/j.ceramint.2013.12.050
[8] J. Padgurskas, R. Rukuiza, I. Prosyčevas, R. Kreivaitis, Tribological properties of lubricant additives of Fe, Cu and Co nanoparticles, Tribol. Int. 60 (2013) 224-232. https://doi.org/10.1016/j.triboint.2012.10.024
[9] Y. Li, Y. Chen, P. Gao, B. Zhong, F. Ai, L. Li, Y. Xiao, Research on influence of abrasive particles on lubricating performance of the emulsion for cold rolling strip, in: Proceedings of Chinese Materials Conference 2017, 2017, pp. 135-143. https://doi.org/10.1007/978-981-13-0107-0_13
[10] Ú. Arinbjarnar, M. Moghadam, C.V. Nielsen, Application of Calcium Carbonate as Green Lubricant Additive in Sheet Metal Forming, Key Eng. Mater. 926 (2022) 1133-1142. https://doi.org/10.4028/p-x87o62
[11] D.X. Peng, C.H. Chen, Y. Kang, Y.P. Chang, S.Y. Chang, Size effects of SiO2 nanoparticles as oil additives on tribology of lubricant, Ind. Lubric. Tribol. 62 (2010) 111-120. https://doi.org/10.1108/00368791011025656
[12] Calcit, PolyPlex 2, Calcit d.o.o., Stahovica, Slovenia, Jan. 2014. Available online: https://www.calcit.si/assets/PDF/ANG_SPLOSNI_KATALOG_2020_PolyPlex.pdf
[13] Sibelco, Portaryte® B. Sibelco, Maastricht, Netherlands, Mar. 2013. Available online: www.sibelco-specialty-minerals.eu
[14] Sibelco, Silverbond M500. Sibelco, Dessel, Belgium, Oct. 01, 2016. Available online: www.sibelco.eu
[15] X. Ji, Y. Chen, G. Zhao, X. Wang, W. Liu, Tribological properties of CaCO3 nanoparticles as an additive in lithium grease, Tribol. Lett. 41 (2011) 113-119. https://doi.org/10.1007/s11249-010-9688-z

Materials Research Proceedings 28 (2023) 891-898 https://doi.org/10.21741/9781644902479-97

Surface topography effects on galling of hot dip galvanized sheet metal

VENEMA Jenny[1,a *], CHEZAN Toni[1,b] and KORVER Frank[1,c]

[1]Tata Steel, Research & Development, PO BOX 10000, 1970 CA IJmuiden, The Netherlands

[a]jenny.venema@tatasteeleurope.com, [b]toni.chezan@tatasteeleurope.com, [c]frank.korver@tatasteeleurope.com

Keywords: Tribology, Friction, Wear, Zinc Coatings, Galling, Automotive

Abstract. During manufacturing of automotive parts from hot dip galvanized sheet metal, surface asperities of the forming tools can cause breakage of small coating particles. Long and narrow scratches appear on the surface of the form part, a phenomenon known as part surface galling. Laboratory testing using a slider on sheet tests (SOST) are performed in order to investigate surface topography effects on galling. These experiments reveal the dominant effect of tool surface roughness on galling. The tool surface roughness has a large effect on the size of the detached coating particles and the distance before scratch occurrence. If the tool roughness is low enough, no surface scratch formation is observed for the investigated range of sheet surface roughness. At a high tool surface roughness scratches are observed at a very short sliding distance for all tested materials. At an intermediate tool surface roughness, the materials selected for this investigation show measurable differences but no clear trend could be identified.

Introduction

Galling, abrasive surface wear of hot dip galvanized steel (GI) sheet metal can occur during deep drawing, the process commonly used for automotive part manufacturing. Observations of industrial forming processes in the areas with contact with the forming tools revealed two types of contact conditions – normal contact and galling. In normal contact conditions the sheet metal topography is flattened by the tool contact. Such contact areas on the deformed sheet surface can be considerably large, tens of millimeters in the sliding length direction, as the sheet metal slides against the forming tools. In some contact areas unexpected galling behavior in the form of long narrow scratches, in the sheet metal sliding direction [1] was observed. Such scratches are created by tool surface local asperities. The consequence of surface scratch formation might be coating detachment in the form of thin flakes. The flakes might attach to the tool surface resulting in increased tool asperity height and in formation of new tool surface asperities and consequently in acceleration of galling of the following formed part.

In the industry several solution directions exist to prevent galling, namely polishing, hardening and/or coating the forming tool surface and/or the application of extra lubrication. These solution directions indicate already some of the parameters which influence galling, such as tool surface parameters such as roughness and lubrication. Other parameters which influence galling are sheet surface, design (deformation) and process parameters such as pressure, velocity and temperature. In the literature investigations on the mechanisms of galling and the influence of several parameters can be found [2-5]. For example, Van de Heide and Dane [6-7] investigated the influence of lubricant on galling.

In a previous investigation [1] the influence of pressure and tool roughness on galling was investigated with the Slider On Sheet Tester (SOST) on one material with representative roughness. In the current investigations the influence of the tool roughness is investigated for three sheet material roughness levels within the typical intervals found in automotive applications. Both the scratch depth and particle sizes are investigated in great detail.

Content from this work may be used under the terms of the Creative Commons Attribution 3.0 license. Any further distribution of this work must maintain attribution to the author(s) and the title of the work, journal citation and DOI. Published under license by Materials Research Forum LLC.

Material and Methods

An experimental program was started to evaluate the geometrical surface parameter on galling. The experiments were performed using a SOST capable of providing controlled well-defined contact conditions between the tool surface and metal sheet. Tests were performed on three different GI coated steel sheets and three different tool roughness levels (Table 1). The tribological interactions were studied by Scanning Electron Microscopy (SEM) analysis of particles collected from the tool. The dimensional topography measurements of the tool and sheet surfaces were performed by a confocal microscope.

Table 1. Surface parameters of the sheet and tool material according to ISO 25178.

	Sa [µm]	Sq [µm]	Sz [µm]	Ssk [-]	Sku [-]	Sp [µm]	Sv [µm]
Tool ring 1	0.33	0.43	5.22	-0.43	4.25	2.66	2.55
Tool ring 2	0.74	0.99	11.96	-1.27	8.45	3.39	8.55
Tool ring 3	1.19	1.57	15.30	-0.97	4.89	6.89	8.42
Sheet 1	1.00	1.14	6.64	0.45	2.50	3.85	2.79
Sheet 2	1.17	1.36	7.73	-0.08	2.06	3.92	3.81
Sheet 3	1.59	1.89	12.30	-0.42	2.30	6.62	5.70

A cylindrical tool (Fig.1a) with contact width of 6 mm is pressed with 1.5 bar (resulting in a normal load of 205 N) against the sheet material. The contact situation is therefore a line contact, with a nominal pressure of 190 MPa. The cylinder moves in length direction for 250 mm at a velocity of 50 mm/s, lifted up and brought into a new position to make a new track next to the previous one (Fig.1b) within a few seconds. In this way, every time virgin sheet material is in contact with the tool. The amount of tracks is depended on the tool roughness and availability of material (sheet size). For the smoothest tool (Sa 0.3 µm), between 70 and 75 tracks are tested, resulting in 17.5 to 18.8 m sliding length for the three different materials. This sliding length can represent drawing of approximately close to 200 parts. The tool is rotated (approximately 5°) after each unique parameter setting. In this way a fresh tool material is in contact for each test. A pressure sensitive foil is used to align the tool properly, thereby ensuring homogeneous contact at the start of the test.

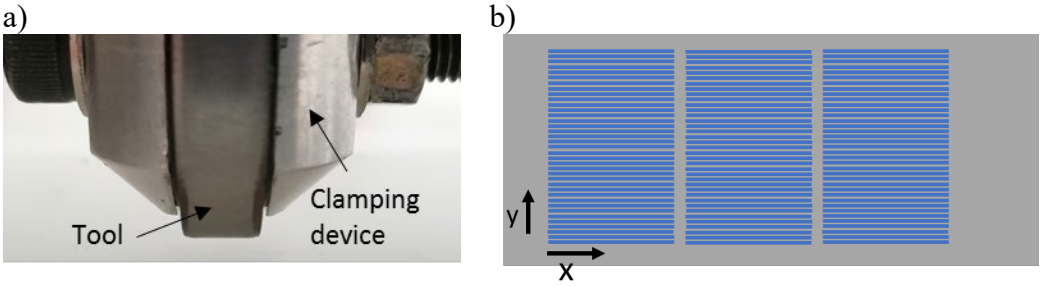

Fig. 1. a) Photograph of cylindrical tool (half) in SOST b) Schematic view of sheet with tracks.

Three different GI coated steel sheets (thickness 0.6 mm) with different surface roughness are tested (Fig. 2). The sheets are cleaned with isopropanol to remove mill applied lubricant on the surface.

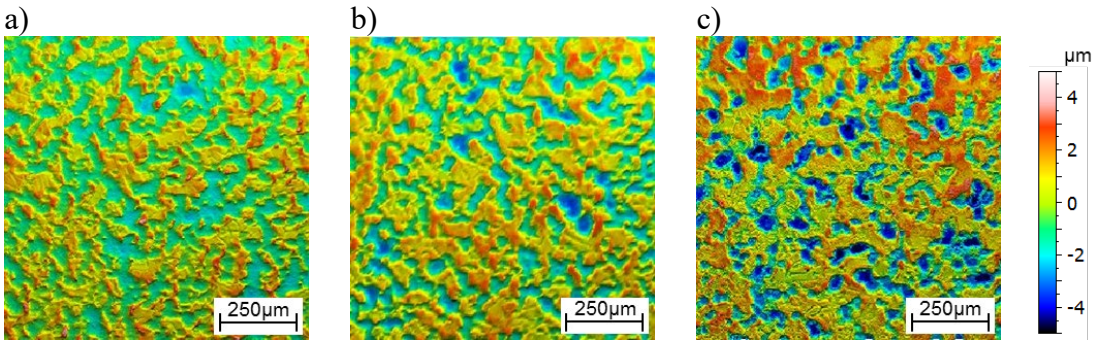

Fig. 2. Confocal measurement sheet surface (size 1x1 mm) a) Sa 1.0 µm b) Sa 1.2 µm c) Sa 1.6 µm.

The slider (diameter of 43 mm) of tool material DIN 1.2379 has a hardness of 60 ± 2 HRC. Three different tool textures with different roughness (Fig. 3) are tested. The tool surface topography has a defined lay with the grinding direction perpendicular to sliding direction.

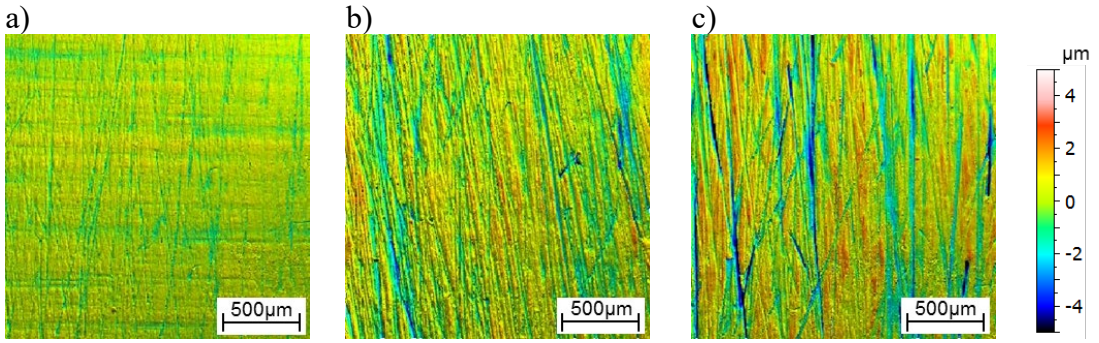

Fig. 3. Confocal measurement tool surface (2x2 mm) a) Sa 0.3 µm b) Sa 0.7 µm c) Sa 1.2 µm. Sliding direction is horizontal.

Results and Discussion

The appearance of the scratches, ploughing tracks and particles are similar to observations on automotive pressed parts and particles collected from stamping tools [1]. The tool wear mechanism is dynamic. Particles of the GI coating break out during sliding and get trapped in different types of tool surface defects (such as grinding scratches). They stick to the tool surface (Fig.4a & 4b). During repeated sliding the particle build up accumulates. Particle accumulation can cause scratches to sheet material, which can become more severe with sliding distance. However, it is also observed that particles break off resulting in a disappearing scratch or a less severe scratch. The process will continue and the particle accumulation will start again at the same or at another position. Loose particles can also cause 3rd body abrasive wear. These scratches do not necessarily follow the same direction as the sliding direction, but could bend off. This wear mechanism was also observed in a few cases in earlier investigations.

In general, the thickness of individual flakes is lower than the thickness of the GI coating and the GI coating is not spalling off. In case of highest tool roughness the scratch depth becomes close to the thickness of the zinc coating. Cross sectional microscopy is planned to further investigate the fracture of the zinc coating.

After the test the particles were collected with adhesive tape for further investigation in the SEM (Fig. 4c). Mapping of the elements of the particles reveals that it mainly consists of Zn (Fig. 4d) and some coating elements (Al). In general, no tool material elements such as Cr are measured. This indicates that no abrasive tool wear occurs. Also, in most cases almost no Fe is measured, suggesting that the scratches are superficial.

The tools are ultrasonic cleaned after collection of the particles. After ultrasonic cleaning of the tools, some Zn particles are still attached to the tool surface (Fig. 4b) in which the sliding direction is visible. Remaining particles on the slider after ultrasonic cleaning represents well the industrial case in which grinding is necessary to remove all particles.

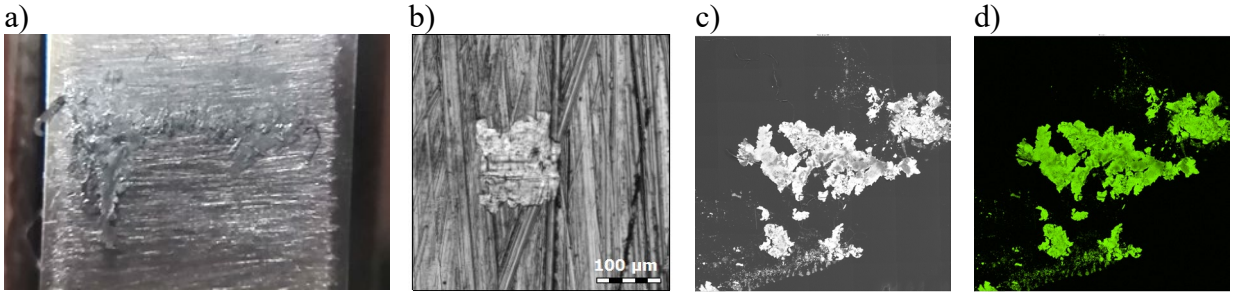

Fig. 4. a) Photo of contact surface of tool after test (tool width 6 mm) b) particle remained after ultrasonic cleaning of tool c) SEM BSE collected particles from tool (size 8.5 x 8.5 mm) Tool Sa 0.7 µm Sheet Sa 1.2 µm. SEM /EDX element mapping of Zn (L) (size 8.5 x 8.5 mm) Tool Sa 0.7 µm Sheet Sa 1.2 µm.

Particles collected from tool.

The collected particles are in the majority of the cases flakes, for one material also some other particle morphology is observed. These flakes are very comparable to the flakes collected from industrial tools at OEMs (Fig. 5). The flakes are only a few microns thick, while the width and length are more than 10 times the thickness.

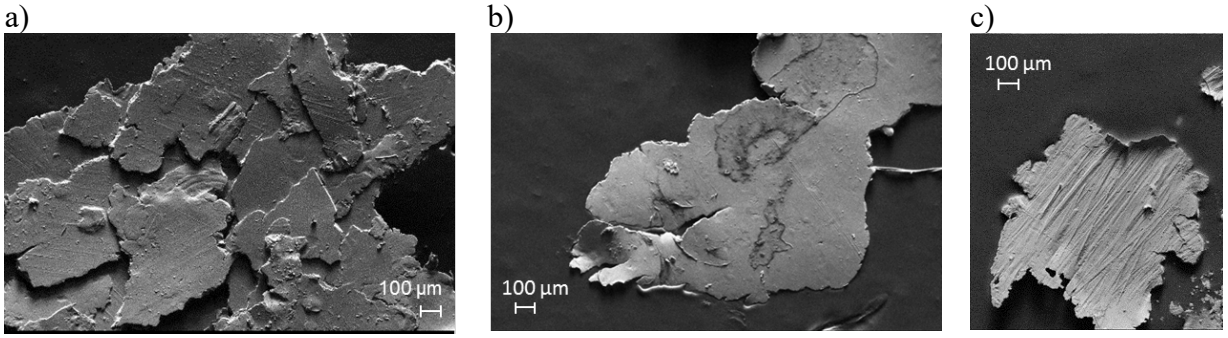

Fig. 5. SEM images a) particles collected from industrial tool b) one particle collected from industrial tool c) one particle collected from SOST sheet Sa 1.2 µm tool Sa 1.2 µm.

The size of the flakes is dependent on the surface roughness, and the average size increases in the majority of cases with increasing tool roughness (Fig. 6).

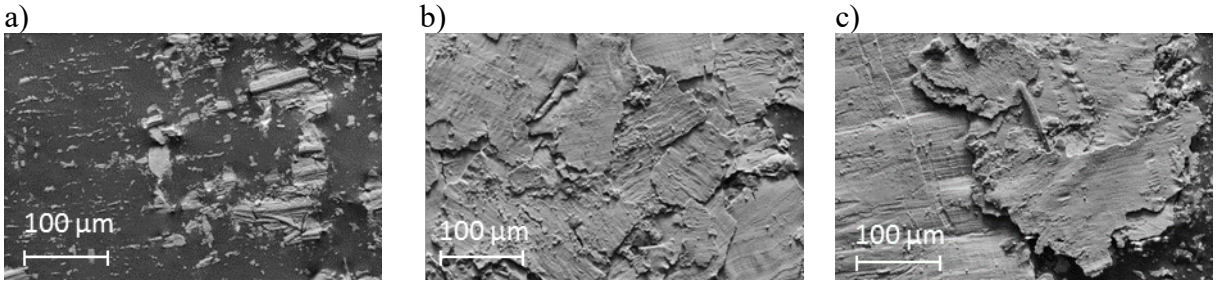

Fig. 6. SEM analysis of particles after test sheet Sa 1.6 µm with tool roughness a) Sa 0.3 µm b) Sa 0.7 µm c) Sa 1.2 µm.

Scratches on the sheet surface.

Three dimensional topography measurements are made at specific track numbers (1,10,20,40,60 and last track). A 2D profile cross section is created and the maximum profile depth determined (Fig. 7a). Criterion for a scratch is a larger than 1 µm increase in max profile depth compared to original material. Fig. 7b shows the maximum profile depth versus the sliding distance for sheet material 1 (Sa=1.0 µm) for several tool roughness. In case of low tool roughness (0.3 µm) no scratch occurs. At medium tool roughness (0.7 µm) scratch occurs at 15 m of sliding distance. And for a high tool roughness (1.2 µm) the scratch occurs immediately after start of test. Thus, the tool roughness plays a major effect on the distance to scratch formation.

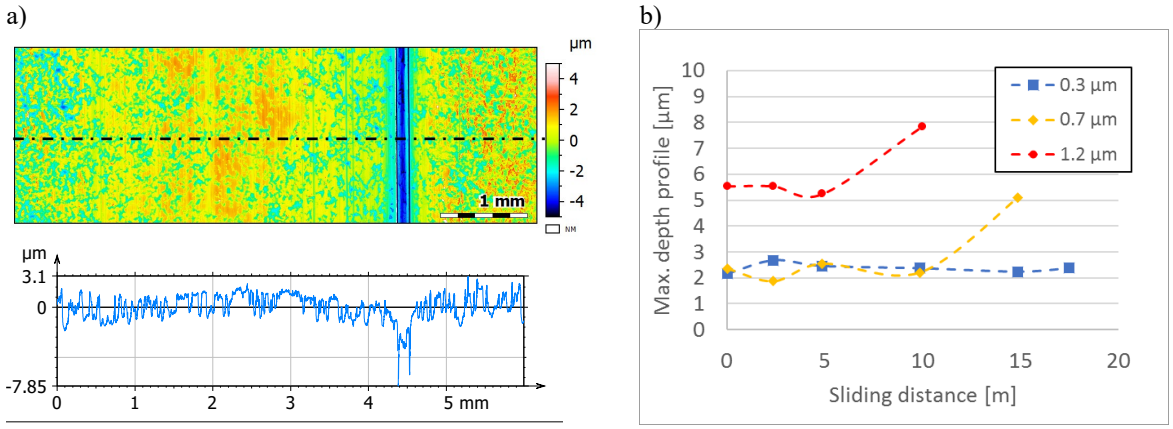

Fig. 7. A) 3D topography measurement sheet Sa 1.0 µm tool Sa 1.2 µm after 10 m sliding. b) max. profile depth versus sliding distance sheet Sa 1.0 µm for the tested tool textures.

For the entire collection of sheet materials no scratches are observed for a low tool roughness of 0.3 µm (Table 2). This shows that the sheet coating can resist relative high contact conditions in case of smooth surface.

In case of intermediate tool roughness the distance before a scratch occurs was different for the three materials considered in this study. A more extended experimental research is necessary to further quantify the sheet coating effect. Also, the number of tests is very limited and further investigations are necessary to determine the range in distance before scratch occurrence for different sheet material and tool roughness combinations. However, trends regarding the increase in tool roughness are observed for each material and each test series (Table 2). An increase in tool roughness results in a decrease in distance to scratch (Table 2) which is probably related to the larger particle size and the presence of more tool surface defects to get stuck. Larger particles can probably be less easily removed out of the contact.

Table 2. Distance [m] to first measured scratch.

	Sheet roughness Sa		
Tool roughness Sa	**1.0 [µm]**	**1.2 [µm]**	**1.6 [µm]**
0.3 [µm]	>17.5	>18.8	>18.5
0.7 [µm]	14.9	4.9	9.9
1.2 [µm]	0.0	2.4	2.4

Materials Research Proceedings 28 (2023) 891-898 https://doi.org/10.21741/9781644902479-97

Fig. 8 reveals the dynamic nature of galling. For example, at a tool roughness of 0.7 µm a large scratch occurs at track 20, which becomes less severe at track 60. Indicating that a part of the adhered particles broke off from the tool. In case of a roughness of 1.2 µm the position of the scratches also changes, indicating that the buildup and breaking of particles on the tool can occur at several position on the tool.

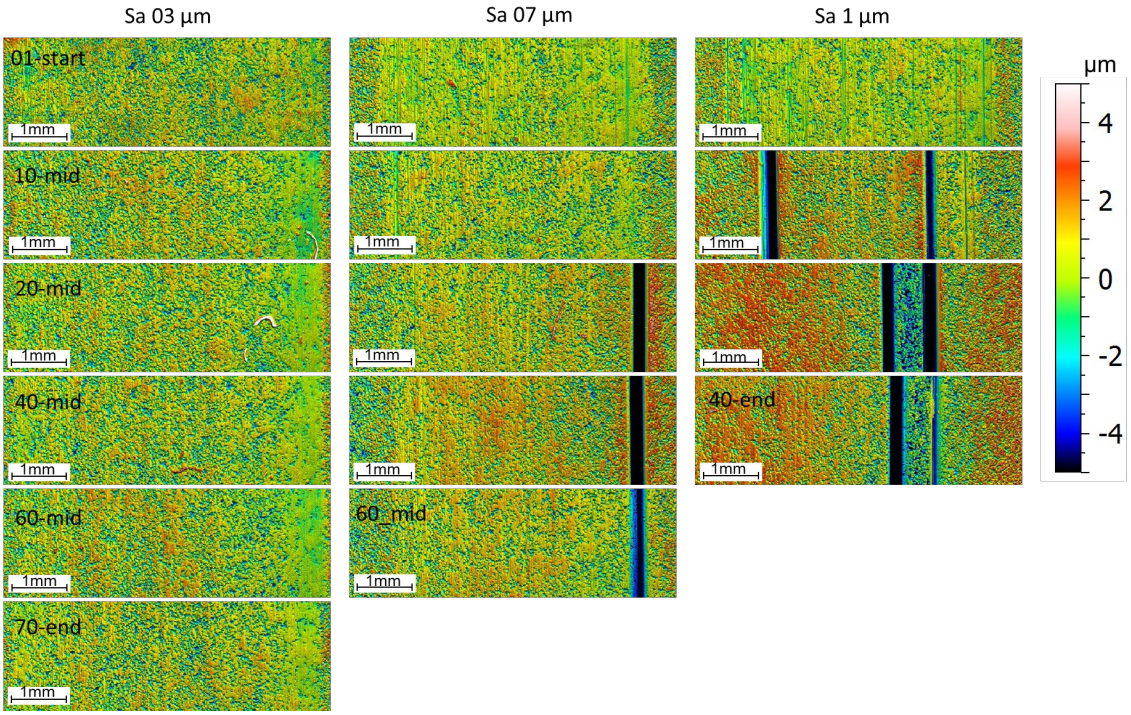

Fig. 8. Confocal measurements for sheet material 2 (Sa 1.2 µm) at positions (# tracks) and for three tool roughness . Sliding in vertical direction.

Coefficient of Friction (COF).

The effect of tool roughness on the COF is also high (Fig.9). With a low tool roughness the friction coefficient is stable and relatively low. Sometimes a certain increase and decrease in COF is related to a scratch, however this certainly is not always the case. The friction coefficient is higher or lower with increasing tool roughness. A different wear regime (cut, wear or ploughing) could cause a different trend in friction coefficient. Recommended is to investigate this effect further with a physical based friction model.

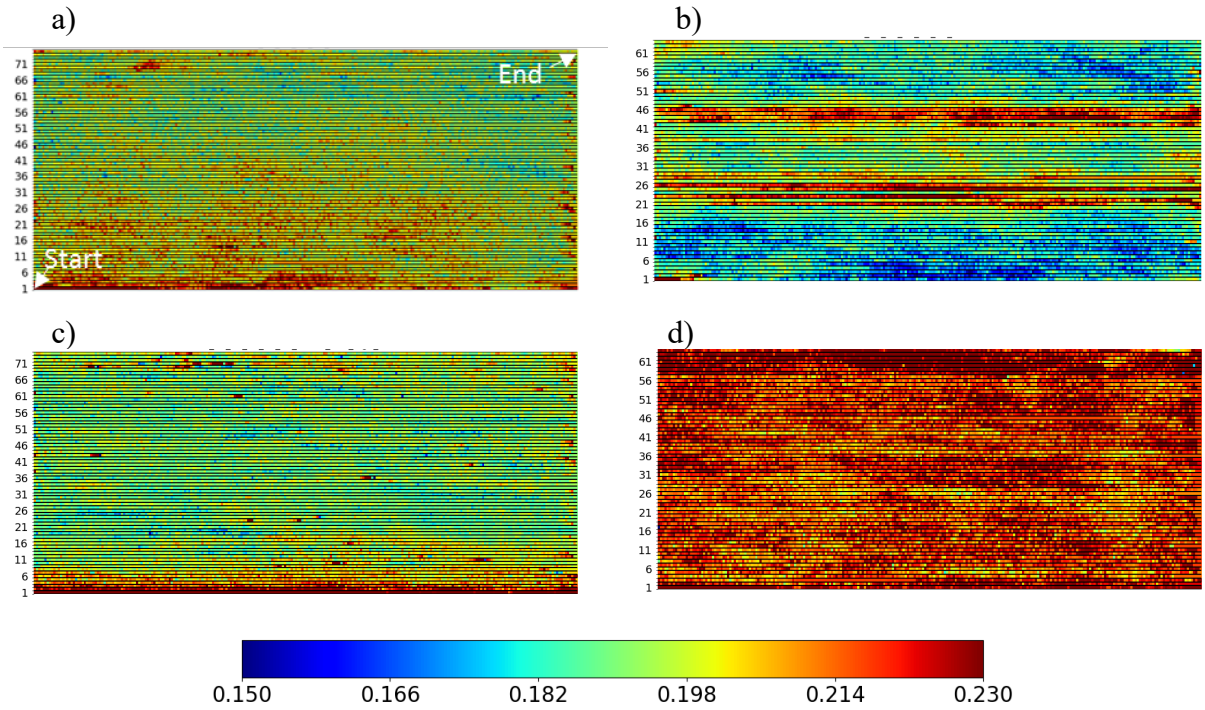

Fig. 9. Colour plot coefficient of friction for the tracks a) Tool Sa 0.3 µm Sheet Sa 1.2 µm b) Tool Sa 0.7 µm Sheet Sa 1.2 µm c) Tool Sa 0.3 µm Sheet Sa 1.6 µm d) Tool Sa 0.7 µm Sheet Sa 1.6 µm.

Summary

The experiments reveal the dominant effect of tool surface roughness on galling of the sheet metal coating. It was found that the detached coating flake size increases with increasing tool surface roughness. A too low or too high tool surface roughness resulted in either no surface scratch formation or deep surface scratches after very short sliding distance for all tested sheet materials. The roughness magnitude of the sheet metal surface appeared to influence the galling resistance performance as well for the tests with intermediate tool surface roughness. The material roughness magnitude differences were less clear while compared to the tool surface roughness effect. Further investigations are planned focused on material coating parameters effect on galling performance.

Acknowledgements

The authors would like to thank Ronald van Goethem, Arne Neelen and Marco Appelman for surface measurement and Jan Wörmann for the SEM analysis.

References

[1] J. Venema, F. Korver, T. Chezan, Slider on Sheet Tester Development for Characterizing Galling, ESAFORM 2022, Key Eng. Mater. 926 (2022) 1204–1210. https://doi.org/10.4028/p-uii69m

[2] E. Schedin, Galling mechanisms in sheet forming operations, Wear 179 (1994) 123-128. https://doi.org/10.1016/0043-1648(94)90229-1

[3] H. Kim, J. Sung, F.E. Gondwin, T. Altan, Investigation of galling in forming galvanized advanced high strength steels (AHSSs) using the twist compression test (TCT), J. Mater. Process. Technol. 205 (2008) 459-468. https://doi.org/10.1016/j.jmatprotec.2007.11.281

[4] W. Wang, K. Wang, Y. Zhao, M. Hua, X. Wei, A study on galling initiation in friction coupling stretch bending with advanced high strength hot-dip galvanized sheet, Wear 328-329 (2015) 286–294. http://doi.org/10.1016/j.wear.2015.02.058

[5] K.G. Budinski, S.T. Budinski, Interpretation of galling tests, Wear 332-333 (2015) 1185-1192. https://doi.org/10.1016/j.wear.2015.01.022
[6] E. van der Heide, A.J. Veld, D.J. Schipper, The effect of lubricant selection on galling in a model wear test, Wear 251 (2001) 973-979.
[7] C.M. Dane, E. van der Heide, Proceedings of the IDDRG '04 Conference, Sindelfingen, Germany, 2004, pp. 182-191.

Materials Research Proceedings 28 (2023) 899-908 https://doi.org/10.21741/9781644902479-98

Influence of increased die surface roughness on the product quality in rotary swaging

FENERCIOĞLU Tevfik Ozan[1,a *], SARIYARLIOĞLU Eren Can[1,b], ADIGÜZEL Erdem[1,c], ŞIMŞEK Ahmet Kürşat[1,d], KOLTAN Umut Kağan [1,e] and YALÇINKAYA Tuncay [2,f]

[1]Repkon Machine and Tool Industry and Trade Inc. Şile/Istanbul/Turkey

[2]Department of Aerospace Engineering, Middle East Technical University, 06800 Ankara/Turkey

[a]ozan.fenercioglu@repkon.com.tr, [b]eren.sariyarlioglu@repkon.com.tr, [c]erdem.adiguzel@repkon.com.tr, [d]kursat.simsek@repkon.com.tr, [e]umut.koltan@repkon.com.tr, [f]yalcinka@metu.edu.tr

Keywords: Metal Forming, Rotary Swaging, Surface Roughness, Finite Element Analysis

Abstract. Rotary swaging is an ascendant forming method for manufacturing axisymmetric parts. High production rate with excellent net shape forming is achieved in recent automation developments. However, precise machine design and tailored process developments are necessary to transfer the high impact type forming loads to workpiece efficiently. The failure of this transfer results in high vibrations of the machine structure and poor product quality, due to the impact loads with high frequencies. The centerpiece of the process development to prevent these disruptive effects is to resolve die specifications such as shape and surface properties. In general forming applications, surface roughness of the dies is perceived as a disruptive element for the product quality and only a small amount is provided to settle lubricants. However, for rotary swaging applications, an optimized surface roughness to increase the load transfer between the die and the workpiece without disrupting the final product surface quality is essential. In this study, for a fixed die shape, the relation between the die surface roughness and the product quality is investigated for macro rotary swaging applications. In particular, the effective transfer of the forming forces to the workpiece is analyzed by using finite element analysis within the scope of surface friction. Consequently, a die set with roughened surface conditions is manufactured by using a novel technique. Real process trials are conducted to validate the results of the analysis.

Introduction

Rotary swaging is an incremental forging operation for tubes and bars. Operation principal of a rotary swaging machine is shown on Figure 1(a). An internal ring with translational sliders is rotated inside a roller cage. Translational sliders hold die assemblies. During the rotation of the internal ring, dies are retracted to an open position due to centrifugal effects and other peripheral supports (support springs). When the die assembly reaches a roller, dies are translated to closed position. Continuous movement of the die assembly results in consecutive blows of dies and cold forging of the workpiece. Hence, the outer diameter of the part decreases with a possible reduction of the cross-section area and with the elongation of the total length. Rod, pipe and tube parts can be shaped by this method and axisymmetric parts can produced. By the addition of a pre-shaped mandrel inside tubular workpiece, it is also possible to form complex shapes inside the workpiece. The mandrel steers the material such that the internal shape of the workpiece reflects the outer shape of the mandrel.

Performance and final mechanical properties of the workpiece are dictated by process parameters and parts (die and mandrel). In particular, dies play the most important role. During

Content from this work may be used under the terms of the Creative Commons Attribution 3.0 license. Any further distribution of this work must maintain attribution to the author(s) and the title of the work, journal citation and DOI. Published under license by Materials Research Forum LLC.

the process, the workpiece is forced to deform with large loads transferred by dies to reduce the outer diameter. To moderate the disruptive effects of the die impact, dies are designed with a tapered entrance. In this way, shearing of the workpiece is prevented. However, this tapered entrance geometrically results in unwanted axial reaction forces. Each blow of the die pushes back the workpiece in the opposite direction of the elongation. These reaction forces show disruptive effects on overall swaging performance. In the open literature, these disruptive effects are studied in detail under the scope of micro metal forming. Small tubes for needles and concentric bimetallic tubes are manufactured using rotary swaging. Vollertsen called these forces, rejection forces and explained that increased rejection forces result in workpiece buckling [1]. To solve this problem, Böhmermann et al. suggested to increase the effective friction on the forging section between die and workpiece to decrease the reaction forces (Fig. 1 (b)) [2]. By increasing the friction, as the die descends, the end of the tapered section pulls the workpiece and the reaction (rejection) force of the sinking section is supported. Herrmann numerically characterized effects of die friction for macro rotary swaging applications using finite element analysis [3]. 50% reduction is achieved in axial reaction forces by increasing friction coefficient from 0.1 to 0.5 in reduction zone.

Similar investigations were also made for radial forging. Rotary swaging and radial forging are similar processes with different machine configurations. Hence, research results are valid for both applications. Apart from the differences in die motions, another difference is observed in workpiece feeding between both applications. Workpiece feeding is usually force controlled and applied by hydraulic cylinders in radial forging which is replaced by position control systems in modern rotary swaging machines. Hence, when reaction forces reach the limit force of the hydraulic cylinders, feeding fails in radial forging. Semiatin suggested not to use any lubricant between die and workpiece when entrance taper angle is more than 6° [4]. In this way, the effective friction is increased between the die and workpiece. In some applications, forging zone of the die is roughened by hardfacing to increase effective friction and to reduce axial reactions. Recent patents are published where hardfacing (conventional method for surface roughening) is replaced by surface structuring (see e.g. [5]). A wave form is machined on the forging zone to create holding forces to balance reaction forces especially for micro rotary swaging applications.

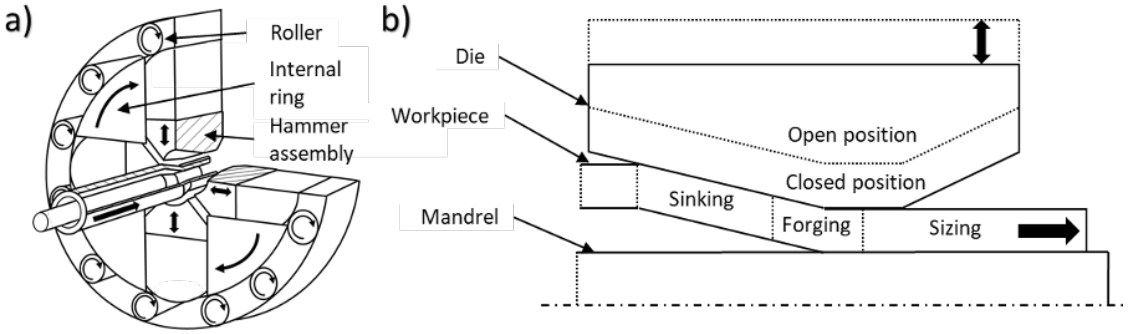

Fig. 1. Schematics of rotary swaging a) Clock-wise rotation of the internal ring rotates die assembly and leads to translational blows when upper surface reaches a roller b) Cross-section of swaging process.

Formerly, effects of the process parameters and parts (die and mandrel) are characterized by process trials. Nevertheless, by the development of reliable metal forming simulations, trial and error methods are evolved to be a final validation tool. Different approaches are found in the literature for the evaluation of rotary swaging and radial swaging. It should be noted that the die-workpiece interactions are similar in rotary swaging and radial forging. Initial studies to foresee the material flow and final mechanical properties are conducted by Grosman and Piela [6]. An

axisymmetric model is developed where the volumetric change of the cross section during forging sequence is imposed by a radial rigid translation in the simulation. Lahoti and Altan derived an analytical expression to determine process forces and resulting stresses using the upper slab method [7]. This analytical study is further pursued by finite element analysis and experimental validations to develop a die design methodology [8]. As a result of these analysis, the relation between effective friction and forging forces are numerically shown. Also, Tseng et al. put a further step by including thermal effects in analytical expressions [9]. After initial studies of Domblesky et al. on the application of flow formulations for radial forging [10], Yamaguchi et al. developed a simulation and experiment method to predict the grain size of radial forged materials [11]. Recently, Poursina et al., Ameli and Movahhedy, Fan et al, Liu et al. applied displacement formulations for swaging operation using ABAQUS/Explicit and the results showed significant compatibility with the experimental results [12-15]. Load predictions converged to experimental results of Uhlig with an error <5% [16].

Validation of different simulations by experiments ensures the reliability of material process simulations. Displacement formulations with an explicit time scheme will be applied in this study to evaluate the process loads and its relation to surface properties. Although, a solution for high axial reactions by roughening die surface is widely suggested in the literature. A correlation between the surface roughness and mechanical vibrations and reactions is not experimentally shown for macro swaging applications. This study aims to clarify the mechanism behind the surface roughening and to evaluate the disruptive effects of reaction forces. A comparison for different friction conditions is numerically conducted through finite element analysis. Results are validated by product contours and also by position feedbacks of the workpiece pusher system. Moreover, a novel simple method is suggested for surface roughening. In this regard, the current study is unique for correlation of reaction forces on product and process quality and proposes an alternative method to hard facing for the swaging industry in die design.

The paper is organized as follows. Rotary swaging method and the effects of the reaction forces on product quality is briefly presented here, section 2 addresses the finite element analysis of the process cycle. Section 3 validates the numerical analysis through experiments. Then the study is concluded in Section 4.

Finite Element Analysis

ABAQUS/Explicit 2016 solver is used in this study after the quasi-static condition is validated using simulation energy outputs. Kinetic energy of the process is compared to internal energy as suggested in the ABAQUS documentation [17]. Less than 2% kinetic energy is calculated during the process. Hence, the method is found valid and doubts about the stimulation of artificial energy modes are removed. Also, this low amount of kinetic energy let the usage of a mass scaling factor (25). Geometrical simplifications are not applied to better converge to further experiments. Schematic shown on Fig. 1 (b), is represented in Fig. 2 (a) and (b) in association with rotary swaging machine elements and modelling aspects, respectively. Axial motion of the workpiece into dies is given by using workpiece pusher. Movement and forces of the workpiece pusher is recorded during the analysis to evaluate reaction forces. Fig. 2 (b) shows initial and final steps (total simulation duration: 4 seconds) of the simulation. Workpiece is modeled using reduced integration elements with combined stiffness hourglass control (C3D8R, size: 1.2 mm). Hourglass control method is determined by restricting artificial energy to internal energy ratio (<1% achieved). For boundary conditions, both translation and rotation are applied to the workpiece during feeding. Cylindrical kinematic element is used to control the feeding motion. A torsional spring is added to cylindrical connector to prevent the torsion on the workpiece with an extrapolated nonlinear elasticity definition (48kNmm/rad). Elastoplastic properties of the workpiece are constructed from the experiments of Ceschini et al. for 33CrMoV Steelmaterial [17]. Process tools are modeled using rigid body surface elements (R3D4, size: 1.5 mm). Dies rotate around the

median axis and translates in the radial direction to perform die blows. This kinematic motion is applied to reference points of die surfaces using translator connectors. Penalty contact method with finite sliding is used to model contact interactions between deformable and rigid bodies. Die surface is divided into 3 subsections to separate forging and sizing regions as in Fig. 1 (b). Two models are constructed with forging region having 0.1 and 0.8 friction coefficient values. These two extremum points are selected by considering wall lubricated metal-metal friction (0.1) and non-lubricated (or roughened) metal-metal friction (0.8). Because of the design of the rotary swaging machine, unlike radial forging, a lubricant always operates between workpiece and dies. Hence, suggestions of Semiatin for radial forging in [4] are not possible for rotary swaging process and a roughened surface is the solution.

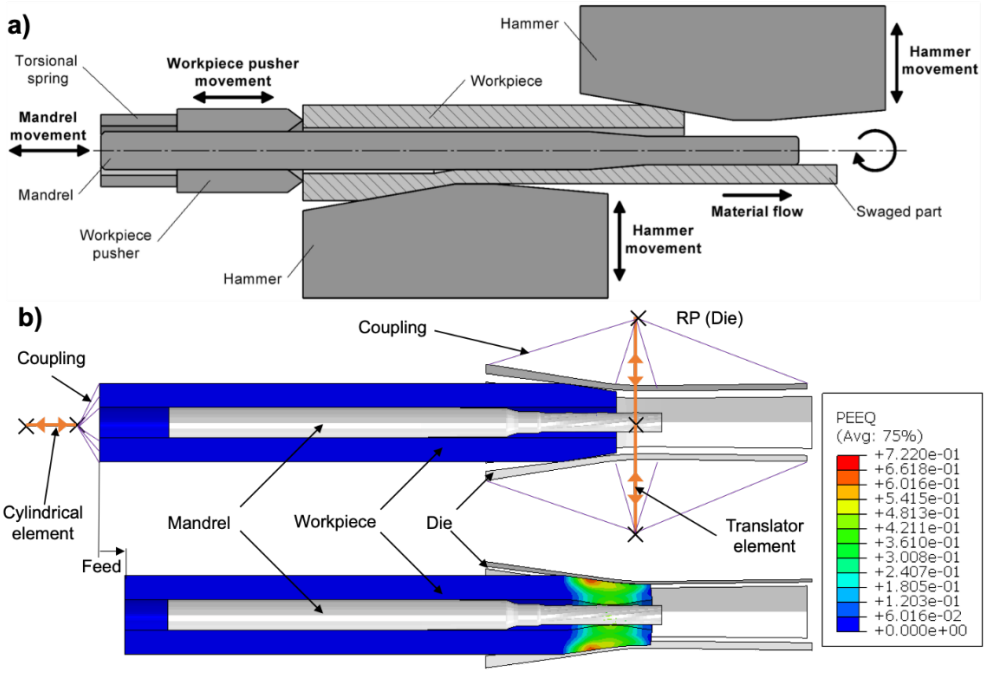

Fig. 2. Rotary swaging analysis model. a) Schematic view of forming section and machine elements, upper and lower die show initial and final position respectively. b) Modelling elements and equivalent plastic strains on deformable body (workpiece) for initial and final steps of the simulation.

Cylindrical element in Fig. 2 represents the workpiece pusher of the rotary swaging machine. Workpiece pusher controls the axial motion of workpiece. Hence, it is exposed to axial reactions. Axial reactions during process simulation are exported from cylindrical element. Fig. 3 shows the load history of the cylindrical connector. When friction coefficient is low (0.1), load profile starts with an increase in each blow. After approximately 2 seconds, a steady load is achieved. This profile is due to entrance tapers of the die and workpiece. Sliding on tapered sections occurs due to low friction. A significant difference is observed for high friction coefficient. During the process, the dies are retracted after the impact. This positive reaction forces prevent the workpiece from escaping back during this retraction. So, upper motion result in a reverse loading with increased friction. The most significant result is the reduction of reaction forces from 12 tons to 7.2 tons when an increased friction is applied between die and workpiece.

Moreover, die torsion force on the workpiece is evaluated for different frictions. Fig. 4 shows relative rotation between the front and rear ends of the cylindrical connector. As can been seen

from Fig. 2, during consecutive flows, the contact area between dies and workpiece increases in the tangential direction as workpiece translates into the sizing region. This is the reason behind the cumulative character of the Fig. 4. As the process continues, the contact area between the die and the workpiece increases and the workpiece also takes the shape of the die profile. The change of friction coefficient in forging region introduced only a small amount of increase (0.03). This increase is small as expected since the main contribution comes from sizing region where friction coefficient is the same for both models. Also, by using V-shaped dies the increase of disruptive effects due to friction are prevented. Contact lengths are controlled in axial and circumferential directions by the help of this shape. A final evaluation is made for the translation of dies to observe if increased friction creates any disruptive effect on die actuation (shown on Fig. 4). No significant difference is observed when reaction forces on translator connectors which actuate dies during analyses are compared. This is related to the angle of the entrance taper. Motion and forces mainly contribute in the horizontal direction. Hence, deviations in the vertical results are relatively small.

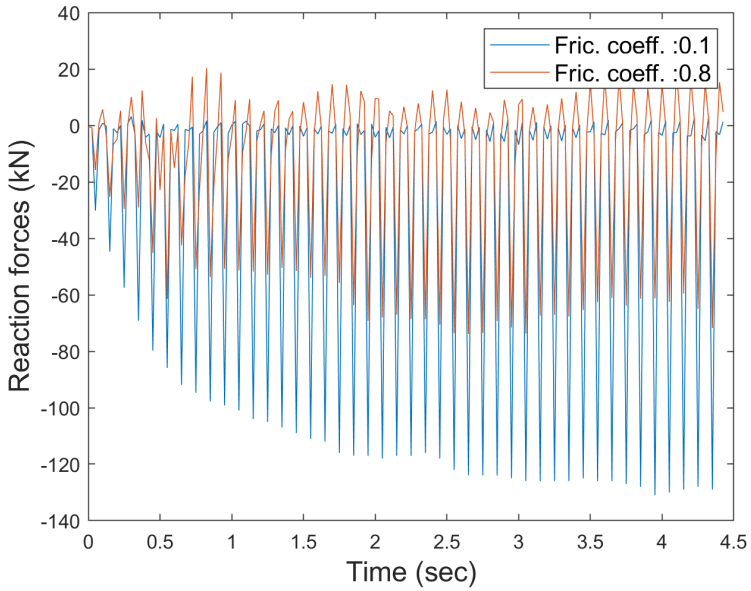

Fig. 3. Reaction forces on workpiece cylindrical connector for different friction coefficients.

The effect of friction coefficient is visualized on Fig. 5 using contact frictional shear pressure outputs. By increasing the surface friction, the contribution of the frictional shearing is increased. During the blow, die pulls the part in the feeding direction which supports the reaction forces created by the tapered section. However, since the die force in vertical direction and contact area are more dependent to workpiece material, contact normal pressures have no significant difference relative to different friction coefficients.

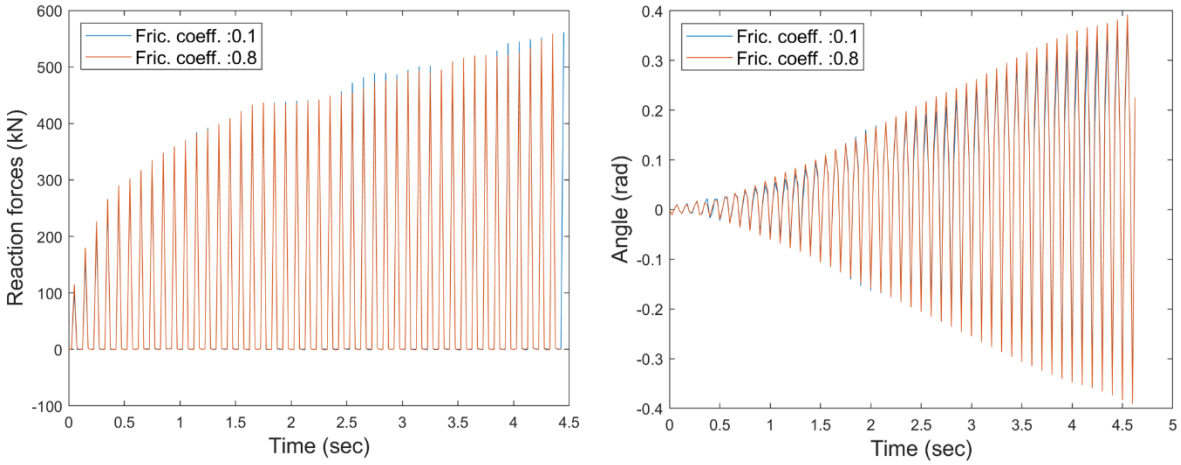

Fig. 4. Reaction forces on die connector for different friction coefficients on the left, Angle between 2 points on cylindrical element for different friction coefficients on the right.

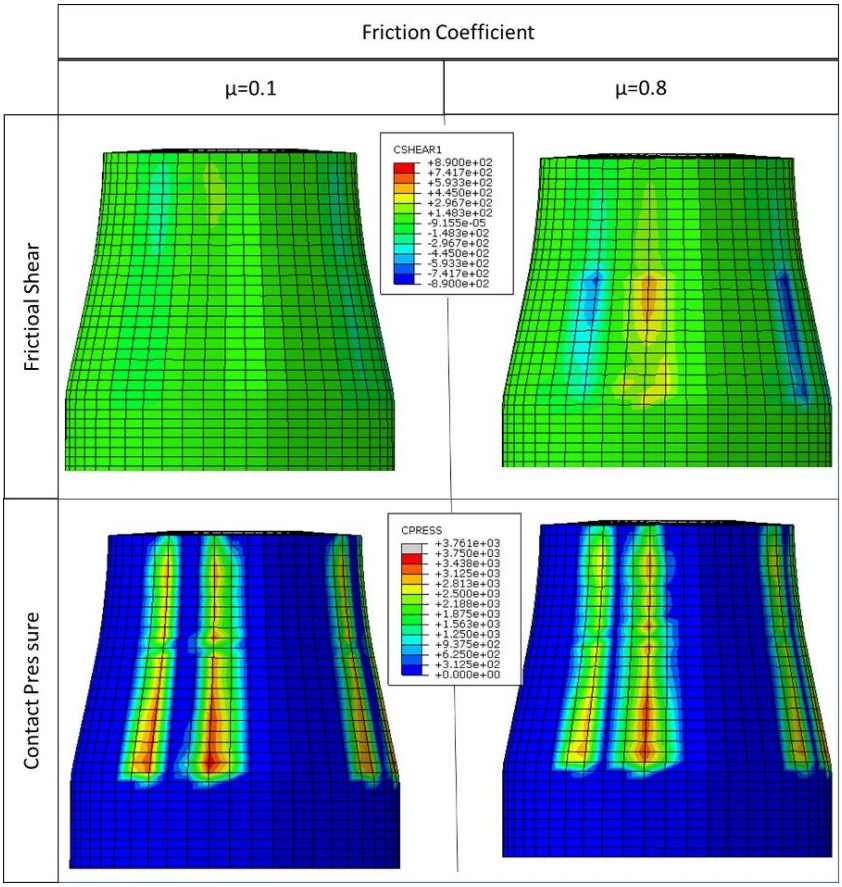

Fig. 5. Frictional shear and contact pressure (in MPa) on the workpiece during forming for different die frictions.

Experimental Validation

In the literature, surface roughening is initially performed using hard facing. Rough areas are coated by hard tungsten layers. During this process, natural pores occur on the surface which creates the necessary roughening. A problem with this method is determined during micro forming studies. During the process, roughening effects disappears as the pores wear out or gets filled by process residues. This problem is especially important for micro forming applications because

workpiece easily buckles due to reaction forces. It is solved by machining a wave form to swaging dies using electro discharge machining (EDM) [e.g. 5-7]. EDM is an advantageous method to create accurate and reliable shapes but it requires special tool (electrode) development, which is costly. An alternative method is used in this study to validate the effects of the increased friction. A 20W laser engravement machine (JNLINK/LXF-20W, China) is used to engrave the die surface.

1.2379 is used as the die material for this trial. Using fixed engravement parameters (given in Table 1), a sample engravement pattern is studied to increase surface roughness. Surface roughness is determined using Mitutoyo Surftest SJ210 (Japan). An engraved V-type die is shown on Fig. 6. Section A-A is the schematic cross-section of the wave.

Table 1. Engravement parameters.

Speed (mm/s)	Power (W)	Freq. (kHz)	Start TC (US)	Laser Off (US)	End TC (US)	Polygon TC (US)	Distance (mm)	Depth (mm)
100	20	20	300	100	300	100	0.4	30

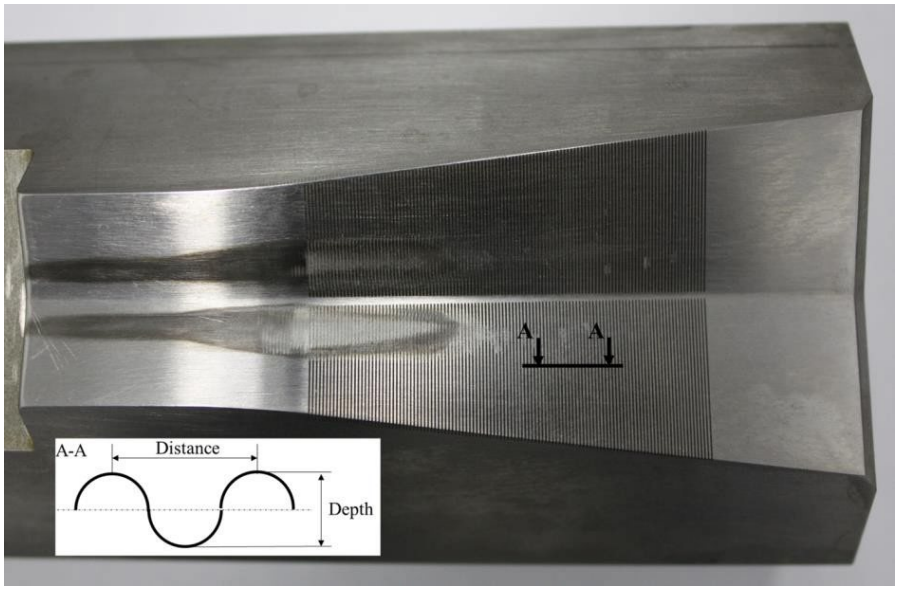

Fig. 6. Engraved swaging die. A-A section shows schematic representation of engravement distance and depth.

V-type dies are composed of 2 sections (left and right) perpendicular to axial direction. Roughness measurements are conducted for these sections separately. Initial and final roughness are presented in Table 2 for 4 dies before and after swaging processes. Initial die geometry is produced using EDM. The difference between the surface roughness parameters for different dies is accepted within tolerances. Surface roughness is measured before and after 3 processes to observe the reliability of the suggested roughening method.

Table 2. Surface roughness of 4 dies before/after engravement and its deviation after 3 processes.

#	Before engravement		After engravement		After 3 processes	
	R_a (right)	R_a (left)	R_a [R_z] (right)	R_a [R_z](left)	R_a [R_z] (right)	R_a [R_z] (left)
1	0.60	0.29	4.37 [43.7]	4.13 [50.0]	3.81 [43.7]	3.00 [39.2]
2	0.71	0.93	3.58 [45.0]	4.03 [40.1]	4.29 [40.1]	3.55 [30.48]
3	0.50	0.69	5.66 [56.7]	6.66 [68.1]	5.97 [33.8]	6.17 [37.56]
4	0.79	0.48	5.75 [58.8]	7.27 [56.7]	8.91 [53.3]	6.09 [48.66]

After the preparation of engraved dies, process trials are performed to evaluate the effects of surface roughness using REPKON RFFM Series, 4-die rotary swaging machine. The hydraulic cylinder, despite the reaction forces generated on the dies, aims to retain its position. As a result, there is a pressure difference at both ends of the cylinder. This pressure difference is then utilized to calculate the reaction force. Since, there was no infrastructure to measure the friction coefficient of the engraved surface in the production facility, it was decided to conduct a comparative study using engraved and non- engraved die sets to verify the analysis concept. During the test, the mechanism that pushes the workpiece into the die set was operated with position control and the reaction forces on the mechanism were measured. Force measurement results are shown in Fig. 7. The introduction of surface roughness on the die has been found to result in a significant reduction of the reaction forces by half. This validates the application of a roughened die surface concept for macro swaging applications. However, a direct correlation is not established due to lack of friction coefficient determination.

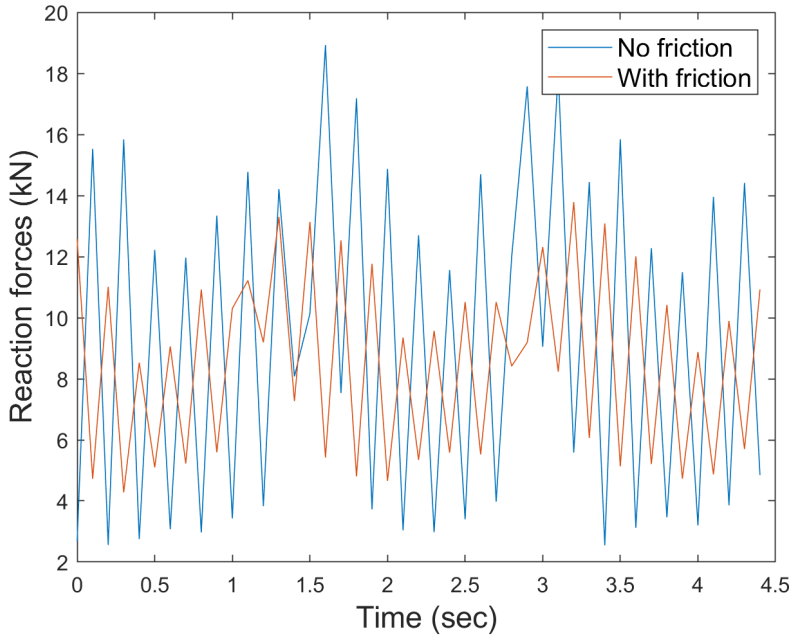

Fig. 7. Workpiece pusher reaction forces during test processes.

Summary

In this study, significant effects of the die surface friction on the rotary swaging process and product quality are determined. Process design requires careful evaluation of benefits and

drawbacks for roughened die surface application. Main highlights of the study which construct a base for this consideration are shared below:

- Die surface friction results in frictional shearing between die and workpiece. During each blow, die pulls the workpiece in the feeding direction which supports the reaction forces created by the tapered section. Hence, reaction forces and machine vibrations decrease.
- The geometric precision of the product is increased by the high friction area created on the dies. In addition, a more matt structure is obtained on the outer surface of the product.
- Die shape and contact surface play an important role for the contact interactions and alter the flow of the material. During rotary swaging, dies pull the surface in the axial and tangential direction. Tangential component results in undesired torsion. For V-shaped dies, tangential contact area is significantly smaller than axial. Hence, increased surface friction does not change the torsion on the workpiece.
- The main drawbacks of the proposed methods are the wear of die surface and tearing of the workpiece surface as a result of the increased frictional shearing. Sustainability of the proposed technique for each trial requires a further study to determine optimum surface roughness and lubrication to prevent deterioration of the product surface quality and to increase die service life.

References

[1] F. Vollertsen, Ed., Micro Metal Forming, Berlin, Heidelberg: Springer Berlin Heidelberg, 2013. https://doi.org/10.1007/978-3-642-30916-8

[2] F. Böhmermann, H. Hasselbruch, M. Hermann, O. Riemer, A. Mehner, H.-W. Zoch, B. Kuhfuss, Dry rotary swaging–approaches for lubricant free process design, Int. J. Precis. Eng. Manuf.-Green Technol. 2 (2015) 325–331. https://doi.org/10.1007/s40684-015-0039-2

[3] M. Herrmann, Schmierstofffreies Rundkneten / Trockenrundkneten, Dry Rotary Swaging, Mar. 2019.

[4] S.L. Semiatin, Ed., Metalworking: Bulk Forming. ASM International, 2005. https://doi.org/10.31399/asm.hb.v14a.9781627081856

[5] F. Binhack, U.S. Patent No. US 2012/0060577 A1. (2012).

[6] F. Grosman, A. Piela, Metal flow in the deformation gap at primary swaging, J. Mater. Process. Technol. 56 (1996) 404–411. https://doi.org/10.1016/0924-0136(95)01854-9

[7] G.D. Lahoti, T. Altan, Analysis of the Radial Forging Process for Manufacturing Rods and Tubes, J. Eng. Indust. 98 (1976) 265-271. https://doi.org/10.1115/1.3438830

[8] G.D. Lahoti, L. Liuzzi, T. Altan, Design of dies for radial forging of rods and tubes, J. Mech. Work. Technol. 1 (1977) 99–109. https://doi.org/10.1016/0378-3804(77)90016-X

[9] A.A. Tseng, S.X. Tong, T.C. Chen, J. Hashemi, Thermomechanical simulation of a radial forging process, Mater. Des. 15 (1994) 87–98. https://doi.org/10.1016/0261-3069(94)90041-8

[10] J.P. Domblesky, R. Shivpuri, B. Painter, Application of the finite-element method to the radial forging of large diameter tubes, J. Mater. Process. Technol. 49 (1995) 57-74. https://doi.org/10.1016/0924-0136(94)01334-W

[11] M. Yamaguchi, S. Kubota, T. Ohno, T. Nonomura, T. Fukui, Grain Size Prediction of Alloy 718 Billet Forged by Radial Forging Machine Using Numerical and Physical Simulation, Superalloys 718. 625. 706 and Various Dcrikatives 1 (2001) 300. https://doi.org/10.7449/2001/Superalloys_2001_291_300

[12] B. Ghasemi, H. Alijani, M. Poursina, Prediction of Residual Stresses for a Hollow Product in Cold Radial Forging Process, Int. J. Eng. 28 (2015) 1209–1218.

[13] A. Ameli, M.R. Movahhedy, A parametric study on residual stresses and forging load in cold radial forging process, Int. J. Adv. Manuf. Technol. 33 (2007) 7-17. https://doi.org/10.1007/s00170-006-0453-2
[14] L. Fan, Z. Wang, H. Wang, 3D finite element modeling and analysis of radial forging processes, J. Manuf. Process. 16 (2014) 329–334. https://doi.org/10.1016/j.jmapro.2014.01.005
[15] L. Liu, L. Fan, Study of Residual Stresses in the Barrel Processed by the Radial Forging, in 2009 Second International Conference on Information and Computing Science, May 2009, vol. 4, pp. 131–134. https://doi.org/10.1109/ICIC.2009.343
[16] A. Uhlig, Investigation of the Motions and the Forces in Radial Swaging, in German, Doctoral dissertation, Technical University Hannover, 1964.
[17] M. Smith, ABAQUS/Standard User's Manual, Version 6.9. Dassault Systèmes Simulia Corp., 2009.
[18] L. Ceschini, A. Morri, A. Morri, S. Messieri, Replacement of Nitrided 33CrMoV Steel with ESR Hot Work Tool Steels for Motorsport Applications: Microstructural and Fatigue Characterization, J. Mater. Eng. Perform. 27 (2018) 3920-3931. https://doi.org/10.1007/s11665-018-3481-9

Materials Research Proceedings 28 (2023) 909-916 https://doi.org/10.21741/9781644902479-99

Design of a new simulative tribotest for warm forming applications having high contact pressure and surface enlargement

GALDOS Lander[1,a *], AGIRRE Julen[1,b] and ARANBURU Elixabet[1,c]

[1]Mechanical and Industrial Production Department, Mondragon Unibertsitatea, Loramendi 4,20500 Mondragon, Spain

[a]lgaldos@mondragon.edu, [b]jagirre@mondragon.edu, [c]earanburue@mondragon.edu

Keywords: Tribology, Warm Forming, Fine Blanking

Abstract. Many tribological tests have been developed in the last decades to emulate real cold forging processes at laboratory conditions and to obtain friction coefficients at different process conditions. In this paper a new tribotester is designed and numerically validated to reach extreme contact conditions, high normal contact pressure and surface enlargement, for warm temperature testing of lubricants starting from material in the form of thick sheets or precuts. The numerical simulations prove that this is possible by the use of a combined bending and ironing test.

Introduction

Fine blanking is a manufacturing process capable of producing sheet metal parts with completely smooth cutting surfaces [1]. The process is sometimes known by other names like fine stamping or precision cutting and like standard shear blanking processes, according to DIN 8580, fine blanking falls under the main category of material separation or parting processes, and is defined according to DIN 8588 under the sub-category dividing [2].

The main differences in comparison with the conventional blanking or punching process are the use of a counterpressure which enables to work in a more compressive stress state and decreases the cambering of the final product, the use of very small clearances (0.5-1% of the material thickness instead of 10-20% in conventional shearing) and the introduction of Vee-Rings in the pressure and/or blanking plates. The Vee-Ring is a physical V-shape feature that is located either in the pressure plate, the blanking plate or in both of them, which has the function to hold the punched material outside the blanking line and so prevents lateral flow of the material during the blanking process. In addition, it serves to apply compressive stress to the sheet metal, improving the flow process and delaying the fracture occurrence.

The main advantages of the process are the increased accuracy (smoother sheared surface and better geometrical tolerances) and the need of less production steps to produce high quality functional components that need to be manufactured by metal forming and final machining instead.

The disadvantages of the technology are the high tool wear of the active elements (punches, dies, plates), the high tool costs and the need of specific presses that are only used for fine blanking, as three actions (force application) are needed to run the process. A compound fine blanking die working principle during the blanking process is shown in Fig. 1.

Content from this work may be used under the terms of the Creative Commons Attribution 3.0 license. Any further distribution of this work must maintain attribution to the author(s) and the title of the work, journal citation and DOI. Published under license by Materials Research Forum LLC.

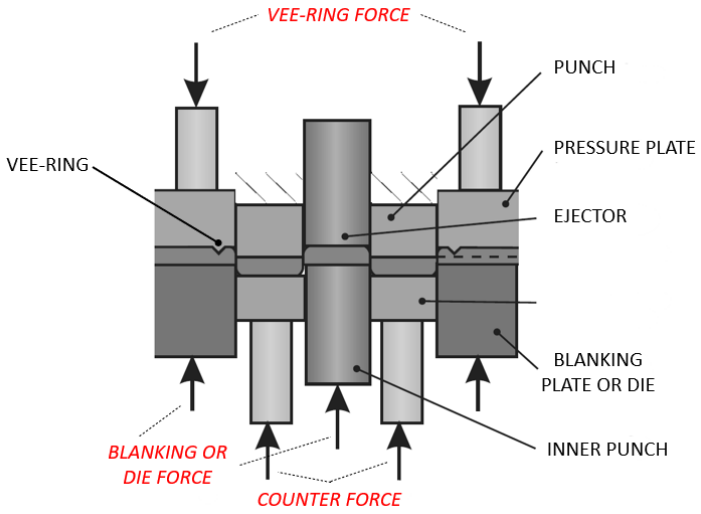

Fig. 1. Compound die set used in fine blanking (recreated from [2]).

Nevertheless, not all the aspects of the fine blanking technology are positive. The main materials that are fine blanked are steels (structural, case hardenable, heat treatable, etc.) which roughly represent the 80-90% of the produced parts all over the world. Other materials like aluminium, cooper and stainless steels are properly processed with the use of proper lubricants that avoid excessive adhesive wear. Anyhow, the elongation capacity of the materials needs to be high enough to guarantee the fine blanking capability of the cut material (complete smooth cutting surface) and this is reached by chemical composition adjustments, a proper thermos-mechanical processing and the soft annealing of the material prior to its processing. For example, in the case of the C45 steel, this annealing heat treatment changes the original microstructure that passes from a ferritic-perlitic typical microstructure to a microstructure that comprises a ferrite matrix with spheroidal cementite embedded in it. This spheroidized microstructure highly increases the fine blanking capability.

Currently, the ultimate tensile strength of fine blanked materials is around 550-600 MPa, both for steel and stainless steels. The current needs for structural lightweighting, especially in the transport industry, are forcing the fine blanking companies to push these material boundaries and to process higher steel grades. Although many attempts have been made by different companies to be able to cut high strength materials, the warm assisted fine blanking seems the most suitable technological approach for this, still causing big challenges to be implemented in serial production.

Warm Assisted Fine Blanking

It is well known that heating of metallic alloys improves their ductility in the absence of blue brittleness or other similar fragility mechanisms. For these reasons, four different research institutes and companies have performed initial fine blanking tests to develop the warm assisted fine blanking process.

Up to the authors best knowledge, researchers of the University of Shanghai were the first ones reporting experimental values in 2020. In their work, aiming to widen the application of the fine-blanking process, the heat-assisted fine-blanking process of AISI 304 stainless steel grade was performed. The cutting of a dog-bone shape component showed that the increase in temperature was beneficial for the final quality of the fine blanked component, being 250ºC the optimal temperature for a cutting quality improvement [3].

Later in 2020, Feintool company together with ETH Zurich published an online web publication about their recently developed Thermo-FineBlanking. Unlike the previous work, both the blank

material and the tool inserts were heated and the aim of the result was to check if conventional steels could be fine blanked without a laborious and expensive heat treatment with a carbide spheroidization level of more than 90%. The cutting force was reduced in a 30% in comparison to the room temperature cutting and fine blanking capability was considerably improved with increased temperature for the 42CrMo4 and 1.4301 (AISI 304) materials [4]. In the same work, authors claimed that new lubricant developments were needed so that a proper tribological condition is obtained with temperatures above 200ºC, the limit for conventional fine blanking mineral-oil based lubricants.

Lastly, researchers of the laboratory for Machine Tools and Production Engineering (WZL) of RWTH Aachen University have published three works where they showed preliminary results of the newly developed warm assisted fine blanking process. In Shemet 2021, the authors presented final microhardness values obtained after fine blanking S700MC, 42CrMo4 and 16MnCr5 steels [5]. Later in Esaform 2021, same group presented the cutting forces at different temperatures for the X5CrNi18-10 (AISI 304) stainless steel. In the same paper, final product tolerances and cutting surface quality of different temperatures were also analysed [6]. Finally, in Esaform 2022, the same research group, presented the results obtained when fine blanking a star shape component and the 40MnB4 and 42CrMo4 steels. The process forces were evaluated depending on the sheet metal temperature and a good fine blanking capability of 40MnB4 was confirmed. Moreover, results showed that process forces and product quality were comparable to 42CrMo4 steel [7].

Following the findings of the previous researchers, Mondragon University, together with the Elay company, has recently performed warm forming fine blanking tests using an industrial Mori hydraulic fine blanking press. Different tests were performed by heating the raw material up to 300ºC and the results of precedent authors were confirmed by cutting a real component. As stated by Zheng et al. from Shanghai University, the critical point of the industrial application of the process is, among others, the loss of properties of conventional lubricants used in fine blanking and thus, the premature tool wear. For this reason, the main objective of the present paper is to develop a new tribotester that can emulate the fine blanking conditions, extreme contact pressures and surface expansions, at warm temperatures, so that the test results can be used for new lubricants screening and new lubricant formulation optimization.

Tribotesters for Extreme Contact Conditions

Several tribotesters have been developed during the last decades to emulate sheet metal forming and forging processes. Among others the ring test for forging and the strip drawing test for sheet metal forming are the most used tests to estimate the coefficient of friction and for the testing of new lubricants.

Groche et al. compared six different well established friction tests for cold forging operations using one state of the art industrial tribosystem, the contact between the 16MnCrS5 steel and tools made of M2 grade steel with a hardness of 61–63 HRC [8]. The tool surfaces were coated with an AlCrN based coating (Balinit Alcrona Pro) and polished to a roughness of Ra < 0.2 mm. In the same study, the different tribotests were numerically simulated and the basic tribological loads, the contact normal pressure, the surface enlargement, the relative sliding velocity and temperature at the interface were compared.

Due to the individual frictional test setups, it is clearly observed that not all the mentioned tribological loads can be set independently. Each of the tribotest has its own characteristic working window and the Sliding Compression Test seems to be the most flexible option to tune the test and get the desired range of contact conditions. All in all, the tribological conditions found in fine blanking and shearing in general are very aggressive [9-10]. Contact pressure can reach levels as high as 5 GPa and surface enlargements bigger than 50 are locally found in the sheared zone for a fine blanking of 8 mm thick S700MC steel. A summary of the numerical results obtained by the authors is shown in Table 1.

Table 1. Summary of the numerical results obtained in [8].

Tribological tests	Contact pressure	Surface expansion	Relative sliding velocity	Temperature
Ring Compression	Low	Low	Low	Low
Combined Forward Rod Backward Can Estrusion	Medium	Low	Medium	Medium
Backward Can Extrusion	Medium-High	High	High	High
Backward Can Extrusion with rotation	High	High	Medium	Medium
Upsetting sliding	Medium	Low	Set value	Low
Sliding compression	Medium	Medium	Set value	Medium

For these limitations, also found in cold forging, and to evaluate different lubricants and surface finishings, Hirose et al. developed an Upsetting-Ironing type tribometer for evaluating the tribological performance of lubrication coatings for cold forging [11]. Numerical simulations of the test prove that the test is able to reach a surface enlargement up to 500 and a contact pressure of around 2GPa for a SWRM 10K steel (tensile strength of 480 MPa). During the test a cylindrical billet is first upset for being later deformed by ironing using three ball bearing made of high chromium steel (SUJ2) of diameter 12 mm. Following this idea, a new tribotester is presented in this work for testing thick sheets and to emulate warm fine blanking conditions.

Design of a New Tribostester

The new tribotester that is proposed for fine blanking is shown in Fig. 2. As in the concept presented by Hirose et al. the test is divided in two steps [11]. First, the initial flat blank is bent to obtain an U-shape. Then punch stroke continues and the ironing phase starts. The U-shaped blank, which has been bent with a clearance of 0.5 mm between the punch and the die (per side) is deformed against bearing balls made by SUJ2 steel of diameter 12 mm. At this moment, a build-up of contact pressure and surface enlargement occurs in the desired contact zone. The ball bearings can be exchanged at every new test due to their low cost and the galling can be studied on them, as well as in the tested sample, following the procedure defined by Hirose et al. Chromium tends to adhere in the tested sample and this is used to determine when the galling starts using an SEM microscope.

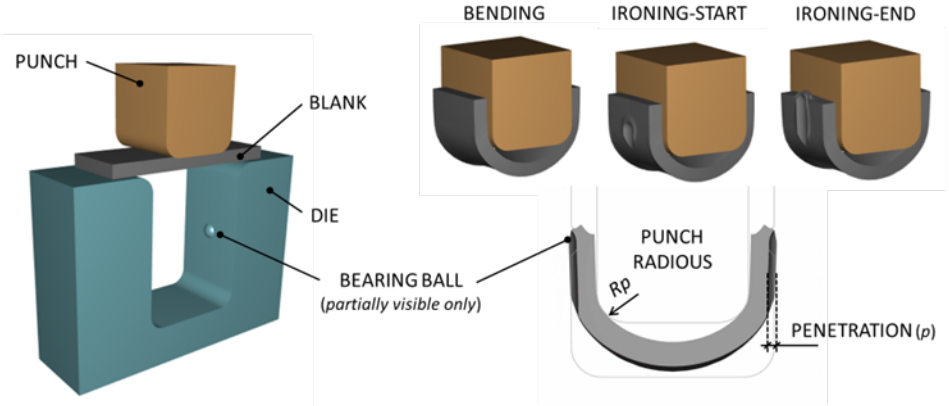

Fig. 2. New tribotester for thick sheet material and extreme tribological conditions.

The parameters that can be changed during the test are the blank temperature, which can be previously heated in a furnace, the ball penetration (see Fig. 2) and the press speed.

Numerical Modelling of the Test

The new testing concept and set-up has been numerically studied to evaluate the contact conditions reached with different testing conditions, varying the penetration (p) and punch radius (R_p). FORGE NxT 3.2 software has been used for running the numerical simulations and the tools have been considered rigid. The blank material is a S700MC steel which has been modelled using solid tetrahedral elements and a simplified Hensel-Spittel hardening law considered as isotropic (r values close to 1 in different directions). Only one half of the blank has been modelled in the study (see symmetry plane in Fig. 3). Young modulus of 210 GPa and a Poisson coefficient of 0.3 were employed. The material temperature has been fixed to room temperature and no temperature influence has been studied in this work. The different simulation conditions are shown in Table 2 and the numerical model is further detailed in Fig. 3.

Table 2. Different simulation conditions.

Material model – Hensel Spittel (MPa)	$\sigma = 1127 \cdot e^{-0.0009 \cdot T} \cdot (\varepsilon - 0.01354)^{0.0833}$
Friction coefficient (Tresca shear model)	0.05, 0.1, 0.2, 0.3
Penetration (p) - mm	2, 3, 4
Punch radious (R_p) - mm	10, 17.5, 25

The main objectives of varying the selected parameters are:

1. To evaluate the sensitivity of the test to different friction coefficients using different test conditions – a higher force increment when changing the friction coefficient is desirable to perform a screening of different lubricants that are suitable for warm fine blanking
2. To evaluate how the penetration changes the contact pressure and surface enlargement
3. To optimize the punch radius value to avoid excessive curving of the tested sample before the ironing phase

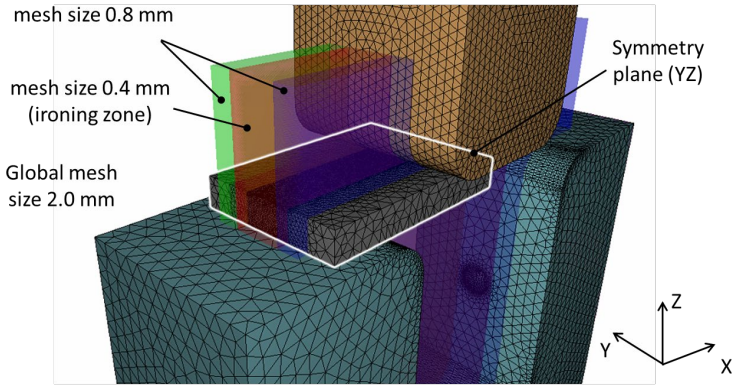

Fig. 3. Numerical model of the bending-ironing tribological test (R10 and p2).

With the purpose of selecting the best tool dimensions of the new tribotester the force evolution curves, surface enlargement variation and the maximum normal contact pressures for each of the simulated case have been evaluated.

A typical force-displacement curve of the punch is shown in Fig. 4a. The curve shows a double dome shape with two force peaks corresponding to the initial bending force and the ironing force respectively. If we solely consider the ironing force, ΔF is defined as the force difference between

Materials Research Proceedings 28 (2023) 909-916 https://doi.org/10.21741/9781644902479-99

the peak forces taking as a reference the m0.05 friction case. A higher force change means a higher sensitivity to detect different friction coefficients and thus to do a proper evaluation of the new lubricants for fine blanking. Fig. 4b clearly shows that sensitivity of the test increases when the punch radius decreases and the penetration increases. Thus, the best testing parameters in terms of friction sensitivity are R_p=10 mm in combination with p=4 mm.

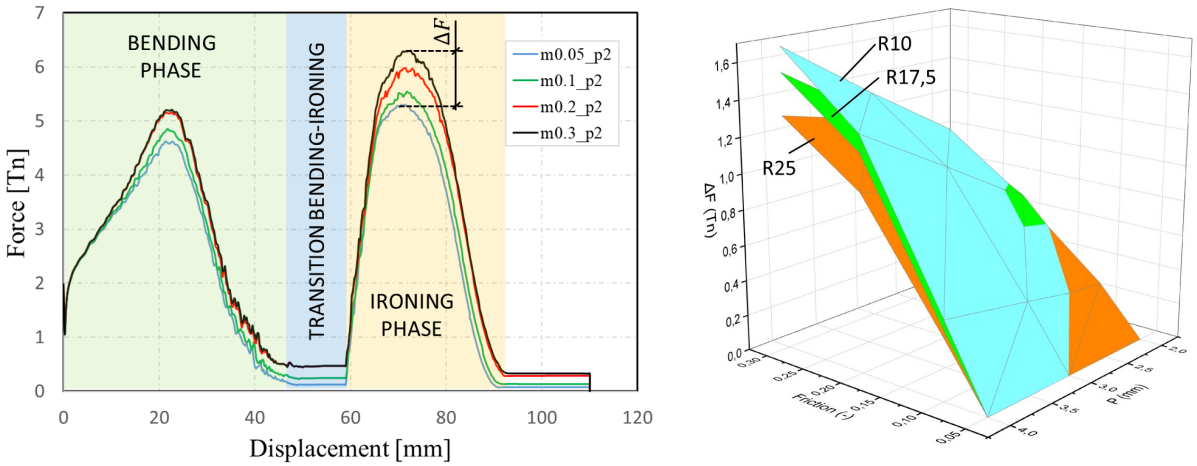

Fig. 4. a) Typical punch Force-Displacement curve for penetration 2 mm and different friction values and b) comparison of ΔF for different configurations.

An example of the numerical results obtained for the field variables maximum surface enlargement and maximum normal contact pressure is shown in Fig. 5a and Fig. 5b respectively. Here, the surface enlargement (named as DSURF) is defined as follows:

$$DSURF = \frac{Surf - Surf_0}{Surf_0} = \frac{Surf}{Surf_0} - 1 \quad (1)$$

where *Surf* is the new expanded surface and $Surf_0$ is the initial surface. Consequently, a DSURF value of 3 means that the new surface is four times greater than the original one.

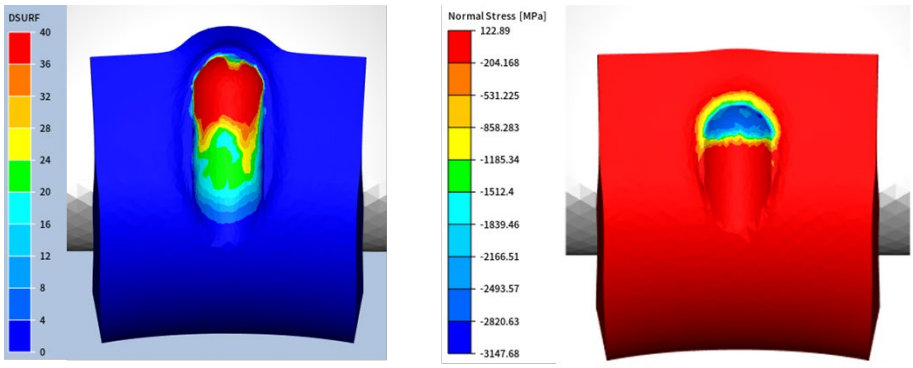

Fig. 5. Example of numerical results for a) Surface enlargement and b) Normal contact pressure.

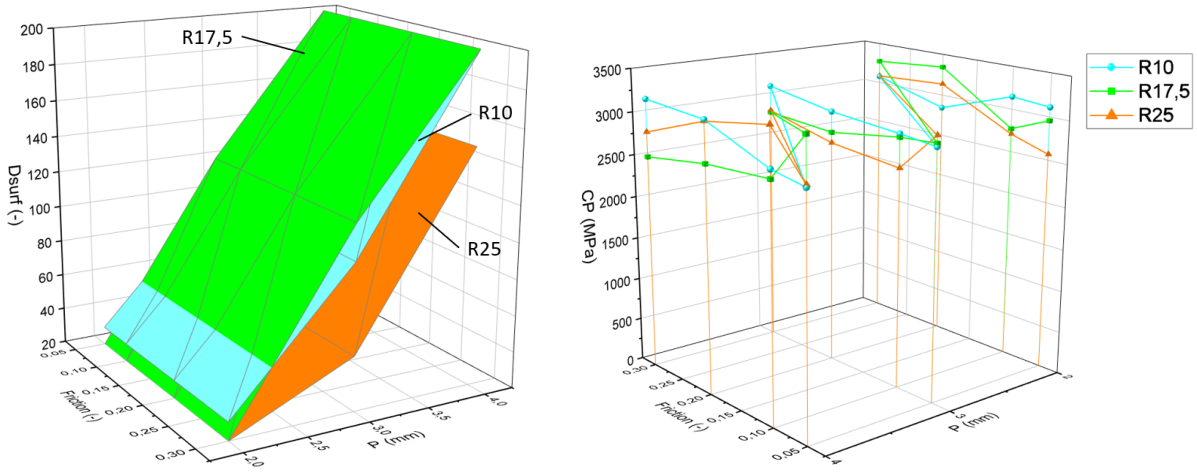

Fig. 6. Influence of parameters on a) Surface enlargement and b) Normal contact pressure.

As it can be observed in Fig. 6a, the maximum surface expansion is mainly dominated by the penetration. Higher penetration results in a higher surface enlargement as already shown by Hirosi et al. where higher amount of upsetting and subsequent ironing achieved higher surface enlargement values. On the contrary, the maximum contact pressure is around 3GPa for all the cases (Fig. 6b). This is probably because the hardening of the material tends to saturate at high strain levels. Nevertheless, both the surface enlargement values and contact pressures are representative of extreme contact conditions and suitable to emulate the fine blanking situation.

Summary

A new tribotester to test lubricants for warm fine blanking has been conceptually defined and numerically validated. The new testing device is simple, can achieve high contact pressures and surface enlargements and uses ball bearings that are cheap and easily exchangeable to analyse wear mechanisms.

The numerical parametric study of the most relevant design dimensions, the ironing penetration (p) and punch radius (R_p), has clearly shown the effect of them on the maximum surface enlargement and contact pressure. The surface enlargement increases with the penetration while the surface enlargement follows a different trend. Similar surface expansion values are obtained for R17.5 and R10 while lower values are observed with R25. This can be probably explained by the fact that using this high punch radius and same sample length, the total extruded length is notably decreased in comparison to the other two cases.

The friction force different between the studied conditions shows that sensitivity to contact condition changes is higher when penetration increases.

Acknowledgments

The authors would like to thank the Spanish Government for the economic support and funding of the HEATFORM European project (SMART Eureka call) and the Elay company for the technical and experimental testing support.

References

[1] R.A. Schmidt, Cold forming and fineblanking, Feintool, Buderus, Wälzholz, Hoesch Hohenlimburg, Germany, 2007.

[2] T. Altan, Metal Forming Handbook /Schuler, Springer-Verlag Berlin Heidelberg, 1998.

[3] Q. Zheng, X. Zhuang, J. Hu, Z. Zhao, Formability of the heat-assisted fine-blanking process for 304 stainless steel plates, Mater. Charact. 166 (2020) 110452. http://doi.org/10.1016/j.matchar.2020.110452

[4] C. Maurer, Development project: Thermo-fineblanking, Feintool, IEPA, 2018. https://blog.feintool.com/en/thermo-fineblanking
[5] I.F. Weiser, A. Feuerhack, T. Bergs, Investigation of the Micro Hardness at the Cut Surface of Fine Blanked Parts with Variation of Sheet Material and Cutting Temperature, Key Eng. Mater. 883 (2021) 269-276.
[6] I.F. Weiser, R. Mannens, A. Feuerhack, T. Bergs, Experimental Investigation of Process Forces and Part Quality for Fine Blanking of Stainless Steel with Inductive Heating, ESAFORM 2021. https://popups.uliege.be/esaform21/index.php?id=2575
[7] I.F. Weiser, T. Herrig, T. Bergs, Fine Blanking Limits of Manganese-Boron-Steel in Fine Blanking Compared to Tempered Steel with Variation of Sheet Metal Temperature, Key Eng. Mater. 926 (2022) 1122-1130. https://doi.org/10.4028/p-7cwhpb
[8] P. Groche, P. Kramer, N. Bay, P. Christiansen, L. Dubar, K. Hayakawa, c. Hu, K. Kitamura, P. Moreau, Friction coefficients in cold forging: A global perspective, CIRP Annals 67 (2018) 261-264. https://doi.org/10.1016/j.cirp.2018.04.106
[9] Y. Abe, R. Yonekawa, K. Sedoguchi, K.I. Mori, Shearing of ultra-high strength steel sheets with step punch, Procedia Manuf. 15 (2018) 597-604. https://doi.org/10.1016/j.promfg.2018.07.283
[10] K.I. Mori, Review of shearing processes of high strength steel sheets, J. Manuf. Mater. Process. 4 (2020) 54. https://doi.org/10.3390/jmmp4020054
[11] M. Hirose, Z.G. Wang, S. Komiyama, An upsetting-ironing type tribo-meter for evaluating tribological performance of lubrication coatings for cold forging, Key Eng. Mater. 535 (2013) 243-246. http://doi.org/10.4028/www.scientific.net/KEM.535-536.243

Incremental and sheet metal forming

Materials Research Proceedings 28 (2023) 919-928 https://doi.org/10.21741/9781644902479-100

Numerical investigation on the deep drawing of sheet metals with an additively applied coating

MÄRZ Raphaela[1,a *], HAFENECKER Jan[1,b], BARTELS Dominic[2,3,c], SCHMIDT Michael[2,3,d] and MERKLEIN Marion[1,e]

[1]Institute of Manufacturing Technology (LFT), Friedrich-Alexander-Universität Erlangen-Nürnberg, Egerlandstraße 13, 91058 Erlangen, Germany

[2]Institute of Photonic Technologies (LPT), Friedrich-Alexander-Universität Erlangen-Nürnberg, Konrad-Zuse-Straße 3/5, 91052 Erlangen, Germany

[3] Erlangen Graduate School in Advanced Optical Technologies (SAOT), Paul-Gordan-Straße 6, 91052 Erlangen, Germany

[a]raphaela.maerz@fau.de, [b]jan.hafenecker@fau.de, [c]dominic.bartels@lpt.uni-erlangen.de, [d]m.schmidt@blz.org, [e]marion.merklein@fau.de

Keywords: Additive Manufacturing, Forming, Hybrid Parts

Abstract. A promising approach to meet ecological and economical challenges in production industry is the combination of additive manufacturing and forming, which enables the production of hybrid parts. The fusion of the two technologies has the potential to use the benefits of both process classes. One example for the combination of additive manufacturing and forming is a process chain consisting of laser-based directed energy deposition (DED-LB/M) to apply a wear resistant coating on a sheet metal and a subsequent deep drawing process to achieve the final geometry of the component. However, the presence of the local reinforcement influences the subsequent sheet metal forming process. In order to gain more knowledge about the process chain a numerical approach is performed. In this work, the influence of a coating using Bainidur® AM applied by DED-LB/M on the formability of the case hardening steel 16MnCr5 in a deep drawing process is evaluated. For this purpose, a numerical model is built and validated by comparison with experimental results. The finite-element-model serves as the basis for the investigation on the influence of the location of the additively applied coating on the deep drawing process and also enables a deeper understanding of the process.

Introduction

Due to governmental requirements and an increasing environmental awareness, modern production technology has to face new ecological and economical challenges [1]. Therefore, a need for resource efficiency and sustainability in the field of production is coming into focus. In addition to lightweight design [2] another approach to meet the current challenges are resource efficient manufacturing processes. Forming technology is known for its resource efficiency as well as for the high output [3]. On the other hand, a disadvantage of the production technology is its low flexibility [3]. In contrast, the use of additive manufacturing enables a high degree of geometric freedom and a customizability of the components [4]. By combining the two technologies, a production of hybrid parts is possible. Synergy effects such as adapted material properties as well as an extension of the process limits appear and the disadvantages of the two process classes can be compensated [5]. One example for the production of hybrid parts is a process chain consisting of DED-LB/M to apply a wear-resistant coating on a circular blank and a subsequent deep drawing process to achieve the final geometry of the component, which is based on the geometry of a barrel sleeve. The forming process enables a resource efficient production of the component compared to current machining of the barrel sleeve. The use of DED-LB/M before

Content from this work may be used under the terms of the Creative Commons Attribution 3.0 license. Any further distribution of this work must maintain attribution to the author(s) and the title of the work, journal citation and DOI. Published under license by Materials Research Forum LLC.

the forming process enables a local reinforcement of the blank. Therefore, global energy-intensive heat treatment strategies can be avoided. The authors in [6] show that DED-LB/M can be used to locally strengthen aluminum sheet metal blanks. The formability of the aluminum blanks is limited due to the heat input [6]. Nevertheless, no investigations have yet been carried out into how a high-strength material applied by DED-LB/M affects the formability of a case hardening steel.

Objective and Methodology

The aim of this work is to investigate the influence of an additively applied coating on a deep drawing process. This is necessary to evaluate the formability of hybrid components where a high-strength coating is applied. The methodology used in this work is shown in Fig.1.

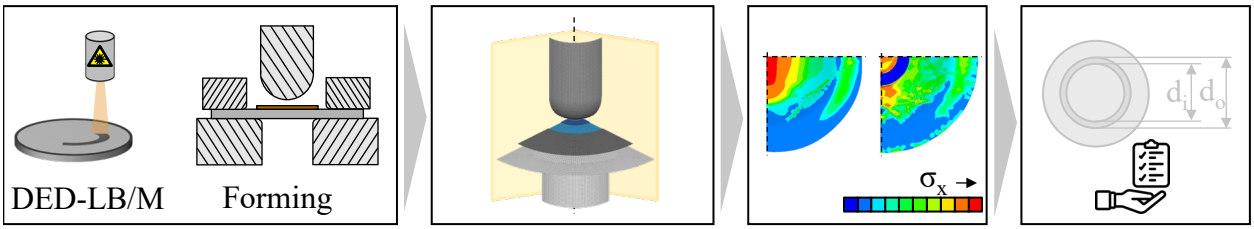

Fig.1. Methodology.

The basis of the investigation is a process combination of DED-LB/M and a subsequent deep drawing process. In a first step, a FE-model of the forming process is built. In addition to the conventional deep drawing process, the model is extended to include the hybrid approach. The validation is done by comparison with experimental results. In addition to the process force, the geometry of the component is compared in order to evaluate the prediction quality of the FE-model. After the validation, an investigation of the stress state of the uncoated and hybrid components is carried out in order to derive conclusions about the formability of hybrid components and the advantageous placement of the additive coating.

Experimental and Numerical Setup

Material and semi-finished product. To produce the hybrid part a process chain consisting of DED-LB/M and a subsequent deep drawing process is used. The geometry of the semi-finished part is shown in Fig. 2a. A circular blank with a diameter of 105 mm and a thickness of 3.5 mm serves as substrate. As material the case hardening steel 16MnCr5 (1.7131) is used. Before the deep drawing process, a wear-resistant coating is applied on the sheet by DED-LB/M. Therefore, the metal powder Bainidur® AM is used. The applied geometry is shown with its variations in Fig. 2b.

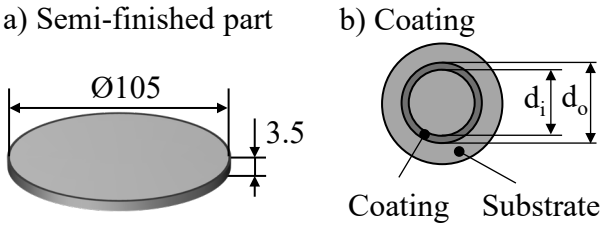

Coating	Inner diameter d_i	Outer diameter d_o
small	16 mm	27 mm
medium	24 mm	35 mm
large	32 mm	43 mm

Fig. 2. a) Geometry of the semi-finished part b) Geometry of the coating and its variations.

The coating is applied in a circle and has a height of 0.5 mm. A difference is made between the listed inner and outer diameters in order to determine the influence of the position of the coating on the forming process. To describe the mechanical properties and the hardening behavior of the substrate material and the coating, true stress-true plastic strain curves are determined, which are used for the numerical simulation. The resulting curves are shown in Fig. 3.

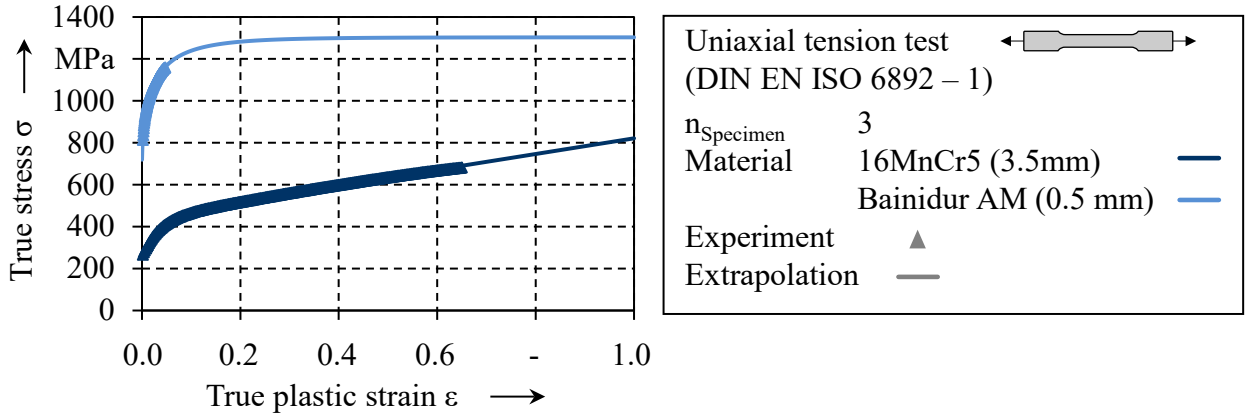

Fig. 3. True stress-true plastic strain curves of the substrate material 16MnCr5 and the coating Bainidur® AM from experimental uniaxial tension tests.

Due to the prevailing stress conditions in deep drawing processes, uniaxial tension tests according to DIN EN ISO 6892-1 [7] at room temperature are carried out. The specimens for the characterization of the substrate material have a measuring length of 50 mm and a width of 12.5 mm. Tensile specimens are also used to characterize the coating. Due to the dimensions of the coating, a smaller specimen geometry with a measuring length of 20 mm and a width of 6 mm is used. The thickness of the specimens corresponds to the thickness of the coating in the experiment. The specimens were first built up as a block through five layers and in the second step separated from the substrate and brought to the final shape by electrical discharge machining. The uniaxial tension tests are carried out using a universal testing machine Zwick Z100 respectively Zwick Z10 for the smaller specimens and a camera-based 3D strain measuring system GOM Aramis. The substrate has a significantly lower initial yield stress of 266 MPa than the coating with a yield stress of 814 MPa. Since higher strains than those determined experimentally

occur in the real process, the two curves were approximated and extrapolated. Voce generalized [8] is chosen as extrapolation approach for the substrate material 16MnCr5. For the coating, the Hockett-Sherby approach [9] was found to be appropriate.

Laser-based directed energy deposition. Before the forming process, circular blanks are coated using DED-LB/M. Therefore, the experiments are performed on an ERLAS UNIVERSAL 50349 machine (ERLAS GmbH). The machine is equipped with a diode laser with a peak power of 4 kW and a characteristic wavelength of 900 to 1080 nm. The nozzle can be moved using three linear axes. In addition, the cell has a sample holder with two rotary axes, which allows the realization of free-form surfaces. The parameter set used for the coating is based on previous investigations [10].

Deep drawing. The subsequent deep drawing process is carried out on a hydraulic press Lasco TSP 100 So with a maximum force up to 1000 kN. The velocity of the punch is set to 4.7 mm/s and the force of the binder is set to 25 kN. The punch geometry is hemispherical with a diameter of 50 mm. The drawing depth, which is set by hard-stops, amounts to 30 mm. In order to reduce the tribological loads, the blanks are lubricated with KTL N 16. The experiments are carried out at room temperature. After the forming process, the parts are measured optically in order to determine the geometry and the sheet thickness. The measurement is carried out with an Atos Core 300 of the company GOM GmbH.

Numerical setup. The numerical model presented in this paper is built with the finite element software LS-Dyna by Ansys, which allows the simulation of nonlinear physical processes. The generation of the input is done with the help of the graphical pre- and post-processor LS-PrePost V.4.7.0. As solver the MPP Double R11.1 is used. Due to the symmetry of the hybrid part, only a quarter is modelled. Therefore, the Keyword “SPC_SET” is applied to the nodes on the x- and y-edges of the part and the coating. For the tools, namely punch, binder and die, rigid shell elements are used. To avoid unwanted movement, constraints in x- and y-direction are defined for the tools. The numerical setup is shown in Fig. 4.

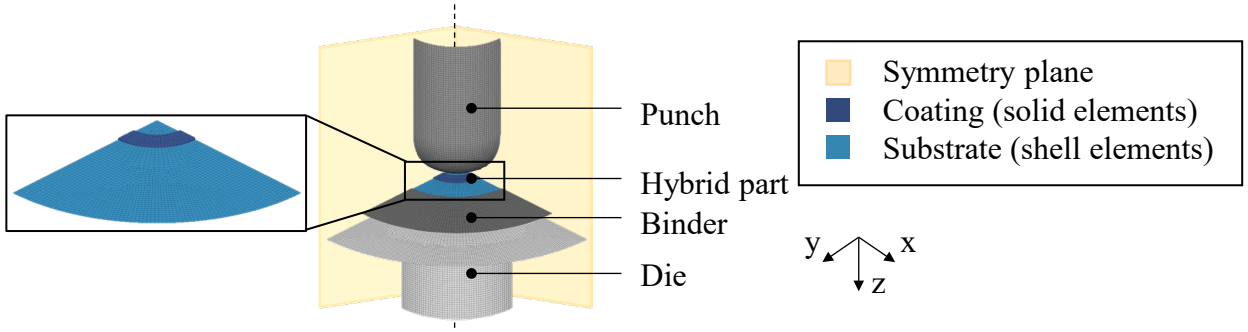

Fig. 4. Setup of numerical model to map the deep drawing process.

The sheet is modeled by fully integrated shell elements. As material model “133-Barlat_YLD2000” is used due to the anisotropic material behavior of the case hardening steel 16MnCr5. In order to map the coating, the material keyword “024-PIECEWISE_LINEAR_PLASTICITY” is applied. In contrast to the substrate material, the coating is modeled with solid elements. To consider the adhesion of the coating to the substrate, the two parts share the same transition nodes. This approach is also chosen in [11]. The contact is modeled with the keyword “CONTACT_FORMING_SURFACE_TO_SURFACE” to avoid penetrations between the tools and the blank.

Results

Validation. In order to evaluate the prediction quality of the presented FE-model, it is validated by comparison with experimental results. In addition to the hybrid part, the conventional deep drawing process is also considered. In Fig. 5, the comparison of the experimentally and numerically determined maximum process forces is shown.

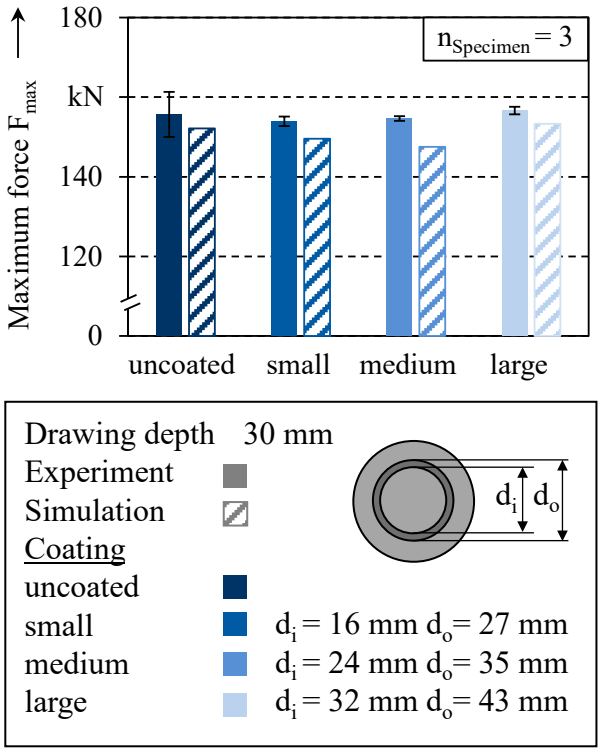

Fig. 5. Comparison of experimental and numerical maximum process force.

Experimentally, a maximum forming force of 155.7 ± 5.1 kN is determined while forming the uncoated blank. In the simulation a maximum forming force of 152.1 kN is reached. With a deviation of 2.6 %, a good agreement between the simulation and the experiment is achieved. Good agreement is also obtained when comparing the numerically and experimentally determined maximum forces of the hybrid components. The largest deviations are evident for the coating with an inner diameter of 24 mm and an outer diameter of 35 mm. Experimentally, a process force of 154.6 ± 0.6 kN is obtained, while the maximum force with 147.5 kN is underestimated in the simulation. However, with a deviation of 4.6 % from the experimentally determined results, a good agreement can be assumed here as well. The influence of the coating on the maximum process force is negligible. The deviations of the variations are within the standard deviation.

In addition to the maximum process forces, the geometry of the part, which was obtained experimentally and calculated numerically, is also compared. The basis for the comparison is the sheet thickness, which was determined at a drawing depth of 30 mm. The sheet thicknesses for the uncoated blank and for the coated blank with an inner diameter of 32 mm and an outer diameter of 43 mm of the coating are shown in Fig. 6. Since only a quarter model was built in the simulation, the resulting thicknesses are mirrored on the y-axis.

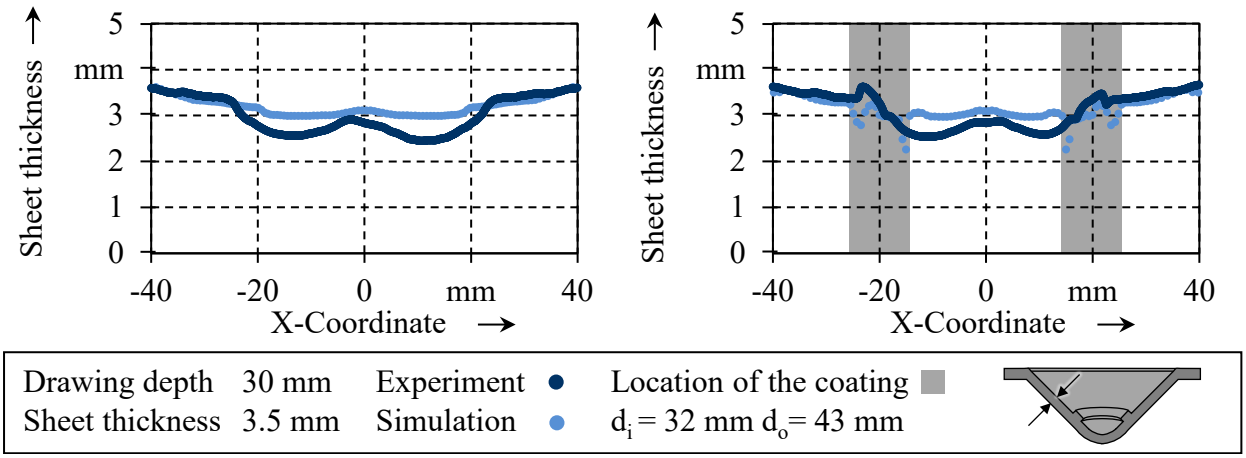

Fig. 6. Experimental and numerical sheet thickness distribution of the a) uncoated part and b) hybrid part.

A good agreement between simulation and experiment is found for the uncoated and the hybrid part in the area of the flange and in the radius area of the die. Deviations are evident in the bottom area of the conventional component. Here, the sheet thickness is overestimated in the simulation for both areas. The reason for this could be the modeling approach of the sheet with shell elements, which is only sufficiently accurate for a sheet with a thickness of 3.5 mm. This upper limit is reached in this case due to the use of a semi-finished part with a sheet thickness of 3.5 mm. Thus, the improvement of the accuracy of the model by using solid elements instead of shell elements has to be verified in future investigations. However, the areas in which the sheet thins out are correctly modeled. Moreover, the determination of the occurring stress states, which is the focus of this contribution, is mainly linked to the process forces, for which only small deviations of less than 5 % are identified. Therefore, it is assumed that the accuracy is adequate for the evaluation of the stress states and the use of the model for further investigations is possible.

Resulting stresses. Different stress states occur during deep drawing. Due to the use of a hemispherical punch, the stress conditions differ from those in conventional deep drawing.

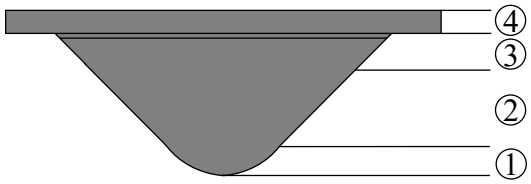

No.	Area	Stresses
1	Punch radius	Biaxial tensile
2	Transition zone	Plane strain/ uniaxial tension
3	Die radius	Bending
4	Flange area	Tensile compressive

Fig. 7. Resulting areas and stress states of a deep drawn part with a hemispherical punch.

The resulting stress states and the corresponding areas are shown in Fig. 7. The bottom area of the part is characterized by biaxial tensile stresses, similar to conventional deep drawing. The subsequent transition area is initially characterized by a plane strain area. As the punch diameter increases, uniaxial tensile stresses occur. In the area of the die radius, the material undergoes a double bending. In the flange area of the component tensile-compressive stresses occur.
By varying the diameter of the coating, it lies in different areas of the deep-drawn component and thus undergoes different stress states. In the following, the influence of the coating diameter on the resulting stresses is investigated. Since radial tensile and compressive stresses occur predominantly in the formed component, the direction-dependent stresses are considered. The resulting stresses in x-direction at a drawing depth of 30 mm and the interface pressure between the punch and the part are shown in Fig. 8.

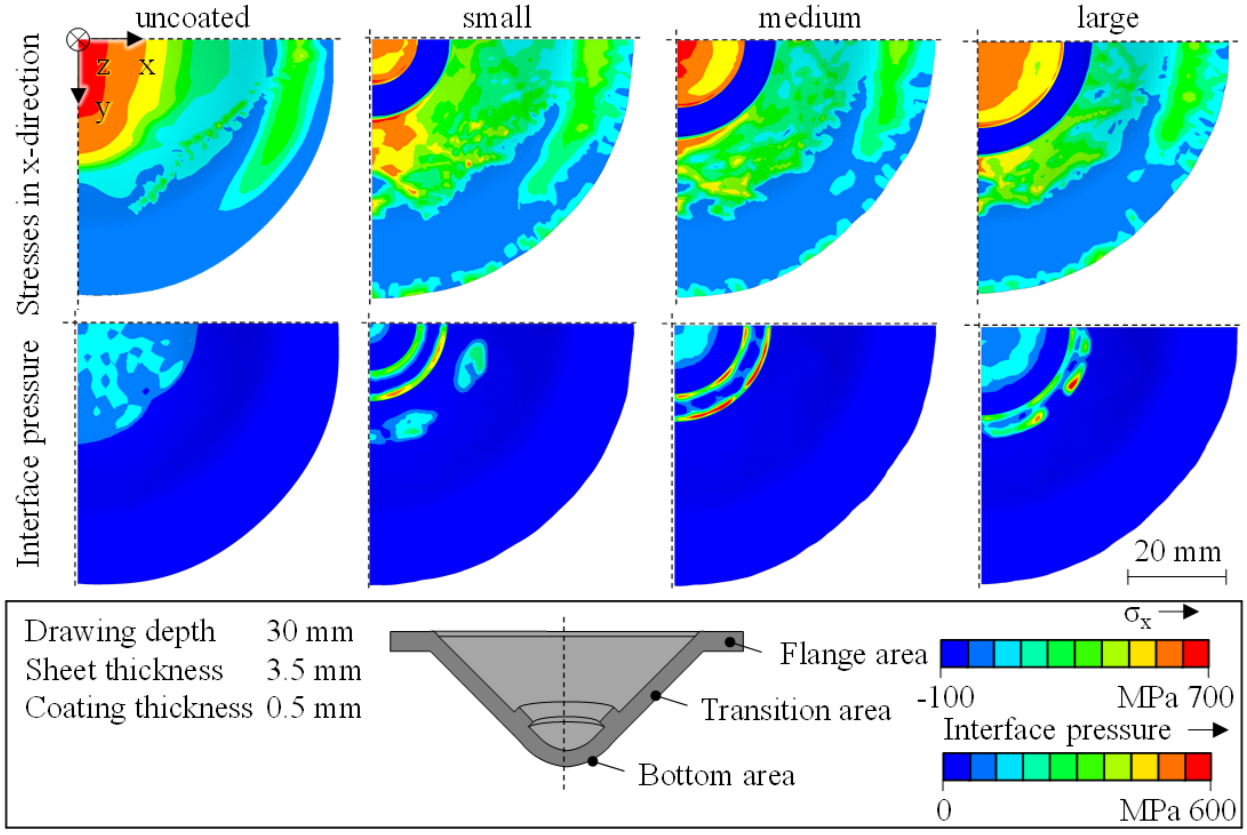

Fig. 8. Comparison of the resulting stresses in x-direction and the interface pressure between the part and the punch in the numerical deep drawing process of the conventional and hybrid parts with coating different diameters.

The maximum tensile stresses occur at the bottom area of the uncoated part. These are more dominant in the y-direction than in the x-direction. The bottom of the component is the most critical area in terms of the formation of cracks due to the maximum stresses in this area. Through the addition of the additively applied coating, the stresses in the bottom area are reduced. The reason for this is the loss of contact with the bottom of the component, as the punch primarily contacts the coating. With an increasing coating diameter, the punch has more contact with the bottom of the component. Therefore, the stresses in the bottom area of the hybrid part increase as well. The use of a coating, however, leads to stress peaks that occur at the inner and outer diameter of the coating, which can be critical regarding a failure of the part at higher drawing depths. A

bigger diameter of the coating leads to lower stresses around the coating. In addition to the stresses in x-directions, the major and minor strains of each finite element are investigated in order to evaluate the stress states of the component. The strains were determined numerically and are shown in Fig. 9.

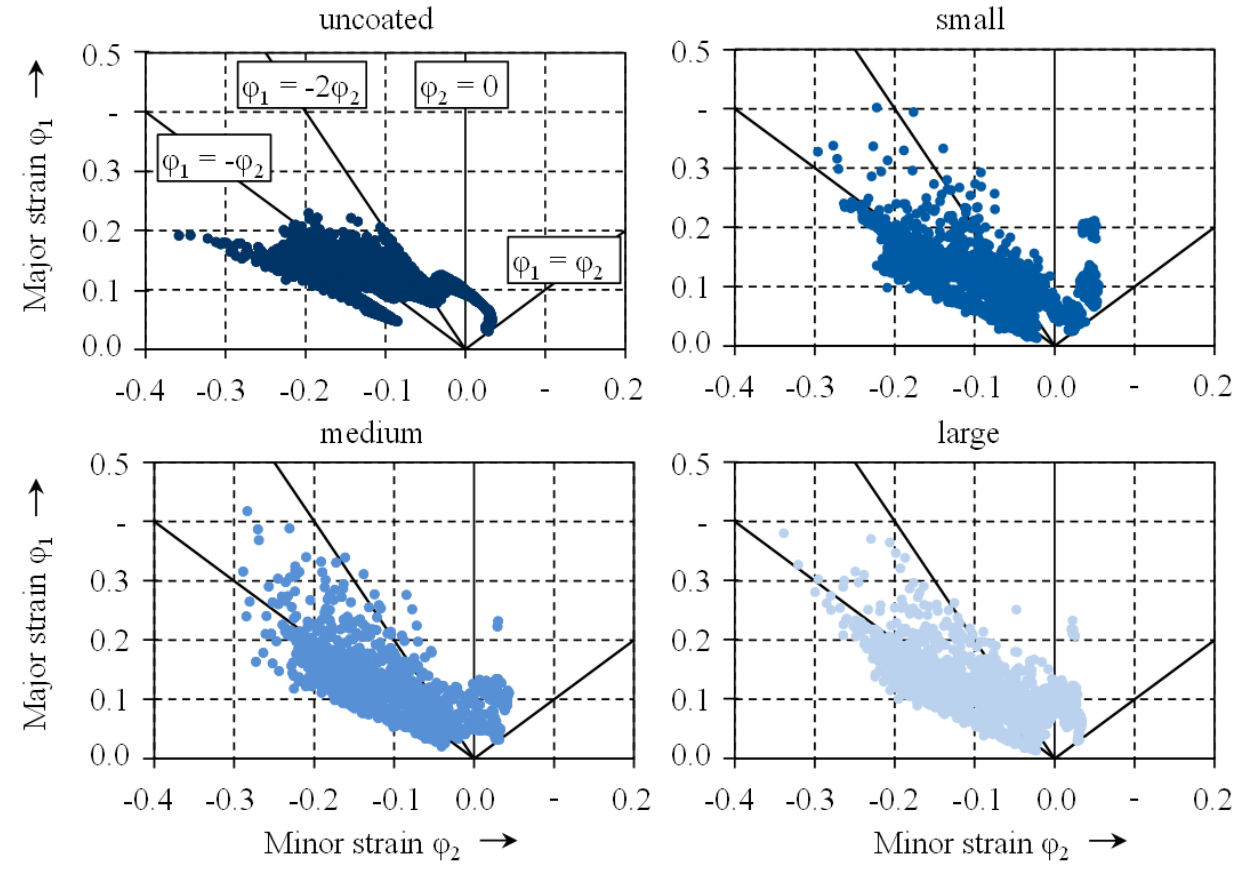

Fig. 9. Major and minor strains from the numerical investigations for the uncoated and hybrid parts.

In the uncoated component, positive major strains and negative minor strains are predominant. This is also observed for the hybrid parts. In the area of the coating positive major and minor strains occur. The major strains are higher at the inner and outer diameter of the coating, especially when using the small coating, and therefore more critical regarding failure. With a bigger diameter of the coating, the load on the coating is more in the area of plane strain with lower major strains. Placing the coating in the plane strain area is therefore more advantageous in terms of formability. Overall, the position of the coating can be used to influence the stress states in the bottom area of the hybrid part. The tensile stresses at the bottom area are reduced through the application of the additive coating. A bigger diameter of the coating leads to reduced stress peaks around the coating, which is due to the plane strain stress condition.

Summary

One approach to meet climate challenges is the combination of different production technologies in order to produce components more resource efficient. An example for this combination is the investigated process chain. In order to evaluate the influence of the additively applied coating on the forming process, a numerical model was built and validated by comparison with experimental

results. A comparison of the resulting maximum process forces from simulation and experiment showed good agreement. There were significant differences in the distribution of the sheet thickness, which can be explained by the modeling approach of the sheet using shell elements. Since the stress state depends mainly on the process force, the model was nevertheless qualified for these investigations. The use of the coating led to reduced tensile stresses in the bottom area of the hybrid component. An enlargement of the diameter of the coating helped to reduce the stress peaks around the coating. A bigger diameter of the coating also led to lower major strains in the area of plane strain. In further investigations, the modeling approach of the sheet with solid elements should be examined. It would also be of interest to model the heat affected area between the coating and the substrate in order to represent the real process more accurately and to better evaluate the influence of the coating.

Acknowledgement
The authors would like to thank the German Federal Ministry for Economic Affairs and Energy for funding the joint project HyConnect (FKZ: 03LB3010*), within the framework of which the present investigations were carried out. Furthermore, the authors would like to thank the Deutsche Edelstahlwerke Specialty Steel GmbH & Co. KG for providing the powder material and the Schaeffler AG for providing the substrate material for the tests.

References
[1] European Commission, A European Green Deal, 2022. https://ec.europa.eu/info/strategy/priorities-2019-2024/european-green-deal_en
[2] A.E. Tekkaya, N.B. Khalifa, G. Grzancic, R. Hölker, Forming of Lightweight Metal Components: Need for New Technologies, Procedia Eng. 81 (2014) 28-37. https://doi.org/10.1016/j.proeng.2014.09.125
[3] F. Klocke, Manufacturing Processes 4, Springer Berlin Heidelberg, Berlin, Heidelberg, 2013.
[4] I. Gibson, D. Rosen, B. Stucker, Additive Manufacturing Technologies, Springer New York, New York, NY, 2015.
[5] M. Merklein, D. Junker, A. Schaub, F. Neubauer, Hybrid Additive Manufacturing Technologies – An Analysis Regarding Potentials and Applications, Phys. Procedia 83 (2016) 549-559. https://doi.org/10.1016/j.phpro.2016.08.057
[6] M. Bambach, A. Sviridov, A. Weisheit, J. Schleifenbaum, Case Studies on Local Reinforcement of Sheet Metal Components by Laser Additive Manufacturing, Metals 7 (2017) 113. https://doi.org/10.3390/met7040113
[7] DIN EN ISO 6892-1:2020-06, Metallic materials - Tensile testing - Part 1: Method of test at room temperature, Beuth publishing, Berlin.
[8] C. Tome, G.R. Canova, U.F. Kocks, N. Christodoulou, J.J. Jonas, The relation between macroscopic and microscopic strain hardening in F.C.C. polycrystals, Acta Metall. 32 (1984) 1637-1653. https://doi.org/10.1016/0001-6160(84)90222-0
[9] J.E. Hockett, O.D. Sherby, Large strain deformation of polycrystalline metals at low homologous temperatures, J. Mech. Phys. Solid. 23 (1975) 87–98. https://doi.org/10.1016/0022-5096(75)90018-6
[10] M. Kreß, D. Bartels, M. Schmidt, M. Merklein, Material Characterization of Hybrid Components Manufactured by Laser-Based Directed Energy Deposition on Sheet Metal Substrates, KEM 926 (2022) 80–89. https://doi.org/10.4028/p-3vlx01
[11] J. Hafenecker, T. Papke, F. Huber, M. Schmidt, M. Merklein, Modelling of Hybrid Parts Made of Ti-6Al-4V Sheets and Additive Manufactured Structures, in: B.-A. Behrens, A. Brosius, W. Hintze, S. Ihlenfeldt, J.P. Wulfsberg (Eds.), Production at the leading edge of technology,

Springer Berlin Heidelberg, Berlin, Heidelberg, 2021, pp. 13-22. https://doi.org/10.1007/978-3-662-62138-7_2

Materials Research Proceedings 28 (2023) 929-936 https://doi.org/10.21741/9781644902479-101

Numerical and experimental investigation of a backward extrusion process for forming geared components from coil

LEICHT Miriam[1,a *], HENNEBERG Johannes[1,b] and MERKLEIN Marion[1,c]

[1]Institute of Manufacturing Technology (LFT), Friedrich-Alexander-Universität Erlangen-Nürnberg, Egerlandstraße 13, 91058 Erlangen, Germany

[a]miriam.leicht@fau.de, [b]johannes.henneberg@fau.de, [c]marion.merklein@fau.de

Keywords: Sheet-Bulk Metal Forming, Extrusion, Cold Forming

Abstract. Stricter political regulations, increasing ecological awareness of society as well as the pursuit for higher performance of components motivate lightweight construction. Functional integration is one way to realize lightweight design, resulting in increased demands on component geometry. Sheet-bulk metal forming (SBMF) offers the potential to enable an economic and ecological production of functional components through short process chains. SBMF from coil also provides additional advantages regarding high output quantity and short cycle times. However, the industrially application of SBMF from coil is limited due to high tool load and coil-specific challenges like an anisotropic material flow, which negatively affects the part accuracy. In this study, a backward extrusion process from coil for forming functional components with gearing is investigated. Therefore, a numerical process model was built and validated based on experimental results. In order to generate a profound process understanding, a combined numerical-experimental approach was chosen for a fundamental process analysis. The influence of the semi-finished product geometry was investigated by forming rotationally symmetric, pre-cut blanks and coil material. The application of the different sheet geometries was compared based on component- and process-side target quantities. The results indicate an anisotropic material flow as a coil-specific challenge, which leads to a direction-dependent component forming.

Introduction

Climate change and the increasing exhaustion of resources are central challenges of the 21st century [1], which leads to an increasing awareness of sustainability and environmental protection among the population and in politics. In the industrial environment in particular, a trend towards reducing environmental pollution and using resources more efficiently is noticeable. Consequently, higher demands are being placed on efficiency and environmental compatibility of manufacturing technologies and products, which require the development of innovative approaches. One effective approach is the implementation of light-weight design in combination with increased functional integration [2]. However, conventional manufacturing processes are reaching their limits [3]. The innovative process class of sheet bulk forming (SBMF) combines the advantages of sheet metal and bulk forming by applying bulk forming operations to sheet metal semi-finished products [4]. SBMF enables the production of thin-walled components with integrated functional elements by means of a three-dimensional material flow [4]. The use of SBMF-processes is currently limited to the forming of pre-cut blanks as semi-finished products, since they offer flexibility in material supply [5]. However, due to the increasing demand for functionally integrated components, manufacturing processes with short cycle times and high output volumes are gaining in importance. With regard to high output rate, the forming from coil offers the possibility to avoid cycle-time limiting handling systems, because the transport of the components between forming stages is realized by coil [6]. Tajul et al. [7] identified an uncontrolled, anisotropic material flow and unequal forming components as challenges of SBMF from coil. Furthermore, Henneberg et al. [8] investigated the forming of rotationally symmetric pins and cups from coil by backward and

Content from this work may be used under the terms of the Creative Commons Attribution 3.0 license. Any further distribution of this work must maintain attribution to the author(s) and the title of the work, journal citation and DOI. Published under license by Materials Research Forum LLC.

lateral extrusion, which provided a basic process understanding of SBMF from coil. Additionally, process-, tool- and workpiece-side measures were investigated to reduce the anisotropic material flow and improve the component accuracy, whereby the greatest potential was achieved for local friction adjustment through the use of a modified blankholder surface [8].The investigation of the transferability of these findings for forming of more complex, functional components with secondary forming elements, such as gearing, is currently a subject of research.

Objectives and Methodology

The objective of this investigation is to develop a fundamental process understanding for the forming of functionally integrated, geared SBMF-parts from coil. The industrial use of SBMF from coil is limited due to significant process challenges. Including the coil-specific, anisotropic material flow, which restricts the dimensional accuracy of the component, as well as high tool stress. Against this background, in this research work a backward extrusion process from the coil for the forming of functional components with external gearing is investigated. The special focus is on the evaluation of the manufacturability of accurately formed gearing elements by extrusion from coil. Therefore, the aim of this research is to obtain a profound process understanding and to analyze causes of the forming limits. A process analysis based on a combined numerical-experimental approach is carried out. Thus, a finite element (FE) model of the process is set up and validated by comparison with experimental target values. In order to investigate characteristics of the coil-specific material flow and its causes, the sheet geometry is varied within the process analysis by examining pre-cut blanks and coil material. For this purpose, geometrical and mechanical component properties as well as the process force are analyzed based on experimental and numerical results.

Process Layout

This chapter gives an overview of the process setup for the backward extrusion process as well as the workpiece target geometry. Subsequently, the material used and the lubricant are explained.

Process setup. In this study, a backward extrusion process from coil for the forming of externally geared components is investigated. With regard to a shortening of process chains, which is considered to be an aim of SBMF [9], the forming is carried out in a single punch stroke. In the reference process, a coil with an initial sheet thickness t_0 of 2.0 mm and a width of 30 mm serves as semi-finished product. During forming, the sheet thickness in the forming zone is reduced to a residual sheet thickness of 1 mm with a punch stroke of 1 mm, forming a blind cavity. The resulting workpiece geometry is a pin with abstracted external gearing, shown in Fig. 1a.

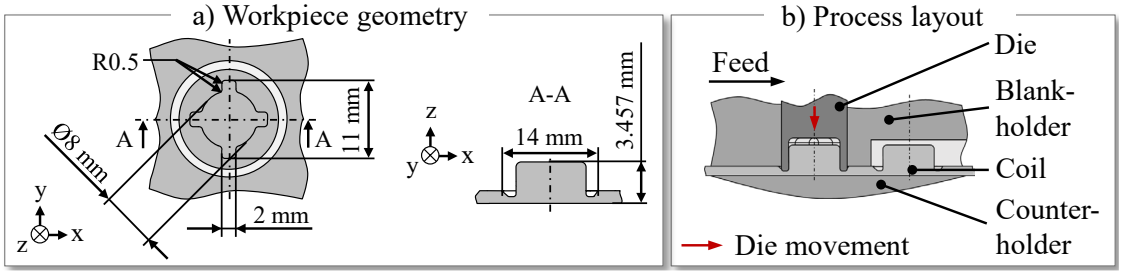

Fig. 1. (a)Workpiece geometry and (b) process layout.

The basic component, the pin, has a diameter of 8 mm and four gearing elements, which are positioned at 90° in and perpendicular to the feed direction. The width of the gearing elements is 2 mm with an outer diameter of 11 mm. The outer diameter of the workpiece has a value of 14 mm. Furthermore, the theoretical pin height with complete material flow into the cavity is 3.4569 mm. To control the material flow into the cavity and to reduce the tool stress, radii are applied at the

edge of the blind cavity and at the edges of the pin and gearing. The geometry of the tool parts as well as the process kinematics were designed based on the workpiece geometry. The tool system, shown in Fig. 1b, consists of a die with an internal gearing, a blankholder and a counter-holder.

In the first process step, the blankholder moves in the negative z-direction and fixes the coil with a force of 130 kN by gas pressure springs. Additionally, the blank holder prevents the material flow out of the forming zone as well as the formation of wrinkles. In the next process step, the die moves downwards and the forming process is carried out with a punch stroke of 1 mm. After forming, the die removes, preventing the lifting of the coil by the blankholder. At the end of the process, the blankholder moves to its initial position and the coil is transported out of the forming zone by feed of 20 mm. In the experimental investigation, the active components are integrated into a tooling system, which is installed in the high-speed press BSTA 510-125B2 from Bruderer in order achieve high output quantities. This stroke-controlled press enables the production of 100 components per minute with a maximum nominal force of 510 kN.

Material and lubrication. The workpiece material used is the cold-rolled, mild deep-drawing steel 1.0338 as coil with a nominal sheet thickness of $t_0 = 2$ mm, which is an established material in SBMF [10]. The steel exhibits a purely ferritic microstructure. In addition, the material has a very good formability, which makes it suitable for the production of car body parts. In order to characterize the mechanical material properties, the flow behavior of the deep-drawing steel was experimentally determined in previous research work [11] in the layer compression test according to DIN 50106 [12] up to a true strain of $\varphi = 0.57$. Specimens with a diameter of 10 mm and a height of 14 mm were used in layer compression test, resulting in a compression ratio greater than one. To represent higher true strains, as occur in SBMF [11], the flow curve (Fig. 2) was extrapolated up to a true strain of $\varphi = 4.0$ using the Hockett-Sherby approach.

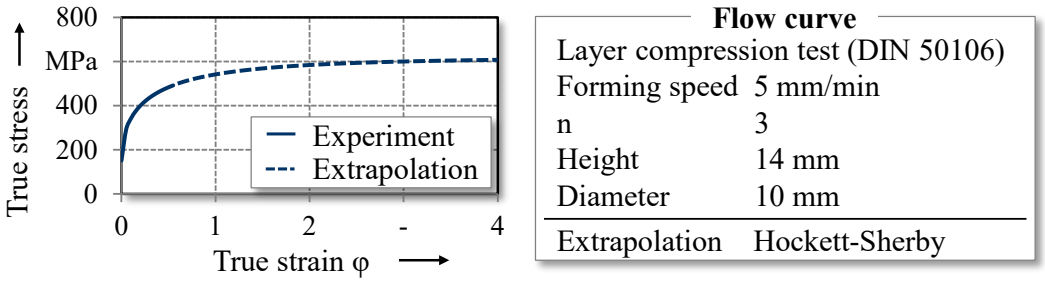

Fig. 2. Flow curve of the workpiece material 1.0338.

The lubricant Beruforge 150 DL from Carl Bechem GmbH, a water-based lubricant with a high solid wax content, was used in the experimental investigation. The suitability of this lubricant for usage in sheet-bulk metal forming has already been demonstrated in [13].

Numerical Process Model and Experimental Validation

In the following, the setup of the simulation model is described. Subsequently, the quality of the numerical model is evaluated by means of an experimental validation.

FE-Model setup. The simulation software Simufact.forming 14.0.1 of Simufact engineering GmbH is used for the numerical investigation of the backward extrusion process. The suitability of this software for SBMF extrusion processes has already been demonstrated in previous research work [11]. Within the analysis of the material flow, the tools are modeled as rigid. To reduce the computational time, the symmetry of the process along the X-axis is applied, resulting in the analysis of a 180° segmented model, as shown in Fig. 3. In addition, a constraint plane was defined in the negative X-direction to represent the influence of the coil.

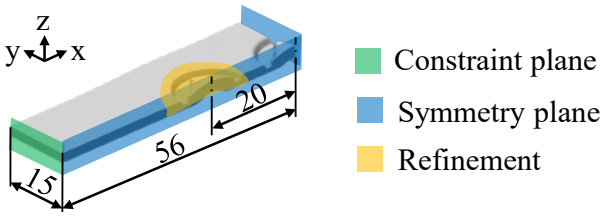

Fig. 3. Setup of the numerical part model.

Two strokes are simulated to evaluate the influence of the preceding forming operation. The workpiece was meshed with hexahedral elements with a maximum element size of 0.5 mm according to the recommendations of Tekkaya [14]. This element type allows an accurate map of the three-dimensional material flow. In addition, a cylindrical refinement box (Fig. 3) with a diameter of 14 mm is applied in the forming zone, reducing the element size to 0.125 mm. The tool components are discretized with tetrahedral elements. The blankholder tension is applied by springs with a low stiffness of 10^{-6} N/mm² and a constant value of 37.8 MPa. Due to the high local contact pressures in SBMF [4], the friction factor model is used to represent the tribological conditions. A global friction factor of m = 0.1 is chosen, which was identified for the material 1.0338 in previous research [11]. The mechanical properties of the workpiece material are mapped by the determined flow curve (Fig. 2).

Experimental validation. For the evaluation of the quality of the virtual process model, the numerical model is validated according to the recommendations of Tekkaya [14]. This includes the comparison of process- and workpiece-related target values of the experiment with the numerical results. The validation is carried out for the reference process with a coil width of 30 mm and a feed rate of 20 mm, which corresponds to the distance between the centers of the components. In the experiment, six components are formed on one coil section. In order to take the influence of the preceding forming into account, only the last five components are considered for validation. First, the numerical process model is validated based on a comparison of workpiece-related target parameters. Fig. 4 represents a comparison of geometric component parameters.

For the validation, the diameter of the blind cavity is evaluated in X- and Y-direction (Fig. 4a). The determined experimental and numerical values show a good agreement with a deviation of 0.39 % in X-orientation and of 2.30 % in Y-direction. Furthermore, differences in X- and Y-direction can be identified in experiment and simulation, with a larger cavity diameter in Y-orientation, which indicates an anisotropic material flow. Consequently, the numerical model depicts the anisotropic material flow during coil forming. As a further component-side target quantities, the distance of the geared elements is analyzed, shown in Fig. 4b. In experiment and in simulation, this geometric target quantities also exhibits differences in the considered directions with higher values in Y-direction, which indicate an unequal material flow. The deviations between experiment and simulation are 1.2 % in X-direction and 1.0 % in the Y-orientation. In addition, numerically and experimentally an incomplete forming of the gearing is observed, as the theoretical distance of 11.0 mm is not achieved. Furthermore, the determined pin height is analyzed quantitatively (Fig. 4c). With a complete material flow into the cavity, a theoretical pin height of 3.46 mm is obtained. Experimentally (3.02 ± 0.02 mm) and simulatively (3.25 mm), however, the theoretical pin height is not achieved because of the partially uncontrolled material flow. Furthermore, a deviation of 7.1 % between simulation and experiment is determined caused by the complex tribological conditions in SBMF, which cannot be mapped in the simulation [5].

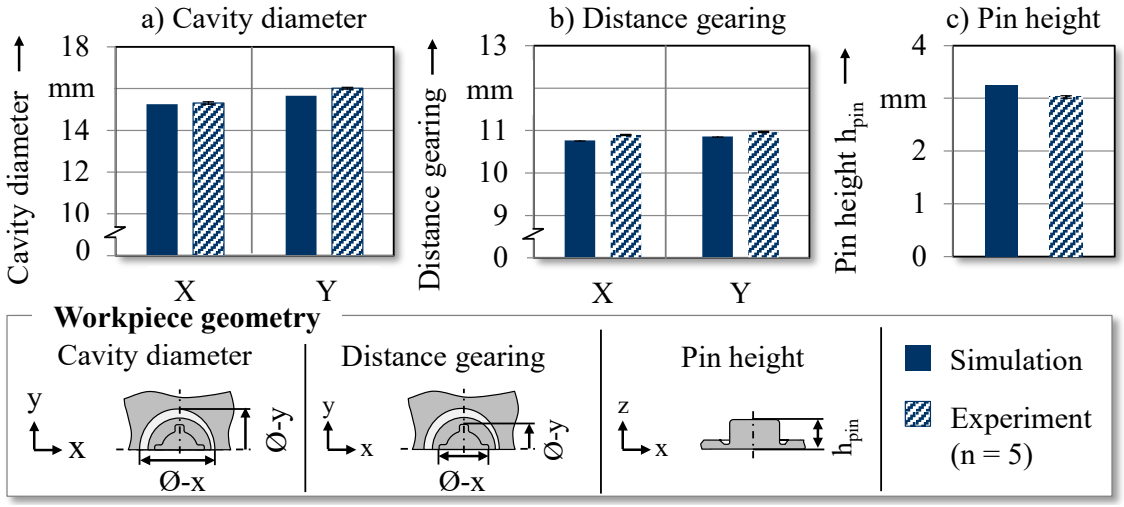

Fig. 4. Validation of the numerical model based on the workpiece geometry: (a) Cavity diameter, (b) distance of the gearing and (c) pin height.

The experimental microhardness distribution is compared with the numerical determined true strain distribution to evaluate the accuracy of the mapping of internal component properties (Fig. 5a). In this regard, a high true strain is considered an indicator of increased strain hardening. The microhardness HV0.05 was determined on sections of the parts with the Fischerscope® HM2000 from Helmut Fischer GmbH according to ISO 14577-1 [15].

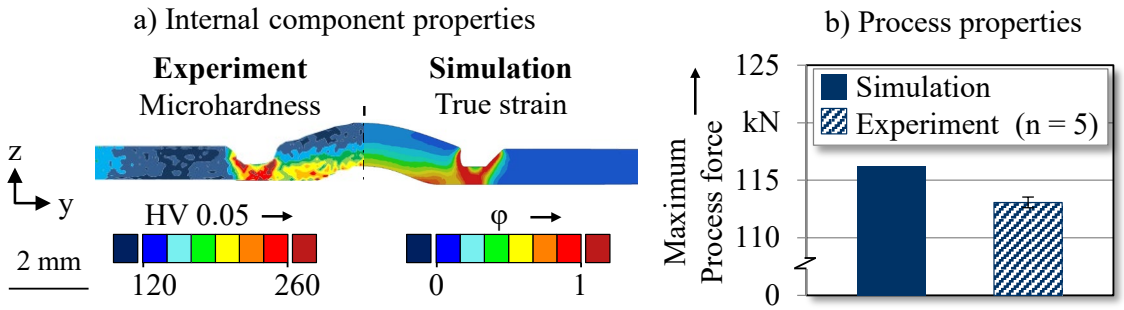

Fig. 5. Comparison of distribution of microhardness and true strain (a) and maximum process (b) force.

The comparison of the microhardness with the true strain distribution shows a high agreement. The maxima of the distributions are achieved in the contact area with the punch. In contrast, low values occur on the upper side of the pin geometry, as the material can flow without flow inhibition in this area. The maximum process force is evaluated as the process-side target variable, which is shown in Fig. 5b. The experimental process force is determined using a piezoelectric load cell 9106A from Kistler AG. In the experiment, a maximum force of 113.08 ± 0.46 kN is required. The maximum numerical force is 116.26 kN. Therefore, the deviation between experiment and simulation is of 2.81 %. In summary, after comparing the part and process-related target values, the numerical process model built up is suitable for realistically representing the forming process.

Materials Research Proceedings 28 (2023) 929-936 https://doi.org/10.21741/9781644902479-101

Process Analysis

The challenge of SBMF from coil is the anisotropic material flow, as demonstrated in the validation by differences in the process results in the X- and Y-direction. The material flow represents a central difference to the SBMF of pre-cut blanks [8], whereby the sheet geometry is considered as a cause for the occurring anisotropic material flow. In order to generate a profound process understanding of coil-specific challenges as well as extrusion of geared components from coil, the influence of the semi-finished product geometry is investigated in the following. A comparison of forming from coil through single stroke with forming from pre-cut blanks is presented. The selected diameter of the blanks corresponds to the coil width of 30 mm. To analyze the material flow, the numerical radial displacement is depicted in Fig. 6, which provides the displacement of the material elements with respect to their initial position. The numerical results were verified by comparison with the experimental component geometry. A negative radial displacement indicates a displacement in the direction of the component center.

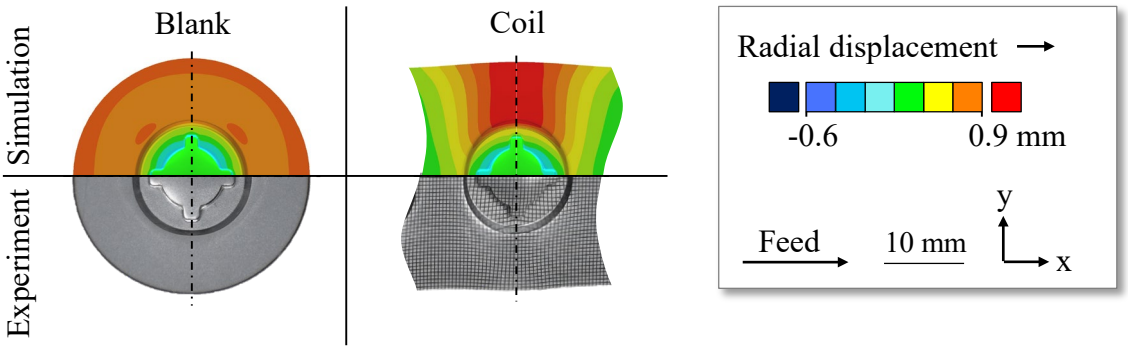

Fig. 6. Influence of the sheet geometry on the radial displacement.

The radial displacement of the circular blank shows a cyclic symmetrical distribution in 90° [5], with an increase in radial displacement outside the bulk forming zone occurring with increasing distance from the centre of the component. Due to the asymmetry of the pin geometry caused by the abstracted gearing, there is also an increased radial displacement locally outwards at an angle of ± 45° to the Y-axis. In contrast to the circular blank, the radial displacement of the coil geometry shows a symmetry with respect to the Y-axis with a high radial displacement perpendicular to the feed direction and a significantly reduced radial displacement in the feed direction. Consequently, an unequal material flow occurs. However, due to the geometry of the coil, the distance from the centre of the part to the outer edge of the coil varies depending on the direction. This leads to a larger contact area between coil and blankholder in X-direction, which reduces the material flow due to the higher friction in this area. In order to analyze the influence of the sheet geometry on the forming of secondary form elements, the form filling of the gearing elements is evaluated by the nominal distance of the abstracted external gearing to the component centre, which is shown in Fig. 7a. The parameter is considered relative to the ideal target values.

When forming the circular blanks, an equal and complete forming of the gearing elements in X- and Y-orientation is achieved with a nominal value of 1.000 ± 0.001. In contrast, the usage of coil results in a difference in nominal distances in the X- and Y-direction, with underfilling of the gearing occurring in both orientations. In Y-direction a value of 0.997 ± 0.001 is determined. In -X-direction a lower nominal distance of 0.993 ± 0.001 occurs. Consequently, the anisotropic material flow leads to an unequal forming and an incomplete form filling of the gearing elements.

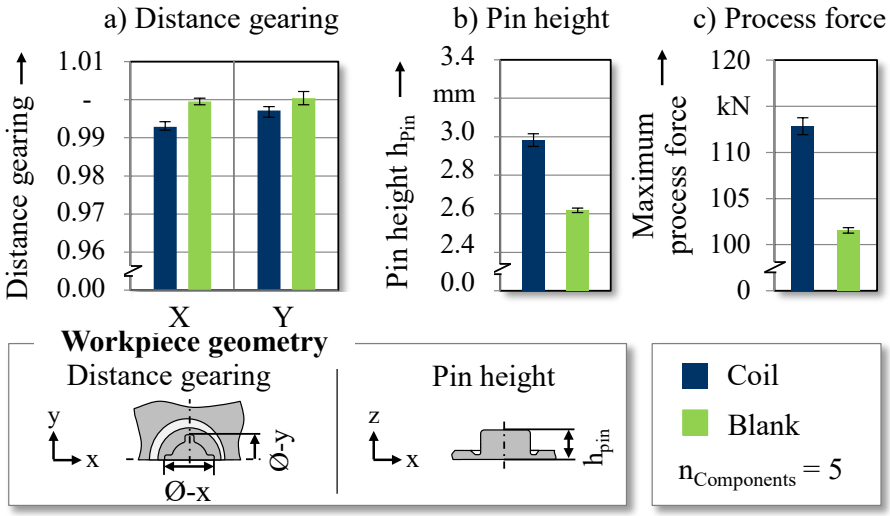

Fig. 7. Influence of the sheet geometry on the distance of the gearing (a), the pin height (b) and the maximum process force (c).

In Fig. 7b, the pin height is considered as further geometric target quantities, which is a parameter for the evaluation of the material utilization. The pin height is 2.62 ± 0.01 mm for the blanks and 2.98 ± 0.03 mm for a coil. Consequently, there is a higher material flow into the cavity when forming the coil. Due to the higher length of the coil in feed direction compared to the diameter of the blank, there is a higher contact between coil and tools as well as a higher material supporting effect, which inhibits the material flow to the outside. Thus, a higher volume of material flows into the die cavity resulting in a greater pin height. The influence of the sheet geometry on the tool stress is evaluated by the maximum process forces (Fig. 7c). When forming the blank, a maximum force of 101.55 ± 0.28 kN is required. For the forming of the coil as sheet geometry, a 10 % higher maximum force results with a value of 112.08 ± 0.84 kN. The increased process force during the forming of the coil is justified by the higher material flow into the bulk forming zone.

Summary

Within this research, a backward extrusion process from coil for the forming of functionally integrated components with geared secondary forming elements is investigated. The focus was on research SMBF- and coil-specific challenges like an anisotropic material flow. In the first step, the process was set up and numerically modeled. Subsequently, the numerical model was validated based on experimental results. In a next step, a combined numerical-experimental approach was used for a fundamental process analysis. The sheet geometry was varied using pre-cut blanks and coils in order to investigate the causes of the anisotropic material flow.

In contrast to the use of circular blanks, the forming of coils leads to an unequal, incomplete forming of the component geometry in and orthogonal to the feed direction. The reason is the non-circular sheet geometry, which causes a higher supporting effect parallel to the feed direction due to the additional material and the higher contact area between coil and tools. Consequently, an anisotropic material flow results. Furthermore, the greater contact between coil and blank holder as well as coil and counter-holder leads to a greater flow of material into the bulk forming zone, resulting in a higher pin height. Therefore, a higher maximum process force is required for the forming of the coil. Despite the higher material flow into the bulk forming zone, the gearing elements were not completely formed, which can be explained by the higher material flow velocity.

In future research work, the influence of the operating mode should be investigated by comparing single stroke and multi-stroke to analyze the influence of previous forming operations.

Furthermore, the investigation of measures for the target control of the material flow represents major research potential to prevent anisotropic material flow and improve part accuracy.

Acknowledgements
The authors would like to thank the German Research Foundation (DFG), which founded this work within the project DFG ME 2043 99-1 'Fundamental investigations on the production of functional components from coil'. The authors would also like to show their gratitude to Mr. Michael Rindl, who supported the execution of this work within the scope of his project thesis.

References

[1] A. Peterburs, Herausforderungen an die dt. Industrie im 21. Jahrhundert, GRIN Verlag, 2012.
[2] A.E, Tekkaya, N.B. Khalifa, G. Grzancic, R. Hölker, Forming of Lightweight Metal Components: Need for New Technologies, Procedia Eng. 81 (2014) 28–37. https://doi.org/10.1016/j.proeng.2014.09.125
[3] M. Merklein, H. Hagenah, T. Schneider, Blechmassivumformung – Stand der Technik und Ausblick, in: M. Merklein (Eds.), Tagungsband zum 2. Workshop, Blechmassivumform-ung, Meisenbach Verlag, 2013, pp. 1–10.
[4] M. Merklein, J. M. Allwood, B.-A. Behrens, A. Brosius, H. Hagenah, K. Kuzman, K. Mori, A. E. Tekkaya, A. Weckenmann, Bulk forming of sheet metal, CIRP Annals 61 (2012) 725–745. https://doi.org/10.1016/j.cirp.2012.05.007
[5] F. Pilz, J. Henneberg, M. Merklein, Extension of the forming limits of extrusion processes in sheet-bulk metal forming for production of minute functional elements, Manuf. Rev. 7 (2020) 9. https://doi.org/10.1051/mfreview/2020003
[6] A. Birkert, S. Haage, M. Straub, Umformtechnische Herstellung komplexer Karosserieteile - Auslegung von Ziehanlagen, Springer, Berlin Heidelberg, 2013. https://doi.org/10.1007/978-3-642-34670-5
[7] L. Tajul, T. Maeno, K. Mori, Successive Forging of Long Plate Having Inclined Cross-section, Procedia Eng. 81 (2014) 2361–2366. https://doi.org/10.1016/j.proeng.2014.10.334
[8] J. Henneberg, Blechmassivumformung von Funktionsbauteilen aus Bandmaterial, PhD Thesis, FAU, 2022. https://doi.org/10.25593/978-3-96147-580-3
[9] K. Mori, T. Nakano, State-of-the-art of plate forging in Japan, Prod. Eng. Res. Devel. 10 (2016) 81–91. https://doi.org/10.1007/s11740-015-0648-1
[10] D. Gröbel, R. Schulte, P. Hildenbrand, M. Lechner, U. Engel, P. Sieczkarek, S. Wernicke, S. Gies, A.E. Tekkaya, B.A. Behrens, S. Hübner, M. Vucetic, S. Koch, M. Merklein, Manufacturing of functional elements by sheet-bulk metal forming processes, Prod. Eng. Res. Devel. 10 (2016) 63–80. https://doi.org/10.1007/s11740-016-0662-y
[11] D. Gröbel, Herstellung von Nebenformelementen unterschiedlicher Geometrie an Blechen mittels Fließpressverfahren der Blechmassivumformung, PhD Thesis, FAU, 2018. https://doi.org/10.25593/978-3-96147-169-0
[12] DIN Deutsches Institut für Normung e.V., DIN 50106 - Prüfung metallischer Werkstoffe - Druckversuch bei Raumtemperatur, Beuth-Verlag, Berlin, 2016.
[13] H. Vierzigmann, M. Merklein, U. Engel, Friction Conditions in Sheet-Bulk Metal Forming, Procedia Engineering 19 (2011) 377–382. https://doi.org/10.1016/j.proeng.2011.11.128
[14] A.E. Tekkaya, A guide for validation of FE-simulations in bulk metal forming, Arab. J. Sci. Engi. 30 (2005) 113–136.
[15] DIN Deutsches Institut für Normung e.V., DIN EN ISO 14577-1:2015-11: Metallische Werkstoffe - Instrumentierte Eindringprüfung zur Bestimmung der Härte und anderer Werkstoffparameter - Teil 1: Prüfverfahren, Beuth-Verlag, Berlin, 2015.

Materials Research Proceedings 28 (2023) 937-942 https://doi.org/10.21741/9781644902479-102

Hot stamping of ultra-thin stainless steel for microchannels

GUO Nan[1,a], ZHANG Xianglu[1,b], HOU Zeran[1,c], YANG Daijun[2,d], MING Pingwen[2,e] and MIN Junying[1,f *]

[1]School of Mechanical Engineering, Tongji University, Shanghai 201804, China

[2]School of Automotive Studies, Tongji University, Shanghai 201804, China

[a]13guonan@tongji.edu.cn, [b]Xianglu_zhang@tongji.edu.cn, [c]zeranhou@tongji.edu.cn, [d]yangdaijun@tongji.edu.cn, [e]pwming@tongji.edu.cn, [f]junying.min@tongji.edu.cn

Keywords: Stainless Steel, Hot Stamping, Microchannel, Dimensional Accuracy

Abstract. Bipolar plate is one of the core components of a proton exchange membrane fuel cell (PEMFC), in which microchannels with regular distribution separate and distribute the fuel gas at the anode and oxygen/air at the cathode, and remove the reaction products from the cell. Dimensional deviations of microchannels affect assembly accuracy, thereby influencing the efficiency and performance of PEMFC. Ultra-thin stainless steel sheet is the most commonly used material for bipolar plate and stamping is an efficient way to form stainless steel microchannels. However, a challenge faced by the stamping process is how to improve the dimensional accuracy of stainless steel microchannels. Hereby we propose a hot stamping process of ultra-thin stainless steel sheet, which is of high potential to improve the dimensional accuracy of micro-channels. Uniaxial tensile tests are performed at room temperature (RT), 300, 600, and 900°C for an ultra-thin stainless steel 316L (SS316L). Results show that the strength of SS316L at 900 °C decreases significantly compared with that at RT, while the elongation is approximately 44%. Hot stamping process for stainless steel microchannels is developed, in which the ultra-thin sheet is heated by resistance heating. Stainless steel microchannels are hot stamped at 900°C, and the 3D profile and cross-sectional thickness distribution of which are measured. The measurement results show that the dimensional deviations of hot-stamped microchannels are lower than that of cold stamping, in terms of channel depth, rib width, and wall angle. Furthermore, the cross-sectional thickness distribution of the hot-stamped micro-channels has a similar trend as that of the cold stamping, and the thickness at the fillet is not significantly different (avg. + 1 μm) from that of the cold stamping.

Introduction

Fuel cell has a high-energy conversion efficiency of more than 40-50% [1], which is regarded as an ideal technology to utilize hydrogen energy. As the key component of a PEMFC, bipolar plates (BPPs) with fine microchannel features play the role of separating and distributing hydrogen and oxygen/air, providing mechanical support to the fuel cell stack, collecting, and conducting current, etc. Dimensional deviations of microchannel features affect assembly accuracy, thereby influencing the efficiency and performance of PEMFC. With the advantage of high electrical conductivity and mechanical strength as well as low cost, stainless steel is widely utilized to fabricate BPPs, and the stamping process is one of the most used methods to manufacture stainless steel BPPs due to its relatively high productivity and low cost. However, dimensional errors are unavoidable on stainless steel BPPs due to the characteristics of residual stress and springback in stamping process, which contributes to uneven pressure distribution, larger contact resistance, and higher GDL porosity [2]. It is reported that fabricating BPPs with fine flow microchannel features, i.e., flow channels with a channel width, a rib width, and a pitch length of 0.5, 0.5, and 1.5 mm, respectively, is a challenge for the current stamping process [3]. Thus, several advanced forming

Content from this work may be used under the terms of the Creative Commons Attribution 3.0 license. Any further distribution of this work must maintain attribution to the author(s) and the title of the work, journal citation and DOI. Published under license by Materials Research Forum LLC.

processes have been developed in the literature to increase the dimensional accuracy and the ultimate flow channel features of BPPs. Based on ultra-thin ferritic stainless steel sheets with thickness of 100 and 75 μm, Bong et al. [4] conducted a two-step stamping process to fabricate microchannels, they found that the two-step forming process evidently increase the forming depth and precision of ferritic stainless steel microchannels. Xu et al. [5] revealed that the depth limit of titanium microchannels is increased from 438.1 μm in single-step forming process to 621.1 μm in three-step forming process. Since increasing forming temperature can reduce the strength of materials, thus reducing residual stress and springback and improving the forming accuracy of parts, some heat-assisted forming processes have been proposed for microchannels. By conducting warm stamping process at the temperature up to 300°C, Lakshmi [6] improved the formability of ferritic stainless steel microchannels. Moreover, they found that increasing forming temperature can reduce the springback of microchannels.

In this work, uniaxial tensile tests were performed at room temperature (RT), 300, 600, and 900°C for an ultra-thin stainless steel SS316L. The variation of strength and elongation of ultra-thin SS316L to temperature was discussed to evaluate the properly forming temperature of ultra-thin SS316L. Then a lab-scale hot stamping platform with an on-site resistance heating device was built to verify the hot stamping process of ultra-thin SS316L microchannels. Channel depth, rib width, and wall angle were measured to characterize the dimensional accuracy of ultra-thin SS316L microchannels under hot stamping process.

Experiments

Uniaxial Tensile Test. An ultra-thin austenitic stainless steel SS316L with a thickness of 100 μm was used in this study. Uniaxial tensile tests were performed to obtain the mechanical properties of ultra-thin SS316L at elevated temperatures. Fig. 1a shows the high-temperature uniaxial tensile testing system with a muffle furnace and digital image correlation technic (DIC). The DIC cameras equipped with blue light bandpass filters record the deformation of the specimen through a glass window on the furnace to calculate strain fields. Additionally, two blue LED lights with a wavelength of 450 nm were used to illuminate the specimen from different directions to ensure sufficient image contrast. The geometric dimension of the uniaxial tensile specimen is shown in Fig. 1b according to the ISO 6892-2 standard. All specimens were cut off along the rolling direction by electrical discharge machining to ensure high edge quality. The test temperature of SS316L includes room temperature (RT), 300, 600, and 900°C, and three samples were tested at each temperature to ensure reproducibility.

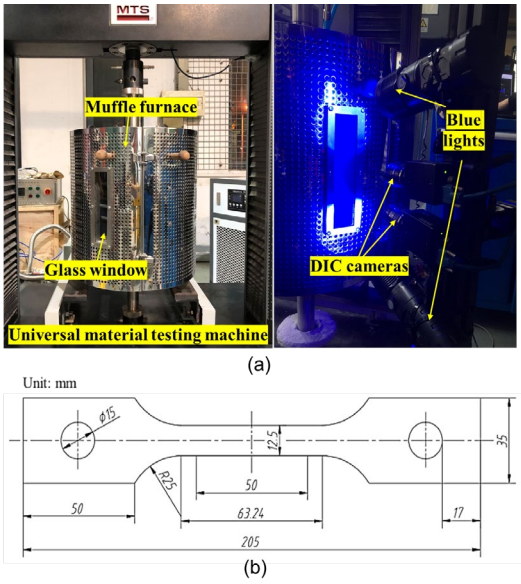

Fig. 1. (a) The high-temperature uniaxial tensile testing system and (b) the geometric dimension of the uniaxial tensile specimen.

Microchannel Hot Stamping Test. The microchannel structure is shown in Fig. 2a, and the cross-sectional geometry of the stamping tool is shown in Fig. 2b, where the dimensions of the channel width, rib width, channel depth, wall angle, and corner radius are also depicted. Fig. 2c illustrates a lab-scale hot stamping platform built in this study, where a pair of electrode clamps is embedded into the system to heat the ultra-thin SS316L sheet by resistance heating. An automatic

tensioning device composed of compression springs and linear guides is assembled to the clamp to prevent ultra-thin SS316L sheet buckling caused by constrained thermal expansion. During the hot stamping process, the initial distance between the upper and lower tool was 150 mm. The ultra-thin SS316L sheet started to be heated by resistance heating with a power of 22.5 kW at 0 s, and the upper tool started to move downward with a velocity of 140 mm/s at 5 s. The ultra-thin SS316L sheet was heated to the target temperature at 6 s, and meanwhile, the upper tool was down to a distance of 10 mm from the lower tool. Then the power was off and the upper and lower tools were closed at 6.1 s. Then the formed microchannel sample was cooled in the tool from 6.1 s to 7 s. Moreover, a solid lubricant boron nitride (BN) was applied to reduce the friction coefficient between the ultra-thin SS316L sheet and tool.

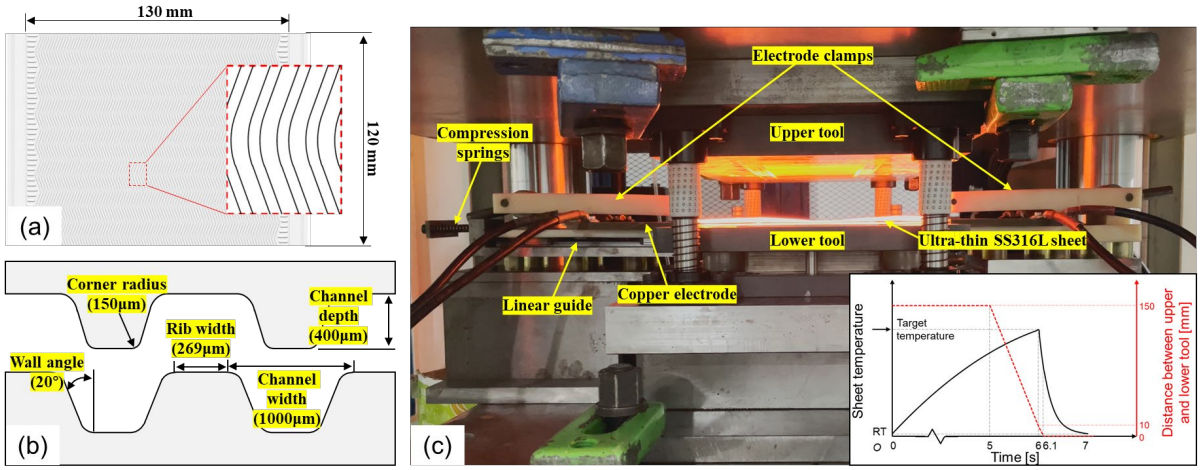

Fig. 2. (a) The designed microchannel structure, (b) the cross-sectional geometry of the stamping tool, and (c) an illustration of the microchannel hot stamping process.

Geometrical and Thickness Measurements. The surface topographies of formed microchannels were measured by a non-contact 3D optical profilometer KEYENCE VR-5000, through which channel width, rib width, and wall angle of the formed microchannels were extracted. Cross-sectional samples were cut along the direction perpendicular to the channels by laser cutting and mounted with resin at room temperature. Then the samples were polished with 800, 1500, and 2500 Grit sandpapers in sequence and observed with an optical microscope to evaluate the thickness of the microchannels.

Results and Discussion

The engineering stress-strain curves of ultra-thin SS316L at different temperatures are shown in Fig. 3a. In the temperature range from RT to 600°C, although the flow stress decreases with the increase of temperature, it can be seen from the stress-strain curves that strain hardening is the dominant. At 900°C, the stress-strain curve of ultra-thin SS316L is more significantly affected by temperature softening, and the strength is reduced to 104 MPa. Fig. 3b represents the variation of ultimate tensile strength and elongation of ultra-thin SS316L with temperature. The ultimate tensile strength (UTS) of ultra-thin SS316L decreases from 620 MPa at room temperature to 104 MPa at 900°C; however, the elongation decreased significantly from room temperature to 600°C, with a minimum value of 26% at 600°C, and with the temperature increasing up to 900°C, the elongation increased to 44%. This indicates that increasing the forming temperature can reduce the strength of the ultra-thin SS316L, thus potentially reduce residual stress and springback to improve the forming accuracy of parts. However, a temperature range, namely 300–600°C, should

be avoided in developing warm/hot stamping process for ultra-thin SS316L, because the elongation of which is much lower than that at room temperature.

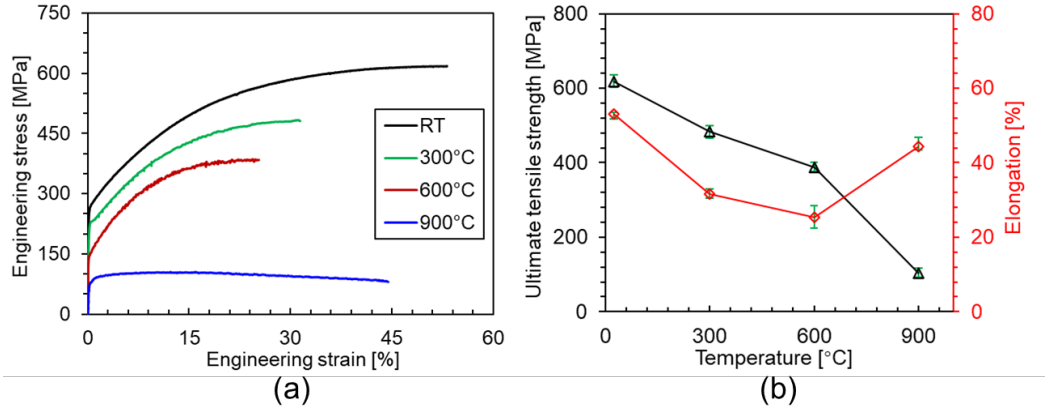

Fig. 3. (a) Engineering stress-strain curves of ultra-thin SS316L at different temperatures and (b) variation of UTS and elongation of ultra-thin SS316L with temperature.

The microchannel features of BPP have significant effects on the distribution of reaction gas, heat and water management, mechanical stability, and consequently on the performance, reliability, and durability of fuel cells [7]. The rib width (a) determines the contact area between the BPP and the MEA, a narrower rib width means a smaller contact area, and a larger contact resistance between the BPP and MEA as well as reduced PEMFC performance. The channel depth (c) and wall angle (β) mainly affect the mass transfer towards MEA and production water removal ability, and a deeper channel depth and a smaller wall angle enhance electrochemical reaction rate and fuel efficiency. Fig. 4 shows a microchannel sample hot-stamped at 900°C, where measurement of microchannel features was conducted within the red dashed wireframe.

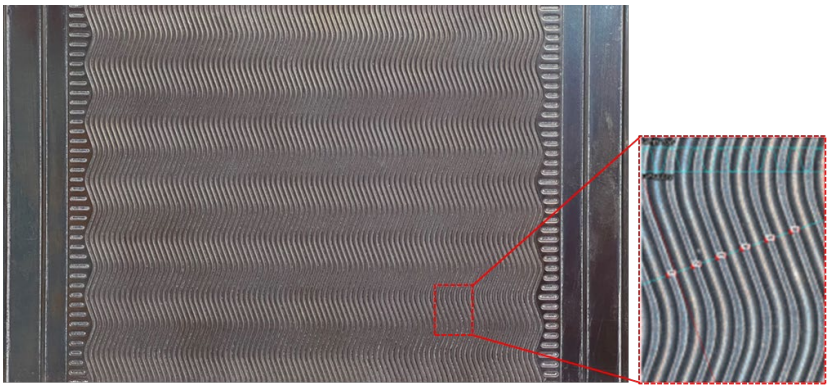

Fig. 4. Hot-stamped microchannel sample.

Measurement results of the microchannel features formed via hot stamping and cold stamping are shown in Fig. 5a. Average c of the hot-stamped microchannel is 394.2 μm, which is closer to the design value (400 μm) compared to that of the cold-stamped microchannel. For a and β, the values of hot-stamped sample are smaller than those of cold-stamped sample, which benefits from the reduced springback under hot stamping process. The dimensional deviations of c, a, and β of the cold-stamped microchannel are larger than that of hot-stamped microchannel. The large dimensional deviations are caused by highly localized stamping force [8]. This indicates that the

hot stamping process improves the dimensional accuracy of ultra-thin SS316L microchannels. Fig. 5b represents the thickness distribution of hot-stamped and cold-stamped microchannels, which have a similar trend, i.e., positions 1, 5, and 9 exhibit a larger thickness, and the maximum thinning appears at the fillet where the sheet metal contacts the lower tool (position 2). There is no significant difference between the minimum thicknesses of the hot-stamped and cold-stamped microchannels (average difference at position 2 is 1 μm).

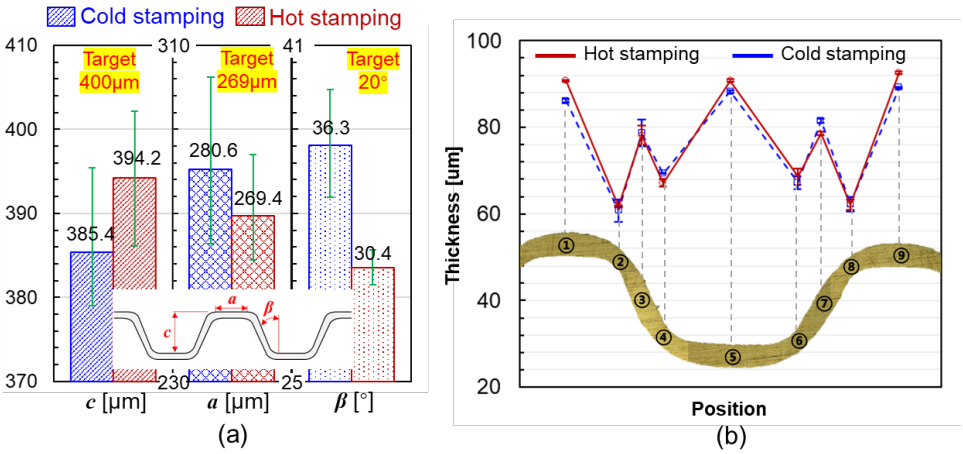

Fig. 5. (a) Comparison of channel depth (c), rib width (a), and wall angle (β) between hot stamping and cold stamping microchannels and (b) cross-sectional thickness distribution of microchannels via hot stamping and cold stamping.

Summary

In this work, the variation of strength and elongation of ultra-thin SS316L at elevated temperatures were investigated by applying high-temperature uniaxial tensile tests. In order to verify the hot stamping process of ultra-thin SS316L microchannels, a lab-scale hot stamping platform with an on-site resistance heating device was built. The dimensional accuracy of hot-stamped ultra-thin SS316L microchannels was characterized, and conclusions can be drawn here:

1) 900°C might be the appropriate hot stamping temperature for ultra-thin SS316L microchannels because of the relative low strength of 104 MPa and an elongation of about 44% of ultra-thin SS316L at 900°C;
2) Compared to cold stamping, hot stamping at 900°C increase the dimensional accuracy of ultra-thin SS316L microchannels in terms of channel depth (from 385.4 μm to 394.2 μm with a target of 400 μm), rib width (from 280.6 μm to 269.4 μm with a target of 269 μm), and wall angle (from 36.3° to 30.4° with a target of 20°).

Acknowledgments

The authors would like to acknowledge the financial support for this research provided through the National Key Research and Development Program of China (No. 2020YFB1505900).

References

[1] K. Sopian, W.R.W. Daud, Challenges and future developments in proton exchange membrane fuel cells, Renewable energy 31(2006) 719-727. https://doi.org/10.1016/j.renene.2005.09.003
[2] L. Peng, Y. Wan, D. Qiu, P. Yi, X. Lai, Dimensional tolerance analysis of proton exchange membrane fuel cells with metallic bipolar plates, J. Power Source. 481 (2021). https://dx.doi.org/10.1016/j.jpowsour.2020.228927
[3] Y. Leng, P. Ming, D. Yang, C. Zhang, Stainless steel bipolar plates for proton exchange membrane fuel cells: Materials, flow channel design and forming processes, J. Power Source. 451 (2020). https://dx.doi.org/10.1016/j.jpowsour.2020.227783

[4] H.J. Bong, J. Lee, J.H. Kim, F. Barlat, M.G Lee, Two-stage forming approach for manufacturing ferritic stainless steel bipolar plates in PEM fuel cell: Experiments and numerical simulations, Int. J. Hydrogen Energ. 42 (2017) 6965-6977. https://dx.doi.org/10.1016/j.ijhydene.2016.12.094
[5] Z. Xu, Z. Li, R. Zhang, T. Jiang, L. Peng, Fabrication of micro channels for titanium PEMFC bipolar plates by multistage forming process, Int. J. Hydrogen Energ. 46 (2021) 11092-110103. https://dx.doi.org/10.1016/j.ijhydene.2020.07.230
[6] R.N. Lakshmi, Forming of ferritic stainless steel bipolar plates, Electronic Theses and Dissertations, 205 (2012). https://scholar.uwindsor.ca/etd/205
[7] J. Wang, Theory and practice of flow field designs for fuel cell scaling-up: A critical review, Appl. Energ. 157 (2015) 640-663. https://doi.org/10.1016/j.apenergy.2015.01.032
[8] C. Turan, Ö.N. Cora, M. Koç, Effect of manufacturing processes on contact resistance characteristics of metallic bipolar plates in PEM fuel cells, Int. J. Hydrogen Energ. 36 (2011) 12370-12380. https://doi.org/10.1016/j.ijhydene.2011.06.091

Materials Research Proceedings 28 (2023) 943-950 https://doi.org/10.21741/9781644902479-103

Approaches for load path design for stretch forming based on part surface geometry

REITMAIER Lisa-Marie[1,a *], BAILLY David[1,b] and HIRT Gerhard[1,c]

[1]Institute of Metal Forming, RWTH Aachen University Intzestraße 10, 52072 Aachen, Germany

[a]lisa-marie.reitmaier@ibf.rwth-aachen.de, [b]david.bailly@ibf.rwth-aachen.de, [c]gerhard.hirt@ibf.rwth-aachen.de

Keywords: Stretch Forming, Sheet Metal, Loading Trajectory, Load Path, CAE Methods

Abstract. Stretch forming enables manufacturing large, slightly curved sheet metal parts. If the curvature is multi-directional and complex, parts often cannot be stretch-formed successfully, due to local or inhomogeneous straining that leads to early material failure, buckling or springback. To control strain distribution, the flexibility of load application needs to be improved. This can be achieved through loading at discrete points based on defined cross-sections of part geometries. However this can be applied only by multi grippers, requiring complex plant technology and control. New parameterized approaches for load path generation based on the part surface geometry for single rigid grippers have been developed to improve the flexibility of load paths. The approaches can be mainly distinguished between Surface Transformation method (ST), which transforms a surface into a curve as the base for tangential path creation and the Tool Path Fitting method (TPF). In TPF, paths are created for several cross-sections, similar to the application for multi grippers, and then compiled into one path. In this paper, the load path approaches have been applied and numerically investigated for parts with positively curved translation surfaces. Results of FE simulation of the stretch forming process show the applicability, potential and limitations of the load path design approaches.

Introduction

Stretch forming is an established industrial process for forming automobile body panels such as doors or roofs and aircraft parts [1]. In general, the process is suitable to manufacture large and slightly curved components for various applications. The stretch forming process typically involves a rectangular sheet metal blank clamped at either two opposite sides, less often at all four sides, formed by a relative movement between the grippers and the die. Within the forming process, the grippers either move in only vertical direction (conventional stretch forming) or in both vertical and horizontal directions simultaneously (tangential stretch forming) so that the load is acting tangentially to the die contour. In general, components produced via tangential stretch forming achieve higher geometrical accuracy [1].

A tangential load path is generated based on a representative curve of the part geometry. In the case of a unidimensional-curved component, the curve equals the cross-sectional part contour. For bi-dimensional and more complex curved components, the cross-section varies in transverse direction. In this case, the creation of stretch forming load path is mainly experience based. To apply loading with respect to the overall part surface and to overcome existing process limits, loading at discrete points along transverse curvature according to the longitudinal cross-sectional profiles has been investigated [2,3]. The flexible loading with respect to the complete part geometry surface improves uniform deformation of the sheet metal and contributes to overcome existing process limits for complex shaped parts in stretch forming. To realize these load profiles, multi grippers with separate modules, complex machinery and process control are required. In order to waive such complex technology systems and work with existing rigid gripping modules, Schmitz et al. [4] used a conventional stretch forming operation and presented a method to

Content from this work may be used under the terms of the Creative Commons Attribution 3.0 license. Any further distribution of this work must maintain attribution to the author(s) and the title of the work, journal citation and DOI. Published under license by Materials Research Forum LLC.

manipulate the strain distribution by selective weakening of the blank with specific hole pattern to homogenize the strain over the part surface. This method involves an optimization algorithm and requires an additional preceding step of laser cutting. In order to avoid complex machinery and additional process steps, alternative parameterized load path design approaches with respect to the overall part surface geometry have been investigated and are presented in this paper.

Approach and Procedure

In this study, different load path design approaches for rigid gripper application based on the surface geometry of bi-dimensional curved components are developed. The approaches can be mainly distinguished between Surface Transformation method (ST), which transforms a surface into a curve as the base for tangential path creation and the Tool Path Fitting method (TPF). In TPF, paths are created for several cross-sections, similar to the application for multi grippers, and then compiled into one path. The part surfaces considered in this work are translation surfaces with positive Gaussian curvature. A translation surface is defined by two curves and is obtained by moving a generator curve, which remains parallel to its initial position, along a guide curve. In this study, the part surfaces and the corresponding stretch forming load paths are created via a developed Python script. Within the scope of this work, the different load path approaches are presented for two different exemplary part geometries. The results are generated through numerical process simulations in LS-Dyna with help of validated stretch forming FE-Models. The criteria for analyzing the different load path approaches are the achieved part geometry and strain distribution.

Material and Methods

Material. The sheet material is 1.4404 austenitic stainless steel in 0.8 mm thickness. The material data is determined via tensile test with samples taken in rolling direction of the sheet. A yield strength of $R_{p0,2}$=279,197 MPa, ultimate tensile strength of R_m =620.043 MPa and ultimate strain A_g=47.697 % were identified.

FE-Model. In order to analyze and compare the forming results after applying different load paths, a FE-Model is established in LS-PrePost 4.3 and the simulations are performed with the explicit solver of LS-Dyna R.11.1.0. The sheet metal blank is 750 x 500 mm in size and discretized with Belytschko-Tsay shell elements with 4 mm. The load is applied on the edge nodes of the short opposite sides of the blank. The sheet is modelled as an elastoplastic deformable body whereas the die is modeled as a rigid body. The die geometry as well as the desired part geometry is limited to bi-dimensional curved translation surfaces with only positive Gaussian curvature. Two-sided stretch forming is conducted.

General approach for load paths determination. To create a conventional load path with only vertical movement, the highest and lowest point of a surface and the final tangential angle α need to be identified (Fig. 1, left). Pre-stretching or post-stretching can be added and involve horizontal movement. A tangential load path (Fig. 1, right) is based on either a cross-sectional curve of the part geometry, or a representative curve that is usually generated based on experience. The path represents an involute of this curve, which can be pictured as wrapping of the sheet metal on the die surface. The involute is defined by the curve and the edge or rather endpoint of the sheet metal. To ensure tensile loads throughout the process a stretching rate of 0.1 % per forming step is applied.

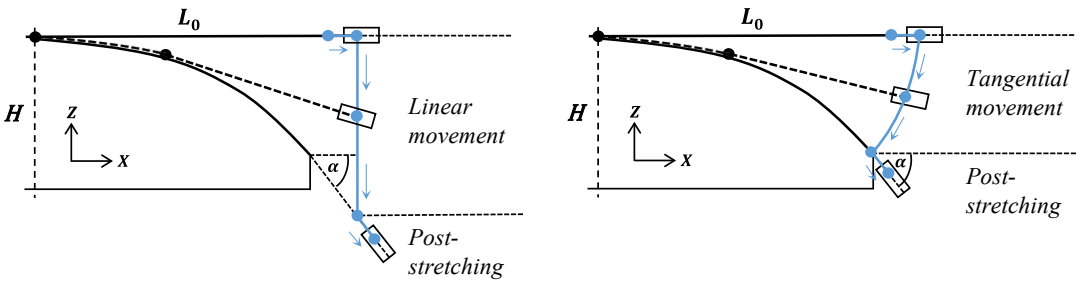

Fig. 1. Schematic drawing of load path determination for a conventional path (left) and a tangential path (right) with an optional pre- or/and post-stretching movement.

Approaches for Load Path Design

The presented approaches for load path design are based on the general approach for tangential stretch forming as stated in the previous section. Therefore, to generate a load path, a defined curve is needed. The Surface Transformation method (ST) transforms a surface into one representative curve as the base for path creation. For the Toolpath Fitting method (TPF), several load paths are created for several cross sections, comparable to the path creation for multi grippers. However, instead of moving multi grippers accordingly, the different paths are compiled into one load path for the rigid single gripper based on different criteria.

Surface Transformation method (ST). In order to transform a multi-curved surface into a single representative curve, all of the surface points are projected onto a plane (cf. Fig. 2). Then, by means of different criteria, a curve is derived from the point cloud. For the first approach, the curve is created based on the lowest points of the surface. Since the first contact point of the sheet metal is always the highest point of a part geometry, respectively the highest point of the lower die, the generated path needs to be corrected by extending the path at the process begin to the same height as the highest point of the part surface geometry.

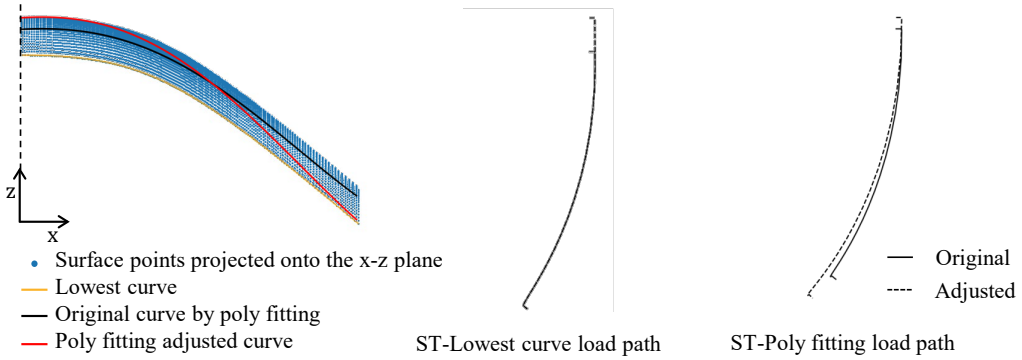

Fig. 2. Projection of coordinate points of a three-dimensional part surface geometry on x-z plane and created representative curves (left) and resulting load paths based on the representative curves (right) generated from two different ST-methods.

In the special case of translation surfaces with only positive Gaussian curvature, the determined lowest curve of the points equals the longitudinal edge curve of the surface. Another load path is based on a curve, which is derived by polynomial fitting through all surface points. The degree of polynomial was set to four. The curve is adapted accordingly in order to include the highest and lowest point of the surface and then the load path is determined based on this curve. Beside the

Materials Research Proceedings 28 (2023) 943-950 https://doi.org/10.21741/9781644902479-103

highest point, the lowest point needs to be included to be able to fully form the desired part geometry.

Coming to the next Surface Transformation method (Fig.3), the surface is cut in transverse direction (y-direction) by several planes. For every transverse cross-section, the points on the curve (black dotted curve) are fitted into a line (red dotted line). All the lines are projected to x-z plane resulting in one red point per cross-section curve. If a sufficient number of transverse cuts are performed, an averaged curve (connecting the red points in the right figure) can be determined. The highest and the lowest point are integrated in the curve as for the poly fitting method.

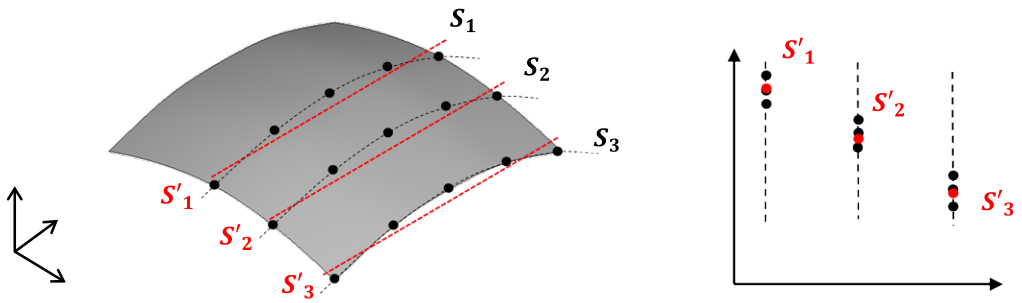

Fig. 3. Simplified sketch of the curve determination by transverse fitting type of Surface Transformation method.

Tool Path Fitting method (TPF). This method (Fig. 4) is based on the generation of load paths determined for each longitudinal cross-sectional curve (black dotted line) of the surface geometry. Within this work, the TPF-method is based on 20 cross-sections. Every load path has the same defined number of steps. So, subsequently for every step, one of the coordinate points of the load paths ($J_{j,\,Ri}$) is picked or fitted into one point. In the first approach, the position that causes the most stretching in the corresponding load step is picked (J_j). In the other approach, this is done by least squares method to find the mean point (T_j).

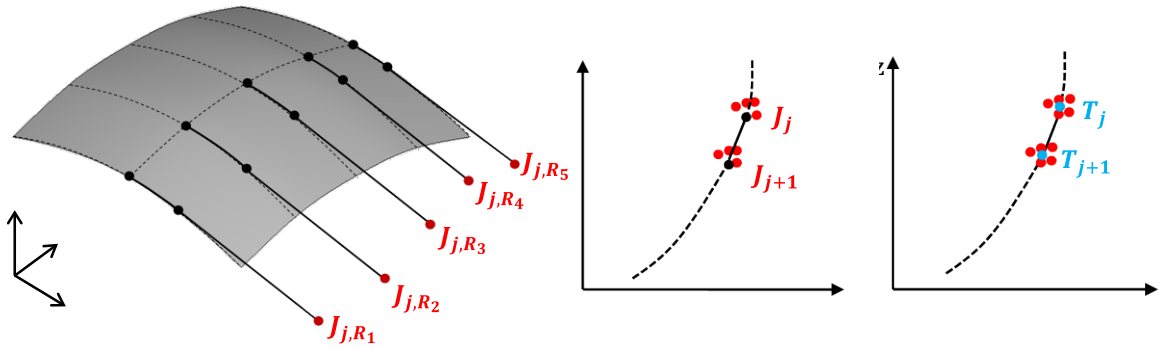

Fig. 4. Simplified sketch of the path determination by Tool Path Fitting method for the lowest point (left) and the mean point (right).

The developed approaches for load path design are summarized in Table 1. The results from the numerical study are presented in the next section.

Table 1. Summary overview of the developed approaches.

Surface Transformation method (ST)	Tool Path Fitting method (TPF)
Transforms a multi-curved surface into a single representative curve. Therefore, all surface points are projected onto a plane and fitted into a curve by means of different criteria. - ST-Lowest Curve - ST-Poly Fitting - ST-Transverse Fitting	Generation of a tangential load path for each specified longitudinal cross-sectional curve of a surface. The paths are compared for every load step and one positions is picked or fitted. The steps are then compiled into one load path. - TPF-Lowest Point - TPF-Mean Point

Results and Discussion

Application of load path design approaches. The presented load path design approaches have been successfully applied for several different translation surface geometries from a defined parameter field. This study focuses on two different exemplary parts shown in Fig. 5 (left), and the corresponding load paths generated via different load path design approaches, shown on the right.

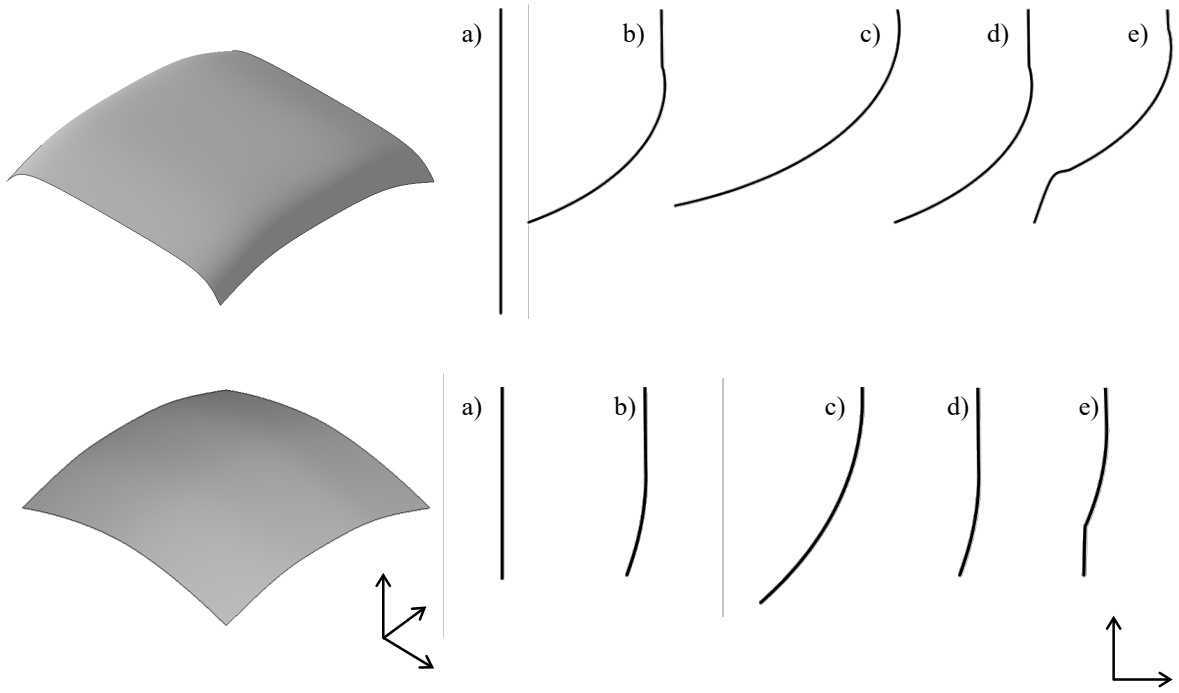

Fig. 5. Visualization of the investigated two different part geometries (left) and load paths a)-e) based on the part surface geometries (right).

Part surface geometry A is relatively flat with a height to length ratio of 0.2 (in both x- and y-direction) and a relatively steep final tangential angle α of 55° towards the edge in x-direction. For part surface geometry B, the height to length ratios in longitudinal and transverse direction are also 0.2 but the final tangential angle α is smaller with 20°. The load paths generated by the different approaches (Fig. 5) are as follows: a) Conventional, b) ST-Lowest Curve, c) ST-Transverse Fitting, d) TPF- Lowest Point, and e) TPF- Mean Point. A generation of a load path by ST-Poly Fitting was not successful, since the generated representative curves were not suitable for

path creation due to multiple change of curvature. All paths presented above are reduced to the motion without pre- or post-stretching. It can be seen that the conventional path is changing significantly with the tangential angle α or rather the curvature in longitudinal direction. The path with the most tangential movement is the path created by Surface Transformation method with Transverse Fitting (Fig. 5, c). Especially the paths based on the lowest curve of the surface geometry (ST-Lowest Curve (Fig. 5, b)) or the lowest tool position (TPF-Lowest Point (Fig. 5, d)) need a significant linear extension to meet the highest point of the surface geometry. To summarize, besides the ST-Poly Fitting approach, all presented approaches seem to lead to reasonable load paths. The applied load varies with the different load path approaches and therefore, influences the forming result as also discussed by [5].

FE-simulation results. FE-simulations were conducted for the different geometries A and B and the presented stretch forming load paths. Fig. 6 shows the resulting plastic strain distribution for geometries A and B after stretch forming with the above developed load paths.

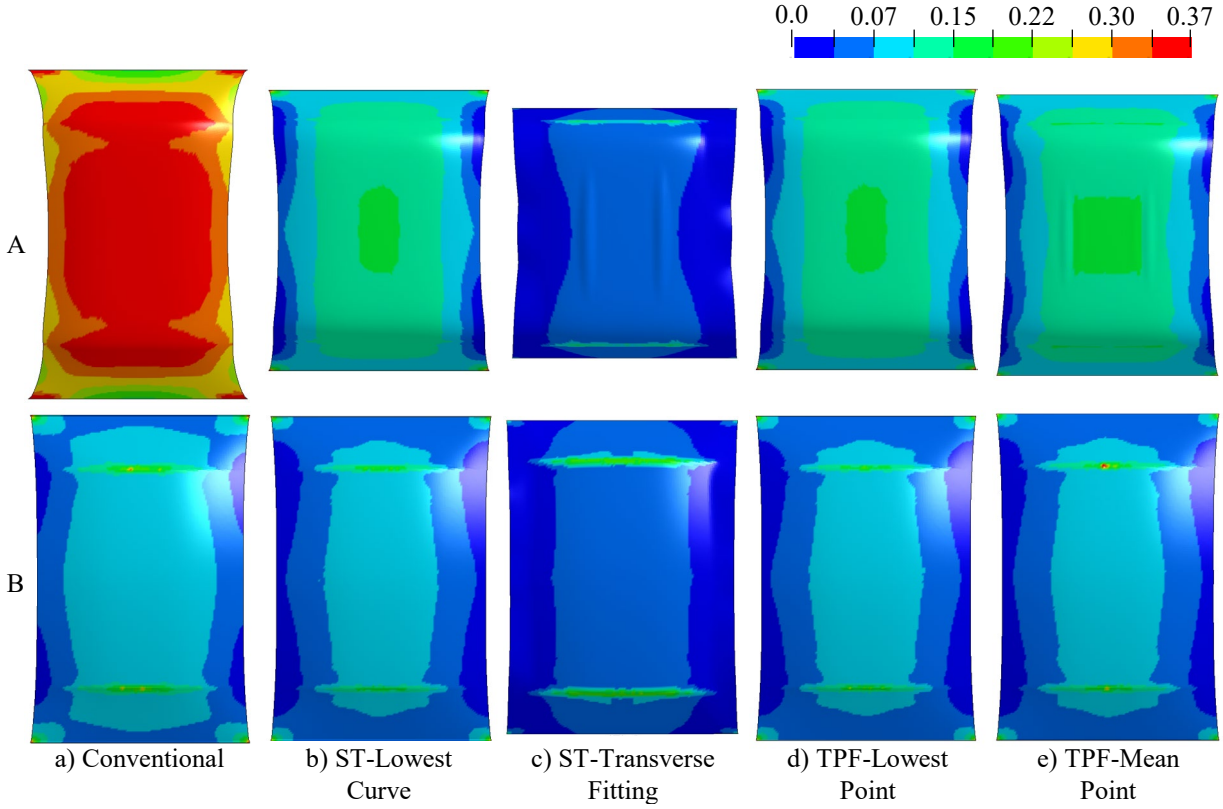

Fig. 6. Effective plastic strain at the final state of deformation under load for geometry A and B.

For the steep curvature of geometry A in longitudinal direction, and the resulting relatively long conventional stretch-forming path, the deformation is expected to cause material failure since the plastic strain of 0.37 exceeds the ultimate strain of the material. Therefore, this part geometry cannot be successfully deformed with the conventional load path.

For load paths b) and d), similar plastic strain distributions can be observed. The path created based on the lowest curve (b) and the choice of the lowest tool position, as in TPF-Lowest Point (d), lead to almost the same resulting path for positively curved translation surfaces. Deviations may be caused by different numbers of data points and consequently different approximations.

As stated before, the load paths based on the ST-Transverse Fitting approach include the most tangential movement. The tangential movement induces less tensile strain and reduces friction

significantly, since the relative movement between die and blank is lowered to a minimum. Therefore, the formed sheet metal blanks show the smallest overall strains for both geometries. So, local straining which leads to early material failure can be avoided. But especially, while forming bi-dimensionally curved components, buckling can occur due to insufficient stretching in the edge area of the sheet. Fig. 7 shows the cross-sections for the geometries A and B, deformed with the original and an adapted load path based on the ST-Transverse Fitting method.

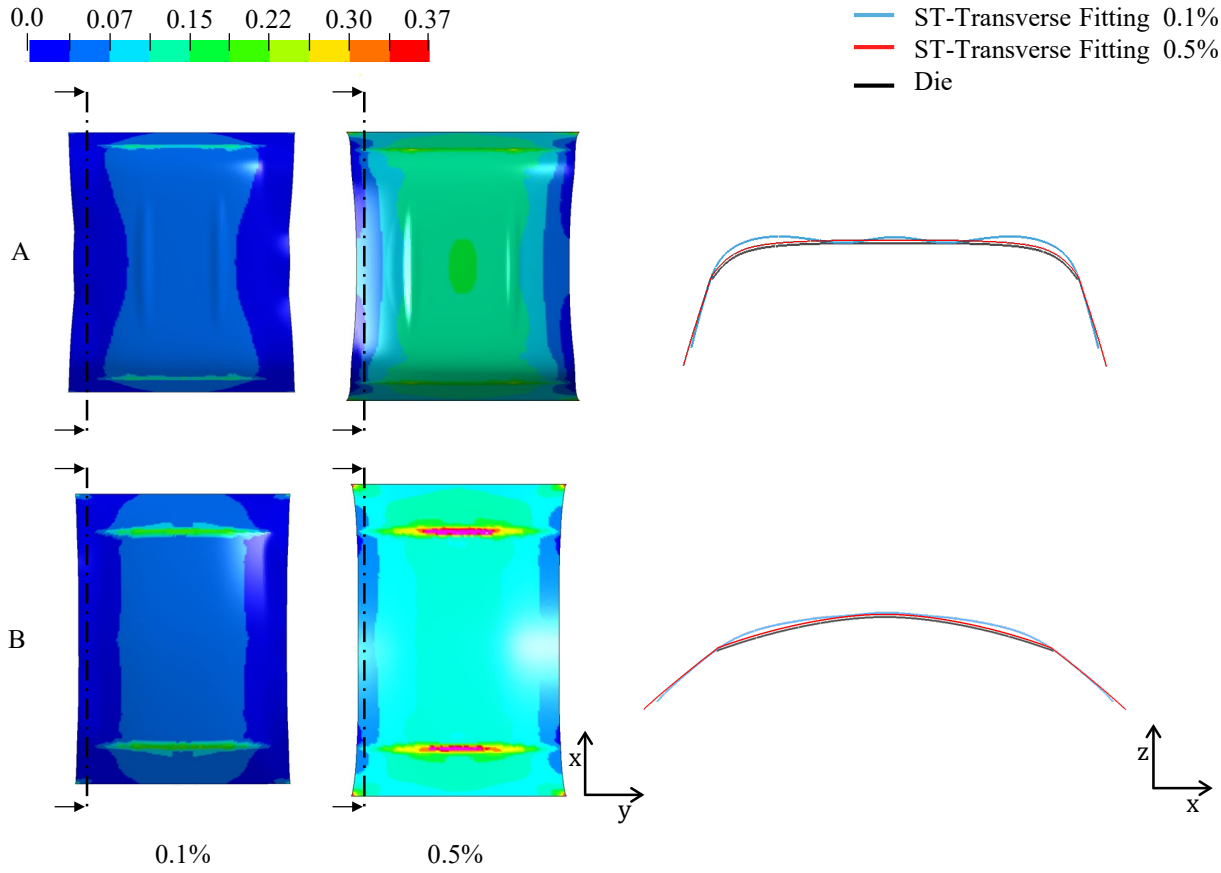

Fig. 7. Effective plastic strain distribution at the final state of deformation under load for geometry A and B for different in-process stretching rates (left) and resulting cross sections (right).

In blue, both cross-sections show deviations from the desired surface geometry denoted in black. Post-stretching is an established measure to apply tensile load at the end of the process. To show the adaptability and therefore flexibility of the load path design approaches, the stretching rate per step was increased from 0.1% to 0.5%. For both geometries, the adaption leads to achievement of the target geometry. The resulting strain distributions are shown in Fig. 7, left. Additional stretching increases the overall strain. The high strains for geometry B for the adapted path can be explained by the simplified die geometries, which are automatically created as shell elements in Python. This leads to element penetration and deformation in the edge area of the simplified die. This example shows that the parameterized path design approaches can be adapted effortlessly and reproducible results can be achieved. For geometry B both simulation results show buckles in the middle area of the blank. The buckles in longitudinal direction occur due to compressive stresses in transvers (y-direction) and cannot be inhibited by additional stretching. The results for a), b)

and d) show no center buckles. This could be referred to increased tensile stretching and therefore increased friction between blank and die at the beginning of the process, which prevents the material from flowing in transverse direction. The individual adaption of in process stretching allow for the control of stress and strain distribution throughout the process in the deformed part and can therefore influence the forming result.

Summary

The presented approaches for load path design based on part geometry, despite the ST-Poly Fitting approach, are shown to be applicable for positively curved translation surfaces. They allow for parametrized load path determination and therefore automated process planning for stretch forming double curved surfaces with rigid grippers. Furthermore, the strain distribution within the sheet during stretch forming could be controlled by the parametrized load path design approaches. Since the material properties and the resulting springback are dependent on the stresses and strains in the sheet metal, the parameterized approaches have the potential to specifically control the strain distribution and the parameters in order to achieve the desired forming result. Further research should verify the results of current approaches in experimental tests and the approaches should also be tested for the applicability to more complex shapes. Furthermore, the potential of the load path approaches to control the springback systematically is of high interest and will be investigated. Additionally, it should be investigated if the achievable geometrical part complexity with simple stretch forming plants without multi grippers can be extended with the presented load path approaches.

References

[1] K. Lange, Handbook of metal forming, Society of Manufacturing engineers, 1985.
[2] Z. Yang, Z.-Y. Cai, C.-J. Che, M.-Z. Li, Numerical simulation research on the loading trajectory in stretch forming process based on distributed displacement loading, Int. J. Adv. Manuf. Technol. 82 (2016) 1353–1362. https://doi.org/10.1007/s00170-015-7470-y
[3] Y. Wang, M. Li, H. Liu, J. Xing, Finite Element Simulation of Multi-gripper Flexible Stretch Forming, Procedia Eng. 81 (2014) 2445–2450. https://doi.org/10.1016/j.proeng.2014.10.348
[4] R. Schmitz, M. Winkelmann, D. Bailly, G. Hirt, Homogenisation of the strain distribution in stretch formed parts to improve part properties, AIP Conference Proceedings 1960 (2018) 160025.
[5] D.E. Hardt, W.A. Norfleet, V.M. Valentin, A. Parris, In Process Control of Strain in a Stretch Forming Process, J. Eng. Mater. Tech. 123 (2001) 496-503.

Materials Research Proceedings 28 (2023) 951-958 https://doi.org/10.21741/9781644902479-104

Modifying mechanical properties of sheet metal materials by work hardening mechanisms induced by selective embossing

HEINZELMANN Pascal[1,a *], BRIESENICK David[1,b] and LIEWALD Mathias[1,c]

[1]Institute for Metal Forming Technology, University of Stuttgart,
Holzgartenstraße 17, 70174 Stuttgart, Germany

[a]pascal.heinzelmann@ifu.uni-stuttgart.de, [b]david.briesenick@ifu.uni-stuttgart.de,
[c]mathias.liewald@ifu.uni-stuttgart.de

Keywords: Embossing, High Strength Steel, Dual-Phase Steel, Tensile Test

Abstract. The selective modification of mechanical properties of sheet metal materials poses a promising approach for realizing lightweight designs, especially when achieved without additional material input. One method for locally adapting the mechanical properties of sheet metal components is to specifically induce work hardening into the sheet metal material by near-surface embossing. Previous studies have already shown this effect for the sheet metal materials DP500 and DP600. The present paper verifies these findings for embossed high-strength steel DP800 considering different blank thicknesses and embossing depths. During experimental investigations, tensile and bending specimens of different sheet thicknesses were manufactured with definite embossing patterns and subsequently tested with regard to their mechanical properties. To verify the true embossing depth, the specimens were measured optically. As a result of this contribution, it was found that the material properties of high-strength sheet metal materials can be modified for lightweight construction and crash properties by selective embossing. Parameter constellations for increasing the yield strength were found for the materials investigated.

Introduction

Today, automotive traffic accounts for a large amount of global greenhouse gas emissions, which is why both the EU and the United States of America are imposing increasingly stringent restrictions regarding the CO_2 output from motor vehicles [1]. Automotive manufacturers must take this into account during the vehicle development phase, not only concerning driving concepts but also the final vehicle weight. But weight optimization of vehicles is not only a crucial development issue in terms of reducing greenhouse gases but also concerns the availability of metallic raw materials [2]. This is exacerbated in the current situation by Russia's invasion of Ukraine and the tense markets associated with it [3], and the increased costs in the energy sector [4]. Against this background, novel approaches to manufacturing lightweight vehicle structures can significantly contribute to overcoming these challenges.

Lightweight constructions of car bodies are in most cases based on weight-optimized designs or the alloy-specific adaptation of the sheet metal materials used. In addition, such metallic lightweight structures can also be realized by modifying the component properties via selective work hardening during their forming [5]. In this context, Namoco et al. carried out experiments with aluminium alloys (A6061-T4 and A5052-H34) [6], which focussed on the targeted introduction of work hardening into the sheet metal material using both embossing and reforming

Content from this work may be used under the terms of the Creative Commons Attribution 3.0 license. Any further distribution of this work must maintain attribution to the author(s) and the title of the work, journal citation and DOI. Published under license by Materials Research Forum LLC.

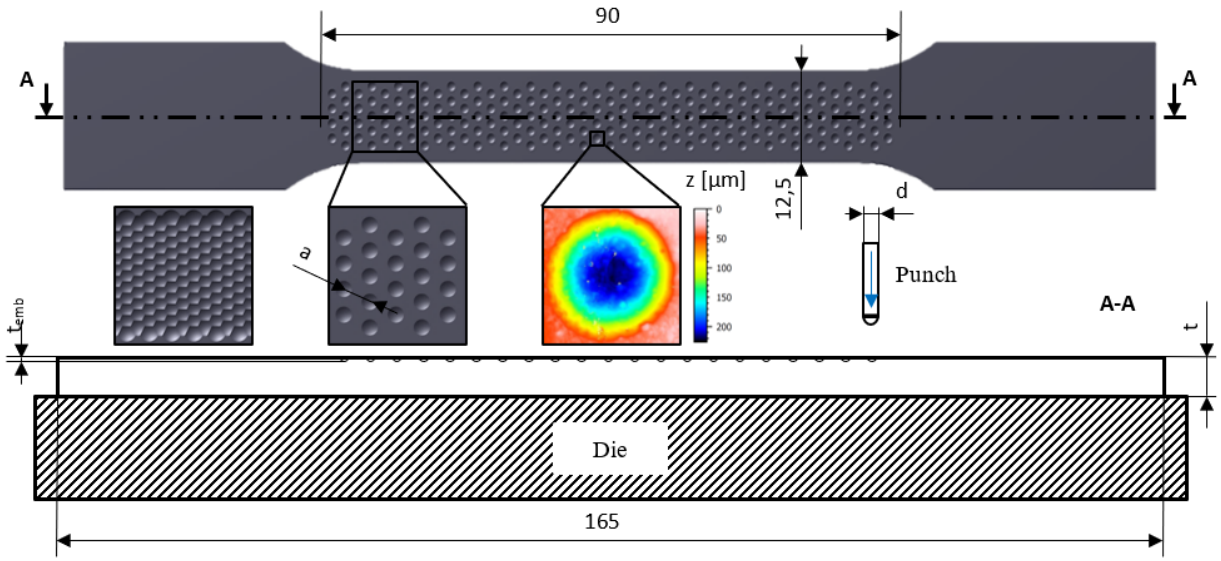

Fig. 1. Schematic of the embossing process with exemplary embossing arrangements.

processes. The results were evaluated based on the obtained values of yield strength, tensile strength and total elongation. Abe et al. examined the formability of embossed deep-drawn components and stated beneficial properties changes due to the embossing process carried out [7]. Walzer et al. investigated DP600 blanks and found that the incorporation of near-surface embossing increased the tensile strength of the sheet metal material [8]. Briesenick et al. carried out bending tests with DP500 blanks embossed in different ways and this way the maximum bending force required was increased by 75 % [9].

Based on these results, the investigations presented in this paper were intended to determine an optimum embossing geometry with regard to the highest possible strength increase of sheet metal structures. The embossing geometry here included the embossing pattern and the embossing depth. Furthermore, the property modifications attainable were evaluated using the example of the two sheet metal materials DP600 and DP800 having different initial yield strengths.

Experimental Method

Previous research work in the field of property modification of sheet materials by means of targeted application of work hardening has predominantly selected DP600 as test material. Materials with higher strengths, however, have not been investigated so far. Due to the existing results with DP600, which serve as a reference, the sheet metal materials DP600 and DP800 were selected for the investigation objectives presented in this paper. In these investigations, the influence of embossing geometries on changes in the mechanical properties yield strength R_p, and elongation at break A was evaluated. In Table *1* the material properties of the unembossed sheet materials are shown.

Table 1. Material properties of the steel blanks used in the tests carried out.

Material	Yield Strength R_p [MPa]	Elongation at Break A [%]
DP600	345.7	26.5
DP800	561.4	18.2

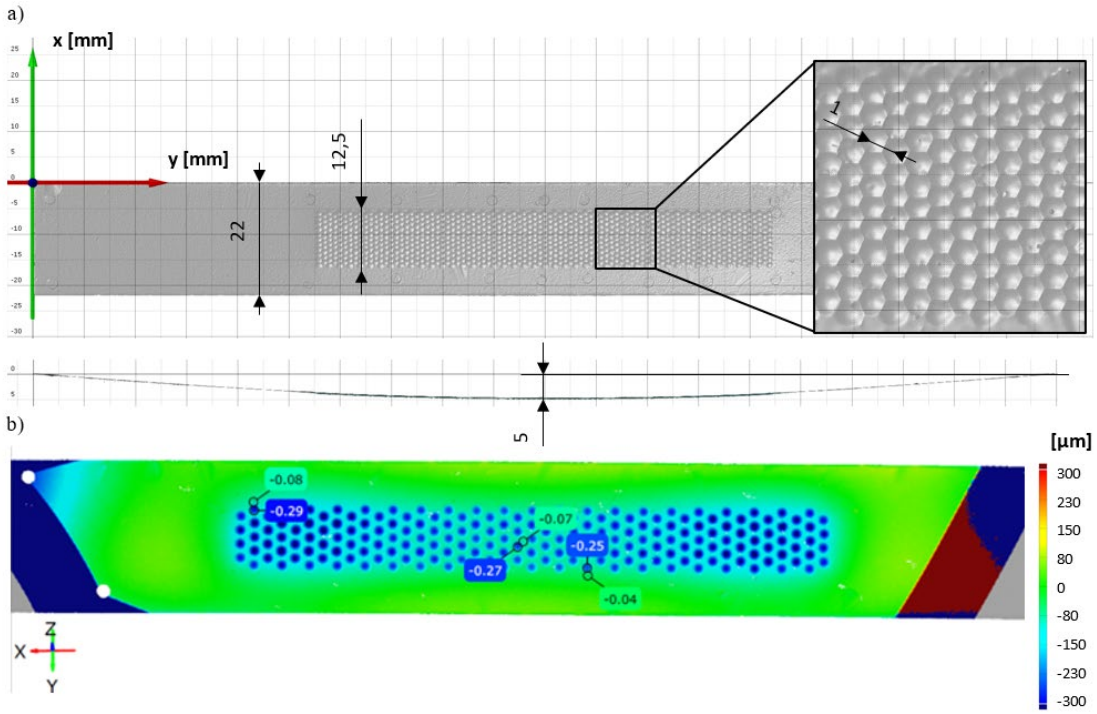

Fig. 2. Measurement of the embossed flat tensile specimens with different embossing geometries.

To evaluate the possible influence of different thicknesses of specimens on the property improvements achievable by means of embossing. The material DP600 was tested with sheet thicknesses *t* of 1.5 mm and 1.77 mm and DP800 was tested with sheet thicknesses of 1.5 mm and 1.85 mm. The different thicknesses were selected due to the availability of the materials used. To examine the mechanical properties changes, tensile tests were performed with embossed and unembossed specimens. The specimen geometry was determined according to DIN EN ISO 6892-1 [12] with form H and a measuring area of 12.5 mm × 50 mm. The embossing patterns to be investigated were applied beyond the measuring area on a surface of 12,5 mm × 90 mm for all specimens, thus ensuring that failure occurred in the measuring area. A hexagonal arrangement was chosen for the embossing patterns, varying the distance *a* between neighbouring embossings by 1 mm, 1,5 mm, and 2 mm as well as the embossing depth t_{emb} by 100 µm and 200 µm. In this respect, Fig. 1 shows an embossed flat tensile specimen with the minimal values *a* of 1 mm and an embossing depth t_{emb} of 100 µm.

A TRUPunch 5000R CNC punching machine was used to emboss the tensile specimen surfaces. This machine can perform up to 1,400 strokes per minute, thus allowing the embossings to be sequentially introduced within relatively short processing times. A modified round punch was used as embossing punch, with the face surface turned into a hemisphere with a diameter *d* of 4 mm. Due to the springback of the sheet metal material, the punch thereby had to penetrate deeper into the material´s surface than the targeted embossing depth. Various test embossing operations were carried out to determine the penetration depth required for this purpose. Furthermore, the embossings were always introduced into the sheet metal material´s surface before cutting out the pre-milled specimen geometry. Subsequently, the embossed sheet metal areas were cut out rectangularly (220 mm × 22 mm) and finally milled into the defined specimen shape to compensate for work-hardening caused by the cut-out. Table *2* lists the manufactured specimen variants in detail. Each variant was manufactured in quadruplicate for the reproducibility of the tensile tests.

Materials Research Proceedings 28 (2023) 951-958 https://doi.org/10.21741/9781644902479-104

Table 2. Specimen designation with details of the material, sheet thickness, embossing distance, and embossing depth.

Specimen Designation	Sheet Metal Material	Sheet Thickness t [mm]	Embossing Distance a [mm]	Embossing Depth t_{emb} [µm]
DP600_T1500_a1000_t100	DP600	1.5	1	100
DP600_T1500_a1500_t100	DP600	1.5	1.5	100
DP600_T1500_a2000_t100	DP600	1.5	2	100
DP600_T1500_a1000_t200	DP600	1.5	1	200
DP600_T1500_a1500_t200	DP600	1.5	1.5	200
DP600_T1500_a2000_t200	DP600	1.5	2	200
DP600_T1770_a1000_t100	DP600	1.77	1	100
DP600_T1770_a1500_t100	DP600	1.77	1.5	100
DP600_T1770_a2000_t100	DP600	1.77	2	100
DP600_T1770_a1000_t200	DP600	1.77	1	200
DP600_T1770_a1500_t200	DP600	1.77	1.5	200
DP600_T1770_a2000_t200	DP600	1.77	2	200
DP800_T1500_a1000_t100	DP800	1.5	1	100
DP800_T1500_a1500_t100	DP800	1.5	1.5	100
DP800_T1500_a2000_t100	DP800	1.5	2	100
DP800_T1500_a1000_t200	DP800	1.5	1	200
DP800_T1500_a1500_t200	DP800	1.5	1.5	200
DP800_T1500_a2000_t200	DP800	1.5	2	200
DP800_T1850_a1000_t100	DP800	1.85	1	100
DP800_T1850_a1500_t100	DP800	1.85	1.5	100
DP800_T1850_a2000_t100	DP800	1.85	2	100
DP800_T1850_a1000_t200	DP800	1.85	1	200
DP800_T1850_a1500_t200	DP800	1.85	1.5	200
DP800_T1850_a2000_t200	DP800	1.85	2	200

To monitor the dimensional accuracy of the produced specimens and their embossings, they were optically measured using a GOM ATOS Compact Scan System, as shown in Fig. 2. Furthermore, the diameters of the embossings on the surface were measured via a Keyence Microscope VHX. Ball segment equations were then used to determine the embossing depths. The Keyence Microscope VHX was used to get fast results to set the right embossing offset. To check all embossing depths over the embossing area the ATOS Compact Scan system was used. Finally, the tensile tests were carried out according to DIN EN ISO 6892-1 [10] using the universal testing machine Roell + Korthaus RKM100.

Results

For assessing the influence of different embossings on the mechanical properties of sheet metal materials, the two characteristic values yield strength R_p and elongation at break A were determined in each of the tensile tests described above. All characteristic values determined in this respect are summarized in Table *3*.

Table 3. Results of the tensile tests.

Experiment	Yield Strength R_p [MPa]	Elongation at Break A [%]
DP600_T1500_a1000_t100	507.35	21.82
DP600_T1500_a1500_t100	500.88	21.95
DP600_T1500_a2000_t100	443.06	22.68
DP600_T1500_a1000_t200	584.34	10.40
DP600_T1500_a1500_t200	545.65	14.48
DP600_T1500_a2000_t200	502.69	19.24
DP600_T1770_a1000_t100	539.41	17.53
DP600_T1770_a1500_t100	486.82	21.23
DP600_T1770_a2000_t100	432.26	24.40
DP600_T1770_a1000_t200	560.92	9.05
DP600_T1770_a1500_t200	528.68	12.67
DP600_T1770_a2000_t200	494.22	17.67
DP800_T1500_a1000_t100	680.81	13.53
DP800_T1500_a1500_t100	655.76	15.44
DP800_T1500_a2000_t100	592.40	16.66
DP800_T1500_a1000_t200	685.00	9.79
DP800_T1500_a1500_t200	661.47	11.81
DP800_T1500_a2000_t200	624.69	14.31
DP800_T1850_a1000_t100	672.87	14.26
DP800_T1850_a1500_t100	649.12	16.69
DP800_T1850_a2000_t100	597.22	17.03
DP800_T1850_a1000_t200	686.07	10.69
DP800_T1850_a1500_t200	673.37	10.88
DP800_T1850_a2000_t200	627.96	13.60

For evaluating these results, the characteristic values achieved must be considered in relation to the respective embossing geometry, i.e., the embossing depth and the embossing distance. Fig. 3 shows these relationships. First, Diagram a) illustrates the yield strengths of those tests performed with specimens having an embossing depth of 100 µm for all test materials and sheet thicknesses investigated. The different embossing distances and respective unembossed reference specimens are shown as coloured bars. Diagram c) shows the same evaluations for the embossing depth of 200 µm. In Fig. 3 b) and d) the evaluation is based on the elongation at break and follows the same scheme then done for the yield strength. The percentage values in the bars of the embossed tests refer to the change in the respective embossing geometry compared to the reference tests of the respective group. For the DP600 material, the increases in yield strength range from 26 % up to 66 %. The range of the DP800 material varies between 5 % and 22 %. When considering the change in elongation at break, a reduction can be observed for all cases. For DP600, this reduction ranges between -66 % and -9 %. For DP800, the reduction occurs in the range of -42 % to -2 %.

An influence of the different plate thicknesses could not be observed for the yield strength. For the elongation at break, a minor influence could be observed.

Considering the influence of the embossing depth on the yield strength, it can be stated that an increase in the embossing depth is accompanied by an increase in the yield strength. This applies more to the lower-strength material DP600 (up to 66 %) than to DP800 (up to 22 %). Thus, some DP600 tests with an embossing depth of 200 µm show similar and partly higher yield strength values than the reference measurements for DP800. An opposite effect can be recognised when considering the influence of the embossing depth on the elongation at break. With an increase in embossing depth, the elongation at break decreases compared to the lower embossing depth. DP600 by up to -66 % and DP800 by up to -45 %. Also, the embossing distance influences the yield strength and the elongation at break. Here, a reduction of the embossing distance leads to an increase in yield strength. This effect is not as high as the effect of the embossing depth, but still considerable. If the yield strength increases due to the reduction of the embossing distance, the elongation at break decreases to a similar extent.

Due to the different patterns, the results of the DP600 material can only be compared with the results of this paper to a limited extent. Qualitatively, it can be said that the results show a similar trend.

Summary

In this paper, the effects of near-surface embossing on yield strength and bearing at fracture were investigated. The dual-phase materials DP600 and DP800 with different plate thicknesses were considered. In general, an increase in the yield strength of the considered DP steel sheets was observed for all tested embossing geometries. In contrast, a reduction was found for the elongation at break for all embossed specimens. The results for the higher-strength material DP800 show property changes due to the introduction of embossing. These changes are overalls smaller in the DP800 material compared to the DP600 material.

When using embossed components, it is therefore important to consider which properties are relevant for the respective application and to what extent the properties should be changed. For this purpose, further research work will be conducted on tests with other materials and embossing geometries. Here, the focus should be when, or in what range, embossing no longer has any influence on higher and highest-strength materials. Moreover, low-strength materials will be considered as well. For a better understanding of the process, additional simulations are needed for providing a more detailed view of the process than just the experimental measurements. Simulations that include the history of the embossing process should also be considered, so the influence of the embossing is also taken into account for further simulative stress analyses. To simulate the whole embossing process, a high computational effort must be made. For faster simulations of embossed parts, the simulation of the processes must be more efficient Possibilities should also be found to transfer the result of the embossing process to simulations of embossed components with little calculation effort.

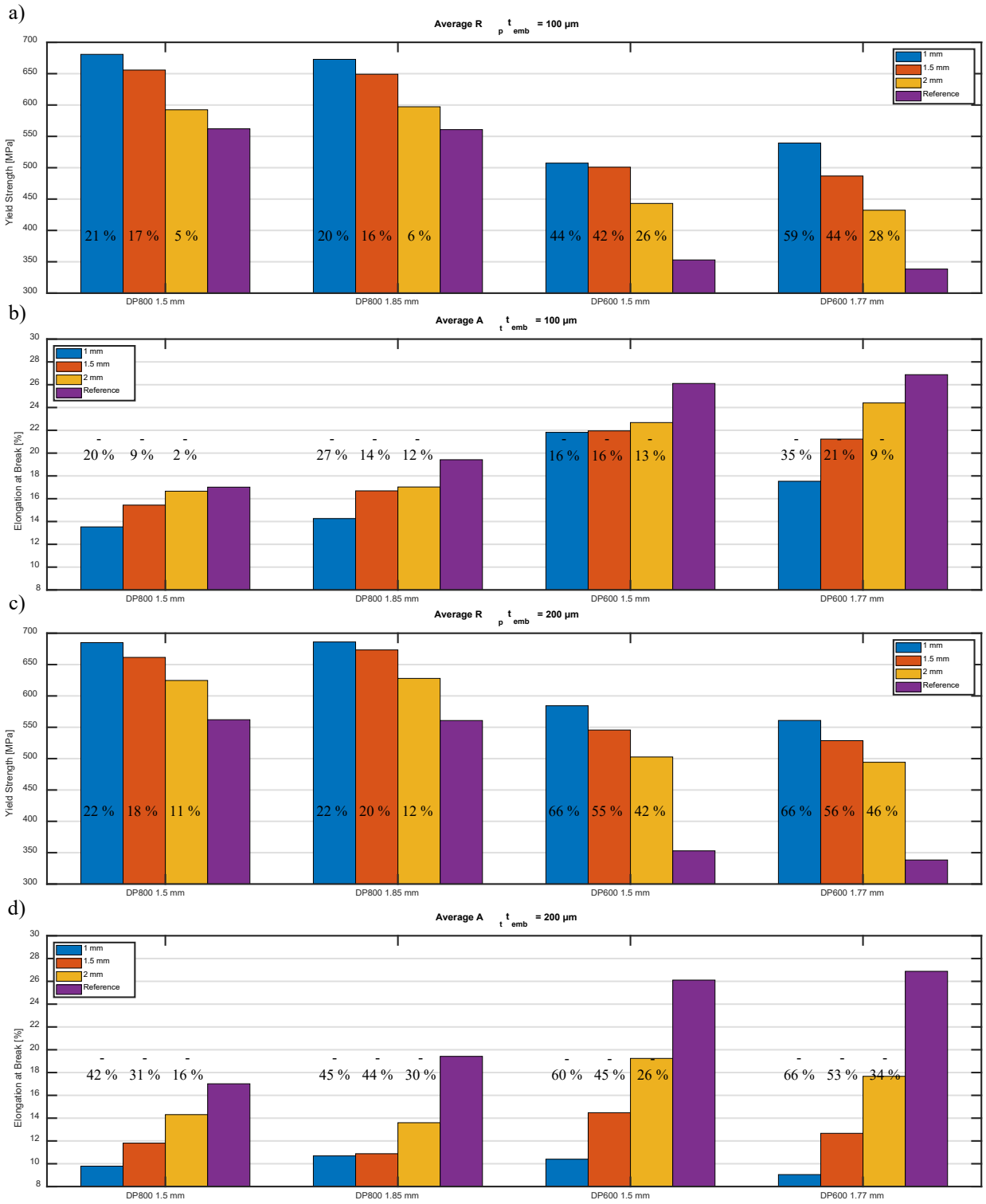

Fig. 3. Evaluation of tensile tests with respect to yield strength for a) t_{emb} = 100 µm, c) t_{emb} = 200 µm and elongation at break for a) t_{emb} = 100 µm, c) t_{emb} = 200 µm.

References

[1] K. Shanmugam, V. Gadhamshetty, P. Yadav, D. Athanassiadis, M. Tysklind, V.K. Upadhyayula, Advanced High-Strength Steel and Carbon Fiber Reinforced Polymer Composite Body in White for Passenger Cars: Environmental Performance and Sustainable Return on Investment under Different Propulsion Modes, ACS Sustainable Chem. Eng. 7 (2019) 4951-4963. https://doi.org/10.1021/acssuschemeng.8b05588

[2] R. Döhrn, Die Lage am Stahlmarkt: Produktion steigt wieder, Probleme bleiben, RWI Konjunkturberichte 72 (2021) 49-58

[3] C. Birkholz, M. Kraus, Die Energiekrise im Standortvergleich: Preiseffekte und Importrisiken. Sonderstudie zum Länderindex Familienunternehmen, München: Stiftung Familienunternehmen, Rep. 978-3-948850-15-9, 2022

[4] O. Holtemöller, S. Kooths, T. Schmidt, T. Wollmershäuser, Gemeinschaftsdiagnose: Energiekrise, Inflation, Rezession und Wohlstandsverlust, Wirtschaftsdienst 102 (2022) 761-765. https://doi.org/10.1007/s10273-022-3291-4

[5] C.S. Namoco, T. Iizuka, R.C. Sagrado, N. Takakura, K. Yamaguchi, Experimental and numerical investigation of restoration behavior of sheet metals subjected to bulging deformation, J. Mater. Process. Technol. 177 (2006) 368–372. https://doi.org/10.1016/j.jmatprotec.2006.03.208

[6] C.S. Namoco, T. Iizuka, K. Narita, N. Takakura, K. Yamaguchi, Effects of embossing and restoration process on the deep drawability of aluminum alloy sheets, J. Mater. Process. Technol. 187-188 (2007) 202–206. https://doi.org/10.1016/j.jmatprotec.2006.11.182

[7] Y. Abe, K. Mori, T. Maeno, S. Ishihara, Y. Kato, Improvement of sheet metal formability by local work-hardening with punch indentation, Prod. Eng. Res. Devel. 13 (2019) 589-597. https://doi.org/10.1007/s11740-019-00910-6

[8] S. Walzer, M. Liewald, Studies on the influence of embossing on the mechanical properties of high-strength sheet metal, AIP Conference Proceedings 2113 (2019) 160006. https://doi.org/10.1063/1.5112703

[9] D. Briesenick, S. Walzer, M. Liewald, Study on the Effect of Embossing on the Bending Properties of High-Strength Sheet Metals, in: Forming the Future: Proceedings of the 13th International Conference on the Technology of Plasticity (Springer eBook Collection), G. Daehn, J. Cao, B. Kinsey, E. Tekkaya, A. Vivek, and Y. Yoshida (Eds.), 1st ed. Cham: Springer International Publishing, Imprint Springer, 2021, pp. 2585-2595.

[10] C. Lesch, N. Kwiaton, F.B. Klose, Advanced High Strength Steels (AHSS) for Automotive Applications − Tailored Properties by Smart Microstructural Adjustments, Steel Res. Int. 88 (2017) 1700210. https://doi.org/10.1002/srin.201700210

[11] F. Ebrahimi, N. Saeidi, M. Raeissi, Microstructural Modifications of Dual-Phase Steels: An Overview of Recent Progress and Challenges, Steel Res. Int. 91 (2020) 2000178. https://doi.org/10.1002/srin.202000178

[12] DIN EN ISO 6892-1:2020-06, Metallische Werkstoffe_- Zugversuch_- Teil_1: Prüfverfahren bei Raumtemperatur (ISO_6892-1:2019); Deutsche Fassung EN_ISO_6892-1:2019, Berlin.

Materials Research Proceedings 28 (2023) 959-968 https://doi.org/10.21741/9781644902479-105

Influence of surface pressure and tool materials on contact heating of aluminum

TRÂN Ricardo[1,a *], PSYK Verena[1,b], WINTER Sven[1,c] and KRÄUSEL Verena[1,d]

[1]Fraunhofer Institute for Machine Tools and Forming Technology, Reichenhainer Straße 88, 09126 Chemnitz, Germany

[a]ricardo.tran@iwu.fraunhofer.de, [b]verena.psyk@iwu.fraunhofer.de, [c]sven.winter@iwu.fraunhofer.de, [d]verena.kräusel@iwu.fraunhofer.de

Keywords: Heating Technology, Contact Heating, Aluminum, Hot Forming, Tool Technology

Abstract. The implementation of lightweight design concepts can significantly benefit from using highly efficient heating technologies such as contact heating in thermo-mechanical processing of sheet metal components. The investigation of the influence of surface pressure and tool material on the heating time and the heating rate during contact heating is the subject of this publication. A specially manufactured contact heating tool with comprehensive temperature and force measurement was used for studying the effects of different contact plate materials (CuZn39Pb3 and CuCr1Zr), surface pressures (3 MPa - 15 MPa) and variable plate thicknesses (1.0 mm - 5.2 mm) during heating of the aluminum alloy EN AW-7075 up to the solution heat treatment temperature of 475 °C. It was observed that heating time is lower for thinner workpieces. Furthermore, heating times decrease and heating rates increase significantly with increasing surface pressure for a pressure range of 3 MPa - 9 MPa. A further increase in surface pressure is not recommended, because the benefit in terms of further reduction of the heating time is marginal and the strength of the contact plate materials at elevated temperatures is limited. Contact heating using copper plates is significantly faster compared to brass plates and the conventionally used steel plates. Brass plates, however, benefit more from an increase in surface pressure. Both investigated materials allow faster heating than conventional steel plates due to their higher thermal conductivity. Depending on the specific process parameters the heating process can be accelerated to less than one second. Thus, contact heating can be realized within the press cycle.

Introduction

In modern manufacturing, the implementation of lightweight design concepts has been becoming more and more important in order e. g. to save resources in aviation [1], reduce fuel consumption and corresponding CO_2 emission in vehicles with conventional combustion machines [2], increase the range that an electrical vehicle can travel without recharging [3], or improve component function and user-friendlyness e. g. in medical engineering products [4]. These concepts involve design changes e. g. in order to realize integration of functions [5] and the use of typical lightweight materials such as high strength steel [6] or light-metal alloys [7]. These materials usually feature limited formability at room temperature so that forming of the complex geometries typically necessary for lightweight components frequently requires thermo-mechanical processes such as press hardening [8], quenching and partitioning [9], or superplastic forming [10]. In this context, fast and energy-efficient heating strategies are an essential prerequisite. Conventionally, the components are heated in roller hearth furnaces by means of thermal radiation. In practice, these furnaces reach lengths of up to 40 m [8] in order to achieve acceptable cycle times despite of the long furnace residence time. Alternative heating technologies requiring less investment costs and floor space and additionally allowing faster heating are based on resistive [11] and inductive heating [12]. However, resistive heating is efficient only for components with favorable - i. e. high

Content from this work may be used under the terms of the Creative Commons Attribution 3.0 license. Any further distribution of this work must maintain attribution to the author(s) and the title of the work, journal citation and DOI. Published under license by Materials Research Forum LLC.

- ratio of length and cross section [13] and uniform heating for complex blank geometries is difficult for both - resistive and inductive heating [8]. Direct contact heating is a relatively new approach (suggested in [14]) with high potential to overcome these limitations. In this technology, the contact plates (typically made of metal or ceramics) that are heated by a heat source (e. g. induction coils [14], gas burners [15], cartridge heaters [16]) serve as energy storage and transfer the heat to the workpiece via thermal conduction. Compared to furnace heating, contact heating excels due to extremely high heating rates, which significantly reduces heating time [17]. The mechanism is very similar to the cooling in direct press hardening. From that process it is known that the heat transfer can be controlled by applying a defined contact force (contact pressure) [18, 19]. This suggests that the contact pressure is also a suitable parameter for adapting the heating rate in contact heating processes, which is e. g. relevant for thermo-mechanical processing of high-strength aluminum alloys [20]. Furthermore, it can be expected that different contact plate materials with significantly varying thermal properties (e. g. heat conduction coefficient) affect the heating rate in contact heating. However, neither the influence of surface pressure nor that of different contact plate materials on the heating behavior during contact heating have been investigated yet. Therefore, providing an analysis of these aspects is the aim of this paper.

Experimental Setup and Process Description

For this purpose, the contact plate tool shown in Fig. 1 was developed and mounted to a hydraulic press HS3-1500 by Dunkes with a press force of 1,000 - 15,000 kN. The setup consists of an insulation box that encases exchangeable contact plates, cooling plates and a gas pressure damper plate, that allows applying different surface pressures. This damper plate is coupled with a gas-pressure-based force measurement that enables recording the time-dependent surface pressure between the contact plates and the workpieces.

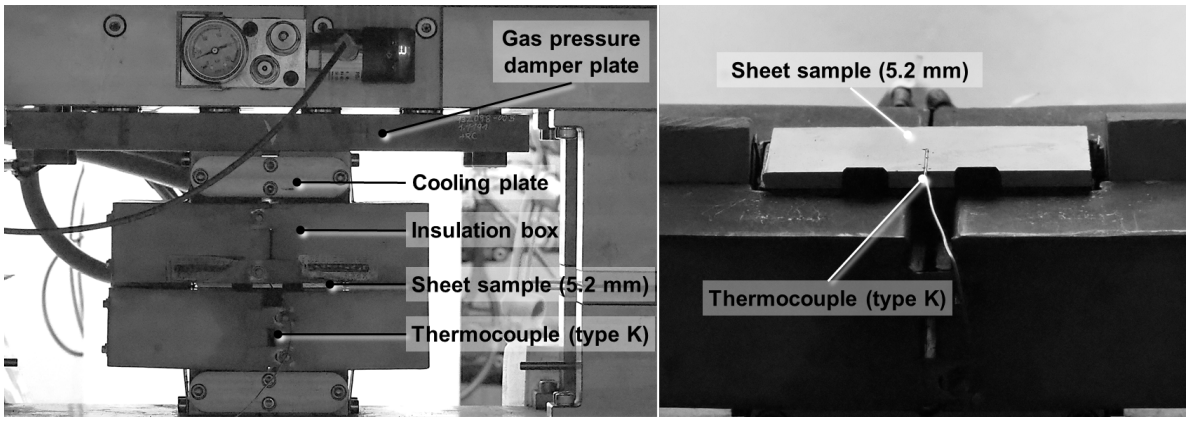

Fig. 1. Experimental setup: front view and view into the open tool with inserted sheet sample.

Materials Research Proceedings 28 (2023) 959-968 https://doi.org/10.21741/9781644902479-105

This study considers contact plates with a heating surface of 100 mm x 60 mm and a height of 35 mm made of the copper alloy CuCr1Zr and the brass alloy CuZn39Pb3, respectively (see Fig. 2). These materials feature approximately the same heat capacity and different thermal conductivity (see Table 1). Thus, the influence of the thermal conductivity of the contact plate material on the heating process can be investigated.

Fig. 2. Contact plates made of different materials.

Table 1. Thermal material properties of the contact plate materials and the workpiece material at room temperature.

	CuCr1Zr	**CuZn39Pb3**	**EN AW-7075**
heat capacity	383 J/kgK	377 J/kgK	862 J/kgK
thermal conductivity	330 W/mK	123 W/mK	145 W/mK

Both, the upper and the lower contact plate were heated with four individually controlled silicon nitride ceramic heating elements by Bach Resistor Ceramics GmbH. These heating elements feature rectangular geometry in order to facilitate homogeneous temperature distribution. The time-dependent temperatures of the contact plates were recorded using type K thermocouples by OMEGA with a sampling rate of 10 Hz during the tests. Furthermore, the pressure in the gas damping plate was measured and served as basis for determining the surface pressure acting on the contact plates and the workpieces to be heated, respectively.

The specimens considered in this study were made of EN AW-7075 with a width w of 60 mm, a length l of 100 mm and thicknesses s of 1.0 mm, 2.0 mm, 3.0 mm; 4.3 mm and 5.2 mm. In order to record the time-dependent temperature of the workpiece, rectangular grooves were milled into the specimens and thermocouples were inserted in the center of the specimen as shown in Fig. 3. For the sheets with 1.0 mm thickness thermocouples with a diameter d of 0.5 mm were used. For all other sheet thicknesses thermocouples with a diameter of 1 mm were used. The groove width was chosen corresponding to the width of the thermocouple. The groove depth amounts to the sum of half of the sheet thickness and half of the height of the thermocouple. Analogous to the temperature measurement of the contact plates also here type K thermocouples by OMEGA were used and the sampling rate was set to 10 Hz.

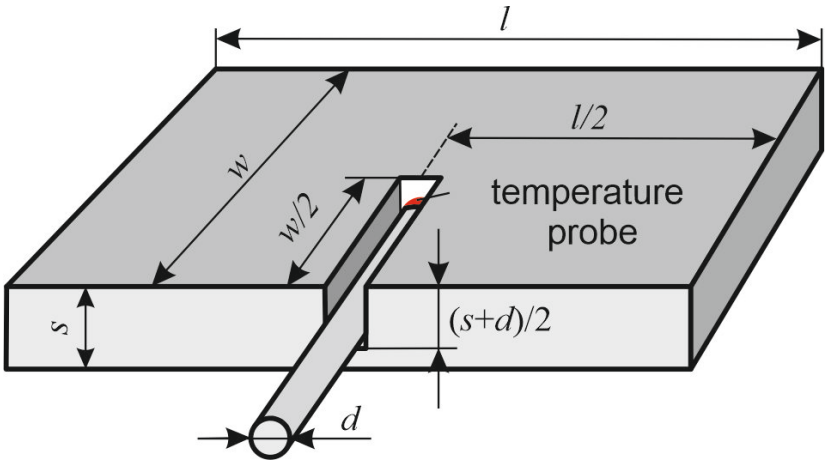

Fig. 3. Principal sketch of the sheet specimen for contact heating tests.

For the contact heating experiments, the contact plates were preheated for 15 minutes in order to achieve homogenous local temperature distribution. As it is known that the temperature rise in the workpiece is very quickly at the beginning of the process, but slows down as it approximates the temperature of the contact plates, the contact plate temperature is usually chosen higher than the target temperature of the workpiece. Here, the contact plates were pre-heated to 500°C in order to achieve the desired specimen temperature of 475°C - i. e. the solution heat treatment temperature of EN AW-7075 - in a reasonable timeframe. Then, a specimen was inserted, the tool was closed within approx. two seconds and a defined surface pressure between the contact plates and the specimen was applied by adjusting the pressure in the gas pressure damper plate correspondingly. For each sample thickness a test series was carried out by varying the surface pressure between 3 MPa and 15 MPa in steps of 3 MPa.

Fig. 4 shows an exemplary process diagram based on the measured time-dependent surface pressure between workpiece and contact plates and corresponding temperatures of workpiece and contact plates for a representative test using copper contact plates. At the moment t=0 s, the contact plates are closed, and the sheet specimen is heated from both sides. From this moment, the surface pressure rises approx. linearly up to the target value that is 9 MPa in the regarded case causing rapid heating of the aluminum specimen. At the same time, a temperature reduction of approx. 20 K of the contact plates can be observed as the heat is transferred into the specimen. Correspondingly, an increase of the workpiece temperature occurs. The measured temperature curve is characterized by an initial fast rise that decreases more and more when it approximates the temperature of the contact plates, which is in good agreement with [16]. After reaching the target temperature of 475°C, the test is completed, the specimen is removed from the tool and quenched in water, and the contact plate temperature is re-adjusted for next test of the test series.

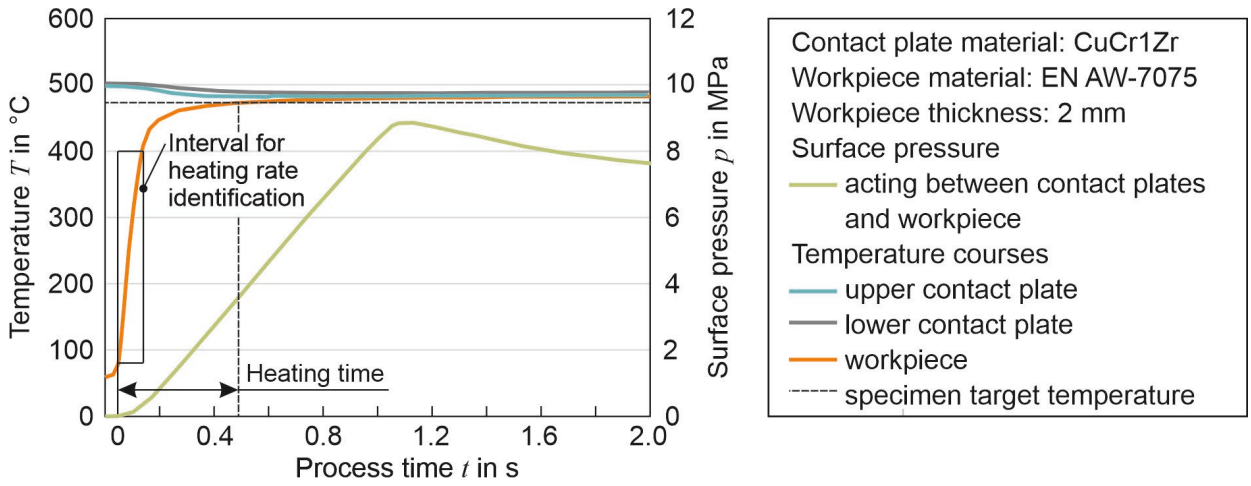

Fig. 4. Time-dependent surface pressure between workpiece and contact plates and corresponding temperatures of workpiece and contact plates.

Based on this measured data, two characteristic values were identified (see also Fig. 4):

1. The heating time t_{heat} was determined as the time interval between closing of the dies (t=0 s) and the moment when the specimen temperature reaches the target temperature of 475°C.
2. The maximum heating rate $\dot{T}$ was determined by referring the temperature difference to the corresponding time difference during the fast (and approximately linear) rise of the temperature. This value allows direct comparison to earlier experiments performed with standard contact plate materials presented in [17].

Influence of the Surface Pressure on the Heating of the Workpiece

Fig. 5 shows the heating times at different surface pressures for five different sheet thicknesses (1.0 mm - 5.2 mm). The contact plate material considered here is the copper alloy. The representative curves for all sheet thicknesses indicate that the heating time decreases with increasing surface pressure. However, the curves show that this effect is limited, because at surface pressures of 9.0 MPa and above higher surface pressures have hardly any further positive influence on the heating time, regardless of the sheet thickness to be heated. This suggests that at lower surface pressure the contact conditions are not ideal. This might be attributed to unevenness or roughness of the sheet. With increasing pressure these deficits are reduced and at a surface pressure of 9 MPa all unevenness or roughness is sufficiently leveled so that the contact conditions are almost constant for even higher pressure. Furthermore, the heating time decreases significantly with reduced sheet thickness. For example, the heating times at the maximum sheet thickness of 5.2 mm and a surface pressure of 3.0 MPa are approx. 13.1 s. With a sheet thickness of 1.0 mm, the heating time drops by approx. 86% to 1.8 s for the same surface pressure.

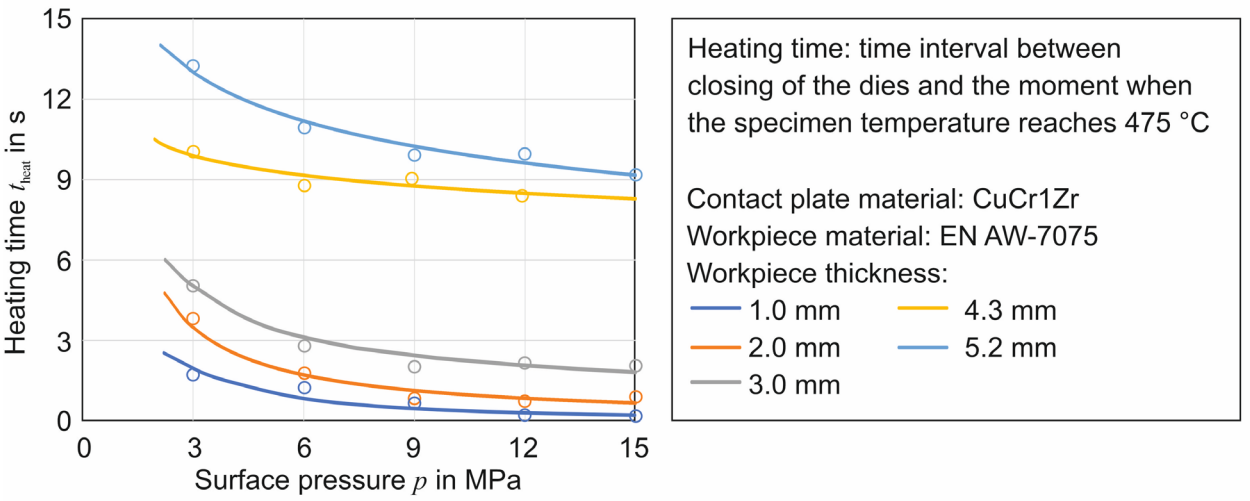

Fig. 5. Heating times for different thicknesses of the aluminum workpiece as function of the surface pressure.

Influence of the Contact Plate Material on The Heating of the Workpiece

In addition to investigating the influence of surface pressure, the material of the contact plates and its influence on the heating rates was studied. For this purpose, additional tests were done using contact plates made of brass alloy. The heating times at varying surface pressures for an exemplary sheet thickness of 2.0 mm are compared to those determined for the copper plates in Fig. 6. In principle, the curves show similar qualitative trends, but the heating times are in general higher in case of the brass plates. This effect can probably be attributed to the lower thermal conductivity of the brass compared to the copper alloy. This means specifically that also in case of heating with brass plates the heating time decreases with increasing surface pressure. The quantitative comparison of the curves determined for the two contact plate materials even shows that in case of heating with brass contact plates the influence of the surface pressure is higher than in case of heating with copper contact plates. For example, the heating under a surface pressure of 3.0 MPa takes more than 10.0 s if brass plates are used, while in case of copper plates such a high heating time was sufficient for heating significantly thicker sheets (see Fig. 5) and heating a sheet with a thickness of 2.0 mm required less than 3.8 seconds. However, also the drop of heating time with increasing surface pressure is more significant if brass plates are used. Already at 6.0 MPa surface pressure, only 4.8 s are required to reach the target temperature, which corresponds to a reduction of 48 %. This percentage reduction is comparable to that of the copper plates (1.9 s at 6.0 MPa). Altogether, the ratio of the heating times for the two contact plate materials (approx. 2.9) corresponds approximately to the inverse ratio of their thermal conductivities (0.37).

Especially if brass plates are used, heating can benefit significantly from a pressure increase, but in addition to the heating time also the temperature dependent stress strain behavior of the contact plate material must be considered when choosing the surface pressure. According to [21], the flow stress of brass alloys similar to the one used here is in the range of 25 MPa - 50 MPa only at a temperature of 550°C, which is only 50 K higher than the contact plate temperature considered here. This means that even though the curves in Fig. 6 suggest that an increase in pressure beyond 15 MPa can still bring a slight reduction of the heating time in case of heating plates made of brass, this advantage must be carefully assessed against the risk of plastic deformation of the contact plates.

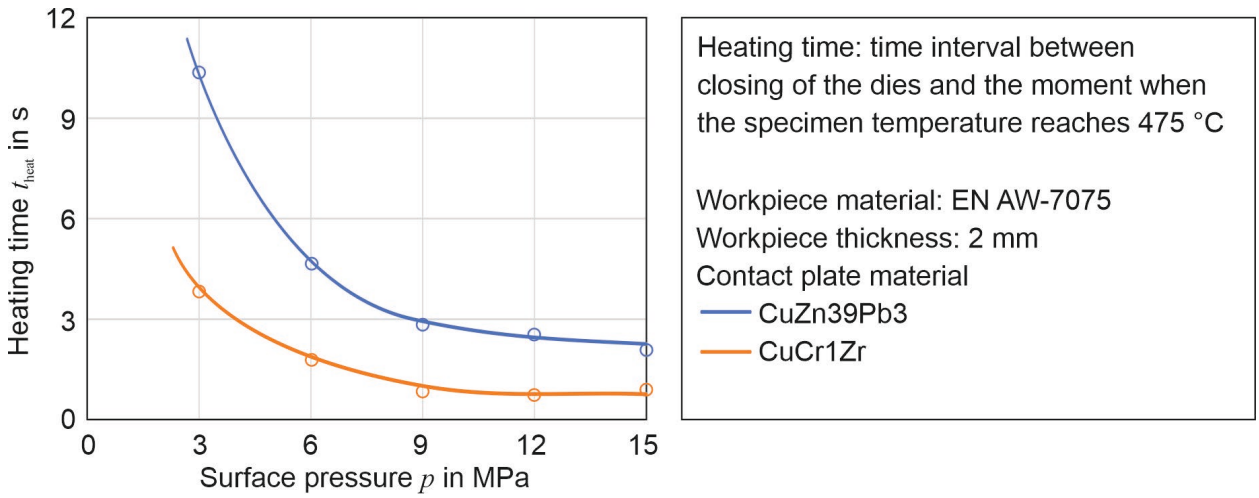

Fig. 6. Heating times for different contact plate materials as function of the surface pressure.

Fig. 7 compares the maximum heating rates $\dot{T}$ of the different contact plate materials for a plate thickness of 2 mm as a function of surface pressure. The heating rates were determined in each case in the range of the linear temperature increase with the maximum slope (see Fig. 4). In addition, the heating rate of the conventionally used contact plate material 1.4828 from [17] was plotted in the diagram for comparison. It can be clearly demonstrated that the maximum heating rates for contact plates made of copper and brass, respectively, are similar at 3 MPa surface pressure. Above 6 MPa surface pressure, however, the values measured for the copper plates increase significantly above the heating rates determined for the brass plates. The maximum heating rates are reached at 12 MPa, but the values for 9 MPa and 15 MPa are at a comparable level. The maximum values amount to approximately 1690 K/s in case of heating plates made of copper and 370 K/s in case of heating plates made of brass. Thus, the maximum heating rate achieved using brass plates is only 23 % of the heating rate achieved using copper plates. At first glance, these results are contrary to those in Figure 6, where the largest difference between the contact plate materials is at 3 MPa and the smallest at 15 MPa. However, the maximum heating rate $\dot{T}$ evaluated here only describes the linear range of the heating process, whereas the heating time t_{heat} covers heating up to 475°C. Heating up to 475°C takes considerably more time and involves strongly non-linear parts of the heating curve (see Fig. 4).

Finally, the heating rate of steel 1.4828 from [17] was plotted. The test conditions were slightly different but still comparable. Especially, the contact plate temperature was slightly lower (480°C instead of 500°C) and the considered workpiece material was a different aluminum alloy with slightly lower heat capacitance but featuring the same thermal conductivity. Moreover, the heating plates and the workpiece were larger in [17], but it can be assumed that this has no significant influence of the heating behavior so the heating rate can be compared. Fig. 7 shows that at a surface pressure of 4.5 MPa, the steel reaches lower heating rates than the predicted heating rates for both materials investigated here. This proves the high potential of the investigated materials in particular the copper alloy for contact heating of aluminum workpieces compared to conventionally used materials as e.g. 1.4828.

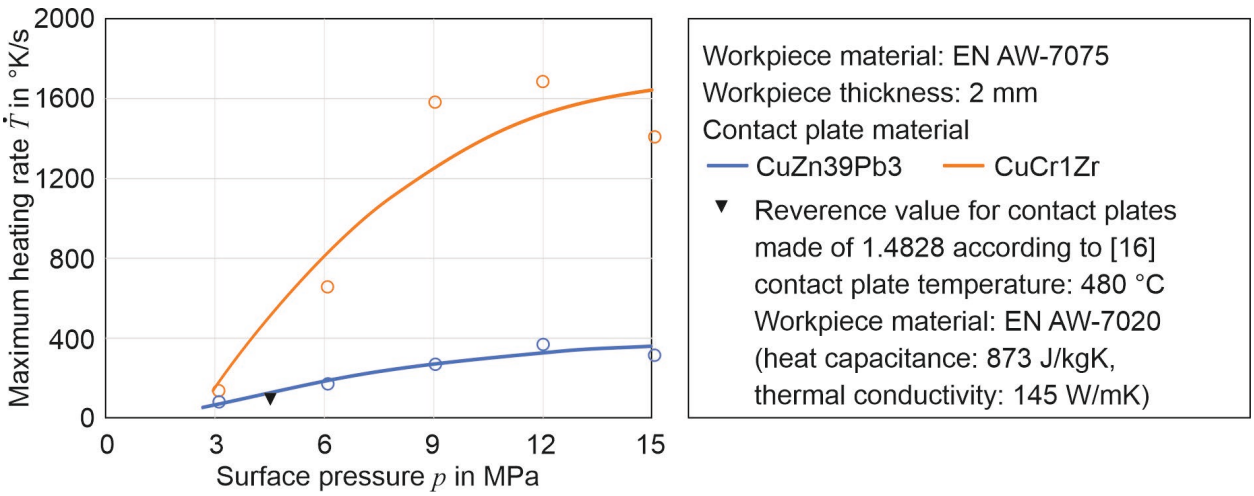

Fig. 7. Maximum heating rates for different contact plate materials as function of the surface pressure.

Summary

In the present study, the effects of two different contact plate materials (copper and brass alloys), five surface pressures and five plate thicknesses on the heating time of the aluminum alloy EN AW-7075 up to the solution heat treatment temperature of 475°C were investigated. A specially manufactured contact heating tool with comprehensive temperature and force measurement was used for this purpose. It was observed for all specimens that fast heating can be realized. Especially at a surface pressure of 9.0 MPa or more, the heating times could be minimized. A further increase in surface pressure is not recommended, because the benefit in terms of further reduction of the heating time is marginal and the strength of the contact plate materials at elevated temperatures relevant for this heating process is limited.

Furthermore, as expected, the heating time decreases significantly with a reduction in sheet thickness. For sheet thicknesses of 1.0 mm and 2.0 mm, heating times of less than 1.0 s could be achieved when heating with the copper plates. The minimum value at 1.0 mm sheet thickness was 0.2 s. The maximum heating rate of 1690 K/s could be achieved at a surface pressure of 12 MPa. This shows the high potential of contact heating especially when heating components with rather small sheet thicknesses. For the highest sheet thicknesses tested here (5.2 mm) and consequently also for the highest volume of the specimen, still a heating rate of 165 K/s could be achieved at the lowest surface pressure. This is significantly more compared to more conventional heating technologies such as furnace heating.

Finally, a comparison of sample heating with brass contact plates was performed. It was found that compared to the heating plates made of copper, especially at low surface pressure significantly higher heating times were necessary, but an increase in surface pressure still allowed reducing the heating time to 2.0 s. Altogether, the following key results were obtained:

- Surface pressures in the range of 9.0 MPa - 12 MPa are recommended for contact heating of aluminum workpieces. Higher pressure brings no further positive effects.
- The lower the sheet thickness, the more positive the contact heating concept. Maximum heating rates of 1690 K/s could be achieved using copper plates.
- Contact heating using copper plates is significantly faster compared to brass plates and the conventionally used steel plates. Heating via brass plates, however, benefits more from an increase in surface pressure.

The presented results prove that contact heating can be realized within the press if suitable surface pressure is applied.

References

[1] M. Hanna, J. Schwenke, L.-N. Schwede, F. Laukotka, D. Krause, Model-based application of the methodical process for modular lightweight design of aircraft cabins, Procedia CIRP 100 (2021) 637-642. https://doi.org/10.1016/j.procir.2021.05.136

[2] C. Koffler, K. Rohde-Brandenburger, On the calculation of fuel savings through lightweight design in automotive life cycle assessments, Int. J. Life Cycle Assess. 15 (2010) 128-135. https://doi.org/10.1007/s11367-009-0127-z

[3] Q. Liu, Y. Lin, Z. Zong, G. Sun, Q. Li, Lightweight design of carbon twill weave fabric composite body structure for electric vehicle, Compos. Struct. 97 (2013) 231-238. https://doi.org/10.1016/j.compstruct.2012.09.052

[4] C.M. Light, P.H. Chappell, Development of a lightweight and adaptable multiple-axis hand prosthesis, Med. Eng. Phys. 22 (2000) 679-684. https://doi.org/10.1016/s1350-4533(01)00017-0

[5] N. Modler, A. Winkler, A. Filippatos, D. Weck, M. Dannemann, Function-integrative Lightweight Engineering - Design Methods and Applications, Chemie Ingenieur Technik 92 949-959. https://doi.org/10.1002/cite.202000010

[6] Z. Tang, Z. Gu, L. Jia, X. Li, L. Zhu, H. Xu, G. Yu, Research on Lightweight Design and Indirect Hot Stamping Process of the New Ultra-High Strength Steel Seat Bracket, Metals 9 (2019) 833. https://doi.org/10.3390/met9080833

[7] M. Linnemann, V. Psyk, N. Kaden, F. Kersten, M. Schmidtchen, V. Kräusel, M. Dix, U. Prahl, Producing and Processing of Thin Al/Mg/Al Compounds, Eng. Proc. 26 (2022) 8. https://doi.org/10.3390/engproc2022026008

[8] H. Karbasian, A.E. Tekkaya, A review on hot stamping, J. Mater. Process. Technol. 210 (2010) 2103-2118. https://doi.org/10.1016/j.jmatprotec.2010.07.019

[9] S. Winter, M. Werner, R. Haase, V. Psyk, S. Fritsch, M. Böhme, M. Wagner, Processing Q&P steels by hot-metal gas forming: Influence of local cooling rates on the properties and microstructure of a 3rd generation AHSS, J. Mater. Process. Technol. 293 (2021) 117070. https://doi.org/10.1016/j.jmatprotec.2021.117070

[10] R. Trân, F. Reuther, S. Winter, V. Psyk, Process development for a superplastic hot tube gas forming process of titanium (Ti-3Al-2.5V) hollow profiles, Metals 10 (2020). https://doi.org/10.3390/met10091150

[11] K. Mori, S. Maki, Y. Tanaka, Warm and hot stamping of ultra tensile strength steel sheets using resistance heating, CIRP Annals—Manuf. Technol. 54 (2009) 209-212.

[12] R. Kolleck, R. Veit, M. Merklein, J. Lechler, M. Geiger, Investigation on induction heating for hot stamping of boron alloyed steels, CIRP Annals—Manuf. Technol. 58 (2009) 275-278.

[13] R. Kolleck, R. Veit, H. Hofmann, F.J. Lenze, Alternative heating concepts for hot sheet metal forming, 1st International Conference on Hot Sheet Metal Forming of High-Performance Steel, Kassel, Germany, 2008, pp. 239-246.

[14] V. Ploshikhin, A. Prihodovsky, J. Kaiser, R. Bisping, H. Linder, C. Lengsdorf et al., New heating technology for furnace-free press hardening process, Tools and Technologies for Processing Ultra-High Strength Materials, Graz, Austria, 2011.

[15] D. Landgrebe, F. Schieck, J. Schönherr, New Approaches for Improved Efficiency and Flexibility in Process Chaines of Press Hardening, International Mechanical Engineering Congress & Exposition (ASME), Houston/Texas, USA, 13 - 19.11.2015.

[16] J.N. Rasera, K.J. Daun, C.J. Shi, Direct contact heating for hot forming die quenching, Appl. Therm. Eng. 98 (2016) 1165-1173.

[17] R. Trân, L. Kertsch, S. Marx, S. Hebbar, V. Psyk, A. Butz, Towards an efficient Industrial Implementation of W-temper Forming for 7xxx Series Al Alloys, in: G. Daehn, J. Cao, B. Kinsey, E. Tekkaya, A. Vivek, Y. Yoshida (Eds.), Forming the Future, Cham: Springer International Publishing, 2021.

[18] C. Hoff, Untersuchungen der Prozesseinflussgrößen beim Presshärten des höchstfesten Vergütungsstahls 22MnB5, Dissertation, Universität Erlangen-Nürnberg, 2007.
[19] W. Xiao, B. Wang, K. Zheng, J. Zhou, J. Lin, A study of interfacial heat transfer and its effect on quenching when hot stamping AA7075, Arch. Civil Mech. Eng. 18 (2018) 723-730. https://doi.org/10.1016/j.acme.2017.12.001
[20] A.A.M. Smeyers, S. Khosla, Production of formed automotive structural parts from AA7xxx-series aluminium alloys, European Patent EP 2 581 218 B1, 2012.
[21] S. Spigarelli, M. El Mehtedi, M. Cabibbo, F. Gabrielli, D. Ciccarelli, High temperature processing of brass: Constitutive analysis of hot working of Cu-Zn alloys, Mater. Sci. Eng. A 615 (2014) 331-339. http://doi.org/10.1016/j.msea.2014.07.091

Materials Research Proceedings 28 (2023) 969-976 https://doi.org/10.21741/9781644902479-106

Low-cost tooling concept for customized tube bending by the use of additive manufacturing

TRONVOLL Sigmund A.[1,a*], TREFFEN Helena[1,b], MA Jun[1,c] and WELO Torgeir[1,d]

[1]Department of Mechanical and Industrial Engineering, Norwegian University of Science and Technology, Trondheim, 7491, Norway

[a]sigmund.tronvoll@ntnu.no, [b]helenatr@stud.ntnu.no, [c]jun.ma@ntnu.no, [d]torgeir.welo@ntnu.no

Keywords: Low-Cost Tooling, Tube Bending, Flexibility, Additive Manufacturing

Abstract. Bending is commonly used in the manufacturing of finished and semi-finished, profile-based products. However, costly profile and bend geometry dependent tooling hampers its applicability for low volume production or prototyping. Additive manufacturing (AM) offers a potential for making tools in low-volume production, which is particularly attractive for customized manufacturing and prototyping with near production intent tooling. In this research, an industrial bending process for tubes and profiles, called rotary drawing bending (RDB), is used as a case. In the RDB process, the mandrel die installed inside the tube or profile blank is of crucial importance to secure the quality of the cross-section of bent shapes. Moreover, this die is normally difficult and expensive to produce. In addition, each mandrel is tailored to a single profile's inner geometry, hence posing an obstacle to acquiring a tooling setup for multiple cross-section dimensions. As a countermeasure, a novel mandrel tooling concept is designed by using a metal rod core with an AM-sleeve fitted to the rod outside, as an easy-to-replicate solution for significantly lowering the costs of offering the capability of forming processes with different cross-section dimensions. Fused filament fabrication (FFF)—a cost-effective AM process—is used for fabricating the mandrel die with various pre-designed and optimized shapes. Using both the AM mandrel in polylactide (PLA) and the conventional metal mandrel in a series of bending experiments of AA6082-T4 Al-alloy tubes, the dimensional and qualitative results of tubes bent with different mandrels is analyzed, discussed, and compared.

Introduction

To meet the increased customer demands for product variety, the manufacturing sector is transforming from mass production to mass customized production, with higher flexibility and on-demand manufacturing [1]. However, for the die-based manufacturing processes such as metal forming, they are increasingly challenged to meet the demands on flexibility [2]. In the metal forming area, the design and fabrication of tools are normally expensive and need a long lead time, which significantly limits the transformation of conventional forming towards the customized forming. This calls for new tooling concepts and methods that allow the time-efficient, cost-effective fabrication of tools for mass customized metal forming.

Additive manufacturing (AM) used for rapid prototyping offers a potential for making tools in low-volume, customized production, which is particularly interested by the industrial metal forming processes. In recent years, some attempts at AM-based tools used in metal forming have been carried out. A typical application of AM as a method for tooling making to realize the metallic dies with optimized cooling channels in hot metal working such as hot stamping [3]. For instance, Komodromos et al. [4] employed a Directed Energy Deposition (DED) to produce the hot stamping tools with integrated cooling channels. After the DED process, the tool surfaces are ball burnished to reduce the surface roughness for more effective heat transfer. Joghan et al. [5] utilized hybrid AM method to make metal laminated forming tools. In this method, laser metal deposition is used

Content from this work may be used under the terms of the Creative Commons Attribution 3.0 license. Any further distribution of this work must maintain attribution to the author(s) and the title of the work, journal citation and DOI. Published under license by Materials Research Forum LLC.

for bonding the sheets and smoothening the edges, and subsequently milling, roller burnishing, and laser treatment are applied as post-processing for improving the strength and surface finish. Similarly, a layer-laminated manufacturing method and a laser melting process were applied in the manufacturing of the dies with conformal cooling channels for extrusion processes [6]. Chantzis et al. [7] proposed a Design for AM (DfAM) method for hot stamping dies which exploits the benefit of lattice structures for reduced thermal conductivity. It shows that the proposed method can significantly improve the cooling performance of a hot stamping die with printing times reduced by at least 12% compared to traditionally manufactured AM dies. This shows that high end AM systems, as those capable of manufacturing metal parts, has a potential for improving process control and manufacturing rate.

For increased flexibility in low-volume manufacturing, more inexpensive AM-solutions would be preferred, as the associated cost and leadtime is the key parameter, rather than geometric complexity. In this case, fused filament fabrication (abbreviated FFF, also called filament-based extrusion AM) has attracted some scientific interest. Strano et al. [8] demonstrated the potential applicability and versatility of FFF as a rapid tool manufacturing technology for different applications in shearing, bending, deep drawing, and injection molding. Frohn-Sörensen et al. [9] utilized the FFF process to manufacture the tooling to draw a small series of sheet metal parts in combination with the rubber pad forming process. In addition, a variety of common polymer materials (PLA, PA, PETG, PC) were comprehensively compared in compressive and flexural tests to provide an guide for material selection in AM-based polymer tools for metal forming [10].

The body of research on AM-based tooling in metal forming is obviously more extensive than the above-summarized ones. However, most of them focus mainly on cold and hot forming of sheets, and in tooling that will be in compression, and are hence not that affected by FFFs tensile anisotropy [11]. The use of AM in making tools for complex tube bending processes has not been explored earlier, and the process that will be discussed in this paper is rotary draw bending (RDB), which is shown in Fig. *1*. This is one of the more popular bending processes, and normally operates with a tooling system including 5-6 complex-shaped tools, in which tooling is one of most important issues affecting the production cost. The tools are also dependent on either or both the bend radius, profile inner- and outer-geometry. Therefore, most workshops keep a limited inventory of tooling variants, which is a significant limitation to their capability in terms of geometric flexibility.

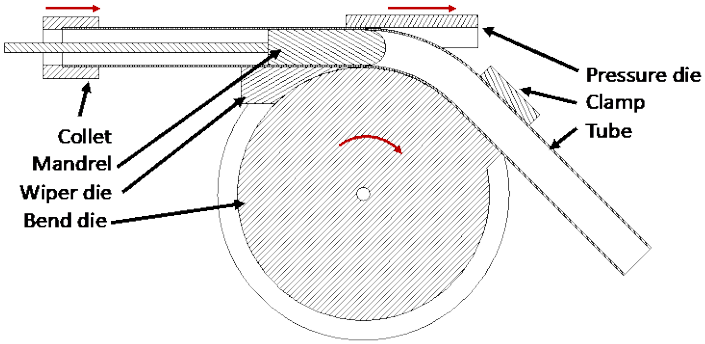

Fig. 1. Conceptual tooling layout of rotary draw bending (RDB).

The aim of this research is to develop a new cost-effective tooling concept for tube rotary draw bending processes by utilizing low-cost FFF manufacturing methods, and initially investigating its applicability to be used for mandrel bending. First, the newly proposed mandrel die concept is introduced. Secondly, using aluminium tubes with different wall thicknesses, a series of bending experiments with and without conventional mandrels and new AM-based mandrels is presented.

Finally, the dimensional accuracy and qualitative aspects of formed tubes is evaluated to verify the feasibility and capability of the new AM-based mandrel die concept for tube bending.

Low-Cost Tooling Concept for Customized Bending

For both product development and low production purposes using RDB, being able to quickly change the wall thickness of tubes or profiles would be beneficial, but requires change of the mandrel, which is a crucial tool for bending components with a high diameter to thickness ratio. Keeping a catalogue of mandrels suitable for all wall thicknesses could be costly, while acquisition on demand through buying or in-house machining might be preferrable. Conventional mandrel shapes, as shown in Fig. *2*, does however require multi-step CNC machining, which often comes with a considerable cost and lead time. It is in this domain we believe additive manufacturing could provide a significant benefit in bringing lead time and cost for changing mandrel to a minimum. As a first step in this effort, we are investigating the feasibility of using spherical end mandrels manufactured using standard FFF process equipment and standard PLA filament material.

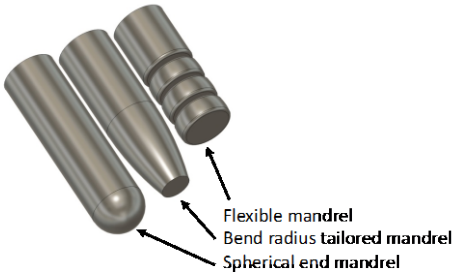

Fig. 2. Mandrel types in tube rotary draw bending.

To provide structural integrity and overcome the inter-layer bonding problems found in FFF parts, the PLA-mandrels used in this study were constructed with a steel core, while adding a bolt-on outer interchangeable PLA sleeve to provide the required geometry, as shown in Fig. *3*. As the suggested hybrid mandrel system is believed to be softer than its metal counterpart, we expect that for getting a comparable result, the mandrel extension (shown in Fig. *3*) would need to be increased.

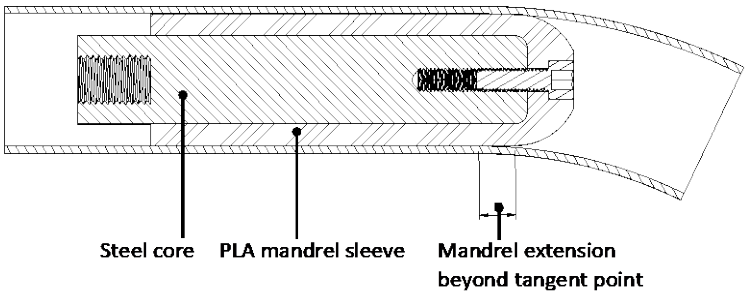

Fig. 3. Hybrid steel/PLA mandrel construction.

Experimental Setup

Using a *Star Technology 800 EVOBEND* tube bending machine, with tooling designed for Ø60 mm profiles and 222 mm bend radius, experiments with tube thicknesses of 3 and 2 mm, and mandrel extension lengths were conducted as shown in Table *1*. The manufactured bends were then evaluated based on the flattening of the cross section radially relative to the bend axis,

measured using a caliper. For the bend radius and outer tube diameter, experience has shown that 3 mm thickness tubes do not exhibit wrinkling defect if manufactured without mandrel, while 2 mm ones do. The 2mm tube experiments are therefore also evaluated qualitatively on the basis of the mandrel's capability of mitigating the wrinkling defect on 2 mm tubes bent without a mandrel. The steel and AM mandrels, and how they are installed in the tool system is shown in Fig. *4*.

Table 1. Experimental matrix.

Experiment #	Mandrel type	Mandrel extension (e)	Tube thickness	Samples
1	No mandrel		3 mm	2
2	Steel	0 mm	3 mm	2
3	AM	0 mm	3 mm	2
4	AM	5 mm	3 mm	2
5	AM	10 mm	3 mm	2
6	No mandrel		2 mm	2
7	AM	5 mm	2 mm	2
8	AM	10 mm	2 mm	2

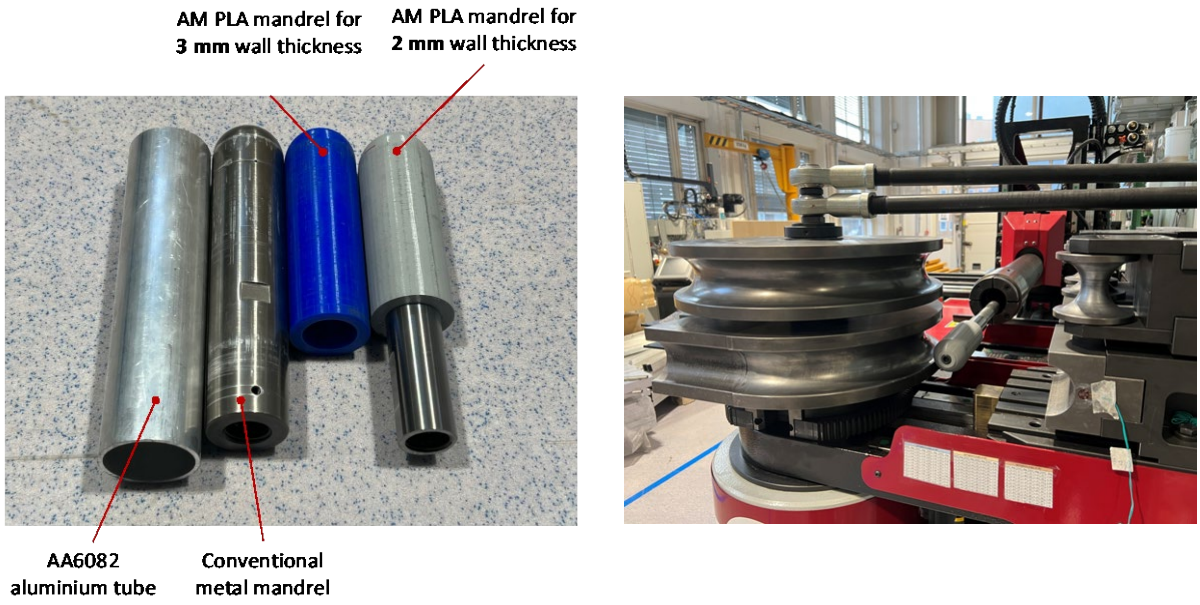

(a) (b)

Fig. 4. (a) AM PLA mandrels and conventional metal mandrel, and (b) assembled tooling in the RDB tooling system.

Results and Discussion

Qualitative and quantitative results for the 3 mm thickness samples are shown in Fig. *5* and in Fig. *6*, respectively. Qualitative assessment does not reveal any major difference between the different mandrels. Quantitatively, the AM mandrel provides a significant support to limit tube flattening and reduces the tube flattening with 50% compared to the samples bent without mandrel. Comparing with the steel mandrel, however, the PLA mandrel is seen to provide less support for 0 extension distance, with 1 mm larger cross section flattening (2-2.5 mm in total), suggesting that the PLA mandrel is significantly softer than the metal version. The flattening is reduced to values comparable to those for steel mandrel if the mandrel extension is increased to 10 mm for the PLA mandrel, which results in approximately 1 to 1.5 mm of flattening. Although increased mandrel extension will increase the contact pressure on the mandrel, there is no indications that the PLA mandrel is being degraded significantly, as it shows no cracks or scuffing marks.

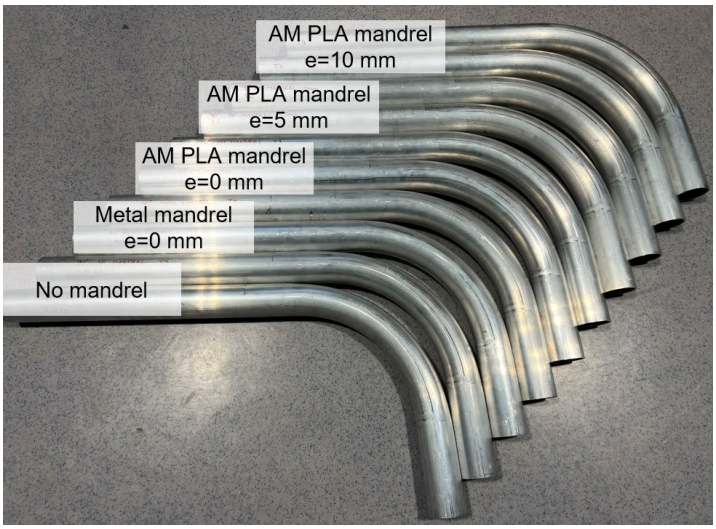

Fig. 5. Qualitative results from tube bending with 2mm wall thickness.

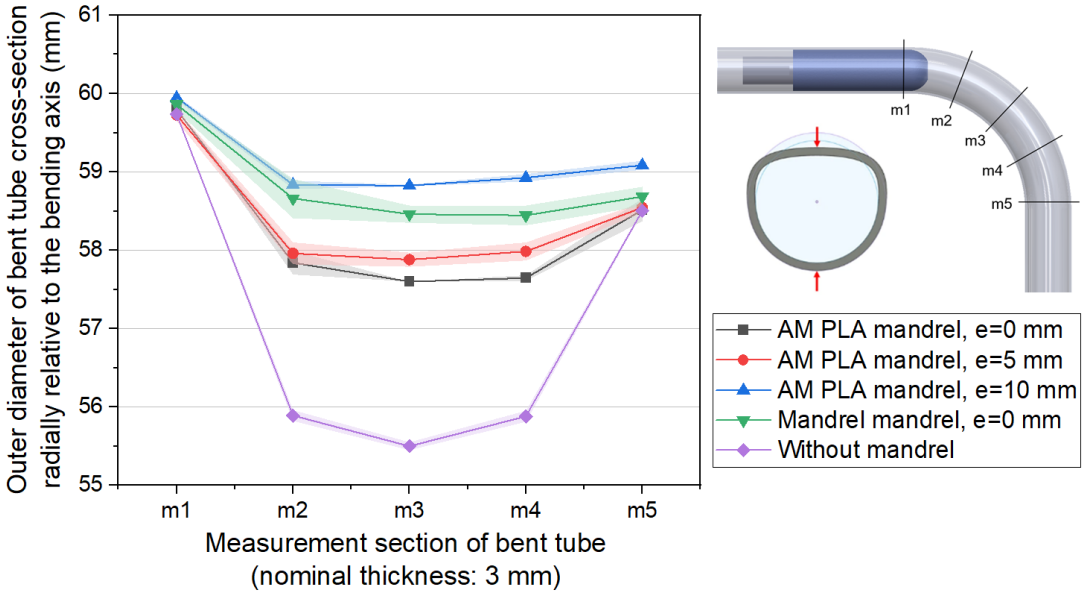

Fig. 6. Radial tube flattening from tube bending with 3 mm wall thickness.

Qualitative and quantitative results for the 2 mm thick samples are shown in Fig. 5 and in Fig. 6, respectively. As shown in Fig. 5, the lowered wall thickness results in pronounced intrados wrinkling when bending without a mandrel, which is effectively mitigated with the use of the AM mandrel. The samples from bending without a mandrel are left out of the quantitative results due to wrinkling. The 2 mm thickness tubes display a slightly higher flattening than for 3 mm thick tubes, with approximately 3 to 4 mm flattening using an extension distance of 5 mm, which is reduced to approximately 2.5 to 3 mm when increasing the extension distance to 10 mm. As in the case with the mandrel for 3 mm wall thickness tubes, there is in this case also no indications that the PLA mandrel is being degraded significantly, as it shows no cracks or scuffing marks as well.

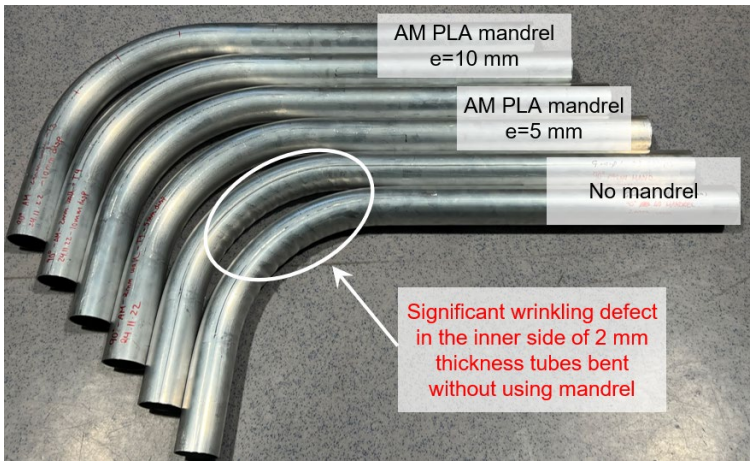

Fig. 7. Qualitative results from tube bending with 2mm wall thickness.

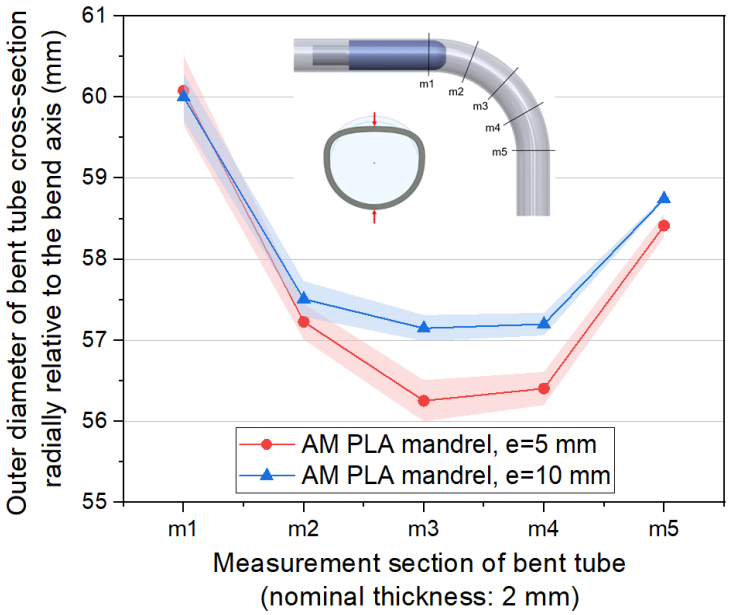

Fig. 8. Radial tube flattening from tube bending with 2 mm wall thickness.

Summary

The proposed tooling concept with a hybrid steel-PLA mandrel is found to provide sufficient support and structural integrity to significantly reduce both the cross section flattening and wrinkling for the investigated cases of tube bending using rotary draw bending of aluminum tubes. With the simplicity of the manufacturing using additive manufacturing, and the low cost associated with the material and manufacturing system for fused filament fabrication, using this type of mandrels provides a significant process improvement over bending without mandrel, and on par with steel mandrels if the mandrel extension length is increased.

As the concept explored in this paper seems promising, replacing other complex tools, as the wiper die could provide additional value. We would also suggest investigating the method's applicability on bending of tubes with higher material strength as steel or titanium. We also believe that further research should target investigating the durability of these AM mandrels, to investigate its applicability for manufacturing larger volumes.

Acknowledgements

The authors gratefully acknowledge the support from NTNU Aluminum Product Innovation Center (NAPIC), and through the *TaFF* project (*Digitally-Controlled, Toolless and Flexible Forming*) in collaboration with *Benteler Automotive Raufoss AS*, funded through *The Research Council of Norway* through grant number 317777.

References

[1] J. Cao, M. Banu, Opportunities and Challenges in Metal Forming for Lightweighting : Review and Future Work, J. Manuf. Sci. Eng. 142 (2020) 1–24. https://doi.org/10.1115/1.4047732

[2] D.Y. Yang, M. Bambach, J. Cao, J.R. Duflou, P. Groche, T. Kuboki, A. Sterzing, A.E. Tekkaya, C.W. Lee, Flexibility in metal forming, CIRP Ann. - Manuf. Technol. 67 (2018) 743-765. https://doi.org/10.1016/j.cirp.2018.05.004

[3] D. Chantzis, X. Liu, D.J. Politis, O. El Fakir, T.Y. Chua, Z. Shi, L. Wang, Review on additive manufacturing of tooling for hot stamping, Int. J. Adv. Manuf. Technol. 109 (2020) 87-107. https://doi.org/10.1007/s00170-020-05622-1

[4] A. Komodromos, F. Kolpak, A.E. Tekkaya, Manufacturing of Integrated Cooling Channels by Directed Energy Deposition for Hot Stamping Tools with Ball Burnished Surfaces, BHM Berg- Und Hüttenmännische Monatshefte. 167 (2022) 428-434. https://doi.org/10.1007/s00501-022-01264-w

[5] H. Dardaei Joghan, M. Hahn, J.T. Sehrt, A.E. Tekkaya, Hybrid additive manufacturing of metal laminated forming tools, CIRP Ann. 00 (2022) 1-4. https://doi.org/10.1016/j.cirp.2022.03.018

[6] R. Hölker, M. Haase, N. Ben Khalifa, A.E. Tekkaya, Hot Extrusion Dies with Conformal Cooling Channels Produced by Additive Manufacturing, Mater. Today Proc. 2 (2015) 4838–4846. https://doi.org/10.1016/J.MATPR.2015.10.028

[7] D. Chantzis, X. Liu, D.J. Politis, Z. Shi, L. Wang, Design for additive manufacturing (DfAM) of hot stamping dies with improved cooling performance under cyclic loading conditions, Addit. Manuf. 37 (2021) 101720. https://doi.org/10.1016/J.ADDMA.2020.101720

[8] M. Strano, K. Rane, M.A. Farid, V. Mussi, V. Zaragoza, M. Monno, Extrusion-based additive manufacturing of forming and molding tools, Int. J. Adv. Manuf. Technol. (2021). https://doi.org/10.1007/s00170-021-07162-8

[9] P. Frohn-sörensen, M. Geueke, T.B. Tuli, M. Manns, B. Engel, P. Manuskript, P. Frohn-sörensen, M. Geueke, T.B. Tuli, M. Manns, B. Engel, 3D printed prototyping tools for flexible sheet metal drawing, (2021) 1-26

[10] P. Frohn-Sörensen, M. Geueke, B. Engel, B. Löffler, P. Bickendorf, Compressive and flexural material properties of PC , PLA , PA and PETG for additive tooling in sheet metal forming, (2022). https://doi.org/10.31224/2239
[11] Q. Sun, G.M. Rizvi, C.T. Bellehumeur, P. Gu, Effect of processing conditions on the bonding quality of FDM polymer filaments, Rapid Prototyp. J. 14 (2008) 72-80. https://doi.org/10.1108/13552540810862028

Materials Research Proceedings 28 (2023) 977-986 https://doi.org/10.21741/9781644902479-107

Experimental investigation of the fluid-structure interaction during deep drawing of fiber metal laminates in the in-situ hybridization process

KRUSE Moritz [1,a,*] and BEN KHALIFA Noomane [1,2,b]

[1]Leuphana University of Lüneburg, Institute for Production Technology and Systems (IPTS), Universitätsallee 1, 21335 Lüneburg, Germany

[2]Helmholtz-Zentrum Hereon, Institute of Material and Process Design, Max-Planck-Straße 1, 21502 Geesthacht, Germany

[a]moritz.kruse@leuphana.de, [b]ben_khalifa@leuphana.de

Keywords: Fiber Metal Laminates, Deep Drawing, In-Situ Hybridization, Fluid-Structure Interaction

Abstract. Matrix accumulations, buckling and tearing of fibers and metal sheets are common defects in the deep drawing of fiber metal laminates. The previously developed in-situ hybridization process is a single-step method for manufacturing three-dimensional fiber metal laminates (FML). During the deep drawing of the FML, a low-viscosity thermoplastic matrix is injected into the dry glass fiber fabric layer using a resin transfer molding process. The concurrent forming and matrix injection results in strong fluid-structure interaction, which is not yet fully understood. To gain a better understanding of this interaction and identify possible adjustments to improve the process, an experimental form-filling investigation was conducted. Using a double dome deep drawing geometry, the forming and infiltration behavior were investigated at different drawing depths with full, partial, and no matrix injection. Surface strain measurements of the metal blanks, thickness measurements of the glass fiber-reinforced polymer layer, and optical analyses of the infiltration quality were used to evaluate the results.

Introduction

Multi-materials allow the engineering of material properties to the specific needs of a given application [1]. Fiber metal laminates (FML) are a multi-material that consists of several layers of fiber-reinforced polymers (FRP) and metal. They were initially developed to address the challenges associated with the use of fiber-reinforced polymers, such as low impact resistance [2]. The material combination offers several advantageous properties, such as improved impact resistance, high strength-to-weight ratio, and little crack propagation [3]. Therefore, FMLs are often used in aircraft body structures, where simple geometries are easy to manufacture [4]. However, their use in other industries, such as the automotive industry, is constrained by the cost and time required to manufacture FML parts with more complex geometries. These parts often require separate forming and bonding steps, as cured FMLs can only be formed to a limited extent [5]. As a result, several investigations have been conducted on one-step manufacturing processes for formed FML, often using half-cured [6, 7] or thermoplastic [8, 9] pre-impregnated fiber materials in a deep drawing process. However, in many cases, strong interactions between fiber, metal and the high-viscosity matrix flow during forming can lead to delamination, inhomogeneous thicknesses of the FRP-layer as well as wrinkling and tearing of the metal sheet and fibers [8,10].

A new manufacturing process for FML was introduced previously [11]. The in-situ hybridization process combines deep drawing with a thermoplastic resin transfer molding process (T-RTM). During deep drawing, a reactive low-viscosity monomeric matrix is injected into the fabric layer (see Fig. 1). After forming, the matrix polymerizes into a thermoplastic and creates

Content from this work may be used under the terms of the Creative Commons Attribution 3.0 license. Any further distribution of this work must maintain attribution to the author(s) and the title of the work, journal citation and DOI. Published under license by Materials Research Forum LLC.

the interface with the metal sheets. Due to the low matrix viscosity, fibers and metal are in direct contact during the forming process. While a low-viscosity matrix is advantageous for fluid flow and fabric drapability during forming, friction between metal and fabric is higher because of high local normal loads at the roving crossings [12]. Previous investigations have shown that this contact under high normal pressures can reduce the formability of the metal sheet by restricting relative movement between fibers and metal [13]. In deep drawing tests of dry FMLs without matrix injection, tool lubrication led to lower metal and fiber strain [14]. Lower friction between fabric and metal improved the forming further by allowing for better interlayer movement.

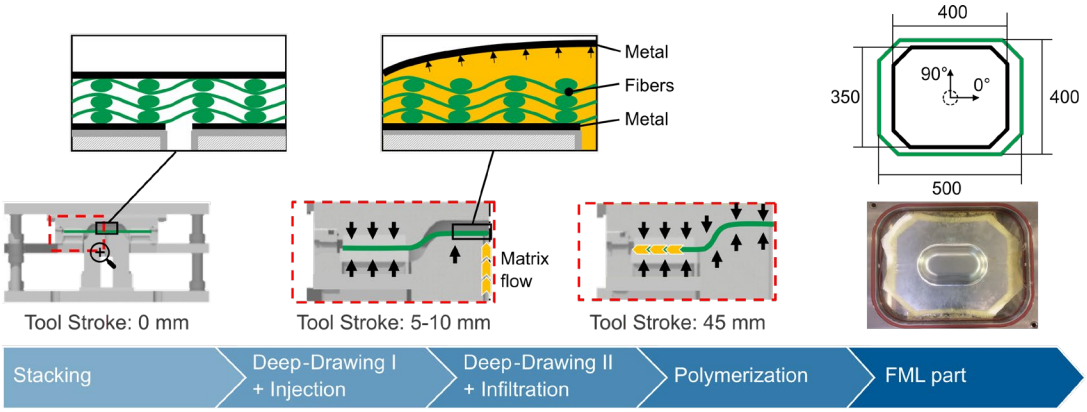

Fig. 1. Combined deep drawing and thermoplastic resin transfer molding (T-RTM) process for the manufacturing of fiber metal laminate parts, as introduced by Mennecart et al. [11].

Double dome geometry parts with a drawing depth of 45 mm could be successfully manufactured without wrinkling or tearing. However, the influence of forming on matrix flow and vice versa has to be investigated to understand fluid-structure interaction in the process and improve infiltration quality and forming. Mennecart et al. [11,15] found that bulging of the metal sheets can occur in regions of high internal pressure due to the matrix injection and low external pressure when no contact with the female die is established. In this work, different amounts of matrix are injected to manufacture parts with different drawing depths, aiming to provide a better understanding of the form-filling behavior. This is necessary to identify the most influential parameters in the process, which are different from those in pure metal deep drawing due to fluid-structure interaction. As a result, possible process improvements are derived.

Materials and Method

The FML specimen consists of a metal layer on the top and bottom, with six layers of a twill 2/2 woven E-glass fabric (280 g/m^2, Interglas 92125 FK800) with good drapability in between. The metal sheets are made of DC04 (1.0338) with a thickness of 1 mm. The dimensions are shown in Fig. 1. The lower metal sheet has a 19 mm diameter hole in the center for matrix injection. A polytetrafluoroethylene (PTFE) foil (0.025 mm) is used between the top metal sheet and tool for lubrication. After stacking the layers in the tool, deep drawing to 15 % of the final drawing depth is performed to plastically deform the metal sheets and achieve sealing between the sheet and punch due to the increased contact pressure. The thermoplastic matrix (Arkema Elium® 150), with an initial viscosity of 100 mPas, mixed with 2.5 % hardener (dibenzoyl peroxide Perkadox® GB-50X), is injected while deep drawing is continued. Deep drawing is performed with a blank holder force of 190 kN, a punch velocity of 1 mm/s and a tool temperature of 70 °C to accelerate matrix polymerization after forming. When the final drawing depth of 45 mm is reached and the tool is fully closed, the position and blank holder force are held for 20 minutes to allow the matrix to fully polymerize before demolding.

The fluid-structure interaction and form-filling behavior during the process are investigated under three different conditions: With full infiltration, partial infiltration and without matrix injection. Deep drawing is performed up to 15 %, 50 % and 100 % of the total drawing depth, where the press is halted and the matrix polymerizes. Additionally, three more drawing depths (80 %, 82.5 %, and 85 %) are analyzed for the full infiltration condition. An overview of the experiments is given in Table 1. The target height of 1 mm for the fabric layer corresponds to a fiber volume fraction of 65% and a matrix volume fraction of 35% for the fabric material used in the experiments. The surface area of the metal sheet is 120,000 mm^2, so the total matrix volume needed for full part infiltration can be calculated to be 42 ml. Approximately 120 ml of matrix are needed to fill the injection channel, so 140 ml are used for the partial infiltration experiments. For the full infiltration experiments, 300 ml are used to ensure that the whole part is infiltrated and any remaining air is flushed out. The formed metal sheets are evaluated with a GOM ARGUS optical surface strain measurement system. The thickness of the glass fiber reinforced polymer (GFRP) layer is measured with a GOM ATOS laser scanning system.

Table 1. Experimental design.

Matrix amount [ml]	Drawing depths [%]
0 (No infiltration)	10, 50, 100
140 (Partial infiltration)	10, 50, 100
300 (Full infiltration)	10, 50, 80, 82.5, 85, 100

In the original process [11], the inner side of the metal sheets is ground in 0° and 90° direction as well as in small circles. A bonding agent (Dynasalan® Glymo by Evonik) is then applied to improve adhesion. For the experiments in this investigation, the inner side of the metal sheet is not ground but treated with a release agent (Henkel Loctite® Frekote HMT2) so that each layer can be investigated separately after manufacturing.

Results

A comparison of parts manufactured with both metal sheet surface treatment methods showed no difference in observed metal strains or fiber draping, which demonstrates the validity of the experiments performed with the release agent. In contrast, previous dry deep drawing experiments without matrix injection demonstrated a strong influence of surface treatment on metal strains [14]. This suggests that the matrix has a lubricating effect on the contact between the fabric and metal, which reduces friction even when the metal sheets are ground.

Full infiltration.

Fig. 2 shows the development of the geometry and strains in the upper metal sheet of the FML during deep drawing. It was previously shown that the strains in the upper metal sheet are more critical regarding tearing than in the lower metal sheet [14]. The vertical distance (major strain) to the forming limit curve (FLC) is used as a measure of how susceptible the metal is to tearing. The applied FLC was obtained as described by Mennecart et al. [13] for DC04 with glass fiber twill fabric interlayer. Because of biaxial tensile strains, the punch radius is the most critical area, even though the die radius has higher major strains.

In the flange, the high blank holder pressure causes high compaction and low permeability of the fabric. As a result, the matrix cannot flow in the flange fast enough during the injection. This causes bulging of the upper metal sheet due to high internal pressure and low external pressure because of the lack of contact with the female die. High friction is present in the flange area between the upper metal sheet and fabric as well as the fabric and lower metal sheet. This hinders the flow of the upper metal sheet and leads to forming similar to a hydro stretch forming process with increased biaxial tensile strains in the bottom and wall area of the part, as can be seen at 50

% drawing depth. In the lower metal sheet, no bulging can occur in the part bottom because external pressure is established due to punch contact. However, slight bulging does occur in the wall area where punch contact is only established during the compression phase towards the end of the deep drawing. The injection is completed at a drawing depth of 45 %. During the injection, the pressure increases linearly from 1 MPa to a maximum of 2.2 MPa. With increasing drawing depth, the injection pressure increases due to higher flow resistance in the die radius and strain hardening in the bulged metal sheet.

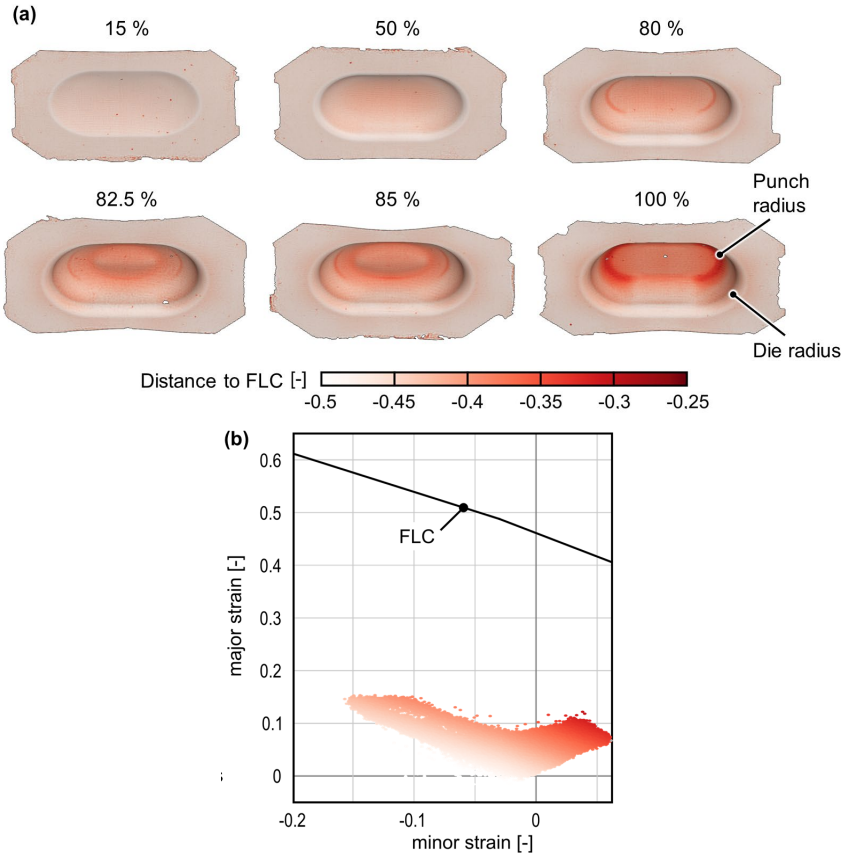

Fig. 2. Development of a part in the in-situ hybridization process with full infiltration (a) Surface strains of the upper metal sheet at different drawing depths (b) Forming limit diagram of the upper metal sheet at 100 % drawing depth (FLC: Forming Limit Curve).

At 80 %, higher strains in the punch radius are present because of metal contact with the fabric, causing the metal to bend over the edge. The wall and bottom area are still bulged. Between 80 % and 82.5 %, the bulge collapses, starting from the center. Comparing the bulge height with the drawing depth shows that die contact is established between 80 % and 82.5 %. When contacting, the die causes the bulge to suddenly collapse inside to achieve a stable condition again. After the brief die contact, there is no contact between the metal sheet and the die at 82.5 % until the die contacts again with further deep drawing between 82.5 % and 85 %. With further closing of the punch and die, the matrix is squeezed to the outside in a donut shape and to the flange with high internal fluid pressure. This is similar to a compression T-RTM process. Because of the bulging and squeezing of the matrix to the outside, high internal fluid pressures lead to high strains in the punch radius of the fully formed upper sheet.

The matrix distribution is shown in detail in Fig. 3a. Because the permeability of the chosen fabric is slightly higher in the 0° direction than in the 90° direction, the flow front initially advances

in an oval shape. At 50 % drawing depth, when the injection is complete, the flow front has not reached the edges of the metal sheets yet. Instead, the matrix accumulates in the bulge due to the high blank holder pressure on the fabric. Furthermore, an air cluster in the middle of the bulge and pores can be observed in the matrix layer. One possible reason for this is that air from the injection channel is pushed into the fabric layer before the matrix. Due to the high injection pressure, matrix and air could mix, resulting in air being trapped inside the matrix bulge. Another probable reason for at least some of the air is gas evolution from the matrix during polymerization. Under high temperatures and pressures, as well as with the formation of thick layers, the thermoplastic matrix can produce carbon dioxide as a byproduct during polymerization. Because of the pores and air cluster, the infiltration quality of the fully formed part is poor in some areas. In the final part, air is trapped inside the GFRP layer as small pores and causes insufficiently infiltrated spots in high compression areas like punch and die radius.

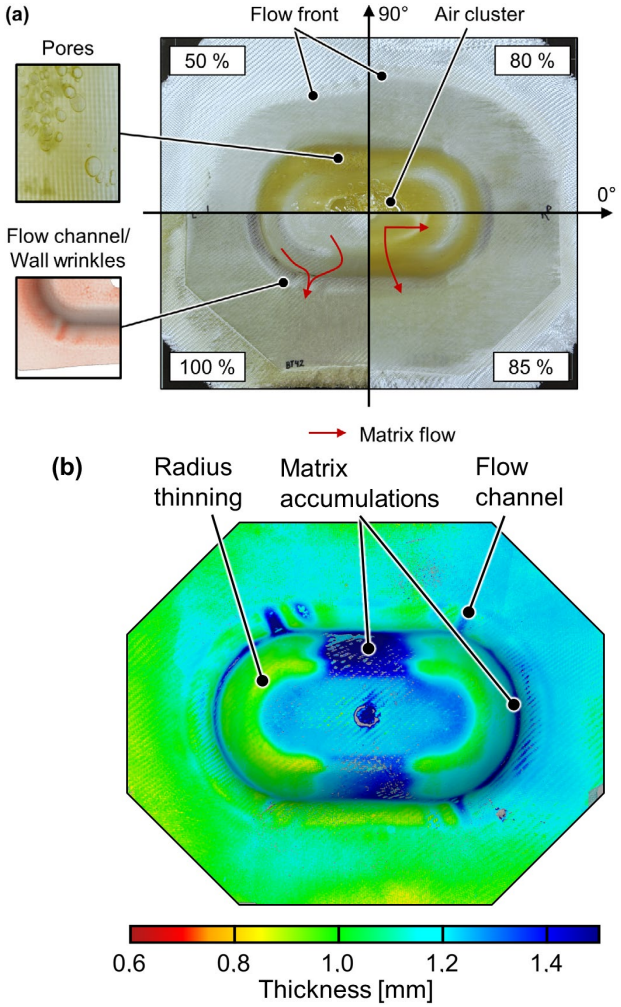

Fig. 3. GFRP layer (a) Matrix flow during the evolution of the geometry (b) Thickness of the cured GFRP layer at 100 % drawing depth.

At 80 %, the flow front has advanced slightly because some matrix is squeezed out of the bulge into the flange. Furthermore, the fabric layer thins out in the punch radius due to high normal compression. When the bulge collapses, the trapped air and matrix are pushed outside and into the flange and wall area. Because of the matrix flow to the outside, the punch radius infiltration is better again at that point. At 85 %, the flange is fully infiltrated. After the collapse, high matrix

flow velocities from the part bottom to the flange lead to the development of flow channels in the GFRP that are still present at 100 %. Towards the end of the deep drawing, the part bottom and wall are compressed between the punch and die. The remaining matrix and air in the bulge are squeezed out to the flange with very high fluid pressures. The matrix flow from bottom to flange predominantly occurs over the edges in the 90° direction, as the double-curved geometry in 0° direction causes high biaxial tensile strains. These result in high compactions and lower permeability of the matrix layer with increasing drawing depth. Due to the fluid-structure interaction, flow channels are formed in the die radius next to the double-curved geometry (Fig. 3). The matrix flows predominantly in the 90° direction in the single-curved area. However, wall wrinkles can occur in free-forming zones without punch and die contact due to tangential compressive stresses in the metal sheet. These wrinkles typically occur in the double-curved wall parts in 0° direction. The stress superposition of the internal fluid pressure from the matrix flow and the tangential compressive stresses from the metal sheet causes the development of the flow channels and wall wrinkles in the transition zone between single and double-curved die radii. Wall wrinkling does not occur in the upper metal sheet because die contact is established due to fluid pressure and forming.

The strong fluid-structure interaction causes an uneven thickness distribution in the GFRP layer of the fully formed part, as shown in Fig. 3b. The flange area is relatively uniform and close to the target thickness of 1 mm because the compression in this area is mainly determined by the blank holder pressure. However, the resulting thickness in the bottom and wall area is influenced by the fluid-structure interaction. The punch radius is thinned out due to high fabric compressions from the metal forming process. The flow channels are still visible in the final part thickness. The presence of a flow channel on the top left but not on the bottom left side may indicate that the punch and die were not perfectly aligned, which affected the matrix flow. In the metal strains, no skew is observed. The part bottom is approximately 1.2 mm thick, while the wall area in 90° direction is around 1.5 mm thick due to the matrix flow and resulting matrix accumulations. Another matrix accumulation is observed in the wall area in 0° direction, where the matrix is squeezed out of the punch and die radius into the wall area. In these experiments, the punch was moved using displacement control. However, the bottom thickness suggests, that the tool was not completely closed so no full compression was present in some parts of the wall and bottom. Further compression of approximately 0.2 mm would likely improve the homogeneity of the thickness by reducing the bottom thickness and further compressing the wall area.

Comparison with partial and no infiltration.

In general, no difference in the strains and forming behavior is observed between partial matrix injection and no matrix injection, as shown in Fig. 4. Only very slight bulging in the wall area occurs with partial infiltration, while no bulging takes place during dry deep drawing. At 15 % drawing depth, almost no plastic strains are observed. At 50 %, higher strains than with full matrix injection are present in the punch radius as the upper metal sheet is in contact with the fabric during the entire process. With full infiltration, there are no strain concentrations at 50 % yet but biaxial tensile strains are present in the entire bottom and wall area due to bulging. Overall, the bulging causes higher strains in the final part, in particular in the bottom and punch radius. When no bulging and matrix accumulation takes place, less matrix has to move towards the flange during the compression phase of the process. Therefore, fluid pressure and flow velocity are lower, which prevents the development of flow channel and wall wrinkles in the partial infiltration experiments.

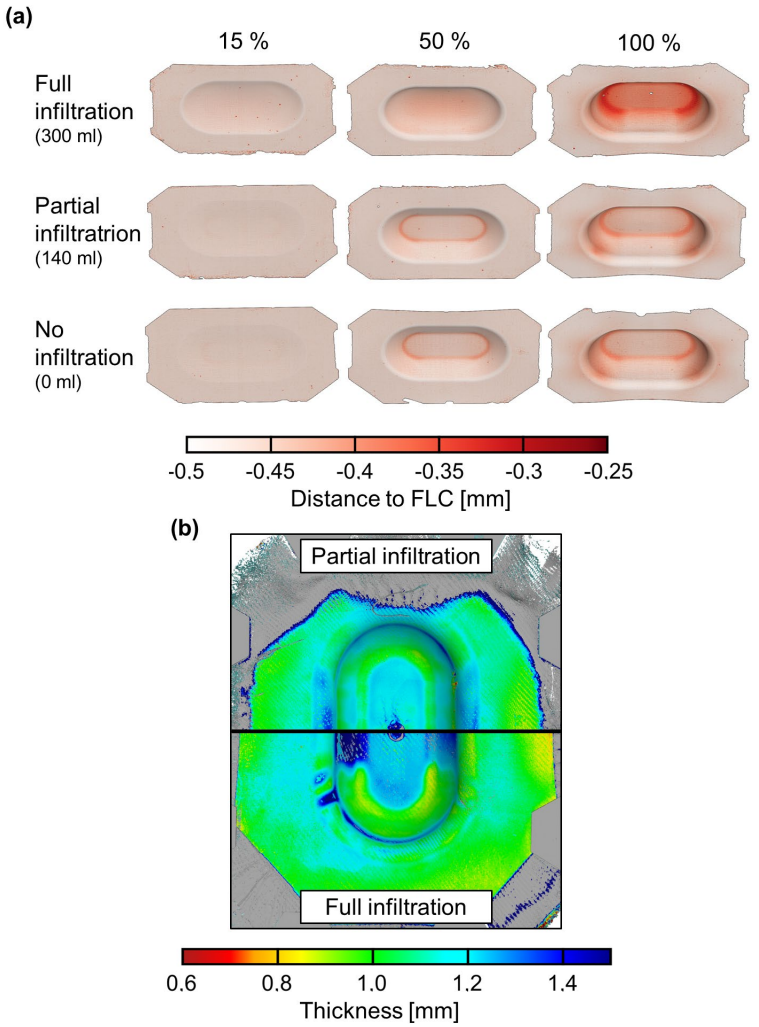

Fig. 4. Comparison with full, partial and without infiltration (a) Development of surface strains in the upper metal sheet at different drawing depths (b) Thickness of the GFRP layer with partial and full infiltration at 100 % drawing depth.

When less matrix is injected, the injection is completed earlier and less bulging is developed on the upper sheet which explains lower injection pressures (1.5 MPa vs 2.2 MPa). With partial infiltration, no air cluster was observed and less matrix accumulates. However, pores are also present at all stages of the process.

When comparing the flow front of the GFRP layer with partial infiltration in Fig. 4b with the flow front in Fig. 3a (full infiltration), a different evolution is observed. With full infiltration, the flow front rather advances in 0° direction because of the fabric's permeability. With partial infiltration, the flow front is further advanced in 90° direction. When comparing the parts at 15 % drawing depth, the flow front with partial infiltration only reaches the die radius, while with full infiltration, parts of the flange have already been infiltrated. With less matrix, the infiltration of the flange area takes place during the later stages of the deep drawing, by squeezing the matrix from part bottom and wall to the flange area. However, the fabric in the punch radius in 0° direction is already compacted further so that the matrix flows in 90° direction when infiltrating the flange. Thus, at small drawing depths and little plastic deformation of the metal sheets, the flow behavior is mainly influenced by the fabric's directional permeabilities. However, with increasing drawing depth, the flow is more influenced by the fabric compaction due to forming.

With partial matrix injection, the thickness distribution of the GFRP layer is much more homogeneous, as shown in Fig. 4b. The part bottom is slightly thinner with partial infiltration and

almost no matrix accumulations are present. This could imply that the compression between punch and die might not be necessary with smaller matrix amounts because the compression due to the forming of the upper metal sheet is sufficient to squeeze the matrix into the flange area during deep drawing.

Discussion

Initially, it was expected, that more matrix would be beneficial for the process because it would flush the remaining air out of the fabric layer into the flange and then out of the part. However, this investigation showed that using more matrix is detrimental to the forming and infiltration quality. The use of another matrix system or evacuating the tool might improve the infiltration quality and reduce pores. It should be noted that it was not possible to evaluate the GFRP layer without polymerizing in this investigation. Hence, slight differences might occur in the actual process, such as the flow front not advancing as far as observed, or less pore formation because the matrix accumulations in the bulge are only present for shorter periods of time.

Bulging of the upper metal sheet and matrix accumulations in the early stages of the process should be avoided altogether. Several strategies can be used to avoid or reduce bulging. In general, early infiltration of the whole fabric layer is advantageous because matrix flow at later deep drawing stages is heavily influenced by the part geometry and fabric compression due to forming. Local high fabric compressions lead to inhomogeneous infiltration and possibly dry spots. Ideally, an improved sealing between the punch and lower metal sheet would allow matrix injection prior to deep drawing. Alternatively, deep drawing could be paused at 10−15 % drawing depth to allow for easier infiltration of the whole part during matrix injection. The injection pressure should be reduced so that no bulging of the metal sheet can occur. In that case, the flange is also infiltrated in an RTM process during matrix injection. The injection time would increase significantly because the fabric's permeability in the flange would be very low due to high compactions. During the deep drawing hold, the blank holder force could temporarily be reduced to allow for faster infiltration. Furthermore, a matrix with lower viscosity would increase the flow velocity. By using only as much matrix as is needed to fill the whole part, injection time and fluid-structure interaction can be reduced. A decrease in punch velocity would further reduce internal fluid pressures because the matrix has more time to be distributed. However, the matrix and tool temperature have to be chosen to avoid increased matrix viscosities during forming.

Summary

A form-filling investigation with different matrix amounts was performed to enhance the understanding of geometry evolution and fluid-structure interaction in the in-situ hybridization process. High matrix amounts lead to stronger fluid-structure interaction, particularly bulging of the upper metal sheet during injection, which results in matrix accumulations in the final part. The matrix flow is significantly influenced by the local fabric compaction due to compression from the formed metal sheets. Inversely, high fluid pressures can influence the metal forming, resulting in increased metal strains and the development of wrinkling in areas where stress superpositions from fluid pressure and forming occur. Overall, using smaller amounts of matrix leads to weaker fluid-structure interaction, resulting in more homogeneous thickness distributions and reduced metal strains in the final part. However, pores are still present in all manufactured parts, possibly due to gas development from the matrix or remaining air in the part and tool because no vacuum was applied before the injection. Apart from evacuating the tool, strategies were presented to improve the process by avoiding bulging. Lower injection pressures, temporarily pausing the deep drawing process or reducing the blank holder force during injection could lead to reduced fluid pressures and fluid-structure interaction. The derived process improvements should be investigated in the future. Presumably, more complex geometries and higher drawing depths can be achieved with adjusted process parameters.

Acknowledgements
The authors would like to thank the German Research Foundation (DFG) for funding the projects BE 5196/4-1 and BE 5196/4-2. The matrix system and hardener were kindly provided by the Arkema Group. The bonding agent was kindly provided by Evonik Industries AG. The authors would like to thank Mr. Marvin Gerdes for the help in performing experiments and Mr. Henrik O. Werner for the help in planning experiments and discussing results.

References
[1] S. Bruschi, J. Cao, M. Merklein, J. Yanagimoto, Forming of metal-based composite parts, CIRP Annals 70 (2021) 567-588. https://doi.org/10.1016/j.cirp.2021.05.009
[2] S. Krishnakumar, Fiber Metal Laminates — The Synthesis of Metals and Composites, Mater. Manuf. Process. 9 (1994) 295–354. https://doi.org/10.1080/10426919408934905
[3] H.E. Etri, M.E. Korkmaz, M.K. Gupta, M. Gunay, J. Xu, A state-of-the-art review on mechanical characteristics of different fiber metal laminates for aerospace and structural applications, Int. J. Adv. Manuf. Technol. 123 (2022) 2965–2991. https://doi.org/10.1007/s00170-022-10277-1
[4] A. Vlot, Glare: History of the development of a new aircraft material, Kluwer Acad. Publ, Dordrecht, 2001. https://doi.org/10.1007/0-306-48398-X
[5] H. Blala, L. Lang, S. Khan, L. Li, A comparative study on the GLARE stamp forming behavior using cured and non-cured preparation followed by hot-pressing, Int. J. Adv. Manuf. Technol. 115 (2021) 1461-1473. https://doi.org/10.1007/s00170-021-07196-y
[6] H. Blala, L. Lang, L. Li, S. Alexandrov, Deep drawing of fiber metal laminates using an innovative material design and manufacturing process, Compos. Commun. 23 (2021) 100590. https://doi.org/10.1016/j.coco.2020.100590
[7] T. Heggemann, W. Homberg, H. Sapli, Combined Curing and Forming of Fiber Metal Laminates, Procedia Manuf. 47 (2020) 36–42. https://doi.org/10.1016/j.promfg.2020.04.118
[8] A. Rajabi, M. Kadkhodayan, M. Manoochehri, R. Farjadfar, Deep-drawing of thermoplastic metal-composite structures: Experimental investigations, statistical analyses and finite element modeling, J. Mater. Process. Technol. 215 (2015) 159-170. https://doi.org/10.1016/j.jmatprotec.2014.08.012
[9] T. Wollmann, M. Hahn, S. Wiedemann, A. Zeiser, J. Jaschinski, N. Modler, N. Ben Khalifa, F. Meißen, C. Paul, Thermoplastic fibre metal laminates: Stiffness properties and forming behaviour by means of deep drawing, Arch. Civ. Mech. Eng. 18 (2018) 442-450. https://doi.org/10.1016/j.acme.2017.09.001
[10] Z. Ding, H. Wang, J. Luo, N. Li, A review on forming technologies of fibre metal laminates, Int. J. Lightweight Mater. Manuf. 4 (2021) 110-126. https://doi.org/10.1016/j.ijlmm.2020.06.006
[11] T. Mennecart, H. Werner, N. Ben Khalifa, K.A. Weidenmann, Developments and Analyses of Alternative Processes for the Manufacturing of Fiber Metal Laminates, in: Volume 2: Materials; Joint MSEC-NAMRC-Manufacturing USA, American Society of Mechanical Engineers, 2018. https://doi.org/10.1115/MSEC2018-6447
[12] M. Kruse, H.O. Werner, H. Chen, T. Mennecart, W.V. Liebig, K.A. Weidenmann, N. Ben Khalifa, Investigation of the friction behavior between dry/infiltrated glass fiber fabric and metal sheet during deep drawing of fiber metal laminates, Prod. Eng. Res. Devel. (2022). https://doi.org/10.1007/s11740-022-01141-y
[13] T. Mennecart, S. Gies, N. Ben Khalifa, A.E. Tekkaya, Analysis of the Influence of Fibers on the Formability of Metal Blanks in Manufacturing Processes for Fiber Metal Laminates, JMMP 3 (2019) 2. https://doi.org/10.3390/jmmp3010002
[14] M. Kruse, J. Lehmann, N. Ben Khalifa, Parameter Investigation for the In-Situ Hybridization Process by Deep Drawing of Dry Fiber-Metal-Laminates, in: WGP 2022, LNPE, 2023. https://doi.org/10.1007/978-3-031-18318-8_13

[15] T. Mennecart, L. Hiegemann, N.B. Khalifa, Analysis of the forming behaviour of in-situ drawn sandwich sheets, Procedia Eng. 207 (2017) 890-895. https://doi.org/10.1016/j.proeng.2017.10.847

Materials Research Proceedings 28 (2023) 987-996 https://doi.org/10.21741/9781644902479-108

Modification of the surface integrity of powder metallurgically produced S390 via deep rolling

HERRMANN Peter[1,a], HERRIG Tim[1,b] and BERGS Thomas[1,2,c]

[1]Laboratory for Machine Tools and Production Engineering (WZL) of RWTH Aachen University, Campus-Boulevard 30, 52074 Aachen

[2]Fraunhofer Institute for Production Technology IPT, Steinbachstr. 17, 52074 Aachen

[a]p.herrmann@wzl.rwth-aachen.de, [b]t.herrig@wzl.rwth-aachen.de, [c]t.bergs@wzl.rwth-aachen.de

Keywords: Deep Rolling, Powder-Metallurgical Steel, Surface Integrity, Residual Stress

Abstract. Fine blanking is an economical process for manufacturing sheet metal workpieces with high sheared surface quality. When machining high-strength steels, material fatigue leads to increased punch wear, which reduces the economic efficiency of the process. This fatigue of the cutting edge and lateral punch surface can be counteracted by mechanical surface treatments. Deep rolling has proved particularly useful for such surface modification, as it allows both: machining of the lateral punch surface and the application of the cutting edge rounding required for fine blanking. For the precise design of the fine blanking punch contour especially the macroscopic deformation of the workpiece is decisive. In this paper, the possibility of specifically modifying the surface integrity of hardened and powder metallurgically produced S390 by means of the incremental surface treatment process deep rolling is investigated. By varying the decisive process parameters rolling pressure, ball diameter and step over distance, their influence on surface integrity is determined. The surface integrity is afterwards characterized by macro hardness, surface topography and residual stress state and microstructural images.

Introduction

Due to the limited availability of geo resources, their use has to be made more efficient by reducing demand and by responsible handling. In mechanical engineering, this results in high demands on the functional integration of technical components. From an economic point of view, short and efficient process chains are required, from which the need for fewer and technologically more complex tools derives. Thus, the demand on the dimensional accuracy and the mechanical properties of tools increase [1].

In particular, fine blanking offers a suitable potential for the economical production of functional components with high quality, due to the high sheared surface quality. Fine blanked components often have to withstand significant loads, which is why high-strength materials are increasingly used in fine blanking [2]. The challenge in processing higher-strength materials is to control the increased tool loads [3]. The highest stress is present on the lateral surface of fine blanking punches. This challenge can be met by improving wear resistance of active surfaces of fine blanking punches.

Deep rolling is a promising technology for increasing the service life of alternately loaded fine blanking punches [4]. Deep rolling is an industrially established process that is used to increase the service life of dynamically loaded components [5]. The process principle is based on incremental elastic-plastic deformation of the component edge zone with a hard rolling body. The local forming of the surface-near edge zone leads to a smoothing of the roughness peaks, induction of residual compressive stresses and strain hardening. These edge zone properties have proven a positive effect on the fatigue strength of components [6].

Content from this work may be used under the terms of the Creative Commons Attribution 3.0 license. Any further distribution of this work must maintain attribution to the author(s) and the title of the work, journal citation and DOI. Published under license by Materials Research Forum LLC.

The cause-and-effect relations between the process kinetics in incremental forming processes, such as deep rolling, and the resulting surface integrity are widely known phenomenologically. However, to extend the application field of deep rolling to include the knowledge-based design of deep rolling processes, material-specific knowledge is required. The overall objective of the studies performed is thereby to reduce abrasive wear on fine blanking punches by means of introducing compressive stresses and surface smoothing. For this reason, specific cause-and-effect relations between the process parameters of deep rolling and the surface integrity of powder metallurgically produced S390 high-speed steel are investigated in this work by means of an experimental parameter study. Powder metallurgically produced S390 high-speed steel is a typical material for fine blanking punches that are conventionally hardened and PVD-coated [7].

Materials and Methods

First, the material of the cylindrical hardened S390 specimens is discussed. Then the experimental setup for the deep rolling within a lathe is presented and the experimental plan is explained. Finally, the measurement methods and the parameters obtained are presented.

The cylindrical specimens (diameter d = 49 mm; length l =60 mm) were set to a hardness of 722 HV30 (61.1 HRC) in preparation for the test. The final specimen geometry was then adjusted by grinding. The material used is the powder-metallurgical S390 from BÖHLER (VOESTALPINE BÖHLER EDELSTAHL GMBH & CO KG, Kapfenberg, Austria), which has the chemical composition given in table 1.

Table 1. Chemical Composition of powder-metallurgical S390 in m-% [8].

C	Si	Mn	P	S	Cr	Mo	Ni	V	W	Co	O
1.63	0.30	0.26	0.018	0.018	4.91	2.28	0.20	5.12	10.09	8.32	0.0041

Due to the chemical composition and the powder-metallurgical microstructure, the compressive strength of the material after heat treatment is in the range of 2,800 to 3,900 MPa. At the same time, the material achieves high toughness: with a hardness of up to 68 HRC, bending strengths of over 4,000 MPa are achieved. The material is characterized by a homogeneous microstructure and, in particular, by the alloying elements tungsten and cobalt, by high wear and high-temperature strength. [8]

Deep Rolling Setup.

The practical test was carried out with a hydrodynamic deep rolling tool from ECOROLL (ECOROLL AG, Celle, Germany) on a conventional lathe. Fig. 1 shows a schematic representation of the test setup and the operating principle of the hydrodynamic deep rolling tool. The lubricant and hydraulic fluid for the hydrodynamic deep rolling tool is the machine's lubricant supply.

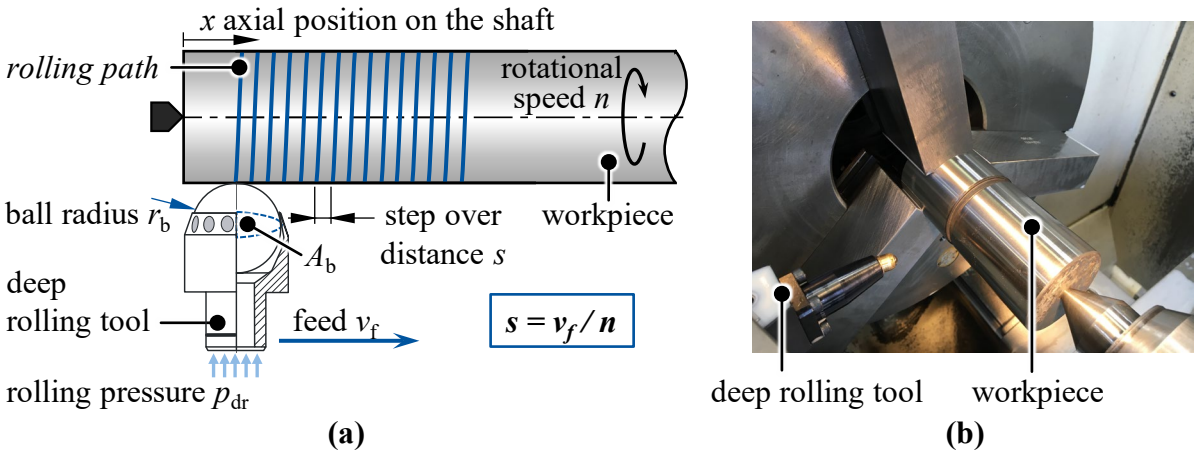

Fig. 1. (a) Test setup including tool and workpiece and properties of the hydrodynamic deep rolling tool from the ECOROLL AG according to [9] and (b) Arrangement of tool and specimen in the lathe.

Fig. 1a shows the schematic test setup. While the workpiece rotates at a constant rotational speed n, the tool moves in axial direction along the workpiece at the feed v_f. From the rotational speed n and feed v_f, the step over distance s results to $s = v_f/n$.

Fig. 1a schematically shows the characteristics of the hydrodynamic deep rolling tool. The rolling ball can be moved dynamically by an infeed during the process. This ensures that the rolling ball and the workpiece are in constant contact during the process. The rolling force F_{dr} is proportional to the rolling pressure p_{dr} and the ball cross-section area A_b and results from the linear relation:

$$F_{dr} = A_b \cdot p_{dr} \cdot (1 - \delta) \text{ with } A_b = d_b^2/4 \cdot \pi. \quad (1)$$

The friction loss δ characterizes the pressure loss between the hydraulic unit and the real pressure applied to the rolling ball. Different loss terms result for different ball diameters d_b and the correspondingly different rolling ball holder:

- $d_b = 3$ mm $\rightarrow \delta_{3mm} = 0.261$
- $d_b = 6$ mm $\rightarrow \delta_{6mm} = 0.236$
- $d_b = 13$ mm $\rightarrow \delta_{13mm} = 0.297$

To determine the friction loss, the rolling force applied at a set pressure was determined for each ball diameter. For this purpose, a test workpiece was fixed on a force measurement platform and the rolling forces for different rolling pressures were determined for each of the three tools ($d_b = 3$ mm, $d_b = 6$ mm and $d_b = 13$ mm). By knowing F_{dr}, p_{dr} and d_{dr}, the friction loss delta could be determined according to Eq. 1, which is specific and constant for each of the three tools.

Test Design.

As a first step it was demonstrated that a significant modification of roughness, hardness and/or residual stress state can be induced by incremental surface treatment. To demonstrate this modification experimentally and to grant a deeper understanding around cause-effect relationships between the deep rolling parameters and the resulting surface integrity, a full factorial experimental design with twofold repetition was used. The process parameters that can be set at the process directly, are the rolling ball diameter d_{dr}, the rolling pressure p_{dr} and step over distance s, which have already been described in the section *Deep Rolling Setup*. The actual parameter values used are shown in Table 2.

Table 2. Parameters of the executed deep rolling experiments.

Deep Rolling Parameter	Parameter Values
Rolling Pressure p_{dr} /MPa	10; 25; 40
Ball diameter d_{dr} /mm	3, 6, 13
Step over distance s /µm	100; 300; 500

In the case of the ECOROLL tool used, the rolling pressure p_{dr} can be varied continuously in the range from 0 to 40 MPa, with this maximum value being fully utilized by the test plan. The step over distances s are selected in such a way that complete machining of the surface is ensured even with the smallest ball impression, but at the same time no excessive machining time occurs. In contrast to the other two parameter variations, the ball diameter d_{dr} increments are not selected equidistantly, since only the three specified diameters are available as tools here. In total, 27 different test setups result from the full-factorial test plan. In the following, the samples are denoted by p_{dr}/MPa-d_{dr}/mm-s/µm (Ex. p_{dr} =10 MPa; d_{dr} = 3 mm; s = 100 µm → 10-3-100).

Measurement methods and objectives.

After the practical test execution, roughness measurements were carried out according to EN ISO 25178. The arithmetical mean height of the surface (S_a) and the maximum height of the surface (S_z) were determined as 3d-surface roughness parameters. To describe the waviness, the value *WDsm* (Mean period length of the dominant waviness) was used in accordance with VDA 2007. These topography measurements were made on a MAHR LD 260 equipped with a MAHR LP C 45-20-5/90° probe (MAHR GMBH, Göttingen, Germany). Furthermore, HV5 and HV30 hardness tests according to Vickers (EN ISO 6507) were carried out. For statistical validation, these test values were recorded five times each. The test values given below are the average of these five values, each of which was measured on a ZWICKROELL ZHU 50 measuring instrument (ZWICKROELL GMBH & CO. KG, Ulm, Germany). In order not to modify the surface condition, the surfaces were specially prepared for the test. The residual stress states presented were analyzed by means of X-ray diffraction using XSTRESS 3000 Mythen (STRESSTECH GMBH, Rennerod, Germany). The depth increments at which the residual stresses were measured are noted at the corresponding position in the diagram.

Results

In order to derive cause-effect relations between the deep rolling parameters and the surface integrity, the smoothing of roughness peaks, the hardness and the residual stress state of the results were investigated. In the following, the results of these investigations are presented and corresponding interactions are derived.

Roughness Measurements. The roughness was reduced with almost all deep rolling setups. The maximum roughness reduction from S_a = 0.44 µm to S_a = 0.21 µm was achieved with a rolling pressure p_{dr} = 40 MPa, ball diameter d_b = 6 mm and step over distance s = 100 µm. On average, S_a was reduced by 27% to 0.32 µm. Fig. 2 shows these influences deep of the rolling parameters on the roughness S_a and additionally on S_z. A measuring point corresponds in each case to the arithmetic mean of the nine corresponding measured values.

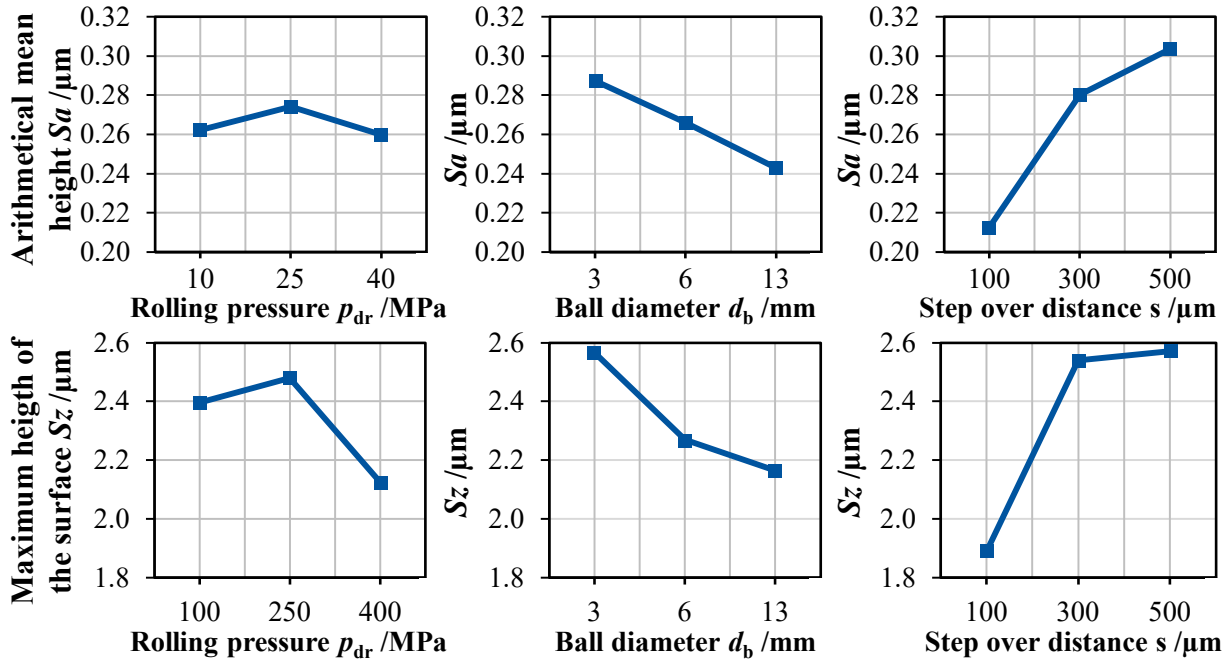

Fig. 2. Main effect plots of the influences of the deep rolling parameters on the arithmetical mean height and the maximum height of the surface.

With respect to S_a, the rolling pressure shows the smallest influence of the three parameters. With increasing rolling pressure p_{dr}, no clear trend in S_a can be identified. There is a clear correlation between the rolling ball diameter d_b and S_a. S_a decreases significantly with increasing d_b. The opposite behavior is found for the dependence on step over distance s. With increasing s, S_a also increases. The results for S_z show similar dependencies as for S_a. With regard to the rolling pressure p_{dr}, no clear trend is established, S_z decreases with increasing ball diameter d_b and increases with larger step over distance s.

In addition to roughness, the waviness of the topography was investigated. In the initial state, the length of the dominant waviness *WDsm* was determined to 0.363 mm. Fig. 3 shows the measured values for *WDsm* for all test setups.

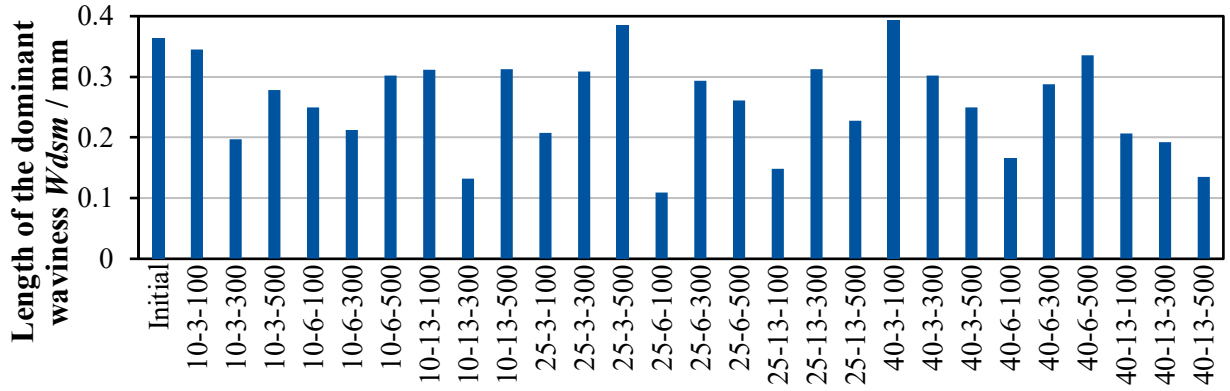

Fig. 3. Length of the dominant waviness Wdsm.

None of the three test parameters shows a correlation with the length of the dominant waviness *WDsm*. In test series carried out with an identical test setup but an initial hardness of 51 HRC, the

selected step over distance *s* and *WDsm* are identical. This expected value is not achieved here. The results rather suggest that there is no correlation between test parameters and *WDsm*.

Hardness tests.

Fig. 4 shows an overall summary of the Vickers hardness tests (HV30). Significant hardness increase was achieved with all deep rolling setups. The maximum hardness increase from 722 HV30 in the initial condition (61.3 HRC) to 882 HV30 (65.7 HRC) was obtained with a rolling pressure p_{dr} = 40 MPa, a ball diameter d_b = 13 mm and a step over distance s = 500 µm. Overall, the hardness values vary in a range of 90 HV30.

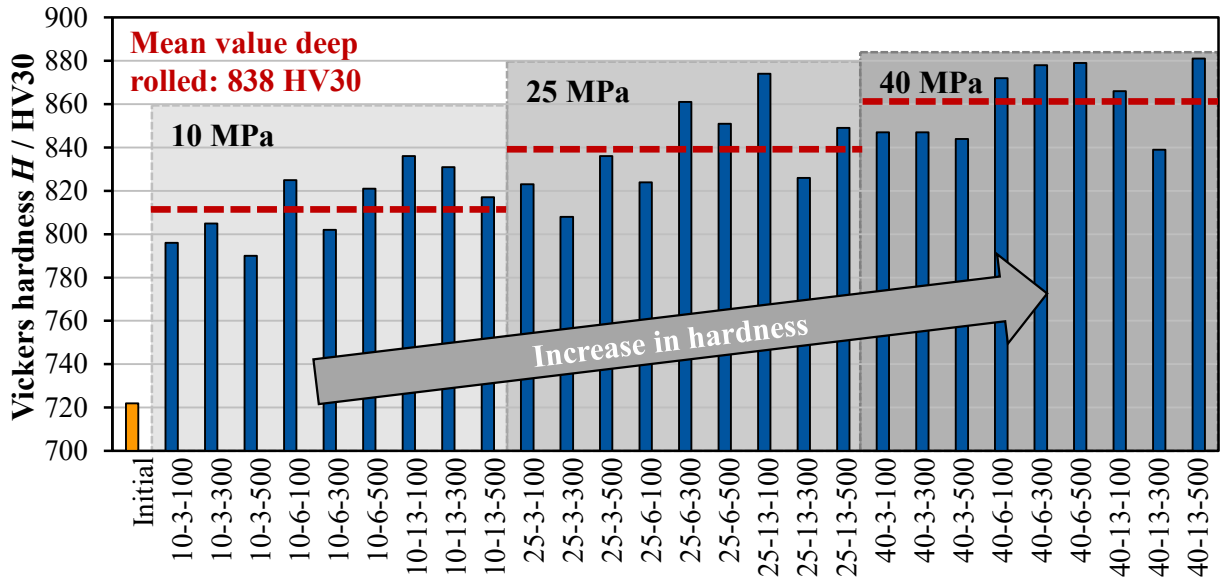

Fig. 4. Overview over the Vickers hardness HV30 for each setup.

On average, a hardness increase of 16% (116 HV30) to 838.6 HV30 was achieved. All hardness values obtained for a rolling pressure p_{dr} = 10 MPa are below this average, whereas all hardness values for p_{dr} = 40 MPa are above this value. The values for p_{dr} = 25 MPa are in between. This tendency can also be seen in the main effect diagrams shown in Fig. 5. The data shown include test values for HV5 as well as HV30. The comparison of the two test forces with each other shows significantly higher HV5 values than HV30 values for a majority of the data points.

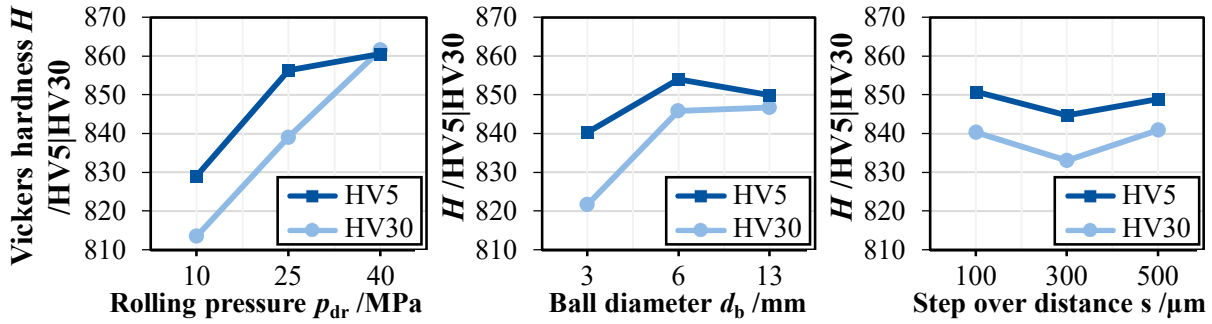

Fig. 5. Main effect plots of the influence of the deep rolling parameters on Vickers hardness HV5 and Vickers hardness HV30.

Due to the lower depth of penetration of the indenter at the low selected test load (HV5), the area of the edge zone closer to the surface has a higher hardness than the edge zone depth covered by the HV30 test. Furthermore, for the HV30 values there is a correlation between the rolling pressure p_{dr} and the Vicker hardness H. H also increases with the rolling ball diameter d_b, although only marginally between d_b = 6 mm and d_b = 13 mm; for the HV5 values this trend is even regressive. In contrast, no clear trend emerges with regard to the step over distance s. Similar hardness values are achieved with all three step over distances s. The test values of H and s do not correlate with each other, which is why s is no longer considered in the following analysis.

In Fig 6. interaction diagrams of the Vickers hardness HV30 as a function of rolling pressure p_{dr} and rolling ball diameter d_b and as a function of d_b and p_{dr} are represented.

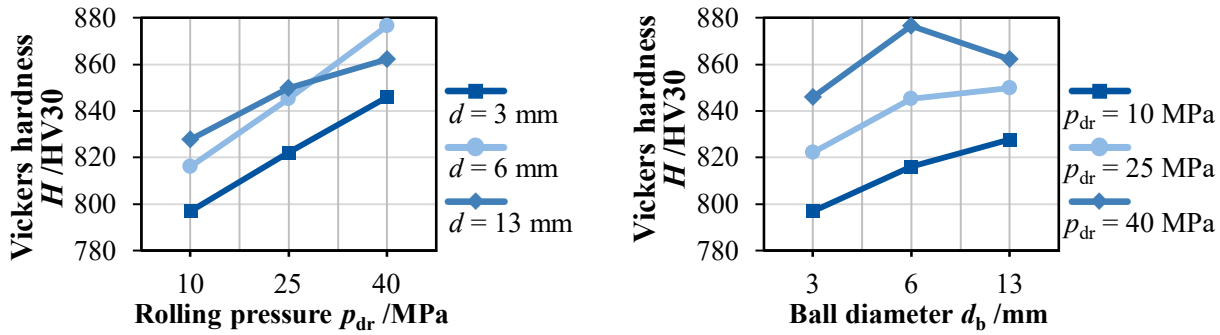

Fig. 6. Interaction diagram of Vickers hardness HV30 as a function of rolling pressure and rolling ball diameter and as a function of rolling ball diameter and rolling pressure.

For each set ball diameter d_b, an increase in rolling pressure is accompanied by a significant increase in hardness. It should be noted that, except for one data point, the largest ball diameter d_b produces the highest hardness at the same pressure. This trend is illustrated in the right hand diagram. The two diagrams show that the differences between the ball diameters of d_b = 6 mm and d_b = 13 mm are comparatively small. The hardness values for d_b = 3 mm are always lower than those of the other two ball diameters at constant pressure. Nevertheless, even with d_b = 3 mm, an increase in hardness can be achieved which is significantly above the hardness value obtained on average.

In contrast to the previous diagrams, in Fig. 7 the Vickers hardness H is not given as a function of one of the three process parameters listed in the test design, but as a function of a resulting variable. The rolling forces F_{dr} given in Fig. 7 are determined according to Eq 1.

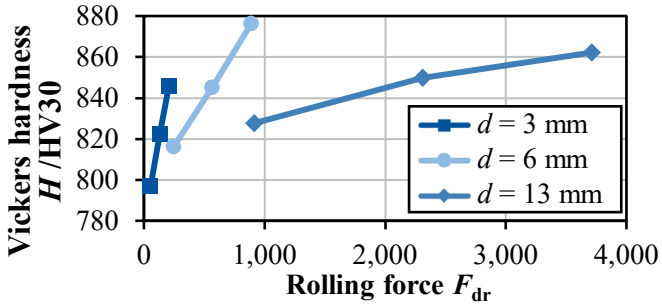

Fig. 7. Interaction diagram of Vickers hardness HV30 as a function of rolling force and rolling ball diameter.

For each of the three ball diameters d_b, the Vickers hardness H correlates with the rolling force F_{dr}. While the smallest hardness increase also occurs at lowest F_{dr} used, the largest hardness values do not occur at $F_{dr,max} \approx 3{,}711$ N but at $F_{dr} \approx 912$ N and the average ball diameter $d_b = 6$ mm. On average, the smallest increases in hardness are obtained with $d_b = 3$ mm and the largest with $d_b = 13$ mm. Nevertheless, even with $d_b = 3$ mm and the comparatively low rolling force $F_{dr} = 208$ N, a hardness increase up to 846 HV30 can be achieved, which is higher than the 839 HV30 achieved on average.

Residual stress analysis.

In addition to the results presented so far, exemplary residual stress curves were measured. All graphs in Fig. 8 show the residual stresses in the axial direction of the specimens, respectively orthogonal to the rolling path. The three graphs show the residual stress curves for the non-deep-rolled initial condition; a rolling pressure $p_{dr} = 40$ MPa, the rolling ball diameter $d_b = 3$ mm and a step over distance s = 500 µm, as well as $p_{dr} = 10$ MPa, $d_b = 3$ mm and $s = 100$ µm.

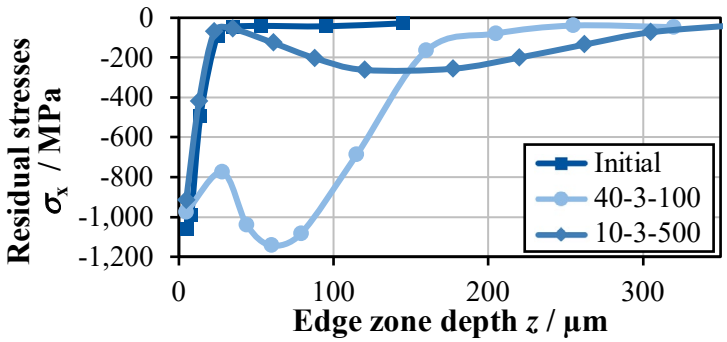

Fig. 8. Depth profile of the residual stress state of selected parameter setups.

In the initial state, a compressive residual stress state is present up to a edge zone depth of $z \approx 25$ µm. At the surface, these residual stresses reach a value of $\sigma_x \approx$ -1,000 MPa. A similar value remains after deep rolling with the rolling pressure $p_{dr} = 10$ MPa. However, here a slight compressive residual stress state is evident at deeper edge zone depths in contrast to the initial condition. For the deep rolling setup with $p_{dr} = 40$ MPa, a similar value of $\sigma_x \approx$ -1,000 MPa is again present at the surface. Here, the maximum residual compressive stresses are, at a depth $z = 60$ µm, at $\sigma_x \approx$ -1,240 MPa. In the range $z > 150$ µm, however, the test setup with lower $p_{dr} = 10$ MPa exhibits greater residual compressive stresses.

Discussion

The surface integrity of powder-metallurgical S390 with an initial hardness of 722 HV30 (61.1 HRC) and an arithmetical height of 0.44 µm can be significantly modified by hydrodynamic deep rolling. With regard to the smoothing of roughness peaks, large rolling ball diameters and a small step over distance have a particularly positive effect. Minimal roughness can be achieved with small rolling ball diameters, but not with large step over distances. Since the influence of rolling pressure on roughness does not show a clear tendency, it can also be assumed that the rolling force, which is proportional to the rolling pressure, has only a subordinate influence in the parameter space considered. It remains unclear to what extent a further reduction in step over distance or larger rolling ball diameters will cause further smoothing.

The results of the waviness analysis show that the spherical ball impression is not introduced into the surface as a distinct path. It is not possible to create a defined path as an impression of the rolling ball at the high initial hardness. Otherwise, the length of the dominant waviness would result directly from the step over distance used. Since this is possible at lower initial hardness, it

can be assumed that the tool is deflected by the material accumulation next to the rolling path that occurs during deep rolling.

The increase in hardness was achieved in particular by using large rolling ball diameters and rolling pressures. A more detailed examination reveals that the rolling ball diameter has only a minor influence, since the maximum hardness increase was not achieved with the largest rolling ball diameter and large hardness increases were achieved independently from the ball diameter. Since neither the rolling pressure nor the rolling force are the main influencing parameters, it can be assumed that the surface pressure present in the contact has a decisive influence.

By comparing HV5 and HV30 test results, it could be shown that the near-surface edge zone achieves a higher hardness than deeper material regions. Furthermore, the HV5 and HV30 test values converge strongly with increasing rolling pressure and increasing rolling ball diameter. This circumstance shows that with increasing rolling pressure and increasing rolling ball diameter, deeper edge zone layers (tested with HV30) reach a similarly high hardness as the near-surface edge zone region (tested with HV5). The work hardening is introduced correspondingly deeper into the workpiece.

Furthermore, it was found that despite the comparatively low rolling force of 208 N, high residual compressive stresses of over 1,100 MPa were introduced into the surface-near edge zone. In contrast to the hardness increase, which was already significant at a rolling force of 52 N, the same parameter setup shows a clear but only slight residual compressive stress introduction. Due to the significantly higher hardness values achieved with a larger rolling ball diameter and greater rolling force, it can be assumed that, with appropriate parameter selection, significantly higher residual compressive stresses will also occur.

Summary

In order to achieve the overall objective of increasing the strength of fine blanking punches with regard to abrasive wear, an experimental study was carried out in this paper. The cause-effect relationships determined are used to design a knowledge-based deep rolling process that increases the service life of fine blanking punches by specifically modifying the surface integrity.

Since it can be assumed that low roughness, high hardness values, and the highest possible near-surface compressive residual stresses lead to high strength, several recommendations can be made for the design of a suitable deep rolling process:

- Minimum roughness can be achieved with any rolling ball diameter. The main parameter influencing the resulting roughness is the step over distance, which should be selected as small as possible.
- High hardness increases can be induced in particular with high rolling pressures. In addition, high rolling pressure causes deeper work hardening.
- Larger rolling ball diameters tend to have a positive effect on hardness, but maximum hardness is not achieved at the largest rolling ball diameter selected. It is assumed that in the process the highest possible surface pressure leads to large increases in hardness.
- Significant residual compressive stresses occur even at low rolling forces. It can also be assumed that higher and deeper residual compressive stresses are produced with greater energy input.

For the design of a fine blanking die, the hardness to which the material is to be set before deep rolling must be taken into account. In addition, a suitable cutting edge rounding must be selected, taking into account the macroscopic deformation caused by deep rolling.

Based on the known phenomenological relationships, it can be assumed that increased strength can be achieved by the shown modifications of the surface integrity. Nevertheless, it remains to provide this evidence experimentally. For this purpose, the possible change in surface integrity due to the subsequent coating process must be determined. Subsequently, practical fine blanking

tests must be carried out on higher-strength sheets in order to provide practical proof of the strength increase.

Funding
This work was funded by the Deutsche Forschungsgemeinschaft (DFG, German Research Foundation) – project number 423492562

References
[1] T. Bergs, M. Wilms, O. Henrichs, S. Weber, G. Stepien, T. Dannen, M. Prümmer, K. Arntz, Individual process chains in toolmaking through data and model-based forecasts, in: Laboratory for Machine Tools and Production Engineering (WZL) of RWTH Aachen University (Ed.), 30th Aachen Machine Tool Colloquium 2021, Aachen, 2021, pp. 80-102.
[2] U. Aravind, U. Chakkingal, P. Venugopal, A Review of Fine Blanking: Influence of Die Design and Process Parameters on Edge Quality, J. Mater. Eng. Perform. 30 (2021) 1-32. https://doi.org/10.1007/s11665-020-05339-y
[3] Y. Abe, T. Kato, K-i, Mori, S. Nishino, Mechanical clinching of ultra-high strength steel sheets and strength of joints, J. Mater. Process. Technol. 214 (2014) 2112–2118. https://doi.org/10.1016/j.jmatprotec.2014.03.003
[4] M. Krobath, T. Klünsner, W. Ecker, M. Deller, N. Leitner, S. Marsoner, Tensile stresses in fine blanking tools and their relevance to tool fracture behavior, Int. J. Machine Tool. Manuf. 126 (2018) 44–50. https://doi.org/10.1016/j.ijmachtools.2017.12.005
[5] D. Meyer, J. Kämmler, Surface Integrity of AISI 4140 After Deep Rolling with Varied External and Internal Loads, Procedia CIRP 45 (2016) 363-366. https://doi.org/10.1016/j.procir.2016.02.356
[6] X. Wang, X. Xiong, K. Huang, S. Ying, M. Tang, X. Qu, W. Ji, C. Qian, Z. Cai, Effects of Deep Rolling on the Microstructure Modification and Fatigue Life of 35Cr2Ni4MoA Bolt Threads, Metals 12 (2022) 1224. https://doi.org/10.3390/met12071224
[7] K. Bobzin, C. Kalscheuer, M. Carlet, D.C. Hoffmann, T. Bergs, L. Uhlmann, Low-Temperature Physical Vapor Deposition TiAlCrSiN Coated High-Speed Steel: Comparison Between Shot-Peened and Polished Substrate Condition, Adv. Eng. Mater. 24 (2022) 2200099. https://doi.org/10.1002/adem.202200099
[8] voestalpine Böhler Edelstahl GmbH & Co. KG, S390 DE: Microclean, Karpfenberg, 2010.
[9] F. Klocke, Fertigungsverfahren 4, Springer Berlin Heidelberg, Berlin, Heidelberg, 2017.

Materials Research Proceedings 28 (2023) 987-1006 https://doi.org/10.21741/9781644902479-109

Electrically-assisted deep drawing of 5754 aluminium alloy sheet

DOBRAS Daniel[1,a *], ZIMNIAK Zbigniew[1,b] and ZWIERZCHOWSKI Maciej[1,c]

[1]Department of Metal Forming, Welding and Metrology, Wrocław University of Science and Technology, 7-9 Ignacego Łukasiewicza Street, 50-371 Wrocław, Poland

[a]daniel.dobras@pwr.edu.pl, [b]zbigniew.zimniak@pwr.edu.pl, [c]maciej.zwierzchowski@pwr.edu.pl

Keywords: Electrically-Assisted Forming, Aluminium Alloys, Deep Drawing

Abstract. The effect of current pulse application on the mechanical behaviour and plasticity of the 5754 aluminium alloy was studied. Tensile and deep drawing tests were conducted. The 5754 aluminium alloy in two different states of hardening was used: H111 and H22. The results show that the application of current pulses can significantly increase the plasticity of the examined alloys in the case of the tensile test. The dynamic recovery process is the main process responsible for the increase in plasticity of the material. However, in the case of the deep drawing process, it was observed that the increase in the material formability is low, and further studies are needed.

Introduction

Aluminium alloys have become very popular in the automotive industry owing to their good specific strength and corrosion resistance. However, the formability of many aluminium alloys at room temperature is low [1,2]. Warm and hot forming methods are applied in metal forming processes because they improve the formability of materials such as aluminium or magnesium alloys [3]. However, these methods have many drawbacks, such as increased adhesion of the die and decreased die strength and lubrication effectiveness [4].

Electrically-Assisted Forming (EAF) is proposed as an alternative method to the warm and hot forming methods. It is commonly known that the application of current pulses during plastic forming of metals can significantly increase their formability, reduce flow stress, and avoid or reduce some of the above-mentioned drawbacks [5–7]. Jeong et al. [8] showed that the application of current pulses during tension can increase the material elongation by over 200% in the case of the 5052-H32 aluminium alloy (AA) [9] and the as-extruded AZ91 magnesium alloy. Because this significant increase of the material plasticity during EAF processes cannot be explained only by the simple Joule heat law, many scientists have tried to explain this phenomenon [10]. There is still no unequivocal proof of existence of non-thermal effects such as the electroplastic effect [11], the magnetoplastic effect [12] or others [13]. The microscale Joule heat theory, more popular in the recent years, has been confirmed by the simulation [14], grain boundary melting [15] or such processes as dynamic recovery and recrystallization [8,16]. However, it does not explain all the observed phenomena [16]. Recently, it has been proved that the application of even low energy current pulses can lead to defect reconfiguration and a change in the dislocation pattern [17–19].

Many industrial metal forming processes have been supported by the application of current pulses. EAF processes such as wire drawing [20,21] or rolling [22,23] have been successfully realized. However, more difficult processes, in terms of EAF, such as deep drawing and press stamping, still need to be developed due to the unsatisfactory results. Only in the case of magnesium alloys the increase of plasticity has been meaningful [24,25]. In the electrically-assisted deep drawing processes, the following problems should still be overcome: excessive heat transfer from the sample to the dies, limited possibility of measuring the temperature or the need to apply higher currents [26–28].

Content from this work may be used under the terms of the Creative Commons Attribution 3.0 license. Any further distribution of this work must maintain attribution to the author(s) and the title of the work, journal citation and DOI. Published under license by Materials Research Forum LLC.

Materials and Methods

The tested material was the 5754 aluminium alloy, delivered in two different states of hardening: H111 and H22. The thickness of both as-received sheets was 1 mm. In the present work, two different electrically-assisted forming processes were conducted: the tensile test and the deep drawing test. The tensile samples with a gauge length of 75 mm and a gauge width of 12 mm were prepared by way of milling along the rolling direction of the sheet. The tensile tests were performed at a strain rate of 0.0025 s^{-1} until fracture using an INSTRON 3369 tensile machine.

The deep drawing tests were carried out at the punch speed of 0.4 mm/s until fracture using an Erichsen 142 Sheet Metal Testing Machine. The experimental study proved that a greater contact between the sample and the dies results in more heat transfer. Therefore, to avoid excessive heat transfer from the sample to the dies, the Erichsen machine was working in the sheet holder quick release (SHQR) mode. This means that, when the set draw depth is reached, the blank holder force is released, and the test continues until stopped. For the same reason, the dies were made of stainless steel because of its low thermal conductivity and high electrical resistance. Before the SHQR, the blank holder force was 35 and 40 kN, in the case of the H111 and the H22 state, respectively. A circular punch with a diameter of 30 mm and a radius of 4 mm as well as a matrix with a diameter of 33.5 mm and a radius of 4 mm were used in the deep drawing tests. A special sample, with experimentally fitted dimensions visible in Fig. 1, was used for the tests. The distance of 130 mm (Fig. 1) is the distance between the edges of the electrodes attached to the sample. The central, circular part of the sample with a radius of 32 mm was cut on the sides in order to obtain the highest current density. The dies were isolated from the machine. The sample mounted to the electrodes before the deep drawing process is visible in Fig. 2.

During all the tests, the electric pulses were generated by a self-constructed current pulse generator working at 2.52 V [29] and applied to the sample through copper electrodes attached to it. The applied current was pulsed with a pulse duration of t_d and a period of t_p, and its shape was created by the function generator device. The first pulse of electric current was applied after a time of t_p from the beginning of the tensile test, and from the moment of sheet holder force release in the case of deep drawing. An oscilloscope and a Rogowski coil were used to measure the current flowing through the samples. Each test was repeated three times. One side of the sample was sprayed with black paint, and its temperature was measured by a FLIR T440 infrared thermal imaging camera during the test.

The microstructural observations of the selected specimens were conducted with a VEGA3 TESCAN Scanning Electron Microscope (SEM) operating at 20 kV, and equipped with an Electron Backscattered Diffraction (EBSD) detector (Oxford Instruments). Mechanical grinding and electrolytic polishing using A2 Struers reagent were applied to prepare the specimen surfaces for the EBSD analysis. The applied step size was 0.2 μm. In the case of the non-EA specimen, the single-iteration grain dilation cleanup procedure was performed only one time and affected less than 4% of the measurement pixels.

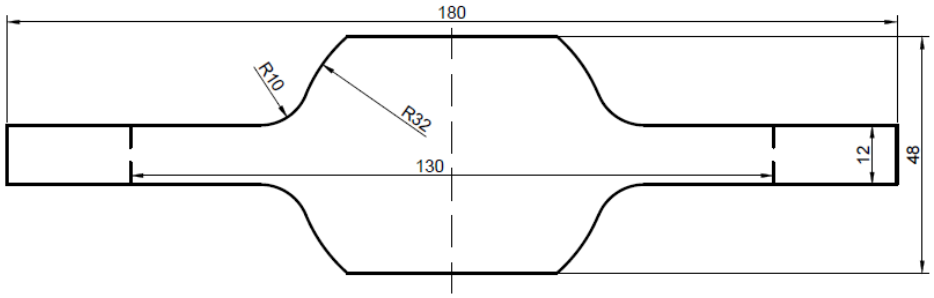

Fig. 1. The shape and dimensions (in mm) of the samples used in the deep drawing tests.

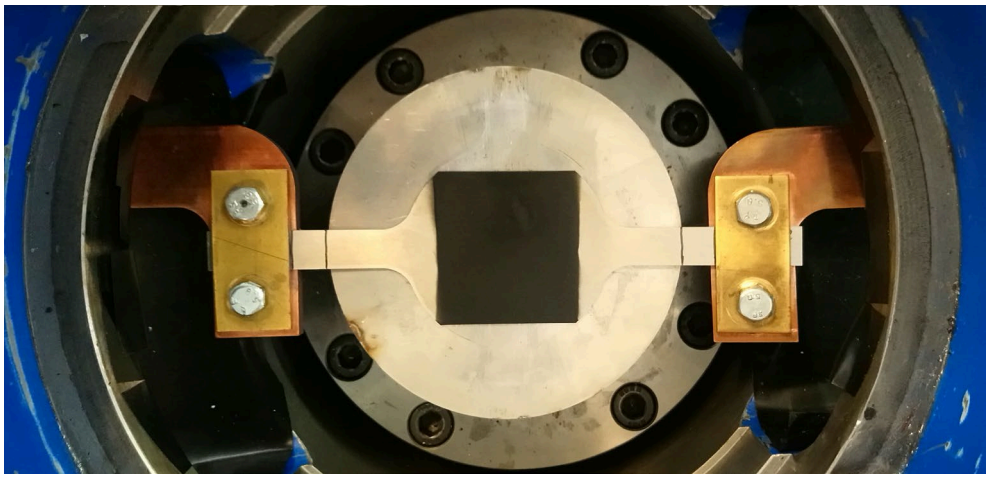

Fig. 2. The setup of the deep drawing sample before the process.

Results and Discussion

One of the most important current parameters in the EAF processes is the current density. Here, the nominal current density is defined as the current measured by the Rogowski coil divided by the cross-sectional area of the sample. The obtained values of the current density, depending on the applied process type and current parameters, are given in Table 1 and 2. Note that the current density in the case of deep drawing is about four times lower than in the case of the tensile test as a result of a four time higher width of the deep drawing samples and no possibility to increase the current. Therefore, as can be seen in Table 1 and 2, the pulses were applied more often in the case of deep drawing.

Table 1. Influence of current parameters on the current density for tensile test.

t_d / t_p [ms / s]	Current density [A/mm^2]	
	5754-H111	5754-H22
400 / 50	190	-
400 / 24	-	200

Table 2. Influence of current parameters on the current density for deep drawing test.

t_d / t_p [ms / s]	Current density [A/mm^2]	
	5754-H111	5754-H22
400 / 2	45	45
400 / 1.2		
500 / 2.5		
500 / 1.5		

The engineering stress-strain curves of AA5754-H111 and AA5754-H22 with and without the current pulse application are shown in Fig. 3a-b. It is clearly seen that the application of the current pulses increase the material elongation. As can be seen, when the current pulse is applied, immediately, the engineering stress decreases and the temperature increases. The significant engineering stress drop is, among others, correlated with the sample's thermal expansion. However, before the next pulse application, the temperature drops almost to the room value. In the case of the annealed state (H111), the average value of engineering strain increased from 22.86 to 32.73% (increase to about 143% of the basic value). However, in the case of the hardened alloy (H22), the

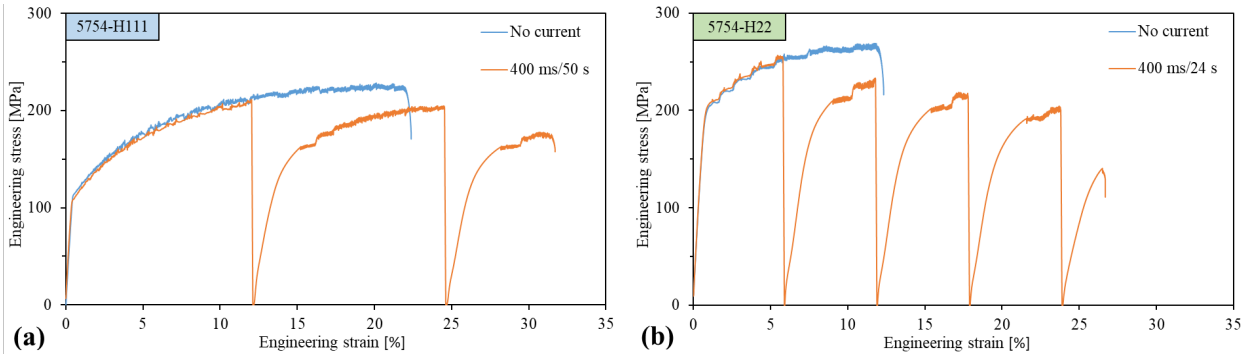

Fig. 3. Engineering stress-strain curves of 5754 AA in the a) H111 and b) H22 state with and without current application.

average value of engineering strain increased from 12.27 to 27.13% (increase to about 221% of the basic value). It is worth mentioning that the ratio of t_d/t_p was 1/60 in the case of the hardened alloy, and it was the best ratio in terms of increasing the material elongation. Nevertheless, in the case of the annealed alloy the similar increase the material elongation occurred for a wide range of t_d/t_p ratios. The average values of the maximal registered temperatures during tensile tests were 364 and 390ºC, for AA5754-H111 and AA5754-H22, respectively. However, in both cases, the average temperature during all the tensile tests was under 200ºC, which is generally a lower temperature than the warm forming temperature for these alloys.

Fig. 4a-b present the deep drawing force-displacement curves of the 5754 aluminium alloy. The force represents the force at the punch in the deep drawing process and the displacement is the displacement of the punch, which corresponds with the depth of the drawpiece. The SHQR took places 5.4 and 3.4 mm from the beginning of the tests for the annealed and the hardened alloy, respectively. The above-mentioned values were experimentally designated, and the obvious decrease of the force corresponds to the SHQR moment. Unlike the tensile tests, in the deep drawing tests, the application of the current pulses did not lead to a significant increase of the drawpieces' heights. Only in one case, the height of the drawpiece increased noticeably, when the 500 ms/1.5 s current parameters were applied to the 5754-H111 aluminium alloy (Fig. 4a). In this case, the displacement at the punch increased about 8% in comparison with the baseline value (Fig. 5a), but in other cases, the displacement increase or decrease were not greater than 2% (Fig. 5a-b). The average values of the maximal registered temperatures during the deep drawing tests, for the different current parameters, are presented in Fig. 6a-b. The temperature did not exceed 80ºC in any case. A picture of an example drawpiece of 5754-H22 AA is visible in Fig. 7. A characteristic fracture is visible on the top edge of the drawpiece.

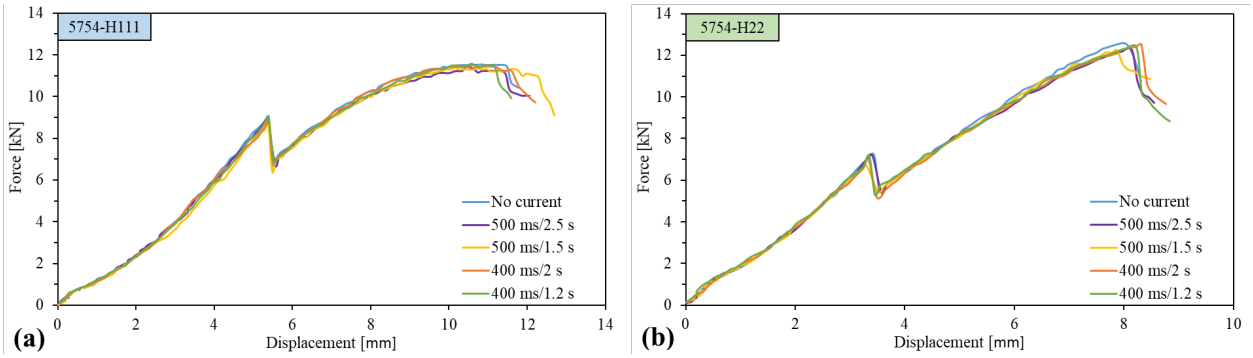

Fig. 4. Deep drawing force-displacement curves of 5754 AA in the a) H111 and b) H22 state with and without current application.

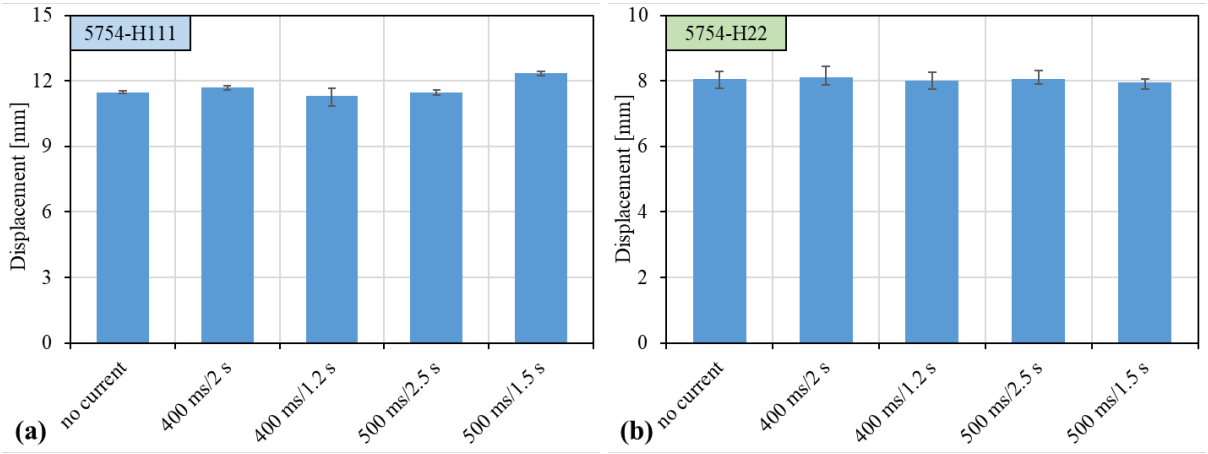

Fig. 5. Influence of the current parameters on the height of the drawpieces of 5754 AA in the a) H111 and b) H22 state.

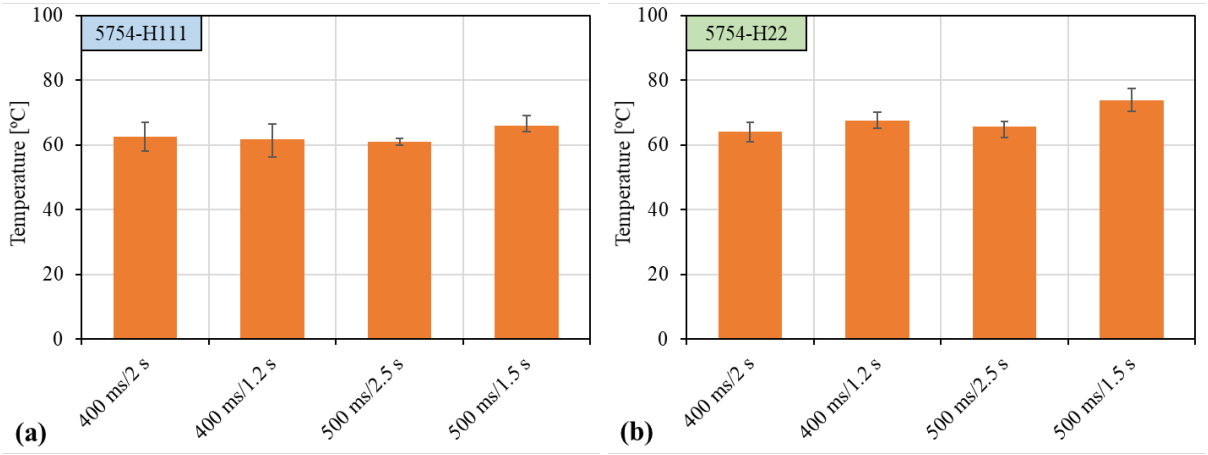

Fig. 6. Influence of the current parameters on the maximal temperature of the drawpieces of 5754 AA in the a) H111 and b) H22 state.

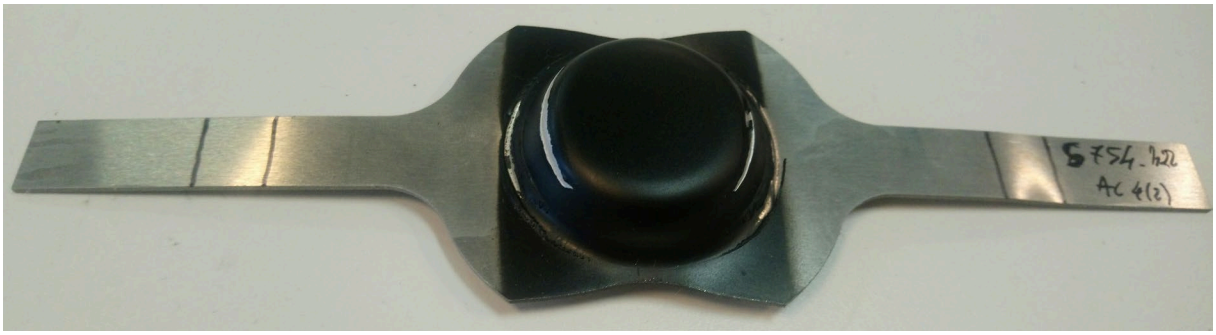

Fig. 7. The example drawpiece of 5754-H22 AA.

Even if the application of the current pulses leads to a significant increase of the material elongation in the tensile tests, it is difficult to reproduce the same conditions and results in the deep drawing process. The current density present during deep drawing is about four times lower than in the case of a tensile, and it is the main reason for the insignificant increase of the material formability. Low current density resulted in low temperature of the tested samples, which did not increase even when the pulses were applied more often. Finally, the dynamic recovery and recrystallization processes cannot take place and increase the material plasticity when the temperature is too low. The solution of the above-mentioned problems will be the application of a large high-current pulse generator, with the possibility of applying high currents. However, this solution increases the process costs and makes it more difficult, yet it will be necessary in potential industrial applications.

The highest increase of the material plasticity, owing to the pulsed current application, occurred in the case of the 5754-H22 AA tensile sample. Therefore, the specimens from the 5754-H22 AA tensile tests were selected for the microstructural analysis. In order to better analyze the effect of the current pulses on the structural changes, two additional tests were conducted. In the first case, the EA tensile test was immediately stopped after the fourth pulse application (Fig. 3b). It happened at 90% elongation of the EA tensile sample. In the second case, the non-EA tensile sample was stretched to a 90% value of its initial elongation and then the test was also stopped. The specimens for the microstructural analysis were cut from the middle of the above-mentioned tensile samples.

The Inverse Pole Figure (IPF) maps of the non-EA and EA specimens are presented in Fig. 8 a) and b), respectively. Due to the high deformation of the crystal lattice, the initial Hit Rate value of the non-EA specimen was only about 60%, which is typical for highly deformed materials. Although the EA specimen was deformed to a greater extent (about two times greater elongation, Fig. 3b), the obtained Hit Rate in this case was more than 80%. It means that the crystal lattice deformation is lower than for the specimen without the current application. If the material has been deformed more, but its lattice is less deformed, then the application of the current pulses and the increase of temperature resulting from it lead to a lattice structure rebuild. The IPF maps represent the above-mentioned case.

Many small grains are visible (Fig. 8b) at grain boundaries of the big and medium size grains in the case of specimen with the pulsed current application. It could mean that the dynamic recrystallization process occurred, especially because, for a while, the temperature during the EA tensile tests reached the value of $0.6T_m$, where T_m is the homologous temperature of aluminium. However, a more detailed analysis is needed to verify this hypothesis.

To analyze the recrystallization process, the Grain Orientation Spread (GOS) parameter was used. Generally, it is assumed that the GOS parameter for recrystallized grains is less than 1.5-2 º. However, this threshold value in the literature ranges from 1 to 3 º [9,30]. In this study the

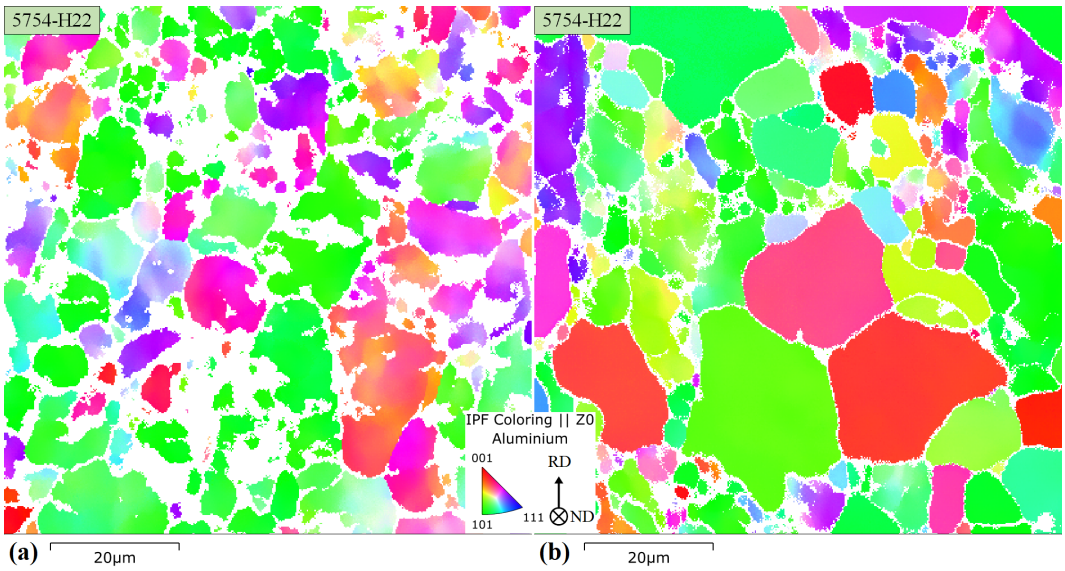

Fig. 8. IPF maps of 5754-H22 AA from a stopped a) non-EA and b) EA tensile test.

recrystallized grains are defined by the GOS less than 1.5 º. The GOS map of non-pulsed specimen is presented in Fig. 9a. It is clearly seen that the most grains are characterized by the GOS higher than 2 º, and only about 13% indexed pixels - by the GOS less than 1.5 º. It could mean that these grains with lower GOS parameter were not deformed or deformed in a small range. Completely different results are shown by the GOS map of the pulsed specimen (Fig. 9b). The effect of temperature resulted in a significant increase in the surface of grains, with the GOS less than 1.5 º. It this case about 62% indexed pixels is characterized by the GOS less than 1.5 º. However, mainly the large grains take small values of the GOS parameter. Therefore, it can be concluded that the intense dynamic recovery process occurred in these large grains. This recovery process led to a structure rebuild of the crystal lattice in grains and thus to the low GOS parameter. On the other hand, many small grains with the GOS less than 1.5 º are visible at grain boundaries of the bigger grains. It could mean that the dynamic recrystallization process started in these places, however, a more detailed analysis using transmission electron microscopy should be performed to prove it.

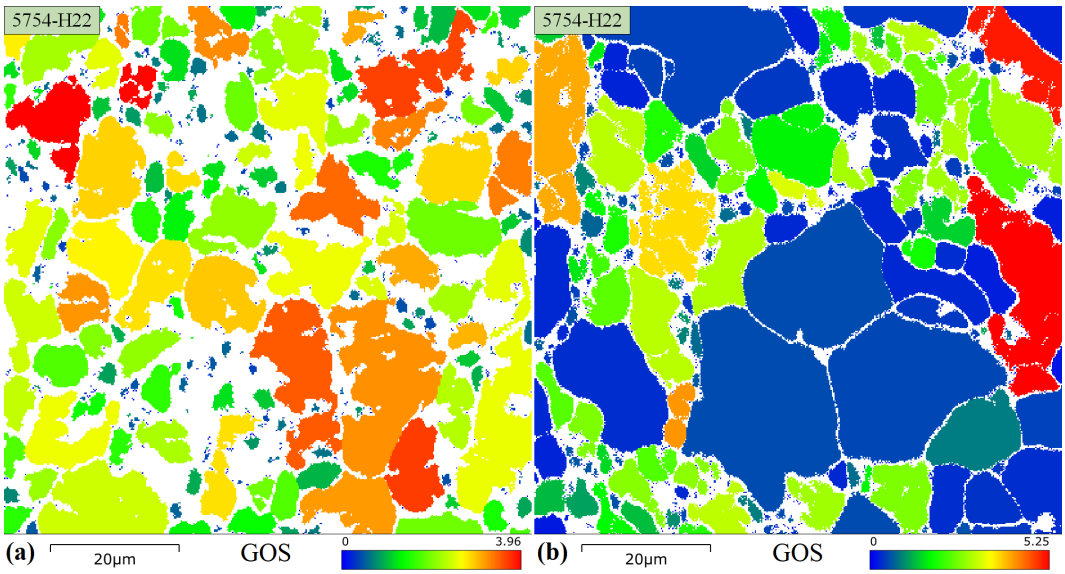

Fig. 9. GOS maps of 5754-H22 AA from a stopped a) non-EA and b) EA tensile test.

Summary

In the present work, electrically-assisted tensile tests and deep drawing processes of the 5754 aluminium alloy in different states of hardening were carried out. The main conclusions are:

1. The application of current pulses can lead to a significant increase of the material elongation in the tensile test, especially in the case of the H22 state.
2. The EBSD analysis proved that the intense dynamic recovery is the main factor responsible for the structure rebuild of the crystal lattice and thus the increase of the material plasticity.
3. The application of the sheet holder quick release mode, new in terms of electrically-assisted forming, can lead to a decrease of the excessive heat transfer from sample to the dies.
4. The application of the current pulses did not lead to a significant increase of the material formability in the case of the deep drawing process. The main difficulties in effective implementation of the electrically-assisted deep drawing processes are the necessity of the application of high currents and an excessive heat transfer from the sample to the stamping dies.

References

[1] Z. Gronostajski, K. Jaśkiewicz, P. Kaczyński, M. Skwarski, S. Polak, J. Krawczyk, W. Chorzępa, P. Trzpis, W-Temper forming of B-pillar from 7075 aluminum alloy, CIRP Ann. 71 (2022) 221–224. https://doi.org/10.1016/j.cirp.2022.03.019

[2] H. Deng, Y. Mao, G. Li, X. Zhang, J. Cui, AA5052 failure prediction of electromagnetic flanging process using a combined fracture model, Arch. Civ. Mech. Eng. 22 (2022) 1-17. https://doi.org/10.1007/s43452-022-00390-z

[3] S. Toros, F. Ozturk, I. Kacar, Review of warm forming of aluminum-magnesium alloys, J. Mater. Process. Technol. 207 (2008) 1–12. https://doi.org/10.1016/j.jmatprotec.2008.03.057

[4] W.A. Salandro, J.T. Roth, Formation of 5052 aluminum channels using Electrically-Assisted Manufacturing (EAM), Proc. ASME Int. Manuf. Sci. Eng. Conf. 2009, MSEC2009. 2 (2009) 599-608. https://doi.org/10.1115/MSEC2009-84117

[5] H.R. Dong, X.Q. Li, Y. Li, Y.H. Wang, H.B. Wang, X.Y. Peng, D.S. Li, A review of electrically assisted heat treatment and forming of aluminum alloy sheet, Int. J. Adv. Manuf. Technol. 120 (2022) 7079–7099. https://doi.org/10.1007/s00170-022-08996-6

[6] E. Simonetto, S. Bruschi, A. Ghiotti, Electroplastic effect on AA1050 plastic flow behavior in H24 tempered and fully annealed conditions, Procedia Manuf. 34 (2019) 83-89. https://doi.org/10.1016/j.promfg.2019.06.124

[7] B.J. Ruszkiewicz, T. Grimm, I. Ragai, L. Mears, J.T. Roth, A Review of Electrically-Assisted Manufacturing with Emphasis on Modeling and Understanding of the Electroplastic Effect, J. Manuf. Sci. Eng. Trans. ASME. 139 (2017) 1–15. https://doi.org/10.1115/1.4036716

[8] J.H. Roh, J.J. Seo, S.T. Hong, M.J. Kim, H.N. Han, J.T. Roth, The mechanical behavior of 5052-H32 aluminum alloys under a pulsed electric current, Int. J. Plast. 58 (2014) 84-99. https://doi.org/10.1016/j.ijplas.2014.02.002

[9] H.J. Jeong, M.J. Kim, J.W. Park, C.D. Yim, J.J. Kim, O.D. Kwon, P.P. Madakashira, H.N. Han, Effect of pulsed electric current on dissolution of Mg17Al12 phases in as-extruded AZ91 magnesium alloy, Mater. Sci. Eng. A. 684 (2017) 668-676. https://doi.org/10.1016/j.msea.2016.12.103

[10] N.K. Dimitrov, Y. Liu, M.F. Horstemeyer, Electroplasticity: A review of mechanisms in electro-mechanical coupling of ductile metals, Mech. Adv. Mater. Struct. 0 (2020) 1-12. https://doi.org/10.1080/15376494.2020.1789925

[11] K. Okazaki, M. Kagawa, H. Conrad, A study of the electroplastic effect in metals, Scr. Metall. 12 (1978) 1063-1068. https://doi.org/10.1016/0036-9748(78)90026-1

[12] M.I. Molotskii, Theoretical basis for electro- and magnetoplasticity, Mater. Sci. Eng. A. 287 (2000) 248-258. https://doi.org/10.1016/s0921-5093(00)00782-6

[13] B.J. Ruszkiewicz, L. Mears, J.T. Roth, Investigation of Heterogeneous Joule Heating as the Explanation for the Transient Electroplastic Stress Drop in Pulsed Tension of 7075-T6 Aluminum, J. Manuf. Sci. Eng. Trans. ASME. 140 (2018) 1–11. https://doi.org/10.1115/1.4040349
[14] J. Zhao, G.X. Wang, Y. Dong, C. Ye, Multiscale modeling of localized resistive heating in nanocrystalline metals subjected to electropulsing, J. Appl. Phys. 122 (2017). https://doi.org/10.1063/1.4998938
[15] R. Fan, J. Magargee, P. Hu, J. Cao, Influence of grain size and grain boundaries on the thermal and mechanical behavior of 70/30 brass under electrically-assisted deformation, Mater. Sci. Eng. A. 574 (2013) 218–225. https://doi.org/10.1016/j.msea.2013.02.066
[16] M.J. Kim, S. Yoon, S. Park, H.J. Jeong, J.W. Park, K. Kim, J. Jo, T. Heo, S.T. Hong, S.H. Cho, Y.K. Kwon, I.S. Choi, M. Kim, H.N. Han, Elucidating the origin of electroplasticity in metallic materials, Appl. Mater. Today. 21 (2020) 100874. https://doi.org/10.1016/j.apmt.2020.100874
[17] S. Zhao, R. Zhang, Y. Chong, X. Li, A. Abu-Odeh, E. Rothchild, D.C. Chrzan, M. Asta, J.W. Morris, A.M. Minor, Defect reconfiguration in a Ti–Al alloy via electroplasticity, Nat. Mater. 20 (2021) 468-472. https://doi.org/10.1038/s41563-020-00817-z
[18] X. Li, J. Turner, K. Bustillo, A.M. Minor, In situ transmission electron microscopy investigation of electroplasticity in single crystal nickel, Acta Mater. 223 (2022) 117461. https://doi.org/10.1016/j.actamat.2021.117461
[19] X. Zhang, H. Li, M. Zhan, Z. Zheng, J. Gao, G. Shao, Electron force-induced dislocations annihilation and regeneration of a superalloy through electrical in-situ transmission electron microscopy observations, J. Mater. Sci. Technol. 36 (2020) 79-83. https://doi.org/10.1016/j.jmst.2019.08.008
[20] Z. Zimniak, G. Radkiewicz, The electroplastic effect in the cold-drawing of copper wires for the automotive industry, Arch. Civ. Mech. Eng. 8 (2008) 173–179. https://doi.org/10.1016/S1644-9665(12)60204-0
[21] G. Tang, J. Zhang, M. Zheng, J. Zhang, W. Fang, Q. Li, Experimental study of electroplastic effect on stainless steel wire 304L, Mater. Sci. Eng. A. 281 (2000) 263-267. https://doi.org/10.1016/s0921-5093(99)00708-x
[22] Z. Xu, G. Tang, S. Tian, F. Ding, H. Tian, Research of electroplastic rolling of AZ31 Mg alloy strip, J. Mater. Process. Technol. 182 (2007) 128-133. https://doi.org/10.1016/j.jmatprotec.2006.07.019
[23] H.D. Nguyen-Tran, H.S. Oh, S.T. Hong, H.N. Han, J. Cao, S.H. Ahn, D.M. Chun, A review of electrically-assisted manufacturing, Int. J. Precis. Eng. Manuf. - Green Technol. 2 (2015) 365-376. https://doi.org/10.1007/s40684-015-0045-4
[24] H. Xie, X. Dong, Z. Ai, Q. Wang, F. Peng, K. Liu, F. Chen, J. Wang, Experimental investigation on electrically assisted cylindrical deep drawing of AZ31B magnesium alloy sheet, Int. J. Adv. Manuf. Technol. 86 (2016) 1063–1069. https://doi.org/10.1007/s00170-015-8246-0
[25] Z. Lv, Y. Zhou, L. Zhan, Z. Zang, B. Zhou, S. Qin, Electrically assisted deep drawing on high-strength steel sheet, Int. J. Adv. Manuf. Technol. 112 (2021) 763-773. https://doi.org/10.1007/s00170-020-06335-1
[26] G.F. Wang, B. Wang, S.S. Jang, K.F. Zhang, Pulse current auxiliary thermal deep drawing of SiCp/2024Al composite sheet with poor formability, J. Mater. Eng. Perform. 21 (2012) 2062-2066. https://doi.org/10.1007/s11665-012-0165-8
[27] H.G. Park, B.S. Kang, J. Kim, Numerical modeling and experimental verification for high-speed forming of Al5052 with single current pulse, Metals 9 (2019). https://doi.org/10.3390/met9121311

[28] Y. Zhao, L. Peng, X. Lai, Influence of the electric pulse on springback during stretch U-bending of Ti6Al4V titanium alloy sheets, J. Mater. Process. Technol. 261 (2018) 12–23. https://doi.org/10.1016/j.jmatprotec.2018.05.030
[29] G. Lesiuk, Z. Zimniak, W. Wiśniewski, J.A.F.O. Correia, Fatigue lifetime improvement in AISI 304 stainless steel due to high-density electropulsing, Procedia Struct. Integr. 5 (2017) 928–934. https://doi.org/10.1016/j.prostr.2017.07.118
[30] M.H. Alvi, S. Cheong, H. Weiland, A.D. Rollett, Recrystallization and texture development in hot rolled 1050 aluminum, Mater. Sci. Forum. 467–470 (2004) 357–362. https://doi.org/10.4028/www.scientific.net/msf.467-470.357

Materials Research Proceedings 28 (2023) 1007-1014 https://doi.org/10.21741/9781644902479-110

Effect of shear angle in shearing on stretch flangeability of ultra-high strength steel sheets

YAGITA Ryo[1,a *], KIMURA Shunsuke[1,b] and ABE Yohei[1,c]

[1]Toyohashi University of Technology, 1-1, Hibarigaoka, Tempaku, Toyohashi, Aichi 441-8580 Japan

[a]yagita@plast.me.tut.ac.jp, [b]kimura@plast.me.tut.ac.jp, [c]abe@plast.me.tut.ac.jp

Keywords: Stretch Flangeability, Ultra-High Strength Steel Sheets, Shearing

Abstract. The effect of the shear angle in shearing on the stretch flangeability of 980 MPa ultra-high strength steel sheets was examined. The sheared edges of the ultra-high strength steel sheets sheared at different shear angles were investigated, and then the cracking on the sheared edge after stretch flanging was observed. The length of the fracture surface in the sheared edge was decreased by shearing with the punch with a shear angle, whereas many cracks and burrs at the edge of the fracture surface were caused, and the boundary between the burnished and fracture surfaces became rougher. In stretch flanging, the cracks in the fracture bottom side rapidly increased with the bending length. The stretch flangeability increased at a shear angle, where the number of cracks per unit length was the highest, i.e. this indicates that the large number of cracks in the sheared edge were effective in suppressing penetration cracking to fracture in the stretch flanging.

Introduction

To improve the fuel consumption of automobiles, the reduction in weight is intensively required in the automobile industry. To reduce the weight, the application to automotive parts using high strength and ultra-high strength steel sheets increases. The ultra-high strength steel sheet having a tensile strength above 1000 MPa is effective for automotive parts. However, in cold stamping of ultra-high strength steel sheets, there are many resolving problems such as large stamping load [1], large springback [2], low formability [3], tool failure [4] and hydrogen-induced delayed fracture [5].

Steel sheets are typically cut by shearing, and then are formed by stamping to the parts. When steel sheets are bent into a concave shape in stamping, tensile stress are generated at the concave shape edges. Because the sheared edge of the sheet has large plastic deformation and fracture in shearing, the sheared edge qualities was usually changed. Yagita et al. [6] showed that the sheared edge of the ultra-high strength steel sheets was affected by the shear angle in the punch and the blankholding force. The sheared edge qualities for edge cracking in the hole expansion [7] and the stretch flange abilities [8] were investigated. Sartkulvanich et al. [9] showed that the damage value is related to the blanking clearance in the hole expansion of 590 MPa steel sheet.

On the other hand, the studies have been performed to improve stretch flanging ability through material composition and crystalline structure. Pan et al. [10] produced 780 MPa steel sheet with different compositions and showed that stretch flangeability was affected by the strength difference between ferrite and martensite, and that the addition of Nb could increase ferrite strength and improve stretch flangeability. Gwon et al. [11] showed that in the stretch flanging of TWIP steels, cracking occurs mainly at the grain boundaries between ferrite and martensite, and that grain refinement can improve stretch flangeability. Choi et al. [12] stretch flanged three different types of steel sheets and showed that the alternation of FCC and BCC layers in the steel resulted in lower stretch flangeability due to voids at the phase interfaces. Wang et al. [13] improved the stretch flangeability of TRIP steel by annealing the steel to generate a banded structure of soft ferrite phases, which caused cracks to propagate in the rolling direction.

Content from this work may be used under the terms of the Creative Commons Attribution 3.0 license. Any further distribution of this work must maintain attribution to the author(s) and the title of the work, journal citation and DOI. Published under license by Materials Research Forum LLC.

Materials Research Proceedings 28 (2023) 1007-1014 https://doi.org/10.21741/9781644902479-110

A schematic illustration of crack initiation in a stretch flanging is shown in Fig. 1. In stretch flanging, a tensile stress is generated at the blank edge, which is deformed in bending. If the roughness of the sheared edge is large, cracks will occur in the product after stretch flanging, triggered by cracks at the blank edge. If the cracks penetrate, the product will be defective, so it is necessary to stretch flange the product to prevent the cracks from penetration. Since the presence of cracks on sheared surfaces increases the potential for crack penetration, it is important to investigate the formation of cracks by shear and their expansion by stretch flanging.

In this paper, the sheared edges of ultra-high-strength blanks sheared at different shear angles were investigated, and the size of the cracks when stretch-flanged was observed.

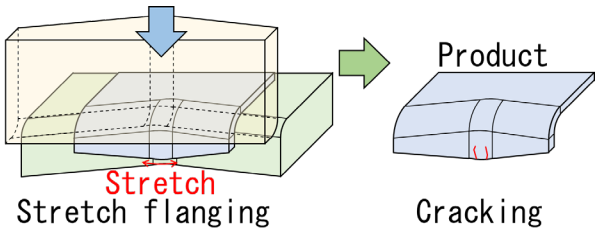

Fig. 1. Crack initiation in stretch flanging.

Materials and Methods

The mechanical properties of the sheet measured by uniaxial tension test are shown in Table 1. The sheet that the nominal tensile strength was 980 MPa was used. Steel sheet was galvanized alloy zinc (GA) steel sheet. The nominal thickness was 1.2 mm.

Table 1. Mechanical properties of steel sheets.

Steel sheets	Thickness [mm]	Galvannealed	Tensile strength [MPa]	Elongation [%]	Reduction in area [%]	*n*-value [-]
980 MPa	1.20	Yes	1003	14.1	58.5	0.128

The method of measuring cracks in the stretch flanging of a sheared steel sheets is shown in Fig. 2. A 150 mm wide steel sheet was sheared to an appropriate length, and the sheared edges were observed. The sheared steel sheets were then stretch flanged, and cracks were observed at the bending deformed edges.

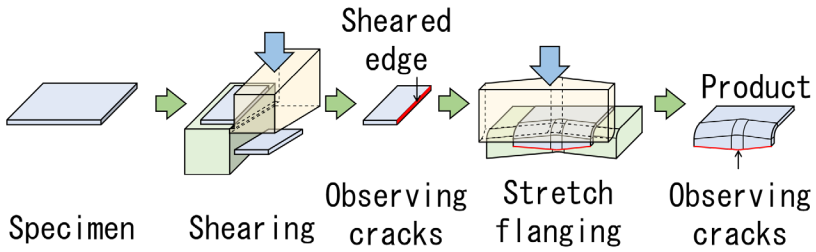

Fig. 2. Method of measuring cracks in stretch flanging of sheared steel sheets.

Shearing conditions are shown in Fig. 3. Each steel sheet was sheared by a die mounted on a servo press (AMADA, SDE-8018). The mean punch speed was 90 mm/s, the shear angles of the punches α, were 0.0, 0.5, and 1.5°, and the clearance between the punch and die was 0.12 mm. The steel sheets were fixed to the die by a blankholder bolted to the die. Counter blocks of urethane rubber (Shore hardness A90) were attached to the under the punch to prevent steel sheets from dropping.

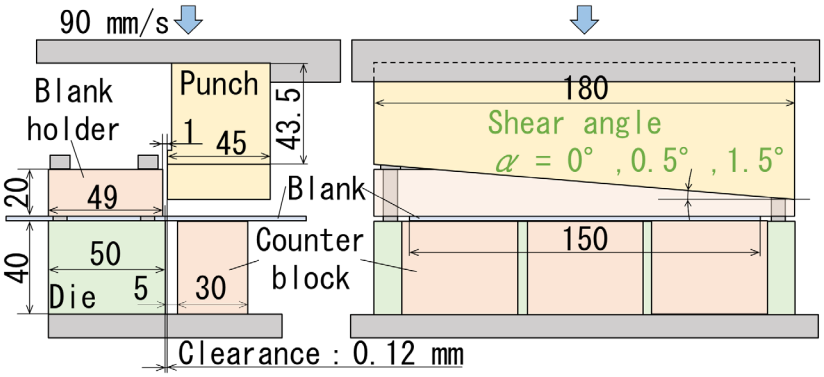

Fig. 3. Shearing conditions.

Stretch flanging conditions are shown in Fig. 4. Each steel sheet was stretch flanged by a die mounted on a servo press (AMADA, SDE-1522). The punch and die had a center angle of 155°, the center was rounded at R50, and the clearance was 1.32 mm. The maximum distance between the sheared edges of the steel sheets and the center of the die was defined as the bend length *l*. The steel sheets were formed in 5 mm increments from 15 mm to 45 mm.

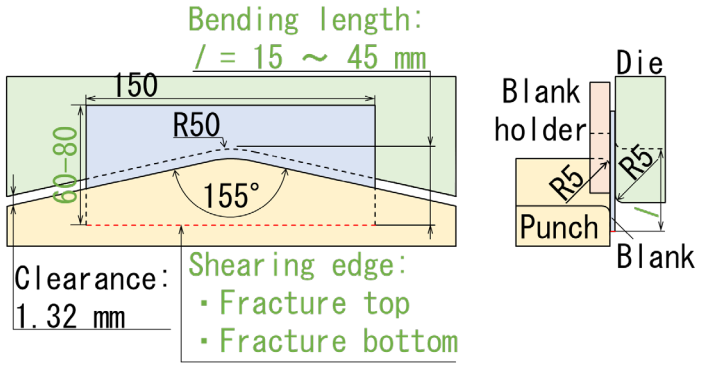

Fig. 4. Stretch flanging conditions.

The steel sheets were mounted on the die by blankholders bolted to the die under two conditions: the fracture top side, where the fracture surface was inside the bend, and the fracture bottom side, where the fracture surface was outside the bend. Anti-rust oil was used as the lubricant.

Results

Sheared Edges of Steel Sheets. The shearing load - punch stroke curve is shown in Fig. 5. The peak shearing load increases with decreasing shear angle, whereas the total stroke decreases.

The sheared edges are shown in Fig. 6(a) to 6(c), and the qualities of sheared edges of sheared sheets are summarized in Fig. 6(d). The sheared edges consisted of the rollover, the burnished surface, and the fracture surface. The ratio of burnished surface was increased by shearing with the punch with shear angle, i.e. the ratio of fracture surface was

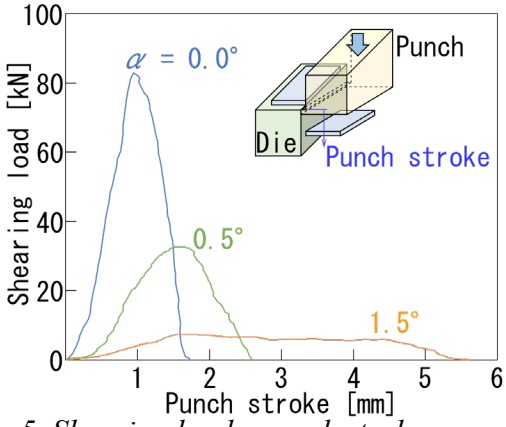

Fig. 5. Shearing load - punch stroke curve.

decreased. In particular, the burnished surface ratio was highest at α =0.5°.

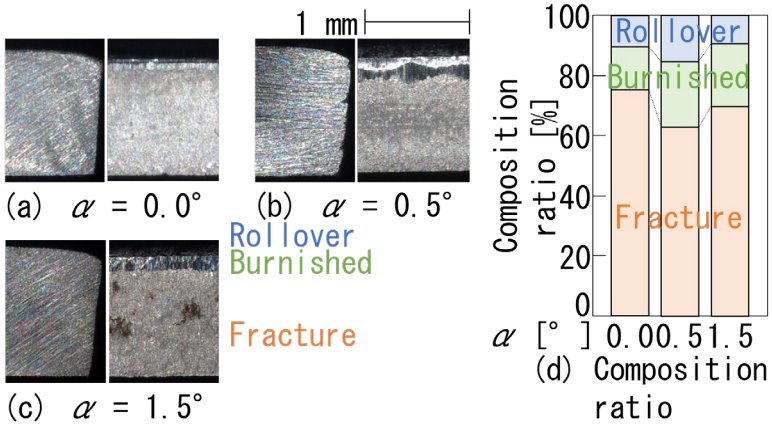

Fig. 6. Sheared edges and quality of sheared edge of sheared sheet.

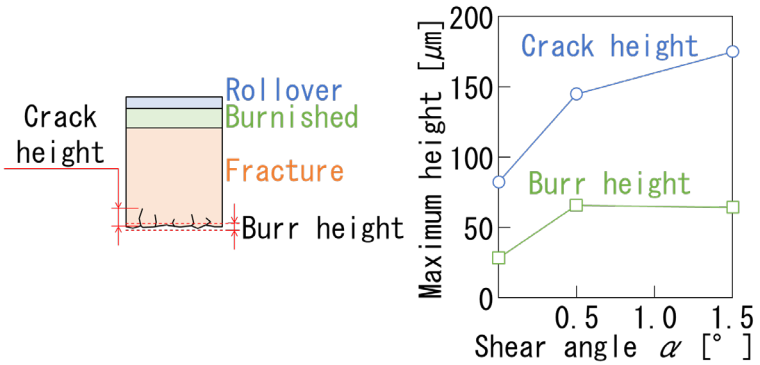

Fig. 7. Maximum crack height and burr height.

In the fracture surface of the sheared edges, cracks that extend into the inside of the fracture surface and small burrs at the edges of the fracture surface were observed. The crack height was defined as the length of the crack from the bottom edge of the fracture surface. The burr height was the length of the burr from the sheet bottom surface. The maximum crack height and burr height sheared at each shear angles are shown in Fig. 7, and the number of cracks per unit width was shown in Fig. 8. The maximum crack height and burr height in the sheared edge with the punch having the shear angle were larger than those in the sheared edge in α = 0.0°. The cracks per unit width in α = 0.5° was the largest.

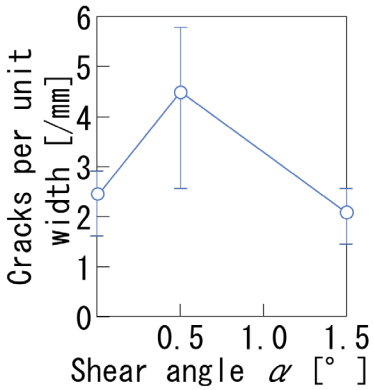

Fig. 8. Number of cracks per unit width.

Materials Research Proceedings 28 (2023) 1007-1014 https://doi.org/10.21741/9781644902479-110

The boundary edges between the burnished and fractured surfaces of the sheared edge are shown in Fig. 9. The burnished surfaces with the punch having the shear angle were rougher. The boundary edge between the burnished and fractured surfaces was rough with a punch having the shear angle α = 0.5°.

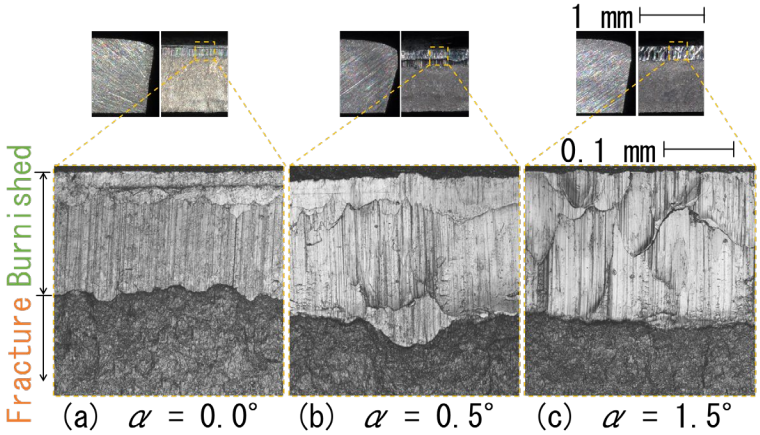

Fig. 9. Boundary between burnished and fractured surfaces.

Cracks after stretch flanging. The stretch flanging ratio with α = 0.0°, the fracture bottom and l = 45 mm is shown in Fig. 10. The stretch flanging ratio was calculated by the difference of gage length on the blank before and after stretch flanging. The initial gage length s was 2 mm. The stretch flanging ratio was the largest at the center of the blank, and deformation was concentrated in a range of approximately -15 mm to +15 mm from the center.

The definition of the crack height after stretch flanging is shown in Fig. 11. Cracks were observed at the bending center of the stretch flanging, and the maximum crack height was classified into the following three types;

i) No cracks: crack height less than 100 µm,
ii) Cracking: crack height larger than 100 µm that do not penetrate in the thickness direction,
iii) Penetration: cracks penetrating in the direction of the sheet thickness.

Cracks were further classified into two types with a threshold value of 300 µm (1/4 of the sheet thickness).

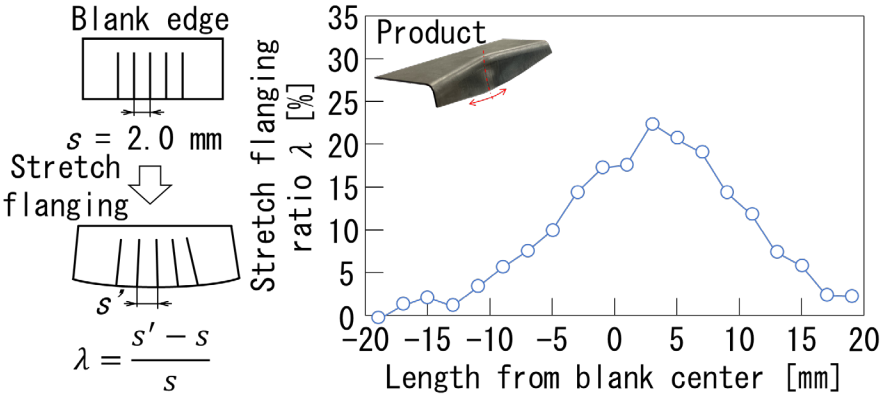

Fig. 10. Stretch flanging ratio with α = 0.0°, fracture bottom side and l = 45 mm.

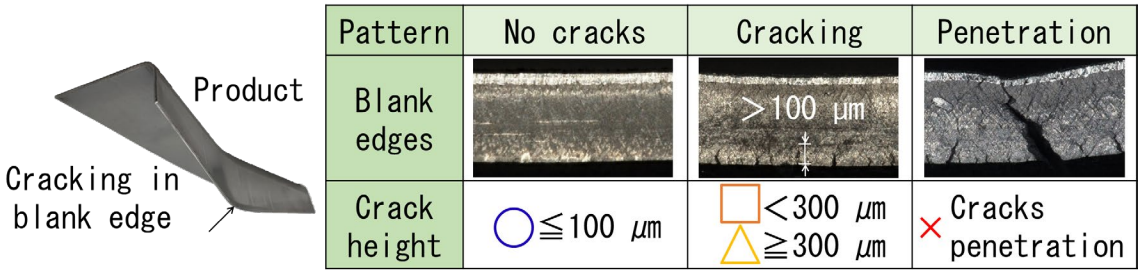

Fig. 11. Definition of crack height after stretch flanging.

The crack heights after stretch flanging on the fracture top and bottom sides are shown in Fig. 12. For both the conditions, as the bending length increased, the crack heights in the sheared edges increased at α = 0.0° and 1.5°, although the cracks did not penetrate. On the other hand, the increment of crack height at 0.5° was small. The crack height after stretch flanging was affected by the sheared edge cut by the punch with the shear angle.

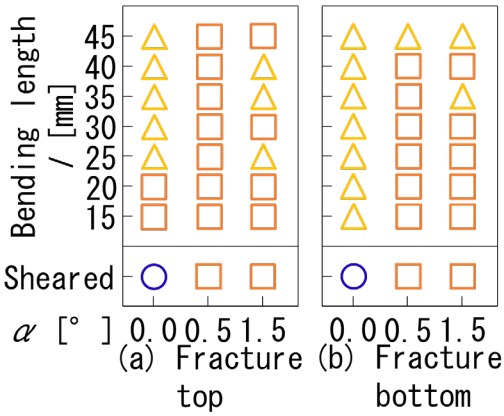

Fig. 12. Crack heights after stretch flanging on the fracture top and bottom sides.

The maximum crack heights for each shear angle after stretch flanging are shown in Fig. 13. A maximum crack height in the sheared edge after stretch flanging was measured in each bending length. On the fracture top side, the maximum crack heights tended to increase as the bending length increased, especially in α = 0.0° and 1.5°. On the fracture bottom side, the maximum crack height was large in α = 0.0°, whereas, the height did not increase significantly. On the other hand, in α = 0.5° and 1.5°, the maximum crack heights increased with increasing bending length, especially at l = 45mm where the crack extended significantly in α = 1.5°. It seems that the maximum crack height and the increment of the height in α = 0.5° were small, although the increment was depending on the sheared edge and the bending side.

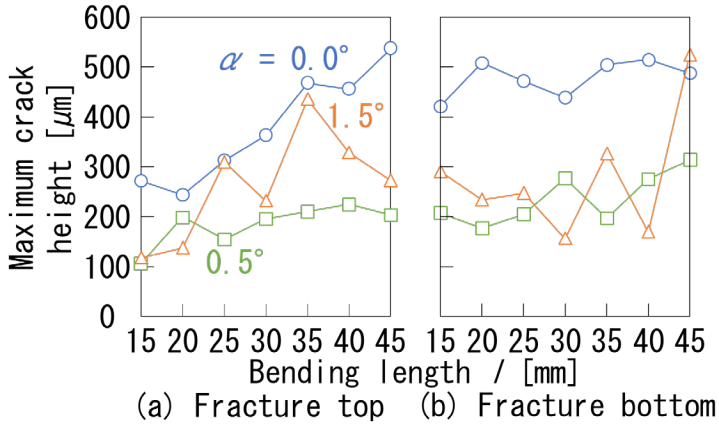

Fig. 13. Maximum crack heights for each shear angle.

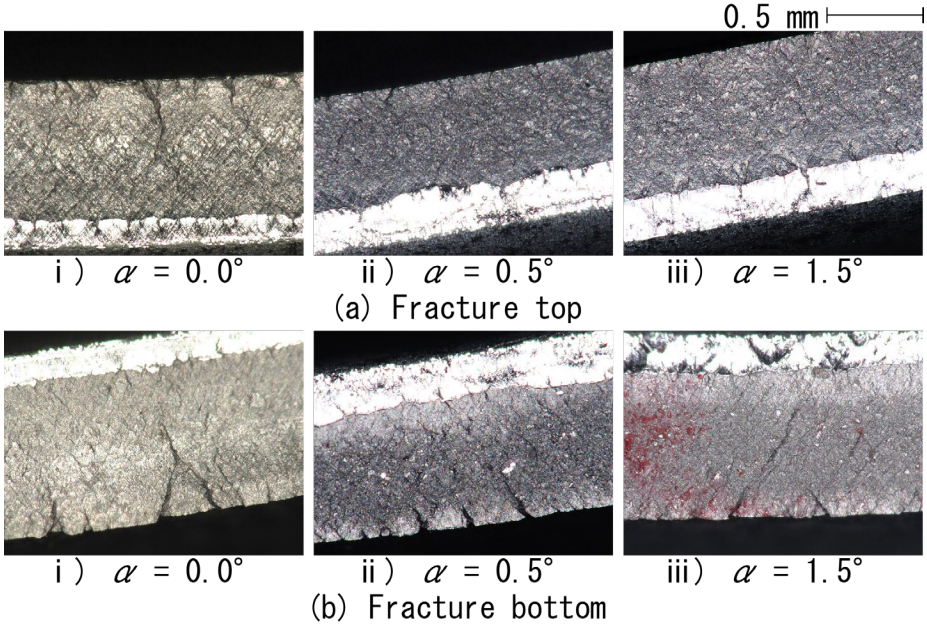

Fig. 14. Edge cracks after stretch flanging with l = 45 mm.

The edge cracks after stretch flanging for each shear angle at l = 45 mm are shown in Fig. 14. Not only in the fracture surface but also in the boundary portion between the burnished and fractured surfaces, the cracks occurred. Although the large cracks with small number are observed in α = 0.0° and 1.5°, the small cracks with large number in fracture surface are observed in α = 0.5°. It seems that a large number of initial cracks as shown in Fig. 8 in the sheared edge distributed the deformation in stretch flanging, and then the occurrence of the large crack was prevented.

Summary

In this paper, the edges of ultra-high-strength blanks sheared with three different shear angles were investigated, and then the size and growth of the cracks in the sheared edge after stretch flanging were observed, with the following results:

1) The ratio of burnished surface was increased by shearing with the punch with shear angle, i.e. the ratio of fracture surface was decreased, and in particular, the burnished surface ratio was highest in the shear angle of 0.5°.
2) The crack height increase after stretch flanging was suppressed in the shear angle of 0.5° in both the fracture top and bottom sides.

3) It seemed that the maximum crack height and the crack increment in the shear angle of 0.5° after stretch flanging were small, although the increment of the maximum crack height was depending on the sheared edge and the bending side.
4) It seemed that a large number of cracks are effective in suppressing penetration cracking caused in stretch flanging, because the stretch flangeability increased in the shear angle of 0.5°, where the number of cracks per unit length were the largest.

References

[1] M.S. Billur, T. Altan, Challenges in forming advanced high strength steels, Proc. New Developments in Sheet Metal Forming (2012) 285-304.
[2] K. Mori, K. Akita, Y. Abe, Springback behaviour in bending of ultra-high-strength steel sheets using CNC servo press. Int. J. Mach. Tools Manuf. 47 (2007) 321-325. https://doi.org/10.1016/j.ijmachtools.2006.03.013
[3] M. Kaupper, M. Merklein, Bendability of advanced high strength steels - A new evaluation procedure, CIRP Annals - Manuf. Technol. 62 (2013) 247-250. https://doi.org/10.1016/j.cirp.2013.03.049
[4] Y. Abe, T. Ohmi, K. Mori, T. Masuda, Improvement of formability in deep drawing of ultra-high strength steel sheets by coating of die, J. Mater. Process. Technol. 214 (2014) 1838-1843. https://doi.org/10.1016/j.jmatprotec.2014.03.023
[5] K. Mori, Y. Abe, K. Sedoguchi, Delayed fracture in cold blanking of ultra-high strength steel sheets, CIRP Annals - Manuf. Technol. 68 (2019) 297-300. https://doi.org/10.1016/j.cirp.2019.04.111
[6] R. Yagita, Y. Abe, Y. Munesada, K. Mori, Deformation Behaviour in Shearing of Ultra-High Strength Steel Sheets under Insufficient Blankholding force, Procedia Manuf. 50 (2020) 26-31. https://doi.org/10.1016/j.promfg.2020.08.006
[7] S. Nasheralahkami, W. Zhou, S. Golovashchenko, Study of Sheared Edge Formability of Ultra-High Strength DP980 Sheet Metal Blanks, J. Manuf. Sci. Eng. 141 (2019) 091009. https://doi.org/10.1115/1.4044098
[8] Y. Abe, R. Yonekawa, K. Sedoguchi, K. Mori, Shearing of ultra-high strength steel sheets with step punch, Procedia Manuf. 15 (2018) 597-604. https://doi.org/10.1016/j.promfg.2018.07.283
[9] P. Sartkulvanich, B. Kroenauer, R. Golle, A. Konieczny, T. Altan, Finite element analysis of the effect of blanked edge quality upon stretch flanging of AHSS, CIRP Annals - Manuf. Technol. 59 (2010) 279-282. https://doi.org/10.1016/j.cirp.2010.03.108
[10] L. Pan, J. Xiong, Z. Zuo, W. Tan, J. Wang, W. Yu, Study of the stretch-flangeability improvement of dual phase steel, Procedia Manuf. 50 (2020) 761-764. https://doi.org/10.1016/j.promfg.2020.08.137
[11] H. Gwon, J.H. Kim, J-K. Kim, D-W. Suh, S-J. Kim, Role of grain size on deformation microstructures and stretch-flangeability of TWIP steel, Mater. Sci. Eng. A 773 (2020) 138861. https://doi.org/10.1016/j.msea.2019.138861
[12] Y.T. Choi, P. Asghari-Rad, J.W. Bae, H.S. Kim, Effect of phase interface on stretch-flangeability of metastable ferrous medium-entropy alloys, Mater. Sci. Eng. A 852 (2022) 143683. https://doi.org/10.1016/j.msea.2022.143683
[13] Y. Wang, Y. Xu, X. Wang, J. Zhang, F. Peng, X. Gu, Y. Wang, W. Zhao, Improving the stretch flangeability of ultra-high strength TRIP-assisted steels by introducing banded structure, Mater. Sci. Eng. A 852 (2022) 143722. https://doi.org/10.1016/j.msea.2022.143722

Materials Research Proceedings 28 (2023) 1015-1020 https://doi.org/10.21741/9781644902479-111

Effect of reduction ratio in flow forming process on microstructure and mechanical properties of a 6082 Al alloy

MUTLU Mehmet[2,a,*], ÖZSOY Atasan[1,b], FENERCIOĞLU Tevfik Ozan[2,c], KARAKAŞ Aptullah[2,d] and BAYDOĞAN Murat[3,e]

[1]Repkon Production Technologies Contracting Industry & Trade Inc., 34980 Şile, Istanbul, Türkiye

[2]Repkon Machine and Tool Industry and Trade Inc., 34980 Şile, Istanbul, Türkiye

[3]Istanbul Technical University, Department of Metallurgy and Materials Engineering, 34469 Maslak, Istanbul, Türkiye

[a]mehmet.mutlu@repkon.com.tr, [b]atasan.ozsoy@repkon.com.tr, [c]ozan.fenercioglu@repkon.com.tr [d]aptullah.karakas@repkon.com.tr, [e]baydogan@itu.edu.tr

Keywords: 6082 Al Alloy, Age Hardening, Flow Forming, Strain Hardening

Abstract. Flow forming is a cold deformation process in which hollow cylindrical or conical parts with different geometric configurations are produced using tools such as balls, rollers, or flow forming wheels on specialized mandrels. Because it enables the production of parts without any further modifications or with minimal modifications before their use in service, the process is categorized as an NSF technology (net-shape forming), and therefore the flow formed parts can be considered as a final product. The aim of this study is to investigate the microstructure and mechanical properties of a flow formed 6082 Al alloy, which was initially in W-temper condition. Hollow cylindrical preforms were first manufactured by machining, and subsequently solution heat treated and quenched. Then, the parts were flow formed with 3 different reduction ratios (45%, 55% and 65%) prior to aging at 177 °C for 8 h to achieve T8 temper condition. Microstructures of the flow formed parts were examined by an optical microscope, and hardness and tensile tests were conducted. The results revealed that increasing reduction ratio slightly decreases hardness and strength with almost constant ductility.

Introduction

Al-Mg-Si alloys (6xxx series alloys) are commonly used heat treatable Al alloys because they offer a combination of high strength, high corrosion resistance, good weldability and low density. In order to obtain appropriate mechanical strength, 6xxx Al alloys are frequently extruded, shaped, and then artificially aged. During these forming processes, the material is subjected to different levels of stress and deformation, precipitation of the second phases occurs in the microstructure of the deformed material during subsequent aging, and the pre-deformation history significantly affects the precipitation behavior and the aging response [1]. Cold working after solution heat treatment and quenching causes nucleation sites for finer precipitates, which further increases strength [2].

The flow forming is a metal forming method which is used to produce hollow cylindrical parts or conical elements by using tools in the form of balls, rollers, or flow forming wheels on a particular mandrel. In order to extrude the material under pressure in the axial direction, the material must first be brought to the state of plastic flow. As a result, the workpiece's length increases and its diameter decreases [3]. During flow forming, the amount of applied plastic deformation is controlled by various process parameters. The most important parameter among them is reduction ratio, namely, percent deformation through the thickness direction.

Content from this work may be used under the terms of the Creative Commons Attribution 3.0 license. Any further distribution of this work must maintain attribution to the author(s) and the title of the work, journal citation and DOI. Published under license by Materials Research Forum LLC.

Most of the studies concerning flow forming processes include surface roughness prediction depending on the flow forming parameters [4], residual stress estimation [5], forming forces arising from the process variables, and investigation the relationships between the microstructure and the mechanical properties of flow formed materials. In this context, De et al [4] investigated the surface roughness of an H30 aluminum alloy after being flow formed, and established a correlation between the surface roughness and the flow forming parameters. Srivastwa et al [6] measured the flow forming forces depending on the feed rate and the rotational speed of the mandrel during flow forming process of 2014 and 7075 Al alloys in annealed condition. They found that effect of varying feed rate had a higher effect on the resulting forming forces than the effect of the varying rotational speed. They also reported that axial force was the dominant force with respect to radial and circumferential forces. Haghshenas et al [7] investigated the mechanical properties 5052 and 6061 Al alloys after 20 to 60% flow forming. They reported that the yield strength of both alloys increased after the flow forming, with the increment in 5052 Al alloy was 47% higher than that of 6061 alloy due to a higher strain hardening coefficient of 5052 Al alloy. Gao et al [8] investigated the effect of recrystallization and solution annealing heat treatments on the microstructures and mechanical properties of a flow formed 2219 Al alloy. They reported that the flow forming increased strength and decreased ductility. Following the recrystallization annealing at 435°C for 30 min, strength of the flow formed samples decreased first, and increased again with increased recrystallization temperature. For the solution annealing heat treatment conducted after the flow forming, both strength and ductility increased with increasing solution annealing temperature. As seen from the previous works, aluminum alloys were subjected to flow forming process to investigate their response to flow forming in the view point of their surface quality and the final mechanical properties after being flow formed. It is therefore, the main aim of the present work is to investigate the effect of reduction ratio during flow forming process, and subsequent aging on the microstructure and mechanical properties of a 6082 Al alloy.

Experimental Procedure

6082 Al preform tubes were first solution annealed (W-temper condition) at 530 °C for 1 h, and then quenched in 20 vol.% polymer containing water [9]. The flow forming process was performed on solution treated alloy in W-temper condition in three different reduction ratios (45%, 55% and 65%), and finally the tubes were aged at 177°C for 8 h. Fig. 1 shows an image of preform material (left) and flow-formed materials (with increasing reduction ratio from left to right). The preform and the flow formed tubes were hereafter designated as Preform, S45, S55 and S65 samples according to the reduction ratio.

Fig. 1. General view of the preform (left) and flow formed 6082 Al tubes with increasing reduction ratios of 45%, 55%, and 65% from left to right.

Microstructures of the preform and the flow formed samples were examined under an Olympus BX53M optical microscope after being prepared by standard metallographic procedure [10] and etched by 25 s immersion into the Groesbeck's reagent (100 ml water, 4 g NaOH, 4 g KMnO4). Hardness of the samples was measured by an Emco Test DuraScan 20 tester using a Vickers pyramid indenter and 300 g load according to ASTM E384 standard [11]. The hardness measurement was carried out through the thickness of the samples at regular intervals from the outer surface (in contact with the rollers) to the inner surface (in contact with the mandrel). The tensile tests were conducted on an Instron 3382 model universal testing machine using the samples, which were prepared according to ASTM E8/E8M standard [12] in the longitudinal direction to the forming direction.

Results and Discussions

Fig. 2 shows optical micrographs of the flow formed samples. As seen in Fig. 2a, the grains are clearly visible in S45 sample, as being approximately 20 μm length and 5 μm width grains, which were elongated along the flow direction. In the microstructures of S55 and S65 samples (Fig. 2b and c), the reduction ratio was higher, and the grains were not clearly visible due to higher amount of reduction on those samples. Despite all samples were subjected to aging heat treatment at 177°C for 8 h, there was no recrystallization in the microstructures due to a lower temperature of aging, which is insufficient for recrystallization. Considering the fact that recrystallization takes place easier when the reduction rate increases [13], it was seen that even 65% of reduction in the thickness direction did not lead to recrystallization of the samples.

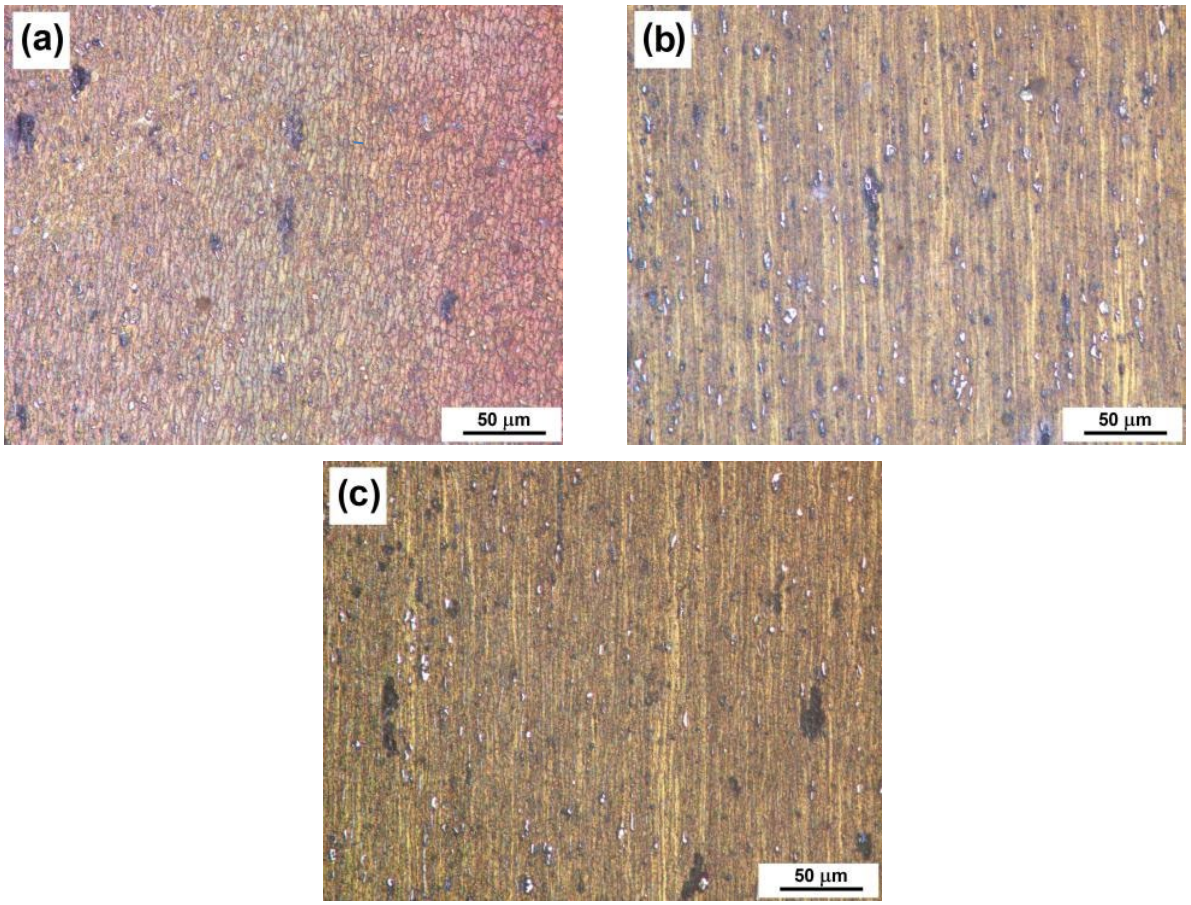

Fig. 2. Optical micrographs of the flow formed samples (a) S45, (b) S55, and (c) S65.

Table 1 lists the hardness of the flow formed samples. It is interesting to note that hardness of the flow formed and the aged samples slightly reduced when the reduction ratio increased. On the other hand, even though hardness of S45 sample close to the inner surface was slightly higher, there was no clear correlation between the hardness values depending on the hardness measurement locations.

Table 1. Hardness measurements of the flow formed and aged samples.

Hardness measurement locations	Hardness, HV0.3		
	S45	S55	S65
1 (close to outer surface)	99	92	93
2	103	96	96
3	98	93	99
4	101	92	93
5 (close to inner surface)	110	93	95

Tensile test results are listed in Table 2, and the stress – strain graphs are presented in Fig. 3. Similar to the hardness variation, strength values of S45 sample are slightly higher than those of S55 and S65 samples. However, the ductility, in terms of elongation, almost remained constant when the reduction ratio increases. Considering that lower reduction ratio results in a higher hardness and strength, and lack of hardness increment with increased reduction ratio, it was concluded that that age hardening mechanism is more effective than strain hardening mechanism in determining the final mechanical properties.

Table 2. Tensile test results of the flow formed and aged samples.

Properties	S45	S55	S65
Yield strength, [MPa]	272	262	268
Ultimate tensile strength, [MPa]	290	275	282
Elongation at fracture, [%]	11.8	11.3	10.8

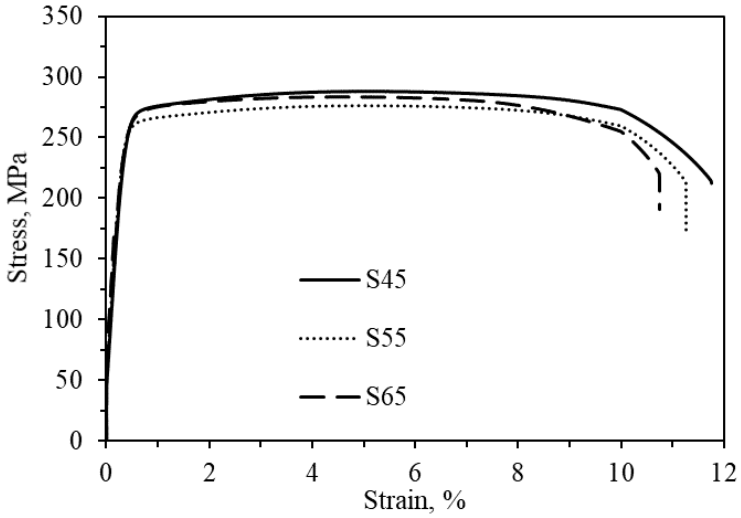

Fig. 3. Stress strain graphs of the flow formed and aged samples.

Summary

The effect of cold deformation by the flow forming on microstructure and mechanical properties of a 6082 Al alloy after the aging was investigated. As the reduction ratio increases from 45% to 65%, the grains are elongated along the flow direction. For lower reduction ratio (S45 sample), the grains are still visible, while, the grains were almost invisible in the samples subjected to reduction ratio (S55 and S65 samples). There was no recrystallization in the microstructures indicating the aging temperature (177°C) after the flow forming is insufficient for recrystallization to take place. Hardness and strength are the highest for the samples subjected to a lower reduction ratio during the flow forming. Increasing deformation slightly reduced hardness and strength, with exhibiting almost constant ductility. The obtained results finally indicate that age hardening mechanism in the present 6082 Al alloy is more effective in determining the final mechanical properties.

References

[1] M. Kolar, K.O Pedersen, , S. Gulbrandsen-Dahl, K. Marthinsen, Combined effect of deformation and artificial aging on mechanical properties of Al–Mg–Si Alloy, Transactions of Nonferrous Metals Society of China 22 (2012) 1824-1830, https://doi.org/10.1016/S1003-6326(11)61393-9

[2] Karakaş, T.O. Fenercioğlu, T. Yalçınkaya, The influence of flow forming on the precipitation characteristics of Al2024 alloys, Mater. Lett. 299 (2021) 130066. https://doi.org/10.1016/j.matlet.2021.130066

[3] Standard Practice for Heat Treatment of Wrought Aluminum Alloys, ASTM B918/B918M-20a, January 2022.

[4] T.N. De, B. Podder, N.B. Hui, C. Mondal, Experimental study and analysis of surface roughness of the flow formed H30 alloy tubes, Materials Today: Proceedings 38 (2021) 3190-3197. https://doi.org/10.1016/j.matpr.2020.09.647

[5] D. Tsivoulas, J. Quinta da Fonseca, M. Tuffs, M. Preuss, Effects of flow forming parameters on the development of residual stresses in Cr–Mo–V steel tubes, Mater. Sci. Eng. A 624 (2015) 193–202. https://doi.org/10.1016/j.msea.2014.11.068

[6] A.K. Srivastwa, P.K. Singh, S. KumarExperimental investigation of flow forming forces in Al7075 and Al2014 – A comparative study, Materials Today: Proceedings 47 (2021) 2715-2719. https://doi.org/10.1016/j.matpr.2021.02.781

[7] M. Haghshenas, J.T. Wood, R.J. Klassen, Investigation of strain-hardening rate on splined mandrel flow forming of 5052 and 6061 aluminum alloys, Mater. Sci. Eng. A 532 (2012) 287-294. https://doi.org/10.1016/j.msea.2011.10.094

[8] P.F. Gao, Z.P. Ren, M. Zhan, L. Xing, Tailoring of the microstructure and mechanical properties of the flow formed aluminum alloy sheet, J. Alloy. Compd. 928 (2022) 167139. https://doi.org/10.1016/j.jallcom.2022.167139
[9] J. Friis, B. Holmedal, Ø. Ryen, E. Nes, O.R. Myhr, Ø. Grong, T. Furu, K. Marthinsen, Work Hardening Behaviour of Heat-Treatable Al-Mg-Si-Alloys, Mater. Sci. Forum 519–521 (2006) 1901–1906. https://doi.org/10.4028/www.scientific.net/msf.519-521.1901
[10] Standard Guide for Preparation of Metallographic Specimens, ASTM E3-11, June 12, 2017.
[11] Standard Test Method for Microindentation Hardness of Materials, ASTM E384-17, June 1, 2017.
[12] Standard Test Methods for Tension Testing of Metallic Materials, ASTM E8/E8M-22, July 19, 2022.
[13] J.D. Verhoeven, Fundamentals of Physical Metallurgy, First ed., Wiley, Michigan, 1975. ISBN 0471906166.

Materials Research Proceedings 28 (2023) 1021-1028 https://doi.org/10.21741/9781644902479-112

Flow forming and recrystallization behaviour of CuZn30 alloy

MUTLU Mehmet[1,a,*], KARAKAŞ Aptullah[1,b], KUŞDEMIR Hakan[1,c], KOLTAN Umut Kağan[1,d] and YALÇINKAYA Tuncay [2,e]

[1]Repkon Machine and Tool Industry and Trade Inc., 34980 Şile, Istanbul, Turkey

[2]Department of Aerospace Engineering, Middle East Technical University, 06800 Ankara, Turkey

[a]mehmet.mutlu@repkon.com.tr, [b]aptullah.karakas@repkon.com.tr, [c]hakan.kusdemir@repkon.com.tr, [d]umut.koltan@repkon.com.tr, [e]yalcinka@metu.edu.tr

Keywords: Flow Forming of CuZn30, Recrystallization of CuZn30

Abstract. CuZn30, which is also called cartridge brass, is an alloy used commonly in the production of large-calibre round cartridge cases. They are usually produced via cupping of a disc and consecutive deep drawing steps to decrease the wall thickness, with an annealing process in between each step to restore formability. In this study the manufacturing of cartridge brass (CuZn30) tubes is conducted through the flow forming process. In order to evaluate the flow forming behaviour, the preforms are manufactured by machining the CuZn30 billets, then the flow forming processes is applied. Thereafter, different temperature ranges (350, 450, and 550ºC for 1 h) are applied to flow formed samples in order to determine the proper recrystallization annealing temperature. The obtained microstructures and the mechanical properties are studied and revealed that the flow forming process is successfully realized, and the microstructure of the material is mapped with respect to the subsequent heat treatment temperature for recrystallization. Spherical and new grains are precisely generated after recrystallization annealing at 450 and 550ºC, but only partial recrystallization is obtained at 350ºC.

Introduction

The alloy CuZn30, also known as cartridge brass, is best known for its use in the production of large-calibre round cartridge cases. In order to reduce the wall thickness in a series of deep drawing steps, they are typically produced by cupping a disc, followed by each deep drawing step being followed by an annealing step to regain formability [1].

Flow forming could also be a suitable alternative method for decreasing the wall thickness of the case. It is an efficient technique for manufacturing precision tubular products and is an incremental forming process in which the wall thickness of a product is decreased by passing rollers over the material once or multiple times [2]. For the flow forming process, in addition to process parameters such as the feed rate, rotation speed, and reduction ratio, which concern the process window, material properties are also a major factor that determines the process outcome. Bylya et al. [3] investigated the influence of the elastic-plastic properties on the formability of the material and pointed out resilience, strain hardening, and tensile area reduction as significant parameters, which affect the material's ability to redistribute its volume along the mandrel. For a material with high strain hardening, the deformed material at the top strengthens and restricts the upward elastic expansion of the material at the bottom. This directs the expansion along the mandrel and allows large elongations under hydrostatic compression. A higher resilience means a higher elastic compression and, therefore, expansion.

Cartridge brass has excellent cold forming and high strain hardening capability. However, its resilience is not as high as for example high strength steel due its lower yield strength. In this work, the flow forming behaviour of CuZn30 is studied considering its plastic properties within the scope

Content from this work may be used under the terms of the Creative Commons Attribution 3.0 license. Any further distribution of this work must maintain attribution to the author(s) and the title of the work, journal citation and DOI. Published under license by Materials Research Forum LLC.

of cartridge case production as well as its recrystallization behaviour to determine the optimum process for the best final product. Heat treatment is required in between the cold forming steps for further forming by recrystallization and is usually done at around 500 to 650ºC for the deep drawing processes according to reduction ratios. [4].

Experimental Procedure

CuZn30 alloy is procured in hot extruded condition. Optical emission spectroscopy is employed to confirm the material grade. The material composition matches with the composition of CuZn30 (C26000) according to ASTM B19 as seen in Table 1 [5].

Table 1. Chemical composition of the preform.

	Zn	Pb	Sn	P	Fe	Ni	Al	Bi	Cu
Value [%]	28.67	0.022	0.014	0.004	0.023	0.01	0.0027	< 0.001	71.2066

Fig. 1 Preform (PRE) part on the left and Flow-formed (FF1) on the right.

For the flow forming operations, the materials are machined into preforms in the form of hollow cylinders closed at one end with an outer diameter of 125.20 mm, wall thickness of 5.2 mm and a length of 300 mm. Preform is then flow formed with a feed rate of 110 mm/sec and rotation speed of 160 rpm with 40% thickness reduction ratio at one cycle which are illustrated in Fig.1. In this work, a preform and a flow formed parts are investigated through the microstructural analysis and the mechanical testing. Metallographic specimens from longitudinal and transverse sections for each case is prepared according to ASTM E3 [6]. The specimens are etched with Klemm's III Reagent 3 minutes and Acidic Ferric Chloride 1 minute by immersion, separately. After etching, microstructures are analyzed under an optical microscope, Olympus BX53M. The hardness measurements are conducted with a Vickers micro indentation method using EmcoTest DuraScan – 20 according to ASTM E384 [7]. For longitudinal and transverse sections of specimens, the hardness is measured 10 times, starting from the forming surface in contact with the rollers, along

Materials Research Proceedings 28 (2023) 1021-1028 https://doi.org/10.21741/9781644902479-112

the diameter at specified intervals. Tensile testing specimens are prepared by machining as shown in Fig. 2 and tested three times according to ASTM E8 [8] using an Instron 3382 model Universal Testing Machine.

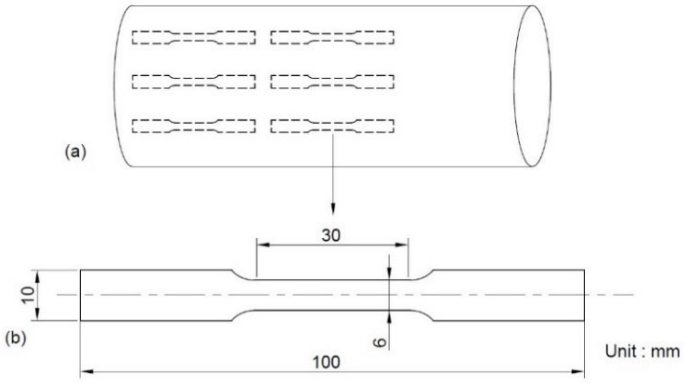

Fig. 2. The cutting position of the specimen for tensile testing (a); and (b) the specimen dimensions for tensile testing.

To investigate the recrystallization behaviour, flow formed samples (abbreviated as FF1) with dimensions around 5x5 cm are cut for microstructure analysis and hardness measurements and tensile testing specimens are machined from the preform and the flow formed parts. After manufacturing the specimens, analysis and testing are carried out, afterwards, the specimens are subjected to recrystallization heat treatment by open atmosphere laboratory furnace. The data given for 40% cold worked CuZn30 (FF1) is used as a reference for determining the recrystallization heat treatment temperature. However, the recrystallization behaviour is expected to vary with the amount of cold work as plastic deformation increases the internal energy of the material. Three heat treatment temperatures, 350, 450 and 550°C, are determined for examination. The specimens are heated with a rate of 10°C/min and held at the respective temperatures for 1 hour followed by air cooling. Microstructure analysis, hardness measurements and tensile tests of the heat-treated specimens are carried out accordingly.

Results and Discussions

The hardness of the preform is measured in the range of 75 – 85 HV. After the flow forming process, the hardness increased to 190 – 235 HV. Near the outer surface where the rollers contact occur, hardness is around 235 HV, and it drops to 190 HV at the inner surface which is in contact with the mandrel. The amount of deformation is higher at the outer surface where the force is applied by the rollers. The hardness values obtained from the longitudinal sections are similar to the transverse section. Microstructure image taken from the preform is presented in Fig. 3. CuZn30 contains approximately 30% Zn. At this concentration, only α phase forms in the microstructure. As illustrated inn Fig. 3, α grains and annealing twins are observed.

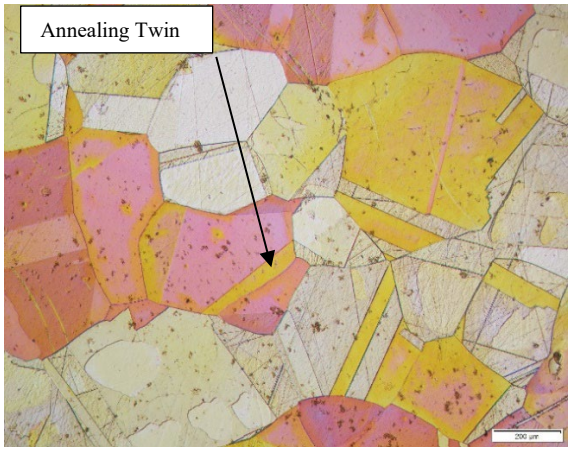

Fig. 3. Microstructure images from transverse cross-sections of PRE-specimen at 100X, Klemm's III Reagent-3min.

The microstructures of flow formed FF1 samples are presented in Fig. 4. The effective hardening mechanism in CuZn30, which consists of a single phase, is deformation hardening. Since α phase has a low stacking fault energy, it is difficult for screw dislocations to perform a cross-slip. Due to this restriction in dislocation movement, the material has high strain hardening properties [9].

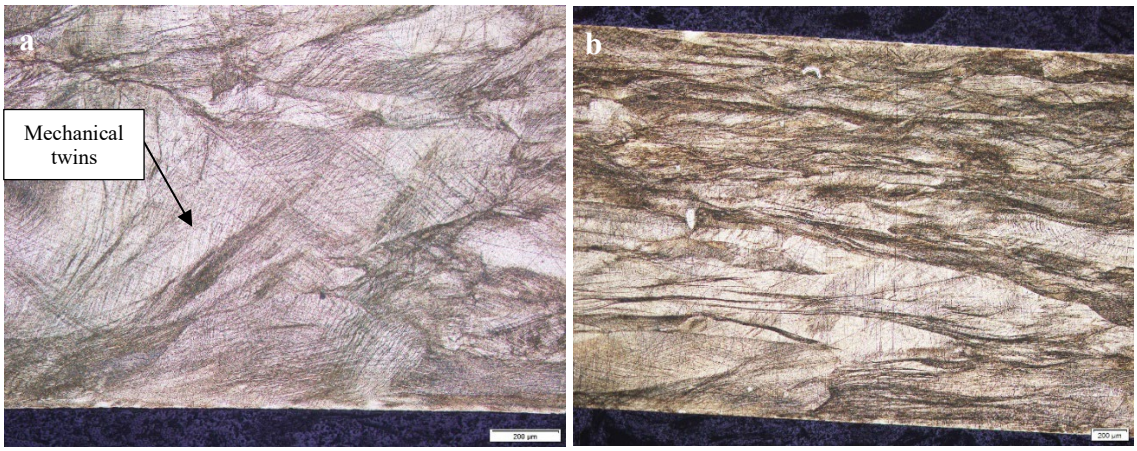

Fig. 4. Microstructure images from transverse cross-section of FF1 specimen at (a) 100X and (b) 50X, Acidic Ferric Chloride-1min.

Since slip systems are limited in materials with low stacking fault energy, mechanical twins are observed in microstructure after the deformation. In flow formed sample (FF1), the mechanical twins are seen as thin parallel lines side by side. These are the local high shear strain zones seen in ductile materials that caused by a high amount of deformation [10]. The ultimate tensile strength (UTS) hardening exponent n of flow-formed (FF1) is calculated as 0.12 and as for the preform (PRE), it is calculated as 0.48. This shows that the preform has a higher strain hardening ability compared to FF1 specimen.

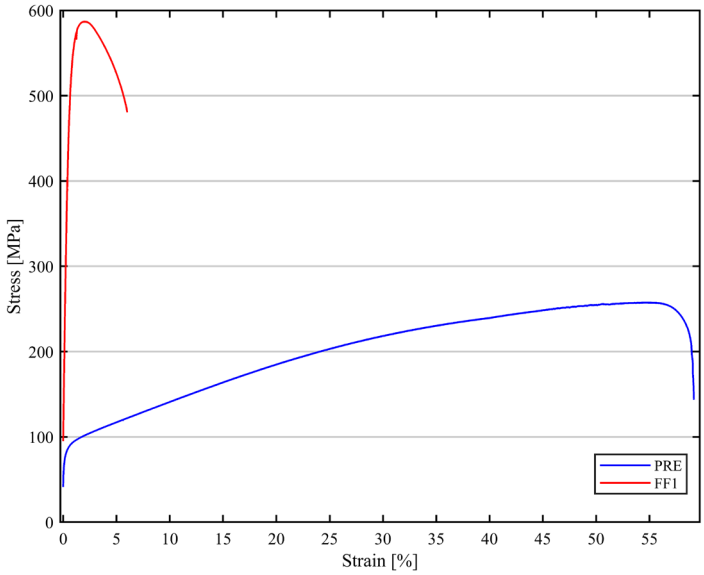

Fig. 5. Stress-strain curves of PRE and FF1 specimens.

The hardness values of heat-treated parts at 350, 450 and 550ºC, are measured between 120 – 130 HV, 90 – 110 HV and 75 – 90 HV respectively. The hardness dropped to preform hardness values after heat treating at 550ºC. The microstructure of heat-treated samples at 350ºC, 450ºC and 550ºC are given in Fig. 6, 7 and 8 respectively. The microstructure of the transverse, longitudinal and planar sections are similar to each other. As shown in Fig. 6, the mechanical twins did not completely disappear in FF1 after the heat treatment at 350ºC. Grain morphology could not occur completely in microstructure, but it could be observed that the number of mechanical twins decreased and partial recrystallization occurred. The recrystallization of FF1 can be completed by increasing the heat treatment time at the application temperature. The microstructures after the heat treatment at 450°C and 550°C are presented in Fig. 7 and 8 respectively. It is observed that recrystallization has taken place in the microstructure. At the higher heat treatment temperature, the grain sizes increased as shown in the figures.

Fig. 6. FF1 heat treated at 350ºC taken at 500X, Acidic Ferric Chloride-1min.

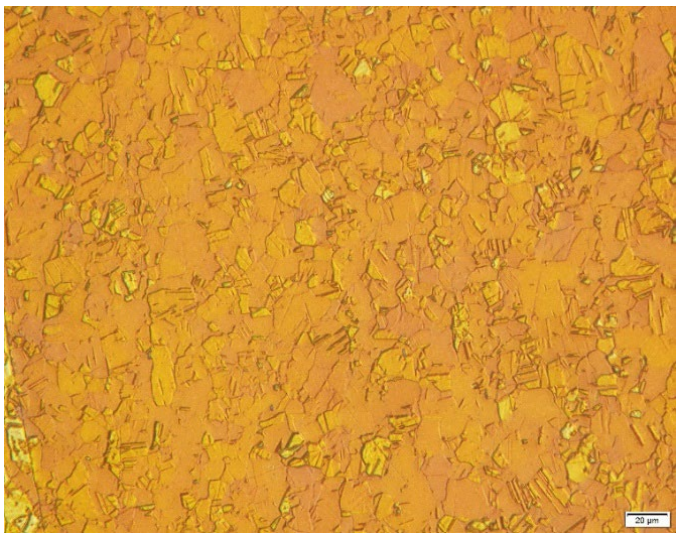

Fig. 7. FF1 heat treated at 450 ºC taken at 500X, Klemm's III Reagent-3min.

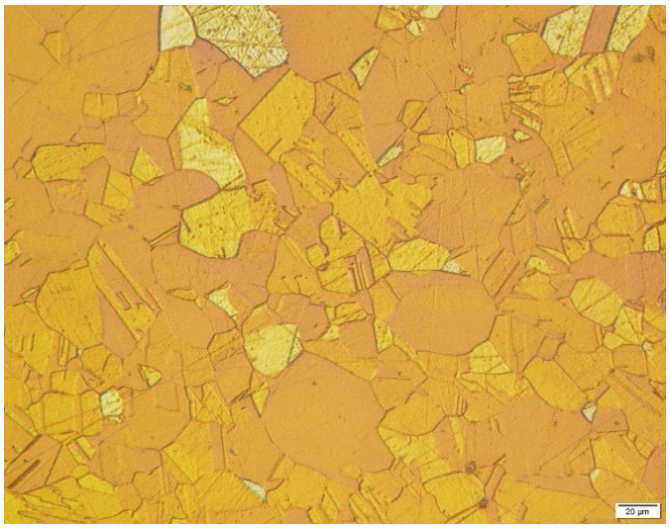

Fig. 8. FF1 heat treated at 550 ºC taken at 500X, Klemm's III Reagent-3min.

The tensile test results of the heat-treated samples are shown in Fig. 9 As the heat treatment temperature increases, the strength of the material decreases and its ductility increases. The strength level of FF1 specimen heat treated at 550°C approaches quite close to the strength levels of preform.

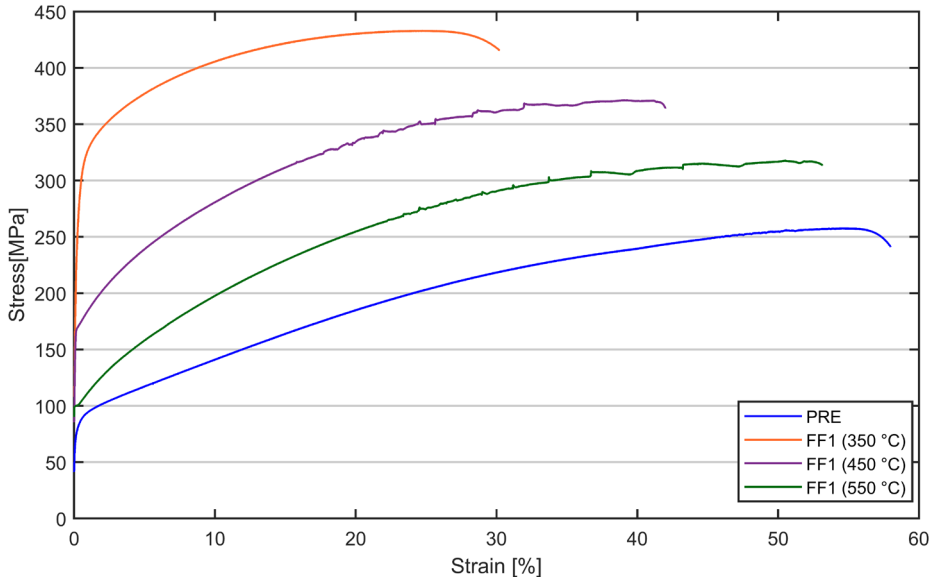

Fig. 9. Stress-strain curves of recrystallization heat treated specimens.

Summary

This paper investigates the formability of cartridge brass using flow forming process as well as the behaviour of recrystallization following cold deformation by heat treatment at three different temperature levels, which are 350°C, 450°C, and 550°C. After the flow forming process, a substantial strain-hardening is obtained, with tensile strength increasing twofold and yield strength increasing fivefold, while elongation decreasing to 5% from 55%. This elongation level makes the material quite brittle, therefore, it is very difficult to use the cartridge brass at this elongation levels because of its low toughness. In order to eliminate brittleness, both recrystallization and annealing procedures are carried out. The annealing processes are applied at three different temperature values. Microstructural analysis and mechanical testing revealed that the recrystallization process succeeds at 450°C and 550°C, while recrystallization could not be completely affected at 350°C. As for tensile testing of the FF1 specimen, which is annealed at 350°C, it is observed that elongation increases which could be related to recovery. The recrystallization mechanism necessitates more temperature in order to lower dislocation density; therefore, only the recovery mechanism occurs at 350°C.

References

[1] A. Doig, Military Metallurgy, 1998, pp. 23 - 29. https://doi.org/10.1201/9781003059400

[2] A. Karakaş, T. Ozan Fenercioğlu, T. Yalçinkaya, The influence of flow forming on the precipitation characteristics of Al2024 alloys, Mater. Lett. 299 (2021) 130066. https://doi.org/10.1016/j.matlet.2021.130066

[3] O. Bylya, T. Khismatullin, P. Blackwell, R. Vasin, The effect of elasto-plastic properties of materials on their formability by flow forming, J. Mater. Process. Technol. 252 (2018) 34-44. https://doi.org/10.1016/j.jmatprotec.2017.09.007

[4] E. El-Danaf, M. Soliman, A. Al-Mutlaq, Correlation of Grain Size, Stacking Fault Energy, and Texture in Cu-Al Alloys Deformed under Simulated Rolling Conditions, Adv. Mater. Sci. Eng. 2015 (2015) 1-12. https://doi.org/10.1155/2015/953130

[5] ASTM, B19-Standard Specification for Cartridge Brass Sheet, Strip, Plate, Bar, and Disks, Annual Book or ASTM Standards, American Society for Testing and Materials, Vol. 02.01

[6] ASTM, E3-11- Standard Guide for Preparation of Metallographic Specimens, Annual Book or ASTM Standards, American Society for Testing and Materials, Vol. 3.01

[7] ASTM, E384-17- Standard Test Method for Microindentation Hardness of Materials, Annual Book or ASTM Standards, American Society for Testing and Materials, Vol. 3.01
[8] ASTM, E8-13. Standard Test Methods of Tension Testing of Metallic Materials, Annual Book or ASTM Standards, American Society for Testing and Materials, Vol. 3.01
[9] G. Xiao, N. Tao, K. Lu, Microstructures and mechanical properties of a Cu–Zn alloy subjected to cryogenic dynamic plastic deformation, Mater. Sci. Eng. A 513-514 (2009) 13-21. https://doi.org/10.1016/j.msea.2009.01.022
[10] S. Cronje, R.E. Kroon, W.D. Roos, J.H. Neethling, Twinning in copper deformed at high strain rates, Bull. Mater. Sci. 36 (2013) 157–162. https://doi.org/10.1007/s12034-013-0445-4

Materials Research Proceedings 28 (2023) 1029-1035 https://doi.org/10.21741/9781644902479-113

Mechanical and microstructural properties of AISI 4140 after flow-forming process

YAZGAN Elif[1,a *], MUTLU Mehmet[2,b], AYDIN Güneş[1,c], KARAKAS Aptullah[2,d], FENERCIOGLU Tevfik Ozan [2,e] and BAYDOGAN Murat[3,f]

[1]Repkon Production Technologies Contracting Industry & Trade Inc., 34980 Şile, Istanbul, Türkiye

[2]Repkon Machine and Tool Industry and Trade Inc., 34980 Şile, Istanbul, Türkiye

[3]Istanbul Technical University, Department of Metallurgy and Materials Engineering, 34469 Maslak, Istanbul, Türkiye

[a]elif.yazgan@repkon.com.tr, [b]mehmet.mutlu@repkon.com.tr , [c]gunes.aydin@repkon.com.tr, [d]aptullah.karakas@repkon.com.tr, [e]ozan.fenercioglu@repkon.com.tr, [f]baydogan@itu.edu.tr

Keywords: Flow Forming, Heat Treatment, AISI 4140

Abstract. Flow-forming is a cold deformation process to form dimensionally precise and rotationally symmetrical parts. Strain hardening effect of the flow forming process, and possibility of producing cylindrical part are the advantages especially for aerospace industry. The purpose of this study is to investigate the effect of initial microstructure of an AISI 4140 steel on the microstructure and mechanical properties after being flow formed by 70% as the reduction ratio in the thickness direction. In this context, as-received steel was heat treated to standard quenched and tempered condition, and an additional annealing was also performed. Before and after the flow forming process, the microstructure was examined, hardness and tensile tests were conducted. The results revealed that the additional annealing was beneficial to obtain a crack free material after the flow forming process of a heat treated material.

Introduction

Flow forming is a cold deformation process commonly used in metal forming industry. With this process, dimensionally accurate and rotationally symmetrical parts can easily be produced [1,2]. Cold deformation during flow forming improves hardness and strength properties of the formed parts due to strain hardening mechanism, which occurs as a result of generation of the dislocations within the material and their interactions with each other [3]. In the flow forming process, a relatively short and thick starting material in tube form (preform) is formed into a longer and thinner tube by means of a rotating mandrel inside the preform, and one or more rollers outside the preform. There are basically two flow forming methods depending on the flow direction of the material. When the flow direction of the material is towards the front of the roller, it is called as forward flow forming, and when the flow direction of the material is the rear of the roller, it is called as backward flow forming. Higher dimensional accuracy, higher inner and outer surface quality, improved hardness and strength, and finer and uniform directional grain structure can be achieved by the flow forming process [4].

Flow forming is an active research area both in academic and industrial point of view. In this context, several works have been published so far focusing on Al alloys [5], Mg alloys [6], Ti alloys [7] and steels. Beside experimental works concerning the relationship between input parameters of the flow forming, and final microstructure and mechanical properties of the flow formed alloys, numerical modelling coupled with the experiments was also made. For example, Banerjee et al [8] studied efficiency of two artificial neural network architectures to estimate the final dimensions of large tubes with respect to the input parameters, by using three optimization

Content from this work may be used under the terms of the Creative Commons Attribution 3.0 license. Any further distribution of this work must maintain attribution to the author(s) and the title of the work, journal citation and DOI. Published under license by Materials Research Forum LLC.

techniques, and concluded that BFGS (Broyden–Fletcher–Goldfarb–Shanno) tuned Elman Neural Network (ENN) provided satisfactorily statistical performance with a faster computational time with respect to LM (Levenberg–Marquardt) tuned method. In another work, Roula et al [9] conducted mechanical tests and finite element analysis to model the flow forming behavior and predict the necking behavior during flow forming. On the other hand, Xu et al [10] studied fatigue crack growth rate of a 34CrMo4 steel which was flow formed after hot drawing. They reported that the hot drawn and cold flow formed steel exhibited a higher resistance to the crack growth than the base metal, fatigue crack growth rate increased with increasing stress ratio, and the sample direction had a little effect on fatigue crack growth rate. Karakaş et al [11] investigated the mechanical properties of an annealed 5140 steel tube after being flow formed in comparison to the annealed condition. They reported that after the flow forming, hardness, yield strength and tensile strength were all significantly improved by a factor of 1.2, 2.6 and 1.6 times, respectively, with a corresponding decrease in elongation at fracture by 50%. They also found that hardness through the thickness direction of the flow formed tube significantly decreased from the outer surface to the inner surface.

AISI 4140 alloy is a medium carbon low alloy steel, which is generally used in quenched and tempered condition to meet the strength and hardness specifications in industrial applications. Although the flow forming has a potentiality to modify the microstructure and mechanical properties of AISI 4140 steel, to the best of our knowledge, its mechanical properties have not been studied so far. It is therefore, in this study, it is aimed to investigate the effect of the initial microstructure of an AISI 4140 low alloyed steel on the microstructure and mechanical properties after flow forming.

Methodology

AISI 4140 steel is used as the starting material (the preform) for the flow forming process. Table 1 shows the chemical composition of a hot rolled and annealed AISI 4140 steel use as the preform material in the present study. Preform tubes have the dimensions of 730 mm in length and 5.5 mm in wall thickness. They were subjected to the flow forming process with a 70% reduction ratio in the thickness direction. Flow forming process parameters were as follows; feed rate was 0.5A mm/min, spindle rate was 1.95A rpm, and a cooled emulsion was used as the lubricant (A is factor of company know-how.). Final dimensions of the tubes were 1965 mm in length and 1.6 mm in wall thickness. In the present study, the preform and flow formed parts were shown in Fig. 1.

Table 1. Chemical composition of the AISI 4140 steel used as the preform in this study.

Element	C	Si	Mn	P	S	Cr	Mo	Ni	Al	Cu	Fe
wt.%	0.41	0.23	0.68	0.008	0.013	0.97	0.19	0.12	0,012	0,18	Balance

In order to investigate the effect of initial microstructure, three samples were prepared including as-received (AR), quenched and tempered (QT), and further annealed samples (QTA) in addition to QT condition. For QT condition, the samples were first austenitized at 845°C for 30 min, quenched in oil at room temperature, and tempered at 500°C for 30 min. Additional annealing was carried out at 600°C for 3 h. The microstructures of the preform and the flow formed samples were examined on an Olympus BX53M optical microscope after being prepared by the standard manner [12] and etched with 2% Nital. The hardness was measured on the cross sections of the tubes at specified intervals along the thickness direction by an Emco Test Dura Scan – 20 hardness tester using a Vickers indenter under a load of 300 g according to ASTM E384-17 standard [13].

Fig. 1. Preform tube (Left) and flow formed tube (Right).

The tensile tests were conducted on an Instron 3382 model universal testing machine by using longitudinal samples prepared along the forming direction according to ASTM E8M standard [14]. Three tensile specimens were tested for each condition.

Result and Discussion

Microstructural examinations.

Fig. 2 shows the optical micrographs of the preforms and the flow formed samples representing each condition of the AISI 4140 steel. The microstructure of AR sample preforms has an equiaxed grain structure composed of ferrite and pearlite (Fig. 2a). The flow forming strongly affected this microstructure resulting in severely elongated grains along the forming direction, as expected (Fig. 2b). QT sample has a tempered martensite structure before the flow forming (Fig. 2c), and exhibited a cold worked structure after the flow forming (Fig. 2d). Additional annealing led to a tempered martensite structure (Fig. 2e), which was coarser with respect to that of QT sample. The flow forming of QTA sample resulted in elongated grains (Fig. 2f) as in the case of the previous conditions. The microstructures of all flow formed samples were similar to each other, which are characterized by severely deformed grains along the forming direction without any remarkable discontinuities in the microstructure.

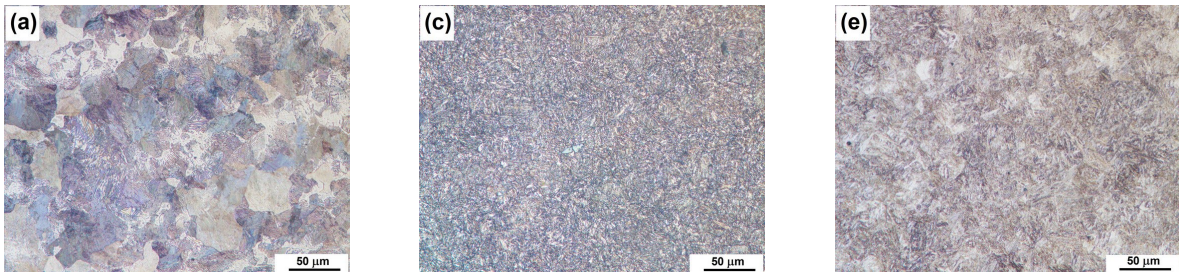

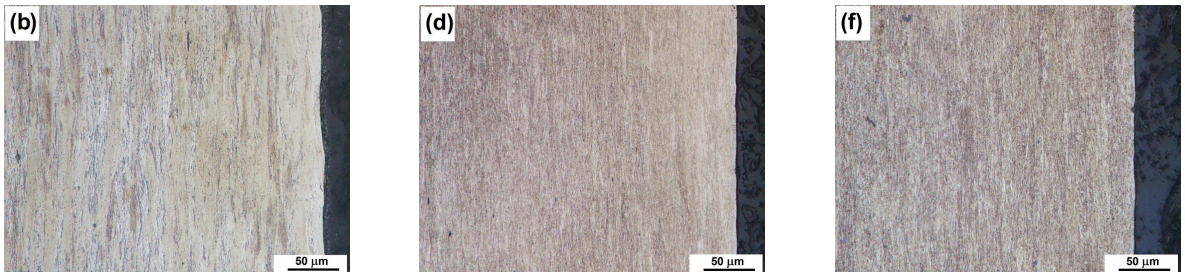

Fig. 2. Optical micrographs of the preform samples (Fig. 2a, c and e) and the flow formed samples (Fig. 2b, d and f). AR samples (Fig. 2a and b), QT samples (Fig. 2c and d), and QTA samples (Fig. 2e and f).

Hardness test results.

Hardness of the samples before and after the flow forming process was listed in Table 2. Among the preform samples, hardness increased with an increasing order for AR, QTA and QT samples. QT samples had the highest hardness, additional annealing slightly reduced hardness, as a result of a higher tempering temperature. Depending on the measurement location, the hardness slightly reduce from the outer surface to the inner surface for AR sample preforms, suggesting that the outer rollers are more effective for hardness increment. However, there was no systematic correlation depending on the measurement locations for QT and QTA samples. After being flow formed, the hardness of all samples increased due to strain hardening. The highest increment (approximately 50%) was observed for AR sample. QT and QTA samples had almost the same hardness, exhibiting a hardness increment by approximately 10-15% after the flow forming process. This indicates that strain hardening mechanism is less effective for heat treated samples than AR sample. No significant variation is observed among the hardness values of the samples from the outer and the inner surface of the flow formed samples.

Table 2. Hardness of the preforms and the flow formed samples.

Distance from the outer surface, [mm]	Hardness, [HV0.3]					
	Preform			Flow formed		
	AR	QT	QTA	AR	QT	QTA
0.15	204	396	354	312	422	435
0.30	212	374	366	305	431	419
0.44	203	388	357	308	417	424
0.60	189	389	379	310	419	413
Average	202	387	364	309	422	423

Tensile test results.

Tensile test results were listed in Table 3, and stress – strain graphs were given in Fig. 3. Among the preform samples, QT samples have the highest strength values with an elongation at fracture of 11.2% as a measure of ductility. Additional annealing reduced strength and ductility. This is a result of the coarser microstructure of QTA sample with respect to QT sample. When the samples were flow formed, regardless of their initial conditions, their strength values were improved with a corresponding decrease in ductility. This shows that hardness and strength values generally

varied similar to each other, except for strength decrement in QTA sample. Although its hardness was equivalent with that of QT sample after the flow forming, strength values of QTA sample were significantly lower than those of QT samples after the flow forming, with slightly higher ductility. On the other hand, for both preform and the flow formed samples, AR samples exhibited lower strength and higher ductility. Similar to the hardness increment upon the flow forming, the strength values increased more in AR samples (approximately 110% for yield strength, and 50% for ultimate tensile strength). On the other hand, for the heat treated samples (QT and QTA samples), this increment was significantly lower (approximately 10-25%). It is also interesting to note that mechanical properties of QTA sample before the flow forming were almost similar to those of AR sample after the flow forming. The tensile test results revealed that initial microstructures of AISI 4140 steel was highly effective in determining the final properties after the flow forming.

Table 3. Tensile test results of the preforms and the flow formed samples.

Properties	Preform			Flow formed		
	AR	QT	QTA	AR	QT	QTA
Yield strength, [MPa]	345	1118	962	738	1342	1059
Ultimate tensile strength, [MPa]	692	1209	1074	1057	1483	1363
Elongation of fracture, %	16.2	11.2	9.3	8.8	5.1	6.6

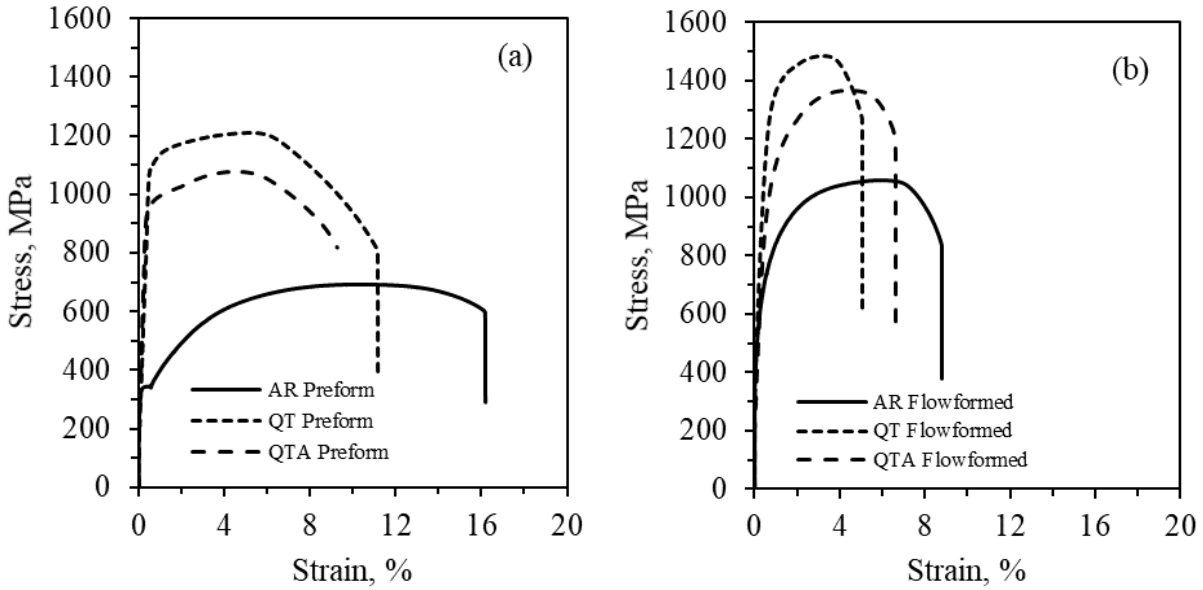

Fig. 3. Stress – strain graphs of (a) the preform and (b) flow formed parts.

Visual examination.

Visual examination of the samples after the flow forming process revealed that AR and QTA samples exhibited no visible defect inside or outside the formed tubes. However, there was a small surface crack inside QT sample as seen in Fig. 4, despite that QT sample preform has slightly higher ductility than QTA sample. The observed crack on QT sample was possibly resulted from its tempered martensite microstructure exhibiting the highest hardness and yield strength. This suggests that additional annealing after quenching and tempering is beneficial to avoid crack

formation during the flow forming, and might be attributed to a coarser tempered martensite microstructure with a lower hardness and yield strength of QTA sample.

Fig. 4. Small surface crack formed inside QT sample.

Summary

In this study, the effect of various initial microstructures of AISI 4140 steel preforms on the microstructure and mechanical properties, and surface quality after being flow formed was investigated. Heat treatments significantly affected the microstructure and mechanical properties of AISI 4140 steel after the flow forming Comparative study of three initial microstructures, namely, as-received (AR), quenched and tempered (QT), additionally tempered after quenching and tempering (QTA) leads to following conclusions:

1. The initial microstructure of AISI 4140 steel significantly affects the microstructure and mechanical properties of the flow formed parts. In this context, AR microstructure exhibited higher increment (approximately 50%) in strength values after the flow forming with a corresponding decrease (approximately 45%) in ductility. On the other hand, the strength increment after the flow forming of QT and QTA samples was lower (10-25%) when compared to that of AR sample.
2. Ductility of all samples in terms of elongation at fracture decreased by the flow forming. However, the highest decrement was observed in QT samples (approximately 55%), while QTA sample exhibited the lowest decrement in ductility (approximately 30%).
3. The highest hardness (387 HV) and strength (1483 MPa) were obtained from QT sample. However, this condition leads to a crack formation on the surface during the flow forming, Additional annealing after quenching and tempering avoided the crack formation during the flow forming. This suggest that a coarser tempered microstructure developed by the additional annealing is beneficial to produce crack free parts for the investigated AISI 4140 steel.

References

[1] A. Karakaş, T.O. Fenercioğlu, T. Yalçinkaya, The influence of flow forming on the precipitation characteristics of Al2024 alloys, Mater. Lett. 299 (2021) 1-4. https://doi.org/10.1016/j.matlet.2021.130066

[2] S. Kalpakjian, S. Rajagopal, Spinning of Tubes: A Review, J. Appl. Metal Work. 2 (1982) 211–223. https://doi.org/10.1007/BF02834039

[3] M.J. Roy, R.J. Klassen, J.T. Wood, Evolution of plastic stra.in during a flow forming process, J. Mater. Process. Technol. 209 (2009) 1018-1025. https://doi.org/10.1016/j.jmatprotec.2008.03.030

[4] D. Marini, D. Cunningham, J.R. Corney, A review of flow forming processes and mechanism, Key Eng. Mat. 651-653 (2015) 750-758. https://doi.org/10.4028/www.scientific.net/KEM.651-653.750

[5] X. Zeng, X.G. Fan, H.W. Li, M. Zhan, S.H. Li, K. Q. Wu, T.W. Ren, Heterogeneous microstructure and mechanical property of thin-walled tubular part with cross inner ribs produced by flow forming, Mat. Sci. Eng. A-Struct. 790 (2020) 139702. https://doi.org/10.1016/j.msea.2020.139702

[6] Q. Xia, J. Long, G. Xiao, S. Yuan, Y. Qin, Deformation mechanism of ZK61 magnesium alloy cylindrical parts with longitudinal inner ribs during hot backward flow forming, J. Mater. Process. Technol. 296 (2021) 117197. https://doi.org/10.1016/j.jmatprotec.2021.117197

[7] Z. Lei, P. Gao, X. Wang, M. Zhan, H. Li, Analysis of anisotropy mechanism in the mechanical property of titanium alloy tube formed through hot flow forming, J. Mater. Sci. Technol. 86 (2021) 77–90. https://doi.org/10.1016/j.jmst.2021.01.038

[8] P. Banerjee, R. Laha, M.K. Dikshit, N.B. Hui, S. Rana,V.K. Pathak, K.K. Saxena, C. Prakash, D. Buddhi, A study on the performance of various predictive models based on artificial neural network for backwardmetal flow forming process, Int. J. Interact. Des. Manuf. *(*IJIDeM) (2022). https://doi.org/10.1007/s12008-022-01079-6

[9] A.M. Roula, K. Mocellin, H. Traphöner, A.E. Tekkaya, P-O Bouchard, Influence of mechanical characterization on the prediction of necking issues during sheet flow forming process, J. Mater. Process. Technol. 306 (2022) 117620. https://doi.org/10.1016/j.jmatprotec.2022.117620

[10] X. Xu, C. Lu, Y. Li, X. Ma, W. Jin, Fatigue Crack Growth Characteristics of 34CrMo4 Steel for Gas Cylinders by Cold Flow Forming after Hot Drawing, Metals 11 (2021) 133. https://doi.org/10.3390/met11010133

[11] A. Karakaş, A.C. Kocabıçak, S. Yalçınkaya, Y.Şahin, Flow Forming Process for Annealed AISI 5140 Alloy Steel Tubes. in: M. Abdel Wahab (Ed.), Proceedings of the 8th International Conference on Fracture, Fatigue and Wear, FFW 2020 2020, Lecture Notes in Mechanical Engineering. Springer, Singapore. https://doi.org/10.1007/978-981-15-9893-7_10

[12] Standard Guide for Preparation of Metallographic Specimens, ASTM E3-11, June 12, 2017.

[13] Standard Test Method for Microindentation Hardness of Materials, ASTM E384-17, June 1, 2017.

[14] Standard Test Methods for Tension Testing of Metallic Materials, ASTM E8/E8M-22, July 19, 2022.

Materials Research Proceedings 28 (2023) 1037-1046 https://doi.org/10.21741/9781644902479-114

Simulation of incremental sheet metal forming for making U-channel in two light-weight alloys

BHUSHAN Bharat[1,a], RAMKUMAR Janakarajan[1,b *] and DIXIT Uday Shanker[2,c]

[1]Department of Mechanical Engineering, Indian Institute of Technology Kanpur, Kanpur, Uttar Pradesh 208016, India

[2]Department of Mechanical Engineering, Indian Institute of Technology Guwahati, Guwahati, Assam 781039, India

[a]bharatb@iitk.ac.in, [b]jrkumar@iitk.ac.in, [c]uday@iitg.ac.in

Keywords: Incremental Sheet Metal Forming, Finite Element Method, U-Channel, Shell Element

Abstract. Incremental sheet metal forming (ISMF) is a viable method for fabricating complicated three-dimensional structures from sheet metal. It is characterized by localized deformation and is effective for both rapid prototyping and low-volume manufacturing. ISMF technology is suitable for quick product development time with affordable tooling and for deforming difficult-to-form materials. Simulation of the process reduces costly hit-and-trial attempts for manufacturing an accurate product. This article presents the simulation for producing a U-channel made of aluminum (Al 6061-T6) and titanium (Ti-6Al-4V) alloys. A finite element method (FEM) package, ABAQUS®, has been used for simulation using shell elements. The effect of various parameters on the forming forces is discussed using two different tools, flat and hemispherical-end.

Introduction

For the past few decades, numerical simulations have been playing a vital role in understanding the underlying physics of various manufacturing processes. In processes where the machine operation and raw material costs are very high, simulation results assist in reducing the expensive hit-and-trial attempts. Sheet metal forming is a metal forming process where a sheet of metal is shaped into a product by deforming it plastically. Incremental sheet metal forming (ISMF) is one of the advanced and innovative techniques in sheet metal forming processes. This die-less process has gained popularity thanks to its high flexibility and cost-effectiveness for small-batch production. This process can form difficult-to-form materials such as titanium, aluminium, and magnesium [1]. Because of its capability to produce high geometric accuracy and surface finish, ISMF finds many applications in the automotive, aerospace, and medical sectors. Numerical modelling of the ISMF is an active area of research [2]. Modelling and simulation can provide all the information about the distribution of stresses and strains, which is crucial for finding out spring back and the possibility for defects. Many advanced finite element methods (FEM) software packages such as ABAQUS®, LS-DYNA, and PAM-STAMP are used to simulate ISMF. Among these packages, ABAQUS® /Explicit is a general-purpose package and hence, has wider availability in organizations. One can model the ISMF process using explicit or implicit dynamic methods [3].

A single-point incremental forming is an ISMF process wherein a tool presses the clamped sheet from the top without having any support from the bottom. The tool can be of different shapes, which is plunged into the sheet incrementally; path planning of the tool is also important. During the deformation, a very high reaction force is developed on the tool, depending on the sheet thickness and material. Arens et al. [4] developed a mathematical relation for the approximate prediction of axial force in ISMF. In the force prediction model, the axial force was the function

Content from this work may be used under the terms of the Creative Commons Attribution 3.0 license. Any further distribution of this work must maintain attribution to the author(s) and the title of the work, journal citation and DOI. Published under license by Materials Research Forum LLC.

of the tensile strength (not the yield strength) with other parameters. No effect of strain hardening was included. Chang et al. [5] highlighted that due to localized and step-wise deformation in the ISMF process, the axial forming force is drastically reduced compared to conventional sheet forming processes. They noted that elastic deformation of the sheet was the major cause of the axial force fluctuation.

Petek et al. [6] demonstrated that the forming force in ISMF is very small as compared to deep drawing and is independent of the size of the product. Forming angle, tool diameter, and step-depth were the major influencing factors for the force distribution during the ISMF process. The authors also observed that the rotation of the tool has no effect on the force, but it affects the surface quality of the product. Asghar et al. [7] observed a good agreement between the forces obtained from FEM and the experimental study. The axial force is greater than the radial force on the deep-drawn component; comparatively, the tangential component of force is much smaller. Hence, geometrical accuracy is mainly influenced by axial and radial forces.

ISMF process provides good formability, low surface roughness, and high geometric accuracy. Formability improvement is one of the major advantages offered by ISMF. Shamsari et al. [8] carried out a single and two-stage ISMF for 70° wall angle truncated cone. Two-stage forming provided 26% improvement in forming depth compared to a single stage; sheet thinning was also reduced by around 45%. The effect of a hemispherical-end and flat-end tool on deformation behavior was also studied. A straight tool path has been used for each simulation, with different step depths as per the number of stages. Najm et al. [9] observed that a flat-end tool with a small corner radius offered the best thickness distribution stability. Ziran et al. [10] found that as compared to hemispherical-end tools, flat-end tools provided greater profile accuracy and formability.

The primary objective of this work is to carry out FE simulations for the forming of Al 6061-T6 and titanium (Ti-6Al-4V) alloys. Although simulations of ISMF have been performed by several researchers; however, many research articles provide only partial information about the results. This work attempts to understand the efficacy of simulations for proper process planning of ISMF. Alloys chosen for simulations are used in the automobile, aerospace, and medical sectors. Simulations were performed for making U-channels and evaluating the effects of step depth and coefficient of friction between the tool and workpiece.

Problem Definition

The deformation in the ISMF process is due to the horizontal and vertical linear movement of the tool along the defined tool path over the workpiece. Due to the motion of the tool, plastic deformation takes place, resulting in the development of stresses, reaction forces, and strains in the workpiece. Fig. 1 shows a forming tool starting from its initial position and moving forward in a horizontal direction at a certain depth. After one pass, more depth is provided depending on step-size. Then the tool moves backward and reaches its original position. This process is continued till the desired form is produced. During the deformation of the workpiece, high reaction forces act on the tool, and thinning of the sheet also takes place. Fig. 1 shows the schematic of the process along with the tool path. Here a spherical-end tool is shown, but the simulations were carried out with a flat-end tool too.

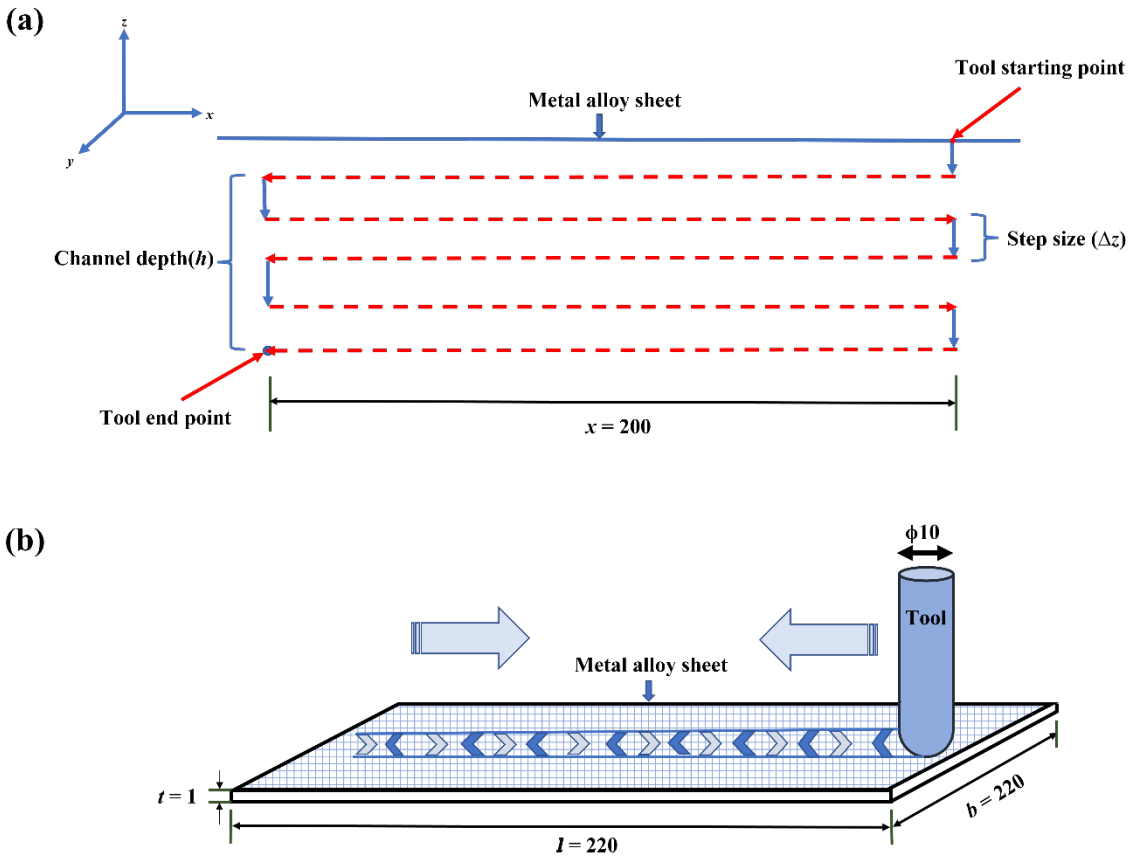

Fig. 1. Forming of U-channel: (a) tool path, (b) total imparted depth h = 5 mm with step size Δz = 1 mm. (All dimensions shown in the figure are in mm).

Numerical Simulation

Simulations were performed in ABAQUS®/Explicit FE software (SIMULIA™ by Dassault Systems®, France). Explicit analysis has been chosen because of its computational efficiency. Considering that strains are small and the sheet is already hardened, strain hardening has been neglected. The sheet blank of aluminum alloy Al 6061-T6 of thickness 1 mm was modeled. Considering the low thickness of the sheet, shell elements were chosen. The use of shell elements provided much less computational time than that required with solid elements [11]. The plasticity model used for numerical simulations for both materials is the 'Perfectly plastic isotropic hardening model based on von Mises yield criterion'. The S4R four-node square shell element was used to mesh the sheet. S4R is a 4-node double curved thin or thick shell with reduced integration, hourglass control, and finite membrane strains. For various parameters, the approximate element sizes of 1 mm, 2 mm, and 4 mm were taken. Simulations were performed to obtain different output parameters such as stress, strain, reaction force on the tool, the thickness of the sheet at different values of coefficient of friction between tool and workpiece, number of stages, and two different types of the tool.

Fig. 2 shows the hemispherical-end tool and the flat-end tool with a diameter of 10 mm. A corner radius of 2.5 mm was given to the flat-end tool. As the analytical rigid property was given to both tools, no material properties were assigned to them. Additionally, no rotational speed was given to the tool, as the effect of rotation was manifested in the form of friction.

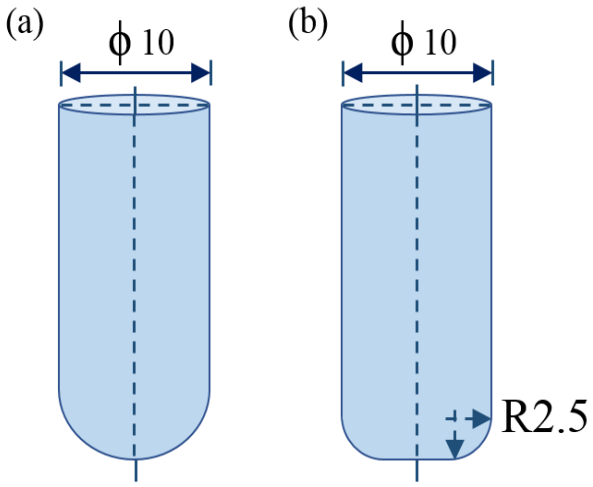

Fig. 2. Incremental sheet metal forming tools: (a) hemispherical-end, and (b) flat-end with chamfered edges. (All dimensions are in mm).

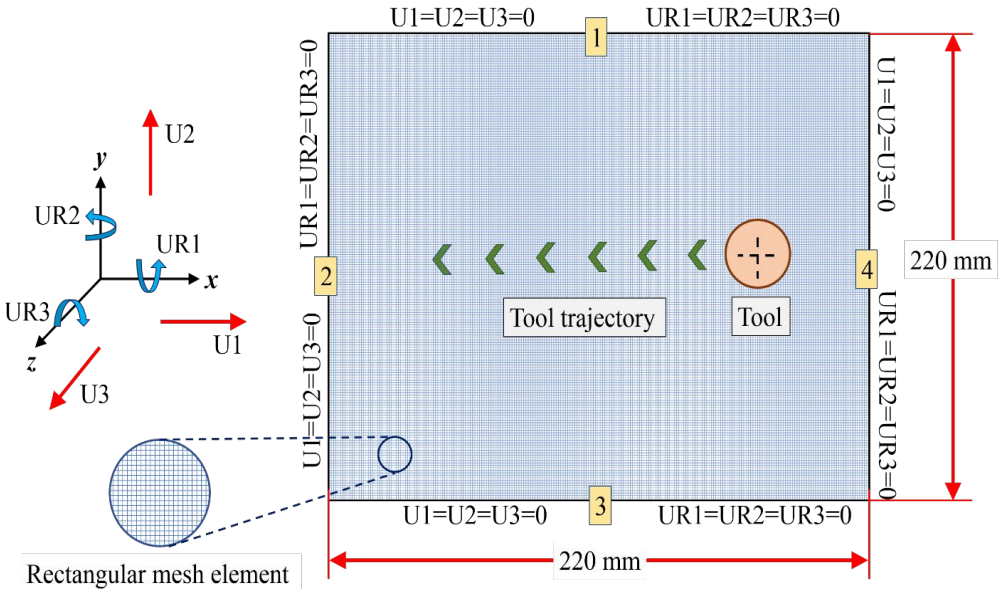

Fig. 3. Domain with boundary conditions. U1, U1, and U3 represent displacement, and UR1, UR2, and UR3 represent rotation about the x, y, and z axes, respectively. The sheet thickness is kept at 1 mm, and the edge length of the square mesh element is 2 mm.

Fig. 3 shows that the sheet was square in shape, with cross-sectional dimensions of 220 mm × 220 mm and a thickness of 1 mm. The sheet was modeled using a deformable, shell, planer type base feature. All edges of the blank sheet were fixed by applying an ENCASTRE (U1=U2=U3=UR1=UR2=UR3=0) boundary condition. In this type of displacement boundary condition sheet was clamped with all its edges. The translation and rotational motion along the *x*, *y*, and *z* axis were restricted. The boundary condition provided for the tool path was of amplitude type. In this type of boundary condition, the field variable varied with time. Co-ordinates of tool path were the field variables. Surface-to-surface explicit type contact property was given for dynamic explicit analysis. A master-slave algorithm was used to describe the frictional contact between tool and work. The tool moves from one edge to the other edge and repeated its path as per the number of stages provided.

The mesh sensitivity analysis was performed. Square S4R shell elements of 1 mm, 2 mm, and 4 mm size were taken by considering the effect of friction. Reaction force was estimated with different mesh sizes. CPU time increased drastically as mesh size decreased. Simulation time was about 20 minutes, 85 minutes, and 225 minutes for the element sizes of 4 mm, 2 mm, and 1 mm, respectively, for one problem. The material properties of the different materials are listed in Table 1.

Table 1. Physical and mechanical properties of Aluminum 6061- T6 and Titanium Ti-6Al-4V [12, 13].

Properties	Aluminum	Titanium
Density [g/cc]	2.7	4.43
Tensile Yield Strength [MPa]	276	880
Ultimate Tensile Strength [MPa]	310	950
Poisson's Ratio	0.33	0.34
Modulus of Elasticity [MPa]	68900	113800

Results and Discussion

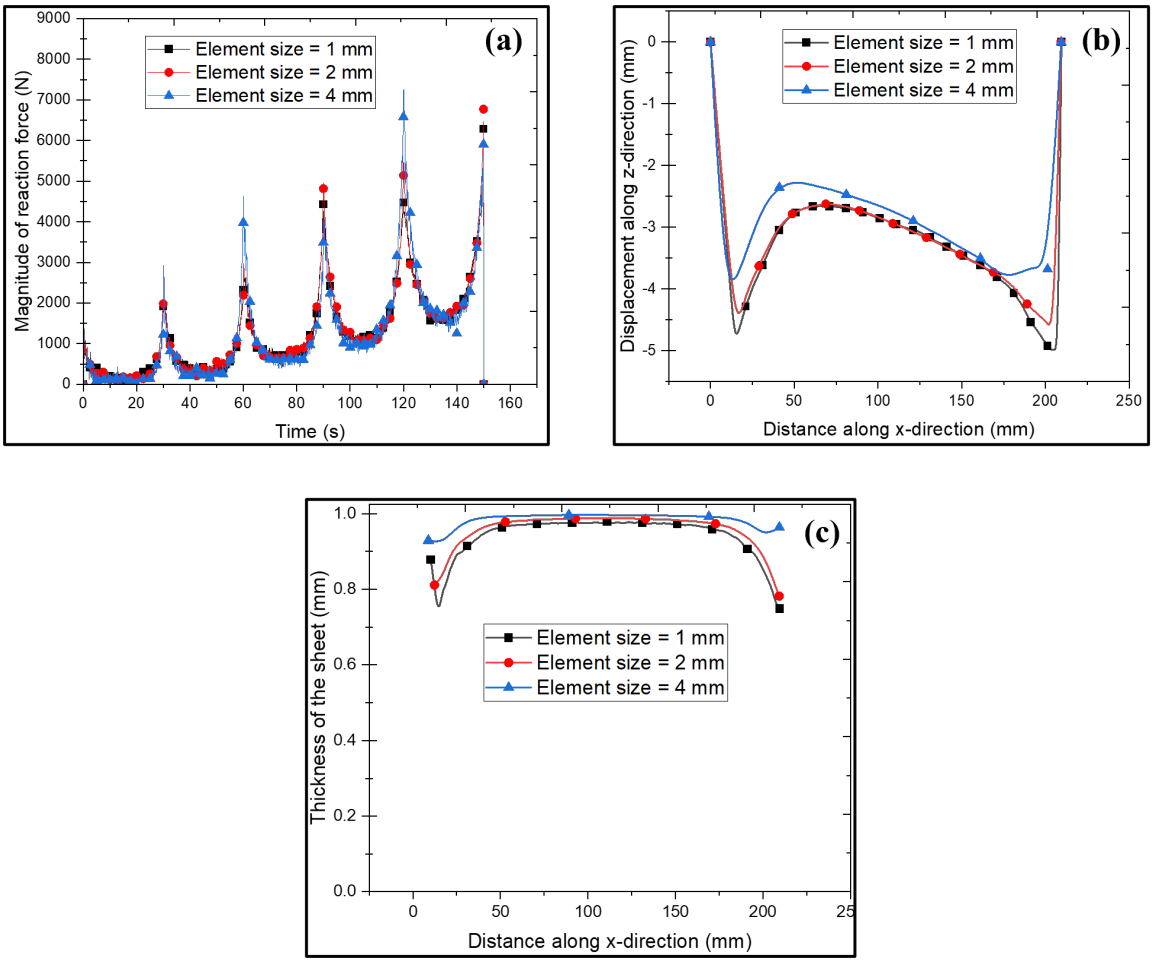

Fig. 4. Element size effect on (a) reaction force developed on the tool, (b) displacement achieved in the z-direction, and (c) thickness of the sheet after deformation.

Mesh sensitivity analysis.

For simulation, mesh size plays a vital role. In Fig. 4, an aluminium alloy has been used to investigate the mesh sensitivity. Smaller element size becomes too costly in terms of simulation time. Mesh sensitivity affects the magnitude of the reaction force developed on the tool, as shown in Fig 4 (a). Element size effect on the magnitude of reaction force developed was insignificant, but it affects the other process parameters significantly. Fig 4 (b) shows that with an element size of 1 mm, the spring back effect is high compared to the element size of 2- and 4-mm. Fig. 4 (c) showed that thickness distribution with larger element size was better, and low thickness reduction was observed. Considering a trade-off between accuracy and computational time, a 2 mm element size was chosen for subsequent parametric study. Fig. 5 shows the von Mises stress developed in aluminium alloy sheet.

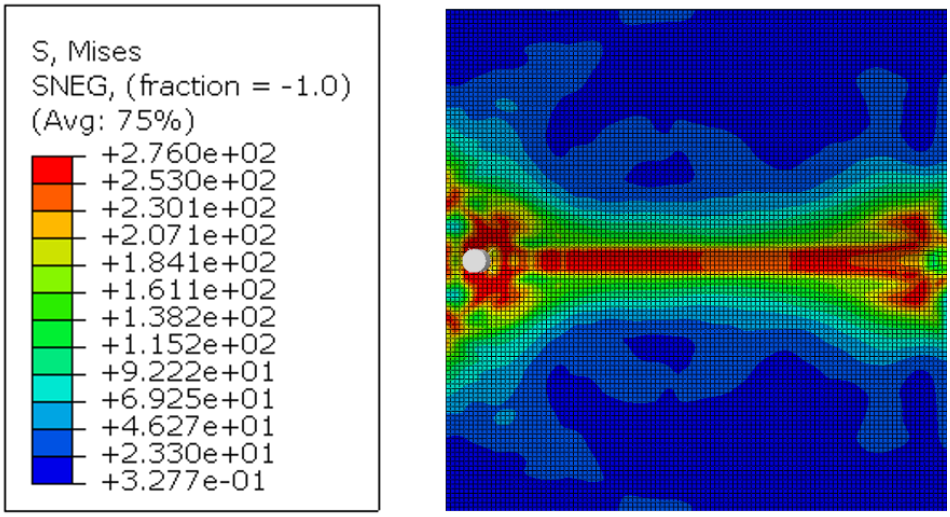

Fig. 5. Numerical simulation response of deformation with aluminium alloy.

Effect of different parameters on the reaction force.

In ISMF, the forming forces depend upon the tool path, and the feasibility of forming a reliable component also depends upon it. In the present case, the straight tool path was chosen for simulation, and forming forces were determined for different process parameters. One of the input process parameters was the coefficient of friction. The penalty-based condition with a hard contact surface was given between the tool and the workpiece.

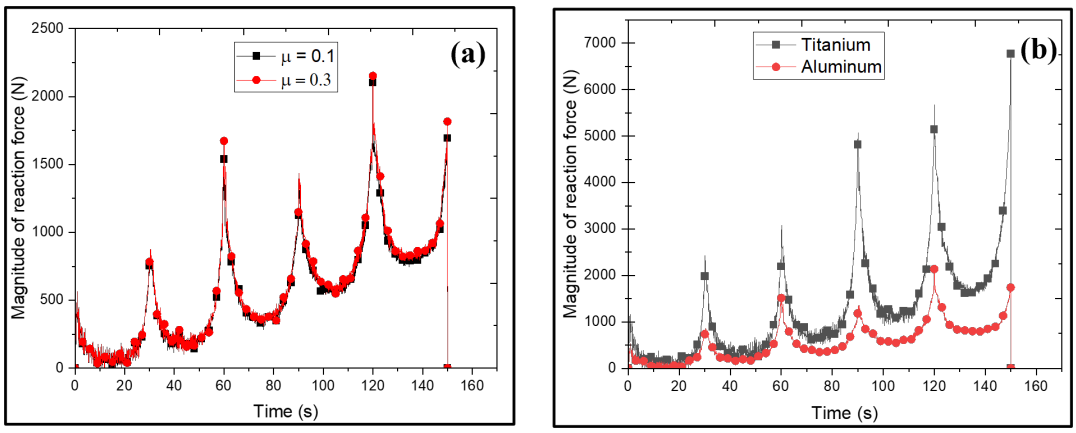

Fig. 6. Time-history plots of resultant reaction force with (a) different coefficients of friction values and (b) different materials.

Force was measured by taking every 0.1 s unit of time in field output request in the step module of ABAQUS. It was observed that the friction coefficient has very little influence on the reaction forces acting on the tool Fig 6 (a). A tool with a hemispherical-end was used by taking μ=0.1 and μ=0.3 with a 2 mm mesh size, i.e., (approximate global size). The observed magnitude of force was the same for these friction coefficient values. These results inferred that the coefficient of friction had an insignificant effect on the reaction force developed on the tool in any direction. When the tool stopped and reversed back during its motion along the assigned path and simultaneously moved in the *z*-direction in accordance with step size, it resulted in a sudden increase in reaction force. Thus, a sharp spike in reaction force was observed at the edges.

Fig. 6 (b) showed that the magnitude of the reaction force on the tool depends upon the type of material used. The developed reaction force with titanium alloy was more compared to aluminum alloy. It was due to the high tensile strength of the titanium alloy. For the same amount of deformation, by keeping all other parameters the same, force developed with titanium should obviously be high.

For making channels by ISMF process, different types of tools can be used, such as hemispherical-end tool, flat-end tool, and flat-end tool with corner radius. Simulation results suggest that the magnitude of reaction force required for making a channel is relatively less with the hemispherical-ended tool, as shown in Fig. 7.

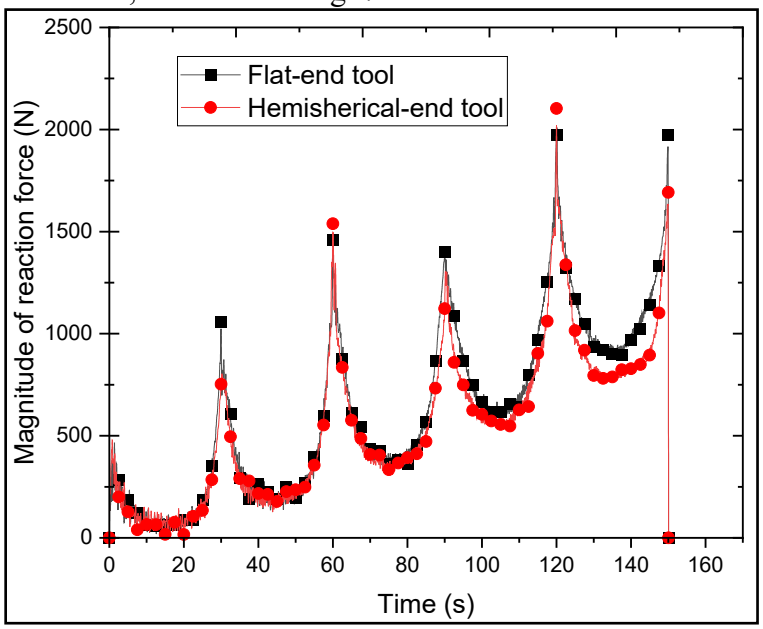

Fig. 7. Time-history plots of magnitude of resultant reaction force with different types of tools.

Effect of the step size.

The effect of step depth on different response parameters was investigated. Forming tool was treated here as a rigid body with no deformation. Reaction force developed on the tool, displacement achieved in the *z*-direction, and final thickness of the sheet were analyzed for two different step sizes. Fig 8 (a) showed that the reaction force developed was high with a large step size.

Sheet thinning is the major factor in sheet forming. Here, it was observed that with different step sizes, there was not much difference in the final thickness of the sheet. The spring back effect with a small step was more compared to a high step size, and the depth achieved in the *z*-direction was more with a large step size Fig. 8 (b), (c).

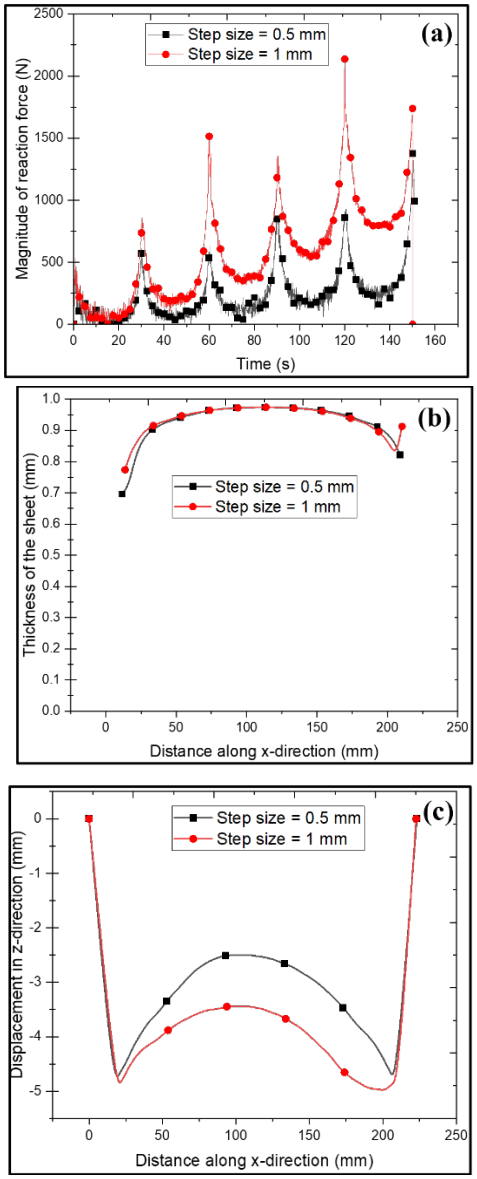

Fig. 8. Effect of step size on (a) reaction force developed on the tool, (b) thickness of the sheet after deformation, and (c) displacement achieved in the z-direction.

Experimental validation was carried out qualitatively from published literature. The trend of various parameters is observed to be in good agreement with numerical simulation data. It was observed that reaction force increases with an increase in step size [14]. From this reference, it is noted that the trend of force is in good agreement as it was done in the simulation in this article. Formability was higher with a large step size, but the thickness distribution was better with a low step size [15]. Strain hardening has a negligible effect on the force developed. There is less effect of the coefficient of friction on the formability and reaction force [16].

Summary

In recent years, the ISMF process has been intensively investigated using the FEM. In this work, numerical simulations were performed for ISMF in the U-channel model. Aluminum and titanium alloys were deformed with flat-ended and hemispherical-ended tools. To obtain a depth of 5 mm, simulations were performed with various step sizes. Based on the analysis of simulation results, the following conclusions can be drawn:

1. The size of the element has a significant effect on the resulting values of some output parameters. However, decreasing the element size makes the simulation computationally intensive, time-consuming, and cost-ineffective.
2. No significant difference was observed with different coefficient of friction values on reaction force.
3. It is observed that the reaction force developed on the tool was higher with high-strength alloy and the flat-end tool experienced a high magnitude of reaction force compared to a hemispherical end tool.
4. Step size affects the reaction force devolved on the tool and formability (measured in the form of depth achieved) but has little influence on the thickness reduction of the sheet.

Future work aims to validate the results with in-house experiments and study formability.

References

[1] I. Bagudanch, G. Centeno, C. Vallellano, M.L. Garcia-Romeu, Forming force in single point incremental forming under different bending conditions, Procedia Eng. 63 (2013) 354-360. https://doi.org/10.1016/j.proeng.2013.08.207
[2] M. Tisza, Numerical modelling and simulation in sheet metal forming, J. Mater. Process. Technol. 151 (2004) 58-62. https://doi.org/ 10.1016/j.jmatprotec.2004.04.009
[3] L. Taylor, J. Cao, A.P. Karafillis, M.C. Boyce, Numerical simulations of sheet metal forming, J. Mater. Process. Technol. 50 (1995) 168-179. https://doi.org/10.1016/0924-0136(94)01378-E
[4] R. Aerens, P. Eyckens, A. van Bael, J.R. Duflou, Force prediction for single point incremental forming deduced from experimental and FEM observations, Int. J. Adv. Manuf. Technol. 46 (2010) 969–982. https://doi.org/ 10.1007/s00170-009-2160-2
[5] Z. Chang, J. Chen, Analytical model and experimental validation of surface roughness for incremental sheet metal forming parts, Int. J. Mach. Tools Manuf. 146 (2019) 103453. https://doi.org/10.1016/j.ijmachtools.2019.103453
[6] A. Petek, K. Kuzman, J. Kopač, Deformations and forces analysis of single point incremental sheet metal forming, Arch. Mater. Sci. Eng. 35 (2009) 107-116. http://www.amse.acmsse.h2.pl/vol35_2/3527.pdf
[7] J. Asghar, R. Lingam, E. Shibin, N.V. Reddy, Tool path design for enhancement of accuracy in single-point incremental forming, Proceedings of the Institute of Mechanical Engineers Part: B J. Eng. Manuf. 228 (2014) 1027-1035. https://doi.org/10.1177/0954405413512812
[8] M. Shamsari, M.J. Mirnia, M. Elyasi, H. Baseri, Formability improvement in single point incremental forming of truncated cone using a two-stage hybrid deformation strategy, Int. J. Adv. Manuf. Technol. 94 (2018) 2357-2368. https://doi.org/10.1007/s00170-017-1031-5
[9] S.M. Najm, I. Paniti, Study on effecting parameters of flat and hemispherical end tools in spif of aluminium foils, Tehnicki Vjesnik 27 (2020) 1844-1849. https://doi.org/10.17559/TV-20190513181910
[10] X. Ziran, L. Gao, G. Hussain, Z. Cui, The performance of flat end and hemispherical end tools in single-point incremental forming, Int. J. Adv. Manuf. Technol. 46 (2010) 1113-1118. https://doi.org/10.1007/s00170-009-2179-4
[11] H.Y. Shahare, A.K. Dubey, P. Kumar, H. Yu, A. Pesin, D. Pustovoytov, P. Tandon, A comparative investigation of conventional and hammering-assisted incremental sheet forming processes for aa1050 h14 sheets, Metals 11 (2021). https://doi.org/10.3390/met11111862
[12] Information on https://asm.matweb.com/search/SpecificMaterial.asp?bassnum=ma6061t6
[13] Information on https://asm.matweb.com/search/SpecificMaterial.asp?bassnum=mtp641

[14] J. Duflou, Y. Tunçkol, A. Szekeres, P. Vanherck, Experimental study on force measurements for single point incremental forming, J. Mater. Process. Technol. 189 (2007) 65-72. https://doi.org/10.1016/j.jmatprotec.2007.01.005
[15] H.B. Lu, Y.le Li, Z.B. Liu, S. Liu, P.A. Meehan, Study on step depth for part accuracy improvement in incremental sheet forming process, Adv. Mater. Res. 939 (2014) 274-280. https://doi.org/10.4028/www.scientific.net/AMR.939.274
[16] B. Lu, Y. Fang, D.K. Xu, J. Chen, H. Ou, N.H. Moser, J. Cao, Mechanism investigation of friction-related effects in single point incremental forming using a developed oblique roller-ball tool, Int. J. Mach. Tool. Manuf. 85 (2014) 14-29. https://doi.org/10.1016/j.ijmachtools.2014.04.007

Materials Research Proceedings 28 (2023) 1047-1056 https://doi.org/10.21741/9781644902479-115

Flange wrinkling in incremental shape rolling

ESSA Abdelrahman[1,a] *, ABEYRATHNA Buddhika[1,b], ROLFE Bernard[2,c], and WEISS Matthias[1,d]

[1]Institute for Frontier Materials, Deakin University, Waurn Ponds, Pigdons Rd., Geelong, VIC 3216, Australia

[2]School of Mechanical Engineering, Deakin University, Waurn Ponds, Pigdons Rd., Geelong, VIC 3216, Australia

[a]aessa@deakin.edu.au, [b]buddhika.abeyrathna@deakin.edu.au, [c]bernard.rolfe@deakin.edu.au, [d]matthias.weiss@deakin.edu.au

Keywords: Incremental Shape Rolling, Flexible Roll Forming, Finite Element Analysis, Wrinkling

Abstract. Automotive structural components from Advanced High Strength Steels (AHSS) can be manufactured with Flexible Roll Forming (FRF). Flange wrinkling is a common shape defect in FRF, this restricts the application of FRF in the automotive industry. The new Incremental Shape Rolling process (ISR) showed that a high tensile transverse strain is developed in the flange and that assists the plastic deformation in the flange. Hence, wrinkle severity can be significantly reduced when weight-optimized components are formed. In this study, the ISR process is applied to a variable width profile from DP600. This investigated profile is a modified automotive component. The forming strains and wrinkling severity in ISR are compared with those obtained from the FRF case. The ISR and the FRF experimental trials are performed on a prototype FRF facility and then used to validate the numerical models which are applied to analyse the deformation behaviour in both processes. The ISR results show a significant reduction in wrinkling. This is due to the high tensile transverse strain that is developed in the ISR flange which facilitates the plastic deformation and hence the flange is stably compressed to the required shape.

Nomenclatures

d_y	Increment size
f	Flange length
MAE	Mean absolute error
n	Number of points considered for the wrinkling evaluation
R	Radius of the pre-cut blank
R_n	Roll nose radius
r_i	Inner radius of the part
t	Material thickness
XYZ	Global coordinate system
xyz	Local coordinate system
xi	X coordinate of the deformed flange edge
$\hat{x}_i$	X coordinate of the ideal flange edge
ε_{th}	Theoretical required longitudinal strain
φ	Bend angle

Content from this work may be used under the terms of the Creative Commons Attribution 3.0 license. Any further distribution of this work must maintain attribution to the author(s) and the title of the work, journal citation and DOI. Published under license by Materials Research Forum LLC.

Materials Research Proceedings 28 (2023) 1047-1056 https://doi.org/10.21741/9781644902479-115

Introduction

Advanced High Strength Steels AHSS are increasingly used in the automotive industry for structural components due to their high strength-to-weight ratio [1, 2]. Roll Forming (RF) is a common forming process for the manufacturing of lightweight automotive structural components from high-strength and low-ductility materials [3]. However, RF is limited to the forming of simple components that have a constant cross-section [4]. Flexible roll forming was therefore developed to enable the forming of complex components with cross-sections that vary along the length of the profile [5]. Flange wrinkling is one of the common shape defects in FRF [6] and occurs if the required longitudinal compressive strain in the flange cannot be achieved by stable compression [7]. Limited practical solutions have been proposed to eliminate flange wrinkling, this restricts the shape complexity achievable with FRF from AHSS [6, 8].

Recently, a prototype flexible roll forming facility has been introduced [9, 10] and special forming tooling developed that supports the flange during the deformation and reduces flange wrinkling. However, wrinkling is still observed when flexible roll forming high-strength sheet metal [9] and this limits the widespread application of FRF in the automotive industry.

Incremental Sheet Forming (ISF) processes such as metal spinning and single-or-two point incremental forming are characterized by localized deformation which improves the formability and shape quality [11]. The axial tensile deformation that is formed during the forward paths in metal spinning balances the compressive hoop stress and this allows the forming of wrinkle-free spun [12, 13]. However, due to the limited working range of the ISF milling machines, forming long automotive structural sections is not feasible [14]. In addition, ISF of high-strength materials needs warm forming techniques to reduce the material strength [15].

The new Incremental Shape Rolling process has been recently developed and applied for the forming of long and straight U-profile components [16]. Similar to ISF, a high transverse tensile strain is developed in the flange and this promises to facilitate the plastic deformation in the flange when ISR is applied to weight-optimized components from AHSS.

In this study, the new ISR process is applied to manufacture the critical region of a simplified automotive component with a changing width cross-section. The same component shape is formed with the conventional FRF process on the same prototype forming facility [9] and the material deformation and shape defects are compared between both processes. Abaqus implicit is then used to further analyse the deformation behaviour in both processes.

Profile Geometry and Material

The investigated component has a cross-section that varies in width along its length, see Fig. 1a. The component has a flange length of f = 18 mm, an inner radius r_i = 5 mm and a material thickness of t =1.5 mm. Wrinkling is only expected to occur in the compression side of the component, where the flange is longitudinally compressed. On the other side, the flange is longitudinally stretched. Therefore, only the compression side of the component is considered in this study and due to shape symmetry around the X-Y plane, only one-quarter of the component is investigated (the highlighted quarter). The pre-cut blank corresponding to the investigated quarter of the component is shown in Fig. 1b. Standard tensile tests were carried out on an Instron 5967 with a 30 kN load cell according to ASTM E8/E8M [17]. The tensile tests were done along the rolling direction and at a test speed of 0.025 mm s^{-1}. The averaged true stress–true strain curve of the DP600 sheet is shown in Fig. 1c. The mechanical properties are obtained by fitting the Hollomon's power law of the tested material and are shown in Table 1.

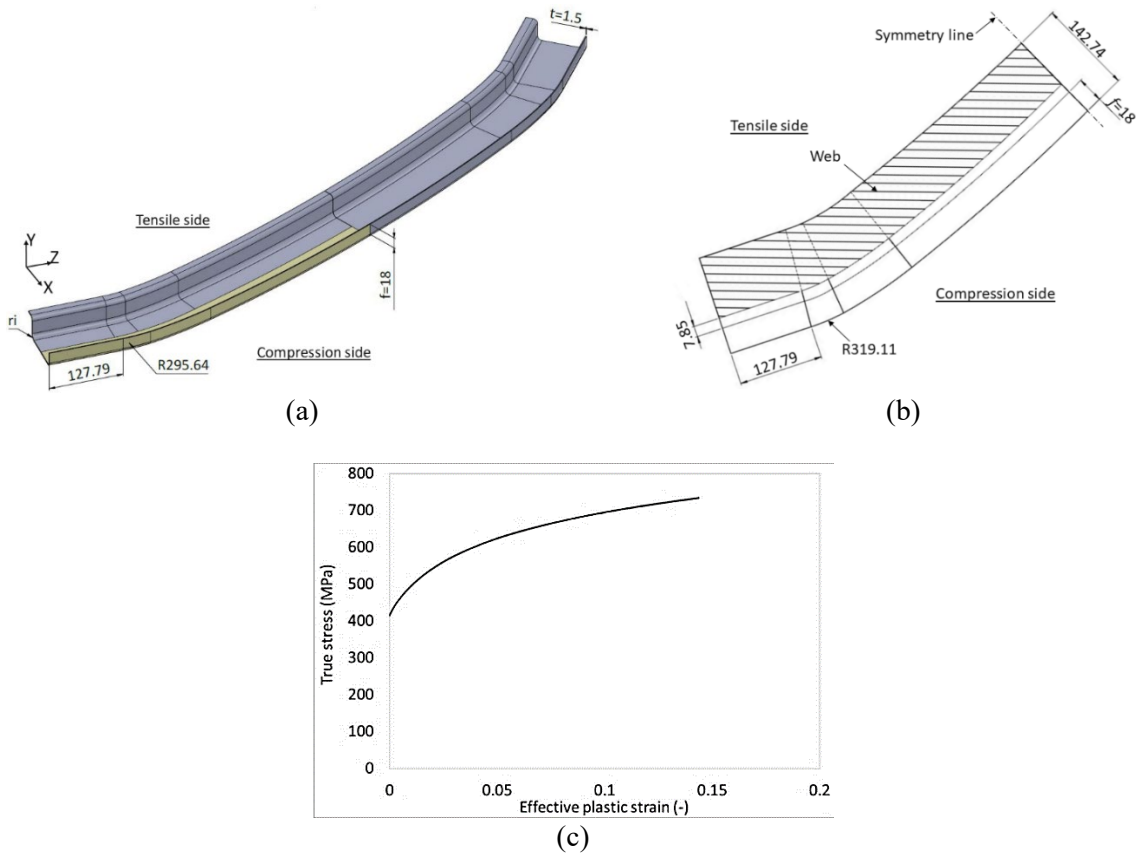

Fig. 1. Schematic showing (a) the full variable width profile and (b) the pre-cut blank corresponding to the investigated quarter of the component and (c) the average true stress-effective plastic strain curve of the DP600 sheet (dimensions in mm).

Table 1. Tensile data of the DP600 sheet.

Material	Thickness t (mm)	0.2% Yield strength (MPa)	Ultimate tensile strength (MPa)	Strain hardening	Strength coefficient (MPa)
DP600	1.5	414.5	733.5	0.11	897

Experimental Trials

Incremental Shape Rolling.

In ISR, the pre-cut blank is held between the clamping dies with the force applied by six hydraulic cylinders. A cylindrical forming roll with a roll nose radius, R_n=1 mm was used, see Fig. 2, and an initial clearance between the forming roll and the top die set to the sheet thickness, *t*. The hexapod which carries the forming roll has six degrees of freedom. During forming the roll is first moved up incrementally in Y-direction, d_y, and then moved in the X-Z plane to follow the top die contour while keeping the initial clearance, *t*. The roll rotates around the Y-axis to keep its axis perpendicular to the roll path. At the same time, the clamping dies move linearly in the longitudinal Z-direction. This roll path is repeated several times until the blank is fully formed over the top die.

Materials Research Proceedings 28 (2023) 1047-1056 https://doi.org/10.21741/9781644902479-115

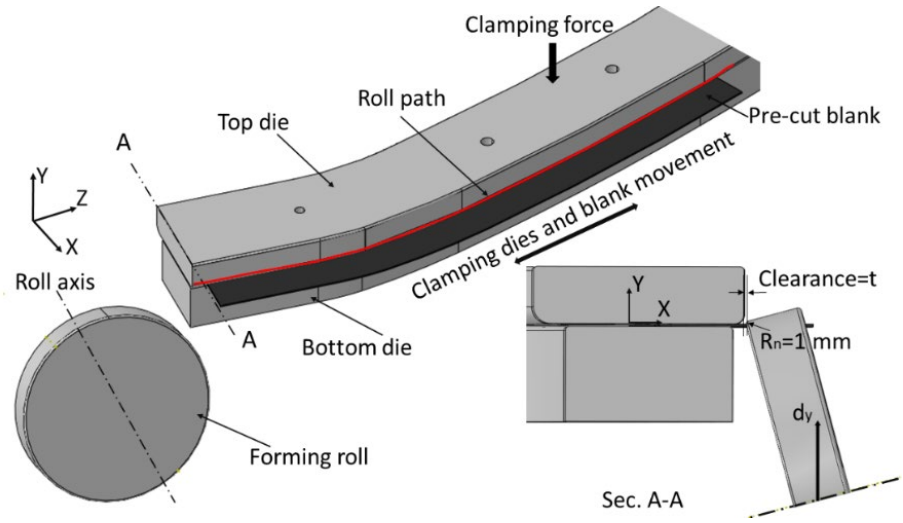

Fig. 2. Schematic drawing of the ISR process of the variable width profile.

The same ISR forming sequence as applied for the ISR of straight components in previous work [16] was implemented in this investigation, where the flange incrementally wraps over the roll nose radius in each pass, and in this way, the flange is formed upwards until the pre-cut is fully formed to the desired shape. In this study, the smallest possible increment size d_y=1 mm was used, as it is reported that the transverse tensile strain increases with decreasing the increment size, d_y [16] which provides the best possible flange quality.

Flexible Roll Forming.

The flexible roll forming trials were done on Deakin's FRF facility, where the blank is held between the clamping dies by six-hydraulic cylinders. One bottom roll (B1) is used to incrementally bend the pre-cut blank into shape with 14 forming passes. This represents the simplest forming and tool approach. More complex forming tools using finger rolls have been applied in previous studies to significantly reduce wrinkling and improve part shape [18]. In this study, a higher winkling tendency was desired to provide a clear difference in forming modes between the ISR and the FRF approach. The corresponding bend angle increment in FRF is 11°, 7°, 10°, 5°, 8°, 5°, 6°, 6°, 6°, 6°, 5°, 5°, 5°, 5°. The left side of Fig. 3 shows the schematic of the relative contact between the roll and the flange during forming, while the FRF bend sequence is shown on the right side of Fig. 3.

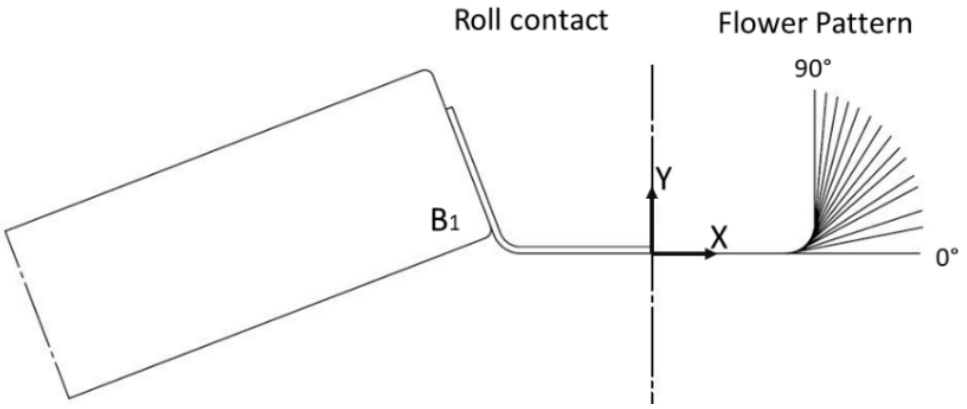

Fig. 3. Schematic of the roll set used in the FRF process and the implemented flower pattern.

Shape Analysis and Strain Measurement.
A 3D laser scanner "CreaForm HandyScan 700" [19] has been used to scan the flange after the final forming pass and before the part was released from the clamping dies. The data was then imported into the Geomagic Qualify software [20] to evaluate the flange quality and to compare it to the ideal shape of the flange. For this, a X-Z plane section cut was created along the length of the flange and located at a distance of 1 mm under the flange edge, see Fig. 4.

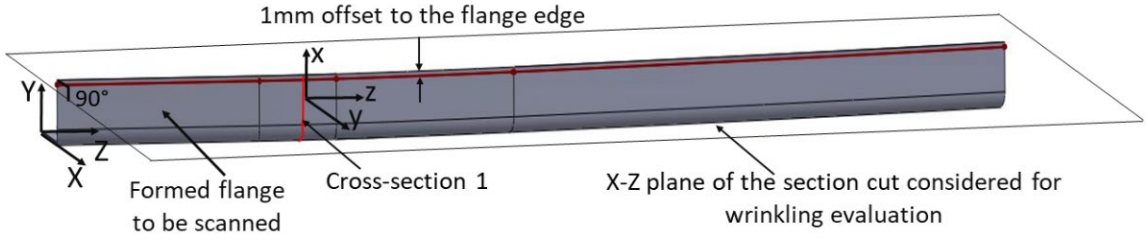

Fig. 4. Formed flange and the path considered for wrinkling evaluation.

Eq. 1 was used to calculate the mean absolute error (MAE) of the flange edge [9] to quantitatively evaluate flange wrinkling. The wrinkles were observed at a *Z*-coordinate of 70 to 320 mm measured from the lead end of the component and the MAE was therefore calculated in this region, see Fig. 5. Note that, the lead end is the component end where the forming pass starts while the tail end is where the forming pass ends.

$$MAE = \frac{1}{n} \sum_{i=1}^{n} |x_i - \hat{x}_i|. \quad (1)$$

Where, $\hat{x}_i$ is the corresponding *X* coordinate of the ideal flange edge, *xi* is the *X* coordinate of the deformed flange edge and *n* is the number of points considered for the wrinkling evaluation.

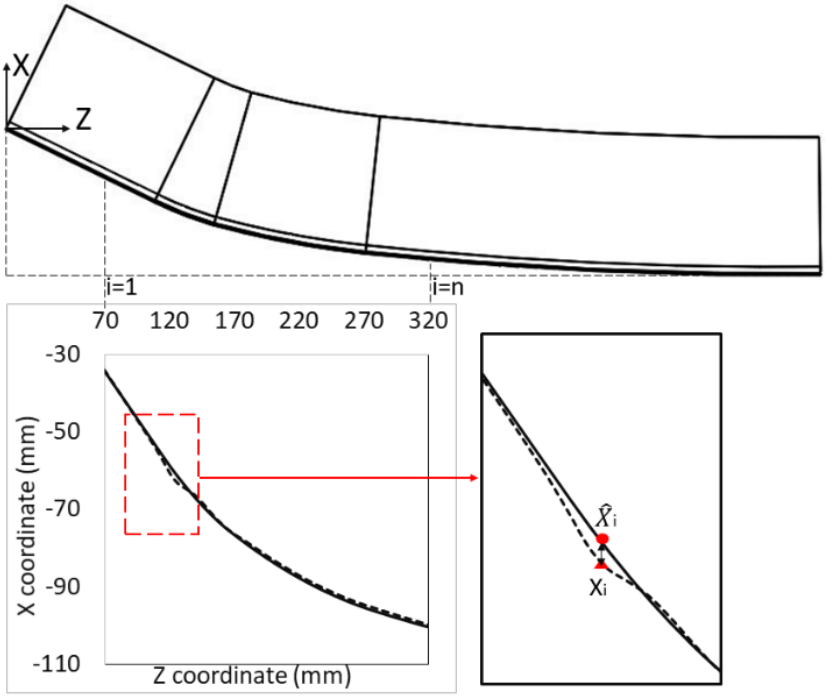

Fig. 5. Flange edge considered for the wrinkling analysis.

The AutoGrid strain measuring system [21] was used to measure the true major and minor strains after the final forming pass and after the component had been removed from the clamping dies. For this, a 2 mm × 2 mm grid was printed on the pre-cut blank and pictures of the formed grid were taken with a camera. The strain components were evaluated in cross-section 1 (S1) in the middle of the critical radius, R=295.64 mm (see Fig. 1a and 6). The local coordinate system (xyz) which follows the formed material was used to plot the strain components; where PExx is the transverse strain and PEzz is the longitudinal strain, while (XYZ) is the global coordinate system, see Fig. 4.

Eq. 2 was used to calculate the theoretical longitudinal strain, ε_{th}, required to form the flange. The R319.11 mm is the most critical radius in the compression side of the pre-cut blank (see Fig. 1a) and this results in the highest longitudinal compression strain in the flange, and severe wrinkling is expected to occur in this critical radius [9]. Based on Eq. 2 the theoretical longitudinal strain that is needed to form the flange in this critical radius is ε_{th} = -0.054.

$$\varepsilon_{th} = ln\frac{R - f(1-cos\varphi)}{R}. \quad (2)$$

Where ε_{th} is the theoretical required longitudinal strain, R is the radius of the pre-cut blank, f is the flange length and φ is the required bend angle of 90°.

Finite Element Analysis

The finite element simulation of the ISR process and FRF process have been performed with Abaqus Implicit. The clamping dies and the forming roll were modelled as rigid bodies, while the pre-cut blank has been discretized with reduced integration, hexahedral, linear brick elements (C3D8R). Four elements through the blank thickness were used with an element size of 1 mm and 2.5 mm in the X and the Z directions, respectively. A "frictionless contact" was assumed between the forming roll and the blank surfaces to avoid convergence issues [22]. To minimize the penetration of the rigid bodies into the blank surfaces at the constraint locations, the "hard contact condition" was applied [23]. The true stress-effective plastic strain curve shown in Fig. 1c was used together with isotropic hardening and the von Mises yield criteria to define the plastic material behaviour of the DP600 sheet [24, 25]. The elastic properties were defined with Poisson's ratio, ν, which is assumed to be 0.3 [9] and a Young's modulus of 200 GPa [26]. For the analysis of the forming results, the same procedure as used in the experimental trials is applied.

Results

Evaluation of Flange Wrinkling.

Fig. 6a compares the formed flange shape with the ideal shape of the flange after the final forming pass for both FRF and ISR. For a clear presentation, a 10 mm X-offset is applied between each forming case. The experimental results show that a clear wrinkle is formed in the FRF flange while the final shape of the ISR flange is close to the ideal shape. The FEA results underestimate the shape error and only indicate the formation of a buckle in the FRF flange, while there is no wrinkling predicted for the ISR process which correlates with the experimental results. Fig. 6b shows the calculated MAE for each forming case. The FEA results of the MAE accurately predict the experimental trend.

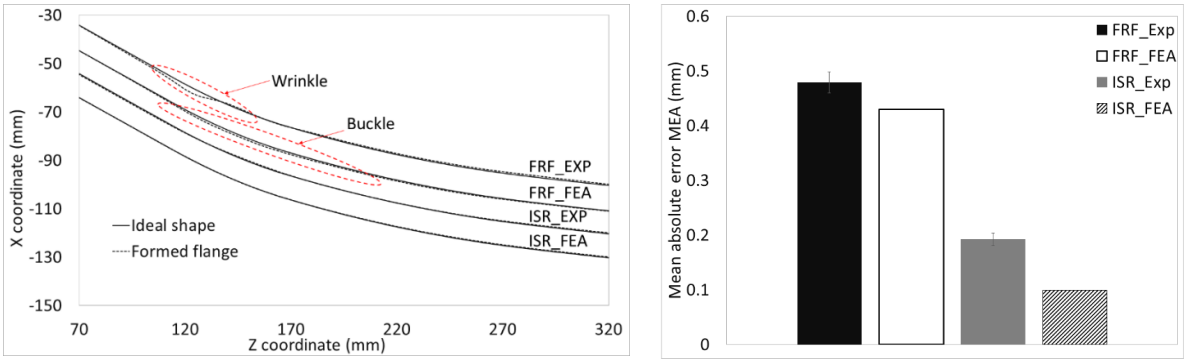

(a) (b)

Fig. 6. (a) Comparison of the flange edge shape after the final forming pass and (b) MAE of the flange edge.

Material Deformation in the Flange.

The distribution of the transverse and the longitudinal residual strain along Section 1, i.e., in the middle length of the critical radius (see Fig. 4) was measured after the final forming pass and is given in Fig. 7a and b, respectively. The Autogrid system gives a good measurement along the flange length, while a strain measurement was not possible in the profile radius area zone, r_i. The experimental results and the FEA results suggest that a high transverse and longitudinal strain develops in the ISR flange, while there is only a very small level of transverse tensile strain and longitudinal strain in the FRF flange, see Fig. 7. The longitudinal compressive strain that is formed in the ISR flange reaches the theoretically required longitudinal, ε_{th}, in the flange edge, see Fig. 7b. In contrast, the longitudinal compressive strain that develops in the FRF flange is significantly lower than the theoretically required strain, ε_{th}.

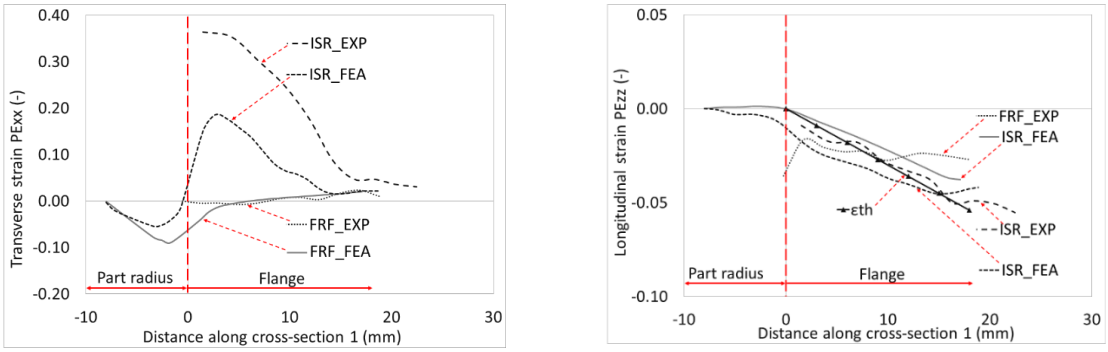

(a) (b)

Fig. 7. Residual strain along cross-section 1 after the final forming pass (a) transverse direction and (b) longitudinal direction.

Discussion

The Effect of the Forming Method on Wrinkling Severity.

In ISR, the flange is wrapped over the roll nose radius to a larger extent in the early forming passes compared to that in the later forming passes [16]. Thus, the formed transverse tensile strain in ISR reaches its maximum level above the part radius, r_i, and then drops back to reach a minimum at the flange edge, see Fig. 7a.

To produce a complex part contour without wrinkling, the flange needs to compress longitudinally [7]. Eq. 2 was used to calculate the theoretical longitudinal strain, ε_{th}, required in

the flange to produce the investigated component. As can be seen in Fig. 7a, ISR results in a high tensile transverse strain. This high transverse strain assists in forming the longitudinal compressive strain that is required to form the investigated flange. As shown in Fig. 7b, the formed longitudinal compressive strain in the flange reaches the theoretically required longitudinal strain. This indicates that the material is stably compressed in the critical zone without wrinkling.

In FRF, bending is the major deformation mechanism in the transverse direction and therefore the transverse tensile strain is low. This results in a small compressive longitudinal strain that is lower than that theoretically required. This means that in FRF the edge length remains longer than required and that therefore the compressive longitudinal stress is released in form of wrinkling rather than stable compression. This explains the severe flange wrinkling that occurred when FRF the component with the simple tooling, see Fig. 6a.

Both the experimental result and the FEA result of the FRF case suggest the formation of a buckle after pass 5, which forms into a wrinkle after pass 7 in the experimental trials. The longitudinal membrane stress, S_{zz}, is investigated along the selected node path in the flange edge (see Fig. 8a) for both the FRF (Fig. 8b) and the ISR case (Fig. 8c). For both processes, the maximum longitudinal compressive stress occurred in the critical radius, R295.64, see Fig. 1a. In FRF, the longitudinal compressive stress increases with the forming passes and reaches the critical buckling initiation stress of 527 MPa [9] after pass 5 (Fig. 8b), which is where the initial buckle was observed. Note that as soon as the buckle initiates the stress will release, i.e., there will be no further stress increase. The residual longitudinal stress formed in ISR is lower than the critical buckling stress and decreases with the forming passes (Fig. 8c). This suggests that the transverse tensile stress that is generated in the flange reduces the longitudinal compressive stress and therefore prevents the development of a wrinkle.

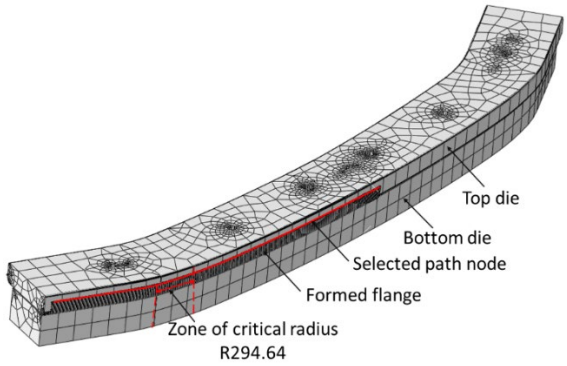

(a)

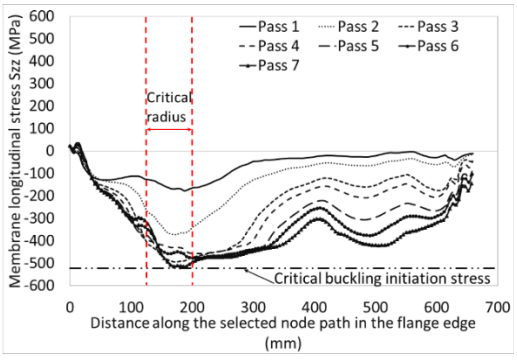

(b)

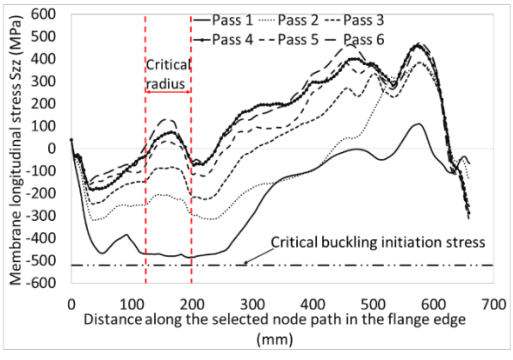

(c)

Fig. 8. (a) Node path considered for analysis of longitudinal stress, (b) evaluation of membrane longitudinal stress at the selected node path for FRF and (c) for ISR.

Summary

In this study, the incremental shape rolling of an automotive component with variable width was investigated and the deformation mechanisms and shape quality compared with those obtained from FRF. The major outcomes of this study are:

- ISR enables the manufacture of weight-optimized automotive components from high-strength steel by eliminating the wrinkling severity.
- In ISR, the transverse tensile strain results from the material wrapping over the roll radius.
- The transverse tensile strain that is developed in the ISR flange assists in the forming of the longitudinal compressive strain that is required to form the part contour. In FRF, the transverse and longitudinal strains are low. This leads to wrinkling instead of stable longitudinal compression in the flange.
- ISR represents a promising alternative to conventional sheet forming processes where excessive wrinkling leads to issues.

Acknowledgements

The authors acknowledge data M Sheet Metal Solutions GmbH for the development and manufacture of the 3D roll forming prototyping facility. The authors would like to thank Deakin University Postgraduate Research Scholarships (DUPRS) for their financial support.

References

[1] N. Baluch, Z.M. Udin, C.S. Abdullah, Advanced high strength steel in auto industry: an overview, Eng. Appl. Sci. Res. 4 (2014) 686-689. https://doi.org/10.48084/etasr.444

[2] G. Sun, M. Deng, G. Zheng, Q. Li, Design for cost performance of crashworthy structures made of high strength steel, Thin-Walled Struct. 138 (2019) 458-472. https://doi.org/10.1016/j.tws.2018.07.014

[3] A.D. Deole, M.R. Barnett, M. Weiss, The numerical prediction of ductile fracture of martensitic steel in roll forming, Int. J. Solids. Struct. 144-145 (2018) 20-31. https://doi.org/10.1016/j.ijsolstr.2018.04.011

[4] C. Jiao-Jiao, C. Jian-Guo, Z. Qiu-Fang, L. Jiang, Y. Ning, Z. Rong-guo, A novel approach to springback control of high-strength steel in cold roll forming, Int. J. Adv. Manuf. Technol. 107 (2020) 1793-1804. https://doi.org/10.1007/s00170-020-05154-8

[5] Y. Yan, H. Wang, Q. Li, B. Qian, K. Mpofu, Simulation and experimental verification of flexible roll forming of steel sheets, Int. J. Adv. Manuf. Technol. 72 (2014) 209-220. https://doi.org/10.1007/s00170-014-5667-0

[6] M.M. Kasaei, H.M. Naeini, G.H. Liaghat, C.M.A. Silva, M.B. Silva, P.A.F. Martins, Revisiting the wrinkling limits in flexible roll forming, J. Strain. Anal. Eng. Des. 50 (2015) 528-541. https://doi.org/10.1177/0309324715590956

[7] M.M. Kasaei, H.M. Naeini, B. Abbaszadeh, M. Mohammadi, M. Ghodsi, M. Kiuchi, R. Zolghadr, G. Liaghat, R.A. Tafti, M. S. Tehrani, Flange wrinkling in flexible roll forming Process, Procedia Eng. 81 (2014) 245-250. https://doi.org/10.1016/j.proeng.2014.09.158

[8] P. Groche, A. Zettler, S. Berner, G. Schneider, Development and verification of a one-step-model for the design of flexible roll formed parts, Int. J. Mater. Form. 4 (2010) 371-377. https://doi.org/10.1007/s12289-010-0998-3

[9] B. Abeyrathna, S. Ghanei, B. Rolfe, R. Taube, M. Weiss, Optimising part quality in the flexible roll forming of an automotive component, Int. J. Adv. Manuf. Technol. 118 (2021) 3361-3373. https://doi.org/10.1007/s00170-021-08176-y

[10] S. Ghanei, B. Abeyrathna, B. Rolfe, M. Weiss. Analysis of material behaviour and shape defect compensation in the flexible roll forming of advanced high strength steel. In: IOP Conf Ser Mater Sci Eng.vol. 651. IOP Conf Ser Mater Sci Eng; 2019. https://doi.org/10.1088/1757-899x/651/1/012064.

[11] S. Gatea, H. Ou, G. McCartney, Review on the influence of process parameters in incremental sheet forming, Int. J. Adv. Manuf. Technol. 87 (2016) 479-499. https://doi.org/10.1007/s00170-016-8426-6
[12] O. Music, J.M. Allwood, K. Kawai, A review of the mechanics of metal spinning, J. Mater. Process. Technol. 210 (2010) 3-23. https://doi.org/10.1016/j.jmatprotec.2009.08.021
[13] Z. Jia, L. Li, Z. R. Han, Z. J. Fan, B. M. Liu, Experimental study on wrinkle suppressing in multi-pass drawing spinning of 304 stainless steel cylinder, Int. J. Adv. Manuf. Technol. 100 (2018) 111-116. https://doi.org/10.1007/s00170-018-2712-4
[14] A.K. Behera, R.A. de Sousa, G. Ingarao, V. Oleksik, Single point incremental forming: An assessment of the progress and technology trends from 2005 to 2015, J. Manuf. Process. 27 (2017) 37-62. https://doi.org/10.1016/j.jmapro.2017.03.014
[15] A. Kumar, V. Gulati, P. Kumar, H. Singh, Forming force in incremental sheet forming: a comparative analysis of the state of the art, J. Braz. Soc. Mech. Sci. Eng. 41 (2019). https://doi.org/10.1007/s40430-019-1755-2
[16] A. Essa, B. Abeyrathna, B. Rolfe, M. Weiss, Prototyping of straight section components using incremental shape rolling, Int. J. Adv. Manuf. Tech. 121 (2022) 3883-3901. https://doi.org/10.1007/s00170-022-09600-7
[17] ASTM Standard, Standard Test Methods for Tension Testing of Metallic Materials, in, ASTM International, 2016.
[18] A. Sreenivas, B. Abeyrathna, B. Rolfe, M. Weiss, Longitudinal strain and wrinkling analysis of variable depth flexible roll forming, J. Manuf. Process. 81 (2022) 414-432. https://doi.org/10.1016/j.jmapro.2022.06.063
[19] Information on https://www.creaform3d.com/en;
[20] Information on http://www.geomagic.com/en/;
[21] Information on https://www.vialux.de/en/;
[22] M. Weiss, B. Abeyrathna, D.S. Gangoda, J. Mendiguren, H. Wolfkamp, Bending behaviour and oil canning in roll forming a steel channel, Int. J. Adv. Manuf. Technol. 91 (2017) 2875-2884. https://doi.org/10.1007/s00170-016-9892-6
[23] Y.Y. Woo, S.W. Han, I.Y. Oh, Y.H. Moon, Shape defects in the flexible roll forming of automotive parts, Int J Automot. Technol. 20 (2019) 227-236. https://doi.org/10.1007/s12239-019-0022-y
[24] B. Abeyrathna, B. Rolfe, L. Pan, R. Ge, M. Weiss, Flexible roll forming of an automotive component with variable depth, Adv. Mater. Process. Technol. 2 (2016) 527-538. https://doi.org/10.1080/2374068x.2016.1247234
[25] B. Abeyrathna, B. Rolfe, J. Harrasser, A. Sedlmaier, G. Rui, L. Pan, M. Weiss. Prototyping of automotive components with variable width and depth. In: 36th IDDRG Conference.vol. 36th IDDRG Conference; 2017. https://doi.org/10.1088/1742-6596/896/1/012092
[26] B. Abeyrathna, B. Rolfe, M. Weiss, The effect of process and geometric parameters on longitudinal edge strain and product defects in cold roll forming, Int. J. Adv. Manuf. Technol. 92 (2017) 743-754. https://doi.org/10.1007/s00170-017-0164-x

Innovative joining by forming technologies

Materials Research Proceedings 28 (2023) 1059-1066 https://doi.org/10.21741/9781644902479-116

Clinching with divided punch to prevent critical neck thicknesses

FALK Tobias[1,a *], KROPP Thomas[1,b] and DROSSEL Welf-Guntram[1,c]

[1] Fraunhofer Institute for Machine Tools and Forming Technology IWU, Nöthnitzer Straße 44, 01187 Dresden, Germany

[a]tobias.falk@iwu.fraunhofer.de, [b]thomas.kropp@iwu.fraunhofer.de, [c] welf-guntram.drossel@iwu.fraunhofer.de

Keywords: Clinching, Divided Punch, Critical Neck Thickness, Crack Prevention

Abstract. Clinching thin sheet metal into a thicker part can result in low neck thicknesses or even neck cracks. How these critical low values for neck thickness can be counteracted is described in this paper, using a two-part punch, which is devided in an inner and outer unit. At the beginning, both move parallel in the direction of the die until the outer punch stops at a defined position and only the inner one moves further down and forms the clinch point, with its characteristic contour and the geometric values of interlock and neck thickness. Due to the large punch diameter at the beginning of the process, more material initially flows into the neck area than in conventional clinching, so that a greater neck thickness can be achieved. Numerical simulation was used to create the concept and verify it experimentally. The greater neck thickness has a positive effect on the shear tensile strength and can also be transferred to the typical joining direction for clinching (thick into thin material).

Introduction

Mechanical joining technology is widely used to join different sheet materials with different thicknesses and tensile strengths. In contrast to welding, for example, the sheet metal partners can be of different types, as is the case when steel is joined into aluminum. Depending on the specific joining process, there is a recommended arrangement of the sheets (see Fig. 1). For example, in self-pierce riveting, the thinner part, which is more difficult to form, should be positioned on the punch side for optimum joint formation [1]. This is different for clinching, where the harder material should also be on the punch side, but it is recommended that the thicker sheet should be joined into the thinner part [2].

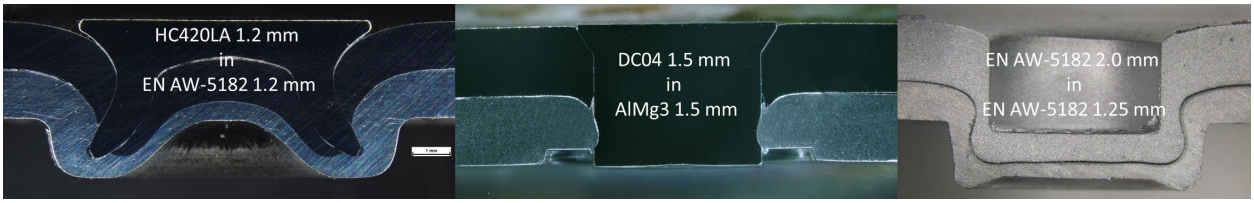

Fig. 1. Cross sections of three different mechanical joining processes (materials and blank thicknesses in the figure): Self-pierce riveting with semi-tubular rivet (left); Self-pierce riveting with solid rivet (middle); Clinching (right).

Clinching

In general, clinching is a simple way to join two or more sheets mechanical. It is frequently used because this joining process does not require a rivet or any other auxiliary joining part and is therefore easier to implement in terms of equipment and has weight advantages over other joining processes. On the other hand, clinching cannot compete with other mechanical joining processes regarding to joint strength. [3]

Content from this work may be used under the terms of the Creative Commons Attribution 3.0 license. Any further distribution of this work must maintain attribution to the author(s) and the title of the work, journal citation and DOI. Published under license by Materials Research Forum LLC.

There are several process variants for clinching, such as clinching with cutting component [4], clinching with preformed hole [5], clinching without point elevation [6] or clinching with flat die [7]. Since these and other special variants are not used in this paper, their description will not be discussed in detail.

In current automotive production, rigid and radial opening clinching dies are mostly used. The rigid dies are characterized by their simple, rotationally symmetrical design. The advantage of radial opening dies is that the material flow is positively influenced by flexible, movable segments, thus the formation of interlock is supported [8].

The actual joining process is similar for both presented die variants. First, the sheets are positioned between the blankholder and die (Fig. 2, I), the moving punch presses the sheet partners toward the die contour (Fig. 2, II), and the joining point is finally formed by radial material flow (Fig. 2, III). This results in a strength-relevant interlock with a sufficiently large neck thickness. [2]

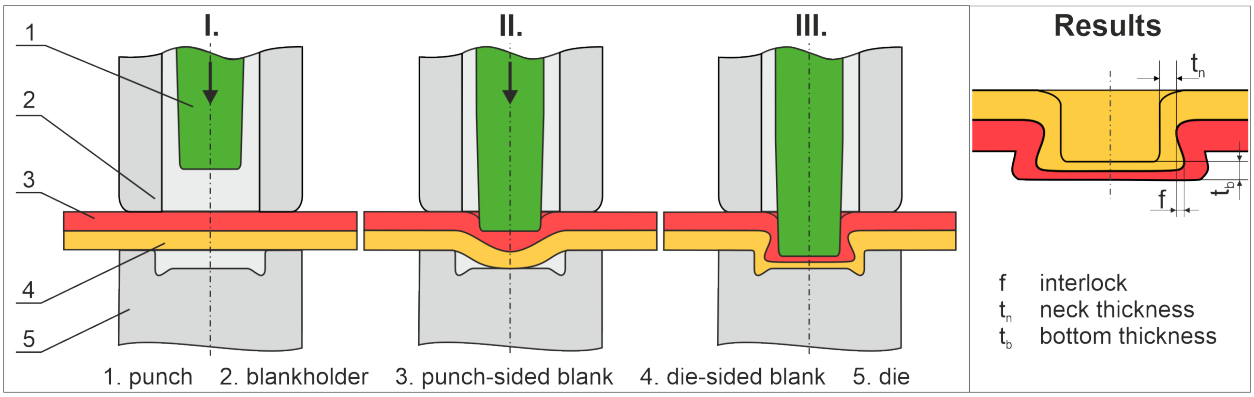

Fig. 2. Three steps of a clinching process (left); characteristic results of a clinching joint (right).

Due to the relatively simple joining process (no intended material cutting as, for example, in the case of semi-tubular self-piercing riveting when piercing the punch-side blank), the clinching process can be simulated easily with the help of numerical computation. Particularly when rigid, rotationally symmetrical dies are used, but also certainly in the case of radial opening dies, it is even possible to use two-dimensional simulations [9], which significantly reduces the complexity and calculation time. Thus, in addition to the pure joining point contour and force-displacement data, critical neck thicknesses and cracks can also be identified and predicted by numerical simulations, as shown in Fig. 3.

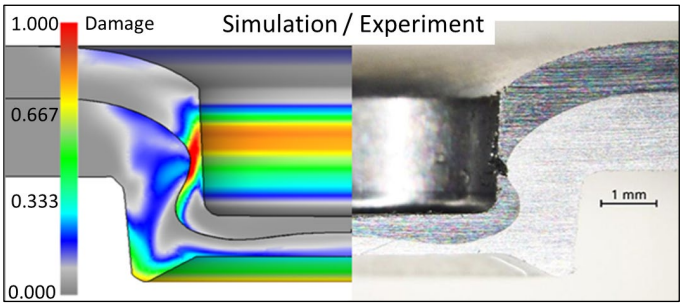

Fig. 3. Comparison of numerical simulation (left) and experimental result (right): HC340LA t = 1.0 mm in EN AW- 5754 t = 1.5 mm) [9].

Sampling

For this study of increasing the neck thickness, a joint with unfavorable sheet metal arrangement and small thickness in the neck region is used. As described above, this tends to be the case for clinching when joining thin into thick material. A steel joint of S350GD $t_1 = 2.0$ mm into S350GD $t_2 = 3.0$ mm is selected (as presented in [10]). As can be seen in Fig. 4(left), a bottom thickness of 1.06 mm results in a clinch point that has significantly lower values for neck thickness than interlock, with average $t_n = 0.25$ mm and $f = 0.42$ mm. A maximum joining force of 80 kN was required for this joint. The rather high force value for clinching can be explained by the large thicknesses and the die diameter of 10 mm.

Furthermore, the cross-section for the typical joining direction is shown on the right in Fig. 4. With an identical joining force (80 kN), almost the same bottom thickness of $t_b = 1.05$ mm is achieved. The neck thickness, averaging $t_n = 0.72$ mm, is significantly greater. The thicker steel sheet on the punch side almost triples the neck thickness but the the interlock ($f = 0.30$ mm) is decreasing. However, the loss of 29 % interlock is not as extreme as the increase of the neck thickness.

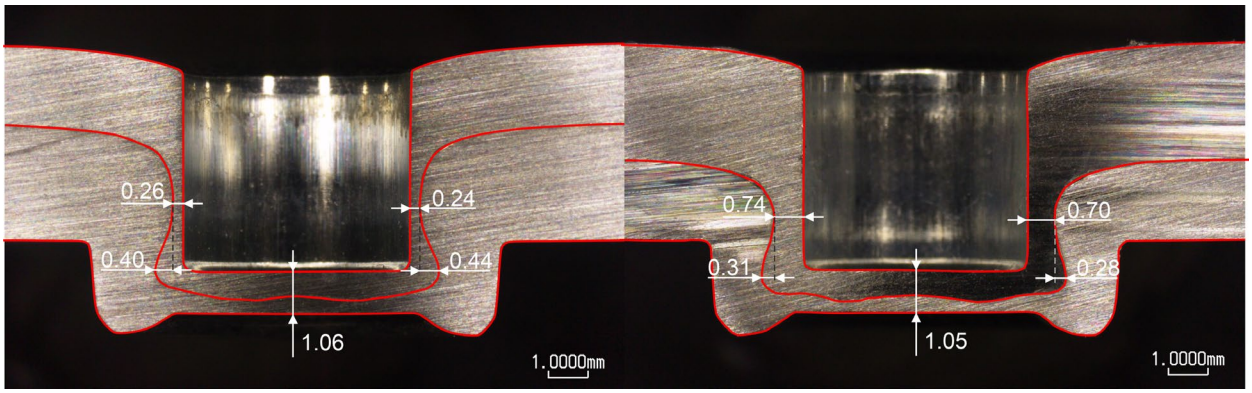

Fig. 4. Cross-sections of S350GD t = 2.0 mm in S350GD t = 3.0 mm (left) and opposite joining direction (right); red line added afterwards for better detection of the contour.

Numerical Simulation

In addition to the available information of the geometric dimensions of the tools, the spring rate of the blankholder and the joining speed, the friction conditions as well as the material properties are important for an exact modeling of the numerical simulation. Due to numerous past projects in which clinch simulations were considered [9, 11, 12], the gained expertise is used and the shear approach is applied for the friction. The selected friction factors have been determined on the base of the already performed numerical computations of the clinching process.

For the integration of the material behavior into the simulations, compression tests [13] are first carried out (Fig. 5, left). Since significantly higher degrees of deformation are achieved during clinching than can be determined in the compression tests, an extrapolation of the data is necessary [14]. For this purpose, individual factors are obtained for different approximation approaches with the experimental data in the initial range and the different results are compared with each other. The least squared error can then be used to find the extrapolation approach that most appropriately reflects the material behavior. For the used S350GD the approximation approach by Orowan is the best fit for the experimental data. The extrapolated and in the simulation used flow curve is shown in Fig. 5 (right).

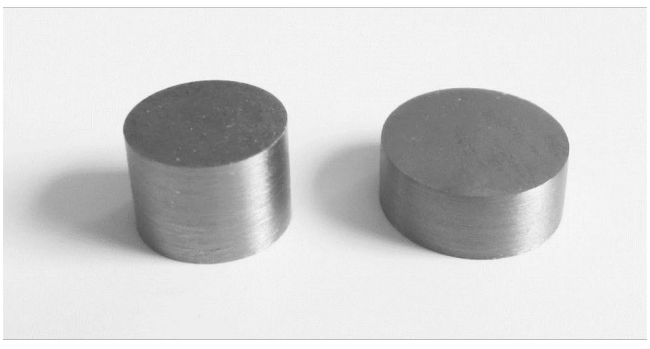

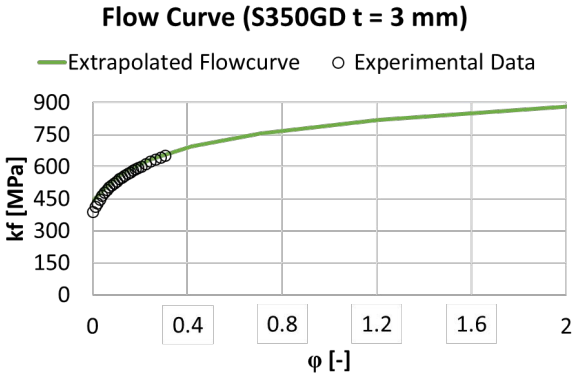

Fig. 5. Original and compressed cylinder sample of the compression test (left); extrapolated flow curve of S350GD t = 3.0 mm with approximation approach by Orowan.

Since only rotationally symmetric tools are used for the experiments, the more simple 2D simulations are used as mentioned above. Using the FEA software DEFORM, a simulation model was built, which can be seen in Fig. 6. Only the two blanks are modeled as elastic-plastic, the tools punch, blankholder and die are defined as rigid for simplification.

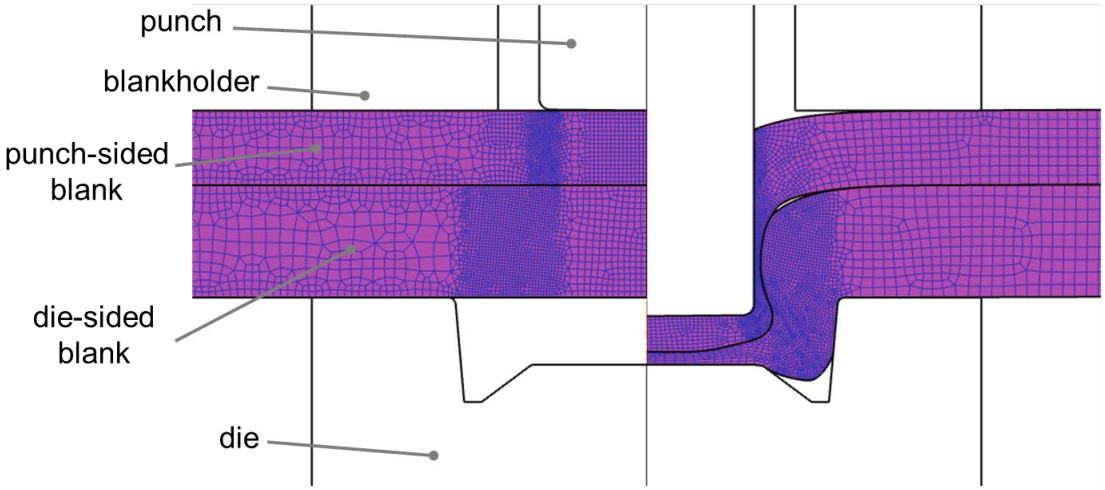

Fig. 6. Numeric simulation model of the clinching process build with the software DEFORM.

Verification

To ensure that the simulation can be used in further investigations, a comparison must be made between the experiment and the numerical calculation. Only if the results of both match sufficiently (geometry and load-stroke-curve), further use is reasonable.

Unlike in Fig. 4, in the following graph (Fig. 7) the colored contour is the result of the simulation. The results of the numerical simulation were generated using Deform V12 software from SFTC. In it, the minimum bottom thickness t_b achieved in the experiments was defined as a stopping criterion in the simulation. With these, areas of high deformation such as interlock and neck areas are generated finer meshes than at the edge of the simulated blanks. For the implementation of friction, a constant shear friction value per contact pair (such as punch/upper blank or die/bottom blank) was determined in parameter studies.

The difference between experimental cross-section and calculated clinch contour is hardly visible. The values of the characteristic geometrical parameters generated by the simulation are also at the same level as those of the experiments. Therefore, the simulation can be considered to have a high accuracy and prediction and can be used in further investigations instead of costly experiments.

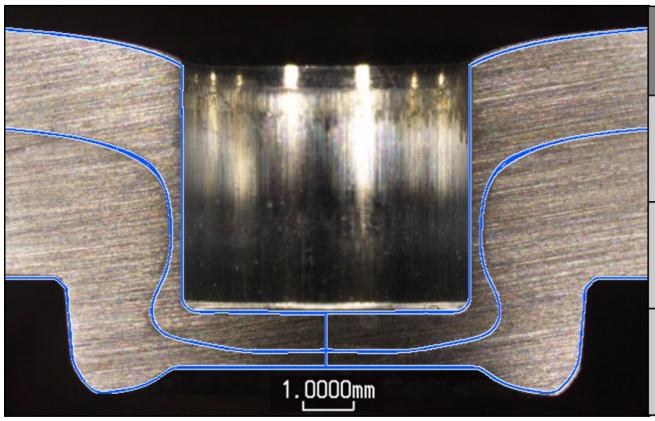

Experiment/ Simulation		left	right
t_n [mm]	Exp.	0.26	0.24
	Sim.	0.22	
f [mm]	Exp.	0.40	0.44
	Sim.	0.39	
t_b [mm]	Exp.	1.06	
	Sim.	1.06	

Fig. 7. Comparison of experiment and simulation: cross-section and simulated contour of the clinch joint (left); characteristic geometrical values (right).

Divided Punch

One approach to bring joints with small neck thicknesses into a non-critical state is to allow more material to flow into the neck area at the beginning of the clinching process. The idea developed here is to use a larger punch diameter which displaces more volume into this neck area. The joining point is then formed by a smaller punch. This does not necessarily have to involve a punch change; the division of the punch into two different diameters is already used in shear clinching [15] (Fig. 8, numbers in the figure are part of the patent [16], where all components are explained by numbers).

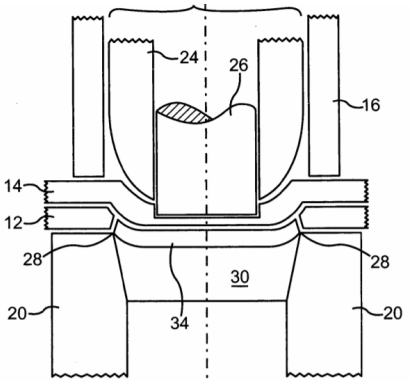

Fig. 8. Division of the punch for clinching with cutting components [16].

Described in more detail, clinching with a divided punch can be structured into four phases. First, just as in the conventional method, the sheets to be joined are positioned between the die and the blankholder (Fig. 9, I.). Then the larger outer punch and the smaller inner punch move simultaneously until a defined stroke is reached (Fig. 9, II.). At this point, the outer punch stops, and only the inner punch continues to move towards the die (Fig. 9, III.) and, as in the conventional case, forms the joining point with its characteristic contour (Fig. 9, IV.).

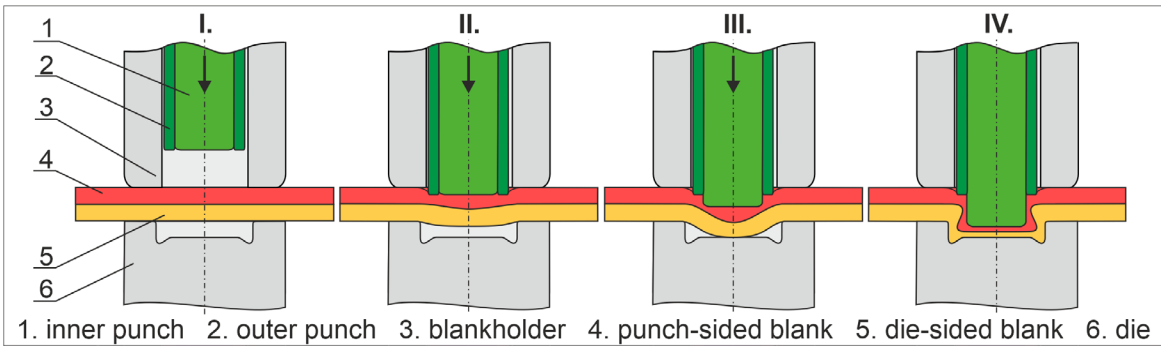

Fig. 9. Four steps of clinching with divided punch.

The validated simulations and the concept of punch division are now being used to first develop simulative tool combinations that generate an increase of the neck thickness. In the case of the outer punch, it is not only the pure geometry that is important, but also at which stroke it should stop moving.

In order to show whether a compression of the material at the end of the process has the same effect as pre-compression, a stepped punch is also considered. This stepped punch has a smaller diameter which, after a defined height, has a shoulder where the diameter becomes larger. This punch shape is one-piece and therefore much simpler in design than a tool division.

Fig. 10 shows the results of the simulations and at the same time also those of the experiments. The left subgraph is already known from Fig. **7** and is only included here for better comparison. First of all, it is noticeable that for all three punch variants the simulation accurately predicts the actual experimental result. This is the case for the pure contours as well as for the measured values for neck thickness and interlock.

The differences between the two conventional punch designs (left and center) are marginal, there is no increase of neck thickness by using the stepped punch. The situation is different with the divided tool (the punch contour is based on the one of the stepped punch): Due to the large outer punch, so much material flows into the neck area at the start of the process that the average neck thickness could be increased from 0.25 mm to 0.39 mm (+77 %). Since experience shows that neck thickness and interlock are always in opposite trends, it is not surprising that the interlock decreases with the divided punch. Compared to the significant increase in neck thickness, however,

the loss of only 17 % (from 0.42 mm to 0.35 mm) is significantly lower.

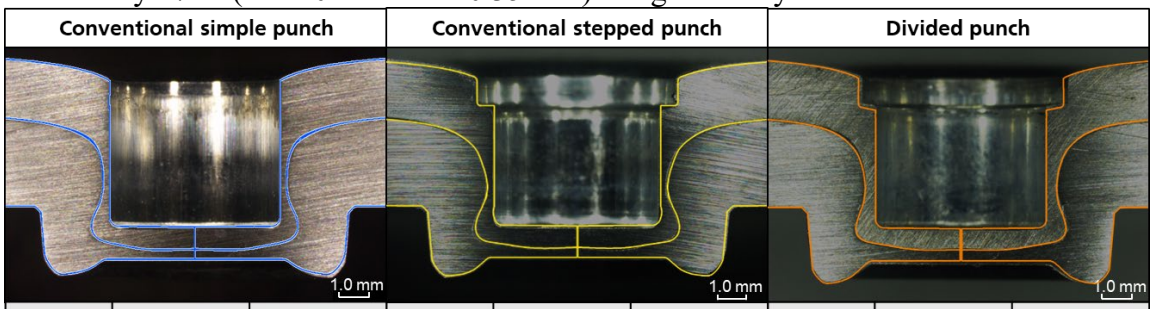

Result	Simulation	Experiment	Result	Simulation	Experiment	Result	Simulation	Experiment
t_n [mm]	0.22	0.26 / 0.24	t_n [mm]	0.23	0.24 / 0.23	t_n [mm]	0.36	0.37 / 0.40
f [mm]	0.39	0.40 / 0.44	f [mm]	0.41	0.45 / 0.42	f [mm]	0.32	0.36 / 0.33

Fig. 10. Comparison of experiments and simulations (colored contours): conventional simple punch (left); conventional stepped punch (middle); divided punch (right).

The declared goal of increasing neck thickness by using a two-part punch appears to be successful. The concept developed is appropriate for the present case. How and whether the larger neck thickness with simultaneously smaller interlock affects the joint strength will be determined in the next step.

Strength Analysis

Since the use of the stepped punch does not have any advantage in the present case, this punch variant is not included in the joint strength investigations. Fig. 11 shows results from shear tensile tests. As discussed in the last chapters, the sheet pairing S350GD 2.0 mm in S350GD 3.0 mm as well as the reverse joining direction can be found in it. In addition, a distinction is made in each case between the conventional simple punch and the divided die.

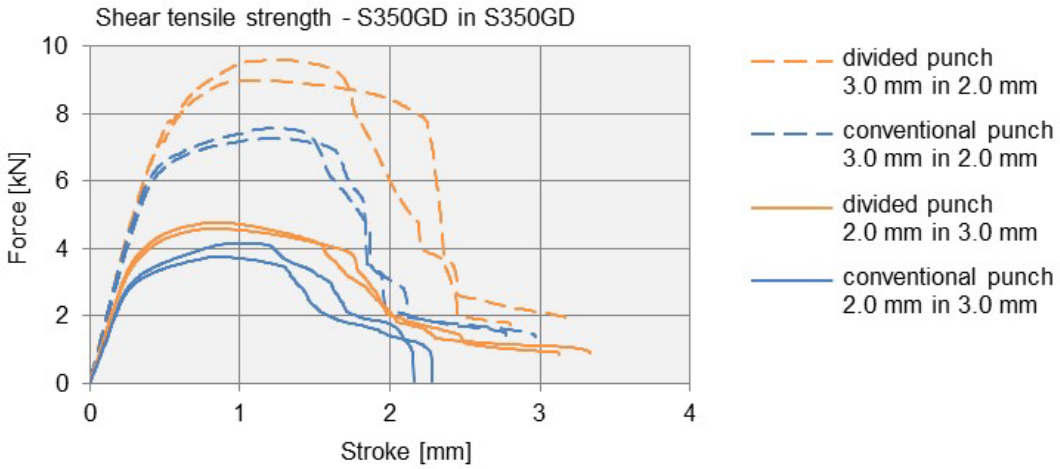

Fig. 11. Results of shear tensile strength: S350GD (2 mm in 3 mm) vs. (3 mm in 2 mm) and conventional simple punch vs. divided punch with pre-stamping.

It can be seen, that for both joining directions (thick in thin and thin in thick) the use of the divided punch has a positive effect on the joint strength under shear tensile load. This is the case both for the maximum forces and for the energy absorption capacity (in connection with the extended strokes). The fact that the use of the thicker blank on the punch side achieves fundamentally higher values than the thinner blank reflects experience. For the untypical blank arrangement for clinching (2 mm in 3 mm), the average maximum force for the variant with pre-stamping can be increased by 19% with the larger punch compared to the simple tool. For reversed blank positioning, even an increase of 25% on average is achieved.

Further Investigations

For the outer punch, not only the diameter is essential, but also how far it moves with the inner punch has an influence on the joint contour. For the sheet pairing S350GD $t = 2$ mm in S350GD $t = 3$ mm investigated in this paper, a small sensitivity analysis is therefore carried out with the help of simulation in order to be able to evaluate the effect on neck thickness and interlock.

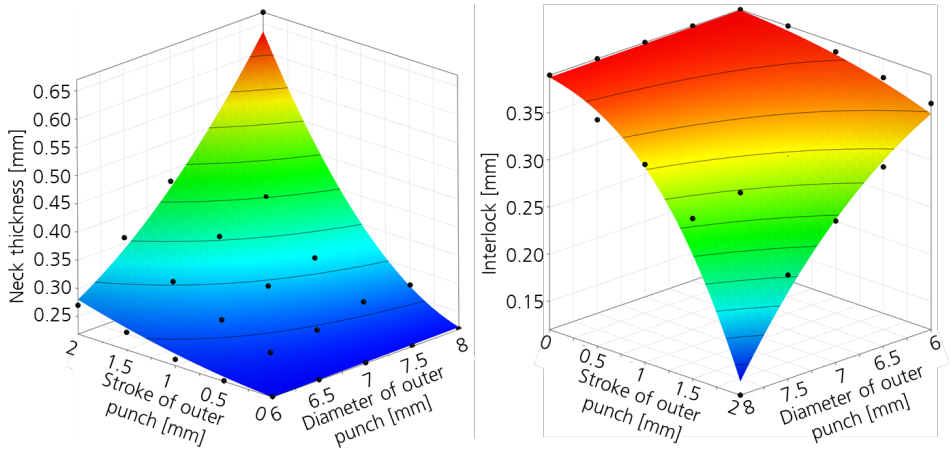

Fig. 12. Results of a sensitivity analysis to show the influence of stroke and diameter of the outer punch on neck thickness (left) and interlock (right).

Fig. 12 shows that the larger the diameter and stroke of the outer punch, the greater the neck thickness. Here, the stroke has a greater influence than the diameter. On the other hand, increasing punch stroke and diameter of the outer tool have a negative effect on the interlock. Depending on the initial situation and requirements, it is therefore also necessary to find a tool setup for the espective compound. The punch division can help to achieve a balanced and target-oriented relationship between neck thickness and interlock.

In further investigations, other joint components should be tested and whether the punch division has a positive effect on the joint contours and strengths. Both different sheet thicknesses and materials (steel, aluminum) in different strengths are of interest here and will be part of the project in the future work. For these other materials, it is also planned to test not only the shear tensile strength but also in head tensile direction, in each case for the reference experiments as well as the optimized with punch division tests. If there is an upper limit of material strengths that can be used with respect to the divided punch, these future investigations will show.

In addition to the rigid dies used here, further studies should analyze the influence when using more flexible designs such as dies with radially opening segments.

The sensitivity analyses presented above could be extended to consider all tools and kinematics and thus provide a fully comprehensive picture of neck thickness increase using punch division. Of course, not only the stroke and diameter of the outer punch influence the relationship between neck thickness and interlock, so the interaction of all parameters should be investigated in more detail.

The obvious disadvantage of the punch division presented here is the need for two decoupled drives. The subject of further research should therefore be whether there are alternative possibilities for pre-stamping. It is conceivable, for example, to use spring units instead of several drives, to carry out the stamping by using a modified blankholder with an integrated stamping ring. This simple tool geometry naturally leads to a loss of flexibility in terms of a freely adjustable punch stroke for pre-stamping.

Summary

In this paper, the issue of small neck thicknesses in clinching was first described and demonstrated using the joint S350GD 2.0 mm in S350GD 3.0 mm. By using a validated simulation model, the

concept of punch division and the positive effect on a neck thickness increase were first simulatively proven. This could be verified by experiments, the comparison to the simulation was convincing and consequently the neck thickness could be increased in these real investigations as well. This led to significantly higher shear tensile strengths for the above-mentioned joint, but also for the joining direction more typical of clinching (thick material joined into thin material).

Acknowledgement
The presented results are part of the research project "Extending the process limits of clinching through pre-stamping" of the European Research Association for Sheet Metal Working (EFB) funded by the program for "Industrial Research" (IGF) of the Federal Ministry of Economic Affairs and Climate Action and the AiF (22329 BR).

References

[1] Technical Bulletin DVS 3410, Self-pierce riveting – basics, Working Group V10 „Mechanical Joining“ by the joint committee for DVS and EFB, 2021.
[2] Technical Bulletin DVS 3420, Clinching – basics, Working Group V10 „Mechanical Joining“ by the joint committee for DVS and EFB, 2021.
[3] X. He, Clinching for sheet materials, Sci. Technol. Adv. Mater. 18 (2017) 381-405. https://doi.org/10.1080/14686996.2017.1320930
[4] M. Merklein, G. Meschut, M. Müller, R. Hörhold, Grundlegende Untersuchungen zur Verbindung von pressgehärtetem Stahl und Aluminium mittels Schneidclinchen, 2013.
[5] Company information of Eckold GmbH & Co. KG, St. Andreasberg, https://www.eckold.de/de/technologien/clinchen/, accessed 11.11.2022.
[6] Company information of TOX Pressotechnik GmbH & Co. KG, Weingarten https://de.tox-pressotechnik.com/verfahren/clinchen/clinchpunkt-formen/uebersicht-clinchpunkt-formen/, accessed 11.11.2022.
[7] S. Dietrich, Grundlagenuntersuchungen zu neuen matrizenlosen Umformfügeverfahren, Dissertation, Verl. Wiss. Scripten 2007.
[8] M.M. Eshtayeh, M. Hrairi, Recent and future development of the application of finite element analysis in clinching process, Int. J. Adv. Manuf. Technol. 84 (2016) 2589-2608. https://doi.org/10.1007/s00170-015-7781-z
[9] W.-G. Drossel, et al. Unerring planning of clinching processes through the use of mathematical methods, Key Eng. Mater. 611 (2014).
[10] W.-G. Drossel, et al. Mechanisch gefügte Stahlstrukturen in Fahrzeugbau und Bauwesen, FOSTA Bericht P1172, 2020.
[11] M. Götz, F. Leichsenring, T. Kropp, P. Müller, Data mining and machine learning methods applied to A numerical clinching model, Comput. Model. Eng. Sci. 117 (2018) 387-423. http://doi.org/10.31614/cmes.2018.04112
[12] N. Vancraeynest, M. Jäckel, S. Coppieters, W.G. Drossel, Data-Based and Analytical Models for Strength Prediction of Mechanical Joints, Key Eng. Mater. 926 (2022) 1556-1563. https://doi.org/10.4028/p-a33855
[13] S. Coppieters, et al. Large Strain Flow Curve Identification for sheet metal: Process informed method selection, Forming Technology Forum (2019).
[14] V. Thoms, W. Voelkner, D. Süße, Methoden zur Kennwertermittlung für Blechwerkstoffe, EFB Forschungsbericht 187, 2002.
[15] D. Han, R. Hörhold, M. Müller, S. Wiesenmayer, M. Merklein, G. Meschut, Shear-clinching of multi-element specimens of aluminum alloy and ultra-high-strength steel, Key Eng. Mater. 767 (2018) 389-396. https://doi.org/10.4028/www.scientific.net/KEM.767.389
[16] S. Busse, et. al. Joining device for connecting parts to be joined in a stamping process comprises a stamping unit having moving concentric stamps, disclosure document, DE 10 2006 028 568 A1, 2006.

Materials Research Proceedings 28 (2023) 1067-1074 https://doi.org/10.21741/9781644902479-117

An ANN based approach for the friction stir welding process intrinsic uncertainty

QUARTO Mariangela[1,a *], BOCCHI Sara[1,b], GIARDINI Claudio[1,c] and D'URSO Gianluca[1,d]

[1]Department of Management, Information and Production Engineering, University of Bergamo, Via Pasubio 7/b, 24044 Dalmine (BG), Italy

[a]mariangela.quarto@unibg.it, [b]sara.bocchi@unibg.it, [c]claudio.giardini@unibg.it, [d]gianluca.d-urso@unibg.it

Keywords: Artificial Neural Network, Process Variability, Friction Stir Welding

Abstract. Friction Stir Welding is a solid-state bonding process that during last years has caught the researcher's attention for the mechanical characteristics of the welded joints that are quite similar to the properties of the base material. The Friction Stir Welding is affected by several process parameters leading to intrinsic variability in the process. The present paper would introduce a new approach for predicting the surface hardness in different areas of the welded parts. Specifically, this method is based on the hypothesis that multiple Artificial Neural Networks, characterized by the same architecture but different weights, can be used for forecasting both the punctual value of the local hardness and its confidence interval, resulting in taking into account the intrinsic variability of the process.

Introduction

Friction Stir Welding (FSW) is one of the most significant technological developments in metal joining of the last thirty years and it is also considered a sustainable technology thanks to its energy efficiency. Indeed, the energy involved is on average 30% - 40% lower than conventional welds. In addition, the emission of greenhouse gases in FSW is about 30% lower than in traditional welds.

Friction Stir Welding is a welding technology patented by The Welding Institute (TWI) in 1991 [1]. This solid state mechanical joining technique is used to make joints between similar or dissimilar materials that are difficult to be welded with conventional fusion techniques, such as sintered materials, magnesium, copper, Inconel, titanium, metal matrix composites and thermoplastics. In particular, it is used for high-strength aluminum alloys, which are difficult to join using traditional techniques due to their typical microstructural alteration during aging hardening.

From a structural point of view, the FSW introduces welded joints without overlapping edges and allows the elimination of connecting parts, such as rivets, with a consequent reduction in the weight and costs of the structures. This process, still relatively young, has produced great interest in the industrial world so as to achieve enormous development, especially in naval applications, but also in the aerospace, railway and automotive industries. The difficulty of the traditional welding processes is linked to the problems developed due to the high temperatures during processing. Conversely, in Friction Stir Welding, which is a friction process by plastic deformation, fusion temperature is never reached during processing, therefore, the formation of the problems that occur in conventional welds is avoided.

In general, welds made using FSW have a different microstructure with respect to the joints welded with fusion processes because the maximum temperature reached in the heat-affected zone is significantly lower than the melting temperature [2]. By basing the microstructural characterization of the joints on the size of the grains and precipitates, it is possible to divide the structure of the FSW joint into four characteristic zones: the nugget, the thermo-mechanically

Content from this work may be used under the terms of the Creative Commons Attribution 3.0 license. Any further distribution of this work must maintain attribution to the author(s) and the title of the work, journal citation and DOI. Published under license by Materials Research Forum LLC.

affected zone, the heat affected zone and the base material. The nugget is the area of completely recrystallized material close to the welding line; near to the nugget, the thermo-mechanically affected zone (TMAZ) is detectable. In the TMAZ the material undergoes both plastic deformation and heating, whilst only alterations of the microstructure and mechanical properties due to the welding thermal cycle are present in the heat affected zone (HAZ) [3].

For these FSWed joints characteristics, it is evident that the process parameters greatly influence the flow of the plastically deformed material [4]. In particular, there is a strong relationship between the microstructure and the quality of the joints is mainly due to the closed connection between the mechanical properties of the FSWed joints and the microstructural variations of the above-mentioned different zones of the welds. Therefore, particular attention must be paid in the choice of parameters to ensure adequate processing conditions, in order to avoid the formation of potential defects or weakness points in the identified welding areas [2].

Due to the large number of variables that must be considered simultaneously, it is not easy to optimize and predict with a good level of accuracy the process performance and the weld quality as a function of both the process conditions and the weld zones considered. For this reason, optimizing process performance by considering each process parameter individually is not an applicable approach. To overcome this problem, various artificial intelligence techniques have recently been used, among which the Artificial Neural Network stands out [5,6].

An Artificial Neural Network (ANN) is a mathematical model capable of reproducing the reasoning mode of the human brain, simulating its processing capabilities through the connection of neurons, which are the elementary computational elements of any neural network. The ANN, once it has been adequately trained, is able to solve even non-linear problems easily and quickly. To do this, the ANN is composed by an oriented network formed by different layers: the input layer, which collects the external data, the hidden layers, which process the information through the activation functions and the weights of each connection, and the outputs layer.

The training of the neural network is based on the use of a dataset thanks to which the network is able to determine the weights of the interconnections and of the activation function. These weights define the reliability of the prediction and can vary as a function of trainings; in fact, repeating the training defines different weights configurations which generate different results in the prediction. Consequently, it is evident that if the same weights are always considered, the ANN produces a constant predictive response with respect to a specific set of inputs. However, this aspect is a distorted version of reality. Indeed, it is known that every process is characterized by an intrinsic variability caused by external conditions that can influence systems in different and, often unpredictable, ways. The possibility of considering this uncertainty in the analysis and prediction of complex systems is a topic of considerable importance [7]. For all these reasons, the main objective of this work is to develop a model capable of predicting not only the punctual mechanical characteristics reached in the different areas of the weld starting from the welding parameters, but also of being able to evaluate the intrinsic variability of the process.

The proposed approach aims at forecasting the welding properties considering the process' natural variability by means of a group of Artificial Neural Network (ANN) having the same architecture, but different weights. The hypothesis of this work is that predicting the output using this approach allows to define an upper and a lower limit in which the proper results are placed. This idea was applied to the FSW process for the prediction of the hardness value reached by an aluminum alloy (AA 2024-T3) as a function of the main welding parameters (considered as input nodes of the ANN).

Methodology

Experimental tests.

AA2024-T3 sheets were friction stir welded perpendicularly to the rolling direction. The FSW process was performed using a CNC machine tool with a tool characterized by a smooth plane shoulder (16-mm diameter) and a frustum of cone pin shape (maximum and minimum diameters equal to 6 and 4 mm, height equal to 3.9 mm). The tool was realized from a drawn bar of carbon steel C40 without any heat treatment. Table 1 reports the welding parameters considered for the experimental campaign. The difference in the feed rate combined to 1200 rpm and 1500 rpm is linked to the presence of macro and micro defects in the joints welded with 1500 rpm-40 mm/min and 1500 rpm-100 mm/min. These defects led the authors to eliminate these combinations of parameters from further evaluation, considering them not suitable for the material considered.

Table 1. Parameters set-up for experimental tests.

Rotational speed (rpm)	Feed rate (mm/min)
1200	40
1200	70
1200	100
1500	70

All the other process parameters, such as the clamping system for the sheets, the tool inclination (fixed at 3°), and the tool penetration depth into the sheets (fixed at 3.99 mm), were kept constant.

Rockwell B hardness tests (HRB) were performed for all the welding conditions, following a 5mm spaced grid in the central zone of the top of the specimens, according to ISO 6508. For each sample, three profiles of indentations were carried out moving from the joint axis to the base material.

Developed approach.

One of the main issues in the FSWed joints is represented by the desire to obtain welds having mechanical properties as close as possible to those of the base material. In this context, one of the most important characteristics is the surface hardness of the joints.

Due to the importance of the prediction of these kind of properties without the need to execute experimental tests, the prediction models have become very useful in the scientific research. Nevertheless, these forecasting models are characterized by a limitation in the prevision since they supply a deterministic constant result for the same inputs, not considering the intrinsic variability of the process. This is a huge limitation typical also of the trained artificial neural networks (ANN). Indeed, the hypothesis behind the development of this models is that, even if the same architecture is considered, the ANN can be characterized by different connection weights and activation functions, obtainable through different training iterations. This means that same architecture, but different weights, generate different, even if still reliable, forecasts. This means that it might be possible to develop a model able to predict not only the required punctual value but also its confidence interval. This kind of model has been developed following the flow-chart reported in Fig. 1.

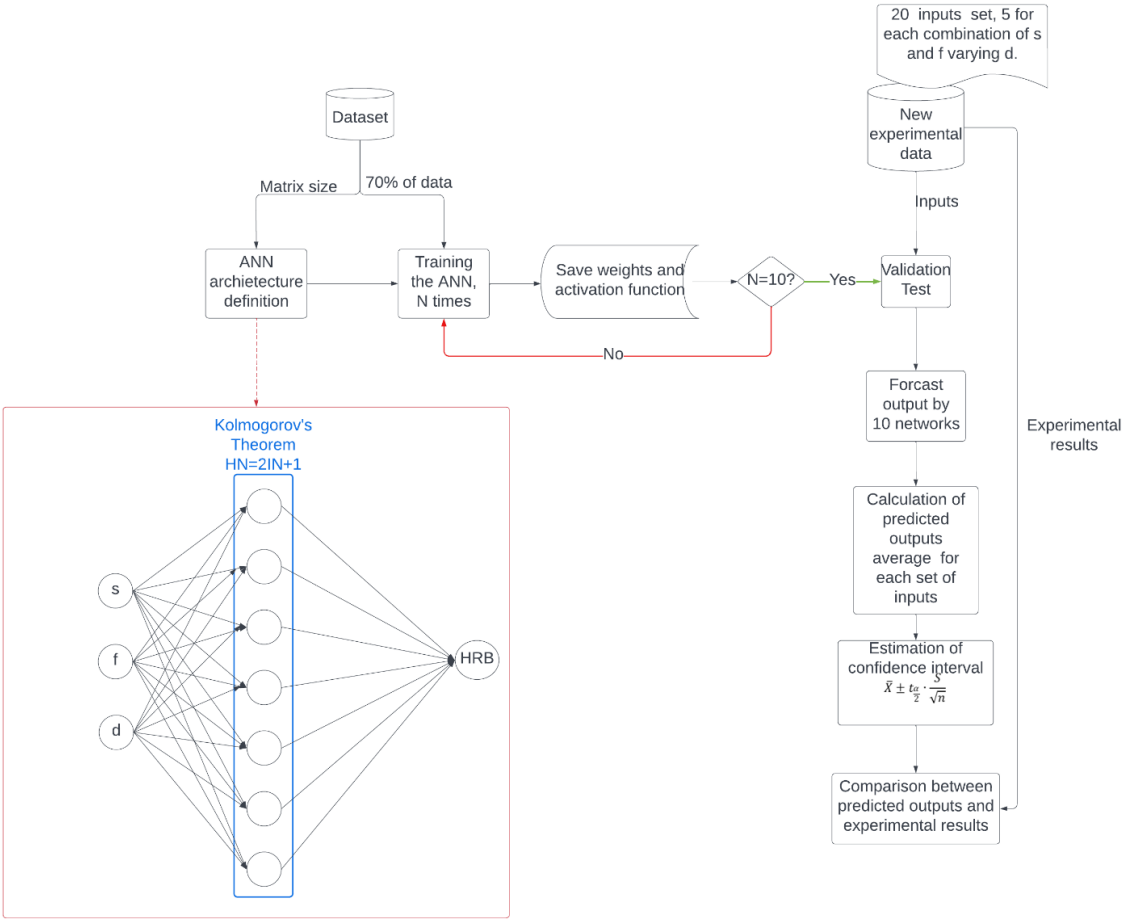

Fig. 1. Algorithm flow-chart.

The following stages are considered:

1. ANN architecture definition. The inputs and the outputs layers were defined according to the welding parameters and the final characteristic to be evaluated. Specifically, the input nodes (IN) were three and represented respectively the rotational speed of the tool (s), the feed rate of the tool (f) and the distance from the welding line (d) where the hardness, which represented the output node (ON), has to be known. A single hidden layer was introduced since the literature supports the idea of introducing few hidden layers to avoid unnecessary complexity of the network. The number of hidden nodes (HN) was selected based on one of the most applied heuristic techniques found in the literature: the Kolmogorov's Theorem, which demonstrates that a network with a single hidden layer can compute any arbitrary function of its input [8]. This theorem allows to estimate the size of the hidden layer as reported in Eq.1.

$$HN = 2 \cdot IN + 1 \tag{1}$$

2. ANN training. The dataset used for the ANN training contained 470 inputs combinations and the relative outputs, considered as target values. The dataset dimension fit with the requirements defined by Alwosheel A. et al. [9]. The dataset was based on the data of experiments performed to evaluate the surface hardness of the welded joints. Through a Matlab code, the ANN was trained to identify the weights, defining N=10. N indicated the number of ANN, with fixed architecture, considered for the multiple ANN approach trained.

This allows to obtain 10 ANNs with the same size, but with the layers differentiated from the weights of the connections and the activation functions. Levenberg–Marquardt algorithm was chosen as the training function for all the ANNs.

3. Forecasting tests. A new group of experimental data were considered for the verification of the applicability of the algorithm. Specifically, 20 combinations of input parameters were selected, and the relative experimental results were collected, ensuring to consider inputs always included in the training interval of the network. These sets of inputs were introduced in the group of the trained ANNs obtaining 10 predictions for each combination, for which the average value was calculated. At this point, the idea of confidence interval was introduced to verify the reliability of the previsions and to forecast the intrinsic variability of the process.
4. Confidence interval definition. Since the standard deviation of the data distribution was unknown, it was necessary to estimate the interval of the population average (μ) using, in addition to the sample mean ($\bar{X}$), the sample standard deviation (S), allowing to estimate the population standard deviation (σ). This can be done assuming that the random variable was normally distributed and, as a consequence, that the confidence interval can be defined by introducing the t-distribution. The t-distribution is similar to the normal distribution (symmetrical, bell-shaped, with mean and median equal to 0), but with a higher probability to fall into its queues than in the central part of the bell. Moreover, increasing the number of degrees of freedom (n), the random variable t tends to the normal distribution. Thus, considering α as the confidence level and n as the sample dimension (represented by the number of repetitions of inputs combination introduced into the dataset), the confidence interval is estimated as reported in Eq. 2. Considering the degrees of freedom equal to 3 and an α equal to 5%, from the statistical table, $t_{\frac{\alpha}{2}} = 4.3027$. The confidence interval was estimated based on the training dataset.

$$\bar{X} - t_{\frac{\alpha}{2}} \cdot \frac{S}{\sqrt{n}} \leq \mu \leq \bar{X} + t_{\frac{\alpha}{2}} \cdot \frac{S}{\sqrt{n}} \quad (2)$$

In this way, the estimated upper and lower bounds allowed to predict and define the interval where the results, in this case the surface hardness, can be placed if the experiments will be repeat more than once. Specifically, from the practical point of view, it was possible to predict HRB with a certain level of variability reproducing the intrinsic variability of the process, linked to external and uncontrollable factors.

Results and Discussion

The validation was performed by comparing the experimental and forecasted data and verifying their placement considering the predicted confidence interval. 20 combinations of inputs, indicating different welding conditions and hardness locations, were selected from the experimental tests (not used for ANN training): five hardness measurements for each combination of welding parameters by randomly selecting the distance from the welding line (d). Table 2 reports the combination used for the validation and the related results obtained from the experiments (performed as reported in previous section) and the average of previsions. It is important to underline that the data used for the validation are not related to a unique welding joint, thus resulting in a nonlinear distribution of the obtained hardness values in the typical FSW W-shape. This choice was made because the main aim of this step was to demonstrate the validity of the developed method considering the totality of the dataset and not limiting it to a determined couple of inputs and their related output. Each ANN responds with a slightly different result from the others and this ANN behavior allows to assimilate these simulation repetitions to the intrinsic variability of the process, such as possible to observe by the standard deviation and the dispersion

of the data is coherent with a stable and feasible process. Furthermore, the error in prevision is very low showing a maximum error equal to 6.25%. As it is possible to observe more clearly in Figure 2, all the average values of the predictions are contained in the estimated confidence interval, the same for the ten predicted values. The validation process allows to demonstrate the reliability of the developed approach not only in the prediction performed by a single ANN, but also in the identification of a confidence interval in which the process results can vary due to the intrinsic variability.

Table 2. Inputs combinations and ANN previsions.

INPUTS			TARGET	PREDICTED OUTPUT		
S	**f**	**d**	**HRB exp**	**MEAN**	**Std. Deviation**	**%Error**
1200	40	75	79	79.5	1.4	0.58%
1200	40	60	79	78.9	0.5	-0.12%
1200	40	10	75	70.3	1.2	-6.25%
1200	40	-2.5	70	67.9	2.3	-2.93%
1200	40	-35	77	77.4	1.0	0.56%
1200	70	50	80	78.4	0.7	-2.05%
1200	70	20	72	74.9	0.8	4.05%
1200	70	2.5	75	71.6	1.2	-4.50%
1200	70	-17.5	74	75.1	0.8	1.45%
1200	70	-45	80	78.4	1.0	-2.03%
1200	100	20	73	75.5	0.6	3.46%
1200	100	2.5	76	73.0	0.6	-3.98%
1200	100	0	76	73.0	0.6	-3.93%
1200	100	-5	71	73.4	0.7	3.31%
1200	100	70	79	78.8	0.5	-0.29%
1500	70	25	79	77.0	1.0	-2.53%
1500	70	10	78	74.5	0.9	-4.46%
1500	70	0	76	73.4	1.3	-3.46%
1500	70	-10	77	74.4	0.8	-3.36%
1500	70	-12.5	79	77.4	1.2	-2.06%

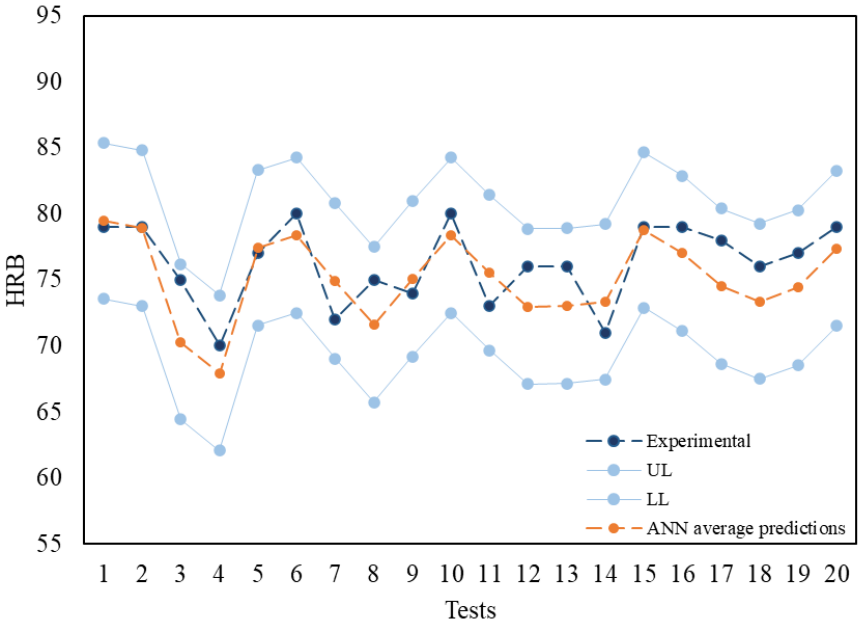

Fig. 2. Validation results.

Summary

A new approach for the prevision of Rockwell B hardness values as a function of the distance from the center of the welding line of joints obtained by the FSW process was developed. The novelty of the model regarded the possibility to predict the results considering the intrinsic variability of the process linked to uncontrollable factors of the process.

This means that, through the proposed approach, it was possible to correctly predict the surface hardness obtainable after a welding process, performed with the welding parameters used for the training. Furthermore, the approach was also able to show the confidence interval of the previsions.

The present approach identifies a new method for the use of ANN in manufacturing processes. In this way, with the same input, it is possible to obtain different outputs, placed in a confidence interval acceptable from the statistical point of view thanks to the different distribution of the weights of the connections, reflecting more a real process that is always characterized by a slight variability in the results.

References

[1] W.M. Thomas, E.D. Nicholas, J.C. Needham, M.G. Murch, P. Templesmith, C.J. Dawes, GB Patent application no. 9125978.8, 1991. Avalible: https://patentimages.storage.googleapis.com/66/60/ad/5f784d0b8653b7/US5460317.pdf (accessed 28 February 2019).

[2] P. Kah, R. Rajan, J. Martikainen, R. Suoranta, Investigation of weld defects in friction-stir welding and fusion welding of aluminium alloys, Int. J. Mech. Mater. Eng. 10 (2015) 1-10. https://doi.org/10.1186/s40712-015-0053-8

[3] M. Jariyaboon, A.J.J. Davenport, R. Ambat, B.J.J. Connolly, S.W.W. Williams, D.A.A. Price, R. Ambat, A.J.J. Davenport, The effect of welding parameters on the corrosion behaviour of friction stir welded AA2024–T351, Corros. Sci. 49 (2007) 877-909. https://doi.org/10.1016/j.corsci.2006.05.038

[4] M. Aissani, S. Gachi, F. Boubenider, Y. Benkedda, Design and optimization of friction stir welding tool, Mater. Manuf. Process. 25 (2010) 1199-1205. https://doi.org/10.1080/10426910903536733

[5] K. Deepandurai, R. Parameshwaran, Multiresponse Optimization of FSW Parameters for Cast AA7075/SiCp Composite, Mater. Manuf. Process. 31 (2016) 1333-1341. https://doi.org/10.1080/10426914.2015.1117628
[6] K. Mallieswaran, R. Padmanabhan, V. Balasubramanian, Friction stir welding parameters optimization for tailored welded blank sheets of AA1100 with AA6061 dissimilar alloy using response surface methodology, Adv. Mater. Process. Technol. 4 (2018) 142-157. https://doi.org/10.1080/2374068X.2017.1410690
[7] W.L. Oberkampf, J.C. Helton, C.A. Joslyn, S.F. Wojtkiewicz, S. Ferson, Challenge problems: Uncertainty in system response given uncertain parameters, in: Reliab. Eng. Syst. Saf., Elsevier, 2004: pp. 11–19. https://doi.org/10.1016/j.ress.2004.03.002
[8] R. Hecht-Nielsen, Kolmogorov's Mapping Neural Network Existence Theorem, in: SOS Printing, 1987.
[9] A. Alwosheel, S. van Cranenburgh, C.G. Chorus, Is your dataset big enough? Sample size requirements when using artificial neural networks for discrete choice analysis, J. Choice Model. 28 (2018) 167-182. https://doi.org/10.1016/J.JOCM.2018.07.002

Materials Research Proceedings 28 (2023) 1075-1082 https://doi.org/10.21741/9781644902479-118

Modelling of the weld seam in the forming simulation of friction stir welded tailored blanks

BACHMANN Maximilian[1,a *], RIEDMÜLLER Kim[1,b], LIEWALD Mathias[1,c] and MERTEN Mathias[2,d]

[1]Institute for Metal Forming Technology, Holzgartenstraße 17, 70174 Stuttgart, Germany

[2]DYNAmore GmbH, Stralauer Platz 34, 10243 Berlin, Germany

[a]maximilian.bachmann@ifu.uni-stuttgart.de, [b]kim.riedmueller@ifu.uni-stuttgart.de, [c]mail@ifu.uni-stuttgart.de [d]mathias.merten@dynamore.de

Keywords: Tailor Welded Blanks, Material Modelling, Sheet Forming

Abstract. In former papers methods to join different aluminium or different steel plates having same thicknesses are presented. These blanks are often joined by friction stir welding using flat tools. In order to increase the lightweight potential, the Materials Testing Institute of the University of Stuttgart developed a modified friction stir welding process to join aluminium and steel plates of different thicknesses. The process differs from the conventional method in stir welding tool used, which consists of a stepped welding pin and enables combined lap-and-butt joints to be produced. In this paper, a suitable material model is presented to describe this weld seam, allowing the forming behavior of hybrid sheet metal compounds to be realistically simulated.

Introduction

In car body construction, lightweight design approaches are becoming more common, in which weight of components is reduced by substituting one material by a comparatively lighter material (lower density). On the one hand, the weight reduced this way can extend the range of vehicles, which is particularly important in terms of the future or acceptance of electromobility, as charging cycles per kilometre driven play a significant role. On the other hand, lightweight components contribute to regulatory compliance as they lead to a reduction in the CO_2 footprint of vehicles by lowering the energy consumption to drive the vehicle and by requiring less material to be used in production [1]. One challenge arising in the substitution of known materials consists in the required adaptation of the component geometries and the joining processes used [2]. When combining high-strength aluminium alloys or even combinations of aluminium and steel alloys lightweight construction potentials increases. In particular, joining processes established in car body construction, such laser beam and resistance spot welding, show limitations regarding the combination of such materials.

Sheet metal components made of different high-strength aluminium alloys and different sheet thicknesses can be used in the same applications as conventional materials, providing better properties like higher strength and lower density. However, joining of such high-strength aluminium alloys (e.g. 6000-series alloys) by established joining processes such as laser beam welding proves to be difficult due to the materials' tendency to hot cracking during or after welding [3]. In addition, the high heat input of the laser beam welding process causes a reduction of the strength of aluminium alloy, resulting finally in a reduced strength of the joint (weld seam) [4]. For resistance spot welding, high wear of electrodes poses a problem when welding such materials. These problems in joining high-strength aluminium alloys were circumvented in 1991 with the friction stir welding process patented by Thomas et al [5]. In this process, the process energy required is introduced by means of a rotating welding tool, which is pressed into and moved along the joint gap [6]. Since the melting temperature is principally not reached during friction stir

Content from this work may be used under the terms of the Creative Commons Attribution 3.0 license. Any further distribution of this work must maintain attribution to the author(s) and the title of the work, journal citation and DOI. Published under license by Materials Research Forum LLC.

welding due to the method of energy input, the materials to be joined remain in the solid phase during the entire process. Joining of different sheet materials with different sheet thicknesses allows application-specific lightweight solutions to be realized. When joining different sheet materials with different sheet thicknesses, however, the welding tool in general has to contact the joint area flatly. Furthermore, for the joining of aluminium and steel, a joining method is required that minimises the appearance of intermetallic phases, as these reduce the strength of the weld seam, and at the same time the surface of the steel is sufficiently activated to form the joint with the aluminium. To ensure this, the Materials Testing Institute of the University of Stuttgart (MPA) developed a variation of the friction stir welding process to join different aluminium or aluminium and steel blanks of different thicknesses. In this process a combined overlap and butt joint is used as shown in Fig. 1. Here, the thicker metal sheet is provided with a milled step in sheet thickness into which the thinner sheet is inserted before the stir welding process [7].

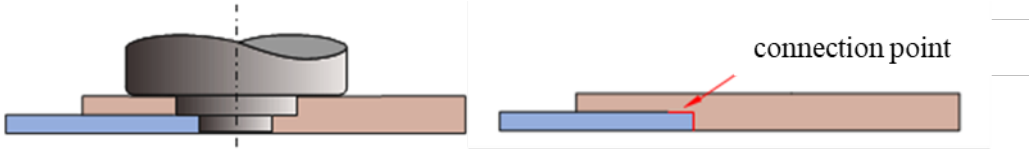

Fig. 1. Combined lap and butt joint; left: with welding tool, right: connection point [1].

Design of the pin of the welding tool shown in Fig. 1 is shaped in a way that both the front face and the surface of the steel sheet are activated. Additional the tool shoulder only rests on the aluminium and therefore does not rub on the steel as with conventional butt joints. The tool live, especially of the tool shoulder significantly is increased. The presented friction stir welding process can therefore be used both to join high-strength aluminium alloys and to produce mixed aluminium-steel joints [8,9]. The use of mixed aluminium-steel joints has a considerable potential for lightweight materials, as load-adapted components can be produced in which higher stressed sections can be provided with a steel sheet and the remainder with an aluminium sheet. In addition to the possibility of joining different materials of different sheet thicknesses, the developed welding process serves as solution annealing. Components of different materials, sheet thicknesses and material grades manufactured with friction stir welding are known as Tailor Welded Blank (TWB).

Previous studies [10] show that TWBs made of aluminium and steel having the same sheet thickness of the base materials show relatively good forming properties as cups with drawing depths similar to the base materials could be drawn. However, [10] considered only 5000-series alloys on the aluminium side in his investigations. Singar [11] investigated the forming capacity of aluminium-steel TWBs made of HX340LAD (0.8mm) and AA 6014 T4 (1.2mm) joined by the cold metal transfer welding process. However, the investigations shown, that the values achieved for elongation at break (approx. 7%) and forming limits from the forming limit diagram required further work to produce TWBs suitable for industrial use.

By using the friction stir welding process presented in this paper hybrid TWBs consisting of DX54 (1.0 mm) and AA 6016 T4 (2.0 mm) can be produced showing a new potential for forming operations [12]. For these hybrid TWBs a simulative mapping approach is developed with focus on the question how the hybrid TWB has to be modelled in order to describe the forming process realistically. First the material characterization in form of tensile tests and the determination of the forming limit curves is carried out for the base materials and the weld seam. With the results from these characterizations a simulative approach of TWBs is set up by mapping the properties of the three components aluminium, steel and weld seam in separate parts in order to map the forming behaviour and thus increase acceptance of aluminium-steel TWBs in the industry.

Material Characterization

For deriving the material model for the forming simulation, the mechanical properties and the forming limit curves (FLC) of both the base materials (DX54 and AA6016 T4) and the weld seam of the TWBs were determined. Concretely, tensile tests were performed at the DYNAmore GmbH to obtain yield curves and Nakajima tests were carried out at the Institute for Metal Forming Technology (IFU) for determining the FLCs. The weld seam was furthermore characterized by the area of the combined lap and butt joint. The yield curves measured via the tensile tests are shown in Fig. 2. Here, for the base materials specimens were testes with 0°, 45° and 90° to rolling direction and for the weld seam, specimens were tested with 0° and 90° to the welding orientation. Each characterization test was performed using 5 samples. The extrapolation of the data from the tensile test was done using Hockett-Sherby. In Fig.2 the yield curves for AL6016 T4 and DX54 in 0° are presented as these are the rolling directions with the lowest loading limits. In this context, Fig. 2 shows the flow curve of the weld seam specimen taken 0° to the welding orientation which is above the flow curve of the base material AA6016 T4, but below the flow curve of the base material DX54. In contrast, the yield curve of the weld seam taken 90° to the welding orientation is below the yield curve of both base materials. Considering these properties, it can be seen weld seams should be positioned in 0° to the welding orientation in order to obtain components with a correspondingly strength.

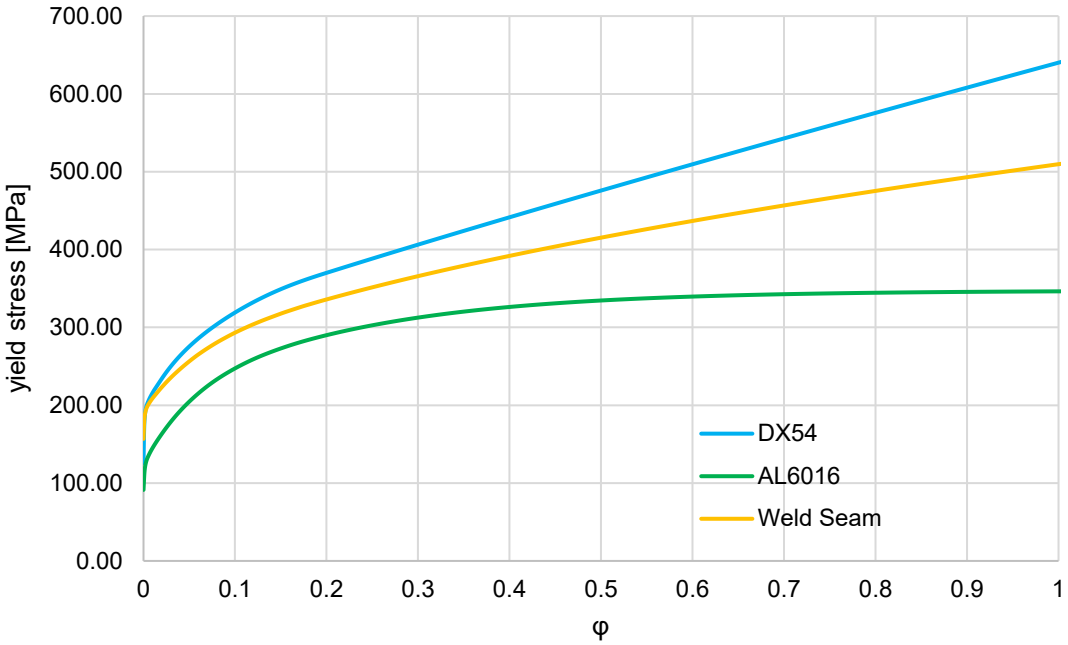

Fig. 2. Yield curves of AA6016 T4, DX54 and weld seam.

The forming limit curves of the TWBs were determined on the basis of 5 support points (waist of 30 mm, 60 mm, 100 mm, 140 mm and 200 mm) according to ISO 12004 [13] using a workshop press of the IFU (see Fig. 3, left and middle). For each of the 5 support points, Nakajima specimens were produced with a welding orientation of 0° and 90°. Each support point was determined using 4 valid samples. The smaller sheet thickness of the aluminium sheet of the TWB was compensated by means of a shim plate, thus ensuring a uniform force application during the testing procedure. The phenomenon of weld seam migration during forming in the direction of the aluminium could be minimized by increasing the pressure of the gas springs of the blank holder.

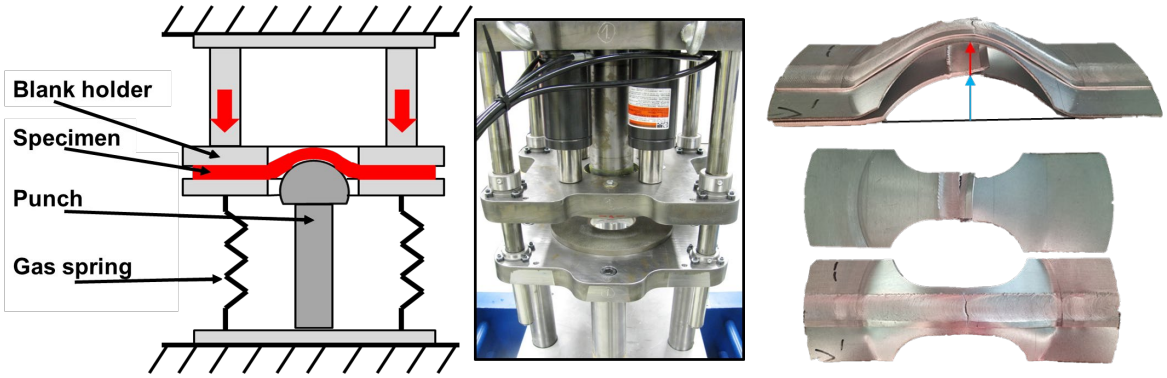

Fig. 3. Principal of the Nakajima test used (left), Nakajima testing device at IFU (middle), TWBs with a welding orientation of 0° and 90° (right).

Depending on the weld direction in the specimens, different results were observed with regard to crack initiation. For the specimens with 0° welding orientation, the crack forms, as usual for Nakajima tests of monolithic specimen, starting from the weld in the middle in the direction of the sheet edge (Fig. 3, right bottom). In this case, the load applied by the punch is absorbed by the weld seam and the base materials. Here, the GOM aramis system could be used to determine the major and minor strains before cracking. Determining the crack initiation for specimen with a welding orientation of 90° proved more difficult. Here, the failure was also initiated in the weld seam, but could not be identified as a local crack on the upper side of the sheet. The applied force of the punch is absorbed only from the weld seam which forces the weld seam to open up from the bottom side of the sheet. Therefore, no crack could be detected on the upper side of the sheet. On the upper side of the sheet only the separation of the weld seam was detected, (see Fig.3 right, middle). In this case, the crack initiation moment could be determined from the history curve of the major and minor strain, since they showed a rapid decrease after separation of the sheets due to the force of the punch. This moment was defined as the crack initiation moment for TWB with welding orientations of 90°.

The different forming behavior of TWBs considering the welding orientation is shown in Fig. 3 (right, top), illustrating the lateral plan view of Nakajima specimens with a waist of 30 mm. The drawing depth at 90° welding orientation is given in blue and the drawing depth at 0° welding orientation is shown in red. Such differences in the forming capability of the TWB could be observed for all waists and are shown in the forming limit diagram for both cases (0° and 90° orientation of the welding seam) in Fig. 4.

Comparison of the two FLCs reveals that TWBs show different forming capability depending on the weld orientation for each loading condition (uniaxial, plain strain, biaxial). These results correspond to those from the tensile tests already presented, as the forming capability of TWBs with a welding orientation of 90° is below the forming capability of 0° at the critical plane strain load.

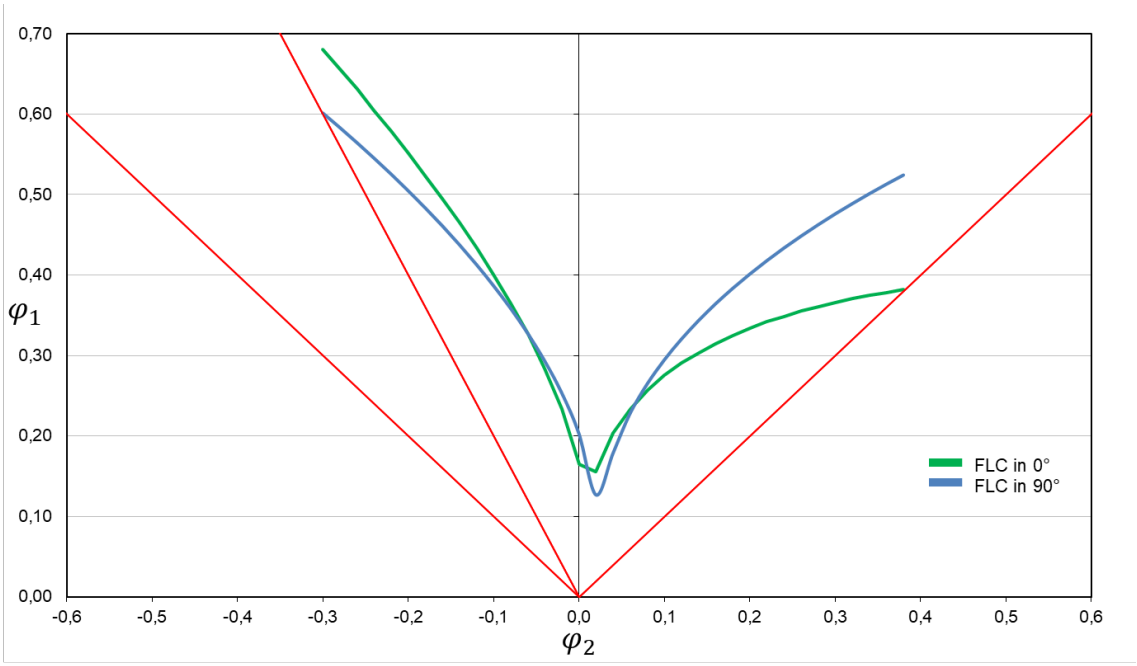

Fig. 4. Forming limit diagram for DX54/AL6016 TWBs in 0° and 90° welding orientation.

Numerical Simulation Setup

The mechanical properties determined for the base materials DX54 and AA6016 T4 as well as the weld seam were subsequently used to set up material models for the simulation of a Nakajima test performed. As described before the failure behavior varies due to the welding orientation and in this approach the welding orientation of 0° was further investigated. The simulations aimed to model the forming behavior of the TWB specimen with different waists and welding orientation of 0° during the Nakajima test as accurately as possible. For simulation setup and performing, the simulation software DYNAFORM and LS-PREPOST were used. Previous simulation work in this field was mainly concerned with the modeling of TWBs consisting of the same material using the software ABAQUS [14], TWBs consisting of different aluminium alloys [15] or TWBs produced by laser welding [16]. In laser-welded TWBs, the width of the weld seam is only a few millimeters compared to friction stir welded TWBs. Moreover, the higher process temperatures of laser welding as opposed to friction stir welding lead to significantly differing forming behavior, especially of the weld seam but also of aluminium sheets as part of a TWB. To account for these characteristics, a new modeling approach was developed for the numerical study on the forming behavior of friction stir welded TWBs presented in this paper, distinguishing it from previous work on laser welded TWBs. The distinction from [14] and [15] is made by considering different materials (aluminium and steel) with different thicknesses. In contrast to [17] this modelling approach on the one hand considers anisotropic material behavior and on the other hand describes the weld seam not only by node definitions, but as an independent material with its specific forming behavior.

In the model approach, the welded blank was divided into three parts (the aluminium side, the weld seam and the steel side) as shown in Fig. 5 a). The weld seam was designed with a width of 20 mm, which corresponds to the area of the combined lap and butt joint of the real TWB. The interface from AA6016 T4 to the weld seam and from the weld seam to DX54 were modeled using the weld function of DYNAFORM. Normally, failure values are assigned to these weld functions to implement the failure behavior at this location. However, as shown during the Nakajima tests, the TWB considered did not fail on the interfaces between the base materials and the weld seam, but within the weld seam. For this reason, the weld function was assigned with ‘no failure’. Each of the three parts was assigned with its determined mechanical properties using the material model

MAT_036-3-Parameter_Barlat. The entire welded blank was meshed with shell elements having a size of 1 mm, which means the weld seam has been represented with 20 elements in width. Fig. 5 b) shows the entire simulation setup with punch, blank holder, die and TWB in lateral plan view.

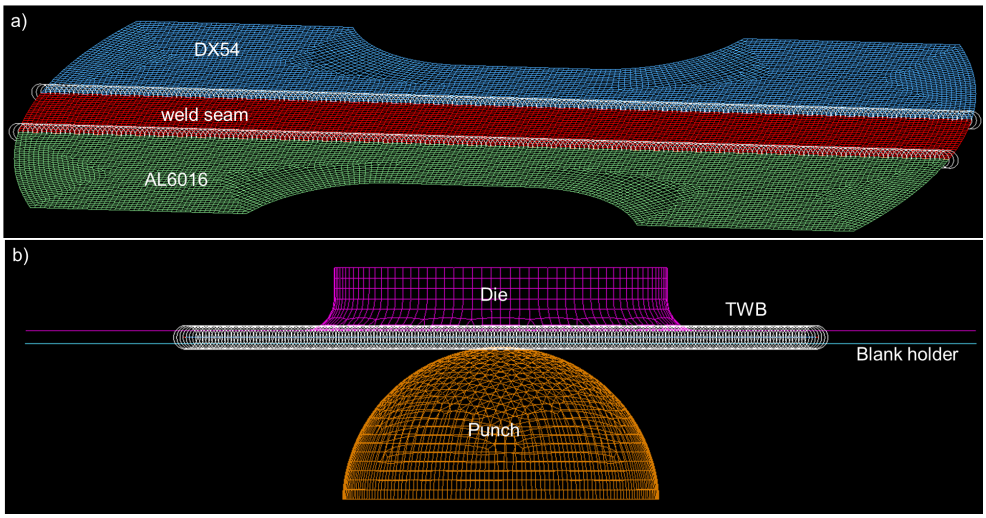

Fig. 5. a) Separation of the blank in 3 parts; b) Simulation setup of Nakajima test considered.

Validation Of Simulation Model

For validation of the simulation results, the strain values measured in the corresponding Nakajima test were compared with the strain values calculated from the simulation. Furthermore, by importing the forming limit curve for the welding orientation of 0°, the crack initiation moment was determined based on the simulation results and compared with the crack initiation observed in the experiment. In this context, Figure 6 shows the major strain distribution of a Nakajima specimen with a waist of 60 mm calculated by simulation on the left side and measured in the experiment on the right side. On the right side the measurement results from the experiment of three samples are shown. The average value for the major strain at crack initiation moment is $\varphi_1 = 0{,}283$ in contrast, the simulative determined main strain is $\varphi_1 = 0{,}31$. Comparison of these strain results revealed the strain distribution could be calculated quite accurately with the established simulation model for TWB consisting of DX54 and AA 6016 T4, but the strain values at crack initiation were overestimated relative to the strain values measured in the experiment. In Fig. 6 the location of crack initiation is highlighted with black arrows. The simulation differs slightly from the experiment with respect to the predicted location of crack initiation. The simulation result indicates this allocation slightly closer to the transition between the weld seam and the base material. The reason for these deviations in the simulation is probably the weld seam exhibits a different mixture of aluminium and steel in the transition area to the base materials compared to the weld seam center. This was not considered in the characterization tests of the weld seam carried out so far.

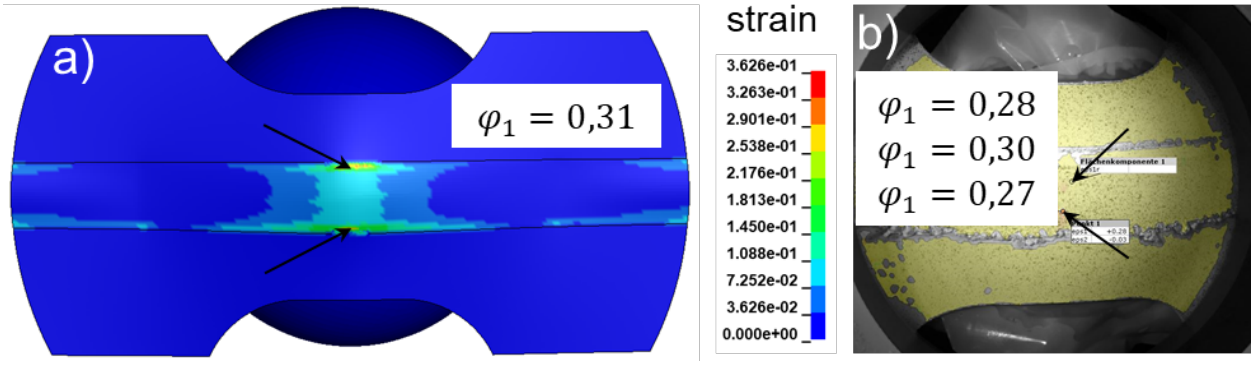

Fig. 6. Strain values before crack initiation moment a) major strain in simulation, b) major strain in experiment.

Summary

In this paper, a modelling approach for the numerical forming simulation of TWBs with a special focus on the consideration of the weld seam is presented. First, the base materials DX54 and AA6016 T4 as well as the weld seam of the TWB considered were characterized. Based on these tests, a simulation model of one of the Nakajima tests was set up and validated using the strains numerically calculated and experimentally measured. The simulation results revealed that the forming behavior of the TWBs could be described quite accurately by mapping the properties of the three components aluminium, weld and steel separately, but the behavior of the weld seam still needs to be represented in more detail as the predicted location of crack initiation varies from the experiments.

In the future, in addition to the strain values, the force curves from simulation and experiment will be compared to base validation on 2 values. Furthermore, a simulative representation of the weld seam with shell and volume elements will be aimed in order to implement hardness measurements of the weld seam in the simulation and thus to consider the transition of the weld seam to the base materials in more detail. Possible variations of the properties of the weld seam will thus considered in further investigations by implementing the hardness profile of the weld seam and linking it to a prior damage. In addition, other connection methods will be considered to map the crack initiation at the correct location. Moreover, simulation of the Nakajima test with welding orientation of 90° will be considered in the future as they have a different failure behavior which was described in this work.

Acknowledgement

The work of this paper was carried out within the framework of the project CO2-HyChain, which is funded by the Technologietransfer-Programm Leichtbau (TTP LB) of the Federal Ministry of Economic Affairs and Climate Action.

References

[1] A. Birkert, S. Haage, M. Straub, Umformtechnischer Herstellung komplexer Karosseriebauteile – Auslegung von Ziehanlagen. Springer Verlag Berlin Heidelberg, 2013.

[2] F. Henning, E. Moeller, Handbuch Leichtbau – Methoden, Werkstoffe, Fertigung. Carl Hanser Verlag München Wien, 2020.

[3] M.W. Mahoney, C. Rhodes, J.G. Flinott, W.H. Bingel, RR. Spurling, Properties of friction stir-welded 7075 T651 aluminium, Metall. Mater. Trans. A 29 (1998) 1955-1964. https://doi.org/10.1007/s11661-998-0021-5

[4] A.K. Lakshminarayanan, V. Balasubramanian, K. Elangovan, Effect of welding processes on tensile properties of AA 6061 aluminium alloy joints, Int. J. Adv. Manuf. Technol. 40 (2009) 286-296. https://doi.org/10.1007/s00170-007-1325-0

[5] W.M. Thomas, E. Nicholas, J. Needham, M. Murch, P. Temple-Smith, C.J. Dawes, Great Britain Patent Application No. 9125978.8 (1991).
[6] H.B. Schmidt, J.H. Hattel, Thermal Modelling of friction stir welding, Scirpta Mater. 58 (2009) 332-337. https://doi.org/10.1016/j.scriptamat.2007.10.008
[7] M. Werz, Experimentelle und numerische Untersuchungen des Rührreibschweißens von Aluminium- und Aluminium-Stahl-Verbindungen zur Verbesserung der mechanischen Eigenschaften, Materialprüfungsanstalt (MPA) Universität Stuttgart, Dissertation, 2020.
[8] T. Wanatabe, H. Takayama, A. Yanagiswa, Joining of aluminium to steel by friction stir welding, J. Mater. Process. Technol. 178 (2006) 342-349. http://doi.org/10.1016%2Fj.jmatprotec.2006.04.117
[9] H. Uzun, C. Donne, A. Arganotto, T. Ghidini, Friction stir welding of dissimilar AL 6013-T4 to X5CrNi18-10 stainless steel, Mater. Des. 26 (2005) 41-46. https://doi.org/10.1016/j.matdes.2004.04.002
[10] T. Tanaka, T. Hirata, N. Shinomiya, N. Shirakawa, Analyses of material flow in sheet forming of friction-stir welds on alloys of mild steel and aluminium, J. Mater. Process. Technol. 22 (2015) 115-134. https://doi.org/10.1016/J.JMATPROTEC.2015.06.030
[11] O. Singar, M. Merklein, Study on the formability characteristics of the weld seam of Aluminium Steel Tailor Hybrid Blanks, Key Eng. Mater. 549 (2013) 302-310. https://doi.org/10.4028/www.scientific.net/KEM.549.302
[12] F. Panzer, M. Schneider, M. Werz, S. Weihe, Friction stir welded and deep drawn multi-matieral tailor welded blanks, Materials Testing, Carl Hanser Verlag, München, 2019.
[13] DIN Deutsches Institut für Normung e.V., Metallische Werkstoffe – Bestimmung der Grenzformänderungskurve für Bleche und Bänder – Teil 2: Bestimmung von Grenzformänderungskurven im Labor, Beuth Verlag GmbH, Berlin, 2021.
[14] W. Lee, K.-H. Chung, D. Kim, J. Kim, C. Kim, K. Okamoto R.H. Wagoner, K. Chung, Experimental and numerical study on formability of friction stir welded TWB sheets based on hemispherical dome stretch tests, Int. J. Plast. 25 (2009) 1626–1654. http://doi.org/10.1016/j.ijplas.2008.08.005
[15] C. Leitao, B.K. Zhang, R. Padmanabhan, D.M. Rodrigues, Influence of weld geometry and mismatch on formability of aluminium tailor welded blanks: numerical and experimental analysis, Sci. Technol. Weld. Join. 16 (2011) 662–668. https://doi.org/10.1179/1362171811Y.0000000055
[16] X. Qiu, The study on Numerical Simulation of Tailor Welded Blanks in Square Cup Stamping, Adv. Mater. Res. 189-193 (2011) 3932-3935. https://doi.org/10.4028/www.scientific.net/AMR.189-193.3932
[17] O. Singar, D. Banabic, Numerical Simulation of Tailored Hybrid Blanks, Proceedings of Romanian Academy, Sereis A, Volume 22, Number2/2021, pp. 177-184.

Materials Research Proceedings 28 (2023) 1083-1090 https://doi.org/10.21741/9781644902479-119

Comparative investigation of partial cooling methods for induction heating of hybrid bulk components for hot forming

INCE Caner-Veli[1,a *], KATZ Fabian[1] and RAATZ Annika[1,b]

[1]Leibniz University Hannover, Institute of Assembly Technology, An der Universität 2, 30823 Garbsen, Germany

[a]ince@match.uni-hannover.de, [b]raatz@match.uni-hannover.de

Keywords: Partial Cooling, Form Variable Handling, Function Integrated Handling, Tailored Forming

Abstract. The novel Tailored Forming process chain enables the combination of crucial properties of different materials by manufacturing hybrid components. Thereby, the limitations of monolithic components are surpassed. However, manufacturing hybrid bulk components introduces new challenges for hot forming. For example, when combining steel and aluminium, the main challenge is establishing and maintaining a temperature gradient in the component to match the differing flow stresses of the materials for a successful forging. For establishing the gradient, a particular heating strategy, including inductive heating of the steel and parallel partial cooling of the aluminium, is necessary. After reaching the target temperature, the heated component has to be transferred to the forging die by a robot while maintaining the essential temperature gradient. Therefore, a portable spray nozzle cooling system attached to the robot's end effector was designed in former work. This paper aims to validate spray nozzles for establishing a temperature gradient in a hybrid workpiece with a particular heating strategy compared to a currently used immersion cooling. For the validation, the nozzles will cool a hybrid steel aluminium shaft, whereby the nozzles' operation parameters influence on the temperature gradient will be investigated. Finally, the performance of the nozzles will be compared against the currently used immersion cooling.

Introduction

Nowadays, the research and development of increasingly high-performance and lightweight materials are becoming essential for resource efficiency. With these challenges, conventional mono-material components reach their limits to an increasing degree. To improve these limitations, hybrid components are developed that allow the use of different material properties by combining them. For example, a shaft that carries a high local mechanical load consists of a material that withstands the load and has a high inherent weight. If instead, only the loaded areas consist of the high-strength material, and the remaining part uses a lighter and, therefore, lower-strength material, the shaft would still be suitable for its application and, at the same time, reduce its weight.

Conventional hybrid manufacturing processes merge the different materials in a near-net shape at the end of the process chain, which restricts the geometry and the quality of the joining [1]. To overcome this limitation, a novel process chain for producing solid hybrid components that pairs the materials in a semi-finished workpiece and then forges them together, called “Tailored Forming” has been developed [2]. The early joining process results in better mechanical properties in the joining zone as well as a wider range of possible final geometries for the hybrid components [3]. However, the early joining leads to a new challenge of establishing and maintaining a temperature gradient in the workpiece during the whole process chain. The combined materials have deviating yield stresses, which must be equalized before forging. In the Tailored-Forming-Process steel-steel, steel-aluminium and titan-aluminium pairings are investigated. Steel and titan require forging temperatures that exceed the melting temperature of aluminium. To prevent

Content from this work may be used under the terms of the Creative Commons Attribution 3.0 license. Any further distribution of this work must maintain attribution to the author(s) and the title of the work, journal citation and DOI. Published under license by Materials Research Forum LLC.

melting of the aluminium, which destroys the component, special heating strategies were developed for several hybrid components [4, 5]. The heating takes place locally using induction heating. In this way, only the material requiring higher temperatures for forming is heated. Simultaneously, the aluminium is actively cooled down in order to prevent exceeding the melting temperature. As a result, this treatment establishes a step-like temperature gradient in the component. Unfortunately, the current heating and cooling strategies can only be used stationary, resulting in the temperature gradient not being maintained during a transfer from the induction coil to the forming machine. As a result, equalization processes occur in the component, which can lead to critical temperatures in the joining zone, resulting in a renewed threat of melting.

In order to eliminate the risk of melting during transfer, a handling system was developed with an integrated cooling device [6]. The handling system consists of a form variable gripper that can handle hot forged objects and spray nozzles as a cooling unit. The form variable gripper allows handling diverse geometries without retooling time, whereby the handling gets more versatile as conventional two-finger grippers adjusted for only one geometry. The nozzles are attached to the gripper by an adaptable mounting system, whereby they can be aligned so that only a predefined area is cooled. Utilizing this handling system enables local cooling during the transfer phase, eliminating the risk of melting. The nozzles' cooling parameters must be selected to prevent melting and avoid an undercooling of the steel side.

This paper aims to validate the cooling system to prove the cooling effect needed for the sufficient forging of hybrid bulk components. For this purpose, the cooling system is initially considered stationary, i.e. without handling equipment integration and compared with the currently utilized immersion bath cooling. An example process from the Tailored-Forming-Process is used for the validation. For this purpose, immersion cooling and spray cooling are presented first to introduce and compare the methods. Based on this knowledge, the chosen methodology is described in more detail, and the experimental setup is explained. Afterwards, the results are examined and evaluated in detail. Finally, the paper concludes with a summary and an outlook.

Cooling Methods

Active cooling through controlled heat dissipation is described as quenching and is defined as cooling occurring more rapidly than in static air [7]. Such quenching techniques as immersion cooling and spray cooling can be utilized to establish the necessary temperature gradient. This chapter discusses the primary cooling techniques used for the particular heating strategy.

Immersion cooling. Immersion cooling means that a workpiece is immersed in a liquid bath and thereby cooled. Water, oil and polymers serve as coolants for immersion cooling. Depending on the coolant, the cooling rate can be influenced. For example, the cooling rate of water is higher than that of quenching oil. Further parameters with which the cooling rate can be influenced are the temperature and the flow velocity of the coolant. During immersion cooling, different phases may occur depending on the workpiece temperature, resulting in different cooling rates. A vapor layer forms on the workpiece at a high surface temperature, which has a heat-insulating effect and thus leads to a low cooling rate. This phenomena is called Leidenfrost-Effect [8] and demonstrated in Fig. 1.

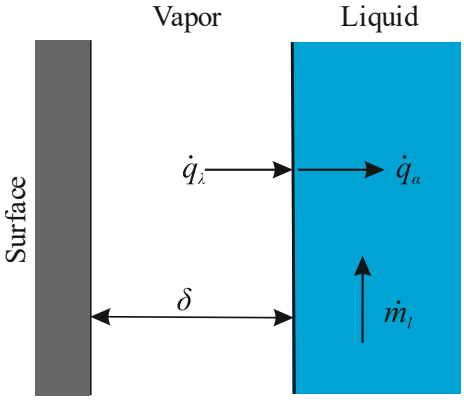

Fig. 1. Leidenfrost scheme demonstrating formation of a vapor layer.

The surface temperature is higher than the boiling point of the surrounding liquid. The vapor layer formed separates the liquid from the object and has the thickness δ and the corresponding

coefficient of thermal conductivity, leading to a heat flux $\dot{q}$. In the fluid media, thermal conduction occurs with a different heat transfer coefficient (HTC), for which heat flux is given as a function. Each phase has a specific range for its coefficients, whereby gas coefficients are smaller than coefficients of liquids, which explains the insulating effect of the vapor [9]. The heat flows from the object into the vapor, and then into the liquid, generating free convection $\dot{m}$ in both phases. As soon as the temperature decreases beneath the liquid's boiling temperature, which is also called the Leidenfrost temperature, the vapor layer breaks down, and the heat dissipation increases again. The induction of a flow into the cooling medium influences the Leidenfrost temperature so that the vapor film forms at higher temperatures.

Spray cooling. Another cooling technique is spray cooling, where a nozzle atomizes a liquid coolant and sprays it onto the workpiece to be cooled. This cooling technique serves, for example, for locally varying cooling rates [10]. Atomization can be performed with single-substance or dual-substance nozzles. In the case of single-substance nozzles, the liquid coolant is atomized directly, and in the case of dual-substance nozzles, it is atomized with pressurized air. Compared with single-substance nozzles, dual-substance nozzles achieve higher heat transfer coefficients (HTC) [11]. The impingement density is the quantity of water or liquid that hits the surface of the workpiece per time and area. Furthermore, an increase in the coolant pressure improves the impingement density, positively affecting the cooling rate and, thus, the HTC [12, 13]. This correlation can be utilized in spray cooling to allow flexible adjustment of the cooling rate by varying the pressure. Another feature is that the heat transfer is highest at the center of the spray and decreases radially from it. However, by overlapping the spray cones, the dissipated heat and, consequently, the heat transfer coefficient can be increased [12]. Thus, the radially decreasing intensity of the heat transfer can be counteracted.

Methods

The previously presented cooling methods will now be compared, utilizing a Tailored-Forming-Process, concerning their cooling performance. Initially, the process and its current heating strategy will be presented, followed by a description of the experimental setup and execution.

Investigated Process. To validate the cooling process to establish and maintain the temperature gradient during heating and transport of the manufacturing process of a hybrid shaft developed by Behrens et al. is used [14]. The shaft consists of steel and aluminium (Fig. 2). Friction welding merges the two materials into a semi-finished workpiece. Induction heating of the steel side then prepares the workpiece for the forging process, while the aluminium side remains in a cooling immersion bath with water. This heating strategy achieves the required steel side temperatures of up to 900°C while the aluminium side remains below the melting point. During the following handling into the forging machine, the aluminium is not cooled, whereby the temperature gradient disappears. Therefore, a spray nozzle cooling unit integrated into the handling equipment was developed that maintains the temperature gradient while handling [6]. To confirm the cooling performance of the nozzles, they will be evaluated in stationary use instead of immersion cooling to establish the temperature gradient. If the same temperature gradient as immersion cooling is achieved, the functionality is verified and the handling equipment integrated configuration can be evaluated.

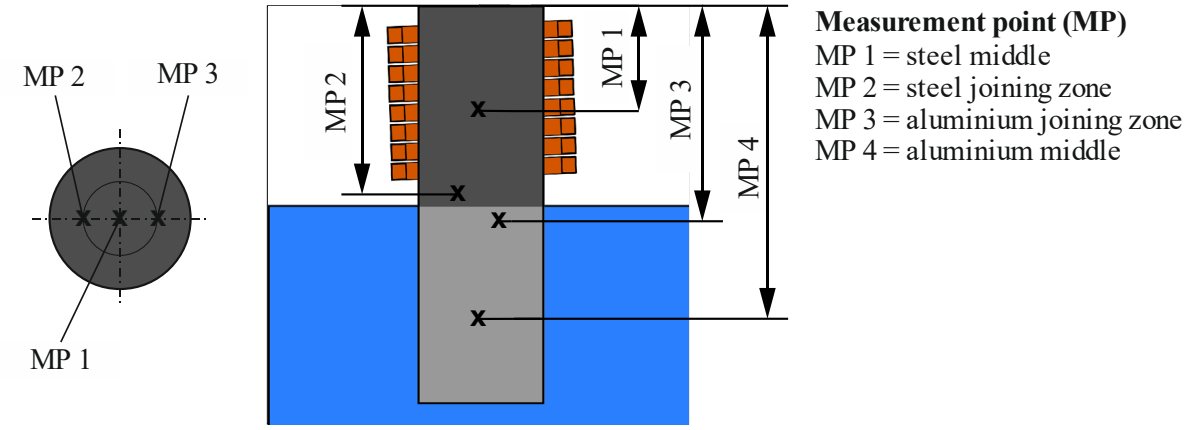

Fig. 2. Scheme of immersion cooled shaft workpiece during inductive heating with marked measurement points (MP).

Experimental Setup. For the validation, the workpiece's steel side is inductively heated, while the the nozzles cool the aluminium. Thermocouples attached to the workpiece measure the temperatures near the joining zone (MP 2 & MP 3) and the center of the respective material volume (MP 1 & MP 4)(Fig. 2) with 10 Hz. Drilled holes permit the thermocouples to be located at the defined positions to measure the temperature. The thermocouples for MS 1 - MS 3 are inserted on the steel end face, while MS 4 passes through the lateral surface of the aluminium. A workpiece can only be used once because the heating and cooling alter the material properties, whereby a second heating would lead to falsified results. Fig. 3 shows the experimental setup, where the workpiece is located in the induction coil. The nozzles are arranged around the aluminium part instead of the immersion bath. Further, the cooling system records the pressurized air and water mass flows. The adjustment of these mass flows occurs through pressure regulation. A valve sets the air pressure, while pressurized air adjusts the water pressure through a tank, where the pressurized air flows in and the water out.

The induction coil heats the workpiece for 28 seconds with a particular power profile, which is designed for immersion cooling, while the nozzles cool the aluminium. The inductive heating unit has a max. power of 44 kW, while the workpiece is heated for 9 s with 55%, then 9 s with 35% and finally 10 s with 20% power to establish the step-like temperature gradient. In order to determine the parameter's influence on the temperature gradient, different parameters for the air and water mass flow are tested. The experimental design includes three parameter sets shown in Tab. 1, each repeated three times in a randomized order. While the pressure parameters are set, the mass flow of the fluids is measured. The air pressure influences the water mass flow antipropotional and is considered insofar as keeping the water pressure constant while varying the air pressure. The original handling process

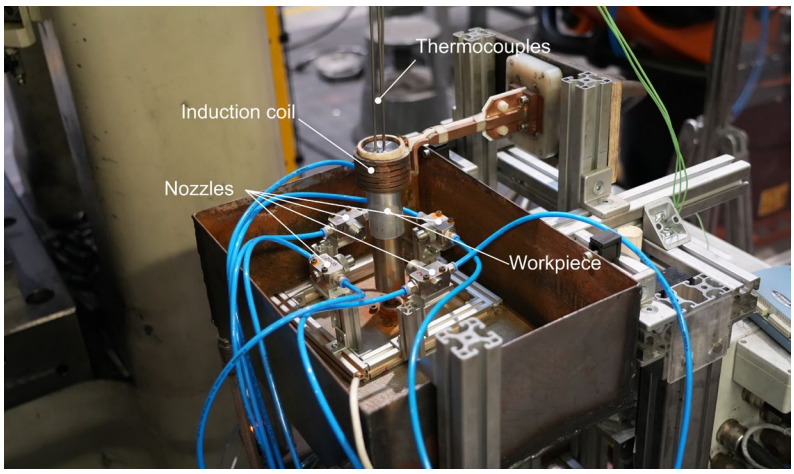

Fig. 3. Experimental setup of the heating unit with spray nozzles.

specifies the pressure limits of each fluid because the utilized robot and surrounding components are not sealed against water and could be damaged. The chosen parameters enable a safe system operation for the tested stationary as well as for the prospective gripper integrated operation.

Table 1. Investigated parameter sets (pressure) and resulting mass flow depending on the parameter.

	Pressure [bar]		Mass flow	
Set	Water	Air	Water [l/min]	Air [m³/h]
1	0.7	1.1	1.6	8.58
2	0.7	1.35	1.02	10.03
3	0.7	1.6	0.7	11.2

Results

In order to compare the cooling performance of the spray cooling with that of the currently utilized immersion bath cooling, the heating process described above is carried out, and the temperatures at the defined measuring points (MS 1 - MS 4) are recorded. The temperature data at the individual points are already available from earlier tests for the immersion bath and serve as a reference. A step-like temperature gradient must be established in the component for spray cooling to be confirmed as a suitable cooling method that should be visible in the temperature curves of the individual measuring points. Furthermore, the aluminium must not exceed its melting point during heating, which would damage the component. Ideally, spray cooling should achieve the same temperature distribution in the component as immersion cooling.

Fig. 4 shows the temperature curve of the workpiece during heating, considering the different parameter sets. All three graphs show the same course, which indicates a good and equal connection in the joining zone, increasing the measurements' significance. If there were strongly deviating joining zone properties of the materials in the individual samples, this would lead to different heat conduction behavior, which would be reflected in the temperature curves. Further, in the curves of MS 2 and MS 3 in all three plots, there is a brief rise in the temperature after finishing the heating of 30 s. This is caused by removing the workpiece's thermocouples towards the end of the heating period. The two thermocouples are inserted in a drilling that leads straight through the steel to the joining zone. Consequently, the sensors pass through the hot steel when they are removed.

One essential factor for a successful forming process is the step-like temperature gradient. For this purpose, Fig. 5 summarizes the temperatures achieved for the corresponding parameter sets. The maximum temperatures during the process were determined for every repetition of each parameter set and measurement point. The first parameter set achieved the best cooling performance in the tests, while the highest air pressure (parameter set 3) resulted in the worst cooling performance. The lowest amount of water is sprayed through the nozzles with high air pressure, which explains the inferior cooling performance of parameter set 3. However, it should be noted that in parameter set 1 at measuring point 4, a strongly deviating maximum temperature occurred. Thermocouple displacement occurred by the spray was observed depending on the orientation of the drilling to the nozzles. The workpiece is manually placed in the induction coil, which causes the rotational orientation of the cylindrical workpiece could vary. Due to the possible displacement of the thermocouple, it experiences a different electric field through the induction coil, which can lead to a significant deviation [15]. Since the parameter sets investigated were restricted by external factors, the temperature gradient may be a local optimum, which would have to be investigated further. Nevertheless, it can already be seen that there is a correlation between the amount of water, the air pressure and the cooling power.

Materials Research Proceedings 28 (2023) 1083-1090 https://doi.org/10.21741/9781644902479-119

Currently, the process utilizes immersion for the thermal preparation, whereby the component reaches a temperature gradient sufficient for successful forming. Here, the temperature gradient serves as a comparison to demonstrate the applicability of spray cooling. Immersion cooling achieves a lower cooling performance, which the Leidenfrost effect can explain. In the experiments, the aluminium reaches temperatures of approx 110 °C, causing the water to boil and form a vapor phase. The steel also heats up and exceeds the 900 °C limit, which is ideal for steel forming. In the case of spray cooling, the steel side reaches approx 800 °C. The influence on the formability requires further investigation.

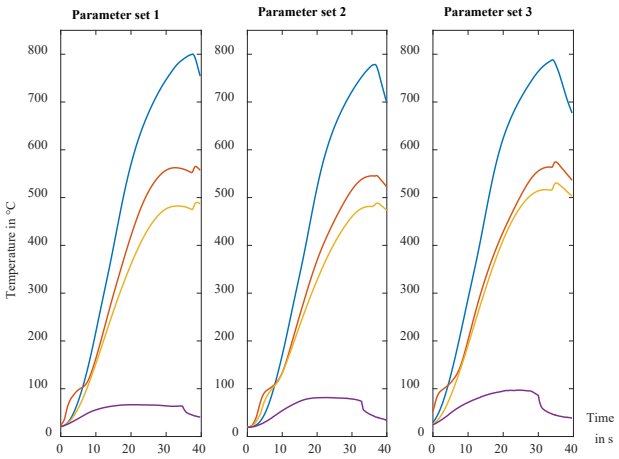

Fig. 4. Temperature in different measurement point (MS) during inductive heating and simultaneous spray cooling.

The cooling of the hybrid workpiece with spray nozzles compared to immersion bath cooling is more intensive. The parameters investigated also show that the cooling performance of the spray nozzles can be variably adjusted, which permits even more precise adjustment of the temperature gradient. Accordingly, it can be assumed that the spray nozzles are suitable for setting the temperature gradient.The results indicate that the necessary cooling performance can be achieved with the nozzles integrated into the handling equipment.

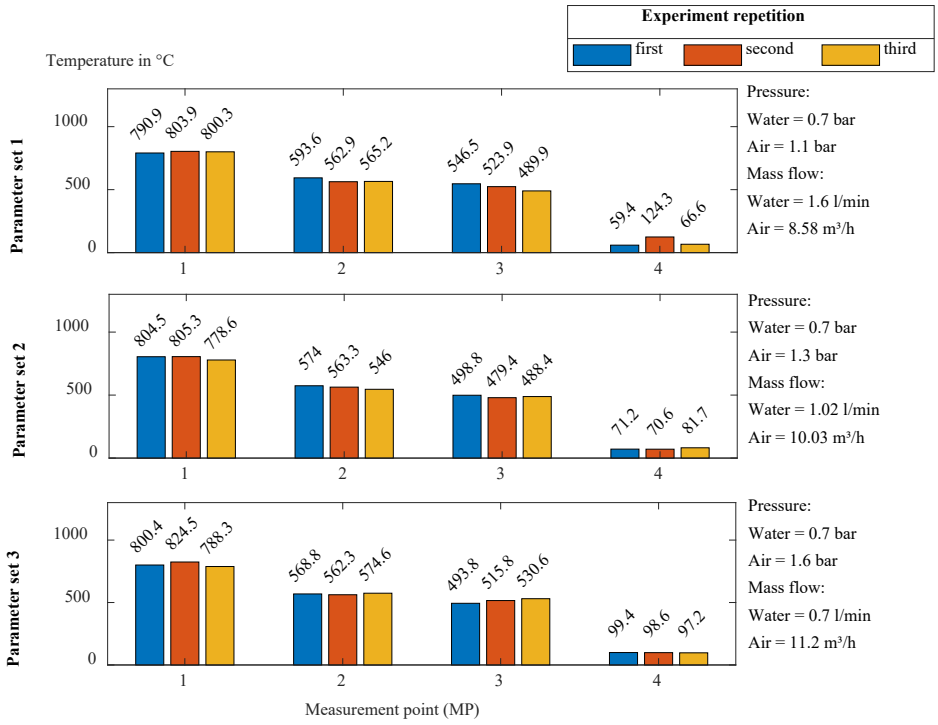

Fig. 5. Bar plot of the experimental results showing the maximal measured temperatures for each parameter set and repetition.

Summary

This paper aimed to validate spray nozzles for establishing a temperature gradient in a hybrid workpiece with a particular heating strategy compared to a currently used immersion bath. The nozzles have the advantage of being able to be integrated into the handling equipment and permit cooling during transport. With immersion cooling, no cooling can be performed during handling, which means that the temperature gradient due to equalization processes disappears.

For the validation, one manufacturing process for hybrid steel aluminium shafts was utilized. The workpiece attached with thermocouples is inductively heated at the steel side, while the aluminium side is cooled with the nozzles. The nozzles operate with compressed air and water, with the pressures of the two fluids as parameters. Three-parameter pairings were made, where the air pressure varies and the water pressure remains constant. The tests were subsequently performed with the corresponding settings. The results show that the mass flows of the two fluids primarily depend on the pressure of the compressed air. Furthermore, parameter combinations with a greater mass flow of water achieve a more effective cooling performance.

Finally, the performance of the nozzles with the best parameter set was compared against the currently used immersion bath cooling. As a result of the comparison, the semi-finished workpiece reached lower temperatures in both materials when cooled with nozzles. Thus, the nozzles can be used for this application, as the nozzle parameters allow a variable cooling performance, which can be further adjusted to approximate the immersion bath cooling.

Outlook

In the future, the parameter range of nozzle cooling must be investigated in more detail since only a small range could be investigated in this work. In these experiments, the forming should also be carried out so that the influence of the cooling capacity on the forming result can be tested simultaneously. Thereby, the effect of 100 °C lower temperature in the steel side on the forming can be investigated, since it is unclear to what extent this precisely influences the forming.

Another aspect to be examined is the nozzle's integration into the handling system and the robotized operation. The robot will be suited with the handling system to grasp the shaft, and the grasping position is essential because that surface cannot be cooled, whereby local heat spots can emerge and possibly damage the workpiece.

Acknowledgement

The results presented in this paper were obtained within the Collaborative Research Centre 1153 ’Process chain to produce hybrid high-performance components by Tailored Forming’ - 252662854 in subproject C07. The authors would like to thank the German Research Foundation (DFG) for the financial and organizational support of this project.

References

[1] P. Groche, S. Wohletz, M. Brenneis, C. Pabst, F. Resch, Joining by forming - a review on joint mechanisms, applications and future trends, J. Mater. Process. Technol. 214 (2014) 1972-1994. https://doi.org/10.1016/j.jmatprotec.2013.12.022

[2] J. Uhe, B.A. Behrens, Manufacturing of Hybrid Solid Components by Tailored Forming, in: J.P. Wulfsberg, W. Hintze, B.A. Behrens (Eds.), Production at the leading edge of technology, Springer Vieweg, Berlin, Heidelberg, 2019. https://doi.org/10.1007/978-3-662-60417-5_20

[3] B.-A. Behrens, K.-G. Kosch, Production of strong steel-aluminum composites by formation of intermetallic phases in compound forging, Steel Res. Int. 82 (2011) 1261-1265. https://doi.org/10.1002/srin.201100055

[4] B.-A. Behrens, H. Wester, S. Schäfer, C. Büdenbender, Modelling of an induction heating process and resulting material distribution of a hybrid semi-finished product after impact extrusion, ESAFORM 2021, Apr.2021. https://doi.org/10.25518/esaform21.574

[5] C.-V. Ince, A. Chugreeva, C. Böhm, F. Aldakheel, J. Uhe, P. Wriggers, B.-A. Behrens, A. Raatz, A design concept of active cooling for tailored forming workpieces during induction heating, Prod. Eng. 15 (2021) 177-186. https://doi.org/10.1007/s11740-021-01027-5
[6] C.-V. Ince, J. Geggier, C. Bruns, A. Raatz, Development of a form-flexible handling technology with active cooling for hybrid components in forging processes, Procedia CIRP 97 (2021) 27-32. https://doi.org/10.1016/j.procir.2020.05.200
[7] A. Buczek, T. Telejko, Investigation of heat transfer coefficient during quenching in various cooling agents, Int. J. Heat Fluid Flow 44 (2013) 358-364. https://doi.org/10.1016/j.ijheatfluidflow.2013.07.004
[8] M. Shirota, M.A.J. van Limbeek, C. Sun, A. Prosperetti, D. Lohse, Dynamic Leidenfrost Effect: Relevant Time and Length Scales, Phys. Rev. Lett. 116 (2016). https://doi.org/10.1103/PhysRevLett.116.064501
[9] P. Stephan, B1 fundamentals of heat transfer, in: VDI Heat Atlas, Springer Berlin Heidelberg, Berlin, Heidelberg, 2010, pp. 15–30. https://doi.org/10.1007/978-3-540-77877-6_115
[10] S. Schüttenberg, J. Lütjens, M. Hunkel, U. Fritsching, Adapted spray quenching for distortion control, Mat.-wiss. u. Werkstofftech. 43 (2012) 99-104. https://doi.org/10.1002/mawe.201100895
[11] I. Stewart, J.D. Massingham, J J. Hagers, Heat transfer coefficient effects on spray cooling, Iron Steel Eng. 73 (1996) 17-23.
[12] S. Herbst, K.-F. Steinke, H.J. Maier, A. Milenin, F. Nürnberger, Determination of heat transfer coefficients for complex spray cooling arrangements, in: International Conference on Distortion Engineering, Bremen, 2015, pp. 247–256.
[13] A. Pola, M. Gelfi, G.M. La Vecchia, Simulation and validation of spray quenching applied to heavy forgings, J. Mater. Process. Technol. 213 (2013) 2247-2253. https://doi.org/10.1016/j.jmatprotec.2013.06.019
[14] B.-A. Behrens, J. Uhe, T. Petersen, F. Nürnberger, C. Kahra, I. Ross, R. Laeger, Contact Geometry Modification of Friction-Welded Semi-Finished Products to Improve the Bonding of Hybrid Components, Metals 11 (2021) 115. https://doi.org/10.3390/met11010115
[15] A. Smalcerz, R. Przylucki, Impact of Electromagnetic Field upon Temperature Measurement of Induction Heated Charges, Int. J. Thermophys. 34 (2013) 667-679. https://doi.org/10.1007/s10765-013-1423-1

Materials Research Proceedings 28 (2023) 1091-1100 https://doi.org/10.21741/9781644902479-120

FSW process mechanics and resulting properties for dissimilar Al-Ti T-joints

RANA Harikrishna [1,a*], BUFFA Gianluca [1,b], FRATINI Livan [1,c]

[1]Department of Engineering, University of Palermo, Viale Delle Scienze, 90128 Palermo, Italy

[a]hairkrishnasinh.rana@unipa.it, [b]gianluca.buffa@unipa.it, [c]livan.fratini@unipa.it

Keywords: FSW, T-Joint, Dissimilar, Skin, Stringer, Titanium, Aluminum, Material Flow

Abstract. Emergent manufacturing demands for superior performance but lightweight structures have pinpointed the development of multi-material and hybrid structures specifically in the aerospace and automotive industrial sectors. Friction stir welding (FSW), a solid-state joining technique has been proven very effective to produce joints between materials possessing extremely diverse thermal and mechanical properties. The present research aims to investigate the feasibility of Al-Ti skin-stringer joints with different plate geometries and placements. The effect of different approaches on material flow, grain morphology, intermittent phases, joint resistance, and microhardness are discussed in depth.

Introduction

Multi-material components are enticing recognition for their unique application base catering to automotive, aerospace, and transportation industries. Multi-material components not only present the unique benefits of demonstrating the properties of the individual materials but their advantages as a union too. The joining between titanium(Ti) and aluminum(Al) can be proposed for numerous applications in aeronautic and automotive sectors, wherein the higher strength-to-weight ratio is crucial in terms of body weight reduction and fuel savings. Conventional thermo-fusion joining techniques struggle with metallurgical challenges owing to a substantial disparity in physical properties, inadequate mutual solubility, and formation of brittle intermetallics (IMCs) [1,2].

The solid-state welding process was adopted into Al-Ti dissimilar joining and had been proven to be an efficacious technology by a few works of literature [3,4]. However, the formation of brittle IMCs like $TiAl_3$, $TiAl_2$, TiAl, Ti_3Al, Ti_2Al_5, $TiAl_2$, and Ti_2Al_5 was difficult to control during the welding. Alternatively, FSW has been proven to be an efficient process to eradicate the formation of IMCs up to a certain extent as compared to other solid-state welding processes [3,5,6]. This technique has been efficient to produce extremely arduous dissimilar welding joints owing to its less heat input feature. Moreover, with an innovative approach to in-process cooling Patel et al. [3] have reported a considerable decrease in the quantity of IMCs, which increased joint efficiency. To date, numerous investigations featuring butt and lap configuration joints with different process parameters have been reported [7-9]. According to these studies, the IMC layer thickness can be downed up to 2µm with a proper set of FSW parameters. Moreover, from the literature mentioned, the ideal range for revolutionary pitch (RP) during FSW with butt configuration joints was 0.05-0.10 which delivered 80-110% joint efficiency [7,9,10]. Apart from common process parameters like tool rotation speed (TRS), tool traverse speed (TTS), tool tilt angle, etc. Li et al.[8] experimented with the tool offset and reported the turbulent material flow in the nugget zone (NZ) during FSW with an increase in tool offset and a decrease in RP. However, vortex material flow is desirable during FSW as it distributes the fine Ti particle in Al substrates and makes a uniform composite structure delivering enhanced properties[3]. A few investigations have reported the reduction in the IMCs by using a thin interlayer during the FSW of Al-Ti butt configuration joints. The interlayer alloy having the higher affinity to the substrate withholds the formation of brittle IMCs, ensuing enhanced properties of the prepared joints [11]. Yet, Al-Ti "T" configuration joints

Content from this work may be used under the terms of the Creative Commons Attribution 3.0 license. Any further distribution of this work must maintain attribution to the author(s) and the title of the work, journal citation and DOI. Published under license by Materials Research Forum LLC.

produced by FSW have not been reported in the literature (except one reported by own research group) as per author's best knowledge owing to the complexities involved.

The literature survey discussed to the point indicates a lack of literature available in the field of Al-Ti "T" configuration FSW joints despite having a huge potential and promising sectors to explore. The objective of the present investigation is to produce successful Al-Ti "T" configuration FSW joints experimenting with parameters including substrate plate position swap and geometrical features. The influence of these variables on the mechanical and microstructural features like joint strength, microhardness, and IMCs distribution is studied in detail. This investigation is an extension of the work carried out by authors elaborating on the influences of several FSW parameters like TRS, TTS, and material positioning as skin/stringer[12].

Materials and Procedure

Materials and Process.

Substrates of aluminum alloy 6156 (Si 1 wt.%, Mg 0.9 wt.%, Cu 0.9 wt.%, Fe 0.1 wt.%, Mn 0.55 wt.%, Cr 0.125 wt.%, Zn 0.4 wt.%, Al – bal) and commercially pure titanium grade 2 with plate dimensions 140 × 90 × 3 mm and 140 × 90 × 2 mm respectively were used for experiments. A fully automatic FSW machine (Make: ESAB, Model: LEGIO 3ST) was used for conducting the experiments. An experimental setup with fixture and tool is displayed in Fig.s 1(a) and (b). Each experiment was conducted with position control mode and using a push roller on the leading edge of the Tungsten-Rhenium conical tool to ensure uniform contact conditions and plunge. TRS and TTS were chosen from the best welding conditions derived from the authors' recent publication [12]. The experiments were repeated thrice with each processing condition to ensure the credibility of the results. To understand the effect of slots in the skin, specimens were prepared with three different slot depths of 0 mm, 0.5mm and 1 mm longitudinally. Table 1 summarises each parametric condition with its unique experiment ID.

Table 1. Parametric sets with relative specimen IDs.

Specimen ID	**A**	**B**	**C**	**D**	**E**	**F**	**G**	**H**	**I**
Skin Material	**Titanium Grade 2**			**Al 6156**					
Skin Slot Depth [mm]	**0**	**0.5**	**1**	**0**	**0.5**	**1**	**0**	**0.5**	**1**
Tool Feed, F [mm min^{-1}]	40			50			70		
Tool Rotation Speed [rev. min^{-1}]	400			800			1000		
Tool Tilt Angle	2.5°								

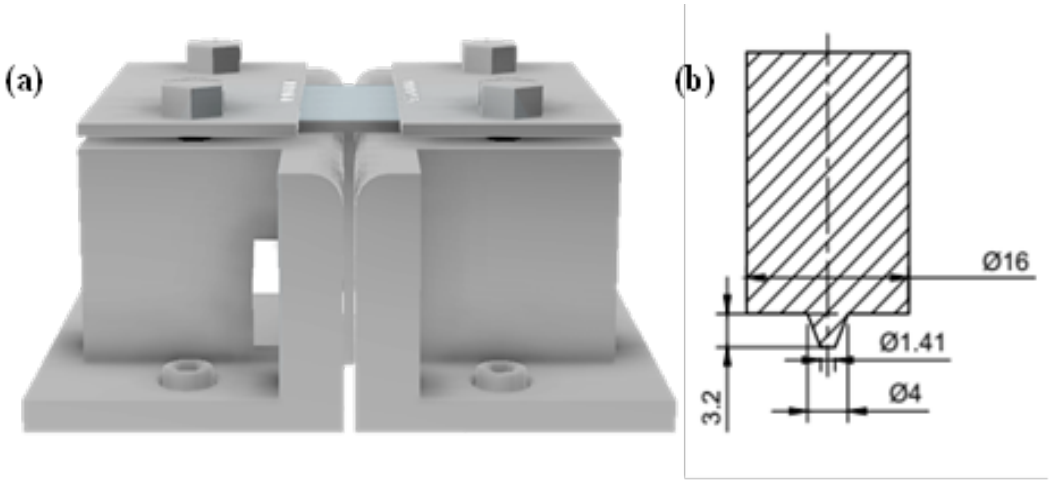

Fig. 1. Experimental setup (a) T-joint custom-designed fixture (b) WC-Re FSW tool geometry.

Microstructural Characterization

The specimens for microstructural examinations were obtained by sectioning at the center of the weld. They were further mounted, ground, and polished finally with 0.5µm diamond paste. Each joint specimen was etched with Keller's reagent (HF 2% vol. + HCL 3% vol. + HNO_3 5% vol. + H_2O 90% vol.) for the AA 6156 section and Kroll's reagent (HF 3% vol. + HNO_3 5% vol. + H_2O 90% vol.) for Ti Grade 2 section. Further, microstructural characterization was carried out through optical microscopy (OM) (OLYMPUS, Model-Inverted Metallurgical Microscope GX51), scanning electron microscopy (SEM), and energy dispersive spectroscopy (EDS) (Make: Zeiss, Model: Ultra-55 SEM).

Hardness and Tensile Testing

Each joint specimen was examined for microhardness using Eseway 4302 Vickers hardness tester (according to ASTM E-384). A square-based pyramid diamond indenter (136^o intersects) was employed for tests with load and dwell time of 5 kg and 15 seconds, respectively. A specially designed fixture as displayed in Fig. 2 was used for conducting T- pull tests on a conventional tensile testing machine with a velocity of 2 mm/minute. The fractured specimens were further examined by SEM fractographic analysis.

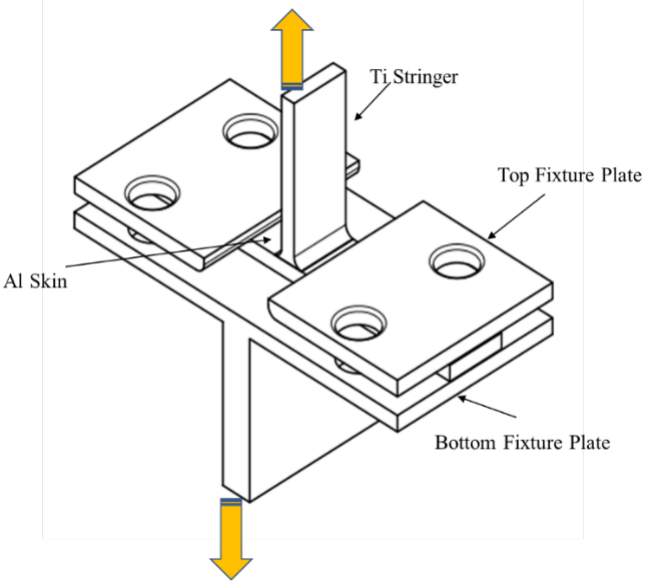

Fig. 2. Schematic of T-pull test fixture.

Results & Discussion

Macro- and Microstructural Analysis

Macrostructural insights.

Macrostructural images of T-joint specimens prepared with Al and Ti as skin and stringer alternatively are displayed in Fig. 4 and Fig. 5. The macrostructure was characterized by very distinctive featured flow arms of different materials and dimensions. These arms are generated by distinctive material flow patterns recorded with varied slot sizes and welding conditions. The size of the flow arm greatly influences the resulting properties owing to the skin/stringer material interlocking. During FSW of T-joints, as soon as the rotating tool pin penetrates the stringer material, it pushes the material underneath the tool to get extruded in the opposite direction, being constrained by the surrounding skin material. Simultaneously, the skin material flows downwards to the sides of the stringer material. As a result, engendered flow arms can be noticed in the vicinity of the thermo-mechanically affected zone (TMAZ) area as schematically represented in Fig.s 6 (a) and (b). Chen et al [13] have reported and corroborated the matching phenomenon of "extruded hook" during the FSW of Al-Ti lap joint configurations. The specific thermal contribution (STC) ensuing from distinct RP majorly contributes to the size of this flow arm, too.

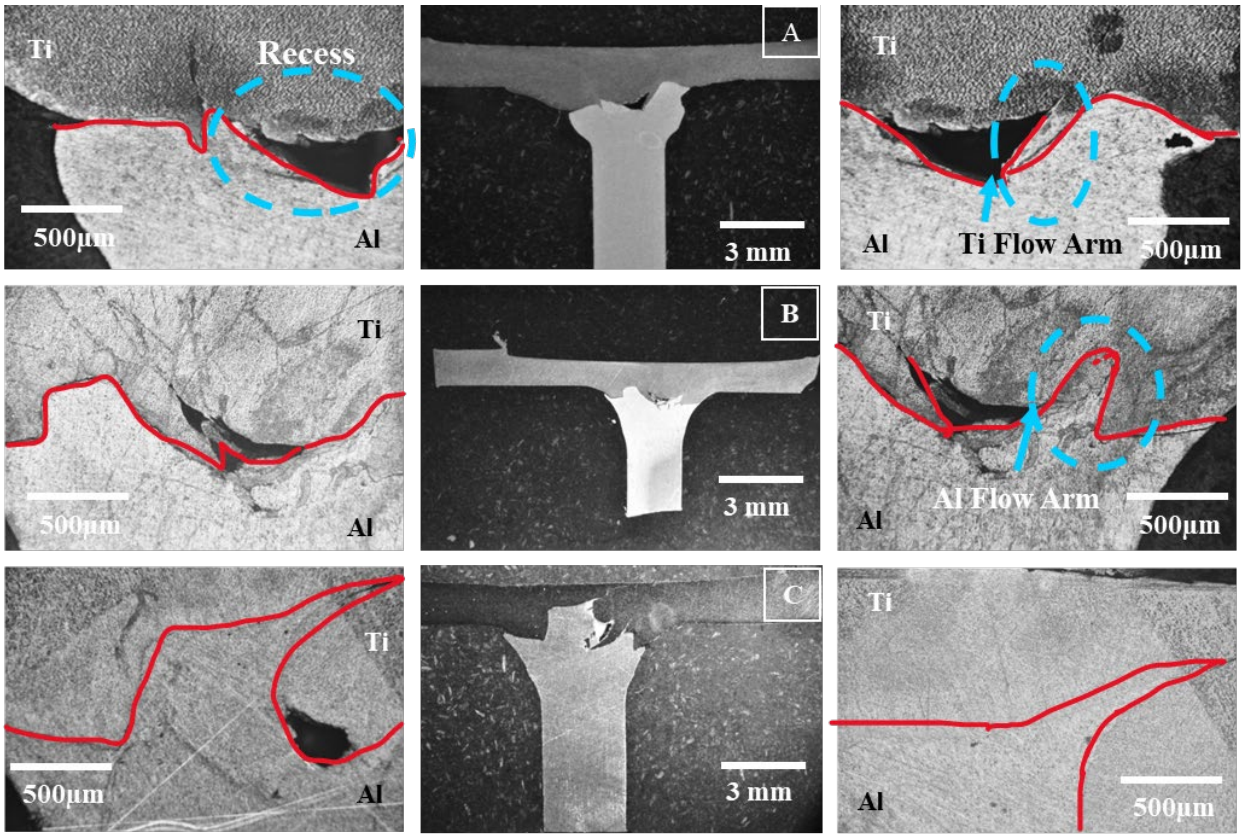

Fig. 4. Macrostructures of Ti skin Al stringer T-joints prepared with the skin-slot depth of (A) 0 mm (B) 0.5 mm (C) 1 mm.

As indicated earlier in the introduction section, FSW parameters were finalized using the author's previous publication. Ti skin/Al stringer samples were prepared with TRS and TTS of 400 rev. min^{-1} and 40 mm min^{-1}. However, the microstructure of this sample was characterized by a recess defect in the NZ. Such defects incurred owing to a huge property mismatch between skin and stringer materials, making it extremely challenging to get a synchronized material in the NZ. The flow stress at room temperature for Al is ¼ of the Ti, making Al soften in the advanced stage

of the FSW stirring, while Ti resists the deformation. Although such mismatch can be minimized at elevated temperatures with a low RP value parametric set, it is not possible to eradicate. Hence, to minimize the flow resistance of the Ti skin material a novel strategy proposing a longitudinal slot in the skin was experimented as schematically exhibited in Fig. 6(c). Therefrom, the samples with 2 longitudinal slots with depths of 0.5 mm and 1 mm were milled prior to the FSW. The slot width was kept equal to the stringer plate thickness. It was believed that the slot shall not only reduce the volume of the Ti material to be deformed and stirred but increase the flow arm size as indicated schematically in Fig. 6(c). The micrographs of the Ti skin samples welded with the 0.5 mm and 1 mm slot depth are displayed in Fig. 4(B) and (C) respectively. As the proposed strategy, the tool pin not only minimized the recess defect size in NZ up to a great extent but allowed the Al flow arm to penetrate the Ti skin material. Still, it was not possible to omit the recess/pocket in the NZ completely. Moreover, the small Ti flow arms engendered by tool-driven extrusion were also identified in these samples indicating the greater softening of the Ti skin. The flow arm interlocking was also visible in these samples.

Nevertheless, the material flow that happened in the Al skin samples was quite different than in Ti skin and it was possible to extract a few defect-free samples at different processing conditions. As far as the Al skin samples are concerned, these samples were characterized by the longer Ti flow arm penetrating the Al skin as displayed in Fig. 5. As discussed in the preceding work, with a decrease and increase in the RP and STC values respectively the flow arm length was reportedly increased delivering the best joint strength. Therefrom, to further increase the flow arm size, a slot design was proposed. As the proposed strategy, the Ti flow arm size was drastically increased with the greater tool-driven extrusion. However, at the same time the larger extent of the extrusion created a larger void to fill in between two Ti flow arms ensuing into the recess/pocket in each sample prepared with slot (see Fig. 5 (E), (F), (H) and (I)). As mentioned earlier, the profile of this stringer arm is quite important for an interlocking mechanism during the T-pull test. It was observed that, while on one hand its vertical alignment (perpendicular to the skin), creates the least disturbance to material momentum while stirring, on the other hand, the horizontal alignment barricades the material flow toward the center and results in recess/pocket defects[9]. It is worth noticing that the flow arm length grows in the vertical direction with slot depth, but once it crosses a threshold value it starts bending towards the center of the weld as schematically represented in Fig. 7. This can be explained as when the slot depth is increased the shoulder rotates closer to the extruded stringer arm, engendering tremendous pressure on the stirring material, which bends the flow arm in the plane parallel to the shoulder face as visible in specimens F and I. This Ti flow arm boundary barricades the skin material to flow toward the center of NZ leaving back unfilled voids. Hence, as far as the slot depth is concerned the joints prepared with 0.5 mm slot exhibited longer and vertically aligned flow arms compared to others.

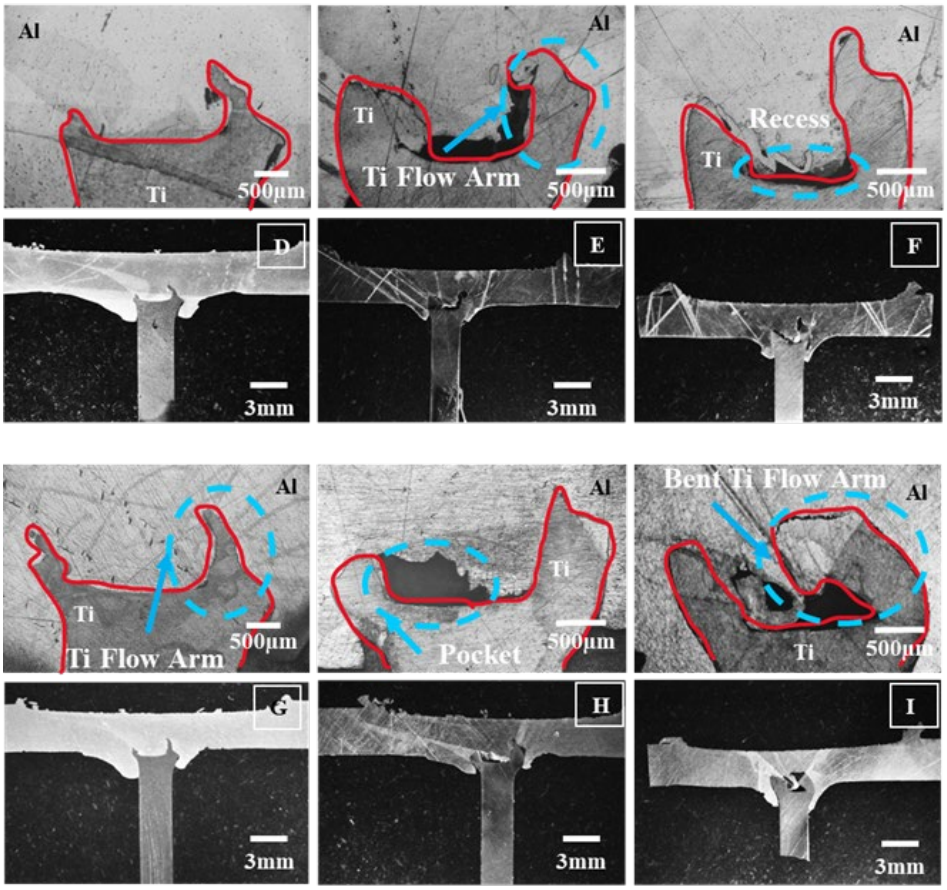

Fig. 5. Macrostructures of Al skin Ti stringer T-joints prepared with slot depth, TRS, and TTS of (D) 0 mm, 800 rev. min^{-1},50 mm min^{-1} (E) 0.5 mm, 800 rev. min^{-1},50 mm min^{-1} (F) 1 mm, 800 rev. min^{-1},50 mm min^{-1} (D) 0 mm, 1000 rev. min^{-1}, 70 mm min^{-1} (E) 0.5 mm, 1000 rev. min^{-1}, 70 mm min^{-1} (F) 1 mm, 1000 rev. min^{-1}, 70 mm min^{-1}.

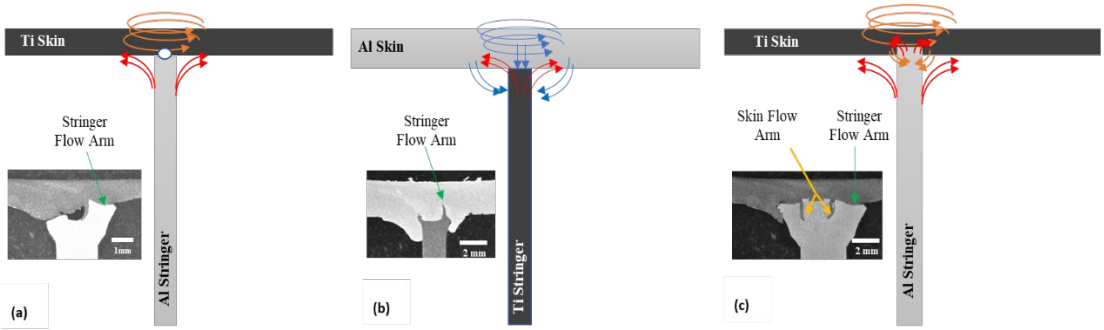

Fig. 6. Schematic exhibits for proposed material flow phenomenon in (a) Ti skin Al stringer (b) Al skin Ti stringer (c) proposed Ti skin with slot Al stringer.

Apart, defects like skin thinning and kissing bonds were also observed in the few samples (viz., B, C, H, I). Kissing bonds are reportedly formed either when the substrate materials are extremely asymmetric or they are inadequately heated and stirred. This eventually promotes the formation of residual oxide layers (e.g. TiO_2 in the present investigation) detached from the other substrate [14]. These layers wane the material attachment and raise the localized stresses during weld solidification. Especially for T-joint configuration, as the tool pin rotation plane is parallel to the joint interface, it becomes difficult to slash these oxide layers [12].

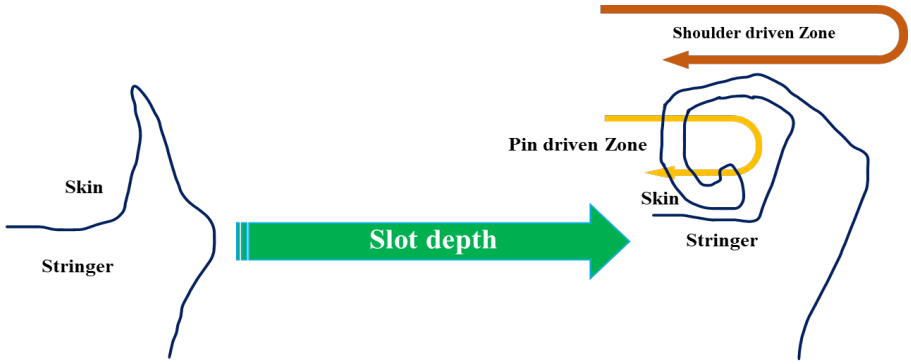

Fig. 7. Schematic representation of change in stringer flow arm profile concerning slot depth.

Microstructural insights.

The SEM and EDS mapping were carried out for the samples with no skin slot and maximum slot depth viz., G and F respectively. The mapping indicated the composite structure near the extruded Ti flow arm for both samples as displayed in Fig. 8. During FSW, when the extruded Ti stringer flow arm reaches the threshold length value, it starts interacting with the rotating shoulder. Further, the Ti flow arm experiences grinding led by the shoulder, leaving fine Ti particles in the vicinity of the flow arm. Rostami et al.[7] have reported the identical occurrence of the composite structure close to the Ti hook profile generated during FSW of Al-Ti lap joints.

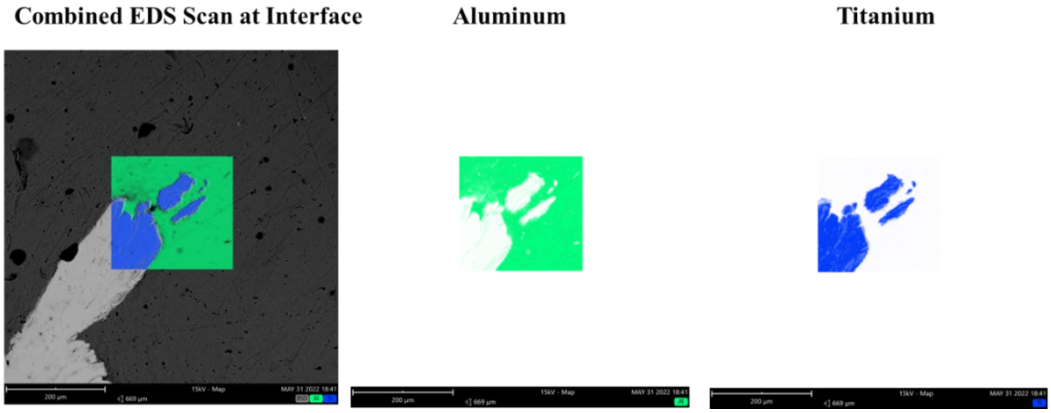

Fig. 8. SEM-EDS mapping of the composite structure near the Ti Flow Arm.

Moreover, the obtained results during the SEM-EDS analysis indicated a very thin and intermittent layer of $TiAl_3$ intermetallic close to the Al-Ti interface as exhibited in Fig. 9. It is noteworthy that the IMC layer thickness ranged from ~ 1 µm to 5 µm, which may be believed to be very lean considering the observed thickness for FSW butt and lap configuration joints [10, 13]. However, a thicker IMC layer was identified in the vicinity of the extruded Ti flow arm. This variable layer thickness at different locations may be understood by the successive events taking place while FSW. On the one side, when the rotating plunges adjacent to the Al-Ti interface, owing to softening of the Al skin led by high frictional heat, the Ti face is pressed downward and extruded as a flow arm leaving an unfilled void. This void remains empty until the tool progress along the joint line and stirring Al enters at the back of the tool.

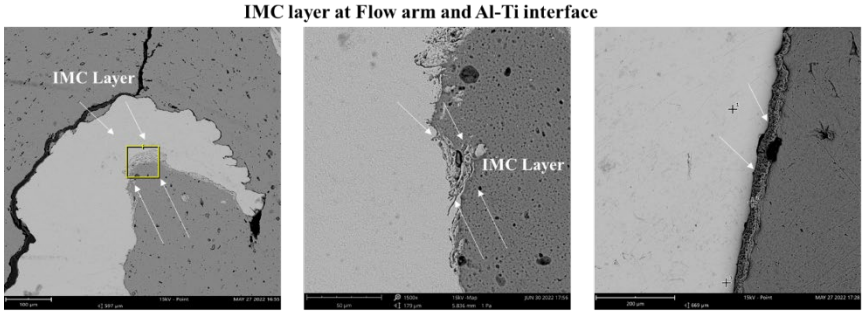

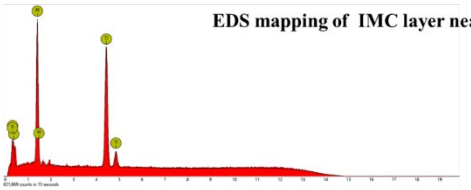

Element Symbol	Atomic Conc.	Weight Conc.	Oxide Symbol	Stoich. Wt.% Conc.
Al	69.11	55.78	Al_2O_3	58.83
Ti	30.89	44.22	TiO_2	41.17

Fig. 9. SEM/EDS mapping of Intermetallic Layer at Al-Ti interface and near the extruded Ti flow arm.

However, by the time Al fills the void completely, the temperatures of both Al and Ti are slightly dropped to a level at which the occurrence of Al-Ti diffusion is very minimal. While of the other side, when the extruded Ti flow arm penetrates Al, the temperatures of both substrates are elevated, leading to the Al-Ti diffusion and formation of a thick layer of IMC. The prevalent IMC phase identified in the NZ was $TiAl_3$. The mechanical properties of the prepared FSW joints are greatly influenced by the location, size, and amount of such IMCs.

Mechanical Properties

The joint strengths observed with T-pull test of all the samples are graphically displayed in Fig. 10. Concerning Ti skin samples, they were characterized by a moderate joint strength, which can be attributed to defects like porosity, recess, etc., and lack of appropriate flow arm interlocking phenomenon. Although the slots allowed the Al flow arm to enter into the Ti skin, there was a lack of proper interlocking. Still, a slight improvement in the joint strength can be observed for the samples prepared with the skin slots. While concerning the Al skin samples, the highest joint strengths of 146 MPa and 144 MPa were observed for sample G and sample D, respectively which were prepared without any skin slot. Although T-joints created with skin slots demonstrated longer extruded flow arms, they were characterized by recess and unfilled cavity defects as described earlier in section 3.1. Alternatively, quite comparable strength of 107 MPa was recorded with the sample I which was prepared with 1 mm slot depth. While comparing the performance of the slot depth in terms of joint strength, the deeper skin slot of 1 mm exhibited considerably superior results which can be attributed to the longer flow arm accompanied by the superior flow arm interlocking with skin in the NZ.

As far as the hardness results are concerned, the substrate materials Ti grade 2 and AA 6156 exhibited a hardness of 115 HV and 40 HV respectively. The hardness values recorded in the NZ of sample G were almost 50 % higher than the unprocessed substrate. The increased hardness values can be attributed to the Al-Ti composite structure, grain refinement, and IMCs present in the NZ of the welded samples [3,15,16]. Such rise in the hardness values can be backed by several strengthening mechanisms viz., shear lag mechanism and dislocation strengthening mechanism. According to the shear lag mechanism, as NZ is characterized by Ti particulate composite structure, during testing when the specimen is loaded the load is transferred from the Al matrix to very hard Ti particulates. The shear stress is generated at the Al-Ti interface due to this load shift, which eventually hinders the dislocation motion and ensures higher properties. As per dislocation

strengthening, owing to a large mismatch of coefficient of thermal expansion between two substrates, geometrically indispensable dislocations are engendered at the Al/Ti interface and in the vicinity to the Ti particulates and IMCs, during the cooling period post-thermos-plastic deformation led by FSW. These dislocations impede crack growth and thereby increase joint strength and hardness. In the nutshell, the T-joints prepared with FSW not only exhibited the metallurgical bonding but the mechanically interlocked bonding too which promises an effective approach for the production of dissimilar material T-joints.

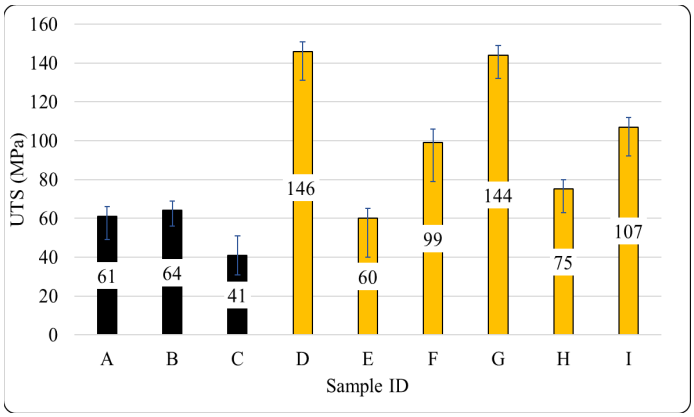

Fig. 10. Joint strength for Ti and Al skin samples.

Summary

This novel investigation describes the successful fabrication of dissimilar T-joints using Ti Gr 2 and AA6156 substrates, wherein the effects of mutual sheet position and innovative skin slot design on macrostructural, microstructural, and mechanical properties of the joints have been discussed in depth. The obtained conclusions are as under:

- AA 6156 substrate skin samples displayed substantially better properties than Ti substrate skin samples.
- The dissimilar material T-joint was characterized by interesting material flow patterns. Particularly, the development and geometry of the extruded flow arm were found to be crucial for mechanical interlocking resulting in improved joint strength. The length of this flow arm is directly proportional to the amount of heat input during the process and skin-slot depth. However, too large values of any of them can bend the flow arm which hinders the appropriate material flow leaving behind defects like cavities, recess, etc, and eventually reducing the mechanical properties.
- The samples produced without skin-slot exhibited superior joint strength as compared to skin-slot samples, owing to the formation of the defects like cavities and recesses in skin-slot samples. However, samples joined with a maximum slot depth of 1 mm exhibited superior joint strength as compared to 0.5 mm slot depth, owing to better mechanical interlocking of the flow arm with Al skin substrate.
- The hardness values of prepared T-joints were improved by 50% and 20% as compared to the unprocessed Al skin substrate and Ti stringer. Such an increase can be attributed to the Ti-particulate composite structure, grain refinement, and IMCs-led strengthening mechanisms.

References

[1] W. Vaidya, M. Horstmann, V. Ventzke, B. Petrovski, M. Koçak, R. Kocik, G. Tempus, Improving interfacial properties of a laser beam welded dissimilar joint of aluminium AA6056 and titanium Ti6Al4V for aeronautical applications, J. Mater. Sci. 45 (2010) 6242-6254. https://doi.org/10.1007/s10853-010-4719-6

[2] W. Shouzheng, L. Yajiang, W. Juan, L. Kun, Research on cracking initiation and propagation near Ti/Al interface during TIG welding of titanium to aluminum, Kovove Mater. 52 (2014) 85-91. http://doi.org/10.4149/km2014285
[3] P. Patel, H. Rana, V. Badheka, V. Patel, W. Li, Effect of active heating and cooling on microstructure and mechanical properties of friction stir–welded dissimilar aluminium alloy and titanium butt joints, Weld World 64 (2020) 365-378. https://doi.org/10.1007/s40194-019-00838-6
[4] Y.-C. Kim, A. Fuji, Factors dominating joint characteristics in Ti–Al friction welds, Sci. Technol. Weld. Join. 7 (2002) 149-154.
[5] L. Fratini, G. Buffa, L.L. Monaco, Improved FE model for simulation of friction stir welding of different materials, Sci. Technol. Weld. Join. 15(3) (2010) 199-207.
[6] A. Simar, M.-N. Avettand-Fènoël, State of the art about dissimilar metal friction stir welding, Sci. Technol. Weld. Join. 22(5) (2017) 389-403. https://doi.org/10.1080/13621718.2016.1251712
[7] H. Rostami, S. Nourouzi, H.J. Aval, Analysis of welding parameters effects on microstructural and mechanical properties of Ti6Al4V and AA5052 dissimilar joint, J. Mech. Sci 32 (2018) 3371-3377. https://doi.org/10.1007/s12206-018-0640-8
[8] B. Li, Z. Zhang, Y. Shen, W. Hu, L. Luo, Dissimilar friction stir welding of Ti–6Al–4V alloy and aluminum alloy employing a modified butt joint configuration: Influences of process variables on the weld interfaces and tensile properties, Mater. Des 53 (2014) 838-848. http://doi.org/10.1016/j.matdes.2013.07.019
[9] A. Kar, S. Suwas, S.V. Kailas, Multi-length scale characterization of microstructure evolution and its consequence on mechanical properties in dissimilar friction stir welding of titanium to aluminum, Metall. Mater. Trans. A 50 (2019) 5153-5173.
[10] Z. Ma, X. Sun, S. Ji, Y. Wang, Y. Yue, Influences of ultrasonic on friction stir welding of Al/Ti dissimilar alloys under different welding conditions, Int. J. Adv. Manuf. Technol. 112 (2021) 2573-2582. https://doi.org/10.1007/s00170-020-06481-6
[11] A. Kar, S.K. Choudhury, S. Suwas, S.V. Kailas, Effect of niobium interlayer in dissimilar friction stir welding of aluminum to titanium, Mater. Charact. 145 (2018) 402-412. http://doi.org/10.1016/j.matchar.2018.09.007
[12] H. Rana, D. Campanella, G. Buffa, L. Fratini, Dissimilar titanium-aluminum skin-stringer joints by FSW: process mechanics and performance, Mater. Manuf. Process. 38 (2023) 471-484. https://doi.org/10.1080/10426914.2022.2116044
[13] Y. Chen, C. Liu, G. Liu, Study on the joining of titanium and aluminum dissimilar alloys by friction stir welding, Open Mater. Sci. 5 (2011). http://doi.org/10.2174/1874088X01105010256
[14] Y. Su, W. Li, F. Gao, A. Vairis, Effect of FSW process on anisotropic of titanium alloy T-joint, Mater. Manuf. Process. 37 (2022) 25-33. https://doi.org/10.1080/10426914.2021.1942911
[15] H. Rana, V. Badheka, A. Kumar, A. Satyaprasad, Strategical parametric investigation on manufacturing of Al–Mg–Zn–Cu alloy surface composites using FSP, Mater. Manuf. Process. 33 (2018) 534-545. https://doi.org/10.1080/10426914.2017.1364752
[16] E. Lertora, C. Mandolfino, C. Gambaro, Effect of welding parameters on AA8090 Al-Li alloy FSW T-joints, Key Eng. Mater. 554c(2013) 985-995. http://doi.org/10.4028/www.scientific.net/KEM.554-557.985

Materials Research Proceedings 28 (2023) 1101-1110 https://doi.org/10.21741/9781644902479-121

Influence of process parameters on mechanical properties of lamination stacks produced by interlocking

MARTIN Daniel Michael[1,a *], KUBIK Christian[1,b], KRÜGER Martin[1,c] and GROCHE Peter[1,d]

[1]Technical University of Darmstadt, Institute for Production Engineering and Forming Machines, Otto-Berndt-Straße 2, 64287 Darmstadt, Germany

[a]daniel.martin@ptu.tu-darmstadt.de, [b]kubik@ptu.tu-darmstadt.de, [c]martin@apo-wetzlar.de, [d]peter.groche@ptu.tu-darmstadt.de

Keywords: Interlocking, Lamination Stacks, Electrical Steel

Abstract. Interlocking is mainly used in the manufacture of lamination stacks for the cores for electrical energy converters. The process involves the embossing of nubs, which are subsequently stacked and joined by an interference fit. For an optimal design of interlocked joints, sufficient knowledge of the relationships between various influencing parameters in the manufacture and the resulting stack properties is essential. In addition to the design parameters nub geometry, size and embossing depth, the process parameters embossing clearance, counterpunch and blankholder force influence the joint strength. In addition to these fixed parameters, continuously varying uncertainty such as wear, which can lead to a rounding of the tool edges, affects relevant stack properties like the joint strength. The mechanical loads in the area of the tool edge which are responsible for this rounding mainly act immediately before material separation and have to be considered in the embossing process. However, the influence of punch edge radii on the joint properties during the interlocking process has not yet been investigated. In order to describe the interdependencies between different influencing parameters on the achievable mechanical strength, experimental investigations are carried out. Therefore, cylindrical nubs are interlocked with varying embossing depth, clearance and edge radii. The joint strength is determined via tensile tests. Key findings are that the joint strength of nubs with increasing abrasive wear on the cutting edge of the embossing tool are compensated by a higher embossing depth. The minimum embossing depth required for stacking and the embossing depth at which the optimum strength is achieved depend on the embossing edge radius and thus on the current abrasive wear state.

Introduction

Interlocking is a process for manufacturing iron cores in the stators and rotors of electric motors. These are assembled from thin sheets that are electrically insulated from each other in order to minimise iron losses. To build up a lamination stack, interlocking nubs are introduced into the sheets by an embossing operation and then pressed into each other, creating a force-fit joint. For electrical insulation, the sheets are coated in advance. Various coating materials are used for this purpose, which are classified according to their chemical composition, insulating capacity and the area of application [1]. Common coating types are organic coatings of type C3 and the completely or predominantly inorganic C5 coatings. C3 coatings can contribute to an improvement in punchability compared to uncoated materials. The same applies for C5 coatings depending on the fillers and additives. Therefore, both are in principle suitable for use in punch-stacked components [2]. Since the working principle of interlocking is based on friction and is therefore dependent on the tribological conditions, the choice of the coating material potentially influences the joint quality.

Fig. 1(a) shows the schematic sequence of the punch-stacking process chain consisting of punching, embossing and stacking. For use in electric drives, both the magnetic and the mechanical

Content from this work may be used under the terms of the Creative Commons Attribution 3.0 license. Any further distribution of this work must maintain attribution to the author(s) and the title of the work, journal citation and DOI. Published under license by Materials Research Forum LLC.

Materials Research Proceedings 28 (2023) 1101-1110 https://doi.org/10.21741/9781644902479-121

properties (joint strength) have to be taken into account when designing interlocked lamination stacks. In order to achieve a high torque density and low power losses, the magnetic properties must be optimised and additional losses caused by the manufacturing process minimised [3].

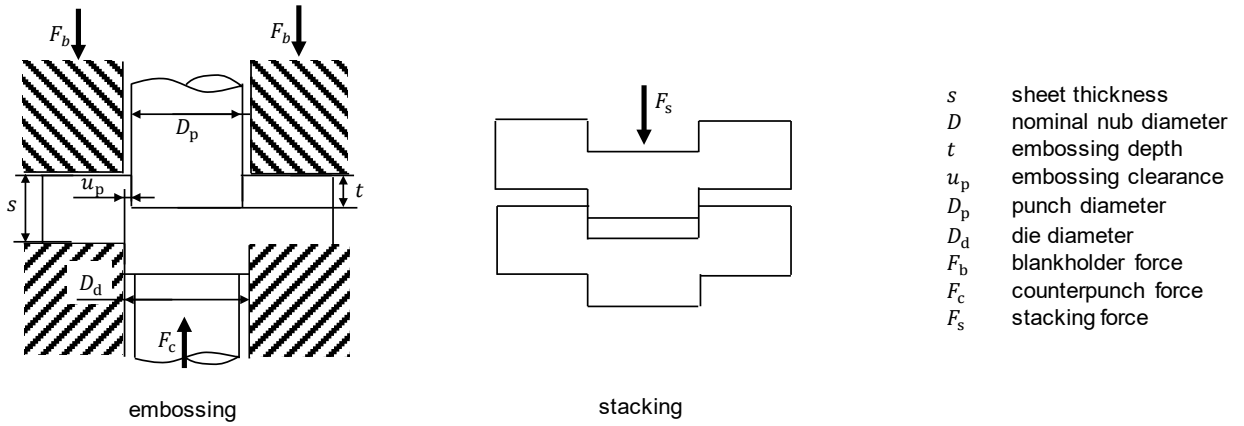

Fig. 1. Schematic illustration of the interlocking process chain.

From a mechanical point of view, the joint strength between the sheet metal lamellae plays a decisive role. To ensure a reliable connection of the lamination stacks in the subsequent assembly steps, a minimum strength is required for robust process handling. The resulting strength of the punch-stacked joint depends on a complex interaction of a multitude of parameters. The geometry, position and number of nubs as well as the material properties (sheet thickness, alloy combination, coating material) are determined during product design of the electric drive. Parameters such as the embossing clearance, the blankholder and counterpunch force as well as the stacking force are determined by the tool design and can be varied within a specific range. The tool parameter embossing clearance and the process parameter embossing depth have been shown to have the greatest influence on the joint strength in previous investigations [4,5]. As an uncontrollable parameter, wear causes alterations in the tool configuration and thus directly affects the mechanical properties of the embossed nubs. Since the embossing process is a punching process that is stopped just before cracks are initialized into the material, wear on the edge of the embossing tool plays an important role.

From the literature it is known that the so-called punch phase in which the blanking tool separates the products from the sheet metal strip causes abrasive wear on the cutting edge of the tool [6]. This abrasive wear is influenced by the acting contact normal stresses, which correlate with the maximal punch force $F_{\max}$. The maximal punch force is defined as the cutting force $F_{\max} = l \cdot s \cdot k_s$, with the cutting line l, the sheet thickness s and the shear strength shear strength k_s, according to Lange [7]. The shear strength depends on a various number of variables such as tool parameters (clearance, tool wear, surface conditions of the active elements), material parameters (tensile strength, elongation at break, alloy composition) and other process parameters (lubrication, temperature, cutting speed) [8].

Due to high accuracy requirements in the cutting step and the influence of the embossing gap on the joint strength, very small clearances between punch and die are selected for both the cutting step and the embossing step in interlocking, which leads to high contact normal stresses and promotes the occurrence of abrasive wear. As mentioned above the embossing step corresponds to a shear cutting process in which the slug is not sheared off completely until it breaks, but remains connected to the base sheet due to a sufficiently small immersion depth of the punch. Because the maximum force occurs shortly before the material fails by tearing off the slug, it can be assumed

that only abrasive wear in the form of rounding of the punch edge has to be considered. Further wear phenomena such as adhesions, scratches and chipping are found on the lateral surface and can be neglected during the embossing process. Literature in area of shear cutting demonstrates that abrasive wear directly affects the properties of the manufactured part.

Former studies prove that the occurring tool wear plays a significant role in the shear cutting of electrical sheet and can also have an effect on the magnetic properties [9,10] in addition to the influence on the mechanical properties and the cutting contour [10,11]. Although this correlation for punching tools is present in recent studies, abrasive wear on embossing tools and its effect on the stack properties have not yet been investigated.

An established method of monitoring the wear condition of punching tools is the measuring of force signals during the process [12]. Previous studies have shown that it is possible to estimate the current punch edge radius [13] and the resulting workpiece characteristics [14] based on time series, for example using machine learning algorithms. This methodology can potentially be used to monitor the current wear condition during punch stacking and to adapt to it by appropriate countermeasures. The hypothesis put forward in this paper is that by monitoring the wear condition in-situ, the optimum range in the process window in terms of joint strength can be determined in real time and abrasive wear can be counteracted by adjusting the process parameters. In order to lay the foundation for this, the correlations between the parameters embossing depth, embossing clearance and punch edge radius and the resulting joint strength are to be investigated experimentally in this paper.

Approach

In order to investigate the influence of the main process parameters and the tool wear state on the joint strength, experimental investigations are carried out. For the experiments electrical steel sheets of grade M270-50A according to DIN EN 10106 [15] are used with two different coating materials (C3 and C5). The sheet thickness is 0.5 mm and the specimen have a size of 35x35 mm containing one cylindrical nub per layer. The nubs have a circular cross section with a diameter of 6 mm. The single sheets where stacked using a punch with the same diameter. For the investigation the parameters blankholder force and counterpunch force are kept constant. The embossing depth is varied in the range 60 % to 125 % in relation to the sheet thickness. The embossing gap is 2 % or 1 % of the sheet thickness. Table 1 gives an overview over the experimental parameters.

Table 1. Dimensions and parameters used in the experimental investigation.

material and design parameters		constant process and tool parameters		varied properties and parameters	
sheet thickness s	0.5 mm	stroke height	35 mm	coating type	C3, C5
specimen size	35 x 35 mm	stroke speed	15 strokes/min	embossing depth t	60 % - 125 %
material	M270-50A	blankholder force F_b	3,000 N	embossing clearance u_p	2 %, 1 %
punch diameter D_p	6 mm	counterpunch force F_c	800 N	punch edge radius	sharp (R00), 0.1 mm (R01), 0.2 mm (R02), 0.3 mm (R03)
		stacking force F_s	5,654 N		

Fig. 2(a) shows the test tool used for the embossing step and the test set-up for stacking the nubs. The tool used for embossing is a test tool for simple shear cutting operations with a closed cutting contour. A round punch with a diameter of 6mm is used. To investigate the influence of tool wear in the form of abrasion, punches with an artificially rounded embossing punch edge (indicated in Fig. 2(a)) with different radii (see Table 1) are used for embossing in addition to a

punch with a sharp edge. The tool is equipped with a piezoelectrical force washer (Kistler 9015A) to acquire the embossing force and an eddy current sensor (µEpsilon EU8) to acquire the motion sequence of the tool.

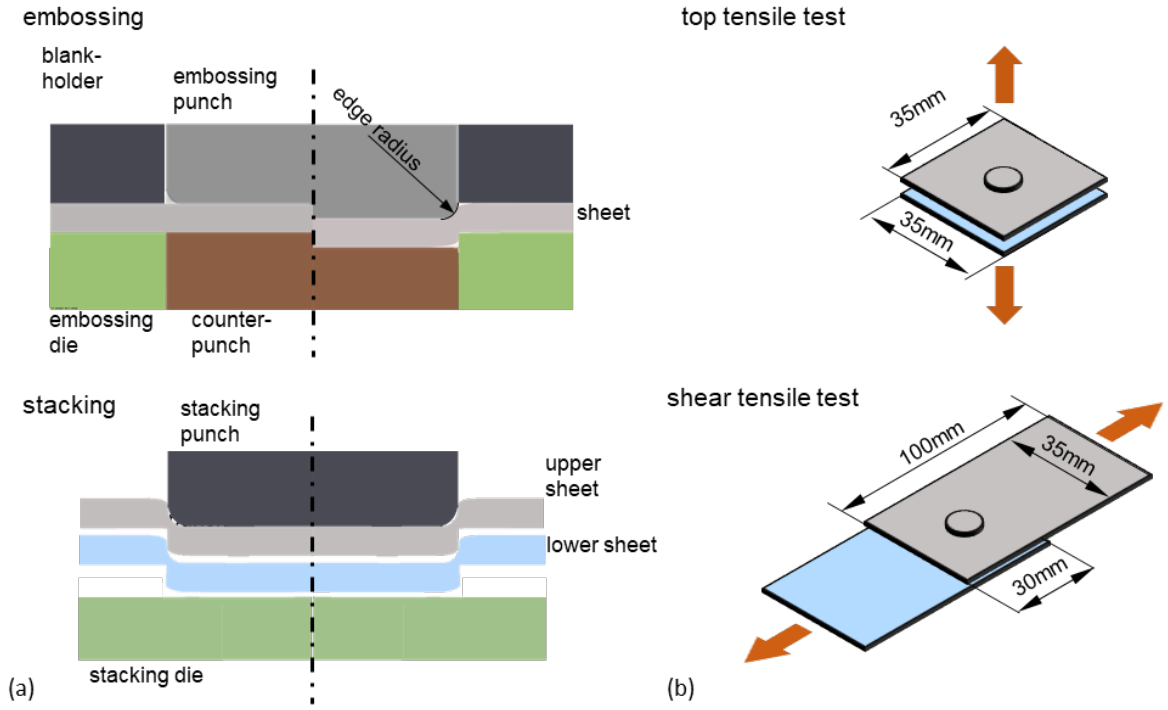

Fig. 2. Experimental setup for embossing, stacking and tensile testing.

The samples are stacked on a tensile-pressure testing machine, whereby the lower sheet is placed on the convex side of the nub on a flat pressure plate and a punch with the same geometry as the embossing punch presses the nub of the upper sheet into the lower nub. The punch movement is force-controlled at 500 N/s until a defined upper force limit is reached, for which a value of 5,654 N was empirically determined, which corresponds to a compressive stress of 200 MPa in relation to the nub cross-section. In order to prevent the lamination stack from sticking to the punch due to radial clamping forces caused by elastic deformation, the stacking punch has an edge radius that is 0.1 mm larger than that of the embossing punch.

Fig. 3 shows the curves of the punch force over time for both materials as a function for different embossing depths using a sharp punch (R00) and for a slightly rounded punch with an edge radius of 0.1 mm (R01). The graphs are synchronised so that the times of impact of the blankholder coincide. Since the embossing depth is varied by adjusting the bottom dead centre of the press, the punch speed changes with the embossing depth, therefore the time at which the punch hits the sheet also changes, as can be seen from the rapid increase at between 0.5 s and 0.6 s. With the rounded edge, the punch consistently hits the sheet a little later, as the length of the punch is slightly shorter with the artificially worn rounded-edge punches, but the hold-down is set the same. In the embossing phase, different characteristic progressions can be seen depending on the embossing depth. At high embossing depths, the typical force curve of shear cutting results with an abrupt drop in force after reaching the critical breaking stress. Using a sharp punch, this can be observed at embossing depths of 100 %. In this case, fracture initiation already takes place at embossing depths in the range of 80 % to 85 %. Below this, the curve of the punch force is decisively dominated by the punch travel and the corresponding counterpunch and blankholder forces.

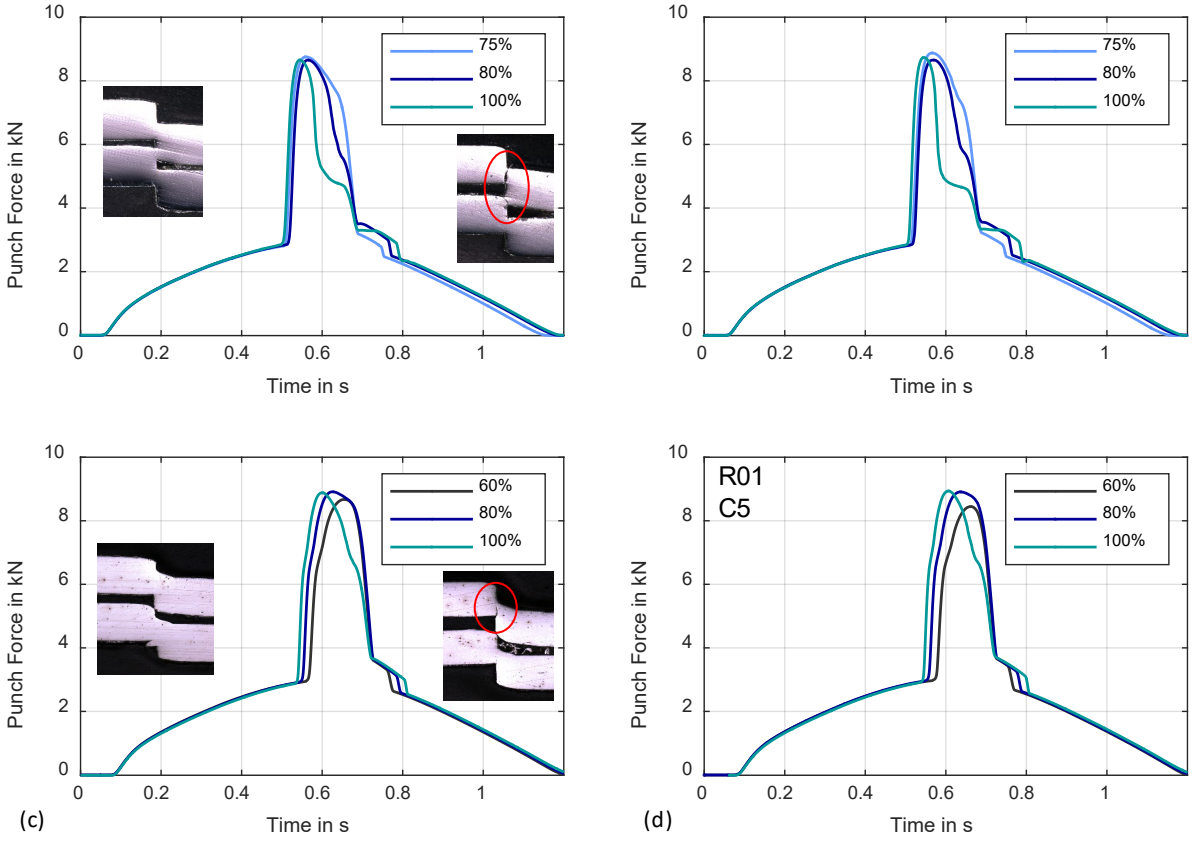

Fig. 3. Punch force curves for different embossing depths (in relation to the sheet thickness) with sharp (R00) embossing tool, (a) and (b), and rounded tool (R01) with edge radius 0.1 mm, (c) and (d); (a) and (c) show the curves for the material with C3 coating, (b) and (d) the material with C5 coating.

When using a worn punch, the material breaks at higher embossing depths. In this state, tensile and compressive stresses are superimposed in the forming zone, local stress peaks are reduced, and the material allows greater plastic deformations. As a result, the embossed nubs do not tear off at embossing depths of 90 % and below.

Fig. 4 demonstrates how the punch force changes with different edge radii at the same embossing depth (100 %). It can be seen that the maximum force increases with increasing edge radius. This is consistent with investigations of force signals during shear cutting [16]. Since the edge radius increases, the effective clearance decreases depending on the depth the tool penetrates the die. As a result of a smaller clearance, the maximum cutting force is reduced. This effect is counteracted by an increasing radius, due to the greater load which must be applied to the tool system to induce cracks in the material. According to Kubik et al., the effect of superimposed tensile and compressive stresses dominates, resulting in an increased maximal force [16].

Furthermore, it can be observed that in the case of a slight fillet, the shape of the curve changes significantly. There is a sharp drop in the force and a kink in the curve immediately before reaching the bottom dead centre (which is passed through at approximately 0.63 s), which indicates that the tensile strength of the material has been reached locally and damage and possibly initial cracking occurs in the area of the tool edges, so that a further increase in the embossing depth can be expected to cause the punching nub to tear off. It is noticeable that the curves for R01 and R02 are very close together. Only a further increase of the edge radius to 0.3mm causes the critical

embossing depth to shift upwards until breakage occurs to such an extent that cracking does not yet occur at 100 % embossing depth. Due to these characteristic changes in the force curve, it is possible to predict the state of wear, expressed by the edge radius for the case at hand, using known methods [6].

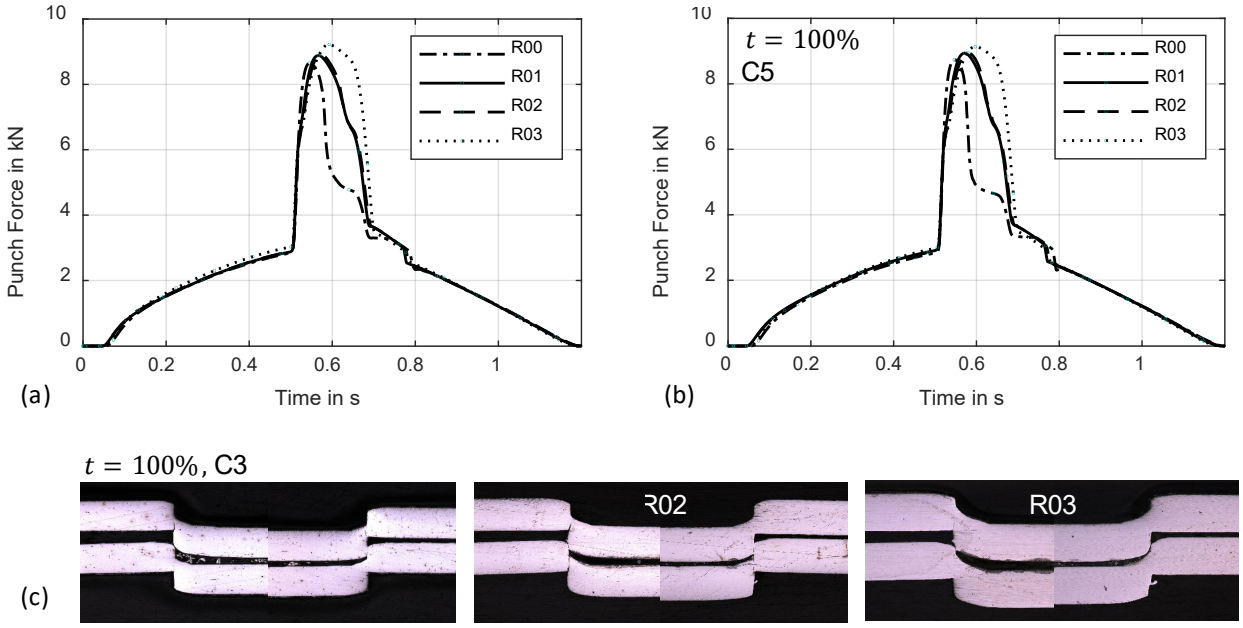

Fig. 4. Punch force curves for different edge radii of the embossing tool for the materials with C3 coating (a) and C5 coating (b) at a stamping depth of 100%.

The joint strength was determined by quasi-static tensile tests, as illustrated in Fig. 2(b) with five repetitions per process parameter set whereby the focus is on the maximum force achieved in the load direction until separation of the stack. For the case R01 shear as well as top tensile tests were performed and evaluated. The results for stamping depths of 80 %, 90 % and 100 % show that the shear strength is significantly higher than the pull-off strength in top tensile test in all cases (see Fig. 5), which can be explained by the fact that in the direction of loading in the sheet plane, in addition to the force-fit connection, they are also joined by a form-fit force component. Nevertheless, both tests show the same qualitative correlation when varying the embossing depth. In the following, only the results from the top tensile tests are used to simplify the investigation of the influence of edge radius, embossing depth and embossing clearance.

Results

In order to find out how the relationship between embossing depth and joint strength changes with increasing tool wear, investigations are carried out with one sharp and three rounded embossing tools. Nubs with different embossing depths are introduced into the samples and then two sheets are pressed together. In the following, the maximum forces achieved in the top tensile test are used to evaluate the joint strength.

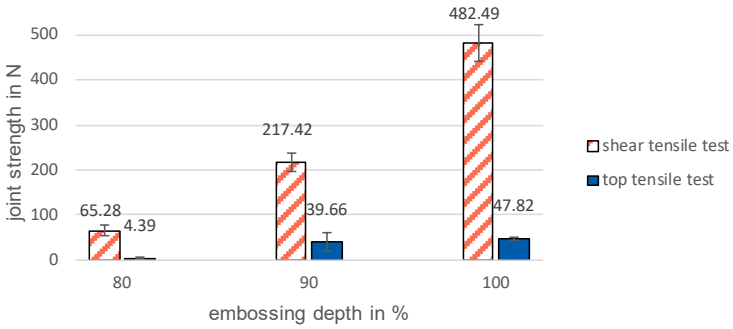

Fig. 5. Comparison of shear and top tensile test for an embossing radius of 0.1 mm.

The results are intended to provide the basis for making a real-time prediction of the joint strength by monitoring the wear condition on the basis of force signals. In addition, it will be investigated whether a targeted rounding of the tool edge can have a positive effect on the joint strength.

Fig. 6 shows the results of the tensile tests for the materials with C3 and C5 coating. Using a sharp tool (R00), a stacking with the present configuration is possible from an embossing depth of 70% (with C3) or 75% (with C5). Below this, no permanent joint can be created. The strength values for R00 of 13.75N at 70% and 14.09N at 75% are at an almost constant, low level in this range. Further increase of the embossing depth to 80% leads to a slightly decreased joint strength. For C5, the lowest embossing depth with which a successful package was produced is 75%. The strength values of 9.45N and 9.69N for 75% and 80% are also very close to each other, whereas the maximum strength value of 12.5 N is measured at 85%. The maximum achievable embossing depth before the nub breaks off is 80% for the C3 material and 85% for C5.

In the tests with rounded tool edges, three main observations can be made:

1. Both the minimum embossing depth at which a laminations stack can be joined and the maximum embossing depth before nub breakage occurs increase significantly compared to a sharp tool. The increase in the minimum embossing depth is due to the fact that, because of the rounded tool edge, there is a significant radius on the inside of the dimple as well as on the underside of the sheet in the rollover zone of the nub, which increases with increasing tool edge radius. This reduces the remaining actual contact area on which the contact normal stress can act in the radial direction. The maximum stamping depth increases because with a rounded punch, the stress peaks at the sharp edges are lowered, causing cracking to occur later. For C5, in all cases with a rounded tool, regardless of the edge radius, a joint can only be made from an embossing depth of 90%. With the largest radius of 0.3mm (R03), nubs with a maximum embossing depth of 125% can be successfully stacked for both C3 and C5.

2. After reaching an optimum, the strength decreases again with a further increase in the embossing depth. This could indicate that if the embossing depth is increased too much, the crack formation is already initiated at least locally and the thus pre-damaged nub no longer has the necessary strength in the subsequent stacking process to build up a press-fit with the same joint strength.

3. The maximum achievable strength with optimal choice of embossing depth increases significantly compared to the case with sharp embossing tool. It can be clearly seen that the maximum achievable joint strength in all cases with a rounded tool edge is above the strength with a sharp tool, regardless of the radius. The optimum is achieved at 100% embossing depth with a slight rounded tool with a radius of 0.1mm and is 47.82N with C3 coating or 44.42N with C5 coating. With further increase, the maximum strength decreases again and tends to occur at higher embossing depths.

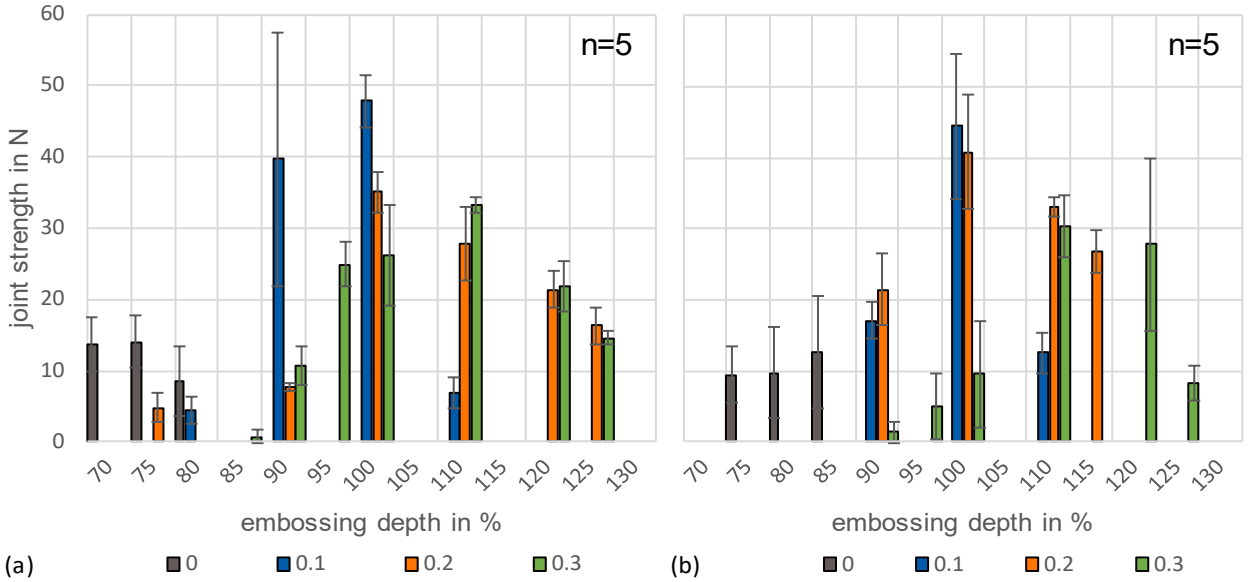

Fig. 6. Results of top tensile tests for different embossing depths and embossing tool radii at samples with C3 coating (a) and coating of type C5 (b).

Based on the tests carried out, the process window for the present joint configuration with a cylindrical nub of 6mm diameter can be determined empirically using an embossing clearance of 2%. In Fig. 7 this is shown as a function of the punch edge radius and the embossing depth. On this basis, both an upper and a lower limit can be read off for the respective radius. These differ only slightly for the two materials examined with different coatings.

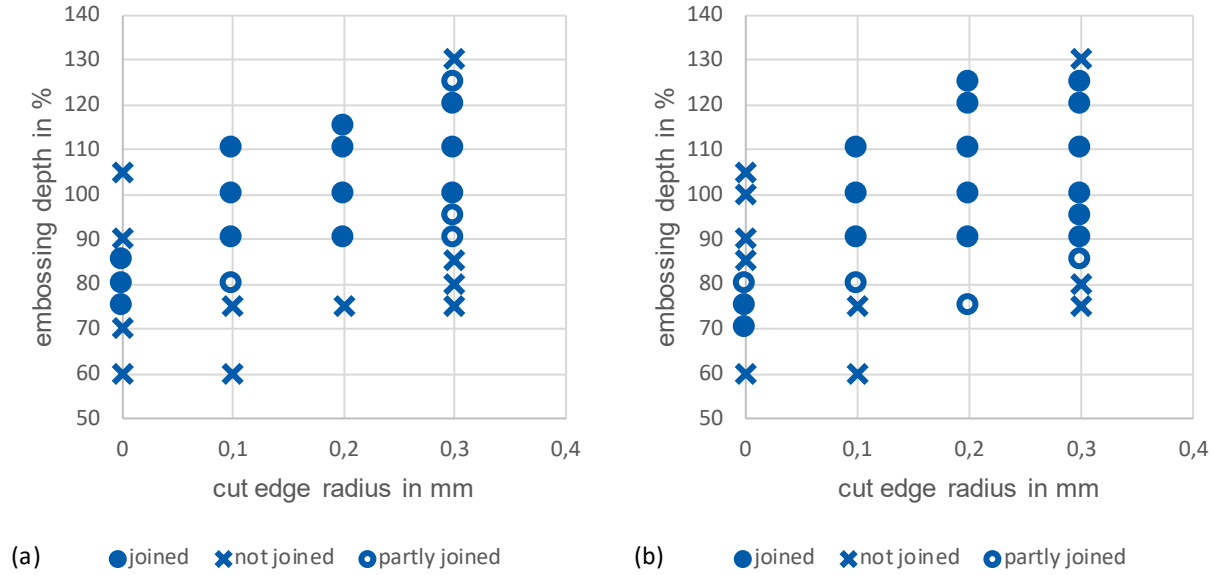

Fig. 7. Process windows for the investigated interlocking setup for test stacks of C3 (a) and C5 (b) coated sheets.

For achieving high-quality lamination a small clearance between the embossing punch and die is favorable [4]. Therefore, the influence of the embossing clearance is further investigated. Fig. 8 shows that the joint strength increases when the embossing clearance decreases from 2 % to 1 %, which is in accordance with studies by Lin et al. [4], where the same relationship between the embossing clearance and the joint strength was established with a sharp punch of 2mm diameter. In addition, the results indicate that the maximum embossing depth at which successful stacking

is possible is about the same as with a smaller gap, although higher local stresses are expected in the embossing step. Furthermore, the lower process limit for the embossing depth is lower with a smaller embossing gap, which leads to a significantly larger process window. This is valid for both C3 and C5 coated material.

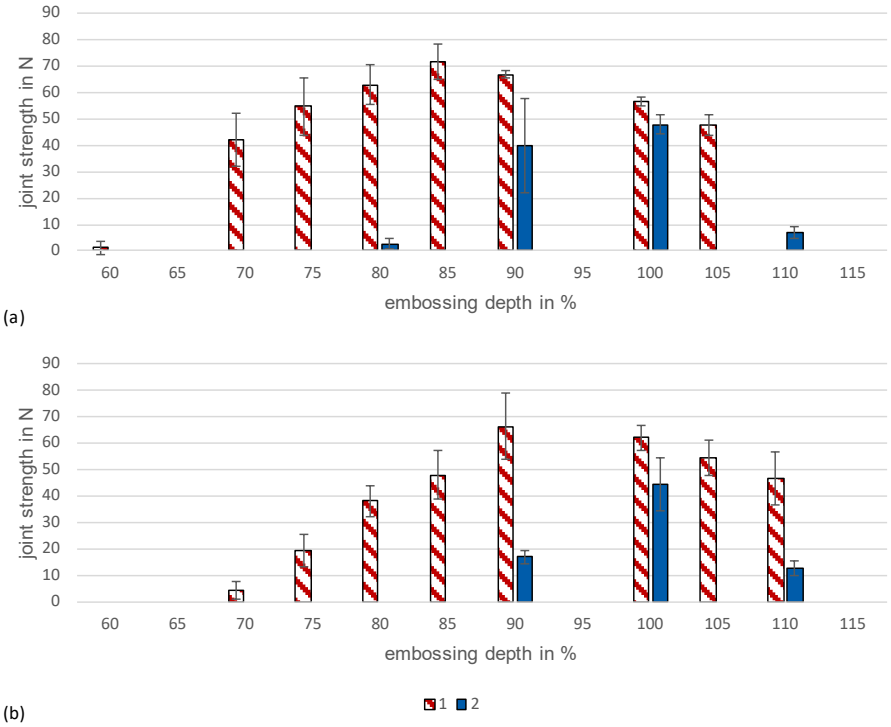

Fig. 8. Joint strength determined in top tensile tests for different embossing clearances 1 % and 2 % at various embossing depth with (a) C3 and (b) C5 coating.

Summary

In this work the influence of tool wear expressed by a rounding of the embossing tool edge on the joint strength of interlocked lamination stacks with cylindrical nubs was investigated.

It can be found that the achievable embossing depth increases when using an embossing punch with a rounded tool edge. Coincidently, the minimum embossing depth required for stacking and the embossing depth at which the optimum strength is achieved depend on the punch edge radius. If the embossing depth is regarded as a control variable, this knowledge can be used to react to wear occurring on the tool edge by adjusting the process parameter embossing depth. Another approach, which is obvious in order to design the interlocking die with regard to optimum mechanical joint strength, is to design the tools for stamping from the outset in such a way that an edge radius is provided in order to achieve the optimum of the achievable joint strength.

The comparison of the two different coating types C3 and C5, which are commonly used for blanking of electrical sheets shows no clear difference in the suitability for interlocked lamination stacks.

Acknowledgement

The presented results are part of the research projects “Production-induced properties in interlocking of lamination stacks for stator cores” of the European Research Association for Sheet Metal Working (EFB). The authors would like to thank the German Federation of Industrial Research Associations (AiF) and the German Federal Ministry for Economic Affairs and Climate Action (Bundesministerium für Wirtschaft und Klimaschutz, BMWK) for funding within the framework of project no. IGF 22036 N. Further thanks go to Dirk A. Molitor for the constructive technical discussions during the preparation of this paper. Furthermore, the authors would like to

thank Bruderer AG for providing the high-speed press BSTA 810-145 on which the tests were carried out.

References

[1] DIN EN 10342:2005-09, Magnetic materials - Classification of surface insulations of electrical steel sheet, strip and laminations; German version EN 10342:2005. https://doi.org/10.31030/9643607

[2] M. Lindenmo, A. Coombs, D. Snell, Advantages, properties and types of coatings on non-oriented electrical steels, J. Magnet. Magnet. Mater. 215-216 (2000) 79-82. https://doi.org/10.1016/S0304-8853(00)00071-8

[3] E. Lamprecht, Der Einfluss der Fertigungsverfahren auf die Wirbelstromverluste von Stator-Einzelzahnblechpaketen für den Einsatz in Hybrid- und Elektrofahrzeugen, Fertigungstechnik - Erlangen vol. 247, PhD thesis, 2014. ISBN 9783875253627

[4] H.-S. Lin, H.-C. Fu, L.-H. Liu et al., Stacking with cylindrical spots in lamination of stamped electrical steel sheets, Procedia Eng. 207 (2017) 992-997. https://doi.org/10.1016/j.proeng.2017.10.864

[5] D.M. Martin, F. Bäcker, B. Deusinger, C. Kubik, P. Gehringer, J. Schröder, P. Groche, Design Guidelines for interlocked stator cores made of CoFe sheets, IOP Conf. Ser.: Mater. Sci. Eng. 1238 (2022) 012036. https://doi.org/10.1088/1757-899X/1238/1/012036

[6] C. Kubik, M. Becker, D.A. Molitor, P. Groche, Towards a systematical approach for wear detection in sheet metal forming using machine learning, Prod. Eng. Res. Devel. 17 (2022) 21-36. https://doi.org/10.1007/s11740-022-01150-x

[7] K. Lange, Handbook of Metal Forming, J. Appl. Metalwork. 4 (1986) 188. https://doi.org/10.1007/BF02834383

[8] C. Kubik, D.A. Molitor, M. Rojahn, P. Groche, Towards a real-time tool state detection in sheet metal forming processes validated by wear classification during blanking, In: IOP Conference Series: Mater. Sci. Eng. 1238 (2022). https://doi.org/10.1088/1757-899X/1238/1/012067

[9] M. Regnet, A. Kremser, M. Reinlein, P. Szary, U. Abele, Influence of Cutting Tool Wear on Core Losses and Magnetizing Demand of Electrical Steel Sheets, 9th International Electric Drives Production Conference (EDPC), 2019, pp. 1-6. https://doi.org/10.1109/EDPC48408.2019.9011866

[10] K. Senda, M. Ishida, Y. Nakasu, M. Yagi, Influence of shearing process on domain structure and magnetic properties of non-oriented electrical steel, J. Magnet. Magnet. Mater. 304 (2006) e513-e515. https://doi.org/10.1016/j.jmmm.2006.02.139

[11] H.A. Weiss, N. Leuning, S. Steentjes, K. Hameyer, T. Andorfer, S. Jenner, W. Volk, Influence of shear cutting parameters on the electromagnetic properties of non-oriented electrical steel sheets, Journal of Magnetism and Magnetic Materials, 2017. https://doi.org/10.1016/j.jmmm.2016.08.002

[12] P. Groche, J. Hohmann, D. Übelacker, Overview and comparison of different sensor positions and measuring methods for the process force measurement in stamping operations, Measurement 135 (2019) 122-130. https://doi.org/10.1016/j.measurement.2018.11.058

[13] W. Klingenberg, T.W. de Boer, Condition-based maintenance in punching/blanking of sheet metal, Int. J. Mach. Tool. Manuf. 48 (2008) 589-598. https://doi.org/10.1016/j.ijmachtools.2007.08.013

[14] R. Hambli, Prediction of burr height formation in blanking processes using neural network, Int. J. Mech. Sci. 44 (2002) 2089-2102. https://doi.org/10.1016/S0020-7403(02)00168-6

[15] DIN EN 10106:2016-03, Cold rolled non-oriented electrical steel strip and sheet delivered in the fully processed state, German version EN10106:2015. https://doi.org/10.31030/2315581

[16] C. Kubik, J. Hohmann, P. Groche, Exploitation of force displacement curves in blanking – Feature Engineering beyond defect detection, Int. J. Adv. Manuf. Technol. 113 (2021) 261-278.

Materials Research Proceedings 28 (2023) 1111-1118 https://doi.org/10.21741/9781644902479-122

Versatile self-piercing riveting with a tumbling superimposed punch

WITUSCHEK Simon[1,a *], ELBEL Leonie[1,b] and LECHNER Michael[1,c]

[1]Institue of Manufacturing Technology, Friedrich-Alexander-Universität Erlangen-Nürnberg, Egerlandstr. 13, 91058 Erlangen, Germany

[a]Simon.Wituschek@fau.de, [b]Leonie.Elbel@fau.de, [c]Michael.Lechner@fau.de

Keywords: Joining, Multi-Material-System, Versatile Joining, Self-Piercing Riveting

Abstract. Increasing resource efficiency is a major challenge and affects almost every aspect of social and economic life. The mobility sector in particular is responsible for a large share of primary energy consumption and is increasingly in the focus of public interest. One possibility to adress these challenges is to reduce the vehicle weight by means of lightweight construction technologies such as multi-material systems. These assemblies consist of workpieces with different mechanical and geometrical properties, which poses a major challenge for joining technology. Mechanical joining processes such as semi-tubular self-piercing riveting are often used in the production of these assemblies, but due to their process characteristics, they are rigid and can only react to changing process variables to a limited extent. One way to increase the versatility of self-piercing riveting is to superimpose a tumbling kinematics on the punch. During tumbling, an angular offset of the punch axis to the tool axis is set and the contact area between punch and workpiece is reduced. In this work, investigations were carried out to determine how the tumbling strategy, consisting of the parameters tumbling angle, tumbling onset and tumbling kinematics, affects the material flow of the rivet element. For this purpose, experimental tests are conducted with the typical materials of conventional multi-material systems and the geometric joint formations are determined by means of macrographs.

Key findings

- Analysis and identification of the significant influencing parameters of the tumbling strategy on the process combination and their interactions
- Evaluation of possibilities of a targeted material flow control to influence the geometric joint formation

Introduction

The energy and climate crisis demands a more efficient use of resources and technology. A major part of this ongoing change has to take place in the mobility sector [1]. Stricter limits for CO_2 emissions were imposed recently [2]. One way of increasing efficiency in automotive engineering is weight reduction [3]. Especially the battery weight in electric vehicles can be partially reduced this way [3]. Since the body in withe is an important part of the vehicle's total weight, efforts are often focused on replacing conventional steel used in body design with lightweight materials such as aluminum, fiber-reinforced plastics or high strength steel [4]. Reducing the overall mass of a passenger car with an internal combustion engine by 100 kg can save about 0,5 l of fuel per 100 km [5]. In addition to reducing weight and increasing efficiency, the mechanical strength and crash behaviour of a vehicle can also be improved by the selective use of materials [4]. This approach is generally called multi-material design [3]. The spectrum of materials used in this strategy includes light metals, such as titanium or aluminum, as well as plastics and composites [6], up to ceramics [7]. Due to the different chemical, mechanical and thermal properties of these materials, joining technology is one of the greatest challenges of multi-material design [6]. While conventional

Content from this work may be used under the terms of the Creative Commons Attribution 3.0 license. Any further distribution of this work must maintain attribution to the author(s) and the title of the work, journal citation and DOI. Published under license by Materials Research Forum LLC.

thermal joining processes reach their limits when it comes to joining dissimilar materials [8], mechanical joining technologies such as semi-tubular self-piercing riveting (SPR) are becoming increasingly important [9]. Since SPR is a rather rigid process with limited flexibility, it cannot comply with the increasing demand for rapid response to individual product configurations [3]. One way to improve the variability of SPR is to superimpose the process with a tumbling kinematics on the punch. The punch is tilted by a certain angle, which reduces the contact area between the tool and the workpiece [10], as shown in Fig. 1b). As a result, the joining forces are reduced, and the process limits are increased [11], due to a higher number of parameters. Furthermore, the flexibility and versatility of the process can be enhanced [3].

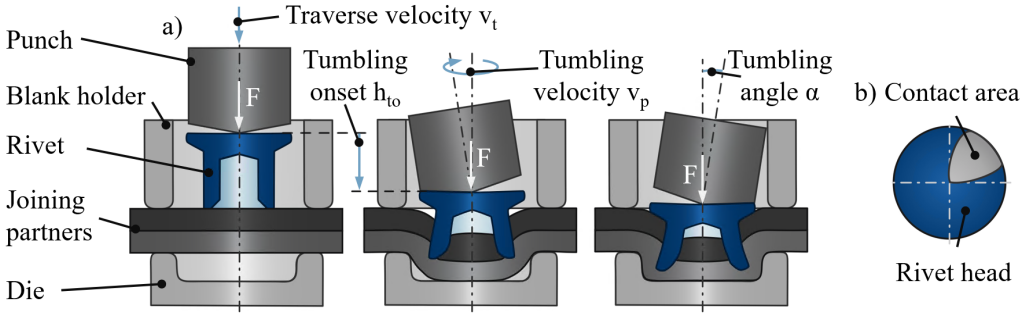

Fig. 1. a) Components and process parameters [13] of semi-tubular self-piercing riveting with tumbling punch and b) resulting contact area.

At present, the potential of this process combination cannot be exploited to its full extent, since no holistic understanding about the correlation of the process parameters with the geometrical joint formation of the SPR joints exists. To improve the process knowledge, an extensive series of experiments was planned and executed, analyzing the effects of various parameters and tumbling strategy combinations based on macrographs. Therefore, the tumbling angle α, the tumbling speed v_t, the tumbling kinematics, and the tumbling onset h_{to} were varied. These parameters are further illustrated in Fig. 1a) and are explained in more detail below. The results of the analysis provide a basis for the efficient use of the process combination to achieve a higher versatility. In particular, conclusions regarding the process and material flow control in semi-tubular self-piercing riveting are drawn.

Tumbling Self-Piercing Riveting Process

For the investigation of the process combination of a tumbling superimposed semi-tubular self-piercing riveting process, the tool shown in Fig. 2 is utilized. The tool design provides the ability to investigate a variety of parameters of the joining and tumbling strategy [3]. The core of the tool setup is the combination of a rotating and a linear axis, which enables predominantly rotating and linear kinematic models to be executed and a free path planning of the contact surface between punch and rivet head can be implemented. Furthermore, the adjustment mechanism for the tumbling angle and the punch movement is excluded from the force path of the tool, thus enabling highly dynamic movements. The tool is installed in a conventional universal testing machine of the type Walter-Bai, which performs the tool stroke in the z-direction. As materials for the investigations, the steel HCT590X with a sheet thickness of $t_0 = 1.5$ mm and the aluminium alloy EN-AW6014 with a sheet thickness of $t_0 = 2.0$ mm are selected. Due to their mechanical and geometric properties, these two materials and sheet thicknesses represent common multi-material systems and their challenges for joining technology. The die type used is a flat die with a diameter of 8.5 mm, a depth of 1.7 mm and a draft angle of 5°. The rivet element is a C-rivet with a shaft diameter of 5.3 mm and a rivet height of 5.0 mm from industrial applications.

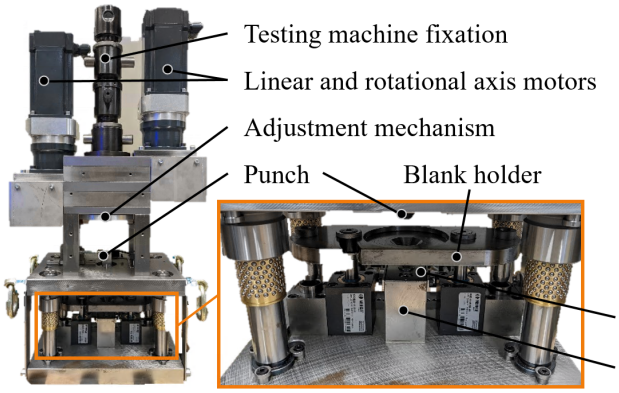

Parameter	
Rivet	C 5,3 x 5 H4
Die	FM_85_2117
Punch-side joining partner	HCT590X+Z t_0=1.5 mm
Die-side joining partner	EN AW-6014 t_0=2.0 mm
Traverse velocity v_t	10 mm/min

Fig. 2. Semi-tubular self-piercing riveting tool with detail views and tool parameters.

The investigations are carried out to identify the influences of individual parameters and their interactions with each other. For this purpose, the four process parameters of the tumbling strategy consisting of the tumbling angle α, the tumbling velocity v_t, the tumbling kinematics and the tumbling onset h_{to} are varied and evaluated. An overview of the variations of the process parameters are shown in Fig. 3. The tumbling angle is investigated in three stages. As a lower limit, the tumbling angle α = 1° is selected, since at an angle of α = 0° no tumbling angle is applied and the process is similar to a conventional semi-tubular SPR process. As a result, no correlations can be identified between the tumbling and the joining process. The upper limit of the investigated tumbling angles is set at α = 5°. Previous studies have shown that in certain circumstances cracks in the rivet shaft of multi-material systems occur at angles higher than α = 5° [3]. For a finer gradation, the tumbling angle α = 3° is also investigated. Furthermore, the tumbling kinematics is varied as a process variable. A distinction can be made between predominantly rotating and predominantly linear movements. For the rotating kinematics models, circular and spiral kinematics are applied. The two models differ mainly in the adjustment of the maximum tumbling angle, which is approached in the first revolution in case of circular kinematics and is built up over the entire joining process in case of spiral kinematics. As a predominantly linear kinematics model, the kinematic shown in Fig. 3d) is investigated, which has fundamentally different motion characteristics. The motion has a significantly higher proportion in the radial direction and thus affects the material flow during the joining process.

a)

Parameter			
Tumbling angle α	1°	3°	5°
Kinematics	Circle	Spiral	Linear
Tumbling speed v_p	180 °/s		360 °/s
Tumbling onset h_{to}	3.0 mm		4.5 mm

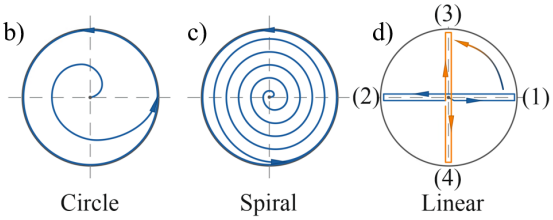

Fig. 3. a) Overview of the process parameter variation and schematic illustration of b) circular c) spiral and d) linear kinematics.

As a further process parameter, the influence of the tumbling velocity on the joining process is investigated. This parameter is varied in the steps 180 °/s and 360 °/s. Since the traverse speed, which generates the z-stroke of the punch, is constant at v_t = 10 mm/min, an increase in the movement speed enhances the distance moved by the contact surface during the joining process, which can be described in terms of the number of revolutions in case of a rotating movement pattern. For the investigations with linear kinematics, the same path speeds are applied as for the

rotating models. The fourth parameter of the tumbling strategy is the tumbling onset. As shown in Fig. 1a), the tumbling onset corresponds to the stroke of the punch from the first contact with the rivet to the start of the tumbling motion. It is selected based on the process phases of conventional semi-tubular SPR with h_{to} = 3.0 mm and h_{to} = 4.5 mm. A tumbling motion of the punch before the cutting phase of the punch-side joining partner is completed causes a large angular misalignment of the rivet in the joint. Therefore, the influence of an onset of the punch movement during spreading with h_{to} = 3.0 mm and setting with h_{to} = 4.5 mm is examined. The process phases are identified during sampling with a tumbling angle α = 0° using force signals [12].

In the investigation, a total of three tests per parameter combination are conducted in order to identify statistical and process uncertainties. In total, the test setup comprises 108 tests. The geometric joint formations, shown in Fig. 4, are determined to evaluate the influences of the individual parameters on the joint and their interactions. For this purpose, macrographs are prepared and the standard geometric parameters relevant for the joint quality are determined. These consist of the undercut, the rivet head end position and the residual sheet thickness [13].

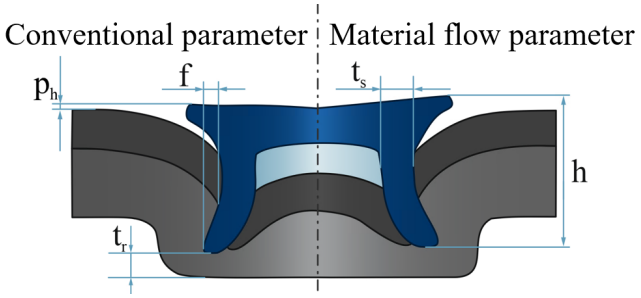

Parameter	
f	Undercut
h	Rivet height
p_h	Rivet head end position
t_r	Residual sheet thickness
t_s	Shaft thickness

Fig. 4. Geometric joint parameter for conventional and material flow parameter.

The investigations are also intended to identify and determine the material flow components. For this reason, the maximum rivet shaft thickness is measured in order to be able to identify radial material flow components in the joint. Furthermore, the rivet height is determined, which also provides insights into the effects of the individual parameters on the joint.

Evaluation of the Influencing Parameters

To determine the influence of the parameter variation, the rivet head geometry was analysed using 3D images. Fig. 5 shows three profile geometries of rivet heads, which differ in the tumbling angle. The other parameters remain constant. Therefore, the circular kinematics, the tumbling onset of h_{to} = 3.0 mm, and the tumbling velocity of v_p = 180 °/s were chosen since the influence of the tumbling angle can be visualized best with this configuration. The colours of the rivet heads indicate how far the rivet extends above the surface of the punch-side joining partner. It is evident that the rivet head sits significantly lower when the tumbling angle is increased. Accordingly, by using a greater tumbling angle it is possible to directly regulate the rivet head end position for example to obtain a plane surface of rivet head and joining partner. The planarity improves with increasing angle and the conical shape caused by the punch is reduced.

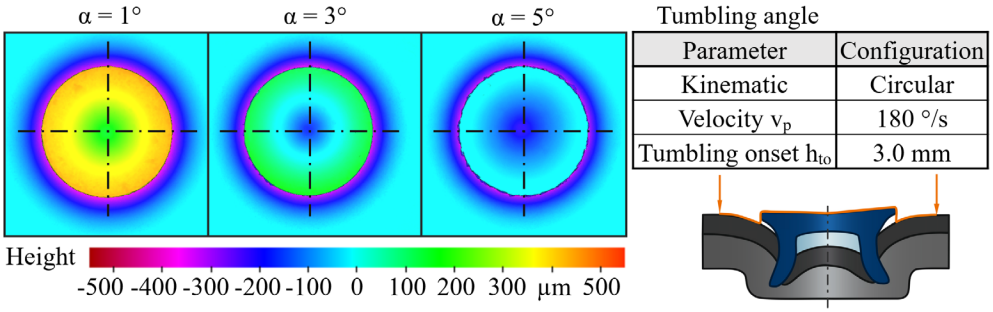

Fig. 5. Analysis of the rivet head geometry with varying tumbling angle.

Thus, it can be determined, the rivet head end position decreases when the tumbling angle is increased. In order to identify process characteristics about the material flow, the residual sheet thickness is examined. Fig. 6 shows the correlation of the residual sheet thickness with the kinematics, the tumbling angle, and the tumbling onset. Since the tumbling velocity has shown hardly any influence on the residual sheet thickness, both velocities are included in the average values plotted. It can be stated that the tumbling onset has a major influence on the residual sheet thickness when circular or spiral kinematics are applied. The linear kinematics leads to significantly more inhomogeneous results and is therefore statistically unstable. If tumbling starts after a 3.0 mm stroke, the residual sheet thickness increases with the tumbling angle. The difference from $\alpha = 1°$ to $\alpha = 3°$ is significantly greater compared to the variation from 3° to 5°. However, if the tumbling starts at $h_{to} = 4.5$ mm, the residual sheet thickness remains almost constant and is barely affected by other parameters. This means that the effect of the tumbling angle on the residual sheet thickness is a characteristic attribute of the tumbling punch, which only occurs if the effective tumbling process is sufficiently applied. It can be seen that not only the onset but also the duration of the tumbling has a significant influence on the geometric joint formation.

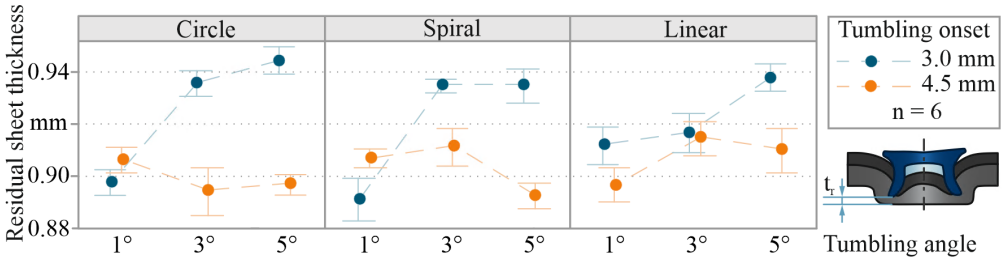

Fig. 6. Average residual sheet thickness depending on kinematics, tumbling angle and onset.

The fact that the residual sheet thickens as the tumbling angle increases contradicts decreasing rivet head end position. Hence, the tumbling punch must result in a deformation of the rivet. Therefore, the rivet height and the thickening of the rivet shaft were investigated to identify the direction of the material flow. Fig. 7 shows the correlation of the rivet height with the kinematics, the tumbling angle, the tumbling velocity, and a constant tumbling onset. It is apparent that the rivet is significantly compressed as a large tumbling angle is selected. The residual sheet thickness can therefore increase as the change in the rivet height is greater than the change in the rivet head end position. The figure also indicates that the deformation of the rivet is significantly less when linear kinematics are used. This shows that the effects of the tumbling punch are not well utilized by linear kinematics. Additionally, it can be seen that increasing the tumbling velocity leads to an enhanced rivet height change, especially with a large tumbling angle. To understand the effect of the velocity on the joint, process limits can be examined. If the tumbling velocity is increased infinitely, the tumbling process is equal to the conventional SPR. Accordingly, a very high velocity

neutralizes the effects of the tumbling punch. A similar case applies to a tumbling velocity approaching zero. Hence, there must be an interval, in which the tumbling velocity ideally amplifies the effects of the tumbling punch however, detailed investigations with additionally varying velocities of the traverse are required therefore.

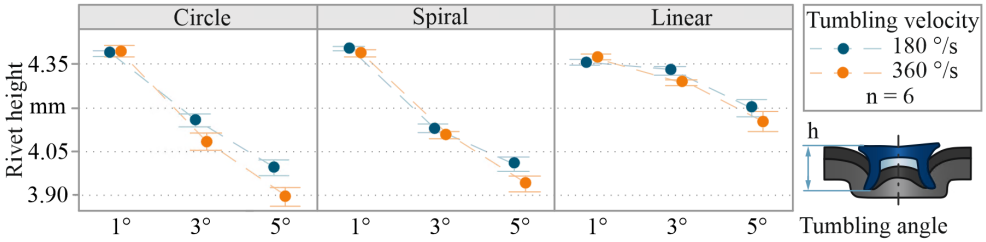

Fig. 7. Average rivet height depending on kinematics, tumbling angle, and tumbling velocity.

A reduction in rivet height leads to a partial radial material flow. The thickening of the rivet shaft increases the clamping effect of the joint and improves the force fit. Fig. 8 can be used to estimate the material flow. The outlines of rivet geometries extracted from the macrographs are shown. The reduction of the rivet height as well as the thickening of the rivet shaft by increasing the tumbling angle can be clearly seen in Fig. 8a). A significant part of the material flows radially inwards, as there is a flow constraint to the outside. The thickening of the rivet shaft also influences the undercut of the joint. For instance, the analysis showed that the undercut does not increase any further above a tumbling angle of $\alpha = 3°$, since the shaft thickening pushes the lowest and innermost point of the punch-side joining partner, at which the undercut is measured, further outward. This effect can be observed particulary well, when taking the average undercut for circular kinematics with 3.0 mm tumbling onset as an example. When the tumbling angle is increased from $\alpha = 1°$ to $\alpha = 3°$, the undercut changes from $f_{1°} = 0.32$ mm to $f_{3°} = 0.37$ mm. However, if the angle is further increased to 5°, the measured undercut even decreases slightly, resulting in an average value of $f_{5°} = 0.35$ mm.

In Fig. 8c) the influence of the kinematics is shown. While the outline is barely distinguishable for circular and spiral kinematics, the outline of the linear kinematis stands out from the other two kinematics, especially on the left side. As shown before, the rivet height remains greater with this kinematics. As a result, the radial material flow is reduced and the rivet shaft barely thickens. Also, the rivet head end position remains higher and the rivet foot is pushed outwards significantly less compared to the other kinematics. Thus, it can be confirmed that the effects of the tumbling punch vary in intensity due to the selection of the kinematics.

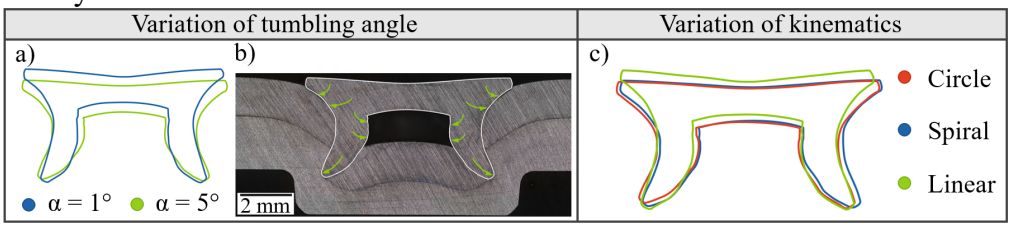

Fig. 8. Comparison of rivet outlines depending on a) tumbling angle and c) kinematics to determine b) material flow behaviour using 3.0 mm tumbling onset and a velocity of 180 °/s.

Summary

In this work, a semi-tubular self-piercing riveting process with superimposed tumbling kinematics on the punch was investigated. This involved deliberately varying the tumbling strategy in order to examine the effects of the process parameters tumbling angle, kinematics, tumbling onset and tumbling velocity on the geometric joint formation. In addition to the conventional geometric parameters such as rivet head end position, residual sheet thickness and undercut, the rivet height

and the thickness of the rivet shaft were analysed to obtain findings on the material flow. It can be stated that the rivet geometry can be significantly influenced by the selected parameters, especially by the tumbling angle. When varying the tumbling kinematics, the circular and spiral kinematics show similar results. The linear kinematics weakens the effects of the tumbling punch and partly causes statistically uncertain results. Accordingly, the following findings refer primarily to the predominantly rotational kinematics.

The analysis of tumbling onset showed that the characteristics of tumbling are less identifiable when onset is delayed. This is particularly important for the residual sheet thickness since it can only be affected by the tumbling angle when the tumbling onset is in an early process stage. This understanding improves the flexibility of the process, as different sheet thickness combinations can thus be joined without having to exchange the die or the rivet. In general, a low rivet head end position is targeted in semi-tubular self-piercing riveting, ensuring that the surface of the rivet head and the punch-sided joining partner form a plane surface. It can be identified that the rivet head end position can be improved by increasing the tumbling angle. Furthermore, it was determined that an early tumbling onset in combination with a large tumbling angle and a high tumbling velocity cause a reduction of the rivet height. This leads to a thickening of the rivet shaft and thus to radial material flow. As a result, the force fit of the joint can be strengthened and the load-bearing capacity affected.

The results of this work provide a solid basis for the process control of tumbling semi-tubular self-piercing riveting. Nevertheless, some aspects offer further research potential. For example, due to the thickening of the rivet shaft the undercut can no longer be increased above a certain tumbling angle. However, since the undercut is decisive for the joint strength, the correlation between these two parameters could be investigated in more detail. Furthermore, there is potential for varying the kinematics, as only one configuration per kinematics was examined here. To separate the effects of tumbling onset and tumbling duration more precisely, it would also be interesting to conduct experiments with a tumbling motion only in the respective process phase. In addition, it is advisable to analyse the significance of the radial material flow for the load-bearing capacity and the joint strength of the connection in more detail.

Acknowledgment
Funded by the Deutsche Forschungsgemeinschaft (DFG, German Research Foundation) - TRR 285-Project-ID 418701707.

References
[1] European Commission, European Green Deal, Brussels, 2021.
[2] Regulation (EU) 2019/631 of the european parliament and of the council: of 17 April 2019, 2022. Available online: https://eur-lex.europa.eu/legal-content/EN/TXT/HTML/?uri=CELEX:32019R0631&from=EN. (accessed 23 November 2022).
[3] B. Bader, E. Türck, T. Vietor, Multi Material Design, A current overview of the used potential in automotive industries, in: Lehnert, Dröder (Eds.), Technologies for economical and functional lightweight design, Springer Berlin Heidelberg, Berlin, Heidelberg, 2019, pp. 3-13.
[4] G. Meschut, V. Janzen, T. Olfermann, Innovative and Highly Productive Joining Technologies for Multi-Material Lightweight Car Body Structures, J. Mater. Eng. Perform. 23 (2014) 1515-1523. https://doi.org/10.1007/s11665-014-0962-3
[5] Federal Ministry for Economics Affairs and Climate, Lightweighting. BMWI. Available: https://www.bmwk.de/Redaktion/EN/Dossier/lightweighting.html, 2022. (accessed 10 November 2022).
[6] S. Kleemann, D. Inkermann, B. Bader, E. Türck, T. Vietor, A Semi-Formal Approach to Structure and Access Knowledge for Multi-Material-Design, 21st International Conference On Eengineering Design, Vancouver (2017) pp. 289-298.

[7] H.E. Friedrich, Leichtbau in der Fahrzeugtechnik, Springer Fachmedien Wiesbaden, Wiesbaden, 2013.
[8] K. Martinsen, S.J. Hu, B.E. Carlson, Joining of dissimilar materials, CIRP Annals 64 (2015) 679-699. https://doi.org/10.1016/j.cirp.2015.05.006
[9] F. Kappe, S. Wituschek, M. Bobbert, G. Meschut, Determining the properties of multi-range semi-tubular self-piercing riveted joints. Prod. Eng. Res. Devel. 16 (2022) 363-378. https://doi.org/10.1007/s11740-022-01105-2
[10]M. Plančak, D. Vilotić, M. Stefanović, D. Movrin, Igor Kačmarčik, 2012. Orbital Forging - A plausible alternative for bulk metal forming, J. Trend. Develop. Machin. Associat. Technol. 16 (2022) 35-38.
[11]M. Merklein, D. Gröbel, M. Löffler, T. Schneider, P. Hildenbrand, Sheet-bulk metal forming - forming of functional components from sheet metals, MATEC Web of Conferences 21 (2015) 1001. https://doi.org/10.1051/matecconf/20152101001
[12]S. Wituschek, M, Lechner, Investigation of the influence of the tumbling angle on a tumbling self-piercing riveting process, Proceedings of the Institution of Mechanical Engineers Part L-J. Mater. Des. Appl. 236 (2022) 1151-1345. https://doi.org/10.1177/14644207221080068
[13]G. Meschut, M. Merklein, A. Brosius, D. Drummer, L. Fratini, U. Füssel, M. Gude, W. Homberg, P.A.F. Martins, M. Bobbert, M. Lechner, R. Kupfer, B. Gröger, D. Han, J. Kalich, F. Kappe, T. Kleffel, D. Köhler, C.-M. Kuball, J. Popp, D. Römisch, J. Troschitz, C. Wischer, S. Wituschek, M. Wolf, Review on mechanical joining by plastic deformation, J. Adv. Join. Process. 5 (2022) 100-113. https://doi.org/10.1016/j.jajp.2022.100113

Lionel Fourment MS on optimization and inverse analysis in forming

Materials Research Proceedings 28 (2023) 1121-1130 https://doi.org/10.21741/9781644902479-123

On the comparison of heterogeneous mechanical tests for sheet metal characterization

GONÇALVES Mafalda[1,a *], OLIVEIRA Miguel Guimarães[1,2,b], THUILLIER Sandrine[2,c] and ANDRADE-CAMPOS António[1,d]

[1]Centre for Mechanical Technology and Automation (TEMA), LASI – Intelligent Systems Associate Laboratory, Department of Mechanical Engineering, University of Aveiro, Portugal

[2]Univ. Bretagne Sud, UMR CNRS, IRDL, F-56100 Lorient, France

[a]mafalda.goncalves@ua.pt, [b]oliveiramiguel@ua.pt, [c]sandrine.thuillier@univ-ub.fr, [d]gilac@ua.pt

Keywords: Heterogeneous Tests, KPIs, Material Behavior, Sheet Metal

Abstract. The characterization of sheet metal behavior is of utmost importance for the accurate virtualization of sheet metal forming processes. Newly proposed mechanical testing approaches are overcoming the use of standard mechanical tests. Test configurations with more complex geometries present richer mechanical fields and, therefore, provide a higher quantity of valuable information about the material behavior in a more efficient manner. To extract that information, full-field measurement techniques such as Digital Image Correlation are being used. Although several test designs have already been proposed, the choice of the best one to calibrate a chosen mechanical model is still an issue. This work aims at proposing Key Performance Indicators (KPIs) that are able to rank mechanical tests by their potential to enhance the material behavior characterization process. These metrics evaluate quantitatively the quality and the importance of the data that each test can provide. The potential of three test designs to characterize accurately sheet metal mechanical behavior is analyzed using the proposed KPIs. From a uniaxial tensile loading test up to rupture, the numerical mechanical information is extracted, and the performance of each test is evaluated and compared.

Introduction

Sheet metal forming processes play a major role in the development of mechanical parts for several industries such as automotive and aircraft. The virtualization of these processes has gained wide popularity in the transition to a more sustainable industry. Reduced costs, time, and material waste associated with the experimental task can be achieved. However, an accurate digitalization of the forming process is only possible when the numerical model can represent reality. For instance, the material constitutive model chosen to define the material behavior has to be well calibrated, having a huge repercussion on the obtained results. A classical model calibration procedure demands a huge quantity of data from several standard mechanical tests. The time and costs associated with this task led to the emergence of new ways of mechanical testing. The so-called heterogeneous testing consists in test configurations that have the potential to provide a significant amount of data with just a single test. Whether they present more complex boundary conditions or geometries, heterogeneities in the mechanical fields are induced, leading to a more informative test.

Several innovative designs have already been proposed to overcome the standardized mechanical testing. The design process of these tests has been led mainly by two approaches searching for: (i) the heterogeneity of the mechanical fields that are induced on the specimen [1–7] and (ii) the quality of the material model parameters that are indentified [8–11]. A more comprehensive review of the mechanical tests commonly used for material characterization and model calibration can be found in [14].

The use of heterogeneous mechanical tests is only achievable due to the emergence of full-field measurement techniques, such as Digital Image Correlation [15]. As an optical technique, it has

Content from this work may be used under the terms of the Creative Commons Attribution 3.0 license. Any further distribution of this work must maintain attribution to the author(s) and the title of the work, journal citation and DOI. Published under license by Materials Research Forum LLC.

the ability to extract information about the strain fields at each material point. Therefore, a larger quantity of information can be extracted from one heterogeneous test using full-fields techniques. With this data, it is possible to calibrate material constitutive models more efficiently using inverse methodologies such as the Finite Element Model Updating (FEMU) technique [16] and the Virtual Fields Method (VFM) [17]. The quality of the identification depends on the quality of the mechanical information that can be retrieved from the specimen. For instance, the heterogeneity of the mechanical fields, the magnitude and distribution of the equivalent plastic strain and the sensitivity of the induced fields to the parameters to be identified are aspects that have a huge influence on the identification quality.

Several designs of tests have been proposed with the aim of trying to characterize material behavior more accurately and cost-effectively. However, it is still unclear how to choose the best test geometry to calibrate a chosen material model. The choice of the most suitable test is not straightforward, so appropriate metrics should be established to evaluate and compare the performance of each test in the model calibration and material identification procedures.

This work aims at filling this gap and establishing Key Performance Indicators (KPIs) that analyze the potential of each test design to provide valuable data for the material characterization and model calibration procedures. Three heterogeneous tests, deformed up to rupture under a uniaxial load, were chosen to be analyzed. The investigation is in a first step purely numerical. Based on the mechanical fields, the potential of each test was evaluated using the proposed KPIs.

Heterogeneous Tests Analysis

Key Performance Indicators. The aim of this work consists in evaluating and comparing the potential of each test to provide relevant information for the material identification and model calibration procedures. For that, some scalar metrics are here proposed. The first metric consists in a mechanical indicator proposed by Souto et. al. [12] that can be defined as

$$I_{\mathrm{T}} = w_{\mathrm{r1}} \frac{\mathrm{Std}(\varepsilon_2/\varepsilon_1)}{w_{\mathrm{a1}}} + w_{\mathrm{r2}} \frac{(\varepsilon_2/\varepsilon_1)_{\mathrm{R}}}{w_{\mathrm{a2}}} + w_{\mathrm{r3}} \frac{\mathrm{Std}(\bar{\varepsilon}^{\mathrm{p}})}{w_{\mathrm{a3}}} + w_{\mathrm{r4}} \frac{\bar{\varepsilon}^{\mathrm{p}}_{\mathrm{max}}}{w_{\mathrm{a4}}} + w_{\mathrm{r5}} \frac{\mathrm{Av}(\bar{\varepsilon}^{\mathrm{p}})}{w_{\mathrm{a5}}}, \quad (1)$$

where ε_1 and ε_2 are the principal major and minor strains in the sheet plane, respectively. The equivalent plastic strain, $\bar{\varepsilon}^{\mathrm{p}}$, and its maximum value, $\bar{\varepsilon}^{\mathrm{p}}_{\mathrm{max}}$, are also considered as evaluation criteria for the test. This indicator evaluates different features: the strain state standard deviation, the strain state range, the standard deviation, the maximum, and the average value of the equivalent plastic strain. The importance of each term is adjusted and normalized using absolute values ($w_{\mathrm{a}i}$, with $i \in [1,5]$) and relative weights ($w_{\mathrm{r}i}$, with $i \in [1,5]$). The chosen values for these parameters can be seen in Table 1. A more detailed description of the indicator as well as the established values for the normalization are described in [12], however, a higher indicator value means a more informative and richer test in terms of strain heterogeneity.

Table 1. Absolute and relative weights for the adjustment and normalization of the indicator terms.

ω_{a1}	ω_{a2}	ω_{a3}	ω_{a4}	ω_{a5}	ω_{r1}	ω_{r2}	ω_{r3}	ω_{r4}	ω_{r5}
1	4	0.25	1	1	0.3	0.03	0.17	0.4	0.1

In a similar way, the scalar indicator proposed by Barroqueiro et. al. [7] is used to evaluate the stress states heterogeneity, in this case, considering only tension, compression, and shear. It can be stated as

$$\boldsymbol{id} = \prod_{s=1}^{3} \left[\frac{3}{\sum_{e=1}^{n} \boldsymbol{X_e}} \sum_{e=1}^{n} (\boldsymbol{\delta_e^s Z_e X_e}) \right]. \quad (2)$$

Materials Research Proceedings 28 (2023) 1121-1130 https://doi.org/10.21741/9781644902479-123

The index *s* relates to the stress state, compression, shear, and tension, respectively. The term $\boldsymbol{Z_e}$ stands for the penalization of stress concentrations and unstressed material while the parameter $\boldsymbol{\delta_e^s}$ is responsible for identifying the stress state in each element $\boldsymbol{e}$. In this case, the term $\boldsymbol{X_e}$ corresponds to the volume of each finite element. The ideal solution would present the same amount of material in the three stress states (tension, compression, and shear) without stress concentrations or unstressed material. The multiplicative behavior of the indicator leads to values close to zero most the elements are subjected to tensile loading, being only a few subjected to shear and compression. More information on the computation of the indicator can be found in [7].

Another metric, proposed by Oliveira et. al. [18], evaluates the sensitivity of the test to anisotropy. It was derived from Mohr's circle equations, and it was introduced for a plane stress state. Based on the principal angle's formulation, it considers the maximum principal stress in absolute value, and the range of tensile orientations typically used to calibrate the material's anisotropic behavior. Represented by γ and denominated by rotation angle, it refers to the principal direction associated with the maximum principal stress in absolute value and, it ranges from 0° and 90°, being given by

$$\gamma = \begin{cases} 45 & \text{if } \sigma_{xx} = \sigma_{yy} \text{ and } \sigma_{xy} \neq 0 \\ 45(1-q) + q|\beta| & \text{otherwise} \end{cases} \quad (3)$$

where β is the principal angle and q is an integer that ranges between -1 and 1, that can be defined as

$$q = \frac{\sigma_{xx}-\sigma_{yy}}{|\sigma_{xx}-\sigma_{yy}|}\frac{|\sigma_1|-|\sigma_2|}{||\sigma_1|-|\sigma_2||} \quad (4)$$

where σ_1 and σ_2 are the principal major and minor stresses, respectively. Since a rotation angle value is related to each material point, an average metric needs to be defined to characterize the sensitivity to anisotropy of each test. Therefore, it is proposed to use the standard deviation measure of the rotation angle to evaluate each test.

Specimen designs. In this work, three specimen designs proposed in the literature were chosen to be analyzed. To improve the quality of the information that can be extracted from a single mechanical test, their geometries were designed from different approaches. The first design was proposed by Rossi et. al. [19] and is usually referenced as Notched. Jones et. al. [2] developed the second specimen geometry, referred as D, via an iterative geometry design process aided by engineering intuition. The last specimen was obtained from a topology-based design methodology [20], designed with the goal of presenting the most heterogeneous displacement field. This will be referred to as TopOpt. The selected geometries are depicted in Fig. 1 along with their dimensions. The three specimen geometries were considered to be machined at 45° with respect to the rolling direction (along the x-direction) in order to enhance the heterogeneity of the mechanical fields.

Material behavior. The material considered in this work is a dual-phase steel (DP600) [21] with a thickness of 0.8 mm. The elastic behavior is considered isotropic, being modeled by Hooke's law. The plastic behavior is anisotropic and is defined by the Yld2000-2d anisotropy yield criterion [22]. The isotropic hardening is characterized by the Swift Law. The material parameters that describe the proposed behavior are in Table 2.

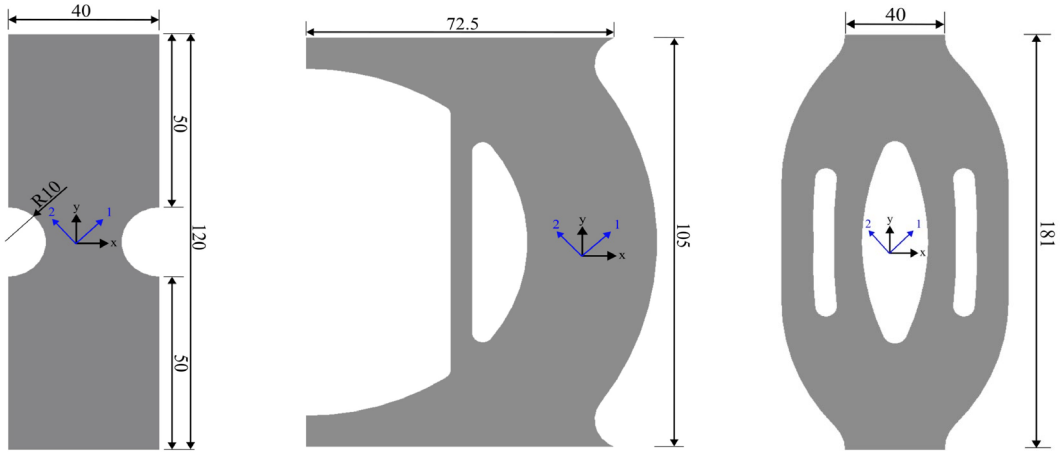

Fig. 1. Specimen designs selected to be analysed in this work: (a) Notched, (b) D and (c) TopOpt.

Table 2. Elastic and constitutive model parameters for the Swift's law and the Yld2000-2d yield function of the DP600 [21].

E[GPa]	ν	K[MPa]	ε_0	n				
210	0.3	979.46	0.00535	0.194				
α_1	α_2	α_3	α_4	α_5	α_6	α_7	α_8	a
1.011	0.964	1.191	0.995	1.010	1.018	0.977	0.935	6

Numerical simulation. Finite element simulations were carried out using Abaqus/Standard to submit each test configuration to a uniaxial tensile loading. Four-node shell elements were used with reduced integration and hourglass control. An element size of 0.5 mm was used for each specimen. The numerical simulations were performed with automatic time stepping and a maximum increment size of 0.02. The material behavior was described with the aid of a UMMDP (User Material Model Driver for Plasticity). Regarding the boundary conditions of the test, the bottom edge of the specimen was constrained in all degrees of freedom while the displacement at the top edge was constrained in *x*- and *z*- directions. A displacement was applied in y- direction. Each mechanical test is performed up to rupture, being the stopping condition established through the Forming Limit Curve (FLC), which is represented in the major and minor strains diagrams of each test. Therefore, the values of the applied displacement that led to rupture were 2.45 mm, 6.38 mm, and 12.45 mm, for the Notched, D and TopOpt, respectively.

Results and Discussion

In this section, the numerical information extracted is used to evaluate the potential of each test. Fig. 2 exhibits the principal stress and strain diagrams and the distribution of the equivalent plastic strain in the specimen just before rupture. Each line stands for the information of one test configuration. The principal strains and stresses diagrams provide huge information on the heterogeneity of the strain and stress fields induced on the specimens as well as the stress and strain state ranges. The equivalent plastic strain distribution on the specimen allows us to understand the areas where a higher magnitude of the variable is achieved. The material points in the elastic regime are represented in grey since these do not provide much information for the characterization of the plastic behavior. By contrast, the color associated with each material point in the plastic regime corresponds to the magnitude of its equivalent plastic strain. All the diagrams present the same scale between tests for easier comparison. `

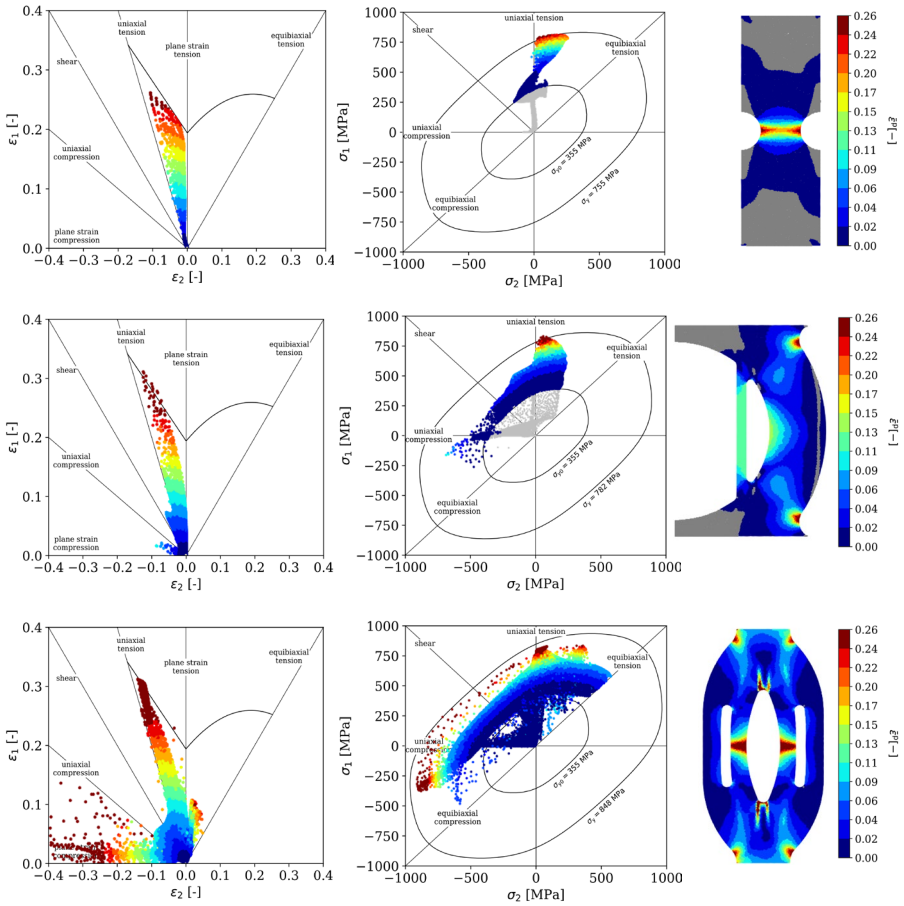

Fig. 2. Principal strains and stresses diagrams and equivalent plastic strain distribution for each test design at the moment just before rupture. Both the initial surface and the one associated with the maximum yield stress are plotted in the principal stress diagrams.

It can be noted that the Notched specimen is the one that presents the smallest stress state range, being limited to uniaxial tension. Similarly, the strain states are mainly located between uniaxial tension and plane strain tension. Regarding the equivalent plastic strain, the higher values of this variable are located in the center part of the specimen. The other material points in the plastic regime are under low values of plastic strain.

In contrast, both D and TopOpt specimens present strain states ranging from plane strain compression and plane strain tension. Although both specimens present material points from uniaxial compression to plane strain compression, the distribution is much denser in the TopOpt specimen. Regarding the principal stresses diagram, there are material points between equibiaxial compression and equibiaxial tension in both specimens, D and TopOpt. However, the latter is the one that presents the largest stress state range. When compared to the Notched specimen, both the D and TopOpt specimens present higher values of plastic strains as well as a larger part of the material points in the plastic regime. In the case of the D specimen, the distribution is more spread, being mainly placed along the curve part of the specimen. The TopOpt specimen presents all the material points in the plastic regime at the moment just before rupture, being the one that achieves higher values of plastic strain. However, these are concentrated in small areas and near the specimen boundaries. This makes the extraction of the information difficult using full-field measurement techniques. It is worth noting that there are material points with plastic strains that are located inside the initial yield surface. This is due to the non-monotonic behavior of some material points. During the test, they enter the plastic regime, but as of a certain point, their strain

paths change direction, leading to a decrease in the induced stresses. Since the equivalent plastic strain consists in a cumulative value, at the moment of rupture, these points are located inside the yield surface but present plastic strains.

With the aim of analyzing quantitatively the information given by the diagrams presented in Fig. 2, the mechanical indicator proposed by [12] has been computed. In Fig. 3, the values of the mechanical indicator for each test configuration are presented as well as its terms individually. All the terms, except for the ones involving the standard deviation computation, were normalized taking into account the size and the number of elements for a fair comparison of the designs.

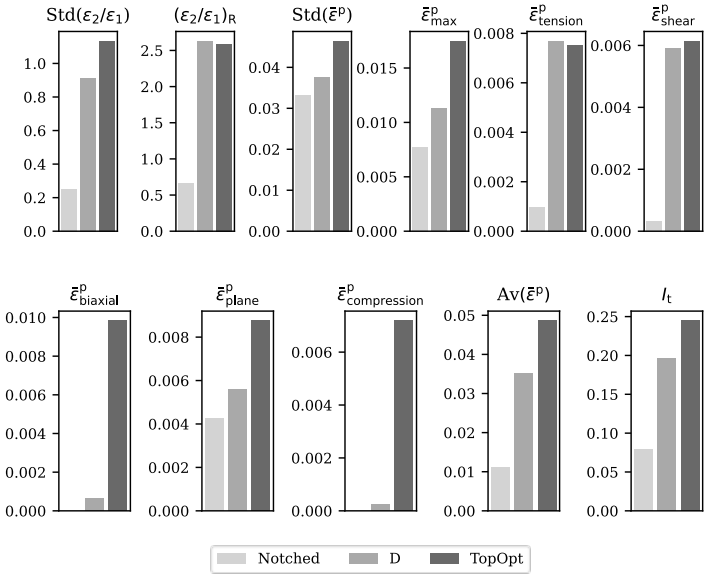

Fig. 3. Values of the mechanical indicator proposed by Souto et. al. [12] and its terms computed individually for all the test designs.

It can be noted that the TopOpt specimen presents the highest overall value of the indicator, followed by the D and the Notched specimens. The higher the indicator value, the more informative the test design is. Regarding the equivalent plastic strain, as has already been referred to previously, the TopOpt presents the highest values and the largest distribution of this variable. It is also the one that presents the most material points in the plastic regime under the strain states evaluated with this indicator. The D specimen also presents an interesting diversity of strain states and equivalent plastic strain distribution. Concerning the strain states range, both specimens present similar performance. Fig. 4 depicts the elements distribution of the D and TopOpt specimens over the strain state range that is limited between -15 and 1. The TopOpt specimen presents a more even distribution of the elements over the presented range although two peaks located around uniaxial tension and between plane strain and uniaxial compression can be noted. In the D specimen, the majority of the material points are between uniaxial tension and shear. Therefore, the standard deviation is higher in the TopOpt specimen than in the D one. However, the second term that evaluates the difference between the maximum and minimum values of the principal strains' ratio is equal for both specimens since these values correspond to the imposed limits. The final value is different due to the normalization of the term concerning the size and number of the elements of each specimen. In previous works [12,23], it was proposed a ranking of the indicator value for well-known standard tests and for new geometries that have been proposed since then. Despite the modification of the strain state range for the computation of the indicator in this work, an updated ranking can be seen in Fig. 5. Also, in the work developed by Thoby et. al [24], it was made a comparison of several specimen designs and this mechanical indicator was used to compare them. Although some terms have been adapted, a similar ranking was obtained.

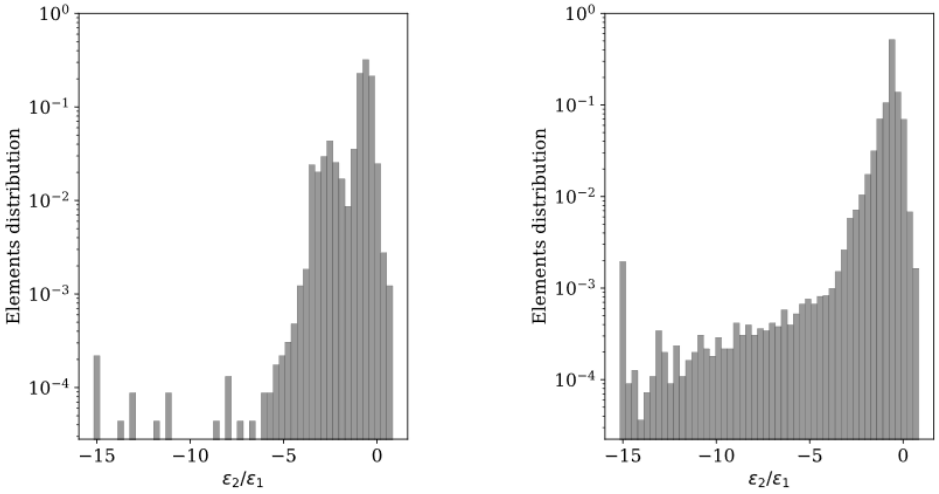

Fig. 4. Elements distribution over the strain state range induced in the (a) D and (b) TopOpt specimens.

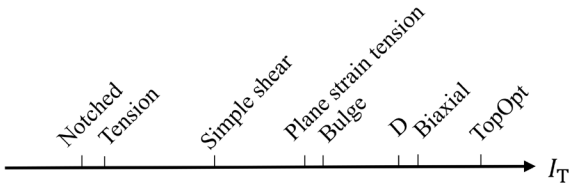

Fig. 5. Ranking for the tests evaluated in [8] and for the Notched, D and TopOpt test designs.

The other mechanical indicator proposed to evaluate the performance of the specimens is the one proposed by [7]. Fig.6 provides the value of the indicator as well as the terms corresponding to each stress state analyzed. Overall, the TopOpt specimen is the one that presents the highest heterogeneity of stress states (tension, compression, and shear). It can be noted that the stress states under which all the specimens present more material points is tension, followed by shear. In compression, there is a significant difference between the TopOpt and the others. The TopOpt specimen was designed considering this indicator, so it is expected that this design presents the highest value.

The rotation angle provides information on the sensitivity of the test to anisotropy. Fig. 7 represents the distribution of the material points over the range of rotation angle values (0° to 90°) for each test configuration. The more dispersed the distribution, the higher the sensitivity to the anisotropic behavior it presents. Therefore, to evaluate quantitatively the information given by the diagrams, it is represented the standard deviation value of the rotation angle of each test design in Table 3. Since the material orientation is 45° in relation to the loading direction, it is expected that most of the material points present rotation angle values in the same order as the material orientation, being the mean value of the rotation angle around 45° for all the test designs. Although the distribution is well dispersed between 0° and 90°, the Notched specimen is the test with the lowest standard deviation value, presenting the majority of the points in the elastic regime with rotation angle values around 45°. However, there is a significant spread of material points in the plastic regime with rotation angle values between -15° and 75°. In contrast, the D specimen presents most of the material points in the plastic regime between rotation angle values of 30° and 60°. The rotation angle standard deviation of the D specimen is considerably higher than the

Notched one, pointing out the difference between both distributions. The TopOpt specimen presents the best range of rotation angle values, presenting material points in the plastic regime between 0° and 90°, covering the whole range. Although this leads to a lower density of points over the range, it presents the highest standard deviation value of all the tests, allowing us to notice a good sensitivity to anisotropy.

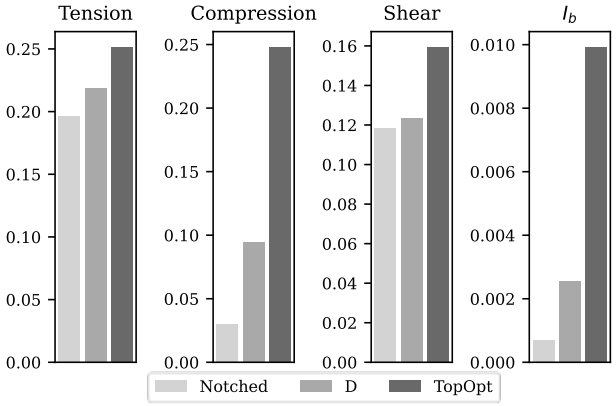

Fig. 6. Values of the performance indicator proposed by Barroqueiro et. al [7] and its terms for all test designs.

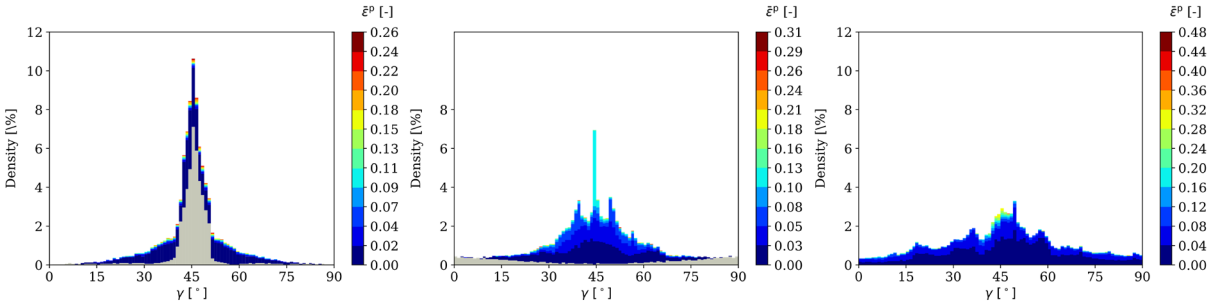

(a) (b) (c)

Fig. 7. Rotation angle values for each test configuration: (a) Notched, (b) D and (c) TopOpt.

Table 3. Mean and standard deviation values of the rotation angle distribution for each test design.

	Notched	D	TopOpt
Av(γ) [°]	45.33	44.92	45.70
Std(γ)	10.16	17.38	19.70

Summary

This work aimed at proposing a set of KPIs to evaluate the performance of several test designs in providing the most informative quantity of data for the material behavior characterization and model calibration procedures.

Three specimen designs were subjected numerically to a uniaxial loading test up to rupture. Based on the obtained mechanical fields, the potential of each test design was analyzed and compared with the others. Firstly, the information given by the principal strains and stresses diagrams was quantified by the computation of the mechanical indicator proposed by Souto et. al. [12]. The obtained values allow us to conclude that the TopOpt specimen presented the larger strain state range and most interesting equivalent plastic strain distribution, followed closely by the D specimen. The stress states heterogeneity present in the specimen was also evaluated by the

mechanical indicator proposed by Barroqueiro et. al. [7]. Due to the tensile conditions of the test, all the specimens presented the majority of their material points under tension, being the TopOpt specimen the one with higher heterogeneity of stress states and, therefore, with the higher indicator value. Based on the rotation angle values distribution, it can be concluded that the TopOpt and the D specimens are the ones that present the higher sensitivity to anisotropy due to the higher standard deviation values. Regarding the TopOpt specimen, due to its complex geometry, it may suffer from buckling when tested. However, this situation may lead to a better performance as long as this behavior can be captured by the full-field measurement technique.

This work already consists in a step closer to a more straightforward approach to choose the most informative heterogeneous mechanical test. At this stage, these KPIs evaluate each test based on the diversity of mechanical phenomena and strain and stress states that are covered. However, there is still a need for metrics that take into account the inverse identification quality, for example, the sensitivity of each test to the model parameters and, also, the full-field measurement technique.

Acknowledgments
This project has received funding from the Research Fund for Coal and Steel under grant agreement No 888153. The authors also acknowledge the financial support under the projects UIDB/00481/2020 and UIDP/00481/2020 – FCT – Fundação para a Ciência e Tecnologia; and CENTRO-01-0145-FEDER-022083 – Centro Portugal Regional Operational Programme (Centro2020), under the PORTUGAL 2020 Partnership Agreement through the European Regional Development Fund. M. Gonçalves is grateful to the FCT for the Ph.D. grant Ref. UI/BD/151257/2021.

Disclaimer
The results reflect only the authors' view, and the European Commission is not responsible for any use that may be made of the information it contains.

References
[1] J.H. Kim, F. Barlat, F. Pierron, M.G. Lee, Determination of Anisotropic Plastic Constitutive Parameters Using the Virtual Fields Method, Exp. Mech. 54 (2014) 1189-204. https://doi.org/10.1007/s11340-014-9879-x
[2] E.M.C. Jones, J.D. Carroll, K.N. Karlson, S.L.B. Kramer, R.B. Lehoucq, P.L. Reu, D.Z. Turner, Parameter covariance and non-uniqueness in material model calibration using the Virtual Fields Method, Comput. Mater. Sci. 152 (2018) 268-290. https://doi.org/10.1016/j.commatsci.2018.05.037
[3] T. Pottier, P. Vacher, F. Toussaint, H. Louche, T. Coudert, Out-of-plane Testing Procedure for Inverse Identification Purpose: Application in Sheet Metal Plasticity, Exp. Mech. 52 (2012) 951–963. https://doi.org/10.1007/s11340-011-9555-3
[4] N. Souto, A. Andrade-Campos, S. Thuillier, Mechanical design of a heterogeneous test for material parameters identification, Int. J. Mater. Form. 10 (2016) 353-367. https://doi.org/10.1007/s12289-016-1284-9
[5] M. Conde, Y. Zhang, J. Henriques, S. Coppieters, A. Andrade-Campos, Design and validation of a heterogeneous interior notched specimen for inverse material parameter identification, Finite Elem. Anal. Des. 214 (2023) 103866.
[6] M. Gonçalves, A. Andrade-Campos, B. Barroqueiro, On the design of mechanical heterogeneous specimens using multilevel topology optimization, Adv. Eng. Softw. 175 (2023) 103314.
[7] B. Barroqueiro, A. Andrade-Campos, J. Dias-de-Oliveira, R.A.F. Valente, Design of mechanical heterogeneous specimens using topology optimization, Int. J. Mech. Sci. 181 (2020) 105764. https://doi.org/10.1016/j.ijmecsci.2020.105764
[8] P. Wang, F. Pierron, M. Rossi, P. Lava, O.T. Thomsen, Optimised experimental characterisation of polymeric foam material using DIC and the virtual fields method, Strain 52 (2016) 59-79.

https://doi.org/10.1111/str.12170
[9] L. Chamoin, C. Jailin, M. Diaz, L. Quesada, Coupling between topology optimization and digital image correlation for the design of specimen dedicated to selected material parameters identification, Int. J. Solids Struct. 193-194 (2020) 270-286. https://doi.org/10.1016/j.ijsolstr.2020.02.032
[10] X. Gu, F. Pierron, Towards the design of a new standard for composite stiffness identification, Compos. Part A Appl. Sci. Manuf. 91 (2016) 448-460.
https://doi.org/10.1016/j.compositesa.2016.03.026
[11] M. Rossi, M. Badaloni, P. Lava, D. Debruyne, F. Pierron, A procedure for specimen optimization applied to material testing in plasticity with the virtual fields method, AIP Conf. Proc. 1769 (2016) 200016. https://doi.org/10.1063/1.4963634
[12] N. Souto, S. Thuillier, A. Andrade-Campos, Design of an indicator to characterize and classify mechanical tests for sheet metals, Int. J. Mech. Sci. 101-102 (2015) 252-271.
https://doi.org/10.1016/j.ijmecsci.2015.07.026
[13] M. Conde, A. Andrade-Campos, M.G. Oliveira, J.M.P. Martins, Design of heterogeneous interior notched specimens for material mechanical characterization, Esaform 2021, Liège, Belgique, 2021.
[14] F. Pierron, M. Grédiac, Towards Material Testing 2.0. A review of test design for identification of constitutive parameters from full-field measurements, Strain 57 2021) 1-22.
https://doi.org/10.1111/str.12370
[15] M. Grédiac, The use of full-field measurement methods in composite material characterization: Interest and limitations, Compos. Part A Appl. Sci. Manuf. 35 (2004) 751-761.
https://doi.org/10.1016/j.compositesa.2004.01.019
[16] S. Avril, M. Bonnet, A.S. Bretelle, M. Grédiac, F. Hild, P. Ienny, F. Latourte, D. Lemosse, S. Pagano, E. Pagnacco, F. Pierron, Overview of identification methods of mechanical parameters based on full-field measurements, Exp. Mech. 48 (2008) 381-402. https://doi.org/10.1007/s11340-008-9148-y
[17] F. Pierron, M. Grédiac, The virtual fields method: Extracting constitutive mechanical parameters from full-field deformation measurements, Springer Verlag, 2012.
[18] M.G. Oliveira, S. Thuillier, A. Andrade-Campos, Evaluation of heterogeneous mechanical tests for model calibration of sheet metals, J. Strain. Anal. Eng. Des. 57 (2022) 208-224.
https://doi.org/10.1177/03093247211027061
[19] M. Rossi, F. Pierron, M. Štamborská, Application of the virtual fields method to large strain anisotropic plasticity, Int. J. Solids. Struct. 97-98 (2016) 322-335.
https://doi.org/10.1016/j.ijsolstr.2016.07.015
[20] M. Gonçalves, A. Andrade-Campos, S. Thuillier, On the topology design of a mechanical heterogeneous specimen using geometric and material nonlinearities, IOP Conf. Ser. Mater. Sci. Eng. 1238 (2022) 012055. https://doi.org/10.1088/1757-899X/1238/1/012055
[21] F. Ozturk, S. Toros, S. Kilic, Effects of Anisotropic Yield Functions on Prediction of Forming Limit Diagrams of DP600 Advanced High Strength Steel, Procedia Eng. 81 (2014) 760-765.
https://doi.org/10.1016/j.proeng.2014.10.073
[22] F. Barlat, J.C. Brem, J.W. Yoon, K. Chung, R.E. Dick, D.J. Lege, F. Pourboghrat, S.-H. Choi, E. Chu, Plane stress yield function for aluminum alloy sheets - Part 1: Theory, Int. J. Plast. 19 (2003) 1297-1319. https://doi.org/10.1016/S0749-6419(02)00019-0
[23] J. Aquino, A. Andrade-Campos, J.M.P. Martins, S. Thuillier, Design of heterogeneous mechanical tests: Numerical methodology and experimental validation, Strain 55 (2019) 1-18.
https://doi.org/10.1111/str.12313
[24] J.D. Thoby, T. Fourest, B. Langrand, D. Notta-Cuvier, E. Markiewicz, Robustness of specimen design criteria for identification of anisotropic mechanical behaviour from heterogeneous mechanical fields, Comput. Mater. Sci. 207 (2022) 111260. https://doi.org/10.1016/j.commatsci.2022.111260

Materials Research Proceedings 28 (2023) 1131-1142 https://doi.org/10.21741/9781644902479-124

On the inverse identification of sheet metal mechanical behaviour using a heterogeneous Arcan virtual experiment

HENRIQUES Joao[1,2,a *], ANDRADE-CAMPOS António[1,2,b] and XAVIER José [2,3,c]

[1]Centre for Mechanical Technology and Automation (TEMA), Department of Mechanical Engineering, University of Aveiro, Campus Universitário de Santiago, 3810-193 Aveiro, Portugal

[2]Intelligent Systems Associate Laboratory (LASI), 4800-058 Guimarães, Portugal

[3]Research and Development Unit for Mechanical and Industrial Engineering (UNIDEMI), Department of Mechanical and Industrial Engineering, NOVA School of Science and Technology, NOVA University Lisbon, 2825-149 Lisbon, Portugal

[a]joaodiogofh@ua.pt, [b]gilac@ua.pt, [c]jmc.xavier@fct.unl.pt

Keywords: Sheet Metal Forming, Anisotropic Plasticity, Arcan Test, Heterogeneous Test Evaluation, Inverse Identification, Digital Image Correlation, Synthetic Images

Abstract. Modelling and simulation are critical stages of product development in modern industry. Simulation tools in solid mechanics use constitutive models and their parameters to describe the behaviour of materials. Nowadays, with the use of heterogeneous test configurations and full-field measurements, it is possible to measure a combination of multiple strain states, allowing for the identification of multiple parameters from a single test with reduced cost and time. This work aims to investigate the potential for obtaining heterogeneous states of strain\stress with the Arcan test configuration. A finite element model was developed using a specimen with a smooth arc section in which the loading and material directions varied, producing tensile, shear, or mixed mode responses. The most heterogeneous test configuration was selected using a heterogeneous criterion and the numerical results were used to generate synthetic speckle pattern images and further processed by digital image correlation (DIC). The DIC results were used as input for the identification procedure through the virtual fields method (VFM) for the simultaneous calibration of the Swift hardening law and the Hill'48 anisotropic yield criterion. The identified solution was compared with the ground truth material parameters. The results show the potential of combining the Arcan test with the VFM to simultaneously identify material parameters for anisotropic plasticity models of sheet metals.

Introduction

Computer-aided engineering systems are a powerful tool used in modern industry to optimise costs and time consumption in the design of new products. Nowadays, in metal forming technology, the development of sheet metal parts tends to be more virtual through the use of numerical simulation. Sheet metal anisotropy is a critical property that greatly influences the accuracy of the numerical results [1]. This anisotropy is a result of the rolling process that produces preferential orientations in the material texture [2], which induces differences in the yield stress along different orientation angles from the rolling direction (RD). Therefore, the accuracy of the simulation is heavily reliant on the calibration of the model that describes the behaviour of the materials during the forming process including the anisotropy. The improved accuracy of complex constitutive models is related to increased flexibility in the mathematical formulation, which translates to a greater number of constitutive parameters to calibrate, resulting in increased calibration complexity [3]. Classically, the calibration procedure was done using standard homogeneous tests [4]. However, as models become more accurate and complex, their calibration has become a difficult task, increasing the number of experimental tests required to accurately calibrate such models.

Content from this work may be used under the terms of the Creative Commons Attribution 3.0 license. Any further distribution of this work must maintain attribution to the author(s) and the title of the work, journal citation and DOI. Published under license by Materials Research Forum LLC.

Recent developments in optical full-field measurement techniques, such as digital image correlation (DIC) [5], have been changing the approach to the calibration procedure of material constitutive models. The increased amount of measurable kinematic data has enabled the transition from simple statically determinate tests to innovative tests with complex geometries that produce heterogeneous states of stress and strain, allowing for the collection of more data and thus reducing the experimental effort [6]. However, there is no closed-form formulation relating local kinematic data to constitutive parameters. As a result, in recent years, there has been an increased interest in the development of robust inverse identification techniques, most notably the virtual fields method (VFM) [7] and the finite element model updating (FEMU) method [8]. These approaches have altered the way mechanical tests are conducted, eventually leading to the development of new standards as cameras gradually replace strain gauges and extensometers in both academia and industry. Nonetheless, the ability to reduce the number of experimental tests required to simultaneously identify material parameters is highly dependent on the test configuration used, which implies that optimised test configurations are required to fully benefit from this new paradigm [6,9].

The mechanical testing scientific community has made significant efforts in recent years to find methodologies for developing optimised specimens [6]. There has been an increase in the development of heterogeneous tests through different methodologies, for instance, using empirical knowledge [10,11] or numerical optimisation procedures [9,12,13]. The specimen design by empirical knowledge is tied to the author's previous experience. However, this approach frequently results in unoptimised specimen shapes, especially when using complex constitutive models, since the relationship between the constitutive parameters and strain measurements can be quite complex [6]. A more logical approach that permits the use of various design variables is the use of numerical optimisation procedures. The design variables can range from the strain states [4,9], identification quality [14] or full-identification chain quality [15,16]. For a more comprehensive review of the state-of-the-art of heterogeneous specimen design, the reader is referred to the work of Pierron and Grédiac [6].

The Arcan test is an interesting test configuration since it allows varying the loading direction in a standard uniaxial tensile testing machine. In the framework of sheet metal plasticity, the majority of the previously mentioned authors focused on optimising the shape of the specimen or using geometries with holes or notches. However, changing the loading direction can also be used to increase strain heterogeneity, which in the case of the Arcan test can result in tension, shear or mixed mode responses. Wang *et al.* [15,16] designed orthotropic foam tests using the Arcan fixture by varying the loading direction and the material orientation. The authors were able to successfully calibrate the orthotropic linear elastic constitutive model with a single test when using the optimised design parameters. Although some authors used the Arcan test in sheet metal plasticity [17,18], it is seldom used in heterogeneous test design for the calibration of plastic constitutive models. Nonetheless, the Arcan test has the potential to provide interesting heterogeneous test configurations when used for test design in sheet metal plasticity.

The goal of this work is to evaluate the heterogeneity of stress/strain states for different Arcan test configurations using a specimen with a smooth arc section [18]. A finite element model was developed in which the loading and material directions varied, producing tensile, shear, or mixed mode responses. The reference constitutive parameters for the DP600 steel were used [19] to select the most promising test configuration using a heterogeneous criterion [4,12]. To get closer to real experimental data, the FEA results for the most heterogeneous test configuration were used to generate synthetic speckle pattern images, which were further processed by DIC. The parameters for the Hill'48 yield criteria and the Swift hardening law were simultaneously identified using the VFM and compared to the ground truth parameters.

Methodology

Numerical model.

In this work, a finite element model of the Arcan test was developed using a specimen with a smooth arc section [18] under quasi-static loading conditions. The load direction angle (α) and the RD angle (θ) with the x-axis were varied, producing tensile, shear, or mixed mode responses. The angles θ and α assumed the values of 0º, 45º or 90º, totalling nine possible test configuration combinations. The finite element model was implemented in ABAQUS/Standard software [20] assuming plane stress conditions and a thickness of 0.8 mm for the specimen. A mesh convergence study was performed and a total of 2596 four-node plane stress elements (CPS4R) were used with displacement-driven loading conditions. The forming limit curve (FLC) is used as the rupture criteria and the test was conducted until the failure of the specimen with a total of 40 load steps. Fig. 1a depicts the specimen geometry and dimensions (in mm) and Fig. 1b shows the FEA mesh and boundary conditions, including the variation of the material and load direction angles.

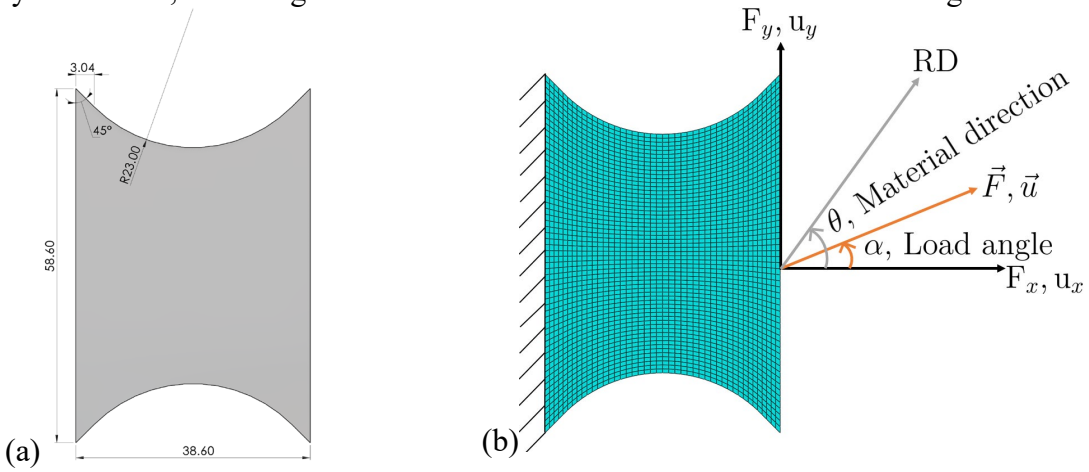

Fig. 1. (a) Geometry and dimensions [mm] of the specimen with smooth arc section [18], (b) Finite element mesh and boundary conditions, showing the variation of the material and load direction angles.

Material and constitutive model.

A sheet metal of DP600 dual-phase steel with 0.8 mm thickness was considered in this work. The elastoplastic behaviour of the material was modelled using phenomenological models, namely isotropic elasticity described by Hooke's law ($E = 210$ GPa and $\nu = 0.3$) and anisotropic plastic behaviour described by the Hill'48 yield criteria [21] and Swift hardening law. The reference parameters of the DP600 steel [19] are presented in Table 2. In this work, the commonly used condition G+H=1 is assumed [3], which deduces that the yield stress in the rolling direction corresponds to the yield stress (σ_y). A user-defined material subroutine, Unified Material Model Driver for Plasticity (UMMDp) [22], was used to model the material behaviour.

Test evaluation.

The selection of the most heterogeneous test configuration is not an obvious task. Therefore, two heterogeneity indicators were used to evaluate the richness of strain/stress in each of the test configurations used. The first indicator was initially proposed by Souto *et al.* [4], and is based on the maximization of five quantities that the ideal test should exhibit and can be written as:

$$IT_1 = w_{\mathrm{r1}} \frac{\mathrm{Std}(\varepsilon_2/\varepsilon_1)}{w_{\mathrm{a1}}} + w_{\mathrm{r2}} \frac{(\varepsilon_2/\varepsilon_1)_{\mathrm{R}}}{w_{\mathrm{a2}}} + w_{\mathrm{r3}} \frac{\mathrm{Std}(\bar{\varepsilon}^{\mathrm{P}})}{w_{\mathrm{a3}}} + w_{\mathrm{r4}} \frac{\bar{\varepsilon}^{\mathrm{P}}_{\mathrm{max}}}{w_{\mathrm{a4}}} + w_{\mathrm{r5}} \frac{\mathrm{Av}(\bar{\varepsilon}^{\mathrm{P}})}{w_{\mathrm{a5}}}, \quad (1)$$

where ε_1 and ε_2 are the major and minor principal strains, respectively, $\bar{\varepsilon}^{\mathrm{P}}$ is the equivalent plastic strain, $\bar{\varepsilon}^{\mathrm{P}}_{\mathrm{max}}$ is the averaged maximum value of the equivalent plastic strain for each stress/strain state and w_{r}, w_{a} are relative and absolute weighting factors, respectively. Since the ratio between

Materials Research Proceedings 28 (2023) 1131-1142 https://doi.org/10.21741/9781644902479-124

the minor and major principal strains represents various strain states, the first two quantities presume that its distribution should be as wide as possible. The final three quantities are related to the equivalent plastic strain, which should be as heterogeneous and widely distributed as possible, as well as have a high global plastic strain level. The quantities are further normalised and adjusted in terms of importance according to the different weights. The weights used in this work were the recommended from the original work by Souto *et al.* [4] and are presented in Table 1.

Table 1. Absolute and relative weighting factors used for the definition of IT_1[4].

w_{a1}	w_{a2}	w_{a3}	w_{a4}	w_{a5}	w_{r1}	w_{r2}	w_{r3}	w_{r4}	w_{r5}
1	4	0.25	1	1	0.3	0.03	0.17	0.4	0.1

The second heterogeneity indicator is the rotation angle (γ) which evaluates the sensitivity of the specimen to anisotropy and is based on the principal angle formulation [23]. This indicator varies between 0º and 90º and represents the principal direction for the maximum principal stress in absolute value and can be written as:

$$\gamma = \begin{cases} 45 & \text{if } \sigma_{11} = \sigma_{22} \text{ and } \sigma_{12} \neq 0 \\ 45(1-q) + q|\beta| & \text{otherwise} \end{cases}, \quad (2)$$

where σ_{11}, σ_{22}, σ_{12} are the components of the Cauchy stress tensor in the material coordinate system and β is the principal angle in degrees and q is an integer that assumes the value of 1 or -1 that can be calculated from:

$$q = \frac{\sigma_{11} - \sigma_{22}}{|\sigma_{11} - \sigma_{22}|} \frac{|\sigma_1| - |\sigma_2|}{\big||\sigma_1| - |\sigma_2|\big|}, \quad (3)$$

where σ_1, σ_2 are the major and minor principal stresses, respectively. The formulation is written in such a way that it can represent most of the conceivable stress/strain states in Mohr's circle [23], except for being undefined in the purely biaxial stress state ($\sigma_{11} = \sigma_{22}$ and $\sigma_{12} = 0$).

Synthetic images and digital image correlation.

The numerical results of the most heterogeneous test configuration were used to synthetically deform a speckle pattern image using the FE Deformation module from the MatchID software [24]. The synthetic speckle pattern images were then further processed with the subset-based 2D-DIC using the MatchID software [24]. The goal of this approach is to simulate a real experiment in which the results are measured by using the DIC filter, where spatial averaging is used to reduce the inherent experimental noise. This approach makes it possible to capture the full uncertainty propagation through the identification chain and leads to more realistic identification results that can also be applied to test design [6].

Furthermore, the choice of DIC settings has a significant impact on measurement accuracy [8]. Therefore, the MatchID Performance Analysis module [24] was used to analyse several combinations of these settings in order to find a good balance between spatial resolution and accuracy. The hardware and DIC settings used here are equal to those used in a previous work (see [25]).

Materials Research Proceedings 28 (2023) 1131-1142 https://doi.org/10.21741/9781644902479-124

Virtual fields method.

The material constitutive parameters were identified using the VFM, which is based on the principle of virtual work. The objective function for the VFM can be written in static conditions while ignoring body forces as:

$$R = \left(- \int_V \boldsymbol{\sigma}\left(\boldsymbol{\chi}, \boldsymbol{\varepsilon}\right) : \operatorname{grad} \mathbf{u}^* \, \mathrm{d}V + \int_{\partial V} \mathbf{T} \cdot \mathbf{u}^* \, \mathrm{d}S \right)^2 \approx 0, \quad (4)$$

where R is the residual, $\boldsymbol{\sigma}$ is the Cauchy stress tensor which is a function of the material parameter set $\boldsymbol{\chi}$ and the strain tensor $\boldsymbol{\varepsilon}$, and $\mathbf{u}^*$ is the virtual displacement vector. The internal virtual work is then calculated for the volume V of the given solid. $\mathbf{T}$ is the traction vector acting on the boundary of the solid and ∂V is the boundary where the loading is applied.

The idea behind the use of VFM for the identification of constitutive parameters is to find the material parameters set that minimises the gap between the internal and external virtual works. Another important aspect of VFM is the selection of appropriate virtual fields $\mathbf{u}^*$, which can be done either manually or automatically. The manual selection of the virtual fields is done by user experience. These must, however, meet the following requirements: (i) $\mathbf{u}^*$ must be kinematically admissible, (ii) $\mathbf{u}^*$ should be constant at the boundary ∂V, in order to use the global force rather than its distribution, which is unknown in experimental tests and (iii) $\mathbf{u}^*$ must be collinear with $\mathbf{T}$ to eliminate components of the loading forces that are unknown [3]. For more details on automatic strategies for the selection of virtual fields see [26,27].

Results and Discussion

Test evaluation. The IT_1 heterogeneity criterion was calculated using the numerical results of each test configuration. To simplify the evaluation, only the results from the last increment before failure were used, since these are a good indication of the stress and strain states observed in a specimen under monotonic loading [4,23]. Each term of the IT_1 criterion was also evaluated separately to see the relative advantages of each test configuration. Fig. 2 depicts the results computed for the IT_1 criterion as well as each of its terms as a function of the load angle (α) for each RD angle (θ).

The results indicate that the shear test configurations (α=90º) are the most heterogeneous, owing to the higher standard deviation of the ratio between the minor and major principal strains, as well as the higher average and maximum value of the equivalent plastic strain. Tensile test configurations (α=0º), on the other hand, provide the least amount of information about the mechanical behaviour of the material, which is not surprising given the relatively simple specimen geometry used, which promotes primarily the tensile stress/strain state localised in a narrow area of the specimen. According to the results, the mixed-mode response test configuration (α=45º) provides more information about the material's mechanical behaviour than the tensile test configurations, but it is still less heterogeneous than the shear test configurations. Furthermore, it can be seen that the shear test configuration with the 90º RD (θ=90º) gives the most information regarding the mechanical behaviour of the material in accordance with the criteria being used. This is primarily due to the larger equivalent plastic strain, average and standard deviation values.

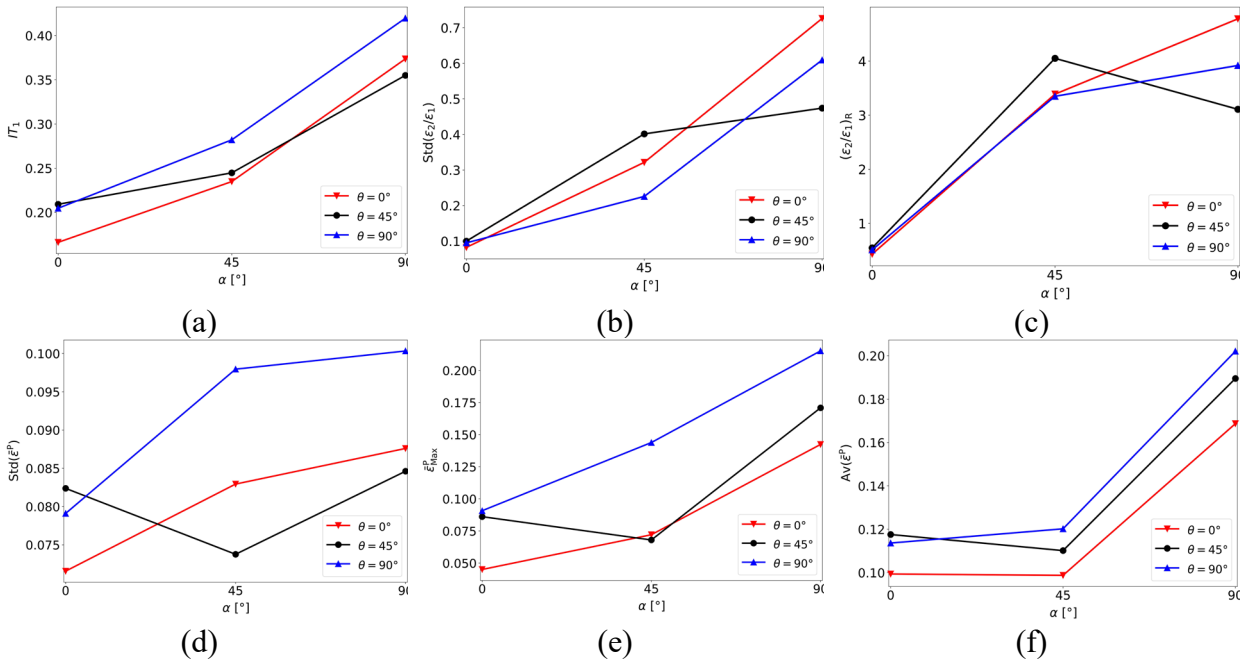

Fig. 2. Mechanical test heterogeneity indicator results for all test configurations: (a) IT_1, (b) $Std(\varepsilon_2/\varepsilon_1)$, (c) $(\varepsilon_2/\varepsilon_1)_R$, (d) $Std(\bar{\varepsilon}^P)$, (e) $\bar{\varepsilon}^P_{max}$ and (f) $Av(\bar{\varepsilon}^P)$.

A qualitative analysis was also carried out by investigating the major and minor principal stresses and strains as well as the rotation angle criterion for the most heterogeneous test configuration of each assessed load angle (see Fig. 3).

According to the principal strains and stresses diagrams, the shear load test with θ=90º exhibits the greatest variety of stress/strain states, ranging from uniaxial compression to pure shear to uniaxial tension. The other test configurations, on the other hand, mostly provide the uniaxial tension state, with the uniaxial tensile test configuration approaching plane strain tension. These qualitative results support the previous analysis using the IT_1 criterion, which indicates that the shear load test configuration is the most heterogeneous, with a higher standard deviation in the ratio between the principal strains.

It is also interesting to locate the material points of higher equivalent plastic strain in both strain and stress diagrams, the rotation angle histogram and the contour represented in the specimen geometry inside the rotation angle diagram. For instance, in Fig. 3a, the points with the highest equivalent plastic strain are in the specimen's centre and are primarily in the uniaxial tension state, with rotation angles ranging from 30º to 60º. According to the rotation angle histogram results, the material points for the loading angles of 45° and 90° (Figs. 3b and 3c) are primarily on the right side (between 45° and 90°), with some points also on the left side of the histogram, but with low levels of equivalent plastic strain, and in the case of the test with a loading angle of 45º, they still are in the elastic regime. On the other hand, the rotation angle histogram for the tensile load test (Fig. 3a) shows a wide distribution of points, with the highest equivalent plastic strain occurring between 30º and 60º, which indicates that this test may be the most sensitive to anisotropy out of the three tests investigated in this qualitative analysis.

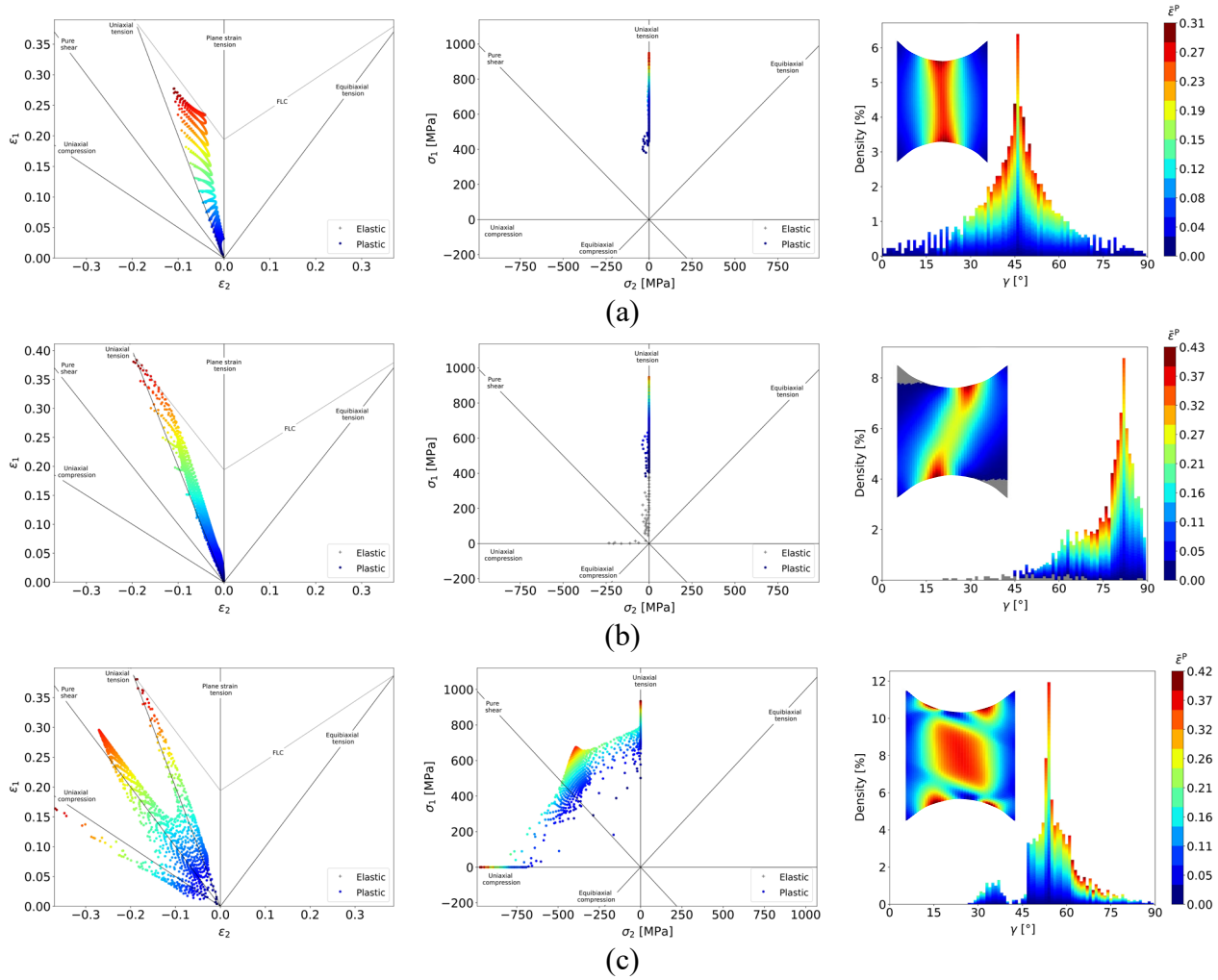

Fig. 3. Numerical results regarding principal strains diagram (left), the principal stresses diagram (center) and rotation angle (right) for the most heterogeneous test configuration of each load angle: (a) α = 0° and θ = 45°, (b) α = 45° and θ = 90° and (c) α = 90° and θ = 90°.

While it can be difficult to quantitively rank all the test configurations, the test with a loading angle of 45º can generally be considered to be the least interesting one. The shear load test appears to outperform the tensile load test in the heterogeneity of strain/stress states. However, the opposite can be said about the rotation angle distribution. Nonetheless, the shear load test with the 90º RD was chosen for the identification process due to significantly higher performance in the stress/strain states and IT_1 criterion results, despite having a narrower distribution of the rotation angle.

Inverse identification.

The numerical results of the shear load test with the 90º RD were used to generate synthetic speckle images, which were then processed by DIC. The DIC results were then used for the inverse identification with VFM with one uniform virtual field, using the VFM module from the MatchID software [24]. Four identification runs were carried out, each with a unique initial set of parameters that were generated using the Latin hypercube sampling (LHS) method. Table 2 lists the reference parameters for the DP600 steel [19], the lower and upper bounds for each parameter, the initial set of parameters used for each identification run, the residual value, the identification results and the absolute relative error.

Table 2. Reference [19] and initial set of parameters, lower and upper bounds, identification results, final residual value and absolute relative error of each of the identification runs.

	F	G	H	N	K [MPa]	ε_0	n
Ref. parameters	0.3748	0.5291	0.4709	1.1125	979.46	0.00535	0.194
Lower bound	0.2624	-	0.3296	0.7787	685.62	0.00370	0.136
Upper bound	0.4872	-	0.6122	1.4462	1273.30	0.00700	0.252
Run 1 - Final residual = 0.6632							
Initial parameters	0.3467	-	0.4356	1.3628	759.08	0.00580	0.238
Id. parameters	0.4185	0.6697	0.3303	1.2970	1054.00	0.00534	0.199
|Relative error| [%]	11.66	26.57	29.86	16.58	7.61	0.19	2.58
Run 2 - Final residual = 0.7142							
Initial parameters	0.4591	-	0.5769	1.0290	1052.92	0.00490	0.179
Id. parameters	0.3925	0.6699	0.3301	1.25	1036	0.00559	0.201
|Relative error| [%]	4.72	26.61	29.90	12.36	5.77	4.49	3.61
Run 3 - Final residual = 0.4432							
Initial parameters	0.2905	-	0.5062	0.8621	906.00	0.00410	0.209
Id. parameters	0.4872	0.6704	0.3296	1.4280	1086.00	0.00371	0.1875
|Relative error| [%]	29.99	26.71	30.01	28.36	10.88	30.65	3.35
Run 4 - Final residual = 0.8209							
Initial parameters	0.4029	-	0.3649	1.1959	1199.84	0.00660	0.150
Id. parameters	0.4872	0.6704	0.3296	1.2430	1043.00	0.00700	0.209
|Relative error| [%]	29.99	26.71	30.01	11.73	6.49	30.84	7.73

The results show that the identified constitutive parameters related to the swift hardening law have a lower absolute relative error than the results for the Hill'48 anisotropy yield criterion. This was expected, given that the qualitative analysis conducted previously indicated that this test configuration contained richer information regarding the stress/strain states than the material anisotropy. Though the difference in residual between all the identification runs was relatively low, identification run 3 had the lowest final residual of all the runs that were performed. However, some parameters seem to have higher absolute errors when compared to the reference parameters. This result is the consequence of the noise and uncertainty propagation throughout the whole identification process when using DIC and experimental images. The results could also be improved by using more virtual fields, as previous research has shown that the number of virtual fields has a significant impact on the performance of VFM identification, with the number of virtual fields increasing the accuracy of the identification [28]. Fig. 4 shows the evolution of the residual between internal and external virtual works during the identification procedure, as well as a comparison of the external virtual work and the final calibrated internal virtual work for each identification run.

The evolution of the residual during the identification process (Fig. 4a) shows that the initial parameters set have a significant impact on the initial and final calibrated residual values, and consequently, on the identification results. The difference in the final residuals between the identification runs, on the other hand, is small, as can be seen in the difference between the external and virtual works (Fig. 4b), where all the curves are nearly coincident. The small difference in

residuals with the variation of the identified parameters also suggests the need for more virtual fields to be used in the identification process, as using just one virtual field could filter out crucial kinematic data about the mechanical behaviour related to a particular constitutive parameter.

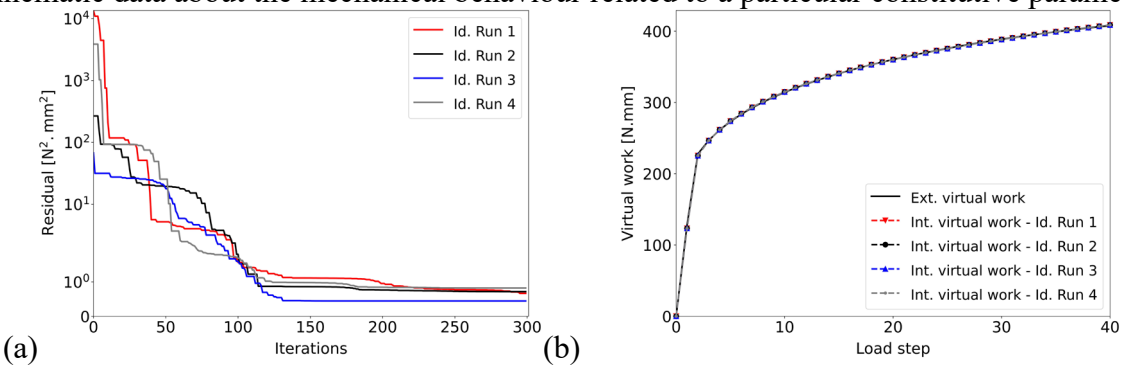

Fig. 4. Identification results in terms of: (a) evolution of the residual during the identitication process and (b) final difference between external and internal virtual works.

In Fig. 5, the Swift hardening law curves and the Hill'48 yield surfaces are compared as part of cross-validation between the reference parameters and the identification results. The numerical results for this test configuration are also plotted in the normalised stress space (see Fig. 5b), with the yield stress calculated from the reference parameters.

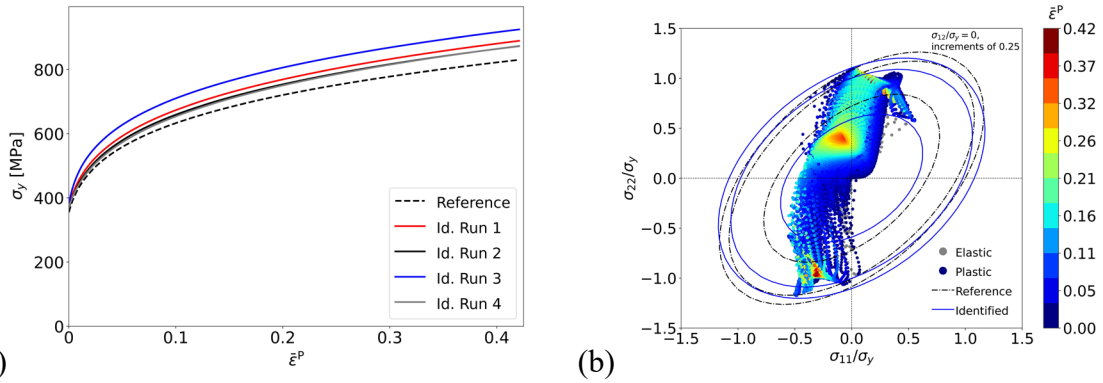

Fig. 5. Results obtained with the identified parameter sets for: (a) Swift law hardening curve for all identification runs and (b) comparison of the reference yield surface with the identified yield surface for the identification run 3 for different levels of σ_{12}/σ_y.

The identified Swift hardening law curves present some divergences from the hardening curve with the reference parameters. These differences become more pronounced as the equivalent plastic strain increases. These results seem to be a consequence of the overall uncertainty propagation in the identification process, in which the global minimum of the residual between the external and internal virtual works may differ from the ground truth parameters due to experimental image noise and the DIC technique's different filtering and spatial resolution. Nevertheless, increasing the number of virtual fields used, even if they are uniform, may improve the accuracy of the parameters identified. Moreover, when comparing the reference and the identification run with the lower residual value (identification run 3), the differences appear to be larger where there is a lack of information in the stress space and lower where there is a higher concentration of points in the stress space. These results are consistent with the previous qualitative analysis of the rotation angle, which revealed a narrower distribution of the rotation angle criterion for this test configuration. A heterogeneous distribution of material points across the whole stress

space would almost certainly improve the accuracy of the identified parameters regarding the anisotropic yield criterion.

Summary

This work investigated the use of different indicators to evaluate the heterogeneity of the mechanical behaviour of distinct test configurations when using the Arcan test. The numerical results from the most interesting test configuration were used to generate synthetic speckle images and processed through DIC and further used in the inverse identification with VFM. The main conclusions that can be drawn from this work are as follows:

- Even with a simple specimen geometry, the Arcan test provided interesting heterogeneous test configurations, demonstrating the potential of its use for heterogeneous test design in the context of metal plasticity.
- The IT_1 criterion proved to be a good quantitative evaluation of the diversity of the material's stress/strain states, which appears to have a significant influence on the inverse identification of the hardening parameters. It is, however, inappropriate for quantifying the identifiability of anisotropy parameters.
- The rotation angle parameter seems to be a suitable qualitative criterion for the evaluation of the sensitivity of mechanical tests to anisotropy.
- When using experimental images and DIC, the propagation of noise and uncertainty throughout the identification process has a significant impact on the identified parameters, resulting in deviations from the ground-truth parameters.

In future works, other test configurations could be used for the inverse identification of the isotropic hardening and anisotropic yielding parameters by finding a good balance between the IT_1 and the rotation angle criterions. Additionally, a greater number of uniform virtual fields could be used in the inverse identification of the constitutive parameters, as could automatic virtual field selection strategies such as sensitivity-based virtual fields. Other specimen geometries could also be used to increase the heterogeneity of stress/strain states of the material, which might become even more important when using more complex constitutive models, such as Yld2000-2D.

Acknowledgements

J. Henriques is grateful to the Portuguese Foundation for Science and Technology (FCT) for the Ph.D. grant 2021.05692.BD. This project has received funding from the Research Fund for Coal and Steel under grant agreement No 888153. The authors gratefully acknowledge the financial support of the FCT under the project PTDC/EMEAPL/29713/2017 by UE/FEDER through the programs CENTRO 2020 and COMPETE 2020, and UID/EMS/ 00481/2013-FCT under CENTRO-01-0145-FEDER-022083. The authors also acknowledge the FCT (FCT - MCTES) for its financial support via the projects UIDB/00667/2020 (UNIDEMI).

Disclaimer

The results reflect only the authors' view, and the European Commission is not responsible for any use that may be made of the information it contains.

References

[1] A. Lattanzi, F. Barlat, F. Pierron, A. Marek, M. Rossi, Inverse identification strategies for the characterization of transformation-based anisotropic plasticity models with the non-linear VFM, Int. J. Mech. Sci. 173 (2020) 105422. https://doi.org/10.1016/j.ijmecsci.2020.105422

[2] P.D. Wu, S.R. MacEwen, D.J. Lloyd, M. Jain, P. Tugcu, K.W. Neale, On pre-straining and the evolution of material anisotropy in sheet metals, Int. J. Plast. 21 (2005) 723-739. https://doi.org/10.1016/j.ijplas.2004.05.007

[3] J.M.P. Martins, A. Andrade-Campos, S. Thuillier, Calibration of anisotropic plasticity models using a biaxial test and the virtual fields method, Int. J. Solids Struct. 172 (2019) 21-37. https://doi.org/10.1016/j.ijsolstr.2019.05.019
[4] N. Souto, S. Thuillier, A. Andrade-Campos, Design of an indicator to characterize and classify mechanical tests for sheet metals, Int. J. Mech. Sci. 101-102 (2015) 252-271. https://doi.org/10.1016/j.ijmecsci.2015.07.026
[5] M. Sutton, J. Orteu, H. Schreier, Image correlation for shape, motion and deformation measurements: basic concepts, theory and applications, first ed., Springer, New York, 2009. https://doi.org/10.1007/978-0-387-78747-3
[6] F. Pierron, M. Grédiac, Towards Material Testing 2.0. A review of test design for identification of constitutive parameters from full-field measurements, Strain 57 (2021) 12370. https://doi.org/10.1111/str.12370
[7] F. Pierron, M. Grédiac, The virtual fields method. Extracting constitutive mechanical parameters from full-field deformation measurements, first ed., Springer, New York, 2012. https://doi.org/10.1007/978-1-4614-1824-5
[8] J. Henriques, J. Xavier, A. Andrade-Campos, Identification of Orthotropic Elastic Properties of Wood by a Synthetic Image Approach Based on Digital Image Correlation, Materials 15 (2022) 625. https://doi.org/10.3390/ma15020625
[9] J. Aquino, A. Andrade-Campos, J.M.P. Martins, S. Thuillier, Design of heterogeneous mechanical tests: Numerical methodology and experimental validation, Strain 55 (2019) 12313. https://doi.org/ 10.1111/str.12313
[10] J. Fu, W. Xie, L. Qi, An Identification Method for Anisotropic Plastic Constitutive Parameters of Sheet Metals, Procedia Manuf. 47 (2020) 812-815. https://doi.org/10.1016/j.promfg.2020.04.251
[11] T. Pottier, P. Vacher, F. Toussaint, H. Louche, T. Coudert, Out-of-plane Testing Procedure for Inverse Identification Purpose: Application in Sheet Metal Plasticity, Exp. Mech. 52 (2012) 951-963. https://doi.org/10.1007/s11340-011-9555-3
[12] M. Conde, Y. Zhang, J. Henriques, S. Coppieters, A. Andrade-Campos, Design and validation of a heterogeneous interior notched specimen for inverse material parameter identification, Finite. Elem. Anal. Des. 214 (2023) 103866. https://doi.org/10.1016/j.finel.2022.103866
[13] M. Gonçalves, A. Andrade-Campos, B. Barroqueiro, On the design of mechanical heterogeneous specimens using multilevel topology optimization, Adv. Eng. Softw. 175 (2023) 103314. https://doi.org/10.1016/j.advengsoft.2022.103314
[14] L. Chamoin, C. Jailin, M. Diaz, L. Quesada, Coupling between topology optimization and digital image correlation for the design of specimen dedicated to selected material parameters identification, Int. J. Solids. Struct. 193-194 (2020) 270-286. https://doi.org/10.1016/j.ijsolstr.2020.02.032
[15] P. Wang, F. Pierron, O.T. Thomsen, Identification of Material Parameters of PVC Foams using Digital Image Correlation and the Virtual Fields Method, Exp. Mech. 53 (2013) 1001-1015. https://doi.org/10.1007/s11340-012-9703-4
[16] P. Wang, F. Pierron, M. Rossi, P. Lava, O.T. Thomsen, Optimised Experimental Characterisation of Polymeric Foam Material Using DIC and the Virtual Fields Method, Strain 52 (2016) 59-79. https://doi.org/10.1111/str.12170
[17] M. Shifa, Strength of Aluminum Alloys Under Static Mixed-Mode I/II Loading Conditions, J. Test. Eval. 46 (2018) 294-304. https://doi.org/10.1520/JTE20160475
[18] A. Kumar, M.K. Singha, V. Tiwari, Structural response of metal sheets under combined shear and tension, Structures 26 (2020) 915-933. https://doi.org/10.1016/j.istruc.2020.05.006

[19] F. Ozturk, S. Toros, S. Kilic, Effects of Anisotropic Yield Functions on Prediction of Forming Limit Diagrams of DP600 Advanced High Strength Steel, Procedia Eng. 81 (2014) 760-765. https://doi.org/10.1016/j.proeng.2014.10.073
[20] Dassault Systèmes. Abaqus 2017 documentation, 2017
[21] R. Hill, A theory of the yielding and plastic flow of anisotropic metals, Proc. R. Soc. Lond. A 193 (1948) 281-297. https://doi.org/10.1098/rspa.1948.0045
[22] H. Takizawa, T. Kuwabara, K. Oide, J. Yoshida, Development of the subroutine library 'UMMDp' for anisotropic yield functions commonly applicable to commercial FEM codes, J. Phys.: Conf. Ser. 734 (2016) 032028. https://doi.org/10.1088/1742-6596/734/3/032028
[23] M. Guimarães Oliveira, S. Thuillier, A. Andrade-Campos, Analysis of Heterogeneous Tests for Sheet Metal Mechanical Behavior, Procedia Manuf. 47 (2020) 831-838. https://doi.org/10.1016/j.promfg.2020.04.259
[24] MatchID: Metrology beyond colors. MatchID version 2022.2, 2022.
[25] J. Henriques, M. Conde, A. Andrade-Campos, J. Xavier, Identification of Swift Law Parameters Using FEMU by a Synthetic Image DIC-Based Approach, Key Eng. Mater. 926 (2022) 2211-2221. https://doi.org/ 10.4028/p-33un7m
[26] S. Avril, M. Grédiac, F. Pierron, Sensitivity of the virtual fields method to noisy data, Comput. Mech. 34 (2004) 439-452. https://doi.org/10.1007/s00466-004-0589-6
[27] A. Marek, F.M. Davis, F. Pierron, Sensitivity-based virtual fields for the non-linear virtual fields method, Comput. Mech. 60 (2017) 409-43. https://doi.org/10.1007/s00466-017-1411-6
[28] J.M.P. Martins, S. Thuillier, A. Andrade-Campos, Calibration of Anisotropic Plasticity Models with an Optimized Heterogeneous Test and the Virtual Fields Method, Residual Stress, Thermomechanics & Infrared Imaging and Inverse Problems 6 (2020) 25-32. https://doi.org/10.1007/978-3-030-30098-2_5

Materials Research Proceedings 28 (2023) 1143-1154 https://doi.org/10.21741/9781644902479-125

On the constraints and consistency in implicit constitutive modelling using ANNs and indirect training

LOURENÇO Rúben[1,2,a], CUETO Elías[3,b], GEORGIEVA Pétia[4,c] and ANDRADE-CAMPOS António[1,2,d *]

[1] Dept. of Mechanical Engineering, Centre for Mechanical Technology and Automation, University of Aveiro, Portugal

[2] LASI, Intelligent Systems Associate Laboratory, Guimarães, Portugal

[3] Aragon Institute of Engineering Research (I3A), University of Zaragoza, Spain

[4] Institute of Electronics and Informatics Engineering of Aveiro (IEETA); Dept. of Electronics, Telecommunications and Informatics, University of Aveiro, Portugal

[a]rubenl@ua.pt, [b]ecueto@unizar.es, [c]petia@ua.pt, [d]gilac@ua.pt

Keywords: Constitutive Model, Elastoplasticity, Neural Networks, Indirect Training, Constrained Optimization

Abstract. The training of an Artificial Neural Network (ANN) for implicit constitutive modelling mostly relies on labelled data pairs, however, some variables cannot be physically measured in real experiments. As such, the training should preferably be carried out indirectly, making use of experimentally measurable variables. The unconstrained training of an ANN's parameters often leads to spurious responses that do not comply with the physics of the problem. Applying constraints during training ensures not only the physical meaning of the ANN predictions but also potentially increases the convergence to a global minimum, while improving the model's performance. An ANN material model is trained using a novel indirect approach, where the local and global equilibrium conditions are ensured employing the Virtual Fields Method (VFM). An example of physical constraint is analyzed and applied during the training process.

Introduction

ANNs are powerful function approximators that can be used to implicitly learn constitutive relations directly from data, without having to postulate a mathematical formulation [1–3]. Several successful applications of ANNs for implicit modelling of material behavior have been reported in the literature (e.g., [4–6] among others). Most of the approaches rely on training the ANNs with paired data, usually stress-strain, from numerically generated datasets. Nevertheless, in a real experiment, certain variables, such as stresses, are not measurable and, therefore, the training should preferably be carried out indirectly making use of experimentally measurable variables only.

Although a standard ANN could be able to learn the constitutive behavior of a material, given enough data, it usually works as a black-box model in which its structure is not easily interpretable and there is no guarantee that its predictions are usable, as they can violate fundamental laws of mechanics and thermodynamics [3–5]. Thus, it is necessary to enforce physics-based constraints when using ANNs for implicit constitutive modelling. The incorporation of this knowledge into the network allows it (i) to learn the structure of the underlying constitutive relations, (ii) reduce its sensitivity to noise and (iii) increase its performance regarding inputs outside the training domain [7]. Physics-based constraints act as a regularization agent for ANNs, reducing the space of admissible solutions and allowing the network to learn with smaller datasets, as it already does not have to learn those relationships from data [6,7]. These constraints can be enforced using

Content from this work may be used under the terms of the Creative Commons Attribution 3.0 license. Any further distribution of this work must maintain attribution to the author(s) and the title of the work, journal citation and DOI. Published under license by Materials Research Forum LLC.

custom ANN architectures [3], model constraints (e.g., weight constraints) [7] or penalty/regularization terms [5,8]. Some examples of constraints are shown in Table 1.

In the present work two single layer perceptron models are used to model the linear elastic response of a virtual material. A novel indirect training methodology employing the sensitivity-based Virtual Field Method (VFM) [17] is used to train both models and study the application of constraints during training. Here, the applied constraint was the positive definiteness of the tangent stiffness, which in the absence of plastic deformation, degenerates into the elastic stiffness matrix **D**.

Table 1. Examples of material model constraints to enforce during ANN training.

	Formulation	Description
1st law of thermodynamics	$\gamma_{\mathrm{loc}} = \boldsymbol{\sigma} : \dot{\boldsymbol{\epsilon}} + \theta\dot{\eta} - \dot{\mathbf{E}}$	The work done by stress must either be stored as recoverable internal energy in the solid or dissipated as heat [8,9]
2nd law of thermodynamics	$\gamma_{\mathrm{loc}} \geq 0$	For a sample of material subjected to a cycle of deformation, starting and ending with identical strain and internal energy, the total work must be positive or zero [8,9]
Drucker's postulate	$\Delta\sigma_{ij}\Delta\varepsilon_{ij} \geq 0$	The work done by the tractions through the displacements is positive or zero [12]
Symmetric positive definiteness of tangent stiffness	$\frac{\partial \boldsymbol{\sigma}}{\partial \boldsymbol{\varepsilon}} = \mathbf{H} > 0$	The tangent stiffness matrix is symmetric positive definite, ensuring that the strain energy is weakly convex [13]
Time consistency	$\lim_{\Delta\boldsymbol{\varepsilon}\to 0} \Delta\boldsymbol{\sigma} = 0$	A consistent material law maps a state of zero strain onto a state of zero stress [13]

The Drucker's stability criterion bears no physical meaning. Not all materials are stable in this sense, however, issues will arise for materials that do not respect it, when used to solve boundary problems [9,17].

Mechanical Test and Dataset Creation

A heterogeneous test was used to generate synthetic data to train the ANN models. The geometry consists of 3 × 3 mm^2 plate with thickness t = 0.1 mm. The initial mesh, geometry and boundary conditions are depicted in Fig. 1. Symmetry boundary conditions are applied to the boundaries at x = 0 and y = 0 and a surface traction is applied to the boundary at x = 3 mm. The traction follows a non-uniform distribution with a single component along the x-direction, varying linearly in the y-direction, according to: $f_x(y) = my + b$, where m and b, respectively, control the slope and intercept of the distribution.

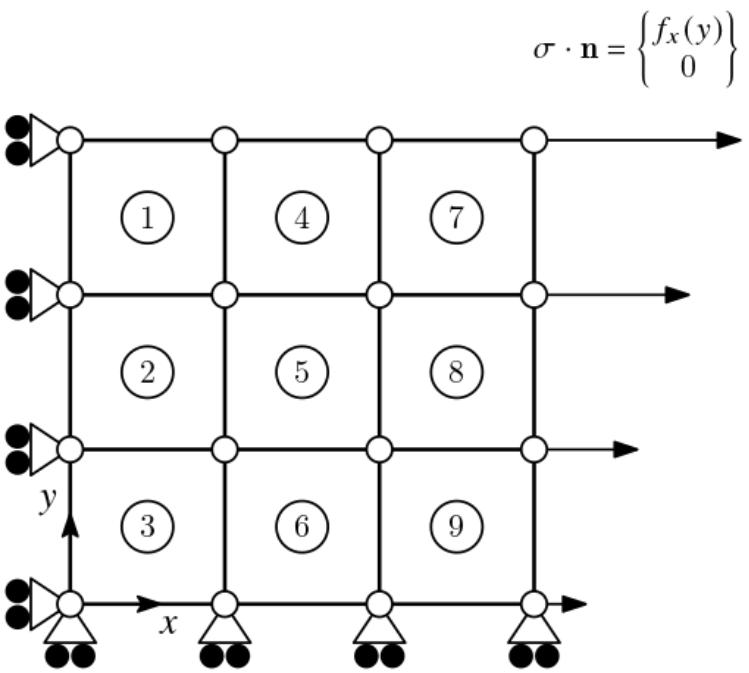

Fig. 1. Heterogeneous test: initial geometry, mesh and boundary conditions, adapted from [14].

The numerical simulations were conducted using the commercial finite element code Abaqus. The model was built with CPS4R elements (bilinear reduced integration plane stress). The elastic parameters were defined as E = 210 GPa and ν = 0.3. To generate a training dataset, various simulations were performed with the time period set to 1 and a fixed time increment Δt = 0.001. For each time step, the strain tensor at the centroid was extracted for all the elements and the resultant force computed from the equilibrium of the internal forces, such that:

$$Fl = \sum_{i=1}^{n} \sigma_i A_i t \tag{1}$$

where F is the global force, l the length of the solid**,** A is the element's area and t is the thickness. The training and validation datasets were generated for different load distribution parameters, depicted in Table 2. Prior to training and for each mechanical test, the dataset was organized into batches of 9 elements per time increment and shuffled before being split into training (67%) and test data (33%). The input features were scaled in order to have zero mean and unit variance.

Table 2. Loading parameters for the generation of the training and validation datasets.

Training set	m = {60,80,100,120} [N/mm]	b = {60,80,100} [N]
Validation set	m	b
	50	50
	70	90
	90	65

Neural Network Model

A single layer perceptron with linear activation was chosen to predict the elastic response. The inputs were the components of the strain tensor at a given time t and the outputs were the components of the corresponding stress tensor, as depicted in Fig. 2.

Fig. 2. Single layer perceptron with linear activation.

The model outputs the stress directly according to the following relationship during the forward pass:

$$\boldsymbol{\sigma} = \mathbf{W}\boldsymbol{\epsilon}+\mathbf{b} \iff \begin{Bmatrix}\sigma_{xx}\\ \sigma_{yy}\\ \tau_{xy}\end{Bmatrix} = \begin{bmatrix}w_{11} & w_{12} & w_{13}\\ w_{21} & w_{22} & w_{23}\\ w_{31} & w_{32} & w_{33}\end{bmatrix}\begin{Bmatrix}\epsilon_{xx}\\ \epsilon_{yy}\\ \epsilon_{xy}\end{Bmatrix} + \begin{Bmatrix}b_{11}\\ b_{21}\\ b_{31}\end{Bmatrix} \tag{1}$$

where w_{ij} are the layer weights and b_{ij} the biases. An analogy can be established between the terms of the weight matrix **W** and the elasticity matrix **D** in the Hooke's law, for an isotropic material under plane stress:

$$\boldsymbol{\sigma} = \mathbf{D}\boldsymbol{\epsilon} \Leftrightarrow \begin{Bmatrix}\sigma_{xx}\\ \sigma_{yy}\\ \tau_{xy}\end{Bmatrix} = \frac{E}{(1+\nu)(1-2\nu)}\begin{bmatrix}1\text{-}\nu & \nu & 0\\ \nu & 1\text{-}\nu & 0\\ 0 & 0 & \frac{1\text{-}2\nu}{2}\end{bmatrix}\begin{Bmatrix}\epsilon_{xx}\\ \epsilon_{yy}\\ \epsilon_{xy}\end{Bmatrix} \tag{2}$$

with **D** defined in terms of the elastic constants E, the Young's modulus and ν, the Poisson's ratio. For the material chosen for this work, the elasticity matrix **D** is the following:

$$\mathbf{D} = \begin{bmatrix}230769.231 & 69230.769 & 0\\ 69230.769 & 230769.231 & 0\\ 0 & 0 & 80769.231\end{bmatrix} \tag{3}$$

The architecture presented above was used to train two models in order to learn the elastic response of the material. One of the models was trained following an unconstrained optimization approach, while the other model was trained using a constrained optimization, in order to study how adding constraints would influence the resulting stress predictions.

Indirect Training for Linear Model

Implicit constitutive modelling using ANNs relies on paired data, usually strain and stress tensors, in order to learn the material behavior. However, variables such as stress cannot be obtained from experiments [15]. Therefore, the training must be carried out indirectly, using only measurable data. The VFM, first introduced by Grédiac [16], is a state-of-the-art method employed in the identification of constitutive parameters, known by its computational efficiency and does not resort to FEM for any forward calculations [17]. The key elements behind the VFM are the Principle of Virtual Work (PVW) and the choice of virtual fields. According to the PVW, the internal virtual work must be equal to the external virtual work performed by the external forces and is written by [18]:

$$-\int_V \boldsymbol{\sigma} : \boldsymbol{\varepsilon}^* \, dV + \int_{\partial V} \mathbf{T} \cdot \mathbf{u}^* \, dS = 0 \tag{4}$$

where $\boldsymbol{\varepsilon}^*$ is the virtual strain, $\mathbf{u}^*$ is the virtual displacement, V is the volume of the solid and T is the traction vector. The virtual entities work can be defined independently of the measured displacements/strains. Any number of virtual fields can be used; however, the following conditions should be honored [5,6]: the functions defining the virtual fields should be piece-wise differentiable and kinematically admissible, in order satisfy the displacement boundary conditions. The virtual fields can be manually defined, though the choice is tied to the user's own experience and intuition. Moreover, manually defined virtual fields do not show a temporal evolution [17]. Nonetheless, systematic procedures to automatically define these virtual entities exist, namely: the stiffness-based and the sensitivity-based virtual fields [4,7].

In the present work, sensitivity-based virtual fields were employed to indirectly train a single-layer perceptron for implicit constitutive modelling, following the workflow presented in Fig. 3.

The key concept of the sensitivity-based virtual fields is to apply a perturbation to each of the model's parameters in order to obtain a stress sensitivity and its temporal evolution [17]. The stress field is the only quantity that depends directly on the constitutive parameters in the VFM, so the stress sensitivity maps highlight areas that strongly depend on a given parameter [20]. In the context of this work, the single-layer perceptron from Fig. 2 is taken as a representation of the constitutive model. The spatial sensitivity of stress to each model parameter is computed as:

$$\delta\boldsymbol{\sigma}^{(i)}(\boldsymbol{\epsilon}, \mathbf{W}, t) = \boldsymbol{\sigma}(\boldsymbol{\epsilon}, \mathbf{W}, t) - \boldsymbol{\sigma}(\boldsymbol{\epsilon}, \mathbf{W}+\delta w_i, t) \,, \; \delta w_i = -0.1 w_i \tag{5}$$

with i being the i-th term of the perceptron's weight matrix $\mathbf{W}$ and t the time step. The virtual displacements $\mathbf{u}^*$ are found starting from the following system of equations applied to a virtual mesh:

$$\delta\boldsymbol{\sigma}^{(i)} = \mathbf{B}\mathbf{u}^{*(i)} \tag{6}$$

where $\mathbf{B}$ is the global strain-displacement matrix, used to map the virtual displacements at the nodes to every virtual strain. If the displacement is prescribed at the boundaries, the traction is unknown and, as such, the displacements are set to zero. If, on the other hand, the traction distribution is unknown and only the resultant force is known, a constant virtual displacement is set at the boundaries. By applying these constraints, a modified global strain-displacement matrix $\overline{\mathbf{B}}$ is obtained and the virtual displacements $\mathbf{u}^*$ can finally be computed as follows:

$$\mathbf{u}^{*(i)} = \mathrm{pinv}(\overline{\mathbf{B}}) \, \delta\boldsymbol{\sigma}^{(i)} \tag{7}$$

with $\mathrm{pinv}(\overline{\mathbf{B}})$ being the pseudo-inverse of the modified strain-displacement matrix. The virtual strains $\boldsymbol{\varepsilon}^*$are then computed as:

$$\boldsymbol{\varepsilon}^{*(i)} = \mathbf{B}\mathbf{u}^{*(i)} \tag{8}$$

The training process is carried out, with the virtual fields $\mathbf{u}^{*(i)}$ and $\boldsymbol{\varepsilon}^{*(i)}$ being updated multiple times in order to evaluate the loss resulting from the application of the PVW and update the weight matrix $\mathbf{W}$ accordingly. The loss to be minimized is the following:

$$\mathcal{L}(\mathbf{W}, \mathbf{b}, \boldsymbol{\epsilon}) = \sum_{i=1}^{n_{\mathrm{VFs}}} \left[\frac{1}{(\alpha^{(i)})^2} \sum_{t=1}^{n_{\mathrm{t}}} \left(\sum_{j=1}^{n_{\mathrm{pts}}} \boldsymbol{\sigma}^j(\mathbf{W}, \mathbf{b}, \boldsymbol{\epsilon}, t) \cdot \boldsymbol{\varepsilon}^{*j^{(i)}}(t) \cdot S^j - \mathrm{W}^*_{\mathrm{ext}}(t) \right)^2 \right] \tag{9}$$

with S^j being the surface area of the j-th measurement point and $\alpha^{(i)}$ the scaling factor of the i-th virtual field, employed to guarantee similar magnitudes between different virtual fields. In the present work, the scaling factor was defined based on the mean of the 30% highest internal virtual work values.

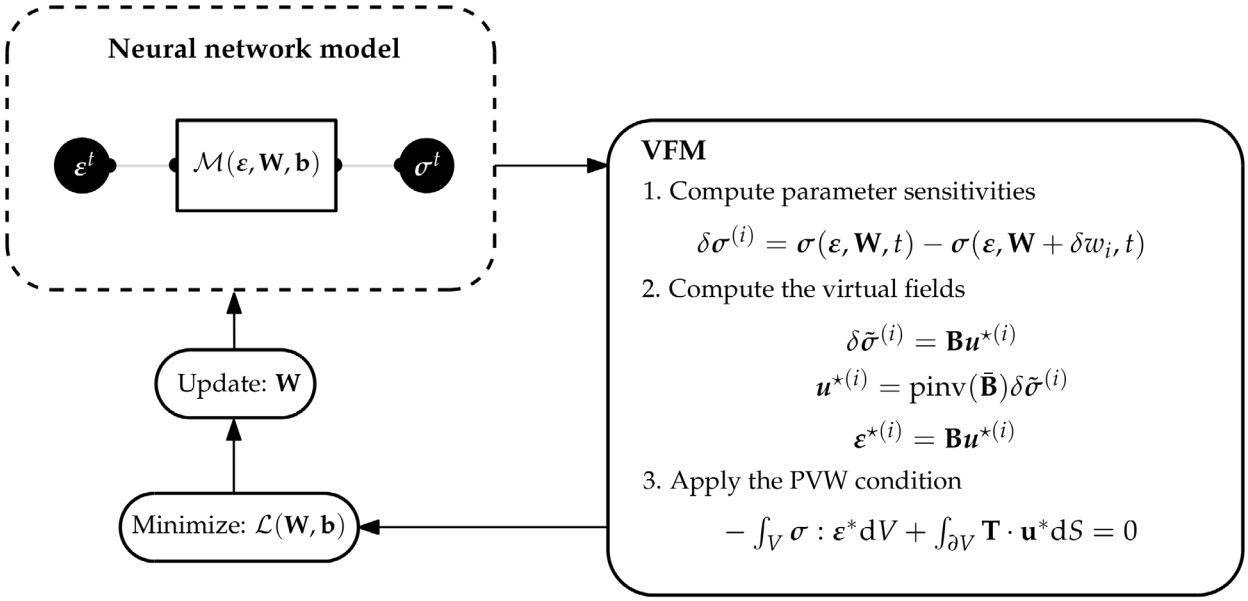

Fig. 3. Coupled ANN-VFM method for implicit constitutive modelling

Unconstrained Training Analysis

The Adam algorithm was used to optimize the network weights, with an initial learning rate set to 0.1, scheduled to be reduced using a multiplier of 0.2 if no improvement in the training loss was registered after 3 epochs. For the unconstrained training model, the network was set to train during a maximum of 10000 epochs. However, an early-stopping criterion was triggered when no further improvement was observed in the test loss, after 2886 epochs. The learning curves are plotted in Fig. 4, showing a sharp decline during training with a low value in the order of 10^{-3} achieved at the end and almost no gap being observed between the train and test curves, indicating the model did not overfit the data.

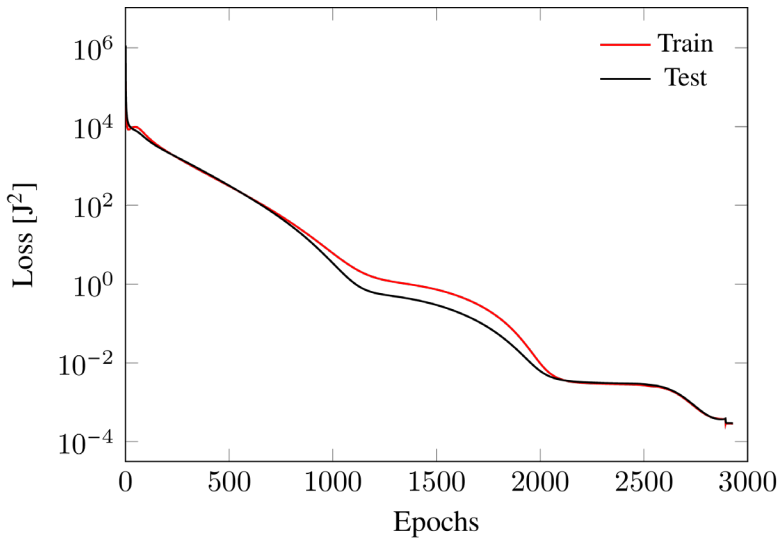

Fig. 4. Learning curves for the unconstrained training model.

Materials Research Proceedings 28 (2023) 1143-1154 https://doi.org/10.21741/9781644902479-125

During training, the layer weights should evolve in such a manner that, at the end of the process, the unscaled matrix **W** approximates **D** as much as possible, with the bias vector **b** being equal to or almost zero. Due to the scaling of the inputs, the parameters hold no significance, so the inverse scaling is needed here to compare both entities. An overview of both scaled and unscaled model parameters obtained after training is shown in Table 3.

Table 3. Scaled and unscaled model parameters for the unconstrained model after training.

	Layer weights **W**	Biases **b**
Scaled	$\begin{bmatrix} 76.6645 & 0.01328 & 0.0159 \\ 23.1111 & 27.4231 & 0.0667 \\ 0.6532 & 0.3366 & 5.1392 \end{bmatrix}$	$\{111 \quad 0.0997 \quad 5.80\}^T$
Unscaled	$\begin{bmatrix} 209891.4619 & 101.9638 & 234.9259 \\ 63273.3868 & 210502.5075 & 981.5443 \\ 1788.5317 & 2584.3104 & 75627.5458 \end{bmatrix}$	$\{0.0305 \quad -0.0369 \quad -0.286\}^T$
Rel. error [%]	$\begin{bmatrix} 9.047 & 99.853 & N/A \\ 8.605 & 8.782 & N/A \\ N/A & N/A & 6.366 \end{bmatrix}$	N/A

Examining the unscaled parameters, one can observe that although the single layer perceptron was able to naturally learn nonnegative terms, it was not able to replicate the symmetry of the elasticity matrix, thus failing to guarantee the isotropy of the material. Furthermore, there are significant errors between the unscaled parameters and the terms of the elasticity matrix **D**. Nevertheless, the indices of the most dominant terms (w_{11}, w_{22}, w_{33}) correlate well with those from **D**. The unscaled bias vector holds very small terms in comparison, however not close to zero. From here, we conclude that the model is not able to fully predict the linear elastic response. This is confirmed by observing the plots comparing the real and predicted elastic curves corresponding to two example elements, shown on Fig. 5. The differences stated above, caused the single layer perceptron predictions to achieve correlations ranging from 0.85 to 0.999 and mean absolute errors (MAE) from 0.266 to 5.173.

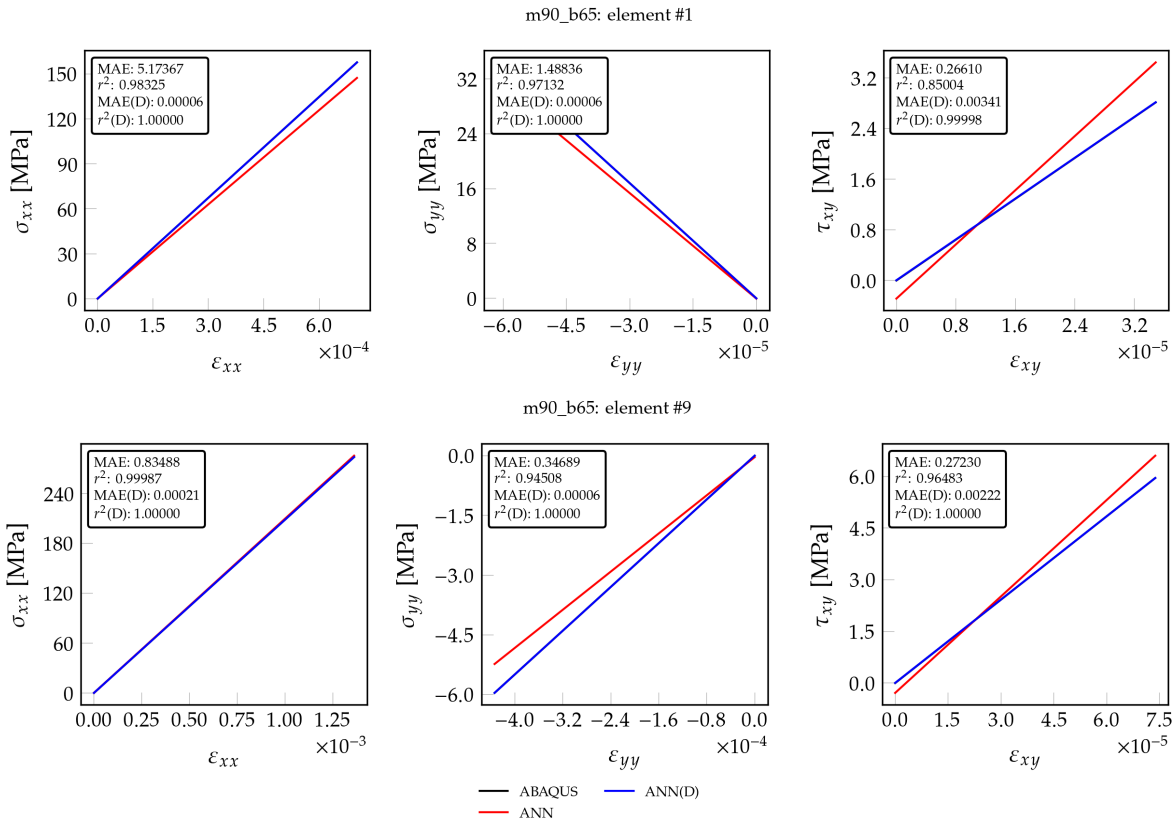

Fig. 5. Validation results for the unconstrained training model for elements 1 and 9.

Constrained Training Analysis

For the constrained training model, the same training parameters were used, with the only difference being that the following set of constraints were applied to the entries of the parameter matrix **W**:

$$w_{ij} > 0 \wedge w_{13} = w_{31} = 0 \wedge w_{23} = w_{32} = 0 \tag{10}$$

meaning all the terms of **W** are forced to be nonnegative and some terms set to be zero, matching the indices of the terms with zero values in **D**. The training progressed with the early-stopping criterion being triggered when no further improvement was observed in the test loss, after 5381 epochs. The resulting learning curves are plotted in Fig. 6, showing a sharp decline during training with a lower value of loss being achieved at the end (order of 10^{-9}) when compared to the unconstrained model. Similarly, almost no gap is observed between the train and test curves, indicating the model did not overfit the data.

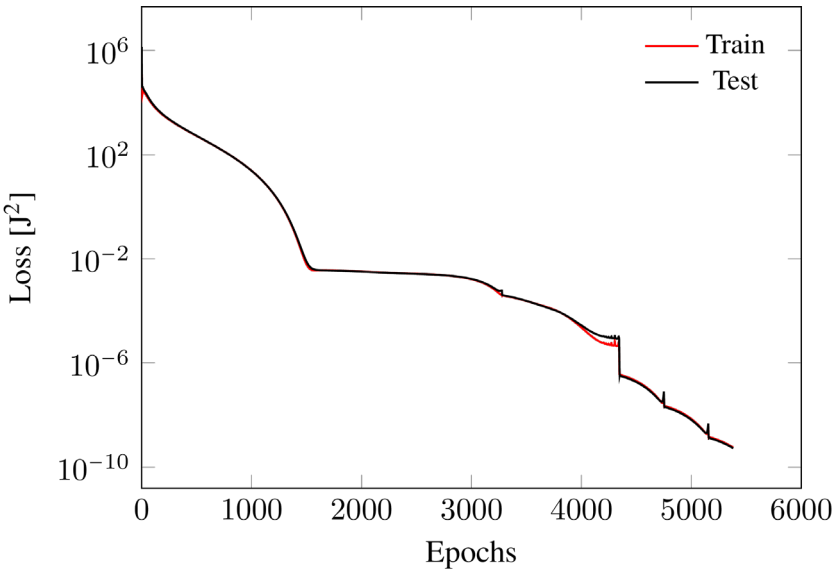

Fig. 6. Learning curves for the constrained training model.

An overview of both scaled and unscaled model parameters obtained after training is shown in Table 4. Examining the unscaled parameters, one can observe that enforcing the constraints defined in (10 was enough for the single layer perceptron to naturally replicate the symmetry of the elasticity matrix, thus guaranteeing the isotropy of the material. Although no constraints were applied to the biases, the unscaled bias vector holds values very close to zero, as it was expected. The model perfectly predicts the elastic response, as it is confirmed by the plots comparing the real and predicted elastic curves corresponding to two example elements, shown on Fig. 7. There are some differences between the unscaled parameters and the terms of the elasticity matrix **D**, however these are not significantly high to cause de model to output badly predicted curves. The constraints allowed the model to achieve lower mean absolute errors and the highest possible correlations r^2.

Table 4. Scaled and unscaled model parameters for the constrained model after training.

	Layer weights **W**	Biases **b**
Scaled	$\begin{bmatrix} 78.4168 & 8.2999 & 0 \\ 23.5103 & 27.8005 & 0 \\ 0 & 0 & 4.9949 \end{bmatrix}$	$\{104.3700 \quad 0 \quad 5.4179\}^T$
Unscaled	$\begin{bmatrix} 230643.294 & 68815.410 & 0 \\ 69149.634 & 230497.092 & 0 \\ 0 & 0 & 80669.215 \end{bmatrix}$	$\{-0.0043 \quad -0.0001 \quad -0.0007\}^T$
Rel. error [%]	$\begin{bmatrix} 0.054 & 0.600 & \text{N/A} \\ 0.117 & 0.118 & \text{N/A} \\ \text{N/A} & \text{N/A} & 0.124 \end{bmatrix}$	N/A

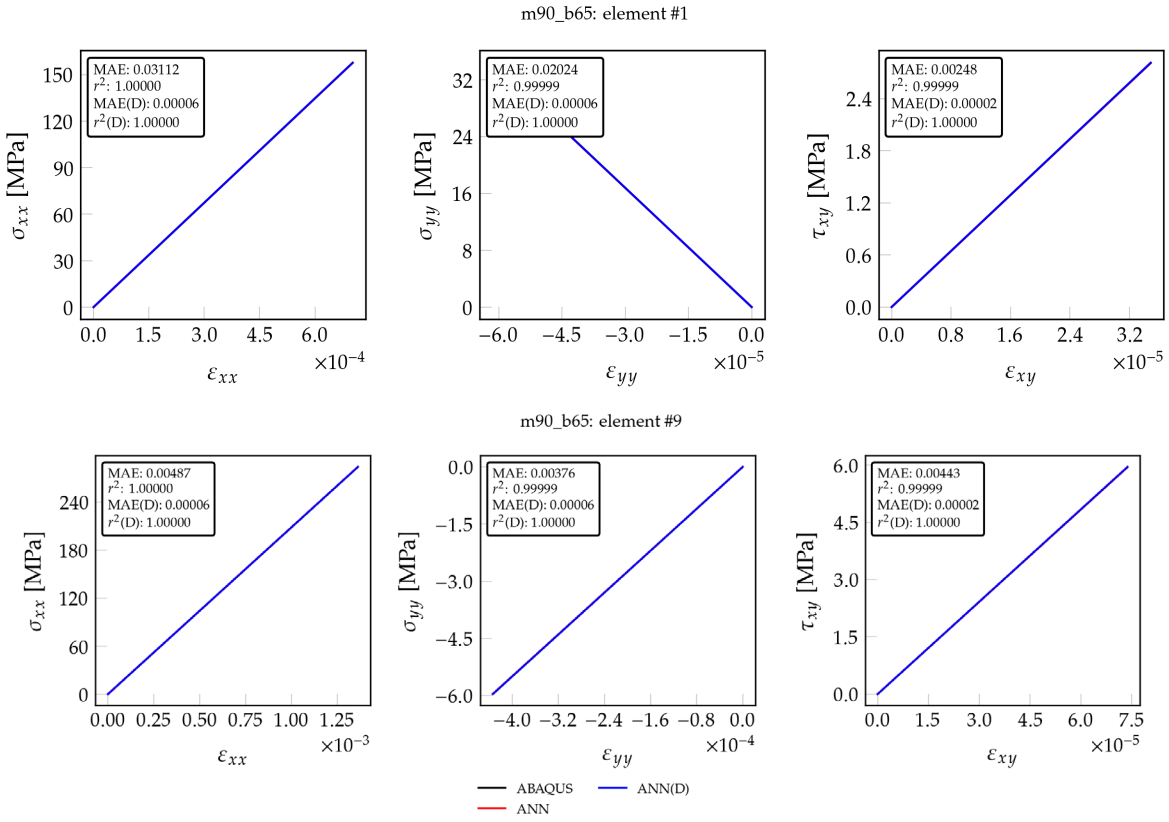

Fig. 7. Validation results for the constrained training model for elements 1 and 9.

Summary

A single layer perceptron model was trained without stress labels employing a new indirect training methodology based on the Virtual Fields Method, which makes use of the Principle of Virtual Work and sensitivity-based virtual fields to guarantee the equilibrium between the external and virtual work. The sensitivity-based virtual fields are a more robust approach than the manually defined virtual fields, providing a systematic way of generating virtual fields that are not static and do not dependent on the user's intuition.

Two different perceptron models with the same architecture were trained in order to learn the linear elastic response of a virtual material and to study the influence of the application of constraints during training. Considering a single layer perceptron with 3 inputs and 3 outputs, an analogy could be established between the mathematical description of the forward pass and the Hooke's law under plane stress, with the perceptron's weight matrix **W** resembling the elasticity matrix **D**. There are several possible ways to constrain the space of admissible solutions of a neural network model. In the present work, by adapting the perceptron's model to the real material model, its parameters gain a real meaning, thus making it easier to control their evolution during training and ensure the predictions are physically admissible. As such, the constraints were applied directly to the perceptron's parameters in order to guarantee nonnegative terms in **W** and force some of its terms to be zero, matching those in the elasticity matrix **D**. It was shown that by applying these constraints, the single layer perceptron naturally learned the symmetry of the elasticity matrix **D**, respecting the isotropy of the material, and replicated its terms without significant errors, being able to predict a linear elastic response that matches the real one.

Disclaimer

The results reflect only the authors' view, and the European Commission is not responsible for any use that may be made of the information it contains.

Acknowledgements

Rúben Lourenço acknowledges the Portuguese Foundation for Science and Technology (FCT) for the financial support provided through the grant 2020.05279.BD, co-financed by the European Social Fund, through the Regional Operational Programme CENTRO 2020. The authors also gratefully acknowledge the financial support of FCT under the projects UID/EMS/00481/2013-FCT under CENTRO-01-0145-FEDER-022083. This project also supported by the Research Fund for Coal and Steel under grant agreement No 888153.

References

[1] Y. C. Lin, J. Zhang, J. Zhong, Application of neural networks to predict the elevated temperature flow behavior of a low alloy steel, Comput. Mater. Sci. 43 (2008) 752-758. https://doi.org/10.1016/j.commatsci.2008.01.039

[2] K. Hornik, M. Stinchcombe, H. White, Multilayer feedforward networks are universal approximators, Neural Networks 2 (1989) 359-366. https://doi.org/10.1016/0893-6080(89)90020-8

[3] K. Linka, E. Kuhl, A new family of Constitutive Artificial Neural Networks towards automated model discovery, Arxiv (2022). https://doi.org/10.48550/arxiv.2210.02202

[4] J. Ghaboussi, D.A. Pecknold, M. Zhang, R.M. Haj-Ali, Autoprogressive training of neural network constitutive models, Int. J. Numer. Methods Eng. 42 (1998) 105-126. https://doi.org/10.1002/(SICI)1097-0207(19980515)42:1<105::AID-NME356>3.0.CO;2-V

[5] A. Zhang, D. Mohr, Using neural networks to represent von Mises plasticity with isotropic hardening, Int. J. Plast. 132 (2020) 102732. https://doi.org/10.1016/j.ijplas.2020.102732

[6] F. Masi, I. Stefanou, P. Vannucci, V. Maffi-Berthier, Thermodynamics-based Artificial Neural Networks for constitutive modeling, J. Mech. Phys. Solids 147 (2021) 104277. https://doi.org/10.1016/j.jmps.2020.104277

[7] F. As'ad, P. Avery, C. Farhat, A mechanics-informed artificial neural network approach in data-driven constitutive modeling, Int. J. Nume.r Methods Eng. 123 (2022) 2738-2759. https://doi.org/10.1002/NME.6957

[8] L. Borkowski, C. Sorini, A. Chattopadhyay, Recurrent neural network-based multiaxial plasticity model with regularization for physics-informed constraints, Comput. Struct. 258 (2022) 106678. https://doi.org/10.1016/J.COMPSTRUC.2021.106678

[9] M. Raissi, P. Perdikaris, G.E. Karniadakis, Physics-informed neural networks: A deep learning framework for solving forward and inverse problems involving nonlinear partial differential equations, J. Comput. Phys. 378 (2019) 686-707. https://doi.org/10.1016/j.jcp.2018.10.045

[10] E. Cueto, F. Chinesta, Thermodynamics of learning physical phenomena, 2022.

[11] A. Danoun, E. Prulière, Y. Chemisky, Thermodynamically consistent Recurrent Neural Networks to predict non linear behaviors of dissipative materials subjected to non-proportional loading paths, Mech. Mater. (2022) 104436. https://doi.org/10.1016/j.mechmat.2022.104436

[12] A. Bower, Appl. Mech. Solids, CRC Press, 2009.

[13] K. Xu, D.Z. Huang, E. Darve, Learning constitutive relations using symmetric positive definite neural networks, J. Comput. Phys. 428 (2021) 110072. https://doi.org/10.1016/j.jcp.2020.110072

[14] J.M.P. Martins, A. Andrade-Campos, S. Thuillier, Comparison of inverse identification strategies for constitutive mechanical models using full-field measurements, Int. J. Mech. Sci. 145 (2018) 330–345. https://doi.org/10.1016/j.ijmecsci.2018.07.013

[15] X. Liu, F. Tao, H. Du, W. Yu, K. Xu, Learning nonlinear constitutive laws using neural network models based on indirectly measurable data, J. Appl. Mech. Trans. ASME 87 (2020) 1-8. https://doi.org/10.1115/1.4047036
[16] M. Grédiac, Principe des travaux virtuels et identification, Comptes Rendus de l'Académie des Sciences 309 (1989) 1–5.
[17] A. Marek, F.M. Davis, F. Pierron, Sensitivity-based virtual fields for the non-linear virtual fields method, Comput. Mech. 60 (2017) 409–431. https://doi.org/10.1007/s00466-017-1411-6
[18] F. Pierron, M. Grédiac, The virtual fields method: extracting constitutive mechanical parameters from full-field deformation measurements. Springer Science & Business Media, 2012.
[19] M. Grediac, F. Pierront, S. Avrilt, E. Toussaint, The Virtual Fields Method for Extracting Constitutive Parameters From Full-Field Measurements: a Review, Strain 42 (2006) 233-253. https://doi.org/10.1111/j.1475-1305.2006.tb01504.x
[20] A. Marek, F.M. Davis, M. Rossi, F. Pierron, Extension of the sensitivity-based virtual fields to large deformation anisotropic plasticity, Int. J. Mater. Forming 12 (2019) 457-476. https://doi.org/10.1007/S12289-018-1428-1/FIGURES/13
[21] T.B. Stoughton, J.W. Yoon, Review of Drucker's postulate and the issue of plastic stability in metal forming, Int. J. Plast. 22 (2006) 391–433. https://doi.org/10.1016/J.IJPLAS.2005.03.002

Materials Research Proceedings 28 (2023) 1155-1166 https://doi.org/10.21741/9781644902479-126

Forming process optimisation for variable geometries by machine learning – Convergence analysis and assessment

ZIMMERLING Clemens[1,a *] and KÄRGER Luise[1,b]

[1]Karlsruhe Institute of Technology, Institute of Vehicle System Technology, Karlsruhe, Germany

[a] clemens.zimmerling@kit.edu, [b] luise.kaerger@kit.edu

Keywords: Forming Optimisation, Surrogate, Machine Learning, Variable Geometries

Abstract. For optimum operation, modern production systems require a careful adjustment of the employed manufacturing processes. Physics-based process simulations can effectively support this process optimisation; however, their considerable computation times are often a significant barrier. One option to reduce the computational load is surrogate-based optimisation (SBO). Although SBO generally helps improve convergence, it can turn out unwieldy when the optimisation task varies, e.g. due to frequent component adaptations for customisation. In order to solve such variable optimisation tasks, this work studies how recent advances in machine learning (ML) can enhance and extend current surrogate capabilities. More specifically, an ML-algorithm interacts with generic samples of component geometries in a forming simulation environment and learns to optimise a forming process for variable geometries. The considered example of this work is blank holder optimisation in textile forming. After training, the algorithm is able to give useful recommendations even for new, non-generic geometries. While the prior work considered initial recommendations only, this work studies the convergence behaviour upon component-specific algorithm refinement (optimisation) at the example of two geometries. The convergence of the new pre-trained ML-approach is compared to classical SBO and a genetic algorithm (GA). The results show that initial recommendations indeed converge to the process optimum and that the speed of convergence outperforms the GA and compares roughly to SBO. It is concluded that – once pretrained –the new ML-approach is more efficient on variable optimisation tasks than classical SBO.

Introduction

Most modern production systems are complex systems and require a careful optimisation during production ramp-up. In current practice, this often involves resource-intensive trial-error campaigns combined with expert-judgment based on experience from prior parts. However, shrinking lot sizes, ever shorter development cycles and increasing product diversity severely challenge such empirical approaches and call efficient process optimisation tasks.

Thus, it is found that recurring optimisation tasks for ever-changing geometries or materials, respectively, are a significant economical barrier [1]. This holds all the more when processing delicate materials, such as textiles used for continuous-fibre reinforced plastics (CoFRP). They are usually processed in elaborate, multi-step processes and most often comprise a forming process of a textile. The wide range of adjustable process parameters and the complex, non-linear material behaviour require place high demands on a suitable process configuration and pose a challenging development task.

Content from this work may be used under the terms of the Creative Commons Attribution 3.0 license. Any further distribution of this work must maintain attribution to the author(s) and the title of the work, journal citation and DOI. Published under license by Materials Research Forum LLC.

Materials Research Proceedings 28 (2023) 1155-1166 https://doi.org/10.21741/9781644902479-126

To reduce the cost of an experimental process development, numerical simulations have gained attention over the last decades [2]. They allow for detailed analyses of complex processes and help concentrate costly experiments on the most promising variants. Also, their inherently digital nature allows a combination with optimisation algorithms. However, they usually involve significant computational efforts and especially repetitive simulations, e.g. iterative optimisation, quickly renders them impracticable in practice.

One option to reduce the numerical effort in such cases is surrogate-based optimisation (SBO) [3]. Surrogates are numerically efficient, data-driven approximations of expensive simulations based on input-output-observations. Once sufficiently trained, optimisation can be done on the surrogate in short time. Overall, SBO results in significant optimisation speed-ups. However, current SBO-approaches are mostly application-specific and fall short on reusability in new scenarios. Even subtle problem variations, e.g. geometry variations in manufacturing, instantly invalidate the surrogate and require resampling of data and reconstructing the surrogate. Thus, demand for generalised models arose.

At the same time, developments in Machine Learning (ML) have achieved remarkable results in complex tasks and may open up new avenues for advanced surrogates . The overarching concept is to sample process observations for a range of generic geometries and analyse it with ML-techniques [4-6]. Recurring patterns in the data may then guide a process optimisation of a new component. Owing to their reconfigurability and ease of evaluation, physics-based numerical process simulations are used for data sampling. Prior work has shown that such models can issue useful process recommendations for new components [4]. However, although the recommendations are useful, they are not strictly optimal but show some deviations to the true optimum. Thus, this work studies whether or not the initial ML-recommendations converge to the true optimum upon component-specific refinement.

Optimisation Methodology

Optimisation Approaches.

Formally, a forming simulation can be seen as a function $\varphi: P \overset{G}{\rightarrow} Q$ which maps variable process parameters $p \in P$ to a part quality descriptor $q \in Q$ for a given component geometry $g \in G$. Process optimisation then amounts to searching the optimal process parameters $p^* = \arg\min q(p)$ which yield the best quality[1]. Finding this optimum is a profound task, though, and this work compares three different workflows as shown in Fig. 1.

One approach is to directly couple optimisation algorithms with the simulation φ, e.g. genetic algorithms as Fig. 1a) shows. For a given geometry g, they determine the process parameter optimum p^* by iterative evaluation, variation and combination of parameter combinations. However, φ is generally costly to evaluate and thus, iterating p^* until convergence quickly become prohibitively computation-intensive.

In order to increase efficiency, surrogate-based optimisation (SBO) constructs a numerically efficient substitute function $\mu_{\mathrm{srg}}: P \rightarrow Q$, the "surrogate". The surrogate seeks approximates φ from a set of pre-sampled observations and allows to do the optimisation in short time on μ_{srg} instead of φ, cf. Fig. 1b) [3]. The obtained candidate solution p^*_{srg} is in turn validated in a simulation run and this new observation is fed back to the database. The procedure then repeats until convergence.

Numerous case studies across disciplines have reported substantial optimisation speed-ups by SBO, see e.g. [7]. However, current SBO-strategies provide mostly application-specific, one-off models and struggle with unforeseen task variations. This impairs reusability in new scenarios:

[1] In manufacturing the part quality q is often expressed by the extent of defects like cracks or wrinkles which are sought to be minimised, not maximised.

Even a subtle problem variation, e.g. a change of material or geometry, instantly invalidates the surrogate and requires resampling of data and reconstructing the surrogate [4]. Thus, demand for generalised models has been identified early on [8].

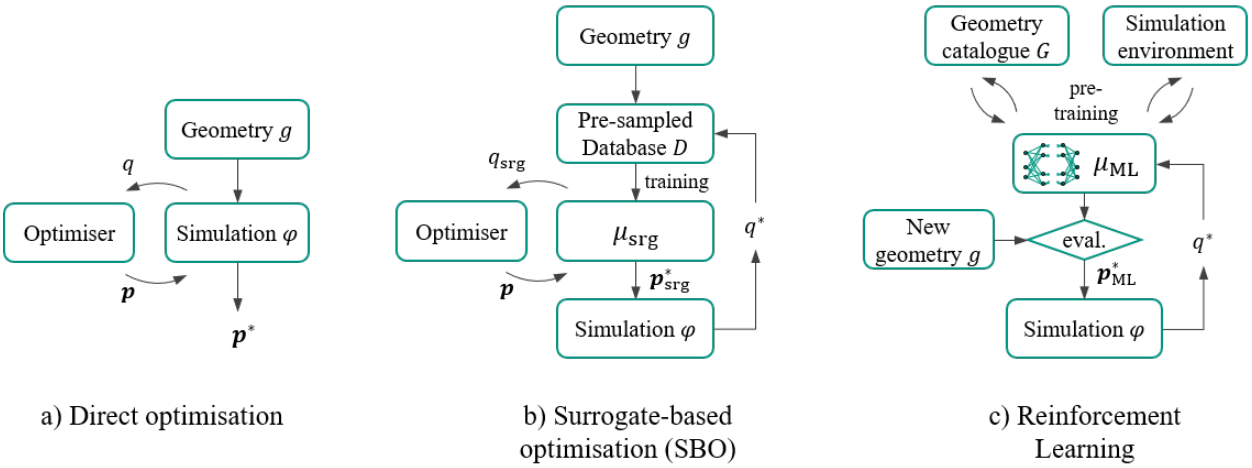

a) Direct optimisation

b) Surrogate-based optimisation (SBO)

c) Reinforcement Learning

Fig. 1. Workflows of a) direct, b) surrogate-based optimisation (SBO) and c) Reinforcement Learning on multiple geometries.

As a remedy, prior work of the authors [4] and [9] suggests to give up on classical surrogate models μ_{srg} in favour of a more generalised function $\mu: G \rightarrow P$. While classical surrogate models are in most cases used for fix geometries or consider parametric geometries only, μ is meant to learn the underlying part-process-relations from a whole set of non-parametric generic training geometries. After training, it shall be able to give parameter recommendations even for new geometries which are not part of the training geometries. A detailed description of the implementation is given in the prior publications [4] and [9] and thus, only a brief glimpse is provided in this work.

Reinforcement Learning for process optimisation.

The overarching idea is that the ML model function interacts with a set of generic geometries (geometry catalogue G) in a simulation environment. The workflow is visualised in Fig. 2a).

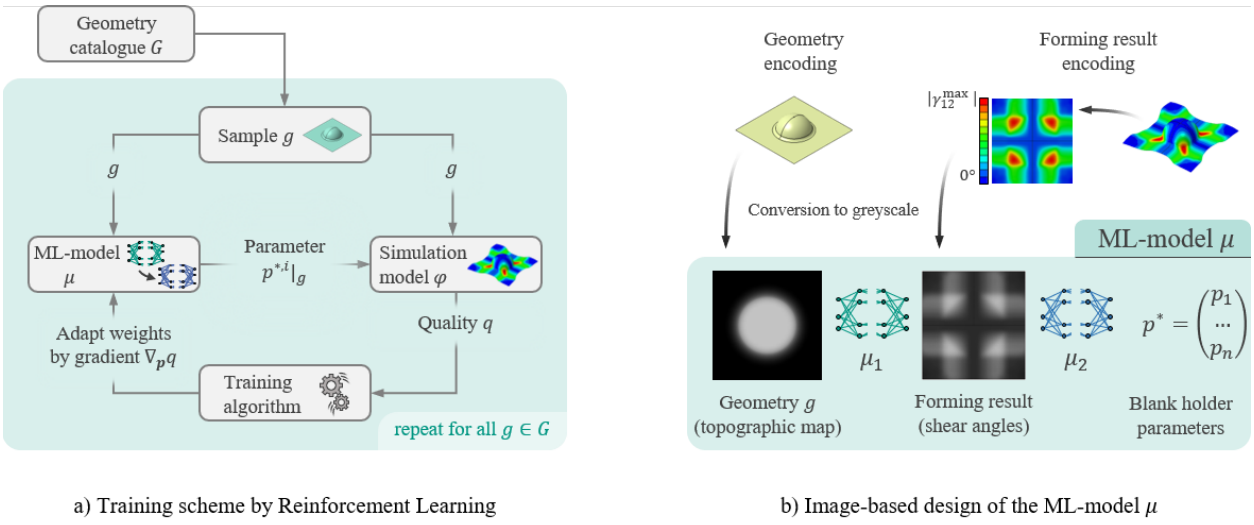

Fig. 2. a) Training scheme via Reinforcement Learning and b) image-based design of the ML-model $\boldsymbol{\mu}$ [4,9].

In each training iteration i, a geometry g is drawn from the geometry catalogue. Then the ML-model μ analyses g and issues an estimation of optimal parameters $p^*|_g$. This parameter recommendation is then evaluated in a simulation run φ to determine the resulting part quality q. If $p^*|_g$ indeed improves the part quality, then the ML-model is encouraged to give similar recommendations for similar geometries in the future. Formally, this means that the gradient $\nabla_{\boldsymbol{p}} q$ is determined and used to adapt μ's parameter recommendations in direction of increasing quality q. The procedure iterates until the forming quality across all geometries in the catalogue seizes to improve.

In the context of material forming, image-based approaches for μ – as illustrated in Fig. 2b) – have been proposed [4-6]. Compared to conventional geometry parameters, e.g. length, width, fillet radii or angles, image-based geometry descriptions have proven robust and versatile when applicability to variable geometries is key. In this work and the prior works of the authors, μ consists of two nested functions, μ_1 and μ_2, both of which are image-processing neural networks, so-called convolutional neural networks. The functions serve different purposes as Fig. 2b) visualises: μ_1 interprets the geometry and issues an estimation where and to what extent material strains are likely to occur. More specifically, the shear strain is evaluated as in-plane shear is the dominant deformation mechanism in engineering fabrics. Then, μ_2 interprets this strain-estimation and devises a parameter recommendation p^*.

Simulation Model and Optimisation Task

This work picks up on the models from the prior works [4,9] and is based on experimentally validated simulation approaches. It considers forming of cuboid geometries with the aid of pressure pads, cf. Fig. 3a). The cuboids can be varied in their dimensions w_1 and w_2 (width and length) as sub-image b) shows. For all geometries, the pads can be positioned freely around the perimeter of the geometries in order to control the draw-in of the fabric during forming.

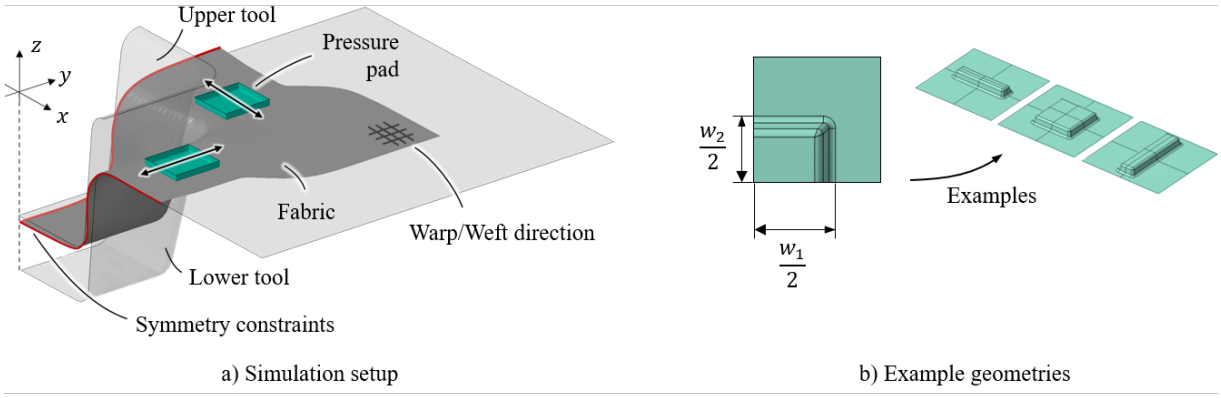

Fig. 3. a) Simulation setup for fabric forming with pressure pads; b) sample geometries in the geometry catalogue. Images are adapted from the prior work [4].

The cuboids are deliberately severe and show a strong tendency towards wrinkling. The overall quality goal during forming is to obtain a wrinkle-free forming result. As a direct measure of wrinkling, the fabric curvature κ is evaluated according to [11]. More specifically, the 99.5 % percentile κ_{qnt} of a Weibull fit to the fabric curvature distribution quantifies the quality, cf. Fig. 4a). The contour plot in Fig. 4b) shows κ_{qnt} for a single geometry as a function of the position of the pressure pads $p_{1,2}$ along with a top-view-visualisation of the pressure pads. The plot has been established by a fine grid-sampling of all possible pad positions for a single geometry. Note that these grid-samples are *by no means* involved in algorithm training but serve only for visualisation of κ_{qnt} (objective function) from an 'omniscient' perspective. The yellow marker illustrates how a specific pad position relates to the contour plot and vice-versa. Note that the plot is normalised so as to facilitate comparability with the following plots.

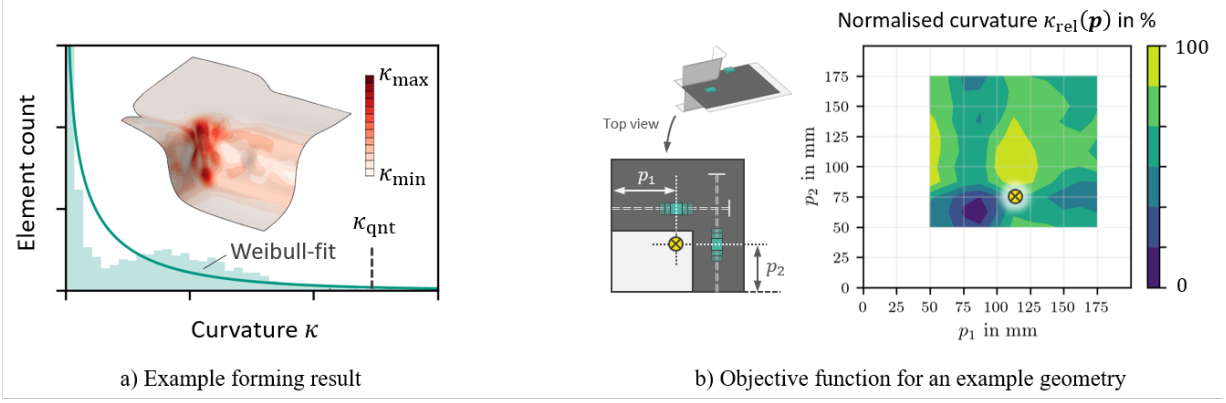

Fig. 4. a) Exemplary forming result with wrinkling, histogram of the fabric curvature plus Weibull fit; b) Contour plot of the obtained curvature (quality) depending on the pad positions $\boldsymbol{p_{1,2}}$*. Images adapted from prior work [4].*

Clearly, different pad positions significantly alter the obtained curvature and a distinct optimum, i.e. minimal curvature, can be observed. All geometries show such an optimum; however, its location varies and μ shall estimate its position for each geometry in the catalogue.

Materials Research Proceedings 28 (2023) 1155-1166 https://doi.org/10.21741/9781644902479-126

Results and Discussion

In the prior work [9], μ is trained on a set of box-geometries shown in Fig. 3b). The results show that it gives useful estimations not just for new box-geometries but also – to a certain degree – for 'non-box' geometries. See [9] for further details on the results. Two of these test geometries shall be further analysed in this work. They are shown in Fig. 5 on the left: A rotational symmetric shell with conical tips (g_1) and a double-dome geometry (g_2).

The contour plots in Fig. 5 show the forming quality (curvature) for all pad positions obtained by a grid-sampling approach. Note that they are not a subset of the box-geometries but, as they are doubly-symmetric and near-convex, they will still show a similar forming behaviour: Both contour plots feature a minimum similar to the box-geometry in Fig. 4b). Some qualitative differences can be observed, though: For g_1, the optimum is not a sharp point but a plateau-like region in the bottom-left of the plot. In contrast, the optimum for g_2 is comparably distinct and surrounded by two, connected maxima in a funnel-like shape while the majority of the plot is of approximately constant, mediocre quality.

Additionally, the plots feature three types of markers, namely two large and 30 small markers. The blue large marker visualises the best quality obtained during grid-sampling which is assumed to be the 'true optimum' p^*. The yellow large marker denotes μ's initial process recommendation $p_{\mathrm{ML}}^{*,0}$ immediately after training on box-geometries. If both the blue and the yellow marker coincided, that would imply that μ had made a perfect estimation of the process optimum. However, such a perfect estimation is highly unlikely since μ makes inference for a new geometry on the basis of generic box-geometries. Thus, the two markers are close to each other but still lie some distance apart. More specifically, an overestimation of $\approx 18\,\%$ (g_1) $\approx 13\,\%$ (g_2) relative to the parameter range $25\ \mathrm{mm} \leq p_{1,2} \leq 200\ \mathrm{mm}$ is observed.

However, the question arises, whether the yellow marker approaches the blue marker (true optimum) upon component-specific continuation of training. That is, having been pretrained on generic boxes, μ interacts now only with geometry g_1 or g_2, respectively. Thereby μ can iteratively refine on these specific geometries. The evolution of μ's recommendation $p_{\mathrm{ML}}^{*,i}$, is visualised by the smaller markers whose hue denotes their order of appearance, i.e. refinement iteration $i_{\mathrm{rfn}} = 1$ (black) to $i_{\mathrm{rfn}} = 30$ (white).

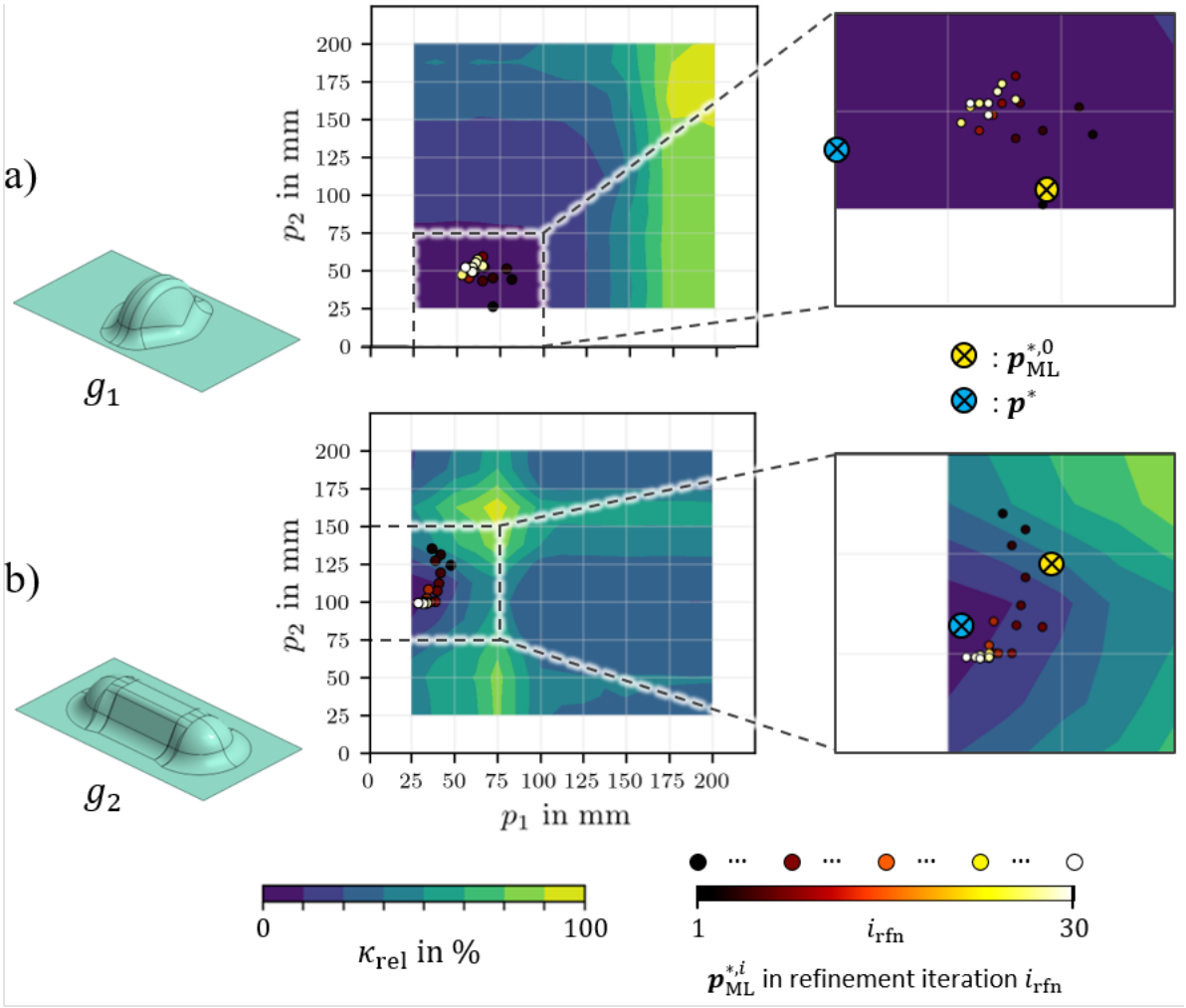

Fig. 5. Contour plots with $\boldsymbol{\mu}$'s process recommendations during component-specific continuation of training for a) geometry $\boldsymbol{g_1}$ (rotational symmetric shell) and b) $\boldsymbol{g_2}$ (double-dome).

However, the question arises, whether the yellow marker approaches the blue marker (true optimum) upon component-specific continuation of training. That is, after the training on generic box-geometries, μ interacts now only with geometry g_1 or g_2, respectively. Thereby μ is meant to iteratively refine its recommendations on these specific geometries. The evolution of μ's recommendation $p^{*,i}_{\mathrm{ML}}$, is visualised by the smaller markers, while their hue denotes their order of appearance, i.e. refinement iteration $i_{\mathrm{rfn}} = 1$ (black) to $i_{\mathrm{rfn}} = 30$ (white).

The plots reveal a disparate refinement behaviour: For geometry g_1 in subplot a), the refined markers appear somewhat incoherently scattered around the initial recommendation. At most, a light tendency to the top left can be observed. In contrast, for g_2 (double-dome) in subplot b), the markers do accumulate and show a coherent evolution: At first, the markers move to the top left. But, since this deteriorates the results, they reverse and gradually move downwards before concentrating near the minimum.

These observations can be explained when examining the objective functions in the contour plots: For g_1 in subplot a), the plateau-characteristic makes it difficult to identify a gradient for an improved pad position. Accordingly, the recommendations (markers) appear erratic. In contrast, a distinct optimum is observable for g_2 and – after a few iterations for 'orientation' – the markers move in direction of improved part quality. For some reason however, they only approach but do

not reach the observed optimum (blue marker). This may be due to numerical noise when evaluating the forming simulation.

Ultimately, Fig. 6 illustrates the optimisation progress for both geometries by means of the objective function. The diagrams support the above line of thought: Sub-image a) shows that the forming quality κ_{rel} stays practically constant for g_1 through all refinement iterations, while it improves (declines) for g_2 after correction of an initial peak. Overall, the results indicate that– like a regular surrogate – μ can indeed refine its initial recommendations with new evidence.

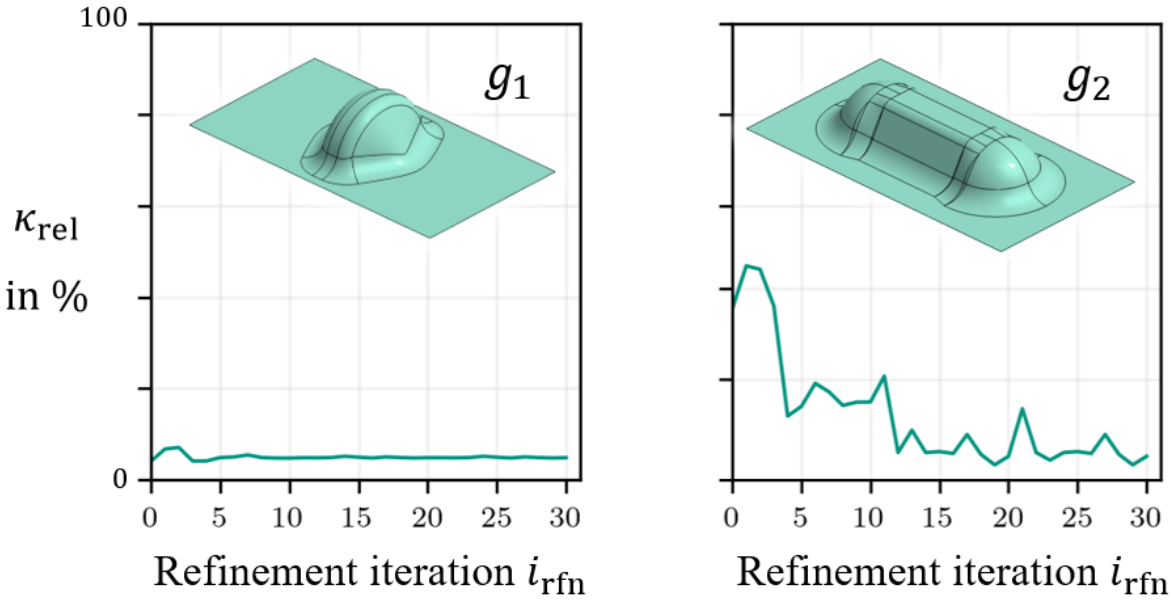

Fig. 6. Evolution of the optimisation objective $\boldsymbol{\kappa_{rel}}$ *during component-specific refinement of* $\boldsymbol{\mu}$ *on* $\boldsymbol{g_1}$ *and* $\boldsymbol{g_2}$.

Summary

Having seen that the RL-based optimisation method indeed shows optimisation behaviour, the three optimisation approaches from Fig. 1 – direct optimisation with a genetic algorithm (GA), SBO and RL – can be compared to each other. Each method is applied to the geometries g_1 and g_2 for inspection of the optimisation behaviour. The GA stems from the publicly available optimisation toolbox 'Dakota' [12] and the SBO reference method is described in detail in [13].

Note that the optimisation approaches employ different iterative schemes: The GA utilises a generation-based principle with each generation comprising $n_{\mathrm{idv}} = 20$ individuals. It is set to terminate after $n_{\mathrm{g}} = 15$ generations, i.e. after a total of $n_{\mathrm{g}} \cdot n_{\mathrm{idv}} = 15 \cdot 20 = 300$ simulations. This limit prevents excessive computation times and was determined empirically in a prior analysis on a fast – but much simpler – substitute model, cf. [4]. The limit is set such that at least one individual becomes (near-)optimal; yet it does not necessarily imply full convergence of the whole population around the optimum. For prevention of a potential quality-loss, the best found solution from the previous generation is (unaltered) carried over to the next generation (so-called 'elitist' selection). Both SBO and RL employ $n_i = 30$ refinement iterations (simulations). However, SBO requires a component-specific sampling – in this work Latin Hypercube Sampling – which accounts for additional $n_s = 20$ a-priori simulations before optimisation start. Also note, that RL needs no specific sampling due to its pretraining on box-geometries. Thus, it can directly start refining its recommendations for optimisation.

Geometry g_1.

For a direct comparison, Fig. 7 plots the progress of each optimiser on the objective κ_{rel} in one diagram along with a detail view for closer inspection (grey shade). Besides the sheer sequence of κ_{rel} (thin dashed line), the plots also show their lower envelope (bold solid line). Essentially, it gives for each iteration the 'so-far-best' solution and visualises, how fast each optimiser reduces the objective function. Overall, all graphs show a successful optimisation behaviour as they all approach the minimum ($\kappa_{\mathrm{rel}} = 0\,\%$).

However, although all approaches improve the solution over the iterations, the gain during additional optimisation iterations is limited as the first solutions are already near-optimal ($\kappa_{\mathrm{rel}} \approx 1\ldots5\,\%$). Thus, they offer little room for improvement with further iterations. This phenomenon can be explained by inspection of the contour plot, cf. Fig.5a): Since the optimum is not a sharp point but a comparably large plateau, the optimisers find it right at the beginning and thus have no room for improvement during iterations.

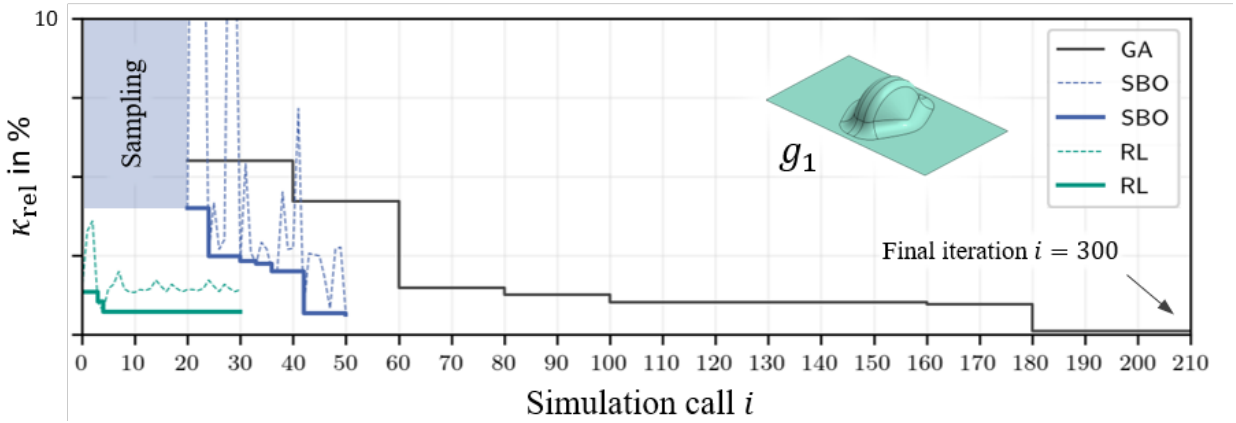

Fig. 7. Juxtaposition of $\boldsymbol{\kappa_{rel}}$ during optimisation on $\boldsymbol{g_1}$ for the GA, SBO and the RL-approach. The plots of GA and SBO are offset to account for the simulations until a first iteration occurs. Note that $\boldsymbol{\kappa_{rel}}$ is near-optimal directly from the beginning ($\boldsymbol{\kappa_{rel} \approx 1\ldots5\,\%}$). In accord, the plot is magnified with a y-axis focus on the lower 10%.

Despite the limited gain, the GA finds the overall-best solution ($\kappa_{\mathrm{rel}} = 0.2\,\%$), while both RL and SBO ($\kappa_{\mathrm{rel}} = 0.82\,\%$) remain slightly inferior ($\kappa_{\mathrm{rel}} = 0.78\,\%$). Note however, that RL and SBO require far fewer iterations to reach their final value, i.e. they converge faster. Also note that all algorithms involve elements of randomness. Thus, re-running them will probably lead to slightly different graphs and optimisation results.

Geometry g_2.

In a similar manner, Fig. 8 shows graphs for each optimisation approach on g_2 (double-dome) The overall behaviour of the algorithms stays the same as before: A successful optimisation can be observed. However, this time a notable effect of additional iterations is observed. Due to the majority of mediocre process responses (plateaus), all methods start at $\kappa_{\mathrm{rel}} \approx 40\ldots50\,\%$ in their first iteration, but then the progresses differ.

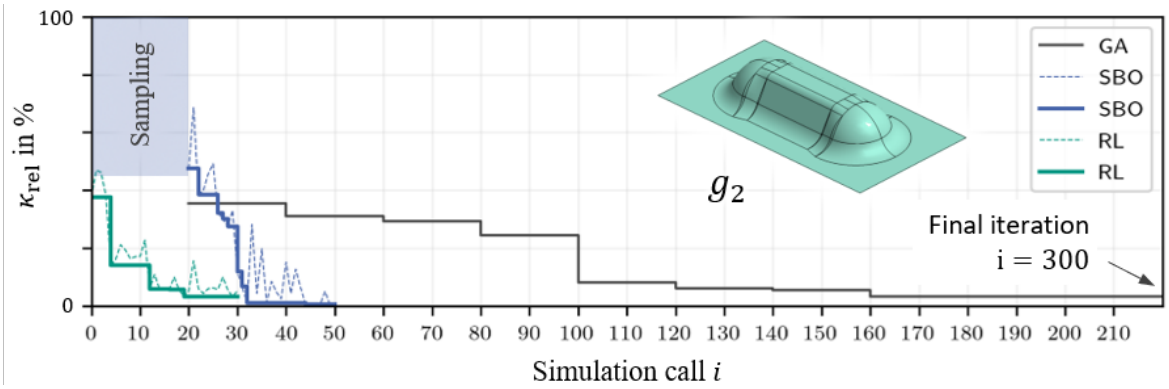

Fig. 8. Juxtaposition of $\boldsymbol{\kappa_{rel}}$ during optimisation on $\boldsymbol{g_2}$ (double-dome) for the GA, SBO and the RL-approach. The plots of GA and SBO are offset to account for the number of simulations until a first iteration.

Overall, the plot resembles the previous: The graphs decline in a monotonous manner to the minimum ($\kappa_{\mathrm{rel}} = 0\%$) and RL and SBO outperform the GA. However, this time all graphs show a substantial improvement of the objective function κ_{rel} during optimisation. All optimisers find a solution within a 5 %-range around the optimum, while SBO finds the overall best-solution with $\kappa_{\mathrm{rel}} \approx 2\,\%$. The GA reaches the 5 %-range after 160 simulations and RL after 18 iterations.

Speed of convergence. Ultimately, the speed of convergence shall be briefly assessed. To this end, the convergence metric

$$C = \int_{i=0}^{i_{\max}} \kappa_{rel}(i)\,\mathrm{d}i = \sum_{i=0}^{i_{\max}} \kappa_{rel}(i)\,\Delta i = \sum_{i=0}^{i_{\max}} \kappa_{rel}(i) \tag{1}$$

is used. Essentially, it is the area under the (solid) graphs until each optimiser has reached its final value in iteration $i_{\max}$. Due to the integer-abscissa, $di = \Delta i = 1$ holds which simplifies the integral to a sum. Overall, a smaller value of C implies faster convergence. If an approach finds a good solution early on, the following summands and thus C becomes smaller. This reflects the desired behaviour during optimisation of expensive functions, i.e. rapid minimisation with only few function evaluations. Table 1 below summarises the convergence metrics C and numbers of simulations $i_{\max}$ each optimisation approach required until its final value.

Table 1: Convergence comparison of GA, SBO and RL according to the convergence metric $\boldsymbol{C}$ and the required number of iterations $\boldsymbol{i_{max}}$.

	GA		SBO		RL	
Geometry	C	$i_{\max}$	C	$i_{\max}$	C	$i_{\max}$
g_1	4.39	180	0.79	42	0.31	4
g_2	37.13	160	13.50	32	4.02	19
sum	-	340	-	74	-	23

For both geometries, g_1 and g_2, SBO and the new RL-based method outperforms the GA by a large margin: While the GA requires 160 or 180 simulations, respectively, SBO and RL require less than 50 simulations to reach an approximately equal forming result. Equally large differences can be observed for the C. When comparing SBO and RL directly, RL appears more efficient than SBO. This is mainly because the RL-based approach does not require a component-specific sampling due to its pretraining on generic (box-)geometries. It must be noted however, that the computational effort for this pretraining may considerable.

The advantage of the pretrained RL-model becomes even more evident when optimising multiple geometries: Suppose, both geometries g_1 and g_2 need to be manufactured and their processes must be optimised. Optimising both geometries with SBO requires in total 74 simulations of which $2 \cdot n_s = 40$ simulations are required just for sampling. In contrast, the RL-model can do without component-specific sampling due to its pretraining on boxes and takes only 23 simulations in total. Although the exact numbers will certainly vary in different applications, the non-necessity of the a-priori sampling substantially cuts the computational effort.

Summary

This work studies the convergence behaviour of a previously proposed RL-based approach for process optimisation of variable geometries. The approach centres around an ML-model which interacts iteratively with a catalogue of generic geometries in a simulation environment. It thereby learns which geometry requires which optimal process configuration. The approach is studied at an example from prior work, namely optimisation of pressure pad positions during textile forming. Prior work has shown that – after the (pre-)training on generic geometries – the RL-approach indeed gives useful, near-optimal process recommendations [4,9]. This work picks up on these results and investigates, whether the recommendations converge to the true optimum upon component-specific refinement and if so, how fast.

The results are twofold: First, the results on two demonstrator geometries hint that the proposed RL-model indeed converges to the true process optimum. Second, a comparison to two conventional optimisation approaches – a genetic algorithm (GA) and a 'classical' surrogate-based approach (SBO) – shows that RL and SBO outperform the GA and show a similar convergence during refinement iterations. However, SBO needs a component-specific a-priori sampling while the RL-based method is pre-trained on generic geometries and can directly start refining its recommendations. Thus – once trained – it speeds up the optimisation process similar to a classical surrogate but beneficially cuts the component-specific sampling effort. However, this comes at the cost of substantial numerical efforts for algorithm pretraining.

The results of this work and the prior work show that it is indeed possible to extract usable part-process-relations from generic samples and use them during process optimisation for new components. While this work outlines their principal potential, the developed techniques yet need to be advanced to more complex and application-centred use-cases from industrial practice. Regarding textile-forming, this means the integration of more complex process scenarios, e.g. more complex geometries, additional process parameters and variable material properties. In the wider sense, the methods can also be tested on other processes inside and outside material forming.

Acknowledgment

This work is part of the IGF research project *OptiFeed* (21949 N) of the research association *Forschungskuratorium Textil e.V.*, Reinhardtstraße 14-16, 10117 Berlin, funded via the *AiF* within the program for supporting the Industrial Collective Research (IGF) from funds of the Federal Ministry of Economic Affairs and Climate Protection (BMWK). It is also part of the Young Investigator Group (YIG) *Green Mobility*, generously funded by *Vector Stiftung*.

References

[1] N. Shamsaei, A. Yadollahi, L. Bian, S.M. Thompson, An overview of direct laser deposition for additive manufacturing - part 2, Additive Manuf. 8 (2015) 12-35. https://doi.org/10.1016/j.addma.2015.07.002

[2] L. Kärger, A. Bernath, F. Fritz, S. Galkin, D. Magagnato, A. Oeckerath, A. Schön, F. Henning, Development and validation of a cae chain for unidirectional fibre reinforced composite components, Compos. Struct. 132 (2015) 350-358. https://doi.org/10.1016/j.compstruct.2015.05.047

[3] S. Koziel, L. Leifsson, Surrogate-Based Modeling and Optimization: Applications in Engineering. Springer Science+Business Media, New York, 2013. https://doi.org/10.1007/978-1-4614-7551-4
[4] C. Zimmerling, C. Poppe, O. Stein, L. Kärger, Optimisation of manufacturing process parameters for variable component geometries using reinforcement learning, Mat. Des. 214 (2022) 110423. https://doi.org/10.1016/j.matdes.2022.110423
[5] H.R. Attar, H. Zhou, A. Foster, N. Li, Rapid feasibility assessment of components to be formed through hot stamping: A deep learning approach, J. Manuf. Process. 68 (2021) 1650-1671. https://doi.org/10.1016/j.jmapro.2021.06.011
[6] H. Zhou, Q. Xu, Z. Nie, N. Li, A study on using image-based machine learning methods to develop surrogate models of stamp forming simulations, J. Manuf. Sci. Eng. 144 (2022) 021012. https://doi.org/10.1115/1.4051604
[7] R.T. Haftka, D. Villanueva, A. Chaudhuri, Parallel surrogate-assisted global optimization with expensive functions – a survey, Struct. Multidisc. Optimization 54 (2016) 3-13. https://doi.org/10.1007/s00158-016-1432-3
[8] H. El Kadi, Modeling the mechanical behavior of fiber-reinforced polymeric composite materials using artificial neural networks - a review, Compos. Struct. 73 (2006) 1-23. https://doi.org/10.1016/j.compstruct.2005.01.020
[9] C. Zimmerling, C. Poppe, L. Kärger, Estimating optimum process parameters in textile draping of variable part geometries - A reinforcement learning approach, Procedia manuf. 47 (2020) 847-854. https://doi.org/10.1016/j.promfg.2020.04.263
[10] C. Zimmerling, D. Trippe, B. Fengler, L. Kärger, An approach for rapid prediction of textile draping results for variable composite component geometries using deep neural networks, AIP Conference Proceedings 2113, ESAFORM 2019 in Vitoria-Gasteiz/Spain (2019), Art. 020007. https://doi.org/10.1063/1.5112512
[11] S. Haanappel, Forming of UD fibre reinforced thermoplastics: A critical evaluation of intra-ply shear. PhD-Thesis, Universiteit Twente, 2013. https://doi.org/10.3990/1.9789036535014
[12] Sandia National Laboraties. DAKOTA user's manual - version 6.15, www.dakota.sandia.gov/sites/default/files/docs/6.15/Users-6.15.0.pdf (2021), last accessed: 31.08.2022.
[13] C. Zimmerling, P. Schindler, J. Seuffert, L. Kärger: Deep neural networks as surrogate models for time-efficient manufacturing process optimisation. PoPuPS of ULiège Library, ESAFORM 2021 in Liège/Belgium (2021). https://doi.org/10.25518/esaform21.3882

Materials Research Proceedings 28 (2023) 1167-1174 https://doi.org/10.21741/9781644902479-127

Identification of the large strain flow curve of high strength steel via the torsion test and FEMU

VANCRAEYNEST Niels[1,a *], COOREMAN Steven[2,b] and COPPIETERS Sam[1,c]

[1]Elooi lab, Department of Materials Engineering, KU Leuven, KU Leuven-Gent Campus, Gebroeders De Smetstraat 1, 9000 Ghent, Belgium

[2] Applications & Solutions department, ArcelorMittal Global R&D Gent / OCAS NV, Belgium

[a]niels.vancraeynest@kuleuven.be, [b]steven.cooreman@arcelormittal.com, [c]sam.coppieters@kuleuven.be

Keywords: Large Strain Flow Curve, Torsion Test, Inverse Identification

Abstract. A torsion specimen is removed from the as-received thick high strength steel sheet (S700MC with a nominal thickness of 12 mm). The test material has a maximum uniform tensile strain of about 12 %. The torsion test is conducted up to fracture. The experimentally acquired torque-angle curve is then used to inversely identify the large strain flow curve up to an equivalent plastic strain of approximately 1. The identification strategy is based on the Finite Element Model Updating (FEMU) approach.

Introduction

Nowadays, numerical simulations are widely used in industry, hence generally considered to be a common engineering tool. However, the quality of simulations highly depends on the accuracy of the inputs. In metal forming simulations, it is well-known that the accuracy of the digital representation of the plastic material behaviour, i.e. the so-called material model, is of crucial importance for the predictive accuracy of the simulation. Commercially available finite element codes are still confined to phenomenological material models. In the case of metal plasticity, such models mostly rely on the concept of a yield surface, a hardening law and the associated flow rule. Experimental data is used to calibrate the governing material model parameters. Obviously, the type, quality and the amount of data determines the calibration accuracy. For example, the work hardening behaviour, also referred to as the flow curve, is conventionally calibrated using a standard tensile test in the Rolling Direction (RD). Since the majority of the metal forming processes generate plastic deformations beyond the maximum uniform tensile strain, the standard tensile test is of limited usefulness to determine the work hardening at large plastic strains, i.e. the large strain flow curve. In the case of sheet metal, several dedicated experiments enable to determine the large strain flow curve. Coppieters et al. [1] recently provided a comprehensive review on methods to determine the large strain flow curve of thin sheet metal. However, the majority of these methods cannot be applied to thick steel sheets. Zhang et al. [2] showed that it is possible to inversely extract the large strain flow curve from the diffuse neck in a tensile test. Alternatively, a torsion test can be used to probe large plastic strains without pronounced necking phenomena [3]. As opposed to a compression test, there is no influence of friction in the torsion test. To acquire the flow curve, the experimentally acquired torque-angle curve can be analytically converted to an equivalent stress-strain curve. The rotation angle directly yields the shear strain which is then converted to the equivalent plastic strain. However, for large plastic deformations, the validity of this analytical approach is violated since the relation between shear strain and equivalent strain does not remain linear [4,5]. The analytical post-processing is further complicated by the inhomogeneous stress and strain distribution within the torsion specimen. Indeed, the stress and strain radially increases in the cross section of the specimen. Thin-walled tubes circumvent

Content from this work may be used under the terms of the Creative Commons Attribution 3.0 license. Any further distribution of this work must maintain attribution to the author(s) and the title of the work, journal citation and DOI. Published under license by Materials Research Forum LLC.

this problem, yet often buckle due to eccentricity of the inner and outer diameter or an unfavourable ratio between the wall thickness and radius [6]. Consequently, this work aims at extracting the post-necking work hardening behaviour of thick high-strength steel through a torsion test on a cylindrical bar. According to Petrov et al. [7], the analytical methods lack accuracy and it is recommended to inversely post-process the experimental data acquired during a torsion test. For example, Gavrus et al. [8] proposed a FEMU method to inversely identify the large strain flow curve. A similar approach is followed in this paper to identify a suitable phenomenological hardening law enabling to describe the pre- and post-necking hardening behaviour of a S700MC sheet with a nominal thickness of 12 mm. The paper is structured as follows. In the first section the experimental details of the torsion experiment are described. The second section embarks on the numerical counterpart of the torsion test. The third section introduces the FEMU method. In section four, the results are presented and discussed.

Experimental

The torsion test is conducted on a custom-made tension-torsion machine (see Fig 1). Consequently, one grip (twisting head) is able to rotate and the other grip (weighing head) is restricted to only translational movement along the rotation axis. The rotation is induced by a servo motor and the angle of rotation of the twisting head is measured with an internal encoder. At the weighing head, gripping the other side of the specimen, the twisting moment is measured using a piezoelectric load cell with a moment and tensile capacity of 100 Nm and 5 kN, respectively. To obtain a pure torsion test, the weighing grip is free to move along the rotation axis.

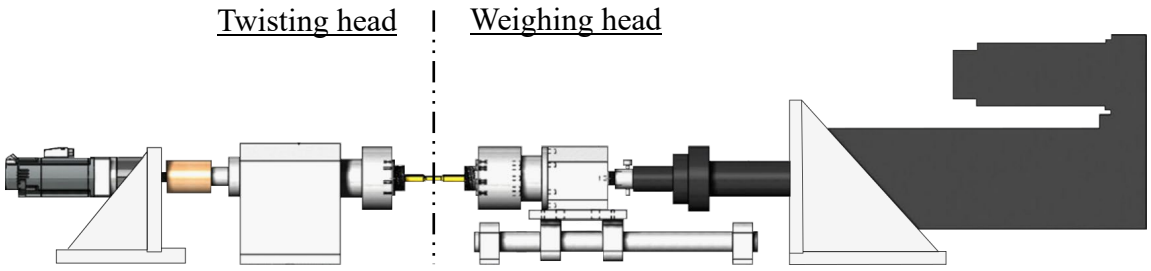

Fig. 1. Schematic overview of the tension-torsion machine. Left: Twisting head controlled by a servo motor; Right: Weighing head capable of measuring torque and tensile force with the possibility to connect a linear actuator to induce tension/compression.

The test material is a high strength low alloy (HSLA) steel S700MC with a nominal thickness of 12 mm. The ‘M’ and the ‘C’ indicate that the grade is made by a Thermomechanical Controlled Process (TMCP) and can be cold formed, respectively. Standard tensile tests were conducted and reported in [9], showing that the material exhibits a maximum uniform tensile strain of 0.12. The torsion samples are manufactured from the steel sheet in the RD. This is schematically visualized in the left panel of Fig. *2*. First, rectangular samples were removed by waterjet cutting. Through precision turning the final torsion samples were obtained as shown in the right panel of Fig. 2.

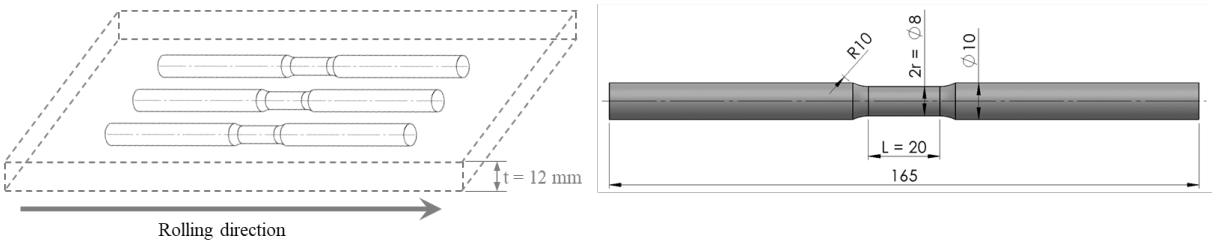

Fig. 2. The orientation of the torsion samples in the steel sheet (left) and geometry of the torsion sample after precision turning (right).

The torsion test is conducted under quasi-static conditions with a nominal strain rate in the order of $\dot{\varepsilon}_{eq} \approx 10^{-3}\frac{1}{s}$. For small rotational angles, the shear strain γ can be converted to the equivalent strain [4]:

$$\dot{\varepsilon}_{eq} = \frac{\dot{\gamma}}{\sqrt{3}} = \frac{r \cdot \dot{\theta}}{L \cdot \sqrt{3}} \tag{1}$$

With *r* the radius and *L* the length of the gauge section. $\dot{\theta}$ is the rotational speed of the twisting head. For the dimensions shown in the right panel of Fig. *2*, Eq. (1) yields a maximum rotational speed $\dot{\theta}$ of *30 °/min* to ensure quasi-static conditions. Three experiments were conducted using a constant speed of rotation *(20 °/min*) up to fracture of the sample. The results can be seen in Fig. *3*. The three repetitions are shown by the dashed grey lines. The solid black line is the average of the three experiments. All experiments easily reached *600* ° of rotation prior to fracture. Identical flat fracture surfaces perpendicular to the rotation axis were obtained in the three experiments.

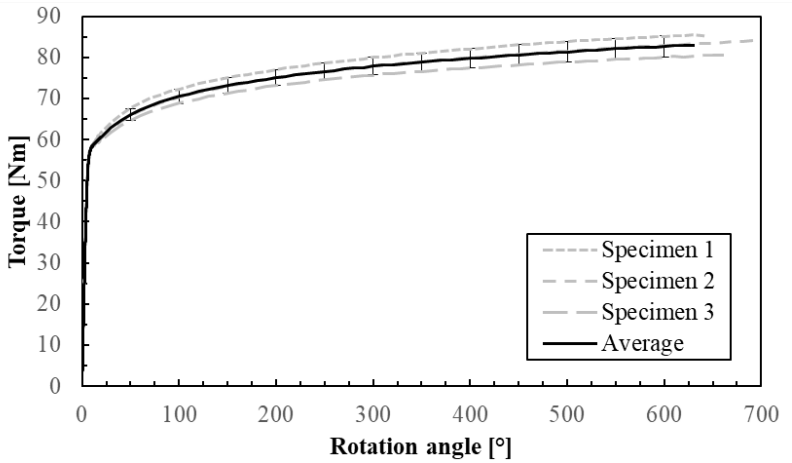

Fig. 3. Experimentally aquired Torque-rotation angle curves.

Numerical

The quasi-static torsion test is simulated using Abaqus/Standard. The torsion sample shown in the right panel of Fig. 2 is modelled in 3D using brick elements. The gripping areas are kinematically coupled with reference points onto which the boundary conditions are applied. The reference point referring to the twisting head is constrained in all degrees of freedom but the rotation angle. The reference point associated with the weighing head fixes all degrees of freedom but the translation along the rotation axis. The specimen is meshed with hexahedral elements (C3D8R) with an average size of 0.3 mm in the gauge section. The material is assumed to be elastically and plastically isotropic. Young's modulus and Poisson's ratio are assumed to be equal to 210GPa and 0.3, respectively. The plastic material behaviour is modelled using the von Mises yield criterion and a phenomenological hardening law.

It has been shown in [9] that the pre-necking hardening behaviour of S700MC can be accurately described by Swift's hardening law. Thus, Swift's hardening law can be fitted to pre-necking

hardening data acquired with a uniaxial tensile test (UTT). As opposed to Swift's hardening law, Voce's hardening law enables to predict saturation of the work hardening. Given that the large strain flow curve is a composite curve, several researchers proposed to combine existing hardening laws. An example of such approach is the p-model proposed by Coppieters and Kuwabara [10]. The p-model essentially combines Swift's and Voce's hardening and was recently successfully adopted to capture the large strain flow curve of 5182-O aluminium alloy [11].

Table 1. Selected phenomenological hardening laws.

Hardening law	Model description
Swift [12]	$\sigma_{eq} = K\left(\varepsilon_0 + \varepsilon_{eq}^{pl}\right)^n$
Voce [13]	$\sigma_{eq} = C\left[1 - me^{-B\varepsilon_{eq}^{pl}}\right]$
p-model [10]	$\sigma_{eq} = \begin{cases} K\left(\varepsilon_0 + \varepsilon_{eq}^{pl}\right)^n, & \varepsilon_{eq}^{pl} \le \varepsilon_{max} \\ K(\varepsilon_0 + \varepsilon_{max})^n + \frac{Kn(\varepsilon_0 + \varepsilon_{max})^{n-1}}{p}\left[1 - e^{-p\left(\varepsilon_{eq}^{pl} - \varepsilon_{max}\right)}\right], & \varepsilon_{eq}^{pl} > \varepsilon_{max} \end{cases}$

Table 1 summarises the hardening laws considered in this work. The model parameters will be inversely identified using FEMU. Swift's and Voce' hardening law both involve three unknowns. The p-model was constructed under the assumption that the large strain flow curve can be extracted from the diffuse neck in UTT. The pre-necking data is then readily available, hence the parameters $K, \varepsilon_0, \varepsilon_{max}$ and n are considered to be known and only the post-necking parameter p is subjected to inverse identification. To increase the flexibility of the p-model in the large strain range probed in the torsion test, however, p and ε_{max} are considered to be the unknown hardening parameters in this work. For the p-model, K, ε_0 and n are fixed and equal to the values found when fitting Swift to the pre-necking data of the UTT. Given that FEMU is driven by a gradient-based optimization, a good initial parameter guess is important to robustly identify the sought parameters. The pre-necking data of the UTT is used to determine the initial guess values, see Table 2.

Table 2. Initial guess values of the unknown hardening parameters.

Hardening law	Initial guess values
Swift	$K = 1250{,}62\ MPa\ ;\ \varepsilon_0 = 0{,}02409\ ;\ n = 0{,}1533$
Voce	$C = 1231{,}49\ ; m = 0{,}4012\ ;\ B = 3{,}52$
p-model	$p = 5\ ;\ \varepsilon_{max} = 0{,}15$

Finite Element Model Updating (FEMU)

With FEMU, the goal is to minimize the discrepancy between the experimental and numerical data and hereby inversely identifying the sought hardening parameters [7], [14]. To compare both datasets, here the torque-angle curves, a cost function $C(\boldsymbol{p})$ is used:

$$C(\boldsymbol{p}) = \frac{1}{2}\left[\boldsymbol{T}_{exp} - \boldsymbol{T}_{num}(\boldsymbol{p})\right]^T \cdot \left[\boldsymbol{T}_{exp} - \boldsymbol{T}_{num}(\boldsymbol{p})\right] \quad (2)$$

With $\boldsymbol{T}_{exp}$ and $\boldsymbol{T}_{num}(\boldsymbol{p})$ the column matrices of the torque for specific rotation angles obtained through the experiment and the FE model, respectively. The vector of the unknown parameters $\boldsymbol{p}$ is iteratively tuned to minimize $C(\boldsymbol{p})$.

To find a local minimum of $C(\boldsymbol{p})$, Cooreman [15] described two local optimization algorithms, namely Gauss-Newton and Levenberg-Marquardt. Both methods rely on the sensitivity matrix $\boldsymbol{S}$. This sensitivity matrix captures the influence of a parameter perturbation on the numerical response $\boldsymbol{T}_{num}$. The construction of the sensitivity matrix via finite differentiation requires an additional simulation per unknown parameter. The parameter update following Levenberg-Marquardt in each iteration reads as:

$$\Delta\boldsymbol{p} = [\boldsymbol{S}^T \cdot \boldsymbol{S} + \alpha \cdot \boldsymbol{I}]^{-1} \cdot \left[\boldsymbol{S}^T \cdot \left[\boldsymbol{T}_{exp} - \boldsymbol{T}_{num}\right]\right] \tag{3}$$

With α a scalar that is strictly positive. If α is zero, then the Gauss-Newton (GN) algorithm is retrieved. Levenberg-Marquardt (LM) is typically used to mitigate stability problems. The implemented optimization strategy follows the work of Denys [16] in which a combination of GN and LM is proposed. The FEMU starts with GN. While looping through the FEMU code the smallest value of the cost function $C(\boldsymbol{p}_{min})$ is stored in the memory. Upon the first increase of the cost function $C(\boldsymbol{p}_k)$ after a parameter update in iteration *k*, the optimization switches to the LM algorithm using an initial damping factor α equal to 10^{-7}. In iteration *(k+1)*, the parameters obtained in iteration (*k*-1) are used to predict the parameters update using LM. If $C(\boldsymbol{p}_{k+1})$ is lower than $C(\boldsymbol{p}_{min})$, the damping factor α will be divided by ten. Otherwise, α will be multiplied by ten to increase the damping behaviour. Convergence is assessed based on the relative change between the current and minimum cost function, $C(\boldsymbol{p})$ and $C_{min}(\boldsymbol{p})$, respectively. The FEMU code stops when the change is below 0.5 %.

Results

In a first step, the torsion test was simulated using Swift's hardening law calibrated based on the pre-necking data obtained from UTT. The parameters can be found in Table 2. The results are shown in Fig. 4 with the dotted line indicating the rotation angle where the maximum plastic strain in the simulation is equal to the maximum uniform tensile strain during the UTT. It can be inferred that the discrepancy with the experiment increases when the torsion test starts to probe strains beyond the maximum uniform tensile strain, i.e. beyond a rotation angle of approximately *75* °. This clearly indicates that the extrapolation of the hardening behaviour by Swift's hardening law is not valid, hence the need to identify the large strain flow curve based on experimental data beyond the maximum uniform tensile strain.

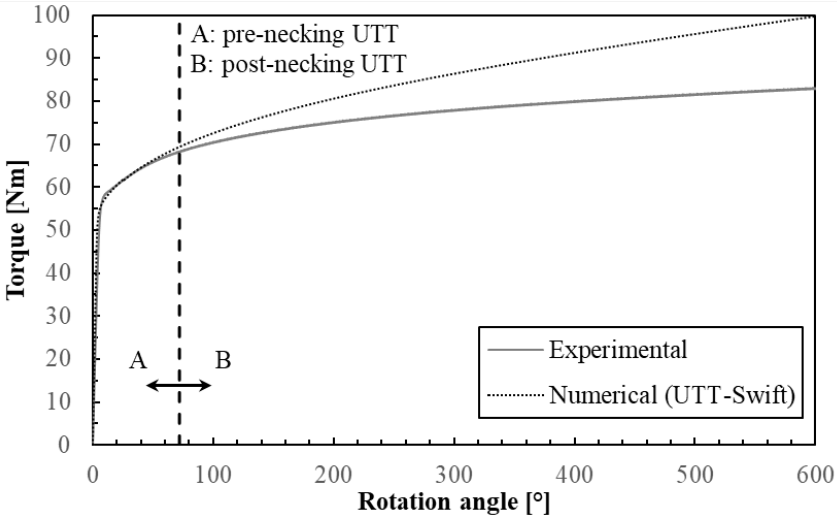

Fig. 4. Comparison between the experimental and the numerical torque-angle curve. With the material behaviour calibrated based on pre-necking data obtained from an UTT.

The FEMU code is fed with the torque-angle curve from 25° until 600°, ensuring that the torsion sample is sufficiently plastically deformed. The rotation angle of 25° is chosen arbitrarily and corresponds to a maximum ε_{eq}^{pl} of 0.04. The upper bound of 600° corresponds to a maximum ε_{eq}^{pl} of 1 without any visible damage. Each 2.5° of rotation, the torque value is probed to accurately capture the material response.

Table 3. The identified hardening parameters.

Hardening law	Hardening parameters	Accuracy Rank
Swift	$K = 1013{,}51\ MPa\ ;\ \varepsilon_0 = 0{,}003643\ ;\ n = 0{,}05792$	3
Voce	$C = 980{,}5754\ ; m = 0{,}2302\ ;\ B = 8{,}48$	1
p-model	$p = 13{,}65\ ;\ \varepsilon_{max} = 0{,}066$	2

The FEMU started with the initial parameters shown in Table 2. The inversely identified hardening parameters are shown in Table *3*. The accuracy rank shown in Table 3 is based on the value of the cost function upon convergence, also referred to as the cost function residual. The lower the cost function residual, the better the similarity between the experimentally acquired and numerically computed torque-angle curves. Consequently, the cost function residual gives an indication of the accuracy of the identified large strain flow curve. It can be inferred that Voce yields the lowest cost function residual, hence deemed to be the best choice for capturing the overall work hardening behaviour of S700MC during a torsion test. Fig. 5 shows the inversely identified hardening laws along with the extrapolated Swift law (UTT). It can be seen that the inversely identified hardening behaviour exhibits saturation at an equivalent stress of approximately 980MPa. Since Swift's hardening law cannot describe such saturation behaviour, and FEMU merely seeks for lowest cost function residual, a trade-off is found for the inversely identified Swift law. Indeed, the accuracy in the pre-necking region is lost to compensate for the inherent inaccuracy of Swift's hardening law in the post-necking regime. In this regard, the p-model is more flexible than Swift's hardening law. Nevertheless, the p-model cannot reproduce the Voce model in the complete strain range when only ε_{max} and p are considered to be the unknowns. Fig. 6 shows the predicted torque-rotation angle curve using the inversely identified hardening laws along with the experiment. It can be inferred that both the Swift law and the p-model predict an overshoot in a particular strain range, while Voce accurately predicts the experiment in the complete strain range.

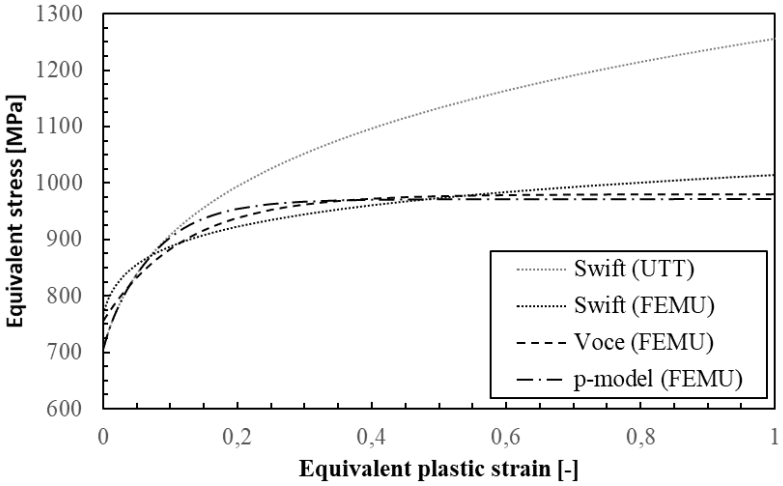

Fig. 5. The inversely identified flow curves compared with the extrapolated Swift law using the UTT.

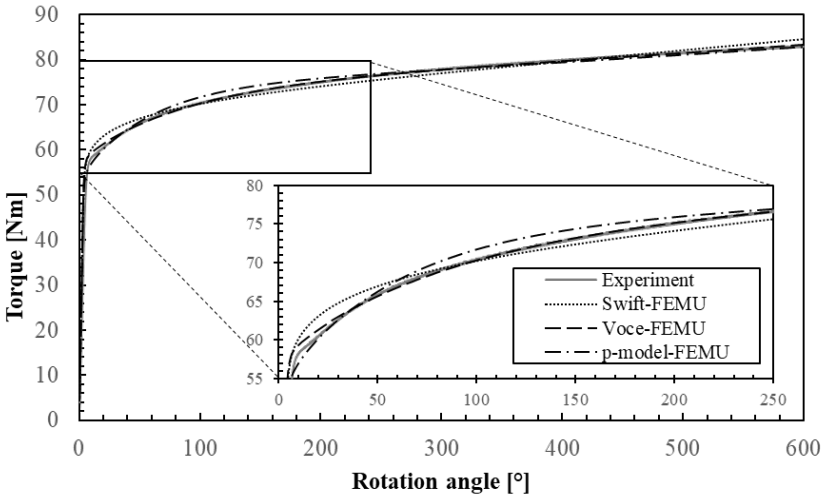

Fig. 6. Torque-rotation angle predicted by the FE model using the inversely identified hardening law. The solid grey line shows the experimental data.

Summary

The torsion test is used to inversely identify the large strain flow curve of a thick S700MC steel sheet. The FEMU approach uses the torque-twist curve to identify the parameters of three phenomenological work hardening laws. The methodology assumes the availability of a standard tensile test in the rolling direction to determine a reasonable initial guess of the sought parameters. It is shown that the hardening behaviour of S700MC, with a nominal thickness of 12mm, during a torsion test up to an equivalent plastic strain of 1 can be accurately described by Voce's hardening law. The following observations will be considered in future work:

- During the torsion test, limited spiral necking in the gauge length could be observed. It must be noted that the adopted FE model did not reproduce this phenomenon. It will be investigated if this is stemming from ignoring plastic anisotropy or an experimental error, e.g. an eccentricity problem.
- The influence of plastic anisotropy on the inverse identification of the large strain flow curve will be investigated.
- A multi-linear hardening law will be implemented to mitigate limitation imposed by the predefined character of phenomenological hardening laws.
- With a direct current potential drop (DCPD) measuring system, the objective is to determine the onset of damage. This would then enables to guarantee that only the undamaged part of the torque-twist curve is fed to the FEMU code.

Acknowledgements

This research was supported by the Research Fund for Coal and Steel under grant agreement No. 888153.

References

[1] S. Coppieters, H. Traphöner, F. Stiebert, T. Balan, T. Kuwabara, A.E. Tekkaya, Large strain flow curve identification for sheet metal, J. Mater. Process. Technol. 308 (2022) 117725. https://doi.org/10.1016/J.JMATPROTEC.2022.117725

[2] H. Zhang, S. Coppieters, C. Jiménez-Peña, D. Debruyne, Inverse identification of the post-necking work hardening behaviour of thick HSS through full-field strain measurements during diffuse necking, Mech. Mater. 129 (2019) 361-374. https://doi.org/10.1016/j.mechmat.2018.12.014

[3] M.V. Erpalov, E.A. Kungurov, Examination of Hardening Curves Definition Methods in Torsion Test, Solid State Phen. 284 (2018) 598. https://doi.org/10.4028/www.scientific.net/SSP.284.598
[4] N. Pardis, R. Ebrahimi, H.S. Kim, Equivalent strain at large shear deformation: Theoretical, numerical and finite element analysis, J. Appl. Res. Technol. 15 (2017) 442-448. https://doi.org/10.1016/j.jart.2017.05.002
[5] S.C. Shrivastava, J.J. Jonas, G. Canova, Equivalent strain in large deformation torsion testing : theoretical and practical considerations, J. Mech. Phys. Solids 30 (1982) 75-90. https://doi.org/10.1016/0022-5096(82)90014-X
[6] A.H. Stang, W. Ramberg, G. Back, Torsion Tests of Tubes, Jan. 1937, Accessed: Nov. 15, 2022. [Online]. Available: https://digital.library.unt.edu/ark:/67531/metadc66259/m1/14/
[7] P. Petrov, D. Shishkin, Y. Kalpin, I. Burlakov, S. Vydumkina, D. Kapitanenko, Determination of the flow curve based on the torsion of conical specimen, Procedia Manuf. 50 (2020) 520-528. https://doi.org/10.1016/J.PROMFG.2020.08.094
[8] A. Gavrus, E. Massoni, J.L. Chenot, An inverse analysis using a finite element model for identification of rheological parameters, J. Mater. Process. Technol. 60 (1996) 447-454. https://doi.org/10.1016/0924-0136(96)02369-2
[9] D. Debruyne et al., Towards Best Practice for Bolted Connections in High Strength Steels, 2019.
[10] S. Coppieters, T. Kuwabara, Identification of Post-Necking Hardening Phenomena in Ductile Sheet Metal, Exp. Mech. 54 (2014) 1355–1371. https://doi.org/10.1007/S11340-014-9900-4/FIGURES/16
[11] H. Shang, C. Zhang, S. Wang, Y. Lou, Large strain flow curve characterization considering strain rate and thermal effect for 5182-O aluminum alloy, Int. J. Mater. Forming 16 (2023) 1-20. https://doi.org/10.1007/S12289-022-01721-4/FIGURES/16
[12] H.W. Swift, Plastic instability under plane stress, J. Mech. Phys. Solids 1 (1952) 1-18. https://doi.org/10.1016/0022-5096(52)90002-1
[13] E. Voce, The relationship between stress and strain for homogeneous deformation, J. Inst. Metals 74 (1948) 537-562.
[14] M. di Donato, S. Bruschi, G. Hirt, M. Franzke, Flow curve determination by torsion tests using inverse modelling, 2016.
[15] S. Cooreman, Identification of the plastic material behaviour through full-field displacement measurements and inverse methods, PhD Thesis, VRIJE Universiteit Brussel, (2008).
[16] K. Denys, Investigation into the plastic material behaviour up to fracture of thick HSS using multi-DIC and FEMU, PhD Thesis, KU Leuven, (2017).

Materials Research Proceedings 28 (2023) 1175-1182 https://doi.org/10.21741/9781644902479-128

Investigating the suitability of using a single heat transfer coefficient in metal casting simulation: An inverse approach

VASILEIOU Anastasia[1,a *], VOSNIAKOS George-Christopher[2,b] and PANTELIS Dimitrios I.[3,c]

[1]The University of Manchester, Department of Mechanical, Aerospace & Civil Engineering, Dalton Nuclear Institute, Oxford Rd, Manchester M13 9PL, United Kingdom

[2]National Technical University of Athens, School of Mechanical Engineering, Manufacturing Technology Laboratory, Heroon Politehniou 9, 15773 Athens, Greece

[3]National Technical University of Athens, School of Naval Architecture and Marine Engineering, Shipbuilding Technology Laboratory, Heroon Politehniou 9, 15773 Athens, Greece

[a]anastasia.vasileiou@manchester.ac.uk, [b]vosniak@central.ntua.gr, [c]pantelis@central.ntua.gr

Keywords: Metal Casting, Casting Modulus, Heat Transfer Coefficient, Genetic Algorithm

Abstract. In metal casting simulation the Heat Transfer Coefficient (HTC) is unknown as it depends on melt and mold materials, on the casting modulus at different regions of the casting and on local conditions at the mold-casting gap. In this paper, thermocouple measurements at three regions of a brass investment casting provided reference cooling curves. A genetic algorithm (GA) determined the optimum 3-step time-dependent HTC for the whole of the casting in a simulation program for which cooling curves are as close as possible to the reference curves. The resulting prediction of solidification times is satisfactory but prediction of qualitative characteristics such as start / end of solidification in different regions was not accurate enough.

Introduction

Casting simulation can assist in selection of optimal process parameters, namely melt temperature, mold preheat temperature, melt inlet pressure and velocity, as well as design of the feeding system. The computational power which is available nowadays allows 'virtual casting' involving thermal, mechanical and flow domains, thus replacing costly real-life experiments [1]. Although the definition of the model is dictated by experimental conditions [2], heat transfer through the casting-mold interface is to be guessed; this is described by the "Interfacial Heat Transfer Coefficient (IHTC)" or simply "Heat Transfer Coefficient (HTC)". Heat transfer across the interface is determined by solid-to-solid conduction, conduction through the gas phase and radiation [3]. HTC is affected by the thermo-physical properties of the materials at the interface (cast metal, mold, coating) such as fluidity or solidification range [4]. At least three different representations of the HTC evolution have been proposed, namely: a step function of temperature, a step function of time (which is implicitly associated with solidification phases) [4] and an exponential function of time as a continuous approximation of the latter [5,6].

The well-known Chvorinov's rule [7] depicts a strong relation between solidification time and casting modulus (volume over surface area of the casting) implying that the different regions of the casting exhibit different solidification times [8]. Although it is commonly acknowledged that different HTCs should be assigned to regions of the casting with "significantly different" geometrical characteristics [9], only few publications investigate this issue [1,4,10,11].

In determining HTC, most commonly, temperature transients are measured close to the metal/mold interface using thermocouples despite their embedding close to the interface. This data can then be used combined with either an inverse calculation [12] or with repetitive simulations

Content from this work may be used under the terms of the Creative Commons Attribution 3.0 license. Any further distribution of this work must maintain attribution to the author(s) and the title of the work, journal citation and DOI. Published under license by Materials Research Forum LLC.

[13], until an HTC is identified that results in good agreement with the experiment. These methods can become substantially complex by employing, e.g., 3D instead of 2D models, various "local" HTCs tied to corresponding casting moduli or intricate optimization algorithms. Partitioning the casting shape into different complementary regions differing to a significant enough extent in casting modulus might be challenging, therefore an approach adopting a single HTC is a welcome simplification.

In order to avoid such complexity the present paper aims to answer the following questions: (a) Is it feasible to determine one 'equivalent' HTC and apply this to the whole casting domain during simulation instead of applying several different HTCs for different sub-domains? (b) How efficient is the use of genetic algorithms in the determination of HTCs?

The next section describes the experiment that provided the reference cooling curves. This is followed by two sections presenting the numerical simulation setup that was used in the evaluation function of the genetic algorithm that determines the optimum HTC and the setting up of this algorithm as well. Results and their discussion in the context of alternative genetic algorithm hyperparameters follow. Last, conclusions and further work are briefly summarized.

Experimental

A particular experiment was conducted to provide reference cooling curves to be used in the simulation through which optimum HTC is to be determined.

Lost wax investment casting was performed for a part with a stepwise increase in cross section made of CuZn33 alloy (brass), Fig. 1(a,b). The casting consists of three coaxial consecutive cylinders, namely a large (L), a medium (M) and a small (S) one. Length of the cylinders is 8 mm and their diameter measures 16 mm, 10 mm and 4 mm, respectively. Thus, casting modulus results as 2.30, 1.98 and 0.89, for L, M and S regions respectively.

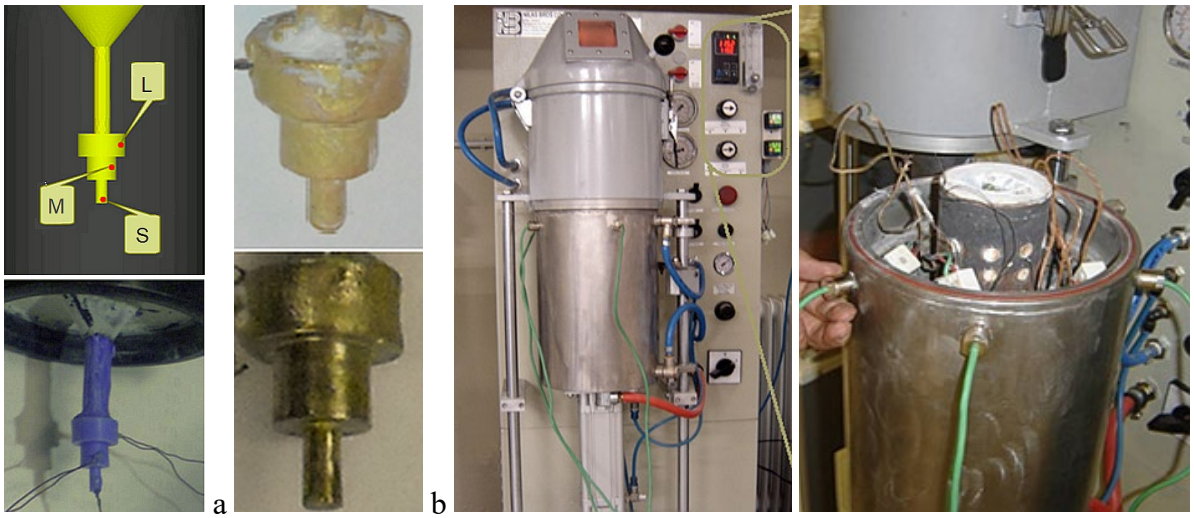

Fig. 1. Experiment setup (a) part/feeder: design (up), wax model with thermocouples (down) (b) casting: rough (up), cleaned (down). (c) casting machine: open with flask (left), closed (right)

The vacuum-pressure casting machine employed (NILAS BROS^{TM}) comprises a melting and a casting chamber, see Fig. 1(c). The former contains a graphite crucible with embedded thermocouple openings for temperature monitoring. Melting takes place under inert atmosphere of Ar. The mold is placed in the casting chamber which is sealed so that vacuum can be created and maintained. The machine is equipped with temperature and pressure displays allowing monitoring of the casting conditions in real time and performing corrections, as needed.

Materials Research Proceedings 28 (2023) 1175-1182 https://doi.org/10.21741/9781644902479-128

The casting parameters were as follows: casting chamber pressure: 0.03 bar (99.7% vacuum), pouring temperature: 990ºC and mold preheating temperature: 600ºC. One K-type thermocouple for each region was embedded in the mold cavity, as close to the metal-mold interface as possible, Fig. 1(a).

An A/D converter (Personal Daq/55 ™) fed raw temperature measurements to a laptop computer where they were processed by the Savitzky-Golay smoothing filter followed by cubic spline interpolation yielding the experimental temperature evolution curves. As shown in Fig. 2. each curve consists, as expected, of a short period of abrupt cooling (1st stage), a long period of mild cooling (2nd stage – solidification) and a third period of more pronounced cooling (3rd stage – post solidification).

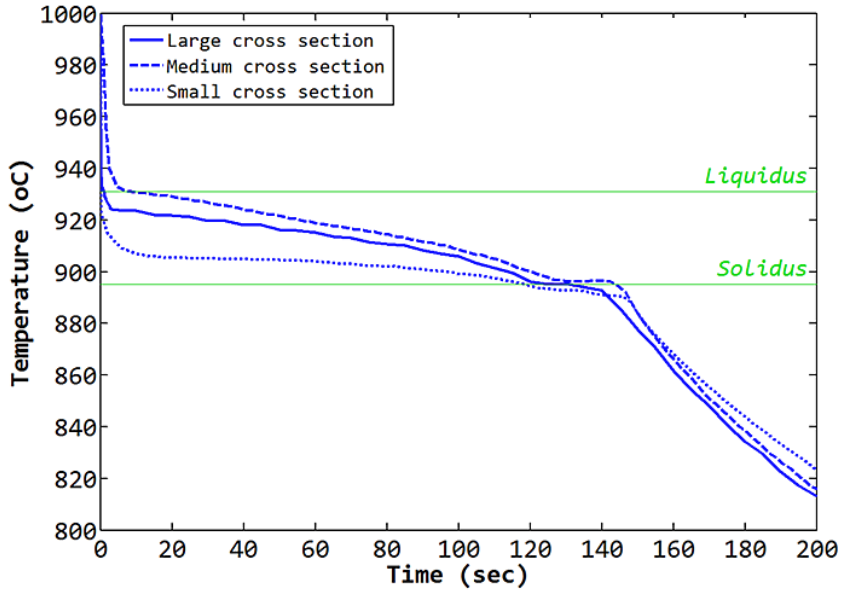

Fig. 2. Experimental temperature evolution curves.

Numerical Simulation Setup

ProCAST 2004.1® was used as the dedicated simulation platform implementing Finite Element Analysis to model coupled heat transfer, fluid flow and stress.

Determination of the initial conditions and the boundary conditions of the problem, i.e. temperature and pressure values during casting (mold preheating temperature, temperature of the outer surface of the mould, vacuum chamber pressure) followed the pertinent experimental settings, see previous Section.

HTC in the part of the sprue section filled by the melt was assumed to be the same as that of the small cylinder part of the casting (S), Fig. 1(a). This is a valid assumption as only a very small height of the sprue is actually filled by melt. The free surface of the melt is assigned radiation losses with an emissivity coefficient equal to 0.3 [14] and convective losses corresponding to air at 600°C with a film coefficient of 20 W/m^{2}K [15]. The pouring cup as such is treated exactly as the outer wall of the flask, i.e. it is assigned a Dirichlet boundary condition.

Melt flow rate was calculated as 1.13 kg/s using Bernoulli equation and considering the dimensions of the vacuum casting machine and of the casting tree.

Cast material properties were defined by interpolating the corresponding data available in literature. For brass CuZn33, liquidus was 931ºC and solidus was 886ºC; latent heat was 205 KJ/kg. Variation curves of thermal conductivity, density, specific heat, viscosity and fraction solid as a function of temperature are taken from [11].

HTC is modelled as a step function of time corresponding to three stages as first documented in [16] and is depicted in Fig. 3(a) and represented by the five element vector [h_1 t_1 h_2 t_2 h_3].

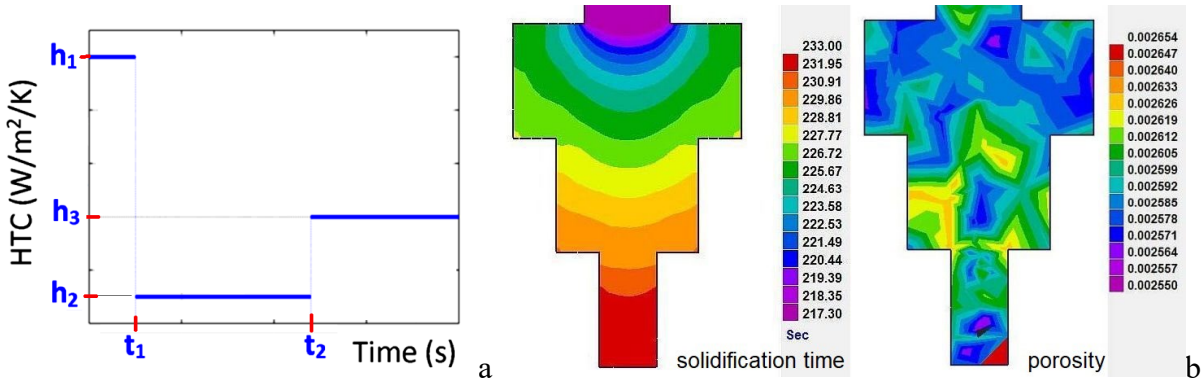

Fig. 3. (a) HTC representation (b) solidification time and porosity indicative simulation results.

Indicative simulation results regarding solidification time and porosity are shown in Fig. 3(b). Note that the right HTC needs to be employed if these results are to be credible, hence the need for inverse optimization approach.

The most valuable simulation result is temperature evolution at the three finite element mesh nodes corresponding to thermocouple locations by analogy to the experimentally obtained counterpart shown in Fig. 2.

Genetic Optimisation Setup

A classic GA was employed in order to determine the optimum HTC values that would cause the predicted temperature evolution curves to be as close as possible to the experimentally obtained ones. It was implemented on Matlab and made use of integer encoding of the chromosome.

The chromosome consists of the five variables that are necessary to define the HTC as a function of time, namely [h1 t1 h2 t2 h3], see Fig. 3(a). For each one of these variables its definition domain was discretised into 150 intervals. Each value is thus mapped to the corresponding interval, i.e. to a number from 1 to 150. The range of values for each variable was determined approximately from literature [11], thus for h_1, which is applicable during filling and generally above solidus, it is 200-30000 W/m^{2}K, whilst for h_2, which is applicable during solidification, it is 10 – 1500 W/m^{2}K; for h_3, which is applicable after the end of solidification, it is 20-3000 W/m^{2}K. The stepwise transitions occur at times t_1 and t_2 roughly corresponding to transition under liquidus and under solidus temperature respectively. Their value ranges are estimated by observing the experimental temperature evolution curves, Fig. 2, as 0.2-30 sec, and 105 – 165 sec respectively.

The fitness of any chromosome is calculated as the RMS metric of the difference in ordinates between 200 points defined on the experimental cooling curve and its simulation counterpart. This is done at the same time for all three curves corresponding to the small medium and large sections, see Fig. 2 and Fig. 1(b). The points are denser in regions where more sudden changes of temperature are expected. The fitness value is stored in a database so that the former does not have to be calculated anew each time the same input vector values are required. Obviously, fitness evaluation presumes that simulation curves of temperature evolution are obtained, which requires running the casting simulation programme with the particular HTC.

Several values were tried for the GA's hyperparameters, namely: for mutation rate: [0.1, 0.4, 0.7] for crossover rate: [0.2, 0.4, 0.5 , 0.8], for maximum iterations: [10, 20, 40, 100] and for population size: [4, 10, 20, 100]. The best result (best coincidence of experimental and simulation cooling curves) was obtained for mutation rate=0.1, population size = 20, crossover rate = 0.8, max iterations=100 and the evolution of the objective function is shown in Fig. 4. Note that if a

much higher number of generations were allowed, e.g. 1000, a further decrease in the value of the objective function might have resulted, since GAs cannot guarantee convergence to the minimum. However, such extravagance is not practical, in view of the high computational cost of each evaluation, as this requires execution of a casting simulation scenario typically lasting several minutes depending on the hardware employed.

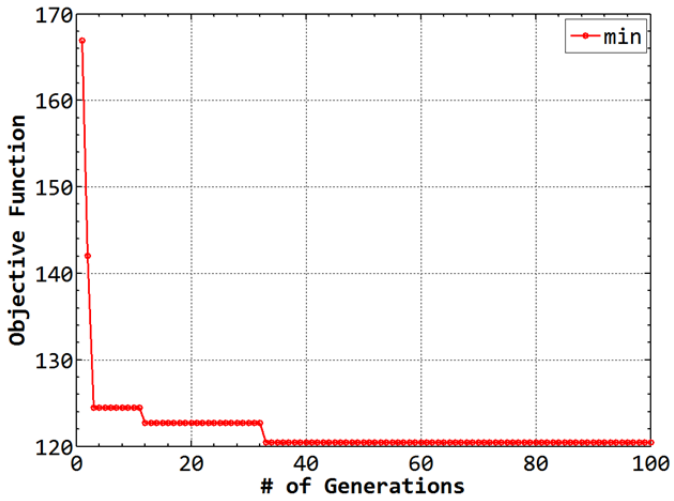

Fig. 4. Genetic algorithm cost evolution for the best chromosome in each generation.

HTC Optimisation Results and Discussion

The optimum HTC value determined by the GA is: [h1 t1 h2 t2 h3] = [102 38 70 3 35] in integer form, whilst in real number terms it is: h1=20400 W/m^{2}K, h2= 6 W/m^{2}K, h3=700 W/m^{2}K, t1=7 sec, t2=117 sec. This solution corresponds to a minimum in objective function equal to 120.4.

Fig. 5 depicts the cooling curves obtained by running the casting simulation for the optimum HTC in comparison to the experimental curves obtained by the corresponding thermocouples.

Referring to Fig. 5 comparison of experimental and simulation curves is generally satisfactory. The slope of the experimental and simulation cooling curves in the 2nd stage (during solidification) and in particular in the 3rd stage (post solidification) are similar.

Regarding the μ section, approximation of the experimental by the simulation curve is fairly good. Regarding the M section, approximation is good for the 2nd stage (solidification) but not so good for the 3rd stage (post solidification). Regarding the m section, approximation is unsatisfactory in the 1st and 2nd stages but fairly good in the 3rd stage. Furthermore, the lag in cooling of the m section with respect to the μ and M sections is not clearly captured by the simulation.

The end of solidification stage as determined by simulation at all three points is not far from the corresponding one that has been experimentally determined. However, the solidification start is not predicted so accurately by simulation.

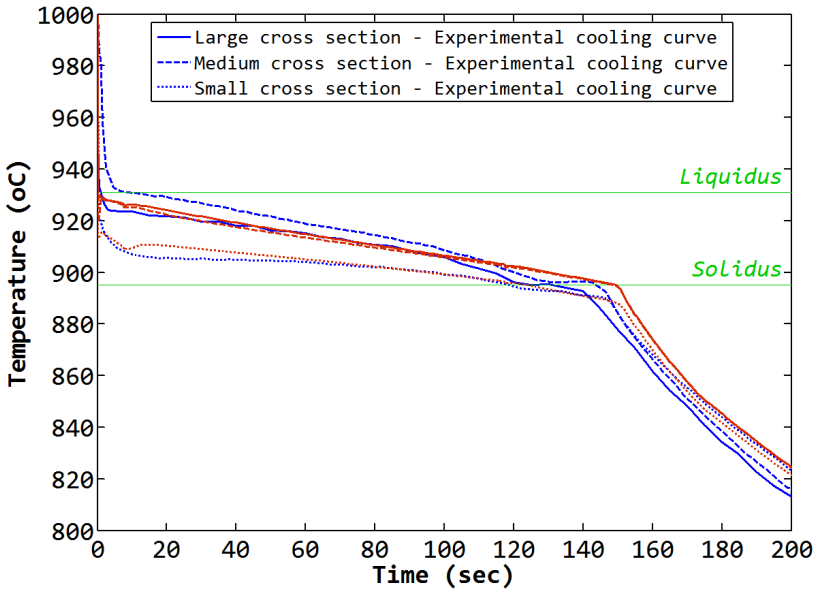

Fig. 5. Experimental and simulation cooling curves comparison.

Table 1 provides quantitative evidence for these observations. Note that the first few seconds after pouring are very important due to their influence on microstructure formation of the casting. Yet, the predicted duration of the 2nd stage (solidification) is in relatively good agreement with the experiment.

For comparison purposes, Table 1 also provides the respective results from a similar exercise considering three separate HTCs that have been reported earlier [11]. Three HTCs are a better alternative to a single HTC but the difference is tolerable especially for the larger sections. The corresponding objective function attains a significantly lower value than that attained in the single HTC case, i.e. 38.50 compared to 120.4. Recalling that this metric denotes the RMS of the ordinate differences between experimental and simulation cooling curves, i.e. a representation of temperature difference in time at the particular points monitored, this improvement is important but not spectacular.

Table 1. Solidification start (S) and end (E) times and duration (D) for large, medium and small (M, m, μ index) according to experiment and simulation.

		Single HTC			3 separate HTCs		
	Experiment	Simulation	Error (sec)	Error (%)	Simulation	Error (sec)	Error (%)
S_M (sec)	0.97	0.13	0.84	86.6%	1.97	-1.10	-103.09%
E_M (sec)	131.8	149.7	-17.9	-13.6%	147.5	-147.64	-11.91%
D_M(sec)	130.83	149.57	-18.74	-14.3%	145.53	-145.67	-11.24%
S_m (sec)	8.5	0.12	8.38	98.6%	2.75	-1.76	67.65%
E_m (sec)	144.1	148.7	-4.6	-3.2%	149.35	-149.38	-3.64%
D_m(sec)	135.6	148.58	-12.98	-9.6%	146.6	-146.70	-8.11%
S_μ (sec)	0.28	0.09	0.19	67.9%	0.24	0.44	14.29%
E_μ (sec)	119.2	124.1	-4.9	-4.1%	119.2	-119.24	0.00%
D_μ(sec)	118.92	124.01	-5.09	-4.3%	118.96	-119.00	-0.03%

Summary

In this work the suitability of simulation modelling vacuum casting of brass with a single HTC that is applicable throughout a casting different casting moduli of different regions was investigated.

An acceptable single HTC can be determined using a single casting experiment for reference, but this of course is case-dependent, i.e. it should be repeated every time any of the process parameters change, e.g. melt temperature, mold temperature and even pouring rate and, of course, if casting or mold geometry or materials change. However, the methodology of determining the HTC is generic and universally applicable

In general, agreement between simulation predictions and experimental measurements concerning temperature evolution at characteristic points of the different regions is fair. In particular, prediction of solidification duration is acceptable. However, qualitative characteristics such as the differences in solidification starting time between different regions are not captured accurately. Yet, predictive performance of the simulation when using a single HTC is tolerably inferior to that achieved when using 3 HTCs as revealed by comparison to pertinent work reported before. However, this is certainly connected to the relatively moderate differences in casting moduli.

In cases of intense differences in casting moduli, most probably different HTCs should be assigned to different regions, but this has to be proved in future extension of this work.

Acknowledgments

This work is funded by the European Commission in the framework HORIZON-WIDERA-2021-ACCESS-03, project 101079398 ‘New Approach to Innovative Technologies in Manufacturing (NEPTUN)’

References

[1] N. Pagratis, N. Karagiannis, G.-C. Vosniakos, D. Pantelis, P. Benardos, A holistic approach to the exploitation of simulation in solid investment casting, Proc. Inst. Mech. Engs, Part B: J. Eng. Manuf. 221/6 (2007) 967–979. https://doi.org/10.1243/09544054JEM465

[2] D. Furer, S.L. Semiatin (eds.), ASM Handbook Vol. 22B: Metals Process Simulation, ASM Intern., Ohio, 2010.

[3] K. Ho, R.D. Pehlke, Metal-mold interfacial heat transfer, Metall. Trans. B 16 (1985) 585-594. https://doi.org/10.1007/BF02654857

[4] G Palumbo, V. Piglionico, A. Piccininni, P. Guglielmi, D. Sorgente, L. Tricarico, Determination of interfacial heat transfer coefficients in a sand mould casting process using an optimised inverse analysis, Appl. Therm. Eng. 78 (2015) 682-694. https://doi.org/10.1016/j.applthermaleng.2014.11.046

[5] D. O’Mahoney, D.J. Browne, Use of experiment and an inverse method to study interface heat transfer during solidification in the investment casting process, Exp. Therm. Fluid Sci. 22 (2000) 111–122. https://doi.org/10.1016/S0894-1777(00)00014-5

[6] Y. Dong, K. Bu, Y. Dou, D. Zhang, Determination of interfacial heat-transfer coefficient during investment-casting process of single-crystal blades, J. Mater. Process. Technol 211 (2011) 2123-2131. https://doi.org/10.1016/j.jmatprotec.2011.07.012

[7] N. Chvorinov, Theorie der Erstarrung von Gussstucken, Giesserei, 27 (1940) 177-188.

[8] F. Havlicek, T. Elbel, Geometrical modulus of a casting and its influence on solidification process. Arch Foundry Eng. 11 (2011) 170-176.

[9] G. Zhi-peng, S.-M. Xiong, B.-C. Liu, L. Mei, A. John, Determination of the heat transfer coefficient at metal–die interface of high pressure die casting process of AM50 alloy, Int. J. Heat Mass Transfer 51 (2008) 6032-6038. https://doi.org/10.1016/j.ijheatmasstransfer.2008.04.029
[10] Z. Sun, H. Hu, X. Niu, Determination of heat transfer coefficients by extrapolation and numerical inverse methods in squeeze casting of magnesium alloy AM60, J. Mater. Proc. Technol. 211 (2011) 1432-1440. https://doi.org/10.1016/j.jmatprotec.2011.03.014
[11] A. Vasileiou, G.-C. Vosniakos, D. Pantelis, Determination of local heat transfer coefficients in precision castings by genetic optimisation aided by numerical simulation, Proc. Inst. Mech. Eng. Part C: J. Mech. Eng. Sci. 229 (2014) 735-750. https://doi.org/10.1177/0954406214539468
[12] W. Zhang, G. Xie, D. Zhang, Application of an optimization method and experiment in inverse determination of interfacial heat transfer coefficients in the blade casting process, Exp. Therm. Fluid Sci. 34 (2010) 1068–1076.
[13] A. Long, D. Thornhill, C. Armstrong, D. Watson, Determination of the heat transfer coefficient at the metal–die interface for high pressure die cast AlSi9Cu3Fe, Appl. Therm. Eng. 31 (2011) 3996-4006. https://doi.org/10.1016/j.applthermaleng.2011.07.052
[14] ASM, ASM Handbook Volume 02 - Properties and Selection: Nonferrous Alloys and Special-Purpose Materials, ASM International, Ohio, 1990.
[15] L.C. Burmeister, Convective Heat Transfer, 2nd ed, New York, Wiley-Interscience, 1993.
[16] F. Lau, W.B. Lee, S.M. Xiong, B.C. Liu, A study of the interfacial heat transfer between an iron casting and a metallic mould, J. Mater. Process. Technol. 79 (1998) 25-29.

Materials Research Proceedings 28 (2023) 1183-1192 https://doi.org/10.21741/9781644902479-129

Sensitivity analysis of the of the square cup stamping process using a polynomial chaos expansion

PEREIRA André F. G.[1,2,a *], MARQUES Armando E.[1,b], OLIVEIRA Marta C.[1,2,c] and PRATES Pedro A.[1,3,4,d]

[1] Centre for Mechanical Engineering, Materials and Processes (CEMMPRE), Department of Mechanical Engineering, University of Coimbra, Portugal

[2] Advanced Production and Intelligent Systems Associated Laboratory (ARISE), 4200-465 Porto, Portugal

[3] Centre for Mechanical Technology and Automation (TEMA), Department of Mechanical Engineering, University of Aveiro, Portugal

[4] Intelligent Systems Associate Laboratory (LASI), 4800-058 Guimarães, Portugal

[a] andre.pereira@uc.pt, [b]armando.marques@uc.pt, [c]marta.oliveira@dem.uc.pt, [d]prates@ua.pt

Keywords: Sobol's Indices, Polynomial Chaos Expansion, Square Cup, Uncertainty

Abstract. The stochastic modelling and quantification of the various sources of uncertainty associated with sheet metal forming processes, usually requires a large computational cost to obtain accurate results. In this work, a polynomial chaos expansion metamodel is used in order to reduce the computational cost of the uncertainty quantification (through Sobol's indices). The metamodel allows to establish mathematical relationships between the square cup forming results and the uncertainty sources associated with the material behaviour and process conditions. Then, sensitivity indices are estimated with the trained metamodel, without resorting to additional numerical simulations. The indices obtained with the metamodel were compared to those obtained with the traditional approach based on a quasi-Monte Carlo method. The metamodel allowed to reduce the computational cost in about 90% when compared to the traditional approach, without compromising the accuracy of the results.

Introduction

Sheet metal forming processes are among the most common and important metal working operations associated with the automotive, aeronautics and metalworking industries [1]. Numerical simulation is a well-established tool for the design and optimization of these processes [2]. However, the traditional use of the finite element method (FEM) is based on a deterministic approach [3], which does not take into account the various sources of uncertainty that are inevitable in a real industrial environment. These sources of uncertainty have a significant effect on the quality of the final product [4,5], leading to an inefficient production and, eventually, to the expensive redesign of the forming process. For all these reasons and due to the increasing availability of big data coupled with the growth of computer performance, the uncertainty analysis of these processes is a current scientific and industrial interest [1,6-8].

In recent years, distinct methods, such as, Monte Carlo Simulation [7-9], design of experiments [3,8] and metamodels [1,10] have been used to model the influence of uncertainty. Sensitivity analyses are used to quantify the influence of each uncertainty source in the variability of the forming results [3,11-13]. Variance-based sensitivity analysis (Sobol's indices [14]) is one of the most common methods to quantify this influence [6]. However, this analysis usually requires a large computational cost in order to obtain accurate sensitivity results [6]. This drawback contributes to the computational inefficiency of the uncertainty analysis, delaying its full and suitable employment in industry.

Content from this work may be used under the terms of the Creative Commons Attribution 3.0 license. Any further distribution of this work must maintain attribution to the author(s) and the title of the work, journal citation and DOI. Published under license by Materials Research Forum LLC.

This work presents a numerical study on the influence of the material and process uncertainty in the results of a square cup forming process. The square cup test was chosen for two main reasons: (i) it is a commonly used benchmark test to represent sheet metal forming processes [1,6,15-18]; (ii) it is a relatively fast process to simulate, which is suitable for performing a large number of numerical simulations. A polynomial chaos expansion (PCE) metamodel is used for reducing the computational cost of the Sobol's indices assessment [19]. The PCE metamodel establishes mathematical relationships between the square cup forming results and the uncertainty sources associated with the elastoplastic material properties of the blank (Hooke's law parameters, hardening law parameters, anisotropy coefficients) and process conditions (blank thickness, friction coefficient and the blank holder force). Then, Sobol's indices are estimated with the trained PCE metamodel, without resorting to additional numerical simulations. The indices obtained with the PCE metamodel were compared to those obtained with the traditional approach based on a quasi-Monte Carlo (q-MC) method.

Stochastic Model

Numerical Model. The square cup forming process was modelled with the same numerical model used in a previous work [6], as shown in Fig. 1. The geometry of the tools was adapted from the NUMISHEET' 93 benchmark [18]. The square blank has an initial thickness t_0, and a side length of 75 mm. The numerical simulation of the forming process consists of three phases: (i) First, the blank holder moves downwards, pressing the blank against the die, until a prearranged black holder force (BHF) is reached; (ii) Then, the punch moves 40 mm downwards, drawing the blank into the die, with a constant BHF; (iii) The final step consists in removing the tools (black holder, punch and die), resulting in the springback of the square cup. The numerical simulations were performed with the software DD3IMP (Deep Drawing 3D Implicit Code) [20]. Only a quarter of the model is simulated due to symmetries in the material, geometry and boundary conditions, and to reduce the computational cost. The blank is discretized with 1800 (8-node hexahedral solid) elements, with 2 elements in thickness and 30x30 elements in the sheet plane. The contact between the blank and the tools is described by the Coulomb's law with a constant friction coefficient, μ_0. In average, the duration of each simulation is approximately 4 minutes and 34 seconds in a computer equipped with an Intel® Core™ i7-8700K Hexa-Core processor (4.7 GHz).

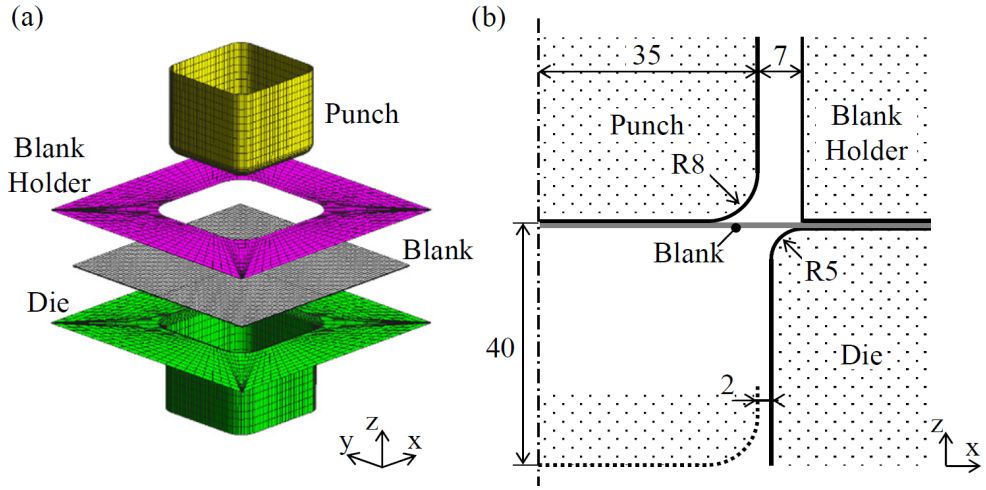

Fig. 1. Square cup forming process: (a) Numerical model [6]; (b) Dimensions of the tools in mm [6].

The mechanical behaviour of the metal sheet is modelled by: (i) the generalized Hooke's law, where E and ν are the Young's modulus and the Poisson's ratio, respectively; (ii) the Swift hardening law; (ii) and the Hill'48 yield criterion. The yield criterion is defined by:

$$F(\sigma_{yy}-\sigma_{zz})^2+G(\sigma_{zz}-\sigma_{xx})^2+H(\sigma_{xx}-\sigma_{yy})^2+2L\tau_{yz}^2+2M\tau_{xz}^2+2N\tau_{xy}^2=Y^2, \quad (1)$$

where σ_{xx}, σ_{yy}, σ_{zz}, τ_{xy}, τ_{yz} and τ_{xz} are the components of the Cauchy stress tensor; Y is the yield stress; F, G, H, L, M and N are anisotropy parameters. The parameters follow the condition $G+H=1$ and L= M = 1.5 (von Mises). F, G, H and N are obtained from the anisotropy coefficients r_0, r_{45} and r_{90}, by:

$$F={r_0}/{r_{90}(r_0+1)};\ G={1}/{r_0+1};\ H={r_0}/{r_0+1}$$

$$N={(r_0+r_{90})(2r_{45}+1)}/{2r_{90}(r_0+1)} \quad (2)$$

The Swift hardening law is given by:

$$Y=C(\varepsilon_0+\bar{\varepsilon}^p)^n \quad (3)$$

where $\bar{\varepsilon}^p$ is the equivalent plastic strain; n, C and ε_0 are hardening parameters. The initial yield stress is $Y_0=C(\varepsilon_0)^n$.

Input and Output Parameters. The sensitivity analysis is focused on 11 input parameters, 8 associated with the material behaviour (E, ν, n, C, Y_0, r_0, r_{45} and r_{90}) and 3 associated with the blank thickness, t_0, friction coefficient, μ_0, and blank holder force, BHF. The uncertainty of the input parameters is assumed to follow a normal distribution characterized by a mean, μ, and a standard deviation, σ, whose values are given in Table 1 [6].

Table 1. Mean and standard deviation of the normal distribution associated to the uncertainty of each input parameter [6].

	E [GPa]	ν	n	C [MPa]	Y_0 [MPa]	r_0	r_{45}	r_{90}	t_0 [mm]	μ_0	BHF [N]
μ	206.00	0.300	0.259	565.32	157.12	1.790	1.510	2.270	0.780	0.1440	2450.0
σ	3.85	0.015	0.018	26.85	7.16	0.051	0.037	0.121	0.013	0.0288	122.5

The uncertainty influence was analysed for 4 output parameters associated with the forming results, namely, the punch force (PF), the equivalent plastic strain ($\bar{\varepsilon}^p$), the thickness change (TC) and the geometry change (GC). The PF and the $\bar{\varepsilon}^p$ values are directly obtained from the numerical simulation, while the TC and the GC are defined by [6]:

$$TC\ [\%]=100\times(t_0-t_f)/t_0 \quad (4)$$

$$GC\ [mm]=\sqrt{(\bar{x}_f-x_f)^2+(\bar{y}_f-y_f)^2+(\bar{z}_f-z_f)^2} \quad (5)$$

where t_0 and t_f are the initial and final sheet thickness, respectively, in a given region of the square cup; (x_f, y_f, z_f) and $(\bar{x}_f, \bar{y}_f, \bar{z}_f)$ are, respectively, the final spatial position of a given node for the numerical simulation with and without uncertainty (i.e., using the mean values of Table 1). The GC quantifies the positional difference of a given node between the deterministic and the stochastic simulation. In this work, only the maximum values of the four outputs were analysed.

Sensitivity Analysis

Sobol's Indices. Sobol's Indices are a sensitivity measure of the influence of the input parameters on the output parameters [14]. Two distinct sensitivity indices can be used to quantify this influence, the 1st order indices, S_i, and the total sensitivity indices, S_i^T, which can be defined as follows [14]:

$$S_i = {V[E(\mathrm{y}|x_i)]}/{V(\mathrm{y})} \tag{6}$$

$$S_i^T = 1 - \left({V[E(\mathrm{y}|x_{\sim i})]}/{V(\mathrm{y})}\right) \tag{7}$$

where $V(\mathrm{y})$ is the unconditional variance of the result y; $V[E(\mathrm{y}|x_i)]$ is the conditional variance of the expected value of y when all input parameters, but x_i, are fixed; and $V[(\mathrm{y}|x_{\sim i})]$ is the conditional variance of the expected value of y when only the input parameter x_i is fixed. The 1st order indices, S_i, quantify the individual influence of each input parameter, x_i, on the result y; while the total sensitivity indices, S_i^T, quantify not only the individual influence of each input parameter, x_i, on the result y, but also the influence of the interactions between the input parameter x_i and the remaining, on the result y.

The indices S_i and S_i^T were already computed and published for the above model of the square cup forming process [6]. These indices were computed with the traditional method proposed in [21], and using the estimators proposed by [22], which allow to significantly improve the stabilization of the indices for a lower number of numerical simulations. A base sample of 3000 simulations was generated with a Sobol's sequence [23], in order to also achieve a faster stabilization. For a base sample of 3000 simulations, a total of 39000 simulations were needed to evaluate the sensitivity indices for the 11 input parameters, accordingly to the traditional procedure [21]. The chosen size of the base sample guarantees the stabilization of the sensitivity indices [6].

Polynomial Chaos Expansion. A Polynomial Chaos Expansion (PCE) metamodel is used to reduce the computational cost of the Sobol's indices evaluation [21]. The PCE metamodel allows to estimate the outputs (i.e., forming results), $\mathrm{y}^{PCE}(\mathbf{x})$, as a function of the input parameters (i.e., uncertainty sources), $\mathbf{x}$, by using an orthogonal polynomial basis, $\Psi_{\boldsymbol{\alpha}}$. The output value predicted by the PCE metamodel is given by [19]:

$$\mathrm{y}^{PCE}(\mathbf{x}) = \sum_{\boldsymbol{\alpha} \in \mathbf{A}} \beta_{\boldsymbol{\alpha}} \Psi_{\boldsymbol{\alpha}}(\mathbf{x}) \tag{8}$$

where $\beta_{\boldsymbol{\alpha}}$ are expansion coefficients and $\mathbf{A}$ is a set of pre-selected multi-index $\boldsymbol{\alpha} = [\alpha_1, \alpha_2, \dots, \alpha_k]$ (k is the number of input parameters). The elements α_i indicates the degree of the polynomial associated with the input parameter x_i. Hermite polynomials are used to build the polynomial basis, $\Psi_{\boldsymbol{\alpha}}$, since the input variables follow a gaussian distribution (see Table 1) [19]. The set $\boldsymbol{\beta}$ of expansion coefficients $\beta_{\boldsymbol{\alpha}}$ is determined with the ordinary least squares method [24]:

$$\boldsymbol{\beta} = (\boldsymbol{\Psi}(\mathbf{x})\boldsymbol{\Psi}(\mathbf{x})^{\mathrm{T}})^{-1}\boldsymbol{\Psi}(\mathbf{x})\mathbf{y}^{*}(\mathbf{x}) \tag{9}$$

where, $\mathbf{y}^{*}(\mathbf{x})$ is a set of q output results obtained with the q training simulations of the numerical model; and $\boldsymbol{\Psi}(\mathbf{x})$ is a $q \times q$ matrix of Hermitian polynomials of degree m. More details about the construction of $\boldsymbol{\Psi}(\mathbf{x})$ can be found in [19]. To avoid a high computational cost, only polynomials up to degree $m \leq 3$ and low order iterations between input variables are considered, following a hyperbolic truncation scheme [25].

Due to the orthogonality property of the polynomial basis, it is possible to directly evaluated the 1st order Sobol's indices by [26]:

$$S_i^{PCE} = \sum_{\boldsymbol{\alpha} \in \mathbf{A}^*} (\beta_{\boldsymbol{\alpha}}^2) \Big/ \sum_{\boldsymbol{\alpha} \in \mathbf{A}} (\beta_{\boldsymbol{\alpha}}^2) \tag{10}$$

where **A*** is a subset of **A** in which the multi-index $\boldsymbol{\alpha}$ is only associated to the input variable x_i (i.e., no other input variable is associated to the multi-index). The total Sobol's indices can be evaluated by [26]:

$$S_i^{T^{PCE}} = \sum_{\boldsymbol{\alpha} \in \mathbf{A}^{\mathbf{T}}} (\beta_{\boldsymbol{\alpha}}^2) \Big/ \sum_{\boldsymbol{\alpha} \in \mathbf{A}} (\beta_{\boldsymbol{\alpha}}^2) \tag{11}$$

where $\mathbf{A}^{\mathbf{T}}$ is a subset of **A** in which the multi-index $\boldsymbol{\alpha}$ is associated to the input variable x_i, even if $\boldsymbol{\alpha}$ is simultaneously associated with other input variables. Based on the above equations it is evident that the Sobol's indices are instantaneously calculated after the evaluation of the expansion coefficients $\beta_{\boldsymbol{\alpha}}$, i.e., after the metamodel training.

The metamodel was trained with the same 3000 base simulations, previously used to compute the indices S_i and S_i^T with the traditional approach. Four metamodels were trained each one for a given output PF, $\bar{\varepsilon}^p$, TC and GC. The metamodel was tested for other 1000 simulations by comparing the predicted PCE output, $\mathrm{y}^{PCE}(\mathbf{x}^*)$, with the one assessed with the testing simulations $\mathrm{y}(\mathbf{x}^*)$. The performance of each metamodel was evaluated with the root-mean-square error, $\sqrt{\epsilon}$, and the coefficient of determination, R^2, given by [26]:

$$\sqrt{\epsilon} = \sqrt{1/q^* \sum_{i=1}^{q^*} \left(\mathrm{y}(\mathbf{x}_i^*) - y^{PCE}(\mathbf{x}_i^*)\right)^2} \tag{12}$$

$$R^2 = 1 - \epsilon / V(\mathbf{y}(\mathbf{x}^*)) \tag{13}$$

where q^* is the number of testing simulations, $\mathrm{y}(\mathbf{x}_i^*)$ and $y^{PCE}(\mathbf{x}_i^*)$ are the simulation and predicted output for the set of input parameters, $\mathbf{x}_i^*$, of the i^{th} testing simulation. $V(\mathbf{y}(\mathbf{x}^*))$ is the variance of the outputs evaluated for the q^* testing simulations. The root-mean-square error, $\sqrt{\epsilon}$, and the coefficient of determination, R^2, of the metamodels trained for each output, are indicated in Table 2.

The PCE metamodels for the outputs PF, $\bar{\varepsilon}^p$ and TC achieved the best performances, with R^2 values close to 1. On the other hand, the PCE metamodel for the output GC had the poorest performance, with a R^2 value of 0.8834. Fig. 2 compares the simulated outputs of the testing dataset, $\mathrm{y}(\mathbf{x}_i^*)$, with those predicted by the PCE, $y^{PCE}(\mathbf{x}_i^*)$. It can be observed that the PCE metamodels were able to accurately predict the simulation outputs, with the exception of GC.

Table 2. Root-mean-square error and coefficient of determination of the metamodels trained for the outputs PF, $\bar{\varepsilon}^p$, TC and GC.

	PF	$\bar{\varepsilon}^p$	TC	GC
$\sqrt{\epsilon}$	0.2207[kN]	0.0036	0.0841%	0.0412[mm]
R^2	0.9956	0.9734	0.9845	0.8834

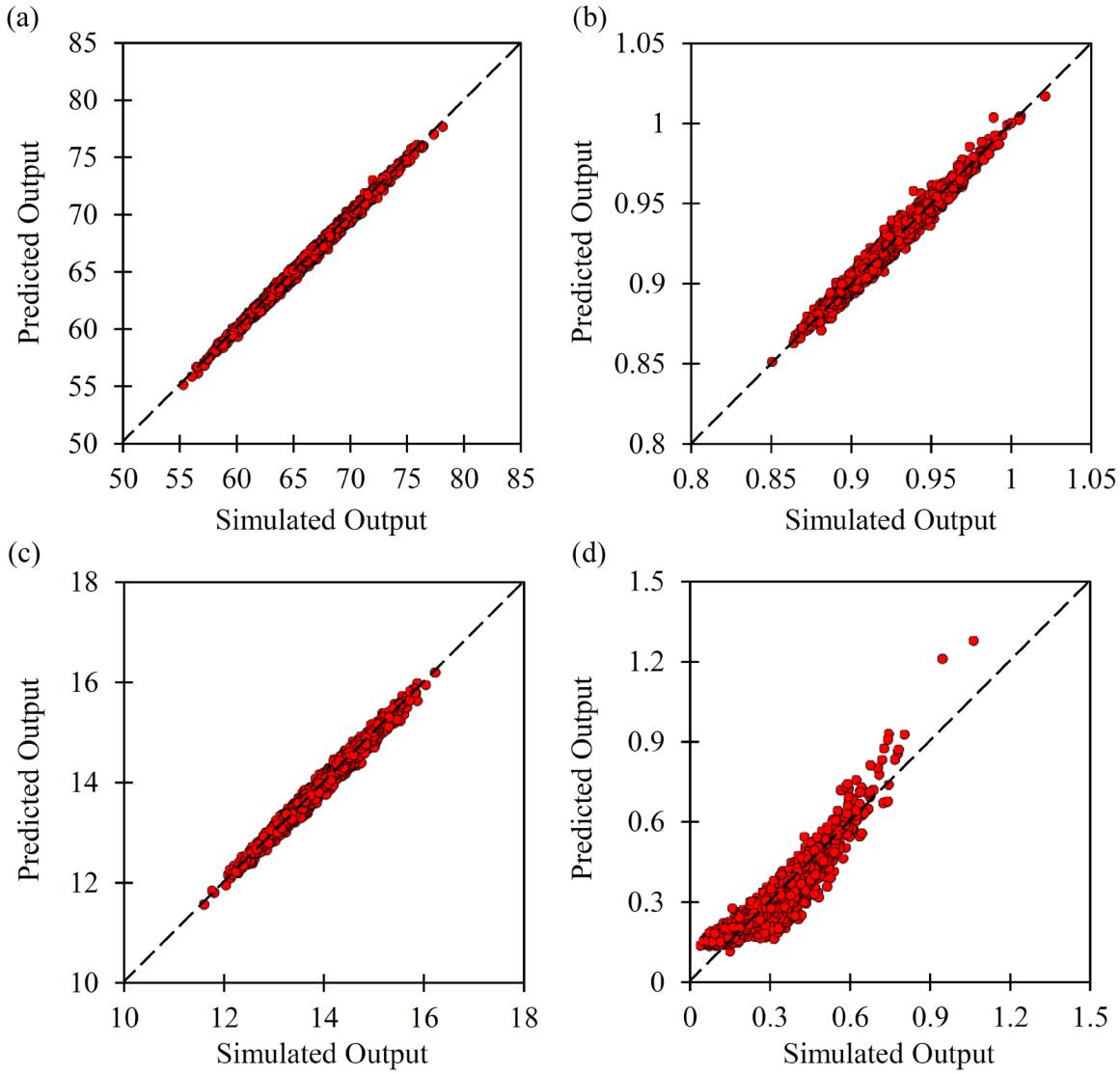

Fig. 2. Predicted (PCE metamodel) and simulated outputs: a) PF [kN]; b) $\bar{\varepsilon}^p$; c) TC [%]; and d) GC [mm]. The dashed line represents the optimal metamodel response, in which predicted outputs are equal to simulated outputs.

Sensitivity Results

In this section, the Sobol's sensitivity indices evaluated with the traditional approach are compared with those evaluated using the PCE metamodel. In this context, Fig. 3 and Fig. 4 show the 1st order and the total Sobol's sensitive indices, respectively, for the outputs PF, $\bar{\varepsilon}^p$, TC and GC.

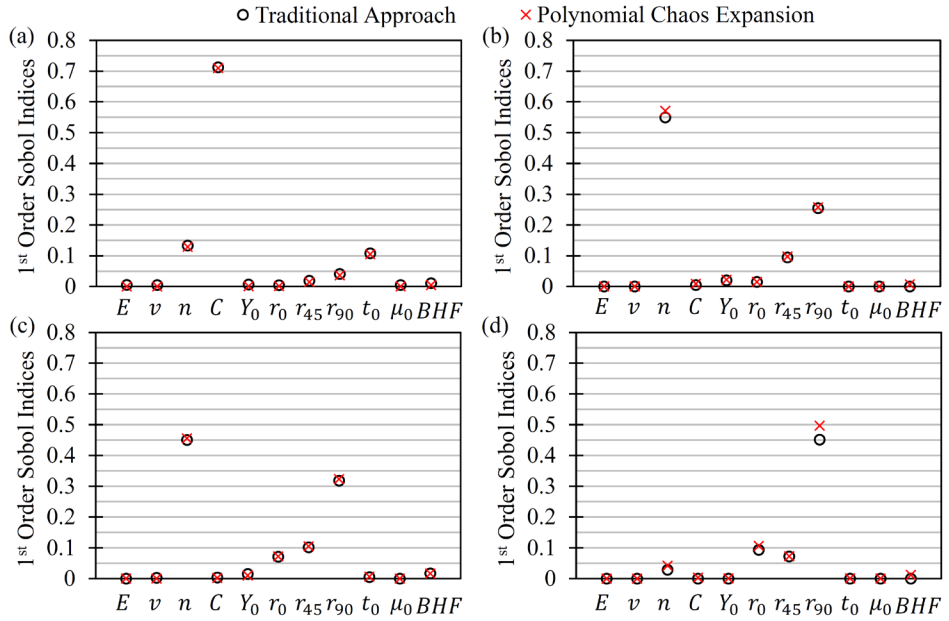

Fig. 3. 1st order Sobol's indices, computed with the traditional approach and with the PCE metamodel, for the outputs: a) PF; b) $\bar{\varepsilon}^p$; c) TC; and d) GC.

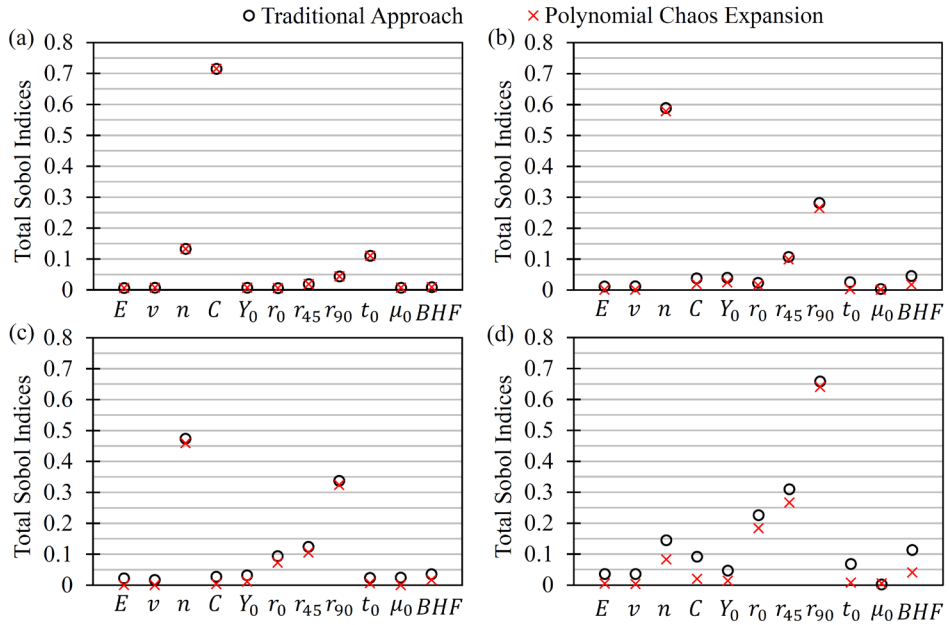

Fig. 4. Total Sobol's indices, computed with the traditional approach and with the PCE metamodel, for the outputs: a) PF; b) $\bar{\varepsilon}^p$; c) TC; and d) GC.

Based on Fig. 3 and Fig. 4, it can be observed that the PCE metamodels are able to accurately predict both sensitivity indices. The only significant difference between the indices computed with the traditional and PCE metamodel is observed for the output GC, where the maximum absolute difference between the sensitivity indices of both methodologies is 0.073. This occurs due to the lower accuracy of the metamodel to predict the GC output, as shown in Fig. 3 (d). Nevertheless, even in this case the accuracy of the sensitivity indices computed by the PCE metamodels is suitable to quantify and rank the influence of the input parameters. It is noteworthy that, that the

computation of the Sobol indices with the traditional approach required 39000 simulations, while the computation with the PCE metamodel only required 4000 simulations (3000 for training and 1000 for testing the metamodel).

In summary, the PCE metamodel allowed to evaluate the Sobol's indices with accuracy and computational efficiency, requiring about 90% less numerical simulations when compared to the traditional approach.

Summary

In this work, a polynomial chaos expansion (PCE) metamodel is used to compute sensitivity indices, with the goal of reducing the computational cost associated with the traditional approach. The sensitivity indices were assessed with both methodologies for 4 outputs/results: the punch force (PF), the equivalent plastic strain ($\bar{\varepsilon}^p$), the thickness change (TC) and the geometry change (GC) of the square cup forming process. In this study was assumed uncertainty in 11 input parameters, namely, elasticity parameters, anisotropy coefficients, hardening parameters, blank thickness, friction coefficient and blank holder force.

The PCE metamodel allowed to establish mathematical relationships between the square cup forming results and the sources of uncertainty. The predictive performance of the PCE metamodels was tested, and it was concluded that the metamodels were able to accurately predict the simulation outputs. Then, Sobol's indices were estimated with the trained PCE metamodels and the traditional approach based on a quasi-Monte Carlo (q-MC) method. Both methodologies obtained similar 1st order and total Sobol's indices for the PF, the $\bar{\varepsilon}^p$ and the TC. Small differences in the Sobol's indices were observed for the GC output, but without compromising the sensitivity results.

In summary, the PCE metamodel allowed to reduce the computational cost in 90%, when compared to the traditional approach, without compromising the results accurately. In future works, other metamodel techniques will be tested to further improve the prediction accuracy, particularly, in the case of the geometry change. Furthermore, it is also intended to optimise the number of base simulations required to train and test the metamodel to further reduce the computational cost.

Acknowledgements

This work was sponsored by FEDER funds through the program COMPETE (Programa Operacional Factores de Competitividade), by national funds through FCT (Fundação para a Ciência e a Tecnologia) under the projects UIDB/00285/2020, UIDB/00481/2020, UIDP/00481/2020, CENTRO-01- 0145-FEDER-022083, LA/P/0104/2020 and LA/P/0112/2020. It was also supported by the project RealForm (reference 2022.02370.PTDC), funded by Portuguese Foundation for Science and Technology. A.E. Marques was supported by a grant for scientific research from the Portuguese Foundation for Science and Technology (ref. 2020.08449.BD). All supports are gratefully acknowledged.

References

[1] A.E. Marques, P.A. Prates, A.F.G. Pereira, M.C. Oliveira, J.V. Fernandes, B.M. Ribeiro, Performance Comparison of Parametric and Non-Parametric Regression Models for Uncertainty Analysis of Sheet Metal Forming Processes, Metals 10 (2020) 457. https://doi.org/10.3390/met10040457

[2] A.F.G. Pereira, P.A. Prates, M.C. Oliveira, J.V. Fernandes, Normal Stress Components during Shear Tests of Metal Sheets, Int. J. Mech. Sci. 164 (2019) 105169. https://doi.org/10.1016/j.ijmecsci.2019.105169

[3] P.A. Prates, A.S. Adaixo, M.C. Oliveira, J.V. Fernandes, Numerical Study on the Effect of Mechanical Properties Variability in Sheet Metal Forming Processes, Int. J. Adv. Manuf. Technol. 96 (2018) 561-580. https://doi.org/10.1007/s00170-018-1604-y

[4] W. Hancock, M. Zayko, M. Autio, D. Ponagajba, Analysis of components of variation in automotive stamping processes, Qual. Eng. 10 (1997) 115-124. https://doi.org/10.1080/08982119708919114
[5] K.D. Majeske, P.C. Hammett, Identifying Sources of Variation in Sheet Metal Stamping, Int. J. Flexib. Manuf. Syst. 15 (2003) 5-18. https://doi.org/10.1023/A:1023993806025
[6] A.F.G. Pereira, M.F. Ruivo, M.C. Oliveira, J.V. Fernandes, P.A. Prates, Numerical Study of the Square Cup Stamping Process: A Stochastic Analysis, ESAFORM 2021 (2021). https://doi.org/10.25518/esaform21.2158
[7] M. Arnst, J.-P. Ponthot, R. Boman, Comparison of Stochastic and Interval Methods for Uncertainty Quantification of Metal Forming Processes, Comptes Rendus Mécanique 346 (2018) 634-646. https://doi.org/10.1016/j.crme.2018.06.007
[8] M. Dwivedy, V. Kalluri, The Effect of Process Parameters on Forming Forces in Single Point Incremental Forming, Procedia Manuf. 29 (2019) 120-128. https://doi.org/10.1016/j.promfg.2019.02.116
[9] V.J. Shahi, A. Masoumi, P. Franciosa, D. Ceglarek, Quality-Driven Optimization of Assembly Line Configuration for Multi-Station Assembly Systems with Compliant Non-Ideal Sheet Metal Parts, Procedia CIRP 75 (2018) 45-50. https://doi.org/10.1016/j.procir.2018.02.022
[10] M.A. Dib, N.J. Oliveira, A.E. Marques, M.C. Oliveira, J.V. Fernandes, B.M. Ribeiro, P.A. Prates, Single and Ensemble Classifiers for Defect Prediction in Sheet Metal Forming under Variability, Neural Comput. Appl. 32 (2019) 12335-12349. https://doi.org/10.1007/s00521-019-04651-6
[11] J. Fruth, O. Roustant, Kuhnt, S. Support Indices: Measuring the Effect of Input Variables over Their Supports, Reliab. Eng. Syst. Saf. 187 (2019) 17-27. https://doi.org/10.1016/j.ress.2018.07.026
[12] P. Zhu, L. Zhang, R. Zhou, L. Chen, B. Yu, Q. Xie, A Novel Sensitivity Analysis Method in Structural Performance of Hydraulic Press, Math. Probl. Eng. 2012 (2012) 1-21. https://doi.org/10.1155/2012/647127
[13] S.H. Kim, H. Huh, Design Sensitivity Analysis of Sheet Metal Forming Processes with a Direct Differentiation Method, J. Mater. Process. Technol. 130-131 (2002) 504-510. https://doi.org/10.1016/S0924-0136(02)00797-5
[14] I.M. Sobol′, Global Sensitivity Indices for Nonlinear Mathematical Models and Their Monte Carlo Estimates, Math. Comput. Simul. 55 (2001) 271-280. https://doi.org/10.1016/S0378-4754(00)00270-6
[15] T. Hama, M. Takamura, A. Makinouchi, C. Teodosiu, H. Takuda, Effect of Tool-Modeling Accuracy on Square-Cup Deep-Drawing Simulation, Mater. Trans. 49 (2008) 278-283. https://doi.org/10.2320/matertrans.P-MRA2007885
[16] Y.Q. Li, Z.S. Cui, X.Y. Ruan, D.J. Zhang, CAE-Based Six Sigma Robust Optimization for Deep- Drawing Process of Sheet Metal, Int. J. Adv. Manuf. Technol. 30 (2006) 631-637. https://doi.org/10.1007/s00170-005-0121-y
[17] J.M. Gutiérrez Regueras, A.M. Camacho López, Investigations on the Influence of Blank Thickness (t) and Length/Wide Punch Ratio (LD) in Rectangular Deep Drawing of Dual-Phase Steels, Comput. Mater. Sci. 91 (2014) 134-145. https://doi.org/10.1016/j.commatsci.2014.04.024
[18] E. Bayraktar, S. Altintaş, Square Cup Deep Drawing Experiments, Proceedings of the NUMISHEET ’93: Proceedings of the 2nd International Conference Numerical Simulation of 3-D Sheet Metal Forming Processes, Isehara, Japan, 1993, p. 441.
[19] B. Sudret, Global Sensitivity Analysis Using Polynomial Chaos Expansions, Reliab. Eng. Syst. Saf. 93 (2008) 964-979. https://doi.org/10.1016/J.RESS.2007.04.002

[20] L.F. Menezes, C. Teodosiu, Three-Dimensional Numerical Simulation of the Deep-Drawing Process Using Solid Finite Elements, J. Mater. Process. Technol. 97 (2000) 100-106. https://doi.org/10.1016/S0924-0136(99)00345-3
[21] A. Saltelli, M. Ratto, T. Andres, F. Campolongo, J. Cariboni, D. Gatelli, M. Saisana, S. Tarantola, Global Sensitivity Analysis, The Primer, 2008.
[22] A. Janon, T. Klein, A. Lagnoux, M. Nodet, C. Prieur, Asymptotic Normality and Efficiency of Two Sobol Index Estimators, ESAIM - Probability and Statistics 18 (2014) 342-364. https://doi.org/10.1051/ps/2013040
[23] I.M. Sobol', On the Distribution of Points in a Cube and the Approximate Evaluation of Integrals, USSR Computat. Math. Math. Phys. 7 (1967) 86-112. https://doi.org/10.1016/0041-5553(67)90144-9
[24] J. Lebon, G. le Quilliec, R.F. Coelho, P. Breitkopf, P. Villon, Variability and Sensitivity Analysis of U-Shaped Deep Drawn Metal Sheet, Proceedings of the 11e colloque national en calcul des structures, Giens, France, May 2013.
[25] G. Blatman, B. Sudret, Adaptive Sparse Polynomial Chaos Expansion Based on Least Angle Regression, J. Comput. Phys. 230 (2011) 2345-2367. https://doi.org/10.1016/j.jcp.2010.12.021
[26] B. Sudret, Risk and Reliability in Geotechnical Engineering, In Risk and Reliability in Geotechnical Engineering, K.-K. Phoon, J. Ching (Eds.), CRC Press: Boca Raton, 2018, ISBN 9781482227222.

Materials Research Proceedings 28 (2023) 1193-1202 https://doi.org/10.21741/9781644902479-130

Coupling machine learning and synthetic image DIC-based techniques for the calibration of elastoplastic constitutive models

PRATES Pedro A.[1,2,a *], HENRIQUES Joan D. F.[1,b], PINTO Jose[1,c], BASTOS Nelson [1,d] and ANDRADE-CAMPOS Antonio[1,2,e]

[1]TEMA – Centre for Mechanical Technology and Automation, Department of Mechanical Engineering, University of Aveiro, 3810-193 Aveiro, Portugal

[2]LASI – Intelligent Systems Associate Laboratory, 4800-058 Guimarães, Portugal

[a]prates@ua.pt, [b]joaodiogofh@ua.pt, [c]josemiguel99@ua.pt, [d]kevinbastos@ua.pt, [e]gilac@ua.pt

Keywords: Constitutive Model Calibration, Elastoplasticity, Machine Learning, DIC

Abstract. Today, most design tasks are based on simulation tools. However, the success of the simulation depends on the accurate calibration of constitutive models. Inverse-based calibration methods, such as the Finite Element Model Updating and the Virtual Fields Method, have been developed for identifying constitutive parameters. These methods are based on mechanical tests that allow heterogeneous strain fields under the "Material Testing 2.0" paradigm in which digital image correlation plays a vital role. Although these methods have been proven effective, constitutive model calibration is still a complex task. A machine learning approach is developed and implemented to calibrate elastoplastic constitutive models for metal sheets, using datasets populated with finite element simulation results of strain field data from mechanical tests. Feature importance analysis is conducted to understand the importance of the different input features and to reduce the computational cost related with model training. Synthetic image DIC-based techniques were coupled with the numerically generated database, enabling the construction of a virtual experiments database that accounts for sources of uncertainty that can influence experimental DIC measurements. A robustness analysis of the methodology is performed for the boundary conditions of the test.

Introduction

The numerical simulation of sheet metal forming processes has become an essential tool to obtain high-performance components for automotive and aerospace industries. The quality of numerical simulations depends on the quality of the constitutive modelling that describes the material behaviour, which is related to the type of constitutive laws and the strategy to identify their parameters. Inverse identification strategies based on Finite Element Model Updating (FEMU) and Virtual Fields Method (VFM) have been proposed (e.g. [1–3]), which make use of full-field measurements of heterogeneous strain field data collected from non-standardized mechanical tests. However, the computational time and a complex implementation process are still major drawbacks of such identification strategies [4–5]. More recently, machine learning based approaches have been explored to identify material parameters (e.g. [6–8]), showing to be a promising alternative to both FEMU and VFM [3]. The authors of the current work have previously proposed a machine learning approach to identify material parameters (isotropic hardening law + orthotropic yield criterion), using a numerically generated database populated with finite element simulation results of cruciform tensile tests and the XG-Boost algorithm [6]. In this work, synthetic image DIC-based techniques are coupled with the numerically generated database, enabling the construction of a virtual experiments database that accounts for sources of uncertainty that can influence experimental DIC measurements. A robustness analysis on the ML approach is performed for the boundary conditions of the finite element model. In particular, the orientation of the material axes

Content from this work may be used under the terms of the Creative Commons Attribution 3.0 license. Any further distribution of this work must maintain attribution to the author(s) and the title of the work, journal citation and DOI. Published under license by Materials Research Forum LLC.

was varied with reference to the global axes system of the cruciform test to emulate specimen misalignments that may occur in material testing.

Methodology and Implementation

General Approach.

Fig. 1 schematizes the proposed approach for calibrating elastoplastic constitutive models. First, a database was established using numerically generated features (i.e. strain fields and loads) obtained from FEA simulations of an heterogenous mechanical test. Different combinations of constitutive parameters were considered while maintaining the same sample geometry and boundary conditions; a Python script was created to enhance the whole process and automatize the generation of the database. Then, a feature importance step was performed to evaluate how useful the data is at predicting the constitutive parameters. A virtual experiments database was created from the FEA-generated database, where synthetic images were generated and processed via DIC. The virtual experiments database was then split into training (90%) and testing (10%) sets. The training set was used to establish an ML model for predicting the material parameters from the strain fields and loads. Finally, the predictive performance of the ML model was evaluated using the testing set.

Numerical model.

The mechanical test selected for this study is the biaxial tensile test on a cruciform sample. The sample geometry was designed in a previous work, enabling heterogeneous stress and strain fields and a wide range of stress and strain paths that are commonly observed in sheet metal forming processes [9]. Fig. 2(a) shows the geometry and the dimensions of the cruciform sample in the sheet plane. The numerical simulation model only considers one fourth of the sample (see grey region in Fig. 2(a)) due to symmetries in the boundary conditions, sample geometry and material behaviour. Moreover, plane stress conditions and a constant thickness of the sheet equationual to 1 mm are assumed. Fig. 2(b) shows the boundary conditions and finite element mesh of the numerical model. Symmetry boundary conditions were prescribed on the 0x and 0y axes ($u_x = u_y = 0$ mm), and displacement boundary conditions were applied to the nodes located at the ends of both arms of the sample to promote equal displacements along both 0x and 0y axes ($u_x = u_y = 2$ mm). The numerical model is discretized with a regular mesh made of 405 CPS4R elements (bilinear shape functions and reduced integration). All FEA simulations were performed using ABAQUS CAE software [10]. Each simulation was carried out for twenty equally spaced time-steps, where the force and the strain field (ε_{xx}, ε_{yy}, and ε_{xy}) was obtained for each time-step.

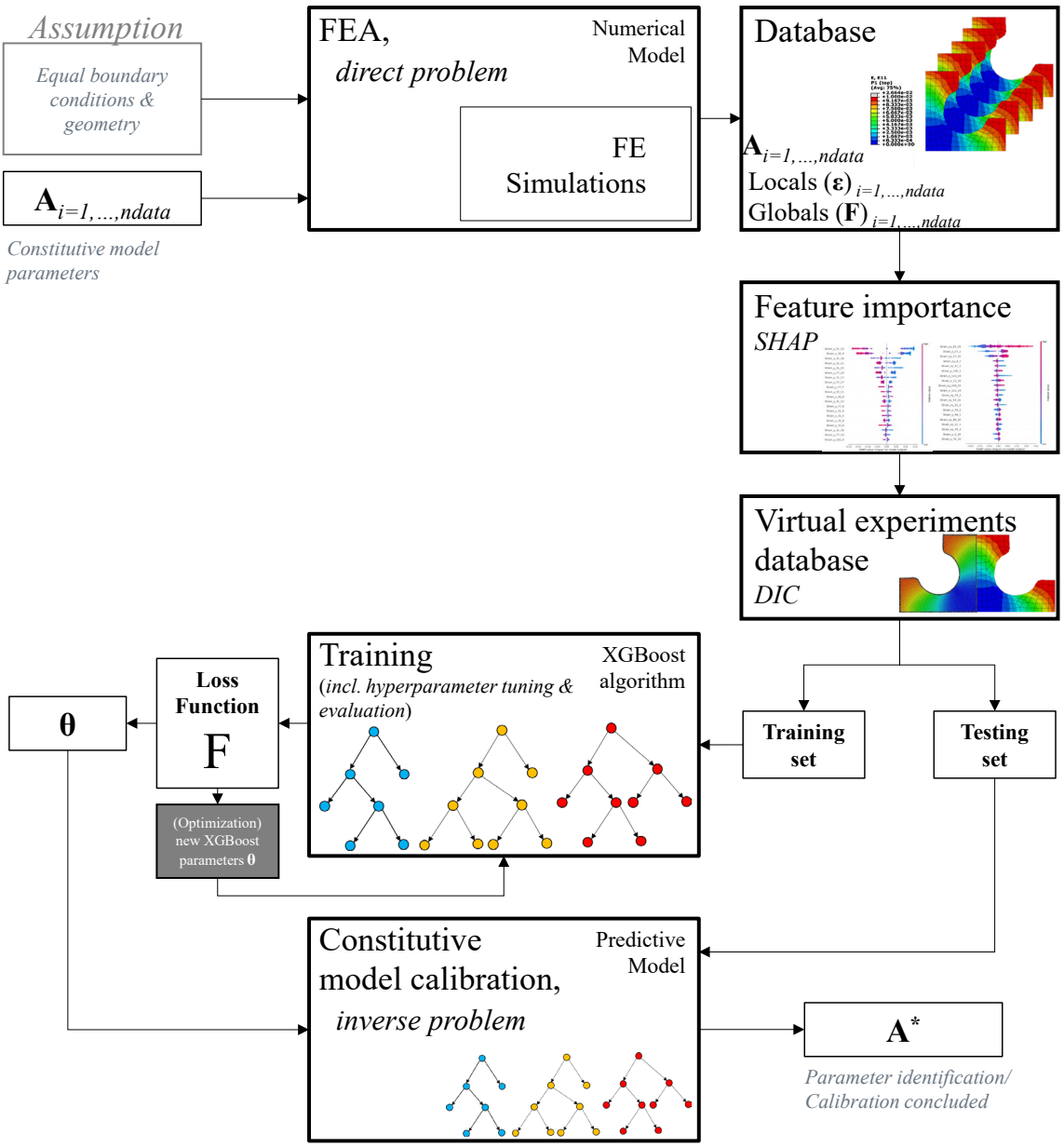

Fig. 1. Flowchart of the proposed identification approach.

The material constitutive model assumes an isotropic elastic behavior, described by the Hooke's law (with Young's modulus E = 210 GPa and Poisson's ratio ν = 0.3), and an orthotropic plastic behavior, described by Hill'48 yield criterion with isotropic hardening described by Swift law under an associated flow rule. Under plane stress conditions, the Hill'48 yield criterion can be written as follows:

$$(F+H)\sigma_{yy}^2+(G+H)\sigma_{xx}^2-2H\sigma_{xx}\sigma_{yy}+2N\tau_{xy}^2=Y^2 \quad (1)$$

where F, G, H and N are anisotropy coefficients, σ_{xx}, σ_{yy} and τ_{xy} are the components of the Cauchy stress tensor in the material axes system of the metal sheet, and Y is the yield stress.

The condition G+H=1 (i.e. $\sigma_{xx} = Y$) was assumed, which corresponds to the following relationships:

$$F = \frac{r_0}{r_{90}(r_0+1)};\ G = \frac{1}{r_0+1};\ H = \frac{r_0}{r_0+1};\ N = \frac{1}{2}\frac{(r_0+r_{90})(2r_{45}+1)}{r_{90}(r_0+1)} \tag{2}$$

where r_0, r_{45} and r_{90} are the Lankford ratios obtained at 0º, 45º and 90º w.r.t. the rolling direction of the sheet, respectively. The Swift law describes the yield stress evolution during plastic deformation as follows:

$$Y = K\left[\left(\frac{Y_0}{K}\right)^{\frac{1}{n}} + \bar{\varepsilon}^{\mathrm{p}}\right]^n \tag{3}$$

where $\bar{\varepsilon}^{\mathrm{p}}$ is the equivalent plastic strain and Y_0, K and n are material parameters.

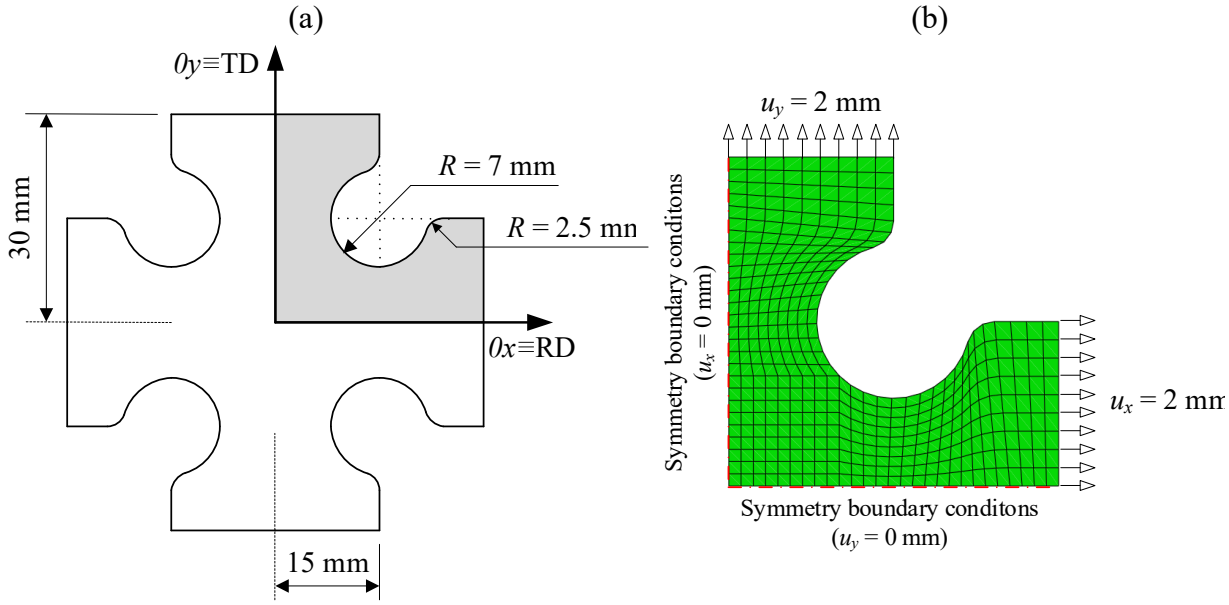

Fig. 2. Biaxial tensile test on a cruciform sample: (a) geometry and dimensions [9]; (b) boundary conditions and finite element mesh.

The database was populated with synthetic data generated by FEA simulations of the cruciform tensile test with different combinations of plasticity material parameters while maintaining the same geometry, boundary conditions and elastic properties. Table 1 shows the range of values of the plasticity material parameters considered as input space for the numerical simulations. Then, 2000 sets of parameters were generated using the Latin Hypercube Sample method, and numerical simulations of the cruciform tensile test were performed for each set. Fig. 3 presents an example of numerical results of the cruciform test that were used to build the database.

Table 1. Input space of plasticity material parameters.

Plasticity material parameters	Range
Y_0 [MPa]	80-300
n	0.1-0.3
K [MPa]	280-700
r_0	1-2.5
r_{45}	1-2.5
r_{90}	1-2.5

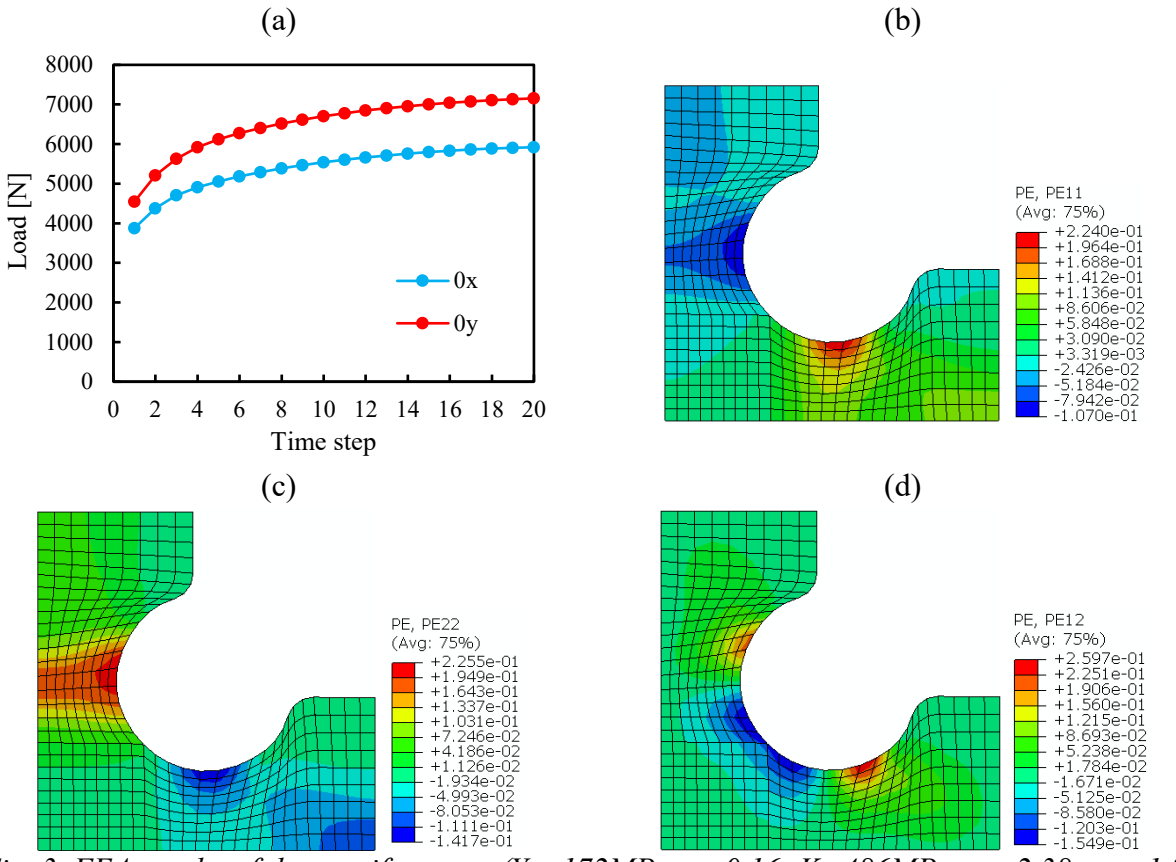

Fig. 3. FEA results of the cruciform test (Y_0=172MPa, n=0.16; K=486MPa; r_0=2.38; r_{45}=1.8; r_{90}=1.06): (a) load vs. displacement along the 0x and 0y axes; strain fields (b) ε_{xx}, (c) ε_{yy}, and (d) ε_{xy}. The strain fields (ε_{xx}, ε_{yy}, and ε_{xy}) were obtained for $u_x = u_y = 2$ mm.

Feature importance.

Many ML systems are essentially considered black boxes, as it is hard to understand and explain how they work after training. Shapley Additive exPlanations (SHAP) are considered state of the art in Machine Learning explainability [11]. SHAP analysis explain how each feature (i.e. loads, strain fields) affects the outputs (i.e. material parameters) of the ML model. As an example, Fig. 4 presents the 20 most important features for predicting the hardening parameters Y_0, n and K. In Fig. 4a, the feature "Force_y_1" (i.e. force 0y at time step 1) is the most relevant feature to predict the initial yield stress, Y_0; moreover, higher values of "Force_y_1" (towards red color) have a positive contribution on the prediction of Y_0 (i.e. higher SHAP values), leading to higher values of Y_0. SHAP analysis confirmed that it is possible to substantially reduce the number of features in

the dataset, by excluding the less important ones and reducing the computational cost without compromising predictive performance.

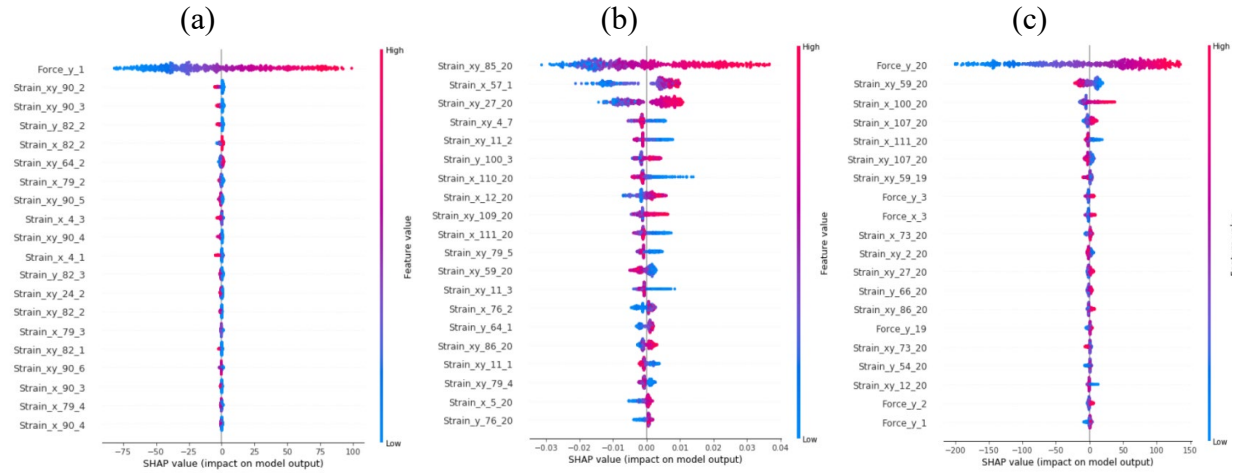

Fig. 4. SHAP analysis of the 20 most important features for predicting the hardening parameters (a) Y_0; (b) n and (c) K.

Virtual experiments.

Virtual experiments enable a proper comparison between simulations and experiments by overcoming issues that arise from the direct numerical-experimental comparison (e.g. alignment, data locations, discretization, filtering effects, experimental uncertainties, etc.) and making the database features one step closer to measurements collected from real experiments. After finishing the feature importance step, the numerical results of the cruciform test were used to generate synthetic images that were then processed with DIC. The DIC setting were selected using the Performance Analysis module from MatchID [12], representing a good compromise between spatial and measurement resolution, as shown in Fig. 5. Each sample was divided into 6455 subsets. In each subset, the location in pixels and the strains ε_{xx}, ε_{yy}, and ε_{xy} were recorded. 2000 samples were generated, 1800 for training and 200 for testing.

XGBoost algorithm.

Extreme Gradient Boosting (XGBoost) is an efficient open-source implementation of the gradient boosted trees algorithm [13]. Gradient boosting is an algorithm in which new models are created from previous models' residuals (weak models) and then combined to make the final prediction (strong models). When adding new models, it uses a gradient descent algorithm to minimize the loss. XGBoost attempts to minimize the regularized objective as follows:

$$obj(\boldsymbol{\theta}) = \sum_i L\left(\hat{y}_i(\boldsymbol{\theta}), y_i\right) + \sum_k \Omega(\boldsymbol{\theta}) \tag{4}$$

where $\boldsymbol{L}$ is the training loss function that measures the deviation between the value $\hat{\boldsymbol{y}}_{\boldsymbol{i}}$ predicted by the model and the actual value $\boldsymbol{y}_{\boldsymbol{i}}$ of sample i; $\boldsymbol{\Omega}$ is the regularization function (i.e. a penalty term) that measures the complexity of the model, which tends to prevent overfitting; $\boldsymbol{\theta}$ represents the set of parameters to be calibrated during training.

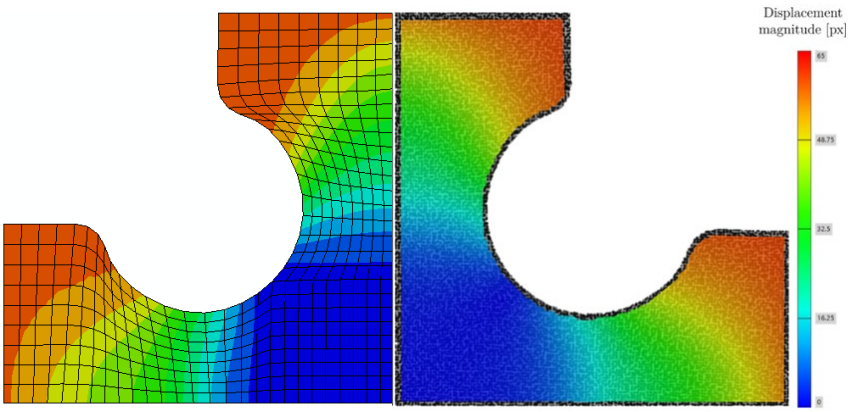

Fig. 5. Comparison of the displacement magnitude in the cruciform test, between FEA (left) and virtual experiments (right).

Performance metrics.

The performance of the ML model was evaluated by comparing the predicted and simulated parameters using the Coefficient of Determination (R^2), given by:

$$R^2 = 1 - \frac{\sum_{i=1}^{j}\left(y_i - y_i^*\right)^2}{\sum_{i=1}^{j}\left(y_i - \overline{y}\right)^2} \tag{5}$$

where y_i and y_i^* are respectively the real and predicted values for the constitutive parameters of simulation i from the test set, $\overline{y}$ is the average of the real values of the constitutive parameters, and j is the total number of simulations of the test set.

Results and Discussion

Performance evaluation.

Fig. 6 compares the Y_0, n and K, r_0, r_{45} and r_{90} values predicted by the ML model with the real values considered in the FEA simulations. In general, the ML model has superior predictive performance, which is confirmed by the values of R^2 presented in the figures.

Robustness Analysis.

The robustness of the ML model was analyzed in relation to the boundary conditions of the cruciform test. In fact, the ML model was trained keeping the boundary conditions unchanged; however, during the performance of experimental tests there may be, to a greater or lesser extent, misalignments in the placement/test of the specimen, which may influence the measurements and consequently the calibration of the constitutive models. In this context, one of the samples from the testing set was chosen (Y_0=172 MPa, n=0.16; K=486 MPa; r_0=2.38; r_{45}=1.8; r_{90}=1.06) and the orientation of the material axes was varied w.r.t. the global axes system 0xy (see Fig. 2) to simulate various cases of sample misalignments that may occur in material testing. Fig. 7 shows the relative error in the prediction of each material parameter, for rotations of the material axes ranging between 0º and 10º w.r.t. the global axes system (the 0º case is taken as reference for calculating the relative error in predictions); this figure also includes an extreme case of 45º. In general, the parameter predictions remain robust regarding possible sample misalignments in-between 0º and 10º; in this interval, the maximum variation of the relative error occurs for parameter r_0 (about 2.65%). This preliminary robustness analysis suggests that sample misalignments do not significantly influence the predictive performance of the ML model, regardless of the overall quality of predictions obtained for each parameter (poor quality for parameters n, r_{45} and Y_0, which requires careful analysis to assess the cause).

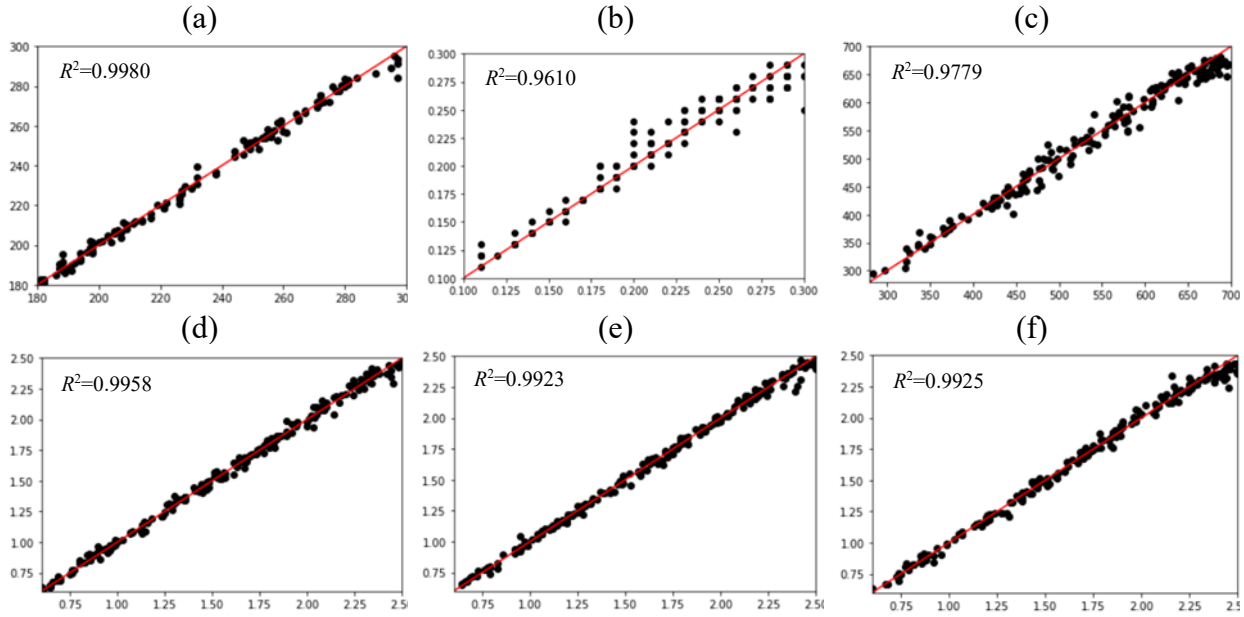

Fig. 6. Predicted (vertical axis) vs. real (horizontal axis) values of the constitutive parameters: (a) Y_0; (b) n; (c) K; (d) r_0; (e) r_{45}; (f) r_{90}. The R^2 values are also presented.

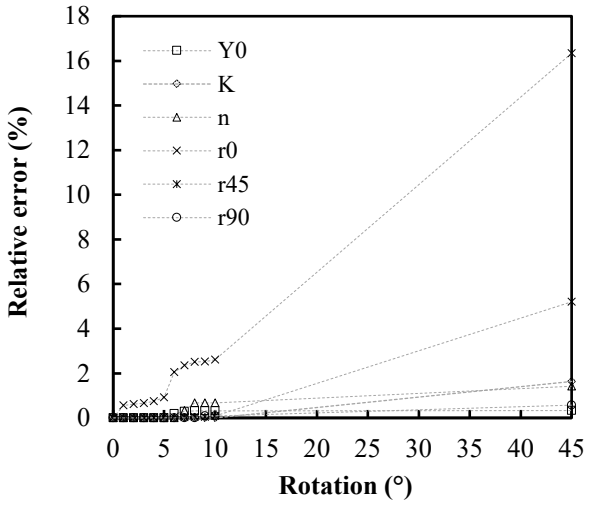

Fig. 7. Relative error in the prediction of the material parameters as a function of the rotation of the material axes w.r.t. the global axes system.

Summary

A machine learning approach was developed for calibrating constitutive models that describe the plastic behaviour of metal sheets. The database was populated with numerically generated features (strain fields and loads) collected from FEA simulations of the biaxial tensile test on a cruciform sample. Feature importance analysis allowed to identify the most relevant features in the database for identifying the constitutive parameters of the Swift hardening law and the Hill'48 yield criterion. A virtual experiments database was established from the FEA-generated database using synthetic images and DIC processing, making the numerically generated features one step closer to measurements collected from real experiments. A robustness analysis on the ML approach was performed for the boundary conditions to simulate possible misalignments that may occur in

material testing, namely on the rotation of the material axes w.r.t. the global axes system. It was concluded:

- Feature importance enabled the identification of the most important features of the database for identifying constitutive parameters. ML training was greatly accelerated, without compromising predictive performance;
- Virtual experiments allow for accurate model predictions of the constitutive parameters, bridging the gap between simulation results and experimental measurements;
- Sample misalignments do not significantly influence the performance of the ML model.

The trained ML model enables an almost instantaneous parameter identification, without being significantly influenced by sample misalignments. On the other hand, it is limited to the identification of Hill'48+Swift law parameters, which can be unsuitable for materials whose plastic behaviour is best described using more advanced constitutive models; also, the trained ML model considers uniform displacements imposed at the end of both arms of the sample. Therefore, it is envisaged to extend the robustness analysis to the displacement boundary conditions (i.e. when it is not possible to achieve uniform displacement at both arms of the sample), and to the type of material constitutive model that describes the plastic behaviour of the material.

Acknowledgments

This research has received funding from the Research Fund for Coal and Steel under grant agreement No 888153. This research was also sponsored by FEDER funds through the program COMPETE (Programa Operacional Factores de Competitividade), by national funds through FCT (Fundação para a Ciência e a Tecnologia) under the projects UIDB/00481/2020, UIDP/00481/2020, CENTRO-01-0145-FEDER-022083 and LA/P/0104/2020. J. Henriques was supported by a grant for scientific research from the Portuguese Foundation for Science and Technology (ref. 2021.05692.BD). All supports are gratefully acknowledged.

References

[1] S. Avril, M. Bonnet, A.-S. Bretelle, M. Grédiac, F. Hild, P. Ienny, F. Latourte, D. Lemosse, S. Pagano, E. Pagnacco, F. Pierron, Overview of identification methods of mechanical parameters based on full-field measurements, Exp. Mech. 48 (2008) 381–402. https://doi.org/10.1007/s11340-008-9148-y

[2] P.A. Prates, A.F.G. Pereira, N.A. Sakharova, M.C. Oliveira, J.V. Fernandes, Inverse strategies for identifying the parameters of constitutive laws of metal sheets, Adv. Mater. Sci. Eng. 2016 (2016) 4152963. https://doi.org/10.1155/2016/4152963

[3] A. Andrade-Campos, N. Bastos, M. Conde, M. Gonçalves, J. Henriques, R. Lourenço, J.M.P. Martins, M.G. Oliveira, P. Prates, L. Rumor, On the inverse identification methods for forming plasticity models using full-field measurements, IOP Conf. Ser. Mater. Sci. Eng. 1238 (2022) 012059. https://doi.org/10.1088/1757-899X/1238/1/012059

[4] J. Martins, A. Andrade-Campos, S. Thuillier, Comparison of inverse identification strategies for constitutive mechanical models using full-field measurements, Int. J. Mech. Sci. 145 (2018) 330–345. https://doi.org/10.1016/j.ijmecsci.2018.07.013

[5] N. Souto, A. Andrade-Campos, S. Thuillier, Mechanical design of a heterogeneous test for material parameters identification, Int. J. Mater. Form. 10 (2017) 353-367. https://doi.org/10.1007/s12289-016-1284-9

[6] N. Bastos, P. Prates, A. Andrade-Campos, Material parameter identification of elastoplastic constitutive models using machine learning approaches, Key Eng. Mater. 926 (2022) 2193-2200. https://doi.org/10.4028/p-zr575d

[7] A.E. Marques, A.F.G. Pereira, B.M. Ribeiro, P.A. Prates, On the identification of material constitutive model parameters using machine learning algorithms, Key Eng. Mater. 926 (2022) 2146-2153. https://doi.org/10.4028/p-5hf550

[8] R. Schulte, C. Karca, R. Ostwald, A. Menzel, Machine learning-assisted parameter identification for constitutive models based on concatenated loading path sequences, Eur. J. Mech. A-Solid. 98 (2023) 104854. https://doi.org/10.1016/j.euromechsol.2022.104854
[9] J. Martins, A. Andrade-Campos, S. Thuillier, Calibration of anisotropic plasticity models using a biaxial test and the virtual fields method, Int. J. Solids Struct. 172 (2019) 21-37. https://doi.org/10.1016/j.ijsolstr.2019.05.019
[10] Dassault Systèmes. Abaqus 2017 documentation, 2017.
[11] S. Lundberg, S. Lee, A Unified approach to interpreting model predictions, 2017.
[12] MatchID: Metrology beyond colors. MatchID version 2022.2, 2022.
[13] T. Chen, C. Guestrin, XGBoost: A scalable tree boosting system, in Proceedings of the 22nd ACM SIGKDD International Conference on Knowledge Discovery and Data Mining, 2016, pp. 785-794.

Materials Research Proceedings 28 (2023) 1203-1210 https://doi.org/10.21741/9781644902479-131

A hybrid VFM-FEMU approach to calibrate 3D anisotropic plasticity models for sheet metal forming

ROSSI Marco[1,a *], LATTANZI Attilio[1,b] and AMODIO Dario[1,c]

[1]Department of Mechanical Engineering and Mathematical Sciences, Università Politecnica delle Marche, via brecce bianche 12, 60131, Ancona, Italy

[a]m.rossi@staff.univpm.it, [b]a.lattanzi@staff.unvipm.it, [c]a.amodio@staff.univpm.it

Keywords: Inverse Methods, 3D Anisotropic Plasticity, Full-Field Measurements

Abstract. Recently, inverse methods such as the Virtual Fields Method (VFM) or the Finite Element Model Updating (FEMU), coupled with a full-field measurement technique, have been distinguished as efficient strategies for the calibration of complex plasticity models [1]. The use of heterogeneous strain fields, in fact, offers a larger amount of material information compared to the classical standard test, enriching the identification process and, in general, reducing the experimental effort for the calibration [2]. Here, an inverse identification framework is proposed for the calibration of a full-scale anisotropic plasticity model. The inverse identification procedure employs full-field information from two main experiments: a tensile test on double notched specimens for the calibration of the coefficients expressing the planar anisotropy, and an innovative Iosipescu-like test for the through-thickness shear ones. A hybrid approach is used with the VFM employed to identify the planar coefficients and the FEMU for the through thickness ones.

Introduction

Sheet metals are characterized by an anisotropic behavior which plays a crucial role in the prediction of their plastic deformation and failure. Generally, their constitutive response is modeled and calibrated by mainly considering the in-plane material behavior, while the through-thickness one is often neglected based on the plane stress assumption. However, in some applications - for instance the sheet metal forming of complex geometries - the state of stress can deviate from the plane stress assumption and a complete 3D description is necessary [1].

Over the years, several testing protocols have been developed to capture in detail the complex mechanical response under different types of loading conditions and to infer a comprehensive description of the material deformation. Traditionally, the common material testing approach relies on the use of quasi-homogeneous tests, where the relation between stress and strains can be directly obtained from experiments properly designed; on the other side, the application of full-field techniques to material testing has allowed to analyze and simultaneously exploit multiple stress and strain conditions produced through heterogenous tests [2,3].

However, mechanical data from heterogeneous tests cannot be directly used in the calibration process, and are generally coupled with inverse methods. Inverse methods have been already used to identify, for instance, the plastic behavior of metals by resorting to numerical simulations [4,5]: the method is often referred as Finite Element Model Updating (FEMU) since, essentially, performs the identification by iteratively changing the constitutive parameters of a numerical simulation of the test until the difference between the numerical and experimental results, in terms of loading force and strain fields, is minimized. Other examples for the identification of the hardening behavior can be found in [6,7] using an energy balance approach called the Virtual Fields Method (VFM) [8]. The VFM has been applied also to anisotropic plasticity [9-11] and to investigate multiaxial loading conditions such as cruciform specimens [12] and the bulge test [13].

Content from this work may be used under the terms of the Creative Commons Attribution 3.0 license. Any further distribution of this work must maintain attribution to the author(s) and the title of the work, journal citation and DOI. Published under license by Materials Research Forum LLC.

However, experimental procedures to calibrate full 3D anisotropic plasticity models of sheet metals are still not well addressed. The aim of this work is to demonstrate that such calibration can be effectively carried out using inverse methods and simple experiments.

Methods

The aim of this paper is the identification of a full 3D anisotropic model trying to reduce the experimental effort and the number of tests required to make the identification. A similar problem was already tackled in [14] by Denys et al., who introduced a double drilled specimen employed for the full calibration of the Hill48 yield surface, by means of the FEMU approach. However, especially for sheet metals, often it is not possible to perform a hole along the thickness of the specimen, so the previous method can only be applied to thick materials.

A different approach is used here, employing specimens that can be easily machined from a sheet metal blank and tested using a standard uniaxial machine, so that the experimental procedure can be readily implemented in almost each material testing lab. The proposed method also requires the use of a full-field optical measurement technique, e.g. digital image correlation (DIC), to obtain the strain field in a region of interest (ROI) of the specimen, following the Material Testing 2.0 logic [2].

Virtual experiments are used to verify the feasibility of the developed procedure; the three-dimensional anisotropic behavior of the material was reproduced using the Hill48 yield function:

$$f(\boldsymbol{\sigma}) = \sqrt{F(\sigma_y - \sigma_z)^2 + G(\sigma_z - \sigma_x)^2 + H(\sigma_x - \sigma_y)^2 + 2L{\tau_{yz}}^2 + 2M{\tau_{xz}}^2 + 2N{\tau_{xy}}^2} \quad (1)$$

where F,G,H,LM and N are constants that must be identified from experiments, in particular, in this case, we set L=M so that the shear behavior through the thickness in the *y*-*z* plane is equal to the one in the *x*-*z* plane. The hardening was described by a Swift law:

$$\sigma_{eq} = k\left(\varepsilon_0 + \varepsilon_{eq}\right)^n \quad (2)$$

where σ_{eq} and ε_{eq} are the equivalent stress and strain, respectively, and k, ε_0 and n are parameters that must be identified. Summarizing, to fully characterize the three-dimensional anisotropic behavior of the material, it is necessary to identify a total of 8 parameters, 5 for the yield function and 3 for the hardening law.

A two-steps identification process was developed using a double notched (DN) specimen to identify the in-plane anisotropic properties and the hardening law, i.e. parameters F, G, H, N, k, ε_0 and n; and a through-thickness shear (TTS) test to identify the shear behavior along the thickness, i.e. parameter L.

FE models of the two tests were developed using ABAQUS and used to generate synthetic data that replicate the load history and the strain maps obtained during a real test. The synthetic data were accordingly used as input for the identification procedure.

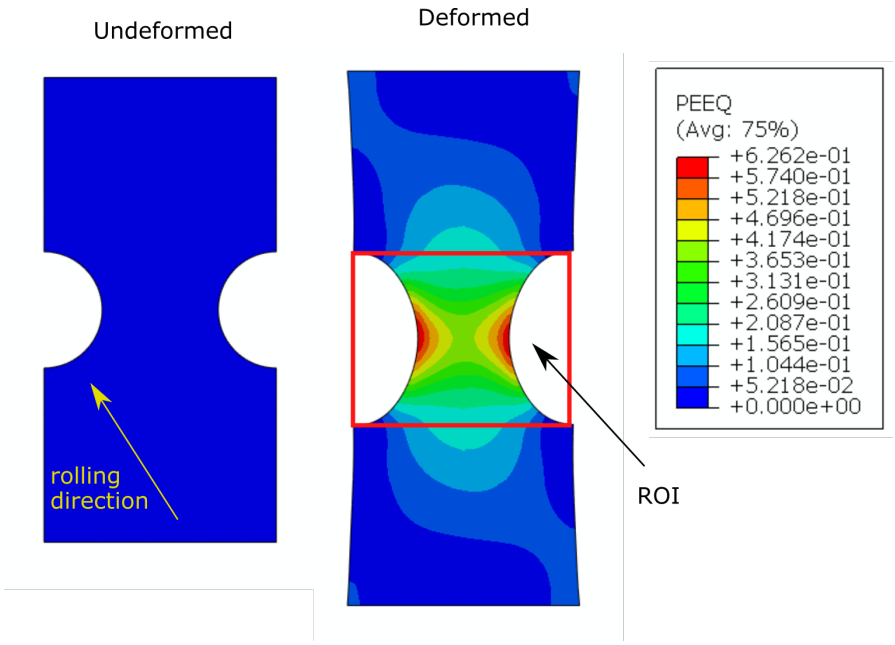

Fig. 1. Double notched specimen used to evaluate the in-plane properties.

Fig. 1 shows the geometry of the DN specimen and the ROI where the full-field strain measurement is performed through DIC. In this case, the FEM data were used to simulate a DIC measurement with 151 × 51 strain points in the ROI. The rolling direction of the material was inclined with an angle of 22.5° with respect to the force direction.

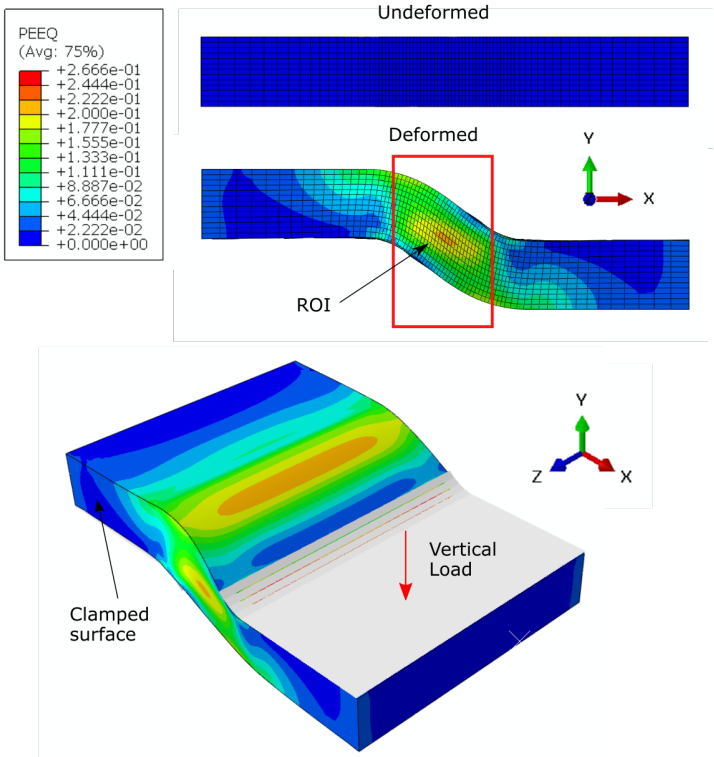

Fig. 2. Through-thickness shear test.

Fig. 2 illustrates the TTS test used to identify the parameters governing the through-thickness shear behavior. In this case, the ROI was placed along the thickness surface with 200 × 200 simulated measurement points, see Fig. 2. For both tests, the thickness of the sheet metal is 2 mm.

The identification of the constitutive parameters was performed using a hybrid VFM-FEMU approach, where the VFM was used with the DN specimen to identify 7 parameters and the FEMU was used with the TTS test to identify 1 parameter. Indeed, the VFM cannot be employed on the TTS test because the problem is three-dimensional and the plane stress or plane strain assumption is not valid, i.e. the strain measured along the thickness surface with DIC is different from the strain inside the material.

The advantage of combining the two methods is that VFM is usually less computationally expensive, so it can be used to quickly identify 7 parameters while FEMU is restricted to the identification of 1 parameter. The hybrid procedure is sequential, first the VFM is applied and then the FEMU using different cost functions, this is possible because the behavior of the DN specimen is not influenced by the parameter L, which is subsequently identified with FEMU. Theoretically, VFM and FEMU could also be put in the same optimization loop, using a common cost function, but such approach will be more complex and less efficient. Test design is essential to develop tests that are uncoupled with respect to different parameters, in order to simplify the identification procedure.

Both methods are implemented in Matlab using the in-built minimization functions to solve the inverse problem. A brief description of the two methods is given below, more details can be found in the references.

VFM Approach

The Virtual Fields Method (VFM) is an inverse method based on the weak form of the equilibrium through the Principle of Virtual Work (PVW) and allows to identify the coefficients of a given constitutive model starting from full-field kinematic and loading data. In the case of quasi-static problems where the body forces are neglected, the VFM is generally expressed for large deformations using the following cost function:

$$\Psi(\boldsymbol{\xi}) = \sum_{i=1}^{N_{vf}} \sum_{j=1}^{N_{step}} \left| \int_V \boldsymbol{T}_j^{1PK} : \delta \boldsymbol{F}_i^* dV - \int_{\partial V} \left(\boldsymbol{T}_j^{1PK} \boldsymbol{n} \right) \cdot \delta \boldsymbol{u}_i dS \right| \quad (3)$$

where $\mathbf{T}_j^{1PK}$ indicates the 1st Piola-Kirchhoff stress tensor, $\delta\mathbf{u}_i$ is any kinematically admissible virtual displacement field, $\delta\mathbf{F}_i^*$ is the corresponding virtual displacement gradient tensor, V is the volume of the inspected solid, ∂V is the boundary surface and $\mathbf{n}$ the surface normal. The first integral term represents the Internal Virtual Work, where the stress tensor is calculated from the full-field strain data of the test according to the model constitutive parameters $\boldsymbol{\xi}$; the second integral indicates the External Virtual Work and accounts for the loading condition on the boundaries. The cost function is evaluated for all the N_{step} timesteps of the test and for all N_{vf} virtual fields introduced. In this study, the constitutive behaviour is described by a non-linear relation, therefore, the identification is achieved through the minimization of the cost function $\Psi(\boldsymbol{\xi})$ until the equilibrium equation of the PVW is satisfied. The method is widely described in the literature and more details can be found in the book and papers cited in the introduction see [6-13].

The selection of the virtual fields (VFs) directly affects the identification results since they activate and weight the constitutive information contained in each material point. For this reason, the definition of the VFs employed in the cost function minimization is not trivial. Different approaches can be found in literature [15, 16] which, basically, classify the VFs in manually defined VFs and automatically generated VFs. In this work, we adopt the latter approach, where the virtual kinematic fields are produced starting from the sensitivity of the computed stress field to the single material parameter:

$$\delta \boldsymbol{T}_{(i)}^{1TPK}(\boldsymbol{\xi}, t) = \boldsymbol{T}^{1TPK}(\boldsymbol{\xi} - \delta\xi_i, t) - \boldsymbol{T}^{1TPK}(\boldsymbol{\xi}, t) \quad (4)$$

in other words, by perturbing the material parameter ξ_i, it is possible to highlight the material points where ξ_i effectively affects the stress calculation; the sensitivity distribution can be used as $\delta\mathbf{F}_i^{\bullet}$ and can be integrated to get the $\delta\mathbf{u}_i$ through a piecewise approach, as discussed in detail in [17].

FEMU Approach

The FEMU is based on the minimization of a cost function that represents a weighted difference between the numerical and experimental results. In this particular case, the compared results are the vertical load force applied by the tensile machine (see Fig. 2) and the full-field strain map measured in the ROI. In a real test, the boundary conditions (BC) are a critical factor, in fact possible misalignments or sliding on the clamping zone of the specimen can influence the deformation history. To reduce the bias due to BC, the FEMU is conducted only on a portion of the material within the ROI, see Fig. 3. The boundary conditions are applied using the displacement measured by the full-field measurement at the border. The central zone is not subjected to friction and the vertical load force measured by the machine can always be obtained from the FE model as sum of the nodal reactions along the vertical direction.

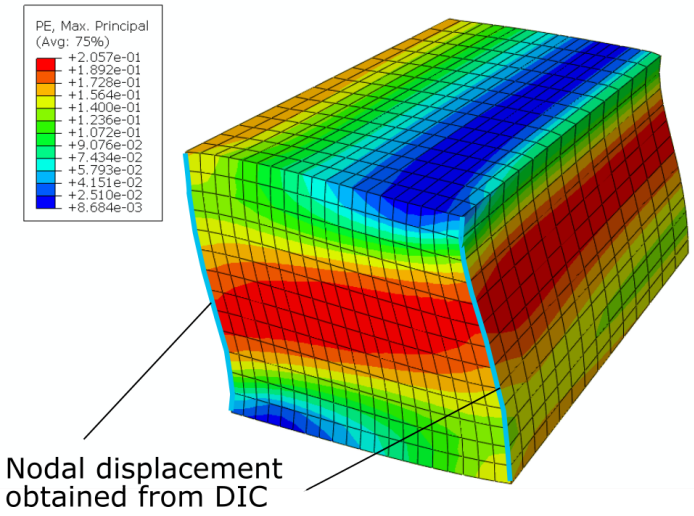

Fig. 3. Portion of the specimen used in the FEMU.

Results and Discussion

The results of the identification are listed in Table 1 in terms of identified parameters and percentage error. The reference parameters are the ones input in the FE model used to create the simulated experiment and can be viewed as the ground truth of the inverse problem. The identification is reasonably good except for parameter ε_0, however it is well known that this parameter has a minor impact in the description of the hardening curve. Moreover, often, the sole parameter identification error is not a proper criterion to evaluate the accuracy of the identification method, instead, it is preferable to verify the results in terms of plastic behavior, i.e. yield surface and hardening curve.

Table 1. Reference and identified parameters.

	VFM							FEMU
	K	ε_0	n	F	G	H	N	L=M
Reference	1000	0.02	0.5	0.3819	0.3125	0.6875	1.389	2.5
Identified	1041	0.0123	0.4846	0.3980	0.3308	0.6692	1.4033	2.66
Error %	-4.1	38.5	3.0	-4.2	-5.8	2.6	-1.03	-6.4

Fig. 4 shows the results in terms of yield surface and hardening curve. Since it is not possible to represent a 6-dimensional anisotropic yield surface, Fig. 4a shows the yield surface in terms of the normal stress components, i.e. σ_x σ_y σ_z, and Fig. 4b shows the yield surface for the shear stress components, i.e. in-plane (τ_{xy}) vs out of plane (τ_{xz} or τ_{yz}). Finally, Fig. 4c illustrates the identified hardening curve. It is worth noting that the computation was performed on a workstation and the VFM algorithm took around 20 seconds to solve the inverse problem while FEMU more than 5 hours. Such huge difference is due to the fact that each iteration of FEMU needs to run a complex three-dimensional FE simulation, on the other hand, parameter L can only be identified with FEMU. Moreover, the hybrid approach allows to simplify the FEMU part since only 1 parameter needs to be identified, reducing the computational effort of the minimization algorithm.

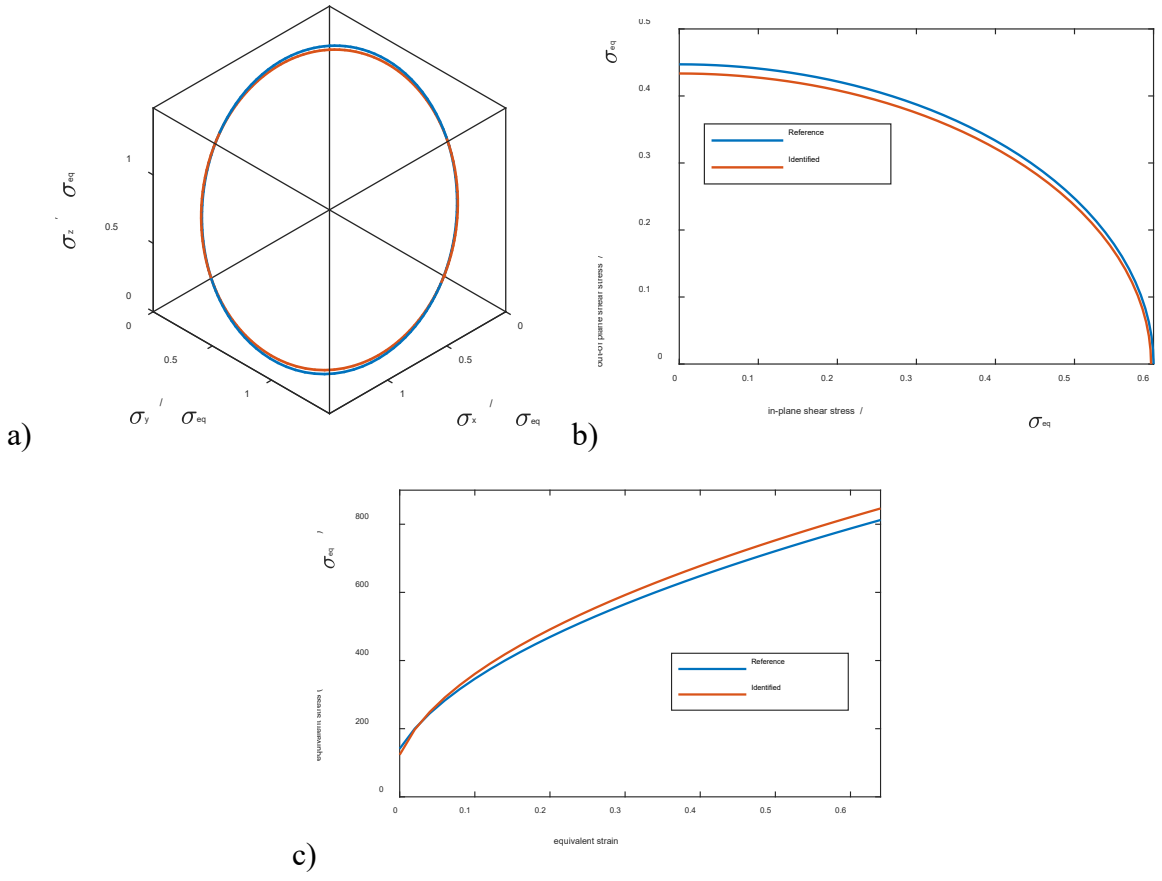

Fig. 4. Comparison of the identification results: a) yield surface for the normal stress components, b) yield surface for the shear components, c) hardening law.

Acknowledgment
This project has received funding from the Research Fund for Coal and Steel under grant agreement No. 888153.

Summary
In this paper an inverse identification procedure to characterize the 3D anisotropic behavior of a metal is proposed and validated through simulated experiments. Two tests are used to identify 8 constitutive parameters combining two well-known inverse methods, i.e. the VFM and FEMU. The identified parameters provides an accurate description of the plastic behavior, with an average error below 5%. In the future, an experimental validation will be conducted and the possibility of identify more complex 3D constitutive model will be evaluated.

References
[1] L. Ma, Z. Wang, The effects of through-thickness shear stress on the formability of sheet metal-A review, J. Manuf. Process. 71 (2021) 269-289. https://doi.org/10.1016/j.jmapro.2021.09.019
[2] F. Pierron, M. Grédiac, Towards Material Testing 2.0. A review of test design for identification of constitutive parameters from full-field measurements, Strain 57 (2021) 12370. https://doi.org/10.1111/str.12370
[3] M. Rossi, A. Lattanzi, L. Morichelli, J.M. Martins, S. Thullier, A. Andrade-Campos, S. Coppieters, Testing methodologies for the calibration of advanced plasticity models for sheet metals: A review, Strain 58 (2022) 12426. https://doi.org/10.1111/str.12426
[4] D. Lecompte, S. Cooreman, S. Coppieters, J. Vantomme, H. Sol, D. Debruyne, Parameter identification for anisotropic plasticity model using digital image correlation, Eur. J. Comput. Mech. 18 (2009) 393-418. https://doi.org/10.3166/ejcm.18.393-418
[5] F. Grytten, B. Holmedal, O.S. Hopperstad, T. Børvik, Evaluation of identification methods for YLD2004-18p, Int. J. Plast. 24 (2008) 2248-2277. https://doi.org/10.1016/j.ijplas.2007.11.005
[6] M. Grédiac, F. Pierron, Applying the Virtual Fields Method to the identification of elasto-plastic constitutive parameters, Int. J. Plast. 22 (2006) 602-627. https://doi.org/10.1016/j.ijplas.2005.04.007
[7] M. Rossi, A. Lattanzi, F. Barlat, A general linear method to evaluate the hardening behaviour of metals at large strain with full-field measurements, Strain 54 (2018) 12265. https://doi.org/10.1111/str.12265
[8] F. Pierron, M. Grediac, The virtual fields method: Extracting constitutive mechanical parameters from full-field deformation measurements, 2012.
[9] M. Rossi, F. Pierron, Identification of plastic constitutive parameters at large deformations from three dimensional displacement fields, Comput. Mech. 49 (2012) 53-71. https://doi.org/10.1007/s00466-011-0627-0
[10] M. Rossi, F. Pierron, M. Štamborská, Application of the virtual fields method to large strain anisotropic plasticity, Int. J. Solids Struct. 97-98 (2016) 322-335. https://doi.org/10.1016/j.ijsolstr.2016.07.015
[11] A. Lattanzi, F. Barlat, F. Pierron, A. Marek, M. Rossi, Inverse identification strategies for the characterization of transformation-based anisotropic plasticity models with the non-linear VFM, Int. J. Mech. Sci. 173 (2020) 105422. https://doi.org/10.1016/j.ijmecsci.2020.105422
[12] J.M.P. Martins, A. Andrade-Campos, S. Thuillier, Calibration of anisotropic plasticity models using a biaxial test and the virtual fields method, Int. J. Solid. Struct. 172-173 (2019) 21-37. https://doi.org/10.1016/j.ijsolstr.2019.05.019
[13] M. Rossi, A. Lattanzi, F. Barlat, J.H. Kim, Inverse identification of large strain plasticity using the hydraulic bulge-test and full-field measurements, Int. J. Solid. Struct. 242 (2022) 111532. https://doi.org/10.1016/j.ijsolstr.2022.111532

[14] K. Denys, S. Coppieters, M. Seefeldt, D. Debruyne, Multi-DIC setup for the identification of a 3D anisotropic yield surface of thick high strength steel using a double perforated specimen, Mech. Mater. 100 (2016) 96-108. http://doi.org/10.1016/j.mechmat.2016.06.011
[15] S. Avril, M. Grédiac, F. Pierron, Sensitivity of the Virtual Fields Method to noisy data, Comp. Mech. 34 (2004) 439-452.
[16] A. Marek, F. Davis, F. Pierron, Sensitivity-based virtual fields for the non-linear Virtual Fields Method, Comp. Mech. 60 (2017) 409-431. https://doi.org/10.1007/s00466-017-1411-6

Machining and cutting

Materials Research Proceedings 28 (2023) 1213-1222 https://doi.org/10.21741/9781644902479-132

Manufacturing of graded grinding wheels for flute grinding

DENKENA Berend[1,a], BERGMANN Benjamin[1,b] and RAFFALT Daniel[1,c*]

[1]Institute of Production Engineering and Machine Tools (IFW), Leibniz University Hannover, An der Universität 2, 30823 Garbsen, Germany

[a]denkenaifw@uni-hannover.de, [b]Bergmannifw@uni-hannover.de, [c]raffalt@ifw.uni-hannover.de

Keywords: Graded Grinding Wheels, Field-Assisted-Sintering, Flute Grinding, Cemented Carbide

Abstract. In this paper, two different methods for manufacturing of graded grinding wheels for two different metal bonds are presented. One method is based on the use of a mask and manual moulding and the other on a height-adjustable holder for moulding. For this purpose, a brittle and a ductile bronze bond are compared. The graded grinding wheels are fabricated through sintering with Field Assisted Sintering Technology (FAST). An analysis of the grain distribution is used to demonstrate the reproducibility of the manufacturing methodology. For analysis, light microscope images of cross-sections of the abrasive layers are taken. The grain distribution is determined using image processing software and a greyscale method. Finally, the advantages of each method are compared. As a result, both manufacturing methods are evaluated in terms of precision, feasibility and efficiency. From this, a recommendation on the implementation and further development of the methods is derived. This method enables the manufacturing of graded grinding wheels for an effective reduction of wear differences for grinding cemented carbide end mill cutters.

Introduction

Cemented carbide end mill cutters are used in a wide range of applications. These include, for example, the aerospace industry, medical technology or electrical engineering [1]. High demands are therefore placed on the quality of the workpieces that are machined with these end mill cutters. In particular, this requires a high level of precision and surface quality. To ensure this, the end mill cutters used must also meet the highest standards. The quality of the flutes of the end mill cutters has a major influence on their performance [2,3]. However, the deep grinding process of the flutes is characterised by high and varying thermomechanical loads. The high thermomechanical loads result from the high depth of cut associated with the process kinematics and the properties of the cemented carbide [4-6]. Cemented carbide possesses a high degree of hardness and wear resistance [4,5]. In addition, the engagement conditions vary significantly along the width of the grinding tool [6,7]. This is a consequence of the flute geometry. These factors result in a high and at the same time uneven radial wear.

This causes an increasing number of defects in the flute bottom and the cutting edges as well. A defect-free flute, however, is decisive for the operational behaviour of the end mill cutters [2]. To counteract this effect, the dressing intervals must be shortened. This ensures the contour accuracy of the grinding wheel. That is decisive for the necessary manufacturing accuracy. However, the frequent dressing intervals reduce the efficiency of the grinding process. This is due to higher downtimes caused by the more frequent dressing on the one hand and the resulting increased dressing wear on the other. The lifetime of the grinding tools is thus shortened.

Another method of ensuring contour accuracy is to adapt the abrasive layer properties to the local wear conditions. By levelling the radial wear occurring, this allows the dressing intervals to be increased. Economic efficiency will be increased as a result, too. The radial wear can be reduced, for example, by increasing the grain retention forces [8]. Likewise, an adjustment of the

Content from this work may be used under the terms of the Creative Commons Attribution 3.0 license. Any further distribution of this work must maintain attribution to the author(s) and the title of the work, journal citation and DOI. Published under license by Materials Research Forum LLC.

bond properties can be made. By using a more ductile bronze bond, the wear can be reduced compared to a brittle bronze [9]. Both methodologies are not applicable in the present case due to quantification limitations. The reason for this is that in the state of the art there is no sufficient accurate model of the influence of the bond properties as well as the grain retention forces on the resulting wear. Another approach is to adjust the number of abrasive grains. An increasing number of abrasive grains reduces the thermomechanical load per individual grain. As a result, this decreases the radial wear occurring [7,10,11]. Depending on the bond properties, the maximum number of abrasive grains is limited. The grains act as defects in the bond. If the number of abrasive grains is too high, the forces acting on the abrasive layer will cause the bond to fail. Wear then increases in turn. These so-called percolation limits depend on the toughness of the bond and the load occurring during the process [12]. Influencing the number of abrasive grains can therefore be used to affect the radial wear.

First approaches have already shown that the adjustment of the grain concentration in the abrasive layer in two steps can level the resulting radial wear [13]. The authors of the present paper have introduced a model in previous work enabling the radial wear differences to be reduced by up to 50 % compared to conventional grinding wheels on the basis of adapting the number of grains to the occurring loads. The model is based on a simulation-supported analysis of the locally occurring load on the grinding wheel. The resulting abrasive grain numbers for a defined application are shown in Fig. 1 [14].

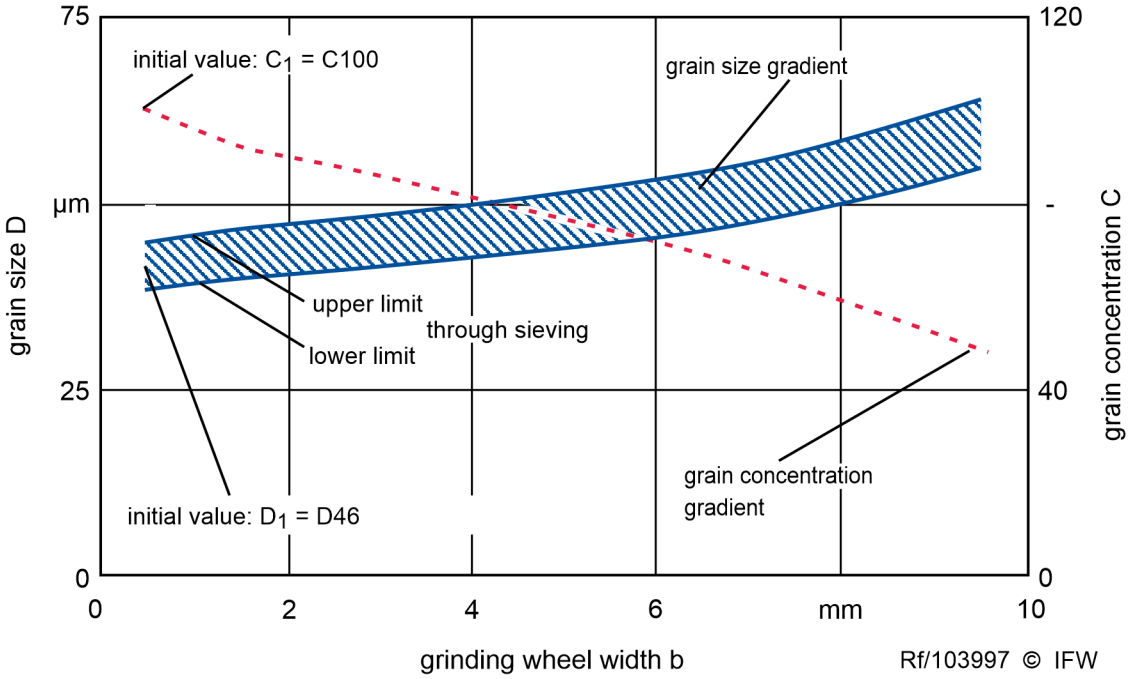

Fig. 1. Comparison of different types of grain number gradients, based on [14].

Two adaptation options are shown. One is via the grain size and the other via the grain concentration. The adjustment via the grain size turned out to be too inaccurate due to the differences in grain sizes after sieving them. This can be seen in the scatter band marked in blue. The grain concentration, on the other hand, can be applied individually in the necessary increments. This is shown in the red line. It has been shown that the implementation of a continuous gradient of the grain concentration is not possible. There are sharp transitions between the concentration ranges [15]. The present work follows on from the preceding research work. So far, only the production of test specimens has been investigated. Therefore, a methodology for the efficient and process-safe production of graded grinding wheels is presented in the following. At

the same time, the moulding method is optimised in order to accurately adjust the heights of the grain concentration ranges. This has led to fluctuations in grain concentration differences in the previously used method based on bulk density.

Materials and Methods

First, grinding layer specimens were sintered. These were used to adjust the moulding accuracy through powder dosing. Specimens are cylindrical with a diameter of 22 mm and a height of 6 mm. The process is comparable to the production of grinding wheels and therefore offers good transferability. The manufacturing of the specimens and the later grinding wheels is shown in Fig. 2.

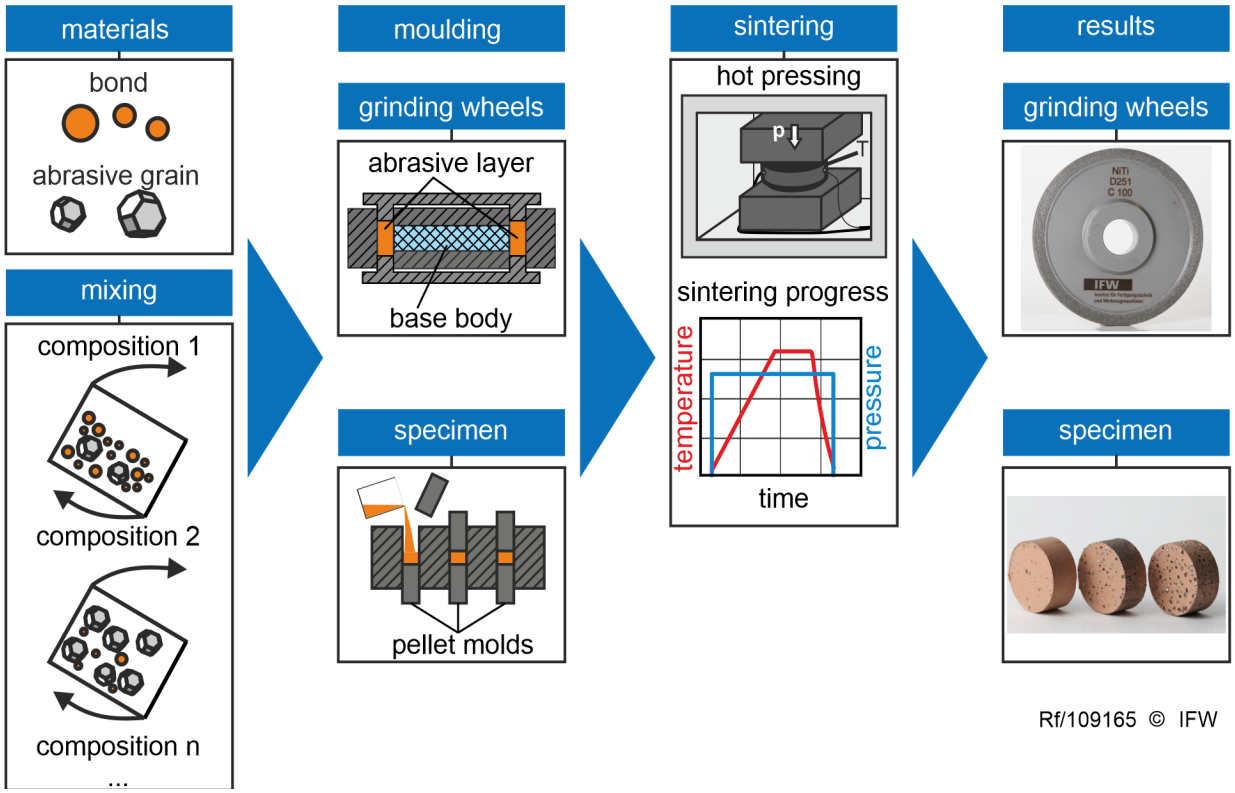

Fig. 2. Grinding wheel and specimen manufacturing.

From this, Fig. 2, also follows the comparability of the two methods. For their production, the components of the abrasive layer must first be mixed and pre-compacted to form a green body.
A Turbula mixer is used for mixing. The mixing time was 30 minutes. The components consist of a bronze bond and diamond grains. Two different pre-alloyed powders were used to evaluate influences on the manufacturing accuracy depending on the components. The composition was 60 wt.% copper and 40 wt.% tin (60/40 bronze), respectively 80 wt.% copper and 20 wt.% tin (80/20 bronze) with an irregular particle shape and an average diameter of 40 µm. Alloys similar to those used are also used in the industrial environment. The sintering temperature used was 420°C for the 60/40 bronze and 620°C for the 80/20 bronze. The holding time was 240 seconds in each case at a pressure of 35 MPa. The diamond grain chosen was an irregular shape grain of size D54 according to the FEPA standard. For each bond type, test specimens with the concentration C0, C25, C50, C75, C100 and C125 were produced. The C specification also complies with the FEPA standard. C100, for example, corresponds to a volume fraction of 25 % of the used grain. Weighting was carried out according to the following equation:

$$m_{bond} = V_{Specimen} \cdot \left(100 - V_{grain}\right) \cdot \rho_{bond} \cdot 0.98 \quad (1)$$

The target parameter is the mass of the bond m_{bond}. $V_{specimen}$ describes the target volume of the grinding layer specimen, respective the grinding wheel abrasive layer. The volume of the bond is calculated by the difference to the volume of the grains, corresponding to the grain concentration, V_{grain}. The density of the used bond material is given by ρ_{bond}. Based on the available knowledge, porosities smaller than 2 % occur during FAST sintering of metallic bonds. Therefore, the correction factor 0.98 was chosen for the metal content to compensate for its larger volume due to porosity. The test specimens were then measured to ensure the accuracy of the process. The method was verified by sintering graded specimens of composition C100/C0/C50 (gradient 1) and the composition C0/C50/C100 (gradient 2). Each layer was 2 mm thick. Accuracy was evaluated using light microscope images.
Based on the results, the graded grinding wheels were manufactured. Both bonding systems were used for this. The variation of the grain concentrations is shown in Table 1:

Table 1. Composition of the graded grinding wheels for the 60/40 bond.

Layer number and position	Grain concentration	Bronze powder mass	Diamond grain mass	Total mass
1 (0 – 1 mm)	C125	11.974 g	1.949 g	13.923 g
2 (1 – 2 mm)	C121	12.149 g	1.887 g	14.035 g
3 (2 – 3 mm)	C114	12.453 g	1.778 g	14.231 g
4 (3 – 4 mm)	C102	12.976 g	1.590 g	14.566 g
5 (4 – 5 mm)	C83	13.803 g	1.294 g	15.097 g
6 (5 – 10 mm)	C47	76.854 g	3.664 g	80.518 g

The gradients were chosen for future application tests so that they would match the corresponding application. There, they should lead to uniform radial wear when grinding a cemented carbide rod with a diameter of 16.8 mm at an engagement width and depth of 6 mm. The calculation was carried out according to the results from [14]. For comparison, a non-graded reference wheel was manufactured for each bond system. The concentration of the reference wheels was set at C125 over the total grinding wheel with. The composition of the graded grinding wheel with the 80/20 bond corresponds to the same concentration steps. The mass of the bond and diamonds were adjusted concerning this.

Moulding Methods

Two different moulding methods were investigated. For both, the sinter die was placed on a turntable to avoid unsteady rotation. This is to prevent segregation of the abrasive layer components. In the first moulding method, the powder for each abrasive layer was weighed out in i (i = 6; 12; 24) portions. These were filled into the mould along a taped-on mask in the corresponding portioning. The smoothing of the powder layers was done by manual drawing using a metallic plate. The number of steps i is used to evaluate how high the effort must be for reproducible filling. A too high number reduces the economic efficiency. The mould was filled using an aluminium hopper. This counteracted the adhesion of powder.

A height-adjustable holder was used for the second moulding method. The powder for a segment was filled in evenly by turning the sintering mould as required by eye. Subsequently, the powder was smoothed by means of the holder and an appropriate metal plate. In the first step, the height of the holder was adjusted in such a way that a pile of powder was first pushed in front of the plate when the powder was being smoothed out. By raising the height of the plate, an even surface was gradually generated. This was repeated for all layers. Both methods were first carried out using an analogue sintering mould made of acrylic glass. This allowed a visual evaluation of

the moulding process for adhesions on the mould edge or the grinding wheel base body. Concept 2 with the analogue mould can be seen in Fig. 3.

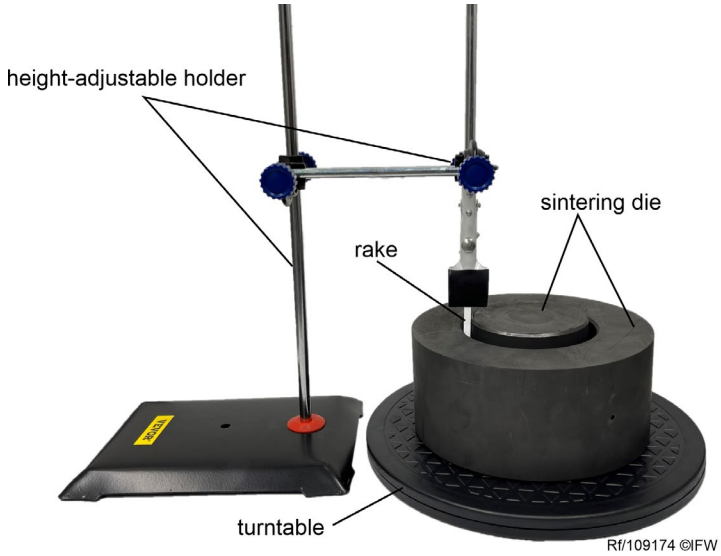

Fig. 3. Manufacturing method using a height-adjustable holder.

All grinding wheels were sintered with the parameters of the test specimens. The evaluation was carried out on the basis of cross-sections of the abrasive layers. Images of these were taken using an optical microscope and a scanning electron microscope. The evaluation of the grain concentration curves was carried out using the evaluation software ImageJ. The method is shown in Fig. 4.

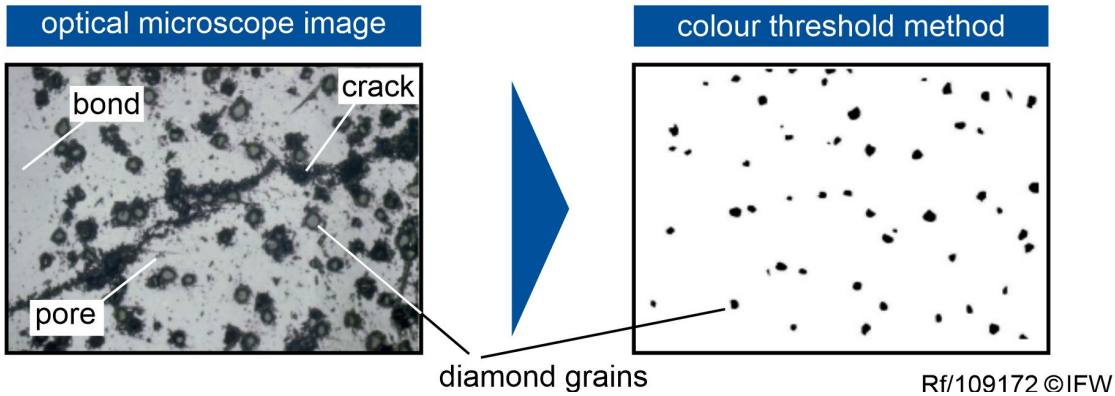

Fig. 4. Evaluation method for the grain concentration.

Analysis of the Specimen Height

As a first step, an assessment of the achieved heights of the abrasive layer specimen was carried out in order to evaluate Eq. 1. This is necessary in order to be able to accurately reproduce the gradients of the grinding wheels. The results of the evaluation are shown in Fig. 5.

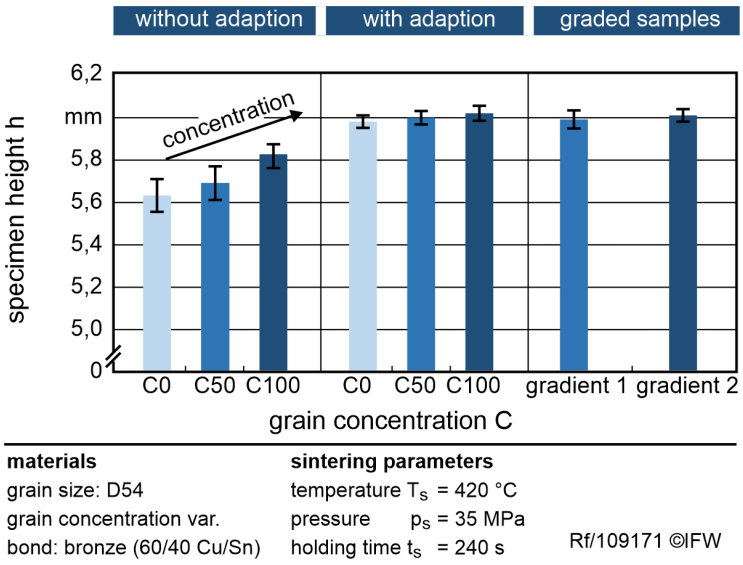

Fig. 5. Evaluation of the sample height adjustment.

The figure shows the inaccuracy in the height of the abrasive layer, as demonstrated in a previous study [15]. Moulding based on bulk density, or a high final porosity, shows that the specimen height decreases correspondingly with an increasing proportion of bond compared to the diamond grain. This is due to the increasing influence of the bond on the specimen height after sintering. The deviations from the target width of the segments can be considered uncritical if the grain concentration differences between them are small. This is the case due to the continuous load progression during deep grinding of the flutes. With larger grain concentration differences, the deviations from the target width can lead to increased radial wear. If, for example, the segment with a lower grain concentration is in the area of a higher load due to the higher shrinkage, the radial wear will increase there. This then counteracts the load design. The deviations should therefore not be greater than a few grain layers. The adjustment of the filling quantities according to Eq. 1, or based on a remaining porosity of 2 %, allows the abrasive layer specimens to be produced at the required target height. This can also be repeated for graded specimens, gradient 1 and gradient 2. Nevertheless, small deviations occur due to inaccuracies caused by the manual manufacturing process and the process chain. Since the deviations correspond to only a few grain layers, it can be assumed that these have only a minor influence on the operational behaviour.

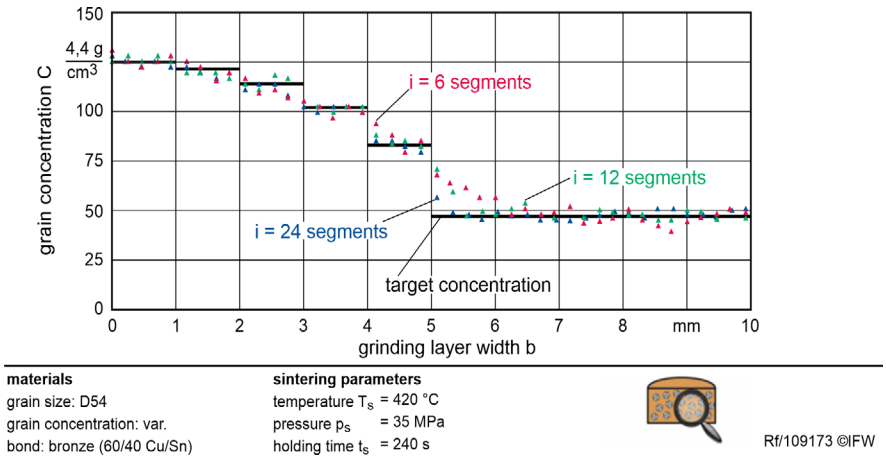

Fig. 6. Concentration gradients of the manufacturing

Fig. 6 shows the process as a microscope image for the evaluation of the single layer heights within the specimen of gradient 1 and 2. From this it is visible that the presented moulding methodology allows an accurate adjustment of the gradients as well. Within the specimen, the deviations from the target concentration are quite small. The presented methodology is therefore suitable for the dimensioning of the moulding-in amounts for graded grinding wheels.

Comparison of the moulding methods

Using the previously presented moulding quantity calculation, the two moulding methods from the previous chapter were compared. Fig. 7 shows the grain concentration curves for the moulding method using the taped mask and manual smoothing for the different divisions of the masks in i segments (i = 6; 12; 24).

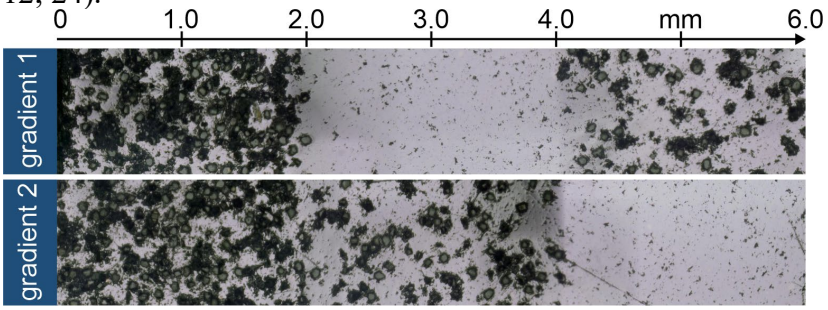

Fig. 7. Evaluation of the gradient course within the samples.

The figure shows that the method with filling based on 6 up to 24 portions of the respective abrasive layer amount enables the production of graded grinding wheels. A smaller quantity of subdivisions (i = 6) results in less accurate production compared to 12 or 24 subdivisions. This can be seen in the more pronounced transitions between the concentration zones. The deviation from the target concentration is particularly noticeable in the transition between C83 and C47. However, the gradient is still within the range of the target gradient. Especially the transition areas between the concentration levels are not to be regarded as disadvantageous. Softer transitions between them are to be aimed for, as the load in the application case is also continuous and not discrete (see Fig. 1). However, a continuous course cannot be implemented in production with current methods. But the inaccuracy, as in the case of production by means of 6 subdivisions, enables an approximation to a continuous course. In addition, the method with fewer subdivisions is advantageous because the moulding time is reduced. If high manufacturing accuracy is required, this can be reached by using 24 subdivisions. The transitions between the concentration zones are strongly pronounced. The fluctuations occurring are in the range of concentration differences >C5. These also appear in non-graded abrasive layers. The outlier in the transition area from C83 to C47 is explained by the smoothing of the layers. Since this was done manually, there are slight variations in their heights. When evaluating the grain concentration in image sections, it is therefore possible that both layers are measured partially in the corresponding section. Nevertheless, the overall small number of outliers also shows that the width of the concentration ranges was fulfilled for all grinding wheels.

Equally, the method based on a height-adjustable holder without individual single weighted amounts was investigated. The results of these investigations are shown in Fig. 8.

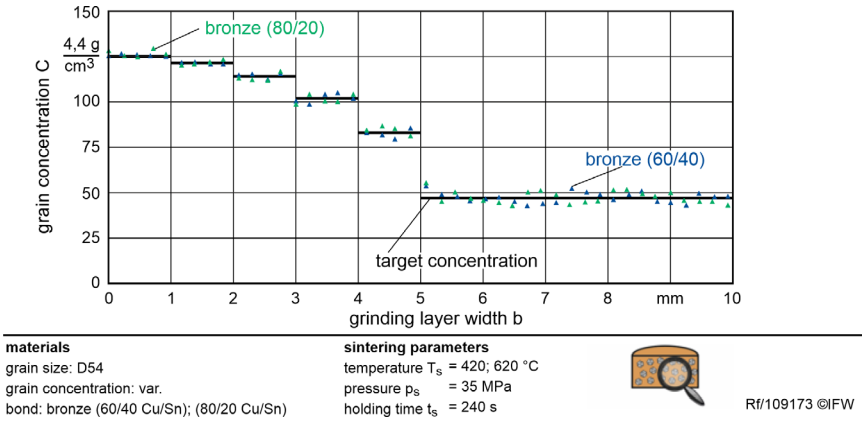

Fig. 8. Concentration gradients of the manufacturing method with the height-adjustable holder.

Two main observations can be drawn from this. First, it shows, as was expected, that the bond has no effect on manufacturing accuracy. Both the (60/40) bronze and the (80/20) bronze can be moulded and sintered into a graded abrasive layer. The differences exist only in local and small variations of the grain concentration. Secondly, the method with the height-adjustable holder shows that the transitions between the grain concentration ranges are even more accurate than the method with the mask. The higher accuracy is due to the fact that the layer heights can be set to the appropriate height without manual influence. A small inaccuracy is again only seen in the transition from C82 to C47. However, this is very slight for both bonds. The grain concentration steps, that can be quantitatively evaluated, are visually indistinguishable. This can be seen in the section of a microscope image of the grinding wheel with the (60/40) bronze. Regardless of the manufacturing method, the more brittle bronze (60/40) has been found to have a tendency to crack. This can be seen in Fig. 9.

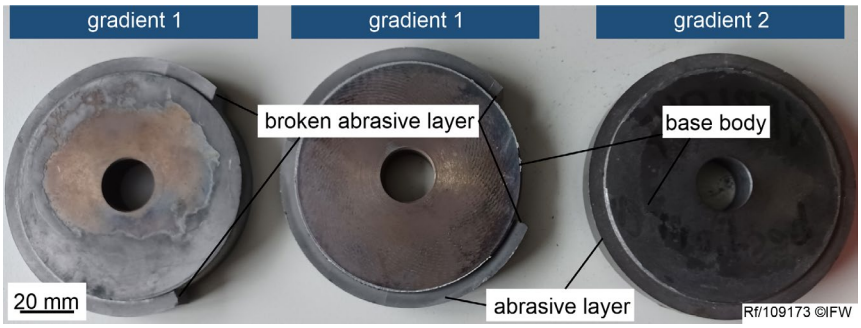

Fig. 9. Graded grinding wheels manufactured on the basis of (60/40) bronze.

The cracks only occurred in the brittle (60/40) bronze. Due to the different diamond concentrations, it can be assumed that the shrinkage of the segments varies with different grain concentrations. Segments with high concentrations are expected to shrink less. This is the case because diamond has a very low coefficient of thermal expansion compared to bronze. As a result, residual stresses in the abrasive layer are to be expected. Unfortunately, these cannot be determined analytically. The reason for this is the geometry of the abrasive layer, the large diamond grains and the fact that some of the residual stresses are already removed after fracture. It was also observed that the non-graded grinding wheels of the (60/40) bronze with C125 also break more frequently than those with C100. The reason for this could be the additionally reduced abrasive layer strength due to the increased number of grains, as discussed in the introduction [12]. As a

solution, an additional gradient was manufactured, starting at C100 (Fig. 9 gradient 2). The structure of the segments is analogous to the gradients from the methods chapter with the steps (C100/C96/C91/C82/C66/C47). As can be seen in Fig. 9, graded grinding wheels with the (60/40) bronze can be manufactured with these gradations. The last segment with C47 was deliberately not chosen lower in order to keep the shrinkage differences small and because concentrations significantly below C50 would lead to increased bond friction when using the grinding wheels.

Summary

In the present work, two methods for moulding and one method for weighing graded grinding wheels were investigated. In the investigation of the weighing-in method, it was demonstrated that the presented Eq. 1 enables an exact implementation of the gradients. This is the case regardless of the bond chosen. With regard to the methods for moulding in, it was shown that the method based on the height-adjustable holder produces the highest precision for moulding in. In addition, this method significantly reduces the time required compared to the method of filling in portions and manual smoothing. The latter method also achieves a high degree of accuracy when using 12 or 24 filling portions per segment. The reduction to 6 portions reduces the time required, but also the interface sharpness. This can be considered favourable with regard to the operational behaviour, as the loads also proceed in non-discrete steps. With regard to the moulding-in method, the use of the height-adjustable holder is therefore nonetheless considered appropriate for the highest reproducibility and productivity. The adjustment of smooth transitions can be achieved, for example, by using a notched metal plate or a rake for smoothing. Future investigations can take this as a starting point.

The layer cracking occurring with brittle bronze could be countered by reducing the grain concentration. Due to the brittleness, the bronze bond (60/40) is more challenging in the manufacturing process than the more ductile bond (80/20). Nevertheless, the more brittle bond results in better operational behaviour due to the improved operational preparation, the self-sharpening during the process and the higher contour accuracy due to the lower ductility. In order to reduce the rejects during the production of graded grinding wheels based on brittle bronzes, two approaches are conceivable for future investigations: First, the use of coated abrasive grains to increase bond strength. Second, the use of specific annealing steps during sintering or quenching to optimise the residual stress states.

In conclusion, it can be stated that the present work represents a functional approach to the production of metal-bonded graded grinding wheels. Furthermore, attempts were presented that will be followed up by subsequent investigations in order to optimise the manufacturing. In addition, the profiling and sharpening of the graded grinding wheels will be the subject of future research.

Acknowledgment

The authors thank the German Research Foundation (DFG) for financially supporting the research project "Operational behavior of sintered metal-bonded diamond grinding wheels with abrasive grain concentration gradient" under grant number “DE 447/228-1”.

References

[1] H. Ortner, H. Kolaska, P. Ettmayer, The history of the technological progress of hardmetals, Int. J. Refract. Met. Hard Mater. 44 (2014) 148-159. https://doi.org/10.1016/j.ijrmhm.2013.07.014
[2] B. Denkena, Lasertechnologie für die Generierung und Messung der Mikrogeometrie an Zerspanwerkzeugen, Ergebnisbericht des BMBF Verbundprojektes GEOSPAN, 2005.
[3] K. Dröder, B. Karpuschweski, E. Uhlmann, A comparative analysis of ceramic and cemented carbide end mills, Prod. Eng. 14 (2020) 355-364. https://doi.org/10.1007/s11740-020-00966-9

[4] S. Malkin, C. Guo, Grinding technology: theory and application of machining with abrasives, 2nd Edition, Industrial Press Inc, 2008. ISBN: 9780831132477, 0831132477
[5] J. Mayr, R. Barbist, Untersuchung und Bewertung der Schleifbarkeit von Hartmetall, Der Stahlformenbauer 31 (2014) 74 – 79.
[6] E. Uhlmann, C. Hübert, Tool grinding of end mill cutting tools made from high performance ceramics and cemented carbides, CIRP Annals 60 (2011) 359-362. https://doi.org/10.1016/j.cirp.2011.03.106
[7] T. Heymann, Gezielte Nut- und Schneidkantenpräparation von Vollhartmetall - Zerspanwerkzeugen durch Polierschleifen, Spanende Fertigung / Prozesse – Innovation – Werkstoffe, Vulkan-Verlag Essen 6. Ausgabe, 2012, pp. 104-110.
[8] B. Denkena, A. Krödel, R. Lang, Fabrication and use of Cu-Cr-diamond composites for the application in deep feed grinding of tungsten carbide, Diam. Relat. Mater. 120 (2021). https://doi.org/10.1016/j.diamond.2021.108668
[9] B. Bergmann, P. Dzierzawa, Understanding the properties of bronze-bonded diamond grinding wheels on process behaviour, CIRP Annals 71 (2022) 293-296. https://doi.org/10.1016/j.cirp.2022.04.014
[10] P. Brevern, Untersuchungen zum Tiefschleifen von Hartmetall unter besonderer Berücksichtigung von Schleiföl als Kühlschmierstoff. VDI Fortschrittsberichte Reihe 2, 1996.
[11] T. Friemuth, Schleifen hartstoffverstärkter keramischer Werkzeuge. Dr.-Ing. Dissertation, Universität Hannover, 1999.
[12] F.L. Kempf, A. Bouabid, P. Dzierzawa, T. Grove, B. Denkena, Methods for the analysis of grinding wheel properties, 7. WGP Jahreskongress, 2017, pp. 87-96.
[13] E. Uhlmann, N. Schröer, A. Muthulingam, B. Gülzow, Increasing the productivity and quality of flute grinding processes through the use of layered grinding wheels, Procedia Manuf. 33 (2019) 754-761. https://doi.org/10.1016/j.promfg.2019.04.095
[14] B. Denkena, B. Bergmann, D. Raffalt, Operational behaviour of graded diamond grinding wheels for end mill cutter machining, SN Appl. Sci. 4 (2022). https://doi.org/10.1007/s42452-022-04970-9
[15] B. Denkena, B. Bergmann, D. Raffalt, Manufacturing Of Graded Grinding Layers, World PM2022 - Session 37: Hard metals, cermets and diamond tools - Processing II, 2022.

Materials Research Proceedings 28 (2023) 1223-1234 https://doi.org/10.21741/9781644902479-133

Modeling of surface hardening in burnishing process

TEIMOURI Reza[1,a *], GRABOWSKI Marcin[1,b] and SKOCZYPIEC Sebastian[1,c]

[1] Cracow University of Technology, Faculty of Mechanical Engineering, Chair of Production Engineering, al. Jana Pawła II 37, 31-864, Kraków, Poland

[a]reza.teimouri@pk.edu.pl, [b]marcin.grabowski@pk.edu.pl, [c]sebastain.skoczypiec@pk.edu.pl

Keywords: Burnishing, Twining-Induced Hardening, Phase Change, Simulation

Abstract. In the present paper, a multiphysic model was developed to identify the underlying mechanism of surface layer hardening in burnishing of stainless steel 304. The mechanic of burnishing process was firstly modeled to obtain deformation parameters i.e. strain and strain rate by incremental plasticity. Then the strengthening mechanisms were identified association of constitutive equations regarding twinning-induced hardening and phase change. It was found that the twining-induced hardening has greatest contribution in strengthening the surface layer. Moreover, among the process parameters, the burnishing depth has greatest effect on hardness magnitude and corresponding depth.

Introduction

Burnishing is categorized as surface finishing operations which are being used for surface smoothening, and mechanical properties enhancement of the engineering materials [1,2]. Compared to other mechanical surface treatment processes such as shot peening, laser shock peening, or ultrasonic peening, burnishing results in better surface quality and induces compressive residual stress at deeper layers [3]. Moreover, it is easily implemented and does not require complex instrumentations and machines. Thus, it is finding its importance at industrial levels such as aerospace and automotive for the superfinishing of hard materials.

During burnishing, the microstructure evolution is corresponded to different microstructure phenomena that can result in hardening of burnished surface layer. However, in majority of conducted research, the underlying mechanism of surface strengthening has been reported as grain refinement Based on the type of material, hardening mechanisms such as dislocation accumulation, crystal twinning and phase change can be also effective in strengthening of surface layer. Starman et al. [4] reported that the martensitic phase transformation corresponds to the surface hardening of AISI 304 processed by shot-peening and laser shock peening. Laine et al. [5] revealed that the twining-induced hardening beside grain size evolution has contribution in surface hardening of shot-peened Ti64 alloy. Rinaldi et al. [6] identified that the strengthening mechanism of CP-T alloy in hard machining process is mainly attributed to twining induced plasticity and grain refinement.

In order to identify the main strengthening mechanism, complex microscopic examination and mechanical testing is required. However, providing such examination techniques for considerable amount of experiments are too expensive and time consuming. In this context, development of material model based on multiphysics of different metallurgical phenomena can be considered as a fundamental means to afford the lack of capabilities of measurement instrumentation and to identify the underlying mechanisms.

In the present study, a theoretical approach based on multiphysics of contact mechanic and multiscale micro-mechanical material model is developed to identify the underlying strengthening mechanism AISI 304 samples processed by burnishing process. Here, firstly the deformation parameters of process like stress, strain and strain rate are modeled by expanding cavity model. Then the strengthening mechanisms are identified by developing a material model including grain

Content from this work may be used under the terms of the Creative Commons Attribution 3.0 license. Any further distribution of this work must maintain attribution to the author(s) and the title of the work, journal citation and DOI. Published under license by Materials Research Forum LLC.

refinement, twinning-induced hardening and phase change. Confirmation of developed theoretical model has been carried out by series of burnishing experiments including different processing parameters.

Theoretical model

Deformation parameter.

Fig. 1 illustrates the schematic diagram of the rolling of a roller on the flat surface that is the main concept of roller burnishing process. In order to calculate the deformation parameters, theory of expanded cavity model (ECM) proposed by Gao et al. [7] utilized here. Accordingly, the mean contact pressure applied by burnishing roller to the surface of the power law hardening material can be calculated by following equation:

$$p_m = \frac{\sigma_y}{\sqrt{3}}\left[1 + \frac{1}{n}\left(\frac{r_p^{2n}}{a^{2n}} - 1\right)\right] + k\varepsilon_{eq}^{n} \tag{1}$$

where r_e, n and k are, respectively, the outer radius of cylinder, strain hardening exponent and material constant for power law. Also, r_p and ε_{eq} are the the plastic boundary of deformation and equivalant plastic strain of contact which can be calculated by following formulation [8].

$$\varepsilon_{eq} = \sqrt{6}\frac{\sigma_y}{E}\frac{r_p^2}{r^2} \quad , \quad r_p = \sqrt{\frac{2Ea^3}{\sqrt{3}R\sigma_y}} \tag{2}$$

Once the mean contact pressure is identified, the burnishing force of an each individual roller induces to a surface can be obtained by following formula:

$$F = 2aLp_m \, , \; a = \sqrt{2R\delta} \tag{3}$$

where L is roller length, a is the penetration radius and δ is the burnishing depth.

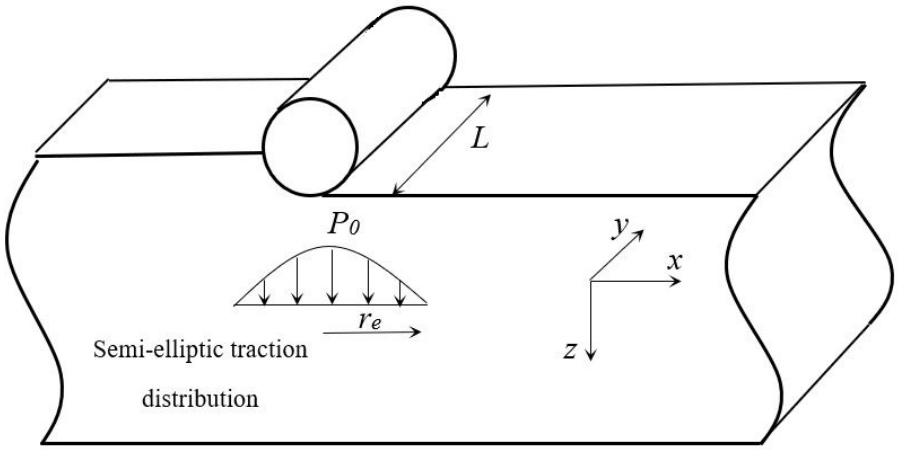

Fig. 1. Schematic illustration of contact of a cylindrical roller to flat surface.

In order to calculate the deformation parameters during motion of the roller over the surface, the theory of incremental plasticity for rolling contact that is suggested by McDowel is utilized [9]. Based on this theory, the loading initiates by elastic stresses and it incrementally increases up to reaching plastic region. Finally, by moving the tool too far from the point of interest, the unloading occurs. The elastic stresses at point of interest *M(x,z)* can be calculated using integration

of Boussineq solution for the normal traction *p(s)* and tangential traction *q(s)* in semi-infinite half space over the region of contact [10].

$$\begin{cases} \sigma_{xx}(x,z) = -\dfrac{2z}{\pi}\int_{-a}^{a}\dfrac{p(s)(x-s)^2}{[(x-s)^2+z^2]^2}ds - \dfrac{2}{\pi}\int_{-a}^{a}\dfrac{q(s)(x-s)^3}{[(x-s)^2+z^2]^2}ds \\ \sigma_{zz}(x,z) = -\dfrac{2z^3}{\pi}\int_{-a}^{a}\dfrac{p(s)}{[(x-s)^2+z^2]^2}ds - \dfrac{2z^2}{\pi}\int_{-a}^{a}\dfrac{q(s)(x-s)}{[(x-s)^2+z^2]^2}ds \\ \tau_{xz}(x,z) = -\dfrac{2z^2}{\pi}\int_{-a}^{a}\dfrac{p(s)(x-s)}{[(x-s)^2+z^2]^2}ds - \dfrac{2z}{\pi}\int_{-a}^{a}\dfrac{q(s)(x-s)^2}{[(x-s)^2+z^2]^2}ds \end{cases} \tag{4}$$

More specifically, by assuming semi-elliptic distribution of tangential and normal traction based on boussinesque formulation, following relationship between the axial and tangential tractions and burnishing force are established.

$$p(s) = \frac{F}{a}\sqrt{1-\left(\frac{2s}{a}-1\right)^2}\ ,\ q(s) = \frac{\mu F}{a}\sqrt{1-\left(\frac{2s}{a}-1\right)^2} \tag{5}$$

By identifying the values of elastic stresses, the elastic strain can be obtained using Hook's law taking into account the plain strain condition i.e. $\varepsilon_{yy}=0$.
In order to calculate the value of plastic stress and strains at any individual poit, the yielding criteria by comparing the value of effective stress and Johnson-Cook constitutive model is identified as follows:

$$\begin{cases} g = \dfrac{1}{2}(S_{ij}-a_{ij})(S_{ij}-a_{ij}) - Y^2 \\ Y = \dfrac{1}{\sqrt{3}}(A + B{\varepsilon_{eff}}^n)\left[1 + C\ln\left(\dfrac{\dot{\varepsilon}_{eff}}{\dot{\varepsilon}_0}\right)\right]\left(\dfrac{T-T_0}{T_m-T_0}\right)^m \\ S_{ij} = \sigma_{ij} - \dfrac{1}{3}\delta_{ij}\sigma_{kk} \end{cases} \tag{6}$$

where S_{ij} is deviatoric stress, and a_{ij} is back stress tensors. Also, Y is the effective stress based on Johnson-Cook (J-C) yield criterion. A, B and C are the *J-C* constants, ε_{eff} and $\dot{\varepsilon}_{eff}$ are effective strain and effective strain rate, respectively, which are calculated based on incremental plasticity theory that will be described in following part. Furthermore, T is the temperature term which can be neglected in burnishing process [11]. According to Eq. 6, when the g>0, the loading at the point of interest is elastic, and the stress and strain can be calculated using Eq. 4, and Hook's law. When g>0, the plastic loading occurs, and to obtain values of plastic strain and stress, the systems of three equations suggested by McDowel need to be solved.

$$\begin{cases} d\varepsilon_{xx} = \dfrac{1}{E}\left[d{\sigma_{xx}}^p - \vartheta\left(d{\sigma_{yy}}^p + d{\sigma_{zz}}^p\right)\right] + \left[\dfrac{n_{xx}}{h+c}\left(d{\sigma_{xx}}^p n_{xx} + d{\sigma_{yy}}^p n_{yy} + d{\sigma_{zz}}^p n_{zz} + 2d{\tau_{xz}}^e n_{xz}\right)\right] = \\ \Psi\left\{\dfrac{1}{E}\left[d{\sigma_{xx}}^e - \vartheta\left(d{\sigma_{yy}}^p + d{\sigma_{zz}}^e\right)\right] + \left[\dfrac{n_{xx}}{h+c}\left(d{\sigma_{xx}}^e n_{xx} + d{\sigma_{yy}}^p n_{yy} + d{\sigma_{zz}}^e n_{zz} + 2d\tau_{xz}{}^e n_{xz}\right)\right]\right\} \\ d\varepsilon_{yy} = \dfrac{1}{E}\left[d{\sigma_{yy}}^p - \vartheta\left(d{\sigma_{xx}}^p + d{\sigma_{zz}}^p\right)\right] + \left[\dfrac{n_{yy}}{h+c}\left(d{\sigma_{xx}}^p n_{xx} + d{\sigma_{yy}}^p n_{yy} + d{\sigma_{zz}}^p n_{zz} + 2d{\tau_{xz}}^e n_{xz}\right)\right] = 0 \\ d{\sigma_{yy}}^p = \dfrac{1}{2}\left(d{\sigma_{xx}}^p + d{\sigma_{zz}}^p\right) \end{cases} \tag{7}$$

The other terms of above formula can be calculated

$$n_{ij}=\frac{S_{ij}-a_{ij}}{\sqrt{2k}},\ da_{ij}=cd\varepsilon_{ij}{}^{p},\ \Psi=1-\exp\left(-\kappa\frac{3h}{2G}\right),\ G=\frac{E}{2(1+\vartheta)} \tag{8}$$

where h and is isotropic and kinematic hardening coefficients.

Our pilot experiemnts on processing of stainless steel 304 showed that the main contributed mechanisms on strengthening the surface layer after burnishing proess are formation of twinning and alpha ferrite. The next step after the calculation of the deformation parameter is to calculate the stress as results of twinning-induced hardening and phase changes.

Twinning-induced hardening.

The stress related to twining induced material strengthening has been presented in following equation [12]:

$$\begin{cases}\sigma_{TW}=M\beta_{TW}Gb\left(\dfrac{1}{d_{cell}}+\dfrac{1}{l}\right)\\ \dfrac{1}{l}=\dfrac{1}{2t}+\dfrac{f_{TW}}{1-f_{TW}}\end{cases} \tag{9}$$

where the σ_{TW} is the term of strengthening stress as result of twinning, M is Taylor factor, β_{TW} is the constant, t is the twin lamellae (that is 18nm) and f_{TW} and is the twining volume fraction that is calculated by following differential equation:

$$df_{TW}=(1-f_{TW})A_f d\varepsilon \tag{10}$$

where A_f is the constant that equals to 1.916 for twining induced plasticity austenitic stainless steels [13].

Phase change.

Transformation of austenite to ferrite usually occurs in cold working of austenitic stainless steel. The increasing rate of the ferrite during deformation is obtained by [14]:

$$f_m^{\bullet}=(1-f_m)v_m N_m^{\bullet} \tag{11}$$

where $f_m^{\bullet}$ is the rate of increase of ferrite volume fraction, f_m is the ferrite volume fraction, v_m is the average ferrite volume and $N_m^{\bullet}$ is the increase rate of ferrite that is related to its nucleation probability (P) on shear bands and the total number of ferrite nucleation (N_I).

$$N_m^{\bullet}=PN_I^{\bullet}+N_I P^{\bullet}H(P^{\bullet}) \tag{12}$$

where H is Heaviside step function. Possible nucleation of ferrite is also affected by number of shear bands. Accordingly;

$$N_I^{\bullet}=\frac{rC\left(f_{sb}^{\bullet}\right)^{r-1}}{v_I},\ f_{sb}^{\bullet}=\alpha(1-f_{sb})\varepsilon^{\bullet} \tag{13}$$

where r and C are materials constant, $f_{sb}^{\bullet}$ is the increase rate of shear band volume fraction.

The ferrite nucleation probability was assumed to follow a Gaussian distribution,

$$P = \frac{1}{\sqrt{2\pi}\sigma_g} \int_{-\infty}^{g} \exp\left[-\frac{1}{2}\left(\frac{g' - \bar{g}}{\sigma_g} \right)^2 \right] dg' \tag{14}$$

where the terms σ_g and $\bar{g}$ are dimensionless mean and standard deviation, respectively. The thermodynamic driving force g is related to the stress states (Σ) and the temperature (T), and is approximated by:

$$g = g_0 + g_1 T + g_2 \Sigma \tag{15}$$

where g_0, g_1, and g_2 are constants. A fraction function (χ) of the plastic deformation is assumed cause temperature rise (ΔT) as:

$$\Delta T = \int_0^{\varepsilon} \frac{\chi}{\rho C_p} \sigma(\varepsilon) d\varepsilon \tag{16}$$

where ρ is material density and C_P is the specific heat capacity.

As per the foresaid strain-induced phase transformation kinetics, the increase rate of the ferrite can then be obtained through combination of above-calculated equations:

$$\begin{cases} f_m^{\bullet} = (1 - f_m)\left(A\varepsilon^{\bullet} + B\Sigma^{\bullet} \right) \\ A = r\alpha\beta P (1 - f_{sb})(f_{sb})^{r-1} - B_f \dfrac{g_1 \chi}{\rho C_P} \sigma(\varepsilon) \qquad B = B_f g_2 \\ B_f = \dfrac{\beta}{\sqrt{2\pi}\sigma_g} (f_{sb})^r \exp\left[-\dfrac{1}{2}\left(\dfrac{g' - \bar{g}}{\sigma_g} \right)^2 \right] H(P^{\bullet}) \\ \alpha = \alpha_0 + \alpha_1 T + \alpha_2 T^2 + \alpha_3 \Sigma \end{cases} \tag{17}$$

By identifying the ferrite volume fraction, the hardness development can be obtained as:

$$\Delta h = \sum_{i=1} f_i h_i - h_0 \tag{18}$$

where f_i is the fraction of phase i in the element, h_0 is the initial bulk microhardness, h_i is the hardness of phase i, and v represents the number of phases present in the element.

Accordingly, the final hardness of the sample after SSPD can be calculated by:

$$h = h_0 + k_D \sigma_D + k_{TW} \sigma_{TW} + \Delta h \tag{19}$$

Experiments

In the present investigation, surface sever plastic deformation experiments carried out by multi-roller rotary burnishing tool. The tool includes four rollers with diameter of 3mm and length of 10mm as shown in Fig. 2. The tool, as shown in the figure, has been mounted on a CNC milling machine to process the surface of the samples made of AISI 304. During the experiments, the burnishing force is controlled by a force dynamometer KISTLER 9257B as shown in Fig. 2. Samples were prepared in sizes of 70mm length, 30mm width and 10mm thickness. Before conducting the experiments, all the samples were milled with a same machining parameters to assure their flatness. The properties of the AISI 304, including the material's constitutive models,

i.e. Johnson-Cook, Isotropic-Kinematic hardening, dislocation density model, twinning-induced plasticity, and ferrite phase transformation constants, have been listed in Tables 1-4, respectively.

Table 1. Johnson-Cook constants of AISI 304 [15].

A (MPa)	B (MPa	C	n
452	694	0.0067	0.311

Table 2. Isotropic-kinematic hardening constants of AISI 304 [15].

h (GPa)	c (GPa)
2.7	0.8

Table 3. Coefficients of austenite-ferrite phase change constitutive equation [14].

α_0	α_1	α_2	α_3	g_0	g_1	g_2	β
-2e-	4.52e-2	11.8	0.8	0.05	-1.2	78.3	4.5

The samples were mechanically polished on a suspension of ethylene glycol and diamond pastes with a gradation of 1 and 6μm. Then, they were electrolytically etched using a voltage of 12V and a exposure time of 30s in a solution of 10g CrO3 and 100 ml of distilled water. The microstructure was observed using a scanning electron microscope (SEM) JSM-IT200. The microhardness measurements were carried out using an Innovatest microhardness tester at a load of 0.245 N.

Fig. 2. Experimental setup.

A series of experiments was carried out to confirm the results obtained by the analytical models. Among the process factors, it was found that the burnishing depth has the most prominent effect on burnishing force and hardness. Thus, a total of three experiments under different burnishing

depths, i.e. 0.2mm, 0.25 mm, and 0.3mm were carried out, and the values of force and hardness distribution were taken into account to compare with the analytical model and understand the effect of factors on the hardening mechanism. During the experiments, spindle speed and feed rate were kept constant at 500 RPM and 200 mm/min, respectively. It needs to be pointed out that each experiment has been repeated three times, and the average values of performance measures (i.e., force and hardness) were reported in the paper.

Results and Discussion

In order to confirm the analytical model, the results of burnishing forces which were derived from the developed model was compared with those experimentally measured values. Fig. 3 demonstrates the comparison of measured and predicted values of burnishing axial force for the experimental data presented in Table 6. It is seen from the figure that there are good agreements between the measured and predicted values of burnishing force. According to the quantified results, the prediction errors vary between 5.2% and 8.7%. It can also be seen that the trend of variation of the main force with respect to process factors for those data calculated by the analytical model is well consistent with the experimental value. It is seen that, as a result of higher values of burnishing depth, the burnishing force increases. The higher value of burnishing depth increases the engagement radius and results in greater force.

Influence of burnishing depth on microhardness and influential parameters have been shown in Fig. 4. According to the figure, it is seen that for all three samples, there is close agreement between the measured and predicted values of microhardness. The error values are in the range of 14.3% to 21.5%, which seems acceptable based on the previous works carried out by different researchers [15]. Moreovr, it is clear in the figure that the microhardness hardness significantly increases by increasing the burnishing depth. This trend can be observed in both experimental results and modeled values. Therefore, the developed analytical model is accurate enough and can be utilized to find the influence of process factors on the microhardness.

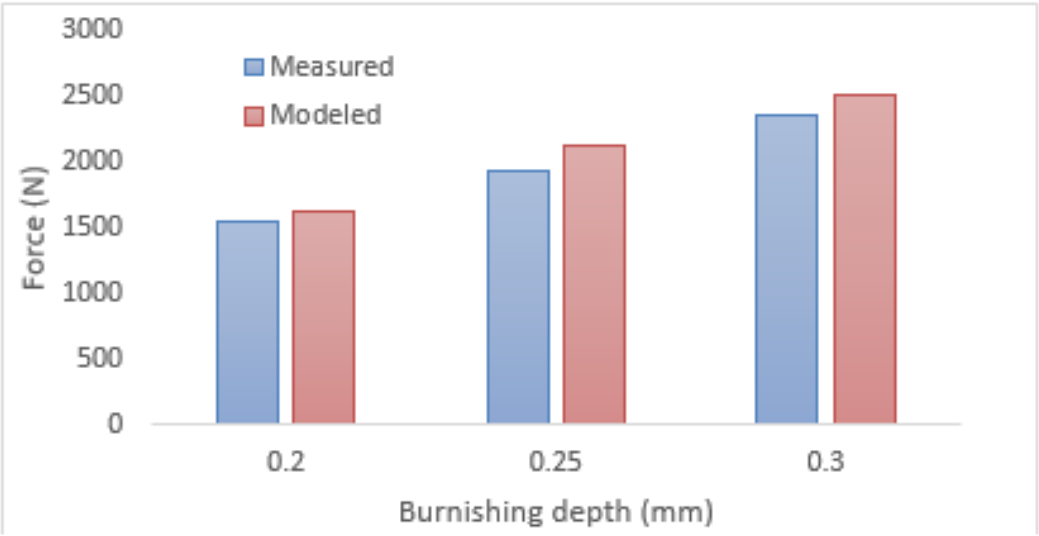

Fig. 3. Comparison between measured and predicted values of burnishing force.

As a result of increasing the burnishing depth, the burnishing axial force increases correspondingly (Fig. 3), which results in further values of plastic strain as shown in Fig. 5a. The greater value of plastic strain corresponds to a higher plastic strain rate under constant values of spindle speed and feed velocity, as shown in Fig. 5b. As result of further values of plastic strain and strain rate, the twinning volume fraction and ferrite volume fraction increase consequently as shown in Fig. 6a and 6b.

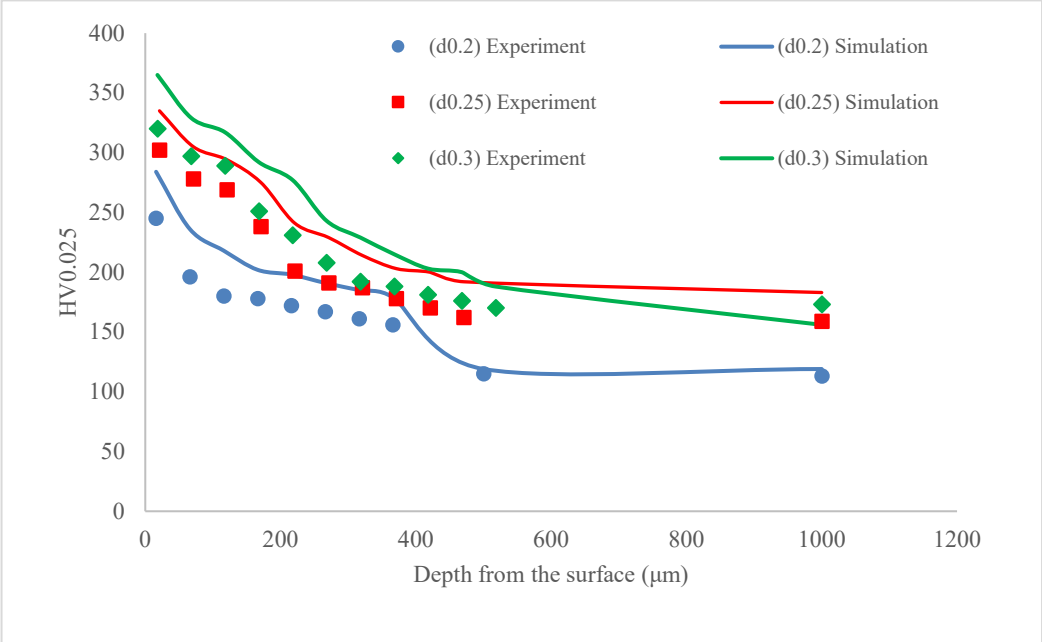

Fig. 4. Comparison between measured and predicted values of microhardness.

In order to check the results derived from the analytical model, scanning electron microscopic images of the surface and subsurface of the samples processed by burnishing at depths of 0.2 mm and 0.3 mm were captured and presented in Fig. 7. According to the figure, it is seen for the sample processed by 0.2mm burnishing depth, amount of twinning and ferrite contents which distributed in subsurface layers (as shown in Fig. 7a) are less than those of sample processed by burnishing depth of 0.3mm (as shown in Fig. 7b). It is seen that for the sample that was processed by further burnishing depth, the twinning, re-twinning, and ferrite content have been distributed up to the entire cross section of the sample that yields hardness development. It is also seen in Fig. 7a that in the deeper surface layer, the twinning induced hardening and austenite-ferrite phase change exist up to a certain depth, which can be considered a validation of the analytic model. This trend was predicted by the analytical model, where the twinning volume fraction is distributed at further depth (Fig. 6a), while the ferrite volume fraction is only available at a limited depth from the surface of the sample (Fig. 6b).

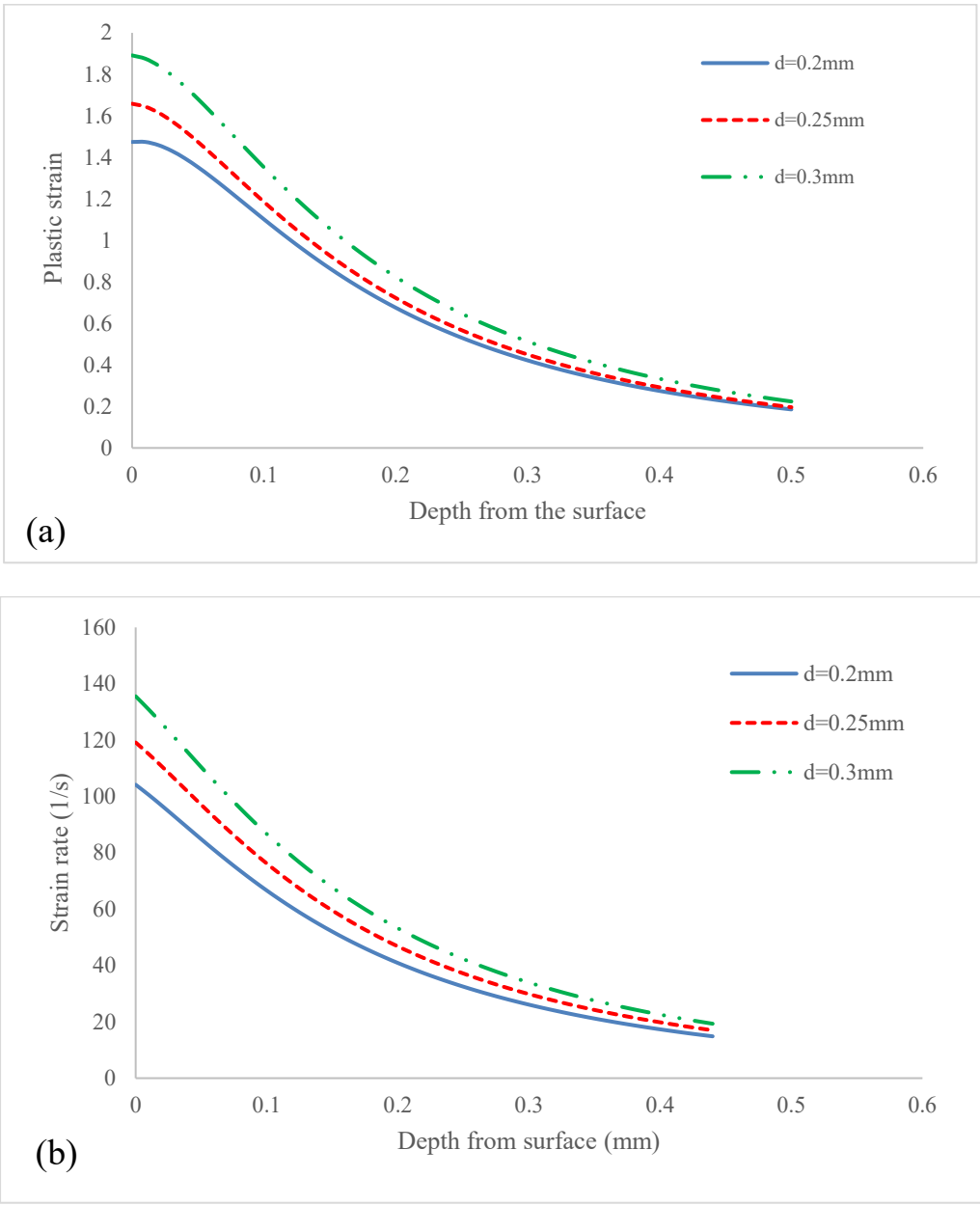

Fig. 5. Effect of burnishing depth on (a) strain and (b) strain rate.

Summary

The obtained results can be summarized as follows:

- There are close agreements between the measured and predicted values of burnishing force where the prediction error in worst case was around 9.1%. Moreover, microhardness distributions modeled by analytical approach were compatible with experiemental values where the maximum prediction error was 21.3%. Also, the trend of variations of hardness and burnishing force which were modeled by analytical approach were consistent well with experiemtnal findings.
- It was found that thanks to contributions of different hardening mechanisms, the micorhardness of the samples can be improved up to 200%. Among the different hardening mechanisms,

twinning-induced plasticity followed by phase change have the gretest effect on hardness development.

- It was found from the results that the phase change-induced hardening is only available in the layers very close to the surface e.g. 50μm in the best case; however, the twining volume fraction exists in much deeper surface layers.

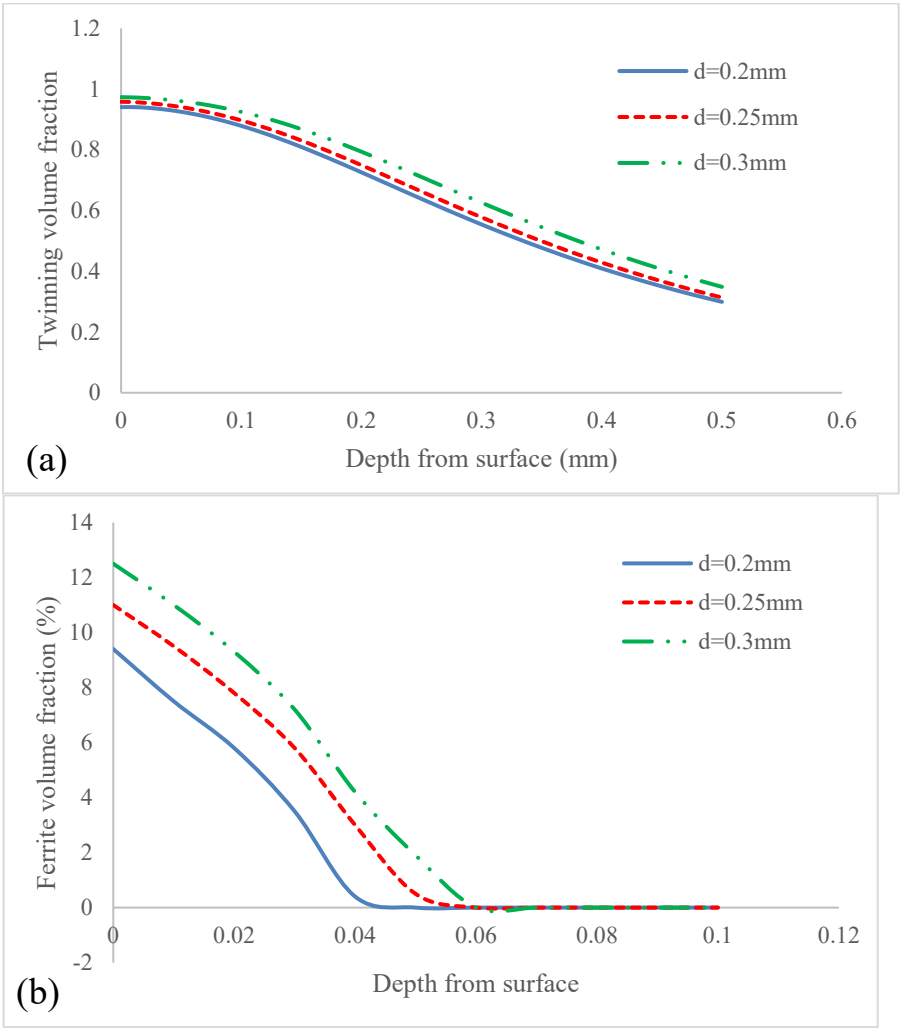

Fig. 6. Effect of burnishing depth on (a) twinning volume fraction and (b) ferrite volume fraction.

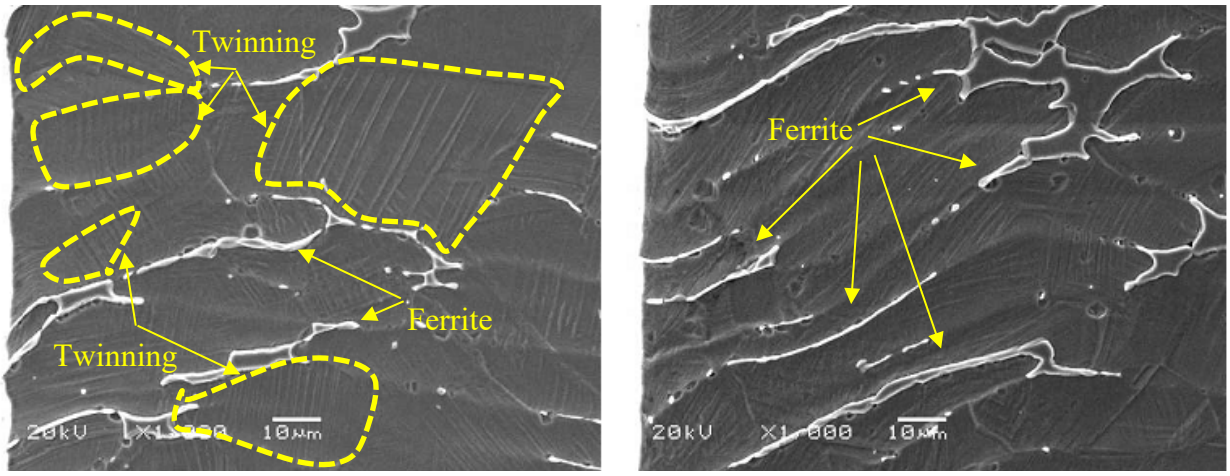

Fig. 7. SEM image of cross section of near surface layers processed by different burnishing depth (a) 0.2mm (b) 0.3 mm (Spindle speed=500 RPM and feed velocity=200mm/min).

References

[1] S. Attabi, A. Himour, L. Laouar, A. Motallebzadeh, Mechanical and wear behaviors of 316L stainless steel after ball burnishing treatment, J. Mat. Res. Tech. 15 (2021) 3255-3267. https://doi.org/10.1016/j.jmrt.2021.09.081

[2] Z.Y. Zhou, G.L. Yu, Q.Y. Zheng, G.Z. Ma, S.B. Ye, C. Ding, Z.Y. Piao, Wear behavior of 7075-aluminum after ultrasonic-assisted surface burnishing, J. Manuf. Process. 51 (2020) 1-9. https://doi.org/10.1016/j.jmapro.2020.01.026

[3] Y. Hua, Z. Liu, B. Wang, X. Hou, Surface modification through combination of finish turning with low plasticity burnishing and its effect on fatigue performance for Inconel 718, Surf. Coat. Technol. 375 (2019) 508-517. https://doi.org/10.1016/j.surfcoat.2019.07.057

[4] B. Starman, H. Hallberg, M. Wallin, M. Ristinmaa, M. Halilovič, Differences in phase transformation in laser peened and shot peened 304 austenitic steel, Int. J. Mech. Sci. 176 (2020) 105535. https://doi.org/10.1016/j.ijmecsci.2020.105535

[5] S.J. Lainé, K.M. Knowles, P.J. Doorbar, R.D. Cutts, D. Rugg, Microstructural characterisation of metallic shot peened and laser shock peened Ti–6Al–4V, Acta Mater. 123 (2017) 350-361. https://doi.org/10.1016/j.actamat.2016.10.044

[6] S. Rinaldi, D. Umbrello, S.N. Melkote, Modelling the effects of twinning and dislocation induced strengthening in orthogonal micro and macro cutting of commercially pure titanium, Int. J. Mech. Sci. 190 (2021) 106045. https://doi.org/10.1016/j.ijmecsci.2020.106045

[7] X.L. Gao, X.N. Jing, G. Subhash, Two new expanding cavity models for indentation deformations of elastic strain-hardening materials, Int. J. Solid Struct. 43 (2006) 2193-2208. https://doi.org/10.1016/j.ijsolstr.2005.03.062

[8] R. Teimouri, M. Grabowski, R. Bogucki, Ł. Ślusarczyk, S. Skoczypiec, Modeling of strengthening mechanisms of surface layers in burnishing process, Mater. Des. 223 (2022) 111114. https://doi.org/10.1016/j.matdes.2022.111114

[9] D.L. McDowell, G.J. Moyar, Effects of non-linear kinematic hardening on plastic deformation and residual stresses in rolling line contact, Wear 144 (1991) 19-37. https://doi.org/10.1016/0043-1648(91)90004-E

[10] K.L. Johnson, K.L. Johnson, Contact mechanics, Cambridge university press, 1987.

[11] Y. Liu, L. Wang, D. Wang, Finite element modeling of ultrasonic surface rolling process, J. Mater. Process. Technol. 211 (2011) 2106-2113. https://doi.org/10.1016/j.jmatprotec.2011.07.009

[12] F. Liu, W.J. Dan, W.G. Zhang, Strain hardening model of twinning induced plasticity steel at different temperatures, Mater. Des. 65 (2015) 737-742. https://doi.org/10.1016/j.matdes.2014.10.008
[13] G. Dini, R. Ueji, A. Najafizadeh, S.M. Monir-Vaghefi, Flow stress analysis of TWIP steel via the XRD measurement of dislocation density, Mater. Sci. Eng. A, 527 (2010) 2759-2763. https://doi.org/10.1016/j.matdes.2014.10.008
[14] W.J. Dan, W.G. Zhang, S.H. Li, Z.Q. Lin, A model for strain-induced martensitic transformation of TRIP steel with strain rate, Comput. Mater. Sci. 40 (2007) 101-107. https://doi.org/10.1016/j.commatsci.2006.11.006
[15] W. Zhang, X. Wang, Y. Hu, S.Wang, Predictive modelling of microstructure changes, micro-hardness and residual stress in machining of 304 austenitic stainless steel, Int. J. Mach. Tool. Manuf. 130 (2018) 36-48. https://doi.org/10.1016/j.ijmachtools.2018.03.008

Materials Research Proceedings 28 (2023) 1235-1244 https://doi.org/10.21741/9781644902479-134

Orthogonal cutting with additively manufactured grooving inserts made from HS6-5-3-8 high-speed steel

KELLIGER Tobias[1,a *], MEURER Markus[1,b] and BERGS Thomas.[1,2,c]

[1]Laboratory for Machine Tools and Production Engineering (WZL) of RWTH Aachen University, Campus-Boulevard 30, 52074 Aachen, Germany

[2]Fraunhofer Institute for Production Technology (IPT), Steinbachstr. 17, 52074 Aachen, Germany

[a]t.kelliger@wzl.rwth-aachen.de, [b]M.Meurer@wzl.rwth-aachen.de, [c]t.bergs@wzl.rwth-aachen.de

Keywords: Orthogonal Cutting, Chip Formation, Additive Manufacturing, LPBF, HSS, ASP 2030, HS6-5-3-8

Abstract. Additive manufacturing (AM) of cutting materials such as high-speed steel (HSS) is very challenging. So far, the impact of the layer-by-layer manufacturing technique onto the AM tool performance during machining is widely unknown. In this study, the performance characteristics of AM grooving inserts manufactured from HS6-5-3-8 (ASP 2030) in AM Laser Powder Bed Fusion (LPBF) process were investigated in fundamental cutting experiments. Six different workpiece materials were analyzed and two different parameter sets for the LPBF process investigated. All AM grooving inserts withstood the thermal and mechanical stresses during machining of the investigated materials. Based on these results, AM threading tools manufactured from HS6-5-3-8 will be investigated in a next step, using the geometrical freedom of the AM process for an adapted channel and outlet nozzle design of the internal cutting fluid supply.

Introduction

Additively manufactured (AM) cutting tools enable new design concepts in tool development including benefits such as lightweight construction [1], damping behavior [2] and internal cutting fluid supply [3]. So far, mainly basic bodies of indexable cutting tools were additively manufactured from steel materials, with conventional cutting inserts mounted. AM tools such as drills, grooving toolholders or indexable milling tools can be already found in industrial applications [4-6]. AM processing of cutting materials is rather rare due to the high requirements to geometrical accuracy, defect-free production and the high demands for the material regarding thermal and mechanical resistance in use. Even though some studies dealing with the processing of cutting materials in different AM techniques exist, only very few works investigating the performance behavior of AM processed cutting tools during machining are known. Examples for AM cutting materials can be found in processing of tungsten-carbide in Binder Jetting [7], slurry-based three-dimensional printing (3DP) technology [8] as well as in Laser Powder Bed Fusion (LPBF) [9], processing of ceramics in Lithography-based Ceramic-Manufacturing (LCM) [10] or LPBF processing of HSS [11].

High-speed steel (HSS) still is a very relevant cutting material. Due to its favorable characteristics of high ductility and bending strength, HSS is widely used for drilling and threading tools but also in broaching of difficult-to-cut high-temperature resistant materials, fine blanking tools and high-performance bearings. [12]

LPBF (also known as SLM or DMLS) is the most commonly used AM technique [13]. Due to LPBF machine concepts with preheated base plate, processing of HSS materials became possible during the last years. Thus, even in hard-to-weld materials with high carbon content, such as HSS, crack formation can be prevented. Kempen et al. [14] manufactured AISI M2 HSS with a relative

Content from this work may be used under the terms of the Creative Commons Attribution 3.0 license. Any further distribution of this work must maintain attribution to the author(s) and the title of the work, journal citation and DOI. Published under license by Materials Research Forum LLC.

density of 99.8 % and a hardness of 57 HRC. Zumofen et al. [15] used higher preheating temperatures to further reduce residual stresses in processing of AISI M2 HSS. Saewe et al. [11] processed defect-free AISI M50 HSS with a relative density up to 99.5 % and a hardness of up to 65 HRC for the application in roller bearings.

So far, no studies regarding the performance behavior of LPBF-processed HSS cutting materials in machining experiments are known. In this work, as-built grooving inserts manufactured from HS6-5-3-8 (ASP 2030) were investigated in orthogonal cutting experiments. Main evaluation criteria were cutting force components, tool wear and chip form. Thus, the potential of the AM HSS for an application in geometrical adapted AM threading tools with individualized cutting fluid supply should be assessed.

Tool Characteristics

In a first step, grooving insert test specimens were additively manufactured by LPBF from HS6-5-3-8 on a modified machine Aconity Midi at Fraunhofer Institute for Laser Technology (ILT). The cutting edges had a slight allowance for the downstream grinding process. Two different LPBF parameter settings were applied with focus on high density (Standard, relative density of 99.96 %) and high productivity (Productive, relative density of 99.87 %), see Fig. 1. As the inserts with a total height of 26 mm were built vertically, a slight increase of hardness between +3.2 % to +4.9 % could be detected between edge 1 close to the build plate and edge 2 in distance to the build plate. The hardness of the specimens built with the parameter setting Standard was around 24 % higher than for the parameter setting Productive. This can be explained by the longer exposure time of the laser per area and the resulting differences in heat generation and dissipation. As no heat-treatment was carried out, this difference in mechanical properties had to be considered for the machining experiments.

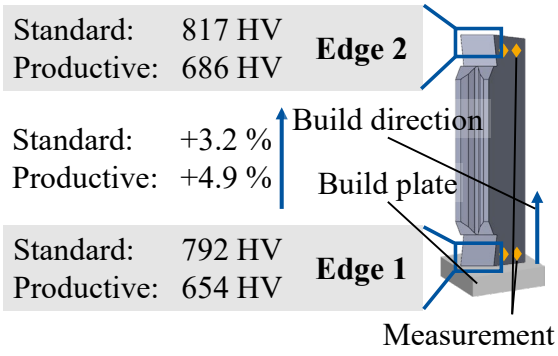

LPBF parameter settings

		Standard	Productive
Laser power	P_L / W	250	300
Scan speed	v_s / mm/s	940	1340
Hatch distance	Δy / µm	80	100
Layer thickness	D_s / µm	30	
Preheating	T / °C	350	

Fig. 1. Micro hardness measurement in dependency of build height and LPBF process parameters.

Both cutting edges of all inserts were then uniformly grinded by the company Meyer + Dörner Räumwerkzeuge GmbH. The cutting edges were measured on an optical microscope Algona Mikro CAD (cutting edge radius r_β) and a tactile contour measurement device MarSurf PCV (rake angle γ and clearance angle α). The mean values are given in Fig. 2, a. The tools were uncoated.

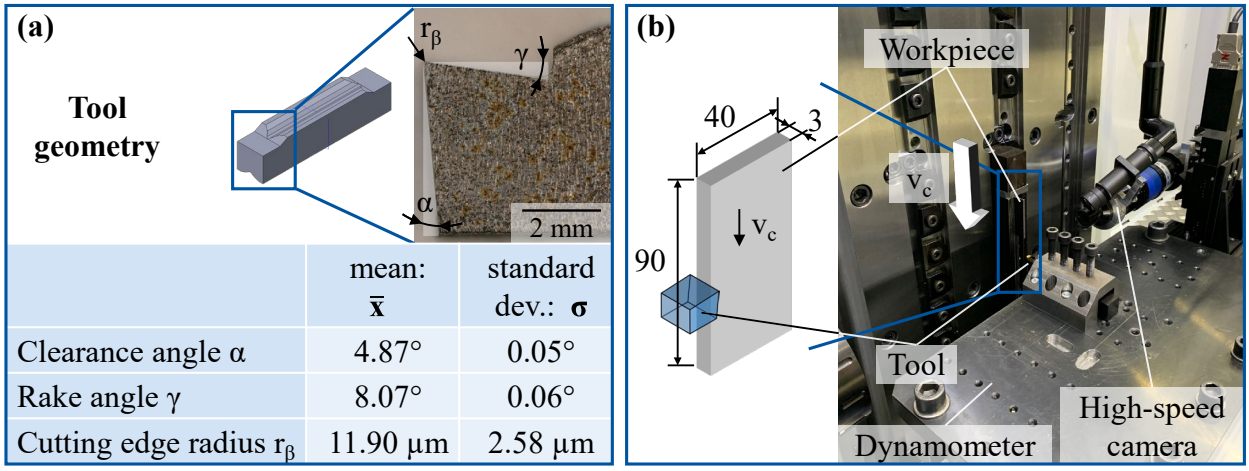

	mean: $\bar{x}$	standard dev.: σ
Clearance angle α	4.87°	0.05°
Rake angle γ	8.07°	0.06°
Cutting edge radius r_β	11.90 µm	2.58 µm

Fig. 2. Measured tool geometry over all investigated cutting edges (a) and experimental setup (b).

Experimental Setup

The experimental setup inside an external vertical broaching machine Forst RASX 2200x800x600 M / CNC is shown in Fig. 2, b. The tool holder was mounted on a dynamometer Kistler Z21289 on the machine table. The workpiece was clamped into the broaching stroke. The chip formation was captured with a high-speed camera Vision Research Phantom v7.3. In order to evaluate the performance behavior of the AM tools, chip formation, chip shape, cutting force and tool wear were investigated. Six different workpiece materials were analyzed with different cutting speed v_c and undeformed chip thickness h each. The cutting parameters are given in Table **1**. The applied materials were two steel alloys (X5CrNiMo17-12-2 (1.4401) and 42CrMo4+QT), one copper alloy (CuZn21Si3P (Ecobrass)), one cast iron (GJL 250) as well as two difficult-to-cut materials (Ti6Al4V (β-annealed) and Inconel 718).

Table 1. Cutting parameters for all investigated workpiece materials.

Workpiece material	v_c [m/min]	h [mm]
42CrMo4+QT	30	0.15
X5CrNiMo17-12-2 (1.4401)	30	0.15
CuZn21Si3P	60	0.2
GJL 250	60	0.2
Ti6Al4V	15	0.1
Inconel 718	5	0.05

For the evaluation of the force signal, cutting force F_c and cutting normal force F_{cN} (respective thrust force) were averaged within the range from 30 % to 70 % of the total signal of one cut (see Fig. 3). Each insert was only used for nine consecutive cuts within one workpiece material. Tool wear was analyzed by optical light microscopy and optical 3D measurement Alicona FocusG5.

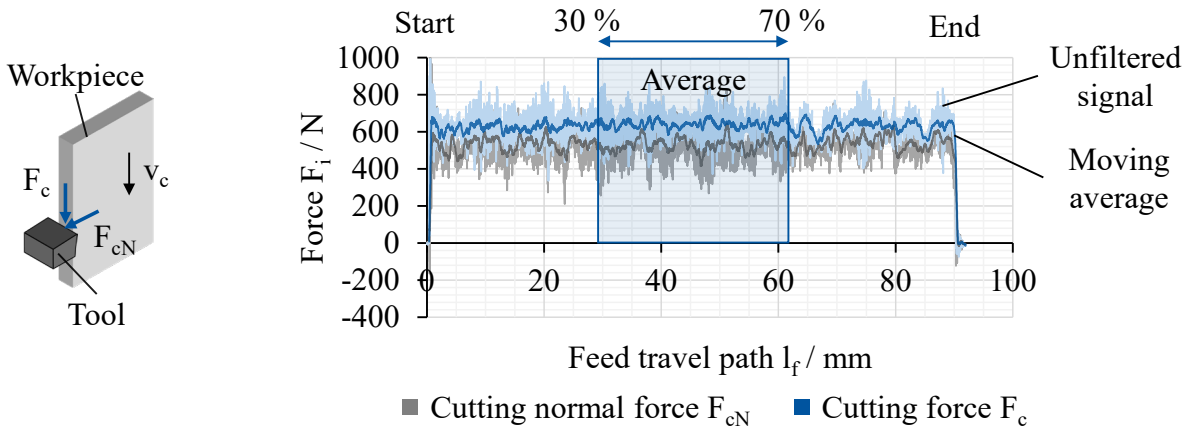

Fig. 3. Evaluation of force signal.

Results and Discussion

In the following section, different comparisons are made in order to evaluate influencing factors onto the tool performance within the scope of the experiments. Not all inserts were tested in each combination of edge number, LPBF parameter setting and workpiece material. A comparison between different materials is not useful as every material was machined with individual cutting parameters. The focus of the analysis was on the comparison between built height and LPBF parameter settings as well as on information regarding the performance behavior of the AM inserts in use with a wide range of different workpiece materials.

In Fig. 4 the influence of the build height (edge 1 and 2) onto the force development is shown for cutting of 42CrMo4 and Inconel 718 with inserts “Standard”. A significant change of the force amplitudes between cut no. 1 and no. 2 to 9 was observed for all experiments. This can be traced back to inaccuracies in the positioning of the machine table and thus the cutting edge relative to the workpiece surface for the first cut, leading to a slightly deviating undeformed chip thickness. For all following analyses, the mean value of cut 2 to 9 is taken into account. The growing mean forces F_c and F_{cN} can be explained by a changing cutting edge microgeometry and blunting of the cutting edge. For 42CrMo4, no significant change in the mean forces could be detected, whereas for hard-to-cut Inconel 718 the mean cutting force F_c was around 7 % lower for edge 2. The higher hardness in bigger distances to the build plate (see Fig. 1, edge 2) seems to increase the edges resistance to blunting. For the application in threading tools, which are also build up in vertical direction, the functional part should thus be positioned on the top relative to the build plate. As the force difference for Inconel 718 could be in the deviation range, further tests with a higher number of inserts should be conducted in the future.

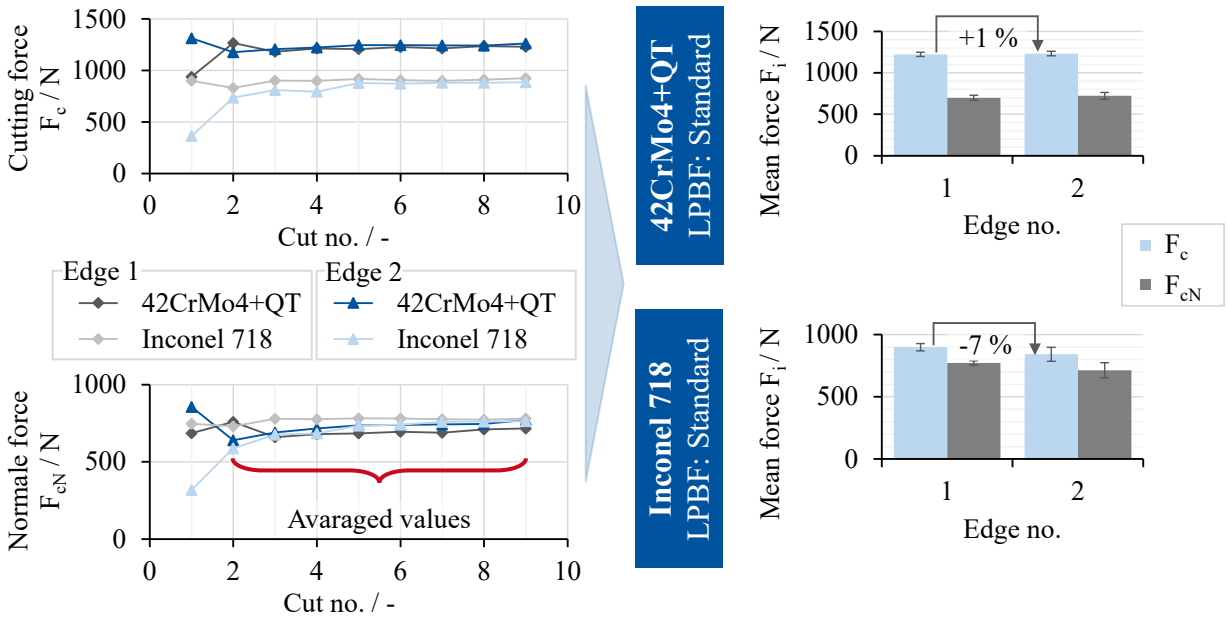

Fig. 4. Influence of build height onto force development (LPBF: Standard).

The LPBF parameter settings Standard and Productive did not influence the development and amplitude of the force signals for cutting of 42CrMo4 (Fig. 5). For cutting of Inconel 718, F_c and F_{cN} did grow along the number of cuts, with F_c being 11 % and F_{cN} 21 % higher for the insert produced with the productive LPBF parameters. The lower hardness of the productive parameters (see Fig. 1) led to a faster wear progression of the cutting edge in the hard-to-cut material even though forces for the standard parameters were comparable (F_{cN}) or lower (F_c).

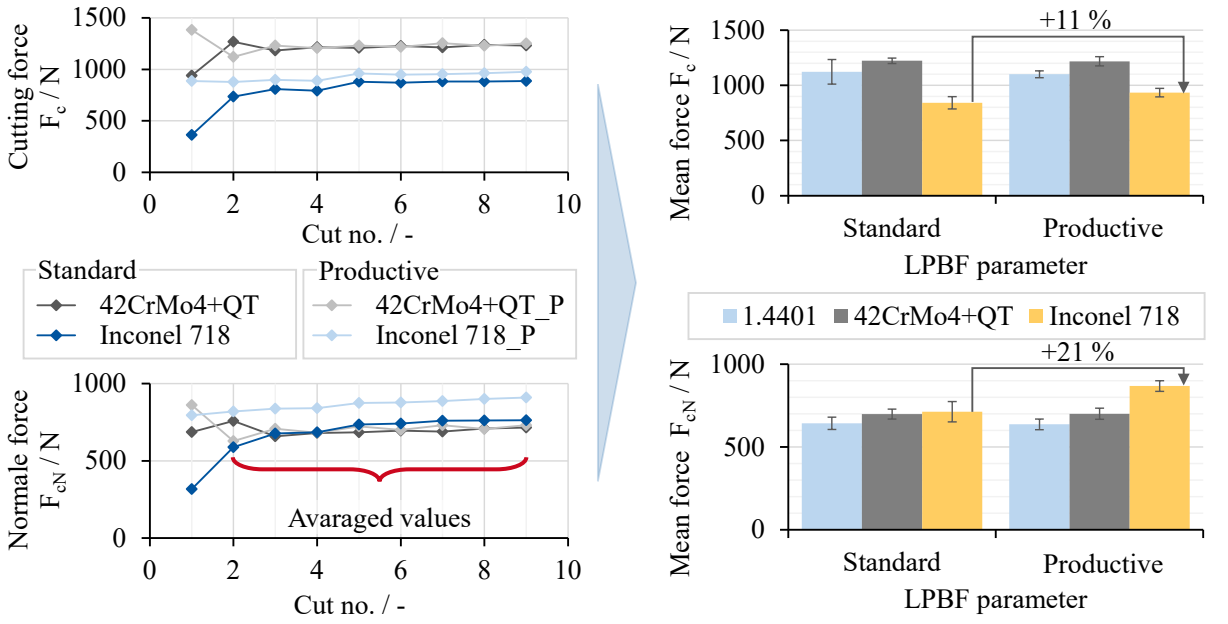

Fig. 5. Influence of LPBF parameter setting onto force development (1.4401: edge 1, 42CrMo4: edge 1, Inconel 718: edge 2).

A visual influence of the LPBF parameter setting and the build height on tool wear and cutting force progression for machining of 42CrMo4 could not be detected neither in the records of flank and rake face nor in the 3D scans, Fig. 6. A thermal influence, similar in size and shape and visible as an annealed rake face and flank face surface, was detected for all four inserts. The high thermal load can be explained by the high tensile strength of the quenched and tempered workpiece material. Chipping occurred on several inserts due to the high mechanical load and abrasive wear caused by the martensitic microstructure. The rising force amplitudes along the feed travel path l_f, which occurred during every cut, could not be explained by growing tool wear. The mean forces F_c and F_{cN} remained nearly constant along the number of cuts, see Fig. 4. A possible explanation might be the rising contact area between chip and rake face as visible in the high-speed video recording in Fig. 7 (42CrMo4+QT). Due to the rising chip up-curl radius, the contact length is constantly increasing, leading to more friction-induced force in and perpendicular to the direction of cut.

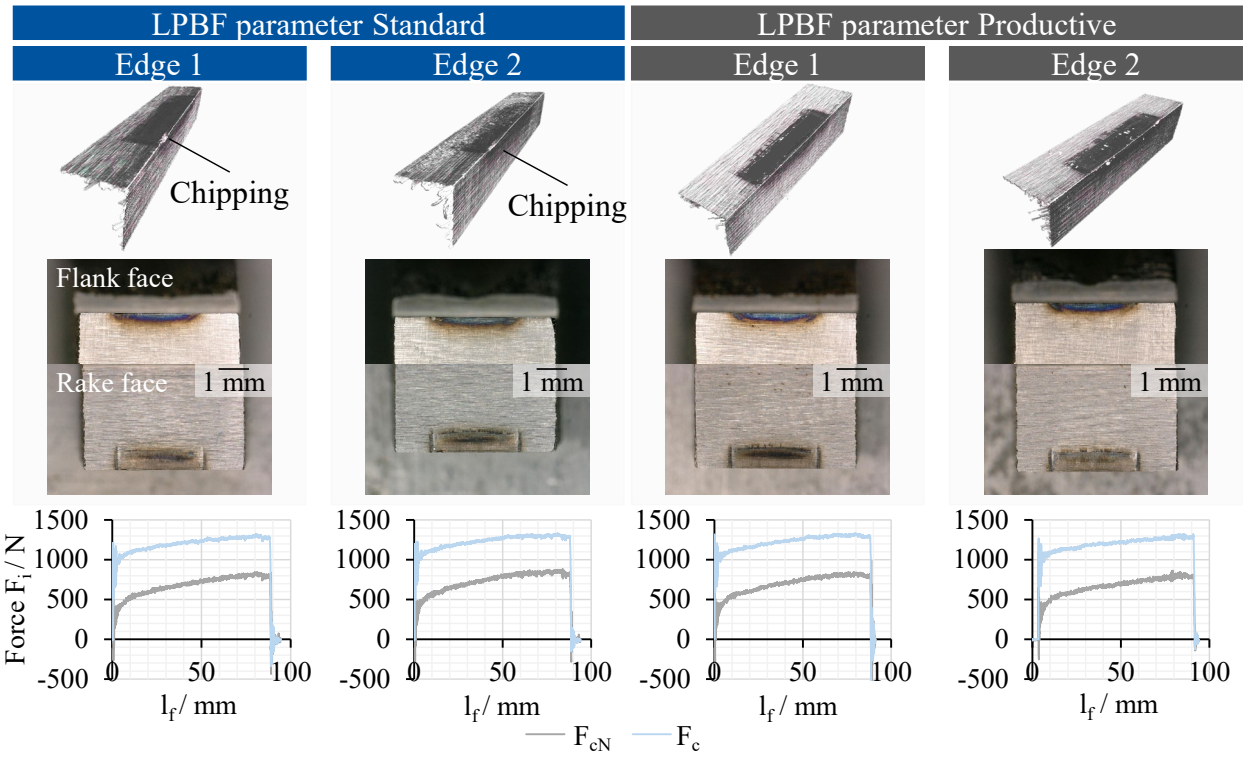

Fig. 6. Tool wear and force signal after nine consecutive cuts in 42CrMo4+QT.

Fig. 7 shows the chip formation captured by the high-speed camera as well as the resulting chip forms. 42CrMo4 exhibited a mainly continuous chip. In the first section of the chip, annealing colors were visible, indicating a high temperature evolution during cutting of the material. For 1.4401, mainly segmented chip formation occurred with material adhesions on the backside of the chip. CuZn21Si3P offered short, discontinuous chips due to the chipbreaking characteristics of the alloy elements. Cast iron GJL 250 with its brittle characteristics of the pearlite lamellae led to very short, dusty chips, whereas for Ti6Al4V a discontinuous lamellar chip formation was observed. Inconel 718 caused a thin, segmented chip with very regular chip up-curl radius.

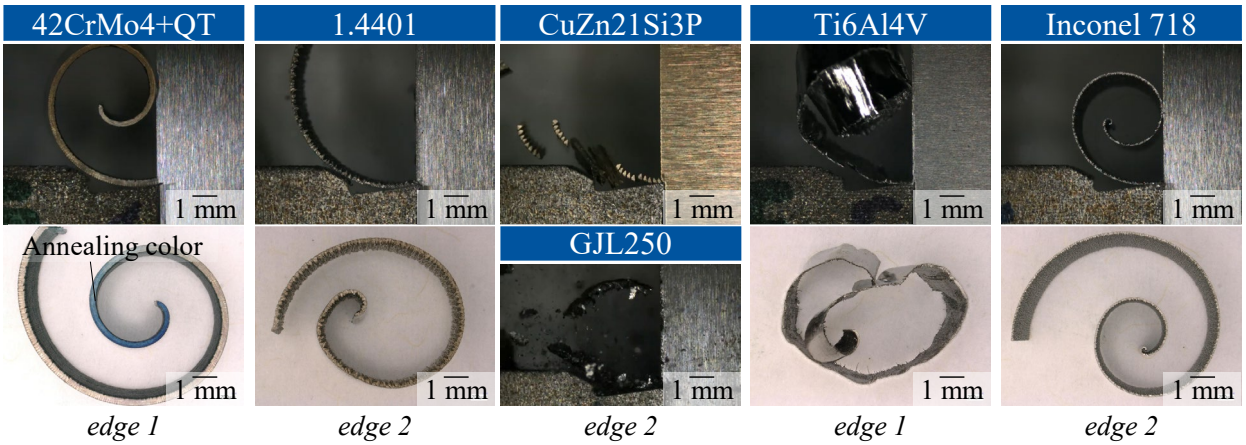

Fig. 7. Chip formation and chip form for all investigated materials (cut no. 3, LPBF: Standard).

As visible in Fig. 8, the forces F_c and F_{cN} did only grow significantly for hard-to-cut materials Inconel 718 and Ti6Al4V along the number of cuts. The cutting inserts seemed to withstand the mechanical load applied during the tool-workpiece-contact for all steel, cast and copper alloys.

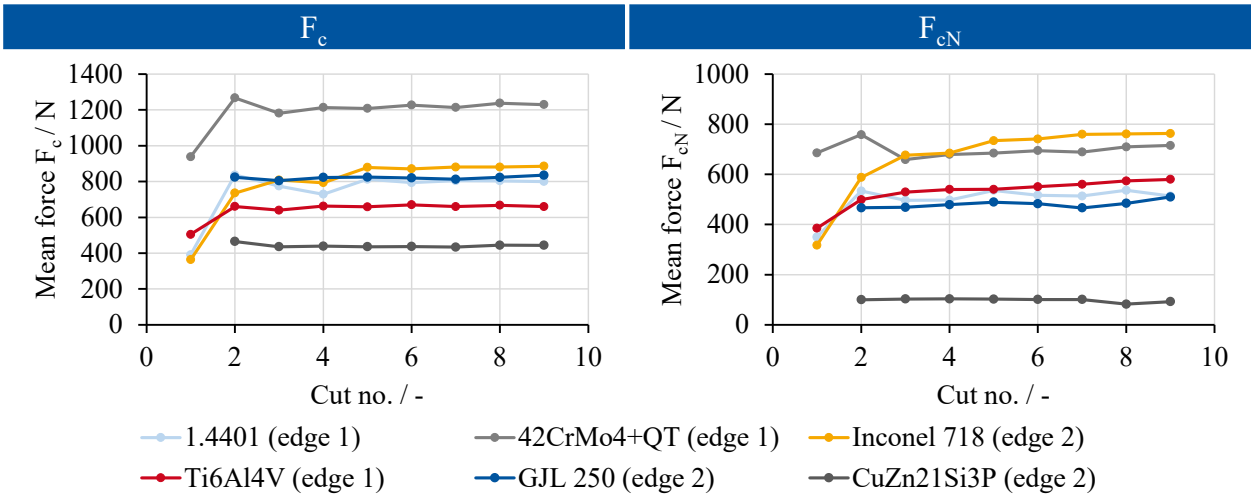

Fig. 8. Force growth along all number of cuts (LPBF: Standard).

The tool wear and force progression for all other materials is presented in Fig. 9. Adhering material could be detected on the rake face for cutting of 1.4401. The thermal load led to discolorations especially on the flank face for cutting of 1.4401 and Ti6Al4V caused by the low thermal conductivity of the materials. A relatively high flank wear was visible for Ti6Al4V and Inconel 718 due to high abrasive wear. The insert used for cutting of CuZn21Si3P appeared nearly unused after nine cuts, whereas strong material adhesions became visible on the flank and rake face for GJL 250. The continuous or discontinuous chip forms correlated with the force signal in terms of fluctuation. Especially for cutting of CuZn21Si3P and GJL 250, a high signal noise appeared in the force measurement, whereas for Inconel 718 nearly no fluctuations were detected.

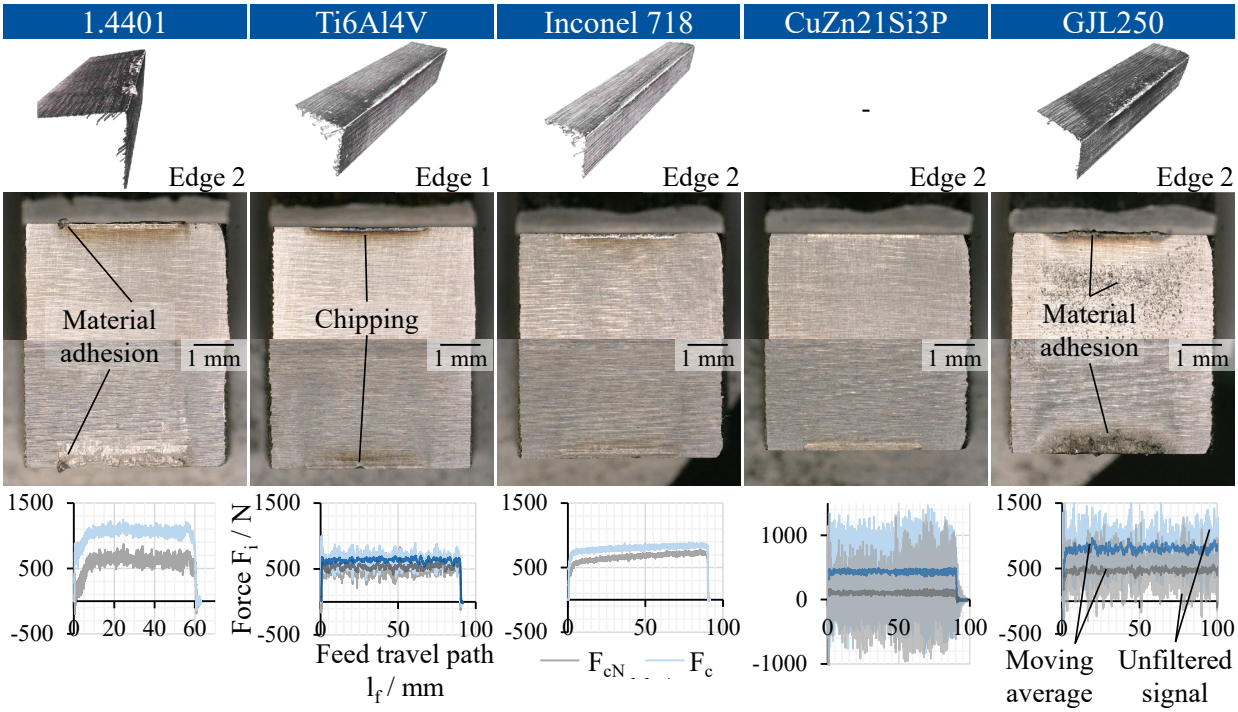

Fig. 9. Tool wear and force signal after nine consecutive cuts for different workpiece materials (LPBF: Standard).

Summary

All as-built, uncoated AM grooving inserts withstood the thermal and mechanical load during machining of the investigated materials within the scope of the experiments. The following findings were made:

- The hardness of the as-built test specimens varied along the distance to the build plate as well as between the two LPBF parameter settings with reduced hardness for small distances and productive LPBF parameters.
- The differences in the material properties of the cutting edge were negligible for machining of the steel alloys 42CrMo4+QT and 1.4401. An influence of the LPBF parameters and build height could be detected only during machining of Inconel 718 with a rising cutting force and cutting normal force over various cuts. The more productive LPBF parameter setting and a small distance to the build plate led to higher forces and faster tool wear development, respective faster tool wear rate of the cutting edge.
- For hard-to-cut materials Inconel 718 and Ti6Al4V, the cutting force rose over various cuts. Chipping phenomena appeared for cutting of Ti6Al4V, whereas high thermal loads resulting in discoloration on the tool flank and rake face, as well as on the chip surface occurred for cutting of 42CrMo4+QT. Adhesion phenomena on the rake face could be detected for alloyed steel 1.4401.

The findings show the capabilities of AM tools made from HS6-5-3-8 even in hard-to-cut materials. As only a limited amount of cuts was performed, tool wear development and thus tool life should be closer analyzed in future investigations, taking into account long-term phenomena. Based on these results, the use of coatings for the AM processed HSS substrate appears reasonable. Thus, thermal influences and material adhesion can be reduced. In future works, the influence of a heat treatment on microstructure and mechanical properties of the AM HSS will be analyzed and compared to conventionally manufactured HSS. In a next step, AM threading tools manufactured from HS6-5-3-8 will be investigated, using the geometrical freedom for an adapted channel and

outlet nozzle design of the internal cutting fluid supply, extending tool life and reducing scrap parts. Another possible application for additively processed HSS can be the manufacturing or repairing of AM broaching tools.

Acknowledgements
The IGF-research project 21581 N (Acronym: “AddBo”) of the Forschungsgemeinschaft Werkzeuge und Werkstoffe e.V. (FGW) is funded by the AiF within the program to promote joint industrial research (IGF) by the Federal Ministry for Economic Affairs and Climate Action (BMWK), following a decision of the German Bundestag. The LPBF manufactured parts within the research project were provided by the Fraunhofer Institute for Laser Technology (ILT) in Aachen, Germany with kind support from Tim Lücke. The authors would like to thank the companies Deutsche Edelstahlwerke Specialty Steel GmbH & Co. KG and Meyer + Dörner Räumwerkzeuge GmbH for their support within the project.

References
[1] T. Scherer, Beanspruchungs- und fertigungsgerechte Gestaltung additiv gefertigter Zerspanwerkzeuge, Dissertation, TU Darmstadt, Darmstadt, 2020.
[2] F.A.M. Vogel, S. Berger, E. Özkaya, D. Biermann, Vibration Suppression in Turning TiAl6V4 Using Additively Manufactured Tool Holders with Specially Structured, Particle Filled Hollow Elements, Procedia Manuf. 40 (2019) 32-37. https://doi.org/10.1016/j.promfg.2020.02.007
[3] T. Lakner, High-pressure cutting fluid supply in milling, Dissertation, RWTH Aachen University, Aachen, 2021.
[4] Dr. Mapal, K.G. Kress, Lasersintern erweitert Fertigungsmöglichkeiten von Präzisionswerkzeugen, Diamond Business, 2017.
[5] A.G. Urma Werkzeugfabrik, Serien-Drehwerkzeug mit innenliegenden Kanalstrukturen, Maschinenbau Schweiz No. 11 (2019) 14-15.
[6] T. Kulmala, Geringeeres Gewicht - höhere Leistung, 2019. Available: https://www.sandvik.coromant.com/de-de/mww/pages/t_cm390am.aspx. (accessed 20 July 2020).
[7] M. Padmakumar, Additive Manufacturing of Tungsten Carbide Hardmetal Parts by Selective Laser Melting (SLM), Selective Laser Sintering (SLS) and Binder Jet 3D Printing (BJ3DP) Techniques, Laser. Manuf. Mater. Process. 7 (2020) 338-371. https://doi.org/10.1007/s40516-020-00124-0
[8] B.D. Kernan, E.M. Sachs, M.A. Oliveira, M.J. Cima, Three-dimensional printing of tungsten carbide-10wt% cobalt using a cobalt oxide precursor, Int. J. Refract. Metal. Hard Mater. 25 (2007) 82-94. https://doi.org/10.1016/j.ijrmhm.2006.02.002
[9] T. Schwanekamp, Pulverbettbasiertes Laserstrahlschmelzen von Hartmetallen zur additiven Herstellung von Zerspanwerkzeugen, Dissertation, Ruhr-Universität Bochum, 2021. https://doi.org/10.13154/294-7802
[10] M. Weigold, T. Scherer, E. Schmidt, M. Schwentenwein, T. Prochaska, Additive Fertigung keramischer Schneidstoffe, wt Werkstattstechnik online 110 (2020) 2-6.
[11] J. Saewe, C. Gayer, A. Vogelpoth, J.H. Schleifenbaum, Feasability Investigation for Laser Powder Bed Fusion of High-Speed Steel AISI M50 with Base Preheating System, BHM Berg- und Hüttenmännische Monatshefte 164 (2019) 101-107. https://doi.org/10.1007/s00501-019-0828-y
[12] F. Klocke, Manufacturing Processes 1: Cutting, Springer, Berlin, Heidelberg, 2011.
[13] Wohlers Associates, Wohlers Report 2022: 3D printing and additive manufacturing global state of the industry, Wohlers Associates, Fort Collins (Colorado), 2022.
[14] K. Kempen, B. Vrancken, S. Buls, L. Thijs, J. van Humbeeck, J.-P. Kruth, Selective Laser Melting of Crack-Free High Density M2 High Speed Steel Parts by Baseplate Preheating, J. Manuf. Sci. Eng. 136 (2014). https://doi.org/10.1115/1.4028513

[15] L. Zumofen, C. Beck, A. Kirchheim, H.-J. Dennig, Quality Related Effects of the Preheating Temperature on Laser Melted High Carbon Content Steels, Industrializing Additive Manufacturing - Proceedings of Additive Manufacturing in Products and Applications - AMPA2017 (2018) pp. 210-219. https://doi.org/10.1007/978-3-319-66866-6_21

Materials Research Proceedings 28 (2023) 1245-1253 https://doi.org/10.21741/9781644902479-135

Machining of PAM green Y-TZP: Influence of build and in-plane directions on cutting forces and surface topography

SPITAELS Laurent[1,a *], RIVIÈRE-LORPHÈVRE Edouard[1,b]
MARTIC Grégory[2,c], JUSTE Enrique[2,d] and DUCOBU François[1,c]

[1] Machine Design and Production Engineering Lab - Research Institute for Science and Material Engineering - University of Mons, Place du Parc 20, Mons, Belgium

[2] Belgian Ceramic Research Centre, Avenue Gouverneur Cornez 4, Mons, Belgium

[a] laurent.spitaels@umons.ac.be, [b] edouard.rivierelorphevre@umons.ac.be, [c] g.martic@bcrc.be, [d] e.juste@bcrc.be, [e] francois.ducobu@umons.ac.be

Keywords: Green Ceramics, Pellet Additive Manufacturing, Milling, Surface Topography, Hybrid Manufacturing

Abstract. The combination of the pellet additive manufacturing (PAM) process and green ceramic machining within the same hybrid machine is a very promising route to obtain green ceramic parts with complex shapes, smooth surface topography and tight tolerances. However, there is still a lack of data due to the novelty of this manufacturing route. This article studies the possible influence of the build and in-plane directions on the cutting forces and surface topography during the milling of Y-TZP green ceramic parts obtained by the PAM process. The RMS cutting forces, arithmetic and total roughness (Ra and Rt, respectively) were measured. The in-plane direction (aligned with one of the horizontal part edges) did not have a significant influence neither on the cutting forces nor on the surface topography. Conversely, the build direction has a significant effect on the cutting forces recorded. The layers deposited the furthest from the build platform required 57.5% less force to be milled than those in contact with it. The surface topography was not significantly modified across the build direction, all values of Ra were within the 0.8 μm Ra class while all Rt values were < 5 μm.

Introduction

Context. Advanced ceramic materials (such as zirconia) are essential for a large set of sectors thanks to their properties (very high melting point and hardness, chemical inertness, *etc.*) [1,2]. However, the conventional manufacturing routes for ceramics are limited to relatively simple designs and require finishing operations (machining, polishing, grinding or lapping) which can represent up to 80% of the total manufacturing costs [2]. Indeed, these operations are usually performed on the fully sintered part which has the final properties of the material.

On the one hand, green ceramic machining has demonstrated its potential to ease the finishing of the part while reducing the costs and risk to generate macro defects as cracks [3,4]. On the other hand, additive manufacturing (AM) processes open new possibilities to generate near net shape parts with complex design while enabling the production of small or unique part in an economical way [5,6].

Material extrusion process, one of the seven AM processes defined in ISO 52900 standard, is feeding great hopes in a ten year horizon [7]. Indeed, it allows the generation of parts made of metal or ceramics at low cost [8]. Moreover, its variant relying on pellets and screw extrusion, Pellet Additive Manufacturing (PAM) can be fed with feedstock developed for the Ceramic Injection Molding (CIM) or Metal Injection Molding (MIM) industry to shape green parts with complex design. Though, the surfaces generated by the PAM process still suffer from the staircase effect and exhibits high arithmetic roughness (Ra ranging from 9 μm to 40 μm) impacting their

Content from this work may be used under the terms of the Creative Commons Attribution 3.0 license. Any further distribution of this work must maintain attribution to the author(s) and the title of the work, journal citation and DOI. Published under license by Materials Research Forum LLC.

fatigue resistance and tribological properties [9-11]. Finishing these parts is then required before foreseeing their usage for demanding applications such as contact (requiring Ra < 1.6 µm, *e.g.*). Nonetheless, even if green ceramic machining can be very attractive thanks to its advantages, it is still limited to simple designs. Lattice, internal surfaces and channels, which can be required in the freeform designs of biomedical implants, are then impossible to finish by machining operations [4,12].

The combination of the green ceramic machining and PAM process inside the same hybrid machine can overcome the disadvantages of both processes [4,13]. Indeed, the subtractive and additive processes can be successively executed so that the milling tool can reach the surfaces to machine when they are still accessible, while the PAM process can ensure an enhanced freedom of design. Hybrid machines are already commercialized, but they are all relying on AM processes which directly produce a fully dense part as Selective Laser Sintering (SLS) or Direct Energy Deposition (DED) [4,13]. As a result, the machining is carried out in fully dense state and leads to higher cutting stresses, wear of the tool and lower material removal rates, making this technology expensive. Developing a machine able to obtain green parts and to machine them at the green state is then an elegant solution to reduce costs, while ensuring new design possibilities for difficult materials such as ceramics. However, except for highly used alloys (Ti6Al4V, *e.g.*), only few data are available for the machining of additively manufactured materials [12].

Goal and motivation of the study. This study aims to determine if the build or in-plane directions within a zirconia green part obtained by the PAM process can have a non-negligible influence on the cutting forces and surface topography generated during finishing operation performed with milling.

Material and Method

Part geometry and printing. The geometry of the part consists of a cube (side of 20 mm) on top of a cylinder (diameter of 15 mm and height of 15 mm). Both are linked using a 3 mm fillet radius. The milling operations are performed on the cube while the cylinder surface is used for the part fixture. Fig. 1 gives the geometry of the part as well as the reference frame (located at one of the part top corners) which was used for the experiments and the build direction selected for the part printing. The X and Y axes are aligned with two horizontal edges of the cube, while the Z axis is aligned with a vertical edge (Z axis is the inverse of the build direction as shown in Fig. 1).

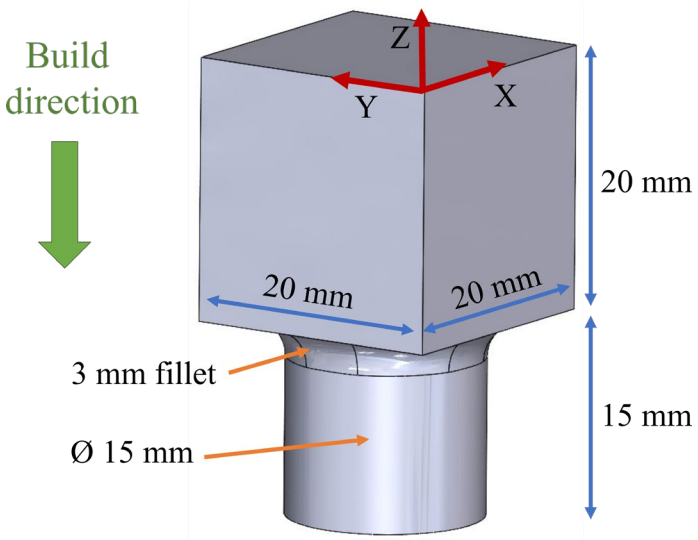

Fig. 1. Part geometry and reference frame.

The part was printed using a Pollen AM Series MC PAM printer by setting the build direction across the part Z axis (see Fig. 1). K2015 pellets from Inmatec were used as feedstock. They are composed of 15wt% polyamide and 85wt% zirconium oxide. The cube is first printed, followed by the cylinder to avoid the need of support structure. The nozzle diameter and layer thickness selected were of 1 mm and 0.35 mm, respectively. These parameters allowed to have a printing time of 25 minutes for the part.

Part machining. A three-jaw chuck was used to clamp the part and the milling operations were conducted with a Stäubli TX200 fitted with a Teknomotor ATC71 electrospindle (maximal power and speed of 7.8 kW and 24000 rpm, respectively). The milling tool used for the operation is supplied by Hoffmann (reference 209425-6, 6 mm diameter, 3 teeth, maximal depth of cut of 19 mm). The cutting conditions were chosen to comply with finishing operations of AM parts. As a result, the axial depth of cut (a_p) was set at 3 mm while the radial depth of cut (a_e) chosen was 0.5 mm. According to a preliminary study, the cutting speed and feed rate were of 339 m/min and 1458 mm/min, respectively.

As depicted in Fig. 2, the part was divided into six zones (each of 3 mm thick) across the build direction (Z axis) and six other zones (each of 3 mm wide) across its in-plane direction (Y axis). Each zone of the in-plane direction corresponds to six different passes. All passes were machined along the part X axis. In total, 216 passes were performed totalizing about 3 minutes of cut within the material.

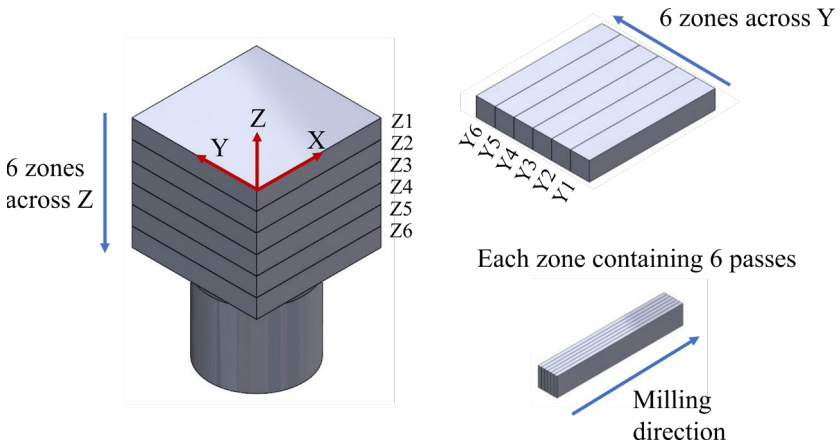

Fig. 2. Zones considered for the milling operations.

Cutting forces and surface topography evaluation. The cutting forces were recorded using a Kistler 9256C2 force sensor coupled with a Kistler charge amplifier 5070A. The DynoWare software executed on a computer as well as a Kistler 5697A2 data acquisition system sampling data at 5 kHz complete the acquisition chain. The reference frame of the cutting sensor is not the same as the frame of the part. Consequently, the total value (Eq. 1) of the X, Y and Z cutting forces components was considered. Fig. 3 gives an example of the total cutting forces signal for three passes of the tests. Finally, the RMS value of the total cutting forces was computed for each pass to have a value representing each pass. These RMS values were then averaged over the six passes contained in each defined zone.

$$F_{tot} = \sqrt{\frac{1}{3} \cdot (F_x^2 + F_y^2 + F_z^2)} \quad (1)$$

Materials Research Proceedings 28 (2023) 1245-1253 https://doi.org/10.21741/9781644902479-135

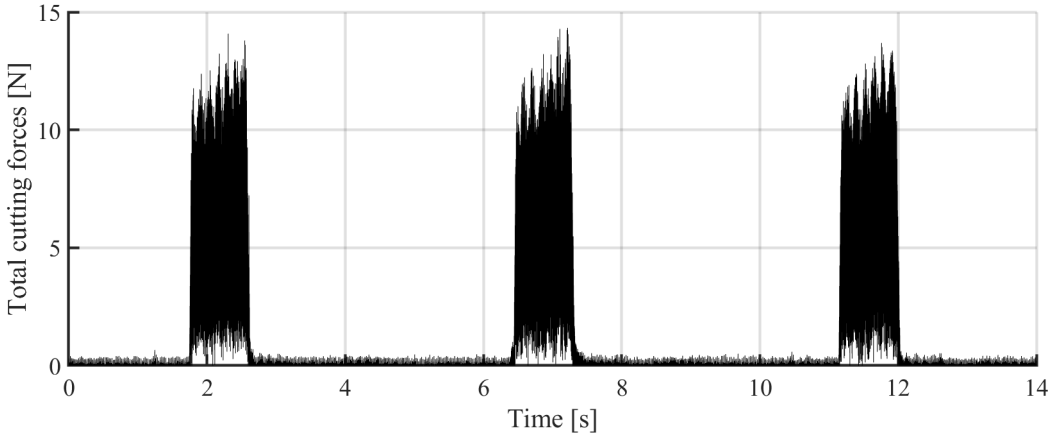

Fig. 3. Example of total cutting forces signal for three passes of the tests.

The surface topography was analyzed qualitatively using a Dino-Lite digital microscope AM7013MZT with DinoCapture software (monitoring of the generation of material pull-out and the existence of porosities inside the parts) and quantitatively with a Diavite DH6 roughness measuring instrument (measurements of Ra and Rt). The evaluation and cut-off lengths (4.8 mm and 0.8 mm, respectively) were selected according to the ISO 4288 standard. The surface topography was evaluated every three passes on the vertical surface generated by side-milling and following the X axis direction.

Results and Discussion

Cutting forces analysis. The cutting forces across the Y and Z zones of the part are depicted in Fig. 4 and 5, respectively. Each graph is given with error bars corresponding to ± σ.

As it can be seen in Fig. 4, the RMS total cutting forces remain stable across the different Y zones with an average of 3.97 N. However, the relative standard deviation ranges between about 29.7% and 38.5%, which is very high. Every bar on the graph represents a total of 6 different tests of 6 passes at different Z heights for a given Y zone. Consequently, the build direction (Z axis) has a non-negligible effect on the cutting forces because of the large standard deviations recorded between the measurement of a given Y zone. Conversely, the in-plane direction (Y axis) does not influence the results since the mean value across the different Y zones is nearly constant.

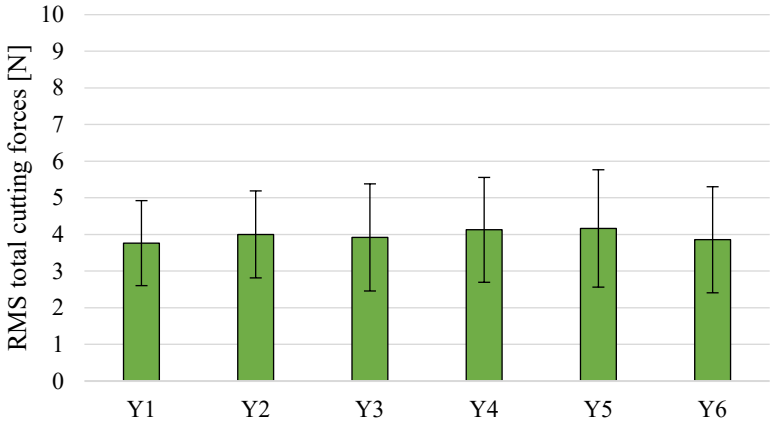

Fig. 4. RMS total cutting forces across the Y zones.

Materials Research Proceedings 28 (2023) 1245-1253 https://doi.org/10.21741/9781644902479-135

The same conclusions can be retrieved from Fig. 5. Indeed, the graph shows a global decreasing trend across the different Z zones. The maximal value is 6.35 N while the minimal value stands at 2.70 N. The cutting forces in the Z6 zone are 57.5% lower than in the Z1 zone.

This confirms the influence of the build direction (Z axis) on the cutting forces. Moreover, it shows that the zones of the part in contact with the build platform of the printer need more force to be cut than those further away. Indeed, Z1 zone corresponds to the first layers deposited on the build platform while Z6 zone is related to the layers near the cylindric part. This difference of cutting forces may originate from the different thermal history applied to the layers in contact with the build platform in comparison with the higher layers. The deposited layers can then exhibit different properties in terms of mechanical properties (micro-hardness, for example). At the knowledge of the authors, no study in literature mentioned this influence for green ceramics parts obtained neither by the PAM process, nor by other AM processes.

Conversely, the average relative standard deviation is stable through all Z zones with values between 9.5% and 13.6%. This confirms that in-plane direction (Y axis) does not influence much the cutting forces. This decreasing tendency is not asymptotical and, since the Z6 zone is near the cylindric part of the part, this change of section and geometry may have an influence on the required cutting forces because of stresses distribution.

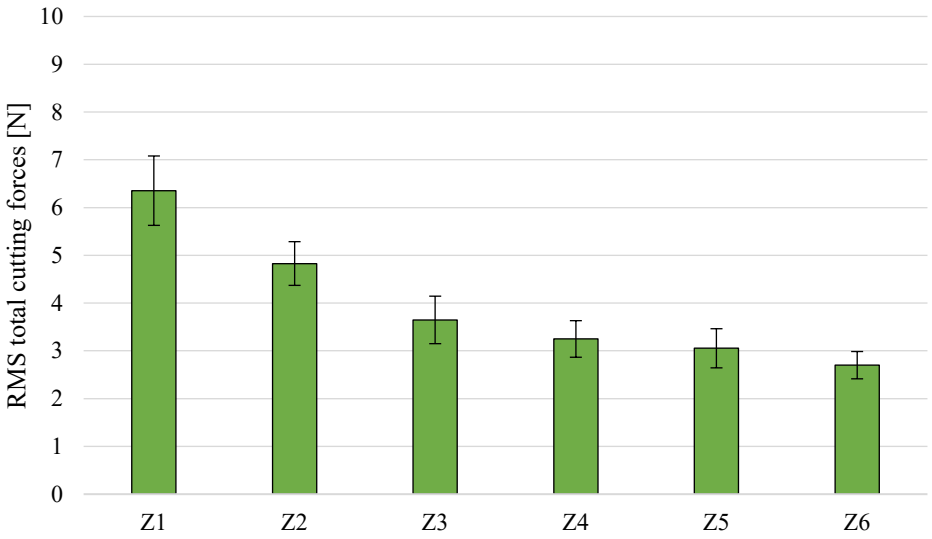

Fig. 5. RMS total cutting across the Z zones.

Surface topography quantitative analysis. Fig. 6 and 7 show the arithmetic roughness evolution across the Y and Z zones of the part. Each graph was given ± σ error bars as well as two red horizontal bars showing the boundaries of the 0.8 µm Ra class, to which the results belong.

As shown in Fig. 6, the Ra results across the Y zones were all within the 0.8 µm Ra class. The values ranged from 0.45 µm to 0.49 µm with a relative standard deviation between 8.5% and 13.4%. Each bar represents the average Ra measured for 6 different tests of 6 passes realized at six different Z positions. Consequently, it shows that neither the in-plane direction (Y axis), nor the build direction (Z axis) significantly influence the arithmetic roughness results.

Materials Research Proceedings 28 (2023) 1245-1253 https://doi.org/10.21741/9781644902479-135

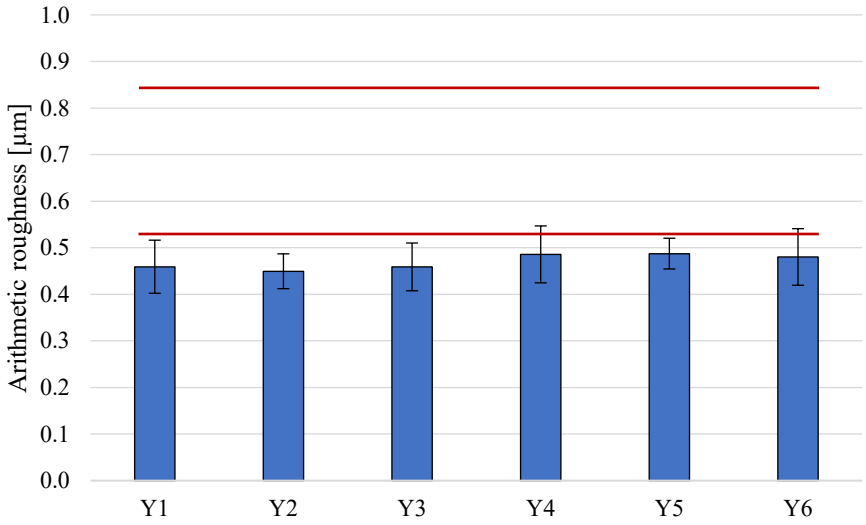

Fig. 6. Arithmetic roughness evolution across the Y zones.

This is also confirmed in Fig. 7 with Ra results across the Z zones between 0.45 µm and 0.49 µm and a relative standard deviation representing from 6.3% to 15.0% of the mean value. This confirms the non-influence of the in-plane and build directions on the arithmetic roughness results. Both graphs also demonstrate the adequacy of cutting parameters to generate a smooth surface topography. Indeed, every pass generates a Ra lower than 1.6 µm with results in the 0.8 µm Ra class. The relatively low standard deviation shows that results are repeatable.

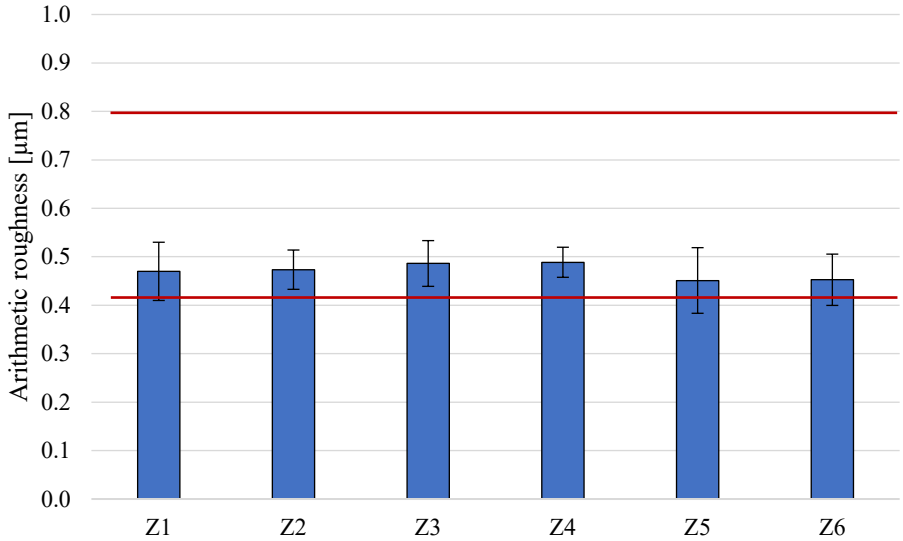

Fig. 7. Arithmetic roughness evolution across the Z zones.

Fig. 8 and 9 give the total roughness measurements obtained across the Y and Z part zones, respectively. Again, each bar of the graph was given a ± σ error bar.

As depicted in Fig. 8, the Rt results across the Y zones were between 2.76 µm and 3.54 µm. The relative standard deviation ranged between 8.6% and 16.6%, except for the Y4 zone where it reached 22.6%. The Y4 zone corresponds to the center of the part and exhibited higher results of Rt compared to the other zones (about 20% higher on average). Some porosities were detected at the center of the part and may influence slightly the Rt measurements.

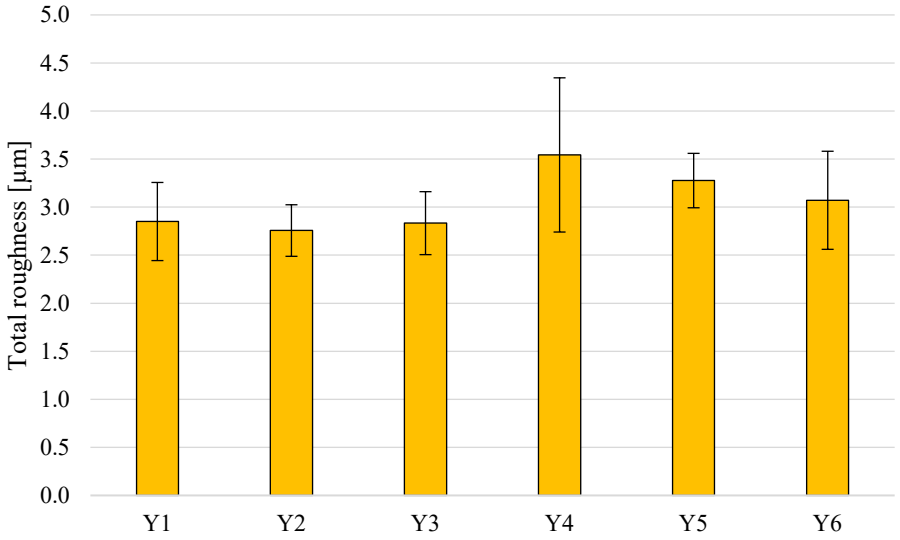

Fig. 8. Total roughness evolution across the Y zones.

By following the build direction (Z axis), the Rt results were between 2.88 µm and 3.30 µm while the relative standard deviation ranged from 7.8% to 19% (see Fig. 9). Even if the mean value varies, all the results are of the same order of magnitude (< 5 µm). Consequently, neither the in-plane nor the build direction (Y axis and Z axis, respectively) influence the total roughness.

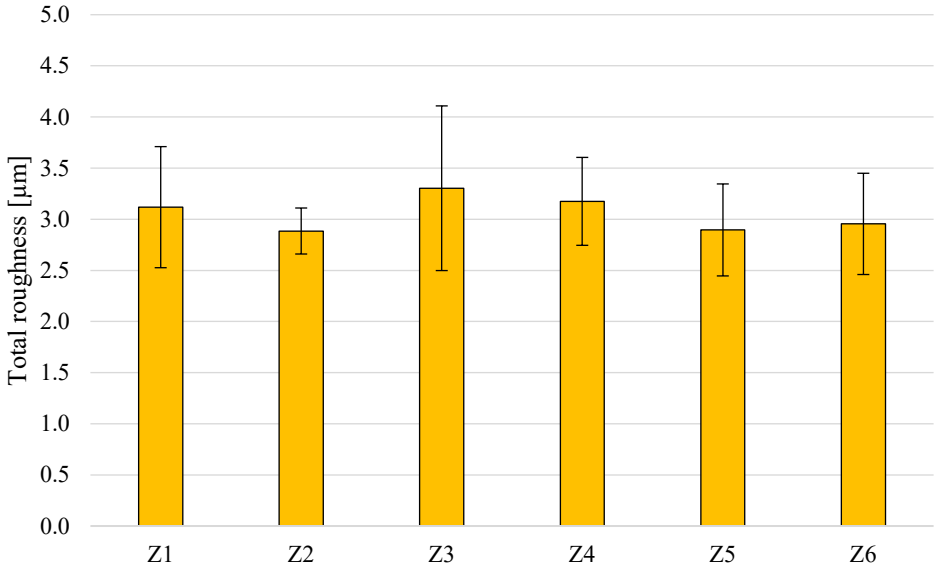

Fig. 9. Total roughness evolution across the Z zones.

Surface topography qualitative analysis. Fig. 10 shows the typical surface topography generated by the milling operation (bottom) compared to the as-built part (top). The bottom part of the picture corresponds to the zones Y1 and Z4. The surface topography obtained after milling is shiny and very smooth.

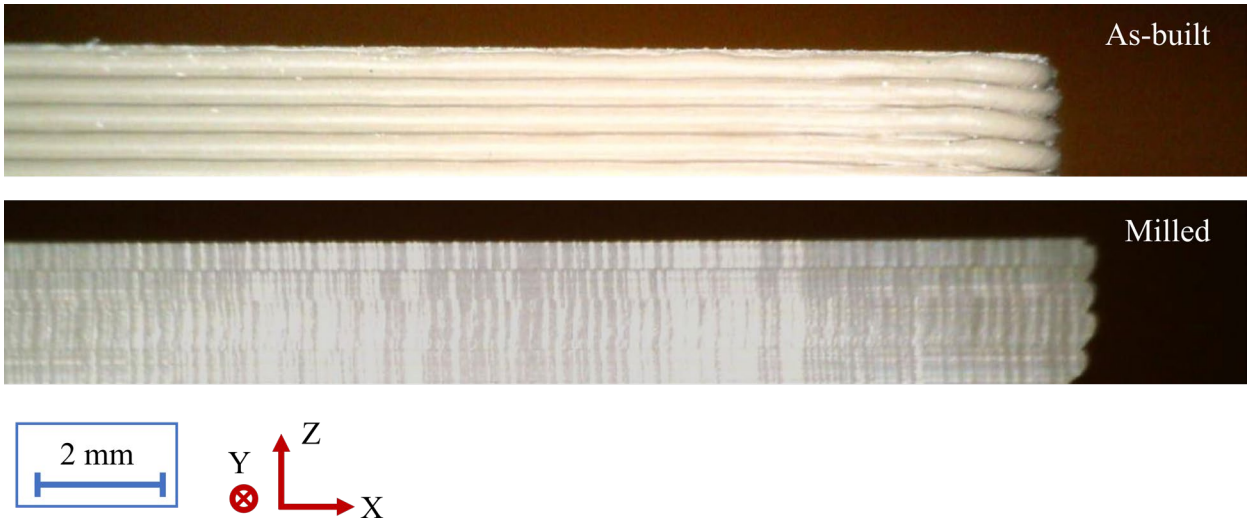

Fig. 10. As-built surface (top) and milled surface of zones Y1 and Z4 (bottom).

Summary

Conclusion. The main findings of this study are:

- The build direction of the part (Z axis) has a significant influence on the cutting forces required to carry out the milling operations. The nearest from the build platform, the higher the cutting forces. When the milling is performed further from the build platform, the cutting forces decrease (up to 57.5% in this study). The experiments do not allow to foresee if this decreasing tendency is asymptotical. The geometry change occurring in Z6 zone (last cubic zone before the transition to the cylindric part) may have an influence on the cutting forces. The in-plane direction (Y axis) does not have a significant influence on the cutting forces.
- From a qualitative point of view, the surface topography generated by the milling operations is smooth and light reflective.
- The arithmetic and total roughness are neither influenced by the build direction (Z axis), nor by the in-plane direction (Y axis) across the part. Indeed, all Ra results belonged to the 0.8 µm Ra class with a maximal relative standard deviation of 15%. So do the Rt results with all values in the same order of magnitude (< 5 µm) with a maximal standard deviation of 22.6%. The center of the part (Y4 zone) exhibited 20% higher Rt results than in the other zones. This may originate from the existence of porosities inside the part.

Perspectives. These are the main perspectives of the work:

- The cutting forces decreasing tendency across the build direction when moving away from the build platform can be further studied. The use of a different part designs with only one geometrical shape (a cube with higher dimensions, *e.g.*) will allow to determine if the cutting forces reach a plateau after a dedicated number of layers deposited. Moreover, micro hardness measurements as well as thermal monitoring can help understanding what physically causes this tendency.
- The influence of the transition between geometrical features (the cube and the cylinder of the part design presented) on the cutting forces can be further investigated by using a different part design.

Acknowledgements
The Wallonian regional government funded this research thanks to a Win²Wal funding instrument (HyProPAM research project, grant number: 2110084). The authors are grateful to the Belgium Ceramic Research Centre (BCRC) for the usage of their Pollen AM Series MC printer and especially to Julien Bossu (UMONS) who printed the part.

References
[1] D. Galusek, K. Ghillányová, Ceramic Oxides, in: R. Riedel, I.-W. Chen (Eds.), Ceramics Science and Technology, Wiley-VCH Verlag GmbH & Co., Weinheim, Germany, 2014, pp. 1-58. https://doi.org/10.1002/9783527631940.ch13
[2] E. Ferraris, J. Vleugels, Y. Guo, D. Bourell, J.P. Kruth, B. Lauwers, Shaping of engineering ceramics by electro, chemical and physical processes, CIRP Ann. 65 (2016) 761-784. https://doi.org/10.1016/j.cirp.2016.06.001
[3] A. Demarbaix, M. Mulliez, E. Rivière-Lorphèvre, L. Spitaels, C. Duterte, N. Preux, F. Petit, F. Ducobu, Green Ceramic Machining: Determination of the Recommended Feed Rate for Y-TZP Milling, J Compos. Sci. 5 (2021) 231. https://doi.org/10.3390/jcs5090231
[4] P. Parenti, S. Cataldo, A. Grigis, M. Covelli, M. Annoni, Implementation of hybrid additive manufacturing based on extrusion of feedstock and milling, Procedia Manuf. 34 (2019) 738-746. https://doi.org/10.1016/j.promfg.2019.06.230
[5] M.K. Thompson, G. Moroni, T. Vaneker, G. Fadel, R.I. Campbell, I. Gibson, A. Bernard, J. Schulz, P. Graf, B. Ahuja, F. Martina, Design for Additive Manufacturing: Trends, opportunities, considerations, and constraints, CIRP Ann. 65 (2016) 737-760. https://doi.org/10.1016/j.cirp.2016.05.004
[6] J. Gonzalez-Gutierrez, S. Cano, S. Schuschnigg, C. Kukla, J. Sapkota, C. Holzer, Additive manufacturing of metallic and ceramic components by the material extrusion of highly-filled polymers: A review and future perspectives, Materials 11 (2018) 840. https://doi.org/10.3390/ma11050840
[7] Smartech Analysis, Ceramics Additive Manufacturing Markets 2017-2028, an opportunity analysis and ten-year market forecast, 2018. https://www.smartechanalysis.com/reports/ceramics-additive-manufacturing-markets-2017-2028/
[8] S.C. Altıparmak, V.A. Yardley, Z. Shi, J. Lin, Extrusion-based additive manufacturing technologies: State of the art and future perspectives, J. Manuf. Processes 83 (2022) 607-636. https://doi.org/10.1016/j.jmapro.2022.09.032
[9] M.A. Krolikowski, M.B. Krawczyk, Does Metal Additive Manufacturing in Industry 4.0 Reinforce the Role of Substractive Machining, in: J. Trojanowska, O. Ciszak, J.M. Machado, I. Pavlenko (Eds.), Advances in Manufacturing II, Springer International Publishing, Cham, 2019, pp. 150-64. https://doi.org/10.1007/978-3-030-18715-6_13
[10] B.N. Turner, S.A. Gold, A review of melt extrusion additive manufacturing processes: II. Materials, dimensional accuracy, and surface roughness, Rapid Prototyp. J. 21 (2015) 250-261. https://doi.org/10.1108/RPJ-02-2013-0017
[11] W. Hung, Post-Processing of Additively Manufactured Metal Parts, in: D.L. Bourell, W. Frazier, H. Kuhn, M. Seifi (Eds.), Additive Manufacturing Processes, ASM International, 2020, pp. 298-315 https://doi.org/10.31399/asm.hb.v24.a0006570
[12] N. Uçak, A. Çiçek, K. Aslantas, Machinability of 3D printed metallic materials fabricated by selective laser melting and electron beam melting: A review, J. Manuf. Process. 80 (2022) 414-457. https://doi.org/10.1016/j.jmapro.2022.06.023
[13] J.M. Flynn, A. Shokrani, S.T. Newman, V. Dhokia, Hybrid additive and subtractive machine tools - Research and industrial developments, Int. J. Mach. Tool. Manuf. 101 (2016) 79-101. https://doi.org/10.1016/j.ijmachtools.2015.11.007

Materials Research Proceedings 28 (2023) 1255-1264 https://doi.org/10.21741/9781644902479-136

Analysis of Ti-6Al-4V micro-milling resulting surface roughness for osteointegration enhancement

CAPPELLINI Cristian[1,a *], MALANDRUCCOLO Alessio[1,b], KIEM Sonja [1,c] and ABENI Andrea[2,d]

[1]University of Bergamo,Via Pasubio 7/b, 24044, Dalmine, Bergamo, Italy

[2]University of Brescia, Via Branze 38, 25123, Brescia, Italy

[a]cristian.cappellini@unibg.it, [b]alessio.malandruccolo@unibz.it, [c]sonja.kiem@natec.unibz.it, [d]andrea.abeni@unibs.it

Keywords: Ti-6Al-4V, Osseointegration, Roughness, Micro-Milling, Additive Manufacturing

Abstract. In the last period, the demand of prostheses has massively increased. To guarantee their reliability, properties of durability, biocompatibility, and osseointegration results to be mandatory. Possessing these attributes, Ti-6Al-4V alloy represents the most employed material for implants realization, and because of its microstructure, it can be manufactured by different processing methods, i.e., machining, and additive manufacturing. Considering the necessity of patient-tailored implants, and the capability of additive manufacturing to produce single batch, and complex shapes, at relatively low cost and short time, this latter represents a rewarding process. Compared to biocompatibility, that is mainly function of material chemistry, durability and osteointegration concern mostly surface roughness that affects cells growth at bone-prosthesis interface. After additive manufacturing process and prior to be inserted in the human body, a prosthetic implant is finished by machining operations, hence, the attainment of an appropriate resulting surface roughness is crucial for obtaining a successful implant. Thus, roughness forecasting capability, as a function of the employed finishing process, permits its optimization, avoiding expensive scraps. For this reason, this paper deals with the development of predictive models of surface roughness when micro-milling Ti-6Al-4V alloy specimens.

Introduction

Considering the substitution predictions of actually world-widespread prosthetic implants, such as orthopaedical and dental ones, that are estimated around 3 billion by 2030, they are requested to endure in the human body for a long period [1,2]. For guaranteeing this permanence, implants' materials must own intense resistance to corrosion in body fluids, high strength, wear and fatigue resistance, together with low density and elastic modulus [3]. Amongst metallic biocompatible materials answering to these requirements, Ti-6Al-4V titanium alloy is the most employed for bone and dental replacements [4]. This is related to its characteristics of bio-inertness [5], passivation by titanium dioxide (TiO2) layer formation [6], for avoiding inflammatory reactions, appropriate weight distribution in the human body by high strength-weight ratio [7], paramagnetism, limited stress yielding phenomena [3], osseointegration enhancement due to cementless joints creation [7], and high fatigue strength, mandatory in the normal body-cyclic load conditions [3]. Ti-6Al-4V microstructure is characterized by the coexistence of α-phase with a hexagonal close-packed (hcp) lattice and β-phase having a body-centered cubic (bcc) one, providing good ductility and making it processable by different technologies, such as forming and additive manufacturing (AM) [8]. Considering its capabilities in complex shapes realization and porosity ratios control [9], AM of titanium alloys, in particular Electron Beam Melting (EBM) methodology [10], is largely employed in biomedical field, permitting the production of optimized

Content from this work may be used under the terms of the Creative Commons Attribution 3.0 license. Any further distribution of this work must maintain attribution to the author(s) and the title of the work, journal citation and DOI. Published under license by Materials Research Forum LLC.

and patience-tailored implants at reasonably costs [11]. AM is identified as a net-shape process, but often a milling or micro-milling operation is required for cleaning external surface defects such as lack of fusion and not-melted particles [12,13]. These processes must ensure a suitable surface roughness of the implant for facilitating osseointegration [14]. Contingently from the implant typology, roughness needs are different, and can range from values smaller than a micron up to few microns of the parameters S_a [15]. S_a parameter is usually considered instead of the R_a one since less influenced by scratches and measurement noise [16]. Beyond roughness, there are other functional parameters, such as fatigue, wear, and corrosion resistance, to be taken into account for guaranteeing implant permanence inside human body [17]. Table 1 shows these latter and their trend as a function of the implant type.

Table 1. Functional parameters qualitative values for implant permanence enhancement.

	Implant type		
Parameters	Dental implants	Bone plates and screws	Ball joints
Surface roughness	↑	↔	↓
Mechanical and fatigue resistance	↓	↔	↑
Wear resistance	↓	↑	↑
Pitting corrosion resistance	↑	↓	↓
Fretting resistance	↓	↔	↑
Crevice corrosion resistance	↓	↑	↓
Table legend: ↑ = high values; ↔ = medium values; ↓ = low values			

Pondering all these aspects, the analysis of micro-milling resulting surface roughness is essential to evaluate the capability of this process for promoting osteointegration. This study analyses the achievable roughness in micro-milling of Ti-6Al-4V EBM AM-ed specimens, with different cutting parameters. An Analysis of Variance (ANOVA) of S_a experimental results individuated the most affecting parameters, and mathematical models for S_a calculation were derived. Once validated by further micro-milling tests, these latter can be employed as predictive tools for S_a estimation starting from a set of known process parameters, or to optimize them as a function of the desired S_a values.

Materials and Methods

The analyzed results were attained form an experimental campaign of micro-milling of differently manufactured Ti-6Al-4V specimens. Two groups of cubic samples with a dimension of 10x10x10 mm^3 were processed: the first one extracted from 20 mm diameter bars resulting from rolling process, and the second one produced by EBM process, named As-received and EBM respectively. EBM specimens were fabricated with an EBM SYSTEM MODEL A2 machine (ARCAM, Designvägen 2 SE-435 33 Mölnlycke Sweden) in vacuum conditions, from ARCAM Ti-6Al-4V powders. Chemical composition, density, and particle size of these latter are reported in Table 2, where the particle size has been assessed as a function of its distribution for different percentiles (d10, d50, and d90), as indicated by ASTM B214-16 standard. Printing parameters were beam power 1250 W with a focus of 80 µm, printing speed 4530 mm/s, hatch spacing 100 µm, slice thickness 50 µm, and alternating the deposition angle amongst layers 90°. After their realization, the specimens were sonically cleaned in an acetone-isopropanol solution [18].

Cutting operations were performed on a five axis Nano Precision Machining Center KERN Pyramid Nano (Kern Micro Technik, Olympiastr. 2, D-82418 Murnau-Westried Germany) having a Heidenhain iTCN 530 numeric control. Each specimen was previously roughed by face milling it with a three flutes flat bottom mill (nominal diameter of 3 mm) at a depth of cut of 100 µm, a

cutting speed of 100 m/min, and a feed of 7.5 µm/tooth/rev for reaching a planar surface. Then, micro-milling of micro-channels along the whole length in the central part of the samples, by a two-flutes micro-mill, RIME HM79/05, was accomplished. The tool had a diameter of 0.5 mm, an edge radius of 5 µm, a helix angle of 30°, and the material was tungsten carbide (WC) coated with titanium aluminum nitride (TiAlN).

Table 2. Dimensional and chemical properties of Ti-6Al-4V powders.

Percentile of particle size distribution[1]	Particle size [µm]
d10	50
d50	68
d90	98
Powder apparent density [g/cm³]	2.57
Chemical composition [%wt]	
Al	6.42
V	3.88
O	0.13
Fe	0.18
Ti	Balance
[1] ASTM B214-16 Standard Test Method for Sieve Analysis of Metal Powders	

Micro-channels were realized maintaining a constant axial depth of cut a_p equal to 0.03 mm and changing cutting speed V_C and feed f_Z in a range of 30-50 m/min and 2-4 µm/tooth/rev respectively, following the central composite design (CCD) experimental plan [19], with an α value of 2 (Fig. 1). The CCD central point with $V_C = 40$ m/min and $f_Z = 3.0$ µm/tooth/rev was repeated three times for statistical reliability purposes [20]. The 11 tests shown in Fig. 1 were performed for both the As-received and EBM specimens, giving a total number of 22 experiments.

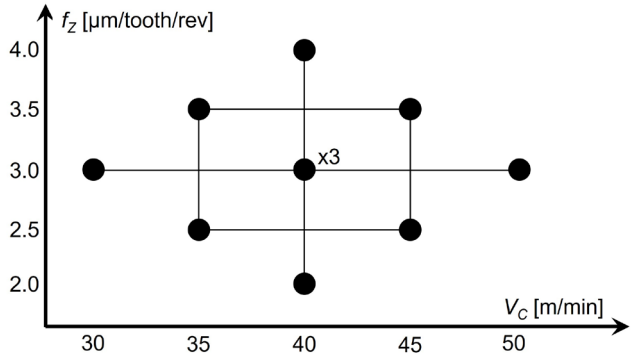

Fig. 1. The employed CCD experimental plan.

A new tool was utilized for each micro-machined channel for avoiding undesired effects of the surface roughness related to tool wear occurrence.

Surface roughness parameters S_a were measured exploiting an optical microscope, namely Mitaka PF60 (Mitaka Kohki.Co.,Ltd., Japan). Consistent with ISO 25178 standard for three-dimensional parametric definition of surface texture, irregularities' heights S_a can be evaluated by Eq. 1:

$$S_a = \frac{1}{LB}\int_0^L \int_0^B |\eta(x,y)|\, dx\, dy \quad (1)$$

where $\eta(x,y)$ is the surface irregularities deviation from base plane, L is the length and B the width of the explored section. In this work, this latter was positioned at the center of the micro-channel with $L = 0.245$ mm and $B = 2.3$ mm, with a magnification of 400x. Fig. 2 shows a S_a measurement example, while Table 3 the acquired S_a results.

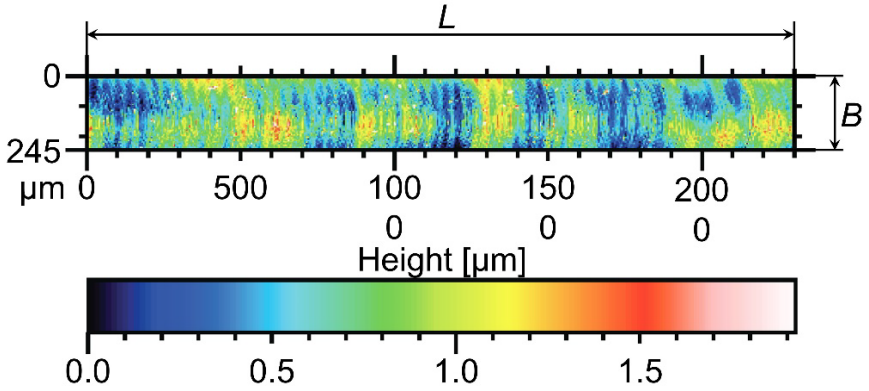

Fig. 2. Example of the acquired S_a measurement (V_C = 40 m/min, f_Z = 30 μm/tooth/rev).

Table 3. Summary of the S_a experimental values for all the tests.

V_C [m/min]	f_Z [μm/tooth/rev]	As-received S_a [μm]	EBM S_a [μm]
40	4.0	0.36	0.27
45	3.5	0.27	0.20
35	3.5	0.29	0.24
50	3.0	0.27	0.25
40	3.0	0.37	0.26
40	3.0	0.34	0.34
40	3.0	0.35	0.29
30	3.0	0.44	0.25
45	2.5	0.37	0.25
35	2.5	0.32	0.29
40	2.0	0.39	0.23

Results and Discussion

With the intent of evaluating which are the process parameters most influencing S_a, and how it is affected by their variation, an ANOVA of the whole set of experimental values, for both As-received and EBM, was performed. The ANOVA results and the related developed regression models' consistency is directly associated to data normality [21]. Therefore, for checking the normal distribution of S_a data, their probability plots were determined. These are reported in Fig. 3, where the central line denotes the cumulative probability, while the upper and lower curves delimit the 95 % confidence interval (CI) boundaries. For verifying the normality assumption, the analyzed data must remain within the CI curves and close to the probability line. Fig. 3a and 3b, representing the probability plots of As-received and EBM S_a values respectively, underline the data normality.

Analysis of As-received S_a.

Table 4 reports ANOVA results for As-received S_a values. Source column indicates the examined process parameters, where it can be observed that their single effects, interactions, and squared contributions were considered. The other columns represent the number of degrees of

freedom (DoF), the adjusted sum of squares (Adj. SS), the adjusted mean of squares (Adj. MS), the F-value, and the p-value of each source. The ANOVA individuated that the S_a value related to the parameter combination V_C = 35 m/min and f_Z = 3.5 µm/tooth/rev had a high standardized residual, indicating it as an outlier. As described in [20], the presence of outliers can be related to several factors, such as the measurer's experience, or the randomization and sequence of the measurements. Anyway, if the value of standardized residual is greater than 4 times the standard deviation, the outlier can be removed without compromising the ANOVA reliability [20]. Since the standardized residual of the outlier had a value of 2.12, 40 times the standard deviation, it was removed in the Response Surface Methodology (RSM) regression analysis.

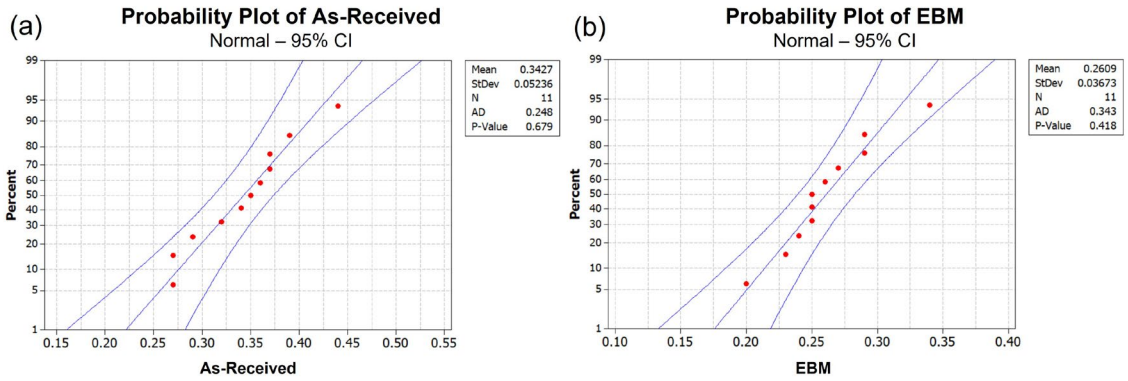

Fig. 3. Probability plots of S_a for (a) As-received, and (b) EBM specimens.

Table 4. ANOVA results for As-received S_a values.

Source	DoF	Adj SS	Adj MS	F-Value	p-Value
f_Z	1	0.000057	0.000057	0.16	0.712
V_C	1	0.015858	0.015858	43.93	0.003
$f_Z \times f_Z$	1	0.000600	0.000600	1.66	0.267
$V_C \times V_C$	1	0.000006	0.000006	0.02	0.900
$f_Z \times V_C$	1	0.008901	0.008901	24.66	0.008
Error	5	0.001444	0.000361		
Total	10	0.024360			

The assessment of the source parameter significant influence on response (S_a) is indicated by the p-value. In the common practice, in fact, if p-value is lower than the significance level, the null hypothesis H0, stating that there is no source-response relation, is rejected. Significance level is directly correlated to CI, thus, considering a CI of 95 % for the present analysis, its value is equal to 1 – 95 % = 0.05. Therefore, when p-value is lower than 0.05 the alternative hypothesis H1 is accepted, concluding that there is a statistically significant source-response relationship [21].

Table 4 results indicate that the variations of V_C and its interaction with f_Z have significant effects on S_a for the As-received material. This outcome is confirmed by the main effects plots of Fig. 4a as well, where an increase of V_C improves the surface quality, reducing the S_a value. A similar trend is also detected when considering the f_Z variation (Fig. 4b), even if a significant influence is not revealed. The surface and contour plots of Fig. 5a and 5b evidently depict the V_C - f_Z interaction effect, while report, once again, that how f_Z affects S_a is not clear. At high values of V_C, in fact, an increase of f_Z lead to a S_a reduction, but at low V_C values, S_a behavior is the opposite. Due to this, further investigations to clarify the f_Z impact are needed.

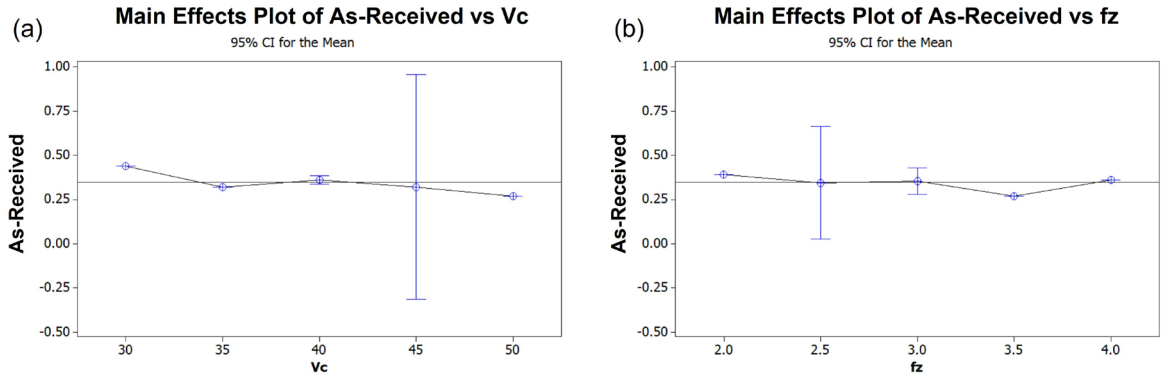

Fig. 4. Main effects plots for As-received S_a.

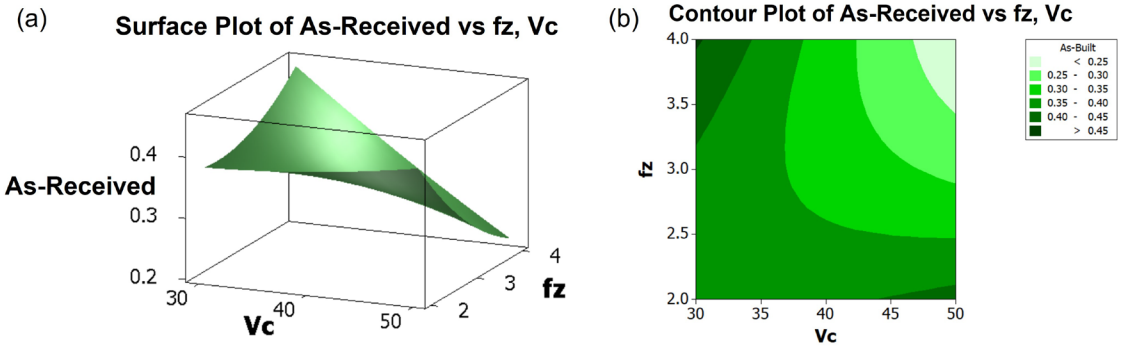

Fig. 5. Surface (a) and contour (b) plots for As-received S_a.

Analysis of EBM S_a.

The ANOVA results of S_a data for EBM micro-milled specimens are reported in Table 5.

Table 5. ANOVA results for EBM S_a values.

Source	DoF	Adj SS	Adj MS	F-Value	p-Value
f_Z	1	0.001408	0.001408	3.05	0.141
V_C	1	0.005208	0.005208	11.29	0.020
$f_Z \times f_Z$	1	0.000647	0.000647	1.40	0.290
$V_C \times V_C$	1	0.000056	0.000056	0.12	0.741
$f_Z \times V_C$	1	0.000225	0.000225	0.49	0.516
Error	5	0.6598	0.13196		
Total	10	12.7408			

Table 5 highlights that only V_C significantly influences S_a. In particular, when augmenting V_C the surface roughness decreases, and this comportment is represented by the negative slope of the related main effects plot in Fig. 6a. Feed shows an analogous behavior (Fig. 6b), but, as in the case of As-received specimens, a statistical significance of it on S_a is not detectable by ANOVA, therefore its final contribution requires to be further explored. Surface and contour plots in Fig. 7 reveal the deep effect of V_C on S_a for EBM samples, pointing to the negligible influence of f_Z, mainly at the higher V_C values.

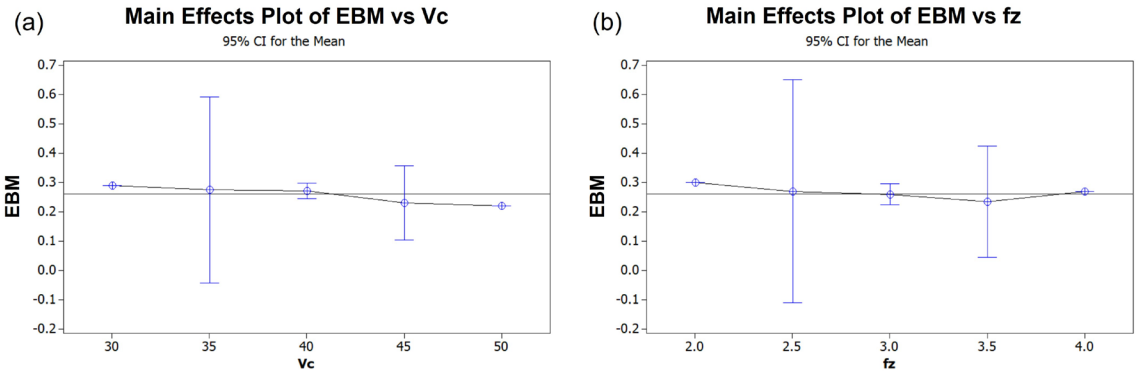

Fig. 6. Main effects plots for EBM S_a.

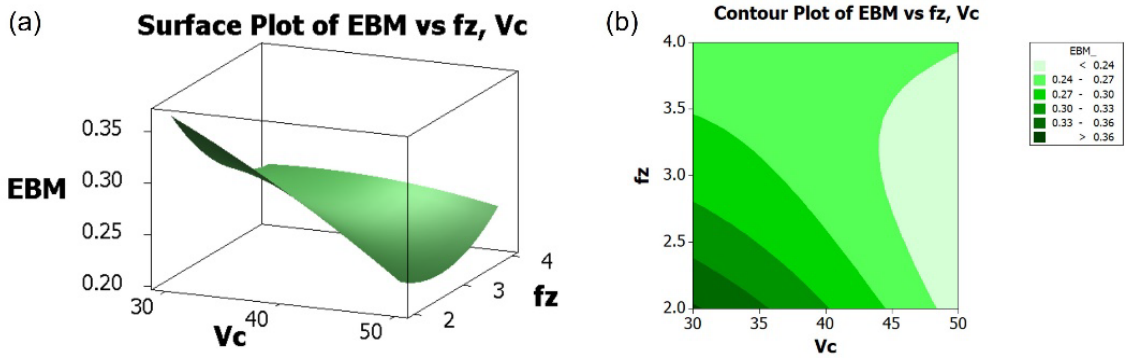

Fig. 7. Surface (a) and contour (b) plots for EBM S_a.

Response Surface Methodology (RSM) regression models.

With the aim of developing mathematical models for predicting S_a as a function of the micro-milling parameters, response surface methodology (RSM) on the whole set of S_a experimental measurements was employed. The developed regression models are reported in Eq. 2 and Eq. 3 for the calculation of As-received (S_{a_AR}) and EBM (S_{a_EBM}) resulting surface roughness respectively.

$$S_{a_AR} = 1.9 + 0.79f_Z + 0.060V_C + 0.022f_Z^2 + 0.000023V_C^2 - 0.23f_ZV_C \quad (2)$$

$$S_{a_EBM} = 0.23 - 0.041f_Z + 0.011V_C + 0.023f_Z^2 - 0.000068V_C^2 - 0.003f_ZV_C \quad (3)$$

The calculated S_a values for each combination of V_C and f_Z, for As-received and EBM materials, are reported in Table 6. For comparison, Table 6 shows the experimental measurements and the percentage error ($e_{\%}$) of the calculations as well.

Discussion.

ANOVA results disclose that, freely from the initial furniture status of the material, V_C heavily influences the final part surface quality. A diminution of V_C increases S_a, and this can be correlated to the vibrational effect induced by the non-homogeneous properties of the material, and to the built-up-edges (BUEs) generation at lower V_C [22]. The V_C-f_Z interaction effect can be argued considering that a f_Z increment reduces the micro-tool vibrations permitting to achieve low roughness and higher quality [23]. On the other hand, a reduction of f_Z increases the contribution of ploughing mode cutting mechanism that enlarges the surface plastic deformation lowering the paths' traces and S_a [24]. However, the analysis of further experimental tests is mandatory to clarify f_Z influence.

Table 6. Experimental and estimated S_a values comparison for As-received and EBM specimens.

V_C [m/min]	f_Z [µm/tooth/rev]	Exp S_{a_AR} [µm]	S_{a_AR} [µm]	$e_{\%_AR}$	Exp S_{a_EBM} [µm]	S_{a_EBM} [µm]	$e_{\%_EBM}$
40	4.0	0.36	0.369	2.4	0.27	0.258	4.3
45	3.5	0.27	0.257	4.7	0.20	0.222	11.0
35	3.5	0.29	0.452	56.0	0.24	0.278	3.1
50	3.0	0.27	0.274	1.6	0.25	0.209	5.1
40	3.0	0.37	0.351	5.2	0.26	0.257	1.2
40	3.0	0.34	0.351	3.2	0.34	0.257	7.1
40	3.0	0.35	0.351	0.3	0.29	0.257	11.4
30	3.0	0.44	0.432	1.8	0.25	0.292	0.6
45	2.5	0.37	0.378	2.1	0.25	0.259	3.5
35	2.5	0.32	0.341	6.5	0.29	0.285	1.7
40	2.0	0.39	0.378	3.2	0.23	0.302	0.7

The EBM S_a values result to be lower than the ones of As-received specimens. This is ascribable to the higher brittleness, and lower ductility, of EBM samples, related to the localized higher cooling rate of EBM process. Therefore, the superior ductility of As-received material causes an increased material adhesion on the tool cutting edge that negatively affects quality [25].

The calculation errors in Table 6 stand below the 11 %, the only exception is related to a $e_{\%}$ of 56 % related to the detected outlier, for which the significance of the value must not be taken into consideration. Overall, the low error values achieved highlight the applicability of the proposed models. Further tests need to be performed to finally validate Eq. 2 and 3 and permitting to exploit a reliable tool to forecast the attainable S_a once V_C and f_Z have been selected, or to optimize the cutting parameters as a function of the desired S_a. It should be noted that the assessment of S_a for promoting osseointegration concerns surface chemistry and morphology as well, giving the necessity of a deeper analysis to establish optimal conditions [26]. Additionally, different S_a requirements are crucial for different biomedical applications [27]. As an example, the outcomes of the accomplished micro-milling tests do not warrant to achieve the optimal combination of material, production process, and cutting parameters for a S_a value suitable for dental applications ($S_a \approx 1.5$ µm). Therefore, additional investigations should be made for analyzing the possibility of micro-machining processes employment in the dental field. Anyway, the achieved S_a values are applicable for prosthetic implants and culture cell grows.

Summary

This paper presents the study of micro-milling cutting parameters effects on the resulting surface roughness S_a as a function of different states of furniture of the material, with the aim of promoting osseointegration of prosthetic implants made of Ti-6Al-4V biocompatible alloy. The ANOVA of the data, obtained by means of an extensive experimental campaign, allowed to identify the most affecting cutting parameters, revealing V_C as the most significant. The application of RSM on data lead to the development of regression models capable to estimate S_a with good approximation, underlining their potential to predict and optimize roughness. A general increase of S_a has been observed when both V_C and f_Z decrease, even if, other tests should be performed to clarify f_Z contribution. The optimum roughness value establishment remains, in fact, a difficult task, being it not merely manufacturing process dependent, but implant application, material chemistry, mechanical and corrosion resistance related as well (Fig. 8). Consequently, ulterior studies and in vitro osseointegration tests are needed to identify the optimal topography combining all requirements.

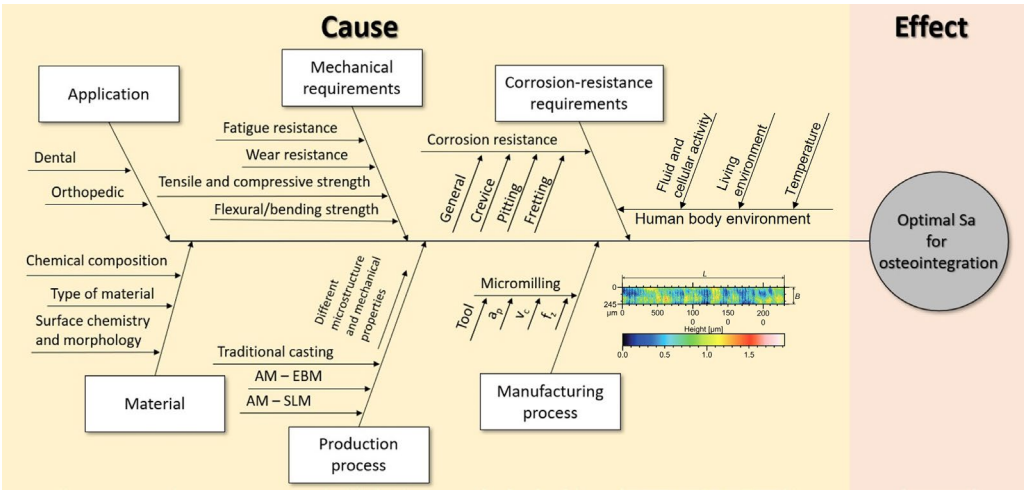

Fig. 8. Summary of influencing parameters on optimal S_a for osseointegration.

References

[1] Y.L. Hao, S.J. Li, R. Yang, Biomedical titanium alloys and their additive manufacturing, Rare Met. 36 (2016) 661-671. http://doi.org/10.1007%2Fs12598-016-0793-5

[2] M. Sarraf, G.E. Rezvani, S. Alipour, S. Ramakrishna, N.L. Sukiman, A state of the art review of the fabrication and characteristics of titanium and its alloys for biomedical applications, Biodes. Manuf. 5 (2022) 371–395. https://doi.org/10.1007/s42242-021-00170-3

[3] R.B. Heimann, Biomaterials – characteristics, history, applications, in: R.B. Heimann (Eds.), Materials for Medical Applications, Walter de Gruyter, Berlin/Boston, 2020, pp. 1-74.

[4] S.A. Aghili, K. Hassani, M. Nikkhoo, A finite element study of fatigue load effects on total hip joint prosthesis, Comput. Methods Biomech. Biomed. Eng. 24 (2021) 1545-1551. https://doi.org/10.1080/10255842.2021.1900133

[5] G.S. Kaliaraj, T. Siva, A. Ramadoss, Surface functionalized bioceramics coated on metallic implants for biomedical and anticorrosion performance-a review, J. Mater. Chem. B 9 (2021) 9433-9460. https://doi.org/10.1039/D1TB01301G

[6] P. Pedeferri, Corrosion in the human body, in: L. Lazzari, M.P. Pedeferri (Eds.), Corrosion Science and Engineering, Springer Cham, Switzerland, 2018, pp. 575-587.

[7] J.W. Nicholson, A.J. Connor, Biological interactions with materials, in: J.W. Nicholson (Eds.), The Chemistry of Medical and Dental Materials, RSC, 2020, pp. 186-226.

[8] S. Gialanella, A. Malandruccolo, Titanium and Titanium Alloys, in: Aerospace Alloys, Springer Cham, Switzerland, 2020, pp. 129-189.

[9] C. Cappellini, Y. Borgianni, L. Maccioni, C. Nezzi, The effect of process parameters on geometric deviations in 3D printing with fused deposition modelling, Int. J. Adv. Manuf. Technol. 122 (2022) 1763-1803. https://doi.org/10.1007/s00170-022-09924-4

[10] J. Tong, C.R. Bowen, J. Persson, A. Plummer, Mechanical properties of titanium-based Ti–6Al–4V alloys manufactured by powder bed additive manufacture, Mater. Sci. Technol. 33 (2017) 138-148. https://doi.org/10.1080/02670836.2016.1172787

[11] W.Y. Yeong, C.K. Chua, A quality management framework for implementing additive manufacturing of medical devices, Virtual Phys. Prototyp. 8 (2013) 193-199. https://doi.org/10.1080/17452759.2013.838053

[12] T. Özel, E. Ceretti, T. Thepsonthi, A. Attanasio, Machining Applications, in: T. Özel, P.J. Bartolo, E. Ceretti, J. De Ciurana Gay, C.A. Rodrigez, J.V. Lopes Da Silva (Eds.), Biomedical devices – Design, prototyping and manufacturing, Wiley, Hoboken, NJ, US, 2017, pp. 99-120.

[13] A. Abeni, C. Cappellini, P.S. Ginestra, A. Attanasio, Analytical modeling of micro-milling operations on biocompatible Ti6Al4V titanium alloy, Procedia CIRP 110 (2022) 8-13. https://doi.org/10.1016/j.procir.2022.06.004
[14] A. Wennerberg, T. Albrektsson, Effects of titanium surface topography on bone integration: A systematic review, Clin. Oral Implants Res. 20 (2009) 172-184. https://doi.org/10.1111/j.1600-0501.2009.01775.x
[15] T. Albrektsson, A. Wennerberg, On osseointegration in relation to implant surfaces, Clin. Implant Dent. Relat. Res. 21 (2019) 4-7. https://doi.org/10.1111/cid.12742
[16] A. Abeni, A. Metelli, C. Cappellini, A. Attanasio, Experimental optimization of process parameters in CuNi18Zn20 micromachining, Micromachines 12 (2021) 1293. https://doi.org/10.3390/mi12111293
[17] L. Lin, H. Wang, M. Ni, Y. Rui, T.Y. Cheng, C.K. Cheng, X. Pan, G. Li, C. Lin, Enhanced osteointegration of medical titanium implant with surface modifications in micro/nanoscale structures, J. Orthop. Translat. 2 (2014) 35-42. https://doi.org/10.1016/j.jot.2013.08.001
[18] P.S. Ginestra, R.M. Ferraro, K. Zohar-Haubert, A. Abeni, S. Giliani, E. Ceretti, Selective laser melting and electron beam melting of Ti6Al4V for orthopedic applications: a comparative study on the applied building direction, Materials 13 2020 5584. https://doi.org/10.3390/ma13235584
[19] Y. Men, J. Liu, W. Chen, X. Wang, L. Liu, J. Ye, P. Jia, Y. Wang, Material parameters identification of 3D printed titanium alloy prosthesis stem based on response surface method, Comput. Methods Biomech. Biomed. Eng. (2022). https://doi.org/10.1080/10255842.2022.2089023
[20] D.C. Montgomery, Design and Analysis of Experiments, 10th ed.; John Wiley & Sons, Hoboken, NJ, US, 2019.
[21] F. Concli, L. Maccioni, L. Fraccaroli, C. Cappellini, Effect of Gear Design Parameters on Stress Histories Induced by Different Tooth Bending Fatigue Tests: A Numerical-Statistical Investigation, Appl. Sci. 12 (2022) 3950. https://doi.org/10.3390/app12083950
[22] G. Kiswanto, A. Mandala, M. Azmi, T.J. Ko, The effects of cutting parameters to the surface roughness in high speed cutting of micro-milling titanium alloy Ti-6Al-4V, Key Eng. Mater. 846 (2020) 133-138. https://doi.org/10.4028/www.scientific.net/KEM.846.133
[23] A. Roushan, U. Srinivas Rao, K. Patra, P. Sahoo, Multi-Characteristics Optimization in Micro-milling of Ti6Al4V Alloy, J. Phys.: Conf. Ser. 1950 (2012) 012046. https://doi.org/10.1088/1742-6596/1950/1/012046
[24] H.K. Rafi, N.V. Karthik, H. Gong, T.L. Starr, B.E. Stucker, Microstructures and mechanical properties of Ti6Al4V parts fabricated by selective laser melting and electron beam melting, J. Mater. Eng. Perform. 22 (2013) 3872-3883. https://doi.org/10.1007/s11665-013-0658-0
[25] S.P.L. Kumar, D. Avinash, Experimental biocompatibility investigations of Ti–6Al–7Nb alloy in micromilling operation in terms of corrosion behavior and surface characteristics study, J. Braz. Soc. Mech. Sci. Eng. 41 (2019) 364. https://doi.org/10.1080/10667857.2021.1903671
[26] A. Kemény, I. Hajdu, D. Károly, D. Pammer, Osseointegration specified grit blasting parameters, Mater. Today: Proc. 5 (2018) 26622-26627.
[27] R. Krishna Alla, K. Ginjupalli, N. Upadhya, M. Shammas, R.R. Krishna, R. Sekhar, Surface roughness of implants: A review, Trends Biomater. Artif. Organs 25 (2011) 112-118.

Materials Research Proceedings 28 (2023) 1265-1274 https://doi.org/10.21741/9781644902479-137

Comparison of cutting tool wear classification performance with artificial intelligence techniques

COLANTONIO Lorenzo[1,a *], EQUETER Lucas[1,b], DEHOMBREUX Pierre[1,c] and DUCOBU François[1,d]

[1]Machine Design and Production Engineering Lab, University of Mons, 7000 Mons, Belgium

[a]lorenzo.colantonio@umons.ac.be, [b]lucas.equeter@umons.ac.be, [c]pierre.dehombreux@umons.ac.be, [d]francois.ducobu@umons.ac.be

Keywords: Machining, Turning, Cutting Tool, Artificial Intelligence, Monitoring, Classification

Abstract. Optimal replacement of machining cutting tools is a major challenge in today's manufacturing industry. Due to the degradation of the tool during machining, late replacement of the tool leads to the risk of producing parts that do not meet technical specifications, while early replacement increases machine downtime and tool costs. To replace tools at the right time, it is necessary to monitor their degradation. Therefore, this paper compares the classification performance of different artificial intelligence approaches to classify the condition of cutting tools from cutting signals. Different approaches, namely: Artificial Neural Network (ANN), Support Vector Classifier (SVC), Random Forest (RF) and k-Nearest Neighbour (k-NN) are tested, and their performance is compared. It is highlighted that ANN and RF methods obtain better classification performances (88.8% and 86.4%, respectively) than the rest of the approaches (80%). Nevertheless, all approaches can monitor the degradation of cutting tools in a satisfactory manner (i.e., 80% accuracy). A comparison of training times highlights that training a neural network takes longer than the other approaches. However, with the computational power currently available, this is not an obstacle for their implementation in real applications as this training can still be achieved in a couple of minutes.

Introduction

The condition of a cutting tool is of critical importance to the machined surface and the associated machining tolerances. A worn tool or a tool in an unsatisfactory condition does not allow the creation of machined surfaces of sufficient quality, which in consequence increases the cost of production [1]. Different tool replacement policies exist [2], but often tool replacement maintenance policies attempt to address this problem by replacing the tool well before its end of life which creates waste. This results in higher tool costs and increased machine downtime, further increasing production costs. As tool wear is an extremely complex and non-stationary phenomenon [3], the determination of the tool condition can be complex. Monitoring the degradation of the tool is thus necessary.

There are two types of monitoring: direct and indirect. The direct approach consists of measuring tool wear directly on the tool, but this requires the machining process to be stopped and results in increased machine downtime [4]. The indirect approach consists of measuring signals during the machining process to try to predict the state of the tool [5]. This has the advantage of allowing a continuous machining process with the least intrusive sensor installation possible. A review of the type of signals that can be recovered during machining is available in [6]. Several indirect monitoring methods exist, but lately, artificial intelligence methods are predominant as they can learn from machining data and adjust their prediction on a case-by-case basis. A systematic literature review describing all approaches present in the literature shows that there are mainly two approaches with AI: classification and regression [7]. Classification aims to monitor

Content from this work may be used under the terms of the Creative Commons Attribution 3.0 license. Any further distribution of this work must maintain attribution to the author(s) and the title of the work, journal citation and DOI. Published under license by Materials Research Forum LLC.

the state of the tool via discrete values listing the state of the tool. Regression aims to follow the evolution of the tool by directly monitoring the wear. In some applications, it is not necessary to know exactly how the tool wear is evolving, so classification methods are used because of their ease of understanding.

In the literature, there are only a few comparisons of performance between different classification approaches. These comparisons are often made to highlight the particularity of one model compared to another, but a more general comparison is almost never made. This paper, therefore, proposes to compare the performance of some common artificial intelligence methods, namely: Artificial Neural Network (ANN), Random Forest (RF), Support Vector Classifier (SVC) and k-Nearest Neighbour (k-NN) implemented on the same database. The choice of these approaches is based on their ease of implementation and their ability to perform a classification for this application. All approaches are optimised and tested on identical data that homogeneously represents the different degradation states of the tool. The comparison of the quality of the results and the efficiency of the approach is realised.

Methodology

To compare the performance of the different AI approaches, the database and the experimental conditions are described. Signals from the database correlated with tool wear are identified and used as input for the different AI approaches. The database is then divided into classes and a split between training and test data is made. Finally, all approaches, namely: ANN, RF, SVC and k-NN, are presented and optimised, and their results are highlighted. A comparison of the results is then made.

Experimental Setup and Database

The database comes from experimental tests carried out on a CNC lathe (Weiler E35), which ensures a constant cutting speed throughout the machining process (Fig. 1). It is used to machine (longitudinal turning operation), C45 steel bars at variable cutting speeds with a CNMG120404-MF3 TP40 tool from SECO. This tool is one of the lower-grade tools to limit the amount of material wasted during testing. Table 1 shows the different cutting conditions used during the tests, only variations in cutting speeds are considered. The machine is instrumented with a force sensor (Kistler 9257B) that collect the cutting forces (Fi) and torques (Mi) during the machining operation. The sensor is mounted at the base of the tool and in the machine frame of reference, Fx corresponds to the feed force, Fy is the radial force and Fz is the cutting force. This sensor is mounted for indirect monitoring, i.e., to be as minimally intrusive as possible. Wear and cutting forces are measured every 2.8 minutes (corresponding to one piece). Wear is assessed according to ISO 3685 [8], which defines wear as the value of Vb (Fig. 2) measured directly on the tool using a microscope (Byameyee EU-1000X 3). Vb is measured as the size of the wear in zone B. This B area is located between the corner radius on one side and 1/4 of the wear area (area C where is located the notch wear) on the other side (Fig. 2)

A total of 30 tools are used to create the database, with the degradation of each tool being measured 6.4 times on average during its lifetime. The database therefore consists of 192 data points evenly distributed over the tool degradation. The measured cutting force corresponds to a 20 s signal sampled at 10 kHz and is processed to recover statistical and frequency values. The statistical analysis corresponds to the calculation of the average, the RMS value and the frequency analysis identifies the frequency and the maximum amplitude of the power spectral density.

To identify the relationships between the signals measured during machining and tool degradation, a Spearman correlation analysis is used on all signals. This correlation analysis is adapted to the size and non-normality of the data. The correlation analysis shows that the features most correlated with wear are the following: Mz RMS (correlation indicator: 0.89), Fx RMS (0.87), machining duration (0.84), chip length (total length machined) (0.84) and Fz RMS (0.79).

As cutting forces are strongly correlated with tool wear, they will be used in the following as inputs for the AI methods. It should be noted that the machining time and the chip length have the same correlation score as they are both dependent. The chip length is also dependent on the cutting speed. In this case, since only variations in the machining speed are taken into account, this indicator allows the method to indicate the change in cutting conditions.

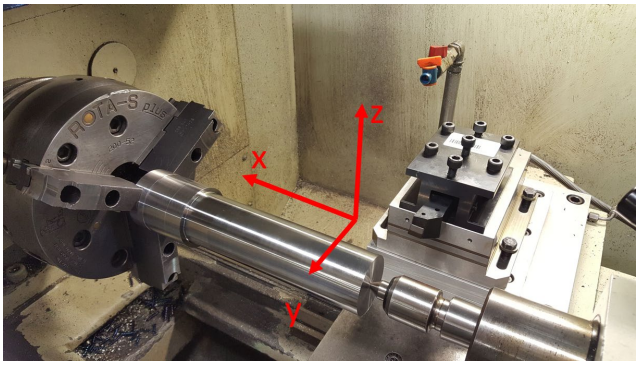

Fig. 1. Experimental turning setup, the tool is mounted into the cutting force and torque sensor.

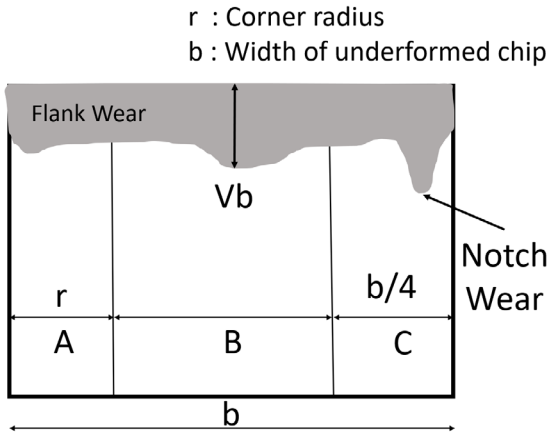

Fig. 2. Flank wear degradation Vb on the flank face.

Table 1. Experimental Cutting Condition.

Tool n°	Feed [mm/rev]	Cutting Speed [m/min]	Depth of cut [mm]
1 to 10	0.2	260	1
11 to 15	0.2	250	1
16	0.2	240	1
17 to 20	0.2	265	1
21 to 30	0.2	Variable: 240 to 260 (for each tool)	1

Features Preparation for Tool Wear Classification

In a classification problem, it is necessary to define classes whose purpose is to define the different possible states of the tool. The degradation of a cutting tool is divided into 3 successive phases (Fig. 3): the first phase corresponds to the beginning of the tool's life, it shows little wear but degrades rapidly. This phase is generally short in relation to the life of the tool. The second phase is the longest and consists of a quasi-linear degradation of the tool, it is a regime phase in which the tool will spend most of the time. Finally, the third phase is the end of the tool's life, which can last more or less time depending on the cutting conditions.

Based on the ISO 3685 standard, it is often accepted that the end-of-life criterion for a cutting tool is when the size of the flank wear reaches 300 µm [8]. This flank wear is called Vb and is presented in Fig. 2. It is therefore proposed that class 1 corresponds to wear between 0 and 150 µm, class 2 corresponds to a wear between 150 and 300 µm and class 3 corresponds to the end of the tool's life with wear exceeding 300 µm. These values (150 and 300 microns) were chosen as they are generally used in the literature as end-of-life criteria.

The database is not uniform across all these classes, indeed, there are significantly more points in class 1 than in class 3 for example. To increase the number of points in each class, data augmentation is performed. This data augmentation consists of linearly interpolating 2 points of

the tool degradation and calculating an intermediate measurement point. This simple type of interpolation is sufficient given the number of measurements points in a complete trajectory; the interpolation error is low. This increases the number of possible points for training the AI but does not change the distribution of points in the different classes (73 % in class 1, 19% in class 2 and 8% in class 3). Nevertheless, with more data points, there will be more points to propose for training AI methods, which generally allows for faster convergence [9].

Artificial intelligence methods need training data to learn the relationships between the data and test data to verify that the model has learned correctly. It was chosen to select 15 points randomly per class to create the test database. For class 3, 15 data points correspond to 40% of the data in this class. This value is quite high (usually 25% of the data is used in testing) but this value does not impact the results presented in the following. By ensuring that each class contains the same number of data points, this ensures that an error in one class has the same overall importance regardless of the class.

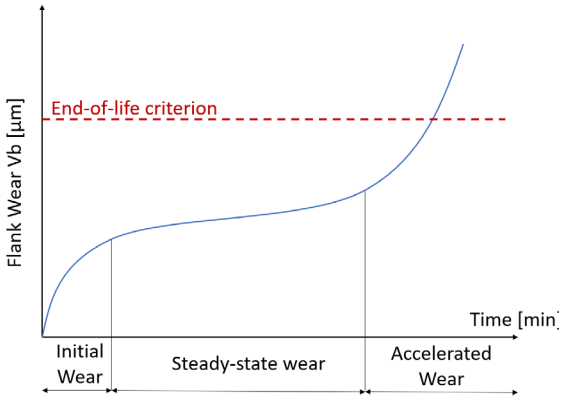

Fig. 3. Typical tool degradation for a given cutting condition.

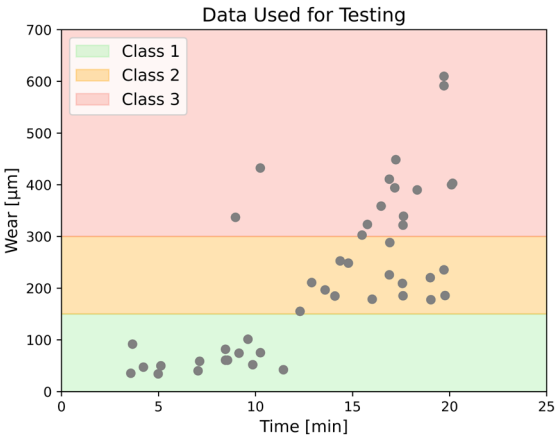

Fig. 4. Testing data randomly selected and their repartition in different classes.

Artificial Neural Network

Neural networks are certainly the most popular intelligence method. Inspired by the way the brain works, this AI can represent highly non-linear relationships between input and output and is extensively represented in the literature [10]. There are multiple hyperparameters that influence the quality of the results, the most common are: the network architecture, the activation function used in each layer, the batch size, and the number of epochs. The most important hyperparameter is the network architecture which will create the relationship between the input and output of the network and is often chosen by trial and error. Table 2 shows the different hyperparameters used to obtain the best classification results. These and all other parameters presented in this paper are optimised by testing the influence of each parameter individually. In this case, for example, different architectures have been tested but the one chosen is the one that gives the best results. The network architecture is presented in Fig. 5.

The results are presented Fig. 6, the overall accuracy is 88.88%. Class 1 is always correctly classified but classes 2 and 3 present an accuracy of 86.7% and 80% respectively.

Table 2. Optimized hyperparameters for ANN.

Hyperparameter	Value
Algorithm	TensorFlow (Python) [11]
Architecture	2 hidden layers each containing 8 neurons
Activation function	1st layer: Tanh, 2nd layer: Relu, output: Softmax
Batch size	5
Epoch	1000

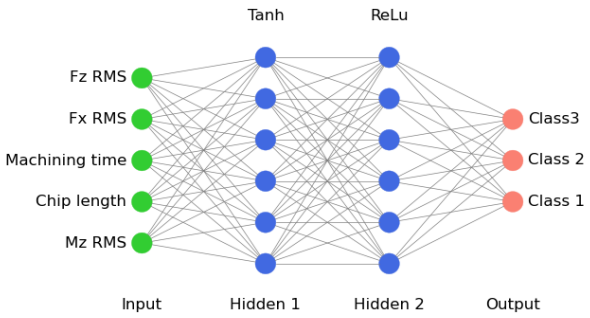

Fig. 5. Best Artificial Neural Network architecture.

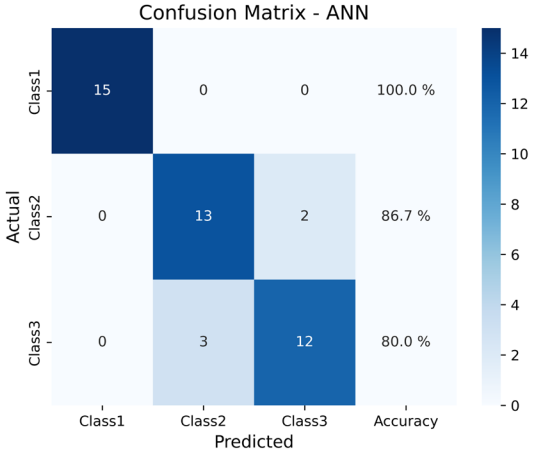

Fig. 6. ANN Confusion matrix – Overall accuracy : 88.8 %.

Random Forest

The random forest classifier is a combination of classical tree classifiers. The Random Forest classifier consists at producing a set of tree classifiers (i.e., Number of estimator) to create an ensemble of classifiers, called forest [12]. To classify a state, each tree of the forest is interrogated, and the most given class is the predicted class (Fig. 7). Combining the results has the advantage of being more accurate than if each tree were taken individually, as the probability of a tree being wrong is higher than the probability of most trees being wrong.

Table 3 shows the different hyperparameters used to create the classifier. The number of estimators corresponds to the number of trees in the forest. The variation of this value can change the accuracy of the approach. The number of 500 is chosen as more estimators do not improve the overall accuracy. The maximum complexity of the trees is controlled by the “maximum depth”, the variation of this parameter slightly improves the results, a value too low leads to bad accuracy while a high value does not improve the results. To measure the quality of a split, the Gini impurity criteria is used [13].

The results obtained with the combination of hyperparameters previously identified are presented Fig. 8. The overall accuracy of the approach is 86.6%. Performance is consistent across all classes 2 and 3 with 80% accuracy.

Table 3. Optimized hyperparameters for RF.

Hyperparameter	Value
Algorithm	Sci kit Learn (Python) [13]
Number of estimators	500
Maximum depth	6
Criterion	Gini

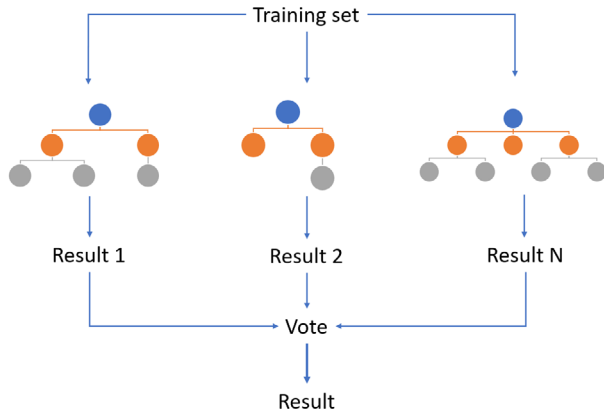

Fig. 7. Random Forest principle.

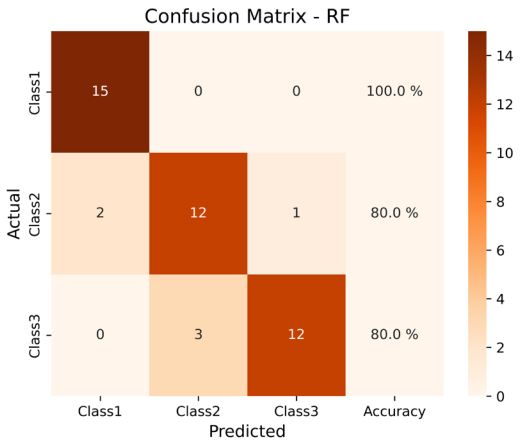

Fig. 8. Random Forest Confusion Matrix – Overall accuracy: 86.8%.

Support Vector Classifier

Support vector machines, and more specifically the support vector classifiers, aim at finding an optimal hyperplane to separate different classes of data [14] (Fig. 9). In this application the kernel function that defines the different classes is the Radial Basis Function (RBF). This approach uses mainly 2 parameters: gamma and C. Gamma controls the curvature of the data separation and so controls the influence of samples selected by the model to be support vectors. The parameter C control the error rate by compromising between the correct classification against the maximization of the decision function. A compromise between these two parameters allows an efficient classification by controlling the shape of the classification area and the influence of outliers. Different combinations of parameters were tested but the combination of parameters that gives the best results is listed Table 4.

Fig. 10 shows the results obtained by the approach described above. The overall accuracy is 80%. Class 1 has no error, class 2 has the highest error rate with an accuracy of 66.7%, and class 3 has a performance of 73.3%.

Table 4. Optimized hyperparameters for SVC.

Hyperparameter	Value
Algorithm	Sci Kit Learn (Python) [13]
C	2
Gamma	1
Kernel	Radial Basis Function

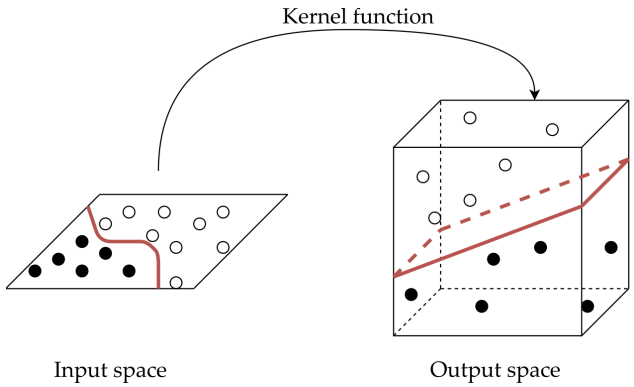

Fig. 9. SVC approach, under Creative Commons Attribution License [7].

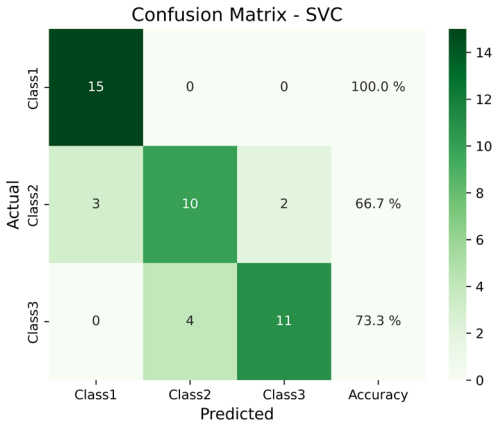

Fig. 10. SVC confusion matrix – Overall accuracy : 80%.

k-Nearest Neighbour

K-Nearest Neighbour in classification uses the k nearest neighbour in the dataset reference of the input to determine the class of a new input [15]. The weight of each neighbour generally depends on the distance to the new inputs. Fig. 11 shows the example of the classification of a new element with a k value of 5. The 5 nearest data items and their distances are used to determine the class of the new item. Table 5 shows the most important parameters for this approach: the number of neighbour and the weight of the connection. In this approach, the best results were obtained with a number of neighbours of 8 and weight depending on the distance.

Fig. 12 presents the results. The overall accuracy is 80%. Only class 1 is correctly classified, class 2 and 3 have 66.7% and 73.3% accuracy respectively.

Table 5. Optimized hyperparameters for k-NN.

Hyperparameter	**Value**
Algorithm	Sci Kit Learn (Python) [13]
Number of neighbours	8
Weight	Distance
Algorithm	Auto

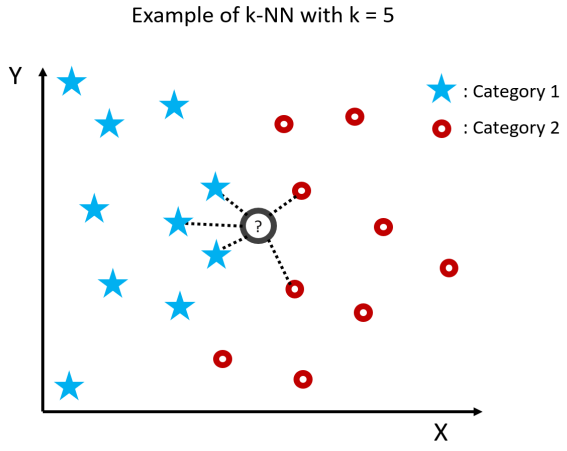

Fig. 11. k-NN approach with k = 5.

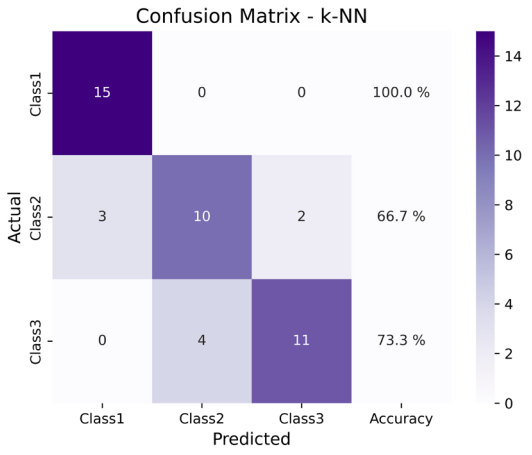

Fig. 12. k-NN confusion matrix – Overall accuracy: 80%

Discussion

Table 6 compares the results obtained by the different approaches and the one with the highest overall score is the ANN method. It can be noted, however, that all approaches score well, with an average accuracy above 80%. Each method has its advantages and disadvantages, and the simple comparison of results does not allow to highlight them. For example, approaches such as k-Nearest Neighbour does not give good results if the dataset is not complete for all cutting conditions. On the other hand, approaches such as Neural Networks generally allow for a generalisation of the results when faced with never seen before cutting conditions.

Table 6. Comparison of the overall accuracy, training and inference time for different AI approach.

Approach	Overall accuracy	Training Time	Inference Time
ANN	88.8%	84.870s	0.080s
RF	86.6%	0.650s	0.050s
SVC	80%	<0.008s	<0.001s
k-NN	80%	<0.008s	<0.001s

An important point when using these approaches is also the computational time and resources required to obtain the results. All results presented in this paper are obtained on a single core of an Intel I7-9750H @ 2.6 GHz CPU. The different computational times, including training and validation are presented in Table **6**. The training time considers the approach initialisation and computing time to fit the dataset. The inference time refers to the time needed by the approach to predict the classes presented in this paper. It is observed that the ANN approach has the longest training time compared to the other approaches. This is due to its training scheme. These considerations must be considered in relation to the available computational resources. However, it is important to note that the training only must be done once. With current computational resources, this is not a limitation as even ANN only takes less than 2 minutes to converge. It should also be noted that this interpretation is only valid for the amount of data in this database. For larger databases, the inference time of methods other than ANNs can increases considerably. In general, ANN methods have a longer training time but a relatively short inference time, which is not the case for other methods. Since training only needs to be done once, it is preferable to use methods with a constant low inference time such as ANN.

The position of the misclassification is also important. If the state of a tool is misclassified at the transition between two classes, this misinterpretation is less critical than if the tool is misclassified at middle of the class interval. Indeed, the misclassification reflects an error of some µm which does not significantly impact the quality of the machined surface. Fig. 13 shows the different positions of the wear incorrectly classified for each approach presented in this paper. From the figure, it appears that there are some data that are often misclassified in the middle of class 2. On this aspect, ANN has the lowest error than any other approaches. For each approach, the transition from class 2 to 3 leads to misclassification of the wear. As stated previously, this misclassification is not critical as this is only an error of less than 25 µm in the estimation of Vb. SVC is the only approach that misclassified a very worn tool.

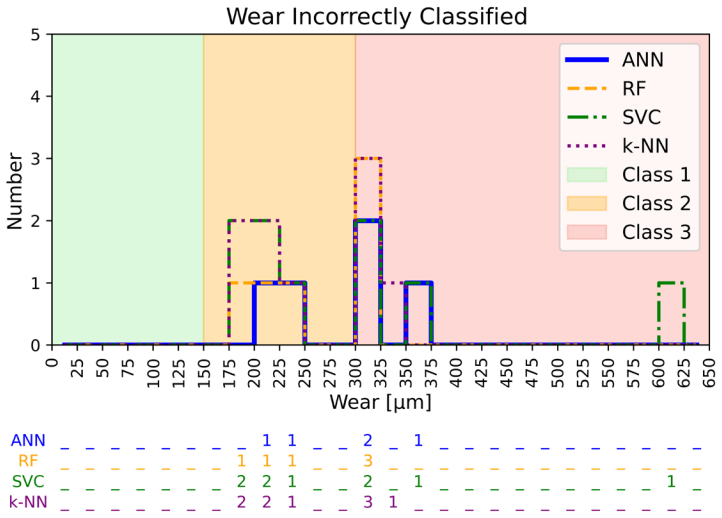

Fig. 13. Misclassified wear class for different techniques.

Summary

Tool condition classification is an effective approach when the tool condition needs to be monitored. artificial intelligence methods are suitable for this purpose, but their performance can vary depending on the approach used. In this paper, a turning database from which cutting signals highly correlated with the wear are used with the following AI classification methods: ANN, RF, SVC, and k-NN. The tool condition is divided into 3 classes, each representing a phase of the tool life. The classes are defined based on the flank wear degradation of the tool (Vb). Each AI approach is optimised to obtain the best achievable results and to be able to compare their relative performances. From the results, it appears that the ANN approach has the best accuracy with an overall accuracy of 88.8%. The second-best approach that achieves similar results is the RF with an accuracy of 86.6%. The other approaches have an average accuracy of 80%. Despite having the best accuracy, neural networks have by far the longest learning time (85s) compared to less than 1 s for all the other approaches. This learning time must be considered as with a larger and more complete database, the learning and inference time can greatly grow. Nonetheless, with the actual computing power, these considerations should not represent any obstacle to real applications as the training can be realised off-line. The results presented in this paper are limited to an ideal case to compare the performance of the different approaches presented. In industrial practice, it is necessary to consider the changes in cutting conditions as well as other variables that can influence the process. Nevertheless, the results of this paper allow a comparison of the approaches presented.

Conflicts of interest

The authors declare that they have no conflicts of interest.

References

[1] W. Xu, L. Cao, Optimal tool replacement with product quality deterioration and random tool failure, Int. J. Prod. Res. 53 (2015) 1736-1745. https://doi.org/10.1080/00207543.2014.957878

[2] A. Jeang, Reliable tool replacement policy for quality and cost, European J. Operat. Res. 108, (1998) 334-344. https://doi.org/10.1016/S0377-2217(96)00368-2

[3] F. Klocke, Manufacturing Processes 1, RWTHedition, Springer, Berlin/Heidelberg, Germany, 2011.

[4] D.E.D. Snr, Sensor signals for tool-wear monitoring in metal cutting operations—a review of methods, Int. J. Mach. Tool. Manuf. 40 (2000) 1073-1098. https://doi.org/10.1016/S0890-6955(99)00122-4

[5] M. Kuntoğlu, A. Aslan, D.Y. Pimenov, Ü.A. Usca, E. Salur, M.K. Gupta, T. Mikolajczyk, K. Giasin, W. Kaplonek, S. Sharma, A review of indirect tool condition monitoring systems and decision-making methods in turning: Critical analysis and trends, Sensors 21 (2020) 108. https://doi.org/10.3390/s21010108
[6] A. Siddhpura, R. Paurobally, A review of flank wear prediction methods for tool condition monitoring in a turning process, Int. J. Adv. Manuf. Technol. 65 (2013) 371-393. https://doi.org/10.1007/s00170-012-4177-1
[7] L. Colantonio, L. Equeter, P. Dehombreux, F. Ducobu, A systematic literature review of cutting tool wear monitoring in turning by using artificial intelligence techniques, Machines 9 (2021) 351. https://doi.org/10.3390/machines9120351
[8] ISO 3685—Tool Life Testing with Single-Point Turning Tools. 1993, Available online: https://www.iso.org/fr/standard/9151.html (last accessed 01/12/2022)
[9] T. Zhao, Y. Liu, L. Neves, O. Woodford, M. Jiang, N. Shah, Data augmentation for graph neural networks, in Proceedings of the AAAI Conference on Artificial Intelligence 35 (2021) 11015-11023.
[10] A. Abraham, Artificial Neural Networks, in: Handbook of Measuring System Design, John Wiley & Sons, Ltd.: Chichester, UK, 2005.
[11] Tensorflow, Available online: https://www.tensorflow.org/?hl=en (accessed 01 December 22)
[12] A. Parmar, R. Katariya, V. Patel, A review on random forest: An ensemble classifier, in: International Conference on Intelligent Data Communication Technologies and Internet of Things, Springer, Cham, 2018, pp. 758-763.
[13] Sci-Kit Learn, Available online: https://scikit-learn.org/stable/ (accessed 01 December 22)
[14] I. Steinwart, A. Christmann, Support vector machines, Springer Science & Business Media, 2008.
[15] L. Jiang, Z. Cai, D. Wang, S. Jiang, Survey of improving k-nearest-neighbor for classification, in: Fourth international conference on fuzzy systems and knowledge discovery (FSKD 2007), 1 (2017) 679-683).

Materials Research Proceedings 28 (2023) 1275-1284 https://doi.org/10.21741/9781644902479-138

Hardware implementation of Monte Carlo and RSM method for the optimization of cutting force during turning of NiTi shape memory alloy

KOWALCZYK Małgorzata[1,a *]

[1]Chair of Production Engineering, Mechanical Faculty, Cracow University of Technology, Avenue Jana Pawła II 37, PL 31-864 Cracow, Poland

[a]malgorzata.kowalczyk@pk.edu.pl

Keywords: NiTi Shape Memory Alloy, Monte Carlo and RSM Methods, Optimization

Abstract. This study was conducted to understand the exact turning of the NiTi shape memory alloy and consisted of four stages: experimental work, function modelling using RSM method, Monte Carlo method optimization and hardware implementation of Monte Carlo method . This article has the following main objectives: to develop a framework for solving machining optimization problems using the Monte Carlo method and hardware implementation of MC method. The solutions presented in this paper are important from the point of view of practical solutions related to the prediction and optimization of the cutting forces components F_c, F_p and F_f during turning of NiTi shape memory alloy.

Introduction

Cutting forces components which have an impact on the tool and on the workpiece causes a certain change in the position of the tool relative to the workpiece. Any displacement of the tool relative to of the workpiece occurring during machining, can adversely affect accuracy dimension of the machined surface. Prediction and optimization of cutting force before real machining can provide significant guidelines to the planning of turning process in particular such difficult to machine of NiTi alloys [1-4].

The shape memory materials are innovative materials with the high application potential. These materials can be used as the smart materials and multifunctional materials due to their memory shape and superelasticity properties [5-7]. But due to their specific properties NiTi alloys are known to be difficult-to-cut materials particularly by using conventional techniques. Their high ductility, high degree of strain hardening, poor thermal conductivity, very low “effective” elastic modulus and unconventional stress–strain behavior are the main properties responsible for their poor machinability [5,6,8,9].

In order to manufacture new products from difficult-to-machine materials, such as shape memory alloys, there is a need to search for more and more effective treatment methods that exceed technological barriers [10-12]. Therefore, an adapted process strategy, prediction and optimization of cutting force is very important when machining NiTi [2,3,13].

The ability to predict and optimization cutting force before machining has attracted great interest from many scientists, being the main goals of many research studies. The prediction and optimization of cutting force is currently determined by using various techniques such as theoretical models [14-15], FE method [4,15-17], the Taguchi procedure [1,2,11,17-20], response surface methodology (RSM) [13, 21-23], the Multi-Objective Ant Lion Optimizer MOALO [21] the multi-response TOPSIS method [3,19], artificial intelligence through the use of the artificial neural networks (ANNs) [15,2-25], genetic algorithms (GAs) [18] and fuzzy logic (FL) [26]. any research works show the use of these methods in the forecasting and also optimization of cutting force [13]. Researchers usually do not use only one modeling approach in their works, but look for

Content from this work may be used under the terms of the Creative Commons Attribution 3.0 license. Any further distribution of this work must maintain attribution to the author(s) and the title of the work, journal citation and DOI. Published under license by Materials Research Forum LLC.

a mutual compilation of the above strategies [18,21,23]. The benefits of using cutting force prediction methods include an increase in the productivity and competitiveness of the production process [1,2,27].

Analyzing the relevant literature regarding the prediction and optimization of machining processes, it can be easily noticed that the current trend is the use of RSM, ANNs, GAs, and the Taguchi procedure for these purposes. The author of this study note that despite the many application possibilities of the MC method [5,10], its application for solving the problems related to the prediction and optimization of machining has not been given much attention in the literature.

Taking into account the above literature review, this paper presents a procedure for model for prediction cutting components force (F_f– the feed force, F_p – the thrust force, F_c – the cutting force) in the turning of NiTi alloy (A_f =60ºC) with PCD tool. The main objective is to develop a model based on response surface methodology (RSM) to the cutting force in terms of machining parameters such as depth of cut (a_p), cutting speed (v_c) and feed rate (f). The computational model enabled to select optimal machining parameters for minimizing cutting forces values. The generation of mathematical models was necessary for the subsequent optimization with the Monte Carlo method, the purpose of which was to find for which cutting parameters the minimum values of the cutting force components are obtained. The algorithm consisted of performing random draws of input parameters from specified ranges for depth of cut, feed rate and cutting speed in a loop.

The next the hardware implementation of the Monte Carlo method was written in the form of code in the software environment, which was uploaded to the microcontroller.

Material Properties

The NiTi alloy used for the experiment was 57.88Ni-42.12Ti (wt%) obtained from Baoji Hanz Metal Material Co.,Ltd. (China). The diameter of the workpiece was 20 mm. The austenite finish temperature was, A_f =60^o C. Table 1 shows the chemical composition (wt. %) of NiTi. The physical, thermal and mechanical properties of the materials of β-TiNi: Tensile Strength, Ultimate, 1364 MPa, Tensile Strength, Yield, 649 MPa, Modulus of Elasticity, 28 GPa, Thermal conductivity, 18 W/m·°C, Hardness, 231 HV, Density, 6500 kg/m^3 , Structure (phase), hi-temp B2 [28-29].

Table 1. The spectroscopy (EDS) analysis results.

β-TiNi		
Element	wt.%	at.%
TiK	42.12	47.15
NiK	57.88	52.85
Total	100	100

Cutting tool

The 80^o rhombic insert of PCD with single-top corner, brazed tip and a positive rake angle was selected for turning of NiTi. The symbol of insert: CCMT 060202 ID5. The new cutting edge was used for each test sample. Each cutting insert was attached to the designated tool holder SCACR 1616K – 06S. The recommends cutting conditions for insert: depth of cut a_p = 0.08- 3.0 mm, feed f = 0.05 – 0.3 mm/rev;. The literature recommends cutting conditions during precise turning of NiTi alloy; cutting speed v_c = 10-50 m/min; feed rate f <0.2 mm/rev; depth of cut a_p<0.5 mm [6-9].

Experimental design

Turning tests were performed in according Taguchi experiment design at three different cutting parameters (feed f, cutting speeds v_c and depth of cut a_p); Taguchi L9 orthogonal array. For the cutting parameters in turning of NiTi, three factors and three levels, as shown in Table 2 [11]. The

parametric design of Taguchi is a very useful technique for elastic design since it provides a simple and systematic empirical effective design at a low cost. It is a method to design an experiment, as it creates the set of arrays with variable factors arranged in such a way that only significant variation is pointed out and the rest insignificant set of variations are neglected thus reducing the number of experiments [2].

Table 2. Cutting parameters.

Parameters	Code	Levels		
		1	2	3
Feed rate, f [mm/rev]	A	0.038	0.058	0.077
Depth of cut, a_p [mm]	B	0.03	0.08	0.13
Cutting speed, v_c [m/min]	C	30	40	50

The following testing equipment was prepared: precise lathe (Masterturn 400), the workpiece (NiTi alloy), CCMT 060202 PCD insert, tool holder SCACR 1616K – 06S, Kistler dynamometer with DynoWere software to visualize measurements [Fig. 1].

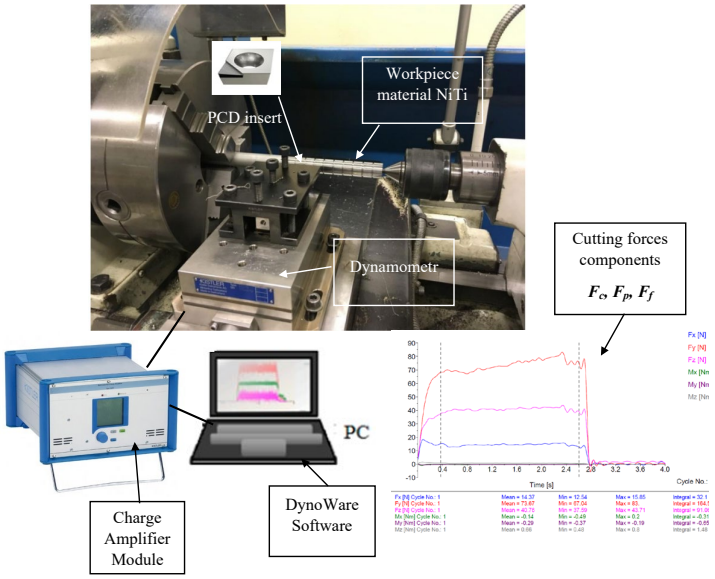

Fig. 1. Experimental set-up for turning of NiTi.

Method

This study was worked out in order to optimize the cutting forces components F_c, F_p and F_f during turning of NiTi shape memory alloy and includes four main stages: experimental work, function modelling using RSM method, Monte Carlo method optimization and hardware implementation of Monte Carlo method. Fig. 2 shows the flow chart which constitutes the overall representation of the methodology developed in the paper. This research has the following main objectives: to develop a framework for solving machining optimization problems using the Monte Carlo method and hardware implementation of MC method.

Experimental work.

The following testing equipment was prepared: precise lathe, work piece (NiTi alloy), tool holder and insert, Kistler dynamometer. Turning tests were carried out in according to Taguchi experiment design (with different feed, cutting speeds and depth of cut). The values of the cutting force components were recorded by the dynamometer and then the cutting force components were in DynoWere software processed (Table 3).

Modelling.

The mathematical relationships between input data and the output parameter-response i.e. cutting force components (F_f , F_p, F_c) Taguchi design was selected. The model for finding parameters of cutting force was appointed using the Response Surface Methodology algorithm.

Monte Carlo Method.

The generation of mathematical models was necessary for the subsequent optimization with the Monte Carlo method, the purpose of which was to find for which cutting parameters the minimum values of the cutting force components are obtained. The algorithm consisted of performing draws of input parameters from specified ranges for depth of cut, feed rate and cutting speed, in a loop.

Hardware implementation.

the Monte Carlo method was written in the form of code in the software environment, which was uploaded to the microcontroller.

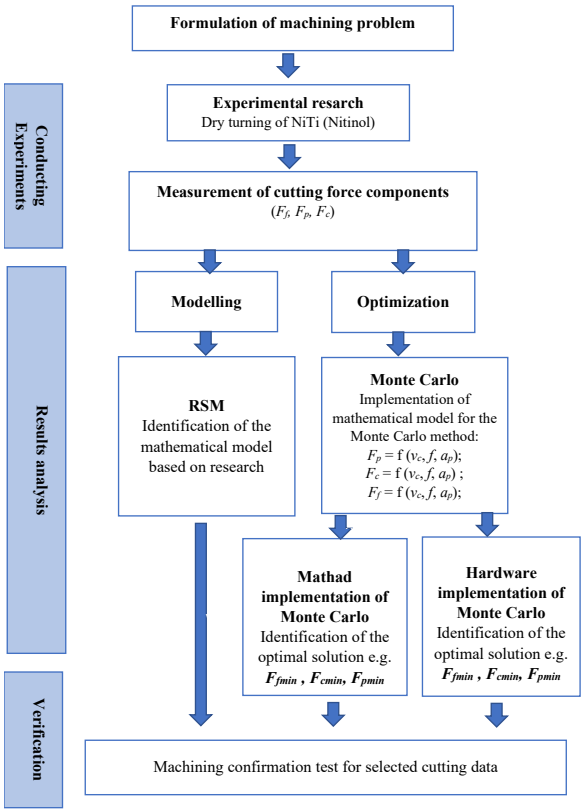

Fig. 2. Flow chart for overall representation of the work methodology.

Results and Discussion

Response surface methodology (RSM).

Response Surface Methodology (RSM) is a series of statistical and mathematical techniques useful for optimizing processes [1,30]. This method is a very effective tool for prediction and modeling the manufacturing problems. It provides more information with a small number of investigations. It is a research strategy to study the limits of input parameters and the emerging experimental statistical model for the measured response, by approximating the existing correlation between the response surface and input process parameters. The limit of the process parameters has to be defined in response surface method, and the first set of experiments was performed to identify machining parameters, which have an impact on the cutting force and to find selected range of cutting parameters [30]. In this study, the cutting speed v_c , depth of cut a_p and the feed f were considered as cutting parameters for monitoring cutting conditions, and the cutting forces components are measured as a response variable (Table 3).

The mathematical model suitable for predicting suitable value is Quadratics model (Eq. 1) where y is a parameter value, describing the investigated physical phenomenon, i.e., the cutting force F_c; b1, b2, …, bi are constant coefficients; and x1, x2, …, xi are factors, which influence the investigated parameter, by considering the full quadratics model as shown in Eq. 2 (F_f – the feed force), Eq. 3 (F_c – the cutting force) and Eq. 4 (F_p – the thrust force).

$$y = bo + b1x1 + b2x2 + b3x3 + b4x4 + b11x12 + b22x22 + b33x32 + b44x42 + b12x1x2 + b13x1x3 + b14x1x4 + b23x3x3 + b24x2x4 + b34x3x4 \quad (1)$$

The mathematical model was established by neglecting the insignificant coefficients of the cuttings forces components (Eq. 2-4):

$$F_f(f, a_p, v_c) = 1.6 + 60.15 \cdot f + 494.26 \cdot a_p - 0.82 \cdot v_c - 5596.04 \cdot f^2 - 3783.73 \cdot a_p^2 \cdot 0.003593 \cdot v_c^2 + 4826.64 \cdot f \cdot a_p + 10.27 \cdot f \cdot v_c \quad (2)$$

$$F_c(f, a_p, v_c) = -381 - 900.2 \cdot f + 2460.6 \cdot a_p + 19.4 \cdot v_c - 14727.8 \cdot f^2 + 7257.6 \cdot a_p^2 - 0.4174 \cdot v_c^2 - 55636.6 \cdot f \cdot a_p + 214.6 \cdot f \cdot v_c \quad (3)$$

$$F_p(f, a_p, v_c) = -24.2 + 1045.5 \cdot f + 1318.1 \cdot a_p - 1.228 \cdot v_c - 17431.4 \cdot f^2 - 4092.9 \cdot a_p^2\ 0.01768 \cdot v_c^2 - 3756.8 \cdot f \cdot a_p + 39.46 \cdot f \cdot v_c \quad (4)$$

The mathematical model was used to for prediction cutting components force (F_f– the feed force, F_p – the thrust force, F_c – the cutting force) in the turning of NiTi alloy (A_f=60°C) with PCD tool by replacing the values of the machining parameters. The impact of cutting cutting parameters was examined using the developed model.

The information in Table 3 shows the result from the comparison between actual value and forecasting value which found that the forecasting values of mean of the feed force F_f has the maximum error of only 1.67%, for mean of the cutting force F_c – 3,93% and for mean of thrust force F_p – 0.23%.

Table 3. Experimental results.

Test no.	Control factors			Measured value (Mean)			Predicted value RSM			% Error		
	f [mm/rev]	a_p [mm]	v_c [m/min]	F_f [N]	F_c [N]	F_p [N]	F_{fRSM} [N]	F_{cRSM} [N]	F_{pRSM} [N]	F_f	F_c	F_p
1	0.038	0.03	30	3.10	32.70	14.20	3.07	31.42	14,17	0.92	3.90	0.23
2	0.038	0.08	40	14.40	73.70	40.80	14.36	72.01	40,76	0.26	2.29	0.09
3	0.038	0.13	50	7.50	67.50	43.40	7.45	65.41	43,36	0.63	3.09	0.10
4	0.058	0.03	40	2.90	108.50	21.30	2.86	106.81	21,26	1.39	1.56	0.18
5	0.058	0.08	50	21.80	53.30	48.50	21.75	51.20	48.46	0.23	3.93	0.09
6	0.058	0.13	30	19.50	121.30	67.60	19.47	119.98	67.56	0.16	1.09	0.05
7	0.077	0.03	50	3.20	169.00	26.50	3.15	166.89	26.45	1.67	1.25	0.17
8	0.077	0.08	30	20.50	66.30	47.50	20.47	64.98	47.46	0.16	1.99	0.07
9	0.077	0.13	40	26.30	118.80	61.70	26.26	117.06	61.66	0.17	1.46	0.07

Monte Carlo method.

The Monte Carlo method is often used in engineering, finance, statistics and other fields of science. Fig. 3 shows a block diagram of the applied MC method for determining the optimal (minimum) values of the factors as shown in Eq.2 (F_f – the feed force), Eq. 3 (F_c – the cutting force) and Eq. 4 (F_p – the thrust force). The optimization task was solved using Mathcad software and hardware implementation. After optimization using the Monte Carlo method, the optimization results were verified experimentally.

The program implementing the assumptions of the Monte Carlo algorithm was written in the Arduino IDE environment, and then uploaded to the Arduino UNO board with the Atmega 328P microprocessor, which is responsible for performing the calculations necessary to carry out the optimization process. In the first part of the program code 'string' and 'int' variables were initialized. They were used to send numbers (in the form of characters) to the microprocessor, which will define the ranges of input parameters (depth of cut a_p, cutting speed v_c, feed rate f, and number of MC draws). Then 'float' values are declared, which will determine the output values (cutting components force F_f– the feed force, F_p – the thrust force, F_c – the cutting force and the values of optimal cutting parameters (v_c, a_p, f). Auxiliary variables have also been introduced, i.e. m - number of MC draws and time - variable responsible for calculating the time program duration. The 'random' function is responsible for generating pseudo-random numbers from a specific range. The program initialization was included in the void setup() function. The void loop function is defined in the following part( ) in which the main part of the code was placed. It contains the way in which the microcontroller reads character type values entered into its memory. The functions responsible for displaying the ranges of input parameters on the terminal were generated. Next a loop implementing the algorithm was placed in the function void loop() Monte Carlo in the final part. The code contains functions responsible for displaying the results received from the microcontroller on the terminal.

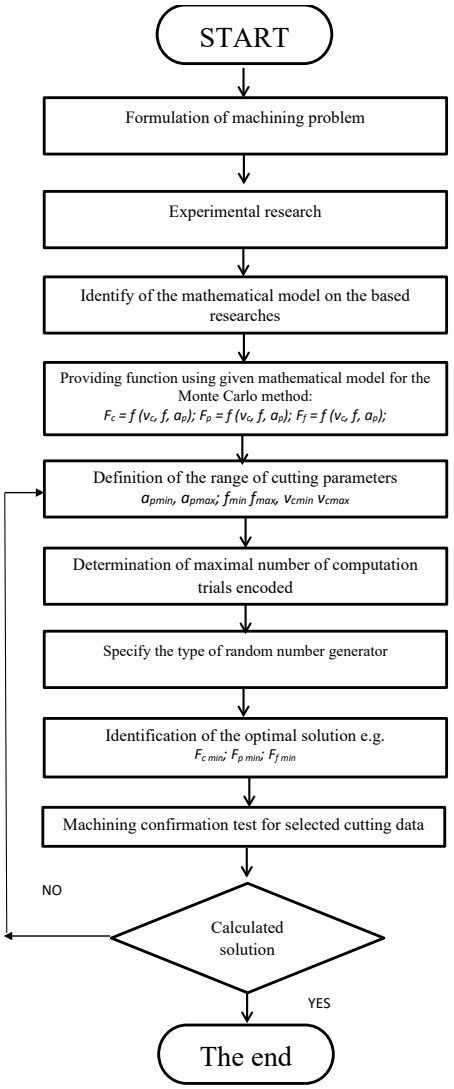

Fig. 3. Monte Carlo method algorithm for solving machining optimization problems [10].

Monte Carlo optimization result.

Table 4 summarizes the results of the calculations of the minimum values (rows 2, 9 and 16) of the functions described by Eq. 2, 3 and 4 and defined by F_f MC min, F_c MC min and F_p MC min for the case of three different numbers of MC draws (the first row): 10^4, 10^5, and 10^6 for Mathcad software and hardware implementation. For the values of the functions F_f MC min, F_c MC min and F_p MC min for all Monte Carlo trials, the corresponding drawing number m (rows 3,10 and 17), the values of parameters f, a_p, and v_c (rows 4–6, 11-13 and 18–20), the measure values of F_f, F_p and F_c (rows 7, 14 and 21) and error of method are determined for Mathcad software and hardware implementation.

Table 4. Calculation results of the minimum value of Eq. 2, Eq. 3 and 4 by using the MC method.

No.	Parameters/Factors	Results MC (Mathcad)			Hardware implementation		
1	MC[no.]	10^4	10^5	10^6	10^4	10^5	10^6
2	$F_f{}^{MC}{}_{min}$	1.028	1.608	1.859	1.037	1.698	1.889
3	m [no.]	4.3	4.787	9.326	4.3	4.787	9.326
4	f [mm/rev]	0.077	0.077	0.077	0.077	0.077	0.077
5	a_p [mm]	0.031	0.03	0.03	0.031	0.03	0.03
6	v_c [m/min]	32.64	30.064	30.042	32.64	30.064	30.042
7	$F_{f\ measure}$	1.81	1.81	1.81	1.81	1.81	1.81
8	*%Error*	43.20	11.16	2.71	42.71	6.19	4.36
9	$F_c{}^{MC}{}_{min}$	71.697	72.503	82.307	71.89	72.78	82.205
10	m [no.]	3.876	8.194	1.169	3.876	8.194	1.169
11	f [mm/rev]	0.038	0.039	0.038	0.038	0.038	0.038
12	a_p [mm]	0.031	0.034	0.032	0.03	0.03	0.03
13	v_c [m/min]	49.285	49.55	49.967	48.94	48.49	48.87
14	$F_{c\ measure}$	79.25	79.25	79.25	79.25	79.25	79.25
15	*%Error*	9.53	8.51	3.86	9.29	8.16	3.73
16	$F_p{}^{MC}{}_{min}$	6.229	6.13	7.75	6.34	6.18	7.83
17	m [no.]	3.876	1.291	4.492	3.876	1.291	4.492
18	f [mm/rev]	0.038	0.039	0.038	0.038	0.038	0.038
19	a_p [mm]	0.031	0.03	0.03	0.03	0.03	0.03
20	v_c [m/min]	49.285	49.766	49.792	48.83	48.26	48.95
21	$F_{p\ measure}$	7.71	7.71	7.71	7.71	7.71	7.71
22	*%Error*	19.21	20.49	0.52	17.77	19.84	1.56

Based on the mathematical model, cutting components force F_f– the feed force, F_p – the thrust force, F_c – the cutting force were optimized using Monte Carlo method. The optimal solution is the following for :

For the feed force F_f *(Mathcad)*: number Monte Carlo trials: 9.326 x10^6, F_f = 1.859 N, f = 0.077 mm/rev, a_p = 0.03 mm, v_c = 30.042 m/min, %error of method: 2.71% .

For the feed force F_f *(hardware implementation)*: number Monte Carlo trials: 9.326 x10^6, F_f = 1.91 N, f = 0.077 mm/rev, a_p = 0.03 mm, v_c = 30.042 m/min, %error of method 4.36% .

For the thrust force F_p *(Mathcad)*: number Monte Carlo trials: 4.492 x10^6, F_p= 7.75N, f = 0.038 mm/rev, a_p = 0.03 mm, v_c = 49.766 m/min, %error of method: 0,52%

For the thrust force F_p *(hardware implementation)*: number Monte Carlo trials: 4.492 x10^6, F_p= 7.82N, f = 0.077 mm/rev, a_p = 0.03 mm, v_c = 48.95 m/min, %error of method: 1.56%

For the cutting force F_c *(Mathcad)*: number Monte Carlo trials: 1.169 x10^6, F_c= 82.307 N, f = 0.038 mm/rev, a_p = 0.032 mm, v_c = 49.967 m/min, %error of method: 3.86%

For the cutting force F_c *(hardware implementation)*: number Monte Carlo trials: 1.169 x10^6, F_c= 81.95 N, f = 0.038 mm/rev, a_p = 0.03 mm, v_c = 48.87 m/min, %error of method: 3.73%

Summary

This paper proposes the Monte Carlo method to predicted and optimized cutting forces based on cutting parameters (cutting speed, feed rate and depth of cut).

The procedure presented in this paper, which is devoted use of Monte Carlo Method for optimization of the cuting forces components (F_c, F_f, F_p) during turning of NiTi alloys , allows for an easy and quick assessment of the obtained results related to the prediction and optimization carried out in the process of conventional machining of NiTi alloys.

The work demonstrates that this method is a quick and effective tool, that enables defining optimal cutting parameters to minimize the cutting force during turning of NiTi alloys.

The important findings are summarized as follows:

1) Prediction accuracy of cutting forces by MC method developed models is efficient both for implementation of MC method in Mathcad software like and hardware implementation of MC method.

2) Comparison of experimental and predicted values of the cutting forces show that a good agreement has been achieved between them (Table 4). The maximum method error was 4.36% for MC draws 10^6. The method is more effective for more MC draws.

3) The Monte Carlo optimization show that the optimal combination of cutting parameters are found to be cutting speed of 50 m/min, feed rate of 0.038 mm/rev, cutting depth of 0.03 mm for the thrust force F_p and the cutting force F_c *and* cutting speed of 30 m/min, feed rate of 0.077 mm/rev, cutting depth of 0.03 mm for feed force F_f .

In this study, the optimization methodology proposed is a powerful approach and can offer to scientific researchers as well industrial metalworking a helpful optimization procedure for various combinations of the workpiece and the cut material tool. The procedure for the cutting force optimization during the turning proposed in this paper can be used to optimize costs and ensure maximum efficiency during applications of turning for NiTi alloy.

References

[1] M. Kowalczyk, Cutting force prediction in ball-end milling of Ni-Ti alloy, Proc. of SPIE 11176 (2019) 11176650-1-11176650-12. https://doi.org/10.1117/12.2536757

[2] R. Agrawal, N. Kumar, K. Parvez, A. Srivastava, M. Sarfaraz Alam, Optimization of cutting force via variable feed rate in dry turning lathe of AISI 304, Mater. Today Proc. 64 (2022) 1182-1187. https://doi.org/10.1016/j.matpr.2022.03.479

[3] S. Lakshmanan, M. Pradeep Kumar, M. Dhananchezian, Optimization of turning parameter on surface roughness, cutting force and temperature through TOPSIS, Mater. Today Proc. in press (2022). https://doi.org/10.1016/j.matpr.2022.09.209

[4] A. Tzotzis, N. Tapoglou, R. K. Verma, P. Kyratsis, 3D-FEM Approach of AISI-52100 Hard Turning: Modelling of Cutting Forces and Cutting Condition Optimization, Machines 10 (2022) 1-16. https://doi.org/10.3390/machines10020074

[5] M. Kowalczyk, K. Tomczyk, Procedure for Determining the Uncertainties in the Modeling of Surface Roughness in the Turning, Mater. 13 (2020) 1-14. https://doi.org/10.3390/ma13194338

[6] B. Dash, M. Das, M. Das, T.R. Mahapatra, D. Mishra, A concise review on machinability of NiTi shape memory alloys, Mater. Today Proc. 18 (2019) 5141-5150. https://doi.org/10.1016/j.matpr.2019.07.511

[7] E. Kaya, I. Kaya, A review on machining of NiTi shape memory alloys: the process and post process perspective, Int. J. Adv. Manuf. Technol. 100 (2019) 2045-2087. https://doi.org/10.1007/s00170-018-2818-8

[8] H. Shizuka, K. Sakai, H. Yang, K. Sonoda, T. Nagare, Y. Kurebayashi, K. Hayakawa, Difficult cutting property of NiTi alloy and its mechanism, J. Manuf. Mater. Process. 4 (2020) 1-15. https://doi.org/10.3390/jmmp4040124

[9] Y. Zhao, K. Guo, J. Li, J. Sun, Investigation on machinability of NiTi shape memory alloys under different cooling conditions, Int. J. Adv. Manuf. Technol. 116 (2021) 1913-1923. https://doi.org/10.1007/s00170-021-07563-9
[10] M. Kowalczyk, Application of the Monte Carlo method for the optimization of surface roughness during precise turning of NiTi shape memory alloy, Proc. of SPIE 10808 (2018) 58 108084P-1 - 108084P-9. https://doi.org/10.1117/12.2501421
[11] M. Kowalczyk, Application of Taguchi method to optimization of surface roughness during precise turning of NiTi shape memory alloy, Proc. of SPIE 10445 (2017) 104455G-1 104455G-11. https://doi.org/10.1117/12.2281062
[12] Y.Z. Zhao. K. Guo, V. Sivalingam, J.-F. Li, Q.-D. Sun, Z.-J. Zhu, J. Sun, Surface integrity evolution of machined NiTi shape memory alloys after turning process, Adv. Manuf. 9 (2021) 446-456. https://doi.org/10.1007/s40436-020-00330-1
[13] H. Zahia, Y.M. Athmane, B. Lakhdar, M. Tarek, On the application of response surface methodology for predicting and optimizing surface roughness and cutting forces in hard turning by PVD coated insert, Int. J. Ind. Eng. Comput. 6 (2015) 267-284. https://doi.org/10.5267/j.ijiec.2014.10.003
[14] Y. Sun, F. Ren, D. Guo, Z. Jia, Estimation and experimental validation of cutting forces in ball-end milling of sculptured surfaces, Int. J. Mach. Tools Manuf. 49 (2009) 1238-1244. https://doi.org/10.1016/j.ijmachtools.2009.07.015
[15] Y. Song, H. Cao, W. Zheng, D. Qu, L. Liu, C. Yan, Cutting force modeling of machining carbon fiber reinforced polymer (CFRP) composites: A review, Compos. Struct. 299 (2022). https://doi.org/10.1016/j.compstruct.2022.116096
[16] R.A. Mali, M.D. Agrahari, T.V.K. Gupta, FE based simulation and experimental validation of forces in dry turning of aluminium 7075, Mater. Today Proc. 27 (2019) 2319-2323. https://doi.org/10.1016/j.matpr.2019.09.120
[17] C.S. Sumesh, A. Ramesh, Optimization and finite element modeling of orthogonal turning of Ti6Al4V alloys: A comparative study of different optimization techniques, Eng. Solid Mech. 11 (2023) 11-22. https://doi.org/10.5267/j.esm.2022.11.002
[18] S.M. Abdur Rob, A.K. Srivastava, Turning of Carbon Fiber Reinforced Polymer (CFRP) Composites: Process Modeling and Optimization using Taguchi Analysis and Multi-Objective Genetic Algorithm, Manuf. Lett. 33 (2022) 29-40. https://doi.org/10.1016/j.mfglet.2022.07.012
[19] N. A. Sristi, P. B. Zaman, N. R. Dhar, Multi-response optimization of hard turning parameters: a comparison between different hybrid Taguchi-based MCDM methods, Int. J. Interact. Des. Manuf. 16 (2022) 1779-1795. https://doi.org/10.1007/s12008-022-00849-6
[20] N. Li, Y.J. Chen, D.D. Kong, Multi-response optimization of Ti-6Al-4V turning operations using Taguchi-based grey relational analysis coupled with kernel principal component analysis, Adv. Manuf. 7 (2019) 142-154. https://doi.org/10.1007/s40436-019-00251-8
[21] B. Hamadi, M.A. Yallese, L. Boulanouar, M. Nouioua, A. Hammoudi, RSM-based MOALO optimization and cutting inserts evaluation in dry turning of AISI 4140 steel, Struct. Eng. Mech. 84 (2022) 17-33. https://doi.org/10.12989/sem.2022.84.1.017
[22] A. Thakur, V. Guleria, R. Lal, Multi-response optimization in turning of EN-24 steel under MQL, Eng. Res. Express. 4 (2022). https://doi.org/10.1088/2631-8695/ac7a0c
[23] R. Kluz, W. Habrat, M. Bucior, K. Krupa, J. Sęp, Multi-criteria optimization of the turning parameters of Ti-6Al-4V titanium alloy using the Response Surface Methodology, Eksploat. i Niezawodn. 24 (2022) 668-676. https://doi.org/10.17531/ein.2022.4.7
[24] T. Palaniappan, P. Subramaniam, Experimental Investigation and Prediction of Mild Steel Turning Performances Using Hybrid Deep Convolutional Neural Network-Based Manta-Ray Foraging Optimizer, J. Mater. Eng. Perform. 31 (2022) 4848-4863. https://doi.org/10.1007/s11665-021-06552-z

[25] D. Peng, H. Li, Y. Dai, Z. Wang, J. Ou, Prediction of milling force based on spindle current signal by neural networks, Measurement 205 (2022) 112153. https://doi.org/10.1016/j.measurement.2022.112153
[26] A. Alalawin, W.H. AlAlaween, M.A. Shbool, O. Abdallah, L. Al-Qatawneh, An interpretable predictive modelling framework for the turning process by the use of a compensated fuzzy logic system, Prod. Manuf. Res. 10 (2022) 89-107. https://doi.org/10.1080/21693277.2022.2064359
[27] E. Altas, O. Erkan, D. Ozkan, H. Gokkaya, Optimization of Cutting Conditions, Parameters, and Cryogenic Heat Treatment for Surface Roughness in Milling of NiTi Shape Memory Alloy, J. Mater. Eng. Perform. 31 (2022) 7315–7327. https://doi.org/10.1007/s11665-022-06769-6
[28] Y. Kaynak, H.E. Karaca, R.D. Noebe, I.S. Jawahir, Tool-wear analysis in cryogenic machining of NiTi shape memory alloys: A comparison of tool-wear performance with dry and MQL machining, Wear 306 (2013) 51-63. https://doi.org/10.1016/j.wear.2013.05.011
[29] K. Weinert, V. Petzoldt, D. Kötter, Turning and drilling of NiTi shape memory alloys, CIRP Ann. - Manuf. Technol. 53 (2004) 65-68. https://doi.org/10.1016/S0007-8506(07)60646-5
[30] M. Subramanian, M. Sakthivel, K. Sooryaprakash, R. Sudhakaran, Optimization of cutting parameters for cutting force in shoulder milling of Al7075-T6 using response surface methodology and genetic algorithm, Procedia Eng. 64 (2013) 690-700. https://doi.org/10.1016/j.proeng.2013.09.144

Materials Research Proceedings 28 (2023) 1285-1294 https://doi.org/10.21741/9781644902479-139

Investigation of surface finish and chip morphology in cryogenic machining biomedical grade polyetheretherketone

SAJJA Nikhil Teja[1,a*], BERTOLINI Rachele[1,b], GHIOTTI Andrea[1,c] and BRUSCHI Stefania[1,d]

[1]Department of Industrial Engineering, University of Padova, Via Venezia 1, 35131, Padova, Italy

[a]nikhilteja.sajja@studenti.unipd.it, [b]rachele.bertolini@unipd.it, [c]andrea.ghiotti@unipd.it, [d]stefania.bruschi@unipd.it

Keywords: Cryogenic Machining, PEEK, Surface Finish, Chip Morphology

Abstract. Polyetheretherketone (PEEK) is attracting the attention of the biomedical field, thanks to its high biocompatibility and wear resistance. Nevertheless, the attainment of good quality surfaces when machining PEEK is still challenging. In this framework, the aim of the paper is to investigate the viability of using cryogenic machining to enhance the surface finish of PEEK compared to the outcomes of dry cutting. To do that, turning trails were executed at varying cooling strategy and depth of cut, and the resultant surface finish and chip morphology were evaluated. The obtained results indicated that cryogenic machining carried out at the highest depth of cut greatly enhanced the PEEK machinability.

Introduction

Polyetheretherketone (PEEK) is a thermoplastic semi-crystalline polymer characterized by an elasticmodulus close to that of human bones, high biocompatibility, stable chemical resistance, and good wearresistance [1]. Thanks to these characteristics, PEEK has been used as a biomaterial in the biomedical area for orthopedic implants since 1987 [2] and is still assessed as one of the most promising polymers for biomedical applications. The conventional route to manufacture PEEK parts comprises machining steps carried out without any cutting fluid to avoid oil residues on the machined surface. Davim and Mata

[3] performed dry turning trials on PEEK bars and studied the effect of PCD tool inserts at varying cuttingspeed and feed. They found that the cutting speed increase and feed decrease contributed to reduce the surface roughness. Abdullah et al. [4] dry-turned the biomedical grade PEEK using carbide tools and optimized the machining parameters, namely cutting speed, feed, and depth of cut to minimize the surfaceroughness. However, dry machining of PEEK is still challenging as the increase in temperature at the cutting zone usually prompts a drastic reduction of the surface quality. A reduced surface finish increasesfriction and accelerates polymer wear rate during the lifespan of the implant: an example is given by acetabular cups, which must be characterized by smooth surfaces when coupled with femoral heads to increase the hip implant performances [5].

To this extent, cryogenic machining can be seen as a possible alternative to dry cutting, which can effectively remove the cutting-generated heat, whilst still preserving the cleanliness of the machined surfaces.

Bertolini et al. [6] investigated the machinability of the polyamide 6 under cryogenic cooling conditions and showed smoother and harder surfaces compared to the ones obtained using a conventionalcutting fluid. Aldwell et al. [7] submerged ultra-high molecular weight polyethylene (UHMWPE) in liquid nitrogen for nearly 24 hours before machining: this process chain was found to lead to a stiffer surface compared to dry conditions. Dhokia et al. [8] froze ethylene-vinyl acetate using liquid nitrogen showing the polymer surface hardening, which, in turn, allowed a 1% dimensional error after machining.Putz et al. [9] studied the influence of cryogenic cooling on

Content from this work may be used under the terms of the Creative Commons Attribution 3.0 license. Any further distribution of this work must maintain attribution to the author(s) and the title of the work, journal citation and DOI. Published under license by Materials Research Forum LLC.

cutting forces and surface integrity of the nitrile-butadiene-rubber elastomer. It was found that, by using the cryogenic coolant, the cutting forceswere increased, but the surface deformation was reduced, promoting a better surface quality compared to that obtained under dry cutting conditions.

According to the literature survey, cryogenic machining of PEEK has been scarcely researched, in particular as regards the impact of the depth of cut on the polymer machinability. In this context, the paper investigates the effect of cryogenic cooling on the PEEK surface finish and the onset of surface defects in comparison with the outcomes from dry cutting. Further, the chip morphology was analyzed and correlated to the machined surface characteristics.

Experimental - Material

The polymer material under investigation was the TECAPEEK^{TM} supplied by Ensinger Plastics. Thisis a biomedical grade used specifically to fix spinal traumas, cruciate ligaments, and meniscal tears. Thematerial was purchased in form of a bar of 42 mm diameter. The PEEK mechanical and thermal properties in the as-received state are listed in Table 1.

Table 1. PEEK mechanical and thermal properties in the as-received state [10].

Property	PEEK
Modulus of elasticity (MPa)	4200
Tensile strength at yield (MPa)	116
Hardness ASTM D2240 (Shore D)	85
Glass transition temperature, T_g (°C)	150
Melting temperature, T_m (°C)	341
Density (g/cm^3)	1.31
Thermal conductivity (W/(k·m))	0.27
Specific heat (J/(g·K))	1.1

Machining Trials

The Mori Seiki^{TM} NL 1500 CNC lathe with the experimental apparatus shown in Fig. 1 (a) was usedto carry out the turning tests. A left-hand tool insert, namely the VCEX 11 03 01L-F 1125 purchased from Sandvik Coromant^{TM}, was used, see Table 2 for its nomenclature. The cutting speed (*Vc*) and feed (*f*) were selected on the basis of the tool manufacturer's guidelines and kept fixed for all the turning trials.On the contrary, it was chosen to vary the depth of cut (*ap*) to evaluate its impact on the PEEK machinability.

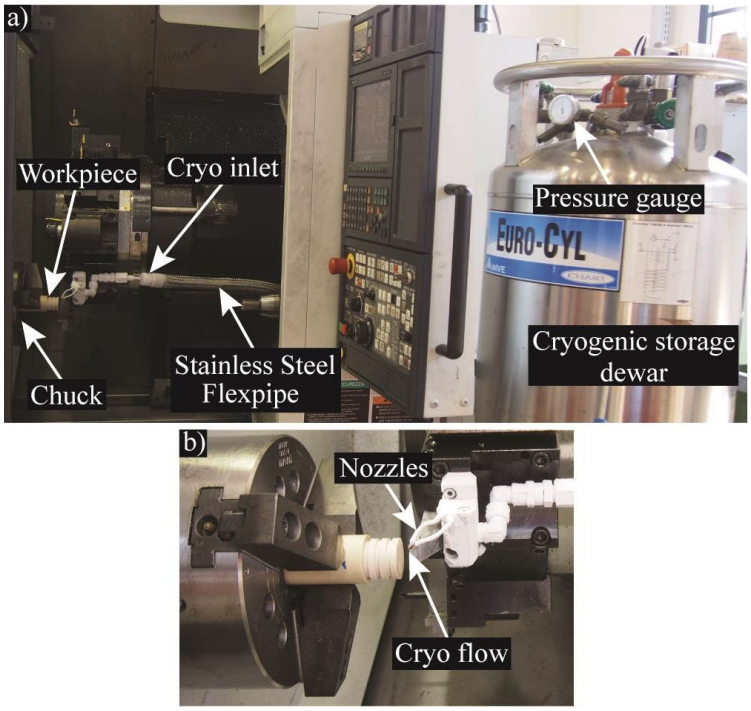

Fig. 1. (a) Machining setup; (b) Closer view of the cutting zone when applying cryogenic cooling.

Table 2. Cutting tool nomenclature and specifications.

ISO code	VCEX 11 03 01L-F 1125
Cutting edge effective length (mm)	10.971
Corner radius (mm)	0.1
Major cutting edge angle (°)	93
Insert thickness (mm)	3.175
Rake angle (°)	5.5
Clearance angle major (°)	7

At first, the external layer of the as-received PEEK bar was removed to eliminate any defect and dimensional error. On this basis, a turning step was performed to achieve a 40 mm diameter by using a cutting speed of 100 m/min, feed of 0.1 mm/rev, and depth of cut of 1 mm.

The turning tests were conducted under both dry and cryogenic cooling conditions with three repetitions for each experimental condition. The liquid nitrogen was stored in a Dewar tank at 15 bars. Two copper nozzles of 0.9 mm diameter were used to spray the liquid nitrogen to the tool flank and rakefaces simultaneously (see Fig. 1 (b)). In each experimental run, the approximate lead time for liquid nitrogen to stabilize was 30 seconds. Table 3 reports the experimental plan of the machining trails.

Table 3. Cutting parameters.

Cutting speed (m/min)	200
Feed (mm/rev)	0.1
Depth of cut (mm)	0.15, 0.25, 0.5
Cooling condition	Dry, Cryogenic
Liquid nitrogen mass flow rate (Kg/s)	0.0058
Length of cut (mm)	5

Surface Quality and Chip Morphology Characterization

The Sensofar PLu Neox™ optical profiler with a 20x magnification Nikon™ confocal objective wasused to analyze the machined surface finish. The scanned surfaces were then assessed using the SensoView™ software.

According to the ISO 25178-2:2012 standard, the surface texture was evaluated in terms of surface roughness, namely the arithmetical mean height (*Sa*), reduced peak height (*Spk*), and reduced valley depth (*Svk*). These surface texture parameters were selected as indicative of the machining quality. According to [11], *Spk* can be related to the wear properties of a surface, while *Svk* to characteristics such as fluid retention properties. The *Spk*/*Svk* ratio was also evaluated to assess the distribution of valleys and peaks on the machined surface.

Scanning electron microscope (SEM) analysis was carried out using a FEI™ QUANTA 450 to evaluate the possible presence of defects on the machined surfaces. To do such analysis, the samples were gold-sputtered with 25 mA for 3 minutes using the Denton Vacuum™ Desk V machine.

After each turning trial, the chips were collected and analyzed using light optical microscope (LOM)and SEM with the aim of evaluating their morphology at varying cutting parameters. In addition, the cutting ratio (*r*) was calculated on the basis of Eq. 1:

$$r = \frac{t_0}{t_c} \tag{1}$$

where t_o is the uncut chip thickness, equal to the feed, and t_c the chip thickness measured using LOM.

Results and Discussion

Surface texture of the machined samples.

Fig. 2 reports the average values of *Sa* along with their standard deviation bars as a function of the depth of cut and cooling strategy.

In the case of dry cutting, a clear trend cannot be identified since the surface roughness was improvedby varying *ap* from = 0.15 mm to = 0.25 mm, and later it was increased at *ap*=0.5 mm, On the contrary,when using the cryogenic cooling strategy, a strong reduction of the surface roughness was observed at increasing depth of cut. 25% and 36% decreases were found for *ap*=0.25 mm and *ap*=0.5 mm with respectto the lowest depth of cut, respectively. At the highest depth of cut, the section of the chip was increasedas well as its brittleness when deformed at lower temperatures. This made its breakage easier, as it will be later documented.

Regardless of the depth of cut, cryogenic cooling was effective in reducing the surface roughness compared to dry cutting. This is due to the fact that the cryogenic fluid cools down the polymer materialvery rapidly, reducing its elongation at rupture and, therefore, overall ductility.

On the contrary, in case of dry cutting, the much higher ductility induced by the higher cutting temperatures results in uneven surfaces, as the material is too easily deformed.

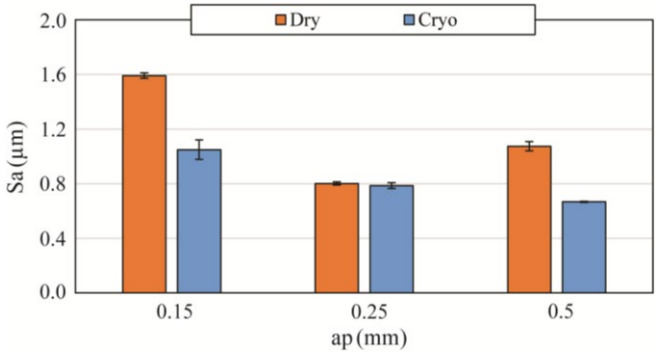

Fig. 2. Sa under dry and cryogenic cooling conditions as a function of the depth of cut.

Further, *Svk* and *Spk* values were analyzed and the results are reported in Fig. 3. For both the coolingstrategies, except at the highest depth of cut that induced both peaks and valleys almost characterized bythe same height, wider valleys and shallow peaks were produced compared to the lowest depth of cut. Both the height of the valleys and depths of the peaks were reduced at increasing depth of cut, regardlessof the cooling strategy. Specifically, the cryogenic strategy assured the heights of the peaks increased by37% and 6% for *ap*=0.15 mm and *ap*=0.25 mm compared to *ap*=0.5 mm, respectively. Similarly, the depths of the valleys increased by 271% and 124% for *ap*=0.15 mm and *ap*=0.25 mm compared to *ap*=0.5mm, respectively.

Cryogenic machining helped in reducing the height of the peaks and especially in increasing the depthof the valleys. The latter was increased by 35%, 12% and 7% at *ap*=0.15 mm, *ap*=0.25 mm, and *ap*=0.5mm compared to the dry cases, respectively.

Having a surface characterized by shallow peaks and deep valleys may help to increase the surface wear resistance as this kind of surface can assure both fluid accessibility and accumulation of the wear debris. In general, deep valleys function as fluid reservoirs to decrease friction and wear by reserving and supplying fluid to the bearing surfaces. Additionally, wear debris can accumulate within deep valleyfeatures. Consequently, abrasive wear produced by third-body wear particles can be reduced [12].

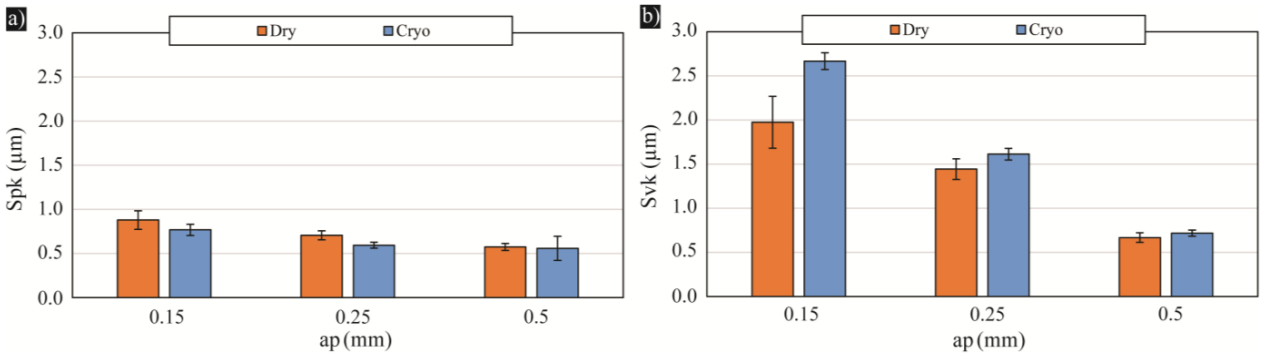

Fig. 3. Spk and Svk under dry and cryogenic cooling conditions as a function of the depth of cut.

The *Spk*/*Svk* ratio was calculated to understand the peculiar nature of the surface texture. In particularthis ratio refers to the average distributed ratio of the peaks and valleys on the machined surfaces. In all the investigated cases, the lowest depth of cut and the use of cryogenic cooling led to the *Spk*/*Svk* reduction, meaning that the surface is dominated by valleys, see Fig. 4.

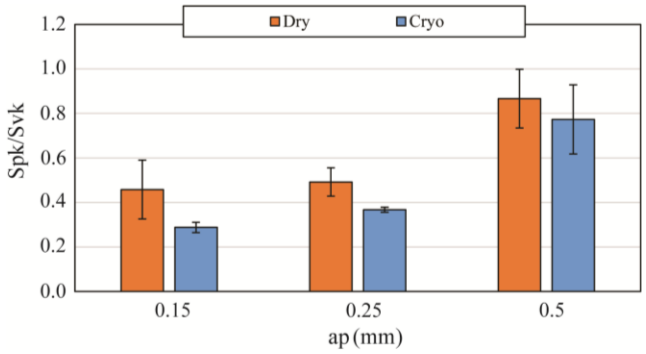

Fig. 4. Spk/Svk under dry and cryogenic cooling conditions as a function of the depth of cut.

The SEM images of the machined surfaces at varying depth of cut are given in Fig. 5. Regardless of the depth of cut, grooves adjacent to feed marks, flakes, and tearing caused by micro-peeling were observed in dry conditions. The highest density of defects was found at the lowest depth of cut, whereasthe lowest density of defects was at the intermediate depth of cut.

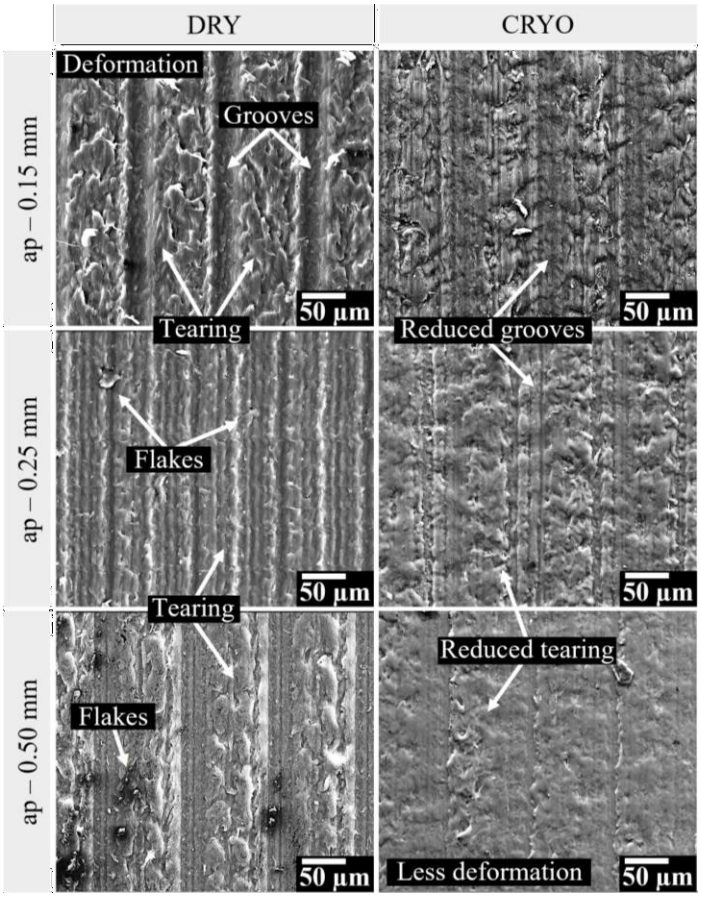

Fig. 5. Dry and cryogenic machined surfaces appearance as a function of the depth of cut.

When applying cryogenic cooling, defects were significantly reduced: the grooves disappeared as wellas the tearings. On the other hand, the cryogenic machined surfaces were characterized by bump-shapedfeatures. A nearly defects-free surface was obtained at the highest depth of cut. These findings on the surface appearance well match the surface roughness data shown in Fig. 2.

The attainment of surfaces with a lower amount of defects in the case of cryogenic machining can beascribed to the cutting temperature. In fact, dry machining can drastically increase the polymer temperature in the cutting zone, which induces a significant increase in its ductility, leading to the material tearing instead of a proper cutting [13].

The chip morphology was assessed as well to be correlated with the surface finish. Fig. 6 and Fig. 7 show the chips at different magnifications as a function of the cutting conditions. The chip morphology was determined according to the ISO 3685-1977 (E) standard [14]. In dry machining, the increase in thedepth of cut led to a change of the chip morphology from continuous tubular snarled to continuous ribbonsnarled chips. This can be ascribed to the increase of ductility given by the temperature increases when adopting more severe process parameters. This is confirmed by the higher magnification images reportedin Fig. 7, which show the presence of a higher amount of shear marks that are indicative of attainment ofhigh strain in the chip.

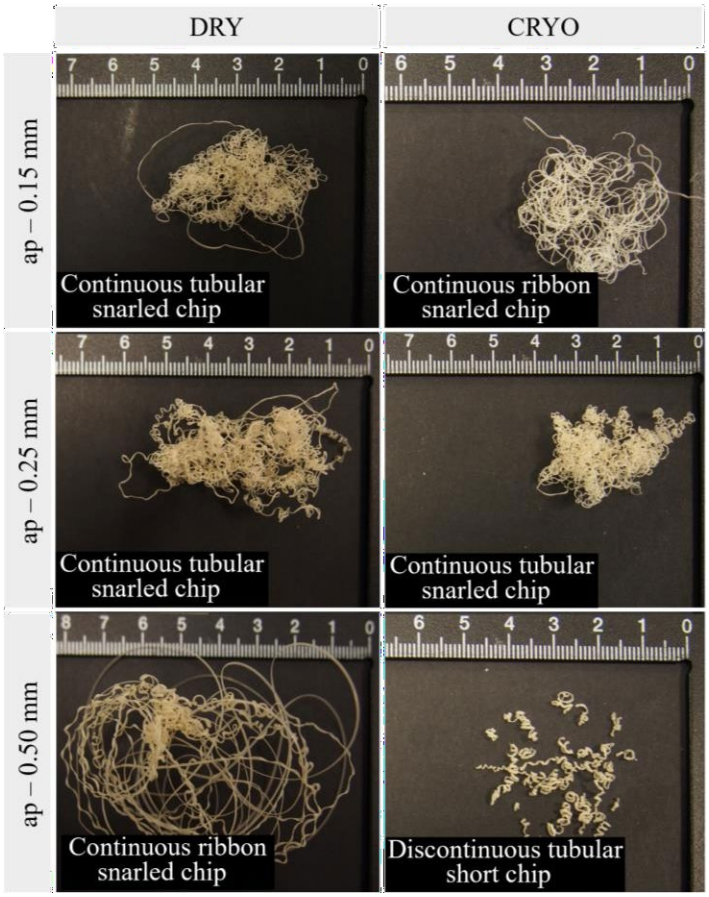

Fig. 6. Morphology of the chips obtained under dry and cryogenic cooling conditions as a function of the depth of cut.

In the case of cryogenic machining, continuous ribbon snarled chips, continuous tubular snarled chips,and discontinuous tubular short chips were formed at *ap*=0.15 mm, *ap*=0.15 mm, and *ap*=0.5 mm, respectively. The breakage of the chip at the highest depth of cut can be ascribed to the synergistic presence of low temperatures and high stresses due to the highest material removal rate. Discontinuous chips can indeed be produced when high compressive stresses are involved or when a brittle material is machined [15].

Actually, Fig. 7 evidences that the shear marks are more emphasized and more frequently observed in the case of the highest depth of cut as a result of the brittleness of the material as a

consequence of thelow temperature during cryogenic machining. A fracture can be more likely to nucleate from these shearbands, and then propagate leading to the macroscopic rupture of the chip.

Similar, even if not equal, evidences were found at the lowest and intermediate depths of cut: even though cryogenic machining did not induce a change in the chip morphology, it reduced the bulkiness and lengths of the formed chips with the respect to the dry case.

The presence of discontinuous chips assures the formation of a surface characterized by a lower amount of defects as shown in Fig. 5. If the cutting temperature is kept well below the polymer rubbery region, the polymer is subjected to a lower deformation, which reduces defects like tearings.

It is worth underlining that discontinuous chips are usually desired in turning operations because theyare less likely to entangle on the machine surfaces and machine tools [5].

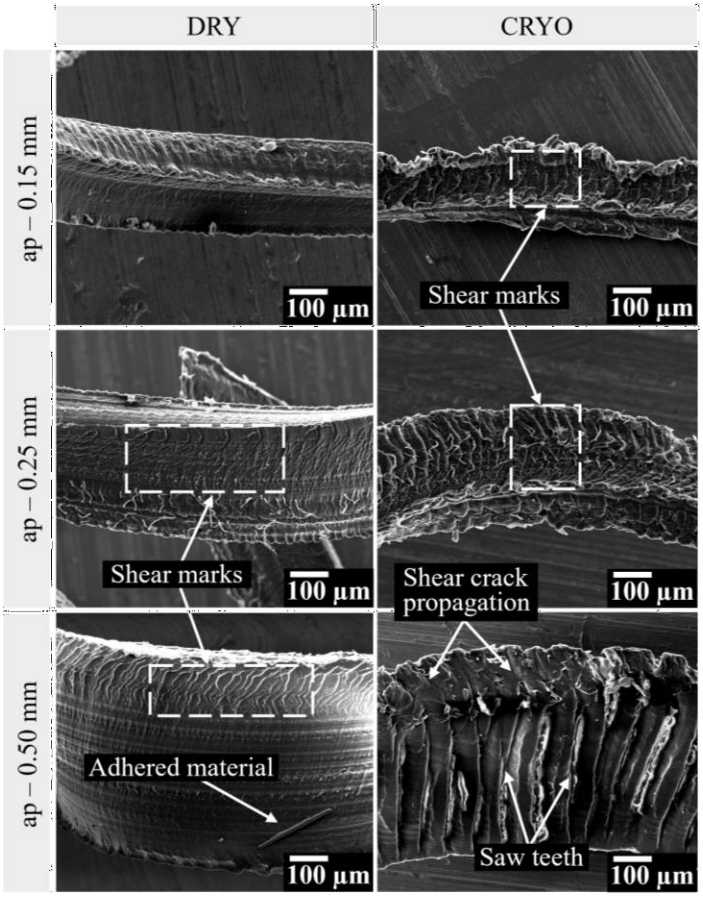

Fig. 7. SEM images of free surfaces of the chips obtained under dry and cryogenic cooling conditions as a function of the depth of cut.

The cutting ratio (r) can be considered a machinability index, being influenced by the nature of the chip-tool interaction, chip contact length, and morphology.

Fig. 8 reports the cutting ratio as a function of the process parameters. Regardless of the depth of cut,the cutting ratio is higher under cryogenic cooling conditions compared to dry ones. To a higher cuttingratio corresponds a higher shear angle and a lower shear plane area that leads to a decrease in the shear force needed to form the chip. This can be attributed to a reduction in the friction angle thanks to the application of cryogenic cooling. This in accordance with [16], where it was stated that the lower the friction coefficient the higher the shear angle.

Only in the case of dry cutting, a slight cutting ratio increase was observed at increasing depth of cut.This confirms the predominance of the temperature effects over the mechanical ones in a dry environment.

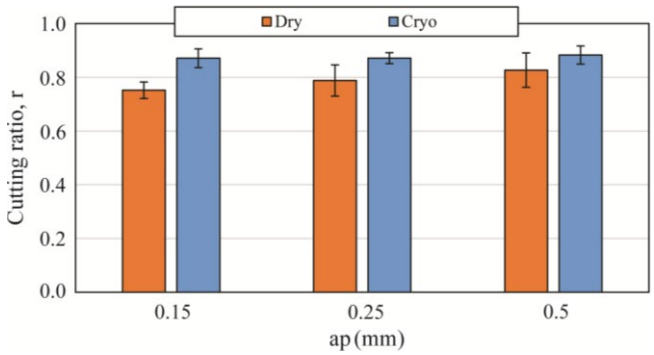

Fig. 8. Cutting ratio under dry and cryogenic cooling conditions as a function of the depth of cut.

Summary

The paper investigated the influence of the depth of cut and coolant strategy on the surface finish andchip morphology in machining biomedical grade PEEK.
The following results can be drawn:

- At increasing depth of cut, smoother surfaces were obtained in cryogenic machining, whereas noclear effect was found in dry machining.
- Cryogenic machining led to a decrease in the height of the peaks, resulting in a surface finish improvement, compared to dry machining. On the other hand, at increasing depth of cut, the height of the peaks was reduced, with consequent improvement of surface finish, regardless of the cooling condition.
- Under cryogenic cooling condition and at the lowest depth of cut, a reduction in the *Spk*/*Svk* ratiowas observed.
- Cryogenic machining lowered the amount of surface defects compared to dry machining. An increase in the depth of cut under cryogenic cooling condition contributed to improve the machined surface quality.
- The chip breakage was obtained solely when the highest depth of cut and cryogenic cooling condition were applied. For the other depths of cut considered, cryogenic machining reduced the bulkiness and lengths of the formed chips with the respect to the dry case.
- The cutting ratio values under cryogenic cooling condition were higher than those obtained underdry conditions at all the depths of cuts.
- A slight increase in the cutting ratio was observed at increasing depth of cut, solely in the case ofdry cutting.

Acknowledgements

This project has received funding from the European Union's Horizon 2020 research and innovationprogram under the Marie Skłodowska-Curie grant agreement No. 956097.

References

[1] Y. Li, X. Cheng, S. Ling, G. Zheng, H. Liu, He, Study of milling process basics for the biocompatible PEEK material, Mater. Res. Exp. 7 (2020) 015412. https://doi.org/10.1088/2053-1591/AB6A5A
[2] S. Kurtz, PEEK Biomaterials Handbook, 2012. https://doi.org/10.1016/C2010-0-66334-6

[3] J.P. Davim, F. Mata, Chemical vapour deposition (CVD) diamond coated tools performance in machining of PEEK composites, Mater. Des. 29 (2008) 1568-1574. https://doi.org/10.1016/j.matdes.2007.11.002
[4] R. Izamshah, A. Long, M.A. Md Ali, M. Kasim, M.H. Abu Bakar, S. Subramonian, Optimisation of Machining Parameters for Milling Polyetheretherketones (PEEK) Biomaterial, Appl. Mech. Mater. 699 (2014) 198-203. https://doi.org/10.4028/www.scientific.net/AMM.699.198
[5] K. Arora, A.K. Singh, Magnetorheological finishing of UHMWPE acetabular cup surface and its performance analysis, Mater. Manuf. Process. 35 (2020) 1631-1649. https://doi.org/10.1080/10426914.2020.1784928
[6] R. Bertolini, A. Ghiotti, S. Bruschi, Machinability Of Polyamide 6 Under Cryogenic Cooling Conditions, Procedia Manuf. 48 (2020) 419-427. https://doi.org/10.1016/j.promfg.2020.05.064
[7] B. Aldwell, J. O'Mahony, G.E. O'Donnell, The Effect of Workpiece Cooling on the Machining of Biomedical Grade Polymers, Procedia CIRP 33 (2015) 305-310. https://doi.org/10.1016/j.procir.2015.06.058
[8] V.G. Dhokia, S.T. Newman, P. Crabtree, M.P. Ansell, A methodology for the determination of foamed polymer contraction rates as a result of cryogenic CNC machining, Robot. Comput.-Integr. Manuf. 26 (2010) 665-670. https://doi.org/10.1016/j.rcim.2010.08.003
[9] M. Putz, M. Dix, M. Neubert, G. Schmidt, R. Wertheim, Investigation of Turning Elastomers Assisted with Cryogenic Cooling, Procedia CIRP 40 (2016) 631-636. https://doi.org/10.1016/j.procir.2016.01.146
[10] Biocompatible PEEK medical grade - TECAPEEK MT natural, Ensinger, Available: https://www.ensingerplastics.com/en/shapes/products/medical-peek-tecapeek-mt-natural (accessed 06 February 2023)
[11] M. Giordano, F. Villeneuve, L. Mathieu, Product Lifecycle Management: Geometric Variations. 2013. https://doi.org/10.1002/9781118557921
[12] Q. Allen, B. Raeymaekers, Surface Texturing of Prosthetic Hip Implant Bearing Surfaces: A Review, J. Tribol. 143 (2021) 040801. https://doi.org/10.1115/1.4048409
[13] R. Ghosh, J. Knopf, D. Gibson, T. Mebrahtu, G. Currie, Cryogenic Machining of Polymeric Biomaterials: An Intraocular Lens Case Study, in: In Medical Device Materials IV: Proceedings of the Materials &Processes for Medical Devices Conference, 2007, p. 54. https://doi.org/10.1361/cp2007mpmd054
[14] Z. Viharos, S. Markos, C. Szekeres, ANN-based chip-form classification in turning, In Proceedings of the XVII. IMEKO World Congress-Metrology in the 3rd Millennium. (2003) 1469-1473.
[15] M. Kaiser, F. Fazlullah, S. Ahmed, A comparative study of characterization of machined surfaces of some commercial polymeric materials under varying machining parameters, Journal of Mechanical Engineering, Automation and Control Systems. 1 (2020) 75-88. https://doi.org/10.21595/jmeacs.2020.21643
[16] H. Autenrieth, M. Weber, J. Kotschenreuther, V. Schulze, D. Löhe, P. Gumbsch, J. Fleischer, Influence of friction and process parameters on the specific cutting force and surface characteristics in micro cutting, Proceedings of the 10th CIRP International Workshop on Modeling of Machining Operations 6 (2007) 539-548. https://doi.org/10.1080/10910340802518728

Materials Research Proceedings 28 (2023) 1295-1302 https://doi.org/10.21741/9781644902479-140

Cutting force in peripheral milling of cold work tool steel

TAMURA Shoichi [1,a *] and MATSUMURA Takashi [2,b]

[1]Ashikaga University, 268-1 Omae-cho, Ashikaga-shi, Tochigi, 326-8558, Japan

[2]Tokyo Denki University, 5 Senjyu Asahi-cho, Adachi-ku, Tokyo, 120-8551, Japan

[a]tamura.shoichi@g.ashikaga.ac.jp, [b]tmatsumu@cck.dendai.ac.jp

Keywords: Cutting Force, Residual Stress, Surface Finish, Heat Treatment

Abstract. Tool steels have been commonly applied to die and mold parts because of the high strength and the high abrasive wear resistance obtained by the heat treatments. In order to achieve high machining rate, the heat-treated tool steels have recently finished with end mills coated by hard thin layers. The cutting force in milling of the tool steel should be controlled to improve the fatigue lives of die and mold, which are associated with not only the surface qualities but also the microstructure in the subsurface. This paper discusses the cutting process in milling of a cold work tool steel in terms of the cutting force and the residual stress in finished subsurface.

Introduction

Tool steels have been applied to die and mold manufacturing due to their excellent mechanical strengths, and wear resistances. Milling of tool steel has been usually performed before quenching of workpiece, then the hardened product has been finished in polishing so far. Because hard milling without polishing is required to improve productivity and product quality, advanced cutting tool and coating materials, such as gradient cemented carbide with different grain sizes, has been developed [1].

Durakbasa et al. [2] performed milling of AISI H13 hot work tool steel to optimize end cutting parameters by Taguchi method. The authors summarized that an end mill coated with AlTiN showed better performance regarding the surface finish and the tool wear resistance in comparison to TiAlCN and ZrN coatings. Aramcharoen et al. investigated the effects of coating materials in milling of hardened tool steel H13 with a 0.5 mm diameter micro end mill [3]. They concluded TiN coated tool was effective to control the tool wear, the chipping, the surface finish, and the burr formation.

Furthermore, the die and molding manufacturing has recently required for control of the affected layer and the residual stress in subsurface in terms of lives of die and mold. Denkena et al. conducted hard millings for AISI H13 [4]. They reported that the undercut geometry of the flank face reduced the tensile residual stress and the tool wear. Caruso et al. investigated the residual stress in subsurface in dry orthogonal cutting of AISI 52100 steel [5]. The large compressive residual stress was obtained in cutting of a harder workpiece with a chamfered tool. Although a large number of experiments have been conducted to investigate the cutting characteristics of tool steels so far, the analytical works have not yet been done so much to discuss the cutting process of hardened tool steels in terms of the properties of surface and subsurface.

The paper studies the cutting process in peripheral milling of a hardened cold tool steel comparing with a carbon steel. The cutting tests are conducted to measure the cutting force and the residual stresses and observe the surface finish. The cutting processes, then, are discussed in an analytical force model. The residual stress in subsurface was associated with the shear plane cutting model.

Content from this work may be used under the terms of the Creative Commons Attribution 3.0 license. Any further distribution of this work must maintain attribution to the author(s) and the title of the work, journal citation and DOI. Published under license by Materials Research Forum LLC.

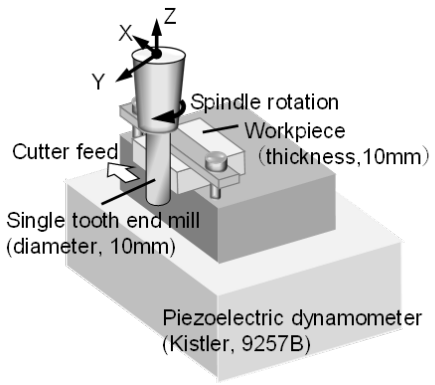

Fig. 1 Cutting test in peripheral milling.

Table 1 Cutting conditions.

Axial depth of cut [mm]	10
Radial depth of cut [mm]	0.1
Cutting speed [m/min]	25
Feed rate [mm/tooth]	0.05
Cutting direction	Down-cut
Lubrication	Dry

Cutting Test

The cutting tests in peripheral milling were conducted on a 3-axis machining center (FANUC Robodrill α-T14iF), as shown in Fig. 1. A 10 mm thick plate of tool steel (JIS, SKD11) was employed as a workpiece for the cutting test. The workpiece was quenched and tempered at 1020℃ and 220℃ in a vacuum furnace, and controlled the hardness of 54 HRC before the cutting test. In addition, a plate of carbon steel (JIS, S50C) with a controlled hardness of 14 HRC was also used as a reference. The workpiece was clamped on a piezoelectric dynamometer (Kistler, 9257B) mounted on the machine table to measure the cutting force. A single tooth square end mill coated with AlCN thin layer, which was ground off one tooth from the original two teeth end mill, was employed to exclude the influence of the cutter runout. The tool diameter and the helix angle were 10 mm and 30°, respectively. The end mill was clamped to the spindle of the machine tool with a collet chuck. The reference surface was machined to control the radial depth of cut before the cutting test. The end mill was fed along +X direction in down-cut peripheral milling at an axial depth of cut of 10 mm, and a radial depth of cut of 0.1 mm, as shown in Table 1. In order to reduce the vibration occurring in the initial cutting state with the sharp edge, the flank wear land was control so as to contact the workpiece in a width of approximately 20 μm by preliminary cutting, where the cutting speed, the feed rate, and the feed travel were 25 m/min, 0.1 mm/tooth, and 30 mm, respectively. The low cutting speed for milling of steel was set to reduce tool vibration, even though the cutting speed was possibly associated with the surface finish. Then, the residual stresses of the machined surfaces were measured in the feed direction (X-axis) and the axial direction (Z-axis) to compare with the residual stress measured before machining, where the machined surfaces were not processed for the measurements. The residual stresses were measured with an X-ray residual stress analyzer (Pulstec, μ-X360s) based on the cos α method [6]. The measurements for each workpiece were conducted at three points on the center line of workpiece thickness.

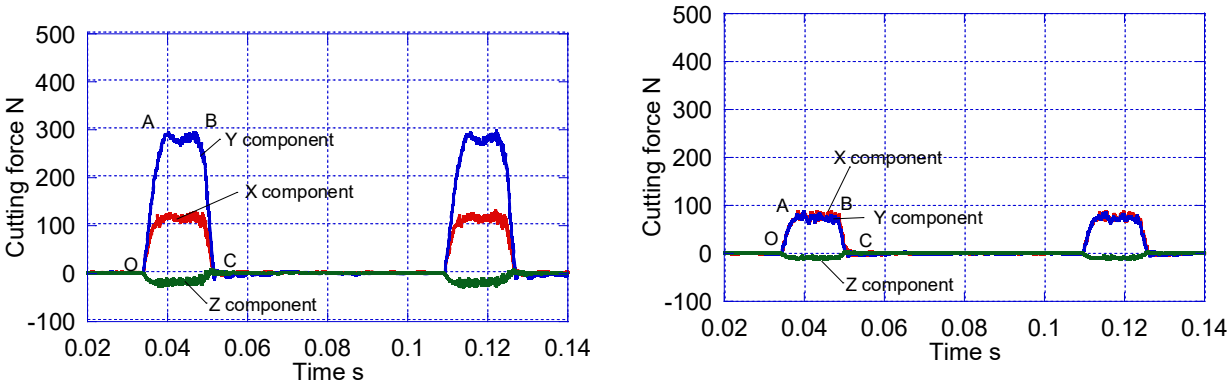

(a) Tool steel (b) Carbon steel

Fig. 2 Cutting forces.

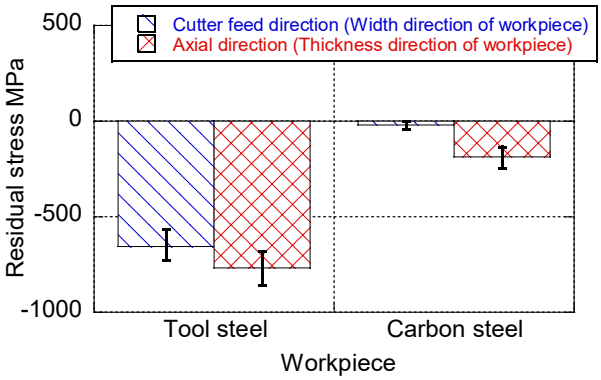

Fig. 3 Residual stresses in subsrface.

Cutting Force in Milling of Cold Work Tool Steel

Figure 2 compares the measured cutting forces in milling of tool steel and carbon steel at a cutting speed of 25 m/min and a feed rate of 0.05 mm/tooth. The cutting force changes periodically in 0.75 s of the tool rotation cycle. Since the cutting area of the helical end mill changes with the cutter rotation, the cutting force changes as:

1) the lowest point on the edge penetrates the bottom of the workpiece plate at O;
2) cutting force increases with the cutting area in O−A;
3) the cutting area moves upward and the cutting force becomes constant without changing the cutting area in A−B;
4) the cutting force decreases in B−C with the cutting area after the cutting edge exits from the top of the workpiece plate.

The large cutting force in milling of tool steel is confirmed because of the higher hardness, where the X and Y components of tool steel are 1.5 and 3.9 times larger than those of carbon steel. The Y component becomes significantly large in comparison to the X component in milling of tool steel. It suggests that the indentation effect of the edge radius is greater than that in milling of carbon steel, as described later.

Materials Research Proceedings 28 (2023) 1295-1302 https://doi.org/10.21741/9781644902479-140

Surface Finish and Residual Stress

Fig. 3 shows the residual stresses of tool steel and carbon steel, where the positive value is estimated as tensile. The compressive residual stress of tool steel is much larger than that of carbon steel. The surface finishes and the height distributions were observed with a laser microscope (Keyence, VK9700), as shown in Fig. 4. The relatively better surface was obtained in milling of tool steel, as shown in Fig. 4(a), even though chatter marks are slightly left on the finished surface. Regarding the height distributions of the surface finishes, as shown in Fig. 4(b) and (d), the height differences are 9 and 20 μm tool steel and carbon steel, respectively. The built-up edge may overcut the workpiece in milling of carbon steel.

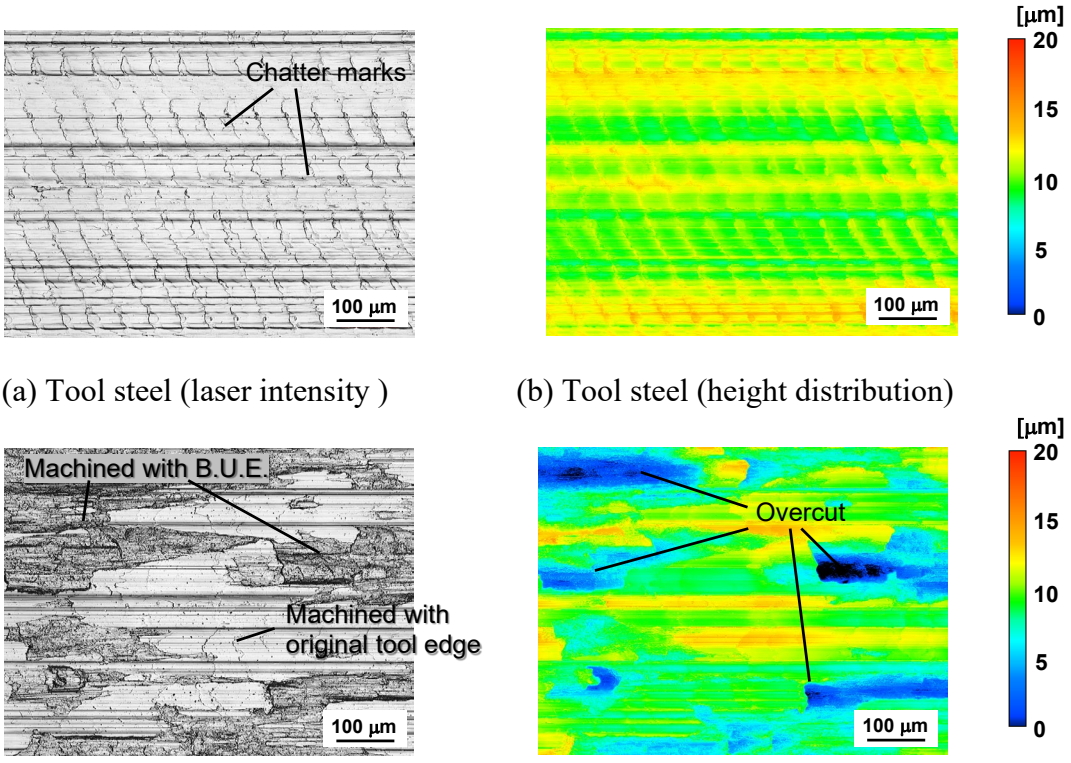

(a) Tool steel (laser intensity) (b) Tool steel (height distribution)

(c) Carbon steel (laser intensity) (d) Carbon steel (height distribution)

Fig. 4 Surface finishes.

Analytical Force Model in Milling

A force model is applied to characterize the cutting process in peripheral milling of tool steel. The force model in milling was presented in Reference [7]. The force model is briefly described here. A three-dimensional chip flow in milling is interpreted as a piling up of the orthogonal cuttings in the planes containing the cutting velocities V and the chip flow velocities V_c, as shown in Fig. 5. Although plastic deformation occurs in the chip formation, the interaction between each orthogonal cutting plane is ignored on the assumption that a rigid chip flows at an angular velocity. The orthogonal cutting models are given by the following equations:

$$\left.\begin{aligned}\phi &= \exp(A_{00}V + A_{01}t_1 + A_{02}\alpha + A_{03})\\ \tau_s &= \exp(A_{10}V + A_{11}t_1 + A_{12}\alpha + A_{13})\\ \beta &= \exp(A_{20}V + A_{21}t_1 + A_{22}\alpha + A_{23})\end{aligned}\right\} \quad (1)$$

Materials Research Proceedings 28 (2023) 1295-1302 https://doi.org/10.21741/9781644902479-140

where ϕ, τ_s and β are the shear angle, the shear stress on the shear plane, and the friction angle. V, t_1 and α are the rake angle, the cutting velocity, and the uncut chip thickness in the orthogonal cutting. A_{ij} (i = 0,1,2; j=0,1,2,3) are parameters acquired in the orthogonal cutting tests. The data can also be identified or refined with referring to the actual cutting force in milling by inverse analysis [8]. The cutting force should be regarded as the sum of the indentation force component due to the ploughing and the chip generation force component due to shearing in the shear zone and friction on the rake face. For the sake of simplicity, this study employs the orthogonal cutting data expressed as Eq. (1) on the assumption that the chip generation force component is the major effect here, where the indentation force component is implicitly associated with the parameters for the uncut chip thickness. Regarding friction on the rake face, the friction angle associated with the friction coefficient is controlled by the third equation in Eq. (1). Because the orthogonal cutting data are acquired in the actual cutting tests for the combination of the tool and the workpiece materials, friction in the interface between the tool face and the chip is characterized in the actual cutting. The shear angle and the shear stress on the shear plane depend on the material behavior. The thermal effect on the material behavior may be mainly controlled by the first term related to cutting velocity dependency, which is associated with the cutting temperature. Because the cutting energy is consumed into the shear energy in the shear plane and the friction energy on the rake face, the cutting energy is estimated in the chip flow model consisting of the orthogonal cuttings. Because the cutting energy depends on the chip flow direction, the chip flow angle is determined to minimize the cutting energy. Therefore, the cutting force is predicted in the determined chip flow model.

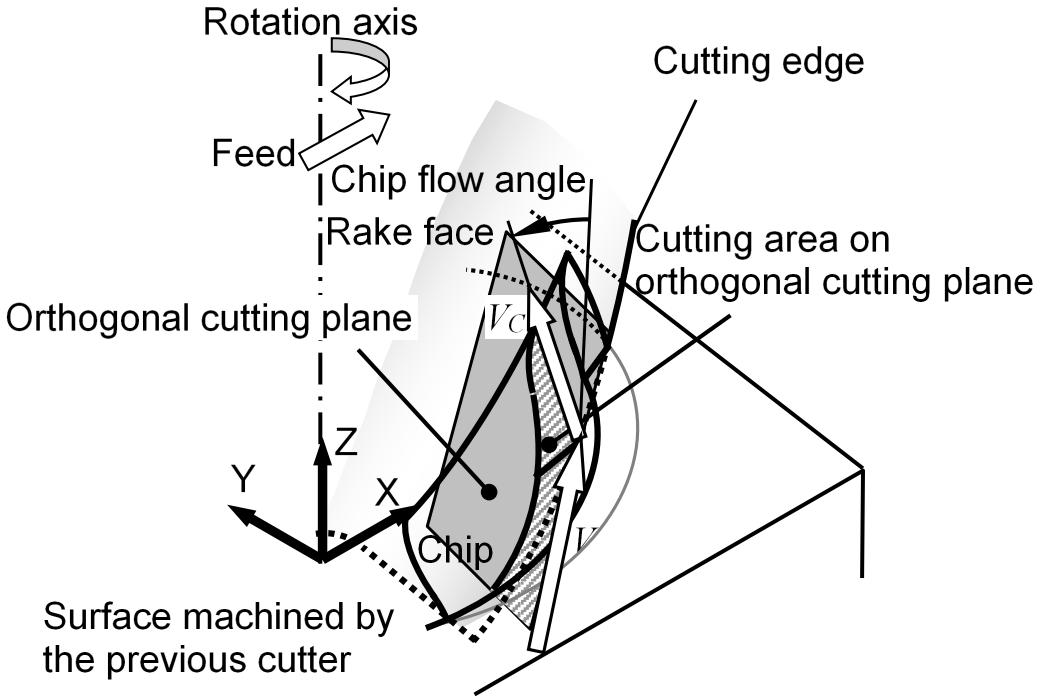

Fig. 5 Chip flow model in analysis.

Materials Research Proceedings 28 (2023) 1295-1302 https://doi.org/10.21741/9781644902479-140

Cutting Model in Cold Work Tool Steel

Based on the results of the cutting tests, the orthogonal cutting data were acquired as:
Tool steel:

$$\left.\begin{aligned}\phi &= \exp(0.189V + 34380t_1 - 6.781\alpha - 0.429)\\ \tau_s &= \exp(0.046V - 2172t_1 + 0.002\alpha + 21.25)\\ \beta &= \exp(-0.095V - 27280t_1 + 1.795\alpha + 0.1696)\end{aligned}\right\} \quad (2)$$

Carbon steel:

$$\left.\begin{aligned}\phi &= \exp(0.254V - 11450t_1 + 0.487\alpha - 3.037)\\ \tau_s &= \exp(-0.001V - 2121t_1 + 0.009\alpha + 20.10)\\ \beta &= \exp(-0.042V - 5414t_1 - 1.357\alpha - 0.266)\end{aligned}\right\} \quad (3)$$

Figure 6 compares the simulated and the measured cutting forces at the same cutting conditions in Fig. 2. The force model and the orthogonal cutting data are verified in the agreement of the

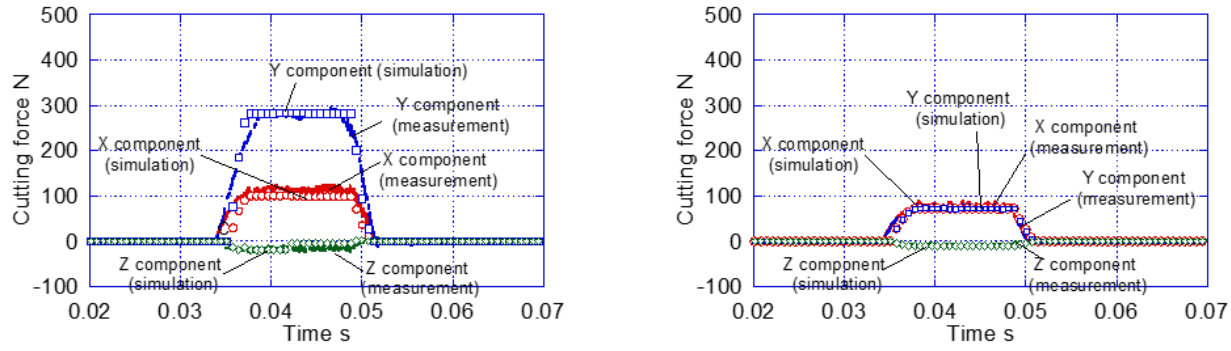

(a) Tool steel (b) Carbon steel

Fig. 6 Cutting force simulations.

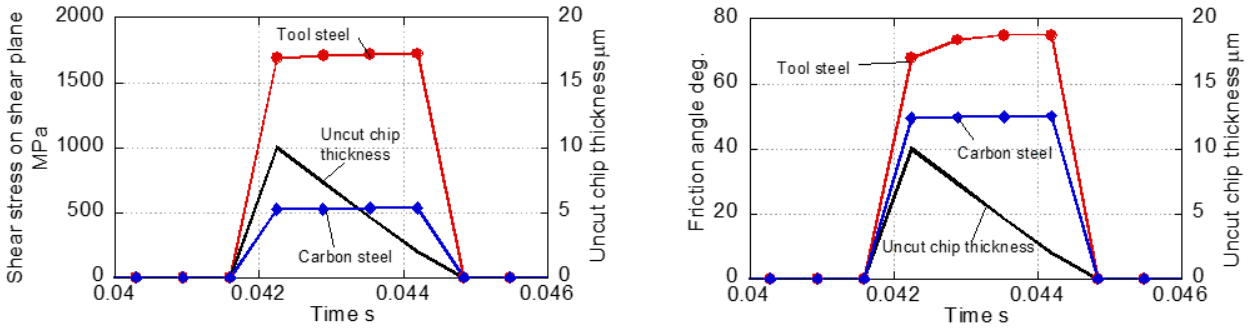

(a) Shear stress on shear plane (b) Friction angle

Fig. 7 Changes in cutting models at a center of axial depth of cut.

simulated cutting force with the measured force. Figure 7 shows the change in shear stress on the shear plane and the friction angle at the center of the plate thickness of the workpiece, where the uncut chip thickness is also shown as a reference. The uncut chip thickness decreases with the cutter rotation in down-cut process. The shear stress on the shear plane in milling of tool steel reaches about 3.3 times larger than that of carbon steel. The shear stresses of both materials are

nearly constant for the change in the uncut chip thickness. Then, the friction angle of tool steel becomes about 1.4 times larger than that of carbon steel at the edge engagement and increases with decreasing the uncut chip thickness. Meanwhile, the friction angle of carbon steel does not increase significantly. Since the coefficients in the second terms of uncut chip thickness in friction angle in equations (2) and (3) involve the indentation effect of the edge radius, the result shows that the indentation effect of the cutting edge in milling of tool steel is relatively much larger than that of carbon steel. Burnishing on the interface between the finished surface and the cutting edge promotes the compressive residual stress in subsurface [9]. Therefore, in milling of tool steel, a large compressive residual stress is induced by burnishing with a large indentation force on the edge radius. On the other hand, the original tool edge does not finish the machined surface and does not promote the burnishing effect on the machined surface in milling of carbon steel, because the built-up edge generates the overcut surface, as shown in Fig. 4(d). The compressive residual stress in subsurface of carbon steel is not expected with less burnishing.

Summary

The paper has been studied the peripheral milling of hardened cold work tool steel to characterize the cutting process. The results are summarized as:

1) In milling of tool steel, the cutting force components in the feed and radial directions of the tool are 1.5 and 3.9 times greater than those of carbon steel.
2) According to the analytical cutting simulation, the shear stress on the shear plane and the friction angle of tool steel becomes much larger than that of carbon steel. Because of the large negative terms of uncut chip thickness in friction angle, the indentation effect of the cutting edge in milling of tool steel is larger than that of carbon steel
3) The large indentation force on the edge radius enhances burnishing to induce a large compressive residual stress in milling of tool steel. In contrast, the original tool edge does not finish the machined surface and does not promote the effect of burnishing on the machined surface in milling of carbon steel, because the built-up edge generates the overcut surface. As consequence, the effect of burnishing is small in milling of carbon steel.

References

[1] V.F.C. Sousa, F.J.G. Silva, Recent advances on coated milling tool technology-a comprehensive review, Coatings, 10 (2020), 3, https://doi: 10.3390/coatings10030235

[2] M.N. Durakbasa, A. Akdogan, A.S. Vanli, and A.G. Bulutsuz, Optimization of end milling parameters and determination of the effects of edge profile for high surface quality of AISI H13 steel by using precise and fast measurements, Measurement 68 (2015) 92-99, https://doi: 10.1016/j.measurement.2015.02.042

[3] A. Aramcharoen, P.T. Mativenga, S. Yang, K.E. Cooke, and D.G. Teer, Evaluation and selection of hard coatings for micro milling of hardened tool steel, Int J Mach Tools Manuf. 48 (2008), 14, 1578–1584, http://doi: 10.1016/j.ijmachtools.2008.05.011

[4] B. Denkena, J. Köhler, and B. Bergmann, Development of cutting edge geometries for hard milling operations, CIRP J Manuf Sci Technol, 8 (2015), 43-52, https://doi: 10.1016/j.cirpj.2014.10.002

[5] S. Caruso, D. Umbrello, J.C. Outeiro, L. Filice, and F. Micari, An experimental investigation of residual stresses in hard machining of AISI 52100 steel, Procedia Engineering, 19 (2011), 67-72. https://doi: 10.1016/j.proeng.2011.11.081

[6] M. Matsuda, K. Okita, T. Nakagawa, and T. Sasaki, Application of X-ray stress measurement for residual stress analysis by inherent strain method - Comparison of cosα and sin2Ψ method-, Mechanical Engineering Journal, 4 (2017), 5, 17-00022-17–00022, https://doi: 10.1299/mej.17-00022

[7] T. Matsumura and E. Usui, Predictive cutting force model in complex-shaped end milling based on minimum cutting energy, Int J Mach Tools Manuf, 50 (2010), 5, 458-466, https://doi: 10.1016/j.ijmachtools.2010.01.008
[8] T. Matsumura, T. Shirakashi, and E. Usui, Adaptive cutting force prediction in milling processes, International Journal of Automation Technology, 4(2010), 3, 221-228, https://doi: doi.org/10.20965/ijat.2010.p0221
[9] H. Mizutani and M. Wakabayashi, Influence of cutting edge shape on residual stresses of cut surface (Effects of rake angle and contact width of flank face), Transactions of the Japan society of mechanical engineers. C, 72 (2006), 715, 247-251

Materials Research Proceedings 28 (2023) 1303-1312 https://doi.org/10.21741/9781644902479-141

Evaluation of the surface integrity characteristics of internal threads machined on lead-free brass alloy

ZOGHIPOUR Nima[1,2,a *], TORAMAN Yaren[1,b], KARA Koray[1,c], BAS Kaan Can[1,2,d] and KAYNAK Yusuf[2,e]

[1]Torun Metal Alloy Ind. & Ltd. Inc., GOSB, İhsan Dede St. No: 116 41480 Gebze,Kocaeli, Turkey

[2]Department of Mechanical Engineering, Marmara University, 34722 Goztepe Campus-Istanbul, Turkey

[a]nima.zoghipour@gmail.com, [b]yaren.toraman@torunmetal.com, [c]koray.kara@torunmetal.com, [d]kaan.bas@torunmetal.com, [e]yusuf.kaynak@marmara.edu.tr

Keywords: Tapping, Threading, Surface Integrity, Lead-Free Brass Alloy

Abstract. Tapping is a typical machining method being utilized in manufacturing internal threads. However, it contains few difficulties to be dealt with since during the process, many cutting edges involve synchronized axial and rotational movements. This work presents the results of an experimental study on the material type considering the influences of the manufacturing process (extrusion and forging) and tap type on the surface integrity characteristics of lead-free brass alloys. Experimental data on the surface quality of the threads, subsurface characteristics including microhardness is presented and analyzed. This study demonstrates that the manufacturing methods have a robust effect on microstructural aspects of low-lead brass alloy and resulting in hardening of the surface and subsurface.

Nomenclature

Ext.	Extruded	F+Ann.	Forged+Annealed

Introduction

In line with advancing technology, the necessity for brass alloys in industry is rising daily. A variety of these alloys are employed in the production of the parts that are primarily used in the food, water, and pumping industries. These parts are manufactured by extrusion or hot forging processes and go through machining processes such as threading in order to be assembled. Addition of some elements into the chemical composition results in enhanced machinability, one of which is Pb [1]. However, due to its use in drinking water, the element's hazardous properties have resulted in the adoption of rigorous regulations and the widespread use of Pb [2]. As a result, recent years have seen a surge in hopes for the creation of lead-free brass alloys due to the rapid advancement of technology. However, the issue that modern industry must face to stay competitive is the manufacture of consumer goods, which is built on a triangle consisting of low costs, low production times, and excellent quality. A new problem that needs to be resolved in this situation is the poor machinability. Industrial methods for producing profiled parts are constantly evolving and competing for market share based on both product quality and price. The utilization of efficient processes is required to achieve these goals [3]. Using both cut and form taps, internal threads can be produced. Cut tapping is a type of machining; chip removal produces the thread. When form tapping is used, the work material is the sole thing that moves to create the thread.

Content from this work may be used under the terms of the Creative Commons Attribution 3.0 license. Any further distribution of this work must maintain attribution to the author(s) and the title of the work, journal citation and DOI. Published under license by Materials Research Forum LLC.

According to Fromentin et al. [4], the main benefit of form tapping is that no chips are produced. The authors claim that by doing this, time-consuming cleaning of the threaded area can be avoided because chips can cause interference when the components are assembled. In another study, the plastic strain and the high strain stress produced by the form tapping were explored by Fromentin et al. [5]. The authors came to the conclusion that form tapping is a good alternative to the conventional tapping procedure. However, it might be argued that the production of forming threads only has a significant potential for materials with high ductility. This is due to the external form tapping's superior surface and stronger threads compared to conventional tapping for thread profiles [6]. The size of the split crest at the top of the thread following the form tapping operation will depend on the diameter of the hole. Both high ductile alloys, such as non-ferrous metals [7–10], and hardened steels, as demonstrated by [7, 11], can be formed using this method. On AISI 304 austenitic stainless steel, tapping operations were performed by Uzun et al. [12] utilizing taps of various sizes and cutting parameters. The depth of cut for each cutting feed and the cutting torques generated during threading were used to calculate the cutting performances of the taps. In the tapping forming process of the 7075-T6 aluminum alloy, Oliveira et al. [13] examined the effects of the tapping speed, tap coating, and the tapered region of the tap. They used a sophisticated statistical analysis to determine the impact of the key factors on the thrust force, torque, and connection of these factors with microhardness and thread profile quality. Burr development during the form tapping process was investigated by Filho et al. [14]. With uncoated and coated taps, internal threads in workpieces made of the 7075-aluminum alloy were completed, and the burr formation at the entrance and exit was examined. The impact of new vegetable oil formulations on the precision of AISI 316L parts and the integrity of their surfaces during reaming and tapping were examined by Belluco et al. [15]. They studied surface roughness and surface metallurgy as part of their investigation of surface integrity. Profilometry was used to evaluate roughness, while optical metallography and microhardness testing were used to investigate the subsurface. The surface characteristics of the threads produced by form tapping were investigated by Fromentin et al. [4]. The two main factors affecting the process are the work material's tensile strength and the lubricant's influence, and a relationship with tapping torque was suggested. In their study, Coelho et al. [16] concentrated on the usage of a minimum quantity of lubricant and emulsion during the machine and form tapping of 7075-T651 aluminum alloy while using both tapping techniques at three forming/cutting speeds. Numerous studies on the methods of tapping various materials have been conducted [17-20].

A comparison of the various types of tools on brass alloys has not been done, according to the research that is currently available in the literature. This paper presents the findings of an experimental investigation on the material type taking into account the influences of the manufacturing method (extrusion and forging) and tap type on the surface integrity properties of lead-free brass alloys. Experimental data on cutting forces, torques, thread surface quality, geometrical accuracy, and subsurface parameters including microhardness are presented and examined.

Methodology

Materials.

Extruded CuZn40Pb2 (CW617N), CuZn38As (CW511L), and CuZn21Si3P (CW724R), each with a diameter of 60 mm and a length of 30 mm, were the three different types of brass alloys employed as test materials in this study. In a Hydromec 550 eccentric press machine with a press load of 165 tons, a portion of these materials was hot forged at 730±10°C at a rate of 11 strokes per minute. The forged specimens underwent a 150 min. annealing process at 550°C. Table 1 and 2 list the chemical composition and mechanical properties of the test materials.

Table 1. Chemical composition of the studied brass alloys [21].

Composition		Cu	Zn	Pb	Sn	Fe	Ni	Al	As	Mn	P	Si
CW617N	%Min.	57.0	Rem.	1.6	-	-	-	-	-	-		-
	%Max.	59.0	Rem.	2.5	0.3	0.3	0.3	0.05	-	-	-	-
CW511L	%Min.	61.5	Rem.	-	-	-	-	-	0.02	-	-	-
	%Max.	63.5	Rem.	0.2	0.1	0.1	0.3	0.05	0.15	-	-	-
CW724R	%Min.	75.0	Rem.	-	-	-	-	-	-	-	0.02	2.7
	%Max.	77.0	Rem.	0.09	0.3	0.3	0.2	0.05	-	0.05	0.10	3.5

Table 2. Mechanical properties of the studied brass alloys [21].

Material	*E*(GPa)	ρ (g/cm^3)	Machinability
CW617N	96	8.43	%95
CW511L	100	8.25	%80
CW724R	100	8.41	%40

Experimental setup.

The internal threading operation using Gühring's C type M10x1.5 form and cut taps on a Fanuc α-D21LiB5 CNC milling center was the main focus of the machining experiments. Fig. 1 depicts the experimental configuration. Through all holes, the experiments were the primary focus and coolant fluid was used. Throughout the testing, the spindle rotational speed was maintained at constant 800 rpm. The cutting forces were measured for 15 seconds at a sampling frequency of 100 Hz using a Kisteler dynamometer type 9129AA. Using a Keyence digital optical microscope, a Mitutoyo Contracer CV-2100M4, and other tools, the integrity of the machined surfaces was assessed. According to ASTM E 384 standards, measurements were taken using an MHVD 1000 IS microhardness tester at various depths beneath the machined surfaces. The dimensional accuracy of the threads was controlled by M10 tap gauge as well as Keyence digital optical microscope according to the illustrated Metric ISO thread dimensions as illustrated in Fig. 2.

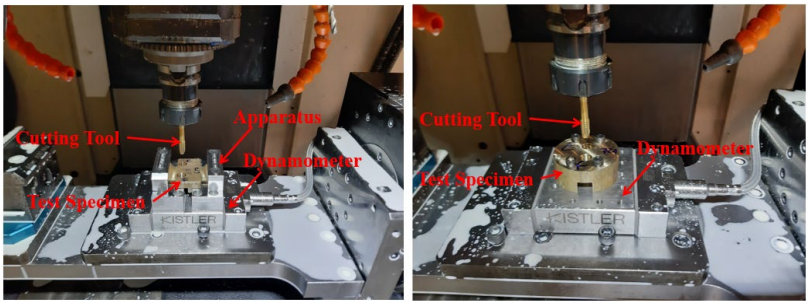

Fig. 1. The experimental setup; a) Ext., b) F+Ann. specimen.

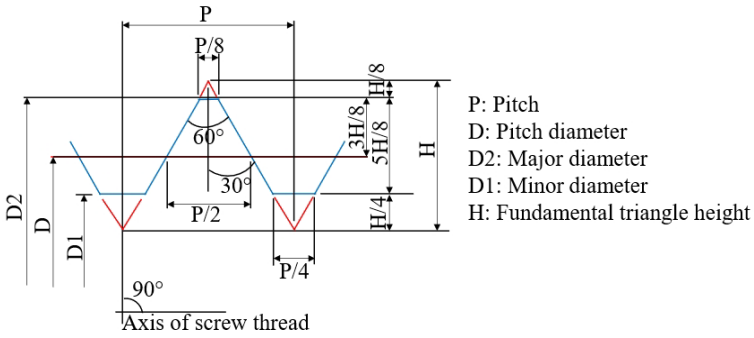

Fig. 2. Metric ISO thread control dimensions.

Results and Discussions

Microstructural Analysis.

Fig. 3 illustrates the microstructure of the Ext. and F+Ann. CW617N, CW511L, and CW724R brass alloys. α and β phases are observed in CW617N and CW511L, while α, γ and κ are seen in CW724R. The β phase content for CW617N has increased from%46 to %51 as a result of multi-directional hot forging and annealing. For CW511L, this rate was gauged between %5 and %17. This augmentation and elongation can be attributed to the phase's superplastic deformation characteristic during the forging process. In CW724R, κ and γ phases have increased from %16 to %19. The looming up of κ phase and the smaller percentages of γ phases compared to κ phases make it seem possible to ignore them and conclude that forging. Table 3 illustrates the measured average grain sizes of two test specimens. The lowest grain size was measured for F+Ann. CW724R as equal to 6.44 µm. The highest grain size was observed for Ext. CW511L as 8.13 µm. It is seen that the average grain size has been reduced by hot forging followed by annealing due to the movement of the dislocations, boundaries, breakages in grain structure and replacement with finer grains.

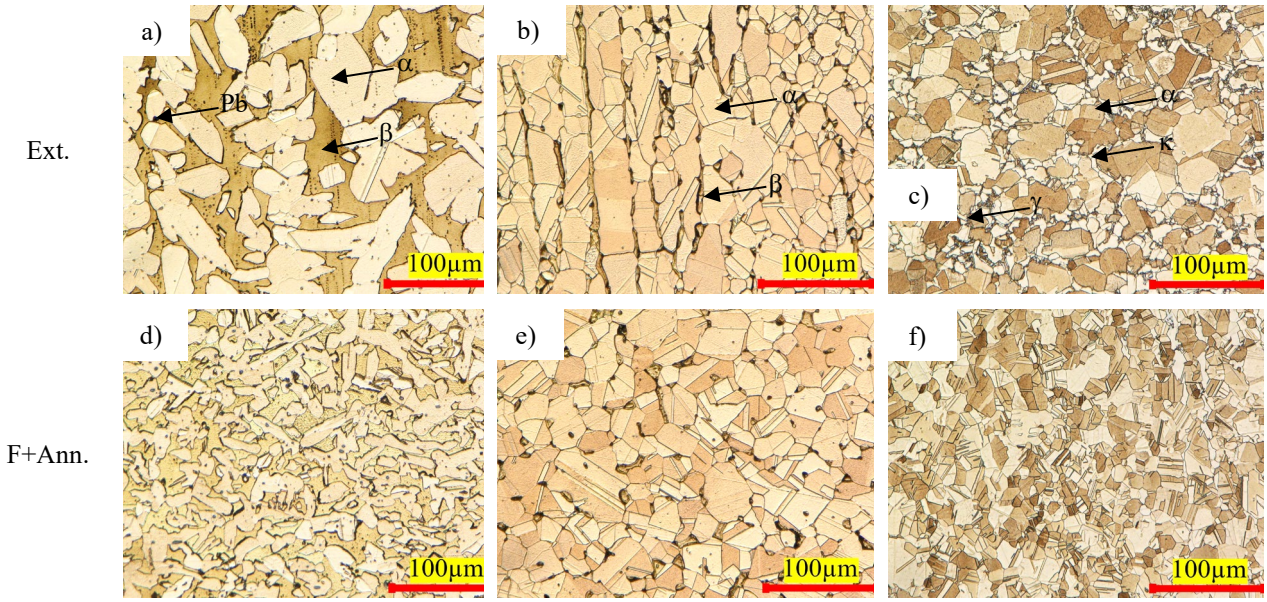

Fig. 3. Microstructure of the test speciemens; Ext.; a) CW617N, b) CW511L, c) CW724R, F+Ann.; d) F+Ann. CW617N, e) CW511L, f) CW724R.

Table 3. Measured average grain sizes and microhardness of the test specimens.

Ave. Grain size (μm)	Ext.	F+Ann.	Ave. Microhardness (HV)	Ext.	F+Ann.
CW617N	7.87	7.14		91.2	112.35
CW511L	8.31	7.74		85.5	102.80
CW724R	6.91	6.44		119	139..35

Cutting Forces and Torques Analysis.

The thrust cutting forces and torques of the tapping operation of the CW724R is illustrated in Fig. 4. Focusing on Fig. 5 b, when the form tap was inserted into the hole, a transition regime was seen for 0.2 to 0.4 seconds. The procedure was halted and reversed in the second of 1.4, leading to the taps returning and a large decrease in the force values. Similar to full immersion of the tapping, the return likewise exhibits a proportional constant zone with a cylindrical component and a slope. The torque increases asymptotically in region I of the torque graph, which represents the point of contact between the surfaces of the tap and the workpiece. Region I's tapered design of the tap produces the thread profiles by causing material deformation. Contrarily, area II experiences a steadying of the torque. The maximum torque is measured at the end of region II, where it shows a slight variance that may have resulted from friction variation. It should be highlighted that area III experiences an abrupt decrease in effort as a result of the process of tapping coming to an end. Region IV has a reversed tap spindle speed and entirely withdrawn tap returns from the hole. Additionally, in area IV, it should be noticed that the spindle's reversal counteracted the force applied in the forward direction before the tap emerged from the hole. On the other hand, when the operation was carried out deploying cut tap, the graph is formed of two regions: the engagement of the conical profile and then the hole diameter. The F+Ann. CW511L was machined utilizing cut and form taps, and the greatest thrust forces were measured as 183.7 N and 872.6 N, respectively. The lowest values, however, for Ext. CW617N were recorded at 110.3 and 660.5 N, respectively, utilizing cut and form taps. The same pattern was seen for the torque values of 711.98 N.m. and 29.83 N.m. in F+Ann. CW511L. Additionally, utilizing cut and form taps, the lowest values were determined to be 6.13 N.m and 14.64 Ext. CW617N, respectively. It is clear that the plastic movement of the material without chip removal in form taps led to larger frictional forces and coefficients, which in turn resulted in thrust forces and torque values that are almost four times those of cut taps. The F+Ann. specimens had greater measured thrust cutting forces and torques than the Ext. specimens. This phenomenon is primarily caused by an increase in the β-phase in the microstructure of CW617N and CW511L acquired by applied forging and annealing processes as well as κ-phase in the CW724R. It is obvious that the presence of Pb results in lower cutting forces and torques by retaining more lubricant on its surface, assisting in the decrease of wear or friction during contact. The measured thrust force and torque values were lower in CW724R than CW511L, despite the decreased Pb content. This is explained by the melting points of CW724R and CW511L, which are 600 and 900°C, respectively. Because of all this, softening during machining may also account for the reduced cutting forces of CW724R compared to CW511L. The silicon-rich κ -phase in the material's microstructure is another factor that contributes to the achieved result. In silicon-free brasses, the κ -phase is harder than the α- and β-phase and also has a BCC lattice structure, supporting the findings of [7].

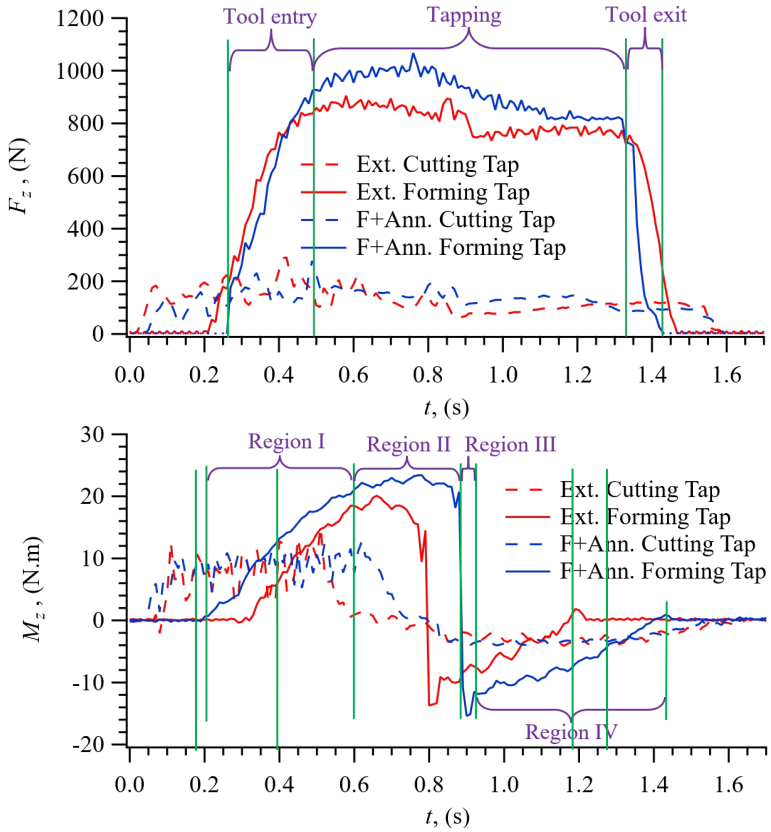

Fig. 4. The measured cutting forces and torques for CW724R.

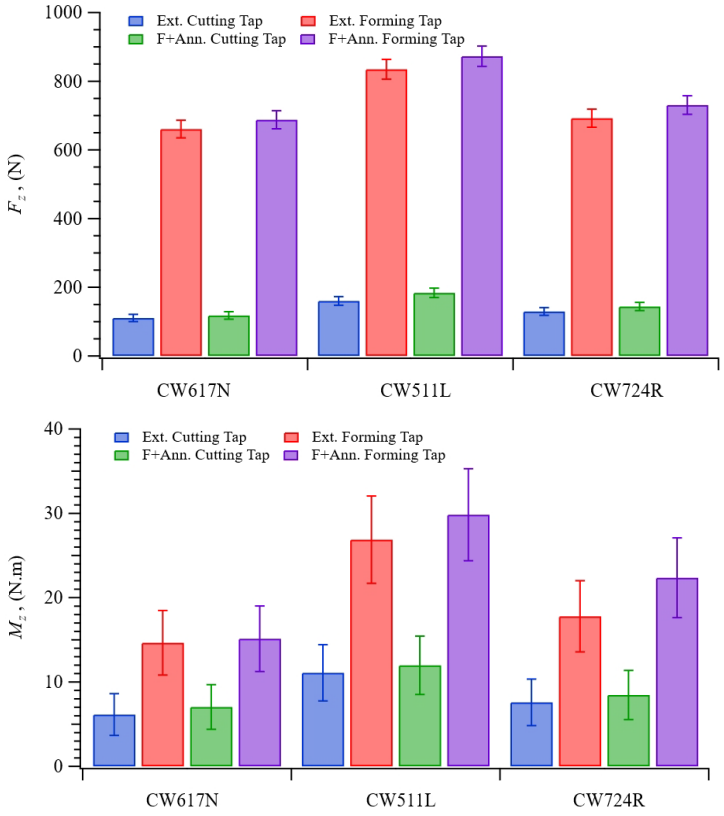

Fig. 5. The measured cutting forces and toques during the experiments.

Surface Quality Analysis and Geometrical Characteristics.

In the form tapping operation, on the top of the threads a split crest was observed due to no metallographic transformation. As demonstrated in Fig. 6b, the highest zone of deformation takes place in Z2 thread's root which during formation is in direct contact with the lobes. The work material flows from Z2 to Z3 on the flank of the thread which is a highly deformed zone and experiences significant displacements. In Z4 no significant deformation is observed. In the cutting tapping operation as shown in Fig. 6a, the thread form was achieved by material removal. Therefore, there were no formed crests on the top of the threads, and the triangle shape was clearly seen. The thread pitch, thread angles, flank straightness and minor, major diameters were inspected by optical Mitutoyo Contracer as well as tap gauges. The geometrical characteristics of all the threads in terms of dimensional tolerances were confirmed by the carried-out inspections and it was determined that the only different zone is Z4 of the threads generated between the tools. The length of Z4 was higher in formed threads than cut ones. It was seen that although in the dimensional tolerance range, the Z4 area in F+Ann. forming threads were much smoother as compared to Ext. specimens which might be attributed to the change in the materials' microstructure in terms of deformation, dislocation, phase content and microhardness. However, no remarkable differences in shape of the threads generated with the cutting tap were observed in all the experiments. Furthermore, some impurities and chip marks were observed on the surfaces Ext. CW511L and CW724R. On the other hand, the quality of the thread surfaces of the CW617N was excellent. The highest impurities belong to CW511L which is also as verification to the force measurements of this paper.

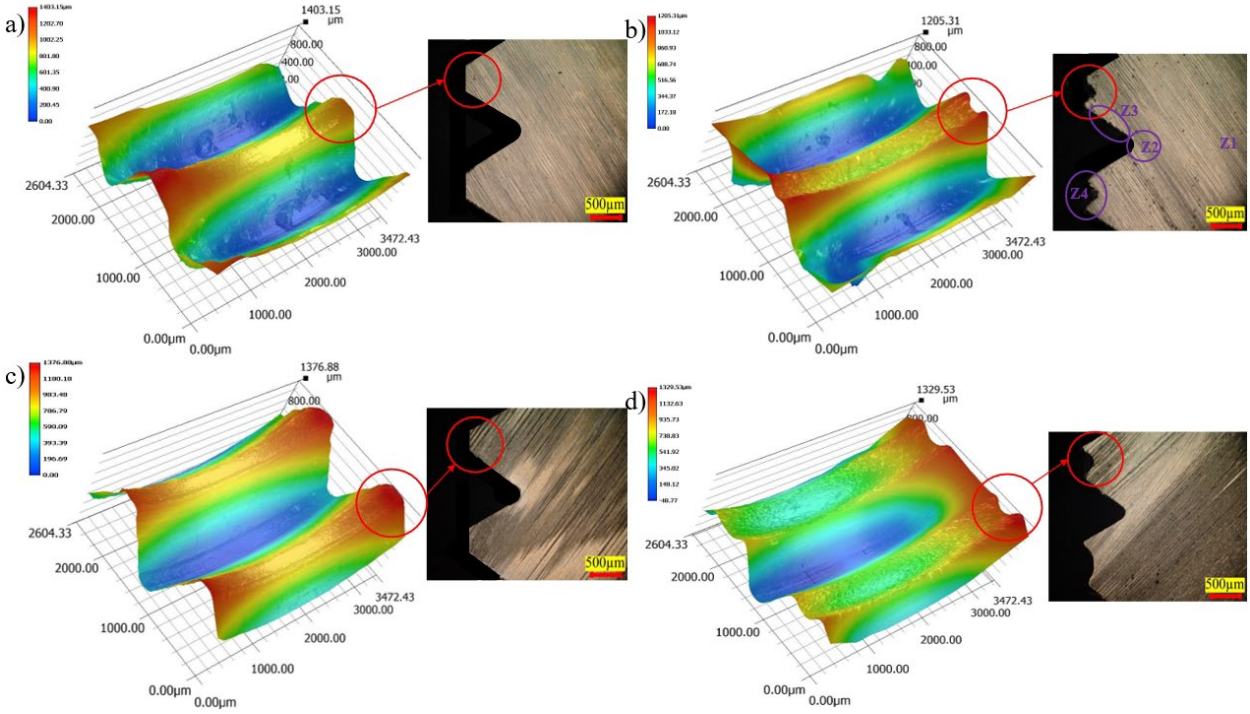

Fig. 6. The formed threads; Ext. CW511L a) cutting, b) forming, F+Ann. CW511L c) cutting, d) forming.

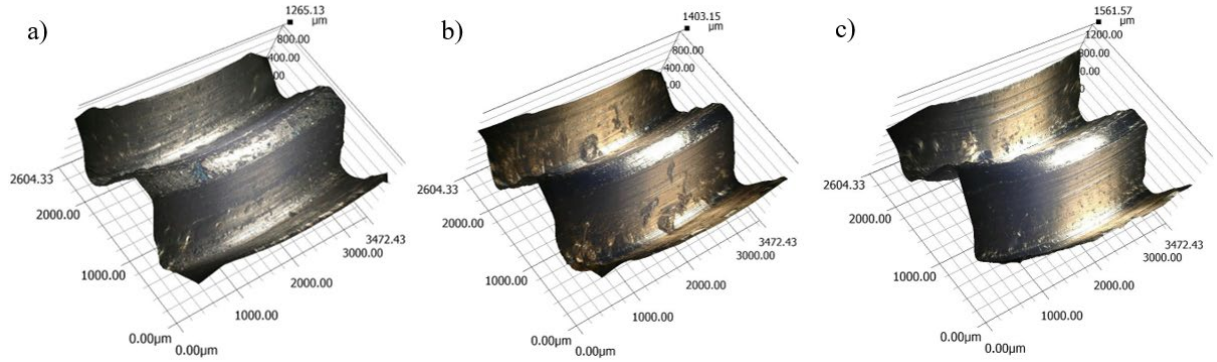

Fig. 7. The cut threads on Ext.; a) CW617N, b) CW511L, c) CW724R.

Surface and Subsurface Microhardness Analysis.

Fig. 8 shows the measured machined surface and sub-surface microhardness of the threads in at 0, 15, 30, 50, 75, 150, 300 and 600 µm distances from the surface. All measurements have been carried out from the most deformed zone, the root of the thread and the average value of two measurements is reported. The properties of the base material could be assessed 600 µm beneath the surface due to the generated strain hardening. The highest microhardness was measured at the machined surface of F+Ann. CW511L with %234.6 increase with respect to the base material using cutting tap. Tapping with cutting tool resulted in higher variations in the surface and sub-surface microhardness. The obtained results show that the tapping tool type plays a significant role in the sub-surface strain hardening. This phenomenon is generated by the deformation of the material structure by the friction and forces between tap and work specimen.

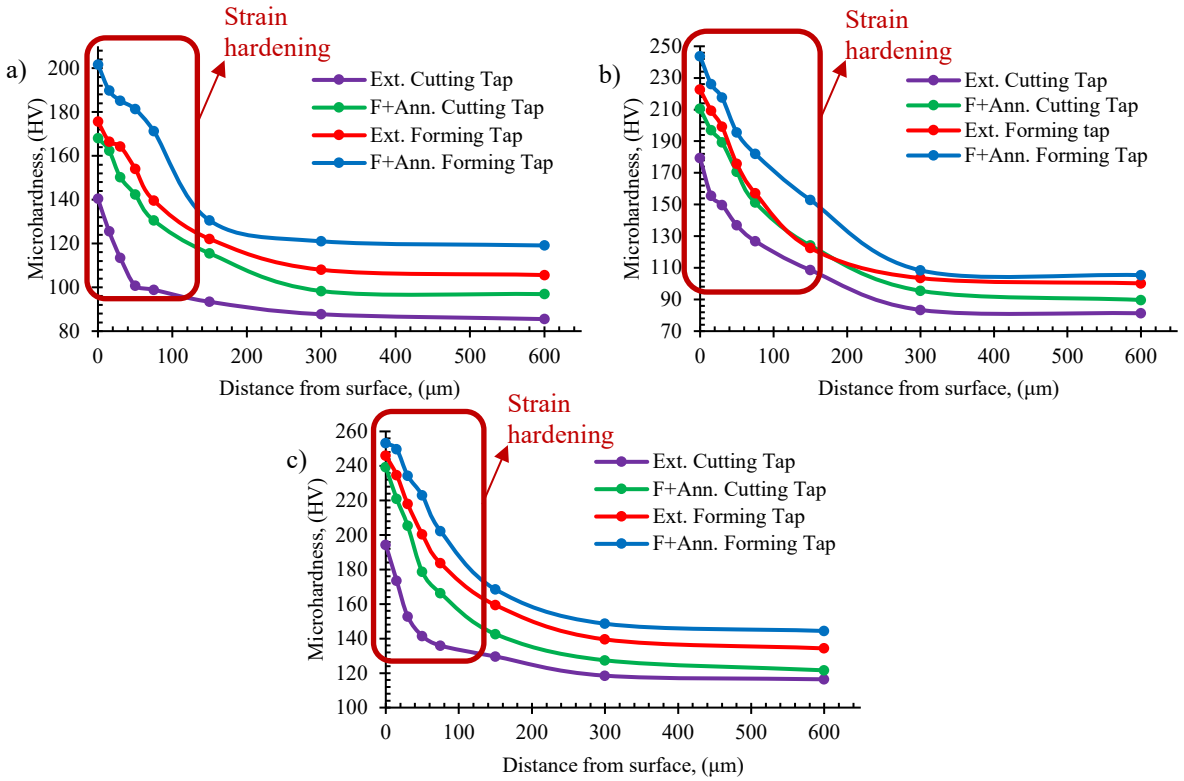

Fig. 8. The measured machined surface and sub-surface microhardness; a) CW617N, b) CW511L, c) CW724R.

Summary
An investigation was carried out to compare cutting and forming tap tool efficiency with respect to thread accuracy, surface quality, generated cutting forces, torques and microhardness in internal threading operation on different types of lead-free brass alloys. Tool type, as well as materials manufacturing method were found to have a significant effect on surface integrity and process responses. In form tapping compared to cutting, higher cutting forces and torques were recorded. It was observed that the phase contents and grain refinement were obtained by multi-directional hot forging operation in the test specimens' microstructure.
The cutting tap tool determined higher strain hardening, but lower thickness of the plastically deformed sub-surface layer and enhanced thread quality in terms of form and dimension.

Acknowledgements
The authors thank TUBITAK (The Scientific and Technological Research Council of Turkey) for partially supporting this work under project number 118C069.

References
[1] N. Zoghipour, E. Tascioglu, G. Atay, Y. Kaynak, Machining-induced surface integrity of holes drilled in lead-free brass alloy, Procedia CIRP 87 (2020) 148-152. https://doi.org/10.1016/j.procir.2020.02.102
[2] Information on:
https://rohs.exemptions.oeko.info/fileadmin/user_upload/RoHS_Pack_9/Exemption_6_c_/
[3] G.M. Sicoe, D. Iacomi, M. Iordache, E. Nitu, Research on numerical modelling and simulation of the form tapping process to achieve profiles, Int. J. Modern Manuf. Technol. 5 (2013).
[4] G. Fromentin, G. Poulachon, A. Moisan, Thread forming tapping of alloyed steel, ICME Proceedings, Naples, Italy, 2002, pp. 115-118.
[5] G. Fromentin, G. Poulachon, A. Moisan, B. Julien, J. Giessler, Precision and surface integrity of threads obtained by form tapping, CIRP Annals 54 (2005) 519-522. https://doi.org/10.1016/S0007-8506(07)60159-0
[6] V. Ivanov, V. Kirov, Rolling of internal threads: part 1, J. Mater. Process. Technol. 72 (1996) 214–220.
[7] J.S. Agapiou, Evaluation of the effect of high-speed machining on tapping, J. Manuf. Sci. Eng. Technol. ASME 116 (1994) 457- 462.
[8] V. Ivanov, Rolling of internal threads: Part 2, J. Mater. Process. Technol. 72 (1996) 221-225.
[9] S. Chowdhary, S.G. Kapoor, R.E. DeVor, Modeling forces including elastic recovery for internal thread forming, J. Manuf. Sci. Eng. ASME 125 (2003) 681-688. https://doi.org/10.1115/1.1619178
[10] R. Chandra, S.C. Das, Forming taps and their influence on production, J. India Eng. 1975.
[11] G. Fromentin, G. Poulachon, A. Moisan, Metallurgical aspects in cold forming tapping, NCMR Proceedings, Leeds, UK, 2002, pp. 373-377.
[12] G. Uzun, I. Korkut, The effects of cutting conditions on the cutting torque and tool life in the tapping process for AISI 304 stainless steel, Mater. Technol. 50 (2016) 275–280. http://doi.org/10.17222/mit.2015.044
[13] J.A. de Oliveira, S.L.M. R. Filho, L.C. Brandão, Investigation of the influence of coating and the tapered entry in the internal forming tapping process, Int. J. Adv. Manuf. Technol. 101 (2018) 1051-1063.
[14] S.L.M. R. Filho, J.A. de Oliveira, É.M. Arruda, L.C. Brandão, Analysis of burr formation in form tapping in 7075 aluminum alloy, Int. J. Adv. Manuf. Technol. 84 (2015). http://doi.org/10.1007/s00170-015-7768-9

[15] W. Belluco, L. De Chiffre, Surface integrity and part accuracy in reaming and tapping stainless steel with new vegetable based cutting oils, Tribol. Int. 35 (2002) 865-870. http://doi.org/10.1016/S0301-679X(02)00093-2
[16] C.C.F. Coelho, R.B.D. Pereira, C.H. Lauro, L.C. Brandao, Performance evaluation of tapping processes using a 7075 aluminium alloy with different cooling systems and threading heads, Proc IMechE Part C: J. Mech. Eng. Sci. 203-210 (2019). http://doi.org/10.1177/0954406219867730
[17] H.J. Patel, B,P, Patel, S,M, Patel, A review on thread tapping operation and para-metric studym Int, J, Eng, Res, Appl. 2 (2012) 109–113.
[18] EMUGE-FRANKEN, Threading Technology, InnoForm Cold-forming Taps - Chipless production of internal threads, Germany, 2009, 28.
[19] ISO 68-1:1998 – a (1998a) ISO general purpose screw threads—basic profile—Part 1: metric screw threads, 1ft ed, pp. 3.
[20] ISO 68-2:1998 – b (1998b) ISO general purpose screw threads—basic profile—Part 2: metric screw threads, 1ft ed., pp. 4.
[21] Information on http:\\www.sarbak.com\document\pdf

Materials Research Proceedings 28 (2023) 1313-1322 https://doi.org/10.21741/9781644902479-142

Analytical method for determining cutting forces during orthogonal turning of C45 steel

ŚLUSARCZYK Łukasz[1,a] and FRANCZYK Emilia[1,b *]

[1]Cracow University of Technology, Faculty of Mechanical Engineering, Chair of Production Engineering, Al. Jana Pawła II 37, 31-864, Cracow, Poland

[a]lukasz.slusarczyk@pk.edu.pl, [b]emilia.franczyk@pk.edu.pl

Keywords: Cutting Forces, Orthogonal Turning, Johnson-Cook Model

Abstract. The authors present a method for determining cutting forces during orthogonal turning of C45 steel. The method utilizes Oxley's chip formation model as well as Johnson-Cook (J-C) constitutive equation and is based on the assumption that the tool is perfectly sharp and the chip formation process is continuous. It is also assumed that the heat exchange between the workpiece, the tool and the chip is carried out by conduction with negligibly small loses caused by convection and radiation and that the thickness of the chip contacting the rake face is constant. The adoption of the above assumptions, together with the knowledge of cutting parameters (including the tool rake angle) as well as of material constants of J-C equation, allows to estimate the thermal-mechanical state of the cutting process and to determine feed and tangential components of the cutting force. Average values of feed and tangent components of the cutting force are calculated using an algorithm implemented in the Matlab environment. The method is based on iterative determination of the minimum difference between stress values in the secondary shear zone. Considered tangential and normal stress values are expressed by formulas based on Oxley's cutting mechanics and the J-C model. The cutting force components obtained in the described method have been compared with the results obtained during experimental studies and with the results obtained in computer simulations using the FEM numerical calculation method.

Introduction

Understanding the phenomena that occur in the cutting zone during machining as well as examination of their impact on process efficiency and quality of machined parts is practically impossible without the use of appropriate models. The issue of modeling of the machining process usually relates to a mechanistic model of the cutting zone, a model of heat generation and distribution or a model of cutting edge wear. Analytical and numerical calculation models are used for forecasting the course of machining process. When describing the behaviour of the machined material at decohesion during the orthogonal turning, it is assumed that there is a slip in the Primary Shear Zone (PSZ), while in the Secondary Shear Zone (SSZ) the friction of the chip against the cutting tool face is taken into account. A good example of using analytical models of the machining process are temperature models determining the partitions of heat penetrating the chip and the workpiece. The examples that can be found in the literature include the Loewen and Shaw's model [1], Trigger and Chao's model [2], the Boothroyd's model [3] and the Oxley's model based on it [4]. The mentioned models allow estimating average temperature the in the slip zone and average contact temperature at the chip-cutting edge interface.

Numerical calculation models for simulating the machining process are a separate group used for process forecasting. Paper [5] describes the use of the ABAQUS application and the FEM method for determination of the impact of friction between the workpiece, chip and the tool on the distribution of forces, strain and temperature in the cutting zone during the turning of AISI 4340 steel. In [6], Özel used the DEFORM application for modelling the friction on the chip-cutting edge interface. The author showed the impact of the friction model used on the chip shape. Another

Content from this work may be used under the terms of the Creative Commons Attribution 3.0 license. Any further distribution of this work must maintain attribution to the author(s) and the title of the work, journal citation and DOI. Published under license by Materials Research Forum LLC.

example of using numerical calculation methods for machining process simulation is [7] where authors used the AdvantEdge application to investigate the impact of protective coatings applied on the cutting tools on heat partition in the cutting zone. Computer simulations are now considered as one of the most important aspects of research on machining processes. They allow for a safe and non-invasive view of the process, also in places inaccessible to conventional monitoring methods. Thus, they make it possible to check how individual changes introduced in the cutting zone or the process itself affect the tested output characteristics. Further, through parameter studies, computer simulations allow to analyze various solutions without the need to conduct costly research.

The aforementioned analytical methods can also be used in order to determine the cutting forces during orthogonal turning. In [8,9], the authors presented methods of determination of the cutting forces based on the known machining parameters and cutting tools geometries. The other input into the method is the workpiece mechanical properties and the constants of J-C constitutive equation. The described method for prediction of cutting forces during orthogonal turning is a less expensive and faster alternative for computer applications based on numerical calculation methods.

Methodology

The described approach is an alternative for numerical calculation methods that use complex calculation algorithms. The presented method is based on the chip forming model proposed by Oxley [9,10]. The principal part of the method is the algorithm which allows determination of the tangential feed components and the of the cutting force during orthogonal turning. In this paper, the method has been used to determine the cutting force components in a wider range of input parameters. The chip forming model during orthogonal turning is presented Fig. 1.

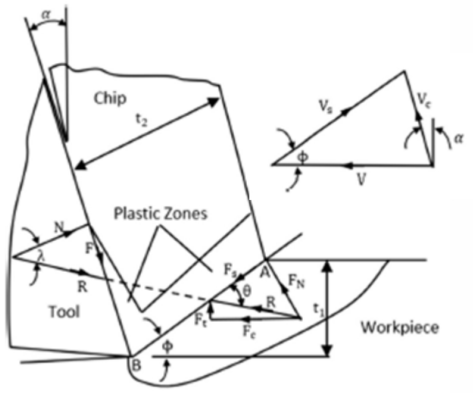

Fig. 1. Chip formation model for orthogonal turning [11].

Where α is the rake angle, ϕ is the shear angle, λ is the average friction angle at tool-chip interface, θ is the angle between resultant cutting force R and primary shear zone AB. Parameters t_1 and t_2 are the depth of cut and the chip thickness respectively. V, V_s, and V_c are the cutting velocity, shear velocity, and chip velocity, respectively. Parameter w is the cutting width that is not shown. The cutting forces are determined by recurrently changing the values: ϕ, C_0 and δ. C_0 is the ratio of shear plane length to the thickness of the PSZ -$l/\Delta s_2$ and δ is the ratio of the thickness of SSZ to chip thickness - $\Delta s_1/t_2$. The described parameters are presented in Fig. 2.

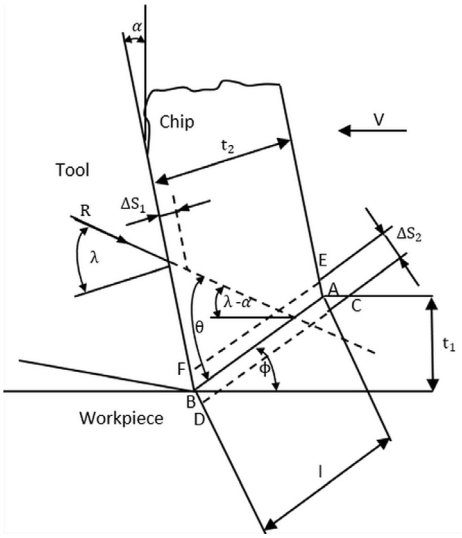

Fig. 2. Parallel-sided shear zone model [11].

Presented method includes calculation of stress values in the PSZ, on the sear plane AB and in the SSZ. Values of the shear flow stress (k_{AB}), strain (ε_{AB}) and strain rate ($\dot{\varepsilon_{AB}}$) on the shear plane in the PSZ are determined from the following equations:

$$k_{AB} = \frac{\sigma_{AB}}{\sqrt{3}} = \frac{1}{\sqrt{3}}(A + B\varepsilon^{n}{}_{AB})\left(1 + Cln\frac{\dot{\varepsilon_{AB}}}{\dot{\varepsilon_0}}\right)\left(1 - \left(\frac{T_{AB}-T_r}{T_m-T_r}\right)^{m}\right) \quad (1)$$

$$\varepsilon_{AB} = \frac{\gamma_{AB}}{\sqrt{3}} = \frac{cos\alpha}{2\sqrt{3}sin\phi\cos(\phi-\alpha)} \quad (2)$$

$$\dot{\varepsilon_{AB}} = \frac{\dot{\gamma_{AB}}}{\sqrt{3}} = C_0\frac{V_s}{\sqrt{3}l_{AB}} \quad (3)$$

The length of the shear zone (l_{AB}), the tool-chip interface length (h), the shear velocity (Vs), the chip velocity (Vc) and the chip thickness (t_2) are determined as follows:

$$l_{AB} = \frac{t_1}{sin\phi} \quad (4)$$

$$h = \frac{t_1 sin\phi}{cos\lambda\sin\phi}\left(1 + \frac{C_0 n_{eq}}{3\left(1+2\left(\frac{\pi}{4}-\phi\right)C_0 n_{eq}\right)}\right) \quad (5)$$

$$V_s = \frac{Vcos\phi}{cos(\phi-\alpha)} \quad (6)$$

$$V_c = \frac{Vsin(\phi)}{cos(\varphi-\alpha)} \quad (7)$$

$$t_2 = \frac{t_1 cos(\phi-\alpha)}{sin\phi} \quad (8)$$

Secondly, in the SSZ, the shear flow stress in the chip with von Mises criterion are determined on the basis of the equation:

$$k_{chip} = \frac{1}{\sqrt{3}}(A + B\varepsilon_{int}^{n})\left(1 + Cln\frac{\dot{\varepsilon_{int}}}{\dot{\varepsilon}_0}\right)\left(1 - \left(\frac{T_{int}-T_0}{T_m-T_0}\right)^{m}\right) \quad (9)$$

while strain ($\varepsilon_{\mathrm{chip}}$) and strain rate ($\dot{\varepsilon_{\mathrm{chip}}}$) are calculated as stated below:

$$\varepsilon_{chip} = \frac{\gamma_{int}}{\sqrt{3}} = 2\varepsilon_{AB} + \frac{h}{2\sqrt{3}\delta t_2} \quad (10)$$

$$\dot{\varepsilon_{chip}} = \frac{\dot{\gamma_{int}}}{\sqrt{3}} = \frac{V_c}{2\sqrt{3}\delta t_2} \quad (11)$$

Basing on [12], a portion of heat conducted to the workpiece from the shear zone (β) is expressed as:

$$\beta = 0.5 - 0.35log_{10}(R_T tan\phi) \qquad for\ 0.04 \le R_T tan\phi \le 10$$
$$\beta = 0.3 - 0.15 = log_{10}(R_T tan\phi) \qquad for\ R_T tan\phi\ \ge 10 \quad (12)$$

where R_T is a non - dimensional thermal number.

$$R_T = \frac{\rho C_p V t_1}{K} \quad (13)$$

The average temperature in PSZ along AB is given by [12]:

$$T_{AB} = T_0 + \eta\Delta T_{sz} \quad (14)$$

$$\Delta T_{sz} = \frac{(1-\beta)F_s V_s}{\rho V t_1 w C_p} \quad (15)$$

where: T_0 - initial work temperature (25°C in present analysis), η - heat partition factor (90% in present analysis), ΔT_{sz} - the temperature rise in the PSZ.

The temperature at the SSZ (T_{int}) is calculated using a heat partition Eq. 16.

$$T_{int} = T_0\Delta T_{sz} + \psi\Delta T_M \quad (16)$$

Where ψ - is a factor to allow for the fact that the T_{int} is average value (ψ =0.9 in present analysis), ΔT_M is the maximum temperature rise in the chip occurring at the interface. By assuming a rectangular heat source at the interface Boothroyd developed the following equation to find ΔT_M:

$$log_{10}\left(\frac{\Delta T_M}{\Delta T_C}\right) = 0.06 - 0.195\delta\sqrt{\frac{R_T t_2}{t_1}} + 0.5log_{10}\left(\frac{R_T t_2}{h}\right) \quad (17)$$

$$\Delta T_C = \frac{FV_c}{\rho V t_1 w C_p} \tag{18}$$

where ΔT_C is the average temperature rise in the chip.
The angles and forces in Fig. 1 are expressed by formulas:

$$\theta = arctan\left(1 + 2\left(\frac{\pi}{4} - \phi\right) - C_0 n_{eq}\right) \tag{19}$$

$$\lambda = \theta - \phi + \alpha \tag{20}$$

$$n_{eq} \approx \frac{nB\varepsilon_{AB}^n}{(A+B\varepsilon_{AB}^n)} \tag{21}$$

$$F = Rsin\,\lambda \tag{22}$$

$$N = Rcos\,\lambda \tag{23}$$

$$F_s = Rcos\big((\phi + \lambda - \alpha)\big) = k_{AB} l_{AB} w \tag{24}$$

$$N_s = Rsin(\phi + \lambda - \alpha) \tag{25}$$

$$F_c = Rcos(\lambda - \alpha) \tag{26}$$

$$F_t = Rsin(\lambda - \alpha) \tag{27}$$

where: F and N are the shear force and normal force at the tool-chip interface, respectively, F_s and N_s are the shear force and normal force at the PSZ, respectively, F_c is the cutting force and F_t is the thrust force and n_{eq} is the strain hardening constant. The normal stress (σ_N) and the shear stress (τ_{int}) and at the tool-chip interface are calculated from the Eq. 28 and 29:

$$\sigma_N = \frac{N}{hw} \tag{28}$$

$$\tau_{int} = \frac{F}{hw} \tag{29}$$

The normal stress $\dot{\sigma}_N$ is determined from J-C model and stress boundary conditions on the primary shear zone - Eq. 30,

$$\dot{\sigma_N} = k_{AB}\left(1 + \frac{\pi}{2} - 2\alpha - 2C_0 n_{eq}\right) \tag{30}$$

Values of the shear angle ϕ and the strain-rate constant C_0 are determined when the differences between τ_{int} and k_{chip} as well as σ_N and σ_0, respectively, are minimal. Also the strain-rate constant δ is determined when the calculated F_c is minimal. With determined shear angle ϕ, and strain rate constants C_0 and δ, the machining forces are calculated. A detailed scheme of the algorithm for determining the tangential (F_c) and the feed (F_f) components of the cuttning force has been presented in the article [12]. The results obtained by means of the presented method were compared with the results of experimental studies as well as with the results obtained from computer simulations based on FEM (Finite Element Method).

Laboratory Test

Laboratory tests included performing a series of orthogonal turning tests. The workpiece was a AISI1045 steel pipe with outer diameter of D=50 mm and wall thickness of d=3mm. The test stand consisted of a TUJ 50 conventional lathe and a measuring track enabling the measurement of cutting forces, which consisted the following elements:

- Kistler (Winterthur, Switzerland) 9257B piezoelectric dynamometer together with a Kistler 9403 tool holder (sensitivity: F_f: -7.70 pC/N; F_p: -7.82 pC/N; F_c: -3.71 pC/ N; threshold: <0.01 N) attached to the lathe support,
- Kistler multichannel charge amplifier type 5019B with a set of filters (scale: F_f, F_p: 50 N/V, F_c: 200 N/V),
- PC with DynoWare Software (Kistler) for archiving and analysis of cutting force components.

The measuring stand with the parameters given above made it possible to measure the components of the total cutting force with a frequency of 1000 Hz and with the following inaccuracies: F_f, F_p: ±0.25 N, F_c: ±1N. The schematic diagram of the test stand is shown in Figure 3. The figure also shows the distribution of cutting force components occurring in the process of orthogonal turning.

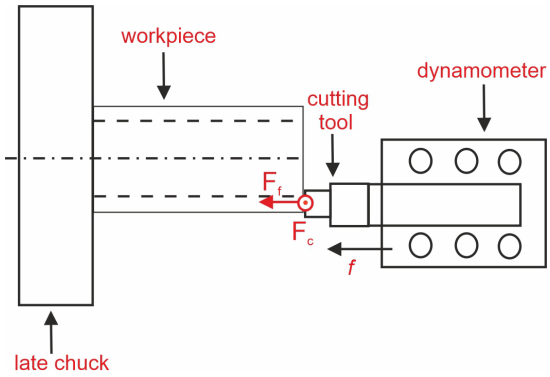

Fig. 3. The schematic diagram of the test stand.

The chemical composition of the AISI 1045 steel in accordance with the PN-EN ISO 683-1:2018-09 standard is presented in Table 1.

Table 1. The percentage chemical composition of AISI 1045 steel.

Symbol	C	Si	Mn	Cr	Ni	Mo	Cu	S	P
	0.42-0.50	0.10-0.40	0.50-0.80	≤0.30	≤0.30	≤0.10	≤0.30	≤0.40	≤0.40

The parameters variability range was chosen on the basis of catalogue data and is presented in Table 2.

Table 2. Values of cutting parameters.

Cutting parameters	Parameter values		
f [mm/rev]	0.1		
V [m/min]	100	200	300
Rake angle α [deg]	-12	-6	0

The tools used in the tests, shown in Fig. 4, were made of P10 carbide without a protective coating. They had a flat rake surface and the length of the cutting edge was 5 mm.

Fig. 4. The tools used in the tests.

Simulation Researches

Computer simulation of the cutting process was carried out using FEM. The simulation was carried out from the moment of first contact of the tool and the workpiece and was continued until a steady state was obtained, that is, until stable stress and temperature values were observed. Both the workpiece and the cutting edge were discretized. Stress of the tool material was calculated using a software package based on a numerical model of the chip formation process, the so-called two-dimensional Lagrange model. In the initial stage of building the material model of the workpiece, three sets of material constants were used. Tables 3 and 4 below present constans of J-C flow stress model and thermo physical properties of AISI 1045 steel, respectively.

Table 3. Constans of J-C flow stress model for AISI 1045 steel.[10,13]

Set number	A(MPa)	B(MPa)	C	n	m	T_0[°C]	T_m[°C]
1	553.1	600.8	0.0134	0.234	1	25	1460
2	731.63	518.7	0.00571	0.94054	0.3241	25	1460
3	546.83	609.35	0.01376	0.94053	0.2127	25	1460

Table 4. Thermo physical properties of AISI 1045 steel.[10]

Specific heat, S (J/kgK)	Thermal conductivity, λ_c (W/mK)	Density ρ (kg/m^3)
420+0.504*T*	52.61-0.0281*T*	7850

After verifying the results and comparing them with empirical data, set no. 1 was selected for further research. This set of constants was also used in the analytical method for determining the cutting forces described in this article.

Results

Fig. 5 includes mean values of cutting forces determined by means of:

- experiment: F_{c_EXP}, is the tangential component, F_{f_EXP} is the feed component,
- simulation (FEM): F_{c_FEM}, F_{f_FEM},
- analytical method: F_{c_CALC}, F_{f_CALC}.

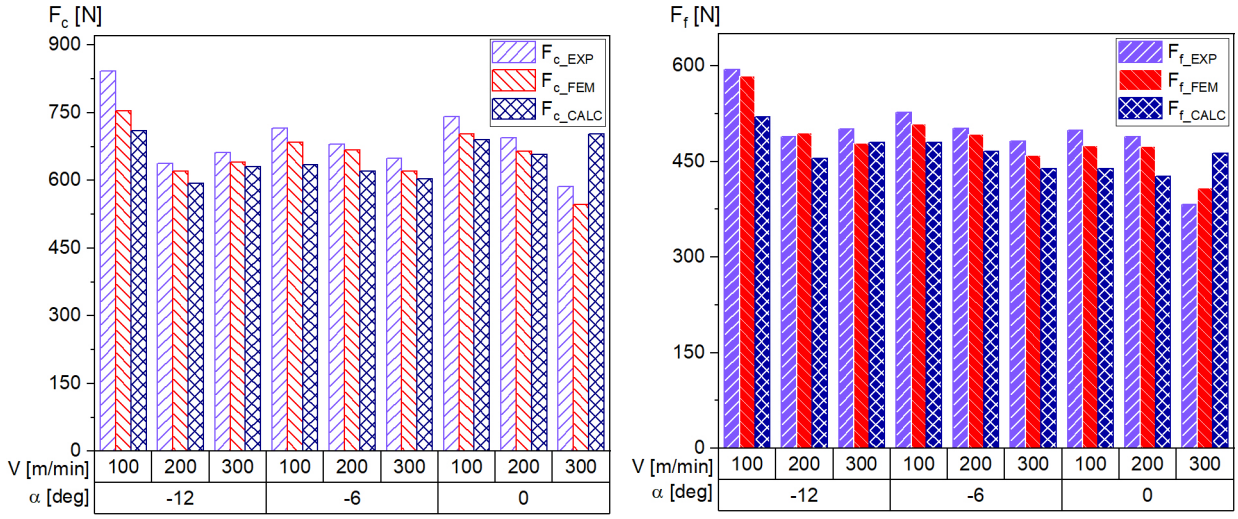

Fig. 5. Mean values of cutting forces determined by various means.

Values of the relative error for the results obtained by means of the FEM and analytical methods as well as for the results obtained from the laboratory test are presented in Figure 6 and were determined according to the formulas:

$$\Delta F_{c_FEM}=abs(F_{c_EXP}-F_{c_FEM})/F_{c_EXP}*100\%$$

$$\Delta F_{f_FEM}=abs(F_{f_EXP}-F_{f_FEM})/F_{f_EXP}*100\% \quad (31)$$

$$\Delta F_{c_CALC}=abs(F_{c_EXP}-F_{c_CALC})/F_{c_EXP}*100\%$$

$$\Delta F_{f_CALC}=abs(F_{f_EXP}-F_{f_CALC})/F_{f_EXP}*100\%$$

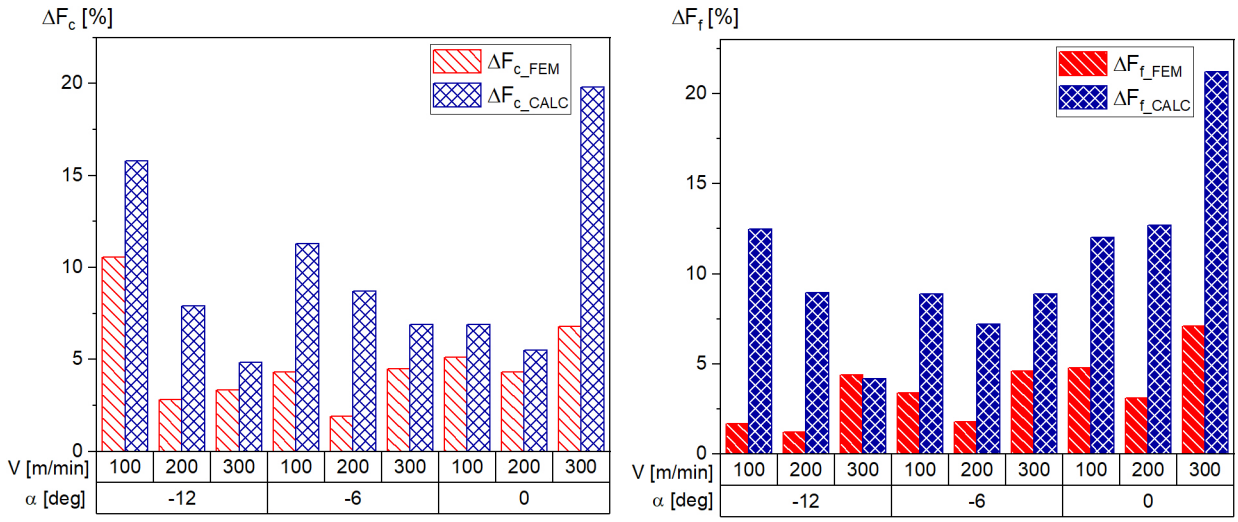

Fig. 6. Relative error for obtained results.

Summary

The presented analytical method for determination of cutting forces during orthogonal turning is characterized by a low calculational complexity and can be an alternative for very complex numerical programs. The input parameters include cutting parameters, tool geometry and the constants of J-C constitutive equation. The analysis of forces obtained in experimental studies allows the following conclusions to be drawn:

- The cutting forces obtained using the FEM simulation have a good conformity with the forces obtained experimentally. The maximum relative error between the results is 10.56% for the F_c component and 7.1% for the F_f component;
- The cutting force values used in the analytical method are closest to the experimental results for the rake angle of α=-6°. In this case, the maximum relative error at V=100 m/min is 11.3% for F_c and 8.9% for F_f;
- In the remaining trials, where rake angles were -12° and 0°, respectively, the relative error between the results obtained experimentally and with the analytical method was greater;
- The maximum relative error for angle α =-12 and V =300 m/min was ΔF_{c_CALC}=19.8%, ΔF_{f_CALC}=21.2%.
  The proposed analytical method is sensitive to the values of the constants of J-C constitutive equation.

References

[1] Goyal, S. Kumar, D. Shailendra, R. Suresh, R. Sharma, Studying Methods of Estimating Heat Generation at Three Different Zones in Metal Cutting, A Review of Analytical models, Int. J. Eng. Trend. Technol. 8 (2014) 532-545. https://doi.org/10.14445/22315381/IJETT-V8P296

[2] G. Hao, L. Zhanqiang, The heat partition into cutting tool at tool-chip contact interface during cutting process: a review, Int. J. Adv. Manuf. Technol. 108 (2020) 393-411. https://doi.org/10.1007/s00170-020-05404-9

[3] J. Davim, C. Maranhão, P. Faria, A. Abrao, J. Campos Rubio, L. Silva, Precision radial turning of AISI D2 steel, Int. J. Adv. Manuf. Technol. 42 (2009) 842-849. https://doi.org/10.1007/s00170-008-1644-9

[4] Yun, L. Huaizhong, W. Jun, Further Development of Oxley's Predictive Force Model for Orthogonal Cutting, Machin. Sci. Technol. 19 (2015) 86-111. https://doi.org/10.1080/10910344.2014.991026

[5] P.J. Arrazola, T. Özel, Investigations on the effects of friction modeling in finite element simulation of machining, Int. J. Mech. Sci. 52 (2010) 31-42. https://doi.org/10.1016/j.ijmecsci.2009.10.001
[6] T. Özel, The influence of friction models on finite element simulations of machining, Int. J. Mach. Tool. Manuf. 46 (2006) 518-530. https://doi.org/10.1016/j.ijmachtools.2005.07.001
[7] W. Grzesik, M. Bartoszuk, P. Nieslony, Finite element modelling of temperature distribution in the cutting zone in turning processes with differently coated tools, J. Mater. Process. Technol. 164-165 (2005) 1204-1211. https://doi.org/10.1016/j.jmatprotec.2005.02.136
[8] J. Ning, S. Y.Liang, Inverse identification of Johnson-Cook material constants based on modified chip formation model and iterative gradient search using temperature and force measurements, Int. J. Adv. Manuf. Technol. 102 (2019) 2865-2876. https://doi.org/10.1007/s00170-019-03286-0
[9] L. Xiong, J. Wang, Y. Gan, B. Li, N. Fang, Improvement of algorithm and prediction precision of an extended Oxley's theoretical model, Int. J. Adv. Manuf. Technol. 77 (2015) 1-13. https://doi.org/10.1007/s00170-014-6361-y
[10] M. Aydın, Cutting temperature analysis considering the improved Oxley's predictive machining theory, J. Braz. Soc. Mech. Sci. Eng. 38 (2016) 2435-2448. https://doi.org/10.1007/s40430-016-0514-x
[11] J.A. Williams, Mechanics of machining: an analytical approach to assessing machinability: By P.L.B. Oxley, published by Ellis Horwood, Chichester, 1989.
[12] D.I. Lalwani, N.K. Mehta, P.K. Jain, Extension of Oxley's predictive machining theory for Johnson and Cook flow stress model, J. Mater. Process. Technol. 209 (2009) 5305-5312. https://doi.org/10.1016/j.jmatprotec.2009.03.020
[13] J.Ning, S.Y. Liang, Article Predictive Modeling of Machining Temperatures with Force-Temperature Correlation Using Cutting Mechanics and Constitutive Relation, Materials 12 (2019) 284. https://doi.org/10.3390/ma12020284

Materials Research Proceedings 28 (2023) 1323-1330 https://doi.org/10.21741/9781644902479-143

Novel methodology for burr extension estimation on machined SLM surfaces

GINESTRA Paola[1,a *], QUARTO Mariangela[2,b], ABENI Andrea[1,c], ATTANASIO Aldo[1,d], CERETTI Elisabetta[1,e], D'URSO Gianluca [2,f] and GIARDINI Claudio[2,g]

[1]Department of Management, Information and Production Engineering, University of Bergamo, via Pasubio 7/b, 24044 Dalmine (BG)

[2]Department of Mechanical and Industrial Engineering, University of Brescia, via Branze 38, 25123 Brescia (BS)

[a]paola.ginestra@unibs.it, [b]mariangela.quarto@unibg.it, [c]andrea.abeni@unibs.it, [d]aldo.attanasio@unibs.it, [e]elisabetta.ceretti@unibs.it, [f]gianluca.d-urso@unibg.it, [g]claudio.giardini@unibg.it

Keywords: Additive Manufacturing, Metals, Micromachining, Surface Characterization

Abstract. Additive manufacturing techniques can cover the needs of these components thanks to their high level of customization of the products and the ability to realize complex shapes without high effort. Despite the benefits derived from AM processes, these techniques are characterized by a low-quality of surface finish, one of the most important requirements for medical devices. Considering this aspect, it is important to develop a solution able to improve the surface finish in order to enjoy the low lead times and the high level of customization typical of these processes. A characteristic element of micro-machining is the presence of burrs on the machined surface which can affect the surface texture of micro-features. For this reason, a novel technique for the evaluation of burr was defined. The burrs were evaluated by means of an autofocus variation digital microscope Keyence VHX-7100, on 17-4 PH steel samples produced by laser bed fusion. A 3D reconstruction of the channels and holes surfaces was performed and through the analysis of the peaks distribution, a threshold was defined to discriminate between the original surface of the part and the burrs. In this way, it was possible to estimate and approximate the value of the extension of the burrs in terms of volume and area, where the area is referred to the projected area. Specifically, in micro-machining, not only the extension of the burrs is significant, but also the variability is particularly high, preventing a priori consideration of the defect.

Introduction

Laser bed fusion technologies are widely used to produce complex metal parts not obtainable with traditional and conventional machining processes. Selective Laser Melting (SLM) is a popular and suitable technique for the production of metal components from powder melting by the passage of a laser source in a controlled atmosphere. This technology has been highlighted for the acceptable structural integrity (i.e. density) of the produced parts and the wide range of materials available for this process [1]. On the contrary, such technology, as all the powder bed processes, suffers from an inadequate final surface finishing that is often characterized by high variability affecting the dimensional accuracy of the specimens.

The poor surface quality derived by powder bed fusion is influencing the technical properties of the parts and compromising their tolerances, leading to a limited range of applicability, extremely related to the post-processing requirements [2]. Other defects, such uncontrolled internal porosities, are deeply under study, to exploit the possible applications of these products. The high surface roughness reached by the final parts produced with SLM is easily explained by the

Content from this work may be used under the terms of the Creative Commons Attribution 3.0 license. Any further distribution of this work must maintain attribution to the author(s) and the title of the work, journal citation and DOI. Published under license by Materials Research Forum LLC.

presence of partially melted powder and layer thickness requirements typical of the building process.

The surface finishing and mechanical properties of the metal 3D printed parts are highly related and therefore, an adequate post-processing technique needs to be identified and applied. Among the wide range of traditional processes used for high precision surface finishing, considering the final applications of 3D components that can require low roughness values (i.e. biomedical applications where the surface roughness can influence bacterial adhesion), micro milling is the most convenient manufacturing process when considering the volume and cost ratio [3,4].

Micro-size features of considerable complexity can be obtained by the mechanical removal of material using micro tools on a variety of substrates and materials. Micro milling is a high efficiency process but requires an extended selection of tools and part miniaturization as well as an optimal process optimization before being applied to complex parts especially 3D printed ones. Before considering the usage of this technology on a SLM sample, the micro milling forces and chip thickness formation have to be analyzed and optimized to avoid any material removal behavior that could decrease the precision of the technique [5]. Specifically, the cutting energy and forces are highly influenced by the undeformed chip thickness causing side effects. When the uncut chip thickness is too low, the cutting process is not anymore guided by an elastic deformation (shearing) but by a ploughing regime, which is an elasto-plastic deformation that causes an incorrect chip formation.

The undeformed chip thickness has been identified as one of the causes of the burrs formation during micro milling operations, affecting the quality of the product and the specified dimensional accuracy [6]. Burrs removal is often cost and time consuming since it is extremely difficult on small size components and rarely performed by conventional processes [7]. Therefore, the controls on burrs formation has assumed a lot of importance for a lot of applications, especially in the biomedical field that requires burrs free components.

For this reason, numerous studies focus on the timely and direct characterization of the burrs to provide prompt feedback on the process. Most of the optical systems used for burrs estimation are not able to provide accurate information on geometry or surface roughness and thus specific additional systems are often required to access this information (profilometers, micro-probes or SEM) [8]. Usually, studies on obtaining burrs data by SEM images are conducted manually, meaning that time and practice are required [9].

In this work, a prior evaluation of the machinability and material removal behavior on 17-4PH steel SLM samples has been performed, and a fast and user-friendly solution for measuring burr formation at the micro-scale requiring only one image as input, is proposed. The use of the data acquired through the optical profilometer allows a geometrical characterization of the machined sample with high accuracy, including the burrs geometrical characteristics in terms of morphology and volume evaluation.

Materials and Methods

Micromilling assessment

17-4 PH samples were produced by the laser powder bed fusion machine ProX 100 (© 3D Systems, Rock Hill, South Carolina, United States) as 25x25x5 mm^3 square samples, with four holes on the corners for the micro milling machine positioning.

The process parameters were: 50W of laser power, 30 microns of layer thickness and 300 m/s of scan speed. The samples were micro-machined by using the five axes Nano Precision Machining Center Kern Pyramid Nano (© Kern Microtechnik GmbH, 82438 Eschenlohe, Germany). The machining tests consist in channel fabrication with a single tool pass from the outer to the center of the sample at a constant depth (a_p) of 200 μm (Fig.1).

Materials Research Proceedings 28 (2023) 1323-1330 https://doi.org/10.21741/9781644902479-143

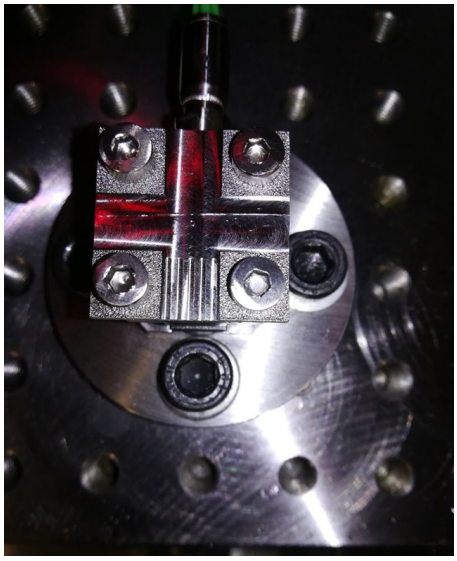

Fig. 1. Reference picture of the machining setup.

Tests can be grouped in two different categories: (i) micro machining at constant cutting speed and different feed per tooth (f_z) values as reported elsewhere [10]; (ii) micro machining with a constant feed rate and three different cutting speeds in order to evaluate the dynamic effects on the burrs developing.

In the first group of tests, a cutting speed (v_c) of 40 m/min was kept constant for each cut. Twenty micro channels were machined by using twenty feed per tooth values ranging between 10 μm and 0.5 μm. The microchannels were produced using a coated two flutes micro mill with a nominal diameter of 0.8 mm.

These tests were designed to identify the MUCT as a function of the feed per tooth. A Labview code was implemented to calculate the cutting force by the cutting load components and the signal was filtered in order to identify the cutting force maximum peak on the flutes (z=2) for each rotation.

The tool run-out has been taken into account when normalizing the cutting force: with two flutes (A and B), the maximum chip thickness for one flute (h_{Amax}) will be different than the thickness for the other flute (h_{Bmax}). This asymmetric condition causes two cutting force peaks (F_{c_maxA}; F_{c_maxB}) which should be normalized by considering the effective thickness (for further details please refer to [10]). The second group of channels were fabricated with a constant depth of cut and by changing the cutting speed on three different levels. It is well known that the cutting speed has a major effect on the size of the burrs in micromachining [11,12].

The tests were finalized to evaluate the burrs formation on the inner and outer side of the channel. Two different dimensional scales were investigated by using a coated two flutes micro mill with a nominal diameter of 0.8 mm and a coated two flutes micro mill with a nominal diameter of 0.2 mm. Two sizes were tested in order to verify the procedure to estimate the burr dimensions at different dimensional scales. With the 0.2 mm micro mill a feed per tooth of 1 μm/tooth and cutting speed of 18, 22 and 26 m/min were tested, while with the 0.8 mm micro mill was chosen a feed per tooth of 3 μm/tooth and cutting speed of 30, 40 and 50 m/min. Each test was repeated three times to statistically validate the results.

Burrs estimation methodology

The new developed method assumes that it is possible to extract more information from surface topography. Specifically, the purpose is to define a method able to quantify burrs extensions exploiting the capabilities of an optical profilometer.

The use of this instrument enables a complete characterization of the machined micro-channels, since the data acquired on the bottom part of the channels can be used for the surface texture evaluation (roughness and amplitude parameters), profiles on different sections can be used for the geometrical characterization of the channels, the data acquired on the top part can be used for the burrs evaluation.

In this paper the focus is on this last point. Since the burrs have complex and irregular geometry, their surface results are difficult to be measured with direct measurement techniques. The proposed method for burrs evaluation leverages the 3D topography enabling the evaluation of burrs volume and projected area. The process flow-chart describing the proposed methodology is reported in Fig. 2.

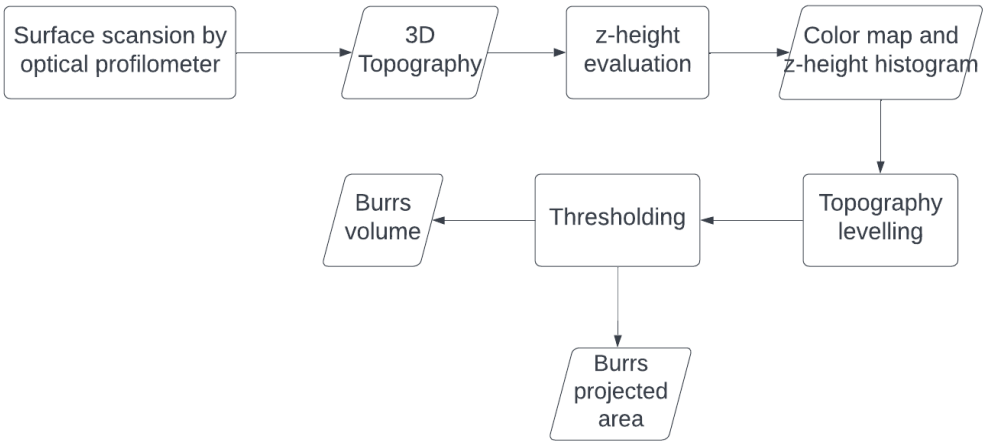

Fig. 2. Flow-chart of proposed method.

The optical profilometer (Sensofar S-neox© Copyright 2021 by Sensofar, Barcelona, Spain) allows the acquisition of a points cloud containing spatial distribution of the scanned points along the 3 main directions (x,y,z). An example of the 3D topography of a micro-machined channel is reported in Fig. 3 where it is possible to distinguish two main regions: the bottom of the channel and the top plane which indicate the rough surface.

The top region is used for the 3D alignment procedure. A roto-translation matrix is determined by applying a least-square algorithm between the top region points and a plane. A linear least-square fitting is applied, using a polynomial plane equation. The coefficients of the equation are then used for the matrix creation, referring to the x-y plane. The obtained matrix is then applied to the entire point cloud along the three main directions x,y,z. The alignment of the top plane is necessary for the thresholding procedure. This step is applied on the height map in order to exclude all the points below the top plane.

The thresholding criterion is based on the points height distribution around the fitted plane, specifically, the limits of the threshold was set in correspondence of the starting point of the positive queue of the z-height distribution which allows to identified only the points characterized by a z-height higher than the as-built surface.

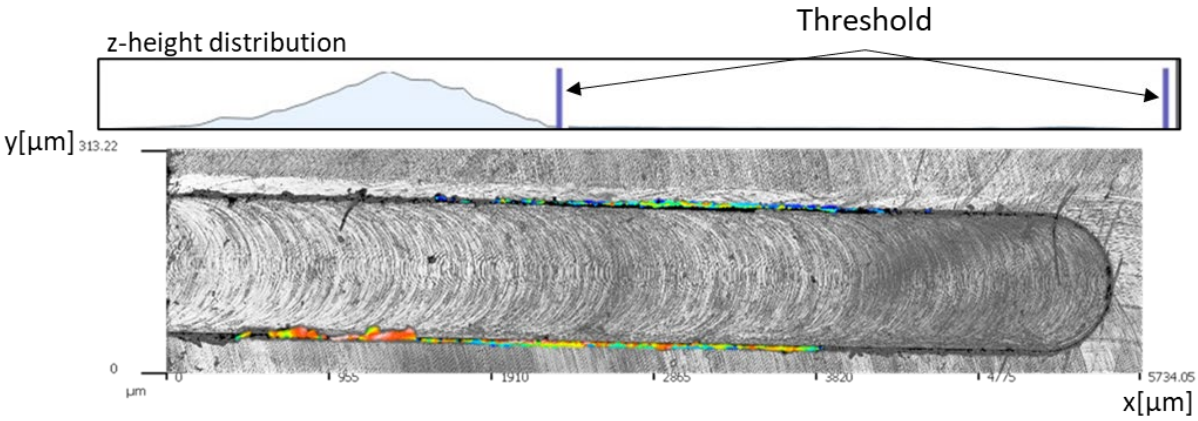

Fig. 3. Portion of burrs identification on the 3D reconstructed machined samples.

Results and Discussion

Identification of the MUCT

As shown in Fig. 4 with a feed per tooth equal or lower than 2 microns, the difference between the cutting force peaks of the two flutes increases. This behavior can be related to a ploughing condition involving flute B that causes an increment of the undeformed depth of cut for flute A. The normalization performed on the resulting cutting force values allowed us to investigate the cutting regime of the material by making the tool run out effects negligible.

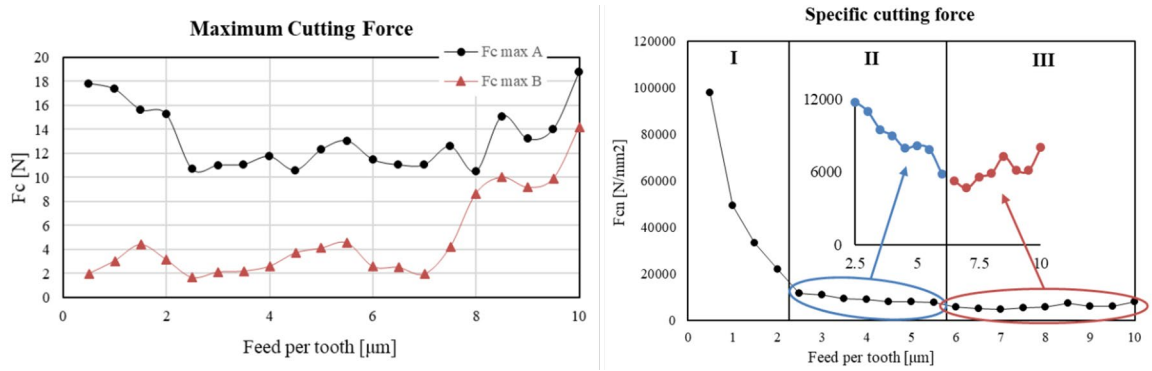

Fig. 4. Cutting force peaks as a function of the feed per tooth (left) and Specific cutting force maximum values for different feed rates (right).

Furthermore, from Fig. 4 it is evident that the specific cutting force changes during the process due to different deformation regimes. Below a f_z of 2.5 µm/tooth, the normalized cutting force increases significantly. For this reason, the MUCT for this analysis was set at 2.5 µm, which falls within the range of the 20-40% of the cutting-edge radius of the tool (0.8 mm). In fact, the region I reported in Fig. 4 is indicating a ploughing deformation region.

The region II instead, is a transition region between the deformation mechanism where the ploughing is progressively substituted by the shearing regime of region III, characterized by the independence of the cutting force in relation to the feed per tooth values.

Influence of cutting speed on burr formation

An overview of the machined channels is reported in Fig. 5, specifically Fig. 5(a) reports the 0.2 mm micro-channels, whilst the Fig. 5(b) shows the 0.8 mm micro-channels.

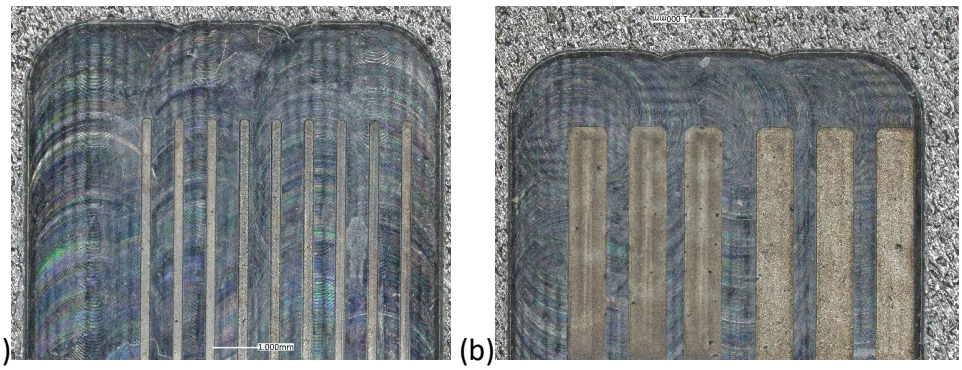

Fig. 5. Reference image of the burrs on the machined samples with 0.2 mm (left) and 0.8 mm (right) tools.

As reported in Fig. 6 the extension of the burrs for this micro milling operation is significant, and the variability between the measured values is particularly high, preventing a priori consideration of the defect.

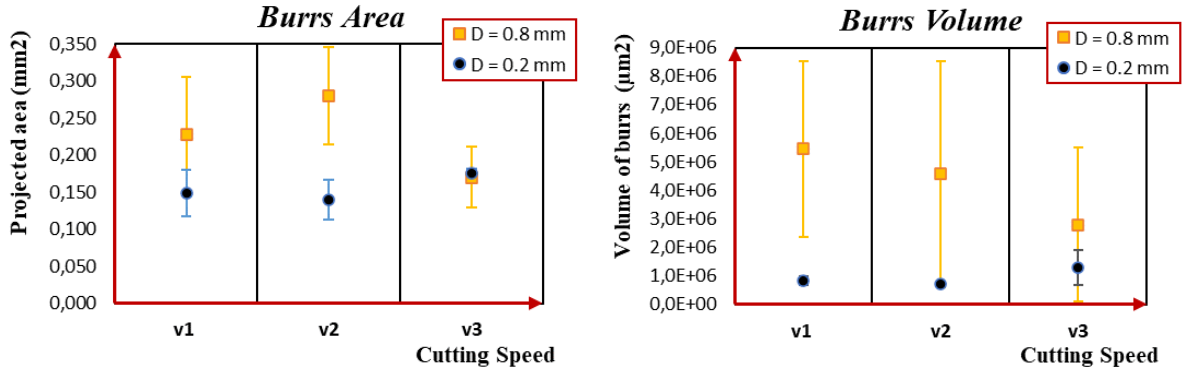

Fig. 6. Burrs Area (left) and volume (right) reported as a function of the cutting speed values for the two used tools.

As visible in Fig. 6, the burrs area on 0.8 mm channels is higher than the 0.2 mm channels, except with the higher cutting speed when it is comparable. There is not a significant dependence of burrs area on cutting speed. The variability of data is calculated as the standard deviation of the measurements, and it resulted lower with 0.2 mm channels. About the volume, the gap between the burrs on 0.2- and 0.8-mm channels increases. The data show a great variability with the 0.8 mm channels and a decrease of the average volume as cutting speed increases. Higher cutting speeds promote higher deformation rates, with a consequent work-hardening of the material. The resulting decrease of the workpiece ductility facilitates the chip evacuation with a consequent reduction of burrs. With 0.2 mm channels, the volume of burrs is almost constant, and it does not depend on cutting speed because on the micro scale, other phenomena are prominent, such as the development of undesired cutting regimes.

The ratio between the burrs area and cross section of the channels (*ratio A*), and the ratio between the burrs volume and the channel volume (*ratio V*), were calculated in order to compare the dimensions of the burrs on channels with different diameters.

$$Ratio\ A = \frac{Burrs\ Area}{D * a_p} \tag{1}$$

$$Ratio\ V = \frac{Burrs\ Volume}{D * a_p * L_C} \quad (2)$$

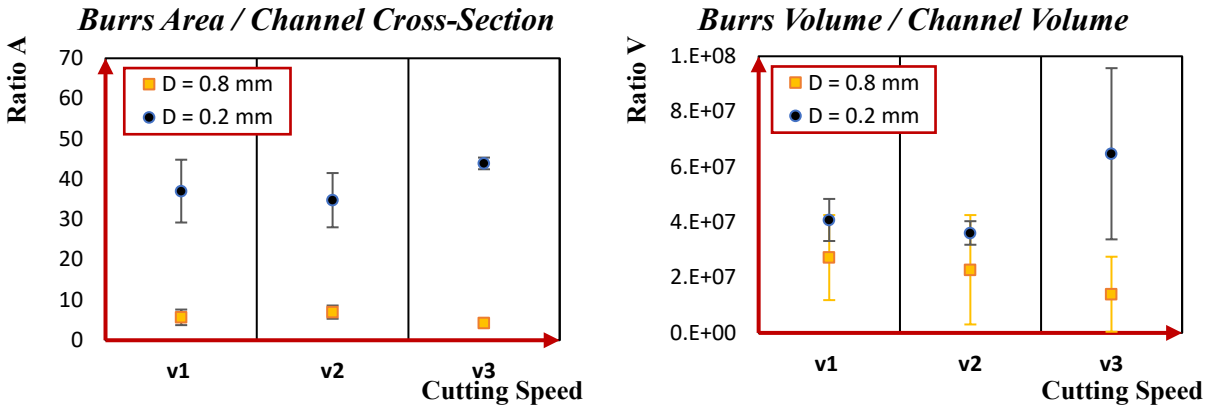

Fig. 7. Ratio A (left) and Ratio V (right) reported as a function of the cutting speed values for the two used tools.

As visible in Fig. 7, the coefficients *A* and *V* are higher for the 0.2 mm channels if compared with 0.8 mm channels. It means that the relative dimension of the burrs is higher with the channels machined with 0.2 mm micro-mill. The miniaturization of the machined features determines a worsening of the surface integrity due to the size effect. It is related to the promotion of negative rake angles due to the decrease of the ratio between the chip thickness and the cutting-edge radius. The compression of the material, known as ploughing, avoids the correct chip formation with a consequent increasement of the materials collected on both sides of the channels. The size effect has more impact on the ratio *A* then the ration *V*. It means that the morphology of burrs strictly depends on the size of the machining process. With the 0.2 mm diameter micro-mill, the burrs are more developed on the xy plane (see Fig. 3), while they are less developed on the z-direction. On the other hand, as the size increases, the burr are more developed in the z-direction. Each micro-mill has the same helix angle, consequently this trend can be related with the compression of the material in ploughing regime.

Summary

This paper deals with the micro milling of a 3D printed stainless steel material for the post-processing of poorly finished samples. Moreover, this paper introduces an easy-to-handle and time efficient procedure for the burrs identification and characterization after micro milling. From the reported results on the micro milling process, it was possible to notice the occurrence of two deformation regimes as a function of the feed per tooth values. Specifically, at low fz, ploughing dominates the material removal behavior while at higher feed rates, the shearing deformation regime becomes predominant. As a result, the cutting forces during shearing are ten times lower than the forces calculated during ploughing.

Moreover, during shearing the cutting force is not related to the feed per tooth values. The measured transition corresponds to a MUCT of 2.5 microns which is 30-35% of the actual tool edge radius, according to literature [13]. The optimal feed rates have been highlighted to reduce the cutting forces and reduce the tool damage, which causes severe tool wear. We moved beyond the state of the art by introducing a quick and easy-to-handle method for burrs estimation on micro-machined samples. Specifically, a threshold has been established and the software automatically selected the volume and the projected areas based on the z-height of the samples.

Moreover, our method avoids the binary transformation of the values and the consequent projection of the area, which leads to an approximation of the area extension in relation to the

projection. Therefore, we based our work on the estimation of the burrs 3D extension and not only the burrs 2D dimension.

References

[1] C. Ransenigo, M. Tocci, F. Palo, P. Ginestra, E. Ceretti, M. Gelfi, A. Pola, Evolution of Melt Pool and Porosity During Laser Powder Bed Fusion of Ti6Al4V Alloy: Numerical Modelling and Experimental Validation, Laser. Manuf. Mater. Process. 9 (2022) 481-502. https://doi.org/10.1007/s40516-022-00185-3

[2] P. Ginestra, L. Riva, E. Ceretti, D. Lobo, S. Mountcastle, V. Villapun, S. Cox, L. Grover, M. Attallah, O. Addison, D. Shepherd, M. Webber, Surface finish of additively manufactured metals: Biofilm formation and cellular attachment. ESAFORM 2021 - 24th International Conference on Material Forming (2021) art. no. 2089. https://doi.org/10.25518/esaform21.2089

[3] M. Carminati, M. Quarto, G. D'Urso, C. Giardini, C. Borriello, A Comprehensive Analysis of AISI 316L Samples Printed via FDM: Structural and Mechanical Characterization, Key Eng. Mater. 25th International Conference on Material Forming, ESAFORM (2022) 926:46-55. https://doi.org/10.4028/p-szzd04

[4] G. D'Urso, C. Giardini, G. Maccarini, M. Quarto, C. Ravasio, Analysis of the surface quality of steel and ceramic materials machined by micro-EDM. European Society for Precision Engineering and Nanotechnology, Conference Proceedings - 18th International Conference and Exhibition, EUSPEN, 2018.

[5] A. Abeni, P.S. Ginestra, A. Attanasio, Comparison Between Micro Machining of Additively Manufactured and Conventionally Formed Samples of Ti6Al4V Alloy, Lecture Notes in Mech. Eng. (2022) 91 - 106. https://doi.org/10.1007/978-3-030-82627-7_6

[6] P. Cardoso, J.P. Davim, A brief review on micromachining of materials, Rev. Adv. Mater. Sci. 30 (2012) 98-102.

[7] B.Z. Balázs, N. Geier, M. Takács, J.P. Davim, A review on micro-milling: recent advances and future trends, Int. J. Adv. Manuf. Technol. 112 (2021) 655–684. https://doi.org/10.1007/s00170-020-06445-w

[8] F. Medeossi, M. Sorgato, S. Bruschi, E. Savio, Novel method for burrs quantitative evaluation in micro-milling, Precis. Eng. 54 (2018) 379-387. https://doi.org/10.1016/j.precisioneng.2018.07.007

[9] F. Akkoyun, A. Ercetin, K. Aslantas, D.Y. Pimenov, K. Giasin, A. Lakshmikanthan, M. Aamir, Measurement of Micro Burr and Slot Widths through Image Processing: Comparison of Manual and Automated Measurements in Micro-Milling, Sensors. 21 (2021) 4432. https://doi.org/10.3390/s21134432

[10] A. Abeni, P.S. Ginestra, A. Attanasio, Micro-milling of Selective Laser Melted Stainless Steel, Lect. Note. Mech. Eng. (2021) 1 - 12. https://doi.org/10.1007/978-3-030-57729-2_1

[11] A.K. Yadav, M. Kumar, V. Bajpai, N.K. Singh, R.K. Singh, FE modeling of burr size in high-speed micro-milling of Ti6Al4V, Precis. Eng. 49 (2017) 287-292. https://doi.org/10.1016/j.precisioneng.2017.02.017

[12] Z. Kou, Y. Wan, Y. Cai, X. Liang, Z. Liu, Burr controlling in micro milling with supporting material method, Procedia Manuf. 1 (2015) 501-511. https://doi.org/10.1016/j.promfg.2015.09.015

[13] M. Malekian, M.G. Mostofa, S.S. Park, M.B.G. Jun, Modeling of minimum uncut chip thickness in micro machining of aluminum, J. Mater. Process. Technol. 212 (2012) 553-559. https://doi.org/10.1016/j.jmatprotec.2011.05.022

Materials Research Proceedings 28 (2023) 1331-1340 https://doi.org/10.21741/9781644902479-144

On the impact of tool material and lubrication in ball end milling of ceramic foams

ROTELLA Giovanna[1,a], SANGUEDOLCE Michela[2,b*], SAFFIOTI Maria Rosaria[2,c], TESTA Flaviano[3,d], UMBRELLO Domenico[2,e] and FILICE Luigino[2,f]

[1]Department of Management, Finance and Technology, University LUM Giuseppe Degennaro, Casamassima-Bari BA 70100, Italy

[2]Department of Mechanical, Energy and Management Engineering, University of Calabria, CS 87036, Italy

[3]Department of Computer Engineering, Modeling, Electronics and Systems Engineering, University of Calabria, CS 87036, Italy

[a]giovanna.rotella@unical.it, [b]michela.sanguedolce@unical.it, [c]mariarosaria.saffioti@unical.it, [d]f.testa@unical.it, [e]domenico.umbrello@unical.it, [f]luigino.filice@unical.it

Keywords: Milling, Ceramic Foams, Tool Wear, Surface Quality

Abstract. High porosity materials, such as ceramic foams, can be used for several applications spanning from thermal insulators, biomedical implants, molten metal filters, and others. The general practice is to adjust the shape of those ceramic foams in a pre-sintering stage to obtain complex shapes. This work aims to investigate the workability of ceramic foams in a post-sintering condition as an alternative way to overcome premature product failure during production and inhomogeneous shrinkage during sintering. An experimental campaign of ball end milling of alumina-based ceramic foams in a sintered state was carried out herein. Two different tool materials (aluminum oxide-based, diamond-coated) have been tested using two levels of spindle speed under minimum quantity lubrication (MQL) and flood lubrication regimes. The most important findings are: (i) the influence of lubricant is more pronounced analyzing the tool wear, but it has a smaller effect on surface characteristics of the workpiece, (ii) higher spindle speed improves workpiece surface quality (ii) diamond coated tools are the best available choice in terms of both tool wear and surface quality.

Introduction

Porous ceramics are classified as advanced materials which, in general, are capable to supply additional functionalities compared to conventionally used ones; these materials include a wide range of structures based on several morphologies and compositions. High porosity materials can be used for different applications embracing thermal insulators [1], biomedical implants [2], molten metal and other fluids filters [3-7], gases porous burners [6], monolithic catalyst supports [7-9] because of their elevated surface-volume ratio, coatings to enhance lubrication during mechanical processing [10]; some of these applications may require a high level of refractoriness, creep and corrosion endurance, as properties belonging to ceramic materials.

To manufacture ceramic foams several processes are available, some of them involve other materials like polymers as precursors, to provide the lattice shape after sintering [11]. Usually, to change the structure of the obtained ceramic foams, it is possible to modify the precursor shape or work the material ahead of sintering [12]. Nowadays, many studies are being carried out about new sustainable production processes and complex shape development [13], also involving extrusion [14] and additive manufacturing [15], to avoid premature product failure during the production process and inhomogeneous shrinkage in the sintering phase [16,17]. However,

Content from this work may be used under the terms of the Creative Commons Attribution 3.0 license. Any further distribution of this work must maintain attribution to the author(s) and the title of the work, journal citation and DOI. Published under license by Materials Research Forum LLC.

additive manufacturing still shows limitations (e.g. thermal shrinkage, surface quality, resolution), thus it is increasing the use of additive processes in combination with subtractive ones [18]. Processing is often supported by sustainable techniques, such as cryogenic and minimum quantity of lubricant (MQL), allowing to perform machining using a lower amount of cutting fluids to reduce waste and the spread of hazardous substances [19]. Concerning conventional and non-conventional machining methods of bulk ceramic materials [18] many studies were carried out while there is still poor knowledge about the machinability of porous ceramic materials. These latter are considered difficult to machine, since they lead to accelerated tool wear [19], together with poor final surface quality. In fact, they are characterized by a high brittleness combined with the complex lattice shape and porosity, that impact on workability.

Ceramic foam components are mainly used as molten metal filters due to their specific properties in terms of creep and thermal-shock resistance, high functional porosity, low molten metal wetting and specific heat capacity, erosion and corrosion resistance, chemical affinity with inclusions to be removed. Thus, the microstructure and the associated mechanical and thermal properties have a critical influence on the suitability of materials for these types of filters [20]. Many studies demonstrated that the performance of porous ceramics depends on pore size and shape, matrix grain size, intergrain bonding, and pore volume fraction [21-23]. Further analysis has shown that geometric parameters and roughness affect the performance of the ceramic foam in the molten metal filtering process [24], as a result of different inclusion filtering mechanisms such as direct particle impact to the filter, adhesion, and entrapment into recirculation areas [25].

It is very necessary to find innovative, cheap, and easy to perform production methods to guarantee high performance, reliable, long lifetime ceramic filters. At the same time, it is important to optimize resources minimizing the maintenance costs and downtime arising from the failure of a filter element ensuring compliance with the environmental constraints.

This paper aims to assess the machinability of alumina based ceramic foams for molten metal filter applications. In fact, it is worth noting that the effective machining of ceramic foams has not been yet comprehensively assessed. Most commonly used machining techniques for bulk ceramics involve conventional methods (e.g. abrasive wheel cutting, diamond or wire saw cutting), non-conventional machining (e.g. wire electrical discharge machining WEDM, laser beam machining LBM, abrasive water jet machining AWJM) and hybrid machining (e.g. hybrid laser waterjet machining, electrochemical discharge assisted wire machining) and the most commonly used tools are diamond-based ones, for their durability [26]. However, studies based on these techniques [20] demonstrated that the machinability of bulk ceramics still represents an issue for both tool wear and surface integrity of the obtained components.

Thus, this paper presents the evaluation of the machinability of alumina based ceramic foams by spherical end milling process using different lubrication methods and tools materials.

Materials and Methods

The samples under investigation are cylindrical alumina-based ceramic foams, with a diameter of 30 mm, the height of 30 mm, and pore density of 30 pores per inch (ppi). The foams, produced via the replica process [16,27], consist of a network of randomly-oriented dodecahedral-shaped cells interconnected through struts.

Two different tool materials (Fig. 1) were chosen for the experimental campaign on spherical end milling process: vitrified hard bond pink aluminum oxide and electroplated diamonds on a metal substrate with an average grit size of around 120 μm. The reason of these choices lies within to the common use of diamond-coated tools to process ceramics, as explained in the review of the state of the art, and the opportunity to differentiate material removal mechanisms by comparison with abrasive tools. Aluminum oxide tools were provided by Meusburger Georg GmbH & Co KG while diamond coated ones were provided by SICUTOOL S.p.A.

A full factorial experimental campaign, as a complement to a preliminary campaign performed under the same conditions [28] was carried out at fixed axial depth of cut, feed rate, and number of passes and varying tool material, lubrication conditions (flood and minimum quantity of lubricant - MQL) and spindle speed. The parameters of the experimental campaign were recommended by the tool manufacturer since a comprehensive literature on the machining of porous ceramics does not exist.

The setup for milling tests is shown in Fig. 2 while the factors considered for the experimental campaign and their levels are reported in Table 1.

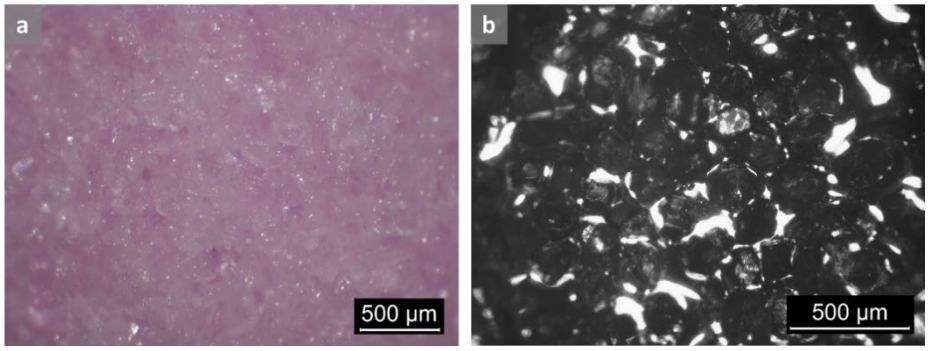

Fig. 1. Micrographs of as received pink aluminum oxide (a) and diamond coated (b) tools.

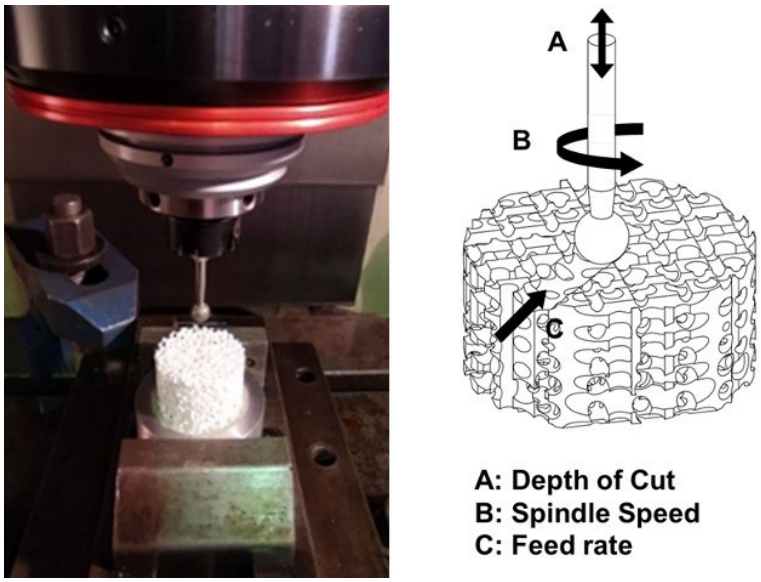

Fig. 2. Schematic of the experimental setup and spherical end milling process.

Materials Research Proceedings 28 (2023) 1331-1340 https://doi.org/10.21741/9781644902479-144

Table 1. Design of experiments for the full factorial experimental campaign.

Factor	Level 1	Level 2
Tool material	Aluminum oxide	Diamond coated
Lubrication conditions	MQL	Flood
Spindle speed [RPM]	10000	40000
Number of Passes	2	
Depth of Cut [mm]	0.5	
Feed Rate [mm/min]	50	

After processing, samples and tools were inspected through a Scanning Electron Microscope to assess the surface characteristics before and after milling, and the tool wear mechanisms.

Results and Discussion

Tool wear is a direct expression of tool life, and it is strictly related to machined surface and subsurface quality. Fig. 3 shows the surfaces of aluminum oxide tools, and the damage is immediately recognizable. For the test at 40000 RPM and using MQL, the tool surface appears flattened (Fig. 3d), the same phenomenon appears to be attenuated for the remaining tests. Also, adhesive wear takes place during the process since a certain amount of adhered foam material was found on the tool surface.

Tool surface flattening and materials mixing can be explained by tool and sample material affinity in terms of composition and mechanical properties. Fig. 4 shows the aluminum oxide worn tools at varying spindle speed, highlighting how different parameters can affect the tool life. Lower spindle speed (Fig. 4a) shows a more marked wearing effect in terms of build-up edge and plastic deformation while rising the speed (Fig. 4b) leads to a lower content of workpiece material adhering to the tool, even though brittle cracks are detectable. Also, adhesion is reduced in the case of flood lubrication which results, by nature, in a more efficient lubrication effect.

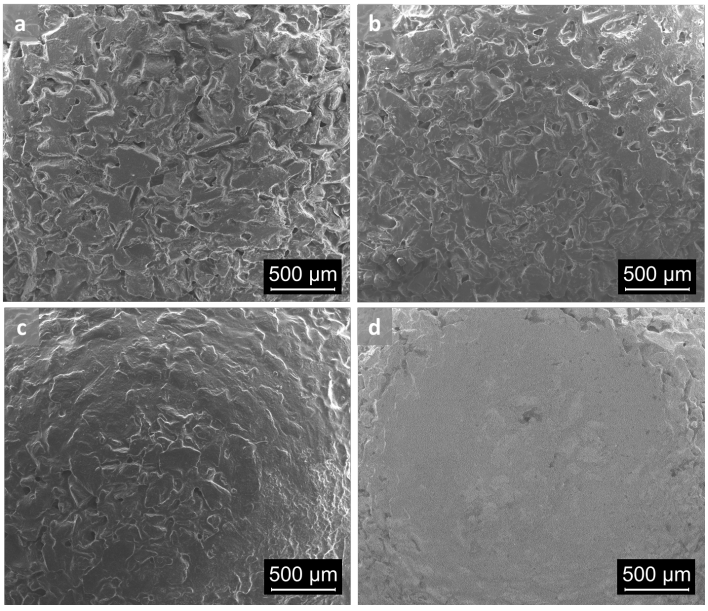

Fig. 3. Aluminum oxide tools after milling at (a) spindle speed 10000 rpm, flood lubrication [28], (b) spindle speed 40000 rpm, flood lubrication, (c) spindle speed 10000 rpm, MQL, (d) spindle speed 40000 rpm, MQL.

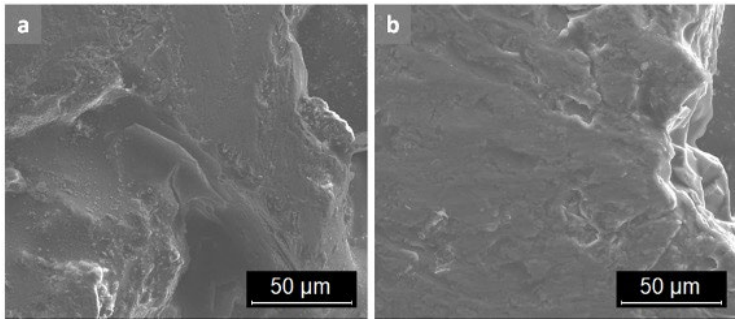

Fig. 4. Details of aluminum oxide tools after milling at different spindle speeds (a) 10000 rpm, (b) 40000 rpm.

As regards diamond coated tools, the damage is not easily recognizable at low magnification, as shown in Fig. 5. A low amount of residual adhered foam material can be seen (Fig. 5d), greater in the case of tests involving MQL. Furthermore, Fig. 6a shows a void left by a diamond being pulled out while Fig. 6b the adhesion phenomenon [28].

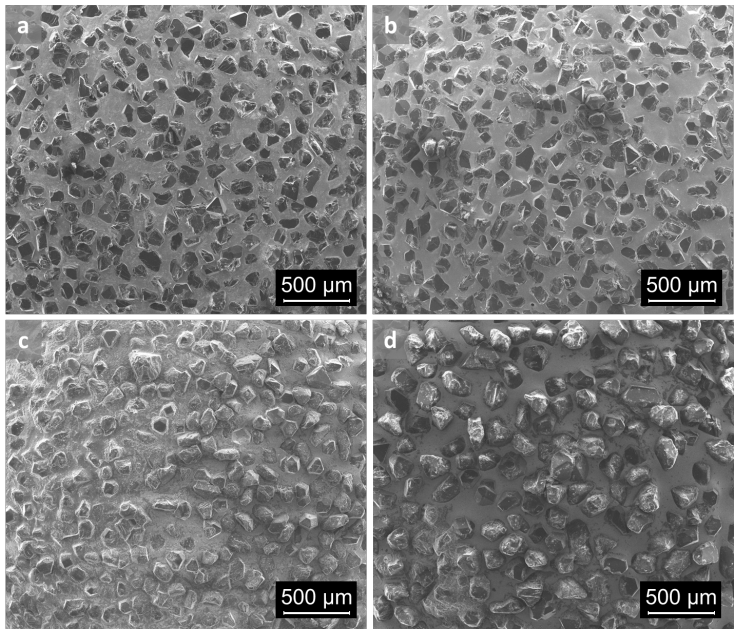

Fig. 5. Diamond coated tools after milling at (a) spindle speed 10000 rpm, flood lubrication [28], (b) spindle speed 40000 rpm, flood lubrication, (c) spindle speed 10000 rpm, MQL, (d) spindle speed 40000 rpm, MQL.

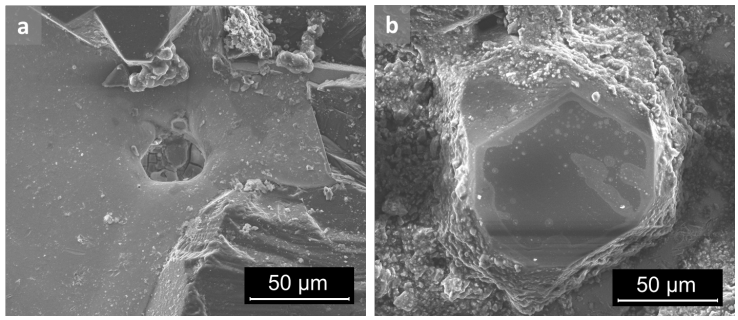

Fig. 6. Details of diamond coated tools after milling (a) diamond pull out, (b) adhesion phenomenon [28].

The process described, inevitably brings both brittle and ductile fractures in workpieces due to the multitude of scratches and their relative interactions when abrasive grains cut into ceramic specimens. The machined surface results ideally deformed similarly to that left by an indentation process, but other mechanisms also take place, like adhesion between tool/workpiece surfaces, as reported above. Furthermore, excessive local forces can generate different defects like chips, fissures, and cracks. The above issues are worsened by the geometric characteristics of the investigated workpieces.

When aluminum oxide tools are used, the adhesion effect evidently affects the fracture mechanism, as shown in Fig. 7. In fact, the chemical affinity between the foam and the tool brings to machined surfaces characterized by a higher content of brittle fractures. The analysis here reported also confirms adhesive wear on the tool.

The effect of lubrication methods can also be evaluated by analyzing Fig. 7 and 8, where no appreciable difference in the final quality of the ceramic surface can be detected. This finding suggests the possibility of effectively machining the samples by avoiding the massive use of lubricants.

On the other hand, the spindle speed influences the machined surface quality as shown by Fig. 7. However, such difference cannot be appreciated at higher magnifications, as Fig. 8 highlights.

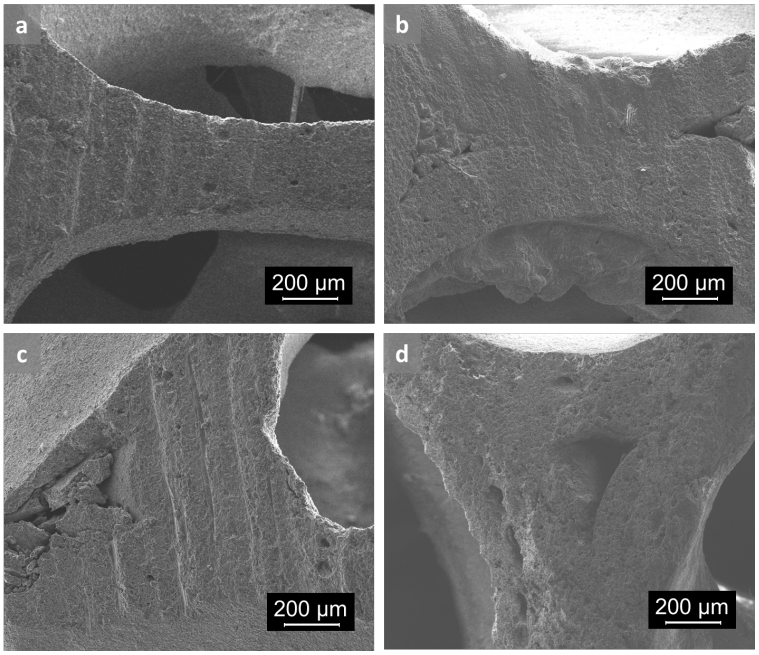

Fig. 7. Ceramic foam surface after milling with aluminum oxide tools at (a) spindle speed 10000 rpm, flood lubrication [28], (b) spindle speed 40000 rpm, flood lubrication, (c) spindle speed 10000 rpm, MQL, (d) spindle speed 40000 rpm, MQL.

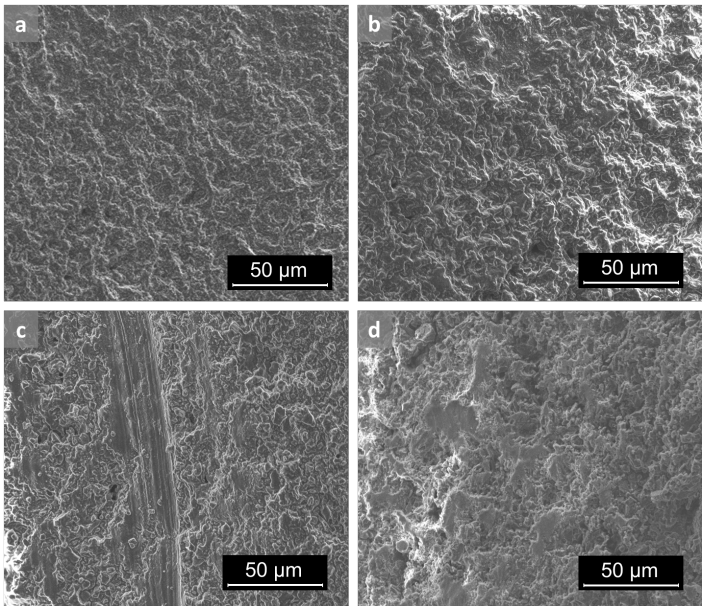

Fig. 8. Details of ceramic foam surface after milling with aluminum oxide tools at (a) spindle speed 10000 rpm, flood lubrication [28], (b) spindle speed 40000 rpm, flood lubrication, (c) spindle speed 10000 rpm, MQL, (d) spindle speed 40000 rpm, MQL.

Diamond coated tools result in a more efficient cutting process since less adhesion effect is present. Fig. 9 and 10 show both ductile and brittle fracture areas, which are typical of the process. The diamond abrasive grains exposed on the milling tool are of random distribution, with a consequent difference in the exposure highness of each diamond. The overall machining is achieved by the combined actions of what can be thought of as several micro-cutting edges with locally different depths of cut, causing areas of both ductile and brittle fracture when machining ceramics. Furthermore, it is possible to state that the effect of lubricant is minimum and that the spindle speed has the same effects as those reported for the aluminum oxide tool.

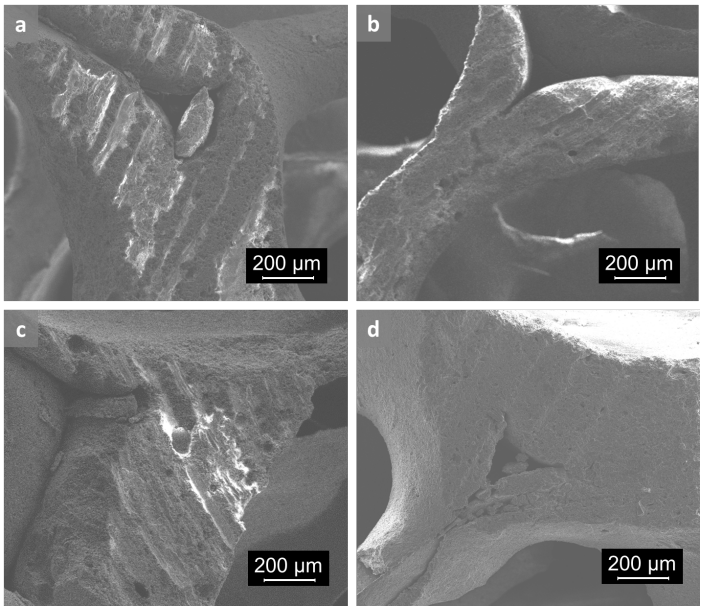

Fig. 9. Ceramic foam surface after milling with diamond coated tools at (a) spindle speed 10000 rpm, flood lubrication [28], (b) spindle speed 40000 rpm, flood lubrication, (c) spindle speed 10000 rpm, MQL, (d) spindle speed 40000 rpm, MQL.

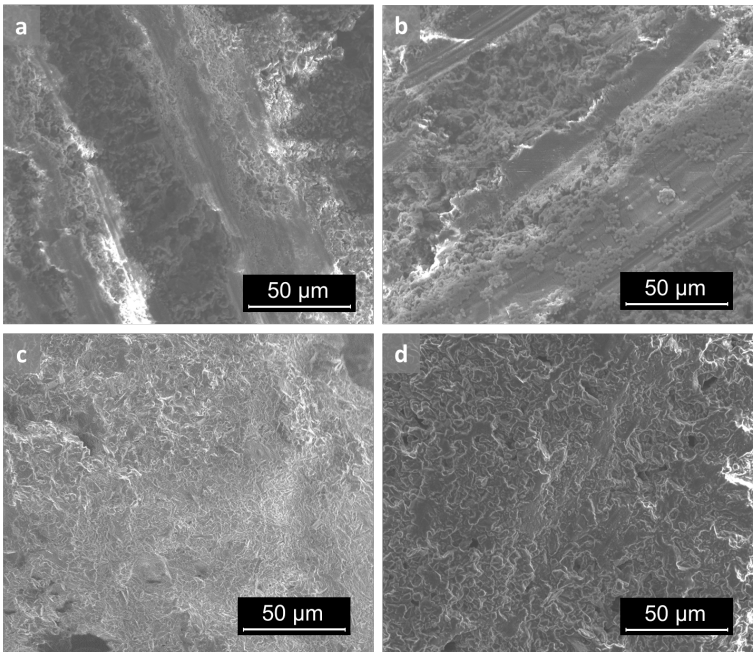

Fig. 10. Details of ceramic foam surface after milling with diamond coated tools at (a) spindle speed 10000 rpm, flood lubrication [28], (b) spindle speed 40000 rpm, flood lubrication, (c) spindle speed 10000 rpm, MQL, (d) spindle speed 40000 rpm, MQL.

Summary

This paper presents an analysis of the workability of alumina based ceramic foam. Such materials combine the issues of machining conventional ceramics with those related to the machinability of geometrically complex parts. The experimental campaign involved the spherical end milling of the workpieces at varying cutting tools, lubricant conditions, and spindle speed.

The results highlighted the tendency of such a process to fast wearing the tools and the combination of ductile and brittle deformation modes on the machined surfaces. The influence of lubricant is more pronounced analyzing the tool wear, where the flood lubrication ensures a longer tool life. Concerning the surface characteristics, lubrication has a smaller effect. On the other hand, the spindle speed plays instead a key role in the deformation mechanism showing a better surface quality when higher speeds are employed.

The results obtained allow the authors to state that ceramic foams can be machined by spherical end milling to obtain a variety of complex shapes and that diamond coated tools are, up to now, the best available choice. In future works, a more comprehensive study of the involved phenomena will be investigated, involving the transition from ductile to brittle material removal, related to locally different depths of cut.

It should be noted that the overall process needs to be optimized to define a workability window able to minimize the tool wear and maximize the surface quality.

References

[1] M. Fukushima, Y.I. Yoshizawa, Fabrication of highly porous silica thermal insulators prepared by gelation-freezing route, J. Am. Ceram. Soc. 97 (2014) 713-717. https://doi.org/10.1111/jace.12723

[2] K. Sharma, M.A. Mujawar, A. Kaushik, State-of-Art Functional Biomaterials for Tissue Engineering, Front. Mater. 6 (2019) 1-10. https://doi.org/10.3389/fmats.2019.00172

[3] J.R. Brown, Foseco Non-Ferrous Foundryman's Handbook, Butterworth-Heinemann, 2000.

[4] J.R. Brown, Foseco Ferrous Foundryman's Handbook, Butterworth-Heinemann, 2000.

[5] A. Salomon, M. Dopita, M. Emmel, S. Dudczig, C.G. Aneziris, D. Rafaja, Reaction mechanism between the carbon bonded magnesia coatings deposited on carbon bonded alumina and a steel melt, J. Eur. Ceram. Soc. 35 (2015) 795-802. https://doi.org/10.1016/j.jeurceramsoc.2014.09.033
[6] P. Wang, K. Zhang, R. Liu, Influence of air supply pressure on atomization characteristics and dust-suppression efficiency of internal-mixing air-assisted atomizing nozzle, Powder Technol. 355 (2019) 393-407. https://doi.org/10.1016/j.powtec.2019.07.040
[7] T. Granato, F. Le Piane, F. Testa, A. Katović, R. Aiello, MCM-41 deposition on alumina ceramic foams, Mater. Lett. 64 (2010) 1622-1625. https://doi.org/10.1016/j.matlet.2010.03.063
[8] T. Granato, F. Testa, R. Olivo, Catalytic activity of HKUST-1 coated on ceramic foam, Microporous Mesoporous Mater. 153 (2012) 236-246. https://doi.org/10.1016/j.micromeso.2011.12.055
[9] F. Jun, Z. ZengFeng, C. Wei, M. Hong, L. JianXing, Computational fluid dynamics simulations of the flow field characteristics in a novel exhaust purification muffler of diesel engine, J. Low Freq. Noise Vib. Act. Control. 37 (2018) 816-833. https://doi.org/10.1177/1461348418790488
[10] G. Ambrogio, F. Gagliardi, Temperature variation during high speed incremental forming on different lightweight alloys, Int. J. Adv. Manuf. Technol. 76 (2015) 1819-1825. https://doi.org/10.1007/s00170-014-6398-y
[11] A.R. Studart, U.T. Gonzenbach, E. Tervoort, L.J. Gauckler, Processing routes to macroporous ceramics: A review, J. Am. Ceram. Soc. 89 (2006) 1771-1789. https://doi.org/10.1111/j.1551-2916.2006.01044.x
[12] M.V. Twigg, J.T. Richardson, Fundamentals and applications of structured ceramic foam catalysts, Ind. Eng. Chem. Res. 46 (2007) 4166-4177. https://doi.org/10.1021/ie061122o.
[13] G.V. Franks, C. Tallon, A.R. Studart, M.L. Sesso, S. Leo, Colloidal processing: enabling complex shaped ceramics with unique multiscale structures, J. Am. Ceram. Soc. 100 (2017) 458-490. https://doi.org/10.1111/jace.14705
[14] F. Gagliardi, C. Ciancio, G. Ambrogio, Optimization of porthole die extrusion by Grey-Taguchi relational analysis, Int. J. Adv. Manuf. Technol. 94 (2018) 719-728. https://doi.org/10.1007/s00170-017-0917-6
[15] G. Liu, Y. Zhao, G. Wu, J. Lu, Origami and 4D printing of elastomer-derived ceramic structures, Sci. Adv. 4 (2018) 1-11. https://doi.org/10.1126/sciadv.aat0641
[16] P. Colombo, H.P. Degischer, Highly porous metals and ceramics, Mater. Sci. Technol. 26 (2010) 1145-1158. https://doi.org/10.1179/026708310X12756557336157
[17] B. Su, S. Dhara, L. Wang, Green ceramic machining: A top-down approach for the rapid fabrication of complex-shaped ceramics, J. Eur. Ceram. Soc. 28 (2008) 2109-2115. https://doi.org/10.1016/j.jeurceramsoc.2008.02.023
[18] R. Rakshit, A.K. Das, A review on cutting of industrial ceramic materials, Precis. Eng. 59 (2019) 90-109. https://doi.org/10.1016/j.precisioneng.2019.05.009
[19] G. Rotella, M. Sanguedolce, M.R. Saffioti, L. Filice, F. Testa, Strategies for Shaping of Different Ceramic Foams, Procedia Manuf. 47 (2020) 493-497. https://doi.org/10.1016/j.promfg.2020.04.345
[20] D.A. Hirschfeld, T.K. Li, D.M. Liu, Processing of porous oxide ceramics, Key Eng. Mater. 115 (1996) 65-80. https://doi.org/10.4028/www.scientific.net/kem.115.65
[21] Porosity of Ceramics by Roy W. Rice (z-lib.org).pdf, (n.d.).
[22] H. Deng, B. Latella, T. Liu, Y. Ke, L. Zhang, Processing and Property Assessment of Porous Alumina and Mullite-Alumina Ceramics, Mater. Sci. Forum. 437-438 (2003) 423-426. https://doi.org/10.4028/www.scientific.net/msf.437-438.423
[23] J.H. She, T. Ohji, Porous mullite ceramics with high strength, J. Mater. Sci. Lett. 21 (2002) 1833-1834. https://doi.org/10.1023/A:1021576104859

[24] E. Werzner, M. Abendroth, C. Demuth, C. Settgast, D. Trimis, H. Krause, S. Ray, Influence of Foam Morphology on Effective Properties Related to Metal Melt Filtration, Adv. Eng. Mater. 19 (2017) 1-10. https://doi.org/10.1002/adem.201700240
[25] O. Dávila-Maldonado, A. Adams, L. Oliveira, B. Alquist, R.D. Morales, Simulation of fluid and inclusions dynamics during filtration operations of ductile iron melts using foam filters, Metall. Mater. Trans. B Process Metall. Mater. Process. Sci. 39 (2008) 818-839. https://doi.org/10.1007/s11663-008-9190-2
[26] R. Rakshit, A.K. Das, A review on cutting of industrial ceramic materials, Precis. Eng. 59 (2019) 90-109. https://doi.org/10.1016/j.precisioneng.2019.05.009
[27] P. Colombo, Conventional and novel processing methods for cellular ceramics, Philos. Trans. R. Soc. A Math. Phys. Eng. Sci. 364 (2006) 109-124. https://doi.org/10.1098/rsta.2005.1683
[28] G. Rotella, M. Rosaria, M. Sanguedolce, F. Testa, L. Filice, F. Micari, Milling of Alumina-Based Ceramic Foams: Tool Material Effects, Meccanica.

Materials Research Proceedings 28 (2023) 1341-1346 https://doi.org/10.21741/9781644902479-145

Superfinishing processes applied on the biomedical implants surface to improve their performance

SAFFIOTI Maria R.[1,a *], ROTELLA Giovanna[2,b] and UMBRELLO Domenico[1,c]

[1]Dept. of Mechanical, Energy and Management Engineering, Univ. of Calabria, CS 87036, Italy

[2]Dept. of Management, Finance and Technology, Univ. LUM, 70010 Casamassima BA, Italy

[a]mariarosaria.saffioti@unical.it, [b]giovanna.rotella@unical.it, [c]domenico.umbrello@unical.it

Keywords: Burnishing, Biomechanics, Surface Integrity

Abstract. The demand of biomedical implants characterized by more and more advanced performances is expected to grow as well as their service life is expected to increase. Therefore, the necessity to research new material properties and production techniques in producing biomedical implants, characterized by higher durability, is strongly required. Regarding permanent prosthesis, the surface conditions play a key role on the prostheses overall mechanical performance. This work aims, through the application of burnishing process, to combine innovative machining finishing operations coupled with environmentally friendly lubricooling techniques to improve the surface integrity of biomedical devices in order to increase their quality, durability and reliability.

Introduction

Nowadays, the demand of products characterized by advanced performances that can provide great societal and environmental benefits is continuously increasing, especially in the biomedical field [1]. Surface integrity modification is one of the available strategies that can be used to enhance the in-service life of a component. As a matter of fact, Severe Plastic Deformation (SPD) processes have been extensively reported for modifying surface properties by altering the surface metallurgical characteristics (e.g. microstructure, hardness, precipitates amount and characteristics, roughness, residual stresses) [2]. Not only mechanical processes are used to change surface characteristics but also thermal processes as laser are employed to modify the surface properties, for example in adhesive joints of non-ferrous materials as shown in this study [3].

Burnishing is a SPD process since it is capable to greatly affect surface integrity due to the high level of strain induced in the workpiece material.

Several studies on different metals of industrial interest were carried out to understand the relationship between the burnishing parameters and post-processed surface integrity. As example in [4] roller burnishing tests were performed on the *Ti6Al4V* titanium alloy, enabling to find a set of processing parameters and lubrication conditions capable to significantly improve the surface quality of the final component. Furthermore, according to [4], the burnishing process aided to improve the surface finish and hardness, also generating compressive residual stresses that contributed to extend the fatigue life [5].

Burnishing is applied to titanium alloys, which represent the most used material for producing orthopedic prostheses like hip and knee implants. Generally, these prostheses, which stay permanently in the human body, need to be revised as a consequence of wear, corrosion and oxidation, which all initiate at the implant surface and may lead to leakage of ions dangerous for the human body [6]. In this case, burnishing is applied in order to increase the wear resistance of titanium alloys. An experimental campaign of burnishing process on cylindrical bars of *Ti6Al4V* was carried out. In particular, the tests were performed under MQL lubrication conditions and by varying process parameters, such as burnishing force, at fixed burnishing speed, feed rate and tool

Content from this work may be used under the terms of the Creative Commons Attribution 3.0 license. Any further distribution of this work must maintain attribution to the author(s) and the title of the work, journal citation and DOI. Published under license by Materials Research Forum LLC.

radius. The choice of using MQL lubricant condition was taken in order to achieve sustainable machining [7] and because the provider of the burnishing tool recommended to not work in dry conditions but to use lubricant as in this case vegetable oil emulsion. Afterwards, the surface integrity was assessed by means of microstructural analysis, roughness and micro-hardness measurements below the machined surface with the aim to analyze the mechanical property improvements after burnishing.

Results showed that the advanced manufacturing technology was able to thoroughly modify surface integrity of the investigated biomaterials. Furthermore, burnishing process enhances surface integrity in correspondence of the subsurface region of *Ti6Al4V*, in terms of grain refinement, surface roughness reduction, and hardness increase, in accordance with the fundamental characteristics required in the biomedical field to achieve the highest product performance and increasingly durable implants.

Experimental Procedure

The titanium alloy involved into the ongoing experimental campaign was the *Ti6Al4V*, grade 5. The as-received material was in form of a bar, with microstructure consisting of α equiaxed grains and intergranular β with 5 μm mean grain size. The bar roughness before processing was equal to 1.2 μm while after the turning process reached a value of 0.8 μm and up to a minimum value of 0.4 μm post burnishing.

Burnishing is a chipless SPD process, which allows increasing the product performance modifying the surface quality by smoothing the roughness, refining the grain structure and increasing the hardness [8. 9].

A deeper analysis concerning the influence of the burnishing process parameters on the *Ti6Al4V* surface integrity was carried out. The burnishing tests were performed using cylindrical bars of *Ti6Al4V* with 30 mm starting diameter, under MQL lubrication conditions. Roller burnishing tests were carried out on a high-speed CNC turning center equipped in particular with Quick Turn Nexus 200-II CNC machine. The lubricant, consisting of a vegetable oil, was delivered at the tool-workpiece interface through an external nozzle.

Table 1. Experimental plan for burnishing.

Burnishing	Value
Cutting speed v (m/min)	150
Feed f (mm/rev)	0.05
Force F (N)	1000 – 1500 – 2000 – 2500
Tool radius R (mm)	2.5
Number of passes	2

The burnishing tool was the SKUV20 (Yamato) with the roller made of hardened steel. Before performing the burnishing process, the bar was previously turned with standard semi finishing parameters, namely 30 m/min of cutting speed, feed of 0.15 mm/rev and 0.1 mm of depth of cut, while the burnishing parameters are reported in Table 1.

In order to control the effective achievement of the fixed burnishing force and monitor the temperature evolution, a three components piezoelectric dynamometer and an infrared thermo-camera were used during the tests. Fig. 1 shows the burnishing process set-up.

The burnished samples were cut in the transverse direction. The cross section was firstly mounted using a thermosetting black epoxy hot mounting resin, and then mechanically polished. These operations were carried out to obtain a mirror-like surface suitable for the metallographic analysis. Before performing the metallographic analysis with the optical microscope (Leica), the samples were etched using the Kroll's reagent able to oxidize the samples in order to highlight and

Materials Research Proceedings 28 (2023) 1341-1346 https://doi.org/10.21741/9781644902479-145

measure the grain edges, then using an automatic procedure provided by ImageJ software, the grain size was measured. Furthermore, a portable surface profilometer (Pocket Surf®) was used to measure the mean surface roughness (Ra) while the Vickers micro-hardness (HV0.1) of the surface and subsurface layer was measured by means of an instrumented micro indenter.

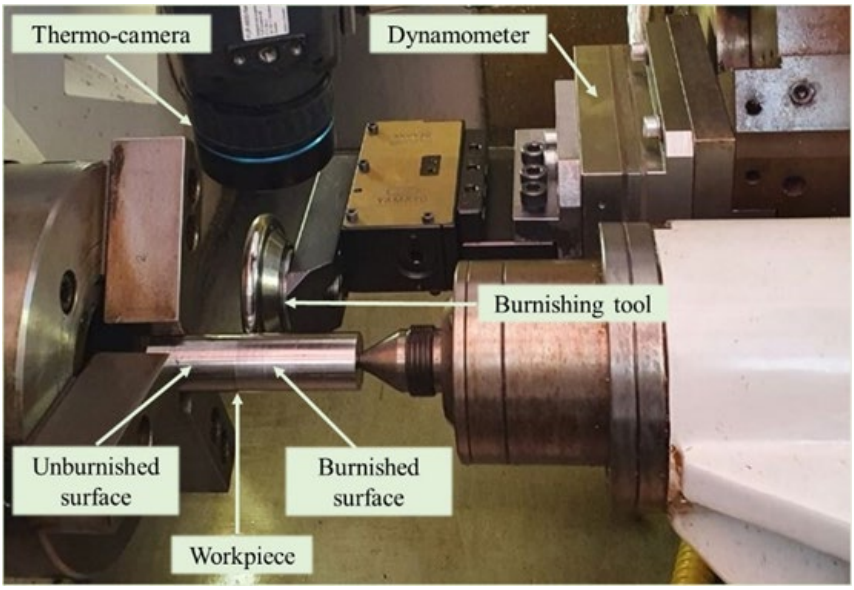

Fig. 1. Burnishing process set-up.

Results

In this preliminary analysis, the overall results were classified analyzing the influence of the burnishing force (B1000, B1500, B2000, B2500), which, according to literature [10], it is considered one of the parameters that mostly affects the surface integrity. Concerning the microstructure, Fig. 2 shows the changes between the different process conditions, in particular the As-Received (AR), As-Turned (AT), and As-Burnished (AB) samples, with 150 m/min burnishing speed, 0.05 mm/rev feed, 2500 N burnishing force, and 2.5 mm tool radius. Focusing on the AB sample, the grain distortion is visible along the working direction. Comparing the AB and AT samples, the AB one appears more deformed due to the larger amount of plastic strain induced by the burnishing process. Fig. 3 allows a better evaluation of the microstructural modifications, outlining the grain size evolution, showing that the surface grain size reduced during machining and even more during burnishing at the highest burnishing force. Although, during burnishing process significant rise in temperature was observed (temperature varied from 20°C to a maximum of 30°C), and therefore dynamic recrystallization did not occur, nevertheless the plastic deformation caused a noticeable grain refinement. This grain refinement is often the outcome of improvements in wear and corrosion resistance, generating compressive residual stresses enabling fatigue life enhancement. In terms of surface roughness, as Fig. 4 shows, an increase in the burnishing force led to a gradually decrease of the surface roughness up to 50% compare to AR sample. Burnishing process was able to give high brightness at the worked surface, also thanks to the MQL lubrication condition, which according to [4] is the optimal solution to obtain a lower roughness.

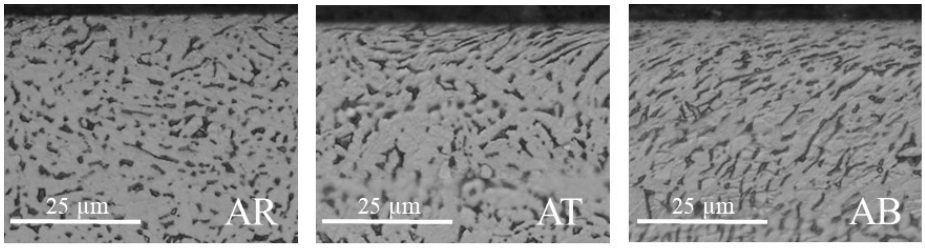

Fig. 2. Microstructure of the AR, AT and AB samples.

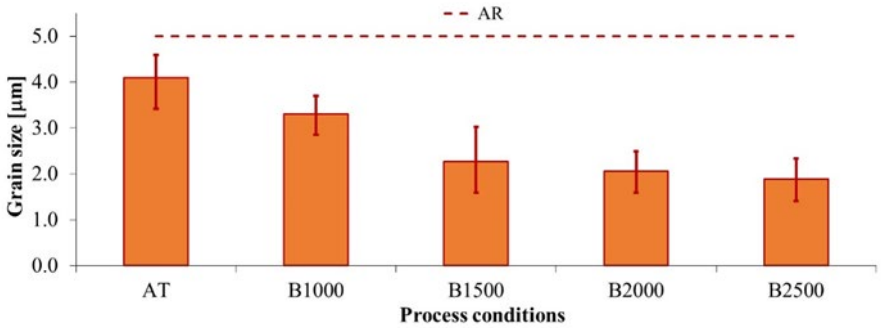

Fig. 3. Grain size evolution at varying burnishing force.

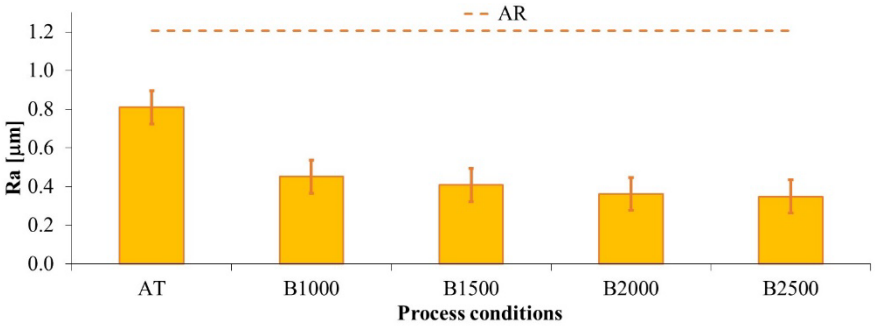

Fig. 4. Roughness at varying burnishing force.

Fig. 5 presents the hardness trend below the machined surface at varying burnishing forces. The hardness of the AR sample was measured equal to 390 HV. Thus, a slight change in the surface hardness resulted after burnishing compared to turning. Furthermore, the deformed layer was deeper after burnishing, which proves an increased work hardening, up to 400 µm from the machined surface, which increased at increasing burnishing force.

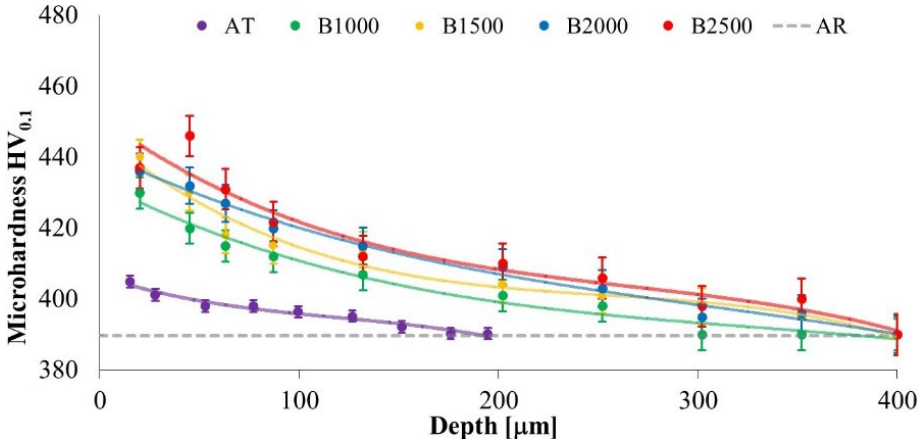

Fig. 5. Microhardness below the machined surface at varying burnishing force.

Summary

Burnishing process is shown to be viable SPD routes for achieving surface integrity enhancement in correspondence of the subsurface region of the biomedical grade *Ti6Al4V* alloy.

The burnishing process of *Ti6Al4V* highlighted enhancements in terms of grain refinement, surface roughness reduction, and hardness increase, which are fundamental characteristics required especially in the biomedical field to achieve the highest products performance.

Future studies will be devoted to investigate the influence of the different processing technologies on in-service life performances of the investigated biomaterials after being processed through burnishing. Specifically, further analysis concerning the influence of other burnishing process parameters as for instance the influence of the feed or tool radius on the *Ti6Al4V* wear resistance will be performed.

Acknowledgements

This research was carried out in the framework of the project PRIN 201742RB8R_002 “Bionic” funded by the Italian Ministry of University and Research.

References

[1] S. Affatato, Recent developments and future trends in total hip arthroplasty (THA), in: Perspectives in Total Hip Arthroplasty, Elsevier, 2014, pp. 76-95.

[2] J.S. Ansari, G.S. Matharu, H. Pandit, Metal-on-metal hips: current status, Orthop. Trauma 32 (2018) 54-60. https://doi.org/10.1016/j.mporth.2017.11.010

[3] M. Alfano, G. Ambrogio, F. Crea, L. Filice, F. Furgiuele, Influence of Laser Surface Modification on Bonding Strength of Al/Mg Adhesive Joints, J. Adhes. Sci. Technol. 25 (2011) 1261-1276. https://doi.org/10.1163/016942410X533381

[4] G. Rotella, L. Filice, Surface modifications induced by roller burnishing of Ti6Al4V under different Cooling/Lubrication conditions, Lect. Note. Mech. Eng. (2021) 141-151.

[5] S. Thamizhmnaii, B. Bin Omar, S. Saparudin, S. Hasan, Surface roughness investigation and hardness by burnishing on titanium alloy, J. Achiev. Mater. Manuf. Eng. 28 (2008) 139-142.

[6] K.L. Urish, N.J. Giori, J.E. Lemons, W.M. Mihalko, N. Hallab, Trunnion Corrosion in Total Hip Arthroplasty—Basic Concepts, Orthop. Clin. North Am. 50 (2019) 281-288. https://doi.org/10.1016/j.ocl.2019.02.001

[7] R.S. Revuru, N.R. Posinasetti, V.R. Vsn, M. Amrita, Application of cutting fluids in machining of titanium alloys—a review, Int. J. Adv. Manuf. Technol. 91 (2017) 2477-2498. https://doi.org/10.1007/s00170-016-9883-7

[8] V. Schulze, F. Bleicher, P. Groche, Y.B. Guo, Y.S. Pyun, Surface modification by machine hammer peening and burnishing, CIRP Ann. - Manuf. Technol. 65 (2016) 809-832. http://doi.org/10.1016%2Fj.cirp.2016.05.005

[9] I.S. Jawahir, Y. Kaynak, T. Lu, The impact of novel material processing methods on component quality, life and performance, Procedia CIRP 22 (2014) 33-44. https://doi.org/10.1016/j.procir.2014.09.001
[10] J. Caudill, J. Schoop, I.S. Jawahir, Correlation of surface integrity with processing parameters and advanced interface cooling/lubrication in burnishing of Ti-6Al-4V alloy, Adv. Mater. Process. Technol. 5 (2019) 53-66. https://doi.org/10.1080/2374068X.2018.1511215

Materials Research Proceedings 28 (2023) 1347-1356 https://doi.org/10.21741/9781644902479-146

Evolution of contact lengths during the turning of treated Ti64β

WAGNER Vincent[1,a *] and DESSEIN Gilles[1,b]

[1]Laboratoire Génie de Production, Ecole Nationale d'Ingénieurs de Tarbes, Université de Toulouse, Tarbes Cedex, France

[a]vincent.wagner@enit.fr, [b]gilles.dessein@enit.fr

Keywords: Contact Length, Ti64β, Tool Wear

Abstract. One of the main ways to increase productivity during the machining of titanium alloy parts is to control the wear mechanisms and consequently the life of the cutting tools. The state-of-the-art shows wear phenomena generated mainly by diffusion. The latter is due to the intrinsic physical properties of titanium generating high temperatures on the cutting and relief faces. Concerning the secondary cutting zone, the wear phenomena result from thermomechanical actions induced by the contact between the secondary zone of the chip and the cutting face of the tool. The analysis of the contact lengths, divided into two parts (sliding contact and sticking contact), is then a strong indicator to be privileged in order to allow the understanding of the present mechanisms. This analysis is even more important when machining processed Ti64 β in which chip formation is no longer periodic but a function of the angle between the primary shear band and the orientation of the individual colonies comprising the titanium. The purpose of this article is the analysis of the contact lengths during the machining of Ti64 treated β . After having presented the experimental device allowing visualising the evolution of the contact length between the chip and the cutting face, a statistical analysis based on the collected images makes it possible to put forward the differences of sliding behaviour on the cutting face. It appears that the distribution of the collected values allows explaining and extrapolating the wear appearing on the cutting face.

Introduction

When machining titanium alloys, two types of tool wear occur. Because of their high mechanical properties and low thermal properties, the wear encountered is flank wear and edge collapse. Tool wear has been studied for many years [1] and [2]. To avoid or limit tool wear, one of the solutions is then to define an optimal tool geometry and reduce the cutting conditions. The aim is to reduce the phenomena of diffusion. These phenomena appear mainly on the rake face and result from the high thermomechanical stresses applied to the cutting face over a distance called the contact length. Some studies concern the analysis of the parameter but it is always considered as constant and function of the cutting conditions, the cutting tool geometry and the workpiece behaviour. For example, Lee and Shaffer [3] and Abdulaze and al. [4] some pioneers in this filed developed an analytical tool-chip contact length models for standard steel. With this model, they link the geometrical aspect such as rake angle, uncut chip thickness or shear angle. Zhang et al. introduced the effect of cutting speed on the model of these lengths and in application for low-carbon steel [5]. Oxley provide a model based on coefficients traducing the strain hardening of the material [6]. Moufki et al attempt to take into account the effect of temperature of the friction law between the chip and the tool, where most of the studies use a Coulomb contact [7]. Moreover, it is commonly accepted that the contact length decreases with increasing cutting speed and rake angle and decreases with the feed rate [8]. A major part of these models are dedicated to a sharp cutting edge. However, when machining with chamfered tools, the cutting process is relatively different. Indeed, the chamfered edge will often lead to the formation of a dead metal zone under itself. This dead metal zone will replace the missing nose of the tool and form a small edge radius, changing the

Content from this work may be used under the terms of the Creative Commons Attribution 3.0 license. Any further distribution of this work must maintain attribution to the author(s) and the title of the work, journal citation and DOI. Published under license by Materials Research Forum LLC.

shear angle. With this specific shape will appear a stagnation point around which the material will flow. Recently, Barelli and al. [9] showed there is a particular evolution of contact lengths during machining. They show from a statistical analysis of the contact lengths over a short period of time that the contact evolves and generates more or less significant deposits. However, this analysis, although accurate, is limited to a single alloy.
Wagner and al. [10] shows that chip formation during the machining of Ti64 β does not follow the cutting process introduced by [11]. It then appears that chip formation is not constant over time but is a function of the orientation of the structure encountered during the creation of the shear band. The morphology of the harvested chips is then very variable.

The objective of this study is to provide an analysis of the contact lengths during the machining of Ti64 β in order to identify if the particular process of chip formation, which is not constant, impacts the contact lengths. After having presented the alloy and the chip formation process, this study is based on an experimental device allowing measuring at each moment the contact lengths during machining. The images collected and analysed allow correlating the contact lengths with the cutting conditions and to compare their variability with the more common structure.

Studied Material

The objective of this part is to present the machined material as well as the experimental device. The alloy used is a Ti64 composed of titanium, 6% aluminium and 4% vanadium. The recrystallisation process is defined by different steps (Fig. 1). The difference between this structure and the more common structure results in the addition of a solution phase in the βdomain between the forging and tempering phases. Indeed, the microstructure of Ti64 is a function of the different stages of the recrystallisation process. The heat treatment is divided in four steps. The first one corresponds to the homogenisation of the structure. The second step is the forging carried out only in the domain α +β . This is followed by solution heat treatment starting in the β range and followed by a long cooling phase. Ultimately, a tempering is performed at a temperature below β transus.

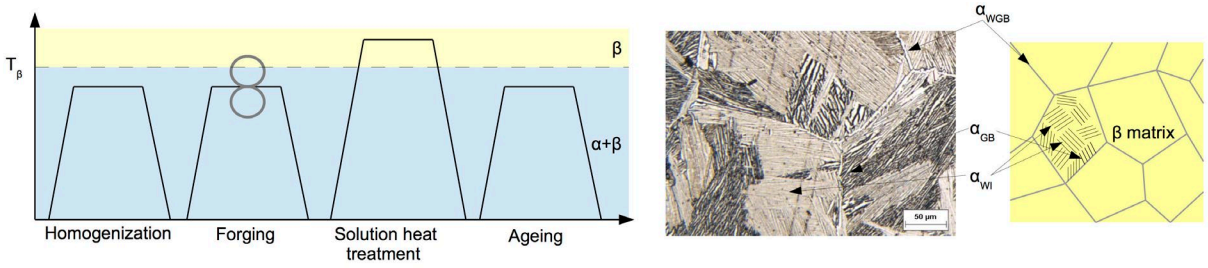

Fig. 1. Heat treatment (left) and structure of Ti64β (two figures on the right).

In contrast to the classical Ti64 structure (with nodular grain [11]), the structure of the alloy studied is fully lamellar (Fig. 2). The α phase is transformed into an acicular phase α ' in the matrix β. It is also possible to observe the α_{BG} phase near the grain boundaries. It appears as the continuous line around the old grains β. Concerning the α_{WBG} phase, it germinates from the grain boundary to the centre and appears as lamellae. Finally, the α_{W1} phase germinates inside the old grain β. The whole phases are immersed in the matrix β.

Materials Research Proceedings 28 (2023) 1347-1356 https://doi.org/10.21741/9781644902479-146

Experimental Device

For these tests, Genymab 900 turning lathe was used. The inserts used were CCMX 120408 with TiN PVD coating, the rake angle was 20° and inserts had a chamfer edge preparation of 0.02 mm. The tests were carried out on tubes in order to be in simple, generalisable cutting conditions. The chip flow will not be unidirectional insofar as a slight angle of inclination of the edge appears. These tests were carried out without lubrication in order not to disturb the image acquisition. The tubes used for these tests have a thickness of 3 mm. Force measurements during machining were performed using a Kistler 9129A dynamometer, a 5019A amplifier and Dynoware software.

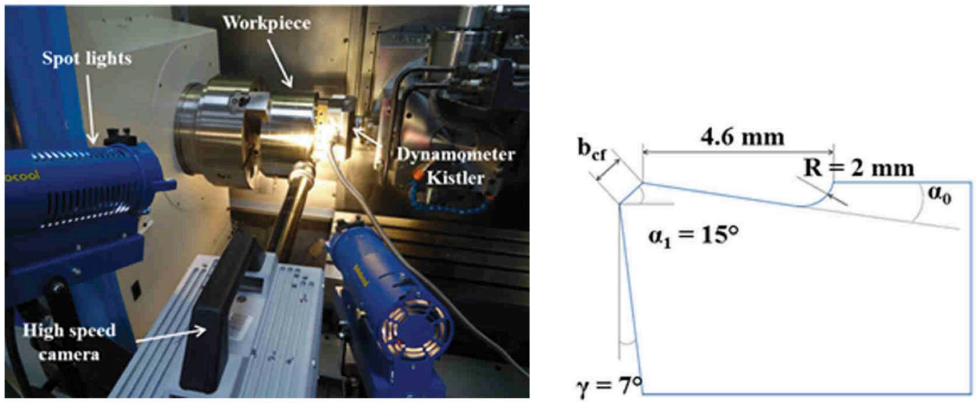

Fig. 2. Experimental setup.

The observations of the chip flow during the machining process were carried out with the help of the PhotronFastcam SA1 high-speed camera whose acquisition characteristics of 5000 images/s^{-1} is chosen. The resolution used is 1024x1024 pixels2 allowing an acquisition time of about 1s. For these tests, two cold light projectors were used to limit their influence on the cutting temperature. Definitely, rings were added between the cell and the x100 zoom lens. The resolution obtained is 5µ m. The experimental setup is shown in Fig. 2.

Chip Formation

For this alloy, the study shows that chip formation does not follow the classical process developed in many works [11-1]. Indeed, the chip formation is not only due to shears generated between the tool tip and the root of the chip. Several phenomena mainly due to the structure composed of lamellar colonies α +β oriented whose orientation varies appear (Fig. 3). The purpose of this section is to highlight these phenomena in order to explain, subsequently, the evolution of the contact lengths.

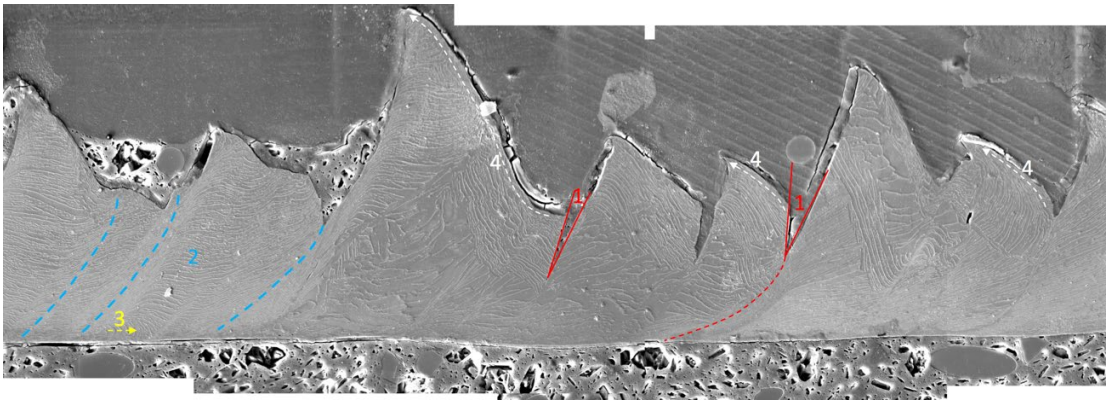

Fig. 3. Example of a micrograph of a Ti64 β chip.

The study of the chip formation allowed to put forward 4 configurations (Table 1).

Configuration 1

Whatever the cutting conditions, cracks can appear near the primary shear bands. There are two possible causes. The first one is similar to the one observed on more classical structures. The crack is then explained by intense shears. The second cause is specific to this alloy. The crack is then explained by a strong accumulation of plastic deformation at the interface of two strongly disoriented colonies (Colony 3 compared to Colony 4 and Colony 1 compared to Colony 2) (Table 1). In this case, the stress accumulation is explained by the difficulty of providing dislocations between two differently oriented colonies.

Configuration 2

The shear bands will appear in a privileged way in colonies whose orientation is transverse to the shear propagation. If the interfacesα /β are not a brake to the propagation of dislocations, a stress gradient exists between the different lamellaeβ going towards an increase of the stress near the interface. Consequently, the strain required to shear the interfaces is greater than that required to shear the laminae α .

Configuration 3

It appears that colonies relatively collinear to the main shear direction can be sheared transversely. The latter is initiated by the movement between the various colonies surrounding it.

Configuration 4

In this configuration, it appears that a continuous shearing of the colony takes place near the free edges of the chip. The chip thus follows the movement imposed between the end and the interface of the closest colony.

This initial study thus shows the randomness of chip formation. A study from [10] concerning the influence of cutting conditions on chip formation then shows that adiabatic shear and cracking become regular when the feed rate and therefore the shear forces are high enough to generate them despite the orientation of the colonies.

The objective of the next part is then to observe the effect of this particular chip formation on the chip flow length.

Table 1. Summary of the different configurations found.

Configuration 1	Configuration 2
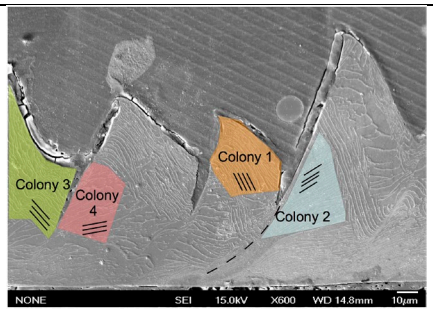	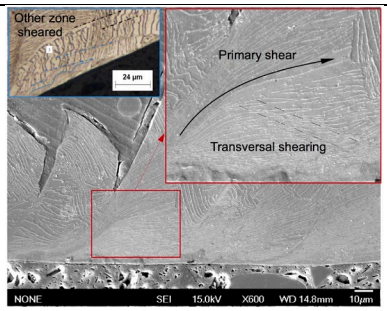
Configuration 3	**Configuration 4**
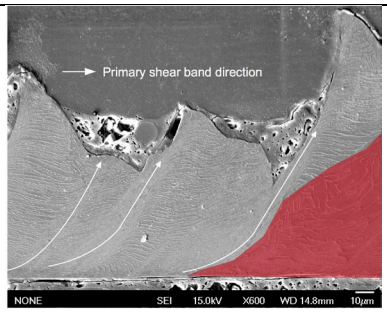	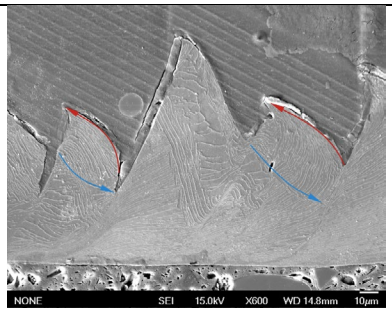

Cutting Length Measurements

The images are then processed using Matlab © software following an algorithm detailed in Fig. 4. The first step consists in locating the cutting edge by defining in X and from the left of the image, the last black pixel (grey level 0). This same operation is performed in Y. From the coordinates of the cutting edge, the algorithm recreates the cutting edge. For this and for each column, the program defines the last pixel with gray levels equal to 255 (white). Then, the chip being one of the elements reflecting the lightest, it is easy to determine a threshold value of gray level delimiting the lower surface of the chip in the background. This value is specific to each serie of images, the algorithm artificially defined that all gray levels below this threshold value are equal to 0. From the points belonging to the edge, the algorithm searches column by column, in the direction of the positive Y, for the last pixel with a gray level of 0. These pixels then belong to the lower surface of the chip. The set of coordinates of the edge and the cutting face being known, it is then possible by difference to calculate the contact lengths between the chip and the cutting face.

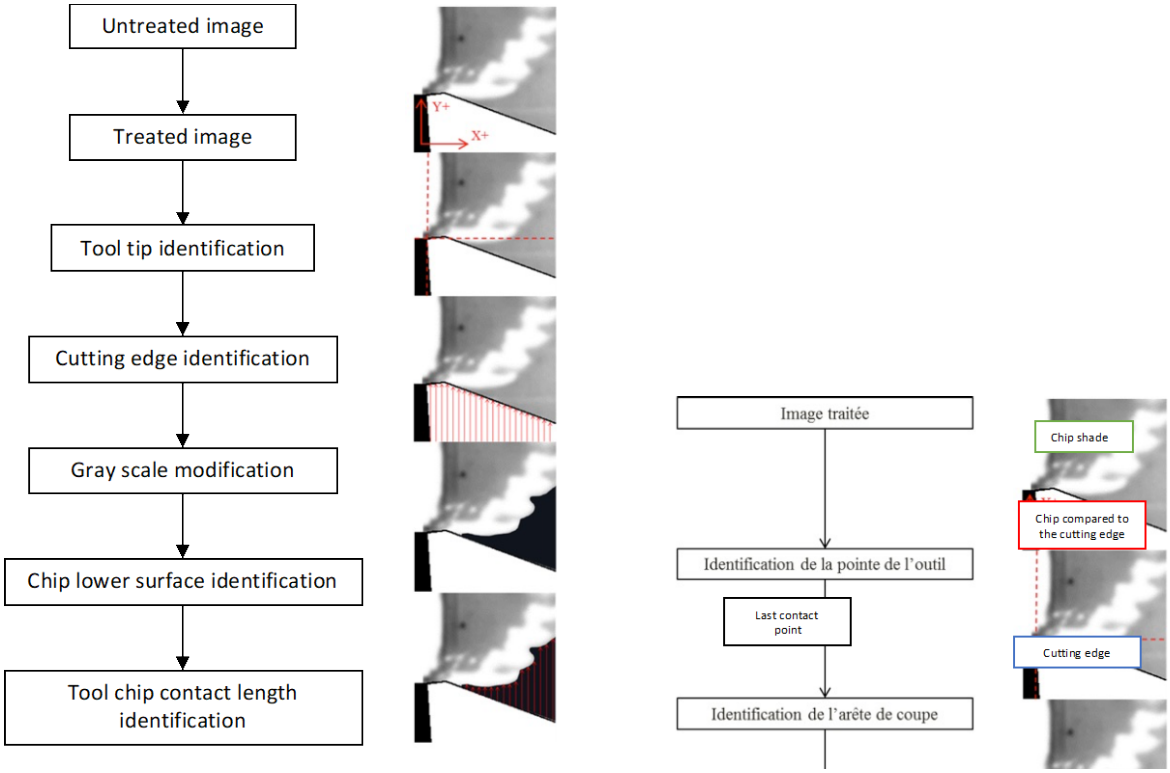

Fig. 4. Image processing.

Given the large number of values obtained, a statistical analysis was carried out. The results obtained are presented in the form of a moustache box (Fig. 5). This choice makes it possible to highlight the distribution of the data and the preferred values taken by the contact lengths. On the representations exposed in this article will be exposed the 5th percentile (the low end of the segment), the 1 st quartile (the low part of the box), the median (the line in the middle of the box), the 3rd quartile (the high part of the box) and finally the 95th percentile (the end of the segment). Each result sums up measurements made on 1000 images of tool-chip contact lengths within cutting process.

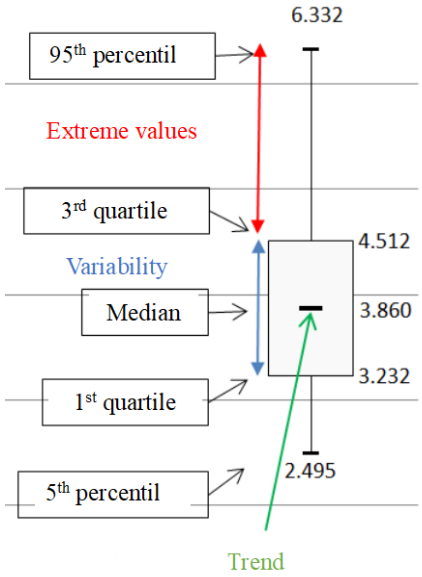

Fig. 5. Moustache box.

When machining Ti64 with a classical structure, the general trend observed is a quasi-linear increase in contact lengths with the feed rate. The increase of the cutting speed has the effect of slightly reducing the contact lengths but in lesser proportions compared to the feed rate.
For this microstructure, the trends are slightly different (Fig. 6). The classical relationship between contact length and feed rate does not appear. For all three cutting speeds tested, increasing the feed rate results in an increase in contact length. From these tests, it is not possible to define the conditions giving the greatest contact length. Concerning their extent, the most variable conditions appear for Vc=30 m/min. Indeed, whatever the quantile or the percentile observed, the greatest differences appear for Vc=30 m/min.

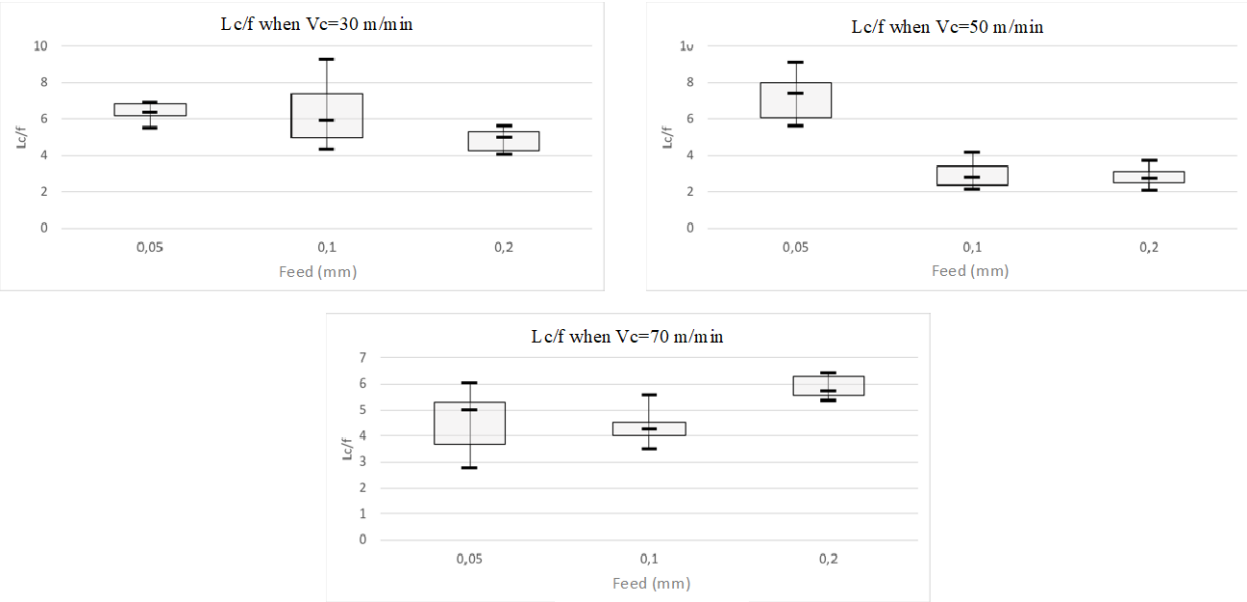

Fig. 6. Evolution of contact lengths for Vc=30 m/min, Vc=50 m/min and Vc=70 m/min.

This trend appears to follow the cutting process and chip formation developed earlier. The variability also seems to correlate with the effect of cutting conditions on chip formation.
Contrary to the analysis made on the more classical structure, it appears that whatever the analysis time, the radius of curvature is not impacted. Table 2 shows the chip formation observed at different times (at the beginning of the analysis, in the first quarter, in the middle, in the third quarter and at the end). It appears that the chip never touches the chip breaker, never segments and because of the edge inclination never meets the machined face (in this example out of the field). Moreover, the tests showed that over the recording period, the chip weight did not influence the contact lengths. Indeed, as the chip does not segment, the chip weight could impact the radius of curvature and consequently the contact lengths. The change in contact lengths can then be explained by the formation of chips.

Table 2. Evolution of chip formation over the duration of the statistical analysis.

Start	Duration / 4	Duration /2	End
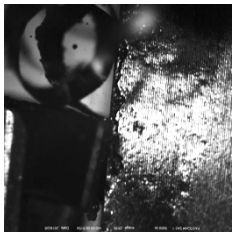	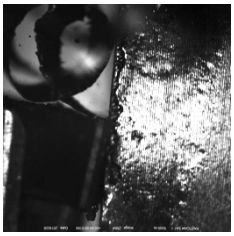		

The study of the effect of cutting conditions on chip formation shows a strong correlation between cutting speed, feed rate and chip geometry. In contrast to the more classical structures where the chips remain, whatever the cutting conditions, more or less scalloped chips, the shape of the chips is much more evolutive. Table 3 shows the effect of cutting conditions on chip formation. At low cutting speeds, the chips are continuous. As the cutting conditions increase, it appears that the chips become scalloped with increasingly constant distances between scallops. However, unlike other alloys, the scalloping becomes more regular as the cutting conditions increase. This relationship is explained by the level of stress that appears at high cutting conditions. As said before, the creation of shear bands is initiated especially when the colonies are oriented perpendicular to the band formation. This initiation is the result of high thermomechanical stress accumulation at the boundary of highly disoriented colonies. Higher stress accumulation then facilitates the creation of primary shear bands. An increase in cutting conditions results in higher stresses and temperatures which then facilitate the appearance of shear bands. Wagner also shows that for certain cutting conditions, shear bands are created regardless of colony orientation [1].
In the study of contact lengths, it would appear that the lengths and especially the variability are a function of chip formation.
For Vc=30 m/min and when fz=0.05 mm, the variability is the lowest. For these conditions, the thermomechanical stresses are so low that the chip is continuous, whatever the structure. In this case, the variability is the lowest. When the feed rate increases, the stresses also increase and the chip formation becomes a function of the orientation of the microstructure. Its morphology becomes variable as well as the contact length. When Vc=50 m/min, there is a significant variability regardless of the feed rate. This disparity is explained by transient phenomena. For the lowest feed rate, the stresses are too low to generate a shear band each time. Conversely, when the feed rate increases, the stresses are greater but above all the probability of the primary bands crossing colonies increases and the chips, like the contact lengths, remain stable.

Table 3. Chip morphology as a function of cutting conditions.

Vc=30 m/min - fz=0,1 mm	Vc=50 m/min - fz=0,1 mm	Vc=70 m/min - fz=0,1 mm
	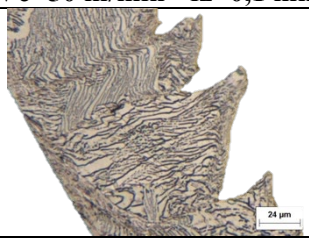	
Vc=65 m/min - fz=0,13 mm	**Vc=65 m/min - fz=0,15 mm**	**Vc=65 m/min - fz=0,20 mm**
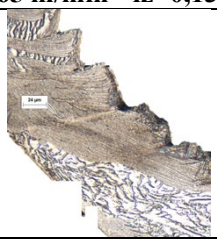		

Summary

Through an innovative experimental device, the objective of this study is to observe the evolution of contact lengths during the machining of Ti64β . After having detailed the microstructure and the particularities of the chip formation, the study develops the method of statistical analysis of the collected images. It appears that this evolution is mainly a function of the chip formation process. The study also shows a strong variability of the contact lengths explained by various points like, for example, the weak cutting conditions obtained during certain tests. In order to complete this analysis and to clearly define the relationship between contact length and tool wear, the next step is to chemically analyse the inserts and to propose a diffusion model complementary to those already existing based on a large experimental campaign.

References

[1] V. Wagner, E. Duc, Study of Ti-1023 milling with toroidal tool, Int. J. Adv. Manuf. Technol. 75 (2014) 1473-1491. https://doi.org/10.1007/s00170-014-6217-5

[2] V. Wagner, M. Baili, G. Dessein, The relationship between the cutting speed, tool wear, and chip formation during Ti-5553 dry cutting, Int. J. Adv. Manuf. Technol. 76 (2015) 893-912. https://doi.org/10.1007/s00170-014-6326-1

[3] E.H. Lee, W. Shaffer; The theory of plasticity applied to the problem of machining, J. Appl. Mech. T ASME 18 (1951) 405-413.

[4] N.G. Abuladze. Character and the length of tool-chip contact (in Russian), in: Proceedings of the machinability of heat-resistant and titanium alloys, Kuibyshev, 1962, pp. 68-78.

[5] H.T. Zhang, P.D. Liu, R.S. Hu, A three zone model and solution of shear angle in orthogonal machining, Wear 143 (1991) 29-43. https://doi.org/10.1016/0043-1648(91)90083-7

[6] P.L.B. Oxley, Mechanics of machining: an analytical approach to assessing machinability, Chichester: Ellis Horwood Limited, 1989.

[7] A. Moufki, A. Molinari, D. Dudzinski, Modelling of orthogonal cutting with a temperature dependent friction law, J. Mech. Phys. Solid. 46 (1998) 2103-2138. https://doi.org/10.1016/S0022-5096(98)00032-5

[8] N.N. Zorev, Metal cutting mechanics, Oxford: Pergamon Press, 1966.

[9] F. Barelli, V. Wagner, R. Laheurte, G. Dessein, P. Darnis, O. Cahuc, M. Mousseigne, Orthogonal cutting of TA6V alloys with chamfered tools: Analysis of tool-chip contact lengths,

Proceedings of the Institution of Mechanical Engineers, Part B: J. Eng. Fabric. 231 (2017) 2384-2395.
[10] V. Wagner, F. Barelli, R. Laheurte, G. Dessein, P. Darnis, O. Cahuc, M. Mousseigne, Thermal and Microstructure Study of the Chip Formation During Turning of Ti64 β Lamellar Titanium Structure, J. Manuf. Sci. Eng. 140 (2018) 031010. http://doi.org/10.1115/1.4038597
[11] R. Komanduri, B.F Von Turkovicz, New Observations on the Mechanism of Chip Formation When Machining Titanium Alloys, Wear 69 (1981) 179-188. https://doi.org/10.1016/0043-1648(81)90242-8

Materials Research Proceedings 28 (2023) 1357-1366 https://doi.org/10.21741/9781644902479-147

Investigation of machining performance of lead-free brass materials forged in different conditions after cooling with liquid nitrogen

ATAY Gokhan[1,a *], ZOGHIPOUR Nima[1,2,b] and KAYNAK Yusuf[2,c]

[1]Torun Metal Alloy Ind. & Ltd. Inc., GOSB, İhsan Dede St. Gebze,Kocaeli, Turkey

[2]Department of Mechanical Engineering, Marmara University, Istanbul, Turkey

[a]gokhan.atay@torunmetal.com, [b]nima.zoghipour@gmail.com, [c]yusuf.kaynak@marmara.edu.tr

Keywords: Lead-Free Brass, Microstructure, Hot Forging, Machining, Cryogenic Cooling

Abstract. The forging process, which is one of the hot forming methods, is used to produce plumbing systems, valves, batteries, fittings, condensers, pipes, etc. from brass alloys in duplex structures. Compared to leaded brasses, machining becomes very difficult due to reasons such as long and continuous chips, burrs, built-up edge in the tool, and unacceptable surface quality problems. In this study, studies have been carried out to improve the machining process that minimizes the mentioned machining problems by controlling the microstructural of lead-free brass materials. Therefore, by examining the effect of the copper content of the forged material, forging temperature, the cryogenic cooling method input parameters after forging on the phase ratio of the material, investigations were carried out on obtaining a high-performance machining process close to the machinability performance of leaded brass materials with good chip breakability. The change in the distribution of beta phases in the material after forging was investigated and machining tests were performed as a hole drilling operation. Cutting forces, surface roughness, and dimensional accuracy analyzes were evaluated within this purpose. The relationship between the beta phase ratio in the material and the machinability has been revealed and it has been observed that the CW511L alloy produced in three different ratios in the standard range and although they are the same material, the Cu% ratio causes significant changes in terms of machinability.

Introduction

Forging process is one of the widely used plastic deformation methods in terms of shaping the material. In this method, in which components from copper alloys are widely produced, the deformability of the billet material increases by heating it in the furnace and it is easily shaped. Zinc element in body-centered cubic crystal lattice structure, which is one of the elements that increase the forging ability. Brass is generally known as copper alloys containing 5% to 40% zinc in concentrations. While brass is manufactured, strength, corrosion resistance, machinability etc. Different alloying elements can be added to change the properties [1]. The most important element in this context is lead, which is associated with excellent chip breaking, low tool wear, and high cutting parameters. However, lead poses a danger to humans and nature and is included in the 2nd class carcinogen group, which cannot be eliminated by human body [2,3]. Pipes, fittings, etc., are produced from brass alloys, especially in contact with drinking water. The lead element ratio in the alloy in the components should not be more than 0.20%. CW511L material standard alloy ratios also support this [4]. In this study, the material that was shaped by hot forging and on which the machining tests were carried out is CW511L from lead-free brass materials. In the brass alloy, the semi-fluid lead layer reduces friction during cutting, acts as a lubricant, and encourages the formation of small discontinuous chips, improving machinability [5,6], cutting forces generated during machining, and thus cutting tool life are improved. The fact that lead is such an important element for machinability and its elimination causes various problems in terms of machinability

Content from this work may be used under the terms of the Creative Commons Attribution 3.0 license. Any further distribution of this work must maintain attribution to the author(s) and the title of the work, journal citation and DOI. Published under license by Materials Research Forum LLC.

in lead-free brass alloys and results in a decrease in productivity and disruption of processes with long chips and reduced tool life that occur during the processing of these materials [6].

Pantazopoulos et al. [7] investigated the microstructure analysis, mechanical behavior and fracture mechanisms of traditional leaded brass materials CuZn39Pb3 (CW614N) and CuZn36Pb2As (CW602N). It has been revealed in their studies that CW602N material with high copper content contains lower β phase compared to the other, has lower hardness, and decreases in toughness due to phase structure. Nobel et al. [6] examined and compared the machinability of lead-free alloys CW510L, CW511L, CW724R, CW508L and leaded alloys CW614N. After the machining of these materials by turning using carbide cutting tools were used in different coatings, temperature and force results investigations were carried out in terms of chip breakability, chip form and tool life. Toulfatzis et al. [8] evaluated the microstructures and β phase ratios of extruded cylindrical lead-free brass materials after heat treatment and looked at the impact of these outputs on the material's machinability in their study. In a different investigation [9], they used heat treatment to lead-free brass alloys to explore the chip breakability, the change in β phase following this heat treatment, and the machining test that followed. The fracture energy and fatigue life of lead-free brass alloy (CW510L and CW511L) materials as determined by the material's notch impact test were examined by Pantazopoulos et al. [10]. The drilling process of hot forged lead-free brass alloys was investigated experimentally by Zoghipour et al. [11] using a form cutting tool. The cutting forces, dimensional accuracy, and surface quality of the holes were tested while taking into account the tools' varied geometries, feed rates, and rotating speeds on hot-forged lead-free brass alloys with different copper contents. Then, to predict and improve the machining process, they applied genetic algorithm-based optimization techniques and modeling of artificial neural networks.

It is anticipated that changes in the material's copper ratio in the Cu-Zn equilibrium diagram will have a significant impact on the material's forgeability and recrystallization temperature, as well as on its microstructural distribution, α and β phase distribution, and consequently its machinability performance. After being hot forged into the desired shape, the brass alloy material is cooled either on its own or in fan conveyor systems, depending on the desired microstructural and mechanical qualities. There are several studies in the literature that demonstrate the use of the cryogenic cooling method in various operations for the machining of different materials [12–14], that it improves machinability performance [15], and that it has no negative effects on human health or the environment [16]. It is crucial to conduct systematic studies to enhance the machinability performance of lead-free brass materials because there are not any available studies examining the impact of forging parameters and cooling process on β phases in the material and the change in machinability performance as a result. In the study, a major breakthrough was made in terms of machinability since the β phases of the cryogenic cooling approach were restrained in the structure without dissolving with rapid cooling. Therefore, it has been attempted to investigate the effects of the forged material's copper content, the sample temperature prior to forging, the cryogenic cooling method input parameters following forging, and the material's phase ratio on achieving a high-performance machining process that is comparable to the machinability performance of materials containing lead. The microstructural characteristics of the material are significantly affected by forging process parameters including the material's percentage Cu alloy, the post-forging cooling technique, the forging temperatures, etc. These consequences have been shown along with this study. Several process characteristics, such as machinability, have a substantial impact on the β%, which are crucial in terms of machinability.

Experimental Setup

Hot forged extruded bars with dimensions of Ø50x66 mm and three different Cu% rates were put through machining testing. The shaped workpieces formed by the hot forging technique are shown in Fig. 1a. Before being employed in the machining experiments, Fig. 1b depicts the burr cutting

procedure and the final shape shown in Fig. 1c. Based on the results of the spectral analysis, the chemical composition of the CW511L alloy material generated at three different Cu% ratios is shown in Table 1.

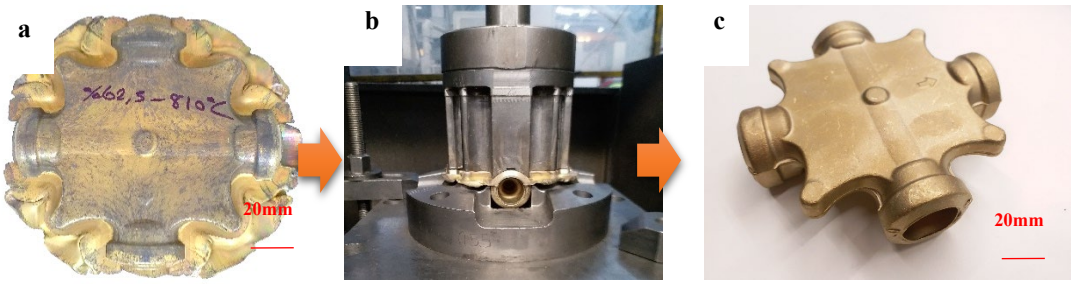

Fig. 1. a) Forged CW511L sample with burrs, b) burr cutting process c) final shape.

Table 1. Chemical composition of the CW511L material with different %Cu.

Material	Cu	Zn	Pb	As	Al	Sn	Ni	Bi	Si	Sb
%61.7 Cu	61.7	Rem.	0.181	0.106	0.003	0.00	0.000	0.003	0.011	0.004
%62.9 Cu	62.9	Rem.	0.174	0.117	0.003	0.00	0.001	0.003	0.002	0.003
%63.4 Cu	63.4	Rem.	0.164	0.106	0.003	0.00	0.002	0.003	0.006	0.002
EN12165 Standart [4]	61.5 63.5	Rem.	- 0.2	0.02 0.15	- 0.05	- 0.1	- 0.3	-	-	-

In a Hydromec-550 tons automated press, forging tests were performed. Forging temperatures of 750, 780 and 810°C were selected during the forging process. All test samples were subjected to a 1 minute cryogenic cooling process in a chamber made of 304L stainless steel, which has a low heat transfer coefficient and is resistant to cryogenic temperatures, after forging. This has been performed in order to apply the coolant (liquid nitrogen) to the component uniformly during cryogenic cooling. During this time, the test samples at forging temperatures between 750 and 810°C were cooled to an average temperature of 200°C. The machining tests were conducted on Fanuc-Robodrill α-D21MiB5 CNC machine as shown in Fig. 3. Boron coolant flood was used during the machining tests. Ø12 spherical carbide cutting tools were particularly made and utilized in the tests as part of the experimental investigation. A thermal camera was used to monitor this process for each sample. Table 2 provides the experiments specific conditions and parameters. Following the machining tests, the CMM was used to measure the dimensional accuracy in the hole diameters.

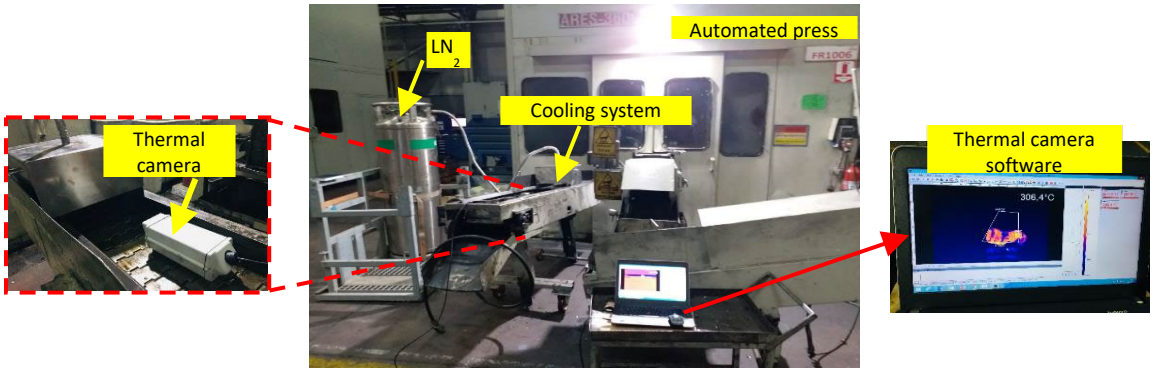

Fig. 2. Forging press and experimental setup.

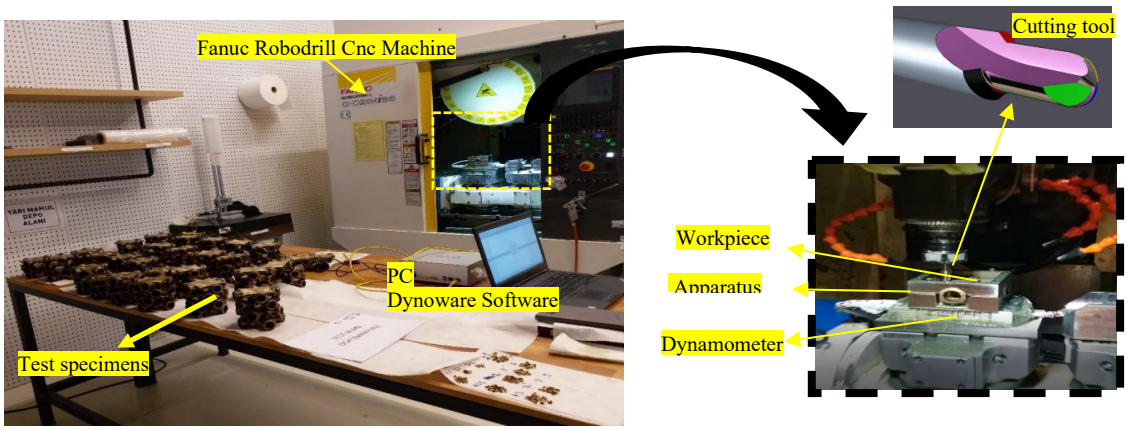

Fig. 3. The used experimental setup for the machining tests.

Table 2. The utilized parameters in hot forging and machining experiments.

Cu (%)	Forging Temperature (°C)	Cooling Duration (min.)	Rotational Speed (rpm)	Feed rate (mm/min.)
61,7	750			
62,9	780	1 (LN_2)	3000	300
63,4	810			

Results and Discussions

β Phase Analysis.

The β% phase ratio and its distribution are the most important factors affecting machinability. In this section, β phases are more clearly expressed by the red color in phase analysis microstructural distributions while the yellowish colors represent α phase. In the case of the material with the lowest Cu content of 61.7%, its intermetallic β% phase is higher compared to the other materials. In the Cu-Zn equilibrium diagram, the percentage of the β phase is controlled by the percentage of Zn, subsequently the Cu% content, and the thermomechanical process. The β phase percentage increased with Zn content, as expected, in the case where the zinc-rich and associated Cu% was the lowest. The β phase (Cu-Zn), an ordered type of intermetallic phase with a body-centered cubic crystal structure, (Cu) is a face-centered cubic crystal which expresses the solid solution, is structurally harder and less ductile than the α-phase. Zinc has the hexagonal close-packed (HCP) lattice structure [17]. The distribution and sizes of these phases have a significant effect on machinability [18]. The presence of the beta phase reduces the ductility of the alloy and thus the segmentation of the chips formed after machining. The morphology exhibited by the β phases and the increase in the percentage distribution in the structure cause a slight increase in hardness and low ductility, as a result, machinability, and chip breakability during machining increase with the increasing beta phase [8, 19]. The measured results from the microstructural analysis of β phase distributions in Fig. 4 demonstrate the effect of the %Cu and forging temperature on the distribution of β% phases in the material. The β phases in the structure showed a decreasing trend in terms of distribution and percentage with the increase of Cu%. This situation can be explained by the decreasing zinc distribution with the increase of Cu% in the structure. β phase is rich in zinc elements. Especially at high forging temperatures, the 61.7% Cu material rises to the point where the percent β phases are at their maximum during the process. By rapid cryogenic cooling, these β phases are being restrained in the brass material's internal structure [20]. In other words, the

necessary time duration and temperature are not given for the β phases in the structure, such as slow cooling, to dissolve and turn into the α phase. In the case of forging at 750 °C forging temperature, approximately 70% less β phase distribution is obtained from the 61.7% Cu sample, whereas in 63.4% Cu specimen this value is around 63%. While there was no significant change in the β% phase ratios of the forging temperature in the 61.7% Cu sample, there was a decrease of approximately 22% from 750 °C to 810°C in the 62.9% Cu specimen, and an increase of approximately 25% was observed in the 63.4% Cu workpieces. There were no significant changes in the β phase distribution of the forging temperature in the samples with a low %Cu, but no clear distributions in the β% phase in the material with an increase in the Cu% could be obtained. It can be said that this is caused by the decrease in the percentage of zinc in the structure with the increase of %Cu.

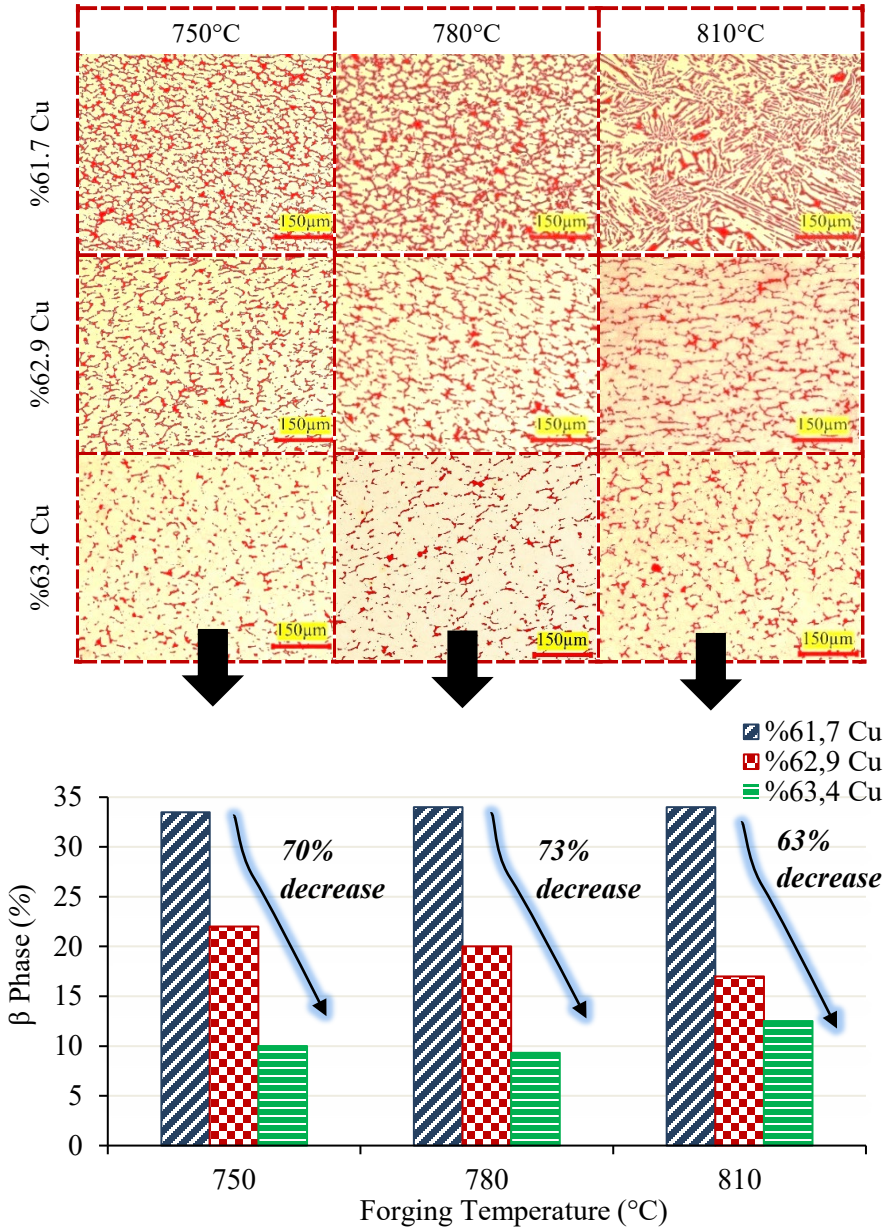

Fig. 4. Effect of Copper content and forging temperature on the beta phases of material.

Cutting Forces.

One of the copper alloys, CW511L, is a low lead alloy that is difficult to machine than other brass alloys [15]. This may therefore result in excessive cutting forces and other machining operations [2]. The feed force is the primary cutting force affecting the cutting tool. Under normal conditions, major variations in cutting forces and machinability qualities are primarily influenced by machining cutting parameters such as speed, feed, and cutting tool geometry. Alloy microstructure and mechanical characteristics affect an alloy's machinability. While the machinability of the metal depends on the metal's microstructural changes, the power consumption depends on the metal's mechanical characteristics [20]. In this instance, β phases and hence hardness is also impacted. The size of the interphase boundaries, which are influenced by the β-phase content and the size of the α-phase crystals, can be increased to enhance machining. In general, soft materials use less energy than hard metals, and tool wear is reduced. Finer grain sizes are advantageous for mechanical qualities, and since they are stronger and more ductile than coarser grains and possess higher machinability. Additionally, imperfections in the material's structure may have an impact on chip breakability and therefore machinability [18].

The average of three repetition cutting forces generated during drilling operation are presented in Fig. 5 according to the Cu% and the forging temperature. A close examination of the graph reveals a considerable impact of the Cu% ratio. It has been noted that the alterations made result in considerable variations in terms of machinability, especially given that these three Cu% ratios are CW511L despite being the same material. The dispersion of the β phases increased with the reduction of Cu%, and as a result, greater β phase distribution and finer α crystals tend to produce longer interphase boundaries, and microstructural distributions significantly influence on the machinability [18]. With an increase in the Cu%, it is seen that the cutting forces increase and the machinability decreases. An increase in cutting forces with significant friction in the contact area may occur in alloys with a ductile phase and low lead content in high FCC lattice structures [6]. This is confirmed by the fact that cutting forces rise with higher phases due to an increase in the Cu%. Once again, in different research [21], machinability tests on various copper alloys were conducted, and it was found that the alloys that we may refer to as zinc-poor or copper-rich yielded the greatest results in terms of cutting forces. At 750°C of forging temperature, 885 N force was attained at a rate of 61.7% copper, a rise of about 23% at a rate of 62.9% copper, an average of 1092 N, and an increase of roughly 36% at a rate of 63.4% copper, resulting in a force value of 1207 N. As can be observed, when the Cu ratio is lowest, the dominating β phases, and smaller grain sizes of the α phases facilitate cutting. In comparison to coarse grains, grains with a finer structure in terms of grain sizes enhance the structure and improve workability [20]. At 780°C forging temperature, 864 N force was measured in 61.7% Cu material, while an increase of roughly 27% at 62.9% Cu, an average of 1099 N, and 63.4% Cu, an increase of nearly 42%, and a force value of 1224 N was recorded. According to the obtained results, forging temperature has no impact on the cutting forces needed for machinability. 869 N force was obtained at 810°C forging temperature at a rate of 61.7% Cu, whereas 1183 N average force was obtained with an increase of almost 36% at a rate of 62.9% Cu, and this ratio was the highest percent increase compared to lower forging temperatures. There was a rise of about 43% and a force value of almost 1240 N was generated at the rate of 63.4% Cu.

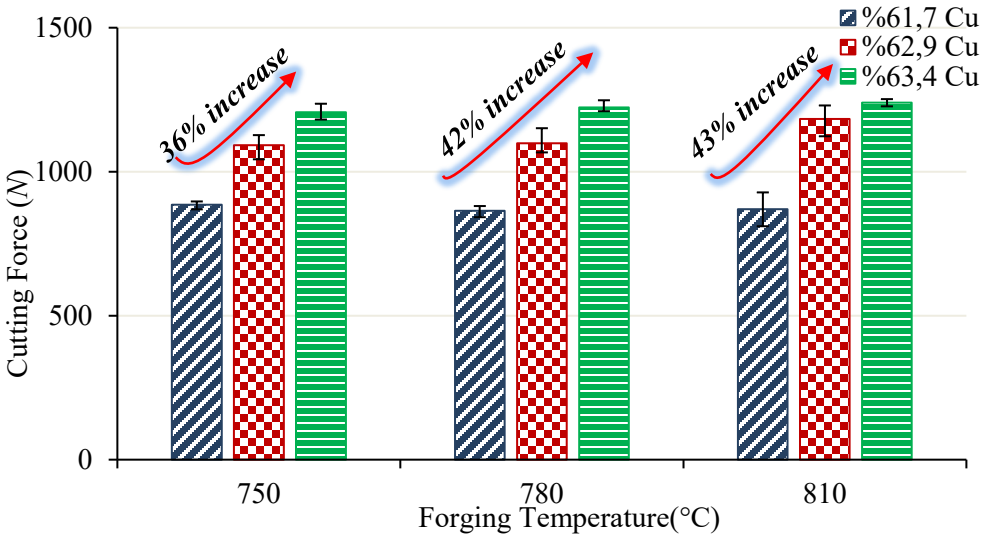

Fig. 5. The average measured cutting forces.

Surface Roughness.

The surface quality of the machined components is a desired characteristic and maintaining high surface quality is always one of the most crucial duties after machining. Surface roughness is known to impact a part's heat conductivity, friction, corrosion, and fatigue life [22]. In specific situations, machining factors such as feed and cutting tool tip radius have an impact on surface roughness [23]. However, since consistent speed, feed, and cutting tools were employed in this investigation, additional knowledge was gained about how the forging parameters and therefore the change in the material effect the machining and hence the change in the desired surface quality. Cutting tools that have been improperly ground have a propensity to scratch soft materials, like brass, leading to a poor surface finish. Fig. 6 shows the variations in surface roughness (Ra) values of the three different Cu% samples formed at 750-780 and 810°C forging temperatures as a result of changes in parameters following the cryogenic cooling process. The illustrated results represent the average of five measurements. When the graph is inspected, the roughness values decrease as Cu% increases. This means that improving the ductility of the outer surface with an increase in Cu% will result in a higher surface quality. While hard materials produce more clastic chips, it may be claimed that ductile materials provide superior surfaces with somewhat more continuous chip formation. Considering the roughness values at 750°C forging temperature, the highest roughness value was found in the material with a Cu content of 61.7%. The measured value in this condition is typically 0.52 µm. With an average roughness value of 0.43 µm measured at 62.9% Cu, it produces a value that is around 17% less than that of 61.7% Cu, while a 17–18% change was seen at 63.4% Cu ratio. At 780°C forging temperature, the highest roughness value was found in the material with a Cu content of 61.7%. In this condition, the measured value is around 0.49 µm on average. With an average roughness value of 0.37 µm measured at 62.9% Cu, a value was approximately 24% less than that of 61.7% Cu material, while a decrease of approximately 18% was observed in 63.4% Cu material. It can be interpreted that the rate of change in the roughness values of Cu% ratio decreases to minimum levels under the condition of the highest forging temperature in the experiments.

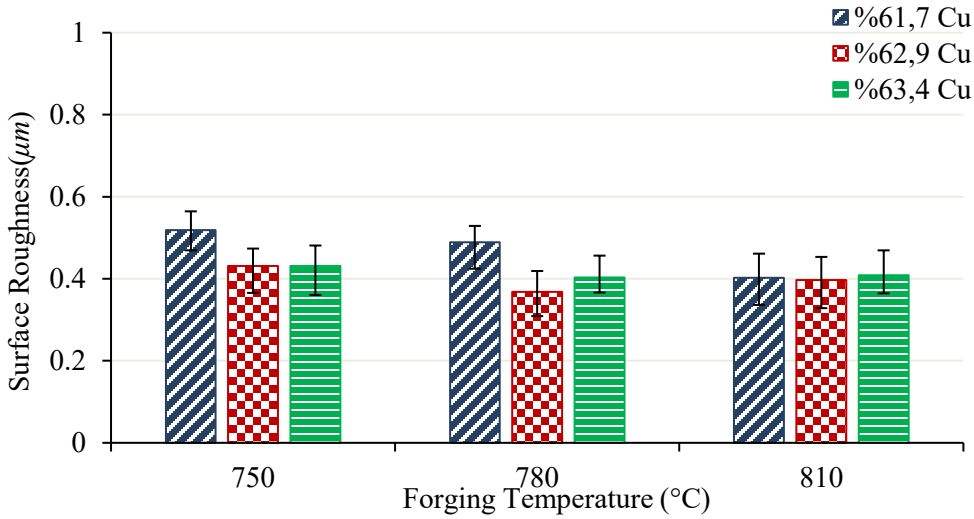

Fig. 6. The average values of the surface roughness (Ra) of the generated holes.

Dimensional Accuracy.

The dimensions and geometric tolerances in the component geometry are extremely important, much as the surface quality attributes of the machined item. After the manufacturing of parts, significant efforts are undertaken, particularly in industry, to obtain products with the appropriate dimensions and quality. Softer materials are more prone to bend when subjected to cutting tool pressure, decreasing dimensional accuracy. High-strength alloys may require carbide tools, grinding, and in certain conditions heat treatment for optimal manufacturing, whereas soft coppers and brasses may be machined rather readily [20]. The diametrical variations of the Ø12 holes that were produced after drilling in materials with various Cu contents of test specimens that were forged at different forging temperatures and treated to cryogenic cooling are shown in Fig. 7. Examining the graph reveals that the Cu% has some influence because, under all conditions, the hole sizes fall within the specified tolerance range. Additionally, it can be observed that holes in samples with a Cu ratio of 63.4% take values that are closer to the nominal size. The ductility of the material allows for a superior surface topography in the scenario when the Cu% ratio is at its highest, and the surface roughness values shown in the preceding section further corroborate this claim. However, experiments with the cutting tool in sequential conditions are required before it can be said that this is long-term. Because issues like lengthy chips, continuous chip status, and surface roughness that can result from chip removal from ductile materials can damage cutting tools and result in additional quality issues. It is typical for these graphical findings to show little fluctuations since the correct cutting tool dimensions are the most crucial aspect of dimensional variations. However, even if there is a change at low levels, the impact of this will be assessed as the impact of material and forging parameters will be explored within the scope of the research.

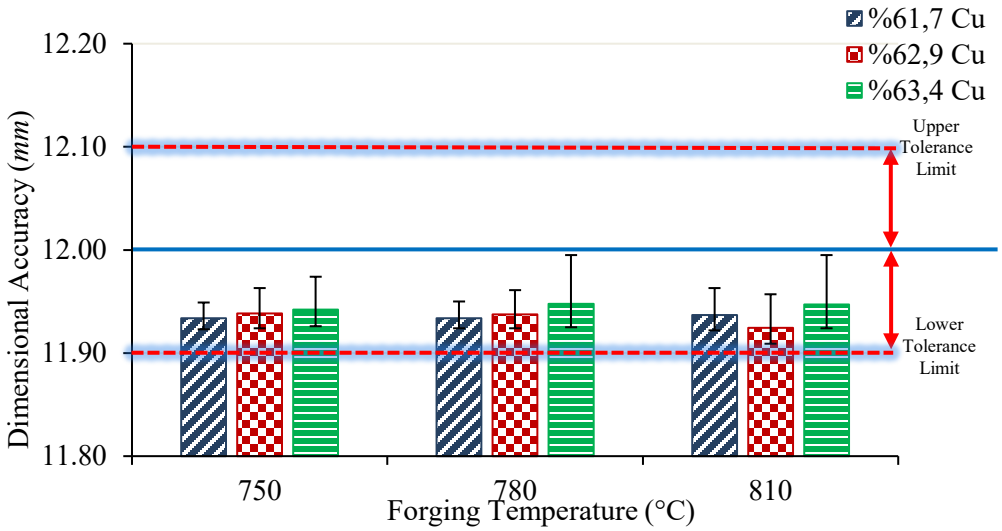

Fig. 7. The variation of the dimensional accuracy values of the generated holes.

Summary

In this research, the machining performance of CW511L material—one of the copper alloy-based lead-free brass materials—was explored by comparing its microstructural characteristics after forging. With the hot forging of the test sample at the correct temperature values, the β% phases in the structure increase to extremely high levels, and in this instance, the Cu% ratio has a major impact. This is a crucial step for machining because it ensures that most of these β phases remain in the structure without transformation (starting with the regular structure) by the action of cryogenic cooling. Additionally, the cutting forces clearly indicate the influence of the forging temperature, the Cu% ratio, and indirectly the distribution of β phases, as well as the influence of the input parameters on the outcomes for roughness and dimensional accuracy. The study is notable because, despite the fact that all of the samples used for the testing were CW511L, there was a substantial variation in the machinability of three distinct CW511L materials that were chosen from the standard range and in the machining tests.

References

[1] R. Francis, The corrosion of copper and its alloys: a practical guide for engineers, NACE International, 2010.

[2] X. Chen, A. Hu, M. Li, D. Mao, Study on the properties of Sn–9Zn–xCr lead-free solder, J. Alloy. Compd. 460 (2008) 478-484. https://doi.org/10.1016/j.jallcom.2007.05.087

[3] H. Atsumi, H. Imai, S. Li, K. Kondoh, Y. Kousaka, A. Kojima, High-strength, lead-free machinable α–β duplex phase brass Cu–40Zn–Cr–Fe–Sn–Bi alloys, Mater. Sci. Eng. A 529 (2011) 275-281. http://doi.org/10.1016/j.msea.2011.09.029

[4] TSE, TS EN 12165, in Copper and copper alloys - Wrought and unwrought forging stock, 2016.

[5] A.L. Fontaine, V. Keast, Compositional distributions in classical and lead-free brasses, Mater. Charact. 57 (2006) 424-429.

[6] C. Nobel, F. Klocke, D. Lung, S. Wolf, Machinability enhancement of lead-free brass alloys, Procedia CIRP 14 (2014) 95-100. https://doi.org/10.1016/j.procir.2014.03.018

[7] G.A. Pantazopoulos, A.I. Toulfatzis, Fracture modes and mechanical characteristics of machinable brass rods, Metallogr. Microstruct. Anal. 1 (2012) 106-114. https://doi.org/10.1007/s13632-012-0019-7

[8] A.I. Toulfatzis, G. Pantazopoulos, A. Paipetis, Microstructure and properties of lead-free brasses using post-processing heat treatment cycles, Mater. Sci. Technol. 32 (2016) 1771-1781. https://doi.org/10.1080/02670836.2016.1221493
[9] A.I. Toulfatzis, G. Pantazopoulos, C. David, D.S. Sargis, A. Paipetis, Final heat treatment as a possible solution for the improvement of machinability of pb-free brass alloys, Metals 8 (2018) 575. https://doi.org/10.3390/met8080575
[10] A.I. Toulfatzis, G. Pantazopoulos, A. Paipetis, Fracture mechanics properties and failure mechanisms of environmental-friendly brass alloys under impact, cyclic and monotonic loading conditions, Eng. Fail. Anal. 90 (2018) 497-517. https://doi.org/10.1016/j.engfailanal.2018.04.001
[11] N. Zoghipour, G. Atay, Y. Kaynak, Modeling and optimization of drilling operation of lead-free brass alloys considering various cutting tool geometries and copper content, Procedia CIRP 102 (2021) 246-251. https://doi.org/10.1016/j.procir.2021.09.042
[12] A. Gharibi, Y. Kaynak, The influence of depth of cut on cryogenic machining performance of hardened steel, J. Faculty Eng. Archit. Gazi University 34 (2019) 582-596.
[13] Y. Kaynak, H. Karaca, I. Jawahir, Cutting speed dependent microstructure and transformation behavior of NiTi alloy in dry and cryogenic machining, J. Mater. Eng. Perform. 24 (2015) 452-460. https://doi.org/10.1007/s11665-014-1247-6
[14] Y. Kaynak, H. Karaca, R.D. Noebe, I. Jawahir, Analysis of tool-wear and cutting force components in dry, preheated, and cryogenic machining of NiTi shape memory alloys, Procedia CIRP 8 (2013) 498-503. https://doi.org/10.1016/j.procir.2013.06.140
[15] Y. Kaynak, H. Karaca, R.D. Noebe, I. Jawahir, Tool-wear analysis in cryogenic machining of NiTi shape memory alloys: A comparison of tool-wear performance with dry and MQL machining, Wear 306 (2013) 51-63. https://doi.org/10.1016/j.wear.2013.05.011
[16] O. Pereira, A. Rodríguez, A.I. Fernández-Abia, J. Barreiro, L.N. López de Lacalle, Cryogenic and minimum quantity lubrication for an eco-efficiency turning of AISI 304, J. Clean. Prod. 139 (2016) 440-449. https://doi.org/10.1016/j.jclepro.2016.08.030
[17] L. Collini, Copper Alloys: Early Applications and Current Performance-Enhancing Processes, 2012, BoD–Books on Demand.
[18] A.I. Toulfatzis, G.J. Besseris, G. Pantazopoulos, C. Stergiou, Characterization and comparative machinability investigation of extruded and drawn copper alloys using non-parametric multi-response optimization and orthogonal arrays, Int. J. Adv. Manuf. Technol. 57 (2011) 811-826. https://doi.org/10.1007/s00170-011-3319-1
[19] G. Pantazopoulos, A. Vazdirvanidis, Characterization of the microstructural aspects of machinable-phase brass, Microscopy and Analysis (2008) 13.
[20] J.R. Davis, Copper and copper alloys, ASM international, 2001.
[21] C. Nobel, U. Hofmann, F. Klocke, D. Veselovac, Experimental investigation of chip formation, flow, and breakage in free orthogonal cutting of copper-zinc alloys, Int. J. Adv. Manuf. Technol. 84 (2016) 1127-1140. https://doi.org/10.1007/s00170-015-7749-z
[22] M. Kurt, Y. Kaynak, E. Bagci, H. Demirer, M. Kurt, Dimensional analyses and surface quality of the laser cutting process for engineering plastics, Int. J. Adv. Manuf. Technol. 41 (2009) 259-267. https://doi.org/10.1007/s00170-008-1468-7
[23] S. Vajpayee, Analytical study of surface roughness in turning, Wear 70 (1981) 165-175. https://doi.org/10.1016/0043-1648(81)90151-4

Material behaviour modelling

Materials Research Proceedings 28 (2023) 1369-1378 https://doi.org/10.21741/9781644902479-148

Process-informed material model selection

CONDE Mariana[1,a *], COPPIETERS Sam[2,b] and ANDRADE-CAMPOS António[1,c]

[1]Department of Mechanical Engineering, TEMA - Centre for Mechanical Technology and Automation, LASI - Intelligent Systems Associate Laboratory, University of Aveiro, Campus Universitário de Santiago, 3810-193 Aveiro, Portugal

[2]Department of Materials Engineering, KU Leuven - Ghent Campus, Gebroeders De Smetstraat 1, Ghent, 9000, Belgium

[a]marianaconde@ua.pt, [b]sam.coppieters@kuleuven.be, [c]gilac@ua.pt

Keywords: Material Model Selection, Numerical Simulation, Hole Expansion Test, Analysis of Variance (ANOVA)

Abstract. The efficient development of metal products with high quality usually requires realistic numerical simulations before the manufacturing procedure. The choice of the constitutive model has a considerable influence on the predicted material behavior's description. Several material constitutive models have been proposed to describe different mechanical phenomena. However, its selection is a labored task that requires expertise. This lack of knowledge can lead to errors in the numerical predictions and, consequently, large costs and delays in the manufacturing procedure. To overcome this problem, an automatic material model selection tool is necessary. This work aims to compare the impact of different constitutive models and their features on the simulation of a forming process and develop a rational and systematic strategy for model selection. The approach focuses on the study of a hole expansion test using Abaqus and a statistical analysis of variance (ANOVA). It was possible to establish a ranking for the importance of the types of models that can help with model selection decision-making and efficient parameter calibration for accurate predictions.

Introduction

Nowadays, the aeronautics and automobile industries are in high demand for quality and efficiency. The design and development of products must be precise, with low costs and no delays. Thus, the trend is to virtualize the design of parts, the prototyping, and the manufacturing processes, through numerical simulations. However, in some cases, the lack of knowledge and time to correctly describe the material behavior is observed. This can lead to errors in the numerical simulations and, consequently, large costs and delays in the development and manufacturing processes. When conducting an accurate Finite Element (FE) simulation, an adequate constitutive model and accurately calibrated material parameters are necessary. In the last decades, many models were developed [1-4], implemented in numerical simulations and validated experimentally [1-3]. There are models that account for the microstructural characteristics of the material (i.e. physics-based) but require large computational efforts [1,2]. However, other models describe macroscopically the phenomenological behavior of materials [4-8]. Generally, phenomenological models are an aggregation of formulations that individually try to capture macroscopic phenomena, such as hardening or the elastic-plastic transition. These can be divided into hardening laws [5,8], anisotropic yield functions [3,6,7] and damage models [3,9]. Regarding metals, the prediction of different mechanical phenomena and effects of the material behavior, such as springback, ratcheting, twinning, transformation-induced plasticity (TRIP) and the Bauschinger effect, have been vastly studied in [1,2,10-13]. One of the problems that a simulation software user faces is the selection of the constitutive equations that describe the material behavior. Although there is a vast number of constitutive models and equations, its selection for a specific material

Content from this work may be used under the terms of the Creative Commons Attribution 3.0 license. Any further distribution of this work must maintain attribution to the author(s) and the title of the work, journal citation and DOI. Published under license by Materials Research Forum LLC.

and process usually requires high expertise, an exhaustive investigation and mechanical experimentation. Most of the authors have been comparing different models with experimental data to determine which is more adequate for a specific material and process mainly based on geometrical measurements [1,10-14] and stress-strain curves, or load-displacement curves and yield loci [1,11-15]. Yet, this comparison can be time-consuming since it starts with several mechanical experiments for the identification of different models' parameters, the accurate calibration of the latter and the simulation and validation of the analyzed mechanical process. A flexible and automatic tool or strategy for model selection is lacking in the industry and scientific community.

This work aims at proposing a rational and systematic strategy for the recommendation of constitutive equations that can guide inverse identification methods, such as in [16], with the goal of accurate forming process simulations. The approach involves the numerical simulation of a hole expansion test using the Abaqus FEA software [17] and the analysis of measurements of interest using the analysis of variance (ANOVA) [18]. This statistical methodology was already implemented as a Design of Experiments (DoE) approach to determine the influence of some geometric factors on the springback of sheet metal parts [19-22], but it can be extended to a more general analysis that helps with constitutive model selection.

Methodology

General Methodology. The proposed methodology is based on the analysis of the influence of the material constitutive models used in the numerical simulation of a sheet metal forming process. Some quantities of interest or critical aspects that are present in a metal-forming process were investigated. These quantities can be related to the premature rupture of the blank, its thickness variation, the geometry of the final shape of the sheet or other errors that one can expect in the considered forming process. This data was analyzed using the ANOVA approach which allows us to find a relation between the implemented material constitutive models and the observable quantities of interest in the forming process simulation and, finally, establish an importance ranking for the models. A flowchart describing the general methodology is presented in Fig. 1.

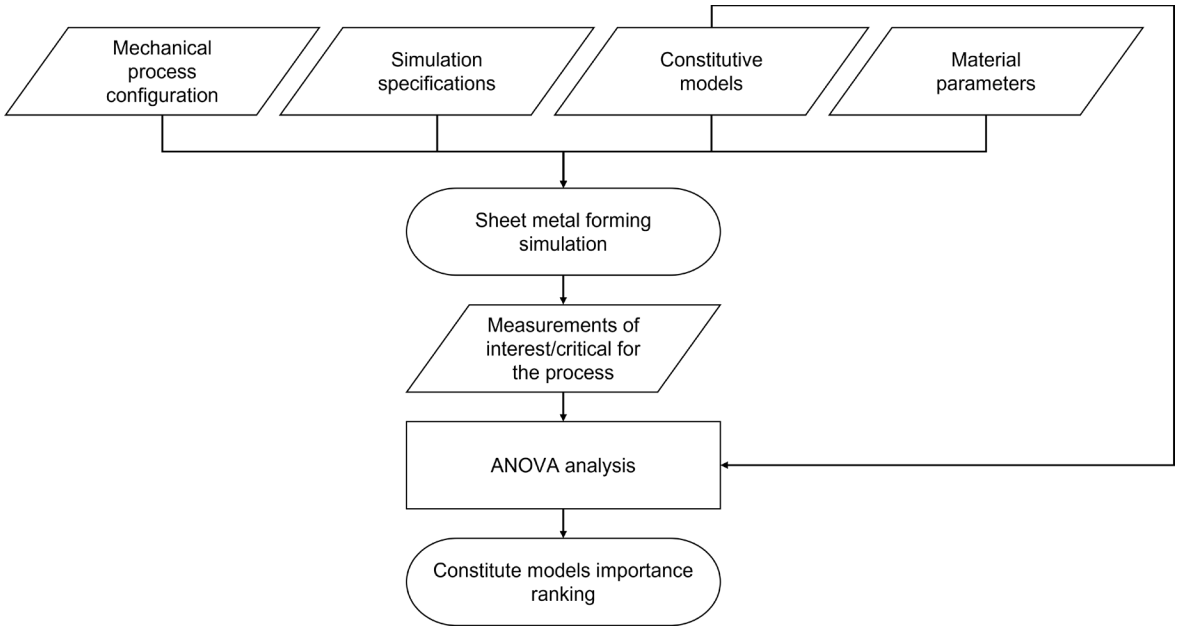

Fig. 1. Flowchart with the general methodology for the material model selection strategy.

ANOVA Strategy. The ANOVA approach is a systematic analysis that allows us to understand the effect of each factor or group (also denoted as independent variables) in the chosen observables

(also denoted as dependent variables) [18]. In this statistical analysis, a hypothesis is tested. The null hypothesis is that there is no difference among the groups' means. The alternative hypothesis is that the averages are not all equal, meaning that at least one group differs significantly from the overall means of the dependent variables. If any of the group means is significantly different from the overall mean, then the **null hypothesis** is rejected. The rejection of the hypothesis can be decided by observing the *p*-value. The *p*-value is defined as the probability of obtaining the observed results, assuming that the null hypothesis is true. It is calculated using the F-statistic and the degrees of freedom for the numerator and denominator. Generally, a *p*-value of 0.05 or lower considers the statistical meaning of the analyzed factor. The smaller the *p*-value is, the more significant the result should be. The F-statistic follows an F-distribution with $(\boldsymbol{k-1})$ and $(\boldsymbol{n-k})$ degrees of freddom, where $\boldsymbol{k}$ is the number of groups and $\boldsymbol{n}$ is the total sample size.

Implementation

Hole Expansion Test Simulation Specifications. As a case study, the sheet metal forming process implemented and analyzed in the model selection strategy was the hole expansion test, which was based on [23]. Its configuration and dimensions are depicted in Fig. 2. The simulation was conducted in Abaqus/Standard software [17] using one 3D deformable shell revolution part for the 150 mm diameter blank with 0.8 mm thickness and 35 mm diameter of the hole. Moreover, two 3D analytical rigid shell revolution parts were modeled for the tools (the punch and the die). Concerning the assembly of the parts, the distance between the blank and the die at the beginning of the simulation was 0.4 mm, whereas between the blank and the punch was 0.5 mm.

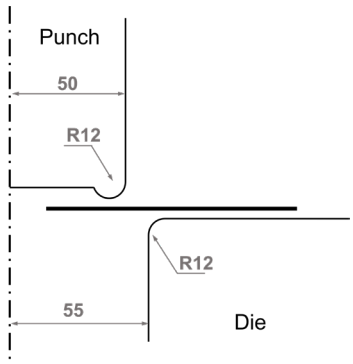

Fig. 2. Hole expansion test configuration (dimensions in mm).

Surface-to-surface contacts were used to define the interactions between the parts with a tangential behavior with penalty and 0.1 friction coefficient and normal behavior of "hard" contact. Besides, contact controls with an automatic stabilization factor of 0.01 were used to avoid convergence issues.

Two static general steps were defined to simulate the non-linear analysis. Initially, two symmetries are established in the blank. In the first step, the punch was moved down with a displacement condition, making sure rupture was not reached independently of the material model and parameters used. Meanwhile, the blank was fixed on the outer edge and the die was also fixed. In the second step, the interactions between the parts were disabled and the vertical displacement of one point of the blank was restricted, to observe the springback behavior of the material.

Regarding the mesh definition, four-node shell elements with reduced integration (S4R) [17] were used in a structured mesh with a total of 6400 elements for the blank, as can be seen in Fig. 3. Furthermore, 9 integration points were calculated along the thickness.

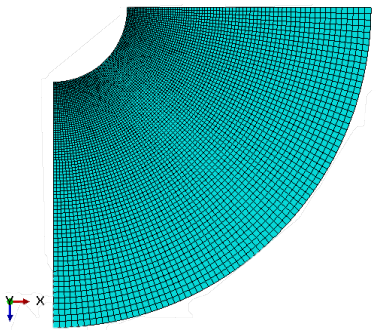

Fig. 3. Mesh of the blank implemented for the hole expansion test.

Material and Constitutive Models Under Analysis. The materials used in the simulations were the DP600 dual-phase steel and the AA3104 aluminum alloy, which behaviors were modelled using the UMMDp (Unified Material Model Driver for Plasticity) from Jancae (Japan Association of Nonlinear CAE) [24]. Concerning the constitutive models under analysis, the Swift hardening law [5], the Voce law [25], the Yld2000-2D for the yield criterion [6] and the Armstrong-Frederick 1966 model (denoted as A-F model) [26] for the kinematic hardening were implemented. The material parameters referring to DP600 [27,28] and AA3104 [29] for the mentioned constitutive models are presented in Table 1. To define the rupture criterion, the Forming Limit Diagram was used [27,30]. Voce's hardening law was fitted to the strain hardening behavior represented by Swift's hardening law.

Table 1. Elastic properties, Swift law, Voce law, Yld2000-2D criterion and Armstrong-Frederick 1966 (A-F model) material parameters for the DP600 steel [27,28] and the AA3104 [29].

DP600									
Elastic properties	E [GPa] 210.000				ν 0.300				
Swift law	K [MPa] 979.460			ε_0 0.00535			n 0.194		
Voce law	σ_{y0} [MPa] 815.600			Q 407.922			b 7.869		
Yld2000-2D criterion	α_1 1.011	α_2 0.964	α_3 1.191	α_4 0.995	α_5 1.010	α_6 1.018	α_7 0.977	α_8 0.935	a 6.00
A-F model	C [MPa] 28896.000				γ 121.000				
AA3104									
Elastic properties	E [GPa] 68.950					ν 0.330			
Swift law	K [MPa] 363.128			ε_0 0.000229			n 0.0275		
Voce law	σ_{y0} [MPa] 351.260			Q 62.400				b 27.205	
Yld2000-2D criterion	α_1 0.594	α_2 1.177	α_3 0.818	α_4 0.892	α_5 0.967	α_6 0.627	α_7 0.947	α_8 1.152	a 8.00
A-F model	C [MPa] 22885.000				γ 400.000				

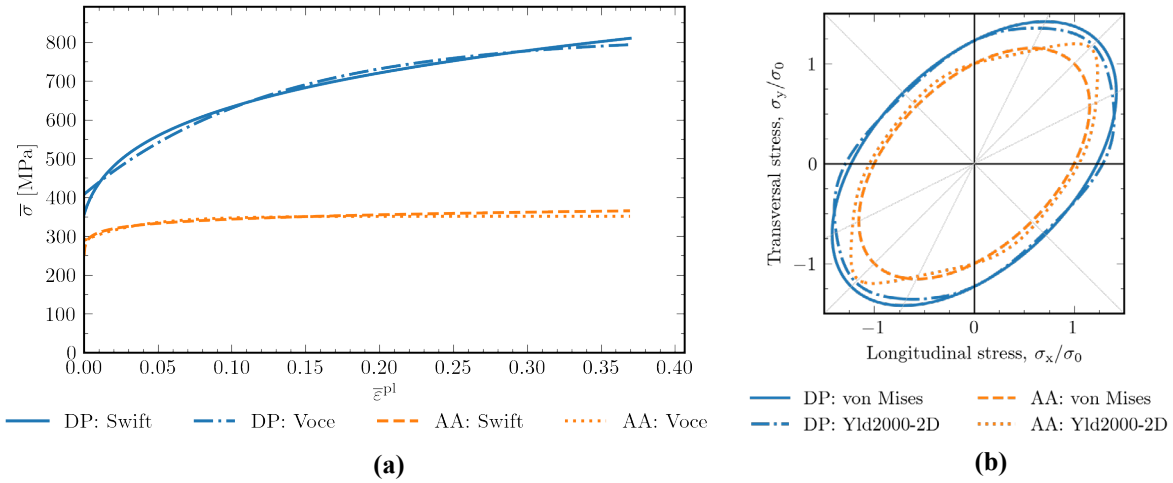

Fig. 4. (a) Plastic strain and stress curves and (b) yield loci for the DP600 and the AA3104 with different material constitutive models.

ANOVA Approach for Model Selection. In this application, the ANOVA approach allows us to establish a relation between each type of constitutive model and its effect in the forming simulation. The type of isotropic, kinematic hardening laws and yield criterion were the independent variables analyzed, whereas the dependent variables were the hole's circularity, the maximum punch force and the springback factor. The hole's circularity is defined as the ratio between the minimum hole's diameter and the maximum hole's diameter, at the end of the simulation. Whereas the springback factor is the ratio between the angle of the deformed sheet before and after the tools' release. Only two levels were analyzed for each factor, being the implementation of the presented models or a simplification of them. In the case of isotropic hardening, the Swift's law or the Voce's law was implemented; for the yield function it was the Yld2000-2D function or the von Mises criterion and for the kinematic hardening it was the A-F model, or no kinematic model was considered. The calculations were made using XLSTAT Cloud add-in for Excel [31].

Results

The hole expansion test simulations using the eight different combinations of the constitutive models presented in Table 2 were conducted for both materials. The obtained outputs of the simulation (dependent variables) are shown in Fig. 5. It can be observed that the hole's circularity is very sensitive to the used yield function (run 1, 3, 5 and 7). For this factor, the AA3104 demonstrates larger sensitivity than the DP600, because the first shows larger variations in the hole's circularity depending on the implemented yield function. Both the maximum punch force and the springback factor are sensitive to the isotropic and kinematic hardening laws used. On contrary, for these dependent variables, the DP600 indicates more sensitivity than the AA3104.

Table 2. Independent variables of the ANOVA approach used for the hole expansion test.

Run	Isotropic hardening law	Yield function	Kinematic hardening law
1	Voce's law	von Mises	Not considered
2	Voce's law	von Mises	A-F model
3	Voce's law	Yld2000-2D	Not considered
4	Voce's law	Yld2000-2D	A-F model
5	Swift's law	von Mises	Not considered
6	Swift's law	von Mises	A-F model
7	Swift's law	Yld2000-2D	Not considered
8	Swift's law	Yld2000-2D	A-F model

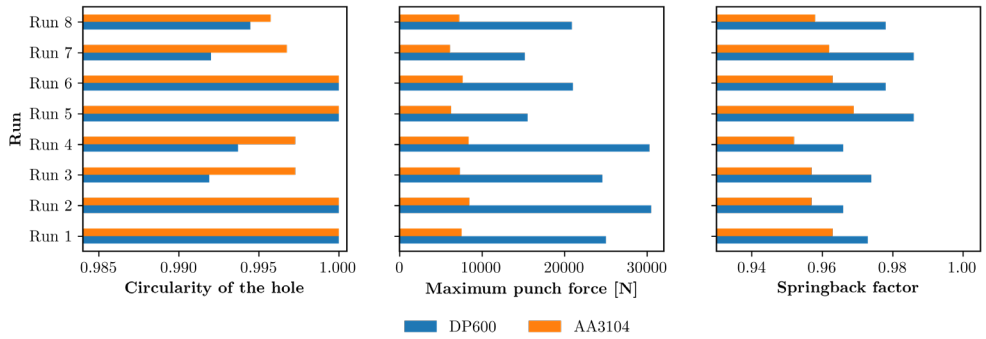

Fig. 5. Hole's circularity, maximum punch force and springback factor obtained from the DP600 and AA3104 simulations using the combination of material models presented in Table 2.

In Table 3, the ANOVA computed results are presented, showing the *p*-values for each factor and dependent variable, the average *p*-value for each factor and the constitutive model's ranking of importance for both materials. As expected, it can be concluded that the yield function is the factor that most influences the hole's circularity, having the lowest *p*-value, independently of the material used. This factor shows a *p*-value lower than 0.05, thus the null hypothesis is rejected. On contrary, and still referring to the hole's circularity, the isotropic and kinematic hardening rules show *p*-values larger than 0.05. Thus, there is no statistical significance of this factor in the hole's circularity. Regarding the maximum punch force, the three factors demonstrate statistical influence on its variation, except for the yield function of AA3104. Both the isotropic and kinematic hardening rules produce a large influence on the maximum punch force, having a very small *p*-value. A similar tendency is observed for the springback factor variation.

Table 3. ANOVA's computed p-values and constitutive model's ranking for the DP600 and AA3104.

Factors	Hole's circularity *p*-value	Maximum punch force *p*-value	Springback factor *p*-value	*p*-value average	Ranking
		DP600			
Isotropic hardening law	7.131×10^{-1}	1.078×10^{-8}	2.534×10^{-7}	2.377×10^{-1}	2
Yield function	2.342×10^{-4}	1.436×10^{-2}	9.715×10^{-1}	3.287×10^{-1}	3
Kinematic hardening law	1.282×10^{-1}	8.716×10^{-8}	1.444×10^{-6}	4.274×10^{-2}	1
		AA3104			
Isotropic hardening law	2.020×10^{-1}	3.099×10^{-4}	9.909×10^{-6}	6.743×10^{-2}	2
Yield function	6.778×10^{-4}	8.624×10^{-2}	1.037×10^{-5}	2.898×10^{-2}	1
Kinematic hardening law	4.913×10^{-1}	2.881×10^{-4}	1.569×10^{-5}	1.639×10^{-1}	3

Analyzing the overall results for the DP600, the kinematic hardening rule has the lowest computed *p*-value average, meaning that this factor has the largest influence on the average of the considered

dependent variables. Besides, it is also possible to establish a constitutive model's importance ranking for the studied material and mechanical process. The kinematic hardening rule shows the largest influence on the simulation results, followed by the isotropic hardening rule and, finally, the yield function. Indeed, looking at the yield locus of this material (see Fig. 4 (b)), a weak plastic anisotropy can be observed. With this information, simplifying the yield function using von Mises is considered adequate, being not necessary to calibrate a complex yield function to describe the anisotropic phenomena of this material for the considered mechanical process. Moreover, this process deals with continuous bending and unbending of the sheet, which might indicate the relevance of the kinematic hardening rule. Yet, the materials reveal different importance for this model. In Fig. 7, the Schmitt parameter [32] is displayed over time for elements shown in Fig. 6, which are distributed along the radial direction of the sheet metal. This parameter can be used to describe strain path changes and is defined as the cosine of the angle in the strain space between the strain rate tensors during the pre-strain and subsequent strain path. It assumes a value of 1 for monotonic, -1 for reversed and 0 for orthogonal strain paths. Indeed, the three types of strain paths can be observed, especially at the end of the drawing (where the time is equal to 1) and during the tools' release.

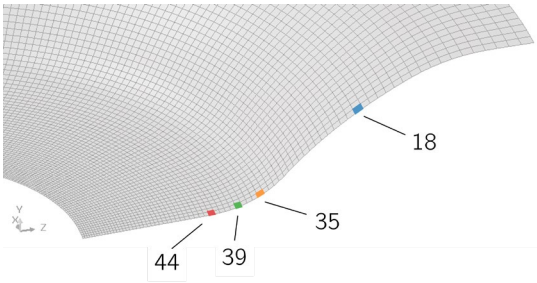

Fig. 6. Location of the elements used to calculate the Schmitt parameter in the deformed blank.

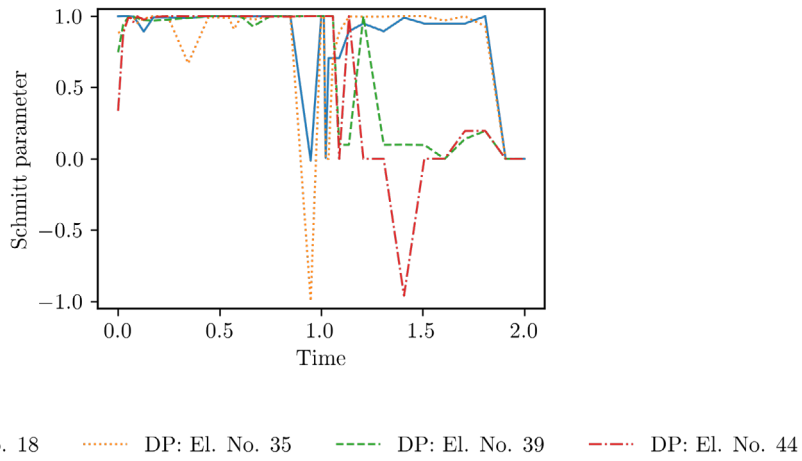

Fig. 7. Schmitt parameter calculated over time in the selected elements for the DP600 (Run 8).

On the contrary, the yield function is the type of model that mainly influences the observables of the AA3104 simulation. This outcome could be expected by looking at the yield locus of the material in Fig. 4 (b). For AA3104, the kinematic hardening rule is the type of model that shows the largest *p*-value, meaning that it is the factor that hardly influences the analyzed observables. In this case, it is recommended to put efforts into the correct calibration of a complex yield function and discard the kinematic hardening rule. Although the mechanical process considered is the same

as the one used with the DP600 and similar load conditions are imposed, in the case of the AA3104, the ANOVA analysis indicates no significance in the implementation of a kinematic hardening rule to correctly describe the hardening behavior. Fig. 8 displays the Schmitt parameter of some elements along the forming of the AA3104 sheet. Indeed, differences can be detected in the strain paths between the materials. For the AA3104, the instants after the tools' release (time greater than 1.0) show fewer strain path changes, compared with the DP600. This can be explained by the different punch's displacements. The punch's displacement in the DP600 analysis was 16.5 mm whereas in the AA3104 analysis was 12 mm, due to the differences in the rupture of the material.

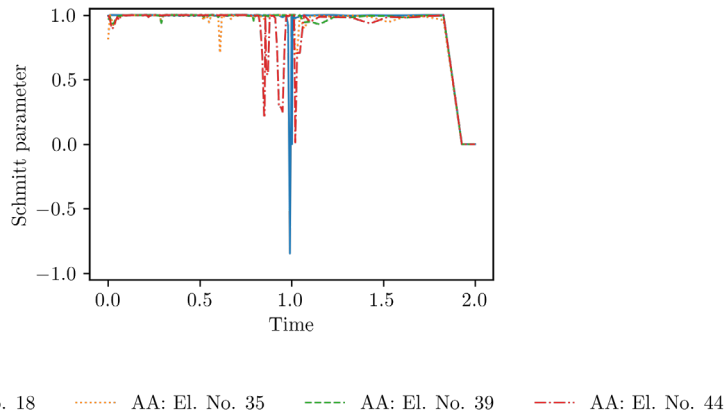

Fig. 8. Schmitt parameter calculated over time in the selected elements for the AA3104 (Run 8).

Summary

In the present work, a process-informed material constitutive model comparison and selection strategy was proposed. The ANOVA methodology was used to establish a relation between the implemented constitutive models in a sheet metal forming simulation and the measures of interest or critical aspects of the process. The outcome of the approach was a constitutive models' importance ranking that indicates the influence of the types of models and mechanical phenomena on the considered forming process. This information is relevant to indicate in which direction should someone focus their efforts concerning material model calibration.

In the study, a hole expansion test simulation was conducted using DP600 dual phase steel and AA3104 aluminum alloy. The ANOVA approach was computed using three factors, the isotropic and kinematic hardening laws, and the yield function. The hole's circularity, the maximum punch force and the resulting springback factor were the dependent variables of the analysis. The differences in the materials' behaviors were clearly observed in the ANOVA results. For the DP600, the most important model was the kinematic hardening, whereas the least important was the yield function. On the contrary, the most important model for the AA3104 was the yield function, whereas the least important was the kinematic hardening rule. These results were expected and confirmed the empirical knowledge by means of a systematic strategy. It must be highlighted that this methodology is material and process-dependent, meaning that for each considered material and mechanical process, a new ANOVA study must be conducted. In the study, the variations in the process conditions, such as friction, temperature and strain rate were not considered and could be interesting to investigate as future works.

Acknowledgements

This project has received funding from the Research Fund for Coal and Steel under grant agreement No 888153. The authors also acknowledge the financial support under the scope of projects UIDB/00481/2020 and UIDP/00481/2020—FCT—Fundação para a Ciência e a Tecnologia and CENTRO-01-0145-FEDER022083—Centro Portugal Regional Operational

Programme (Centro2020), under the PORTUGAL 2020 Partnership Agreement, through the European Regional Development Fund. Mariana Conde is grateful to the Portuguese Foundation for Science and Technology (FCT) for the PhD grant 2021.06115.BD.

Disclaimer

The results reflect only the authors' view, and the European Commission is not responsible for any use that may be made of the information it contains.

References

[1] R. Jafari Nedoushan, M. Farzin, D. Banabic, Simulation of hot forming processes: Using cost effective micro-structural constitutive models, Int. J. Mech. Sci. 85 (2014) 196-204. https://doi.org/10.1016/j.ijmecsci.2014.04.026

[2] D.S. Connolly, C.P. Kohar, K. Inal, A novel crystal plasticity model incorporating transformation induced plasticity for a wide range of strain rates and temperatures, Int. J. Plast. 152 (2022) 103188. https://doi.org/10.1016/j.ijplas.2021.103188.

[3] D. Banabic, F. Barlat, O.Cazacu, T. Kuwabara, Advances in anisotropy of plastic behaviour and formability of sheet metals, Int. J. Mater. Form. 13 (2020) 749-787. https://doi.org/10.1007/s12289-020-01580-x

[4] A. Taherizadeh, D.E. Green, J.W. Yoon, Anisotropic hardening model based on non-associated flow rule and combined nonlinear kinematic hardening for sheet materials, AIP Conf Proc 1567 (2013) 496. https://doi.org/10.1063/1.4850020

[5] H.W. Swift, Plastic instability under plane stress, J. Mech. Phys. Solid. 1 (1952) 1-18. https://doi.org/10.1016/0022-5096(52)90002-1

[6] F. Barlat, J.C. Brem, J.W. Yoon, K. Chung, R.E. Dick, D.J. Lege, F. Pourboghrat, S.-H. Choi, E. Chu, Plane stress yield function for aluminum alloy sheets - Part 1: Theory, Int. J. Plast. 19 (2003) 1297-1319. https://doi.org/10.1016/S0749-6419(02)00019-0

[7] D. Banabic, F. Barlat, O. Cazacu, T. Kuwabara, Advances in anisotropy and formability, Int. J. Mater. Form. 3 (2010) 165-189. https://doi.org/10.1007/s12289-010-0992-9.

[8] A.C.S. Reddy, C.B. Reddy, D.V. Paleswar, Review on Different Hardening Models for Computation of Deep Drawing Process Simulation n.d. https://doi.org/10.31224/osf.io/4a28r

[9] D. Banabic, Sheet Metal Forming Processes - Constitutive Modelling and Numerical Simulation, Spinger, 2010. https://doi.org/10.1007/978-3-540-88113-1

[10] S. Ben-Elechi, M. Khelifa, R. Bahloul, Sensitivity of friction coefficients, material constitutive laws and yield functions on the accuracy of springback prediction for an automotive part, Int. J. Mater. Form. 14 (2021) 323-340. https://doi.org/10.1007/s12289-020-01608-2

[11] Y. Hou, J. Min, J. Lin, Z. Liu, J.E. Carsley, B. Thomas, Springback prediction of sheet metals using improved material models, Procedia Eng. 207 (2017) 173-178. https://doi.org/10.1016/j.proeng.2017.10.757

[12] J. Lin, Y. Hou, J. Min, Effect of constitutive model on springback prediction of MP980 and AA6022-T4, Int. J. Mater. Form. 13 (2020) 1-13. https://doi.org/10.1007/s12289-018-01468-x

[13] K. Chatziioannou, Y. Huang, S.A. Karamanos, Simulation of Cyclic Loading on Pipe Elbows Using Advanced Plane-Stress Elastoplasticity Models, J. Press. Vessel. Technol. 143 (2021) 021501-10. https://doi.org/10.1115/1.4047876

[14] V. Prakash, D.R. Kumar, A. Horn, H. Hagenah, M. Merklein, Modeling material behavior of AA5083 aluminum alloy sheet using biaxial tensile tests and its application in numerical simulation of deep drawing, Int. J. Adv. Manuf. Technol. 106 (2020) 1133-1148. https://doi.org/10.1007%2Fs00170-019-04587-0

[15] Z. Tuo, Z. Yue, X. Zhuang, X. Min, H. Badreddine, L. Qiu, Comparison of two uncoupled ductile damage initiation models applied to DP900 steel sheet under various loading paths, Int. J. Damage Mech. 30 (2021) 25-45. https://doi.org/10.1177/1056789520945002

[16] M. Conde, Y. Zhang, J. Henriques, S. Coppieters, A. Andrade-Campos, Design and validation of a heterogeneous interior notched specimen for inverse material parameter identification, Finite Elem. Anal. Des. 214 (2023) 103866. https://doi.org/10.1016/j.finel.2022.103866
[17] Dassault Systèmes. Abaqus 6.14 Online Documentation 2014.
[18] H. Scheffe, The analysis of variance, Vol. 72, John Wiley & Sons, 1999.
[19] P. Teixeira, A. Andrade-Campos, A.D. Santos, F.M.A. Pires, J.M.A. César de Sá, Optimization strategies for springback compensation in sheet metal forming. First ECCOMAS Young Investig, Conf., Aveiro, Portugal, 2012, p. 24-27. https://doi.org/10.1016/B978-0-85709-481-0.00003-3
[20] A. Maia, E. Ferreira, M.C. Oliveira, L.F. Menezes, A. Andrade-Campos, Numerical optimization strategies for springback compensation in sheet metal forming, Comput. Meth. Prod. Eng. Res. Dev. (2017) 51-82. https://doi.org/10.1016/B978-0-85709-481-0.00003-3
[21] H. Naceur, Y.Q. Guo, S. Ben-Elechi, Response surface methodology for design of sheet forming parameters to control springback effects, Comput. Struct. 84 (2006) 1651-1663. https://doi.org/10.1016/j.compstruc.2006.04.005
[22] S. Zhang, L. Léotoing, D. Guines, S. Thuillier, Potential of the Cross Biaxial Test for Anisotropy Characterization Based on Heterogeneous Strain Field, Exp. Mech. 55 (2015) 817-835. https://doi.org/10.1007/s11340-014-9983-y
[23] J. Ha, S. Coppieters, Y.P. Korkolis, International Journal of Mechanical Sciences On the expansion of a circular hole in an orthotropic elastoplastic thin sheet, Int. J. Mech. Sci. 182 (2020) 105706. https://doi.org/10.1016/j.ijmecsci.2020.105706
[24] H. Takizawa, T. Kuwabara, K. Oide, J. Yoshida, Development of the subroutine library "UMMDp" for anisotropic yield functions commonly applicable to commercial FEM codes, J. Phys. Conf. Ser. 734 (2016). https://doi.org/10.1088/1742-6596/734/3/032028
[25] E. Voce, The Relationship between Stress and Strain for Homogeneous Deformation, J. Inst. Met. (1948) 537-562.
[26] P.J. Armstrong, C.O. Frederick, A Mathematical Representation of the Multi Axial Bauschinger Effect, Mater. High Temp. 24 (2007) 1-26. https://doi.org/10.1179/096034007X207589
[27] F. Ozturk, S. Toros, S. Kilic, Effects of anisotropic yield functions on prediction of forming limit diagrams of DP600 advanced high strength steel, Procedia Eng. 81 (2014) 760-765. https://doi.org/10.1016/j.proeng.2014.10.073
[28] J. Fu, F. Barlat, J. Kim, F. Pierron, Identification of nonlinear kinematic hardening constitutive model parameters using the virtual fields method for advanced high strength steels, Int. J. Solid. Struct. 102-103 (2016) 30-43. https://doi.org/https://doi.org/10.1016/j.ijsolstr.2016.10.020
[29] M. Iadicola, Data for Numisheet 2020 uniaxial tensile and tension/compression tests, Natl. Inst. Stand. Technol., 2020. https://doi.org/10.18434/M32202
[30] S.M. Mirfalah-Nasiri, A. Basti, R. Hashemi Forming limit curves analysis of aluminum alloy considering the through-thickness normal stress, anisotropic yield functions and strain rate, Int. J. Mech. Sci. 117 (2016) 93-101. https://doi.org/10.1016/j.ijmecsci.2016.08.011
[31] Addinsoft. XLSTAT n.d. https://www.xlstat.com/en/ (accessed November 21, 2022).
[32] J.H. Schmitt, E. Aernoudt, B. Baudelet, Yield loci for polycrystalline metals without texture, Mater. Sci. Eng. 75 (1985) 13-20. https://doi.org/https://doi.org/10.1016/0025-5416(85)90173-9

Materials Research Proceedings 28 (2023) 1379-1386 https://doi.org/10.21741/9781644902479-149

Simple multiaxial tests to assess dynamic ductility of 17-4PH

MANCINI Edoardo[1,a *], CORTIS Gabriele[2,b], CORTESE Luca[2,c], UTZERI Mattia[3,d] and SASSO Marco[3,e]

[1] Università degli Studi dell'Aquila, DIIIE, Piazzale Ernesto Pontieri I, 67100 L'Aquila, Italy

[2] Sapienza University of Rome, Via Eudossiana 18, 00184 Rome, Italy

[3] Università Politecnica delle Marche, DIISM, Via Brecce Bianche, 60121 Ancona, Italy

[a]edoardo.mancini@univaq.it, [b]gabriele.cortis@uniroma1.it, [c]luca.cortese@uniroma1.it, [d]m.utzeri@pm.univpm.it, [e]m.sasso@staff.univpm.it

Keywords: Ductile Damage Modelling, High Strain Rate, Material Characterization

Abstract. To investigate material ductility, the use of simple multiaxial specimens which can be tested through a common tensile machine or by a Split Hopkinson bar facility would allow avoiding the use of more complex equipment to induce different stress states in the investigated material. In this work, experimental dynamic tests have been performed on four different specimen geometries on a 17-4PH steel by a direct Split Hopkinson Bar (SHB). Finite element models of the experiments are set up and used jointly with experimental data to calibrate and validate a strain rate dependent plasticity model, and to extract the local values of stress and ultimate strain in the most critical point of the samples, at fracture. These latter results allowed the calibration of a ductile damage model, whose predictions, compared with a previous calibration using tests carried out in quasi-static conditions, confirmed the effectiveness of the proposed specimens and test methodology to assess material ductility under dynamic conditions.

Introduction

To provide an accurate evaluation of material plastic strain at failure which is crucial in different fields of mechanical design, different ductile damage models have been developed in the literature to describe how a material gets damaged with plastic deformation until reaching its ultimate strength. They can be classified according to their driving principle: starting from those thermodynamically based [1,2], through criteria relying on the evolution of micro-void [3] up to empirical-based formulations [4]. All of them require different experimental tests for their calibration (such as tensile tests on round smooth or notched bar, torsion or compression tests and often multi-axial tests) and often special testing set-ups, involving a complex experimental phase and tuning procedures, which are non-trivial and not suitable for companies which sometimes may not have specific facilities available. These difficulties are greater under dynamic conditions due to the special devices required for multiaxial tests execution, as to achieve combined tension-torsion [5].

The aim of this paper is to validate, under dynamic conditions, the effectiveness of simple specimen geometries capable of inducing different multi-axial stress states in the material, to be tested using a conventional SHB, in order to simplify the experimental phase of material characterization. Starting from the geometry proposed by Driemeier et al. [6] and improved by Cortis et al. [7], different simulations have been carried out to identify the most suitable sample proportions and dimensions for dynamic tests. In order to reproduce additional loading conditions, round bar (RB) and round notched bar (RNB) specimens have been tested too. Using the results obtained from the dynamic tests made on these new simple specimens, a ductile damage model

Content from this work may be used under the terms of the Creative Commons Attribution 3.0 license. Any further distribution of this work must maintain attribution to the author(s) and the title of the work, journal citation and DOI. Published under license by Materials Research Forum LLC.

Materials Research Proceedings 28 (2023) 1379-1386 https://doi.org/10.21741/9781644902479-149

has been calibrated, and its prediction was compared with that one obtained from a previous calibration obtained by testing the same sample geometries under quasi-static conditions.

Material and Methods

Plasticity Model. Among the constitutive models available in the literature, suitable to describe the flow stress in a material as a function of strain, strain rate and temperature, the Johnson and Cook (JC) [8] was considered. The model is based on Mises Plasticity and accounts for strain hardening, strain rate and thermal softening:

$$\sigma = (A + B\varepsilon^n)\left[1 + C\ln\left(\frac{\dot{\varepsilon}}{\dot{\varepsilon}_0}\right)\right]\left[1 + \left(\frac{T - T_0}{T_{melt} - T_0}\right)^m\right] \quad (1)$$

In Eq. 1 ε, $\dot{\varepsilon}$, $\dot{\varepsilon}_0$, T_0 and T_{melt} are the equivalent plastic strain, the plastic strain rate, the reference strain rate, the room temperature and the melting temperature of the material while *A, B, n, C* and *m* are the constants to be calibrated.

Damage model. Ductile damage models belonging to the class of empirical formulations are represented by a scalar *D* that increases proportionally with the equivalent plastic strain ε_p weighted on a function of the stress state $f(T, X)$;

$$D = \int_0^{\varepsilon_f} f(T, X) d\varepsilon_p \quad (2)$$

where the triaxiality *T* and the Lode parameter *X* are the two scalars describing the stress state (Eq. 3).

$$T = \frac{1}{3}\frac{I_1}{\sqrt{3J_2}}; X = \frac{27}{2}\frac{J_3}{\left(\sqrt{3j_2}\right)^3} \quad (3)$$

Where I_1 is the first stress invariant, J_2 and J_3 are the second and the third deviatoric stress invariants, respectively. Material failure occurs when *D* reaches a critical value set equal to 1.

Under proportional loading conditions, which implies *T* and *X* constant with plastic strain, it is possible to invert Eq. 2 to obtain the following expression:

$$\varepsilon_f = f^{-1}(T, X) \quad (4)$$

which represents a "Fracture Surface" in the space (T, X, ε_f). $f^{-1}(T, X)$ can be described by different expressions; in the present work, the Coppola-Cortese (CC) [9] formulation was adopted:

$$\varepsilon_f = \frac{1}{A_1} e^{-A_2 T}\left(\frac{cos\left[\beta\frac{\pi}{6} - \frac{1}{3}arccos(\gamma)\right]}{cos\left[\beta\frac{\pi}{6} - \frac{1}{3}arccos(\gamma X)\right]}\right)^{\frac{1}{n}} \quad (5)$$

Materials Research Proceedings 28 (2023) 1379-1386 https://doi.org/10.21741/9781644902479-149

where A_1, A_2, β and γ are material constants that define the surface shape, while n represents the strain hardening exponent of a Hollomon's power law fit of the stress-strain curve: $\sigma = K\varepsilon^n$.

Materials. All specimens were manufactured from a single wrought bar. The investigated material is a 17-4PH steel that was characterised already under static conditions by some of the authors [7]. In order to compare the fracture surface obtained at a high strain rate with that one in static conditions, the calibration will be performed using multiaxial tests similar to those used in the static investigation, namely the improved "Driemeier" specimens and the RB and RNB specimens. In this work, two different configurations of the central holes of the Driemeier geometry were selected, corresponding to two different angles (α) of 10° and 30°, hereafter referred to as Pos10 and Pos30, respectively. The two angles were chosen to generate proper combinations of tensile-shear stress states. Moreover, to obtain similar strain rates from all tests, an optimization procedure was used to identify the sample dimensions, as reported in the next sub-section, "Samples for Dynamic Tests".

The final specimen dimensions are shown in Fig. 1. They were machined from metal bars with a diameter of 20 mm. The thickness of the gauge region of samples (a) and (b) is constant and equal to 2 mm.

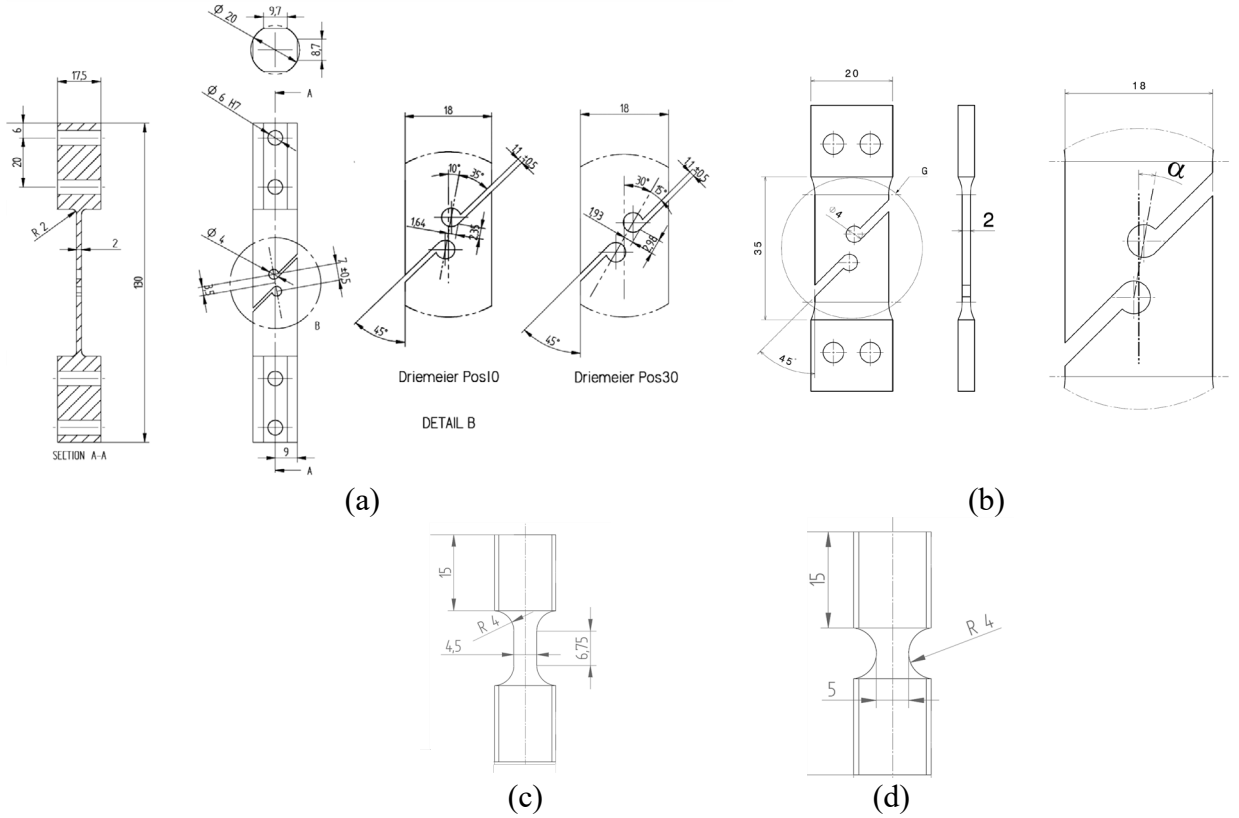

Fig. 1. Optimised geometries: Driemeier Pos10 and Pos30 for quasi-static (a) and dynamic tests (b); RB (c) and RNB (d) for dynamic tests.

Equipment. Quasi-static tests were performed in [7] by a universal servo-hydraulic MTS with 250 kN maximum load. Instead, a custom direct split Hopkinson bar [10] was used for dynamic tests. It consists of three aligned bars, named the pre-stressed, input and output bars. A tensile input wave (σ_i) is generated by pre-loading the pre-stressed bar in compression; the subsequent sudden release of this pre-load generates the waves that deform dynamically the sample (Fig. 2). By acquiring the transmitted and reflected waves (σ_t, σ_r) using properly placed strain gages and assuming uniaxial wave propagation in the bars and dynamic equilibrium in the sample, the dynamic properties, as well as the displacements u at the lateral faces of the specimen, can be assessed [10]. Moreover, digital images of all tests have been acquired using a FastCam at 100 kfps.

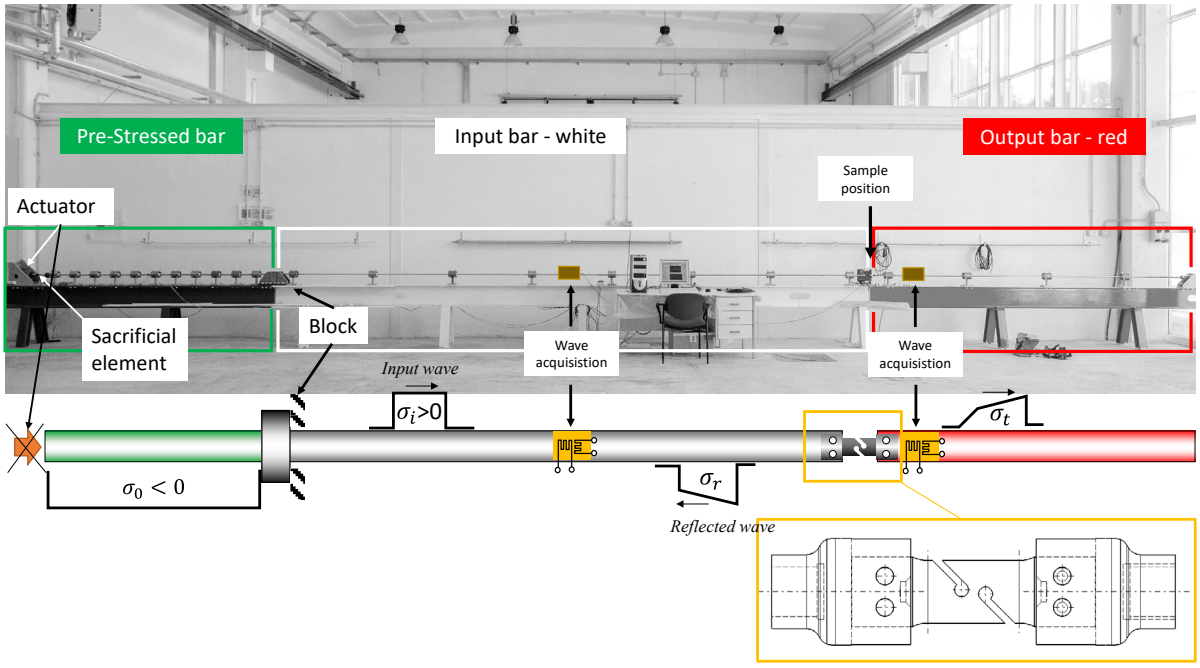

Fig. 2. Direct Split Hopkinson bar, and details the improved Driemeier sample and fasteners.

Samples for Dynamic Tests. The geometries of the samples used in the dynamic tests essentially consist of modifications of those used in the quasi-static tests, to adapt them to the available SHB equipment. Basically, the dynamic tests specimens must meet the geometric requirements in length and cross-section, to be mounted and successfully tested on the Hopkinson bar; in addition, the same equivalent plastic strain rate should be achieved in all tests. To meet these requirements, an inverse Finite Element (FE) approach was implemented according to a previously developed procedure [11,12], where the tests on RB, RNB and Driemeier samples are reproduced by FE simulations. The shape and size of the Driemeier specimens were maintained, whereas the cross-section diameter and the fillet of the RB and RNB specimens were iteratively varied according to a full factorial Design of Experiment plan; moreover, the impact intensity, i.e. the boundary velocity, was varied as well. Eventually, a combination of parameters has been found that permits the achievement of similar average plastic strain rates in the four different tests.

Of course, this is an approximate method, in which reasonable values for the material stress-strain curve as well as for the material strain to failure are assumed, not being known a priori.

The final dimensions adopted in the tests for RB and RNB samples are reported in Fig. 1.

Materials Research Proceedings 28 (2023) 1379-1386 https://doi.org/10.21741/9781644902479-149

Results and Discussion

The experimental results were first used to calibrate the JC constitutive material model. The material constants were derived through an inverse procedure by means of Finite Element simulations of the tests, minimizing the difference between experimental and numerical load-displacement global data. The comparison of the experimental curves with those obtained by the FE simulations using best fit JC material constants are shown in Fig. 3, where the red dots represent the onset of failure. Three repetitions were performed for each text and the experimental curves in the graphs represent the average data.

Concerning the RB and RNB tests an excellent numerical-experimental match is observed, even for Driemeier Pos10 and Pos30, although small discrepancies are shown, the match is fairly good. In Fig. 4 the distribution of equivalent plastic strain is reported, which fulfils one of the design requirements, namely the concentration of the maximum plastic strain value at its critical point in the centre of the gauge.

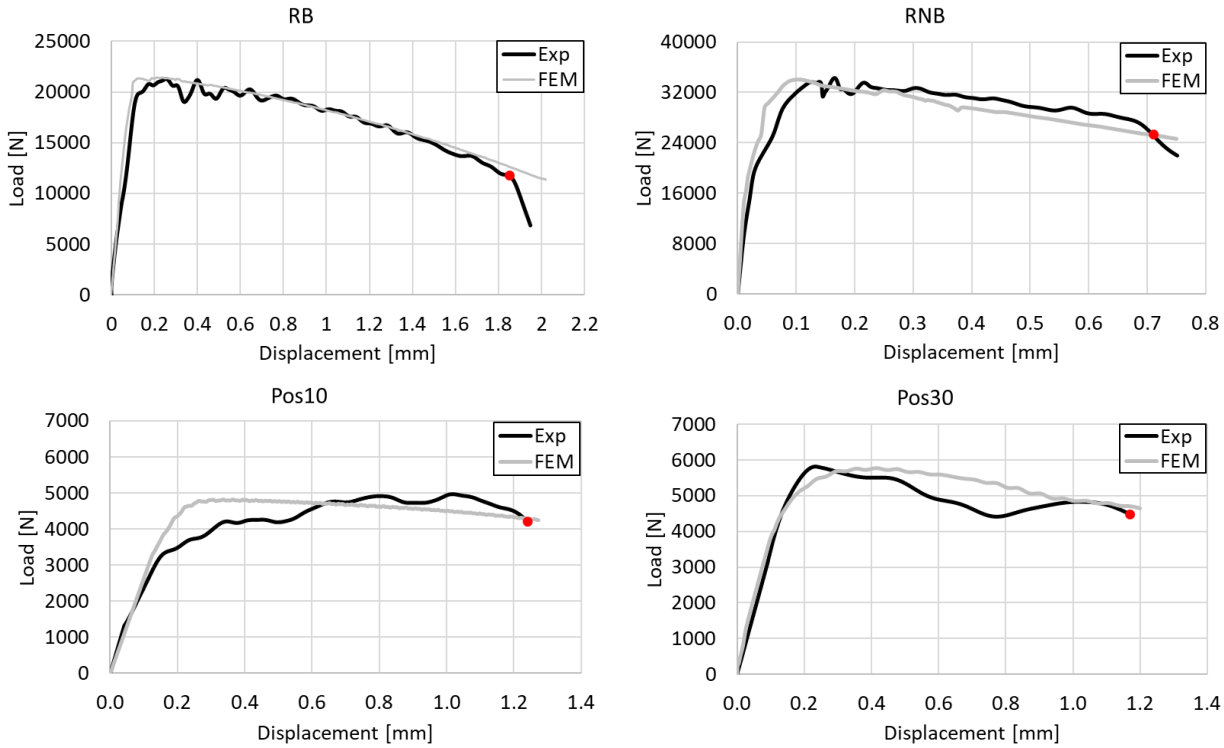

Fig. 3. Comparison between experimental and numerical load-displacement curves for RB, RNB, Pos10 and Pos30 tests. The red dots represent the onset of failure.

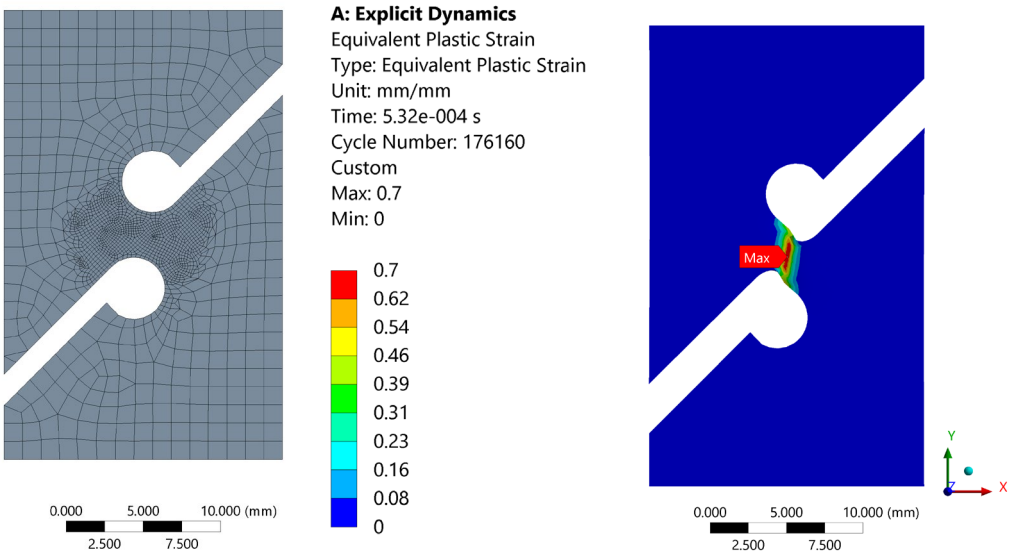

Fig. 4. Driemeier Pos 10°, mesh detail and contour plot of equivalent plastic strain.

After validating the FEM models by means of the numerical-experimental comparison presented above, the parameters T, X and ε_p were derived, for each test, at the critical point and at the instant of failure. These data are reported in Table 1, for both static and dynamic conditions. Subsequently, the CC damage model was calibrated through a minimisation algorithm, namely the calibration constants (A_1, A_2, β, γ) were derived such that the resulting fracture surface was as close as possible to the T, X and ε_p experimental points.

Table 1. Values of $\boldsymbol{T}$, $\boldsymbol{X}$ *and* $\boldsymbol{\varepsilon_p}$ *for static and dynamic tests.*

	Static			Dynamic		
	T	X	ε_p	T	X	ε_p
Pos10	0.05	0.16	0.33	0.13	0.41	0.70
Pos30	0.10	0.38	0.46	0.26	0.71	0.83
RB	0.61	0.99	1.17	0.67	0.99	0.78
RNB	0.76	0.99	0.81	1.07	0.99	0.40

Fig. 5a illustrates the dynamic and static fracture surfaces predicted by CC damage model, using the JC as plasticity model. In addition, a two dimensional view of ε_p as a function of the T along curves at constant X has been reported (Fig. 5b).

The dynamic fracture surface showed a good match with the experimental points (Fig. 5b). It is worth noting that the static-dynamic comparison suggests an increase in the ductility of the 17-4PH as the strain rate is increased, overall. More in detail, the dynamic fracture surfaces were slightly below the static fracture surfaces at high triaxialities (T around 1), remaining higher for medium and low triaxialities.

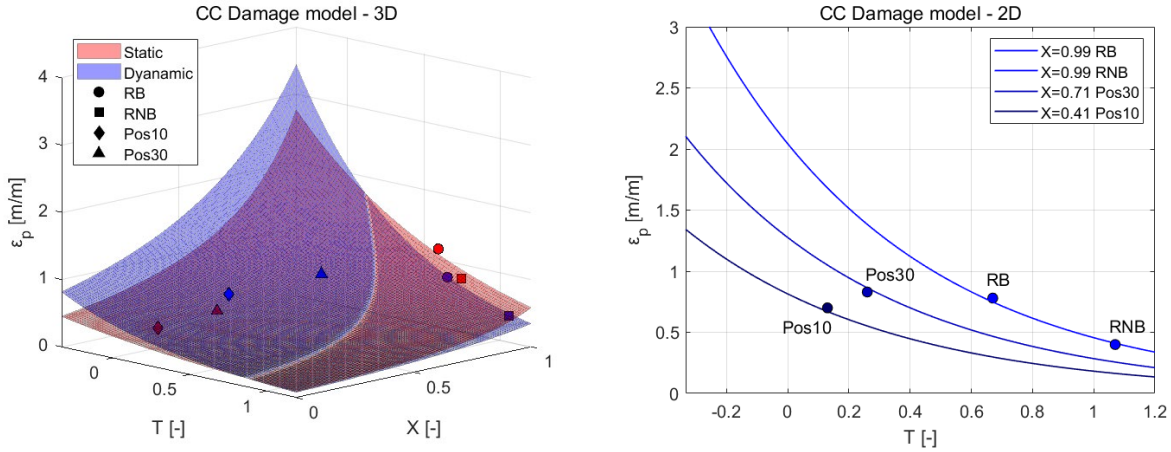

(a) (b)

Fig. 5. 3D (a) and 2D (b) views of 17-4PH fracture surfaces obtained under quasi-static and dynamic conditions, with indications of the strain to fracture of the RB, RNB, Pos10 and Pos30 tests.

Summary

In this work, the possibility of adopting simple multiaxial specimens for material characterization tests at high strain rates was investigated. The ductility of a 17-4PH steel alloy at high strain rates, as estimated by a damage model proposed by one of the authors, was evaluated and compared with the corresponding material behaviour under static conditions. Tensile specimens, such as round bars and round notched bars, together with the simple multiaxial specimens, were used. The dynamic experimental campaign was carried out by a direct split Hopkinson bar. The results highlighted the differences in terms of static-dynamic ductility of 17-4PH, and showed the suitability of the proposed approach to calibrate a ductile damage model at a high strain rate, using a standard dynamic testing equipment.

References

[1] J. Lemaitre, A continuous damage mechanics model for ductile fracture, J. Eng. Mater. Technol. 107 (1985) 83-89.

[2] N. Bonora, A nonlinear CDM model for ductile failure, Eng. Fract. Mech. 58 (1997) 11-28.

[3] J.W. Hancock, A.C. Mackenzie, On the mechanism of ductile failure in high-strength steel subjected to multi-axial stresses, J. Mech. Phys. Solids 24 (1976) 147-169.

[4] D.M. Jr Norris, J.E. Reaugh, B. Moran, D. F. Quinnones, A plastic-strain mean-stress criterion for ductile fracture, J. Eng. Mater. Technol. 100 (1978) 279-286.

[5] M. Sasso, E. Mancini, Feasibility Study of a Combined Tension-Torsion Hopkinson Bar, EPJ Web Conf. Volume 250, 2021, DYMAT 2021 - 13th Int. Conference on the Mechanical and Physical Behaviour of Materials under Dynamic Loading

[6] L. Driemeier, M. Brünig, G. Micheli, M. Alves, Experiments on stress-triaxiality dependence of material behavior of aluminum alloys, Mech. Mater. 42 (2010) 207-217. https://doi.org/10.1016/j.mechmat.2009.11.012

[7] G. Cortis, F. Nalli, M. Piacenti, A direct methodology for the calibration of ductile damage models from a simple multiaxial test, IOP Conf. Ser. (2021), Mater. Sci. Eng. 1214 (2021) 012016. https://doi.org/10.1088/1757-899X/1214/1/012016

[8] G.R. Johnson, W.H. Cook, A constitutive model and data for metals subjected to large strains, high strain rates, and high temperatures, Proceedings of the Seventh International Symposium on Ballistics, International Ballistics Committee, Hague, The Netherlands, 19-21 (1983) 541-547.

[9] T. Coppola, L. Cortese, P. Folgarait, The effect of stress invariants on ductile fracture limit in steels, Eng. Fract. Mech. 76 (2009) 1288-1302. https://doi.org/10.1016/j.engfracmech.2009.02.006
[10] E. Mancini; M. Sasso, M. Rossi, G. Chiappini, G. Newaz, D. Amodio, Design of an Innovative System for Wave Generation in Direct Tension-Compression Split Hopkinson Bar, J. Dyn. Behav. Mater.1 (2015) 201-213. https://doi.org/10.1007/s40870-015-0019-1
[11] M. Sasso, E. Mancini, L. Cortese, F. Nalli, Design and Optimization of Dynamic Test Samples for Ductile Damage Assessment, In Proceedings of the DYMAT 2018 - 12th International Conference on the Mechanical and Physical Behaviour of Materials under Dynamic Loading, Arcachon, France, 9-14 September 2018. https://doi.org/10.1051/epjconf/201818301061
[12] G. Cortis, F. Nalli, M. Sasso, M. L. Cortese, E. Mancini, Effects of Temperature and Strain Rate on the Ductility of an API X65 Grade Steel, Appl. Sci. 12 (2022) 2444. https://doi.org/10.3390/app12052444

Materials Research Proceedings 28 (2023) 1387-1396 https://doi.org/10.21741/9781644902479-150

Nonlinear elastic stress triaxiality dependent constitutive model for fibre-reinforced polymer composites

OBID Štefan[1,a], HALILOVIČ Miroslav[1,b] and STARMAN Bojan[1,c *]

[1]University of Ljubljana, Faculty of Mechanical Engineering, Aškerčeva 6, 1000 Ljubljana, Slovenia

[a]stefan.obid@fs.uni-lj.si, [b]miroslav.halilovic@fs.uni-lj.si, [c]bojan.starman@fs.uni-lj.si

Keywords: Constitutive Model, Stress Triaxiality Dependency, Anisotropic Material

Abstract. A novel constitutive model is proposed to describe fibre-reinforced polymer composite materials. The model covers three fundamental phenomena of such materials: anisotropy, tension-compression asymmetry, and nonlinear material behaviour. The model is based on the one-dimensional Ramberg-Osgood relation, which is extended to a multiaxial anisotropic form. Tension-compression asymmetry is then implemented with the introduction of stress triaxiality dependency. Finally, the model is verified using experimental data where the material response in uniaxial tension, uniaxial compression and shear stress states were measured.

Introduction

Fibre-reinforced polymer composites are increasingly used in many manufacturing fields due to their high strength-to-weight ratio and low cost. Their main property is an anisotropic material response which is a consequence of reinforcement fibres orientation. Another essential property caused by reinforcement fibres is tension-compression asymmetry. In tension loading, fibres stretch and increase overall material stiffness, which is not the case in compression loading, where they can buckle due to matrix porosity [1]. The third important property is a nonlinear material response which is mainly a consequence of the polymer matrix and can be observed even at low strains [2]. All three properties must be addressed to accurately model the material response of fibre-reinforced materials.

One of the first attempts at modelling 2D orthotropic material with tension-compression asymmetry was proposed in [3], where different values of compliance tensor components were prescribed depending on the sign of stress tensor components. The problem with this model was thermodynamical inconsistency due to asymmetric compliance tensor, which was later solved in [4] and [5]. Similar variations of tension-compression asymmetry modelling with sign manipulation can be found in [6,7] and later in [8], where this idea was generalised to a 3D constitutive model. Recently, 3D tension-compression asymmetric damage model for fibre-reinforced materials was introduced in [9], where the damage initiation criterion is defined based on a sign of individual stress components or a sign of two stress components sum. For modelling nonlinear material response in large deformations, the hyperelastic approach was used in [10,11], where asymmetry was implemented with the dependency of constitutive parameters based on signs of principal strain or main stress components. Another approach for modelling material asymmetry was introduced in [12,13], where stress triaxiality dependency was implemented in a linear anisotropic model with an additional term to model polymer matrix nonlinear response.

As seen from the literature, there is no unified approach to model the phenomena mentioned above. In the following, we present a novel elastic constitutive model based on the Ramberg-Osgood relation [14], which is extended to a multiaxial anisotropic model. To implement asymmetric material response new approach is used, where constitutive relation consists of two parts defining material response in tension and compression separately. The two parts are weighted

Content from this work may be used under the terms of the Creative Commons Attribution 3.0 license. Any further distribution of this work must maintain attribution to the author(s) and the title of the work, journal citation and DOI. Published under license by Materials Research Forum LLC.

depending on the value of stress triaxiality, which serves as a tension-compression indicator. In this paper, the derivation of the model is shown, including verification based on experimental data.

Derivation of constitutive relation

The derivation of constitutive relation consists of two parts. In the first part, we take the Ramberg-Osgood nonlinear relation and generalise it to obtain a nonlinear anisotropic model. In the second part, we introduce the dependency of stress triaxiality to implement asymmetric material response.

Nonlinear anisotropy.

To ensure thermodynamic consistency, the strain energy function of the developed model must remain a potential function. Therefore, rather than generalising the Ramberg-Osgood relation itself, we generalise its strain energy potential, which we can write as

$$C = \frac{\sigma^2}{2G} + \frac{\zeta^{n+1}}{n+1}\frac{\sigma^2}{K} \tag{1}$$

where σ is stress, G is shear modulus, K is secant modulus, ζ is stress invariant defined as $\sqrt{(\sigma/K)^2}$ and n is an exponent. As stated, we generalise Eq. 1 to multiaxial anisotropic form as

$$C = \frac{1}{2}\boldsymbol{\sigma}:\mathbb{S}:\boldsymbol{\sigma} + \frac{\zeta^{n-1}}{n+1}\boldsymbol{\sigma}:\mathbb{N}:\boldsymbol{\sigma} \tag{2}$$

where $\boldsymbol{\sigma}$ represents the stress tensor, $\mathbb{S}$ linear compliance tensor and $\mathbb{N}$ nonlinear compliance tensor. From the comparison of Eq. 1 and Eq. 2, we can see that linear compliance tensor $\mathbb{S}$ takes the role of shear modulus G, and nonlinear compliance tensor $\mathbb{N}$ takes the role of secant modulus. Stress invariant ζ is generalised in a similar manner to $\sqrt{\boldsymbol{\sigma}:\mathbb{N}:\mathbb{N}:\boldsymbol{\sigma}}$. With derivation of expression Eq. 2 with respect to stress tensor, we obtain nonlinear anisotropic constitutive relation

$$\boldsymbol{\varepsilon} = \frac{\partial C}{\partial \boldsymbol{\sigma}} = \mathbb{S}:\boldsymbol{\sigma} + \frac{\zeta^{n-1}}{n+1}\left((n-1)\frac{\boldsymbol{\sigma}:\mathbb{N}:\boldsymbol{\sigma}}{\zeta^2}\mathbb{N} + 2\mathbb{I}^{sym}\right):\mathbb{N}:\boldsymbol{\sigma} \tag{3}$$

where $\mathbb{I}^{sym}$ represents 4-th order symmetric identity.

Tension-compression asymmetry.

The dependency of stress triaxiality is used to implement asymmetric material response. Stress triaxiality η is stress invariant defined as the ratio between hydrostatic pressure p and von Mises stress q

$$\eta = -\frac{p}{q} \tag{4}$$

The absolute value of stress triaxiality indicates how uniform is stress state distributed between three material axes. The crucial property for implementing asymmetric behaviour is the stress triaxiality sign, which is positive in tensile stress states, and negative in compressive stress states. We can now define strain energy as a function of stress triaxiality as

$$\mathrm{C} = \mathrm{C_t}\,\psi_t(\eta) + C_c\,\psi_c(\eta) \tag{5}$$

where C_t and C_c are tensile and compressive strain energy functions defined the same as Eq. 2, where separate tensors $\mathbb{S}$, $\mathbb{N}$ and exponent n are assigned to each one. Both parts of Eq. 5 contain weight functions $\psi_t(\eta)$ or $\psi_c(\eta)$ which are piecewise defined, as shown in Fig. 1.

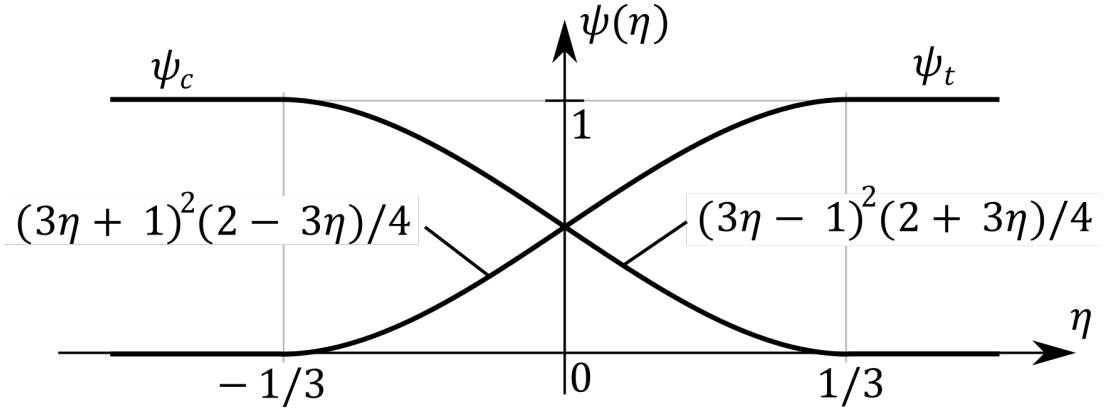

Fig. 1. Weight functions $\psi_t(\eta)$ and $\psi_c(\eta)$.

With such defined weight functions energy part C_t only affect material behaviour in tensile stress states and vice versa, C_c only has an effect in compressive stress states. In the transition zone between uniaxial compression ($\eta = -1/3$) and uniaxial tension stress state ($\eta = 1/3$), where both energy parts are intertwined, the weight functions are defined as a third-order polynomial.

Taking the derivative of strain energy density (Eq. 5) with respect to stress tensor yields final constitutive relation, which in shortened form can be written as

$$\boldsymbol{\varepsilon} = \left(\frac{\mathrm{d}\psi_t(\eta)}{\mathrm{d}\eta} C_t + \frac{\mathrm{d}\psi_c(\eta)}{\mathrm{d}\eta} C_c\right)\frac{\partial \eta}{\partial \boldsymbol{\sigma}} + \psi_t(\eta)\frac{\partial C_t}{\partial \boldsymbol{\sigma}} + \psi_c(\eta)\frac{\partial C_c}{\partial \boldsymbol{\sigma}} \tag{6}$$

Constitutive relation (Eq. 6) is valid for general nonlinear anisotropic and asymmetric material. If no tension-compression asymmetry is observed, the relation simplifies to Eq. 3. Furthermore, if material behaviour is linear, the model reduces to classic linear anisotropic form written as

$$\boldsymbol{\varepsilon} = \mathbb{S} : \boldsymbol{\sigma} \tag{7}$$

Compliance Tensor Structure

In this section, the compliance tensor structure and containing parameters are shown. For simplicity sake, we will restrict from general anisotropy to orthotropic material. In this case, linear compliance tensors $\mathbb{S}_t$ and $\mathbb{S}_c$ take the following form in Voigt notation

$$[\mathbb{S}_\alpha] = \begin{bmatrix} 1/E_1^\alpha & -\nu_{12}^\alpha/E_1^\alpha & -\nu_{13}^\alpha/E_1^\alpha & 0 & 0 & 0 \\ -\nu_{12}^\alpha/E_1^\alpha & 1/E_2^\alpha & -\nu_{23}^\alpha/E_2^\alpha & 0 & 0 & 0 \\ -\nu_{13}^\alpha/E_1^\alpha & -\nu_{23}^\alpha/E_2^\alpha & 1/E_3^\alpha & 0 & 0 & 0 \\ 0 & 0 & 0 & 1/G_{12}^\alpha & 0 & 0 \\ 0 & 0 & 0 & 0 & 1/G_{13}^\alpha & 0 \\ 0 & 0 & 0 & 0 & 0 & 1/G_{23}^\alpha \end{bmatrix}, \quad \alpha \in \{t, c\} \tag{8}$$

where E_i^α is an elastic modulus, G_{ij}^α is a shear modulus and ν_{ij}^α is a Poisson's ratio. Nonlinear compliance tensors $\mathbb{N}_t$ and $\mathbb{N}_c$ have a similar form to linear compliance tensors and are formulated as

Materials Research Proceedings 28 (2023) 1387-1396 https://doi.org/10.21741/9781644902479-150

$$[\mathbb{N}_\alpha] = \begin{bmatrix} 1/A_{11}^\alpha & 1/A_{12}^\alpha & 1/A_{13}^\alpha & 0 & 0 & 0 \\ 1/A_{12}^\alpha & 1/A_{22}^\alpha & 1/A_{23}^\alpha & 0 & 0 & 0 \\ 1/A_{13}^\alpha & 1/A_{23}^\alpha & 1/A_{33}^\alpha & 0 & 0 & 0 \\ 0 & 0 & 0 & 1/B_{12}^\alpha & 0 & 0 \\ 0 & 0 & 0 & 0 & 1/B_{13}^\alpha & 0 \\ 0 & 0 & 0 & 0 & 0 & 1/B_{23}^\alpha \end{bmatrix}, \quad \alpha \in \{t, c\} \tag{9}$$

where A_{ij}^α and B_{12}^α are parameters defining nonlinear material response. We can see that linear compliance tensors contain well-known parameters for describing linear elastic properties, whereas, in nonlinear compliance tensors, parameters have no direct physical meaning.

Parameter Identification Procedure

The derived constitutive model (Eq. 6) has four compliance tensors $\mathbb{S}_t$, $\mathbb{N}_t$, $\mathbb{S}_c$, $\mathbb{N}_c$ and two exponents n_t, and n_c. Each parameter dictates a particular part of the model response (see Table 1).

Table 1. Parameter influence on the model response.

model response	*compressive*	*tensile*
linear	$\mathbb{S}_c$	$\mathbb{S}_t$
nonlinear	$\mathbb{N}_c, n_c$	$\mathbb{N}_t, n_t$

This property enables parameters to be separately identified in four groups, as indicated in Table 1. Identification procedure is performed in the following steps:

1) Uniaxial tensile tests are used, from which linear tensile parameters are identified based on initial slopes of strain-stress curves, yielding a linear system of equations from which parameter values are calculated.
2) With linear parameters known, we can proceed to nonlinear parameter identification. The same test set is used in the first step, whereas whole strain-stress curves are now used, not just initial slopes. In this step, parameters cannot be directly calculated. Therefore, optimisation methods are used to minimise the deviation between model response and experimental data. In our case, the procedure is carried out in Wolfram Mathematica software by applying the BFGS quasi-Newton method to a scatter of points randomly distributed over the parametric hyperspace.
3) 1. and 2. steps are repeated where compressive linear and nonlinear parameters are identified based on uniaxial compression tests.

Fig. 2 shows which part of the material response and which model parameters are determined in which identification step.

Materials Research Proceedings 28 (2023) 1387-1396 https://doi.org/10.21741/9781644902479-150

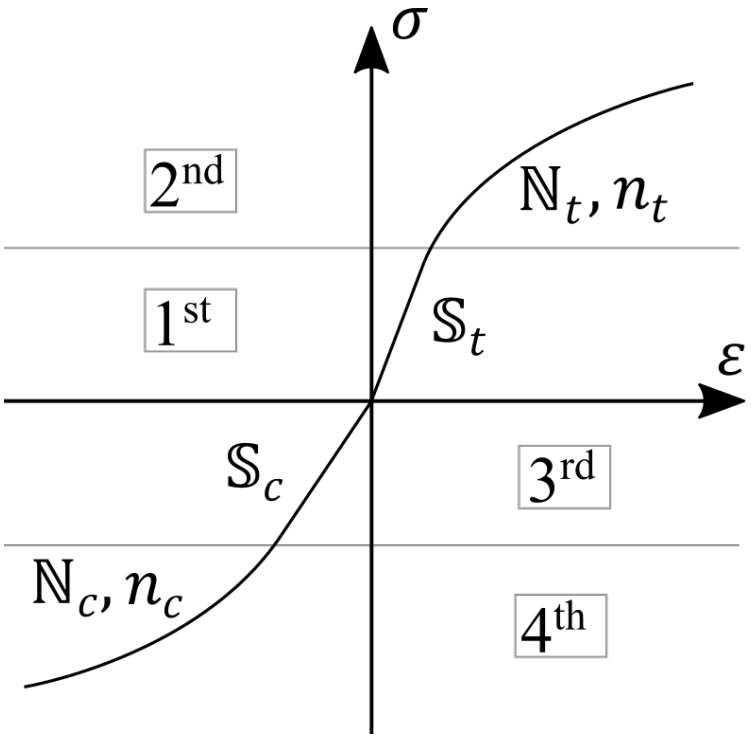

Fig. 2. Four-step identification procedure.

In each step, uniaxial tests performed in different material orientations are used to identify all parameters in compliance tensors. The choice of specimen orientations is identical as in the identification of classic linear anisotropic or orthotropic material.

Validation

To validate the developed model, we used the material properties of a unidirectional glass-fibre epoxy composite carried out in [1]. In this study, besides linear orthotropic properties, tension-compression asymmetry of elastic moduli and nonlinear material response in an off-axis direction were also determined. The nonlinear material response was separately described with three parametric Ramberg-Osgood relation

$$\gamma_{ij} = \frac{\sigma_{ij}}{G_{ij}} + \left(\frac{\sigma_{ij}}{K_{ij}}\right)^{1/N_{ij}}, \qquad \text{ij} \in \{12, 13, 23\} \tag{10}$$

Material properties determined in [1] which have the same values in tension and compression, are listed in Table 2, and elastic moduli are separately listed in Table 3.

Table 2. Material properties from [1].

ij	12	13	23
ν_{ij}^{α}[/]	0.29	0.27	0.41
G_{ij}^{α}[GPa]	4.25	4.16	4.47
K_{ij}^{α}[MPa]	211	191	∞
N_{ij}^{α}[/]	0.237	0.219	/

$\alpha \in \{t, c\}$

Materials Research Proceedings 28 (2023) 1387-1396 https://doi.org/10.21741/9781644902479-150

Table 3. Elastic moduli from [1].

α	t	c
E_1^α[GPa]	49.1	47.9
E_2^α[GPa]	12.8	12.5

These experimental data are useful for validating the developed model because of its ability to describe all fundamental phenomena of this material behaviour, namely, orthotropy, nonlinearity and asymmetry. Since our model also use classic parameters for the description of linear material response, values from Table 2 and Table 3 can be directly used to determine linear compliance tensors $\mathbb{S}_t$ and $\mathbb{S}_c$. Since our model is also based on the Ramberg-Osgood relation, one would expect that nonlinear properties $\mathbb{N}_\alpha$ and n_α will be directly computed from K_{ij}^α and N_{ij}^α from Table 2, which is not the case. The reason is the exponent N_{ij}^α, which has different values in different directions, not alike in our model, which has the same value of the exponent n_α for all material directions. Therefore, nonlinear properties have to be determined using optimisation and are listed in Table 4.

Table 4. Optimised values of nonlinear parameters.

A_{ij}^α[MPa]$\star$	B_{12}^α[MPa]	B_{13}^α[MPa]	B_{23}^α[MPa]	n^α [/]
∞	154.3	151.5	∞	4.404

$\alpha \in \{t, c\}, \quad \star\, i, j \in \{1, 2, 3\}$

To validate the developed model properly, we compared the 3-point bending test finite element simulation results carried out in [1] and the simulation done with our constitutive model, which was implemented in the Abaqus finite element software via the VUMAT subroutine. Fig. 3 shows the comparison of both simulation results. Since the bending test is symmetrical, only half of the field is shown in the figure with symmetry plane on the left side. The compared strain fields are almost identical, where only a minuscule difference can be observed in the shear strain field.

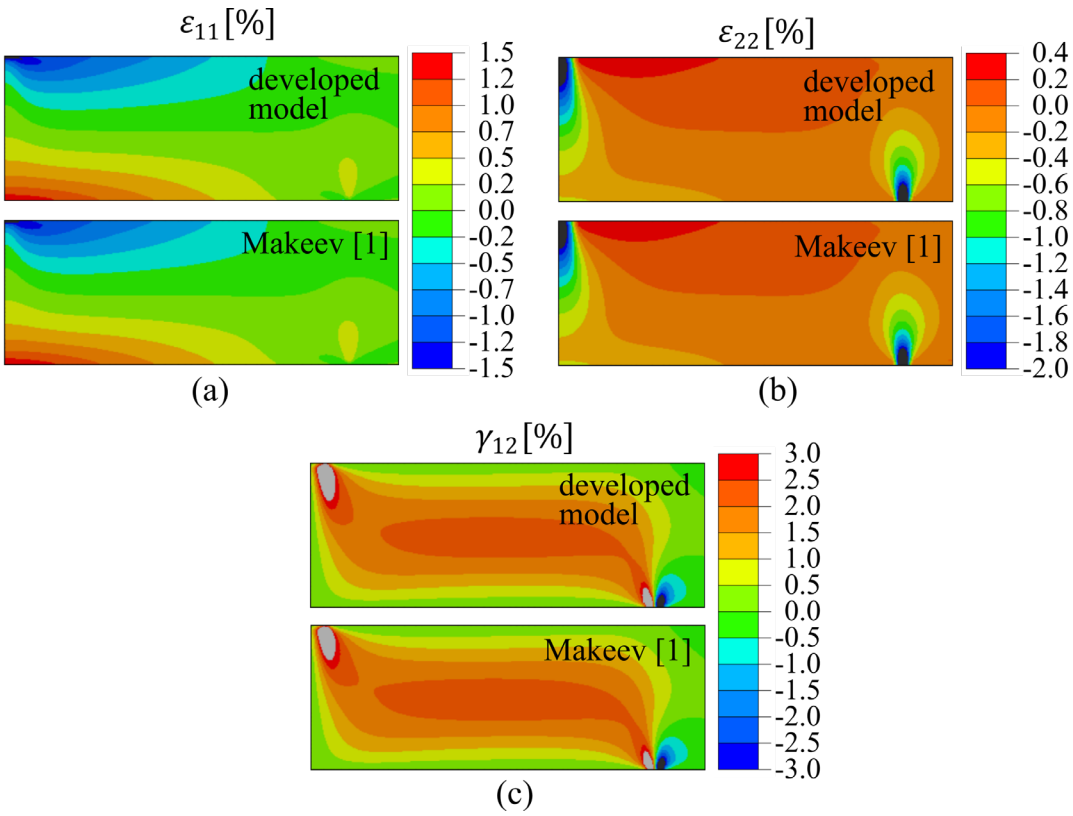

Fig. 3. Comparison of 3-point bending FEM simulation results.

Verification

In this section, verification of the developed model is presented. Redundant experimental data set is used, where more data are available than needed for model calibration, which enables us to verify whether the model prediction agrees with the rest of the experimental data, which were not used for calibration.

Experimental data used for verification were carried out in [15], where multiple in-plane tests were performed for woven roving glass fibre composite plates. Specimens were cut from the plate at 0°, 22.5° and 45° angles with respect to fibre orientation. For each direction, uniaxial tension, uniaxial compression and shear tests were performed, where longitudinal and transversal strains were measured. In total, 9 tests and 18 strain-stress curves were carried out (shown in Fig. 4).

For model calibration, only tension and compression tests in 0° and 45° directions are used, which is 4 out of 9 tests. With four step identification procedure, the parameter values in Table 5 were determined.

Table 5. Calibrated values of model parameters from experimental data.

α	E_1^α [GPa]	E_2^α [GPa]	G_{12}^α [GPa]	ν_{12}^α [/]	A_{11}^α [GPa]	A_{22}^α [GPa]	A_{12}^α [GPa]	B_{12}^α [GPa]	n_α [/]
t	19.8	14.2	4.86	0.152	1.69	174	7.46	0.223	2.43
c	18.2	13.1	4.15	0.199	∞	1.77	-2.27	0.130	3.57

A comparison of experimental curves and model response is shown in Fig. 4, where columns represent different material orientations, and rows represent different loading cases.

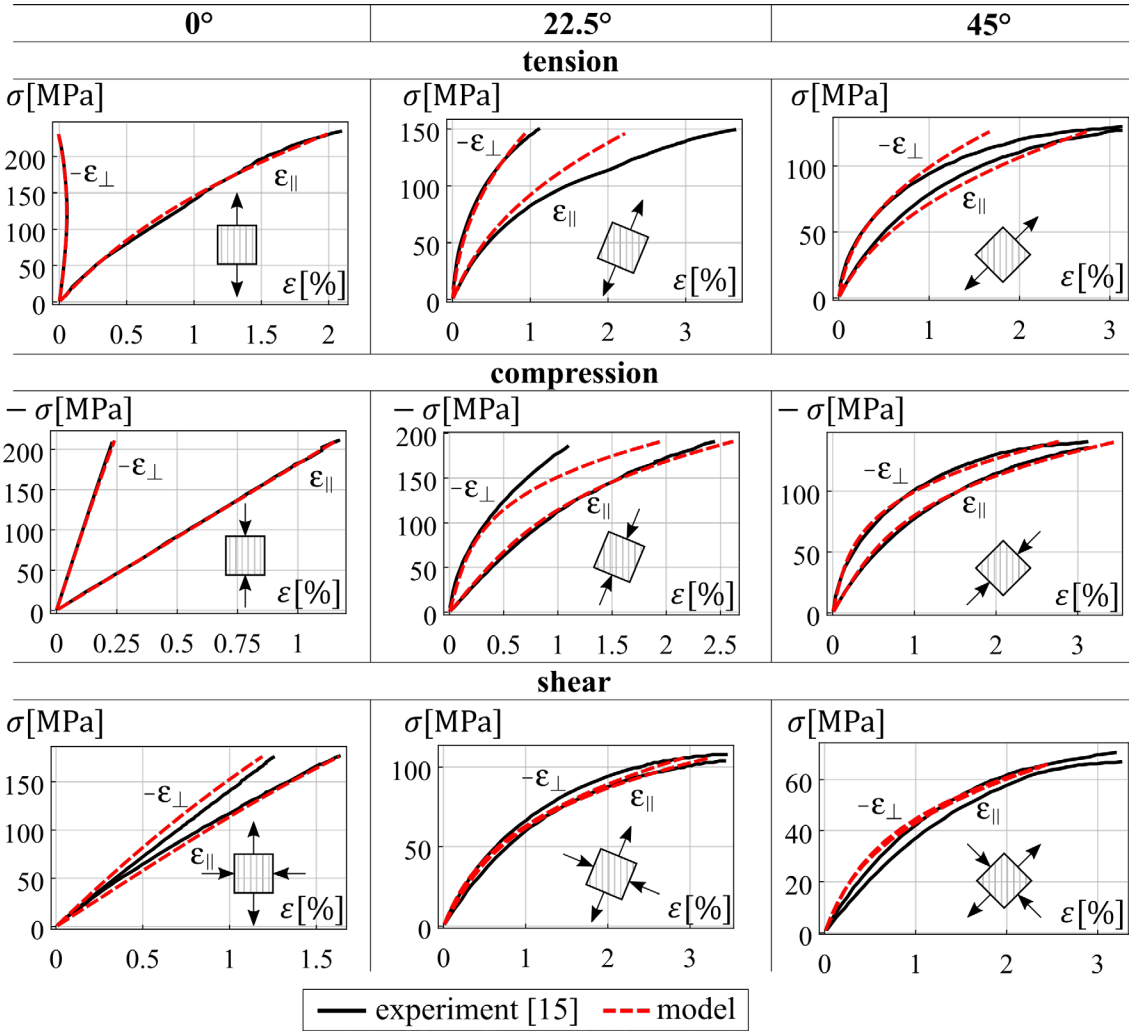

Fig. 4. Comparison of experimental and model strain-stress curves.

For a more quantitative comparison, an absolute relative error between experimental data and model response strain energy density was calculated using the equation below

$$err = \left|\frac{C_{model} - C_{exp}}{C_{exp}}\right| \cdot 100\% \tag{11}$$

where model strain energy C_{model} is calculated by equation (5), and experimental strain energy C_{exp} is calculated as the area under the stress-strain diagram. Calculated error values represent a relative difference in the area below the model and experimental curves. The calculated values are specified in Table 6.

Table 6. Calculated relative error for each loading case.

relative error *err* [%]	0°		22.5°		45°	
	∥	⊥	∥	⊥	∥	⊥
tension	0.721	1.537	10.914	0.687	3.766	3.813
compression	0.424	1.874	0.005	18.353	0.052	0.447
shear	20.950	25.367	4.183	5.907	8.618	2.670

It is not surprising that model responses show good agreement with experimental curves from which the model was calibrated (colored green in Table 6), where maximal error is 3.766%. Values, colored yellow in Table 6, represent relative error in loading cases which were not included in the calibration procedure. High error values in some responses could be lowered with inclusion of all experimental data in calibration procedure. However, ideally one would want to capture material behaviour from as few experiments as possible. Therefore, it is more important to see that model can correctly predict material behaviour from just uniaxial tension and compression test in two different orientations.

Summary

The novel constitutive model for the description of anisotropic, nonlinear and asymmetric material behaviour was presented. The nonlinear Ramberg-Osgood relation was generalised to an anisotropic form, where stress triaxiality dependency was introduced to achieve tension-compression asymmetry.

Quite a few parameters are needed to capture all the phenomena mentioned above, which are identified in separate groups in a four-stage identification procedure. The model uses classic linear anisotropic parameters to describe the linear part of the model response, which is convenient when values of those parameters are already given. Another good property of the model is that it reduces to a simpler form or, ultimately, to a linear anisotropic model if the material does not exhibit all the aforementioned phenomena. In that case, also the number of parameters is drastically decreased.

A redundant experimental data set was used for verification, where good prediction properties of the model were shown. The model was able to predict a comparable response to experimental data in a 22.5° direction and in a shear stress state, both of which were not included in the calibration procedure.

References

[1] E.V. Lomakin, Y.N. Rabotnov, A theory of elasticity for an isotropic body with different moduli in tension and compression, Mech. Solid. 13 (1978) 25-30.

[2] Y. He, A. Makeev, Nonlinear shear behavior and interlaminar shear strength of unidirectional polymer matrix composites: A numerical study, Int. J. Solid. Struct. 51 (2014) 1263-1273. https://doi.org/10.1016/j.ijsolstr.2013.12.014

[3] S.A. Ambartsumian, A.A. Khachatrian, Basic equations in the theory of elasticity for materials with different resistance to tension and compression, Inzhenernyi zhurnal – Mekhanika tverdogo tela (1966) 44–53.

[4] R.M. Jones, Stress-strain relations for materials with different moduli in tension and compression, Aiaa J. 15 (1977) 16-23.

[5] C.W. Bert, Models for fibrous composites with different properties in tension and compression, J. Eng. Mater. Technol. 99 (1977) 344-349. https://doi.org/10.1115/1.3443550

[6] B.P. Patel, K. Khan, Y. Nath, A new constitutive model for bimodular laminated structures: Application to free vibrations of conical/cylindrical panels, Compos. Struct. 110 (2014) 183-191. https://doi.org/10.1016/j.compstruct.2013.11.008

[7] K. Vijayakumar, K.P. Rao, Stress-strain relations for composites with different stiffnesses in tension and compression, Comput. Mech. 2 (1987) 167-175. https://doi.org/10.1007/BF00571022

[8] L. Zhang, H.W. Zhang, J. Wu, B. Yan, A stabilised complementarity formulation for nonlinear analysis of 3D bimodular materials, Acta Mech. Sin. 32 (2016) 481-490. https://doi.org/10.1007/s10409-015-0517-3

[9] J. Park, J.W. Yoon, A general FRC (fiber reinforced composite) constitutive model considering transverse isotropy and accumulated damage, J. Mech. Sci. Tech. 36 (2022) 6147-6156. https://doi.org/10.1007/s12206-022-1129-z

[10] M. Latorre, F.J. Montáns, Bi-modulus materials consistent with a stored energy function: Theory and numerical implementation, Comput. Struct. 229 (2020) 106176. https://doi.org/10.1016/j.compstruc.2019.106176
[11] Z. Du, G. Zhang, T. Guo, S. Tang, X. Guo, Tension-compression asymmetry at finite strains: A theoretical model and exact solutions, J. Mech. Phys. Solid. 143 (2020) 104084. https://doi.org/10.1016/j.jmps.2020.104084
[12] E.V. Lomakin, B.N. Fedulov, Nonlinear anisotropic elasticity for laminate composites, Meccanica 50 (2015) 1527-1535. https://doi.org/10.1007/s11012-015-0104-5
[13] E.V. Lomakin, O.P. Shchendrigina, Stresses and strains in a disk of physically nonlinear material with stress state dependent properties, Mech. Solid. 55 (2020) 475-481. https://doi.org/10.3103/S0025654420040081
[14] W. Ramberg, W.R. Osgood, Description of stress-strain curves by three parameters, Technical Report NACA-TN-902, 1943.
[15] E.W. Smith, K.J. Pascoe, The role of shear deformation in the fatigue failure of a glass fibre-reinforced composite, Compos. 8 (1977) 237-243.

Materials Research Proceedings 28 (2023) 1397-1406 https://doi.org/10.21741/9781644902479-151

Calibration of thermo-viscoplastic constitutive model under biaxial loadings: A Feasibility Study

WANG Zhihao[1,a], GUINES Dominique[1,b] and LEOTOING Lionel[1,c *]

[1] Univ Rennes, INSA Rennes, LGCGM (Laboratoire de Génie Civil et Génie Mécanique), F-35000 Rennes, France

[a]zhihao.wang@insa-rennes.fr, [b]dominique.guines@insa-rennes.fr, [c]lionel.leotoing@insa-rennes.fr

Keywords: Thermo-Viscoplastic Model, Thermal Biaxial Tensile Test, Calibration

Abstract. In this study, an inverse identification strategy based on the finite element model updating (FEMU) method is proposed to calibrate the parameters of a temperature and strain rate dependent constitutive model. The mechanical responses of a dedicated cruciform specimen with heterogeneous temperature field under biaxial loading are employed to supply information to the inverse scheme. A combination of Particle Swarm Optimization (PSO) and SIMPLEX optimization algorithm is employed to find the optimal values of the material parameters. In order to validate the proposed identification strategy, a virtual experiment is designed and performed with a reference material constitutive model. The proposed strategy is proved to be feasible as all seven parameters of the constitutive model are accurately identified. In addition, the influences of measurement noise of force, temperature, and strain data are analyzed by means of a sensitivity study. The experimental data after the localized necking should be avoided for parameter identification. The proposed inverse identification strategy shows good robustness to strain noise.

Introduction

Advanced processes in engineering, such as hot stamping, high-speed metal forming or electrically-assisted manufacturing, involve complex mechanical behaviors and multi-axial loading conditions [1]. For a numerical analysis of these forming processes, it is necessary to construct the constitutive model that takes into account the thermo-visco-plastic hardening relations. Over the years, a number of phenomenological or physical constitutive models have been proposed to describe the temperature and strain rate dependent flow stress of sheet metals. Phenomenological models usually incorporate strain hardening models with temperature softening and strain rate hardening multiplicative or additive factors, such as Johnson-Cook model [2] or Khan-Huang-Liang model [3]. The physical-based models are usually based on the thermodynamics and kinetics of dislocations, such as Zerilli-Armstrong model [4] or Voyiadjis-Abed model [5]. In recent years, machine-learning approaches have also made significant progress in the phenomenological representation of the material macroscopic responses [6].

The constitutive models are strongly nonlinear and often involve many parameters to allow high fitting potential and flexibility. Therefore, strategies for the identification of model parameters are crucial. The conventional strategy relies on some conventional tests, such as the uniaxial tensile test or bulge test, to calibrate the parameters from analytical solutions based on the assumption of homogeneous stress distribution. However, in the case of high temperature and quasi-static forming, the necking strain of certain ductile materials can be at extremely low levels [7]. Necking introduces unreliability to the parameter identification since it breaks the assumption of homogeneous stress distribution. In addition, most of the sheet metals are deformed with a heterogeneous stress field in practical production. Adopting a conventional strategy may lead to an incomplete characterization of mechanical responses for the multi-axial loading conditions [8]. An inverse identification strategy based on full-field measurements is considered as a promising

Content from this work may be used under the terms of the Creative Commons Attribution 3.0 license. Any further distribution of this work must maintain attribution to the author(s) and the title of the work, journal citation and DOI. Published under license by Materials Research Forum LLC.

alternative to overcome the drawbacks of conventional strategies [9, 10]. Avril et al. [11] presented a complete overview and comparison of five mainstream methods of this strategy. Among them, the FEMU is a very intuitive one, it can be applied to non-linear constitutive models and complex specimen shapes with heterogeneous stress fields. The principle of the FEMU is to minimize the gap between the numerical predictions and experimental measurements by iteratively updating the model parameters. The mapping relationship between the prediction and experiment can be established based on displacement, strain, force, etc. In addition, the minimization of the gap requires efficient and robust optimization algorithms, such as gradient-based algorithms (e.g., the Levenberg–Marquardt method) or metaheuristics (e.g., the genetic algorithms (GA) [12], particle swarm optimization (PSO) [13]).

For the FEMU method, the finite element (FE) model should reproduce the experiment as close as possible, including the specimen geometries, loadings, and boundary conditions. In addition, the mesh refinement of the FE model is also crucial, as it directly affects the precision and time consumption of the method. It should be noted that the computational cost is the main factor limiting the application of the FEMU method since the FE analysis is required at each iteration. Investigating the sensitivity of the FEMU method to the measurement noise is also essential. For complex experiments with heterogeneous strain and temperature fields, the full-field measurements obtained by the Digital Image Correlation (DIC) method or infrared cameras always contain data noise. Sensitivity studies allow the evaluation of possible biases in parameter identification caused by data noise.

In recent years, the combination of biaxial tensile testing with inverse identification strategies has shown great potential in characterizing the mechanical properties of metal sheets. Biaxial stretching is a special case of multi-axial loading. It can be used to identify anisotropic yield criterion parameters by achieving very heterogeneous strain and stress distributions through cruciform specimen design [14, 15], and also to determine the forming limits at various strain paths by adjusting the biaxial tensile ratios [16]. In addition, Liu et al. [17] employed a cruciform specimen and the FEMU method to identify the sheet metal hardening at large strains. The geometry of the specimen was carefully designed and the thickness reduction in the central zone permitted to reach a high level of homogeneous deformation under equi-biaxial tension. To the best of the authors' knowledge, studies combining biaxial tensile tests with inverse strategies to calibrate constitutive models that consider both temperature and rate effects are very unusual. Thus, the aim of this study is to conduct a feasibility study on the application of the FEMU method combined with biaxial tensile tests for the calibration of a thermo-viscoplastic constitutive model. A virtual experiment based on the thermal biaxial tensile test with a dedicated cruciform specimen [17] is designed and performed with a reference thermo-viscoplastic constitutive model in ABAQUS software. The advantage of the virtual experiment is that it can provide ideal full-field data for the parameters identification and the identified results can be directly validated by the reference model. This is very convenient for feasibility and sensitivity studies. In the following sections, the framework of FEMU and the details of the FE model are introduced. The effects of mesh size, plastic heat, and optimization algorithm are discussed. In addition, the robustness of the proposed inverse identification scheme is investigated by adding Gaussian noise to the force and strain data and considering the reconstruction errors of the temperature field.

Virtual biaxial tensile test

Reference thermo-viscoplastic constitutive model.

A Voce-type model [18] is used to define the temperature and strain rate-dependent plastic behavior of the virtual material with the following equations:

$$\bar{\sigma} = \sigma_0(T) + K_1 \exp(-K_2 T) \times \sqrt{1 - \exp\left[-K_3 \exp(K_4 T)\bar{\varepsilon}_p\right]} \times \dot{\varepsilon}^{m_0 \exp(m_1 T)} \quad (1)$$

$$\sigma_0(T) = \{1 - T/T_m \times \exp[K_0(1 - T_m/T)]\} \times \sigma_0(T_0) \quad (2)$$

where K_i and m_i are material parameters. K_1 defines the hardening potential of the material. The hardening potential decreases exponentially with increasing temperature, and this temperature softening effect is defined by K_2. m_0 and m_1 define the hardening effect of strain rate on flow stresses and this effect is temperature dependent. K_3 and K_4 introduce the effect of temperature on strain hardening. T is the temperature and T_m= 617°C is the melting temperature. $\dot{\varepsilon}$ is the strain rate. $\sigma_0(T)$ is the initial yield stress with consideration of temperature effect. The values of these parameters are presented in Table 1, and Fig. 1 illustrates the effect of temperature and strain rate on the flow stresses.

Table 1. Material parameters for the reference model.

Parameter	K_0	K_1 (MPa)	K_2 (1/°C)	K_3	K_4 (1/°C)	m_0	m_1 (1/°C)
Value	0.2295	334.2	0.00307	2.293	0.00633	0.00564	0.00811

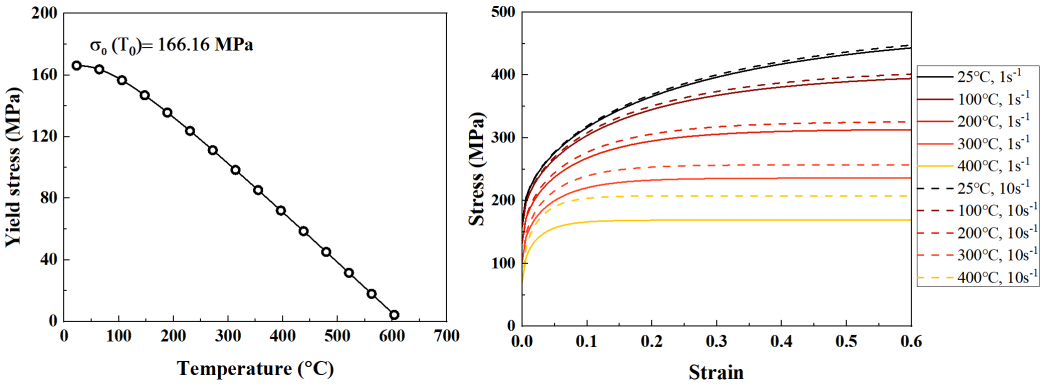

Fig. 1. Effect of temperature and strain rate on flow stresses.

FE model of the virtual biaxial tensile test

The virtual test is based on the thermal biaxial tensile test using induction heating method and employs the cruciform specimen proposed by Liu et al. [17]. The induction heating method has a faster heating rate compared to the conventional furnace heating method, and eliminates the space requirement of the furnace or insulated box and its limitation on the full-field measurements of the specimen. The heating principle works as follows: an induction coil heats a circular steel plate with a given power, and the plate heats the specimen through heat conduction and heat radiation. The top surface of the steel plate is just in contact with the specimen bottom surface and covers the specimen central area. Since an open local heating approach is adopted, the heat balance of the specimen is achieved by constant power induction heating and heat conduction to the air and grips, so the temperature distribution of specimen is non-uniform.

The virtual biaxial tensile test is modeled with the ABAQUS FE code and performed with the fully coupled temperature-displacement procedure. It consists of three stages: heating, thermal expansion, and thermal stretching. The material thermal properties (Young's modulus, Poisson's ratio, Thermal conductivity, etc.) used for the simulations are from [19], and the thermo-viscoplastic constitutive model is implemented in a UHARD subroutine. For the first stage, as shown in Fig. 2(a), the cruciform specimen is heated to the target temperature by the hot plate (in grey) positioned below the specimen and reaches thermal balance after a holding period. The plate is heated by setting a body heat flux in the central area to simulate a constant power heating situation. The bottom surface of the specimen is just in contact with the plate and the heating of the specimen is achieved by defining heat conduction and heat radiation properties between the specimen and the plate. In addition, to simulate the air heat transfer, an interaction of the surface film condition is defined to the surfaces of the specimen and plate; to simulate heat transfer in the grip regions of the specimen, surface film condition is also adopted but with a larger film coefficient. By adjusting the value of body heat flux, thermal balance can be reached in the specimen central area for different targeted temperatures (100°C, 200°C and 300°C). In the second stage, as shown in Fig. 2(b), a quarter of the specimen geometry is employed and thermal expansion of the specimen is simulated by introducing the historical temperature fields obtained from the heating stage. In the third stage, the specimens at different temperatures are equi-biaxial stretched at 0.02, 2, and 200 mm/s, respectively. For the velocity of 0.02 mm/s, the effect of plastic work on the specimen temperature is not considered. While, for the 2 and 200 mm/s cases, the simulation of the specimen temperature is based on the adiabatic condition assumption, i.e., without considering the heat transfer from the plate and air to the specimen. This is an omission of the thermal balance between the heating of the plate and the heat dissipation by the air in order to reduce the simulation time. To verify this, simulation results based on the assumption of adiabatic and isothermal conditions are compared at room temperature (RT, 23°C). The reason for choosing the RT condition is that the flow stress is higher at this temperature ensuing in a larger plastic work. As shown in Table 2, with 0.02 mm/s velocity and isothermal condition, the temperature of the specimen central element shows a slight increase. In the cases of 2 and 200 mm/s, the temperature increases significantly, but the temperatures obtained under adiabatic and isothermal conditions are approximately the same. The cruciform specimen is discretized through the eight-node brick solid elements with reduced integration (C3D8R). In order to balance simulation accuracy and computation time, mesh refinement with convergence check is performed for the specimen central area. As can be seen in Fig. 3, the equivalent strain of the specimen center element converges at a mesh size of 0.15 mm and the corresponding computation time is about 202 s (CPU processes: 8 cores, 2.2 GHz). In addition, three elements in the thickness direction are applied.

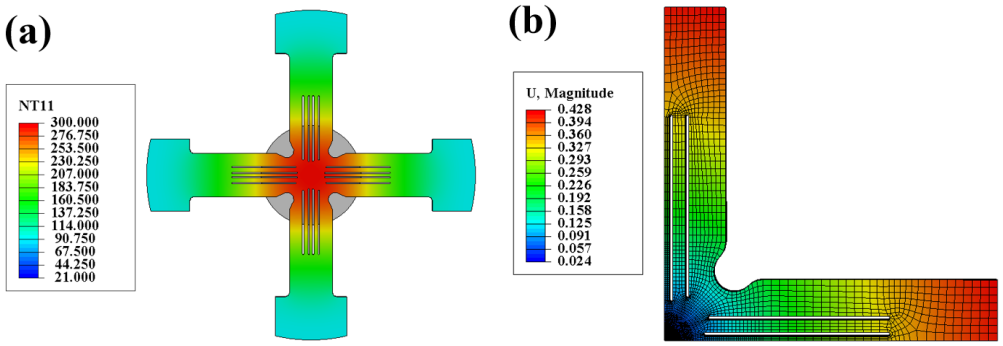

Fig. 2. (a) FE model with predicted temperature field for the heating stage (300°C), and (b) displacement field of the specimen after the thermal expansion.

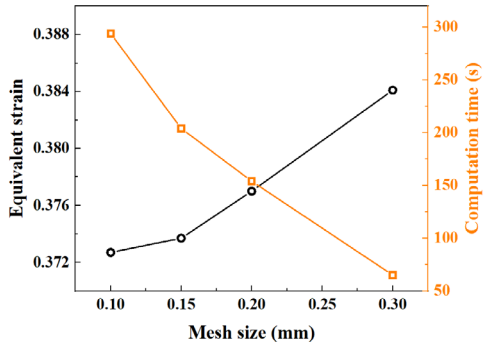

Fig. 3. Convergence analysis for the mesh refinement of the specimen central area.

Table 2. Temperature of the center element predicted based on the assumption of adiabatic and isothermal conditions.

0.02 mm/s	2 mm/s		200 mm/s	
Isothermal	Adiabatic	Isothermal	Adiabatic	Isothermal
23.1°C (Strain 0.3)	39.8°C (Strain 0.317)	39.7°C (Strain 0.317)	54.9°C (Strain 0.274)	55.4°C (Strain 0.277)

In total, the virtual biaxial tensile tests under four temperatures (RT, 100°C, 200°C, 300°C) and three tensile velocities (0.02, 2, and 200 mm/s) are performed. Afterwards, the temperature fields of the specimens, the major and minor principal strains of the center element, and the force data of the two tensile axes are extracted. These data will be used for the inverse identification procedure.

Inverse Identification Procedure Based on FEMU Method

The flowchart of the FEMU method is shown in Fig. 4. The inverse identification procedure is divided into two steps: identification of parameters K_i followed by m_i. The other material parameters (Young's modulus, Poisson's ratio, Thermal conductivity, etc.) are kept the same as in the virtual experiment. Firstly, the temperature-dependent parameters (K_i) are identified under quasi-static loading (0.02 mm/s, corresponding to an average strain rate of 0.01 s^{-1}). Then, strain rate-dependent parameters (m_i) are identified for all the considered strain rate and temperature conditions. The FEMU method is achieved by using the mode-FRONTIER software platform allowing the coupling between the FE simulation code (ABAQUS software) and optimization

algorithms. The FE models of the third stage (in section 2) with the corresponding temperature fields are imported into the procedure, while the loadings on the two tensile axes are controlled by the virtual measured forces. The tensile forces are directly influenced by temperature and strain rate-dependent flow stresses. A cost-function is used to quantify the gap in the major and minor principal strains of the specimen center element between the simulation and the virtual experiment, which can be expressed as follow:

$$Q = \frac{1}{N_T+N_R}\sum_{T,R=1}^{N_T,N_R} Q_{N_T,N_R}(p) \tag{3}$$

$$Q_{N_T,N_R}(p) = \frac{1}{N_i}\sum_{i=1}^{N_i}\left\{\sqrt{\left[\varepsilon_1^{sim}(i)-\varepsilon_1^{exp}(i)\right]^2/\left[\varepsilon_1^{exp}(i)\right]^2}+\sqrt{\left[\varepsilon_2^{sim}(i)-\varepsilon_2^{exp}(i)\right]^2/\left[\varepsilon_2^{exp}(i)\right]^2}\right\} \tag{4}$$

where p represents a set of material parameters. ε_1 and ε_2 are the major and minor principal strains, respectively. ε^{sim} and ε^{exp} are the principal strains obtained from simulation and virtual experiment, respectively. N_T is the number of temperature conditions, and N_R is the number of strain rate conditions. N_i is the total number of equally spaced time points defined in each simulation. The cost-function is calculated using a MATLAB script.

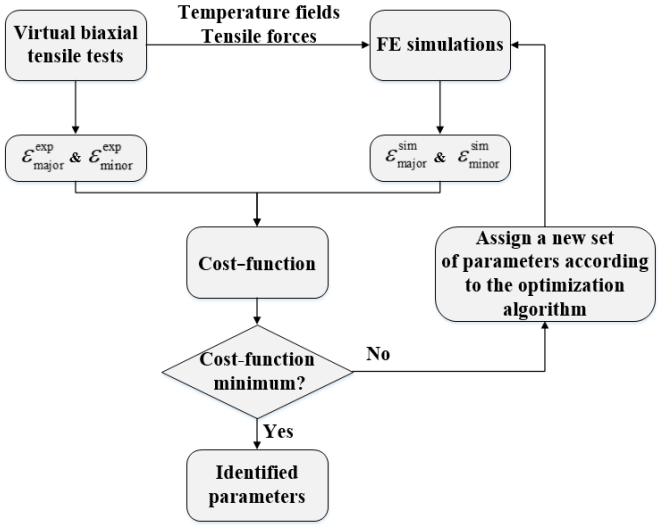

Fig. 4. Flowchart for the FEMU method.

The FEMU method minimizes the cost function by finding the optimal set of parameters, and the update iteration of the parameters is achieved by coupling an optimization method with the cost-function. In this work, a combination of PSO and SIMPLEX optimization algorithms is employed to identify the parameters K_i, while the parameters m_i are identified using only the SIMPLEX algorithm. The PSO consists of a swarm of potential solutions called particles [20]. These particles move through the search domain at a specified velocity to find the best solution. Each particle maintains a memory which helps it in keeping the track of its previous best position. In addition, the path of the particle also takes into account the global best position shared by the particle swarm. Since PSO does not use the gradient of the problem being optimized, it enables the parameters to be close to the global optimal position, but does not guarantee to find the exact value. Therefore, the SIMPLEX algorithm is employed to further determine the exact values of the parameters. For the parameters of PSO, the number of particles is 10, the inertia weight is 0.6, cognitive learning weight is 2, social learning weight is 0.5 and turbulence is 0.01. The Uniform

Latin Hypercube algorithm is adopted to define the initial set of parameters for each particle, which allows for a regular equally spaced over the parameter ranges. For the identification of K_i, 1400 iterations are performed using PSO and 266 iterations are performed by SIMPLEX. Table 3 lists the parameter ranges, the identified parameter values and the relative errors with respect to the reference values. It could be found that the PSO locates the approximate values of the parameters within a large parameter range. Based on this, the ranges of parameters are reduced and then the exact values of the parameters are obtained by the SIMPLEX. For the identification of parameters m_0 and m_1, 12 FE simulations are required for each iterative cycle, which implies a huge computational time. Therefore, only the SIMPLEX algorithm is used for the identification of m_i, considering that it is an efficient algorithm with a fast convergence rate. For the identification of m_i, 60 iterations are performed. Overall, the relative errors of the identified parameters are at a low level, which proves the feasibility of the proposed inverse identification procedure.

Table 3. Identified parameters of the constitutive model.

	Parameter	PSO			SIMPLEX		
		Range	Identified value	Error	Range	Identified value	Error
Step 1	K_0 (MPa)	[0.1, 0.4]	0.252	9.9%	[0.2, 0.3]	0.2267	1.2%
	K_1	[200, 400]	340.7	1.9%	[300, 350]	333.4	0.23%
	K_2 (1/°C)	[0.001, 0.005]	0.00316	2.9%	[0.002, 0.004]	0.00306	0.32%
	K_3	[1, 5]	2.199	4.1%	[2, 4.5]	2.299	0.26%
	K_4 (1/°C)	[0.001, 0.1]	0.00626	1.1%	[0.003, 0.008]	0.00633	0%
Step 2	m_0				[0.001, 0.009]	0.00544	3.5%
	m_1 (1/°C)				[0.005, 0.01]	0.00821	1.2%

Sensitivity analysis

In Section 3, the parameters of the constitutive model are accurately identified based on the tensile forces, principal strains, and temperature fields obtained from the virtual tests. However, noises are inevitable when physical measurements are done. Therefore, in this section, the effects of measurement noises are evaluated. A comparison study is performed with and without noise using the simulation of thermal biaxial tensile test under a temperature of 300°C and a tensile velocity of 200 mm/s. White Gaussian noises are added to the tensile force data of the two tensile axes, and the disrupted force is given by $\tilde{F}(t) = F(t) + n(0, s)F_{max}$. Where $n(0,s)$ is a normal (Gaussian) distribution with zero mean and standard deviation s, F_{max} is the maximum value of the force. As shown in Fig. 5(a), two levels of noise (s = 0.005 and s = 0.01) are tested. The relative error of the principal strains between the simulations with and without noise is also shown in this figure. It can be found that the significant increase in the relative error occurs at the decrease of the tensile force, which usually means the occurrence of necking. While, during the uniform deformation stage, both levels of noise bring weak influence on the principal strains of the specimen center element. Therefore, identification using the test data before the occurrence of necking seems to be effective.

During the test, factors such as the offset of the heat source location and suboptimal contact can cause asymmetric distribution and shift of the specimen temperature field. Although the temperature field can be measured by an infrared thermal camera, the temperature field reconstruction in the FE simulation inevitably contains errors. To evaluate the influence of temperature field reconstruction errors, the center of the originally symmetrically distributed temperature field in the simulation is shifted so that the highest temperature is moved from the original center of the specimen to 5 mm off-center, and the temperature of the center point is

decreased from 300 °C to 290 °C. The tensile forces of the two tensile axes are then compared, and the results are shown in Fig. 5(b). It can be seen that the deviation of the force curve appears at the beginning of the necking stage. This indicates that the temperature field reproduced in the FE model should refer to the experimentally measured results and the data from the force decrease stage should be avoided for parameter identification.

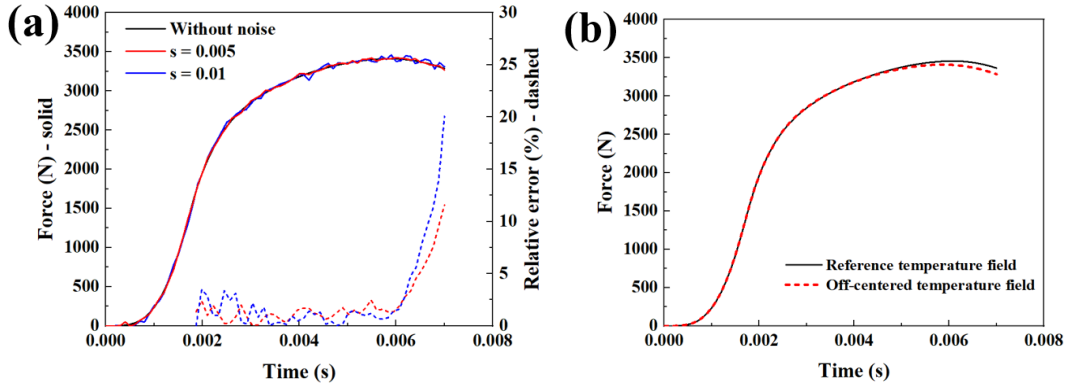

Fig. 5. (a) Tensile force (acquisition rate 10000Hz) with and without gaussian noise, and the relative error of the principal strains between the cases with and without noise. (b) Tensile force predicted with reference temperature field and off-centered temperature field.

In order to evaluate the effect of strain noise, white Gaussian noises (n = 0,0.1) are added to the principal strain data, then the identification of parameters K_i is performed based on the procedure introduced in section 3. The identified values of K_i with the corresponding errors are given in Table 4, and a comparison between the flow stresses of reference model and the identified model is given in Fig. 6. The result indicates that K_0 exhibits a significant sensitivity to the strain noise. K_0 is the parameter that determines the temperature-dependent initial yield stress, so the principal strain data from the initial deformation stage are dominant for its identification. The added Gaussian noise is multiplied by the maximum value of strain, which makes the magnitude order of the noise excessive for the strain of the initial stage. This can be the reason for the large error in K_0 identification. From Fig. 6, the flow stress of the identification model is in good agreement with that of the reference model, therefore the proposed inverse identification process is considered to have good robustness to the strain noise.

Table 4. Identified parameters K_i based on the strain data with Gaussian noise.

Parameter	K_0	K_1 (MPa)	K_2 (1/°C)	K_3	K_4 (1/°C)
Identified value	0.2804	341.8	0.00323	2.196	0.00617
Error	22.1%	2.2%	5.2%	4.2%	2.5%

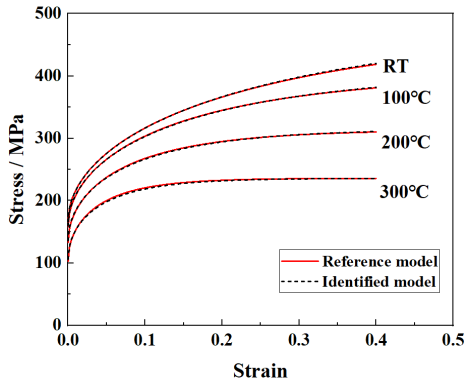

Fig. 6. Comparison of flow stresses between the reference model and the identified model.

Summary

In this work, the feasibility of the proposed inverse identification strategy for identifying the thermo-viscoplastic constitutive model is analyzed. A virtual biaxial tensile test is designed and used to supply information for the constitutive model parameters identification. The main conclusions are as follow:

- The proposed inverse identification strategy is based on the FEMU method with biaxial tensile test. The parameters K_i and m_i are accurately identified based on the force, temperature and strain data obtained from the virtual tests.
- The PSO algorithm is used to track the approximate values of the parameters and reduce the ranges of parameters, then the exact values of the parameters are obtained by the SIMPLEX algorithm.
- Sensitivity study shows that using force and temperature data before the occurrence of necking is preferable in order to reduce the effect of data noise. The identification of the parameter K_0 is sensitive to strain noise. The proposed inverse identification strategy exhibits a sufficient robustness to strain noise.

References

[1] R. Zarea, J. Fernández-Sáez, An implicit consistent algorithm for the integration of thermoviscoplastic constitutive equations in adiabatic conditions and finite deformations, Int. J. Solid. Struct. 43 (2006) 1594-1612. https://doi.org/10.1016/j.ijsolstr.2005.03.070

[2] G.R. Johnson, W.H. Cook, A constitutive model and data for metals subjected to large strains, high strain rates and high temperatures, In Proceedings of the 7th International Symposium on Ballistics, The Hague, The Netherlands, 19–21 April 1983, pp. 541-547.

[3] A.S. Khan, Y.S. Suh, R. Kazmi, Quasi-static and dynamic loading responses and constitutive modeling of titanium alloys, Int. J. Plast. 20 (2004) 2233-2248. https://doi.org/10.1016/j.ijplas.2003.06.005

[4] F.J. Zerilli, R.W. Armstrong, Dislocation-mechanics based constitutive relations for material dynamics calculations, J. Appl. Phys. 61 (1987) 1816-1825.

[5] G.Z. Voyiadjis, F.H. Abed, Microstructural based models for bcc and fcc metals with temperature and strain rate dependency, Mech. Mater. 37 (2005) 355-378. http://doi.org/10.1016/j.mechmat.2004.02.003

[6] X. Li, C.C. Roth, C. Bonatti, D. Mohr, Counterexample-trained neural network model of rate and temperature dependent hardening with dynamic strain aging, Int. J. Plast. 151 (2022) 103218. https://doi.org/10.1016/j.ijplas.2022.103218

[7] H. Shang, P. Wu, Y. Lou, J. Wang, Q. Chen, Machine learning-based modeling of the coupling effect of strain rate and temperature on strain hardening for 5182-O aluminum alloy, J. Mater. Process. Tech. 302 (2022) 117501. https://doi.org/10.1016/j.jmatprotec.2022.117501

[8] J.M.P. Martins, A. Andrade-Campos, S. Thuillier, Comparison of inverse identification strategies for constitutive mechanical models using full-field measurements, Int. J. Mech. Sci. 145 (2018) 330-345. https://doi.org/10.1016/j.ijmecsci.2018.07.013

[9] Z. Wang, S. Zang, X. Chu, S. Zhang, L. Leotoing, Identification of 7B04 aluminum alloy anisotropy yield criteria with conventional test and Pottier test at elevated temperature, Results. Phys. 15 (2019) 102655. https://doi.org/10.1016/j.rinp.2019.102655

[10] P. Prates, A. Pereira, N. Sakharova, M. Oliveira, J Fernandes, Inverse strategies for identifying the parameters of constitutive laws of metal sheets, Adv. Mater. Sci. Eng. 2016 (2016) 1-18. https://doi.org/10.1155/2016/4152963

[11] S. Avril, F. Pierron, Y. Pannier, R. Rotinat, Stress reconstruction and constitutive parameter identification in plane-stress elasto-plastic problems using surface measurements of deformation fields, Exp. Mech. 48 (2008) 403-419. https://doi.org/10.1007/s11340-007-9084-2
[12] J.H. Holland, Adaptation in natural and artificial systems: an introductory analysis with applications to biology, control, and artificial intelligence, Ann. Arbor., MI, University of Michigan Press.
[13] J. Kennedy, R.C. Eberhart, Particle Swarm Optimization, in: Proceedings of the IEEE International Conference on Neural Networks, Piscataway, vol. IV, 1995, pp. 1942-1948.
[14] P.A. Prates, M.C. Oliveira, J.V. Fernandes, A new strategy for the simultaneous identification of constitutive laws parameters of metal sheets using a single test, Comp. Mater. Sci. 84 (2014) 102-120. http://doi.org/10.13140/RG.2.2.25692.80004
[15] S. Zhang, L. Leotoing, D. Guines, S. Thuillier, S. Zang, Calibration of anisotropic yield criterion with conventional tests or biaxial test, Int. J. Mech. Sci. 85 (2014) 142-151. https://doi.org/10.1016/j.ijmecsci.2014.05.020
[16] Z. Wang, D. Guines, X. Chu, L. Leotoing, Characterization of forming limits at fracture from shear to plane strain with a dedicated cruciform specimen, Int. J. Mater. Form. 7 (2022) 15. http://doi.org/10.1007/s12289-022-01658-8
[17] W. Liu, D. Guines, L. Leotoing, E. Ragneau, Identification of sheet metal hardening for large strains with an in-plane biaxial tensile test and a dedicated cross specimen, Int. J. Mech. Sci. 101-102 (2015) 387-398. https://doi.org/10.1016/j.ijmecsci.2015.08.022
[18] J. Liang, D. Guines, L. Leotoing, Effect of temperature and strain rate on the plastic anisotropic behavior characterized by a single biaxial tensile test, Procedia Manuf. 47 (2020) 1532-1539. https://doi.org/10.1016/j.promfg.2020.04.346
[19] J. Gao, Y. Cao, L. Lu, Z. Hu, K. Wang, F. Guo, Y. Yan, Study on the interaction between nanosecond laser and 6061 aluminum alloy considering temperature dependence, J. Alloy. Compd. 892 (2022) 162044. https://doi.org/10.1016/j.jallcom.2021.162044
[20] A.G. Gad, Particle Swarm Optimization Algorithm and Its Applications: A Systematic Review, Arch. Computat. Meth. Eng. 29 (2022) 2531-2561. http://doi.org/10.1007/s11831-021-09694-4

Materials Research Proceedings 28 (2023) 1407-1416 https://doi.org/10.21741/9781644902479-152

Extension of the modified Mohr-Coulomb fracture model by a strain rate and temperature dependence

VASQUEZ RAMIREZ Dominyka[1,a *], WESTER Hendrik[1,b], ROSENBUSCH Daniel[1,c] and BEHRENS Bernd-Arno[1,d]

[1]Gottfried Wilhelm Leibniz Universität, Institute of Forming Technology and Machines, An der Universität 2, 30823 Garbsen, Germany

[a]vasquezramirez@ifum.uni-hannover.de, [b]wester@ifum.uni-hannover.de, [c]rosenbusch@ifum.uni-hannover.de, [d]behrens@ifum.uni-hannover.de

Keywords: Fracture Characterisation, MMC Fracture Model, Dual-Phase Steel

Abstract. During industrial sheet metal processes such as shear cutting, high temperatures and strain rates occur. Due to materials dependency on temperature and strain rate, the numerical fracture modelling should consider these both highly influential factors for accurate simulation results. Since the widely used Modified Mohr-Coulomb (MMC) fracture model does not take the dependency on temperature and strain rate into account, the objective of this research is therefore to extend the MMC fracture model. For the fracture characterization, miniaturised tensile tests under variation of specimen geometry, temperature and strain rate are conducted. Additionally, tensile tests with butterfly specimens under varying stress states are carried out. In order to determine material specific MMC parameters, the experimental tests are numerically depicted in Abaqus. The temperature and strain rate extension of the MMC fracture model is based on the Johnson-Cook failure model. With this approach, a temperature and strain-rate dependent MMC fracture model is developed for the dual phase steel DP980.

Introduction

Any sheet metal procedure, whether it is cutting or forming, begins with a suitable process design to describe materials forming behaviour under specific process conditions [1]. A cost- and time-efficient possibility for such investigations is the Finite Element (FE) method, which is built upon a specific material model [2]. Based on a thorough material investigation, it is possible to predict material fracture depending on stress or strain in a specific process using FE [3]. This research therefore covers an extension of a fracture model regarding temperature and strain rate on a DP980 sheet metal. For this purpose, Modified Mohr-Coulomb (MMC) fracture model was extended with Johnson-Cook (J-C) [4] strain rate hardening and thermal softening effect terms using experimental results from various tensile tests that cover a specific stress, temperature and strain rate field.

The Mohr-Coulomb (MC) fracture model combines the normal stresses σ_1, σ_2 and σ_3 to calculate material failure in dependence on friction coefficient c_1 and shear resistance c_2 [5]:

$$c_2 = max\left\{\frac{1}{2}|\sigma_1 - \sigma_2| + c_1(\sigma_1 + \sigma_2), \frac{1}{2}|\sigma_2 - \sigma_3| + c_1(\sigma_2 + \sigma_3), \frac{1}{2}|\sigma_3 - \sigma_1| + c_1(\sigma_3 + \sigma_1)\right\} \quad (1)$$

In [5] it was also shown that the normal stresses can be given as a function of mean stress σ_m, stress triaxiality η and normalised Lode angle $\bar{\theta}$. Subsequently, the MC model can be represented as a function of the equivalent stress $\bar{\sigma}$, η and $\bar{\theta}$. However, the model only describes failure in a stress based space, which is not accurate when modelling materials fracture. Nonetheless, the transformation of the equation from a solely stress based into a stress and strain based space under condition of monotonic loading allowed to define the MMC failure model in terms of equivalent plastic strain at fracture $\bar{\varepsilon}_\mathrm{p}^\mathrm{f}$ [6]. Therefore, with A and n as strength and work hardening exponents

Content from this work may be used under the terms of the Creative Commons Attribution 3.0 license. Any further distribution of this work must maintain attribution to the author(s) and the title of the work, journal citation and DOI. Published under license by Materials Research Forum LLC.

Materials Research Proceedings 28 (2023) 1407-1416 https://doi.org/10.21741/9781644902479-152

of the Swift hardening law, respectively, as well as c_3 as a material constant, the MMC failure model is defined as follows [7]:

$$\bar{\varepsilon}_{\mathrm{p}}^{\mathrm{f}} = \left\{\frac{A}{c_2}\left[c_3 + \frac{\sqrt{3}}{2-\sqrt{3}}(1-c_3)\left(\sec\left(\frac{\bar{\theta}\pi}{6}\right)-1\right)\right]\left[\sqrt{\frac{1+c_1^2}{3}}\cos\left(\frac{\bar{\theta}\pi}{6}\right)+c_1\left(\eta+\frac{1}{3}\sin\left(\frac{\bar{\theta}\pi}{6}\right)\right)\right]\right\}^{-\frac{1}{n}} \quad (2)$$

However, the MMC fracture model does not directly take the temperature nor the strain rate into account. In [6] it was shown, that DP980 changes its characteristics when exposed to higher temperatures. For this reason, in [6] it was investigated whether the temperature influence reflects on the MMC fracture model. As a result, it was depicted that the MMC fracture model and its parameters are highly dependent on materials behaviour under increasing temperatures. Another investigation was conducted in [8] on a DP590 steel, where the strain rate influence on the Hosford-Coulomb fracture model was demonstrated. These examples conclude, that a varying material behaviour, influenced by temperature and strain rate, is an important factor when parametrising a fracture model and should therefore be taken into account for accurate modelling.

An exemplary solution was proposed in [9], where a failure model DF2014 was successfully extended using the strain rate hardening and thermal softening effect terms of the J-C failure model for a AA7075 sheet material. Similar approach is applied in this research as well by using the MMC fracture model as the basis with an extension by the strain rate and thermal effect terms of the J-C failure model to define the following equation:

$$\bar{\varepsilon}_{\mathrm{p}}^{\mathrm{f}} = \left\{\frac{A}{c_2}\left[c_3 + \frac{\sqrt{3}}{2-\sqrt{3}}(1-c_3)\left(\sec\left(\frac{\bar{\theta}\pi}{6}\right)-1\right)\right]\left[\sqrt{\frac{1+c_1^2}{3}}\cos\left(\frac{\bar{\theta}\pi}{6}\right)+c_1\left(\eta+\frac{1}{3}\sin\left(\frac{\bar{\theta}\pi}{6}\right)\right)\right]\right\}^{-\frac{1}{n}} \cdot \left[1 + d_1\left(\frac{T-T_{ref}}{T_{melt}-T_{ref}}\right)\right]\left[1 + d_2 ln\left(\frac{\dot{\bar{\varepsilon}}^{pl}}{\dot{\varepsilon}_0}\right)\right] \quad (3)$$

With d_1 and d_2 indicated as material parameters, T as current temperature, T_{ref} as reference temperature of 20°C, T_{melt} as melting point of the material at 1520°C [10], $\dot{\bar{\varepsilon}}^{pl}$ as equivalent plastic strain and $\dot{\varepsilon}_0$ as refence strain rate at 0.001 1/s. For the determination of the individual temperature and strain rate dependent material parameters, such as plastic strain at fracture, normalised Lode angle and stress triaxiality, various material characterization tests and subsequent simulations with Abaqus are carried out, which are presented in the next chapters.

Experimental Tests

Miniaturised tensile tests. Miniaturised specimens of three different geometries were used to conduct isothermal tensile tests at various temperatures on a quenching and forming dilatometer DIL 805A/D+T. Additionally, an optical measurement system Aramis was applied to correctly indicate the length change at fracture by means of digital image correlation (DIC). The schematic setup of the dilatometer and its corresponding components is presented in [6]. A uniaxial and two notched specimen geometries with a radius of 3 and 10 mm were chosen as miniaturised tensile specimens, which are shown in Fig. 1 (a). Geometry variation during the miniaturised tensile tests served to induce different stress states on the material in order to cover various stress triaxiality and normalised Lode angle values. The tensile tests were conducted at temperatures between 20 and 600 °C, while the strain rate was held constant at 0.001 s^{-1}.

Tensile tests on butterfly specimens. The butterfly specimen, shown in Fig. 1 (b), was tested under different loading angles in an interval of 15.5°, as shown in Fig. 1 (c), thus varying the stress state from shear to uniaxial tension. Five loading angles were tested at 20°C with a constant forming speed of 0.001 1/s. The tests were conducted on a tensile testing machine S100/ZD with an optical measurement system Aramis to track the displacement in x and y direction. A stochastic pattern was applied on both miniaturised and butterfly tensile specimens for the DIC

measurements. A more detailed setup of the butterfly tensile testing equipment and its corresponding components is presented in [2] and [11].

High speed tensile tests. The high speed uniaxial tensile tests were conducted on a high speed tearing machine SZM500 with the specimen geometry shown in Fig. 1 (d). The deformation was recorded by means of a high speed camera and subsequently evaluated using greyscale correlation. Strain gauges were applied due to the expected high vibrations caused by the high strain rates. The testing temperature was held constant at 20 °C, whereas the strain rate variated between 100, 500 and 1000 1/s to cover a wide range of strain rates that occur in various sheet metal processes, e.g. in shear cutting. The sheet metal thickness of the DP980 material used was 1 mm for each test.

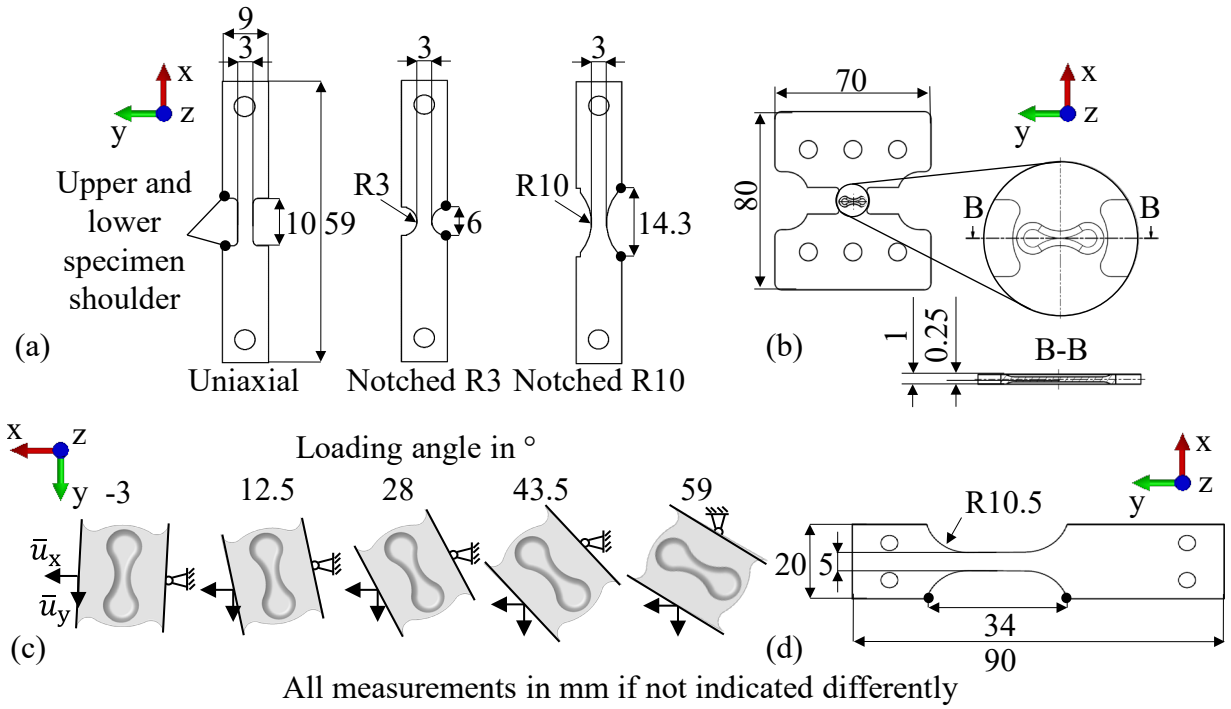

Fig. 1. Miniaturised tensile specimens (a), butterfly specimen (b), loading angles of butterfly tensile tests (c) and high speed tensile specimen (d).

Numerical Modelling

Each of the conducted experimental tests were simulated in Abaqus/implicit to determine the parameters of the extended MMC fracture model. For this purpose, temperature and strain rate dependent flow curves were modelled using uniaxial tensile test results of miniaturised and high speed specimens. Then, the acquired flow curves were extrapolated via a combined approach of Swift [12] and Voce [13] with k_{Comb} as flow stress, ε as plastic strain, ε_0 as starting plastic strain, σ_0 as yield stress, σ_s and E as material parameters and α as a weighting factor of 0.7, which was determined using the least squares method:

$$k_{\mathrm{Comb}}(\varepsilon) = \alpha \cdot A(\varepsilon_0 + \varepsilon)^n + (1-\alpha)(\sigma_S + (\sigma_0 - \sigma_S))e^{\left(-\frac{\varepsilon}{E}\right)} \quad (4)$$

Anisotropic parameters, determined experimentally using miniaturised uniaxial tensile tests on specimens produced in 0°, 45° and 90° to rolling direction, were calculated using Hill'48 approach and implemented as R_{11}, R_{22}, R_{33}, R_{12}, R_{13} and R_{23} variables in the numerical calculation. Moreover, time-displacement curves of each experimental test were determined and applied as an amplitude input in the numerical simulation with the exception of the butterfly tests, where the time-displacement curves in x and y direction were used as displacement boundary condition. In

the numerical simulation of the experimental tests, one end of the specimen was always fixed, while the other was exposed under translatory motion according to the amplitude. During the simulation of the butterfly tests, fracture was indicated when the maximum displacement in x and y directions was reached. For the miniaturised and high speed tensile tests, the length change was measured between the upper and lower specimen shoulder, exemplary shown in Fig. 1 (a) and (d), until the length change at fracture from experiments was reached, thus indicating fracture.

Solid eight node elements type C3D8R were used for the simulations with an element edge length of 0.1 mm and an application of symmetries on miniaturised and high speed tensile specimens both in y and z directions. Symmetry in the z direction was used for butterfly tensile specimens. Direct method was applied as a solver with a full Newton solution technique. Equivalent plastic strain at fracture $\overline{\varepsilon_{\mathrm{p}}^{\mathrm{f}}}$, stress triaxiality η and normalised Lode angle $\bar{\theta}$ were determined for each simulated test. Since the stress state varied during the deformation, integral calculation of η and $\bar{\theta}$ over the plastic strain at fracture was carried out to determine the average stress triaxiality η_{av} and average normalised Lode angle $\overline{\theta_{av}}$ [7]:

$$\eta_{\mathrm{av}} = \frac{1}{\varepsilon_{\mathrm{p}}^{\mathrm{f}}} \int_0^{\varepsilon_{\mathrm{p}}^{\mathrm{f}}} \eta(\varepsilon_{\mathrm{p}}) d\varepsilon_{\mathrm{p}} \qquad \overline{\theta_{av}} = \frac{1}{\varepsilon_{\mathrm{p}}^{\mathrm{f}}} \int_0^{\varepsilon_{\mathrm{p}}^{\mathrm{f}}} \theta(\varepsilon_{\mathrm{p}}) d\varepsilon_{\mathrm{p}} \tag{5}$$

The aforementioned tensile simulations were conducted for each specimen geometry, temperature and strain rate to determine the parameters of the extended MMC fracture model, given in Eq. 3. For this reason, experimental tests at 20°C and 0.001 1/s with subsequent numerical results were used to determine parameters c_1, c_2 and c_3, shown in Eq. 2. Miniaturised and butterfly tensile test results were applied for this purpose. Subsequently, results from miniaturised tensile tests between 100 and 600°C at 0.001 1/s were used to determine material constant d_1 of the temperature extension term. A similar approach was applied to determine material constant d_2 of the strain rate extension term using miniaturised uniaxial and high speed tensile test results at 20 °C, which were conducted at strain rates between 0.001 and 1000 1/s. Parameters A, n, c_1, c_2 and c_3 were held constant during the determination of d_1 and d_2.

Results and Discussions

Tensile test results. Experimental test results from miniaturised uniaxial and high speed tensile tests are shown in Fig. 2 in form of extrapolated flow curves using the aforementioned approach in Eq. 4. Fig. 2 (a) shows flow curves at 0.001 1/s of the miniaturised uniaxial specimens at all considered temperatures, whereas Fig. 2 (b) illustrates flow curves at various strain rates of the uniaxial specimens at 20°C. An interesting phenomenon can be pointed out in Fig. 2 (a), which is the so called blue-brittleness [6]. It indicates, that at specific temperatures materials strength does not decrease with increasing temperature due to foreign atom diffusion at dislocations. Therefore, the flow curve behaviour between 20 and 300 °C barely deviates from each other. Starting at 400 °C, however, materials thermal softening overcomes the blue-brittleness effect, resulting in a strong decrease of flow stress with increasing temperature. The strain rate influence, shown in Fig. 2 (b), portrays an interesting behaviour as well in which the flow stress at 0.001 and 100 1/s as well as at 500 and 1000 1/s begins with a similar yield stress. However, with an increasing plastic strain, the flow curve at a higher strain rate overcomes the one at a lower strain rate. This is due to the logarithmic dependence of the yield stress on the strain rate, in which only small differences are observed regarding the yield stress within the quasi-static and medium strain rates of 0.001 and 100 1/s as well as between the dynamic strain rates of 500 and 1000 1/s [14]. The logarithmic strain rate dependence is therefore the reason for the yield stress leap between the strain rates of 0.001 - 100 1/s and 500 - 1000 1/s. Moreover, dual phase steels have been proven to have a low strain rate sensitivity in regard of yield stress [15]. The portrayed flow curves were implemented

in the numerical simulation of each tensile geometry for the corresponding temperature and strain rate, including the ones of the notched and butterfly tensile specimens.

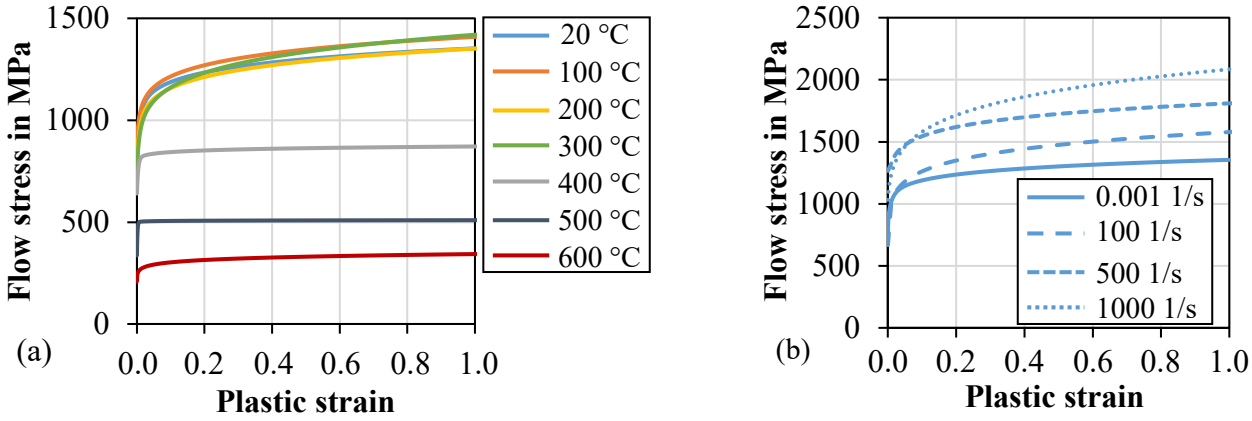

Fig. 2. Extrapolated flow curves of uniaxial tensile tests: at 0.001 1/s varying the forming temperature (a) and at 20 °C varying the strain rate (b).

Numerical results. Each numerically depicted tensile test was verified by comparing force-displacement curves with the experimentally determined results. This verification approach is exemplary shown in Fig. 3, illustrating a comparison of the numerically and experimentally determined force-displacement curves of the miniaturised uniaxial tensile tests for all temperatures at 0.001 1/s. For a better visualisation, the force-displacement curves are split into (a) and (b).

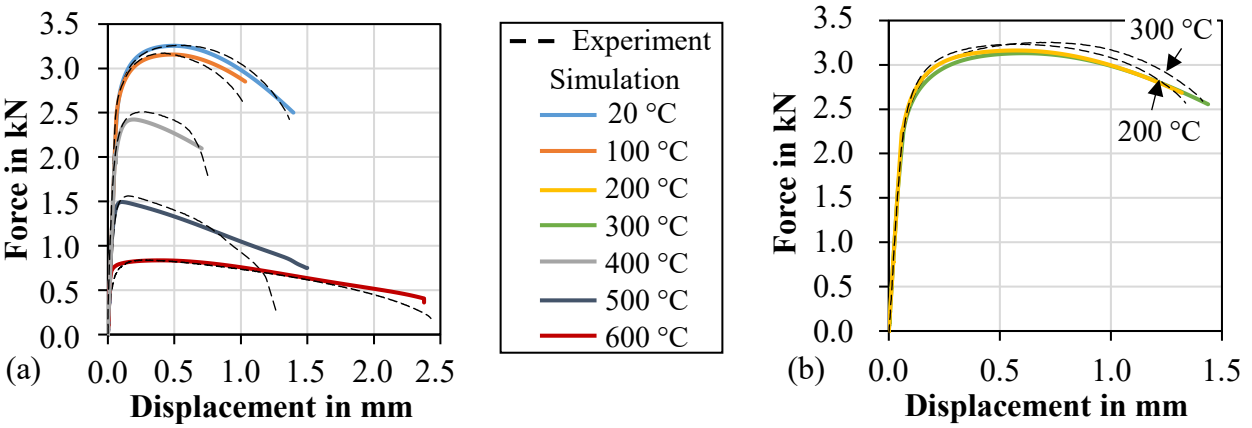

Fig. 3. Verification of numerically determined force-displacement curves with experimental results of miniaturised uniaxial tensile tests at 20, 100, 400 - 600 °C (a) and at 200 - 300 °C (b).

Overall, good agreement was observed. The force-displacement curves at 400 and 500°C show the largest deviation between the numerical and experimental results, in particularly after reaching maximal tensile strength. This is due to the fact that no damage was taken into account when simulating the tensile tests. Damage consideration serves for a better depiction of material softening when localized necking occurs, since it takes the effect of decreased loading capacity caused by defect structure development into account [16]. Moreover, in Fig. 3 the blue-brittleness effect can be depicted once more, in particularly between 20 and 200°C regarding both the maximal force and maximal displacement. The blue-brittleness effect was mainly observed in the miniaturised uniaxial specimens and not in the notched specimens.

Finally, the verified numerical results from each tensile test were used to determine the extended MMC fracture model parameters. Fig. 4 shows exemplary curves of plastic strain as a function of

stress triaxiality (a) and normalised Lode angle (b) for all tensile specimens at 20°C and 0.001 1/s. As mentioned in the introduction, stress triaxiality and normalised Lode angle change over the course of plastic strain, which is particularly visible on the miniaturised tensile specimens. For this reason, Eq. 5 is used to calculate the average values of η_{av} and $\overline{\theta_{av}}$. A stress triaxiality ranging from -0.1 to 0.99 and a normalised Lode angle between -0.04 and 0.5 were covered at 20°C and 0.001 1/s, while reaching a plastic strain of fracture up to 0.75.

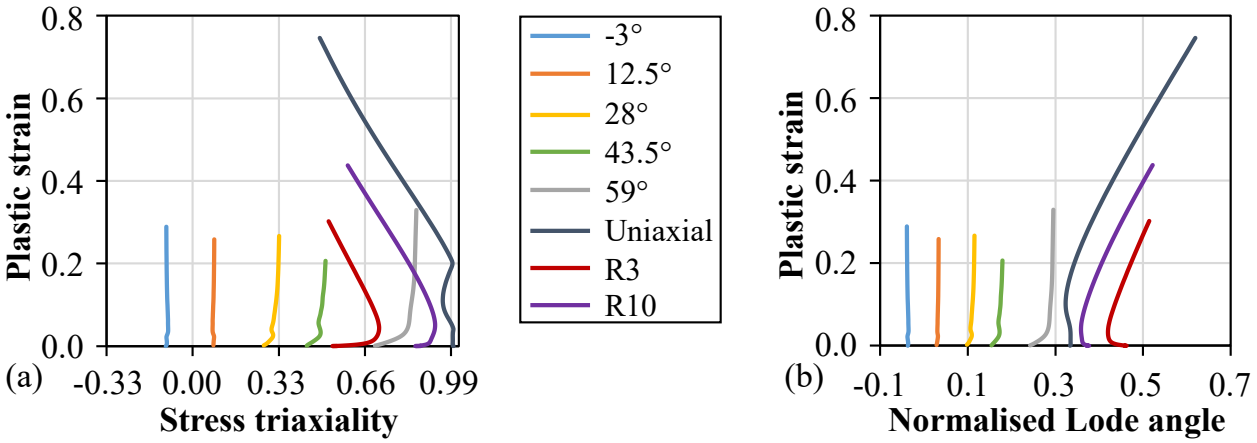

Fig. 4. Plastic strain over stress triaxiality (a) and plastic strain over normalised Lode angle (b) for all tensile specimens at 20°C and 0.001 1/s.

Fig. 5 (a) shows average normalised Lode angle over average stress triaxiality of the tested specimens between 20 and 600°C at 0.001 1/s. The black lines in Fig. 5 indicate the two-dimensional plane strain and plane stress states which occur in sheet metal forming. Fig. 5 (b) serves for a better illustration of η_{av} and $\overline{\theta_{av}}$ at a temperature field of 20 - 300°C. Here, blue-brittleness effect can be depicted again, in which the average values of stress triaxiality for uniaxial specimen are lower in the field of 100 - 300°C than at 20°C.

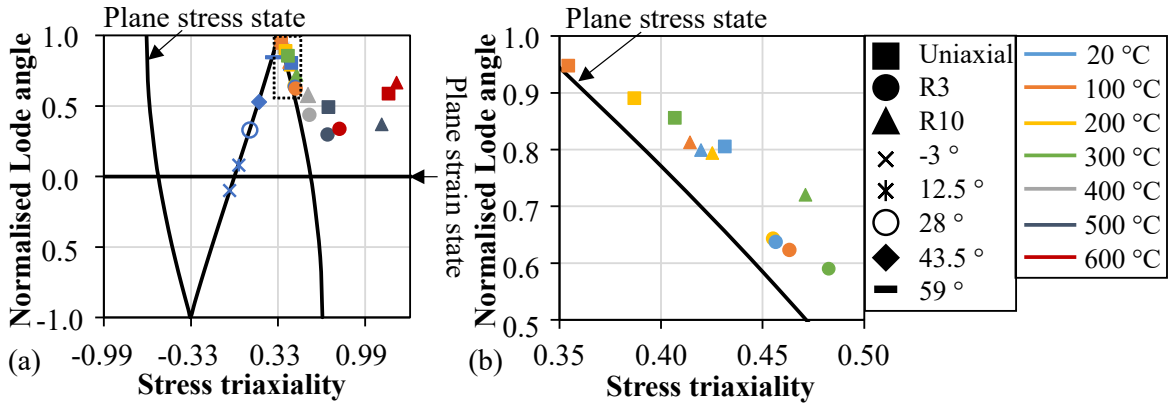

Fig. 5. Normalised Lode angle over stress triaxiality of miniaturised and butterfly tensile specimens at all temperatures at 0.001 1/s (a), a detailed illustration of $\overline{\theta_{av}}$ over η_{av} at temperatures 20 - 300 °C (b).

Similar diagrams of normalised Lode angle over stress triaxiality were generated for high speed tensile tests at 20°C. Subsequently, the abovementioned results were used to parametrise the MMC failure model and to determine the temperature and strain rate extension terms.

MMC failure surfaces. At first, the numerical results were used to parametrise c_1, c_2 and c_3 of the MMC fracture model at 20°C and 0.001 1/s. For this purpose, the results of the tensile tests on miniaturised and butterfly specimens at 20°C and 0.001 1/s were used, specifically the ascertained

plastic strain at fracture, average stress triaxiality and average normalised Lode angle. The parameters c_1, c_2 and c_3 were fitted to the experimental results of the miniaturised and butterfly tensile tests by the least square method. The resulting fracture surface is shown in Fig. 6 a). In Fig. 6 b), the fitted plastic strain at fracture is shown as a function of stress triaxiality in a plane stress state, together with the experimentally determined values.

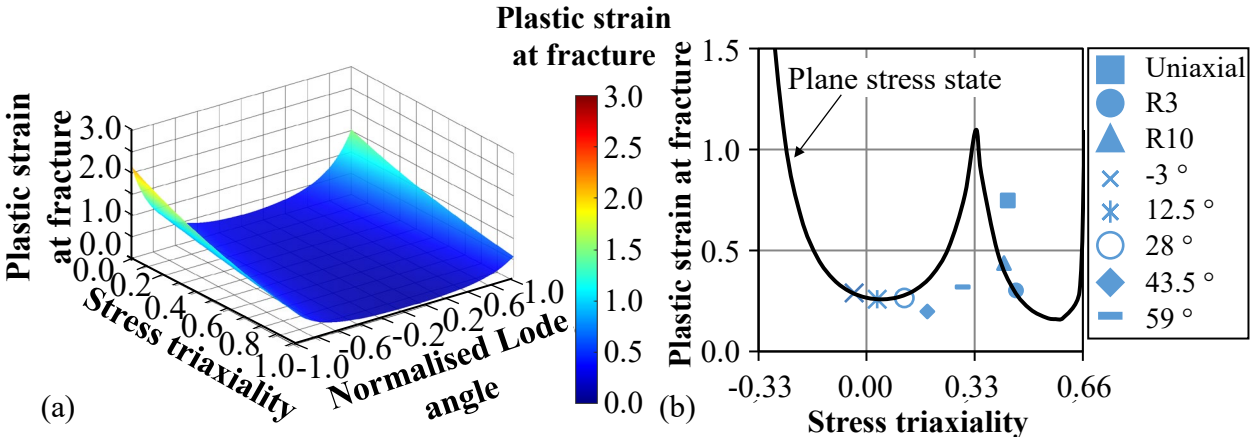

Fig. 6. MMC failure surface at 20 °C and 0.001 1/s (a), plastic strain at fracture over stress triaxiality of miniaturised and butterfly tensile tests at 20 °C and 0.001 1/s in a plane stress state (b).

Subsequently, the parametrisation of the temperature term d_1 was carried out, using the miniaturised tensile tests at various temperatures. As mentioned above, DP980 sheet material shows a non-typical steel behaviour called blue-brittleness in a temperature range of 20 - 300°C. For this reason, the parameter d_1 was determined for two different temperature fields: 20 - 300°C and 400 - 600°C, while the parameters A, n, c_1, c_2 and c_3 were held constant. The failure surfaces of the MMC fracture model, extended by the temperature term d_1, are shown in Fig. 7 (a) for the temperature field of 20 - 300°C and in Fig. 7 (b) for the temperature field of 400 - 600°C, both at 0.001 1/s. It can be clearly seen, that the rising temperature increases the plastic strain at fracture. Lastly, the parametrisation of the strain-rate factor d_2 was carried out using miniaturised uniaxial and high speed tensile tests at 20°C, while the parameters A, n, c_1, c_2, c_3 and d_1 were held constant. The acquired MMC failure surfaces of the extended equation are shown in Fig. 7 (c) for 20°C. The built failure surfaces clearly indicate, that an increasing strain rate decreases the plastic strain at fracture.

It can be therefore concluded, that it is possible to consider the strain rate and temperature dependant material behaviour by implementing the strain rate hardening and thermal softening effect terms directly in the MMC fracture model. Such parametrised equation can be furtherly used to execute numerical simulations of various sheet metal forming processes, such as shear cutting, to correctly predict material failure while taking strain rate and temperature influence into account.

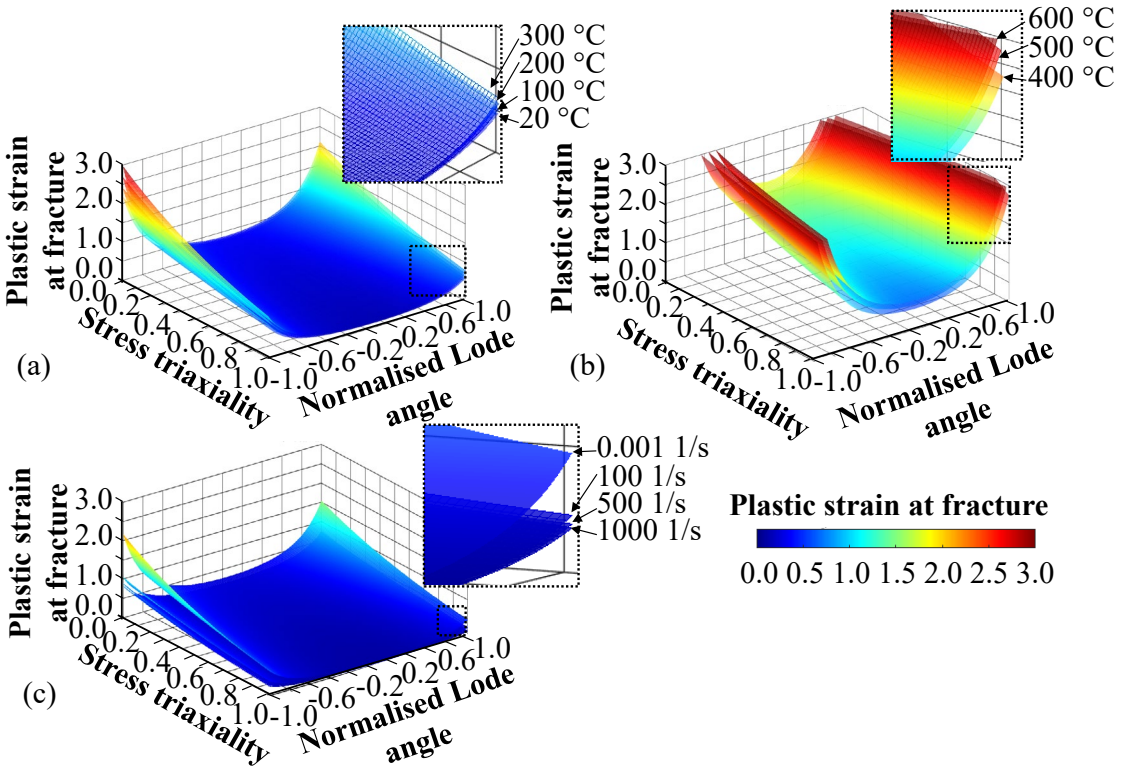

Fig. 7. Extended MMC failure surfaces of: a temperature field between 20 - 300°C at 0.001 1/s (a), a temperature field between 400 - 600°C at 0.001 1/s (b), a strain-rate field between 0.001 - 1000 1/s at 20°C (c).

The individual values of average stress triaxiality, average normalised Lode angle and plastic strain at fracture, determined numerically and used to parametrise the MMC fracture model, are listed in the following tables. Table 1 shows the values regarding temperature dependency, obtained from the miniaturised tensile test specimens of uniaxial, both notched R3 and R10 geometries at 0.001 1/s. Table 2 shows the values regarding the load angle of the butterfly tensile tests at 20°C and 0.001 1/s (left) and the high speed tensile tests at 20°C (right). Lastly, Table 3 holds the individual parameters of the extended MMC failure model.

Table 1. Temperature dependent average stress triaxiality, average normalised Lode angle and plastic strain at fracture of the miniaturised tensile test specimens of uniaxial, R3 and R10 geometries at 0.001 1/s.

	Uniaxial			R3			R10		
Temperature in °C	η_{av}	$\overline{\theta_{av}}$	$\overline{\varepsilon_p^f}$	η_{av}	$\overline{\theta_{av}}$	$\overline{\varepsilon_p^f}$	η_{av}	$\overline{\theta_{av}}$	$\overline{\varepsilon_p^f}$
20	0.43	0.81	0.75	0.46	0.64	0.30	0.42	0.79	0.44
100	0.35	0.95	0.39	0.46	0.62	0.32	0.41	0.81	0.41
200	0.36	0.89	0.57	0.46	0.64	0.31	0.42	0.79	0.48
300	0.41	0.86	0.67	0.48	0.59	0.49	0.47	0.72	0.68
400	0.37	0.91	0.36	0.57	0.44	0.67	0.56	0.58	0.84
500	0.71	0.49	1.43	0.71	0.29	1.02	1.12	0.37	1.60
600	1.17	0.59	1.81	0.79	0.34	1.70	1.23	0.67	1.89

Table 2. Average stress triaxiality, average normalised Lode angle and plastic strain at fracture of butterfly tensile tests at 20 °C and 0.001 1/s (left), and of high speed tensile tests at 20 °C (right).

Butterfly tensile tests				High speed tensile tests			
Load angle in °	η_{av}	$\overline{\theta_{av}}$	$\overline{\varepsilon_p^f}$	Strain rate 1/s	η_{av}	$\overline{\theta_{av}}$	$\overline{\varepsilon_p^f}$
-3	-0.04	-0.09	0.29	100	0.36	0.93	0.33
12.5	0.03	0.08	0.26	500	0.39	0.81	0.26
28	0.12	0.33	0.26	1000	0.33	0.99	0.06
43.5	0.19	0.53	0.19				
59	0.29	0.85	0.32				

Table 3. Parameters of the extended MMC fracture model.

c_1	c_2	c_3	A	n	d_1 (T = 20 - 300 °C)	d_1 (T = 400 - 600 °C)	d_2
0.04	760	1.005	1450	0.0775	2	15	-0.045

Summary

Due to the temperature and strain rate increase in certain industrial sheet metal processes such as shear cutting, it is essential to considerate material's dependency on aforementioned parameters in material modelling to ensure accurate simulation results. Therefore, the aim of this paper is to extend the Modified Mohr-Coulomb fracture model by a temperature and strain rate dependant term for a DP980 steel sheet. For this purpose, Johnson-Cook strain rate hardening and thermal softening effect terms were applied as extension parameters. For the variable parametrisation of the extended MMC model, experimental results from various tensile tests were used, which covered a process relevant stress, temperature and strain rate field. Subsequently, the acquired experimental tests were simulated in Abaqus/implicit to obtain the required parameters of average stress triaxiality, average normalised Lode angle and plastic strain at fracture. Finally, the results were used to determine the individual parameters of the MMC model as well as of the temperature and strain rate dependant terms, which served as an extension of the MMC failure model. In future investigations, the extended model will be applied in a shear cutting simulation and validated using experimental data, so it can be subsequently considered in the simulation of an industrial sheet metal process to improve material's failure prediction and subsequently the process design.

Acknowledgement

The authors are much obliged to the DFG (German Research Foundation) for the financial support of the project "Improved FE simulation of the shear cutting process using a temperature and strain rate-dependent extension of the MMC model" (project number: 199808648).

References

[1] M. Schneider, I. Peshekhodov, A. Bouguecha, B.-A. Behrens, A new approach for user-independent determination of formability of a steel sheet sheared edge, Prod. Eng. 10 (2016) 241-252. https://doi.org/10.1007/s11740-016-0677-4

[2] B.-A. Behrens, D. Rosenbusch, H. Wester, P. Althaus, Comparison of three different ductile damage models for deep drawing simulation of high-strength steels, IOP Conf. Ser.: Mater. Sci. Eng. 1238 (2022) 12021. http://doi:10.1088/1757-899X/1238/1/012021

[3] X. Xiao, H. Pan, Y. Bai, Y. Lou, L. Chen, Application of the modified Mohr-Coulomb fracture criterion in predicting the ballistic resistance of 2024-T351 aluminum alloy plates impacted by blunt projectiles, Int. J. Impact Eng. 123 (2019) 26-37. https://doi:10.1016/j.ijimpeng.2018.09.015

[4] G. R. Johnson, W. H. Cook, Fracture characteristics of three metals subjected to various strains, strain rates, temperatures and pressures, Eng. Fract. Mech. 21 (1985) 31-48. https://doi:10.1016/0013-7944(85)90052-9
[5] Y. Bai, T. Wierzbicki, Application of extended Mohr-Coulomb criterion to ductile fracture, Int. J. Fract. 161 (2010) 1. https://doi:10.1007/s10704-009-9422-8
[6] B.-A. Behrens, K. Brunotte, H. Wester, C. Kock, D. Kildonaviciute, Determination of temperature dependence in Modified-Mohr-Coulomb failure model for process simulation of shear cutting, IOP Conf. Ser.: Mater. Sci. Eng. 1238 (2022) 12028. http://doi:10.1088/1757-899X/1238/1/012028
[7] M. J. Mirnia, M. Shamsari, Numerical prediction of failure in single point incremental forming using a phenomenological ductile fracture criterion, J. Mater. Process. Technol. 244 (2017) 17-43. https://doi:10.1016/j.jmatprotec.2017.01.029
[8] C. R. Roth, D. Mohr, Effect of strain rate on ductile fracture initiation in advanced high strength steel sheets: Experiments and modeling, Int. J. Plast. 56 (2014) 19-44. https://doi:10.1016/j.ijplas.2014.01.003
[9] J. Cao, Z. Sun, L. Huang, Z. Yin, A unified model of ductile fracture considering strain rate and temperature under the complex stress states, J. Mater. Process. Technol. 297 (2021) 117275. https://doi:10.1016/j.jmatprotec.2021.117275
[10] R. Indhu, S. Soundarapandian and L. Vijayaraghavan, Yb: YAG laser welding of dual phase steel to aluminium alloy, J. Mater. Process. Technol. 262 (2018) 411-421. https://doi:10.1016/j.jmatprotec.2018.05.022
[11] B.-A. Behrens, K. Brunotte, H. Wester, M. Dykiert, Fracture Characterisation by Butterfly-Tests and Damage Modelling of Advanced High Strength Steels, Key Engineering Materials 883 (2021) 294-302. https://doi:10.4028/www.scientific.net/KEM.883.294
[12] H. W. Swift, Plastic instability under plane stress, J. Mech. Phys. Solids 1 (1952) 1-18. https://doi:10.1016/0022-5096(52)90002-1
[13] E. Voce, The relationship between stress and strain for homogeneous deformations, J. Inst. Met. 74 (1948) 537-562
[14] J. Qin, R. Chen, X. Wen, Y. Lin, M. Liang, F. Lu, Mechanical behaviour of dual-phase high-strength steel under high strain rate tensile loading, Materials Science and Engineering: A 586 (2013) 62-70. http://doi:10.1016/j.msea.2013.07.091
[15] E. Cadoni, N. Singh, D. Forni, M. K. Singha, N. K. Gupta, Strain rate effects on the mechanical behavior of two Dual Phase steels in tension, The European Physical Journal Special Topics 225 (2016) 986-993. http://doi:10.1140/epjst/e2016-02638-3
[16] F. Gutknecht, F. Steinbach, T. Hammer, T. Clausmeyer, W. Volk, A. E. Tekkaya, Analysis of shear cutting of dual phase steel by application of an advanced damage model, Procedia Struct. Integr 2 (2016) 1700-1707. https://doi:10.1016/j.prostr.2016.06.215

Materials Research Proceedings 28 (2023) 1417-1426 https://doi.org/10.21741/9781644902479-153

Optimizing crystal plasticity model parameters via machine learning-based optimization algorithms

JUAN Rongfei[1,a], BINH Nguyen Xuan[1,b], LIU Wenqi[1,c] and LIAN Junhe[1,d *]

[1]Advanced Manufacturing and Materials, Department of Mechanical Engineering, Aalto University, 02150 Espoo, Finland

[a]rongfei.juan@aalto.fi, [b] binh.nguyen@aalto.fi, [c] wenqi.liu@aalto.fi, [d] junhe.lian@aalto.fi

Keywords: Crystal Plasticity Model, Machine Learning, Parameter Calibration

Abstract. The field of materials science and engineering is constantly evolving, and new methods are being developed to improve our understanding of the relationship between microstructure and properties. One such method is crystal plasticity (CP) modeling, which is widely used for predicting the mechanical properties of crystals and phases. However, determining the constitutive parameters for CP models has been a significant challenge, with current methods relying on either direct chemical composition or inverse fitting, both of which can be time-consuming and lack accuracy. In this study, we propose an automated, advanced, and more efficient method for determining constitutive parameters by using a genetic algorithm (GA) optimization method coupled with machine learning. Our proposed method is applied to two widely used CP models, and the reference data for the calibration is the stress-strain curve from tensile tests. The results of the automated calibration process are then compared to numerical simulation results of CP models with known parameters, demonstrating the efficiency and accuracy of our proposed method.

Introduction

In the field of materials science and engineering, the integrated computational materials and engineering (ICME) approach provides a comprehensive and quantifiable description of the relationship between microstructure and properties. One such approach is crystal plasticity (CP) modeling, which is widely employed for predicting the crystal and phase-level mechanical properties of materials. The CP model has been successfully used to predict the number of ears formed during the cupping process, the anisotropic deformation behavior, the yield locus, the hardening curves, and the residual stress formation during deformation. Currently, there are two prominent crystal plasticity constitutive laws: the phenomenological (PH) and the dislocation-based (DB) constitutive laws. These laws diverge in explaining the dislocation evolution and the interaction laws between slip planes at the microscopic level [1]. In other words, the two laws define the strain-hardening process differently with their own set of equations and resultant fitting parameters. Both constitutive laws aim to define the kinetic equation for the shear rate $\dot{\gamma}$ on the slip system α. The phenomenological law defines the shear rate formula through empirical observation [2], while the law based on dislocation density derives the shear rate from physical kinetic equations that depend on material properties [3, 4].

Previous studies have used these two CP models to predict different types of nonlinear loading deformation with varying success [5-9]. However, the process of determining the constitutive parameters for CP models has been a significant challenge, with current methods relying on either direct chemical composition [10,11], which may lack a certain level of accuracy for specific applications, or inverse fitting of fitting constitutive parameters via a manual procedure that relies on the researcher's experience and is highly subjective and time-consuming.

In light of these challenges, several recent studies attempted to determine the optimal constitutive parameters by different optimization algorithms[12,13]. It is shown that the optimization algorithms, e.g., genetic algorithm (GA), could provide very accurate parameter

Content from this work may be used under the terms of the Creative Commons Attribution 3.0 license. Any further distribution of this work must maintain attribution to the author(s) and the title of the work, journal citation and DOI. Published under license by Materials Research Forum LLC.

calibration for both models. However, the procedure to use the GA for the optimization process of CP models is not straightforward and a manual process shall be involved in formulating an empirical function serving as the response surface to save the computational time for GA.

Therefore, in the current study, it is aimed to formulate an automated, advanced, and more efficient method for determining constitutive parameters by using the GA optimization method. The main focus is to improve the efficiency and simplify the formulation of the response surface that is needed in the GA optimization process. A machine-learning-based approach is proposed for this purpose to be coupled with GA. The new method is applied to both CP models: four fitting parameters ($\tau_0, \alpha, h_0, \tau_{sat}$) in the phenomenological law and six fitting parameters ($\hat{d}^{\alpha}$, i_{slip}, Ω, p, q, τ_{sol}) in the dislocation-density-based law [5,9]. The reference data for the calibration is the stress-strain curve from tensile tests, which is also the most used case for single-phase materials [14]. In the study, numerical simulation results of CP models with known parameters are used as the target or "experimental" curve, which can be used to verify and compare the results of the parameters by the automated calibration process.

Methodology

The response surface methodology (RSM) is a frequently used mathematical model to analyze the response of interest [15]. RSM aims to accurately predict the response variables given an unknown set of explanatory variables. For example, in CP parameter calibration, the explanatory variables are the fitting parameters (four in PH law and six in DB law) and the response variables are the corresponding stress values. Therefore, the essential aspect of RSM is the true reflection of regional continuity around the global optima. This study uses the multilayer perceptron (MLP) as the RSM for the genetic algorithms. An MLP is a feedforward artificial neural network comprising an input layer, several hidden layers, and an output layer. The MLP structure used in this project consists of three layers: the input layer (parameters) with 4-6 neurons and the output layer (stress values) with varying neurons depending on the number of interpolated stress values. There is only one hidden layer, and the number of nodes in the hidden layer is calculated as:

$$N_{hidden} = round(\frac{2}{3} N_{input} + N_{output}) \quad (1)$$

The approximation depends on the hidden layer, where each neuron is the weighted linear sum of the neurons in the previous layer or the input layer. The output layer derives from the transformation of the hidden layer by the activation function, whose outputs depend on whether the inputs pass their respective thresholds. Rectified Linear Unit (ReLU) is used as the activation function for its common usage and exemplary performance in neural networks:

$$\text{ReLU}(x) = max(x, 0) \quad (2)$$

where x is the value in the hidden nodes. The function returns 0 if x is negative.

Optimization of complex functions with unknown structures is a challenging problem to solve. The genetic algorithm, a commonly used hyperparameter optimization algorithm, is applied in this research to tackle this problem. This algorithm is based on the theory of evolution by Charles Darwin, where survival of the fittest is regarded as the best outcome. A study by Himani Panwar [16] finds that the natural selection process is simulated by choosing the best individuals 11 from each generation determined by the fitness function. According to Sedighiani [12], GA can converge to the global optimum of the objective functions instead of being stuck in local optima like the gradient-based searching methods. For this reason, GA is a robust optimization algorithm that guarantees to find the optimal solution in a probabilistic fashion of biological evolution.

Fig. 1 shows the structure of GA is mainly based on the work of Sedighiani et al. [12], which features eight steps that simulate biological evolution. The goal of GA is to maximize the fitness functions in one iteration.

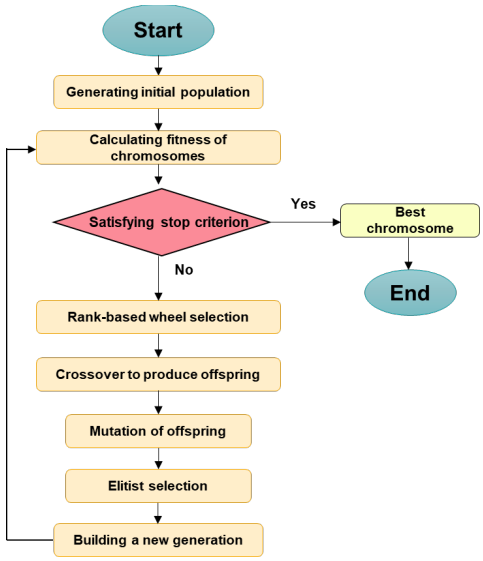

Fig. 1. GA workflow comparison in each iteration.

Objective, Fitness, and Stop Criteria Functions

In this study, a multi-objective optimization approach was developed to improve the precision of simulation results. The optimization process was divided into two stages, with the first stage focusing on optimizing the parameters that control yield strength and the second stage focusing on optimizing the parameters that control hardening behavior.

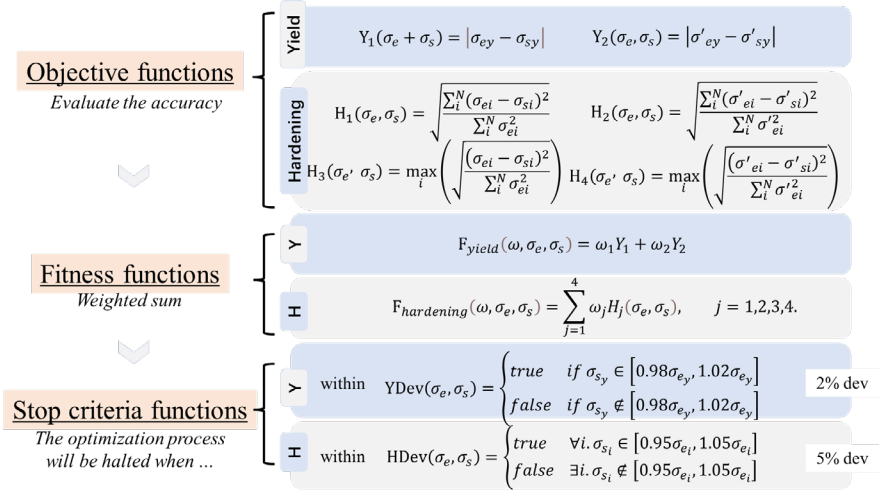

Fig. 2. Overview of the multi-objective optimization approach functions.

Fig. 2 shows all the functions of the optimization, which are the objective, fitness, and stop criteria functions. In the first stage of optimization, two objective functions were employed to evaluate the accuracy of simulated yield strength. The first objective function, Y_1, measured the absolute difference between the experimental and simulated yield strength values, while the second objective function, Y_2, calculated the slope of yield strength.

$$Y_1(\sigma_e,\sigma_s)=|\sigma_{ey}-\sigma_{sy}| \tag{3}$$

$$Y_2(\sigma_e, \sigma_s) = \left|\sigma'_{ey} - \sigma'_{sy}\right| \quad (4)$$

where σ_{ey} and σ_{sy} are the yield strength of the experiment and simulation curves, and σ'_{ey} and σ'_{sy} are the slope of the yield strength of experiments and simulation, respectively. As shown in the fitness function later, a linear combination of these two objective functions, Y1 and Y2, was used to minimize the deviation between the experimental and simulated yield strength values, as well as the deviation in the slope of the yield strength. This approach helped to quantify the yield strength accuracy more precisely and take into account the increasing trend of the experimental and simulated yield strength.

In the second stage of optimization, four objective functions were utilized to evaluate the global fitness of the simulated hardening behavior. The first objective function measured the normalized Euclidean distance between the experimental and simulated hardening curves, while the second objective function measured the normalized slope difference between the two curves. This helped to determine whether the simulated and experimental hardening curves shared the same global shape.

$$H_1(\sigma_e, \sigma_s) = \sqrt{\frac{\sum_i^N (\sigma_{ei} - \sigma_{si})^2}{\sum_i^N \sigma_{ei}^2}} \quad (5)$$

$$H_2(\sigma_e, \sigma_s) = \sqrt{\frac{\sum_i^N (\sigma'_{ei} - \sigma'_{si})^2}{\sum_i^N \sigma'^2_{ei}}} \quad (6)$$

In the two objective functions, the subscript *i* stand for each data point in the hardening part of the stress–strain curves for both experiments and simulations, and *N* represents the total number of data points.

To further penalize the maximum distance and slope difference between the curves, two additional objective functions, H_3 and H_4, were employed which delivered the maximum value point of H_1 and H_2, respectively. These objective functions helped to account for the maximum deviation and slope difference between the experimental and simulated curves. A linear combination of these four objective functions was used to converge to the global optimum and avoid getting stuck in local optima.

$$H_3(\sigma_e, \sigma_s) = \max_i \left(\sqrt{\frac{(\sigma_{ei} - \sigma_{si})^2}{\sum_i^N \sigma_{ei}^2}} \right) \quad (7)$$

$$H_4(\sigma_e, \sigma_s) = \max_i \left(\sqrt{\frac{(\sigma'_{ei} - \sigma'_{si})^2}{\sum_i^N \sigma'^2_{ei}}} \right) \quad (8)$$

The fitness function for each optimization stage was the weighted sum of all objective functions. In the first stage, the yield stress fitness function was the weighted sum of Y_1 and Y_2, while the hardening fitness function in the second stage was the weighted sum of the hardening objective functions. The weights could be manually tuned to improve the results in each stage when certain fitness aspects required emphasis. The sum of the weights was defined to be one, with the difference in the weights being due to the unequal importance and result scale of the objective functions.

$$F_{yield}(\omega, \sigma_e, \sigma_s) = \omega_1 Y_1 + \omega_2 Y_2 \quad (9)$$

$$F_{hardening}(\omega, \sigma_e, \sigma_s) = \sum_{j=1}^{4} \omega_j H_j(\sigma_e, \sigma_s), \; j = 1,2,3,4 \quad (10)$$

The optimization process was halted when the stopping criteria were met. In the first stage, the process stopped when the simulated yield strength value was within a specified deviation from the experimental value, as defined in YDev. A rather small tolerance, 2% is chosen for this case to ensure very good fitness on the yield strength. In the second stage, the process stopped when all simulated stress values were within a specified deviation, 5%, of the experimental stress values, as defined in the HDev function. These stopping criteria ensured that the final simulation results met the desired precision and accuracy.

$$\mathrm{YDev}(\sigma_e,\ \sigma_s) = \begin{cases} true & if\ \sigma_{s_y} \in \left[0.98\sigma_{e_y},\ 1.02\sigma_{e_y}\right] \\ false & if\ \sigma_{s_y} \notin \left[0.98\sigma_{e_y},\ 1.02\sigma_{e_y}\right] \end{cases} \tag{11}$$

$$\mathrm{HDev}(\sigma_e,\ \sigma_s) = \begin{cases} true & \forall i.\ \sigma_{s_i} \in \left[0.95\sigma_{e_i},\ 1.05\sigma_{e_i}\right] \\ false & \exists i.\ \sigma_{s_i} \notin \left[0.95\sigma_{e_i},\ 1.05\sigma_{e_i}\right] \end{cases} \tag{12}$$

Experimental and simulated data were used in this process and precise yield stress values and similar global shapes to the target curves were obtained, which will be shown in the next section. In Table 1, the default weights for the fitness functions used in this study are shown. The developed optimization approach was effective in improving the precision of simulation results and could be applied to various optimization problems in the field. Additionally, the approach allowed for manual tuning of the weights for the objective functions to emphasize specific aspects of the fitness, providing more flexibility in the optimization process.

Table 1. Default weights for two fitness functions.

	F_{yield}		$F_{hardening}$			
	ω_{y1}	ω_{y2}	ω_{h1}	ω_{h1}	ω_{h1}	ω_{h1}
weight	0.999	0.001	0.9	0.025	0.05	0.025

Resutls and Discussion

Before the optimization, we must ensure our target curve and search space for the optimizer. Instead of the experimental data, the target strain-stress curves are taken from the CP simulation for a better comparison of the quality of the fitted parameters by the optimization approach. To prove the general validity of the proposed approach for different types of materials, not only one simulation but three simulation results with very different parameter sets were selected as the target curves to compare the difference between the initial parameter values with the optimal parameters delivered by the calibration process. Next, we need to determine the parameter ranges and step sizes. The range allows the optimizer to limit the search space, and the step size allows for the discretization of continuous parameter values. Therefore, the algorithms only search within the range by the defined step size.

The CP model calibration process begins with converting the true stress-true strain curve into the flow curve in the preprocessing stage. Next, initial simulations are performed, which will yield the final optimal parameters that are dependent on the parameters of the initial simulations. Good initial simulations help direct the optimizing algorithm to the location of the true parameter set. The number of initial simulations in this work is 30. To improve the precision of both yield stress and hardening parameter predictions, the range of all simulated yield stresses must cover the experimental yield stress and the boundaries should cover the experimental global curve. Additionally, the neighboring simulated curves should have a similar global shape to that of the target curve. Fig. 3 shows the relationship between the initial guess simulations and target curves.

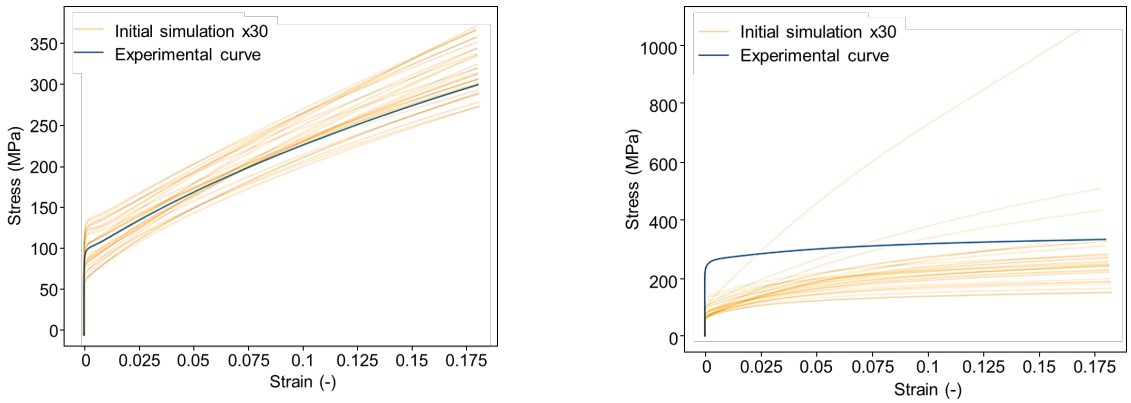

(a) Good initial simulations (b) Bad initial simulations

Fig. 3. Good (a) and bad (b) initial simulations and experimental curve.

The first stage of the optimization process involves adjusting the yield stress parameters, which are represented by τ_0 for the PH model and p, q, and τ_{sol} for the DB model. The hardening parameters are not altered during this stage. The results of this stage are illustrated in Fig. 4a for the PH model, where it can be observed that in the first iteration, the simulated yield stress (σ_{sy}) is approximately 123.5 MPa at $\tau_0 = 52$. In the following iteration, the genetic algorithm predicts $\tau_0 = 51$, resulting in a further increase in σsy. The optimization process concludes in the third iteration, where $\tau_0 = 54$ and σsy deviates by 2% from the experimental yield stress (σ_{ey}) whose true value is $\tau_0 = 55$. It is important to note that the algorithm does not always produce better results in each iteration; instead, it demonstrates an improvement trend, with simulated yield stress values progressively approaching the experimental yield stress. This is because the algorithm explores different parts of the search space in each iteration, gradually honing in on the true parameter set. Similarly, for the DB model, the optimized parameters are (p, q, τ_{sol}) = (0.2, 1.3, 0.3), which results in a 2% deviation in the yield stress from the true parameters (p, q, τ_{sol}) = (0.2, 1.8, 0.4) as shown in Fig. 4b. Despite not being exact, the results are still satisfactory due to the non-uniqueness of optimal parameters. This means that even if one parameter is changed, another varying parameter can exist to balance the outcome.

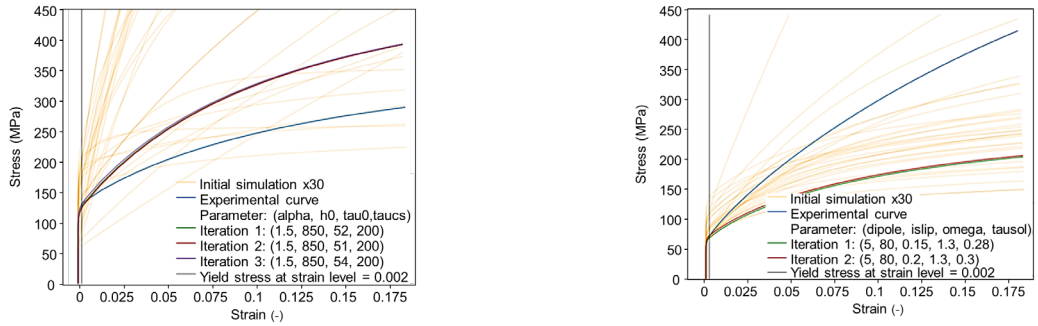

(a) Yield control optimized by GA of PH (b) Yield control optimized by GA of DB

Fig. 4 Strain-stress curve of σ_y at $\varepsilon = 0.002$ in the first optimize stage of PH (a) and DB (b).

In the second stage of the optimization process, the algorithms focus on adjusting the hardening parameters. For the PH model, these parameters are represented by α, h_0, and τ_{sat}, while for the DB model, they are represented by $\hat{d}^{\alpha}$, i_{slip}, and Ω. The values of the yield stress adjusting parameters are obtained from the first stage of the optimization process. The results of this stage are illustrated in Fig. 5 for both the PH and DB models.

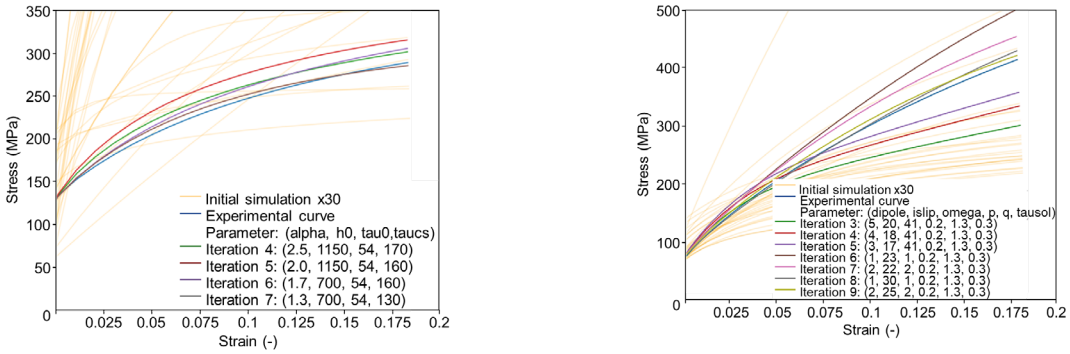

(b) Hardening behavior optimization of PH (b) Hardening behavior optimization of DB

Fig. 5 Strain-stress curve in the second optimization stage of PH (a) and DB (b).

The quality of the fitting simulation curve is evaluated based on two criteria: the loss distance and the number of intersections with the experimental curve. The goal is to achieve a minimum distance loss and to have the simulated curve globally above, below, or exactly overlapping the experimental curve. This is because these conditions indicate that the simulated and experimental curves share the same increasing trend, which is a good indication of the accuracy of the simulation. On the other hand, if the simulated curve intersects with the experimental curve, it indicates contrasting material performance and a loss of the simulated prediction meaning. In the last iteration (7th) of the PH1 model, the simulated curve shares two intersections with the experimental curve, while in the DB1 model, the last iteration (9th) shares no intersections, making the final simulation result of DB1 better than PH1 in terms of the above-mentioned criteria.

Following the procedures demonstrated above, the performance of the final iteration results of the parameter calibration program under GA was then compared and illustrated in Fig. 6. The GA demonstrates good and stable calibration quality for the three initial target curves of both the PH and DB model. Similar conclusions were also observed in the results of the DB laws. Table 2 below records all optimal parameter solutions predicted by GA. It is important to note that in some cases, more than one parameter controls the same aspect of the simulation, and their effects can balance each other out. For example, only τ_0 controls the yield point of PH, while other parameters control the hardening curve, and a and h_0 have opposite effects on the hardening curve.

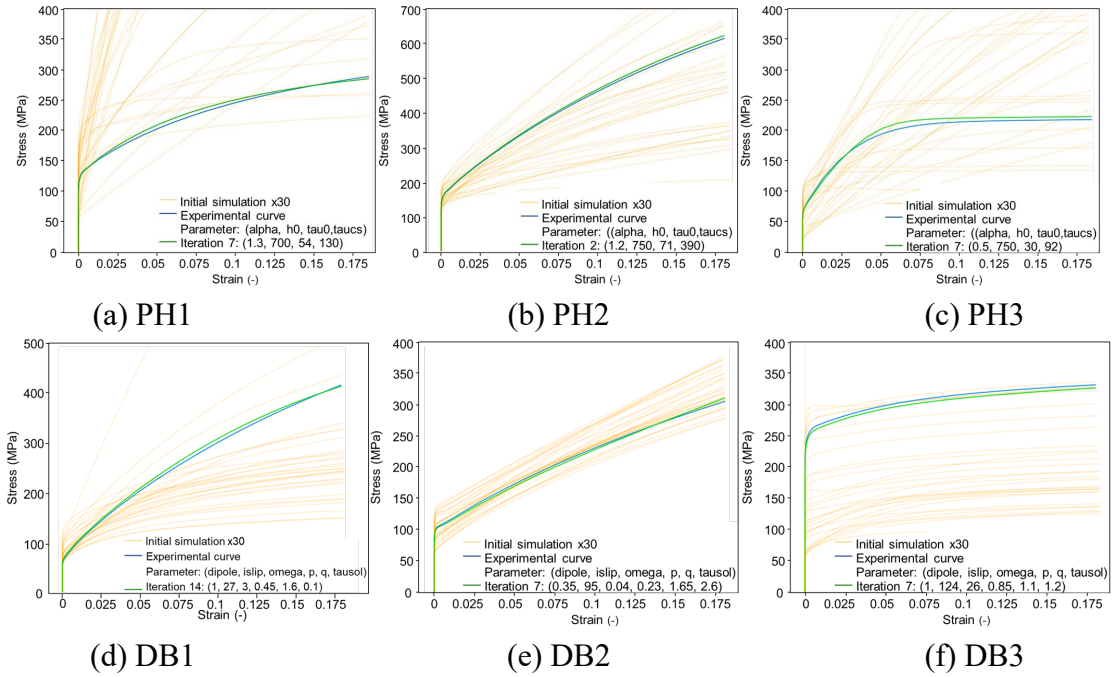

(a) PH1 (b) PH2 (c) PH3

(d) DB1 (e) DB2 (f) DB3

Fig. 6. Final iteration of parameter calibration for target curves in PH and DB laws.

Table 2. Final fitting parameter calibration results for two CP models.

	τ_0	a	h_0	τ_{sat}		$\hat{d}^{\alpha}$	i_{slip}	Ω	p	q	τ_{sol}
PH1	54	1.3	700	130	DB1	1	27	3	0.45	1.6	0.10
True	55	1.6	600	150	True	1	25	3	0.20	1.8	0.40
PH2	71	1.2	750	390	DB2	0.35	95	0.04	0.23	1.65	2.60
True	70	1.9	800	500	True	0.80	80	0.80	0.20	1.10	1.20
PH3	30	0.5	750	92	DB3	2	140	10	0.85	1.10	1.20
True	30	0.8	1000	90	True	2	180	15	0.90	1.10	1.20

Fig. 7 shows the comparison of the yield point error and the root means square error (RSME) of the hardening behavior between experimental data and optimized results. As seen in Fig. 7a, the error analysis of GA at the yield point shows relatively small values, within a 2% deviation from the experimental ones. Meanwhile, in Fig. 7b, the RSME values for the hardening behavior also indicate that the fitting quality for the three cases shows very good quality.

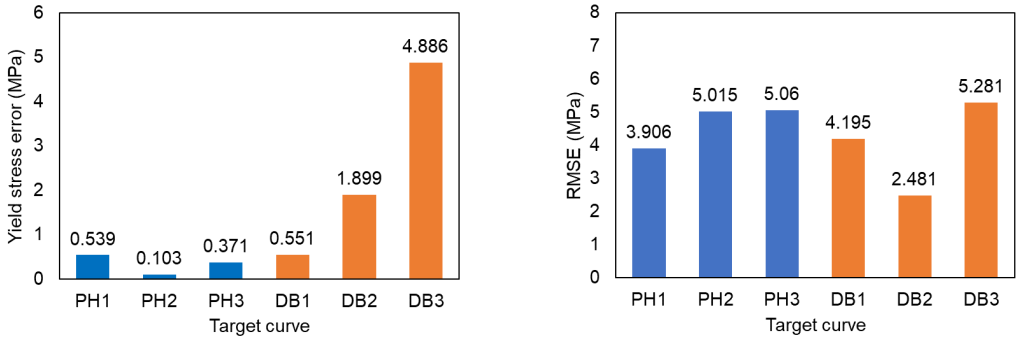

(a) Yield stress error comparison (b) Root mean square error comparison

Fig. 7. Error analysis of the final iteration of parameter calibration for the three target curves.

Summary

The optimization workflow presented in this study solves well the problem of parameter calibration for three chosen target stress-strain curves, which traditionally relies on educated

guessing by experts. Additionally, the use of machine learning-assisted methodology in this article has led to a fully automated process for identifying fitting parameters. Despite the success of the calibration process in identifying optimal fitting parameters, certain challenges and limitations also exist in the current workflow. These include:

- Choosing an appropriate parameter range: If the true parameters do not lie within the specified range, the optimization algorithm may not converge to the correct solution unless the optimal solution is non-unique and another candidate within the range behaves similarly to the target curve.
- Poor initial simulations: Initial simulations should be regenerated when the yield stress is not covered in the range of simulated yield stress values.
- Nonconvergence of simulations in the DB model: Not all combinations of DB fitting parameters result in successfully converging simulations. This problem usually arises from large $\hat{d}^{\alpha}$ and very small p values.
- Nonconvergence of the MLP regressor: This issue can occur due to a large number of data points in the target curve and can be solved by loading point interval omission.

These limitations and challenges present in the current workflow can be overcome by certain adjustments, such as adjusting the chosen parameters, and are currently being solved in a more general and automated matter in ongoing studies.

Acknowledgments
Simulations were performed with computing resources granted by the Finnish IT Center for Science (CSC) services. The authors gratefully acknowledge CSC [project number: 2004956 Optimization of crystal plasticity parameter calibration] for the simulation resources for the project. All the authors also are grateful to Ilari Pajula, Nam Anh Chu, and Lucas Krieger from group 1 of the Computational Engineering project course at Aalto University for preliminary work and related discussion on this study.

References
[1] F. Roters, M. Diehl, P. Shanthraj, P. Eisenlohr, C. Reuber, S.L. Wong, T. Maiti, A. Ebrahimi, T. Hochrainer, H.O. Fabritius, S. Nikolov, M. Friak, N. Fujita, N. Grilli, K.G.F. Janssens, N. Jia, P.J.J. Kok, D. Ma, F. Meier, E. Werner, M. Stricker, D. Weygand, D. Raabe, DAMASK - The Dusseldorf Advanced Material Simulation Kit for modeling multi-physics crystal plasticity, thermal, and damage phenomena from the single crystal up to the component scale, Computat. Mater. Sci. 158 (2019) 420-478. https://doi.org/10.1016/j.commatsci.2018.04.030
[2] E. Voce, The Relationship between Stress and Strain for Homogeneous Deformation, J. I. Met. 74 (1948) 537-562.
[3] S.L. Wong, M. Madivala, U. Prahl, F. Roters, D. Raabe, A crystal plasticity model for twinning- and transformation-induced plasticity, Acta Mater. 118 (2016) 140-151. https://doi.org/10.1016/j.actamat.2016.07.032
[4] F.J. Gallardo-Basile, Y. Naunheim, F. Roters, M. Diehl, Lath Martensite Microstructure Modeling: A High-Resolution Crystal Plasticity Simulation Study, Materials 14 (2021) 691. https://doi.org/10.3390/ma14030691
[5] R. Juan, W. Liu, X. Inza, X. Ureta, J. Mendiguren, J. Lian, Crystal Plasticity Modeling of Al Alloy under Linear and Non-Linear Loading, Key Eng. Mater. 926 (2022) 2099-2108. http://doi.org/10.4028/p-2jqp1v
[6] J. Lian, W. Liu, X. Gastañares, R. Juan, J. Mendiguren, Plasticity evolution of an aluminum-magnesium alloy under abrupt strain path changes, Int. J. Mater. Form. 15 (2022) 40. https://doi.org/10.1007/s12289-022-01692-6

[7] M. Bertin, C.W. Du, J.P.M. Hoefnagels, F. Hild, Crystal plasticity parameter identification with 3D measurements and Integrated Digital Image Correlation, Acta Mater. 116 (2016) 321-331. https://doi.org/10.1016/j.actamat.2016.06.039
[8] D. Raabe, M. Sachtleber, Z. Zhao, F. Roters, S. Zaefferer, Micromechanical and macromechanical effects in grain scale polycrystal plasticity experimentation and simulation, Acta Mater. 49 (2001) 3433-3441. https://doi.org/10.1016/S1359-6454(01)00242-7
[9] W. Liu, J. Lian, N. Aravas, S. Münstermann, A strategy for synthetic microstructure generation and crystal plasticity parameter calibration of fine-grain-structured dual-phase steel, Int. J. Plast. 126 (2020) 102614. https://doi.org/10.1016/j.ijplas.2019.10.002
[10] C.C. Tasan, J.P.M. Hoefnagels, M. Diehl, D. Yan, F. Roters, D. Raabe, Strain localization and damage in dual phase steels investigated by coupled in-situ deformation experiments and crystal plasticity simulations, Int. J. Plast. 63 (2014) 198-210. http://doi.org/10.1016/j.ijplas.2014.06.004
[11] H.J. Bong, H. Lim, M.-G. Lee, D.T. Fullwood, E.R. Homer, R.H. Wagoner, An RVE procedure for micromechanical prediction of mechanical behavior of dual-phase steel, Mater. Sci. Eng. A 695 (2017) 101-111. https://doi.org/10.1016/j.msea.2017.04.032
[12] K. Sedighiani, M. Diehl, K. Traka, F. Roters, J. Sietsma, D. Raabe, An efficient and robust approach to determine material parameters of crystal plasticity constitutive laws from macro-scale stress-strain curves, Int. J. Plast. 134 (2020) 102779. https://doi.org/10.1016/j.ijplas.2020.102779
[13] J. Kuhn, J. Spitz, P. Sonnweber-Ribic, M. Schneider, T. Bohlke, Identifying material parameters in crystal plasticity by Bayesian optimization, Optim. Eng. 23 (2022) 1489-1523. https://doi.org/10.1007/s11081-021-09663-7
[14] K. Zhang, B. Holmedal, S. Hopperstad, S. Dumoulin, J. Gawad, A. Van Bael, P. Van Houtte, Multi-level modelling of mechanical anisotropy of commercial pure aluminium plate: Crystal plasticity models, advanced yield functions and parameter identification, Int. J. Plast. 66 (2015) 3-30. https://doi.org/10.1016/j.ijplas.2014.02.003
[15] D.T. Do, D.H. Lam, T. Nguyen, T.T. Phuong Mai, L.T.M. Phan, H.T. Vuong, D.V. Nguyen, N.T.T. Linh, M.N. Hoang, T.P. Mai, H.H. Nguyen, Utilization of Response Surface Methodology in Optimization of Polysaccharides Extraction from Vietnamese Red Ganoderma lucidum by Ultrasound-Assisted Enzymatic Method and Examination of Bioactivities of the Extract, Scientific World Journal 2021 (2021) 7594092. https://doi.org/10.1155/2021/7594092
[16] P. Himani Panwar, Dharamveer Singh, Abha Singh, Genetic Algorithm for Solving Simple Mathematical Equality Problem, IRJET 07 (2020) 7622-7627.

Materials Research Proceedings 28 (2023) 1427-1434 https://doi.org/10.21741/9781644902479-154

Correlation between porosity level and elastic modulus in a foamed hiped Ti alloy

GUGLIELMI Pasquale[1,a*], CASTELLANO Anna[1,b], CUSANNO Angela[1,c] and PALUMBO Gianfranco[1,d]

[1] Politecnico di Bari, Department of Mechanics, Mathematics and Management, Via Orabona 4 - 70125 Bari – Italy

[a]pasquale.guglielmi@poliba.it, [b]anna.castellano@poliba.it, [c]angela.cusanno@poliba.it, [d]gianfranco.palumbo@poliba.it

Keywords: Ti Alloy, Foaming, Hot Isostatic Pressing, Microstructure, Ultrasonic Tests, Young's Modulus

Abstract. Nowadays, in the manufacturing of highly customized prosthetic implants, the need of devices with mechanical properties close to the human bone's ones plays a key role. In the present work, Ti6Al4V-ELI porous structures obtained by a solid-state foaming process were studied from a microstructural and mechanical point of view, being the aim to control the stiffness of the prostheses in order to be as much as possible close to the human bone's one, thus reducing the stress shielding effect. Samples with different levels of porosity (average diameter variable between a few microns and about 50 microns) were investigated by means of contact ultrasonic tests in order to evaluate changes in terms of elastic properties. Metallographic observations combined with contact ultrasonic tests revealed that a good correlation exists between the foamed structure (quantity and average size of the pores) and the stiffness.

Introduction

The human bone can be considered as anisotropic and non-homogeneous material. Moreover, it is capable to vary its shape dynamically according to the stress conditions to which it is subjected [1]. The capability to withstand external stresses is intimately related to both microstructural and macroscopic properties. Many studies evaluated the relationship between architectural factors and large-scale mechanical properties, in terms of fracture risk. Indeed, anisotropy can be correlated both to the modulus of elasticity and strength [2].

In accordance with these considerations, the manufacture of devices for the replacement/repair of damaged bones capable to adapt in the best way to the natural properties of the specific bone through the adoption of metallic materials is still an aspect of primary importance in the biomedical field. Titanium (Ti) and its alloys are extensively used in orthopaedic applications thanks to their (i) good mechanical properties, (ii) biocompatibility [3] and (iii) corrosion resistance [4]. However, large differences in terms of mechanical properties between the prosthesis and the bone to which it is close can cause an alteration of the stress distribution (stress shielding) [5,6]. When considering metallic prostheses, such an aspect plays an important role and cannot be neglected, even for Ti alloys whose elastic modulus is closer to the human bone's one than stainless steels. Thus, the adoption of materials for producing the implants which are characterised by a porous structure can make their stiffness closer to the human bones' one. Ti alloys obtained by means of the Hot Isostatic Pressing (HIP) process of Ti powders can be used for producing such porous materials, since they can develop cellular structures characterised by average porosity up to about 50% by means of a solid state foaming process (i.e. when subjected to constant temperature up to about 1250°C and for appropriate durations) [7]. As result of the foaming process, the mechanical response of the implant is affected. In addition, porosity also affects the surface properties, thus being able to promote the cellular proliferation [4].

Content from this work may be used under the terms of the Creative Commons Attribution 3.0 license. Any further distribution of this work must maintain attribution to the author(s) and the title of the work, journal citation and DOI. Published under license by Materials Research Forum LLC.

Materials Research Proceedings 28 (2023) 1427-1434 https://doi.org/10.21741/9781644902479-154

Another important aspect in the manufacture of highly customized implants is the need for a perfect fitting between the geometry of the prosthesis and the anatomy of the specific patient; in fact, micro-movements between the two parts can cause the onset of infections [8]. In the light of this non-negligible aspect, increasingly advanced manufacturing technologies, such as additive manufacturing [9], superplastic and incremental forming [10] capable of guaranteeing very complex shapes, are nowadays a functional solution for reducing these risks. In addition, in the specific case of superplastic forming process, which requires the aid of high temperatures, the foaming process could be performed not only after the manufacturing process but also simultaneous with a considerable reduction of both time and costs.

Therefore, the possibility of suitably customising the prosthesis, not only in terms of shape but also of properties (like the stiffness) is a key aspect in the modern medicine. In the present work, according to the one of main goals of the founded national project FabriCARE, the effect of the pressure of the HIP process was evaluated after foaming tests performed at high and constant temperature (1020°C) for 240 minutes. Metallographic aspects, such as the topology of the promoted porosity and the mechanical properties in the elastic field were investigated, respectively by means of light microscopy and ultrasonic tests. Starting from the measurements of the velocity of the bulk (longitudinal and transversal) waves obtained from contact ultrasonic tests, using the linear elastodynamic theory for wave propagation in isotropic material, the elastic moduli of different Ti6Al4V-ELI foam-based specimens were determined. Finally, results from the analyses were correlated and allowed to evaluate the correlation between the average size of the porosities (obtained after the foaming process) and the elastic properties (Young's modulus).

Material and Methods

Material.

The experimental activity was conducted using two different titanium billets produced by Hot Isostatic Pressing (HIP) characterized by process pressure from 80 to 120MPa. For all conditions Ti6Al4V-ELI powders with a diameter from 50 up to 100µm were used. The chemical composition of the investigated material is reported in Table 1.

Table 1. Chemical composition of the investigated Ti6Al4V-ELI alloy.

Al%	V%	Fe%	C%	N%	H%	O%	Ti
5.88	3.87	0.14	0.22	0.006	0.002	0.112	Bal.

Dog-bone specimens (thickness: 3mm) were extracted from the billets using an Electrical Discharge Machine (EDM). The main dimensions of the sample are shown in Fig. 1.

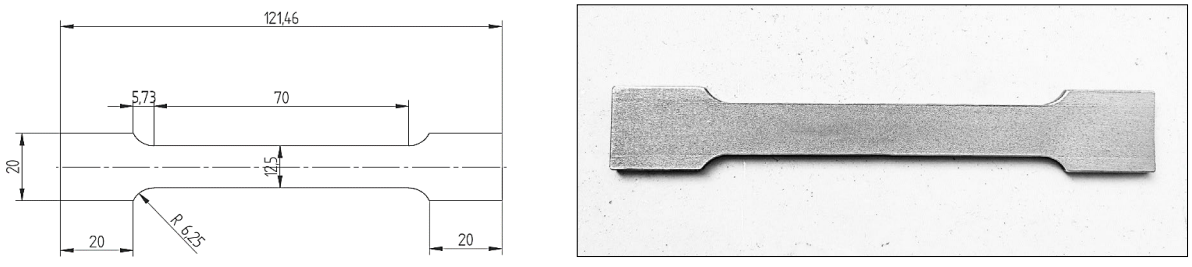

(a) (b)

Fig. 1. (a) Main dimensions [mm] of the dog-bone sample extracted by EDM (b) adopted for the foaming tests.

Methodology

Creation of the porous structure.

The porous structure of the specimens to be subjected to ultrasonic tests (Fig. 1) was obtained by solid state foaming, which consists in a heat treatment in the furnace (T=1020°C for 240 minutes [11]). The samples were extracted from billets produced by compacting Ti6Al4V powders (size is in the range 50-100 micron) placed in a sealed can in which the air was replaced by argon gas (pressure: 0.2 MPa) using the HIP process.

In this work, two different levels of the pressure applied during the HIP process were investigated, as summarized in Table 2.

Table 2 Starting conditions of the HIPed samples subjected to foaming.

	Diameter of titanium powders, μm	Argon pressure, MPa	HIP pressure, MPa
D100-A0.2HIP80	From 50 up to 100	0.2	80
D100-A0.2HIP120	From 50 up to 100	0.2	120

Each foaming test was replicated three times; furthermore, the results achieved and subsequently discussed were compared to the "as received" condition (i.e. concerning the specimen extracted from the billet and not subjected to any foaming process).

The level of porosity (percentage area and average diameter of pores) determined by the foaming process was assessed by analysing samples extracted from the central cross sections of the dog-bone specimens: the samples were prepared in order to be observed by an optical microscope (Nikon MA200 equipped with the ImageJ® software for digital image processing).

Young's modulus evaluation by means of ultrasonic tests

The wave phenomena involved in the ultrasonic tests are usually described by the linearized elastodynamic theory [12], since the ultrasonic waves can be regarded as small perturbations of a reference state of an elastic body. Solutions in the form of progressive plane waves for the equation of motion (Eq. 1) are found

$$\mathrm{Div}(\mathbb{C}[\boldsymbol{\nabla u}]) = \boldsymbol{\rho \ddot{u}}, \tag{1}$$

in absence of the body forces, where $\rho = \rho(\boldsymbol{x})$ is the mass density and $\mathbb{C} = \mathbb{C}(\boldsymbol{x})$ is the incremental fourth order elasticity tensor referred to the initial state of the body, having the first and the second minor symmetries, and $\boldsymbol{u} = \boldsymbol{u}(\boldsymbol{x})$ has the following form:

$$\boldsymbol{u}(\boldsymbol{x},\mathrm{t}) = \mathbf{a}\,\boldsymbol{\varphi}(\boldsymbol{x}\cdot\boldsymbol{n} - \mathrm{v\ t}) \tag{2}$$

and represents a progressive elastic plane wave with propagation direction n, direction of motion a, propagation velocity v; φ is a real valued smooth function.

The propagation of plane progressive elastic waves in an elastic body is ruled by the "Fresnel-Hadamard condition" that is the Christoffel equation:

$$[\boldsymbol{\Gamma}(\boldsymbol{n}) - \boldsymbol{\rho v^2 I}]\,\boldsymbol{a} = \mathbf{o} \tag{3}$$

where Γ(n) is the second order Kelvin-Christoffel propagation tensor for the direction n, related to the elastic tensor $\mathbb{C}$ as follows:

$$\boldsymbol{\Gamma}(\boldsymbol{n}) = \mathbb{C}^{\boldsymbol{t}}[\boldsymbol{n} \otimes \boldsymbol{n}] \tag{4}$$

where the superscript "t" represents the minor transposition for fourth order tensors.

From Eq. 3, if an elastic wave propagates in a given direction n, the square of the propagation velocity v is an eigenvalue of the Christoffel tensor Γ(n) while the direction of motion a is the associated eigenvector. The symmetry properties of the elastic tensor $\mathbb{C}$ strongly influence the

features of progressive elastic waves propagating along a certain direction n. Moreover, according to the "Federov-Stippes theorem", if the elasticity tensor $\mathbb{C}$ is symmetric and strongly elliptic, then at a point x there exists longitudinal (a and n parallel) and transverse (a and n perpendicular) elastic waves. In the case of isotropic material, for each possible direction of propagation n only pure propagation modes like longitudinal waves and transverse waves may propagate. Instead, for anisotropic materials in a generic direction of propagation n, different from a material symmetry axis, elastic waves may propagate in a not pure propagation modes (as "quasi-longitudinal" waves or as "quasi-transverse" waves).

This theoretical framework suggests a non-destructive ultrasonic experimental counterpart: indeed, the results of ultrasonic tests can be employed for facing two major problems in the mechanics of elastic materials: (i) the *classification problem*, that is the determination of the symmetry class and the identification of the material symmetry axes; (ii) the *representation problem*, that is, once known the symmetry class, the determination of the components of the elastic tensor $\mathbb{C}$ characterizing the elastic response of the material.

For the study of acoustic and mechanical behaviour of *porous* Ti6Al4V-ELI specimens the theoretical model of the isotropic material was adopted. So, by the inversion of the Christoffel equation (Eq. 3), the well-known expression in Eq. 5 have been obtained.

$$E = \boldsymbol{\rho v_T^2} \frac{3v_L^2 - 4v_T^2}{\boldsymbol{v_L^2 - v_T^2}}, \qquad G = \boldsymbol{\rho v_T^2}, \qquad \boldsymbol{\nu} = \frac{\left(\frac{\boldsymbol{v_L}}{\boldsymbol{v_T}}\right)^2 - \mathbf{2}}{\mathbf{2}\left[\left(\frac{\boldsymbol{v_L}}{\boldsymbol{v_T}}\right)^2 - \mathbf{1}\right]} \tag{5}$$

between the elastic properties (the Young's modulus E, the shear modulus G and the Poisson's ratio ν), the velocity of longitudinal waves v_L and of transversal waves v_T and the density ρ.

The ultrasonic tests were performed at the Laboratorio Ufficiale Prove Materiali "M. Salvati" (Polytechnic University of Bari). In particular, ultrasonic tests were carried out by contact through the pulse-eco (or back reflection) technique, i.e. a single transducer is employed that emits and receives the ultrasonic signal. For the sake of brevity, only the results of the contact ultrasonic tests are shown. The ultrasonic immersion tests carried out using an innovative goniometric device [13] gave results similar to those of the ultrasonic contact tests.

The experimental setup of the contact ultrasonic tests (Fig. 2a) consists in: (1) an ultrasonic pulser/receiver Panametrics 5072PR for generating and receiving the ultrasonic waves; (2) a digital oscilloscope KEYSIGHT DSOS254A (2.5 GHz, 4 channels) for monitoring the ultrasonic signals; (3) an ultrasonic 5 MHz longitudinal wave contact transducer; (4) an ultrasonic 2.25 MHz transversal waves contact transducer; (5) a PC controlling the test.

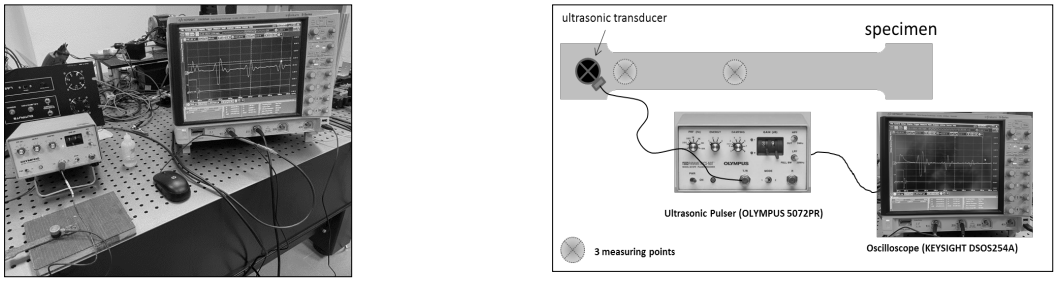

(a) (b)

Fig. 2. Ultrasonic contact tests setup: (a) main components and (b) a schematic drawing showing the TOF measuring points.

In particular, for each of the five samples, three time-of-flight (TOF) measurements of both longitudinal and transverse waves were performed. Such TOF measurements were performed in three different areas of the sample, as shown in Fig. 2b.

It is worth noticing that the TOF measurements were carried out through an averaging process of the acquired and normalized ultrasonic signals for each area of the tested specimens performed by the ad hoc developed Virtual Instrument (VI) created using the software LabView. So, starting from the TOF of the ultrasonic waves, known the thickness s of each of the three measurement zones in the sample, that is the spatial path of the wave in the material, the ultrasonic velocities v of the longitudinal waves and of the transversal waves were determined, respectively, by using:

$$v = \frac{2s}{TOF} \tag{6}$$

being $2s$ the wave path (the double of the thickness of the material).

Finally, known the density of each Ti6Al4V-ELI foam-based specimens, by implementing in the Eq. 5 the average values of the ultrasonic velocities, the elastic moduli were determined.

Results and Discussion

Experimental foaming tests Fig. 3 shows the micrographs of different sections of the foamed samples at a constant temperature of 1020°C for 240 minutes. It is possible to evaluate the effect of the HIP process conditions (in accordance with the values reported in Table 2).

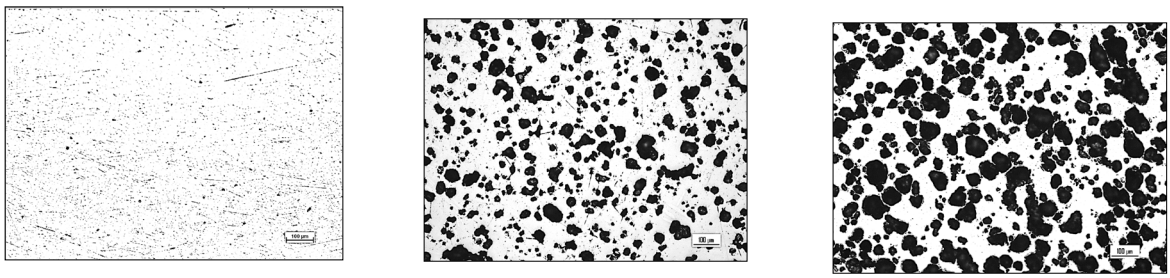

as received D100-A0.2HIP80 D100-A0.2HIP120

Fig. 3. Effect of the HIP conditions on the solid-state foaming after 240 minutes at 1020°C.

In the same Fig. 3 it is possible to appreciate the large difference between the foamed conditions and the as received one. The reported micrographs suggest that by increasing the HIP process pressure the porosity of the structure can be largely affected. It is thus reasonable to expect significant variations in terms of elastic properties of the material.

The images from the metallographic observations were also analysed quantitatively: in particular, the level of porosity was evaluated in terms of both average area (%) and average size (porosity diameter). Results have been reported in Fig. 4.

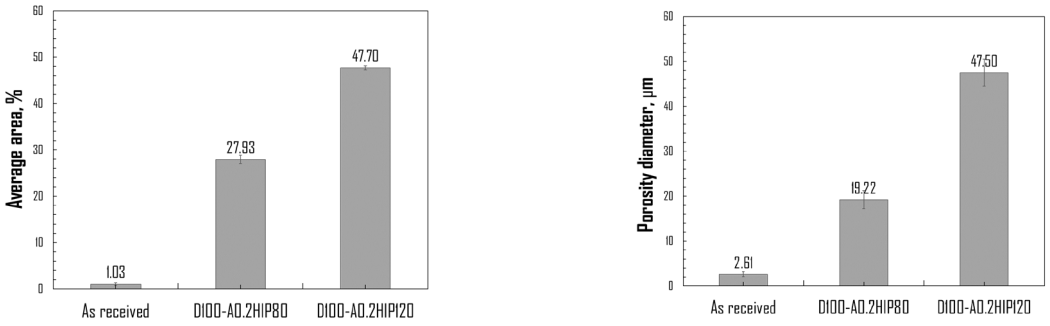

(a) (b)

Fig. 4. Effect of the HIP conditions in terms of Average area (a) and Average size (b) of the porosity.

It is interesting to note that after the foaming process the percentage area of voids varies from a minimum of about 1% (for the as received condition) to a maximum of 47.7% (D100-A0.2HIP120). At the same time, the average size of the pores varies from 2.61 to 47.50µm.

According to the graphs in Fig. 4, an increase in the HIP pressure from 80 to 120 MPa allowed to obtain an increase of the porosity equal to about 42%, while an increase in the average size of about 60%.

Experimental ultrasonic tests.

This section presents some results from ultrasonic tests aimed at determining the elastic properties of the investigated material after the foaming process. In particular, the attention was focused on the Young's modulus, whose values were compared with the elastic modulus obtained same alloy deriving from a conventional process and tested in "as received" condition.

The graphs in Fig. 5 show the results in terms of ultrasonic velocities and level of porosity. In both graphs, it is possible to observe a variation in the acoustic behavior of the specimens and a variation of the level of porosity, as well. In particular, it is worth noticing that as the porosity increases, the values of the velocities of both the longitudinal and the transversal waves decrease.

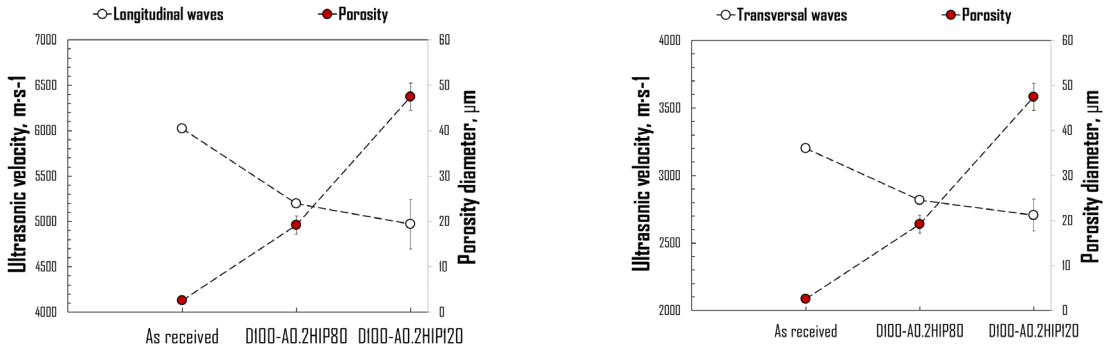

(a) (b)

Fig. 5. Ultrasonic velocities of the longitudinal (a) and transversal (b) waves measured according to the different levels of porosity.

On the contrary, in the graphs in Fig. 6 the values of the elastic moduli determined using Eq. 5 have been plotted together with the levels of porosity.

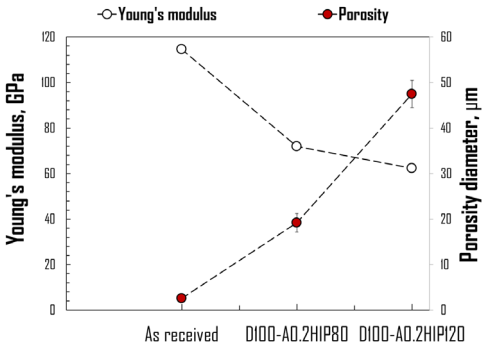

Fig. 6. Young's modulus for each Ti6Al4V-ELI foam-based specimen as a function of the different levels of porosity.

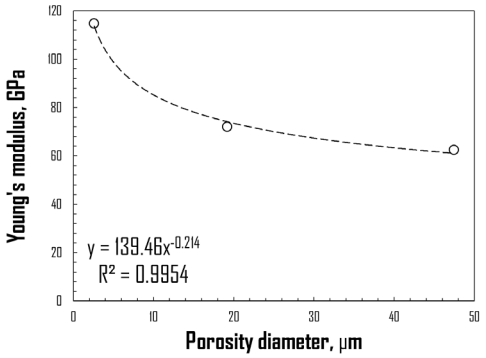

Fig. 7. Correlation between the level of porosity (Average diameter) and the Young's modulus evaluated using the ultrasound technique.

Also in terms of mechanical properties, a large decrease of the elastic moduli can be observed when the porosity increases: the Young's modulus was reduced from 114 GPa (the alloy in the "as received" condition) to about 62 GPa, when the maximum value of the HIP pressure was used. If compared to the "as received" condition, the increase in the HIP pressure allows to produce a porous structure, after the foaming process, able to drastically (about 45 %) reduce the elastic properties.

In addition, it is worthy of notice that a strong correlation between the porosity after the foaming process and the elastic properties could be determined (Fig. 7): using a power law data could be correlated in a robust way (R-squared equal to 0.995), thus demonstrating the possibility to efficiently design the elastic response of the material thought the definition of the porosity level which, in turn, is controlled by the foaming process.

Summary

In the present work different porosity levels after the foaming process (T=1020°C for 240 minutes) were obtained in specimens extracted from a billet produced by means of the Hot Isostatic Pressing (HIP) process of Ti powders.

Results coming from metallographic analyses allowed to evaluate an improved foaming capability (average porosity equal to about 60%) as the HIP pressure was increased from 80 to 120MPa.

In addition, ultrasonic contact tests allowed to evaluate the mechanical properties of the porous material obtained by the foaming process, which revealed to largely affect the stiffness (Young's modulus decreases when the porosity increases). The Young's modulus could be thus correlated to the level of porosity through a power function, thus paving the way to the customization of the prosthesis not anymore only in terms of shape according to the specific anatomy of the patient but also in terms of mechanical properties.

References

[1] E. F. Morgan, G.U. Unnikrisnan, A.I. Hussein, Bone Mechanical Properties in Healthy and Diseased States, Annu. Rev. Biomed. Eng. 20 (2018) 119-143. https://doi.org/10.1146/annurev-bioeng-062117-121139.

[2] D. Wu, P. Isaksson, S.J. Ferguson, C. Persson, Young's modulus of trabecular bone at the tissue level: A review, Acta Biomater. 78 (2018) 1-12. https://doi.org/10.1016/j.actbio.2018.08.001

[3] Y. Guo, F. Liu, X. Bian, K. Lu, P. Huang, X. Ye, C. Tang, X. Li, H. Wang, K. Tang, Effect of Pore Size of Porous-Structured Titanium Implants on Tendon Ingrowth, Appl. Bionics Biomech. 2022 **(**2022). https://doi.org/10.1155/2022/2801229
[4] M. Chimutengwende-Gordon, R. Dowling, C. Pendegrass, G. Blunn, Determining the porous structure for optimal soft-Tissue ingrowth: An in vivo histological study, PLoS One 13 (2018) 1-17. https://doi.org/10.1371/journal.pone.0206228
[5] M. Niinomi, M. Nakai, J. Hieda, Development of new metallic alloys for biomedical applications, Acta Biomater. 8 (2012) 3888-3903. https://doi.org/10.1016/j.actbio.2012.06.037
[6] C. Piao, D. Wu, M. Luo, H. Ma, Stress shielding effects of two prosthetic groups after total hip joint simulation replacement, J. Orthop. Surg. Res. 9 (2014) 1-8. https://doi.org/10.1186/s13018-014-0071-x
[7] S. Oppenheimer, D.C. Dunand, Solid-state foaming of Ti-6A1-4V by creep or superplastic expansion of argon-filled pores, Acta Mater. 58 (2010) 4387-4397. https://doi.org/10.1016/j.actamat.2010.04.034
[8] G. Palumbo, G. Ambrogio, A. Crovace, A. Piccininni, A. Cusanno, P. Guglielmi, L. De Napoli, G. Serratore, A Structured Approach for the Design and Manufacturing of Titanium Cranial Prostheses via Sheet Metal Forming, Metals 12 (2022) 293. https://doi.org/10.3390/met12020293
[9] J. Barrios-Muriel, F. Romero-Sánchez, F.J. Alonso-Sánchez, D.R. Salgado, Advances in orthotic and prosthetic manufacturing: A technology review, Materials 13 (2020) 295. https://doi.org/10.3390/ma13020295
[10] G. Ambrogio, G. Palumbo, E. Sgambitterra, P. Guglielmi, A. Piccininni, L. De Napoli, T. Villa, G. Fragomeni, Experimental investigation of the mechanical performances of titanium cranial prostheses manufactured by super plastic forming and single-point incremental forming, Int. J. Adv. Manuf. Technol. 98 (2018) 1489-1503. https://doi.org/10.1007/s00170-018-2338-6
[11] P. Guglielmi, A. Piccininni, A. Cusanno, A.A. Kaya, G. Palumbo, Mechanical and microstructural evaluation of solid-state foamed Ti6Al4V-ELI alloy, Procedia CIRP 110 (2022)105-110. https://doi.org/10.1016/j.procir.2022.06.021
[12] M.E. Gurtin, The linear theory of elasticity, in: Linear theories of elasticity and thermoelasticity, Springer, 1973.
[13] A. Castellano, P. Foti, A. Fraddosio, S. Marzano, M.D. Piccioni, Mechanical characterization of CFRP composites by ultrasonic immersion tests: Experimental and numerical approaches, Compos. Part B Eng. 66 (2014) 299-310. https://doi.org/10.1016/j.compositesb.2014.04.024

Materials Research Proceedings 28 (2023) 1435-1442 https://doi.org/10.21741/9781644902479-155

Micro-mechanical study of damage evolution in isotropic metallic materials

KNAAK Karl[1,a], REVIL-BAUDARD Benoit[1,b] and CAZACU Oana[1,c *]

[1]Department of Mechanical & Aerospace Engineering, University of Florida, REEF, Shalimar, USA

[a]karl.knaak@ufl.edu, [b]revil@ufl.edu, [c]cazacu@reef.ufl.edu

Keywords: Damage, Finite-Element, Unit-Cell

Abstract. Virtual tests enable the expansion of the knowledge base accessible by direct experimentation. In particular, the role of microstructure on damage can be investigated using unit-cell models for porous materials. Additionally, it is of great interest to assess the role of the loading history on the response. In this paper, we present a dedicated user-defined element (U.E.L.) that was developed and implemented in the finite element (F.E.) code, ABAQUS. Verification of the capabilities of the U.E.L. is provided. The simulation results presented provide insights into the effect of J_3 on the mechanical response and porosity evolution.

Introduction

Assessment of damage of polycrystalline metallic materials is a major concern for any engineering application. Consequently, there have been intense efforts to gain understanding of the dissipative mechanisms leading to damage and ultimately failure. While advancement in diagnostic techniques e.g., X-ray tomography, has led to improved understanding of damage evolution, data is limited to a few loading paths. Numerical studies are needed to provide interpretation of data as well as for gaining insights into the damage evolution for loadings that are inaccessible to direct mechanical testing.

Beginning with the pioneering works of Needleman and collaborators (see [1]) micro-mechanical finite-element (F.E.) studies using a cylindrical unit-cell were conducted. However, for analysis of the response under full 3-D loadings of isotropic materials with randomly distributed voids in three perpendicular directions, the unit-cell should be initially cubic see [2]–[5]. For a comprehensive survey of the literature on plasticity-damage couplings for isotropic materials with matrix obeying von Mises, Tresca, and the isotropic form of the CPB criterion [6], the reader is referred to the monograph [5]. For example, for a porous material, with matrix exhibiting tension-compression asymmetry, the F.E. results obtained using cubic unit-cells showed the importance of the matrix tension-compression asymmetry on the rate of void growth and confirm the predictions of the dilatational model of Cazacu-Stewart [7]. Moreover, anisotropy and creep in porous crystals were investigated with cubic unit-cells in [4] and the results were further explained using an analytical model for porous crystals in [5]. The F.E. results provide insights on the effects of stress triaxiality and Lode parameter on void evolution for ductile single crystals in the dislocation creep.

In this paper, we present results of a micro-mechanical finite-element (FE) study on cubic unit-cells performed using the commercial code ABAQUS [8]. To be able to investigate separately the influence of the invariants of the applied stress on porosity evolution, a user element routine (UEL) has been developed. The FE unit cell model and constitutive assumption is presented in Section 2 and the UEL developed is described in Section 3. Verification and validation of the U.E.L. conducted as well as results concerning the effects of J_3 on the dilatational response for tensile loadings are presented in Section 4. Conclusions of the study are presented in Section 5.

Content from this work may be used under the terms of the Creative Commons Attribution 3.0 license. Any further distribution of this work must maintain attribution to the author(s) and the title of the work, journal citation and DOI. Published under license by Materials Research Forum LLC.

Materials Research Proceedings 28 (2023) 1435-1442 https://doi.org/10.21741/9781644902479-155

General Numerical Setup

It is assumed that the porous solid contains a regular array of initially spherical voids. The inter-void spacing is considered to be the same in any direction. Thus, the unit cell is initially cubic with edge lengths 2 C_0 and contains a single void of initial radius r_0 at its center (see Fig. 1 a.). The void volume fraction is defined as:

$$f = \frac{V_{void}}{V_{cell}} = \frac{V_{cell} - V_{matrix}}{V_{cell}} = 1 - \frac{V_{matrix}}{V_{cell}} \tag{1}$$

so the initial void volume fraction writes as:

$$f_0 = \frac{\pi}{6}\left(\frac{r_0}{C_0}\right)^3 \tag{2}$$

Let **u** denote the incremental displacement between the current and reference configuration, and **t** the prescribed Cauchy stress vector, defined on the current configuration. Symmetry conditions are imposed on the coordinate planes. To simulate the constraints of the surrounding material, we need to enforce that the faces of the unit cell, which are initially parallel to the coordinate planes, remain planes and are shear free. Given the void geometry and the symmetry conditions, only $^1/_8{}^{th}$ of the unit-cell must be analyzed. The F.E. mesh considered in the calculations presented hereafter consists of 22,000 3-D tetrahedral ABAQUS C3D10 elements and is shown in Fig. 1 b. The coordinate axes are principal directions for the stress experienced by the porous material. The normal components, Σ_1, Σ_2, Σ_3 i.e. the tractions over the current areas of the RVE faces are calculated as follows:

$$\Sigma_1 = \frac{1}{C_2 \cdot C_3}\int_0^{C_3}\int_0^{C_2} t_1 dx_2\, dx_3\,, \Sigma_2 = \frac{1}{C_1 \cdot C_3}\int_0^{C_3}\int_0^{C_1} t_2 dx_1\, dx_3\,, \Sigma_3 = \frac{1}{C_1 \cdot C_2}\int_0^{C_2}\int_0^{C_1} t_3 dx_1\, dx_2 \tag{3}$$

C_i with i=1…3 denote the current cell dimensions are calculated using: $C_i = C_0 + U_i(t)$, i=1…3.

The overall principal strains and the von Mises macroscopic effective strain are calculated as:

$$E_1 = ln\left(\frac{C_1}{C_0}\right), E_2 = ln\left(\frac{C_2}{C_0}\right), E_3 = ln\left(\frac{C_3}{C_0}\right), E_e = \sqrt{\frac{2}{3}(E_1^2 + E_2^2 + E_3^2)} \tag{4}$$

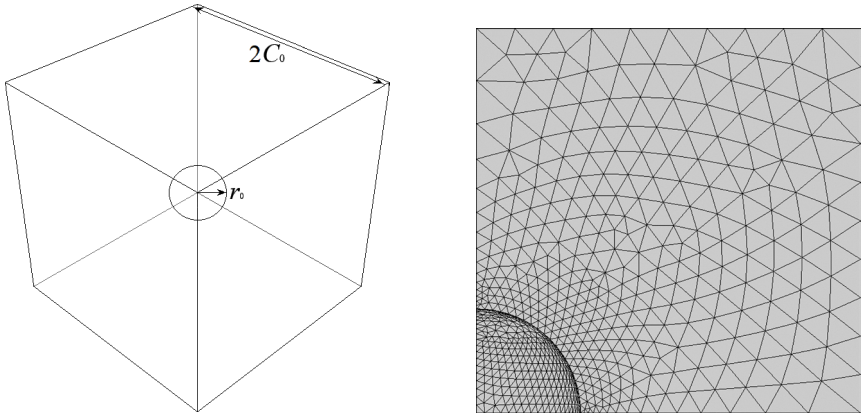

a) b)

Fig. 1. Depiction of a) unit-cell with single centrally located spherical void and fully dense matrix and b) FE mesh of (1/8th) of the unit-cell.

The time histories of the displacements, $U_i(t)$, i=1…3 are determined by the analysis in such a way that the overall Cauchy stresses Σ_1, Σ_2,Σ_3 experienced by the porous material follow a prescribed proportional loading history. Such prescribed proportional loading are of interest for assessing the effects of the stress state (stress invariants) on the response of porous solids and damage evolution. Let us recall that for isotropic materials, the stress state effects are uniquely determined by the following stress invariants: the mean stress, $\Sigma_m = \frac{1}{3}(\Sigma_1 + \Sigma_2 + \Sigma_3)$, and the 2nd and 3rd invariants of the deviatoric stress tensor J2 and J3; the stress triaxiality is defined $T_\Sigma = \frac{\Sigma_m}{\Sigma_e}$, with $\Sigma_e = \sqrt{3J_2}$

U.E.L. Subroutine

The U.E.L. is a 2-node, 6 D.O.F. ($u(i)$, i=1…6), truss element fixed to the R.V.E. at the corner node across the body diagonal from the void. Node 1 of the U.E.L. is the corner node of the R.V.E. and node 2 is free and receives a displacement boundary condition in the x_1, x_2, and x_3 directions. Depending on loading, the "control direction" changes such that U.E.L. change in length is compatible with the sign of the desired applied force. The U.E.L. has 3 input parameters: stress triaxiality T_Σ, sign of third invariant S_{J_3}, and spring stiffness k_{prop}. The U.E.L. calculates the force applied to node 1 (corner node of R.V.E.) in the x_1, x_2, x_3 directions based on a displacement applied to node 2. U.E.L. change in length is calculated first, stress ratio ρ to ensure the prescribed T_Σ is calculated next, then effective spring stiffnesses in the x_1, x_2, x_3 based on the change in length and stress ratios are calculated, and finally the U.E.L. stiffness matrix and force vectors are constructed.

For example, for overall axisymmetric loading, $\Sigma_1 = \Sigma_3$ and $\Sigma_1 = \rho \cdot \Sigma_2$ with ρ constant.
these steps are written out as follows:

1. Calculate the change in length in the 3 orthogonal directions:

$$\Delta u_1 = u(1) - u(4), \Delta u_2 = u(2) - u(5), \Delta u_3 = u(3) - u(6) \tag{5}$$

2. Calculate the necessary stress ratio ρ to impose prescribed stress triaxiality:

$$\rho = \frac{3T_\Sigma - S_{J_3}}{3T_\Sigma + 2 \cdot S_{J_3}} \tag{6}$$

3. Calculate effective stiffness of the 3 orthogonal springs based on load scenario:
   - Control direction along x_2:

$$k_{eff}^{(1)} = \rho k_{eff}^{(2)} \frac{A_1}{A_2} \frac{\Delta u_2}{\Delta u_1}, k_{eff}^{(2)} = k_{prop}, k_{eff}^{(3)} = \rho k_{eff}^{(2)} \frac{A_3}{A_2} \frac{\Delta u_2}{\Delta u_3} \tag{7}$$

   - Control direction along x_1:

$$k_{eff}^{(1)} = k_{prop}, k_{eff}^{(2)} = \frac{k_{eff}^{(1)}}{\rho} \frac{A_2}{A_1} \frac{\Delta u_1}{\Delta u_2}, k_{eff}^{(3)} = \rho k_{eff}^{(1)} \frac{A_3}{A_1} \frac{\Delta u_1}{\Delta u_3} \tag{8}$$

4. Calculate the stiffness matrix of the U.E.L.
5. Calculate the force vector of the U.E.L.

The forces from the force vector are applied to the corner node of the R.V.E. producing incremental displacements $U_i(t)$. Every node on each periodic face has its respective normal displacement defined as the incremental displacement, $U_i(t)$ in the periodic boundary condition.
In the next section, we further verify and use the developed subroutine. For this purpose, we assume that the plastic behavior of the fully dense matrix is governed by the von Mises yield criterion with associated plastic flow rule, i.e. the effective stress is defined as:

$$\bar{\sigma} = \sqrt{3J_2} \tag{9}$$

It is assumed that hardening is isotropic and governed by the equivalent plastic strain, $\bar{\varepsilon}^p$ defined as the work-equivalent measure of the effective stress $\bar{\sigma}$. A Swift -type law is considered, so in the plastic regime:

$$\bar{\sigma} = A(\varepsilon_0 + \bar{\varepsilon}^p)^n \tag{10}$$

where A, ε_0, and n are material parameters. The parameter values used in the FE calculations are as follows: elasticity parameters are Young's Modulus E = 200 GPa and Poisson's coefficient ν = 1/3; the hardening parameters are: A = 728.22 MPa, ε_0 = 0.0025, and n = 0.1. The simulations are conducted using the built-in von Mises material implementation in Abaqus [8]. The unit-cell has initial edge length $2 \cdot C_0$ = 12 mm, and initial void radius r0 = 1.625 mm (see Fig.1), which correspond to an initial porosity of 1.04%.

U.E.L. Verification, Validation and Results

Tensile axisymmetric loadings corresponding to fixed stress triaxiality $T_\Sigma = 1$ were compared with results from the literature [2]. Note that the stress-strain and void evolution predictions match nearly exactly throughout the entire loading path and provide excellent agreement of the U.E.L. subroutine for tensile loadings with $J_3 > 0$ (Fig. 2) or at $J_3 < 0$ (Fig. 3).

a)

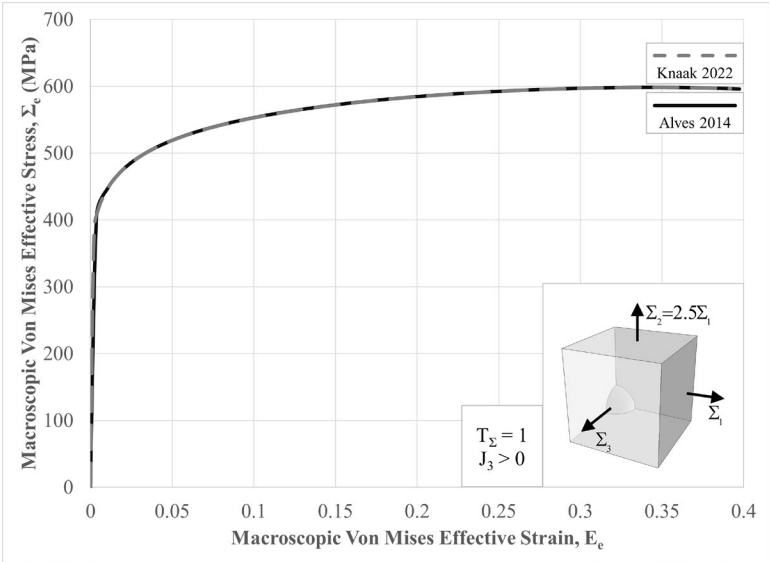

b)

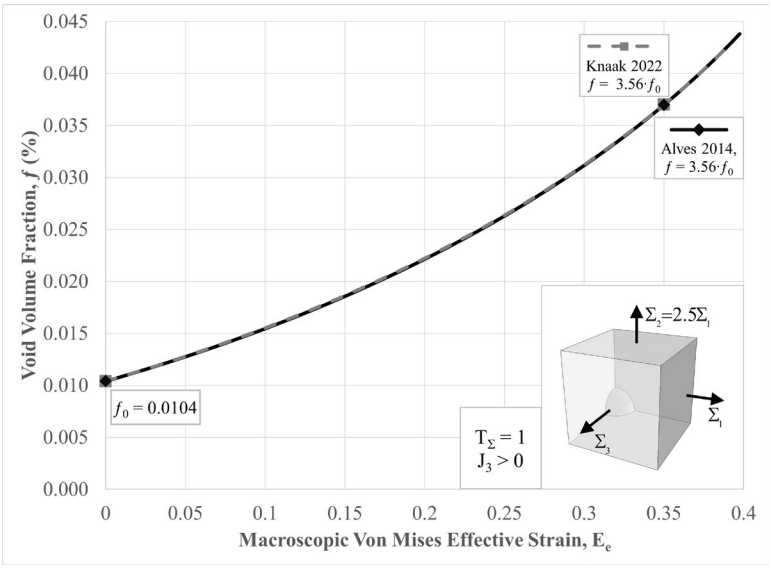

Fig. 2. Comparison of axisymmetric loading corresponding to fixed stress triaxiality $T_\Sigma = 1$ with $J_3 > 0$ obtained with the UEL and results in [2] for a) macroscopic effective stress-strain b) void volume fraction vs. macroscopic effective strain.

a)

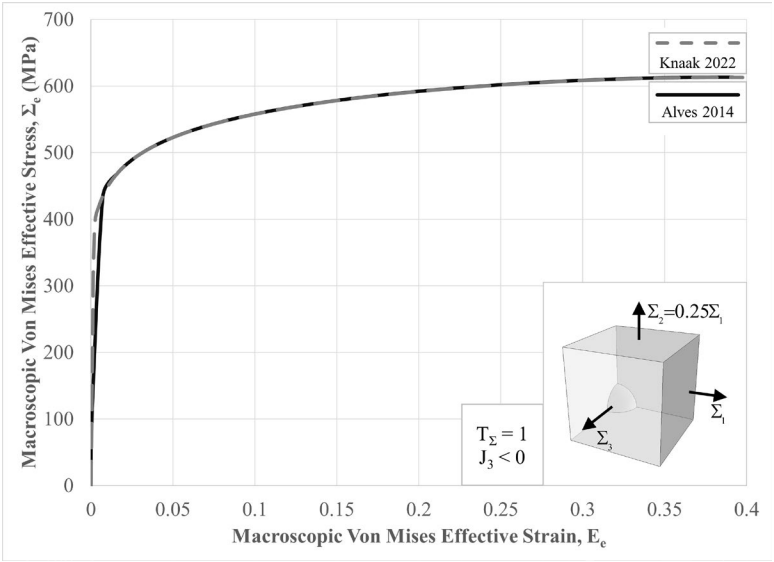

b)

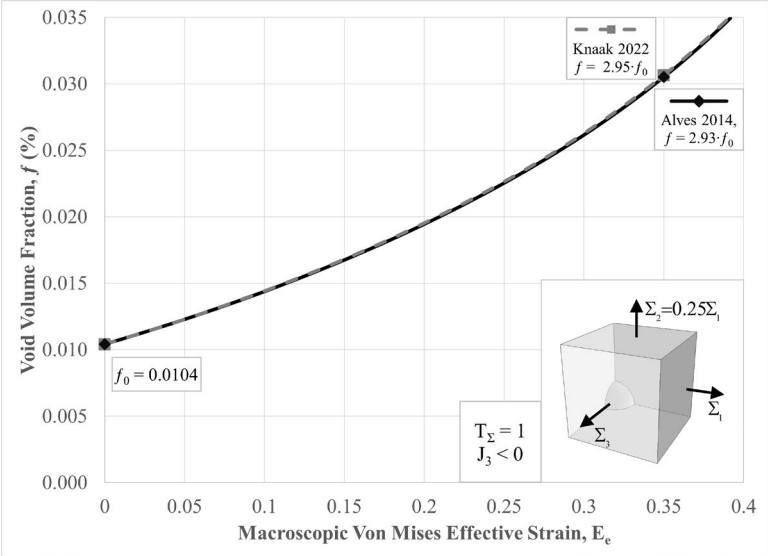

Fig. 3. Comparison of axisymmetric loading corresponding to fixed stress triaxiality $T_\Sigma = 1$ with $J_3 < 0$ obtained with the UEL and results in [2] for a) macroscopic effective stress-strain b) void volume fraction vs. macroscopic effective strain.

Fig. 4 shows a comparison of the stress-strain response predictions and void evolution predictions for loadings at same triaxiality $T_\Sigma = 1$ with $J_3 > 0$ and $J_3 < 0$, respectively.

a)

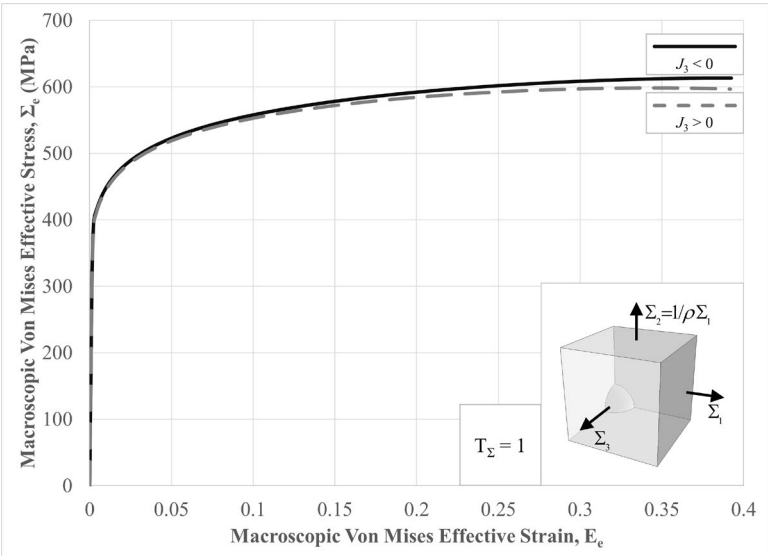

b)

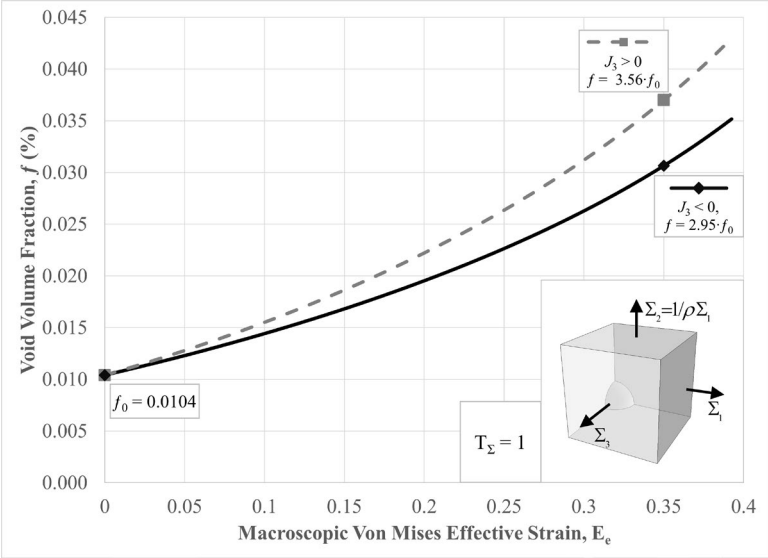

Fig. 4. Comparison of axisymmetric loadings corresponding to fixed stress triaxiality $T_\Sigma = 1$ with $J_3 > 0$ and $J_3 < 0$ predictions in a) macroscopic effective stress-strain response and b) void volume fraction vs. macroscopic effective strain.

Stress-strain response shows the response for loading corresponding to $J_3 < 0$ is stiffer than the response at $J_3 > 0$. This leads to a faster void growth for loading corresponding $J_3 > 0$ than the response for $J_3 < 0$. It can be concluded that there is a significant influence of J_3 (principal stress ordering) on stress-strain response and void evolution for a porous material governed by the von Mises yield criterion.

Summary

The knowledge gained experimentally needs to be complemented with systematic investigations in which the role of each stress invariant can be isolated. To be able to assess the influence of the loading history, and the relative influence of J_3 on both the stress-strain response and porosity evolution, it is essential that during the simulations the triaxiality remains constant. For this purpose, a user element routine was developed for the commercial finite-element code ABAQUS. The verification of the accuracy of the implementation was performed. Most importantly, the F.E. results show that even for isotropic porous von Mises materials, the third invariant, J_3, influences the response.

References

[1] J. Koplik, A. Needleman, Void growth and coalescence in porous plastic solids, Int. J. Solid. Struct. 24 (1988) 835–853. https://doi.org/10.1016/0020-7683(88)90051-0

[2] J.L. Alves, O. Cazacu, Micromechanical study of the dilatational response of porous solids with pressure-insensitive matrix displaying tension-compression asymmetry, European J. Mech. Solid. 51 (2015) 44-54. https://doi.org/10.1016/j.euromechsol.2014.11.010

[3] J. Faleskog, G. Xiaosheng, C.F.Shih, Cell model for nonlinear fracture analysis - I. Micromechanics calibration, Int. J. Fract. 89 (1988) 355-373. https://doi.org/10.1023/A:1007421420901

[4] A. Srivastava, A. Needleman, Porosity evolution in a creeping single crystal, Modell. Simul. Mater. Sci. Eng. 20 (2012) 035010. https://doi.org/10.1088/0965-0393/20/3/035010

[5] O. Cazacu, B. Revil-Baudard, N. Chandola, Plasticity-Damage Couplings: From Single Crystal to Polycrystalline Materials, Springer, 2019.

[6] O. Cazacu, B. Plunkett, F. Barlat, Orthotropic yield criterion for hexagonal closed packed metals, Int. J. Plast. 22 (2006) 1171-1194. https://doi.org/10.1016/j.ijplas.2005.06.001
[7] O. Cazacu, J. B. Stewart, Analytic plastic potential for porous aggregates with matrix exhibiting tension–compression asymmetry, J. Mech. Phys. Solid. 57 (2009) 325-341. https://doi.org/10.1016/j.jmps.2008.10.010
[8] Abaqus, Abaqus - Version 6.14-1. Dassault Systemes Simulia Corp., Providence, RI, 2014.

Materials Research Proceedings 28 (2023) 1443-1452 https://doi.org/10.21741/9781644902479-156

Micromechanical modeling of failure in dual phase steels

AYDINER Ilbilge Umay[1,a], TATLI Berkehan[1,b] and YALÇINKAYA Tuncay [1,c *]

[1]Department of Aerospace Engineering, Middle East Technical University, 06800, Ankara, Turkey

[a]aydiner.umay@metu.edu.tr, [b]btatli@metu.edu.tr, [c]yalcinka@metu.edu.tr

Keywords: Dual-Phase Steel, Cohesive Zone Modelling, Crystal Plasticity

Abstract. Having brittle martensitic islands diffused in a ductile ferrite matrix, dual-phase (DP) steels are known for their high formability and favorable material properties. Although they have already proven their advantages in the industry, there are still discussions regarding their microstructure-macroscopic response link. In order to effectively exploit their advantages and analyze their ductility in metal forming operations, the failure mechanisms of DP steels must be well examined following a micromechanics-based approach. There are a number of failure mechanisms to be addressed at the micro scale such as ferrite-martensite and ferrite-ferrite interface decohesion as well as martensite cracking depending on the different microstructural parameters and stress state. A crystal plasticity based finite element framework for RVE calculations is followed here based on the previous work which focuses solely on the plastic deformation (see [1]). Isotropic J2 plasticity model is employed for the hard martensite phase while the rate-dependent crystal plasticity framework is used for the ductile ferrite phase. Cohesive zone elements are inserted at the ferrite-martensite and ferrite-ferrite interfaces for intergranular cracking analysis, besides, intragranular cracking in martensite phase is addressed through an uncoupled damage model. First, a preliminary study was performed in order to identify and calibrate aforementioned failure models, then, various 3D polycrystalline RVEs having different microstructural parameters loaded with different stress triaxialities are analyzed and discussed adding up to the preliminary discussions presented in [2].

Introduction

Dual-phase (DP) steels are one of the material groups most favored by the automotive industry due to their good formability without compromising on high strength. These mechanically advantageous characteristics of dual phase steels stem from the micromechanical cooperation between two different phases, namely the soft ferrite phase and the hard martensite phase. Martensite islands are interspersed between the ferrite grains and this heterogeneous microstructure translates to complex fracture mechanisms that should be studied in the micro scale. Stress concentration and strain localization due to the strength and ductility contrast between two constituent phases lead to various failure mechanisms. Although previous works give various results about the exact location of the failure initiation, three different types of damage nucleation modes have been identified to predominate in DP steels which are ferrite/ferrite (F/F) decohesion, ferrite/martensite (F/M) decohesion and martensite cracking (see [3-6]). Therefore, each failure mechanism should be analyzed with a separate compatible technique and a multiscale approach is essential to establish the macroscale results of plastic deformation, damage evolution and crack initiation occurring at the microscale. The variation of dominant damage nucleation mode is mainly dependent on martensite distribution and volumetric fraction [3,4,6]. Still, according to [7] failure in DP-steels is highly related also with the stress state, and one should place greater emphasis on the effect of triaxiality variation on the material. Most of the previous works [8,9] have been centered around uniaxial tension cases, yet there exist few papers mentioning different stress states [10]. There are examples of modeling DP in either simplified or realistic dual phase

Content from this work may be used under the terms of the Creative Commons Attribution 3.0 license. Any further distribution of this work must maintain attribution to the author(s) and the title of the work, journal citation and DOI. Published under license by Materials Research Forum LLC.

microstructures (see e.g. [8-12]) at representative volume element (RVE) scale. Due to its low ductility, phenomenological models are deemed sufficient to represent the constitutive behavior of martensite phase while ferrite deformation is handled by both phenomenological and crystal plasticity models (see e.g. [1,12]). For the modelling of void nucleation and growth among ferrite grains, Modified Mohr-Coulomb (MMC) [10] and Gurson-Tvergaard-Needleman (GTN) [13,14] models are used in the literature. Martensite cracking on the other hand, has been modeled with various approaches such as the extended finite element method (XFEM) [14], maximum principal stress criterion [10] and Bao-Wierzbicki failure criterion [15]. Ferrite/ferrite [13] and ferrite/martensite [9,11,16] grain boundary decohesion have been observed by the incorporation of cohesive zone model (CZM). Parameter identification of cohesive elements has been performed through nanoindentation tests [16] and compact tension (CT) specimen simulations [13] by obtaining critical failure stress and fracture energy.

In this study, three dimensional RVEs are generated using Voronoi tessellations where J_2 plasticity and crystal plasticity frameworks are employed for the martensite and ferrite phases respectively. The main goal is to predict crack initiation and progression in DP steel by inserting cohesive elements to model the decohesion of ferrite/ferrite and ferrite/martensite interfaces. Moreover, an uncoupled damage model is employed in order to model the intragranular cracking of martensite phase. Each type of decohesion is simulated with a different set of interface parameters to obtain the appropriate constitutive behavior. Both the experimental results from the literature and the numerical techniques are used for parameter identification. Those numerical techniques include an inclusion RVE study, CT specimen and nanoindentation simulations. Crystal plasticity parameters are also obtained through an RVE study of pure ferrite phase. Lastly, polycrystalline dual phase RVEs are analyzed under various stress states, martensite distributions and crystallographic orientations to discuss and compare the failure results with respect to the observations in the literature.

Constitutive Models

Ferrite phase is modeled with rate dependent crystal plasticity framework that links the crystallographic slip at the microscale to the macroscopic deformation measures. In this framework, the two fundamental mechanisms causing the macroscopic deformation are elastic lattice distortion and crystallographic slip caused by dislocation motion on active slip systems (see [17,18]). The deformation gradient is multiplicatively divided into an elastic and a plastic part in the finite strain formulation that serves as the basis for the crystal plasticity model employed here,

$$\mathbf{F}=\mathbf{F}_e\cdot\mathbf{F}_p \tag{1}$$

The rate of change of $\mathbf{F}_p$ is related to the plastic slip rates $\dot{\gamma}^\alpha$ of the α by,

$$\dot{\mathbf{F}}_p\cdot\mathbf{F}_p^{-1}=\sum_\alpha \dot{\gamma}^\alpha \mathbf{m}^\alpha\otimes\mathbf{n}^\alpha, \tag{2}$$

where $\mathbf{m}^\alpha$ and $\mathbf{n}^\alpha$ represent the slip direction and slip normal in the reference configuration. Power law relation is used to obtain the evolution of plastic slip rate $\dot{\gamma}^\alpha$,

$$\dot{\gamma}^\alpha=\dot{\gamma}_0\left|\frac{\tau^\alpha}{g^\alpha}\right|^n \mathrm{sign}(\tau^\alpha) \tag{3}$$

where $\dot{\gamma}_0$ refers to the reference plastic slip rate and n refers to the rate sensitivity exponent. τ^α denotes the resolved shear stress and g^α is the slip resistance on the slip system α that controls the hardening of the single crystal. Evolution of slip resistance is governed by,

$$\dot{g}^{\alpha}=\sum_{\beta} h^{\alpha\beta}\left|\dot{\gamma}^{\beta}\right| \tag{4}$$

where $h^{\alpha\beta}$ and $h^{\alpha\alpha}$ denotes the latent hardening matrix and self-hardening rate respectively. Following basic forms are adapted for the evolution of those,

$$h^{\alpha\alpha}=h_0 \operatorname{sech}^2\left|\frac{h_0\gamma}{g_s-g_0}\right| \tag{5}$$

$$h^{\alpha\beta}=q^{\alpha\beta}h^{\alpha\alpha} \quad (\alpha\neq\beta) \tag{6}$$

where h_0 is the initial hardening modulus, g_0 is the initial slip resistance and g_s is the saturation slip resistance. Crystal plasticity simulations of the ferrite phase in this paper use {112}[111] slip family.

Due to the very limited ductile deformation, the martensite phase is modeled with J_2 plasticity framework with isotropic hardening in order to have a less expensive analysis, while ferrite phase, which accommodates the majority of the deformation in DP steels is simulated through a crystal plasticity model. The martensite plasticity model is described as [19],

$$\sigma_{y,m}=\sigma_{y_0,m}+k_m\left(1-\exp\left(-\varepsilon_p n_m\right)\right) \tag{7}$$

$$\sigma_{y_0,m}=300+1000C_m^{1/3} \tag{8}$$

$$k_m=\frac{1}{n_m}\left[a+\frac{bC_m}{1+\left(\frac{C_m}{C_0}\right)^q}\right] \tag{9}$$

where $\sigma_{y,m}$, ε_p and C_m denotes respectively the current yield strength, accumulated plastic strain and carbon content expressed in wt.%. Initial yield stress, $\sigma_{y_0,m}$, hardening modulus, k_m and hardening exponent, n_m, are material parameters. The values provided by [19] are used for the hardening parameters of the martensite phase throughout this study and given as, C_m=0.3 wt%, a=33 GPa, C_0=0.7, q=1.45, b=360 GPa, n_m=120. Moreover, the Young's modulus and Poisson's ratio are taken to be E=210 GPa and ν=0.3, respectively.

Failure Models

Bao and Wierzbicki failure criterion [20] is adopted to predict the intragranular failure in martensite grains. In this criterion, equivalent plastic strain to fracture $\bar{\varepsilon}_f$ is assumed to be dependent on the stress triaxiality $\eta=\sigma_m/\bar{\sigma}$, in which $\bar{\sigma}$ is the Von Mises equivalent stress and σ_m is the mean stress. The fracture locus can be accurately characterized by a piece-wise function of the following form when stress triaxiality is assumed to be constant throughout the experiment,

$$\bar{\varepsilon}_f=\begin{cases}\dfrac{C_1}{1+3\eta}, & -1/3\leq\eta\leq 0\\ C_2+(C_2-C_1)(3\eta-1), & 0\leq\eta\leq 1/3\\ C_2\exp\left(-\alpha(\eta-1/3)\right), & \eta\geq 1/3\end{cases} \tag{10}$$

where $C_1=\bar{\varepsilon}_f^{ss}$ is the equivalent plastic strain to fracture in pure shear, $C_2=\bar{\varepsilon}_f^{UT}$ is the equivalent plastic strain to fracture in uniaxial tension and α is the fitting parameter used for large triaxiality values. Damage accumulation is calculated by considering the following integral,

$$D(\bar{\varepsilon}_p) = \int_0^{\bar{\varepsilon}_p} \frac{1}{\bar{\varepsilon}_f} d\bar{\varepsilon}_p \tag{11}$$

It follows that, damage only increases as $\bar{\varepsilon}_f$ is always positive according to Eq. 10.

The Park-Paulino-Roesler (PPR) model [21], a unified, mixed-mode, potential based cohesive zone model, is used to simulate the decohesion of the ferrite/ferrite and ferrite/martensite grain boundaries. The framework has already been applied successfully for the intergranular cracking in polycrystalline plasticity (see [22]). The following is a definition of the potential function of PPR,

$$\psi(\Delta_n,\Delta_t)= \min(\phi_n,\phi_t) + \left[\Gamma_n \left(1-\frac{\Delta_n}{\delta_n}\right)^{\alpha} \left(\frac{m}{\alpha}+\frac{\Delta_n}{\delta_n}\right)^{m} +\phi_n-\phi_t\right] \times \left[\Gamma_t \left(1-\frac{|\Delta_t|}{\delta_t}\right)^{\beta} \left(\frac{n}{\beta}-\frac{|\Delta_t|}{\delta_t}\right)^{n} +\phi_t-\phi_n\right] \tag{12}$$

Here, m, n are non-dimensional exponents, α, β are shape parameters, δ_n, δ_t are the normal and tangential final crack opening widths, ϕ_n, ϕ_t are fracture energies in normal and tangential directions, Δ_n is the normal separation, Δ_t is the effective sliding displacement. Γ_n, Γ_t are energy constants that are related to shape parameters and initial slope indicators. Shape parameters α, β define the softening responses and λ_n, λ_t are the initial slope indicators that control cohesive stiffness and cohesive elastic behavior. Fracture energies ϕ_n, ϕ_t are the areas under the pure normal and tangential traction–separation curves. The traction functions are defined as the derivatives of the potential function with respect to corresponding separations,

$$T_n(\Delta_n,\Delta_t)= \frac{\partial \psi}{\partial \Delta_n}, \; T_t(\Delta_n,\Delta_t)= \frac{\partial \psi}{\partial \Delta_t} \tag{13}$$

When separation reaches critical values, the traction is equal to the corresponding cohesive strength (σ_{max}, τ_{max}). Nine input parameters, including normal fracture energy (ϕ_n), tangential fracture energy (ϕ_t), normal cohesive strength (σ_{max}), tangential cohesive strength (τ_{max}), normal shape parameter (α), tangential shape parameter (β), normal initial slope indicator (λ_n), and tangential initial slope indicator (λ_t) are needed to be identified to model the behavior of each interface. For more details about the formulation and applications see [2,23].

The ability of the model to capture the mixed mode fracture makes it very suitable to three-dimensional framework of this study.

Numerical Implementation

Material parameters of ferrite phase are identified through a generated pure ferrite polycrystalline RVE. Cubic elastic parameters are taken from [24] as C_{11}=231.4 GPa, C_{12}=134.7 GPa, C_{44}=116.4 GPa and experimental data presented in [6] is utilized to fit the flow curves obtained from RVE simulations (see [12] for more details). Obtained hardening parameters are tabulated in Table 1. Reference slip rate $\dot{\gamma}_0$ is taken to be 0.001 s^{-1} while rate sensitivity exponent n is determined as 25 and the ratio of latent to self-hardening assumed to be 1.

Table 1. Crystal plasticity parameters for ferrite phase.

Slip Systems	g_s [MPa]	h_0 [MPa]	g_0 [MPa]
{112}⟨111⟩	252	475	98

Eq. 1-6 with the provided material parameters are implemented as a user material subroutine (UMAT) in ABAQUS software based on the framework of Huang (see [25]).

Bao-Wierzbicki uncoupled damage model (see Eq. 3) is applied amongst martensite grains to observe the damage behavior of martensite phase in polycrystal RVEs. The parameter identification of the model is performed by the simulation of a tensile specimen to match the

experimental data of the martensite phase given in [6] (see e.g. [15]). Obtained model parameters are α=1.54, C_1=0.04 and C_2=0.04. This damage model with the provided model parameters is then implemented in ABAQUS by means of a user-defined field subroutine (USDFLD).

Identification of PPR cohesive zone model parameters is a rather comprehensive problem. Since ferrite/ferrite grain boundary decohesion is also considered on top of ferrite/martensite grain boundary decohesion in this study, PPR model parameters of both interfaces must be fitted all together to the experiments. For that, first results provided in [2] are utilized for ferrite/martensite interface. Then, in order to find the critical stress and failure energy of the ferrite/ferrite interface a CT-specimen study is performed as exemplified in [13]. Lastly, ferrite/martensite inclusion problem that includes both ferrite/ferrite and ferrite/martensite interfaces is analyzed for the final parameter calibration of each constituent interface simultaneously. For compactness, details of the parameter identification study for PPR cohesive zone model are not shown here. See Table 2 for the identified model parameters for the ferrite/ferrite and ferrite/martensite interfaces.

Table 2. Calibrated PPR CZM parametes for ferrite/ferrite and ferrite/martensite interfaces.

Interface	σ_{max} [MPa]	τ_{max} [MPa]	ϕ_n [N/mm]	ϕ_t[N/mm]	α	β	λ_n	λ_t
F/F	650	227.5	230	230	4.46	2.74	0.001	0.002
F/M	1500	525	0.4	0.4	4.46	2.74	0.01	0.02

In the FE calculations, 10-node second-order tetrahedral elements (C3D10) are used to simulate bulk elements, while 12-node compatible triangular cohesive elements are used between the interfaces. The Voronoi-based tessellation generator software Neper [26] was used to create 3D microstructures. Input files are modified by an in-house MATLAB code that identifies the ferrite/ferrite and ferrite/martensite interfaces and inserts cohesive elements to those interfaces by considering element connectivity in the original mesh. Updated input files are then run through ABAQUS along with the user material subroutines (UMAT) for both crystal and J2 plasticity, user element subroutine (UEL) for the PPR CZM and user-defined field (USDFLD) for the Bao-Wierzbicki damage model. The next section presents and discusses the findings.

Numerical Examples

This section presents numerical findings in three-dimensional RVEs, and briefly discusses the impact of microstructural parameters on the plastic deformation and failure behavior of dual-phase steels. This is accomplished by producing a number of cubic polycrystalline RVEs, which are non-periodic, with 250 and 280 randomly oriented and distributed grains. There are two main morphologies with different martensite distributions but same volumetric fraction of 15%. The input files for ABAQUS are generated via an in-house MATLAB script as mentioned previously. While the martensite phase is assigned to the classical J_2 plasticity theory with isotropic hardening as given in Eq. 7, the rate-dependent crystal plasticity model that has been presented through Eq. 1–6 with the hardening parameters in Table 1 is assigned to the ferrite phase. Boundary conditions are defined such that RVE analysis can follow the mechanical response of the material under various stress states that have different overall triaxiality values (see [12] for more details). For all simulations, applied strain rate is assumed to be 0.001 s^{-1}. Volumetric averaging method is then used to obtain the true stress-strain curves.

First, six RVEs, each of three having the same martensite distribution, are analyzed. Crystal orientations of ferrite grains are randomly changed for each RVE to study the effect of grain orientation and microstructure on the material response and damage initiation. Fig. 1 shows the homogenized stress-strain curves of the simulations plotted on top of the experimental results [6].

The results from the first morphology show a slight anisotropy due to the relatively lower number of ferrite grains with respect to the second morphology. When Fig. 1a is compared to Fig. 1b, it is very obvious that variation in the martensite distribution and morphology changes the overall response of the material to a great extent. Looking at this figure, the effect of crystal orientation may not be clear enough to distinguish. In order to have a better understanding of how grain orientation affects the stress and damage evolution on the microstructure, von Mises Stress and damage contours are plotted for each morphology at the same cross section and instant in Fig. 2 and Fig. 3. Here, by examining the significant difference between decohesion, deformation and damage accumulation patterns, one can easily deduce that microstructural parameters of DP-steels have a considerable influence on the crack initiation, growth, and propagation. Here, it should be noted that ferrite grains are colored gray in all damage distribution contours as no damage model is employed for the ferrite phase.

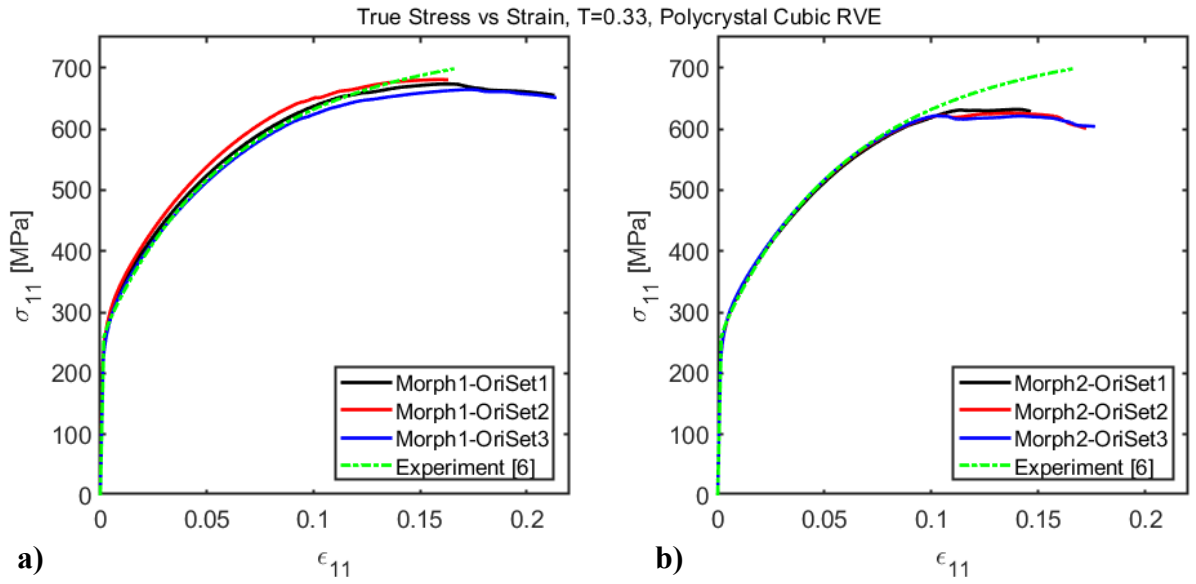

Fig. 1. True stress versus true strain curves of a) the first morphology b) the second morphology with three different orientation sets.

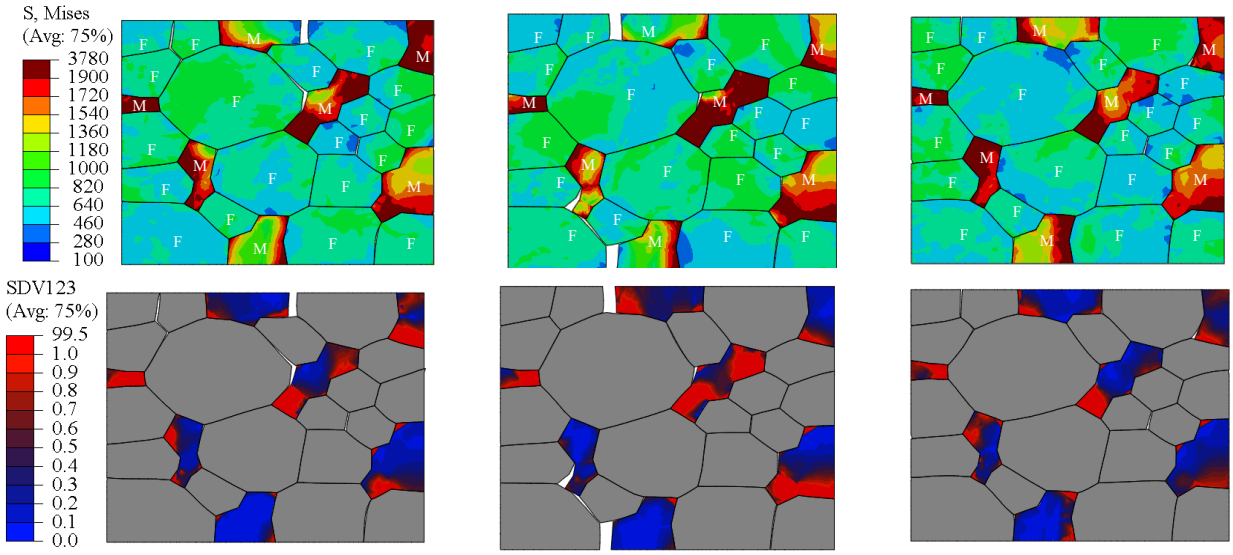

Fig. 2. Von Mises Stress (Top) and Damage (Bottom) distributions of Morph1-Oriset1 (Left), Morph1-Oriset2 (Middle), Morph1-Oriset3 (Right). F: Ferrite, M: Martensite.

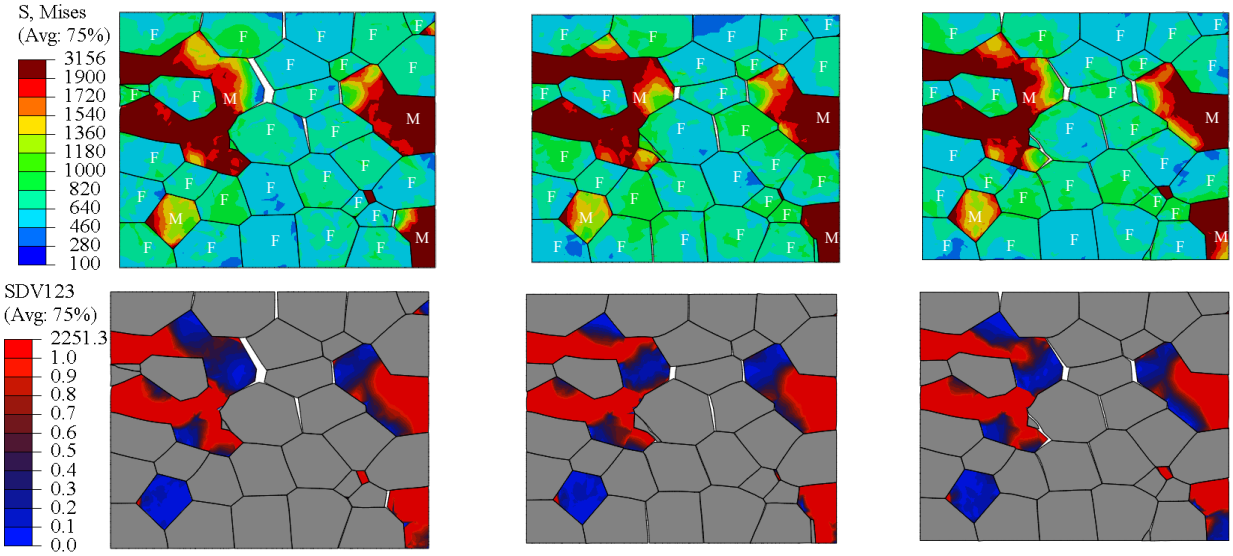

Fig. 3. Von Mises Stress (Top) and Damage (Bottom) distributions of Morph2-Oriset1 (Left), Morph2-Oriset2 (Middle), Morph2-Oriset3 (Right). F: Ferrite, M: Martensite.

Then, the analyses are carried out for three RVEs having the same crystal orientation and martensite distribution with three different stress triaxialities. Martensite distribution selected here is the same as the first morphology to be able to capture the sole effect of stress state on the failure mechanisms and stress distribution. Obtained flow curves are shown in Fig. 4. As per expectations, higher stress triaxiality translates to lower failure strains. From Fig. 5, it can be inferred that when triaxiality is held at 1.5, intergranular decohesion leads to complete failure with the martensite grains remaining below critical damage, in contrast with the other examples.

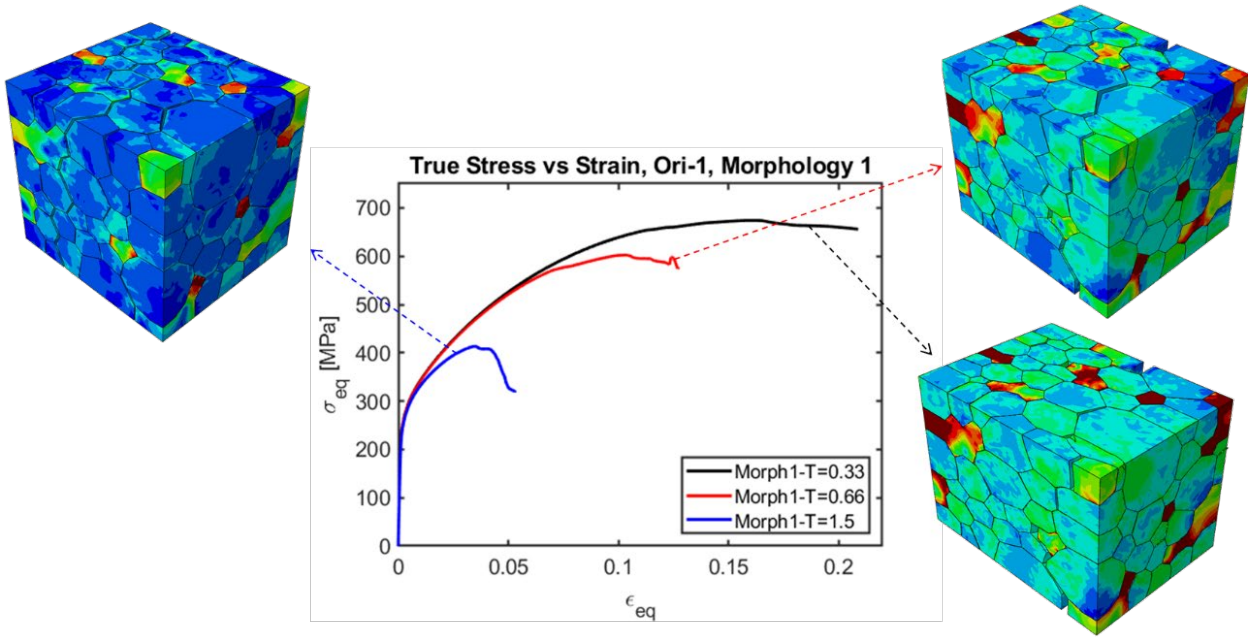

Fig. 4. True stress versus true strain curves of the first morphology with three different stress triaxialities.

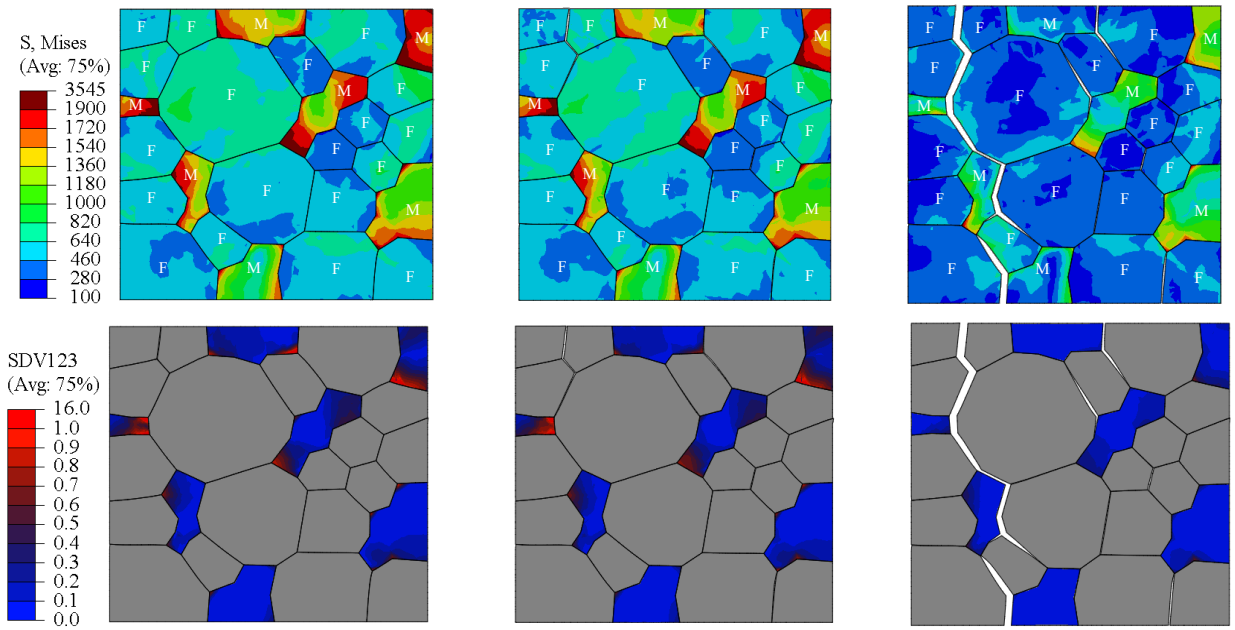

Fig. 5. Von Mises Stress (Top) and Damage (Bottom) distributions of Morph1-T=0.33 (Left), Morph1-T=0.66 (Middle), Morph1-T=1.5 (Right). F: Ferrite, M: Martensite.

Summary

This study makes an attempt to address the microstructure evolution, constitutive response, and failure in three-dimensional dual phase steel microstructures through polycrystalline RVEs employing J_2 and crystal plasticity frameworks in addition to cohesive zone and damage models. Analyses are performed for different orientation sets and morphologies under various stress triaxialities. The study clearly demonstrates how damage and fracture behavior of DP steels at the microstructure scale depend on the orientation set, morphology, and triaxiality. Obtained results prove that for the numerical analysis of failure in DP-steels, an extensive study in microscale is

necessary that includes modeling of inter/intra-granular failure mechanisms, and microstructural evolution.

References

[1] T. Yalçinkaya, S.O. Çakmak, C. Tekoglu, A crystal plasticity based finite element framework for RVE calculations of two-phase materials: Void nucleation in dual-phase steels, Finite Elem. Anal. Des. 187 (2021) 103510. https://doi.org/10.1016/j.finel.2020.103510
[2] T. Yalçinkaya, B. Tatli, I.E. Ünsal, I.U. Aydiner, Crack Initiation and Propagation in Dual-phase Steels Through Crystal Plasticity and Cohesive Zone Frameworks, Procedia Struct. Integrity 42 (2022) 1651-1659. https://doi.org/10.1016/j.prostr.2022.12.208
[3] J. Kadkhodapour, A. Butz, S. Ziaei Rad, Mechanisms of void formation during tensile testing in a commercial, dual-phase steel, Acta Mater. 59 (2011) 2575-2588. https://doi.org/10.1016/j.actamat.2010.12.039
[4] A. Tang, H. Liu, R. Chen, G. Liu, Q. Lai, Y. Zhong, L. Wang, J. Wang, Q. Lu, Y. Shen, Mesoscopic origin of damage nucleation in dual-phase steels, Int. J. Plast. 137 (2021) 102920. https://doi.org/10.1016/j.ijplas.2020.102920
[5] G. Avramovic-Cingara, Y. Ososkov, M.K. Jain, D.S. Wilkinson, Effect of martensite distribution on damage behaviour in DP600 dual phase steels, Mater. Sci. Eng., A 516 (2009) 7-16. https://doi.org/10.1016/j.msea.2009.03.055
[6] Q. Lai, O. Bouaziz, M. Gouné, L. Brassart, M. Verdier, G. Parry, A. Perlade, Y. Bréchet, T. Pardoen, Damage and fracture of dual-phase steels: Influence of martensite volume fraction, Mater. Sci. Eng. A 646 (2015) 322-331. https://doi.org/10.1016/j.msea.2015.08.073
[7] S. Qin, R. McLendon, V. Oancea, A.M. Beese, Micromechanics of multiaxial plasticity of DP600: Experiments and microstructural deformation modeling, Mater. Sci. Eng. A 721 (2018) 168-178. https://doi.org/10.1016/j.msea.2018.02.078
[8] X. Sun, K.S. Choi, W.N. Liu, M.A. Khaleel, Predicting failure modes and ductility of dual phase steels using plastic strain localization, Int. J. Plast. 25 (2009) 1888-1909. https://doi.org/10.1016/j.ijplas.2008.12.012
[9] J. Kadkhodapour, B. Anbarlooie, H. Hosseini-Toudeshky, S. Schmauder, Simulation of shear failure in dual phase steels using localization criteria and experimental observation, Comput. Mater. Sci. 94 (2014) 106-113. https://doi.org/10.1016/j.commatsci.2014.02.046
[10] S. Qin, Y. Lu, S.B. Sinnott, A.M. Beese, Influence of phase and interface properties on the stress state dependent fracture initiation behavior in DP steels through computational modeling, Mater. Sci. Eng. A 776 (2020) 138981. https://doi.org/10.1016/j.msea.2020.138981
[11] H. Hosseini-Toudeshky, P. Parandavar, B. Anbarlooie, Stress–strain prediction of dual phase steels using 3D RVEs considering both interphase hardness variation and interface debonding at grain boundaries, Arch. Appl. Mech. 92 (2022) 255–270. https://doi.org/10.1007/s00419-021-02054-5
[12] T. Yalcinkaya, G.O. Gungor, S.O. Cakmak, C. Tekoglu, A micromechanics based numerical investigation of dual phase steels, Procedia Struct. Integrity 21 (2019) 61-72. https://doi.org/10.1016/j.prostr.2019.12.087
[13] V. Uthaisangsuk, U. Prahl, W. Bleck, Micromechanical modelling of damage behaviour of multiphase steels, Comput. Mater. Sci. 43 (2008) 27-35. https://doi.org/10.1016/j.commatsci.2007.07.035
[14] N. Vajragupta, V. Uthaisangsuk, B. Schmaling, S. Münstermann, A. Hartmaier, W. Bleck, A micromechanical damage simulation of dual phase steels using XFEM, Comput. Mater. Sci. 54 (2012) 271-279. https://doi.org/10.1016/j.commatsci.2011.10.035
[15] Matsuno, C. Teodosiu, D. Maeda, A. Uenishi, Mesoscale simulation of the early evolution of ductile fracture in dual-phase steels, Int. J. Plast. 74 (2015) 17-34. https://doi.org/10.1016/j.ijplas.2015.06.004

[16] H. Hosseini-Toudeshky, B. Anbarlooie, J. Kadkhodapour, Micromechanics stress–strain behavior prediction of dual phase steel considering plasticity and grain boundaries debonding, Mater. Des. 68 (2015) 167-176. http://doi.org/10.1016/j.matdes.2014.12.013
[17] T. Yalcinkaya, W.A.M. Brekelmans, M.G.D. Geers, BCC single crystal plasticity modeling and its experimental identification, Modell. Simul. Mater. Sci. Eng. 16 (2008) 085007. http://doi.org/10.1088/0965-0393/16/8/085007
[18] O. Bulut, S.S. Acar, T. Yalçinkaya, The influence of thickness/grain size ratio in microforming through crystal plasticity, Procedia Struct. Integrity 35 (2022) 228-236. https://doi.org/10.1016/j.prostr.2021.12.069
[19] A.P. Pierman, O. Bouaziz, T. Pardoen, P.J. Jacques, L. Brassart, The influence of microstructure and composition on the plastic behaviour of dual-phase steels, Acta Mater. 73 (2014) 298-311. https://doi.org/10.1016/j.actamat.2014.04.015
[20] Y. Bao, T. Wierzbicki, On fracture locus in the equivalent strain and stress triaxiality space, Int. J. Mech. Sci. 46 (2004) 81–98. https://doi.org/10.1016/j.ijmecsci.2004.02.006
[21] K. Park, G.H. Paulino, J.R. Roesler, A unified potential-based cohesive model of mixed-mode fracture, J. Mech. Phys. Solids 57 (2009) 891–908. https://doi.org/10.1016/j.jmps.2008.10.003
[22] T. Yalçinkaya, İ. Özdemir, A.O. Firat, Inter-granular cracking through strain gradient crystal plasticity and cohesive zone modeling approaches, Theor. Appl. Fract. Mech. 103 (2019) 102306. https://doi.org/10.1016/j.tafmec.2019.102306
[23] A. Cerrone, P. Wawrzynek, A. Nonn, G.H. Paulino, A. Ingraffea, Implementation and verification of the Park–Paulino–Roesler cohesive zone model in 3D, Eng. Fract. Mech. 120 (2014) 26-42. https://doi.org/10.1016/j.engfracmech.2014.03.010
[24] W. Woo, V.T. Em, E.-Y. Kim, S.H. Han, Y.S. Han, S.-H. Choi, Stress–strain relationship between ferrite and martensite in a dual-phase steel studied by in situ neutron diffraction and crystal plasticity theories, Acta Mater. 60 (2012) 6972-6981. https://doi.org/10.1016/j.actamat.2012.08.054
[25] Y. Huang, A User-Material Subroutine Incorporating Single Crystal Plasticity in the ABAQUS Finite Element Program, 1991.
[26] R. Quey, P.R. Dawson, F. Barbe, Large-scale 3D random polycrystals for the finite element method: Generation, meshing and remeshing, Comput. Methods Appl. Mech. Eng. 200 (2011) 1729-1745. https://doi.org/10.1016/j.cma.2011.01.002

Materials Research Proceedings 28 (2023) 1453-1462 https://doi.org/10.21741/9781644902479-157

Local and nonlocal strain gradient approaches for size-dependent plastic deformation

ÜNSAL İzzet Erkin[1,a], GÜNAY Enes[2,b] and YALÇINKAYA Tuncay[3,c *]

[1]Departmant of Aerospace Engineering, Middle East Technical University, Ankara 06800, Turkey

[a]erkin.unsal@metu.edu.tr, [b]enes.gunay@metu.edu.tr, [c]yalcinka@metu.edu.tr

Keywords: Strain Gradient Plasticity, CMSG Theory, Size Effect, Finite Element Method

Abstract. Micro scale manufacturing technologies have been a productive area of research due to the increase in miniaturization in various industries. However, most of the know-how in conventional metal forming processes cannot be readily transferred into micro/meso forming processes due to the size effect. By incorporating the length scale into the formulation, strain gradient theories offer a viable solution to the issues arising from size-dependent complications. This paper aims at implementing a lower-order strain gradient plasticity (SGP) theory developed from the Taylor dislocation model to numerically analyze the impact of the plastic size effect on the forming of metallic materials. The material model together with local and nonlocal approaches for the strain gradient calculations is implemented in a commercial finite element (FE) code through user subroutines. The flat punch indentation problem is examined using the implemented code.

Introduction

Modeling plastic deformation on small scales has seen a significant increase of interest in recent years. Experimental observations show that many metal manufacturing processes are affected by noticeable sensitivity toward non-conventional deformation measures, resulting from size effects. A notable example being flat punch indentation. Having become a popular microforming process, metallic microscale devices fabricated from flat punches have been shown to outperform silicon-based devices [1]. Since the manufacturing processes for these metal-based HARMS (High-aspect-ratio microscale structures) are expensive and time-consuming, it is crucial to understand the mechanical interactions that take place when metals are micromolded. A better understanding of the interactions between the flat punch and the material might contribute to improving the strength and hardness of the final material [2]. Other examples of size dependent plasticity include MEMS, biosensors, and thin film applications which demonstrate significant size effects for sufficiently small specimens [3-5]. As the notion of smaller is stronger prevails, it has become vital to include gradient-dependent effects in the modeling of elastic-plastic materials.

Since there is no internal length scale parameter, the classical continuum models of plasticity can only remain limited at the micron scale [6]. It is a widely known fact that dislocations are created, moved, and stored when a material is deformed, and the storing of dislocations causes the material to harden. Dislocations could be stored in two distinct mechanisms: they can either accumulate by randomly trapping one another or they can be stored as they are necessary for compatible deformation of the material. The former is termed statistically stored dislocations (SSDs) [7] while the latter is known as geometrically necessary dislocations (GNDs) [7-8]. The gradients of plastic shear in a material are related to geometrically necessary dislocations. Consequently, plastic strain gradients can be identified as the result of the response of the material to inhomogeneous deformation.

A number of strain gradient (SG) frameworks have been proposed to bridge the gap between micromechanics and classical continuum-based plasticity theories [9-10]. In literature, strain

Content from this work may be used under the terms of the Creative Commons Attribution 3.0 license. Any further distribution of this work must maintain attribution to the author(s) and the title of the work, journal citation and DOI. Published under license by Materials Research Forum LLC.

gradient theories have been separated into two classes [11]. The first class of SG theories referred to as higher-order theories, initially proposed by [12], uses higher-order stress terms as the work conjugate to the strain gradient. Due to this, the equilibrium equations need to be adapted and additional boundary conditions and tractions must be considered. The second class known as lower-order SG theories, initially proposed by [13], involves the conventional stress description, retains all of the features of classical J_2 theory and requires no additional boundary conditions. These models incorporate the strain gradient effects in the calculation of the flow strength of the material. Therefore, they do not require any change in the equilibrium equations as only the hardening function of the material is modified. This feature essentially makes lower-order theories easy to implement in a commercial finite element code, however, the lack of higher-order stress terms and additional boundary conditions might cause inaccuracies, a notable example being the boundary layer phenomenon [6].

This study aims to use the widely popular Conventional Mechanism-Based Strain Gradient (CMSG) plasticity theory to model size-dependent behavior in small scale metal forming processes. CMSG, which is based on the Taylor dislocation model [14], is the lower-order counterpart of the more general higher-order Mechanism-Based Strain Gradient (MSG) theory. Further, two distinct approaches for calculating strain gradients are implemented. The first approach uses a local, intra-element level numerical differentiation scheme in which the plastic strain increments are interpolated through their values at the integration points and the strain gradient is evaluated as a common value at the centroid of each element. The second approach considers the calculation of strain gradients on an inter-element level by extrapolating the plastic strain from integration points to nodes and performs a nodal averaging scheme to nonlocalize the gradient. Both approaches are implemented in a three-dimensional setting via User Material Subroutines (UMAT) in the commercial finite element solver ABAQUS.

The paper is outlined as follows. The constitutive model together with the strain gradient calculation methods are explained in Section 2, a benchmark problem to verify the implementation is addressed in Section 3. The obtained results for flat punch indentation simulations are presented in Section 4, which is finally followed by summary and outlook in Section 5.

Conventional Mechanism-Based Strain Gradient (CMSG) Plasticity

Taylor Dislocation Model. The conventional mechanism-based strain gradient plasticity theory is based on the Taylor model of dislocation hardening [14]. The shear flow stress is related to the dislocation density by

$$\tau=\alpha\mu b\sqrt{\rho} \tag{1}$$

where μ is the shear modulus, b is the Burgers vector and α is an empirical coefficient, which takes values between 0.3 and 0.5. The dislocation density ρ is decomposed into ρ_S for statistically stored dislocations (SSDs) [7] and ρ_G for geometrically necessary dislocations (GNDs)

$$\rho=\rho_S+\rho_G. \tag{2}$$

Effective strain gradient can be related to the GND density, by

$$\rho_G=\bar{r}\frac{\eta^p}{b} \tag{3}$$

where $\bar{r}$, is a Nye-factor and is around 1.90 for the Face Centered-Cubic (FCC) polycrystals [15]. This parameter reflects the effect of crystallography on the distribution of GNDs. The tensile flow stress σ_{flow} is then related to the shear flow stress τ, by

$$\sigma_{flow}=M\alpha\mu b\sqrt{\rho_S+\bar{r}\frac{\eta^p}{b}} \tag{4}$$

where M is the Taylor factor ($M = 3.06$ for fcc metals), which serves as an isotropic interpretation of the crystalline anisotropy at the continuum level [16].

By using the formula $\sigma_{flow} = \sigma_{ref} f(\varepsilon^p)$, where σ_{ref} is a reference stress and f is a nondimensional function derived from the uniaxial stress-strain curve, it is also possible to link the flow stress for uniaxial tension to the plastic strain ε^p. Since the plastic strain gradient η^p vanishes for the uniaxial tension, the SSD density can be determined from Eq. 4, as

$$\rho_S=[\sigma_{ref} f(\varepsilon^p)/(M\alpha\mu b)]^2 \tag{5}$$

Then the flow stress in Eq. 4 becomes

$$\sigma_{flow}=\sqrt{[\sigma_{ref} f(\varepsilon^p)]^2+M^2\bar{r}\alpha^2\mu^2 b\eta^p}=\sigma_{ref}\sqrt{f^2(\varepsilon^p)+l\eta^p} \tag{6}$$

where l is the is the intrinsic material length scale in strain gradient plasticity and is given explicitly by

$$l=M^2\bar{r}\alpha^2\left(\frac{\mu}{\sigma_{ref}}\right)^2 b=18\alpha^2\left(\frac{\mu}{\sigma_{ref}}\right)^2 b \tag{7}$$

The intrinsic material length l for typical metallic materials is usually on the scale of microns. Note that from Eq. 6, as the material length scale parameter l vanishes, conventional J_2 plasticity relations are recovered.

Constitutive Relations. The governing equations of CMSG plasticity are nearly identical to those of conventional plasticity because higher order terms are not included. The volumetric and deviatoric strain rates are obtained as

$$\dot{\varepsilon}_{kk}=\frac{\dot{\sigma}_{kk}}{3K},\quad \dot{\varepsilon}'_{ij}=\frac{\dot{\sigma}'_{ij}}{2\mu}+\frac{3\dot{\varepsilon}^p}{2\sigma_e}\dot{\sigma}'_{ij} \tag{8}$$

From the Taylor dislocation model, the equivalent plastic strain rate $\dot{\varepsilon}^p$ includes the flow stress. In order to incorporate the gradient effects without higher-order stress terms, $\dot{\varepsilon}^p$ is replaced by a viscoplastic formulation to express plastic strain gradient in terms of effective stress σ_e rather than its rate $\dot{\sigma}_e$ (for more details see [17])

$$\dot{\varepsilon}^p=\dot{\varepsilon}\left(\frac{\sigma_e}{\sigma_{flow}}\right)^m=\dot{\varepsilon}\left[\frac{\sigma_e}{\sigma_{ref}\sqrt{f^2(\varepsilon^p)+l\eta^p}}\right]^m \tag{9}$$

The substitution of Eq. 9 into Eqs. 8 gives the strain rate which then can be inverted to get the stress-rate in terms of the stain-rate as follows

$$\dot{\sigma}_{ij}=K\dot{\varepsilon}_{kk}\delta_{ij}+2\mu\left[\dot{\varepsilon}'_{ij}-\frac{3\dot{\varepsilon}^p}{2\sigma_e}\left(\frac{\sigma_e}{\sigma_{ref}\sqrt{f^2(\varepsilon^p)+l\eta^p}}\right)^m\dot{\sigma}'_{ij}\right] \tag{10}$$

Materials Research Proceedings 28 (2023) 1453-1462 https://doi.org/10.21741/9781644902479-157

Above constitutive relations allow for gradient effects without the higher order stress terms. Since the effective plastic strain gradient reduces the plastic incremental moduli, it falls under the lower-order framework of strain gradient plasticity theories [13]. Effective strain gradient η^p definition is the same with Gao et. al [6]. The quadratic invariants of three models of geometrically necessary dislocations for bending, torsion, and void formation serves as the basis for calculating the effective strain gradient. The resulting expression reads

$$\eta^p=\varepsilon^p_{ik,j}+\varepsilon^p_{jk,i}-\varepsilon^p_{ij,k} \tag{11}$$

Finite Element Implementation. In this study, CMSG framework has been implemented in ABAQUS via user material subroutine (UMAT) in a three-dimensional setting. The only additional task beyond classical plasticity is the assessment of the plastic strain gradient within the UMAT as the equilibrium equations, boundary conditions, and kinematic relationships between the strain and displacement are identical to those in classical plasticity. For the calculation of the effective strain gradient η^p, two different approaches have been utilized, the first approach evaluates the strain gradient at the local element level. Plastic strains are interpolated in the isoparametric space through the shape functions as

$$\varepsilon^p_{ij}=\sum_{k=1}^{8} N_k(\xi,\eta,\zeta)\left(\varepsilon^p_{ij,IPT}\right)_k \tag{12}$$

such that, the plastic strains ε^p_{ij} represents the interpolated values within the element, obtained from the values at the integration points $\left(\varepsilon^p_{ij,IPT}\right)_k$. Where $N_k(\xi,\eta,\zeta)$ is the shape function vector, with three-dimensional linear shape functions adapted as

$$N_k=\frac{1}{8}\left(1+\xi\xi_i\right)\left(1+\eta\eta_i\right)\left(1+\zeta\zeta_i\right) \tag{13}$$

In this context, the implementations are considered on an 8-noded full integration C3D8 elements from ABAQUS Standard element library, with the node and integration points numbering given in Fig. 1.

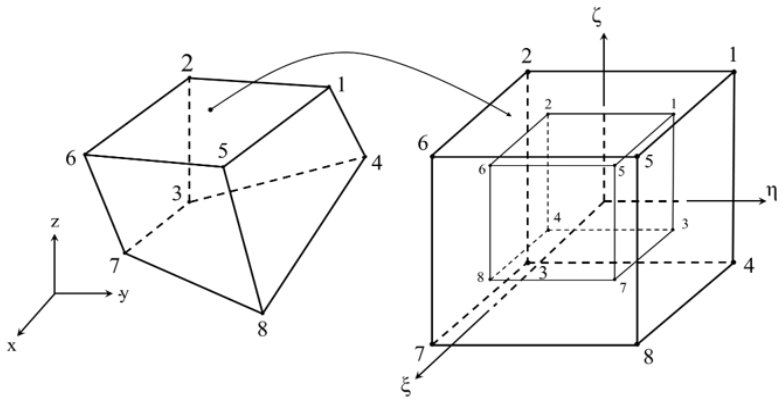

Fig. 1. Numbering scheme used in the Gauss point-based interpolation.

Materials Research Proceedings 28 (2023) 1453-1462 https://doi.org/10.21741/9781644902479-157

Derivatives of the shape functions with respect to global coordinates can be obtained by using the chain rule and the inverse of the Jacobian.

$$\begin{bmatrix} \frac{\partial N}{\partial x} & \frac{\partial N}{\partial y} & \frac{\partial N}{\partial z} \end{bmatrix}^T = J^{-1} \begin{bmatrix} \frac{\partial N}{\partial \xi} & \frac{\partial N}{\partial \eta} & \frac{\partial N}{\partial \zeta} \end{bmatrix}^T \tag{14}$$

where J is the element Jacobian matrix describing the derivatives of the global coordinates in relation to the natural coordinate system. With the plastic strain gradient definition from Eq. 11, components of η^p within the element can be computed as

$$\eta^p_{ijk} = \sum_{m=1}^{8} \frac{\partial N_m}{\partial x_j} \varepsilon^p_{ik,IPT} + \sum_{m=1}^{8} \frac{\partial N_m}{\partial x_i} \varepsilon^p_{jk,IPT} - \sum_{m=1}^{8} \frac{\partial N_m}{\partial x_k} \varepsilon^p_{ij,IPT} \tag{15}$$

where x_i for i=1,2,3 denote x, y, z coordinates respectively. In this method, since the values at the integration points are interpolated, the plastic strains obtained stay within the confines of the element, and effective plastic strain η^p, is a single value evaluated at the centroid. This is clearly a local approach as computations are done on a single element basis. For more details related to this approach the reader is referred to [18].

In the nonlocal approach, the plastic strain values are extrapolated to the nodes. This is done by inverting the shape function matrix used to interpolate nodal values to integration points,

$$\varepsilon^p_{ij,IPT} = \sum_{k=1}^{8} N_k(\xi,\eta,\zeta) \left(\varepsilon^p_{ij,N}\right)_k \tag{16}$$

$$\varepsilon^p_{ij,N} = \sum_{k=1}^{8} N_k^{-1}(\xi,\eta,\zeta) \left(\varepsilon^p_{ij,IPT}\right)_k \tag{17}$$

where $\varepsilon^p_{ij,N}$ denotes the extrapolated nodal values of the plastic strains and $\varepsilon^p_{ij,IPT}$ is again the plastic strains at the integration points. Hence, plastic strain values at the nodes can be obtained. However, because each node is tied to several elements, different plastic strain values will be assigned to the same node for each element to which it is attached. To overcome this and ensure continuity of an otherwise discontinuous field, a nodal averaging scheme is employed. Fig. 2 depicts the basic concept of this technique for a one-dimensional case. After nodal averaging is performed, using the shape function derivatives and the element Jacobian, the gradient of plastic strain can be calculated at the position of each integration point.

$$\nabla \varepsilon^p_{ij,IPT} = \frac{\partial \varepsilon^p_{ij,IPT}}{\partial \mathbf{x}} = \frac{\partial \varepsilon^p_{ij,IPT}}{\partial \boldsymbol{\psi}} \frac{\partial \boldsymbol{\psi}}{\partial \mathbf{x}} = \frac{\partial \left(\sum_{k=1}^{8} N_k \left(\varepsilon^p_{ij,N}\right)_k\right)}{\partial \boldsymbol{\psi}} \frac{\partial \boldsymbol{\psi}}{\partial \mathbf{x}} \tag{18}$$

Following this, the gradient of the plastic strains can be written concisely as

$$\nabla \varepsilon^p_{ij,IPT} = \nabla_{\boldsymbol{\psi}} \left(\sum_{k=1}^{8} N_k\right) \left(\varepsilon^p_{ij,N}\right)_k J^{-1} \tag{19}$$

$\nabla_{\boldsymbol{\psi}} \left(\sum_{k=1}^{8} N_k\right)$ describes the gradient of shape functions with respect to isoparametric coordinates. Therefore, Eq. 11 for the nonlocal approach can be written as

$$\eta^p_{ijk} = \sum_{m=1}^{8} \frac{\partial N_m}{\partial \psi_j} \varepsilon^p_{ik,N} J^{-1} + \sum_{m=1}^{8} \frac{\partial N_m}{\partial \psi_i} \varepsilon^p_{jk,N} J^{-1} - \sum_{m=1}^{8} \frac{\partial N_m}{\partial \psi_k} \varepsilon^p_{ij,N} J^{-1} \tag{20}$$

where ψ_i for i=1,2,3 denote ξ, η, ζ coordinates in isoparametric space respectively. With this approach, the strain gradients are assigned to each integration point separately. Because nodal averaging takes into account the effects of neighboring elements, the strain gradient is nonlocalized.

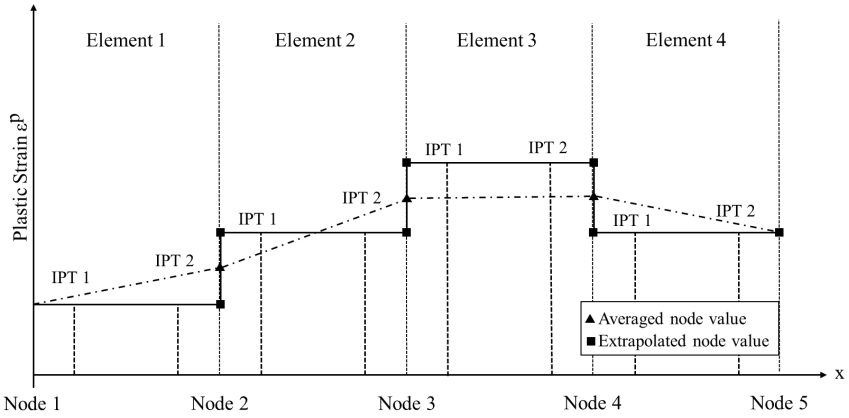

Fig. 2. Plastic strain field along four one-dimensional elements.

Numerical Example

Uniaxial tension subject to a constant body force. A bar subjected to a constant body force is analyzed to evaluate the mechanism-based strain gradient plasticity implementation and assess the capacity for depicting the size dependency. Simulations with local and nonlocal approaches are performed and compared. The model, inspired by the works of [17] is a basic example where gradient effects can be observed, consists of a uniform mesh of 10x10x100 C3D8 elements with 100 elements through the length of the bar.

The nodes at the top of the bar are constrained in all three directions, and the nodes at the bottom of the bar are constrained in z and y directions but not in x direction. A constant body force g is applied to the bar to induce a gradient along x direction. Also, a traction $\bar{\sigma}$ is applied at the far end. A sketch of the model, with the mesh is illustrated in Fig. 3.

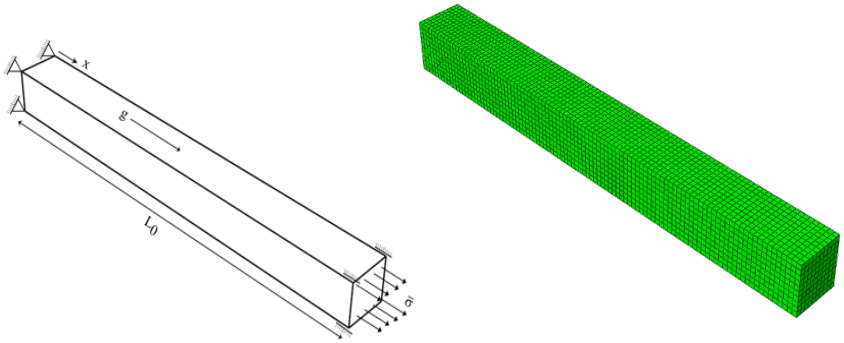

Fig. 3. Boundary conditions and mesh for the gravity loaded bar.

Loads are given in proportion to the yield strength σ_Y, such that for a material with $\nu = 0.3$ and $\sigma_Y/E = 0.002$, the traction boundary condition is $\bar{\sigma} = \sigma_Y$, and the body force, $g = \sigma_Y/L_0$. Further, for isotropic hardening, a classical power law hardening relation is adopted, with $\sigma_{ref} = \sigma_Y(E/\sigma_Y)^N$ and $f(\varepsilon^p) = (\varepsilon^p + \sigma_Y/E)^N$ in Eq. 10. Throughout the study, the strain hardening exponent and the yield strength have been taken as N=0.2 and σ_Y=400 [MPa], respectively.

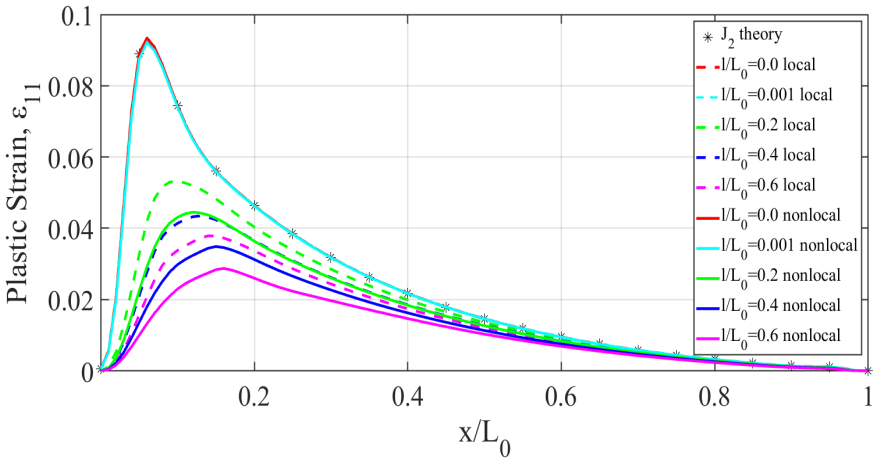

Fig. 4. Plastic strain distribution for bar loaded with

Size dependency for several different length scales is illustrated in Fig. 4. The curves show the plastic strain distribution over the length of the bar. The classical J_2 response is recovered if the length scale for either method is zero or a small value that is non comparable with the characteristic length of the material. Moreover, raising this value leads to a stronger material response. However, results from the two methods are different. Nonlocal approach consistently predicts lower plastic strain distributions. This could be attributed to the nodal averaging scheme, which averages out the high plastic strains onto the neighboring elements, consequently smoothing out the distribution.

Flat Punch Indentation

Flat punch indentation has found many applications with the advance of microforming applications. Experiments on metals such as aluminum showed that, besides the required punch

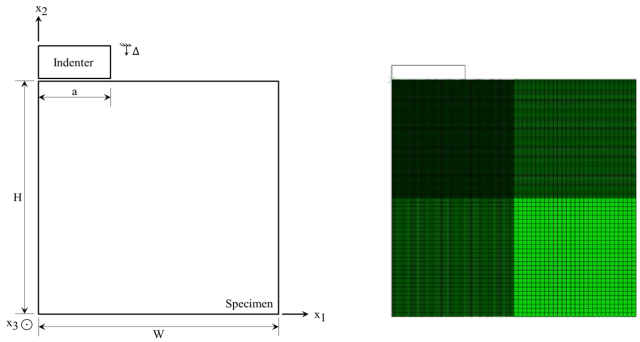

Fig. 5. Frontal view for the flat punch indentation with, W=H=50 μm, a=0.3W and $\Delta = 1.5$ μm.

load, both the size and shape of imprinted features are affected by the scale of the as substantial details are lost when the characteristic length is on the order of 10 μm [19]. Frontal view sketch and mesh of a three-dimensional flat punch indentation problem is highlighted in Fig. 5.

In the mesh, 42849 three-dimensional hex elements are used to model the process using a single layer through x_3. Only half of the sample is modeled by exploiting the symmetry boundary conditions on the left face through x_1 direction. A rigid flat indenter of half width a is given a downward displacement of Δ and the mesh is refined around the edges of the punch where highest stresses are obtained. The material parameters and the hardening function are the same with the earlier example. The downwards displacement is set to be Δ=1.5 μm and the friction between the contact surfaces is modeled with Coulomb friction with a friction coefficient of μ=0.2. The width and the height of the model are equal with, W=H=50 μm and the indenter width a=0.3W=15 μm.

Fig. 6 shows dimensionless displacement versus the dimensionless location for different length scale ratios, together with the classical plasticity solution. Indenter half width a is kept constant. Details of the imprint get lost as the length scale parameter increases. This effect is called indentation size effect (ISE) and agrees well with the experimental observation of [20] and numerical simulations of [19]. Again, the nonlocal approach, predicts higher resistance to deformation in contrast to the local approach though the difference is small.

Fig. 7 shows the equivalent stress contours for the local and nonlocal solution. Expectedly, as the length scale increases stresses also increase. Moreover, even though the patterns of deformations left by the imprint are quite similar, stress contours show a difference. For the nonlocal approach, the stresses are diffused owing to the nodal averaging.

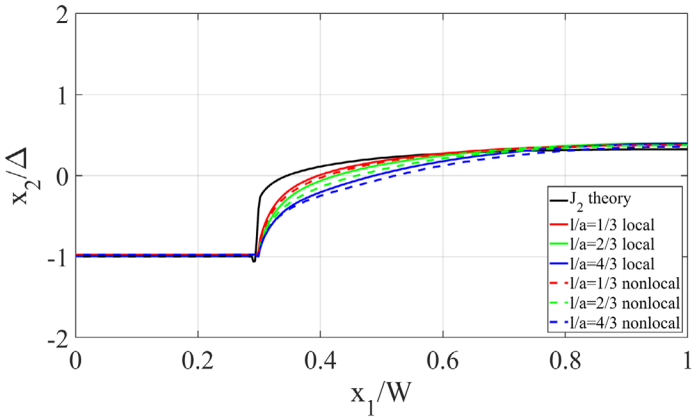

Fig. 6. Deformation patterns of imprints for different ratios of length scale l and constant indenter half width a.

Summary

In this paper, size dependency in plastic deformation is investigated. A lower order strain gradient theory is implemented and two different methods for strain gradient calculations are discussed. It has been observed that nonlocal approach consistently predicts stronger material response, however the difference between the two approaches is small. It is noted that, for the flat punch indentation problem the length scale has a notable effect on the deformation pattern, pile up characteristics, and the stress distributions, yet the simulations done in this paper unfortunately remain at the qualitative level.

Our ongoing focus is on performing more detailed simulations for flat punch indentation accounting for realistic materials with actual experimental data. Using this approach, it would be interesting to predict the behaviors of real materials response and study deeply the underlying mechanisms of plastic gradient effects on micro-sized materials.

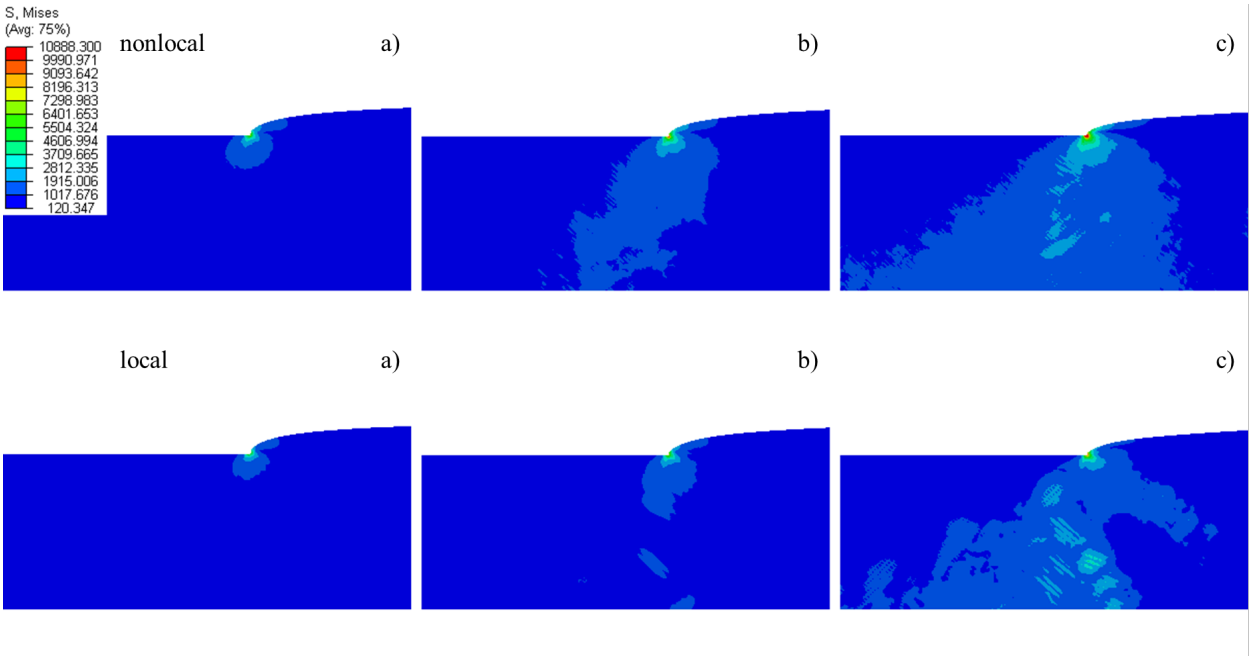

Fig. 3. Stress contours for the flat punch indentation for local and nonlocal approaches for different length scales a) l/a =1/3 b) l/a=2/3 c) l/a = 4/3.

References

[1] J. Jiang, F. Mei, W.J. Meng, Fabrication of metal-based high-aspect-ratio microscale structures by compression molding, J. Vac. Sci. Technol. 26 (2008) 745-751. https://doi.org/10.1116/1.2912078

[2] D.M. Cao, W.J. Meng, Microscale compression molding of AL with surface engineered Liga inserts, Microsyst. Technol. 10 (2004) 662-670. https://doi.org/10.1007/s00542-004-0440-1

[3] T. Yalçinkaya, İ. Özdemir, I. Simonovski, Micromechanical modeling of intrinsic and specimen size effects in microforming, Int. J. Mater. Form. 11 (2017) 729-741. https://doi.org/10.1007/s12289-017-1390-3

[4] A. Darvishvand, A. Zajkani, A new model for permanent flexural deflection of cantilever MEMS actuator by conventional mechanism-based strain gradient plasticity framework, Microsyst. Technol. 25 (2019) 4277-4289. https://doi.org/10.1007/s00542-019-04337-y

[5] F.M. Weafer, Y. Guo, M.S. Bruzzi, The effect of crystallographic texture on stress-induced martensitic transformation in NiTi: A computational analysis, J. Mech. Behav. Biomed. Mater. 53 (2016) 210-217. https://doi.org/10.1016/j.jmbbm.2015.08.023

[6] H. Gao, Y. Huang, W.D. Nix, J.W. Hutchinson, Mechanism-based strain gradient plasticity-I. theory, J. Mech. Phys. Solids. 47 (1999) 1239-1263. https://doi:10.1016/s0022-5096(98)00103-3

[7] M.F Ashby, The deformation of plastically non-homogeneous alloys, Phil. Mag. 21 (1970) 399-424. https://doi.org/10.1080/14786437008238426

[8] J.F. Nye, Some geometrical relations in dislocated crystal, Acta. Metall. 1 (1953) 153-162. https://doi.org/10.1016/0001-6160(53)90054-6

[9] T. Yalçinkaya, W.A.M. Brekelmans, M.G.D. Geers, Deformation patterning driven by rate dependent non-convex strain gradient plasticity, J. Mech. Phys. Solids 59 (2011) 1-17. https://doi.org/10.1016/j.ijsolstr.2004.04.021

[10] T. Yalçinkaya, W.A.M. Brekelmans, M.G.D. Geers, Non-convex rate dependent strain gradient crystal plasticity and deformation patterning, Int. J. Solids Struct. 49 (2012) 2625-2636. https://doi.org/10.1016/j.jmps.2010.10.002

[11] C.F. Niordson, J.W. Hutchinson, Non-uniform plastic deformation of Micron scale objects, Int. J. Numer. Methods Eng. 56 (2003) 961-975. https://doi.org/10.1002/nme.593

[12] E.C. Aifantis, On the microstructural origin of certain inelastic models, J. Eng. Mater. Technol. 106 (1984) 326-330. https://doi.org/10.1115/1.3225725
[13] A. Acharya, A.J. Beaudoin, Grain-size effect in visco- plastic polycrystals at moderate strains, J. Mech. Phys. Solids 48 (2000) 2213-2230. https://doi.org/10.1016/S0022-5096(00)00013-2
[14] G.I. Taylor, The mechanism of plastic deformation of crystals. Part I.—Theoretical, Proc. R. Soc. 145 (1934) 362-387. https://doi.org/10.1098/rspa.1934.0106
[15] A. Arsenlis, D.M. Parks, Crystallographic aspects of geometrically-necessary and statistically-stored dislocation density, Acta Mater. 47 (1999) 1597-1611. https://doi.org/10.1016/S1359-6454(99)00020-8
[16] J.F.W. Bishop, R. Hill, A theoretical derivation of the plastic properties of a polycrystalline face-centred metal, Philos. Mag. J. Sci. 42 (1951) 1298-1307. https://doi.org/10.1080/14786444108561385
[17] Y. Huang, S. Qu, K.C. Hwang, M. Li, H. Gao, A conventional theory of mechanism-based strain gradient plasticity, Int. J. Plas. 20 (2004) 753-782. https://doi.org/10.1016/j.ijplas.2003.08.002
[18] E. Martínez-Pañeda, C. Betegón, Modeling damage and fracture within strain-gradient plasticity, Int. J. Solids Struct. 59 (2015) 208-215. https://doi.org/10.1016/j.ijsolstr.2015.02.010
[19] K.L. Nielsen, C.F. Niordson, J.W. Hutchinson, Strain gradient effects in periodic flat punch indenting at small scales, Int. J. Solids Struct. 51 (2014) 3549-3556. https://doi.org/10.1016/j.ijsolstr.2014.06.009
[20] K. Chen, W.J. Meng, F. Mei, J. Hiller, D.J. Miller, From micro- to nano-scale molding of metals: Size effect during molding of single crystal Al with rectangular strip punches, Acta Mater. 59 (2011) 1112-1120. https://doi.org/10.1016/j.actamat.2010.10.044

Materials Research Proceedings 28 (2023) 1463-1470 https://doi.org/10.21741/9781644902479-158

Suitability evaluation of pre-formed cruciform sample without thickness reduction for high strain values in the center of the specimen under different strains paths

MITUKIEWICZ Grzegorz[1,a *], LEOTOING Lionel[2,b], WANG Guan[1,c], GUINES Dominique[2,d], GOSZCZAK Jarosław[1,e] and BATORY Damian[1,f]

[1]Lodz University of Technology, Department of Vehicles and Fundamentals of Machine Design, Stefanowskiego 1/15, 90-537 Lodz, Poland

[2]Univ Rennes, INSA Rennes, LGCGM (Laboratoire de Génie Civil et Génie Mécanique), F-35000 Rennes, France

[a]grzegorz.mitukiewicz@p.lodz.pl, [b]lionel.leotoing@insa-rennes.fr, [c]guan.wang@dokt.p.lodz.pl, [d]dominique.guines@insa-rennes.fr, [e]jaroslaw.goszczak@p.lodz.pl, [f]damian.batory@p.lodz.pl

Keywords: Cruciform Sample, Biaxial Tensile Test Simulation, Ductile Damage Criterion

Abstract. In this study, the Finite Element (FE) simulation of an initially pre-deformed DC-5 steel cruciform specimen has been carried out and compared to experimental results. A new geometry of the sample with local reinforcements and without thickness reduction allows distribution of plastic deformation and gets high strains in its gauge region. The simulation is divided into two steps. The first one introduces initial deformation to the sample arms. For the second step, the calculated strain field is introduced as an initial pre-strain field before the application of loading along the two perpendicular arms of the cruciform specimen during the in-plane biaxial tensile test. The described numerical study expands the knowledge of material plastic flow using a ductile damage criterion under different biaxial tensile strain paths. The numerical and experimental results are in good agreement for different strain paths, from uniaxial to equibiaxial strain states.

Introduction

Sheet metal forming is a very popular manufacturing process in many industrial sectors. Therefore, the knowledge of the mechanical behaviour of materials under large plastic strain is essential to build reliable numerical models for the prediction of the final shape and quality of formed parts. The characterization of mechanical behaviour needs dedicated tests, able to reproduce the forming conditions of the processes. Different tests have been proposed to characterize anisotropy, flow stress, or forming limits (at necking or at rupture). Some of them are very common and standardized, like the Nakazima [1] or Marciniak [2] tests for the determination of Forming Limit Curves (FLC). Non-conventional tests have been also proposed to improve the knowledge of the material under complex loadings, including multiaxiality or non-linear strain paths for high strains. The use of cruciform shapes [3] stretched along two perpendicular directions in the sheet plane is very promising. Unfortunately, the level of strain reached in the gauge region is generally low and not suitable for the forming applications. Many cruciform shapes have been proposed and optimized to achieve a localization of high strains at the centre of the samples, before necking and rupture onset in the arms.

In order to localize the strains at the centre of the samples, a reduction of sheet thickness is proposed in the gauge region. Besides, longitudinal slots are generally designed to decrease the transversal stiffness of the arms [4]. The number and the position of each slot can have a great influence on the strain and stress fields in the central zone of the samples. Recently, Zhang et al. [5] conducted an extensive review of the existing cruciform specimen designs. The authors

Content from this work may be used under the terms of the Creative Commons Attribution 3.0 license. Any further distribution of this work must maintain attribution to the author(s) and the title of the work, journal citation and DOI. Published under license by Materials Research Forum LLC.

proposed three different geometries of samples which subsequently were evaluated numerically and by experiments.

The reduction of sheet thickness can affect the characterization of the mechanical behaviour. Some defects may occur when reducing the thickness (surface finish, precision for small thicknesses) and the behaviour of the material is not always homogeneous through the sheet thickness. In order to avoid this operation, a new cruciform shape with a constant thickness in the gauge region was proposed [6]. Out of plane deformations were applied around the gauge region to strengthen the connection zone between the arms and the central region.

The aim of this study is to evaluate the potential of this new specimen to achieve large strains in the gauge region for different strain paths. A Finite Element (FE) model of the pre-forming step followed by the in-plane biaxial stretching of the specimen is defined. A comparison is done between the predictive strain fields and the experimental ones from the Digital Image Correlation (DIC) method.

Cruciform Sample

Sample shape. The sample has been designed (arms' length and dimensions of the middle part) according to the capacity of the biaxial testing machine [7]. The geometry is in accordance with the international standard ISO 16842 [8] which recommends that the ratio between the sample thickness "a" and its arm width "B" should be smaller than 0.08 (Fig.1). The width of the arms is B = 30mm and the thickness of the sample is a = 0.5mm.

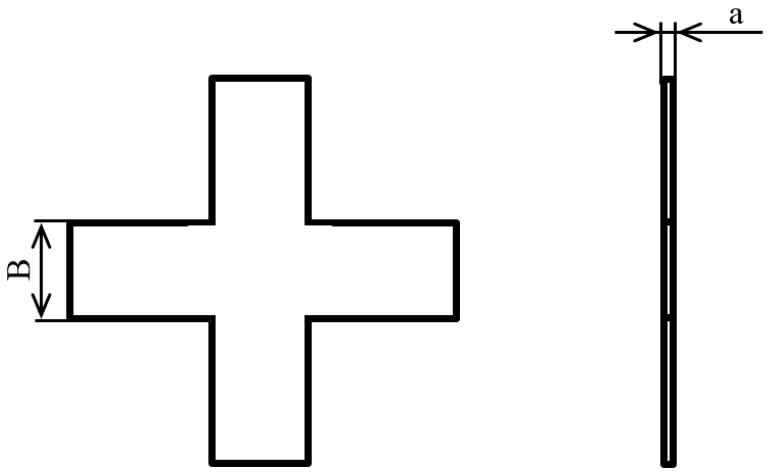

Fig. 1. Sheet thickness "a" and the arm width "B".

In order to achieve higher plastic deformation in the gauge region during biaxial stretching, the sample is preformed (Figs. 2 and 3). The aim of this preforming operation is to strengthen the sample material in the junction area between the arms and the gauge region. This solution has been already described in the previous work of Mitukiewicz and Głogowski [6].

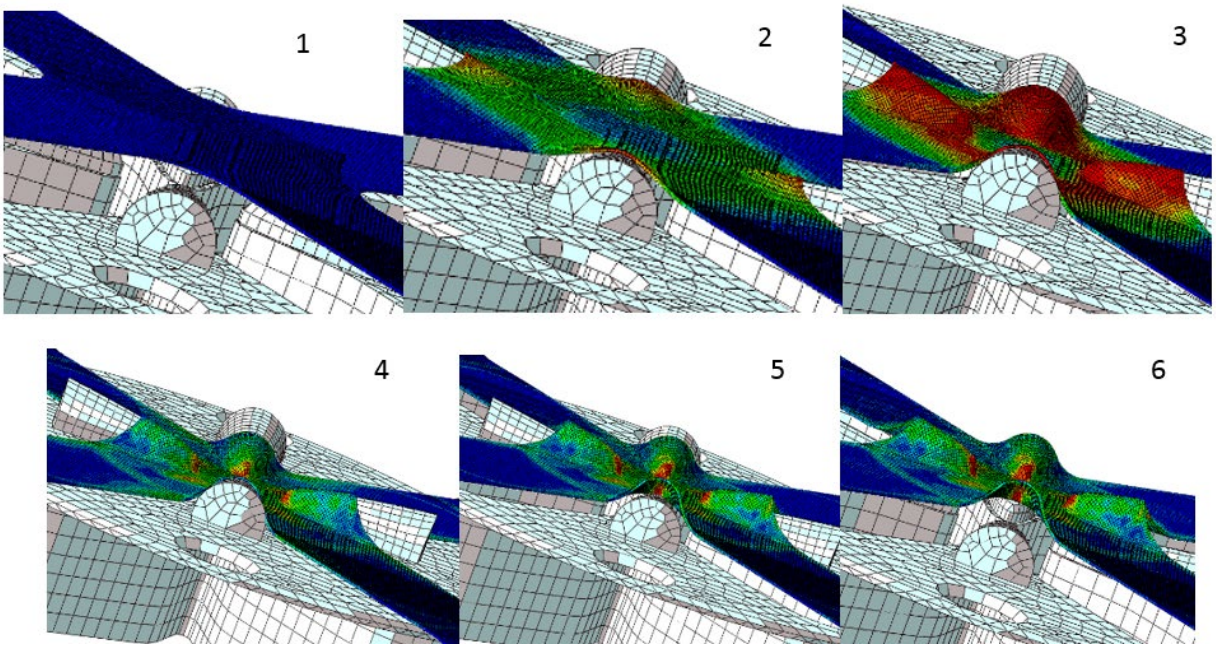

Fig. 2. Cruciform sample preforming (1 to 6 - successive steps).

Material. For this study, a DC-5 low-carbon steel specimen is used. The elastic mechanical properties of this material are as follows: Young's modulus of 210 GPa and Poisson's ratio of 0.3. Regarding the plastic behavior, an isotropic plastic criterion of von Mises is assumed with an initial yield stress of 225 MPa. The plastic strain hardening behavior is described by means of the true stress versus equivalent plastic strain curve from a uniaxial tensile test performed along the rolling direction (Fig. 3).

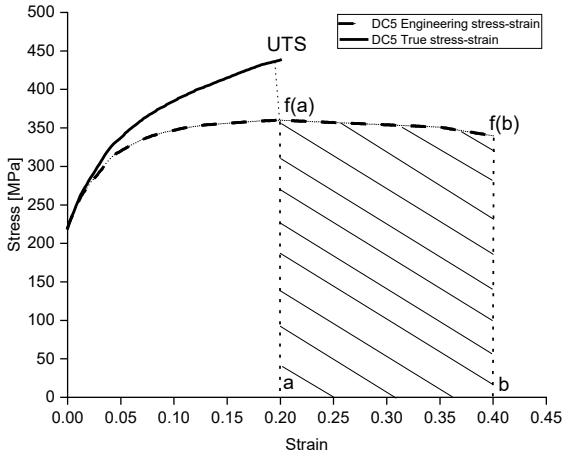

Fig. 3. True stress-plastic strain curve vs. engineering stress-plastic strain curve (UTS - ultimate tensile strength).

In-Plane Biaxial Test

Experimental setup. To test the samples, a servo-hydraulic testing machine provided with four independent dynamic actuators is used (Fig. 4). Thanks to an efficient servo-hydraulic control, the center point of the sample is always maintained stationary during the tests. The loading capacity

Materials Research Proceedings 28 (2023) 1463-1470 https://doi.org/10.21741/9781644902479-158

of the machine is 50KN for each actuator and a wide range of testing velocities can be applied (from quasi-static to 2m/s).

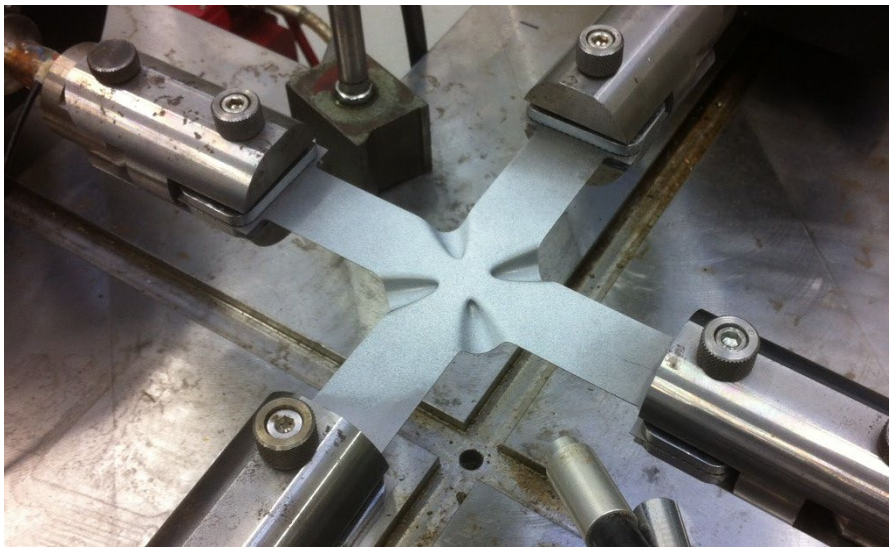

Fig. 4. Experimental setup with the pre-deformed cruciform sample.

During the test, the gauge region of the cruciform sample is filmed. The image resolution is 1024pixels×1024pixels and the acquisition rate is 250 frames/s. A random speckle pattern is applied on the surface of the specimen (Fig. 5). For the calculation of the strain field at the top surface of the specimen, the DIC method is used thanks to the CORRELATE software of the GOM Company.

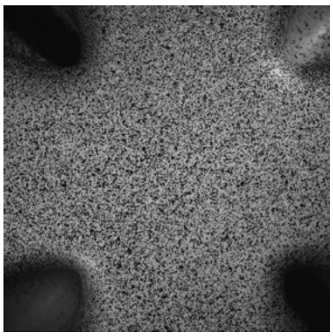

Fig. 5. Random speckle pattern applied on the top surface of the gauge region.

Loading conditions. The strain path measured at the center of the sample is directly linked to the ratio of actuator velocities applied along the two perpendicular directions of the biaxial test. By changing the velocity ratio, all the strain states between uniaxial and equibiaxial stretching can be reached.

Three loading conditions were studied:

- Biaxial stretching (**case 1**): the same velocity ($V=V_X=V_Y=1$mm/s) is applied along the two perpendicular directions
- Near plane strain (**case 2**): the velocity of $V_X=1$mm/s is applied along the rolling direction and a smaller velocity ($V_Y=0.02$mm/s) is applied along the perpendicular direction to compensate the Poisson effect.

- Uniaxial stretching (**case 3**): only the velocity (V_X =1mm/s) along the rolling direction is applied. No velocity is applied along the perpendicular direction, the sample remains free.

FE Model

The finite element modeling is performed using Abaqus software. To simulate the in-plane biaxial tensile test of this reinforced sample, two steps are defined in the FE model: the punching process (Step-I) and the tensile test process (Step-II). A view of the components of the punching die and the 3D model assembly are shown in Fig. 6. The model consists of three parts, the upper part, the cross holder, and the base part. A cruciform sample is placed between the bottom base and the cross holder to prevent any movement of the specimen during the forming process (Step 1).

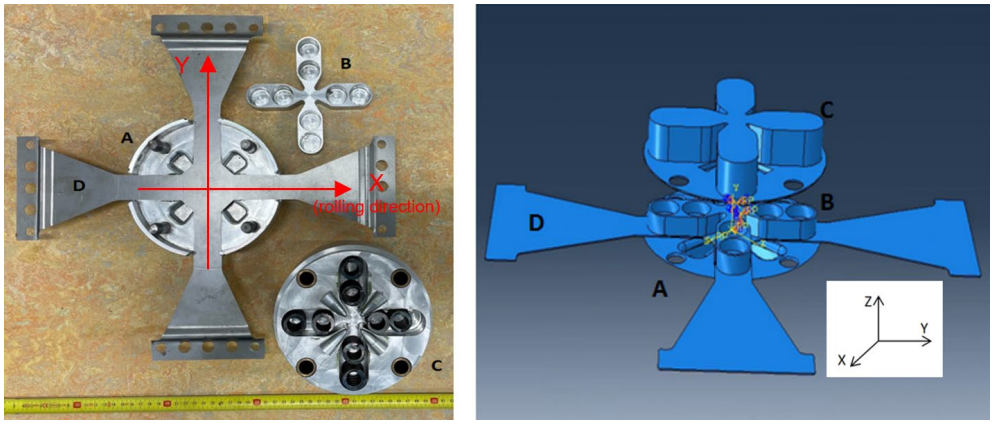

Fig. 6. Components of punching die and view of the 3D model assembly:

A - base part; B - cross holder; C - upper part; D - 0.5 mm cruciform sample.

In the FE model, the different tools are considered rigid. Only the cruciform specimen is considered deformable (C3D8R element type). Tangential contact behaviour is applied for all the contact areas during the punching process. The frictional coefficient is assumed to be 0.1. A refined mesh size of 0.5 mm is defined in the gauge area. Fig. 7 gives the distribution of the plastic equivalent strain at the surface of the specimen at the end of the first step. One can notice that the centre of the specimen does not deform during the punching process of Step 1. For Step 2, a damage evolution criterion [9], calibrated from the uniaxial test (Fig. 2), is introduced.

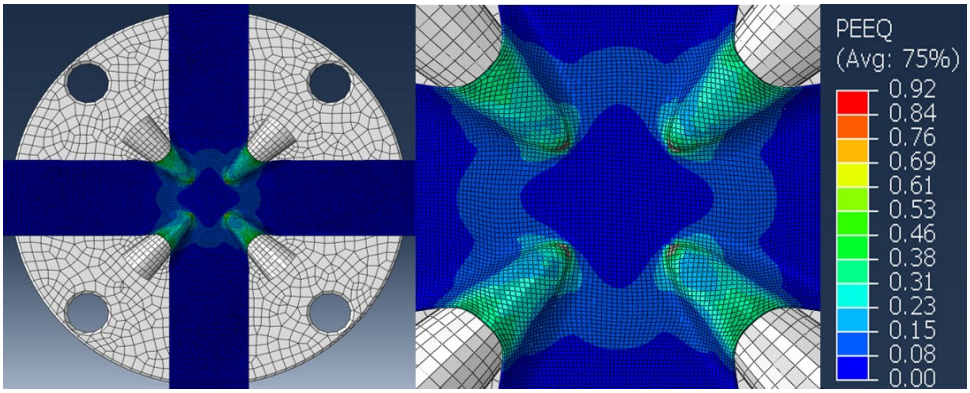

Fig. 7. Plastic equivalent strain distribution at the end of Step 1.

Materials Research Proceedings 28 (2023) 1463-1470 https://doi.org/10.21741/9781644902479-158

Results and Discussion

As mentioned before, three loading conditions (cases 1 to 3) are studied. The following figures (Figs. 8 to 10) show the comparison between experimental and predictive in-plane strain components ε_{11} and ε_{22} along the two perpendicular directions X and Y defined in Fig. 6 respectively. The time for the comparison corresponds to the onset of necking in one of the four arms.

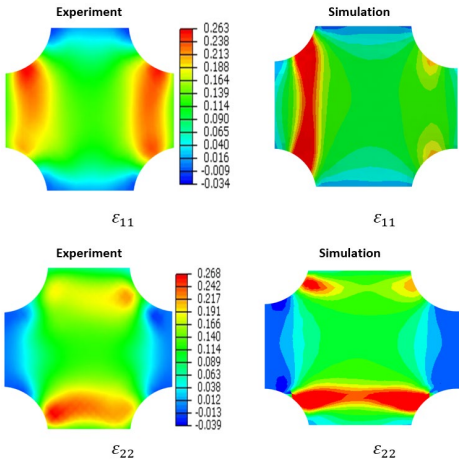

Fig. 8. Case 1 – Biaxial stretching.

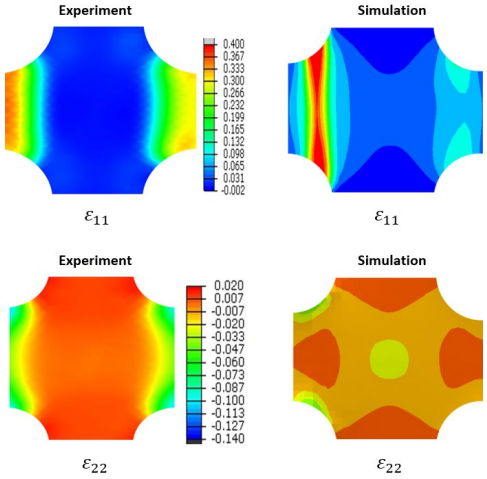

Fig. 9. Case 2 – Near plane strain condition.

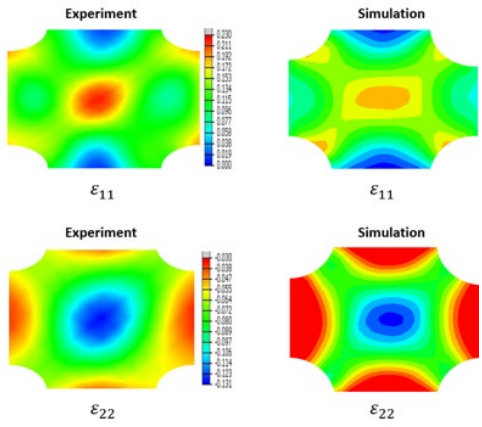

Fig 10. Case 3 – Uniaxial stretching.

Figs. 8 to 10 show a similarity in the strain distribution between the experimental and the predictive results. For cases 1 and 3, the level of strain measured at the centre of the sample is rather high. It leads to values of equivalent strain similar to or higher than the ones measured in the uniaxial test. This is an essential result for the use of this cruciform shape for mechanical characterization (hardening behaviour or anisotropy). The evolution of major and minor strains (in-plane principal strains) can be plotted for the three loading conditions. The comparison of the maximum equivalent strain (failure strain) values for three cases is shown in Table 1. The maximum equivalent strain values represent the starting of the structural failure. The quantitative comparison between simulated and experimental strains at the specimen center can reach up to 30% depending on the considered condition. Fig.11 compares the strain paths for three cases between experimental and numerical results. As expected, the three loading conditions lead to very different strain paths. For this cruciform shape, the strain path measured at the centre of the sample is directly linked to the ratio of actuator velocities. Moreover, as already observed for cruciform samples with reduced thickness [5], the strain paths for the three cases are quasi-linear.

Table 1. Comparison of maximal strain values between experimental and numerical study at the centre point of the specimen.

	Experiment		Simulation		Difference	
	$\varepsilon 11_{max}$	$\varepsilon 22_{max}$	$\varepsilon 11_{max}$	$\varepsilon 22_{max}$	$\Delta\varepsilon 11_{max}$[%]	$\Delta\varepsilon 22_{max}$[%]
Case1 [Biaxial stretching]	0.132	0.121	0.109	0.080	17.4	33.9
Case2 [Plane strain]	0.075	-0.019	0.052	-0.023	30.7	21.1
Case3 [Uniaxial stretching]	0.276	-0.159	0.191	-0.129	30.8	18.9

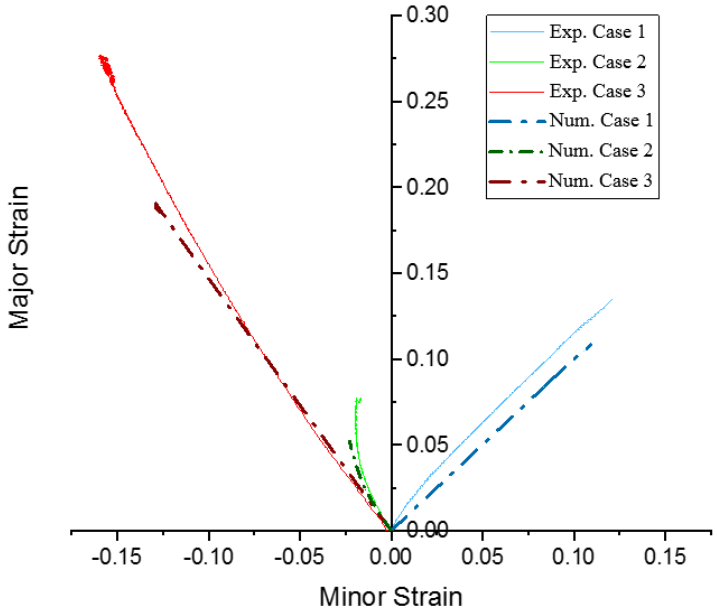

Fig. 11. Comparison of the strain paths for the three loading conditions.

Summary

A numerical model of the forming and testing of an original cruciform sample, without local thickness reduction, was proposed. This cruciform sample was subjected to three different loading conditions (biaxial stretching, near plane strain condition, and uniaxial stretching) in order to evaluate the potential of this sample to characterize advanced mechanical behaviour for different strain states. The predictive qualitative results from the FE model are in agreement with the strain fields measured during the tests for the same loading conditions however the quantitative

comparison between simulated and experimental strains at the specimen center can reach up to 30% of difference depending on the considered condition. Specimen geometry and the dimensions of the preforming die were obtained through FE analysis by a limited number of comparisons. Since the character of the deformations obtained from simulation and experiments is similar, the current numerical model can be used for further optimizations of the proposed geometry in order to emphasize the strain localization at the gauge region and use the sample for mechanical characterization at high strain level (hardening behaviour or forming limits).

References

[1] K. Nakazima, T. Kikuma, K. Hasuka, Study on the formability of steel sheets, Yawata Technol. Rep. 264 (1968) 8517-8530.

[2] Z. Marciniak, K. Kuczynski, Limit strains in the processes of stretch-forming sheet metal, Int. J. Mech. Sci. 9 (1967) 609-620.

[3] T. Kuwabara, S. Ikeda, T. Kuroda, Measurement and analysis of differential work hardening in cold-rolled steel sheet under biaxial tension, J. Mater. Process. Technol. 80–81 (1998) 517-523. https://doi.org/10.1016/S0924-0136(98)00155-1

[4] W. Liu, D. Guines, L. Leotoing, E. Ragneau, Identification of sheet metal hardening for large strains with an in-plane biaxial tensile test and a dedicated cross specimen, Int. J. Mech. Sci. 101-102 (2015) 387-398. https://doi.org/10.1016/j.ijmecsci.2015.08.022

[5] R. Zhang, Z. Shao, Z. Shi, T.A. Dean, J. Lin, Effect of cruciform specimen design on strain paths and fracture location in equi-biaxial tension, J. Mater. Process. Technol. 289 (2021)116932. https://doi.org/10.1016/j.jmatprotec.2020.116932

[6] G. Mitukiewicz, M. Głogowski, Cruciform specimen to obtain higher plastic deformation in a gauge region, J. Mater. Process. Technol. 227 (2016) 11-15. https://doi.org/10.1016/j.jmatprotec.2015.07.016

[7] L. Leotoing, D. Guines, Investigations of the effect of strain path changes on forming limit curves using an in-plane biaxial tensile test, Int. J. Mech. Sci. 99 (2015) 21-28. https://doi.org/10.1016/j.ijmecsci.2015.05.007

[8] ISO 16842:2021 Metallic materials — Sheet and strip — Biaxial tensile testing method using a cruciform test piece.

[9] M. Amraei, M. Dabiri, T. Björk, T. Skriko, Effects of Workshop Fabrication Processes on the Deformation Capacity of S960 Ultra-high Strength Steel, ASME. J. Manuf. Sci. Eng. 138 (2016) 121007. https://doi.org/10.1115/1.4033930

Materials Research Proceedings 28 (2023) 1471-1480 https://doi.org/10.21741/9781644902479-159

Examination of intrinsic and extrinsic size effect in thin specimens through crystal plasticity frameworks

GÜNAY Enes[1,a], BULUT Orhun[1,b] and YALÇINKAYA Tuncay[1,c *]

[1]Department of Aerospace Engineering, Middle East Technical University, Ankara 06800, Türkiye

[a]enes.gunay@metu.edu.tr, [b]orhun.bulut@metu.edu.tr, [c]yalcinka@metu.edu.tr

Keywords: Crystal Plasticity, Size Effect, t/d Ratio Influence

Abstract. Manufacturing devices at the microscale requires a precise analysis for desirable mechanical behavior. As the products of microscale forming operations have a comparable thickness dimension with grain size, the ratio between thickness and grain size (t/d) becomes an important aspect of mechanical behavior. A number of experimental studies investigated this phenomenon and have shown the influence of the t/d ratio in micron-sized sheet specimens. On the other hand, the computational studies addressing this phenomenon employing micromechanics-based models are quite restricted. The current study aims to investigate the t/d ratio effect through finite element method (FEM) simulations with both local and nonlocal crystal plasticity frameworks. The numerical analyses with the local crystal plasticity framework are obtained by utilizing two different methodologies, where the initial slip resistance is taken as constant or modified using a subroutine based on grain size effects and slip system interactions (see [1]).

Introduction

Microelectromechanical systems are commonly used in different areas such as medicine, portable devices, and inertial measurement units. These systems are composed of micron-sized components that necessitate an investigation of their mechanical behavior. At such small scales, material behavior is heavily size dependent. The effect of grain boundaries and grain dimensions begin to dictate the material behavior (see [2]). However, when these specimens become so thin that there are very few grains in thickness direction, it is not enough to consider the grain size effects only (see [3]). Experiments in the literature have shown that the ratio of specimen thickness to average grain diameter is an important factor determining material response (see e.g. [4,5,6]). In these experiments, the t/d ratio is controlled by keeping one parameter (either specimen thickness or average grain diameter) constant while changing the other. The experiments show that the plasticity response from t/d parameter can be categorized in three main regions (see [5]). Very thin materials that lie in $t/d < 1$ region contain one or very few grains in the thickness direction. This results in a large majority of grains lying at the material surface and an independence of material response from the t/d ratio. Beyond this region, the number of grains in thickness direction begins to increase, yielding a multi-crystal behavior and rapid increase of stress response until the critical t/d ratio is achieved. The critical t/d ratio can be thought of as a material property. Upon reaching this value, the material begins to show proper polycrystalline behavior and acts as a bulk material. The influence of t/d ratio becomes insignificant since the surface grains are in very few numbers (see [7]).

In this paper, the behavior of such thin specimens is examined with three different approaches. First, a conventional local crystal plasticity is used. Local crystal plasticity frameworks do not have an intrinsic length scale parameter. Then, a lower order strain gradient crystal plasticity framework is implemented as an ABAQUS UMAT subroutine. Strain gradient methods have an intrinsic length scale parameter that allows them to predict size effects at the microscale (see e.g.

Content from this work may be used under the terms of the Creative Commons Attribution 3.0 license. Any further distribution of this work must maintain attribution to the author(s) and the title of the work, journal citation and DOI. Published under license by Materials Research Forum LLC.

[8]). The higher order strain gradient formulations have higher order stresses which make them challenging to implement (see e.g. [9,10]). However, since the magnitude of the higher order stresses are often small, lower order approaches have also been used to obtain similar result except for boundary layers near interfaces or material surfaces as explained in [11]. The last method used is a subroutine that uses Hall-Petch theory to define initial slip resistance to crystals at each material point. This subroutine is implemented into the crystal plasticity framework. It is modified to work together with Voronoi tessellation geometries obtained from Neper program (see [12]). Grain misorientations and distance to grain boundaries at each point of the crystal structure is taken into account to provide a non-uniform distribution of initial slip resistance throughout the polycrystal specimens. Specimens with different thicknesses are simulated under uniaxial tension condition with all three methods and the results are discussed in detail.

The structure of this paper is as follows. First, the constitutive relations for both local and strain-gradient framework are described. Then, the material constants of aluminum alloy AA6016 in T4 temper condition, as well as the geometry parameters used in the finite element models are given. Additionally, the boundary conditions of the uniaxial tension are explained. Finally, the results are presented and compared with experimental findings in the literature.

Crystal Plasticity Frameworks

In the finite element analysis of the t/d effect, both a rate-dependent local, and a rate-dependent strain gradient crystal plasticity model is employed. This framework is based on a local crystal plasticity ABAQUS user material subroutine (UMAT) (see [13]). The UMAT subroutine is modified to include non-local strain-gradient effects using lower-order formulation following the theory of [10]. Since local crystal plasticity models do not inherently include size effects, it would not be possible to correctly predict the intrinsic size effect due to the change in grain size. The modification to include strain gradient effects in the constitutive formulations allows the size effects of crystal grains to be captured in simulations through geometrically necessary dislocations (GNDs).

The deformation gradient is decomposed into elastic and plastic components,

$$\mathbf{F}=\mathbf{F}^{e}\mathbf{F}^{p} \tag{1}$$

It is assumed that plastic deformation only occurs as a result of plastic slip. The elastic component of the deformation gradient only considers the stretching and rotation of the crystal lattice. The plastic component of the deformation gradient evolves according to the following flow rule

$$\dot{\mathbf{F}}^{p}=\mathbf{L}^{p}\mathbf{F}^{p} \tag{2}$$

where the plastic component of velocity gradient $\mathbf{L}^{p}$ is defined as the integration of plastic slip rate $\dot{\gamma}^{\alpha}$ on each slip system α that has slip direction and normal $\mathbf{m}^{\alpha}$ and $\mathbf{n}^{\alpha}$ respectively. The crystal plasticity framework consists of 12 active slip systems for a face-centered cubic material.

$$\mathbf{L}^{p}=\dot{\mathbf{F}}^{p}\mathbf{F}^{p-1}=\sum_{\alpha=1}^{N}\dot{\gamma}^{\alpha}\left(\mathbf{m}^{\alpha}\otimes\mathbf{n}^{\alpha}\right) \tag{3}$$

The slip rate is expressed in power law form, as,

$$\dot{\gamma}^{\alpha}=\dot{\gamma}_{0}\left|\frac{\tau^{\alpha}}{g_{T}^{\alpha}}\right|^{n}\operatorname{sign}(\tau^{\alpha}) \tag{4}$$

where $\dot{\gamma}_0$ is the reference slip rate, τ^α is the resolved shear stress, g_T^α is the total slip resistance, n is the rate sensitivity exponent, and $\mathrm{sign}(x)$ is the sign function. In this formulation, the total slip resistance is a combination of slip resistance caused by statistically stored dislocations (SSDs) and geometrically necessary dislocations (GNDs).

$$g_T^\alpha = \sqrt{{g_{ssd}^\alpha}^2 + {g_{gnd}^\alpha}^2} \tag{5}$$

The SSD slip resistance is described by the following relation,

$$\dot{g}_{ssd}^\alpha = \sum_{\beta=1}^{N} h^{\alpha\beta} \left|\dot{\gamma}^\beta\right| \tag{6}$$

From [14], the self and latent hardening law is expressed as,

$$h^{\alpha\alpha} = h_0 \, \mathrm{sech}^2 \left|\frac{h_0 \gamma}{g_s - g_0}\right| \tag{7}$$

$$h^{\alpha\beta} = q^{\alpha\beta} h^{\alpha\alpha} \tag{8}$$

where h_0 is the initial hardening modulus, g_s is the saturation slip resistance, g_0 is the initial slip resistance and $q^{\alpha\beta}$ is the latent hardening coefficient. The strain gradient framework assumes that there are no initial GNDs in the model, and GNDs only evolve because of strain gradient effects over time. Hence, the initial slip resistance is purely related to SSDs. The GND slip resistance is a formulation based on internal length scale parameter as well as the GND density of the crystals.

$$g_{gnd}^\alpha = g_0 \sqrt{l \eta_{gnd}^\alpha} \tag{9}$$

The length scale parameter l is defined as,

$$l = \frac{\alpha_T^2 \mu_s^2 b}{g_0^2} \tag{10}$$

Here, α_T is the Taylor coefficient that depends on the dislocation mechanisms of the crystal, μ_s is the shear modulus and b is the Burger's vector length. The GND density is described as,

$$\eta_{gnd}^\alpha = \left|\mathbf{n}^\alpha \times \sum_{\beta=1}^{N} \mathbf{m}^\alpha \mathbf{m}^\beta \nabla \gamma^\beta \times \mathbf{n}^\beta\right| \tag{11}$$

The calculation of strain gradient in a lower-order framework involves finite element operations. Using an 8-node 3D brick element with 8 Gauss integration points, the plastic slip values on each integration point is extrapolated to element nodes (see [15] for details). Then, a nodal averaging of the plastic slip is performed on nodes of neighboring elements. Finally, the gradient of strain is computed at the position of integration points.

Numerical Analysis

The numerical parameters of thickness/grain diameter ratio simulations are given in this section. A user material subroutine (UMAT) in the finite element software ABAQUS is used for crystal plasticity finite element method (CPFEM) simulations. The details of crystal plasticity parameters and the geometry-based initial slip resistance subroutine parameters are provided hereafter.

Using the material data of AA6016 in T4 temper condition from [16], the material parameters for the crystal plasticity framework are identified using a representative volume element (RVE) with 300 grains. This number of grains is sufficient to obtain an isotropic response from a polycrystal RVE in a reasonable computation time. The stress-strain response of the simulations is fitted to experimental material data under symmetric boundary conditions and tensile loading. Since the RVE is not morphologically periodic, symmetry boundary conditions are used to simulate the uniaxial tension at constant stress triaxiality of 0.33. Elastic stiffness coefficients for Al alloy are taken for cubic behavior from [17] as $C_{11} = 108.2$ GPa, $C_{12} = 61.3$ GPa, $C_{44} = 28.5$ GPa. Reference slip rate $\dot{\gamma}_0$ and the rate sensitivity exponent n are $10^{-3}\,s^{-1}$ and 20, respectively. The latent hardening parameter q is taken as 1.4. The hardening parameters are fitted using an RVE are initial hardening modulus h_0, saturation slip resistance g_s and initial slip resistance g_0, which are 190 MPa, 95 MPa and 47 MPa, respectively.

Table 1. Dimensions and total grains of the specimens used in simulations.

thickness [μm]	mean grain diameter [μm]	t/d ratio	Total number of grains	Number of finite elements	Avg. elements per grain
18	59	0.3	665	63368	95.3
35	73	0.48	665	62208	93.5
70	93	0.75	665	51076	76.8
105	105	1	703	50000	71.1
147	105	1.4	985	70000	71.0
189	105	1.8	1266	90000	71.1
211	105	2	1414	110000	77.8
253	105	2.4	1696	130000	76.7
295	105	2.8	1976	150000	75.9
316	105	3	2117	160000	75.6
358	105	3.4	2398	180000	75.1
400	105	3.8	2680	200000	74.6
484	105	4.6	3242	240000	74.0
526	105	5	3524	260000	73.8
568	105	5.4	3805	280000	73.6

The lower-order strain gradient theory requires an intrinsic length scale parameter for the slip resistance contribution of GNDs to be determined and the size effects to be predicted. The relation for the length scale parameter that governs the gradient effects is given in Eq. 10 (see [10]). The details of Taylor alpha coefficient can be found in [18]. In this problem, it is taken as 0.5. The shear modulus of AA6016 T4 is taken as 26 GPa and the Burger's vector magnitude is taken as 0.286 nm from [19]. The length scale parameter is calculated as 23.86 μm. However, above a certain element size in the FEM mesh, the lower-order model is mesh dependent. The GNDs are high in density in regions with non-uniform strain states such as grain boundaries. New dislocations must be introduced to obtain a homogenous plastic deformation in these regions (see [20]). If these regions are not modeled with an adequately fine mesh, strain gradients cannot be realized correctly. In this work, since there are many grains in the polycrystal structure, the computation times would be very long if a finer mesh was used. Hence, the length scale parameter is set to 500 μm after an element size sensitivity analysis to perform a qualitative comparison with the experiments.

A subroutine that calculates initial slip resistance based on the distance to grain boundaries on each integration point is implemented and tested in this work. This subroutine is built into the crystal plasticity framework and is only used to determine g_0. The details can be found in (see [1]). The size effects are realized in the initial slip resistance by the following relation,

$$g_0^{\alpha}=\tau_0+\frac{k^{\alpha}}{\sqrt{L^{\alpha}}} \tag{12}$$

where τ_0 is the critical resolved shear stress of a theoretically infinite crystal, taken as 0.05 MPa. L^{α} is the distance at a material point from grain boundaries in the direction of slip for a slip system. k^{α} is the micro Hall-Petch coefficient calculated as,

$$k^{\alpha}=K\left(1-m^{\alpha'}\right)^{c} \tag{13}$$

K and c are empirical coefficients, taken as 0.414 and 0.134, respectively. These values are obtained by fitting the stress-strain response using a 300 grain RVE with uniform 47 MPa initial slip resistance. $m^{\alpha'}$ is the Luster-Morris parameter for each slip system based on grain misorientation,

$$m^{\alpha'}=\left(\frac{\mathbf{m}_A^{\alpha}.\mathbf{m}_B^{\alpha}}{|\mathbf{m}_A^{\alpha}||\mathbf{m}_B^{\alpha}|}\right)\left(\frac{\mathbf{n}_A^{\alpha}.\mathbf{n}_B^{\alpha}}{|\mathbf{n}_A^{\alpha}||\mathbf{n}_B^{\alpha}|}\right) \tag{14}$$

where $\mathbf{m}^{\alpha}$ and $\mathbf{n}^{\alpha}$ are slip directions and normals respectively of each slip system α for grains A and B.

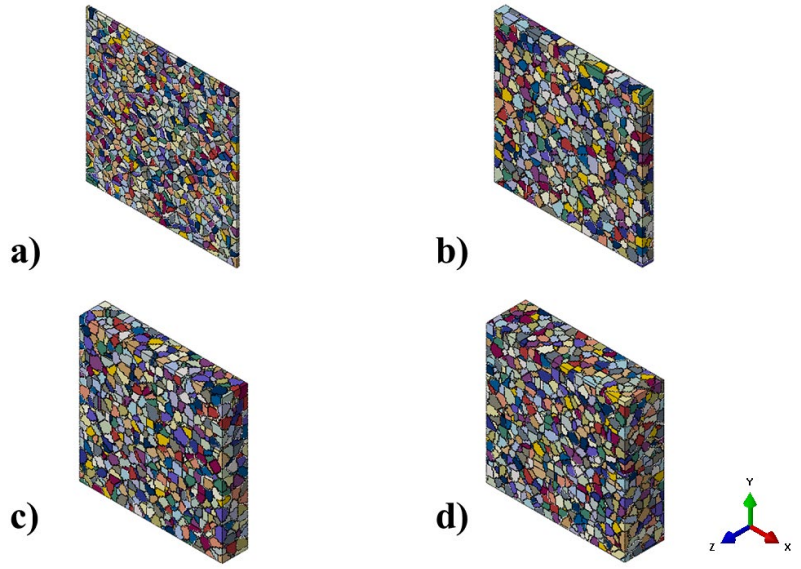

Fig. 1. Polycrystal microstructures of a) t/d = 0.48, b) t/d = 1.4, c) t/d =3, d) t/d = 5.4.

Tensile specimens of 2 mm x 2 mm x t mm thickness are generated through Neper software with dimensions given in Table 1. Examples of polycrystal structures at different t/d ratios are given in Fig. 1. Each grain is given a random crystal orientation. These orientations are random for each specimen with a different t/d ratio. However, they are kept constant while comparing local, strain-gradient, and geometry-based slip resistance simulations. 10% uniaxial tension is applied to each specimen in y-direction with a loading rate of $10^{-3}s^{-1}$ over 100 seconds.

Materials Research Proceedings 28 (2023) 1471-1480 https://doi.org/10.21741/9781644902479-159

Numerical Results

The numerical examples are presented in this section and a qualitative comparison with the experimental observations is conducted. Experimental results of true stress at 0.05 strain for a nickel polycrystal are represented in Fig. 2 from [5].

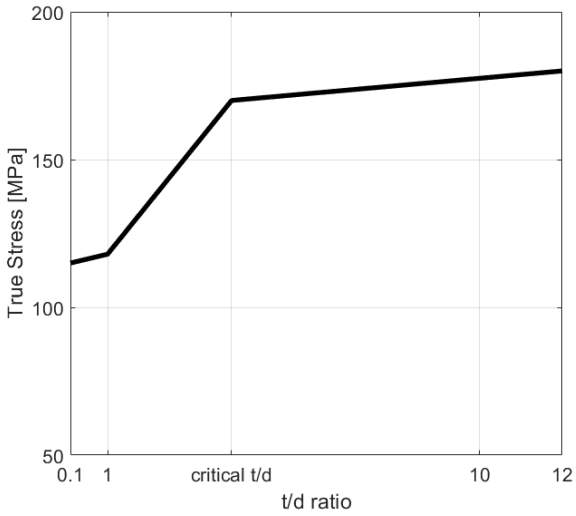

Fig. 2. Experimental values of true stress at 0.05 strain for different t/d ratios of Ni polycrystal (see [5]).

The FEM analysis results using the local crystal plasticity framework shows that, at low t/d ratio specimens (1 and below), the grains do not yield a stronger response despite their lower size compared to large t/d ratios. This is because the local crystal plasticity framework cannot predict intrinsic size effects. As a result, a monotonous increase in strength is observed in this region as seen in Fig. 3a. However, experimental results show that the stress response should not change significantly in t/d < 1 region. Without using a strain gradient framework or modifying the grains to have slip resistance based on their size and geometry, the increased strength of smaller grains cannot be reflected.

Finite element simulation results utilizing the strain gradient crystal plasticity framework are shown in Fig. 3b. The size-dependent solution shows that the strength of specimens in t/d < 1 range does not significantly change, similar to experimental findings. As specimen thickness decreases in this region, the average grain diameter also decreases. Hence, the material response gets stronger, and the significant stress increase in local solution due to surface grains and the presence of additional grains is no longer observed when the size effects are captured. Additionally, the critical t/d value is predicted as t/d = 3. In both Fig. 3a and 3b, a sharp, discontinuous increase can be seen between t/d = 1 and t/d = 1.4. This is a result of increased number of grains in the thickness direction. These grains allow for additional grain boundaries to be created, thus, a jump in stress response is observed.

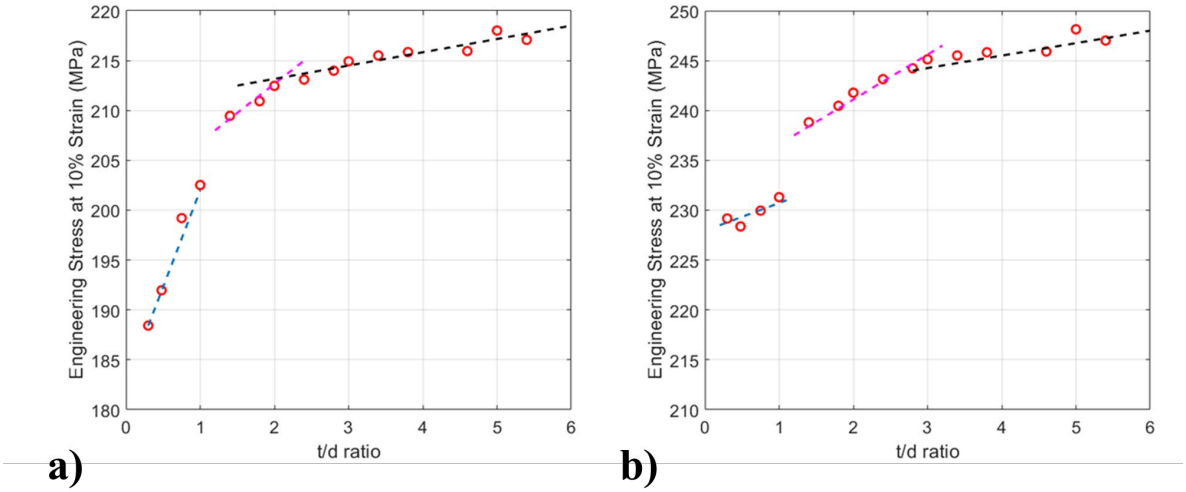

Fig. 3. Flow stress values of different t/d specimens at 10% strain with a) local crystal plasticity framework, b) strain gradient crystal plasticity framework.

After the critical t/d value is reached, the increase in stress response becomes less significant with increasing t/d values. This is in line with the experimental results. In the 1 < t/d < critical t/d region, there is a sharp increase in strength since additional grains in the thickness direction are now appearing and significantly increasing the material's strength. After the critical value, the thickness effect is no longer observed since the specimen approaches bulk size. There are enough grains in thickness direction so that newly formed grain boundaries do not impede dislocation motions significantly. The stress levels reached for every specimen is higher compared to results from local solution since GNDs impede deformation by increasing the slip resistance at locations where their densities are high.

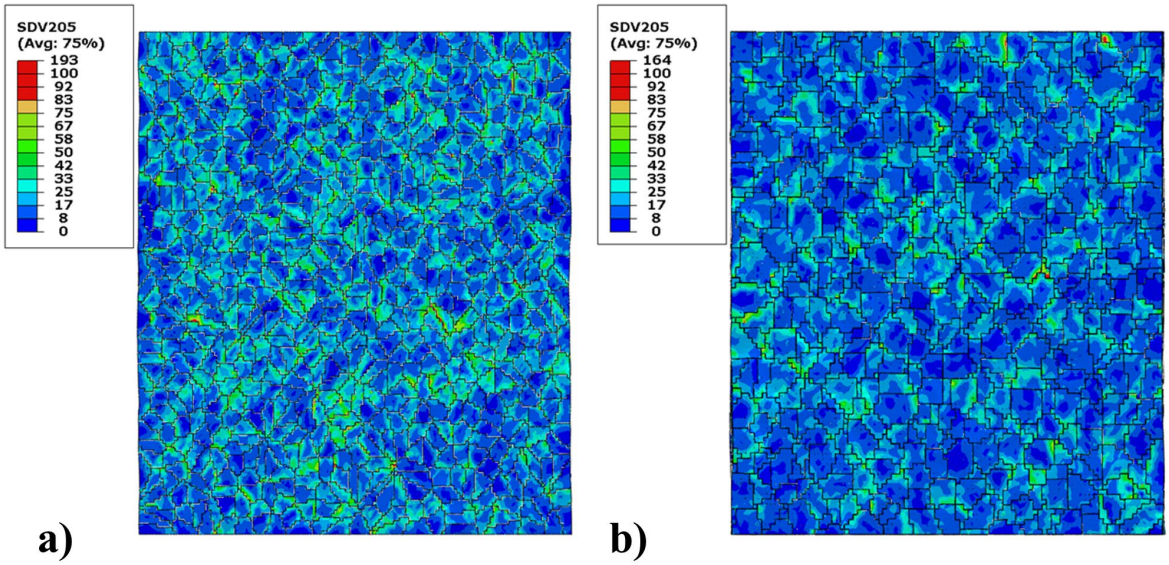

Fig. 4. GND densities [1/mm] of a) t/d = 0.48 and b) t/d = 5.4.

The GND densities of specimens having t/d ratios of 0.48 and 5.4 are presented in Fig. 4. Here, GND densities for each grain are highest at the grain boundaries. Neighboring grains with significant misorientation between each other can be spotted since GND densities would

concentrate at those locations. The density of GNDs is higher in the specimen with smaller t/d ratio, resulting in a higher slip resistance due to smaller grain sizes.

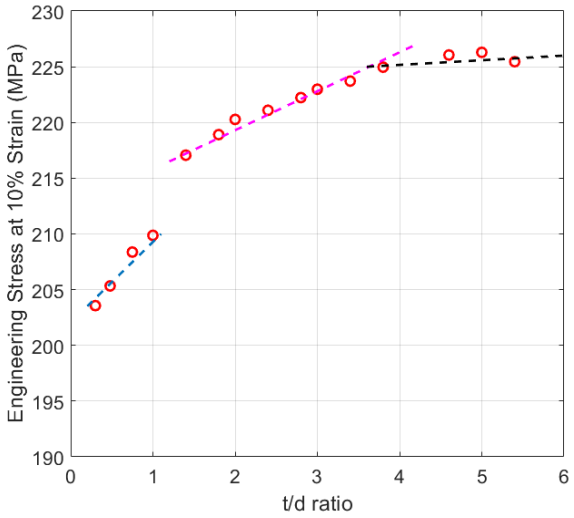

Fig. 5. Flow stress values of different t/d specimens at 10% strain with geometry-based initial slip resistance simulations.

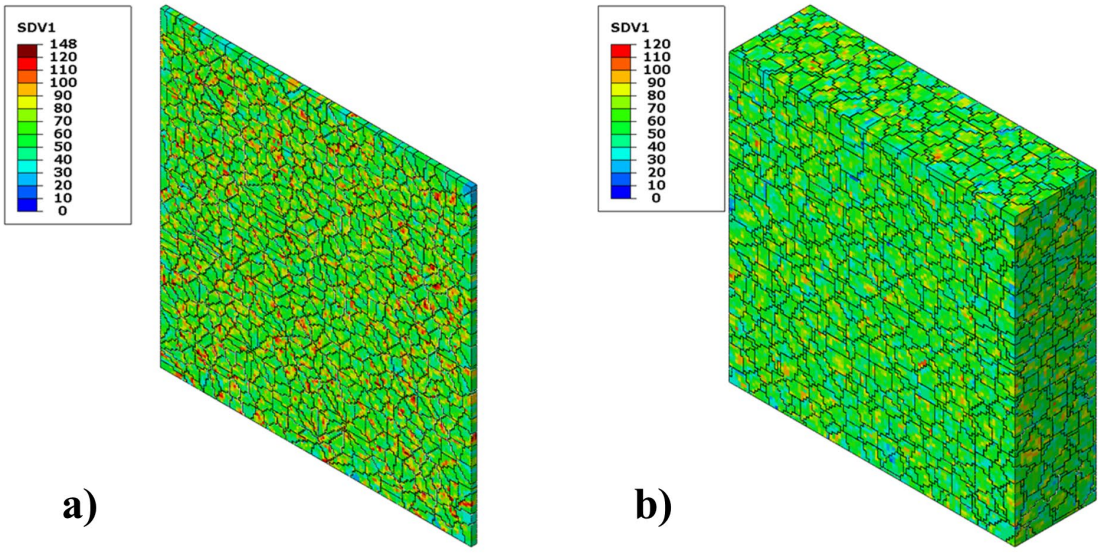

Fig 6. Comparison of initial slip resistance [MPa] at a) t/d = 0.48 and b) t/d = 5.4 for slip system (111)[0$\bar{1}$1].

Finally, the results of simulations where a geometry-based initial slip resistance is used are shown in Fig. 5. The critical t/d value is predicted higher with this method as approximately 4. Since the distance to grain boundaries is a parameter that determines the initial slip resistance at each material point, size effects are taken into account. At t/d < 1, an increase in strength can still be observed with increasing t/d, although at a much lower rate than the local solution. Moreover, after the critical t/d value, the strength increase slows down as expected from the experimental findings. Fig. 6 shows the comparison of initial slip resistance at t/d ratios 0.48 and 5.4 for one of the slip systems. There is a larger initial resistance assigned to elements in $t/d = 0.48$ on average since the grains are smaller and the integration points are closer to grain boundaries as a result.

Summary

In this work, a series of crystal plasticity finite element method simulations are conducted to examine the uniaxial tension loading responses of micron-sized specimens. Three different approaches have been used to obtain these results. Local crystal plasticity frameworks yield size-independent results since there is no information regarding grain or specimen size in their constitutive relations. A subroutine is utilized in a local framework to determine the initial slip resistance of crystals at every material point through a size-dependent approach. While this method does not influence constitutive relations, it is still able to capture the effects seen in experiments since smaller grains in low t/d ratios have their slip resistance increased compared to larger grains. The last method used is the lower-order strain-gradient framework. With this method, the density of GNDs is calculated and used in the constitutive relations directly based on a length scale parameter.

The results show that by using a strain-gradient framework or employing Hall-Petch theory to determine initial slip resistance of crystals, a similar trend to experimental findings in t/d<1 region can be found. As the thickness and t/d ratios of the specimens increase, an increase in their stress/strain response can be seen in every result case. This is attributed to the fact that new grain boundaries and more grains in the thickness direction are developing rapidly. Once the critical t/d value is reached, a different value is obtained with every method. The simulations using local crystal plasticity framework show that the critical t/d is obtained at 2. With the strain gradient framework, the critical value is found as 3. This indicates that there is still a considerable size dependence until this point. On the other hand, when Hall-Petch theory is utilized, the specimens reach this critical value and start showing bulk-material behavior at a t/d value of 4. This is consistent with the trends obtained from experiments as seen in Fig. 2. Additionally, the stress increase in the post-critical region is predicted slightly less in this case.

References

[1] D. Agius, A. Kareer, A. Al Mamun, C. Truman, D.M. Collins, M. Mostafavi, D. Knowles, A crystal plasticity model that accounts for grain size effects and slip system interactions on the deformation of austenitic stainless steels, Int. J. Plast. 152 (2022) 103249. https://doi.org/10.1016/j.ijplas.2022.103249

[2] T. Yalçinkaya, İ. Özdemir, I. Simonovski, Micromechanical modeling of intrinsic and specimen size effects in microforming, Int. J. Mater. Form. 11 (2018) 729-741. https://doi.org/10.1007/s12289-017-1390-3

[3] H.S. Kim, Y.S. Lee, Size dependence of flow stress and plastic behaviour in microforming of polycrystalline metallic materials, Proc. Inst. Mech. Eng., Part C: J. Mech. Eng. Sci. 226 (2012) 403-412. https://doi.org/10.1177/0954406211414473

[4] P.J.M. Janssen, T.H. De Keijser, M.G.D. Geers, An experimental assessment of grain size effects in the uniaxial straining of thin Al sheet with a few grains across the thickness, Mater. Sci. Eng. A 419 (2006) 238-248. https://doi.org/10.1016/j.msea.2005.12.029

[5] E. Hug, C. Keller, Intrinsic effects due to the reduction of thickness on the mechanical behavior of nickel polycrystals, Metall. Mater. Trans. A 41 (2010) 2498-2506. https://doi.org/10.1007/s11661-010-0286-3

[6] C. Keller, E. Hug, R. Retoux, X. Feaugas, TEM study of dislocation patterns in near-surface and core regions of deformed nickel polycrystals with few grains across the cross section, Mech. Mater. 42 (2010) 44-54. https://doi.org/10.1016/j.mechmat.2009.09.002

[7] O. Bulut, S.S. Acar, T. Yalçinkaya, The influence of thickness/grain size ratio in microforming through crystal plasticity, Procedia Struct. Integrity 35 (2022) 228-236. https://doi.org/10.1016/j.prostr.2021.12.069

[8] T. Yalçinkaya, Strain gradient crystal plasticity: Thermodynamics and implementation, in: G. Z. Voyiadjis (Eds.), Handbook of Nonlocal Continuum Mechanics for Materials and Structures, Springer, London/Berlin, 2017, pp.1001-1033.
[9] T. Yalçinkaya, İ. Özdemir, A.O. Firat, Inter-granular cracking through strain gradient crystal plasticity and cohesive zone modeling approaches, Theor. Appl. Fract. Mech. 103 (2019) 102306. https://doi.org/10.1016/j.tafmec.2019.102306
[10] T. Yalçinkaya, İ.T. Tandoğan, İ. Özdemir, Void growth based inter-granular ductile fracture in strain gradient polycrystalline plasticity, Int. J. Plast. 147 (2021) 103123. https://doi.org/10.1016/j.ijplas.2021.103123
[11] C.S. Han, H. Gao, Y. Huang, W.D. Nix, Mechanism-based strain gradient crystal plasticity-I, Theory, J. Mech. Phys. Solids 53 (2005) 1188-1203. https://doi.org/10.1016/j.jmps.2004.08.008
[12] R. Quey, P. Dawson, F. Barbe, Large-scale 3D random polycrystals for the finite element method: Generation, meshing and remeshing, Comput. Methods Appl. Mech. Eng. 200 (2011) 1729–1745. https://doi.org/10.1016/j.cma.2011.01.002
[13] Y. Huang, A user-material subroutine incorporating single crystal plasticity in the ABAQUS finite element program, Mech. Report 178 (1991)
[14] D. Peirce, R.J. Asaro, A. Needleman, An analysis of nonuniform and localized deformation in ductile single crystals, Acta Metall. 30 (1982) 1087–1119. https://doi.org/10.1016/0001-6160(82)90005-0
[15] E.P. Busso, F.T. Meissonnier, N.P. O'dowd, Gradient-dependent deformation of two-phase single crystals, J. Mech. Phys. Solids 48 (2000) 2333-2361. https://doi.org/10.1016/S0022-5096(00)00006-5
[16] H. Granum, V. Aune, T. Børvik, O.S. Hopperstad, Effect of heat-treatment on the structural response of blast-loaded aluminium plates with pre-cut slits, Int. J. Impact Eng. 132 (2019) 103306. https://doi.org/10.1016/j.ijimpeng.2019.05.020
[17]E. Nakamachi, C. Xie, H. Morimoto, K. Morita, N. Yokoyama, Formability assessment of FCC aluminum alloy sheet by using elastic crystalline viscoplastic finite element analysis, Int. J. Plast. 18 (2002) 617–632. https://doi.org/10.1016/S0749-6419(01)00052-3
[18] H. Mughrabi, The α-factor in the Taylor flow-stress law in monotonic, cyclic and quasi-stationary deformations: Dependence on slip mode, dislocation arrangement and density, Curr. Opin. Solid State Mater. Sci. 20 (2016) 411-420. https://doi.org/10.1016/j.cossms.2016.07.001
[19] O. Engler, C.D. Marioara, Y. Aruga, M. Kozuka, O.R. Myhr, Effect of natural ageing or pre-ageing on the evolution of precipitate structure and strength during age hardening of Al–Mg–Si alloy AA 6016, Mater. Sci. Eng. A 759 (2019) 520-529. https://doi.org/10.1016/j.msea.2019.05.073
[20] A. Arsenlis, D.M. Parks, Crystallographic aspects of geometrically-necessary and statistically-stored dislocation density, Acta Mater. 47 (1999) 1597-1611. https://doi.org/10.1016/S1359-6454(99)00020-8

Materials Research Proceedings 28 (2023) 1481-1490 https://doi.org/10.21741/9781644902479-160

Considering the stiffness of the forming tools in the numerical analysis of the ironing process

OLIVEIRA Marta C.[1,a *], NETO Diogo M.[1,b], ALVES José L.[2,c] and MENEZES Luís F.[1,d]

[1]CEMMPRE, Department of Mechanical Engineering, University of Coimbra, Pinhal de Marrocos, 3030-788 Coimbra, Portugal

[2]Microelectromechanical Systems Research Unit, University of Minho, Campus de Azurém, Guimarães, 4800-058, Portugal

[a]marta.oliveira@dem.uc.pt, [b]diogo.neto@dem.uc.pt, [c]jlalves@dem.uminho.pt, [d]luis.menezes@dem.uc.pt

Keywords: Sheet Metal Forming, Ironing Stage, Deformable Tools, Numerical Analysis

Abstract. Ironing can occur in cylindrical cup drawing whenever the thickness of the drawn flange is larger than the gap between the punch and the die. This is particularly relevant for materials that present *r*-values lower than 1.0, such as the aluminium alloys, since they tend to present more thickening of the flange. The aim of this study is to evaluate numerically the impact of the elastic deformation of the forming tools on the final cup geometry, i.e., the earing profile and the evolution of thickness along the circumferential direction, at different heights. Different contact conditions are also analysed since they strongly affect both the thickness strain and the earing profile. The process conditions considered are the ones from EXACT, the ESAFORM Benchmark 2021, enabling the comparison with experimental results. Considering the deformation of the forming tools mainly impacts the ironing stage, enabling predicting wall thickness values larger than the gap between the punch and the die.

Introduction

Ironing processes are commonly adopted in deep drawing to produce cylindrical cups with uniform thickness in the wall. It is mainly a bulk forming process where the wall of the cup is submitted to compression in the radial direction and shear stress in the contact areas with the tools. These compression forces can result in the elastic deformation of the forming tools, changing the desired thickness reduction. Typically, finite element analysis of sheet metal forming processes assume that the forming tools are rigid. This allows a significant reduction of the computational cost of the simulations since only the outer surface of the tools is modelled. Indeed, in most cases this simplification generates accurate results.

The actual increasing accuracy of both the plasticity and the friction models in predicting the material flow raised questions regarding the influence of the elastic deformations of dies and press lines. In fact, nowadays, it is consensual that they are responsible for many of the differences between the forming simulation results and the manufactured geometries. The iterative spotting steps performed during the die try-out aim to homogenize the contact pressure within the die, to compensate for the fact that the elastic deformation is unknown [1]. Different methods for analysis and virtual rework of tool structures and surfaces, including the combination of structural behaviour with sheet metal forming simulations are described in [2]. The results show that the elastic deformation of the tools changes the blank draw-in significantly, leading to considerable changes in the product's quality measures [2]. Nevertheless, many of the methods suggested to combine the structural analysis and forming simulation into one FE-model lead to large models, which are time-consuming to solve when scaled to industrial dies. Therefore, work has been done

Content from this work may be used under the terms of the Creative Commons Attribution 3.0 license. Any further distribution of this work must maintain attribution to the author(s) and the title of the work, journal citation and DOI. Published under license by Materials Research Forum LLC.

to develop methods to include die and press deformations in sheet metal forming simulations, where the die surfaces are still represented as 2D surfaces [3], including some to circumvent the fact that the press stiffness is commonly unknown [4]. The models that enable predicting the elastic deformations of dies can also be used to improve their structure using, for example, topology optimization [1]. Nevertheless, reliable results require accurate plasticity and the friction models, as pointed out in [2,3].

For small industrial or experimental dies, it is possible to combine structural analysis with sheet metal forming simulations, without resorting to model reduction strategies. This allows an improved understanding of the evolution of the contact conditions during the forming process and its impact in the final geometry. This can be particularly relevant for processes that involve high contact forces, such as the ones that occur in the ironing process. The Swift cup drawing test proposed under the benchmark EXACT [5] was adopted in the present study to assess the importance of the stiffness of the forming tools on the numerical predictions, in particular their accurate dimensions. Accordingly, the finite element model considers that the forming tools are modelled either as rigid or as deformable bodies [6]. Then, the numerical results are compared with the experimental ones, highlighting the impact of the tools deformation in the ironing stage.

Finite Element Model

The benchmark EXACT - Experiment and Analysis of Aluminium Cup Drawing Test [5], proposed at ESAFORM 2021, was selected to analyse the effect of the forming tools stiffness on the ironing conditions. The forming process involves a punch, a die and a blank-holder. Nevertheless, due to the thickening of the flange, the drawing operation is followed by an ironing one, promoted by the same forming tools. The blank presents a diameter 107.5 mm and a nominal thickness of 1.0 mm. The cylindrical punch presents 60 mm of diameter while the die opening diameter is 62.4 mm, i.e., the gap between the punch and the die is 1.2 mm. The cylindrical cup is fully drawn considering a constant blank-holder force of 40 kN. To avoid the pinching of the cup rim by the blank-holder, a stopper with the same thickness of the blank was used, guaranteeing a minimum gap between the blank-holder and the die (1.0 mm) [5].

The numerical simulations are performed with the in-house finite element code DD3IMP [7]. Due to geometrical and material symmetry, only a quarter of the geometry was modelled. The blank was discretized with linear hexahedral finite elements, combined with a selective reduced integration technique. Note that the use of solid elements seems to be the more accurate approach to predict the forming forces and strains (see also [5,8]). Two layers of elements were adopted through the thickness, which allows an accurate evaluation of the contact forces and of the through thickness stress gradients. The region corresponding to the bottom of the cup was defined with an unstructured coarse mesh while for the zone corresponding to the cup wall a refined structured mesh was used, yielding a total of 15,408 finite elements and 16,006 nodes.

Typically, the forming tools are modelled as rigid surfaces. Accordingly, Fig. 1 (a) presents the forming tools modelled by Nagata patches [9], which allows the use of a coarse finite element mesh to define the outer surface of the tools. In addition to the classical approach (rigid tools), the forming tools were also modelled as deformable elastic bodies (E=210 GPa and ν=0.3). The prediction of the elastic deformation of the forming tools requires a proper definition of the geometry (volume) of each one, particularly the punch and the die used in the ironing operation. Two different geometries for the die were studied and modelled by solid elements, which are illustrated in Fig. 1 (b) and (c). The main differences are in the outer diameter and height. The model (#1) presented in Fig. 1 (b) presents an outer diameter of 230 mm and 63 mm of height, while the model (#2) presented in Fig. 1 (c) contains an outer diameter of 180 mm and 25 mm of height. Considering the deformable tools, the total number of elements involved in the numerical simulation increased up to 24,704 elements in model #1 and 23,580 elements in model #2. To impose a constant force over the deformable blank-holder, a pliable (E=0.70 GPa) hollow cylinder

(61 mm of inner diameter and 100 mm of outer diameter) was used with a prescribed displacement on the upper face (1.07 mm). The friction conditions between the blank and the forming tools were described with the Coulomb's law. Two different values of the friction coefficient were adopted in the numerical study to best describe the drawing and the ironing force, respectively.

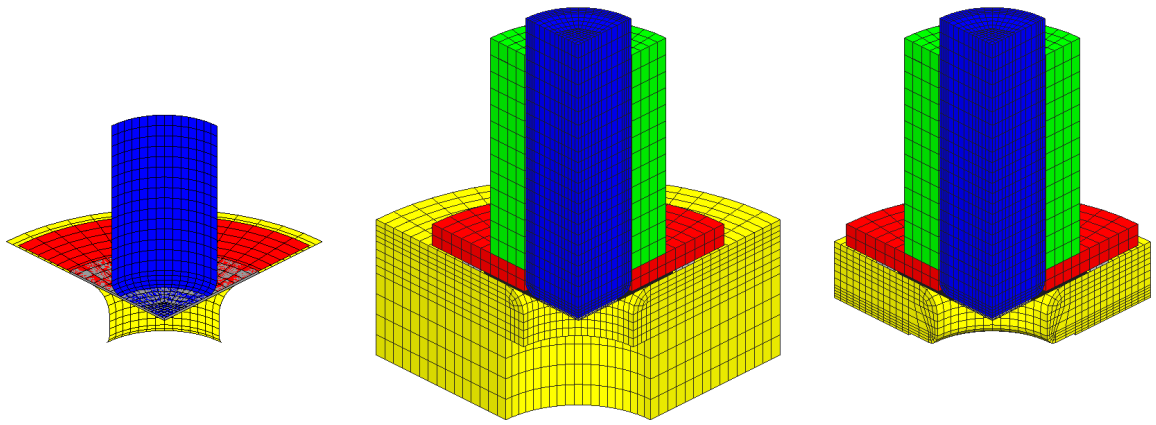

(a) (b) (c)

Fig. 1. Definition of the forming tools used in the numerical simulation: (a) rigid tools described by Nagata patches; (b) deformable tools (#1) described by solid elements; (c) deformable tools (#2) described by solid elements.

Constitutive Model

The mechanical behaviour of the AA 6016-T4 aluminium alloy is assumed to be isotropic in the elastic regime, being described by the Young's modulus, E, and the Poisson ratio, ν. Regarding the hardening behaviour, it was described with the Swift law:

$$Y = K(\varepsilon_0 + \bar{\varepsilon}^{\mathrm{p}})^n \tag{1}$$

where Y is the flow stress, $\bar{\varepsilon}^{\mathrm{p}}$ is the equivalent plastic strain and K, ε_0 and n are material parameters. The values considered for these parameters are the ones suggested by the benchmark committee, as shown in Table 1 [5]. The orthotropic behaviour was described by the yield criterion proposed by Cazacu and Barlat, usually referred as CB2001 [10]. The CB2001 is a generalization of the Drucker's isotropic criterion to orthotropy, such that:

$$\bar{\sigma} = \left\{27\left[\left(J_2^0\right)^3 - c\left(J_3^0\right)^2\right]\right\}^{\frac{1}{6}} \tag{2}$$

where J_2^0 and J_3^0 are the second and third generalized invariants of the deviatoric Cauchy stress tensor, defined as:

$$J_2^0 = \frac{a_1}{6}(\sigma_{11} - \sigma_{22})^2 + \frac{a_2}{6}(\sigma_{11} - \sigma_{33})^2 + \frac{a_3}{6}(\sigma_{11} - \sigma_{33})^2 + a_4\sigma_{12}^2 + a_5\sigma_{13}^2 + a_6\sigma_{23}^2 \tag{3}$$

$$
\begin{aligned}
J_3^0 = {} & (1/27)(b_1+b_2)\sigma_{11}^3 + (1/27)(b_3+b_4)\sigma_{22}^3 + (1/27)[2(b_1+b_4)-b_2-b_3]\sigma_{33}^3 \\
& -(1/9)(b_1\sigma_{22}+b_2\sigma_{33})\sigma_{11}^2 - (1/9)(b_3\sigma_{33}+b_4\sigma_{11})\sigma_{22}^2 \\
& -(1/9)[(b_1-b_2+b_4)\sigma_{11}+(b_1-b_3+b_4)\sigma_{22}]\sigma_{33}^2 \\
& +(2/9)(b_1+b_4)\sigma_{11}\sigma_{22}\sigma_{33} - (\sigma_{13}^2/3)[2b_9\sigma_{22}-b_8\sigma_{33}-(2b_9-b_8)\sigma_{11}] \\
& -(\sigma_{12}^2/3)[2b_{10}\sigma_{33}-b_5\sigma_{22}-(2b_{10}-b_5)\sigma_{11}] - (\sigma_{23}^2/3)[(b_6-b_7)\sigma_{11}-b_6\sigma_{22}-b_7\sigma_{33}] \\
& +2b_{11}\sigma_{12}\sigma_{23}\sigma_{13}
\end{aligned}
\tag{4}
$$

where $a_1,...,a_6$ and $b_1,...,b_{11}$ are the anisotropy parameters and c is a weighting parameter. The procedure adopted for the identification of the anisotropy parameters is detailed in [5] and the corresponding values are listed in Table 2. Note that the a_5, a_6 and b_k $(k = 6, 7, 8, 9, 11)$ are the anisotropy parameters corresponding to the off-plane properties, for which the isotropic values, i.e., 1.0 are assumed. Fig. 2 compares the uniaxial tensile tests experimental results (obtained by the Tokyo University of Agriculture and Technology (TUAT) and by the University of Aveiro (UA)) with the ones predicted by CB2001 yield criterion. Note that the in-plane evolution of the *r*-values is well captured but the same is not valid for the yield stress distribution. Although not shown here, the direction of the plastic strain-rate is also well captured by this yield criterion (see [5]).

Table 1. Elastic properties and hardening parameters used in the Swift law [5].

E [GPa]	ν [-]	K [MPa]	ε_0 [-]	n [-]
70	0.33	498.8	0.0089	0.285

Table 2. Anisotropy parameters of CB2001 yield criterion [5].

a_1	a_2	a_3	a_4	a_5	a_6	c				
1.000	1.900	1.391	0.870	1.000	1.000	1.2				
b_1	b_2	b_3	b_4	b_5	b_6	b_7	b_8	b_9	b_{10}	b_{11}
2.000	0.830	1.500	2.000	0.200	1.000	1.000	1.000	1.000	0.566	1.000

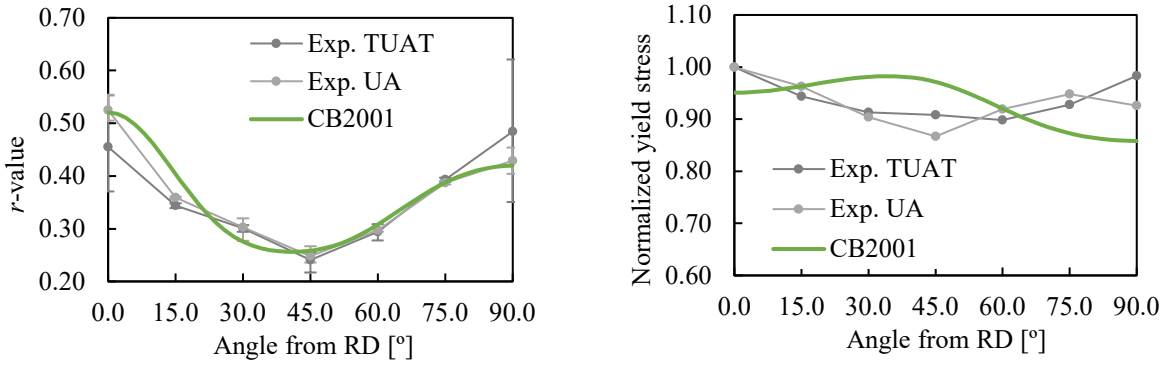

Fig. 2. Comparison between experimental and predicted: (a) r-values and (b) yield stresses.

Results and Discussion

The comparison between predicted and experimental punch force evolution is presented in Fig. 3, using both rigid and deformable tools in the numerical simulation. Besides, as previously mentioned, two different values of friction coefficient were used in the numerical analysis, namely μ=0.1 (Fig. 3 (a)) and μ=0.05 (Fig. 3 (b)). The drawing force is accurately described using μ=0.1 while the ironing force is clearly overestimated. Reducing the friction coefficient to μ=0.05 leads to a global reduction of the punch force during the drawing stage but, the ironing force is still overestimated. The increase of the punch force at approximately 35 mm of punch displacement results from the thickening of the blank during the drawing operation, leading to a thickness larger than the gap between the punch and the die (1.2 mm), i.e., results from the ironing. For both values of friction coefficient, the effect of the elastic deformation of the forming tools on the predicted drawing force is negligible. Nevertheless, the ironing force is reduced when the elastic deformation of the forming tools is considered in the numerical simulation. This is a consequence of the slight increase of the die opening diameter and, consequently, of the gap, due to the high values of contact pressure arising during the ironing stage of the cylindrical cup. Although the die in model #1 is stiffer than the one of model #2 (see Fig. 1), the bigger differences in the punch force only arise after 45 mm of punch displacement, i.e., when the cup wall is sliding over the vertical surface of the tools.

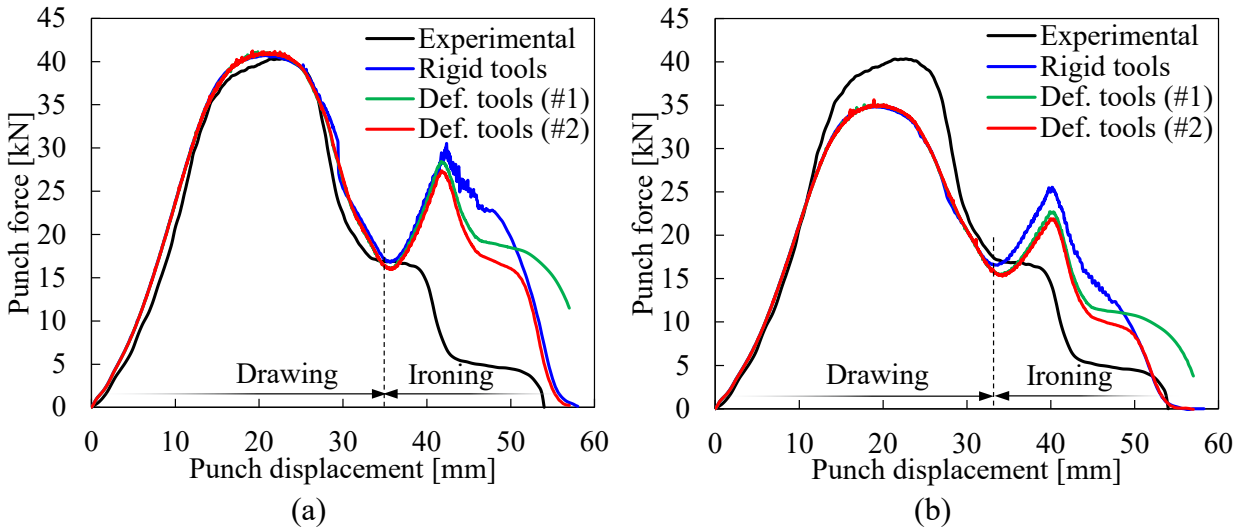

Fig. 3. Comparison between experimental [5] and numerical punch force evolution using different values of friction coefficient in the numerical analysis: (a) μ=0.1; (b) μ=0.05.

The numerical prediction of the blank-holder force evolution is presented in Fig. 4, for the different values of friction coefficient used in the numerical analysis. Regarding the rigid tools, the blank-holder force is kept constant (magnitude of 40±4 kN) by adjusting the position of the blank-holder. On the other hand, when the deformable tools are considered in the numerical model, the blank-holder force is proportional to the axial compression of the hollow cylinder. Thus, the blank-holder force increases slightly until about 25 mm of punch displacement (thickening of the flange) and then decreases quickly. At about 30 mm of punch displacement the stopper is activated, i.e., the gap between the blank-holder and the die decreases to 1.0 mm. The models with a lower friction coefficient predict the loss of contact between the blank and the blank-holder earlier (punch displacement lower than 30 mm) due to the reduction of the restraining forces. This effect is also visible in the punch force evolution, with a sudden drop, as shown in Fig. 3. This also means that

the models that use a lower value for friction coefficient predict lower strain values in the radial direction of the blank during this stage of the forming process.

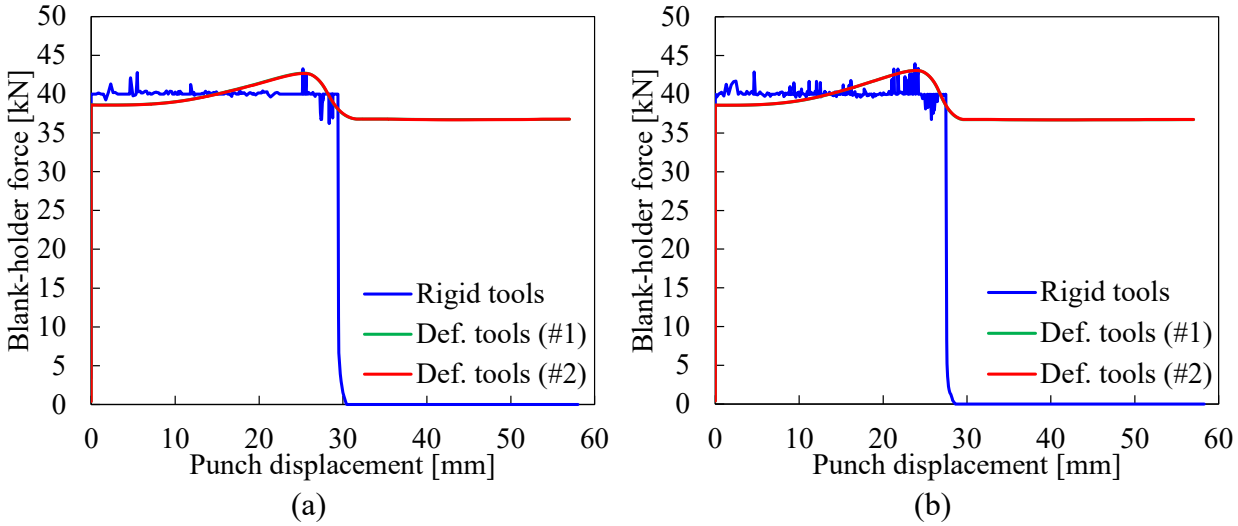

Fig. 4. Numerical prediction of the blank-holder force evolution using different values of friction coefficient in the numerical analysis: (a) μ=0.1; (b) μ=0.05.

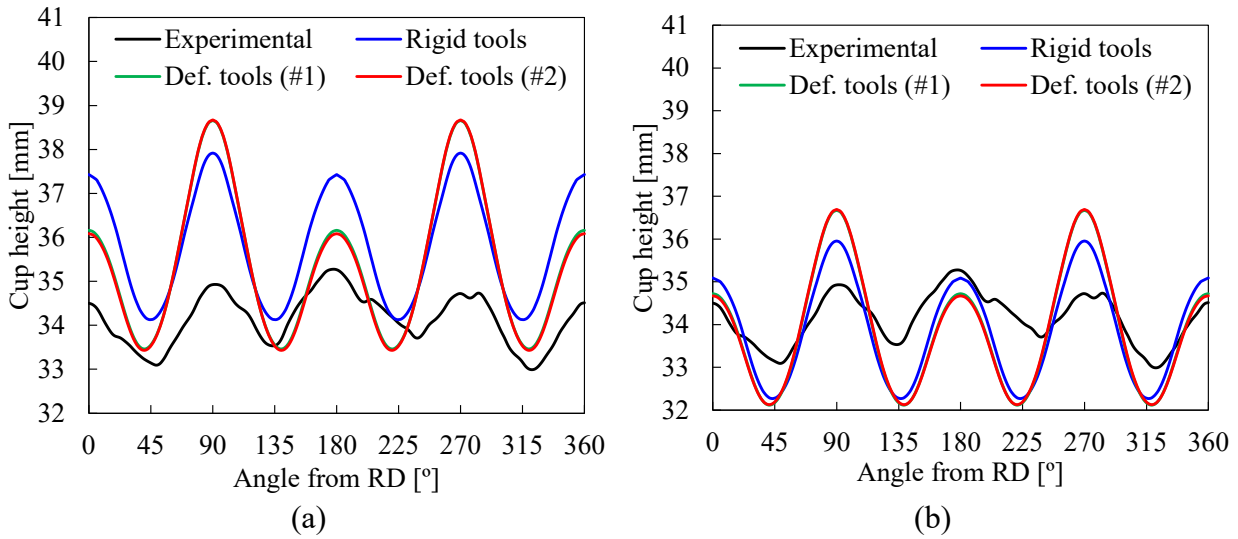

Fig. 5. Comparison between experimental [5] and numerical earing profile using different values of friction coefficient in the numerical analysis: (a) μ=0.1; (b) μ=0.05.

The comparison between the predicted and the experimental earing profile is presented in Fig. 5, using both rigid and deformable tools in the numerical simulation. The stiffness of the die has a negligible effect on this geometrical parameter. The decrease of the friction coefficient from μ=0.1 (Fig. 5 (a)) to μ=0.05 (Fig. 5 (a)) leads to a global decrease of the cup height. The amplitude of the ears experimentally measured is clearly overestimated by the numerical simulation, either using rigid or deformable tools. However, both the number of ears and the position of the valleys/peaks is accurately predicted. This can be related with the accurate description of the in-plane evolution of the *r*-values, while the overestimation of the amplitude of the ears can be associated with the less accurate prediction of the yield stress in-plane distribution, as shown in Fig. 1 and detailed in [5].

Whatever the friction coefficient adopted, the elastic deformation of the forming tools leads to the increase of the cup height in the transverse direction and a decrease in the rolling one. Nevertheless, the effect between the rolling direction and 45º is more evident for μ=0.1, corroborating the uneven distribution of the contact forces in the flange for anisotropic materials [11]. Considering the lower value of friction coefficient (μ=0.05), the elastic deformation of the forming tools leads to a slight increase (about 0.5 mm) of the amplitude of the ears. On the other hand, for μ=0.1 the amplitude of the ears increases about 1.7 mm in comparison with the results obtained using rigid tools. In both cases, the elastic deformation of the forming tools leads to a larger deviation from the experimental earing profile.

The distribution of the equivalent plastic strain is presented in Fig. 6, for the model that considers the deformation of the tools (#2), comparing the two different values of friction coefficient. The global increase of the cup height generated by the increase of the friction coefficient (see Fig. 5) results from a larger plastic strain at the cup bottom, as shown in Fig. 6. The ironing force when the cup wall is sliding between the punch and the die increases from 9.5 kN, when using μ=0.05, to 16.5 kN, for μ=0.1 (see Fig. 3). This increase of the punch force leads to a thinning of the cup bottom. Indeed, the predicted thickness in the middle of the cup bottom is reduced from 0.938 mm for μ=0.05 to 0.900 mm for μ=0.1.

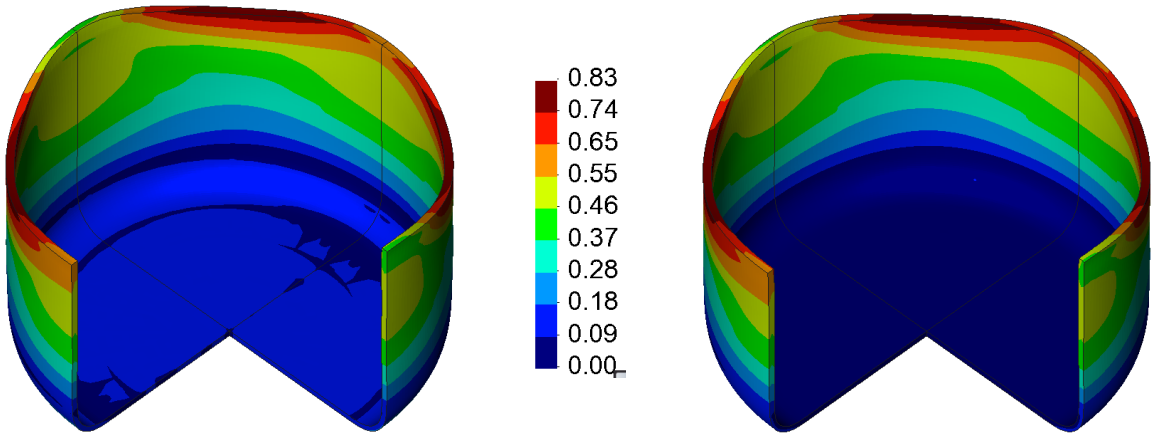

Fig. 6. Predicted equivalent plastic strain distribution considering the deformable tools (#2) described by solid elements using different values of friction coefficient: (a) μ=0.1; (b) μ=0.05.

Fig. 7 (a) compares the position of the outer radius of the blank along the circumferential direction, when using deformable tools (model #2) and the two values of friction coefficient, for two values of punch displacement. For a punch displacement of ~23 mm, there is still a flange (radius higher than 41.2 mm, which corresponds to the die opening radius plus the die shoulder radius). On the other hand, for a punch displacement of ~30 mm, the blank lost contact with the blank-holder (see Fig. 4). The results show a small effect of the friction coefficient on the draw-in, confirming that the increase of the friction coefficient constrains the radial movement of the flange. Fig. 7 (b) compares the thickness of the blank rim along the circumferential direction, for the same instants. The compression of the flange along the circumferential direction imposes an increase of the thickness. On the other hand, some locations present thinning (close to 90º) when the blank partially loses contact with the blank-holder, causing some pinching of the blank still in contact with the blank-holder (see Fig. 7 (a)). Globally, the lower value of the friction coefficient leads to slightly higher thickening, close to 45º. A higher thickness value should correspond to a higher contact pressure between the blank and the ironing tools (die and punch). Nevertheless, this seems to have a negligible impact in the ironing force evolution (see Fig. 3), because of the lower

friction coefficient. In fact, for both values of the friction coefficient in the simulations performed with deformable tools the ironing force presents an identical slope, between a punch displacement of ~ 36 mm and ~ 40 mm. Then, the force starts to drop in the numerical simulations performed with μ=0.05, while it keeps on increasing for μ=0.10, until a punch displacement of ~ 42 mm. This seems to be mainly dictated by the difference in the height of the cup, which is approximately 2 mm higher at the end of the forming, for the simulations performed with μ=0.10 (see Fig. 5). Note that, as previously mentioned, the increase of the friction coefficient constrains the radial movement of the flange, leading to a slightly lower draw-in (see Fig. 7 (a)) and a larger plastic strain at the cup bottom (see Fig. 6).

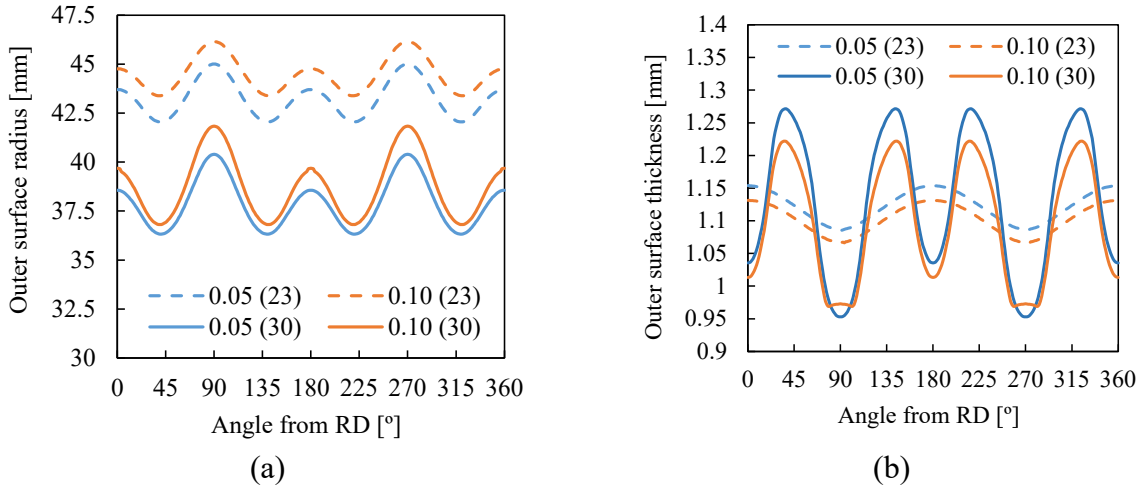

Fig. 7. Comparison between numerical distribution along the circumferential direction in the outer surface: (a) radius and (b) thickness, for a punch displacement of ~23 mm and 30 mm, using different values of friction coefficient (μ=0.1; μ=0.05) and deformable tools (model #2).

The comparison between predicted and experimental cup wall thickness distribution along the circumferential direction is presented in Fig. 8, which was evaluated at three different values of cup height (H), using both rigid and deformable tools in the numerical simulation. The decrease of the friction coefficient from μ=0.1 (Fig. 8 (a)) to μ=0.05 (Fig. 8 (b)) leads to a global increase of the final wall thickness, particularly at locations close to the cup bottom. In fact, using the largest value of friction coefficient (μ=0.1), the cup wall thickness is underestimated by the numerical models (rigid and deformable tools) at all locations, as shown in Fig. 8 (a). The largest difference between numerical and experimental data occurs for H=30 mm, where the numerical simulation considering rigid tools predicts a maximum value equal to the gap between the punch and the die. On the other hand, considering the elastic deformation of the forming tools, the final wall thickness is up to 0.03 mm larger than the nominal gap between the punch and the die. The comparison with the evolution presented in Fig. 7 (b) confirms that the ironing contributes to the uniformization of the thickness.

Due to the material anisotropy, the effect of the deformation of the tools is non-uniform along the circumferential direction. Thus, the thickness predicted using deformable tools is higher around the rolling direction and lower around the transverse direction (in comparison with the prediction obtained with rigid tools). The smaller difference between numerical and experimental thickness was obtained for the lower value of friction coefficient (μ=0.05), for which the predicted ironing force is closer to the experimental measurement (see Fig. 3). Nevertheless, the value is still higher than the experimental one, although the drawing force is clearly underestimated. This corroborates the difficulties in describing both process conditions using a constant value for the friction

coefficient. The results indicate that the friction coefficient between the blank and the die is very low during the ironing operation due to the high levels of contact pressure (see also [5]). The average thickness evaluated both at *H*=10 mm and *H*=20 mm is accurately predicted using the lower friction coefficient (see Fig. 8 (b)), although there is a larger variation of the cup wall thickness predicted by the numerical models along the circumferential direction (anisotropic behaviour). This variation is influenced by the yield criterion adopted, as discussed in [5].

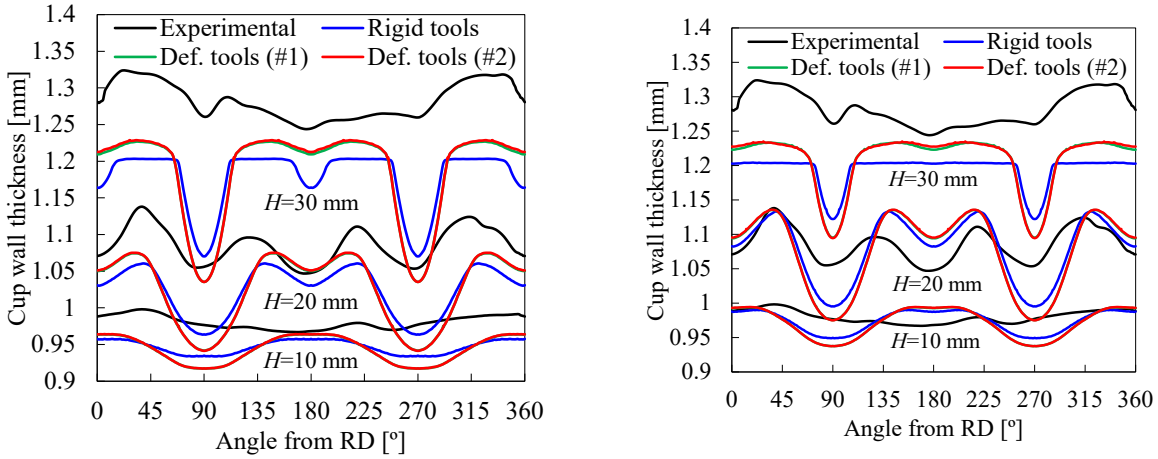

Fig. 8. Comparison between experimental [5] and numerical cup wall thickness distribution along the circumferential direction evaluated at three different cup height values using different values of friction coefficient in the numerical analysis: (a) μ=0.1; (b) μ=0.05.

Summary

The Swift cup drawing test proposed at the benchmark EXACT was used to study the importance of the stiffness of the forming tools on the numerical predictions. Accordingly, the numerical results are compared with the experimental ones. When considering a small value for the friction coefficient, the punch force is underestimated in the drawing stage and overestimated in the ironing stage. Besides, the decrease of the friction coefficient leads to a global decrease of the cup height. The smaller difference between numerical and experimental thickness was obtained for the lower value of friction coefficient. Considering the deformation of the forming tools in the numerical simulation, the main conclusions are:

- The predicted ironing force is significantly reduced, while the effect on the predicted drawing force is negligible;
- The amplitude of the ears is enlarged, particularly for the largest value of friction coefficient;
- The predicted wall thickness is larger than the gap between the punch and the die.

Acknowledgments

The authors gratefully acknowledge the financial support of the Portuguese Foundation for Science and Technology (FCT) under projects with reference 2022.08459.PTDC, UIDB/00285/2020 and LA/P/0112/2020.

References

[1] M. Burkart, P. Essig, M. Liewald, M. Beck, M. Mueller, Compensation of elastic die and press deformations during sheet metal forming by optimizing blank holder design, in: IOP Conf Ser Mater Sci Eng, IOP Publishing Ltd, 2020. https://doi.org/10.1088/1757-899X/967/1/012074.

[2] R. Lingbeek, Virtual tool reworking new strategies in die design using finite element forming simulations, PhD Thesis, University of Twente (2008).

[3] J. Pilthammar, M. Sigvant, S. Kao-Walter, Introduction of elastic die deformations in sheet metal forming simulations, Int. J. Solids Struct. 151 (2018) 76-90. https://doi.org/10.1016/j.ijsolstr.2017.05.009

[4] F. Abbasi, A. Sarasua, J. Trinidad, N. Otegi, E. Saenz de Argandoña, L. Galdos, Substitutive press-bolster and press-ram models for the virtual estimation of stamping-tool cambering, Materials. 15 (2022). https://doi.org/10.3390/ma15010279

[5] A.M. Habraken, T.A. Aksen, J.L. Alves, R.L. Amaral, E. Betaieb, N. Chandola, L. Corallo, D.J. Cruz, L. Duchêne, B. Engel, E. Esener, M. Firat, P. Frohn-Sörensen, J. Galán-López, H. Ghiabakloo, L.A.I. Kestens, J. Lian, R. Lingam, W. Liu, J. Ma, L.F. Menezes, T. Nguyen-Minh, S.S. Miranda, D.M. Neto, A.F.G. Pereira, P.A. Prates, J. Reuter, B. Revil-Baudard, C. Rojas-Ulloa, B. Sener, F. Shen, A. van Bael, P. Verleysen, F. Barlat, O. Cazacu, T. Kuwabara, A. Lopes, M.C. Oliveira, A.D. Santos, G. Vincze, Analysis of ESAFORM 2021 cup drawing benchmark of an Al alloy, critical factors for accuracy and efficiency of FE simulations, Int. J. Mater. Forming 15 (2022) 1-96. https://doi.org/10.1007/s12289-022-01672-w

[6] D.M. Neto, J. Coër, M.C. Oliveira, J.L. Alves, P.Y. Manach, L.F. Menezes, Numerical analysis on the elastic deformation of the tools in sheet metal forming processes, Int. J. Solids Struct. 100 (2016) 270-285. https://doi.org/10.1016/j.ijsolstr.2016.08.023

[7] L.F. Menezes, C. Teodosiu, Three-dimensional numerical simulation of the deep-drawing process using solid finite elements, J. Mater. Process. Technol. 97 (2000) 100-106. https://doi.org/10.1016/S0924-0136(99)00345-3

[8] J. Coër, H. Laurent, M.C. Oliveira, P.Y. Manach, L.F. Menezes, Detailed experimental and numerical analysis of a cylindrical cup deep drawing: Pros and cons of using solid-shell elements, Int. J. Mater. Forming 11 (2018) 357-373. https://doi.org/10.1007/S12289-017-1357-4/FIGURES/21

[9] D.M. Neto, M.C. Oliveira, L.F. Menezes, J.L. Alves, Applying Nagata patches to smooth discretized surfaces used in 3D frictional contact problems, Comput. Methods Appl. Mech. Eng. 271 (2014). https://doi.org/10.1016/j.cma.2013.12.008

[10] O. Cazacu, F. Barlat, Generalization of Drucker's yield criterion to orthotropy, Math. Mech. Solids 6 (2001) 613-630. https://doi.org/10.1177/108128650100600603

[11] D.M. Neto, M.C. Oliveira, R.E. Dick, J.L. Alves, L.F. Menezes, Non-Uniform Effect of the Contact Conditions on the Earing Profile in Cylindrical Cups of Anisotropic Materials, Key Eng. Mater. 926 (2022) 1188-1194. https://doi.org/10.4028/p-9i8j3o

Materials Research Proceedings 28 (2023) 1491-1502 https://doi.org/10.21741/9781644902479-161

ESAFORM 2021 cup drawing benchmark of an Al alloy: Critical follow up analysis of its potentials

OLIVEIRA Marta C.[1,a], CAZACU Oana[2,b], REVIL-BAUDARD Benoit[2,c], NETO Diogo M.[1,d], FROHN-SÖRENSEN Peter[3,e], MA Jun[4,f], LIU Wencheng[5,g], CRUZ Daniel J.[6,h], SANTOS Abel D.[6,i], VAN BAEL Albert[7,j], GHIABAKLOO Hadi[7,k] and HABRAKEN Anne M.[8,l *]

[1]CEMMPRE, Department of Mechanical Engineering, University of Coimbra, Polo II, Pinhal de Marrocos, 3030-788 Coimbra, Portugal

[2]Department of Mechanical and Aerospace Engineering, University of Florida, REEF, 1350N. Poquito Rd, Shalimar, FL 32579, USA

[3]Forming Technology (UTS), Institute of Production Technologies, University of Siegen, Breite Strasse, 11, 57076 Siegen, Germany

[4]Department of Mechanical and Industrial Engineering, Norwegian University of Science and Technology, 7491 Trondheim, Norway

[5]School of Civil Aviation, Northwestern Polytechnical University, Taicang 215400, China

[6]Institute of Science and Innovation in Mechanical and Industrial Engineering (INEGI), R. Dr. Roberto Frias 400, 4200-465 Porto, Portugal

[7]Department of Materials Engineering, Katholieke Universiteit Leuven, Kasteelpark Arenberg 44- box 2450, 3001 Leuven, Belgium

[8]ArGEnCo department, University of Liege, 9 Allée de la Découverte, 4000 Liège, Belgium

[a] marta.oliveira, [b]cazacu@reef.ufl.edu, [c]revil@ufl.edu, [d]diogo.neto@dem.uc.pt, [e]peter.frohn@uni-siegen.de, [f]jun.ma@ntnu.no, [g]wencheng.liu@usst.edu.cn, [h]dcruz@inegi.up.pt, [i]abel@fe.up.pt, [j]albert.vanbael@kuleuven.be, [k]ghiabakloo@gmail.com, [l]anne.habraken@uliege.be

Keywords: Benchmark, 6016-T4, Deep Drawing Modelling, Thickness Prediction, Ironing Force Prediction, Plastic Anisotropic Models

Abstract. The 1st ESAFORM Benchmark, called EXACT [1], enabled an in-depth study of the factors that contribute to the accuracy of predictions and efficiency of finite element (FE) simulations of deep drawing of a cup from AA 6016-T4 sheet through the joint work of 11 teams. FE analyses were conducted with elasto-plastic models or crystal plasticity approaches using commercial or academic FE codes. This paper reminds the content of EXACT benchmark and gives new results that highlight the importance of the tool stiffness and various contact conditions to predict the ironing forces and the thickness distribution along the cup wall. The use of the Benchmark experimental data and virtual tests performed with DAMASK crystal plasticity code to identify and validate a two-surface kinematic hardening model based on Yoshida and Uemori approach is also discussed.

Content from this work may be used under the terms of the Creative Commons Attribution 3.0 license. Any further distribution of this work must maintain attribution to the author(s) and the title of the work, journal citation and DOI. Published under license by Materials Research Forum LLC.

Materials Research Proceedings 28 (2023) 1491-1502 https://doi.org/10.21741/9781644902479-161

Introduction

Hereafter, the work performed within ESAFORM 2021 benchmark is described and the structure and content of the quite extensive article (96 pages) [1] are reminded. Indeed, this detailed paper provides both theoretical equations and details on the identification methodologies, before the analysis of the FE results *versus* experiments. As pointed out in the next section, some discrepancies between measurements and predictions justify further investigations and the current article summarizes the ongoing activities around all the gathered data.

ESAFORM 2021 Benchmark consisted of a cup drawing process of a 1 mm thick AA 6016-T4 sheet with a strong cube component (52% volume fraction of grains). As shown in Fig. 1, the main goal is to accurately predict the punch force-displacement curve, the earing profile, the thickness distribution and the wall height. Another objective was to provide the dataset necessary to identify advanced models, both elasto-plastic macroscopic models or models accounting for the behavior of the constituent grains. Mechanical characterization tests and texture measurements post tests were also performed, including measurements of the texture of the fully-drawn cup (see Fig. 1)

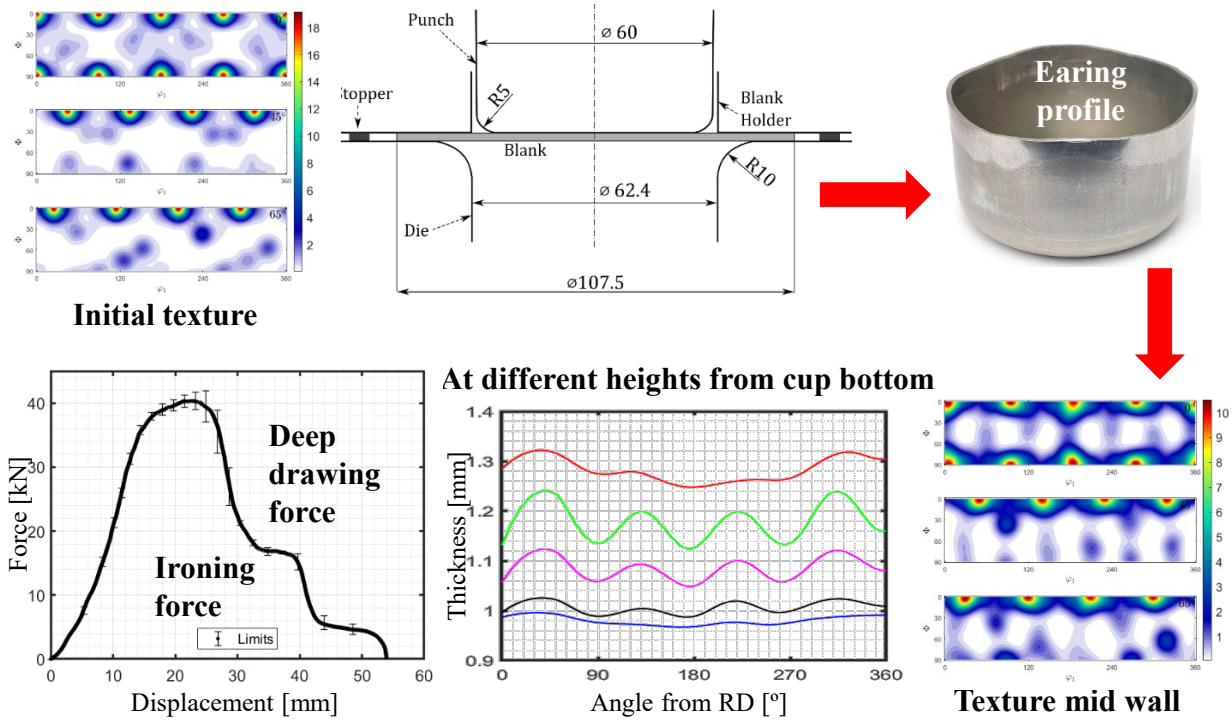

Fig. 1. Cup drawing of a circular blank (Φ =107.5mm) of AA 6016 sheet, adapted from [1].

Specifically, cup drawing tests done at University of Porto (UPorto) were complemented with extensive mechanical characterization by 2 independent teams: tensile tests in 7 orientations (true stress-strain curves and Lankford coefficients, obtained from several repeats of any given test, measured at Tokyo University of Agriculture and Technology (TUAT), and at the University of Aveiro (UA)), biaxial tests in TUAT, shear and reverse shear tests in UA and in the University of Liege (ULiege). For a detailed discussion of testing procedures and experimental errors see [1].

Finally, the initial texture and the one present after forming in the middle and at the top of the cup were measured at UA from coupons taken in the rolling direction (RD), 45° and 90° to the RD. The benchmark results (earing, wall height, thickness distribution, deep drawing, and ironing forces) were measured by UPorto (see [1]).

Eleven institutions participated using either commercial codes with built-in models or their implementation of other models in ABAQUS implicit or explicit, LS-DYNA, MSC.MARC, PAMSTAMP or academic FE Softwares (DD3IMP from Coimbra University (UCoimbra) or Lagamine from University of Liege (ULiege)). Some participants used various models.

The organization of the result presentation in article [1] is shown in Fig. 2. After describing the experimental tests, and a general discussion on friction effects, the choices made by the participants concerning material description, finite element models and FE type were described. Tables 10-12 in article [1] identify the hardening law, yield criterion and homogenization approaches. Fig. 2 summarizes where to find in [1]: the description of the numerous laws used (also reminded in Fig. 3), their identification and how results were presented. Finally, it points to some of the conclusions.

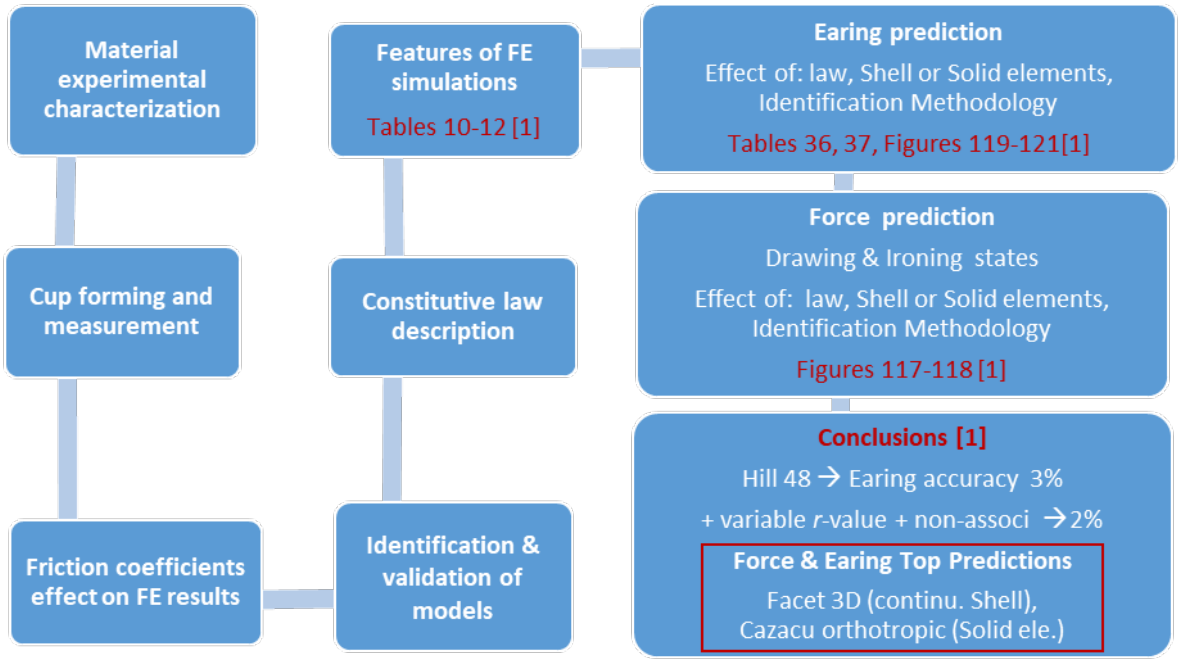

Fig. 2. Sections of article [1] describing the ESAFORM Benchmark 2021.

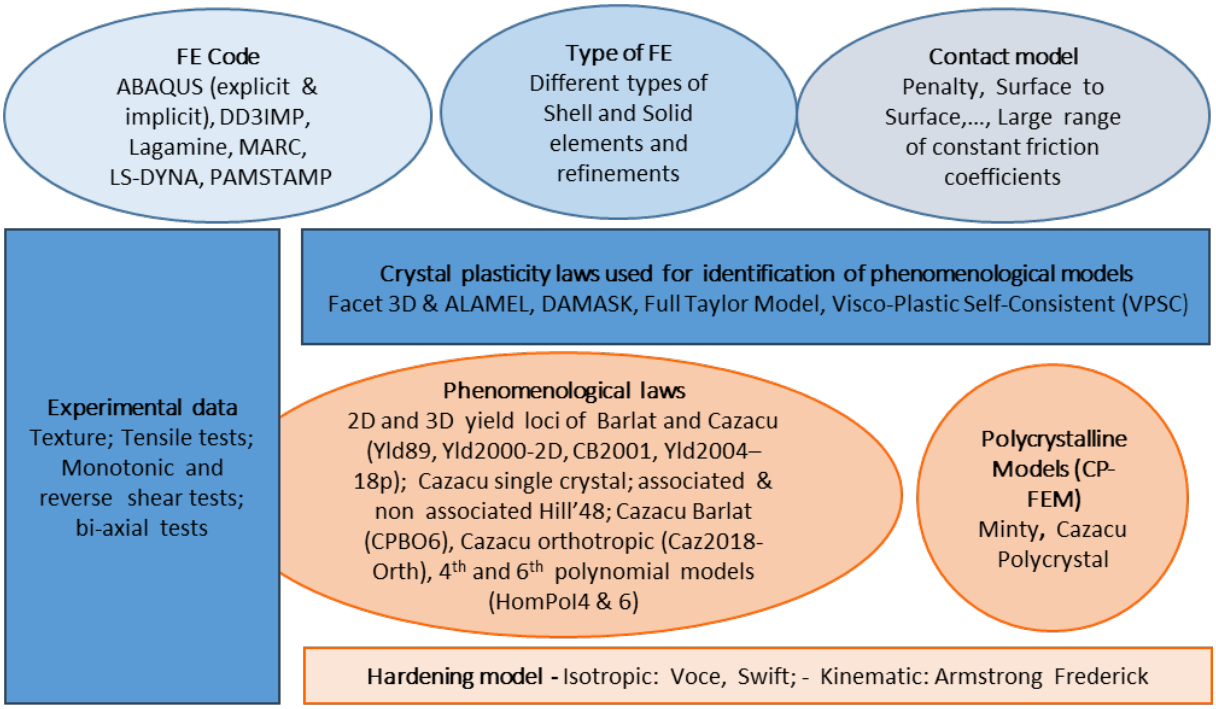

Fig. 3. Different model features involved in ESAFORM 2021 Benchmark: light blues define the FE codes, elements, contact models, while pink color points the constitutive laws used and dark blue rectangles explain how they are identified.

Fig. 3 summarizes all the material models used. An extensive discussion on model identification is provided in [1]. Here we just mention that for crystal plasticity models (CPM), it was detailed: i) the choice of the set of representative grains to model the texture; ii) the detailed methodology for identification of the parameters of the CPM; with tables for all parameter values, iii) predictions of Lankford coefficient variation and yield stress variation (see a summary in Fig. 4.). For both classical and recent anisotropic yield functions, the data set used for identification was either based on physical tests or on virtual tests computed with CPM, as synthesized in Fig. 5.

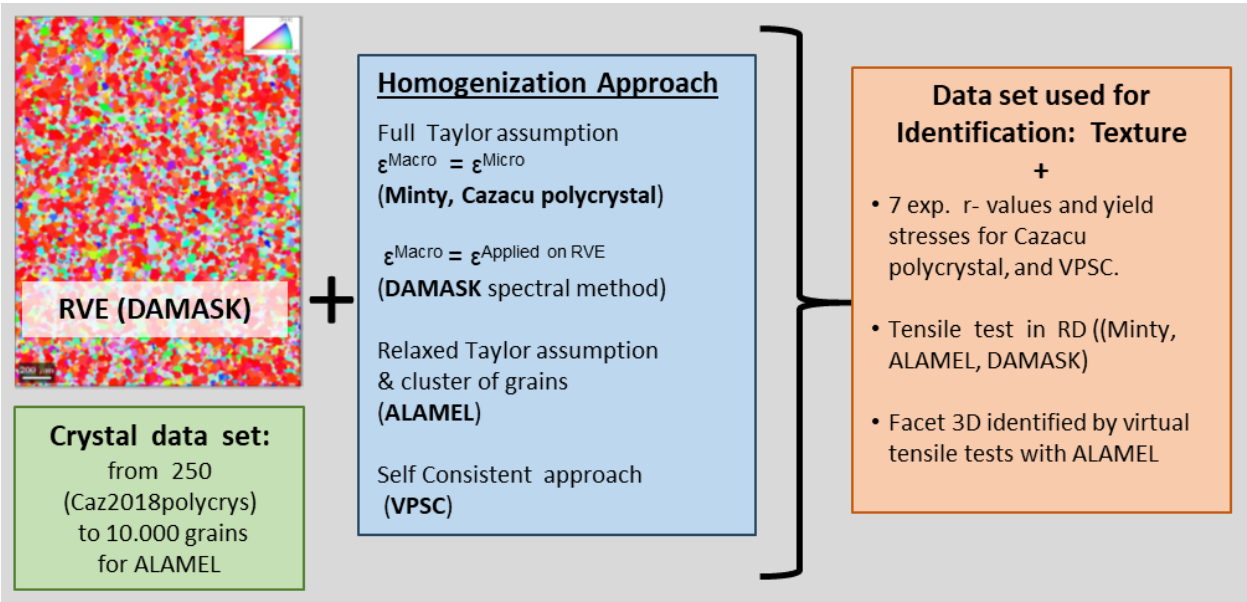

Fig. 4. Identification methodology and main homogenization schemes of the CPM.

Mechanical tests	Tensile	Lankford 0° 45° 90°	Yield stress 0°	Yield stress 45° 90°	Yield 15° 30° 60° 75°	Bi-axial =	Bi-axial ≠	Shear
Identification based on experiments - Phenomenological law	UCoimbra Hill48(A)							
	USakarya Yld89							
	REEF Caz2018-Orth - ULiege Hill48(A) - USakarya HomPol 4 & 6							
	UGent Yld200-2D*, POSTECH Yld200-2D & Yld2004-18p, NTNU Yld2004-18p*							
	UCoimbra CB2001							
	UAalto Hill48 (NA)							
	UCoimbra CPBO6 ex2							

Fig. 5. List of mechanical physical or virtual (CPM) tests used for the identification of the anisotropic yield functions used by the participants (see [1] for more details).*

To check the validity of the parameter identification of the anisotropic yield functions and respective CPM models, the participants had to provide the predicted in-plane evolutions for the Lankford coefficients and the yield stresses, for tensile directions varying from 0° to 90° to the RD. Cup drawing simulation results were discussed in detail in several subsections. First the FE results (solid and shell FE simulations) obtained using anisotropic yield functions, identified either from physical or virtual tests, and then FE results of cup drawing obtained with polycrystalline model results. It can be concluded that Hill48 provides satisfactory earing results (within 3% of earing measurements, see Fig.2); small differences in results obtained with Hill48, between various teams, due to FE modelling features. An overestimation of the ironing force was observed when using shell elements. Various possible improvements using a non-associated flow rule or variable Lankford coefficients were also discussed. Two models provided very accurate results for both earing and force: Facet 3D constitutive law [2], with continuum shell elements and identification based on CPM; and Cazacu orthotropic law [3], with solid elements and an identification relying on the 7 available physical tensile tests. The reader is referred to [1] for more details.

Influence of the Tool Stiffness

A part of the EXACT benchmark reported data was the measurement of the thickness at the top of the cup. It was roughly 0.1 mm larger than the gap between the punch and the die. Explanations were sought and discussed, one being that the gap was slightly bigger than initially reported, i.e., enough to justify the measured values. However, the geometry for the EXACT benchmark was done very carefully (see [1]), which did not support this assumption.

Here, we discuss further investigations done to provide explanations for attaining a cup with a thickness higher than the gap between the punch and the die. This could be related with the elastic deformation of the tools during the process. Note that the modelling of the tool deformation can be performed using different approaches, namely by adjusting the stiffness of the surfaces that describe the tool or modelling them as deformable bodies. The latter approach was adopted and simulations were conducted with the academic code DD3IMP, considering the Swift law and the Hill48 yield criterion, with the parameters provided by the benchmark committee. A friction coefficient of 0.06 was assumed between the blank and the tools, to improve the description of the drawing force. More details concerning the constitutive model and the friction coefficient adopted are presented in Table 1 (column Def1). For reference, simulations were performed considering rigid tools (Rig1 results).

Materials Research Proceedings 28 (2023) 1491-1502 https://doi.org/10.21741/9781644902479-161

Table 1. FE code, tool modelling approach, type of finite element for the blank, constitutive model and friction coefficient adopted in each model.

	Rig1	Rig2	Rig3	Def1	Def2	Def3
Software	DD3IMP	PAMStamp	Abaqus	DD3IMP	PAMStamp	AutoForm
Forming tools	Rigid	Rigid	Rigid	Deformable	Deformable	Deformable
Finite elements: type	Solid	Solid	Solid-Shell	Solid	Solid	Solid-Shell
and number	15408	55560	9743**	23313	171405	9390***
Hardening law	Swift	Swift	Swift	Swift	Swift	Swift
Yield criterion	Hill48	Hill48	Facet-3D	Hill48	Hill48	Facet-3D
Friction coefficient	0.06	0.075	0.09	0.06	0.075	0.09
CPU time*	3h02m	3h33m	2h46m	16h04m	37h48m	1h18m

* Note that different meshes (blank and tools) and CPUs were used with different codes; ** 5 through thickness integration points; *** 11 through thickness integration points

A similar approach was adopted at University of Siegen (USiegen) and simulations were conducted using the commercial code PAMStamp considering also hexahedral solid elements and the same constitutive model. The results were compared with those obtained with rigid tools, which were presented in [1]. To be noted that with rigid tools, a slightly higher value for the friction coefficient was considered, to capture the maximum punch force in the drawing stage in [1]. The model with deformable tools uses the same value such as to allow for direct comparison, as shown in Table 1 (Rig 2 and Def2).

In ESAFORM 2021 benchmark, the use of Facet-3D yield function with Abaqus/Explicit led to an accurate cup height profile and punch force curves. However, the thickness measured at different height sections was underestimated. In the follow up research, Facet-3D was used in AutoForm R10, since it allows implementing a user material and enables a convenient adjustment of the tool stiffness. In this work, the value of 10 GPa/mm was used for the punch, while for the die and the blank holder a higher value of 60 GPa/mm was adopted. This combination was found by trial and error to somehow trade-off the ironing force and the thickness distribution. With lower tool stiffnesses, the maximum sheet thickness increases and the ironing force decreases. Other details about these models are presented in Table 1 (Rig3 and Def3).

Fig. 6 (a) presents the comparison of the punch force evolution with its displacement, obtained with the different models, as well as the experimental results. Globally, the adoption of rigid or deformable tools has a negligible impact on the drawing stage, where the maximum value attained is mainly dictated by the value of the friction coefficient. Nevertheless, the maximum value of the ironing force drops when adopting deformable tools and solid elements for the blank. When the blank is discretized with solid-shell elements, the model with deformable tools shows a slight increase of the ironing force, but these results are not directly comparable, because different codes were used. Regarding the earing profile, although models Rig1 and Rig2 present quite similar average height and trend (see Fig. 6 (b)), the effect of considering deformable tools leads to a lower cup height for Def1, while for Def2 it increases. On the other hand, for the models adopting solid-shell elements the impact of considering deformable tools is negligible (Rig3 and Def3). Note that in this case the earing profile is not symmetric, because the initial position of the blank was off set, to improve the comparison with the experimental results [1].

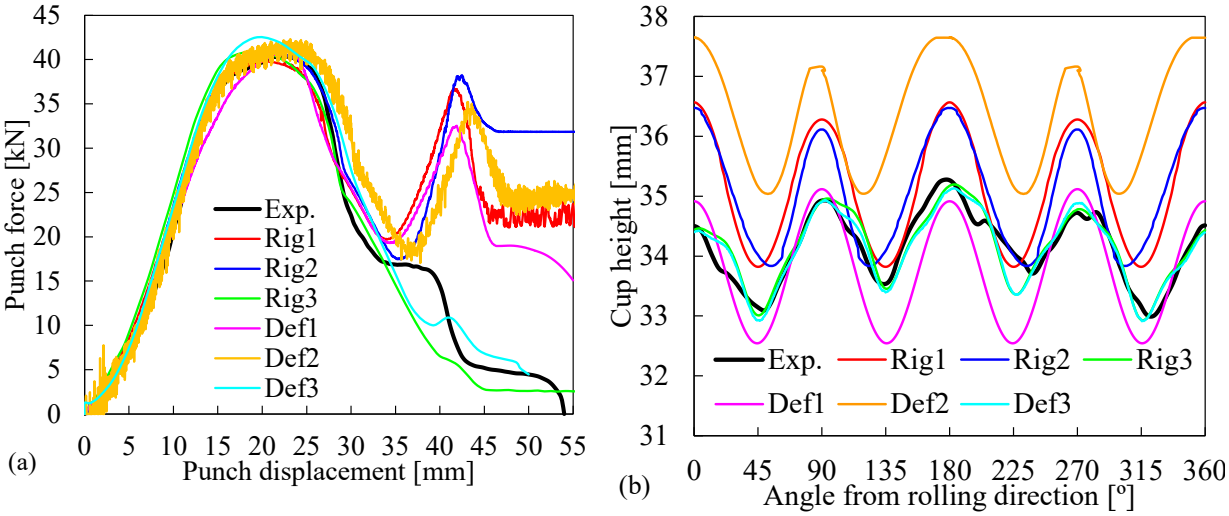

Fig. 6. Comparison between experimental and predicted results using rigid and deformable tools: (a) punch force-displacement and (b) earing profile.

The thickness distribution along the circumferential direction is presented in Fig. 7, for two values of cup height, 20 mm and 30 mm. The models that use rigid tools and solid elements (Rig 1 and Rig2) led to a trend like the experimental one for the lower height. For the higher height, the thickness is constant and equal to the value of the gap (1.2 mm) for Rig 1 while Rig2 predicts a slightly higher value, which indicates that the contact algorithm implemented in DD3IMP imposes the contact constraints more strictly. When adopting deformable tools, the models that use solid elements present different trends, with Def1 leading to higher thickness values for both heights, while Def2 underestimates the thickness value for both heights. These results seem to be coherent with the average cup height because lower thickness values result in a higher cup and *vice-versa* (see Fig. 6 (b)). Although the results are not directly comparable for solid-shell elements (Rig3 and Def3), one can see that the thickness estimation improves when considering deformable tools. In brief, deformable tools lead to thickness values on the top of the cup higher than the gap between the die and the punch, like in the experiment. In this context, it should be mentioned that the option of adjusting the stiffness of the surfaces has a negligible impact on the CPU time, when compared with the use of solid deformable tools (see Table 1).

The lower punch force value predicted for the ironing stage when adopting solid-shell elements had already been reported in [1]. The differences observed in the models obtained with solid elements and deformable tools seem to be related with distinction features in the treatment of the contact conditions. In fact, although not shown here, it was observed that the adoption of the penalty algorithm instead of the hard contact one, adopted in this work for PAMStamp, would lead to a clearly lower value for the force during the ironing stage. Thus, even when adopting deformable tools, an evolutional friction law is suggested to capture the drawing and the ironing forces in a more realistic way [4]. In this context, some of the authors are working on an improved analysis of the contact conditions, considering the experimental analysis of the contact conditions using flat strip drawing friction tests.

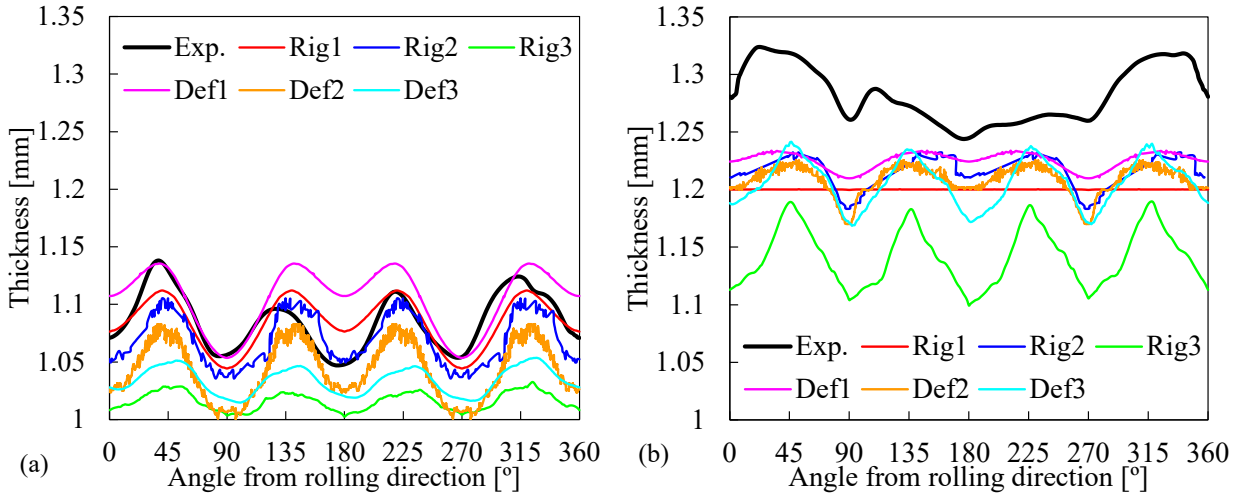

Fig. 7. Comparison between experimental and numerical wall thickness distribution along the circumferential direction evaluated at different cup height values: (a) H=20 mm; (b) H=30 mm.

CP-Based and Phenomenological Modelling of Kinematic Hardening Behavior

The experimental cyclic shear deformation behavior of AA 6016-T4 sheet, observed in Fig.12 of [1] and reported in Fig. 8 (b) hereafter, presents a kinematic hardening phenomenon. To capture this phenomenon, a two-surface model was proposed by Yoshida and Uemori (YU) and has been widely used in sheet metal forming analysis [5-6]. It consists of a yield surface and a bounding surface, in which the kinematic hardening is described by moving the yield surface within the bounding surface. Hereafter, an associated flow rule (AFR) based two-surface hardening model is proposed, which is modified from the non-AFR based two-surface model proposed by Ghaei et al. [7]. The YU hardening model was incorporated with an advanced yield function to describe the complex deformation behavior in sheet metal forming. In this model, the yield criterion f_y determines the boundary between the elastic and plastic zone using the yield stress y in the stress space and the function $\boldsymbol{F}$ determines the shape of the bounding surface, as given by:

$$f_y(\boldsymbol{\eta}) - y = 0 \tag{1}$$

$$F(\boldsymbol{\Sigma} - \boldsymbol{\alpha_2}) - b_0 - r(p) = 0$$

$$\boldsymbol{\eta} = \boldsymbol{\sigma} - \boldsymbol{\alpha}$$

where $\boldsymbol{\sigma}$ is the Cauchy stress tensor in current state, $\boldsymbol{\Sigma}$ is the stress tensor corresponding to the bounding surface, and $\boldsymbol{\alpha}$ is the backstress tensor controlling the movement of the yield surface. $\boldsymbol{\eta}$ is substituted into the yield criterion to calculate the effective stress. $\boldsymbol{\alpha_2}$ is the corresponding backstress tensor and b_0 is the initial size of the bounding surface. r controls the expansion of the bounding surface, which is governed by the equivalent plastic strain p:

$$r(p) = Q[1 - \exp(-bp)] \tag{2}$$

where the Q and b are the material constants that need to be calibrated. In this model, the kinematic hardening behaviour is governed by the state of the backstress $\boldsymbol{\alpha}$, which can be decomposed as $\dot{\boldsymbol{\alpha}} = \dot{\boldsymbol{\alpha}}_1 + \dot{\boldsymbol{\alpha}}_2$. $\dot{\boldsymbol{\alpha}}_1$ is dependent on the rate of equivalent plastic strain $\dot{p}$, and can be described by:

$$\dot{\boldsymbol{\alpha}}_1 = \gamma_1 \left(\frac{b_0 + r - y}{y} \boldsymbol{\eta} - \boldsymbol{\alpha_1} \right) \dot{p} \tag{3}$$

where γ_1 is the material constant. $\boldsymbol{\alpha_1}$ is the deviation between the central position of the yield surface and the bounding surface, whose motion is controlled through $\dot{\boldsymbol{\alpha}}_2$, as given by:

$$\dot{\boldsymbol{\alpha}}_2 = \gamma_2 \left(\frac{c_2}{y} \boldsymbol{\eta} - \boldsymbol{\alpha_2} \right) \dot{p} \tag{4}$$

where c_2 and γ_2 are the material parameters. $\boldsymbol{\alpha_2}$ is the central position of the bounding surface in the stress space. To obtain the equivalent plastic strain rate $\dot{p}$, the classical AFR is employed:

$$\dot{\boldsymbol{\epsilon}}^{\boldsymbol{p}} = \dot{\lambda} \frac{\partial f_y}{\partial \boldsymbol{\sigma}} = \dot{\lambda} \boldsymbol{m} \tag{5}$$

where $\dot{\boldsymbol{\epsilon}}^{\boldsymbol{p}}$ is the rate of the plastic strain tensor and $\dot{\lambda}$ is the plastic multiplier, which is equal to the equivalent plastic strain rate in AFR, i.e., $\dot{p} = \dot{\lambda} \boldsymbol{m}$ is the first order of the yield function, which makes the plastic potentials normal to the yield surface. A consistency condition in the yield surface and bounding surface is utilized to solve the equivalent plastic strain rate:

$$\frac{\partial f_y}{\partial \boldsymbol{\sigma}} : \dot{\boldsymbol{\sigma}} + \frac{\partial f_y}{\partial \boldsymbol{\alpha_1}} : \dot{\boldsymbol{\sigma}}_1 + \frac{\partial f_y}{\partial \boldsymbol{\alpha_2}} : \dot{\boldsymbol{\sigma}}_2 = \boldsymbol{m} : \dot{\boldsymbol{\eta}} = 0 \tag{6}$$

Here, the elastic stress tensor follows Hooke's law, and hence the rate of the stress tensor is obtained by:

$$\dot{\boldsymbol{\sigma}} = \boldsymbol{D} : \left(\dot{\boldsymbol{\epsilon}} - \dot{\boldsymbol{\epsilon}}^{\boldsymbol{p}} \right) = \boldsymbol{D} : \left(\dot{\boldsymbol{\epsilon}} - \dot{\lambda} \boldsymbol{m} \right) \tag{7}$$

where $\boldsymbol{D}$ is the elastic stiffness matrix, and $\dot{\boldsymbol{\epsilon}}$ is the rate of the total strain tensor. The plastic multiplier can thus be represented by:

$$\boldsymbol{m} : \boldsymbol{D} : \left(\dot{\boldsymbol{\epsilon}} - \dot{\lambda} \boldsymbol{m} \right) - \boldsymbol{m} : \dot{\boldsymbol{\alpha}}_1 - \boldsymbol{m} : \dot{\boldsymbol{\alpha}}_2 = 0 \tag{8}$$

Therefore, the plastic multiplier (equivalent plastic strain rate) can be obtained:

$$\dot{p} = \frac{\boldsymbol{m} : \boldsymbol{D} : \dot{\boldsymbol{\epsilon}}}{\boldsymbol{m} : \boldsymbol{D} : \boldsymbol{m} + \boldsymbol{m} : \frac{\dot{\boldsymbol{\alpha}}_1}{\dot{p}} + \boldsymbol{m} : \frac{\dot{\boldsymbol{\alpha}}_2}{\dot{p}}} \tag{9}$$

In addition, the tangent consistent modulus $\boldsymbol{D^{ep}}$ of the two-surface hardening model is determined:

$$\dot{\boldsymbol{\sigma}} = \boldsymbol{D^{ep}} : \dot{\boldsymbol{\epsilon}} = \left(\boldsymbol{D} - \frac{(\boldsymbol{D} : \boldsymbol{m}) \otimes (\boldsymbol{D} : \boldsymbol{m})}{\boldsymbol{m} : \boldsymbol{D} : \boldsymbol{m} + \boldsymbol{m} : \frac{\dot{\boldsymbol{\alpha}}_1}{\dot{p}} + \boldsymbol{m} : \frac{\dot{\boldsymbol{\alpha}}_2}{\dot{p}}} \right) \tag{10}$$

Besides the permanent softening, workhardening stagnation is observed at the early stage of reverse loading [5]. To describe this phenomenon, a stagnation surface is introduced to limit the expansion of the bounding surface. In this method, the expansion of the bounding surface is only

Materials Research Proceedings 28 (2023) 1491-1502 https://doi.org/10.21741/9781644902479-161

allowed when the central position of the bounding surface is within the range of the stagnation surface. This stagnation surface is given as follows:

$$f_s(\boldsymbol{\alpha_2} - \boldsymbol{\alpha_s}) - y_s = 0 \tag{11}$$

where y_s and $\boldsymbol{\alpha_s}$ are the initial size and the central location of the stagnation surface in stress space, respectively. A non-linear kinematic hardening law is utilized to describe the translation of the bounding surface:

$$\dot{\boldsymbol{\alpha}}_s = \dot{\mu}(\boldsymbol{\alpha_2} - \boldsymbol{\alpha_s}) = \dot{\mu}\boldsymbol{\xi} \tag{12}$$

where the tensor $\boldsymbol{\xi}$ and rate $\dot{\mu}$ are achieved using the following criterion:

$$\frac{\partial f_s}{\partial \boldsymbol{\alpha_2}} : \dot{\boldsymbol{\alpha}}_2 + \frac{\partial f_s}{\partial \boldsymbol{\alpha_s}} : \dot{\boldsymbol{\alpha}}_s - \dot{y}_s = 0 \tag{13}$$

where the $\dot{\mu}$ is obtained by,

$$\dot{\mu} = \frac{\boldsymbol{n} : \dot{\boldsymbol{\alpha}}_2 - \dot{y}_s}{\boldsymbol{n} : (\boldsymbol{\alpha_2} - \boldsymbol{\alpha_s})} \tag{14}$$

where $\boldsymbol{n} = \frac{\partial f_s}{\partial \boldsymbol{\alpha_2}}$. The rate of y_s is defined as:

$$\begin{cases} \dot{y}_s = h\boldsymbol{n} : \dot{\boldsymbol{\alpha}}_2, & when \quad \dot{r} > 0 \\ \dot{y}_s = 0, & when \quad \dot{r} = 0 \end{cases} \tag{15}$$

where h is the calibrated material constant, which controls the expansion level of the stagnation surface. The $\dot{r}$ determines that the stagnation surface is only allowed to expand associated with the expansion of the bounding surface.

Kinematic hardening model calibration and validation was based on the results of DAMASK solver, a CPM model (see [1] Norwegian University of Science and Technology (NTNU) participant approach) used to predict the stress response of AA6016-T4 during the cyclic deformation. The parameters of the modified YU kinematic hardening model are identified with a virtual uniaxial tension-compression test in RD (1.5 cycles), as given in Table 2. To evaluate the performance of the calibrated hardening model at various strain levels, a comparison between the stress-strain curves predicted by CPM simulation and YU model for five tension-compression cycles was illustrated in Fig. 8 (a). It was found that the calibrated YU hardening model can well capture the tension-compression full-CPM history stress-strain response. Fig. 8 (b) shows that the modified YU model identified by the virtual uniaxial tension-compression tests coupled with Yld2004-18p yield function is capable of accurately predicting the experimental mechanical response of AA6016-T4 in the shear-reverse shear deformation mode measured in [1].

Table 2. The parameters of the modified two-surface kinematic model for the AA6016-T4 sheet.

y(MPa)	b_0(MPa)	γ_1	c_2(MPa)	γ_2	Q(MPa)	b	h
101.2	105.3	850	25.2	391.3	158.3	12.8	0.18

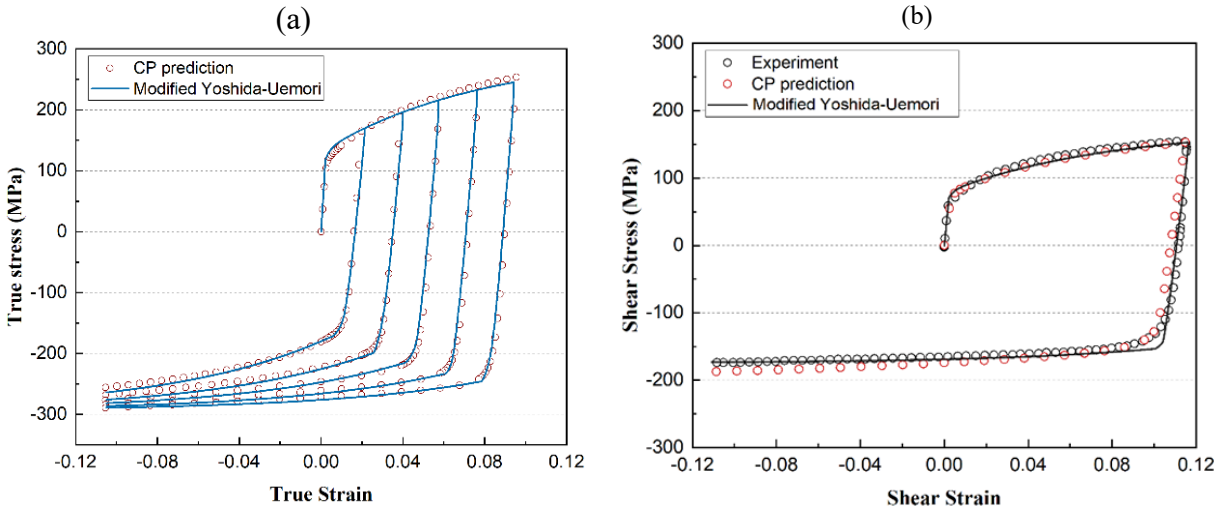

Fig. 8. (a) Comparison of stress-strain response of 5 tension-compression cycles by CPM simulations and modified YU model. (b) comparison of shear-reverse shear stress-strain responses from experiment [1], DAMASK CPM predictions, results of Yld2004-18p yield function coupled with modified YU model.

Summary

The ESAFORM Benchmark series is an ongoing adventure (https://esaform.org/grants/), do not hesitate to apply. It allows a whole community to exchange ideas about an issue that poses difficulties to realize reliable and efficient forming processes and, or simulations.

In 2021 cup drawing benchmark, the simulations pointed out that phenomenological laws identified using only physical experiments or completed by crystal plasticity results could reach accurate predictions of force evolution, final earing and thickness distribution. Additionally, an issue about the ironing force, the wall thickness distribution and the punch-die gap drew attention to the question of friction and tool elasticity. The current article demonstrates that both effects are important and it suggests that a variable friction parameter could be required to improve ironing force prediction. Nevertheless, even with a single tuned friction coefficient, the Facet 3D model, considering the tool deformation available in AutoForm R10 was able to improve its thickness prediction accuracy at the top of the cup compared to its results based on rigid tools. Models with rigid and deformable tools, built in DD3IMP and PAMStamp, led to physically consistent results, coherent with the experimental ones.

The extensive experimental results gathered in [1] allow the identification of advanced anisotropic elastoplastic models, as shown by the work of NTNU and Northwestern Polytechnical University (Taican, China), with their advanced two-surface model. Validated on experimental reverse shear tests, pointing the need of an accurate kinematic behaviour model, their work is still ongoing to present a cup deep drawing application.

The reader can consult the open access article [1] for a more detailed analysis of all the benchmark results and access to the data (https://zenodo.org/record/6874577#.Y4YhzHbMKyA).

References

[1] A.M. Habraken, T.A. Aksen, J.L. Alves, R.L. Amaral, E. Betaieb, N.Chandola, L. Corallo, D.J. Cruz, L. Duchêne, B. Engel, E. Esener, M. Firat, P. Frohn-Sorensen, J. Galan-Lopez, H. Ghiabakloo, L.A.I. Kestens, J. Lian, R. Lingam, W. Liu, Jun Ma, L.F. Menezes, T.Nguyen-Min, S.S. Miranda, D.M. Neto, A.F.G. Pereira, P.A. Prates, J. Reuter, B. Revil-Baudard, C. Rojas-Ulloa, B. Sener, F. Shen, A. Van Bael, P. Verleysen, F. Barlat, O. Cazacu, T. Kuwabara, A. Lopes, M.C. Oliveira, A.D. Santos, G. Vincze, Analysis of ESAFORM 2021 cup drawing benchmark of an Al alloy, critical factors for accuracy and efficiency of FE simulations, Int. J. Mater. Form. 15 (2022) 61. https://doi.org/10.1007/s12289-022-01672-w

[2] P. Van Houtte, S.K. Yerra, A. Van Bael, The facet method: a hierarchical multilevel modelling scheme for anisotropic convex plastic potentials, Int. J. Plast. 25 (2009) 332-360. https://doi.org/10. 1016/j.ijplas.2008.02.001

[3] O. Cazacu, New yield criteria for isotropic and textured metallic materials, Int. J. Solids Struct. 139 (2018) 200-210. https://doi.org/10.1016/j.ijsolstr.2018.01.036

[4] M.C. Oliveira, D.M. Neto, A.F.G. Pereira, J.L. Alves, L.F. Menezes, Evaluating the influence of the deformation of the forming tools in the thickness distribution along the wall of a cylindrical cup, IOP Conf. Series: Mate. Sci. Eng. 1238 (2022) 012079. https://doi.org/10.1088/1757-899X/1238/1/012079

[5] F. Yoshida, T. Uemori, A model of large-strain cyclic plasticity describing the Bauschinger effect and workhardening stagnation, Int. J. Plast. 18 (2002) 661-686. https://doi.org/10.1016/S0749-6419(01)00050-X

[6] F. Yoshida, H. Hamasaki, T. Uemori, Modeling of anisotropic hardening of sheet metals including description of the Bauschinger effect, Int. J. Plast. 75 (2015) 170-188. https://doi.org/10.1016/j.ijplas.2015.02.004

[7] A. Ghaei, A. Taherizadeh, A two-surface hardening plasticity model based on non-associated flow rule for anisotropic metals subjected to cyclic loading, Int. J. Mech. Sci. 92 (2015) 24-34. https://doi.org/10.1016/j.ijmecsci.2014.11.017

Materials Research Proceedings 28 (2023) 1503-1510 https://doi.org/10.21741/9781644902479-162

Combined material model to predict flow curves of cold forging raw materials having high strain hardening exponent

ZEREN Doğuş[1,a *], KOCATÜRK Fatih[1,b] and TOPARLI M. Burak[1,c]

[1]R&D Center, Norm Fasteners

[a]dogus.zeren@normfasteners.com, [b]fatih.kocatuerk@univie.ac.at, [c]burak.toparli@tubitak.gov.tr

Keywords: Metal Forming, Voce Material Model, Flow Curve Prediction, Finite Element Method

Abstract. In order to increase the accuracy of cold forging simulations, flow curves obtained by experimental compression tests are used instead of the material models existing in the software library. The parameters of Ludwik material model were determined with respect to the constructed experimental flow curves at different temperatures and strain rates. Then, the flow curves were defined into the software by using these parameters. While Ludwik model can represent the material flow curve with high accuracy at low plastic strain values, the error rate between the experimental flow curve and the Ludwik model increases at high plastic strain values. Voce material models were known to predict the flow curve of materials with high strain hardening exponents more accurately, especially at high temperature and strain values. In this study, the performance of Ludwik material model was compared to four Voce material models given in the literature and a more accurate combined material model was defined for each flow curve at different temperature and strain rates for 42CrMoS4 material. All experimental flow curves were predicted with a minimum R^2 of 0.99 and the lowest mean absolute error value with the new combined material model.

Introduction

The accuracy of cold forming process simulations using finite element analysis (FEA) software depends on the true stress -plastic strain curves used. In cases where plastic deformation is high, the stress and strain distributions are not uniform, that is, they do not show a certain trend. For this reason, it is difficult to predict the flow curves of steel materials with a high strain hardening exponent, where high plastic strain values are observed in the flow curves, using a single material model. Defining the flow curves of such materials separately according to the deformation transitions increases the accuracy of the prediction models. Plastic deformation transitions in flow curves can be listed as follows: i) the part from the beginning of plastic deformation to the maximum compression stress value, ii) after the maximum compression stress value, the material exhibits strain softening part until the actual rupture of the material. In the literature, there are models such as Hollomon [1], Ludwigson [2], Ludwik [3], Swift [4] and Voce [5] that consider the work hardening rate for material flow curve prediction. However, these models are insufficient to represent the hardening and softening behavior of materials at high plastic strain values. Guo et al. [6] suggested a model that includes both the hardening and softening phases by combining the Voce Model for Hardening [5] and a linear softening model (Voce Model with Linear Softening). The developed model was able to predict the flow stress over a wide plastic strain range. Nguyen [7] has proposed a combination of Voce hardening and Voce softening models. On the other hand, Rotpai et al. [8] proposed a new piecewise model for flow curve prediction at room and elevated temperatures in order to minimize the deviation between the predicted flow curves and the experimental flow curves. A Swift-Voce model to describe the large deformation behavior of 7050-T7451 aluminum alloy under uniaxial stress, notched stress, and pure shear operations was developed by Cao et al [9]. The combination of Swift model and the 4th order polynomial was

Content from this work may be used under the terms of the Creative Commons Attribution 3.0 license. Any further distribution of this work must maintain attribution to the author(s) and the title of the work, journal citation and DOI. Published under license by Materials Research Forum LLC.

also proposed in order to describe the large deformation behavior of the Ti-6Al-4V alloy in the same study. In addition to predicting material flow curves with mathematical models, there are also studies carried out to predict flow curves with machine learning or regression models [10,11]. An artificial neural network model was suggested by Kocatürk et al. [10] to estimate experimental flow curves of a medium carbon steel material at different temperatures and strain rate values, and the flow curve predictions with high accuracy were obtained with this method. In another study, Aydın et al. [11] proposed a model that can obtain true stress-strain curve from experimental compression test data. Moreover, machine learning models and various regression models were used to predict the flow curves for the intermediate temperature and strain rate values where experimental flow curves are not available and promising flow curves were estimated. In this study, flow curves at different temperatures and strain rates, which were constructed by using the compression test results of a medium carbon alloy steel material, were employed. The parameters of Ludwik Model, Voce Model for Hardening [7], Voce Model for Softening [5], Voce Model with Linear Softening [2] and Voce Model for Hardening and Softening [5] were determined using the "curve_fit" function in the Scipy library on the Python programming language for every temperature and strain rate values. Voce Model for Hardening and Softening best-predicted the flow curve up to maximum compression stress point while Voce model with linear softening and Ludwik Model best-predicted the part from maximum compression stress to the maximum loading point. A new combined material model based on plastic strain subintervals was proposed for the flow curves at different temperatures and strain rates.

Materials and Method

The flow curves were obtained from the experimental compression test results of 42CrMoS4 medium carbon alloy steel material. To obtain the flow curves from the experimental compression test data of the materials, the model suggested by Aydın et al. [11] was used. Compression tests were carried out at different temperatures and strain rates in accordance with ASTM E9 standard [12]. Compression tests were performed with a ZWICK universal tensile/compression testing machine for temperatures at 25, 100 and 200°C and strain rates of 0.001 and 0.275 s^{-1}. Before each compression test, MoS_2 based lubricant was used for test plates in order to minimize the friction effects. A model was developed in the Python programming language to compare the performance of the material models used to predict the experimental flow curves obtained. In this model, the material models are defined firstly, then the model coefficients that give the best prediction are determined with the curve fitting method according to the defined plastic strain intervals, and the performances of the models are reported according to the coefficients obtained. The determined coefficients, R^2 and mean absolute error (MAE) were used for the performance comparison of the obtained flow curves. Functions in the Numpy library were used to calculate the performance criteria. The "curve_fit" function in the Scipy library was used to find the model parameters according to the experimental flow curves. Finally, the Matplotlib library was used to plot the resulting flow curves. The material models used to predict flow curves are defined below. In these models, σ represents the true stress, ε the true plastic strain, n is the hardening exponent, and $\sigma_0, \beta, K, A, B, C, D, k$ represent the material coefficients, respectively.

Ludwik model [9]:

$$\sigma = \sigma_0 + K\varepsilon^n \tag{1}$$

Voce hardening model [12]:

$$\sigma = \sigma_0(1 - Ae^{-\beta\varepsilon}) \tag{2}$$

Voce softening model [12]:

$$\sigma = \sigma_0(1 - Ae^{\beta\varepsilon}) \tag{3}$$

Voce linear softening model [8]:

$$\sigma = \sigma_0\left(1 - Ae^{-\beta\varepsilon}\right) - k\varepsilon \tag{4}$$

Voce hardening and softening model [3]:

$$\sigma = \sigma_0 + A(1 - e^{-B\varepsilon}) + C(1 - e^{D\varepsilon}) \tag{5}$$

Comparison of Ludwik and Voce Models

In this section, the flow curve prediction performances of Ludwik and Voce material models in the true plastic strain range of [0, 1.8], which is the whole plastic strain range for 42CrMoS4 material, were compared for 3 different temperatures and 2 different strain rates. The results obtained are given in Table 1. In order to compare the models fairly, the "curve_fit" function in the Scipy library is used with initial parameter values for all models. The Voce Hardening and Softening model best predicted the flow curves at all temperatures and strain rate value of 0.001 s^{-1} with a minimum R^2 value of 0.97. For 25°C and 0.275 s^{-1} strain rate, the Voce Linear Softening model best predicted the flow curve with 0.97 R^2, while the Ludwik model best predicted the flow curves at 100 and 200°C, 0.275 s^{-1} strain rate with 0.65 and 0.78 R^2, respectively. Flow curve predictions obtained at 100 °C and strain rate values of 0.001 and 0.275 s^{-1} were shown in Fig. 1 for the plastic strain range of [0, 1.8].

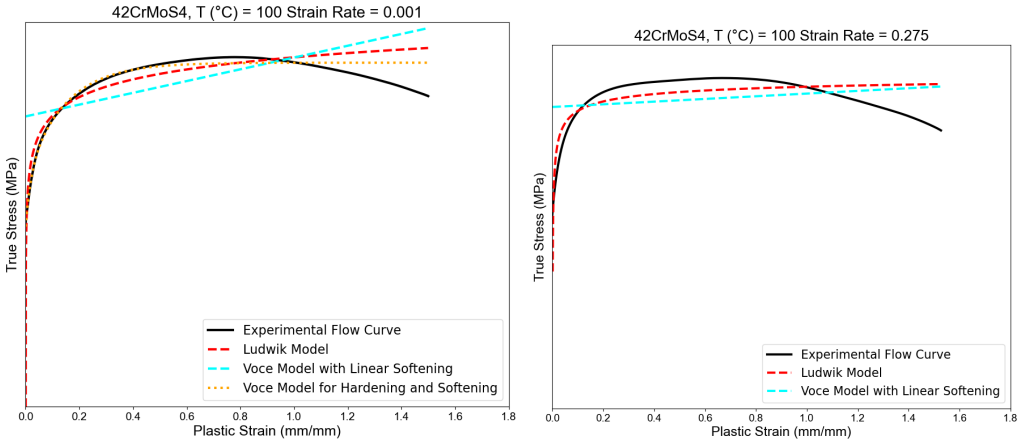

Fig. 1. Flow curve predictions in the plastic strain range of [0, 1.8] for 100°C, 0.001 and 0.275 s^{-1} strain rates.

Table 1. Model comparison for plastic strain range of [0, 1.8].

Temperature (°C)	Strain Rate	Model Name	Pl. Str. Inverval	R^2	MAE
25	0.001	Ludwik	0.0-1.8	0.900	1117751
25	0.001	Voce with Linear Softening	0.0-1.8	0.440	2825240
25	0.001	**Voce with Hardening and Softening**	0.0-1.8	**0.980**	**446045**
25	0.275	Ludwik	0.0-1.8	0.600	9942
25	0.275	**Voce with Linear Softening**	0.0-1.8	**0.970**	**2822**
100	0.001	Ludwik	0.0-1.8	0.870	1019870
100	0.001	Voce with Linear Softening	0.0-1.8	0.390	2332653
100	0.001	**Voce with Hardening and Softening**	0.0-1.8	**0.970**	**438462**
100	0.275	**Ludwik**	0.0-1.8	**0.650**	**7555**
100	0.275	Voce with Linear Softening	0.0-1.8	0.050	12002
200	0.001	Ludwik	0.0-1.8	0.880	893179
200	0.001	Voce with Linear Softening	0.0-1.8	0.400	2079574
200	0.001	**Voce with Hardening and Softening**	0.0-1.8	**0.970**	**370809**
200	0.275	**Ludwik**	0.0-1.8	**0.780**	**6440**
200	0.275	Voce with Linear Softening	0.0-1.8	0.190	12061

In order to obtain closer results to the experimental flow curves for 42CrMoS4 material, and to identify models that predict the hardening and softening phases during plastic deformation more accurately, the model predictions for the lower plastic strain ranges were also compared. In order to determine the model that best predicts material behavior up to the maximum compression stress value, the flow curve prediction performances of Ludwik and Voce material models in the true plastic strain range [0, 0.6] were compared for 3 different temperatures and 2 different strain rates. Flow curve predictions obtained at 100 °C and strain rate values of 0.001 and 0.275 s^{-1} were shown in Fig. 2 for the plastic strain range of [0, 0.6]. The results obtained for the true plastic strain range of [0, 0.6] were tabulated in Table 2. The Voce Hardening and Softening model best predicted the flow curves at all temperatures and strain rate values with a minimum R^2 value of 0.999.

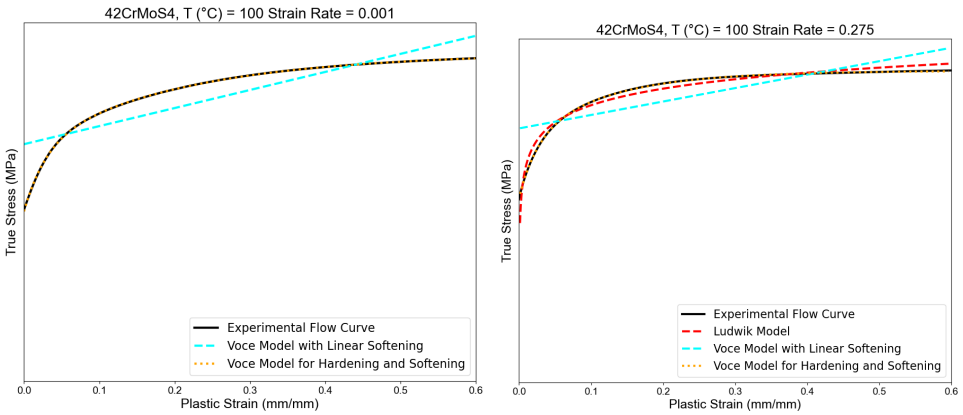

Fig. 2. Flow curve predictions in the plastic strain range of [0, 0.6] for 100°C, 0.001 and 0.275 s^{-1} strain rates.

Materials Research Proceedings 28 (2023) 1503-1510 https://doi.org/10.21741/9781644902479-162

Table 2. Model comparison for plastic strain range of [0, 0.6].

Temperature(°C)	Strain Rate	Model Name	Pl. Str. Interval	R^2	MAE
25	0.001	Voce with Linear Softening	0.0-0.6	0.800	1121473
25	0.001	**Voce for Hardening and Softening**	0.0-0.6	**0.999**	**9083**
25	0.275	Ludwik	0.0-0.6	0.980	1642
25	0.275	Voce with Linear Softening	0.0-0.6	0.660	6054
25	0.275	**Voce for Hardening and Softening**	0.0-0.6	**0.999**	**86**
100	0.001	Voce with Linear Softening	0.0-0.6	0.780	922398
100	0.001	**Voce for Hardening and Softening**	0.0-0.6	**0.999**	**11076**
100	0.275	Ludwik	0.0-0.6	0.970	1474
100	0.275	Voce with Linear Softening	0.0-0.6	0.630	5177
100	0.275	**Voce for Hardening and Softening**	0.0-0.6	**0.999**	**87**
200	0.001	Voce with Linear Softening	0.0-0.6	0.750	849120
200	0.001	**Voce for Hardening and Softening**	0.0-0.6	**0.999**	**22864**
200	0.275	Voce with Linear Softening	0.0-0.6	0.730	4821
200	0.275	**Voce for Hardening and Softening**	0.0-0.6	**0.999**	**42**

In order to determine the model that can predict the hardening and softening behavior of 42CrMoS4 material more accurately, model predictions were compared. For this purpose, the flow curve prediction performances of Ludwik and Voce material models in the plastic strain range of [0.6, 1.8] were compared for three different temperatures and 2 different strain rates. The results were given in Table 3. Flow curve predictions obtained at 100 °C and strain rate values of 0.001 and 0.275 s^{-1} were shown in Fig. 3 for the plastic strain range of [0.6, 1.8]. The Voce Linear Softening model with a minimum R^2 of 0.78 obtained the best prediction for the flow curves with strain rate of 0.001 s^{-1} and for all temperature values. The Voce Linear Softening model also obtained the best prediction with 0.92 R^2 for the flow curve at 200°C and 0.275 s^{-1} strain rate. The best predictions for both flow curves at 25 and 100°C and 0.275 s^{-1} strain rate were obtained with the Ludwik model with 0.999 R^2.

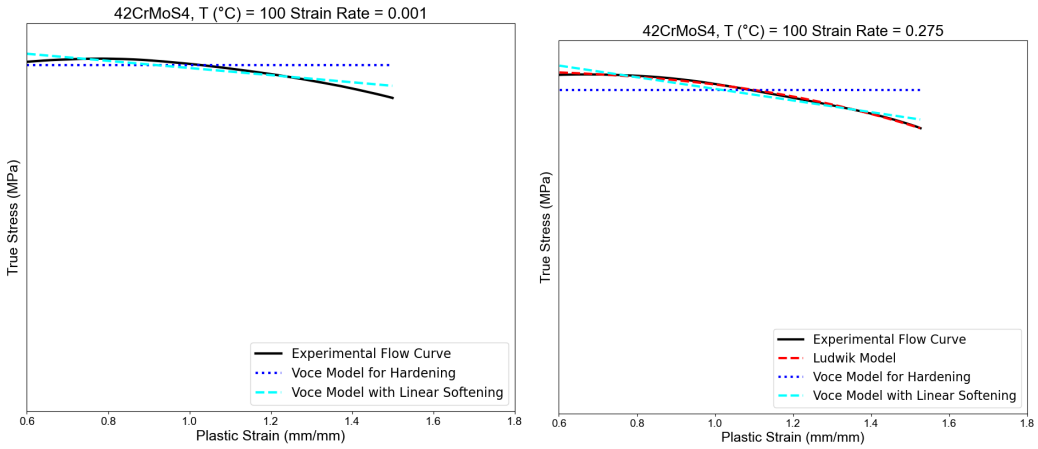

Fig. 3. Flow curve predictions in the plastic strain range of [0.6, 1.8] for 100°C, 0.001 and 0.275 s^{-1} strain rates.

Table 3. Model comparison for plastic strain range of [0.6, 1.8].

Temperature(°C)	Strain Rate	Model Name	Pl. Str. Interval	R^2	MAE
25	0.001	**Voce with Linear Softening**	0.6-1.8	**0.850**	**117884**
25	0.275	**Ludwik**	0.6-1.8	**0.999**	**157**
25	0.275	Voce for Hardening	0.6-1.8	0.000	4152
25	0.275	Voce with Linear Softening	0.6-1.8	0.980	617
100	0.001	Voce for Hardening	0.6-1.8	0.000	334923
100	0.001	**Voce with Linear Softening**	0.6-1.8	**0.810**	**165377**
100	0.275	**Ludwik**	0.6-1.8	**0.999**	**205**
100	0.275	Voce for Hardening	0.6-1.8	0.000	3482
100	0.275	Voce with Linear Softening	0.6-1.8	0.930	900
200	0.001	Voce for Hardening	0.6-1.8	0.000	298707
200	0.001	**Voce with Linear Softening**	0.6-1.8	**0.780**	**159582**
200	0.001	Voce for Hardening and Softening	0.6-1.8	0.000	298707
200	0.275	Voce for Hardening	0.6-1.8	0.000	2607
200	0.275	**Voce with Linear Softening**	0.6-1.8	**0.920**	**734**

According to the flow curve prediction results, while the Voce Hardening and Softening model best predicted the material behavior up to the maximum stress point, the Voce Linear Softening and Ludwik models best predicted the hardening and softening behaviors observed after the maximum compression stress value. In order to determine the transition points for these stages, analyzes were carried out to find the model that gives the best estimate in each interval by dividing the whole plastic strain range into 9 equal parts with a true plastic strain range of 0.2. As a result, a new combined material model was determined for each flow curve, which predicts the flow

curves very close to the experimental data. The performances of the combined models that give the best predictions at each determined subinterval of true plastic strain range for the flow curves at each temperature and strain rate value were reported in Table 4. Flow curve predictions obtained with the combined model for strain rate values of 0.001 and 0.275 at 100°C were shown in Fig. 4.

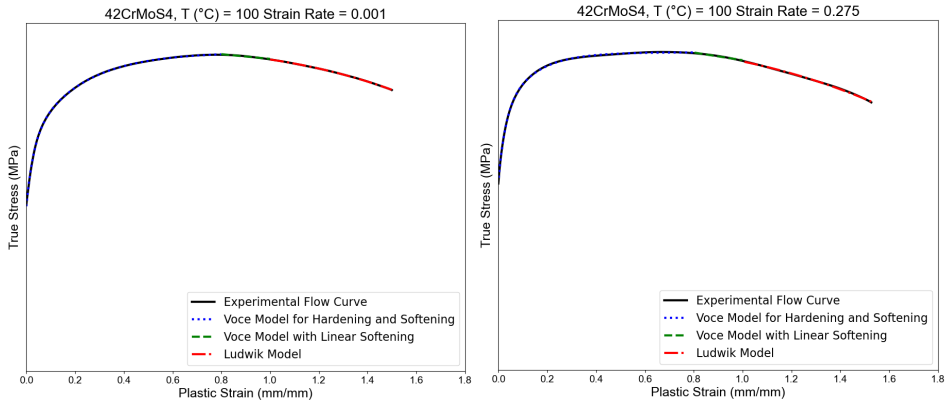

Fig. 4. Combined model flow curves of 42CrMoS4 in the plastic strain range of [0, 1.8] for 100°C, 0.001 and 0.275 s^{-1} strain rates.

Table 4. Combined model performances for 42CrMoS4 material based on plastic strain range.

Temperature (°C)	Strain Rate	Model Name	Pl. Str. Interval	R^2	MAE
25	0.001	Voce for Hardening and Softening	0.0-0.8	0.999	44344
25	0.001	Voce with Linear Softening	0.8-1.0	0.993	1080
25	0.001	Ludwik	1.0-1.8	0.999	709
25	0.275	Voce for Hardening and Softening	0.0-0.6	0.9999	86
25	0.275	Voce with Linear Softening	0.6-1.0	0.968	119
25	0.275	Ludwik	1.0-1.8	0.999	40
100	0.001	Voce for Hardening and Softening	0.0-0.8	0.999	16048
100	0.001	Voce with Linear Softening	0.8-1.0	0.963	3838
100	0.001	Ludwik	1.0-1.8	0.999	830
100	0.275	Voce for Hardening and Softening	0.0-0.8	0.9999	145
100	0.275	Voce with Linear Softening	0.8-1.0	0.981	17
100	0.275	Ludwik	1.0-1.8	0.999	41
200	0.001	Voce for Hardening and Softening	0.0-0.8	0.999	41638
200	0.001	Voce with Linear Softening	0.8-1.0	0.946	4050
200	0.001	Ludwik	1.0-1.8	0.999	1993
200	0.275	Voce for Hardening and Softening	0.0-0.8	0.999	63
200	0.275	Voce with Linear Softening	0.8-1.0	0.987	12
200	0.275	Ludwik	1.0-1.8	0.999	14

Summary
Within the scope of the study, flow curves obtained from experimental compression test results of medium carbon alloyed 42CrMoS4 steel were used. The coefficients of both material models were determined for different temperature and strain rate values. In order to fit the curve with model equations, "curve_fit" function in the Scipy library has used on Python programming language. The performances of different material models were also examined by dividing the total plastic strain range into subintervals, and combined piecewise material models were proposed according to the true plastic strain values for each temperature and strain rate value. Flow curve prediction performances of Ludwik material model and four different Voce material models were compared. In the comparisons, the flow curve up to the maximum compression stress point was best predicted by the Voce Hardening and Softening model, while the Ludwik and Voce Linear Softening models best predicted the part after the maximum compression stress point to the breaking point. For the flow curves at different temperatures and strain rates, the new combined material model depending on plastic strain ranges were proposed by using Ludwik and four different Voce models. All experimental flow curves were predicted with a minimum R^2 of 0.99 and lower absolute error values with the new combined material model while Ludwik model predicted the flow curves with a maximum R^2 of 0.90.

References
[1] H. Hollomon, Tensile deformation, Aime Trans. 12 (1945) 1-22.
[2] D.C. Ludwigson, Modified stress-strain relation for FCC metals and alloys, Metall. Trans. 2 (1971) 2825-2828. https://doi.org/10.1007/BF02813258
[3] P. Ludwik, Elemente der Technologischen Mechanik, Springer, 1909. https://doi.org/10.1007/978-3-662-40293-1
[4] H.W. Swift, Plastic instability under plane stress, J. Mech. Phys. Solids 1 (1952) 1-18. https://doi.org/10.1016/0022-5096(52)90002-1
[5] Voce, The relationship between stress and strain from homogenous deformation, J. Inst. Met. 74 (1948) 537-562.
[6] J.H. Guo, S.D. Zhao, G.H. Yan, Z.B. Wang, Novel flow stress model of AA 4343 aluminium alloy under high temperature deformation, Mater. Sci. Technol. 29 (2013) 197-203. https://doi.org/10.1179/1743284712Y.0000000140
[7] D.T. Nguyen, A new constitutive model for AZ31B magnesium alloy sheet deformed at elevated temperatures and various strain rates, High. Temp. Mater. Process. 33 (2014) 499-508. http://dx.doi.org/10.1515/htmp-2013-0109
[8] U. Rotpai, T. Arlai, S. Nusen, P. Juijerm, Novel flow stress prediction and work hardening behavior of aluminium alloy AA7075 at room and elevated temperatures, J. Alloy. Compd. 891 (2021) 162013. https://doi.org/10.1016/j.jallcom.2021.162013
[9] J. Cao, F. Li, W. Ma, D. Li, K. Wang, J. Ren, H. Nie, W. Dang, Constitutive equation for describing true stress -strain curves over a large range of strains, Philos. Mag. Lett. 100 (2020) 476-485. https://doi.org/10.1080/09500839.2020.1803508
[10] F. Kocatürk, M.B. Toparli, B. Tanrıkulu, S. Yurtdaş, D. Zeren, C. Kılıçaslan, Flow curve prediction of cold forging steel by artificial neural network model, 24th International Conference on Material Forming, 2021.
[11] T. Aydın, F. Kocatürk, D. Zeren, A Model to Construct and Predict Flow Curve of Materials from Compression Test Results with Machine Learning Models Using Python, Key Eng. Mater. 926 (2022) 2022-2030. https://doi.org/10.4028/p-18kwo6
[12] ASTM E9-19, Standard Test Methods of Compression Testing of Metallic Materials at Room Temperature, ASTM International, West Conshohocken, PA, 2019.

Materials Research Proceedings 28 (2023) 1511-1520 https://doi.org/10.21741/9781644902479-163

Modelling of yield point phenomenon in bake-hardening grade steel

DESHMANE Nachiket S.[1,2,a*], PERDAHCIOGLU Semih E. [1,b], and VAN DEN BOOGAARD Ton[1,c]

[1]University of Twente, Drienerlolaan 5, 7522 NB Enschede, Netherlands

[2]Stichting Materials innovation institute, Van der Burghweg 1, 2628 CS Delft, Netherlands

[a]nsdeshmane@gmail.com, [b]e.s.perdahcioglu@utwente.nl, [c]a.h.vandenboogaard@utwente.nl

Keywords: Yield Point Phenomenon, Lüders Bands, Strain Localization, Strain Gradient, Mesh Size Dependency

Abstract. In this study the yield point phenomenon in Bake-Hardening grade steel is predicted using a physically based thermo-mechanical model. A modified Taylor equation is proposed with a physically based dislocation density evolution approach. The softening that follows the higher yield point is incorporated with a Voce type decaying exponential function. The strain rate dependency of the plastic hardening is also incorporated in the model. The yield point in the decay function is also strain rate dependent but does not follow the same dependency of plastic hardening. This was solved by making the decay function strain rate dependent by adding a modified strain rate stress term to the exponential function. This parameter is calculated based on tensile experiments. Due to the softening behavior of the material, the numerical model is mesh size sensitive. Hence, a lower order strain gradient enhanced approach is implemented. The gradient is in a form of an additional hardening term assigned in the locally strained bands based on the plastic strain gradient. Hill48 yield criterion is used to assimilate the anisotropy in the steel grade. The numerical results show good correspondence with experimental tensile tests. The regularization significantly reduced the mesh size dependency of the numerical results.

Introduction

The yield point phenomenon creates an inhomogeneous plastic yielding in steels during forming, which results in unfavorable surface defects in form of stretcher marks on the formed steel products. Hence, modeling the yield point phenomenon has been a point of interest for many researchers in past few decades.

In a tensile test, the yield point phenomenon exhibits a distinct higher yield point followed by softening and a constant stress yield elongation, prior plastic hardening. Hahn [1] attributed the higher yield point to the extra stress required to unpin the locked dislocations by the Cottrell atmosphere. The unpinned dislocations are now mobile and multiply due to short range interaction with other dislocations resulting in a softening of the curve. A locally strained shear band(s) is(are) formed near the specimen shoulder at about 54° to the tensile axis and propagates along the tensile axis to the other shoulder of the specimen, termed as Lüders band. Hahn [1] was among the earlier researchers to propose an analytical model for the yield point phenomenon as an extended Orowan's equation based on dislocation density evolution and the dependency of the Lüders band velocity on the applied stress. Yoshida et al. [2] further proposed a constitutive model based on an extended Hahn model. They considered two modes the Lüders propagation and the subsequent plastic deformation with different sets of constitutive equations, the transition between the two was governed by a change in strain rates. Similarly, Estrin et al. [3, 4] and McCormick et al. [5] proposed a constitutive model for yield phenomena incorporating the dislocation dynamics based on diffusion of the dislocations to active slip systems on surrounding grains and their short-range interaction with immobile dislocations and solutes.

Content from this work may be used under the terms of the Creative Commons Attribution 3.0 license. Any further distribution of this work must maintain attribution to the author(s) and the title of the work, journal citation and DOI. Published under license by Materials Research Forum LLC.

Contrary to Hahn's theory, Akama et.al [6] and Nes et al. [7] observed that the phenomenon is triggered not only by the release of dislocations locked by the Cottrell atmosphere but also by substitutional elements segregated at the grain boundaries. Nes et al. [7], therefore proposed a Taylor based dislocation density evolution equation [8] to incorporate grain size and dislocation cell size dependency, along with a thermally dependent parameter. Similarly, Ballarin et al. [9] developed a physically based model for bake-hardening steels to predict the macroscopic behavior based on carbon solute concentration, wherein the band propagation was modeled with a Voce type equation. Kyriakides et al. [10] modelled the Lüders phenomenon with a trilinear stress-strain curve with an intermediate softening response in bending of steel tubes. Span and van Liempt [11], proposed a physically based dislocation density evolution model for temper rolling that quantitatively described the Lüders band behavior in conjugation to temper rolling parameters and chemical composition of a particular steel grade. The softening in the model was attributed to the Lüders front velocity.

As stated earlier, in a tensile test, the yield point phenomenon is accompanied by a peak stress followed by a softening, which results in an inhomogeneous localized plastic shear band. In a finite element framework, this shear band is associated with the localization of strain along row(s) of elements. Simultaneously, the adjoining elements along this localized strain band undergo softening to compensate for the instability. Therefore, the band width, the strain gradient across the band and the resultant macroscopic flow stress (within Lüders strain elongation region) are mesh dependent [2,9,10,12]. Therefore, a regularization solution serves two objectives: firstly, to attain mesh–independent finite element results and secondly to account for the correlation of numerical Lüders band width to the actual observed in experiments. The regularization can be achieved by either introducing rate dependency to the model [10] or by introducing a higher order strain gradient to the model [12,13]. Kyriakides et al. introduced a mild rate dependency in the model via a strain rate power law, for the regularization of the solution. Mazière et al. [12] introduced the Aifantis strain gradient plasticity model, wherein a higher order modulus and a characteristic length scale is introduced, the latter being fitted with experiments. In this study, the mesh size dependency is reduced by using a lower-order gradient enhanced approach by the addition of a hardening term based on studies by Perdahcioglu et al. [14].

In the current study, a novel approach is modelled expanding on Taylors equation to incorporate thermal and strain rate dependency of the yield phenomena. The softening, or decay, function expands on the similar concept of dislocation density evolution and its short range interaction with immobile or mobile dislocations and solutes. This gives a better prediction of the Lüders phenomena in the model. Tensile tests to characterize Lüders phenomenon are elaborated in *Section Tensile Experiment*. The strain distribution and evolution over the specimen surface are captured with digital image correlation (DIC). A constitutive model detailed in section *Model* is proposed based on underlying physical dislocation density evolution. An extended Taylor model [8] is proposed, wherein the evolution of dislocation density is given by an extended Bergstrom model [15,16] for plastic hardening. For the softening an exponential equation is proposed. The model further incorporates strain rate dependency of the material based on Krabiell and Dahl [17] model. Based on experiments an anisotropic yield criteria Hill48 is used. The Lüders band width and strain distribution is observed to be mesh size sensitive. Hence a regularization method as proposed by Perdahcioglu et al. [14] is adopted to reduce the mesh size dependency of the numerical results; detailed in the section *Gradient Plasticity*. Finally the experimental and model results are discussed in the *Results and Discussion* as well as in the section *Conclusion*.

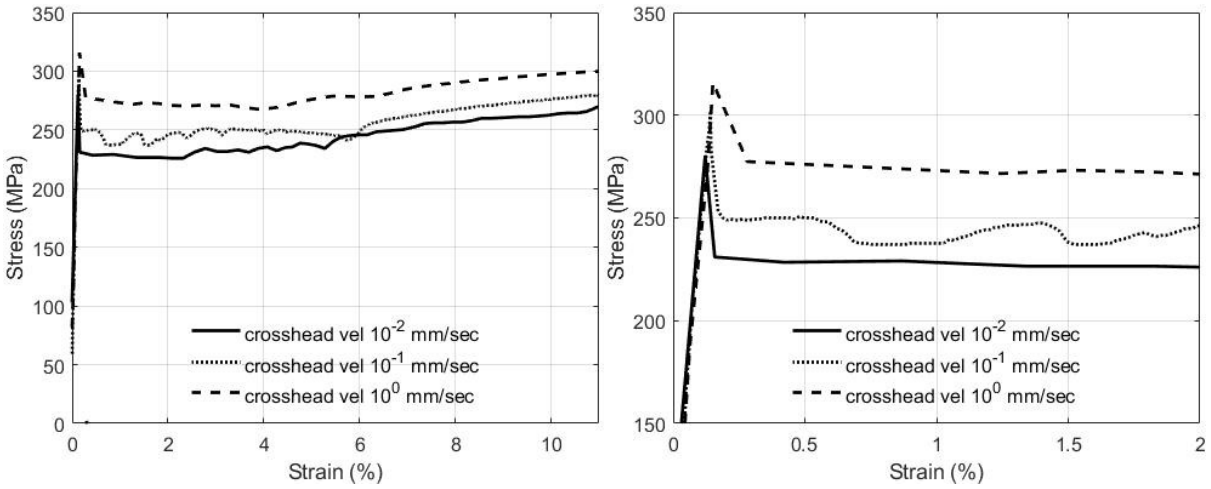

Fig. 1. Experimental tensile test of as-received Bake Hardened steel at three cross-head velocities.

Tensile Experiments

Bake hardening steel utilized in this study is in as-received state without undergoing temper rolling. Thus, the steel displays a distinctive yield point phenomenon with an elongated Lüders strain at a constant lower yield stress, see Fig. 1. The band is observed to nucleate just prior to higher yield point near the specimen shoulder and propagates across the specimen gauge length as the test progresses at a constant stress. The specimen is tested at three different cross-head velocities 10^0, 10^{-1}, 10^{-2} mm/s and at rolling, transverse and 45° direction. The local strain distribution and evolution across the specimen surface is measured with DIC during the tensile test. The surface of the specimen (gauge length) is therefore covered with a speckled pattern for the DIC (Aramis) measurement.

The higher yield point is observed to be linearly dependent to strain rate. Similarly, the Lüders stress and elongation are observed to be strain rate dependent. In each test, the band nu- cleated near the specimen shoulder at approximately 54° to the tensile loading axis and propagated along the loading axis across the gauge length. The band and its strain gradient could be seen in the DIC full field measurements Fig. 2 over the gauge length for the tensile test results at 10^{-1} cross head velocity. The band width is measured at half height with reference to the band (strain rate) peak height in this study. The mean peak width thus measured at half height was 5.6mm with a standard deviation of 0.79. The Lüders strain elongation is also observed to be directly proportional to the test cross-head velocity, and is in accordance with studies by Yoshida et al. It is also peculiar to see that the band does not limit to a single shear band, but forms a combination of two bands in a 'V' shape. A few tests also showed multiple bands being nucleated at both specimen shoulders during the test. It can be speculated that the band nucleation and propagation in a tensile test is a product of two factors: the dislocation density mechanics and the geometry of the test specimen. During band nucleation, the local shearing strain in a grain expands to neighboring grains, which deform in a preferred orientation resulting in a macroscopic shear band. Furthermore, the limitation imposed by the specimen width, causes the band to propagate during tensile loading.

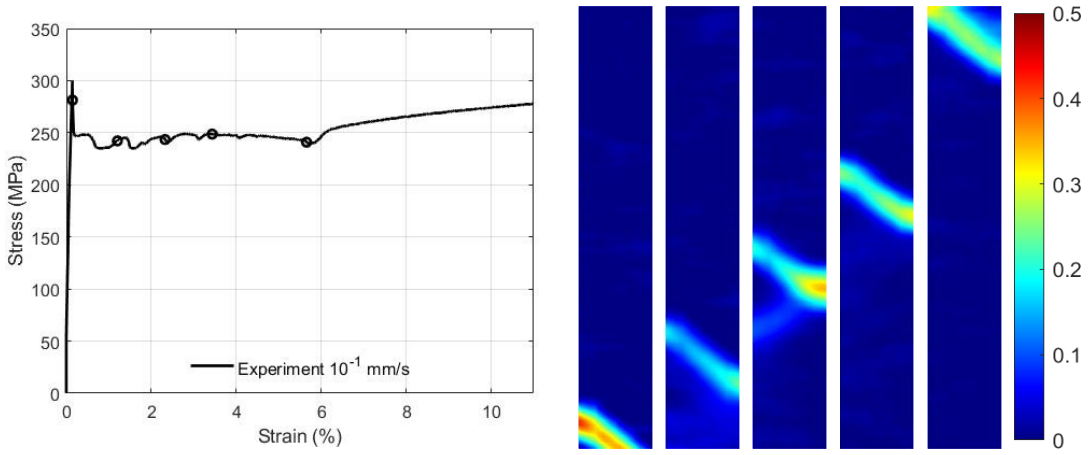

Fig. 2. Strain rate across the gauge length is plotted by DIC field measurements at stages highlighted in the flow stress.

Model

Work hardening.

A physically-based model, based on extended Taylor's equation is proposed in this study. The model therefore includes the dependency of flow stress in material on strain rate and temperature, and dislocation density evolution as a product of strain hardening.

$$\sigma(\epsilon) = \sigma_0 + \sigma_{thermal} + \sigma_{decay} + \alpha G b\sqrt{\rho(\epsilon)} \quad (1)$$

Where, σ_0 is the initial flow stress (MPa), $\sigma_{thermal}$ is the dynamic stress based on Krabiell and Dahl model [17], σ_{decay} is the softening function, α is constant parameter depending on immobile dislocations distribution, G is the shear modulus for steel, b is the Burgers vector, $\rho(\epsilon)$ is the dislocation density. Van Liempt [18] proposed an extended Bergstrom model [15] to show the dislocation density ρ development with strain. Eq. 2 describes the hardening as a development of the dislocation structure with strain.

$$\frac{d\rho}{d\epsilon} = M[B\rho^c\, g(\epsilon_t)] - \Omega\rho. \quad (2)$$

Where, ϵ gives total accumulated strain, B_u is the proportional constant for the increase of immobile dislocation in the cell walls, c is the exponent describing the influence of the dislocation density on the decrease of dislocation cell size, given by $d_{cell} = k\rho^{-c}$, M is the Taylor constant, parameter Ω is the strain rate and temperature dependent and represents the remobilization (dynamic recovery) of immobile dislocations. Here Ω is taken constant, β term provides for the linear hardening behavior at higher strains. The function $g(\epsilon)$ was introduced by van Liempt [18] to describe the change in dislocation mean free path due to change in dislocation cell geometry at higher strains. Vegter et al. [16,19] postulated that at high strains dislocation cell walls within the grains are deformed, and the small orientation difference between the cells influences the dislocation mean free path. This influence of the cell shape distortion on the mean free path is given with an exponential function $g(\epsilon) = \exp(\beta\epsilon)$. The first order term of Taylor series expansion of the function was used to avoid unexpected deflection at high strains in the flow stress giving the function: $g(\epsilon) = 1 + \beta\epsilon$. This gives a linear hardening at high strains, and by substituting the same in Eq. 2 the following is obtained:

$$\frac{d\rho}{d\epsilon} = M[B\rho^c\,(1 + \beta\epsilon_t)] - \Omega\rho. \quad (3)$$

Eq. 3 is integrated between the limits $\epsilon = 0$ and $\epsilon + \epsilon_0$, where ϵ_0 is the pre-deformation parameter accounting for the existing dislocation density prior to deformation, finally giving the dislocation density evolution as a function of equivalent strain as presented in Vegter et al. [19]:

$$\rho(\epsilon)^{\frac{1}{1-c}} = \frac{B_u}{\Omega}\left[\beta(\epsilon+\epsilon_0) + \left(1 - \frac{\beta}{M\Omega(1-c)}\right)\left[1 - \exp\left(-M\Omega(1-c)(\epsilon+\epsilon_0)\right)\right]\right] \quad (4)$$

This physically based density evolution is then substituted in Eq. 1 making the expression of the flow stress as a function of equivalent strain. The constants for the equation shown in Table 1 are referenced from [19].

Table 1. Parameters used for the hardening model.

σ_0	[MPa]	80
M	[-]	2.7
A	[-]	0.88
G	[MPa]	80.0E3
B	[-]	2.5E-7
Ω	[-]	2.1
B_u	[-]	8.3E8
B	[-]	0.38
ϵ_0	[-]	0.005
C	[-]	0.0

Dynamic stress.

The dynamic stress as postulated by Krabiell and Dahl [17], was incorporated into the model to account for the strain rate dependency of the material. The dynamic term describes the thermal activation of mobile dislocation past obstacles with regard to its dependency on strain rate and temperature.

$$\sigma_{thermal}(\dot{\epsilon}, T) = \begin{cases} 0 & \dot{\epsilon} < \dot{\epsilon}\exp\left(-\frac{\Delta G_0}{k_{boltz}T}\right) \\ \sigma_0^*\left(1 + \frac{k_{boltz}T}{\Delta G_0}\ln\frac{\dot{\epsilon}}{\dot{\epsilon_0}}\right)^p & \dot{\epsilon}\exp\left(-\frac{\Delta G_0}{k_{boltz}T}\right) < \dot{\epsilon} < \dot{\epsilon_0} \\ \sigma_0^* & \dot{\epsilon} > \dot{\epsilon_0} \end{cases} \quad (5)$$

Where, σ_0^* is the dynamic stress at zero thermal activation, ΔG_0 is the maximum activation enthalpy, p is the exponent for thermally activated contribution, $\dot{\epsilon_0}$ is a structure parameter pertaining to density of mobile dislocation and obstacle distribution; effectively the limiting strain rate for thermally activated movement, k_{boltz} is the Boltzmann constant and T is the temperature.

Decay stress.

The higher yield point can be attributed to either the additional stress required to unpin the locked dislocations in Cottrell atmosphere [1], or due to interaction of dislocation with grain boundaries [7] and the solutes segregated at grain boundaries [6]. Once the dislocations are 'free' from the obstacles, they become mobile. This can be considered as an instant drop in the number of immobile dislocations which causes a drop in the flow stress. An exponential Voce type equation is therefore proposed to represent the decay in the flow stress. It was also observed that the higher yield point is strain rate dependent and does not follow the work hardening strain rate

dependency. Thus, a modified Krabiell and Dahl [17] strain rate dependency model was implemented in σ_{decay} resulting in following equation:

$$\sigma_{decay} = \left(\Delta\sigma + \sigma_t^d\right) \exp(-n\epsilon) \tag{6}$$

Table 2. Thermal stress and Decay stress model parameters.

σ_0^*	[MPa]	1083
k_{boltz}	[mJ/K]	1.38E-20
T	[K]	300
ΔG_0	[mJ]	1.6E-16
$\dot{\epsilon}_0$	[-]	10.0E8
m	[-]	3.982
A	[-]	40
n	[-]	300

Where $\Delta\sigma$ corresponds to stress difference between higher yield point and yield point without the yielding phenomenon; the later estimated from Interstitial Free (IF) grade steel tests. This will correspond to the higher stress required to unpin the dislocations and set them to mobile phase. The exponential decay corresponds to the softening as a result of mobile dislocations multiplying by interaction with other dislocation networks and solutes. The constant n influences the softening rate due to dislocation multiplication. σ^d gives an additional stress term to the yield point, enabling strain rate dependency of the yield point. The parameters shown in Table 2 are fitted to experimental data by adjusting σ^* (from Eq. 5) keeping rest parameters constant.

Yield criterion.

The material exhibited anisotropy, with a variation in yield stress when tested under uniaxial and shear loading. Hill48 yield function was therefore used:

$$\phi = F\left(\sigma_y - \sigma_x\right)^2 + G(\sigma_z - \sigma_x)^2 + H\left(\sigma_x - \sigma_y\right)^2 + 2L\tau_{yz}^2 + 2M\tau_{zx}^2 + 2N\tau_{xy}^2 - \sigma_y^2 \tag{7}$$

The anisotropy coefficients, in terms of R values, were calculated from uniaxial and shear experiments. The model thereby showed a good fit with uniaxial tensile and shear test with same hardening parameters.

Gradient Plasticity.

The band size and strain gradient over the band showed mesh size dependency. Hence, the mesh size dependency is reduced using a lower-order gradient enhanced approach using an additional hardening term based on studies by Perdahcioglu et al. [14]. This non-local hardening term is calculated from the plastic strain gradients across the band. Perdahcioglu et al. [17] referred to this phenomenon as stress created by the evolution of geometrically necessary dislocations (GNDS) within a locally sheared zone and thus calculated them from incremental plastic strain and Burgers vector. The rate of change of the additional dislocations generated due to the strain gradient is therefore given by:

$$\dot{\rho}_{grad} = \frac{2\dot{\eta}^p}{b} \tag{8}$$

Where $\dot{\eta}^p$ is the rate of equivalent plastic strain gradient, b is the Burgers vector. The total change in dislocation density for a given strain increment ρ_{grad} is then placed in Eq. 1, resulting in an additional hardening stress across the band during its evolution and propagation.

$$\sigma(\epsilon) = \sigma_0 + \sigma_{thermal} + \sigma_{decay} + \alpha G b \sqrt{\rho(\epsilon) + \rho_{grad}} \quad (9)$$

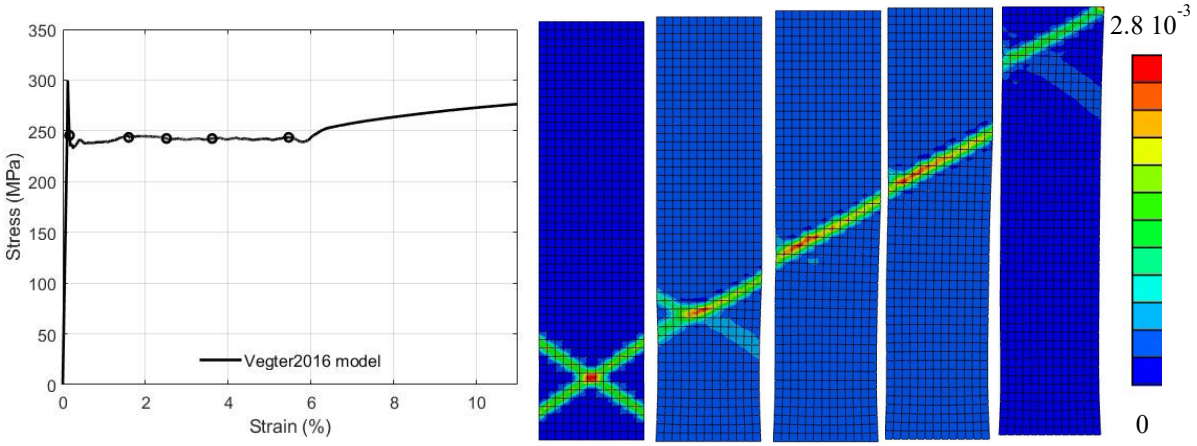

Fig. 3. Numerical tensile test strain-rate stages highlighted in flow stress.

Results and Discussions

The model was validated with a numerical tensile test. The gauge area 50x12.5x0.74 mm (length x width x thickness) was subjected to uniaxial loading. To replicate the material's inhomogeneity, numerical instability was incorporated by introducing fluctuating yield stress in a range 0 – 1 MPa randomly assigned to integration points. In Abaqus software, the arc-length method to solve for iterations during softening. The resultant flow stress and Lüders band are presented in Fig. 3. Fig. 4 shows the results of the simulations incorporating the hardening model combined with the anisotropic yield criterion tested at three cross-head velocities and shows a good fit with the experiments. The higher yield point is predicted well in the three velocities, attributed to the independent strain-rate model included in the decay function. The strain-rate dependency of the decay function also results in an increase in Lüders strain elongation with increasing test velocity. The thermal stress model's implementation shows a good fit with experimental tests at varying cross-head velocities. The band inclination is also observed between 52°-55° in accordance with the experiments.

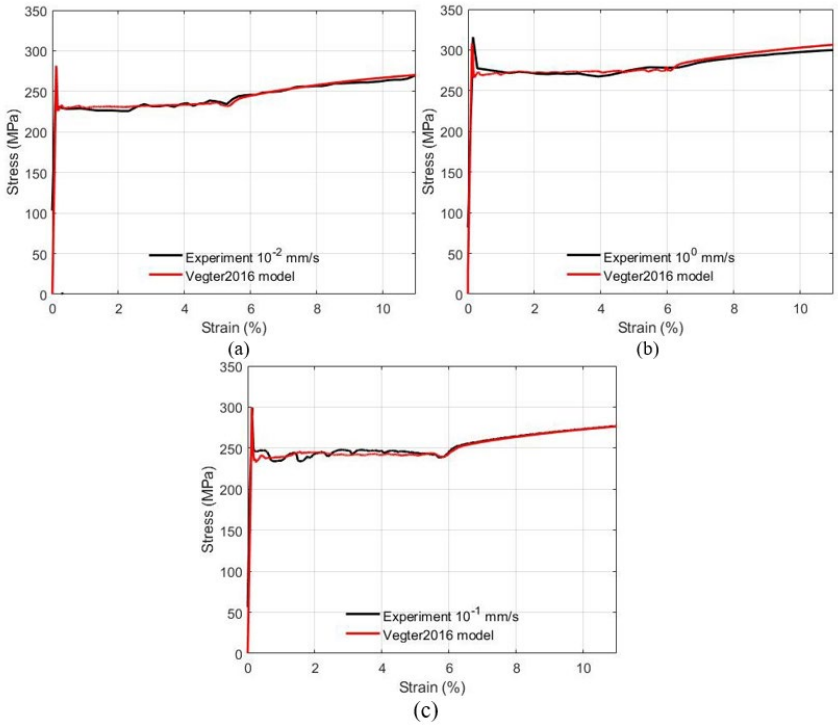

Fig. 4. Numerical tensile test compared with tensile experiments at three different cross-head velocities (a) 10^0 (b) 10^{-1} and (c) 10^{-2} mm/s.

Due to the softening and strain rate dependency in the model, the numerical test result is mesh dependent. Hence the first step was to test the mesh dependency of the model, by conducting the numerical tensile test by varying mesh sizes. Thus, numerical uniaxial tensile test was conducted with three-dimensional quadratic mesh with reduced integration at varying mesh sizes of 0.5, 0.75 and 1mm. The mean band peak width is calculated at every increment and plotted with reference to nodal displacement (Fig. 5 a). The mean peak width (calculated at half height of the peak) observed for mesh sizes 0.5, 0,75 and 1 mm are 1.30, 1.42 and 1.83mm. In either case the strain-rate peak is observed to be higher with a lower mesh size which further ascertains the mesh dependency of the Lüders band. The implementation of the gradient model results in an additional hardening term implemented only at the regions with localized strains, and is determined with a number of integration points within a prescribed radius. The integration points within the assigned radius experience an additional hardening term influencing the gradient width. This could be seen in the peak width determined from simulations with the gradient model, in Fig. 5b. Although a major difference could not be seen in the average peak widths for different mesh sizes, the variation of the peak width with different mesh sizes has more overlap with each other.

Summary

The modified dislocation density evolution model gives a good approximation of the experimental data. The dynamic stress factor implemented in the decay function enables predicting the higher yield point as well as Lüders elongation in coordination with applied strain rates. The decay function also facilitates understanding the underlying dislocation dynamics behavior: a higher yield stress term required to unpin the dislocations and an exponential decay to accommodate the softening by dislocation multiplication and short range interaction [1]. This includes its interaction with solutes at grain boundaries in accordance with [6]. It is also postulated that apart from dislocation dynamics, the specimen geometry in combination with its loading condition influences

formation of shear band and its propagation. The mesh size dependency of the strain bands was reduced by inclusion of the gradient model, however the simulated band size could not be achieved as observed in experiments. This could be further improved by modifying the decay function to control the rate of softening in the model.

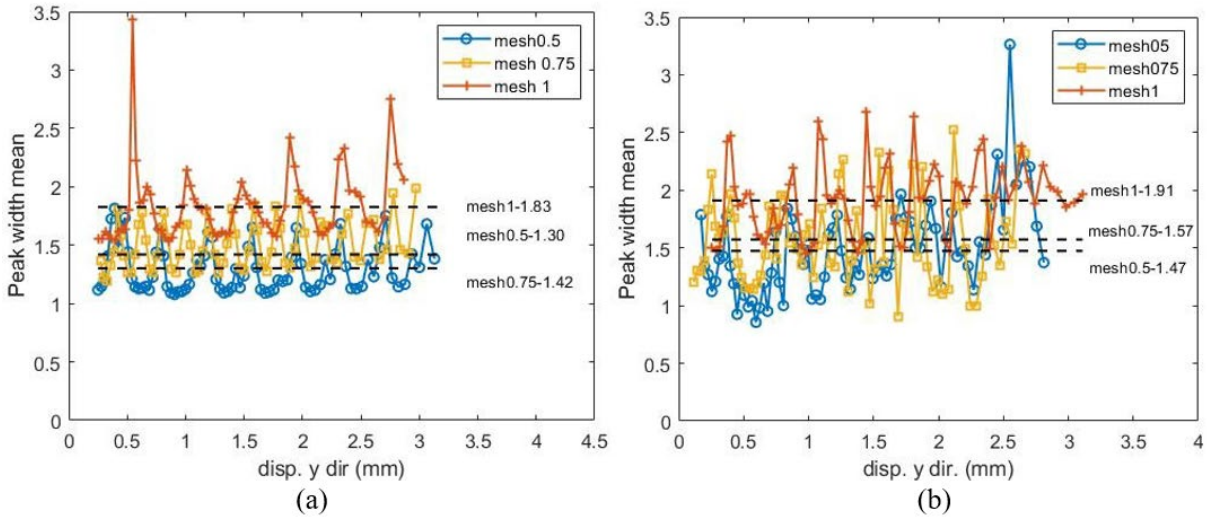

Fig. 5. For mesh sizes 0.5, 0.75 and 1mm band width with respect to displacement (a) without inclusion of gradient term (b) with inclusion of gradient term.

References

[1] G. Hahn, A model for yielding with special reference to the yield-point phenomena of iron and related bcc metals, Acta Metall. 10 (1962) 727–738. https://doi.org/10.1016/0001-6160(62)90041-X

[2] F. Yoshida, Y. Kaneda, S. Yamamoto, A plasticity model describing yield-point phenomena of steels and its application to fe simulation of temper rolling, Int. J. Plast. 24 (2008) 1792–1818. https://doi.org/10.1016/j.ijplas.2008.05.004

[3] Y. Estrin, L. Kubin, A unified phenomenological description of work hardening and creep based on one-parameter models, Acta Metall. 34 (1986) 2455–2464.

[4] Y. Estrin, L. Kubin, Plastic instabilities: phenomenology and theory, Mater. Sci. Eng. A 137 (1991) 125–134. https://doi.org/10.1016/0921-5093(91)90326-I

[5] P. McCormick, C. Ling, Numerical modelling of the portevin - le chatelier effect, Acta Metall. Mater. 43 (1995) 1969–1977. https://doi.org/10.1016/0956-7151(94)00390-4

[6] D. Akama, N. Nakada, T. Tsuchiyama, S. Takaki, A. Hironaka, Discontinuous yielding induced by the addition of nickel to interstitial-free steel, Scripta Mater. 82 (2014) 13–16. http://doi.org/10.1016/j.scriptamat.2014.03.012

[7] E. Nes, B. Holmedal, E. Evangelista, K. Marthinsen, Modelling grain boundary strengthening in ultra-fine grained aluminum alloys, Mater. Sci. Eng. A 410-411 (2005) 178–182. https://doi.org/10.1016/j.msea.2005.08.121

[8] G. Taylor, The mechanism of plastic deformation of crystals. part i. - theoretical, Royal Society 145 (1934).

[9] V. Ballarin, A. Perlade, X. Lemoine, O. Bouaziz, S. Forest, Mechanisms and modeling of bake-hardening steels: Part ii. complex loading paths, Metall. Mater. Trans. A 40 (2009) 1375–1382. http://doi.org/10.1007/s11661-009-9812-6

[10] S. Kyriakides, J. Miller, On the propagation of Luders bands in steel strips, J. Appl. Mech. 67 (2001) 645–654. https://doi.org/10.1115/1.1328348
[11] P. Span, J. van Liempt, Modelling of the impact of chemical composition on important metallurgical processes during cold strip production, EU technical Steel Res. (2005) 145–06.
[12] M. Mazière, S. Forest, Strain gradient plasticity modeling and finite element simulation of Lüders band formation and propagation, Cont. Mech. Thermodyn. 27 (2013) 83–104. https://doi.org/10.1007/s00161-013-0331-8
[13] M. Mazière, C. Luis, A. Marais, S. Forest, M. Gaspérini, Experimental and numerical analysis of the Luders phenomenon in simple shear, Int. J. Solid. Struct. 106 (2017) 305–314. https://doi.org/10.1016/j.ijsolstr.2016.07.026
[14] E. Perdahcıoglu, C. Soyarslan, T. Asık, E van den Boogaard, A class of rate-independent lower-order gradient plasticity theories: Implementation and application to disc torsion problem, Materials 11 (2018) 1425. https://doi.org/10.3390/ma11081425
[15] Y. Bergstrom, A dislocation model for the stress-strain behaviour of polycrystalline alpha-fe with special emphasis on the variation of the densities of mobile and immobile dislocations, Mater. Sci. Eng. 5 (1969) 193–200. https://doi.org/10.1016/0025-5416(70)90081-9
[16] H. Vegter, H. Mulder, P. van Liempt, J. Heijne, Tailored work hardening descriptions in simulation of sheet metal forming, Int. J. Plast. (2013) 474–481. https://doi.org/10.1063/1.4850016
[17] W. Krabiell, A. Dahl, Zum einfluß von temperatur und dehngeschwindigkeit auf die streckgrenze von baustählen unterschiedlicher festigkeit, Archiv fuer das Eisenhuettenwesen 52 (1982) 429–436.
[18] P. van Liempt, Workhardening and substructural geometry of metals, J. Mater. Process. Technol. 45 (1994) 459 – 464. https://doi.org/10.1016/0924-0136(94)90382-4
H. Vegter, H. Mulder, P. van Liempt, J. Heijne, Work hardening descriptions in simulation of sheet metal forming tailored to material type and processing, Int. J. Plast. 80 (2016) 204–221. https://doi.org/10.1016/j.ijplas.2015.11.002

Materials Research Proceedings 28 (2023) 1521-1530 https://doi.org/10.21741/9781644902479-164

Digital twin development for the sensitivity analysis of near solidus forming process

MUHAMMAD Sajjad[1,a *], GORKA Plata[1,b], JOKIN Lozares[2,c] and JOSEBA Mendiguren[1,d]

[1]Mondragon Unibertsitatea, Faculty of Engineering, Mechanics and Industrial Production, Loramendi 4, Mondragon 20500, Gipuzkoa, Spain

[2]Department of Mechanics, Design and Industrial Management, University of Deusto, Avda. of Universities 24, 48007, Bilbao, Spain

[a]msajjad@mondragon.edu, [b]gplata@mondragon.edu, [c]jokin.lozares@deusto.es, [d]jmendiguren@mondragon.edu

Keywords: NSF (Near Solidus Forming), Digital Twin (DT), FORGE NxT®, Design of Experiments (DOE)

Abstract. Near Solidus Forming (NSF) process, performed at semi-solid material state is gaining popularity due to its good physical properties, low manufacturing cost and material waste. Although the process possesses many advantages over traditional hot forging, the nature of the process itself is very complex and due to this the researcher struggles to identify the material behavior at NSF conditions. Especially the material model in this condition has not been stated clearly before and therefore it is important to develop a reliable digital twin (DT) strategy which can validate the material model efficiently. Therefore, the objective of this work is to investigate the influence of all DT parameters like billet material and dimensions, billet and dies temperature, heat transfer coefficient, emissivity, ambient temperature, and friction coefficient, in two industrial components such as H spindle and R spindle. The Taguchi Design of Experiments (DOE) approach combined with numerical simulation in FORGE NxT® is employed to develop the sensitivity analysis of the process. The impact of all parameters in the DT are evaluated in terms of die filling and forming forces, and its importance in the material model is studied. Results show that the newly developed approach proposed a novel optimum NSF-DT calibration strategy for material-model validation. Which can be used to develop an accurate model of the NSF process at the laboratory and industrial scale

Introduction

Forging is a widely used technology in the field of automotive, aerospace, and other engineering sectors around the world. The process is important due to its cost efficient and reliable spectrum of manufacturing for planes, cars, and ships components. Furthermore, the processed components possess superior mechanical properties which are best suited for critical applications. The process is done either at room or high temperature based on the material and the desired properties of the components. In particular, Near solidus Forming (NSF) process is referred to the one developed critically close to the solid temperature and it is gaining popularity due to its good physical properties, low manufacturing cost and material waste compared to traditional hot forging process [1,2]. Although gaining popularity, the process is not still fully developed, and it is not clear how the physics behind the NSF develops [1]. This is due to the complex behavior of the material at such a high temperature. Previous NSF-DT studies have shown an important gap on the prediction of forces and filling [2]. Researchers suggested that material is the key factor influencing the process and developing a correct model can be a key object to understanding how this process

Content from this work may be used under the terms of the Creative Commons Attribution 3.0 license. Any further distribution of this work must maintain attribution to the author(s) and the title of the work, journal citation and DOI. Published under license by Materials Research Forum LLC.

works [3]. Others investigated that the boundary conditions play a significant role in the process and by controlling certain parameters the processes could be developed accurately [2].

Talking about the history of the process the main development was gained in the semi-solid forming processes initially from the investigation of low melting point alloys [4], even some trials were carried out with stainless steels [5]. However, the high costs associated with the production of globular aluminum alloys, compared with the die casting ones, made this process infeasible for industrial production. Despite this drawback, some electronic consumer goods and automotive parts were manufactured by taking advantage of this technology [6].

Nevertheless, in 1992 the first investigations about semi-solid forming of steels at high solid content were performed by P. Kapranos et al. [7]. Since then, many researchers have tried to manufacture sound components by gaining the advantage of this near-net-shape technique to bring it closer to industry without fortune[8, 9]. Gourlay et al. studied material behavior at a high solid fraction, typical in NSF processes [10]. For instance, at values from 0.9 to 1, granular behavior was reported. Another important aspect is the process temperature as maximum load and ductility were shown to decrease when the temperature is increased [11].

To learn the process deeply, the investigation of certain factors is necessary such as the values of the heat transfer coefficient (HTC) and friction factor during the process. This knowledge is necessary to achieve realistic simulations and generate reliable, and useful results about the process.. As friction is a universal phenomenon influencing the metal forming process and it is inevitable for friction to exist between dies and workpieces. In addition, friction gives rise to redundant energy usage by increasing the process load requirement. The forming load, the die wear and the surface finish of the product are significantly influenced by the friction. For this reason, an appropriate evaluation of this parameter is very essential in metal forming. To obtain precise friction characterization during the forming process, several experimental methods were presented. There are several friction tests, some of which has advantages over another and also shortcomings. Noticeable among them are the ones employed in metal forming: the ring test, double-cup extrusion test and the spike test [12,13]. Specifically for the case of NSF, a T-Shape spike test which is developed by Zhang et al. can be used to avoid the difference of friction conditions on the cylinder surface and end surface of a round billet [13,14]. Deformations, including both extrusion and compression, are involved in this test and only the cylindrical surface of the billet is in contact with the punch and die.

Furthermore, Dadras and Burte et al. investigated the interface HTC [15]. Later, Burte and Stone extended the work of Dadras and predicted HTC values and simulated forging operations [16]. To understand the heat transfer under lubricated condition, Azushima et al. conducted the compression and compression-sliding tests of aluminum-coated 22MnB5 under dry and lubricated conditions using the hot fat drawing test simulator [17]. Similarly, Y. Chang et al. also investigate factors that influencing the HTC and an actual hot-formed automotive B-pillar was obtained in experiment to validate its formability under various contact pressures [18, 19].

Bai et al. introduced an efficient closed-form technique for the determination of HTC at different forming and contact conditions based on finite element (FE) heat transfer analysis using FE software DEFORM [20]. Similarly, Chang and Bramley used FE tools to determine the HTC at the work-piece/die interface for forging process by conducting an upsetting test where the surface temperature of the die was recorded [19]. Then the measured and predicted temperatures were combined using an inverse algorithm to determine the HTC.

The nature of the NSF process is that the real-time experiments are time-consuming and costly [21]. To overcome this, the Finite Element Method (FEM) tools are widely used to model and simulate forming processes and results such as temperature changes, stress, strain, deformation and load history in the die, and in the workpiece can be studied [22]. However, advances in the numerical analysis of complex forming processes require the better understand of interface

characteristics for heat transfer and friction. For example, Petersen et al. proposed the FEM in conjunction with metal experiments to verify the general feasibility of the proposed test geometry and pointed out that the practical ring-compression test was more commonly used for the quantitative evaluation of the tribological conditions at the die/work-piece interface in metal forming [23].

Nevertheless, many authors compared the DT material models to their experiments and concluded that the material model plays a vital role in the forming processes and the actual models are not capable of correctly representing the NSF phenomenon[24]. However, NSF-DT are strongly depended on the process parameters noise and BC uncertainty, e.g., HTC, friction coefficient, billet tolerances. Therefore, without having all these dependencies under control one can does not assure that the differences shown between experimental, and NSF-DT are coming from the material model. This work has a double objective. On the one hand, by means of a DOE approach, the sensitivity to the main outputs (force and filling) to the material model and other influencing parameters is studied. In this way, the impact of each factor can be evaluated. On the other hand, once the influencing parameters and their impact are established, the optimum NSF-DT strategy is developed in order to be able to rely on the DT for material model validation purposes.

Material and Methods

The material used in this process is 42CrMo4 steel and its chemical composition is shown in the Table 1. The material is suited for high-temperature forming due to its fatigue strength and ductility properties. The industrial process used as a reference in this study consists of three major steps, shown in Fig.1. Initially, the billet is heated homogeneously in the furnace to the desired temperature by maintaining a uniform temperature throughout the furnace. Next, the billet is transferred from the furnace to a worktable through a mechanical arm as quickly as possible to minimize heat loss. The deformation die-set consists of top and bottom dies while a punch which deforms the billet. Finally, in the last step, the punch moves from the top dead center to the bottom dead center and the deformation takes place, this way the desired shape is achieved.

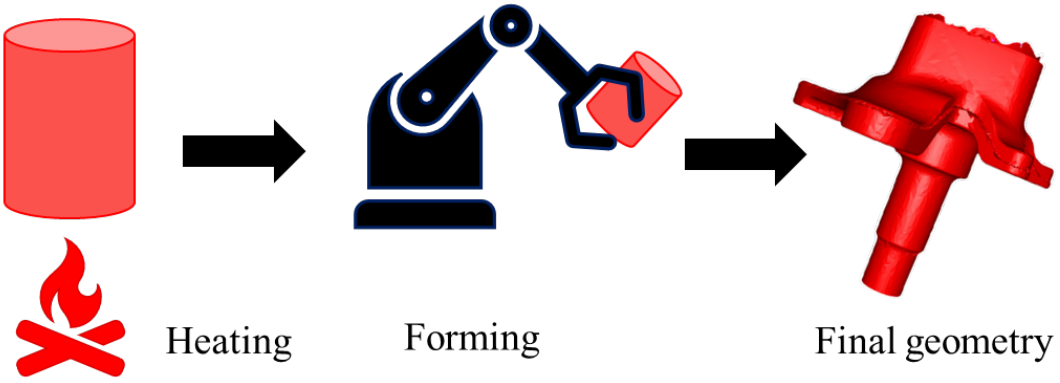

Fig. 1. NSF process flow detail.

The two industrial components used in this study which were recently manufactured at Mondragon University are shown in Fig. 2. The weight of H spindle workpiece is a ~2.3 kg and the R Spindle a ~3 kg.

Materials Research Proceedings 28 (2023) 1521-1530 https://doi.org/10.21741/9781644902479-164

Table 1. Chemical composition of 42CrMo4 steel %wt.

Cr	Mn	C	Mo	Si	P	S
1.05	0.75	0.41	0.22	0.20	0.02	0.02

The numerical tool FORGE NxT® is used to reproduce the entire NSF process in order to analyze the effect of all parameters during forming. The simulation procedure includes all the steps such as heating of the billet in the furnace, transfer of the billet and lastly the deformation phase. A servomechanical press with a capacity of 400 tons was used and its specification of forces, ram speed and ram position during deformation can be seen in work from Lozares et al. [2].

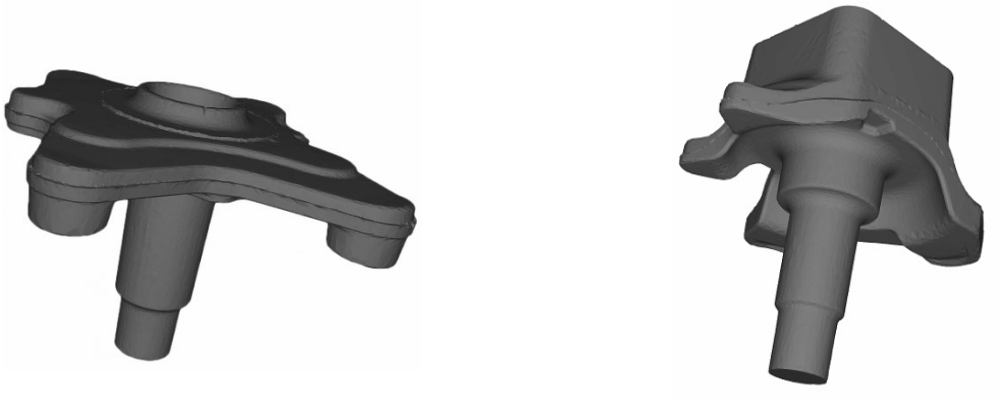

(a) (b)

Fig. 2. NSF industrial components (a) H spindle and (b) R spindle.

In the study, the effect of 10 parameters such as material, billet dimensions and temperature, (HTC), friction coefficient (FC), ambient temperature and emissivity are investigated. To study the effect of material on the process the strength of the material is reduced by changing the constitutive parameters. The level of each individual parameter is presented with symbol letters from V1 to V10, shown in the table 2. Since a list of parameters are considered in this study and to fully investigate the effect of individual parameter a design of experiment Taguchi DOE approach is used where the effect on input parameters is studied in relation to the forming force and fillings. However, based on the available data, the L16 orthogonal array is selected. The experimental design table is generated by employing data into Minitab software. Overall, total of 32 simulation were run, 16 of which for the H spindle and 16 for the R spindle and their result has been presented in the results section.

Table 2. Parameters detail and its Levels in Taguchi Method.

Component	Symbol	H-Spindle		R-Spindle	
		Level 1	Level 2	Level 1	Level 2
Billet Location (four points)	V1	1,2	3,4	1,2	3,4
Billet Diameter (mm)	V2	64.7	65.3	68.7	69.3
Billet Length (mm)	V3	89.5	90.5	92.5	93.5
Material Strength %	V4	50%	100%	50%	100%
Billet Temperature (°C)	V5	1360	1370	1360	1370
Dies Temperature (°C)	V6	200	270	200	270
Heat Transfer Coefficient (kW/m^2.K)	V7	2000	20000	2000	20000
Emissivity	V8	0.35	1	0.35	1
Ambient Temperature (°C)	V9	50	70	50	70
Friction Coefficient	V10	0.25	0.45	0.25	0.45

For filling calculation, horizontal and vertical filling has been selected and based on the components shapes five points have been selected for the R and H spindle. The filling has been calculated from these reference points at three different punch strokes in each case. Similarly, the forces were also calculated at three different strokes.

Results and Discussion

NSF process strongly depends on the temperature and a small variation can make a big difference in the output. Therefore, knowledge of the process cycle during heating and also in the transfer phase is mandatory. A typical example of the billet heating phases from heating to the deformation stage is shown in Fig. 3. Fig. 3(a) represents the temperature field of the billet inside the furnace when heated up to 1370°C. The temperature distribution seen in Fig. 3 (a) shows clearly that the outer surface of the billet has the highest temperature reading as it is directly in contact with the heat source. Overall, it can be seen that uniform temperature distribution is achieved at the end of the heating phase. Fig. 3(b) represents the temperature plots after the transfer phase, which indicates that the surface of the billet cold fairly fast even for the transfer time of ~3 seconds. The temperature field after the stand-by time of workpiece for ~2 seconds on the compression tool is given in Fig. 3(c), where the temperature range is between 411°C and 1370°C. This? shows how quickly the heat can be transferred from the billet to the contacting surfaces especially the ones with lower temperatures. That's why it is always preferred to deform the billet as soon as it is placed inside the forming tool.

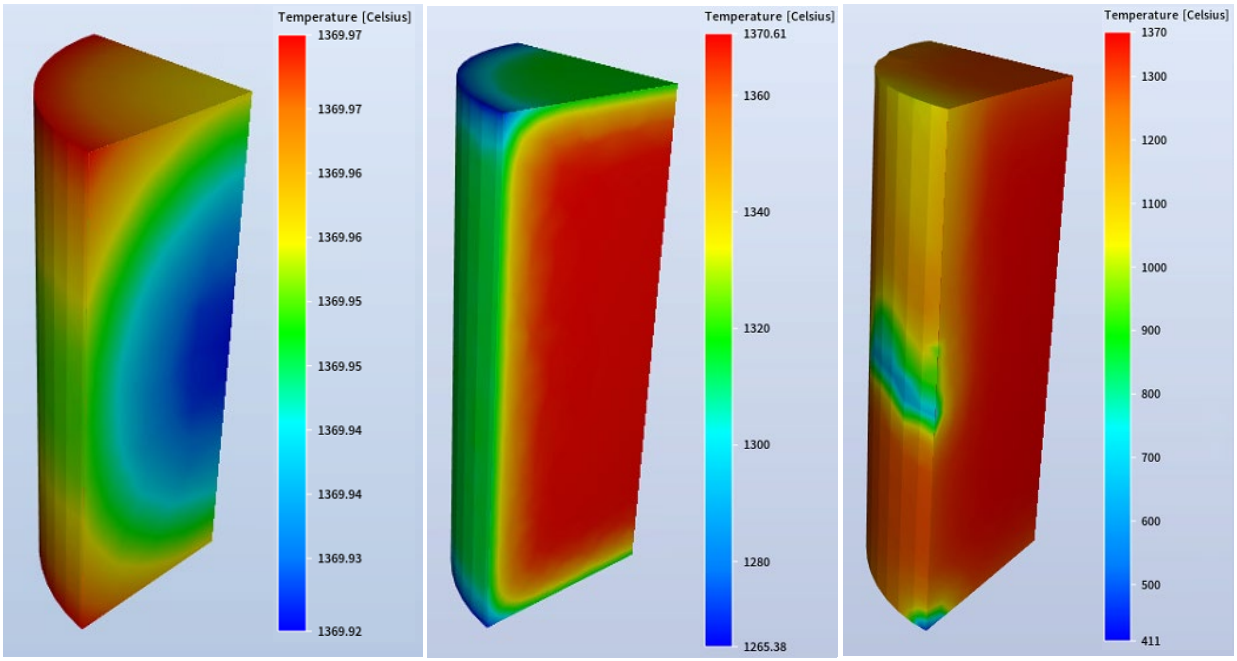

(a) (b) (c)

Fig. 3. Temperature distribution (a) After heating the billet up to 1370 ºC (b) temperature field at 1370 ºC after transport to compression table (c) temperature field after waiting time.

The deformation phases of R spindle during simulation from start to end is shown in Fig. 4. The equivalent strain representation shows that the higher values of stresses are develop in the contacting area of the billet and the punch at the initial stages of the process. Once the process crosses through a certain threshold, the stress concentration shifts to the lower side of the billet where the deformation is intense as can be seen in the Fig. 4 right side geometries. Similar behavior is noticed in H spindle as well.

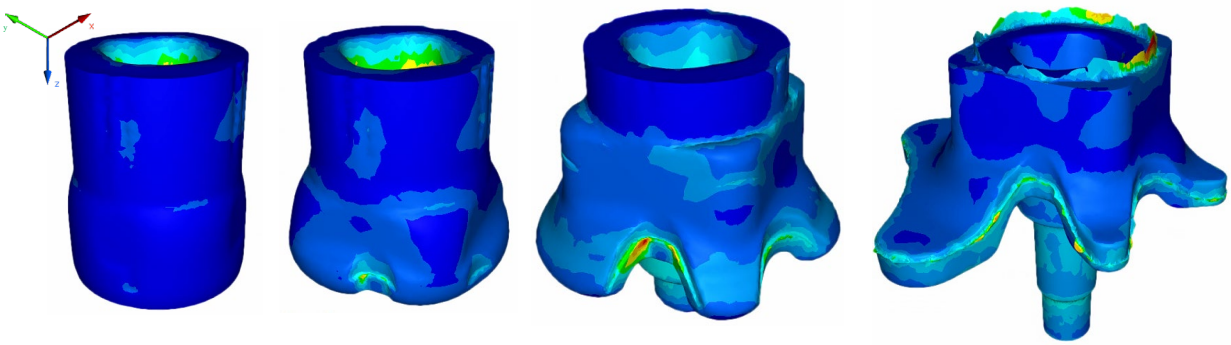

Fig. 4. Deformation phases of the R spindle from the start to the end of the process.

The results of the die filling and forces are indicated in Fig. 5. The x-axis of the plots shows the ten parameters while the y-axis represents the nominal value percentage of filling and forces values. As mentioned before that we have two types of filling, Fig. 5(e) represents the filling calculation in the punch direction which will be in the z-axis according to the Fig. 4, while Fig. 5(a-d) indicates the filling in the horizontal axis horizontal to the z plan. The forces are indicated in Fig. 5(f). The plots are calculated at three different strokes in each benchmark in order to have an overall view of the parameters effect by taking the average of the outputs values.

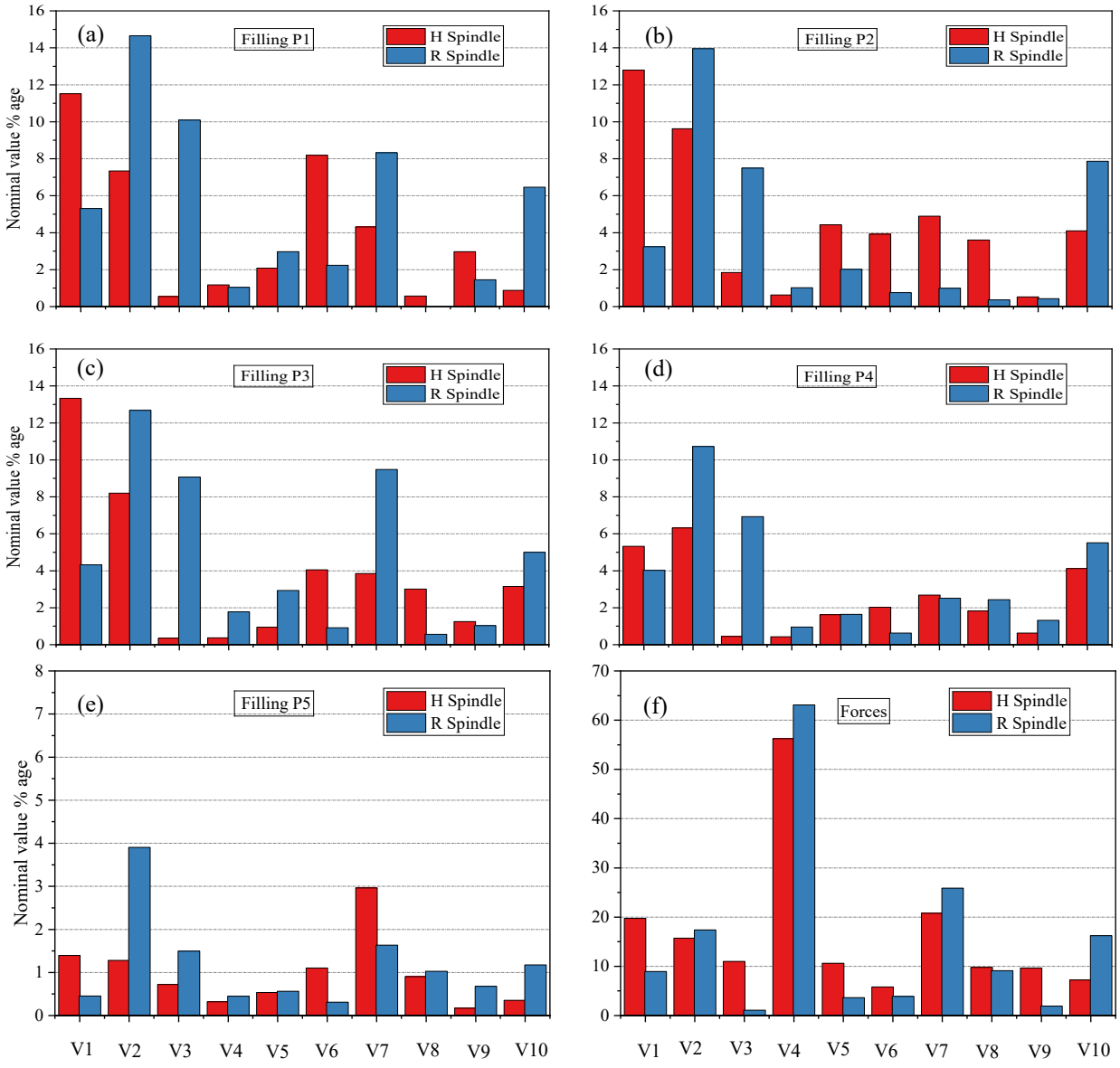

Fig. 5. Nominal value percentage of H and R spindle (a-e) die filling (f) punch forces.

Nevertheless, it is clear that the filling in the horizontal axis strongly depends on the location of the billet placement as shown in Fig. 5(a-d). Where in terms of forces the location plays a minor role in this process, see Fig. 5(f). The billet location can be optimized by trial and error, and it can be always different for every single component. Next when it comes to the dimension of the billet, its effect is always found to be high seen in Fig 5(a-e). For example, filling in any axis is strongly dependent on the diameter and length of the billet meaning the billet with a bigger size can achieve better and complete fillings whereas a smaller billet can cause pores or unfinished surfaces in the part.

In the boundary conditions parameters, which can be of the most interest for the NSF process. The major influencing factors are the heat transfer coefficient, friction coefficient (FC) and material strength which is having a nominal value percentage effect of up to 9 % on the process as shown in Fig. 5. The result suggested that by increasing the FC from 0.25 to 0.45 the material flow in the process was reduced and similar behavior was noticed for HTC and material strength. Other boundary condition parameters such as ambient temperature, billet and dies temperature are

negligible as they have on average of 2-3 % effect and changes in its values had a minor effect on the process.

Next, the punch forces are found to be strongly dependent on the material of the component as shown in Fig. 5(f), with a whopping value of 55-65 %. It is obvious, a material with high strength will require more force to deform compared to ductile material. The most interesting thing to notice here besides material is the effect of HTC and FC on the forces. The effect of HTC is found to be 24 % and FC at 15 %. From the calculation, the forces are found to be rising by making an increase in the values of these two individual factors. And the remaining parameters are found to be least influencing factors with the individual effect below 9 %.

Overall, we can conclude from the DT of the NSF process, to optimize the filling it is important to focus on the location, billet dimensions, HTC and FC. While to reduce the punch forces it is important to study and optimize the material properties, HTC and FC. And by characterizing these parameters and optimizing their values at the NSF condition, one can create a material model with good accuracy.

Summary

The effect of process parameters and boundary conditions in the NSF process is numerically investigated for 42CrMo4 steel. Taguchi design methodology combined with Minitab is employed and the data were simulated in the FORGE NxT®. The outcome of the process is stated in terms of forces and material filling in the dies. The following conclusions are drawn from the present work:

- Among all ten factors, the most significant factor which affects the filling is the location and dimensions of the billet, which are subjective factors and can be optimized by trial and error.
- The important parameters which can be of scientific interest for the development of the NSF process model are the material strength, HTC and FC, and their impact is also high on the filling.
- For the forces, the major influencing factor is the material, and this factor contributes 55-65 % of the total force values. Other factors such as HTC and FC are found to be up to 30 %.
- The remaining factors such as billet and dies temperature, emissivity and ambient temperature can be neglected and always remember that these parameters can have a different effect on the process if their ranges are different to the assumed ones. But since NSF is performed at high temperatures these ranges are considered based on the temperature requirements of the process.
- With all this knowledge in hand, it is concluded that to develop an accurate model of the process it is important to characterize first the most influencing factor both in filling and also for forces. These factors can be characterized by using experiment tests such as spike test for FC and compression test for HTC and so on.

Overall, the developed DT strategy provides useful information regarding NSF process at the industrial level and using this result one can develop an accurate material model by focusing on the major influencing factors in the process.

Acknowledgments

The authors would like to acknowledge Hybrid Semi-Solid Forming project funded by the "Research Fund for Coal and Steel" (RFCS) program of the European union, with the grant number 800763. Also, we sincerely thank CIE Automotive for their technical support.

References

[1] G. Plata, J. Lozares, A Sánchez, I. Hurtado, C. Slater, Preliminary study on the capability of the novel near solidus forming (NSF) technology to manufacture complex steel components, Materials 13 (2020) 1-14. https://doi.org/10.3390/ma13204682
[2] J. Lozares, G. Plata, I. Hurtado, A Sánchez, I. Loizaga, Near solidus forming (NSF): Semi-solid steel forming at high solid content to obtain as-forged properties, Metals 10 (2020). https://doi.org/10.3390/met10020198
[3] J. Rakhmonov, M. Qassem, D. Larouche, K. Liu, M. Javidani, J. Colbert, X.-G. Chen, A New Approach to Determine Tensile Stress-Strain Evolution in Semi-Solid State at Near-Solidus Temperature of Aluminum Alloys, Metals 11 (2021) 396. https://doi.org/10.3390/met11030396
[4] D.H. Kirkwood, Semisolid metal processing, 1994.
[5] K.P. Young, R.G. Riek, M.C. Flemings, Structure and properties of Thixocast steels, Metal. Technol. 6 (1979) 130-137. https://doi.org/10.1179/030716979803276552
[6] P. Kapranos, Semi-Solid Metal Processing. Thixoforming, Explorer, Hayward, 2001.
[7] P. Kapranos, D.H. Kirkwood, C.M. Sellars, Semi-solid processing of tool steel, Le Journal de Physique IV 03 (1993) C7-835-C7-840. https://doi.org/10.1051/jp4:19937131
[8] P. Cezard, T. Sourmail, Thixoforming of Steel: A State of the Art from an Industrial Point of View, Solid State Phenom. 141-143 (2008) 25-35. https://doi.org/10.4028/www.scientific.net/SSP.141-143.25
[9] G. Hirt, W. Bleck, A. Bührig-Polaczek, H. Shimahara, W. Puttgen, C. Afrath, Semi Solid Casting and Forging of Steel, Solid State Phenom. 116-117 (2006) 34-43. https://doi.org/10.4028/www.scientific.net/SSP.116-117.34
[10] C.M. Gourlay, A.K. Dahle, Dilatant shear bands in solidifying metals, Nature 445 (2007) 70-73. https://doi.org/10.1038/nature05426
[11] K. Traidi, V. Favier, P. Lestriez, et al, Thermomechanical steels behaviors at semi-solid state, in: AIP Conference Proceedings. American Institute of Physics Inc., 2016.
[12] L. Deng, X.T. Li, J.S. Jin, X.Y. Wang, J.J. Li, T-shape upsetting-extruding test for evaluating friction conditions during rib-web part forming, J. Mater. Process. Technol. 214 (2014) 2276-2283. https://doi.org/10.1016/j.jmatprotec.2014.04.021
[13] Q. Zhang, E. Felder, S. Bruschi, Evaluation of friction condition in cold forging by using T-shape compression test, J. Mater. Process. Technol. 209 (2009) 5720-5729. https://doi.org/10.1016/j.jmatprotec.2009.06.002
[14] Q. Zhang, M. Arentoft, S. Bruschi, l. Dubar, E. Felder, Measurement of friction in a cold extrusion operation: Study by numerical simulation of four friction tests, Int. J. Mater. Form. 1 (2008) 1267-1270. https://doi.org/10.1007/s12289-008-0133-x
[15] W.M. Dale, Temperature, Its Measurement and Control in Science and Industry, Int. J. Radiat. Biol. Relat. Stud. Phys. Chem. Med. 6 (1963) 610-610. https://doi.org/10.1080/09553006314550741
[16] P.R. Burte, Y.-T. Im, T. Altan, S.L. Semiatin, Measurement and Analysis of Heat Transfer and Friction During Hot Forging, 1990.
A. Azushima, K. Uda, H. Matsuda, Thermal behavior of aluminum-coated 22MnB5 in hot stamping under dry and lubricated conditions, J. Mater. Process. Technol. 214 (2014) 3031-3036. https://doi.org/10.1016/j.jmatprotec.2014.07.003
[17] C.C. Chang, A.N. Bramley, Determination of the heat transfer coeecient at the workpiece — die interface for the forging process, Proc. Inst. Mech. Eng. Part B: J. Eng. Manuf. B 216 (2002) 1179-1186. https://doi.org/10.1243/095440502760272449
[18] Chang Y, Li S, Li X, et al Effect of contact pressure on IHTC and the formability of hot-formed 22MnB5 automotive parts. Appl Therm Eng 99 (2016) 419-428. https://doi.org/10.1016/j.applthermaleng.2016.01.053

[19] Q. Bai, J. Lin, L. Zhan, T.A. Dean, D.S. Balint, Z. Zhang, An efficient closed-form method for determining interfacial heat transfer coefficient in metal forming, Int. J. Mach. Tool. Manuf. 56 (2012) 102-110. https://doi.org/10.1016/j.ijmachtools.2011.12.005
[20] Ł. Rogal, J. Dutkiewicz, H.V. Atkinson, L. Lityńska-Dobrzyńska, T. Czeppe, M. Modigell, Characterization of semi-solid processing of aluminium alloy 7075 with Sc and Zr additions, Mater. Sci. Eng. A 580 (2013) 362-373. https://doi.org/10.1016/j.msea.2013.04.078
[21] P. Hartley, I. Pillinger, Numerical simulation of the forging process, Comput, Meth. Appl. Mech. Eng. 195 (2006) 6676-6690. https://doi.org/10.1016/j.cma.2005.03.013
[22] S.B. Petersen, P.A.F. Martins, N. Bay, An alternative ring-test geometry for the evaluation of friction under low normal pressure, J. Mater. Process. Technol. 79 (1998) 14-24. https://doi.org/10.1016/S0924-0136(97)00448-2
[23] H.V. Atkinson, Modelling the semisolid processing of metallic alloys, Prog. Mater. Sci. 50 (2005) 341-412. https://doi.org/10.1016/j.pmatsci.2004.04.003

Materials Research Proceedings 28 (2023) 1531-1540 https://doi.org/10.21741/9781644902479-165

Finite element model for micro-stamping titanium bipolar plate

KHADEMI Maziar[1,a], ZHANG Peng Neo[1,b *], PEREIRA Michael[2,c], SREENIVAS Achuth[1,d] and WEISS Matthias[1,e]

[1]Deakin University, Institute for Frontier Materials, Waurn Ponds, Pigdons Rd., Geelong,VIC. 3216, Australia

[2]Deakin University, School of Engineering, Waurn Ponds, Pigdons Rd., Geelong,VIC. 3216, Australia

[a]maziar.khademi@gmail.com; [b]zhangp@deakin.edu.au, [c]michael.pereira@deakin.edu.au, [d]achut@deakin.edu.au, [e]matthias.weiss@deakin.edu.au

Keywords: Bipolar Plates, Micro-Stamping, Thin Foil, Finite Element Method

Abstract. Bipolar plates are the essential components of a Proton Exchange Membrane Fuel Cell. Lightweight bipolar plates can be micro-stamped from an ultrathin metallic foil. A major concern is the manufacturability of the foil in the micro-stamping process. The typical stamped micro-channels have end cavities or corners where the deformation mode can be different from the two-dimensional plane strain conditions that occur at the straight sections of the micro-channels. The thin foil has a large ratio of length (or width) to thickness, and shell elements were often used for three-dimensional models. Currently, it is unknown if the shell elements available in commercial software packages are able to predict the ultrathin material behaviour correctly. In addition, the deformation behaviour and forming limits of titanium foil in the micro-stamping process are not well understood. The current study uses a micro-stamping tool to produce straight micro-channels from commercially pure titanium foil. The experimental data are used to validate a two-dimensional and a three-dimensional finite element model of the process. It is shown that there are deviations between the experimental and the numerical thinning results. Material thinning is different between the straight and the cavity end sections suggesting that three-dimensional process models are required to accurately analyze forming.

Introduction

Fuel cells are capable of producing clean energy and reducing greenhouse gas emissions and are considered a suitable alternative to internal combustion engines [1]. The bipolar plate is an essential component of the Proton Exchange Membrane Fuel Cells (PEMFC) to distribute gas (hydrogen, air) uniformly through micro-channels and to conduct current [2].

Bipolar plates can be made of various materials, and metal bipolar plates have been considered to reduce weight and enable high-volume manufacture at low cost [3]. Aluminium alloys [4], titanium [5], and stainless steel [6] have been applied for metal bipolar plates and formed with stamping [7], rubber pad forming [8], and hydroforming [9]. Liu and Hua [10] applied rubber pad forming to manufacture multi-row micro-channels from SS304. They investigated process control parameters (rubber hardness, internal and outer radii, draft angle) by two-dimensional (2D) finite element (FE) simulation. Kolahdooz et al. [11] studied the rubber pad forming of SS316L bipolar plates with 0.1 mm thickness and considered three-dimensional (3D) shell elements in their simulation. Osia et al. [12] used a 3D FE model to investigate two convex and concave hydroforming methods to form SS304 bipolar plates. Bong et al. [13] implemented a multi-stage micro stamping process and according to the major deformation mode of plane strain employed 2D plane strain elements in the numerical analysis. In contrast, Karacan et al. [14] applied 3D shell elements to study the forming of different channel depths in micro stamping. They found that the dominant stress state in micro-stamping was a combination of biaxial and plane strain. Modanloo

Content from this work may be used under the terms of the Creative Commons Attribution 3.0 license. Any further distribution of this work must maintain attribution to the author(s) and the title of the work, journal citation and DOI. Published under license by Materials Research Forum LLC.

et al. [15] studied the micro stamping of titanium bipolar plates with parallel flow channels and predicted fracture using different ductile fracture criteria in combination with a 3D FE model.

Typical stamped micro-channels have end cavities or corners where the deformation mode can be distinctly different from the two-dimensional (2D) plane strain that occurs in the straight U-section profile of the micro-channels[16]. This requires 3D models to represent the different deformation conditions. The thin foil has a large ratio of length (or width) to thickness, and shell elements are often used for 3D models. However, limited research has been done to study the effect of the element type on the thinning or strain predictions in micro stamping. Currently, it is unknown if shell elements available in commercial software packages can predict the ultrathin material behaviour correctly. The situation becomes more complicated when analysing the forming of titanium foil. The current study uses a micro-stamping tool to produce straight micro-channels from commercially pure titanium foil. The experimental data are then used to validate a 3D FE model of the process. The findings of this study will help guide future FE analysis and will give insights into the micro-stamping of titanium foil.

Material Properties

A commercially-pure titanium (CP-Ti) foil with a thickness of 0.1 mm was used. To determine the tensile properties of the titanium sheet, samples were prepared at 0° to the rolling direction and tensile tests were performed based on the ASTM standard (E8M-04) [17]. "Orange peel" was obtained on the dogbone sample surfaces after the tensile tests, which indicates that the limited number of grains within the thickness may lead to local deformation before fracture [18]. The true stress-strain curve was determined, and the Swift law (Eq. 1) fitted to the plastic part of the curve, as shown in Fig. 1. In future work, a biaxial stretching experiment will be conducted for fitting the Swift law at a larger plastic range.

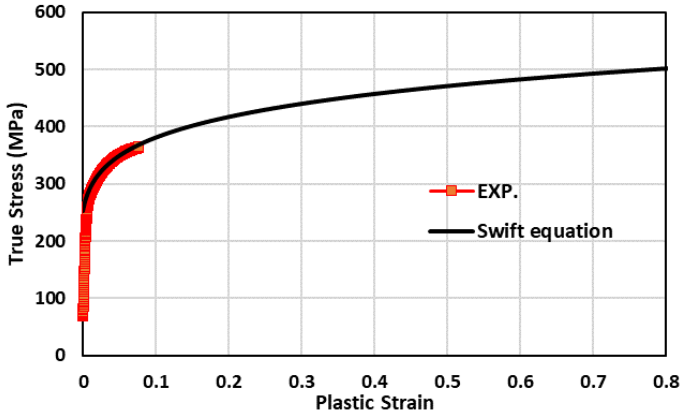

Fig. 1. True stress-strain curve and calibrated swift law results of Titanium foil

$$\sigma = K(\varepsilon + \varepsilon_0)^n \quad (1)$$

where σ and ε are the true stress and plastic strain obtained from the uniaxial tensile test. k, n and ε_0 are the constants of a particular material. The mechanical properties are listed in Table 1.

Table 1. Mechanical properties of the titanium sheet.

	E (GPa)	υ	K (MPa)	n	ε_0
titanium	120[15]	0.361[15]	517.2	0.135	0.005

Experimental Tests

The micro stamping tool was installed in an Instron 500 kN universal testing machine. A CP-Ti strip with dimensions of 195 mm × 97.5 mm was guillotined from the coil and the rolling direction

was aligned with the transverse direction of the channel. Fig. 2 presents the experimental setup [16]. Fig. 3 illustrates the dimensions of the designed micro-channels.

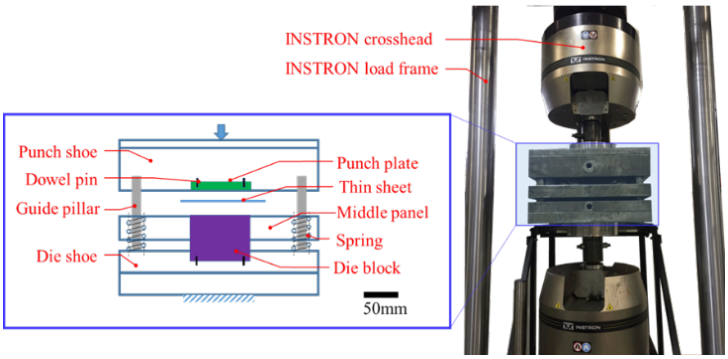

Fig. 2. The experimental equipment for the micro stamping trials [16].

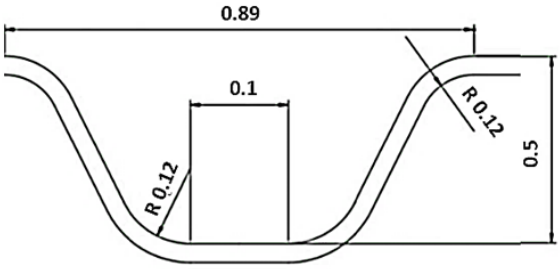

Fig. 3. Schematic of cross-section shape of one micro-channel, units in mm.

The top crosshead travelled at a load-controlled speed of 35 kN/min. The tests were stopped at a force of 90kN when cracks were found on all seven micro-channels and then repeated with more tests that stopped at sequentially reduced loads. After each test, the formed sheet was taken out for crack examination using the white-light method [16]. This identified a pinhole at a load of 78 kN (Fig. 4). The punch (male tooling) displacement at fracture initiation of the sheet was determined using an Alicona profilometer and determined to be approximately 0.32 mm when the pinhole initiated.

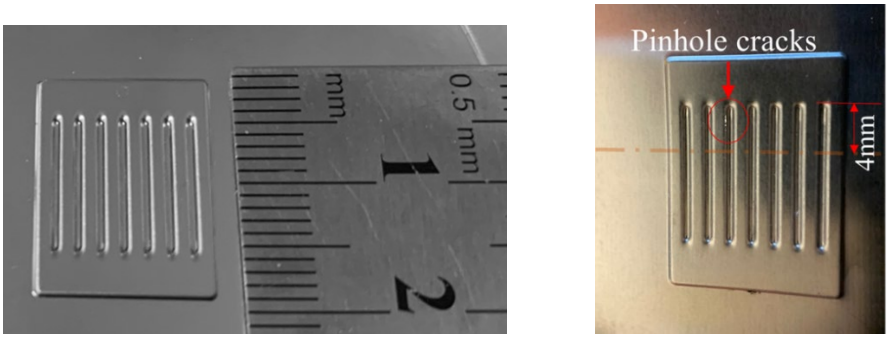

(a) (b)

Fig. 4. CP-Ti bipolar micro channel plate produced by micro-stamping. (a) Formed without cracks and (b) with pinhole cracks, the location of cross-section for microscope observation is 4mm from the end cavities.

For evaluating the thinning, a segment of the sample was cut from the formed sheet at the cutting location marked in Figure 4-b. Then the sample was mounted in resin, ground and polished to a flat surface. An Olympus DP71 microscope with a digital camera system was used to capture images at 5× magnification (Fig. 5). The thickness was measured based on the captured image. A

line perpendicular to both sides of the surfaces was constructed at each measurement location, and the line length was measured [19] with Digimizer Image Analysis software [20]. This measurement approach can achieve subpixel (~0.001mm) accuracy. The thinning values are measured from two different channels (No. 2 & 3 in Fig. 5) and the averaged value is presented in this paper

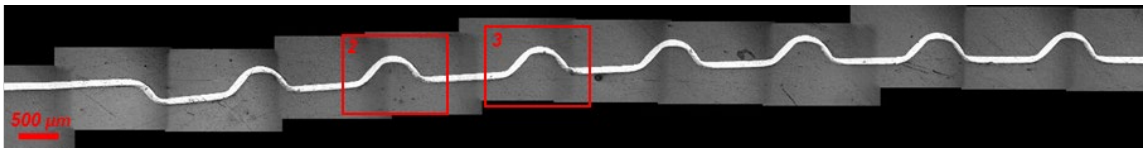

Fig. 5. Microscope image of a cross-section of the micro-stamped channel titanium

In this research, the thinning is used as the target parameter. Therefore, the thinning is defined as:

$$\%Thinning = \frac{t_0 - t_f}{t_0} \quad (2)$$

where $t_0$is the initial blank thickness, and t_f is the thickness of the final formed part.

The forming die (female tooling) surfaces were also scanned, and Fig. 6-a and b show the 3D image of the surface scan obtained with the Alicona for one single corrugation. The cross-section tool profiles in the transverse and the longitudinal direction were determined by performing a section cut on the scanned 3D surface, as illustrated in Fig. 6-c and d. In this study the point cloud of the tool surface scan of the top and bottom die was used to generate the tool surfaces in the FE model. For this, the tool radii were approximated with smooth arcs, and the radii of the punch and die represent the best fit from a group of 10 points distributed at the corner. The tool dimensions and geometric features of the experimental set up are shown in Fig. 6-d.

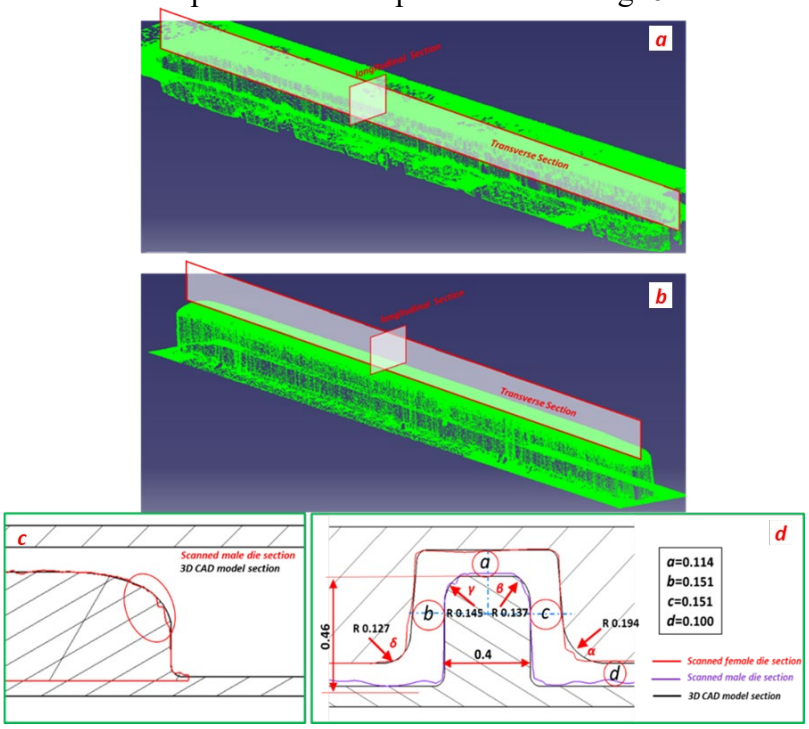

Fig. 6. a) Point cloud of female die. b) Point cloud of male die. c) Male die cross-section in longitudinal diection. d) Top and bottom die cross sections in transverse direction.

Finite Element Simulation

The commercial software package Abaqus explicit was used. Only one half of one channel was modelled in the 3D FE model. The model set up is shown in Fig. 7-a. In order to apply the force on the sheet, a displacement boundary condition is applied to the punch while the die is constrained in all directions. A symmetry boundary conditions was applied to the sheet on the symmetry axis as illustrated in Fig. 7-b (right end of the sheet). The left end was fixed to simulate the clamping of the sheet. According to the distance of the channels in transverse direction, the individual channel patterns do not influence each other during the forming process and therefore the two sides of the channel can be assumed to be fixed.

In this research, a 2D simulation was also considered to investigate the effect of different elements. Fig. 7-c demonstrates the 2D FE model. All the dimensions of FE models were considered based on the experimental set up.

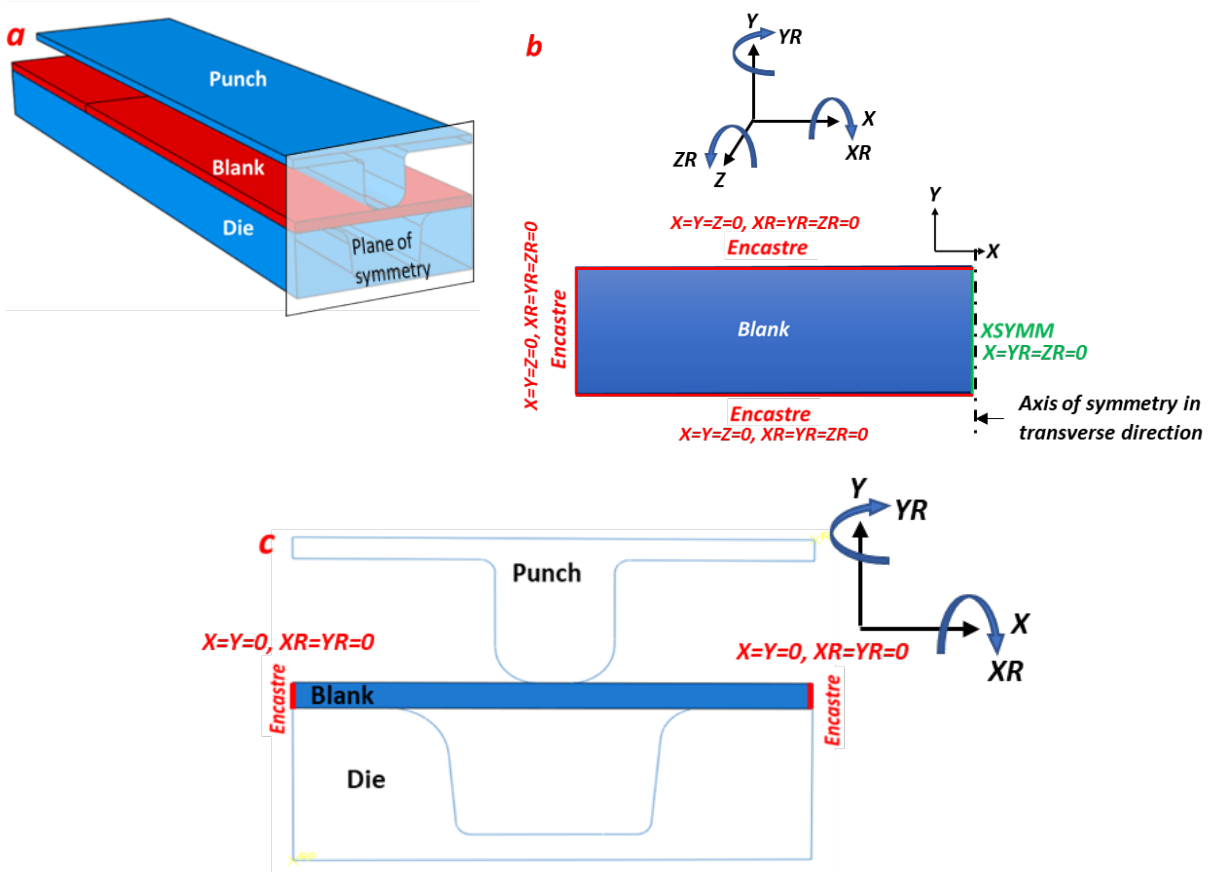

Fig. 7. a) 3D FE model for punch, die and blank. b) The boundary conditions of the blank in 3D FE model c) 2D FE model with blank boundary conditions.

The 3D geometry of the scanned punch and die surfaces profiles were converted to CAD and imported to the Abaqus explicit. The blank was modelled as a deformable part and was meshed with 3D stress, eight-node solid, reduced integration elements (C3D8R) with 10 elements through the material thickness. A mesh sensitivity study was performed to reach convergence. This gave an optimum mesh size of 0.01 mm (Fig. 8-a). For the 3D simulation with shell elements, a 4-node doubly curved thin shell (S4R) with 5 thickness integration points, reduced integration and hourglass control was used (Fig. 8-b).

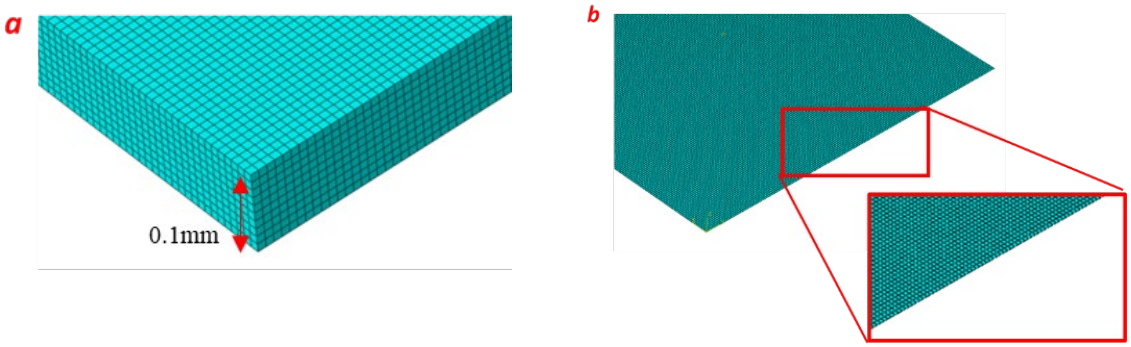

Fig. 8. FE model of the blank. a) Solid element (C3DR8) b) Shell element (S4R).

The die sets were meshed as discrete rigid bodies with four nodes of 3D bilinear rigid quadrilateral element (R3D4). The mesh size of the tools was considered in a way to discretise the geometry of the parts completely and with the desired accuracy. A refined mesh size of 0.01 mm was used in the critical contact locations of the die and the punch radius as shown in Fig. 9.

The 2D simulation was performed according to the geometry of Fig. 6, and the blank meshed with plane-strain, reduced integration CPE4R elements. The mesh size for 2D simulation was chosen the same as in previous research [16]. The Punch and die were meshed with 2-node 2-D linear discrete rigid element (R2D2). A surface-to-surface condition was implemented to define interaction between die setup and sheet.

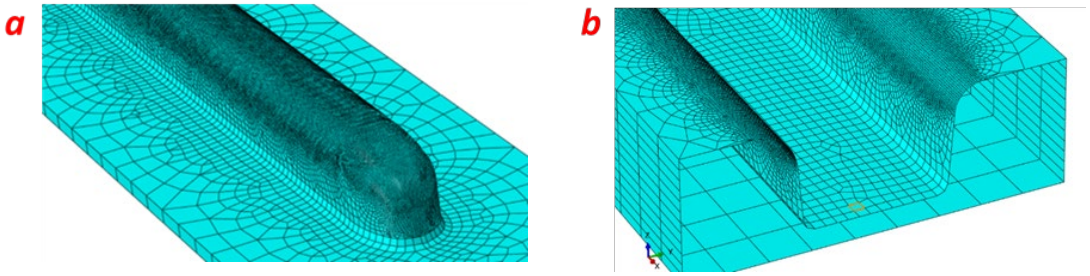

Fig. 9. FE model of the (a) punch and (b) die.

The friction coefficient between the tooling and sheet was assumed to be 0.4 in all simulations (2D and 3D) [16]. The mechanical properties of the sheets were applied in the simulation based on the material parameters given in Table 1 assuming isotropic material behaviour.

The explicit solution method used mass scaling to reduce the simulation time. The value of the mass scale coefficient (10^9) was determined in such a way that the ratio of kinetic energy to internal energy during the process was less than 1% to maintain the quasi-static nature of the problem.

Results and Discussion

The experimental thinning curves of the titanium blank are compared in the straight channel cross-section 4 mm away from the end cavities and at a punch stroke of 0.32 mm, which is when the pin hole originated. As shown in Fig. 10, the maximum thinning occurs in the die radius area. It should be noted that this is the smallest radius of the tool. Therefore, the critical forming regions are identified near the bending area of the die (δ region). The FE model represents the experimental thinning results but there is some error. This might be due to the presence of sharp points in the physical male and female tooling profile (Fig. 6-d) that were not considered in the FE model. This leads to severe deformation and, as a result, severe thinning in this area. In the FE model these

Materials Research Proceedings 28 (2023) 1531-1540 https://doi.org/10.21741/9781644902479-165

points are simplified as perfect arcs which could be why the FE model underpredicts deformation severity in this region.

There is only a minor difference in thinning prediction between the 2D and the 3D model. This may be due to material deformation being mostly plane strain tension in the investigated cross-section which is located in the straight channel and not in the end cavity. This allows for the simplification to 2D plane strain forming.

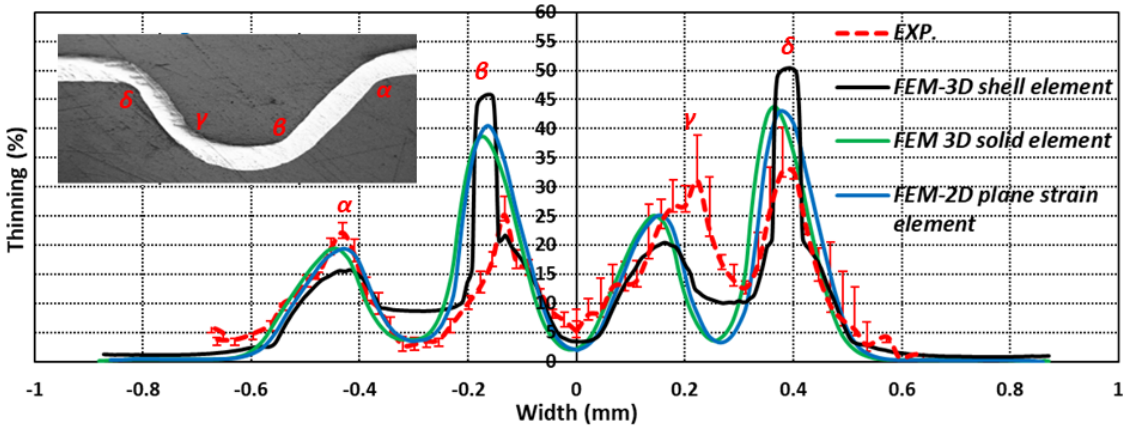

Fig. 10. Thinning prediction compared with the experimental (EXP.) results for titanium sheet.

The shell element is not able to accurately predict the distribution and level of material thinning (Fig. 10). In fact, when the punch displacement reaches to 0.26 mm, the shell element becomes extremely thin at the end of the cavity in the die area (δ region), and then thinning continues along the channel in longitudinal direction.

The thinning curves numerically predicted with the solid 3D element model for the straight channel region and the end cavity, sections 1 and 2, are shown in Fig. 11-a. There is a clear difference in the thinning behaviour between the two cross-sections (Fig. 11-b).

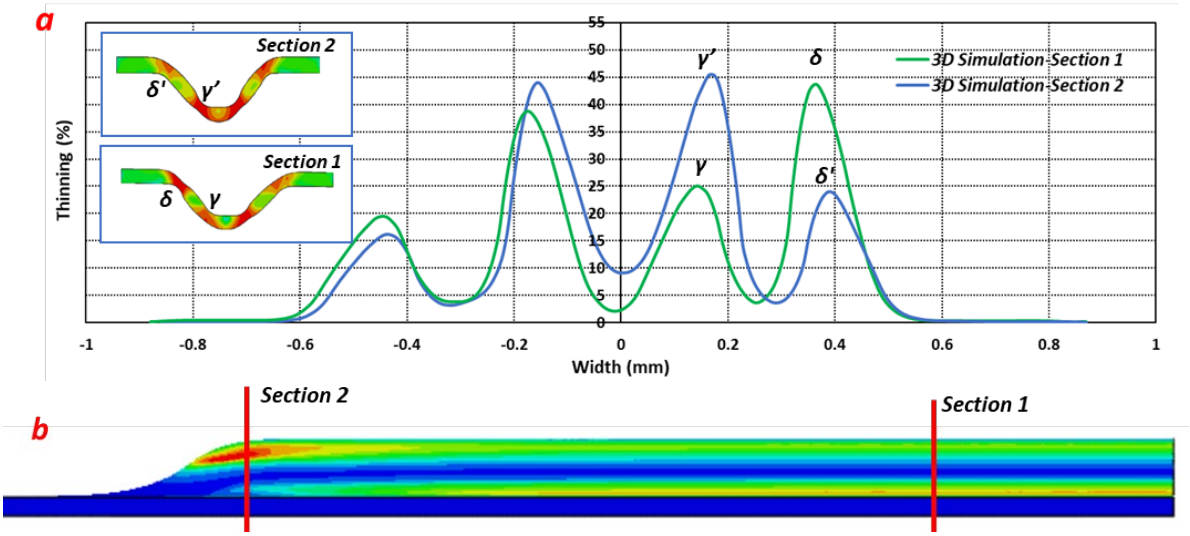

Fig. 11. a) Comparison of material thinning in sections 1 and 2. b) The location of section 1 and 2 in the simulation model.

The maximum thinning is transferred from the die radius in section 1 (region δ) to the punch radius area in section 2 (region γ'). The strain path of a node in the different radius areas was measured for both cross-sections during the process, and the result is shown in Fig. 12.

At the straight region, the strain path of the micro-channel corner regions that contact with the male and female tool radius are plane strain deformation (γ and δ Fig.12-b). The sheet at the cavity regions shows different strain path. The corner that was formed by the male tool radius region has a strain path starting with the biaxial stretching initially, but deviating to plane strain as the channel formed deeper (γ' in Fig.12-b). The female tool gives the bottom sheet corner negative minor strain (along the longitudinal of the channel direction), but the deformation mode shifts to plane strain towards the end of forming (δ' in Fig.12-b). In the cavity end area (section 2), the thinning is higher compared to the straight channel section and therefore closer to material failure. This, however, does not correlate well with the experimental pinhole location, which was in the straight channel section (Fig. 4b).

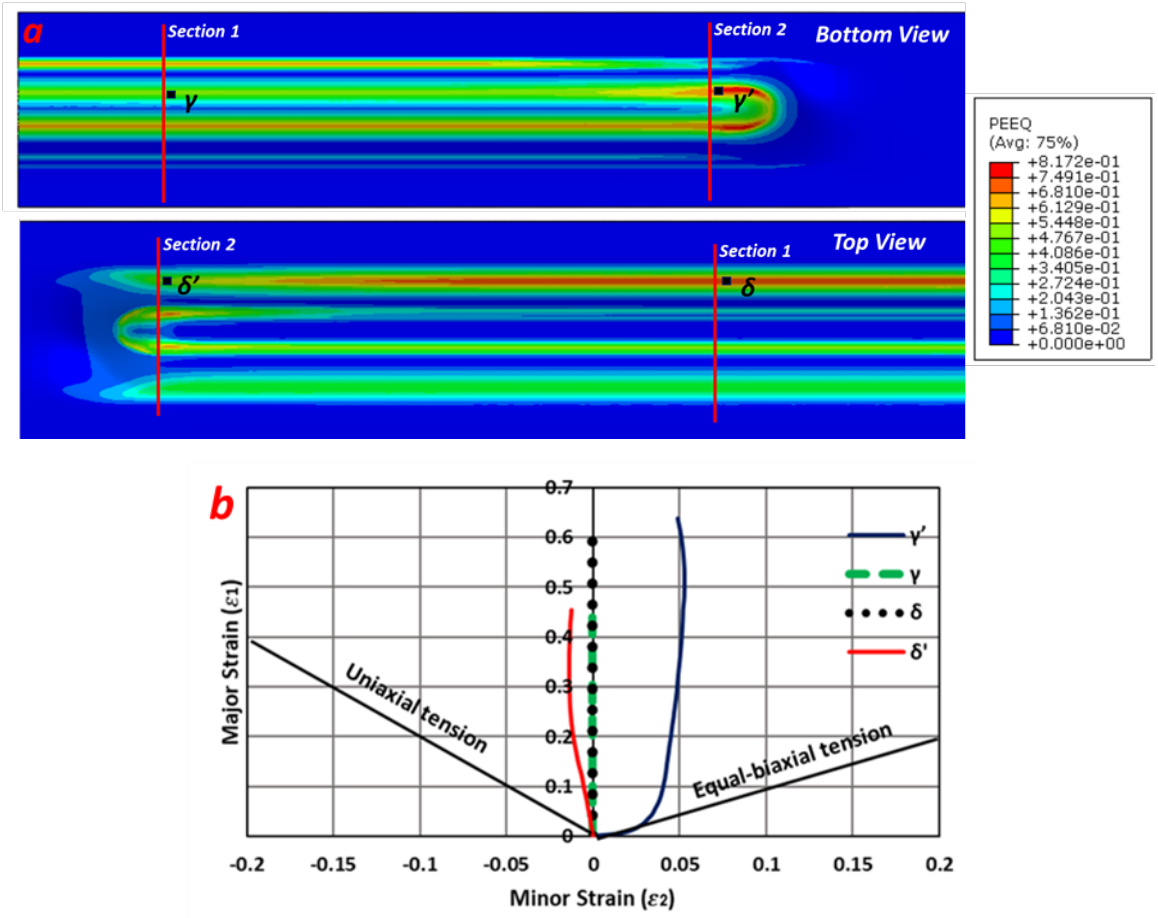

Fig. 12. a) The location of the considered nodes in the different sections, showing contours of equivalen plastic strain (PEEQ) on the bottom and top surfaces of the blank. b) The strain path of the bending area elements at both sections during the process.

Summary

- Titanium foil was micro-stamped, and the 3D FE model predictions did not match the experimental data in some of the channel regions. More research is required to accurately model the material behaviour and fracture limits of titanium foil in micro stamping.
- The analysis of solid and shell elements in the 3D model suggests that the shell elements cannot accurately represent material thinning.

- The stress state at the end cavity of the channels is different from that in the straight channel region. The assumption of 2D conditions for micro-channel deformation is therefore only valid in the straight section but does not represent the higher material deformation in the cavity that was observed in this study.
- As future work, implementing a comprehensive model that includes microstructural properties, and anisotropic properties, and performing accurate fracture criteria will be considered for the micro-stamping of the titanium foil.

References

[1] A. Hermann, T. Chaudhuri, P. Spagnol, Bipolar plates for PEM fuel cells: A review, Int. J. Hydrogen Ener. 30 (2005) 1297-1302. https://doi.org/10.1016/j.ijhydene.2005.04.016
[2] L. Carrette, K. Friedrich, U. Stimming, Fuel cells-fundamentals and applications, Fuel cells 1 (2001).
[3] J.-C. Hung, T.-C. Yang, K.-c. Li, Studies on the fabrication of metallic bipolar plates-Using micro electrical discharge machining milling, J. Power Source. 196 (2011) 2070-2074. https://doi.org/10.1016/j.jpowsour.2010.10.001
[4] L. Soler, J. Macanás, M. Munoz, J. Casado, Aluminum and aluminum alloys as sources of hydrogen for fuel cell applications, J. Power Source. 169 (2007) 144-149. https://doi.org/10.1016/j.jpowsour.2007.01.080
[5] N. Abdullah, S. Kamarudin, Titanium dioxide in fuel cell technology: An overview, J. Power Source. 278 (2015) 109-118. https://doi.org/10.1016/j.jpowsour.2014.12.014
[6] M. Weiss, P. Zhang, M.P. Pereira, B.F. Rolfe, D.E. Wilkosz, P.D. Hodgson, Understanding size effects and forming limits in the micro-stamping of industrial stainless steel foils, Metals 11 (2020) 38. https://doi.org/10.3390/met11010038
[7] R. Backes, A.M. Herring, J. Berger, J. Turner, H. Wang, Evaluation of stamping methods for stainless steel bipolar plates using finite element analysis, ECS Meeting Abstracts, IOP Publishing, 2008, p. 70. https://doi.org/10.1149/MA2008-02/1/70
[8] M. Elyasi, H.T. Ghadikolaee, M. Hosseinzadeh, Investigation of dimensional accuracy in forming of metallic bipolar plates with serpentine flow field, Int. J. Adv. Manuf. Technol. 96 (2018) 1045-1060. https://doi.org/10.1007/s00170-018-1650-5
[9] L. Peng, X. Lai, P. Hu, J. Ni, Flow channel shape optimum design for hydroformed metal bipolar plate in PEM fuel cell, J. Power Source. 178 (2008) 223-230. https://doi.org/10.1016/j.jpowsour.2007.12.037
[10] Y. Liu, L. Hua, Fabrication of metallic bipolar plate for proton exchange membrane fuel cells by rubber pad forming, J. Power Source. 195 (2010) 3529-3535. https://doi.org/10.1016/j.jpowsour.2009.12.046
[11] R. Kolahdooz, S. Asghari, S. Rashid-Nadimi, A. Amirfazli, Integration of finite element analysis and design of experiment for the investigation of critical factors in rubber pad forming of metallic bipolar plates for PEM fuel cells, Int. J. Hydro. Ener. 42 (2017) 575-589. https://doi.org/10.1016/j.ijhydene.2016.11.020
[12] M. Balali Osia, S. Jamal Hosseinipour, M. Bakhshi-Jooybari, A. Gorgi, Forming metallic micro-feature bipolar plates for fuel cell using combined hydroforming and stamping processes, Iranian (Iranica) J. Ener. Environm. 4 (2013). 10.5829/idosi.ijee.2013.04.02.03
[13] H.J. Bong, J. Lee, J.-H. Kim, F. Barlat, M.-G. Lee, Two-stage forming approach for manufacturing ferritic stainless steel bipolar plates in PEM fuel cell: Experiments and numerical simulations, Int. J Hydro. Ener. 42 (2017) 6965-6977. https://doi.org/10.1016/j.ijhydene.2016.12.094

[14] K. Karacan, S. Celik, S. Toros, M. Alkan, U. Aydin, Investigation of formability of metallic bipolar plates via stamping for light-weight PEM fuel cells, Int. J. Hydro. Ener. 45 (2020) 35149-35161. https://doi.org/10.1016/j.ijhydene.2020.01.251
[15] V. Modanloo, H. Talebi-Ghadikolaee, V. Alimirzaloo, M. Elyasi, Fracture prediction in the stamping of titanium bipolar plate for PEM fuel cells, Int. J. Hydro. Ener. 46 (2021) 5729-5739. https://doi.org/10.1016/j.ijhydene.2020.11.088
[16] P. Zhang, M.P. Pereira, B.F. Rolfe, D.E. Wilkosz, P. Hodgson, M. Weiss, Investigation of material failure in micro-stamping of metallic bipolar plates, J. Manuf. Process. 73 (2022) 54-66. https://doi.org/10.1016/j.jmapro.2021.10.044
[17] ASTM International Standard, E8M-04: Standard test methods for tension testing of metallic materials, testing of metallic materials, 2004.
[18] T. Furushima, H. Tsunezaki, K.-i. Manabe, S. Alexsandrov, Ductile fracture and free surface roughening behaviors of pure copper foils for micro/meso-scale forming, International J. Mach. Tool. Manuf. 76 (2014) 34-48. https://doi.org/10.1016/j.ijmachtools.2013.10.001
[19] B. Abeyrathna, P. Zhang, M.P. Pereira, D. Wilkosz, M. Weiss, Micro-roll forming of stainless steel bipolar plates for fuel cells, Int. J. Hydro. Ener. 44 (2019) 3861-3875. https://doi.org/10.1016/j.ijhydene.2018.12.013
[20] Information on https://www.digimizer.com/download/

New and advanced numerical strategies for material forming

Materials Research Proceedings 28 (2023) 1543-1550 https://doi.org/10.21741/9781644902479-166

Advanced CFD investigations of electromagnetic stirring of molten steel in continuous caster tundish

ZIELIŃSKA Monika[1,2,a *], YANG Hongliang[3,b], MADEJ Łukasz[2,c] and MALINOWSKI Łukasz[1,d]

[1]Corporate Technology Center CTC, ABB Sp. z o. o., Zeganska 1 st., 04-713 Warsaw, Poland

[2]Department of Applied Computer Science and Modelling, AGH University of Science and Technology, Mickiewicza 30 av., 30-059 Krakow, Poland

[3]ABB AB/Metallurgy, Terminalvagen 24, Bldg 340, Vasteras 72159, Sweden

[a]monika.zielinska@pl.abb.com, [b]hongliang.yang@se.abb.com, [c]lmadej@agh.edu.pl, [d]lukasz.malinowski@pl.abb.com

Keywords: Computational Fluid Dynamics, Metallurgy Industry, Electromagnetic Stirring

Abstract. The continuous casting process is one of the initial operations in the entire metal forming chain used in the metallurgical industry. The phenomena of solidification and unification of properties that occur during slab casting are highly dependent on the steel composition and the purity of the metal. The high cleanliness of steel is the determinant of the good quality of the final products, without internal cracks or inhomogeneities in mechanical, thermal or electrical properties. Therefore, one of the production goals is to avoid the non-metallic inclusions in the molten steel by intensifying their removal processes. One of the most important metallurgy equipment responsible for cleaning the steel is the ladle furnace, where special mixing processes are executed to increase the removal process of unfavourable elements. Another critical piece of equipment is the tundish, located just before the slab casting, which can additionally improve the microstructure final composition and homogeneity. Therefore, the investigations presented in the paper are centred on the development of an advanced Computational Fluid Dynamic (CFD) model of the flow behaviour of the molten steel inside the tundish. The key element of the model is to include the effect of an additional electromagnetic stirring device which can improve the cleanliness and the composition of the steel and hence its final properties. The role of this device is often omitted during practical research, but its direct influence on the properties of the steel has a clear impact on the characteristics of the formed metallic parts under further processing operations. Therefore, optimization of the process inside the tundish is essential from an industrial point of view. The paper includes a detailed analysis of the flow and stirring energy distributions to predict and understand the active and dead zones inside the tundish to avoid the regions with stagnant velocity distribution. As an outcome of such a developed coupled electromagnetic/fluid dynamic model, optimizing the mixing processes to control the product's properties is possible.

Introduction

In the metallurgical industry, intensive investigations are conducted to obtain the best properties of the products and, at the same time, reduce production costs and environmental pollution. The steel composition and microstructure significantly influence material behaviour during further metal forming processes and need to be optimized early in the production stages. Thus, researchers have been working to improve the steel's cleanliness by, e.g., minimizing the amount of non-metallic inclusions leading further to, e.g., crack initiation. In reality, the proper classification and detection of inclusions is a crucial aspect of developing the production process. Zhang and Thomas in [1] reviewed the different sources of inclusions which occur during the whole continuous casting process. The phenomena leading to the generation of inclusions in molten steel are complex. Many

Content from this work may be used under the terms of the Creative Commons Attribution 3.0 license. Any further distribution of this work must maintain attribution to the author(s) and the title of the work, journal citation and DOI. Published under license by Materials Research Forum LLC.

aspects influence their formation, e.g., the high oxidizing atmosphere in the electrical arc furnace (EAF), which is the first stage of the process, reoxidation or slag entrainment in the next steps of the production etc. Researchers also focus on the improvement of steel cleanliness, mainly in the ladle, tundish and directly, in the slab casting operation. The common practice is the absorption of inclusions to the slag layer [2], intensification of the removal process by the additional inert gas injection [3-5], introduction of special channels with induction heating [6] or finally, dedicated control devices can be added to improve the stirring of the melt like baffle walls or electromagnetic stirrers (EMS) [7,8]. Currently, the research in this area mainly focuses on mathematical or numerical modelling due to the difficulties with the measurements under real production conditions. The numerical approach of Computational Fluid Dynamics (CFD) enables the wide investigation of the flow and inclusions behaviour for each metallurgical equipment starting from the electrical arc furnace, ladle furnace, and tundish. It also enables the solidification phenomena predictions occurring during the casting.

Therefore, the main goal of this research is the development of a complex coupled electromagnetic/fluid dynamic model of the steel behaviour in the tundish equipped with electromagnetic stirrers. Material flow in the tundish is critical as it is the last production stage with fully liquid metal. The overall goal is to simulate the molten steel flow, the velocity and stirring energy distributions to understand the development of so-called active and dead zones inside the tundish. As a result, the mixing process could be appropriately designed to increase the homogeneity of the steel and avoid areas with the stagnant flow or inhomogeneous temperature distribution. Both phenomena lead to catastrophic problems related to the quality and clogging of outlets. These issues are dangerous from a safety point of view and can lead to production faults, exposing the company to unexpected costs.

Methodology

The numerical investigations of the flow behaviour inside the tundish were conducted in the commercial CFD software Ansys Fluent. The geometry of the tundish was prepared according to the industrial specification of the real device. Simulations focused on the different computational scenarios within the tundish with additional control devices namely baffle walls, electromagnetic stirrers and stoppers, to control the mass flow rate through outlets. The tundish geometry used during the research is presented in Fig. 1a, as a case with additional stoppers and in Fig. 1b, as a case with a baffle wall to control the flow distribution. In both cases, additional electromagnetic stirring is also considered.

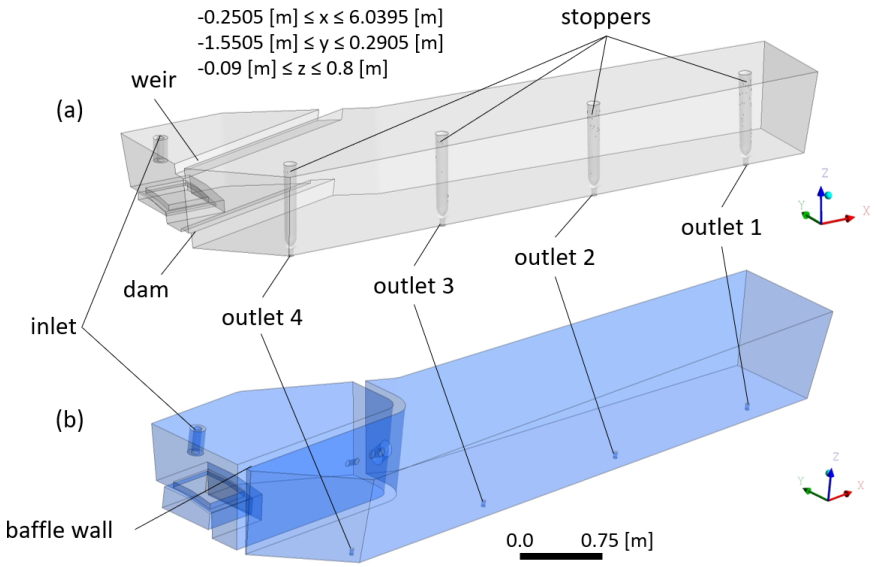

Fig. 1. The geometry of the tundish used in the numerical simulations (a) with stoppers and (b) with baffle wall.

The parametric study included comparing the different scenarios of the current applied during EMS operation to understand the influence of such additional stirring mechanism on the mixing process and optimize the power input to avoid energy losses. The list of cases which were conducted to compare the velocity and stirring energy distributions is presented in Table 1.

Table 1. List of cases to compare the flow behaviour.

Case no.	Description
1	without EMS, without baffle wall
2	with 100% of EMS, normal direction of stirring
3	with 100% of EMS, reversed direction of stirring
4	without EMS, with baffle wall
5	with 100% of EMS, without baffle wall, with stoppers
6	with 84% of EMS, without baffle wall, with stoppers
7	with 69% of EMS, without baffle wall, with stoppers
8	with 60% of EMS, without baffle wall, with stoppers
9	with 31% of EMS, without baffle wall, with stoppers

Electromagnetic stirring used to induce the steel flow is realized by the additional momentum source terms introduced into the momentum equation. Forces from the electromagnetic stirring are mapped into the fluid computational domain and depend on the velocity. The following equation describes this dependence:

$$\vec{F} = \overrightarrow{F_0}\left(1 - \frac{\overrightarrow{F_0} \bullet \vec{V}}{2\tau f \bullet \left|\overrightarrow{F_0}\right|}\right), \quad (1)$$

where $\overrightarrow{F_0}$ - stirring force calculated for stationary melt [N/m3], $\vec{F}$ - stirring force after compensation with moving melt [N/m3], τ - pole pitch [m], f - frequency [Hz], $\vec{V}$ - velocity of melt [m/s].

Materials Research Proceedings 28 (2023) 1543-1550 https://doi.org/10.21741/9781644902479-166

The exemplary force field mapping operation to include the effect of electromagnetic stirring in the tundish is presented as a force density in Fig. 2.

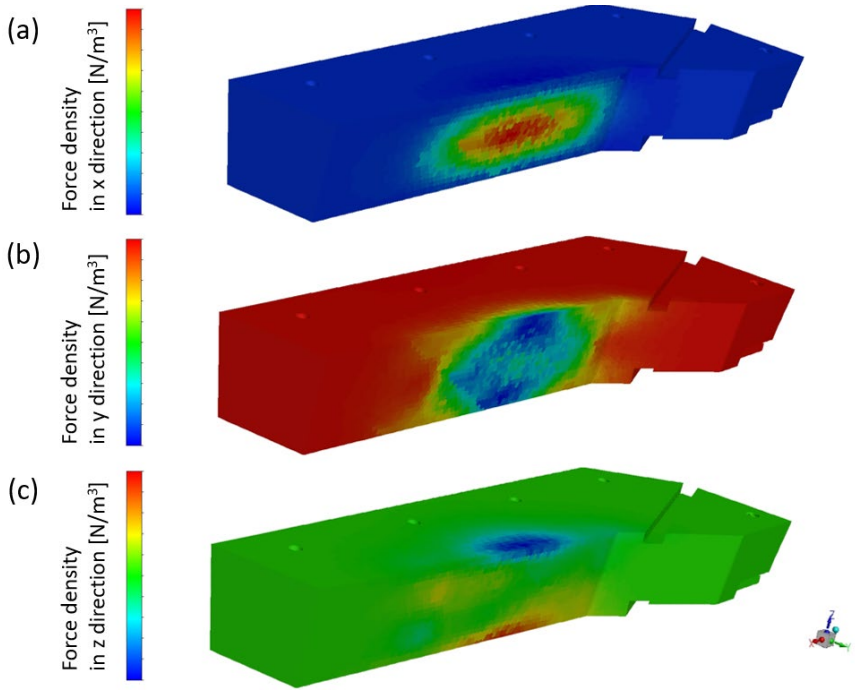

Fig. 2. Force densities in (a) x-direction, (b) y-direction and (c) z-direction, respectively.

During the investigations, the mixing process was also taken into consideration. Visualization of the mixing operation in the molten steel is realized by additional discrete phase particles available in the Discrete Phase Model (DPM), which interact with the continuous phase. To understand the flow behaviour, the massless particles were injected into the domain in accordance with the boundary conditions of the stream. The particles, as a tracers, travel with the continuous phase and enable observation of the liquid steel's movement.

Results and Discussion

CFD simulations help to understand the flow inside the tundish under the additional electromagnetic forces. Based on the evaluated turbulent dissipation rate that occurs in the molten steel, the stirring energy can be calculated. The simulations were performed for different cases to evaluate the influence of the applied current scenarios, which directly correspond to the force factor of the EMS, on the velocity distribution and stirring effectiveness. The first comparison between the velocity and stirring energy distribution for 100% , 84%, 69%, 60% and 31% of EMS stirring force and for the case with stoppers is presented in Fig. 3. It should also be pointed out that inside the tundish, the clogging of outlets is a rather common phenomenon and depends on the solidification of the molten steel, mainly in the areas of the dead zones and sedimentation process, where different remains detach from walls are clogged up the outlets. This issue is very often inside the tundish because of the relatively low stirring energy inside compared with the ladle furnace, where the mixing process is the most intensive. Based on that, the analysis of the stirring energy close to the outlets can improve the design process and optimization of the work of the device. The comparison between the stirring energy distribution in the area of each outlet for cases with stoppers for 100% and 31% of EMS is presented in Fig. 4.

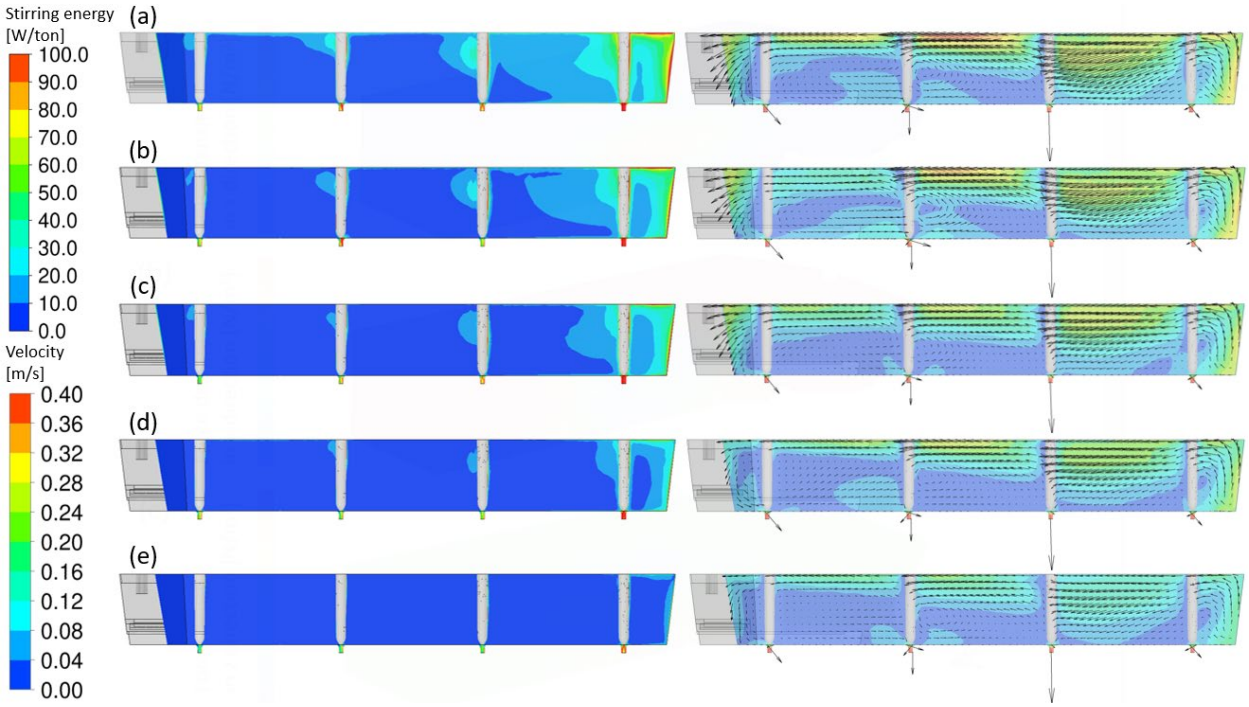

Fig. 3. Stirring energy (left) and velocity (right) distribution for different EMS force factors (a) 100% - case no. 5, (b) 84% - case no. 6, (c) 69% - case no. 7, (d) 60% - case no. 8, (f) 31% - case no. 9.

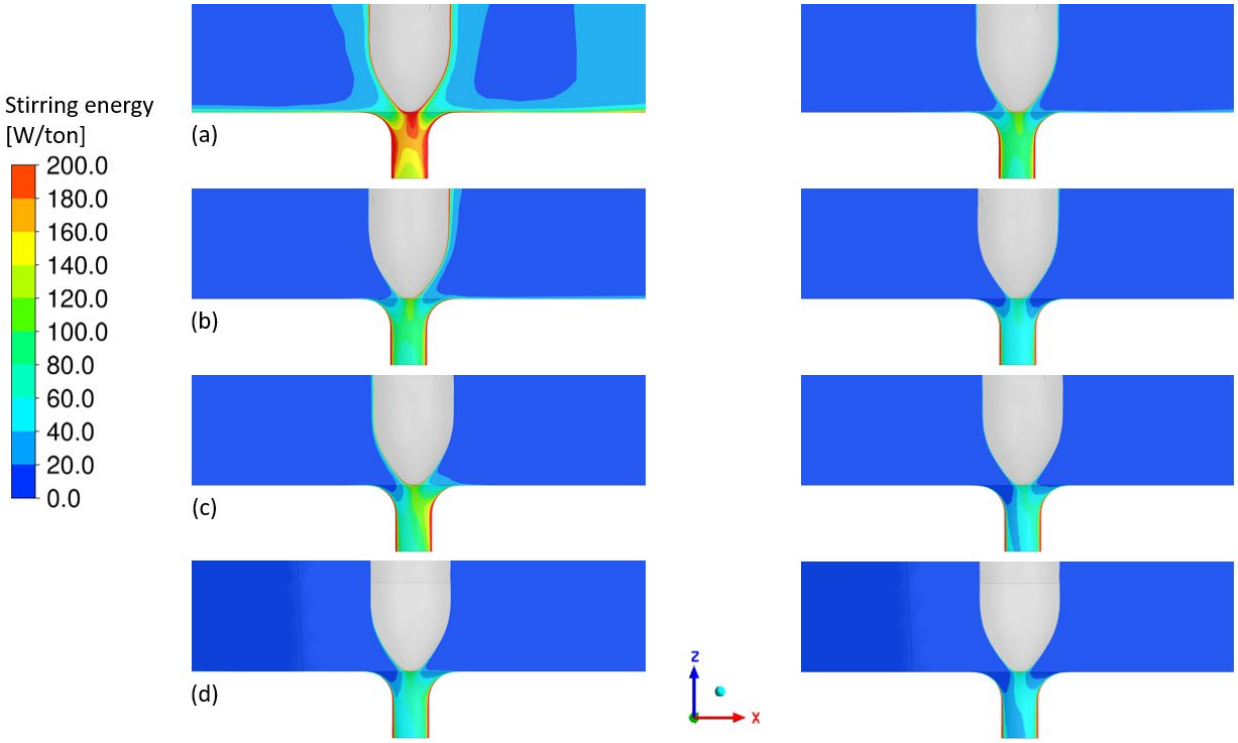

Fig. 4. Stirring energy distribution for case no. 5, 100% of EMS (left) and case no. 9, 31% of EMS (right) for different outlets: (a) outlet 1, (b) outlet 2, (c) outlet 3, (d) outlet 4.

Based on Fig. 4, stirring energy distribution close to outlet 3 has the most asymmetric character, and the gradients of the values are the highest.

Another important investigation is the evaluation of the molten steel mixing inside the tundish. This mixing can be easily visualized by the mentioned massless particles whose behaviour is dependent on the steel flow in the tundish. The observation of the tracers in the numerical model can be compared to the analysis of the dye injected into the water during the water model tests. The particles flow inside the device is presented in Fig. 5 and Fig. 6, where different types of cases were compared to each other. The simulation model without any additional control devices is presented as a reference case. Then, the results for the case with 100% of EMS are shown. The investigation also included the reversed direction of the stirring to compare the behaviour of particles and the results with a common control device like a baffle wall with openings used to improve the liquid steel mixing process. The comparison confirms that the best mixing is presented for the case with 100% EMS stirring. The results are much better than the baffle wall and indicate the high efficiency of homogenising velocities and temperatures. Obtained results also indicate an increase in the inclusions removal process, which is important to the steel's quality.

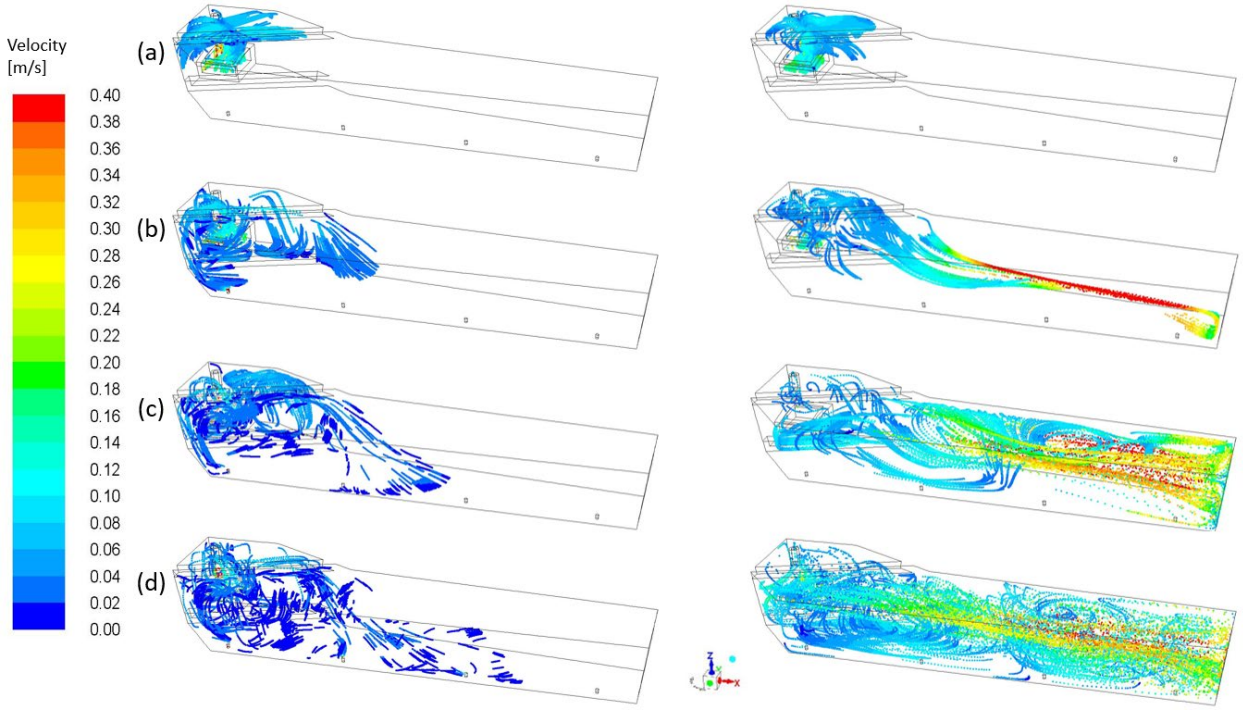

Fig. 5. Massless DPM tracers to visualize the mixing process for case no. 1 without EMS, without baffle wall (left) and for case no. 2 with 100% of EMS, the normal direction of stirring at (a) 20 [s], (b) 50 [s], (c) 100 [s], (d) 200 [s].

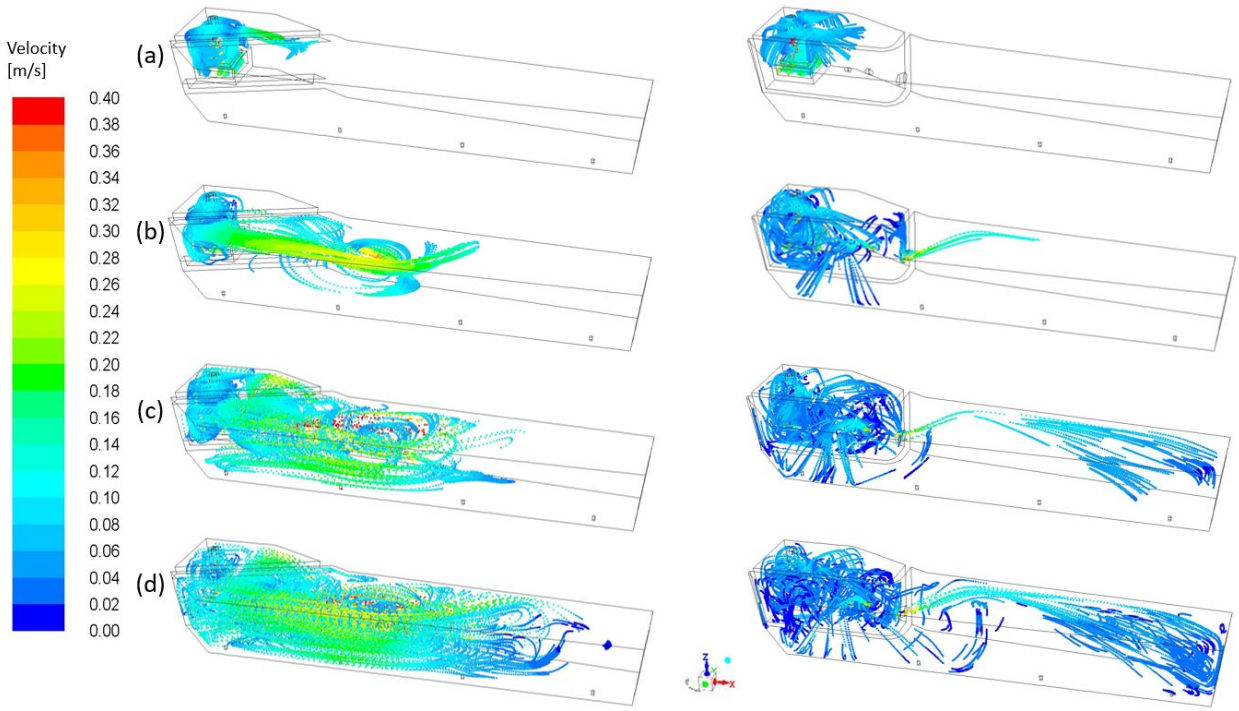

Fig. 6. Massless DPM tracers to visualize the mixing process for case no. 3 with 100% of EMS, reversed direction of stirring (left), and for case no. 4 without EMS, with baffle wall at (a) 20 [s], (b) 50 [s], (c) 100 [s], (d) 200 [s].

Summary

Based on the presented research, the following conclusions can be formulated:

- CFD simulations enable to understand the issues in the steelmaking industry and optimize the continuous casting process to improve the effectiveness of the work of metallurgical devices.
- The molten steel flow inside the tundish can be highly improved by the electromagnetic stirrers. In this case relatively low power input significantly improves the effectiveness of the mixing. As a result the homogenization of the structure and purity of the steel is improved. At the same time, agglomeration of inclusions into the slag occurs due to the prevention of the dead zones. So areas with stagnant flow influencing the velocity, temperature and inclusions distribution are minimized. All those aspects directly influence the final products' quality,
- The EMS stirring also prevents uncontrolled solidification and sedimentation, which is dangerous from a safety point of view due to the risk of clogging and faults of the production line.
- The above-mentioned advantages confirm that the structure of the molten steel can be controlled by the usage of electromagnetic stirrers, which also influence further metal forming operations .

Acknowledgments

The research within the industrial doctorate project co-financed by the Ministry of Science and Education.

References

[1] L. Zhang and B.G. Thomas, Inclusions in continuous casting of steel, XXIV National Steelmaking Symposium, Morelia, Mich, Mexico, 2003.

[2] B.H. Reis, W.V. Bielefeldt, A.C.F. Vilela, Efficiency of inclusion absorption by slags during secondary refining of steel, ISIJ Int. 54 (2014) 1584-1591. https://doi.org/10.2355/isijinternational.54.1584
[3] S. Chang, X. Cao, Z. Zou, M. Isac, R.I.L. Guthrie, Micro-bubble formation under non-wetting conditions in a full-scale water model of a ladle shroud/tundish system, ISIJ Int. 58 (2018) 60-67. https://doi.org/10.2355/isijinternational.ISIJINT-2017-390
[4] H. Yang, S.P. Vanka, B.G. Thomas, Mathematical modeling of multiphase flow in steel continuous casting, ISIJ Int. 59 (2019) 956-972. https://doi.org/10.2355/isijinternational.ISIJINT-2018-743
[5] G.M. Souza, A.F.G. Mendonça, R.P. Tavares, Physical and mathematical modeling of inclusion behavior in a tundish with gas curtain, Int. J. Eng. 73 (2020) 531-538. https://doi.org/10.1590/0370-44672020730010
[6] H. Lei, B. Yang, Q. Bi, Y. Xiao, S. Chen, C. Ding, Numerical simulation of collision-coalescence and removal of inclusion in tundish with channel type induction heating, ISIJ Int. 59 (2019) 1811-1819. https://doi.org/10.2355/isijinternational.ISIJINT-2019-118
[7] L. Zhang, S. Taniguchi, K. Cai, Fluid flow and inclusion removal in continuous casting tundish, Metall. Mater. Trans. B. 31 (2000) 253-266. https://doi.org/10.1007/s11663-000-0044-9
[8] B. Li, H. Lu, Y. Zhong, Z. RensZ. Lei, Numerical simulation for the influence of ems position on fluid flow and inclusion removal in a slab continuous casting mold, ISIJ Int. 60 (2020) 1204-1212. https://doi.org/10.2355/isijinternational.ISIJINT-2019-666

Materials Research Proceedings 28 (2023) 1551-1558 https://doi.org/10.21741/9781644902479-167

Evaluation of data transfer influence in coupled Monte Carlo finite element model on microstructure evolution predictions

WERMIŃSKI Mariusz[1,a *], PERZYŃSKI Konrad[1,b], SITKO Mateusz[1,c] and MADEJ Łukasz[1,d]

[1]AGH University of Science and Technology, 30 Mickiewicza Avenue, 30-059 Krakow, Poland

[a]marwer@agh.edu.pl, [b]kperzyns@agh.edu.pl, [c]msitko@agh.edu.pl, [d]lmadej@agh.edu.pl

Keywords: Interpolation, Monte Carlo, Finite Element Method, Welding

Abstract. The processes of microstructure evolution under thermal loading occurring during welding or additive manufacturing are highly complex and challenging to observe experimentally. Therefore, in this work, to support experimental investigation, a hybrid numerical model based on the combination of the Monte Carlo (MC) and Finite Element (FE) method was developed to simulate both temperature profiles and corresponding grain growth phenomena at a micro scale explicitly. The welding simulation was selected as a case study. The discrete MC microstructure evolution model is based on the temperature distribution provided by the FE simulation with the Goldak heat source model. The temperature data are transferred from 3D FE space to cubic MC Pott's domain in each time step. Direct coupling between the MC cells and FE cubic elements provides accurate results but significantly increases the simulation time. Therefore, coarser FE meshes are used in the research, but this requires applying reliable data interpolation techniques between the two methods. As a result, the temperature field stored in a coarse FE cloud of points is interpolated into regular high-resolution MC cell space in each time step. Evaluation of the influence of various interpolation methods, along with their parameters on the final microstructure morphology after welding, is presented within this work.

Introduction

Modern industry requires efficient and durable methods of joining various metallic parts. The most popular techniques in this area are the welding operations [1], which are based on melting both materials in the joining zone by the focused heat sources, e.g. laser or electron based. However, similar material processing routes are also used in other applications like additive manufacturing or soldering [2,3]. Despite the final application, phenomena controlling microstructure evolution in all those processes are very complex to analyze experimentally. During the high-heat loading of metallic materials, various phenomena should be considered, involving melting, crystallization, grain growth, phase transformation, etc. Most of the time, experimental observations of these phenomena are done after the end of the process. As a result, drawing direct conclusions about local microstructure behavior during the process is not straightforward. Therefore, numerical simulations are frequently used to support experimental observations and visualize phenomena that are difficult or impossible to observe in laboratory conditions [4].

To investigate both the temperature evolution and corresponding microstructural changes in the welding and heat-affected zones, a hybrid Finite Element (FE) - Monte Carlo (MC) model was developed. The FE part based on the classical Goldak movable heat source model is responsible for the evaluation of the temperature fields during the process. The MC model is used as a full-field approach allowing explicit representation of complex grain morphology in the weld line area [5–7]. The MC method was selected in this case due to a straightforward definition of cell transition rules. However, in this case, coupling both methods is a crucial stage in successful model development.

Content from this work may be used under the terms of the Creative Commons Attribution 3.0 license. Any further distribution of this work must maintain attribution to the author(s) and the title of the work, journal citation and DOI. Published under license by Materials Research Forum LLC.

The direct coupling assumes linking each cubic FE element with a corresponding cubic MC cell, as presented in Fig. 1a. In this case, the data transfer is straightforward as both computational domains operate on the space discretized exactly in the same way. However, a high-resolution MC space is required to capture the grain growth during the process, which directly leads to a high-resolution FE mesh. As a result, the computational times for large-scale models may be quite excessive. Therefore, the solution is to use a coarser FE mesh that does not directly correspond to the MC cells. However, in this case, the data transfer between the two incompatible meshes in each time step has to be developed based on the interpolation technique, as seen in Fig. 1b.

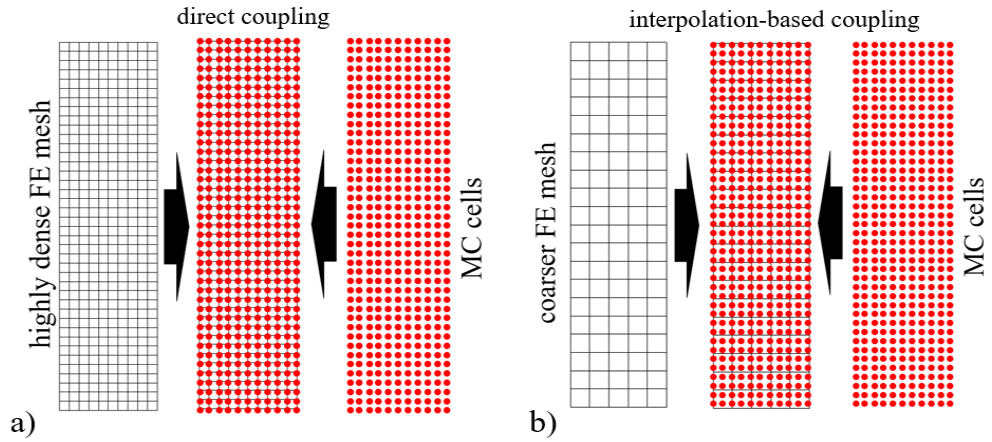

Fig. 1. Concepts of the FE-MC models based on a) direct and b) interpolation-based coupling.

Evaluation of the influence of various interpolation methods and their parameters on the final microstructure morphology after welding simulated by the MC model is the primary goal of the current research to confirm the quality of the results.

Hybrid FE-MC Model Description

The essential step in simulating the effect of thermal loading on the microstructure evolution during welding is to acquire sensible temperature data in specified conditions. The presented approach assumes that the thermal loading during welding is performed by the moving heat source incorporated into the FE framework. The welding operation of two high-purity aluminium plates was selected as a case study for the current investigation. The applied moving heat source model is based on Goldak's ellipsoid [8] in the form of:

$$q(x,y,z,t)=\frac{6\sqrt{3}Q}{abc\pi\sqrt{\pi}}e^{\frac{-3x^2}{a^2}}e^{\frac{-3y^2}{b^2}}e^{\frac{-3[z+v(\tau-t)]^2}{c^2}} \tag{1}$$

where: q – heat flux at a given point in the coordinate system; a, b, c – semi-axes of the ellipsoid; Q – energy input rate; v – welding velocity; τ – lag factor.

The FE model provides information on the temperature evolution during the subsequent process stages, as presented in Fig. 2.

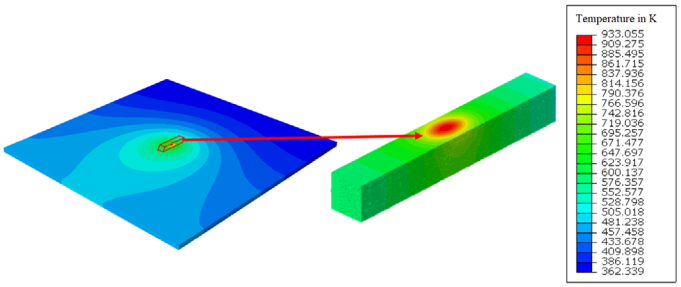

Fig. 2. FE temperature field in [K] during welding with the highlighted section of interest for interpolation analyses.

The acquired data for a particular time step is called a frame in the current work. Data from each frame has to be then transferred to the regular cubic MC space. To reduce the computational time, the MC space is associated only with the heat-affected zone during the welding.

The developed MC microstructure evolution model is based on Pott's approach [9]. The initial microstructure morphology required for simulation (Fig. 3) is generated using the cellular automata grain growth algorithm from the DigiCore library [10]. The average grain diameter is 0.143 [mm], and the resolution of generated MC space is 102×92×701, with the cell's edge length set to 0.02 [mm] to properly capture grain boundaries geometry (Fig. 3). The main idea of the MC method is to calculate the probability p of, a randomly selected, cell state change and set it to a new state according to the following equation:

$$p = \begin{cases} M(T_i)e^{\frac{-\Delta E}{kT}} & \Delta E \le 0 \\ M(T_i) & \Delta E > 0 \end{cases} \tag{2}$$

where: ΔE – change in the energy; kT – model factor; $M(T_i)$ – grain mobility; T_i – temperature of a cell.

The Eq. 3 describes change in the free energy:

$$\Delta E = E_{new} - E \qquad E = \sum_{j=1}^{Z} 1 - \delta_{SS_j} \tag{3}$$

where: E – free energy for an initial state, E_{new} – free energy for a new state, Z – number of neighbors, δ – Kronecker delta of state between current and neighboring cell. The probability p is calculated for every cubic cell in MC space. This computation is applied for every FE frame of welding simulation by performing an arbitrary set number of iterations known as the Monte Carlo Steps (MCS).

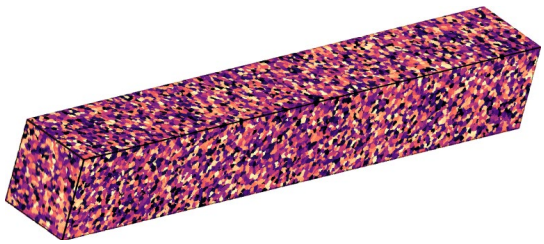

Fig. 3. Initial microstructure.

Materials Research Proceedings 28 (2023) 1551-1558 https://doi.org/10.21741/9781644902479-167

The temperature field from the FE model is used to calculate the grain mobility $M(T_i)$, which involves activation energy Q for specific material and given temperature T_i of MC cell in Arrhenius equation (Eq. 4). In the current model Eq. 4 is normalized to 0 – 1 range by M_0 scaling factor, where 1 means the value for a melting point:

$$M(T_i) = M_0 e^{-\frac{Q}{kT_i}} \tag{4}$$

Data transfer between the two models is performed by interpolating temperature values from FE cloud of points into regular high-resolution 3D MC space. As pointed out, selecting appropriate interpolating functions is crucial to reproduce a final microstructure representation after welding. Four different methods were implemented and used in the current FE-MC hybrid model. The first is an Inverse Distance Weighting (IDW) method [11]. This approach is based on the evaluation of the temperature value in a particular cell by averaging the values of neighboring FE data points (Eq. 5). The weights from Eq. 6 depend on the distance and the parameter n (Eq. 6):

$$u(x) = \begin{cases} \dfrac{\sum_{i=1}^{N} w_i(x) u_i}{\sum_{i=1}^{N} w_i(x)} & d(x, x_i) \neq 0 \\ u_i & d(x, x_i) = 0 \end{cases} \tag{5}$$

$$w_i(x) = \frac{1}{d(x, x_i)^n} \tag{6}$$

The second interpolation algorithm is based on Smoothed-Particle Hydrodynamics (SPH) approach [12], where the evaluated value u depends on the weighting kernel function k (Eq. 7). The kernel function determines the weight of value using the neighborhood radius r and distance d between the current point x and neighboring one x_i. Two different kernel functions: *Epanechnikov* (Eq. 8) and *Quartic* (Eq. 9), were used during the current investigation:

$$u(x, r) = \frac{\sum_{i=1}^{N} k(x_i, r) u_i}{\sum_{i=1}^{N} k(x_i, r)} \tag{7}$$

$$k_{epanechnikov}(x, r) = \frac{3}{4}\left(1 - \left(\frac{x}{r}\right)^2\right) \tag{8}$$

$$k_{quartic}(x, r) = \frac{15}{16}\left(1 - \left(\frac{x}{r}\right)^2\right)^2 \tag{9}$$

Additionally, two other approaches are considered due to their simplicity and low computational complexity. The third interpolation method is a particular variant of the IDW method with n set to 0. This provides a simple average method (AVG) that only takes unweighted values into the computations. The last interpolation technique is based on finding the nearest point and applying its value (NEAREST).

Comparison of Interpolation Methods

In order to study the impact of interpolation methods and their parameters on the evolution of microstructure in the MC space, two simulations of the thermal loading of an aluminium plate were carried out. The first computation was made with the most time-consuming direct coupling where FE points are equidistant from each other, and the size of the FE elements is the same as MC cells (Fig. 1a). In this case, the data are directly transferred from the particular FE integration point into the corresponding MC cell, and there is no interpolation. The simulation results from Fig. 4 are assumed to be a benchmark for further investigation. The second set of simulations is realized on a coarser FE mesh, and as described earlier, different interpolation methods were used to transfer the data into the MC model.

Fig. 4. Final microstructure obtained from the direct coupling between FE and MC models.

Each interpolation test was then conducted according to the parameters collected in Table 1. Corresponding final microstructure morphologies from hybrid FE-MC simulations are gathered in Fig. 5 – 9. For presentation purposes, only the middle section of the heat-affected zone is presented. Besides that, skeletonization of the top view of the microstructure was done to emphasize the difference in the shape of grains. Finally, obtained computational times and average grain sizes are summarized in Table 2.

Table 1. Combination of applied interpolation methods and their parameters.

Case no.	1	2	3	4	5	6	7	8	9	10	11	12	13
Interpolation method	IDW	IDW	IDW	SPH/ Q	SPH/ Q	SPH/ Q	SPH/ E	SPH/ E	SPH/ E	AVG	AVG	AVG	NEARES T
Radius of range	0.2	0.4	0.4	0.2	0.4	0.8	0.2	0.4	0.8	0.2	0.4	0.8	-
n parameter	2	1	2	-	-	-	-	-	-	-	-	-	-

Table 2. The results of applied interpolation methods and reference microstructure.

Case no.	1	2	3	4	5	6	7	8	9	10	11	12	13	Ref.
Average computation time per frame [s]	46	46	45	21	22	20	4	4	3	18	21	26	17	-
Average central grain area [mm^2]	0.012	0.03	0.018	0.013	0.029	0.032	0.014	0.033	0.033	0.035	0.037	0.029	0.031	0.043
Average elongated grain area [mm^2]	0.030	0.108	0.085	0.062	0.127	0.168	0.083	0.148	0.162	0.123	0.147	0.123	0.134	0.167

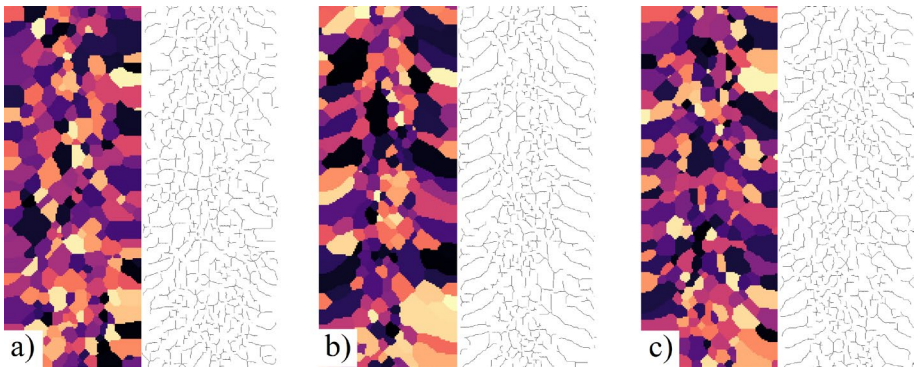

Fig. 5. Top view of the microstructure and its skeletons after thermal loading using IDW method: a) Case 1, b) Case 2, c) Case 3.

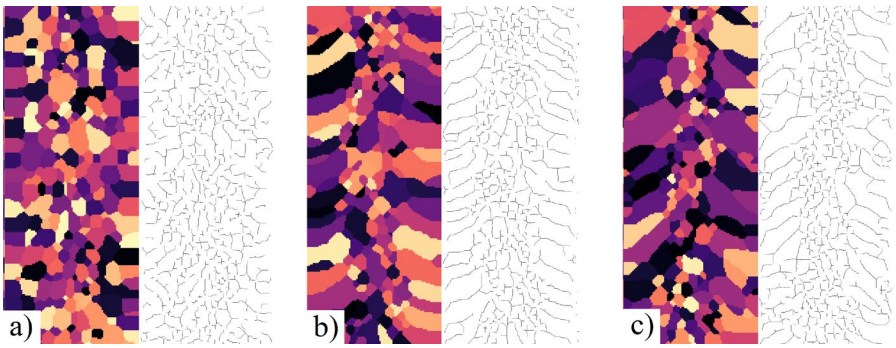

Fig. 6. Top view of the microstructure and its skeletons after thermal loading using SPH-Quartic method: a) Case 4, b) Case 5, c) Case 6.

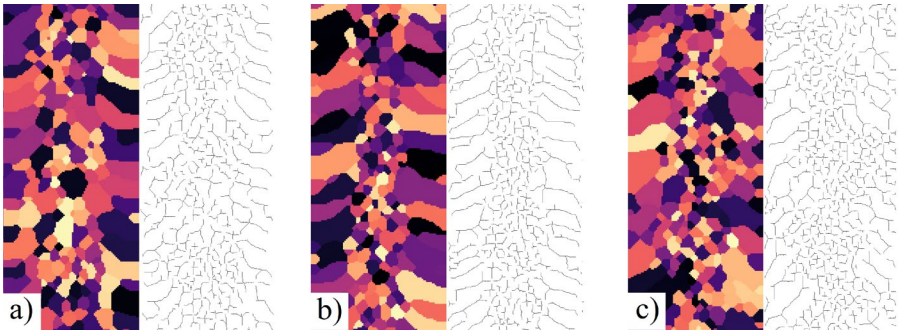

Fig. 7. Top view of the microstructure and its skeletons after thermal loading using SPH-Epanenchnikov method: a) Case 7, b) Case 8, c) Case 9.

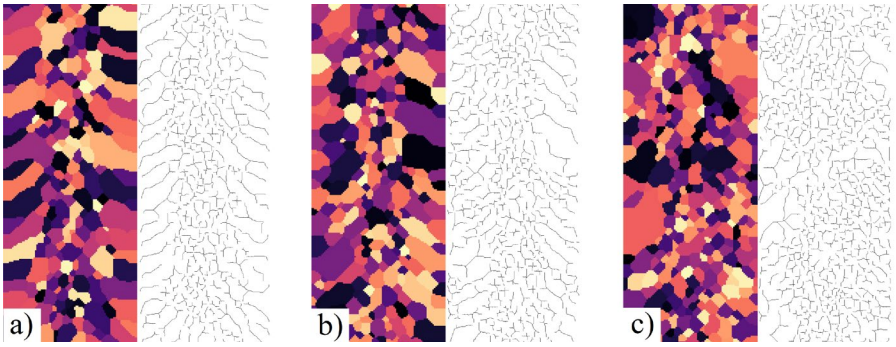

Fig. 8. Top view of the microstructure and its skeletons after thermal loading using AVG method: a) Case 10, b) Case 11, c) Case 12.

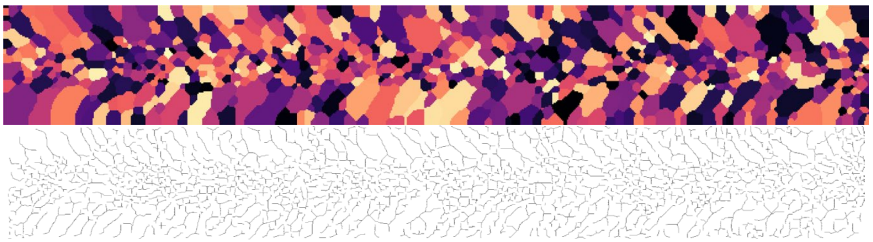

Fig. 9. Top view of the microstructure and its skeletons microstructure after thermal loading using NEAREST method (Case 13, entire model).

As presented, the applied methods and their parameters highly impact the resulting microstructures. Presented top views of the microstructures (Fig. 5 – 9) can be easily distinguished into two sections: the central part, which results in new and not fully grown grains, and the second one, with elongated grains after the grain growth. This division is particularly evident in the presented skeletons. Size, curvature, and a fraction of elongated grains depend on selected interpolation algorithms and their parameters. It is observed that SPH method in both variants produces the most elongated and curved shapes of grains that are related to the number of points taken into account in the neighborhood. However, at 0.8 [mm] neighborhood radius, the shapes of elongated grains are more irregular. According to the AVG method, if fewer values are considered in the averaging, the final structure is similar to the referenced one. The IDW approach shows the curvature of grains depends on the number of points taken into consideration, and the size relies on a parameter $\boldsymbol{n}$ value. The NEAREST method, despite its simplicity, provides a very similar microstructure to the reference one. From the presented approaches, similar microstructures are produced by the SPH (Fig. 6b and Fig. 7b), the AVG (Fig. 8a), and the NEAREST. These methods differ in two points: the shape and size of elongated grains, which are the largest in the SPH, and the angle of direction of grain growth from the fusion zone to HAZ boundary, which is more perpendicular in the case of SPH and AVG. These methods present significantly different results from the reference, especially regarding the elongated-to-center grains ratio. Despite this, it seems that the NEAREST method most closely reflects the reference microstructure relative to the others.

Summary

Based on the presented research, it can be concluded that:

1) temperature fields mapped from macro to micro scale by interpolation methods slightly vary from the direct transfer case. There are also minor differences in the shape and size of new grains.

2) the most similar microstructure can be obtained by using an appropriately tailored method. The most effective results are produced using SPH interpolation (using *Epanechnikov* and *Quartic* kernel functions with 0.4 radii of range), AVG method (with the application of 0.2 radii of range) and the nearest neighbor approach. NEAREST provides the closest results to the benchmark case among these three methods.

3) approaches based on averaging (all cases of the IDW and the AVG second and third case) introduce some disorder in temperature fields, which results in a lack of elongated grains.

More simulations will be carried out on a larger computational MC domain as the subject of future work. The research will also include an examination of geometric parameters and velocity of the heat source and its influence on the microstructure evolution.

Acknowledgement

The financial assistance of the National Science Centre project No. 2019/35/B/ST8/00046 is acknowledged.

References

[1] B. Wang, S.J. Hu, L. Sun, T. Freiheit, Intelligent welding system technologies: State-of-the-Art review and perspectives, J. Manuf. Syst. 56 (2020) 373-391. https://doi.org/10.1016/J.JMSY.2020.06.020

[2] A.V. Müller, D. Dorow-Gerspach, M. Balden, M. Binder, B. Buschmann, B. Curzadd, T. Loewenhoff, R. Neu, G. Schlick, J.H. You, Progress in additive manufacturing of pure tungsten for plasma-facing component applications, J. Nucl. Mater. 566 (2022) 153760. https://doi.org/10.1016/J.JNUCMAT.2022.153760

[3] S. Mercan, The effect of the amount of soldering wire on fatigue strength in joining steels and sockets, Int. J. Fatigue 127 (2019) 157–164. https://doi.org/10.1016/J.IJFATIGUE.2019.06.004

[4] J. Yanagimoto, D. Banabic, M. Banu, L. Madej, Simulation of metal forming – visualization of invisible phenomena in the digital era, CIRP Annals 71 (2022) 599-622. https://doi.org/10.1016/J.CIRP.2022.05.007

[5] F. Villaret, B. Hary, Y. de Carlan, T. Baudin, R. Logé, L. Maire, M. Bernacki, Probabilistic and deterministic full field approaches to simulate recrystallization in ODS steels, Comput. Mater. Sci. 179 (2020) 109646. https://doi.org/10.1016/J.COMMATSCI.2020.109646

[6] C.L. Park, P.W. Voorhees, K. Thornton, Application of the level-set method to the analysis of an evolving microstructure, Comput. Mater. Sci. 85 (2014) 46-58. https://doi.org/10.1016/J.COMMATSCI.2013.12.022

[7] D. Tourret, H. Liu, J.L. Lorca, Phase-field modeling of microstructure evolution: Recent applications, perspectives and challenges, Prog. Mater. Sci. 123 (2022) 100810. https://doi.org/10.1016/J.PMATSCI.2021.100810

[8] J. Goldak, A. Chakravarti, M. Bibby, A new finite element model for welding heat sources, Metall. Mater. Trans. B 15 (1984) 299-305. https://doi.org/10.1007/BF02667333

[9] A. Williamson, J.P. Delplanque, Investigation of Dynamic Abnormal Grain Growth Using the Monte Carlo Potts method, Comput. Mater. Sci. 124 (2016) 114-129. https://doi.org/10.1016/J.COMMATSCI.2016.07.025

[10] K. Boguń, M. Sitko, M. Mojżeszko, L. Madej, Cellular automata-based computational library for development of digital material representation models of heterogenous microstructures, Archiv. Civ. Mech. Eng. 21 (2021) 61. https://doi.org/10.1007/s43452-021-00211-9

[11] P.M. Bartier, C.P. Keller, Multivariate interpolation to incorporate thematic surface data using inverse distance weighting (IDW), Comput. Geosci. 22 (1996) 795-799. https://doi.org/10.1016/0098-3004(96)00021-0

[12] L.D.G. Sigalotti, O. Rendón, J. Klapp, C.A. Vargas, F. Cruz, A new insight into the consistency of the SPH interpolation formula, Appl. Math. Comput. 356 (2019) 50-73. https://doi.org/10.1016/j.amc.2019.03.018

Materials Research Proceedings 28 (2023) 1559-1564 https://doi.org/10.21741/9781644902479-168

Evaluation of data transfer methods efficiency in the random cellular automata model of dynamic recrystallisation

PAWLIKOWSKI Kacper[1,a *], SITKO Mateusz[1,b], CZARNECKI Michał[1,c] and MADEJ Łukasz[1,d]

[1]AGH University of Science and Technology in Krakow, Poland

[a]kpawliko@agh.edu.pl, [b]msitko@agh.edu.pl, [c]mczarneck@student.agh.edu.pl, [d]lmadej.agh.edu.pl

Keywords: Random Cellular Automata, Dynamic Recrystallisation, Microstructure

Abstract. Numerical simulations can help predict microstructure morphology evolution under hot forming conditions and support final material properties determination. Cellular Automata (CA) is a commonly used full-field method to model changes in microstructure morphology during different metal-forming processes. However, in the case of microstructure evolution changes during high deformation levels, at higher temperatures, the CA method has some limitations related to computational domain geometry changes. The use of random cellular automata (RCA) allows for a more realistic representation of this phenomenon. However, it involves much more effort during model implementation to optimise the algorithm in terms of execution time, which has to be at an acceptable time. This paper is a part of a larger research aiming at developing the dynamic recrystallisation model (DRX) using the RCA directly incorporated into the finite element (FE) framework. The main goal of the current work is to evaluate the efficiency of data transfer approaches between the two mentioned coupled model components. Particular attention is on shortening the execution time thanks to data streams opened in binary mode.

Introduction

Because of the rapid development of computer technology, current numerical methods can consider not only the macroscopic response of the material but also can track the microstructural changes explicitly. Advanced multiscale models often use different numerical simulation methods to reflect given phenomena at subsequent scales. In general, three major phenomena are responsible for microstructure evolution during the deformation of metallic materials: recrystallisation, phase transformation, and texture development. The former group of phenomena, particularly dynamic recrystallisation (DRX), is critical when evaluating hot metal forming conditions. This phenomenon leads to microstructure restoration during hot working conditions, which eventually influences their final mechanical properties [1].

In principle, DRX consists of two main stages: nucleation and growth of new dislocation-free grains. It is a process driven mainly by a reduction of the dislocation density accumulated in the material during plastic deformation conditions under elevated temperatures. This process occurs directly during deformation at high temperatures, so its direct experimental observations are very demanding. Therefore, various numerical models are used to support and complement experimental analysis [2,3]

The cellular automata (CA) is one of the advanced full-field numerical methods commonly used to represent the microstructure evolution during plastic deformation. This method has been used for DRX simulations for many years, starting from the first simple model that did not consider computational domain deformation developed by Goetz and Seetharaman [4]. They showed that even a straightforward model could approximate the material properties observed during experiments. More and more advanced models appeared over the following years. Xiao et al. [5] introduced the DRX model based on the CA coupled with the topology deformation technique to

Content from this work may be used under the terms of the Creative Commons Attribution 3.0 license. Any further distribution of this work must maintain attribution to the author(s) and the title of the work, journal citation and DOI. Published under license by Materials Research Forum LLC.

account for the influence of grains' topology change during deformation on the kinetics of the DRX. Gawad and Pietrzyk introduced the Cellular Automata Finite Element model (CAFE) [6] with a simplified way to account for the microstructure's evolution in the FE simulation. Complex and more flexible models combining the CA method with FE were also developed [7]. However, all these examples also showed that an accurate description of the deformation of the cellular automata computational domain under plastic forming conditions is a significant limitation of the classic CA approach, which is based on a regular grid of cells (Fig. 1a). Many solutions have been proposed to deal with that issue in recent years. In some works, authors introduced a simple CA space elongation algorithm along a selected axis [8], and as a result, new recrystallised grains were also artificially elongated. Another research developed a technique based on mapping the computational space between two separate coordinate systems [9]. It eliminated many disadvantages of previously reviewed approaches but still considered a series of geometrical assumptions during simulation. An exciting concept of space deformation was introduced in [10]. The authors coupled the CA method with the FE approach and introduced the CA space deformation algorithm directly based on FE mesh geometry. However, because of the regularity of CA space, the remeshing operations were limited in FE software at higher deformation degrees. Therefore, the current paper's authors introduced the concept of coupling the FE deformation model with the random cellular automata (RCA) model of microstructure evolution presented in [11].

In this case, the RCA modifies the definition of a regular CA space and considers it as a cloud of points (Fig. 1).

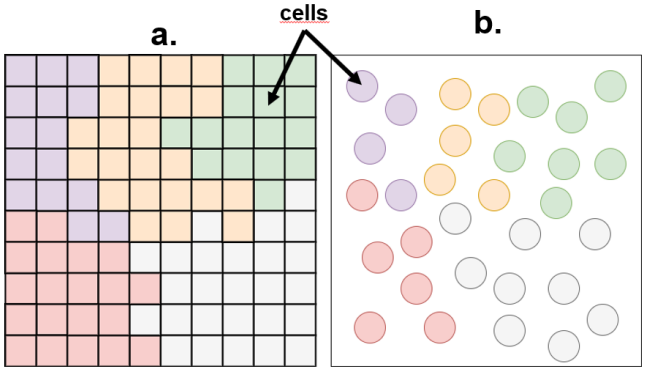

Fig. 1. Comparison of a) CA and b) RCA computational space.

The method retains all general properties of CA without introducing errors during coupling with finite element integration points, which deal with deformation calculations. As a result, the coupled RCAFE model reflects the material's behaviour during deformation more accurately, as it directly considers CA space deformation.

RCAFE DRX Simulation

The material deformation simulations are carried out in the classical J2 plasticity FE framework of Abaqus software. Additionally, each RCA cell from the microstructure evolution model is associated with a single FE integration point (Fig. **2**). Therefore, coordinates of integration points, their displacements and equivalent plastic stresses are transferred from the FE to RCA models in each time step. The described coupling between RCA with the FE model carries the risk that some areas of the material may not be discretized with the correct number of cells, and it can influence the final results. Proper initial FE mesh discretization and remeshing operations should overcome this issue. The RCA model presented in this work can easily incorporate changes introduced by FE remeshing algorithm.

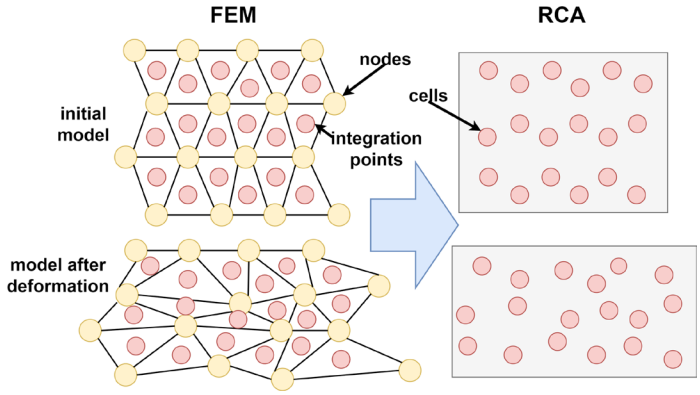

Fig. 2. Transformation of integration points into RCA cells.

In general, the simulation in such a coupled RCAFE model consists of several steps. A the beginning of each iteration, cells in the RCA space are translated based on corresponding integration points coordinates in the FE model. After that, dislocations in each cell are evaluated based on the stress value from Abaqus software:

$$\overline{\rho} = \frac{1}{\rho_0}\left(\frac{\sigma_i}{a_6 G b}\right)^2 \tag{1}$$

where: G is the shear modulus, σ_i is the equivalent stress value calculated by the Abaqus, a_6 is the model constant, b is the magnitude of the Burgers vector, and ρ_0 is the initial dislocation density. When the critical value of dislocation density is reached, new nuclei are incorporated into RCA space with the nucleation rate described by:

$$\dot{N} = c\dot{\varepsilon}\exp\left(-\frac{Q_n}{RT}\right) \tag{2}$$

where: c is constant, $\dot{\varepsilon}$ is the strain rate, Q_n is the activation energy for nucleation, T is the temperature, and R is the universal gas constant.
Finally, in each time step, the cell changes its state from unrecrystallised to recrystallised based on its size and growth velocity value calculated as:

$$V = M_0 \exp\left(-\frac{Q_m}{RT}\right) 2\alpha\tau\left(\rho_{(k,l)} - \rho_{(i,j)}\right) \tag{3}$$

where: M_0 is the initial grain boundary mobility, Q_m is the activation energy for grain boundary motion, α is a coefficient from the range (0,1), $\rho_{(k,l)}$ - dislocation density in the analysed and neighbouring cell, and τ is the energy required for dislocation movement.

The flow of the simulation in such a basic version of the DRX model is presented in Fig. 3.

Materials Research Proceedings 28 (2023) 1559-1564 https://doi.org/10.21741/9781644902479-168

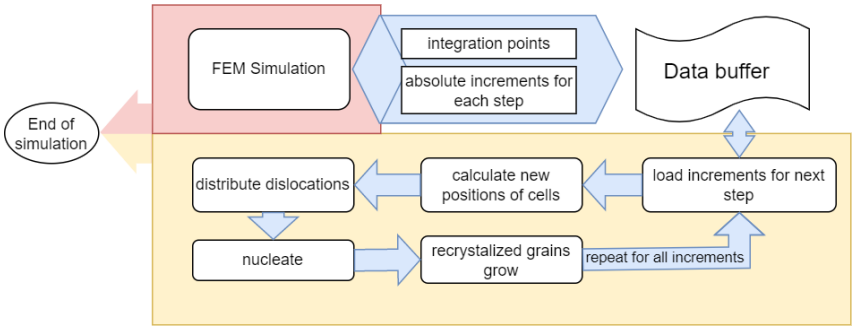

Fig. 3. Flow of implemented DRX simulation process.

Initial research on this topic clearly pointed out that the major disadvantage of the coupled RCAFE solution is the excessive computational time. The improvements in the RCA code itself, related to designing specific neighbourhood types and neighbourhood search algorithms, have already been carried out in [15]. Therefore, the current research is directly focused on further optimising the algorithmic solution to increase the model efficiency, particularly developing effective data transfer mechanisms between the RCA and FE methods.

Results

A two-dimensional digital material representation (DMR) model consisting of six grains discretised by 50 000 elements was selected as a case study for the current research (Fig. 4). The DMR model was deformed by 30% at 1100°C within the FE framework. In each FE element time step, the data from FE integration points were directly transferred to the corresponding RCA points, where the progress of dynamic recrystallisation was simulated within the in-house code.

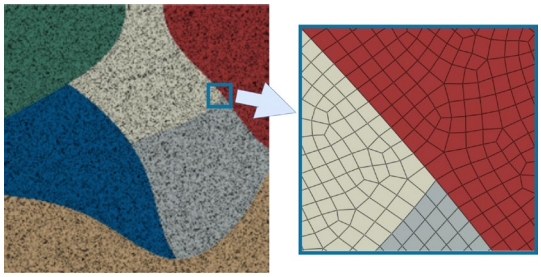

Fig. 4. Illustration of the DMR model used for the FE simulations.

Obtained microstructure evolution results in the RCA computational domain are presented in Fig. 5; blue cells represent unrecrystallised grains, and cells in the red-scale colours represent new, recrystallised ones. It is seen that nucleation starts from grain boundary regions, where higher dislocation densities are expected. The nuclei can also appear inside grains, but only after reaching significant deformation levels, which replicates well-known experimental observations. It should be clearly pointed out that despite the very small model used as a case study, the calculation time was quite long, reaching approx. 28 s. This time in the case of models with a larger number of grains and significantly refined FE mesh in 3D space, will lead to unacceptable simulation times. While the RCA simulation itself can be accelerated with the use of parallelisation techniques, the bottleneck of the coupled RCAFE solutions is transferring a large amount of data between the two models. In the evaluated case, the data transfer took about 30% of the entire simulation time.

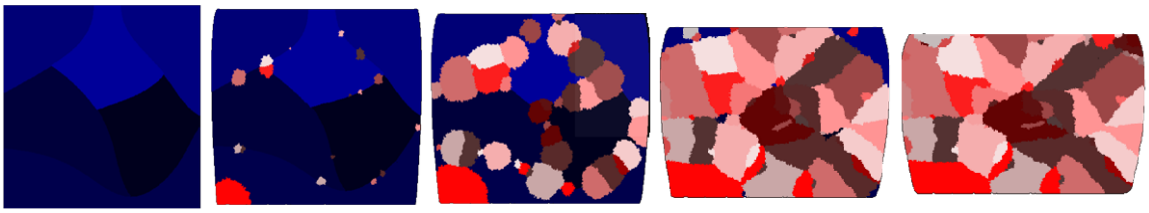

Fig. 5. The results of subsequent simulation steps for a model consisting of 50 000 elements.

As mentioned, the described technique should ultimately simulate much larger DMR models in 3D space. Therefore, as the first step, we decided to look at the possibility of reducing the time of data transfer. Two different methods of handling data transition from FE to RCA were implemented and compared. Both approaches differ in the format of the files stored in the buffer linking the two models. In the basic approach, data files from Abaqus with subsequent changes in stress values and positions of FE integration points were saved in a standard text form. In the second approach, files were saved and loaded in binary mode. The concept of communication between FE and RCA models is presented in Fig. 6.

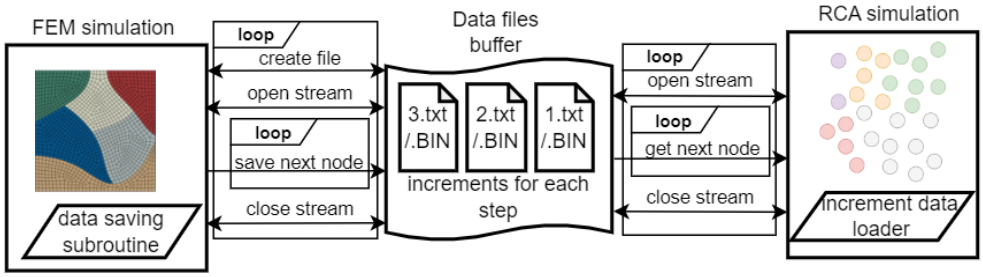

Fig. 6. Diagram of communication between FE and RCA models.

A series of simulations with increasing FE discretization levels was carried out to evaluate the differences between the two solutions. The summary of realised measurements shown in Fig. 7 proves that thanks to the application of binary files, it is possible to save up to 10% of the time for the largest model. Nevertheless, the time effort associated with the data transfer is still quite excessive in comparison to the pure simulation time.

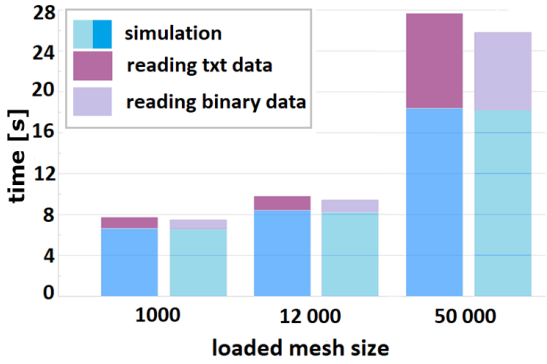

Fig. 7. Comparison of simulation and data transfer times for the text and binary files, respectively.

Summary

The use of the RCA concept allowed for the implementation of the DRX microstructure evolution model that, thanks to the flexibility of this solution, can be directly coupled with material

deformation data obtained from FE simulations. As a result, it is possible to take into account the influence of cellular automata space deformation on the progress of dynamic recrystallisation. At this research stage, the developed RCA DRX model considers only basic components like dislocation distribution, nucleation and dislocation density-driven grain growth and will be further developed. It was proven that in the coupled RCAFE simulation, the data transfer procedure between the commercial and in-house codes generates a major overhead in total simulation time. It was shown that the use of binary files could already speed up the analysis in comparison to the standard text files; however, further improvements in this aspect are also required. The further concept assumes direct information exchange inside subroutine code to eliminate the need for the files.

Acknowledgement
The financial assistance of the National Science Centre project No. 2019/35/B/ST8/00046 is acknowledged. This research was supported in part by PLGrid Infrastructure.

References
[1] K. Huang, R.E. Logé, A Review of Dynamic Recrystallization Phenomena in Metallic Materials, Mater. Des. 111 (2016) 548-574. https://doi.org/10.1016/j.matdes.2016.09.012
[2] M. Bernacki, R.E. Logé, T. Coupez, Level Set Framework for the Finite-Element Modelling of Recrystallization and Grain Growth in Polycrystalline Materials, Scripta Mater. 64 (2011) 525-528. https://doi.org/10.1016/j.scriptamat.2010.11.032
[3] T. Takaki, A. Yamanaka, Y. Tomita, Phase-Field Modeling for Dynamic Recrystallization, Adv. Struct. Mater. 64 (2015) 441-459. https://doi.org/10.1007/978-3-319-19440-0_20
[4] R.L. Goetz, V. Seetharaman, Modeling Dynamic Recrystallization Using Cellular Automata, Scripta Mater. 38 (1998) 405- 413. https://doi.org/10.1016/S1359-6462(97)00500-9
[5] N. Xiao, C. Zheng, D. Li, Y. Li, A Simulation of Dynamic Recrystallization by Coupling a Cellular Automaton Method with a Topology Deformation Technique, Comput. Mater. Sci. 41 (2008) 366-374. https://doi.org/10.1016/j.commatsci.2007.04.021
[6] J. Gawąd, M. Pietrzyk, Application of Cafe Multiscale Model to Description of Microstructure Development during Dynamic Recrystallization, 2007.
[7] Ł. Madej, M. Sitko, K. Radwanski, R. Kuziak, Validation and Predictions of Coupled Finite Element and Cellular Model: Influence of the Degree of Deformation on Static Kinetics Case Study, Mater. Chem. Phys. 179 (2016) 282-294. https://doi.org/10.1016/j.matchemphys.2016.05.040
[8] H. Hallberg, M. Wallin, M. Ristinmaa, Simulation of Discontinuous Dynamic Recrystallization in Pure Cu Using a Probabilistic Cellular Automaton, Comput. Mater. Sci. 49 (2010) 25-34. https://doi.org/10.1016/j.commatsci.2010.04.012
[9] N. Yazdipour, C.H.J. Davies, P.D. Hodgson, Microstructural Modeling of Dynamic Recrystallization Using Irregular Cellular Automata, Comput. Mater. Sci. 44 (2008) 566-576. https://doi.org/10.1016/j.commatsci.2008.04.027
[10] H. Li, X. Sun, H. Yang, A Three-Dimensional Cellular Automata-Crystal Plasticity Finite Element Model for Predicting the Multiscale Interaction among Heterogeneous Deformation, DRX Microstructural Evolution and Mechanical Responses in Titanium Alloys, Int. J. Plast. 87 (2016) 154-180. https://doi.org/10.1016/j.ijplas.2016.09.008
[11] L. Madej, M. Sitko, A. Legwand, K. Perzynski, K. Michalik, Development and Evaluation of Data Transfer Protocols in the Fully Coupled Random Cellular Automata Finite Element Model of Dynamic Recrystallization, J. Comput. Sci. 26 (2018) 66-77. https://doi.org/10.1016/j.jocs.2018.03.007

Materials Research Proceedings 28 (2023) 1565-1574 https://doi.org/10.21741/9781644902479-169

Visual quality prediction of plastic product based on thermographic images

LE GOFF Ronan[1,a *], MARCHAL Nils[1,b] and AGAZZI Alban[1,c]

[1]IPC, 2, rue Pierre et Marie Curie, 01100 Bellignat, France

[a]ronan.legoff@ct-ipc.com, [b]nils.marchal@ct-ipc.com, [c]alban.agazzi@ct-ipc.com

Keywords: Injection Moulding, Quality Prediction, Thermography

Abstract. The main purpose of this study is to control the visual quality in plastic injection moulding using an infrared camera after the ejection of the plastic part. Quality indicators have been extracted from the thermal image and from the data recorded by the sensors in the plastic injection machine and in the mould. After cooling, visual quality has been labelled by plastic experts based on 3 aesthetic defects: spot, flow line and streak mark. Three methods of reducing the dimension of the thermal image were studied: Quantiles, Principal Component Analysis (PCA), and Linear Discriminant Analysis (LDA). The visual quality can be predicted efficiently using dimension reduction of the image and Partial Least Square (PLS) regression. The PLS results allow to identify the root causes that explain the apparition of visual defects.

Introduction

The injection moulding process is one of the most used processes in the thermoplastic industry. It allows the manufacturing of parts having various shapes with low production time. The quality requirements of injected plastic parts are increasing to guarantee the final product functionality.

For this reason, quality control is widely used in this industry. Methods are often based on statistical grounds [1,[2] and multivariate analysis have been successfully used [3-[5]. In the past, neural networks coupled with fuzzy logic have shown to be efficient in predicting the quality from the parameter settings of the injection machine [6-[11].

However, these works were focused on the modelling of the injection process and have to target a dimensional quality or a weight. The visual quality is more difficult to characterize and to estimate quantitatively [12]. Existing inspection of defects in appearance relies mainly on manual visual inspection, which is neither efficient nor accurate enough to ensure the manufacturing quality. It is all the more difficult to estimate it on a plastic part right after its ejection since its appearance is not yet stabilized due to residual shrinkage.

To analyse the visual quality online, the most straightforward way to proceed is to take a picture of the plastic part right after the ejection, detect any anomaly and evaluate it in order to decide if the product should be accepted or rejected. Artificial Intelligence techniques to extract relevant information about the visual quality can be used. Since the part is still hot right after the ejection, a picture taken with an infrared camera can be a good candidate. Indeed, it has been shown in [13] that the image of the plastic part and its dimensional quality can be efficiently found by taking the hot part of the thermal image.

The most recent advances in this field were summarized in [14]. As noted in this review, studies have been mainly focused on the variation of the injection machine setting parameters. Nagorny [15] presents image analysis techniques based on neural network. It is very powerful to predict the visual quality of the part from the image but the method demands a large number of data to train the model.

In this paper, an alternative technique is introduced to handle the problem, based on dimensional reduction. It is assumed that the relevant information contained in the whole thermal image can be efficiently summarized in a small numbers of components obtained by dimensional reduction.

Content from this work may be used under the terms of the Creative Commons Attribution 3.0 license. Any further distribution of this work must maintain attribution to the author(s) and the title of the work, journal citation and DOI. Published under license by Materials Research Forum LLC.

These components are used as inputs of a machine learning algorithm to predict the visual quality. The good results obtained with this prediction justify our assumption that the thermal image can be summarized in a few components.

This paper is organized as follows: first, the methodology of our work is explained. Secondly, the experimental setup of the work is presented. Next, the different quality criteria used to estimate the visual quality is discussed. Finally, the main results are shown and compared, and the best results are detailed in the last section.

Methods

Our approach is based on the use of dimensional reduction of the image to extract the relevant information in an automatic way.

After different attempts, two dimensional reduction methods were selected: the first one is Principal Component Analysis (PCA), which is well known in data analysis and consists in looking for the axes in the space of variables, which carry the greatest inertia. The second one is Linear Discriminant Analysis (LDA), where best representative axes are looked for taking into account the target quality to be predicted. LDA is also target oriented, since it takes into account the quality we want to predict. For this reason, LDA is expected to be more efficient. This better efficiency will be checked in the results. In this work, both of these methods are implemented using the Scikit-learn package [16] in Python [17].

These two methods provide us with components of the image ranked by decreasing order of importance. Concerning the choice of the number of components to be kept, different ways to proceed exist, but none of them has ever emerged. For this reason, the simplest method, which also seems to be the most reliable, is used [18]. This method consists in plotting the explained variance with respect to the number of components. In the obtained curve, the last inflexion point before the explained variance tends to be constant and vanishing, which gives the number of components, looked for. For instance, we keep components 0, 1, 2 and 3 in Fig. 1 below.

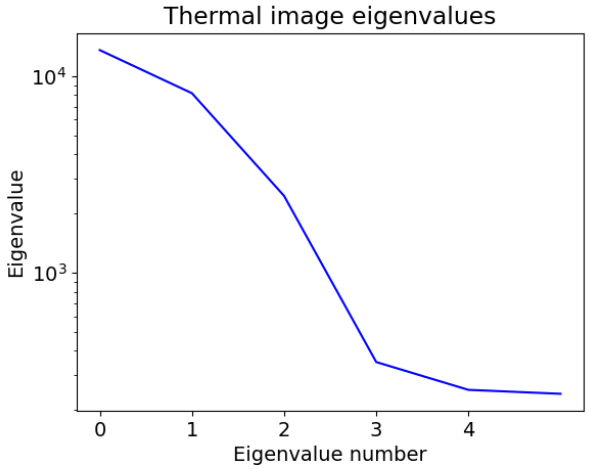

Fig. 1. Illustration of the method to choose the number of thermal image components.

To exhibit the interest of such dimension reduction methods, some quantiles of the thermal image are also computed and used in a way similar to what was done with the dimensional reduction components.

After having selected the correct number of components of the image, the next step is to use them to predict the visual quality. Since this work aims to compare the predictive power of the thermal image indicators and more classical indicators of the process, thermal image indicators and indicators given by sensors in the machine (partially from [19]) are placed in the same dataset. Prediction was then carried out using PLS (Partial Least Square) regression. This regression is

similar to an ordinary multilinear regression but is adapted to non-orthogonal input data, which is indeed the case here.

Among the results of this PLS regression, the ranking of all the input variables is shown according to their power to predict the target visual quality. This will also allow us to compare them for this goal, and to show the importance of the thermal image.

Lastly, PLS regression allows making a detailed analysis of the prediction mechanism, which leads to an interpretation of the results in terms of physical root causes. Indeed, PLS regression defines intermediate latent variables, called PLS components, which are orthogonal with each other and which are the basis for an ordinary multilinear regression. These PLS components are computed through a rigorous algorithm, and their number is fixed by prediction tests. The user has no choice to make for these prediction tests that makes the whole process very rigorous. These PLS components can be interpreted as root causes for the output variable we try to predict. PLS regression was performed using the plsRglm package [20-23].

Experimental Setup

A Billion 200T H150/470-200 plastic injection moulding machine was used for the experiments. The plastic material chosen for all the experiments was a black polypropylene "ExonMobil EXXTRAL CMU201" which is often used in the automotive industry. The plastic part was produced by an experimental mould chosen for simplicity to define quality criteria. The plastic part is shown in Fig. 2 below. Its dimensions are approximately 100×100×50 mm.

Fig. 2. Plastic part.

A Staubli robot arm takes the part out of the mould at the ejection and puts it in front of an Optris thermal camera sensitive in a wavelength range from 7.5 to 13 micrometres. For our purpose, it is enough to use the bare thermal camera image. The elapsed time between the mould opening and the image capture was constant and equal to 10 seconds.

The thermal camera picture was reshaped to isolate the plastic part from the background, especially the reflection from the robot arm. This reshaping has been performed using K-Means clustering and DBSCAN algorithm [16] in Python. This is made easy by the fact that the plastic part and the background are clearly separated on the statistical distribution of the pixels. An example of an obtained picture is shown in Fig 3. below. As can be seen on the left, the hot part is limited to the centre near the injection point and the extremity of the plastic part are the parts that have cooled down the quickest. On the right, the cumulative distribution function shows the proportion of pixels below a given temperature: this allows the easy determination of quantiles as the abscissa corresponding to a given ordinate in this curve.

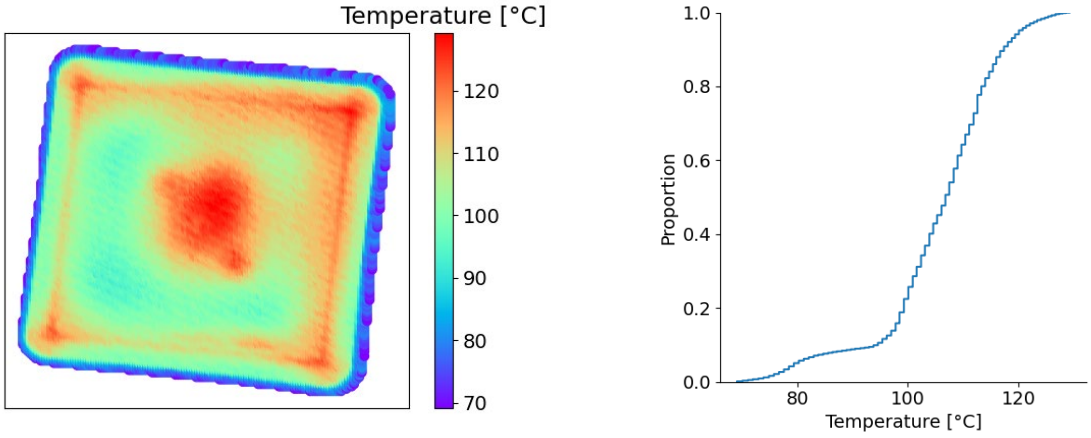

Fig. 3. Reshaped thermal camera picture (left) and empirical cumulative distribution function (right).

The dataset was produced using a L12 Plackett-Burman Design of Experiments [18]. The 11 setting parameters of the injection machine are listed in Table 1 below (together with their minimum and maximum value in this DoE), and have been chosen to ensure repeatability and automatic inline control.

Table 1. Setting parameters for the DoE.

Setting parameters	Minimum	Maximum
Clamping force	100 t	200 t
Injection stroke	80 cm^3	86 cm^3
Injection speed	50 cm^3/s	90 cm^3/s
Holding pressure	100 bars	300 bars
Controller temperature	20 °C	60 °C
Dosing delay	1 s	10 s
Screw speed	50 tr/min	150 tr/min
Barrel Temperature	220 °C	260 °C
Feeding stroke	90 cm^3	110 cm^3
Opening speed	100 mm/s	120 mm/s
Back Pressure	30 bars	70 bars

Since the thermal picture cannot vary directly, this DoE on the machine parameter setting paramters is the best way to get enough variance on the thermal pictures to be able to build a reliable statistical model to predict the visual quality.

Measurements

Once produced, the plastic parts are cooled down and plastic experts evaluate their quality 2 days later. This delay ensures that the plastic part has fully stabilized. A label is given, ranging from one (perfect) to 10 (the worse), for each of the three following criteria:

1) The presence of spots or sink marks, which come from concave zones in the part and indicate that not enough material has been injected during the holding phase to compensate for the shrinkage. This is because the holding phase was not sufficient.
2) The presence of flow lines (run-out), which come from an excessively large opening time of the mould. While the mould is open, a residual pressure exists in the nozzle that makes

the plastic material flow into the opened mould. If the opening time is long, a drop of cold material is formed and then crushed by the mould when it closes. In the subsequent process, it forms on the final part a mark around the injection point when surrounded by new material.

3) The presence of streaks around the injection point. When the plastic material is not sufficiently dried before being injected, residual humidity forms water droplets in the part around the injection point, that are visible as white marks in the part.

Finally, a total visual quality is computed as the product of the three qualities defined just above.

Overview of Results

As explained in the previous section, quantiles or dimensional reduction components from the thermal image are extracted, and concatenated to the indicators. A PLS regression is performed in order to predict a visual quality. This is done for Spots quality, Flow lines quality, Streaks quality and Total visual quality. For each quality, a separate PLS regression model is computed. Quality of the prediction is given by R2 (usual measure of quality in regression), which measures the ratio of the variance explained by regression divided by the total variance. Results are given in Table 2 below.

Table 2. Obtained R2 as a function of the considered quality and the input data.

Data Set	Spots quality	Flow lines quality	Streaks quality	Total visual quality
indicators and quantiles of the thermal image	0.780	0.647	0.148	0.349
indicators and principal components of the thermal image	0.839	0.764	0.349	0.343
indicators and LDA components of the thermal image	0.919	0.950	0.830	0.400

As can be seen from Table 2, a much more powerful way to predict the visual quality is to use the dimensional reduction instead of using only quantiles from the thermal image. In fact, R2 is better for each quality in the last two lines of Table 2 rather than in the first one, which concerns quantiles. For each quality, Table 2 shows that the best R2 result is obtained for LDA reduction. This is expected, since LDA reduction computes the components taking into account the target quality, which is not the case with the other dimension reduction methods.

In the last column of Table 2, it is noticed that the prediction performance of the total visual quality remains poor (R2=0.4) whatever the dimensional reduction of the thermal image is. This is because the total visual quality is the product of the three basic qualities (spots, flow lines and streaks). This product has great uncertainty compared to the uncertainties of the basic qualities since some values of the basic qualities can be important. This makes the total visual quality more difficult to predict.

Detailed Results

As seen in Table 2 above, LDA dimensional reduction provides the best regression. In this section, these results are analysed using the interpretation allowed by PLS regression.

Spots quality.

With the criterion of the inflexion point in the explained variance (see section “Methods”), six LDA components are kept. Main standardized coefficients (i.e. those greater than 0.1 in absolute value) of the PLS regression for spots quality prediction are given in Table 3 below.

Table 3. Main standardized coefficients for spots quality prediction.

Variable	Standardized Coefficient
First LDA component	0.259
Viscosity during the holding phase	0.241
Third LDA component	0.202
Mould viscosity during the holding phase	0.180
(…)	(…)
Second LDA component	-0.275

This table shows that the thermal image summarized by LDA component is highly relevant to explain spots quality: the interpretation of each LDA component is not available, but it can be noticed that the highest positive coefficient is held by the first LDA component and the smallest negative coefficient is held by the second LDA component. Since they are the most important LDA components, they are connected to the global homogeneity of the image and spots are connected with visual defects that have an importance on the global scale. This is expected from a visual inspection of the plastic parts.

Moreover, spots are due to a lack of material caused by an insufficient holding. In Table 3, it is found that a high viscosity in the holding phase, in the machine and in the mould, increases the spots quality. The viscosity is computed as the pressure integral in the holding phase. So Table 3 says that having a high pressure during holding increases the spots quality, that is what is expected from the definition of spots (sink marks) in section “Measurements”.

In the next table, such an interpretation is examined to identify the root causes of the spots quality in a more detailed way than with the standardized coefficients (Table 3). For the spots quality, the algorithm tells us to keep 4 PLS components.

The root causes to improve the spots quality provided by PLS components are summarized in Table 4 below. To keep the paper brief, we shall skip the detailed analysis and the justification of these results.

Table 4. Summary of PLS component interpretation for spots quality.

PLS component	Interpretation
1	Increase the pressure integral during the holding phase
2	Same as 1, plus increase the volume of polymer available for injection; also look at the thermal image in detail
3	Analyse the thermal image
4	Same as 3

Flow lines quality.

With the criterion of the inflexion point in the explained variance (see section “Methods”), 6 LDA components are kept. Main standardized coefficients (i.e. those greater than 0.1 in absolute value) are shown in Table 5 below.

Table 5. Main standardized coefficients for the flow lines quality prediction.

Variable	Coefficient
First LDA component	0.659
Fifth LDA component	0.149
Injected volume during the dynamic phase	0.106
(…)	(…)
Third LDA component	-0.109
Fourth LDA component	-0.121
Viscosity during the holding phase	-0.159
Viscosity during the dynamic phase	-0.196
Second LDA component	-0.307

The Table 5 shows that the standardized coefficients are clearly dominated by the thermal image and, in particular, the first and second LDA components. This shows that flow lines are visible on a global scale on the thermal image, and so that the thermal image is very relevant to explain the presence of flow lines (the LDA components have been calculated with respect to the flow lines quality, and have also changed compared to the spots quality case). Compared with the spots quality, it is noticed that the viscosity in the holding and dynamical phase acts negatively this time. Indeed, to have a good flow lines quality, the residual pressure after mould opening must be low, that is easier if the pressure imposed during the injection and the holding has been low (see section "Measurements" for physical causes).

Statistical tests on prediction power indicate to keep 4 PLS components. The root causes obtained for the interpretation of the four PLS component are summarized in Table 6 below.

Table 6. Summary of PLS component interpretation for flow lines quality.

PLS component	Interpretation
1	Inject the polymer early and not during the holding phase right before the mould opening, which may cause some flow of the polymer in the opened mould
2	Cool down the plastic part efficiently to avoid flow lines, which means that an efficient cooling must solidify the sprue
3	Inject a large quantity of polymer for the residual quantity of polymer in the machine to become low, and to have a low residual pressure
4	Inject all the available polymer volume, so there remains nothing to flow in the mould during mould opening

Streaks quality.

With the criterion of the inflexion point in the explained variance (see section "Methods"), we keep 4 LDA components. Main standardized coefficients (i.e. those greater than 0.05 in absolute value) are shown in Table 7 below.

Table 7. Main standardized coefficients for the streaks quality prediction.

Variable	Coefficient
First LDA component	0.831
Viscosity during the dynamic phase	0.095
Thermal controller mean flow rate	0.076
Fourth LDA component	0.072
(…)	(…)
Third LDA component	-0.055
End of feeding time	-0.069

What is visible in this Table 7 is that almost everything is explained by the first LDA component. For consistency with other analysed qualities, we look also at the PLS components. Statistical tests on prediction power tell to keep 4 PLS components.

The interpretation of the four PLS component as root causes are summarized in Table 8 below.

Table 8. Summary of the PLS component interpretation for streaks quality.

PLS component	Interpretation
1	Lower the polymer temperature at all stages to avoid the formation of water vapour bubbles
2	Increase the pressure during the holding phase to avoid droplets to form.
3	Augment the pressure drop in the nozzle to avoid shear in the mould (which causes heating and formation of water vapour bubbles)
4	Decrease pressure and injected volume during the holding phase, which decreases the shear in the mould and so the polymer heating.

Total visual quality.

The PLS regression leads to a R2 equal to 0.4, which is too small for the interpretation of the coefficients to be possible.

Summary

In this paper, the visual quality prediction of injected plastic boxes based on dimensional reduction is studied. Three methods of reducing the dimension of the thermal image are studied: quantiles, Principal Component Analysis (PCA), and Linear Discriminant Analysis (LDA). The prediction of the quality marks is achieved from a dataset gathering dimensional reduction and from indicators calculated from the machine and mould sensors. The best results are obtained with the LDA dimensional reduction whose interpretation enable to define root causes explaining the phenomena.

The presented work shows that the dimensional reduction method is validated and is a much simpler alternative for visual quality prediction than neural networks, which demand a huge amount of data. The statistical analysis interpretation shows also that it is possible to refine human experts' evaluation and knowledge, to evaluate their notation and can help ~~to~~ define a human evaluation procedure.

Acknowledgement

The authors gratefully acknowledge the SYMME laboratory and INMODELIA for technical support.

References

[1] S. Kumar, H. Park, C.M. Lee, Data-driven smart control of injection molding process, CIRP-JMST 31 (2020) 439-449. https://doi.org/10.1016/j.cirpj.2020.07.006
[2] F. Finkeldey, J. Volke, J.-C. Zarges, H.-P. Heim, P. Wiederkehr, Learning quality characteristics for plastic injection molding processes using a combination of simulated and measured data, J. Manuf. Process. 60 (2020) 134-143. https://doi.org/10.1016/j.jmapro.2020.10.028
[3] D. Kazmer, S. Westerdale, D. Hazen, A comparison of statistical process control (SPC) and on-line multivariate analyses (MVA) for injection modling, Int.. Polym. Process. 23 (2008) 5. https://doi.org/10.3139/217.2192
[4] R. Gao, X. Tang, G. Gordon, D. Kazmer, Online product quality monitoring through in-process measurement, CIRP Annals 63 (2014) 493-496. https://doi.org/10.1016/j.cirp.2014.03.041
[5] D.O. Kazmer, L. Hutson, D. Hazen, Machine learning and multi-objective optimization of industrial extrusion, SPE ANTEC (2020).
[6] H. Lau, T. Wong, K. Pun, Neural-fuzzy modeling of plastic injection molding machine for intelligent control, Expert. Syst. Appl. 17 (1999) 33-43. https://doi.org/10.1016/S0957-4174(99)00019-6
[7] B.H.M. Sadeghi, A BP-neural network predictor model for plastic injection molding process, J. Mater. Process. Technol. 103 (2000) 411-416. https://doi.org/10.1016/S0924-0136(00)00498-2
[8] P. Yarlagadda, C. Khong, Development of hybrid neural system for prediction of process parameters in injection moulding, J. Mater. Process. Technol. 118 (2001) 110-116. https://doi.org/10.1016/S0924-0136(01)00901-3
[9] E. Li, L. Jia, J. Yu, A genetic neural fuzzy system-based quality prediction model for injection process, Comput. Chem. Eng. 26 (2002) 1253-63. https://doi.org/10.1016/S0098-1354(02)00092-3
[10] W.-C. Chen, P.-H. Tai, M.-W. Wang, W.-J. Deng, C.-T. Chen, A neural network-based approach for dynamic quality prediction in a plastic injection molding process, Expert Syst. Appl. 35 (2008) 843-849. https://doi.org/10.1016/j.eswa.2007.07.037
[11] F. Yin, H. Mao, L. Hua, A hybrid of back propagation neural network and genetic algorithm for optimization of injection molding process parameters, Mater. Des. 32 (2011) 3457-3464. https://doi.org/10.1016/j.matdes.2011.01.058
[12] N. Baudet, M. Pillet, J.L. Maire, Visual inspection of products: a comparison of the methods used to evaluate surface anomalies, Int. J. Metrol. Qual. Eng. 2 (2011) 31-38. https://doi.org/10.1051/ijmqe/2011006
[13] P. Nagorny, T. Lacombe, H. Favreliere, M. Pillet, E. Pairel, R. Le Goff, M. Wali, J. Loureaux, P. Kiener, Generative Adversarial Networks for geometric surfaces prediction in injection molding, IEEE ICIT, (2018). https://doi.org/10.1109/ICIT.2018.8352405
[14] R. Farooque, M. Asjad, S.J.A. Rizvi, A current state of art applied to injection moulding manufacturing process - A review, Mater. Today: Proc. 43 (2021) 441-446. https://doi.org/10.1016/j.matpr.2020.11.967
[15] P. Nagorny, Contrôle automatique non-invasif de la qualité des produits - Application au procédé d'injection-moulage des thermoplastiques, Grenoble: Université Grenoble Alpes, (2020).
[16] F. Pedregosa, G. Varoquaux, A. Gramfort, V. Michel, B. Thirion, O. Grisel, M. Blondel, P. Prettenhofer, R. Weiss, V. Dubourg, J. Vanderplas, A. Passos, D. Cournapeau, M. Brucher, M. Perrot, E. Duchesnay, Scikit-learn : Machine learning in Python, J. Mach. Learn. Res. 12 (2011) 2825-2830. https://doi.org/10.48550/arXiv.1201.0490
[17] G. Van Rossum, F.L. Drake Jr, Python reference manual, Centrum voor Wiskunde en Informatica Amsterdam, (1995).
[18] G. Saporta, Probabilités, analyse de données et statistique, third ed., Technip, (2011).

[19] J.-Y. Chen, V.-V. Tseng, M.-S. Huang, Quality Indexes Design for Online Monitoring Polymer Injection Molding, Adv. Polym. Technol. ID 3720127 (2019). https://doi.org/10.1155/2019/3720127
[20] F. Bertrand and M. Maumy-Bertrand, Partial Least Squares Regression for Generalized Linear Models, R package version 1.5.0 (2022).
[21] F. Bertrand and M. Maumy-Bertrand, "Partial Least Squares Regression for Generalized Linear Models," in book of abstracts, User2014!, Los Angeles, (2014).
[22] N. Meyer, M. Maumy-Bertrand, F. Bertrand, Comparaison de la regression PLS et de la regression logistique PLS: application aux donnees d'allelotypage, Journal de la Societe Francaise de Statistique (2010). http://journal-sfds.fr/article/view/47,.
[23] R.C. Team, R: A language and environment for statistical, Vienna, Austria: R Foundation for Statistical Computing URL, (2022). https://www.R-project.org/

Materials Research Proceedings 28 (2023) 1575-1582 https://doi.org/10.21741/9781644902479-170

Estimation of rolling process variation by usage of a Monte-Carlo method

WEINER Max[1,a *], RENZING Christoph[1,b], SCHMIDTCHEN Matthias[1,c] and PRAHL Ulrich[1,d]

[1]Institute of Metal Forming, TU Bergakademie Freiberg, 09599 Freiberg, Germany

[a]max.weiner@imf.tu-freiberg.de, [b]christoph.renzing@imf.tu-freiberg.de, [c]matthias.schmidtchen@imf.tu-freiberg.de, [d]ulrich.prahl@imf.tu-freiberg.de

Keywords: Rolling Simulation, PyRolL, Monte Carlo Method, Process Variations

Abstract. Rolling simulation, especially for groove rolling, is heavily dominated by use of finite element methods, but simulating a full pass sequence often takes several hours. Simpler models offer high-speed simulation within seconds at the expense of resolution and accuracy. In mechanical engineering, Monte-Carlo approaches are well known for analysis of fabrication tolerances in component assembly. By usage of fast simulation cores, this technique becomes available for analysis of process variations in groove rolling, since computational costs are crucial due to the need of hundreds or thousands of simulation runs. Rolling process variations can be classified in two groups: first, variations of the input material, such as actual dimensions, temperature and microstructure state; second variations occurring during processing, such as transport times, environment temperature and tool wear. The regarded process was the operation of the experimental semi-continuous rolling plant at the Institute of Metal Forming (IMF). Simulations were carried out by use of the open source rolling framework PyRolL, developed at IMF. The main part of process parameters was considered as constant, but some were described as a statistical distribution. For each simulation run a set of actual sample values of the distributed parameters was drawn using a random number generator. Selected result values were described by use of statistical methods to analyze the variational behavior of the process in behalf of the two variation classes.

Introduction

The term Monte Carlo Method (MCM) generally refers to a class of methods, which are characterized by the use of random numbers. These methods are rather diverse and serve different purposes. Here, the term shall be used for the concept of drawing random numbers as input for a function and analysing the results of several evaluations of this function, with different random inputs, with statistical methods. A detailed overview on this type of Monte Carlo methods is given by Lemieux [1]. The nature of the function can be complex, even of a black-box type, where nothing about the internals of the function is known but the input and output interfaces. In this case, Monte Carlo methods can provide valuable information about the behavior of the function while altering inputs.

Here, the function equals the simulation procedure, so it is generally known, but complex. For example, it is generally not possible, to compute derivatives of the outputs in dependence on the inputs in an analytical way. Even numerical derivation is hard, due to the multi-dimensional nature of most natural or technical systems.

The use of Monte Carlo methods for the analysis of variations in technical processes was reported before in the field of assembly of complex structures, like in mechanical engineering and building construction (f.e. [2-7]). However, in the field of rolling processes, there was no such attempt yet to the knowledge of the authors. The authors have previously used a similar approach to model powder morphology influences in sintering processes [8, 9]. The current work shall show

Content from this work may be used under the terms of the Creative Commons Attribution 3.0 license. Any further distribution of this work must maintain attribution to the author(s) and the title of the work, journal citation and DOI. Published under license by Materials Research Forum LLC.

the possibility of the application of Monte Carlo methods for the analysis of process variations in rolling processes. The focus lies hereby on the estimation of the workpiece temperature evolution. The temperature evolution is crucial for the microstructure development of the workpiece, which shall be investigated in a following work. The influence of variations in the initial workpiece and within the regarded process route is analysed and evaluated. Due to the need of a large number of function evaluations (simulation runs), the evaluation speed of the process model is crucial to the applicability of this approach.

Rolling simulation is currently dominated by the use of finite element (FE) based models. These are offering high accuracy and high resolution results at the expense of high computational resource usage. So, these methods are inconvenient for the current need. Therefore, one-dimensional approaches shall be used here. These offer less accuracy and limited resolution, but are computable within fractions of seconds on typical personal computer systems. The current work is based on the open-source rolling simulation framework PyRolL [10], developed by the authors, which is a fast, open and flexible software package mainly aimed at groove rolling in reduction passes. The models used for the different parts of the problem can be exchanged and extended with low effort to the user's needs.

Method

The Institute of Metal Forming operates a semi-continuous pilot rolling plant, which is the object of the current investigation. It consists of a two-high reversing roughing stand and four continuous finishing stands. The pass schedule of the current work consists of 10 oval-round reversing passes followed by 4 oval-round continuous finishing passes. A 50 mm round workpiece made of a mild structural steel is rolled down to 8 mm diameter. Details of the schedule are provided in the supplemental material [11], as the exact properties of the pass schedule are of minor importance for the statements of this work.

Monte Carlo Approach.

The basic idea of the approach shown here is to simulate the rolling process several times with different input values, which are drawn by a random number generator according to predefined statistical distributions. Afterwards, the distribution of the results can be analysed by classic methods of descriptive statistics to obtain information about the process' variational behavior. The principle is shown in Fig. 1.

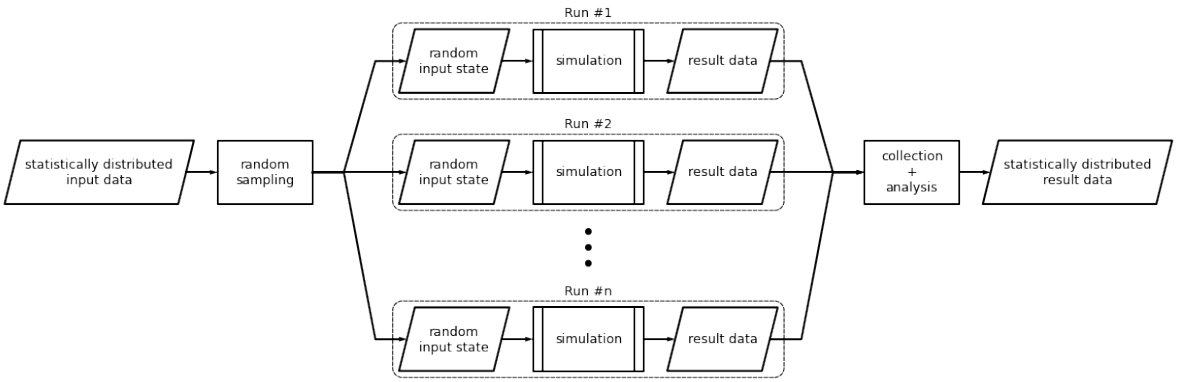

Fig. 1. Chart of the Concept of Variation Estimation Using Monte Carlo Techniques.

This approach provides information about the overall variational behavior of the process. If a single source of variation is introduced in the input, the reaction of the process on this variable can be analysed. The count of variation sources introduced is generally unbounded. The tracing back of result variations to the input can be done using classic correlation methods of descriptive statistics, however, with the same typical caveats. The main benefit of the approach is, that no information about the internals of the simulation procedure is needed for variational analysis,

especially there is no need for derivatives of result values in dependence on the input. The simulation procedure can generally be treated as black box with defined input and output interfaces.

The key problem is to obtain data describing the variations of the input variables. In this work two showcases shall be regarded: first the variation of the initial workpiece in diameter and temperature, second the variation of the inter-pass durations between the reversing passes. This choice was taken, since two fundamentally different types of variation sources were suspected. First, sources in the initial workpiece, which are applied only once, but traverse the whole process line. Second, variations in the process itself, which affect the workpiece state in each process step anew.

The question of varying inter-pass durations is crucial for scientific experiments on microstructure evolution, but currently often neglected. Mostly, only flat durations between the reversing passes are included in the design calculations. Due to manual transport and feed of the workpiece to the following roll pass, the scheduled inter-pass durations are never realized in practice. Although, these deviations from the schedule influence the microstructure evolution of the sample, as well as the actual conditions in the roll passes. The current approach is aimed to help quantifying these deviations.

Data Acquisition.

The pilot plant at IMF is equipped with several measurement and data collection systems. Data from a number of rolling trials have been collected and analysed to obtain the inter-pass durations t between the reversing passes. The complete dataset and analysis routines are available in the supplemental material [11].

For the approximative description of the durations' distribution, a gamma distribution was used, which is a generalized exponential distribution. The probability density function (PDF) of the gamma distribution is defined as in Equation 1, where Γ is the gamma function and $\alpha > 0$ and $\beta > 0$ are parameters.

$$f(x) = \frac{\beta^{\alpha}}{\Gamma(\alpha)} x^{\alpha-1} \exp(-\beta x) \tag{1}$$

Since the gamma distribution is only defined for $x > 0$, but no inter-pass durations below a certain value occur due to technical restrictions, the distribution was modified by introducing a minimal inter-pass duration t_0 with $x = t - t_0$. So, there are three free parameters α, β and t_0 for fitting of the distribution function. The fitting was done using least squares optimization of the resulting PDF function on the density histogram of the data. Statistical analysis and model fitting were done by use of the SciPy [12] and Pandas [13, 14] software packages.

Core Simulation Procedure.

In the current work, the open-source rolling simulation framework PyRolL [10] was used to simulate the rolling process. Generally, the shown approach can be used with every rolling simulation software available, since the procedure does not depend on any internals of the simulation. A fast simulation approach, however, is favourable, since the simulation has to be done several, up to hundreds of, times. The models used here are of one-dimensional type, thus, they lack of resolution in other directions as the rolling direction and provide only limited accuracy, but at the benefit of high solution speed. They typically combine empirical approaches with simplified analytical solutions. PyRolL is designed to offer simple exchangeability of the used model approaches. The model set can be chosen in a modular way by loading plugin packages. The current simulation was done with the basic configuration of PyRolL, which includes the empirical roll force and torque model of Hensel and Spittel [15], an integral thermal model approach according to Hensel et al. [16], contact area estimation according to Zouhar [16] and roll flattening

according to Hitchcock and Trinks [18]. Spreading was simulated using the equivalent flat pass according to Lendl [19-21] in conjunction with the spreading equation of Wusatowski [22]. The calculation time of one simulation run is below 1 s on typical current desktop computer systems. Details of software construction and model equations are provided in the documentation of PyRolL [10].

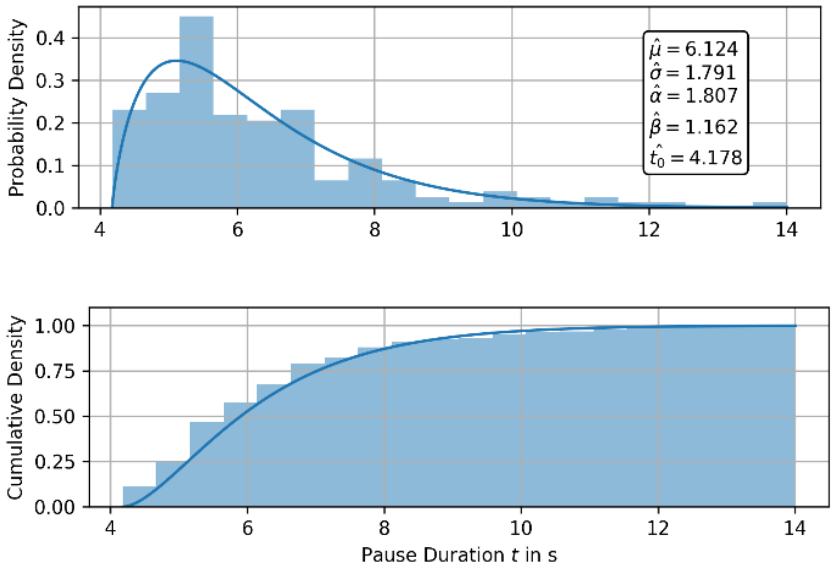

Fig. 2. Histograms of Inter-Pass Duration Between Roll Passes of the Reversing Mill.

Results

Inter-pass Durations For the analysis of the inter-pass durations a set of 29 rolling trials was analysed. The histograms of the obtained dataset are shown in Fig. 2 in conjunction with the fitted distribution parameters. The mean inter-pass duration was about $\mu(t) = 6.1$ s. The 90 % confidence interval is between 4.50 s and 9.32 s. Data points larger than 15 s were capped as outliers, since they occurred very rarely and are related to operational problems.

Simulation Showcases.

In the following, two showcases of the Monte Carlo approach described above shall be shown. For each case 100 sample conditions were drawn using a random number generator. The current analysis was limited to the aspect of temperature evolution as example for the possibilities of the method, although other key problems such as roll force and torque, spreading and filling, as well as elastic rolling stand behavior are included in the simulation core. The temperature evolution was selected, because it is the most vivid property of the process to show the importance of variation analysis. It influences directly and substantially the plastic material behavior and the evolution of the microstructure, while it is quite sensitive to most process conditions. More detailed data is included in the supplemental material [11].

The first showcase is the analysis of variations solely in the input workpiece. Exemplary, the diameter d of the round profile and the mean initial temperature T of the workpiece were chosen. Their variations were modelled using normal distributions with the nominal values as mean $\mu(d) = 50.0$ mm resp. $\mu(T) = 1373$ K and standard deviations of $\sigma(d) = 1.0$ mm resp. $\sigma(T) = 10$ K. The inter-pass durations were here chosen as an approximate constant of $t = 6.1$ s (corresponding to the mean inter-pass duration above) for the reversing passes, but were calculated directly from rolling velocity and distance for the continuous passes.

The resulting temperature evolution is shown in Fig. 3. The variations of the incoming and outgoing temperatures at each roll pass are plotted as boxplots in the respective positions. Two

line plots show the results of the simulation using only the nominal values and the mean curve of the Monte Carlo results. These were rather equivalent in this case. The variations of the simulation results tended to decrease along the pass schedule, compare also Fig. 5. In the continuous passes, the variations of the workpiece temperatures were rarely significant. This is in accordance to practical experience.

The second showcase is the consideration of the varying inter-pass durations during operation of the reversing mill due to manual feeding. The durations were drawn from the gamma distribution created above. The remaining parameters were the same as in the first case.

The resulting temperature distribution is shown in Fig. 4 similarly to the first case. The standard deviations of both cases are compared in Fig. 5. In contrast to the first case, the variations of the workpiece temperature are not decreasing along the pass schedule but in the finishing passes, since additional variation is introduced between each pass of the reversing mill. So the variation of the utput workpiece is higher than that of the input. Additionally, the mean of the Monte Carlo results tends to deviate from the nominal results, unlike the first case.

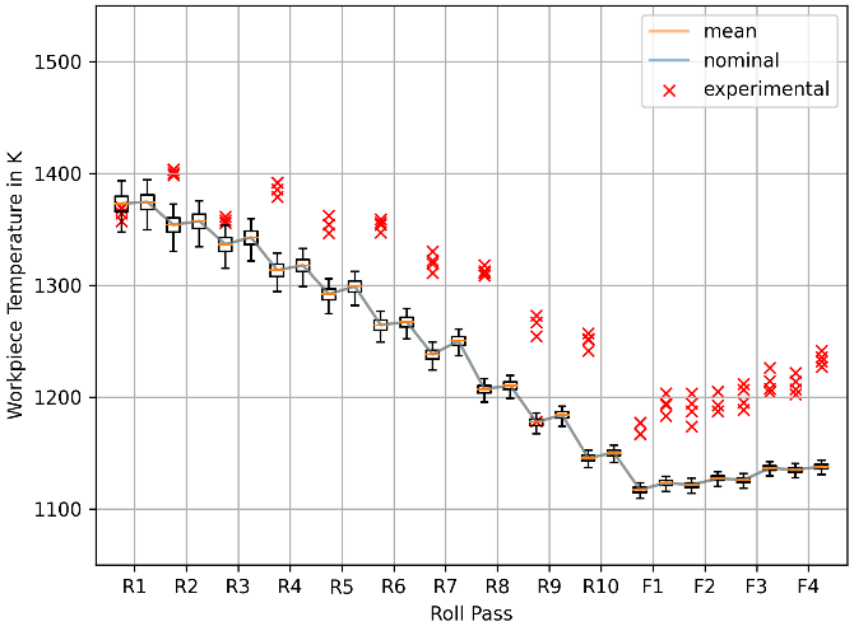

Fig. 3. Temperature Evolution Within the Rolling Process Under Variation of the Initial Workpiece.

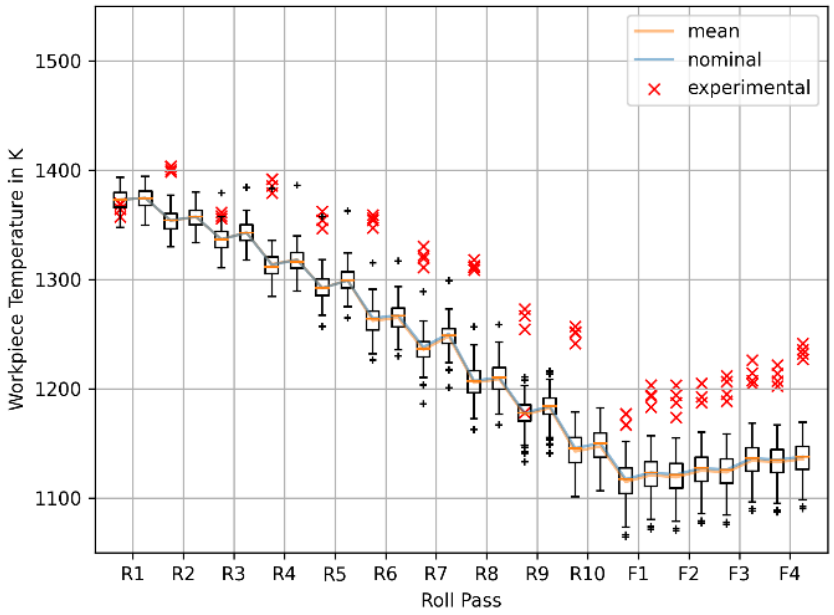

Fig. 4 Temperature Evolution Within the Rolling Process Under Variation of the Initial Workpiece and of the Inter-Pass Durations.

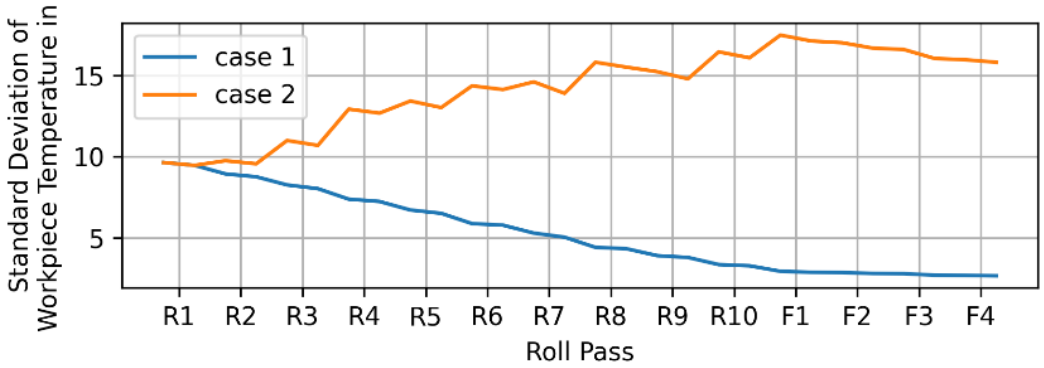

Fig. 3. Evolution of the Temperature Standard Deviation.

Summary

The current work showed the general applicability of Monte Carlo method based variation estimation techniques on the variational behavior of rolling processes. Two different kinds of variation sources in rolling processes were identified: first, variations in the input workpiece, second, variations within the process. They showed fundamentally different behavior. While variations in the input workpiece tend to vanish along the process, variations in the process itself accumulate and lead to high variations in the product. This leads to the conclusion, that the control of variations within the process is crucial in comparison to variations in the input material.

Especially in the case of manual feeding of a reversing mill, as common in pilot plants, this has to be kept in mind. It can be stated, that a well-controlled process should tend to decrease the variations of its input workpiece. These findings are in accordance to practical experience. In following work, the concept will be extended by the use of more advanced models within the simulation core. However, this has to be done always with the computational effort in mind, since the core simulation must be carried out up to hundreds of times. With the use of locally resolved models, estimations regarding the variation of local workpiece state can be carried out. Especially in terms of microstructure evolution, this would be a valuable contribution to the interpretation of

experimental results. In the future, this approach can help to identify sources of variations within a process and evaluate their influence on the resulting output variations.

A key is the acquisition of a statistical description of the process parameters. A first estimate can be given by a normal distribution with a certain standard variation around the nominal parameter value. For more accurate results, the collection of data in the running process may be appropriate, as was shown for the inter-pass durations. The method's reliability is dependent on both, the accuracy of the simulation models and the statistical parameter description.

References

[1] C. Lemieux, Monte Carlo and Quasi-Monte Carlo Sampling, Springer New York, (2009). ISBN: 978-0-387-78165-5. https://doi.org/10.1007/978-0-387-78165-5.

[2] C.-Y. Lin, W.-H. Huang, M.-C. Jeng, J.-L. Doong, Study of an Assembly Tolerance Allocation Model Based on Monte Carlo Simulation, J. Mater. Process. Technol. 70 (1997) 9-16. https://doi.org/10.1016/S0924-0136(97)00034-4.

[3] Zhengshu Shen, Gaurav Ameta, J.J. Shah, J.K. Davidson, A Comparative Study Of Tolerance Analysis Methods, J. Comput. Inform. Sci. Eng. 5 (2005) 247-256. https://doi.org/10.1115/1.1979509.

[4] J.-Y. Dantan, A.-J. Qureshi, Worst-Case and Statistical Tolerance Analysis Based on Quantified Constraint Satisfaction Problems and Monte Carlo Simulation, Computer-Aided Design 41 (2009) 1-12. https://doi.org/10.1016/j.cad.2008.11.003.

[5] A.-J. Qureshi, J.-Y. Dantan, V. Sabri, P. Beaucaire, N. Gayton, A Statistical Tolerance Analysis Approach for Over-Constrained Mechanism Based on Optimization and Monte Carlo Simulation, Computer-Aided Design 44 (2012) 132-142. https://doi.org/10.1016/j.cad. 2011.10.004.

[6] H. Yan, X. Wu, J. Yang, Application of Monte Carlo Method in Tolerance Analysis, Procedia CIRP. 13th CIRP Conference on Computer Aided Tolerancing 27 (2015) 281-285. https://doi.org/10.1016/j.procir.2015.04.079.

[7] C. Rausch, M. Nahangi, C. Haas, W. Liang, Monte Carlo Simulation for Tolerance Analysis in Prefabrication and Offsite Construction, Automat. Constr. 103 (2019) 300-314. https://doi.org/10.1016/j.autcon.2019.03.026.

[8] M. Weiner, M. Schmidtchen, U. Prahl, A New Approach for Sintering Simulation of Irregularly Shaped Powder Particles - Part I: Model Development and Case Studies, Adv. Eng. Mater. 24 (2022). https://doi.org/10.1002/adem.202101513.

[9] M. Weiner, T. Zienert, M. Schmidtchen, J. Hubálková, C.G. Aneziris, U. Prahl, A New Approach for Sintering Simulation of Irregularly Shaped Powder Particles - Part II: Statistical Powder Modelling, Adv. Eng. Mater. (2022) 202200443. https://doi.org/10.1002/adem.202200443.

[10] M. Weiner, C. Renzing, M. Stirl, and M. Schmidtchen. PyRolL. Version 1.0.5. Institute of Metal Forming, TU Bergakademie Freiberg. URL: https://pyroll-project.github.io.

[11] M. Weiner, C. Renzing, R. Pfeifer, M. Schmidtchen, U. Prahl. Supplemental Material to 'Estimation of Rolling Process Variation by Usage of a Monte-Carlo Method' at ESAFORM2023. 2022. https://doi.org/10.25532/OPARA-195.

[12] P. Virtanen, R. Gommers, T.E. Oliphant, M. Haberland, T. Reddy, D. Cournapeau, E. Burovski, P. Peterson, W. Weckesser, J. Bright, S.J. van der Walt, M. Brett, J. Wilson, K. Jarrod Millman, N. Mayorov, A.R.J. Nelson, E. Jones, R. Kern, E. Larson, C.J. Carey, I. Polat, Y. Feng, E. W. Moore, J. VanderPlas, D. Laxalde, J. Perktold, R. Cimrman, I. Henriksen, E.A. Quintero, C.R. Harris, A.M. Archibald, A.H. Ribeiro, F. Pedregosa, P. van Mulbregt, SciPy 1.0 Contributors, SciPy 1.0: Fundamental Algorithms for Scientific Computing in Python, Nat. Methods 17 (2020) 261-272. https://doi.org/10.1038/s41592-019-0686-2

[13] pandas-dev/pandas: Pandas (2020). https://doi.org/10.5281/zenodo.3509134

[14] W. McKinney, Data Structures for Statistical Computing in Python, Proceedings of the 9th Python in Science Conference (2010), pp. 56-61. https://doi.org/10.25080/Majora-92bf1922-00a
[15] A. Hensel, T. Spittel. Kraft- und Arbeitsbedarf bildsamer Formgebungsverfahren, VEB Deutscher Verlag für Grundstoffindustrie, 1978.
[16] A. Hensel, P. Poluchin, W. Poluchin, Technologie der Metallformung. Deutscher Verlag für Grundstoffindustrie, 1990.
[17] G. Zouhar, Umformungskräfte beim Walzen in Streckkaliberreihen, Akademie Verlag Berlin, 1960.
[18] J. H. Hitchcock, W. Trinks, Roll Neck Bearings. Report of Special Research Committee on Roll Neck Bearings, ASME (1935) 51.
[19] A. E. Lendl, Rolled Bars - Part I - Calculation of Spread between Non Parallel Roll Surfaces, Iron and Steel 21.14 (1948) 397-402.
[20] A. E. Lendl, Rolled Bars - Part II - Application of Spread Calculation to Pass Design, Iron and Steel 21 (1948) 601-604.
[21] A. E. Lendl, Rolled Bars - Part III - Application of Spread Calculation to Diamond Passes, Iron and Steel 22 (1949) 499-501.
[22] Z. Wusatowski, Fundamentals of Rolling, Pergamon Press, 1969.

Materials Research Proceedings 28 (2023) 1583-1592 https://doi.org/10.21741/9781644902479-171

Influence of mesh in modelling of flow forming process

KRISHNAMURTHY Bhaskaran[1,a *], SHITIKOV Andrei A.[2,b], BLACKWELL Paul[3,c] and BYLYA Olga[1,d]

[1]AFRC, University of Strathclyde, 85 Inchinnan Drive, Inchinnan, Renfrew PA49LJ, UK

[2]QuantorForm LLC, 2nd Yuzhnoportovyy Proyezd, 16/2, Moscow 115088, Russia

[3]DMEM, University of Strathclyde, 75 Montrose Street, Glasgow G11XJ, UK

[a]bhaskaran.krishnamurthy@strath.ac.uk, [b]aa-shitikov@yandex.ru, [c]paul.blackwell@strath.ac.uk, [d]olga.bylya@strath.ac.uk

Keywords: Incremental Bulk Forming, Flow Forming, Meshing, Coarse Meshing

Abstract. Flow forming is an incremental bulk forming process used to produce tubular components from high-strength alloys. One of the features complicating its modelling is the small contact area of the workpiece with the tools. Taken along with cyclic non-monotonic loading from three rollers deforming the workpiece with complicated kinematics, this demands a very fine mesh and time step throughout the simulation. The typical approach of using a tetrahedral mesh with strain-based remeshing can introduce errors in the results due to the highly localized deformation and can also prolong the computation time. In the present study, in parallel to using tetrahedral mesh with remeshing, two different approaches of hexahedral mesh without any remeshing were also modelled for the workpiece, retaining all the other setup parameters, and the results compared. In both cases, local mesh adaptations were used to ensure a very fine mesh in the zone of contact with the rollers. Results from the simulations clearly showed that the key outputs such as stress state parameters (triaxiality and Lode stress parameters) and plastic strain values were very sensitive to the mesh and remeshing method used and careful consideration is required before employing the outputs for further analysis.

Introduction

Flow forming is an incremental bulk forming process employing two or three rollers that produce localized zones of deformation to manufacture near-net shape tubular components [1,2]. It is a flexible and effective method to produce parts from high-strength alloys with limited ductility at room temperature[3]. It is highly flexible as it affords the possibility of independent setting of up to seven process parameters (mandrel rotation speed, axial and radial displacement speeds of three independent rollers) as detailed in [4,5] and this enables different forming strategies depending on the material, component shape and machine capabilities. In addition, for large thickness reduction ratios of thick-walled workpieces with wall thinning of up to 80–90%, the process can be carried out in several passes [5,6].

However, the process is innately complex and deciding on a forming strategy or solving particular problems such as component fracture are not straight-forward. Finite-element (FE) modelling of the process can provide some much needed insight into the complicated process mechanics, but it is not without its fair share of complications, as detailed in the work of Bylya et al. [7]. One of the features of the flow forming process that complicates its modelling is the small contact area of the workpiece with the rollers. This circumstance imposes special requirements on the choice of the finite element mesh and the time step of the calculation. Consequently, the choice of mesh size and time step influences the output from the model considerably. The inaccuracy and errors resulting from the choice of mesh will impact further analysis such as fracture prediction

Content from this work may be used under the terms of the Creative Commons Attribution 3.0 license. Any further distribution of this work must maintain attribution to the author(s) and the title of the work, journal citation and DOI. Published under license by Materials Research Forum LLC.

that uses the outputs from the simulation and therefore cannot be overlooked in the case of robust modelling required for industrial applications.

For finite deformations in bulk forming processes, typically, a tetrahedral mesh is employed in many commercial metal forming software and a strain-based remeshing algorithm is used to remesh the nodes and elements when the strain reaches a certain value, which can be set by the user. The remeshing is helpful to avoid distortion of meshes at very high strains and can be beneficial is most metal forming modelling for improving the accuracy of the model. However, in incremental bulk forming processes, such as flow forming, remeshing can introduce errors in the results due to highly localized deformation and can also prolong the computation time. The influence of mesh size and remeshing formulation has been reported in few earlier works [8,9]. The focus therein was limited to sensitivity analysis against a specific output value (von Mises stress) [9] or the differences between different formulation of the problem, i.e., Euler, Lagrangian or ALE[8]. In the present work, in parallel to the typical approach of using tetrahedral mesh with remeshing, alternative use of hexahedral mesh for the workpiece without any remeshing was also modelled, using the same Lagrangian formulation and retaining all the other setup parameters. The key output parameters from the models were analyzed and compared against actual experimental findings.

Experimental Data Used for Modelling

A relatively short process involving a single pass flow forming of Ti6Al4V tube of thickness 12 mm is taken for simulation and for comparison of the models. It was found experimentally with repeatability that Ti6Al4V preforms fractured before the roller reached a final depth of 9 mm (i.e., reduction of 3 mm (25%)). A finite-element simulation of the process will play a crucial role in understanding the reason behind the failure. Furthermore, owing to the short duration of the actual process prior to failure, i.e. 16 s, the process can be simulated completely using a full 3D elasto-plastic formulation and with fine mesh and time-step settings. A schematic of the process and process parameters used in the model setup are provided in Fig. 1 and the kinematics parameter used for the model setup are summarized in Table 1.

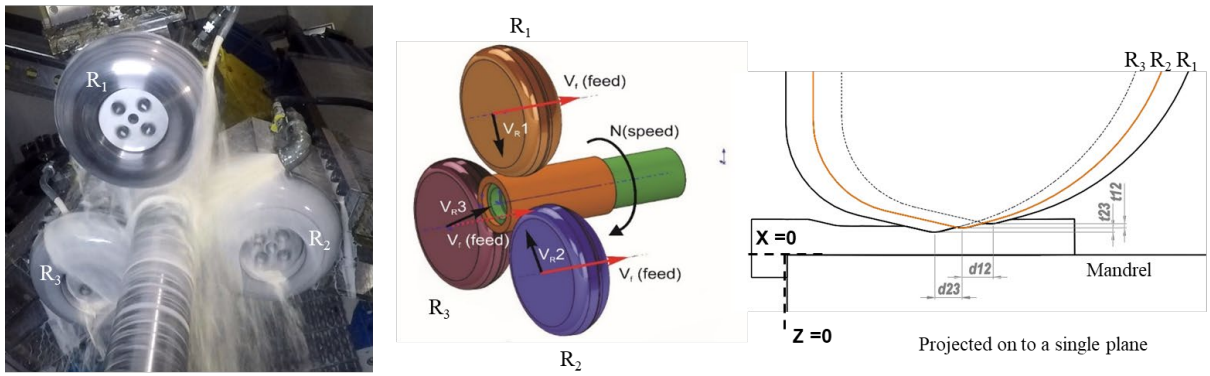

Fig. 1. Three-roller flow forming process - (a) capture of process carried out at AFRC, University of Strathclyde, (b) schematic of the process representing the main process parameters and (c) schematic showing the axial and radial positions of the three rollers when projected on to a single axial plane.

The rollers are located 120° apart in the circumferential direction as shown in Fig. 2 (a) and (b), with Roller 1 directly above the workpiece in what is designated as the vertical axis for the whole setup. The rollers are staggered both axially and radially. The total reduction is split between the rollers in such a way that Roller 1 has a bite of 1 mm, Roller 2 goes further deep with a radial

offset of 1 mm between Roller 1 and 2 (t_{12}) and Roller 3 goes even further deep with a radial offset of 1 mm between Roller 2 and 3 (t_{23}); in summary, the total bite of Roller 2 and Roller 3 are set to be 2 and 3 mm, respectively. In addition, Roller 2 trails behind Roller 1 by 4 mm (d_{12}), and Roller 3 trails behind Roller 2 by 4 mm (d_{23}) in the axial direction. When projected onto a single plane the roller offset will appear as shown in Fig. 2(c). A constant rotation speed of 150 RPM is prescribed to the mandrel and a tailstock is used to apply pressure across the face of the workpiece such that the workpiece rotates along with Mandrel without slipping. The rollers do not have their own spindle drives but rotate only due to the friction on contact with the workpiece.

Table 1. Summary of main process parameters used in experimental trials studied.

Speed, N [RPM]	Feed, V_f [mm/s]	Initial Thickness, t_0 [mm]	Final Thickness, t_f [mm]
150	1	12	9
Radial offset b/w Roller 1 and 2, t_{12} [mm]	Radial offset b/w Roller 2 and 3, t_{23} [mm]	Axial offset b/w Roller 1 and 2, d_{12} [mm]	Axial offset b/w Roller 2 and 3, d_{23} [mm]
1	1	4	4

Modelling Approach

To obtain a smooth deformation field when simulating the process, the roller must pass the contact zone in at least three time steps. The typical size of the contact spot according to experimental measurements for the case of the simulated process is approximately 9 × 16 mm, please refer to Fig. 2(a). With a workpiece rotation speed of 150 rpm and the external diameter of the part being 164 mm, the calculated time step should not exceed 4 ms. In order for at least 8–10 workpiece nodes to be in contact with the roller (blue dots in Figure 2a), the required size of the finite element mesh element should not exceed 2 mm; this is also necessary for the correct modelling of the plastic deformation gradient, and the resulting residual stresses, across the thickness of the workpiece (Fig. 2(b)). Furthermore, elastic deformation of the rest of the workpiece and secondary plastic deformation of the already deformed regions also play a crucial role, and therefore a relatively fine mesh is also required in regions that are in the vicinity of contact with rollers and also in already deformed regions.

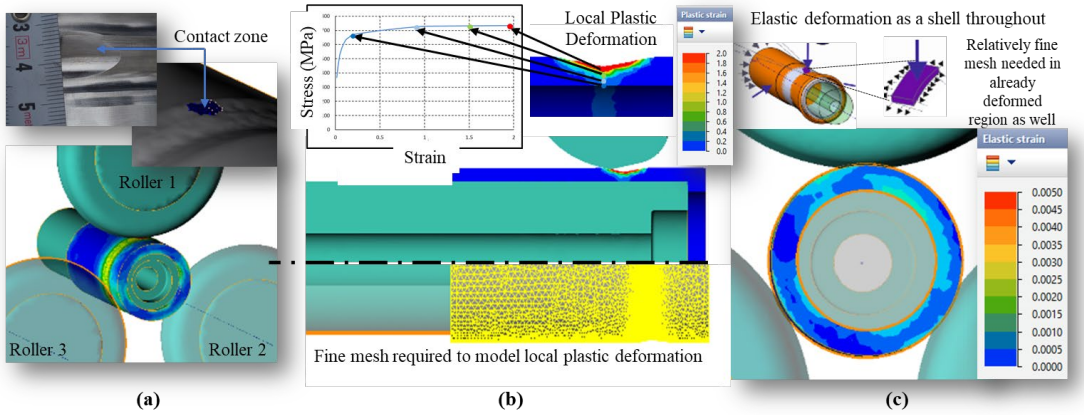

Fig. 2. Factors influencing the finite element mesh when modelling flow forming: a) small contact area between the workpiece and rollers (inset: measurement from experiment and that observed in FE simulation), b) local plastic deformation (showing the gradient of plastic strain along thickness), c) elastic deformation of workpiece as a shell throughout.

To analyze the influence of mesh settings, 3 different cases were simulated as shown in Fig. 3: Case I - default tetrahedral mesh with strain-based remeshing (Fig. 3 (b)); Case II – a coarse hexahedral mesh with less than 2 mm element size in the contact zone without remeshing through the process (Fig. 3 (c)); Case III - a finer hexahedral mesh with less than 1 mm element size in the whole deforming region of workpiece without remeshing through the process (Fig. 3 (d)). Only the first 16 s of the process leading to the fracture were simulated in each case. In Case I and II, a local mesh adaptation covering the expected contact zone with the three rollers through the process was used to refine the initial mesh to 1 mm and 2 mm, respectively. In regions outside the mesh adaptation, an average mesh sizes of 5-8 mm were used in both cases. In Case III, a fine mesh with average element size of 1 mm was used in the region covering the expected start of contact with rollers to the end of the workpiece as shown in Fig. 3 (d). The nose region in the rollers, which typically contact the workpiece, were also meshed fine as shown in Fig. 3 (a) to ensure proper contact area calculations.

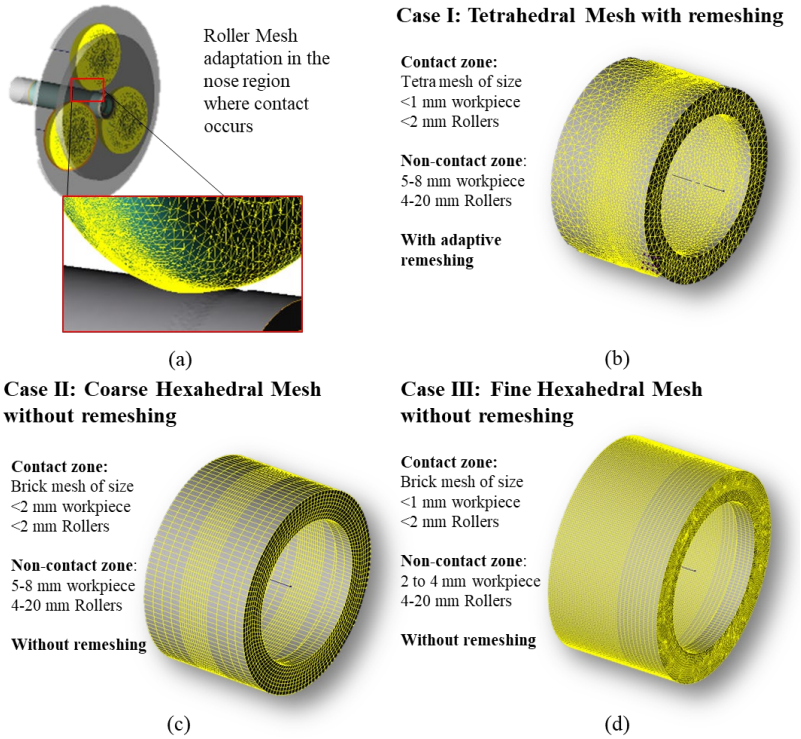

Fig. 3. Mesh settings used in the study – (a) Mesh adaptation used in the nose region for meshing of rollers to simulate accurate contact with workpiece; Workpiece mesh settings used in (b) Case I with tetragonal mesh and strain-based remeshing, (c) Case II with relatively coarse hexagonal mesh and without remeshing through process, and Case III with finer hexagonal mesh and without remeshing through process.

All the cases were simulated using commercial metal-forming software, QForm. The tool kinematics in the model setup were maintained as close to the real process as possible and were the same in all 3 cases. A full 3D elasto-plastic model with isotropic hardening material model obtained from room-temperature tensile tests carried out with the same batch of Ti6Al4V as used in the flow forming trials was used for the simulations. A constant timestep of 1 ms was used everywhere. The friction condition at mandrel and roller contact were maintained the same in all cases well. A low friction (Levanov friction factor of 0.2) and high friction (Levanov friction factor of 0.2) condition were specified at the workpiece interface with mandrel and rollers, respectively.

The temperature in the workpiece was observed to not rise beyond 50°C in experiments owing to strong coolant flow. Hence, the thermal simulation was neglected in all cases.

Results and Discussion

All three simulated cases showed reasonable agreement with roller reaction forces and final geometry observed in the experimental trials. In the experiments, it was observed that the fracture initiated on the inner surface of the workpiece in contact with the mandrel, as shown in Fig. 4(a). The trials were stopped at different instances and the fracture was identified to originate just under where roller 3 would be when it reached a depth of approx. 10 mm. Three points in the same axial plane at different depths along the thickness – Outer (surface), Mid (6 mm deep), and Inner (12 mm deep, in contact with mandrel) – corresponding to this section were identified in the simulations for further analysis, with Inner marking the location of fracture, as shown in Fig. 4(b). The same three points with exact XYZ coordinates in all three cases of simulation were tracked through the whole process, and the history of key output parameters, particularly accumulated plastic strain, triaxiality and Lode angle parameters, were traced. Furthermore, the timestamps of key events during the process, namely, Roller 1 Contact, Roller 2 Contact, Roller 3 Contact and the instance of fracture initiation with respect to the 3 identified points were recorded as shown in Fig. 4(c) and these were converted to mandrel revolutions for easy comparison.

A through-process comparison of the key output parameters from all 3 cases for the 3 identified points are presented in the following section:

Accumulated Plastic Strain.

Accumulated plastic strain or the Odquist parameter, calculated using Eq. 1 below, is an important representative scalar of the total strain path during the process and is often used in further calculations such as residual stress and fracture prediction.

$$\varepsilon^P = \int_0^t \dot{\bar{\varepsilon}}^p dt \tag{1}$$

Fig. 5 below shows a comparison of the history of accumulated plastic strain in the three cases simulated. As can be seen from Fig. 5(a), the ε^P in Case I exhibits kinks or jumps in values, which are absent in Case II and III. This can be attributed to the remeshing in Case I, wherein remeshing introduces errors in plastic strain value when remapping the calculated strain from previous time step to the newly generated mesh. Transportation of tensor values from old mesh to the new mesh poses considerable challenges and different software employ different assumptions to carry out this operation, and this introduces small errors during remapping. On repeating the operation for a few times in the case of large deformations, the errors become pronounced. This issue is not limited to QForm but is observed in other commercial FE software as well and is a challenge that warrants further in-depth study.

In addition to this, the calculated values for plastic strain in Outer and Mid points in Case I are considerably higher than those calculated in Case II and III. Given that the total reduction in thickness was 2 mm at failure, and the Mid point is 6 mm from the initial surface of the workpiece, the extremely high value of plastic strain, $\varepsilon^P = 2$, predicted for the point in Case I appears erroneous.

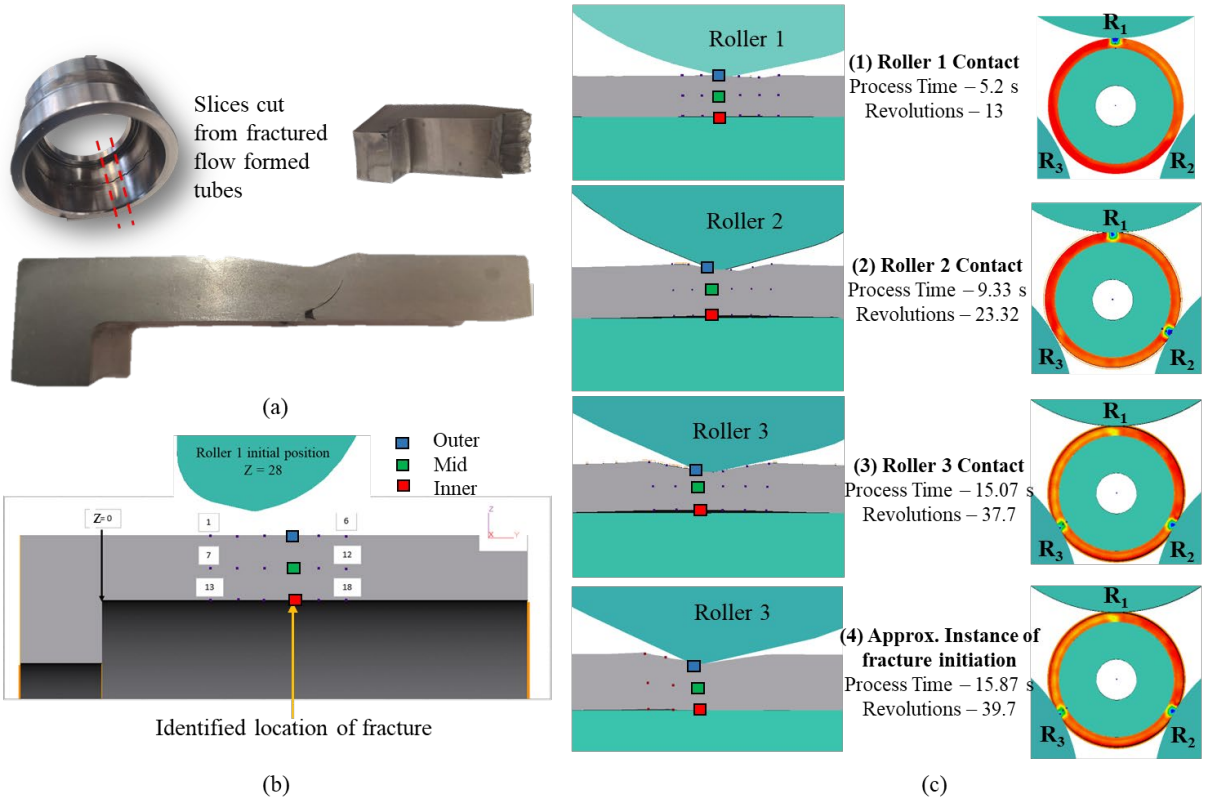

Fig. 4. Tools used for analysis of results – (a) fracture observed in experimental trials showing the location of fracture initiation, (b) points traced through the whole process in all three simulations, and (c) the timestamps of key events during the process, namely, Roller 1 Contact, Roller 2 Contact, Roller 3 Contact and instance of Fracture initiation w.r.t the points traced.

The ε^P values predicted in Case II and III appear more reliable. The difference observed in values between those calculated in Case II and Case III shows the sensitivity of the results to the mesh size used. Case III with a finer mesh can be expected to provide more accurate results in this case. Unfortunately, since the value of plastic strain cannot be directly measured but only inferred through other measurements and observations, novel calibration strategies are required to further validate the results, which are beyond the scope of this present work.

Stress-state Parameters.

Triaxiality and Lode angle parameters are important stress-state parameters that are most commonly used in fracture criteria [10, 11]. Triaxiality parameter (η), defined as the ratio of mean stress (σ_m) to equivalent or effective stress ($\bar{\sigma}$), as expressed in Eq. 2 below, is a useful parameter to represent the 3D stress-state in a point. A Triaxiality parameter of $\eta = -1/3$ represents purely uniaxial compressive stress, $\eta = 0$ represents pure shear, $\eta = 1/3$ represents purely uniaxial tensile stress and intermediate points represents a combined stress state in a point. Experimental investigation on fracture locus in Ti6Al4V show that the material is prone to fail under a tensile stress state earlier than in other conditions and $\eta >= 1/3$ are unsafe [12].

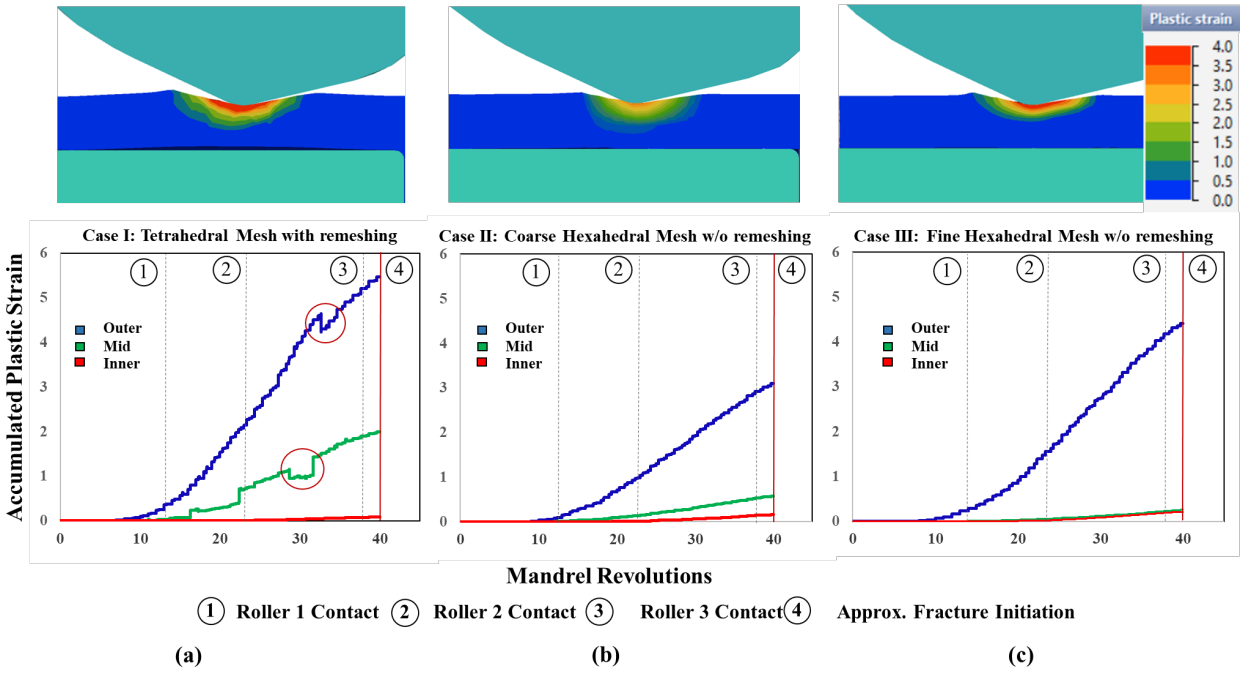

Fig. 5. Comparison of history of accumulated plastic strain in all 3 cases simulated: (a) Case I – tetrahedral mesh with remeshing, (b) Case II – Coarse hexahedral mesh, (c) Case III – fine hexahedral mesh. (Top inset: Plastic strain profile across thickness at the instance of fracture initiation in all 3 cases).

Looking at the fracture observed in flow formed Ti6Al4V tubes, the fracture appears on the inner surface where plastic strain is almost 0 and fracture surface was observed to be brittle and most probably resulted from the tensile stress state along the inner edge of the tubes directly under the rollers (refer to Fig. 6(a) and 6(b)).

$$\eta = \frac{\sigma_m}{\bar{\sigma}} \tag{2}$$

Fig. 6(c-e) shows a comparison of the history of triaxiality parameter for the same three points in all three cases studied. As can be observed, the history is considerably different in the three cases, and in Cases I and III employing a fine mesh, the deviations about the mean values are higher compared to Case II with a relatively coarser mesh. Case II and III using a Hexahedral Mesh show a trend with predominantly tensile stresses ($\eta = 1/3$) in the Inner point where fracture occurred and also in the Mid point in the initial stages closer to the contact with Roller 1. The stress state in the Mid point then transitions towards compressive stress ($\eta = -1/3$) as the reduction increases under Roller 2 and 3, which appears logical.

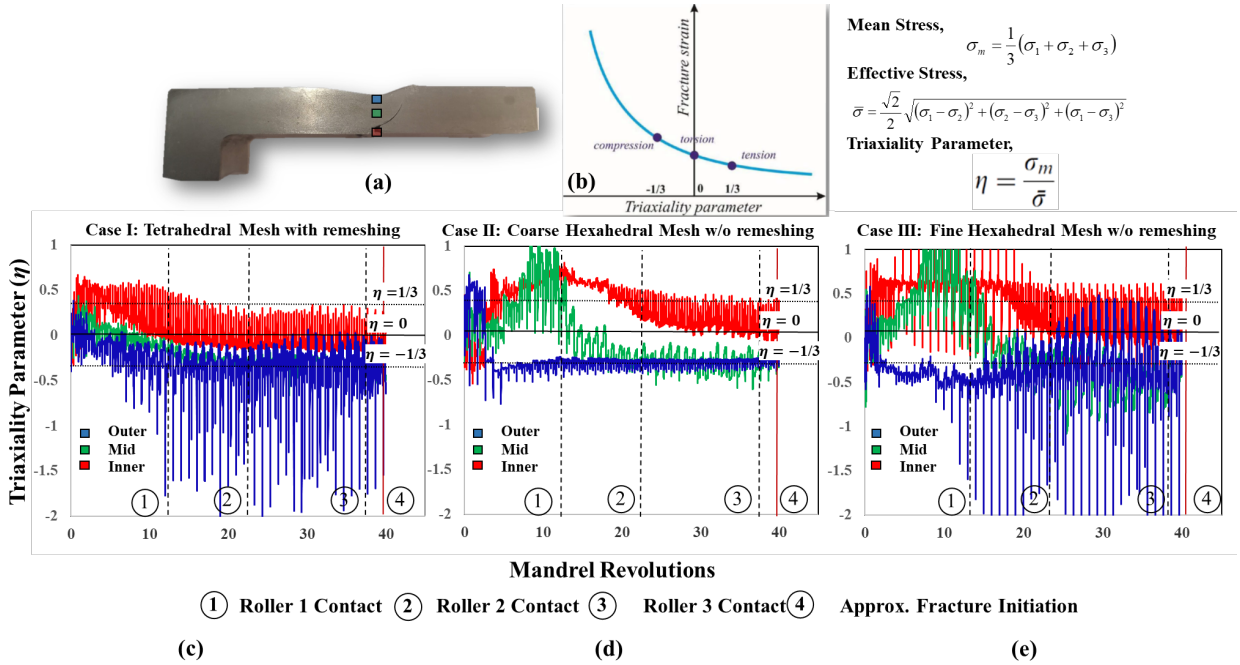

Fig. 6. Comparison of history of triaxiality parameter in all 3 cases simulated: (b) Case I – tetrahedral mesh with remeshing, (c) Case II – coarse hexahedral mesh, (d) Case III – fine hexahedral mesh. (Top inset: (a) Key: Location of points with respect to observed fracture, (b)) relationship between fracture strain and triaxiality parameter).

The duration from Roller 3 contact (Revolution 38) to the time of fracture initiation (Revolution 40) was examined further in-depth as shown in Fig. 7. The three peaks observed within a single revolution corresponds to the instant when the points are directly under the influence of the 3 rollers. As can be clearly seen in the figure, Case II and III predict tensile stresses in Inner Point, which correlates well with the main hypothesis that fracture originated in this location due to unsafe tensile stress-state prevalent at this point, while Case I does not. Case III predicts higher triaxiality and additional peaks, which warrants further investigation to be taken up in future work. Similar differences were observed in the case of Lode angle parameter as well but are not presented herein for brevity.

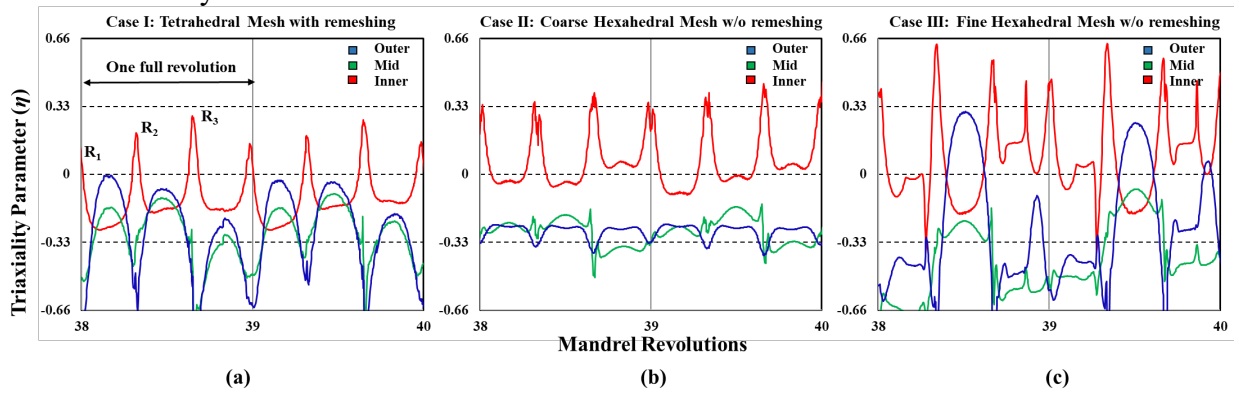

Fig. 7. In-depth comparison of history of triaxiality parameter in all 3 cases simulated in the last 2 revolutions leading up to fracture initiation.

Computation time.

The total simulation time for the three cases differed considerably and were – (i) Case I – 93 hr 24 min 48 s; (ii) Case II - 24 hr 17 min 59 s; (iii) Case III – 63 hr 49 min 13 s. It is understood that the total node count dictates the number of equations to be solved and directly influences the computation time. The total node count in the three cases simulated were - (i) Case I – 22525; (ii) Case II - 13806; (iii) Case III – 40956. As can be observed, the total simulation time in Case III was lower than that in Case I, despite having higher node count. This implies that remeshing is the chief time-consuming operation. Furthermore, in the case of hexahedral meshes, the absence of errors introduced by the remeshing operation could also lead to faster convergence of solution.

For the present case involving flow forming of Ti6Al4V tubes, hexahedral mesh appears to provide more reliable results. For cases involving large deformations and multiple passes of forming, distortion of mesh cannot be avoided without remeshing and appropriate strategies for restoring the mesh and more accurate methods for remapping the results to the restored mesh have to be investigated.

Summary

Flow forming an incremental bulk forming process with localized plastic deformations, owing to the process nature, imposes special requirements on the choice of finite element mesh and time step in simulations. Therefore, the results are highly sensitive to the mesh used. To gain a better understanding of the influence of mesh settings, 3 different cases were simulated herein - tetrahedral mesh with strain-based remeshing and two hexahedral mesh settings (relatively coarse and fine) without remeshing. A relatively short process involving a single pass flow forming of Ti6Al4V tube exhibiting fracture in the initial stages was used as the basis for model development and comparison.

- Although all cases modelled displayed comparable prediction of roller forces and output geometry, they exhibited stark differences in key output parameters, namely, accumulated plastic strain and triaxiality and Lode angle parameters that are used in critical analysis such as fracture prediction.
- For the process considered, hexahedral mesh without remeshing provided more reliable results in terms of accumulated plastic strain. Tetrahedral with remeshing provided erroneous plastic strain values in critical points in the workpiece and also introduced jumps in plastic strain history when remapping the calculated strain from previous time step to the newly generated mesh during remeshing. For short single pass flow forming, use of hexahedral mesh without remeshing is suggested as a reliable method. However, for cases involving large deformations and multiple passes of forming, distortion of mesh cannot be avoided without remeshing and more accurate methods for remapping the results during remeshing needs to be researched.
- Triaxiality and lode angle parameter from hexahedral mesh simulations without remeshing also indicate tensile stress state in the point of origin of failure, supporting the hypothesis that the fracture in question originated due to unsafe tensile stress state along the inner edge of the tube during roller penetration. The history of triaxiality and Lode angle parameters predicted using tetrahedral mesh simulation with remeshing exhibit a different trend to that observed in hexahedral mesh simulations. Before employing the results for particular problem solving such as fracture prediction, it is required to make sure that the results obtained are robust and trustable.
- Although the differences between the results are apparent and results from hexahedral mesh appear reliable when compared with experimental observation, further validation is required to improve trustworthiness of the results. Novel and intelligent validation techniques are required for this as these key output parameters are not readily measurable from experiments.

References

[1] C.C. Wong, T.A. Dean, J. Lin, A review of spinning, shear forming and flow forming processes, Int. J. Mach. Tools Manuf. 43 (2003) 1419-1435. https://doi.org/10.1016/S0890-6955(03)00172-X

[2] M. Sivanandini, S. Dhami, B. Pabla, Flow Forming Of Tubes–A Review, Int. J. Sci. Eng. Res. 3 (2012) 1-11.

[3] A. Plewiński, T. Drenger, Spinning and flow forming hard-to-deform metal alloys, Arch. Civ. Mech. Eng. 9 (2009) 101-109. https://doi.org/10.1016/s1644-9665(12)60043-0

[4] G. Ray, D. Yilmaz, M. Fonte, R.P. Keele, Metalworking: Bulk Forming, in: S. L. Semiatin (Ed.), Metalworking: Bulk Forming, ASM International, Volume 14a, 2005, pp. 516–521.

[5] Leifeld Metal Spinning AG, Spinning and Shear Forming Manual, Leifeld Metal Spinning AG, Ahlen, 2002.

[6] O.I. Bylya, T. Khismatullin, P. Blackwell, R.A. Vasin, The effect of elasto-plastic properties of materials on their formability by flow forming, J. Mater. Process. Technol. 252 (2018) 34-44. https://doi.org/10.1016/j.jmatprotec.2017.09.007

[7] O.I. Bylya, M. Ward, B. Krishnamurty, S. Tamang, R.A. Vasin, Modelling challenges for incremental bulk processes despite advances in simulation technology: Example issues and approaches, Procedia Eng. 207 (2017) 2358-2363. https://doi.org/10.1016/j.proeng.2017.10.1008

[8] M. Houillon, E. Massoni, E. Ramel, R. Logé, 3D FEM simulation of the flow forming process using lagrangian and ALE methods, AIP Conf. Proc. 908 (2007) 257-262. https://doi.org/10.1063/1.2740821

[9] H. Shinde, P. Mahajan, A.K. Singh, R. Singh, K. Narasimhan, Process modeling and optimization of the staggered backward flow forming process of maraging steel via finite element simulations, Int. J. Adv. Manuf. Technol. 87 (2016) 1851-1864. https://doi.org/10.1007/s00170-016-8559-7

[10] Y. Bao, T. Wierzbicki, On fracture locus in the equivalent strain and stress triaxiality space, Int. J. Mech. Sci. 46 (2004) 81-98. https://doi.org/10.1016/j.ijmecsci.2004.02.006

[11] G.R. Johnson, W.H. Cook, Fracture characteristics of three metals subjected to various strains, strain rates, temperatures and pressures, Eng. Fract. Mech. 21 (1985) 31-48. https://doi.org/10.1016/0013-7944(85)90052-9

[12] J.T. Hammer, Plastic deformation and ductile fracture of ti-6al-4v under various loading conditions, PhD Thesis, The Ohio State University, 2012. http://rave.ohiolink.edu/etdc/view?acc_num=osu1354700435

Materials Research Proceedings 28 (2023) 1593-1602 https://doi.org/10.21741/9781644902479-172

Phase field modeling of ductile fracture and application in metal forming

WASEEM Sarim[1,a], ERDOGAN Can[1,b] and YALÇINKAYA Tuncay [1,c *]

[1]Department of Aerospace Engineering, Middle East Technical University, 06800 Ankara, Türkiye

[a]waseem.sarim@metu.edu.tr, [b]cane@metu.edu.tr, [c]yalcinka@metu.edu.tr

Keywords: Phase Field Fracture, Ductile Fracture, Finite Element Method

Abstract. A phase field model for ductile fracture is coupled with the Modified Mohr Coulomb (MMC) model for plastic damage evolution and subsequent crack growth. An energy-based damage threshold is applied to control degradation due to ductile damage. The model is implemented through a user subroutine. MMC parameters from the literature are utilized and found to be compatible with the model, accurately reproducing material response curves in a variety of loading conditions for 6016-T4 aluminum alloy. The influence of model parameters is demonstrated and additionally the Nakazima test is simulated to demonstrate the capability of the model predicting the formability of the material through a failure locus. The model is found capable of reproducing experimentally observed crack paths and quantitative material behavior.

Introduction

The phase field methodology has been applied to an increasing variety of fracture cases over the last few years. Based on Griffith's energy balance [1], the variational approach to fracture was developed by Francfort and Marigo [2], providing solutions to several limitations of the original theory. Bourdin et al. [3] regularized this approach through the introduction of a functional to describe the crack surface and this became the basis for the phase field model for brittle fracture, later formalized by Miehe et al. [4]. The framework is expanded to encompass more complex mechanisms such as dynamic crack growth (e.g. [5]), anisotropic crack growth (e.g. [6]) and fatigue crack growth (e.g. [7]) among many.

Adapting the phase field method to a ductile fracture framework involves the introduction of a plasticity related component in addition to the elastic energy density and fracture surface energy terms. The defining characteristic of the various models introduced in the literature is the coupling mechanism for plasticity. Duda et al. [8] opted to not couple the plastic damage with phase field evolution, leading to a model described as a brittle fracture model applied to an elastoplastic solid, with limited plastic deformation at the crack tip before failure. Ambati et al. [9] coupled their model by introducing a coupling term that acts through the degradation function. Models in [10,11] act through the introduction of a separate degradation function for the plastic dissipation term. It should be noted that the latter incorporates non-local plastic effects as well in their formulation. In a framework inspired by the phase field approach to fatigue, Yin et al. [12] degrade the fracture toughness through the accumulated plastic strain. To control the degradation over the material loading history, some models introduce a plastic damage threshold, where plastic damage influences the material response once this value is passed. Both plastic strain thresholds (e.g. [13]) and energy thresholds (e.g. [10]) have been employed in the literature.

The micromechanical mechanisms of ductile fracture demonstrate a high dependency on the stress state characterized by stress triaxiality and Lode parameter (see [14,15]). Ductile fracture models incorporating both parameters have been applied to numerical studies of metal forming (e.g. [16,17]). Recently, attempts have been made to incorporate these effects in ductile phase field models. Borden et al. [10] incorporate stress triaxiality through the addition of a section of the

Content from this work may be used under the terms of the Creative Commons Attribution 3.0 license. Any further distribution of this work must maintain attribution to the author(s) and the title of the work, journal citation and DOI. Published under license by Materials Research Forum LLC.

Johnson-Cook damage model to the plastic damage accumulation. Li et al. [18] introduced a damage threshold that evolves with the modified Mohr Coulomb model (MMC). Vajari et al. [19] introduced a model that degrades the fracture toughness through the Stress-Weighted Ductile Fracture Model.

While most studies are focused on demonstrating the ability of various ductile models to recreate known crack paths from literature, quantitative studies accurately capturing the load-displacement response of the material remain limited. This study aims to simulate a ductile phase field model, capable of reproducing crack paths for various boundary value problems as well as the material response as accurately as possible. In the scope of this study, we introduce the MMC model to the plastic damage evolution, potentially allowing the model to accurately capture the material response in a broad range of loading conditions.

In this work, a non-linear J2 plasticity model is coupled with the phase field paradigm through coupled-temperature displacement elements, with temperature acting as the phase parameter. This is done by employed by exploiting a similarity between the phase field driving force and steady state heat transfer equation (see [20]). The in-built finite strain framework in the commercial finite element (FE) solver Abaqus is employed in conjunction with user subroutines. The framework is assessed through a comparative study with the experimental and numerical data from [21] while utilizing their hardening and MMC parameters. Load displacement curves are corroborated for various specimens. Furthermore, to demonstrate the utility of the phase field framework in metal forming processes, we utilize the Nakazima test [22], which is employed to determine a material's formability for deep drawing operations. Sheet specimens of various dimensions are subjected to a punch test, with the results subsequently used to plot a failure limit curve for the studied material.

The paper is organized as follows. Section 2 addresses the theory behind the ductile fracture phase field model employed in this paper and its various features. Section 3 covers several benchmark examples, as well as their load-displacement curves recreated through simulations. Section 4 includes the Nakazima test simulations and the achieved failure limit curve. The paper is concluded with a summary.

Theory and Methodology

Phase field fracture relies on the introduction of an auxiliary variable known as the phase field parameter $\phi \in [0,1]$ where a value of 0 represents undamaged material and 1 represents a complete loss of stress carrying capacity. The incorporation of plasticity in the phase field paradigm is based on an additional plastic term introduced to the variational form of Griffith's energy balance, as

$$E=E^s+E^e+E^p \tag{1}$$

where E^s is the fracture surface energy, while E^e and E^p refer to the elastic and plastic energy components of the total energy functional, respectively. Both the fracture and elastic contributions may be studied in more detail from [4]. The plastic contribution is thus defined by

$$E^p(\phi,\varepsilon^p)=g(\phi)W^p(\varepsilon_p) \tag{2}$$

where W^p is the energy corresponding to the plastic damage and g is the degradation function taken identical for both elastic and plastic contributions of energy. This brings certain computational advantages, allowing the retention of the original yield function without any phase field components as the yield surface and equivalent stress degrade identically. A very simple alteration to the brittle strong form becomes adequate to incorporate plastic damage leading to

$$G_c\left(\frac{\phi}{l_0}-l_0\Delta\phi\right)+g'(\phi)(H+W^p)=0 \tag{3}$$

where G_c represents the fracture toughness and l_0 is the length scale parameter governing the diffusiveness of the crack. H is the local history variable given by the maximum elastic energy over the deformation history. The definition of W^p is the dominating factor in the evolution of damage as it quantitatively dominates H. Commonly represented by plastic energy dissipation, it is given as follows:

$$W^p = \int \sigma_{eq} \dot{\varepsilon}^p_{eq} dt \tag{4}$$

where $\dot{\varepsilon}^p_{eq}$ is the equivalent plastic strain rate and σ_{eq} is the equivalent stress. This particular formulation has its drawbacks. In the case of brittle fracture, the elastic damage accumulates at an accelerating pace due to the linear elastic nature of the problem. Plastic contribution to damage, however, accumulates significantly slower, leading to a gradual degradation over a large strain range rather than a dramatic drop past a critical strain level, which is a far more realistic representation. The addition of a plastic dissipation threshold W^p_c solves this problem, with significant changes made to the role of existing parameters. G_c no longer represents the fracture toughness of the material, with this role passed on to W^p_c. Furthermore, the length scale is demoted back to a regularization parameter, no longer influencing the material fracture toughness. Instead, G_c only influences the rate of degradation past the threshold, controlling the reduction in stress following critical damage, where it may be inflated to ease convergence issues. W^p is now replaced by $\langle W^p - W^p_c \rangle$ where $\langle . \rangle$ is the Macaulay operator. An alternative family of degradation functions proposed by Alessi et al. [23] was chosen over the more common quadratic function.

$$g = \frac{(1-\phi)^2}{(k-(k-1)(1-\phi)^2)} \tag{5}$$

where k=1 retrieves the original quadratic function. Lower values of k delay premature degradation, though lowering the value has consequences in terms of convergence issues. A value of 0.5 was found to sufficiently reduce premature degradation while presenting no serious convergence problems.

Furthermore, the equivalent plastic strain at failure, ε_f, for the MMC model (see [21]) is given as follows:

$$\varepsilon_f = \left\{ \frac{K}{\widehat{C}_2} \left[\widehat{C}_3 + \frac{\sqrt{3}}{2-\sqrt{3}} (\widehat{C}^*_4 - \widehat{C}_3)\left(\sec\left(\frac{-L\pi}{6}\right) - 1 \right) \right] \times \left[\sqrt{\frac{1+\widehat{C}_1^2}{3}} \cos\left(\frac{-L\pi}{6}\right) + \widehat{C}_1 \left(T + \frac{1}{3}\sin\left(\frac{-L\pi}{6}\right)\right) \right] \right\}^{1/n} \tag{6}$$

$$\widehat{C}^*_4 = \begin{cases} 1 & \text{for } -1 \le L \le 0 \\ \widehat{C}_4 & \text{for } 0 < L \le 1 \end{cases}$$

where K, n and $\widehat{C}_i$ are material specific constants. L is the Lode parameter and T is the stress triaxiality with both defined as

$$T = \frac{\sigma_h}{\sigma_{eq}}, \qquad L = \frac{2\sigma_2 - \sigma_1 - \sigma_3}{\sigma_1 - \sigma_3} \tag{7}$$

where σ_1, σ_2 and σ_3 are principal stresses while σ_h and σ_{eq} are the hydrostatic and equivalent stresses, respectively.

The incorporation of the MMC model opens up the range of specimens and deformation cases that may be studied, where the model can accurately capture damage at evolving stress states.

While in the classic approach, damage evolves through equivalent plastic strain and failure strain, as

$$D=\int \frac{\dot{\varepsilon}^{p}_{eq}}{\varepsilon_f} dt \tag{8}$$

where D=1 represents complete fracture and ε_f is the failure strain. In the context of the phase field paradigm, damage evolves through plastic dissipation that drives the phase field parameter to retain an energy-based framework. We employed the following definition for W^p:

$$W^P=\int \frac{\sigma_{eq}\dot{\varepsilon}^{p}_{eq}}{\varepsilon_f} dt \tag{9}$$

In the current implementation, the addition of the MMC model helps scale the plastic contribution in regard to the stress state. While classical uncoupled fracture models, employ a strain-based incremental measure of damage where the material is considered fully broken at a damage value of 1, this framework uses W_c^p as the fracture indicator. J2 plasticity model with non-linear isotropic hardening is coupled with the phase field paradigm through a staggered scheme, where plastic and elastic damage contributions from the previous increment influence the evolution of the phase field parameter in the current one. An extended Voce hardening rule given below is utilized to define isotropic hardening.

$$\sigma_y=\sigma_0+\sum_{i=1}^{3} Q_i (1-\exp(-C_i\varepsilon^{p}_{eq})) \tag{10}$$

where σ_y is the yield stress, σ_0 is the initial yield stress value, and Q_i and C_i are hardening parameters. The plasticity framework and the phase field evolution are coupled through the degradation function $g(\phi)$. J2 plasticity model is solved with classical radial return algorithm in the user subroutine (UMAT) and at the end of each increment stress and material stiffness are degraded through $g(\phi)$ retrieved from the previous converged increment, as

$$\sigma=g(\phi)\sigma_{0,} \quad \mathbb{C}=g(\phi)\mathbb{C}_0 \tag{11}$$

where $\sigma_{0,}$ and $\mathbb{C}_0$ are the undegraded stress tensor and material tangent stiffness tensor, respectively, retrieved from the J2 plasticity solution. The phase field evolution is solved by using the heat generation subroutine (HETVAL) exploiting the similarities between the phase field strong form (Eq. 3) and steady-state heat transfer equation (see [20] for the details of the implementation). Elastic and plastic energy contributions from the previous converged increment are used to drive the phase field evolution in the current increment.

Ductile Failure Simulations

Several benchmark examples are simulated to gauge the proposed model's ability to capture ductile failure crack paths as well as the material response. Firstly, 4 specimen geometries, namely notched tension (NT3, NT10), plane strain tension (PST) and in-plane shear (ISS), are solved using the proposed phase field formulation for 6016-T4 aluminum alloy. The details of the specimen dimensions and experimental data are given in [21]. The MMC model variables, calibrated and tested in the aforementioned paper, are used in the ductile fracture phase field model. The parameter set given in Table 1 is employed in the presented phase field framework.

Table 1. Material and model parameters.

E [MPa]	ν	l_0 [mm]	G_c [N/mm]	W_c^p [N.mm]		
70000	0.3	1	50	275		
σ_0 [MPa]	Q_1 [MPa]	C_1	Q_2 [MPa]	C_2	Q_3 [MPa]	C_3
135	19.04	87.05	142.22	10.06	75	3.08
K	$\widehat{C}_1$	$\widehat{C}_2$	$\widehat{C}_3$	$\widehat{C}_4$	n	
0.9969	0.01	0.5075	0.8820	1.0056	0.01122	

All simulations are performed with the implicit finite element solver Abaqus. Models are meshed with a fully integrated 3D (hexahedral) temperature-displacement coupled element (C3D8T in Abaqus) as shown in Fig. 1. NT3, NT10 and ISS are pulled from the center of the top pin and held from the center of the bottom pin while allowing for rotation around the pins. Pin centers are connected to the specimen with the MPC beam constraint. For the PST specimen, the clamped regions are assumed to be rigid and modeled as rigid bodies in FE as shown in Fig. 1. The PST specimen is pulled upwards from the top rigid section and held fixed from the bottom rigid section. Only the middle portion of the ISS specimen is modeled for FE simulations to save computational time. In order to apply boundary conditions, top and bottom pin centers are connected to the FE mesh with the MPC beam constraint as shown in Fig. 1 with black lines. The details of the specimen dimensions and experimental procedure can be found in [21]. The average element size in the gauge section is 0.05 mm with 5 elements in the thickness direction in all FE models. Solutions are performed using automatic step size control with a maximum step size of 0.001 s and a total time of 1 s which is found to be an efficient value in terms of solution time and convergence.

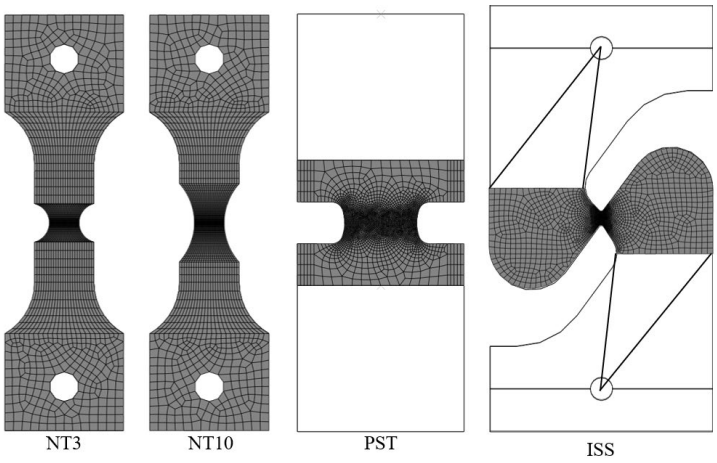

Fig. 1. FE models of the tensile test specimens.

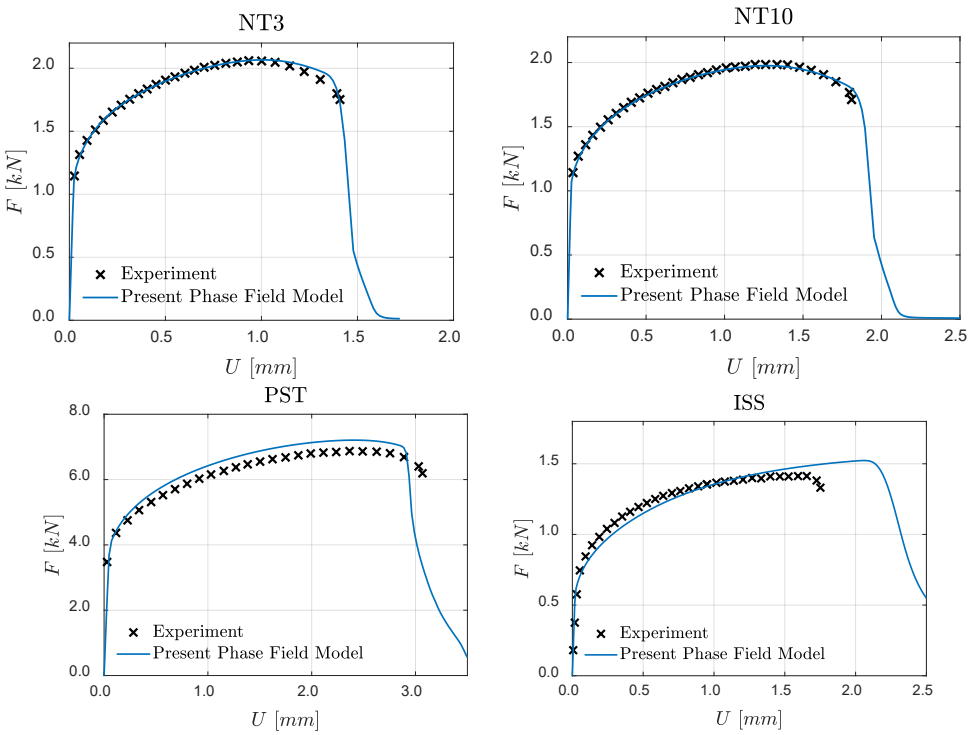

Fig. 2. Comparison of experimental [21] and the present phase field results. Load vs. Displacement curves for 4 specimen geometries.

In Fig. 2, the comparison of force vs. displacement is depicted for 4 specimens. For the given MMC parameters, the material response performed well for each of the four specimens compared to experimental data. The fracture strain for the ISS specimen is exaggerated slightly, but referring to [21] confirms that this is a feature of the MMC fit, not the phase field model. It can be concluded that the developed phase field framework is compatible with classical uncoupled ductile failure models such as Johnson-Cook and MMC. The simulated crack paths are shown in Fig. 3. A straight horizontal crack is developed in the tension specimens resulting in a cup-cup fracture surface. For the ISS test, a slanted crack is developed in the gauge region. All crack paths are compatible with the experimental results presented in [21].

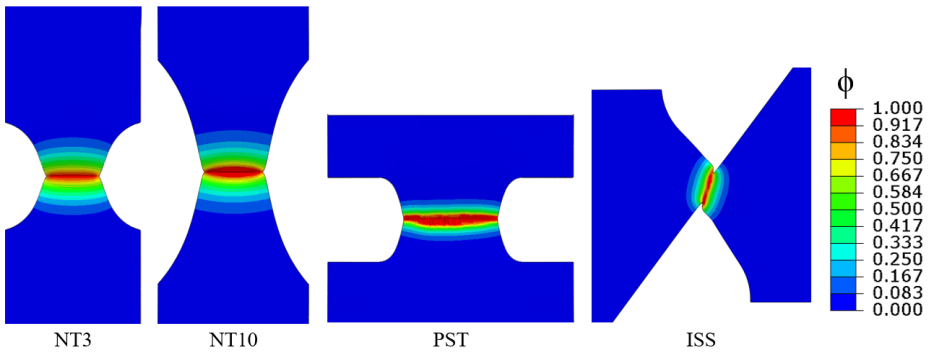

Fig. 3. Distribution of phase field parameter (ϕ) after fracture.

In order to illustrate the effect of length scale in the current model, two additional simulation results are shown in Fig. 4 with the PST specimen. It is clear that the length scale has an insignificant effect on the failure strain but the diffusiveness of the phase field is increased with increasing length scale. Using a smaller length scale is desirable to have relatively precise crack

paths; however, this requires an equivalently finer mesh as comparable scales for both can lead to the mesh distribution influencing the crack path. In all simulations, we set the length scale as 1 mm. Furthermore, in Fig. 4, the effect of critical plastic dissipation, W_c^p, is depicted. This is the main calibration parameter of the proposed model that defines the ductility limits of the material where larger critical dissipation delays the fracture strain value.

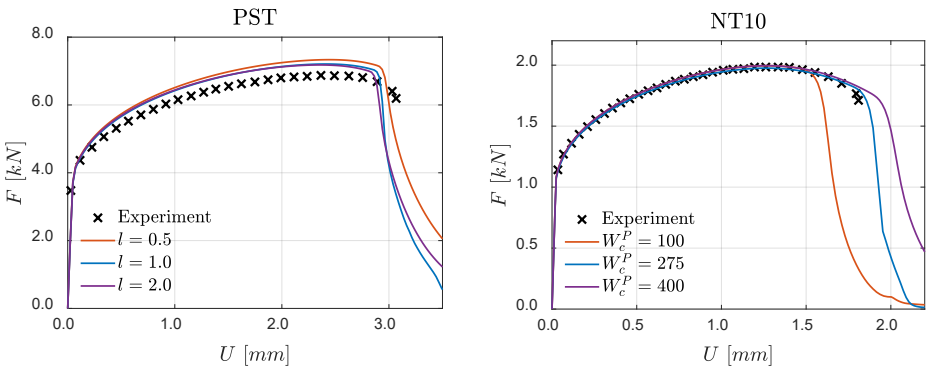

Fig. 4. Effect of length scale and critical plastic dissipation, W_c^p, on fracture.

Nakazima Forming Test Simulations

In order to demonstrate the capability of the presented framework in predicting material formability, the Nakazima test [22] is simulated to reproduce a failure limit curve which assesses the formability of a material in the context of the deep drawing process. The dimensions of the Nakazima setup are adopted from [24]. Specimen thickness is taken as 1mm. The finite element model of the test is given in Fig. 5. Both the punch and the die are taken as rigid bodies and the test sample is meshed with fully integrated 3D (hexahedral) temperature-displacement coupled elements. Outer edge of the Nakazima sample and the die is fixed in all three directions. Displacement boundary condition is applied to the punch while fixing the displacement in transverse directions. Incrementation is retained from the previous section. Frictionless contact is assumed between all interacting surfaces. The punch is pushed vertically until the specimen experiences crack initiation and subsequent crack growth.

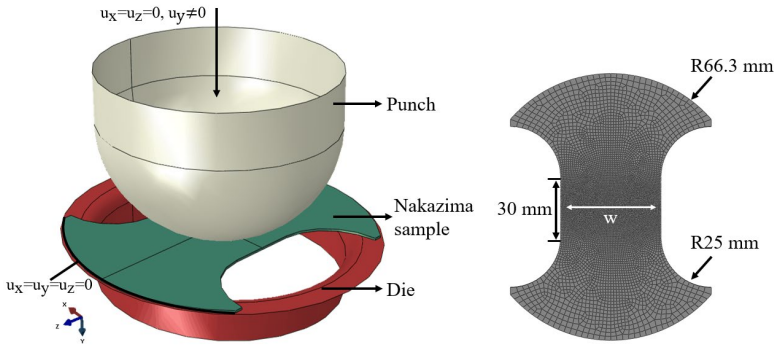

Fig. 5. Finite element model of Nakazima test setup. For the dimensions of the setup see [24].

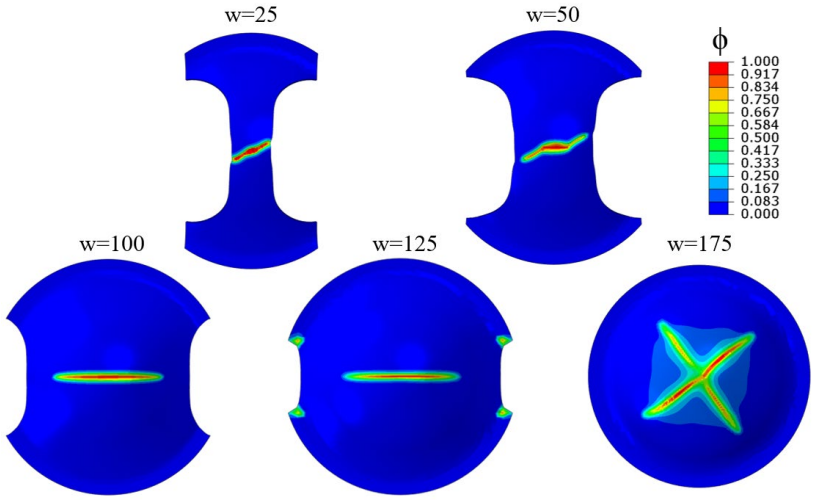

Fig. 6. Crack paths for the Nakazima simulations. Here, w refers to the specimen width.

In Fig. 6, the crack pattern developed for the various specimens may be observed. For narrow specimens, the crack initiates horizontally at the center followed by slanted crack growth which is a pattern that can be observed experimentally (see [24,25]) but most damage models fail to capture it. A horizontal crack development is obtained for wider specimens in agreement with the experimental observations.

The failure limit curve is plotted by taking the major and minor strain histories at the center point of each specimen. The curves are depicted in Fig. 7. A critical facet of plotting a forming limit curve (FLC) is choosing the failure point for the specimen. In this study, we choose the point right before the crack initiation predicted by the phase field model. Hence, we preferred to refer to the curve as a failure limit curve rather than a forming limit curve. The shape of the curve obtained matches the prevalent trend in the literature. A possible source of inaccuracies in the current study may be the assumption of isotropic hardening behavior as sheet metals tend to be anisotropic. The study in [25] compared the performance of an anisotropic yield function vs. an isotropic one and concluded that the anisotropic yield function is found to be more successful at reproducing major-minor strain history curves.

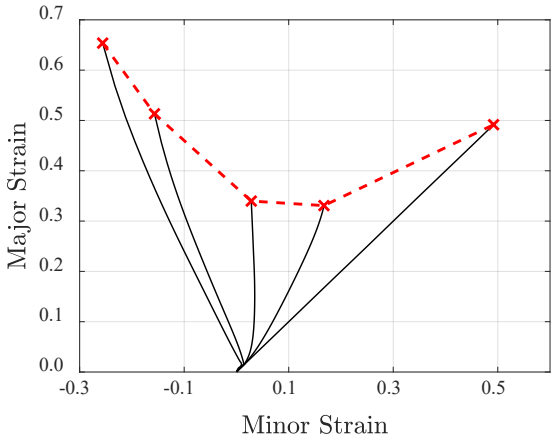

Fig. 7. Failure loci plot for Nakazima specimens.

Summary

A ductile phase field fracture model is developed to simulate crack paths and accurate material responses for various benchmark cases. It demonstrates compatibility with the MMC model allowing the use of existing calibrated parameters for various materials. The framework provides

a route for the non-local coupled implementation of classically uncoupled damage models. Finite element simulation results demonstrated good correspondence with experimental data in terms of both crack paths and material force-displacement response. The Nakazima test is analyzed in FE to show a possible forming application of the developed phase field model, and the results are found to be promising. The framework is a simplistic implementation of a non-local coupled ductile failure model functioning with an implicit solver. The versatility of this methodology could allow future works to simulate more complex ductile fracture behavior such as anisotropic plasticity and damage models.

References

[1] A.A. Griffith, The phenomena of rupture and flow in solids, Philos. Trans. Royal Soc. A. 582-593 (1921) 163-198. https://doi.org/10.1098/rsta.1921.0006

[2] G.A. Francfort, J.J. Marigo, Revisiting brittle fracture as an energy minimization problem, J. Mech. Phys. Solid. 46 (1998) 1319-1342. https://doi.org/10.1016/S0022-5096(98)00034-9

[3] B. Bourdin, G.A. Francfort, J.J. Marigo, Numerical experiments in revisited brittle fracture, J. Mech. Phys. Solids 48 (2000) 797-826. https://doi.org/10.1016/S0022-5096(99)00028-9

[4] C. Miehe, F. Welschinger, M. Hofacker, Thermodynamically consistent phase-field models of fracture: Variational principles and multi-field FE implementations, Int. J. Numer. Methods Eng. 83 (2010) 1273-1311. https://doi.org/10.1002/nme.2861

[5] M.J. Borden, C.V. Verhoosel, M.A. Scott, T.J.R. Hughes, C.M. Landis, A phase-field description of dynamic brittle fracture, Comput. Methods Appl. Mech. Eng. 217–220 (2012) 77-95. https://doi.org/10.1016/j.cma.2012.01.008

[6] S. Teichtmeister, D. Kienle, F. Aldakheel, M.-A. Keip, Phase field modeling of fracture in anisotropic brittle solids, Int. J. Non Linear Mech. 97 (2017) 1-21. https://doi.org/10.1016/j.ijnonlinmec.2017.06.018

[7] S. Waseem, I.E. Unsal, T. Yalçinkaya, Phase Field Modelling of Fatigue Crack Growth at Constant and Variable Amplitude Loading, Procedia Struct. Integr. 42 (2022) 1692-1699. https://doi.org/10.1016/j.prostr.2022.12.213

[8] F.P. Duda, A. Ciarbonetti, P.J. Sánchez, A.E. Huespe, A phase-field/gradient damage model for brittle fracture in elastic–plastic solids, Int. J. Plast. 65 (2015) 269-296. https://doi.org/10.1016/j.ijplas.2014.09.005

[9] M. Ambati, T. Gerasimov, L.D. Lorenzis, Phase-field modeling of ductile fracture, Comput. Mech. 55 (2015) 1017–1040. https://doi.org/10.1007/s00466-015-1151-4

[10] M.J. Borden, T.J.R. Hughes, C.M. Landis, A. Anvari, I.J. Lee, A phase-field formulation for fracture in ductile materials: Finite deformation balance law derivation, plastic degradation, and stress triaxiality effects, Comput. Methods Appl. Mech. Eng. 312 (2016) 130-166. https://doi.org/10.1016/j.cma.2016.09.005

[11] C. Miehe, F. Aldakheel, A. Raina, Phase field modeling of ductile fracture at finite strains: A variational gradient-extended plasticity-damage theory, Int. J. Plast. 84 (2016) 1-32. https://doi.org/10.1016/j.ijplas.2016.04.011

[12] B. Yin, M. Kaliske, A ductile phase-field model based on degrading the fracture toughness: Theory and implementation at small strain, Comput. Methods Appl. Mech. Eng. 366 (2020) 113068. https://doi.org/10.1016/j.cma.2020.113068

[13] H. Ulmer, M. Hofacker, C. Miehe, Phase field modeling of brittle and ductile fracture, PAMM 13 (2013) 533-536. https://doi.org/10.1002/pamm.201310258

[14] Y. Bao, T. Wierzbicki, On fracture locus in the equivalent strain and stress triaxiality space, Int. J. Mech. Sci. 46 (2004) 81-98. https://doi.org/10.1016/j.ijmecsci.2004.02.006.

[15] Y. Bai, T. Wierzbicki, Application of extended Mohr–Coulomb criterion to ductile fracture, Int. J. Fract. 161 (2010). https://doi.org/10.1007/s10704-009-9422-8

[16] H. Vural, C. Erdogan, T.O. Fenercioğlu, T. Yalçinkaya, Ductile failure prediction during the flow forming process, Procedia Struct. Integr. 35 (2022) 25-33. https://doi.org/10.1016/j.prostr.2021.12.044
[17] C. Erdogan, H. Vural, T.O. Fenercioğlu, T. Yalçinkaya, Effect of process parameters on the ductile failure behavior of flow forming process, Procedia Struct. Integr. 42 (2022) 1643-1650. https://doi.org/10.1016/j.prostr.2022.12.207
[18] C. Li, J. Fang, C. Wu, G. Sun, G. Steven, Q. Li, Phase field fracture in elasto-plastic solids: Incorporating phenomenological failure criteria for ductile materials, Comput. Methods Appl. Mech. Eng. 391 (2022) 114580. https://doi.org/10.1016/j.cma.2022.114580
[19] S.A. Vajari, M. Neuner, P.K. Arunachala, A. Ziccarelli, G. Deierlein, C. Linder, A thermodynamically consistent finite strain phase field approach to ductile fracture considering multi-axial stress states, Comput. Methods Appl. Mech. Eng. 400 (2022) 115467. https://doi.org/10.1016/j.cma.2022.115467
[20] Y. Navidtehrani, C. Betegón, E. Martínez-Pañeda, A simple and robust Abaqus implementation of the phase field fracture method, Appl. Eng. Sci. 6 (2021) 100050. https://doi.org/10.1016/j.apples.2021.100050
[21] H. Granum, D. Morin, T. Børvik, O.S. Hopperstad, Calibration of the modified Mohr-Coulomb fracture model by use of localization analyses for three tempers of an AA6016 aluminium alloy, Int. J. Mech. Sci. 192 (2021) 106122. https://doi.org/10.1016/j.ijmecsci.2020.106122
[22] K. Nakazima, T. Kikuma, K. Hasuka, Study on the Formability of Steel Sheets, Yamata Technical Report 264 (1968) 8517-8530.
[23] R. Alessi, J.J. Marigo, S. Vidoli, Gradient Damage Models Coupled with Plasticity and Nucleation of Cohesive Cracks, Arch. Rational Mech. Anal. 214 (2014) 575-615. https://doi.org/10.1007/s00205-014-0763-8
[24] R. Amaral, A.D. Santos, C. de Sá José, S. Miranda, Formability prediction for AHSS materials using damage models, J. Phys. Conf. Ser. 843 (2017) 012018. http://doi.org/10.1088/1742-6596/843/1/012018
[25] M.B. Gorji, D. Mohr, Predicting shear fracture of aluminum 6016-T4 during deep drawing: Combining Yld-2000 plasticity with Hosford–Coulomb fracture model, Int. J. Mech. Sci. 137 (2018) 105-120. https://doi.org/10.1016/j.ijmecsci.2018.01.008

Materials Research Proceedings 28 (2023) 1603-1610 https://doi.org/10.21741/9781644902479-173

A phase-field numerical framework to study ductile damage to fracture transition: An application to material forming processes

PINO MUÑOZ Daniel[1,a *], BOUCHARD Pierre-Olivier[1,b], ELDAHSHAN Hazem[1,2,c], ALVES José[2,d] and PERCHAT Etienne[2,e]

[1] MINES Paris, PSL Research University, CEMEF - Center for Material Forming, CNRS UMR 7635, BP 207, 1 rue Claude Daunesse, 06904 Sophia Antipolis Cedex, France

[2] Transvalor SA, E-Golf Park, 950 Avenue Roumanille, 06410 Biot, France

[a]daniel.pino_munoz@minesparis.psl.eu, [b]pierre-olivier.bouchard@minesparis.psl.eu, [c]hazem.eldahshan@minesparis.psl.eu, [d]jose.alves@transvalor.com, [e]etienne.perchat@transvalor.com

Keywords: Ductile Damage to Fracture Transition, Phase Field, Forming Processes

Abstract. In this work we present a phase-field based method to accurately predict the nucleation and evolution of damage. The damage pattern is then used as a criterion for automatic, remeshing-based, 3D crack insertion and propagation. The proposed framework has been implemented in Forge® finite element software and it offers a robust numerical tool for the modeling of damage to fracture transition in complex industrial processes. A bar shearing simulation will be used to show the robustness and efficiency of the approach. The flexibility of the approach is presented through the use of different damage criteria introduced into the phase-field formulation.

Introduction

Material forming processes take advantage of the ductility of materials, in particular metals, to obtain a given geometry of a part. Depending on the complexity of the part, different stages might be needed. From a mechanical perspective, the material will be submitted to a non-proportional loading path and large deformation. As a result of these processes damage and fracture might appear within the material. Depending on the process, damage, and subsequent fracture, should be either avoided or controlled. In either case the simulation of the kinetics of the evolution of damage is fundamental in order to design new parts and manufacturing processes. The damage to fracture transition becomes particularly necessary in order to study processes where damage should be controlled (*e.g.,* blanking and cutting processes). To this end, the first step consists in being able to predict the damage kinetics. Then the damage prediction should be used to initiate and propagate cracks into the material.

Regarding the prediction of damage, when dealing with brittle materials Griffith theory can be used to explain the evolution of fracture. In fact, this energetic approach can be used to reproduce experiments of fracture of brittle materials [1]. On the other hand, when dealing with ductile materials the literature about models that allow to predict the evolution of damage is often restricted to specific material and/or particular loading conditions. It is thus fair to say that there is no unified theory that quantitatively explains the kinetics of ductile damage and fracture phenomena. However, we can say that there are three main stages on the process:

1. void nucleation
2. void growth and distortion
3. void coalescence.

Voids are nucleated due to stress concentrations and the presence of defects in the materials. These voids will grow under plastic deformation and their growth will be significantly affected by the

Content from this work may be used under the terms of the Creative Commons Attribution 3.0 license. Any further distribution of this work must maintain attribution to the author(s) and the title of the work, journal citation and DOI. Published under license by Materials Research Forum LLC.

material's stress state. And finally void coalescence is the result of the merging of previously nucleated voids [2,3].

The numerical modeling of these ductile damage mechanisms has been done by using different numerical approaches: *uncoupled* and *coupled* approaches. Uncoupled approaches can be seen as a post processing tool that allows to compute the local damage state of the material by using a set of thermomechanical variables integrated over time. These approaches are easy to implement and do not affect the convergence of the finite element solver[1]. They present an important drawback: uncoupled approaches do not allow to reproduce the drop of stress experimentally observed once damage has been initiated. On the other hand, coupled models link the evolution of damage to the elastoplastic properties of the material. This allows to capture the softening behavior experimentally observed but this brings along some drawbacks. The softening of the materials leads to numerical difficulties that are well documented in literature [9] and the numerical solver must be adapted to tackle these challenges.

Extensive literature can be found in the context of ductile fracture applied to material forming as in [5] and [6] (and the references therein). The phase-field community has also proposed remarkable contributions to the field such as [7,8]. Such approaches often focus on capturing the drop of loading carrying capacity of the material. However, the degradation of the material is taken into account within a continuum mechanics framework and thus no actual crack is introduced in the computational domain.

Once damage has developed in the material, a discontinuity should be introduced. Early attempts to introduce the discrete cracks based on a remeshing approach in 2D were proposed in [9]. Crack propagation direction is given by the maximum damage at different distances from the crack tip, which led to wrong crack directions especially in the case of complex crack patterns (*e.g.,* merging, branching and multiple cracks) and its extension to 3D was complicated. An alternative to this approach based on the marching ridges method was introduced in [10]. The idea was to find the local maximum of the damage field and propagate the crack by introducing a segment linking these local maximum points. It is worth mentioning that there exist alternatives to discrete crack insertion methods (such as the XFEM [11] or the GFEM [12]) which suffer from difficulties when it comes to large plastic strain and remeshing. But these methods will not be covered in this work.

In this article, the phase-field based damage modeling strategy proposed in [13] is briefly discussed. The proposed method, based on a phase-field-inspired approach to predict the evolution of damage, will be presented in the next section. Then the phase-field damage is used to drive the crack insertion and propagation following the *Crack Insertion and propagation using the Phase Field and Adaptive Remeshing* (CIPFAR) algorithm introduced in [14]. Finally, some results are presented.

Phase-Field Inspired Damage Formulation

Phase-field approaches to simulate damage and fracture can be seen as an extension of the generalized formulation of Griffith theory introduced by Francfort and Marigo [15]. The idea is to use a regularized representation of the crack by introducing a damage variable (d). The evolution of this damage problem is driven by the minimization of an energy functional that links the mechanical behavior of the material to its damage evolution. The energy functional is given by:

$$\mathcal{E}_l(u,d) = \int_\Omega g_e(d) W_e(\epsilon^e) d\Omega + \int_\Omega \frac{G_c}{2l_c}\left(d^2 + {l_c}^2 \nabla d^2\right) d\Omega \quad (1)$$

Materials Research Proceedings 28 (2023) 1603-1610 https://doi.org/10.21741/9781644902479-173

Where ε^e is the elastic strain tensor, W_e is the elastic energy density, G_c is the fracture toughness, l_c is the regularization length and $g_e(d)$ is the degradation function given by:

$$g_e(d) = (1-d)^2 \tag{2}$$

The choice of the degradation function satisfies the following conditions: $g_e(0) = 1$, $g_e(1) = 0$ and $g'_e(d) = 0$. The minimization of the energy functional leads to the following set of equations:

$$d - {l_c}^2 \nabla^2 d = -g'_e(d)H \qquad \text{(Phase-field evolution)} \tag{3}$$

$$H = \frac{2l_c}{G_c} max W_e(\epsilon^e) \qquad \text{(Local history functional)} \tag{4}$$

$$\nabla d.n = 0 \qquad \text{(Neumann boundary condition)} \tag{5}$$

A similar set of equations is found when a non-local continuum damage formulation is used. The main difference is that phase-field evolution includes the term $g'_e(d)$ which vanishes when the material is completely damaged ($d = 1 \rightarrow g_e(d = 1) = 0$). This vanishing term prevents spurious diffusion of the damage variable [13].

The previous set of equation corresponds to the classic phase-field damage formulation for brittle materials. If we were to extend this formulation to ductile damage modeling while keeping the phase field philosophy, we would need to come up with an energy functional that accounts for the plastic dissipation which should also account for the plasticity-damage coupling. Real material exhibit complex damage behavior often involving a strong coupling damage, stress triaxiality and/or even the Lode parameter [2]. Obviously proposing a general energy functional that fulfills all these requirements is not an easy task.

In order to overcome this problem of finding an appropriate energy functional, we simply replace the local history functional by a phenomenological law. The idea is to introduce any of the existing *Uncoupled* damage criterion into the local functional:

$$H = \eta_c \langle D - D_{thresh} \rangle \tag{6}$$

Where D is the local damage (damage criterion), η_c is a material parameter used to control the post-peak stress response of the material by controlling the amount of effective energy needed to create the crack surfaces once the crack is initiated and D_{thresh} is a damage threshold value used to delay the softening of the material. The effect of η_c and D_{thresh} is shown in Fig. 1, which corresponds to the 1D homogeneous solution of the phase-field equation.

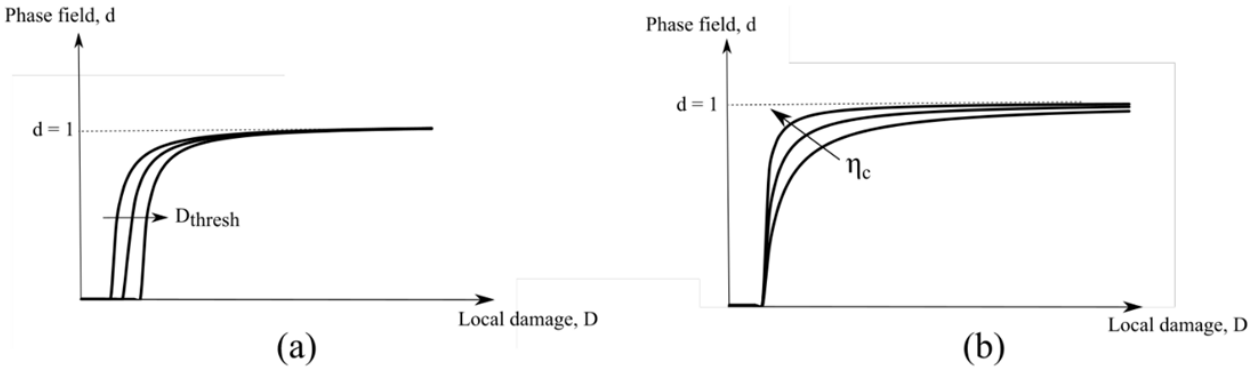

Fig. 1. The effect of model parameters on the evolution of the phase field in a 1D homogeneous solution [16].

Once the phase-field is computed, the crack insertion strategy presented in [14] is used in order to introduce the crack discontinuity into the mesh. In the next section, a forming application is presented and discussed.The implementation and validation of the different building blocks of the proposed approach has been done in Forge®.

Results

The proposed strategy has already been validated and tested [13,14]. It has been proven that the approach is very robust and flexible as different damage criterion could be used to study a given problem. In fact, as it has been mentioned before, there is not a unified theory that explains the evolution of ductile damage and therefore the choice of the damage criterion is done depending on the material and the loading conditions.

Here we will present a simple case of a bar shearing. The boundary conditions of the problem are shown in Fig. 2. Depending on the choice of damage criterion, the failure pattern predicted by the model will be different. The different failure criteria tested are listed in Table 1 and the corresponding properties used in the simulations are shown in Table 2.

Table 1. Damage criteria used for the coupled phase-field simulations [16].

Model number	Damage criterion	Driving force (DF)	Parameters
1	$D = \int_0^{\bar{\varepsilon}} \frac{\sigma_1}{\bar{\sigma}} d\bar{\varepsilon}$	Maximum principal stress σ_1	-
2	$D = \int_0^{\bar{\varepsilon}} \frac{\bar{\sigma}}{A} d\bar{\varepsilon}$	Von Mises stress $\bar{\sigma}$	A
3	$D = \int_0^{\bar{\varepsilon}} C_1 exp C_2 \eta d\bar{\varepsilon}$	Stress triaxiality η	C_1 and C_2
4	$D = \int_0^{\bar{\varepsilon}} \frac{\sigma_1 - \sigma_3}{\bar{\sigma}} d\bar{\varepsilon}$	Maximum shear stress $2\tau_{max} = \sigma_1 - \sigma_3$	-

Materials Research Proceedings 28 (2023) 1603-1610 https://doi.org/10.21741/9781644902479-173

Table 2. Material and model parameters [16].

Quantity		Value	Units
Young's modulus	E	200 000	MPa
Poisson's ratio	ν	0.3	-
Yield stress	σ_y	$A\,\overline{\varepsilon}^{\,0.1845}\,\dot{\overline{\varepsilon}}^{\,0.012}$	MPa
A		818	MPa
Charasteristic length	l_c	0.5	mm
Damage model 1			
Damage threshold	D_{thresh}	0.1	-
Fracture parameter	η_c	200	-
Damage model 2			
Damage threshold	D_{thresh}	0.1	-
Fracture parameter	η_c	50	-
Damage model 3			
Damage threshold	D_{thresh}	0.05	-
Fracture parameter	η_c	200	-
C_1		2	-
C_2		1	-
Damage model 4			
Damage threshold	D_{thresh}	0.2	-
Fracture parameter	η_c	100	-

The different crack patterns are shown in Fig. 3 for each of the models in Table 1. For each model the upper row shows the phase-field damage level (d) and the lower row represents the cracks that have been inserted. Fig. 3a shows the results obtained when using the Normalized Latham-Cockcroft model (number 1 in Table 1) at different macroscopic loading states. It can be seen that two cracks are initiated at the left and right boundaries of the sheared zone. It is important to highlight that the approach is robust enough to handle the two cracks that propagate independently and that end up merging into a single crack that breaks the rod into two pieces.

Crack patterns obtained when using models 2 and 4 in Table 1 present a similar kinetics: first two cracks near the boundary of the rod are initiated and these cracks merge at the end in order to fully break the rod. Interestingly the crack initiation region from these two models is different from the one observed in model 1. This time, the two branches are initiated in the upper and lower boundaries of the rod. This change on the initiation region can be explained by the driving term of the damage criterion used (Column 3 in Table 1).

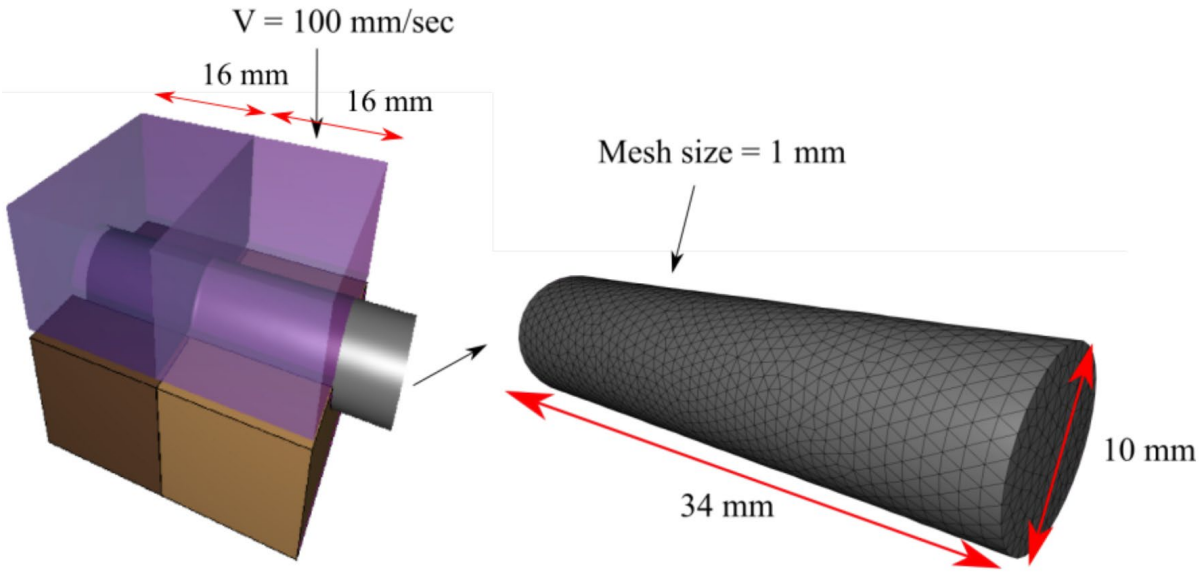

Fig. 2. Geometry and boundary conditions of a bar subjected to shear loading [16].

The von Mises stress as well as the maximum shear stress are concentrated over the regions that are in contact with the tools in the shearing regions. On the other hand, the normalized maximum principal stress is maximum over the left and right boundaries of the rod, which explains the pattern observed in model 1. Finally, model 3 (triaxiality driven) leads to a completely different crack pattern. In fact, the regions that present high triaxiality are located behind the shearing region. Therefore, the crack nucleates in the upper and lower regions of the rod but inside of the tool.

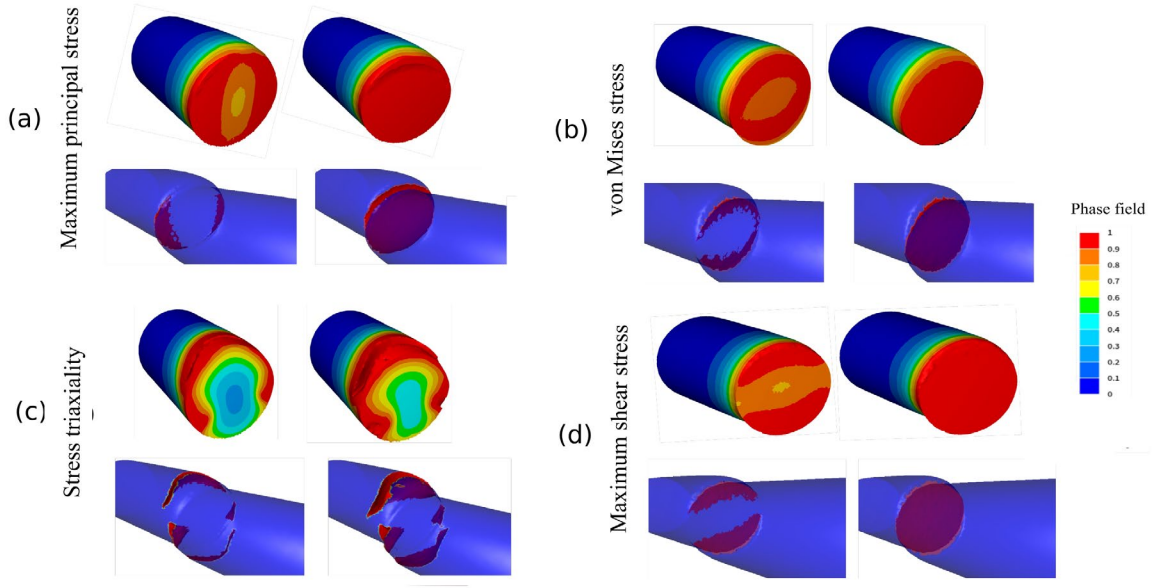

Fig. 3. Illustration of the phase field damage evolution (upper row) and the inserted cracks surfaces (lower row) for the four different damage criteria introduced in Table 1.

Summary

To conclude, the presented examples confirm the ability of the proposed approach to accurately model the damage to fracture transition under complex loading conditions. In addition, the model provides a general framework for crack initiation and propagation in 3D that can be adopted for different applications. Since there is no a universal model that accurately predicts the ductile damage evolution, the use of custom damage criteria (often developed in the context of *uncoupled* approaches) combined with the phase-field formulation allows to account for complex damage phenomena experimentally observed. Once the damage has initiated, the CIPFAR algorithm is used to insert cracks into the computational domain while being robust and reliable. Further developments and tests should be carried out in order to study the impact of different damage criteria in the case of multistage non-proportional loading processes.

References

[1] T.L. Anderson, Fracture mechanics: fundamentals and applications, CRC press, 2017.
[2] Y. Bao, T. Wierzbicki, On fracture locus in the equivalent strain and stress triaxiality space, Int. J. Mech. Sci. 46 (2004) 81-98. https://doi.org/10.1016/j.ijmecsci.2004.02.006
[3] Y. Lou, J.W. Yoon, H. Huh, Modeling of shear ductile fracture considering a changeable cut-off value for stress triaxiality, Int. J. Plast. 54 (2014) 56-80. https://doi.org/10.1016/j.ijplas.2013.08.006
[4] M. Jirásek, Mathematical analysis of strain localization, Revue européenne de génie civil 11 (2007) 977-991.
[5] K. Saanouni, On the numerical prediction of the ductile fracture in metal forming, Eng. Fract. Mech. 75 (2008) 3545-3559. https://doi.org/10.1016/j.engfracmech.2007.02.023
[6] T.S. Cao, Models for ductile damage and fracture prediction in cold bulk metal forming processes: a review, Int. J. Mater. Form. 10 (2017) 139-171. https://doi.org/10.1007/s12289-015-1262-7
[7] M. Ambati, T. Gerasimov, L. De Lorenzis, Phase-field modeling of ductile fracture, Computat. Mech. 55 (2015) 1017-1040. https://doi.org/10.1007/s00466-015-1151-4
[8] C. Miehe, F. Aldakheel, A. Raina,. Phase field modeling of ductile fracture at finite strains: A variational gradient-extended plasticity-damage theory, Int. J. Plast. 84 (2016) 1-32. https://doi.org/10.1016/j.ijplas.2016.04.011
[9] J. Mediavilla, R. Peerlings, M. Geers, Discrete crack modelling of ductile fracture driven by non-local softening plasticity, Int. J. Numer. Meth. Eng. 66 (2006) 661-688. https://doi.org/10.1002/nme.1572
[10] S. Feld-Payet, V. Chiaruttini, J. Besson, F. Feyel, A new marching ridges algorithm for crack path tracking in regularized media, Int. J. Solid. Struct. 71 (2015) 57-69. https://doi.org/10.1016/j.ijsolstr.2015.04.043
[11] T. Belytschko, T. Black, Elastic crack growth in finite elements with minimal remeshing, Int. J. Numer. Meth. Eng. 45 (1999) 601-620. https://doi.org/10.1002/(SICI)1097-0207(19990620)45:5%3C601::AID-NME598%3E3.0.CO;2-S
[12] A.M. Aragón, A. Simone, The discontinuity-enriched finite element method. Int. J. Numer. Meth. Eng. 112 (2017) 1589-1613. https://doi.org/10.1002/nme.5570
[13] H. Eldahshan, D. Pino Muñoz, J. Alves, E. Perchat, P.-O. Bouchard, 3D crack initiation and propagation applied to metal forming processes, Int. J. Mat. Form. 15 (2022) 1-26. http://doi.org/10.1007/s12289-022-01702-7
[14] H. Eldahshan, J. Alves, P.-O. Bouchard, E. Perchat, D. Pino Munoz, CIPFAR: A 3D unified numerical framework for the modeling of ductile fracture based on the phase field model and adaptive remeshing, Comput. Meth. Appl. Mech. Eng. 387 (2021) 114171. https://doi.org/10.1016/j.cma.2021.114171

[15] G.A. Francfort, J.-J. Marigo, Revisiting brittle fracture as an energy minimization problem, J. Mech. Phy. Sol. 46 (1998) 1319-1342. http://doi.org/10.1016/S0022-5096(98)00034-9
[16] H. Eldahshan, 3D crack initiation and propagation in a fully parallel framework applied to metal forming applications, PhD thesis, Mines Paris, PSL University, 2021.

Materials Research Proceedings 28 (2023) 1611-1620 https://doi.org/10.21741/9781644902479-174

A meshless numerical solution of thermo-mechanics of hot-rolled steel bars on a cooling bed

VUGA Gašper[1,a], MAVRIČ Boštjan[1,2,b], HANOGLU Umut[1,3,c] and ŠARLER Božidar[1,3,d *]

[1]Faculty of Mechanical Engineering, University of Ljubljana, Slovenia

[2]Department of Information Technology, Uppsala University, Sweden

[3]Institute of Metals and Technology, Ljubljana, Slovenia

[a]gasper.vuga@fs.uni-lj.si, [b]bostjan.mavric@it.uu.se, [c]umut.hanoglu@imt.si, [d]bozidar.sarler@fs.uni-lj.si

Keywords: Cooling Bed, Steel Bars, Thermo-Mechanics, Strong Form Meshless Method

Abstract. After the continuous hot-rolling process, steel bars are immediately placed on the cooling bed. At the beginning of the cooling, the material is at high temperatures, and the yield strength is low. Due to thermal load, yield strength can be exceeded, and permanent plastic strains start accumulating, resulting in possible unwanted shape changes and residual stresses. The present paper aims to develop a thermo-mechanical model for studying and eliminating undesirable phenomena before the products leave the cooling bed. The governing equations are solved for the two-dimensional slice in a strong form, and a modified version of the radial basis function generated finite difference (RBF-FD) method [1]. The initial bar geometry is obtained from the existing meshless hot-rolling simulation system [2]. The thermal and mechanical models are one-way coupled, i.e. the temperature solution represents a driving force for the stress and strain solution. The temperature field is obtained with explicit propagation in time. The convective and radiative heat fluxes on the boundary are updated at each time step using the ray tracing procedure to determine the radiative heat flux. The mechanical part is solved by considering the small strain elasto-plasticity, where the isotropic von Mises temperature-dependent hardening is employed. The global system of nonlinear equations of the mechanical part is solved by the Newton-Raphson method. The closest point projection method is used to solve the constitutive relations. A sensitivity study is performed on the influence of cooling intensity on a rectangular steel bar's temperature, stress and strain field. We defined the most influential factors for defect formation. For the first time, a novel meshless RBF-FD method is successfully used for solving such a complex industrial problem. The model will be perspectively upgraded from the slice to the three-dimensional model to enable also bending.

Introduction

The meshless strong form radial basis function generated finite difference (RBF-FD) method has gained popularity in modelling different steel production processes. It has been successfully applied to solve large spectra of continuous casting problems, such as diffusion-convection with phase change [1], natural convection influenced by magnetic stirring [3], turbulence phenomena [4], 2D microsegregation with grain growth [5], and 2D thermo-mechanics [6]. Also, multi-pass hot-rolling has been successfully modelled with RBF-FD [2,7], including the grain size prediction [8].

This work represents the first use of RBF-FD for solving the thermo-mechanical response of the last stage of hot-rolling, where the hot-rolled steel bars are cooled. Previous attempts at modelling this step were performed in 1D [9], 2D [10,11] and 3D [12,13]. In [9], the friction with the supports was investigated. In [12], a simple thermo-elastic description has been used and later

Content from this work may be used under the terms of the Creative Commons Attribution 3.0 license. Any further distribution of this work must maintain attribution to the author(s) and the title of the work, journal citation and DOI. Published under license by Materials Research Forum LLC.

extended in [13], including contact with the supports and gravitational load. In [10], the bending of the bars and the residual stresses were computed, and in [11], the flow of surrounding air was included to better predict heat transfer at the boundary. All of the above studies were performed for symmetric and asymmetric rail profiles where the geometry significantly impacts the bending and residual stress formation.

An example of round steel bars cooling on the cooling bed (CB) is shown in Fig. 1 left. A cross-section scheme with rectangular bars (80×39 mm) used in this work is presented in Fig. 1 right. The heat shield with the length of p_l is positioned on top of the CB, raised by p_y from the lowest point of the CB. Each bar starts from the left at the position p_1. After a time t_p, the bar is moved for a distance x_{bp} to the position p_2, and a new bar occupies the position p_1. This movement is repeated until the final position p_n is reached, where the bars leave CB.

The influence of the position of the heat shield above the bars p_y and the distance between the bars x_{bp} on the thermo-mechanical response is investigated.

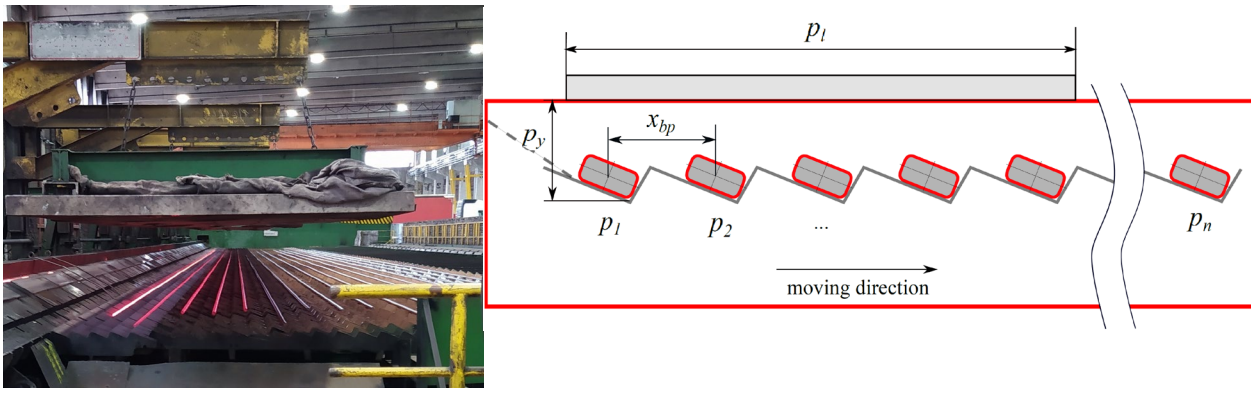

Fig. 1. Left: Photo of the cooling bed. Right: cross-section of the cooling bed with rectangle steel bars present on each position p_i.

Thermal Model

Cooling of the steel bars is governed by the heat diffusion equation

$$\frac{\partial}{\partial t}(\rho c_p T) = \nabla k \cdot \nabla T + k\nabla^2 T \tag{1}$$

where ρ, c_p, k and T stand for the density, the specific heat at constant pressure, the heat conductivity and the temperature, respectively. Material parameters ρ, c_p and k are temperature-dependent. Neumann boundary condition is employed as

$$\mathbf{q}\cdot\mathbf{n} = -k\frac{\partial T}{\partial \mathbf{n}} = q_{conv} + q_{rad} \tag{2}$$

where **q** represents the total heat flux and **n** is normal at the boundary. The prescribed value on the right-hand side is composed of convective q_{conv} and radiative q_{rad} terms, defined as

$$q_{conv} = h(T - T_{amb}), \qquad q_{rad} = \varepsilon\sigma(T^4 - T_{amb}{}^4) \tag{3}$$

Materials Research Proceedings 28 (2023) 1611-1620 https://doi.org/10.21741/9781644902479-174

where h, T_{amb}, ε and σ stand for the heat transfer coefficient, the ambient temperature, the emissivity coefficient, and the Stefan-Boltzmann constant, respectively. Since the bars are positioned close to each other, and a heat shield is present above the cooling bed, information about the geometry and the positioning is effectively introduced in q_{rad}. The boundary of the system, composed of the bars and heat shield, is discretized and enclosed inside another discretized closed-loop virtual boundary. The net radiative heat flux of the i-th discretized boundary surface $q_{rad,i}$ is defined as a difference between the emitted heat flux from the surface and the received heat flux from the surroundings as

$$q_{rad,i} = \varepsilon_i \sigma T_i^4 - \sum_{j=1}^{J} \varepsilon_j \sigma T_j^4 \frac{A_j}{A_i} F_{j \to i} \tag{4}$$

where the received part is defined as a sum over all J discrete surfaces (DSs). DS visibility is defined by the view factor $F_{j \to i} \in [0,1]$. It represents the portion of the radiation emitted by the surface A_j received by the surface A_i [14].

Mechanical Model

This work considers small strain elasto-plasticity with von Mises flow rule and isotropic hardening. The mechanical equilibrium of the steel bar is described by the balance law

$$\nabla \cdot \boldsymbol{\sigma} = \mathbf{f} \tag{5}$$

where $\boldsymbol{\sigma}$ is the stress tensor and f is the body force. The strain tensor is defined in terms of displacement $\mathbf{u}$ as $\boldsymbol{\varepsilon} = 1/2\left(\nabla \mathbf{u} + \nabla \mathbf{u}^{\mathsf{T}}\right) = \nabla^s \mathbf{u}$. It can be split into elastic $\boldsymbol{\varepsilon}^e$ and plastic $\boldsymbol{\varepsilon}^p$ terms $\boldsymbol{\varepsilon} = \boldsymbol{\varepsilon}^e + \boldsymbol{\varepsilon}^p$. The relationship between stresses and strains is defined by the Hooke's law

$$\boldsymbol{\sigma} = \mathsf{D}^e \boldsymbol{\varepsilon}^e = \mathsf{D}^e (\boldsymbol{\varepsilon} - \boldsymbol{\varepsilon}^p) \tag{6}$$

where D^e represents the fourth-order elasticity tensor. The employed von Mises yield criterion states that the material yields when von Mises stress $\sigma_{vm} = \sqrt{3J_2}$ exceeds the yield stress obtained from the uniaxial tensile test σ_y. J_2 represents the second invariant of the deviatoric part $\mathbf{s} = \boldsymbol{\sigma} - \mathbf{I}\mathrm{tr}(\boldsymbol{\sigma})/3$ of the stress tensor, where $\mathbf{I}$ is the identity tensor. The evolution of the yield stress is defined by a hardening law $\sigma_y = \sigma_y(\bar{\varepsilon}^p, T)$, assumed to be a nonlinear function of the temperature and the accumulated plastic strain $\bar{\varepsilon}^p = \sqrt{2/3}\,\|\boldsymbol{\varepsilon}^p\|$. Johnson-Cook strain rate independent hardening law is used

$$\sigma_y(\bar{\varepsilon}^p, T) = \left(A + B\left(\bar{\varepsilon}^p\right)^n\right)\left(1 - \left(\frac{T - T_0}{T_m - T_0}\right)^m\right) \tag{7}$$

where all constants are determined by fitting 46MnVS5 steel data obtained by the JMatPro software. Admissible stress states are compactly specified with a yield function

$$\Phi(\boldsymbol{\sigma},\sigma_y)=\sqrt{3J_2(\mathbf{s}(\boldsymbol{\sigma}))}-\sigma_y\le 0 \tag{8}$$

where $\Phi(\boldsymbol{\sigma},\sigma_y)<0$ holds in the elastic regime and $\Phi(\boldsymbol{\sigma},\sigma_y)=0$ holds in the plastic regime. The evolution of the plastic strain is defined in the rate form by a plastic flow rule

$$\dot{\boldsymbol{\varepsilon}}^p=\dot{\gamma}\frac{\partial\Phi}{\partial\boldsymbol{\sigma}}=\dot{\gamma}\sqrt{\frac{3}{2}}\frac{\mathbf{s}}{\|\mathbf{s}\|} \tag{9}$$

where γ represents the plastic multiplier and connects the strain and the stress space. Lastly, a set of loading/unloading conditions is given as

$$\Phi(\boldsymbol{\sigma},\sigma_y)\le 0,\quad \dot{\gamma}>0,\quad \Phi(\boldsymbol{\sigma},\sigma_y)\dot{\gamma}=0 \tag{10}$$

that have to be fulfilled. Since the material response is path-dependent, Eq. 5 is solved incrementally. For a $(n+1)$-th load increment, it can be written in the form $\mathbf{f}^{\text{int}}|_{n+1}-\mathbf{f}^{ex}|_{n+1}=\mathbf{r}(\mathbf{u}_{n+1})=0$, where $\mathbf{r}$ represents the residual that should be zero, $\mathbf{f}^{ex}$ external load, and $\mathbf{f}^{\text{int}}$ internal force defined as $\mathbf{f}^{\text{int}}=\nabla\cdot\boldsymbol{\sigma}\left(\nabla^s\mathbf{u}\right)$. Due to a nonlinear relationship between stress and strain, the residual is linearized as

$$\nabla\cdot\left(\mathsf{D}\nabla^s\right)\Big|_{n+1}^{k}\delta\mathbf{u}=-\mathbf{r}\Big|_{n+1}^{k} \tag{11}$$

where $\mathsf{D}=\partial\boldsymbol{\sigma}/\partial\boldsymbol{\varepsilon}$. Eq. 11 is iteratively (index k) solved for $\delta\mathbf{u}$. After each k-th iteration, the displacement increment is updated as $\Delta\mathbf{u}^k=\Delta\mathbf{u}^{k-1}+\delta\mathbf{u}$. From here, the strain increment $\Delta\boldsymbol{\varepsilon}^k$ is determined and inserted into the integration model, where all other state variables are updated, solving Eqs. 6-10. When $\delta\mathbf{u}$ is sufficiently small, the displacement is updated as $\mathbf{u}_{n+1}=\mathbf{u}_n+\Delta\mathbf{u}$. Since only temperature load is applied on the steel bars, the external load is defined as $\mathbf{f}^{ex}_{n+1}=\nabla\cdot((3\lambda+2G)\alpha\Delta T\mathbf{I})\big|_{n+1}$, where λ,G,α and ΔT stand for the first and the second Lamé's constants, the linear expansion coefficient, and the temperature difference ($\Delta T=T_{n+1}-T_n$), respectively. Between bars and the cooling bed, no contact is assumed. The Neumann type of boundary condition is prescribed on the whole boundary $\mathbf{t}=\boldsymbol{\sigma}\cdot\mathbf{n}=0\,\text{N/m}$, where $\mathbf{t}$ represents the traction vector. Since only the derivatives of the displacement field are defined, two additional conditions are enforced to obtain a unique solution

$$\int_\Omega\mathbf{u}(\mathbf{r})d\Omega=0\quad,\quad\int_\Omega\left(\mathbf{u}(\mathbf{r})\times\mathbf{r}\right)d\Omega=0 \tag{12}$$

where Ω represents the bar cross-section area, and $\mathbf{r}$ is a position vector. The posed equations are solved within a plane strain assumption.

Numerical Method

Spatial discretization is performed using the RBF-FD method. The observed domain is discretized by a homogeneous distribution of the scattered discretization nodes - collocation nodes (CNs). For each CN, a set of closest local neighbours is determined that constructs the so-called local

subdomains ${}_l\Omega, l \in [1, N_{all}]$, where N_{all} represents the number of all CNs. Inside each ${}_l\Omega$, the interpolation of a general function can be written as

$$ {}_l y_\xi(\mathbf{r}) \approx \sum_{i=1}^{{}_l N} {}_l\alpha_{i,\xi}\ {}_l\Phi_i(\mathbf{r}) + \sum_{i=1}^{M} {}_l\alpha_{({}_l N+i),\xi}\ p_i(\mathbf{r}) = \sum_{i=1}^{{}_l N+M} {}_l\alpha_{i,\xi}\ {}_l\Psi_i(\mathbf{r}) \tag{13} $$

where ξ is the index that runs over space dimensions n_d, ${}_l N$ is the number of CNs inside ${}_l\Omega$ and is here set to ${}_l N = 13$, ${}_l\alpha_{i,\xi}$ represents weight coefficients, and ${}_l\Phi_i(\mathbf{r})$ is the Radial Basis Function (RBF). Various types of RBFs can be used in the RBF-FD method. Here, 3rd order polyharmonic splines [15] (PHSs) are employed as ${}_l\Phi_i(\mathbf{r}) = (\| \mathbf{r} - {}_l\mathbf{r}_i \| / {}_l h)^3$, where ${}_l h$ represents the average distance from the centre of ${}_l\Omega$ to its neighbours inside ${}_l\Omega$. The interpolant is augmented with monomials $p_i(\mathbf{r}), i \in [1, M]$, where $M = 3$ for the 2nd order augmentation $p_1 = x, p_2 = y, p_3 = 1$ used here. Eq. 13 can be compactly written as a system of $n_d({}_l N + M)$ linear equations

$$ \sum_{\chi=1}^{n_d} \sum_{i=1}^{{}_l N+M} {}_l A_{ji,\chi\xi}\ {}_l\alpha_{i,\chi} = {}_l\gamma_{j,\xi} $$

where

$$ {}_l A_{ji,\xi\chi} = \begin{cases} \Psi_i({}_l\mathbf{r}_j)\delta_{\xi\chi} & \text{if } {}_l\mathbf{r}_j \in \Omega \cup \Gamma \\ p_{j-{}_l N}({}_l\mathbf{r}_j)\delta_{\xi\chi} & \text{if } j > {}_l N \text{ and } i \le {}_l N \\ 0 & \text{otherwise} \end{cases}, \quad {}_l\gamma_{j,\xi} = \begin{cases} y_\xi({}_l\mathbf{r}_j) & \text{if } {}_l\mathbf{r}_j \in \Omega \cup \Gamma \\ 0 & \text{otherwise} \end{cases} \tag{14} $$

Application of a linear differential operator L on the interpolation function Eq. 13 acts only on the basis functions

$$ L_l\mathbf{y}(\mathbf{r})_\xi = \sum_{\chi=1}^{n_d} L_{\xi\chi}\, {}_l y_\chi(\mathbf{r}) \approx \sum_{\chi=1}^{n_d} \sum_{i=1}^{{}_l N+M} {}_l\alpha_{i,\chi}\ L_{\xi\chi}\, {}_l\Psi_i(\mathbf{r}) \tag{15} $$

Expressing weight coefficients from Eq. 14, we arrive at

$$ L_l\mathbf{y}(\mathbf{r})_\xi \approx \sum_{\zeta=1}^{n_d} \sum_{j=1}^{{}_l N+M} {}_l\gamma_{j,\zeta} \sum_{\chi=1}^{n_d} \sum_{i=1}^{{}_l N+M} {}_l A^{-1}_{ij,\chi\zeta}\ L_{\xi\chi}\, {}_l\Psi_i(\mathbf{r}) = \sum_{\zeta=1}^{n_d} \sum_{j=1}^{{}_l N+M} {}_l\gamma_{j,\zeta}\ {}_l W_{j,\xi\zeta}(\mathbf{r}) \tag{16} $$

where the operator's action on a function is now expressed as a weighted sum of known values ${}_l\gamma_{j,\zeta}$ and operator coefficients ${}_l W_{j,\xi\zeta}(\mathbf{r})$. So, in order to discretize differential operators, the operator coefficients (OCs) should be determined for each ${}_l\Omega$. This is done as a pre-prosses step only once.

Regarding the governing equation of the thermal model Eq. 1, OCs for the gradient and the Laplacian operator of the scalar field are computed. Time marching is performed with the forward Euler method. View factor matrix **F**, which includes the view factor $F_{j\to i}$ for each (j,i) DS pair,

is computed with the Monte Carlo method. Here $N_{vf} = 10^5$ particles are shoot in random directions from *j*-th DS and checked which *i*-th DS is hit. Based on the number of hit particles in the *i*-th DS the $F_{j \to i}$ component is determined. In case DS is reflective, the $N_{vf} \cdot \zeta$ number of random particles is bounced off, where ζ is the reflection coefficient.

Discretization of the differential operators in the governing equation Eq. 11 of the mechanical model is performed slightly differently than in the thermal model for increasing stability. OCs of ∇^s operator are not evaluated in CNs but on the 2nd order finite difference (FD) stencils prescribed separately to each CN when CN lies inside the domain. Then, the divergence operator is evaluated via the FD method. The distance between CN and its nearest point on the FD stencil equals $h/2$, where h is the distance to the nearest CN. On the boundary, where only OCs of ∇^s are needed, the position of evaluation of COs is moved for $h/2$ in the opposite side of the outward-facing normal vectors. With the OCs computed, a sparse global system of equations is assembled and solved to obtain the solution. Our future work will publish a more detailed description of the procedure.

Simulation Procedure

The thermal simulation starts by importing the bar's discretized domain (CNs), placing it on the first stage p_1, and setting the material parameters based on the initial temperature $T_{bar,0}$. For the determination of radiative heat fluxes, the CB is enclosed inside the virtual rectangle shown with the red contour in Fig. 1. The boundary of the first bar (also shown with the red contour in Fig. 1) is discretized on DSs. Then, the view factor matrix **F** is computed with DSs of the rectangle and the first bar. Three types of DSs are considered: the first one belongs to the heat shield with reflectivity ζ_{pl}, the second to the steel bars with reflectivity ζ_{bar}, and the third to all other surfaces with reflectivity ζ_{sur}. The heat shield temperature and ambient temperature are set to T_{pl} and T_{sur}, respectively. With **F** computed, heat fluxes on the boundary are calculated using the remaining parameters shown in Table 1. The simulation runs until t_p is reached, where during time marching, the heat fluxes on the boundary and material parameters are updated before each time step. After that, the bar is moved to p_2, and a new bar is positioned on p_1. Since 2 bars are now included, a new **F** is computed. The simulation runs again until t_p where 2 bars are now cooled. This process is repeated with 3, 4, and so on bars until the last position p_n is reached. Then a new cycle is run where the bar on p_n position is removed from the system. Adding the bars on the CB (from the left side) and removing them (from the right side) is repeated until the temperature difference at the time t_p in the centre of the bar on the last stage p_n between two cycles is less than $\Delta T_{\max}$. With this procedure, the quasi-steady state temperature solution is obtained.

The temperature solution is position (or stage) dependent $T(\mathbf{r}, t_j, p_i), t_j \in [0, t_p]$. For mechanical simulation, it is transformed to $T(\mathbf{r}, t_j), t_j \in [0, t_p\ p_n]$ since an arbitrary bar can be picked for the analysis. The mechanical model then incrementally applies the temperature load and considers the updating of the material parameters.

In this work, we show the influence of the distance between bars x_{bp} and the position of the heat shield p_y on the thermal and mechanical solution fields. The study is performed for three different x_{bp} s (R1, R2, R3). To study the same time window $t_{\max} = t_p \cdot p_n$, different times on each stage t_p and a different number of maximum stages p_n are applied. Also, three different p_y s (P1, P2, P3) are investigated, as shown in Table 2.

Table 1. Constants used in the thermal model.

$\varepsilon_{pl}, \varepsilon_{bar}, \varepsilon_{sur}$ [/]		ζ_{pl}, ζ_{bar} [/]	ζ_{sur} [/]	T_{pl} [°C]	$T_{bar,0}$ [°C]	T_{sur} [°C]	h [W/m²K]	ΔT_{max} [°C]
0.8		0.2	0	300	900	25	20	0.5

Table 2. Parameters used in the case studies.

	x_{bp} [m]	t_p [s]	p_n [/]		p_y [m]
R1	0.15	5	30	P1	0.3
R2	0.3	10	15	P2	0.7
R3	0.45	15	10	P3	1.3

Results of the Thermal Model

In Fig. 2, the temperature solution in the centre of the bar for the P1R1 case (T_{P1R1}) and the difference to other cases $T_{\mathrm{diff}} = T_{\mathrm{P1R1}} - T_{\mathrm{PiRi}}$ are shown over time. In the P1R1 case, the bars are close to each other, and the heat shield is at its lowest point. Due to that, the slowest cooling is obtained. In all cases, the temperature sensitivity to the position of the heat shield is small. With a larger p_y, the bar's centre is additionally cooled for ~1°C. A comparison of R1 and R2 shows that x_{bp} has a more significant impact on the solution than p_y. In the end, the centre point is cooled for ~5°C more. In case of increased spacing between the bars (compare R2 and R3), the temperature drop is much lower ~1°C.

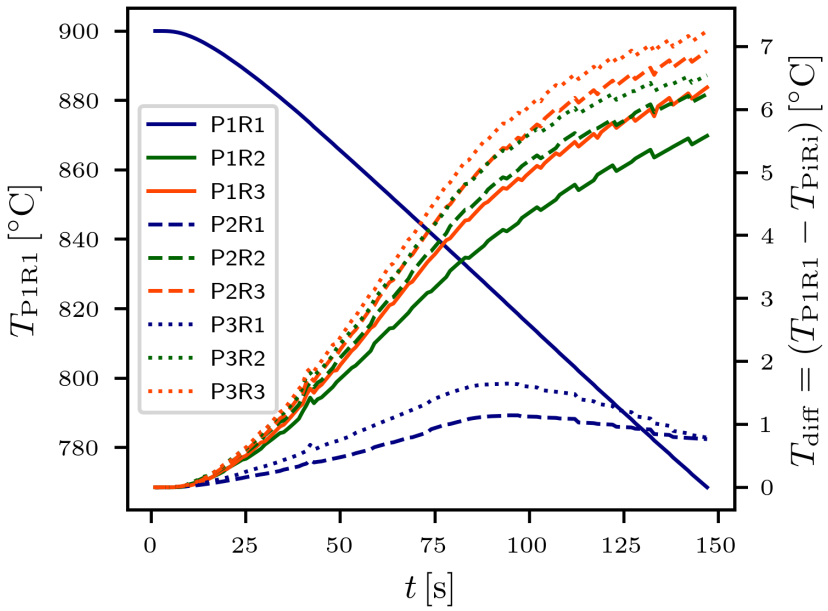

Fig. 2. P1R1 temperature solution in time at the centre of the bar and the difference to other cases.

Fig. 3 shows the temperature solution at the end of the simulation over the field for all investigated cases. As shown before, observing cases from left to right (increasing x_{bp}), the temperature decreases more than changing the cases from top to bottom (increasing p_y). One can also observe that the field is not symmetric. This is a consequence of nonuniform heat fluxes that change with time. In all cases, the right half of the bar is cooled more. This happens since a bar on the right-hand side of some other observed bar is colder than the bar on the left-hand side, so the heat flux on the right is larger.

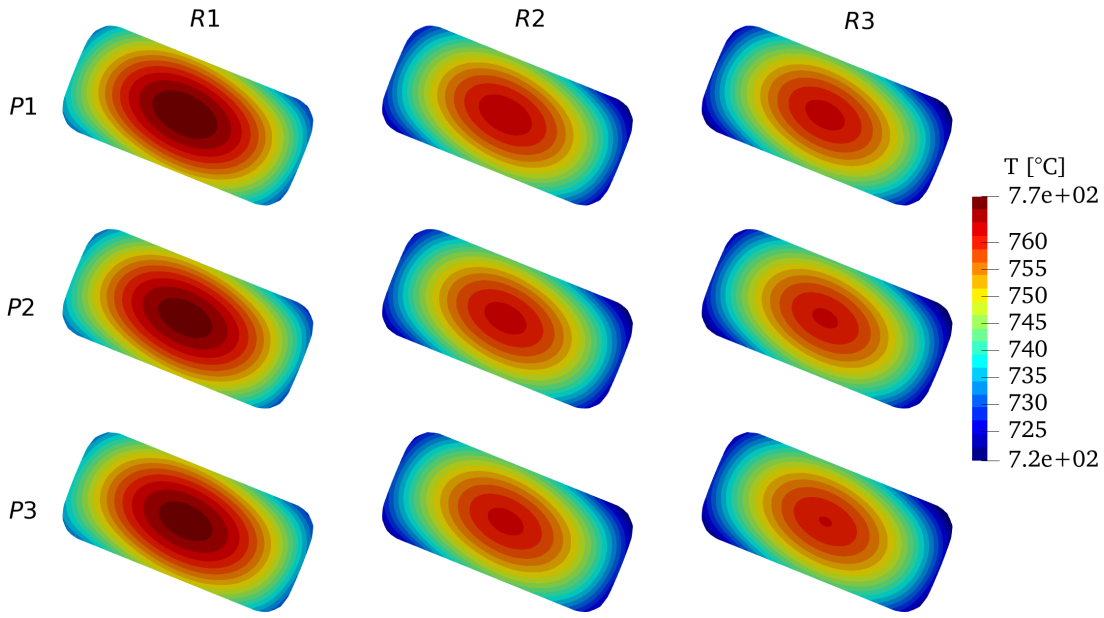

Fig. 3. Temperature of all cases as a function of x_{bp} and p_y at $t_{max} = 150$ s.

Results of the Mechanical Model

In Fig. 4, the results of the von Mises stress σ_{vm} and the accumulated plastic strain $\bar{\varepsilon}^p$ are shown over time obtained in the centre point of the bar. Up to $t \approx 5$ s, the elastic response occurs where no plastic strain is present. Then the slope of the σ_{vm} changes and the bar is plastically deformed. One can see that σ_{vm} and $\bar{\varepsilon}^p$ are changing mostly linearly with time. Small differences in solutions at the end of the simulation are obtained. As in the temperature solution, cases with the same x_{bp} have a similar solution.

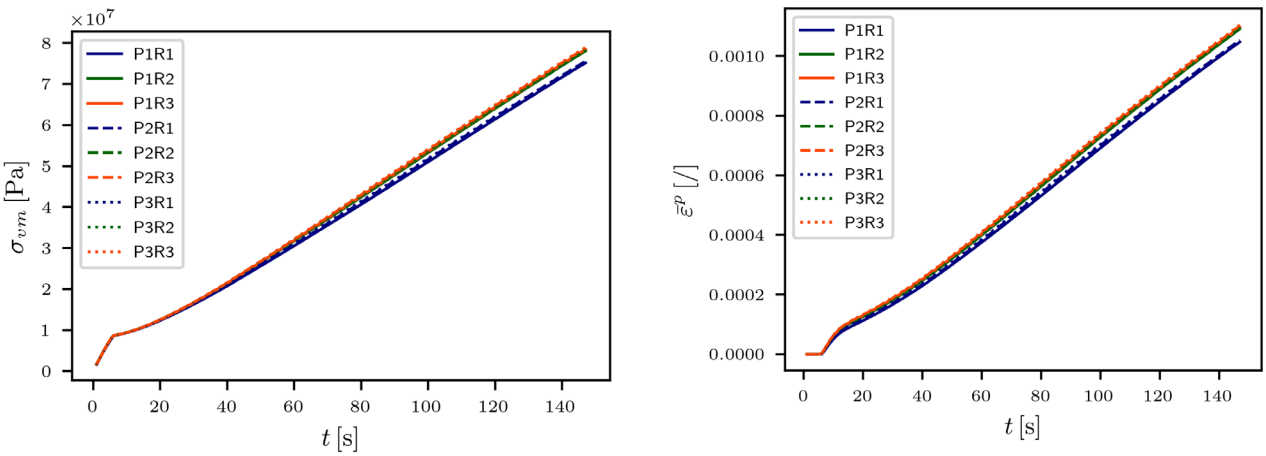

Fig. 4. Von Mises stress (left) and accumulated plastic strain (right) in the centre of the bar over time.

In Fig. 5, the von Mises stress is shown over the field for all cases at the end of the simulation. Similar asymmetry as in the temperature field can be observed. The highest stresses occur in the same area as the lowest temperatures.

In Fig. 6, the initial shape is shown with a grey colour contour. For comparison with deformed shapes, it is shrunk by a factor of 16. The deformed contours, also shown in Fig. 6, are obtained by applying the displacement field solution, multiplied by 300, onto the initial geometry to make

the change visible. In the R1 case, the shrinkage is the smallest, and in the R3 case is the largest. All deformed shapes have a more elliptic shape and are also slightly tilted to the left.

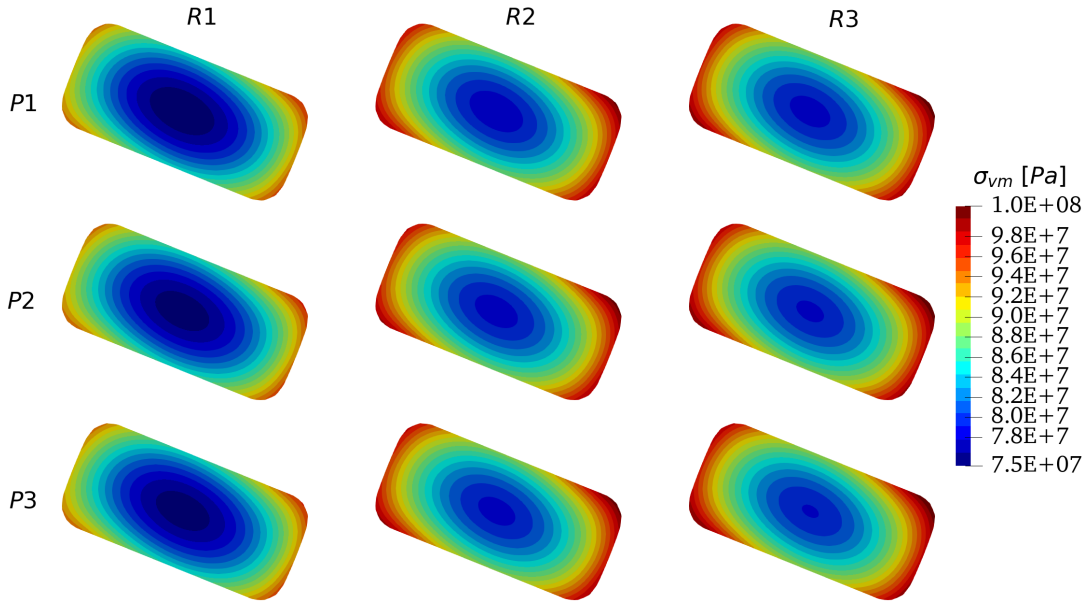

Fig. 5. Von Mises stress of all cases as a function of x_{bp} and p_y at $t_{\max} = 150$ s.

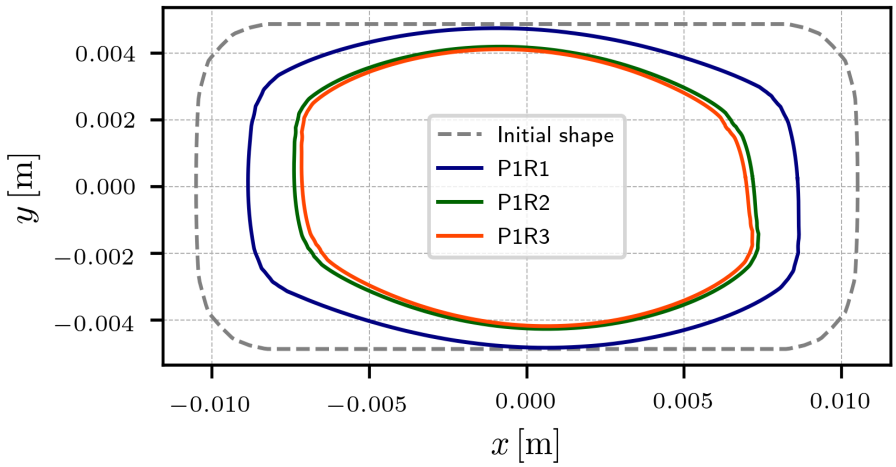

Fig. 6. Initial shape contour shrank by a factor of 16. Deformed contours are obtained by applying the displacement solution multiplied by a factor 300.

Summary

In this work, we presented the modelling of a thermo-mechanical response of steel bars on the cooling bed with the RBF-FD method. Nine cases with varying distances between bars and the position of the heat shield were investigated. We have shown that the solution fields and the final geometry are not symmetric. A reduction of distance between bars has proven to be much more dominant in reducing the cooling rate than the reduction of spacing between bars and the heat shield. The calculated accumulated plastic strain in all considered cases ranges up to ~0.1%, and the maximum von Mises stresses obtained are ~100 MPa.

With this work, we have successfully demonstrated the use of the RBF-FD method on a complex industrial problem. In future work, a three-dimensional model will be implemented to capture also bending of the bars.

Acknowledgements
The Slovenian Grant Agency (ARRS) funded this research by core funding P2-0162, a young researcher programme, and project L2-2609 - co-funded by Štore-Steel Company (www.store-steel.si).

References
[1] R. Vertnik, B. Šarler, Meshless local radial basis function collocation method for convective-diffusive solid-liquid phase change problems, Int. J. Numer. Meth. Heat Fluid Flow 16 (2006) 617-640. https://doi.org/10.1108/09615530610669148
[2] U. Hanoglu, B. Šarler, Multi-pass hot-rolling simulation using a meshless method, Comput. Struct. 194 (2018) 1-14. https://doi.org/10.1016/j.compstruc.2017.08.012
[3] K. Mramor, R. Vertnik, B. Šarler, Simulation of Natural Convection Influenced by Magnetic Field with Explicit Local Radial Basis Function Collocation Method, CMES - Comput. Model. Eng. Sci. 92 (2013) 327-352.
[4] K. Mramor, R. Vertnik, B. Šarler, Meshless approach to the large-eddy simulation of the continuous casting process, Eng. Anal. Bound. Elem. 138 (2022) 319-338. https://doi.org/10.1016/j.enganabound.2022.03.001
[5] B. Šarler, R. Vertnik, A. Lorbiecka, I. Vušanović, B. Senčič, A multiscale slice model for continuous casting of steel, IOP Conf. Ser. Mater. Sci. Eng. 33 (2012). https://doi.org/10.1088/1757-899X/33/1/012021
[6] B. Mavrič, T. Dobravec, R. Vertnik, B. Šarler, A meshless thermomechanical travelling-slice model of continuous casting of steel, IOP Conf. Ser. Mater. Sci. Eng. 861 (2020) 012018. https://doi.org/10.1088/1757-899x/861/1/012018
[7] U. Hanoglu, B. Šarler, Hot Rolling Simulation System for Steel Based on Advanced Meshless Solution, Metals 9 (2019) 788. https://doi.org/10.3390/met9070788
[8] U. Hanoglu, B. Šarler, Developments towards a Multiscale Meshless Rolling Simulation System, Materials 14 (2021) 4277. https://doi.org/10.3390/ma14154277
[9] L.V. Nikitin, F.D. Fischer, E.R. Oberaigner, F.G. Rammerstorfer, M. Seitzberger, R.I. Mogilevsky, On the frictional behaviour of thermally loaded beams resting on a plane, Int. J. Mech. Sci. 38 (1996) 1219-1229. https://doi.org/10.1016/0020-7403(96)00009
[10] J. Basu, S.L. Srimani, D.S. Gupta, Rail behaviour during cooling after hot rolling, J. Strain Anal. Eng. Des. 39 (2004) 15-24. https://doi.org/10.1177/030932470403900102
[11] A. Pernía-Espinoza, F.J. Ascacibar, E. Martínez-de-Pisón, J. Blanco, Analysis of rail cooling strategies through numerical simulation with instant calculation of thermal expansion coefficient, Rev. Metal. 46 (2010). https://doi.org/10.3989/revmetalm.0911
[12] M. Abouaf, J.-L. Chenot, J.-L. Marcelin, A two-dimensional finite element idealization for thermo-elastic deflection in beams, Int. J. Numer. Methods Eng. 19 (1983) 1453-1465. https://doi.org/10.1002/nme.1620191004
[13] I.I. Boyadjiev, P.F. Thomson, Y.C. Lam, Prediction of the deflection and residual stress in controlled cooling of hot-rolled steel beams including load and arbitrary support: Part I. Computational model, J. Mater. Process. Technol. 147 (2004) 370-376. https://doi.org/10.1016/j.jmatprotec.2004.01.009
[14] A. Jaklič, F. Vode, T. Kolenko, Online simulation model of the slab-reheating process in a pusher-type furnace, Appl. Therm. Eng. 27 (2007) 1105-1114. https://doi.org/10.1016/j.applthermaleng.2006.07.033
[15] G.E. Fasshauer, Meshfree Approximation Methods with Matlab: (With CD-ROM), World Scientific 6 (2007). https://doi.org/10.1142/6437

Materials Research Proceedings 28 (2023) 1621-1630 https://doi.org/10.21741/9781644902479-175

Physics-informed machine learning in the determination of effective thermomechanical properties

SOYARSLAN Celal[1,2,a *] and PRADAS Marc[3,b]

[1]Chair of Nonlinear Solid Mechanics, University of Twente, The Netherlands

[2]Fraunhofer Innovation Platform, University of Twente, The Netherlands

[3]School of Mathematics and Statistics, The Open University, United Kingdom

[a]c.soyarslan@utwente.nl,[b] bmarc.pradas@open.ac.uk

Keywords: PINNs, Computational Homogenization, Thermomechanics, Effective Properties

Abstract. We determine the effective (macroscopic) thermoelastic properties of two-phase composites computationally. To this end, we use a physics-informed neural network (PINN)-mediated first-order two-scale periodic asymptotic homogenization framework. A diffuse interface formulation is used to remedy the lack of differentiability of property tensors at phase interfaces. Considering the reliance on the standard integral solution for the property tensors on only the gradient of the corresponding solutions, the emerging unit cell problems are solved up to a constant. In view of this and the exact imposition of the periodic boundary conditions, it is merely the corresponding differential equation that contributes to minimizing the loss. This way, the requirement of scaling individual loss contributions of different kinds is abolished. The developed framework is applied to a planar thermoelastic composite with a hexagonal unit cell with a circular inclusion by which we show that PINNs work successfully in the solution of the corresponding thermomechanical cell problems and, hence, the determination of corresponding effective properties.

Introduction

Accurate prediction of the effective (macroscopic) material properties is crucial for the high-fidelity simulation of the deformation processes of heterogeneous media. Although there exist analytically derived bounds, e.g., (arithmetic) Voigt and the (harmonic) Reuss averages;
and effective-medium theories, e.g., the Maxwell, self-consistent, and differential effective-medium approximations, these fall short of providing accurate predictions for materials systems, including high property contrast and varying phase volume fractions [1]. This is due to the limited microstructural descriptors considered in their formulation, e.g., the phase volume fraction and shape. As a remedy, full-field computational micro-macro transfer techniques, e.g., finite element method-based computational homogenization schemes, have been proposed [2-5]. This requires solving the boundary value problem, in this context also referred to as the *cell problem*, over the discretized periodic unit cell, or, in general, a representative volume element (RVE).

Since the founding work of Lagaris *et al*., [6] deep neural networks (DNNs) have emerged as an alternative method to solve partial differential equations (PDEs). Physics-informed neural networks (PINNs) use the universal approximation property [7-9] of DNNs in approximating the solution of PDEs in physical problems[10]. This is accomplished through an optimization procedure in which the DNN hyper-parameters are found by minimizing loss functions.
Whereas the classical machine learning approaches identify the corresponding error in terms of distance to a dataset, it is the residual norm of the governing differential equation and associated initial and boundary conditions (BCs) which forms the loss function in PINNs [6, 11-13]. As opposed to standard discretization techniques, e.g., the finite element method (FEM), which

Content from this work may be used under the terms of the Creative Commons Attribution 3.0 license. Any further distribution of this work must maintain attribution to the author(s) and the title of the work, journal citation and DOI. Published under license by Materials Research Forum LLC.

requires domain discretization and construction of a weak form, PINNs allow solving the PDE in its strong form and in a meshless manner providing a differentiable solution which proves helpful in subsequent calculations[6]. For an extensive survey regarding the state of the art of PINNs, the reader is referred to [14].

This work considers the determination of the effective thermomechanical properties of periodic two-phase composites. This is accomplished by two-scale asymptotic and computational homogenization. Unlike many references that conventionally use FEM in the solution of the cell problem, see, e.g., [2-5], we use PINNs by considering that the micro- (constituent-level) \MP{scale} is described by Duhamel-Neumann and Fourier laws. Solving the unit cell problems up to a constant and an exact imposition of the periodic boundary conditions eliminates loss contributions from the boundary conditions of different kinds. It should be noted that the property tensor computations rely on the integrals of the gradient of the corresponding solutions.
DeepXDE is used as the scientific ML and physics-informed library[10]. A 2D periodic hexagonal unit cell with a central circular inclusion is selected as an application problem. Our work shows that PINNs successfully solve the cell problem, i.e., the local thermomechanical boundary value problem, and determine corresponding effective properties. For an extended treatment of the framework in generic elliptic PDEs, with $n-$dimensional applications including phase contrast and interface sharpness effects on the solution accuracy, see [15].

Planar Thermoelasticity

We consider planar thermoelasticity in which the relation between mechanical and thermal fields is constructed through the following Duhamel-Neumann law [16,17] for *i,j,k,l* = 1,2

$$\sigma_{ij} = \mathrm{C}_{ijkl}\epsilon_{ij} - \beta_{ij}\Theta \tag{1}$$

$$\beta_{ij} = \mathrm{C}_{ijkl}\alpha_{kl} \tag{2}$$

Here, C_{ijkl}, β_{ij}, and α_{kl} denote components of the fourth-order planar elasticity tensor C, and planar second-order thermal expansion tensors β and κ, respectively. The temperature field is denoted by Θ whereas σ represents the stress tensor. Letting x denote the position vector, the components of the strain tensor ϵ are computed from the displacement field u with

$$\epsilon_{ij} = \frac{1}{2}\left[\frac{\partial u_i}{\partial x_j} + \frac{\partial u_j}{\partial x_i}\right] \tag{3}$$

Letting κ denote the second-order thermal conductivity tensor; it is assumed that Fourier law relates the heat flow vector to the temperature with

$$q_i = -\kappa_{ij}\frac{\partial \Theta}{\partial x_j} \tag{4}$$

In view of Eq. 1 and 4, and letting b and f denote the internal body force and heat source density, respectively, the linear momentum balance and the stationary heat balance equations respectively read

$$\frac{\partial \sigma_{ij}}{\partial x_j} = b_i \qquad and \qquad \frac{\partial q_i}{\partial x_i} = f \tag{5}$$

Considering planar thermoelastic isotropy, we have

$$C_{ijkl} = \lambda\delta_{ij}\delta_{kl} + \mu\left[\delta_{il}\delta_{jk} + \delta_{ik}\delta_{jl}\right], \qquad \beta_{ij} = \beta\delta_{ij}, \qquad and \qquad \kappa_{ij} = \kappa\delta_{ij} \tag{6}$$

for *i, j, k, l* = 1, 2. Here, λ and μ represent planar Lamé constants, whereas β and κ denote isotropic thermal expansion and heat conduction coefficients. In matrix notation, the isotropic property tensors C, β, and κ whose indicial representations are given in Eq. 6, correspond to the following 3 x 3, 2 x 2, and 2 x 2 matrices, respectively

$$[C] = \begin{bmatrix} \lambda + 2\mu & \lambda & 0 \\ \lambda & \lambda + 2\mu & 0 \\ 0 & 0 & \mu \end{bmatrix}, \quad [\beta] = \begin{bmatrix} \beta & 0 \\ 0 & \beta \end{bmatrix}, \quad [\kappa] = \begin{bmatrix} \kappa & 0 \\ 0 & \kappa \end{bmatrix} \tag{7}$$

First-Order Asymptotic Homogenization

We are interested in material systems of two periodically distributed phases showing linear physical properties. For such systems, a repeating material domain *v*, which is also referred to as a unit cell, encapsulates all material characteristics. Henceforth, let *x* denote the cell-scale (microscale) position and capture fast field variations. It is linked to the macroscale position ${}^{M}x$ which captures fields slow variations, with $x = {}^{M}x/\epsilon$, where $0 < \epsilon << 1$ scale separation parameter. Following [17], we apply a two-scale asymptotic expansion of the *nondimensional* thermoelastic problem-solution in terms of the displacement and temperature fields $u^{\epsilon}({}^{M}x)$ and $\Theta^{\epsilon}({}^{M}\boldsymbol{x})$ results in the following representation

$$u^{\epsilon}\left({}^{M}x\right) = u^{(0)}\left({}^{M}x, x\right) + \epsilon u^{(1)}\left({}^{M}x, x\right) + \epsilon^2 u^{(2)}\left({}^{M}x, x\right) + O(\epsilon^3) \tag{8}$$

$$\Theta^{\epsilon}\left({}^{M}x\right) = \Theta^{(0)}\left({}^{M}x, x\right) + \epsilon u\Theta^{(1)}\left({}^{M}x, x\right) + \epsilon^2 u\Theta^{(2)}\left({}^{M}x, x\right) + O(\epsilon^3) \tag{9}$$

Here, $u^{(i)}$ and $\Theta^{(i)}$ are *v* periodic functions in *x*. Using Eq. 1 and 4 to derive the expansions for the stress tensor and heat flux vector, σ^{ϵ} and q^{ϵ}, substituting the expansions in Eq. 5 and comparing coefficients of powers in ϵ and applying separation of variables, we reach the following macroscopic property tensors $C^{\star}$, $\beta^{\star}$, and $\kappa^{\star}$, respectively

$$C^{*}_{ijkl} = \frac{1}{|v|}\int_{v} \left[C_{ijkl} + C_{ijmn}\frac{\partial U^{kl}_{m}(x)}{\partial x_n}\right] dV \tag{10}$$

$$\beta^{*}_{ij} = \frac{1}{|v|}\int_{v} \left[\beta_{ij} - C_{ijmn}\frac{\partial L_m(x)}{\partial x_n}\right] dV \tag{11}$$

$$\kappa^{*}_{ij} = \frac{1}{|v|}\int_{v} \left[\kappa_{ij} - \kappa_{nj}\frac{\partial M^{i}(x)}{\partial x_n}\right] dV \tag{12}$$

In Eq. 10, 11 and 12, ${U^{kl}}_{m}$, L_m and M^i for *m, k, l, i* = 1, 2 correspond to v - periodic corrector functions which constitute the solutions of the following cell-problems, respectively

$$\frac{\partial}{\partial x_j}\left[C_{ijkl}\frac{\partial U^{mn}_{k}(x)}{\partial x_l}\right] = -\frac{\partial C_{ijmn}(x)}{\partial x_j} \tag{13}$$

$$\frac{\partial}{\partial x_j}\left[C_{ijkl}\frac{\partial L_k(x)}{\partial x_l}\right] = \frac{\partial \beta_{ij}(x)}{\partial x_j} \tag{14}$$

$$\frac{\partial}{\partial x_j}\left[\kappa_{jl}\frac{\partial M^{i}(x)}{\partial x_l}\right] = -\frac{\partial \kappa_{ij}(x)}{\partial x_j} \tag{15}$$

Physics-Informed Neural Networks (PINNs)

In the representation of the corresponding theory, we follow the works by Lu *et al.* [10] and Haghighat *et al.* [13]. Let $N^L(x;\Theta) : \mathrm{R}^{\dim_{in}} \rightarrow \mathrm{R}^{\dim_{out}}$ represent the surrogate model, an L-layer neural network with L - 1 number of hidden layers, that gives the approximate solution for the unknown u of the differential equation. Let x and y denote the input and output vectors, respectively, and $\Theta := \{W, b\}$ represent the set of trainable network parameters, i.e., the weight matrix W and the bias vector b. $\dim_{in}$ and $\dim_{out}$ denote the network input and output dimensions, respectively. With the input-output relations $z^0 \leftarrow x$ and $y \leftarrow z^L$, the propagation of the input through the layers of a feed-forward network is accomplished with the following sequence of operations

$$z^k = \sigma(W^k z^{k-1} + b^k), \qquad 1 \leq k \leq L-1 \tag{16}$$

$$z^L = W^L z^{L-1} + b^L \tag{17}$$

Here, σ is the nonlinear activation function, and q_k, $z^k \in \mathrm{R}^{q_k}$, $W^k \in \mathrm{R}^{q_k \times q_{k-1}}$ and $b^k \in \mathrm{R}^{q_k}$ denote the number of neurons, the outputs, the weight matrix, and the bias vector of each layer k, espectively.

Fig. 1 depicts a schematic plot of a PINN used in the solution of PDEs for the input x and output $\hat{u}$, as an approximation of the actual solution u. P and B respectively denote the differential and boundary operators and the subscripts P and B associations with the PDE and the boundary operators, respectively. For a given training set (collocation points) T, the loss function $L(\boldsymbol{\theta}; T)$ then comprises a weighted sum (with ω_P and ω_B denoting the loss weights) of the residuals of the PDE and the boundary terms which are denoted by $L_P(\boldsymbol{\theta}; T_P)$) and $L_B(\boldsymbol{\theta}; T_B)$), respectively, to give

$$L(\theta; T) = \omega_P L_P(\theta; T_P) + \omega_B L_{PB}(\theta; T_B) \tag{18}$$

The neural network minimizes the loss function by varying the network parameters θ by means of a process referred to as training. At the end of the training, a converged parameter set $\boldsymbol{\theta}^\star$ is reached, providing the optimum output.

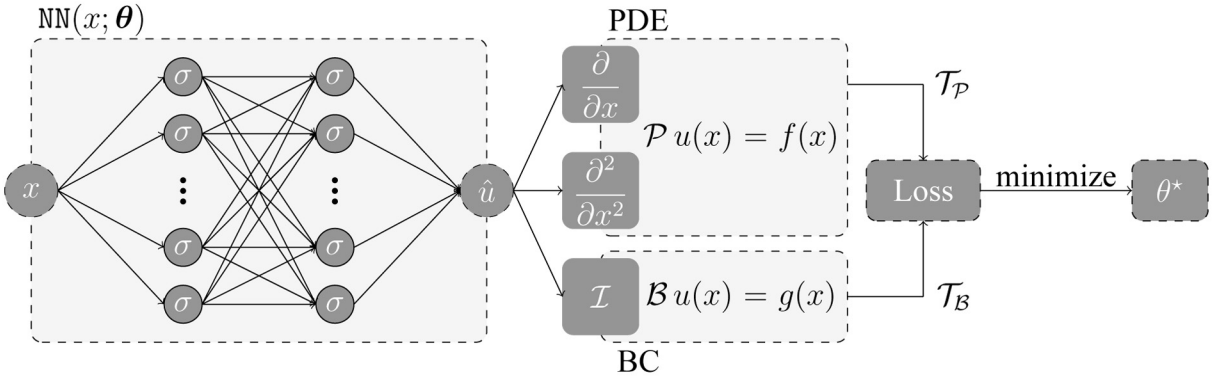

Fig. 1. Schematics of a PINN used in the solution of a PDE with P and B denoting differential and boundary operators, respectively. The image is adapted from [10].

Applications

As an illustrative example, we consider a two-dimensional hexagonal composite domain with a circular inclusion. The selected unit cell corresponds to the Wigner-Seitz cell of the hexagonal Bravais lattice; see Fig. 2. An inclusion volume fraction of $\phi_i = 0.30$ is selected.

Letting $a(x)$ denote a generic isotropic property; the inclusion and matrix properties are denoted as a_i and a_m, respectively. For convenience we consider the values $a_i = \lambda_i = \mu_i = \beta_i = \kappa_i = 2$ and $a_m = \lambda_m = \mu_m = \beta_m = \kappa_m = 1$. This corresponds to a property contrast of 2. The case for phase interchange with $a_i = 1$ and $a_m = 2$ is also investigated.

Considering Eq. 13, 14 and 15, the computation of the source terms requires property derivatives with respect to position. To make this possible, we use a diffuse interface approach given by

$$a(x) = a_m + \frac{a_i - a_m}{2}\left[1 - \tanh\left(\frac{|x|-r}{\xi}\right)\right] \tag{19}$$

where the regularization parameter ξ is chosen to satisfy $L/\xi = 200$. In view of Neumann's principle [18, 19], the macroscopic thermoelastic properties of the material system represented by the periodic composite unit cell given in Fig. 2 possess planar isotropy. Consequently, we can compute the thermoelastic property tensor components through the solutions $U^{kl}{}_m$, L_m and M^i of Eq. 13, 14 and 15 using only one source term in each, which we denote by b^U, b^L and f^M, respectively, and are given in matrix form as

$$[b^U] = \begin{bmatrix} \frac{\partial[\lambda(x)+2\mu(x)]}{\partial x_1} \\ \frac{\partial \lambda(x)}{\partial x_2} \end{bmatrix}, \qquad [b^L] = \begin{bmatrix} \frac{\partial \beta(x)}{\partial x_1} \\ \frac{\partial B(x)}{\partial x_2} \end{bmatrix}, \qquad and \qquad f^M = \frac{\partial \kappa(x)}{\partial x_1} \tag{20}$$

The above problem is implemented into DeepXDE, a scientific ML and physics-informed library [10]. As for the NN hyperparameters, the density and depth of the neural network are selected as 50 and 3, respectively. 25000 collocation points are selected over the problem domain. In optimization studies, a learning rate of 0.01 is used with 30000 epochs. The first 5000 of the 30000 epochs belong to adam optimizer, whereas the remaining 25000 to the L-BFGS optimizer.

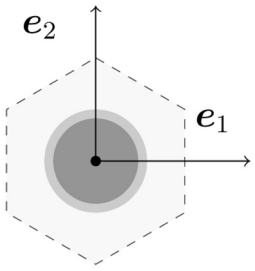

Fig. 2. The selected hexagonal unit cell centered at the origin of the selected Cartesian plane (e_1, e_2). The regular hexagon has an edge length of L and the circular inclusion a radius of r. A diffuse phase interface formulation makes the function differentiable when computing the source terms.

Results and Discussions

Using the PINNs framework, the cell problems dictated by Eq. 13, 14 and 15 are solved for the load cases given in Eq. 20 considering phase properties with $a_i/a_m = 2$ and $a_m/a_i = 2$. Fig. 3 gives the normalized loss function training histories for the PINN solutions. During the iterations, the

first 5000 epochs belonged to the first-order and stochastic adam optimizer. It is observed thatat the latter stages of adam optimization, the loss hardly improves. Reverting to L-BFGS optimizer considerably reduces loss by providing a monotonic convergence.

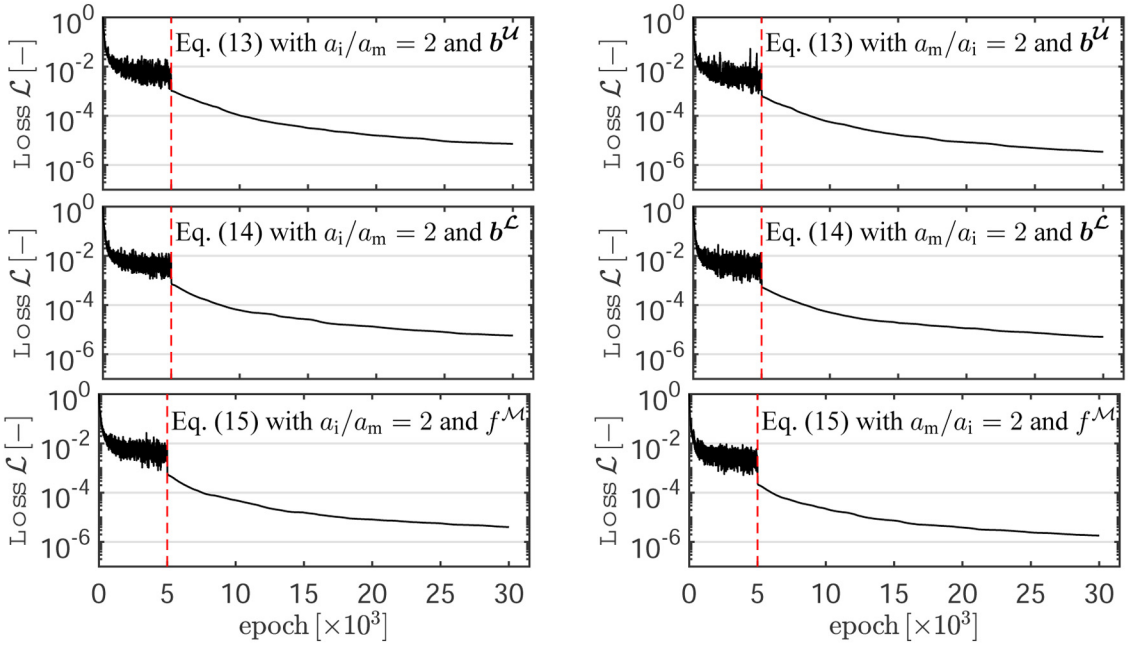

Fig. 3. Training histories of the loss function for the PINN solution of the cell problems given in Eq. 13, 14 and 15. The first 5000 epochs (marked with a red dashed line) belong to adam optimizer, whereas the remaining to L-BFGS. All results are normalized with respect to the initial state.

Resultant contour plots for the property, as well as resultant fields, are given in Figs. 4, 5, and 6. The symmetry and periodicity in the solution fields match that of the composite unit cell. The phase interchange results in the interchange of zones of maximum and minimum in the field distributions.

Computing the integral expressions given in Eq. 10, 11 and 12, we determine the effective property tensors. For $a_i/a_m = 2$ and phase content of $\phi_i = 0.30$, the (arithmetic) Voigt and the (harmonic) Reuss averages yield $a^*_V = 1.300$ and $a^*_R = 1.176$, respectively, which also correspond to upper and lower bounds, respectively.

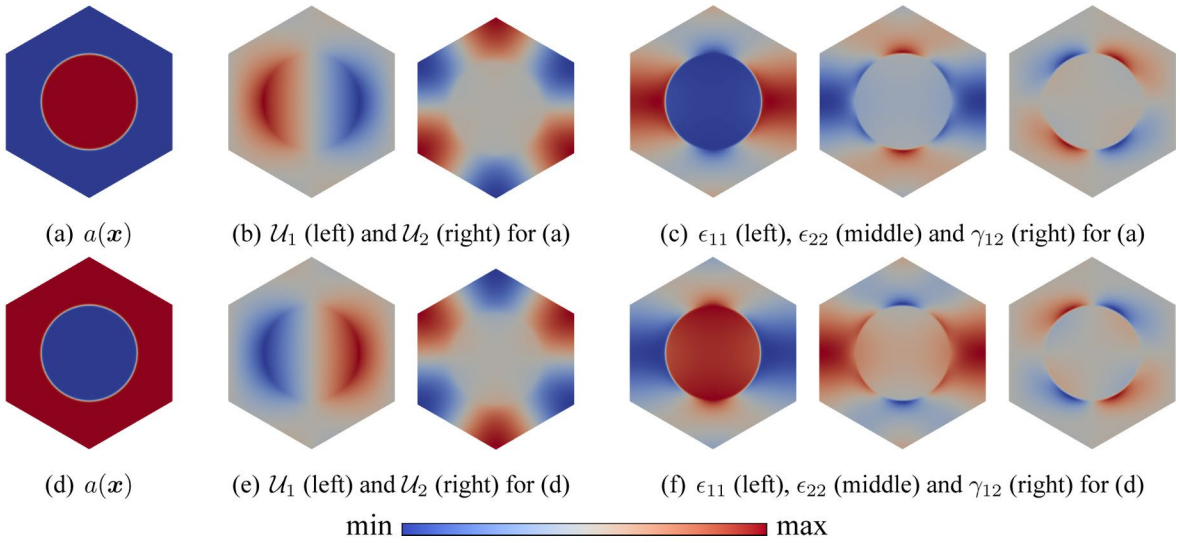

Fig. 4. The contour plots for the solution of Eq. 13 considering the load case b^U given in Eq. 20. The property field a(x) is given for $a_i/a_m = 2$ in (a) and for $a_m/a_i = 2$ in (d). The strain components are computed using the corresponding corrector function U with $\epsilon_{11} = \partial U_1/\partial x_1$, $\epsilon_{22} = \partial U_2/\partial x_2$ and $\gamma_{12} = [\partial U_1/\partial x_2 + \partial U_2/\partial x_1]$.

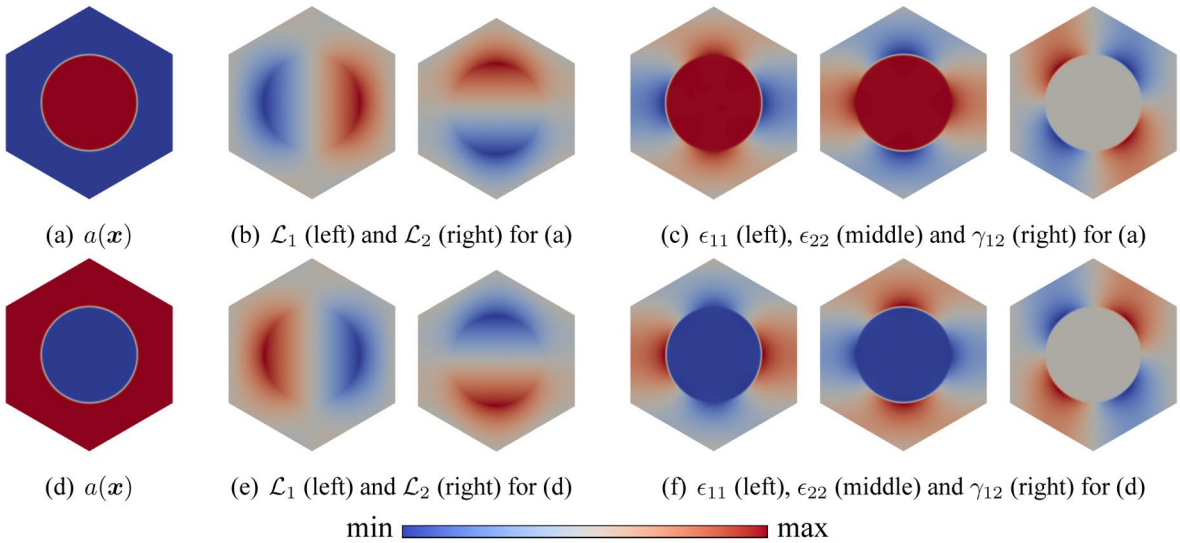

Fig. 5. The contour plots for the solution of Eq. 14 considering the load case b^L given in Eq. 20. The property field a(x) is given for $a_i/a_m = 2$ in (a) and for $a_m/a_i = 2$ in (d). The strain components are computed using the corresponding corrector function L with $\epsilon_{11} = \partial L_1/\partial x_1$, $\epsilon_{22} = \partial L_2/\partial x_2$ and $\gamma_{12} = [\partial L_1/\partial x_2 + \partial L_2/\partial x_1]$.

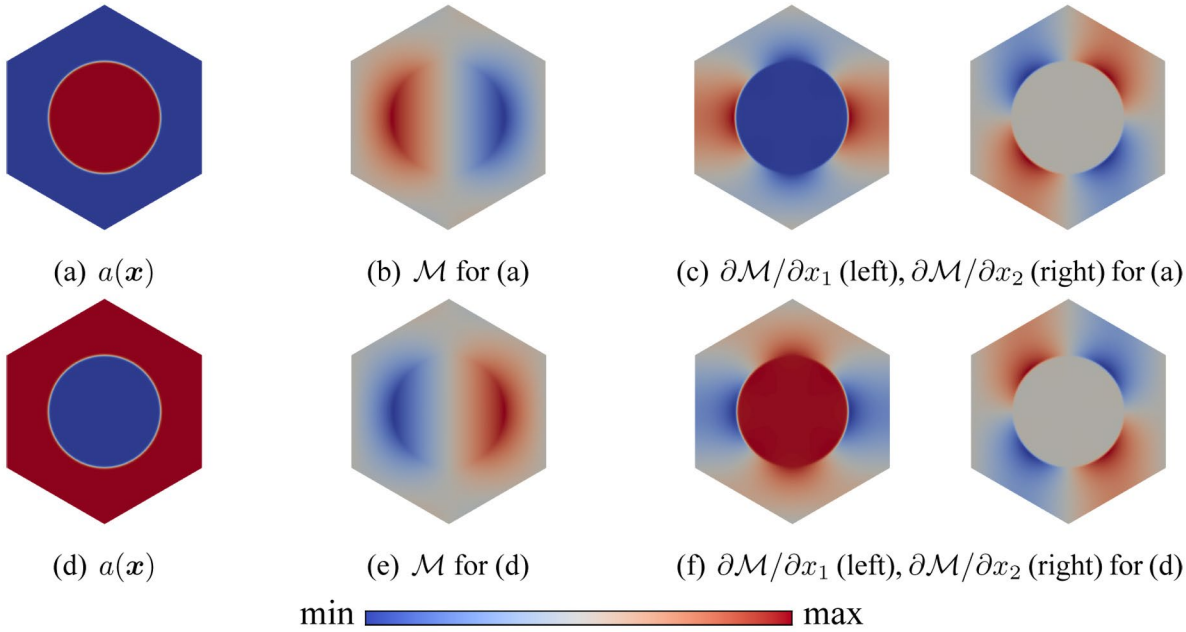

Fig. 6. The contour plots for the solution of Eq. 15 considering the load case $f^{\mathcal{M}}$ given in Eq. 20. The property field a(x) is given for $a_i/a_m = 2$ in (a) and for $a_m/a_i = 2$ in (d).

This is, however, under sharp interface conditions, which is not the case in our PINN computations. In our PINN solution, we have the following matrix representations

$$[C^*] = \begin{bmatrix} 3.621 & 1.207 & 0 \\ 1.207 & 3.621 & 0 \\ 0 & 0 & 1.207 \end{bmatrix}, \quad [\beta^*] = \begin{bmatrix} 1.207 & 0 \\ 0 & 1.207 \end{bmatrix}, \quad [\kappa^*] = \begin{bmatrix} 1.224 & 0 \\ 0 & 1.224 \end{bmatrix}$$

This corresponds to the effective planar Lamé constants of $\lambda^* = \mu^* = 1.207$. Selecting $\lambda = \mu$ and keeping a constant ratio between the λ, μ, and β values of the matrix and the inclusion corresponds to the assumption of an identical thermal expansion coefficient α for the phases. Consequently, one expects to recover $\alpha^* = \alpha_i = \alpha_m = 1/4$ as the effective thermal expansion coefficient for the composite. Our solutions with $\beta^* = \lambda^* = \mu^*$ agree with this statement and confirm our computations. Taking $a_m/a_i = 2$ and phase content of $\phi_i = 0.30$, the (arithmetic) Voigt and the (harmonic) Reuss averages, considering sharp interface conditions, yield $a^*_V = 1.700$ and $a^*_R = 1.538$, respectively. In our PINN solution, we have the following matrix representations

$$[C^*] = \begin{bmatrix} 4.830 & 1.610 & 0 \\ 1.610 & 4.830 & 0 \\ 0 & 0 & 1.610 \end{bmatrix}, \quad [\beta^*] = \begin{bmatrix} 1.610 & 0 \\ 0 & 1.610 \end{bmatrix}, \quad [\kappa^*] = \begin{bmatrix} 1.638 & 0 \\ 0 & 1.638 \end{bmatrix}$$

This corresponds to the effective planar Lamé constants of $\lambda^* = \mu^* = 1.610$. As before, our solutions with $\beta^* = \lambda^* = \mu^*$ agree with the condition of $\alpha^* = \alpha_i = \alpha_m = 1/4$. Although these results show that the emerging effective properties lie between those of the constituent phases and the analytical bounds, the computed magnitudes do not follow conventional rules of mixtures.

Summary

We presented a physics-informed neural network-based first-order two-scale periodic asymptotic computational homogenization framework to determine the effective (macroscopic) thermoelastic properties of two-phase composites. The developed framework allowed the exact imposition of the periodic boundary conditions. Solving the relevant thermomechanical unit cell problems up to

a constant was sufficient to compute the integrals giving the effective properties. These allowed the training loss terms devoid of boundary condition contribution, eliminating the need for identifying the associated weights. We applied the developed framework to a planar composite with a circular inclusion of a hexagonal periodic unit cell. We showed that PINNs work successfully to solve emerging cell problems yielding the determination of effective thermomechanical properties.

References

[1] S. Torquato, Random Heterogeneous Materials, Microstructure and Macroscopic Properties, 1st ed. Interdisciplinary Applied Mathematics 16, Springer-Verlag New York, 2002.

[2] D. Lukkassen, L.-E. Persson, P. Wall, Some engineering and mathematical aspects on the homogenization method, Compos. Eng. 5 (1995) 519–531. https://doi.org/10.1016/0961-9526(95)00025-I

[3] C. Soyarslan, S. Batgmann, M. Pradas, J. Weissmuller, 3D stochastic bicontinuous microstructures: Generation, topology and elasticity, Acta Mater. 149 (2018) 326-340. https://doi.org/10.1016/j.actamat.2018.01.005

[4] C. Soyarslan, M. Pradas, S. Bargmann, Effective elastic properties of 3D stochastic bi-continuous composites, Mech. Mater. 137 (2019) 103098. https://doi.org/10.1016/j.mechmat.2019.103098

[5] C. Soyarslan, J. Havinga, L. Abelmann, T. van den Boogaard, Asymptotic homogenization in the determination of effective intrinsic magnetic properties of composites, Result. Phys. 44 (2023) 106188. https://doi.org/10.1016/j.rinp.2022.106188

[6] I. Lagaris, A. Likas, D. Fotiadis, Artificial neural networks for solving ordinary and partial differential equations, IEEE Transactions on Neural Networks 9 (1998) pp. 987-1000. https://doi.org/10.1109/72.712178

[7] G. Cybenko, Approximation by superpositions of a sigmoidal function, Mathematics of Control, Signals and Systems 2 (1989) 303–314. https://doi.org/10.1007/BF02551274

[8] K. Hornik, M. Stinchcombe, H. White, Multilayer feedforward networks are universal approximators, Neural Networks 2 (1989) 359–366. https://doi.org/10.1016/0893-6080(89)90020-8

[9] K. Hornik, M. Stinchcombe, H. White, Universal approximation of an unknown mapping and its derivatives using multilayer feedforward networks, Neural Networks 3 (1990) 551-560. https://doi.org/10.1016/0893-6080(90)90005-6

[10] L. Lu, X. Meng, Z. Mao, G.E. Karniadakis, DeepXDE: A Deep Learning Library for Solving Differential Equations, SIAM Review 63 (2021) 208–228. https://doi.org/10.1137/19M1274067

[11] I. Lagaris, A. Likas, D. Papageorgiou. Neural-network methods for boundary value problems with irregular boundaries, IEEE Transactions on Neural Networks 11 (2000) 1041-1049. https://doi.org/10.1109/72.870037

[12] J. Sirignano K. Spiliopoulos, DGM: A deep learning algorithm for solving partial differential equations, J. Computat. Phys. 375 (2018) 1339–1364. https://doi.org/10.1016/j.jcp.2018.08.029

[13] E. Haghighat, M. Raissi, A. Moure, H. Gomez, R. Juanes, A physics-informed deep learning framework for inversion and surrogate modeling in solid mechanics, Comp. Meth. Appl. Mech. Eng. 379 (2021) 113741.

[14] S. Cuomo, V. Schiano di Cola, F. Giampaolo, G. Rozza, M. Raissi, F. Piccialli, Scientific Machine Learning through Physics-Informed Neural Networks: Where we are and What's next, arXiv preprint (2022), arXiv: 2201.05624

[15] C. Soyarslan, M. Pradas, Physics-informed machine learning in asymptotic homogenization of elliptic equations. arXiv preprint (2023), arXiv: 2301.09725

[16] W. Nowacki, Dynamic Problems of Thermoelasticity, Polish Scientific Publishers Warszawa, Poland, 1975.

[17] R. Guinovart-Díaz, R. Rodriguez-Ramos, J. Bravo-Castilero, F.J. Sabina, G.A. Maugin, Closed-Form Thermoelastic Moduli of a Periodic Three-Phase Fiber-Reinforced Composite, J. Therm. Stress. 28 (2005) 1067–1093. https://doi.org/10.1080/014957390967730
[18] F.E. Neumann. Vorlesungen über mathematische Physik: Vorlesungen über die Theorie der Elasticität der festen Körper und des Lichtäthers. B. G. Teubner, Leipzig, 1885.
[19] J.F. Nye, Physical properties of crystals: their representation by tensors and matrices, Oxford University Press, 1985.

Materials Research Proceedings 28 (2023) 1631-1640 https://doi.org/10.21741/9781644902479-176

Through process stochastic model of hot strip rolling

SZELIGA Danuta[1,a *], CZYŻEWSKA Natalia[2,b], KUSIAK Jan[1,c], OPROCHA Piotr[2,d], PIETRZYK Maciej[1,e] and PRZYBYŁOWICZ Paweł[2,f]

[1]Faculty of Metals Engineering and Industrial Computer Science, AGH University of Science and Technology, Al. Mickiewicza 30, 30-059 Kraków, Poland

[2]Faculty of Applied Mathematics, AGH University of Science and Technology, Al. Mickiewicza 30, 30-059 Kraków, Poland

[a]szeliga@agh.edu.pl, [b]nczyzewska@gmail.com, [c]kusiak@agh.edu.pl, [d]oprocha@agh.edu.pl, [e]maciej.pietrzyk@agh.edu.pl, [f]pprzybyl@agh.edu.pl

Keywords: Internal Variables, Stochastic Model, Hot Strip Rolling, DP Steel, Microstructure Evolution

Abstract. Advanced numerical models, which predict heterogeneity of microstructural features, are needed to design modern multiphase steels. Models based on stochastic internal variables meet this requirement. Our objective was to account for the random character of the recrystallization and to transfer this randomness to equations describing the evolution of the dislocations and the grain size during hot deformation. The idea of the internal variable model with the dislocation density and the grain size being stochastic variables is described briefly in the paper. Histograms of the grain size measured in the experimental compression tests were used to identify the coefficients in the model. Inverse analysis with the objective function based on the distance between histograms was applied. The model was used to simulation of the various technological routes in the industrial process of the hot strip rolling.

Introduction

Continuous development of the industry is associated with the search for new construction materials that combine high strength with good formability, as well as high strength-to-density ratio. These features can be obtained for steels with heterogeneous microstructures, in which hard constituents of bainite, martensite and retained austenite are dispersed in a soft ferrite matrix [1]. Advanced numerical models are needed to gain knowledge on the local heterogeneities of the microstructural features and resulting properties. As it was shown in [2] internal variable stochastic models, which can predict heterogeneity of the microstructure, would be a support for the design of multiphase materials.

Majority of the models, which can predict heterogeneity of the microstructure, is based on the explicit representation of the microstructure using Representative Volume Elements (RVE). These models require long computing times. Development of the fast mean field model with a capability to predict distributions of the selected microstructural features is the motivation for our research. The papers, which deal with an application of the mean-field stochastic approach to describe heterogeneity of the microstructure, are rare and they usually consider problem of a correlation between material microstructure and in-use properties of products. Among the recent papers, authors of [3] used statistics for geometry description in homogenization methods and in [4] *n*-point statistics was applied to predict crack probability. In few papers random distribution of selected parameter is used as an input for the deterministic material model, e.g. the Authors of [5] studied an influence of various distributions of the austenite grain size prior to recrystallization on the recrystallization kinetics. Our objective was to account for the random character of the recrystallization which occurs during deformation and after deformation at elevated temperatures and to transfer this randomness to equations describing evolution of the dislocation populations

Content from this work may be used under the terms of the Creative Commons Attribution 3.0 license. Any further distribution of this work must maintain attribution to the author(s) and the title of the work, journal citation and DOI. Published under license by Materials Research Forum LLC.

and the grain size. The idea of the model is presented in [6] and its identification for hot deformation processes is described in [2,7]. Since the model incorporates stochastic character of the phenomena, it may predict the distribution of parameters instead of their average values. The general objectives of the present work were twofold. The first was identification and validation of the stochastic approach to modelling hot deformation of the dual phase (DP) steel including dynamic processes during deformation and static processes during interpass times. The second was application of this model to the simulation of various technological routes for the hot strip rolling process. Application of the results from the stochastic model as input for the simulation of phase transformations during laminar cooling recapitulates the paper.

Model

Description of the model.

The model is discussed in details in [6] and only main equations are repeated here for a completeness of the presentation. The model origins from Kocks-Estrin-Mecking (KEM) approach [8,9] with the stochastic dynamic recrystallization term added. After discretization in time, the evolution of the dislocation density is governed by the equation:

$$\rho(t_i) = \rho(t_0)\left[1-\xi(t_i)\right] + \left\{\rho(t_{i-1}) + \left[A_1\dot{\varepsilon} - A_2\rho(t_{i-1})\dot{\varepsilon}^{1-a_7}\right]\Delta t\right\}\xi(t_i) \tag{1}$$

where: t - time, $\dot{\varepsilon}$ - strain rate, a_7 - coefficient accounting for the influence of the strain rate on the recovery, Δt - time step, A_1, A_2 - coefficients responsible for hardening and recovery defined in [6] and in Fig. *1*.

The parameter $\xi(t_i)$, accounts for a random character of the recrystallization and its distribution is described by the following conditions:

$$\begin{aligned} &\mathbf{P}\left[\xi(t_i)=0\right] = \begin{cases} p(t_i) & if\ \ p(t_i)<1 \\ 1 & otherwise \end{cases} \\ &\mathbf{P}\left[\xi(t_i)=1\right] = 1-\mathbf{P}\left[\xi(t_i)=0\right] \end{aligned} \tag{2}$$

In Eq. 2 $p(t_i)$ is a function, which bounds together the probability that the material point recrystallizes in a current time step and present state of the material:

$$p(t_i) = a_4\rho(t_{i-1})^{a_6}\frac{3\gamma(t_i)\tau}{D_\gamma(t_{i-1})}\exp\left(\frac{-a_5}{RT}\right)\Delta t \tag{3}$$

where: D_γ - grain size in μm, τ - energy per unit dislocation length, a_4, a_5, a_6, a_{17} - coefficients.

In Eq. 3 variable γ represents a mobile fraction of the recrystallized grain boundary and depends on the distribution of $\xi(t_{i-1})$ in previous step, as it is explained in [6]. In the work [7] the model was further extended by including interpass times and static phenomena into simulations. Several trajectories of Eq. 1 were calculated, each time using randomly generated values of $\rho(t_0)$ and $D_\gamma(t_0)$. These individual trajectories were then aggregated into histograms at consecutive time steps t_i. Strictly speaking, we start with the grain size $D_\gamma(t_0) \equiv D_0$ which is a random variable described by the Weibull distribution with the shape parameter $k = 10$, which was determined on the basis of measured grain size distributions shown in [2]. The scale parameter of the distribution was established as the average grain size measured after roughing rolling.

The changes of the grain size during deformation and during the interpass times were calculated based on the fundamental works of Sellars [10], who proposed equations describing grain size after static and dynamic recrystallization, as well as after grain growth.

When during the calculation the random parameter $\xi(t_i) = 0$, the considered point recrystallizes and its new grain size $D_\gamma(t_i)$ is drawn from the Gauss distribution with the expected value of the grain size calculated by the deterministic model either for the static or for the dynamic recrystallization [10]. The standard deviation in the Gauss distribution is an optimization variable a_{16} in the model. The chart showing flow of calculations in the model is shown in Fig. *1*, where: *Np* - number of the Monte Carlo points, *Nt* - number of the time steps, $\dot{\varepsilon}$ - strain rate, *b* - module of the Burgers vector, *l* - mean free path for the dislocations, - *R* - universal gas constant, *T* - temperature in K.

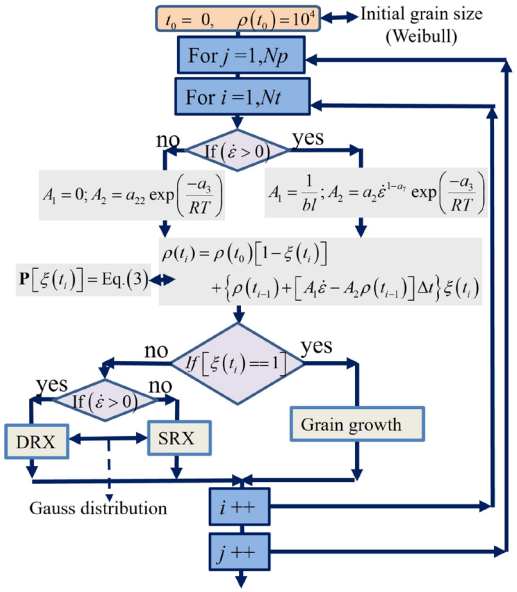

Fig. 1. Selected results of a comparison of measured and calculated flow stress in uniaxial compression.

Beyond the histograms of the selected parameters, the model allows calculation of the average dislocation density ρ_{av} and further the flow stress σ_p, as follows:

$$\sigma_p = \alpha G b \sqrt{\rho_{av}} \qquad \rho_{av} = \frac{1}{Np}\sum_{i=1}^{Np}\rho_i \quad (4)$$

where: *G* - shear modulus, *b* - module of the Burgers vector, *Np* - number of points in the Monte Carlo solution, α - coefficient.

The model contains 22 coefficients, which are grouped in the vector **a**. These coefficients were identified on the basis of the experimental data.

Identification and validation of the model.

Details of the identification procedure are described in [2,6]. Inverse algorithm developed in [11] was applied.

The conventional objective function used in the identification of the deterministic models [11] was extended by including the metric of the distance between measured and calculated histograms of the grain size. The experimental data published in [12] were used. Steel DP600 with the symbol S406 in that publication was considered. The tests composed uniaxial compression of the samples measuring ϕ10×12 at various temperatures and strain rates. The total strain was 1 in all the tests and the expected value of the austenite grain size after preheating was 30 μm. Full set of the experimental data for these test, including micrographs taken at various stages of the deformation and after the deformation, can be found in the RFCS report [13]. The model with optimal coefficients was validated and the selected results are shown in Fig. *2* for the flow stress and in Fig. *3* for the austenite grain size. The experimental flow stress was calculated by the inverse solution [11] for the forces measured in the uniaxial compression tests. Reasonably good agreement between measurements and predictions of the model was obtained for all the experiments.

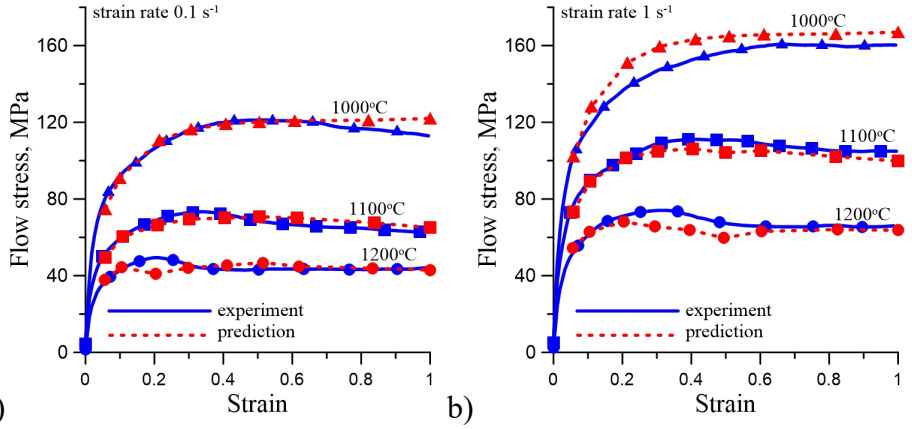

Fig. 2. Selected results of a comparison of measured and calculated flow stress in uniaxial compression.

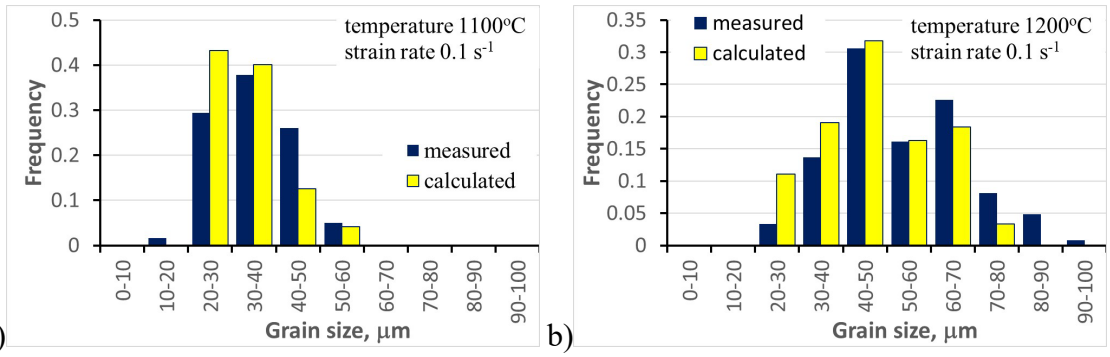

Fig. 3. Selected results of a comparison of measured and calculated histograms of the grain size after uniaxial compression at the strain rate 0.1 s^{-1} and temperature 1100°C (a) and 1200°C (b).

We assumed further that the model, which was validated in the laboratory experiments for various deformation/temperature cycles, will give good results for the industrial conditions.

Numerical Tests of the Model

Numerical tests were performed to evaluate model's predictive capability in the varying conditions of deformation. The stochastic model was implemented into the finite element (FE) program [14] and it was solved in selected points of the FE mesh. The two experiments were simulated: i) Interrupted compression of the uniaxial samples with various holding times between deformations, ii) Varying strain rate test.

Interrupted compression of the uniaxial samples [15].

This test is usually used to develop static recrystallization model. In the present work simulation of the 2 step compression of the sample measuring ϕ10×12 mm were performed. Results for the strain of 0.4 in both deformations and various interpass times are shown in Fig. *4* and in Fig. *5*. The deformation temperature was 1000°C and the strain rate was 1 s^{-1}. Changes of the flow stress calculated following Eq (4) are shown in Fig. *4*. The flow stress during the interpass time decreases asymptotically to zero but it can be concluded that the recrystallization is completed in 2 s after the end of deformation. Histograms of the grain size and dislocation density at the beginning of the second deformation for various interpass times are shown in Fig. *5*. It is confirmed that after 2 s the static recrystallization is completed.

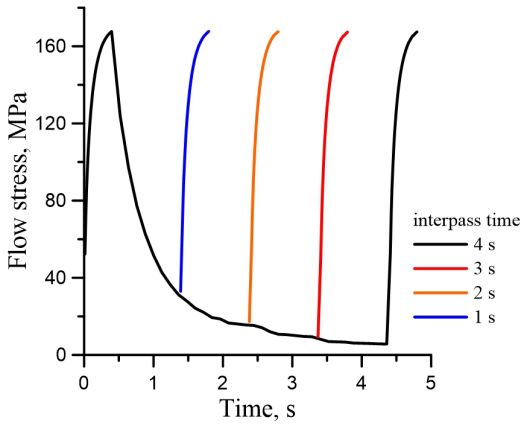

Fig. 4. Results of simulations of the interrupted compression of the cylindrical samples with different interpass times.

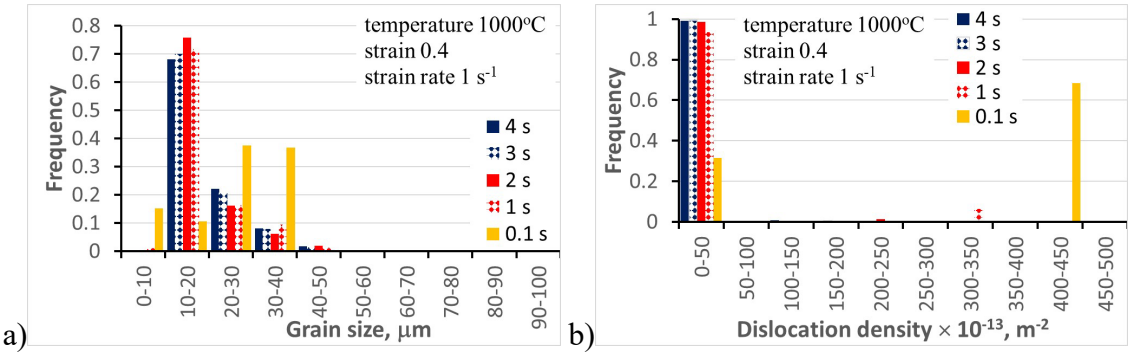

Fig. 5. Histograms of the grain size (a) and dislocation density (b) calculated for various times after the end of deformation.

Varying strain rate test.

In this test the strain rate was changed by an order of magnitude at various stages of the deformation. When external variable models are used, after the change of the conditions the response of the model moves immediately to a new equation of state. On the other hand, it was observed experimentally by many researchers that the response of the material is delayed [16]. This delay is larger for pure metals but it is also observed for alloys (steels) [17]. Below we present the results for the tests when at the strain of 0.4 the strain rate is changed by an order of magnitude (between 0.1 and 1 s^{-1}). The test temperature was 1100°C what means that at the strain of 0.4 the dynamic recrystallization has already begun. Changes of the flow stress during varying strain rate tests are shown in Fig. *6*a. Delay of the material response is well seen in this figure. Histograms of the dislocation density during these tests are shown in Fig. *6*b. Full bars represent dislocation density at the strain 0.4, when the strain rate was changed. The bars with a pattern represent dislocation density at the strain 0.5 (additional strain of 0.1 after the strain rate was changed). It is seen that after this additional strain the state of the system has not reached the state, which was predicted for the constant strain rate.

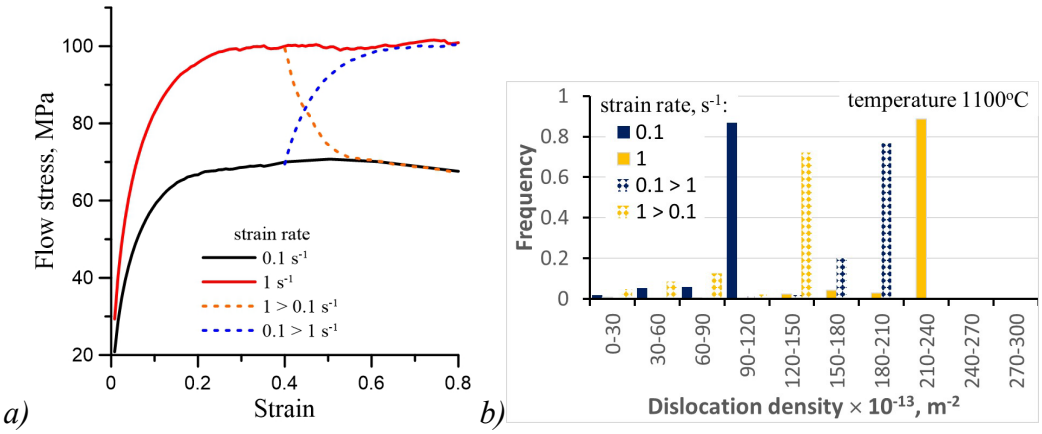

Fig. 6. Changes of the flow stress (a) and histograms of the dislocation density (b) during varying strain rate tests.

Hot Strip Rolling

The hot strip mill composed of reverse roughing mill, 6-stand continuous finishing mill and 2-section laminar cooling was considered. Rolling of the strip 1500×3 mm was simulated. The results for the finishing mill only are presented below. The work roll radius was 400 mm in all stands and the distance between stands was 5 m. The rolling schedule is given in Table 1, where: *h* - thickness, *r* - reduction, *v* - velocity, *t* - interpass time, *rpm* - rotational velocity of the rolls.

Table 1. Rolling schedule considered in the paper.

pass	*h*, mm	*r*	*v*, m/s	*t*, s	*rpm*
0	67	-	0.36	-	-
1	40.6	0.385	0.59	8.5	14.1
2	19.1	0.53	1.26	4	30
3	9.4	0.508	2.56	2	61
4	5.4	0.426	4.44	1.1	106.2
5	3.7	0.315	6.49	0.8	154.9
6	3	0.189	8	0.6	191.1

Two rolling strategies were considered: i) Classical rolling with the end of rolling temperature about 900°C followed by a laminar cooling (V1); ii) Rolling with intensive cooling in finishing mill between 4th and 5th stands as well as between 5th and 6th stands. The end of rolling temperature is below 850°C (V2). Laminar cooling followed and phase transformation model for partially recrystallized material was applied. The objective of V2 was to show the model's capability to predict effect of the austenite deformation on the kinetics of transformations. Calculated time-temperature profiles and load parameters for both variants are shown in Fig. *7*. An effect of additional cooling between stands on loads was evaluated, as well, and it was small.

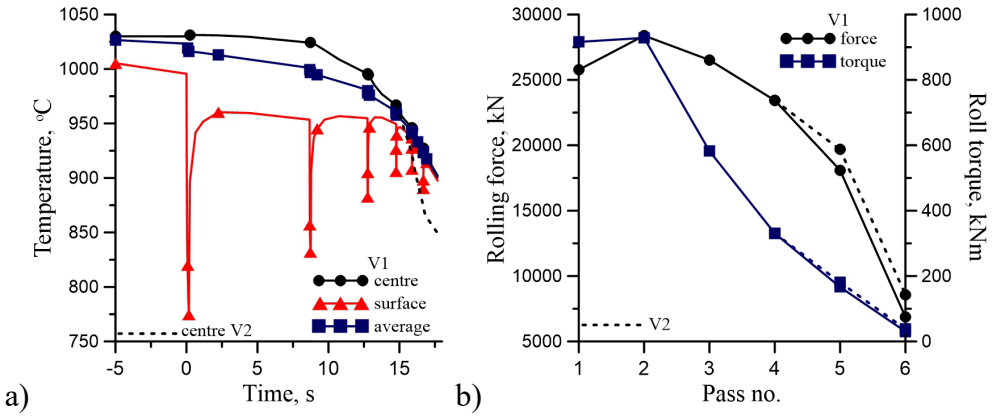

Fig. 7. Calculated time-temperature profiles (a) and load parameters (b) for the two rolling routes.

The stochastic model was applied to calculate distribution of the microstructural parameters during rolling. The selected results for the last 2 passes are shown in Fig. *8*. These results show that decrease of the end of rolling temperature leads to an increase of the dislocation density at the beginning of transformations. These results were used as an input data for simulations of the phase transformations during laminar cooling. At this stage the deterministic model of phase transformations described in [12] was applied but the input data were stochastic. The typical laminar cooling system composed of 2 sections and described in [18] was considered. This system allows a 3-stage cooling sequence: fast/slow/fast cooling. In consequence the DP microstructure composed of ferrite and martensite can be obtained. Since the input data for the deterministic phase transformation model were stochastic, calculated phase composition was obtained in the form of histograms, which are shown in Fig. *9*a. It is seen in this figure that deformation of the austenite (V2) results in an increase of the ferrite volume fraction. Beyond the ferrite, martensite and small amount of bainite (below 0.02) was predicted by the model.

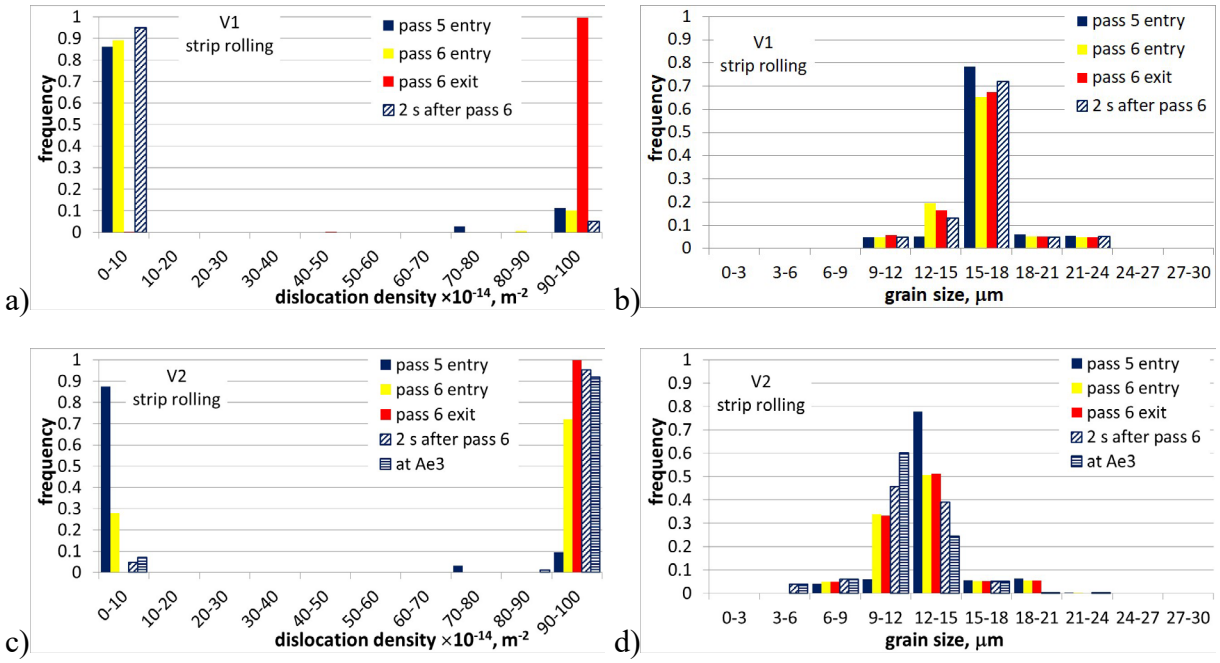

Fig. 8. Calculated histograms of the dislocation density (a,c) and the grain size (b,d) in the last 2 passes of the hot strip rolling according to the rolling schedule V1 (a,b) and V2 (c,d).

Ferrite grain size was calculated by the model, as well. The following deterministic equation proposed in [19] was used:

$$D_\alpha = \left(1-0.45\varepsilon_r^{1/2}\right)\left\{\left(-0.4+6.37\,\mathrm{C_{eq}}\right)+\left(24.2-59\,\mathrm{C_{eq}}\right)C_r^{-0.5}+22\left[1-\exp\left(-0.015D_\gamma\right)\right]\right\} \quad (5)$$

where: ε_r - deformation of the austenite at the beginning of transformation, C_{eq} - carbon equivalent for the steel calculated as C_{eq} = C + Mn/6 + (Cr + Mo)/5, C_r - average cooling rate during ferritic transformation, $D\gamma$ - austenite grain size prior to transformations in μm.

Deformation of the austenite was zero for the V1 and for the V2 it was evaluated from the dislocation density using reverse KEM model. Although Eq. 5 is deterministic, the input parameters (grain size, dislocation density) are stochastic. In consequence the ferrite grain size was obtained in the form of histograms, which are shown in Fig. *9*b. As expected, deformation of the austenite accelerates nucleation of the ferrite and finer grain size was predicted for the rolling schedule V2. Accounting for the random character of the nucleation during phase transformation will be an objective of our future works.

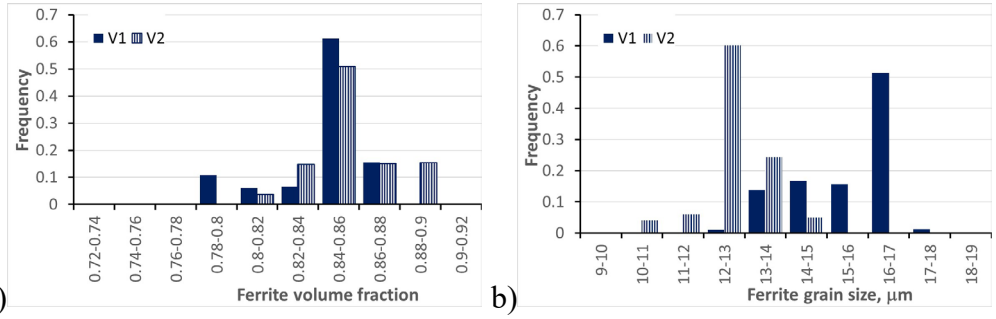

Fig. 9. Calculated histograms of the ferrite volume fraction (a) and the ferrite grain size (b) after laminar cooling of the steel strip.

Summary

The stochastic model describing evolution of the microstructure during hot strip rolling and laminar cooling is presented in the paper. Numerical tests of the model allowed to draw the following conclusions:

- Identification based on the inverse analysis for the compression tests yielded coefficients in the model, which give good agreement between predictions and measurements of both average values and distributions of various parameters.
- Capability to predict histograms of different microstructural features instead of their average values is the main advantage of the model.
- The model was validated in the interrupted compression test and in the varying strain rate test. Prediction of the model were in qualitative agreement with published information about these tests.
- The model is classified as mean-field model and it does not need explicit representation of the microstructure. In consequence, its computing costs are low.
- The model was applied to simulation of various novel strategies for the industrial hot strip rolling. The results are in agreement with our knowledge about this process, what confirmed model's capability to support a design of the optimal rolling technology.
- The stochastic model for the hot deformation is completed. When this model is coupled with the FE program, it can be applied to any hot forming process. In the phase transformations part it is still the work in progress. In the present work we used deterministic phase

transformation model with stochastic input data (histograms of the dislocation density and the grain size calculated by the hot deformation model). Accounting for the random character of the nucleation during phase transformations will be the objective of future works.

Acknowledgements
Financial assistance of the National Science Foundation in Poland (NCN), project no. 2021/43/B/ST8/01710, is acknowledged.

References

[1] R. Kuziak, R. Kawalla, S. Waengler, Advanced high strength steels for automotive industry, Arch. Civil Mech. Eng. 8 (2008) 103-117. https://doi.org/10.1016/S1644-9665(12)60197-6
[2] D. Szeliga, N. Czyżewska, K. Klimczak, J. Kusiak, R. Kuziak, P. Morkisz, P. Oprocha, V. Pidvysotsk'yy, M. Pietrzyk, P. Przybyłowicz, Formulation, identification and validation of a stochastic internal variables model describing the evolution of metallic materials microstructure during hot forming, Int. J. Mater. Form. 15 (2022) 53. https://doi.org/10.1007/s12289-022-01701-8
[3] M. Tashkinov, Statistical methods for mechanical characterization of randomly reinforced media, Mech. Adv. Mater. Modern Process. 3 (2017) 18. https://doi.org/10.1186/s40759-017-0032-2
[4] B.C. Cameron, C.C. Tasan, Microstructural damage sensitivity prediction using spatial statistics, Scientif. Report. 9 (2019) 2774, https://doi.org/10.1038/s41598-019-39315-x
[5] G. Napoli, A. Di Schino, Statistical modelling of recrystallization and grain growth phenomena in stainless steels: effect of initial grain size distribution, Open Eng. 8 (2018) 373-376. http://doi.org/10.1515/eng-2018-0049
[6] K. Klimczak, P. Oprocha, J. Kusiak, D. Szeliga, P. Morkisz, P. Przybyłowicz, N. Czyżewska, M. Pietrzyk, Inverse problem in stochastic approach to modelling of microstructural parameters in metallic materials during processing, Math. Probl. Eng. (2022) 9690742. https://doi.org/10.1155/2022/9690742
[7] D. Szeliga, N. Czyżewska, K. Klimczak, J. Kusiak, R. Kuziak, P. Morkisz, P. Oprocha, M. Pietrzyk, Ł. Poloczek, P. Przybyłowicz, Stochastic model describing evolution of microstructural parameters during hot rolling of steel plates and strips, Arch. Civil Mech. Eng. 22 (2022) 239. https://doi.org/10.1007/s43452-022-00460-2
[8] H. Mecking, U.F. Kocks, Kinetics of flow and strain-hardening, Acta Metall. 29 (1981) 1865-1875.
[9] Y. Estrin, H. Mecking, A unified phenomenological description of work hardening and creep based on one-parameter models, Acta Metall. 32 (1984) 57-70.
[10] C.M. Sellars, Physical metallurgy of hot working, in: Hot working and forming processes, C.M. Sellars, G.J. Davies, (Eds), The Metals Society, London, 1979, pp. 3-15.
[11] D. Szeliga, J. Gawąd, M. Pietrzyk, Inverse analysis for identification of rheological and friction models in metal forming, Comput. Meth. Appl. Mech. Eng. 195 (2006) 6778-6798.
[12] K. Bzowski, J. Kitowski, R. Kuziak, P. Uranga, I. Gutierrez, R. Jacolot, L. Rauch, M. Pietrzyk, Development of the material database for the VirtRoll computer system dedicated to design of an optimal hot strip rolling technology, Comput. Meth. Mater. Sci. 17 (2017) 225-246.
[13] J. Kitowski, Ł. Rauch, M. Pietrzyk, A. Perlade, R. Jacolot, V. Diegelmann, M. Neuer, I. Gutierrez, P. Uranga, N. Isasti, G. Larzabal, R. Kuziak, U. Diekmann, Virtual Strip Rolling Mill VirtRoll, European Commission Research Programme of the Research Fund for Coal and Steel, Technical Group TGS 4, Final Report from the Project RFSR-CT-2013-00007, 2017.
[14] M. Pietrzyk, Finite element simulation of large plastic deformation, J. Mater. Process. Technol. 106 (2000) 223-229. https://doi.org/10.1016/S0924-0136(00)00618-X

[15] R.A. Petković, M.J. Luton, J.J. Jonas, Recovery and recrystallization of carbon steel between intervals of hot working, Canadian Metallurgical Quarterly 14 (1975) 137-145.
[16] J.J. Urcola, C.M. Sellars, Effect of changing strain rate on stress-strain behaviour during high temperature deformation, Acta Metall. 35 (1987) 2637-2647.
[17] K.P. Rao, Y.K.D.V. Prasad, E.B. Hawbolt, Hot deformation studies on a low-carbon steel: Part 2 - An algorithm for the flow stress determination under varying process conditions, J. Mater. Process. Technol. 56 (1996) 908-917. https://doi.org/10.1016/0924-0136(95)01903-0
[18] M. Pietrzyk, J. Kusiak, R. Kuziak, Ł. Madej, D. Szeliga, R. Gołąb, Conventional and multiscale modelling of microstructure evolution during laminar cooling of DP steel strips, Metall. Mater. Trans. B, 46B (2014) 497-506.
[19] P.D. Hodgson, R.K. Gibbs, A mathematical model to predict the mechanical properties of hot rolled C-Mn and microalloyed steels, ISIJ Int. 32 (1992) 1329-1338. https://doi.org/10.2355/isijinternational.32.1329

Non-conventional processes

Materials Research Proceedings 28 (2023) 1643-1652 https://doi.org/10.21741/9781644902479-177

Design of a user-friendly human machine interface for jet electrochemical machining

DAMM Philipp[1,a *], MEICHSNER Gunnar[1,b], LEREZ Christoph[1,c] and HACKERT-OSCHÄTZCHEN Matthias[1,d]

[1]Chair of Manufacturing Technology with Focus Machining, Institute of Manufacturing Technology and Quality Management (IFQ), Faculty of Mechanical Engineering, Otto von Guericke University Magdeburg, Universitätsplatz 2, 39106 Magdeburg, Germany

[a]philipp.damm@ovgu.de, [b]gunnar.meichsner@ovgu.de, [c]christoph.lerez@ovgu.de, [d]matthias.hackert-oschaetzchen@ovgu.de

Keywords: Human Machine Interface, Jet-ECM

Abstract. Electrochemical machining with a closed free jet (Jet-ECM) is a flexible ablating manufacturing technology. With this manufacturing technology, surface structures in the micrometer range can be generated without tool wear occurring. Until now, the technology has mainly been developed in research institutions. Therefore, the aspect of a user-friendly human machine interface has not been in the focus of the machine tool design. The aspect of a user-friendly human machine interface was considered in the construction and development of a new Jet-ECM prototype system at the Otto von Guericke University Magdeburg (OVGU). The prototype system is intended for teaching and research purposes. Users, who will operate the prototype system, have different knowledge of the Jet-ECM process and machine control. Therefore, it was necessary to develop a user-friendly interface, that is easy to learn and easy to use.In the present study, the procedure for creating a user-friendly human-machine interface will be introduced, and the resulting design will be explained. The design was developed according to established design guidelines for machine systems and can also serve as a template for industrial operation. To arrange the operating elements ergonomically and according to the material, energy and information flow, a suitable mask layout was developed. Furthermore, the user interface is suitable for future expansion. Based on the realised user interface, the main components of the Jet-ECM prototype system can be controlled, various process functions can be executed, and different process variables can be analysed.

Introduction

To create a graphical user interface (GUI) for Jet-ECM, the fundamental understanding of this manufacturing technology is necessary to conduct various user tasks. Jet-ECM is an electrochemical machining process based on the anodic dissolution of the workpiece under the influence of electric charge exchange [1,2]. The dissolution takes place between the workpiece and the liquid ion conductor, called electrolyte. Reaction products are carried out by the continuous electrolyte flow. In Jet-ECM an electrolyte jet localises the electric direct current between the anodic workpiece and the cathodic tool, as seen in Fig. 1. The nozzle is positioned at a defined position above the workpiece surface. This nozzle is made of stainless steel and has an inner diameter of e.g. 100 µm [3]. An electrolyte is pumped through the nozzle and hits perpendicular upon the surface of the workpiece. The ejecting jet is forming a closed free jet, because there is no mixing between the surrounding fluid and the ejecting jet, due to the lower density of the atmospheric air in comparison to the electrolyte [4].

Content from this work may be used under the terms of the Creative Commons Attribution 3.0 license. Any further distribution of this work must maintain attribution to the author(s) and the title of the work, journal citation and DOI. Published under license by Materials Research Forum LLC.

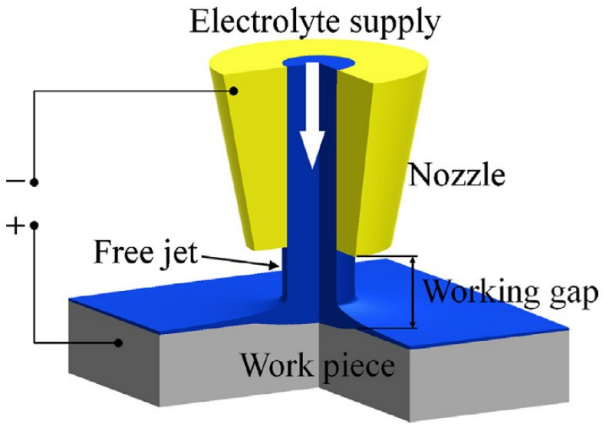

Fig. 1. Scheme of Jet-ECM [3].

The current density, which amounts up to 1000 A/cm², is localised due to the shape of the closed free jet [5]. Therefore, a high localisation and a high precision of the removal geometry can be achieved. Different removal geometries can be realised by changing the movement strategies of the nozzle and the on-time of the electric current.

Machined examples are shown in Fig. 2 and Fig. 3. Without movement of the nozzle in the machining process, point removals can be generated. The depth of a point removal depends mainly on the on-time of electric current. An array of point removals shows Fig. 2a). The shape of a point removal is a typical calotte geometry.

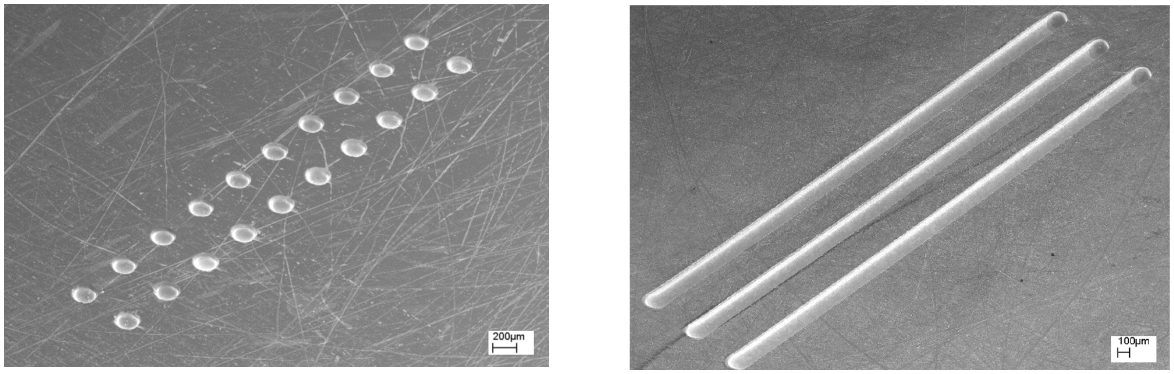

a) Point removals b) Line removals

Fig. 2. SEM images of point and line removals generated with Jet-ECM [6].

With movement of the nozzle and constant process parameters, different forms of removal geometries can be machined, such as line removals, plane surfaces and contour removals. Line removals occur during a line movement of the nozzle with a switched-on electric current. The depth of a line removal depends on the dwell time over the machined workpiece surface and can be influenced by nozzle velocity and number of repetitions of the same line removal. By using complex nozzle geometries, the whole line removal geometry can be affected [7]. The line removals, as seen in Fig. 2b), were each machined with three superimposed lines [6]. Noticeable is the reproducibility and the high quality of the line removal.

A machined plane surface can be realized by an overlay of line removals, as seen in Fig. 3a). The line removals have a defined distance to each other. This defined line distance is caused

through a specific motion in one direction. In order to avoid additional removal, this motion takes place without switched-on electric current. To reach a high surface quality, the kinematic roughness has to be considered. Hackert [8] shows, that the kinematic roughness is nearly steady, if the line distance is smaller than the inner diameter of the nozzle. By a rise of the line distance, the kinematic roughness increases to a maximum. The maximum is reached if the line distance has the width of 1.9-fold of the nozzle diameter [8].

Another removal movement is the contour removal, where the removal takes place along a contour path. The contour removals can be executed through a programmed trajectory with different motion commands. Contour removals are applied to machine for example channels for a microreactor. To get a constant depth for the microstructure, the nozzle velocity has to be equal for each motion commands. Fig. 3b) shows an example of a machined microstructure in form of a microreactor. The cavities are machined in stainless steel with a depth of 60 µm and a width of 200 µm [2].

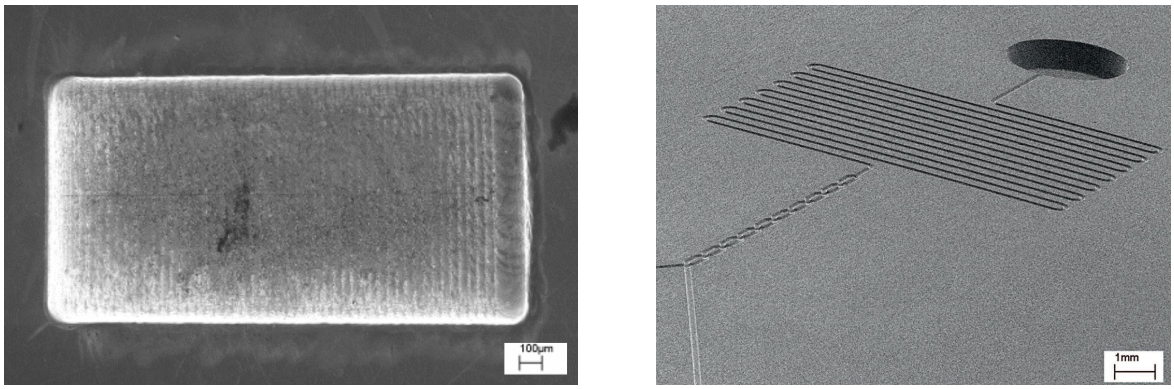

a) Plane surface removal [8] b) Contour removal (microreactor) [2]

Fig. 3. SEM images of a plane surface and a microreactor generated with Jet-ECM.

Jet-ECM prototype system

The design of the Jet-ECM prototype system at the OVGU is shown in Fig. 4. The prototype system is housed in a casing to prevent reaching into the system during processing. The extraction system vacuums and filters the removal gases. A granite portal is mounted on the carrying frame. The linear stages are mounted on this granite portal, that is designed in a gantry design. The nozzle system is mounted on the z-axis and the processing chamber is mounted on the x-axis. To separate the processing area and the electrolyte system, a partition wall is implemented. The electrolyte system consists of fresh electrolyte tank, filter, pump and measurement system for electrical conductivity, electrolyte temperature and pH-value.

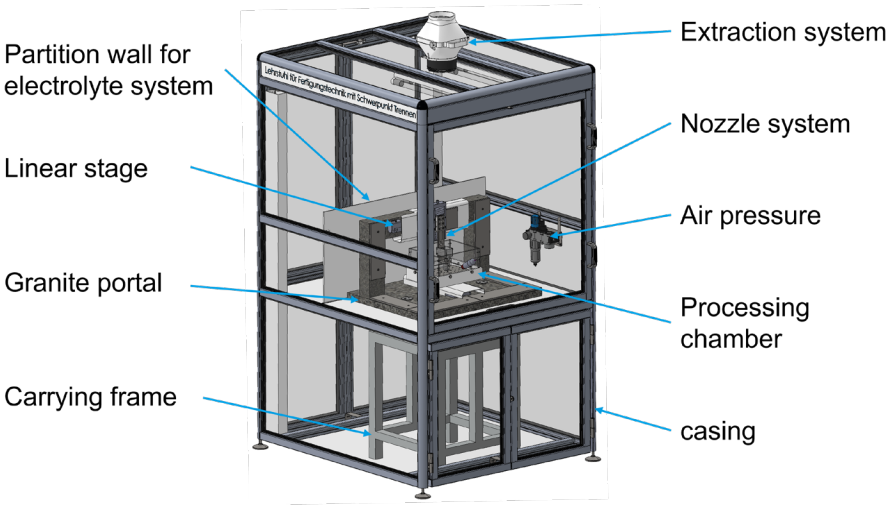

Fig. 4. Design of the Jet-ECM prototype system.

According to Fig. 5 the Jet-ECM prototype system consists of different components, that can be divided into the main parts electrolyte system, power supply, nozzle system, data acquisition, positioning system and control system.

The electrolyte system supplies the Jet-ECM prototype system with an electrolyte. A micro annular gear pump pumps the electrolyte through a filter out of an electrolyte tank. The flow rate of this micro gear pump is in range of 0.048 ml/min to 288 ml/min. The electrolyte is transported to the nozzle system and is ejected perpendicular to the workpiece surface. The used electrolyte is collected in the processing chamber. Afterwards, the electrolyte is discharged to the disposal tank.

A maximum voltage of 50 V and a maximum current of 7 A can be set with a digital laboratory power supply, which is locally and remotely programmable.

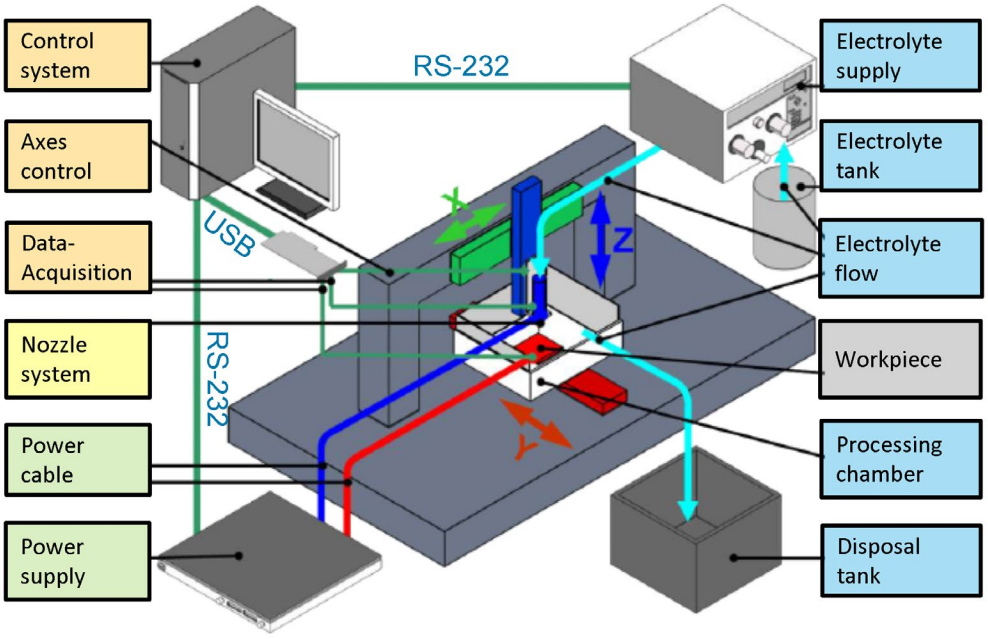

Fig. 5. Components of the Jet-ECM prototype system according to [2].

The nozzle system consists of a nozzle, nozzle holder, cathode contact and connections for the electrolyte and air pressure. The nozzle system defines the position of the nozzle to the workpiece. Furthermore, the nozzle system supplies electrolyte and electric current.

To measure analogue signals and to generate digital output signals, a data acquisition device is used. Through analogue inputs for instance the process voltage, working gap voltage and the process current are measured. The digital outputs are used to switch the process voltage and the air pressure.

The positioning system consists of three linear stages and a motion control. A motion controller is utilized to control the nozzle movement in three axes. Various motion profiles, e.g. multi-axis point-to-point, multi-axis segmented motion or third order profiles can be executed.

To control the whole machining process, a control system, called Jet-Control, was programmed based on the commercial software LabVIEW. All process operations and tasks can be controlled by using Jet-Control. To add a possibility for the user to interact with the Jet-ECM process, a user-friendly human machine interface was designed. Based on the interface, the user can observe, adjust and control the Jet-ECM process. Caused by the variety of different components and by adding new features, the GUI becomes quickly too complex and confusing. Therefore, the GUI was redesigned, using established design guidelines for machine systems.

Concept of the Human Machine Interface

To design a human machine interface, it is recommended to consider the function first and the presentation later [9]. Therefore, the user tasks have to be analysed and sorted due to their importance and their frequency. Accordingly, a task flow is analysed, that shows the sequence for machining a microstructure. As seen in Fig. 6 the task flow can be separated in three main tasks: preparation, processing and post-processing. In the preparation task, the user has to enter the motion commands of a trajectory into a process file. The user loads the process file into the software Jet-Control. Furthermore, the process parameters, for example process voltage, nozzle velocity, flow rate, etc., have to be set. To set the working gap, the user can choose an assisted program which is included in the GUI. To do this, the user manually moves the nozzle to a desired position over the workpiece and enters the required distance of the working gap. With starting of the assisted program, the nozzle is moved into the workpiece direction until an electrical contact is determined. After reaching the electrical contact with the workpiece surface, the working gap is set automatically. For this purpose, the nozzle is moved in opposite direction from the electrical contact position and positioned at the required distance from the workpiece surface.

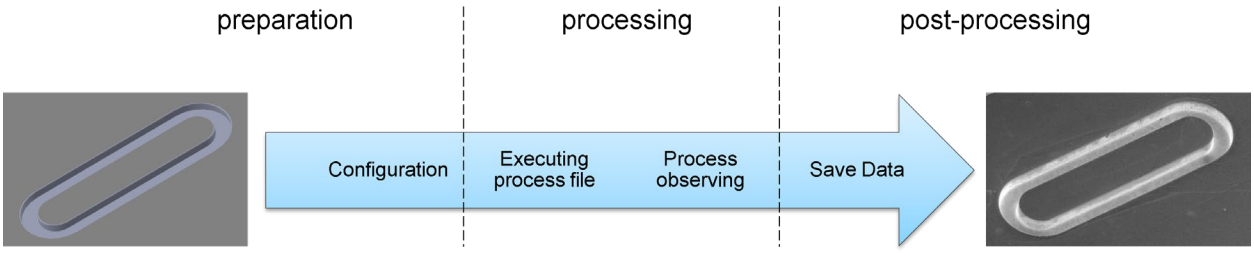

Fig. 6. Task flow to generate a microstructure with Jet-ECM from CAD to machined sample (picture on right hand side from [6]).

After the preparation, the processing task can be started by the user. During the processing task, the removal process takes place based on the set process parameters and the process file. The user

can observe the process via GUI by checking different diagrams, LED's, text or number inserts. Furthermore, the user can interact anytime for warnings and errors.

After the removal process, the post-processing task begins. In the post-processing task, Jet-Control saves selected measurements, such as process current, nozzle position or nozzle velocity, that were recorded during the machining process. Based on the stored measurements, the current characteristics can be determined and the electric charge can be calculated.

Throughout the analyses of the task flow, the common user tasks can be derived. These tasks are listed in Fig.7 and are weighted of their importance and their frequency. Fig. 7a) shows the importance of user tasks. For the Jet-ECM process, it is necessary to switch the process units, such as power supply or electrolyte supply, check for warnings, observing the process parameters and control manually the movement of the nozzle. These functions should always be visible during the whole process.

Less important tasks are configuration or adjusting the working gap, because these tasks have to be performed once during the process. That's why, these tasks shouldn't be visible during the whole process and should be selectable than needed.

Tasks such as save data or implement new features are not required for the process or for the user. Accordingly, these tasks should play a minor role and not be focused or visible.

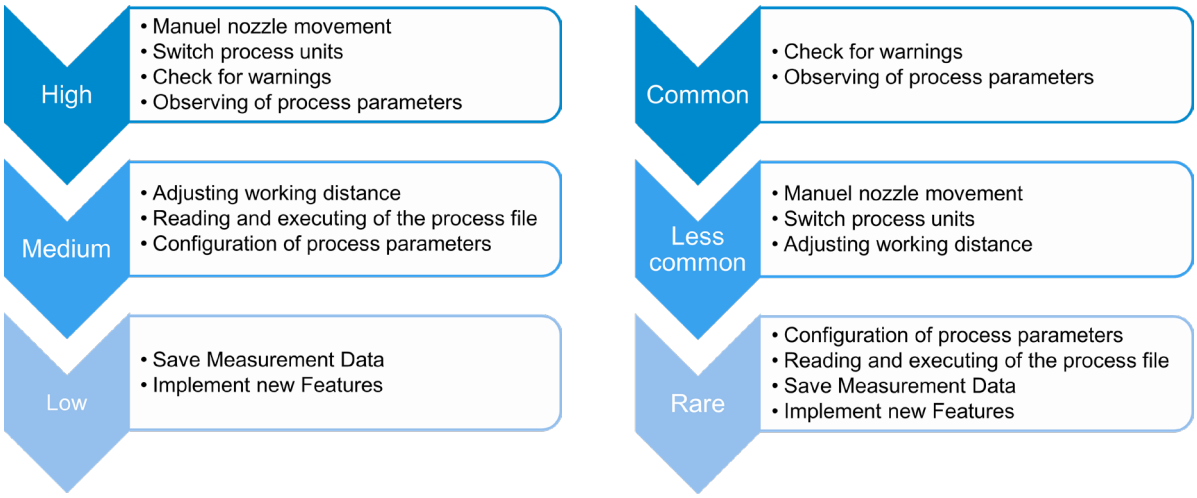

a) Importance of user tasks b) Frequency of user tasks

Fig. 7. List of common user tasks weighted by their importance and frequency.

Fig. 7b) shows the frequency of the user tasks, according to which the visibility should be based. Therefore, the warnings and process parameter should take up the most space. The less common user tasks, such as manual movement or switching process units, should be less visible. The rare user tasks shouldn't be visible, only visible during selecting.

To design the presentation of the GUI, a layout is being used according to Zühlke [10]. The presentation consists of a two-dimensional mask layout, which covered the whole window, as seen in Fig.8. The window is separated into single sections. Each section has its own unique function or task. The section on the top right is called status domain. This domain shows the operating mode of the prototype system. Next to the status domain are the error domain and the command domain. The error domain displays the warning and error messages. The command domain displays, which operations are currently executed. These three domains are located on the top and are always visible. On the right side, the domain of direct functions is located. This domain is used to trigger direct operation functions, that are independent of the activated mask, but dependent on the state

of the prototype system. An example of an independent function is the emergency stop, which is always useable.

The domain of direct functions is also visible and operable during the whole machine process. The working domain is placed in the centre of the window. The working domain displays specific functions, which contains the main tasks and information. The navigation domain is located below the working domain. Due to the navigation domain, the user can choose specific functions, that are displayed in the working domain.

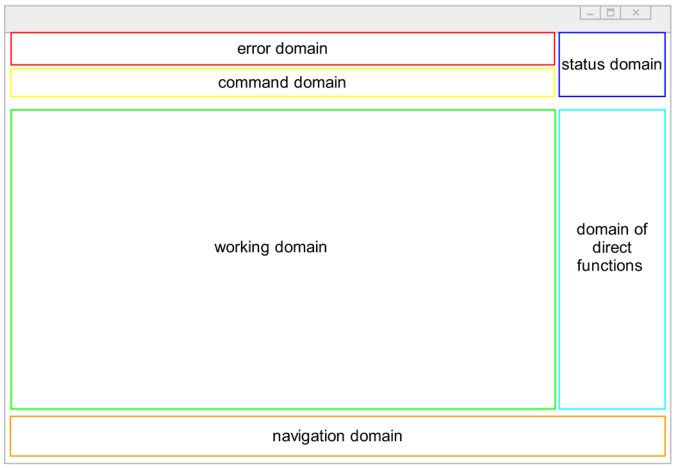

Fig. 8. Conceptional mask layout according to [10].

Based on the mask layout, the GUI was designed. The GUI consists of four different mask layouts, that can be chosen by the navigation domain. The mask layouts are differentiated by the working domain, which are: *overview*, *configuration*, *working gap* and *process file*. The mask layouts for the working domains *overview* and *configuration* are shown in Fig 9.

As described before, the error domain, command domain and status domain are placed on the top, because there is the biggest attention of the user [10]. The domain of direct functions is used for the manual movement of the nozzle, for switching the process units like power supply or electrolyte system and for the emergency stop. The emergency stop is configured to abort the removal process at any time as quickly as possible. When pressed, movements are stopped immediately and all process units, e.g. power supply and electrolyte system, are switched off.

The navigation domain consists of different buttons. Four of these buttons are actually assigned with domains and two of them can be used to add new functionality. The *EXIT* Button on the right is used to end Jet-Control. As seen in Fig. 9a), the working domain *overview* is selected. The overview displays all the important information and measurements in tabular form. In addition, process parameters are visualized in various diagrams that the user can select. Fig. 9b) shows the working domain *configuration*. At the configuration, the user can select different parameter to adjust the processing units. Furthermore, the user has the possibility, to save new process parameters via a save button for each system. To undo the change, the user can click on the default button.

At the mask layout for the working domain working gap, as seen in Fig. 10a), the user can operate the function to adjust the working gap. Firstly, the user starts to select a strategy and set a distance for the working gap. Under the dropdown field, the user can activate the process. Due to the domain of direct functions, the user can move the nozzle to a position, there the user wants to set the defined working gap. After clicking the button *approach contact*, the touching process begins. Through diagrams and LED's, the user can observe the process. The user could cancel the

process anytime. After setting the working gap, each touched position will be display in tabular form for the x, y and z position and could be used for the following removal process.

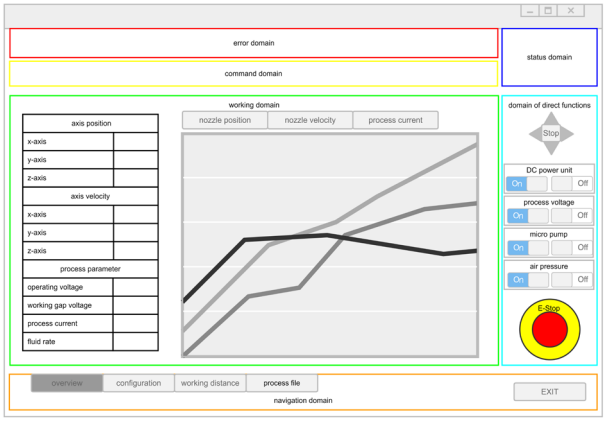

a) Overview-mask: Compilation of process parameters in tabular and diagram form

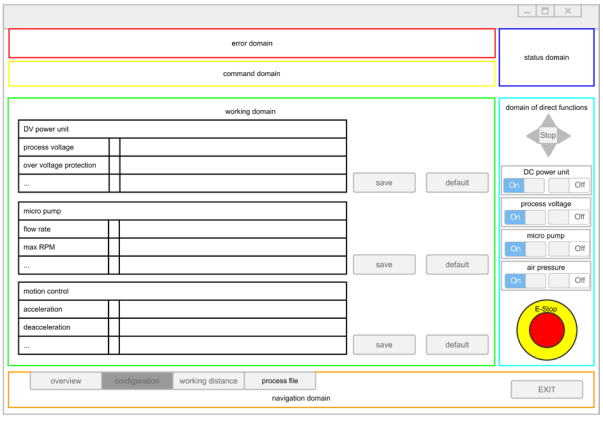

b) Configuration-mask: Setting of process variables

Fig. 9. Mask layouts for the working domains: overview and configuration.

Fig. 10b) shows the mask layout for the working domain *process file*. This working domain is needed to load and execute a process file. The process file contains movement commands and switching commands for the removal process. In the dropdown field, the user chooses the desired process file and load the file over the button *load process file*. Afterwards, the file displayed at the window on the left side. Due to the radio buttons, the user can select different file types for saving the measurement data and can adjust the sampling rate. With clicking on the button *start process file*, the machining process will start and can be stopped with *CANCEL* or the *emergency stop*.

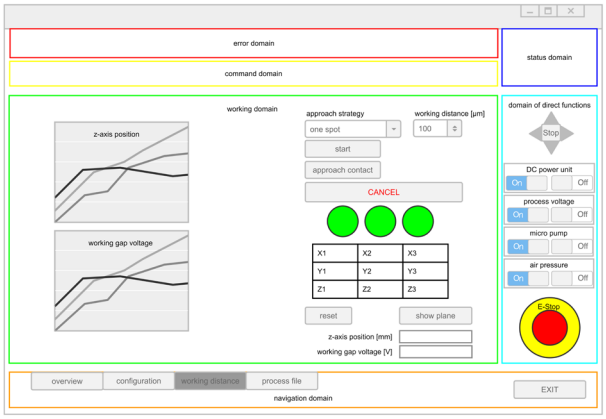

a) Working gap-mask: Program-assisted setting of the working gap

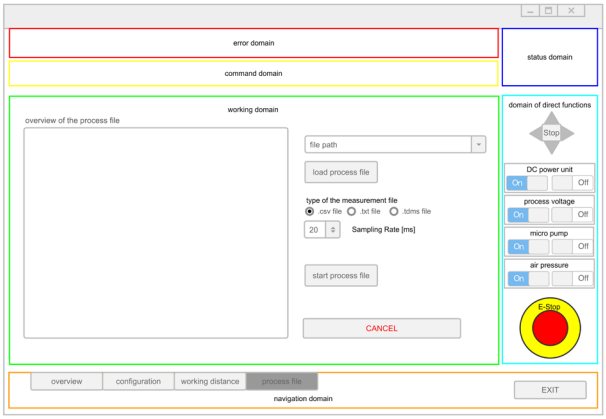

b) Process file-mask: Visualisation and executing of commands for machining

Fig. 10. Mask layouts for the working domains: working gap and process file.

Designed User-Friendly Human Machine Interface

Based on the GUI concept, a human machine interface was designed and implemented with LabVIEW, as seen in Fig. 11. To ensure user-friendliness, the mask layouts are kept minimalist, that each mask only contains the information, that the user needs. Furthermore, identical information is placed at the same location. Operating elements are arranged according to the material, energy and information flow. In Fig. 11 the different sections are framed in colour for a

purpose of presentation. For example, the error domain is framed in red and the command domain is framed in yellow. Due to the importance of these domains, they are additionally placed at the top. Through text inserts, the GUI displays error messages in the error domain and displays executing tasks in the command domain. The status domain consists of an Enum-ring, which contains the status messages: initialization, ready, running and error. These messages represent the status of the machining process and are presented accordingly in text and colour. Green for the status initialization and ready, flashing green for the status running and red for the status error.

On the right side, the domain of direct functions is placed and is framed in light blue. In order to highlight the actors of the process unit, the actors are grouped into clusters. The first cluster contains arrow keys to manually move the nozzle. Furthermore, in the cluster are different buttons located, to set the type of movement, velocity and increment. By clicking the checkbox *automatic control of z-axis,* the readjustment movement of the *z*-axis can be activated or deactivated. The following clusters contain the process units, that can be controlled by *ON* and *OFF* buttons. To highlight the switching state, the background colour of the cluster changes to green when a process unit is activated.

The navigation domain is framed in orange and is realized using a tab control. Each tab activates a different working domain, which is framed in green. With adding new tabs, new features or functions can be implemented to the GUI.

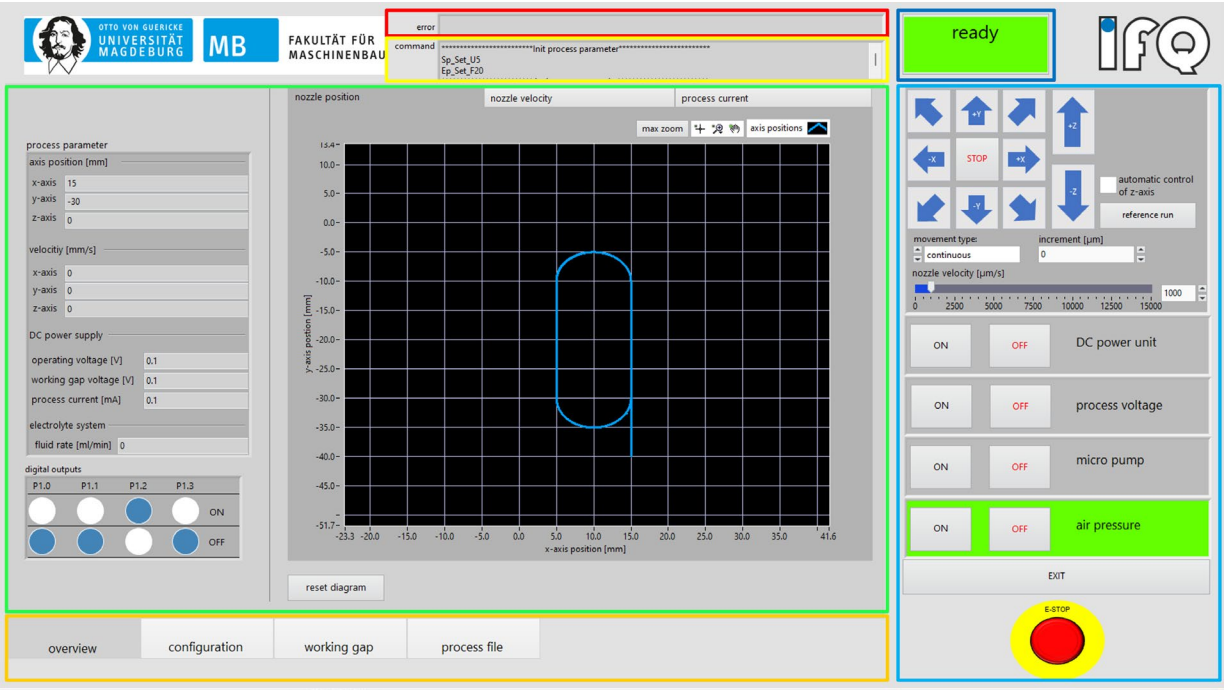

Fig. 11. Implemented GUI concept in LabVIEW with outlined section.

As seen in Fig. 11 the working domain *overview* is selected. On the left side, all process parameters grouped into a cluster. At the bottom, a table is located, which displays the state of the digital outputs. On the right side, a tab control is placed, from which the user can select which diagram to activate.

Summary

The study focused on a design of a user-friendly human machine interface for jet electrochemical machining. Through the developed interface, the Jet-ECM process can be controlled as well as

user tasks can be assisted, for example for the working gap setting. Caused by the variety of different components and by adding new features, the GUI becomes quickly too complex and too confusing. Therefore, established guidelines were applied to design a human machine interface for the Jet-ECM process. To ensure a user-friendly interface, the interface was designed minimalistic and the operating elements were arranged according to the material, energy and information flow. To determine the order and the visibility of user tasks, a task flow of the Jet-ECM process was analysed. Therefore, the frequency and the importance of the user tasks were worked out. The GUI was designed based on a two-dimensional mask layout. The interface can be extended for later functions or features by adding new mask layouts.

References

[1] W. Natsu, T. Ikeda, M. Kunieda, Generating complicated surface with electrolyte jet machining, Precis. Eng. 31 (2007) 33-39. https://doi.org/10.1016/j.precisioneng.2006.02.004

[2] M. Hackert-Oschätzchen, G. Meichsner, M. Zinecker, A. Martin, A. Schubert, Micro machining with continuous electrolytic free jet, Precis. Eng. 36 (2012) 612-619. https://doi.org/10.1016/j.precisioneng.2012.05.003

[3] M. Hackert-Oschätzchen, A. Martin, G. Meichsner, M. Zinecker, A. Schubert, Microstructuring of carbide metals applying Jet Electrochemical Machining, Precis. Eng. 37 (2013) 621-634. https://doi.org/10.1016/j.precisioneng.2013.01.007

[4] E. Truckenbrodt, Fluidmechanik, 4th ed., Springer, Berlin, 2008, ISBN: 978-3-540-79017-4.

[5] M. Yahyavi Zanjani, M. Hackert-Oschätzchen, A. Martin, G. Meichsner, J. Edelmann, A. Schubert, Process Control in Jet Electrochemical Machining of Stainless Steel through Inline Metrology of Current Density, Micromachines 10 (2019) 261. https://doi.org/10.3390/mi10040261

[6] M. Hackert-Oschätzchen, Entwicklung und Simulation eines Verfahrens zum elektrochemischen Abtragen von Mikrogeometrien mit geschlossenem elektrolytischen Freistrahl. Zugl.: Chemnitz, Techn. Univ., Diss., 2010, Verl. Wiss. Scripten, Auerbach, 2010, ISBN: 9783937524955.

[7] J. Mitchell-Smith, A. Speidel, A.T. Clare, Transitory electrochemical masking for precision jet processing techniques, J. Manuf. Process. 31 (2018) 273-285. https://doi.org/10.1016/j.jmapro.2017.11.028

[8] M. Hackert-Oschätzchen, G. Meichsner, A. Schubert, Generating plane and microstructured surfaces applying Jet Electrochemical Machining, in: A. Michaelis (Ed.), Proceedings / Int Symp on ElectroChemical Machining Technology - INSECT 2009., Fraunhofer Verl., Stuttgart, 2009, ISBN: 9783839600764.

[9] J. Johnson, GUI Bloopers 2.0: Common User Interface Design Don'ts and Dos, 2nd ed., Elsevier monographs, s.l., 2007, ISBN: 978-0-12-370643-0.

[10] D. Zühlke, Nutzergerechte Entwicklung von Mensch-Maschine-Systemen: Useware-Engineering für technische Systeme, 2nd ed., Springer Berlin Heidelberg, Berlin, Heidelberg, 2011, ISBN: 978-3-642-22074-6.

Materials Research Proceedings 28 (2023) 1653-1662 https://doi.org/10.21741/9781644902479-178

Digital twin for the determination of process input variables for electrochemical precision machining according to DIN SPEC 91399

THIELECKE Alexander[1,a *], MEICHSNER Gunnar[1,b], and HACKERT-OSCHÄTZCHEN Matthias[1,c]

[1]Chair of Manufacturing Technology with Focus Machining, Institute of Manufacturing Technology and Quality Management (IFQ), Faculty of Mechanical Engineering, Otto von Guericke University Magdeburg, Universitätsplatz 2, 39106 Magdeburg

[a]alexander.thielecke@ovgu.de, [b]gunnar.meichsner@ovgu.de, [c]matthias.hackert-oschaetzchen@ovgu.de

Keywords: Electrochemical Machining, Multiphysics Simulation

Abstract. The ablation results with electrochemical precision machining (PECM) are essentially influenced by the material to be processed and by the current density distribution in the working gap. Therefore, ablation experiments according to DIN SPEC 91399 are essential to determine the material-specific removal characteristics and to derive process input variables for the process design. A main limitation of these experiments is the lack of accessibility at crucial surfaces on the workpiece and on the device, which means that relevant information such as the local current density distribution or the local temperature field cannot be measured. To face the mentioned limitation, the aim of this work was to develop a digital twin for an experiment for PECM according to DIN SPEC 91399. The digital twin is based on a commercial multiphysics simulation software with the main property that the calculation time of the model is less than the real time for the experiment to allow a simultaneous processing of experiment and simulation. Via suitable interfaces, experiment and simulation can be interconnected in future. Based on this, the digital twin can be applied to evaluate parameters, monitor the process in real time and adapt it accordingly. The design and the properties of the digital twin will be shown exemplary for an experiment with the workpiece material steel 1.4301.

Introduction

Electrochemical Machining (ECM) is the generic term for a number of machining processes in which material removal is based on the principle of anodic metal dissolution. The workpiece is polarised as an anode and the tool electrode as cathode. An electrolyte, as a sufficiently electrically conductive medium, provides an electric charge transport between the electrodes. The ECM process is a non-contact machining process without heat input. Disadvantages of conventional cutting methods such as tool wear, negative influence on the component properties or burr formation can be avoided if ECM is applied.

A further development of the EC-countersinking process is electrochemical precision machining (PECM), in which the precision can be further increased by applying an oscillating cathode and a pulsed direct current. The PECM process is a separating manufacturing process and is classified according to DIN 8580 in the 3. main group Machining and further in the groups Ablation and Electrochemical Ablation [1]. Fig. 1 shows the principle of the PECM-process with oscillating cathode.

Content from this work may be used under the terms of the Creative Commons Attribution 3.0 license. Any further distribution of this work must maintain attribution to the author(s) and the title of the work, journal citation and DOI. Published under license by Materials Research Forum LLC.

Materials Research Proceedings 28 (2023) 1653-1662 https://doi.org/10.21741/9781644902479-178

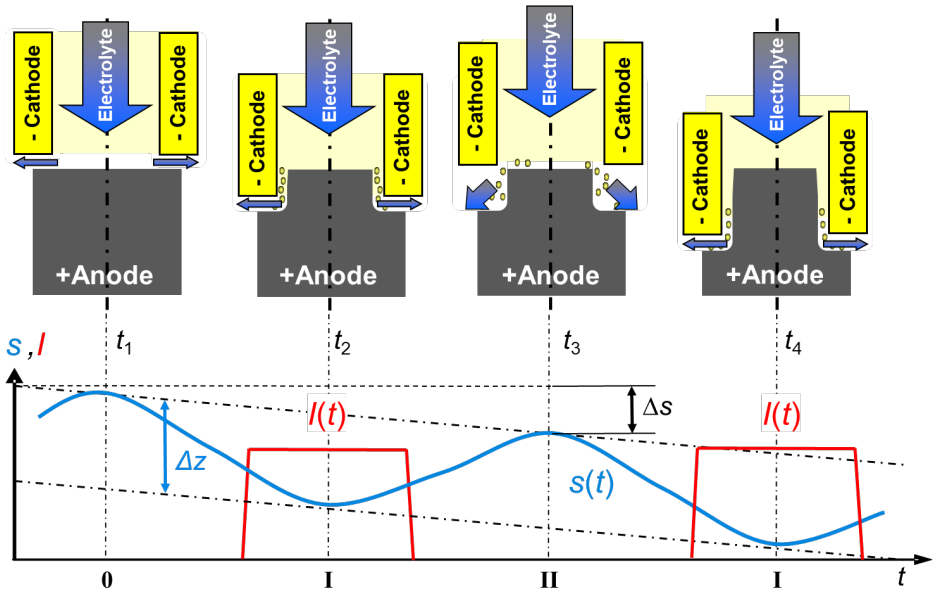

Fig. 1. Principle of a pulsed ECM-process with oscillating cathode according to [2].

In the initial state (0), the cathode is at top dead center, so that a maximum working distance is established between the anode and the cathode. Thus, the working distance is sufficiently supplied with electrolyte. State I describes the time of material removal. Here, the cathode geometry is transferred in the anode.

Shortly before the bottom dead center of the oscillation movement is reached, the machining voltage is switched on so that a current pulse with almost constant current is formed for a defined current pulse width. In the lower dead position of the oscillation movement, the working distance reaches the minimum. After exceeding the bottom dead center, the material is removed until the machining voltage is switched off.

The working distance is extended in state II until the top dead center is reached. This ensures that the working distance is sufficiently supplied with fresh electrolyte to remove reaction and removal products, which are created in state I.

The sequence of state I and state II is repeated until the target sink depth is reached. For this purpose, the oscillation of the cathode is superimposed with a feed movement. [3–5] Due to the reduced working distance in the PECM process, the production of complex shapes in the micrometer range is possible (structure size ≥ 5 µm). [6]

EC-removal is based on a complex mechanism. Material-specific removal parameters and the current density distribution in the working distance are essential process input variables, that cannot be derived with sufficient accuracy from literature values.

The DIN SPEC 91399 describes a method, which is based on determining the material-specific removal rate during PECM using an industrial machine tool. Applying a special removal device and complying with defined boundary conditions, the velocity of the relative movement between the cathode and anode can be evaluated as a comparison variable for determining the material-specific removal parameters.

With the help of systematic ablation experiments, the ablation functions of the material-specific ablation rate and the change of state in the working distance can be determined. From this, process input variables can be determined for the PECM process. [7]

Method

In addition to the time and cost issues, the challenge in PECM ablation experiments is the measurement of physical variables such as the distribution of the current density during the PECM process. A simulation model can serve as a digital twin, that provides missing measurement variables or make ablation experiments more efficient through preliminary investigations. With FEM-based simulation software, such as the commercial software COMSOL Multiphysics, it is possible to build a digital twin, obtain missing information from a PECM process and analyse it. A digital twin is the digital model of physical objects and has the task of generating a comprehensive exchange of information. The basis for this is, that the model not only includes anode, cathode and electrolyte region, but is designed in such a way, that the entire device unit is represented. The aim of the work is to build a simulation model, that confirms the results of a previous experiment with the workpiece material 1.4301. In order to monitor the process in future, it is also necessary for the digital twin to calculate the simulation results in a time which is lower than the machining time of the real process. This should enable real-time data exchange between the digital twin and the real process in future by help of the development of suitable interfaces.

Model Description

In order to create the digital twin, materials and PECM input parameters were taken from previous ablation experiments [8]. The design and the geometry dimensions of the simulation model are based on the recommendations of DIN SPEC 91399. Fig. 2 shows a cross-section of the PECM device and the derived geometry of the simulation model.

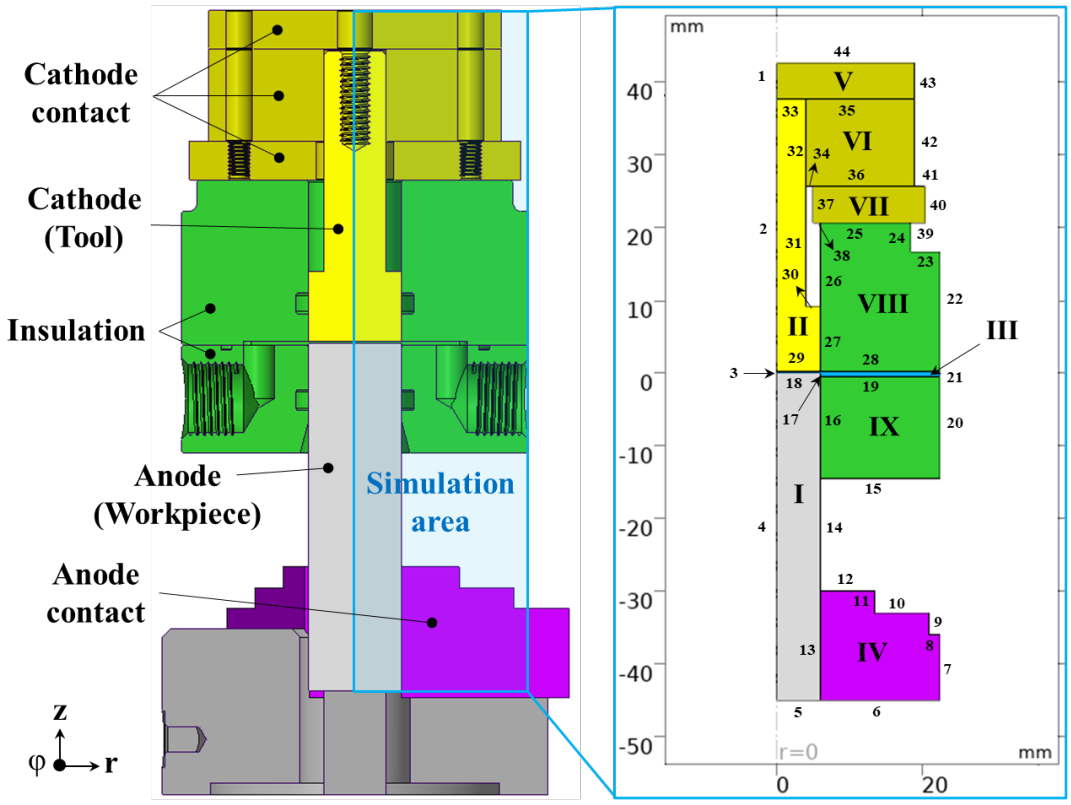

Fig. 2. Cross section of the PECM device and derived *2D axisymmetric model geometry with defined domains and boundaries.*

In the simulation model, the experimental end front working distance $s_{f\text{-}E}$ was set at the beginning of the simulation. The cathode unit was assigned a constant feed with superimposed oscillation

movement for a period $T = 0.02$ s. Electric current flows through the application of a pulsed voltage with a pulse duration $t_p = 1$ ms at the dead center of the oscillating movement of the cathode. In order to keep the simulation time of the digital twin below the real process time, the oscillating movement and pulsed power supply were interrupted after the simulated period. The surface of the workpiece was then removed with calculated velocities for further 30 s. A process time of 30 s was selected in order to comply with DIN SPEC 91399, according to which the removal experiment run for further 30 s after the end front working distance $s_{f\text{-}E}$ has been established [7].

The model is evaluated according to simulation duration and working distance at the end of the 30 s simulated process time.

Due to the desired model solution time below 30 s and the almost rotationally symmetrical design of the device, the model was designed as an axisymmetric model with the coordinates r, φ and z, with the axis of symmetry at r = 0. The two electrodes, can be seen in gray (anode/workpiece) and yellow (cathode/tool). Both electrodes are cylindrical in shape. The workpiece has a diameter of 12 mm and a length of 45 mm. The cathode consists of a stepped shaft with diameters of 7.5 mm and 12 mm and a length of 37.5 mm. In the simulation the electric conduction processes in the cathode and in the workpiece as well as in the electrical contact geometries were considered, since otherwise some effects can be underestimated [9].

The oscillating movement of the tool unit occurs in z-direction. The allocation of the materials to the model domains and the material parameters used for the simulation are summarized in Table 1.

Table 1. Material parameters of the simulation model derived from [8].

Domain	Material	σ [mS/cm]	ε_r
I, II, IV-VII	1.4301	$1.4 \cdot 10^{10}$	1
III	Electrolyte ($NaNO_3$)	67.4	65
VIII, IX	POM	10^{-10}	4

In order to analyse the ECM-specific parameters, the electrical conductivity σ and the relative permittivity ε_r were assigned to the domains. To represent the desired PECM process, 3 physics modes of COMSOL Multiphysics were applied. *Electric Current* mode was applied to supply the PECM process with external electric potential. The *Moving Mesh* was applied to simulate the oscillating motion of the cathode assembly and the flushing chambers as well as the removal of the surface of the workpiece. The *Events Interface* was applied to simulate the various PECM parameters in a precisely timed manner.

Eq. 1 describes the electrical potential $U_{\text{pulsed}}(t)$ which connects and disconnects the voltage according to the lower- and upper time limits. The electrical potential is determined by subtracting the process voltage U_{min} with the sum of overpotentials ΔU [4].

$$U_{pulsed}(t) \begin{cases} 0\,V, if\ t < t_{Low} \\ U_{min} - \Delta U, if\ t_{Low} \leq t \leq t_{Upp} \\ 0\,V,\ if\ t > t_{Upp} \end{cases} \quad (1)$$

with

$$t_{Low} = \frac{T}{4} - \frac{t_p}{2} \quad (2)$$

and

$$t_{Upp} = \frac{T}{4} + \frac{t_p}{2} \quad (3)$$

The pulsed current parameters used in the simulation model are summarised in the Table 2 below.

Table 2. Pulsed electric potential parameters derived from [3,8].

Definition	Symbol	Value	Unit
Process voltage	U_{min}	6.7	[V]
Sum of potentials	ΔU	4.6	[V]
Pulse width	t_p	0.001	[s]
Lower Limit	t_{Low}	0.0045	[s]
Upper Limit	t_{Upp}	0.0055	[s]

The electrical potential $\varphi_{el} = U_{pulsed}(t)$ was applied at boundary 6 and ground at boundary 44 and it was switched via the event interface. Boundary conditions of the electric current mode defined in the model are listed in the Table 3.

Table 3. Boundary conditions of electric current mode.

Condition	Boundary	Property
Axial Symmetry	1-4	-
Electric Insulation	5, 7-12, 14, 15, 20-24, 26, 30, 31, 34, 37-43	-
Ground	44	$\varphi_{el} = 0$ [V]
Electric Potential	6	$\varphi_{el} = U_{pulsed}(t) \cdot C_2$ [V]

The moving mesh mode was applied to simulate the movement of the cathode unit, including the flushing channel and flushing chambers. The oscillation of the cathode was defined as a harmonic oscillation superimposed with a constant movement in z-direction, which is explained in Eq. 4.

$$z(t) = \left(\hat{Z} \cdot \cos\left(2\pi \cdot f \cdot t + \frac{\pi}{2}\right)\right) \cdot C_1 - v_f \cdot t \quad (4)$$

$\hat{Z}$ is the range of the oscillation (amplitude), f is the frequency and v_f the lowering velocity. The discrete variable C_1 is a logical auxiliary variable to control which expression to use in an equation. C_1 is explained in more detail in the Events Interface section. When the oscillation has reached its lowest point in z-direction, $s_{f\text{-}E}$ is set. Table 4 allocates the motion parameters of the cathode.

Table 4. Motion parameters of the cathode derived from [8].

Definition	Symbol	Value	Unit
Period	T	0.02	[s]
Frequency	f	50	[Hz]
Amplitude	$\hat{Z}$	0.185	[mm]
Working distance	$s_{f\text{-}E}$	0.048	[mm]
Feed rate	v_f	0.01	[mm/min]

For numerical reasons, period *T* starts after 1 s simulation time. Figure 3 illustrates the cathode oscillation and the pulsed electrical potential in a period *T*, here the oscillation graph $z(t)$ marked with blue line is plotted as in Eq. 4 and the pulsed voltage $U_{pulsed}(t)$ graph marked with red line is characterized as in Eq. 1.

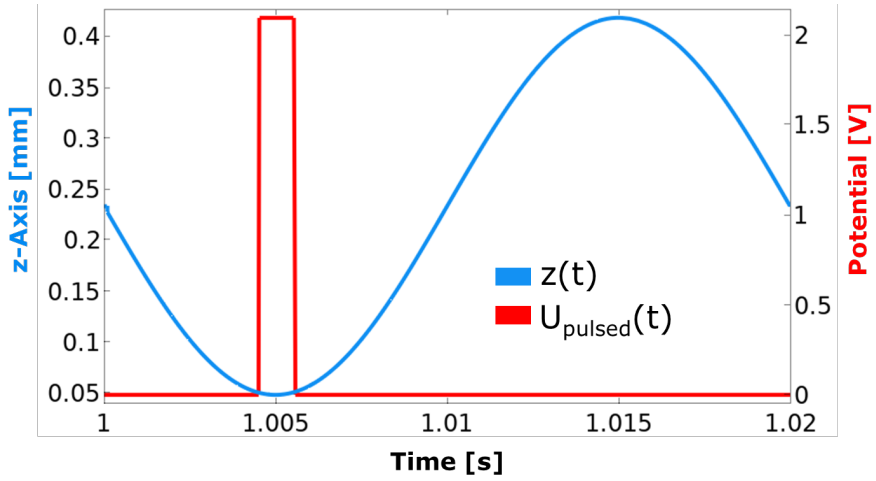

Fig. 3. Cathode oscillation and pulsed potential in one period.

The surface of the workpiece is removed with 2 different removal rates. According to [3,4], the removal rate is recorded as follows during the pulse on time t_p.

$$v_a(J) = ((V_m \cdot J + v_0) \cdot c) \cdot C_2 \tag{5}$$

with

$$c = f \cdot t_p \tag{6}$$

The removal rate is therefore strongly dependent on the current density distribution J [A/cm²] on the workpiece surface. The pulsed current flow is characterized by the duty cycle c, which is composed of the multiplication of the frequency f and the pulse on time t_p. V_m ($0.0106 \frac{mm/min}{A/cm^2}$) and v_o ($-0.063 \frac{mm}{min}$) result from the removal experiment and are described in more detail in [8]. V_m, v_0 and c are thus constant values, while J is calculated during the pulse on time. In order to save computing time of the model, an average removal rate $\hat{v}_a$ is calculated after the time period *T*, with which the workpiece surface is removed for another 30 s.

$$\hat{v}_a = \frac{1}{T} \cdot \int_{1.0045\ s}^{1.0055\ s} v_a(J)dt \cdot C_3 \tag{7}$$

Boundary conditions of moving mesh mode defined in the PECM simulation model are listed in the Table 5.

Table 5. Boundary conditions of moving mesh mode.

Condition	Boundary	Property
Fixed Boundary	5	-
Prescribed Mesh Displacement in Normal Direction	3, 4, 13, 14, 17, 21	$d_n = 0$ [mm]
Prescribed Mesh Displacement	1, 2, 15, 16, 19, 20, 22-44	$d_r = 0$ [mm] $d_z = z(t)$ [mm]
Prescribed Normal Mesh Velocity	18	$v_n = -v_a(J) - \hat{v}_a$ [mm/min]

The event interface is used to trigger events. When an event occurs, the solver stops and provides a possibility to reinitialize the values of variables. The events are controlled with the state variables C_1, C_2 and C_3, which can assume the values 0 and 1. The course of the variables can be seen in Fig. 4.

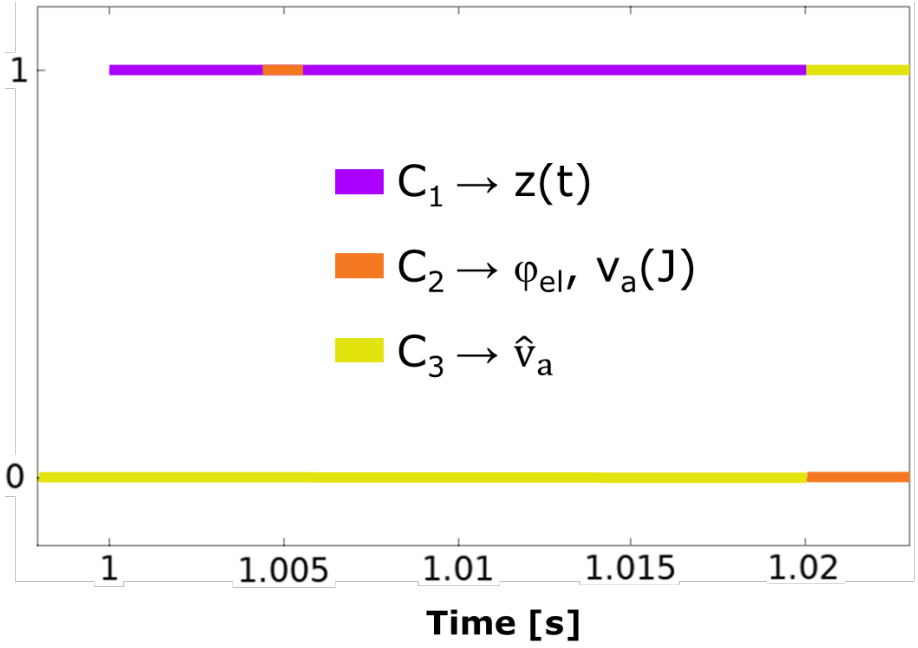

Fig. 4. Discrete auxiliary variables as function of the time.

The variables are linked to the equations and boundary conditions. C_1 triggers the oscillation from $t = 1$ s to $t = 1.02$ s, after that the first term of Eq. 4 becomes zero and the cathode moves on without oscillation with the constant feed motion v_f. C_2 switches from 0 to 1 at $t = 1.0045$ s and back to 0 at $t = 1.0055$ s ($t_p = 0.001$ s). The electrical potential φ_{el} (see Table 3) and the removal rate $v_a(J)$ (Equation 5) are linked to the state variable C_2. Variable C_3 is coupled to $\hat{v}_a$ (Equation 7). The average removal rate is calculated during the pulse, then the workpiece surface is removed with the calculated velocity $\hat{v}_a$ for 30 s.

The mesh for the model was generated using a physics-driven mesh as the sequence type. The physics-controlled mesh is the default mesh setting in COMSOL Multiphysics, which in turn distinguishes different element sizes from very fine to very coarse. The mesh encloses an area of

1356 mm² with 1155 triangular elements. The maximum and minimum element sizes are 5.8 mm and 0.026 mm.

Results

Fig. 5 shows the current density distribution in the entire model at the bottom dead center of the oscillation.

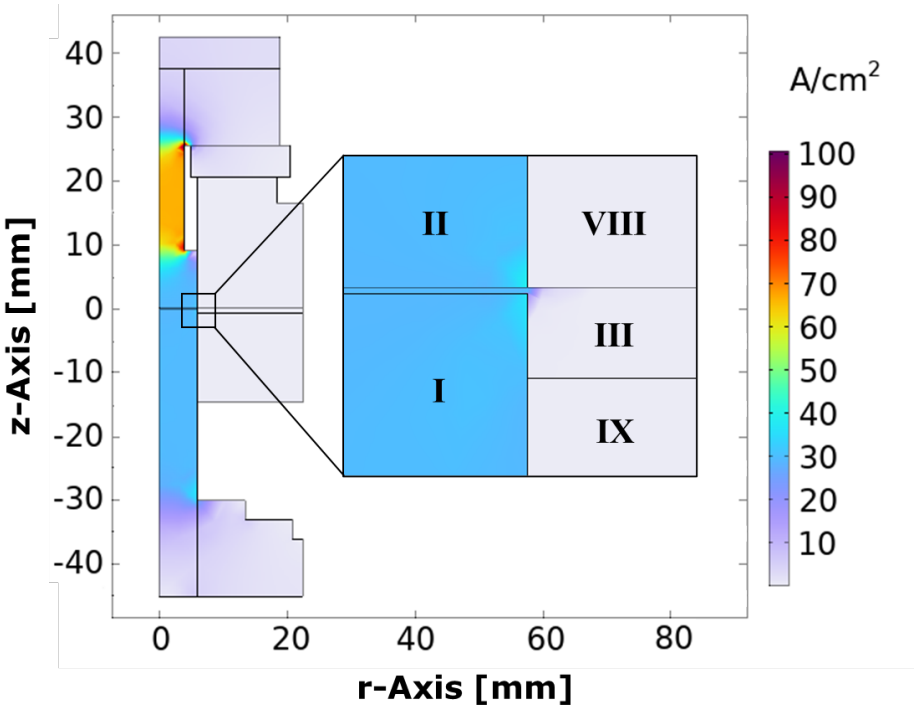

Fig. 5. Current density distribution at time t = 1.005 s.

In the model, a maximum current density J of 101 A/cm² occurs during the pulse on time, which can be attributed to peak effects at points on the cathode. A current density J of 29 A/cm² is established in the working gap between the cathode and the workpiece surface during t = 1.005 s. The removal rate v_a depends on the current density distribution on the workpiece surface (boundary 8). Figure 6 shows the 3 applied velocities, of which v_f represents the constant feed of the cathode while v_a (J) and $\hat{v}_a$ are calculated during the simulation.

Since $v_a(J)$ depends on the current density acting in the pulse, the curve is not linear but increases as the cathode approaches the workpiece surface due to the oscillating movement. The maximum removal rate is reached at the bottom dead center of the oscillation.

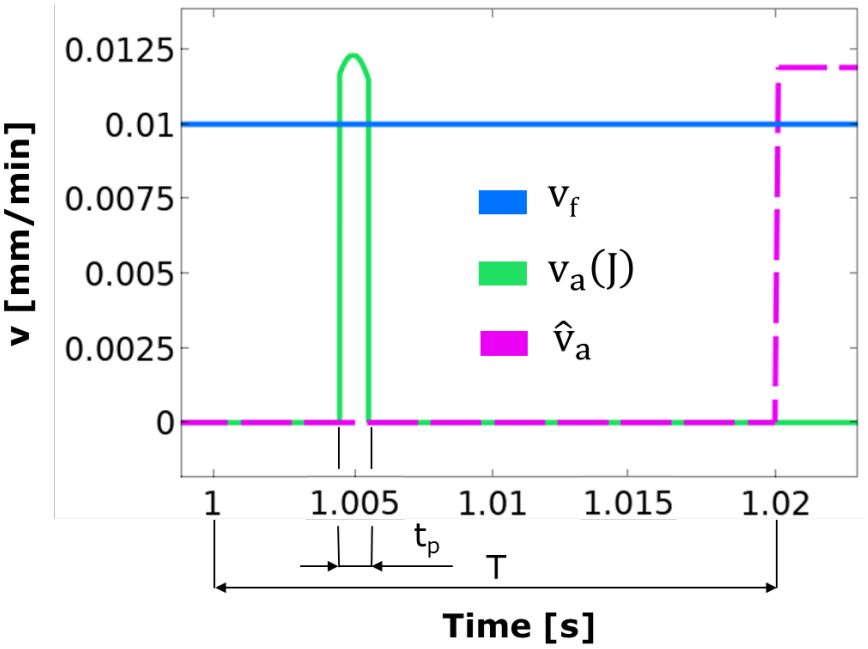

Fig. 6. Course of the velocities vf = 0.01 mm/min, va(J) = 0.0115…0.0123 mm/min and $\hat{v}_a$ = 0.0119 mm/min.

If the cathode moves away from the workpiece surface, the removal rate drops until the pulse ends and no more removal takes place. The effect of the course of $v_a(J)$ is thus an effect of the combination of feed and oscillation of the cathode. After t = 1.02 s, the cathode moves at a constant speed v_f in the z-direction and the workpiece is removed at the average velocity calculated from $v_a(J)$. In Figure 7, the evaluation is based on the final working distance after t = 31.005 s.

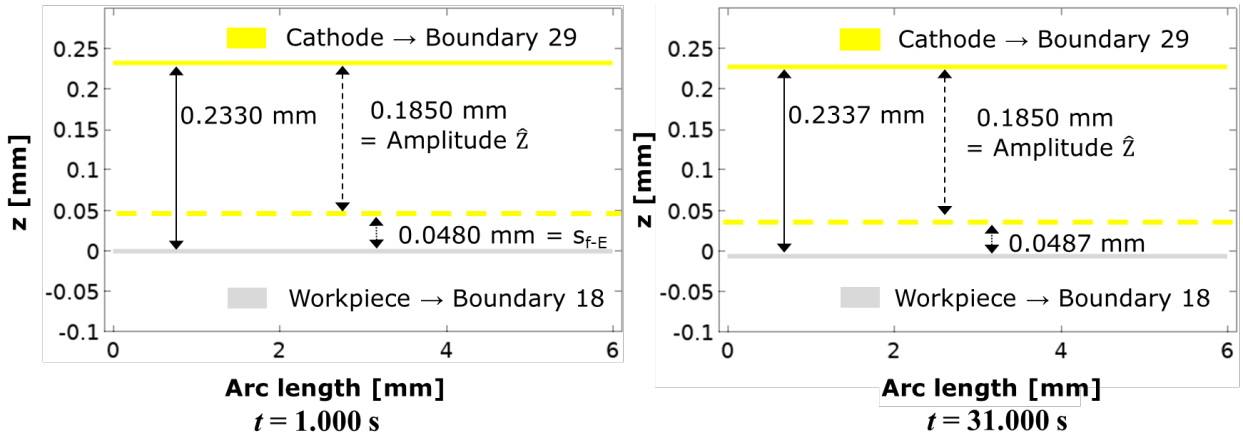

Fig. 7. Comparison of the end front working distance at the initial state and after the process time.

The end front working distance is set at the bottom dead center of the oscillation. After the process time of 30 s, the working distance between the surface of the cathode and the surface of the workpiece is 0.0487 mm. The difference between the defined end front working distance and the calculated working distance after a process time of 30 s is therefore 0.7 µm. The computing time of the simulation model for a real removal time of 30 s was 25 s.

Summary
In this study, a digital twin for the determination of process input variables for electrochemical precision machining according to DIN SPEC 91399 was developed. For this, a simulation model for a PECM process according to DIN SPEC 91399 was build up in COMSOL Multiphysics based on the geometry of an entire device unit. To design the PECM process, the oscillation of the cathode and the current pulse conditions were integrated in the model. The input parameters were set according to previous ablation experiments. A validation was carried out by maintaining the working gap after the process time of 30 s. It was shown, that the simulation time of the developed model is less than the real time of the machining process. The model can be expanded in further work. For example, the effective electrical conductivity of the electrolyte, which is influenced by the generation of heat and the formation of gas bubbles, is also decisive for the removal process in the PECM process. Approaches would be the coupling of further physical interactions like thermodynamics and fluid dynamics, multiscale approaches and the implementation of current control characteristics. In order to carry out parameter studies with this model, it is essential to integrate further ablation periods into the calculation. This will allow the removal rate to be updated as the process progresses, to match the feed of the tool electrode and the removal rate on the workpiece.

References
[1] Deutsche Institut für Normung e. V. (DIN), Fertigungsverfahren – Begriffe, Einteilung, 2020.
[2] A. Schubert, G. Meichsner, M. Hackert-Oschätzchen, M. Zinecker, J. Edelmann, Präzise elektrochemische Bearbeitung von pulvermetallurgischen Stählen, Galvanotechnik (2012).
[3] G. Meichsner, Entwicklung und Realisierung einer Methode zur Bestimmung von Prozesseingangsgrößen für das elektrochemische Präzisionsabtragen, Verlag Wissenschaftliche Scripten, 2018, ISBN: 3957350875
[4] F. Klocke, W. König, Fertigungsverfahren 3, Springer, Berlin, New York, 2005-2008, ISBN: ISBN 978-3-540-48954-2
[5] T.L. Lievestro, Electrochemical Machining, in: ASM handbook, 9th ed., ASM International, Metals Park, Ohio, 1989, pp. 533-541, ISBN: 978-1-62708-188-7.
[6] A. de Silva, H. Altena, J.A. McGeough, Precision ECM by Process Characteristic Modelling, CIRP Annals 49 (2000) 151-155. https://doi.org/10.1016/S0007-8506(07)62917-5
[7] Deutsche Institut für Normung e. V. (DIN), Methode zur Bestimmung von Prozesseingangsgrößen für das elektrochemische Präzisionsabtragen - Anforderungen, Kriterien, Festlegungen, 2018.
[8] G. Meichsner, M. Hackert-Oschätzchen, M. Krönert, J. Edelmann, A. Schubert, M. Putz, Fast Determination of the Material Removal Characteristics in Pulsed Electrochemical Machining, Procedia CIRP 46 (2016) 123-126. https://doi.org/10.1016/j.procir.2016.03.175
[9] M. Hackert-Oschätzchen, Gestaltung von elektrochemischen Abtragprozessen durch Multiphysiksimulation gezeigt an der Endformgebung von Mikrobohrungen, Verlag Wissenschaftliche Scripten, Auerbach/Vogtl., 2015, ISBN: 978-3-95735-028-2

Materials Research Proceedings 28 (2023) 1663-1672 https://doi.org/10.21741/9781644902479-179

Influence of material properties on near dry-EDM process: The discussion of research for titanium grade 2 and Inconel 625 alloy

ŻYRA Agnieszka[1,a*], SKOCZYPIEC Sebastian[1,b] and BOGUCKI Rafał[2,c]

[1]Cracow University of Technology, Faculty of Mechanical Engineering, Chair of Production Engineering, al. Jana Pawła II 37, 31-864, Kraków, Poland

[2]Cracow University of Technology, Faculty of Materials Engineering and Physics, Department of Materials Engineering, al. Jana Pawła II 37, 31-864, Kraków, Poland

[a]agnieszka.zyra@pk.edu.pl, [b]sebastian.skoczypiec@pk.edu.pl, [c]rafal.bogucki@pk.edu.pl

Keywords: Electro Discharge Machining, EDM, Dry EDM, Inconel 625 Alloy, Titanium Grade 2

Abstract. Dry EDM machining with external workpiece cooling is one of the possible modifications of dry EDM process, which enables to reduce the negative impact of EDM machining on the environment and on the machine tool operator. At the same time, it is possible to obtain relatively good machining accuracy and surface quality. Due to the problems with the effective heat dissipation from the machining gap, the application of dry-EDM is still limited to micromachining. In this paper the comparison and discussion of dry-EDM technological factors for two hard to machine materials: Inconel 625 and Titanium Grade 2 have been presented. The tests were carried out in carbon dioxide as a dielectric supplied to the machining gap through the channel in the workpiece electrode. To improve the process effectivity additional workpiece cooling were also applied, however the presence of fluid in machining area makes the process near dry-EDM. The input machining parameters were pulse time, machining voltage, current amplitude and inlet gas pressure. The main aim of this work was to show the significance of the type of machined material on the material removal rate, and surface layer (i.e. roughness, morphology and microhardness). The results analysis will be discussed considering differences in physical properties of machined materials.

Introduction

Nickel and chromium-based superalloys such as Inconel 625 and titanium Grade 2 are widely used in all the branches of industry, such as aviation, space industry, automotive and power generation industry. Inconel alloys account for more than half of the materials used to manufacture the hot sections of turbojet engines [1]. Inconel alloys are used similarly to titanium alloys for the manufacture of turbine blades of high-temperature turbo-machine engine components [2]. Titanium alloys are also used very extensively in the medical industry, particularly because of their biocompatibility, which is very important for implant materials. Due to the physical and mechanical properties of these materials, conventional machining of these materials is very difficult and, moreover, often cost-intensive due to high material losses during machining (material costs) and tool wear [3,4]. Machining methods which may be used for mentioned materials are unconventional machining methods such as electrochemical, electro-discharge or ultrasonic machining [5,6].

The physical phenomena occurring during material removal in EDM are very complex [2,7]. When the potential is applied to both electrodes (workpiece and tool electrode), a pulsed DC is generated between these electrodes. At the time when the gap width is adequate and the breakdown field strength is exceeded, the dielectric breakdown phenomena by gases occurs and electrons are emitted from the working electrode. Accelerated in the electric field electrons collide with the

Content from this work may be used under the terms of the Creative Commons Attribution 3.0 license. Any further distribution of this work must maintain attribution to the author(s) and the title of the work, journal citation and DOI. Published under license by Materials Research Forum LLC.

atoms of the gas leading to atoms' ionization, which results in formation an ionization fronts from anode and cathode. When the fronts are connected, then a flow of high current in a small bridge occurs. It results in forming plasma channel with gas-interface. The rapid thermal processes lead to melting, boiling and evaporating of the workpiece surface and the tool electrode. As a result, a discharge channel consisting of an inner plasma channel and a transition area into the gas phase. The discharge channel close implosively, after the pulse is down and its volume increases continuously with the high internal pressure development, which enables the removal of some of the molten metal from the crater. Dielectric is poured over the molten metal in the craters, causing rapid cooling of the electrode material, so that micro-cracks can also form within the craters formed. The main function of the dielectric fluid is to cool, solidify the molten workpiece material and remove it from the machining zone [8,11].

The undoubted advantage of EDM is the dimensional and form accuracy that can be achieved during the process, even when machined feature size is below 100 μm. During stable machining the machining accuracy might be in range of the machining gap width. Disadvantages include the low machining productivity, high working electrode wear, as well as thermal stresses that occur in the surface layer after machining [12]. There are advantages of EDM such as possibility to machine any material which is electrical conductor (stainless stills, carbides, titanium and nickel alloys, etc., materials which are characterized by high hardness) it is also possible to obtain thin-walled elements, with complicated geometry and at the same time with very good accuracy (even close to 2 μm). However, one of the biggest drawback of EDM is the negative environmental impact when machining in liquid dielectrics, especially when the most commonly used hydrocarbon dielectrics are applied. One possible solution in the entrepreneurship where there is no possibility to use other machining technology than EDM, to reduce the negative influence on the environment and the machine-tool operator might be the usage one of alternative, environmentally neutral dielectrics. These include gaseous dielectrics such as air, oxygen, nitrogen, argon or carbon dioxide [13].

Due to the fact that during dry-EDM process it is still a problem with effective removal of heat from the machining gap, as well as workpiece material surface, adequate selection of process input parameters, dry-EDM is still limited to micromachining and is not used in industrial applications [14]. What is more one of the factors which has major impact on dry-EDM process it the workpiece material. Roth et al. [15] shows in his work, the influence of process stability and dry-EDM efficiency, not only because of the material's' physical properties, but mainly due to the properties which have a direct impact on the nature of the discharges produced during machining.

In this paper the results of dry-EDM milling of Inconel 625 and titanium Grade 2 in the carbon dioxide with the additional external workpiece cooling (sample immersed in the de-ionized water environment) were presented. The goal of this research was to determine the influence of material properties on dry-EDM process, considering gap working voltage, current intensity, pulse on-time, pulse off time and gas pressure. It is also worthy to mention that research of dry-EDM with carbon dioxide as dielectric medium is rarely described in the literature.

Materials and Methods

The near-dry EDM milling was conducted on the research test stand equipped with electro-discharge generator MATRIX MPS – 7163 160V/3A at the Cracow University of Technology [14]. The tool was tubular copper working electrode with an outer diameter of 1 mm. The carbon dioxide as the medium was supplied with pressure to the machining gap through thin - walled pipe electrode, while the workpiece was submerged in the de-ionised water (Fig. 1). Inconel 625 alloy and titanium Grade 2 were machined in the milling kinematics, with the parameters described in Table 1. The polarity during machining Inconel 625 was - working electrode (+), workpiece (-); during machining titanium Grade 2 - working electrode (-), workpiece (+). The electrode polarity was established on the basis of the preliminary tests, where the machining stability and working

electrode wear were verified for machining both Inconel 625 alloy and titanium Grade 2. The difference between used electrodes polarity between Inconel alloy and titanium Grade 2 is caused by the characteristic of used EDM generator type, as well as differences in the materials properties. For the samples 7A and 7B, the average values from three repetitions of the machining are presented in Table 1.

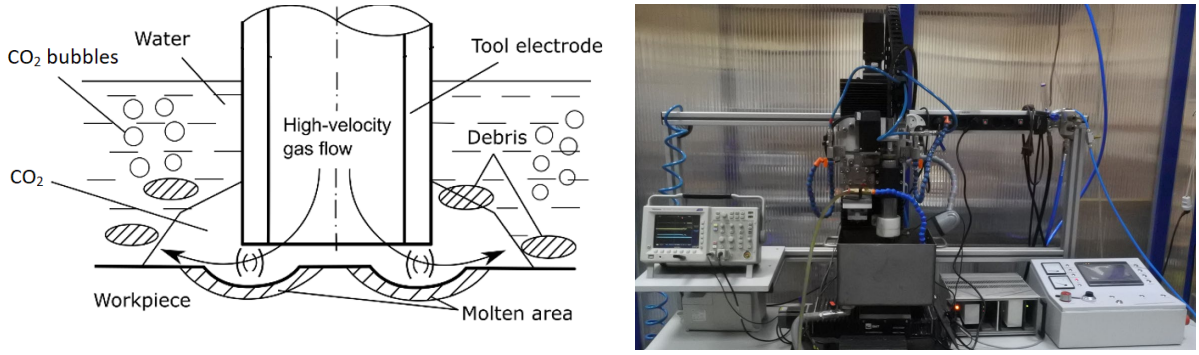

a) b)

Fig 1. a) Scheme of dry-EDM in the deionized water environment [14,16], b) test stand.

Table 1. Samples description with machining parameters, working tool: tubular copper electrode Ø1 mm, gas: carbon dioxide, external coolant type: deionised water (G= 0.01 µS), voltage: U=100 V

Inconel 625 (A)	titanium Grade 2 (B)	Pulse on-time [µs]	Voltage [V]	Current intensity [A]	Gas pressure [bar]
1A	1B	100	100	2.70	6
2A	2B	500	100	2.70	6
3A	3B	300	100	0.90	6
4A	4B	300	100	4.50	6
5A	5B	300	100	2.70	2
6A	6B	300	100	2.70	10
7A (3 repetition)	7B (3 repetition)	300	100	2.70	6

Described below analysis was focused on comparison of selected aspects of surface integrity of Inconel 625 alloy and titanium Grade 2 after dry-EDM in the milling kinematics with external workpiece cooling such as: surface roughness parameters (measured with Taylor Hobson profilometer), SEM photographs and microhardness. The detailed research methodology and research devices which were used during this research were described in [14].

Discussion of the Results

Fig. 2 shows the differences of material removal rate during (MRR) dry-EDM of Inconel 625 and titanium Grade 2 with external workpiece cooling. MRR was determined by the calculation of the workpiece material volume removed and the total milling time in each trial (each time removing 10 layers of material).

It is possible to say that in the most trials, the material removal rate is higher for Inconel 625, or material removal rates for both materials are very close. However, the exceptions are: trials 4B (where the highest current value, I=4.5 A, was used) and 3B (where the lowest current value, I=0.9 A, was used). Trial 3B was interrupted after removal of the one layer of the material, as the

total milling time for this layer exceeded the total milling time for the 10 layers of titanium Grade 2 in all other cases. It was stated that milling with these machining parameters used for trail 3B is inefficient. As a result, in all diagrams trial 3B is marked in a separate color (grey).

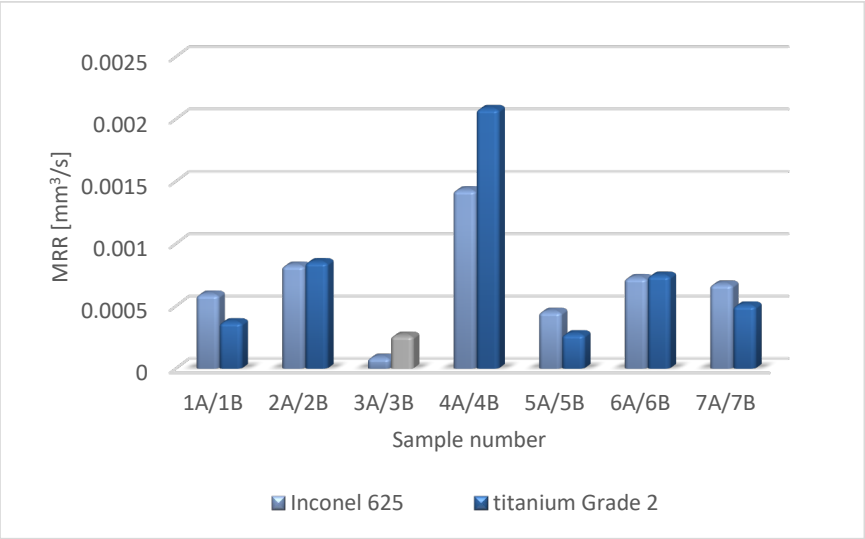

Fig 2. Comparison of material removal rate during dry-EDM of Inconel 625 and titanium Grade 2 with external workpiece cooling.

Considering the results presented in Table 2, Fig. 3, Fig. 4, one can state, that the significant differences between the results of roughness parameters of Inconel 625 and titanium Grade 2 may be observed. Much higher values of Ra and Rz parameters were obtained for Inconel 625 comparing to titanium Grade 2, when machining with higher current intensity (I=4.5 A), sample 4A, and with highest pressure (p=10 bar), sample 6A. What is more the influence of input process parameters to Ra and Rz roughness parameters can be observed. In case of the current intensity and gas pressure similar tendencies may be noticed. Strong linear correlation pattern between Ra and Rz parameters was also observed (r=0.980 for Inconel 625 and r=0.992). The examples of roughness profiles are presented in the Fig. 5.

The value of mean square deviation of the roughness profile Rq in most cases is lower for titanium Grade 2. Rsk parameter gives information about the symmetry of the profile distribution in relation to mean plane. The lower the Rsk value, the flatter the surface and the more rounded the peaks what is which is beneficial during part exploitation. Much lower values of Rsk parameter were obtained after EDM machining of titanium Grade 2.

The value of Rku (kurtosis) is a measure of the sharpness of profile peaks. When the distribution of profile peaks and valleys are normal Rku=3 µm, while for profiles with sharp peaks Rku can be higher than 20 µm. Considering obtained results one can state, that in majority cases Rku is close to 3 µm for Inconel 625, so the profile height distribution is close to normal. Similar, in most cases Rku is close to 3 µm for titanium Grade 2, however it is higher for 4B (I=4.5 A), 6B (p=10 bar) and 7B (research plan center) trial.

Table 2. Surface roughness parameters of Inconel 625 and titanium Grade 2 (mean values based on 3 measurements) after dry-EDM with additional workpiece cooling.

Sample number (var. A/var B)	Ra [µm]		Rz [µm]		Rq [µm]		Rsk [µm]		Rku [µm]	
	A	B	A	B	A	B	A	B	A	B
1A/1B	3.72	3.94	21.00	20.02	4.64	5.08	-0.01	-0.04	3.03	3.66
2A/2B	6.92	3.30	39.53	16.99	8.77	4.20	0.36	-0.30	3.07	3.32
3A/3B	4.80	2.30	24.27	12.46	5.86	2.89	0.63	-0.87	2.79	3.99
4A/4B	5.71	2.93	32.07	14.82	7.12	3.74	0.45	-0.07	3.14	4.11
5A/5B	11.19	4.09	49.27	20.16	13.37	5.16	0.05	-0.14	3.53	3.25
6A/6B	5.73	2.87	35.10	15.68	7.26	4.16	0.48	-0.77	3.23	6.99
7A/7B	5.34	4.20	28.88	21.35	6.58	5.52	0.44	0.18	3.07	5.13

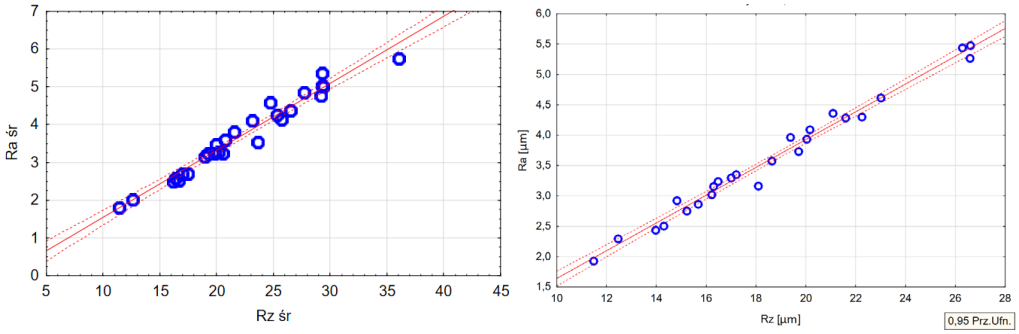

a) b)

Fig. 3. Comparison of correlation coefficient between Ra and Rz parameters for a) Inconel 625 and b) titanium Grade 2.

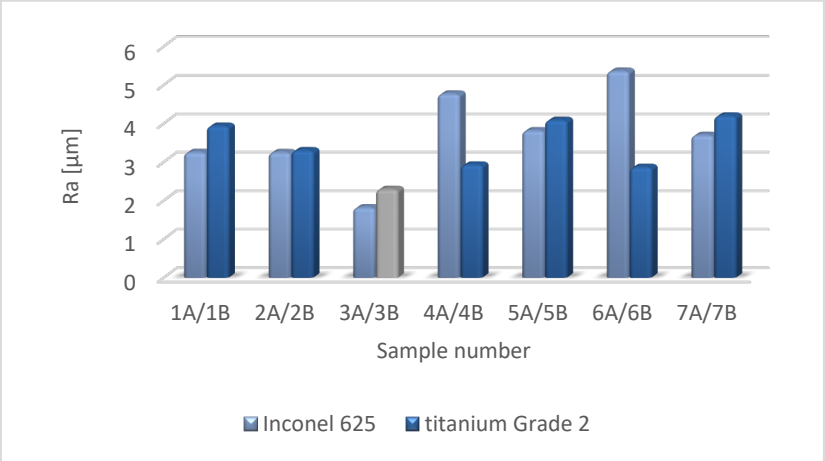

Fig. 4. Comparison of surface roughness parameter Ra for Inconel 625 and titanium Grade 2.

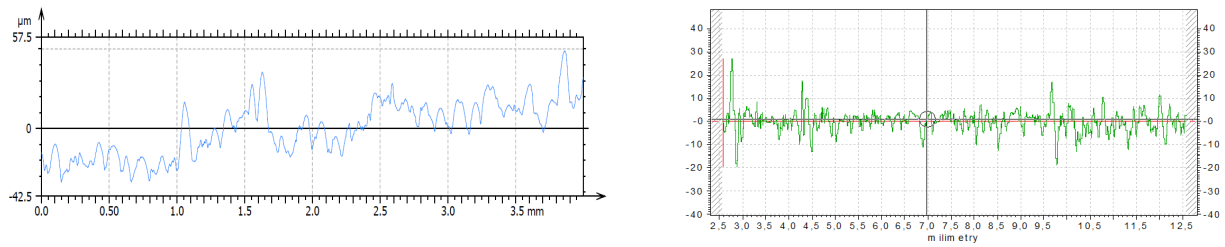

a) Inconel 625 b) titanium Grade 2

Fig. 5. Comparison of surface roughness profiles of Inconel 625 and titanium Grade 2 for the research plan centre t_i=300 µs, U= 100 V, I=2.7 A, p= 6.

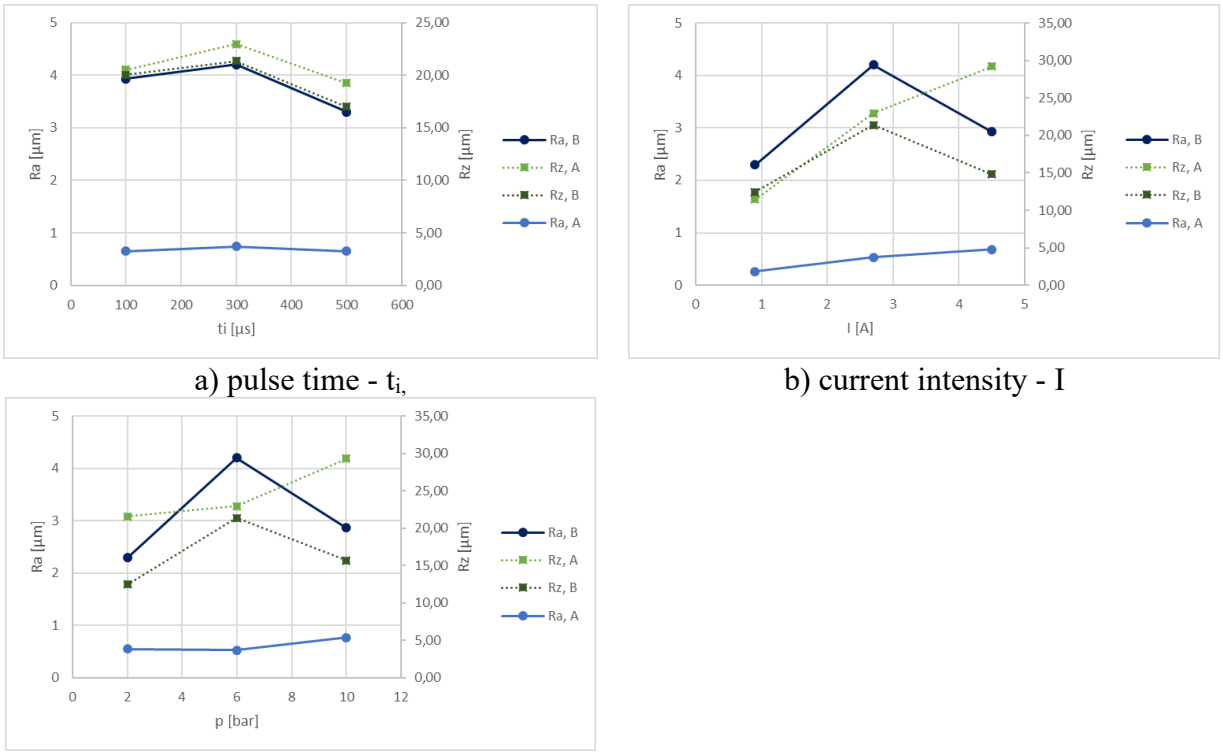

a) pulse time - t_i, b) current intensity - I

c) gas presurre - p

Fig. 6. Comparison of the influence of different process parameters: t_i, I and p on the surface roughness petameters Ra and Rz for Inconel 625 and titanium Grade 2 (relation based on the mean values according to Table 2), Standard deviations of Ra and Rz for samples machined with research plan central parameters (ti=300 µs, I=2.70 A, p= 6 bar): 1A: σRa= 1.65 µm; σRz=7.12 µm, 1B: σRa= 4.2 µm; σRz=21.6 µm.

Titanium grade 2 is characterized by low thermal conductivity and a single-phase α-structure, that is why no phase transformations were observed in the heat-affected zone (Fig. 7-9). The structural changes of the surface layer mainly involved the white layer, which is due to the lack of phase transformations and therefore it is difficult to observe the heat-affected zone. Of course, depending on the machining parameters used, changes in the shape of the grooves can be observed. The bottom of the groove is even and flat, the cross-section seems to reflect the actual shape of the working electrode. In the case of Inconel 625 (Fig. 7-9) surface layer morphology changes can be noticed (Fig. 7-9 A-F). With the increase of pulse time (Fig. 7 A-B), the depth of the milling grooves increases and also the recast layer becomes thicker (t_i= 500 µs). The cross-sections also

show increasing surface irregularities and deepening the discharge craters. Similar relationships can be found with increasing current intensity (Fig. 8 C-D). The increase of gas pressure causes the white layer thickness decrease (Fig. 9 E-F). At the same time discharge craters become shallower and less amount of melted material can be found on the workpiece surface.

Inconel 625 and titanium Grade 2 after dry-EDM milling with additional workpiece cooling are characterized by different hardness. In the Fig. 10 the hardness of each RAW material (Inconel 625 and titanium Grade 2) is given. It is possible to say that the values of microhardness of Inconel 625 and titanium Grade 2 in most cases are lower than for RAW materials. The Inconel 625 hardness decrease comparing to the RAW material may be caused by chipping of the recast layer during preparation of metallographic microsections or the dissolution of the carbides in the heat affected zone. In the case of titanium Grade 2, the decrease of microhardness comparing to RAW material may be related to the changes that have occurred in the material as a result of energy - electrical discharges occurring there. In the initial state, titanium Grade 2 had been cold-formed before treatment and was therefore strengthened. Energy application (electrical discharge) may cause the internal stresses removal and dislocations can be regrouped (dislocations allow the material to deform if they are free to move), as well as the density of dislocations decreases. As a result, strength and hardness decrease, while plastic deformability increases.

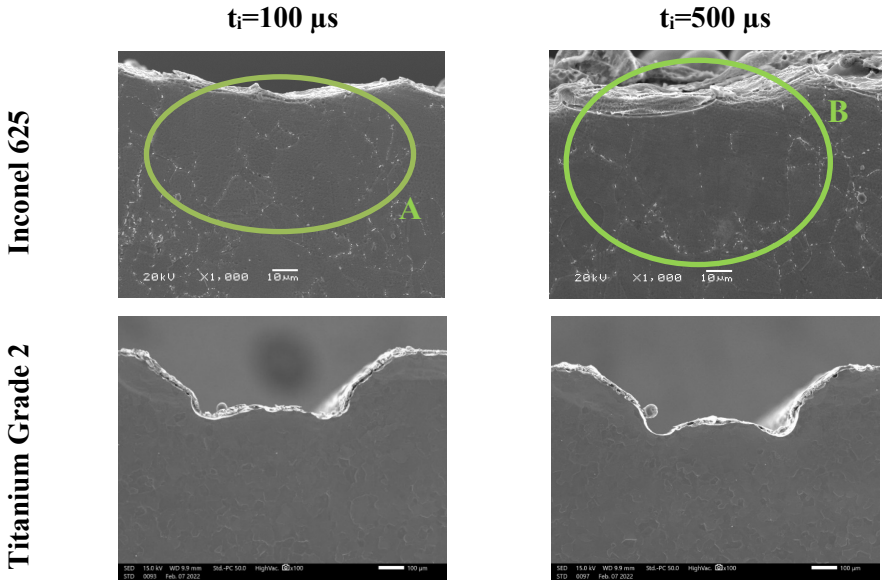

Fig. 7. Comparison of the SEM photos of Inconel 625 and titanium Grade 2 after EDM process with pulse time t_i=100 µs and t_i=500 µs with the following machining parameters: U=100 V, I=2.7 A, p=6 bar.

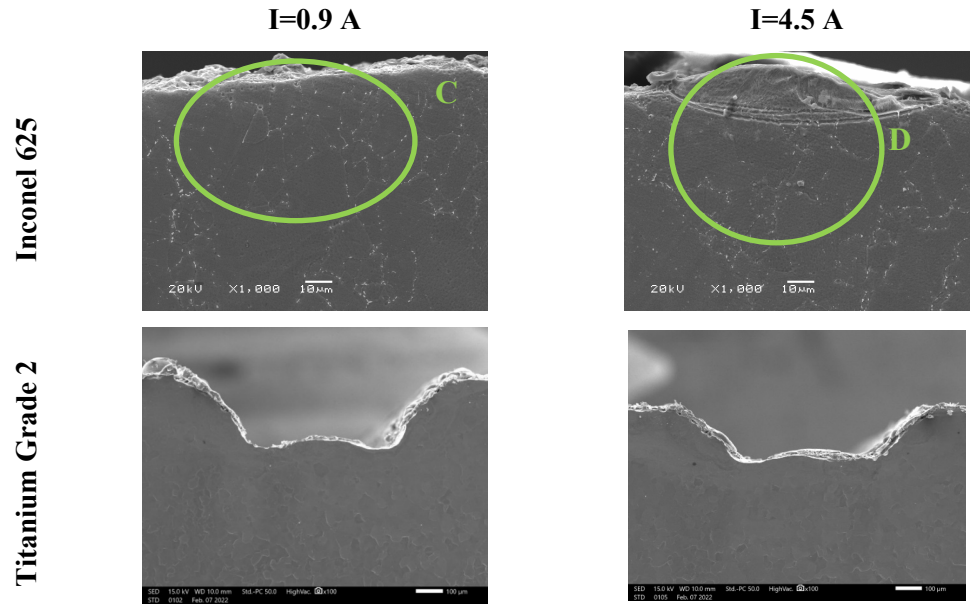

Fig. 8. Comparison of the SEM photos of Inconel 625 and titanium Grade 2 after EDM process with current I=0.9 A and I=4.5 A s with the following machining parameters: t_i= 300 µs, U=100 V, p=6 bar.

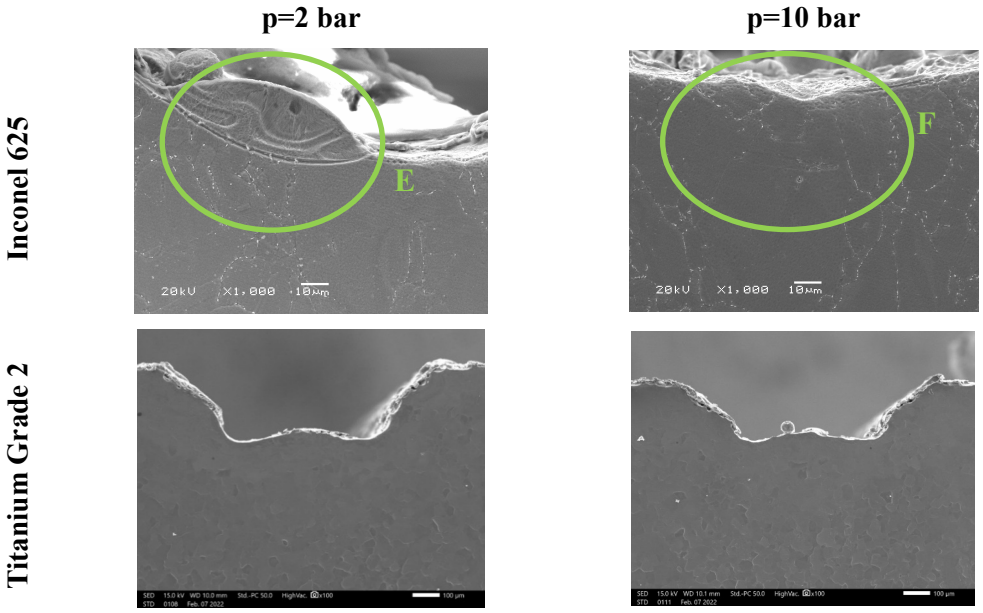

Fig. 9. Comparison of the SEM photos of Inconel 625 and titanium Grade 2 after EDM process with pressure p=2 bar and p=10 bar with the following machining parameters: t_i= 300 µs, U=100 V, I=2.7 A.

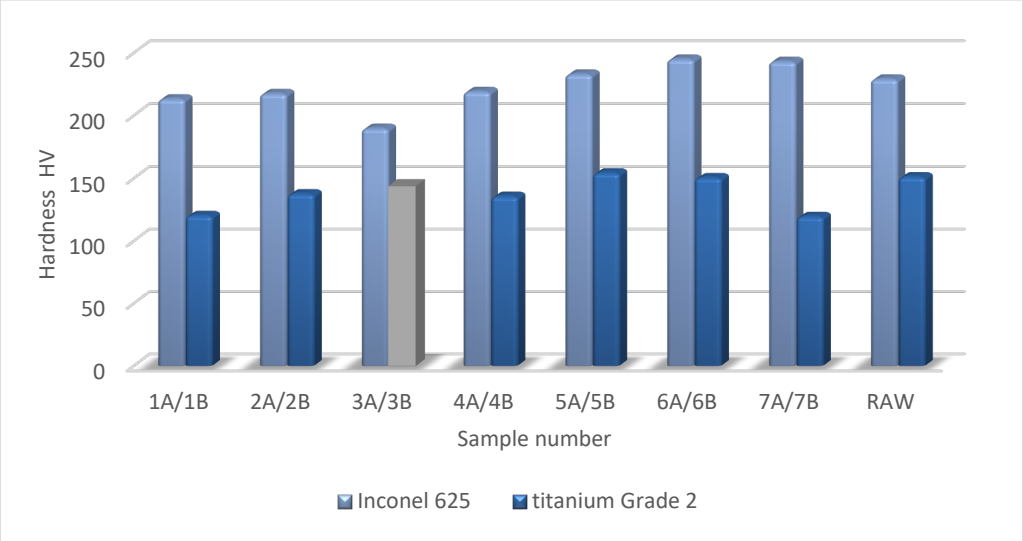

Fig. 10. Results of microhardness measurements of Inconel 625 and titanium Grade 2, average values from repetitions at three levels, RAW material hardness for reference for Inconel 625 and titanium Grade 2.

Summary

According to the research work carried out, the type of material (and, in particular, its internal structure, thermal and electrical conductivity) which was EDM milled in carbon dioxide, is crucial for the conducted machining process, obtained machining efficiency, working electrode wear, as well as surface roughness. However, is worth to underline that, regardless of the type of machined material, the productivity of the process is very low, which favours micro machining as an application area for the investigated process. In this application, the benefits of external cooling, such as better surface layer properties (roughness, lower thermal changes) and lower working electrode wear, result in easier designing of the machining process (it is easier to compensate the occurring lower working electrode wear) and determine the application area (better surface layer properties). It is worthy to underline, that considering the nature of the dry-EDM with additional workpiece cooling, it is hard to identify the relation between roughness parameters. It is caused by the stochastically distribution of discharge craters during the dry-EDM process. The better representation of roughness is considered to be obtained after 3D roughness measurements, which should much better represent the state of the surface roughness (especially given the randomness of the EDM discharges). Therefore, in further research it is recommended to conduct 3D roughness measurements.

References

[1] F. Klocke, A. Klink, D. Veselovac, D.K. Aspinwall, S.L. Soo, M. Schmidt, J. Schilp, G. Levy, J.-P. Kruth, Turbomachinery component manufacture by application of electrochemical, electro-physical and photonic processes, CIRP Ann. - Manuf. Technol. 63 (2014) 703-726. https://doi.org/10.1016/j.cirp.2014.05.004

[2] R. Świercz, Modelowanie i optymalizacja obróbki elektroerozyjnej materiałów trudnoobrabialnych, Warszawa: Oficyna Wydawnicza Politechniki Warszawskiej, 2019.

[3] M. Kumar, S. Datta, R. Kumar, Electro-discharge Machining Performance of Ti–6Al–4V Alloy: Studies on Parametric Effect and Phenomenon of Electrode Wear, Arab. J. Sci. Eng. 44 (2019) 1553–1568. https://doi.org/10.1007/s13369-018-3632-1

[4] B.B. Pradhan, M. Masanta, B.R. Sarkar, B. Bhattacharyya, Investigation of electrodischarge micro-machining of titanium super alloy, Int. J. Adv. Manuf. Technol. 41 (2009) 1094. https://doi.org/10.1007/s00170-008-1561-y

[5] S. Kumar Sahoo, N. Thirupathi, K. Saraswathamma, Experimental Investigation and Multi-Objective Optimization of Die sink EDM Process Parameters on Inconel-625 alloy by using Utility Function Approach, Mater. Today Proc. 24 (2020) 995-1005. https://doi.org/10.1016/j.matpr.2020.04.412
[6] N.K. Singh, Y. Singh, A. Sharma, R. Prasad, Experimental investigation of flushing approaches on EDM machinability during machining of titanium alloy, Mater. Today Proc. 38 (2020) 139-145. https://doi.org/10.1016/j.matpr.2020.06.165
[7] A. Descoeudres, Characterization of electrical discharge machining plasmas (2006).
[8] A. Banu, M.Y. Ali, Electrical Discharge Machining (EDM): A Review, Int. J. Eng. Mater. Manuf. 1 (2016) 3-10. https://doi.org/10.26776/ijemm.01.01.2016.02
[9] B. Jha, K. Ram, M. Rao, An overview of technology and research in electrode design and manufacturing in sinking electrical discharge machining, J. Eng. Sci. Technol. Rev. 4 (2011) 118-130. https://doi.org/10.25103/JESTR.042.02
[10] K.P. Rajurkar, M.M. Sundaram, A.P. Malshe, Review of Electrochemical and Electrodischarge Machining, Procedia CIRP, 6, (2013) 13-26. https://doi.org/10.1016/j.procir.2013.03.002
[11] A. Miernikiewicz, Doświadczalno-teoretyczne podstawy obróbki elektroerozyjnej (EDM), Kraków: Politechnika Krakowska, 2000.
[12] A. Żyra, R. Bogucki, S. Skoczypiec, An influence of titanium alloy Ti10V2Fe3Al microstructure on the electrodischarge process efficiency, Arch. Metall. Mater. 64 (2019) 1005-1010. https://doi.org/10.24425/amm.2019.129487
[13] B.K. Baroi, Jagadish, P.K. Patowari, A review on sustainability, health, and safety issues of electrical discharge machining, J Braz. Soc. Mech. Sci. Eng. 44 (2022) 59. https://doi.org/10.1007/s40430-021-03351-4
[14] A. Żyra, S. Skoczypiec, R. Bogucki, Selected Aspects of Surface Integrity of Inconel 625 Alloy after Dry-EDM in Carbon Dioxide, Key Eng. Mater. 926 (2022) 1681-1688. https://doi.org/10.4028/p-o1809g
[15] R. Roth, F. Kuster, K. Wegener, Influence of oxidizing gas on the stability of dry electrical discharge machining process, Procedia CIRP, 6 (2013) 338-343. https://doi.org/10.1016/j.procir.2013.03.029
[16] A. Żyra, W. Bizoń, S. Skoczypiec, Primary research on dry electrodischarge machining with additional workpiece cooling, in AIP Conf. Proc. 2017 (2018) 020034. https://doi.org/10.1063/1.5056297

Materials Research Proceedings 28 (2023) 1673-1682 https://doi.org/10.21741/9781644902479-180

Development of a method for performance characterisation of PEMEC process considering electrolyte temperature in case of hybrid polishing of 316L steel

KRZAK Daniel[1,a *], ROY Florian[1,b], SALVATORE Ferdinando[1,c], GIDON Antoine[2,d], GUERIN Stéphane [2,e] and RECH Joël[1,f]

[1]University of Lyon, Ecole Centrale de Lyon - ENISE, LTDS UMR5513, 58 Rue Jean Parot, 42000 Saint-Etienne, France

[2]Cetim, rue de la Presse, 42000 Saint-Etienne, France

[a]daniel.krzak@enise.fr, [b] florian.roy@enise.fr, [c] ferdinando.salvatore@enise.fr, [d] antoine.gidon@cetim.fr, [e] stephane.guerin@cetim.fr, [f] joel.rech@enise.fr

Keywords: Polishing, Drag Finishing, Electrochemical Polishing, Surface Roughness, Material Removal

Abstract. This work falls within the context of very rough parts (Ra > 10 µm) polishing using a new hybrid process called PEMEC, which combines a mechanical abrasion action (tribofinishing) and an anodic dissolution action (electrochemical polishing). The study of the performances of a polishing process requires the monitoring of the surface roughness, but also the monitoring of the dimensions and the shape of the parts. This paper proposes a new method for characterising polishing operations that enables all these criteria to be monitored in a single test. This method is applied to the study of the influence of the electrolyte temperature in the PEMEC process.

Introduction

The polishing of complex shaped very rough metallic parts (Ra > 10 µm) is an old subject in industry, often related to parts produced by casting, forging, etc. However, the functional simple shaped surfaces of these parts, such as plane or cylindrical, were usually calibrated using machining processes (turning, milling, grinding, etc.). The polishing of complex shaped very rough metal parts (Ra > 10 µm) is once again becoming a major research topic in the industry with the upgrowing development of additive manufacturing techniques, such as Laser Powder Bed Fusion (L-PBF). Additive manufacturing enables the design of new parts with complex functional surfaces. These complex surfaces are difficult to access and cannot be finished by conventional machining processes. In the case of L-PBF, the surfaces are very rough, and it is common to observe surfaces with Ra roughness values ranging from 10 - 30 µm depending on the area concerned [1]. Numerous recent research projects aimed to optimise conventional polishing processes on these rough and complex surfaces (chemical or electrochemical polishing, tribofinishing, laser polishing, water polishing, plasma electrolytic polishing, etc. [2-5]). Among these recent works, Malkorra et al. [5] have shown that it is possible to reduce the roughness from an Ra of 10 µm to 1 µm using the drag finishing process. However, to achieve this goal, very long treatment times are required. Then, conventional polishing processes tend to severely deteriorate the geometry of the parts (size, shape), especially the sharp edges. In order to solve this problem, new polishing processes have appeared with the objective of reducing surface roughness without deteriorating the shape of the parts. These processes are called "hybrid" processes because they combine the simultaneous and controlled action of several mechanisms (physical, chemical, optical, etc.) and/or energy sources/tools [6]. The main objective of hybrid processes is to increase the material removal during the polishing process through a synergistic effect between the mechanisms. For example, there are several hybrid processes daily used in industry that combine

Content from this work may be used under the terms of the Creative Commons Attribution 3.0 license. Any further distribution of this work must maintain attribution to the author(s) and the title of the work, journal citation and DOI. Published under license by Materials Research Forum LLC.

abrasion and chemical dissolution mechanisms [7-8]. In the scientific literature, there are also several processes that combine abrasion and anodic dissolution mechanisms [9-14]. Unfortunately, these hybrid processes have been designed to polish simple surfaces such as planes or cylinders and are not suitable for complex shapes.

Moreover, it can be stated that all the papers dealing with the polishing of rough and complex parts do not use any standardised method. Each paper develops a specific method for its own samples with respect to its application. It is therefore difficult to compare the performance between several processes. Additionally, the wide majority of the papers are focused on surface roughness. Only few papers have investigated the evolution of part's geometry (dimension, form, edges, …). The objective of this article is to propose a reference method for the characterisation of polishing processes on parts with complex geometries and very high initial roughness ($Ra > 10$ µm). The application case study of this new method concerns the investigation of the influence of electrolyte temperature in a new process called 'PEMEC'. This polishing process was recently proposed in [15]. This process combines an abrasive action (tribofinishing) with an anodic dissolution action (electrochemical polishing - ECP). Among the large variety of technical solutions in tribofinishing, the PEMEC process kinematic uses a drag-finishing machine kinematics that enables to polish complex surfaces thanks to its double rotation. The principle of this process is described in Fig .1

As a reminder, electrochemical polishing (ECP) is one of the most common electrochemical polishing processes used for metallic parts with complex shapes. This process involves the controlled dissolution of the surface to be polished. ECP commonly provides shiny surfaces. When electropolishing, current flows from the anode (the workpiece – Fig.1 A-D) to the cathode (the machine tank – Fig.1 A-D). The anode-cathode assembly is immersed in an electrolyte bath, the concentration and composition of which varies according to the metal being polished. The scientific community has conducted numerous studies on the sensitivity of the process parameters (temperature, electrolyte composition, agitation rate, distance between the electrodes, etc.) [3]. This process requires long treatment periods. Moreover, the concentration of the electric current lines on the sharp edges induces a modification of the geometry of the parts (Fig. 1D).

Drag-finishing is a mechanical polishing process that improves the surface roughness of parts with complex geometries. The parts are dragged through a mixture of a large number of abrasive particles (called abrasive media) immersed in a liquid. The interaction between the abrasive media and the surface to be polished induces 3 mechanisms: plastic deformation of the roughness peaks, scratches and finally it generates micro-chips. These mechanisms lead to an improvement of the surface finish. This process has been studied several times and it has been shown that the efficiency of the process depends on several parameters such as drag velocity, type of liquid and geometry, as well as size and composition of the abrasive media [5]. However, this process requires long polishing periods to achieve a low roughness. In addition, abrasives are particularly aggressive to sharp edges, which changes the geometry of the polished workpieces.

Rech et al. [15] have shown that there is a synergistic effect between abrasion and anodic dissolution during the PEMEC process. It becomes possible to reduce the roughness very quickly from a *Sa* value of 11 µm to 3 µm within 120 minutes on complex 316L stainless steel parts, without significantly modifying the shape of the parts and especially the sharp edges.

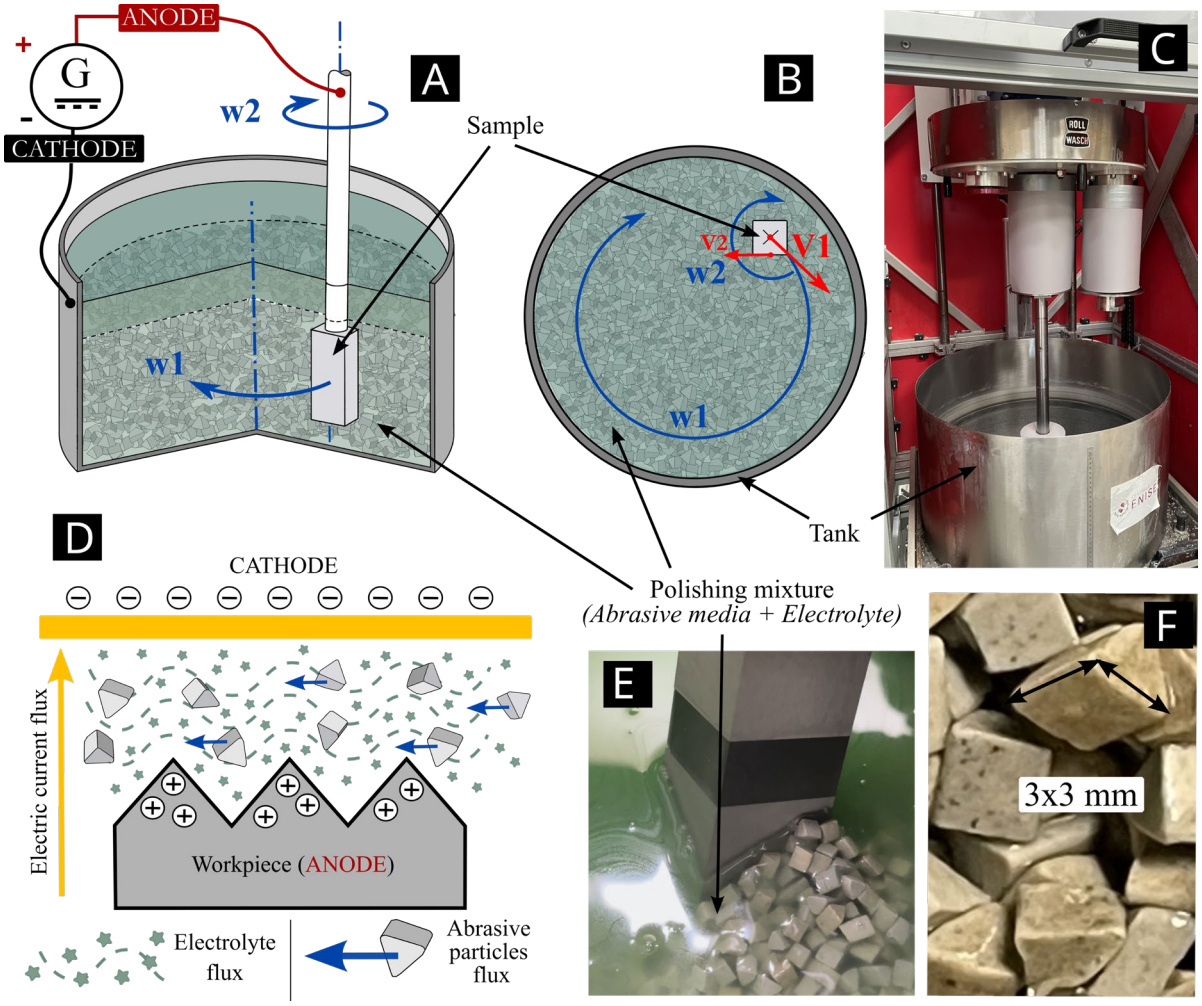

Fig. 1. PEMEC process principle: A) Schematic illustration; B) Schematic illustration; C) PEMEC machine; D) Schematic illustration of PEMEC principle; E) PEMEC polishing mixture (Abrasive media + Electrolyte); F) Elementary abrasive media used in PEMEC process.

Experimental Procedure

Definition of sample geometry.

The first step of the new method, to characterize polishing processes, is to define a new sample geometry with a calibrated geometry and roughness (Fig. 2). The part has rectangular parallelepipedal shape with two *'reference surfaces'* at its upper and lower ends. These *'reference surfaces'* are flat and smooth (Fig. 2A). During the polishing process, these surfaces will be protected and will not be affected by the polishing process (Fig. 2C). These '*reference surfaces'* enable the sample to be relocated in an absolute reference frame. Then there are two groups of so-called *'transition surfaces'* (Fig. 2C). *'Transition surfaces'* are also flat and smooth. They enable to investigate the evolution of the macro-geometry of the sample (flatness, orientation, dimension) and the evolution of edge sharpness. Both the *'reference surfaces'* and *'transition surfaces'* have been generated by grinding. Finally, in the centre of the sample, there is the so-called *'calibrated roughness area'* where a high roughness is generated with a determined shape (Fig. 2B). The analysis of the evolution of the topography in this zone enables the analysis of the polishing mechanisms (plastic deformation, abrasion, dissolution, ...). The principle of this analysis has already been introduced by Malkorra et al. [16].

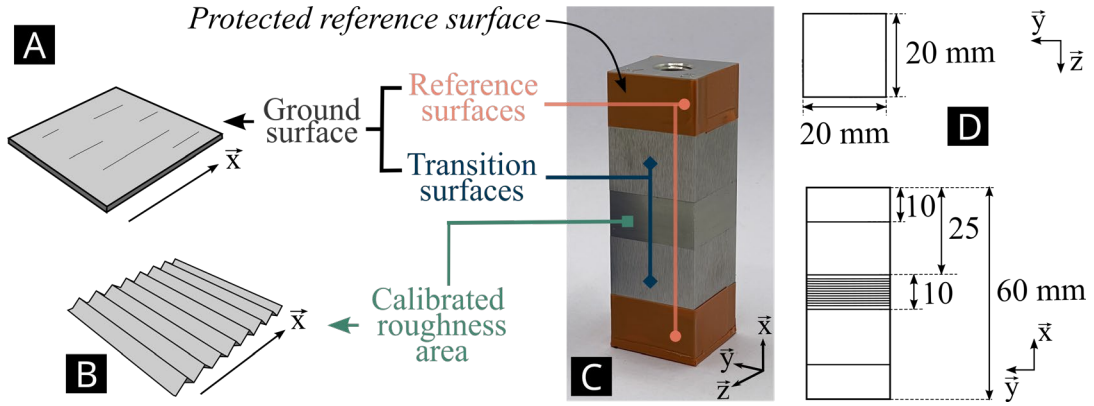

Fig. 2. A) Ground surface schematic; B) Calibrated roughness area schematic; C) Image of sample with protected reference surface; D) Sample dimensions.

Sample fabrication.

The samples were fabricated from austenitic 316L stainless steel. For logistical reasons, it was decided to use 316L stainless steel from laminated bars. After milling, *'reference surfaces'* and *'transition surfaces'* were both manufactured by fine grinding. Before polishing, the *'reference surfaces'* and *'transition surfaces'* cannot be distinguished from each other. The only difference between these two surfaces is that *'reference surface'* will be protected during the polishing process, and thus will not be modified. The edges around the transition surfaces are sharp (Fig. 3E). The so-called *'calibrated roughness area'* was machined by milling (Fig.3 A to D) with the aim of reproducing a microgeometry similar to those obtained after additive manufacturing processes. This step allowed to obtain a high roughness value ($Ra \simeq 12$ µm / $Rz \simeq 50$ µm). The results found when polishing this *'calibrated roughness area'* have the same trends as those obtained when polishing real parts produced by additive manufacturing [15].

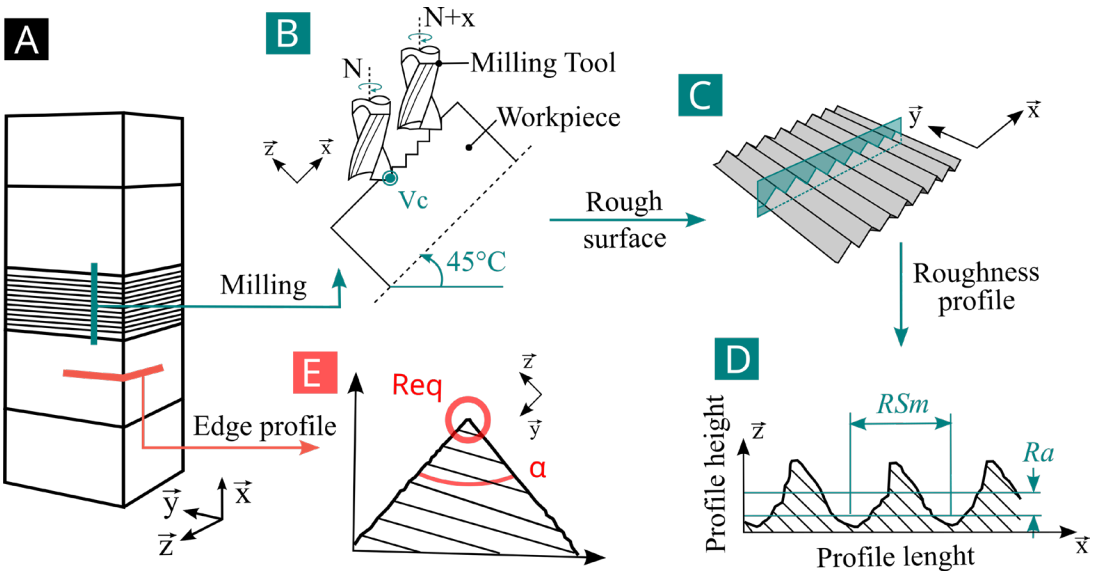

Fig. 3. A) Sample schematic; B) Calibrated roughness milling operation; C) Calibrated surface schematic; D) Periodical calibrated roughness profile; E) Edge profile.

Polishing tests.

The samples were polished by the PEMEC process for 75 minutes. The PEMEC machine is designed within a drag-finishing machine, that enables both polishing processes (abrasion + anodic dissolution) to be carried out. The main rotation (w1 in Fig. 1 A-B) induces a drag velocity V1 responsible for the abrasive mechanisms, while the second rotation (w2 in Fig. 1 A-B) leads to a homogeneous treatment around the workpiece. This kinematic induces a high sliding speed. This set-up has already been used in previous works [15]. During the polishing process, the workpiece is immersed and dragged in the polishing mixture (abrasive media + electrolyte). Table 3 shows the composition of the polishing mixture and the process parameters used. A DC power supply was installed between the tank (cathode) and the workpiece (anode).

Table 1 Polishing mixture composition and process parameters

		PEMEC process	
Drag velocity V_1 [m/s]		0.6	
Rotation speed, w_1 [rpm]		200	
V_2 [m/s]		0.69	
Sample rotation speed, w_2 [rpm]		655	
Temperatures		25 °C	62 °C
"Polishing mixture"	Abrasive particles	Pyramidal shape Al_2O_3 abrasive particles, size 3x3 mm	
	Electrolyte / Lubricant	Phosphoric acid H_3PO_4 (85 wt.%) and deionised water	
Voltage [V]		12	
Current density [A/dm²]		20	

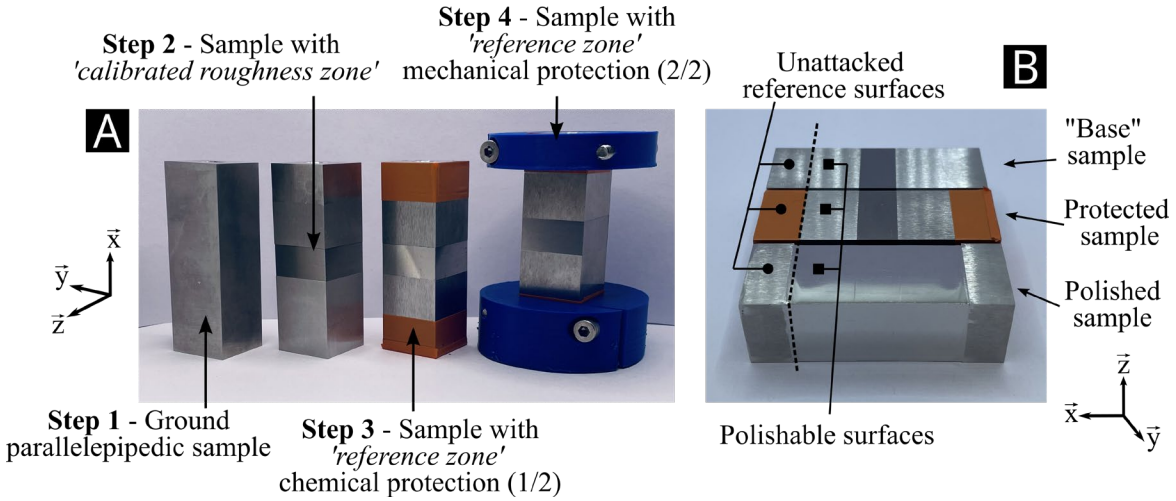

Fig. 4. A) Sample protection process; B) Protected reference surface principle.

The distance between the anode (workpiece) and the cathode (tank), and the drag speed are very influential parameters for the ECP mechanisms. The anode-cathode distance was set at around 30 mm, and this distance oscillates around this value due to the rotation of the workpiece (w2) and the geometry of the workpiece. It should be noted that the distance and drag speed used in this study are significantly higher than the values used in studies conducted by the scientific community on ECP. The temperature of the electrolyte is controlled before and during the treatment to ensure that the temperature is the same throughout the polishing process. In this study, two temperature levels were chosen: T°= 25 °C and 62 °C. The samples are mounted in the machine with a reference surface protection system (Fig. 4). The tests were interrupted every 15

minutes in order to characterise the topography evolution of the 4 calibrated roughness areas and the 8 transition surfaces and edges. This enables to obtain an average value, as well as to quantify the deviation.

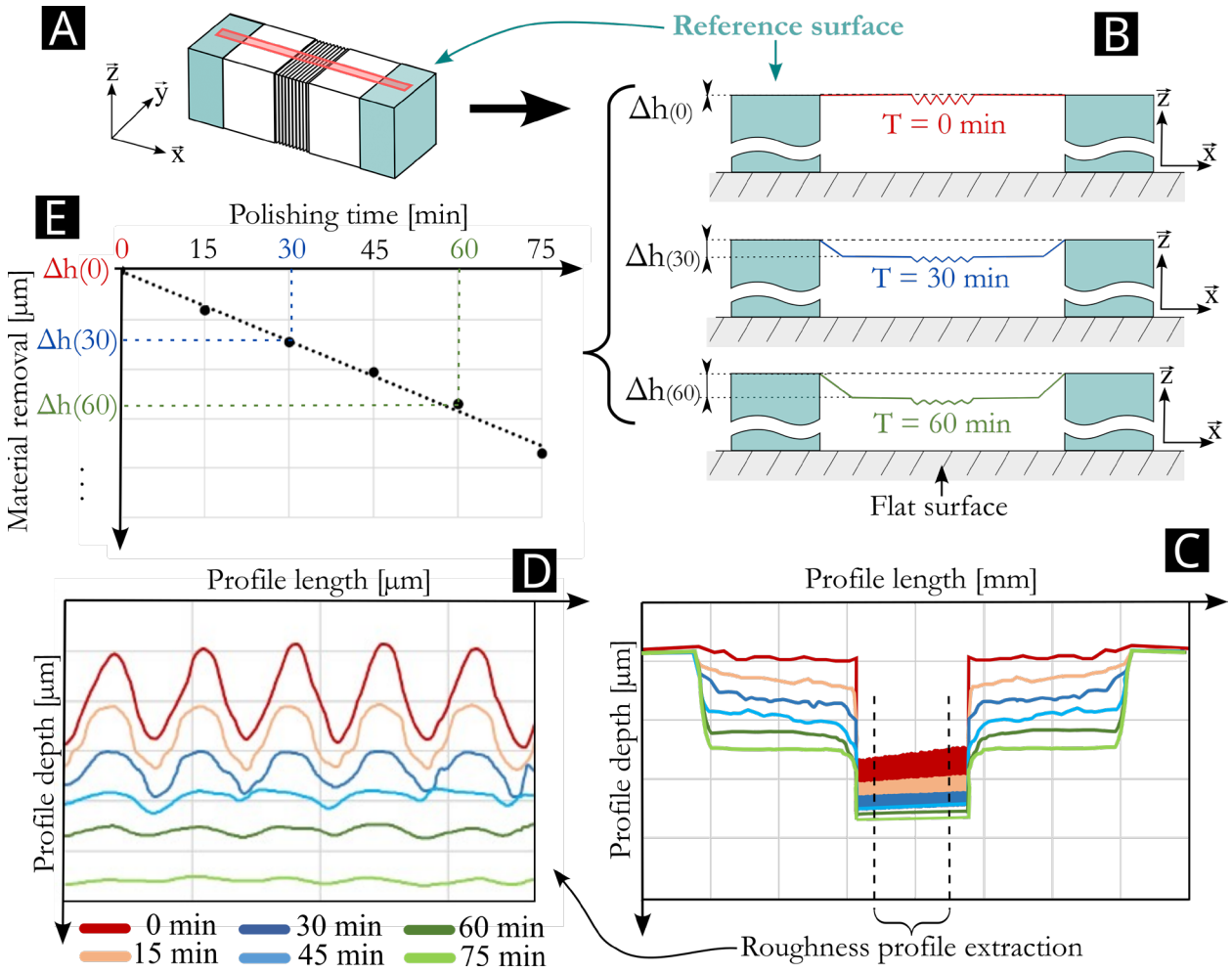

Fig. 5. A) Sample with highlighted reference surfaces schematics; B) Reference surface working principle; C) Profile overlay; D) Roughness profile extraction after profile overlay; E) Material removal evolution obtained.

Results and Discussions

The new method for characterising the performance of polishing processes was applied for two polishing conditions, corresponding to operating conditions, i.e. two different values for electrolyte temperatures. The results are presented in Figures 6, 7 and 8.

Fig. 6A shows the evolution of the amount of material removed (Δh) in the *'transition surfaces'* for both tested conditions. The process for obtaining figure 6 is explained in figures 5A, 5B and 5E. It appears that the material removal rate is much higher at high temperature. Thus, after 75 min, a value of $\Delta h \sim 384$ µm can be observed at 62 °C compared to 74 µm at 25 °C. If we analyse the evolution of material removal, we can observe that at 62 °C, the process removes nearly as much material after 15 min ($\Delta h \sim 65$ µm) as the process at 25 °C after 75 min ($\Delta h \sim 74$ µm). There is a ratio of around 4.5 on the material removal rate between the two different temperatures tested.

Fig. 6B shows the evolution of the *Ra* parameter in the *"calibrated roughness area"*. It can be observed that the roughness is improved much faster when using a high temperature. Thus, after

15 minutes only, *Ra* reaches a value of ~ 0.45 µm at 62 °C, compared to 8.22 µm at 25 °C. The PEMEC process at 25 °C only achieves a *Ra* < 1µm after 75 min.

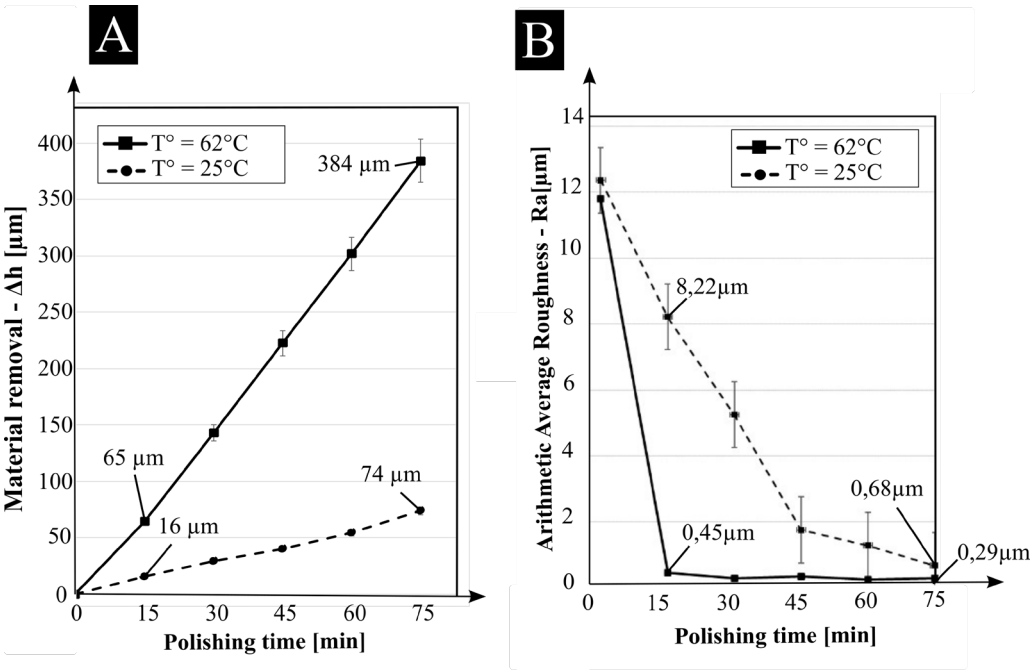

Fig. 6. A) Material removal, Δh[µm], over time; B) Arithmetic Average Roughness, Ra[µm], over time.

Fig. 7A and B show the evolution of the roughness profile, as well as their relative position compared to the reference surfaces. These figures were obtained by overlaying the different measured roughness profiles, using the *"reference surfaces"* as a reference (Fig.5 A-B). This overlay process is explained in Fig. 5 A to D. Fig. 7A and B illustrate clearly that the polishing process at 62 °C completely erases the initial roughness profile in less than 15 minutes. It can also be seen that the amount of material removed is greater than the initial height of the roughness profile. However, after a 15-minutes treatment, a slightly noticeable periodic surface remains from the initial roughness profile. The surface then becomes aperiodic from 30 minutes onwards.

In comparison, at 25 °C the profile remains periodic until 75 min. It can be observed that the valleys of the profiles are not much affected at the beginning of the treatment. This behaviour reveals the abrasion of the roughness peaks, which indicates that abrasion is probably the dominant mechanism. In sharp contrast, at 62 °C there is clearly a combination of homogeneous material dissolution and peak roughness abrasion (synergistic effect of the PEMEC process). These results confirm the findings of the literature regarding the importance of temperature control in electrochemical polishing [5].

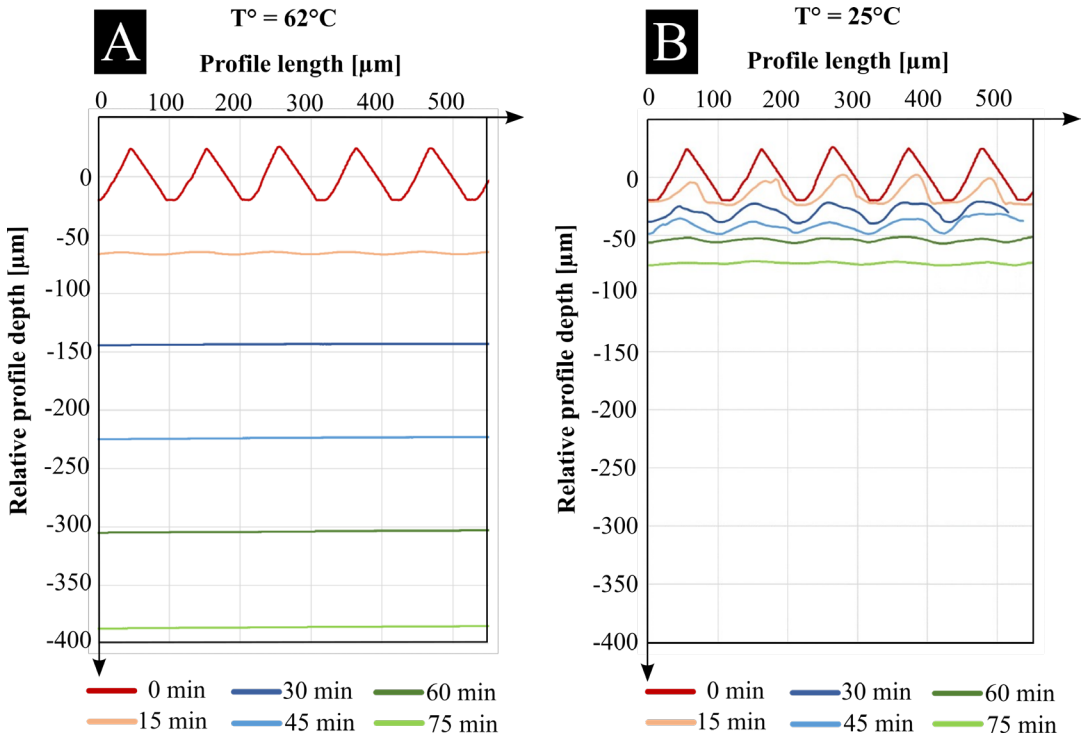

Fig. 7. A) Roughness profile evolution at 62 °C; B) Roughness profile evolution at 25 °C.

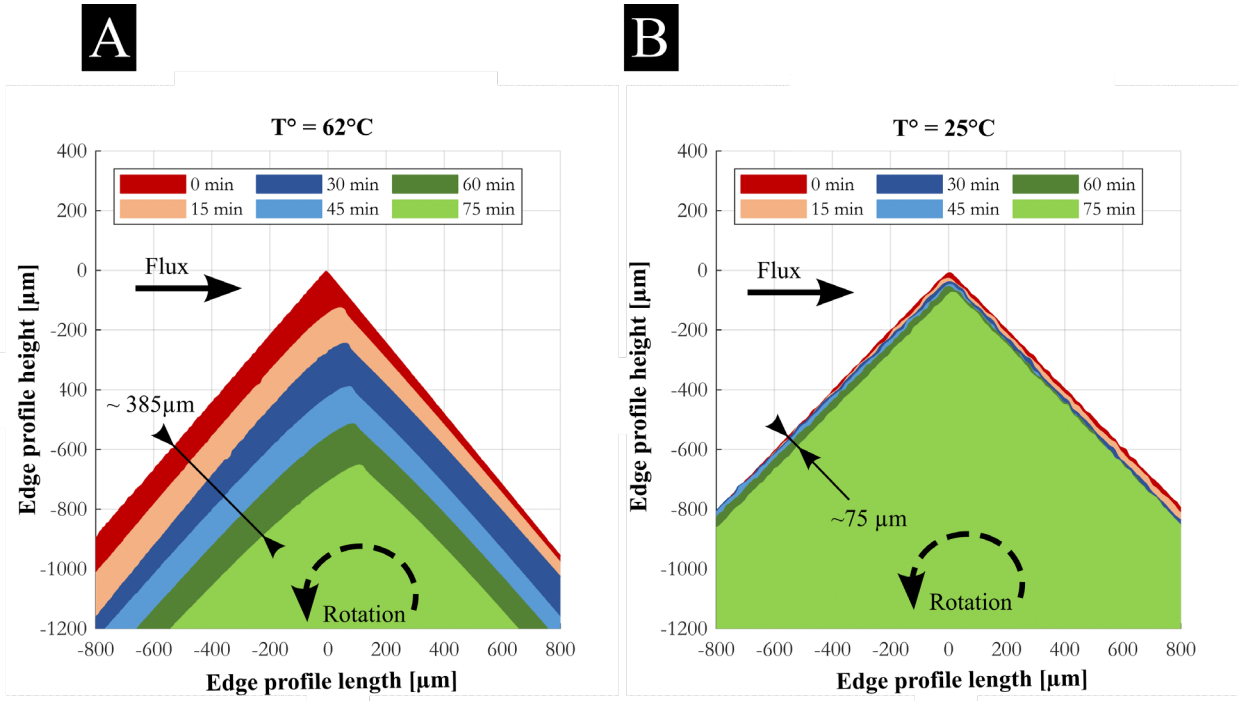

Fig. 8. A) Edge profile evolution at 62 °C; B) Edge profile evolution at 25 °C.

Fig. 8A and B show the evolution of the edge profile, were obtained by overlaying the different measured edge profiles. It is clear that at 25 °C the edges are only slightly affected by the process, while, at 62 °C the change in edge geometry is very rapid. This is in accordance with the previous

results presented in Fig. 7 and 8. A large amount of material is removed. However, the edge sharpness remains quite sharp and not rounded (~ 1 mm) as is commonly seen in drag-finishing processes. A closer look at the profiles shows that the two sides are not symmetrical. On the left side, the shape is more affected by the polishing process than on the right side leaving non-flat surfaces near the edge, as well as a slightly curved edge. This is due to the direction of rotation of the sample in the machine. The w2 speed induces a greater abrasive media impact speed on left side. This asymmetry can be counterbalanced by regularly reversing the direction of rotation in the machine. So, it can be concluded that the PEMEC process enables to preserve edge sharpness thanks to the reduced polishing duration (some minutes).

Summary

This paper has presented a new method to characterise the performance of a polishing process on complex shaped samples with high roughness. This method was applied to the characterisation of the influence of electrolyte temperature in the PEMEC process, which combines an abrasive and an anodic dissolution action. This method has shown its ability to simultaneously quantify the multi-scale evolution of the samples: roughness parameters, roughness profiles, material removal and edge macro-geometry. This method allows to reveal the mechanisms of action of polishing processes.

In the case of the PEMEC process, it was shown that temperature is a key parameter for the efficiency of material removal. While the process is essentially dominated by the abrasive action at low temperature, the dissolving action plays a major role in synergy with the abrasion at higher temperature.

The perspective of this work will now focus on a generalised use of this methodology in order to study the sensitivity of the PEMEC process to all the mechanical parameters (shape and speed of the abrasive particles, ...) and the electrochemical parameters (voltage, electrolyte, ...) so as to identify the best synergistic conditions between the two mechanisms.

This geometry of samples has the potential to compare the efficiency of various polishing processes for complex and rough parts.

References

[1] F. Cabanettes, A. Joubert, G. Chardon, V. Dumas, J. Rech, S. Grosjean, Z. Dimkovski, Topography of as built surfaces generated in metal additive manufacturing: a multi-scale analysis, Precis. Eng. 52 (2018) 249-265. https://doi.org/10.1016/j.precisioneng.2018.01.002

[2] E. Łyczkowska, P. Szymczyk, B. Dybała, E. Chlebus, Chemical polishing of scaffolds made of Ti-6Al-7Nb alloy by additive manufacturing, Arch. Civ. Mech. 14(4) (2014) 586-594. https://doi.org/10.1016/j.acme.2014.03.001

[3] W. Han, F. Fang, Fundamental aspects, and recent developments in electropolishing, Int. J. Mach. Tools Manuf. 139 (2019) 1-23. https://doi.org/10.1016/j.ijmachtools.2019.01.001

[4] S. Han, F. Salvatore, J. Rech, J. Bajolet, J. Courbon, Effect of abrasive flow machining (AFM) finish of selective laser melting (SLM) internal channels on fatigue performance, J. Manuf. Process. 59 (2020) 248-257. https://doi.org/10.1016/j.jmapro.2020.09.065

[5] I. Malkorra, H. Souli, F. Salvatore, P. Arrazola, J. Rech, A. Mathis, J. Rolet, Numerical modelling of the drag finishing process at a macroscopic scale to optimize surface roughness improvement on additively manufactured (SLM) Inconel 718 parts, Procedia CIRP, 108 (2022) 648-653. https://doi.org/10.1016/j.procir.2022.01.002

[6] B. Lauwers, F. Klocke, A. Klink, A.E. Tekkaya, R. Neugebauer, D. Mcintosh, Hybrid processes in manufacturing, CIRP Ann. - Manuf. Technol. 63(2) (2014) 561-583. https://doi.org/10.1016/j.cirp.2014.05.003

[7] E. Atzeni, A.R. Catalano, P.C. Priarone, A. Salmi, The technology, economy, and environmental sustainability of isotropic superfinishing applied to electron-beam melted Ti-6Al-

4V components, Int. J. Adv. Manuf. Technol. 117(1) (2021) 437-453. https://doi.org/10.1007/s00170-021-07739-3
[8] P. Trubacova, S. Atieh, F. Bajard, A.G. Terricabras, G.J. Rosaz, J.P. Rigaud, Niobium micro-mechanical polishing for superconductive radio-frequency applications, euspen's 20th International Conference & Exhibition, Geneva, CH, June 2020.
[9] D.T. Curtis, S.L. Soo, D.K. Aspinwall, C. Sage, Electrochemical superabrasive machining of a nickel-based aeroengine alloy using mounted grinding points, CIRP Ann. - Manuf. Technol. 58(1) (2009) 173-176. https://doi.org/10.1016/j.cirp.2009.03.074
[10] K.P. Rajurka, D. Zhu, Improvement of electrochemical machining accuracy by using orbital electrode movement, CIRP Ann. - Manuf. Technol. 48(1) (1999) 139-142. https://doi.org/10.1016/S0007-8506(07)63150-3
[11] D. Zhu, Y.B. Zeng, Z.Y. Xu, X.Y. Zhang, Precision machining of small holes by the hybrid process of electrochemical removal and grinding, CIRP Ann. - Manuf. Technol. 60(1), (2011), 247-250. https://doi.org/10.1016/j.cirp.2011.03.130
[12] F. Klocke, R. Zunke, Removal mechanisms in polishing of silicon based advanced ceramics, CIRP Ann. - Manuf. Technol. 58(1) (2009) 491-494. https://doi.org/10.1016/j.cirp.2009.03.120
[13] H.S. Lee, D.I. Kim, J.H. An, H.J. Lee, K.H. Kim, H. Jeong, Hybrid polishing mechanism of single crystal SiC using mixed abrasive slurry, CIRP Ann. - Manuf. Technol. 59(1) (2010) 333-336. https://doi.org/10.1016/j.cirp.2010.03.114
[14] R. Komanduri, D.A. Lucca, Y. Tani, Technological advances in fine abrasive processes, CIRP Ann. - Manuf. Technol. 46(2) (1997) 545-596. https://doi.org/10.1016/S0007-8506(07)60880-4
[15] J. Rech, D. Krzak, F. Roy F, F. Salvatore, A. Gidon, S. Guérin, A new hybrid electrochemical-mechanical process (PEMEC) for polishing complex and rough parts, CIRP Ann. 71(1) (2022) 173-176. https://doi.org/10.1016/j.cirp.2022.03.011.
[16] I. Malkorra, H. Souli, C. Claudin, F. Salvatore, P. Arrazola, J. Rech, H. Seux, A. Mathis, J. Rolet, Identification of interaction mechanisms during drag finishing by means of an original macroscopic numerical model, Int. J. Mach. Tools Manuf. 168(A) (2021) 103779. https://doi.org/10.1016/j.ijmachtools.2021.103779

Materials Research Proceedings 28 (2023) 1683-1688 https://doi.org/10.21741/9781644902479-181

Unconventional method for recycling CFRPs by using a milling process

BOCCARUSSO Luca[1,a *], DE FAZIO Dario[1,b], DURANTE Massimo[1,c], FORMISANO Antonio[1,d] and LANGELLA Antonio[1,e]

[1]Department of Chemical, Materials and Production Engineering, University of Naples Federico II, Piazzale V. Tecchio 80, 80125 Napoli, Italy

[*a]luca.boccarusso@unina.it, [b]dario.defazio@unina.it, [c]mdurante@unina.it, [d]aformisa@unina.it, [e]antgella@unina.it

Keywords: CFRPs, Mechanical Recycling, Machining, Impregnation, Bending

Abstract. Composite materials are increasingly employed in many industrial sectors (transportation, infrastructure, electronics). Among the others, carbon fibers are used primarily as reinforcing agents in high-performance composites with synthetic resin matrices such as epoxies, polyimides, vinyl esters, phenolics, and certain thermoplastics. However, when carbon fibers were coupled with a thermosetting matrix, the resulting composites are not easily recyclable. When these products reaching their end-of-life (EoL) there are several difficulties in their recycling and in the reuse of the carbon fiber reinforce. There are several recycling process methods, but one of the most promising and investigated in the last years is the mechanical one that differently from other approaches do not require the use of high temperature or chemical substances to decompose the polymeric matrix. Respect to known mechanical recycling methods like shredding, crushing and hammer milling process, in this work is presented a mechanical recycling that mainly consists in the use of an un-conventional milling process in order to obtain carbon/epoxy chips. Different chips in terms of geometry and size were obtained by fixing the milling process parameters, so the results in terms of chip morphological characteristic were presented. CFRPs chips, after sieving, were then used to manufacture new CFRPs laminates produced starting from recycled materials.

Introduction

Carbon fiber reinforced plastic (CFRP) materials are attracting a significant interest in our day-to-day life because of their interesting mechanical properties combined with the low weight [1].

It is not a surprise that their demand over the last 40 years is grown more and more and during these last years, although the COVID pandemic, the CFRP growing demand reached a current rate of 11% per year due to the increasing need of lightweight materials in different industrial fields. It was estimated that the CFRPs demand was around 120 kTons during the present year [2,3].

It is worth to note that the growing demand of CFPRs is directly connected with an increasing production of virgin carbon fibres (vCF) with expensive and energy intensive processes that generates gases such as ammonia (NH_3), carbon monoxide (CO), carbon dioxide (CO_2) nitrogen oxides (NO_X) and other volatile compounds [4].

It was calculated by a Life Cycle Assessment (LCA) analysis that the amount of energy required for the production of vCF is almost 198 - 595 MJ/kg [5] compared with 13 - 32 MJ/kg required for the production of virgin glass fibre (vGF).

In addition to these considerations, it have to be considered that the growing demand of CFRPs will dramatically increase the amount of waste derives both from scraps produced during the manufacturing of composite products and from the end-of-life products; this latter represents the majority part. A defined waste management and a recycling policy are then required since it is estimated an increasing of CFRP waste of around 20 kTons annually by 2025 also considering that

Content from this work may be used under the terms of the Creative Commons Attribution 3.0 license. Any further distribution of this work must maintain attribution to the author(s) and the title of the work, journal citation and DOI. Published under license by Materials Research Forum LLC.

around 6000 - 8000 commercial aircrafts (with CFRP components) will reach their end-of-life by the 2030 [6,7].

Based on these considerations, it is clear that there is a strong need to recycle CFRPs by adopting an appropriate recycling process that is in the same time cheap, eco-sustainable, suitable for the industrial scale-up and able to obtain rCF to produce recycled CFRPs with interesting mechanical properties. Among different recycling processes, usually classified in chemical, thermal and mechanical processes, one of the most promising for the future is represented by the mechanical one. Chemical e thermal methods were widely investigated in the last years [8,9] and in spite of interesting mechanical properties are achieved by composites produced using these rCF, both methods are characterized by high costs, specific laboratory apparatus that can obstacle an easy industrial scaling up, long processing time and environmental impact.

The mechanical method is usually used to indicate a broader process's categories such as shredding, crushing and hammer milling that lead to a composite fragmentation into small pieces. An overview on the mechanical recycling process [5,10] leads to the conclusion that these methods produce short recovered fibers that due to their geometrical characteristics, size and the presence of residual matrix, severely affect the overall mechanical properties of the recycled composite material [11]. All these aspects compromise the use of mechanical recycled composite as load bearing structure limiting their use sometimes as fillers in low properties composite materials such as SMC and BMC. In addition, the use of shredding or hummer-milling process implies the use of ad-hoc industrial machine with low flexibility and big size.

To overcome this limitation, in this work it is studied the possibility to use the milling process as mechanical recycling method in order to obtain carbon/epoxy chips used to produce recycled CFRP laminates.

Materials and Methods

The CFRP materials used in this experimental campaign were manufactured using 20 unidirectional carbon/epoxy prepregs (0.2 mm in thickness) supplied by Toray. Composite laminates $(0/90)_{20}$ were produced using the compression molding process under a pressure of 8 bar and a temperature of 130°C for 8 hours. At the end of the polymerization phase, the cured composite laminates (4 mm in thickness) were cut in plate 200 mm x 200 mm to allow the machining of the CFRP material. For this purpose, a CNC machine (C.B. Ferrari) and a three flute HSS end mill tool (20 mm in diameter) were used for the peripheral down-mill machining of the produced samples. A radial depth of cut of 3.00 mm with a feed rate, *f*, of 1000 mm/min and a spindle speed, *s*, of 1000 rpm were adopted as machining parameters.

The obtained CFRP chips were then sieved using a shaking table aiming to achieve a satisfying separation between fine and coarse fibers (mean size > 0.1 mm) from powders (mean size < 0.1 mm).

Therefore, in order to produced recycled CFPR samples, the obtained chips were manually impregnated with an epoxy resin and placed in a mold at room temperature for 24 hours. Different typologies of samples were produced, they mainly differ in the size of the recycled reinforcement (greater or smaller than 0.1 mm) and in its percentage weight content equal to 14, 17, 20 and 25%. Then, the flexural behavior of each sample typology was investigated according to ASTM D790 standard testing three specimens for each sample typologies. For this purpose, three-point bending tests were carried out using a universal testing machine (MTS Alliance RT/50) equipped with a 1 kN piezoelectric load cell. Specimens (120 mm x 21 mm x 4 mm) were tested using a span length of 64 mm (span to depth ratio equal to 16). Three un-reinforced samples are also tested as reference. The flexural strength was calculated by means of the following equation:

$$\sigma_f = \frac{3FL}{2bt^2} \quad (1)$$

where σ_f is the maximum stress in the outer fibers at midpoint, F is the maximum load of the load-deflection curve, b is the width of the specimen, t is the thickness of the specimen and L is the support span. The flexural elastic modulus was evaluated as the ratio, within the elastic limit, of stress to corresponding strain.

Results and Discussions

The machining operation of virgin CFRP samples produced chips of different sizes. In detail, the results after sieving are reported in Table 1 and in Fig. 1 are showed typical chip images for each sieving size.

Table 1. Size dimension distribution of CFRP chips obtained after the machining operation.

	Chip size <0.1 mm	**Chip size >0.1 mm**	**Chip size >0.3 mm**	**Chip size >1.5 mm**
Weight content [%]	3.49	20.96	40.98	34.57

In Fig. 2 is instead reported the results of the bending tests. The flexural stress-strain curves can give precious indication about the mechanical properties of the recycled samples in terms of interfacial adhesion efficiency between the surface of the recovered fibers and the new epoxy matrix. In detail, it was observed that for samples produced by using recycled materials with a mean size smaller than 0.1 mm the results were not affected by the reinforcement weight content.

Then, for a better readability of the results, in Fig. 2 it is plotted only one stress-strain curve for representing this sample category.

The results showed that all reinforced samples are characterized by a linear elastic response with a reduction of the strain at breaking in comparison with the reference sample type (pure epoxy sample); this difference decreases as the reinforcement content increases.

Looking at both Fig. 2a and 2b it is clear that the sample reinforced with rCF smaller than 0.1 mm showed the worst performances and despite a flexural modulus improvement respect to reference sample (around 40%) an evident reduction of both the strain at breaking and the flexural strength was detected. The reduction of the flexural strength is due to the small size of the reinforcement phase that acted more as defect than as reinforce, in addition it barely can stop the propagation of internal cracks nucleated in proximity of possible porosity within the sample.

Differently, when the reinforcement phase was represented by rCF chips with a mean size greater than 0.1 mm both the flexural strength and modulus were higher than those of the reference sample and they increase as the rCF chips weight content increases. In detail an increasing of about +46% of the flexural strength was detected when 25 wt.% of rCF chips was adopted.

In spite of this interesting results, it has to be considered that the mechanical properties achieved following this method do not allow the use of this recycled composite for structural applications where high performance are required. This is due to two main reasons: (i) the obtained rCF are short fiber, then the properties cannot reach those of long fibers and (ii) the mechanical recycled fibers are characterized by the presence of matrix residues on their surface and this involves a reduced adhesion efficiency between the recovered fibers and the new resin. By way of example, in Fig. 3 it is showed a magnification of a rCF chip where it is evident the presence of residual matrix on its external surface.

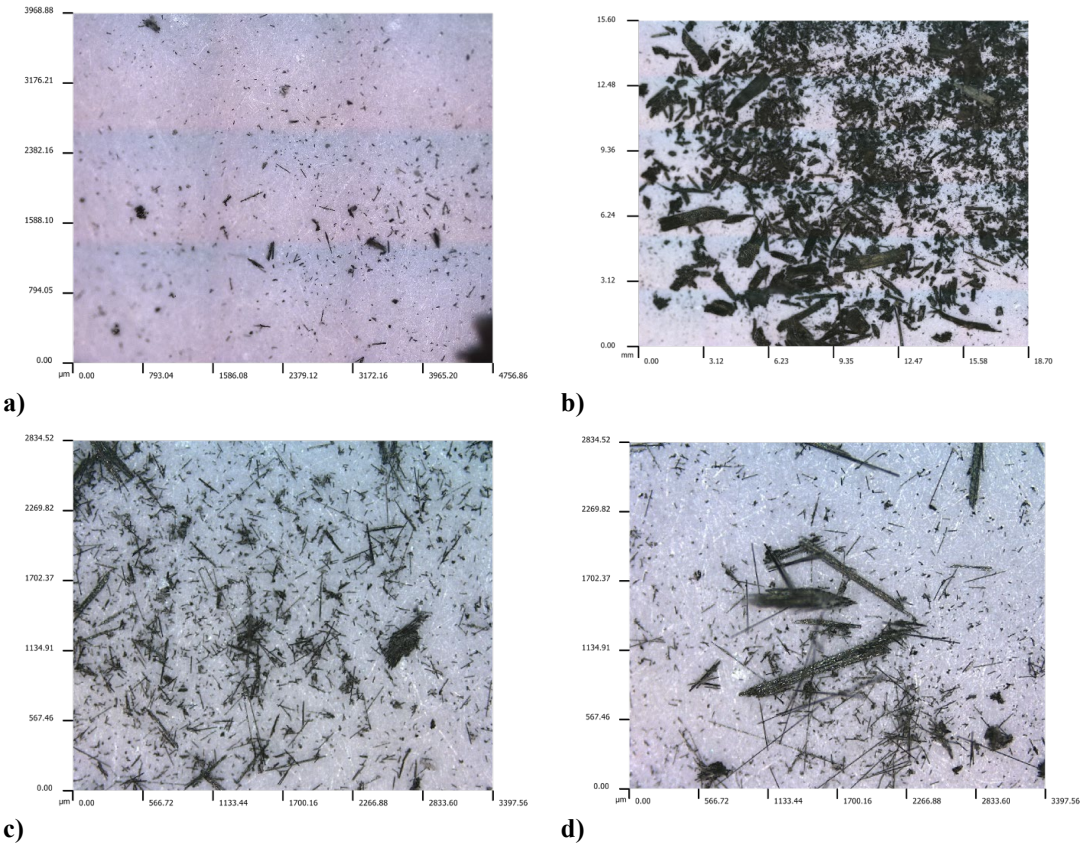

Fig. 1. Typical chips obtained after the milling process: size dimension <0.1 mm (a), size dimension >0.1 mm (b), size dimension >0.3 mm (c), size dimension >1.5 mm (d).

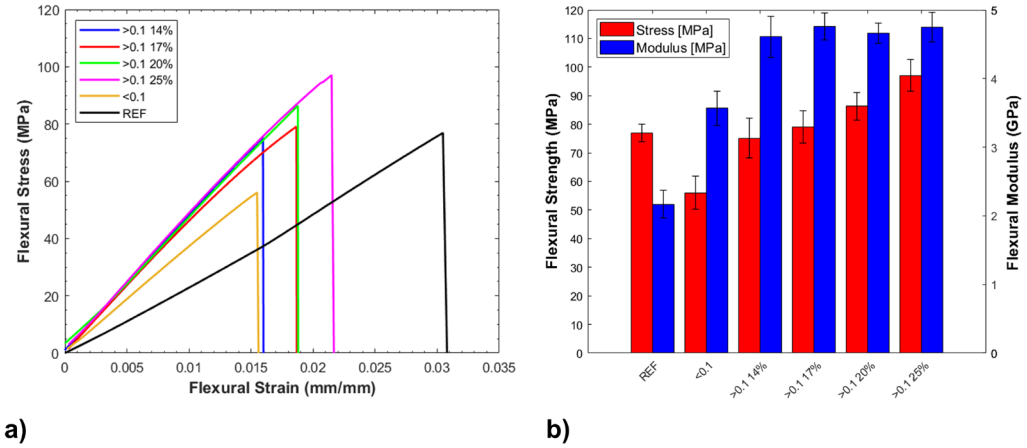

Fig. 2. Typical stress-strain curves (a) and mean flexural strength and modulus (b) for each sample category.

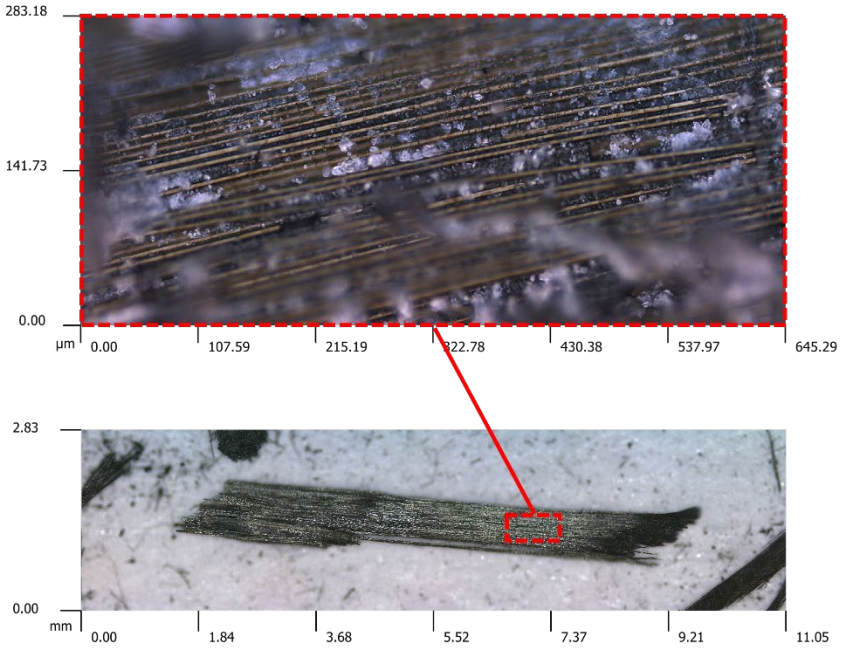

Fig. 3. Details of a rCF chip with the presence of residual matrix on its surface.

Summary

In this work it was presented a preliminary study on the use of a milling process to obtain rCF chip usable as reinforcement for the production of recycled CFRPs. The results showed that the flexural properties were affected by the rCF chip size, in particular the use of the smallest one (mean size < 0.1 mm) did not involve any advantages, contrary to what obtained when greater rCF chips were adopted. Indeed, the use of rCF chips with a mean size greater than 0.1 mm allowed the production of recycled CFRPs characterized by a flexural strength 46 % higher respect to pure epoxy sample. The results showed that according to the proposed procedure, it is possible to use the recycled carbon fibres as reinforcement of the epoxy resin reaching a flexural strength of around 100 MPa and a flexural modulus of around 115 GPa.

It is also important to note that after sieving, it was highlighted that only 3.9 wt.% of the rCF chips was comprised of those with a mean size smaller than 0.1 mm. This means that the proposed recycling procedure is characterized by a high efficiency since the 87.1 % of the obtained waste can be successfully reutilized to produce recycled CFRPs.

References

[1] F. Pinto, L. Boccarusso, D. De Fazio, S. Cuomo, M. Durante, M. Meo, Carbon/hemp bio-hybrid composites: Effects of the stacking sequence on flexural, damping and impact properties, Compos. Struct. 242 (2020) 112148. https://doi.org/10.1016/j.compstruct.2020.112148

[2] L. Lin, A.K. Schlarb, Recycled carbon fibers as reinforcements for hybrid PEEK composites with excellent friction and wear performance, Wear. 432-433 (2019) 202928. https://doi.org/10.1016/j.wear.2019.202928

[3] D. He, V.K. Soo, H.C. Kim, P. Compston, M. Doolan, Comparative life cycle energy analysis of carbon fibre pre-processing, processing and post-processing recycling methods, Resour. Conserv. Recycl. 158 (2020) 104794. https://doi.org/10.1016/j.resconrec.2020.104794

[4] R. Grzanka, The greening of carbon fibre, Reinf. Plast. 58 (2014) 44-46. https://doi.org/10.1016/S0034-3617(14)70143-2

[5] F. Meng, E.A. Olivetti, Y. Zhao, J.C. Chang, S.J. Pickering, J. McKechnie, Comparing Life Cycle Energy and Global Warming Potential of Carbon Fiber Composite Recycling Technologies

and Waste Management Options, ACS Sustain. Chem. Eng. 6 (2018) 9854-9865. https://doi.org/10.1021/acssuschemeng.8b01026
[6] S.R. Naqvi, H.M. Prabhakara, E.A. Bramer, W. Dierkes, R. Akkerman, G. Brem, A critical review on recycling of end-of-life carbon fibre/glass fibre reinforced composites waste using pyrolysis towards a circular economy, Resour. Conserv. Recycl. 136 (2018) 118-129. https://doi.org/10.1016/j.resconrec.2018.04.013
[7] V.P. McConnell, Launching the carbon fibre recycling industry, Reinf. Plast. 54 (2010) 33-37. https://doi.org/10.1016/S0034-3617(10)70063-1
[8] T. Liu, L. Shao, B. Zhao, Y.C. Chang, J. Zhang, Progress in Chemical Recycling of Carbon Fiber Reinforced Epoxy Composites, Macromol. Rapid. Commun. 43 (2022) 2200538. https://doi.org/10.1002/marc.202200538
[9] L. Stieven Montagna, G. Ferreira de Melo Morgado, A.P. Lemes, F. Roberto Passador, M. Cerqueira Rezende, Recycling of carbon fiber-reinforced thermoplastic and thermoset composites: A review, J. Thermoplast. Compos. Mater. 0 (2022). https://doi.org/10.1177/08927057221108912
[10] G.A. Vincent, T.A. de Bruijn, S. Wijskamp, M.I. Abdul Rasheed, M. van Drongelen, R. Akkerman, Shredding and sieving thermoplastic composite scrap: Method development and analyses of the fibre length distributions, Compos. Part. B Eng. 176 (2019) 107197. https://doi.org/10.1016/j.compositesb.2019.107197
[11] G. Colucci, O. Ostrovskaya, A. Frache, B. Martorana, C. Badini, The effect of mechanical recycling on the microstructure and properties of PA66 composites reinforced with carbon fibers, J. Appl. Polym. Sci. 132 (2015) 42275. https://doi.org/10.1002/app.42275

Materials Research Proceedings 28 (2023) 1689-1696 https://doi.org/10.21741/9781644902479-182

Consolidation behaviour of particle reinforced aluminium-matrix powders with up to 50 vol.% SiC_p

SPETH Marco[1,a *], RIEDMÜLLER Kim Rouven[1,b] and LIEWALD Mathias[1,c]

[1]Institute for Metal Forming Technology (IFU), University of Stuttgart, Holzgartenstraße 17, 70174 Stuttgart, Germany

[a]marco.speth@ifu.uni-stuttgart.de, [b]kim.riedmueller@ifu.uni-stuttgart.de, [c]mathias.liewald@ifu.uni-stuttgart.de

Keywords: Metal Matrix Composites (MMC), Compressibility, Powder Pressing

Abstract. Aluminium-matrix composites (AMC) are produced in order to improve specific properties (e.g. mechanical, thermal or tribological) of the matrix alloy using discontinuous reinforcements like fibres or particles. If functional requirements of application specific components such as brake discs have to be met, reinforcement contents of more than 35 % may be required. Therefore, a new manufacturing route is currently being investigated at the Institute for Metal Forming Technology (IFU) of the University of Stuttgart, combining powder pressing with subsequent semi-solid forming to obtain near-net-shape components. A key challenge of this process route includes compacting the green bodies. In this contribution, therefore, powder pressing of AlSi7Mg0.6 and SiC_p powders with up to 50 vol.% SiC_p are investigated in order to gain a deeper understanding of the compacting behaviour of powder with particularly high reinforcement contents. During the investigations, homogenously mixed powders were consolidated to a cylindrical green body by uniaxial powder pressing in order to determine the compressibility of different AMC powder mixtures. At first, the influence of the consolidation pressure onto the reached density was analysed, resulting in compressibility curves as well as process limits for different amounts of reinforcement particles. Subsequently, the influence of particle size onto the achieved density as well as consolidation behaviour could be identified. Furthermore, the high tool wear due to the abrasive behaviour of the reinforcement is quantified in this paper.

Introduction

In comparison to monolithic aluminium alloys, aluminium-matrix composites (AMC) exhibit advanced properties such as increased stiffness, wear resistance, specific strength and vibration damping as well as a decreased coefficient of thermal expansion [1]. However, manufacturing of particle reinforced AMC still is facing technological problems in terms of relatively high processing costs and prevailing production difficulties, which are in the focus of different current research activities [1-3]. Manufacturing processes of AMC investigated in this context in general can be divided into liquid, semi-solid and solid routes. In liquid process routes, the matrix alloy is melted, while solid reinforcement particles are distributed in the melt. This can adversely affect its castability, thus leading to porosity [4] and agglomeration [5] within the final component´s volume. The particle reinforcement content achievable with liquid process routes is therefore up to now limited to 30 vol.% in most cases [6]. In contrast, in the semi-solid (e.g. [7]) and solid (e.g. [8]) process routes, both matrix and reinforcement are solid powders. Therefore, a consolidation step is required in these process routes to produce green bodies for further manufacturing steps. Several approaches can be used for this consolidation respectively cold or hot isostatic pressing, cold uniaxial pressing or direct pressure sintering. For the solid process route, a sinter [1], sinterforging [9] or extrusion [10] step can subsequently be used in order to bond as well as further consolidate the green bodies into the final shape for solid forming. Current investigations in the

Content from this work may be used under the terms of the Creative Commons Attribution 3.0 license. Any further distribution of this work must maintain attribution to the author(s) and the title of the work, journal citation and DOI. Published under license by Materials Research Forum LLC.

field of reinforced aluminium powder mixtures show the influence of size ratio, volume ratio between reinforcement and matrix alloy particles up to 30 vol.%. Hafizpour and Simchi displayed that a size ratio of 1:1 is recommended, especially for higher amounts of reinforcements, in order to reach a high density [3]. O'Donnell and Looney investigated the influence of lubrication onto the consolidation process using insert wall lubrication or mixed-in lubrication, showing no noticeable effects on the sintered specimens [1].

At the Institute for Metal Forming Technology of the University of Stuttgart (IFU), semi-solid routes were initially investigated in terms of producing continuous fibre-reinforced aluminium alloys [11]. Further investigations resulted in the manufacturing of a metallic end connection for pultruded fiber composite tensile rods, which were forged into a metallic end connection [12]. First investigations of particle reinforced AMC were produced by a process route combining direct pressure sintering with subsequent semi-solid forming, resulting in promising material properties as well as complex near-net shape components [2]. However, the direct pressure sintering step should be avoided in order to reduce energy costs. Therefore, a novel process route is currently investigated combining cold uniaxial compression with subsequent semi-solid forming. Thereby, particular focus is now being placed on the forming of AMC with particle loadings higher than 30 vol.% silicon carbide (SiC_p). Currently, no investigations of the compaction behavior of powders with SiC_p reinforcement higher than 30 vol.% were made, while for this novel process route further understanding of the compaction behavior is needed.

The present paper deals with the first step of the novel semi-solid process route and thus with the cold uniaxial compression of aluminium alloy powder with silicon carbide powder (SiC_p). Here, special attention is paid to the production of green bodies with as homogenous as possible particle and density distribution in the green body volume. In this paper the influence of two different composite particle sizes of the powder as well as of compression insert wall lubrication onto the consolidation behaviour is studied.

Materials and Methods

For the investigations of different AMC powder mixtures on the consolidation behaviour, two different particle sizes having a mean particle diameter of 250 µm and 63 µm respectively were analysed. For the matrix aluminium alloy (AlSi7Mg0.6), produced by Ecka Granules GmbH, Germany, nitrogen gas atomized powder with a nearly globular shape was used (Fig. 1a). During production of gas atomized powders larger particle sizes are undesirably produced, due to overspray. This normally would lead to a recycling of those larger particles, since established additive manufacturing routes commonly use particle sizes smaller than 63 µm. To utilize those larger particles for the production of green bodies, a powder particle size having a mean diameter of 250 µm was used. However, a conventional particle size for AM with a mean diameter of 63 µm was investigated as well. Commercially available SiC_p particles having an angular shape, as seen in Fig. 1b, were utilised as reinforcement particles. Dry mixing of both powders (size ratio 1:1) with a particle loading of 30, 40 and 50 vol.% SiC_P was performed by a turbular mixer. With a mixing speed of 20 min^{-1} and 15 min mixing time, a homogenous mixture of both powders could be guaranteed for all powder mixtures. The homogeneity was proven by an image analysis of the different volume fractions based on finite body tessellation and the coefficient of variance (COV) [13].

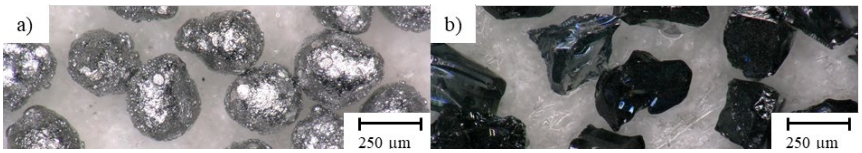

Fig. 1. a) Nitrogen gas atomized aluminium powder b) SiC powder (mean diameter 250 µm).

The tool used for the consolidation tests was designed with a movable compression insert mounted on four springs in order to ensure a two-sided uniaxial compression (Fig. 2). The insert diameter was 56 mm having a g6 fit, while the punches were processed to a H7 fit. The upper and lower punch was attached to a loading cell for measuring the press forces during consolidation. Contact faces of the punches to the workpiece were designed to be changeable due to the expected high abrasive wear by the SiC_p. This was achieved by using changeable punch-chips, which were mounted via a ball catch for a quick changeover. A hydraulic press was used to consolidate the green bodies with different press ram forces. Maximum force of the press is 2000 kN having a maximum stroke of 800 mm with a constant ram speed of 10 mm/s.

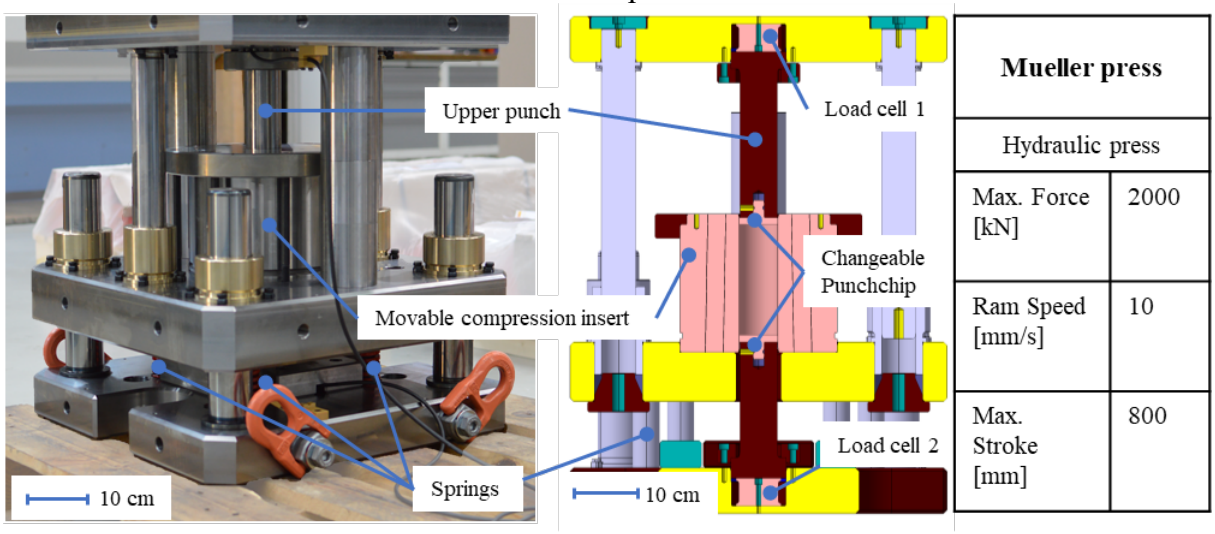

Mueller press	
Hydraulic press	
Max. Force [kN]	2000
Ram Speed [mm/s]	10
Max. Stroke [mm]	800

Fig. 2. Compacting tool and specification of hydraulic press used.

During the consolidation tests, mixed powders all having a size ratio of 1:1 (mean particle diameter of both powders) were compacted using pressures of 300, 450 and 600 MPa respectively (see Table 1). The coarser (F 60) powder was additionally compacted using a hydraulic press at a pressure of 1000 MPa, in order to determine the maximum force that can be applied without defects in the green body for this coarse size. In conventional powder metallurgic process routes often, lubrication is added to the powder mixture. However, for the subsequent semi-solid forming, lubrication is undesirable due to the included remaining lubrication in the final components. The presented experiments were carried out partly without lubricant and partly with molybdenum disulfide (MoS_2). Here, the MoS_2 was only applied to the inner side of the insert and the punch surfaces, aiming to minimize the amount of contamination inside of the green bodies produced. After ejection of the green bodies out of the insert, the green body density was measured using a volumetric approach. Weight measurement was performed on a precision balance with a deviation in measure of 0.001 g, while for dimensional measurement a micrometer with 0.01 mm deviation was used. For all experimental parameter combinations, three green bodies were produced and the mean deviation was used to compare the results in an objective manner.

Table 1. Experimental parameters used.

Experimental parameters				
Powder particle size [µm]	F 60 (250 – 400 µm)		F 220 (40 – 63 µm)	
SiC-Fraction [vol.%]	30	40	50	
Compaction pressure [MPa]	300	450	600	1000 (only F60)
Lubrication	None		Molykote (MoS_2)	

Results and Discussion

At first the obtained results of the unlubricated consolidation experiments are presented. The mixtures of powders with the larger particle size (F 60) could be pressed at all compaction pressure levels to unlubricated green bodies having relative densities dependent on the pressure value. The resulting compressibility curves are shown for all three investigated proportions of SiC-particles in Fig. 3. Thereby, the relative density was calculated from the reached density (volumetric approach) compared to the ideal density of the composite of each respective powder mixture. Lower particle loadings of 30 vol.% SiC_p showed the highest reached density for all pressure values. The reason for this is that the aluminium matrix is plastically deformed during densification, while the harder SiC_p particles are only elastically deformed. At the beginning of the densification a particle rearrangement occurs, as the pressure further increases the plastic deformation and thus the particle deformation of the aluminium particle begins. Elastic deformation of the SiC_p leads to a reduction of the plastic deformation and hence an insufficient bonding strength between the aluminium particles. Given by the uniaxial compression with a movable compression insert, the area of the lowest density is in the middle of the green body. If the plastic deformation is insufficient, a delamination plane appears in the green body, consisting of nearly non-compacted powder with low cohesion. Green bodies having a density below the depicted red line indicating a relative density of 77 % in fact showed such behavior with an insufficient densification. In general, a higher portion of reinforcement amount increases the absorbed elastic pressure and further limits the densification. Green bodies with 50 vol.% SiC_p showed on average a 4% lower relative density compared to green bodies with only 30 vol.% SiC_p. Maximum reached densities were 91.86 % (30 vol.%), 89.51 % (40 vol.%) and 87.69 % (50 vol.%). During ejection, abrasive wear of the insert as well as the punch-chips appeared, while with higher compaction pressure a higher ejection force as well as a higher wear behavior was determined.

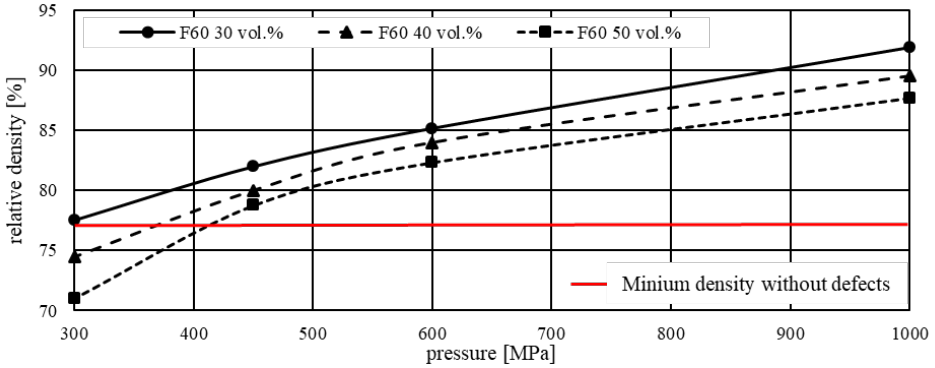

Fig. 3. Compressibility curve of the larger powder mixture without lubrication.

The finer powder of F220 could not be compacted without lubrication, since delamination and shear fractures occurred during ejection, as seen in Fig. 4 (1.). The reason for this is, on the one hand, that smaller aluminium particles have lower limiting strains, reducing the deformation ratio. On the other hand, particle rearrangement of the finer particles represents the dominant mechanism of densification as investigated by [3]. Another reason constitutes the higher friction between insert wall and powder mixture, which lead to sticking effects during ejection. Furthermore, the higher inner friction within the powder leads to a reduced deformation ratio, due to reduced force transmission. This promotes delamination and increases the density gradient inside of the green body, having areas of almost no compaction in the middle plane and highly compacted areas in the contact zones with both punches. Increasing the pressure up to 600 MPa shear cracks appear and the green body additionally cracks during ejection. Thus, the maximum pressure applied was reduced to 600 MPa for the following experiments.

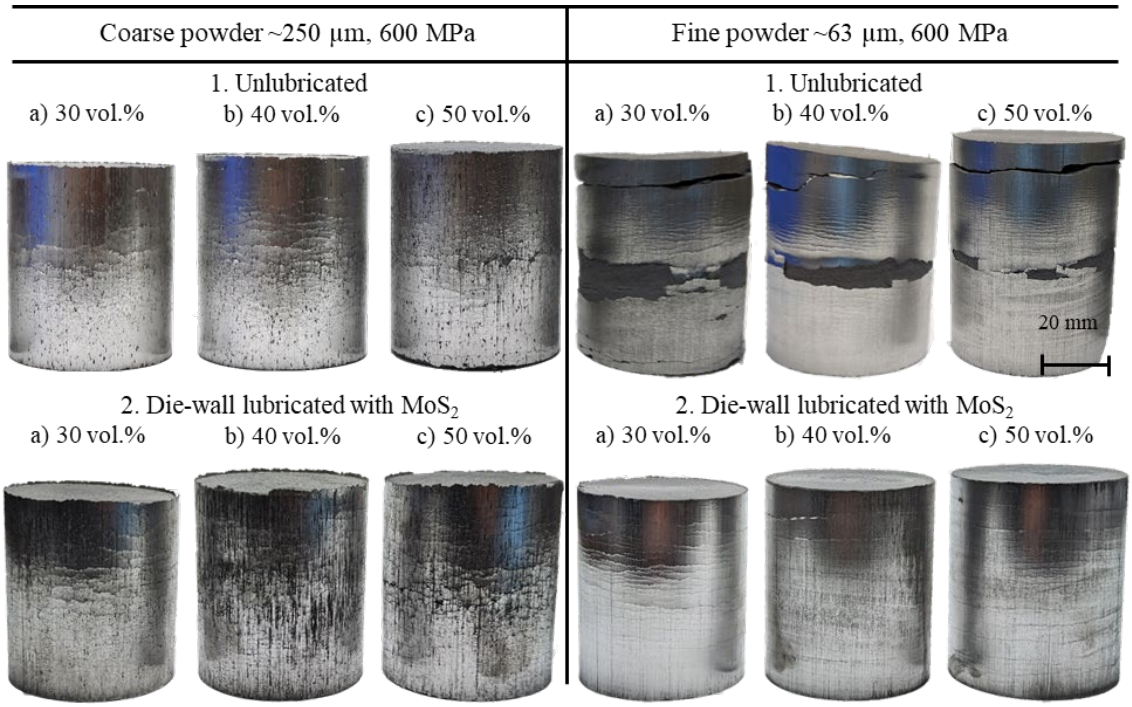

Fig. 4. Produced green billets with a constant pressure of 600 MPa, 1) Unlubricated 2) Insert-wall lubrication.

Compaction with a sprayed insert-wall lubrication, containing MoS_2, at 600 MPa achieved delamination-free green bodies for both the fine as well as the coarse powder mixtures (see Fig. 4 (2.). In the following, the resulting densities obtained from the compression experiments using insert wall lubrication (MoS_2) are presented in Fig. 5. The trend towards lower densities at higher particle loadings could be confirmed for both particle sizes and resulted from the higher amount of elastic energy absorbed by the SiC_p. Compared to the unlubricated densities of F60 particle size, an improvement in compressibility of approximately 2 % could be observed. Again, the lowest pressure of 300 MPa resulted in insufficient compaction for particle loadings of 40 and 50 vol.% as indicated by the red line in Fig. 5.

In conclusion, the fine powder showed a reduced compressibility compared to the coarser powder after consolidation. As already shown by the results of the unlubricated experiments, one reason for this is the friction between insert wall and powder, which is principally higher with fine than with coarser powder. As a consequence, higher friction results in lower consolidation

pressures during densification. In this respect, the difference between measured force of the upper punch compared to the measured force of the lower punch, which corresponds to the friction loss, was 15.2 % higher for fine powder than for coarse powder at 300 MPa. At 450 MPa, the value was 32.0 % higher, and 51.5 % at 600 MPa. Another reason for the lower densification of the finer powder is the inner friction of the powder particles, since the porous structure has more contacts as well as smaller voids in the finer powder mixture.

In addition, the experiments carried out have shown that the limit for the lowest density, at which just sufficient compaction occurs in the middle plane of the green body, in general is nearly the same for fine powder compared to coarser powder. For all three particle loadings and both particle sizes, an insufficient consolidation is reached at densities below 77 % resulting in loose powder in the middle separation plane. Particle loadings of 40 and 50 vol.% SiC_p should be manufactured with pressures of 450 MPa or 600 MPa. Higher pressure than 600 MPa favors shear and delamination cracks without lubrication as well as increases the tool wear during ejection, due to the higher elastic energy absorbed by the SiC. Therefore, higher pressures should only be used for significantly higher required green body densities.

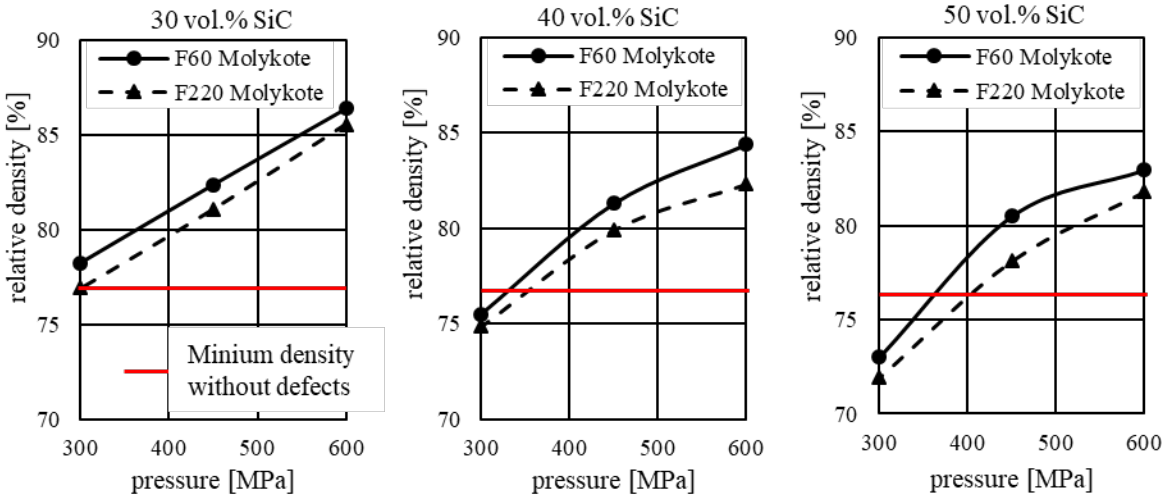

Fig. 5. Compressibility curves for both particle sizes using insert wall lubrication.

Summary

In this paper, the consolidation process of highly reinforced aluminium powders with SiC_p contents up to 50 vol.% were investigated. Thereby, the influence of particle loading and size of the powder mixture on the achieved density of the green bodies to be consolidated was analysed. Subsequently, the compaction parameters regarding compaction pressure as well as lubrication effects onto the produced densities of the green bodies were determined. The main findings are summarized according to the obtained results:

- The coarser powder mixture exhibited a lower wall friction as well as a higher compressibility during compaction, resulting from lower inner friction as well as a high plastic deformation of coarser aluminium particles. In general, it was found for all powder mixtures investigated that the green body must exhibit a density of at least 77 % after consolidation in order to ensure sufficient plastic deformation of the aluminium powder and thus avoid a delamination plane in the middle of the green body.
- Finer powder mixtures showed a higher insert wall friction, especially during the ejection of the green bodies, resulting in shear and delamination fractures. Green bodies without insert wall lubrication could not be compacted. One reason for shear and delamination defects was the higher friction inside the powder. For finer powders the main densification mechanism is particle rearrangement, resulting in high particle to particle contacts as well

as smaller voids inside the green body compared to the green bodies with coarse powder. Thereby, the inner friction reduced the force transmission inside the powder, causing high density gradients inside the green body height and failure of the form-locking bonds.

- Particle loading reduced the achieved density, due to the absorbed elastic energy by the SiC_p for both particle sizes of the powder decreasing the plastic deformation of the aluminium powder. A higher amount of SiC_p results in lower densities of the final green bodies.
- Compaction pressure improved the density achieved for both particle sizes of the powder, which can be attituded to the increased plastic deformation of the aluminium particles and the resulting bonds between the particles.
- Unlubricated experiments using fine powder mixtures resulted in delamination in the middle plane of the green bodies as well as shear cracks near the contact areas of the punches, due to high insert wall friction during compaction as well as during ejection. Insert wall lubrication enabled the manufacturing of green bodies with the finer powders, and reduced the ejection forces acting on the green body. In general, insert wall lubrication improved the achieved densities compared to the unlubricated green bodies by 2 % for the coarser powder mixtures, due to the reduced friction energy absorbed by the insert. Coarser powder reached higher densities compared to the finer powder, resulting from the higher friction energy absorbed by the insert as well as the higher inner friction in the finer powder mixture during compaction.

For future research, the process parameters of lubricated insert wall with a compaction pressure of 600 MPa will be used, as the results showed defect-free green bodies for both particle sizes with sufficient densification. For semi-solid forming of brake disc-shaped components the green bodies will be heated into a semi-solid state and subsequently formed using different process parameters. Thereby, the influence of the process parameters onto the particle distribution of the final component will be further investigated.

Acknowledgement
The authors like to thank German Research Foundation (DFG) for their financial support of the research project (LI1556/72-1) “Manufacturing of application-specific components from particle reinforced aluminium matrix composites using a combination of powder pressing and thixoforging”.

References

[1] G. O’Donnell, L. Looney, Production of aluminium matrix composite components using conventional PM technology, Mater. Sci. Eng. A 303 (2001) 292-301. https://doi.org/10.1016/S0921-5093(00)01942-0

[2] A. Storz, T. Schubert, T. Weissgärber, C. Seyboldt, K.R. Riedmüller, Efficient processing of Metal-Matrix-Composites by combining Direct Pressure Sintering and subsequent Thixoforging, Mater. Sci. Forum 825-826 (2015) 167-175. https://doi.org/10.4028/www.scientific.net/MSF.825-826.167

[3] H.R. Hafizpour, A. Simchi, Investigation on compressibility of Al-SiC composite powders, Powder Metall. 51 (2008) 217-223. https://doi.org/10.1179/174329007X22250

[4] S.N. Ahmad, J. Hashim, M.I. Ghazali, The effects of porosity on mechanical properties of cast discontinuous reinforced metal- matrix composite, J. Compos. Mater. 39 (2005) 451-466. https://doi.org/10.1177/0021998305047096

[5] J. Hashim, L. Looney, M.S.J. Hashmi, Particle distribution in cast metal matrix composites - Part I, J. Mater. Process. Technol. 123 (2002) 251-257. https://doi.org/10.1016/S0924-0136(02)00098-5

[6] J. Grilo, V.H. Carneiro, J.C. Teixeira, H. Puga, Manufacturing methodology on casting-based aluminium matrix composites: Systematic review, Metals 11 (2021) 1-30. https://doi.org/10.3390/met11030436
[7] Y. Wu, G.Y. Kim, Compaction behavior of Al6061 and SiC binary powder mixture in the mushy state, J. Mater. Process. Technol. 216 (2015) 484-491. https://doi.org/10.1016/j.jmatprotec.2014.10.003
[8] J. Sun, G. Chen, B. Wang, G. Chen, W. Tang, Fabrication, microstructures, and properties of 50 vol.% SiCp/6061Al Composites via Hot Pressing, J. Mater. Eng. Perform. 28 (2019) 2697-2706. https://doi.org/10.1007/s11665-019-04071-6
[9] M. Balog, P. Krizik, M. Nosko, Z. Hajovska, M.V.C. Riglos, W. Rajner, D.S. Liu, F. Simancik, Forged HITEMAL: Al-based MMCs strengthened with nanometric thick Al2O3 skeleton, Mater. Sci. Eng. A 613 (2014) 82-90. https://doi.org/10.1016/j.msea.2014.06.070
[10] L.A. Dobrzański, A. Włodarczyk, M. Adamiak, The structure and properties of PM composite materials based on EN AW-2124 aluminum alloy reinforced with the BN or Al2O3 ceramic particles, J. Mater. Process. Technol. 175 (2006) 186-191. https://doi.org/10.1016/j.jmatprotec.2005.04.031
[11] K. Siegert, P. Unseld, J. Baur, F. Kauffmann, E. Arzt, K.v. Niessen, Thixoforging of continuous fiber-reinforced AlSi/AlMg-alloys, Int. J. Mach. Tool. Manuf. 46 (2006) 1227-1232. https://doi.org/10.1016/j.ijmachtools.2006.01.037
[12] K.R. Riedmüller, M. Liewald, Material efficient production of complex (hybrid) components using semi solid forming processes, AIP Conf. Proc. 1769 (2016) 030001. https://doi.org/10.1063/1.4963417
[13] X. Deng, N. Chawla, Modeling the effect of particle clustering on the mechanical behavior of SiC particle reinforced Al matrix composites, J. Mater. Sci. 41 (2006) 5731-5734. https://doi.org/10.1007/s10853-006-0100-1

Materials Research Proceedings 28 (2023) 1697-1702 https://doi.org/10.21741/9781644902479-183

A numerical approach to optimize the toolpath strategy for polymers forming

FORMISANO Antonio[1,a *], DURANTE Massimo[1,b], BOCCARUSSO Luca[1,c] and MEMOLA CAPECE Fabrizio[1,d]

[1]Department of Chemical, Materials and Production Engineering, University of Naples Federico II, P.le V. Tecchio 80, 80125 Napoli, Italy

[a]aformisa@unina.it, [b]mdurante@unina.it, [c]luca.boccarusso@unina.it, [d]capece@unina.it

Keywords: Incremental Sheet Forming, Polymers, FE Analysis, Toolpath Strategy

Abstract. Incremental sheet forming is a relatively new technology with a deformation strategy that resembles the layered manufacturing principle of rapid prototyping; thanks to this, it can represent a viable way to form metal and polymer sheets, guaranteeing high customization and cost-effectiveness. On the other hand, and particularly when considering thermoplastic sheets, the components obtained by this process suffer from peculiar defects like, for example, twisting and wrinkling. A way of reducing the risk of such defects is to optimize the toolpath strategy to lower in-plane forming forces. To pursue this aim, the present work follows a numerical approach; a commercial FE code was used to simulate the incremental forming of polycarbonate sheets by varying the toolpath strategy. The investigation of some features like the forming forces and the deformation states was carried out, with the goal of determining an optimized toolpath strategy for the reduction of the incremental forming forces and the consequent expectation of reduced risk of failures and defects for incremental formed polymer sheets.

Introduction

The interest in the incremental sheet forming (ISF) of thermoplastic polymers has been experiencing a significant increase over the past few years since these important materials can be engineered to reach high specific strength and stiffness values, and the ISF technology guarantees high customization. The products manufactured with this process can cover many fields of application; for example, they are largely considered for aerospace and unmanned aerial vehicles, so as for racing and commercial cars [1], and several applications have been also found in the biomedical sector [2].

When formed by ISF, the polymer sheets (but not only) can suffer from failures and undesired deformation phenomena like, for example, twisting and wrinkling. The first one occurs as the effect of an uncontrolled twist of the sheets with respect to the clamping frame and it is caused by the in-plane shear that, in turn, is generated by the tangential component of the forming forces. The authors, in previous works, observed and quantified this phenomenon both for metal [3] and polycarbonate sheets [4], and the last ones, in the case of axisymmetric components obtained by a unidirectional toolpath, showed very high twisting angles (about 22°) if compared to the corresponding ones on metal sheets (less than 6°). On the other hand, they also observed a dramatic reduction of the twisting angle when adopting an alternate toolpath. All the same, severe forming conditions in terms of sliding forces on thin sheets of not particularly resistant materials like thermoplastics can determine the occurrence of wrinkling [5].

However, the attempt to reduce the sliding forces between the tool and the sheet can also be made for further different aims like, for example, to limit the global forming forces, to reduce the risk of failures of the forming tool and of the sheets, and to improve the surface quality of the incrementally formed parts; in addition, it could be possible to reduce the use of lubricants employed to lower friction and sticking of material to the tool.

Content from this work may be used under the terms of the Creative Commons Attribution 3.0 license. Any further distribution of this work must maintain attribution to the author(s) and the title of the work, journal citation and DOI. Published under license by Materials Research Forum LLC.

Materials Research Proceedings 28 (2023) 1697-1702 https://doi.org/10.21741/9781644902479-183

Considering the above, this work aims to follow a numerical approach for the optimization of the toolpath strategy applied to the incremental forming of polycarbonate sheets, to reduce the forming forces and, with it, reduce the risk of failures and defects. To do this, the manufacture of cone frusta with fixed wall angle by varying the toolpath strategy was simulated by a commercial FE code; from the results of the simulations, some outputs were investigated, like the forming forces and the stress-strain states.

Materials and Methods

The manufacture of cone frusta with a fixed wall angle was simulated by means of the FE commercial code LS DYNA; the goodness-of-fit of the numerical model was evaluated in a previous authors' work [6] on the occurrence of wrinkling when thin polycarbonate sheets were worked by incremental forming.

Polycarbonate sheets with a thickness of 1.5 mm were considered; besides, the forming tool had a hemispherical head, 10 mm in diameter. The main geometrical features of the cone frusta are highlighted in Fig. 1; in particular, α represents the wall angle, h the height and R the radius of the major base.

The sheet and the tool (only its hemispherical head) were modeled, whereas the effects of the blank holder were simulated by setting fixed constraints to the nodes of the sheet periphery (a square of 100 mm × 100 mm in dimensions).

The elements of the sheet are fully integrated shells with five integration points through the thickness and a mean dimension of 1.41 mm. The material model was the MAT PLASTICITY POLYMER. For the tool head, Belytschko-Tsay shell elements with two integration points through the thickness and a mean dimension of 0.2 mm were used, while the MAT RIGID model was chosen, setting typical properties of the steel.

The main materials' properties are summarized in Table 1.

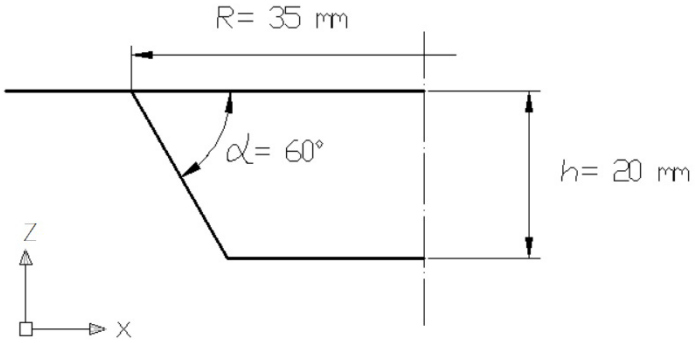

Fig. 1. Geometrical features of the cone frusta.

Table 1. Main materials' properties.

Material	Density [g/cm^3]	Young's modulus [GPa]	Poisson's ratio [-]	Yield stress [MPa]	Ultimate elongation [%]
Polycarbonate (sheet)	1.2	2.3	0.3	60	110
Steel (tool)	7.85	210	0.3	-	-

Materials Research Proceedings 28 (2023) 1697-1702 https://doi.org/10.21741/9781644902479-183

The SURFACE TO SURFACE contact card was selected for the tool/sheet interaction (consider that for this kind of test the sheets can be lubricated with mineral oil for cold forming to reduce friction and sticking of material to the tool and then, to avoid the risk of damages) and x, y, and z displacement laws were set in the BOUNDARY PRESCRIBED MOTION card to impose the tool movement (feed rate of the forming tool V_f=1000 mm/min).

Finally, the run time of the simulations was notably decreased, using mass scaling [3].

Different paths of the forming tool were considered to impress the deformation to the sheet with which comes in contact on points of a spiral path; in particular, the points were equally spaced around θ=6° from each other and the vertical step (*vs*, the vertical distance between two consecutive spirals) was equal to 1 mm (see Fig. 2; five exemplary consecutive points, from A to E, are reported).

Three solutions, reported in a not-to-scale schematization in Fig. 3, were chosen to cover the distance between two consecutive points: in particular, describing:

- one segment;
- a horizontal and a vertical segment;
- an upward (where H_r represents the ramp height) and a vertical segment.

These three typologies are labeled std_tp (standard toolpath), Hr0_tp and Hr1_tp, respectively.

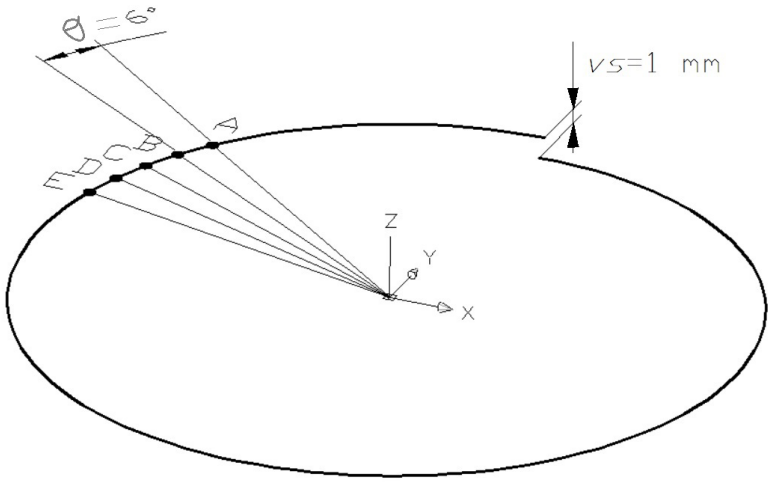

Fig. 2. Details of the spiral path.

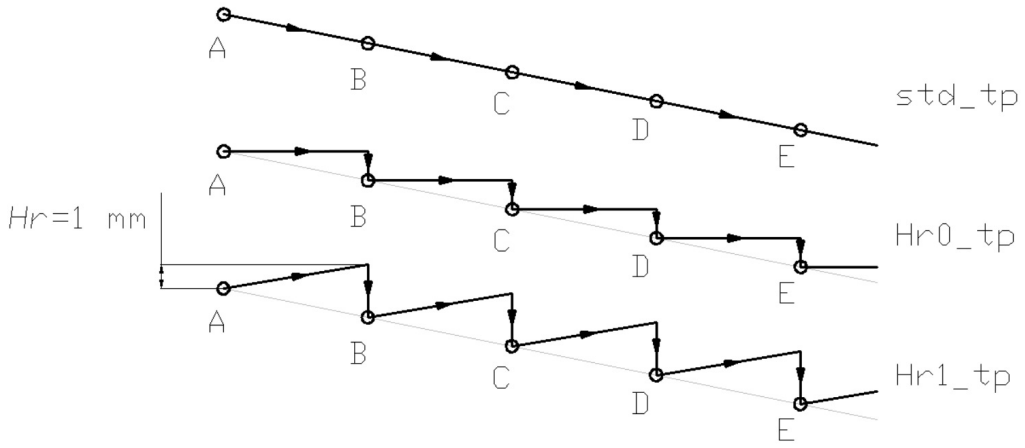

Fig. 3. Toolpath strategies.

Materials Research Proceedings 28 (2023) 1697-1702 https://doi.org/10.21741/9781644902479-183

Results

Fig. 4 shows an example of FE simulation of the ISF process for the Hr1_tp strategy; in particular, it is possible to observe the deformed sheet and the tool head for a z displacement of about 15 mm.

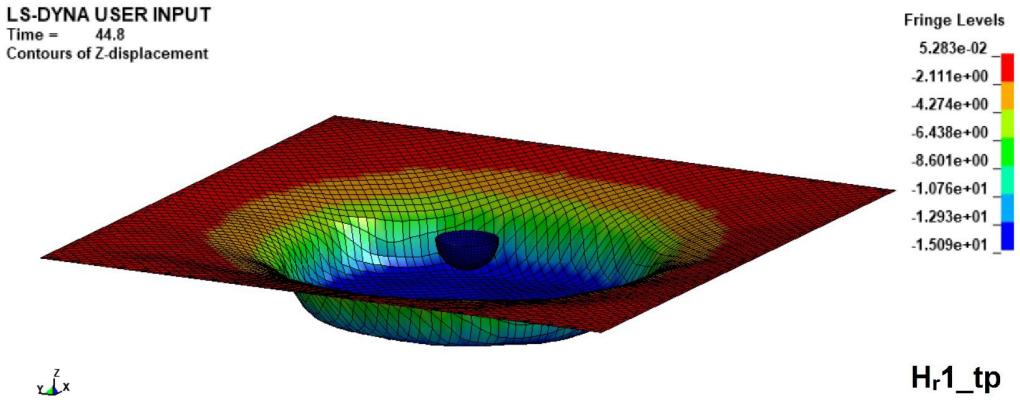

Fig. 4. FE simulation of the ISF process for the Hr1_tp strategy.

Fig. 5 reports the trend of the vertical (F_Z) and of one only horizontal force (F_X) for the different toolpath strategies. It is possible to note that the forces for the first two strategies show the typical trend for the manufacture of cone frusta by ISF with a spiral toolpath [5,7].

Moreover, they are similar, with very slightly lower values for the Hr0_tp compared to the std_tp; in detail, the maximum values of F_Z and F_X (in absolute terms) are of about 400 N and 300 N. This behaviour is an effect of the elastic springback that, despite being lower for the second toolpath, determines a significant tool/sheet contact and, consequently, high forming forces [8].

The third strategy allows a very significant reduction of both the components of the forming forces; F_Z lies below 200 N, while the absolute value of F_X does not exceed 50 N

In addition, the reduced regularity of the forces trend is representative of a noncontinuous contact between the tool and the sheet. On the other hand, the forming time for this last strategy increases, passing from about 40 s of the first two strategies to about 55 s, due to the increase of the length of the toolpath.

Moreover, Fig. 6 reports the max shear strain for three consecutive forming steps related to the std_tp and the Hr1_tp strategy. The figure highlights that the std_tp strategy determines strain accumulation on a large area of the sheet and in an asymmetric way, following the tool movement; this is not so true for the Hr1_tp strategy, which shows a more localized deformation and reduced shells distortion.

By considering the results on the forming forces from Fig. 5 and that the twisting is caused by the combination of continued strain accumulation and asymmetric stress levels [9,10], it can be assumed that the twisting can be reduced with the Hr1_tp strategy.

Finally, despite not being capable of predicting accurately wrinkling (the numerical model does not include wrinkle instability criteria), the results of the simulations let suppose that the occurrence of this defect is less likely for the Hr1_tp strategy.

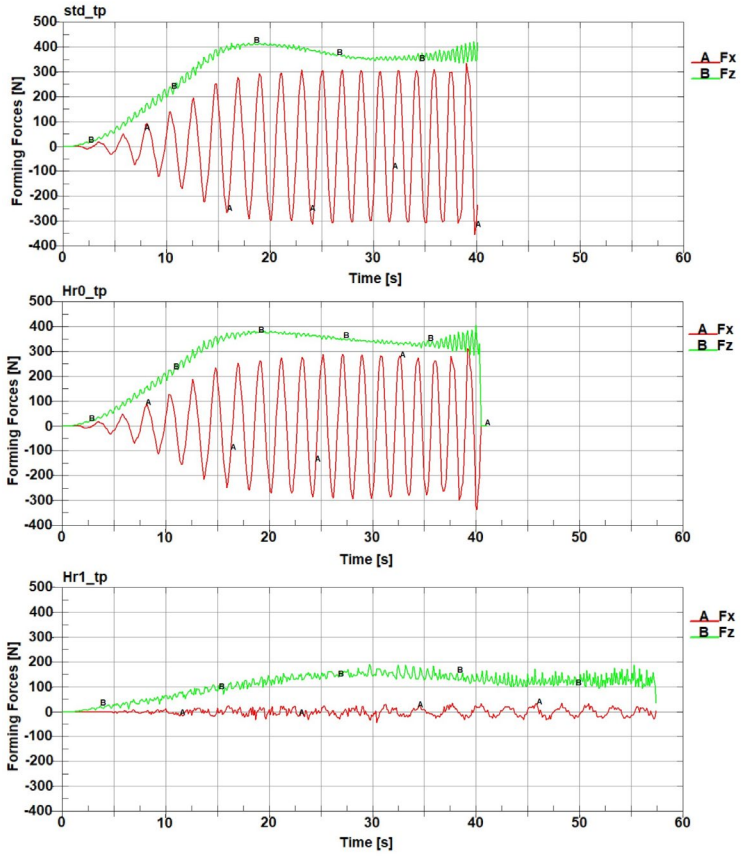

Fig. 5. Trend of the forming forces by varying the toolpath strategy.

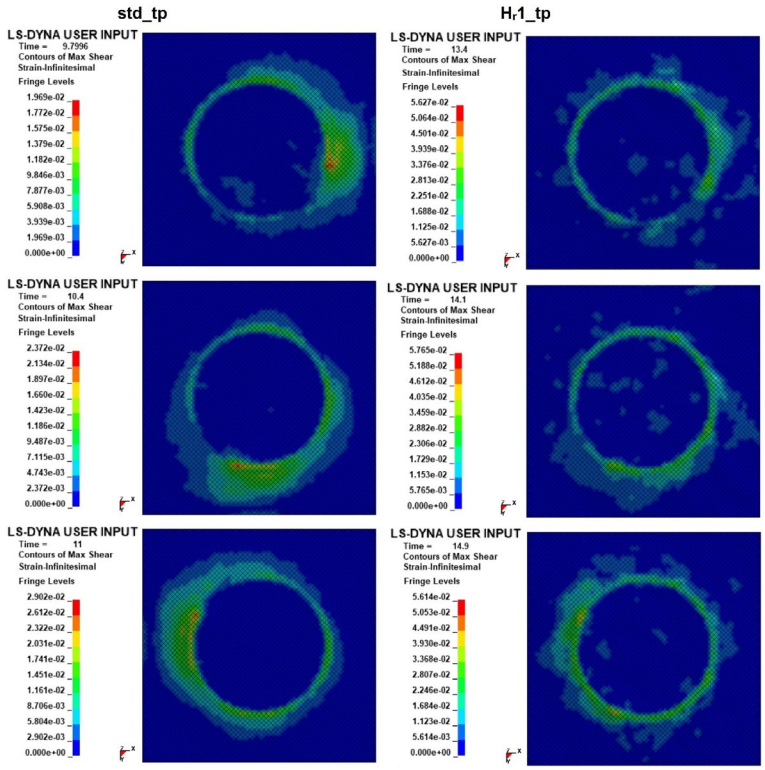

Fig. 6. Max shear strain distribution for std_tp and H_r1_tp strategy.

Summary

In the present work, a commercial FE code was used for the simulation of the incremental sheet forming of polycarbonate, with the aim of investigating different toolpath strategies. From the analysis of the results in terms of forces and strain states, it can be concluded that a stepped path, constituted by a sequence of upward and vertical segments, while showing higher forming times, can reduce drastically both the vertical and the in-plane forming forces, as well as the severity of the deformation states. Consequently, this may involve reduced risk of failures and defects like twisting and wrinkling.

Future works can focus on extending the numerical investigation by considering, for example, different forming tool shapes, and carrying out an experimental campaign for estimating what expected from the numerical analyses, in particular the reduction of the forming forces and of the twisting defect.

References

[1] M. Hassan, G. Hussain, H. Wei, A. Qadeer, M. Alkahtani, Progress on Single-Point Incremental Forming of Polymers, Int. J. Adv. Manuf. Technol. 114 (2021) 1-26. https://doi.org/10.1007/S00170-021-06620-7

[2] G. Centeno, I. Bagudanch, D. Morales-Palma, M.L. García-Romeu, B. Gonzalez-Perez-Somarriba, A.J. Martinez-Donaire, L.M. Gonzalez-Perez, C. Vallellano, Recent Approaches for the Manufacturing of Polymeric Cranial Prostheses by Incremental Sheet Forming, Procedia Eng. 183 (2017) 180-187. https://doi.org/10.1016/J.PROENG.2017.04.059

[3] A. Formisano, L. Boccarusso, F. Capece Minutolo, L. Carrino, M Durante, A. Langella, Negative and Positive Incremental Forming: Comparison by Geometrical, Experimental and FEM Considerations, Mater. Manuf. Process. 32 (2017) 530-536. https://doi.org/10.1080/10426914.2016.1232810

[4] M. Durante, A. Formisano, F. Lambiase, Incremental Forming of Polycarbonate Sheets, J. Mater. Process. Technol. 253 (2018) 57-63. http://doi.org/10.1016/j.jmatprotec.2017.11.005

[5] M. Durante, A. Formisano, F. Lambiase, Formability of Polycarbonate Sheets in Single-Point Incremental Forming, Int. J. Adv. Manuf. Technol. 102 (2019) 2049-2062. https://doi.org/10.1007/s00170-019-03298-w

[6] A. Formisano, M. Durante, A Numerical-Experimental Investigation on the Wrinkling Defect in Incremental Forming of Thin Polycarbonate Sheets, Int. Rev. Model. Simul. 12 (2019) 206-211. https://doi.org/10.15866/iremos.v12i4.17614

[7] N. Rosca, T. Trzepieciński, V. Oleksik, Minimizing the Forces in the Single Point Incremental Forming Process of Polymeric Materials Using Taguchi Design of Experiments and Analysis of Variance, Materials 15 (2022) 6453. https://doi.org/10.3390/ma15186453

[8] H. Wei, L. Zhou, B. Heidarshenas, I.K. Ashraf, C. Han, Investigation on the Influence of Springback on Precision of Symmetric-Cone-Like Parts in Sheet Metal Incremental Forming Process, Int. J. Light. Mater. Manuf. 2 (2019) 140-145. https://doi.org/10.1016/j.ijlmm.2019.05.002

[9] Z. Chang, J. Chen, Mechanism of the Twisting in Incremental Sheet Forming Process, J. Mater. Process. Technol. 276 (2020) 116396. https://doi.org/10.1016/j.jmatprotec.2019.116396

[10] J.R. Duflou, H. Vanhove, J. Verbert, J. Gu, I. Vasilakos, P. Eyckens, Twist Revisited: Twist Phenomena in Single Point Incremental Forming, CIRP Ann. Manuf. Technol. 59 (2010) 307-310. https://doi.org/10.1016/j.cirp.2010.03.018

Materials Research Proceedings 28 (2023) 1703-1710 https://doi.org/10.21741/9781644902479-184

Surface topography investigation during nanosecond pulsed laser engraving of SAE304 stainless steel

NIKOLIDAKIS Evangelos[1,a], KARMIRIS-OBRATAŃSKI Panagiotis[2,3,b *], PAPAZOGLOU Emmanouil-Lazaros[3,c], KARKALOS E. Nikolaos[3,d], MARKOPOULOS P. Angelos[3,e] and ANTONIADIS Aristomenis[1,f]

[1]Technical University of Crete, School of Production Engineering & Management, Micromachining & Manufacturing Modeling Laboratory, University campus, Building E4.026-Kounoupidiana, 73100 Chania, Greece

[2]AGH University of Science and Technology, Faculty of Mechanical Engineering and Robotics, Department of Manufacturing Systems, al. Mickiewicza 30, 30-059 Cracow, Poland

[3]National Technical University of Athens, School of Mechanical Engineering, Laboratory of Manufacturing Technology, Heroon Polytechniou 9, 15780, Athens, Greece

[a]krhthkournas@gmail.com, [b]karmiris@agh.edu.pl, [c]mlpapazoglou@gmail.com, [d]nkark@mail.ntua.gr, [e]amark@mail.ntua.gr, [f]aantoniadis@tuc.gr

Keywords: Surface Topography, Laser Engraving, Nanosecond Pulsed Laser, SAE304 Steel

Abstract. Laser engraving process is widely used for various industrial applications, such as the creation of small and complex geometries with ultra-high precision. As surface topography can affect the functionality of produced surfaces in various ways, it is required to carry out comprehensive experimental work in order to correlate the laser engraving process parameters with surface topography characteristics. In the current paper, the surface topography of SAE304 stainless steel specimens in respect to laser power, scanning speed and pulse repetition rate is studied through microscope observations. The findings indicate that the scanning speed is the most dominant parameter regarding surface roughness and from the viewpoint of surface quality, it is suggested that higher scanning speed, lower power and pulse repetition rate values should be employed.

Introduction

Laser machining and laser assisted machining are a rapidly growing non-conventional manufacturing processes class, with lasers becoming gradually more and more significant as part of the modern industrial environment [1]. In general, by the interaction of the material with the laser beam, the material's electrons absorb a proportion of the laser beam energy and become excited [2]. The temperature of the excited electrons sub-system is raised and subsequently the absorbed energy is transferred to the material's atomic lattice, causing it to heat up until its melting and/or ablation. The high energy densities that are employed during laser-based processes provide a number of significant advantages over the conventional machining that include the potential to create small and complex geometries with ultra-high precision, the reduction of the Heat Affected Zone (HAZ), and the deformations due to the thermal and mechanical stress concentration [3]. Laser engraving consists one of the most widely employed laser-based processes.

In laser engraving, the material is removed layer by layer subsequent to the multiple passes of the laser beam over the material surface. Given that usually, in laser engraving, pulsed lasers are utilized, each layer of material is removed by the overlap of the generated craters that are formed due to material ablation [4]. As it was aforementioned, pulsed lasers are most commonly utilized since, although they have lower nominal power, through their pulsed operation extremely high-

Content from this work may be used under the terms of the Creative Commons Attribution 3.0 license. Any further distribution of this work must maintain attribution to the author(s) and the title of the work, journal citation and DOI. Published under license by Materials Research Forum LLC.

power peak and power density can be achieved [5]. In laser engraving, minimum power density of 10^8 W/cm^2 is required and laser pulse durations in the order of nanoseconds are usually utilized. Finally, the operation wavelength of the laser is also an important parameter, since the material reflectivity is directly related with the laser beam wavelength, and thus, the proper type of laser has to be used for each class of material. Hence, neodymium-doped yttrium aluminum garnet Nd:YAG lasers have prevailed over other types of lasers (e.g., CO_2 lasers) for the engraving of metallic materials since the reflectivity of metals in wavelengths around 1064 nm is significantly lower, in comparison with the reflectivity in the range of 10.6 μm wavelengths where CO_2 lasers operate.

The relevant field of laser machining, including the laser engraving, is an area of active research. The laser milling of aluminum-magnesium alloy has been studied by Campanelli et al. [6] in terms of the material removal depth and the surface roughness as function of the machining parameters. Orazi et al. [7] presented a semi-empirical model regarding the Material Removal Rate (MRR) in machining of aluminum alloy 7075 and mild steel AISI 1040 with fiber pulsed laser. Teixidor et al. [8] studied the surface quality and the dimensional accuracy in respect to the process parameters in laser milling of hardened AISI H13 tool steel. In the work of Campaneli et al. [9], an experimental investigation regarding the laser milling of aluminum alloy 5754 was carried out, where the impact of machining parameters on the material removal depth, the MRR and the mean surface roughness Ra was mainly studied. The deep engraving process of AISI 1045 stainless steel was investigated by Anita Pritam [10], with the engraving depth and the surface roughness being the machining process evaluation indexes. The experimental work of Sugar et al. [11] presents a study regarding the effect of machining parameters on the surface quality of laser processed brass. The machinability of titanium alloy Ti6Al4V with laser milling has been investigated in the work of Ahmed et al. [12], with the MRR and the surface roughness being considered as representative indexes of the alloy's machinability. The MRR and the dimensional accuracy in fabrication of microchannels with Nd:YAG laser on alumina was studied by Mohammed et al. [13], while the machining quality of microchannels on Nickel-Titanium (NiTi) based shape-memory alloys was discussed in the work of Mohammed et al. [14]. From the literature review, the importance and interest on studying the surface quality after laser machining and engraving for different materials and alloys is clearly deduced.

The current paper pertains to the surface topography of SAE 304 stainless steel after its engraving with pulsed Nd:YAG laser. From the literature review it is concluded that laser engraving process is very sensitive to the machining parameters, thus, an extensive and detailed study of how each parameter affects the surface topography is scientifically interesting, but also with practical value. Hence, different laser powers, scanning speeds and repetition rates were utilized in order to cover a wide range of machining conditions and define the impact of each parameter on the surface topography. The Design of Experiment (DOE) was based on Taguchi L9 orthogonal array with three factors at three levels each. More specifically, laser power values of 8, 12 and 16 W were used, as well as scanning speed values of 200, 400 and 600 mm/min and pulse repetition rate values of 30, 50 and 70 kHz. Finally, although commonly the surface topography is evaluated based on the Ra and Rz values, in the current study the analysis of surface topography was done in terms of Sa and Sz, while statistical analysis was followed in order the obtained results to be interpreted.

Materials and Methods

The current series of experiments was carried out on a LASERTEC 40 laser machining center made by DMG MORI, which is equipped with a Nd:YAG pulsed laser that operates in 1064 nm wavelength, with 20W maximum nominal average power, nominal spot diameter of 30 μm and 100 ns pulse duration. A stainless steel SAE304 plate of 5 mm thickness was utilized as workpiece. Square pockets of 4x4 mm dimension were engraved by using unidirectional cross hatching

scanning strategy. The track distance T_d, i.e., the distance between two successive tracks was set equal to the hatching distance H_d, i.e., the distance between two subsequent pulses. The hatch distance is calculated based on Eq. 1 and the overlap between the pulses according to Eq. 2.

$$H_d = \frac{v_{scan}}{f} \tag{1}$$

$$overlap = 1 - \frac{H_d}{D} \tag{2}$$

with H_d the hatching distance in [mm], v_{scan} the laser beam scanning speed in [mm/s], D the nominal laser beam diameter and f the repetition rate in [Hz]. The scanning strategy and its main geometrical features are schematically depicted in Fig. 1.

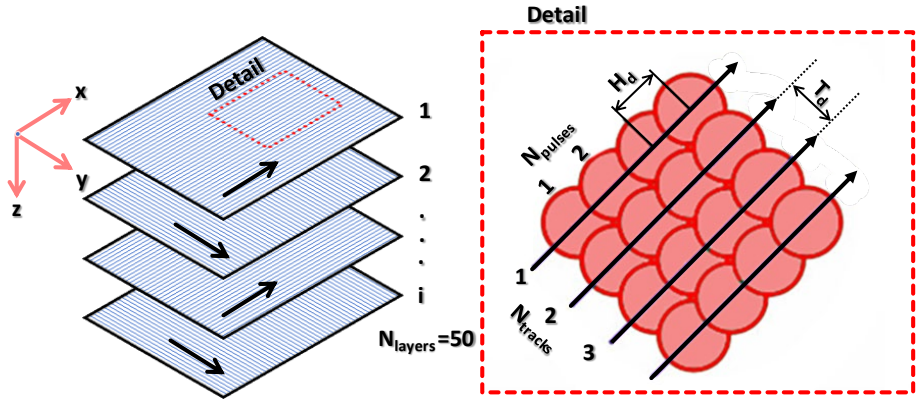

Fig. 1. Unidirectional cross hatching scanning strategy and its main geometrical features.

The DoE was based on Taguchi L9 orthogonal array with three factors at three levels each. Namely, the control parameters were the mean power P, the scanning speed v_{scan} and the repetition rate f. The mean power values were set between 8 and 16 W, the scanning speeds between 200 and 600 mm/s, while the repetition rate took values between 30 and 70 kHz. By utilizing the aforementioned machining parameters, the study covers a wide range of different power densities, hatching distances and track distances, thus, the impact and the significance of each parameter can be assessed. Moreover, in order the process to reach a steady state that will ensure representative and reliable results, each pocket was engraved by 50 successive layers. Finally, by using the touch probe measuring system of the laser machine, the laser beam was initially focused on the top surface of the plate. Thus, the standoff distance was initially zero for the first layer to be engraved, while, for the next layers, the standoff distance was increasing and was equal to the engraving depth. It is worth noting that the maximum applicable engraving depth is almost negligible in relation to the focal length. The machining parameters combinations based on the aforementioned DOE, along with the machining center features are listed in detail in Table 1.

Finally, the study of the surface topography was carried out in terms of Sa and Sz that were defined as:

$$\boldsymbol{Sa} = \frac{\mathbf{1}}{\boldsymbol{A}} \iint_{\boldsymbol{A}} |\boldsymbol{z}(\boldsymbol{x},\boldsymbol{y})|\, dxdy \tag{3}$$

where, A the definition area, and z (x,y) the height of the scale-limited surface at position (x,y) and **Sz** the sum of the largest peak height value and the largest pit height value within a definition area.

The surface roughness values were measured by utilizing the Focus Variation method in a Keyence VHX-7000 optical microscope equipped with specialized lenses. The measurements were

Materials Research Proceedings 28 (2023) 1703-1710 https://doi.org/10.21741/9781644902479-184

conducted by following the ISO 25178-2 standards, while, based on the obtained SR values, the cut off length was defined at 0.8 mm.

Table 1. Machining parameters.

Machining Parameters			
Control Parameters			
#	**Power [W]**	**Scanning Speed [mm/s]**	**Repetition Rate [kHz]**
1	8	200	30
2	8	400	50
3	8	600	70
4	12	200	50
5	12	400	70
6	12	600	30
7	16	200	70
8	16	400	30
9	16	600	50
Constant Parameters			
Spot Size		30 [μm]	
Pulse Duration		100 [ns]	
Number of Layers		50	

Results and Discussion

After the experiments were conducted, the surface topography was investigated by means of Focus Variation microscope. In Fig. 2a and b, the topography of two indicative surfaces produced by laser engraving under two different conditions, namely no.3 and 4, is depicted and in Table 2, the results regarding Sa and Sz are presented for all experiments. From these figures it can be seen that the surface includes various characteristic features, such as craters and peaks due to the intense thermal phenomena induced by the laser beam. Although different process conditions lead to different surface quality, as can be seen from the results of Table 2, this typical morphology is not considerably altered. It is worth noting that this type of surface is similar to the surface produced by other non-conventional processes which involve a high heat input, such as EDM. Although the surface quality is moderate-to-high, with Sa mostly varying between 0.57-1.75 μm, the high values of Sa and Sz observed for the experiments no.4 and 7 can be explained as a result of both high interaction time due to relatively lower value of scanning speed and considerably high overlap values.

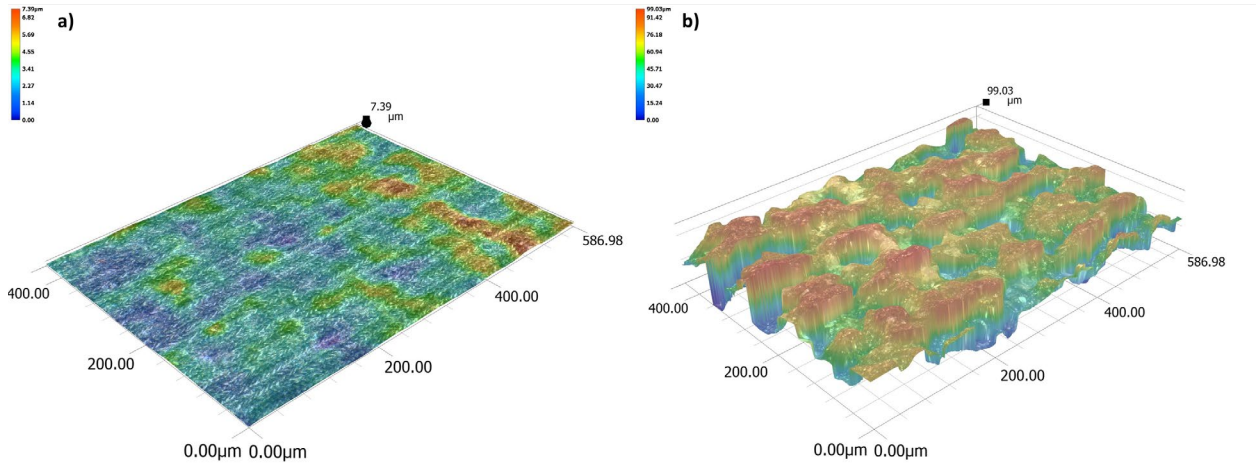

Fig. 2. Surface topography under different process conditions: a) 8 W / 600 mm/s / 70 kHz and b)12 W / 200 mm/s / 50 kHz.

Table 2. Experimental results.

#	Power [W]	Scanning Speed [mm/s]	Repetition Rate [kHz]	Hatching Distance [µm]	Overlap	Sa [µm]	Sz [µm]
1	8	200	30	6.67	0.778	1.75	16.37
2	8	400	50	8.00	0.733	0.84	6.28
3	8	600	70	8.57	0.714	0.57	5.34
4	12	200	50	4.00	0.867	11.57	87.35
5	12	400	70	5.71	0.809	1.50	15.28
6	12	600	30	20.00	0.333	0.76	6.64
7	16	200	70	2.86	0.905	10.81	110.75
8	16	400	30	13.33	0.555	1.03	9.92
9	16	600	50	12.00	0.600	0.67	6.52

Based on the experimental results of Table 2 it is deduced that there is a threshold of overlap beyond which the surface roughness rapidly increases. Namely, for overlap greater that 0.85 there is a significant increase in both Sa and Sz values. The parabolic increase trend of the surface roughness in respect to the overlap that it is depicted in Fig. 3, is in line with the respective literature [14].

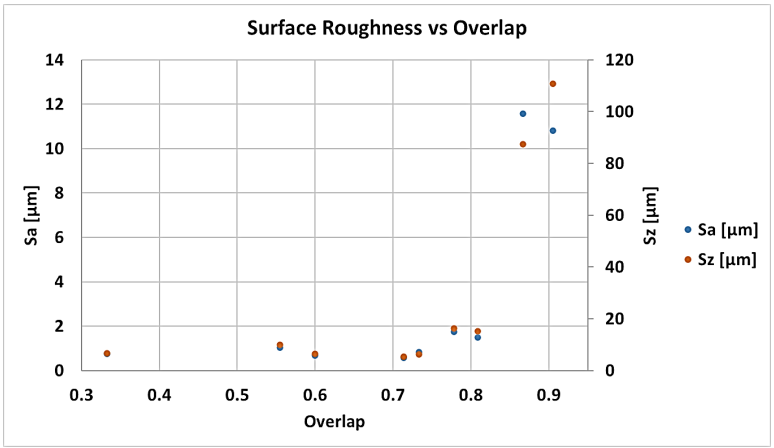

Fig. 3. Surface roughness values (Sa and Sz) in respect to the overlap.

In Fig. 4a and b, the main effects and interactions plots are depicted for Sa. At first, from the main effects plot it can be observed that although all parameters affect Sa, scanning speed causes the most significant variation of Sa values. More specifically, as the scanning speed increases, lower Sa is obtained, with the higher decrease of Sa values being noted between 200 and 400 mm/s. Thus, an appropriate selection of scanning speed values is crucial for achieving a high-quality surface during laser engraving process. Regarding the effect of mean power and pulse repetition frequency on Sa, it can be seen that they have a similar effect on Sa, as they both lead to an increase of average roughness up to a point and then the value of Sa remains almost constant.

Apart from the results presented in Fig. 4a, the interaction plots of Fig. 4b can also reveal more details about the combined effect of process parameters on Sa. Between mean power and scanning speed, a significant interaction is observed at the lowest value of scanning speed (200 mm/s), whereas for the other values of scanning speed, their interaction is negligible. However, the interaction of power and frequency is considerable for all levels of frequency, although a certain trend is not observed, as the correlation between power and frequency for each frequency level is different. Finally, the interaction between scanning speed and frequency is considerable only for the lowest value of frequency (30 kHz). Thus, it can be deduced that although power and frequency have a combined effect on the surface quality, the interaction between them and scanning speed is generally weak.

Various factors related to process parameters, such as the interaction time, overlap and energy per pulse contribute also to the creation of the surface topography. More specifically, if we consider the influence of scanning speed alone, with fixed values of mean power and pulse repetition frequency, due to the decrease of interaction time the heat-induced alterations of the surface are less intense, leading to improved surface roughness. As for mean power, when the other two parameters are fixed, the reason which leads to larger roughness is related to the larger thermal input to the workpiece, which leads to more intense thermal phenomena such as vaporization and remelting, which induce irregularities on the surface.

The effect of pulse repetition frequency, when scanning speed and power values are fixed, can be explained based on the interactions between various factors. More specifically, although the per pulse energy decreases, the hatching distance also decreases and the overlap increases. Thus, the higher number of repeated pulses, leading to a smaller overlap, creates a rougher surface with enlarged craters and other irregularities.

Finally, it can be deduced that, in order to avoid increased average roughness, lower power and frequency values should be used along with higher scanning speed values. However, these values should be selected taking also into consideration the effect of these parameters on the depth of produced pockets and the machining time, which are contradicting goals.

Afterwards, in order to be able to predict the roughness values in respect to process parameters for the specific material, an empirical relationship is established between process parameters and Sa. As a linear regression model was not able to describe the data with high correlation coefficient values, a power law model was adopted, as follows:

$$Sa = 151530 P^{0.354155} v_{scan}^{-2.70297} f^{0.920414} \quad (4)$$

The Mean Square Error (MSE) of the developed equation is 4.28060 μm^2 and the standard error of the regression (S) value is 2.06896 μm. The errors of the empirical equation can be attributed to the reduced number of experiments conducted when conducting the experiments with a DOE method like Taguchi method and some considerably high values occur. However, the choice of an established DOE method provided an excellent compromise between the cost of the experiments and the accuracy of the results.

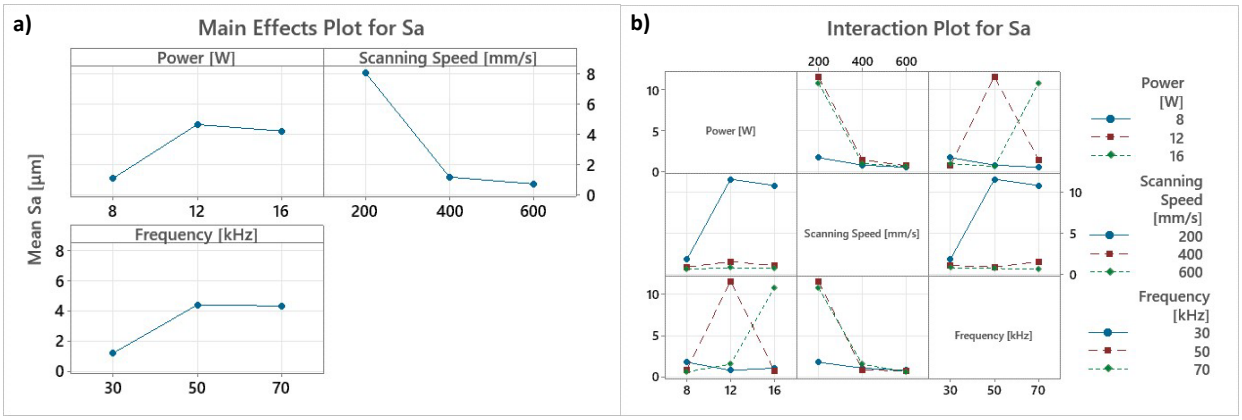

Fig. 4. (a) Main effects plot for Sa and (b) Interaction plot for Sa.

Regarding Sz values, the main effects plot of Figure 5a indicates that the three process parameters have a similar effect on Sz, as on Sa. Thus, it is shown that when laser scanning speed, which is again the most significant parameter, increases, the peak-to-valley height is considerably reduced for speed values up to 400 mm/s and then the decrease is slighter, whereas for both higher mean power and pulse repetition frequency, Sz increases more abruptly at first and then in a more gradual way. Moreover, the interactions plot of Figure 5b is also similar to that of Sa, indicating a higher degree of interaction between power and frequency, whereas the interaction between these parameters and scanning speed is weaker. An empirical relationship was also developed with a power law model with MSE value of 127.179 µm^2 and an S value of 11.2774 µm, in order to correlate the process parameters with Sz, as follows:

$$Sz = 197857 P^{0.818046} \upsilon_{scan}^{-2.52004} f^{0.859392} \quad (5)$$

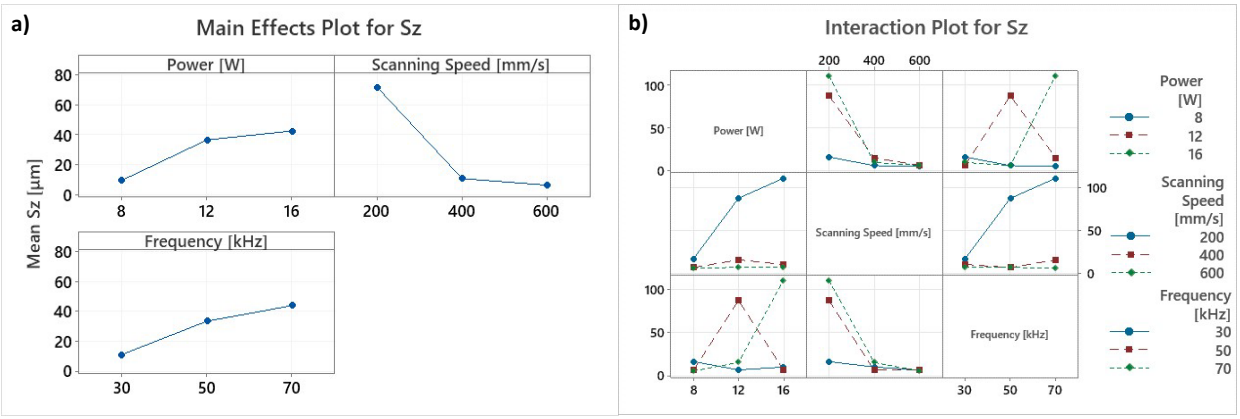

Fig. 5. (a) Main effects plot for Sz and (b) Interaction plot for Sz.

Summary

In this paper, the surface topography obtained during laser engraving of SAE304 is investigated by means of experimental work and statistical analysis. The experiment was designed based on Taguchi L9 orthogonal array for three levels of scanning speed, mean power and pulse repetition frequency in order to determine their effect on surface topography. After the results were analyzed, several conclusions were drawn:

Scanning speed considerably affects the surface topography, as indicated by the results of both Sa and Sz. For fixed mean power and pulse repetition rate, the decrease of interaction time between the laser beam and workpiece leads to lower heat input and less intense thermal phenomena, resulting in surfaces with higher quality and less irregular features.

Mean power and pulse repetition rate affect surface topography to a lower extent than scanning speed. As mean power increases, the heat input to the workpiece increases and a rougher surface is obtained as the more intense thermal phenomena lead to vaporization and remelting of the material and deeper microcraters are formed in the surface. Regarding pulse repetition rate, its increase leads to higher overlap and larger values of surface roughness. Thus, with regard to surface roughness, it is recommended that higher values of scanning speed and lower values of mean power and pulse repetition rate are desirable.

References

[1] Y.C. Shin, B. Wu, S. Lei, G.J. Cheng, Y.Y. Lawrence, Overview of Laser Applications in Manufacturing and Materials Processing in Recent Years, J. Manuf. Sci. Eng. Trans. 142 (2020) 110818. https://doi.org/10.1115/1.4048397

[2] P. Johander, I. Goenaga, D. Gomez, C. Moldovan, O. Nedelcu, P. Petkov, U. Kaufmann, H.J. Ritzhaupt-Kleissl, R. Dorey, K. Persson, Design and manufacturing of micro heaters for gas sensors, 4M 2006 - Second International Conference on Multi-Material Micro Manufacture (2006) pp. 117-121.

[3] E. Nikolidakis, A. Antoniadis, FEM modeling and simulation of kerf formation in the nanosecond pulsed laser engraving process, CIRP J. Manuf. Sci. Technol. 35 (2021) 236-249. https://doi.org/10.1016/j.cirpj.2021.06.014

[4] G. Schnell, U. Duenow, H. Seitz, Effect of Laser Pulse Overlap and Scanning Line Overlap on Femtosecond Laser-Structured Ti6Al4V Surfaces, Materials 13 (2020) 969. https://doi.org/10.3390/ma13040969

[5] K. Anderson, Aluminum Science and Technology, ASM International, 2018.

[6] S.L. Campanelli, G. Casalino, N. Contuzzi, Multi-objective optimization of laser milling of 5754 aluminum alloy, Opt. Laser Technol. 52 (2013) 48-56. https://doi.org/10.1016/j.optlastec.2013.03.020

[9] A. Pritam, Experimental investigation of laser deep engraving process for AISI 1045 Stainless Steel by Fibre Laser, Int. J. Inf. Res. Rev. 03 (2016) 1730-1734.

[10] P. Šugár, J. Šugárová, M. Frnˇcík, B. Ludrovcová, Nanosecond YB fibre laser milling of alluminium bronze: effect of process parameters on the surface finish, Adv. Sci. Technol. Res. J. 12 (2018) 10-15. https://doi.org/10.12913/22998624/93613

[11] N. Ahmed, S. Ahmad, S. Anwar, A. Hussain, M. Rafaqat, M. Zaindin, Machinability of titanium alloy through laser machining: material removal and surface roughness analysis, Int. J. Adv. Manuf. Technol. 105 (2019) 3303-3323. https://doi.org/10.1007/s00170-019-04564-7

[12] M.K. Mohammed, U. Umer, A.U. Rehman, Al-A.M. Ahmari, A.M. El-Tamimi, Microchannels fabrication in alumina ceramic using direct Nd: YAG Laser Writing, Micromachines 9 (2018) 371. https://doi.org/10.3390/mi9080371

[13] M.K. Mohammed, A. Al-Ahmari, Laser-machining of microchannels in NiTi-based shape-memory alloys: experimental analysis and process optimization, Materials 13 (2020) 2945. https://doi.org/10.3390/ma13132945

[14] H. Wan, J. Min, J. Lin, B.E. Carlson, S. Maddela, C. Sun, Effect of laser spot overlap ratio on surface characteristics and adhesive bonding strength of an Al alloy processed by nanosecond pulsed laser, J Manuf. Process. 62 (2021) 555-65. https://doi.org/10.1016/j.jmapro.2020.12.055

Materials Research Proceedings 28 (2023) 1711-1718 https://doi.org/10.21741/9781644902479-185

A numerical procedure to test the effects of the main variables in the submerged arc welding process

CONTE Romina[1,a *], RODRÌGUEZ IZQUIERDO David[1,b], GAGLIARDI Francesco[1,c], AMBROGIO Giuseppina[1,d], FILICE Luigino[1,e]

[1]University of Calabria, Ponte P. Bucci, cubo 45C, 87036 Arcavacata di Rende (CS), Italy

[a]romina.conte@unical.it, [b]david.rodriguez@unical.it, [c]francesco.gagliardi@unical.it, [d]giuseppina.ambrogio@unical.it, [e]luigino.filice@unical.it

Keywords: Fusion Welding, Finite Element Method, Numerical Analysis

Abstract. Arc welding processes (AWPs) are performed by generating an electric arc between a metal electrode and the workpiece to be joined. Submerged arc welding, belonging to AWPs, is characterized by the peculiarity that the arc is not visible. Indeed, a granular fusible material flux is employed in the process to shield the parts to be processed, avoiding arc radiation and fumes and, at the same time, reducing the oxidation risks of the welded metals. The main process variables are current, voltage and welding speed. These variables have to be properly set to balance the specific heat in the weld pool for a proper process optimization.

Introduction

Fusion welding is a flexible technique characterized by high efficiency [1], widely employed in the mechanical industry to join conventional structural steels. To carry out the process, the materials are heated to a temperature below the melting point and a filler material allows the joint [2].

According to the filler material employed it is possible to distinguish several process variants. One of them is the Submerged Arc Welding (SAW), which the authors focused on. The process principle is based on the generation of an electric arc between the electrode and the base material. The arc is protected by a granular flow of flux from the atmospheric contaminants, in addition it is worth pointing out that the flux itself increases the conduction of the generated arc [3].

During the welding, the involved materials are subjected to heating and cooling phases, which occur very quickly affecting the microstructure creating a new metallurgical condition within the heat affected zone (HAZ) [4,5]. More in detail, the heat input depends on the current, voltage and welding speed, which are the main process parameters to set for carrying out the process. The welding current significantly affects the penetration while the voltage is responsible for the bead width and not greatly contributes to its penetration depth. Therefore, the input process parameters have to be set according to the joint typology and to the thickness of the metals to be joined [3]. The employed energy causes changes at its microstructure and, therefore, at the mechanical properties of the final joint.

The scientific literature reports studies which aim at understanding the influence of the process parameters on the joint. Jou [6] carried out experiments aiming at correlating the main process parameters to the weld bead by numerical investigations in order to predict its size. Numerical analyses and optimization techniques have been widely carried out to predict residual stresses and affected zones in different manufacturing processes [7,8]. These numerical techniques have been employed for analyzing thermal and mechanical behavior of welded components [9] as well as for predicting thermal cycles, residual stresses and deformations induced by this joining method [10]. Other authors reported the numerical simulation of the welding and cooling conditions and the subsequent investigation of the melted zone extension as well as of the HAZ and of the hardness profile [9].

Content from this work may be used under the terms of the Creative Commons Attribution 3.0 license. Any further distribution of this work must maintain attribution to the author(s) and the title of the work, journal citation and DOI. Published under license by Materials Research Forum LLC.

The main focus of this work lies in the setting of a numerical model aiming at analyzing the effect of the variables on a multi-pass welding joint in terms of thermal properties, looking at the characteristics of the bead HAZ and of its distortions and residual stresses.

Material and Method

Material. The material investigated in this study is the medium carbon steel alloy ASTM A516 Grade 70, employed as base material and widely used in the construction of welded pressure vessels. The main requirement for its service is the high notch toughness. The EH14 copper coated wire, generally used in the construction of containers or boilers, was selected as filler material. The following tables (Table 1 and Table 2) report, respectively, the chemical composition and the mechanical properties of the employed materials.

Table 1. Chemical composition of the base and filler material.

	Element [%]					
	C	***Mn***	***P***	***S***	***Si***	***Cu***
ASTM A516 Gr 70	0.31	1.2	0.035	0.035	0.45	-
EH-14	0.10	1.8	0.019	0.013	0.05	0.05

Table 2. Mechanical properties of the base and filler material.

	ASTM A516 Grade 70	**EH-14**
Tensile strength [MPa]	[485-620]	550
Yield strength, min [MPa]	[260]	470
Elongation in 8 in. [200 mm], min, %	17	30
Elongation in 2 in. [50 mm], min, %	21	-

The experimental test, performed to calibrate the heat source, was performed on plates characterized by different thicknesses (Fig. 1a), specifically dimensions of 100×400×10 mm^3 and 100×400×25 mm^3 were welded by SAW employing a specific clamping equipment designed to the aim of this investigation (Fig. 1b).

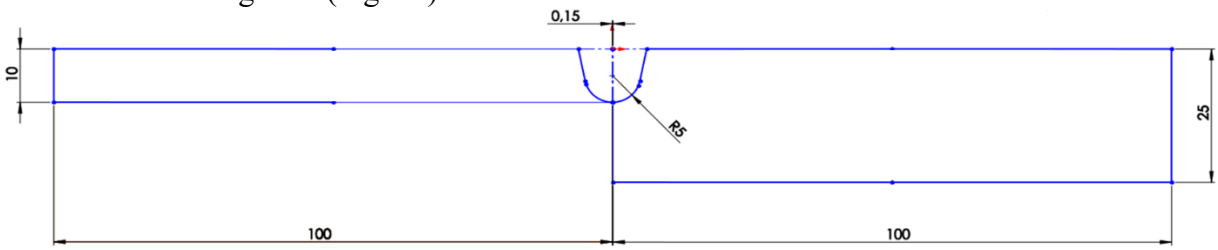

(a)

(b)

Fig. 1. a) Coupon geometry (mm) and b) experimental clamping system.

Method. A three-dimensional numerical model was developed by commercial ESI Sysweld software, which is one of the most widely used software for analyzing welding distortions and residual stresses through the finite element method. In fact, the software allows the welding process simulation providing the thermal analysis, which this work focuses on.

The numerical analysis starts with the calibration of the heat source, which characteristics affect the temperature distribution. The heat source moves along the weld path, for each pass taking into consideration specific experimental evidence. The double ellipsoid proposed by Goldak [11,12] was used to the aim of this study and modeled considering as parameters the arc efficiency η, half width of the fused zone a, its penetration depth b, its front length c_f and its back length c_b (Fig. 2).

The numerical model was built by using 80,500 elements and 87,771 nodes. The boundary conditions were defined to replicate the experimental state. This resulted in imposing constraints at a distance of 50 mm from the plates' extremity. Concerning the thermal boundary conditions, an ambient temperature of 20 °C and a heat transfer coefficient ranging from 0.040 to 0.032 W/mm-K, according to the thermal phases of the analyzed material, were set.

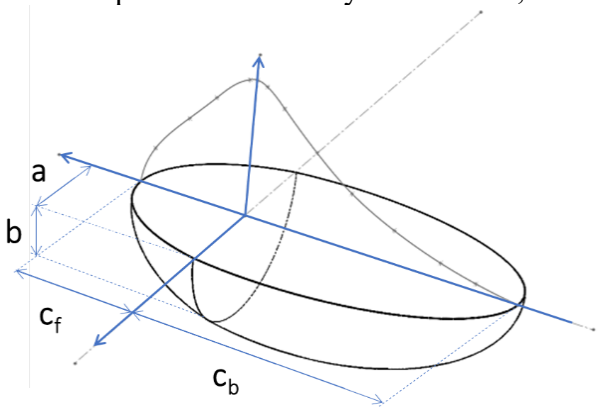

Fig. 2. Goldak's double-ellipsoid and parameters.

A multi-pass welding joint was executed. Specifically, the experimental procedure involves three welding steps. The first one (*Pass 1*) is performed on the bottom side of the plates to be joined and it is aimed at creating a sort of weld cup, while two second passes (*Pass 2*) and all the successive ones (*Pass 3+n*) are performed on the top side, moving on the left and on the right respect to the centerline of the weld bead, until the expected weld bead height is reached. Each pass typology is characterized by a different combination of process parameters and can start just as soon as the temperature measured on the plates is lower than 250°C.

The process parameters considered to the aim of this study are current (I), voltage (V) and welding speed (v). Table 3, below shown, reports the values set for the analyzed case study:

Table 3. Process parameters.

# Pass typology	I **[A]**	V **[V]**	v **[mm/min]**
Pass 1	440	27	320
Pass 2	540	25,4	384
Pass 3+n	675	34	768

Discussion of the Results

The multi-pass welding was investigated by dividing the analysis in two different steps. Specifically, *Pass 1*, being performed on the bottom side of the sheets, was not considered in the analysis. The numerical model starts setting and calibrating *Pass 2* performed in two steps. The first simulation was, therefore, run considering the weld beads obtained experimentally by

overlapping the first two *Pass 2,* hereafter named *Sample A.* To do that, specimens with dimension 70×35×25 mm^3 were firstly cross-sectioned from the center of the test plate and then the surface treated by grinding and polishing and finally etched. Looking at the macrograph (Fig. 4a), each *Pass 2*, and the respective deposit, is clearly visible as well as the HAZ. The geometry of each fused zone, coming from the macrograph, and the process parameters represent the input data for Sysweld. When the process was completely simulated, results were analyzed in terms of temperature distribution (Fig. 4b), comparing the numerical data with the experimental evidence.

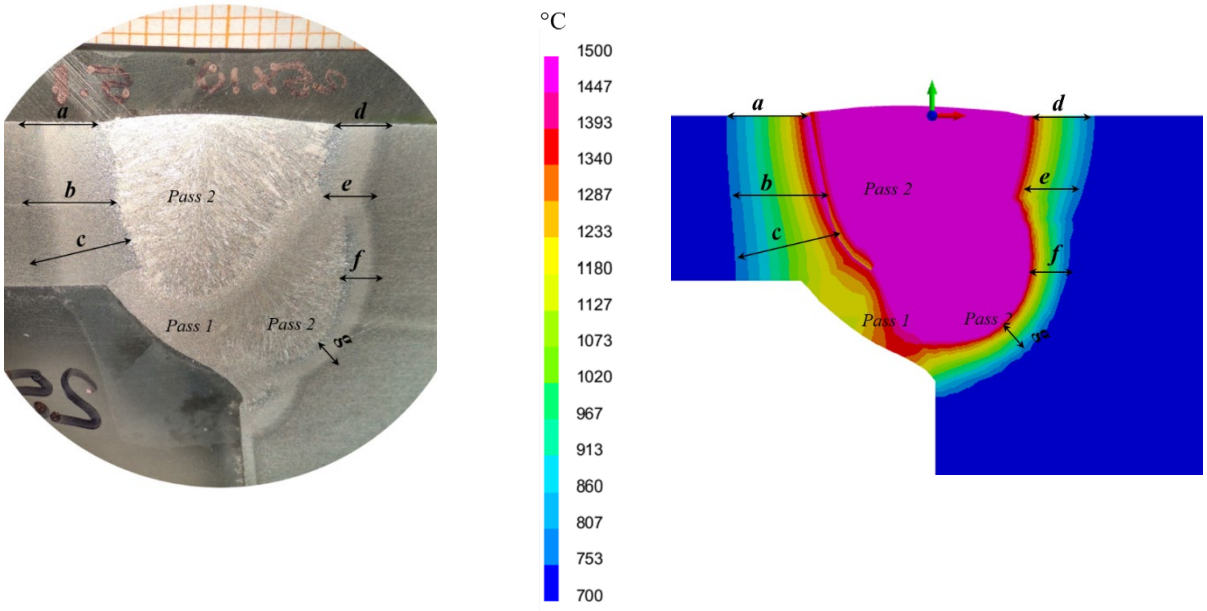

(a) (b)

Fig. 4. HAZ measurement for Sample A: a) experimental test, b) numerical simulation.

In detail, the extension of the HAZ was measured both on the experimental macrograph (five different sections of the same sample were processed) and on the thermal histogram obtained from the simulation. According to that, the upper and lower limits of the temperature scale were set considering, respectively, the beginning of the transition zone in the austenitic field and the melting point of a low carbon steel. For estimating the zone affected by the process temperature, some points were selected and the length defined considering the perpendicular of the tangent to the point. Therefore, the segments a, b, c, d, e, f, g were measured and the values collected for both numerical analysis and experimental test. The comparison of gathered measurements, displayed in Fig. 5, demonstrates that the numerical model was calibrated properly, since the HAZ obtained in *Sample A* is actually equal to the one obtained experimentally.

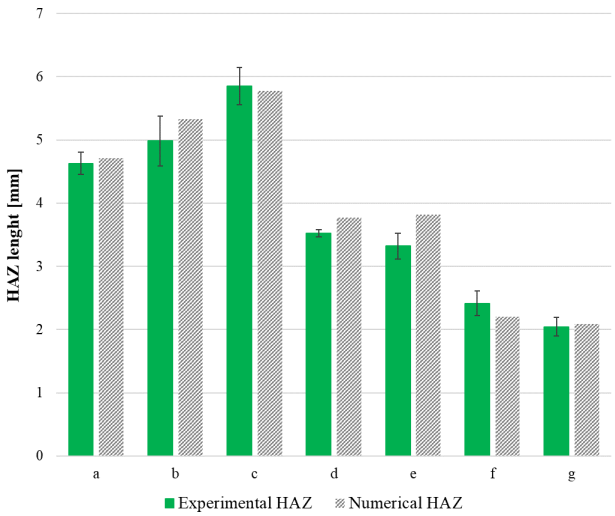

Fig. 5. Sample 1: Comparison of experimental and numerical HAZ lengths.

Once validated the *Pass 2* of the welding sequence, a second joint, hereafter named *Sample B*, was performed overlapping the subsequent *Pass 3+n,* depositing as much as material in order to complete the weld bead, as required by the welding procedure specifications. Two additional welding passes were required, named *Pass 3* and *Pass 4*.

Fig. 6a displays the sectioned joint and each pass can be easily distinguished. It is interesting to look at the 5x enlargement, where the metallurgical transformation, due to the heat influence, of the weld zone, of the heat affected zone and of the base material is observable.

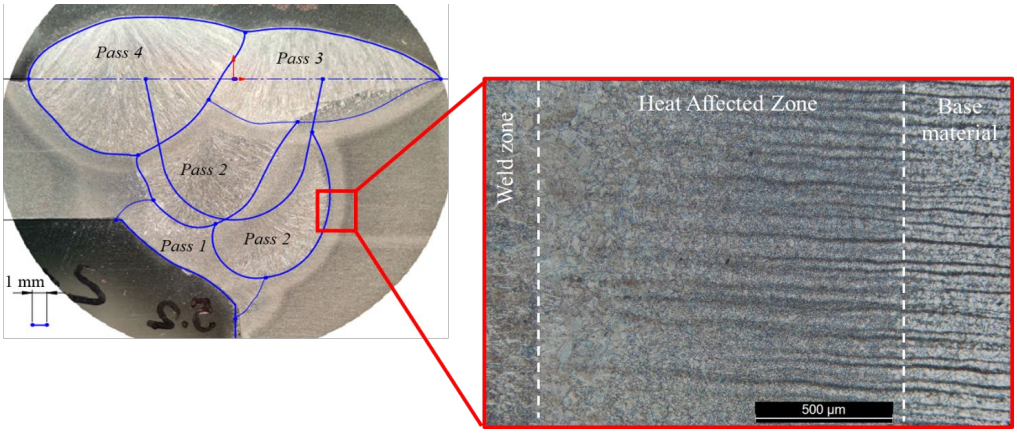

(a) (b)

Fig. 6. a) sectioned view of Sample B and b) its 5x enlargement.

The finite element model was then defined to simulate the welding process on *Sample B*. To be thorough, the measurement of the HAZ was detected as well (Fig. 7), and the comparison between numerical and experimental data, as previously performed for *Sample A*, are synthesized in Fig. 8.

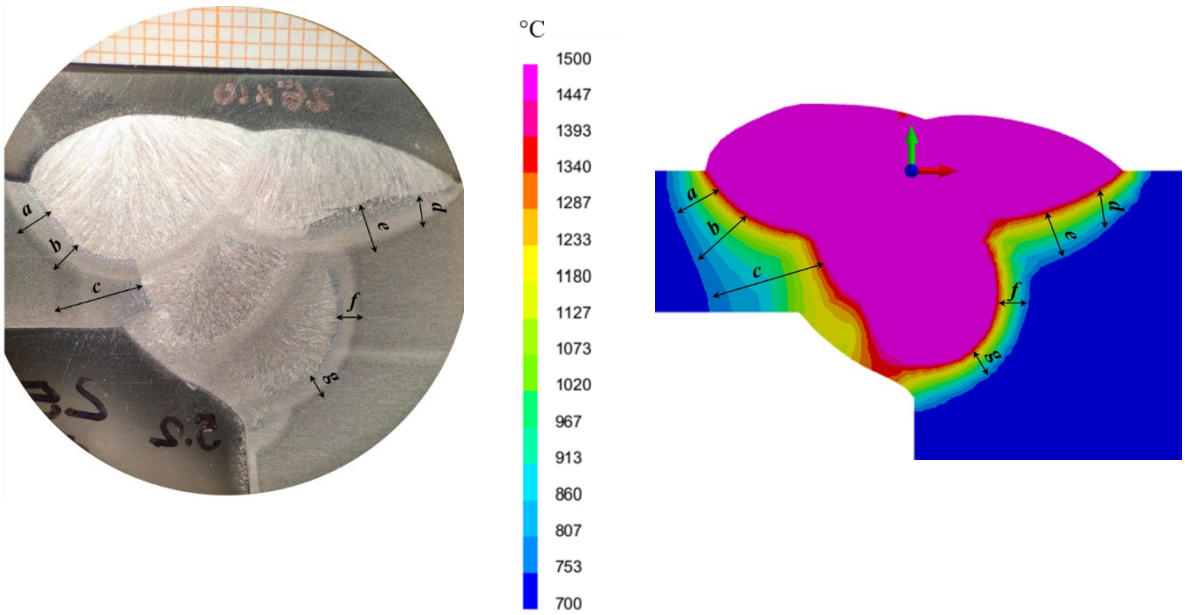

(a) (b)

Fig. 7. Sample B HAZ measurement: a) experimental test, b) numerical simulation.

These further experimental measurements demonstrated the capability of the finite-element simulation in predicting the heat transfer, even if a multi-pass welding is analyzed. The numerical results agree with the experimental data, reasonably. Actually, differences on the left side of the welding bead, especially point *b*, can be detected. The experimental and simulated discrepancies could be attributed to errors related to a possible experimental variance along the length of the weld bead, considering also that the dimension of the samples is far from the usual industrial standards and, therefore, steady-state conditions could be just partially reached. Anyway, additional analyses are required to explain the highlighted inaccuracy, more clearly.

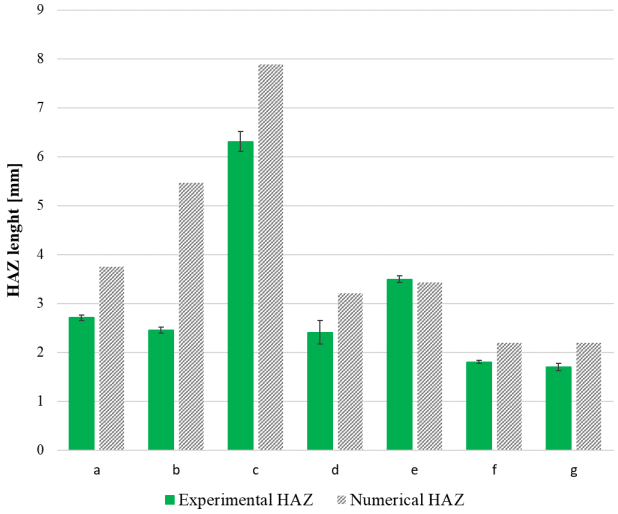

Fig. 8. Sample B: Comparison of experimental and numerical HAZ lengths.

The experimental and numerical comparison proved the effectiveness of the numerical model therefore the potentiality of the obtainable results in improving the performance of jointed parts can be deduced by looking at displacements and residual stresses generated on the parts owing to

the multi-pass welding. Herein, for example, the dishomogeneity related to the different thicknesses of the sheets to be welded are observable, clearly (Fig. 9). Practically, this information can be useful to set a different clamping system and/or welding sequence to compensate for unbalanced stress and strain distributions, important for easier parts' assembly and for their fatigue life behavior.

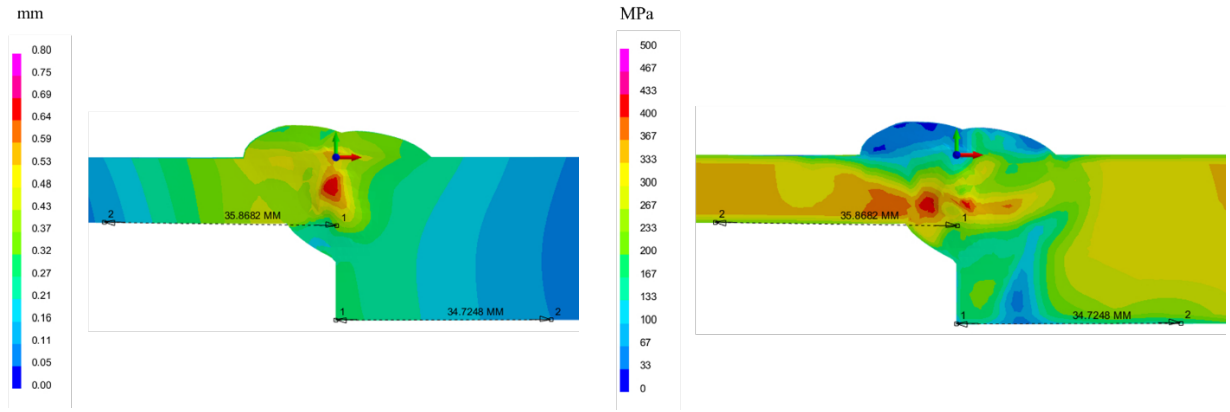

(a) (b)

Fig. 9. a) Displacement and b) residual stress on Sample B at the end of the welding process.

Summary

In this work, the temperature distribution, the distortions and the residual stress within multi-pass welding of plates, characterized by different thickness, were investigated by a finite element simulation properly calibrated by experimental evidence. Specifically, the geometric parameters of the double Goldak's ellipsoid were set and applied on specific positions of the weld beads' geometry extracted by each experimental welding pass. The adjustments of heating source's shape, efficiency and position were performed to achieve a conformity between temperature distribution, obtained by the numerical analysis, and extension of the HAZ, extracted by micrographs of sectioned and prepared samples.

The obtained results showed a good overlap between the numerical and the experimental results, therefore, considering the good calibration of the model, preliminary results on distortions and residual stresses, difficult to analyse experimentally, where observed. Further analyses will be carried out by comparing, in terms of HAZ, distortions and residual stress, more samples processed by different process parameters, in order to speed the welding optimization up.

References

[1] R. Singh, Applied welding engineering: processes, codes, and standards., Butterworth-Heinemann, 2020.

[2] J.A. Schey, Introduction to Manufacturing Processes, 3rd editio, McGraw-Hill Higher Education, 2000.

[3] A. Singh, R.P. Singh, A review of effect of welding parameters on the mechanical properties of weld in submerged arc welding process, Mater. Today Proc. 26 (2020) 1714-1717. https://doi.org/10.1016/j.matpr.2020.02.361

[4] M. Zhang, Y. Han, C. Jia, Z. Zheng, H. Li, C. Wu, Improving the microstructures and mechanical properties with nano-Al2O3 treated wire in underwater submerged arc welding, J. Manuf. Process. 74 (2022) 40-51. https://doi.org/10.1016/j.jmapro.2021.11.056

[5] G. Labeas, I. Diamantakos, Numerical investigation of through crack behaviour under welding residual stresses, Eng. Fract. Mech. 76 (2009) 1691-1702. https://doi.org/10.1016/j.engfracmech.2009.03.006
[6] M. Jou, Experimental Investigation of Resistance Spot Welding for Sheet Metals Used in Automotive Industry., JSME Int. J. Ser. C. 44 (2001) 544-552. https://doi.org/10.1299/jsmec.44.544
[7] Z. Pu, D.Umbrello O., W. Dillon Jr, Jawahir S., Finite Element Simulation of Residual Stresses in Cryogenic Machining of AZ31B Mg Alloy, Procedia CIRP 13 (2014) 282-287. https://doi.org/10.1016/j.procir.2014.04.048
[8] G. Rotella, S. Rinaldi, L. Filice, Roller burnishing of Ti6Al4V under different cooling/lubrication conditions and tool design: effects on surface integrity, Int. J. Adv. Manuf. Tech. 106 (2020) 431-434. https://doi.org/10.1007/s00170-019-04631-z
[9] H.M.E. Ramos, S.M.O. Tavares, P.M.S.T. de Castro, Numerical modelling of welded T-joint configurations using SYSWELD, Sci. Technol. Mater. 30 (2018) 6-15. https://doi.org/10.1016/j.stmat.2018.08.002
[10] G. Romaní, A. Portolés, Modelo tridimensional de simulación por MEF para estudiar la influencia de variables esenciales de soldadura robotizada GMAW en uniones a tope planas., Sold. y Tecnol. Unión. 19 (2008) 22-26.
[11] J. Goldak, A. Chakravarti, M. Bibby, A new finite element model for welding heat sources, Metall. Trans. B. 15 (1984) 299-305. https://doi.org/10.1007/BF02667333
[12] J.H. Chujutalli, M.I. Lourenço, S.F. Estefen, Experimental-based methodology for the double ellipsoidal heat source parameters in welding simulations, Mar. Syst. Ocean Technol. 15 (2020) 110-123. https://doi.org/10.1007/s40868-020-00074-4

Materials Research Proceedings 28 (2023) 1719-1728 https://doi.org/10.21741/9781644902479-186

The sound insulation capacity of some panels made of polymeric materials manufactured by 3D printing

HRIȚUC Adelina[1,a *], DODUN Oana[1,b], MIHALACHE Andrei M.[1,c], SLĂTINEANU Laurențiu[1,d] and NAGÎȚ Gheorghe[1,e]

[1]"Gheorghe Asachi" Technical University of Iași, Department of Machine Manufacturing Technology, Blvd. D. Mangeron, 59 A, 700050 Iași România

[a]adelina.hrituc@student.tuiasi.ro, [b]oanad@tcm.tuiasi.ro, [c]andrei-marius.mihalache@academic.tuiasi.ro, [d]slati@tcm.tuiasi.ro, [e]nagit@tcm.tuiasi.ro

Keywords: Soundproofing, Polymeric Materials, 3D Printing, Research Equipment

Abstract. The soundproofing of certain spaces is necessary primarily to combat noise pollution generated by high-intensity noise sources. One of the ways to reduce the unwanted propagation of high-intensity sound waves is based on the use of panels made of polymeric materials. The expansion in recent decades of the manufacturing processes of parts by 3D printing has led, among other things, to the identification of ways to change the properties of the materials included in the parts manufactured by 3D printing and to modify, in this way, including the sound insulation properties of such materials. For the development of experimental research aimed at allowing the study of the sound insulation capacity of small panels made by 3D printing from polymeric materials, a relatively simple equipment was designed. Equipment includes an enclosure in which the sound source, the small panel, and the sensor of a device used to evaluate the characteristics of sounds. Experimental tests were carried out on panels made of polylactic acid. The experimental results were mathematically processed with the help of specialized software. An empirical mathematical power function model was determined. This empirical mathematical model highlights the intensity of the influence exerted by the thickness of the panel by the speed and volume of the sounds on the acoustic pressure level. It was found that the strongest influence is exerted by the volume of the sound wave.

Introduction

The sound corresponds to a mechanical vibration with a certain frequency and intensity transmitted through a gaseous, liquid, or solid acoustic medium. In principle, it is considered that the frequency of sound sensed by the human ear is between 20 and 20,000 Hertz. From the point of view of vibration frequency, near sounds are infrasound and ultrasound, respectively. When some sounds are appreciated by people as unpleasant, because of their frequency or because of too high intensity, they are called *noises*.

We can talk about *noise pollution* when the noise-producing source cannot be eliminated or removed. This pollution can adversely affect the health of people or other organisms. It is necessary to use solutions that diminish the intensity of the ultrasound transmission process to reduce the negative influence of noise pollution.

There is a wide range of solutions capable of reducing the intensity of the noise transmission process. One of these ways considers insulating materials from a sound point of view [1–4]. Plastic materials are sometimes used as soundproofing materials.

In principle, plastic materials are non-metallic materials with an amorphous structure obtained by melting together several constituents (resins, plasticizers, dyes, lubricants, fillers, and auxiliary materials). Plastic materials are easily shaped at temperatures usually in the range of 140-180 ° C. The technology of obtaining plastic materials by joining several molecules of the same type is called *polymerization*, and the results of its application are *polymers*. The parts made of polymeric

Content from this work may be used under the terms of the Creative Commons Attribution 3.0 license. Any further distribution of this work must maintain attribution to the author(s) and the title of the work, journal citation and DOI. Published under license by Materials Research Forum LLC.

materials can be manufactured by different processes (by pressing, drawing, injection, thermoforming, etc.). Currently, a group of technologies in a remarkable expansion are the technologies based on adding materials, being *additive manufacturing technologies*. One of these technologies is *fused deposition modeling*, which involves the successive addition of layers obtained by advancing and depositing a polymer in a molten state.

For sound insulation, polymer panels manufactured through a fused deposition modeling process can be used in certain situations.

Therefore, it was normal for some researchers to turn their attention to the properties of polymeric materials manufactured by 3D printing processes that could reduce noise pollution. Thus, the problem of manufacturing by 3D printing some lattice structures capable of contributing to the reduction of noise intensity was addressed by Franklin et al. [3]. They used experimental tests, simulations of the studied processes, and appropriate methodologies to reveal the ability of the lattice structures to dampen vibrations with frequencies between 0 and 30,000 Hz.

Perrot and Hoang undertook research to improve the conditions for modeling the sound insulation properties of some structures made of cellular foams and the possibilities of manufacturing such structures [4]. They noted that 3D printing variants of cellular foams are still too expensive for widespread use.

Equipment for the study of sound insulation properties of some panels made of polymeric materials by 3D printing was presented in work [5].

The research, the results of which are presented in this paper, aimed to carry out experimental tests regarding the influence of the thickness of polymer panels, respectively the frequency and intensity of sounds, on the sound insulation capacity of polylactic acid panels manufactured by 3D printing.

Generation and Propagation of Sounds

Sounds can be generated by vibrating a solid body using different forms of energy. Thus, sounds are generated mechanically, electromechanically, hydraulically, pneumatically, etc. As mentioned, sounds can be transmitted through solid, liquid, and gaseous media. When sound passes from one medium to another, part of its energy can be reflected, a part is dissipated (absorbed) in the second medium, and another part passes through that medium (Fig. 1). The propagation of sounds takes place through successive contractions and elongations of some areas in the environment in which the sounds propagate.

If the flow corresponding to the incident energy is denoted by E_i, by E_a – the flow of absorbed energy, and by E_r – the flow of reflected energy, the sound absorption coefficient α at the level of the separation surface between two media can be calculated using relations of the form:

$$\alpha = \frac{E_a}{E_i} \tag{1}$$

or

$$\alpha = 1 - \frac{E_r}{E_i} \tag{2}$$

The different media traversed by the sound contribute to a gradual reduction in its intensity. In such conditions, *an acoustic impedance* can be defined as a quantity with the help of which the opposition of an environment to the propagation of acoustic waves is evaluated:

$$Z = \frac{p}{vS} \tag{3}$$

where p is the sound pressure, v is the velocity of the sound wave, and S - the surface through which the wave propagates.

Different sizes can be used to evaluate the intensity of sounds, one of which is the *sound pressure level* or sound intensity (expressed in decibels). Such a quantity represents the sound intensity level to a reference value.

The intensity of the sound wave absorption process depends not only on the properties of the material through which the sound wave passes, but also on some properties of the sound. Different materials exhibit distinct sound attenuation properties. Materials that absorb a greater amount of acoustic energy are considered soundproof materials.

Equipment for Evaluating the Sound Insulation Capacity of Some Panels Made of Polymeric Materials

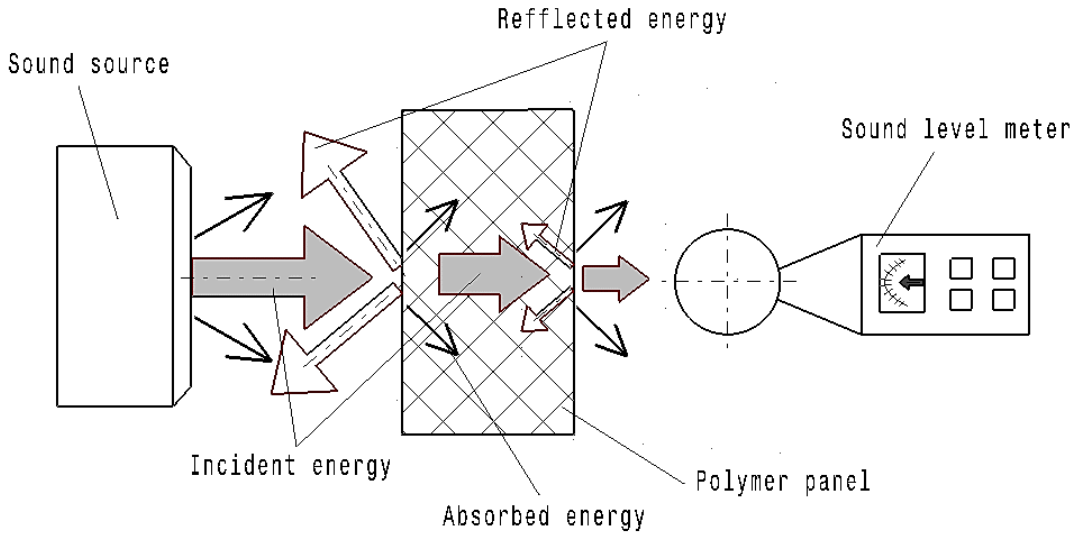

Fig. 1. Schematic representation corresponding to sound propagation from the source to the sound level meter, passing through the polymer panel.

One of the objectives pursued through the research, the results of which are presented in this paper, was to design equipment that would allow the evaluation of the sound insulation capacity of some panels made of polymeric materials.

It is known that for the evaluation of the sound insulation capacity of different materials, equipment incorporating the so-called Kundt tube can be used [6]. Since the accessible Kundt tubes allowed the use of relatively small test sample, the problem of designing and making specialized equipment for evaluating the sound insulation properties of the materials of polymer test samples with surfaces of 100x100 mm^2 and thicknesses of 1-6 mm was formulated.

The main requirements that such equipment had to fulfill were the following:

1. To allow the locating and clamping a test sample in the form of a panel of polymeric material, with an area of 100x100 mm^2 and with thicknesses of up to 6 mm;

2. To include a source of sounds whose characteristics (frequency, volume) can take values

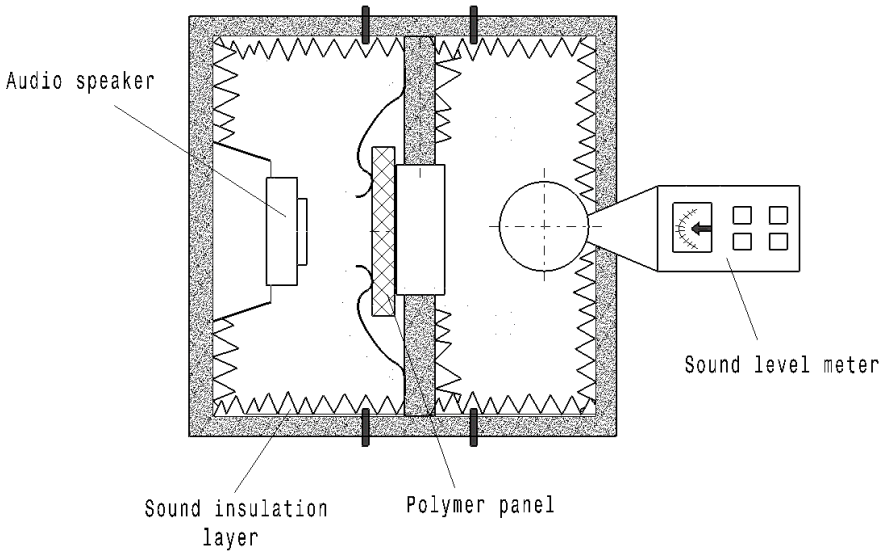

Fig. 2. Schematic representation of the equipment for investigating the sound insulation capacity of some polymer panels.

between certain limits;

3. To include a sound level meter;

4. The different components involved in the generation of sounds and, respectively, in their measurement can be located inside an enclosure to avoid disturbing the results by sounds from outside the equipment;

5. As far as possible, ensure conditions to avoid the sounds reflected by the walls of the enclosure affecting the results of the measurements.

The equipment represented schematically in Fig. 2 was designed to obtain information about the sound insulation capacity of some panels made of polymeric materials. In principle, the equipment includes three distinct compartments, which can be assembled with the help of hook fasteners. In the first compartment, a speaker will have to generate a sound commanded via Bluetooth through a program opened on a mobile phone or a computer. In the second compartment, a polymer sample having a certain thickness can be oriented and fixed. The sensor of a sound level meter (type HY1361 - China) enters the third compartment.

The walls of the three compartments were made of wood to ensure, as much as possible, an avoidance of the results being affected by the sounds existing outside the equipment. Also, to reduce the influence of the sounds possibly reflected by the walls of the compartments, the inner surfaces were covered with a layer of material also characterized by a high sound absorption capacity.

An image of the equipment can be seen in Fig. 3.

Materials Research Proceedings 28 (2023) 1719-1728 https://doi.org/10.21741/9781644902479-186

Fig. 3. Image of equipment used to study the influence exerted by some factors on the transmission of sound through small panels manufactured by 3D printing.

In Fig. 4, it can be observed how pockets were generated in the sample during its manufacture by 3D printing. This way of printing was done in the idea of having not only a 100% infill of the part so that the insulation can be better, but also in the idea of creating a resistance structure for the part considering the next usage of such a part in construction for example.

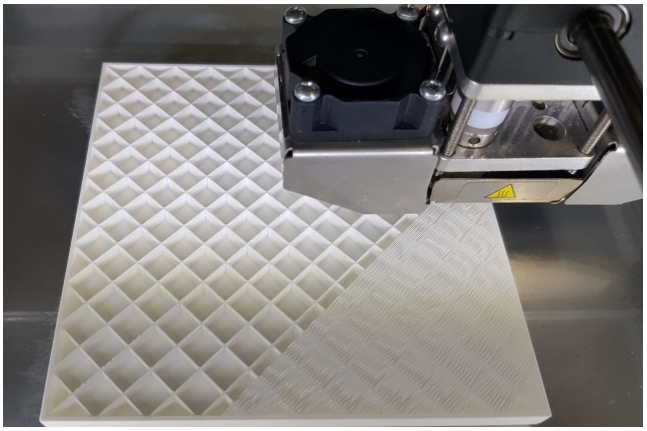

Fig. 4. Image taken during 3D printing of the 6mm thick panel with 10% grid infill.

Modeling Some Research Elements Using the Finite Element Method

A type of harmonic analysis was used to obtain a map of the sound pressure inside a closed enclosure. The 3D model assumes the existence of a speaker box in which there is a panel with a thickness of 1 mm manufactured by 3D printing. The design is similar to the one used in the experimental tests. A 100% cushion box enclosure was modeled (Fig. 5) because the surrounding acoustic environment serves as the domain in which the acoustic waves propagate. Therefore, a mesh of acoustic elements must surround the geometric body considered. In this way, the whole design distributes a certain topology to all elements to have a network control option available.

As excitation, it was necessary to choose between Mass Source, Surface Velocity, Diffuse Sound Field and other types. It was preferred Mass Source because it best suited the experimental setup. Excitation can be applied to vertices, edges or surfaces by introducing a pressure wave inside the system. The mass source is given by the Helmholtz equation (link) and if it is applied to a

surface, one can divide the mass flow by the area it is applied to. A plane wave was simulated in this way [link]. By suppressing the speaker and the test sample, the analysis mode treated the geometry as infinitely rigid, replacing it with voids that will act as sound reflectors. The maximum value of 15 kHz was set for the maximum range using a linear frequency. A far-field sound pressure level (SPL) plot was requested, assuming a 100mm sphere radius and 360o at the end of the theta angle, using the perfectly matched layers (PML) option to model the far-field radiation limit (Fig. 6).

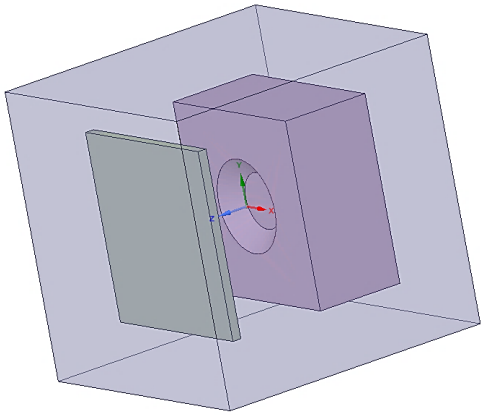

Fig. 5. Proposed 3D model design with 100% cushioned enclosure.

Air was the preferred propagation medium and we added a second enclosure designed to absorb the outgoing acoustic radiation without reflection coupled with PML elements. By adding a second coordinate system relative to the global one the orientation from the main axis (Y) was changed to be defined by the global Z and a construction surface was requested to be able to see the distribution of the results inside the enclosure.

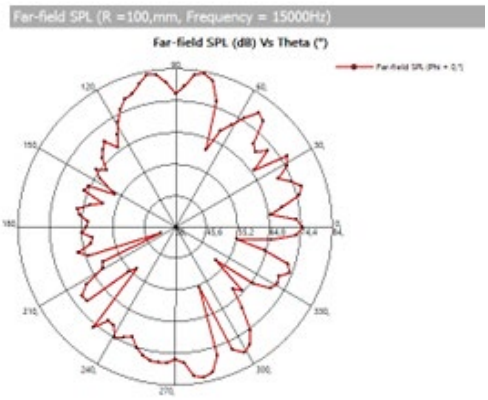

Fig. 6. Far-field sound pressure level at 360º distribution plot.

Fig. 7 highlights the pressure distribution that builds up inside the enclosure, reaching a value of 0.342652 MPa in the center of our panel.

Fig. 8 shows recordings of sound pressure levels recorded at 15 kHz with a peak amplitude of 108.67 dB in amplitude. It can be seen that the space between the speaker box and the panel is the most affected. The edges of the enclosure are all blue, which ensures that our setup works by trapping acoustic radiation without reflecting it.

The authors acknowledge that this analysis is based on an ideal setup and further refinement may be necessary before using the results in other areas of research.

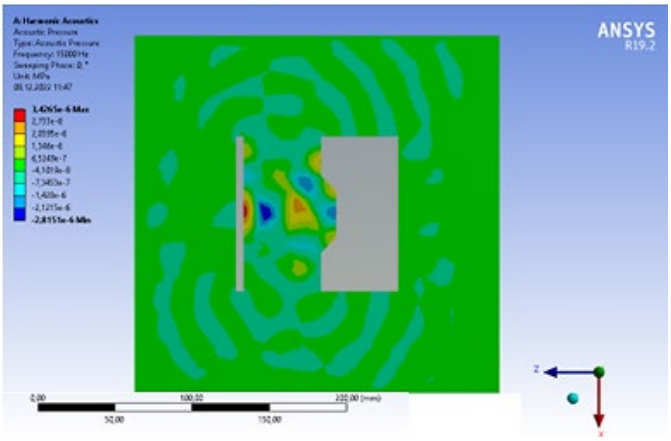

Fig. 7. Acoustic pressure accumulation at 15 kHz.

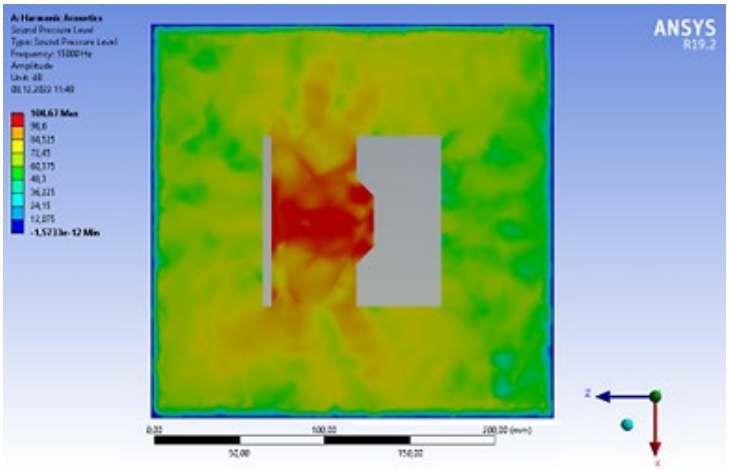

Fig. 8. Sound pressure level map at 15 kHz.

Experimentation of the Equipment for Evaluating the Sound Insulation Capacity of Some Polylactic Acid Panels

An experimental research plan was designed to highlight the influence of several factors on the sound insulation capacity of polylactic acid panels manufactured by 3D printing. These panels were manufactured under the working conditions recommended by the manufacturer of the printing equipment (Ultimaker 2 - Netherlands) with a 100% infill. As previously mentioned, the panels had an area of 100x100 mm^2 and thicknesses of 1 mm and 6 mm, respectively. The material used was PLA, polylactic acid as this is a usual material used in the printing process, but also being an organic material and the focus in the market and industry is on such materials.

Sound pressure level was used as the output parameter. This size was determined with the help of a sound level meter.

The input factors in the measurement process were the thickness t of the polylactic acid panel, the frequency f of the vibrations, and a size V relating to the sound volume. In this way, it was possible to plan the experimental trials according to the requirements of a full factorial experiment, type $L8$, with 3 independent variables at two levels of variation. Two-panel thicknesses (1 mm and

6 mm, respectively), two frequencies (500 Hz and 15,000 Hz, respectively), and two sound volume levels (10 % and 100 %) were used in this way. Generally speaking, the number of the independent variables can be bigger and more complex, but due to the usage of a Taguchi method for experimental research, there is possible to have like a concludent result with this L8 method type, minimizing a lot the number of the variables and the number of the trails for the experiments.

Both the values of the input factors and the results of the experimental tests can be seen in Table 1.

For a more appropriate interpretation of the experimental results, measurements were also performed without the polylactic acid panel, obtaining the following results: a) for V=10 % and f=500 Hz, I_s=95.2 dB; b) for V=100 % and f=15,000 Hz, I_s=95.0 dB; c) for V=100 and f=500 Hz, I_s=107.1 dB; d) for V=100 % and f=15,000 Hz, I_s=110 dB.

The experimental results were mathematically processed using specialized software based on the least squares method [7]. In this way, the following empirical mathematical power function model was obtained:

$$I_s = 123.027 t^{0.0216} f^{-0.0725} V^{0.0734} \quad (4)$$

Table 1. Experimental conditions and results.

Exp. no.	Input factors (coded value/real value)			Output parameter
	Panel thickness, t, mm	Sound frequency f, Hz	Sound volume level V, %	Sound intensity I_s, dB
1	-1/1	-1/500	-1/10	99.2
2	-1/1	-1/500	+1/100	110.1
3	-1/1	+1/15000	-1/10	68.7
4	-1/1	+1/15000	+1/100	84.8
5	+1/6	-1/500	-1/10	97.1
6	+1/6	-1/500	+1/100	109.1
7	+1/6	+1/15000	-1/10	62.7
8	+1/6	+1/15000	+1/100	80.1

By considering the empirical mathematical model constituted by equation (1), the diagram in figure 9 was developed.

The analysis of the determined mathematical model highlights that, among the three input factors considered, the strongest influence is exerted by the sound volume level V since, in relation (4), the exponent with the highest absolute value is attached to this factor. As expected, an increase in the sound volume level V results in an increase in the sound intensity I_s. Increasing the frequency f of the sounds leads to a decrease in the intensity I_s of the sound since the exponent attached to the factor f in equation (4) has a negative value.

Summary

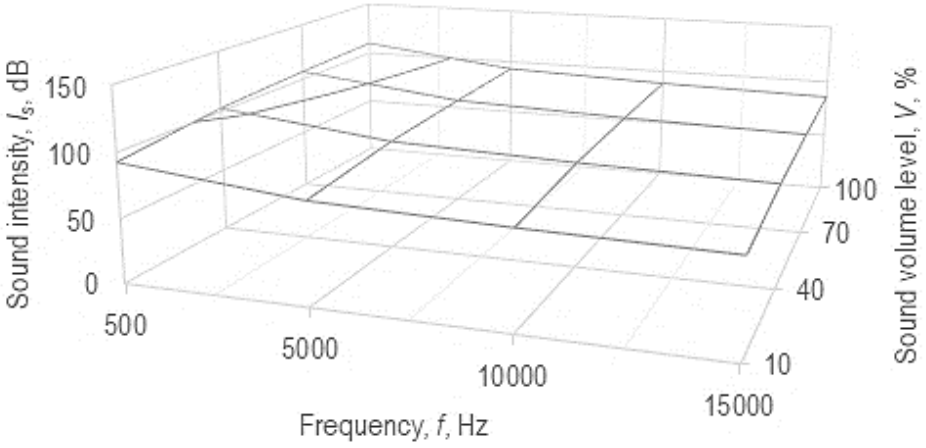

Fig. 9. The influence exerted by the frequency f and by the sound volume level V on the sound intensity I_s (t=1 mm).

The problem of evaluating the ability of some polymeric materials to contribute to the reduction of noise pollution is a current issue. For the experimental research of how different factors contribute to the variation of sound intensity after passing it through a polylactic acid panel, equipment was designed and made to provide conditions for the passage of sound through the polymer panel and the measurement of sound intensity with the help of a sound level meter. In the experimental tests, the panel thickness, frequency, and volume level of the sounds were considered input factors. An empirical mathematical model of the power function type was determined through the mathematical processing of the experimental results with the help of specialized software. It was found that the most significant influence on the intensity of sounds is exerted by the volume level of the sound passing through the panel. Increasing the frequency leads to a decrease in sound intensity after passing through the polylactic acid panel. In the future, it is intended to expand theoretical and experimental research on the influence of different factors on the variation of sound intensity after passing through panels made of different polymer materials or having different structural characteristics.

References

[1] A. Schiavi, A. Prato, Evaluation of sound absorption: an experimental comparative study among reverberation room, impedance tube and airflow resistivity-based models, International Congress on Sound and Vibration, Montreal , 7-11 July, 2019.
[2] A. Borlea (Tiuc), T. Rusu, S. Șimon (Niste), Theoretical consideration on sound absorbtion, Annals of the „*Constantin Brâncuşi*" University of *Târgu Jiu,* Engineering 2 (2011) 89-97.
[3]. J. Franklin, A. Hodge, J.S. Kerween, B. Ramsbottom, Design and Testing of Lattice Structures for Noise Reduction. Major Qualifying Project, Worcester Polytechnic Institute, 2022.
[4] C. Perrot, M. T. Hoang and F. Chevillotte, An overview of microstructural approaches for modelling and improving sound proofing properties of cellular foams: Developments and prospects, 10th International Styrian Noise, Vibration and Harshness Congress, Gratz, Austria, (2018) 1-8. hal-01818223f
[5] A. Hrituc, O. Dodun, A. Mihalache, G. Nagîț, Equipment requirements for the investigation of sound insulation properties of 3d printed polymeric materials, IManEE 2022 conference, Iași, Romania, 17-19 November 2022.

[6] I. Iaşnicu (Stamate), O. Vasile, Radu Iatan, The analysis of sound absorbing performances for composite plates containing recycled textile wastes, U.P.B. Sci. Bull., Series D 78 (2016) 213-220.
[7] G. Crețu, Fundamentals of experimental research. Laboratory handbook (in Romanian). "Gheorghe Asachi" Technical University of Iași, România, 1992.

Materials Research Proceedings 28 (2023) 1729-1738 https://doi.org/10.21741/9781644902479-187

Machining of hybrid structures produced through cold spray technology: A preliminary study

PERNA Alessia Serena[1,a *], VISCUSI Antonio[1,b], ASTARITA Antonello[1,c], BOCCARUSSO Luca[1,d], CARRINO Luigi[1,e] and DURANTE Massimo[1,f]

[1]Department of Chemical, Materials and Production Engineering, University of Naples Federico II, Piazzale V. Tecchio 80, 80125 Napoli, Italy

[a]alessiaserena.perna@unina.it, [b]antonio.viscusi@unina.it, [c]antonello.astarita@unina.it, [d]luca.boccarusso@unina.it, [e]luigi.carrino@unina.it, [f]massimo.durante@unina.it

Keywords: Machining, Cold Spray, Composites, Metal Coatings, Thermal Spray

Abstract. Cold spray is a recently developed manufacturing technology for creating metallic layers on a variety of materials. Metallic particles are accelerated and strike the target surface using a pressurized gas flowing at supersonic speeds. In the last years, cold spray has gained increasing interest in different industrial scenarios, in particular, in the aerospace sector. Given the many fields of application, the need to understand how coated substrates behave when it is necessary to carry out machining operations arises. In this work, low-pressure cold spray equipment was employed to produce metal coatings on epoxy-based glass fibre-reinforced substrates optimized for cold spray deposition employing a layer of polypropylene on the composite surface. An automatic multi-purpose machine was used to drill 4mm diameter holes in the coated specimens considering the rotational speed fixed and varying the feed rate. The machined areas were then analyzed to assess the surface quality of the drilled holes and the burr morphology, considering different feed rate values and different entry surface of the drill-bit.

Introduction

In response to the growing demand for engineered materials capable of responding to the various requests arising during their applications, interest in composite materials such as Polymer Matrix Composites (PMCs), whose properties are completely tailorable due to their anisotropic structure, has increased [1]. Numerous engineering disciplines have been lured to the notion of producing lightweight, high-performance structures, resulting in a recent growth in the use of PMCs for high-end applications [2].

As examined in the literature [3], the metallization of PMCs has been recognized as one of the most promising approaches for further broadening their areas of usage and mitigating the challenges associated with their inherent inadequacies (such as their poor surface characteristics and high sensitivity to heat). In reality, surface metallization can enhance PMC erosion behaviour, boost thermal and electrical conductivity, and assure lightning protection, all of which are important considerations for the aerospace sector [4] .

The functionalization of polymer composite materials using standard processes such as plasma-enhanced chemical vapour deposition (PE-CVD), sputtering, laser ablation and evaporation, and liquid phase deposition is complex and costly, and the resultant coatings are difficult to modify. In reality, these technologies have the following disadvantages: high equipment and processing costs or work-piece size restrictions, low adhesive force, poor stability, lengthy production cycle, distortion of the substrate surface caused by molten particles, and high-temperature flames in thermal spraying (TS) [5].

Because of its capacity to generate thick coatings without compromising the substrate, cold spray (CS) technology has emerged as one of the approaches for metallizing PMC surfaces [6]. In

Content from this work may be used under the terms of the Creative Commons Attribution 3.0 license. Any further distribution of this work must maintain attribution to the author(s) and the title of the work, journal citation and DOI. Published under license by Materials Research Forum LLC.

reality, CS employs kinetic energy to permit the deposition of micron-sized metallic particles (10-100 m in diameter) that do not melt and retain their original properties throughout the process [7].

Cold spray is a revolutionary powder deposition process that is increasingly being used to produce thick functional coatings from a variety of materials, including ceramics [8]. The name "cold deposition" refers to this method's ability to keep processed powder temperatures below the melting point of the particle's substance during the deposition process. As a result, the particles in the solid state strike the substrate at a relatively high velocity, distort, and bond together for coating creation and growth. As a result, CS may be sprayed on temperature-sensitive materials such as polymer matrix composites or plastics without causing considerable thermal degradation, surface deformation, oxide, vacancy development, or phase shift. Furthermore, these coatings reduce residual stress [9].

Cold spray offers resource efficiency benefits, which result in economic and environmental benefits that contribute to long-term sustainability [10]. Cold spray, for example, is a technique that may be described as a green manufacturing process since it releases no harmful emissions, has no discernible environmental impact, and is an important tool for sustainability in a variety of sectors. The heating source is electric and regulated at temperatures below the melting point of the substance being sprayed, thus there are no noxious fumes or other potentially harmful emissions. This prevents the melting of metal powder and the release of hazardous gases. In general, the benefits of cold spray for sustainable production fall into four categories: 1) the process has a minimal environmental effect; 2) repair rather than replacement; 3) better performance, which extends the useable life of components; and 4) an alternative to more polluting and/or less sustainable techniques [11].

Although cold spray has been extensively studied and optimized for the deposition of metal powders on metal substrates, little is known about the deposition of metals on composites, which is far more interesting because it would allow for completely tailored products from the core to the surface.

The majority of the investigations in the literature focus on CS deposition on thermoplastic-based substrates: because there is no other adhesion mechanism other than mechanical interlocking, deformation of the substrate and particles is required for adhesion to occur. This is only conceivable if the substrate is thermoplastic, as it is more ductile because of the weak links that exist between the polymeric chains. Thermosetting polymers, on the other hand, display brittle behaviour, with weakly adherent and inhomogeneous coatings.

However, thermosetting matrix composites are the most appealing in many industries (including automotive and aerospace) due to their high compatibility with fibres and strong mechanical properties. To address this issue, it was presented a unique method that may consist of putting a thermoplastic-based interlayer on the surface of a thermoset-based substrate to achieve excellent CS deposition [12].

However, the application of cold spray for additive, repairing, and coating manufacturing applications is still severely limited by the fact that, due to the poor control over the process, the products require post-processing procedures. Considering that the coatings obtained are substantially thicker than those created with typical coating processes, it is not viable to optimize the processing settings using literature data. In particular, since the drilling process of CS coating on composite involves layers of different materials, it is yet required to do in-depth research on the phenomena that take place during the process.

In this work, for the first time in the literature, a preliminary study on the drilling operations on metal coatings obtained by cold spray on thermoset-based composite substrates optimized for CS deposition is presented.

Materials and Methods

Substrate manufacturing.

By employing plain-woven glass textiles weighing 200 g/m2 and an epoxy infusion technique, square laminates of glass fibre-reinforced plastic measuring 100x100 mm were produced. A total of 16 0/90 cloth layers were piled to achieve a 5 mm thickness. A commercial epoxy resin optimised for infusion applications, with a glass temperature (Tg) onset of 85°C, was employed.

As was mentioned in the preceding paragraphs, several investigations have proven that it is challenging for the sprayed aluminium powder to adhere to the epoxy-based substrate [13]. The particle impact energy is what determines how well cold-sprayed metallic materials adhere to plastic (particle mass and velocity). Even with less impact energy, deformation of the particle is still necessary during the collision. Therefore, only a polymeric substrate that is softer and more ductile, like thermoplastic materials, can allow for the deposition of CS metal and the formation of coatings [12].

Therefore, a unique approach was here suggested based on Polypropylene (PP) film treatments carried out on the epoxy surface, therefore enhancing the metal anchoring, in order to build a metal coating on the composite substrates. Particularly, a heated plate press P 200 E was utilized to promote the PP-composite coupling and a commercial thermoplastic PP film with a thickness of 0.5mm was placed on the surface of each sample. The PP employed has a nominal Tg of -20°C and a melting temperature (Tm) of 170°C.

The dishes were heated to 200 °C, which is slightly higher than the temperature at which polypropylene melts, and then 5 bar of pressure was applied for approximately 5 minutes.

Cold Spray Deposition.

For the cold spray depositions, Dymet 423 low-pressure apparatus with nitrogen as a carrier gas was employed. In order to create the metallic coating on the PP layer, LPW South Europe provided micron-sized powders of the aluminium alloy AlSi10Mg (size range 15-45 μm).

Preliminary experimental results and literature findings served as the foundation for the method chosen for the coating production process [14,15]. Several coating tracks were first created by altering the process parameters in a wide range (inlet gas temperature: 150-600 °C, inlet gas pressure: 4-8 bar, stand-off distance (SoD): 10-80 mm). These coating tracks had a travel speed of the spraying gun equal to 8 mm/s. For the sake of brevity, this process was not described in this article. The optimal process parameters, employed for the deposition of the aluminium layer were determined according to the preliminary study (inlet gas temperature: 160°C, inlet gas pressure: 6 bar, SoD: 45 mm). During the deposition a K-type thermocouple was positioned on the substrate to assess the real process conditions.

To avoid degradation phenomena of the substrate and to ensure softening, the inlet gas temperature was specifically chosen by taking into account that the temperature of the gas flow on the target surface was below the melting point of the polymeric material and, at the same time, greater than the glass transition one. This was done to allow metallic particles to penetrate the polymeric surface. The proper gas pressure was chosen, taking into mind that the substrate will erode more quickly at higher pressures due to the significant shot-peening impact of the particles. Finally, in terms of stand-off distance, greater values of SoD result in particles rebounding, which results in a thin coating since the particles' velocity is reduced upon collision with the substrate. This finding was supported by the literature [16], which indicates that a denser coating forms when the particle momentum is higher.

A 60x60 mm coating was created on the composite substrate specimens' surface by spraying a single layer of Al-based particles. A PosiTest ATM was used to assess the adhesive strength of the coating obtained while complying to the ASTM D4541 standard. Using cyanoacrylate adhesive, aluminum dollies with 10 mm diameter were attached to the top of the cold-sprayed deposits. Using a drill bit, any extra glue or coating around the dolly was taken off. Dolly surfaces were

examined with an optical microscope to measure the quantity of removed coating in order to determine if the test was successful.

Machining of the specimens.

Drilling operations were performed using a 5-axis machining centre (C.B. Ferrari) with a 4mm twist drill bit. As indicated in Table 1, 16 holes were drilled while maintaining the rotational speed constant at 1000 rpm and varying the feed rate.

Table 1. Drilling process parameters employed in this research activity.

Hole	**Feed Rate [mm/min]**	**Hole**	**Feed Rate [mm/min]**
1	20	*9*	20
2	40	*10*	40
3	80	*11*	80
4	160	*12*	160
5	200	*13*	200
6	400	*14*	400
7	800	*15*	800
8	250 *(mean value)*	*16*	250 *(mean value)*

Drilling operations were performed perpendicular to the surface of the substrate. As illustrated in Fig.1, the first eight holes were drilled considering the uncoated composite side as the entry surface, whereas the holes from 9 to 16 were drilled with the coated one as the entry surface.

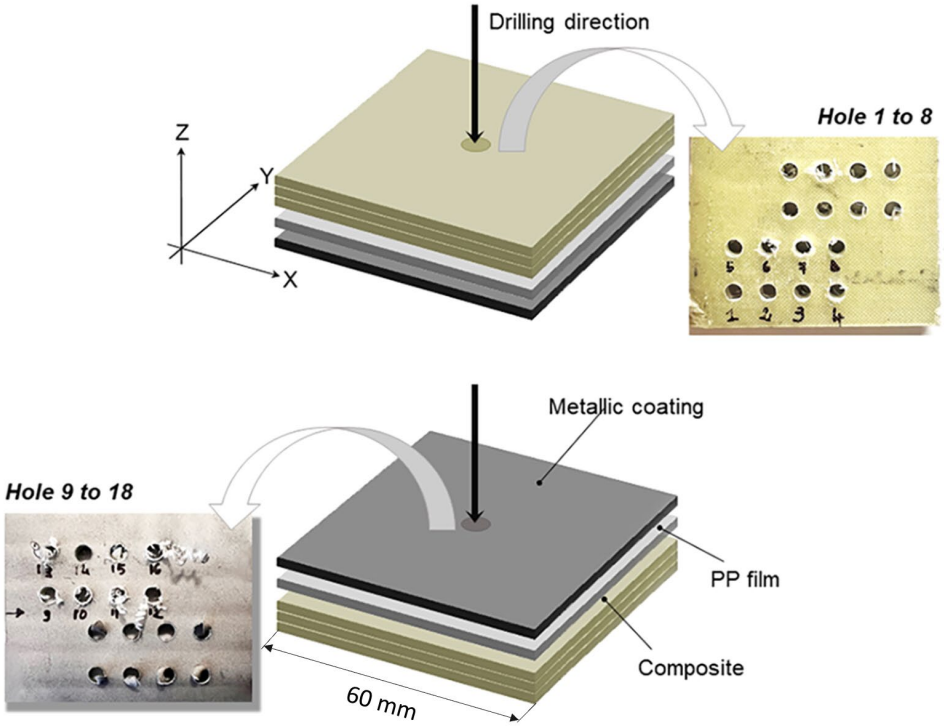

Fig. 1. Schematic illustration of drilling direction considered during the experimental tests.

Results and Discussion

As regards the holes obtained considering the epoxy-based composite as the entry surface the main results obtained by varying the feed rate are highlighted in Fig. 2. When the feed rate is increased it is possible to observe increasing delamination of the surface, defined as the inter-ply failure occurring during the drilling operation of the composite materials[17]. This phenomenon, as highlighted in Fig. 2, may be seen at the drilled-hole entry.

The plies separate from one another and form a peel-up delamination zone around the drilled-hole entry circumference when the drill penetrates the top surface of the laminate. This is caused by the contact between the composite material and the cutting edges of the drill, which creates a peeling force that acts in the Z direction through the slope of the drill [18]. In fact, when the thrust force is greater than the material's interlaminar bond strength, drilling-induced damage manifests as splitting between two adjacent layers.

Delamination is widely acknowledged as the primary mechanism of failure when drilling composite laminates and is regarded as a serious issue since it significantly lowers the material’s fatigue strength [19].

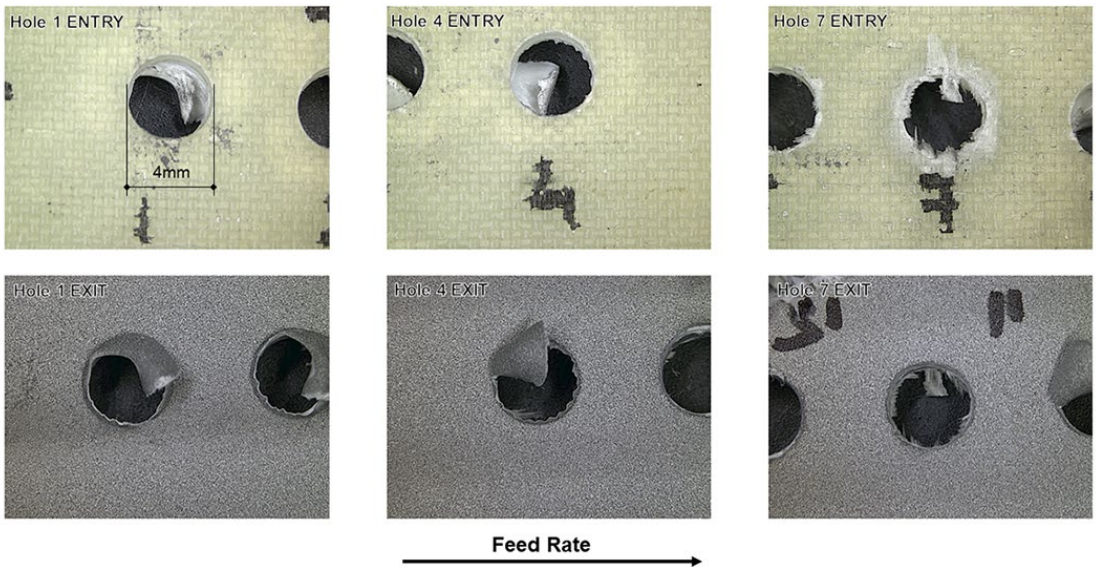

Fig. 2. Macrographs of the holes obtained considering the epoxy-based composite as the entry surface.

As the drill bit travels down the substrate's thickness, it will come into contact with PP film that has been cold-sprayed with aluminium powders. It is possible to observe the formation of burr, a push-out defect due to the deformation during the drilling process of the more ductile material compared to the epoxy-based composite . As the feed rate increases, this defect appears less evident. It is furtherly possible to observe, that the coating remains well adhered to the PP surface.

It, therefore, appears evident that the optimal feed rate value must take into account the opposing trend of delamination of the composite and push-down of the thermoplastic film.

As regards the holes obtained considering the coating as the input surface, the results obtained are portrayed in Fig. 3.

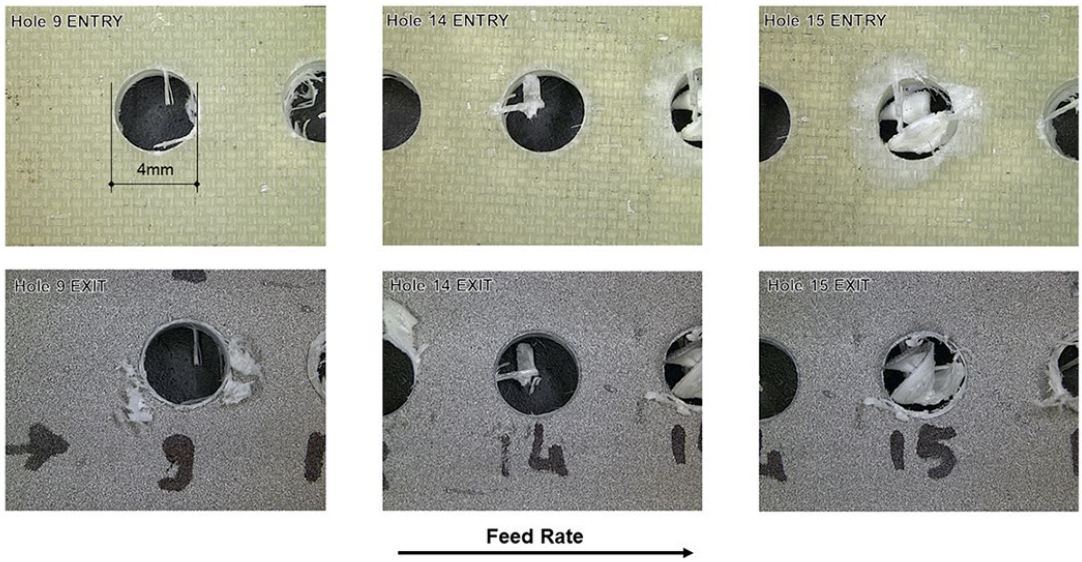

Fig. 3. Macrographs of the holes obtained considering the metallic CS coating as the entry surface.

Materials Research Proceedings 28 (2023) 1729-1738 https://doi.org/10.21741/9781644902479-187

Likewise the previous case, as the feed rate increases, the substrate might delaminate, in this case as a push-out delamination phenomenon. It should be noted that fiber breakage can be observed even at low feed rate values, as illustrated by observing hole 9.

However, in this scenario, we can notice the production of long continuous chips on the inlet surface, where the drilling bit penetrates the CS coating and the Polypropylene film, as shown in Fig. 4.

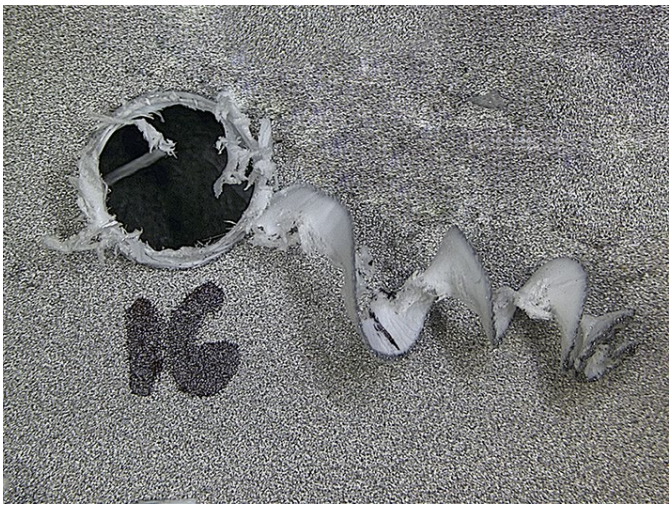

Fig. 4. Long continuous chip obtained with high values of the feed rate.

It is possible to assess that the feed rate strongly influences the length of the chips. Long continuous chips are undesirable as they could frequently tangle around the drilling tool and require hand removal, potentially affecting the operations [20]. In fact, low glass transition temperatures and low heat conductivity of the thermoplastic material are the main factors that contribute to tool clogging in thermoplastic composites. Due to friction, the tool temperature could rise above the glass transition temperature of the polymer during machining, causing the thermoplastic material to become rubbery and deposit on the tool's surface[21].

It is interesting to observe the presence of the CS coating on the surface of the chips created. In fact, the adhesion tests performed on the samples indicate that, despite the creation of the spiral chips, the coatings remain effectively adherent to the composite substrate. As depicted in the macrographic images of the dolly following the adhesion tests illustrated in Fig. 5, the coating is dense and homogenous. The measured average adhesion value is 5 MPa.

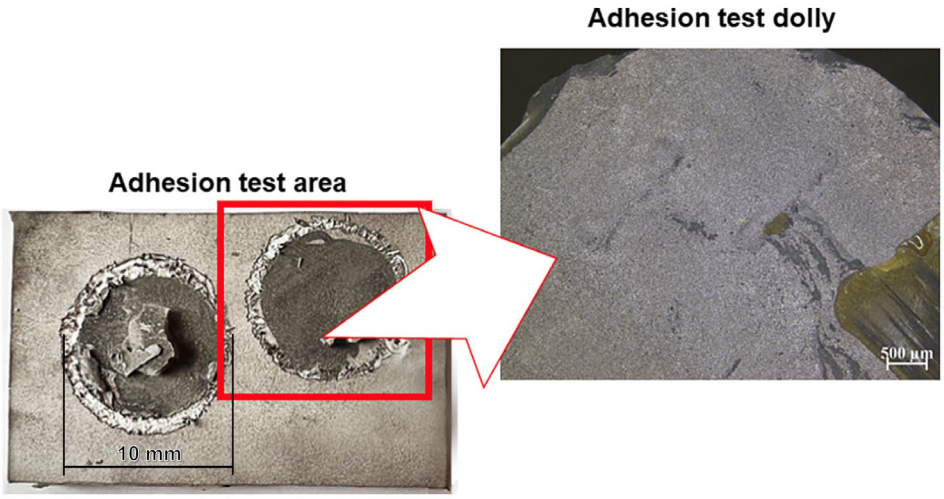

Fig. 5. Adhesion tests performed on the coated specimens. It is possible to observe the CS coating in the macrograph of the adhesion test dolly.

Confronting the results obtained by changing the entry surface of the drill, it is possible to assess that when the drilling operation starts from the composite laminate to the metal coating, no significant changes are observed in the composite to the coating/composite drilling sequence, when increasing the feed rate. However, the formation of long spiral metal/PP chips can be observed when the coating side is chosen as the entry surface, making further machining of the hole necessary and hindering the drilling operations.

Summary

The purpose of the work is to assess the influence of metal-based cold spray coatings on the quality of the holes and burr formation during drilling operations on composite laminates, optimized for CS deposition. The main findings of this work can be summarized as follow:

- the feasibility of drilling operations on cold spray coated samples was assessed
- the surface quality of the machined areas was analyzed by fixing the rotational speed and varying the feed rate
- The feed rate influences the delamination of the composite both at the drilled-hole entry (peel-up delamination) and exit (push-out delamination). Increasing the feed rate, the delamination effects worsen.
- it was shown that the machined-hole entry surface has a strong influence on the burr formation. In particular, long spiral chips are formed when the coating side is chosen as the entry surface.
- The coating remains well adhered to the surface during the drilling operations and remains adhered to the chips. This is further confirmed by adhesion tests performed on the coated surface.

References

[1] S. Kumar, M. Chavan Naveen, Rao D. Srinivasa, Cold spraying: A low temperature variant of thermal spray techniques to deposit metallic materials, Frontiers in Advanced Materials Research 1 (2019) 25-27. https://doi.org/10.34256/famr1914

[2] V.K. Champagne, D.J. Helfritch, Mainstreaming cold spray-push for applications Mainstreaming cold spray-push for applications, Surf. Eng. 30 (2014) 396-403. https://doi.org/10.1179/1743294414Y.0000000277

[3] R. Gonzalez, H. Ashrafizadeh, A. Lopera, P. Mertiny, A. McDonald, A Review of Thermal Spray Metallization of Polymer-Based Structures, J. Therm. Spray Technol. 25 (2016) 897-919. https://doi.org/10.1007/s11666-016-0415-7
[4] A. McIlhagger, E. Archer, R. McIlhagger, Manufacturing processes for composite materials and components for aerospace applications, in: Polymer Composites in the Aerospace Industry, Elsevier, 2020: pp. 59-81. https://doi.org/10.1016/B978-0-08-102679-3.00003-4
[5] P. Fauchais, G. Montavon, Thermal and Cold Spray: Recent Developments, Key Eng. Mater. 384 (2008) 1-59. https://doi.org/10.4028/www.scientific.net/kem.384.1
[6] H. Parmar, F. Tucci, P. Carlone, T.S. Sudarshan, Metallisation of polymers and polymer matrix composites by cold spray: state of the art and research perspectives, Int. Mater. Rev. 67 (2021) 385-409. https://doi.org/10.1080/09506608.2021.1954805
[7] V. Champagne, D. Helfritch, The unique abilities of cold spray deposition, Int. Mater. Rev. 61 (2016) 437-455. https://doi.org/10.1080/09506608.2016.1194948
[8] A. Moridi, S.M. Hassani-Gangaraj, M. Guagliano, M. Dao, Cold spray coating: review of material systems and future perspectives, Surf. Eng. 30 (2014) 369-395. https://doi.org/10.1179/1743294414Y.0000000270
[9] S. Marx, A. Paul, A. Köhler, G. Hüttl, Cold spraying: Innovative layers for new applications, J. Therm. Spray Technol. 15 (2006) 177-183. https://doi.org/10.1361/105996306X107977
[10] G. Prashar, H. Vasudev, A comprehensive review on sustainable cold spray additive manufacturing: State of the art, challenges and future challenges, J. Clean. Prod. 310 (2021). https://doi.org/10.1016/J.JCLEPRO.2021.127606
[11] S. Pathak, G.C. Saha, Development of Sustainable Cold Spray Coatings and 3D Additive Manufacturing Components for Repair/Manufacturing Applications: A Critical Review, Coatings 7 (2017) 122. https://doi.org/10.3390/coatings7080122
[12] A. Viscusi, V. Antonucci, L. Carrino, R. della Gatta, V. Lopresto, I. Papa, A.S. Perna, M.R. Ricciardi, A. Astarita, Manufacturing of an innovative composite structure: Design, manufacturing and impact behaviour, Compos. Struct. 250 (2020) 112637. https://doi.org/10.1016/J.COMPSTRUCT.2020.112637
[13] J. Affi, H. Okazaki, M. Yamada, M. Fukumoto, Fabrication of Aluminum Coating onto CFRP Substrate by Cold Spray, Mater. Trans. 52 (2011) 1759-1763. https://doi.org/10.2320/matertrans.T-M2011807
[14] R. della Gatta, A. Viscusi, A.S. Perna, A. Caraviello, A. Astarita, Cold spray process for the production of AlSi10Mg coatings on glass fibers reinforced polymers, Mater. Manuf. Process. 36 (2021) 106-121. https://doi.org/10.1080/10426914.2020.1813895
[15] A.S. Perna, A. Viscusi, R. della Gatta, A. Astarita, Integrating 3D printing of polymer matrix composites and metal additive layer manufacturing: surface metallization of 3D printed composite panels through cold spray deposition of aluminium particles, Int. J. Mater. Forming 15 (2022) 15. https://doi.org/10.1007/S12289-022-01665-9
[16] W.Y. Li, C. Zhang, X.P. Guo, G. Zhang, H.L. Liao, C.J. Li, C. Coddet, Effect of Standoff Distance on Coating Deposition Characteristics in Cold Spraying, Mater. Des. 29 (2008) 297-304. https://doi.org/10.1016/j.matdes.2007.02.005
[17] G.D. Wang, S.K. Melly, N. Li, T. Peng, Y. Li, Research on milling strategies to reduce delamination damage during machining of holes in CFRP/Ti stack, Compos. Struct. 200 (2018) 679-688. https://doi.org/10.1016/J.COMPSTRUCT.2018.06.011
[18] B.V. Kavad, A.B. Pandey, M.V. Tadavi, H.C. Jakharia, A Review Paper on Effects of Drilling on Glass Fiber Reinforced Plastic, Procedia Technol. 14 (2014) 457-464. https://doi.org/10.1016/J.PROTCY.2014.08.058

[19] J.P. Davim, P. Reis, Study of delamination in drilling carbon fiber reinforced plastics (CFRP) using design experiments, Compos. Struct. 59 (2003) 481-487. https://doi.org/10.1016/S0263-8223(02)00257-X
[20] U.A. Khashaba, Drilling of polymer matrix composites: A review, J. Compos. Mater. 47 (2012) 1817-1832. https://doi.org/10.1177/0021998312451609
[21] M. Alauddin, I.A. Choudhury, M.A. el Baradie, M.S.J. Hashmi, Plastics and their machining: A review, J. Mater. Process. Technol. 54 (1995) 40-46. https://doi.org/10.1016/0924-0136(95)01917-0

Materials Research Proceedings 28 (2023) 1739-1746 https://doi.org/10.21741/9781644902479-188

Process characteristics of constrained friction processing of AM50 magnesium alloy

DE CASTRO Camila C.[1,a *], SHEN Junjun[1,b],
DOS SANTOS Jorge F.[1,2,c] and KLUSEMANN Benjamin[1,3,d]

[1]Helmholtz Zentrum Hereon, Institute of Materials Mechanics, Solid State Joining Processes, Geesthacht, Germany

[2]Pacific Northwest National Laboratory, Richland, WA, United States

[3] Leuphana University Lüneburg, Institute for Production Technology and Systems, Lüneburg, Germany

[a]camila.castro@hereon.de, [b]junjun.shen@hereon.de, [c]jorge.dossantos@pnnl.gov, [d]benjamin.klusemann@hereon.de

Keywords: Constrained Friction Processing, Solid-State Processing, Mg Alloy, Fine Grains

Abstract. Constrained Friction Processing (CFP) is a novel solid-state technique suitable to produce rods especially from lightweight materials. The technology is particularly interesting to overcome the processing challenges associated with Mg due to its hexagonal close-packed (hcp) structure. The process is a variation of the refill friction stir spot welding (refill FSSW) technique, and is performed by plunging the rotating shoulder into the base material, which causes the material to be extruded into the cavity crated by the retraction of the rotating probe and, at the same time, being constrained by it. The complex shear and the heat generated during the process causes metallurgical transformations in the material, such as dynamic recrystallization, allowing for substantial grain refinement to micro- or even submicro- scale. In this study, real time data – torque, axial force and temperature – acquired from the process are analyzed in order to present, for the first time, a description of the CFP technique. Furthermore, the resultant features of the microstructure of a refined rod is explored.

Introduction

The demand for lightweight and environmental-friendly materials has increased over the years as the urge for reduction in greenhouse gas emissions scales [1]. In this scenario, the adoption of Mg and its alloys as structural materials is expected to increase due to their properties such as low density (1.74 g/cm³) and, thus, high strength-to-weight ratio. Nonetheless, the processing of these materials remains a challenge due to Mg's poor workability associated to the hcp crystal structure, which has a limited number of slip systems at room temperature [2].

Severe plastic deformation (SPD) techniques have been investigated for the processing of Mg alloys as means of microstructure tailoring aiming grain refinement and texture modification, which result in improvements on mechanical properties. Among those, Equal-Channel Angular Pressing (ECAP) was demonstrated to produce a refined microstructure on magnesium alloys after multiple passes, which is responsible to enhance the material ductility at moderate temperatures [3]. High-pressure Torsion (HPT) is reported to be capable of producing ultrafine microstructures Mg alloys, with an effect of doubling the strength of the base material [4].

While these techniques have been demonstrated to be able to produce fine-grained Mg and Mg alloy samples both for study of their fundamental properties and for potential applications, they may involve or even require multiple passes, considerable set up and processing times, besides potential dimensional limitations in the samples that can be produced. Most of these limitations

Content from this work may be used under the terms of the Creative Commons Attribution 3.0 license. Any further distribution of this work must maintain attribution to the author(s) and the title of the work, journal citation and DOI. Published under license by Materials Research Forum LLC.

are alleviated or even overcome by using a newly developed technique called Constrained Friction Processing (CFP).

This friction-based technique is suitable for thermo-mechanical processing of lightweight alloys and is based on the fundamentals of the refill friction stir spot welding (refill FSSW) technique [5], but optimized for the production of extruded rods with fine or even ultrafine microstructures. CFP is performed using a 3-part toolset (a stationary clamping ring and the shoulder and probe as the rotating parts), and the processing steps are summarized in Fig. 1. Initially, the toolset reaches the surface of the plate for the clamping of the system using the set clamping force (a). Then, the rotating shoulder plunges into the base material, generating heat due to the friction and plasticizing the material. At the same time, the rotating probe is moved in the opposite direction in order to create a cavity to accommodate the plasticized material displaced by the shoulder and to constrain the material flow (b). Once the desired plunge depth is reached, the rotation of the tools stops and the shoulder is retracted to the level of the probe (c). Finally, the clamping of the plate is released and the tool system is removed, leaving a processed rod (d). The complete process time takes only few seconds depending on the plunge depth, what qualifies the CFP as a fast and simple way to obtain rods with refined microstructure.

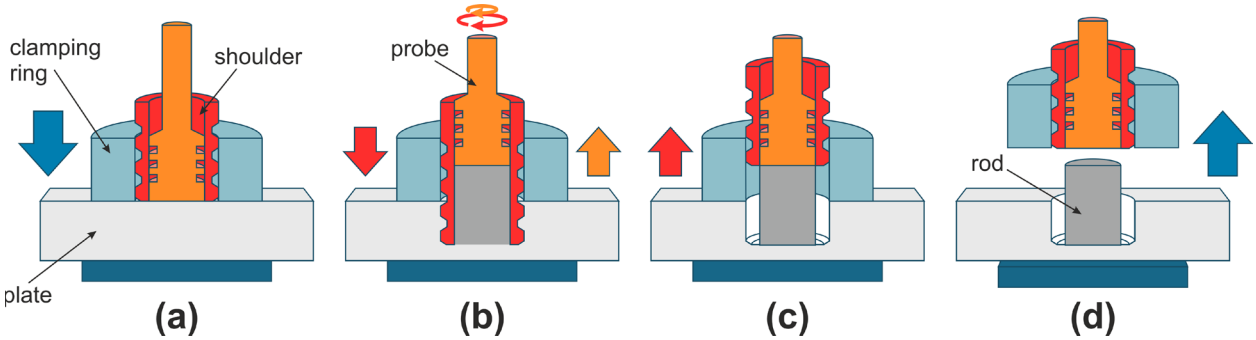

Fig. 1. Schematic representation of CFP: (a) clamping of the plate, (b) plunging, (c) shoulder retraction and (d) releasing steps.

The present study analyzes CFP characteristics in terms of torque, axial force and the temperature evolution in order to better understand the process and enable its further development. Typical CFP rods were processed using as-cast AM50 as base material, and information such as torque and axial force were recorded for each tool part, as well as the process temperature, which was measured using a thermocouple placed at the base of the processed rod. Finally, the microstructure of a typical rod is analyzed in order to demonstrate the potential of CFP on grain refinement.

Materials and Methods

The base material selected in this study is an as-cast AM50 magnesium alloy, obtained via permanent mold casting, as described by Elsayed et al. [6]. The as-cast material features a microstructure with typical dendritic grains (with grain sizes in terms of average diameter varying from 457 to 1023 μm), eutectic β-Mg17Al12 and secondary Al-Mn phases.

In this study, CFP rods were produced using a refill FSSW machine (RPS 200, Harms-Wende GmbH) operated in position control mode. Both axial and rotational movement of each tool part is actuated using individual transducers. The axial forces produced during the process on the rotating parts of the tool can be measured using four shear pancake load cells for each component. Furthermore, the torque produced by the probe and the shoulder is measured using a system consisting of a lever arm attached to the motor spindle that transmits the force to the load cell, also a shear pancake type. A schematic representation of the toolset is given in Fig. 2, which consists

of a molybdenum-vanadium alloyed hot-work tool-steel clamping ring (⌀17 mm) and probe (⌀6 mm), and a G40 tungsten carbide shoulder (⌀9 mm), resulting in an extrusion ratio of 2.25. For the experiment, a total of two samples were produced: one for the torque and axial force measurements, which was subsequently submitted to the microstructural, and one for the acquisition of the temperature evolution. In all cases, the rotation speed (RS) for both shoulder and probe was set as 1800 rpm, combined with a shoulder plunge speed (PS) of 1 mm/s at a constant clamping ring force of 12 kN. The plunge depth (PD) was set as 3.00 mm, resulting in a rod with a total length of 6.75 mm. The process parameters were selected based on preliminary experiments aiming the determination of the suitable processing window. The workpiece used for the CFP with dimensions of 100 x 25 x 6 mm³ was fixed to the stainless steel backing plate attached to the working table, ensuring the stability of the system during the process. No post-processing cooling was used in this study, whereby the produced rods were air cooled.

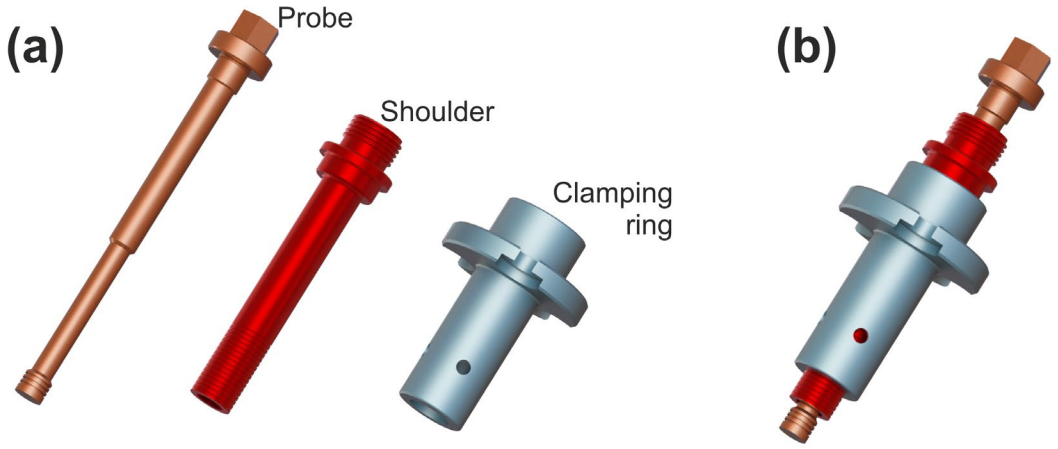

Fig. 2. Schematic representation of the toolset: (a) probe, shoulder and clamping ring, and (b) toolset assembly.

The temperature evolution during CFP was measured using a K-type thermocouple with an acquisition frequency of 50 Hz. The precision of the used thermocouple is ± 2.2 °C or ± 0.75% of the measured temperature, whichever is greater [7]. For this measurement, a 2.5 mm long, 0.6 mm diameter hole was drilled on the back of the workpiece, in a concentric position in relation to the tools. Therefore, the temperature was measured at a point 0.5 mm away from the root of the rod.

For the microstructural analysis, the rod was embedded in acrylic resin, grounded to #4000 Si C foil until the cross-section was reached, and mechanically polished to 0.2-µm water-free colloidal silica suspension. In order to reveal the rod's microstructure, the sample was etched by immersion for 15 s using an acetic-picric solution (180 mL ethanol, 20 mL distilled water, 7.5 mL acetic acid, 4 g picric acid). The metallographic analysis was performed using a VHX-6000 digital microscope. Micrographs were acquired using a Leica DMi8 microscope, where the grain size (d), i.e. average grain diameter, was measured according to ASTM E 112 (grain boundary intersection count method) [8] using the ImageJ 1.52a software [9].

Results and Discussion

Process Characteristics of CFP.

The position of the rotating tools (shoulder and probe) during CFP was recorded and is depicted in Fig. 3(a), along with the RS data. The process starts at t = 0 s, when the toolset just reached the surface of the plate, and the set clamping ring force was applied. In the plots, the tool plunge is indicated with positive values on the *y-axis*, while the retraction of the probe corresponds to negative values. With a set shoulder and probe RS of 1800 rpm, the shoulder starts to plunge the

Materials Research Proceedings 28 (2023) 1739-1746 https://doi.org/10.21741/9781644902479-188

material at a PS of 1.00 mm/s. For this processing route, the displacement of the rotating tools was set to follow a sine profile. The average volume of extruded material is 35.34 mm³/s. In order to constrain this volume of material without imposing any compression, the probe retraction speed is set as 1.25 mm/s, resulting in a total displacement of 3.75 mm at the end of the process.

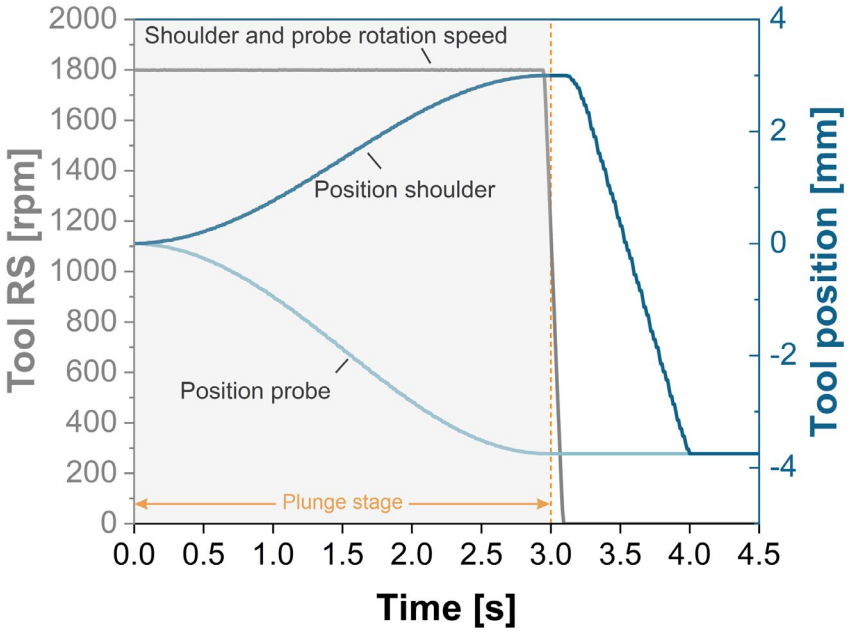

Fig. 3. Position and rotation speed (RS) data acquired for probe and shoulder during CFP.

The torque and axial forces for the probe and the shoulder are presented in Fig. 4. The axial forces correspond to the resistance of the material to the extrusion component of the CFP. For a better understanding of the mechanical efforts associated to the process, it is important to read the results of the actual CFP presented in Fig. 4 (a) along with the plots of the CFP performed without plunging into the workpiece, Fig. 4 (b), that represents the forces and torque related to the friction between the machine components and tool parts. In terms of axial forces, the effect of friction is negligible. The actual CFP axial forces measurement indicates a maximum force during the plunging of around 5.47 kN for the shoulder at t = 0.98 s. For the probe, the maximum axial force (1.66 kN) was measured at the beginning of the process. This likely corresponds to the reaction force to the material stuck between shoulder and probe remaining from the previous processing operation, since the material is not yet plasticized at this moment. Combined with the stuck material, this reaction force is also related to the displaced material produced on the probe due to the beginning of the shoulder plunge.

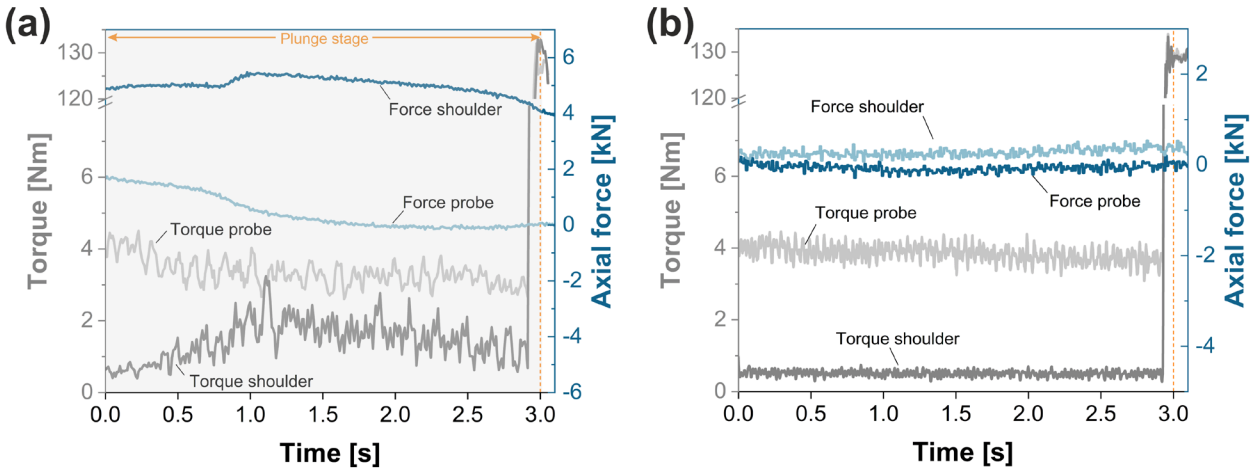

Fig. 4. Torque and axial force data acquired for probe and shoulder during CFP (a) on AM50 workpiece. (b) Measured torques and axial forces due to internal friction, without plunging into the workpiece.

The torque measurements during the CFP indicate the resistance of the material to be stirred due to the rotation of the tool, and are especially interesting for the shoulder. This is attributed to the negligible contribution of the probe to the torque, evidenced by Fig. 4, which shows an average of around 4 Nm. This is somehow expected, since the only contact between probe and material is on its lower surface and the shoulder and probe rotate at the same speed, generating a material flow that doesn't impose significant stresses at this surface. For the shoulder, the torque increases from the beginning of the process until it reaches its peak value of 3.20 Nm around t = 1.10 s. This is an indication of the obvious increase in the resistance of the material to the rotation movement as the shoulder plunging progressively increases. From this peak point on, the torque continuously decreases until the end of the process. It is interesting to point out that the peak values for torque and axial force are reached at the same time, indicating that at this point the material reaches the temperature and shearing conditions leading to plasticization.

As the shoulder approaches the set PD, the control system of the machine starts to drastically reduce the toolset RS to zero at t = 2.94 s for 0.15 s, resulting in a deceleration of 12032 rpm/s (Fig. 3). The deceleration of the tool results in a drastic increase of the torque up to 132 Nm for both probe and shoulder. The process then finishes with the shoulder moved upwards to the same position as the probe (y = -3.75), and releasing the clamping ring force, leaving the processed rod.

The analysis of the temperature measurements, depicted in Fig. 5, indicates that the peak values of torque and axial force for the shoulder occur at around 205°C (478 K). This corresponds to 52% of the AM50 melting temperature, according to differential scanning calorimetry (DSC) measurements reported by Kasprzak et al. [10], i.e. solidus and liquidus temperature of 434°C (707 K) and 640°C (913 K), respectively. Another aspect observed in Fig. 5 is that the peak temperature produced during the plunge stage of the process, Fig. 1(b), measured as 468°C (741 K), is 34°C above the solidus temperature of AM50 alloy and corresponds to 81% of the AM50 liquidus temperature.

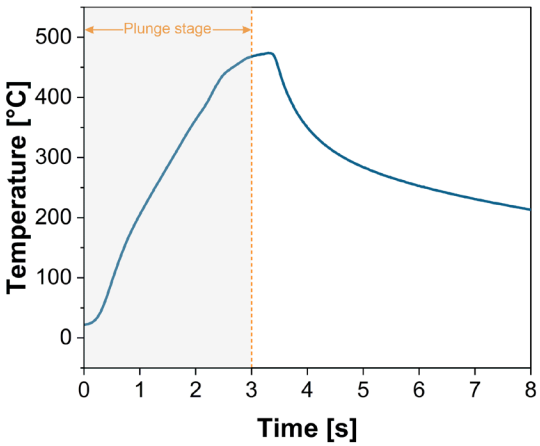

Fig. 5. Temperature evolution during CFP, measured via thermocouple placed at the rod's root.

Microstructure produced by CFP.

The microstructures of the base material and of the rod produced from the conditions presented are depicted in Fig. 6. The comparison of the rod with the surrounding base material indicates a strongly refined microstructure, with average *d* of around 7.7 ± 1.9 µm. This represents a reduction to around 1:96 in comparison to the base material.

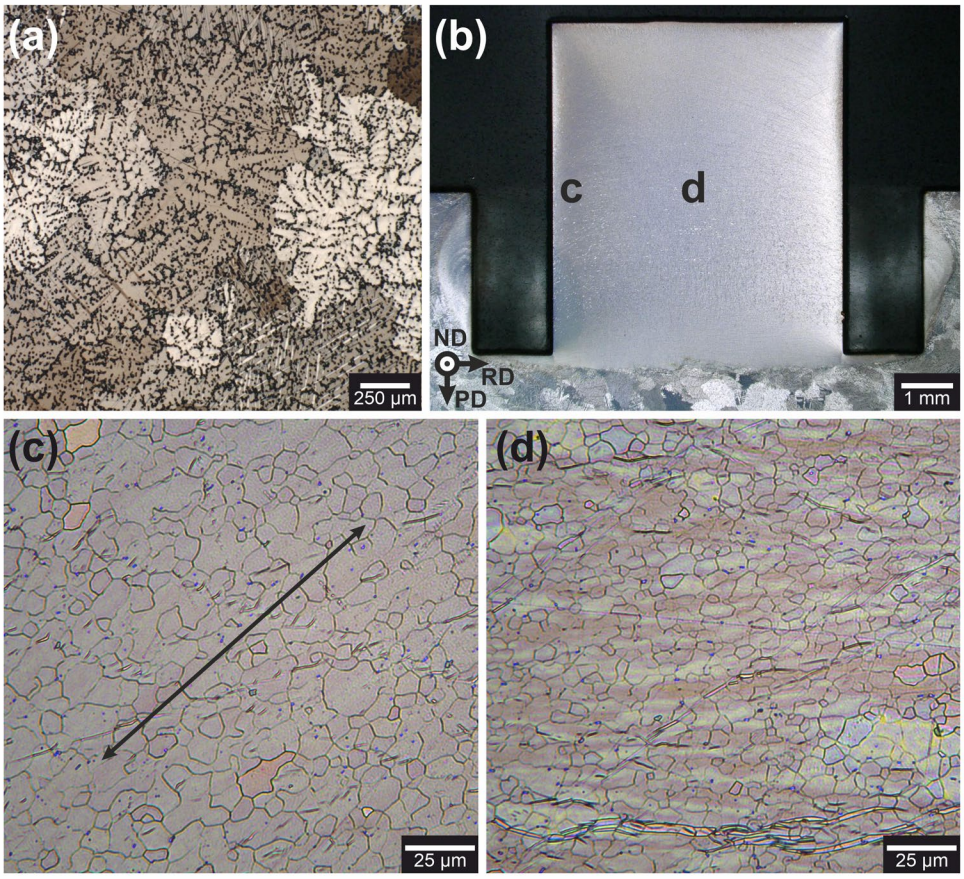

Fig. 6. Micrographs of (a) as-cast AM50 base material, (b) macrostructure of a rod produced by CFP and (c) and (d) micrographs of two selected regions of the rod.

The microstructure of a produced rod varies along the plunge direction (PD) as well as in the radial direction (RD). Two examples of microstructures are depicted in Fig. 6(c) and (d). Along the PD, it is possible to observe a refined and equiaxed microstructure with $d = 8.2 \pm 1.1$ µm. Although the grain structure along the PD is similar for every position, there is a variation in d due to the varying stirring conditions and distinct thermal histories as a function of the height. At the bottom of the rod, the average measured d is considerably smaller than the other positions of the rod, 5.4 ± 0.5 µm, while the average d at the top of the rod is 9.0 ± 0.7 µm.

Along the RD of the rod, less remarkable differences on d are observed, e.g., at the border (9.0 ± 1.8 µm) (c) and at the center (8.2 ± 1.1 µm) (d) of the rod. However, the examination of the grain structure at these two positions indicates some deformation of the grains along the direction of around 47° // PD. This may be attributed to the material flow conditions during CFP, described by Shen et al. [11] as a spiral curve similar to a conical compression spring, and developed layer by layer during the refilling stage of the refill FSSW, which is analogous to CFP.

Summary

In the present study, CFP was introduced and its characteristics were investigated in terms of torque, axial force and temperature evolution during the process. Furthermore, the microstructure of a typical AM50 rod produced via the novel CFP was analyzed. The main findings are summarized below:

- Although the probe plays an important role on the constraint of the material flow, the torque evolution during the process is negligible for this tool part. For the axial force, a peak value of 1.66 kN is found at the beginning of the process and is progressively reduced to roughly zero.
- The data acquired for the shoulder indicates peak values of torque of 3.2 Nm at t = 1.1 s and axial force of 5.47 kN at t = 0.98 s, i.e., roughly at the same moment. In this time interval, the temperature measured at the bottom of the rod reads around 200 °C, suggesting that the temperature of plasticization of AM50 during CFP is at least 52% of AM50's melting temperature.
- The produced microstructure has an average d of around 7.7 ± 1.9 µm, which represents a reduction of the initial as-cast base material of around 1:96. It is interesting to point out that this remarkable d reduction was obtained using a simple process setup in only 3 s of processing time, indicating suitable upscale potential of CFP.

References

[1] European Environment Agency, Greenhouse gas emissions from transport in Europe. Retrieved from https://www.eea.europa.eu/data-and-maps/indicators/transport-emissions-of-greenhouse-gases-7

[2] Z. Wu, R. Ahmad, B. Yin, S. Sandlöbes, W.A. Curtin, Mechanist origin and predicion of enhanced ductility in magnesium alloys, Science 359 (2018) 447-452. https://doi.org/10.1126/science.aap8716

[3] R.B. Figueiredo, T.G. Langdon, Grain refinement and mechanical behavior of a magnesium alloy processed by ECAP, J. Mater. Sci. 45 (2010) 4827–4836. https://doi.org/10.1007/s10853-010-4589-y

[4] R.B. Figueiredo, M.T.P. Aguilar, P.R. Cetlin, T.G. Langdon, Deformation heterogeneity on the cross-sectional planes of a magnesium alloy processed by high-pressure torsion, Metall. Mater. Trans. A Phys. Metall. Mater. Sci. 42 (2011) 3013-3021. https://doi.org/10.1007/s11661-011-0609-z

[5] C. Schilling, J.F. Dos Santos, Method and device for linking at least two adjoining work pieces by friction welding, European Patent Office. EP1230062 (2000)

[6] F.R. Elsayed, N. Hort, M.A. Salgado-Ordorica, K. Kainer, Magnesium permanent mold Castings optimization, Mater. Sci. Forum. 690 (2011) 65-68. https://doi.org/10.4028/www.scientific.net/MSF.690.65
[7] ASTM International, ASTM E230 - Standard Specification for Temperature-Electromotive Force (emf) Tables for Standardized Thermocouples, (2017). https://doi.org/10.1520/E0230_E0230M-17
[8] ASTM International, ASTM E112 - Standard Test Methods for Determining Average Grain Size, (2021). https://doi.org/10.1520/E0112-13R21
[9] C.A. Schneider, W.S. Rasband, K.W. Eliceiri, NIH Image to ImageJ: 25 years of image analysis, Nat. Methods. 9 (2012) 671–675. https://doi.org/10.1038/nmeth.2089
[10] W. Kasprzak, J.H. Sokolowski, M. Sahoo, L. Dobrzanski, Thermal and structural characteristics of the AM50 magnesium alloy, J. Achieve. Mater. Manuf. Eng. 28 (2008) 131-138.
[11] J. Shen, S.B.M. Lage, U.F.H. Suhuddin, C. Bolfarini, J.F. dos Santos, Texture Development and Material Flow Behavior During Refill Friction Stir Spot Welding of AlMgSc, Metall. Mater. Trans. A Phys. Metall. Mater. Sci. 49 (2018) 241-254. https://doi.org/10.1007/s11661-017-4381-6

Materials Research Proceedings 28 (2023) 1747-1758 https://doi.org/10.21741/9781644902479-189

Analysis of the relationship between the properties of selected materials and the parameters of the EDD process

TRAJER Marcin[1,a], CZESZKIEWICZ Adrian[2,b] and MACHNO Magdalena[3,c *]

[1]Division of Surface Engineering, Faculty of Materials Science and Engineering, Warsaw University of Technology, Wołoska 141, 02-507 Warsaw, Poland

[2]Łukasiewicz Research Network–Institute of Aviation, al. Krakowska 110/114, 02-256 Warsaw, Poland

[3]Department of Rail Vehicles and Transport, Faculty of Mechanical Engineering, Cracow University of Technology, al. Jana Pawła II 37, 31-864 Cracow, Poland

[a]marcin.trajer.dokt@pw.edu.pl, [b]adrian.czeszkiewicz@ge.com, [c]magdalena.machno@pk.edu.pl

Keywords: Electrical Discharge Drilling (EDD), Micro-Hole, Difficult-To-Cut Material

Abstract. The thermophysical properties of the electrodes material significantly impact performance of the electrical discharge machining (EDM). The aim of this article was to investigate the influence of thermophysical properties of selected materials on the EDM process. The effect of the thermophysical properties of these materials on process efficiency factors (material removal rate, linear tool wear) and hole geometry (aspect ratio, radial overcut) was analyzed. The results showed that selected thermophysical properties of the workpiece, such as thermal conductivity, melting point, have the most significant impact on the electro-erosion process. Optimal result parameters (material removal rate: 2.58 mm^3/min, linear tool wear: 4.95 mm, aspect ratio: 8.00, radial overcut: 0.046 mm) and no presence of "bottom cone" were obtained for EDM drilling in Inconel 718 and similarly for AISI 1045 steel. On the other end were high resistance alloys such as tungsten carbide and copper alloy.

Introduction

The electrical discharge machining (EDM) process is one of the unconventional methods of manufacturing. The process has been known since around 1943 [1]. However, efforts are still being made to improve its performance, parameters and the accuracy of the manufactured shapes. Experimental research is still being done to increase material removal rate (MRR), reduce tool wear (TW), and reduce surface roughness (SR) [2-4]. Additionally micro-holes requires high dimensional and shape accuracy without burrs and micro-cracks [5].

In the process of electrical discharge machining the workpiece material is removed as a result of phenomena accompanying electric discharges occurring in the inter-electrode gap area. The gap involves area between workpiece and working tool electrode. Energy transferred during the discharge in a form of spark melts and evaporates the metal. For the occurrence of electrical discharges, the electrodes are connected to the electric pulse generator. Space between the electrodes is filled with a working liquid. Also, the selection of parameters and material of the tool should ensure the removal of more material from the workpiece [6,7]. In addition, the EDM enables processing of electrically conductive materials, regardless of their hardness. This is the most important advantage of EDM process comparing to conventional machining methods. Thanks to that technique can be successfully used to produce parts from modern engineering materials in such industries as aviation, automotive and medical. In addition, due to the high accuracy of obtained geometry (approx. 5 μm), this process is also suitable for the production of micro-shapes, including micro-holes in the diameter range of 1-999 μm [6,8,9].

Content from this work may be used under the terms of the Creative Commons Attribution 3.0 license. Any further distribution of this work must maintain attribution to the author(s) and the title of the work, journal citation and DOI. Published under license by Materials Research Forum LLC.

Currently, aviation, automotive and medical industries use engineering materials that are resistant to high temperature conditions, providing at the same time high strength, and high hardness. Within parts such as jet engines turbine blades are equipped with micro-holes which are made to increase their high temperature operational capabilities (up to 1,373 K). These micro-holes are called "cooling holes". When the jet engine is running, cool air flows through them, further reducing airfoil temperature [10]. However, due to the strength properties of the used materials, as well as the size of micro-holes (0.3 - 5 mm in diameter, depth to diameter ratio (40-600:1), the choice of technology for their production is limited. Currently, one of the most frequently chosen technologies for cooling holes manufacturing is electrical discharge drilling (EDD) [11,12].

In conducted research [13], Authors indicate that the thermophysical properties of the workpiece material and the working electrode affect the machinability the EDM process. At the same time also material of the working electrode have a strong impact on the EDM process. Calculated erosion resistance index shows how important it is to analyze such electrode material properties as thermal conductivity, specific heat and melting point. Similar research results are presented in the analysis of the impact of the thermophysical properties of the electrode material on the EDM process of such materials as AISI 304 stainless steel and Ti-6Al-4V alloy in [14]. The results indicated that the greater resistance of the material is (higher erosion resistance index, harder to EDM) lower overcut and lower taper rate are. According to this analysis, despite the low MRR value, good machining accuracy can be achieved. However, in [15], a significant impact of the thermophysical properties of the workpiece (in this case Inconel 718 superalloy) on the EDM process was demonstrated. In the analysis of the results, attention was paid to the change in the behavior of selected thermophysical properties of the superalloy under the influence of temperature. In this case, the thermal conductivity of the material increases with increasing material temperature. Also in [7], when analyzing the parameters of the post EDM surface layer, the high thermal conductivity of workpiece - steel HTCS was taken into account. The analysis of the results showed that the thickness of the white layer was in the range of 5-34.5 μm and depended mainly on the amount of thermal energy supplied to the workpiece. The amount of thermal energy that reaches the material and the speed of its propagation in the surface layer of the material depends on the thermal conductivity of the material.

The above examples of the analysis of the results of EDM process researchers indicate that the impact of the thermophysical properties of the electrodes material (workpiece material and tool electrode) significantly affect the selection of machining parameters and the efficiency of the process or the quality of the machined surface. Thus, the impact of these properties of the electrode material on stock removal, process efficiency or the quality of the treated layer is crucial to obtain effective machining.

The aim of this work is to investigate the influence of the thermophysical properties of five materials such as: tungsten carbide VHM, superalloy Inconel 718, carbon steel AISI 1045, copper alloy CuCr1Zr and aluminum alloy AW-2017A on the EDM process. The EDM process was performed using a brass tubular electrode with an outer diameter of 0.4 mm and a working fluid of deionized water. All tests were performed with same electrical pulse parameters such as gap voltage, current, cycle load (pulse on duration / pulse off duration). Moreover drilling process time was identical. The efficiency of the process was analyzed in terms of the material removal rate and linear wear of the working electrode as well as the geometric characteristics of the micro-holes (radial over cut, aspect ratio - the ratio of the hole length to its diameter). Finally, the results were linked to the thermophysical properties of the materials in which the micro-holes were drilled. The summary of test results in selected materials is also intended to show how strongly the thermophysical properties of the workpiece material affect the course of the process and performance factors.

Materials and methods

Material used for workpiece and tool.

Experimental EDM research was carried out in five selected materials:

- tungsten carbide VHM,
- Inconel 718 superalloy,
- AISI 1045 carbon steel,
- CuCr1Zr copper alloy,
- AW-2017A (AlCu4MgSi) aluminium alloy.

The selection of the materials was guided by their diverse thermophysical properties (see Table 1), as well as by their diverse chemical composition. Following scope of the article and the phenomena the EDM process, knowledge of selected thermophysical properties of the workpiece material is important. This is related to the impact of these properties on the EDM drilling process and on the efficiency of that process. For a more accurate analysis of the results, the chemical composition of each material was measured, which is shown in Table 2. The chemical composition was determined using an X-MET8000 X-ray spectrometer (Hitachi High-Tech, Tokyo, Japan).

Table 1. Thermophysical properties of the selected material.

Property (unit)	Workpiece Materials					Electrode Material
	VHM	Inconel 718 [20,21]	AISI 1045 [22,23]	CuCr1Zr [16,17]	AW-2017A [18,19]	Brass [18,19]
Density [g/cm^3]	15.0	8.19	7.82	8.94	2.75	8.55
Melting point [K]	2,273	1,533-1,609	1,793	1,338-1,356	913	1,263
Thermal conductivity [W/(m·K)]	87.9	11.4	48.1	401	134	159
Specific heat capacity [J/(kg · K)]	150-350	435	570	385	873	385

Table 2. Chemical composition of workpiece materials [%].

Chemical element	Workpiece material				
	VHM	Inconel 718	AISI 1045	CuCr1Zr	AW-2017A
Al	0.77	0.57	-	-	91.89
C	-	-	0.43	-	-
Co	6.04	0.1	-	-	-
Cr	0.79	18.4	0.05	0.6	0.08
Cu	-	0.08	0.07	99.27	4.45
Fe	0.61	16.81	98.47	-	0.72
Mg	-	-	-	-	0.76
Mn	-	-	0.71	-	0.92
Mo	-	3.16	<0.01	-	-
Nb	-	5.37	-	-	-
Ni	-	53.63	0.04	-	-
Re	4.48	-	-	-	-
S	-	-	0.01	-	-
Si	-	0.34	0.03	-	0.63
Ta	0.91	-	-	-	-
Ti	-	0.96	-	-	0.17
W	86.4	0.06	-	-	-
Zn	-	-	-	-	0.23
Zr	-	-	0.01	0.04	-

Brass tubular electrodes with external diameters of 0.4 mm and internal diameters of 0.215 mm were used for EDM drilling. Brass has good heat conductivity as well as low electrical resistance.

According to [24], brass is the best tool material for EDM machining. In addition, selected round electrodes are the best for micro-hole drilling [25].

Experimental details.

The micro-holes were made by electrical discharge machining on the custom made EDM machine. It is equipped with transistor controlled generator as well as NC controlled. In each type of workpiece 9 blind micro-holes were made. The drilling parameters in each material were the same and were selected in such a way as to ensure correct machining (minimize short circuits). The number of holes was chosen to reduce outliers from results evaluation. During the process, the tool electrode moved towards the workpiece with a feed rate controlled by gap voltage value and rotated at a constant rotational speed. The working fluid was fed with constant pressure through a channel in the electrode to the gap area between the electrode and the workpiece. The rotation of the working electrode and the continuous flow of working liquid under the narrow inter-electrode gap were intended to improve the stability of the process. These solutions improve the removal of erosion products (debris, air bubbles), reducing the possibility to occur short circuits or arc discharges. During the test, a new electrode was used in each of the tested materials in order to ensure the same working conditions for each workpiece material. To ensure electrical discharges to occur, both electrodes (tool and workpiece) were connected to an electrical pulse generator. Each hole was made with a fixed spindle displacement in the Z axis. Fig. 1 shows a diagram of the test stand.

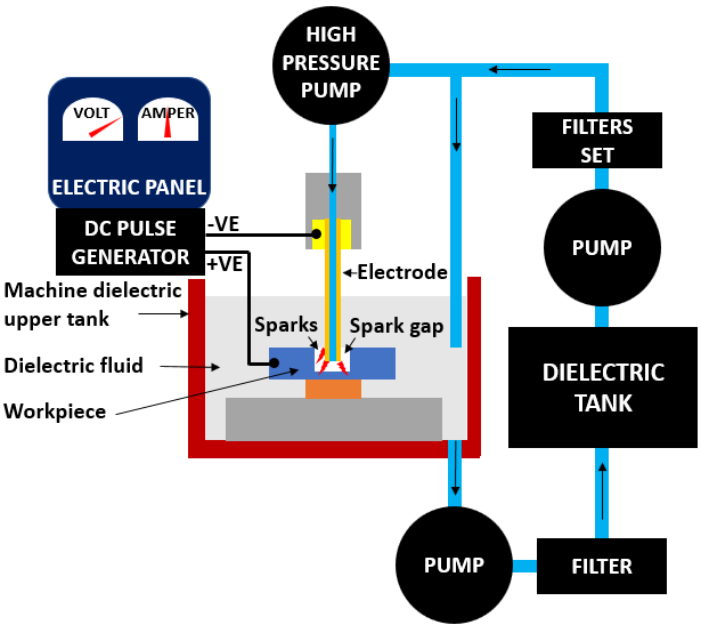

Fig. 1. Scheme of the EDM process test stand.

The drilling process was performed using the following conditions: current amplitude: 10 A, open voltage: 40 V, pulse on duration: 30 µs, pulse off duration: 30 µs, tool rotation speed: 500 rpm, capacitance: 1425 nF, working fluid: deionized water, working fluid temperature: 294 K, electrical conductivity of the working fluid: 10 µS/cm, working fluid pressure: 11 MPa, initial interelectrode gap: 100 V, the value of the spindle displacement in the Z axis: 8.9 mm, load cycle: 50%.
In this work below response parameters were analyzed:

- material removal rate (MRR), was calculated from the following equation:

$$MRR\ (mm^3/min) = V/t. \quad (1)$$

Where: V – volume of material removed, t – drilling time,

- linear tool wear (LTW, mm), determined as the shortening of the electrode along its length and measured after each hollow hole,
- the radial overcut (ROC), was calculated according to the below formula:

$$ROC\ [mm] = (D_{hole} - D_{electrode})/2. \quad (2)$$

where: D_{hole} – average input diameter, $D_{electrode}$ – outer diameter of the tool electrode, aspect ratio (AR), was calculated according to the formula:

$$AR = H_{depth}/D_{hole}. \quad (3)$$

where: H_{depth} – drill hole depth.
Diameter measurements were made using an Alicona C200 microscope (Alicona Imaging GmbH, Raaba/Graz, Austria). A dedicated lens with a high focal length was used for scanning. The vertical scanning resolution was 3 μm. The volume of material removed as well as holes geometry was measured using the GOM Inspect program (ZEISS, Oberkochen – Germany). The volume of the shallowest holes (< 1 mm deep) due to large on fluence of conicity on the volume of hole was directly measured using a volume measuring tool. In contrast, the volume of the deepest holes (> 1 mm deep) was measured as follows:

- a cylinder was created from the scanned hole, using the "best fit 3 sigma" method, which allowed the cylinder to be sufficiently matched to the scanned shape of the hole,
- cylinder diameter was measured,
- hole depth was measured,
- the volume of the hole (V_{hole}) was calculated using the formula:

$$V_{hole} = P_p \cdot H. \quad (4)$$

where: P_p [mm^2] – the surface area of the hole measured at depth 0.1 mm, H [mm] – hole depth.
In the case of holes made in aluminum alloy, due to their significant depth (H_{depth} > 6 mm), the holes had to be cut along the axis. This made it possible to measure accurately the depth of these holes.
The measurement results of the experimental studies are given in Table 3. Table 4 shows the calculated standard deviation for the determined result factors.

Table 3. Results of the experiments (average value).

Workpiece material	Results			
	V [mm^3]	t [s]	D_{hole} [mm]	H_{depth} [mm]
Tungsten carbide VHM	0.05	24	0.47	0.37
Inconel 718 superalloy	0.75	18	0.49	3.94
Carbon steel AISI 1045	0.53	19	0.50	2.67
Copper CuCr1Zr	0.11	47	0,48	0.67
Aluminium alloy AW-2017A	1.32	12	0.51	6.39

Table 4. Calculated standard deviation values for the result factors.

Material workpiece	MRR	LTW	ROC	AR
	Standard deviation			
Tungsten carbide VHM	0.018	0.0058	0.0033	0.0067
Inconel 718 superalloy	0.150	0.0724	0.0025	0.0815
Carbon steel AISI 1045	0.081	0.0727	0.0064	0.0853
Copper CuCr1Zr	0.008	0.0155	0.0025	0.0326
Aluminium alloy AW-2017A	0.162	0.0845	0.0057	0.1496

Results and Discussions

Influence of the thermophysical properties of the electrode material on the efficiency of the process

In the EDM process, performance parameters such as material removal rate (MRR) and linear tool wear (LTW) play a key role [6]. Manufacturers are looking MRR increase options. At the same time tool wear generates about 50% of the crafting costs. Therefore TW reduction is expected. In addition, when producing micro-holes, electrode wear can be as high as 100%. As can be seen in the MRR result tables below, the process efficiency was different for each of the micro-holes analyzed. The highest material removal efficiency is observed for the AW-2017A aluminum alloy (about 6.5 mm^3/min) (Fig. 2a). Also, the other analyzed output factors turned out to have the highest values compared to the other materials (LTW - 2.25 mm, Fig. 2b, AR - 12.49, Fig. 2c). It is also worth mentioning that deep micro-holes production process, the material removal rate parameter is strongly related to the aspect ratio of the hole. This dependence is observed by analyzing the results in Fig. 2a and Fig. 2c.

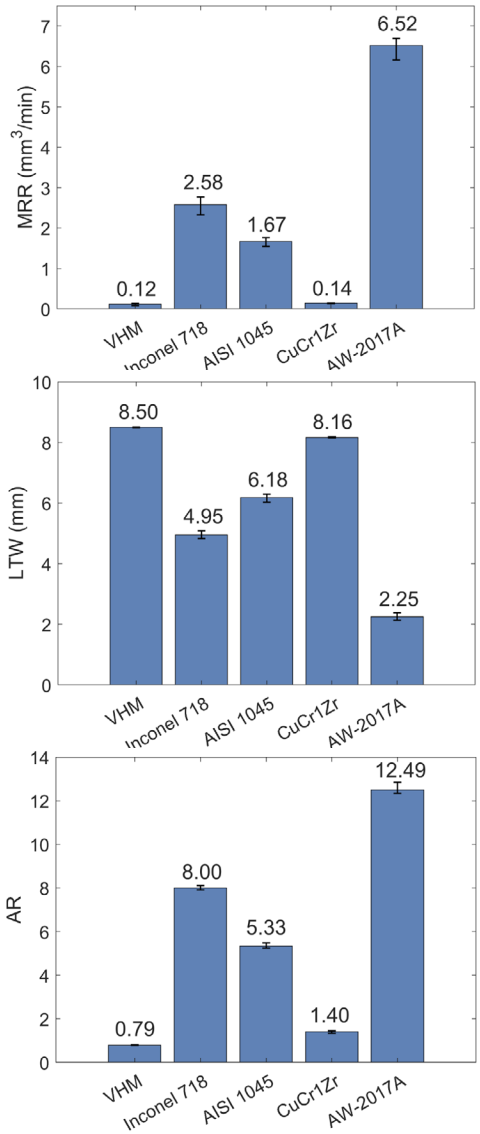

Fig. 2. The results of the EDM process factors: a) material removal rate (MRR), b) linear tool wear (LTW), c) aspect ratio (AR).

In the case of the electro-erosion process, one could conclude that the thermal conductivity of the workpiece material has the main influence on the material erosion process. This is related to the nature of the process. The nature of thermal phenomena that accompany electrical discharges and related extremely high temperature of the created plasma channel, approx. 4,000 – 8,000 K [26]. The consequence here is the non-stationary propagation of heat from the so-called surface sources, which are formed on the surfaces of the electrodes under the pressure of the plasma channel generated during the electro-erosive discharge. However, the analysis of the results shown in Fig. 2a for the MRR shows that it is the melting temperature that drives the performance of the EDM process. The highest MRR value (6.52 mm^3/min) was achieved for aluminum alloy. The thermal conductivity of this material (134 W/(m·K)) is similar to the thermal conductivity of tungsten carbide material (87.9 W/(m·K)). CuCrZr copper alloy, on the other hand, has an even better thermal conductivity than these materials (401 W/(m·K)). After analyzing the remaining thermophysical properties, the AW-2017A alloy has the lowest melting point (913 K) compared to the other analyzed materials (even lower than the melting point of the tool electrode material). This shows that the melting temperature of material is its property, which has a significant impact on the EDM process.

Further analysis of the results confirms the above statement. Analyzing the obtained results, VHM tungsten carbide also has good thermal conductivity (105 W/(m·K)). However, this material has a high melting point (approx. 2,273 K). The same applies to the CuCr1Zr chromium-circus alloy. This alloy also has good thermal conductivity (401 W/(m·K)), but has a high melting point (in the range of 1,338 - 1,356 K). A similar effect on the MRR of the thermal conductivity and melting point of materials can be observed for super alloy Inconel 718 and carbon steel AISI 1045 (thermal conductivity: 11.4 W/(m·K) and 48.1 W/(m·K), respectively, and melting point: 1,533-

1,609 K and 1,793 K, respectively). From the graph of Fig. 2a, it can be concluded that the material removal rate has similar values obtained for drilling in these materials.

Comparable conclusions were presented in [14], The authors indicate that material properties such as the melting point, the specific heat capacity and thermal conductivity affect the material removal rate during electro-erosion treatment of the material. The increase in these properties of the workpiece material cause its lower machinability by EDM, according to the index of resistance to the material erosion process given in [13]. In order to check how well selected materials can be machined by the EDM process, the erosion resistance index was calculated. The erosion resistance index (ER_{index}) calculations were made using the following formula (5) and are summarized in Table 5.

$$ER_{index} = \lambda \cdot c \cdot T^2. \tag{5}$$

where: λ – thermal conductivity (W/(m·K)), c – specific heat capacity (J(kg·K)), T – melting point (K). Calculated values of the erosion resistance index for individual materials presented in Table 5. The values of λ, c, T for the ER_{index} calculation were taken from Table 1 (in the case of a range of values, the maximum value in the range was considered). Equation (5) was used in accordance with the formula for calculating the machinability index by EDM presented in [13]. This formula shows that the square of the material's melting point has the greatest effect on the EDM's machinability of the material.

Table 5. Erosion resistance index of analyzed material (ER_{index}).

Tungsten carbide VHM	Inconel 718	Carbon steel AISI 1045	Copper CuCr1Zr	Aluminium alloy AW-2017A	Brass
Erosion resistance index ER_{index} [x 10^{10} $J^2/(m \cdot s \cdot kg)$]					
15.90	1.28	8.81	28.40	9.75	9.76

The calculated index of resistance to the EDM process confirms that its higher values for tungsten carbide VHM and CuCr1Zr alloy indicate that their EDM machinability is reduced. On the other hand, lower ER_{index} values for Inconel 718 superalloy, AISI 1045 carbon steel and AW-2017A aluminum alloy confirm the higher MRR value obtained. Also, according to the interpretation of the ERindex, a higher value indicates that a given material can be used as a tool electrode material. Certainly, the brass electrode is one of the most appropriate for the machining of Inconel 718 superalloy (the lowest ER_{index} obtained for Inconel 718, and the highest obtained ER_{index} for CuCr1Zr alloy). This is also confirmed by the obtained higher slenderness values (AR about 8) of the micro-holes hollowed out in this nickel-based superalloy.

In addition, the erosion resistance index informs how much wear of the working electrode can be expected when machining a given material. If the ER_{index} is higher, the material removal rate due to its poor EDM machinability will be lower. The working electrode will have to work longer and wear out more to remove the required amount of material.

It is also worth noting that the same drilling parameters and the same type of working electrode (with the same geometry, made of the same material) were used for the experimental research. The obtained results therefore show that the selected parameters and the type of working electrode are appropriate for drilling micro-holes in the AW-2017A alloy. This could also have influenced the most effective parameters for this material, such as MRR and LTW. The selected parameter values in this case ensured the stability of the process. In addition, the authors [14] also draw attention to the importance of thermal conductivity of the tool electrode material. The greater thermal conductivity of the working electrode material causes more heat to be dissipated in it. That turns in to the lower energy density of the electric discharge by that creating smaller craters on the

surface of the workpiece. Analyzing Fig. 2a, lower MRR values for Inconel 718 and carbon steel AISI 1045 can be associated with much lower thermal conductivity of these materials compared to the thermal conductivity of the working electrode material (λ lower by approx. 90% for Inconel 718 and approx. 70% for AISI 1045).

Influence of the thermophysical properties of the electrode material on the accuracy of micro-holes.

In the case of the analysis of micro-holes and their subsequent functionality in production parts, their high dimensional and shape accuracy is crucial. For this purpose, the radial overcut parameter of the micro-holes (ROC) was investigated (Fig. 4). The obtained results show that the ROC values are in the range of 0.03 - 0.06 mm. It can therefore be assumed that this parameter has similar values for analyzed materials. It can also be assumed that drilled holes are characterized by good dimensional accuracy.

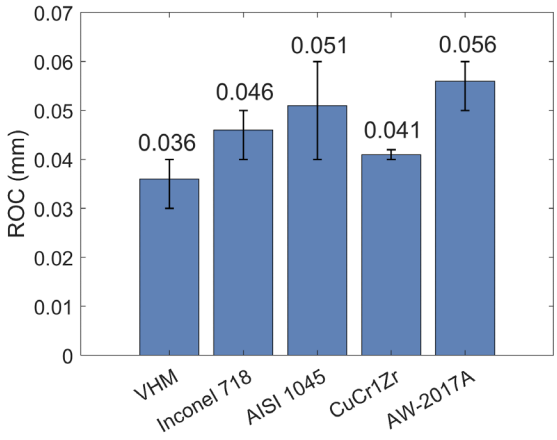

Fig. 4. The results of the geometric factor: radial overcut (ROC).

In addition, SEM images of the entrance of the wells showed the formation of a heat affected zone (HAZ) around the holes (Fig. 5). In case of VHM The HAZ layer includes also a material which has been melted but not fully removed and solidified at the edge of the hole. Such build-up material was not observed for neither Inconel 718 nor steel AISI 1045 which represent similar level of thermal conductivity. Large HAZ collar might result from heat being given off by a significant amount of re-solidified material formed at the edge of the hole drilled in the tungsten carbide. However, this certainly needs further investigation.

The SEM images for drilling in tungsten carbide and CuCr1Zr alloy show unremoved material at the bottom of the hole. In the literature, this phenomenon is called the “residual cylinder” [25] or “cone” [27].

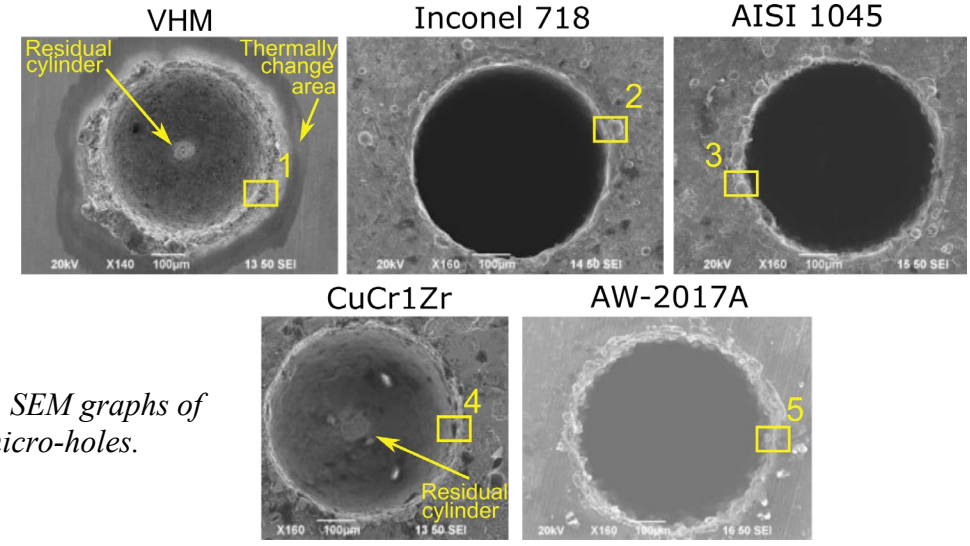

Fig. 5. SEM graphs of micro-holes.

Analysis of the hole entry shows clearly solidified material that has not been removed (Fig. 6). In addition, SEM photos and scans of the hole entry showed the so-called “residual cylinder” formed at the bottom of micro-holes drilled in tungsten carbide and copper alloy. This finding will be analyzed further in the article.

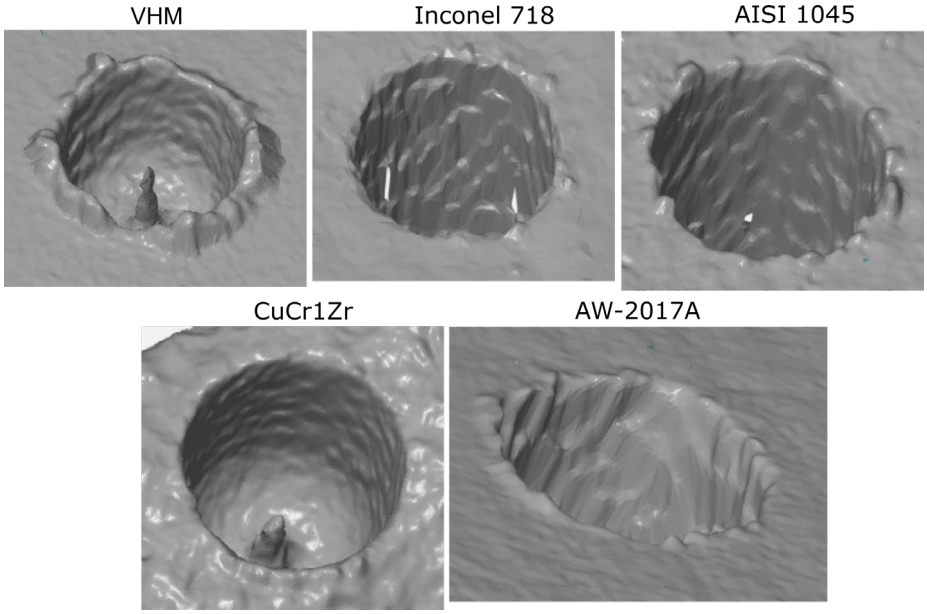

Fig. 6. Visualization of the entrance of micro-holes based on measurements.

Hole edge analysis (see in Fig. 7) showed that the smoothest edge was obtained for Inconel 718 superalloy and aluminum alloy. It is due to the good EDM machinability of these materials. Both have ER_{index} values lower or similar to brass. That is linked to the proper selection of the electrode material. On the other hand, on the edge of holes drilled in other materials, many defects such as microcracks and burrs. That is due to high ER_{index} and not optimized process parameters.

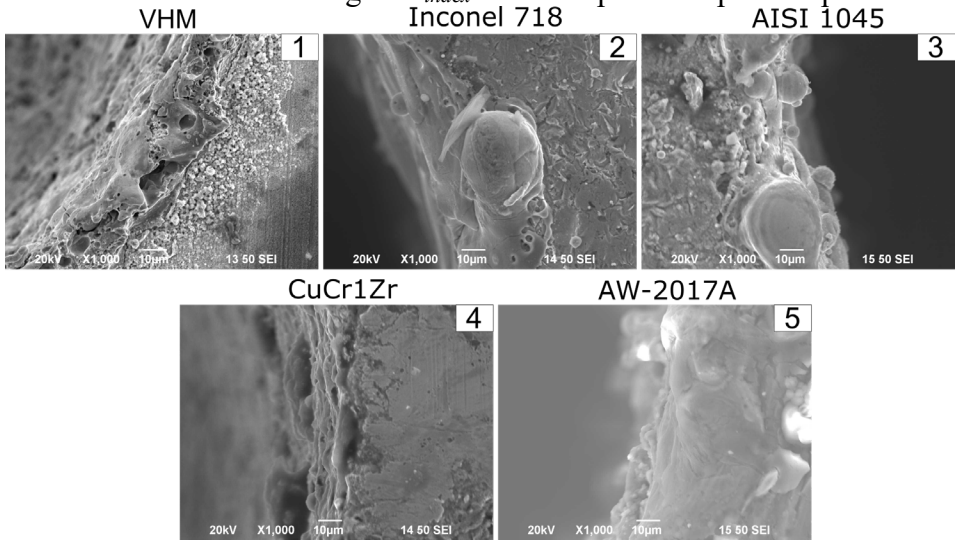

Fig. 7. Magnification of fragments marked as 1, 2, 3, 4, and 5, respectively, in Fig. 5.

In addition, VHM, CuCrZr and AW-2017A micro-holes cross-section reveals presence of residual cylinder located in the center of the hole bottom (Fig. 8). It represents not completely removed material. The measured height of the "residual cylinder" formed at the bottom of the holes drilled in the tungsten carbide, CuCr1Zr alloy and AW-2017A alloy was on average 0.30 mm,

0.17 mm and 0.25 mm, respectively.

The formation of the "residual cylinder" is influenced by the geometry of the working electrode - the tubular electrode, what has been explored in [25]. The front of the working electrode, due to the internal channel has a ring shape. Therefore, during the machining process, the heating of the material in the middle was lower comparing to material below the electrode “ring”. At the same time center of the hole receives more flushing what additionally cools that area. Thus, such conditions together with specific workpiece material properties prevented the effective removal of material in this area. In [27], it is explained that the "residual cylinder" is formed as result of the increased current density in the outside corner of the tool electrode tip. This increases the discharge frequency in the area of the bottom edge of the hole, and a lower frequency in the area on the bottom center. Uneven material removal together with higher flushing results in unremoved cone-shaped material. What interesting, remaining cylinder height increases together with the depth of the hole. In the analyzed test results, clearly visible that the cylinder remaining at the bottom in the holes has different shape or does not exist for different materials. Taking in to account that all holes were drilled with same material electrode and same parameters- all should present similar cone shaped bottom- assuming electric field is a main driver for that. Therefore it is suspected that “bottom cones” present in tungsten carbide and CuCr1Zr alloy results from the low machinability of these materials by EDM. When machining these materials, their thermophysical properties made stable machining much more difficult. What interesting, the aluminum alloy, in which the drilling was the fastest, the remaining cylinder at the bottom of the hole has comparable size to the one in carbide. That might be driven by high (the highest for selected materials) specific heat capacity. That parameter might prevent material removal similarly to high melting temperature of the VHM and high thermal conductivity of the copper alloy. Different properties produce similar result.

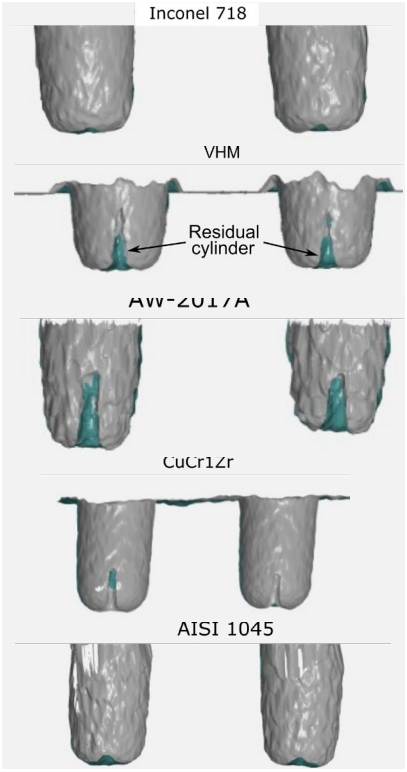

Fig. 8. Cross-sections of the bottom of the micro-holes.

Interestingly, both the Inconel 718 superalloy and AISI 1045 alloy present almost lack of a “residual cylinder” at the bottom of the holes drilled. This can be related to the lowest ER_{index} (for Inconel 718: ER_{index} = 1.28, for AISI 1045: ER_{index} = 8.81). At the same time ER_{index} of the working electrode material is higher brass ER_{index} = 9.75. This shows that in order to improve the accuracy of the bottom of the hole, the appropriate combination of electrodes is crucial. Despite the highest MRR value was obtained for aluminum alloy, the accuracy of the holes in this material requires improvement. On the other hand, the accuracy of holes drilled in Inconel 718 superalloy and AISI 1045 steel is acceptable, despite the lower efficiency of the EDM process.

Summary

The paper analyzes the impact of thermophysical properties of selected materials on the EDM performance. The analysis of the results showed that these material properties significantly affect the analyzed measures of the process such as MRR, LTW, AR. The greatest influence of properties such as melting point and thermal conductivity was observed on the EDM drilling process of micro-holes. The most important conclusions are as follows:

1. The best values were obtained for EDM drilling in aluminum alloy: MRR = 6.52 mm^3/min, LTW = 2.25 mm, and AR = 12.49. However, the accuracy of the geometry of micro-holes in this

material turned out to be unsatisfactory. Unremoved material in form ”residual cylinder” remained at the bottom of the hole.
2. Optimal values and high dimensional and shape accuracy (almost no “residual cylinder“ at the bottom of micro-holes) obtained for micro-holes drilled in Inconel 718 superalloy. Followed by: similar values and almost lack of „residual cylinder” presence in AISI 1045 steel.
3. Acceptable the EDM drilling process performance in Inconel 718 and AISI 1045 steel, was confirmed by the calculated erosion resistance index. The values of this index were the lowest for these workpiece materials (ER_{index} equal to 1.28 and 8.81, respectively for Inconel 718 and AISI 1045 steel), and were also lower than the value of this index for the working electrode material (ER_{index} = 9.76).
4. The results of the research carried out as part of this article show that other properties of modern engineering materials should also be taken into account during EDM process optimization.

References

[1] B.M. Schumacher, R. Krampitz, J.-P. Kruth, Historical phases of EDM development driven by the dual influence of "Market Pull" and "Science Push", Procedia CIRP 6 (2013) 5-12. https://doi.org/10.1016/j.procir.2013.03.001
[2] J.E. Abu Qudeiri, A. Saleh, A. Ziout, A.-H.I. Mourad, M.H. Abidi, A. Elkaseer, Advanced electric discharge machining of stainless steels: assessment of the state of the srt, gaps and future prospect, Materials 13(6) 907 (2019) 2-48. https://doi.org/10.3390/ma12060907
[3] T. Chwalczuk, A. Felusiak, M. Wiciak-Pikuła, Influence of electrode material on surface roughness during die-sinking electrical discharge machining of Inconel 718, Mat. Res. Proc. 17 (2020) 138-145. https://doi.org/10.21741/9781644901038-21
[4] E. Franczyk, M. Machno, W. Zębala, Investigation and optimization of the SLM and WEDM processes’ parameters for the AlSi10Mg-sintered part, Materials 14 (2021) 1-16. https://doi.org/10.3390/ma14020410
[5] D. Kumar, N.K. Singh, V. Bajpai, Recent trends, opportunities and other aspects of micro-EDM for advanced manufacturing: a comprehensive review, J. Braz. Soc. Mech. Sci. Eng. 42 (2020). https://doi.org/10.1007/s40430-020-02296-4
[6] K.H. Ho, S.T. Newman, State of the art electrical discharge machining (EDM), Int. J. Mach. Tools Manuf. 43 (2003) 1287-1300. https://doi.org/10.1016/S0890-6955(03)00162-7
[7] R. Świercz, D. Oniszczuk-Świercz, Experimental investigation of surface layer properties of high thermal conductivity tool steel after electrical discharge machining, Metals 7 (2017) 1-16. https://doi.org/10.3390/met7120550
[8] T. Musazawa, State of the art of micromachining, CIRP Ann. 49 (2000) 473-488. https://doi.org/10.1016/S0007-8506(07)63451-9
[9] S. Thirumalai Kumaran, T.J. Ko, M. Uthayakumar, M.A. Khan, M. Niemczewska-Wójcik, Surface texturing by dimple formation in TiAlSiZr alloy using μ-EDM, J. Aust. Ceram. Soc. 53 (2017) 821-828. https://doi.org/10.1007/s41779-017-0095-x
[10] M. Trajer, Ł. Pyclik, J.R. Sobiecki, The nickel aluminide coatings obtained on small holes produced with the EDD method, Stroj. Vestn./J. Mech. Eng. 68) (2022) 623-634. https://doi.org/10.5545/sv-jme.2022.169
[11] B.K. Sahu, S. Datta, S.S. Mahapatra, On electro-discharge machining of Inconel 718 super alloys: an experimental investigation, Mater. Today 5 (2018) 4861-4869. https://doi.org/10.1016/j.matpr.2017.12.062
[12] L. Zhang, H. Tong, Y. Li, Precision machining of micro tool electrodes in micro EDM for drilling array micro holes, Precis. Eng. 39 (2015) 100-106. https://doi.org/10.1016/j.precisioneng.2014.07.010

[13] D. Reynaerts, P.-H.'s Heeren, H. van Brussel, Microstructuring of silicon by electro-discharge machining (EDM)-part I: theory, Sens. Actuators A: Phys. 60(1-3) (1997) 212-218. https://doi.org/10.1016/S0924-4247(97)01359-9
[14] G. Maccarini, G. Pellegrini, C. Ravasio, Effects of the properties of workpiece, electrode and dielectric fluid in micro-EDM drilling process, Procedia Manuf. 51 (2021) 834-841. https://doi.org/10.1016/j.promfg.2020.10.117
[15] M. Machno, Investigation of the machinability of the Inconel 718 superalloy during the electrical discharge drilling process, Materials 13 (2020) 1-20. https://doi.org/10.3390/ma13153392
[16] B. Khosrozadeh, M. Shabgard, Effects of hybrid electrical discharge machining processes on surface integrity and residual stresses of Ti-6Al-4V titanium alloy, Int. J. Adv. Manuf. Technol. 93 (2017) 1999-2011. https://doi.org/10.1007/s00170-017-0601-x
[17] A. Gholipoor, H. Baseri, M.R. Shabgard, Investigation of near dry EDM compared with wet and dry EDM processes, J. Mech. Sci. Technol. 29 (2018) 2213-2218. https://doi.org/10.1007/s12206-015-0441-2
[18] A.A. Khan, Electrode wear and material removal rate during EDM of aluminum and mild steel using copper and brass electrodes, Int. J. Adv. Manuf. Technol. 39 (2008) 482-487. https://doi.org/10.1007/s00170-007-1241-3
[19] Suhardjono, Characteristics of electrode materials on machining performance of tool steel SKD11 with EDM shinking, ARPN J. Eng. Appl. 11 (2016) 986-991.
[20] Z. Pan, Y. Feng, T.P. Hung, Y.C. Jiang, F.C. Hsu, L.T. Wu, C.F. Lin, Y.C. Lu, S.Y. Liang, Heat affected zone in the laser-assisted milling of Inconel 718, J. Manuf. Process. 30 (2017) 141-147. https://doi.org/10.1016/j.jmapro.2017.09.021
[21] M. Hernándes, R.R. Amriz, R. Cortès, C.M. Gómora, G. Plascencia, D. Jaramillo, Assessment of gas tungsten arc welding thermal cycles on Inconel 718 alloy, T. Nonferr. Metal. Soc. 29 (2019) 579-587. https://doi.org/10.1016/S1003-6326(19)64966-6
[22] J. Selech , D. Ulbrich, D. Romek, J. Kowalczyk, K. Włodarczyk, Nadolny, Experimental study of abrasive, mechanical and corrosion effects in ring-on-ring sliding contact, Materials 13 4950 (2020). https://doi.org/10.3390/ma13214950
[23] J. Ma, N.H. Duong, Sh. Lei, Numerical investigation of the performance of microbump textured cutting tool in dry machining of AISI 1045 steel, J. Manuf. Process. 19 (2015) 194-204. https://doi.org/10.1016/j.jmapro.2014.10.001
[24] R. Velavan, S. Nandhakumar, P. Vijayakumar, Experiment in EDM process by using brass electrode with Inconel material in nano powder mixed dielectric medium, Pakistan J. Biotechnol. 14 (2017) 50-53.
[25] Y. Zhang, Z. Xu, Y. Zhu, D. Zhu, Effect of tube-electrode inner structure on machining performance in tube-electrode high-speed electrochemical discharge drilling, J. Mater. Process. Technol. 231 (2016) 38-49. https://doi.org/10.1016/j.jmatprotec.2015.12.012
[26] S. Vidya, P. Mathiyalangan, R. Wattal, A review on research aspects and trends in micro-electrical discharge machining (micro-EDM), Int. J. Eng. Technol. Sci. Res. 5 (2018) 581-590.
[27] E. Bamberg, S. Heamawatanachai, Orbital electrode actuation to improve efficiency of drilling micro-holes by micro-EDM, J. Mater. Process. Technol. 209 (2009) 1826-1834. https://doi.org/10.1016/j.jmatprotec.2008.04.044

Materials Research Proceedings 28 (2023) 1759-1764 https://doi.org/10.21741/9781644902479-190

Modeling electrochemical machining based on effective parameters

WAIMANN Johanna[1,2,a *], VAN DER VELDEN Tim[2,b], SCHMIDT Annika[2,c], RITZERT Stephan[2,d] and REESE Stefanie[2,e]

[1] Modeling and simulation techniques for systems of polycrystalline materials, RWTH Aachen University, Mies-van-der-Rohe-Str. 1, 52074 Aachen, Germany

[2] Institute of Applied Mechanics, RWTH Aachen University, Mies-van-der-Rohe-Str. 1, 52074 Aachen, Germany

[a]waimann@ifam.rwth-aachen.de, [b]vandervelden@ifam.rwth-aachen.de, [c]schmidt@ifam.rwth-aachen.de, [d]ritzert@ifam.rwth-aachen.de, [e]reese@ifam.rwth-aachen.de

Keywords: Electrochemical Machining, Effective Parameters, Material Modeling, Finite Element Method

Abstract. The process of electrochemical machining uses chemical reactions to dissolve material of the surface layer. This special kind of processing avoids undesired microstructural changes in the surface, such as the formation of dislocations. ECM is thus a very promising processing technique for high-strength materials. To model the complex chemical reactions in a computationally efficient manner, an inner variable is introduced, which describes the dissolution level of the material. The evolution of the inner variable is formulated based on Faraday's law of electrolysis. Furthermore, the use of an effective formulation of the necessary material parameters enables to consider this homogenized description of the dissolution process within an electrical finite element framework. Each effective material parameter is a result of classical mixture rules.

Introduction

Electrochemical machining (ECM) takes advantage of the anodic dissolution of metals, see exemplary in [1]. Due to the absence of mechanical loads during the ECM process, no undesired side effects, like formation of dislocations or residual stresses, occur. It is thus also possible to process even high-strength materials, see for instance [2-5].

The chemical reaction is driven by the electrochemical potential, whereby compared to electropolishing the electric part of the potential – and not the chemical one – is dominant. Fig. 1 schematically shows the idea of the process. The work piece and the tool serve as anode and cathode in the electrically loaded system. Due to the contact with the electrolyte and the already mentioned electrochemical potential the effect of the anodic dissolution takes place. This means that the metallic material depending on its valence dissolves into electrons, which go to the anode, and metal ions that are flushed away by the fluid. In reality – of course – the reactions are much more complicated, for instance due to a developing oxide layer, which would delay the dissolution process, as well as due to reactions at the cathode. The authors propose a new strategy [6], which is kept simple for the beginning and will be further extended step by step in future works. For the consideration of the oxide layer's influence on the dissolution of the work piece, a first approach is proposed in this article.

The next two sections deal with the generalized modeling concept using a smoother description of the dissolution as well as the related evolution equations. The idea has been already introduced in [6]. In the following, an introduced flow function enables to consider the influence of the already mentioned oxide layer. The article is completed by two simulations and conclusions in the later sections, respectively.

Content from this work may be used under the terms of the Creative Commons Attribution 3.0 license. Any further distribution of this work must maintain attribution to the author(s) and the title of the work, journal citation and DOI. Published under license by Materials Research Forum LLC.

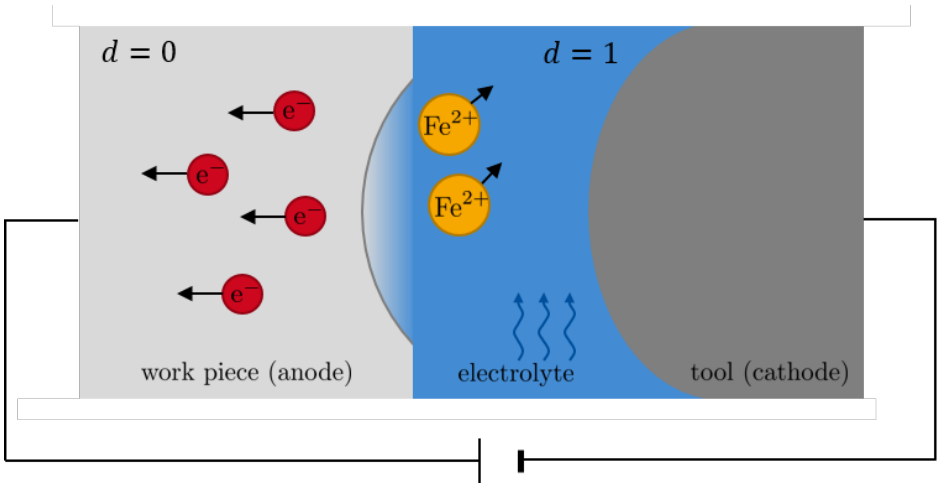

Fig. 1. Concept of the dissolution process with iron-based dissolution, see also [6,7]: dissolution variable $\boldsymbol{d}$ *varying between* $\boldsymbol{d = 0}$ *in the metal and* $\boldsymbol{d = 1}$ *in the electrolyte.*

The Concept of Effective Parameters Using the Dissolution Level as an Inner Variable

The inner variable d describes the state of the dissolution process. Hence, it is zero for the undissolved metal material and one for the completely dissolved material and thus for the electrolyte. At this point, for simplicity, the assumption is made, that the metal ions are permanently removed by the fluid flow. During the chemical reaction, d ranges between zero and one. Each material parameter at each material point within the simulation is then determined using a classical mixture rule. The resulting effective parameters are then marked by $\overline{(\cdot)}$. Depending on the choice of a series or parallel connection, they have one of the following forms

$$\overline{(\cdot)}_S = \left[(1-d)\frac{1}{(\cdot)^{ME}} + d\,\frac{1}{(\cdot)^{EL}}\right]^{-1} \tag{1}$$

$$\overline{(\cdot)}_P = (1-d)(\cdot)^{ME} + d\,(\cdot)^{EL} \tag{2}$$

respectively. Therein, $(\cdot)^{ME}$ and $(\cdot)^{EL}$ correspond to the individual material parameters of the metal and the electrolyte.

The conservation of electric charge that describes the electrical part of the observed multiphysical problem reads

$$\dot{\rho}_E + \mathrm{div}(\boldsymbol{j}) = 0 \tag{3}$$

wherein, the charge density ρ_E and the current density $\boldsymbol{j}$ depend on the field strength $\boldsymbol{E}$. They have the following forms

$$\rho_E = \mathrm{div}(\epsilon_0\,\bar{\epsilon}_r(d)\,\boldsymbol{E}) \tag{4}$$

$$\boldsymbol{j} = \bar{\kappa}_E(d)\,\boldsymbol{E} \tag{5}$$

with the material related and based on Eq. 1 or 2 effectively chosen relative permittivity $\bar{\epsilon}_r(d)$ and electric conductivity $\bar{\kappa}_E(d)$, the electric constant ϵ_0 as well as $\boldsymbol{E}$.

The primary unknown of the electrical problem is the electric potential v. Not yet obvious in the presented equations, its gradient is considered within the electric field strength via

$$\boldsymbol{E} = -\mathrm{grad}(v) \tag{6}$$

The original paper [6] additionally considers a thermally coupled system. There also a more detailed description of the effective parameter approach can be found, which is also later used for the consideration of a relocatable cathode in terms of a moving boundary value problem [7]. Due to simplicity, the additional thermal problem is skipped, here. More information on the finite element formulation and implementation can be found in [6,8].

Evolution of the Dissolution Level Based on Faraday

The anodic dissolution leads to the split of a metal atom into electrons and ions, see also Fig. 1. The temporal amount of the dissolution by this reaction can be described by Faraday's law of electrolysis. Motivated by [9] and introduced in [6,7], one can formulate the evolution equation of the inner variable d. The dissolution level of an incremental reference volume $\mathrm{d}V_{ref}$ reads

$$\dot{d}\ \mathrm{d}V_{ref} = v_{dis}\ \mathcal{A}\ \mathrm{d}I. \tag{7}$$

In Eq. 7, v_{dis} is a material parameter which is experimentally observed by our project partners of the *Werkzeugmaschinenlabor (WZL)* at RWTH Aachen University. It is thus not only related to Faraday's law but also to the efficiency of the performed experiment. The quantity $\mathrm{d}I$ describes the increment of the electric current. Furthermore, the dissolution only takes place if the material has contact to the electrolyte. To account for this constraint, the activation function $\mathcal{A}$ is introduced. The latter becomes one for contact with the electrolyte and is otherwise zero. This ensures that the anodic dissolution only takes place in material layers, which are at the surface.

Consideration of a Formed Oxide Layer and Its Damping Properties

The former sections deal with the state of the art of the new method to describe the ECM process. In the following, the modeling approach is extended to consider the oxide layer formation in dependency on $\boldsymbol{j}$. During the ECM process, one can observe the formation of such a layer on the anodic surface (see Fig. 2), which shows a diode-like influence on the electric problem and, thus, serves with the polarization voltage Δv_p as a barrier that has to be overcome before the dissolution process in the trans-passive regime can start.

The considered modeling strategy to methodologically describe the ECM process, was - due to our origin in mechanics - always driven by the idea of applying general solution schemes of mechanical problems to the electrochemical one. The presented work focuses on the more dominant trans-passive area and for simplicity neglects the removal at low current densities before the passivation of the material. Following the characteristics of a yield function in plasticity, a flow function ϕ^{OX} is introduced. As long as $\phi^{OX} \leq 0$, the oxide layer serves as an isolating barrier, preventing the electric flow. When $\phi^{OX} > 0$, the current flow over the surface as well as the dissolution process are initiated. A first assumption for a one-dimensional formulation of ϕ^{OX} reads:

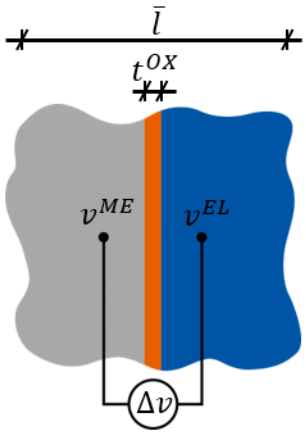

Fig. 2. Unit cell for the surface area with a characteristic length $\bar{\boldsymbol{l}}$: metal (grey) with potential $\boldsymbol{v^{ME}}$, oxide layer (orange) with thickness $\boldsymbol{t^{OX}}$ and electrolyte (blue) with potential $\boldsymbol{v^{EL}}$.

$$\phi^{OX} = |\boldsymbol{v}^{ME} - \boldsymbol{v}^{EL}| - \Delta v_p = \begin{cases} \leq 0 : \text{insulating} \\ > 0 : \text{conducting} \end{cases} \tag{8}$$

The choice of the flow function is based on experimental observations. The electric flow through the oxide layer and, thus, the material dissolution can start when the flow function is positive. Physically, this means that the potential difference

$$\Delta v = |v^{ME} - v^{EL}| \tag{9}$$

is higher than the polarization voltage Δv_p. For the three-dimensional case the formulation of a flow function is much more complicated. The reason for that is that one has to check the potential difference in each direction, especially for curved surfaces. But, this formulation is part of our future works.

Furthermore, the existence of the oxide layer also influences the effective material parameters. According to the chosen approaches in Eq. 1 and 2, they read

$$\overline{(\cdot)}_S = \left[(1-d)\frac{1}{(\cdot)^{ME}} + \frac{t^{OX}}{\bar{l}}\frac{1}{(\cdot)^{OX}} + d\frac{1}{(\cdot)^{EL}}\right]^{-1} \tag{10}$$

$$\overline{(\cdot)}_P = (1-d)(\cdot)^{ME} + \frac{t^{OX}}{\bar{l}}(\cdot)^{OX} + d\,(\cdot)^{EL} \tag{11}$$

Therein, $(\cdot)^{OX}$ corresponds to the parameters of the oxide layer, which are weighted by its thickness t^{OX} in relation to the effective length $\bar{l}$ of the examined unit cell.

Finally, the introduction of a modified current density $\boldsymbol{j}_{mod}$ enables to take into account the insulating character of the oxide layer. It has the form:

$$\boldsymbol{j}_{mod} = \begin{cases} \boldsymbol{0}, & \phi^{OX} \leq 0 \\ \boldsymbol{j} - j_0\boldsymbol{n}, & \phi^{OX} > 0 \end{cases} \tag{12}$$

with the normal $\boldsymbol{n}$ on the metal surface and a reduction term

$$j_0 = \kappa_E^{OX}\left(-\frac{\Delta v_p}{t^{OX}}\right) \tag{13}$$

Numerical Results

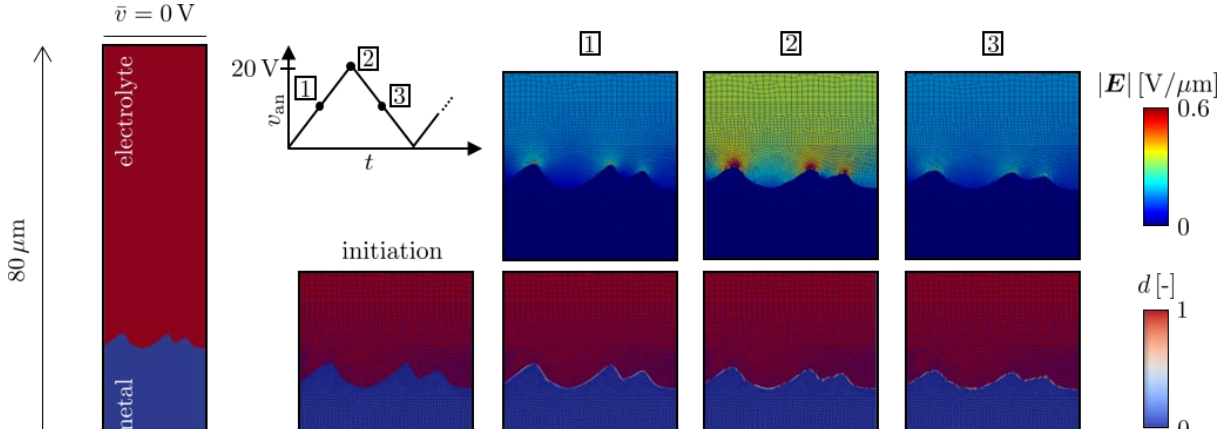

Fig. 3. Pulsed electrochemical machining with initial non-uniform roughness and without consideration of the oxide layer: boundary value problem (left) as well as norm of the electric field strength $\boldsymbol{E}$ and dissolution level $\boldsymbol{d}$ for different load steps during the first cycle (right).

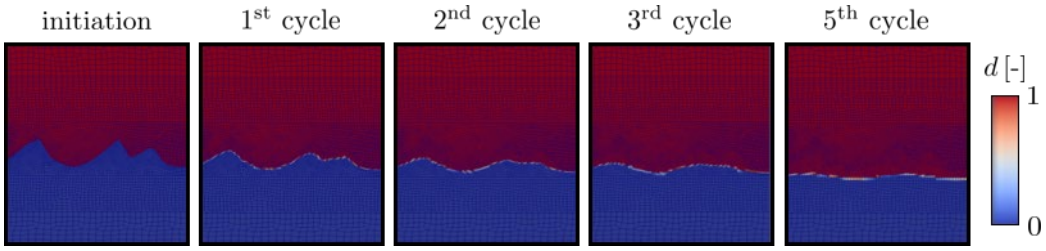

Fig. 4. Pulsed electrochemical machining with initial non-uniform roughness and without consideration of the oxide layer: dissolution level $\boldsymbol{d}$ *after individual load cycles.*

Within this chapter, two simulations are presented. The used material parameters are given in [6]. The first example shows the simulation of a pulsed electrochemical processing of a material surface with an initial non-uniform roughness and without considering the influence of the oxide layer. Fig. 3 (*left*) shows the boundary value problem. The electric potential is prescribed at the anode and linearly varied between 0 V and 20 V. It is zero at the cathode. On the right part of Fig. 3, the norm of the electric field strength and the dissolution level for different time steps of the first pulse are presented: The electric field strength is highest at the peaks of the structure and results in a faster dissolution, there. The flattening of the surface roughness is also presented in Fig. 4. It shows the dissolution level before the first, after the first, second, third and fifth cycle. Similar simulations with a different initial roughness are also given in [6] and [10].

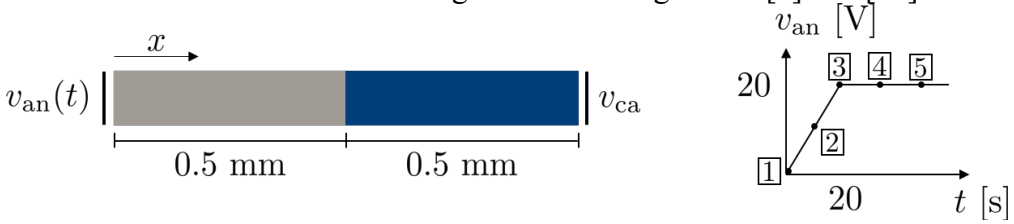

Fig. 5. Electrochemical machining with consideration of the oxide layer: boundary value problem (left) and prescribed electric potential at the anode with marked load steps (right).

In the second example, a one-dimensional academic problem is assumed as presented in Fig. 5. The electric potential at the cathode is prescribed with zero. At the anode the potential is linearly increased to a maximum value of 20 V and then kept constant. The assumed polarization voltage reads $\Delta v_p = 1.5$ V. Fig. 6 shows the resulting dissolution level and the electric potential for some chosen times steps, which are marked in Fig. 5. The results for this first simulation considering the oxide layer show that before the difference between the electric potential in the metal and the electrolyte reaches the critical value of the polarization voltage no material dissolution takes place. After that, the chemical reaction is initiated and the dissolution begins.

Summary

The presented model contributes to the field of modeling the anodic dissolution during electrochemical machining. The formulation is based on the use of effective material parameters.

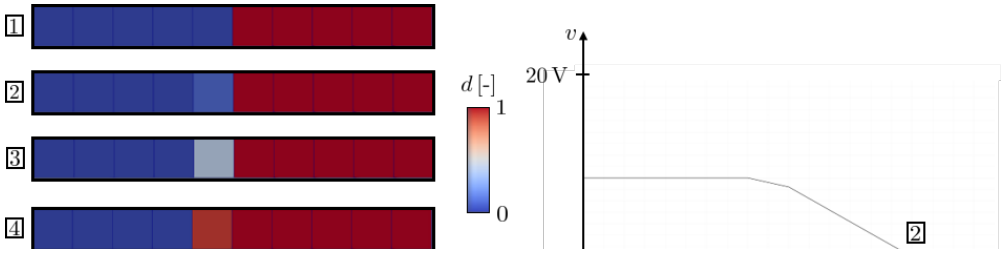

Fig. 6. Electrochemical machining with consideration of the oxide layer: dissolution level $\boldsymbol{d}$ *(left) and electric potential* $\boldsymbol{v}$ *plotted over* $\boldsymbol{x}$ *(right) at marked load steps, see Fig. 5.*

Compared to our earlier works, an idea is proposed how the influence of a formed oxide layer can be taken into account and which thus refers to the trans-passive area of the electrochemical process. The presented numerical results reveal the complex mechanism.

The earlier described material model already accounts for the iron-based dissolution based on Faraday's law of electrolysis. Now, the model also accounts for a polarization voltage which has to be overcome within the trans-passive area, before the removal can start. But, of course, it is still a simplification of the complex and coupled chemical reactions. Besides further three dimensional simulations of the ECM process – also in combination with the removal before passivation – in future works, the modelling approach must be able to consider the full electrochemical potential to describe the material dissolution of the individual alloying elements at the anode. Additionally, a polycrystalline structure and different phases of the metal will be included, which influence the resulting surface roughness. Once the reactions at the anode will be described in more detail, the focus of further works will lie on the reactions at the cathode and the fluid structure interaction. The presented model neglects these local effects on the dissolution process and assumes, so far, that developed heat, gases and ions are permanently transported away by the electrolyte.

Acknowledgements
The authors gratefully acknowledge the financial support of the German Research Foundation (DFG, Deutsche Forschungsgemeinschaft) within the transregional Collaborative Research Center SFB/TRR 136, project number 223500200, subproject M05. We also kindly acknowledge our project partners of the Werkzeugmaschinenlabor (WZL) and the Chair of Corrosion and Corrosion Protection (KKS) at the RWTH Aachen University for many interesting and helpful discussions on the ECM process and the chemical reactions as well as for the essential experimental support.

References
[1] C.H. Hamann, W. Vielstich, Electrochemistry, 3. tot. rev. and enl. ed., Wiley-VCH, Weinheim, 1998.
[2] F. Klocke, A. Klink, D. Veselovac, D.K. Aspinwall, S.L. Soo, M. Schmidt, J. Schilp, G. Levy, J.-P. Kruth, Turbomachinery component manufacture by application of electrochemical, electro-physical and photonic processes, CIRP Ann. - Manuf. Technol. 63 (2014) 703-726. https://doi.org/10.1016/j.cirp.2014.05.004
[3] A.E. DeBarr, D.A. Oliver, Electrochemical Machining, Macdonald & Co., Ltd, London, 1968.
[4] J.A. McGeough, Principles of Electrochemical Machining, first ed., Chapman & Hall, London, 1974. https://doi.org/10.1002/cite.330472314
[5] T. Bergs, S. Harst, Development of a process signature for electrochemical Machining, CIRP Ann. - Manuf. Technol. 69 (2020) 153-156. https://doi.org/10.1016/j.cirp.2020.04.078
[6] T. van der Velden, B. Rommes, A. Klink, S. Reese, J. Waimann, A novel approach for the efficient modeling of material dissolution in electrochemical machining, Int. J. Solids Struct. 229 (2021) 111106. https://doi.org/10.1016/j.ijsolstr.2021.111106
[7] T. van der Velden, S. Ritzert, S. Reese, J. Waimann, Modeling moving boundary value problems in electrochemical machining, accepted in Int. J. Numer. Methods Eng. (2022).
[8] J.L. Pérez-Aparicio, R.L. Taylor, and D. Gavela, Finite element analysis of nonlinear fully coupled thermoelectric materials, Comput. Mech. 40 (2007) 35-45. https://doi.org/10.1007/s00466-006-0080-7
[9] S. Harst, Development of a process signature for electrochemical machining, first ed., Apprimus Wissenschaftsverlag, Aachen, 2019.
[10] J. Waimann, T. van der Velden, A. Schmidt, S. Ritzert, S. Reese, Consideration of chemically-induced damage in a thermo-electrically coupled system, accepted in Proc. Appl. Math. Mech. (2022).

Materials Research Proceedings 28 (2023) 1765-1774 https://doi.org/10.21741/9781644902479-191

Coefficient of friction of cemented carbides machined by sinking EDM

PETERSEN Timm[1,a,*], KÜPPER Ugur[1,2,b], HERRIG Tim[1,c] and BERGS Thomas[1,2,d]

[1]Laboratory for Machine Tools and Production Engineering (WZL) of RWTH Aachen University, Campus Boulevard 30, 52074 Aachen, Germany

[2]Fraunhofer Institute for Production Technology IPT, Steinbachstr. 17, 52074 Aachen Germany

[a]t.petersen@wzl.rwth-aachen.de, [b]u.kuepper@wzl.rwth-aachen.de, [c]t.herrig@wzl.rwth-aachen.de, [d]t.bergs@wzl.rwth-aachen.de

Keywords: Sinking Electrical Discharge Machining, Cemented Carbide, Coefficient of Friction

Abstract. Cemented carbides possess properties that predestine them as a durable tool. However, these properties hinder conventional machining, which is why Electrical Discharge Machining (EDM) is a promising alternative. Three different EDMed cemented carbides were compared with a ground surface in a pin-on-disk test setup. They were evaluated under dry and lubricated conditions with two distinct antibody materials. The tests did not reveal a correlation between the surface roughness of the cemented carbide pins and the coefficient of friction. However, some test sets yielded very different results, which is why particular considerations should be made with new sliding compositions.

Introduction

The requirements for tools used in forming processes are subject to a continuous increase [1]. On the one hand, higher strength materials are used as workpiece material in forming in order to implement lightweight design. On the other hand, the tolerances become narrower to allow net-shape production, reducing subsequent machining steps and increasing material efficiency. Both developments result in higher tool loads and thus shorter tool life time [2,3]. Therefore, it is part of current research to investigate the properties and applicability of new tool materials such as cemented carbides [4,5]. Cemented carbides can resist high compressive stresses and are significantly harder than conventional tool materials. This makes cemented carbides substantially more resistant to wear [6]. However, these properties hinder conventional machining simultaneously. Grinding is only possible in the case of certain geometries and milling proves to be very challenging [7]. One alternative applied to machine forming tools from cemented carbides is electrical discharge machining (EDM) [8]. Due to its thermal working principle, EDM is able to machine workpieces independently from their mechanical properties [9]. EDM employs several thousand discharges per second, which are temporally and spatially very confined. These discharges consist of plasma, which melts and evaporates the adjacent material. On the one hand, not all material that is molten is also removed from the discharge location and thus leads to the formation of a recast layer, also known as white layer due to its appearance in cross sections. On the other hand, not all heat that is transferred from the plasma to the workpiece is involved in melting or evaporating the material. Some of the heat is transported further below the surface but only heats the material up to a certain temperature. In some cases it can reach the corresponding phase transformation temperature. Because the amount of heat is very little for each single discharge, it is quickly dissipated into the periphery. This leads to rapid cooling and in some cases a freeze of the material in the current phase and geometry [10]. The tensions resulting from this process can lead to residual stresses and cracks. Especially cemented carbides are prone to these effects, because they consist of two or more different phases with different thermophysical

Content from this work may be used under the terms of the Creative Commons Attribution 3.0 license. Any further distribution of this work must maintain attribution to the author(s) and the title of the work, journal citation and DOI. Published under license by Materials Research Forum LLC.

properties. One way to reduce the impact on the workpiece is the application of a sequence of different machining steps each subsequent one with lower heat input. This sequence allows for productive machining whilst keeping the effect on the rim zone as small as possible. For cemented carbides, it has been proposed [11] to use needle type discharges in order to optimise production with both objectives in mind. It has been shown that this approach can be applied successfully for fine and ultra-fine grained cobalt cemented tungsten carbides [12]. It could also be seen that the surface roughness changed from one machining step to the other. Therefore, the objective of this research is to identify the influence three different surface topographies of two different cemented carbide grades have on the sliding behavior with two different antibodies and tested in two different lubrication conditions. Several authors have published research regarding the tribological behaviour of cemented carbides [13,14], because of their properties that destine them for the use as forming tools. Another aspect that is regularly researched is the tribological performance of surfaces produced by EDM. It has been shown, that the craters can serve as reservoirs for the lubricant or to reduce particles in the contact zone [15,16]. Additionally, Sari et al. [17] compared the load carrying capacity of wire EDMed gears to those manufactured with profile grinding and found that the characteristic surface structure resulting from the EDM process leads to beneficial tribological conditions in rolling contact. They attributed this to the statistical and non-directional crater structure resulting from EDM, which allows the roughness to get flattened instead of resisting the load and thus reducing the peak stresses in the material. However, it must be expected that the effects are different in this case because the investigated material was hardened 16MnCr5 instead of the present cemented carbide, which will most likely not be reshaped by the counterbody. In contrast, Bergs et al. [18] did not get the same results in a disk-on-disk test comparing wire electrical discharge turning (WEDT) to grinding. In their case, the flattening of the WEDTed surfaced did not yield the same surface roughness as the ground specimen. However, it has to be noted that the WEDT processes is more challenging than WEDM because of an increased punctiform heat input and the need for a precise runout in combination with the moving wire. The present paper aims to combine both elements and investigate the tribological behavior of cemented carbides machined by EDM.

Experimental Setup

The experimental setup was chosen according to previous investigations, however, some alterations have been made. The process of specimen preparation was the same as previously [19]. The only difference lies in the geometry of the tested pin. For the present investigations, the specimens had a convex contact area and the body of the pin was 10 mm by 10 mm. The radius of the convex area was 20 mm. As depicted in Fig. 1 on the left, the cemented carbide pins were cut from blocks via wire electrical discharge machining (WEDM) with an oversize on the top of the pin of 1 mm. This oversize was then removed via sinking electrical discharge machining (SEDM). The oversize and the machining technology of SEDM were chosen in order to make the material experience the roughing steps of the technology whilst still reaching the best available surface finish of Ra = 0.2 µm. The technology was applied three times in a different way. The first pins were created whilst only applying the first machining step. This machining step is called roughing. The second set of pins was created using the first machining step and all steps necessary to reach a surface roughness of Ra = 1 µm. This machining operation is called finishing. The third set of pins was created using all the previous machining steps and all additional machining steps in order to reach a surface roughness of Ra = 0.2 µm. This machining operation is called super-finishing. Both GFMS EDM machines used hydrocarbon oils as dielectric. While the Cut 2000 X Oil Tech used IonoFil 100, the Form 2000 VHP used Ionoplus IME-MH, both by the company oelheld. The tool materials were 0.2 mm brass wire for WEDM and copper tungsten (WCu) with 80 wt% for SEDM. The materials of the pins were CTF30 and UMG01 by Ceratizit [20]. CTF30 consists of 15 wt% cobalt and tungsten carbide grains with a size of 0.8 - 1.3 µm, whereas UMG01 does not

contain a significant amount of binder material and consists of tungsten carbide grains with a size of 0.2 µm. The friction test was conducted according to previous investigations [19, 21]. The setup can be seen in Fig. 1 on the right hand side. The cylindrical antibody was mounted on a lathe and rotated with a constant angular velocity of $\omega = 312.5\ min^{-1}$ resulting in a surface velocity relative to the pin of $v = 6.25\ m \cdot min^{-1}$. Two different antibody materials were used in this investigation: 42CrMo4 and 16MnCr5. The radii of the cylinders were r = 20 mm each. The pins were pressed on the rotating cylinder with a force of $F_n = 5000$ N. The force F_n was controlled with a 9011A force sensor and the resulting force F_t with a 9257B dynamometer, both by Kistler. In order to evaluate the effect the eroded surface has on the transport of lubricant, the tests were conducted with and without minimal quantity lubrication. In the case of lubrication, the Lubrimat L60 by Steidle was used to apply single drops of lubricant every few seconds.

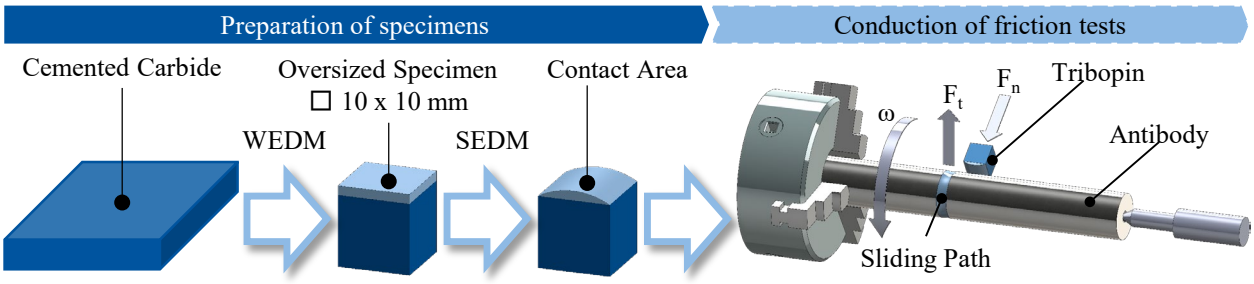

Fig. 1. Process of preparation of specimen and test setup according to [21].

Three different outputs from the tests were evaluated. Firstly, the tangential force F_t resulting from the applied force F_n and the rotation ω were measured. An arrow indicating this force F_t can be seen in Fig. 1 on the right. However, because of the difficulties described in a previous publication [19], where the investigations were conducted according to the setup schematically depicted in Fig. 2, top left was changed. There, the theoretical contact between the specimen and the antibody was a line. Because material was quickly sticking to the surface of the specimen and the antibody was reshaped during the test procedure, the stick-slip effect occurred. This caused strong vibrations and increased the overall level of the detected tangential force, which can be seen in Fig. 2, left bottom. In order to prevent the stick-slip effect and the resulting vibration, the test setup was revised according to the schematic drawing in Fig. 2, right top. Here two cylinders can be seen that are placed orthogonally to each other. The actual pins were only a cuboid cutout of the rear cylinder, which does not affect the contact area. Both cylindrical surfaces have the same radii of r = 20 mm. This setup theoretically causes a point contact, which reduces the risk of vibration. It can be seen in the graphs comparing the two setups that the revised setup is able to measure the force without vibrations or deviations. The subsequent evaluation of the measurements is a lot more stable and reliable since the section to be evaluated does not have to be chosen manually.

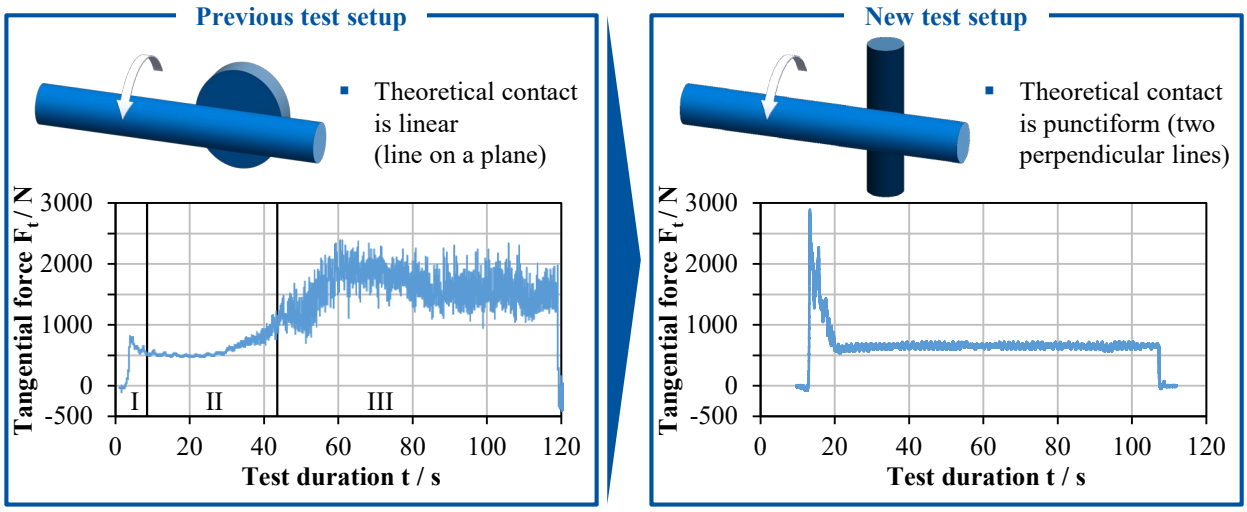

Fig. 2. Comparison of previous and revised test setup [19].

The second and third output from the investigation are the surfaces of the specimen and the antibody. Both were investigated using the optical microscope Smartzoom 5 by Zeiss. For comparison, some cemented carbide pins were ground to the desired shape with a diamond grinding wheel bound with artificial resin. Since each experiment was conducted thrice, the according number of pins had to be created from the corresponding materials. This totaled in a number of 96 pins, 48 from each cemented carbide grade and 12 of each surface finish.

Results

In order to give an idea of the surfaces that were created with the different machining operations described in the experimental setup, Fig. 3, left depicts the average surface roughnesses of all pins used in this investigation. For statistical reasons, all pins were tactilely measured three times with a Waveline 800 by Jenoptik. The colours of the columns indicate the material, with dark blue being CTF30 and light blue being UMG01. As expected, it can be seen that the surface roughness decreases with the increased number of machining steps. However, a clear difference between the two materials can be perceived as well. The surface roughness of UMG01, the small grained and binderfree material is significantly smaller for all compared surface conditions. As described by Bergs et al. [22], this difference cannot entirely be attributed to the smaller grain size. For the roughed specimen, the white layer, which consists of molten and resolidified material, is significantly larger than the largest protruding WC grains.

On the right hand side of Fig. 3 the average coefficient of friction is depicted. The coefficient of friction μ is the quotient of the two forces F_t and F_n as shown in Eq. 1. Because the applied force F_n varied slightly from test to test, both forces were measured and averaged over the same duration as denoted in Fig. 2, right bottom.

$$\mu = \frac{F_t}{F_n} \tag{1}$$

In this part of the investigation, the averages are calculated over all surface conditions of the pins. The purpose of this diagram is to highlight the difference between the two antibody materials. However, the differences are marginal. For both antibody materials, the average coefficient of friction (COF) appears to be the same with respect to the lubrication condition. It can be noted that the coefficients of friction (COFs) with dry 42CrMo4 are slightly larger than those with 16MnCr5, while the deviation is a little larger as well. In the lubricated condition, this result is turned around and the COFs with 42CrMo4 are slightly smaller than those with 16MnCr5. From the present

results it can be presaged that the described effects are a little more dominant with CTF30 than with UMG01, while there is no difference detectable within the cemented carbide pins with 16MnCr5. Regarding this evaluation it can be stated that the antibody materials do not seem to have a strong effect on the COF.

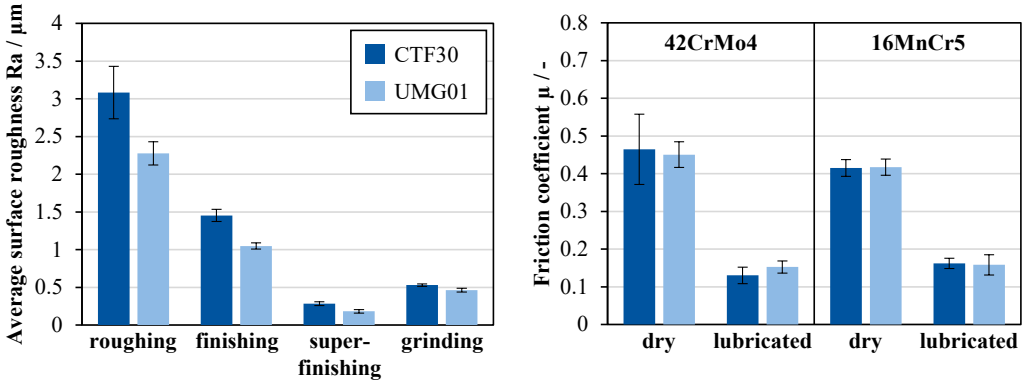

Fig. 3. Average surface roughness of the cemented carbide pins and the average coefficient of friction for both antibody materials and both lubrication conditions.

A more detailed analysis of the COFs is depicted in Fig. 4. Here both cemented carbides and all surface and lubrication conditions are separately displayed for the antibody material 42CrMo4. On the left hand side, the COF is shown as it appeared without any lubrication and on the right hand side it is shown as it appeared with the application of lubricant. Regarding the dry condition, a large deviation can be seen for the ground CTF30 specimens. Here one ground pin yielded a COF of 0.75, which was much higher than all the other results. In general, there is no correlation between the surface roughness and the COF. For CTF30, the worst COF of the eroded specimen resulted from the finished pins. The roughed and super-finished surface conditions resulted in the lowest COFs. For the eroded UMG01 pins, no significant difference between the COFs can be recognized and it should be noted that these results have very little deviations. Only the ground UMG01 pins have significantly lower COF of around 0.4.

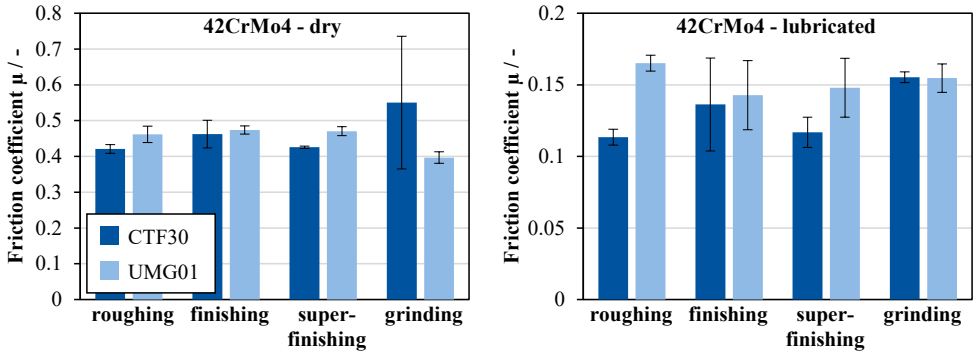

Fig. 4. Coefficients of friction for 42CrMo4, all surface conditions of the cemented carbide pins and for both lubrication conditions.

The deviations appearing in the diagram on the right hand side of Fig. 4 appear to be significantly larger than those from the unlubricated surface condition on the left hand side. However, it needs to be emphasized that the scale is different and the largest deviations on the right are slightly smaller than those of the finished CTF30 pins on the left, which is the largest

without considering the ground CTF30 pins. The lubricated CTF30 pins show a very similar appearance to the unlubricated ones. The finished CTF30 pins result in the largest COF for the eroded pins and the roughed and super-finished pins result in very similar COFs. All eroded CTF30 pins result in a lower COF than the ground pins. This might be caused by an effect suggested by Sari et al. [17]. They described the capability of the discharge craters to transport a lubricating medium into the contact area. They found that the durability of gears machined by EDM can be higher because of this effect and in contrast to the doubts created by the harmful effect EDM has on the surface integrity. However, the same effect cannot be seen for the pins made of UMG01, even though the ground pin has almost exactly the same COF as the one made from CTF30. The finished and super-finished UMG01 pins have a slightly lower average COF, but the deviations are large enough to range them on the same level as the ground pin. Furthermore, in contrast to CTF30, the roughed UMG01 pins have the highest overall COF for this lubrication condition and antibody material. Especially, when comparing the two results for the roughed pins, which both have a very little standard deviation, it becomes apparent that there must be a difference resulting from the material of the specimens.

The second antibody material investigated was 16MnCr5. The resulting COFs are displayed in Fig. 5, where the non-lubricated condition is shown on the left and the lubricated condition is shown on the right. For the dry condition, no successful tests could be conducted for the roughed and the ground UMG01 specimen. The specimen broke or the force was quickly overreaching the measurement scale, indicating an upcoming breakage. This happened for all the specimen of the corresponding test series even though the tests were conducted in a randomized order, which reduces the chances that this result is solely caused by an outlier. All other tests on this antibody material have worked in the same way as on 42CrMo4 and have shown the same force pattern as seen in Fig. 2. The remaining COFs from the dry constellation show very little variance. Neither the material of the specimen nor the applied surface finish seems to have a significant influence. In comparison to the antibody material 42CrMo4, which has an average COF for the dry condition of 0.46, the average COF is slightly lower with a value of 0.42. The lubricated condition displays a very different result. Here, the COFs vary throughout both investigated parameters. For CTF30, the differences are only slight, but it can been seen that the COF shrinks with a decreased surface roughness for the eroded specimens. The ground specimens however, yielded the highest COF, albeit not having the highest surface roughness. All results for CTF30 are within a smaller range than the results of UMG01. Especially, between the roughed and the finished specimens there is a large difference, with the prior having the smallest COF on this antibody material and the latter having the highest COF for all tests conducted under the lubricated condition. The super-finished and the ground UMG01 specimens have a very similar average COF, however, the deviation was larger for the super-finished specimens. When comparing the two antibody materials for the lubricated condition, it becomes apparent that 42CrMo4 yielded a lower average of 0.14 but the deviations in the test were significantly larger. In contrast, the average COF for the lubricated 16MnCr5 was 0.16 with a relatively small deviation. Additionally, the comparison of the cemented carbide pins for the lubricated tests also reveals an interesting difference. For 42CrMo4, UMG01 does not appear to be affected by its surface condition. In contrast, for 16MnCr5, UMG01 yielded different results for different surface conditions. The results for CTF30 can be read vice versa.

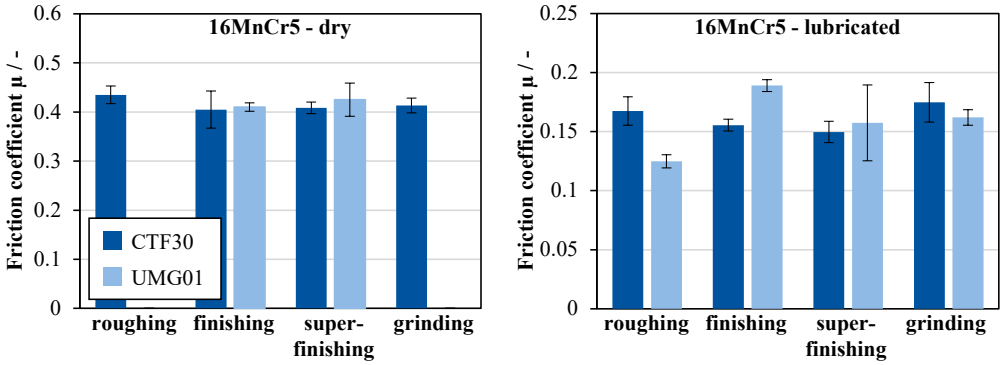

Fig. 5. Coefficients of friction for 16MnCr5, all surface conditions of the cemented carbide pins and for both lubrication conditions.

The results for the COF contrast the results presented by Llanes et al. [23], who found that the COF correlates with the surface roughness. However, they used a scratch test setup, where the indenter was a spherical tip diamond with a radius of 50 µm and the antibody was the EDMed cemented carbide. In general, the results are in good agreement with literature regarding tests conducted in dry conditions [14,24] and are only slightly higher in the lubricated condition than the laser textured specimen tested by Fang et al. [13].

In Fig. 6 and Fig. 7, the surfaces of the cemented carbide pins can be seen after the tests. In Fig. 6, the pins tested with 42CrMo4 as antibody material are depicted and in Fig. 7 the pins tested with 16MnCr5 are shown. In both figures, several broken pins are displayed. However, most of them broke when the test setup was disassembled. In Fig. 6, only the super-finished UMG01 pin number 3 broke during the test. For Fig. 7, all the super-finished and the first roughed UMG01

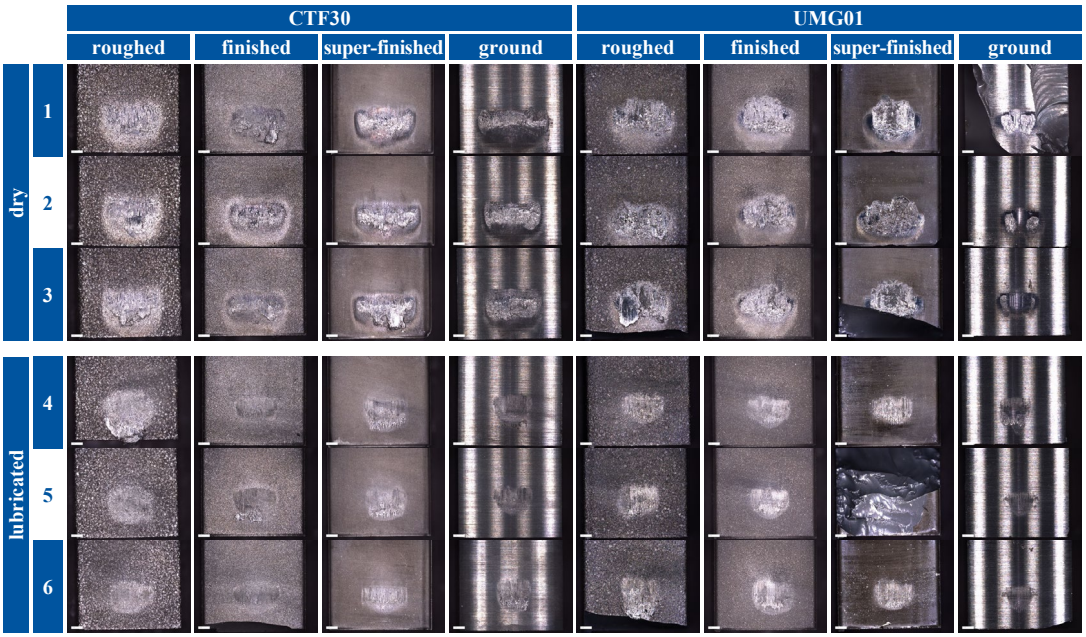

Fig. 6. Microscopic images of the surfaces of all pins tested on 42CrMo4.

pins broke in the test without lubrication. The remaining two roughed UMG01 pins were causing an overload in the measurement system and were therefore stopped. All the pins that broke first caused an overload, which is why these pins were accounted for as broken.

For both antibody materials, different regions are present on most cemented carbide pins. On the one hand, there are regions which appear to be flattened and on the other hand there are regions that have accumulated material. Even though the tested cemented carbides are significantly harder than the tested shafts, profilometry revealed that the tips of the profile have been flattened. An energy dispersive X-ray spectroscopy (EDX) has been conducted to reveal that all the material that appears to be bulged has in fact migrated from the test shafts and is not rearranged material from the cemented carbide pin.

When comparing the microscopic images from Fig. 6 and Fig. 7, a difference in the size of the imprint can be observed. For the antibody material 42CrMo4, the imprint appears significantly smaller than for the antibody material 16MnCr5. Similarly, the imprints on the shafts are larger on 16MnCr5 than on 42CrMo4.

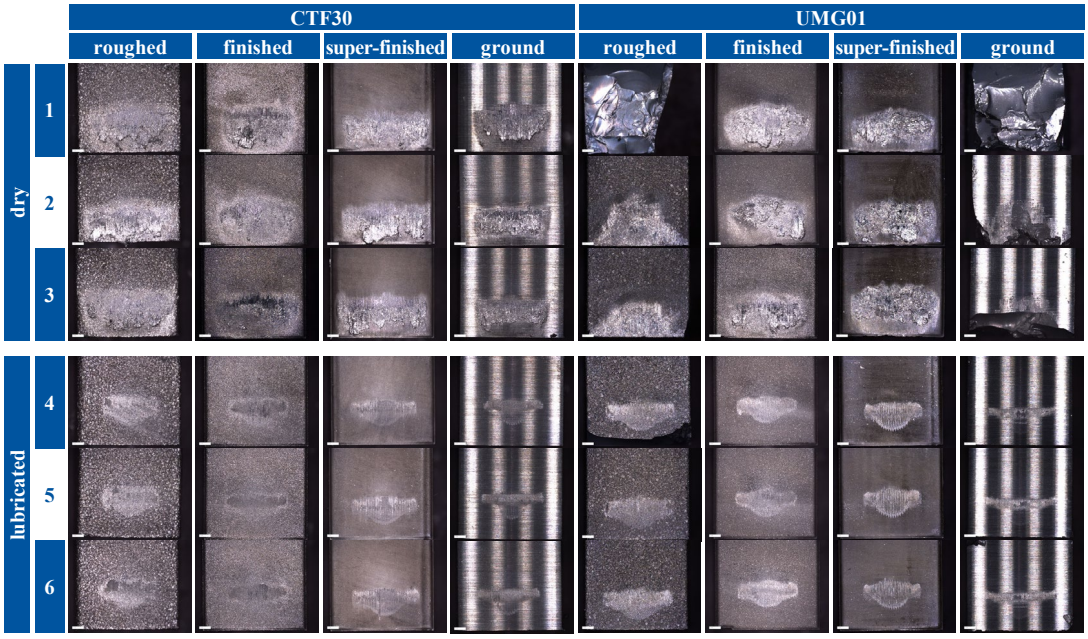

Fig. 7. Microscopic images of the surfaces of all pins tested on 16MnCr5.

Summary

The coefficient of friction of two distinct cemented carbides in contact with two different antibody materials was investigated in a dry and a lubricated setup. The cemented carbide pins were machined through sinking EDM to three different surface finishes and one set of pins was manufactured by grinding as a reference. Even though the surface roughnesses differed from one machining strategy to the other, no general correlations between the surface roughness and the COF could be found. Likewise, both antibody materials yielded similar results in the respective tests. Some test configurations, however, did show significant differences, which indicate the necessity to evaluate each configuration of materials and surface properties independently. This is especially obvious with the broken specimens from the series 16MnCr5, dry, roughed and ground. The friction reducing effect of the craters presumably present in the lubricated setup could not be identified with the same extend as it is in literature, which is attributed to the smaller dimensions of the craters found on cemented carbide surfaces.

Funding

The authors thank the German Research Foundation (DFG) for funding the DFG project BE 2542/42-2: “Analysis of discharge-dependent surface integrity of cemented carbide forming

dies machined by sinking EDM and its influence on the tribological characteristics and the resulting fatigue behaviour"(project number 290130034).

References

[1] F. Klocke, Manufacturing processes: Forming, Springer, Berlin, New York (2013) ISBN: 978-3-642-36772-4.
[2] U. Engel, J. Groenback, C. Hinsel, Tooling solutions for challenges in cold forging, Umformtechnik (2011).
[3] J. Cao, E. Brinksmeier, M. Fu, R.X. Gao, B. Liang, M. Merklein, M. Schmidt, J. Yanagimoto, Manufacturing of advanced smart tooling for metal forming, CIRP Annals, 68 (2019) 605-628. https://doi.org/10.1016/j.cirp.2019.05.001
[4] H. Voigts, R. Hild, A. Feuerhack, T. Bergs, Investigation of Failure Mechanisms of Cemented Carbide Fine Blanking Punches by Means of Process Forces and Acoustic Emission, in Forming the Future, Springer, Cham (2021) 1173-1187. https://doi.org/10.1007/978-3-030-75381-8_98
[5] O. Baer, A. Feuerhack, H. Voigts, T. Bergs, Investigation of the Mechanical Punch Loads during Fine Blanking of High-Strength Steels with Cemented Carbide, Procedia Manuf. 34 (2019) 90-100. https://doi.org/10.1016/j.promfg.2019.06.125
[6] L. Prakash, Editor, Comprehensive Hard Materials: Fundamentals and General Applications of Hardmetals, Elsevier, 2014. ISBN: 9780080965284.
[7] E.L. Silva, S. Pratas, M.A. Neto, C.M. Fernandes, D. Figueiredo, R.F. Silva, Multilayer Diamond Coatings Applied to Micro-End-Milling of Cemented Carbide, Materials 14 (2021) 3333. https://doi.org/10.3390/ma14123333
[8] K. Andreas, M. Merklein, U. Engel, Influence of Combined Hard and Fine Machining on the Surface Properties of Cemented Carbides, Tribology in Industry 34 (2012) 119-127.
[9] F. Klocke, W. König, Fertigungsverfahren: Abtragen, Generieren und Lasermaterialbearbeitung, Springer, Berlin, New York, 2007. ISBN: 9783540236504.
[10] R. Hess, P. Grethe, L. Heidemanns, T. Herrig, A. Klink, T. Bergs, Simulation based derivation of changed rim zone properties caused by thermal loadings during EDM process, Procedia CIRP 113 (2022) 41-46. https://doi.org/10.1016/j.procir.2022.09.117
[11] H. Juhr, H.-P. Schulze, G. Wollenberg, K. Künanz, Improved cemented carbide properties after wire-EDM by pulse shaping, J. Mater. Process. Technol. 149 (2004) 178-183. https://doi.org/10.1016/j.jmatprotec.2004.02.037
[12] T. Petersen, U. Küpper, A. Klink, T. Herrig, T. Bergs, Discharge energy based optimisation of sinking EDM of cemented carbides, Procedia CIRP 108 (2022) 734-739. https://doi.org/10.1016/j.procir.2022.03.113
[13] S. Fang, S. Klein, C.-J. Hsu, L. Llanes, C. Gachot, D. Bähre, Fabrication and tribological performance of a laser-textured hardmetal guiding stone for honing processes, Int. J. Refract. Metal. Hard Mater. 84 (2019) 105034. https://doi.org/10.1016/j.ijrmhm.2019.105034
[14] W. Zhao, N. He, L. Li, Friction and Wear Properties of WC-Co Cemented Carbide Sliding against Ti6Al4V Alloy in Nitrogen Gas, Adv. Mater. Res. 188 (2011) 49-54. https://doi.org/10.4028/www.scientific.net/AMR.188.49
[15] K.W. Liew, C.K. Kok, M.N. Ervina Efzan, Effect of EDM dimple geometry on friction reduction under boundary and mixed lubrication, Tribol. Int. 101 (2016) 1-9. https://doi.org/10.1016/j.triboint.2016.03.029
[16] R. Zhou, J. Cao, Q.J. Wang, F. Meng, K. Zimowski, Z.C. Xia, Effect of EDT surface texturing on tribological behavior of aluminum sheet, J. Mater. Process. Technol. 211 (2011) 1643-1649. https://doi.org/10.1016/j.jmatprotec.2011.05.004
[17] D. Sari, D. Welling, C. Löpenhaus, F. Klocke, A. Klink, Adjusting Surface Integrity of Gears Using Wire EDM to Increase the Flank Load Carrying Capacity, Procedia CIRP 45 (2016) 295-298. https://doi.org/10.1016/j.procir.2016.02.355

[18] T. Bergs, U. Tombul, D. Mevissen, A. Klink, J. Brimmers, Load Capacity of Rolling Contacts Manufactured by Wire EDM Turning, Procedia CIRP 87 (2020) 474-479. https://doi.org/10.1016/j.procir.2020.02.111
[19] T. Petersen, U. Küpper, T. Herrig, A. Klink, T. Bergs, Fracture Toughness and Tribological Properties of Cemented Carbides Machined by Sinking Electrical Discharge Machining, ESAFORM 2021 (2021) 13. https://doi.org/10.25518/esaform21.1518
[20] CERATIZIT, Complete programme wear parts 2015. https://www.ceratizit.com/uploads/tx_extproduct/files/GD_KT_PRO-0272-0915_SEN_ABS_V1.pdf. Accessed 19 June 2020.
[21] P.-M. Mattfeld, Tribologie der zinkphosphatfreien Kaltmassivumformung, Dissertation, RWTH Aachen University, Aachen, 2014. ISBN: 978-3-86359-195-3.
[22] T. Bergs, T. Petersen, U. Tombul, A. Klink, Analysis of the Influence of Surface Integrity of Cemented Carbides Machined by Sinking EDM on Flexural Fatigue, Procedia CIRP 87 (2020) 456-461. https://doi.org/10.1016/j.procir.2020.02.096
[23] L. Llanes, Influence of electrical discharge machining on the sliding contact response of cemented carbides, Int. J. Refract. Metal. Hard Mater. 19 (2001) 35-40. https://doi.org/10.1016/S0263-4368(00)00045-7
[24] K. Bonny, P. de Baets, W. Ost, J. Vleugels, S. Huang, B. Lauwers, W. Liu, Influence of electrical discharge machining on the reciprocating sliding wear response of WC-Co cemented carbides, Wear 266 (2009) 84-95. https://doi.org/10.1016/j.wear.2008.05.009

Materials Research Proceedings 28 (2023) 1775-1780 https://doi.org/10.21741/9781644902479-192

Effects of ultrasonic burnishing on the surface quality of corrosion-resistant tool steel using a hard-carbon-coated burnishing tool

HUUKI Juha[1,a *], ULLAH Rizwan[1,b] and FANGNON Eric[1,c]

[1]Aalto University, Department of Mechanical Engineering, Puumiehenkuja 3, 02150 Espoo, Finland

[a]juha.huuki@aalto.fi, [b]rizwan.ullah@aalto.fi, [c]eric.a.fangnon@aalto.fi

Keywords: Ultrasonic Burnishing, Surface Quality, Carbon Coated Tool

Abstract. Ultrasonic burnishing is a relatively new and effective method for improving the surface finish of metal parts. Burnishing strongly affects the surface quality, improving surface properties such as, surface hardness and surface roughness. Previous studied have observed that changing some burnishing parameters significantly affects the burnished surface quality. In this research, using a carbon-coated burnishing tool, tangential misalignment angles were varied on a corrosion resistant tool steel that has not been previously investigated. Two different burnishing tools were used to study their effect on surface quality and surface hardness. The results revealed that coated tungsten carbide tool has produced superior surface finish compare to non-coated burnishing tool which is the new finding. It is rather surprising that surface roughness has not increased as it typically happens during burnishing but a clear surface roughness enhancement was observed. The results showed a clear improvement in surface roughness (80-86%), whereas surface hardness did not change significantly.

Introduction

Ball burnishing and other forms of burnishing methods have gained popularity in recent years, as they not only affect the workpiece surface but also improve both the physical and mechanical properties of turned parts [1]. The goal of all burnishing methods is to create surface layers of high quality to improve the surface properties of mechanical components, such as surface roughness, hardness residual stress, and microstructure in different applications that require an excellent surface finish and dimensional accuracy [2,3]. Such methods are mainly used on rotating components with high-quality requirements, such as automotive axles, bearing parts, or crankshafts [4].

In manufacturing industries, the burnishing process has proven to be an easy and economical surface enhancement technique in secondary operations like grinding, honing, and lapping [5]. The burnishing process leads to the plastic deformation of the work surface when it comes in contact with a highly polished and hardened tool known as a burnishing tool [5].

Ultrasonic burnishing is less well known than the roller, ball, or diamond methods. This modern method is used for finishing metal surfaces by forging at very high frequency. Forging is performed with a ball-shaped finishing head at extremely high ultrasonic frequency while the workpiece rotates along a fixed axis, as depicted by the schematic in Fig.1. A constant spring load is applied to the burnishing tool to keep it in contact with workpiece surface. The process removes no material from the workpiece. Instead, it causes plastic deformations on the part surface, thereby creating residual stresses and improving surface quality [6].

Content from this work may be used under the terms of the Creative Commons Attribution 3.0 license. Any further distribution of this work must maintain attribution to the author(s) and the title of the work, journal citation and DOI. Published under license by Materials Research Forum LLC.

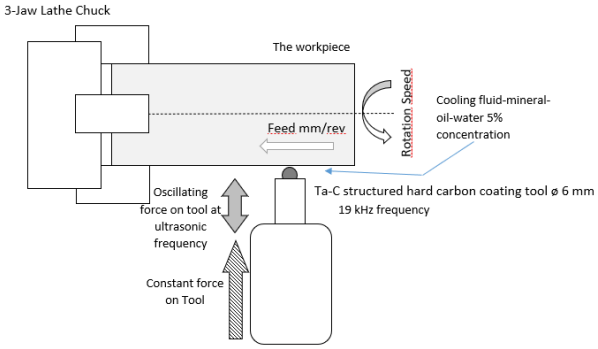

Fig.1. Schematic of the ultrasonic burnishing process.

Raza et al. recently published an extensive overview of past research on surface integrity in different burnishing processes, including ball burnishing, roller burnishing, and low plasticity burnishing (LPB) [5]. The authors found that carbon chromium, TiN coated EN31, tungsten carbide, high carbon and chromium steel, and HSS steel were all common roller materials reported in past research work. The burnishing process is mostly used to improve hardness, surface roughness, fatigue strength, corrosion resistance, wear resistance and microstructure properties, and to generate compressive residual stresses [5]. A ball burnishing tool consists of a hard ball constructed from hard materials. According to Raza et al., most researchers have used carbide material for the ball because of its high modulus of elasticity and high density. However other ball burnishing tool material is also used including alumina carbide, cemented carbide, silicon carbide, silicon nitride, ceramics, and carbon steel [5,6]. Moreover, as Prasad et al. state, most researchers have studied and optimized the burnishing process parameters on the surface roughness and surface hardness of ferrous and nonferrous metals, such as brass and aluminium alloys [5,6].

Little research work has been conducted on tangential misalignment or carbon-coated tools in ultrasonic burnishing, although many authors have examined burnishing methods, such as the ball, roller, or slide effect on material integrity [7-12]. Moreover, to our knowledge, no study has investigated the effect of ultrasonic burnishing on the surface quality of cylindrical stainless-steel workpieces with different tangential alignments a carbon-coated tool. Furthermore, based on our literature review, no researchers have used ultrasonic burnishing to finish Corrax material. The material is used in the mold industry and in different engineering parts [13]. For this reason, there is a clear need to evaluate the effect of ultrasonic burnishing on the surface finish in this context.

Methodology

HIQUSA ultrasonic burnishing equipment was used to burnish a workpiece manufactured from a corrosion resistant-tool steel with an initial hardness of 385 HV. As shown in Fig.2, ultrasonic burnishing was performed on the stainless steel, commercially available as Corrax. The workpiece was pre-machined from a diameter of 90 mm to 88 mm, with a length of 500 mm. The designations and typical compositions of the test material used are shown in Table 1. The test material is well-suited for mould-making parts and it exhibits excellent resistance to corrosion [13].

Table 1: The chemical compositions (wt%) of the tested work material.

Corrax						
C	**Si**	**Mn**	**Cr**	**Ni**	**Mo**	**Al**
0.03	**0.3**	**0.3**	**12.0**	**9.2**	**1.4**	**1.6**

Fig. 2, below, depicts both the HIQUSA ultra burnishing equipment used to undertake the burnishing process and the Tangential Misalignment Angle (TMA), kappa (κ). TMA is defined as

the angle formed between the burnishing tool axis and axis of the shaft. For the tool oriented 90° to the shaft, TMA is considered as 0 and it can increase on either side - hence positive and negative TMA are possible. It is important to study TMAs, since in burnishing process, one semi-spherical (burnishing tool) and a cylindrical surface get in contact with each other and double curved surfaces [2] could form. Beside the possible effect on cylindricity, surface roughness can be vary significantly [2].

In our previous work [2], burnishing was performed on Stavax stainless steel using a wolfram carbide ball with a finishing head 6 mm in diameter. The Ta-C structured hard-carbon coated-tool used in this research is known commercially as BALINIT® MILUBIA [15]. Burnishing in this case was limited to a TMA range of 0°-45°. The burnishing parameters are shown in table 2. The ultrasonic burnishing parameters were 80 rpm for the spindle speed and 0.05 mm/rev for the feed, while forging was performed at a frequency of 19 kHz. The spring preload was 1.5 mm for the workpiece. A cutting fluid (filtered 5% oil-water emulsion) was used to cool the tool in the process.

Table 2. Burnishing process parameters.

Burnishing parameters	Ultrasonic burnishing
Force P	5.40 N
Frequency	19 kHz
Preload on the spring	1.5 mm
Feed	0.05 mm/rev
Speed	80 rpm

However, in the present work, the burnishing parameters were changed to 500 RPM and a ø 6 mm carbon-coated tool was used. The tool feed and burnishing frequency of the tool head were kept constant, as in Fig.1 [2]. With this configuration, burnishing was only possible at 0° TMA, while a higher TMA resulted in deteriorated surfaces.

Surface Roughness

MarSurf PS 10 apparatus was used to measure the surface roughness of the burnished bands along a cylindrical shaft. This equipment uses a stylus measuring probe and the cut-off length value is selected as 2.5 mm. The device was used to measure the roughness of both the pre-machined and burnished surfaces.

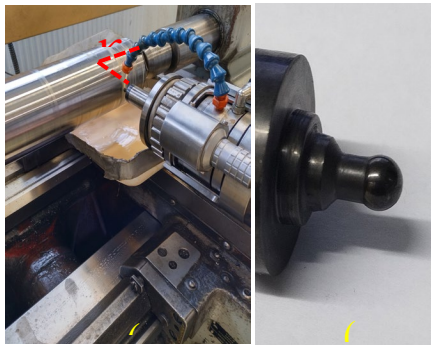

Fig. 2. Burnishing equipment: (a) tangential misalignment angle (TMA) κ, (b) carbon coated tool head.

Surface Hardness

Brickers-220 equipment was used to measure the surface hardness of the burnished bands along the circumference of the shaft. Each burnished band was approx. 5 mm in length. Hardness was measured five times at each location, which corresponded to a different tangential misalignment angle.

Results and Discussion

The test material surface after burnishing is shown in Fig. 3. The surface finish differences between the burnished surfaces produces by the Ta-C hard carbon coated tool (green) and the wolfram carbide tool (red) can be easily distinguished. This demonstrates that tool material and coating significantly affects the surface finish.

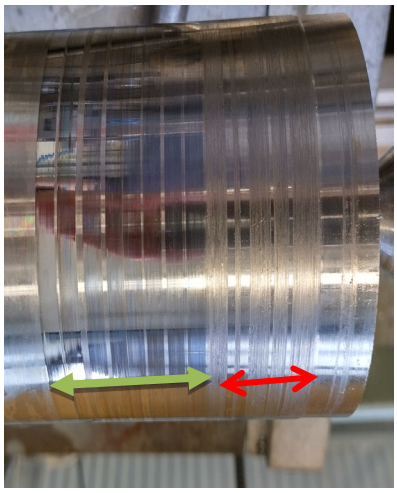

Fig. 3. Surface with carbon coated tool head (green arrow) and a wolfram tungsten carbide (red arrow).

Surface hardness.

The hardness of the machined (after the turning operation) shaft prior to burnishing was measured as 385 on the HV10 scale ± 15. The same value is 41 on the Rockwell C scale (HRC), which is comparable to the as-supplied hardness value provided by the manufacturer of Corrax [13].

The use of coated tools during burnishing, resulted in a rather uniform surface hardness with both positive and negative tangential misalignment angles (TMAs), implying that TMAs has exert no effect on surface hardness (Fig 4). This finding contrasts with the results for Stavax (a stainless steel with a different composition from Corrax) where surface hardness increased (1.5-3.6%) compared to a machined but unburnished surface. This effect could be associated with material behaviour or the use of coated tools and therefore must be further investigated. However, ultrasonic burnishing has been found increase surface hardness by 6.8 % for 34CrNiMo4 steel [14].

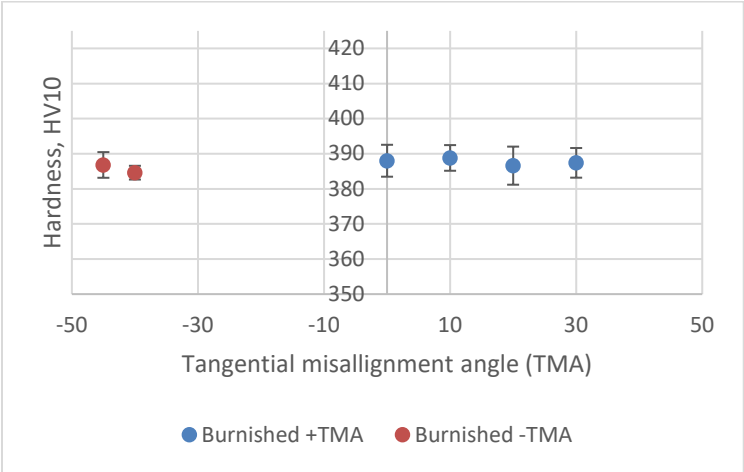

Fig. 4. Surface hardness measured on the Rockwell HRC scale for various test-material tangential misalignment angles.

Surface roughness.

For purposes of comparison, the surface roughness of an unburnished and machined (turning only) surface was measured as 1.6 µm. Surface roughness appeared to be affected by changing TMAs, where 0 degrees yielded a rough surface compared to higher TMAs. The increase in surface roughness compared to the machined surface was a minimum of 80% and maximum of 86%, which is an extremely positive influence. Overall, surface roughness, which reflects superior surface quality, improved significantly compared to the machined surface. This result is comparable to the burnishing of Stavax [2]. Fig 5 demonstrates the significant improvement in surface roughness achieved by using the coated tool. These findings are also in accordance those reported in the literature on the effect of burnishing on surface quality [2,7].

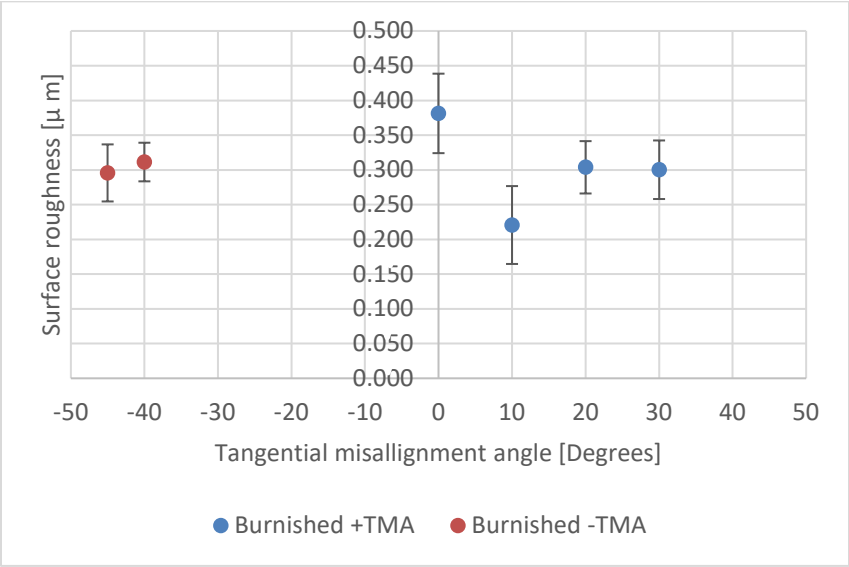

Fig. 5. Surface roughness of Corrax material (Ra).

Summary

Ultrasonic burnishing is a finishing process which imparts beneficial compressive residual stresses and enhanced surface properties. The method is especially suited for shafts and mechanical parts but can be implemented on flat-face surfaces as well. In this study, ultrasonic burnishing was applied to Corrax (a stainless-steel material) using coated tools. The study analysed the effects of changing the tangential misalignment angle (TMA) on surface hardness and on surface roughness. The following conclusions can be drawn:

- For the specific case of Corrax, ultrasonic burnishing exerted very little effect on surface hardness, which is an unusual burnishing behaviour that requires further investigation.
- Coated burnishing tools enhanced surface roughness by 80-86% which is comparable with previous results.
- Performing the ultrasonic burnishing operation with the Ta-C structured hard-carbon coated-tool 6 mm diameter and 19 kHz frequency, the Corrax material is a suitable combination for the application of the process in terms of surface quality enhancement.
- Ultrasonic burnishing treatment process with tungsten carbide (Ta-C) structured hard carbon coated tool has resulted much superior surface quality compared to non-coated burnishing tool.

References

[1] A. Dzierwa, A.P. Markopoulos, Influence of ball-burnishing process on surface topography parameters and tribological properties of hardened steel, Machines. 7 (2019) 11. https://doi.org/10.3390/machines7010011

[2] R. Ullah, E. Fangnon, J. Huuki, Effect of Ultrasonic Burnishing Parameters on Burnished-Surface Quality of Stainless Steel After Heat Treatment, In International Conference on Flexible Automation and Intelligent Manufacturing 2023, Springer, Cham, pp. 38-47. https://doi.org/10.1007/978-3-031-18326-3_4

[3] M. Celik, U. Caydas, M, Akyuz, The influence of roller burnishing process parameters on surface quality and fatigue life of AA 7075-T6 alloy, Materialwissenschaft und Werkstofftechnik 53 (2022) 608-616. https://doi.org/10.1002/mawe.202100291

[4] S. Świrad, The surface texture analysis after sliding burnishing with cylindrical elements, Wear. 271 (2011) 576-581. https://doi.org/10.1016/j.wear.2010.05.005

[5] A. Raza, S. Kumar, A critical review of tool design in burnishing process, Tribol. Int. 174 (2022) 107717. https://doi.org/10.1016/j.triboint.2022.107717

[6] G.D. Devaraya, R. Shetty, S.S. Rao, V.N. Gaitonde, Wear resistance enhancement of titanium alloy (Ti-6Al-4V) by ball burnishing process, J. Mater. Res. Technol. 6 (2017) 13-32. https://doi.org/10.1016/j.jmrt.2016.03.007

[7] J. Huuki, R. Ullah, S. Laakso, Process limitation of ultrasonic burnishing for commercially available martensitic stainless steel, Procedia Manuf. 51 (2020) 885-889. https://doi.org/10.1016/j.promfg.2020.10.124

[8] K.R. Prasad, M.R. John, Optimization of external roller burnishing process on magnesium silicon carbide metal matrix composite using response surface methodology, J. Braz. Soc. Mech. Sci. Eng. 43 (2021) 342. https://doi.org/10.1007/s40430-021-03069-3

[9] J.T. Maximov, G.V. Duncheva, A.P. Anchev, M.D. Ichkova, Slide burnishing—review and prospects, Int. J. Adv. Manuf. Technol. 104 (2019) 785-801. https://doi.org/10.1007/s00170-019-03881-1

[10] Ch. Priyadarsini, V.S.N. Venkata Ramana, K. Aruna Prabha, S. Swetha, A review on ball, roller, low plasticity burnishing process, Mater. Today: Proc. 18 (2019) 5087-5099. https://doi.org/10.1016/j.matpr.2019.07.505

[11] N. Yaman, N. Sunay, M. Kaya, Y. Kaynak, Enhancing Surface Integrity of Additively Manufactured Inconel 718 by Roller Burnishing Process, Procedia CIRP 108 (2022) 681-686. https://doi.org/10.1016/j.procir.2022.03.106

[12] M.H. El-Axir, An investigation into roller burnishing, Int. J. Mach. Tools Manuf. 40 (2000) 1603-1617. https://doi.org/10.1016/S0890-6955(00)00019-5

[13] Uddeholm Finland. Uddeholm Corrax. https://www.uddeholm.com/files/PB_Uddeholm_corrax_english.pdf (accessed 6 December 2022)

[14] J. Huuki, S.V.A. Laakso, Surface improvement of shafts by the diamond burnishing and ultrasonic burnishing techniques, Int. J. Mach. Mach. Mater. 19 (2017) 246-259. https://doi.org/10.1504/IJMMM.2017.084007

[15] Oerlikon Finland. Balinit Milubia coating. https://www.oerlikon.com/ecoma/files/HQ265EN_BALINIT_MILUBIA.pdf?download=true (accessed 6 December 2022)

Materials Research Proceedings 28 (2023) 1781-1788 https://doi.org/10.21741/9781644902479-193

Influences in deep hole sinking (EDM, ECM) that make it difficult to analyze the process status

SCHULZE Hans-Peter[1,a *], HERZIG Mathias[1,b] and KRÖNING Oliver[1,c]

[1]Leukhardt Schaltanlagen Systemtechnik GmbH, NL Magdeburg, Gustav-Ricker-Straße 62, D-39120 Magdeburg, Germany

[a]hans-peter.schulze@leukhardt-system.de, [b]mathias.herzig@leukhardt-system.de, [c]oliver.kroening@leukhardt-system.de

Keywords: EDM, ECM, Hybrid Processes, Process Analysis

Abstract. A particular problem of deep hole sinking is the correct process analysis during the sinking process. It is important to know the primary technological objectives and to design the process regulation accordingly. Due to the objectives high removal rate, minimum roughness of the inner surface, high dimensional accuracy, etc., the analysis criteria are clearly changed and must be made available to process regulation. Another influencing parameter is the structure of the process energy source (PES).

Introduction

When sinking deep holes, it is of particular importance that the current process status of the machining process is precisely analyzed in order to give the process controller the correct signals to continue machining. In the following article, the two basic methods ECM and EDM will first be discussed, with the special features in the areas of the frontal, the lateral and the transition gap being considered. Differences in these areas occur particularly when the feed rate deviates greatly from the current removal rate. Another machining case is when the inner surface of the countersink is to be designed in a defined manner.

When using a hybrid processing method between EDM and ECM, the current and voltage curves analysis becomes even more complex because transient pulses also occur. It must also be noted that the ED parts of the machining take place in an electrolyte and are only local, while the EC removal always takes place over a large area. This raises the question of whether the pulse analysis can be used to regulate the feed rate or not. Finally, the topic of the applied process energy source (PES) is discussed.

Process Analysis ECM

In its process analysis, the ECM must distinguish whether it is used to sink a specified profile into an undefined surface, to rework a profile, or to sink deep holes, whereby aspects greater than 10 are assumed. EC milling is excluded from further considerations.

In the case of maximizing productivity and no special requirements for the inner surfaces of the holes, solutions are possible, as shown in Fig. 1 [1]. In the case of the insulation of the cathode surface, Fig. 1,II, it can be assumed that the current-voltage analyzes relate entirely to the front gap. As a result, this analysis can be used for feed regulation. The size of the lateral gap will depend on the insulation configuration at the edges of the lateral gap. It must be noted that if the lateral gap is too small, the flushing of the frontal gap will be negatively affected.

Content from this work may be used under the terms of the Creative Commons Attribution 3.0 license. Any further distribution of this work must maintain attribution to the author(s) and the title of the work, journal citation and DOI. Published under license by Materials Research Forum LLC.

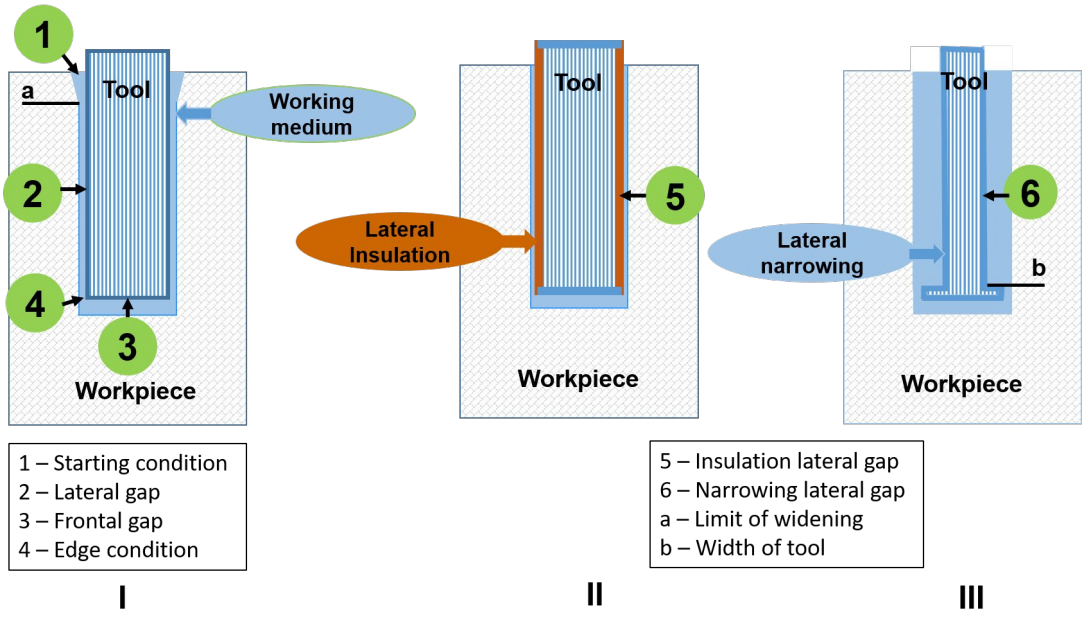

Fig. 1. Different conditions by ECM and EDM.

Fig. 1,I shows the areas of interest for analysis. In area 1, the starting conditions are at the surface. Due to larger stray fields, a larger area is removed than later in the hole area. The frontal erosion is reduced due to the areal removal with ECM. Area 1 can be minimized if the frontal area of the tool electrode is designed as a cone. In area 2, the side gap is widened by the fixed arrangement (a) until the current density no longer allows removal. Therefore, the side gap is usually slightly conical. In contrast to the arrangement in Fig. 1,II, where removal can no longer take place due to the lateral insulation (5), in Fig. 1,III, the active side gap is achieved by narrowing the tool electrode. This intensifies the rinsing effect (6), and which lateral gap is created depending on the front height of the tool electrode (b). The working gap on the front side depends on the ratio of the removal on the front side to the feed rate. It would be ideal if both were the same size, then, there would be a constant front gap. However, the current and voltage recordings only show us the overall picture of the individual ablation areas. It is sufficient for the critical process states such as soft short circuits or discharge since the machining process has to be interrupted or the rinsing has to be improved to achieve the desired surface quality.

Process Analysis EDM in the Electrolyte

If the EDM process is considered in the conventional sense, then we have a dielectric as the working medium and a cathodic polarity for the workpiece [2]. The discharge conditions are determined by the electrical field conditions and the degree of contamination in the working gap. In contrast to the ECM, a small area is removed locally but with a high frequency and constantly changing location. It can be assumed that the electrical discharge binds the entire energy through its plasma channel and that the removal ratios at the anode and cathode can be calculated from this.

Referring to Fig. 1, area 1 is mostly more frayed, while area 2 shows less taper. There is also a rounding in the corner area 4, but not as homogeneously as with the ECM. The primary removal area is the front gap, because there the gap is constantly regulated to a specified gap by the feed rate. Flushing in the side gap reduces the dielectric strength, so isolated discharges also occur there. These discharges determine the roughness of the hole wall. Even with the EDM, we cannot assign the current and voltage curves to the areas defined in Fig. 1, but only look at the effect afterward [3].

If hybrid-machining processes are to be analyzed, then some conditions from the conventional EDM conditions no longer apply [2,3,4].

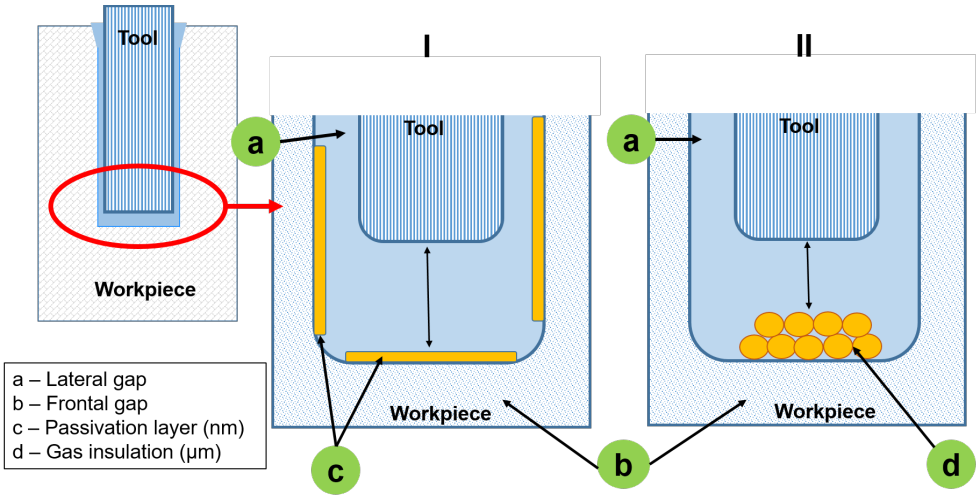

Fig. 2. Changed ED conditions in the hybrid ED-EC process.

In Fig. 2, it can be seen that the electrical breakdowns are not determined by the working medium, but by passivated layers (Fig. 2,c) and/or gaseous deposits (Fig. 2,d**)**. The breakdown takes place in these phases, while the formation of the discharge channel (plasma, gas volume) primarily takes place in the electrolyte. Since in hybrid applications, there is almost exclusively an anodic polarization of the workpiece, the sparks are removed over a larger area than with the original EDM. Passivation in the lateral gap prevents further erosion from a certain lateral gap width and is, therefore, decisive for the surface quality of the inner wall surfaces of the bore. For electrical breakdown, the condition I in Fig. 2, hence electrical breakdown in very thin solid layers, must be considered.

In the case of passivation layers in the nanometer range, a field breakdown occurs because even a small voltage drop across the passive layer leads to high electrical field strength. Assuming a layer thickness of 10 nm and a voltage drop of 1 V, the electric field strength would be 10^8 V/m. At these field strengths, altered effects of electrical conductivity (tunneling, hopping) take place in a dielectric solid. If the insulating effect is eliminated, a combined heat/field breakdown can occur via the remaining front gap. In the electrolyte, the discharge channel spreads out more, depending on the electrical conductivity of the electrolyte, than would be the case in a dielectric. As a result, energy is withdrawn from the discharge base, and the crater formations become smaller and larger.

Fig. 3 shows where one can speak of hybrid machining methods and which basic removal processes cause the main removal.

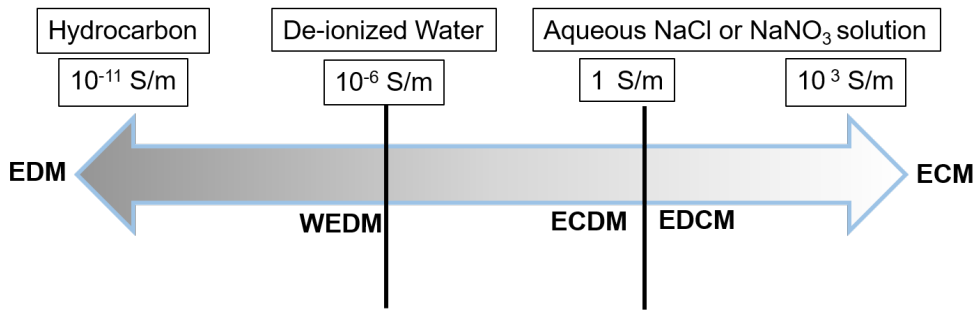

Fig. 3. Dependence of the hybrid ED-EC process on the electrical conductivity of the working medium [5].

A contrast to this is in Fig. 2II where the dielectric layer is a gas layer. The gas accumulations are usually thicker than the passive layers and more mobile in their formation, so the breakdown conditions can change quickly. The tool's rotation or the working gap's flushing can cause these changes, for example. Another special feature can be that the gas layer is accumulated as gas bubbles or as a homogeneous gas layer. In the latter case, the discharge can be described according to the EDM models based on gas discharges. With the accumulation of gas bubbles, a small EC removal can still have an effect, which leads to a heating breakdown due to the extremely reduced working surface with a very high current density.

Fig. 3 shows that the ECD erosion by the discharges is at electrical conductivities below 1 S/m, while the EC-dominant EDC erosion is at electrical conductivities above 1 S/m.

Process Analysis of the Hybrid EDM-ECM Process

For process analysis, two applications are available for comparison, which were intensively examined in two studies. In the first study, a wire EDM system [3] was analyzed in terms of its current and voltage curves, while in the second study, EDC sinking of smaller holes was considered. The primary objective was to assign the current-voltage pairs to a fundamental erosion or disturbance condition and internal surfaces with minimal roughness.

With sinking, the current and voltage curves shown in Fig.4 are typically related to the basic processes. The output data of the process energy source (PES) [6] are 30 A and 50 V, with a reduced EC current resulting from the impedance conditions (Eq. 1–4) of the test arrangement. By increasing the electrical conductivity of the working medium, the EC current could be increased accordingly.

In the case of the short circuit, the full PES current appeared and the voltage drops to almost zero volts. In the EC processing (Fig. 4), it was reduced to approx. 7 A here. The pulse in Fig. 4,B is an exception, which is determined by the characteristics of the PES. The number of partial overshoots (Fig. 4,C) increases with increasing immersion depth, which suggests very short partial discharges due to contamination of the working gap. An ED discharge (D) and an arc discharge (E) can then be seen in the right-hand diagram of Fig. 4. With a pulsing of 5 µs pulse-on and 5 µs pulse-off, these two discharges show a strong negative overshoot in the switch-off range, which can be attributed to the capacitive components (capacitor discharge) of the passive residual layer.

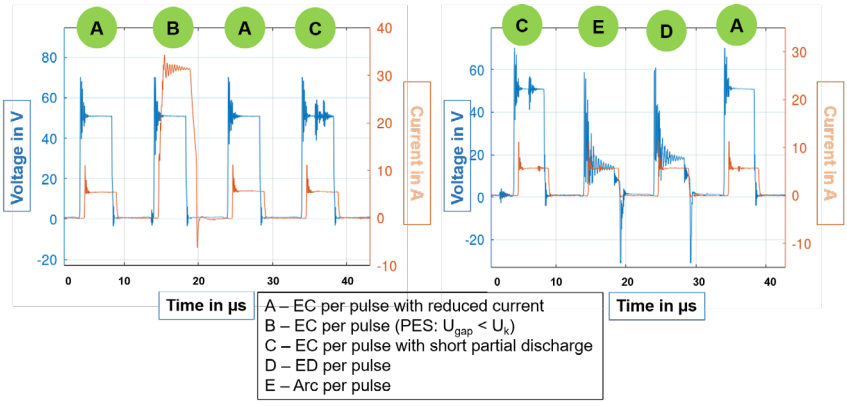

Fig. 4. Basic processes in hybrid hole sinking EDCM [7].

In Table 1, the pulses that occur after the current and voltage curves are selected must be differentiated according to the basic pulses, the pulses with transitions between basic erosion and the pulses that are specifically given by the characteristics of the PES. From the percentage number

of pulse types per time unit, it can be concluded whether the lowering process is ideal or needs to be corrected by the process regulation.

Table 1. Categorization of the pulses according to base, transition, and PES-dependent pulses.

Index	Conditions	Comments	Typ
a	$U_{max} = U_{PES}$ and $I_{gap} = I_{EC}$	EC-Pulse	Basic
b	$U = U_{spark}$ and $I_{gap} = I_{ED}$	ED-Pulse	Basic
c	$U < U_{spark}$ and $I_{gap} = I_{arc}$	Arc-Pulse	Basic
d	U = 0V (very close) and $I = I_{PES}$	Short circuit	Basic
e	U falls below the spark burning voltage	ED-Pulse → Arc-Pulse	Transition
f	U increases to U_{max}	ED-Pulse → EC-Pulse	Transition
g	U_{max} falls to U_{spark}	EC-Pulse → ED-Pulse	Transition
h	U_{max} falls to U_{arc}	EC-Pulse → Arc-Pulse	Transition
i	Solution of the Passivation via ECM		PES
k	Dynamics of the gas layer loosens the insulation		Flushing
l	Collapsing voltage U_k of the PES gives security of processing		PES

In Fig. 5, the pulse transitions are visible, which are defined in Table 1 under the indices e to h. The position in Fig. 5,A corresponds to the transition from the EC phase with an intermediate plateau to the ED phase. The intermediate plateau may be because the final ED erosion arose from thermal breakdown. In Fig. 5,B,C EC ablations can be seen, which are determined by the characteristics of the PES used, which is explained in more detail in the next section. Finally, Fig.5,D shows the transition from the ED phase to the EC phase.
These findings were also found largely in the WEDM investigation [3], which was used to work with a static PES.

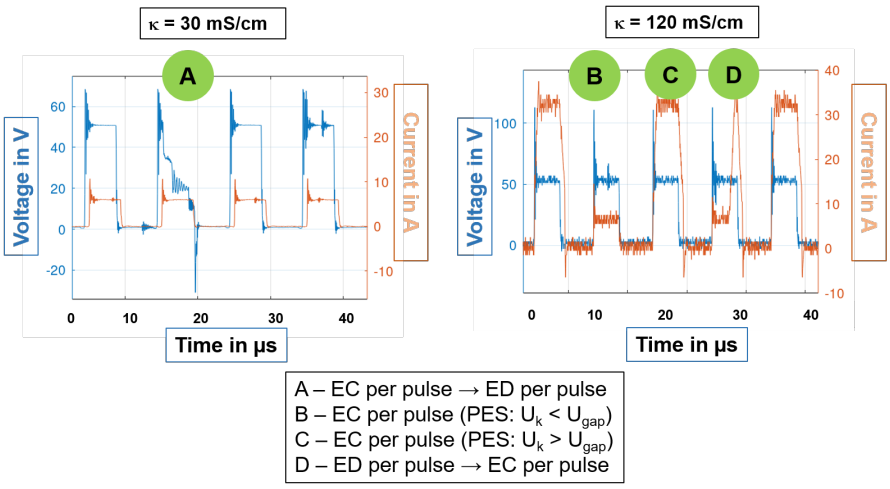

Fig. 5. Pulses with process transitions in ED hole sinking [7].

Influences of PES

A special process energy source (PES) was used for the hole sinking, the characteristics of which are shown in Fig. 6. Up to the break voltage U_k, it acts as a current source. It determines the pulse energy of the ED discharge and the arc discharge with its set current IPES. The operating point of the ECM is then determined by the load characteristic of the working gap. The working point ECM 2 is present when the working voltage is close to the maximum voltage U_{max}. As the electrical

conductivity of the working-gap resistance increases, the voltage drop across the gap decreases compared to the total impedance of the PES load, i.e. smaller currents automatically appear in the working gap.

The total impedance of the PES load is Z_{PES} Eq. 1 and is made up of the components of the contact Z_{ko}, the leads Z_{Li} and the working gap Z_{el}. If the electrolyte has high electrical conductivity, the remaining impedance components must also be small so that the PES voltage drops completely across the working gap. In the case of a current source, however, the same current would always be impressed, which would be important for the ECM. With a voltage source, a desired current can be achieved by changing the voltage, leading to ED discharges in the side gap for a long time. The voltage difference ΔU in Fig. 6 determines how quickly the current falls after exceeding U_k and depends on the structure of the PES.

According to Eq. 2, only the impedance of the working medium Z_{wm} is decisive for EC machining, which depends on the working gap a_x, the machining area A_x and the electrical conductivity κ of the working medium. Due to the passivation (Eq. 3, Z_{pass}) or the formation of gas bubble layers (Eq. 4, Z_{bub}), the impedance changes in that these layers have their impedance, with the capacitive components also playing a role. Furthermore, the impedance of the remaining working gap fluid remains (Eq. 3, Z_{fl1} and Eq. 4, Z_{fl2}). Only the layer impedances are then of interest for the breakdown conditions.

The advantage of the PES used is that it has a self-regulating effect, which means that process regulation can be significantly reduced.

$$\underline{Z}_{PES} = \underline{Z}_{ko} + \underline{Z}_{Li} + \underline{Z}_{el} \tag{1}$$

$$\underline{Z}_{el} = \underline{Z}_{wm} \quad \text{for ECM} \tag{2}$$

$$\underline{Z}_{el} = \underline{Z}_{pass} + \underline{Z}_{fl1} \quad \text{before EDM} \tag{3}$$

$$\underline{Z}_{el} = \underline{Z}_{bub} + \underline{Z}_{fl2} \quad \text{before EDM} \tag{4}$$

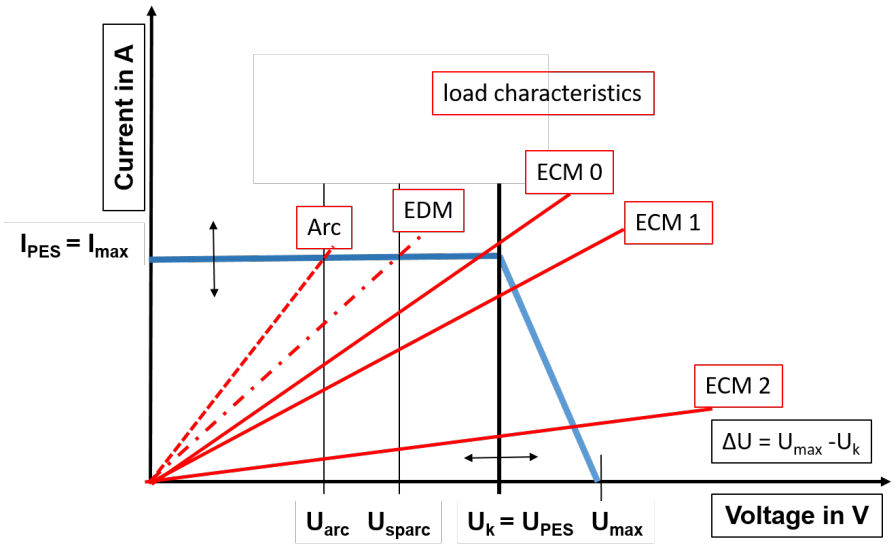

Fig. 6. Characteristic of the PES with different load curves.

Simplifications of the Process Analysis in the Hybrid Process Under Defined Technological Target Parameters

The machining process can be evaluated using pulse analysis for its process regulation but also for the technological objective. The technological objectives can be minimizing the machining time, the quality of the inner surface of the hole or the accuracy of the countersunk hole. In Fig. 7, a processing example is used to show how specific process states and a sequence of process states appear in the voltage-current characteristic [8, 9]. What is not apparent are the transition pulses. In the example, the frequency of the basic processes can be seen, with ED and EC pulses taking place in roughly the same number, while soft short circuits represent around 10% of the processing cases.

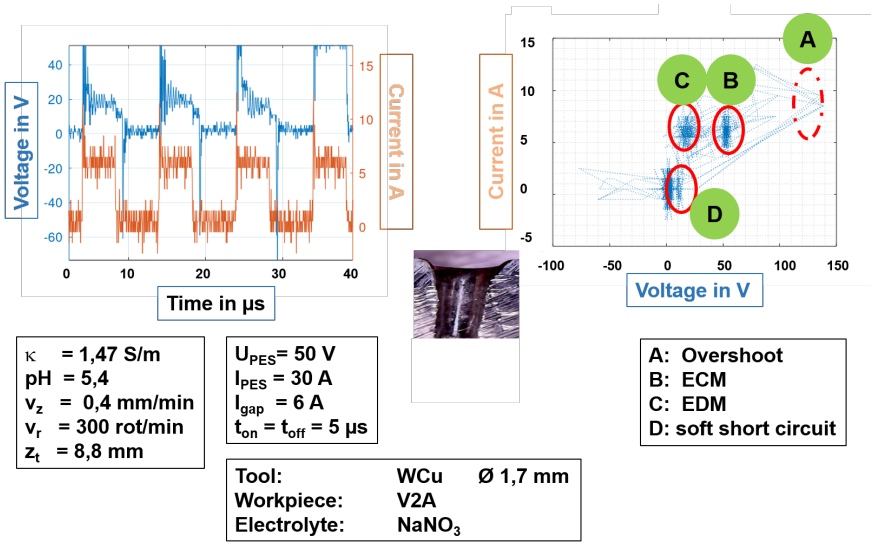

Fig. 7. Voltage – Current curve for 100 pulses in sinking deep of 8.8 mm [7].

If a more precise statement is to be made about the process states for regulation, then the sequence of pulses defined in Tabelle 1 must be made. The current and voltage limit values required for this are known from the literature or can be determined from a test run. With a smooth, shiny inner surface of the holes, the proportion of ED discharges in the side gap should be minimal. From the sequence of the pulse phases, there is a higher probability of isolated ED phases occurring in the side gap, since ED phases in the frontal gap only expose small areas for ECM.

Summary

To predict the processing result with pulsed hybrid EDM-ECM methods, assigning the individual pulses to a specific basic processing or a transitional behavior is necessary. It is difficult to find out where the effects of the removal take place. They are primarily to be found in the front gap because here, the size of the working gap is continuously tracked by the feed rate. In the lateral gap, on the other hand, static behavior can be assumed, which means that no further removal or application mechanisms are effective after the lateral gap has reached a certain size.

In the hole sinking study, a special process energy source was used, which acts as a current source up to a voltage U_k, after which it acts as a voltage source. The advantage of this PES is that it protects itself against working currents that are too high and causes a kind of self-regulation for the critical processing pulses.

The process regulation via the feed regulation can take place through targeted analysis of the pulse processes in terms of their phases and sequence. This makes it possible to achieve smooth, shiny surfaces even for deeper countersinks.

References

[1] G. Meichsner, Entwicklung und Realisierung einer Methode zur Bestimmung von Prozesseingangsgrößen für das elektrochemische Präzisionsabtragen. Diss. TU Chemnitz (2018), Scripts Precision and Microproduction Band 12.

[2] A. Ahmed, M. Rahman, S. Kumar, Spark Erosion based hybrid processes, in: Erosion Machining, Chapter 6, Taylor & Francis Group, 2020.

[3] K. Oßwald, I. Lochmahr, H.-P. Schulze, O. Kröning, Automated Analysis of Pulse Types in High Speed-Wire EDM, Procedia CIRP 68 (2018) 796-801. https://doi.org/10.1016/j.procir.2017.12.157

[4] M. Bellotti, J. Quin, D. Reynaerts, Breakthrough phenomena in drilling micro holes by EDM, Int. J. Mach. Tools Manuf. 146 (2019) 1034-36. https://doi.org/10.1016/j.ijmachtools.2019.103436

[5] H.-P. Schulze, D. Borkenhagen, St. Burkert, Demands on process and process energy sources for the electroerosive and electrochemical micro machining. Int. J. Mater. Form. 1 (2008) 1383-1386. https://doi.org/10.1007/s12289-008-0122-0

[6] A.K.M. De Silva, H.-P. Schulze, J.A. McGeough, M. Zybura, Process Control and Power Systems for Electrochemical-Erosion Sinking (ELESIN), Proceedings of the 16th ISEM 2010, Shanghai, 389-392.

[7] O. Ibrahim, Experimentelle Untersuchungen zum Lochsenken durch Hybride EDM-ECM Prozesse (EDCM) Thesis BA (2022) OvGU Magdeburg.

[8] H.-P. Schulze, St. Burkert, Influence of the electrochemical process on hole structure through hybrid ED-EC process, INSECT 2007, 129 – 134, Scripts Precision and Microproduction Band 1

[9] M. Läuter, H.-J. Trautmann, M. Zybura-Skrabalak, H.-P. Schulze, G. Wollenberg, Structure of process-energy-source for time-parallel combined processes, *J. Mater. Process. Technol*. 149 (2004) 519-523. https://doi.org/10.1016/j.jmatprotec.2004.02.018

Materials Research Proceedings 28 (2023) 1789-1796 https://doi.org/10.21741/9781644902479-194

Out-of-autoclave molding of carbon fiber composites pipes with interlaminar carbon nanotubes

BELLISARIO Denise[1,a *], IORIO Leandro[2,b], PROIETTI Alice[2,c], QUADRINI Fabrizio[2,d] and SANTO Loredana[2,e]

[1]Mercatorum University, p.zza Mattei 10, Rome, Italy

[2]University of Rome Tor Vergata, via del Politecnico 1, Rome, Italy

[a]denise.bellisario@unimercatorum.it, [b]leandro.iorio@uniroma2.it, [c]alice.proietti@uniroma2.it, [d]fabrizio.quadrini@uniroma2.it, [e]loredana.santo@uniroma2.it

Keywords: Carbon Fiber, Composite, Carbon Nanotube, Out-of-Autoclave Molding

Abstract. Carbon fiber reinforced (CFR) composite rings with and without interlaminar carbon nanotubes (I-CNTs) were manufactured starting from high performance prepregs used in aeronautics. Nano-particles deposition was obtained by an innovative easily scalable procedure which does not affect composite processability. A CNTs-solvent solution was sonicated for an established time to reduce bulk CNTs agglomerates. The solution was poured on prepreg stripes and left at room temperature for solvent evacuation. The prepreg stripes were wrapped on steel pipe to obtain the annular configuration and manufactured by an out-of-autoclave (OOA) process. The consolidation pressure was applied through a thermo-shrinkable tube and curing occurred in oven. Stereomicroscopy and mechanical tests were performed on CFR and I-CNTs/CFR rings. A good adhesion among the plies was observed as well as the positive effects of CNTs deposition; an increase of 34%, 15% and 17% was obtained for the stiffness, the peak load and the fracture energy of the functionalized rings, respectively.

Introduction

The extensive use of carbon fiber reinforced polymer (CFRP) composites in highly-valued fields such as Automotive, Aeronautics and Aerospace is mainly due to their high structural performances and light weight if compared to alloys. Currently, the real challenge in these fields requires the development of new qualified materials and new production technologies that are more scalable at industrial level.

Generally, composite stiffness and in-plane strength are governed by reinforcing fibers, whereas matrix and matrix/fibers adhesion are responsible for creep, peeling strength and interlaminar shear strength (ILSS) resistance. Adding fillers in the polymer matrix before fiber impregnation can lead to property improvements, achieving even higher performances. For this reason, more attention must be paid to resin processability which can be negatively affected by changes in its formulation, with detrimental consequences for the final composite. Carbon nanotubes (CNTs) can interact with the matrix at a microscopic level enhancing its rigidity and strength. The CNTs insertion affects the resin mobility with a reduction in all the stages of the curing process. Consequently, the increase of the resin viscosity is responsible for lower reactivity and worse fiber impregnation during manufacturing of composites structures.

In the last decades, many researches discussed the positive effect of CNTs insertion in the resin matrix. All the studies are focused on the definition of an easily implementable and repeatable technique for spreading nanoparticles on dry or wet carbon fibers. Different solutions have been investigated. The most adopted strategies deal with the modification of the polymeric matrix before impregnation (massive mixing), using a massive interlayer between prepreg plies and the use of dispersed nano-reinforcements (interlaminar deposition).

Content from this work may be used under the terms of the Creative Commons Attribution 3.0 license. Any further distribution of this work must maintain attribution to the author(s) and the title of the work, journal citation and DOI. Published under license by Materials Research Forum LLC.

Positive effects arising from mixing nanoparticles with the matrix before wet lamination of CFR fabrics were demonstrated by Leão et al. [1]. In particular, the positive effect was evaluated on the mechanical performances of carbon/epoxy composites with an increase of the ultimate tensile strength and the toughness of about 18% and 62%, respectively. Tefera et al. [2] demonstrated an increase in flexural strength of laminates manufactured by resin transfer molding with CNTs treated and non-treated with nitric acid to obtain carboxylic functional group. These solutions mixed with epoxy resin formed the matrix in 24 h – 96 h. Increments of about 17.4% and 15.3% for manufactured samples were measured for treated CNTs and for the lowest mixing time (24 h). Massive mixing not always ensures benefits to molded composites; in fact, matrix properties can be severely affected as well as the resin processability. For this reason, in industries other solutions are preferred, being the resin of the matrix already qualified for specific applications and changes in its properties are generally undesirable.

Interlaminar deposition of nano-reinforcements is another possible strategy that has a small influence on the resin processability. The insertion, as interlayers of hierarchical short carbon fibers synthetized with CNTs was proposed by Zhou et al. [3] who obtained increase of 125% in the fracture energy of nano-reinforced CFR epoxy laminates. Following this approach, Zheng et al. [4] manufactured CBT/polysulfone nanofiber paper by vacuum filtration, to be used as interleaf. Enhancements in interlaminar toughness both in mode I and mode II were obtained. The former is related to pre-cracked laminate failure governed by peel forces and the latter to the crack propagation by shear stresses. Moreover, interleave thickness greatly affects the interlaminar properties. Ou et al. [5] demonstrated that the interlaminar fracture toughness in mode I increase up to 76% for an interleaf thickness of 10 μm whereas it decreases to 36% by increasing thickness interleaf up to 15 μm. On the other side, mode II fracture toughness increases continuously when increasing the interleaf thickness up to 15 μm. Another important aspect was demonstrated by Nasirmanesh et al. [6] who inserted a CNTs interleaf in the midplane of an 8-ply laminate. In this case, impact tests revealed that crack initiation and propagation is confined around the CNT interleaf whereas it spreads all over the thickness for the base laminate. Moreover, flexural tensile failure is the predominant fracture mechanism on CNTs sheet base laminates compared to interlaminar shear breakage. Static tests revealed that tensile strength is the same whereas residual tensile strength and corresponding strain to failure was higher for CNT based laminates. Superior mechanical performances can be obtained by an aligned CNT configuration over composite plies. This effect is exalted by the use of thin plies as demonstrated by Cohen et al. [7]. In particular, an increase in the ILSS up to 10% compared to traditional laminates were obtained. Kaynan et al. [8] produced thin CNT reinforced adhesive interlayers used to mold interlayered CFR laminates. On one hand, the use of massive interlayers allows to increase the composite mechanical properties, on the other it leads to a lower manufacturability. Drawbacks come from both deposition strategies. Yourdkhani et al. [9] demonstrated that re-agglomeration and filtration of CNTs during liquid processing affect CNTs dispersion in the resin matrix. At first, they evaluated the degradation of CNT dispersion and the results underlined that laminates with interlaminar nano-reinforcements exhibited values slightly greater for compressive strength and electrical conductivity than traditional neat laminates. To date, the most viable solution is integrating CNTs in composites by using functionalized interlayers even if a more complex manufacturing procedure is necesary. This trend is confirmed by Li et al. [10] who inserted CNT buckypaper in the mid-plane of glass fibre reinforced laminates.

In previous works, the authors developed an innovative procedure easily scalable on an industrial level. The process allows CNTs deposition during the lamination sequence without adding intermediate step and thus avoiding to negatively affect the processability of the matrix. Specifically, multiwalled carbon nanotubes (MWCNTs) are mixed with a solvent and sonicated for an established time to exfoliate the bulk agglomerates. After, the mixture is poured on one

surface of the uncured CF prepreg plies and left at room temperature for solvent evacuation before lamination. Finally, increase in peeling and bending strength were obtained compared to neat laminates, when commercial automotive prepreg were used [11], as well as a better bending strength was achieved for aeronautical autoclave-molded prepregs [12].

In this study, MWCNTs were deposited as interlaminar reinforcements (I-CNTs) on a commercial aerospace fabric prepreg with the same procedure described above and developed by the authors. In this case, the laminated prepregs were molded in a tube shape with and without I-CNTs. Specifically, an out-of-autoclave process was used for the molding step as already done previously by authors for thermoplastic composites [13]. Observations with stereomicroscope and compression tests up to failure were carried out to evaluate both the soundness of the manufacturing process and the mechanical performances.

Materials and Methods

Tube shaped composite samples with and without 1wt% I-CNTs were manufactured by an out-of-autoclave (OOA) process. A 1 wt% of I-CNTs was chosen thanks to authors' previous studies [10, 11] that had established a good interaction of MWCNTs with the resin matrix with this percentage. Higher percentages caused an excess of CNTs which worsen the interaction with the resin matrix. Conversely, lower percentages cause less detectability of matrix interaction effects. Commercially epoxy matrix prepregs (40%) CYCOM® 977-2 by Solvay, commonly used in aeronautics, were used in the experimentation as well as commercial MWCNTs. The whole manufacturing process is shown in Fig. 1.

MWCNTs had a length of 10-30 μm, minimum outer diameter of 8 nm, purity higher than 95 wt%, ash lower than 1.5 wt%. Exfoliation of MWCNTs occurred in order to minimize the presence of bulk aggregates, and subsequently interlaminar deposition was performed. A MWCNTs-isopropanol solution was mechanically mixed through a magnetic stirrer for 1h and sonicated for 1h. In this way, a good level of nanoparticles exfoliation was achieved and agglomerates were not visible at naked eye. The solution was poured on prepreg stripes 960 mm in length and left at room temperature for 1 day to allow solvent evacuation. From now on, neat samples have been named CFR while the ones with interlaminar carbon nanotubes have been called I-CNTs/CFR. Prepreg stripes were wrapped around a steel pipe, being the mold, of 50 mm as nominal outer diameter and of 220 mm in height, and about 6 windings were obtained. The assembly was placed inside a thermo-shrinkable tube made of crosslinked polyethylene (PEX) by ELCON. A release film of fluorinated-ethylene-propylene (FEP) was placed on the rings-mold and at rings-PEX interfaces to favor the tube extraction. When heated, the thermo-shrinkable tube reduces its initial non-equilibrium diameter (85 mm) to a smaller equilibrium-diameter (25 mm), exerting a circumferential pressure on the tube surface. Curing was carried out in oven (by Nabertherm) at 180 °C for 1 h, and after cooling at room temperature, the workpieces were extracted. Four rings with and without I-CNTs were produced.

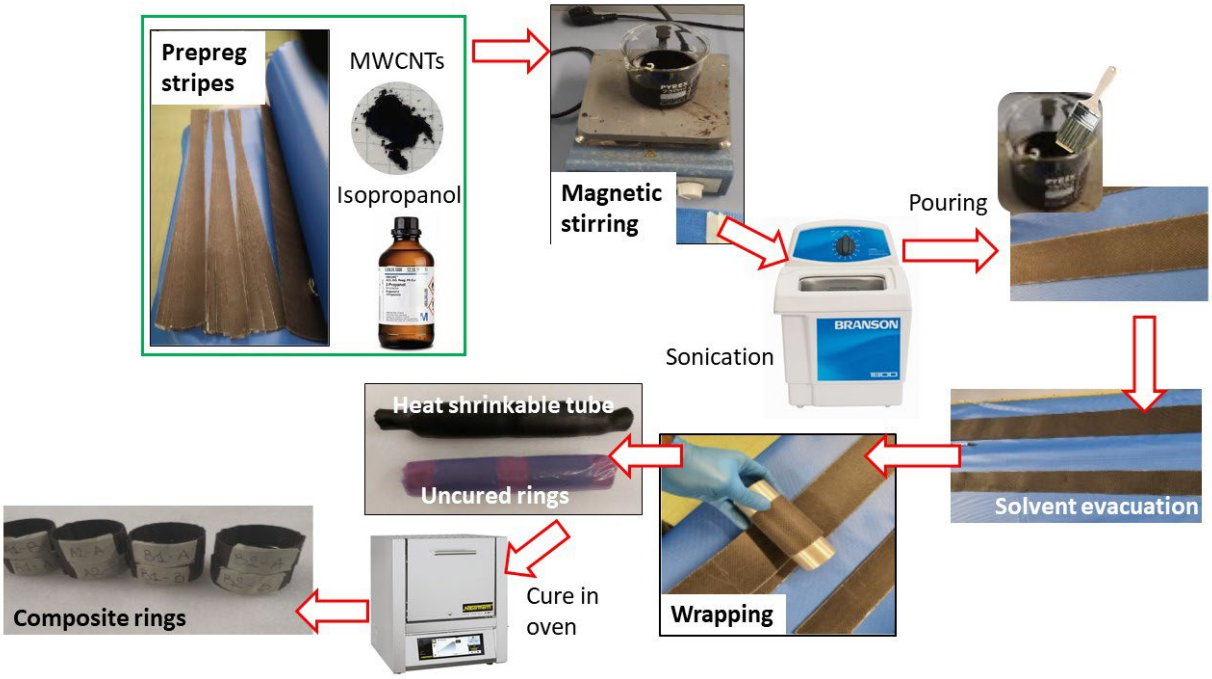

Fig. 1. Procedure of I-CNTs deposition and rings molding by the out-of-autoclave process.

Physical dimensions were measured and densities were evaluated through a hydrostatic scale to reduce the effects of manufacturing defects. Optical observations through a stereomicroscope Leica S9i were made to investigate plies adhesion and compaction. Compression tests up to failure were performed on an MTS Alliance RT/50 Universal testing machine to investigate the effect of I-CNTs on the macroscopic behavior of the composite rings. Transverse compression setup configuration, where the axis of-the movable machine crosshead is perpendicular to the longitudinal axis of the rings was used. A test speed of 1 mm/min and an acquisition frequency of 10 Hz were set.

Results and Discussions

Reduction of the molecular mobility in composites laminates is the key factor to understand the positive effect of the nanoparticles with the polymer matrix. The strongest effect is obtained when interpenetrating structures are placed in the interlaminar region. Also, the resin processability in thermosetting-based composites should be affected as little as possible, and molecular mobility is the main parameter to take into account. Fiber impregnation and diffusion, responsible of high polymerization degrees, are enhanced by low resin viscosity. In light of this, the positive effect of CNTs integration is a compromise between the improvements in the structural behavior and the minimum influences on the resin processability. This aspect represents the main goal of all the new developed technologies.

The proposed manufacturing procedure of interlaminar nanoparticles deposition does not alter the resin composition, minimally affecting its processability. Moreover, the use of additional layers either in the form of interleaves or adhesives is avoided. This procedure only adds a technological step consisting in sonicating the resultant isopropanol-MWCNTs solution to debundle and exfoliate CNTs and to reduce the presence of bulk agglomerates. Also, the solvent is used only to obtain a uniform distribution over the prepreg surfaces and its ease of evacuation allows to leave only the interlaminar nanoparticles. The use of commercially available prepreg, already optimized for industrial applications, requires a good experimental setup for interlaminar nano-reinforcements deposition, in order to enhance the structural behavior of functionalized laminates.

The proposed out-of-autoclave molding process guarantees good compaction among composite layers, after winding. The stereoscope observations, shown in Fig. 2, clearly highlight the six windings obtained after wrapping. Bleeding occurred during curing and a good level of adhesion was reached; fibers interpenetration among the layers was not observed. Defects related to the manufacturing procedure were observed in some areas since the mold was not optimized at this stage of the experimentation. The external surfaces un-homogeneities are due to asperities of the inner surfaces of the PEX tube and these irregularities can be easily overcome optimizing the molding assembly. However, the main objective in the study is to verify the feasibility of the process and this has been confirmed.

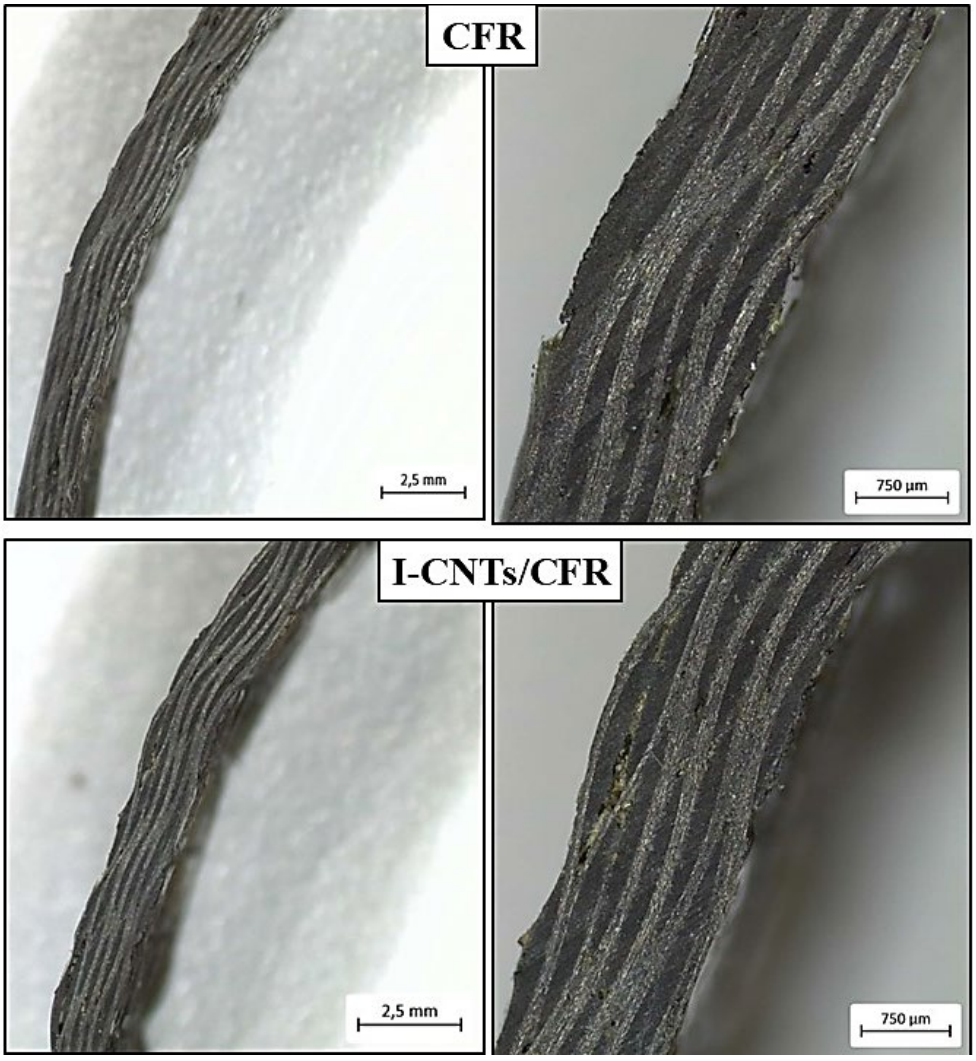

Fig. 2. Stereoscope images of CFR and I-CNTs/CFR ring samples.

CFR and I-CNTs/CFR rings had similar thickness of 2.1±0.2 mm and 2.0±0.3 mm respectively, nearly 0.3 mm for each ply. In Fig. 3 the evolution of thickness for rings with and without CNTs is shown in polar coordinates, that is, ring thickness was measured at a different angular position. Densities of CFR and I-CNTs/CFR rings were 1.37 g/cm^3 and 1.34 g/cm^3 on average. They were measured through a hydrostatic scale because of the irregularities on the rings surface. Lower densities of functionalized composites are due to the presence of interlaminar reinforcements which slightly increase the distance among prepreg plies.

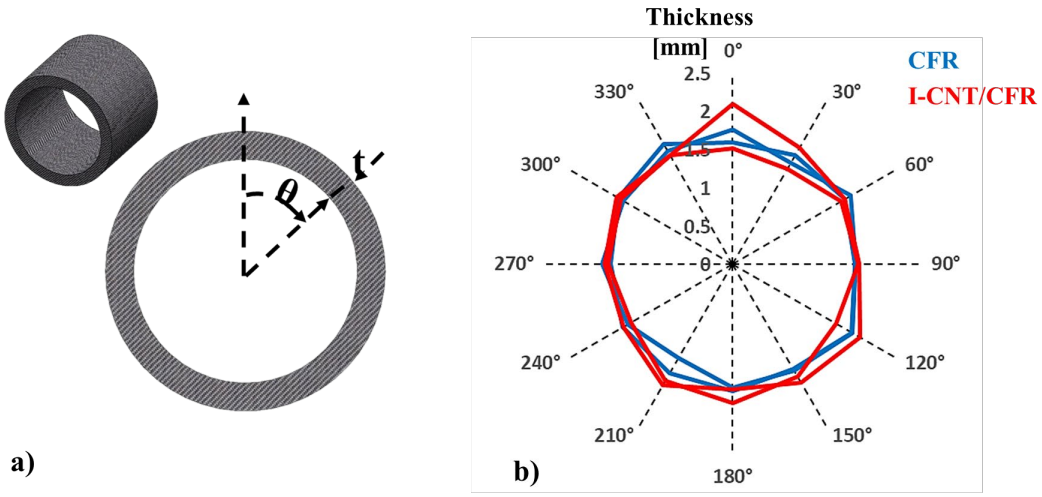

Fig. 3. Evolution of thickness for CFR rings and I-CNTs/CFR rings in polar coordinates.

Improvements by the addition of MWCNTs can be seen at room temperature as a consequence of the molecular mobility reduction mechanism. Compression tests were performed in transverse configuration and results are shown in Fig. 4 as load-displacement curves.

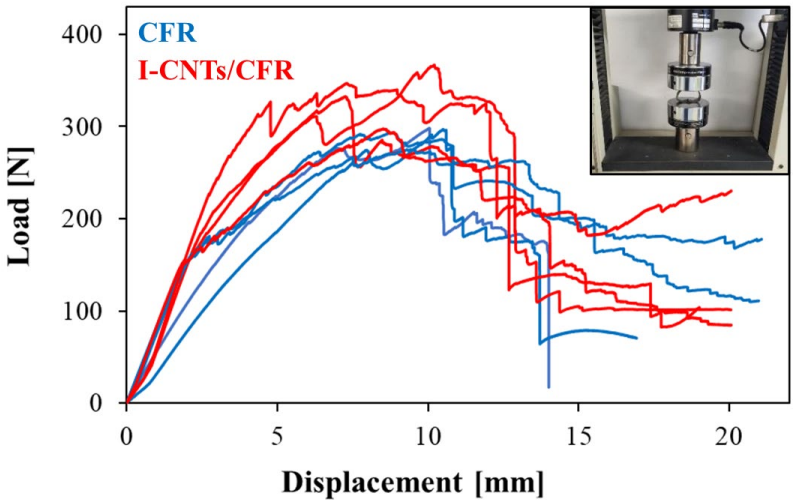

Fig. 4. Compression curves of composite rings.

Table 1. Stiffness, load peak and fracture energy values calculated from the curves.

	Stiffness	Peak Load	Fracture Energy
	N/mm	N	J
CFR	65 ± 20	291 ± 11	3.5 ± 0.7
I-CNT/CFR	86 ± 7	336 ± 34	4.1 ± 0.6

The non-homogeneous nature of the composite rings is responsible for some oscillations in the load-displacement curve, which do not affect the interpretation of the interlaminar CNTs effect. Stiffness, peak load and fracture energy are summarized in Table 1. Despite the lab scale OOA

procedure, stiffness, peak load and fracture energy increase of 32%, 15% and 17%, respectively, for I-CNTs composites compared to traditional ones. In particular, also considering only the better responses for CFR without I-CNTs (e.g. 83 N/mm for stiffness, 283 N for peak load and 4.1 J for fracture energy), the ameliorative effect of the CNTs would be in any case confirmed. The manufacturing process does not affect the positive role of CNTs at all. This preliminary experimentation, aims to highlight the effectiveness of interlaminar CNTs on the global mechanical behavior of I-CNTs composites. The increased structural performances aimed by CNTs insertion confirms what found also by literature review about this topic [9,10].

Summary

The use of commercial materials is the best solution for high-valued engineering applications in which material qualification and certification has strict restrictions. Commercial material innovation is strictly related to the improvement of already high performances which should be enhanced through simple and easily scalable processes. In this light, any proposed improvements in laminate manufacturing should minimally affect the initial structure and composition of the materials. This, in order to avoid the re-designing of the structure or the change of the processing strategies. All these needs have been matched by the proposed manufacturing procedure consisting of interlaminar deposition of CNTs on CFR prepregs by CNTs-solvent solution dispersion. In particular, the proposed additional step for composite functionalization does not alter the commercial material processability. CFR and I-CNTs/CFR composite rings were manufactured by a non-conventional out-of-autoclave process which guarantees plies compaction and repeatable structure quality even if further optimization in the molding setup are needed. The effects of CNTs deposition were demonstrated by the slight density reduction of I-CNTs composite rings with an increase of distance between the plies. Moreover, the compression tests showed a positive effect with an increase in the stiffness and in the peak load of I-CNTs/CFR composite rings. Further analysis could be performed to understand the effects of CNTs insertion on molecular mobility at higher temperature. Moreover, the ideal CNTs' content as function of the adopted manufacturing process is another big issue as well as the investigation on delamination mechanisms.

References

[1] S.G. Leão, M.G. Martins, N.C.F. Menezes, F.L.R.M. Limam, C.F. Silva, G.C. Arantes, A.F. Ávila, Experimental multi-scale analysis of carbon/epoxy composites nano-reinforced by carbon nanotubes/multi-layer graphene, Mater. Res. 20 (2017) 134-142. https://doi.org/10.1590/1980-5373-MR-2017-0976

[2] G. Tefera, G. Bright, S. Adali, Flexural and shear properties of CFRP laminates reinforced with functionalized multiwalled CNTs, Nanocomposites 7 (2021) 141-153. https://doi.org/10.1080/20550324.2021.1961507

[3] H. Zhou, X. Du, H.Y. Liu, H. Zhou, Y. Zhang, Y.W. Mai, Delamination toughening of carbon fiber/epoxy laminates by hierarchical carbon nanotube-short carbon fiber interleaves, Compos. Sci. Technol. 140 (2017) 46-53. https://doi.org/10.1016/j.compscitech.2016.12.018

[4] N. Zheng, Y. Huang, H.Y. Liu, J. Gao, Y.W. Mai, Improvement of interlaminar fracture toughness in carbon fiber/epoxy composites with carbon nanotubes/polysulfone interleaves, Compos. Sci. Technol. 140 (2017) 8-15. https://doi.org/10.1016/j.compscitech.2016.12.017

[5] Y. Ou, L. Wu, M. Hefetz, C. González, J.J. Vilatela, Improving interlaminar properties of woven carbon fibre composite laminates with industrial-scale carbon nanotube fibre interleaves, Compos. Part A 164 (2023). https://doi.org/10.1016/j.compositesa.2022.107283

[6] A. Nasirmanesh, A.K. Singh, D. Villaflor, B. Blandford, Effects of midplane carbon nanotube sheet interleave on the strength and impact damage resistance of carbon fiber reinforced polymer composites, Polym. Compos. 43 (2022) 3085-3095. https://doi.org/10.1002/pc.26601

[7] E. Kalfon-Cohen, R. Kopp, C. Furtado, X. Ni, A. Arteiro, G. Borstnar, M.N. Mavrogordato, I. Sinclair, S.M. Spearing, P.P. Camanho, B. L. Wardle, Synergetic effects of thin plies and aligned carbon nanotube interlaminar reinforcement in composite laminates, Compos. Sci. Technol. 166 (2018) 160-168. https://doi.org/10.1016/j.compscitech.2018.01.007
[8] O. Kaynan, Y. Atescan, E. Ozden-Yeniguna, H. Cebeci, Mixed Mode delamination in carbon nanotube/nanofiber interlayered composites, Compos. Part B 154 (2018) p. 186-194. https://doi.org/10.1016/j.compositesb.2018.07.032
[9] M. Yourdkhani, W. Liu, S. Baril-Gosselin, F. Robitaille, P. Hubert, Carbon nanotube-reinforced carbon fibre-epoxy composites manufactured by resin film infusion, Compos. Sci. Technol. 166 (2018) 169-175. https://doi.org/10.1016/j.compscitech.2018.01.006
[10] N. Li, G.D. Wang, S.K. Melly, T. Peng, Y.C. Li, Q. Di Zhao, S. de Ji, Interlaminar properties of GFRP laminates toughened by CNTs buckypaper interlayer, Compos. Struct. 208 (2019) 13-22. https://doi.org/10.1016/j.compstruct.2018.10.002
[11] L. Iorio, L. Santo, F. Quadrini, D. Bellisario, D. Benedetti, J. Agnelli, Carbon fiber laminates with interlaminar carbon nanotubes, Mater. Plast. 57 (2020) 80-85. https://doi.org/10.37358/MP.20.1.5314
[12] F. Quadrini, D. Bellisario, L. Iorio, A. Proietti, N. Gallo, L. Santo, Autoclave molding of carbon fiber laminates with interlaminar carbon nanotubes, Proceedings of ASME 2022 17th International Manufacturing Science and Engineering Conference, MSEC 2022 volume 2 (2022). https://doi.org/10.1115/MSEC2022-85480
[13] D. Santoro, D. Bellisario, F. Quadrini, L. Santo, Anisogrid thermoplastic composite lattice structure by innovative out-of-autoclave process, Int. J. Adv. Manuf. Technol. 10 (2020) 1941-1952. https://doi.org/10.1007/s00170-020-05671-6

Polymer processing and thermomechanical properties

Materials Research Proceedings 28 (2023) 1799-1808 https://doi.org/10.21741/9781644902479-195

Two-step PM forging for precise fabrication of carbon fiber reinforced engineering plastic gears

AIZAWA Tatsuhiko[1,a *], MIYATA Tomohiro[2, b] and ENDO Kiyoyuki[3, c]

[1]3-15-10 Minami-Rokugo, Ota-City, Tokyo 144-0045, Japan

[2]15-1 Monden Industrial-Park, Aizu-Wakamatsu, Fukushima 965-0845, Japan

[3]4-1-5 Sannoh, Ota-City, Tokyo 143-0023, Japan

[a]taizawa@sic.shibaura-it.ac.jp, [b]aizu5@marutaka-ind.co.jp, [c]endo@igma.co.jp

Keywords: Carbon Fiber Composites, Engineering Plastics, Gears, Powder Metallurgy, Green Compaction, Sinter-Forging, Die Technology

Abstract. Carbon fiber reinforced engineering plastic (CFREP) small-sized parts were fabricated by PM (Powder Metallurgy)-oriented forging process. This manufacturing procedure consisted of the green compaction and sinter-forging steps. In the first step, the CFREP powders were consolidated to a green compact with high density. This preform was further sinter-forged into a final product by hot stamping with the use of the induction heating unit. Hardness distribution was measured to describe the consolidation behavior with increasing the compression load, and to optimize the sinter-forging conditions for solidifying the green compact to the sintered product. X-ray tomography was utilized for non-destructive diagnosis on the residual pores and defects. The eight-teeth gear model was fabricated to demonstrate that two step procedure wrought well to yield the dense and defect-free gear with sufficient strength and integrity.

Introduction

The composite materials have been used to improve its mechanical and functional properties by combining the secondary phase materials and the matrix [1]. In particular, CFRP (Carbon Fiber Reinforced Plastics) and CFRTP (Carbon Fiber Reinforced Thermo-Plastics) have been widely used to produce the light-weight and high strength structural parts and members [2,3]. In those composite materials, their intrinsic properties are controlled not only by the fiber orientation and density in reinforcement but also by the selection of matrix plastics [3,4]. The normal CFRP is made from the epoxy-resin matrix and the carbon long-fibers; the CFRP ply and woven cloth are also used as a staring material for near-net shaping of parts and members. Most of those CFRP parts and members have been fabricated by using the autoclave processing [5] and the hot/warm stamping [6] with the finishing step. In particular, the small-sized parts and structural members are often yielded by hot stamping the laminated ply sheets [7]. The carbon short-fiber reinforced plastics are injection molded into various small- to medium-sized products from the pelletized feedstock [8]. Those processes work well when the composite matrix is made from relatively low glass transition temperature plastics such as epoxy. Most of engineering plastics (EP) have much higher glass transition temperature than normal matrix plastics; they are difficult to be molded or compressed into products. In addition, their feedstock is usually made of powders and particles; a new manufacturing process is necessary to fabricate the small sized EP and CFREP parts from this feedstock.

The mechanical gears are a typical element to transfer the applied load from input to output, to reduce the rotational speed in reducer, and to construct the mechanism of movement [9]. As reported in [10], the light-weight gears with high stiffness play an important role in the reducer at the robot arms and joints and in the automatic mechanics for electric vehicles. In addition, the gears with high radiation resistance are also needed in the robotics working in decommissioning

Content from this work may be used under the terms of the Creative Commons Attribution 3.0 license. Any further distribution of this work must maintain attribution to the author(s) and the title of the work, journal citation and DOI. Published under license by Materials Research Forum LLC.

operations [11]. Most of engineering plastics have sufficient radiation resistance and high specific strength to provide a solution to those demands.

In the present study, the carbon fiver reinforced engineering plastic (CFREP) powders are selected as a feedstock to fabricate the CFREP gears with sufficient hardness and integrity. Two-step powder metallurgy oriented procedure is developed for this fabrication. First, the CFREP powders are poured into a die cavity to consolidate them into the green compact with relatively high density. This green compact is further sinter-forged to an eight-teeth gear-model product. The hardness distribution is measured to describe the green compaction behavior and to investigate the effect of holding temperature and applied load on the sinter-forging process. The X-ray tomography is also employed to make non-destructive evaluation on the defects and porosities left in the green compact and sinter-forged gear. Three dimensional profilometer is used to measure the dimension of gear teeth with reference to the CAD (Computer Aided Design) data.

Methods and Materials

Two-step PM (Powder Metallurgy) oriented method is stated in details on the green compaction step for cold forging the CFREP powders to a green compact and on the sinter-forging step to consolidate the green preform to the final product. How to characterize the green compact and sinter-forged gear product, is also explained in the following.

Two-Step PM-Oriented Procedure.

Two-step PM-procedure to fabricate the CFREP product consists of the green compaction step in cold and dry and the sinter-forging step in hot. As illustrated in Fig. 1, the feedstock powders were poured into a die cavity in the die set. In the green compaction step, the load was applied to the punch to consolidate them into a green compact with the specified density in cold and dry. The incremental compression mode was utilized to deliver the powders to every branch of cavity for uniform consolidation. This green preform was fixed into the other die set to sinter-forge this preform into a sintered product at the elevated temperature. The indirect heating method was employed to preserve the hot forging condition by using the high-frequency induction heating (HF-IH) system (YS-Electrical Industry, Co., Ltd.; Kofu, Japan). In both steps, the CNC (Computer Numerical Control) system (Precise Stamping Laboratory, llc.; Tokyo, Japan) was commonly utilized.

The solid lubrication was utilized to reduce the friction on the contact interface between the punch/core surfaces and the work in these two-step processes. The h-BN sprayed film was formed onto the punch and die surfaces before each operation. After green compaction, the punch is first released and the core-die was reloaded to move down for ejection of formed compact. In nearly the same manner, the sintered work was also ejected from the die-set.

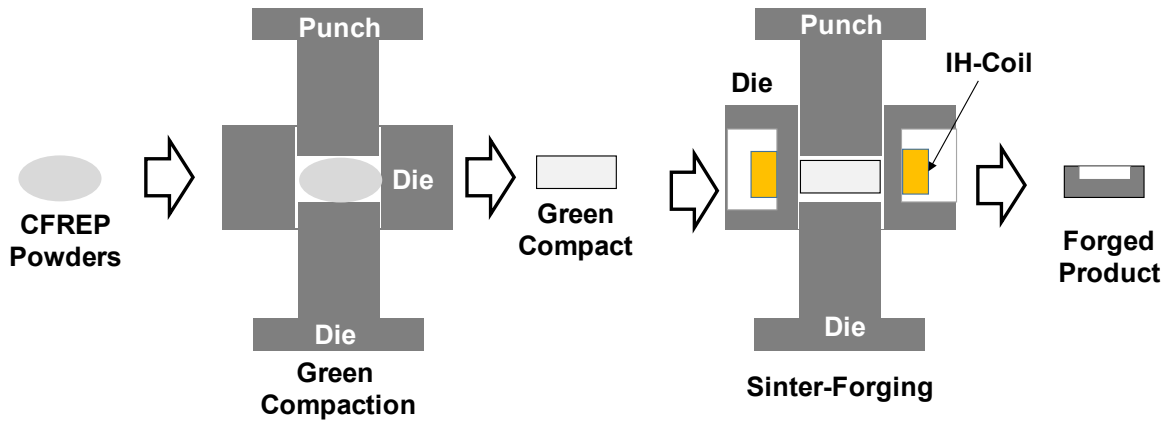

Fig. 1. A schematic view on the two-step PM-oriented procedure from the feedstock powders to the product. a) Green compaction step, and b) sinter-forging step.

Green compaction.

Among several materials, the CFREP powders (Aurum-PD450; Mitsui chemicals, Co., Ltd.) were selected as a feedstock for fabrication of gear models by the two-step procedure. This Aurum-PD450 was a thermoplastic polyimide with Tg (Glass transition temperature) of 518 K (or 245°C) and Tm (Melting temperature) of 661 K (or 388°C). When using the injection molding, the mold temperature could be higher than 673 K; this PD450 must be difficult to be shaped into products by using the injection molding. Table 1 summarized the mechanical properties of this Aurum-PD450. Compared to normal thermoplastic polymers such as PP (polypropylene) and PC (polycarbonate), higher strength and modulus characterizes this feedstock.

Table 1. Mechanical properties of Aurum-PD450.

Item	Typical data	Testing method
Tensile strength	90 MPa	ASTM D 638
Ultimate elongation	90 %	ASTM D638
Bending strength	140 MPa	ASTM D 790
Bending modulus	3 GPa	ASTM D790
Izod impact strength	90 J/m	ASTM D256

Fig. 2 depicts the CFREP powders as an initial material for green compaction. The carbon short-fibers were included into each powder at the preparation of powder feedstock.

Fig. 2. CFREP powders as a feedstock for consolidation via the cold, dry stamping to a green compact.

In the normal powder metallurgy (PM) processes, the original powder feedstock was poured into a die cavity and consolidated by stamping in cold. As stated in [12], the metal and alloyed powders with lubricants were mixed and compressed in the die to build up the green compact. This green compact was further processed to degrease the lubricants from the green compact before sintering and sinter-forging processes. In the present two-step PM procedure, no lubricating oils and waxes were utilized in green compaction and sinter-forging steps to minimize the contamination.

Materials Research Proceedings 28 (2023) 1799-1808 https://doi.org/10.21741/9781644902479-195

In this consolidation process, the relative density of green compact is controlled by varying the applied load. As stated in [12], this relative density of green compact has significant influence on the homogeneity and uniformity of products in the sinter-forging step. Hence, the hardness of green compact is measured by varying the applied load. Figure 3 shows an experimental setup for consolidation of CFREP powders to a green compact, corresponding to its schematic view in Fig. 1a. The load cell was embedded into the lower die. Owing to the programmable loading sequence in the CNC stamping system, the stoke schedule of upper die set was controlled to densify the green compact through the incremental loading sequence.

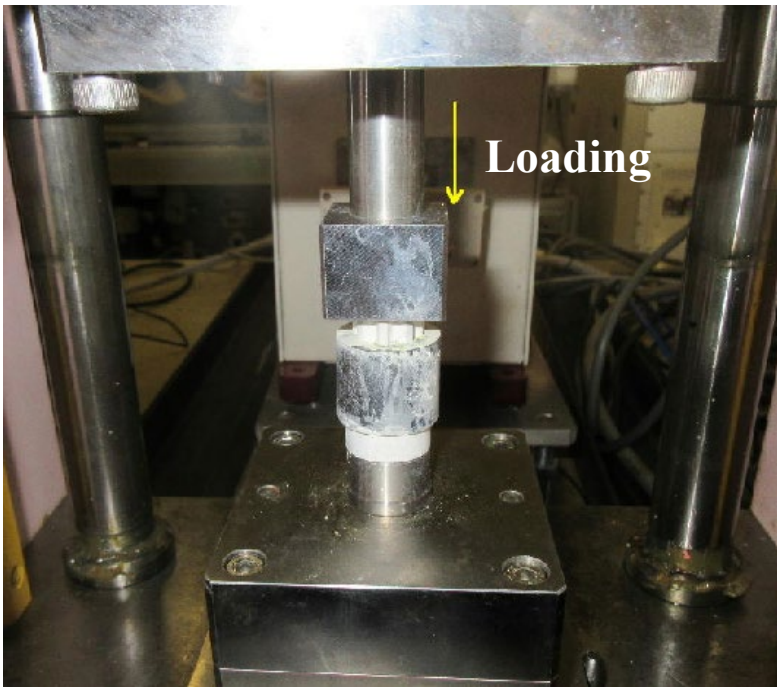

Fig. 3. Experimental setup for consolidation of CFREP powders to green compact in correspondence to its schematic view in Fig. 1a.

Sinter-Forging.

The green compact preform was fixed into the die-set for sinter-forging, as shown in Fig. 4. The HF-IH coil was placed to surround the die set with the designated clearance to optimize the spatial impedance between the dies and the coil. The load was first applied to 2 kN before heating the die set. The load was increased to the holding load at the specified temperature. The holding duration was constant by 600 s. In the following experiment, the holding temperature and applied load were varied to optimize the sinter-forging conditions by measuring the surface hardness. The sprayed h-BN film was also used for solid lubrication on the die surface.

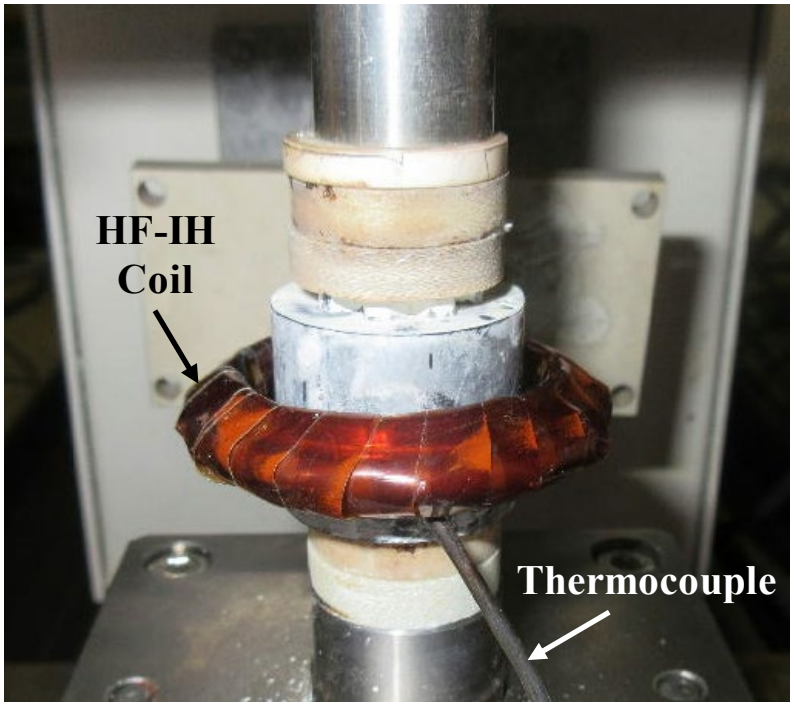

Fig. 4. Experimental setup for sinter-forging of the green compact to the forged gear product in correspondence to the schematic view in Fig. 1b.

Characterization.

A table-top X-ray tomography apparatus (X-1; Ueda, Japan) was employed to make non-destructive evaluation on the residual pored and defects in the green compact as well as the sinter-forged products. The intrinsic spatial resolution is 50 – 100 μm; however, the X-ray penetration capacity must be optimized to improve the spatial resolution in practice. Otherwise, no X-ray images are obtained when the applied power is too much or too low. Through the learning step, the optimal conditions were fixed and used in the following diagnosis. Three dimensional profilometer was also used to measure the part dimension of each tooth in the sintered gear with reference to the original CAD data and to discuss the dimensional accuracy of sintered CFREP gears.

Results

The cold and dry consolidation process is described by measurement of the average and maximum hardness in the teeth of green preforms in each loading condition. The sinter-forging behavior is also described by hardness measurement to search for the optimal processing conditions. The X-ray tomography is utilized to validate the dense green compacts and sinter-forged products. Three dimensional profilometer is utilized to measure the tooth profile and configuration for practical usage as a gear with reference to the standard.

Green compaction behavior.

The CFREP powders were consolidated in cold and dry to green compact preforms, the hardness of which was measured in each green compaction conditions to determine the appropriate load. A typical green compact was depicted in Fig. 5a when the applied load was 3.2 kN. The X-ray tomography was utilized for non-destructive evaluation on the density distribution in the inside of preform. As shown in Fig. 5b, no pores and defects were detected by this diagnosis. Three cross-section X-ray tomographic images proved that the preform had homogeneous density distribution.

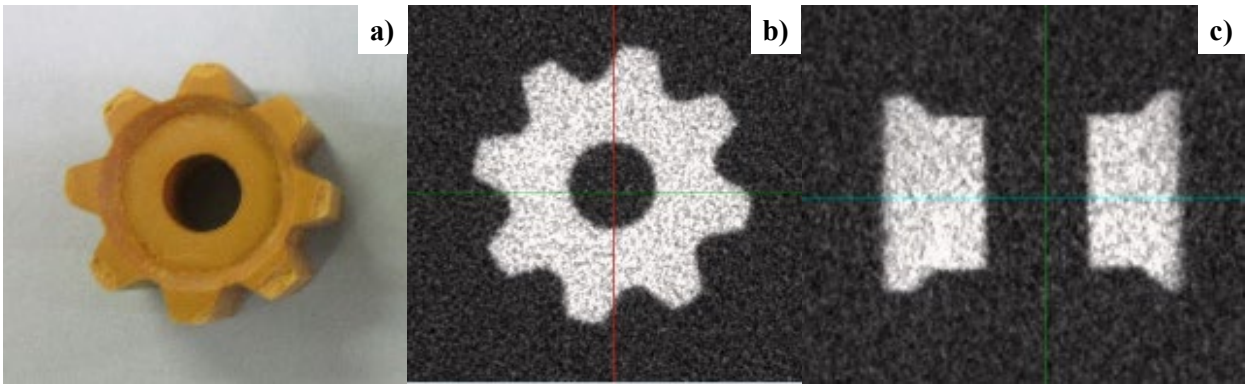

Fig. 5. A green compact after cold, dry stamping by applying the load of 3.2 kN. a) Overview of the green compact, b) X-ray tomographic image on the green compact from the top view, and c) X-ray tomographic image on the green compact from the side view.

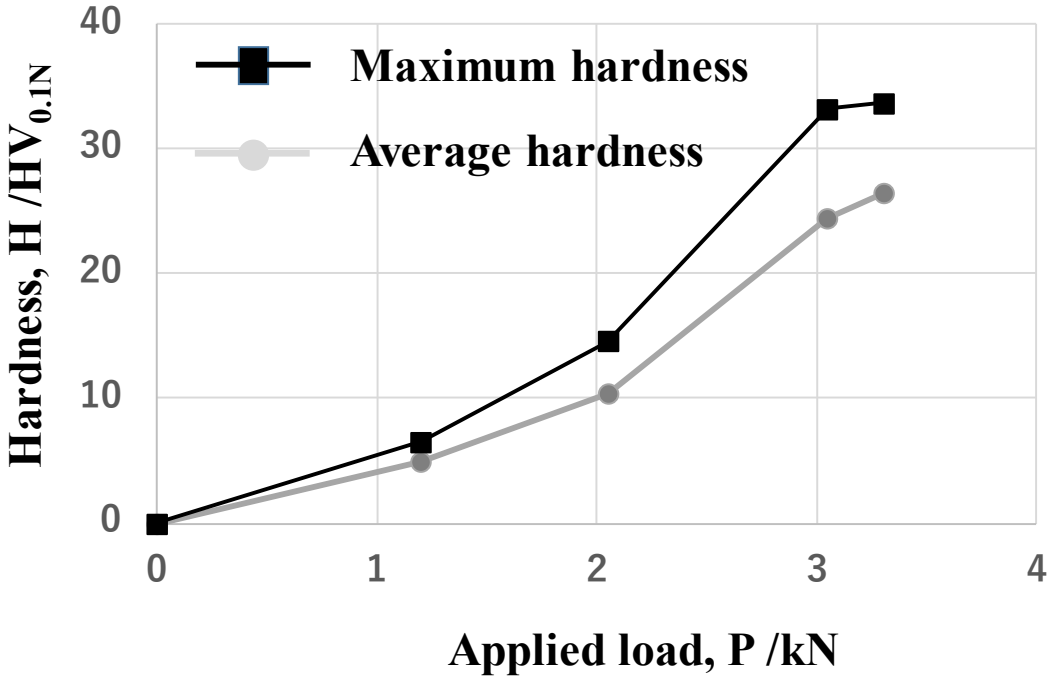

Fig. 6. Variation of the average and maximum hardness with increasing the applied load in the green compaction.

The average and maximum hardness were measured at each tooth of eight-teeth green compact preform. The applied load and duration were constant by 0.1 N (or 10 gf) and 10 s, respectively. As shown in Fig. 6, both hardness increased monotonously with increasing the applied load (P) up to P = 3 kN. This reveals that densification of CFREP powders advances with increasing the applied load during this consolidation process. The deviation of the maximum hardness from the average one increased with increasing P. This might be because of the friction on the surface of dies. When P > 3 kN, both hardness turned to be nearly constant; the green compact is near-fully consolidated in dry and cold. Several green preforms were fabricated by applying the load of 3.2 kN to investigate the hardness distribution among teeth of gear preforms.

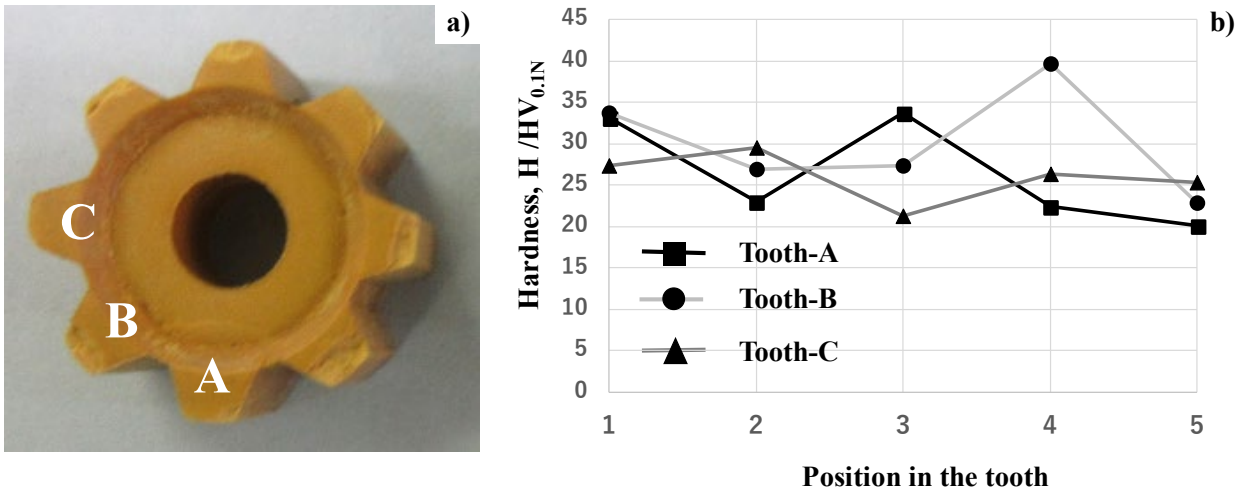

Fig. 7. Deviation of the surface hardness among the teeth of green preform gear when applying the load by 3.2 kN. a) Selected three teeth for measurement in the gear preform, and b) deviation of surface hardness among five positions in each tooth.

Three teeth (A, B, C) of green compact were selected to measure the hardness at the five positions in each tooth as depicted in Fig. 7a. The center point of tooth was denoted by No. 2. No. 1 and No.3 points were located away from this center point in the upper and lower directions by 0.075 mm, respectively. No. 4 and No. 5 points were also located away from No. 2 in the right and left sides by 0.075 mm, respectively.

Fig. 7b shows the hardness distribution in each tooth for A, B and C teeth. Since the average hardness is 27 $HV_{0.1N}$ in Figure 6, the deviation in each tooth ranges from 21 $HV_{0.1N}$ to 34 $HV_{0.1N}$ excluding the extraordinary high hardness. That is, the feasible hardness of green compact is estimated to be 27 $HV_{0.1\,N} \pm 7$ $HV_{0.1N}$; the statistical deviation is controlled to be less than a single standard deviation from the average hardness.

Most of this dimensional deviation comes from the powder flow and deformation behavior under compression. After [13], the rearrangement of CFREP powders by powder flow has more influence on the density of green compact than the deformation of CFREP powders. The incremental compression mode might be necessary to make more uniform densification in the green compact.

Sinter forging behavior.

The green compact specimens were fixed into the die cavity for sinter-forging. The specimen was first compressed and held by 2.0 kN during induction heating as shown in Fig. 4. The die temperature was inline monitored by using the thermocouple, which was embedded into the die. The holding temperature (T_H), the loading sequence, and the holding duration (τ) work as a main parameter in this sinter-forging process. T_H must be higher than Tg; T_H could exceed Tm since the actual specimen temperature might be less than Tm due to the thermal conductivity through die wall and the gap conductance between the specimen and die surface.

At first, the parameters were fixed at T_H = 668 K (or 395°C) and τ = 600 s, the sinter-forged preform was fabricated as shown in Fig. 8a. The X-ray tomography was also employed to investigate the sintering behavior; the X-ray irradiation intensity was lowered to distinguish the pores and defects left after sintering. Figure 8b shows the cross-sectional view of sinter-forged specimen. No pores and defects were seen in the inside of preform.

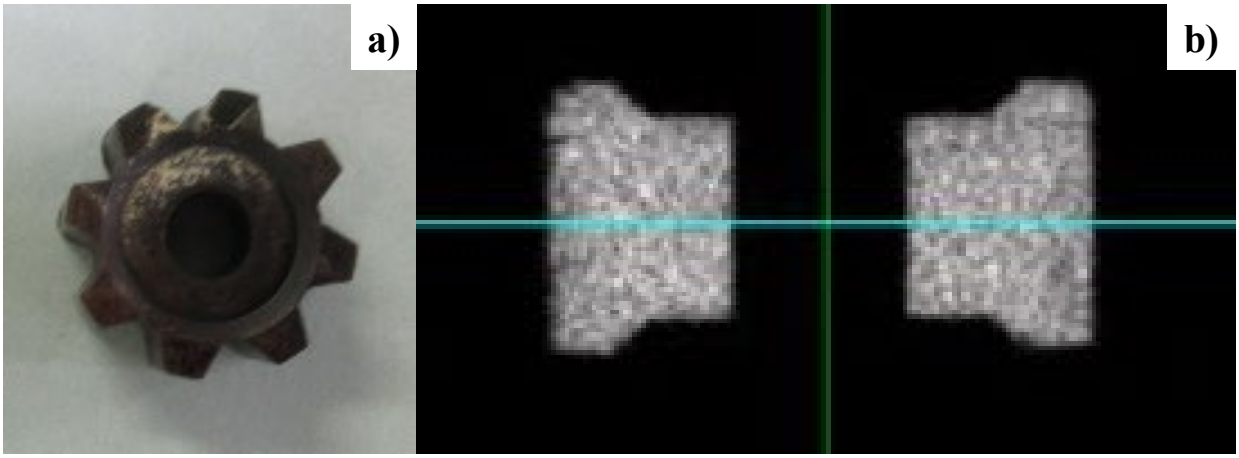

Fig. 8. A sintered gear after hot forging at 668 K for 600 s by 2 kN. a) Overview of the sinter-forged product, and b) X-tomographic image on the sinter-forged product in Fig. 5a with three cross-sectional images.

Table 2. Variation of the maximum hardness by varying the holding temperature just below Tm and the applied load in the sinter-forging.

Specimen	Holding Temperature (T_H) ℃	Applied load (P) kN	Hardness (HV0.1N)
#1	381	2.5	41
#2	387	3.0	38
#3	389	4.0	47

Let us investigate the effect of T_H and applied load (P) on the sintering behavior. T_H was varied below T_m of polyimide matrix. Table 2 summarizes the variation of measured maximum hardness by varying T_H and P. Compared to the hardness distribution of green compact in Fig. 7b, higher hardness was attained by sinter-forging. Different from the sinter-forging of electrically conductive metallic powders [14], the loading schedule must be controlled and optimized to attain much higher hardness at the sinter-forged gear-teeth of non-conductive CFERP.

Table 3. Dimensional measurement of sinter-forged CFREP gear by three dimensional profilometer.

Item	D_c (mm)	D_{cic} (mm)	D_{coc} (mm)
Sinter-forged CFREP gear	4.963	15.969	11.981
Die for sinter-forging	5.02	16.06	12.04

Quantitative evaluation on the CFREP gear.

Three dimensional profilometer in the projector-type (CALYPSO) was utilized to measure the center hole diameter (D_c), the diameter of circumscribing inner and outer circles (D_{cic} and D_{coc}) were measured for the sinter-forged CFREP gear at T_H = 450 ℃, by P = 3 kN and for 300s. Table 2 compares the measured data and original dimensions of die. In every dimension of gears, a negative deviation of 0.5 % is commonly measured in the sinter-forged CFREP gear. This deviation can be improved by optimization the sinter-forging conditions.

Discussion

As stated in [15], most of engineering plastic gears are made from polyacetal (POM) and MC Nylon, which is essentially polyamid resin, U-PE (Ultra High Molecular Weight Polyethylene), and PEEK (Poly-Ether-Ether-Ketone). Although they are characterized by the lightweight, the non-rusting, the quiet operating, and the injection molding enabling low cost, they suffer from the low strength, the tendency to hold heat, and the large dimensional change. In particular, the thermal distortion by relatively large coefficient of thermal expansion influences on the gear performance working in operation, in addition to the geometric distortions by the resist temperature change, the moisture absorption rate and the resistance to chemicals. The present CFREP gear has higher strength, chemical and thermal stability than those normal engineering plastic gears. Especially, this gear is free from the thermal distortion and dimensional change. To be noticed, those normal engineering plastic gears have no ways in hardening and strengthening. This CFERP gear is made from high strength polyimide matrix and carbon short fibers. This high strength composite design reflects on the high hardness even for the green compact.

Let us discuss the radiation resistance of CFREP gears. As discussed in [16], the CFRP has a risk of microstructural damage without CNT modification; this damage might come from the interfaces between the carbon fiber and epoxy matrix. The carbon fiber – poly imide interface is enough strong to reduce the risk of microstructural damage even under γ-irradiation conditions. This superiority in the radiation resistance is attractive to the gear box in reducer and in mechanical control unit of robots working in decommissioning operations.

The PM processing has been utilized to make mass production of small-sized and middle sized automotive parts. Its merits for fabrication of CFREP gears by the two-step PM processing, are as follows: 1) easiness to yield the complex shaped gears as a spur-gear, milter and bevel gears, screw gears and warm gears, 2) adaptivity to join the two gear units into a single working gear by sintering under compression, and 3) strengthening of gear teeth by homogeneous distribution of CFREP powders including the short carbon fibers.

In the present study, the green compaction and sinter-forging is performed in the uniaxial compression mode so that this two-step procedure has no ways to control the short-fiber orientation in the consolidation and forging. The CFREP powder flow control as well as the incremental loading in sinter-forging must be effective to make fiber-orientation control around the tooth part of CFREP gears.

Summary

Two step powder-metallurgy manufacturing procedure is proposed to fabricate the carbon reinforced engineering plastic gears from the powder feedstock. Through the green compaction step, the original powders are consolidated in cold to a solid gear-preform with relatively high density without significant pores and defects. This preform is sinter-forged at the holding temperature below the melting point for 600 s under the applied load to fabricate the CFREP gear with dimensional accuracy. In the further optimization of the processing parameters, the dimensional accuracy is improved with sufficient tolerance within the requirement of highly qualified gears.

Acknowledgements

The authors would like to express their gratitude to S-I. Kurozumi (Nano-Film Coat, Co., Ltd.) for his help in experiments, and, to Mitsui Chemical, Co., Ltd. for his help in feedstock. This study was financially supported in part by METI, Japan on the Go-Tech Program at 2022.

References

[1] I. M. Low, Y. Dong, Composite Materials – Manufacturing, properties and applications -. 1st Ed. Elsevier, London, UK, 2021.

[2] D. Ozkan, M.S. Gok, A.C. Karaoglanli, Carbon fiver reinforced polymer composite materials, their characteristic properties, industrial application areas and their machinability, Eng. Des. Appl. III (2020) 235-253. https://doi.org/10.1007/978-3-030-39062-4_20
[3] K. Terada, Carbon fiber reinforced thermos-plastics – Currently, applications and forecast, J. JSPE 81 (2015) 485-488.
[4] R.J.H. Wanhill, Carbon fiber polymer matrix structural composites, in: N. Eswara Prasad, R.J.H. Wanhill (Eds.), Aerospace Materials and Material Technologies, Springer Singapore, 2017, pp. 309-341. https://doi.org/10.1007/978-981-10-2134-3
[5] C. Dong, J. Zhou, X. Ji, Y. Yin, X. Shen, Study of the curing process of carbon fiber reinforced resin matrix composites in autoclave processing, Procedia Manuf. 37 (2019) 450-458. https://doi.org/10.1016/j.promfg.2019.12.073
[6] M. Okayasu, M. Sato, Hot-stamping technology for carbon fiber reinforced thermoplastic plates based on electrical resistance heating, J. Compos. Mater. 54 (2019) 002199831987755. http://doi.org/10.1177/0021998319877559
[7] C. Guo, J. He, Y. Su, S. Li, Thermo-stamping co-curing process for CFRP/steel hybrid sheets and its interface strength improvement, Compos. Struct. 241 (2020) 112108. https://doi.org/10.1016/j.compstruct.2020.112108
[8] Y. Kageyama, K. Akai, N. Nishio, K. Kageyama, Selection of molding method for CFRP automotive body parts – resin injection vs. Compression, Proc. APMS 2015 (2015) 455-463.
[9] V. Vullo, Gears. Vol. 2: Analysis of load carrying capacity and strength design, Springer, 2020.
[10] Z. Liu, Z. You, Z. Wang, Lightweight design of multistage gear reducer based on continuous variables and discrete neighborhood, Proc. ICMD 2017 (2017) 379-387.
[11] I. Tsitsimpelis, C.J. Taylor, B. Lennox, M J. Joyce, A review of ground-based robotic systems for the characterization of nuclear environments, Progress in Nuclear Energy 111 (2019) 109-124. https://doi.org/10.1016/j.pnucene.2018.10.023
[12] I. Chang, Y. Zhao, Advances in powder metallurgy –properties, processing and applications, Woodhead Publishing, 2013.
[13] K. Peng, H. Pan, Z. Zheng, J. Yu, Compaction behavior and densification mechanisms of Cu – W composite powders, Powder Technol. 382 (2021) 478-490. https://doi.org/10.1016/j.powtec.2021.01.013
[14] A. Fais, A faster FAST: Electro-sinter-forging, Metal powder Rep. 73 (2018) 80-86. https://doi.org/10.1016/j.mprp.2017.06.001
[15] Information on https://khkgears.net/new/plastic_gears.html
[16] M. Yan, L.L. Li, Chen, N. Li, Y. Jiang, Z. Xu, M. Jing, Y. Hu, L. Liu, X. Zhang, Radiation resistance of carbon fiber reinforced epoxy composites optimized synergistically by carbon nanotubes in interface area/matrix, Compos. Part B: Eng. 172 (2019) 447-457. https://doi.org/10.1016/j.compositesb.2019.04.041

Materials Research Proceedings 28 (2023) 1809-1818 https://doi.org/10.21741/9781644902479-196

Exploring sheath-core yarns technology to optimise bio-composite performances

QUEREILHAC Delphine[1,a *], FEMERY Jules[1,b], MOREL Guillaume[1,c], KORYCKI Adrian[1,d], DE LUYCKER Emmanuel[1,e], OUAGNE Pierre[1,f] and CHABERT France[1,g]

[1]Univ. de Toulouse, Laboratoire Génie de Production, LGP, INP-ENIT, F-65016 Tarbes, France

[a]delphine.quereilhac@enit.fr, [b]jfemery@enit.fr, [c]guillaume.morel@enit.fr, [d]adrian.korycki@enit.fr, [e]emmanuel.de-luycker@enit.fr, [f]pierre.ouagne@enit.fr, [g]france.chabert@enit.fr

Keywords: Flax, Biocomposite, Extrusion, Sheath-Core, 3D Printing

Abstract. This work focuses on the design and fabrication of a continuous filament made of flax yarn and bio-based thermoplastic polymer. For this purpose, the sheath-core process has been explored by using an extrusion laboratory line equipped with a wire coating die to manufacture a flax core coated with PLA. The polymer properties were investigated (thermal transition, mechanical properties, melt viscosity) to link the polymer properties, the process and the properties of the resulting filament. The filament diameter decreases and surface defects appear when the pulling speed increases. The mechanical characterization of flax/PLA filaments demonstrates a higher elastic modulus, higher stress at break and lower strain at break as compared with pure PLA filaments. Such PLA coated flax filaments are a relevant option to widespread the use of biobased composites.

Introduction

Generalities about biocomposites.

Working with eco-friendly materials, recycling, and reusing are key challenges to face the demand for renewable resources. According to this statement, biocomposites are a great attraction, as they are produced from biofibers and biopolymers, and can present the required properties and functionalities at a reasonable cost [1]. The biocomposites market forecast report has estimated that the market size is likely to attain $10.89 billion by 2024, and the fabrication of materials from biobased feedstock is likely to raise from 5% in 2004 to 18% in 2020, and ~25% in 2030 [2]. Vegetal fibers such as flax and hemp have attracted significant focus as a potential alternative to synthetic fibers like carbon and glass [3], and biocomposites have been largely employed for several secondary applications in aerospace, automotive, packaging, electronics, and building sectors. It is thus important to keep developing new processes to widen the application panel of these renewable materials.

The choice of reinforcement largely relies upon the inherent chemical and physical characteristics of the fibres. Right from the cultivation to processing phases, various factors such as environmental conditions, processing methods or fiber age, influence the properties of plant fiber. Some of these features also have a direct effect on several biocomposite responses such as fiber-matrix bonding, thermal stability, or moisture sensitivity [4]. On the other hand, considerable research works are being performed in developing fully biodegradable materials (green composites) by combining biodegradable polymer matrix with biofiber [5]. The manufacturing of natural fibre-reinforced biocomposites is based, in general, on the technologies used for conventional synthetic short fibre composites, such as extrusion, injection moulding or compression moulding. Nevertheless, suitable processing methods and conditions must be chosen to manufacture fibre-reinforced biocomposites. To obtain biocomposites with suitable properties,

Content from this work may be used under the terms of the Creative Commons Attribution 3.0 license. Any further distribution of this work must maintain attribution to the author(s) and the title of the work, journal citation and DOI. Published under license by Materials Research Forum LLC.

it is crucial to control their thermal stability, interfacial adhesion, fiber distribution, type and content [6].

Flax fibres.

In this work, flax has been chosen among all vegetal fibres for its good mechanical properties and its availability at industrial level and local scale. After extraction from the flax straw (woody core), fibres are organised in bundles, linked by a middle lamella, which cements the cell walls of adjacent cells together. It is mainly composed of pectic polysaccharides, lignin, and a small amount of proteins [7]. Many industrial processes aim to remove this natural matrix, to improve the separation of elementary fibres and the composite matrix/flax adhesion. However, these processes also bring undesirable side effects such as deterioration of the fibre and loss of mechanical performance [8].

Sheath-core flax/PLA.

Nowadays, flax is often found in composite materials under the form of unidirectional ply, woven, or short fibres, but an emerging technique is the use of long fibres for 3D printed composites. Material extrusion is defined as an additive manufacturing process in which material is selectively dispensed through a nozzle. Additive manufacturing process creates complex 3D parts through directionally orientated extrusion. The simplicity and relatively low price make of material extrusion make it widely used in many research works [9]. Two main options exist to print composites with continuous natural fibres: (i) in-nozzle impregnation in which the yarn and the molten matrix arrive simultaneously inside the noozle, and (ii) pre-impregnated filament printing in which the core yarn is trapped into a matrix sheath. Simultaneous impregnation of thermoset resin and continuous fibre in the extrusion head leads to several process issues, such as fibre content and feed, deposition rate and path [9]. Also, passing fibre and thermoplastic filament through a single nozzle limits control over fibre and can lead to poor overall surface finish and increased voids [10].

In this work, a novel process will be explored to improve the quality of a sheath-core filament, made of flax yarn coated by a PLA (polylactic acid) matrix. PLA is a bio-based polymer which uses have been drastically widen these last years, as it is renewable and biodegradable, and it is obtained from agricultural crops like sugar beet or corn. It demonstrates good mechanical strength, stiffness and can be processed with conventional polymer processing techniques. In addition, when looking at its life cycle, it appears that PLA requires nearly one tenth of the fossil energy when compared to synthetic polymers [11]. These factors make PLA an ideal choice to experiment biodegradable composites. In this research work, material intrinsic parameters were explored such as fibre properties, PLA thermal transitions and melt viscosity. Then, several filaments were manufactured with a wire coating die equipment while varying the pulling speed. Then, the structure and the properties of the resulting filaments were investigated to correlate the PLA properties with mechanical behaviour of the filaments.

Materials and Methods

Flax yarn.

The first test batch was carried out on flax sliver, which is a product originally manufactured for garment-textile fabrication. In order to design a very thin and soft yarn, this flax material has been prepared for wet spinning process: firstly, the fibres have undergone a chemical degumming process with low concentration caustic soda. This step is crucial to separate cellulose and non-cellulose parts and to get rid of all the pectins and sticking agents present on the fibres to keep their cohesion. Also, this process turns the flax from hydrophobic to hydrophilic, which is a major requirement for the wet spinning process. After degumming, fibres were bleached with peroxide to prepare them for further transformation and finishing, such as dyeing. Flax sliver was turned to yarn on a Linimpionti BMR1 wet spinning machine, presented in Fig. 1a. Machine speed was 15m.min^{-1}, with a drawing of 4, and a torsion of 450 revolution.min^{-1}. Final yarn has a count of 66

± 3 Tex. For flax yarn characterisation, the tensile tests are carried out on a Tenso-Lab 4 v. (Mesdan Lab, Italy) apparatus, according to standard NF EN ISO 2062 [12] over a length of 250 mm, with a speed of 250 mm.min^{-1} and a preload of 0.50 cN.Tex^{-1}.

PLA 3 grades.

PLA is a linear thermoplastic aliphatic polyester obtained from lactic acid. As shown in Fig. 1b, lactic acid has two enantiomer form L-Lactic and D-Lactic acid due to its chiral geometry. It results in dimers with three enantiomer forms: L-lactid, D-Lactid and DL-Lactid [13]. In this work, two different grades of PLA are studied from NaturePlast: PLE005 and PLE005-A (called respectively in this work PLA-A and PLA-B). PLE005 (PLA-A) is a homopolymer of L-lactid (>99%) with high crystallisation potential and PLE005-A (PLA-B) is a copolymer of L-Lactid (>95%) and D-Lactid (<5%) with slower crystallisation kinetics due to the presence of D-Lactid [14]. PLA pellets were systematically dried in an oven at 60°C for few hours before any experiment. Indeed, the presence of water in PLA while processing can affect its property by hydrolysis phenomenon and plasticising of the crystalline phase [15].

Extruder and wire coating die.

The wire coating die is presented in the scheme in Fig. 1c. The die is a commercial equipment provided to fit a single screw Rheomex extruder on a Polylab OS system by ThermoFisher. The flax fiber enters through the top and exits at the bottom of the scheme. The molten polymer enters at the left side and it flows into a tube up to join the fiber to coat it. The screw is L/D= 25 and its rotating speed is kept constant at 5 rpm. The temperatures are 180°C for the screw, 170°C inside the die. Then, the fiber coated with the molten PLA exits the die at the bottom of the scheme. The coated fiber is pulled out the die with a system equipped with 2 rollers. The pulling speed has been varied between 0.003 and 0.2 m.s^{-1}. The flow is considered as steady, incompressible and isothermal, the flowing profile is a Poiseuille-type, with a maximum fluid velocity ($V_{r=R}=V_{max}$) at the vicinity of the fiber and a sticking condition at the die wall ($V_{r=0} = 0$). A modular part can be changed to vary the thickness of the polymer coating, the nozzle dimensions chosen in this study are 2 and 4 mm. The maximum shear rate just before exiting the die $\dot{\gamma}$ is calculated by V_m/e, with e the width of the channel where the polymer flows. The maximum shear rate is 200 s^{-1} for a 2 mm diameter filament.

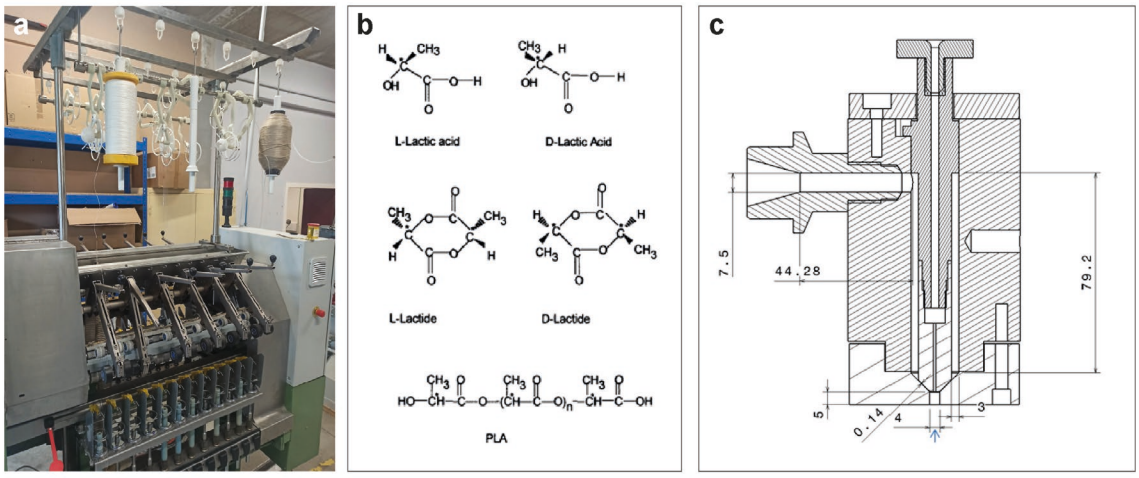

Fig. 1. Wet spinning machine (a), structures of lactic acid, lactid and PLA [15] (b), wire coating dye (c).

Rheological behavior.

The polymer coating thickness could be predicted by considering the process parameters and the polymer rheological properties. For that, we measured the complex viscosity of the two grades of PLA in an oscillatory rheometer MCR501 by Anton Paar, applying the Cox-Merz equivalence.

The experiments were carried out using a 25 mm diameter parallel-plate configuration with a 1 mm gap. Initially, dynamic strain sweeps were performed to determine the linear viscoelastic regime (LVR). Time sweeps were performed to check the thermal stability of the polymer along the experiment duration. Frequency sweeps were performed to measure G' and G'' between 200 and 230°C with 10°C steps, from 100 to 0.1 rad.s^{-1}. Since the angular frequency is limited to 100 rad.s^{-1}, we applied TTS at the reference temperature of 200°C to extend the shear rate range to attain the 200 s^{-1} involved in the process.

DSC.

The thermal transitions and enthalpy were determined using a Mettler Toledo DSC1 under a nitrogen flow rate of 50 mL.min^{-1}. After heating at 210°C to cancel the thermomechanical history, a cooling rate at 10°C.min^{-1} was applied followed by a second heating ramp at 10 °C.min^{-1}.

Mechanical characterisation.

For pure PLA, specimens were injected on a Proxima H120 (Billion, France) at 190°C to 175° from nozzle to rear barrel with mould regulated at 40°C to achieve a low crystallinity. The tensile tests were carried out on a 33R4204 (Instron, United State) testing machine, equipped with a mechanical extensometer 2620-604 (Instron, United State) and a load cell 2525-805 of 5kN (Instron, United State) according to standard NF EN ISO 527 with a speed of 3mm.min^{-1}. In this study, five specimens were tested for each grade of PLA.

Optical observations. A microcutting machine Mecatome T202 (PRESI, France) was used for sample preparation with an ultra-thin wheel UTW-R200U (PRESI, France). Samples were directly observed on their cross-sections with a binocular Leica Wild M420 at magnification of x40. The surfaces of PLA filaments were inspected through a high-resolution microscope Keyence VHX-6000S (Bois-Colombes, France) in a reflection and transmission mode with a magnification of x100.

Results

Mechanical characterization of PLA.

The tensile behaviour of both PLA is shown in Fig. 2. PLA-A and PLA-B show an elastic domain in their first percent of elongation indicating no modification in their microstructure. Then, PLA display a plastic domain where modifications in the microstructure appear, mainly chains' conformation and crystalline slip, until specimens breaking.

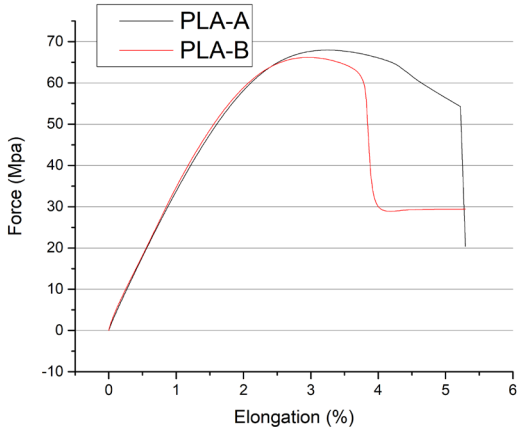

Fig. 2. Tensile curve of PLA-A and PLA-B.

The tensile properties of PLA-A and PLA-B are shown in Table 1. PLA-A, despite its low crystallinity due to high cooling rate during injection molding, has a slightly higher rigidity and strain at yield point than PLA-B. Previous studies have shown that a higher crystallinity of homopolymer of PLLA improves its rigidity and resilience [16]. PLA-B accepts longer elongation

before breaking than PLA-A because of less crystallinity resulting in higher macromolecular mobility.

Table 1. Mechanical properties of PLE005 and PLE005-A

	Young Modulus	**Stress at yield point**	**Elongation at yield point**	**Elongation at break**
	(Mpa)	(MPa)	(%)	(%)
PLA-A	3700	67.6	3.17	4.10
PLA-B	3500	65.2	3.08	>15

Thermal transitions of PLA.

Thermal transitions of PLA upon heating are shown in Fig. 3a. Glass transitions of PLA-A and PLA-B are 66°C and 60°C respectively. Their melting point are 178°C for PLA-A and 155°C for PLA-B. Those temperatures depend of the initial composition of PLA and its molecular weight. Also, the crystalline phase has stronger intermolecular interaction and lower flexibility [17], increasing the melting temperature. As expected, PLA-A reaches a higher crystallinity than PLA-B due to its higher concentration of L-Lactide. In Fig. 3b, DSC thermogram shows that PLA-A starts to crystalize at 117°C when cooling from a molten state. The crystallisation kinetics depends on its concentration of L-Lactid and molecular weight. At a cooling rate of 3°C.min^{-1}, PLA-B does not undergo crystallisation when cooling from a molten state due to presence of D-Lactid. Variation of D-Lactid concentration affects the crystallisation kinetics of PLA, at concentration higher of 15%, its crystallisation is not possible. Authors have shown that the crystallisation of PLA is 60 times faster from a concentration of 6.6% to 0.6% of D-Lactid [13].

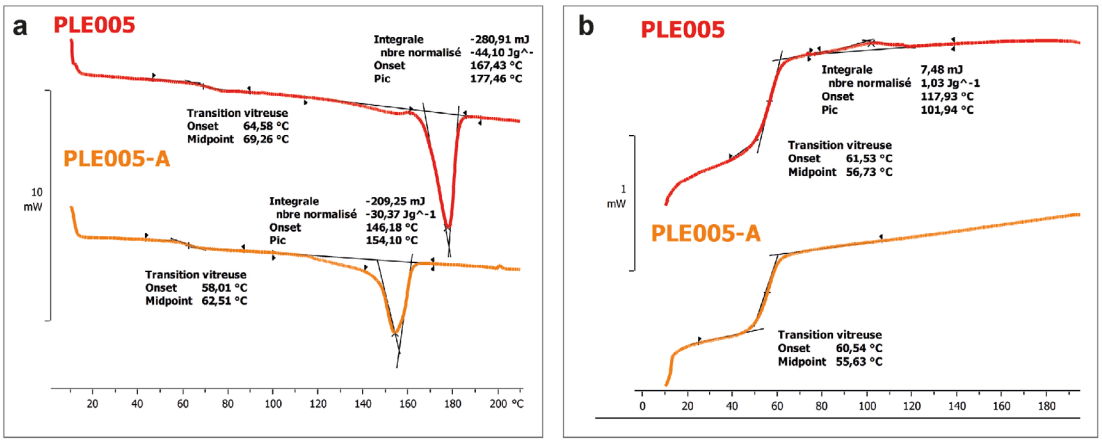

Fig. 3. DSC thermograms of PLA, heating ramp (a) cooling ramp (b).

Viscosity of PLA.

TTS was applied to frequency sweeps at 200, 210 and 220°C to obtain master curves shown in Fig. 4. The curves do not follow the rheological behavior expected for molten polymers, indicating a structural evolution with time. However, the slopes of G' and G'' are closed to the ω^1 and ω^2 dependency. This complex flowing behavior is mentionned in the literature: Lactic acid exists in two enantiomeric forms, L-lactic acid and D-lactic acid, whose co-crystallization forms a stereocomplex with a melting point about 50 °C higher than PLA homocrystals [18]. Neat PLLA demonstrates a Newtonian plateau at low frequencies, typical of polymer melts, while such

behavior is not observed when PLLA is blended with 5% PDLA. In the presence of PDLA, significant deviation of complex viscosity at low frequencies can be associated to the interaction between chains caused by stereocomplex formation [19]. This agrees with our findings, the master curve deviate from the expected trend for PLA-B which contain <5% of PDLA according to the manufacturer. Also, the complex viscosity of PLA- B is higher than those of PLA-A, likely due to the presence of a small concentration of stereocomplex in the PLLA melt. Moreover, measurement of the melt rheological properties of PLA is complicated by degradation effects resulting in chain breakage. Master curves of dynamic viscosity constructed using time-temperature superposition show significant dispersion for unstabilized PLA [20]. Finally, the complex viscosity of PLA-A and PLA-B is about 100 and 250 Pa.s respectively, at the Newtonian plateau.

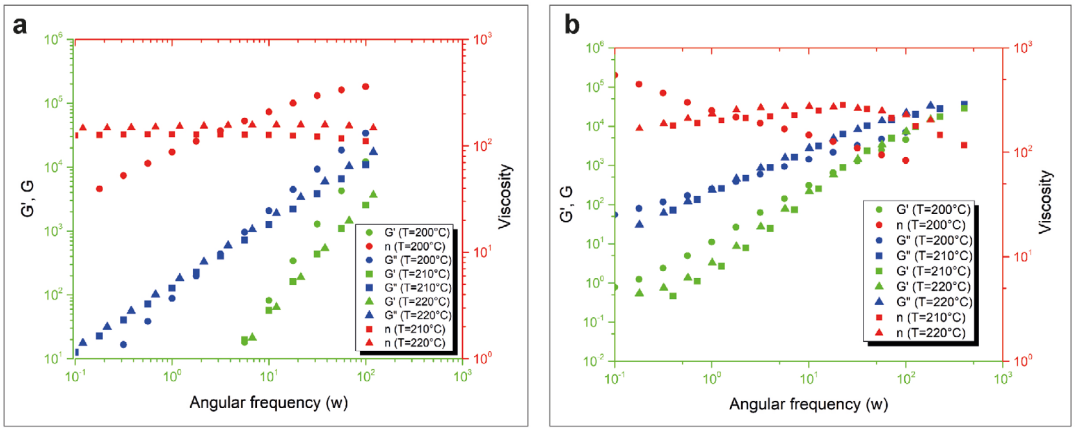

Fig. 4. Viscosity curves of PLA-A (a) and PLA-B (b).

Extrusion rates are often limited by the surface defects that appears at the die exit when the shear stress is too high [21]. At the die exit, the velocity profile goes from a parabolic shape to a plug one, resulting in tensile stresses that can crack the surface of the extrudate. This is known as the shark skin effect. In our cases, this defect is more likely to appear for PLA-B whose viscosity is higher, for the same shear rate, hereby related to the pulling speed. Such surface defects are seen in Fig 5 for both PLA. At low pulling speed, the filament surface of PLA-A is smooth Fig. 5a, whereas air bubbles Fig. 5b and shark skin effect Fig. 5c are visible for higher pulling speed. As expected, no shark skin effect was noticed for PLA-A due to a lower viscosity as seen in Fig. 4. Since PLA and flax fiber were thoroughly dried before processing, these bubbles could not stem from residual water. Another explaination could be associated with the design of the die in which the molten polymer could trap air where it meets the fiber.

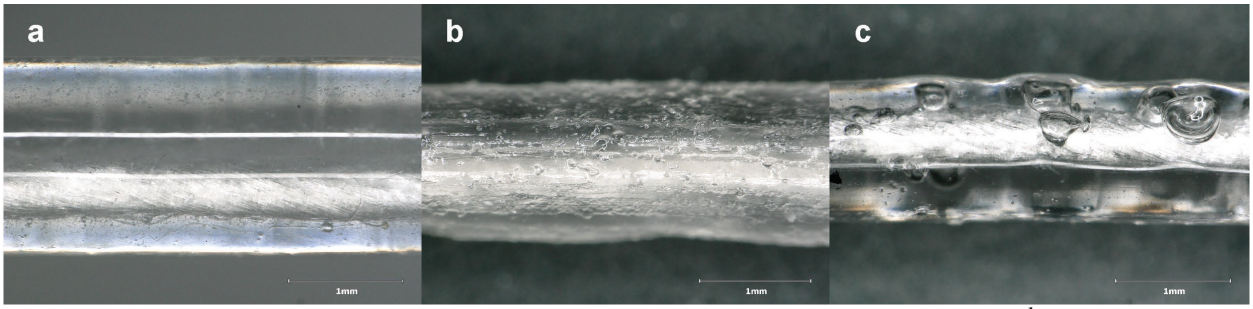

Fig. 5. Optical micrographs of PLA filament surfaces of PLA-A at 0.014 m.s^{-1} (a), PLA-A at 0.040 m.s^{-1} (b), PLA-B at 0.040 m.s^{-1} (c).

Microscopic observations of PLA injected with flax yarn.

Table 2 presents the longitudinal section of PLA extruded with flax yarn. Cross-sections show a clear irregularity in the location of the flax yarn: it tends to go to the side of the filament instead of its centre.

Table 2. Transversal section of the filaments, depending of the pulling speed and grade (PLA-A and PLA-B).

Pulling speed	PLA-A	PLA-B
0,008 $m.s^{-1}$	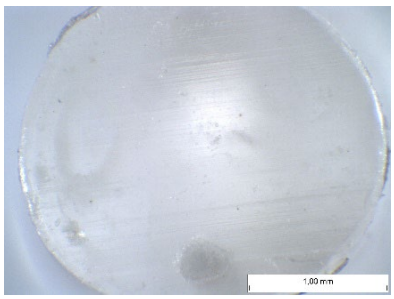	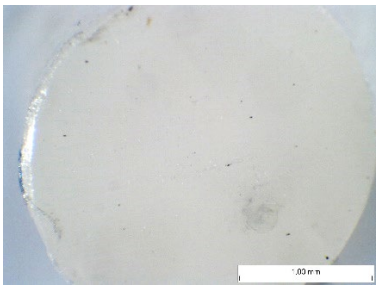
0,014 $m.s^{-1}$	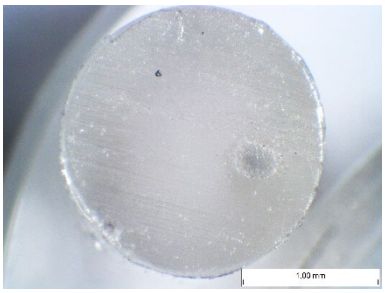	
0,040 $m.s^{-1}$	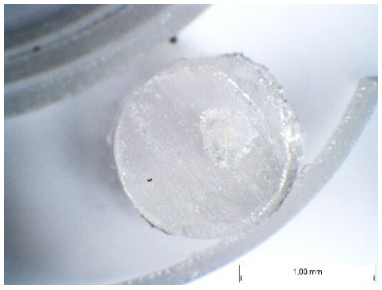	
0,065 $m.s^{-1}$		

Mechanical properties of PLA injected with flax yarn.

Fig. 6a shows the filament diameters for the two grades of PLA. As expected, when the pulling speed increases, the PLA coating thickness around the flax fibre get thinner. No effect of the viscosity is seen, since the diameters are similar for both grades Fig. 6b shows the impact of pulling speed on the stress strain curve of the two PLA/flax (PLA-A and PLA-B) filaments pulled at 0.008,

0.014, 0.040 and 0.065 $m.s^{-1}$. It appears that the highest is the shear rate, the lowest is the strength at break: a fast-pulling speed creates a thinner polymer layer onto the flax yarn.

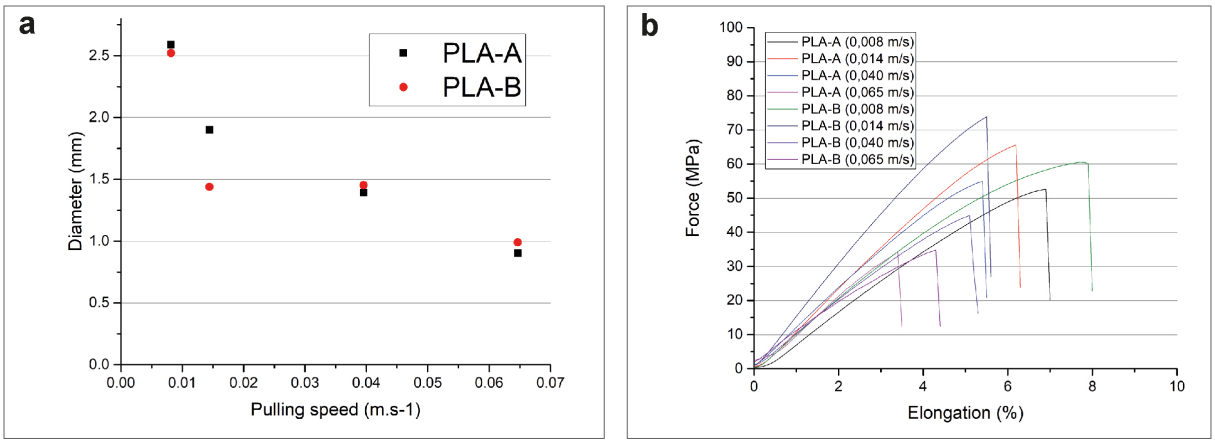

Fig. 6. Evolution of the diameter with the pulling speed (a), Stress strain curve of PLA-A and PLA-B for 4 pulling speed (b).

Fig. 7a presents the stress strain curve of flax yarn, pure PLA filaments and PLA coated flax filaments (referred as PLA injected). It is clear that adding flax yarn, which has naturally a higher stiffness, increases the filament rigidity and decreases the elongation at break compared to pure PLA filaments. The impact of PLA grade and pulling speed is less obvious. Fig. 7b presents the elastic modulus of pure PLA-A and PLA-B for the 4 pulling speed, along with PLA-A and PLA-B coated flax at one speed. The elastic modulus is higher for filaments containing flax. When increasing the pulling speed, the elastic modulus decreases. This could be attributed to the surface defects appearing at high shear rates as seen in Fig 5.

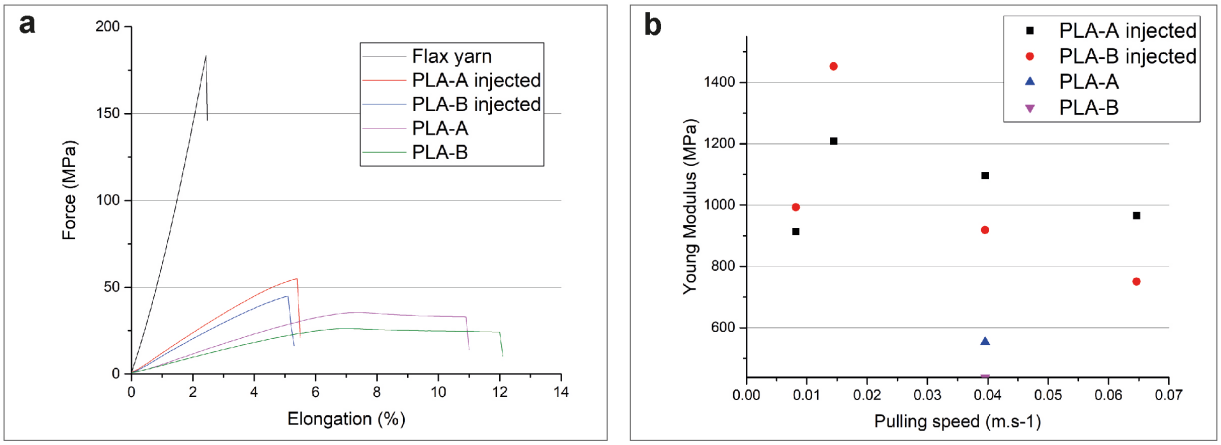

Fig. 7. Stress strain curve (a) and Young's modulus (b) of flax yarn, PLA coated flax and pure PLA filaments.

Summary

In the present work, a wire-coating die was used to manufacture novel filament of flax yarn with a PLA coating. The material properties were assessed to check whether the polymer properties are suitable with the extrusion process.

The main conclusions of this research work are as follows:

- The two grades of PLA are suitable to be extruded in a wire-coating die. A range of filaments with various diameters was successfully achieved.
- The filament diameter decreases when the pulling speed increases
- The tensile properties of the PLA coated flax and better than pure PLA filaments.

This work demonstrates the ability to obtain flax/PLA filaments. Further work will focus on printing composite parts with such filaments. Also, it might be relevant to study the interfacial adhesion between the flax yarn and the PLA matrix to enhance the mechanical properties of the composites obtained by 3D printing.

References

[1] J.J. Andrew, H.N. Dhakal, Sustainable biobased composites for advanced applications: recent trends and future opportunities – A critical review, Compos. Part C: Open Access 7 (2022) 100220. https://doi.org/10.1016/j.jcomc.2021.100220

[2] T. Gurunathan, S. Mohanty, S.K. Nayak, A review of the recent developments in biocomposites based on natural fibres and their application perspectives, Compos. Part A: Appl. Sci. Manuf. 77 (2015) 1-25. https://doi.org/10.1016/j.compositesa.2015.06.007

[3] M.P.M. Dicker, P.F. Duckworth, A.B. Baker, G. Francois, M.K. Hazzard, P.M. Weaver, Green composites: A review of material attributes and complementary applications, Compos. Part A: Appl. Sci. Manuf. 56 (2014) 280-289. https://doi.org/10.1016/j.compositesa.2013.10.014

[4] O. Faruk, A. K. Bledzki, H.-P. Fink, M. Sain, Biocomposites reinforced with natural fibers: 2000–2010, Prog. in Polym. Scie. 37 (2012) 1552-1596.

[5] A.N. Netravali, S. Chabba, Composites get greener, Mat. Today 6 (2003) 22-29. https://doi.org/10.1016/S1369-7021(03)00427-9

[6] L. Pil, F. Bensadoun, J. Pariset, I. Verpoest, Why are designers fascinated by flax and hemp fibre composites?, Compos. Part A: Appl. Sci. Manuf. 83 (2016) 193-205. https://doi.org/10.1016/j.compositesa.2015.11.004

[7] A. Melelli, O. Arnould, J. Beaugrand, A. Bourmaud, The Middle Lamella of Plant Fibers Used as Composite Reinforcement: Investigation by Atomic Force Microscopy, Molecules 25 (2020) 632. https://doi.org/10.3390/molecules25030632

[8] C. Baley, F. Busnel, Y. Grohens, O. Sire, Influence of chemical treatments on surface properties and adhesion of flax fibre–polyester resin, Compos. Part A: Appl. Sci. Manuf. 37 (2006) 1626-1637. https://doi.org/10.1016/j.compositesa.2005.10.014

[9] D. Stoof, K. Pickering, Y. Zhang, Fused Deposition Modelling of Natural Fibre/Polylactic Acid Composites, J. Compos. Sci. 1 (2017) 8. https://doi.org/10.3390/jcs1010008

[10] S. Valvez, P. Santos, J.M. Parente, M.P. Silva, P.N.B. Reis, 3D printed continuous carbon fiber reinforced PLA composites: A short review, Procedia Struct. Integrity 25 (2020) 394-399. https://doi.org/10.1016/j.prostr.2020.04.056

[11] G. Rajeshkumar, S. Arvindh Seshadri, G.L. Devnani, M.R. Sanjay, Suchart Siengchin, J. Prakash Maran, Naif Abdullah Al-Dhabi, Ponmurugan Karuppiah, Valan Arasu Mariadhas, N. Sivarajasekar, A. Ronaldo Anuf, Environment friendly, renewable and sustainable poly lactic acid (PLA) based natural fiber reinforced composites – A comprehensive review, J. Clean. Prod. 310 (2021) 127483. https://doi.org/10.1016/j.jclepro.2021.127483

[12] AFNOR, NF EN ISO 2062 - Textiles - Yarns from packages - Determination of single-end breaking force and elongation at break using constant rate of extension (CRE) tester, 2010

[13] D. Garlotta, A Literature Review of Poly(Lactic Acid), Jour. of Poly. and the Envi. 9 (2001) 63-84. https://doi.org/10.1023/A:1020200822435

[14] J. Huang, M.S. Lisowski, J. Runt, E.S. Hall, R.T. Kean, N. Buehler, J.S. Lin, Crystallization and Microstructure of Poly(L -lactide- *co* - *meso* -lactide) Copolymers, Macromolecules 31(1998) 2593-2599. https://doi.org/10.1021/ma9714629
[15] G.L. Siparsky, K.J. Voorhees, J.R. Dorgan, K. Schilling, Water transport in polylactic acid (PLA), PLA/ polycaprolactone copolymers, and PLA/polyethylene glycol blends, Jour. of Envir. Polym. Degrad. 5 (1997) 125-136. https://doi.org/10.1007/BF02763656
[16] G. Perego, G.D. Cella, C. Bastioli, Effect of molecular weight and crystallinity on poly(lactic acid) mechanical properties, J. Appl. Polym. Sci. 59 (1996) 37-43. https://doi.org/10.1002/(SICI)1097-4628(19960103)59:1<37::AID-APP6>3.0.CO;2-N
[17] Q. Fang, M.A. Hanna, Rheological properties of amorphous and semicrystalline polylactic acid polymers, Industrial Crops and Products 10 (1999) 47-53. https://doi.org/10.1016/S0926-6690(99)00009-6
[18] Y. Ikada, K. Jamshidi, H. Tsuji, S.H. Hyon, Stereocomplex formation between enantiomeric poly(lactides), Macromolecules 20 (1987) 904-906. https://doi.org/10.1021/ma00170a034
[19] S. Saeidlou, M.A. Huneault, H. Li, P. Sammut, C.B. Park, Evidence of a dual network/spherulitic crystalline morphology in PLA stereocomplexes, Polymer 53 (2012) 5816-5824. https://doi.org/10.1016/j.polymer.2012.10.030
[20] H. J. Lehermeier, J.R. Dorgan, Melt rheology of poly(lactic acid): Consequences of blending chain architectures, Polym. Eng. Sci. 41 (2001) 2172-2184. https://doi.org/10.1002/pen.10912
[21] N. El Kissi, J.-M. Piau, F. Toussaint, Sharkskin and cracking of polymer melt extrudates, J. Non-Newtonian Fluid Mech. 68 (1997) 271-290. https://doi.org/10.1016/S0377-0257(96)01507-8

Materials Research Proceedings 28 (2023) 1819-1828 https://doi.org/10.21741/9781644902479-197

Effect of energy director thickness on thermal diffusion and joint quality during ultrasonic welding of CF/PEEK composites

KORYCKI Adrian[1,2,a], CARASSUS Fabrice[1,2,b], GARNIER Christian[1,c *], CHABERT France[1,d] and DJILALI Toufik[2,e]

[1]LGP-ENIT-INPT, University of Toulouse, 47 Avenue d'Azereix, 65016 Tarbes, France

[2]LAUAK FRANCE, 8 Rue Louis Caddau, 65000 Tarbes, France

[a]akorycki@enit.fr, [b]fabrice.carassus@groupe-lauak.com, [c]cgarnier@enit.fr, [d]fchabert@enit.fr, [e]toufik.djilali@groupe-lauak.com

Keywords: Thermal Diffusion, Shear Strength, Energy Director, Composites, Ultrasonic Welding

Abstract. Thermoplastic composites offer new possibilities for the aerospace industry. Large and thin structural parts can be processed rapidly and more cost-effectively than thermoset composites since the latter need to undergo lengthy curing reactions. An additional advantage is the possibility of being assembled by welding processes. However, joining thermoplastic composites remains challenging due to the lack of knowledge of the impact of process parameters (time, pressure, temperature) on the welded joints. A polymer film named energy director (ED) is usually set up at the interface to enhance the weld resistance. A combined experimental-numerical approach was carried out to estimate the influence of ED thickness on the thermal diffusion within the assemblies and the mechanical resistance of welds in the ultrasonic welding (USW) process. The studied materials are unidirectional carbon fibre-reinforced polyetheretherketone (CF/PEEK) and 50 µm and 250 µm polyetherimide (PEI) films as ED. Thermocouples (TCs) are inserted into the PEI layer to measure the temperature evolution during USW. Besides, the thermal profile is obtained based on the simulation of conduction phenomena through the thickness of the material using the finite element method (FEM). The effect of the ED through-thickness model points out the evolution of the temperature profile with time during the USW process for different PEI thicknesses. For both ED thicknesses, the temperature reached is above the PEI glass transition (220 °C) allowing macromolecular interdiffusion. According to our results, only the first ply reaches the melting temperature of PEEK, showing that the composite parts are not thermally affected during USW. Because of the high conductivity of unidirectional CF/PEEK composites, a thinner ED leads to a too-short heating time at the interface. Associated with too high power in a short time, a lower weld resistance of APC-2 parts is obtained by single lap shear for 50 µm PEI layer, 12 MPa, compared to 43 MPa obtained for 250 µm. A higher PEI thickness at the interface slows down the cooling step, resulting in a deeper interdiffusion of PEI and so, a stronger weld.

Introduction

Ultrasonic welding is a process that makes it possible to obtain good-quality welds quickly and affordably [1,2]. In USW, the heat is generated at the interface by friction between the two parts through high-frequency vibrations. Indeed, the process can be easily implemented at an industrial scale and the cycle times are in the order of seconds. Ultrasonic welding does not need any specific material property [3]. No additional device is necessary to generate heat in the welding area compared to induction and resistance welding for which, susceptor and resistor are required, respectively. The development of an industrially viable solution for ultrasonic welding of CF/PEEK would give this family of composite materials an undeniable advantage over thermosetting composites.

Content from this work may be used under the terms of the Creative Commons Attribution 3.0 license. Any further distribution of this work must maintain attribution to the author(s) and the title of the work, journal citation and DOI. Published under license by Materials Research Forum LLC.

Many parameters affect the ultrasonic welding quality, such as welding time, pressure, amplitude and type of energy director [4,5]. Monitoring the thermal diffusion is crucial to relate process parameters to welds' performance. Nevertheless, measuring the temperature during welding processes is challenging and the works related are rare [3]. Non-invasive techniques do not exist yet to assess the temperature profile at the interface during welding. Due to the closed contact between the two composite parts with an integrated PEI layer, it is difficult to measure the temperature and almost impossible to control it. Moreover, the very short cycle times during USW reduce the means available to measure the temperature. Any device placed between the two specimens would alter friction phenomena, thus, changing heat generation [6,7]. Besides, some works report thermal profiles during USW obtained by simulation of thermal transfer [8,9], but none of them focuses on ED thickness.

In this work, the thermal analysis conducted on CF/PEEK composites using different thicknesses of PEI are displayed. The micro-thermocouples were chosen to minimize their influence during welding. The experimental section presents quasi-non-intrusive temperature measurements where temperature profiles are analyzed through the influence of USW parameters. The mechanical resistance of welding joints and process parameters for two PEI thicknesses on CF/PEEK are correlated to the thermal profiles. The thermal diffusion through the sample thickness from the interface is investigated from a FEM analysis in the numerical section.

Materials and Methods

Experimental methods.

Continuous carbon fibre-reinforced polyetheretherketone composite, named APC-2 from Cytec Industries and polyetherimide, named Ultem 1000 from Sabic, have been used.

The composite plates were produced by compression with Pinette Emidecau Industries Lab800 thermo-compression device. Two types of plates are manufactured: (1) APC-2 plates and (2) APC-2 with a 250 µm or 50 µm PEI layer on top plates. A stack of 14 unidirectional plies of APC-2 was made to obtain a mirror symmetry lay-up $[0/90]_7$. The PEI film was integrated on the APC-2 plates.

The thermocouples were 80 µm diameter K-type from Omega. Chromel and Alumel threads were supplied separately and welded using the air arc welding technique. TCs are inserted according to the procedure described by Bonmatin et al. [10]. The TCs were deposited and covered with a metal mass of 5 kg on the composite containing the PEI film to insert them into the polymer layer. The assembly was then placed in an oven for 40 min at 290 °C. Then, the TCs were extended to connect them to a Logger GL980 midi data recorder from Graphtec Corporation.

Omega 4X ultrasonic welder from Mecasonic was used for the experiments. It is welding equipment with a working frequency of 20 kHz and a maximum load of 3000 N. The displacement amplitude of the waves generated by the generator is amplified by a factor of 1.7 by the booster and by a factor of 1.7 by the sonotrode.

The quality of the assemblies was assessed by lap shear strength (LSS). The assemblies tested were made following ASTM D1002, with samples of 100 x 25 mm^2 corresponding to length and width respectively, and an overlapping area of 10 x 25 mm^2. The Single Lap Shear (SLS) tests were performed on the Instron Universal 33R4204 tensile machine equipped with a 100 kN load cell with a crosshead speed of 2800 $N.min^{-1}$. The value of LSS [MPa] was calculated with Eq. 1.

$$LSS = \frac{F_{max}}{l_0 \cdot w} \quad (1)$$

In the SLS test, the strength of a weld depends on the load at the breaking point F_{max} [N], the length of the weld zone l_0 [mm] and the width w [mm].

Numerical methods.

To carry out the simulation, the FEM has been chosen. It consisted of the simplification of differential equations for numerical use. These methods, introduced for many years, are still widely used for the resolution of thermal problems [11,12]. The configuration applied for the simulation was a simple one-dimensional (1D) thermal conduction model in which the in-depth heat diffusion throughout the material part, especially in the first layers of composites was considered. Abaqus software from Dassault System was used for the numerical analysis of heat transfer. The model considered the thermal and physical properties of the polymer changing with temperature and melting heat. In this case, the heat source term was considered to be null because no volumetric internal energy was generated. A non-stationary thermal model was developed, where the software used the local heat equation (Eq. 2).

$$div\left(k\vec{\nabla}T\right) = \rho C_p \frac{\partial T}{\partial t} \quad (2)$$

where k is the thermal conductivity [W.(m.°C)$^{-1}$], T is the temperature [°C], ρ is the material density [kg.m^{-3}] and C_p is the heat capacity [J.(kg.°C)$^{-1}$]. The left-hand term corresponds to diffusion whereas the right-hand term corresponds to the transient heat state.

Results and Discussion

Experimental analysis.

During the welding process, the power [W] and displacement of sonotrode [mm] were recorded over time [s] by the machine, and they were plotted to identify different stages of USW according to Villegas's work. The welding machine can work in different modes, mostly the welding is controlled by time or displacement of the sonotrode. The time-controlled welding allows finding the optimum displacement of the sonotrode where the process is stopped in the stage before degradation of the material [13]. The temperature measurements were taken by thermocouple integrated into the PEI film during welding for every 1 µs. The three curves of power [%], displacement [%], and temperature [°C] are presented as a function of time [s] in Fig. 1. The maximum power of the machine considered for the calculation is 3000 W and the maximum displacement represents the thickness of two PEI layers, 0.5 mm and 0.1 mm.

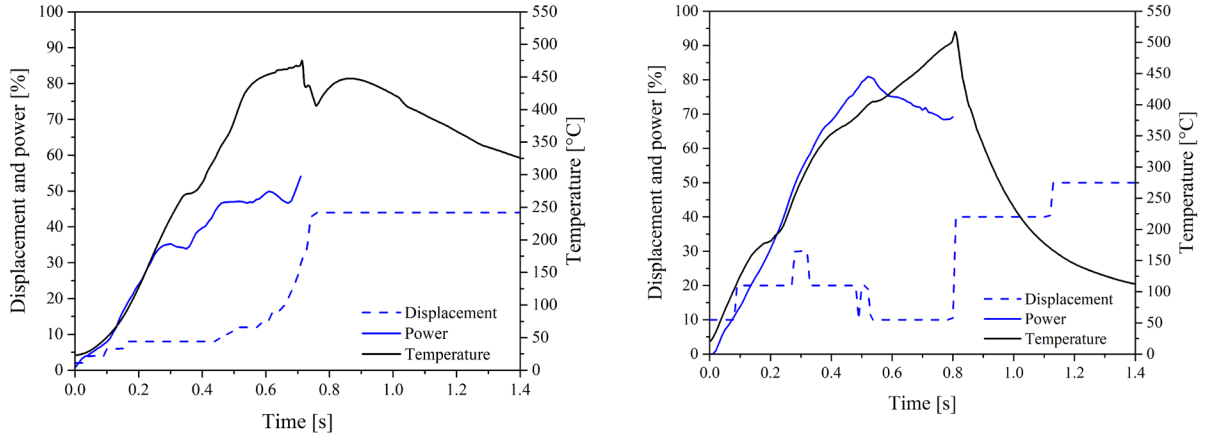

Fig. 1. Temperature monitoring with thermocouples during USW of APC-2 composites with integrated (a) 250 µm PEI for an amplitude of 68 µm, a load of 2.5 bar and a displacement of 30 % (b) 50 µm PEI for an amplitude of 68 µm, a load of 2.5 bar and a time of 0.8 s.

For the assembly of CF/PEEK with 250 µm PEI, the optimized displacement-controlled mode was applied at 30 %, Fig. 1.a, to melt the first plies of adherents. Regarding the welding of CF/PEEK with 50 µm PEI, the displacement-controlled mode at 40 % was not enough to weld the assembly while at 50 % high degradation of material was observed, so the time-controlled mode with optimized 0.8 s has been applied, Fig. 1.b. The same trend on the temperature curves during the welding step from room temperature to the maximum one can be observed. The latter reached 475 °C at 0.714 s and 517 °C at 0.807 s with a heating ramp towards 800 $K.s^{-1}$. Then, very rapid cooling is observed with a ramp towards 600 $K.s^{-1}$ and 1600 $K.s^{-1}$. ED with smaller thickness causes higher power of welding around 80 % with only two stages. At first, heating of the ED at the interface occurs due to the phenomenon of friction. The sonotrode does not move significantly because the materials involved in this step are still rigid and have not yet undergone a change of state. Then, the PEI continues to warm up. It begins to flow as a result of nucleation (viscoelastic heating mechanism controlled by surface friction heating) and the growth of hot spots at various places in the area of overlapped composite parts. The flowing of the energy director after reaching its glass transition causes a decrease in power and a displacement of the sonotrode. It can be assumed that the ED is not completely molten (lack of the third stage) and it seems that the first plies of composites do not reach the melting temperature of PEEK. So, there is no risk of degradation or delamination of PEEK composite parts during USW with these parameters. Displacement of the sonotrode until the end of welding achieves 50 %, which means that the thermocouples were in contact with the composites which explains the fast cooling rate. Due to high conductivity, carbon fibres contribute to very efficient heat diffusion.

After temperature monitoring, the mechanical strength was calculated. LSS are 43 ± 5 MPa and 12 ± 2 MPa for CF/PEEK with PEI of 250 µm and 50 µm, respectively.

Numerical conditions.

The transient thermal model was applied to the same welding configuration as the previous section, i.e. two layers of PEI, as seen in Fig. 2. The composite parts are 2 mm thick, and each PEI layer was 0.25 mm or 0.05 mm thick. A narrow transverse slice corresponding to the stacking of the three materials was designed in two dimensions (2D) by Abaqus. Therefore, a conduction model was performed, allowing to obtain the through-thickness thermal fields. To create this model, the following assumptions were used:

1) The interfaces between PEI and CF/PEEK were not perfect and thermal contact resistance was taken into account,
2) The studied materials were only PEI and CF/PEEK and the material properties varied with the concentration of each one, a mix of both materials was not considered,
3) Taking into account the thermal anisotropy of the composite, only the through-thickness properties of materials were considered,
4) The thermal behaviour of the sonotrode, steel plates or other tools was not considered,
5) Finally, only conduction was considered (neither convection nor radiation).

With these hypotheses, the conduction model gave an approximate thermal evolution at any point of the thickness and the evolution of temperature gradients over time.

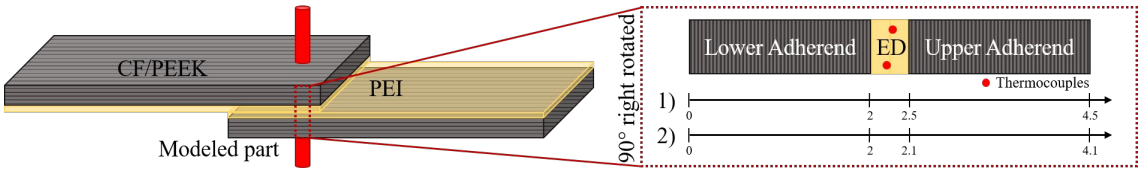

Fig. 2. Through-thickness model of the welding configuration, the distance through the thickness (mm).

The model is concentrated on the thermal properties of the CF/PEEK because such properties evolve much with temperature when PEEK changes from a glassy state to a flow state or a molten state. These properties are presented in Table 1. Those of PEI are presented in Table 2.

Table 1. Thermal properties of APC-2 [14].

Temperature [°C]	Thermal conductivity [W.(m.°C)$^{-1}$]	Specific heat [J.(kg.°C)$^{-1}$]	Density [kg.m^{-3}]
0	0.42	800	1601
50	0.52	930	1598
100	0.60	1040	1593
150	0.70	1260	1586
200	0.70	1300	1575
250	0.70	1400	1563
300	0.75	1550	1551
350	0.68	1650	1537
400	0.65	1700	1524

Table 2. Thermal properties of PEI [15].

Temperature [°C]	Thermal conductivity [W.(m.°C)$^{-1}$]	Specific heat [J.(kg.°C)$^{-1}$]	Density [kg.m^{-3}]
0 - 400	0.22	1248	1270

To consider the interface of CF/PEEK and PEI, the thermal conductance used for the model is presented in Table 3.

Table 3. Thermal conductance between CF/PEEK and PEI.

Temperature [°C]	Thermal conductance [W.(°C)$^{-1}$]
0 - 400	1000

Elements used for the model are four-node linear heat transfer quadrilateral elements, called DC2D4 in Abaqus software. The mesh is composed of two elements across the width of the studied area, as seen in Fig. 3. Two layers of 250 µm PEI have been meshed with 20 elements of 12.5 µm thick while for 50 µm PEI they have been meshed with 5 elements of 10 µm thick. The APC-2 layer is single bias meshed with an element size varying from 12.5 µm to 0.1 mm, and the mesh is increasingly finer near the PEI layer.

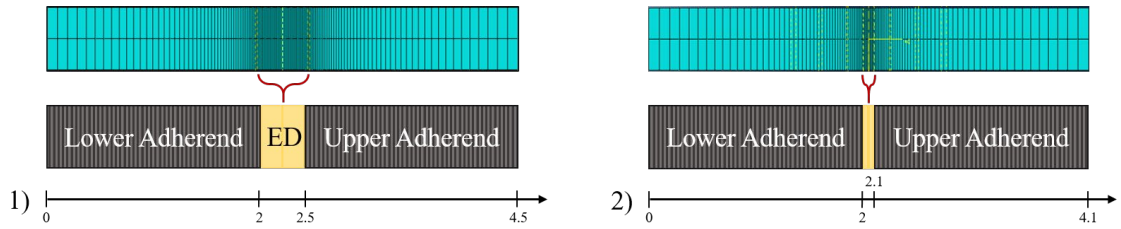

Fig. 3. Mesh elements of the out-of-plane model, the distance through the thickness (mm).

As recorded experimentally, the initial temperature of the specimen was considered to be at 23°C for 250 µm PEI and 20°C for 50 µm PEI. Therefore, this initial temperature was applied to the whole model. Adiabatic boundary conditions were used on the lateral sides, as well as on the upper and lower external surfaces of the composites.

The recorded temperature profile, shown in Fig. 1, was applied to the PEI layer presented in Fig. 3. At $t_0 = 0$ s, the temperature corresponds to the initial temperature. Then, the experimental temperature ramp was applied up to the value of 475°C at 0.714 s for 250 µm PEI and 517°C at 0.807 s for 50 µm PEI. This thermal profile was applied at the interface between the two integrated PEI layers.

Transient heat transfer analysis was used for this model and only the nodal temperature (NT) was computed as output data to understand the time and spatial evolution of the temperature field along the thickness of the assembly. This model contains two steps corresponding to the heating phase and the cooling phase. The heating phase lasts 0.714 s for 250 µm PEI and 0.807 s for 50 µm PEI as measured experimentally and the cooling phase lasts 15 s.

Simulation analysis.

Nodal temperatures were computed and their temporal evolution was compared, during the cooling phase, with the experimental thermogram (black line) recorded and plotted in Fig. 4. Three of the four curves correspond to different locations of the numerical model, showing respectively the interface between two integrated PEI layers (blue dashed line), the interface between APC-2 and the integrated PEI layer (green dashed line) and the interface between first and second composite ply (red dashed line).

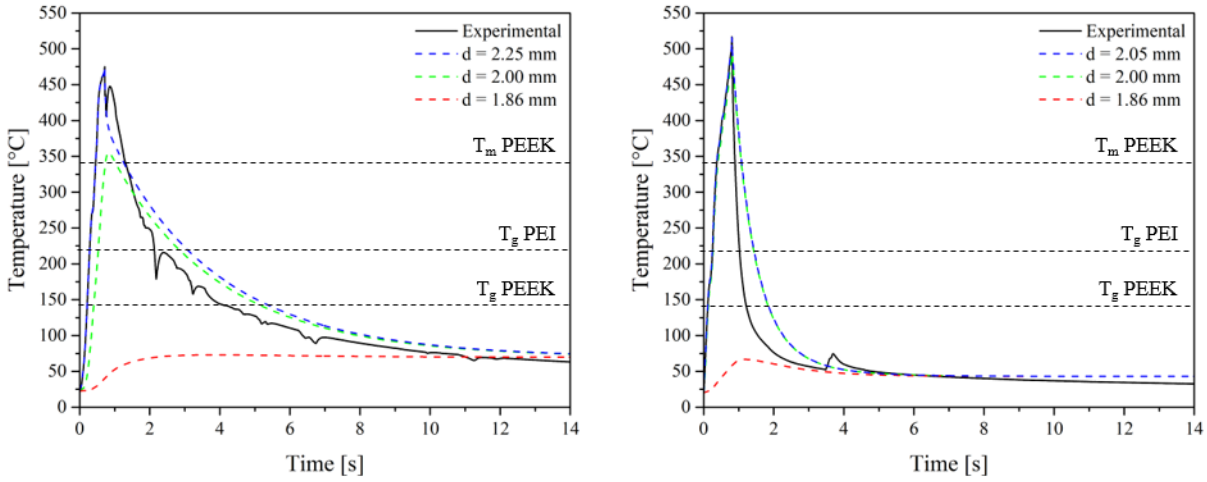

Fig. 4. Experimental and numerical thermograms during UW (a) for 250 µm PEI (b) for 50 µm PEI.

Comparing the experimental value to the numerical thermogram at the interface between the integrated PEI layers (d = 2.25 / 2.05 mm), where the TC are located, a slight difference can be highlighted. The cooling ramp is slower in the model, exhibiting either a too-high numerical contact conductance or a gradient of thermal properties in the interphase zone, which is not considered in the model and the numerical temperature starts to get closer to fit the experimental one. One hypothesis is that input material data from the literature do not fit the studied material. Moreover, the model does not take into account some heat exchanges like convection or exchanges with the jaws (adiabatic upper and lower surfaces boundary conditions). Regarding the material,

the composite is made of unidirectional PEEK thermoplastic with carbon fibre. The thermal conductivity of CF/PEEK is higher than the one of the PEEK and so, when the heat moves to APC-2, it is mostly evacuated by the fibres. Moreover, in the case of CF/PEEK with 50 µm PEI, the TC significantly affects the diffusion of heat. The small thickness of ED and displacement during USW causes contact between TC and carbon fibre. The through-thickness modelisation also does not take into account transverse material properties and only propagates the heat through the thickness. Thus, every simulated temperature could be considered slightly overestimated.

Regarding the curve at the interface between APC-2 and the integrated PEI layer (d = 2.00 mm), the maximum reached temperature is 355°C for 250 µm PEI and 494°C for 50 µm PEI. The APC-2 composite reaches its melting (T_m) during welding in this configuration. It means that PEEK melting occurs within the first ply.

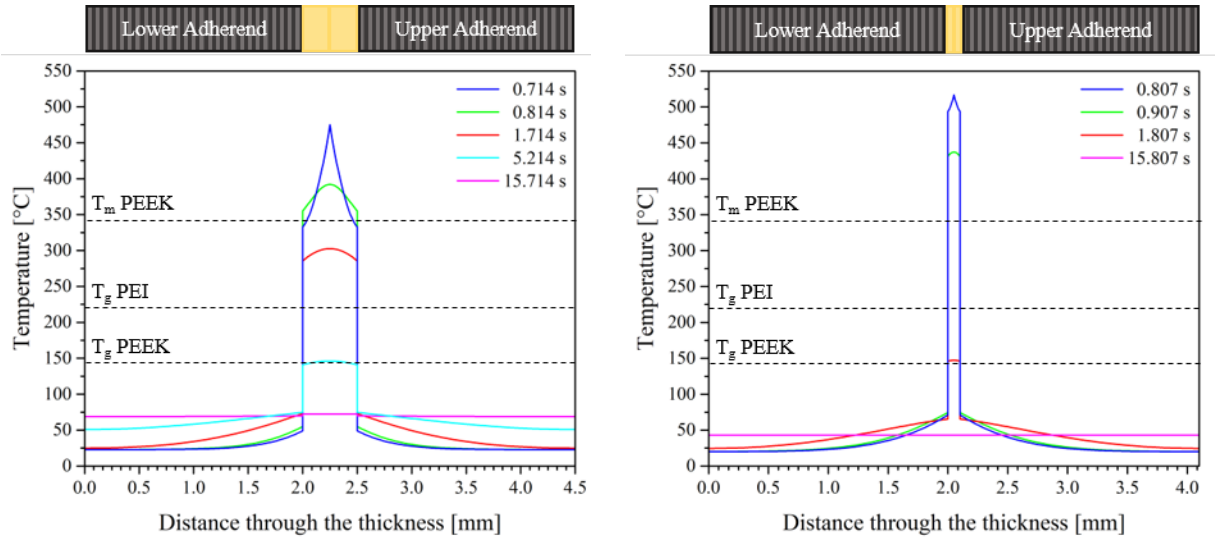

Fig. 5. Temperature profiles through the assembly right after the end of the vibration step with different welding times (a) for 250 µm PEI (b) for 50 µm PEI.

The spatial evolution of the temperature, right after the ultrasonic welding process and during the cooling step, is plotted along the thickness in Fig. 5. The true distance along the path with a reference value between the integrated PEI layers is plotted against the temperature. Different welding times are shown from t_c = 0.714 / 0.807 s (end of vibration step) to t = t_c + 15 s (end of the cooling step). It can be noticed that the profile is symmetrical from the middle of the integrated ED and, as expected, it is due to the symmetry of the stacking sequence of the model (geometry, material and section), loading and boundary conditions. Also, the curves present breaking points at a distance of 2.00 mm (PEI/PEEK interface), 2.25 /2.05 mm (PEI/PEI interface) and 2.50 / 2.10 mm (PEI/PEEK interface). As the thermal contact resistance was taken into account for the non-perfect interface between PEI and PEEK, a drastic drop in temperature is observed after 4.5 s for 250 µm PEI and 1.0 s and 50 µm PEI.

At the temperature t_c as the thermal loading is applied between two integrated PEI layers, the temperature in the middle of ED shows its peak at a value of 475 / 517°C. It is above the T_g of PEI, measured at 220°C, which implies that all the PEI is flowing. Moving to the interface between PEI and the composite layer, it appears that the temperature decreases to reach 355 / 494°C. This thermal evolution highlights the fact that ED, right after the ultrasonic loading, is partially flowing. The flowing material is located at the interface between PEI layers and allows interdiffusion

between those two PEI layers, it is the condition to get a strong weld. Concerning composite parts, the maximum temperature reached during heating is above T_m of PEEK, measured at 340°C, which contributes to interdiffusion of the first plies. The time t_c is the starting point for the transfer of heat from the ED to the composite.

At $t = t_c + 0.1$ s, the heat flux has already started to be transferred from the two integrated PEI layers to CF/PEEK composites. The breaking point is no longer visible because the contact between integrated PEI layers is considered to be perfect. The ED temperature decreases and its maximum temperature is 392 / 437°C in the middle of the ED. The heat moves from the middle to the exterior, i.e. from the highest one to the lowest temperature. Regarding the composite layer, its maximum temperature is 355 / 435°C at the interface and still above its T_m giving mobility to the amorphous phase of the PEEK. At $t = t_c + 1$ s, in the case of thicker ED, the temperature is still above T_g of PEI while for the smaller thickness of ED, the temperature is already below. The same temperature for thicker ED is obtained after 5.214 s.

For the rest of the cooling process, the temperature at the centre of the ED decreases while it increases at the end of the assembly reaching the quasi-thermal equilibrium at the end of the cooling step, $t = t_c + 15$ s.

To conclude, in the studied configuration with a welding time of 714 / 807 ms, the temperature is above the T_g of PEI in almost the entire thickness of ED. This indicates that interdiffusion is possible between the PEI layers. Concerning APC-2, the maximum temperature reached is 355 / 494°C. It can be assumed that the PEEK matrix is thermally affected during welding allowing interdiffusion in the first ply, the second ply remains not affected. However, in the case of 50 µm PEI, the time to create a strong weld between ED and composite was too short causing low mechanical resistance. LSS results agree with the thermal scenario described above: 43 ± 5 MPa and 12 ± 2 MPa for CF/PEEK with PEI of 250 µm and 50 µm, respectively.

Summary

This study focused on the temperature profiles during welding for different thicknesses of ED. CF/PEEK parts with 250 µm and 50 µm thick PEI layers were assembled by USW. A non-intrusive experimental procedure was carried out to measure the temperature at the welding interface. It was observed that the thermocouples must be inserted entirely inside the layer, otherwise, they can alter the temperature measurement.

The curves of power and displacement of the sonotrode over time have shown that different stages and specific points can be identified (heating, flowing of PEI, final flowing and cooling) in comparison with the temperature profiles. As the interface is a closed contact during welding, measuring the temperature at the interface is difficult. However, welding power and displacement have been shown to have a strong connection with thermal history. Too high power during welding distorts the composite.

To evaluate the thermal diffusion from the interfaces between CF/PEEK and PEI layers, a FEM was developed. Considering the input parameters for the model, it is important to mention that thermal contact resistance has a significant impact on thermal diffusion. For both thicknesses, the PEI reaches its T_g, allowing macromolecular interdiffusion between the two parts, the condition to get a strong weld. Besides, the model predicts that only the first ply of the composite parts is thermally affected, in which the temperature within the PEEK matrix exceeds its T_m. Such local heating at the interface prevents composite degradation and deconsolidation. However, in the case of the smallest ED thickness, a too-high power in a short time leads to poor welding of APC-2 parts. It has been confirmed with the mechanical characterization of welds, 12 MPa was obtained for the 50 µm PEI layer, compared to 43 MPa obtained for 250 µm. A higher PEI thickness at the interface slows down the cooling step of highly conductive unidirectional CF/PEEK composites, resulting in a deeper interdiffusion of PEI and so, a stronger weld. These results contribute to a better understanding of the thermal transfer phenomena during USW. By varying the ED thickness,

we demonstrated the possibility to assemble composite parts by USW without affecting the whole composite parts, thus preventing composite degradation and deconsolidation.

Further work will focus on PEEK and other polyaryletherketones (PAEK) as energy directors, to assess the effect of crystallinity at the interface on mechanical strength.

Acknowledgements
This work received financial support from ANR through France Relance plan of the French government in collaboration with the company Lauak Group (France).

References

[1] I. Fernandez Villegas, Ultrasonic welding of thermoplastic composites, Front. Mater. 6 (2019) 291. https://doi.org/10.3389/fmats.2019.00291
[2] S.K. Bhudolia, G. Gohel, K.F. Leong, A. Islam, Advances in ultrasonic welding of thermoplastic composites: a review, Materials 13 (2020) 1284. https://doi.org/10.3390/ma13061284
[3] A. Korycki, C. Garnier, M. Bonmatin, E. Laurent, F. Chabert, Assembling of carbon fibre/PEEK composites: comparison of ultrasonic, induction, and transmission laser welding, Materials 15 (2022) 6365. https://doi.org/10.3390/ma15186365
[4] J. Qiu, G. Zhang, E. Sakai, W. Liu, L. Zang, Thermal welding by the third phase between polymers: a review for ultrasonic weld technology developments, Polym. 12 (2020) 759. https://doi.org/10.3390/polym12040759
[5] W. Tao, X. Su, H. Wang, Z. Zhang, H. Li, J. Chen, Influence mechanism of welding time and energy director to the thermoplastic composite joints by ultrasonic welding, J. Manuf. Process. 37 (2019) 196-202. https://doi.org/10.1016/j.jmapro.2018.11.002
[6] F. Köhler, I. Fernandez Villegas, C. Dransfeld, A. Herrmann, Static ultrasonic welding of carbon fibre unidirectional thermoplastic materials and the influence of heat generation and heat transfer, J. Compos. Mater. 55 (2021) 2087-2102. https://doi.org/10.1177/0021998320976818
[7] G. Palardy, I. Villegas Fernandez, On the effect of flat energy directors thickness on heat generation during ultrasonic welding of thermoplastic composites, Compos. Interface. 24 (2017) 203-214. https://doi.org/10.1080/09276440.2016.1199149
[8] A. Levy, S. Le Corre, I. Fernandez Villegas, Modeling of the heating phenomena in ultrasonic welding of thermoplastic composites with flat energy directors, J. Mater. Process. Technol. 214 (2014) 1361-1371. https://doi.org/10.1016/j.jmatprotec.2014.02.009
[9] A. Benatar, T.G. Gutowski, Ultrasonic welding of PEEK graphite APC-2 composites, Polym. Eng. Sci. 29 (1989) 1705-1721. https://doi.org/10.1002/pen.760292313
[10] M. Bonmatin, F. Chabert, G. Bernhart, T. Cutard, T. Djilali, Ultrasonic welding of CF/PEEK composites: influence of welding parameters on interfacial temperature profiles and mechanical properties, Compos. Part A: Appl. Sci. Manuf. 162 (2022) 107074. https://doi.org/10.1016/j.compositesa.2022.107074
[11] D. Defauchy, G. Regnier, P. Peyre, I. Amran, A. Ammar, Polymer selective laser melting simulation using the C-NEM method, in: Proceedings of the Research & Innovation for Transport Systems of the Future, Paris, France, 2012, pp. 1-10.
[12] F. El Halabi, J.F. Rodriguez, L. Rebolledo, E. Hurtós, M. Doblaré, Mechanical characterization and numerical simulation of polyether-ether-ketone (PEEK) cranial implants, J. Mech. Behav. Biomed. Mater. 4 (2011) 1819-1832. https://doi.org/10.1016/j.jmbbm.2011.05.039
[13] I. Fernandez Villegas, In situ monitoring of ultrasonic welding of thermoplastic composites through power and displacement data, J. Thermoplast. Compos. 28 (2015) 66-85. https://doi.org/10.1177/0892705712475015

[14] C. Ageorges, L. Ye, Y.W. Mai, M. Hou, Characteristics of resistance welding of lap shear coupons. Part I: Heat transfer, Compos. Part A: Appl. Sci. Manuf. 29 (1998) 899-909. https://doi.org/10.1016/S1359-835X(98)00022-0
[15] R. Don, L. Jakobsen, J. Gillespie, Fusion bonding of thermoplastic composites by resistance heating, SAMPE Journal, 26 (1990) 59-66.

Materials Research Proceedings 28 (2023) 1829-1840 https://doi.org/10.21741/9781644902479-198

Laser transmission welding of PEKK: Influence of material properties and process parameters on the weld strength

MATUS AGUIRRE Marcela[1,2,3,a *], GARNIER Christian[1,b], GILBLAS Rémi[2,c], COSSON Benoît[3,d], AKUÉ André[3,e], SCHMIDT Fabrice[2,f] and CHABERT France[1,g]

[1]LGP-ENIT-INPT, 47 Avenue d'Azereix, Tarbes cedex BP1629-65016, France

[2]ICA-IMT Mines Albi, Campus Jarlard, 81013 Albi, CT Cedex 09, France

[3]IMT Nord Europe, Institut Mines Télécom, Univ. Lille, Centre Materials and Processes, F-59653 Villeneuve d'Ascq, France

[a]mmatusag@enit.fr, [b]cgarnier@enit.fr, [c]rgilblas@mines-albi.fr, [d]benoit.cosson@imt-nord-europe.fr, [e]andre.akue.asseko@imt-nord-europe.fr, [f]fabrice.schmidt@mines-albi.fr, [g]fchabert@enit.fr

Keywords: Laser Welding, Thermoplastics, Optical Properties, Single Lap Shear Test

Abstract. Laser transmission welding (LTW) is a suitable process for assembling thermoplastic materials. This joining process is used to assemble most thermoplastics, but high-performance thermoplastics, such as polyetherketoneketone (PEKK), have received less attention until now. The present work deals with joining PEKK parts by LTW in amorphous over semi-crystalline state configuration. The optical properties of amorphous and semi-crystalline states were measured. The effect of the upper part thickness (2 or 4 mm) and those of the laser power reaching the interface was assessed through the determination of the heat affected zone (HAZ) dimensions and the mechanical resistance of the bonds. Single lap shear (SLS) tests were conducted to investigate the influence of the process parameters on the interfacial strength and to validate the weld quality. The highest LSS is obtained around 60 MPa. When increasing the laser power, the dimensions of the HAZ increase, and the mechanical strength decreases.

Introduction

Laser transmission welding (LTW) is an assembly process used for joining thermoplastic materials with a near-infrared (NIR) laser. Parts to be joined are overlapped and clamped together for welding. The laser beam faces the upper part and irradiates the assembly interface. Here, the laser energy is absorbed and converted into heat. This allows the polymers to melt at the interface and, by molecular interdiffusion, a weld seam is created during cooling.

For laser irradiation to reach the interface, the upper substrate needs to be transparent to the laser wavelength. To achieve the absorption at the interface, two techniques can be applied: use an absorbing medium at the joint interface; or assuring that the bottom substrate is absorbent at the wavelength of interest. For the first method, special NIR-absorbent dyes or pigments are applied at the joint interface, like ClearWeld® technology [1].

For the second one, a laser-absorbent part serves as lower substrate to achieve the energy absorption at the interface. However, most thermoplastics are transparent to the NIR laser radiation in their natural state. Although, the bottom substrate can be rendered absorbent by different methods. The first one is filling the polymer with an absorbing additive, like colorants [2,3] or reinforcements [4,5]. And the other and much less studied option is to increase the degree of crystallinity of the lower substrate to modify its optical properties. Indeed, the crystalline structure of semi-crystalline polymers limits the light transmission [6], and increases the light travel path,

Content from this work may be used under the terms of the Creative Commons Attribution 3.0 license. Any further distribution of this work must maintain attribution to the author(s) and the title of the work, journal citation and DOI. Published under license by Materials Research Forum LLC.

leading to higher absorption [5,7], whereas an amorphous polymer is transparent in NIR. Despite its potential, this approach was rarely studied to weld thermoplastics.

High-performance thermoplastics such as Poly-Ether Ether Ketone (PEEK) and Poly-Ether Ketone Ketone (PEKK), can be processed into amorphous and crystalline states, depending on the processing conditions. Few works have studied LTW of PEEK and PEKK without additives. Amanat et al. studied the joining of PEEK films with ClearWeld® at the interface [8]. In their work, semi-crystalline PEKK assemblies showed a higher weld strength than amorphous PEEK joints, for all the laser speeds and power considered. Villar et al. welded PEKK thermo-compressed samples using an 808 nm NIR laser device [9]. They control the degree of crystallinity of PEKK to obtain quasi-amorphous and semi-crystalline samples, to be used as upper-transparent and lower-absorbent substrates, respectively. However, the results of mechanical strength of these welds are scarce in the literature, and none focus on PEKK welds.

In addition to the optical properties of the substrates, the process parameters can influence the bond quality in LTW: laser power, welding speed, laser beam size and, clamping pressure.

In this work, we study the joining process of amorphous and semi-crystalline PEKK by LTW. The optical properties and process parameters are correlated with the size and shape of the weld, as well as its mechanical strength. The originality is to keep constant the laser power reaching the interface while varying the thickness of the upper-substrate.

Materials and Methods

Kepstan® PEKK grade 7002 was supplied by Arkema France in pellets. PEKK 7002 is a semi-crystalline thermoplastic with tunable crystallinity due to its crystallization kinetics.

After drying the pellets at 120°C for 30 hours, specimens were manufactured by an injection molding press Proxima 50 from Billion. Two crystalline morphologies of unfiled PEKK were obtained: amorphous form (PEKK-A) and semi-crystalline form (PEKK-SC). Samples molded were plates of 95 × 95 mm² with 2 and 4 mm thick for amorphous form (PEKK-A2 and PEKK-A4 respectively), and 2 mm thick for PEKK-SC.

The molded plates were cut into 25 ± 3 mm width rectangular samples, then dried at 120°C for more than 24h and kept into a desiccator before welding. Acetone was used to clean the samples surfaces.

Differential Scanning Calorimetry (DSC) scans were carried out in a DSC 1 Stare System Mettler Toledo. Ramps of 10 $K \cdot min^{-1}$ were used for heating from 25°C to 380°C, and cooling from 380ºC to 25ºC. Glass transition temperature (Tg), melting temperature (Tm), cold crystallization temperature (Tcc) and degree of crystallinity (Xc) were obtained at heating. Cooling was used to obtain the crystallization temperature from melt (Tcm) and the maximum crystallinity (Xc-max).

The optical properties were measured using a FTIR spectrophotometer Bruker Vertex 70. Transmission (T) and reflection (R) factors were measured using an integration sphere with an Infragold Lambertian coating. Characterization was made at room temperature for the wavelength range of 0.9 to 2 µm. Absorption factors (A) are obtained using Eq. 1.

$$T + R + A = 1 \quad (1)$$

Transmissivity of clamping glass was experimentally measured using a power-meter Gentec Pronto-500, by comparing the output power measured before and after going through the glass.

Lap-joint configuration (Fig. 1) was used for welding, with an overlap of 12.5 mm, as indicated on ISO 4587:2003. The amorphous substrate was positioned over the semi-crystalline one.

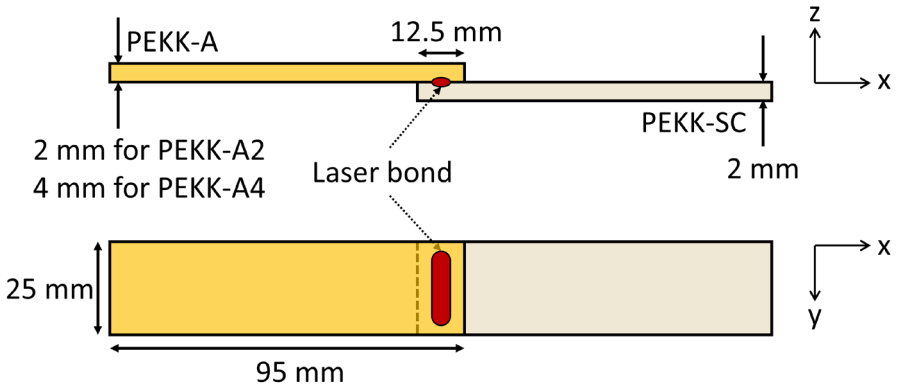

Fig. 1. Schematic diagram of lap-joint configuration used for welding PEKK-A/PEKK-SC (not to scale).

The assembly configuration is kept fixed on the welding machine platform. A support is placed under the amorphous sample to keep the interface parallel to the platform. A 15 mm thick semi-transparent glass plate is positioned over the assembly to apply the clamping pressure necessary to ensure intimate contact at the joint interface. The weld is created at the center of the overlap area using a moving laser. Thus, the interface is heated as the laser beam moves over the samples, following a predefined welding path. This LTW technique is known as *contour welding*.

Samples are welded using an ES weld 200 welding machine from ES Laser with a Diode laser of 975 nm. Output laser power can be set from 0 to 220 W with a resolution of ± 3 W. A circular shape laser beam is used with a beam diameter of 5 mm, obtained at maximum laser defocus. Clamping pressure is constantly applied at 3.8 MPa thanks to the glass plate. The welding path is a straight line: the laser beam moves from its initial position (L0) until the indicated weld length (Lw) of 20 mm, as shown in Fig. 2.

When a constant speed is used to irradiate the interface from L0 to Lw, an ovoidal weld bond is created instead of a thick line, as shown in Fig. 3A. To obtain a more homogeneous weld bond along the line laser path, like in Fig. 3B, a procedure combining static and dynamic irradiation is applied. The procedure starts by statically irradiating the interface for 2 seconds at L0. Then, the laser moves to irradiate at the given speed, from L0 to Lw. Finally, the laser statically irradiates the interface for 1 second at Lw. That allows to melt the interface all along the welding path in a more homogeneous shape of the weld bond (Fig. 3B).

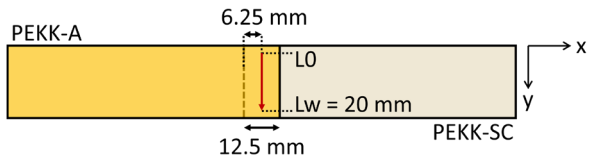

Fig. 2. Schematic diagram indicating the welding path position, direction and dimensions on the PEKK-A/PEKK-SC assembly.

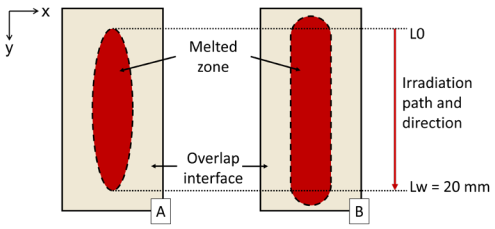

Fig. 3. Schematic diagram of the melted zone's shape created at the interface when irradiating with (A) dynamic condition, (B) static and dynamic condition.

The optimum welding speed to achieve the melting at the interface, regardless of the laser power, is 60 mm/min, as determined by previous tests. Thus, welding speed is kept constant for all welds. After irradiation, clamping pressure is maintained for 120 seconds while cooling.

Two process parameters are varied for this study: the transparent substrate thickness (2 and 4 mm) to obtain PEKK-A2/PEKK-SC and PEKK-A4/PEKK-SC assemblies, and the laser intensity. For the laser power, the preliminary welding tests indicated that the power-range needed at the interface to melt it without burning it is between 75 and 95 W. Thus, four power intensities were selected: 75, 85, 88, and 95 W. That provided eight configurations for the study (Table 1).

Table 1. Assembly configurations.

	75 W	**85 W**	**88 W**	**95 W**
PEKK-A2/PEKK-SC	A2/SC-P1	A2/SC-P2	A2/SC-P3	A2/SC-P4
PEKK-A4/PEKK-SC	A4/SC-P1	A4/SC-P2	A4/SC-P3	A4/SC-P4

Single lap shear (SLS) tests were carried out to characterize the lap-joint welded samples strength. An INSTRON 550R tensile machine was used with a load cell of 50kN and a cross head load rate of 2800 $N \cdot mm^{-1}$. Each sample was tested until failure. The load at failure F_f [N] was recorded and the type of failure mode was identified. Also, the normalized lap-shear strength LSS [MPa] was obtained by dividing the force at failure by the contact area Ac [mm^2]. This area was measured by microscopy for the samples that failed at the interface.

Visual inspection of the welds was carried out with a numerical optical microscopy VHX-6000S from Keyence. Post-failure bond interfaces were characterized to obtain the shape and dimensions of each weld. The weld cross-sections of post-welding bonds were visualized to characterize the HAZ along the weld path.

Results

Thermal transitions.

Fig. 4A shows a typical DSC thermogram of PEKK 7002 amorphous specimens. Tg is 158 ± 2°C and Tm is measured at 317 ± 2°C. Crystallization temperatures are around 202 ± 1°C for Tcc, and 295 ± 1°C for Tcm.

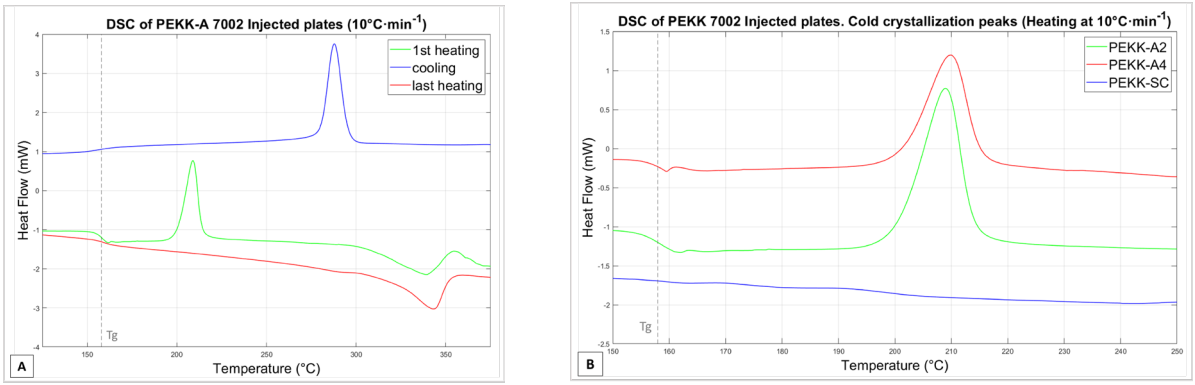

Fig. 4. (A) DSC scans of PEKK 7002 amorphous molded plates. (B) cold crystallization peaks of molded samples obtained on the first heating DSC scan.

In Fig. 4B, an exothermic peak is observed around 200°C for amorphous samples (green and red curves), after glass transition. This indicates cold crystallization, occurring when the sample is not fully crystallized. Indeed, right after Tg, the macromolecules have gained enough mobility to self-organize into crystalline structures. For PEKK-SC, no peak is observed because the sample is

already fully crystallized. To assess the degree of crystallinity, the enthalpy of this peak (ΔHcc) is subtracted from the melting enthalpy of the first heating (ΔHm), then the result is divided by the enthalpy of 100 % crystallized polymer ($\Delta H_{100\%}$), considered as same as PEEK (130 $J \cdot g^{-1}$) [10]. A degree of crystallinity of 4 ± 2% was found for PEKK-A and 20 ± 2% for PEKK-SC.

Optical properties.

The laser irradiation that strokes the samples' surface can be transmitted, reflected and/or absorbed. For that, transmission, reflection and absorption factors of the samples need to be determined. The transmission factor (T) characterizes the quantity of incident laser irradiation that will be able to go through its thickness. The reflection factor (R) indicates the portion of the irradiation that will be reflected by the material surface. Finally, absorption factor (A) will provide the fraction of the incident irradiation that will be absorbed by the material, either at the surface or in the volume. These three factors are related between them by Eq. 1 and they can be expressed in percentage for the desired wavelength.

In the visible light spectral range, PEKK-A has a natural yellow translucent coloration, whereas PEKK-SC samples are opaque with a natural beige color. Their optical properties are necessary to verify their compatibility with LTW at 975 nm. The results are gathered in Table 2.

Table 2. Transmission, reflection and absorption factors of PEKK molded samples.

Substrate	T [%]	R [%]	A [%]
PEKK-A2	75 ± 1.5	13 ± 0.1	12 ± 0.1
PEKK-A4	62 ± 0.7	13 ± 0.1	25 ± 0.1
PEKK-SC	20 ± 0.02	48 ± 1.7	32 ± 1.7

The transmission spectrum of PEKK samples is seen in Fig. 5. At 975 nm, PEKK-A samples have a transmission factor higher than PEKK-SC ones: 75 % for PEKK-A2 and 62 % for PEKK-A4, against 20 % for PEKK-SC. Also, increasing the thickness of PEKK-A decreases the transmission factor by more than 17 %. Based on previous works of LTW on PEKK [9] a transmission factor of 60% is suitable to achieve melting at the interface. Consequently, 2 and 4 mm thick PEKK-A samples seem adequate to be used as transparent upper substrate for LTW.

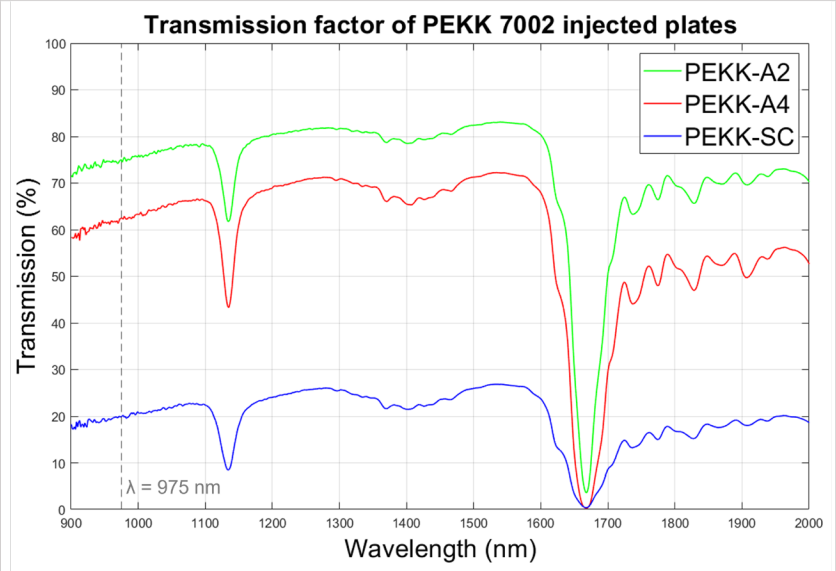

Fig. 5. Transmission spectrums of PEKK 7002 molded samples.

Table 2 pointed out that the sample with the highest absorption factor is the semi-crystalline one. Even if its absorption is low (32 %), it is higher than its transmission factor (20 %). This validates the suitability of PEKK-SC as absorbent substrate for LTW.

To irradiate the assembly interface, the output laser irradiation (Po) will first go through the clamping glass and then through the transparent substrate. Therefore, the output laser power value will decrease after going through each layer, according to the transmission factor of each layer. Hence, the power reaching the assembly interface will be the percentage of output power that the glass and the transparent substrate will allow to transmit. At our laser wavelength, the clamping glass has a transmissivity of 0.82, as evaluated with the power-meter. Then, the transmission factor of the transparent-upper substrate depends on its thickness: 0.75 for PEKK-A2, and 0.62 for PEKK-A4. Thus, the power at the interface (Pint) can be calculated using Eq.2 and Eq.3 for PEKK-A2/PEKK-SC and PEKK-A4/PEKK-SC, respectively.

$$P_{int(A2)} = P_0 \times 0.82 \times 0.75 \quad (2)$$

$$P_{int(A4)} = P_0 \times 0.82 \times 0.62 \quad (3)$$

The power at the interface is set between 75 and 95 W. Table 3 indicates the output laser power used for each type of assembly to obtain the desired power at the interface for each targeted power.

Table 3. Laser power used for LTW.

	P_0 [W]		P_{int} [W]
	for A2/SC	**for A4/SC**	**For both**
P1	123	148	75
P2	139	168	85
P3	144	175	88
P4	154	188	95

Weld characterization.

The cross-section of the weld bond along the weld path is observed to characterize its heat affected zone (HAZ). Fig. 6 shows a micrograph of the assembly cross-section before and after welding for A4/SC-P2. Before welding, we can easily identify the interface line between the overlapped substrates (inside the red dashed rectangle in Fig. 6A). After welding, the HAZ appears as an oval shape replacing the interface line (inside the red dashed contour in Fig. 6B). The color change from yellow to white within the HAZ demonstrates a modification of the crystallinity. All the weld bonds characterized showed this same shape and aspect on their HAZ.

The PEKK-SC shows a yellow coloration within the HAZ: the substrate became amorphous on cooling. This means that PEKK-SC absorbed enough laser power to melt at the interface and that the cooling ramp was faster than the crystallization kinetics. Also, in PEKK-SC, the HAZ is so deep that it almost reaches the bottom of the substrate. It indicates that the laser irradiation penetrated the sample, as stands by Jones et al. [1], and was absorbed on the volume and not only at the interface. The average depth for both types of assemblies is 1.4 ± 0.2 mm. With these parameters, it would not be possible to weld lower parts thinner than 1.4 mm.

In PEKK-A substrate, the HAZ colors go from yellow to white. The melting zone is mainly located at the interface. The white color indicates that PEKK-A sample undergoes cold crystallization. Tcc was measured at 202°C in Fig.4. Following laser absorption at the interface, this temperature was achieved by heat conduction from the lower part. Moreover, the shape and colors of HAZ indicates that the samples really merged at the interface to create a strong bond.

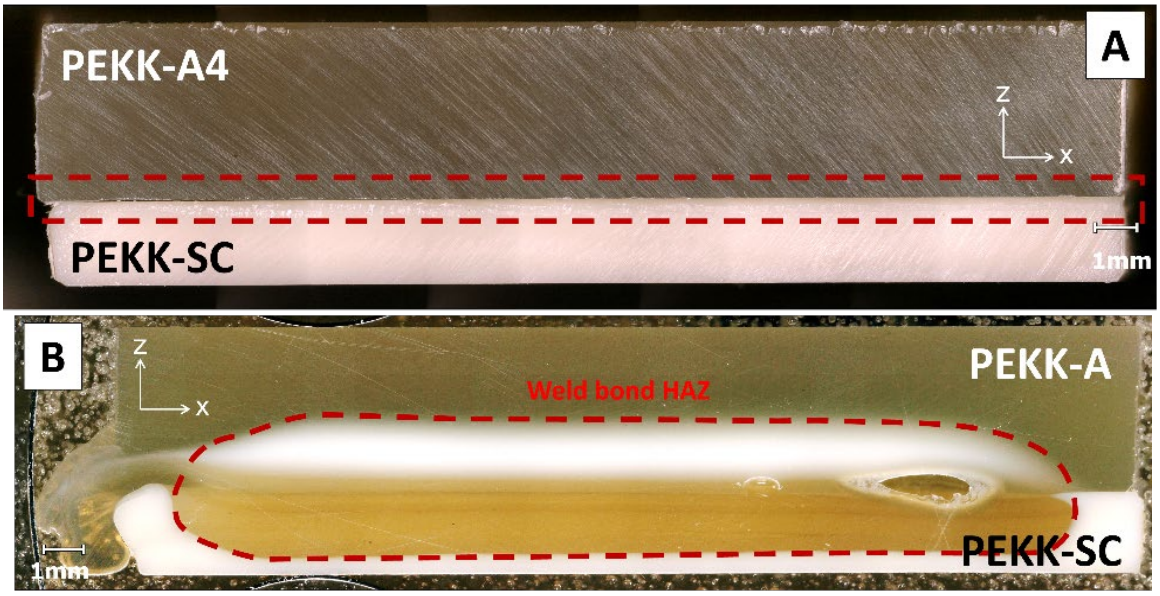

Fig. 6. A4/SC-P2 assembly cross-section along the welding path (A) before and (B) after welding.

HAZ dimensions were measured for each assembly configuration. Its height (along the X axis) and length (along the Z axis) were plotted against the power used for welding in Fig. 7. A notorious increment on the HAZ dimensions with the power is noticed. This increase is almost linear for three of the four intensities (75, 85 and 95 W). The HAZ dimensions obtained at 88 W do not follow the regular trend. A possible explanation is related to the uncertainty of the power. Indeed, the values of power are defined with ± 3%. Thus, the data obtained for 85 and 88 W are expected to be close to each other.

For the HAZ height, almost 1 mm of difference is found from lowest to highest power, for both types of assemblies (A2/SC and A4/SC). Concerning the length of the HAZ, it is quite the same on A4/SC, with only 0.3 mm of difference from the lowest to the highest power. For A2/SC, this length improves considerably with laser intensity, with a gap of 1.6 mm. Moreover, this HAZ length is higher than the welding path used for welding (20 mm) in all the configurations. That indicates that the irradiation procedure used, combining static and dynamic irradiation, had a positive impact on the melting at the interface. This increment of the HAZ dimensions with laser power can be explained by the fact that increasing the laser power maximizes the heat input which leads to a greater volume of melted material at the interface, resulting in a higher welded zone.

The HAZ dimensions also increase with the increase of the transparent substrate thickness for each laser power. This can be caused by the scattering of the laser irradiation through the samples. Thus, PEKK-A4 seems to scatter more the light than PEKK-A2, which increases the distribution of the energy over a larger area.

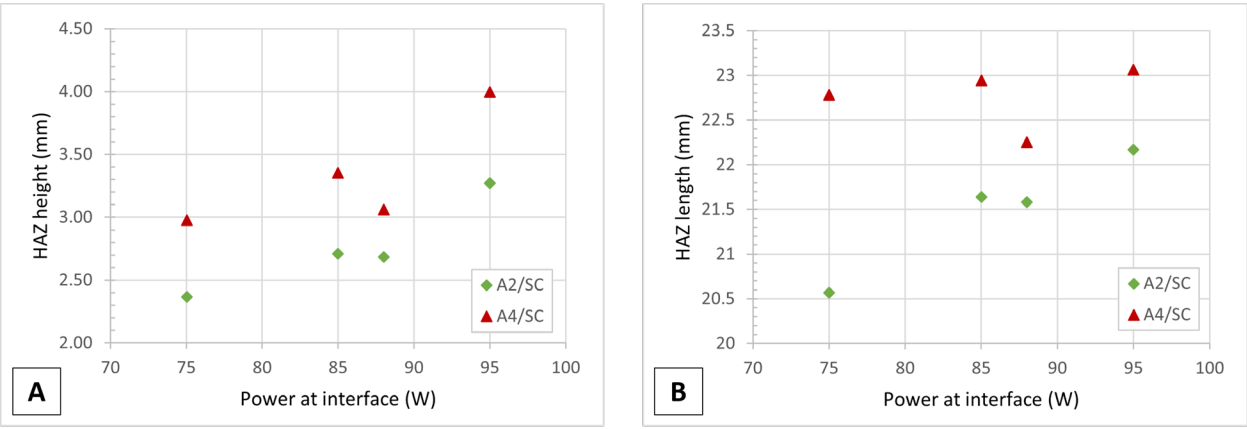

Fig. 7. HAZ dimensions (A) height and (B) length, plotted against the laser power used at the interface.

Different mechanical tests are carried out to quantify the resistance of welded samples by LTW: DCB [2,11], wedge [12], and SLS tests [8,11,13-16]. SLS is the easiest and most used test.
When tested in SLS, lap-joint welded samples failed in different modes. To identify their failure type, four failure modes are defined (Table 4) inspired by the classification proposed by Amanat et al. [8] for LTW on PEEK. Two types of failure were obtained within our assemblies:

- *Cohesive failure*: this indicates that the bond broke and was separated as if it was ripped off. The samples actually fused at the interface, creating a strong weld.
- *Substrate near joint*: one or both substrates broke near the weld bond, but the bond was fully or mostly intact, proving that the bond strength is superior to the substrate strength.

Table 4. Failure modes for LTW samples tested by SLS.

Failure mode	Appearance	Inference	Description
Interfacial	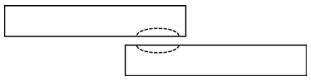	Bond strength << substrate strength	Assembly fails at the interface because no real material cohesion was created at the irradiated interface. Most undesired result.
Cohesive	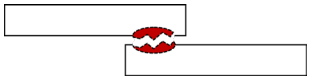	Bond strength ~ substrate strength	Assembly fails at the interface within the weld bond created.
Substrate near joint	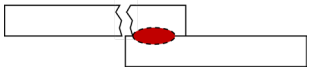	Bond strength > substrate strength	Failure within the substrate but near the interfacial region and weld bond intact (or mostly).
Bulk substrate	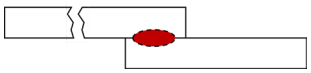	Bond strength >> substrate strength	Bulk substrate results in tensile yield and brakes far from the weld bond. Most desired result.

Even though two failure modes were obtained, only the samples that failed in cohesive mode are analyzed in this paper. The overlap interface is visible so the real contact area can be measured to obtain the LSS value for each cohesively failed assembly. 1 or 3 samples over 5 failed cohesively for each configuration. A hypothesis steaming from this high dispersion is related to the irradiated surface that can vary locally due to heterogeneities of the samples: different macromolecular organization, and micro-voids or particles inside them. These heterogeneities can lead to the scattering of the laser path in the upper substrate, and to an inhomogeneous absorption of the laser irradiation in the bottom substrate. The LSS obtained are plotted with the power for both type of assembly in Fig. 8.

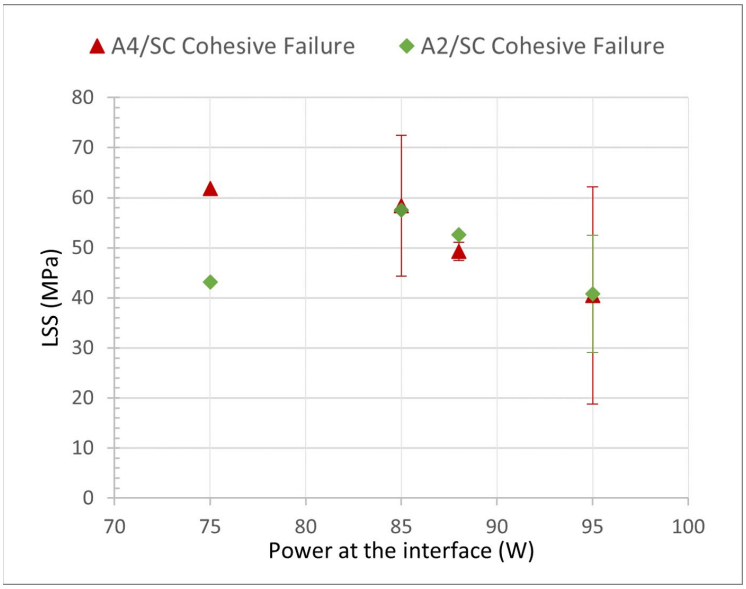

Fig. 8. LSS (MPa) of LTW samples failed cohesively. Bars indicate the measuring range.

The strength obtained at one laser power is the same for both types of assemblies except for the first laser power of 75 W. However, the strength decreases with laser power from 85 W. This drop in weld strength can be caused by different crystalline morphology at the interface. Indeed, the crystallinity of PAEK is strongly impacted by its thermal history. A higher power reaching the interface would result in a higher temperature and slower cooling ramp. As proved on PEEK [17], the refinement of the primary lattice takes place when the temperature is higher than or equal to the previous crystallization temperature. An evolution of the lattice sizes could result in lower ultimate tensile strength. Further studies are needed to clarify this point. Overall, the strength of our assemblies is higher than those achieved by Potente et al. when welding PEEK T-joint specimens with similar thicknesses for the transparent substrate [18]. They achieved a maximum strength of 40 MPa, while our minimum is of the same value for both types of assemblies.

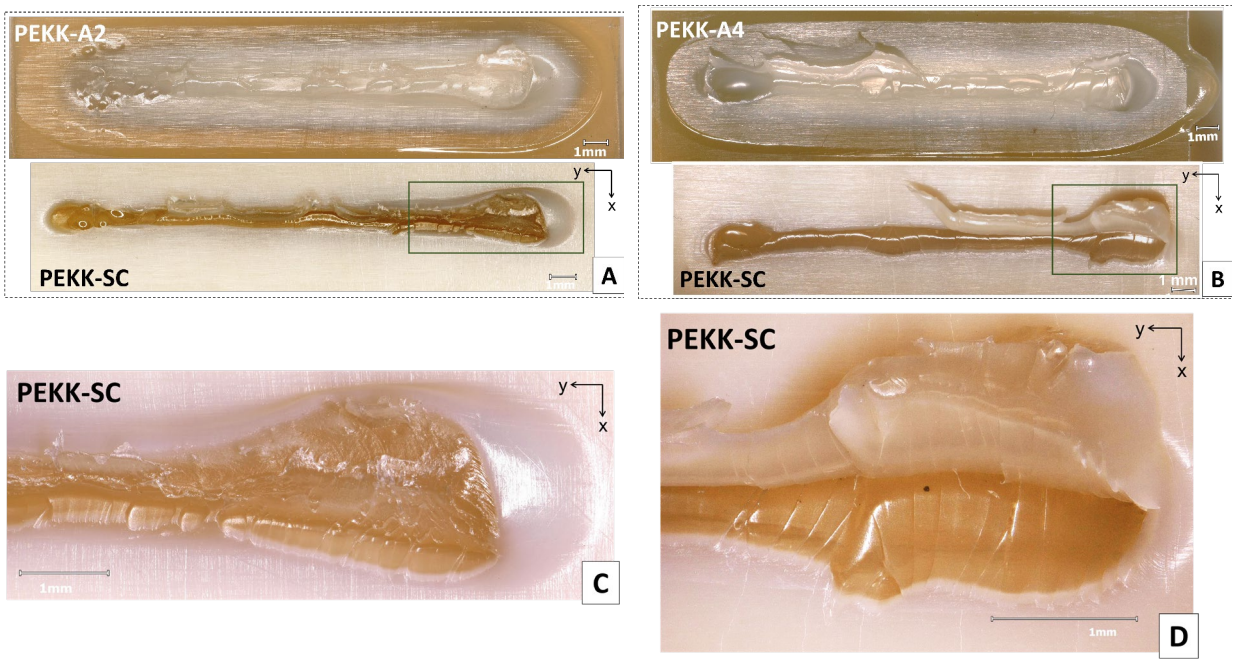

Fig. 9. Weld bond of assemblies failed with cohesive mode. The opened overlapped interfaces allow to visualize the weld bond on each substrate of the assembly for (A) A2/SC-P2 and (B) A4/SC-P2. (C) Magnified view of inset show in (A). (D) Magnified view of inset shown in (B).

The cohesively failed weld bonds were characterized by optical microscopy. Fig. 9 shows the micrograph of the opened overlap of cohesively failed assemblies in the PEKK-A and PEKK-SC substrates. The weld bonds show signs of sheared material on each substrate. That indicates that the samples were melted and fused together at the irradiated zone and that the bonds were shared during mechanical test.

Summary

PEKK 7002 grade is suitable to be welded with amorphous over semi-crystalline sample configuration. The following conclusions are outlined:

- The optical properties of the substrates were measured in injection molded plates:
  - A transmission factor of 40 % is measured on amorphous plates at the wavelength of interest, even with 4 mm thick. Thus, the amorphous state is transparent enough to allow LTW.
  - Increasing the thickness of the amorphous substrate from 2 to 4 mm decreases the IR transmission factor by 17 %.
  - The absorption properties of the semi-crystalline state of PEKK 7002 make it suitable for LTW.
- We targeted to define the process parameters according to the material properties to get a strong and reliable weld.
  - The output laser power was varied to obtain the same laser intensity radiation at the interface considering the transmission factor of the transparent substrate.
  - The welding speed and irradiation procedure were established to allow the materials to melt at the interface all along the welding path.
- Relationships between the process parameters, the material properties and the dimensions of the HAZ, and the mechanical resistance of the welds were determined. The highest LSS

is 60 MPa, demonstrating the ability of LTW in achieving strong welds in amorphous over semi-crystalline PEKK.

Further work will focus on extending the study to other process parameters. A thorough characterization of the HAZ will be carried out to link the crystalline morphology to the thermal history undergone within the HAZ.

References

[1] I. Jones, Laser welding for plastic components, Assem. Autom. 22 (2002) 129-135. https://doi.org/10.1108/01445150210697429

[2] F. Chabert, C. Garnier, J. Sangleboeuf, A.C.A. Asseko, B. Cosson, Transmission Laser Welding of Polyamides: Effect of Process Parameter and Material Properties on the Weld Strength, Procedia Manuf. 47 (2020) 962-968.

[3] N. Amanat, C. Chaminade, J. Grace, N. James, D.R. Mckenzie, Optimal process parameters for thermoplastic polyetheretherketone joints fabricated using transmission laser welding and Lumogen® IR absorptive pigment, J. Laser. Appl. 23 (2011) 012003. http://doi.org/10.2351/1.3552972

[4] S. Berger, F. Oefele, M. Schmidt, Laser transmission welding of carbon fiber reinforced thermoplastic using filler material—A fundamental study, J. Laser. Appl. 27 (2015) S29009. https://doi.org/10.2351/1.4906391

[5] X.F. Xu, A. Parkinson, P.J. Bates, G. Zak, Effect of part thickness, glass fiber and crystallinity on light scattering during laser transmission welding of thermoplastics, Opt. Laser. Technol. 75 (2015) 123-131. https://doi.org/10.1016/j.optlastec.2015.06.026

[6] V. Kagan, R.G. Bray, Advantages and limitations of laser welding technology for semi-crystalline reinforced plastics, Int. Congr. Appl. Lasers Electro-Opt, Jacksonville, Florida, USA, Laser Institute of America, 2001 [cited 2022 Dec 11], 1218-1227. Available from: http://aip.scitation.org/doi/abs/10.2351/1.5059784

[7] V.A. Kagan, R.G. Bray, W.P. Kuhn, Laser Transmission Welding of Semi-Crystalline Thermoplastics—Part I: Optical Characterization of Nylon Based Plastics, J. Reinf. Plast. Compos. 21 (2002) 1101-1122. https://doi.org/10.1177/073168402128987699

[8] N. Amanat, C. Chaminade, J. Grace, D.R. Mckenzie, N. James, Transmission laser welding of amorphous and semi-crystalline poly-ether-ether-ketone for applications in the medical device industry, Mater. Des. 31 (2010) 4823-4830. http://doi.org/10.1016/j.matdes.2010.04.051

[9] M. Villar, C. Garnier, F. Chabert, V. Nassiet, D. Samelor, J.C. Diez, A. Sotelo, M.A. Madre, In-situ infrared thermography measurements to master transmission laser welding process parameters of PEKK, Opt. Laser. Eng. 106 (2018) 94-104. https://doi.org/10.1016/j.optlaseng.2018.02.016

[10] T. Choupin, L. Debertrand, B. Fayolle, G. Regnier, C. Paris, J. Cinquin, B. Brule, Influence of thermal history on the mechanical properties of poly(ether ketone ketone) copolymers, Polym. Cryst. 2 (2019) e10086. https://doi.org/10.1002/pcr2.10086

[11] T.B. Juhl, J. de C. Christiansen, E.A. Jensen, Mechanical testing of polystyrene/polystyrene laser welds, Polym. Test. 32 (2013) 475-481. http://doi.org/10.1016/j.polymertesting.2013.01.009

[12] M.A. Villar montoya, Procédé de soudage laser de polymères haute performance : établissement des relations entre les paramètres du procédé, la structure et la morphologie du polymère et les propriétés mécaniques de l'assemblage, PhD Thesis, Toulouse, INPT, 2018. Available from: http://www.theses.fr/2018INPT0118

[13] A. Korycki, C. Garnier, M. Bonmatin, E. Laurent, F. Chabert, Assembling of Carbon Fibre/PEEK Composites: Comparison of Ultrasonic, Induction, and Transmission Laser Welding, Materials 15 (2022) 6365. https://doi.org/10.3390/ma15186365

[14] T.B. Juhl, J. de Claville Christiansen, EA. Jensen, Investigation on high strength laser welds of polypropylene and high-density polyethylene, J. Appl. Polym. Sci. 129 (2013) 2679-2685. https://doi.org/10.1002/app.39000
[15] V. Wippo, Y. Winter, P. Jaeschke, O. Suttman, L. Overmeyer, The Influence of Laser Welding Processes on the Weld Seam Quality of Thermoplastic Composites with High Moisture Content, Phys. Procedia 83 (2016) 1064-1072. https://doi.org/10.1016/j.phpro.2016.08.112
[16] A.C. Akué Asséko, B. Cosson, É. Lafranche, F. Schmidt, Y. Le Maoult, Effect of the developed temperature field on the molecular interdiffusion at the interface in infrared welding of polycarbonate composites, Compos. Part B Eng. 97 (2016) 53-61. https://doi.org/10.1016/j.compositesb.2016.04.064
[17] L. Martineau, F. Chabert, B. Boniface, G. Bernhart, Effect of interfacial crystalline growth on autohesion of PEEK, Int. J. Adhes. Adhes. 89 (2019) 82-87. https://doi.org/10.1016/j.ijadhadh.2018.11.013
[18] H. Potente, F. Becker, G. Fiegler, Investigations towards application of a new technique on laser transmission welding, Weld World. 45 (2001) 15-20.

Materials Research Proceedings 28 (2023) 1841-1850 https://doi.org/10.21741/9781644902479-199

Influence of roughness in ultrasonic welding of carbon fiber/PEEK composites

CARASSUS Fabrice[1,2,a *], KORYCKI Adrian[1,2,b], GARNIER Christian[1,c], CHABERT France[1,d], YAHIAOUI Malik[1,e] and DJILALI Toufik[2,f]

[1]LGP-ENIT-INPT, University of Toulouse, 47 Avenue d'Azereix, 65016 Tarbes, France

[2]LAUAK FRANCE, 8 Rue Louis Caddau, 65000 Tarbes, France

[a]fabrice.carassus@groupe-lauak.com, [b]akorycki@enit.fr, [c]cgarnier@enit.fr, [d]fchabert@enit.fr, [e]myahiaoui@enit.fr, [f]toufik.djilali@groupe-lauak.com

Keywords: Ultrasonic Welding, Composites, Roughness, Shear Strength

Abstract. In this work on ultrasonic welding of CF/PEEK composites, it was established that the surface roughness of the substrates has an influence on the interfacial strength of a joint. The joint resistance is lower when the roughness increases. Interestingly, a new characteristic time was found, named the healing plateau time (t_{HP}), which is determined by the displacement versus time curves during ultrasonic welding. This time seems to be related to the shear strength of the joint. This is a major finding, because it appears as a non-destructive way of predicting the quality of welds. Besides, DNS test on CF/PEEK unidirectional composite pointed out 40% higher shear strength compared with SLS, performed on CF/PEEK substrates assembled with a 250 µm PEI integrated energy director. Ultrasonic welding was optimized to reach a performance close to the shear strength of bulk.

List of abbreviations

CF	*Carbon fiber*	$QDNSS_{max}$	*Quasi double-notched shear strength maximum value*
D_h	*Healing degree*		
D_{IC}	*Intimate contact degree*	Ra	*Profile's arithmetic mean deviation*
DNS	*Double-notch shear*		
G_{IC}	*Mode I energy release rate*	Rz	*Average profile height*
$G_{IC(\infty)}$	*Bulk material resistance*	SDB	*Sandblasted*
G_{IIC}	*Mode II energy release rate*	SLS	*Single lap shear*
HP	*Healing plateau*	SS	*Shear strength*
LSS	*Lap shear strength*	SS_{bulk}	*Bulk material shear strength*
LSS_{max}	*Lap shear strength maximum value*	STB	*Shotblasted*
$\lambda_{cut\text{-}off}$	*boundary wavelength between roughness and waviness*	STD	*Standard*
		t_h	*Healing time*
PEEK	*Polyetheretherketone*	t_{HP}	*Healing plateau time*
PEI	*Polyetherimid*	t_{ic}	*Intimate contact time*
QDNSS	*Quasi double-notched shear Strength*	t_{rep}	*Reptation time*
		USW	*Ultrasonic welding*

Content from this work may be used under the terms of the Creative Commons Attribution 3.0 license. Any further distribution of this work must maintain attribution to the author(s) and the title of the work, journal citation and DOI. Published under license by Materials Research Forum LLC.

Materials Research Proceedings 28 (2023) 1841-1850 https://doi.org/10.21741/9781644902479-199

Introduction

Composites in aeronautics are currently dominated by thermosets, but the development of high-performance thermoplastic composites is booming. These materials open the way towards new forming and assembling processes. *Ultrasonic welding* (USW) is a joining method that uses ultrasonic vibrations and pressure over time to generate heat at the contact surfaces. Joining is achieved by the formation of a molten interphase which consolidates on cooling under pressure. The use of an energy director, a pure polymer film between both surfaces to be welded, facilitates the surface wetting to achieve intimate contact. *Polyetherimide* (PEI) is often used as energy director for joining *Polyetheretherketone* (PEEK) matrix composites, as both polymers are miscible. Moreover, PEI has the advantage of flowing at a lower temperature than PEEK, which facilitates the mobility of its macromolecular chains through PEEK.

The weld quality in USW depends on several process parameters and material properties, but geometric parameters must also be considered. Besides, interface healing and intimate contact between both surfaces to be welded are still not fully understood. According to Voyutskii [1], surface wetting is not sufficient to develop interfacial strength in polymer welding, the chains must be able to diffuse from one surface to another. Before the polymer chains diffuse from one side to the other one, intimate contact is established by the flow of asperities onto the surface of polymeric materials. Then, healing is generated by the chains diffusing across the interface and their random rearrangement. The highest welding strength is achieved when healing is completed and the interface disappears completely. Intimate contact describes the evolution of physical contact between both materials to be welded. It represents the true contact surface, formed by the asperities in contact, in opposition to the apparent contact surface. Initially, a perfect contact is impossible because of the surface roughness. It is assumed that roughness improves the frictional effect in USW and increases the temperature at the interface. But on the other hand, the imperfections must be flattened under pressure to generate intimate contact. Indeed, the intimate contact is the necessary condition for the polymeric chains to diffuse across the interface. The effect of roughness on weld strength is rarely considered and to date, no experimental study of roughness in USW is available. Usually, the specimens to be welded are prepared from plane plates without considering their roughness. However, various surface qualities are obtained when parts are manufactured in industrial conditions. Therefore, a deeper knowledge is needed to weld despite imperfect geometry or unusual roughness. Some analytical approaches were developed to handle this topic. In the most advanced existing models, the *intimate contact degree* (D_{IC}) has been established by considering the roughness as a set of rectangular asperities [2,3], far from realistic geometry. However, this model may be sufficient to predict the influence of roughness on the joint quality, by linking the roughness parameters to pressure, viscosity and welding time. Further refinement of models may be interesting to fit the realistic roughness parameters. Anyway, such models must be validated with experimental data, which are the purpose of this article.

This work aims to contribute to the prediction of the weld resistance in USW according to the initial part roughness. Thus, the influence of roughness on the interfacial strength is investigated by combining mechanical characterization and analytical approach. Most studies choose the *mode I energy release rate* (G_{IC}) to evaluate the adhesion of an assembly composed of 2 bulk materials [4,5,6]. This energy release rate could be considered as the resistance of welds. It can be compared to the $G_{IC(\infty)}$ corresponding to the bulk material resistance. This energy release rate, attributed to a multiplicative combination of interfacial and bulk effects depends on the adhesion time [7]. Eq. 1 relates it directly to the polymer *reptation time* (t_{rep}). t_{rep} mainly depends on the temperature and the polymer chain hindrance (Eq.2). It defines the average time needed for a polymer chain to completely leave its initial position. The latter is represented in the reptation theory by a tube from which the macromolecule escapes at the extremities.

$$\frac{G_{IC}(t)}{G_{IC\infty}} \approx \left(\frac{t}{t_{rep}}\right)^{\frac{1}{4}} \quad (1)$$

$$t_{rep} = \frac{N^3 lo^3 \mu_M}{N_e k_B T} \quad (2)$$

With: N number of monomers, lo segment length of an ideal chain, μ_M dynamic viscosity, N_e number of monomers between entanglements, k_B Boltzmann constant

In the aerospace industry, it is customary to consider the shear strength of joints instead of energy release rate. It was therefore decided to implement a new approach based on the mode II resistance and to discuss its validity while quantifying the influence of roughness.

Materials and Methods

USW was performed in displacement mode using a Mecasonic Omega 4x pneumatic welding machine. The input parameters were the applied pressure, the amplitude and the sonotrode displacement. Time, displacement, and energy dissipation were recorded by the device during welding. Fig. 1 shows the general layout of the welding system.

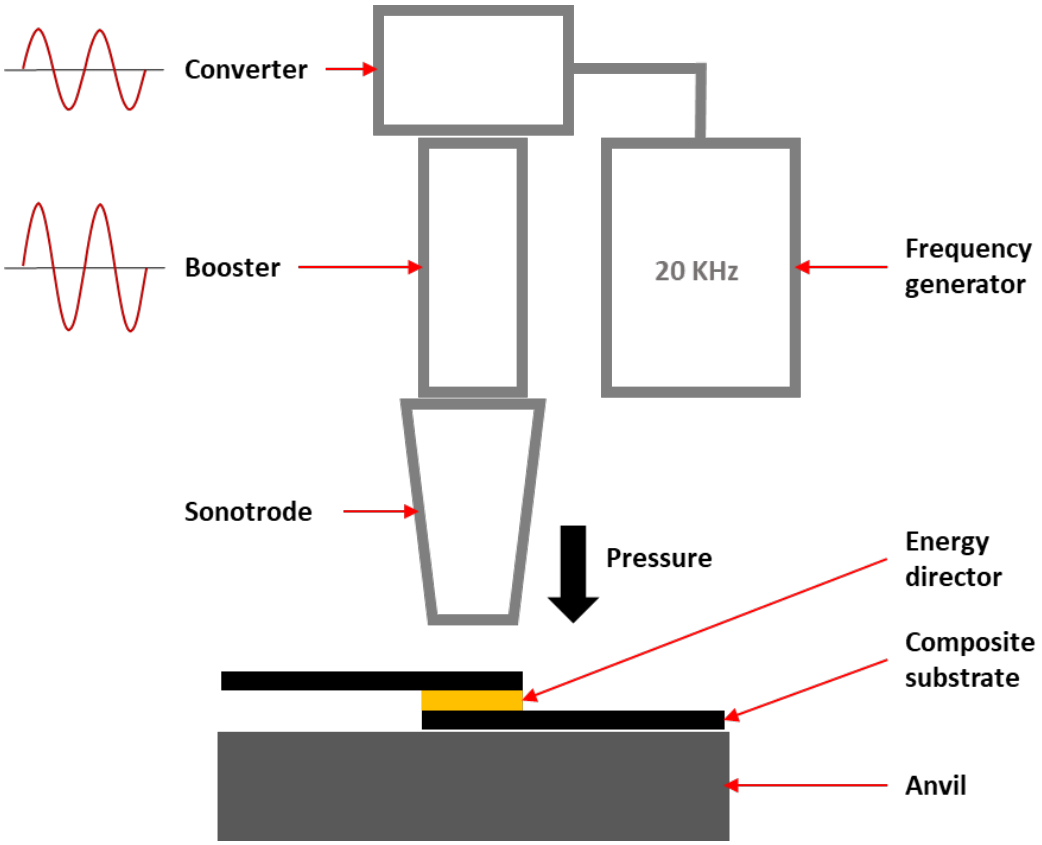

Fig. 1. Layout of the ultrasonic welding device.

Composite plates were manufactured with a Pinette Emidecau Industries Lab800 thermo-compression device. The substrates were made of APC-2 prepreg supplied by Solvay, which is composed of unidirectional *carbon fibers with polyetheretherketone matrix* (CF/PEEK). Composite plates underwent an additional step to integrate a 0.25 mm thick pure polymer film of Ultem 1000 PEI as energy director under compression. To vary the surface finish of these composite plates, steel backplates of different roughness were used. Several surface conditions were tested to obtain different types and values of roughness.

The composite plates were then cut in 100 x 25 x 2 mm substrates. Before welding, their roughness was measured using a Mahr MarSurf PS1 roughness meter, by averaging 5 measurements spread over the area to be welded, in the longitudinal direction on each sample. A comparison between the *profile's arithmetic mean deviation* (Ra) (Eq. 3) and the *average profile height* (Rz) was carried out but did not show a significant difference. Therefore, Ra was chosen as the default measurement parameter. In accordance with roughness tables, the *boundary wavelength between roughness and waviness* ($\lambda_{cut\text{-}off}$) was chosen to be 0.8 mm for roughness below 2 µm, and 2.5 mm for roughness above 2 µm. The limited size of the specimens welded area made it inadequate to take higher values of $\lambda_{cut\text{-}off}$.

$$\mathrm{Ra} = \frac{1}{n}\sum_{i=1}^{n} |Yi| \tag{3}$$

With:Yi deviations of the evaluation profile from the surface mean line.

Two types of mechanical tests are carried out for this study: The specimens were prepared according to, *Double-Notch Shear* (DNS) testing from ASTM D-3846 and *Single Lap Shear* (SLS) testing from ASTM D-1002.

DNS testing specimens measuring 79.50 x 12.70 x 4.05 mm were cut from a plate with all unidirectional fibers oriented in the direction of the compressive load. The specimens were then double-notched. The tests were conducted on a special compression device as shown in Fig. 2A, which allows the specimen to be held vertically without buckling. A micro-torque spanner was required to tighten the equipment's nuts up to 0.1 N.m. In addition, welded specimens were cut to DNS dimensions to characterize assemblies. To compensate the offset, a counterpart of the same material, with same thickness, was glued to each side of the assembled specimen.

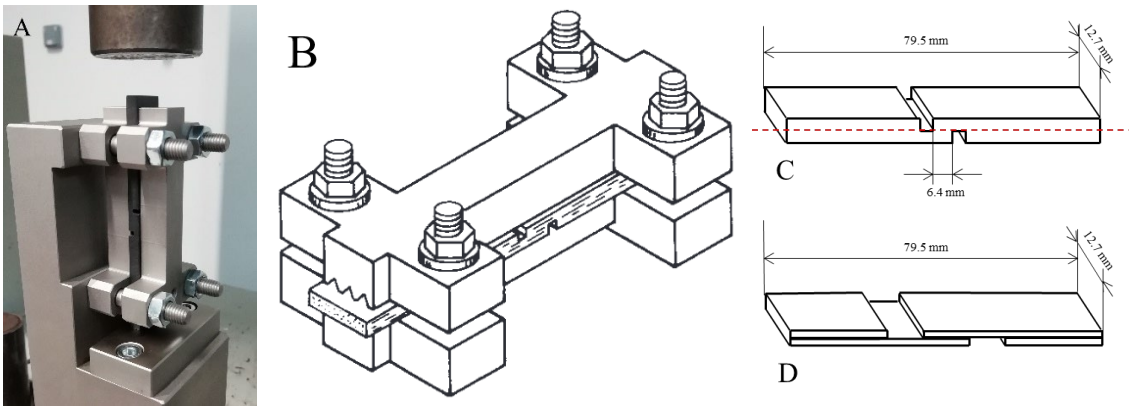

Fig. 2. (A) DNS testing equipment on CF/PEEK composite, (B) scheme of the DNS equipment according to ASTM D-3846, (C) Standard DNS specimen, (D) Quasi-DNS welded specimen.

Then, SLS testing were performed on welded specimens as shown in Fig. 3. An Instron 33R4204 tensile machine with a 100kN cell and adjustable jaws were used. Specimen shear resistances were evaluated, and the fractured surfaces were examined.

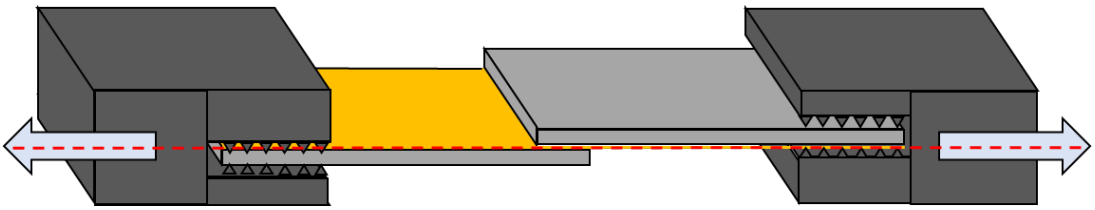

Fig. 3. Principle of the SLS test performed on a CF/PEEK composite with PEI energy director integrated on each welding surface.

Results and Discussion

Rather than establishing a *mode II energy release rate* (G_{IIC}) based on Eq. 1, we chose to compare the *shear strength* (SS) of a joint to the *shear strength of the bulk material* (SS_{bulk}) which is considered to be the maximum shear strength reachable. This ratio could be considered as the *healing degree* (D_h) of the joint and it can be related to the reptation time of the polymer (Eq. 4).

$$\frac{G_{IIC}(t)}{G_{IIC\infty}} \approx \frac{SS(t)}{SS_{bulk}} \approx \left(\frac{t}{t_{rep}}\right)^{\frac{1}{4}} = D_h \quad (4)$$

DNS tests gave a SS_{bulk} value of 73 ± 5 MPa, which is the shear strength value of the bulk material. It is assumed that the strength of assemblies could not reach those of the bulk, due to different entanglement rate in the interface vicinity. It does not mean the quality of assemblies is poor. The welds obtained with optimized welding parameters were characterized. The strength of the bulk was compared with our best assembly configuration by SLS and by a quasi-DNS method, where the assemblies were adapted to fit into the DNS tooling provided. For this comparison, only joints that led to composite fracture were considered. The DNS and SLS tests were performed on a set of 5 specimens, a smaller number for the quasi-DNS test, as several samples were rejected due to failure in the energy director. The advantage of the quasi-DNS test is that the assembly is placed in a pure shear configuration. For the rest of the study, shear strength obtained by SLS test are called Lap Shear Strength (LSS) while strength obtained by quasi-DNS are called Quasi Double Notched Shear Strength (QDNSS). The mean and maximum values for these tests are given in Table 1. The results obtained for both tests are different, +40 % for $QDNSS_{max}$ compared to LSS_{max}, confirming that SLS test does not only imply Mode II fracture. This difference suggests that DNS testing is a more reliable method for the determination of mode II strength than SLS.

The healing degree determined by the QDNSS/SSB ratio is D_h = 93.7 %, which means that the welding parameters were fully optimized. This healing degree should be studied further to see whether it is suitable to define the quality of a joint. Similarly, it would be possible to set a performance ratio for the SLS test. LSS/SS_{bulk} ratio is close to 60 %. Consequently, reaching this value in SLS tests could mean a very good performance is achieved for such assembly. Thereafter, it should be difficult to go beyond this LSS_{max} in SLS testing with the same materials.

Table 1. Shear strength values of CF/PEEK composite assemblies with PEI energy director. LSS is obtained by SLS testing and QDNSS is obtained by quasi-DNS testing method. LSS_{max} and $QDNSS_{max}$ are the maximum values of the corresponding tests.

SSB [MPa]	LSS [MPa]	LSS_{max} [MPa]	QDNSS [MPa]	$QDNSS_{max}$ [MPa]
73 ± 5	43 ± 4	50	68 ± 2	70

Quasi-DNS testing could therefore be a substitute for SLS testing. In addition to a better assessment of the mode II loading, this can lead to cost saving due to smaller specimen sizes and cheaper equipment.

To study the influence of roughness on UW, two surface conditions were tested on the PEI side of the plates. One was generated by thermocompression in contact with a sandblasted backplate (SDB), and the other one with a shotblasted one (STB). The roughness of each specimen was measured before welding. The range is quite large on these specimens: between 9 and 32 µm. The substrates were classified to have pairs of equivalent values. The reference specimens were standard ones (STD), meaning they had a relatively smooth PEI energy director. Their arithmetic roughness was measured between 0.2 and 0.4 µm. The optimized welding parameters for the standard specimens were kept for the rough ones. After welding, the joints were tested in SLS. The results shown in Fig. 4A demonstrate that the higher the roughness, the lower the apparent LSS. Moreover, a high deviation in the results is pointed out. After visual inspection of the fractured surfaces of most joints fractured below 20 MPa, it appears that these welds are incomplete, which means that some portions of the welding area are still intact, and the fracture is located within the energy director. To obtain the true LSS of assemblies, image processing in ImageJ software gives access to the true welded area. The latter is then reported to the true LSS value and plotted versus the roughness in Fig. 4B. A plateau at around 22 ± 4 MPa is identified, which corresponds to the minimum lap shear strength of the weld for these materials, regardless their roughness. Nevertheless, when comparing STB and SDB backplates specimens with STD ones, there is a real gap in roughness, respectively with a minimum value of around 10 µm for rough specimen, and a maximum value of 0.4 µm for smooth ones. Thus, a roughness threshold shall exist between both values, and the fluctuation from 0.4 µm to this threshold should be interesting to study. Unfortunately, no intermediate data are available for this study.

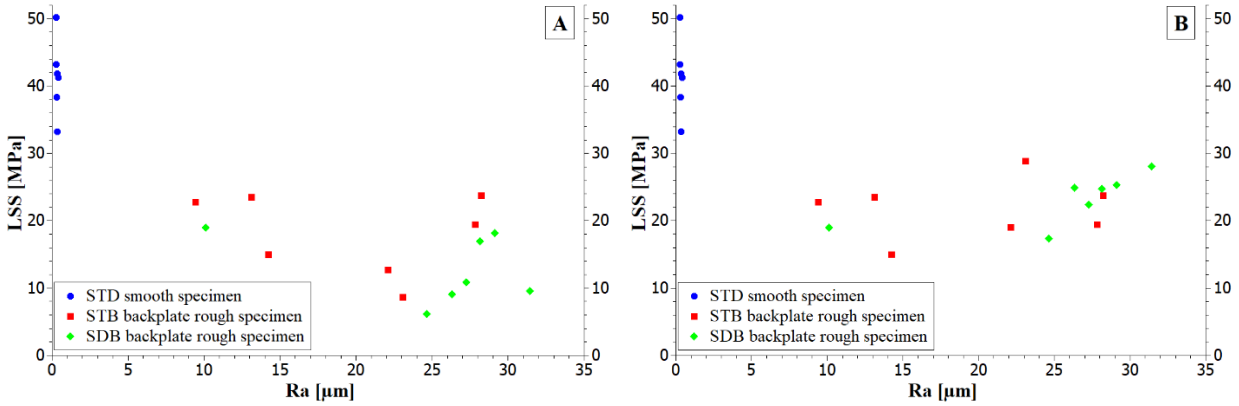

Fig. 4. (A) LSS of CF/PEEK assemblies as a function of PEI energy director roughness. (B) The same results obtained by using the true welded areas in the strength calculation.

To go deeper towards understanding such results, the welding curves are closely examined and compared with the obtained roughness and LSS values. Fig. 5 shows typical welding curves, which highlight the sonotrode displacement over time and the dissipated power during welding. The curves show the main characteristic stages of ultrasonic welding as described by Villegas [8] with slight variations due to different tooling and welding configuration, namely, stage 1) heating of the energy director, stage 2) after a first peak of dissipated power, energy director starts to melt, stage 3) the entire energy director is in a molten state and the sonotrode begins its main displacement, stage 4) includes a second power peak, the matrix at the contact of the energy director starts to melt locally, and stage 5) the matrix at the interphase is completely molten and the degradation begins due to overheating, while the dissipated power starts decreasing.

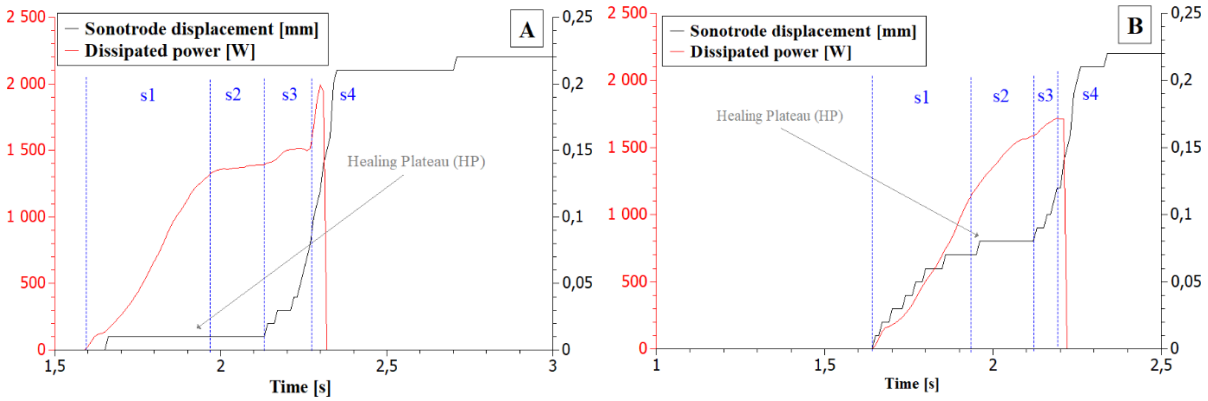

Fig. 5. Welding curves showing sonotrode displacement and dissipated power versus time. Typical curves for (A) standard specimens, (B) rough specimens.

The reference specimens led to the best results by reaching the middle or end of stage 4, which usually involves the joint fracture located within the composite plies. For the rough ones, the welding process more frequently stops during stage 3 or at the very beginning of step 4, and the break often takes place inside the energy director. However, significant differences appear between these graphs' displacement curves. The welding of rough specimens revealed a clearly visible plateau on the displacement curve during stage 1 and 2, which is obvious for all specimens. To date, this phenomenon has never been mentioned in the literature, probably because no study has focused on assembling rough surfaces until now, but smooth specimens. It is similar to fluctuations surrounding the initial point of displacement. However, the sonotrode displacement in stage 1 indicates that this plateau is representative of the beginning of the intimate contact between the welded surfaces. In the following, it will be called *Healing Plateau* (HP). *Intimate contact time* (t_{ic}) is identified as the time required to reach this plateau. Fig. 5b shows a significant power requirement to heat the substrate interfaces and flatten the surface asperities. In this case, rather than getting a first power peak, the change in slope seems to match with the stage 2 transition, which occurs during the HP. In the examples shown, the HP of rough specimens lasts slightly less than half as long as for smooth specimens (here, t_{HP}smooth = 0.53 s and t_{HP}rough = 0.24 s).

There is another important point to consider. In displacement mode in USW, the requested final height arrives too quickly, this is why stage 4 is scarcely reached. The sonotrode travelled distance to reach the plateau is a loss which prevents from achieving the requested displacement and thus, obtain an efficient joining. The roughness could help predicting the height of HP and t_{ic}, as shown in Fig. 6. There seems to be a trend for all roughnesses, but with significant variability for the lowest ones. Therefore, it should be possible to adjust the welding distance depending on the roughness, in order to reach the desired height in displacement mode. For LSS values below 10 MPa, identifying the HP is not obvious.

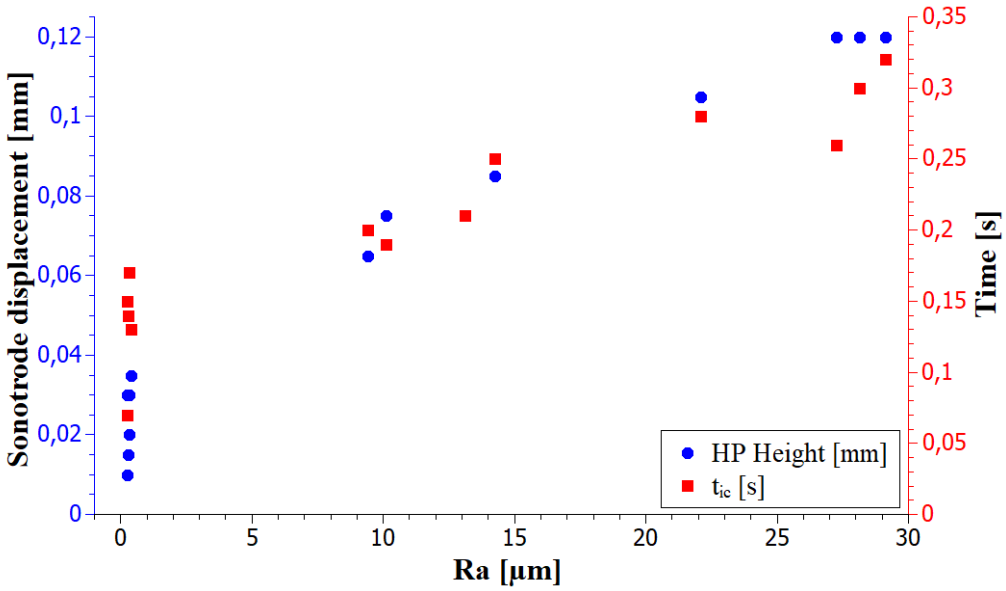

Fig. 6. Healing plateau height position (rounds) and experimental intimate contact time (squares), defined from the welding curves during sonotrode displacement for assemblies with LSS > 10 MPa.

The *healing plateau duration* (t_{HP}), which is finally a characteristic heating time of the interphase, could therefore be responsible for the strength of the assemblies. All plateau durations were measured on the welding curves, using a first-order derivative function to highlight the displacement variations. These results were scaled to the weld area and compared to each joint resistance in Fig. 7. A proportionality appears between t_{HP} and the LSS values. This trend seems to imply that t_{HP} should be maximized to obtain the best welding results. This finding, if confirmed by further studies, could be a simple and non-destructive way of assessing the quality of an ultrasonically welded joint.

To go further in the analysis, the *healing time* (t_h) and t_{HP} are highlighted. It is expected these two values are related. Assuming t_{rep} is considered unitary, and the shear stress of the bulk in SLS is fixed to our maximum value LSS_{max}, the shear stress and time ratios were calculated and plotted in Fig. 8 according to Eq. 4. The resulting trend looks like a line that does not pass through the origin, suggesting t_{HP} is different from t_h.

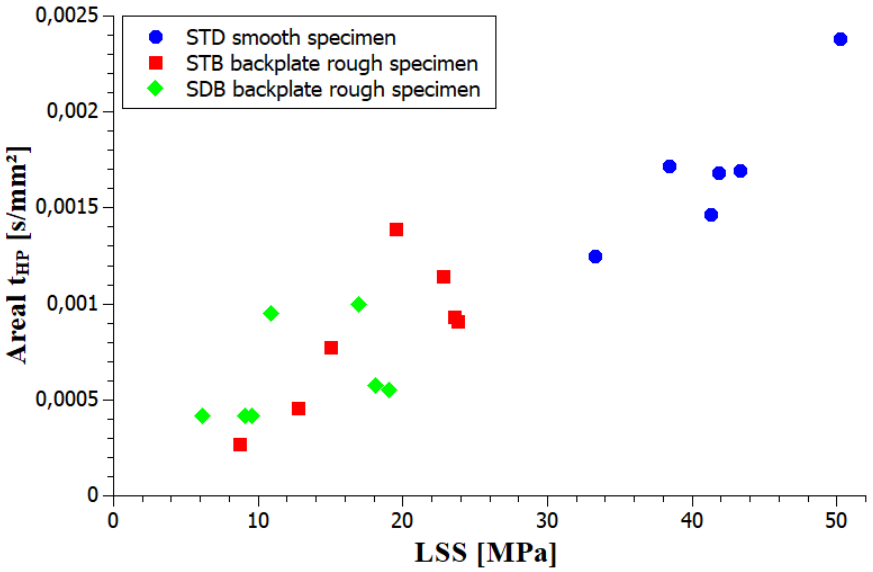

Fig. 7. Link between the healing plateau duration and the shear strength of welded assemblies.

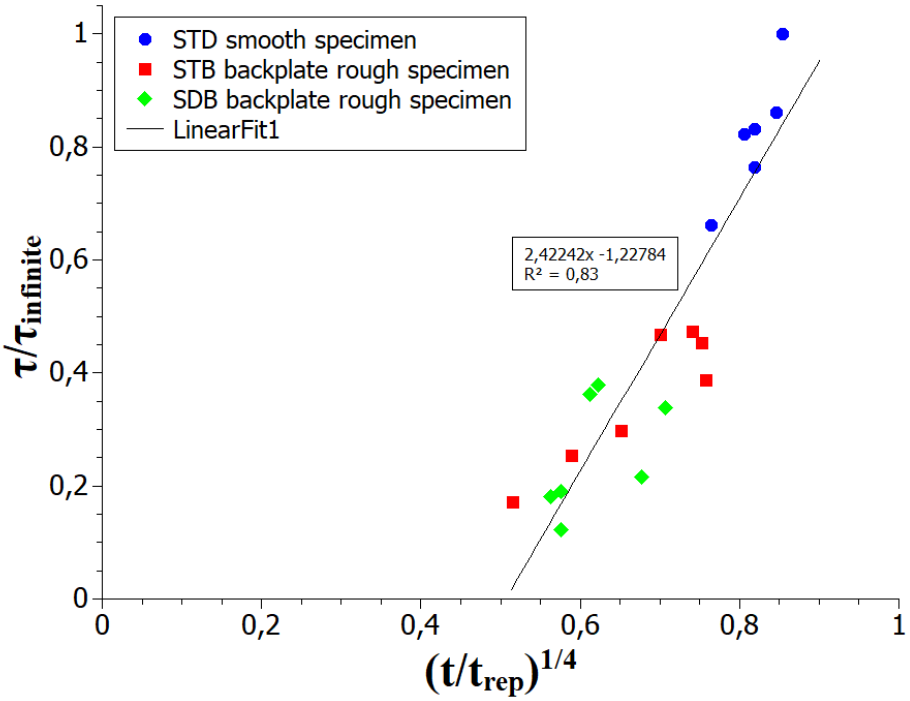

Fig. 8. Healing degree obtained by plotting shear stresses versus time ratios.

Summary

The influence of roughness when assembling composite plates by ultrasonic welding was studied. For that, composite specimens were manufactured with various roughness. For the first time, the intimate contact time was identified experimentally through the power and displacement welding curves. The displacement curves revealed a characteristic plateau duration, particularly evident on rough surfaces, which appears to be directly related to the joint shear strength. Exploiting this knowledge is a first step towards non-destructive examination of assemblies. It was established that this characteristic time is not the healing time of the interface during welding, but the link

between them seems obvious. A high roughness seems to have a negative effect on the strength of a joint welded in displacement mode by USW.

Finally, DNS test as a method of assessing Mode II strength has proven to be more reliable than SLS test, in addition to being less costly in terms of equipment and materials. Nevertheless, it can be established that an SLS test resulting in an LSS/SS_{bulk} ratio of 60% or more demonstrates the high quality of an assembly.

Aknowledgments
This work received financial support from ANR through France Relance plan of the French government in collaboration with the company Lauak Group (France).

References

[1] S.S. Voyutskii, V.L. Vakula, The role of diffusion phenomena in polymer-to-polymer adhesion, J. Appl. Polym. Sci. 7 (1963) 475-491. https://doi.org/10.1002/app.1963.070070207
[2] W.I. Lee, G.S. Springer, A Model of the Manufacturing Process of Thermoplastic Matrix Composites, J. Compos. Mater. 21 (1987) 21. https://doi.org/10.1177/002199838702101103
[3] F. Yang, R. Pitchumani, A fractal Cantor set based description of interlaminar contact evolution during thermoplastic composites processing, J. Mater. Sci. 36 (2001) 4661-4671. https://doi.org/10.1023/A:1017950215945
[4] P.G. de Gennes, Reptation of a Polymer Chain in the Presence of Fixed Obstacles, J. Chem. Phys. 55 (1971) 572. https://doi.org/10.1063/1.1675789
[5] D. Adolf, M. Tirrell, Molecular weight dependence of healing and brittle fracture in amorphous polymers above the entanglement molecular weight, J. Polym. Sci.: Polym. Phys. Ed. 23 (1985) 413-427. https://doi.org/10.1002/pol.1985.180230214
[6] S. Prager, M. Tirrell, The healing process at polymer-polymer interfaces, J. Chem. Phys. 75 (1981) 5194. https://doi.org/10.1063/1.441871
[7] Y.H. Kim, R. P. Wool, A theory of healing at a polymer-polymer interfaces, Macromolecules 16 (1983) 1115-1120. https://doi.org/10.1021/ma00241a013
[8] I.F. Villegas, Strength development versus process data in ultrasonic welding of thermoplastic composites with flat energy directors and its application to the definition of optimum processing parameters, Compos. Part A: Appl. Sci. Manuf. 65 (2014) 27-37. https://doi.org/10.1016/j.compositesa.2014.05.019

Materials Research Proceedings 28 (2023) 1851-1860 https://doi.org/10.21741/9781644902479-200

Insights on the use of PVB nanocomposites as energy directors in ultrasonic welding of epoxy composites

CILENTO Fabrizia[1,a *], PALMIERI Barbara[1,b], SORRENTINO Luigi[1,c], GIORDANO Michele[1,d] and MARTONE Alfonso[1,e]

[1]Institute of Polymers, Composite and Biomaterials (IPCB), National Research Council of Italy, 80055 Portici, Italy

[a]fabrizia.cilento@ipcb.cnr.it, [b]barbara.palmieri@ipcb.cnr.it, [c]luigi.sorrentino@cnr.it [d]michele.giordano@cnr.it, [e]alfonso.martone@cnr.it

Keywords: Nanocomposites, Damping, Ultrasonic Welding, Graphite Nanoplatelets

Abstract. The selection of an adequate coupling film for welding thermoset composites (TSC) is primary for improving the degree of automation in the composite industry. Ultrasonic welding (UW) is a well-established technique for joining composites and has recently been utilized in the aerospace and automotive industries. To achieve an efficient joining, the use of a polymer-based material placed at the welding interface called an energy director (ED) is required. The choice of the coupling layer material is linked to several requirements, such as processing temperature, high adhesion to the TSC adherend and mechanical strength of the resulting welded joints. Most importantly, the viscoelastic dissipation of the ED influences the heating mechanism and the joint behaviour since the hysteresis loops generated during welding are dissipated into viscoelastic heat. In this work, the authors investigated the possibility of using Poly-vinyl-butyral (PVB) reinforced with graphite nanoplatelets (GNPs) as a coupling layer in UW of TSC adherents, showing that an improvement of lap shear strength (LSS) of 80% with respect to neat PVB.

Introduction

Joining of TSCs has been limited to mechanical fastening and adhesive bonding, or a combination of the two [1]. In the first case, the drilling of holes results in stress concentrations and weakening of the thin composite structure, also significantly reducing its lightweight potential [2]. In contrast, adhesive bonding, although not requiring holes, needs rigorous surface preparation, high curing temperatures and pressures and long curing times to preserve the long-term durability of bonded composite joints [3].

Thus, the development of novel joining techniques able to overcome these drawbacks is required. Welding is a highly efficient process for joining composites, being capable of producing joints in relatively short cycle times, characterized by equivalent or better performance than adhesively bonded or mechanically fastened joints. Specifically, ultrasonic welding (UW) is a well-established technique for joining composites and has recently been utilized in the aerospace and automotive industries [4,5]. However, it requires the melting or softening ability of the polymer with increasing temperature, being applicable only in joining fibre-reinforced thermoplastic composites (TPC). To weld TSC, the use of polymer-based films placed at the welding interface is required to promote frictional and viscoelastic heating [6]. These coupling films, called energy director (ED), must satisfy various requirements such as processing temperature, high adhesion to the TSC adherend and mechanical and environmental performance of the resulting welded joint [7].

In contrast to other welding processes, in the UW, heat is generated by the internal damping of an applied ultrasonic vibration. During ultrasonic welding, the parts are subjected to a longitudinal mechanical vibration with a high frequency (typically 10-40 kHz). The mechanical vibration causes a standing wave in the welding parts in the form of heat [8]. The mechanism of heat

Content from this work may be used under the terms of the Creative Commons Attribution 3.0 license. Any further distribution of this work must maintain attribution to the author(s) and the title of the work, journal citation and DOI. Published under license by Materials Research Forum LLC.

generation is via viscoelastic dissipation due to the cyclic deformation of the plastic. In a purely elastic material, the driving force causes deformation rates in the part that is in phase with the force so there is no energy dissipation. The deformation rate in a purely viscous material is proportional to the applied force but has a phase difference of 90° dissipating the energy. Thus, in UW, the driving dynamic welding force depends on the material properties and shape of the product. When the ED heats, melts and flows to fill the interface joining the parts. With increasing temperature, the damping factor grows and the increasing vibrational energy is converted into heat by hysteresis losses [9].

The transformation of mechanical vibration into heat depends on a large number of mechanical and thermal properties of the material: the damping has to reach a certain level to cause high hysteresis losses, which are responsible for the elevation of the temperature. On the other hand, the material has to be stiff enough to successfully transmit the vibrational energy from the horn to the joint interface.

The polymer itself may not reach these mechanical requirements. Nanomaterials can effectively increase the mechanical performances of polymers both in terms of elastic modulus and damping, thanks to the energy dissipation that occurs at the interface with the matrix. Nanoparticles with a lamellar (2D) structure, such as graphene and its analogues (graphene oxide, GO, graphene nanoplatelets, GNP, etc.), can significantly improve the damping capabilities of nanocomposites [10] and also fracture toughness [11]. The nanoparticle shape factor and content can influence the mechanical behaviour of nanocomposites and in particular the damping factor (tanδ) [12].

In this work, the authors investigated the possibility of using Poly-vynil-butyral (PVB) reinforced with graphite nanoplatelets (GNPs) as a coupling layer in UW of TSC adherents. The effect of GNPs' weight content and flake dimensions on the temperature-dependent dynamic characteristics of nanocomposites and their influence on joint quality have been assessed. Specifically, nanocomposites with GNPs content varying from 0.5 wt% to 2.0 wt% and different aspect ratios have been fabricated using a lab mixer. Both the viscoelastic behaviour and morphology of the nanocomposites have been investigated. Finally, the interlaminar shear properties, through lap shear strength and short beam strength of UW joints have been investigated.

Materials and Methods

Poly-vinyl-butyral (PVB) (Mowital B60H) is a tough plastic resin commonly used for bonding. The presence of hydrophilic vinyl alcohol units and the hydrophobic vinyl butyral units confer both high adhesion to inorganic material and elasticity and toughness.

Two-dimensional graphite nanoplatelets (GNPs) are multilayer graphene obtained by the exfoliation of graphite. Nanoplatelets with different aspect ratios have been selected in this study and their geometry is listed in Table 1.

Table 1. Properties of selected nanoplatelets.

Nanoplatelet	SSA*	Lateral size	Thickness	Aspect ratio
MICRO850	14 m^2/g	4 μm	850 nm	4.70
AVA 1240	22 m^2/g	40 μm	12 nm	3333
G2NAN	30 m^2/g	30 μm	14 nm	2143

*SSA=specific surface area

Nanocomposites filled with selected GNPs were produced following a mixing and moulding process. Firstly, the polymer and the nanoplatelets are mixed using a Thermo Haake Rheomix for 10 min at a temperature of 150°C. Then, films of 200 μm thickness are fabricated using a hot platen press at 140°C and 200 bar for 20 min.

A number of 8 different coupons have been fabricated, varying the filler concentration and aspect ratio (Table 2). Also, an unfilled PVB film has been produced as reference.

Table 2. Fabricated nanocomposites.

Sample	***Filler***	***Nominal filler content*** [wt%]
Ref	Neat	-
1	AVA1240	2.0
2	G2Nan	0.5
3	G2Nan	1.0
4	G2Nan	1.5
5	G2Nan	2.0
6	MICRO850	0.5
7	MICRO850	1.5
8	MICRO850	2.0

Thermogravimetric analysis (TGA) (TA Instruments Q500) was conducted to evaluate the real filler/matrix composition of the films. Measurements were performed in an inert atmosphere, using nitrogen gas, with a temperature ramp of 10°C/min from room temperature to 700°C. The weight loss is evaluated at 500°C.

The thermal properties of the PVB/GNPs films were investigated by differential scanning calorimetry (DSC) using the DSC Discovery instrument. Each specimen was heated and cooled twice from 0 to 300°C at a rate of 10°C/min and the glass transition temperature (T_g) values were extracted from the DSC curves.

Dynamic mechanical analysis (DMA) was employed to measure the loss modulus and assess the viscous behaviour of the PVB/GNPs nanocomposites. A TA Instruments Q800 DMA equipped with a single cantilever clamp was used to perform a temperature sweep from 30 to 120°C at a heating rate of 3°C/min and a frequency of 1 Hz and considering an initial amplitude of 20 μm. Data are elaborated according to the ASTM D790 standard for the flexural behaviour of composites [13].

An optical microscope Olympus BX 51M, equipped with Linkam THM600 hot stage, was employed to assess the morphology of the material and the quality of the dispersion of the nanoparticles.

A carbon fabric/epoxy prepreg with a fibre volume content of 58% was used. 8 plies of CF/epoxy prepreg were stacked with a [(0/90)/ (45/-45)/(-45/45)/ (90/0)]s lamination sequences. The CF/epoxy stack were cured in autoclave at 120°C for 2 hours and 3 bar with vacuum bag, resulting in a laminate with a final thickness of 2 mm. Subsequently the CF/epoxy cured adherends were ultrasonic welded using the PVB/GNP film as coupling layer and ED.

Ultrasonic welding of individual coupons was performed using a Rinco Dynamic 3000 ultrasonic welder. The following process parameters were used: 500 N welding force, 36 μm peak-to-peak amplitude, 1000 ms welding time and 500 Ws maximum welding energy.

The coupons were saw cut from the cured CF/epoxy laminates to the dimensions of 36 x 12 mm for the Interlaminar Shear Strength (ILSS) tests (Fig. 1Fig. **1**) and 25 x 100 mm for the Lap Shear Strength (LSS) tests (Fig. 1).

ILSS tests were performed according to ASTM D2344 standard to evaluate the interfacial strength of the ultrasonic welded joints; the bonding characteristics of the ultrasonic welded joint was evaluated by LSS tests, according to ASTM D5868 standard. The tests were carried out with a 50-kN load cell in a Instron 68TM-50 Mechanical tester.

The interlaminar shear strength (ILSS) was calculated by dividing the peak recorded reaction force, F_{max} by the area of the cross section (A_{ILSS}), equal to 40 x 12 mm^2, as shown in Eq. 1.

$$ILSS = \frac{3}{4} \cdot \frac{F_{max}}{A_{ILSS}} \quad (1)$$

The LSS of the joints was calculated as the maximum load divided by the total overlap area. The total overlap area (A_{LSS}) was about 25 x 25 mm^2, Eq. 2.

$$LSS = \frac{F_{max}}{A_{LSS}} \quad (2)$$

A minimum of three specimens were tested per type of PVB/GN coupling layer used in this study.

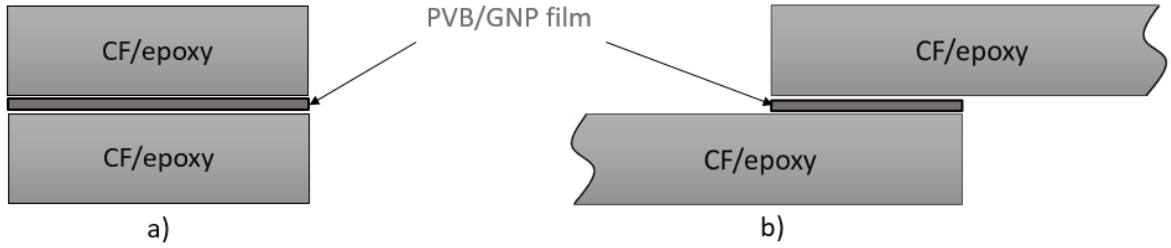

Fig. 1. Schematic representation of the CF/Epoxy/PVB joints in (a) ILSS and (b) LSS configurations.

Results and Discussion

The results of thermal analyses are reported in Table 3. The actual filler content is equal to the nominal value, as confirmed by TGA. Also, the glass transition temperature (T_g) of the polymer is not affected by the inclusions: it is equal to that of the unfilled polymer (73°C) for all samples.

Table 3. Results of thermal analyses conducted on PVB/GNPs nanocomposites.

Sample	***Actual filler content*** [wt%]	T_g [°C]
1	1.7	73
2	0.5	72
3	1.0	73
4	1.5	73
5	2.1	73
6	0.5	72
7	1.5	70
8	1.7	72

Micrographs show excellent dispersion in the case of MICRO850 and G2Nan in contrast to AVA1240. The morphology of the material changes considerably according to the selected GNPs. In the case of AVA1240, the presence of agglomerates can be observed, with a non-uniform distribution of particles (Fig.2). The quality of the dispersion increases significantly in the case of G2Nan (Fig.3). In this case, the distribution of nanoparticles is uniform for all concentrations from

0.5 wt% to 2.0 wt%, with a slight level of agglomeration. Finally, the best dispersion was observed for MICRO850 for all contents, with a very good level of homogeneity and absence of clusters (Fig. 4).

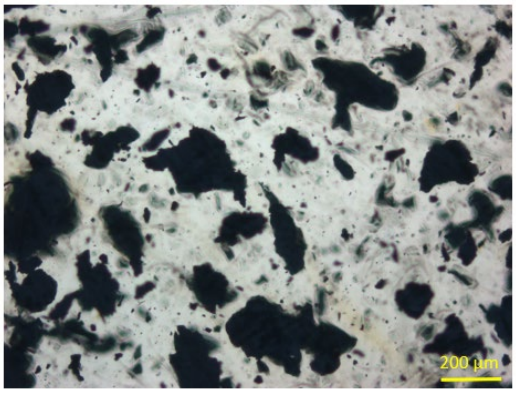

Fig. 2. Micrograph of PVB reinforced with AVA1240 at 2 wt%.

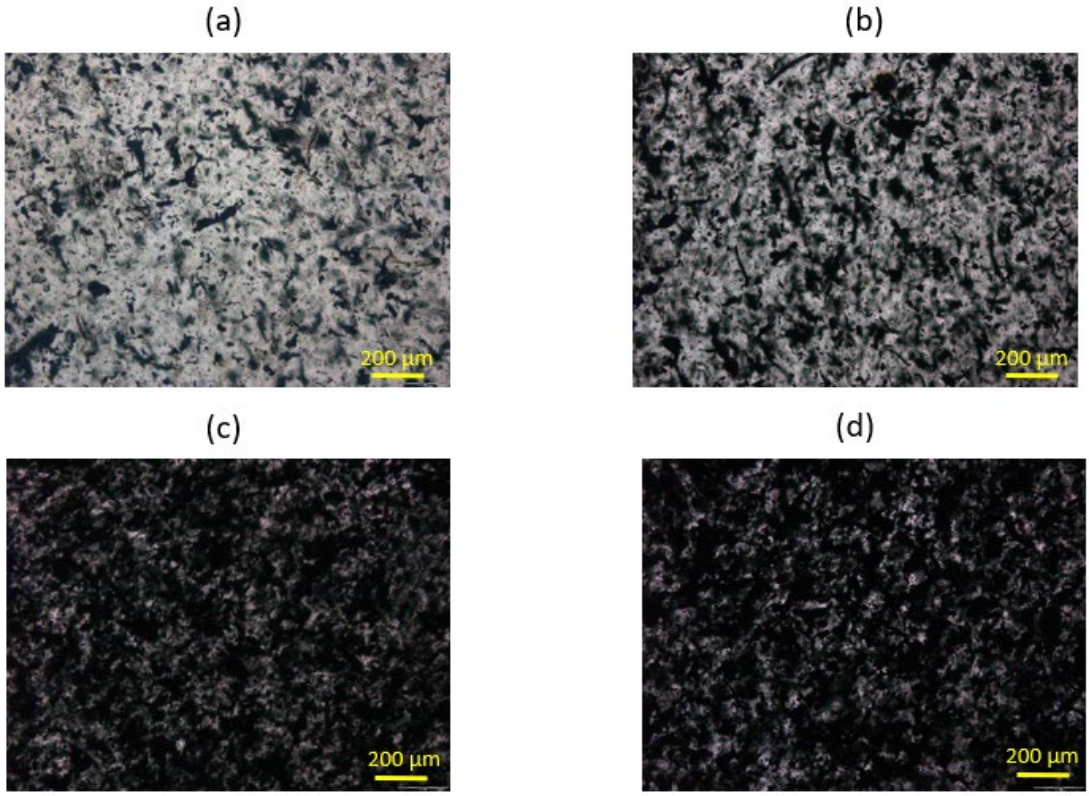

Fig. 3. Micrograph of PVB reinforced with G2Nan at 0.5 wt% (a), 1 wt% (b), 1.5 wt% (c) e 2 wt% (d).

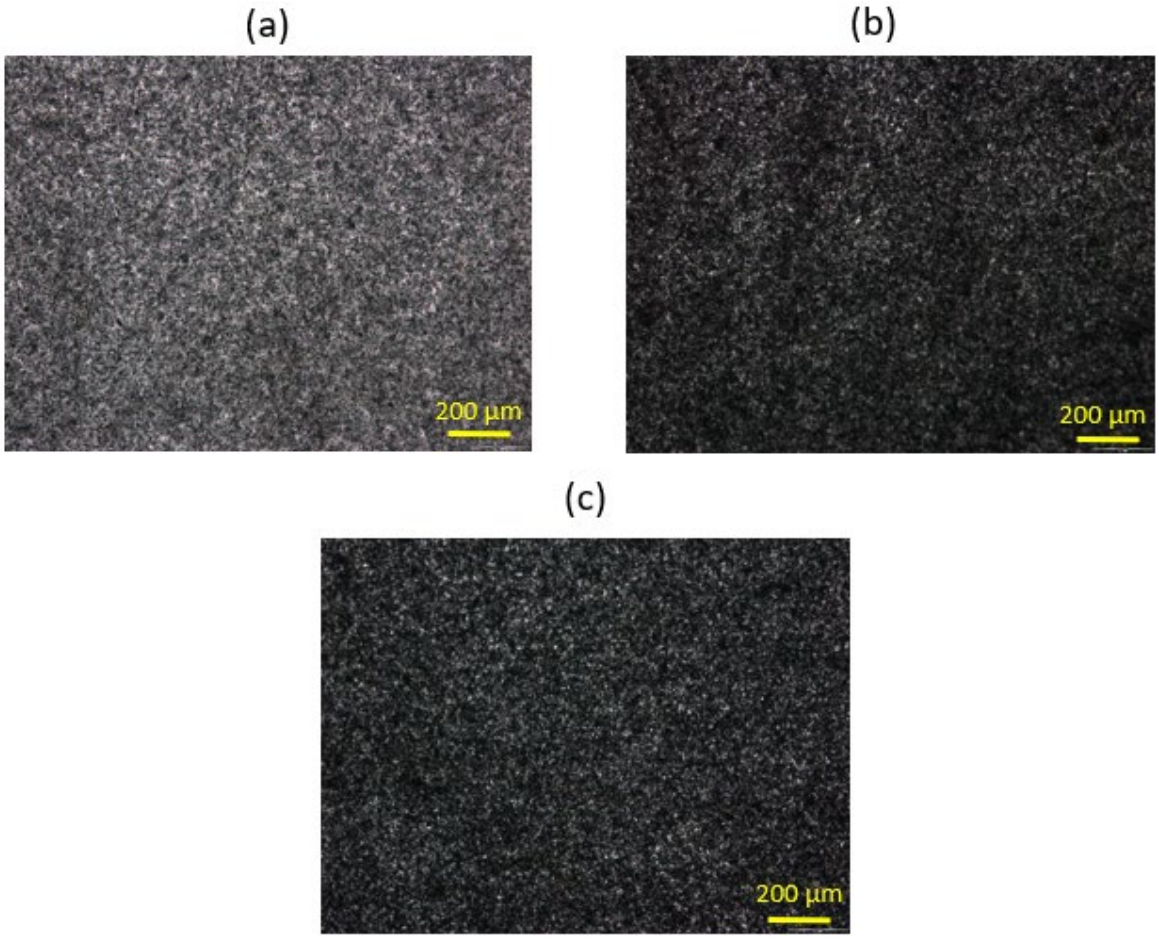

Fig. 4. Micrograph of PVB reinforced with MICRO850 at 0.5 wt%(a), 1.5 wt% (b), 2wt% (c).

The quality of GNPs dispersion is reflected in the mechanical performance of the nanocomposite. The results of the analyses carried out showed an improvement in the mechanical properties in the case of G2Nan and MICRO850 reinforced PVB compared to the unfilled polymer, and a deterioration in the case of AVA1240, both in terms of elastic modulus and damping.

In a viscoelastic material, the properties are intermediate between those of an ideal solid and those of an ideal liquid, as there is a phase lag between strain and deformation due to the time required to obtain molecular rearrangements. A measure of the elastic or pseudo-solid nature of the material is represented by the storage modulus (*E'*), while a measure of the viscous or pseudo-liquid nature of the material is represented by the loss modulus (*E''*). From a physical point of view, the storage modulus is related to the stiffness of the material and the loss modulus reflects the damping capacity of the material. The damping factor, tanδ represents the ratio between the viscoelastic and elastic response of a material and defines the dissipative capacity of the material. The results of the dynamic mechanical analyses conducted on the samples, in terms of storage and tanδ are reported in Fig. 5.

In the case of G2Nan, a maximum elastic modulus is observed for samples with a GNP content of 0.5 wt%, an increase of 9% compared to unfilled PVB. As the filler content increases, the possible presence of clusters leads to a decrease in the elastic modulus with respect to the neat PVB, albeit insignificant. The damping factor increases as the GNP content increases, with a maximum in correspondence of filler content of 1.5 wt%. This configuration provides a 33% increase in tanδ, without altering the elastic modulus of the material (2% reduction).

In the case of MICRO850, due to the small particle size, dispersion is uniform at all concentrations and the elastic modulus increases with increasing filler content. Again, a 30% increase in tanδ is observed for 1.5% GNP content.

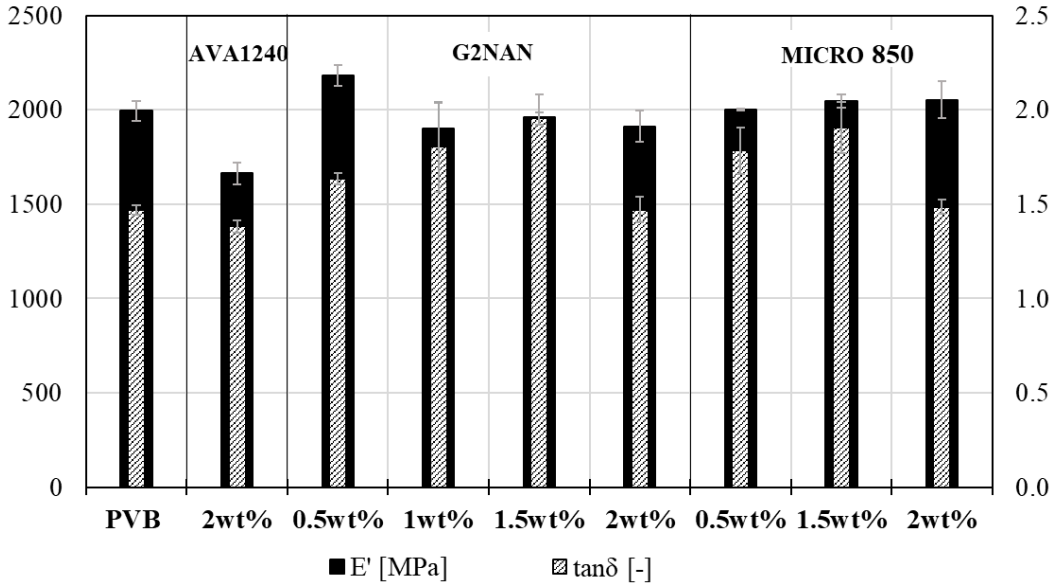

Fig. 5. Comparison between storage modulus at room temperature and damping ratio at peak of the tested nanocomposites.

In UW, the energy directors need to match damping and stiffness requirements to guarantee a certain level of hysteresis losses and to successfully transmit the vibrational energy from the horn to the joint interface respectively. Therefore, AVA1240 has not been considered for further investigation.

A strict correlation between the results of DMA and the short beam shear (SBS) is observed (Fig. 6). The mechanical properties of the coupling layer influence the strength of the joint. Welded joints with nanocomposites with high elastic modulus showed higher SBS with respect to the neat PVB, with a maximum of 40 MPa for PVB filled with 0.5 wt% of G2Nan. At low lamellar nanoparticles content, the fracture toughness of polymers improves, since the inclusions delay crack propagation [11].

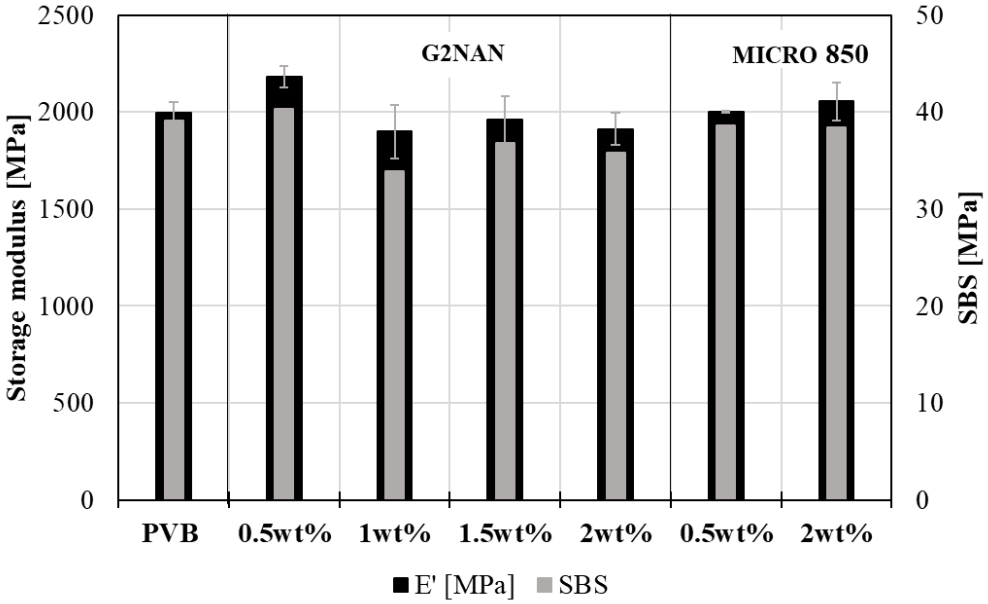

Fig. 6. Comparison between SBS and storage modulus

Lap shear strength has been assessed only for nanocomposites reinforced with G2Nan at different filler content. It is shown in Fig. 7 that this value is always higher than that of the neat PVB and it is maximum for the case of PVB filled with 0.5 wt% of G2Nan.

PVB filled with 0.5 wt% of G2Nan showed an improved quality of the joint with respect to the other samples. According to [14] the higher the material damping and the storage modulus (i.e. the higher the loss modulus) the higher the heat generation during welding and the lower the energy required for the welding process. It means that the ultrasonic weldability significantly depends on the loss modulus of the material [9]. Indeed, the LSS and E'' at 120°C (Fig. 7) show a similar trend.

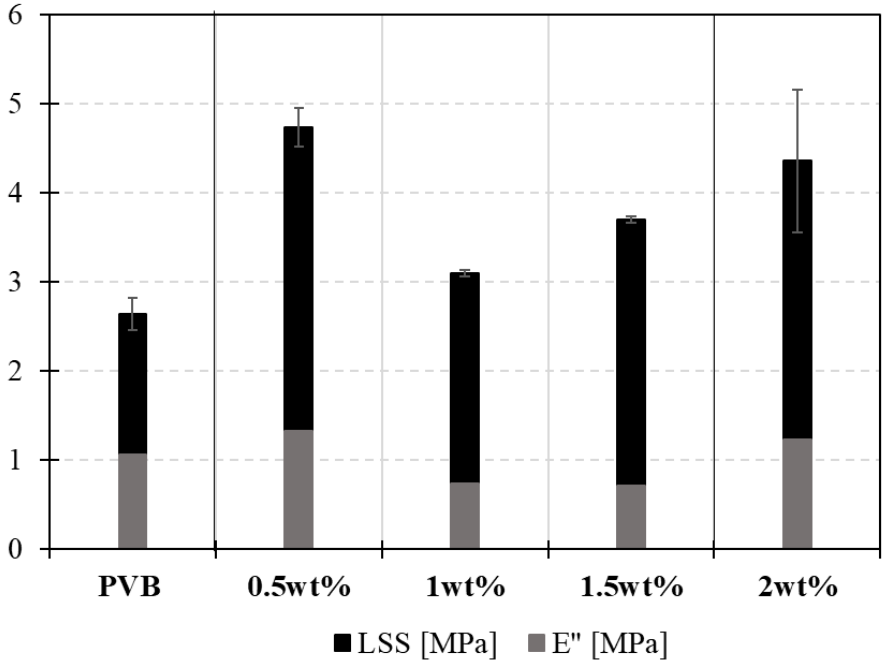

Fig. 7. Comparison between LSS and loss modulus.

Summary

The possibility of using PVB/GNP coupling films as energy directors in UW of TSC has been demonstrated. The influence of GNPs' weight content and flake aspect ratio on the mechanical properties of nanocomposites and joint quality has been assessed.

It was found that the use of lamellar nanoparticles can effectively improve the mechanical performances of polymers both in terms of damping and elastic modulus and consequently weldability. Unlike neat PVB, the inclusions act as reinforcement, supporting part of the load that is transferred from the matrix, both improving the elastic properties and the dissipative capabilities of the material. The high hysteresis losses ensure the elevation of the temperature during welding and the high stiffness ensure the transmission of the vibrational energy from the horn to the joint interface.

An improvement of 28% of loss modulus and 80% of LSS is shown for PVB reinforced with 0.5% of G2Nan, meaning that GNPs positively affect the damping capacity of PVB and therefore the joint strength.

In order to further optimize and increase weld strength future investigations will be addressed. Strategies will be aimed at modifying the thickness of coupling layers and adding the PVB reinforced films as an intermediate material co-cured with the TSC laminates.

References

[1] T. Löbel, D. Holzhüter, M. Sinapius, C. Hühne, A hybrid bondline concept for bonded composite joints, Int. J. Adhes. Adhes. 68 (2016) 229-238. https://doi.org/10.1016/j.ijadhadh.2016.03.025

[2] S.D. Thoppul, J. Finegan, R.F. Gibson, Mechanics of mechanically fastened joints in polymer-matrix composite structures-a review, Compos. Sci. Technol. 69 (2009) 301-329. https://doi.org/10.1016/j.compscitech.2008.09.037

[3] J.R. Vinson, Adhesive bonding of polymer composites, Polym. Eng. Sci. 29 (1989) 1325-1331. https://doi.org/10.1002/pen.760291904

[4] Z. Zhang, X. Wang, Y. Luo, Z. Zhang, L. Wang, Study on heating process of ultrasonic welding for thermoplastics, J. Thermoplast. Compos. Mater. 23 (2010) 647-664. https://doi.org/10.1177/0892705709356493

[5] M. Hou, A. Beehag, Q. Yuan, Welding techniques for polymer or polymer composite components, Google Patents, 25-Nov-2004.

[6] I.F. Villegas, Ultrasonic welding of thermoplastic composites, Front. Mater. 6 (2019) 291. https://doi.org/10.3389/fmats.2019.00291

[7] E. Tsiangou, S. Teixeira de Freitas, I. Fernandez Villegas, R. Benedictus, Investigation on energy director-less ultrasonic welding of polyetherimide (PEI)- to epoxy-based composites, Compos. Part B Eng. 173 (2019) 107014. https://doi.org/10.1016/j.compositesb.2019.107014

[8] C.J. Nonhof, M. Riepen, A.W. Melchers, Estimates for process conditions during the vibration welding of thermoplastics, Polym. Eng. Sci. 36 (1996) 2018-2028. https://doi.org/10.1002/pen.10597

[9] C. Hopmann, A. van Aaken, Ultrasonic welding of polyamide-influence of moisture on the process relevant material properties, Weld. World 58 (2014) 787-793. http://doi.org/10.1007/s40194-014-0158-3

[10] J. Wang, X. Jin, C. Li, W. Wang, H. Wu, S. Guo, Graphene and graphene derivatives toughening polymers: Toward high toughness and strength, Chem. Eng. J. 370 (2019) 831-854. https://doi.org/10.1016/j.cej.2019.03.229

[11] Y.T. Park, Y. Qian, C. Chan, T. Suh, M.G. Nejhad, C.W. Macosco, A. Stein, Epoxy toughening with low graphene loading, Adv. Funct. Mater. 25 (2015) 575-585. https://doi.org/10.1002/adfm.201402553
[12] J. Wang, C. Li, X. Zhang, L. Xia, X. Zhang, H. Wu, S. Guo, Polycarbonate toughening with reduced graphene oxide: toward high toughness, strength and notch resistance, Chem. Eng. J. 325 (2017) 474-484. https://doi.org/10.1016/j.cej.2017.05.090
[13] ASTM D 790-17, Standard Test Methods for Flexural Properties of Unreinforced and Reinforced Plastics and Electrical Insulating Materials1, 2017.
[14] G. Menges, H. Potente, Studies on the weldability of thermoplastic materials by ultrasound, Weld. World 9 (1971) 46-58.

Materials Research Proceedings 28 (2023) 1861-1870 https://doi.org/10.21741/9781644902479-201

Effect of compression during post-treatment to improve the mechanical strength of printed carbon fiber/ PEKK composites

COMBETTES Julien[1,a *], ABADIE Amandine[1,b], FAZZINI Marina[1,c], BORLENGHI Andrea[2,d], BOSSHARD Jonas[2,e], GARNIER Christian[1,f], DESSEIN Gilles[1,g] and CHABERT France[1,h]

[1]LGP-ENIT-INPT, University of Toulouse, 47 Avenue d'Azereix, BP1629-65016 Tarbes Cedex, France

[2]9TLabs, Badenerstrasse 790, 8048 Zürich, Switzerland

[a]jcombett@enit.fr, [b]amandine.abadie@enit.fr, [c]marina.fazzini@enit.fr, [d]andrea@9tlabs.com, [e]jonas@9tlabs.com, [f]christian.garnier@enit.fr, [g]gilles.dessein@enit.fr, [h]france.chabert@enit.fr

Keywords: Additive Manufacturing, Carbon Fiber, Composite, Porosity, Post-Treatment

Abstract. This work aims to understand the effect of consolidation on parts obtained by material-extrusion additive manufacturing process. Three plates were manufactured with carbon fiber/PEKK tapes. Two of them were consolidated under pressure at 334 and 360°C corresponding to the maximum of the melting peak and the end of the melting peak of PEKK respectively. Another plate did not undergo any post-treatment after printing, it is used as a reference. The parts were characterized to measure their porosity by density measurement and X-ray micro-computed tomography. Subsequently, short beam shear tests and dynamic mechanical analysis (DMA) tests were carried out to assess the influence of porosity on the mechanical strength of the plates. As expected, the interlaminar shear strength (ILSS) decreases when the porosity increases. The highest ILSS is obtained for the part consolidated at 360°C due to a lower porosity. The highest storage modulus is obtained for the part consolidated at 334°C whereas the loss factor indicates a lower glass transition for the same part. This could be explained by a lower degree of crystallinity as revealed by DSC, compared to the part consolidated at 360°C.

Introduction

Additive manufacturing offers affordable opportunity to obtain complex shapes [1]. Material-extrusion based processes are the most used techniques of 3D printing. ASTM International's additive manufacturing (AM) technologies committee approved a new standard guide for the use of layer-based material extrusion (MEX) processes in additive manufacturing. MEX processes are used to fabricate polymer, or polymer composite, parts by depositing a filament or bead of material from an extrusion head. Initially, most of raw materials were filaments of polylactic acid (PLA) and acrylonitrile butadiene styrene (ABS). Indeed, because of their low thermal transitions, their printing temperatures fit any basic printing machine [2,3]. However, after printing, such printed parts often suffer from poor interlayer adhesion bonding and high porosity rate [4]. MEX is now driven by high demanding applications, which require high performance polymers. PEEK (polyetheretherketone) and PEKK (polyetherketoneketone) are high performance semi-crystalline thermoplastics whose glass transition and melting temperatures are around, respectively, 150°C and above 360°C [5,6]. Printing PEEK and PEKK is possible with machines equipped with a heating chamber to control the crystallization upon cooling. As shown by Wang et al. [7] who characterized the bending properties of PEEK, printed parts reached 190 MPa for the bending strength compared to around 200 to 300 MPa for an injection molded part [8]. Other works report similar trends regarding mechanical resistance for PEKK printed parts [9]. Indeed, printing of PEKK is a challenge due to its high deposition temperature of around 400°C and its very high viscosity. Such high temperatures induce harsh temperature gradients inside the part during

Content from this work may be used under the terms of the Creative Commons Attribution 3.0 license. Any further distribution of this work must maintain attribution to the author(s) and the title of the work, journal citation and DOI. Published under license by Materials Research Forum LLC.

printing. Consequently, the crystallization of PEKK is not homogeneous along the z-axis direction. This gradient of crystallinity contributes to warpage defects due to anisotropic shrinkage. Also, a too fast crystallization could hinder macromolecular diffusion at the interfaces, the surface contact between filaments. Thus, the mechanical resistance between each layer of PEEK or PEKK printed parts remains very low as demonstrated by Rahman et al. who measure an interlayer resistance between 80 and 100 MPa [10]. A way to improve the mechanical properties of thermoplastics is the association with short or continuous fibers. Among fibers, carbon fibers have the highest elastic modulus and stress at break. Therefore, some studies have focused on printing carbon fiber/polyetherketoneketone (PEKK) composites which target aerospace, medical and any other demanding applications due to outstanding chemical resistance, flame retardancy and low smoke generation and toxicity [11]. When filled with short carbon fibers (100 to 300 μm), the performance of these composites is limited [12,13] as revealed by their brittle behavior under impact [14], but the short fibers increases the tensile strength up to 95 MPa against 80 MPa for the pure PEEK [15]. Addition of continuous fibers makes the material much more resistant [15]. The stiffness, low weight and stress resistance make continuous carbon fiber an ideal material to produce industry-grade composite parts. Unfortunately, long carbon fiber/PEEK printed parts also suffer from high porosity and poor interlayer adhesion as demonstrated by Luo et al. who found an interlaminar shear strength (ILSS) of 4 MPa for a 20%wt long carbon fiber filled composite, compared to an ILSS of 12 MPa when printing pure PEEK [16]. An option to overcome this flaw has been put forward by Van de Werken et al. who studied the effect of hot-pressing as post-treatment after printing. After applying a temperature of 250°C for less than 3 hours at 1.4 MPa, the porosity was decreases by a factor 2 to achieve 5% of porosity with an ILSS of 35 MPa [17].
9Tlabs is a company offering solutions to design and manufacture complex parts in no time. They propose additive manufacturing machines to produce high performance continuous fiber composites (carbon fiber with PEEK or PEKK matrix) with up to 60% fiber volume fraction. High volumes of structural composites can be manufactured in achieving up to 80% weight saving and 50% cost saving in series production, high reproducibility and great quality [18]. Their solution is based on a two step process: 1) a printing step 2) a consolidation step.

In this article, the effect of the consolidation step on the part performance was evaluated. The porosity rate and mechanical properties of the parts were measured on printed parts and after consolidation step at two different temperatures at 334°C and 360°C. The porosity was measured by density measurement and micro-computed tomography (μCT). The benefits and limitations of these techniques are discussed. The mechanical strength of printed parts was measured by interlaminar shear strength (ILSS). The material moduli were determined by dynamic mechanical analysis (DMA). An attempt to correlate these results to the porosity of parts is proposed to highlight the effect of compression post-treatment.

Materials

The composites plates were manufactured with a 9T Labs additive manufacturing machine [18]. 9T Labs offers a whole additive fusion technology including post treatment. The printing strategy is XY/Z with fiber direction along the Y-direction as drawn by the white line in Fig.1.

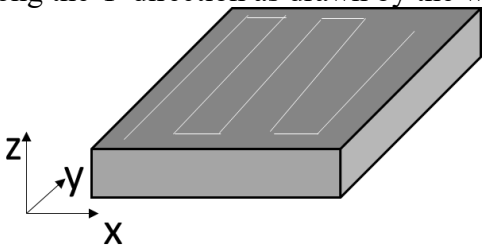

Fig. 1. Orientation of the printed plates with the building strategy (white line).

The material feedstock is a rectangular unidirectionnal carbon fiber pre-impregnated tape whose theoretical fiber volume fraction is 60 % [18]. The deposited tape contains a polyetherketoneketone (PEKK from Arkema company) matrix and AS4 carbon fiber. After printing, the parts are inserted into a mold, and a compression cycle is applied to densify the parts. This process guarantees high resistance complex shape parts. For the sake of clarity, the parts are 2- and 3-mm tick plates in this study. Three cases are compared i) Printed plate without consolidation (named UP), ii) Printed plates with a compression cycle at 334°C (CP-C1) and iii) Printed plates with a compression cycle at 360°C (CP-C2). The compression temperatures were chosen according to the thermal transitions of PEKK matrix. DSC (differential scanning calorimetry) were performed on about 10 mg of PEKK filament in aluminum pans with a Q200 TA Instruments DSC. The heating cycle is as follows: First heating ramp: 10°C.min^{-1} from 25°C to 380°C, cooling ramp: 10°C.min^{-1} from 380°C to 25°C, second heating ramp : 10°C.min^{-1} from 25°C to 380°C. Three samples were tested, only the second heating ramp of one sample is shown in Fig. 2. The filaments were dried at 140°C for 24h before testing. The glass transition is visible at 160°C, then the melting peak spreads from 300 to 360°C. The compression temperatures correspond to the maximum of the melting peak (334°C) and the end of the melting peak (360°C) for CP-C1 and CP-C2 respectively. The consolidation cycle is defined by a heating ramp at 15°C.min^{-1} under 30kN, an isothermal step at 334 or 360°C under 45kN for 180 s, followed by a cooling ramp at 7°C.min^{-1} under 45kN. Then, the parts are demolded when the temperature is below 160°C. The printing and post-treatment parameters are defined respectively in Table 1 and Table 2.

Table 1. Printing parameters.

Plate temperature (°C)	180
Chamber temperature (°C)	Inactive
Fiber Guide/Printing Temperature (°C)	360
Print speed (mm.min^{-1})	1000
Line width (mm)	0,9
Layer height (mm)	0,17

Table 2. Consolidation parameters.

	UP	CP-C1	CP-C2
Heating ramp (°C.min^{-1})	/	15	15
Isothermal Temperature (°C)	/	334	360
Max Pressure (kN)	/	45	45
Cooling ramp (°C.min^{-1})	/	7	7

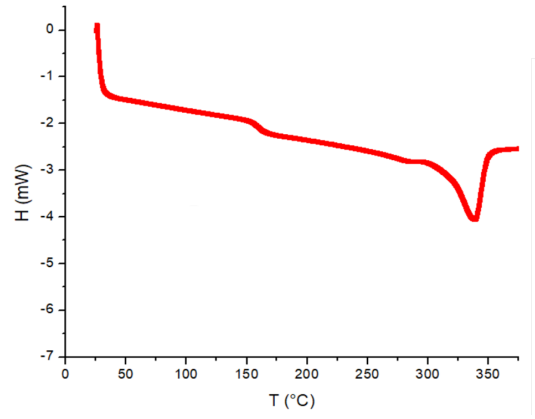

Fig. 2. DSC curve, second heating ramp for PEKK tape, 10°C.min^{-1}.

Methods

Before any characterization, all samples were dried at 140°C for 24h.

Short beam shear (SBS) tests were carried out on an Instron 4204 universal testing machine with a three-point bending device. The radius of the two supports and loading nose were 5 mm and 2 mm respectively, according to NF-EN 2463 standard. The cross-head speed was 1 mm.min^{-1}. For each configuration, at least three specimens were tested, the results were averaged. The strength of the SBS test was calculated from Eq. 1:

$$\tau_{SBS} = \frac{3}{4}\frac{P_{max}}{b.h} \quad (1)$$

with τ_{SBS} : Short-beam strength (SBS) (MPa), P_{max}: maximum load (N), b: sample width (mm), h: sample thickness (mm)
The sample density was measured by hydrostatic weighing in accordance with NF EN ISO 1183-1 standard. The density of the samples, ρ_s (g.cm^{-3}), was calculated by Eq. 2:

$$\rho_s = \frac{m_s}{(m_s - m_e)}\rho_{water} \quad (2)$$

with m_s : apparent mass of the sample in air (g), m_e : apparent mass of sample in water (g)
ρ_{eau} : water density
Then, the porosity was obtained by Eq. 3:

$$P = 1 - \frac{\rho_s}{\rho_f} \quad (3)$$

with ρ_f the density of the raw tape (according to the data sheet ρ_f= 1,58 g.cm^{-3}), ρ_s is the density of the sample and P is the porosity rate.

X-ray micro-computed tomography (µCT) was used to evaluate the porosity of the plates. Volume images were generated by a laboratory tomography device (Easytom RXSolution). The acquisition parameters were a tension of 150 kV and an intensity of 200 µA. 10 x 15 mm specimens were positioned on a rotation stage and 1440 projections of transmitted X-ray intensity field were recorded at each angular step of 0.25° by a flat panel detector (1920 x 1536 pixels) through an X-ray detector. Each projection was obtained by averaging ten images recorded at the same angular position. A volume image of the variations of the linear attenuation coefficient in the specimen was reconstructed from all radiographies by using a filtered back-projection algorithm. The distribution of grey levels in 3D images is due to local differences of density and so corresponds to a 3D representation of the microstructure of the specimen. Each volume image was reconstructed with the same voxel size of 13.48 µm. The pictures were treated with Avizo software. Each sample was divided into six parallelepipedic parts as seen in Fig. 3. The depth of the sample is not represented here but it is considered as well. Using a greyscale, a threshold is applied to separate the matrix and fiber part from the black part, i.e., the pores. The light grey part represents the clamping device used to hold the specimens: so, it is not considered for analysis. Furthermore, the air around the specimen is not counted as pores. The calculation of the global porosity rate is done by averaging the porosity rates of each zone.

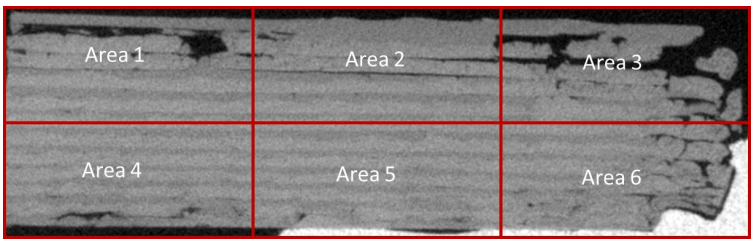

Fig. 3. Separations of area on XZ view.

Dynamic mechanical Analysis (DMA) was investigated using an ARES strain-controlled rheometer from TA Instruments in rectangular torsion mode. For dynamic analysis, sinusoidal strain γ* is imposed with a constant angular frequency ω. Viscoelasticity of polymers leads to a

phase lag between strain and stress σ* giving access to, in the linear viscoelastic domain, the complex dynamic modulus. Storage and loss moduli, G' and G'', were recorded as a function of temperature. Measurements were achieved from 25°C to 325°C with a 3°C.min^{-1} ramp. The angular frequency ω was 1 rad.s^{-1} and the strain γ was 0.1% for UP, 0.05% for CP-C1 and 0.1% for CP-C2 to stay within the linear viscoelastic domain. Sample sizes were 45 x 10 x 3 mm^3.

Results and discussions

Porosity.

Two different methods, hydrostatic weighing and micro-computed tomography were applied to evaluate the porosity. The results are presented in Fig. 4. The porosity for the reference plate (no consolidation) is 15% by tomography and 10% by hydrostatic weighing. The compression step at 334°C results in decreasing the porosity up to 3% by tomography and 7% by hydrostatic weighing. A higher compression temperature, 360°C, leads to a reduction of the porosity, below 1% whatever the technique. A high porosity is often reported for printed parts, for instance in the work by Tao et al. [4]. The compression step reduces the porosity. Indeed, the viscosity of the thermoplastic matrix decreases with temperature, resulting in easier polymer flow and closing of the pores. A representation of the theoretical structure of printed parts is schemed in Fig. 5.

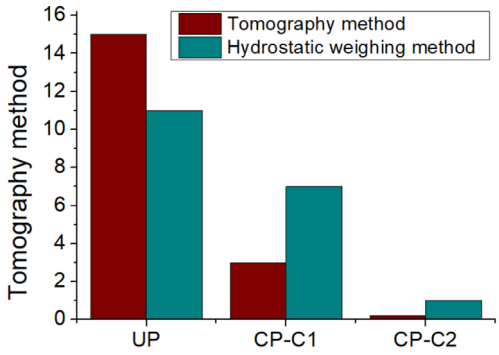

Fig. 4. Porosity for non-consolidated (UP), consolidated at 334°C (CP-C1), consolidated at 360°C (CP-C2) specimens.

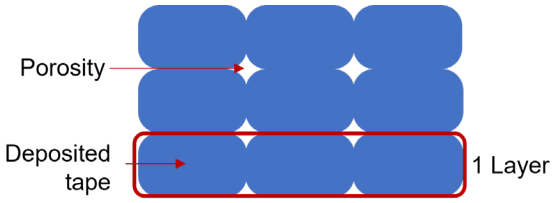

Fig. 5. Representation of the structure of a printing part (view XZ).

In the case of UP, besides pores presented in Fig. 5, delamination of the layers is observed. Indeed, the specimens were printed in a chamber without temperature control, resulting in low adhesion between tapes. Therefore, a higher porosity is measured on the specimen edges compared to the inner structure, as seen in Fig. 6. For the CP-C1 and CP-C2 plates, no delamination is detected by the software, leading to a better accuracy in the calculation of the porosity.

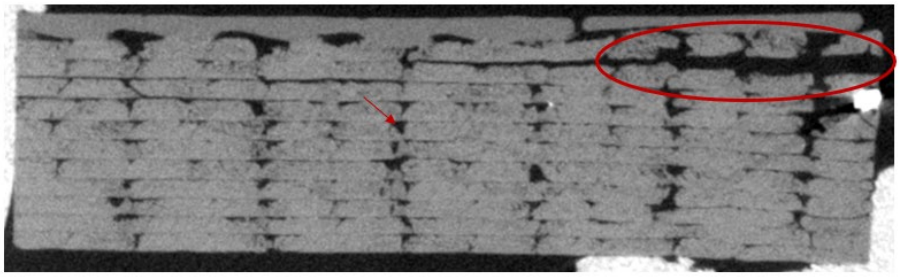

Fig. 6. XZ view of a slice of UP.

For the unconsolidated plate (UP), the porosity obtained by hydrostatic weighing is smaller than the one obtained from the density measurement. This is because external porosities due to

delamination are not considered in weighing, as water can seep into the narrowest pores on the sample edges.

For the consolidated specimens, the porosity is higher for hydrostatic weighing in both cases as seen in Fig. 4 for CP-C1 and CP-C2. The pores below 13,5 µm size (1 pixel) were not detected whereas hydrostatic weighing considers all pores whatever their sizes. A smaller pixel size would be necessary to detect smaller pores and to make both techniques to converge to the same porosity result. To sum up, CP-C2 has a much lower porosity than other specimens. The consolidation step at 360°C allows the PEKK matrix to flow more easily and to close the voids compared to 334°C. This temperature corresponds to the maximum of the melting peak. At this temperature, some crystalline lattices still remain, as a consequence, the viscosity is still too high to make the consolidation step effective.

Effect of compression on mechanical properties.

The results of SBS tests for unconsolidated specimens, compressed specimens at 334 and 360°C are shown in Fig.7a, b and C respectively. Interlaminar Shear Strength (ILSS) is defined by the first drops in stress on the curve. For UP, a more progressive and less brutal fall in stress is pointed out compared to the trend obtained for consolidated plates. ILSS results (calculated from the ISO 14130 standard) for the UP is 4,44$\pm$0,89 MPa whereas 42,54$\pm$2,36 MPa and 69,54$\pm$3,49 MPa were obtained for CP-C1 and CP-C2, respectively. The consolidation step has an impressive effect on ILSS with an increase of more than 800 % for CP-C1 and 1400 % for CP-C2. These results demonstrate the efficiency of the compression post-treatment after printing. A higher dispersion is noticed for UP whereas the curves for consolidated ones are closed one to each other. Moreover, increasing the temperature for the compression step increases the ILSS of about 40% when comparing CP-C2 and CP-C1. ILSS is related to interlayer adhesion. At 360°C, the viscosity is lower than at 334°C, giving more mobility to the macromolecules and a faster macromolecular diffusion across the layers. ILSS is mainly the contribution of two parameters: interlayer adhesion and porosity. We target to determine which one is the most influential on ILSS. For that, ILSS is plotted with the porosity in Fig.8. As expected, the ILSS value decreases with the increase in porosity. When the porosity tends towards zero, the ILSS value sharply increases. A hypothesis explaining such rise is related to the contact surface between tapes: Under pressure, the pore sizes decrease. Because of the elliptical shape of the tape section, this contact surface increases abruptly at the beginning and then slowly until the perfect contact between tapes is reached (flat surface). From a threshold, the effect of porosity is expected to be overlooked, giving a maximum ILSS value.

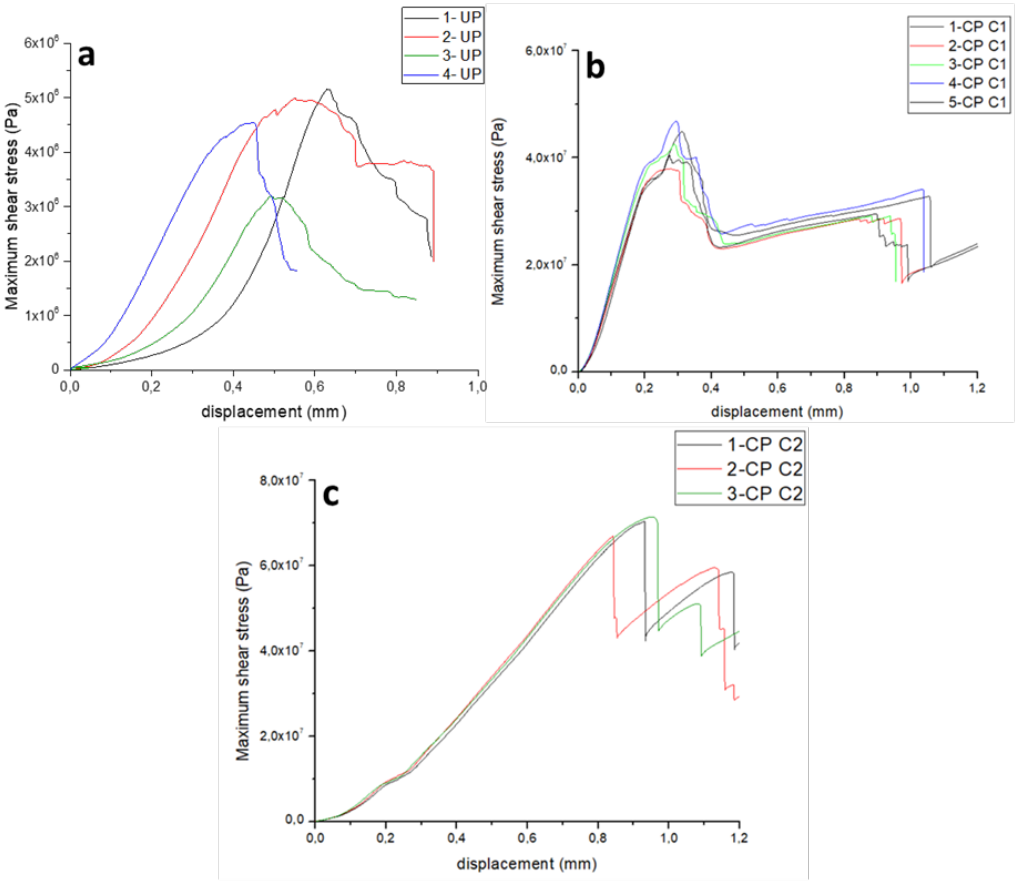

Fig. 7. SBS curves. a: plate UP ; b: plate CP-C1 ; c: plate CP-C2.

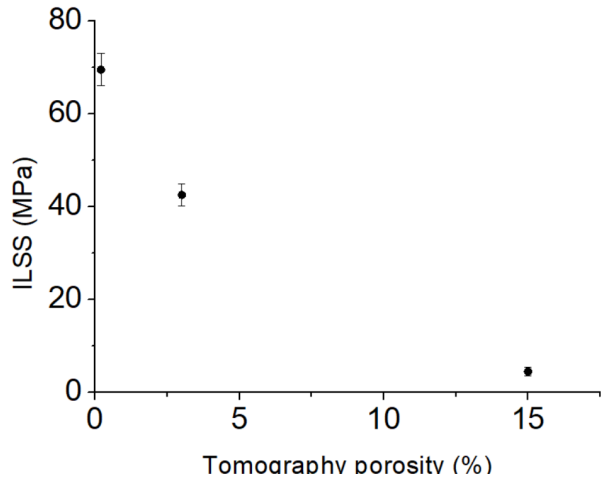

Fig. 8. Variation of SBS test results with porosity obtained by micro-computed. tomography

Effect of compression on dynamic moduli.

The dynamic moduli are presented in Fig. 9. In Fig. 9a, for all the specimens, a quasi-constant storage modulus G' is observed at the lowest temperatures up to 160°C, at this temperature, a sudden drop is associated to the glass transition (Tg). After the rubbery plateau, a last decrease towards 300°C corresponds to the softening of the amorphous phase of PEKK. As expected, G' for the unconsolidated plate is lower than for the consolidated ones. Surprisingly, the storage modulus in the glassy plateau is the highest for CP-C1. It means that the stiffness of the specimen consolidated at 334°C is higher than the one compressed at 360°C. Also, we notice a slight shift in the glass transition, around 170°C, with the lowest Tg for CP-C1. For the loss modulus G'' in Fig. 9b, a peak is observed at Tg and then a drop thereafter. The loss modulus (G'') is also higher in the case of CP-C1, which means that the material needs more energy to deform. In Fig.9c, the maximum of the ratio tan δ=G''/G' is shifted towards lower temperatures for CP-C1. This lower

Tg is associated with a higher macromolecular mobility in the amorphous phase. Also, this peak is broader and less symmetrical than the ones obtained for the UP and the plate consolidated at 360°C. This peak shape is often attributed to a higher polydispersity in chain lengths. In our case, it could stem from a higher dispersity in crystallite sizes. Indeed, in the case of compression at 334°C, the crystalline phase of the material has partially melted. This unmelted crystalline phase could hinder the crystallization during cooling, giving more time to the macromolecules to diffuse across the contact surface of the tapes. G' and G'' of CP-C1 are therefore higher than those of CP-C2. These results are supported by the degree of crystallinity results gathered in Table 3. The degree of crystallinity Xc is calculated from DSC curves with the Eq. 4:

$$Xc = \frac{\Delta Hf}{\Delta H_{100\%} * V_m} \quad (4)$$

With ΔHf the enthalpy of the melting peak of the first heating ramp, ΔH_(100%) the enthalpy of PEEK (considering the crystallinity of PEEK is close to those of PEKK) at 100% of crystallinity [19], V_m the volume fraction of matrix (0,4). Very high standard deviations of the degree of crystallinity are observed for UP and CP-C1 in Table 3 whereas those consolidated at 360°C are less disperse. This deviation indicates a non-homogeneity during crystallization. It means that the crystallization does not occur homogeneously within the part during consolidation at 334°C.

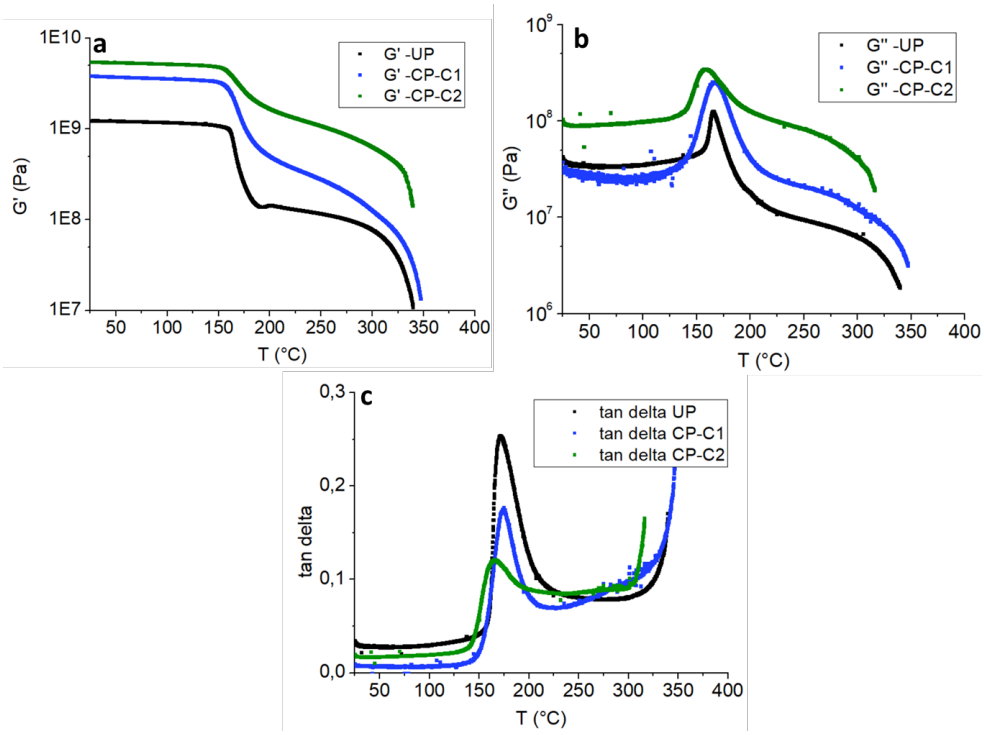

Fig. 9. DMA results for unconsolidated parts (UP), consolidated parts (CP) at 334°C (CP-C1) and 360°C (CP-C2): (a) storage modulus (G'); (b) loss modulus (G''), (c) tan δ.

Table 3. Degree of crystallinity of PEKK tapes and printed plates obtained from DSC curves

Material	Cristallinity (%)
PEKK	29 ± 3
UP	17 ± 2
CP-C1	17 ± 3
CP-C2	39 ± 15

Summary

To conclude, 9T Labs provides a complete additive manufacturing process to obtain printed parts with high mechanical strength. It consists of a printing step followed by a compression cycle. Two compression temperatures, 334 and 360°C were studied to determine the optimized conditions. When comparing to the reference plates (without the compression step), it reveals that the consolidation has a significant impact on part properties. The porosity was measured after printing on unconsolidated and consolidated parts by two techniques: tomography and hydrostatic weighing. The parts were characterized through short-beam strength tests, dynamic mechanical analysis, and differential scanning calorimetry. The aim was to compare the effect of the consolidation temperature at 334 and 360°C on porosity, ILSS and dynamic moduli.

The porosity was considerably reduced when the parts underwent consolidation post-treatment, the lowest porosity was obtained at 360°C, less than 1%, due to the PEKK matrix which is fully melted at this temperature. ILSS was initially near 4 MPa for the non-consolidated plates, whereas for those consolidated at 334°C and 360°C, ILSS were 42 and 69 MPa respectively. This result is higher than the ones found by Van Der Varken et al. [17]. This higher strength could stem from the reduction of porosity and increase of contact surface. ILSS results are clearly related with porosity, but the trend is not linear, indication the contribution of other phenomena such as macromolecular orientation. The highest storage modulus was obtained for the part consolidated at 334°C. A hypothesis could be linked to chains conformation: they are oriented in the extrusion direction whereas this organization is lost at 360°C. The loss factor (tan $\boldsymbol{\delta}$) indicates a lower glass transition for the part consolidated at 334°C. This lower glass transition is consistent with a higher macromolecular mobility in the amorphous phase and a lower degree of crystallinity. Further works will focus on understanding the effect of thermal cycles on crystal morphology and the role of crystallinity on interfilament adhesion.

References

[1] N. Shahrubudin, T.C. Lee, R. Ramlan, An Overview on 3D Printing Technology: Technological, Materials, and Applications, Procedia Manuf. 35 (2019) 1286-1296. https://doi.org/10.1016/j.promfg.2019.06.089

[2] G.W. Melenka, B.K.O. Cheung, J.S. Schofield, M.R. Dawson, J.P. Carey, Evaluation and prediction of the tensile properties of continuous fiber-reinforced 3D printed structures, Compos. Struct. 153 (2016) 866-875. https://doi.org/10.1016/j.compstruct.2016.07.018

[3] B. Brenken, E. Barocio, A. Favaloro, V. Kunc, R.B. Pipes, Fused filament fabrication of fiber-reinforced polymers: A review, Addit. Manuf. 21 (2018) 1-16. https://doi.org/10.1016/j.addma.2018.01.002

[4] Y. Tao, F. Kong, Z. Li, J. Zhang, X. Zhao, Q. Yin, D. Xing, P. Li, A review on voids of 3D printed parts by fused filament fabrication, J. Mater. Res. Technol. 15 (2021) 4860-4879. https://doi.org/10.1016/j.jmrt.2021.10.108

[5] L.M. Maloo, S.H. Toshniwal, A. Reche, P. Paul, M.B. Wanjari, A Sneak Peek Toward Polyaryletherketone (PAEK) Polymer: A Review, Cureus. 14 (2022). https://doi.org/10.7759/cureus.31042

[6] H. Pérez-Martín, P. Mackenzie, A. Baidak, C.M. Ó Brádaigh, D. Ray, Crystallinity studies of PEKK and carbon fibre/PEKK composites: A review, Compos. Part B Eng. 223 (2021) 109127. https://doi.org/10.1016/j.compositesb.2021.109127
[7] Y. Wang, W.-D. Müller, A. Rumjahn, F. Schmidt, A.D. Schwitalla, Mechanical properties of fused filament fabricated PEEK for biomedical applications depending on additive manufacturing parameters, J. Mech. Behav. Biomed. Mater. 115 (2021) 104250. https://doi.org/10.1016/j.jmbbm.2020.104250
[8] A.D. Schwitalla, T. Spintig, I. Kallage, W.-D. Müller, Flexural behavior of PEEK materials for dental application, Dent. Mater. 31 (2015) 1377-1384. https://doi.org/10.1016/j.dental.2015.08.151.
[9] R. Davies, N. Yi, P. McCutchion, O. Ghita, Mechanical property variance amongst vertical fused filament fabricated specimens via four different printing methods, Polym. Int. 70 (2021) 1073-1079. https://doi.org/10.1002/pi.6172
[10] K.M. Rahman, T. Letcher, R. Reese, Mechanical Properties of Additively Manufactured PEEK Components Using Fused Filament Fabrication, in: American Society of Mechanical Engineers Digital Collection, 2016. https://doi.org/10.1115/IMECE2015-52209
[11] D. Veazey, T. Hsu, E.D. Gomez, Next generation high-performance carbon fiber thermoplastic composites based on polyaryletherketones, J. Appl. Polym. Sci. 134 (2017). https://doi.org/10.1002/app.44441
[12] F. Ning, W. Cong, J. Qiu, J. Wei, S. Wang, Additive manufacturing of carbon fiber reinforced thermoplastic composites using fused deposition modeling, Compos. Part B Eng. 80 (2015) 369-378. https://doi.org/10.1016/j.compositesb.2015.06.013
[13] N. van de Werken, H. Tekinalp, P. Khanbolouki, S. Ozcan, A. Williams, M. Tehrani, Additively manufactured carbon fiber-reinforced composites: State of the art and perspective, Addit. Manuf. 31 (2020) 100962. https://doi.org/10.1016/j.addma.2019.100962
[14] D. Garcia-Gonzalez, M. Rodriguez-Millan, A. Rusinek, A. Arias, Investigation of mechanical impact behavior of short carbon-fiber-reinforced PEEK composites, Compos. Struct. 133 (2015) 1116-1126. https://doi.org/10.1016/j.compstruct.2015.08.028
[15] P. Wang, B. Zou, S. Ding, L. Li, C. Huang, Effects of FDM-3D printing parameters on mechanical properties and microstructure of CF/PEEK and GF/PEEK, Chin. J. Aeronaut. 34 (2021) 236-246. https://doi.org/10.1016/j.cja.2020.05.040
[16] M. Luo, X. Tian, J. Shang, W. Zhu, D. Li, Y. Qin, Impregnation and interlayer bonding behaviours of 3D-printed continuous carbon-fiber-reinforced poly-ether-ether-ketone composites, Compos. Part Appl. Sci. Manuf. 121 (2019) 130-138. https://doi.org/10.1016/j.compositesa.2019.03.020
[17] N. van de Werken, P. Koirala, J. Ghorbani, D. Doyle, M. Tehrani, Investigating the hot isostatic pressing of an additively manufactured continuous carbon fiber reinforced PEEK composite, Addit. Manuf. 37 (2021) 101634. https://doi.org/10.1016/j.addma.2020.101634
[18] Solutions Manufacture strong, lightweight, sustainable products like never before 9t Labs, https://www.9tlabs.com/solutions/additive-fusion-solution (accessed December 7, 2022).
[19] M. Doumeng, L. Makhlouf, F. Berthet, O. Marsan, K. Delbé, J. Denape, F. Chabert, A comparative study of the crystallinity of polyetheretherketone by using density, DSC, XRD, and Raman spectroscopy techniques, Polym. Test. 93 (2021) 106878. https://doi.org/10.1016/j.polymertesting.2020.106878

Materials Research Proceedings 28 (2023) 1871-1878 https://doi.org/10.21741/9781644902479-202

Viscoelastic characterization of reformable epoxy vitrimers composites

PALMIERI Barbara[1,a *], CILENTO Fabrizia[1,b], MARTONE Alfonso[1,c], GIORDANO Michele[1,d] and AMENDOLA Eugenio[1,e]

[1]Institute of Polymers, Composite and Biomaterials (IPCB), National Research Council of Italy, 80055 Portici, Italy

[a]barbara.palmieri@ipcb.cnr.it, [b]fabrizia.cilento@ipcb.cnr.it, [c]alfonso.martone@cnr.it, [d]michele.giordano@cnr.it, [e]eugenio.amendola@cnr.it

Keywords: Compression Moulding, Vitrimer, Multifunctional Composites, Epoxy Matrix

Abstract. Epoxy Vitrimers are gathering attention as a development in the field of more easily re-processable and self-healing thermosets. Incorporating a catalyst should activate the transesterification reaction within the polymeric macromolecule inducing topological modification of the network. Reacting epoxy precursors with suitable anhydrides and acids will promote exchange reactions between esters and beta-hydroxyls, adding the vitrimeric behaviour. In the present work, a commercial epoxy system suitable for CFRP manufacturing has been modified to induce vitrimeric behaviour by exploiting the catalytic activity towards the transesterification reaction of Zn2+. Creep experiments confirm that the resin starts to flow above a critical "Vitrimeric" temperature (T_v). Moreover, the thermoformability of vitrimer-CFRP has been investigated by reprocessing CFRP coupons.

Introduction

Unlike thermoplastic polymers, thermosetting resins and their composite materials are very difficult to recycle. A stable cross-linked structure prevents long-range molecular mobility necessary to activate material flow at temperatures high enough to reform and recycle. As a result, thermosetting composites are hardly recycled, and most components are sent to landfills at the end of their service life.

Increasing environmental awareness and industrial competitiveness encourage introduction and development of repairable and recyclable structural materials to reduce polymer waste and extend their service life. Recently, the development of thermoreversible cross-linked networks has been introduced as a viable alternative to produce composite components that can be recycled and reformed as thermoplastic materials [1,2]

Introducing a thermoreversible covalent bond in the cross-linked backbone allows the topological reshuffling of polymeric networks and makes it possible to rework and reform the cross-linked material. The dissociative Diels- Alder reaction between furans and maleimides is a well-established approach for designing and synthesising covalent adaptable networks (CAN) [3]. As a further development in more easily re-processable and self-healing thermosets, vitrimers are gathering attention for outdoing the current drawbacks of CANs [4].

One possible mechanism that enables the vitrimeric behaviour in epoxy resins is based on transesterification exchange reactions between esters and beta-hydroxyls formed by reacting epoxy precursors with suitable acids/anhydrides [1,5]. Incorporating a catalyst activates the transesterification reaction and induces topological variations, stress relaxation and flow in the cross-linked networks, even though the total number of cross-links does not change [6,7].

However, there have been difficulties in realising such behaviour in rigid thermosets until 2011, when Leibler et al. [4] introduced a new group of materials named vitrimers. They applied the

Content from this work may be used under the terms of the Creative Commons Attribution 3.0 license. Any further distribution of this work must maintain attribution to the author(s) and the title of the work, journal citation and DOI. Published under license by Materials Research Forum LLC.

well-established transesterification reaction to the hydroxyl and ester groups in an anhydride-cured epoxy matrix to create a reworkable thermosetting network.

During transesterification, the network's connectivity is altered via exchange reactions, inducing stress relaxation and plastic flow at elevated temperatures without depolymerisation.

In the presence of a transesterification catalyst, it was shown that elastomeric epoxy/acid and rigid epoxy/anhydride networks possess gradually decreasing viscosity with increasing temperature, as is characteristic of other vitreous materials such as inorganic glass. Shi et al. [8] investigated such systems' capability to be welded and reprocessed. Demongeot et al. [9] investigated the mechanism of action of the catalytic zinc species active in these materials.

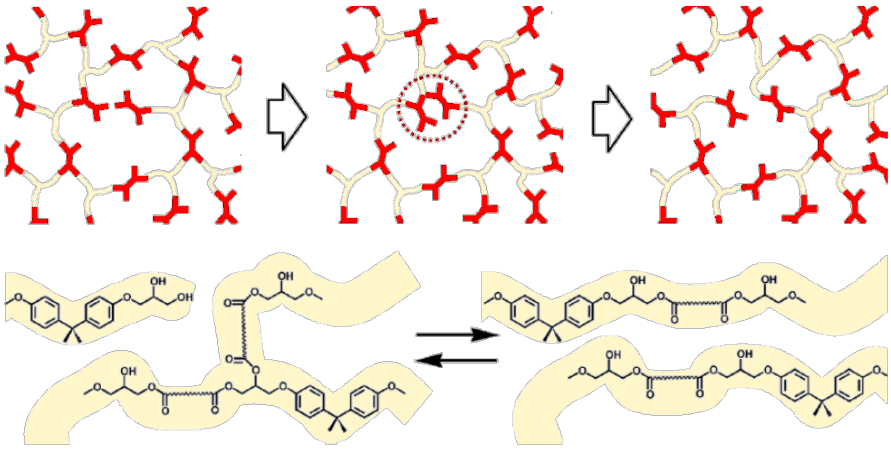

Fig. 1. Exchange reaction scheme and related topological changes. Adapted from [7,9].

In the present work, a commercial epoxy system (*araldite*® LY 3508 and *aradur*® 917-1 by Huntsman Corporation) suitable for CFRP manufacturing was selected for its modification as a vitrimer. Furthermore, zinc acetate was selected as a transesterification catalyst. Two formulations at a different stoichiometric ratio between epoxy precursor and curing agent have been prepared and modified by adding Zinc acetate into anhydride. Creep experiments showed a flow above a critical temperature (about 170°C) that confirms the achievement of a vitrimeric behaviour. In addition, a vitrimer-CFRP was realised using one of the formulations analysed and was thermoformed.

Materials and Methods

The used resin is a mixture of Bisphenol A diglycidyl ether (DGEBA) epoxy resin with an Epoxy Equivalent Weight (EEW) of 196.5 g/eq, tetrahydro-methyl phthalic anhydride (THMPA) curing agent and 2,4,6-tris(dimethyl aminomethyl)phenol as the catalyst, kindly provided by Huntsman corporation with product names *araldite*® LY 3508, *aradur*® 917-1 and Accelerator 960-1 respectively. The vitrimers formulations are based on ester interchange reaction, and Anhydrous zinc acetate (ZnAc2) (99.99%) was used as the catalyst, purchased by Merck Sigma-Aldrich. All reagents were used without further purification.

The Epoxy resin *araldite*® LY 3508 and cross-linking anhydride *aradur* ® 917-1 were mixed at room temperature with a mechanical mixer in a glass beaker until a homogeneous mixture was achieved. Subsequently, the Accelerator 960-1 was added and further mechanically mixed. The total weight of the prepared mixture was in the range of 100 g.

Two different formulations were realised, varying the epoxy to acyl ratio between 0.6 (M2) to 1.0 (M2A).

In addition, zinc acetate is added to the epoxy resin formulations to promote the ester interchange reaction and induce cross-linked resin's vitrimeric behaviour. First, an adduct is synthesised between tetrahydro-methyl phthalic anhydride (THMPA) and zinc acetate. Then, the

required amount of *aradur* 917-1 (20.00 g, 0.120 mol) and zinc acetate (3.22 g, 0.018 mol) are reacted in a round bottom flask at 120°C for 2 hours under nitrogen flow.

The THMPA/zinc acetate adduct is cooled to room temperature and used without further purification. Then, the epoxy vitrimeric mixture is prepared according to the above procedure while substituting *aradur* ® 917-1 with the THMPA/zinc acetate adduct.
After mixing, samples were degassed under a vacuum and cured for 1h @ 120°C and 2h at 140°C. Table 1 summarises the cross-linked sample condition realised.

Table 1. Cross-linked sample composition.

Sample Codex	LY 3508 [phr]	*Aradur* 917-1 [phr]	960-1 acc. [phr]	r epoxy/acyl ratio	$ZnAc_2$ * [%]
M2 **	*100*	*70*	*3*	0.6	-
M2A	100	40	3	1.0	-
M2-V	100	70	3	0.6	5
M2A-V	100	40	3	1.0	5

* $ZnAc_2$ percentage is calculated to the total acyl groups.
** Commercial Huntsman formulation

Experimental Methods

DSC was performed with a *Discovery DSC* of *TA Instruments* under a nitrogen atmosphere with a heating and cooling rate of 10°C min^{-1}, from room temperature to 250°C. About 10 mg samples were encapsulated in aluminium pans before measurements.

DMA experiments were conducted with a *Dynamic Mechanical Analyzer Q800* from *TA Instruments* in the single cantilever mode. Samples were measured from 30 to 160°C at 3 °C/min, a strain amplitude of 15 μm, and a frequency of 1 Hz. The samples were cut into a rectangular shape of 25 mm × 5.5 mm and a thickness of ca. 2.5 mm.

Creep tests were performed using a *Dynamic Mechanical Analyzer Q800* from *TA Instruments*. The Tension Film clamp with preload of 0.1 N was applied. The specimen dimensions were c.a. 10x5.5x2 mm^3. Five minutes of isothermal hold was used before each creep segment, starting from 70°C to 220°C with 50°C incremental steps to evaluate sample strain variation from the glassy to the rubbery state. The stress of 0.1 MPa was applied for 45 minutes.

The ability of the vitrimer composite to be thermoformed has been assessed by applying plastic deformation in a three-point bending configuration with a span of 50 mm. The forming temperature (200°C) was chosen according to the vitrimeric temperature (in the actual epoxy system T_v is expected at 220°C,[10]). The sample was kept at the temperature of 200°C for 600s. Therefore, a load was applied (displacement control mode) with a speed of 500 μm/min up to a maximum deflection of 10 mm. The force needed to deform the sample was 0.1 N.

Results and Discussion

The preparation of cross-linked systems with semi-flexible molecular structures facilitates topological interchange reactions; however, it reduces the glass transition temperature and elastic modulus. Therefore, a balance must be sought between the reactivity of interchange linkages and thermomechanical properties. It is well known that bifunctional epoxy precursors can be cross-linked with monocarboxylic anhydrides using either an excess or a defect of the curing agent. Usually, the reaction is promoted by the presence of substituted amines as the catalyst. If a stoichiometric ratio between epoxy and acyl groups is used, the cross-linked density is lower, but the presence of hydroxyl and ester groups highly facilitates the ester interchange reaction [11].

The transesterification reaction can be activated by the presence of Zn2+ ions at an elevated temperature beyond vitrimeric temperature (T_v), leading to a topological rearrangement.

This study will discuss the influence of the THMPA/ZnAc2 molecular ratio on the epoxy formulations' mechanical properties. In addition, temperature-dependent creep experiments have verified the occurrence of molecular long-range rearrangements.

Epoxy mixture M2 described in Table 1 has been formulated as reference material. The epoxy is used with a stoichiometric defect, with a mole ratio of epoxy/acyl equal to 0.6. The acyl groups in stoichiometric excess can further react with -OH groups formed due to oxirane ring addition to carboxylic acid.

The curing behaviour and glass transition temperature of the M2 system are illustrated in Fig. 2a. The absence of an exothermic peak in the second heating ramp of DSC is a clear indication of a complete conversion. The observed T_g is about 120°C. The epoxy mixture M2A was subsequently prepared with a stoichiometric ratio between epoxy and acyls equal to unity.

The cure of M2A system is illustrated in Fig. 2b (DSC Thermogram). As expected, the T_g drops to 99°C due to a lower cross-linking density.

To obtain a vitrimerized version of M2 and M2A, zinc acetate is introduced as a suitable catalyst for ester interchange reactions. The amount of zinc acetate has been fixed at 5% of the acyl groups, the obtained systems have been named M2-V and M2A-V, respectively.

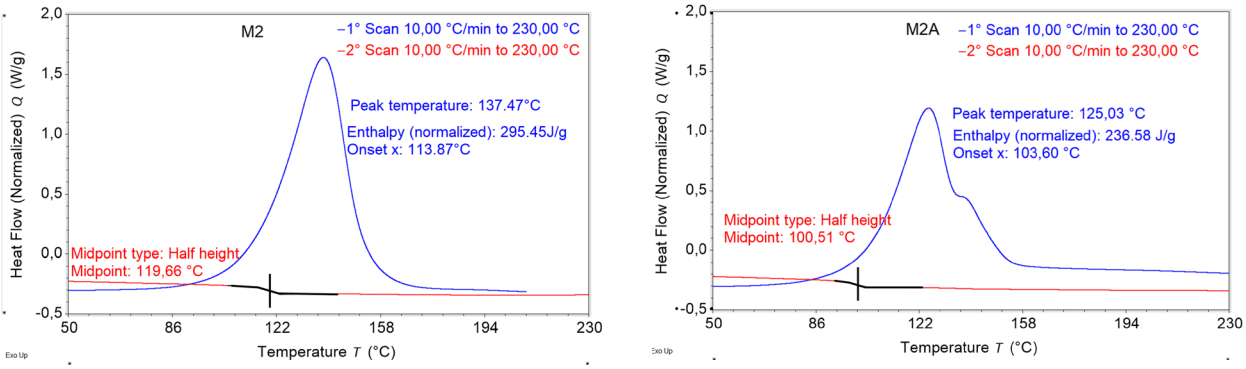

a) b)

Fig. 2. DSC curves of the samples at different epoxy/acyl ratio. Reference resin a); stoichiometric ratio (epoxy/acyl 1.0, M2A) b).

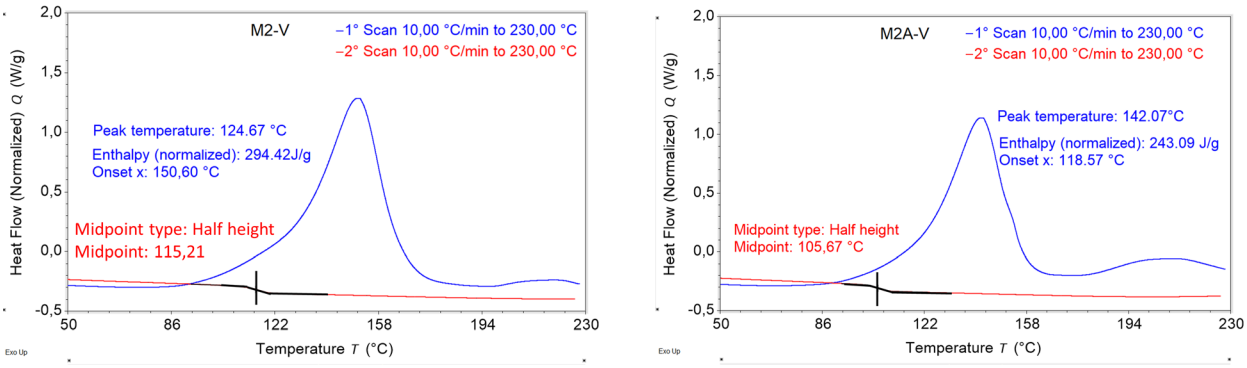

a) b)

Fig. 3. DSC curves of the samples at different epoxy/acyl ratios. Modified formulation, "Vitrimers" M2-V a) and M2A-V b).

The zinc acetate influences the primary cross-linking reaction and activates a secondary reaction in the temperature range between 180 and 230°C, while the T_g of the cross-linked sample appears to be dominated by the ratio between epoxy and acyl groups (Fig. 3).

DMA experiments, shown in Fig. 4, have been performed in the linear viscoelastic deformation range to confirm cross-linked samples' glass transition temperatures and elastic modulus. The

glass transition temperature has been evaluated as the value at the inflection point of the storage modulus diagram.

The effects of catalyst addition and the different stoichiometric ratio between epoxy and acyls are shown in Fig. 5 and highlight three main phenomena:

a) The glass transition temperatures obtained by DMA confirm the corresponding values measured by DSC;
b) The addition of the Zn2+ catalyst produces an increase in the glassy elastic modulus;
c) The tanδ (ratio between loss and storage moduli) of vitrimeric systems (M2-V and M2A-V) @160°C is higher than corresponding conventional formulations (M2 and M2A, respectively). Indeed, this experimental observation could be related to a residual viscous flow, confirmed by following creep experiments.

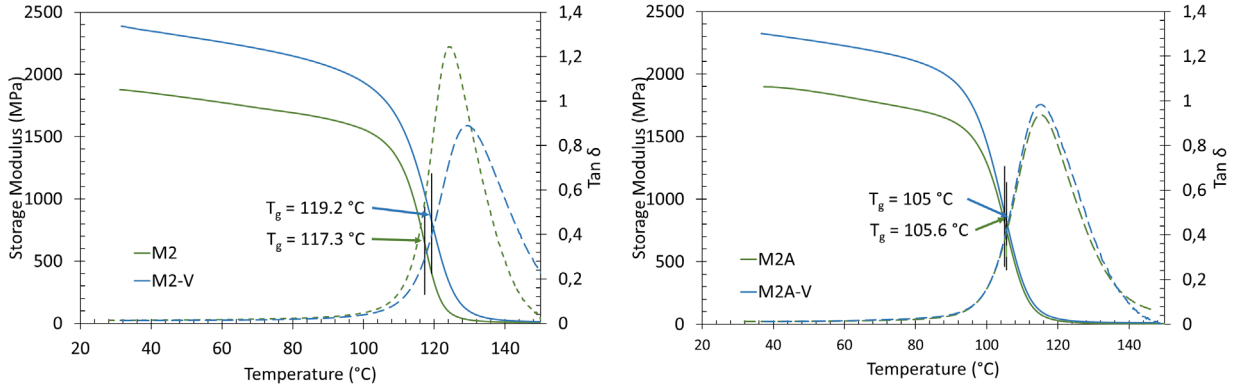

a) b)

Fig. 4. DMA curves at different epoxy/acyl ratios M2 and its vitrimer a); M2A and its vitrimer b).

Table 2 summarises the thermomechanical properties of the analysed systems characterised by DSC, DMA and CREEP experiments.

Table 2. Thermo-mechanical properties.

Description	**T_g (DSC) [°C]**	**T_g (DMA) [°C]**	**Reaction Enthalpy [J/g]**	**Elastic Modulus [GPa]**
M2	119.7	119.2	295.5	1.88
M2A	100.5	105.6	236.6	1.89
M2-V	115.2	117.3	294.4	2.38
M2A-V	105.7	105.0	243.1	2.34

In addition to the DMA experiment, the explicit and robust confirmation of vitrimeric behaviour due to thermoreversible cross-linking rearrangements has been obtained by creep experiments.

Samples in the form of thin slabs have been subjected to creep experiments under tension deformation. The creep experiments have been performed in the temperature range between 70 and 220°C.

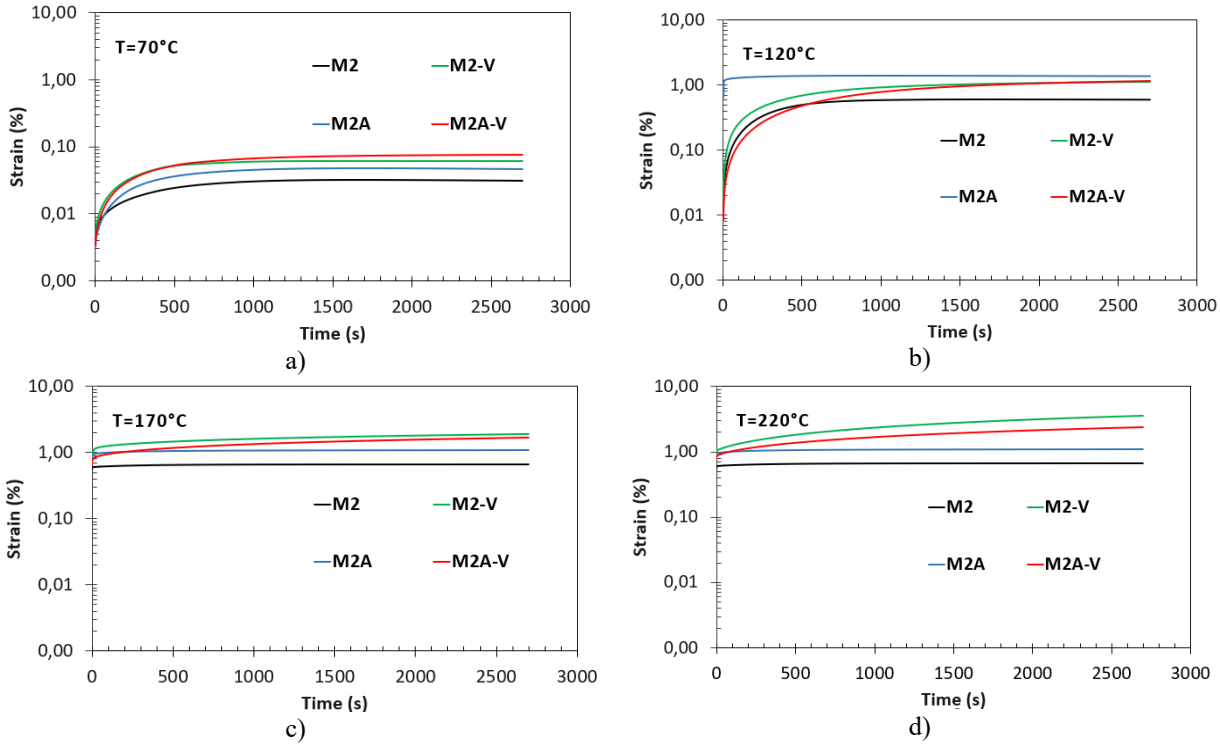

Fig. 5. Creep curves at different temperatures.

Specimen M2 and M2A showed stable behaviour; in fact, creep is negligible at each temperature. Even at temperatures higher than T_g, no molecular flow has been observed.

Things change when zinc acetate is added to the formulation. The presence of metallic ions strongly catalyses the ester interchange reaction, resulting in evident creep of samples subjected to tensile load at different temperatures, as reported in Fig. 5. The effects are higher in the case of the M2A-V sample with an equivalent amount of epoxy and acyls (r=1.0).

To verify the thermoformability of the vitrimeric matrix developed, a carbon fibre-reinforced composite has been realised using the matrix M2A-V.

The vitrimer-CFRP laminates were produced by hand lay-up and vacuum consolidation at 120°C (Fig. 6).

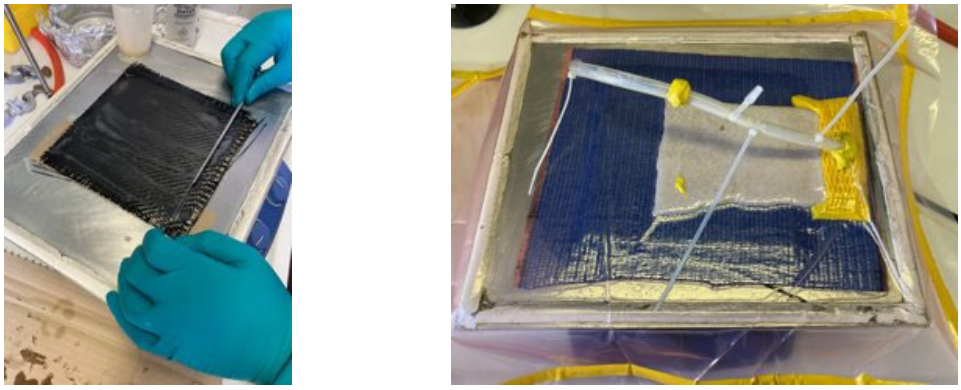

Fig. 6. Manufacturing procedure for vitrimer-CFRP.

Then, test specimens were cut to the dimensions 60x12 mm, and thermoformed following the procedure reported in Fig. 7.

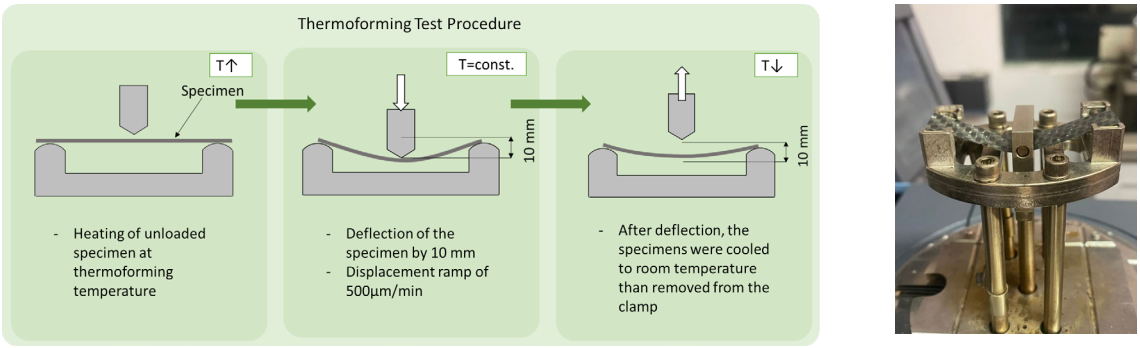

Fig. 7. Experimental set-up and 3-point bending thermoforming test procedure.

After the cooling stage, the sample was frozen in the deformed configuration, even if a spring-back (13%) had been detected. By observing the reshaped sample, no flaws or other defects have been observed, therefore, the polymeric phase is able to flow and is prone to be reprocessed to improve the sustainability of parts made by vitrimers.

Summary

The epoxy groups can efficiently react with carboxylic acids or anhydrides. Therefore, bi/multifunctional epoxy precursors can be efficiently cross-linked with carboxylic anhydrides, resulting in very stable materials with a glass transition temperature of 100-140°C and an elastic modulus in the range of 1.5-2.0 GPa.

In this work, two different formulations with the adjustable stoichiometric ratio between epoxy precursor and curing agent have been prepared. In order to promote the polymer modification into vitrimer, the catalyst Zn2+ has been introduced into the formulation by synthesising an adduct between ZnAc2 and the THMPA curing agent, with a catalyst concentration of 5 % than to acyl groups. The presence of metallic ions strongly catalyses the ester interchange reaction, resulting in evident creep of samples subjected to tensile load at different temperatures. Moreover, an empirical approach to investigate the thermoformability of vitrimer-CFRP has been presented with satisfactory results.

Even if epoxy vitrimers have shown important features for increasing the sustainability of composite materials, major challenges will have to be faced to transfer this from an academic concept into real-world materials. First of all, it is mandatory to increase the glass transition to meet the requirements of structural applications, in addition, industrialisation needs affordable catalysts to sustain mass production, by the way, their development is very promising.

Acknowledgements
This work has been supported by the Research Project LAMPO (code CDS00750), founded by the Ministry of Economic Development. The authors would like to thank M. De Angioletti, F. Docimo, M. R. Marcedula and C. Leone for their support to experiments.

Reference
[1] M. Capelot, M.M. Unterlass, F. Tournilhac, L. Leibler, Catalytic Control of the Vitrimer Glass Transition, ACS Macro Lett. 1 (2012) 789.
[2] L. Imbernon, S. Norvez, From landfilling to vitrimer chemistry in rubber life cycle, Eur. Polym. J. 82 (2016) 347-376. https://doi.org/10.1016/J.EURPOLYMJ.2016.03.016
[3] S. Dello Iacono, A. Martone, A. Pastore, G. Filippone, D. Acierno, M. Zarrelli, M. Giordano, E. Amendola, Thermally activated multiple self-healing diels-alder epoxy system, Polym. Eng. Sci. 57 (2017) 674-679. https://doi.org/10.1002/pen.24570
[4] D. Montarnal, M. Capelot, F. Tournilhac, L. Leibler, Silica-like malleable materials from permanent organic networks, Science (1979). 334 (2011) 965-968. https://doi.org/10.1126/SCIENCE.1212648/SUPPL_FILE/MONTARNAL.SOM.PDF
[5] S. Wang, S. Ma, Q. Li, X. Xu, B. Wang, W. Yuan, S. Zhou, S. You, J. Zhu, Facile: In situ preparation of high-performance epoxy vitrimer from renewable resources and its application in nondestructive recyclable carbon fiber composite, Green Chem. 21 (2019) 1484-1497. https://doi.org/10.1039/C8GC03477J
[6] W. Denissen, J.M. Winne, F.E. Du Prez, Vitrimers: Permanent organic networks with glass-like fluidity, Chem. Sci. 7 (2016) 30 -38. https://doi.org/10.1039/C5SC02223A
[7] M. Capelot, D. Montarnal, F. Tournilhac, L. Leibler, Metal-catalyzed transesterification for healing and assembling of thermosets, J. Am. Chem. Soc. 134 (2012) 7664-7667. https://doi.org/10.1021/ja302894k
[8] Q. Shi, K. Yu, M.L. Dunn, T. Wang, H.J. Qi, Solvent Assisted Pressure-Free Surface Welding and Reprocessing of Malleable Epoxy Polymers, Macromolecules 49 (2016) 5527-5537. https://doi.org/10.1021/ACS.MACROMOL.6B00858
[9] A. Demongeot, S.J. Mougnier, S. Okada, C. Soulié-Ziakovic, F. Tournilhac, Coordination and catalysis of Zn2+ in epoxy-based vitrimers, Polym. Chem. 7 (2016) 4486-4493. https://doi.org/10.1039/C6PY00752J
[10] X. Niu, F. Wang, X. Li, R. Zhang, Q. Wu, P. Sun, Using Zn2+ Ionomer to Catalyze Transesterification Reaction in Epoxy Vitrimer, Ind. Eng. Chem. Res. 58 (2019) 5698-5706. https://doi.org/10.1021/ACS.IECR.9B00090
[11] Y. Yang, G. Peng, S. Wu, W. Hao, A repairable anhydride-epoxy system with high mechanical properties inspired by vitrimers, Polym. 159 (2018) 162-168. https://doi.org/10.1016/j.polymer.2018.11.031

Materials Research Proceedings 28 (2023) 1879-1886 https://doi.org/10.21741/9781644902479-203

Thermal and mechanical properties of Fdmed biocomposites in polylactic acid and food flour waste

PAPA Ilaria[1,a *], LANGELLA Antonio[1,b], NAPOLITANO Francesco[2,c] and RUSSO Pietro[2,d]

[1]Dept. of Chemical, Materials and Production Engineering, University of Naples Federico II, Naples, Italy

[2]Institute for Polymers, Composites and Biomaterials - CNR-Pozzuoli, Naples, Italy

[a]ilaria.papa@unina.it, [b]antgella@unina.it, [c]francesco.napolitano@ipcb.cnr.it, [d]pietro.russo@ipcb.cnr.it

Keywords: Biocomposites, PLA, FDM, Filament, Flour Waste, Mechanical Properties

Abstract. In the last few years, fused deposition modelling (FDM) has been explored as an innovative technology for processing thermoplastic green composite materials. However, not all FDM filaments are ecologically beneficial due to their release of toxic compounds during printing. Moreover, they have a dangerous environmental impact, as they are obtained from petroleum. The researches on biofilament manufacturing for FDM are of great interest, thus attracting a lot of attention. The low cost of such filaments could help minimize the use of petroleum-based plastics. In this frame, this work deals with a 3d printer PLA filament neat and additive by food flour waste percentage was created. The innovative filament was analyzed by calorimetric and thermogravimetric analysis, and its printability was evaluated by manufacturing specimens of suitable dimensions for flexural tests. The mechanical tests were carried out to assess the use of the innovative 3d printed biocomposite in place of traditional plastics in packaging or to make films for food use.

Introduction

Plastics derived from natural sources have attracted extraordinary attention as they do not contribute to the depletion of fossil resources, ensuring reduced carbon dioxide production during synthesis and transformation. Therefore, they generate a lower environmental impact than petroleum-derived ones. As a result, PLA is one of the most widely used bioplastics. Still, its intrinsic characteristics, such as fragility, often limit its use in particularly demanding applications unless strategies such as mixing with other polymers or including suitable additives are used. With these approaches, new environmentally sustainable materials are obtained, with better performance and which guarantee the reduction of environmental contamination associated with plastic [1-5].

The most common manufacturing technologies for thermoplastic-based green composites are extrusion, compression moulding and injection moulding [6]. Nevertheless, fused deposition modelling (FDM) has been explored as an innovative technology for processing thermoplastic green composite materials [7-11]. The many advantages of FDM, the reduction of production time and costs, and the possibility to create highly elaborated geometries are the most interesting aspects that make this manufacturing technique promising for making green composite components [12]. FDM has gained interest in several fields, such as aerospace, automotive, research, medical architecture, food, and design [13-15]. It is an additive manufacturing method which applies different thermoplastics materials for composites and biocomposites [16]. A thermoplastic filament is heated and crushed out on the printing plate by a nozzle. The product is created by depositing material layer by layer that solidifies after fusing to produce the components [17,18].

Content from this work may be used under the terms of the Creative Commons Attribution 3.0 license. Any further distribution of this work must maintain attribution to the author(s) and the title of the work, journal citation and DOI. Published under license by Materials Research Forum LLC.

The market demand for 3D printing filament is estimated to reach high gain values by 2027 at an annual growth rate of about 20%. Plastic filaments have recently led the printing press industry due to the high demand for filaments [19]. However, not all FDM filaments are ecologically beneficial due to their release of toxic compounds during printing. In addition, they have a dangerous impact on the environment, as they are obtained from petroleum [20].

The growing use of industrial and domestic FDM 3D printing further increases plastic waste. Such technology could gradually displace and replace some cheap and non-biodegradable plastic waste in ambient conditions posing a threat to the environment. To address the above-described problems, the researches on biofilament manufacturing for FDM are of great interest thus attracting a lot of attention. The low cost of such filaments could help minimize the use of petroleum-based plastics. Although many works have been done on biomaterials, most concern biomedical applications [21-23].

In this frame, combining biodegradable polymers with agricultural waste, marine waste, or industrial residues from wood processing has gained particular interest in producing composite materials with high mechanical performance [1-5]. Often these fibres come from processing waste typical of the areas of research sites, such as flour deriving from hazelnut processing waste [24] or bamboo [25].

This work created a 3d printer PLA filament neat and additived by food flour waste percentage. The innovative filament was analyzed by calorimetric and thermogravimetric analysis, and its printability was evaluated by manufacturing specimens of suitable dimensions for flexural tests. The mechanical tests were carried out to assess the use of the innovative 3d printed biocomposite in place of traditional plastics in packaging for food use.

Materials

Investigated systems were based on a commercial polylactic acid (PLA) supplied by Biowares.r.l. with the trade name Luminy LX175 (density: 1.24 g/cm3, MFI@210°C/2.16 Kg: 6g/10 min, Tg: 60°C) and food flour waste (FW) supplied by a local pasta factory.

From PLA pellets (100% wt.), cleaned and filled filament (FW) was produced using a 3Devo Composer 450 Filament Maker (Utrecht, The Netherlands) with a single screw extruder equipped with four heating zones, reaching a maximum T=450°C.

For the extrusion of the PLA_FW, the four heat zones reached a temperature between 70° and 190°, in about twenty-five minutes, with a first increasing sequence to favor the melting of the granules of raw material inserted into the feed hopper (Fig. 1), and then decreasing to favor the extraction of the extruded filament. Once the temperature T=190°C was reached, the extruded filament was wound onto a reel via the rotating shaft of the extruder itself. At the exit, the filament is further cooled by two fans, as the extruder expels it through a nozzle at a temperature of about 170°, corresponding to the last heat zone. The diameter of the extruded filament has been controlled by a sensor which guarantees maximum uniformity of the diameter. Finally, neat and filled PLA filaments with a 1.75 ± 0.2 mm diameter were produced.

Materials Research Proceedings 28 (2023) 1879-1886 https://doi.org/10.21741/9781644902479-203

Fig. 1. Granules of raw material neat and infilled by flour waste.

3D Printer Setup

The samples were manufactured using the Sharebot 42 3D printer, which uses FDM (Fused Deposition Modeling) as an additive manufacturing technique. The 3D printer is 450x420x470 mm in size and has a printing volume of 250x220x220 mm, while the Z resolution is 50 microns. CAD 3D of the samples were modelled with Solidworks software. Then, they were imported into the Simplify3D software. The heated printing bed, the printing bed autocalibration system, the easy detach system and the filament sensor are integrated into the 3D printer. 100% infill density, a line infill pattern and a -45°/+45° raster orientation were adopted. Layers height was fixed equal to 0.2 mm. Plate temperature equal to 90°C, a deposition speed equal to 70 mm/s and an extruder temperature equal to 215°C were selected for all samples.

Thermal Analysis

Extruded compounds were thermally analyzed using a TA Instruments DSC Q2000 differential scanning calorimeter (New Castle, DE, USA) by applying a typical three-stage procedure involving a first heating step from 30°C to 220°C, a cooling step from 220°C to 30°C and further heating from 30°C to 220°C. All the steps were carried out on 8-10 mg of material at a rate of 10°C/min. Processing of collected thermograms allowed the evaluation of some typical parameters, such as the temperature and the enthalpy of the main transitions evaluated as the peak temperature and the area underlying the respective calorimetric signal.

Thermogravimetric analyses were carried out by a Perkin Elmer Pyris Diamond analyzer (TGA) model. At this purpose, materials were heated starting from a temperature of 25°C up to a temperature of 800°C in a flow of nitrogen at a heating rate of 10°C/min.

All the investigated materials were compared with neat PLA processed under the same conditions.

Mechanical Tests

Bending measurements determined the mechanical performances of the explored materials. Specifically, bending tests were conducted on 12.7x3.2x4 mm3 specimens, according to ASTM D790 standard [23] using a Galdabini QUASAR 50 materials testing machine with a test speed equal to 3mm/min.

For each sample, five specimens were tested to verify the reproducibility of the data.

Results and Discussion

Calorimetric results.

Table 1 summarises the results obtained from the calorimetric analysis of the materials under study. The glass transition temperature (T_g) and the melting temperature (T_m) values, characteristic of the hosting matrix, are not substantially affected by waste flours. On the contrary, the inclusion of this filler significantly increases the melting and cold crystallization enthalpy values (H_m and H_{cc}, respectively), slightly anticipating the cold crystallization temperature (T_{cc}). In other words, it is evident that the filler alters the crystalline structure of the host matrix and probably favours its crystallization.

Table 1. DSC results.

Material	T_g[°C]	T_{cc}[°C]	ΔH_{cc}[J/g]	T_m [°C]	ΔH_m[J/g]
PLA	59.2	124.2	8.9	150.3	14.9
PLA+1%FW	59.6	116	13.9	149.9	21.9
PLA+3%FW	58.9	117.7	15.9	149.5	21.5
PLA+5%FW	59.4	118.4	13.9	149.6	19.6

TGA results.

The results obtained on all examined samples are collected in Table 2 regarding key parameters. In addition, the temperatures corresponding to a weight loss equal to 1% and 5% ($T_{1\%}$ and $T_{5\%}$, respectively), the temperature at which the massive degradation of the material (T_d) occurs and the residual mass percentage remaining at the end of the applied thermal scan are reported.

The inclusion of waste flours causes a progressive reduction in the material's thermal stability. However, this effect, usually catalyzed in the presence of organic fillers, appears to be not marked up to a composition of 3% by weight.

In the presence of 5 wt% of FW, on the other hand, perhaps also due to the higher moisture content brought internally to the composite by the organic filler included, the first parameter $T_{1\%}$ is strongly anticipated.

Concerning the amount of the residue, this parameter, resulting to be not zero even for the reference matrix, increases with the filler content, assuming values not easily comparable with the nominal content of waste flours included.

Table 2. TGA results.

Material	$T_{1\%}$ [°C]	$T_{5\%}$ [°C]	T_d[°C]	Residue [%]
ExtrudedPLA	290	307	351	0.5
PLA+1%FW	262	285	320	1.1
PLA+3%FW	261	292	324	1.8
PLA+5%FW	160	286	322	3.1

Mechanical results.

Flexural tests results have been reported in Fig. 2 and Table 3 where the flexural strength, σ_f, and the correspondent maximum deflection, d_{max}, are reported for each material tested.

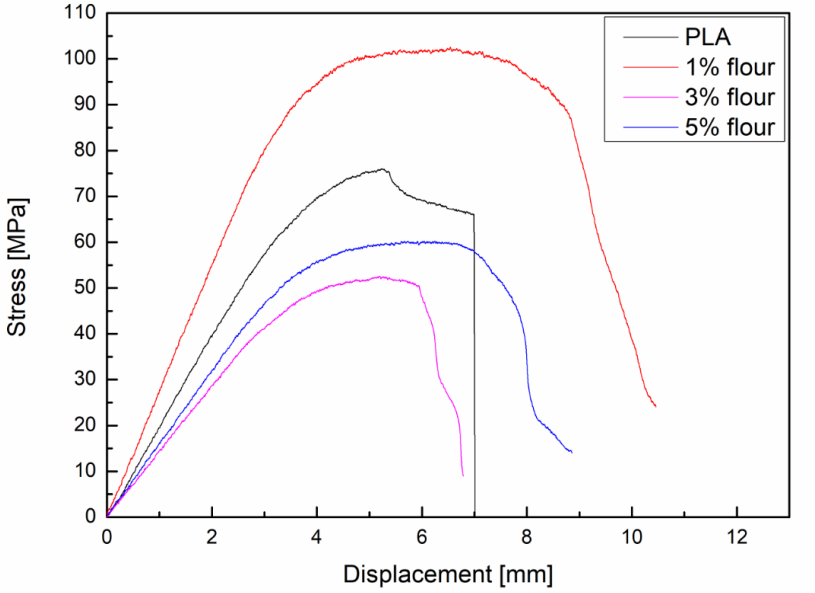

Fig. 2. Stress displacement curves for all materials tested.

As visible in Fig. 2, the printed samples with a percentage of flour waste of 1%wt show a maximum load higher respect to neat PLA, also offering the ability to hold the load over a longer displacement range. On the other hand, increasing the FW content determines increasing material embrittlement, as confirmed by the visual inspections of the bent specimens (see Fig. 3). Clearly, samples of extruded PLA or containing 1% wt of FW show a crack at the load's application point, while ones filled with 3% and 5% by weight of FW yield at the load application point undergo a brittle break.

Table 3. Flexural tests results.

Material	**$б_f$ [MPa]**	**d_{max} [mm]**
ExtrudedPLA	75.91± 2.5	5.20± 0.2
PLA+1%FW	100.21± 3.0	6.66± 0.5
PLA+3%FW	50.99± 2.6	5.30± 0.3
PLA+5%FW	58.61± 3.2	6.00± 0.6

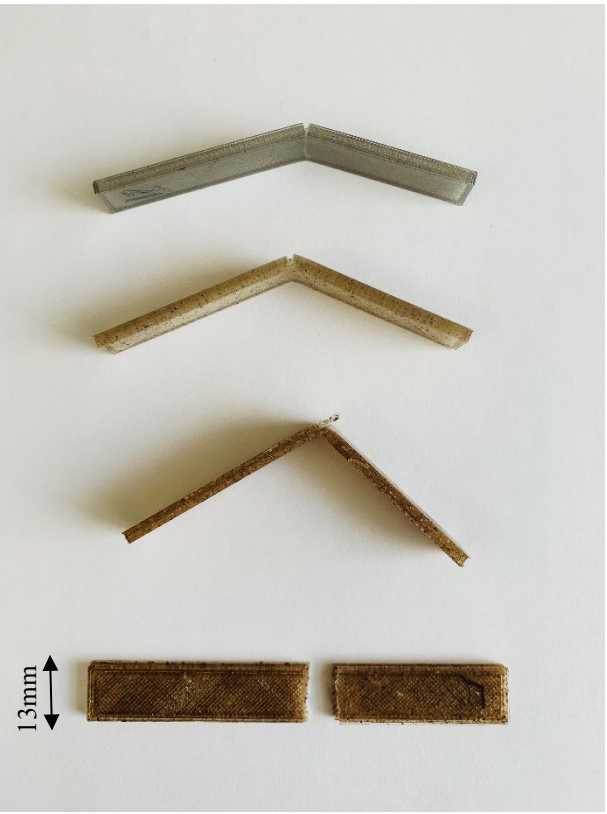

Fig. 3. Bending specimens after test.

These considerations are further highlighted by bending features values at break obtained for all the materials studied on at least 5 specimens tested for each sample (see Table 3).

Summary

The work's aim is to propose innovative biodegradable filament made of PLA and different flour waste percentages to explore the potential of 3d printed composites for sustainable industrial applications. The attention was focused on food flour waste in huge quantities on the national territory, especially in Southern Italy, where there is a large consumption of products such as pasta and bread.

The filament produced appears constant in diameter, equal to 1.75mm. Thermal and mechanical analysis of samples based on poly (lactic) acid-containing food flour waste have indicated an improvement in the mechanical parameters in bending behaviour compared to those characteristics of the polymeric reference matrix only for FW=1%. Also, material toughness decreases with the flour waste content over FW=1%. This behaviour is typical for micro composites, including filler having a poor chemical affinity with the surrounding matrix. It is supported by the morphological observations performed on fractured cryogenic sections of the samples.

References

[1] R. Scaffaro, M.C. Citarrella, E.F. Gulino, M. Morreale, Hedysarum coronarium-Based Green Composites Prepared by Compression Molding and Fused Deposition Modeling, Materials 15 (2022) 465. https:// doi.org/10.3390/ma15020465

[2] J. Armando, K. Rafiee, H. Schritt, D. Pleissner, G. Kaur, S.K. Brar, Biodegradable Green Composites: It's Never Too Late to Mend, Curr. Opin. Green Sustain. Chem. 30 (2021) 100482. https:// doi.org/10.1016/j.cogsc.2021.100482

[3] P. Bordón, R. Paz, C. Peñalva, G. Vega, M. Monzón, L. García, Biodegradable Polymer Compounds Reinforced with Banana Fiber for the Production of Protective Bags for Banana Fruits

in the Context of Circular Economy, Agronomy 11 (2021) 242. https://doi.org/10.3390/agronomy11020242
[4] G. Lo Re, M. Morreale, R. Scaffaro, F.P. la Mantia, Kenaf-Filled Biodegradable Composites: Rheological and Mechanical Behaviour, Polym. Int. 61 (2012) 1542-1548. https://doi.org/10.1002/pi.4243
[5] F.P. La Mantia, M. Morreale, Improving the Properties of polypropylene-Wood Flour Composites by Utilization of Maleated Adhesion Promoters, Compos. Interfaces 14 (2007) 685-698. https://doi.org/10.1163/156855407782106500
[6] A. Gholampour, T. Ozbakkaloglu, A Review of Natural Fiber Composites: Properties, Modification and Processing Techniques, Characterization, Applications; Springer: New York, NY, USA, 2020; Volume 55, ISBN 1085301903990
[7] R. Scaffaro, A. Maio, E.F. Gulino, G. Alaimo, M. Morreale, Green Composites Based on Pla and Agricultural or Marine Waste Prepared by Fdm, Polymers 13 (2021) 1361. https://doi.org/10.3390/polym13091361
[8] Z. Liu, Q. Lei, S. Xing, Mechanical Characteristics of Wood, Ceramic, Metal and Carbon Fiber-Based PLA Composites Fabricated by FDM, J. Mater. Res. Technol. 8 (2019) 3741-3751. https://doi.org/10.1016/j.jmrt.2019.06.034
[9] R. Prabhu, A. Devaraju, Recent Review of Tribology, Rheology of Biodegradable and FDM Compatible Polymers, Mater. Today Proc. 39 (2020) 781-788.
[10] S.D.S. Kopparthy, A.N. Netravali, Review: Green Composites for Structural Applications, Compos. Part C Open Access 6 (2021) 100169. https://doi.org/10.1016/j.jcomc.2021.100169
[11] N.R. Rajendran Royan, J.S. Leong, W.N. Chan, J.R. Tan, Z.S.B. Shamsuddin, Current State and Challenges of Natural Fibre-Reinforced Polymer Composites as Feeder in Fdm-Based 3d Printing, Polymers 13 (2021) 2289. https://doi.org/10.3390/polym13142289
[12] V. Mazzanti, L. Malagutti, F. Mollica, FDM 3D Printing of Polymers Containing Natural Fillers: A Review of Their Mechanical Properties, Polymers 11 (2019) 1094. https://doi.org/10.3390/polym11071094
[13] J. Liu, L. Sun, W. Xu, Q. Wang, S. Yu, J. Sun, Current advances and future perspectives of 3D printing natural-derived biopolymers, Carbohyd. Polym. 207 (2019) 297-316. https://doi.org/10.1016/j.carbpol.2018.11.077
[14] Y. Tao, H. Wang, Z. Li, P. Li, S.Q. Shi, Development and Application of Wood Flour-Filled Polylactic Acid Composite Filament for 3D Printing, Materials 10 (2017) 1-6. https://doi.org/10.3390/ma10040339
[15] I. Papa, A.T. Silvestri, M.R. Ricciardi, V. Lopresto, A. Squillace, Effect of fibre orientation on novel continuous 3d-printed fibre-reinforced composites, Polymers 13 (2021) 2524. https://doi.org/10.3390/polym13152524
[16] Z. Wang, J. Xu, Y. Lu, L. Hu, Y. Fan, J. Ma, X. Zhou, Preparation of 3D printable micro/nanocellulose-polylactic acid (MNC/PLA) composite wire rods with high MNC constitution, Ind. Crop. Prod. 109 (2017) 889-896. https://doi.org/10.1016/j.indcrop.2017.09.061
[17] D. Popescu, A. Zapciu, C. Amza, F. Baciu, R. Marinescu, FDM process parameters influence over the mechanical properties of polymer specimens: A review, Polym. Test. 69 (2018) 157-166. https://doi.org/10.1016/j.polymertesting.2018.05.020
[18] F. Napolitano, E. Cozzolino, I. Papa, A. Astarita, A. Squillace, Experimental integrated approach for mechanical characteristic optimization of FDM-printed PLA in an energy-saving perspective, Int. J. Adv. Manuf. Technol. 121 (2022) 3551-3565. https://doi.org/10.1007/s00170-022-09535-z
[19] Global 3D Printing Filament Market Share Report, Dec. 2020, 2020-2027, www.grandviewresearch.com/industry-analysis/3d-printing-filament-market

[20] A. Manoj, M. Bhuyan, S.R. Banik, M.R. Sankar, Review on particle emissions during fused deposition modeling of acrylonitrile butadiene styrene and polylactic acid polymers, Mater. Today: Proc. 44 (2021) 1375-1383. https://doi.org/10.1016/j.matpr.2020.11.521
[21] R. Verma, K.S. Vinoda, M. Papireddy, A.N.S. Gowda, Toxic Pllutants from Plastic Waste- A Review, Procedia Environ. Sci. 35 (2016) 701-708. https://doi.org/10.1016/j.proenv.2016.07.069
[22] S. Bose, K.D. Traxel, A.A. Vu, A. Bandyopadhyay, Clinical significance of three-dimensional printed biomaterials and biomedical devices, MRS bulletin 44 (2019) 494-504. https://doi.org/10.1557/mrs.2019.121
[23] V.K. Balla, S. Bodhak, P. Datta, B. Kundu, M. Das, A. Bandyopadhyay, S. Bose, In Biointegration of medical implant materials (Second Edition), Woodhead Publishing (2020) 433-482. https://doi.org/10.1016/B978-0-08-102680-9.00016-0
[24] S. Wasti, S. Adhikari, Use of Biomaterials for 3D Printing by Fused Deposition Modeling Technique: A Review, Front. Chem. 8 (2020) 1-14. https://doi.org/10.3389/fchem.2020.00315
[25] F. Özdemir, N. Ayrilmis, E. Yurttaş, Mechanical and thermal properties of biocomposite films produced from hazelnut husk and polylactic acid, Wood Mater. Sci. Eng. (2021) 1-14. https://doi.org/10.1080/17480272.2021.1955972
[26] T.Y. Wang, Y. Weng, Characterization of interfacial compatibility of polylactic acid and bamboo flour (PLA/BF) in biocomposites, Polymer Testing, (2014) 119-125. https://doi.org/10.1016/j.polymertesting.2014.04.001

Materials Research Proceedings 28 (2023) 1887-1896 https://doi.org/10.21741/9781644902479-204

Characterization of the biaxial response of a thermoplastic ABS Sheet using DIC-instrumented bubble inflation technique

VAREDI Rasoul[1,2,a,*], BUFFEL Bart[1,2,b] and DESPLENTERE Frederik[1,c]

[1]Department of Materials Engineering, ProPoliS Research Group, KU Leuven Bruges Campus, Spoorwegstraat 12, 8200 Bruges, Belgium

[2]SIM M3 Program, Technologiepark-Zwijnaarde 48, 9052 Zwijnaarde, Belgium

[a]rasoul.varedi@kuleuven.be, [b]bart.buffel@kuleuven.be, [c]frederik.desplentere@kuleuven.be

Keywords: Vacuum Forming Process, Large Rapid Deformation, Nonlinear Behavior, DIC

Abstract. During the forming of a product with the thermo-vacuum forming process, a heated thermoplastic sheet is subjected to a complex and dynamic multi-axial deformation mode. In order to measure the relevant mechanical response of the material during processing, an experimental method that applies the relevant modes of deformation during forming is required. The bubble inflation technique combined with digital image correlation (DIC) allows having a complete data set regarding displacement, principal strains as well as local thickness reduction for material characterization. Bubble formation as a function of temperature would be investigated to determine the nonlinear terms of a material constitutive model for numerical simulation.

Introduction

Thermoforming is a material processing technology in which a thermoplastic sheet is radiatively heated above its glass transition point. The heated sheet begins to sag under its weight when it is in its softening range. In order to compensate for sag deformation and also make a uniform biaxial pre-stretching before forming into the desired mold shape, positive air pressure is exerted. At the appropriate temperature, the sheet is stretched to get the shape of a mold using both mechanical loading and vacuum. The thickness of the thermoformed product is determined as a critical parameter for product quality definition. In order to predict the thickness distribution of the thermoformed product, it is essential to characterize the strain and temperature dependency of material under relevant modes of deformation when it is subjected to large rapid deformation. Currently, a proper prediction of the thickness is still a challenge, due to a lack of proper understanding of the material behavior and the need for a specific experimental test that applies large and rapid biaxial or multi-axial deformation mode. Experimental work shows that a uniaxial tensile test is not sufficient to characterize the material behavior while it is subjected to the mainly multi-axial direction [1,2] in the vacuum forming process. Therefore, it is essential to examine the extension behavior of the material in biaxial directions with a suitable experimental method. There are different classical experimental methods to determine the biaxial extension behavior of the material. A basic rheometer test is a squeeze-flow technique where the specimen is compressed between two discs with a lubricated surface [3]. This kind of rheometer is well-suited for liquid-like high viscous materials while the forming range of thermoplastic material in vacuum forming is far away from the melting point and it is close to a solid-like state. Moreover, it does not cover large deformations. The biaxial in-plane technique is another well-known displacement-controlled method to characterize the behavior of the material. But gripping the material at an elevated temperature, sag deformation during heating, and the complexity of the clamping introduce uncertainties to this test setup. The plug assist technique is the other common method that is used frequently to capture relevant large deformation at a high strain rate corresponding to the vacuum

Content from this work may be used under the terms of the Creative Commons Attribution 3.0 license. Any further distribution of this work must maintain attribution to the author(s) and the title of the work, journal citation and DOI. Published under license by Materials Research Forum LLC.

forming process. But this method has also a big drawback regarding the effect of friction and heat transfer through contact between plug and specimen. It could be concluded that a large biaxial extension can be achieved under pressurized air within another classical method named the bubble inflation test. This method seems to have the best fit to track the appropriate strain rates and large biaxial elongation deformations. This technique was initially applied by a British scientist, Treloar in 1944 [4]. A very simple conical glass tube was used in his test setup to purge by pressurized air to detect the natural rubber inflation with a thickness of 0.8 mm at ambient temperature. In 1951, Rivlin et al [5] utilized this method to calibrate directly the Neo-Hookean and Mooney-Rivlin rheological parameters of natural rubber by examining the equibiaxial state of the deformation at the pole of the inflated material using membrane theory. In 2001, Reuge et al [6] extracted the equibiaxial stress-strain data of elastomers at ambient temperature by measuring the elongation and curvature radius of the bubble of a specimen with 40 mm diameter at the pole using a 2D CCD video camera technique. In 2008, the bubble inflation test coupled with a 3D digital image correlation (DIC) device was adopted for the first time by Sasso [7] to capture the real-time strain field evolution of the rubbery-like material at ambient temperature. A similar effort was implemented to determine the stress field by computing the curvature tensor during inflating of the material at each surface point by Machado [8]. Cakmak et al. in 2013 [9] performed a biaxial bubble inflation test using a self-constructed test rig with a diameter of 120 mm over two different rubbery-like materials at -20°C, 20°C, and 60°C under low strain rate so that the stretch ratio near to 2 was reported at around 20 seconds. The main goal was to determine a master curve applicable to small and large deformations. To the best of the author's knowledge, the only research aiming to meet the extension modes relevant to vacuum forming process was performed by Turner et al. in 2019 [10] to investigate the biaxial response of 2 mm thickness PEEK in the temperature range between 130 to 160°C at the pole using a small size of bulge diameter 5 cm. Discrepancy reported on principal strain directions at the pole using DIC measurement was attributed to the extrusion process of the material. The tests at different temperatures and very high strain rates (less than 1 second) highlighted the nonlinear viscoelastic behavior of the material. However, the results were limited to the pole of the specimen and the shape of the bubble was not discussed.

As outlined previously, the bubble inflation technique combined with the optic method provides valuable real-time datasets including displacement, strains at different locations as a function of time as well as the local thickness reduction to fully understand the material behavior during the vacuum forming process. The objective of this work is to characterize the biaxial behavior of the Acrylonitrile Butadiene Styrene (ABS) material in the range of thermo-vacuum forming process. ABS is well suited for vacuum forming process fabrication. Formability at relatively low temperature, impact resistance, strength, and stiffness of this material makes it to be a good choice for economical engineering applications, especially for prototyping. In this work, ABS Epsotech single layer (AB AN2 V0, Tg=105°C) was used [11]. Forming temperature range of this material is 140°C up to 180°C. Although the aforementioned literature has provided a comprehensive understanding of the fundamental biaxial deformation behavior of mostly elastomers and PEEK materials, to the best of the author's knowledge, no studies exist concerning the extension behavior of ABS in more than one axis at forming temperatures. In the present work, a specific instrumented bubble inflation test setup with a 300 mm inner diameter was developed. The inner effective diameter is large enough to let the specimen expand avoiding any border effect. Moreover, It helps to investigate the shape of the bubble formation when it is subjected to large deformation at elevated temperatures which is helpful to calibrate the non-linear terms of the material constitutive model as a subsequent step of this work. Two different temperatures in the forming range (140°C and 150°C) were selected to examine the temperature-strain dependency of the material.

Instrumented Bubble Inflation Experimental Test Setup

A schematic view of the custom-made bubble inflation test rig is presented in Fig. 1. A circular ABS disc material with a diameter of 340 mm and thickness of 3 mm is mounted between two metal disks flanges, slightly clamped around the circumference providing an effective diameter of 300 mm of the material to inflate. Thinning of the material underneath the flange due to excessive clamping pre-load must be avoided since the thermoplastic material softens at elevated temperatures.

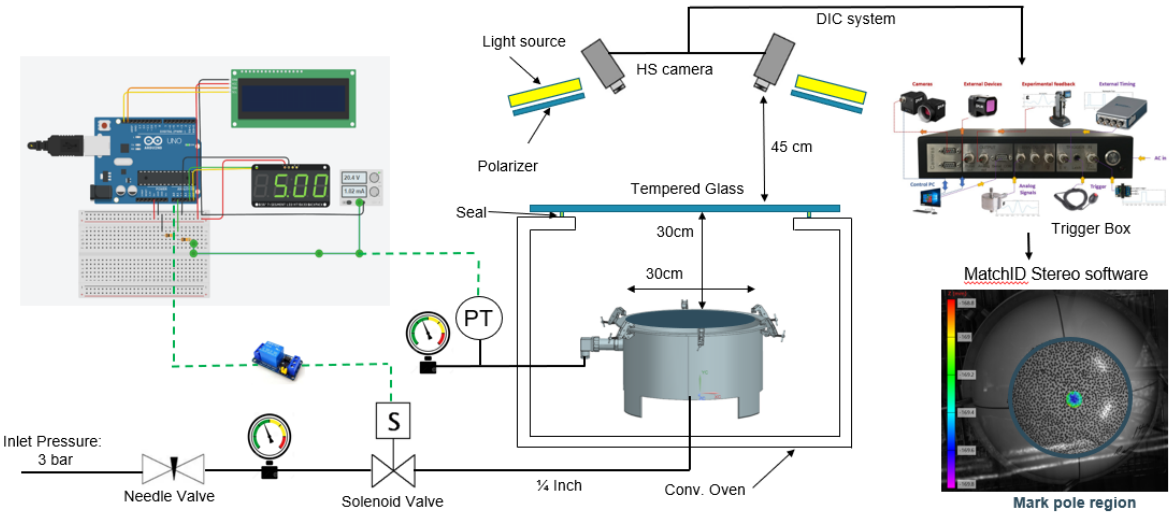

Fig. 1. Schematic annotated diagram of custom-made bubble inflation test rig.

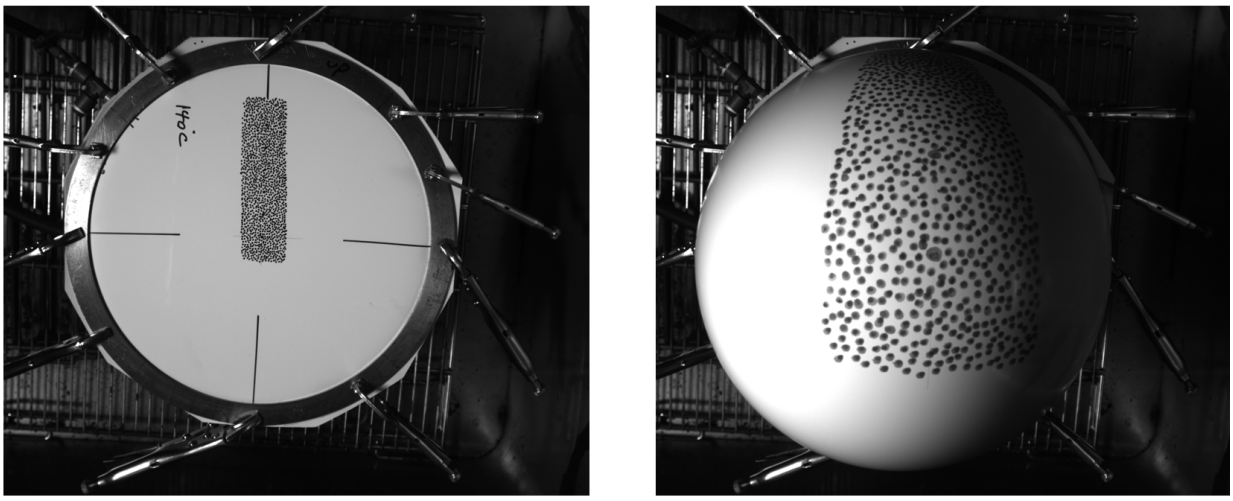

(a) (b)

Fig. 2. 3 mm ABS Epsotech disk with a diameter of 300 mm speckled by permanent marker mounted between flanges using 10 adjustable clamps inside the convection oven, a) reference state, b) deformed state after 3 seconds of applying pressurized air.

This can be troublesome, particularly when conducting high strain rate tests at higher temperatures due to the excessive formability of the material. To avoid this, it needs to balance the clamp pre-load force in such way to avoid the tearing failure of the specimen during inflation. Moreover, the material shows sufficient friction with the steel flanges at elevated temperatures to avoid slippage. It is noted that the polymeric material here works itself like a seal at high temperatures, the application of an additional sealant O-ring is thus unnecessary. A temperature-

control convection oven is used to heat the material to reach the desired temperature. The upstream pressure behind the solenoid valve was fixed at 0.3 MPa for all the tests. This pressure allows a large rapid deformation in less than 3 seconds. It is possible to increase the upstream pressure to 0.7 MPa to meet a higher value of strain rate in case of need. A voltage-type pressure transducer in the range of 0 to 25 kPa (0.5 to 4.5 V RSPRO) with an accuracy of ± 0.25 % is applied to measure the air pressure inside the cavity during inflation. It sends the analog voltage signal to the microcontroller to regulate the solenoid valve condition on 20 kPa as a default triggering set point. Pressure data is then synchronized to the actual DIC data for each image frame for stress calculation during time evolution. The full field surface deformation of the material during inflation is optically measured using two high-contrast 5 Megapixels cameras (Fujinon HF-SA) supports with 3.45µm sensor size with 12.5 mm focal length lenses under MatchID system platform [12]. The cameras are mounted at a 75 cm distance from the disc specimen ensuring that the whole region is under the Field of View (FOV). There is a tempered ultra-clear glass with a thickness of 5 mm in between. The distance between the glass and the specimen is 310 cm. A dotted random, non-repetitive, with high contrast speckle pattern with an average size of 3.7 pixels is made on the Region Of Interest (ROI) with dimensions of 40 x 140 mm using a permanent marker in each test (Fig. 2a). The minimum speckle size adapted by MatchID system is 3 x 3 pixels per speckle [12]. A surface of a combination of 3 to 5 pixels that represents a unique signature so-called subset, is utilized to correlate between the reference state and deformed state per each updated reference. Digital pair images are taken with 20 frames per second during all the following tests. The correlation settings adopted in MatchID stereo software can be found in Table 1. Moreover, in order to enhance the quality of the record images and make uniform light conditioning on the region of interest, a light source was employed. However this light conditioning is valid for the reference state, it makes a shiny reflection on a curved surface during the inflation of the material which moves from the corner to the center of the specimen. This issue is particularly annoying for DIC correlation and post-processing. To avoid this, cross-polarized filtration techniques were implemented by applying linear polarizers in front of camera lenses and light sources.

Table 1. Correlation setting using MatchID stereo software.

Parameters	Method
Correlation algorithm	Zero-Normalized sum of squared differences
Interpolation	Local Bicubic Spline Interpolation
Stereo transformation	Affine
Correlation progress	Spatial + update reference
Subset weight	Uniform
Subset size	45x45
Step size	3
Strain window [pixels]	15
Strain Tensor	Green Lagrange

Results and Discussion

Fig. 2a shows the ABS disc at the reference state which is subsequently inflated beyond the hemispherical stage shown in Fig. 2b at 140°C. It is done under instantaneous purging of 0.3 MPa pressurized air into the cavity by the quick opening action of the solenoid valve. The material was heated inside the oven for 90 minutes to make sure about temperature uniformity distribution across the specimen and through the thickness. The material starts to sag under its weight when it

gets the formability temperature range. The out-of-plane sagging displacement of the material measured using the DIC system is 2.8 mm and 14.93 mm for 140°C and 150°C, respectively at the pole of the material. Then, the 3D displacement of the specimen was incrementally correlated for 3 seconds of evolution time of inflation for all the following tests. Fig. 3 shows a typical contour plot of the out-of-plane correlation images of ABS material at 140°C. Fig. 4a shows the variation of the pressure inside the cavity during the inflation of the material at two different temperatures. The peak pressure value for 140°C and 150°C are 12.68 kPa and 9.66 kPa which occurs after 1.36 and 1.28 seconds of the test, respectively. After that, the pressure value decreases due to the continuous thickness reduction of the material while inflation is still ongoing even at a higher rate. Fig. 4b shows the out-of-plane pole deflection at these two selected temperatures. It is 238 mm and 273 mm at 140°C and 150°C, respectively. It is expected that the bubble deformation is to be truly biaxial only at the pole region [6]. In order to check the equibiaxiality behavior of the material at the pole, the correlation was first performed at the pole region to extract the strain variation of the material. Here, strain is calculated by applying a polynomial fit on the displacement data using MatchID post-processing stereo software. The Green-Lagrange strain was selected due to the large strain field for strain definition. The principal green strain in both directions at the pole at 140°C and 150°C are shown in Fig. 5a. Discrepancy between strains in the principal directions at 140°C is more pronounced which could be attributed to anisotropy generated during extrusion process manufacturing. By enhancing the temperature to 150°C, this effect is less pronounced and the material tends to behave like a truly biaxial extension. For a strain value less than 1, the material extends in the same manner at different temperatures. Strain dependency of the material begins particularly at strain higher than 1 so that the maximum principal strain reaches 11 at 150°C while it is 6 at 140°C. The strain gradient in Fig. 5b reveals how the rate of elongation begins to grow up from 1.5 seconds of the test to be doubled at the same time for higher temperatures.

Upon knowledge of the pole extension behaviour of the material at different temperatures, it is of particular important to detect the shape of the bubble formation during inflation by knowing the extension behavior of the material at different locations. It enhances the accuracy of the curve-fitting process afterward to find the non-linear terms of the mathematical models. The ultimate goal of this work is to calibrate the potential viscoelastic constitutive model using an inverse approach based on Finite Element Model Updating (FEMU).

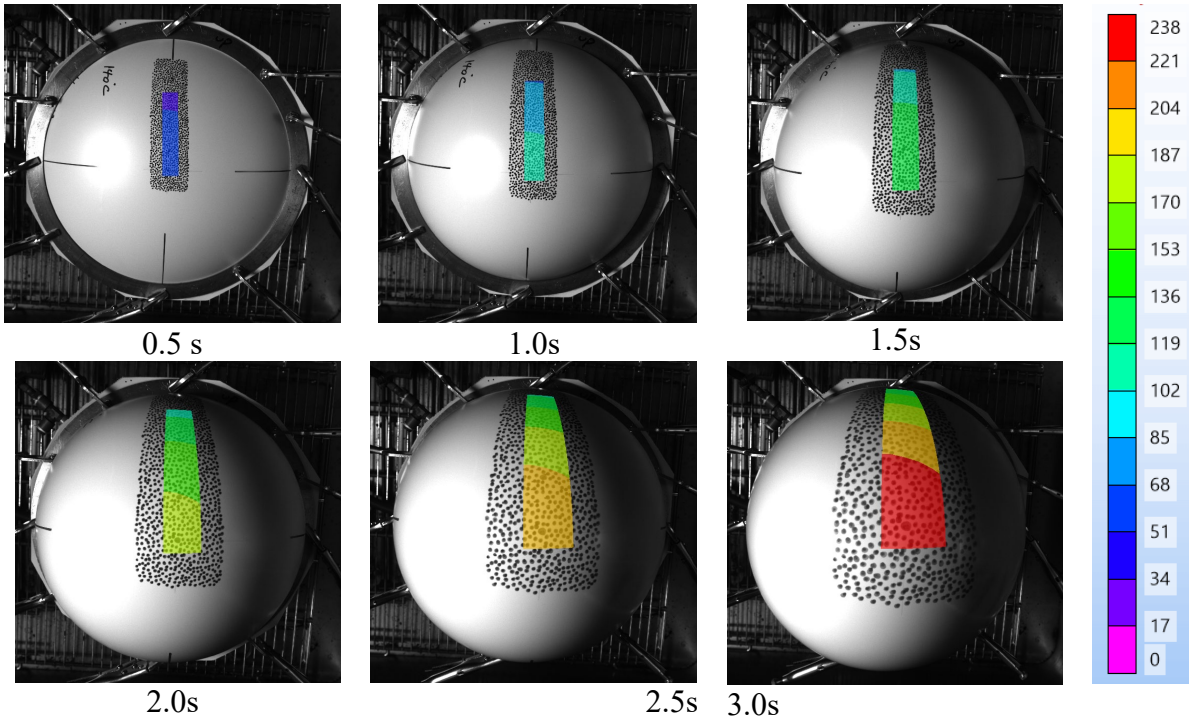

Fig. 3. Displacement magnitude [mm] of DIC inflation images sequence at 140°C during the time evolution.

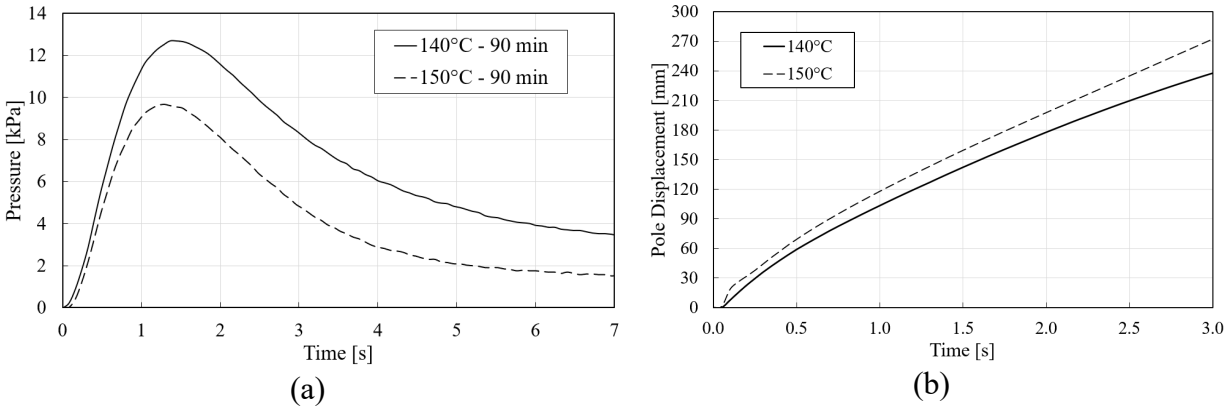

Fig. 4. (a) Pressure profile during inflation of the ABS material at 140°C and 150°C, (b) pole displacement within 3 seconds recording with 20 frames/sec using DIC cameras.

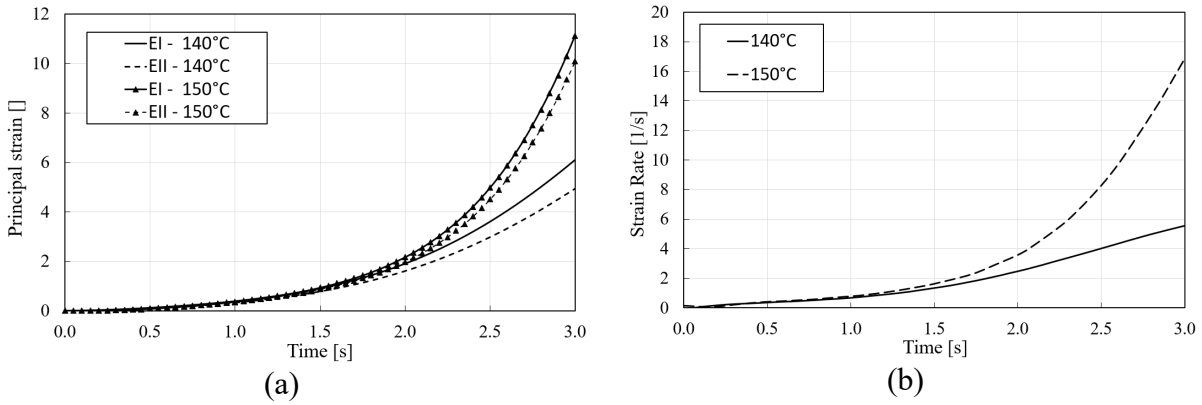

Fig. 5. Strain and strain rate variation at the pole against time during 3 seconds of inflation of 3 mm ABS at 140°C and 150°C, (a) maximum and minimum principal strains (b) strain rate.

To meet this aim, 3 more points have been marked across the centrelines at a distance of 2 cm from each other as shown in Fig. 6(a). DIC data were averaged over a circle with a 5 mm diameter around each marked point shown in the zoomed view in Fig. 6(b). Fig. 7 shows the extension of the material on selected points at different temperatures. It is apparent that temperature increment induces the extension of the material, especially near the pole (ROI 2) which is in agreement with the aforementioned equal biaxial extension in two directions at the pole region versus the off-center location which is mostly unbalanced biaxial extension. It seems that by increasing temperature, a large amount of strain localizes disproportionately in a small region at the pole, resulting in prominent thickness reduction. This kind of extension distribution at higher temperatures tends to make a peaky bubble shape and eventually necks at the pole until failure. Fig. 8 indicates the rate of extension at 150°C versus 140 °C as evidence of the nonlinear behavior of the material. While the specimen at 150°C is softer, this also results in the material deforming at a higher rate than the material tested at 140°C; a maximum strain rate of 3.83 s-1 is observed at ROI 2 in comparison to rates of 10.8 s-1 seen in 150°C. The strain value at ROI 4 varies from 2 to 2.8 when the temperature shifts from 140°C to 150°C. The rate of extension at the locations far away from the pole is less influenced by temperature increment. In fact, thickness reduction at the pole region increases by a greater proportion than the material strain hardening at elevated temperatures.

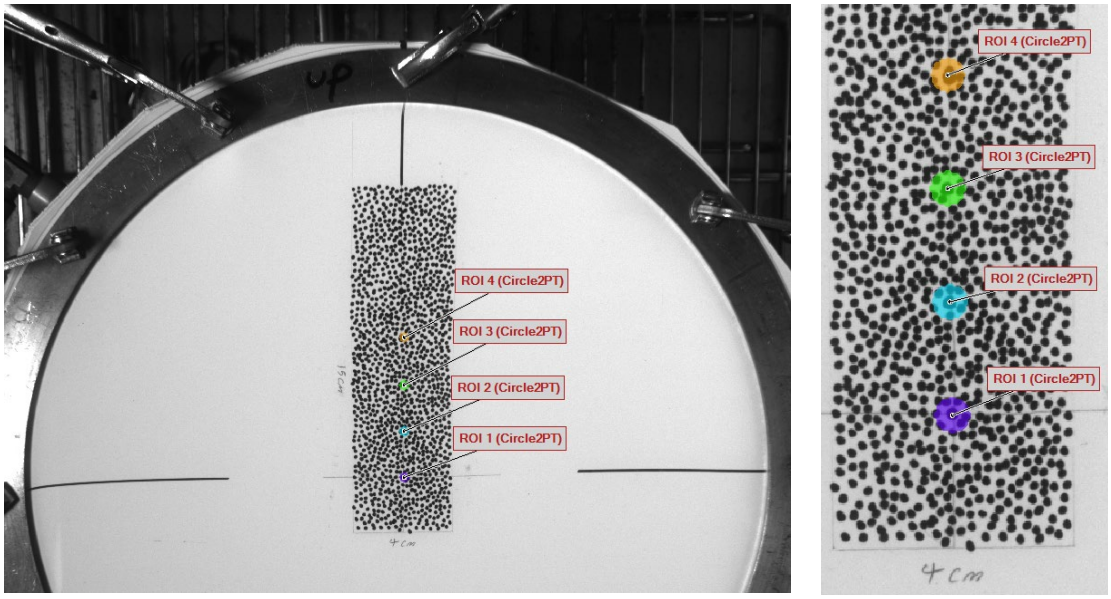

(a) (b)

Fig. 6. (a) Extracting averaged DIC data over circle with 5 mm diameter around the points every 2 cm across the center line, (b) Zoomed view of 4 small circle Region of Interests (ROI).

To make it more tangible, the thickness reduction during the real-time inflation test is calculated considering the Green-Lagrange strain definition through the following formula [13]:

$$t_f = t_i \left(\frac{1}{\sqrt{(1+2\varepsilon_1)(1+2\varepsilon_2)}} \right) \quad (1)$$

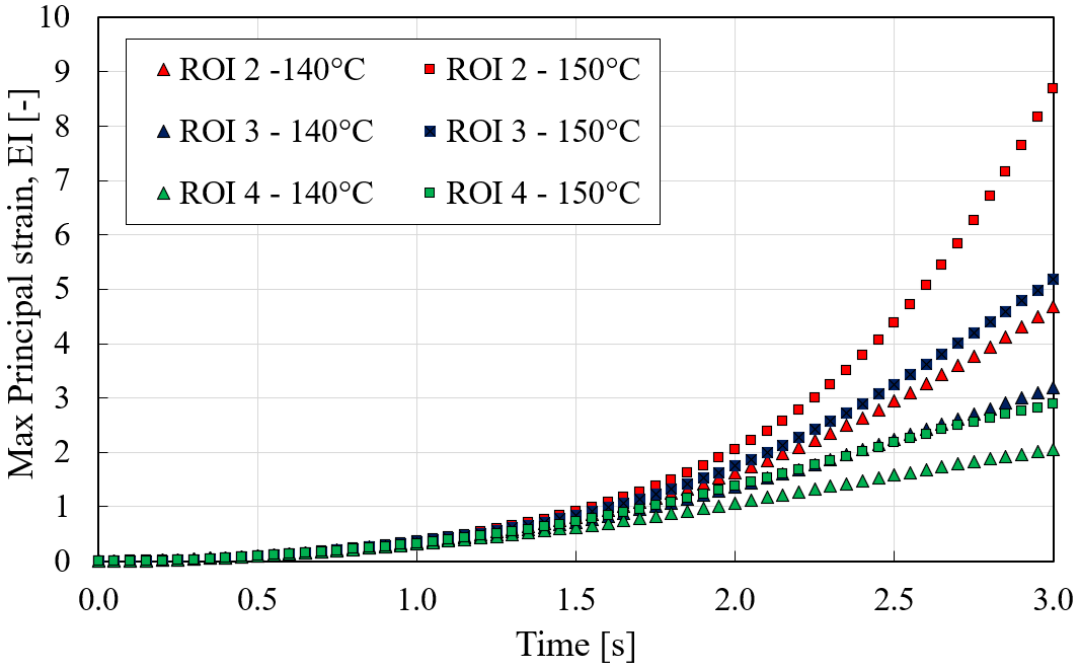

Fig. 7. Average strain of ABS material at three probes across the line with 2 cm distance to each other at 140°C and 150°C.

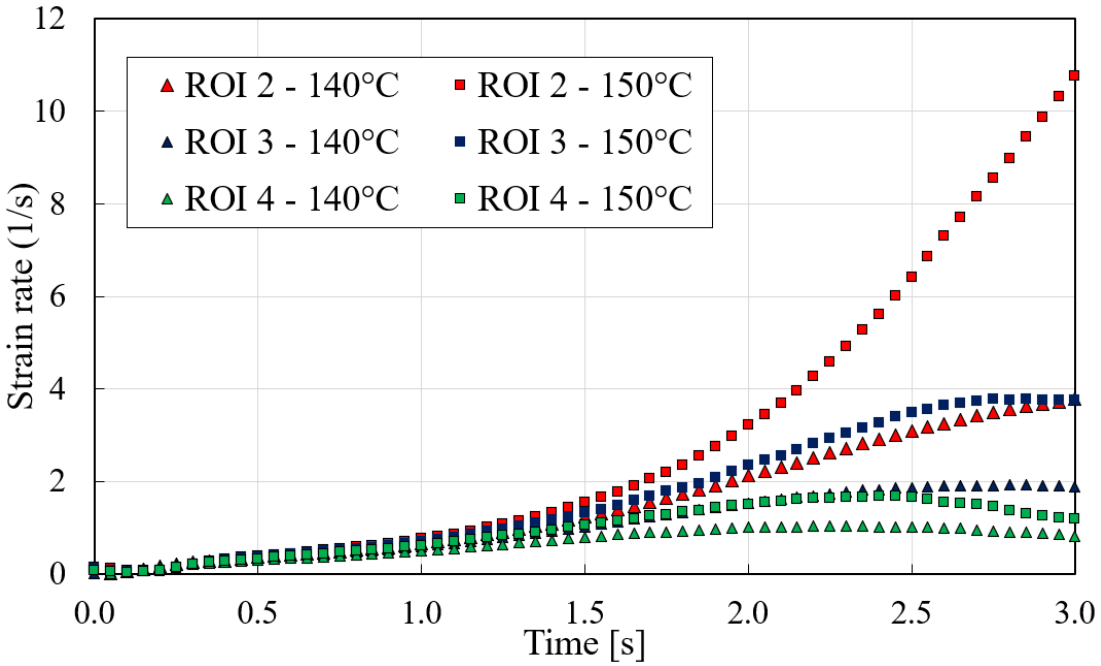

Fig. 8. Strain rate ABS material at three different locations across the line with 2 cm distance to each other at 140°C and 150°C.

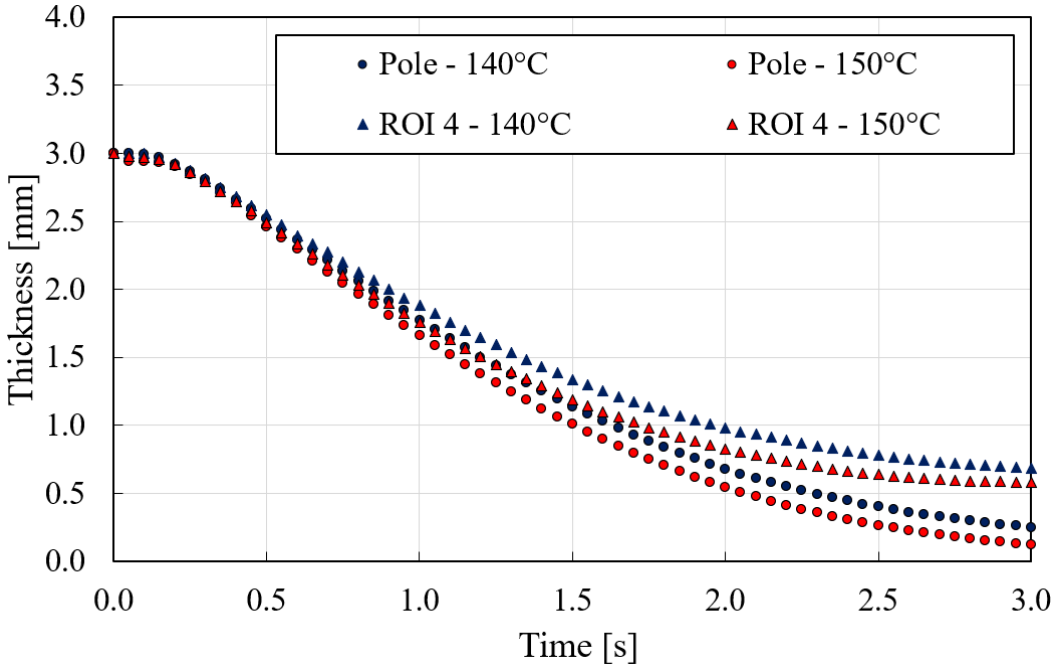

Fig. 9. Thickness variation against real-time at 140°C and 150°C.

Where t_f is the final wall thickness, t_i is the initial thickness, ε_1 and ε_2 are maximum and minimum principal strains, respectively. Equation 1 is only valid with the volume conservation of the sheet during inflation. Fig. 9 shows the effect of temperature increment on thickness variation at pole and ROI 4 (the last and furthest point from center) against time evolution. 52% thickness reduction (From 0.24 mm to 0.12 mm) at pole against 14% at the ROI 4 (From 0.67 mm to 0.57 mm) indicates the tendency of the material behavior to generate a narrow peaky bubble shape formation at elevated temperature. In other hands, strain hardening behavior at lower temperature leads to have more uniform stretching which is exhibited by delaying neck failure while at higher temperature strain hardening is drastically reduced which might be attributed to increasing mobility of the polymer matrix leading to have non-uniform deformation indicated by excessive thickness reduction at the pole.

Summary

In this study, the biaxial extension behaviour of a heated ABS sheet was examined using a custom-made bubble inflation test rig. DIC measurements were focused across the centreline to detect the bubble-shaped formation of the material as a function of temperature during inflation. It was exhibited that increasing the forming temperature results in an overall decreasing pressure level with larger material stretching at a higher strain rate. Biaxial strain discrepancy at the pole, attributed to anisotropy produced during the extrusion process of the sheet, is more prevalent at a lower forming temperature. Increasing the temperature from 140°C to 150°C reduces this effect resulting in a nearly equibiaxial extension in the two principal directions. Real-time strain values at different points across the centreline revealed a large amount of strain localized disproportionately in a small region at the pole by temperature increment, resulting in prominent thickness reduction. This kind of extension distribution tends to make a narrow peaky bubble shape at higher temperatures. The strong dependence of bubble shape as a function of temperature shown in this work is suggested as a convenient representative to calibrate the material non-linear model parameters aiming to elaborate the numerical simulation accuracy.

Acknowledgment
This work has been funded by the ICON project "ProPeL", which fits in the MacroModelMat (M3) research program, coordinated by Siemens (Siemens Digital Industries Software, Belgium), and funded by SIM (Strategic Initiative Materials in Flanders) and VLAIO (Flemish government agency Flanders Innovation & Entrepreneurship). The authors wish to acknowledge the support provided by Dr. Güven Ogus and Dr. Pascal Lava from MatchID team for DIC measurement over the bubble inflation test setup. The authors would like to thank Vitalo group company for preparing and providing the ABS sheet materials with different thicknesses and dimensions.

References
[1] M. Johlitz, S. Diebels, Characterisation of a polymer using biaxial tension tests. Part I: Hyperelasticity, Arch. Appl. Mech. 81 (2011) 1333-1349. https://doi.org/10.1007/s00419-010-0480-1
[2] J.K. Lee, T.L. Virkler, C.E. Scott, Effects of Rheological Properties and Processing Parameters on ABS Thermoforming, Polym. Eng. Sci. 41 (2001). https://doi.org/10.1002/pen.10725
[3] S.H. Catraei, C.W. Maxasko, Lubricated Squeezing Flow: A New Biaxial Extensional Rheometer, J. Rheol. 25 (1981) 433-443. https://doi.org/10.1122/1.549648
[4] L.R.G. Treloar, Strains in an inflated rubber sheet and the mechanism of bursting, Institution of Rubber Industry 19 (1944) 201-212. https://doi.org/10.5254/1.3546716
[5] R.S. Rivlin, D.W. Saunders, Large Elastic Deformations of Isotropic Materials. VII. Experiments on the Deformation of Rubber, Royal Society 243 (1951) 251-288. https://doi.org/10.1098/rsta.1951.0004
[6] N. Reuge, F. Schmidt, Y. Le Maoult, M. Rachik, F. Abbe, Elastomer biaxial characterization using bubble inflation technique. I: Experimental investigations, Polym. Eng. Sci. 41 (2001) 522-531. https://doi.org/10.1002/pen.10749
[7] M. Sasso, G. Palmieri, G. Chiappini, D. Amodio, Characterization of hyperelastic rubber-like materials by biaxial and uniaxial stretching tests based on optical methods, Polym. Test. 27 (2008) 995-1004. http://doi.org/10.1016/j.polymertesting.2008.09.001
[8] G. Machado, D. Favier, G. Chagnon, Membrane Curvatures and Stress-strain Full Fields of Axisymmetric Bulge Tests from 3D-DIC Measurements. Theory and Validation on Virtual and Experimental results. Experimental Mechanics, Exp. Mech. 52 (2012) pp.865-880.
[9] U.D. Çakmak, Z. Major, Experimental Thermomechanical Analysis of Elastomers Under Uni- and Biaxial Tensile Stress State, Exp. Mech. 54 (2014) 653-663. https://doi.org/10.1007/s11340-013-9820-8
[10] J.A. Turner , G.H. Menary, P.J. Martin, Biaxial Characterization of Poly(ether-ether-ketone) for Thermoforming: A Comparison Between Bulge and in-Plane Biaxial Testing, Polym. Eng. Sci. 59 (2019) 1853-1865. https://doi.org/10.1002/pen.25185
[11] Information on https://epsotech.com/files/uploads/epsotech/2020/AB%20AN2%20V0.pdf (epsotech.com) (accessed on 09.02.2023).
[12] Information on https://www.matchid.eu/ (accessed on 09.02.2023)
[13] B. Van Mieghem, P. Lava, D. Debruyne, A. Van Bael, J. Ivens, Digital image correlation for online wall thickness measurements in thick gauge thermoforming, ESAFORM 2013, Annual Conference on Material Forming, 2013, 1583-1591.

Materials Research Proceedings 28 (2023) 1897-1906 https://doi.org/10.21741/9781644902479-205

Experimental measurement of CF/PEKK tapes heating behavior in the laser assisted automated fiber placement process

LE LOUËT Violaine[1,a], LE REUN Adrien[2,b], SOBOTKA Vincent[2,c *] and LE CORRE Steven[2,d]

[1]CAPACITES SAS, 26 bd Vincent Gâche F-44200 Nantes, France

[2]Nantes Université, CNRS, LTEN, UMR 6607, F-44000 Nantes, France

[a]Violaine.Le-louet@univ-nantes.fr, [b]adrien.le-reun@univ-nantes.fr, [c]vincent.sobotka@univ-nantes.fr, [d]steven.lecorre@univ-nantes.fr

Keywords: Heat Transfer, Infrared Camera, Automated Fiber Placement

Abstract. This work takes place within the framework of the study and control of heat transfer taking place during the heating stage of the Laser Assisted Automated Fiber Placement (AFP) process. Understanding the interaction between the composite tape and the incoming laser radiation is a cornerstone for controlling the thermal history of the laminate. Laser incidence, fibre orientation and lay-up velocity have long been identified as key factors influencing the laser absorption by the composite and its increase in temperature. For the sake of simplicity, homogenous model is often used to describe phenomena inside the composite. However, the study of the radiative behaviour of laminates and tapes has shown that absorption occurs over a volume whose size depends on the carbon fibre architecture within the polymer matrix. Investigating heat transfer at micro scale is then crucial to fully understand the thermal phenomena occurring in the AFP process. In order to investigate heat transfer according to process parameters and especially to the orientation of the tape, a specific bench is developed in order to perform static heating a single composite with a laser diode. A full calibration of the bench was first performed including the response of the IR camera as well as the shape and power imposed by the laser source. Then, measurements for several orientations of the tape (0°,45° and 90°) were performed and thermal response measured and analysed.

Introduction

From their potential recyclability, bonding ability and tenacity in comparison with thermoset, the interest for thermoplastic composites steeply increased for years. Development of technical polymers with melting temperatures reaching 400°C made conceivable their use in structural parts, especially in aeronautics.

Among the manufacturing processes, Automated Fibre Placement (AFP) processes have been pointed out as suitable solutions to meet these expectations [1,2]. This process is based on the laying of narrow prepreg tapes with automated systems. The laser-assisted thermoplastic AFP process is promising to enable complex shapes manufacturing and in-situ consolidation. The process is simplified with three steps which are depicted in Fig. 1: heating, adhesion and consolidation phases. First, the laying tape and the substrate are heated such as both reach the matrix melting temperature. Heating phase must ensure that ply and substrate temperatures reach the matrix melting temperature without exceeding the matrix degradation temperature [3-5]. Then, the compaction roller pressurizes the ply (laying tape) and the substrate to increase intimate contact. Pressure and melting of the matrix enable bonding of ply and substrate with the inter-diffusion of polymer chains through the interface, called reptation [6]. Adhesion phase tries to maximize the degree of intimate contact [7,8] between ply and substrate based on pressure of the roller. Finally, the consolidation during cooling phase is an essential step to improve the

Content from this work may be used under the terms of the Creative Commons Attribution 3.0 license. Any further distribution of this work must maintain attribution to the author(s) and the title of the work, journal citation and DOI. Published under license by Materials Research Forum LLC.

mechanical resistance through matrix crystallization. These statements make the prediction and modeling of heat transfers necessary steps to master the process under varying configurations: laying speed, materials properties, shape geometry, etc…

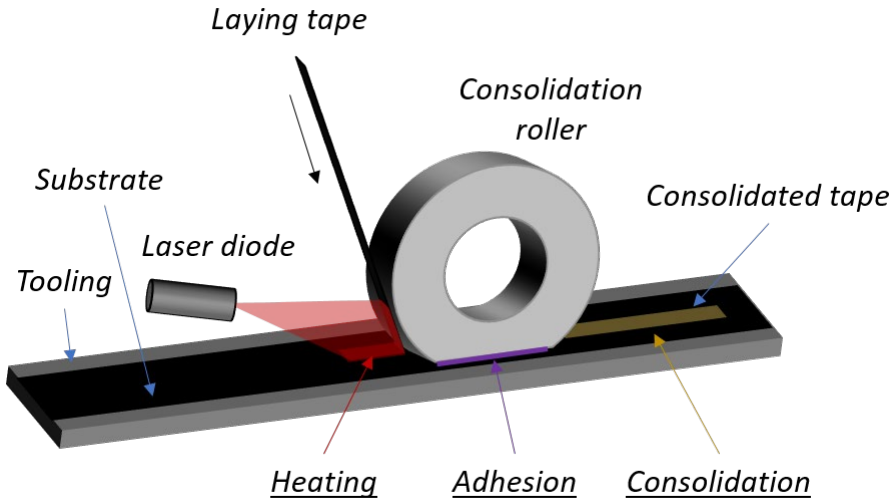

Fig. 1. Laser-assisted AFP process: heating, adhesion and consolidation.

In this article, we propose the development of an original bench representative of an AFP process enabling the precise measurement of a composite tape surface temperature heated by laser. The bench is specifically designed to study the effect of laser incidence angle and fibre orientation. Finally, a comparison with a novel numerical model is presented and discussed.

Material

The studied material is an AS7 carbon fibre [9] reinforced UD prepreg tape with a PEKK7002 [10] matrix. Fibres and matrix properties have been either extracted from datasheet, as density, considered constant in this study, or measured at laboratory with DSC for specific heat capacity and guarded hot plate for thermal conductivity.

A model of fibre conductivity with a weak transverse thermal conductivity (0.5 $W.m^{-1}.K^{-1}$) at core and a higher one on the edge (8.7 $W.m^{-1}.K^{-1}$) has been designed to account for the fibre thermal behavior. The skin thermal conductivity has been identified using the guarded hot plate measurement and a steady microstructure simulation.

Table 1. PEKK7002 and AS7 carbon fibre properties.

	PEKK7002	Carbon fibre AS7
Density ρ [kg/m^{-3}]	1290	1790
Thermal conductivity k [$W/m^{-1}/K^{-1}$]	0.27	Longitudinal: 10 Transverse (core): 0.5 Transverse (skin): 8.7
Specific heat capacity C_p [$J/kg^{-1}/K^{-1}$]	T ≤ 162°C, 3.35 T + 1017.0 162 < T < 334°C, 3.45 T + 1137.6	-0.00295 T(°C)² + 3.493 T(°C) + 578.4

Experimental Setup

In order to remove the instrumentation constraints of the dynamic process, an experimental apparatus is developed to measure the evolution of physical values during laser-heating of a single tape, such as surface temperature and heat flux between tape and tooling.

The system is developed to facilitate unidimensional heat transfer through the tape thickness. It consists of two identical frames made of steel Z35CD17 (AFNOR), whose dimensions 100x20x6 mm, maintained in contact in the plane (O,y,z). Three thermocouples are placed along the central axis at respectively 250 µm, 1.25 mm and 3.25 mm from the surface and form a flux sensor which measures heat transfer between composite and tooling (Fig. 2). This sensor is also used to calibrate the laser heat flux. In both frames, respectively 11 and 10 type K 250 µm diameter thermocouples are placed at 250 µm from the surface to measure 2D heat transfer phenomena. The lower part of the system can be heated up to 400°C thanks to heating cartridges.

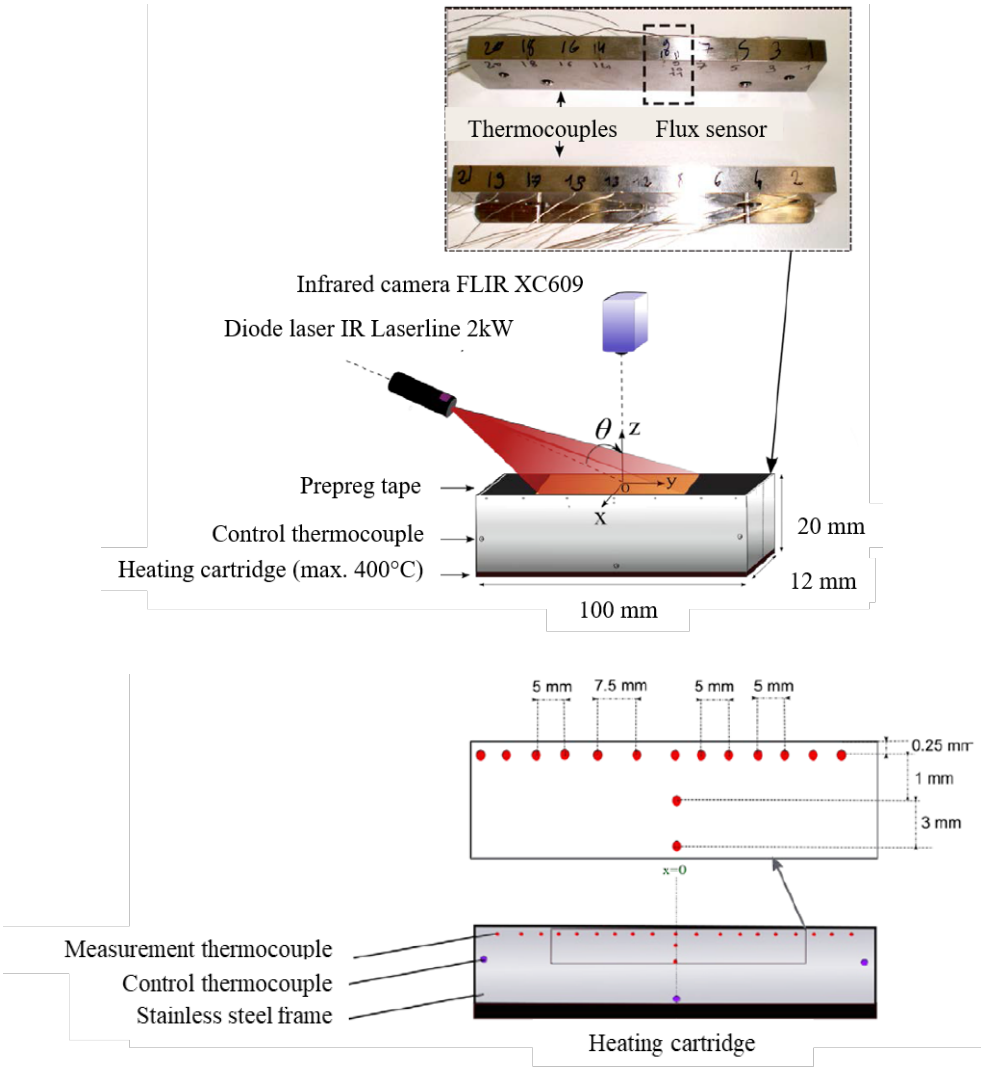

Fig. 2. Thermocouples positioning and flux sensor.

A FLIR XC609 infrared camera (Fig. 3) is maintained perpendicularly to the frame thanks to a metal support whose position is adjustable in the three axes (x,y,z) such as surface temperature is monitored in the plane (O,x,y). Heating of the tape is supplied with a laser diode LDM 2000-30 from Laserline with a maximal output power of 2000 W and of wavelength of 980 nm. The laser is mounted on a rotating arm which enables the adjustment of laser incidence angle from 0° to 70°

with respect to plane (O,x,y) and distance to tape from 150 to 200 mm. Due to bulk issues, the minimal incidence angle is 10° when camera and diode are both installed.

The tape is 12 mm wide, 60 mm long, 0.2mm thick and maintained at the tooling surface thanks to 50 N magnets. For safety issues, the whole system is installed within an opaque box.

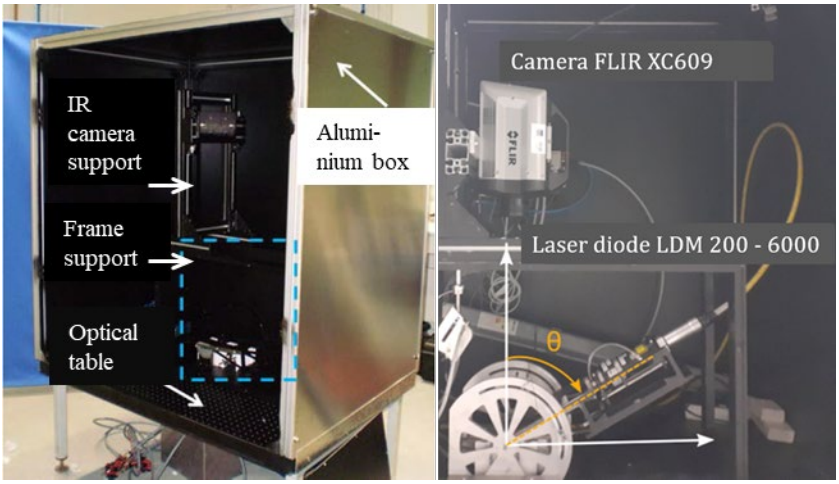

Fig. 3. Experimental apparatus.

Caracterisation of Laser Source in Normal Incidence

The laser spot is a 12x12 mm² square on which intensity is distributed in a top hat shape with a homogeneous and maximal value over a 6x6 mm² area and decreases exponentially on the edges. The nominal intensity, meaning the intensity in the central area is calibrated with the help of the heat flux sensor implemented in the metallic support. The evolution with time of an incoming heat flux irradiating the sensor surface is calculated with the Beck inverse method [11] supplied with the thermocouples responses. The usual algorithm was modified to retrieve the thermocouples response time.

During the campaign, the IR camera is removed so the laser diode can be positioned normally to surface (0°). A graphite coating of known emissivity is sprayed homogenously over the support surface. The thermal resistance of the layer is neglected as its thickness does not exceed a few dozen microns.

Calibration consisted in irradiating the surface during 100 ms at the minimum power of the laser diode. The distance with the surface was varied from 150 mm to 200 mm. Fig. 4 displays the evolution versus time of the heat flux density calculated using Beck algorithm. Overshoots can be observed at the beginning and end of irradiation. These are induced by the algorithm itself. Although its use benefits from making no assumption of the flux behaviour with time, the algorithm lacks accuracy for the identification of Heaviside functions with infinite first derivatives. The actual heat flux evolution with time is indicated with dotted lines on the graph.

The laser beam is slightly divergent and the heat flux density decreases with the distance from the surface. This evolution is linear with distance as displayed in Fig. 5.

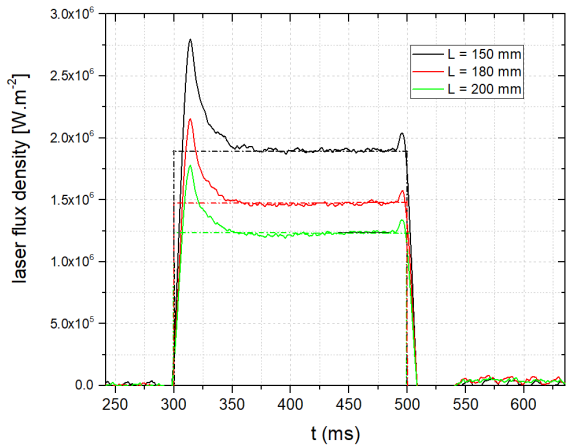

Fig. 4. Measurement of the heat flux density with time during a 100 ms pulse.

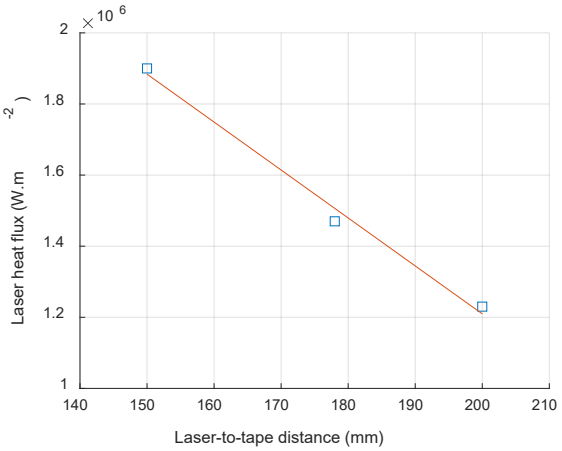

Fig. 5. Evolution of heat flux density with distance.

Tape Surface Temperature: Effect of Fibre Orientation and Incidence Angle

Tape surface temperature is measured regarding fibre orientation φ and laser incidence angle θ (Fig. 6). As temperature decreases with grazing incidences, the laser power density is adjusted in order to reach similar temperatures for every incidence angle and work in the same calibration range of the camera (Fig. 7).

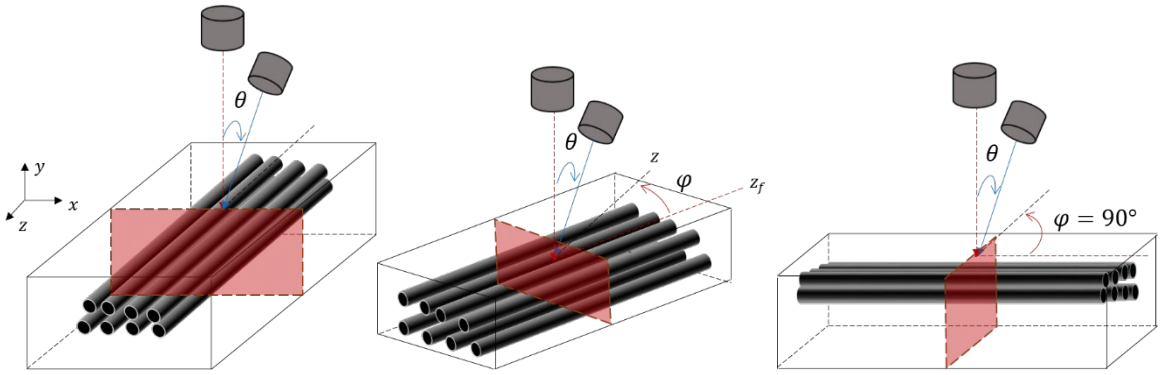

Fig. 6. Angles configuration: fibre orientation φ, incidence angle θ.

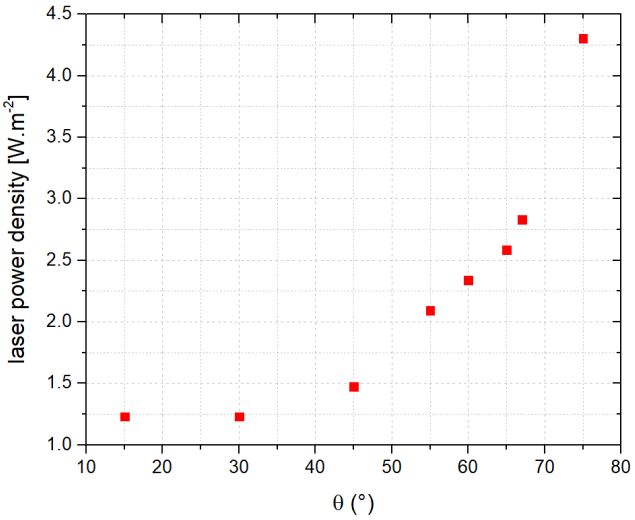

Fig. 7. Power density according to the incidence angle.

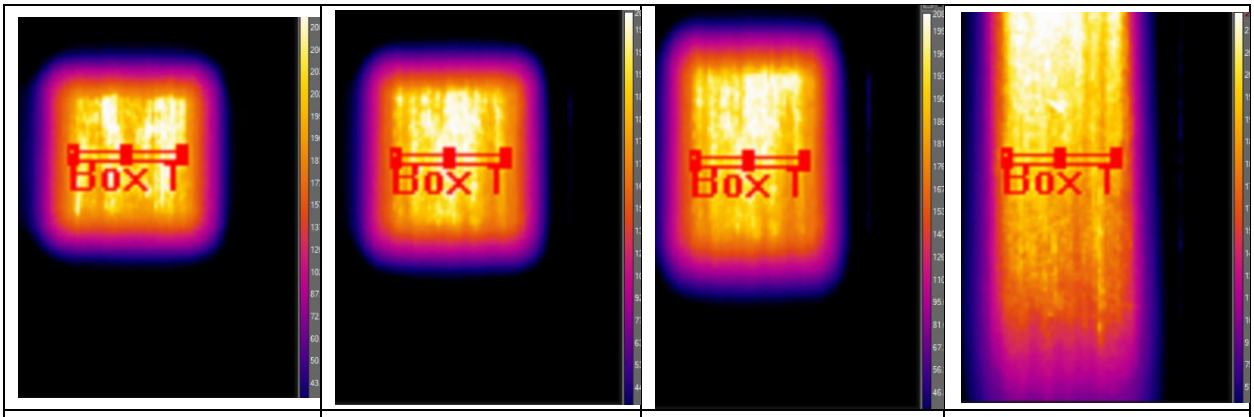

(a) θ = 15°	(b) θ = 30°	(c) θ = 45°	(d) θ = 75°

Fig. 8. Thermographs at φ = 0°.

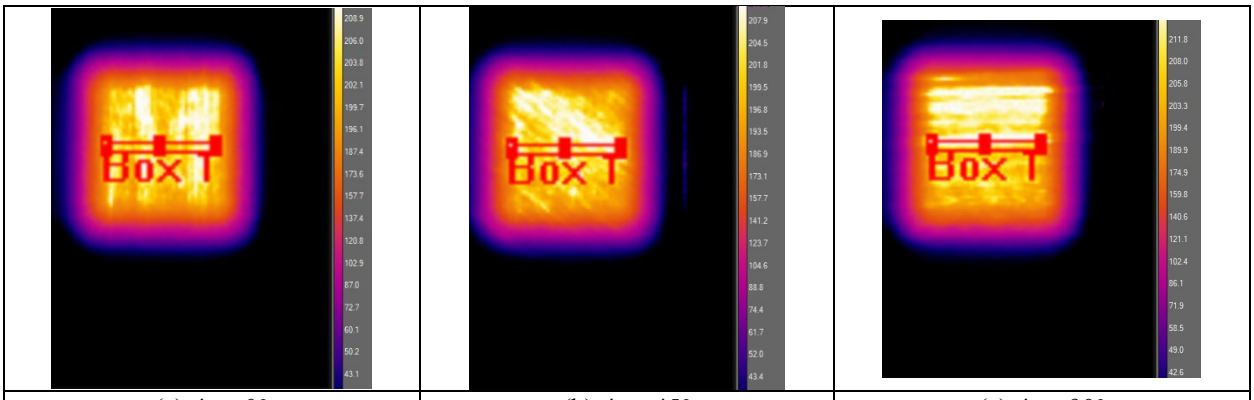

(a) ϕ = 0°	(b) ϕ = 45°	(c) ϕ = 90°

Fig. 9. Thermographs at θ = 15°.

Fig. 8 displays the thermographs at end of heating t = 20 ms for trials on a tape positioned at φ = 0° and for increasing incidence angles θ. The expansion of the laser spot length with incidence is clearly noticeable. The temperature distribution over the irradiated surface also become less homogeneous as the incidence angle decreases. As a result, temperature is extracted and averaged over a slim area (represented by the red box) aligned with pivot point of the laser diode and where

the magnitude of the laser flux has been calibrated. Similarly, thermographs are presented for three fibre orientations: 0, 45 and 90° in near-normal incidence θ = 15 (Fig. 9). The temperature variability is noticeable and due to tape heterogeneity. The color contrast highlights the fibre orientation.

Series of 5 samples have been tested in the configurations φ = 0°, 45° and 90°, and θ = 15°, 45° and 60° on which the average temperature and standard deviation are determined. The measurement uncertainty u is estimated following:

$$u = \sqrt{u(T_{mean})^2 + u(\sigma_{mean})^2} \quad (1)$$

with:

$$u(T_{mean}) = \frac{1}{\sqrt{5}}\sqrt{\frac{1}{n}\sum_{i=1}^{n=5}(T_i - T_{mean})^2} \quad (2)$$

$$u(\sigma_{mean}) = \frac{1}{\sqrt{5}}\sqrt{\frac{1}{n}\sum_{i=1}^{n=5}(T_i - \sigma_{mean})^2} \quad (3)$$

The measurement uncertainty is caused by:

1. The resolution of the camera
2. The heterogeneity of the tape surface
3. The variability of the tape over the batch
4. The variability of the test and of the operator

Results are summarized in Fig. 10. Surface temperature increases during the 20 ms heating time to reach approximately 200°C for every incidence angle. The effect of fibre orientation on the surface temperature is shown negligible as temperature differences between various fibre orientations samples are inferior to the measurement uncertainty. These experimental temperatures are compared with a novel thermo-optical model at the microscale.

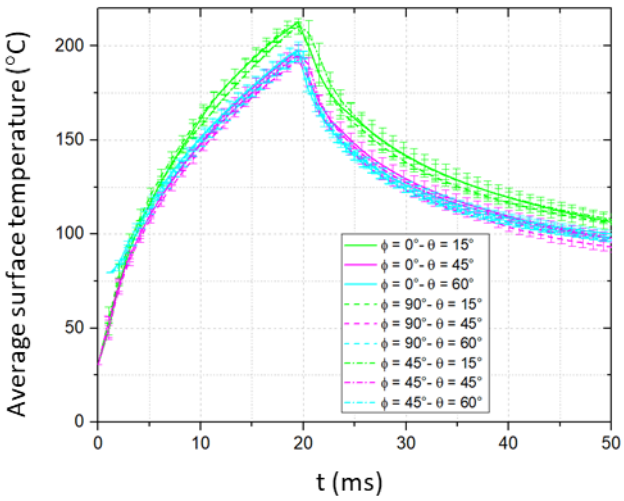

Fig. 10. Evolution of surface temperature as a function of fibre orientation (0, 45, 90°) and incidence angle (15, 45, 60°).

Numerical Model

A numerical thermo-optical model is designed at the micro-scale based on the tape microstructure. A cross-section micrograph (Fig. 11) of the experimental samples is performed and used to characterize the fibre distribution through the thickness. Image points out the heterogeneity of fibre distribution in the thickness with denser area close to the surfaces and a weaker fibre fraction at core.

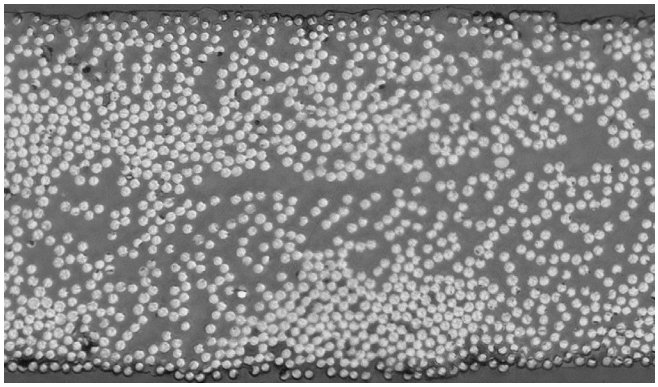

Fig. 11. Cross section micrograph of the tape.

An artificial microstructure is created based on the actual fibre distribution and used to perform a FEM simulation computed with Freefem++ [12].The matrix is considered fully transparent at the laser wavelength. [13]. Therefore, the laser beam is only absorbed by carbon fibres. A ray-tracing algorithm is developed to compute fibres areas heated by the laser beam (Fig.12) depending on fibre orientation and incidence angle. The laser beam is modelled by approximately 4000 scanning lines which are evenly spaced by a fraction of fibre element size. The intersection between the scanning lines and fibres is computed without considering refraction in the polymer matrix. Every heated carbon fibre element is tagged for the following thermal simulation in which a heat flux condition is applied based on the laser power density ϕ_{laser} and the carbon absorption coefficient α_{carbon}.

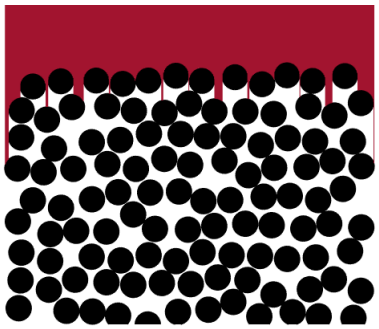

Fig. 12. Ray-tracing algorithm: detection of heated fibres by the laser beam.

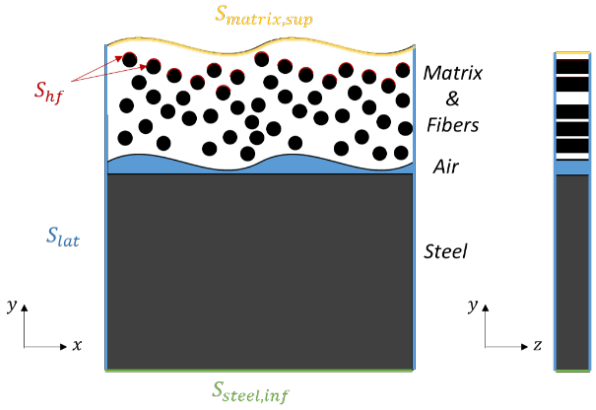

Fig. 13. Schematic of the problem: volume and boundary conditions.

The problem is modeled in Fig. 13. The heat equation is solved in the four physical volumes: fibres, matrix, steel and air.

$$\rho C_p \frac{\partial T}{\partial t} - div\left(\bar{\bar{k}} \cdot \vec{\nabla} T\right) = Q_v \quad (4)$$

with the following boundary conditions:

1. Adiabatic lateral surfaces S_{lat} (heat transfer is 1D): $\vec{\phi}.\vec{n} = 0$
2. Fixed temperature: $T = T_{amb} = 20°C$ on steel lower surface $S_{steel,inf}$
3. Dissipation by air convection on matrix upper surface $S_{matrix,sup}$: $\phi = h_{air}(T - T_{amb})$
4. Laser heat flux absorption on fibres heated elements S_{hf}: $\phi = \alpha_{carbon}\, \phi_{laser}\, \vec{q} \cdot \vec{n}$

where $h_{air} = 5$ W.m^{-2}.K^{-1} the air convection coefficient, $\alpha_{carbon} = 0.9$ the carbon absorption coefficient, $\vec{n}$ the normal vector to the element and $\vec{q}$ the resulting direction vector of laser heat flux, depending on fibre orientation and incidence angle.
The simulation is performed on 50 iterations with a 20 ms heating time which corresponds approximately to the exposure time in a manufacturing process context at a 500 mm.s^{-1} laying speed with a 12 mm laser beam width. It is also chosen to nullify the effect of back surface condition, meaning that diffusion time through the thickness is greater than 20 ms. The total time is set at 40 ms to study the cooling kinetic.

Experimental and Numerical Comparison

Average experimental and numerical surface temperatures are compared in Fig. 14 for near-normal $\theta = 15°$ and grazing $\theta = 60°$ incidences with respectively 1.31 and 2.49 MW.m^{-2} laser power density. Laser heat flux has been corrected to fit experimental and numerical temperatures.

Both incidences show an accurate approximation between experimental and numerical temperatures at the end of heating phase. The simulation confirms that fibre orientation has a negligible effect on surface temperature and the necessity to increase laser power to reach similar surface temperatures. Heating and cooling kinetics are also closed between experimental and numerical temperatures, meaning that heat transfers are rather well described by the model.

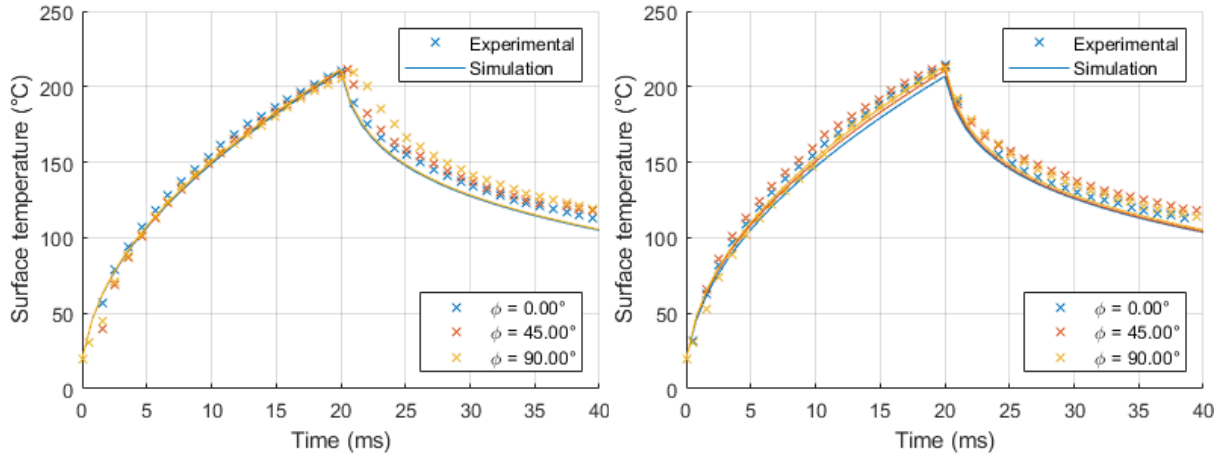

Fig. 14. Evolution of numerical and experimental surface temperature for (a) near-normal θ = 15° and (b) grazing θ = 60° incidences and three fibre orientations.

Summary
A specific experimental bench is designed to study heat transfer in the laser-heating of a single carbon fiber reinforced composite tape in a static configuration. The bench is instrumented with thermocouples and an infrared camera to measure laser heat flux and tape surface temperatures. A thermo-optical model is developed and approximates the evolution of surface temperatures. Both experimentation and simulation results highlighted the negligible effect of fibre orientation on surface temperatures. However, laser power has to be increased with grazing incidences to reach a similar surface temperature.

Acknowledgments
This work was conducted under the framework of HAICoPAS, a PSPC project (projet de recherche et développement structurant pour la compétitivité). Authors are grateful to the partners of the HAICOPAS Project (Hexcel Composites, Arkéma, Coriolis, Institut de Soudure, PEI, Ingecal) for their interest and support to this research.

References
[1] D. H.-J. Lukaszewicz, C. Ward, K.D. Potter, The engineering aspects of automated prepreg layup: History, present and future, Compos. Part B: Eng. (2012) 997-1009. https://doi.org/10.1016/j.compositesb.2011.12.003
[2] Z. August, G. Ostrander, J. Michasiow, D. Hauber, Recents developments in automated fiber placement of thermoplastic composites, Sampe J. 50 (2014) 30-37.
[3] K. Cole, I. Casella, Fourier transform infrared spectroscopic study of thermal degradation in films of poly (etheretherketone), Thermochimica acta 211 (1992) 209-228. https://doi.org/10.1016/0040-6031(92)87021-2
[4] M. Day, D. Sally, D. Wiles, Thermal degradation of poly (aryl-ether-ether-ketone): Experimental evaluation of crosslinking reactions, J. Appl. Polym. Sci. 40 (1990) 1615-1625. https://doi.org/10.1002/app.1990.070400917
[5] P. Tadini, N. Grange, K. Chetehouna, N. Gascoin, S. Senave, I. Reynaud, Thermal degradation analysis of innovative pekk-based carbon composites for high-temperature aeronautical components, Aeros. Sci. Technol. 65 (2017) 106-116. https://doi.org/10.1016/J.AST.2017.02.011
[6] P.-G. De Gennes, Reptation of a polymer chain in the presence of fixed obstacles, J. Chem. Phys. 55 (1971) 572-579. https://doi.org/10.1063/1.1675789
[7] A. Khodaei, F. Shadmehri, Intimate contact development for automated fiber placement of thermoplastic composites, Compos. Part C: Open Access 8 (2022) 100290. https://doi.org/10.1016/j.jcomc.2022.100290
[8] O. Çelik, D. Peeters, C. Dransfeld, J. Teuwen, Intimate contact development during laser assisted fiber placement: Microstructure and effect of process parameters, Compos. Part A: Appl. Sci. Manuf. 134 (2020) 105888. https://doi.org/10.1016/j.compositesa.2020.105888
[9] Hexcel, Datasheet Carbon Fibre AS7.
[10] Arkema, Datasheet Kepstan 7002.
[11] J. Beck, B. Blackwell, A. Haji-Sheikh, Comparison of some inverse heat conduction methods using experimental data, Int. J. Heat Mass Trans. 39 (1996) 3649-3657. https://doi.org/10.1016/0017-9310(96)00034-8
[12] F. Hecht, New development in freefem++, J. Numeric. Math. 20 (2012) 251-265. https://doi.org/10.1515/jnum-2012-0013
[13] M. Villar, C. Garnier, F. Chabert, V. Nassiet, D. Samélor, J. Diez, A. Sotelo, M. Madre, In-situ infrared thermography measurements to master transmission laser welding process parameters of PEKK, Optic. Laser. Eng. 106 (2018) 94-104.

Materials Research Proceedings 28 (2023) 1907-1916 https://doi.org/10.21741/9781644902479-206

Polymer-tool friction coefficient in temperature for thermoforming numerical simulation

CAUBET Benoit[1,2,a *], LÉONARDI Frederic[2,b] and AMAND Sylvain[1,c]

[1]University of Pau, Institut des Sciences Analytiques et de Physico-Chimie pour l'Environnement et les Matériaux, UMR 5254, 2 Av. Du Président Pierre Angot, 64000 Pau, FRANCE

[2]AXYAL, Aéropole Pyrénées, Rue de Bruscos, 64230 Sauvagnon, FRANCE

[a]benoit.caubet@univ-pau.fr, [b]frederic.leonardi@univ-pau.fr, [c]sylvain.amand@axyal.fr

Keywords: Thermoforming, Friction Coefficient, Numerical Simulation, Thickness Distribution, T-SIM®, Polycarbonate

Abstract. In this work, friction coefficient between Polycarbonate and Aluminum was measured over the entire thermoforming temperature range by using a rotational rheometer with a specific geometry, following the B. Hegemann *et al.* [1] method. The effects of velocity, pressure and surface roughness were investigated. Then, numerical simulation were performed using a finite element code package for thermoforming (T-SIM®) with K-BKZ viscoelastic model. The objective of this work is to find which friction coefficient use in T-SIM simulation to be as close as possible to reality. For this, numerical simulation results for different friction coefficient were compared with experimental values to evaluate the predictive capacity. It was shown that friction coefficient is temperature dependent and rapidly increase above glass transition of polycarbonate. At room temperature, friction coefficient increases with an increase in roughness, but after glass transition, trend is reversed. Simulations with measured friction coefficients shows good agreement with experiment data.

Introduction

Thermoforming is a manufacturing process widely used in the industry for making 3D complex parts. An extruded polymer sheet is heated to be easily deformable and then vacuum formed on a cold mold. Despite the apparent simplicity of this process, it is actually a technical process, difficult to optimize, in which the material undergoes very large deformations in an anisotherm environment. Uneven thickness distribution is caused by localized variable deformations during vacuum forming. However, for manufacturers, a uniform thickness distribution and a high average thickness are very important parameters for the manufacture of high-quality parts. This thickness distribution is mainly affected by the viscoelastic behavior of the extruded polymer sheet [2,3,4] but previous work show that contact friction also has a huge impact on thickness distribution [2,5-8]. In the literature, the majority of authors study the effect of friction in the context of plug assist thermoforming. In this work, we will focus on conventional thermoforming, where the slip rate between the polymer and the mold is lower. Some studies claim that the friction coefficient does not depend on the sliding speed [1,5] but others show the opposite [9]. Several friction models exist but in this study we consider that the friction behavior between mold and polymer sheet can be simply represented using Coulomb friction law. This law defines friction coefficient as the ratio between the friction force and the normal force (Eq. 1):

$$\mu = \frac{F}{F_N} \tag{1}$$

Two friction coefficients can be defined : a static coefficient which corresponds to the minimum tangential force necessary to prime the slide and a dynamic coefficient which corresponds to the

Content from this work may be used under the terms of the Creative Commons Attribution 3.0 license. Any further distribution of this work must maintain attribution to the author(s) and the title of the work, journal citation and DOI. Published under license by Materials Research Forum LLC.

tangential force necessary to maintain this slide. In this study, only the dynamic coefficient will be taken into account. The purpose of this work is to measure the impact of different parameters on the coefficient of friction between polycarbonate sheet and aluminum mold. The effects of velocity, pressure and surface roughness were investigated using a rotational rheometer with a specific geometry, following the method developed by B. Hegemann *et al* [1]. Measured friction values will be used in a numerical simulation of the thermoforming process and simulation results were compared with experimental data to evaluate the predictive capacity.

Materials and Methods

Polycarbonate is a technical polymer with excellent mechanical properties and good temperature resistance. It is easily thermoformable thanks to its good flow resistance and is used in many fields such as automotive, aeronautic or medical. For this study a commercial polycarbonate LEXAN 9030 from SABIC was used. The initial sheet thickness was 2,94 ± 0,05 mm. Temperature shrinkage is negligible (< 2%) in the extrusion or transverse direction. The glass transition temperature measured by DSC (rate: 10°C/mn) is around Tg = 149°C. Thermoforming molds and friction coefficient samples used for this study were made with Aluminum 5083 (AW-Al Mg4,5Mn0,7). Aluminum 5083 is a common aluminum-magnesium alloy with 4,5% magnesium.

Torsional Rheometer Test Method.

The friction coefficient measuring device used in this study is based on the B. Hegemann *et al.* [1] method. developed at the IPK-Stuttgart**.** An Anton Paar MCR302 rotational rheometer is used in parallel configuration. The upper moving plate is replaced by the mold material sample and the polymer is fixed on the bottom. The test arrangement is shown in Fig. 1a**.** After contact, the torque required to rotate both parts is measured and converted into a coefficient of friction. Applied normal force and rotation speed are easily adjustable over a wide range of values representative of the thermoforming process. The device is placed in a temperature-regulated chamber, suitable for making measurements from room temperature until forming temperature. Between each measurement, the upper plate is cleaned with acetone to remove any residual traces of polymer. In order to reproduce as much as possible a linear sliding during the test and minimize the velocity gradient, the contact surface is limited to one ring (Fig. 1b). Inner and outer radii are respectively 9 mm and 12.5 mm. As a result, the maximum speed rotation varies only about 15% around the mean value. The tested polymer sample is a 25 mm disc, glued on a disposable plate with a two-component epoxy adhesive resistant up to 180°C. Special attention is paid to the flatness of the experimental setup to ensure optimal contact.

Thus, assuming that the normal force is evenly distributed over the contact surface, and taking into account the geometry used, the average friction coefficient can be calculated from the following relation [Eq. 2] :

$$\mu = \frac{3}{2} \times \frac{\tau}{F_N} \times \frac{R_O^2 - R_i^2}{R_O^3 - R_i^3}. \quad (2)$$

where Γ is the measured torque, F_N the normal force and Ri and Ro are respectively the inner and outer radius of the ring.

Test settings.

With this method, friction coefficients were measured over a wide range of temperature, from room temperature to 180°C. First every 40°C up to 140°C, then, every 10°C from the glass transition temperature of polycarbonate samples (Tg = 149°C). Beyond 180°C, the epoxy adhesive fail and does not maintain the sample properly. This temperature range does not cover the entire forming range (up to 220°C for polycarbonate) but in reality, due to the low thermal effusivity of polycarbonate compared to aluminium, interface temperature is much lower and probably no more than 180°C. Some previous studies [1, 9] show that there is no significant influence of normal

force on friction coefficient. In order to verify this hypothesis, friction coefficients were measured at room temperature for several values of normal force (2, 5 and 10N). For higher temperatures, the normal force was limited to 2N because of MCR302 torque measurement limitation but also to limit compression deformations beyond glass transition temperature.

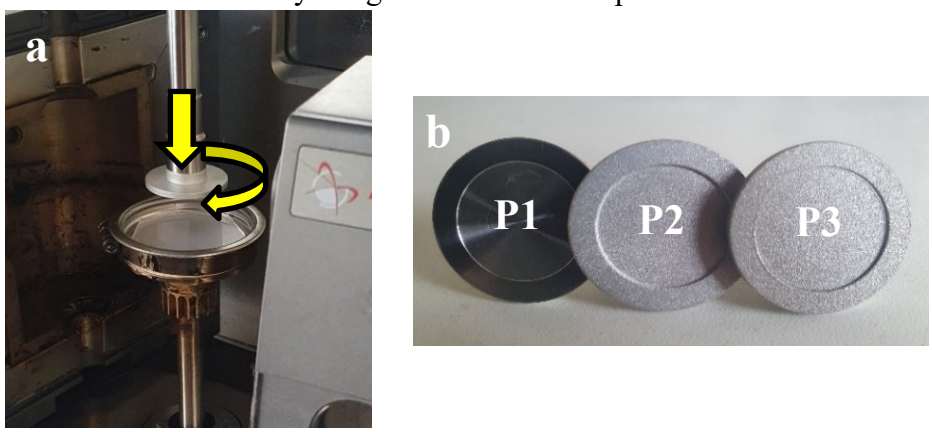

Fig. 1. (a) Modified rotational rheometer with aluminum upper plate and polymer sample on the lower plate. (b) P1, P2 and P3 aluminum plate with roughness of respectively Ra = 0,38 µm, Ra = 2,80 µm and Ra = 8,12 µm. Contact surface is limited to a crown of 9 mm inner radius and 12.5 mm outer radius.

In order to measure the impact of the sliding speed on the friction coefficient, different rotational speeds were investigated. In industry, the mold rising speed is typically within the range 25-100 mm/s. However, glide speed can be considerably less due to the frictional force and the sheet deformation resistance [5, 9]. Thus, for the sake of covering a representative sliding speeds range of the thermoforming process, friction coefficients were measured for three different rotational speeds of 4.4 rpm, 11.1 rpm and 22.2 rpm corresponding respectively to an average sliding speed of 5 mm/s, 12.5 mm/s and 25 mm/s. In addition, all these measurements were carried out for three different aluminium upper plates surface roughness, corresponding to different surface states of industrial moulds (Fig. 1b). The plate 1 (P1) corresponds to a smooth mold with Ra = 0,38 µm while plate 2 (P2) and 3 (P3) have been sanded with roughnesses of Ra = 2,80 µm and Ra = 8,12 µm respectively. The various tested parameters are summarized in Table 1. This experimental design allows the coverage of a wide range of friction coefficients values on all the thermoforming process parameter range.

Friction Measurement Results and Discussions

Fig. 2 shows the evolution of the coefficient of friction at room temperature as a function of the normal force for applied values of 2 N, 5 N, and 10 N. For the P1 plate with the smoothest surface, normal force does not affect the friction coefficient in the measurement range. For P2 and P3 plates, with a rougher surface, the friction coefficient increases slightly with normal force. Increase in the normal force must increase the penetration of the roughnesses into the polymer and therefore the friction.

Table 1. Friction coefficient measurement parameters.

	Roughness (µm)	Temperature range (°C)	Normal Force (N)	Rotation speed (mm/s)
Plate 1 (P1)	0,38	20	2 - 5 - 10	5 - 12,5 - 25
		60-180	2	
Plate 2 (P2)	2,80	20	2 - 5 - 10	5 - 12,5 - 25
		60-180	2	
Plate 3 (P3)	8,12	20	2 - 5 - 10	5 - 12,5 - 25
		60-180	2	

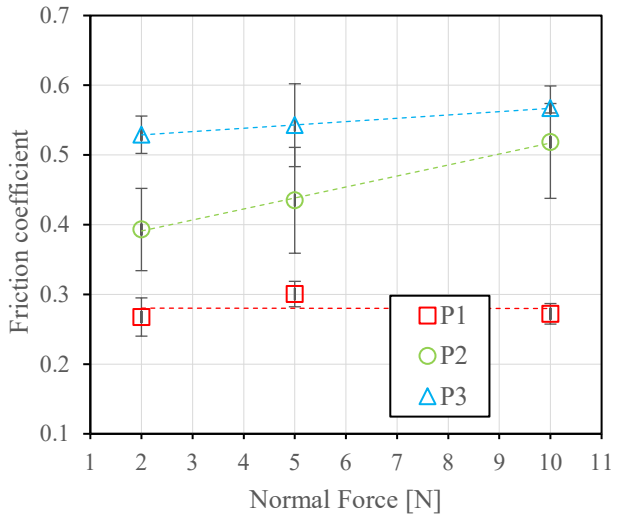

Fig. 2. Friction coefficient at room temperature for an applied normal force of 2N, 5N and 10N (Speed test = 12,5mm/sec).

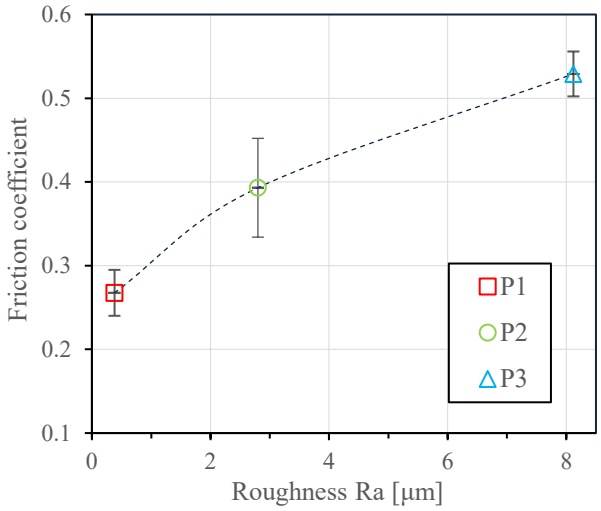

Fig. 3. Friction coefficient in function of roughness (Normal force = 2N, Speed test = 12,5 mm/sec).

Friction coefficient evolution with surface roughness at room temperature is reported in Fig. 3. Contrary to expectation the coefficient of friction increases with the surface roughness by almost following a linear relationship. This result contradicts previous studies [10, 11] assuming that the apparent surface contact reduction due to the roughness decreased friction. One possible explanation is that, in reality, the friction force can be divided into two independent contributions: an adhesive term representing the adhesion phenomena at the real contact level and a deformation term representing volumic deformations by "ploughing". This deformation term is sometimes not negligible at room temperature [12]. It is possible that in the case of the roughness profile of the P2 and P3 plates, the deformation term is important and increases the friction coefficient.

In temperature, for a 2N applied force, Fig. 4 shows that the friction coefficient is stable up to the glassy transition temperature (~150°C) and then increases more or less significantly with roughness. This results is consistent with literature [1, 2, 9]. However, there is a

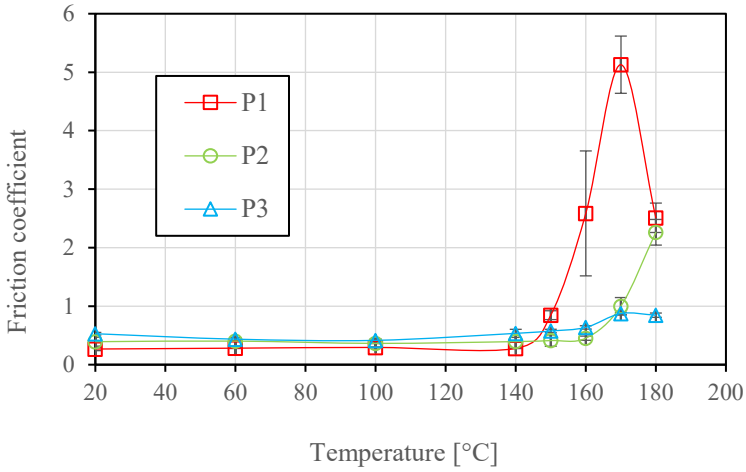

Fig. 4. Effect of temperature on friction coefficient for the three plates (Normal force = 2N, Speed test =12.5mm/sec).

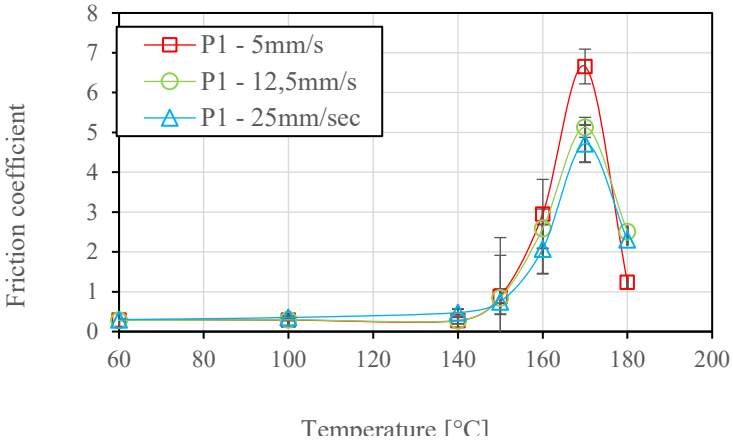

Fig. 5. Effect of speed sliding on friction coefficient in temperature for smooth plate P1 (Normal force = 2N).

decrease of friction coefficient in temperature as a function of the surface roughness. It is deduced that, unlike to ambient temperature, the drop in mechanical properties due to temperature increase reduces the deformation term effect on friction in favor of the adhesion term. Friction coefficient decline from 180°C can be explained by a totally sticky contact, the measured torque being linked to pure shear of the sample [1]. Fig. 5 shows the effect of the sliding speed on the friction coefficient for P1 plate. The decrease in the sliding speed increases friction. This sensitivity to speed and temperature relates the viscoelastic behavior of polymers and Time Temperature Superposition (TTS) principle. This behavior has already been observed in the case of elastomers [12] as well as on impact PS and PP [9]. The behavior is the same with the P2 and P3 plates.

Numerical Simulation and Experimental Comparison

T-SIM software.

The 3D numerical simulations were carried out using the commercial package code T-SIM® version 4.9 (Accuform) based on the finite element method and specially designed for the simulation of the thermoforming process. This software use a K-BKZ [13] type nonlinear viscoelastic constitutive model to describe large polymer deformations during forming. Friction Coulomb's law was applied on contact areas between sheet and mold, and the heat equation allows the calculation of thermal transfers during the process. The thickness distribution and polymer stretching were numerically investigated for the different experimentally measured friction coefficient values. Next, numerical results were compared with experimental thermoforming data obtained with two representative moulds presented in Fig. 8. The mold A has the same surface roughness as plate P1 (Ra = 0,41 μm) and the mold B has the same as plate P3 (Ra = 8,06 μm).

Viscoelastic model parameters.

During thermoforming, polymer materials exhibit nonlinear viscoelastic behavior due to large deformations and high strain rates over a wide range of temperatures. To describe this particular behavior, T-SIM use the K-BKZ type viscoelastic Wagner Model. This model shows good results for the simulation of the thermoforming process for ABS [2, 4], PS [14], or HDPE [15]. The Wagner model is expressed as follows (3):

$$\sigma(t) = \int_{-\infty}^{t} m(t-t')h(I_1, I_2)C^{-1}(t,t') \quad (3)$$

- $C^{-1}(t,t')$ is the finger strain tensor. I_1 and I_2 are invariants and depend on the solicitation type.
- $m(t-t')$ is the time dependent Memory function used to explain the linear viscoelasticity. The memory function is calculated from the discrete relaxation spectra obtained by small amplitude oscillatory shear (SAOS) experiment. Several experiments were carried out at different temperatures and the master curve was reconstructed thanks to the time-temperature equivalence principle and the Williams-Landel-Ferry (WLF) equation.
- $h(I_1, I_2)$ is the Damping of the two strain invariants used to describe the nonlinear viscoelasticity. T-SIM software uses the following damping function Wagner (4) :

$$h(I_1, I_2) = \frac{1}{1 + A\sqrt{(I_1-3)(I_2-3)}} \quad (4)$$

K-BKZ Wagner damping function was numerically determined using T-SIMFIT® v1.41 software from uniaxial tensile test data. Tensile test were carried out at 170, 180 and 190°C and for four different speeds of 1.25, 2.5 and 12.5 mm/sec corresponding to an initial elongation rate

of 0.1, 0.5 and 1 s-1 respectively. Fig. 6 shows the prediction from Wagner model for A = 0,095 in comparison with experimental data at 170°C.

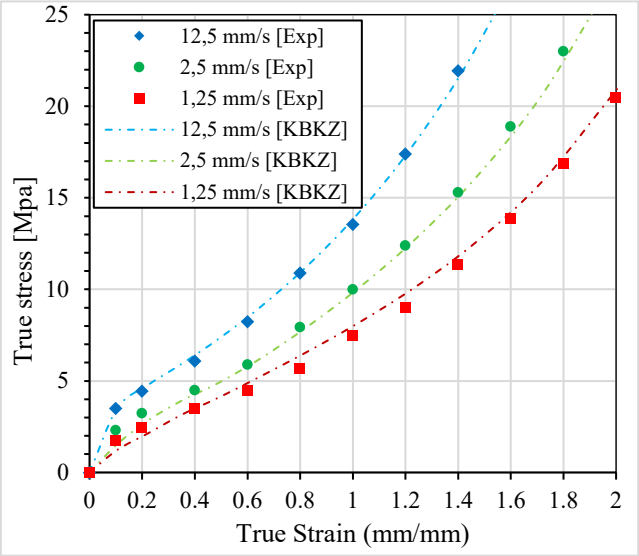

Fig. 6. Lexan 9030 stress/strain curve at 170°C. Experimental data are represented by symbols and KBKZ prediction by dashed lines for A = 0,095.

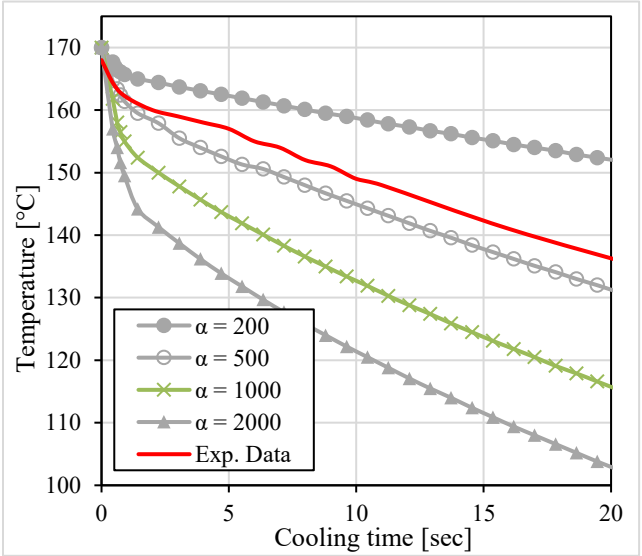

Fig. 7. Cooling of a Lexan 9030 sheet at 170°C during 20sec. Red line correspond to experimental cooling measured by thermal camera and gray lines are simulated cooling for different conductive exchange coefficient.

Heat transfer.

As shown above, the viscoelastic behaviour of polymers is highly temperature dependent. Therefore, it is necessary to well know the temperature throughout the forming cycle. For this purpose, a heat equation makes it possible to account for heat exchanges during the process. The polycarbonate thermal capacity and thermal conductivity were determined on a large temperature range by measurement in modulated DSC and HOT DISK device. The measured values are respectively Cp = 2.140 J/(Kg.K) and λ = 0.22 W/(m.K) at 180°C. In T-SIM, thermal properties are constant but in reality, they are temperature dependent, particularly around the Tg. For mold and sheet heat exchanges, the mold is only represented by its external surface and is assumed to be isothermal throughout the operation. The mold's thermal properties are not involved in it, and it is considered that the sheet-mold heat flow is monitored by a conductive exchange coefficient called "α". It may not hold a tangible sense, but it may however be experimentally determined : the cooling of a Lexan 9030 sheet at a temperature of 170°C, in contact with an aluminum mold at room temperature could be measured and then compared to simulated cooling for different α values (Fig 7). As a result, conductive exchange coefficients were found to be close to 500 W/m²/K, which is similar to a value obtained by Marotta and Fletcher [16]. Likewise, the convection exchange coefficient between polymer and ambient air is 8 W/m²/K.

Friction coefficient.

At the areas of contact between sheet and mold, sliding is managed by the Coulomb friction law. As with thermal properties, the friction coefficient is considered constant throughout the forming cycle. This study showed that in reality, the friction coefficient depends on several parameters and is largely temperature dependent for polymers. Several friction coefficients corresponding to the previously measured coefficients have been tested and the simulation will be compared with the experimental results.

Process parameters.

T-SIM software makes it possible to easily manage the various process parameters to best match the experimental parameters (see *Experimental thermoforming*) . The initial sheet temperature is 215°C. The mold rising speeds are respectively 20 cm/s and 10 cm/s for mold A and mold B. No pre-stretching were performed and a vacuum of - 0.2 bar is applied for 5s. A 60,000 polygons mesh permit to have an optimal compromise between precision and calculation time. Different process parameters are summarized in Table 2.

Experimental thermoforming.

Experimental thermoforming was performed on a laboratory scale thermoforming machine Formech 450DT. A thermal camera placed above the device allows sheet temperature profile recording in real time. The pressure during the forming cycle is measured by a manometer. Fig. 9 shows the experimental setup. The polymer sheet is heated with ceramic radiants until reaching a temperature of 215°C. In order to achieve the most uniform temperature distribution possible, the power of the external radiants is slightly increased to compensate heat losses by convection with ambient air. The rise of the mold is manually controlled. The average mold speed is around 20 cm/sec for mold A and 10 cm/sec for mold B, in order to avoid tearing the sheet on sharp angle. Then, a vacuum of -0.2 bar is applied for 5 to 7 sec to form the sheet on the mold.

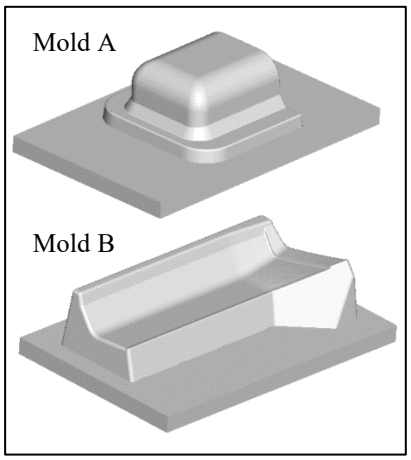

Fig. 8. Molds used for experimental thermoforming and simulation. Mold A has a surface rugosity of R = 0,41 µm corresponding to plate P1 and Mold B, Ra= 8,06 µm corresponding to plate P3.

Fig. 9. Experimental thermoforming setup with Formech 450DT thermoforming machine and thermal camera.

Table 2. Process parameter for numerical simulation with T-SIM®.

Process parameters	Mold roughness	Mold temp.	Sheet temp.	Mold speed	Convection coefficient	Conduction coefficient	Vacuum pressure
Mold A	0,41 µm	70°C	215°C	20 cm/s	8	500	0,2 bar during 5 sec
Mold B	8,06 µm	95°C		10 cm/s			

Simulation and Experimental Comparison Results

Several simulations were carried out with process parameters presented in Table 2. Four coefficients of friction were simulated as a function of the two molds: µ = 0.3 (minimum coefficient of friction for the polycarbonate-plate couple P1), µ = 0.75, µ = 1.5 and µ = 5 (corresponding to total stick) for the mold A and µ = 0.5 (minimum friction coefficient for

polycarbonate-plate P3) μ = 0.75, μ = 1.5 and μ = 5 for mold B. For each mold and friction coefficient, the simulated thickness distribution along the transverse (A-A) and longitudinal (B-B) axis is represented by a continuous line in Fig. 10 and Fig. 11. Experimental thicknesses has been measured on at least two different thermoformed parts using a digital micrometer is represented by diamond symbols. The thickness distribution can be divided in two regions: the upper part and the side parts. For mold A, uppers parts are located from 150 mm to 250 mm for transversal cut and from 225 mm to 375 mm for longitudinal cut. For mold B, uppers parts are located from 150 mm to 275 mm for transversal cut and from 75 mm to 425 mm for longitudinal cut. Other parts are considered as side parts.

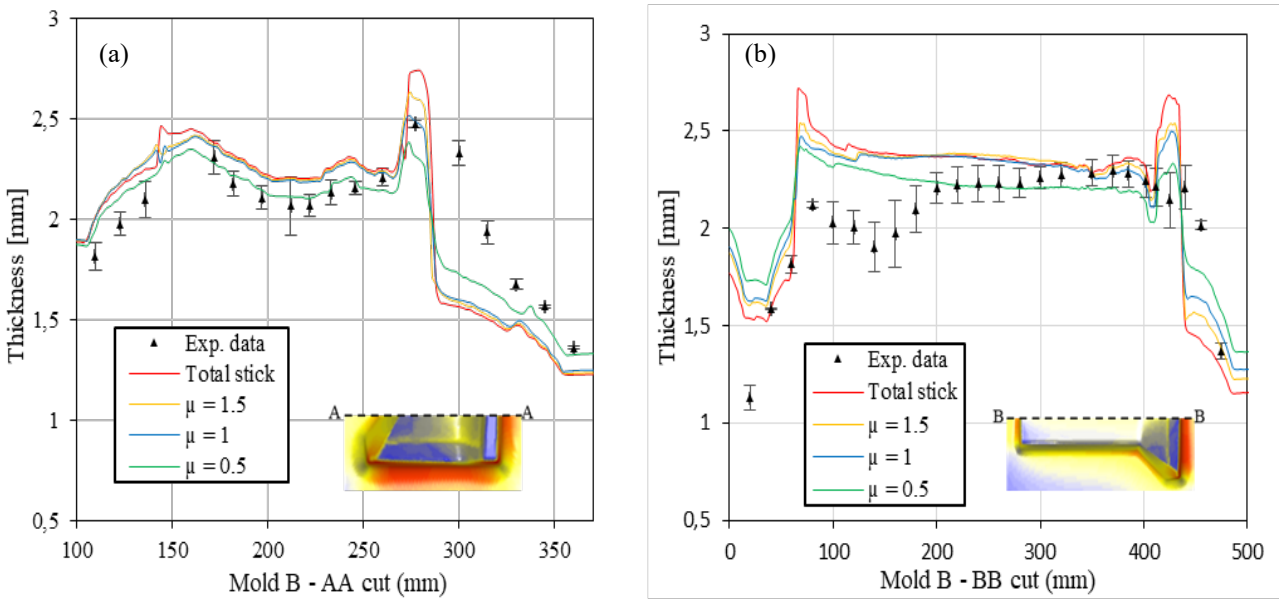

Fig. 11. Mold B thickness distribution along transversal (A-A) axis (a) and longitudinal (B-B) axis (b). Simulated data are in continuous line and experimental data are represented by diamond symbols.

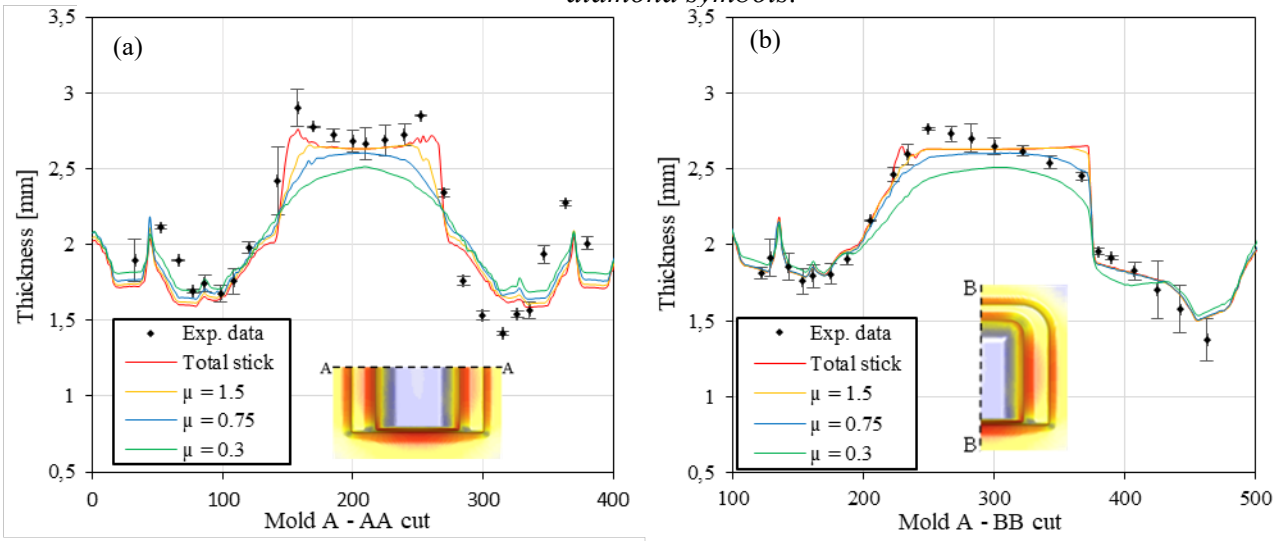

Fig. 10. Mold A thickness distribution along transversal (A-A) axis (a) and longitudinal (B-B) axis (b). Simulated data are in continuous line and experimental data are represented by diamond symbols.

The effect of friction coefficient variation is particularly visible on mold upper parts, the first in contact with polymer sheet during forming. The higher the friction coefficient, the greater the

simulated thickness. Indeed, when the friction coefficient is important or when the contact is completely sticky, the sheet cannot slide on the surface of the mold. Thus, the deformations are mainly concentrated on the side parts and in the corners. This phenomenon is amplified by the sheet cooling in contact with mold, witch limit the polymer ability to deform under stress. We can deduct from its results that a lower friction coefficient promote a more uniform thickness distribution especially when the mold geometry have a large upper planar surface.

Overall, for the two mold, simulated thickness distribution shows good agreements with experimental data. For mold A [Fig. 10a and 10b], average measured thickness on the upper part correspond to simulated thickness for high friction coefficient, see even, for total stick behavior on [Fig. 10a].

Its results confirm the friction coefficients measured previously: since the polymer sheet is still close to 215°C when in contact with the mold, P1 plate friction coefficient measurements predict sticky contact for this temperature. For mold B [Fig. 11a and 11b], average measured thickness on the upper part gets closer to simulated thickness for a friction coefficient between $\mu = 0.5$ and 1. Again, this correspond to friction coefficient value measured for plate P3 at this temperature. Based on this results, the sanding of the thermoforming tools makes it possible to limit the friction with sheet polymer in temperature and thus greatly improve the average thickness distribution.

Summary

A rotational rheometer with a specific geometry allowed us to measure the coefficient of friction from the ambient temperature up to the forming temperature for different speed of rotation and normal force. Effect of surface roughness were explored. It was shown that friction coefficient is temperature dependent and rapidly increase above glass transition. At room temperature, contrary to expectation, friction coefficient increases with an increase in roughness. One possible explanation is that, for this couple of materials, the friction deformation term is not negligible at room temperature and result in an increase of friction for rough plate. After glass transition, this trend is reversed and the smooth plate (P1) exhibit sticky behavior beyond 180°C. Simulations with T-SIM® shows good agreement with experiment data and confirms the friction coefficient values in temperature for the different roughnesses. For mold A (smooth surface corresponding to plate P1), best match is reached for a very high friction coefficient. For sand mold B (corresponding to plate P3), friction coefficients between 0.5 and 1 show best results. Based on this results, the sanding of the thermoforming tools makes it possible to limit the friction with sheet polymer in temperature and thus greatly improve the average thickness distribution.

Acknowledgments

This work was supported by ANRT funding and AXYAL (Sauvagnon, FRANCE) as part of a CIFRE PhD thesis.

References

[1] Information on: Polymer_Polymeric_Hegemann2003_(methode par rhéo).pdf
[2] J.K. Lee, C.E. Scott, T.L. Virkler, Effects of rheological properties and processing parameters on ABS thermoforming, Polym. Eng. Sci. 41 (2001) 240-261. https://doi.org/10.1002/pen.10725
[3] M. Takaffoli, G. Hangalur, R. Bakker, N. Chandrashekar, Thermo-visco-hyperelastic behavior of polycarbonate in forming of a complex geometry, J. Manuf. Process. 57 (2020) 105-113. https://doi.org/10.1016/j.jmapro.2020.06.019
[4] J. Cha, H.Y. Song, K. Hyun, J.S. Go, Rheological measurement of the nonlinear viscoelasticity of the ABS polymer and numerical simulation of thermoforming process, Int. J. Adv. Manuf. Technol. 107 (2020) 2449-2464. https://doi.org/10.1007/s00170-020-04979-7
[5] P.J. Martin, R. McCool, C. Härter, H.L. Choo, Measurement of polymer-to-polymer contact friction in thermoforming, Polym. Eng. Sci. 52 (2012) 489-498. https://doi.org/10.1002/pen.22108

[6] D. Marathe, D. Rokade, L. Busher Azad, K. Jadhav, S. Mahajan, Z. Ahmad, S. Gupta, S. Kulkarni, V. Juvekar, A. Lele, Effect of Plug Temperature on the Strain and Thickness Distribution of Components Made by Plug Assist Thermoforming, Int. Polym. Process. 31 (2016) 166-178. https://doi.org/10.3139/217.3060
[7] R.A. Morales, M.V. Candal, O.O. Santana, A. Gordillo, R. Salazar, Effect of the thermoforming process variables on the sheet friction coefficient, Mater. Des. 53 (2014) 1097-1103. https://doi.org/10.1016/j.matdes.2013.08.009
[8] P. Collins, E.M.A. Harkin-Jones, P.J. Martin, The Role of Tool/Sheet Contact in Plug-assisted Thermoforming, Int. Polym. Process. 17 (2002) 361-369. https://doi.org/10.3139/217.1702
[9] A. Erner, Étude expérimentale du thermoformage assisté par poinçon d'un mélange de polystyrènes, p. 232.
[10] J. Voyer, S. Klien, I. Velkavrh, F. Ausserer, A. Diem, Static and Dynamic Friction of Pure and Friction-Modified PA6 Polymers in Contact with Steel Surfaces: Influence of Surface Roughness and Environmental Conditions, Lubricants 7 (2019) 17. https://doi.org/10.3390/lubricants7020017
[11] V. Quaglini, P. Dubini, D. Ferroni, C. Poggi, Influence of counterface roughness on friction properties of engineering plastics for bearing applications, Mater. Des. 30 (2009) 1650-1658. https://doi.org/10.1016/j.matdes.2008.07.025
[12] B. Briscoe, The friction of polymers : a short review, Proc. 7 th Leeds-Lyon Symposium of tribology, N° 00682, 1980, pp. 9-1281.
[13] E. Mitsoulis, 50 Years of the K-BKZ Constitutive Relation for Polymers, ISRN Polym. Sci. 2013 (2013) 1-22. https://doi.org/10.1155/2013/952379
[14] K. Landsecker, C. Bonten, Thermoforming simulation of heat conductive plastic materials using the K-BKZ model, presented at the Materials characterization using X-rays and related techniques, Kelantan, Malaysia, 2019, p. 030049. https://doi.org/10.1063/1.5088307
[15] S. aus der Wiesche, Industrial thermoforming simulation of automotive fuel tanks, Appl. Therm. Eng. 24 (2004) 2391-2409. https://doi.org/10.1016/j.applthermaleng.2004.03.003
[16] E.E. Marotta, L.S. Fletcher, Thermal contact conductance of selected polymeric materials, J. Thermophys. Heat Trans. 10 (1996) 334-342. https://doi.org/10.2514/3.792

Materials Research Proceedings 28 (2023) 1917-1926 https://doi.org/10.21741/9781644902479-207

A local power law versus a well-identified viscosity curve over a large shear rate range in thermorheology of polymers

LIN Qiao[1,a *], ALLANIC Nadine[1,b], MOUSSEAU Pierre[1,c], BEREAUX Yves[1,d], GIRAULT Manuel[2,e] and DETERRE Rémi[1,f]

[1]GEPEA Nantes Université, Oniris, CNRS, GEPEA, UMR 6144, F-44000 Nantes, France

[2]Institut P' CNRS-ENSMA-Université de Poitiers, UPR 3346, F86961 Futuroscope Chasseneuil Cedex, France

[a]qiao.lin@univ-nantes.fr, [b]Nadine.Allanic@univ-nantes.fr, [c]pierre.mousseau@univ-nantes.fr, [d]yves.bereaux@univ-nantes.fr, [e]manuel.girault@ensma.fr, [f]remi.deterre@univ-nantes.fr

Keywords: Pseudo-Plastic; Annular Flow; Cross Law; Viscous Dissipation; Velocity Field

Abstract. There are always debates on the use of power law to model flows having a local zero shear rate. This paper uses an original method to define a functional shear rate range with respect to the flow condition and identify an equivalent power law from a Cross-law fluid. The numerical and experimental results are compared to show the ability of the power law to model a flow having a low-shear region.

Introduction

Different viscosity models exist to represent the rheology behavior of polymers. The most simple behavior law for non-Newtonian materials is the power law [1,2]. The shortcoming of the power-law model to describe the viscosity at the zero shear rate was pointed out by several studies [3,4]. Some authors claim that the power law can be used with particular attention to the shear stress range [5], while some just use more complex models such as the Cross model [6] and the Carreau model [7] which better describe the low-shear regime.

The power law cannot be totally abandoned. Although the simplifications that the power law (compared to other complex viscosity models) can provide in numerical studies may seem small, it can still bring clarity for sensitivity analyzes [8] or facilitate the development of analytical formulations. It is important to know whether the power law can be used when a low-shear region exists in the flow.

In this paper, a power law, fitted to a Cross law for a specific shear rate range by an innovative thermo-rheological method [8], is used to model an annular polymer flow. The Cross law is also used to model the same flow for comparison. An experimental annular device [9] is used to measure the flow temperature variation due to viscous dissipation. The temperature measurements are compared to the predictions of the viscosity models. The numerical simulation results for the shear rate, viscosity, shear stress and velocity in the flow are compared as well.

Flow Geometry

We propose to perform analyzes on an annular polymer flow, which can be studied by using a Thermo-Rheo Annular Cell (TRAC) [9]. The structure of the TRAC is presented in Fig. 1, with thermocouples T_{1-4} installed on its central axis for flow temperature measurements. The polymer flow enters the duct from the left of the figure and is guided to the annular part ($z \geq 0$) by a 45° cone. The outlet is on the right side (Fig. 1). The central axis is not only for thermocouple instrumentation, but also for generating additional viscous dissipation in the passing flow, to extract information from the rheological behavior of the flow. The details on the flow model of the TRAC can be found in [9].

Content from this work may be used under the terms of the Creative Commons Attribution 3.0 license. Any further distribution of this work must maintain attribution to the author(s) and the title of the work, journal citation and DOI. Published under license by Materials Research Forum LLC.

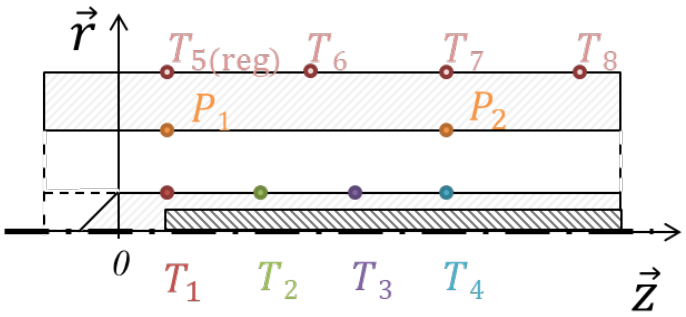

Fig. 1. Illustration of the TRAC.

Viscosity Models

The Cross law [6] (Eq. 1) is employed to represent the rheological behavior of the polymer :

$$\eta = \eta_0 / \left[1 + \left(\frac{\eta_0}{\tau^*}\dot{\gamma}\right)^{1-n}\right] \quad (1)$$

with η the viscosity, $\dot{\gamma}$ the generalized shear rate, η_0 the zero shear rate viscosity, n the power index at high shear rate regime ($0 < n < 1$ for shear thinning materials such as the polymers) and τ^* the critical stress level at the transition to shear thinning. According to the material database of the « Autodesk® Moldflow® » software, the Cross-law parameters for Polypropylene PPC 9642 at 195 °C are: η_0 = 3192.75 Pa.s, τ^* = 19996.2 Pa and n = 0.3387.

The power law [1,2], shown in Eq. 2, is used to compare to the Cross law.

$$\eta = K\dot{\gamma}^{n_p - 1} \quad (2)$$

with K the consistency coefficient and n_p the power-law index ($0 < n_p < 1$ for shear thinning materials). The power law is a straight line in logarithmic scale having the slope: $\left(d\ln\eta / d\ln\dot{\gamma} = n_p - 1\right)$. It should be noted that the Cross law also has a similar slope for $\dot{\gamma} \to \infty$: $\left(\lim_{\dot{\gamma}\to\infty} d\ln\eta / d\ln\dot{\gamma} = n - 1\right)$. The power-law parameters (K and $n_p \neq n$) are carefully chosen to compare with the Cross law of PPC 9642. This is detailed in the next section.

Procedure of the Study

A power-law curve can be drawn from two different viscosity points. In this paper, we use an innovative method to obtain viscosity points from temperature measurements. When the polymer melt flows through the TRAC, the temperature variation due to viscous dissipation is recorded at the central axis of the annular geometry. This temperature variation, for a given flowrate, is sensitive to one point on the material's viscosity curve. The point is called « critical point » in [8]. To identify critical points, the inverse method process can be designed with different approaches. But the process always takes temperature signals as the input variables and a critical point for each flowrate as the output result. Higher flowrates lead to critical points at higher shear rate regime. We need two different flowrates to obtain two critical viscosity points.

In practice, the TRAC is installed as a nozzle at the outlet of an injection unit. During injection, the polymer flows through the TRAC. Experiments are carried out with Polypropylene PPC 9642 at two different injection flowrates: 42.4 $cm^3.s^{-1}$ and 56.5 $cm^3.s^{-1}$. The corresponding simulations are brought off using the finite element model of the TRAC and the Cross-law viscosity model of the same polymer.

The main discussion of this study is whether the power law can perform as well as a more complex viscosity model rather than the identification of material parameters. To find an equivalent power-law curve of the Cross-law one, the identification of the power-law parameters is performed from the results of the simulations with the Cross law, that is to say by using the simulated temperature variation as a reference (Fig. 2). Two critical viscosities (580.3 Pa.s - 61.7 s^{-1} and 500.6 Pa.s - 80.5 s^{-1}) are obtained by applying the inverse method on the Cross-law simulation results, respectively at a flowrate of 42.4 $cm^3.s^{-1}$ and 56.5 $cm^3.s^{-1}$. A power-law curve (K = 5721.2 Pa.s^n, n = 0.4448) is drawn from these two points in Fig. 3.

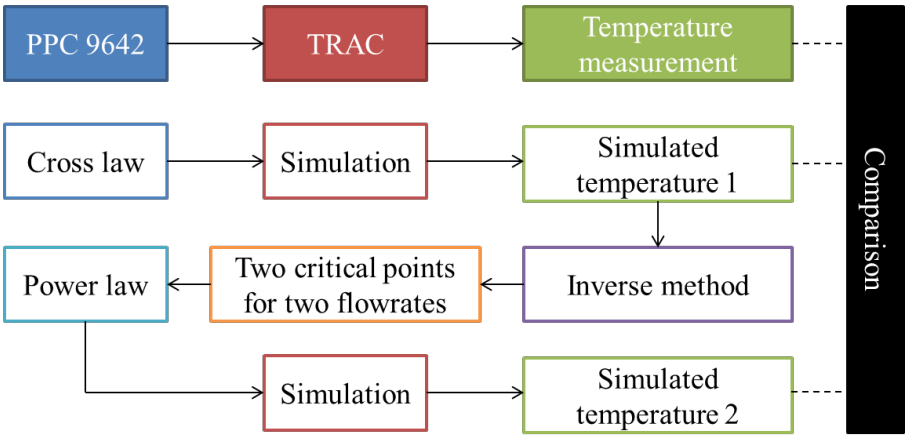

Fig. 2. Procedure of the study.

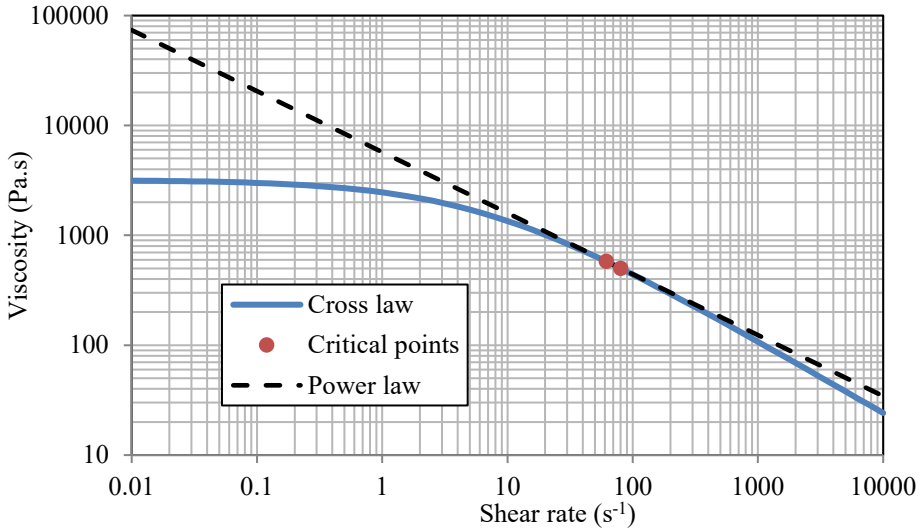

Fig. 3. Viscosity curves of the Cross law and the power law along with the critical points.

Fig. 3 shows that the critical points are on the Cross-law curve, because they are obtained from the Cross-law simulation results. The power-law curve, passing through the critical points, is close to the Cross-law curve only in a specific zone, near the transition region between the low-shear Newtonian zone and the high-shear pseudo-plastic zone. The difference between the two viscosity models can be seen at the high shear rate regime and especially at the low shear rate regime.

Other simulations at the same flowrates are carried out by using the power-law curve in Fig. 3 to replace the Cross-law viscosity model. In the next section, we will find out whether the power-law curve is good enough to describe the flow behavior and whether the critical viscosity points can represent a functional zone of a viscosity curve, by comparing the measurements of the TRAC,

the Cross-law simulations' results and the power-law simulations' results (Fig. 2). The simulation software used is « ANSYS® POLYFLOW® ». Shear rate, velocity and temperature profiles can be exported directly from the simulation tool. The viscosity and shear stress profiles are calculated from the shear rate profiles using analytical expressions (Eq. 1 and Eq. 2).

Results and Discussion

ΔT is the temperature variation relative to that of the initial state. The temperature variations ΔT due to viscous dissipation during injection (at 42.4 $cm^3.s^{-1}$ and 56.5 $cm^3.s^{-1}$) are measured directly by the TRAC and shown in Fig. 4. For an easy reading of the figure, only the temperatures measured by thermocouples T_2 and T_4 (Fig. 1) are presented. These flow configurations are also simulated with the Cross law and the power law. The results of the simulations are presented in Fig. 4 as well.

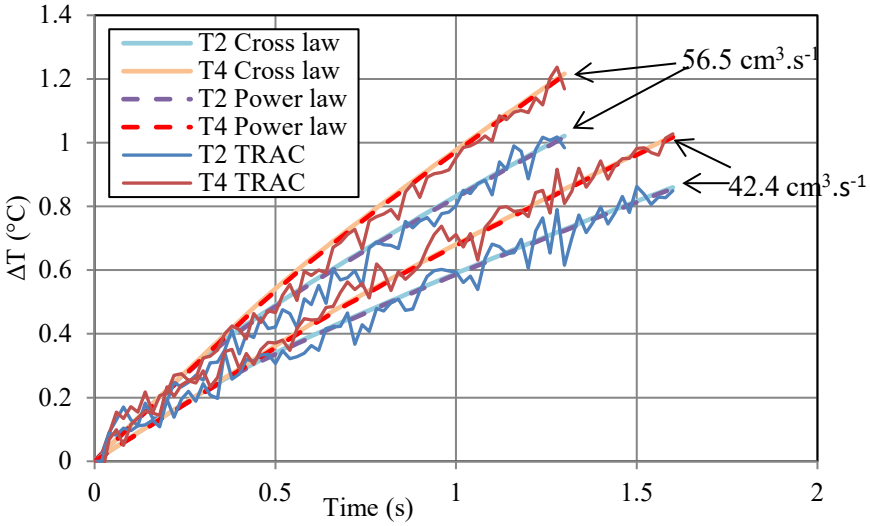

Fig. 4. Temperature variations (due to viscous dissipation during injection) measured by thermocouples T_2 and T_4 of the TRAC and simulated with the Cross law and the power law for different flowrates (42.4 $cm^3.s^{-1}$ and 56.5 $cm^3.s^{-1}$).

The increase in temperature due to viscous dissipation can be observed in Fig. 4. The higher the flowrate, the greater the temperature increases. The injection duration is shorter at the higher flowrate, because the injection volume is limited to the capacity of the machine.

The power law can predict the temperature measurements as well as the Cross law, as the power law is drawn from the critical viscosity points identified using the temperature variations of the Cross-law simulations. Indeed, the heat generated by viscosity dissipation within the flow is brought to the central axis by convection. The viscosity of the flow affects not only the viscous dissipation power (shear rate multiplied by shear stress), but also the velocity field (integral of shear rate) for the convection.

The steady-state shear rate profiles (at 42.4 $cm^3.s^{-1}$ and 56.5 $cm^3.s^{-1}$) as a function of radial position in the annular structure, are calculated respectively with the Cross law and the power law and presented in Fig. 5. The radius of the central axis (inner radius of the annular flow) is 4 mm. The outer radius of the annular flow is 10 mm.

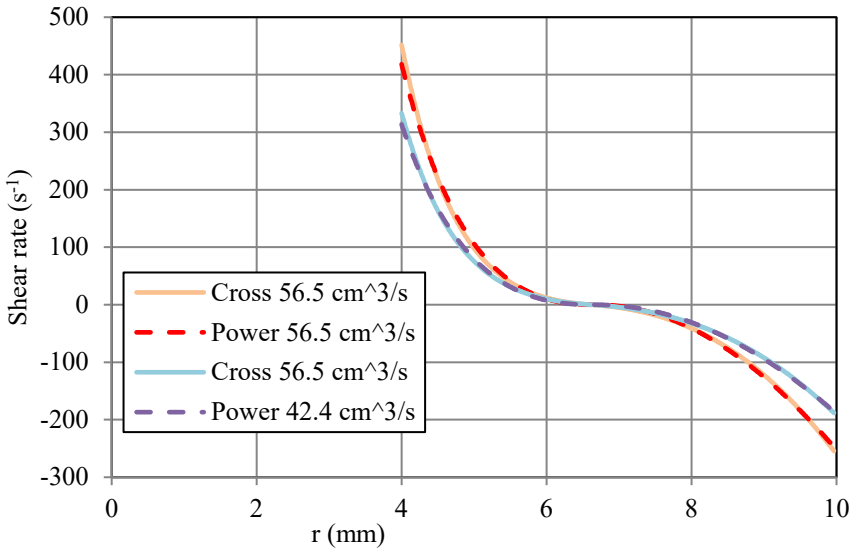

Fig. 5. Steady-state shear rate profiles as a function of radial position in the annular structure, calculated respectively with the Cross law and the power law, at 42.4 $cm^3.s^{-1}$ and 56.5 $cm^3.s^{-1}$.

The power-law calculations show lower absolute values of shear rate close to the inner and outer walls (r = 4 mm and 10 mm) of the annular geometry, compared to those of the Cross law. However, for example at r = 5 mm in the flow, the absolute values of shear rate obtained by the power law become higher than the Cross-law results. Although these differences are minuscule, they reveal that the power-law parameters that we identified with the innovative method minimize the prediction error across a certain depth of the flow domain.

The shear rates of the critical points in Fig. 3 are 61.7 s^{-1} and 80.5 s^{-1}. They have lower values than the maximum shear rates in the annular flow in Fig. 5. The maximum shear rates are on the surface of the central axis ($r = 4$ mm):

- 333 s^{-1} at the flowrate of 42.4 $cm^3.s^{-1}$;
- 452 s^{-1} at the flowrate of 56.5 $cm^3.s^{-1}$.

The power law is capable of delivering accurate predictions, because the power-law curve in Fig. 3 remains close to the Cross-law curve at the shear rate of 452 s^{-1}. The viscous dissipation method does not identify a power-law curve to fit the high-shear region beyond the maximum shear rate in the flow. By not doing so, the identified power law has less error in the relatively low-shear region (from 20 to 60 s^{-1}) on the left side of the critical points in Fig. 3.

Since the viscosity depends on the shear rate for non-Newtonian materials such as the polymers, we can plot the viscosity profile as a function of radial position in Fig. 6a. The main criticism of using the power law is that when a zero shear rate exists in the flow (Fig. 5), the calculated viscosity will reach a high or even infinite value in the low-shear region (Fig. 6a), which is not physical. However, Fig. 6b shows that the calculated shear stress (obtained by multiplying the shear rate by the viscosity) is not affected by the « zero shear rate problem » of the power law.

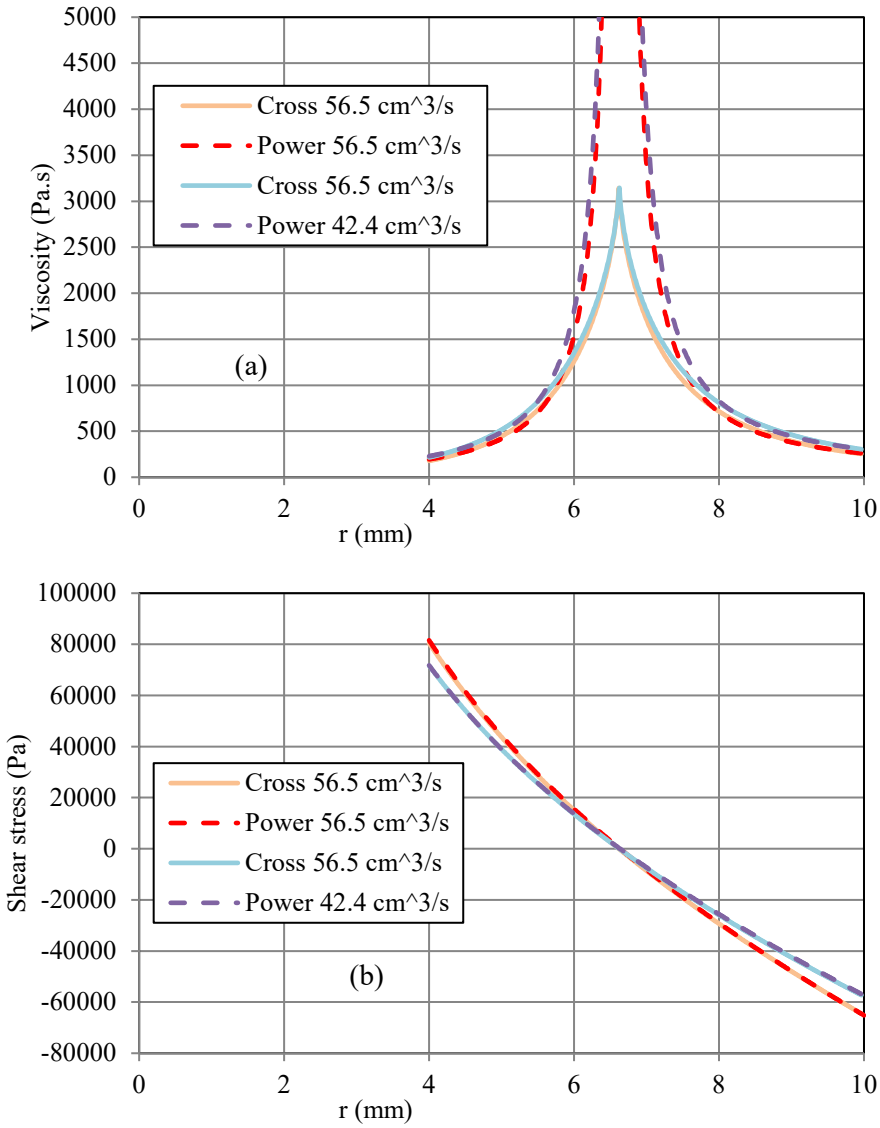

Fig. 6. Steady-state (a) viscosity and (b) shear stress profiles as a function of radial position in the annular structure, calculated respectively with the Cross law and the power law, at 42.4 $cm^3.s^{-1}$ and 56.5 $cm^3.s^{-1}$.

The velocity profiles are presented in Fig. 7. The predictions of the Cross law and the power law are almost the same on the velocity fields.

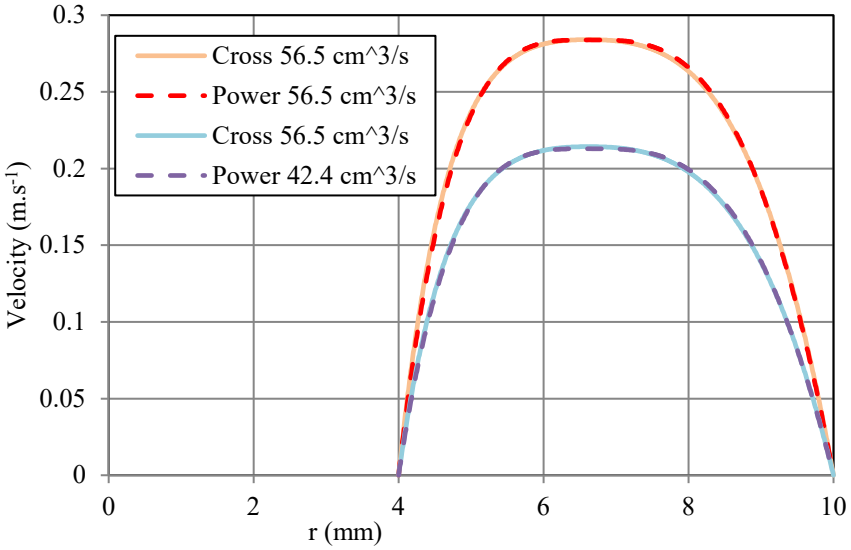

Fig. 7. Steady-state velocity profiles as a function of radial position in the annular structure, calculated respectively with the Cross law and the power law, at 42.4 $cm^3.s^{-1}$ and 56.5 $cm^3.s^{-1}$.

Fig. 7 shows again that the power-law parameters identified using the viscous dissipation method minimize the prediction error across a certain depth of the flow domain. This new method aims to identify parameters to reproduce the same heat exchange between the flow and the central axis of the annular geometry, rather than focusing on the pressure loss (like the classic capillary rheometry method [10]). Viscous dissipation and velocity profile are two of the key factors in this heat exchange.

If we aim to identify the power-law parameters using the simulated pressure measurements corresponding to each flowrate (42.4 $cm^3.s^{-1}$ and 56.5 $cm^3.s^{-1}$) to solve the pressure-flowrate equation of annular flow [11], this power law, different from the one identified with the viscous dissipation method, will be more accurate for pressure loss predictions but can be less accurate to predict velocity profiles especially at the center of the flow (« Power* » in Fig. 8). In general, the power-law calculations in Fig. 8 are still close to the Cross-law calculations. The power law identified with pressure measurements can have good performance as well.

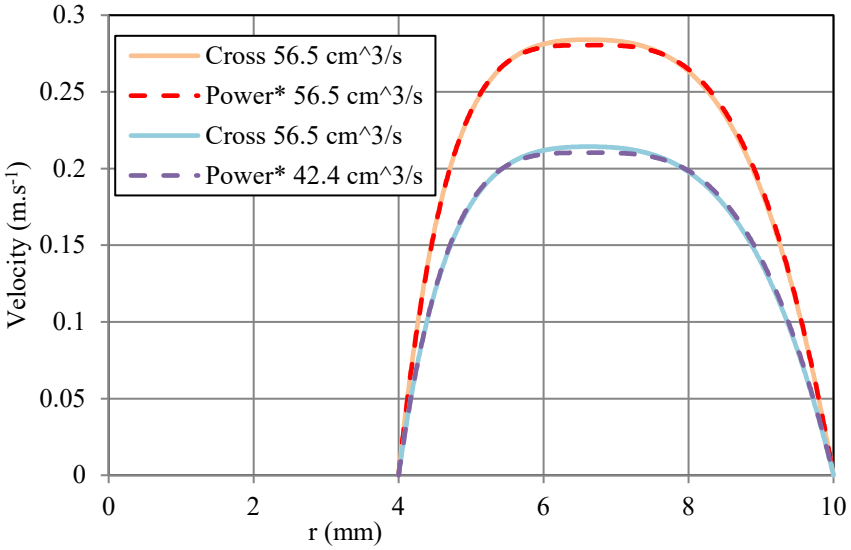

Fig. 8. Steady-state velocity profiles as a function of radial position in the annular structure, calculated respectively with the Cross law and the power law (identified with the pressure method), at 42.4 $cm^3.s^{-1}$ and 56.5 $cm^3.s^{-1}$.

The velocity values can be divided by the average velocity to obtain a dimensionless velocity profile. For a power-law type material, the dimensionless velocity profile depends on the value of the index $\boldsymbol{n_p = [\partial \ln \eta / \partial \ln \dot{\gamma}]}$, and does not depend on the flowrate [8,11]. For a Cross-law type material, the dimensionless velocity profile depends on the flowrate. In Fig. 9, a power-law type dimensionless velocity profile is drawn to compare with Cross-law ones for a large range of flowrates.

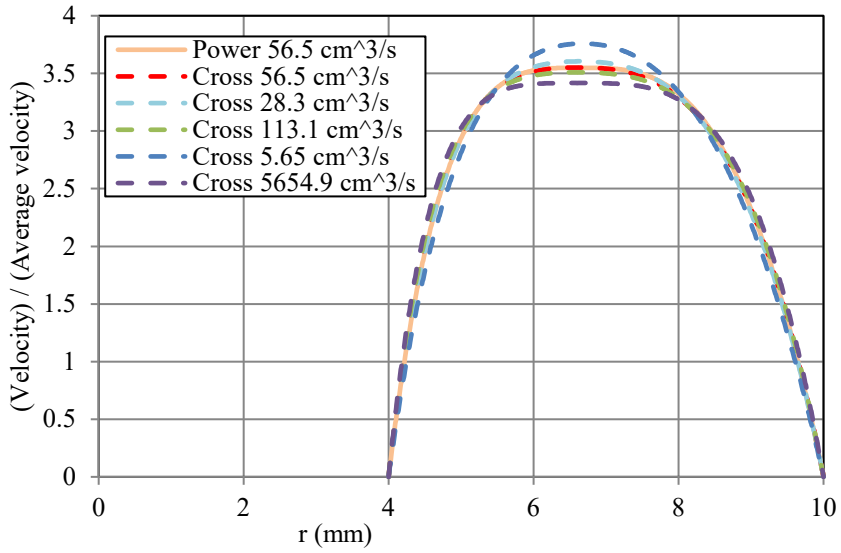

Fig. 9. Dimensionless steady-state velocity profiles as a function of radial position in the annular structure, calculated respectively with the power law (identified with the viscous dissipation method) and the Cross law for a large range of flowrates.

The power law identified with the viscous dissipation method is used to obtain the power-law type dimensionless velocity profile in Fig. 9. When the flowrate at 56.5 $cm^3.s^{-1}$ is multiplied or divided by two. The Cross-law type profiles are still close to the power-law one. When the flowrate is 100 times higher or 10 times lower, differences become significant.

Fig. 9 indicates that the identified local power law has a certain range of validity. For a different range of flowrates, the local power law may need to be re-identified. For example, a local power law with n_p close to 1 will give better results at low flowrates when the material is almost Newtonian. When the local power law is identified at high shear rate regime, it will have a larger range of validity compared to the one identified in the Newtonian-shear thinning transition region (Fig. 3). In this study, the flowrates (42.4 $cm^3.s^{-1}$ and 56.5 $cm^3.s^{-1}$) are chosen on purpose to obtain critical viscosity points in the Newtonian-shear thinning transition region, to show the potential of a power law which fits the Cross law only in a specific range.

Summary

An innovative viscous dissipation method is used to define an equivalent power-law curve from a Cross-law one. The temperature variations due to viscous dissipation, calculated by the power law and the Cross law, are both found to be accurate compared to the experimental measurements. Thanks to numerical tools, the shear rate, viscosity, shear stress and velocity profiles in the flow, respectively obtained with the Cross model and the power-law model, are compared. The comparisons show that it is possible to find a power law to approach to a Cross-law flow for a specific flowrate range. On the viscosity curve, this refers to a dominant functional segment for a specific shear rate range.

Although the calculated power-law flow can be close to the Cross-law one, the power law cannot reproduce exactly the same result of the Cross law. Using different methods to identify the power-law parameters lead to different calculation precisions in the flow domain.

In general, the power law can have competitive performance compared to the Cross law, when the power-law parameters are carefully chosen for a functional shear rate range of the material, even for the transition region between the low-shear Newtonian zone and the high-shear pseudo-plastic zone. This conclusion can be extended to other viscosity models, as long as they can be decomposed into straight line segments in logarithmic scale.

Acknowledgement

This work was supported by the French Ministry of Higher Education, Research and Innovation and held in IUT Nantes.

This work used Polypropylene PPC 9642 kindly supplied by the company TotalEnergies.

References

[1] W. Ostwald, About the rate function of the viscosity of dispersed systems, Kolloid Z. 36 (1925) 99-117.

[2] A. de Waele, Viscometry and plastometry, Journal of Oil and Colour Chemists' Association. 6 (1923) 33-88.

[3] A.G. Fredrickson, Flow of non-Newtonian fluids in annuli, PhD Thesis, University of Wisconsin-Madison, 1959.

[4] R.B. Bird, Experimental tests of generalised newtonian models containing a zero-shear viscosity and a characteristic time, The Canadian J. Chem. Eng. 43 (1965) 161-168. https://doi.org/10.1002/cjce.5450430402

[5] D.W. McEachern, Axial laminar flow of a non-Newtonian fluid in an annulus, AIChE J. 12 (1966) 328-332.

[6] M.M. Cross, Rheology of non-Newtonian fluids: a new flow equation for pseudoplastic systems, J. Colloid Sci. 20 (1965) 417-437.

[7] P.J. Carreau, Rheological equations from molecular network theories, Trans. Soc. Rheol. 16 (1972) 99-127.

[8] Q. Lin, N. Allanic, R. Deterre, P. Mousseau, M. Girault, In-line viscosity identification via thermal-rheological measurements in an annular duct for polymer processing, Int. J. Heat Mass Transf. 182 (2022) 121988. https://doi.org/10.1016/j.ijheatmasstransfer.2021.121988
[9] Q. Lin, N. Allanic, P. Mousseau, Y. Madec, G. Beau, R. Deterre, On-line melt temperature measurements for polymer injection molding through an instrumented annular duct, Polym. Eng. Sci. 62 (2022) 3994-4004. https://doi.org/10.1002/pen.26161
[10] B. Rabinowitsch, Über die viskosität und elastizität von solen, Zeitschrift Für Physikalische Chemie. 145 (1929) 1-26.
[11] R. Deterre, F. Nicoleau, Q. Lin, N. Allanic, P. Mousseau, The flow of power-law fluids in concentric annuli: A full analytical approximate solution, J. Non-Newtonian Fluid Mech. 285 (2020) 104392. https://doi.org/10.1016/j.jnnfm.2020.104392

Sustainability on material forming

Materials Research Proceedings 28 (2023) 1929-1938 https://doi.org/10.21741/9781644902479-208

Energy and resource-efficient forming of gas cylinders by friction-spinning

DAHMS Frederik[1,a *] and HOMBERG Werner[1,b]

[1]Paderborn University, Forming and Machining Technology, 33098 Paderborn, Germany

[a]fd@luf.upb.de, [b]wh@luf.upb.de

Keywords: Friction-Spinning, Flow-Forming, Metal-Spinning, Incremental Forming, Energy and Resource Efficiency, Gas Cylinder Forming, Pressure Vessel

Abstract. Friction-spinning as an innovative incremental forming process enables large degrees of deformation in tube and sheet metal-forming due to a self-induced heat generation in the forming zone. This paper presents new process designs for energy and resource-efficient forming of gas cylinders by friction-spinning without the use of an external heat supply. The self-generated heat enables friction-spinning process to reduce the energy demand in the manufacture of gas cylinders, which are usually manufactured with external heat (mostly fossil fuels), by 95 %. Typical gas cylinder contours, such as flattened and spherical bottom ends and cylinder necks, are manufactured by friction-spinning of AW 6060 tubular profiles with specifically designed tool path strategies. It is shown that friction-spinning enables the manufacture of typical gas cylinder contours with sufficient wall thickness and the required gas tightness without the input of external heat. Thus, this process can contribute to an increase in the energy and resource efficiency of forming processes.

Introduction

Friction-spinning as an innovative incremental hot-forming process enables large degrees of deformation in the field of tube and sheet metal forming due to a friction-induced heat generation in the forming zone in an efficient way [1]. The self-induced partial heating of the components not only enables significantly higher degrees of deformation, but also a defined influence on the mechanical properties such as hardness, microstructure [1] and residual stress distributions [2,3].

However, friction-spinning is also suitable for meeting today's social demand for a reduction in emissions and energy consumption of manufacturing processes. This is illustrated by the example of the manufacture of seamless aluminium gas cylinders, which are usually manufactured using external heat [4]. Comparable incremental processes such as flow-forming [5, 6], metal-spinning [7, 8] or tube-spinning [9] usually use gas burners with fossil fuels for the manufacture of these aluminium gas cylinder contours to enable the necessary degrees of deformation and to ensure the gas-tight sealing [10]. Due to its self-induced heat generation, friction-spinning offers the potential to reduce the energy consumption of comparable manufacturing processes by 95 % [11]. In addition, by eliminating the necessity of external heat supply, the manufacturing process can be realised solely through renewable energy, which provides the possibility of climate neutrality of the manufacturing process.

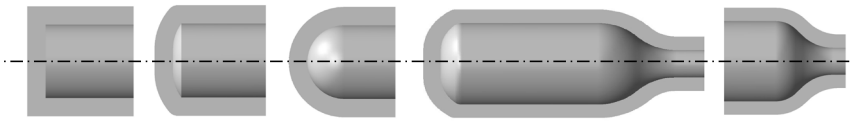

Fig. 1. Example of a gas cylinder and its typical contour elements: flattened and spherical bottom ends and cylinder neck.

Content from this work may be used under the terms of the Creative Commons Attribution 3.0 license. Any further distribution of this work must maintain attribution to the author(s) and the title of the work, journal citation and DOI. Published under license by Materials Research Forum LLC.

Regarding the forming of flattened bottom ends of cylinders it has already been shown that friction-spinning enables the gas and liquid-proof sealing of tube ends with defined wall thickness distributions [12]. Nevertheless, when manufacturing complete gas cylinders, it is necessary to form more complex contours that comply with the standards for aluminium gas cylinders such as DIN EN ISO 7866 [13]. With the aim of energy and resource-efficient manufacturing of gas cylinders, such as the widely used carbonating cylinders, new process designs of the friction-spinning process are developed and investigated. The novelty of this process is that it eliminates the use of gas burners in the manufacture of gas cylinders, thus saving enormous amounts of energy. It also avoids the surface defects of the workpieces (such as surface oxidation) and impacts on the machine and the tools caused by the gas burner. To evaluate this novel process, essential process characteristics, such as force and temperature profiles, and also specific gas cylinder properties such as the workpiece contour, wall thicknesses and gas tightness are determined.

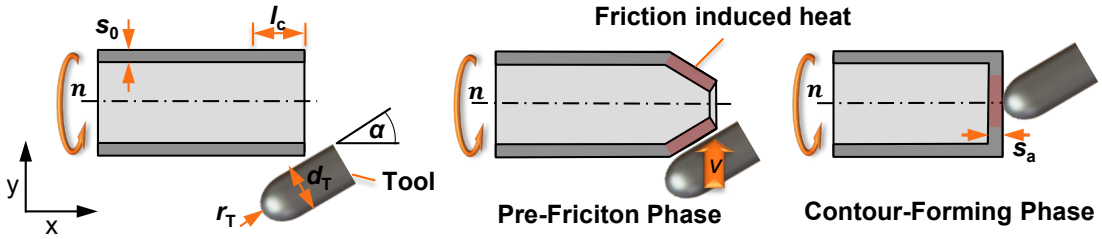

Fig. 2. Friction-spinning process for the forming of sealed-up tubes (flattened cylinder bottom ends. Rotation-speed n, feed rate f, tool-angle α, tool diameter dT, tool radius r_T, initial wall thickness s_0, wall thickness of the cylinder bottom end s_a, tool contact length l_c.

Process Design and Experimental Setup

Typical gas cylinder contours [13], such as flattened and spherical bottom ends and cylinder necks (*cf.* Fig. 1), are manufactured by friction-spinning of tubular profiles with specifically designed tool path strategies. The manufactured parts are assessed concerning their contour, wall thickness and tightness. Generally, the workpieces are manufactured using heat-treatable 3.3206 (EN-AW 6060 initial temper state T6) tubular profiles (100 x 40 x 5 mm) with the LUF in-house design friction-spinning machine (FSV) which is computer controlled by Sinumerik 840D by Siemens AG, Germany. The main spindle drive has a power of 100 kW and enables maximum rotational speeds of 3000 rpm. The tools used have a diameter of 20 mm and are made of the steel alloy 1.3343 (hardened).

The general process-design of the manufacture of sealed-up tubes (flattened bottom ends) by friction-spinning of tubes is subdivided into the pre-friction phase and the contour-forming phase (*cf.* Fig. 2). In the pre-friction phase, a conical basic contour is formed using the large contact area with the tool to induce heat to the workpiece by friction. In the subsequent contour-forming phase, different workpiece contours are formed by specific tool path strategies and the targeted selection of the tool contact area. In the case of a flattened cylinder bottom, the tool path is linear and directed radially (cf. Fig. 3, FB). For the manufacture of more complex contours, such as spherical bottoms and cylinder necks, special curved tool paths have been developed, but due to the limitations of the current version of the FSV machine control, these are interpolated by linear tool paths.

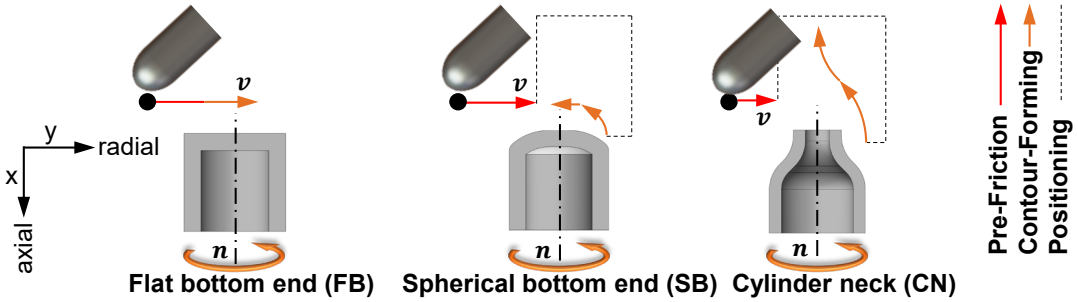

Fig. 3. Tool path designs for flat and spherical bottom ends and cylinder necks.

For the manufacture of the spherical bottom ends (Fig. 3, SB), the pre-friction phase is performed with a large contact area to induce heat and to form an initial cone shape by a linear path in the radial direction. The contour forming then is performed using the tip of the tool, i.e. a point contact and with a curved path that ends in a radial direction. By flattening the path of tool to the end, a centrical flattened bottom section can be realised, too.

For the manufacture of the cylinder necks (Fig. 3, CN), the pre-friction phase is also performed with a large contact area to induce heat and to form an initial cone shape by a linear path in the radial direction. In this case, this path is kept shorter so that the tube is not closed at the end of the process. Contour forming is then performed with the tip of the tool, and therefore a point contact, and with a curved path which does not close the end of the tube by ending in the axial direction. By the combination of tool path design SB and CN complete gas cylinders (*cf.* Fig. 3) are manufactured.

The manufactured parts are evaluated regarding their *contour* by:

- Axial cutting (separating) so that the cut surface lies exactly in the component axis.
- Repeatable positioning of the specimen with a measurement standard on a scanner.
- Image capture with 600 dpi.
- Digital determination of the wall thickness and contour by comparison with the measurement standard.

The *tightness* of the manufactured gas cylinder is demonstrated by applying a hydraulic pressure of 250 bar. For this purpose, a thread is cut into the open end of the gas cylinders to connect them with a pressure gauge, a locking valve and a hydraulic pump by hydraulic hoses (*cf.* Fig. 4, (b)). First, the air is pressed out of the hydraulic hose. Then a hydraulic pressure of 250 bar is applied with the pump, and the valve is closed. After one hour of pressure setting, the pressure is set again to exactly 250 bar and checked with the pressure gauge after 24 hours. The same procedure is also performed with helium at 25 bar.

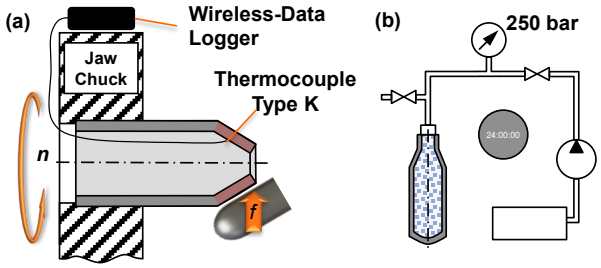

Fig. 4. Telemetric temperature measuring set-up in the friction-spinning process (a) and tightness measuring set-up (b).

The complexity of *temperature measurements* in the friction-spinning process results from its process characteristics (friction of the tool on the surface and rotation of the workpiece), and, with aluminium, especially optical temperature measurements are usually not feasible due to its

complex emissivity characteristics [14]. In addition, a basic black coating on the driven tool does not endure the forming process, so reflections of the ambient heat radiation cannot be ruled out. In a previous work, good results were obtained with a telemetric method using type k thermocouples with a radio data logger (measuring amplifier) [2]. Thermocouples type k are mechanically joined in corresponding holes at two discrete measuring points at 5 mm and 15 mm distance to the end of the tube (*cf.* Fig. 4, (a)). Thus, the measuring amplifier can be mounted on the rotating jaw chuck, and the measured values can be transmitted wirelessly, which will provide new valuable insights into the temperature profile of the friction spinning process even in optically non-measurable areas.

Force measurements are performed using a 6-axis load cell (50 kN, ME-Meßsysteme GmbH, Hennigsdorf, Germany) mounted between the tool holder and the support system. Forces are measured in the radial and axial direction of the workpiece.

Results and Discussion

Essential process characteristics, such as force and temperature profiles and also specific gas cylinder properties, such as the workpiece contour, minimum wall thicknesses were measured and tightness was proved.

Contour and wall thickness.

Starting with an initial wall thickness of 5 mm the thickness is reduced to at least 3.6 mm in the case of the flattened bottom end (a), 3.5 mm in the case of the spherical bottom end (b) and 3 mm in the case of the spherical bottom end (c). The cylinder neck's initial wall thickness of 5 mm is reduced to at least 3.9 mm (d). In all cases, the formation of burrs on the outer contour is observed (*cf.* Fig. 5, red marks). This is attributed to the interpolation of the curved paths by linear paths. Therefore, the burrs of the manufactured gas cylinders were removed by turning (e). It can be concluded from this that the manufacture of typical gas cylinder contours with the friction-spinning process is possible in principle, but the integration of accurate path curves into the process control is necessary. The inner contours of the bottom ends show curved shapes, especially in the centre, where the tube ends are joined. To create a more homogeneous inner contour, auxiliary tools may be used.

All the manufactured bottom ends are sufficiently joined, as shown in Fig. 5 ((a)-(c)). To prove this, three complete cylinders (e) were manufactured by the combination of the process designs of the spherical bottom end SB2 (c) and the cylinder neck CN (d). By testing three of the cylinders as shown in Fig. 4 (b), it can be stated that the manufactured bottom ends are tight, i.e. sufficiently connected to withstand a hydraulic load of 250 bar and are thus suitable as pressure vessels. In addition, the gas tightness of the cylinder was also assessed with helium at 25 bar using the same method. There was no measurable pressure loss over a period of 24 hours.

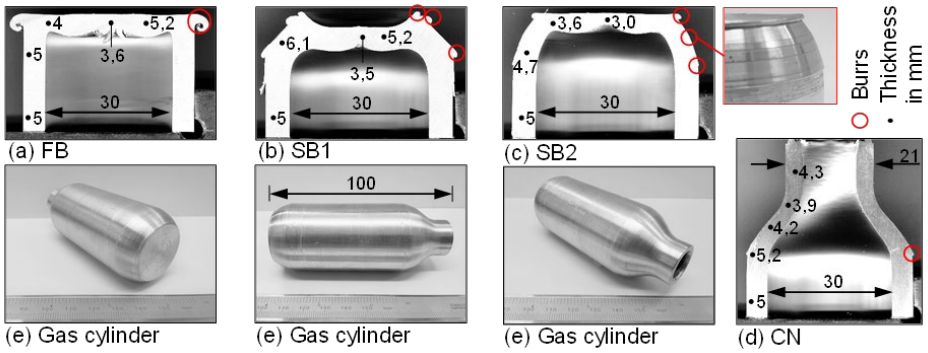

Fig. 5. Manufactured by friction-spinning: (a) flattened bottom end, (b - c) spherical bottom end, (d) cylinder neck and (e) gas cylinder. Rotation speed n = 1500 rpm, feed rate v = 30 mm per min.

Process Forces.

First, the process forces are measured to characterise the new process designs of the friction spinning process. Fig. 6 shows the force profiles and the maximum forces reached in the forming process of the cylinder necks (CN) and spherical bottom ends (SB) in dependence on the process parameters feed rate *v* and rotation speed *n*. In the pre-friction, phase the process forces increase sharply and reach a first peak after 4 seconds (*cf.* Fig. 6, (a-b)). The high level of process forces is maintained for a longer time in the case of the spherical bottom ends due to a longer pre-friction phase. In the contour-forming phase, the process forces do not increase as steeply as in the pre-friction phase. This is because the initial shape was already generated in the pre-friction phase and thus the deformation has a less abrupt onset. The comparatively shorter pre-friction phase of the cylinder neck forming process causes that the forces in the contour-forming phase are significantly greater than those of the bottom end forming process. The highest process forces occur in the horizontal direction (Fx) (*cf.* Fig. 6, (c-d)). They reach their maximum when the feed rate is high (90 mm/min), and the rotation speed is low (500 rpm). In the case of the cylinder necks 5512 N and of the spherical bottom ends 5320 N. Significantly lower maximum process forces are reached with a low feed rate of 30 mm per minute and a higher rotation speed of 1500 rpm. In the case of the cylinder necks 1339 N and of the spherical bottom ends 1767 N. As the process parameters significantly influence the process forces, the temperature profiles are also determined, as these have major influence on the yield stress and therefore can explain the occurring process forces.

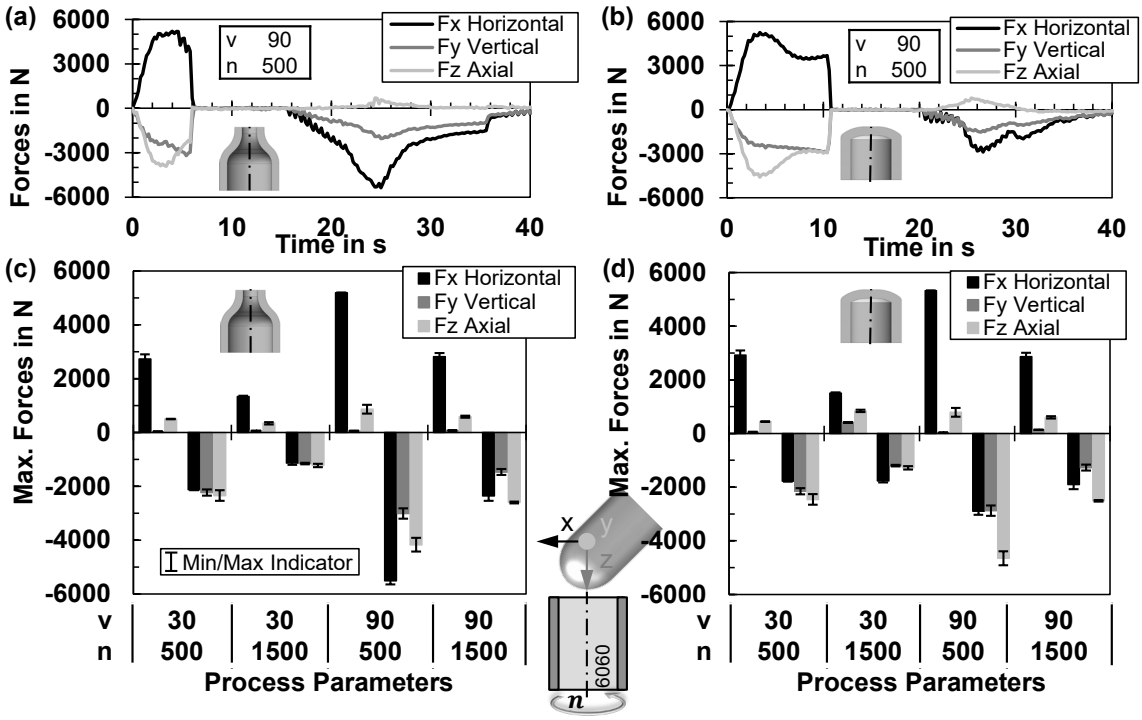

Fig. 6. Force profiles (a-b) and maximum forces (c-d) of the manufacture of the cylinder necks (CN) and spherical bottom ends (SB) by the friction-spinning process in dependence on the process parameters feed rate v [mm/min]and rotation speed n [1/min].

Temperature profiles.

Since the workpiece temperature has a huge influence on the yield stress, and thus on the process forces, corresponding temperature profiles were determined. Fig. 7 shows the temperature profiles of the manufacture of the spherical bottom ends (SB) by the friction-spinning process measured with thermocouple type k at 5 and 15 mm distance to the tube's end in dependence on the process parameters feed rate *v* and rotation speed *n*. Form the first contact with the tool, the

workpiece temperature strongly increases to a first peak at the end of the pre-friction phase. While re-positioning the tool for contour-forming the workpiece temperature decreases. In the contour-forming phase, the temperature again steeply increases to a second peak. In the following, heat is emitted until the reversal point for forming the flat bottom end, where a third peak of workpiece temperature is reached.

The described temperature profile is increased by the rotation speed and decreased by the feed rate so that a maximum workpiece temperature at 5 mm distance to the tube's end of 594°C is reached by a rotation speed of 1500 rpm and a feed rate of 30 mm per min (*cf.* Fig. 7, (a)). With a high feed rate of 90 mm per min and a low rotation speed of 500 rpm the maximum workpiece temperature reaches only 455°C. At a distance of 15 mm to the tube's end the temperature profile follows the same pattern, but with the same process-parameters maximum temperatures of only 558 and 387°C are reached (*cf*. Fig. 7, (b)). This is because the contact time with the tool is lower at this measuring point.

Derived from the determined temperature profiles the material bonding of the tube end in the centre of the bottom end is a solid-state bonding mechanism. This means that the adhesion is achieved by the diffusion of interfacial atoms, resulting in strong and uniform material bonding [15].

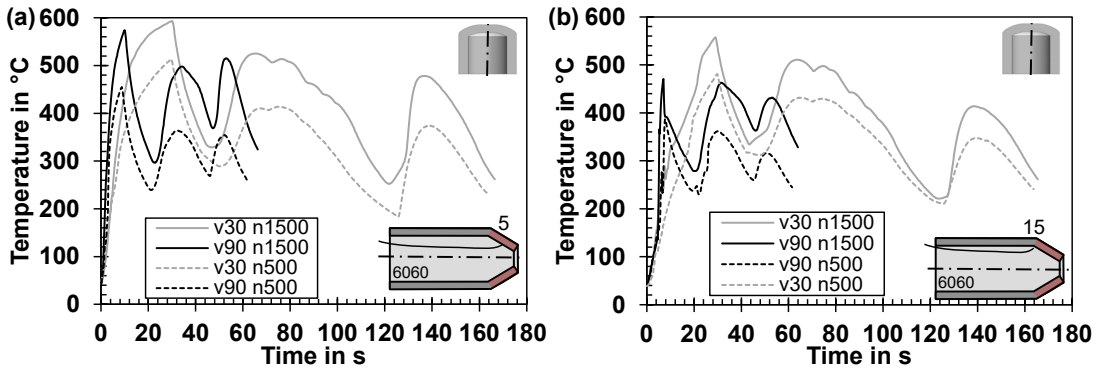

Fig. 7. Temperature profiles of the manufacture of the spherical bottom ends (SB) by the friction-spinning process measured with thermocouple type k at 5 and 15 mm distance to the tube's end in dependence on the process parameters feed rate v [mm/min]and rotation speed n [1/min].

In Fig. 8 the temperature profiles of the manufacture of the cylinder necks (CN) measured with thermocouple type k at 5 and 15 mm distance to the tube's end in dependence on the process parameters feed rate *v* and rotation speed *n* are shown. Form the first contact with the tool, the workpiece temperature increases sharply and reaches a first peak at the end of the pre-foaming phase. With the re-positioning of the tool for the contour-forming the workpiece temperature decreases. then, In the contour-forming phase the temperature again steeply increases to a second peak. In contrast to the manufacture of the spherical bottom ends, the highest temperatures are achieved in the contour-forming phase, which is attributable to the shorter pre-friction phase.

The described temperature profile is increased by the rotation speed and slightly decreased by the feed rate, so that a maximum workpiece temperature at 5 mm distance to the tube's end of 593°C is reached by a rotation speed of 1500 rpm and a feed rate of 30 mm per min (*cf.* Fig. 8, (a)). With a high feed rate of 90 mm per min and a low rotation speed of 500 rpm, the maximum workpiece temperature reaches only 485°C. At a distance of 15 mm from the end of the tube, the temperature profile follows the same pattern, but with the same process parameters only maximum temperatures of 551 and 403°C are reached (*cf.* Fig. 8, (b)).

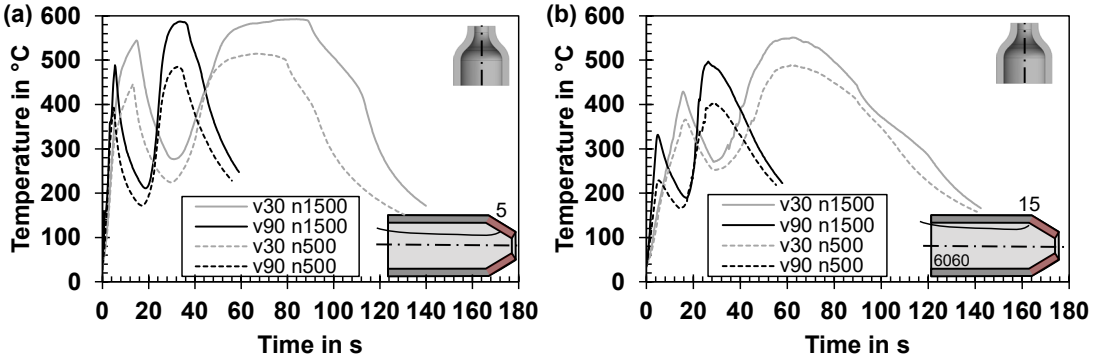

Fig. 8. Temperature profiles of the manufacture of the cylinder necks (CN) by the friction-spinning process measured with thermocouple type k at 5 and 15 mm distance to the tube's end in dependence on the process parameters feed rate v [mm/min]and rotation speed n [1/min].

With both contours, it can be seen that the higher rotation speed increases the workpiece temperature, which is due to more frictional heat input. This also interacts with the feed rate, which, if it is low, allows longer heat input. At the higher rotation speed, however, this effect is less. In this regard, the determined temperature profiles show a causal relationship with the determined maximum process forces. The higher the temperature, the lower the process forces, which is due to the lower yield stress. In this respect, the next step is to clarify to what extent the different temperature profiles cause recrystallization processes. This is investigated in the following through hardness tests.

Hardness.

Since there are process parameter-dependent temperature profiles and temperature gradients along the workpiece contour, corresponding hardness profiles were measured using the Vickers hardness test method according to DIN EN ISO 6507-1 [16] with a Nexus 4000 hardness testing device, Innovatest Company, Maastricht, Netherlands. First, an initial hardness of 86 HV0,3 was determined for the tubular profiles. Fig. 9 (a-b) shows that all specimens are softened by the manufacture process. On average of all measured parts, the hardness value (HV0.3) decreases by 38%. This is attributed to dynamic recovery and recrystallization due to the high workpiece temperatures combined with the high degrees of deformation [17]. Only at measuring point 5 of the bottom end which was manufactured with a high feed rate and a low rotation speed a significantly lower softening of 26% can be observed (*cf.* Fig. 9, (a)). This correlates with the observation that at a distance of 15 mm to the tube's end the maximum temperatures of only 387°C are reached, and thus the temperature at measuring point 5 is even lower (*cf*. Fig. 7, (b)). Under this condition, less dynamic recovery and recrystallization can be assumed and consequently less softening. However, the hardness profile over the entire contour cannot be influenced by the process parameters investigated.

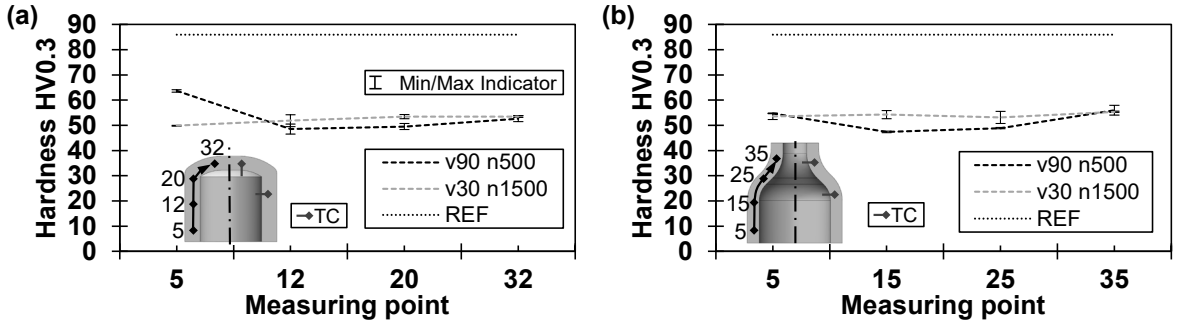

Fig. 9. Hardness profiles of the manufactured cylinder necks (CN) and spherical bottom ends (SB) in dependence on the process parameters feed rate v [mm/min]and rotation speed n [1/min].

Discussion.

In the experimental investigations, the resulting contours and the new process characteristics were evaluated. It is shown that friction-spinning enables the forming of the required contours for the manufacture of gas cylinders, and tightness, i.e. the essential property of gas cylinders, is fulfilled. The reduction of the wall thickness by up to 40 % does not lead to tightness failures. This is attributed to the fact that the friction spinning process allows sufficient material bonding of the cylinder's bottom ends through pressure welding-like processes, i.e. diffusion of interfacial atoms.

However, in terms of lightweight construction, the requirement arises to reduce the wall thickness to a rational minimum. Nevertheless, it can be assumed that there is a critical material-dependent standard dimensional ratio (SDR) to withstand this forming process, which must be determined in the next step. The use of tailored tubes will be investigated to overcome this limitation. For example, the internal flow-forming process developed at LUF can be used to manufacture these tailored tubes [18]. With this process, the wall thickness can be partially reduced to a specified minimum by flow-forming on the inner side of the tube, leaving the necessary wall thickness in the forming zone. The design and evaluation of this new process combination and chain will be part of future research. Additionally, a more homogeneous outer contour can be achieved by real curve paths and a more homogeneous inner contour can be achieved by the use of auxiliary tools. Furthermore, it should be investigated whether functional integrations, such as the forming of a thread, can be realised in the manufacturing process of the cylinder necks.

The investigated process characteristics, forces and temperature profiles are significantly influenced by the process-parameters feed rate and rotation speed. The process forces can be strongly affected and kept relatively low, leading to longer process times and higher workpiece temperatures. These process characteristics cause softening of the material due to recrystallization. However, gas cylinders usually have to be heat-treated before they can be introduced to the market with certification [19]. In the case of aluminium 6060, this is realised by annealing and ageing, which restores the initial mechanical properties. Furthermore, under this constraint, the processes can also be designed for a minimum energy consumption.

However, the actual power and the *total energy consumption* of forming machines strongly depend on their specific characteristics, which is why it is extremely challenging to compare different manufacturing processes performed on different machines, especially if the established processing is not transparent. And it also does not seem plausible to subtract the energy consumption of an empty run to obtain a pure transformation energy consumption, since energy is lost in specific amounts in every process despite the efficiency of the machine, and the actual energy consumption of comparable processes in the manufacture of these contours is unknown. In this work, however, we have demonstrated that the friction-spinning process at least does not require external heat input for the manufacture of these contours.

According to Lossen [11], depending on the process parameters, 70 to 735 kJ of pure forming energy is consumed during the friction-spinning process, which generates heat of about 500°C in the workpiece due to friction and deformation work. In comparison, the energy of 1300 to 1730 kJ is required to generate this heat in the workpiece (tube end of 40 x 5 x 80 mm of aluminium 6060) with an acetylene torch [11]. This calculation is based on a heating time of 30 - 40 seconds, a burner/torch surface of 1.13 cm² and 2.55 cm² and a mixture ratio of 1:3 [11]. In this context, it has to be stated that of course other potential forming processes also induce heat by deformation work, but with the friction-spinning process, the heat and thus the energy of an acetylene torch can be completely dispensed. Although the exact reduction of energy consumption cannot be determined reliably from this, friction-spinning provides the possibility to exclusively use renewable energy for the manufacturing process of gas cylinders and therefore can contribute to an increase in energy and resource efficiency.

Summary

In this paper, new process designs for energy and resource-efficient forming of gas cylinders by friction-spinning are presented. Typical gas cylinder contours, such as flattened and spherical bottom ends and cylinder necks, are manufactured by friction-spinning of AW 6060 tubular profiles with specifically designed tool path strategies. It is investigated how the process parameters influence the process properties and the mechanical properties of the workpiece. These newly developed process designs of the friction spinning process investigated here considerably expand the application possibilities of the process and also offer a great opportunity to increase energy efficiency in the manufacture of high-volume products. An essential factor here is the demonstrated adaptability of the friction-spinning process. The specific variation of the contact area of the bar-shaped standard tool enables, on the one hand, the free forming and, on the other hand, the targeted areal heat input by friction to extend the process limits. The synergetic combination of these two elements in one process design enables, for example, the production of contours typical of gas cylinders, which are difficult to manufacture without the addition of external heat in comparable and established forming processes. Thus, it is possible to limit the energy supply to electrical energy from renewable sources. Nevertheless, the actual energy consumption of this process compared to other processes and also the life cycle of the components manufactured with it, such as a carbonisation cylinder, still need to be investigated in future research.

Acknowledgment

The authors would like to thank the Ministry of Economic Affairs, Industry, Climate Action and Energy of the State of North Rhine-Westphalia (Ministerium für Wirtschaft, Industrie, Klimaschutz und Energie des Landes Nordrhein-Westfalen) for funding the research project “EECC”: "Technology development for energy-efficient vessel construction (Technologieentwicklung für den energieeffizienten Behälterbau)". The research work conducted in this project is the basis of the paper.

References

[1] B. Lossen, A. Andreiev, M. Stolbchenko, W. Homberg, M. Schaper, Friction-spinning - Grain structure modification and the impact on stress/strain behaviour, J. Mater. Process. Technol. 261 (2018) 242-250. https://doi.org/10.1016/j.jmatprotec.2018.06.015

[2] F. Dahms, W. Homberg, Manufacture of defined residual stress distributions in the friction-spinning process: Driven tool and subsequent flow-forming, Key Eng. Mater. 926 (2022) 683-689. https://doi.org/10.4028/p-3rk19y

[3] F. Dahms, W. Homberg, Manufacture of defined residual stress distributions in the friction-spinning process: Investigations and run-to-run predictive control, Metals 12 (2022) 158. https://doi.org/10.3390/met12010158

[4] D. J. Sharman, H. L. Stark, D.W. Kelly, A comparison of potential methods for the alleviation of residual stresses in the necks of aluminium alloy thick-walled gas cylinders, J. Strain Anal. Eng. Des. 32 (1997) 315-323. https://doi.org/10.1243/0309324971513436
[5] X. Song, K.S. Fong, S.R. Oon, W.R. Tiong, P.F. Li, A.M. Korsunsky, A. Danno, Diametrical growth in the forward flow forming process: simulation, validation, and prediction, Int. J. Adv. Manuf. Technol. 71 (2014) 207-217. https://doi.org/10.1007/s00170-013-5492-x
[6] D. Tsivoulas, J. Da Quinta Fonseca, M. Tuffs, M. Preuss, Effects of flow forming parameters on the development of residual stresses in Cr-Mo-V steel tubes, Mater. Sci. Eng. A 624 (2015) 193-202. https://doi.org/10.1016/j.msea.2014.11.068
[7] Z. Li, X. Shu, Residual stress analysis of multi-pass cold spinning process, Chinese J. Aeronaut. 35 (2021) 259-271. https://doi.org/10.1016/j.cja.2021.07.004
[8] O. Music, J.M. Allwood, K. Kawai, A review of the mechanics of metal spinning, J. Mater. Process. Technol. 210 (2010) 3-23. https://doi.org/10.1016/j.jmatprotec.2009.08.021
[9] C.H. Gür, E.B. Arda, Effect of tube spinning and subsequent heat treatments on strength, microstructure and residual stress state of AISI/SAE type 4140 steel, Mater. Sci. Technol. 19 (2003) 1590-1594. https://doi.org/10.1179/026708303225008022
[10] W.F. Maschinenbau, Our machines for high-precision tubes and gas cylinders, Available: https://wf-maschinenbau.com/app/uploads/2021/10/WF-machines-precision-tubes-and-gas-cylinders.pdf, Accessed: Jan. 18 2023
[11] B. Lossen, Ein Beitrag zur Herstellung von hybriden Bauteilen mittels Reibdrücken, 1st ed. Düren: Shaker Verlag, 2019.
[12] W. Homberg, B. Lossen, A. Struwe, An innovative incremental forming process for the manufacturing of functional graded parts, Key Eng. Mater. 554-557 (2013) 1368-1374.
[13] DIN EN ISO 7866:2021-05, Gasflaschen - Wiederbefüllbare nahtlose Gasflaschen aus Aluminiumlegierungen_- Auslegung, Bau und Prüfung (ISO 7866:2012 + Cor 1:2014 + Amd 1:2020); Deutsche Fassung EN ISO 7866:2012 + AC:2014 + A1:2020, DIN Deutsches Institut für Normung e. V., Berlin.
[14] C.-D. Wen, I. Mudawar, Modeling the effects of surface roughness on the emissivity of aluminum alloys, Int. J. Heat Mass Transf. 49 (2006) 4279-4289. https://doi.org/10.1016/j.ijheatmasstransfer.2006.04.037
[15] D. Kumar Rajak, D.D. Pagar, P.L. Menezes, A. Eyvazian, Friction-based welding processes: friction welding and friction stir welding, J. Adhes. Sci. Technol. 34 (2020) 2613-2637. https://doi.org/10.1080/01694243.2020.1780716
[16] Metallische Werkstoffe - Härteprüfung nach Vickers - Teil 1: Prüfverfahren, DIN EN ISO 6507-1:2018-07, Deutsches Institut für Normung e. V., Berlin, Jul. 2018. Available: https://www.beuth.de/en/standard/din-en-iso-6507-1/280959455
[17] H.J. McQueen, J.J. Jonas, Recovery and recrystallization during high temperature deformation, in Treatise on Materials Science & Technology, Plastic Deformation of Materials: Elsevier, 1975, pp. 393-493.
[18] E. Wiens, W. Homberg, Internal flow-turning - a new approach for the manufacture of tailored tubes with a constant external diameter, Procedia Eng. 207 (2017) 1755-1760. https://doi.org/10.1016/j.proeng.2017.10.934
[19] On the harmonisation of the laws of the member states relating to the making available on the market of pressure equipment, European Parliament and the Council of the European Union, Jun. 2014, Available: https://eur-lex.europa.eu/legal-content/DE/TXT/?uri=CELEX:02014L0068-20140717

Materials Research Proceedings 28 (2023) 1939-1946 https://doi.org/10.21741/9781644902479-209

Technological and sustainability implications of wet and dry turning of Ti6Al4V EBM parts

COZZOLINO Ersilia[1,a *], FRANCHITTI Stefania[2,b], BORRELLI Rosario[2,c], PIROZZI Carmine[2,d] and ASTARITA Antonello[1,e]

[1]Dipartimento di Ingegneria Chimica, dei Materiali e della Produzione Industriale, Università degli Studi di Napoli Federico II, Piazzale Tecchio 80, 80125 Napoli, Italy

[2]CIRA (Italian Aerospace Research Center), 81043 Capua CE, Italy

[a]ersilia.cozzolino@unina.it , [b]s.franchitti@cira.it, [c]r.borrelli@cira.it, [d]c.pirozzi@cira.it, [e]antonello.astarita@unina.it

Keywords: Sustainable Manufacturing, Additive Manufacturing, Machining, Turning, Roughness, Electron Beam Melting

Abstract. Sustainability is a crucial topic nowadays and Additive Manufacturing (AM) processes are becoming more and more widely used today also because, among its advantages, is claimed to be green technology. However, AM parts usually require postprocessing to improve their surface finishing and result assemblable. In this study, a Ti6Al4V cylindrical sample has been manufactured by Electron Beam Melting (EBM) and then post-processed by turning. Both dry and wet turning has been performed by using the same process parameters. Surface roughness has been measured both before and after each turning pass along the parallel and perpendicular direction to the cylindrical axis and energy consumption has been recorded during each turning pass. Results showed that both dry and wet turning led to a lower roughness along the perpendicular direction to the cylindrical axis than that along the parallel direction, as a result of the technological signature of the turning process. Also, they depict that the first turning pass results in higher cutting forces and, then, the highest values of energy consumption among all the turning passes, both in wet and dry turning. The Specific Energy Consumption (SEC) index has been investigated to evaluate the energy required to remove a unit volume of material; it reflects lower cutting efficiency in the material removal process.

Introduction

Sustainable Manufacturing (SM) is growing its attention focus more and more today both in the industry and research community [1]. The idea behind this concept is to manufacture parts for industrial applications with the objective to minimize the impact on the environment in terms of energy consumption, carbon footprint, and material waste. Additive Manufacturing (AM) is becoming more and more important today, as it plays a key role in the Industry 4.0 context. It consists in manufacturing 3D parts, previously modeled, by adding material layer by layer. AM is claimed to be a green technology because it holds great potential in improving materials efficiency, reducing life-cycle impacts, and enabling greater engineering functionality compared to conventional technologies [2,3]. However, the surface finishing of AM parts hardly ever meets the quality standard requirements, so postprocessing is always required. Machining processes, such as turning and milling, are widely used to reduce the roughness of the parts. Nevertheless, additional steps to manufacturing processes require unavoidably an additional amount of energy and resources. Cutting fluids are typically adopted in machining processes but their usage is crucial because, on the one hand, it helps to reduce friction, heat, and wear and so to increase the tool life but, on the other hand, it has not a negligible impact on the environment. Some studies exist in the

Content from this work may be used under the terms of the Creative Commons Attribution 3.0 license. Any further distribution of this work must maintain attribution to the author(s) and the title of the work, journal citation and DOI. Published under license by Materials Research Forum LLC.

literature on the dry and wet turning of wrought parts but very few have been carried out on the post-process machining of AM parts [1-3].

In this experimental study, a Ti6Al4V cylindrical sample was manufactured by Electron Beam Melting (EBM) and then machined by both wet and dry turning under the same combination of process parameters to improve the surface finishing. Energy consumption has been recorded during the turning process process with and without lubricant. Also, the roughness has been measured before and after each turning pass. The sustainability index Specific Cutting Energy (SCE) is calculated to evaluate the energy required to remove a unit volume of material, that reflects lower cutting efficiency in the material removal process. The results obtained in this study aim to give some guidelines for better decision-making as a result of a compromise between energy consumption and roughness obtained from a sustainable perspective.

Material and Methods

A cylindrical sample, having a diameter D equal to 30 mm and a height equal to 103.38 mm, has been manufactured by Electron Beam Melting (EBM). Ti6Al4V plasma-atomized powders, having an apparent density of 2.57 g/cm3 [4] and a particle size ranging from 45 μm to 106 μm equal to 93.7%, have been used to manufacture the sample by means of an Arcam A2X machine in a vacuum (10^{-4}- 10^{-5} mbar), that is necessary for metals alloy having high affinity with oxygen and nitrogen. In addition, a helium pressure of 10^{-3} mbar has been applied to prevent electrostatic charging and smoke events leading to eventually process termination and powder spreading. The EBM machine worked in automatic mode: a hot tungsten filament cathode emitted electrons accelerated to 60 kV resulting in a maximum beam power of 3.5 kW. Layer thickness t and line offset h were chosen equal to 50 μm and 0.1 mm, respectively, to manufacture the sample by using the standard Ti6Al4V build theme [5].

Then, the sample was post-processed by turning to improve its surface finishing by means of a parallel lathe FEL-660HG. Turning inserts Sandvik CNMG 12 04 08-SM H13A with a turning tool holder Sandvik PCLNR 2525M have been used to perform the machining processes,
A length of 50 mm of the sample has been turned by using some lubricant oil Siroil Emulg and a length of 50 mm has been turned without the lubricant oil. Two new inserts have been used to perform the machining processes with and without lubricant oil, by selecting the same process parameters, to evaluate the roughness after the postprocessing by avoiding taking into account the wear of the tool. Table 1 contains the process parameters adopted to machine the sample, chosen according to the best results obtained in the literature [6].

Table 1. Process parameters adopted in post-processing of the Ti6Al4V EBM sample by machining.

Feed rate [mm/rev]	Depth of cut [mm]	Spindle speed [rev/min]	Number of cutting passes
0.22	0.6	300	4

The surface finishing of the sample was acquired both before and after the machining process both with and without lubricant by means of the confocal microscope 3D Optical Surface Metrology System Leica DCM3D. Then, Ra roughness parameter was measured, by selecting three profiles, along both the parallel and perpendicular directions to the axis of the cylindrical sample with the Leica Map software.

Energy consumption was measured during the machining processes by means of the power device Quality Analyser CA8331. It is equipped with three current sensors MiniFLEX MA193-350, four tension cables and four crocodile clips. Data over time can be visualized by the Power Analyser Transfer PAT2 software. The lathe adopted for this study has got a three-phase

connection without neutral (32 A 380 V) so three tension cables, three crocodile clips and three current sensors were adopted in this study to measure the tension and current over time, respectively [7]. By the measurements of the current and tension the device gives as output both power and energy consumption second by second.
Then, the sustainability efficiency index Specific Energy Consumption (SEC) for the machining process, with and without the lubricant, was calculated as follows [8]:

$$SEC = E_{removed}/m_{removed} \quad (1)$$

Where $E_{removed}$ is the total energy consumption to perform the turning process and $m_{removed}$ is the material mass removed, that has been measured by using a Gibertini ETERNITY 200 CAL balance. SEC was calculated after each turning pass to investigate its trend and to compare the results obtained in terms of energy consumption.

Results and Discussion

The first result that can be appreciated in this study is that the post-process machining of the Ti6Al4V EBM sample resulted feasible both with and without the lubricant oil, as illustrated in Fig. 1. Also, both solutions led to an improvement of the surface roughness removing the surface material with the process conditions mentioned above. Roughness was measured both before and after the machining process along the two principal directions of the cylindrical sample, according to international standard EN ISO 4287. Table 2 contains the results obtained in terms of surface roughness.

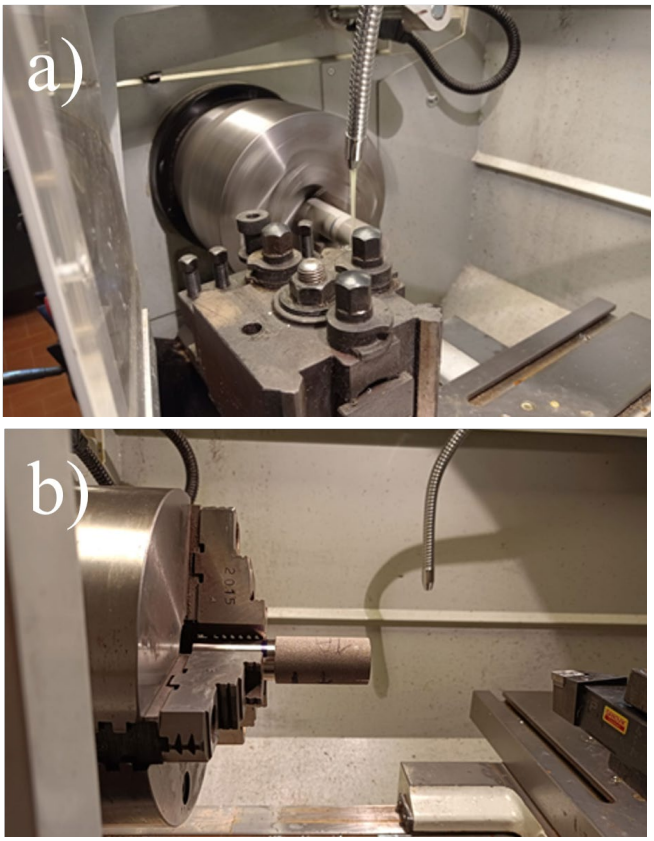

Fig. 1. Turning process of the sample a) with lubrication and b) without lubrication.

Table 2. Results obtained in terms of surface roughness along the parallel and perpendicular direction to the cylinder axis.

$Ra_{//}$ [μm] as built	$Ra_{//}$ [μm] with lubricant	$Ra_{//}$ [μm] without lubricant	Reduction % $Ra_{//}$ with lubricant	Reduction % $Ra_{//}$ without lubricant
30.73	1.86	1.54	93.94	94.99
$Ra_{\perp}$ [μm] as built	$Ra_{\perp}$ [μm] with lubricant	$Ra_{\perp}$ [μm] without lubricant	Reduction % $Ra_{\perp}$ with lubricant	Reduction % $Ra_{\perp}$ without lubricant
30.10	0.29	0.45	99.03	98.50

According to the results obtained, the roughness of the as-built sample along the parallel direction to the cylindrical axis is slightly higher than roughness along the perpendicular one. Then, it can be observable that the process parameters selected for this experimental campaign allowed to reach a roughness along the perpendicular direction $Ra_{\perp}$ to the cylindrical axis lower than that obtained along the parallel direction $Ra_{//}$. Indeed, reduction percentages of 93.94 % and 94.99 %, with and without lubricant oil respectively, have been obtained along the parallel direction whereas reduction percentages of 99.03 % and 98.50 %, with and without lubricant oil respectively, have been obtained along the perpendicular direction. These results are direct consequences of the technological signature of the turning process [7].

As mentioned above, energy consumption was measured during each turning pass as well as the material mass removed was calculated by measuring the sample mass before and after each machining process. Based on these measurements, SEC was calculated according to Eq. 1. Table 3 contains all the results obtained in terms of mass removed, energy consumption and specific energy consumption.

Table 3. Results obtained in terms of mass removed and energy consumption during the turning process.

Number of the turning passes	$m_{removed}$ [g] with lubricant	$m_{removed}$ [g] without lubricant	$E_{removed}$ [Wh] with lubricant	$E_{removed}$ [Wh] without lubricant	SEC [Wh/g] with lubricant	SEC [Wh/g] without lubricant
1	2.4	7.1	34.2	55.8	14.25	7.80
2	8.4	9.9	23.9	24.8	2.84	2.51
3	7.5	8.5	22.2	23.7	2.96	2.79
4	7.4	6	20.7	16.8	2.80	2.80

The first result observable regards the trend of the mass removed during each turning pass. At first, just a little amount of surface material of the sample has been removed, both with and without the usage of lubricants. This is because, in the beginning, the undulations are more pronounced according to the higher surface roughness of the as-built sample. The second turning pass allowed the removal of the highest amount of material both with and without the lubricant, by selecting the same process parameters. Results in Table 3 show that the trend of the mass removed over the number of turning passes is very similar between the two process conditions (with and without lubricant). However, a big difference in amount of removed material for the first pass exists (2.4 g with lubricant and 7.1 g without lubricant). This is due to the fact that the first turning pass is a roughing process, friction between the tool and the part is higher as well as the tool is at the beginning of his life. Thus, these conditions help the mass removal at the beginning. In total, the

mass removed with the lubricant is 25.7 g while the mass removed in total without the lubricant is 31.5 g.

Fig. 2 depicts the trend of the electrical energy consumption during each turning pass. It is important to premise that lubrication is activated by a sub-unite of the machine used for turning. The contribution of this pump in terms of power consumption is negligible. For this reason, in this study the attention was mostly focused on the energy consumption in dry and wet turning as a result of only different cutting forces during the process. Also in this case, the trend of data related to the machining process by adopting the lubrication is very similar to that the one without the usage of the lubricant as well as the curve related to the turning without lubricant is slightly shifted upwards. This is explained by the fact that the use of the cutting fluids reduces the friction between the tool and the workpiece resulting in a reduction of the heat generation and cutting forces [9], both with and without the usage of lubricant, as the power in machining is linearly dependent from the cutting forces [10] and the roughness of the as-built sample is the higher than that after each turning pass. For this reason, at the beginning of the machining process, the cutting forces are higher, and this explains why the highest values of energy consumption have been obtained during the first turning pass.

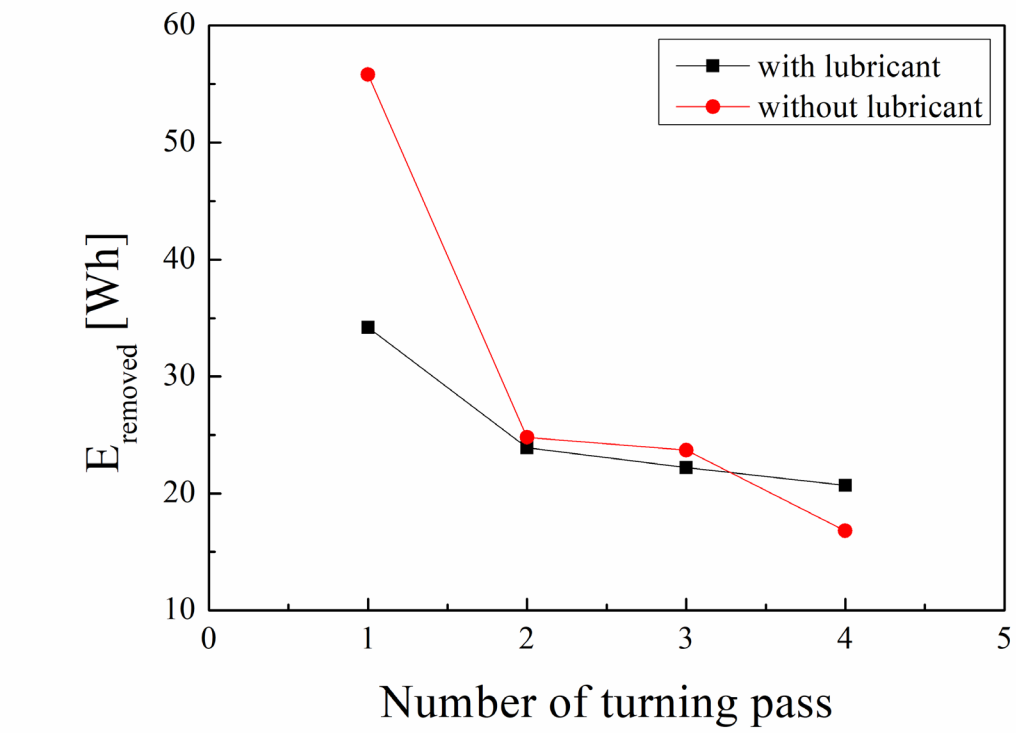

Fig. 2. Energy consumption to remove material after each turning pass with and without the usage of the lubricant.

Nevertheless, Fig. 3 shows that the SEC curve with lubricant oil is shifted upwards to the SEC curve without the lubricant. As indicates that from a sustainability perspective, even if the cutting forces are higher, dry turning can be considered more sustainable in terms of energy consumption than wet turning under the same process conditions. Fig. 3 depicts that at first there is a huge difference in SEC whereas data are very similar from the second turning pass to the end of the process.

By jointly investigating roughness and energy consumption during the turning of an EBM Ti6Al4V sample, it can be said that by selecting the process parameters of our study, it is

worthwhile to choose the dry turning rather than the wet turning since it leads to similar results in terms of surface roughness (Table 2) by reducing specific energy consumption to perform the turning process. This study could be improved by including more than one configuration of turning process parameters on EBM parts printed under the same process conditions and by also considering the cutting tool wear. In general, dry turning shortens tool life as well as lubricant has a negative impact on the environment. In this perspective, a joint investigation of surface roughness, energy consumption and tool wear will demonstrate the possibility to prefer dry turning to wet turning by using optimal process parameters.

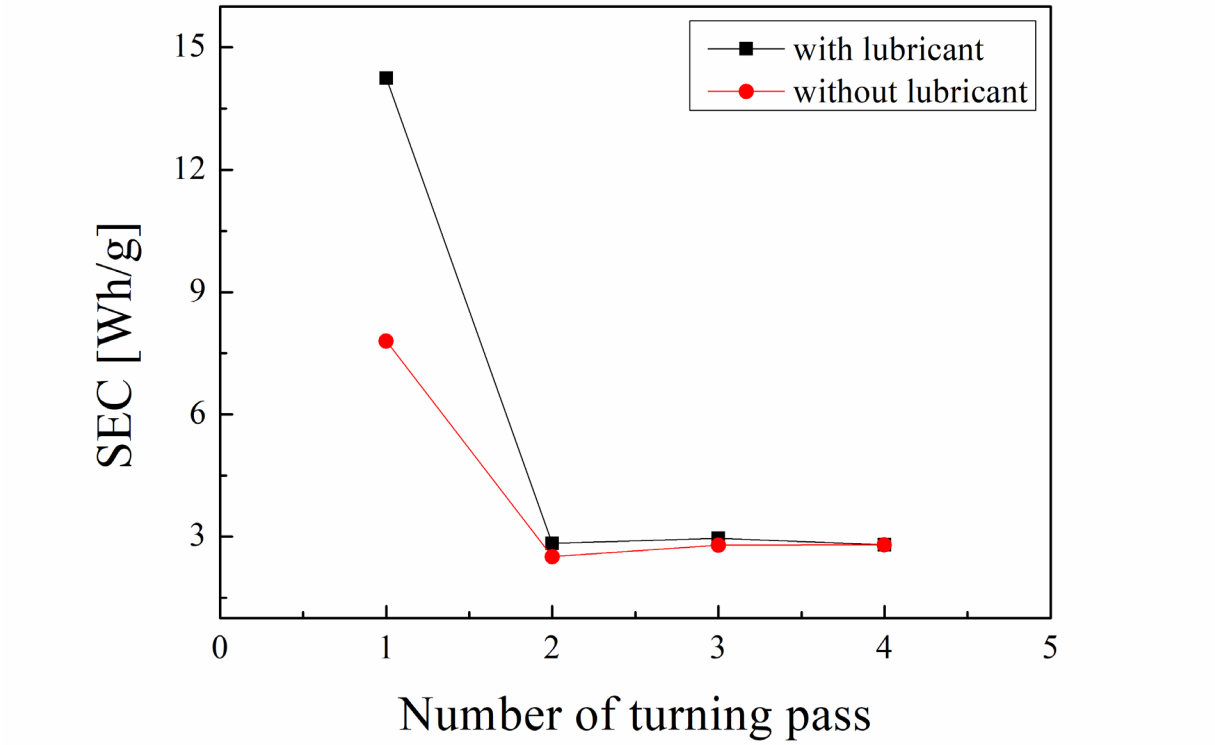

Fig. 3. Specific energy consumption after each turning pass with and without the usage of the lubricant.

Summary

This study demonstrates the possibility of choosing dry turning rather than wet turning as post-process machining for a Ti6Al4V EBMed cylindrical sample by reducing the sustainability index SEC without sacrificing its surface quality. The main results obtained and discussed in this study are:

- Roughness reduction percentages of 93.94 % and 99.03 % have been obtained by wet turning along the parallel and perpendicular directions, respectively. Roughness reduction percentages of 94.99 % and 98.50 % have been obtained by dry turning along the parallel and perpendicular directions, respectively. Thus, for the objective of this study, lubricant is not required to deliver a certain reduction in diameter and final surface finish.
- The same process conditions in machining lead to a lower roughness along the perpendicular direction to the cylindrical axis than that along the parallel direction, according to the technological signature of the turning process.
- The first turning pass, both with and without the lubrication, allows to remove just only a little amount of material as the surface undulations of the as-built sample are more pronounced and the roughness is higher.

- Wet turning leads to a removed mass of 25.7 g whereas dry turning leads to a removed mass of 31.5 g by selecting the same process parameters and by fixing the same number of turning passes.
- The first turning pass results in higher cutting forces and, then, the highest values of energy consumption among all the turning passes, both in wet and dry turning.
- Dry turning can be considered more sustainable in terms of energy consumption than wet turning under the same process conditions as the SEC curve with lubricant oil is shifted upwards to the SEC curve without the lubricant.

This study is among the first steps toward the sustainability assessment of post-process machining of additive manufactured parts. In fact, it is a preliminary investigation of sustainability implications in terms of energy consumption in both dry and wet machining of EBM samples. It is a first step to investigate how different the outputs in terms of both surface roughness and energy consumption are in machining the same parts having a simple cylindrical shape. The next step will regard the sustainability assessment and technological implications in machining a complex EBM part. Also, this study can be extended to other machining operations such as milling. The same cylindrical EBM samples could be post-processed by milling by selecting different process conditions by fixing the output in terms of total depth of cut, and then in terms of final surface roughness.

Also, the wear-cutting tool should be investigated for better decision-making as a result of a compromise between the energy consumption, tool life and roughness obtained from a sustainable perspective.

References

[1] S. Pawanr, G.K. Garg, Selection of optimum Cutting Parameters for Minimization of Specific Energy Consumption during Machining of Al 6061, J. Phys. Conf. Ser. 1240 (2019). https://doi.org/10.1088/1742-6596/1240/1/012064

[2] Y.H. Çelik, E. Kilickap, M. Güney, Investigation of cutting parameters affecting on tool wear and surface roughness in dry turning of Ti-6Al-4V using CVD and PVD coated tools, J. Brazilian Soc. Mech. Sci. Eng. 39 (2017) 2085-2093. https://doi.org/10.1007/s40430-016-0607-6

[3] M. Younas, S.H. Imran Jaffery, M. Khan, R. Ahmad, L. Ali, Z. Khan, A. Khan, Tool Wear Progression and its Effect on Energy Consumption in Turning of Titanium Alloy (Ti-6Al-4V), Mech. Sci. 10 (2019) 373-382. https://doi.org/10.5194/ms-10-373-2019

[4] Standard Test Method for Apparent Density of Free-Flowing Metal Powders Using the Hall Flowmeter Funnel, in: ASTM VOL 02.05.

[5] M. Koike, K. Martinez, L. Guo, G. Chahine, R. Kovacevic, T. Okabe, Evaluation of titanium alloy fabricated using electron beam melting system for dental applications, J. Mater. Process. Technol. 211 (2011) 1400-1408. https://doi.org/10.1016/j.jmatprotec.2011.03.013

[6] V. Upadhyay, P.K. Jain, N.K. Mehta, In-process prediction of surface roughness in turning of Ti-6Al-4V alloy using cutting parameters and vibration signals, Meas. J. Int. Meas. Confed. 46 (2013) 154-160. https://doi.org/10.1016/j.measurement.2012.06.002

[7] E. Cozzolino, A. Astarita, R. Borrelli, S. Franchitti, V. Lopresto, C. Pirozzi, A Preliminary Investigation of Energy Consumption for Turning Ti6Al4V EBM Cylindrical Parts, Key Eng. Mater. 926 (2022) 2355-2362. https://doi.org/10.4028/p-vm4f1y

[8] E. Cozzolino, V. Lopresto, D. Borrelli, A. Caraviello, An integrated approach to investigate the energy consumption for manufacturing and surface finishing 3D printed Inconel 718 parts, J. Manuf. Process. 79 (2022) 193-205. https://doi.org/10.1016/j.jmapro.2022.04.045

[9] M. Mangiaterra, Lubricants impact on cutting forces, Degree Project In Mechanical Engineering, Second Cycle, KTH Royal Institute of Technology, Sweden, 2018.
[10] G.M. Królczyk, M. Wzorek, A.Król, O. Kochan, J. Su, J. Kacprzyk, Sustainable Production : Novel Trends in Energy, Environment and Material Systems Studies in Systems, Decision and Control 198, Springer Cham, 2019. https://doi.org/10.1007/978-3-030-11274-5

Materials Research Proceedings 28 (2023) 1947-1956 https://doi.org/10.21741/9781644902479-210

Energy measurements and LCA of remanufactured automotive steel sheets

FARIOLI Daniele[1,a *], FABRIZIO Matteo[1,b], KAYA Ertuğrul[1,c], MUSSI Valerio[2,d] and STRANO Matteo[1,e]

[1]Politecnico di Milano, Via Privata Giuseppe La Masa, 1, 20156 Milan MI, Italy

[2]Strada della Torre della Razza, 29122 Piacenza, Italy

[a]daniele.farioli@polimi.it, [b]matteo.fabrizio@polimi.it, [c]ertugrul.kaya@polimi.it, [d]valerio.mussi@musp.net, [e]matteo.strano@polimi.it

Keywords: Sheet Metal Remanufacturing, Energy Analysis, Circular Economy, LCA Sustainability

Abstract. New paradigms based on Circular Economy (CE) principles are needed for boosting the ecological transition and improving the energy and material efficiency. In this paper, a novel remanufacturing process chain for End-of-Life (EoL) automotive panels is first presented. The core of the recycling strategy is the reshaping of curved EoL automotive sheets through flattening by means of a hydraulic press. Flattening experiments together with press power consumption measurements have been performed on thin steel parts. While the experimental procedure demonstrated the technical feasibility of flattening "small-scale" steel parts, a more complete analysis on environmental sustainability was required. For this purpose, a Life Cycle Assessment (LCA) of the remanufacturing process chain proposed was set up. The results of the study demonstrated that flattening is a viable solution for reshaping EoL automotive panels, and that, for one kg of reshaped steel, approximately 2.2 kg CO_2 and 24 MJ could be saved.

Introduction

The production of metals accounts for about 8% of total global energy consumption [1]. Concerning the steel industry, the production of 1 ton of solid steel corresponds to a primary energy demand of 23.2 GJ [2]. Cullen et al. (2012) stated that the global steel demand is expected to increase tremendously [3].

Steel production and recycling is also strongly linked to the market dynamics, geopolitical instabilities or pandemic events. Those two factors can have a profound impact on the steel flow, availability and price [4-5]. Considering the presented issues, it is crucial for engineers and researchers to examine the entire process chain of sheet metals, including recycling, looking for potential resource efficiency improvements [6].

Recycling proved to have direct positive, demonstrating to be less energy demanding than raw material extraction and production [7-8].

Considering the recycling of End-of-Life Vehicle (ELV), recyclers use efficient processes to recover valuable materials like steel and aluminum alloys [9]. The quantity of metal recycled from end-of-life vehicles is a result of the technology available and the extent to which the technology is used in the scrap processing industry [10].

The steel production by EAF represents worldwide 28% of the total and reaches 46% in Europe (2017, [11]). EAF plants are mainly fed by metal scraps, thus being much less environmentally impacting than blast furnaces. Nevertheless, EAF has relevant impact on the environment, while approximately the half of the energy input is wasted during the process [12].

Considering the aspects aforementioned, there is the incumbent need of efficient methodologies, such as circular economy paradigms, to improve the material efficiency of EoL

Content from this work may be used under the terms of the Creative Commons Attribution 3.0 license. Any further distribution of this work must maintain attribution to the author(s) and the title of the work, journal citation and DOI. Published under license by Materials Research Forum LLC.

steel sheets [3]. Increasing the material efficiency can be achieved by six strategies: Reduce, Reuse, Repair, Remanufacture, Recycle, and Recover [13]. Applying these strategies is not always straightforward because of practical problems: Cooper and Gutowski [14] listed the enablers and barriers related to the improvement of material efficiency. Political actions, legislations and the collaboration with associations or national institutions can be a driver for implementing sustainable solutions [15].

The the general opinion of the scientific community is that there is margin to find alternatives, whenever possible, to replace the conventional remelting of metal panels [16-17]. These practices can be divided mainly in two approaches: solid state recycling and direct remanufacturing for reuse of metal panels.

Solid state recycling involves the formation of a billet starting from shredded particles and/or powders. Several routes are possible, such as hot compression [18], hot rolling [19], cold/hot extrusion of chips, Spark Plasma Sintering (SPS) with compaction and extrusion [20], friction consolidation through a rotative die plunge [21], Submerged Arc Welding (SAW) of metal chips and metal waste [22]. Although technically feasible, in solid-state recycling, the material must be available in form of small pieces (or powder), requiring a shredding stage in the product's life cycle.

Reshaping strategies instead are meant to directly utilize a metal panel avoiding shredding and compaction and providing new shape or directly performing new stamping operations on it. For example, Ali et al. [23] proposed an innovative recovering strategy for large industrial scrap from the automobile industry producing metal facade systems for buildings. Other researchers such as Ingarao and Takano employed incremental forming to reshape aluminum alloy panels [1,24]. The proposed routines highlight the capability of reshaping panels, but the application of incremental forming could be potentially limited to small batches due to the need of programming the tool path case by case. Two other interesting studies were conducted by Abdullah [25] and Haase [26]. Abdullah developed a methodology for reusing EoL car bodies into mesh steel defining five sustainability indexes. Haase designed a lifecycle based on pre-used material (car roof) to obtain by stamping operations a brake disk cover part.

The present study presents first the main results of remanufacturing tests of thin steel parts through cold and warm flattening with a hydraulic press. The measurements of the press energy consumed during these tests are presented. The measurements were needed to setup a Life Cycle Assessment (LCA) of the remanufacturing routine through the SimaPro software package and to understand the different contributions of power consumption during the flattening cycle. The performed analysis showed the promising results obtained by flattening thin steel parts and the environmental benefits associated with it.

Flattening as a Viable Solution for Remanufacturing Eol Sheet Metals

In the framework of circular economy and environmental sustainability, this paper presents a novel remanufacturing cycle for car body panels. The concept proposed is to exploit EoL car bodies (preferably large panels) to produce metal sheets reusable for a new life, as described in Fig. 1. The largest panels, having often a given curvature, should be first trimmed, then flattened and eventually reshaped. A potential part to be reshaped from an EoL car is the car roof shown in Fig. 2.

The flattening process can be performed through a hydraulic press, whose tools are simply hard steel plates able to flatten car bodies of different models in a "short" time. The tooling costs are expected to be reduced due to the simple geometry. Flattened parts, once characterized, can be then used as regenerated blanks for subsequent forming or shearing applications. The proposed cycle clearly produces blanks which are not uniform and perfect, which might have some defects, but final imperfections are not necessarily a problem for some final intended uses and applications [27].

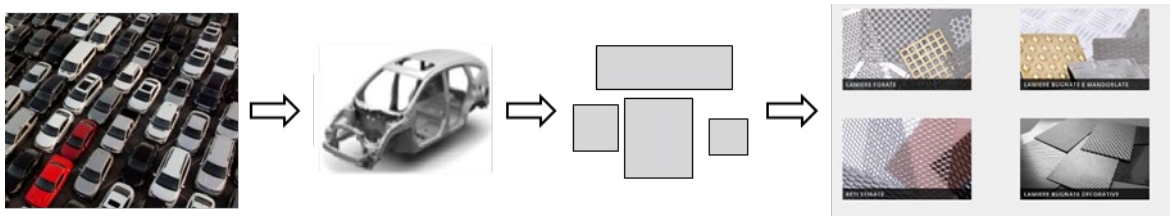

Dismissed fleet cars. *Dismantled EoL car.* *Warehouse of classified and characterized flat or corrugated sheets.* *Regenerated blank.*

Fig. 1. Remanufacturing framework for car bodies.

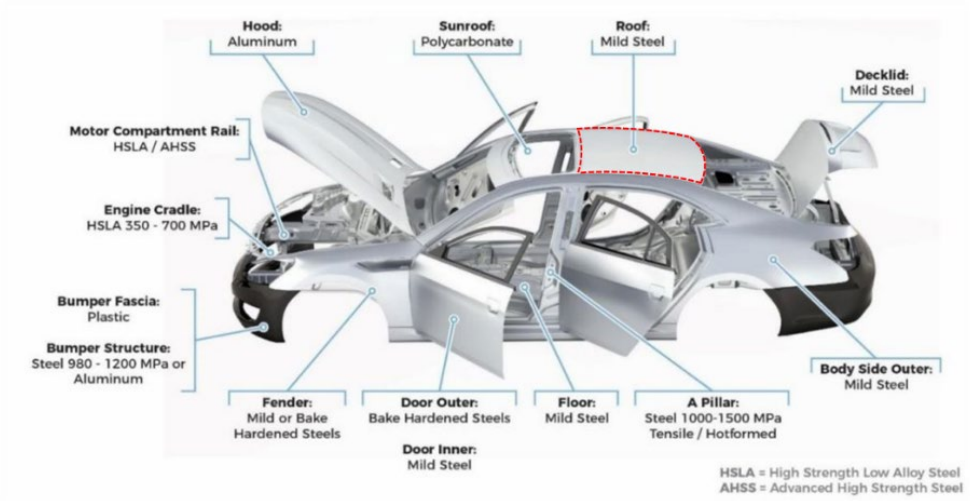

Fig. 2. Example of first use component (car roof) [28].

Flattening Experiments and Press Power Consumption Measurements

Considering the framework presented in the previous Section, tests were carried out to understand the feasibility of flattening curved parts and to test the influence of the main process parameters on the results of the flattening process. The press used for flattening experiments is a SACMI PH150. It is a double effect numerically controlled hydraulic press with maximum tonnage of 150 ton and heated dies (up to 600°C). The control system of the machine uses a pressure sensor applied to the hydraulic cylinder that is governing the press slide, which is in turn used to regulate the applied load. One linear encoder is mounted on the press slide and one on the extracting cylinder to control the vertical position of the punch. Pressure and position can be recorded as analogic signal by an external controller.

The parts to be flattened were obtained by shaping in controlled and repeatable conditions 0.8 mm thick virgin DC 04 sheets (EN 10130, 2006). The shaping process was performed with an Erichsen test machine imposing up to Erichsen Index (EI) equal to 6 mm. The flattening cycle, summarized in Fig. 3, is a sequence of different operations. First, the moving punch (represented in Fig. 3) moves fast (>10 mm/s) approaching the sample. Then, when the punch is close to the sample, the velocity of the piston is reduced to 1 mm/s and continued until the tonnage reaches a predefined set level. The vertical displacement continues at constant velocity until the press tonnage exceeds the set level, called dwell force (F_d). This force is reached when the sample is almost completely flattened. When the tonnage has reached the set value, the piston is held in position for a given dwell time (τ). After the dwell time, the tonnage is released, and the piston moves up.

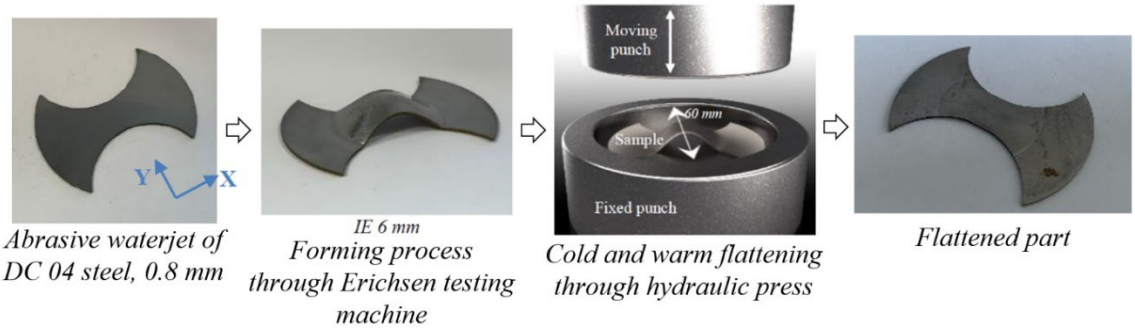

Fig. 3. Experimental procedure followed: shaping thin steel parts and then flattening through hydraulic press.

The main process parameters varied in the tests were: the pre-forming index *EI* (mm), the dwelling time τ (s), the punch and die temperatures T_T (°C), the dwelling force F_d (tons). The experiments showed that the best quality of the flattened part is achieved by warm flattening with short dwell time. Similar results can be achieved also by cold flattening. In general, flattening can be considered as a promising and effective process for recovering EoL panels.

The press power consumption has been measured under different conditions: during idle time, during flattening (considering different tool temperatures) and during the heating phase of the dies (with pump for oil recirculation turned off). Indeed, quantifying the energetic inputs of remanufacturing is fundamental to assess the environmental sustainability of the process and to understand the benefits with respect to conventional recycling by melting.

The press power consumed has been measured through LEM sensors, which can capture the current and voltage of the three phases. From those values, it is possible to compute the electric power absorbed by the machine. The sensors were mounted around the cables of the main power supply unit of the press, thus detecting all possible contributions of press energy consumption.

Results of the Press Power Measurements

The main results of the press power measurements are summarized in Table 1, while Fig. 4 shows the power consumed during one flattening cycle performed at room temperature. the measurements showed that keeping the dies at 160°C consumes around 1.9 kW. Instead, keeping the dies at 300°C requires on average 3.7 kW.

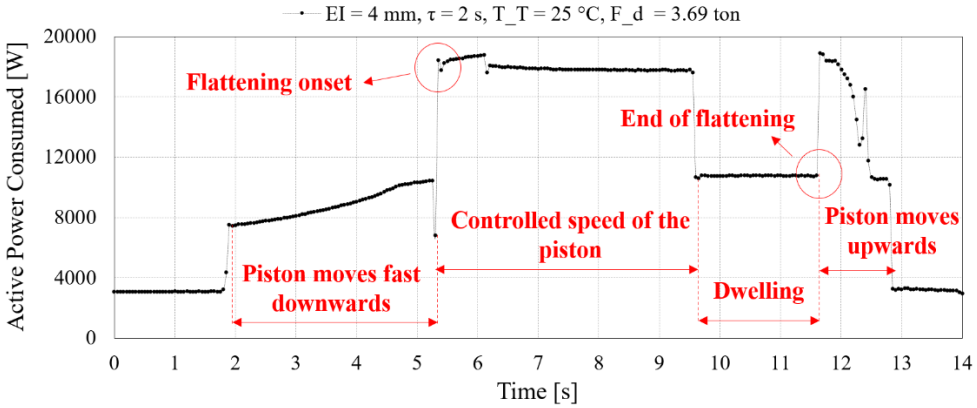

Fig. 4. Press power consumption during the flattening of a DC 04 specimen (0.8 mm) characterized by EI = 4 mm, τ = 2 s, T_T = 25 °C, F_d = 3.69 ton.

Table 1. Power consumption for different conditions tested.

Condition	Power consumption [W]	Duration
Idle phase, T_T = 25 °C	~ 3200	-
During dwelling, EI = 4 mm, T_T = 25 °C, F_d = 3.69 ton	~ 11000	Variable: 2 s or 60 s.
During dwelling, EI = 4 mm, T_T = 25 °C, F_d = 92.15 ton	~ 13000	Variable: 2 s or 60 s.
Heating dies, from 25 °C to 160 °C	~ 11000	≈ 25 min.
Dwelling, EI = 4 mm, T_T = 160 °C, F_d = 3.69 ton	~ 11500	60 s
Keep the dies at 160 °C (steady state)	~ 1900	-
Heating dies, from 160 °C to 300 °	~ 11000	≈ 30 min
Keep the dies at 300 °C (steady state)	~ 3700	-

Life-Cycle Assessment (LCA) of Remanufacturing a Car Roof

The experimental procedure presented in the previous Section is referred to a hydraulic press suited for flattening only parts inscribable in a circle with 6 mm diameter. Nevertheless, the measurements with LEM sensors were helpful to model the profile of power consumption of a press designed for flattening large panels (see Table 2), and to make reasonable hypotheses for setting up the LCA presented in the next Section.

In the framework of sustainable reuse of resources and materials, a LCA of the remanufacturing process was set up, focusing on the remanufacturing by flattening of two EoL panels, cut out of a car roof. In order to define the energetic inputs of flattening large and thin steel panels, the data reported in Table 2 have been used. These data refer to the technical performances of a hydraulic press designed and used exactly for the purpose of flattening sheet metals. The LCA is set-up with the aim of evaluating the embedded energy and the equivalent $kgCO_2$ emissions of the remanufacturing process chain and compare these values with the same indicators of:

- Sheets produced starting from virgin ore. According to a study performed by WorldSteel Association [29], the energy requirement for producing 1 kg or rolled steel (using a "cradle-to-gate" approach) is equivalent to 25.4 MJ, emitting approximately 2.35 $kgCO_2^{Eq}$. These values are close to others published by SSAB [30] and Arcelor Mittal [2].
- Sheets produced from EAF-based recycling plants, without the addition of DRI (Direct Reduced Iron) [31]. According to the work of Suer et al. the production of one kg of rolled steel is associated with a GWP = 0.74 $kgCO_2^{Eq}$ and a CED = 11 MJ.

Assumptions for Setting Up the LCA

- The two panels are extracted by means of an electric cutter from a car roof, which in turn is extracted from the chassis of the EoL car itself in 100 s. The power of the electric cutter is 1400 W. The cutting time of the panels from the roof is 360 s. The same cutter is used for both operations. These disassembly operations at the actual state are not employed by car recyclers, therefore they represent a crucial stage for the reshaping purposes presented. Furthermore, it is fundamental that the EoL panels are not damaged, thus becoming unrecoverable with this routine.
- The two flattened panels have a nominal area of 800x400 mm and 800x700 mm, a nominal thickness of 1 mm and total approximate weight of 6.9 kg. The entire car roof cut from the chassis of the car has a weight of 21 kg. The data presented were directly measured and are referred to a roof extracted from EoL FIAT Punto.
- The portion of the roof not used during flattening is assumed to follow the same recycling path that would have and EoL car, i.e. shredding, magnetic separation, melting in EAF, casting and

rolling. The LCA includes the stage of painting removal as well: for the mechanical de-coating phase, technical data of a commercial sheet metal brusher have been used, whose average power consumption is 4000 W and the operative time for brushing two panels is approximately 280 s. Considering a thickness of paint of 100 μm and the nominal area of the 2 panels (both sides) and considering the average automotive paint density (850 kg/m^3), the amount of paint removed by the brusher is around 150 g. This mass is assumed to be treated in an incineration plant.

- In the analysis, the impacts associated to metal scraps in the second station (namely the roof scrap, see Fig. 5) are not take into account because the study wants to assess the environmental benefits of recycling by reshaping a portion of the roof instead of smelting the same mass (i.e. 6.9 kg). What is not "re-shapable" for a second life by flattening is, in any case, assumed to follow the conventional recycling framework.
- For the calculation of the energy for flattening, Fig. 6 with the relative information reported were used. The analysis is not considering the wear of the various components such as press dies.

Table 2. Technical information of the hydraulic press used for flattening thin sheet metal panels.

Parameter	Value
Max tonnage	420 ton
Max tool temperature	300 °C
Maximum oil pressure	210 bar
Max pump throughput	70 L/min
Oil reservoir volume	500 L
Diameter pressing piston	505 mm
Max power principal electric motor (pump)	15 kW (30 A)
Max power heating system upper die	9.6 kW (14 A)
Max power heating system lower die	9.6 kW (14 A)

Hydraulic press designed for flattening sheet metal panels. Courtesy of Pezzato s.r.l.

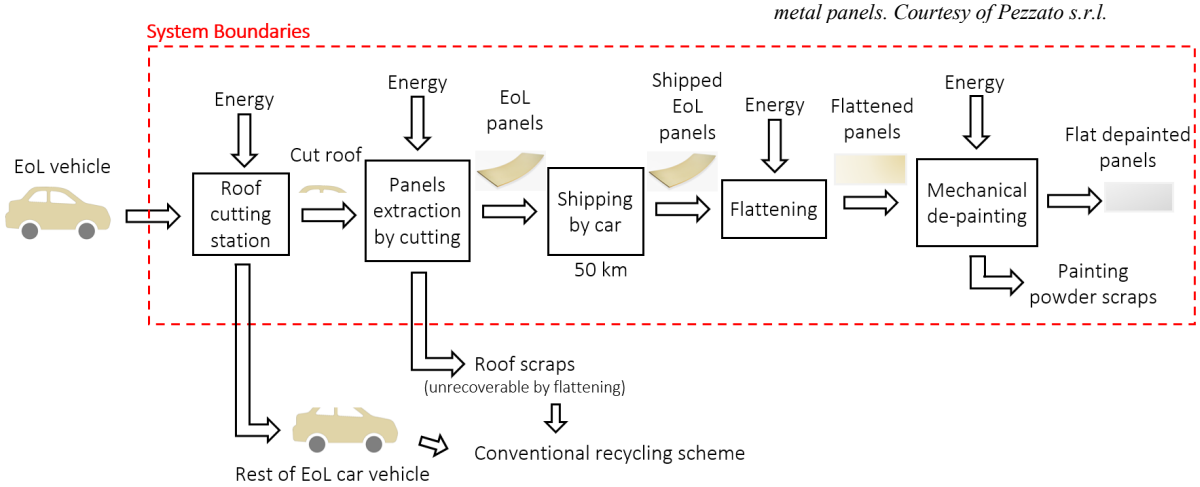

Fig. 5. Definition of the system boundary and flattening process chain with all inputs and outputs.

For determining the energetic input of the press for one flattening cycle, the following assumptions have been used: the press works for 8 hours/day; during the first hour, the press is consuming energy only for heating the dies (for 60 minutes at a power of 20 kW). The other 7

hours the press is performing flattening cycles. During this period, an average power consumption of 10 kW is assumed considering the contribution of idle stage (set-up), flattening and keeping the dies in temperature. Consequently, the total energy consumed is 90 kWh/day. Assuming the duration of one flattening cycle equal to 50s and the available working time, 504 parts per day can be flattened. Each cycle is consuming ≈ 0.18 kWh. For processing two panels, as in this case, a total energy of 0.36 kWh is absorbed by the hydraulic press. The software used for performing the LCA is SimaPro, with Ecoinvent 3 database.

Table 3. Data used for the LCA.

Stage	Input energy [kWh]	Input material	Output material
Roof cutting station	0.038	Dismantled EoL car	Cut roof (21 kg) + Rest of EoL car vehicle*
Extraction of two EoL panels by cutting the roof	0.14	Cut roof (21 kg)	2 bent EoL panels (6.9 kg) + Roof scraps* (14.1 kg)
Shipping by road vehicle of the 2 panels – 50 km by lorry (> 32 ton – EUR 4)	-	2 bent EoL panels (6.9 kg)	2 transported bent EoL panels (6.9 kg)
Flattening 2 panels (2 production cycles)	0.36	2 transported bent EoL panels (6.9 kg)	2 flattened panels (6.9 kg)
Mechanical de-painting of 2 panels (both sides)	0.31	2 flattened panels (6.9 kg)	2 depainted panels (6.9 kg) + paint scrap powder**

* Subjected to conventional recycling by melting, impacts not included in the LCA.
** EoL modelled through landfill incineration.

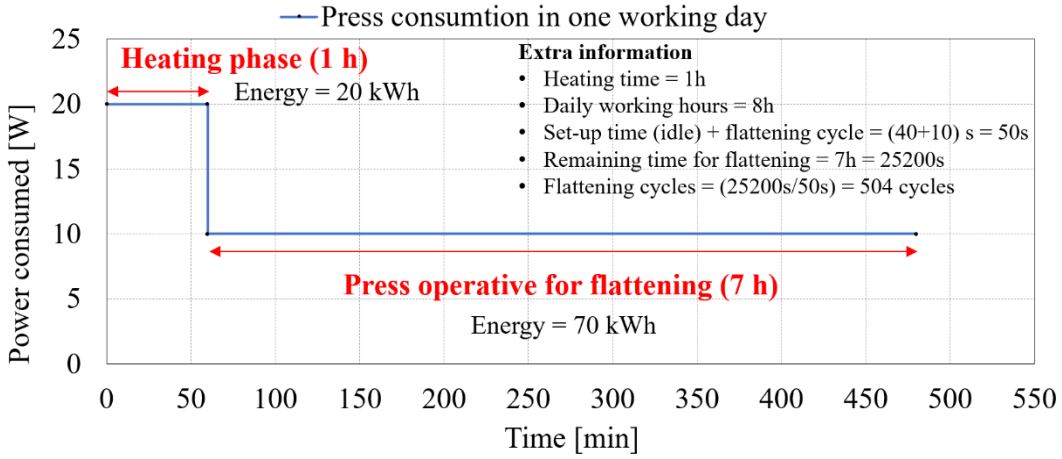

Fig. 6. Press consumption with additional information.

Results of the LCA and Discussion

The main results of the LCA analysis are summarized in Fig. 8, Fig. 7 and Table 4. Data in Table 4 are normalized with respect to 1 kg of flattened automotive steel panel (1 mm thick) or rolled virgin steel. The table highlights the benefits in terms of CO_2 emissions and energy potentially achievable if the proposed reshaping strategy is adopted. The values of Δ_{GWP100} and Δ_{CED} are computed with respect to the case of remanufactured panels.

The left-hand side of Fig. 7 shows clearly that the biggest impacts in terms of CO_2 emissions are related to the painting scrap incineration and electric consumption of flattening (the emissions are computed according to the Italian national energetic mix). The right-hand side of Fig. 7 shows that flattening and de-coating stage have the biggest contributions in energy consumption. Roof cutting station and transportation have negligible impacts, as visible in Fig. 8.

Table 4. Environmental benefits obtained by reshaping EoL panels through flattening.

	GWP100 kg CO_2^{Eq}/kg_{steel}	**CED*** MJ/ kg_{steel}	Δ_{GWP100} kg CO_2^{Eq}/kg_{steel}	Δ_{CED} MJ/ kg_{steel}
Conventional process**	2.35	25.4	≈ **2.2**	≈ **24**
EAF routine + coil production***	0.74	11	≈ **0.6**	≈ **9.6**
Reshaping by flattening***	0.144	1.42	-	-

* CED = Cumulative energy demand.
** Data from literature – Production of steel coils with "cradle-to-gate" approach. [29]
*** Data from literature – Production of steel coils from EAF-based recycling steel production. [31]
**** Modelled in SimaPro, including landfill incineration of the paint.

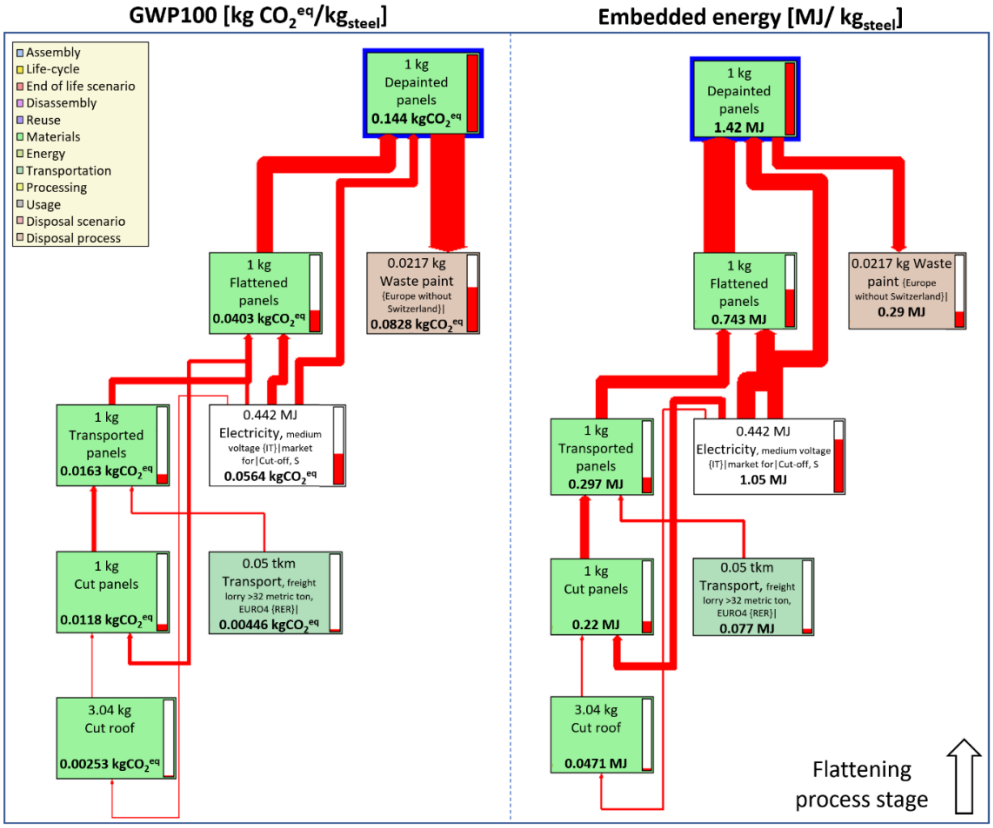

Fig. 7. Results of the LCA analysis with SimaPro.

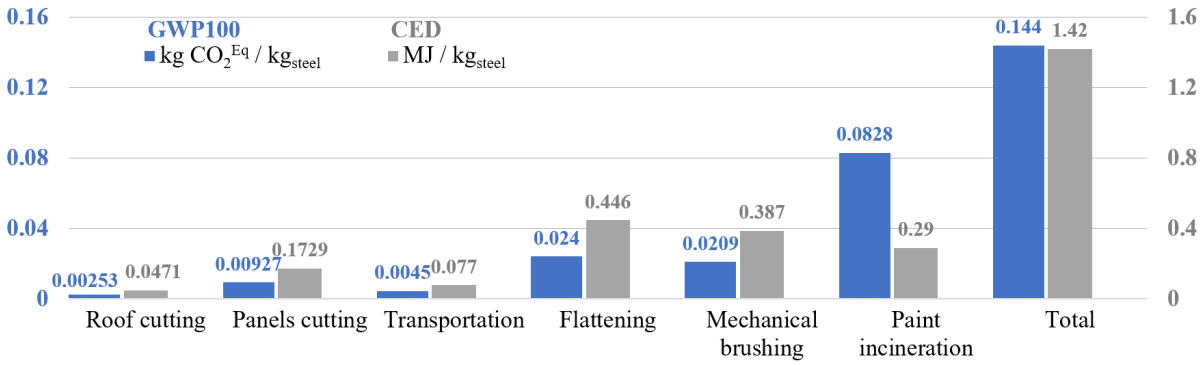

Fig. 8. Different contributions of the different stations in the flattening process chain proposed.

Summary

The work demonstrated different important conclusions, listed below:

- From a technical perspective, flattening is a viable solution for giving a second life to panels deriving from a previous usage (for instance automotive car bodies). The larger the area of the panels to be flattened, the higher the tonnage required by the press, but the higher the "material efficiency" recovered.
- The LEM sensors used for measuring the press power absorption allowed to quantify easily different contributions of energy consumption, such as: moving the piston, idle phases, heating up the dies, keeping the dies in temperature and performing flattening.
- The LCA analysis demonstrates to be a helpful tool to quantify the environmental impacts of all the stages of the flattening process chain. The study showed the tremendous benefits in terms of CO_2^{Eq} emissions and energy that could be potentially achieved by implementing reshaping and remanufacturing strategy of sheet metals.

The implementation of such process chain, considering the huge volumes of EoL cars, could be a potential strategy for reusing efficiently sheet metals in a circular economy business model for automotive car makers or car dismantlers. Enhancing material efficiency through remanufacturing and reshaping is therefore a solution for boosting the ecological transition and meeting the future targets of net zero CO_2 emissions. Lastly, it is important to mention that flattening shaped and formed sheet metals is not always feasible, especially for EoL components with high strains and thinning levels.

References

[1] G. Ingarao, O. Zaheer, L. Fratini, Manufacturing processes as material and energy efficiency strategies enablers: The case of Single Point Incremental Forming to reshape end-of-life metal components, CIRP J. Manuf. Sci. Technol. 32 (2021) 145–153. https://doi.org/10.1016/j.cirpj.2020.12.003

[2] P.A. Renzulli, B. Notarnicola, G. Tassielli, G. Arcese, R. Di Capua, Life cycle assessment of steel produced in an Italian integrated steel mill, Sustain. 8 (2016). https://doi.org/10.3390/su8080719

[3] J.M. Cullen, J.M. Allwood, M.D. Bambach, Mapping the global flow of steel: From steelmaking to end-use goods, Environ. Sci. Technol. 46 (2012) 13048–13055. https://doi.org/10.1021/es302433p

[4] P. Wang, W. Li, S. Kara, Cradle-to-cradle modeling of the future steel flow in China, Resour. Conserv. Recycl. 117 (2017) 45–57. https://doi.org/10.1016/j.resconrec.2015.07.009

[5] Nuove tensioni su logistica e materie prime nel primo trimestre 2022, Lamiera (May 2022), 2022, pp. 7–8.

[6] J.M.C. Julian, M. Allwood, Sustainable materials : with both eyes open. Cambridge, UIT, 2012.

[7] EuRIC AISBL, Metal Recycling Factsheet. Information on: https://www.euric-aisbl.eu/position-papers/download/591/335/32. (accesed on 06.02.2023)

[8] G. Ingarao, R. Di Lorenzo, F. Micari, Sustainability issues in sheet metal forming processes: An overview, J. Clean. Prod. 19 (2011) 337–347. https://doi.org/10.1016/j.jclepro.2010.10.005

[9] J. Cui, H.J. Roven, Recycling of automotive aluminum, Trans. Nonferrous Met. Soc. China (English Ed.) 20 (2010) 2057–2063. https://doi.org/10.1016/S1003-6326(09)60417-9

[10] R. Paul, End-of-life management of waste automotive materials and efforts to improve sustainability in North America, Society of Automotive Engineers International, USA, 120 (2009) 853–861. https://doi.org/10.2495/SDP090802

[11] ESTEP, Green steel by EAF route : a sustainable value chain in the EU Circular Economy scenario, 2019, pp. 1–6.

[12] T. Hay, V.V. Visuri, M. Aula, T. Echterhof, A Review of Mathematical Process Models for the Electric Arc Furnace Process, Steel Res. Int. 92 (2021). https://doi.org/10.1002/srin.202000395

[13] D.R. Cooper, J.M. Allwood, Reusing Steel and Aluminum Components at End of Product

Life, Environ. Sci. Technol. 46 (2012) 10334–10340. https://doi.org/10.1021/es301093a
[14] D.R. Cooper, T.G. Gutowski, The Environmental Impacts of Reuse: A Review, J. Ind. Ecol. 21 (2017) 38–56. https://doi.org/10.1111/jiec.12388
[15] J. Kawai, Development of environmentally-conscious steel products at the Nippon Steel Corporation, Mater. Des. 22 (2001) 111–122. https://doi.org/10.1016/s0261-3069(00)00051-0
[16] D.R. Cooper, J.M. Allwood, Reusing steel and aluminum components at end of product life, Environ. Sci. Technol. 46 (2012) 10334–10340. https://doi.org/10.1021/es301093a
[17] G. Ingarao, R. Di Lorenzo, L. Fratini, An Exploratory Study for Analyzing the Energy Savings Obtainable by Reshaping Processes of Sheet Metal Based Components, Procedia Eng. 183 (2017) 309–315. https://doi.org/10.1016/j.proeng.2017.04.044
[18] N.K. Yusuf, M.A. Lajis, A. Ahmad, Hot press as a sustainable direct recycling technique of aluminium: Mechanical properties and surface integrity, Materials 10 (2017). https://doi.org/10.3390/ma10080902
[19] A.S. Kore, K.C. Nayak, P.P. Date, Formability of aluminium sheets manufactured by solid state recycling, J. Phys. Conf. Ser. 896 (2017). https://doi.org/10.1088/1742-6596/896/1/012007
[20] J.R. Duflou, A.E. Tekkaya, M. Haase, T. Welo, K. Vanmeensel, K. Kellens, W. Dewulf, D. Paraskevas, Environmental assessment of solid state recycling routes for aluminium alloys: Can solid state processes significantly reduce the environmental impact of aluminium recycling?, CIRP Ann. - Manuf. Technol. 64 (2015) 37–40. https://doi.org/10.1016/j.cirp.2015.04.051
[21] D. Baffari, G. Buffa, G. Ingarao, A. Masnata, L. Fratini, Aluminium sheet metal scrap recycling through friction consolidation, Procedia Manuf. 29 (2019) 560–566. https://doi.org/10.1016/j.promfg.2019.02.134
[22] R. Bendikiene, A. Ciuplys, L. Kavaliauskiene, Circular economy practice: From industrial metal waste to production of high wear resistant coatings, J. Clean. Prod. 229 (2019) 1225–1232. https://doi.org/10.1016/j.jclepro.2019.05.068
[23] A.K. Ali, Y. Wang, L. Alvarado, Facilitating industrial symbiosis to achieve circular economy using value-added by design: A case study in transforming the automobile industry sheet metal waste-flow into Voronoi facade systems, J. Clean. Prod. 234 (2019) 1033–1044. https://doi.org/10.1016/j.jclepro.2019.06.202
[24] H. Takano, K. Kitazawa, T. Goto, Incremental forming of nonuniform sheet metal: Possibility of cold recycling process of sheet metal waste, Int. J. Mach. Tool. Manuf. 48 (2008) 477–482. https://doi.org/10.1016/j.ijmachtools.2007.10.009
[25] Z.T. Abdullah, Assessment of end-of-life vehicle recycling: Remanufacturing waste sheet steel into mesh sheet, PLoS One 16 (2021) 1–17. https://doi.org/10.1371/journal.pone.0261079
[26] R. Haase, Remanufacturing of metal components : reforming of sheet metal blanks. Fraunhofer IWU, 2020. Available: https://www.careserviceproject.eu/wp-content/uploads/CarE-Service-Training-on-Metal-reforming-25th-of-May.pdf
[27] A.K. Ali, P.N. Kio, J. Alvarado, Y. Wang, Symbiotic Circularity in Buildings: An Alternative Path for Valorizing Sheet Metal Waste Stream as Metal Building Facades, Waste and Biomass Valorization 11 (2020) 7127–7145. https://doi.org/10.1007/s12649-020-01060-y
[28] Technology Roadmaps: Intelligent Mobility Technology, Materials and Manufacturing Processes, and Light Duty Vehicle Propulsion, Center for automotive research, 2017. https://doi.org/10.32964/tj16.6
[29] W. Asscociation, Life cycle inventory (LCI) study - Seventh global LCI study for steel products, no. Sustainability, 2021.
[30] SSAB, EPD for cold rolled steel sheets and coils.
[31] J. Suer, M. Traverso, N. Jäger, Review of Life Cycle Assessments for Steel and Environmental Analysis of Future Steel Production Scenarios, Sustainability 14 (2022) 14131. https://doi.org/10.3390/su142114131

Materials Research Proceedings 28 (2023) 1957-1966 https://doi.org/10.21741/9781644902479-211

Analysis of temperature effect on strength and microstructure in friction induced recycling process (FIRP)

BORGERT Thomas[1,a *] and HOMBERG Werner[1,b]

[1]Paderborn University, Forming and Machining Technology, Germany

[a]tb@luf.upb.de, [b]wh@luf.upb.de

Keywords: Recycling, Aluminium, Friction-Induced, Energy Efficiency

Abstract. In order to reduce global energy consumption in production and industry along with the associated CO2 emissions, existing resources must be used more efficiently. This includes the energy-efficient and comprehensive recycling of a wide range of metals. Especially for the production of aluminium, there is a large potential for saving energy using efficient recycling processes. With regard to the recycling of aluminium studies have shown that solid-state recycling processes are significantly more efficient considering the used energy and resources compared to the conventional, smelting-metallurgical recycling process. In this paper, the direct and energy-efficient friction-induced recycling process (FIRP) based on the conform process is further described and analysed in terms of the temperature-property relationships. For this purpose, the influence of the processing temperature on the microstructure and properties of the recycled semi-finished products is investigated using the toll system that enables an ECAP forming. Specific sections of the (in theory) infinite, recycled semi-finished product are taken and analysed at different process temperatures of the solid state recycling process. Based on these sections, the properties in terms of mechanical hardness, strength, ductility and grain size are analysed and a degressive relationship between process temperature and mechanical hardness up to a temperature of 270 °C can be shown. Applying the Hall-Petch relationship, it is analysed whether there is a correlation between the strength and the microstructure in the form of the grain size.

Introduction

In order to achieve the climate targets set in the Federal Republic of Germany for 2030 with regard to the CO2 emission reduction, emissions must be reduced in all sectors [1]. Aluminium is used as a construction material in a wide application range. Examples of aluminium applications are building facades or the use in the area of vehicles for lightweight construction. In the automotive sector, aluminium is used for lightweight construction to substitute components that are usually made of steel. Due to the low density of aluminium, the mass of the vehicle in operation can be reduced, thus saving emissions. Other properties that further expand the range of applications for aluminium are its good corrosion resistance and the (theoretical) possibility of infinite recycling [2]. However, due to the high emissions, primary aluminium production represents one of the most energy-intensive production processes. The production of one kilogram of aluminium primarily produced from bauxite requires 155.9 MJ of energy. This amount of energy is determined under the assumption of a parity of the underlying energy supply from coal and hydropower plants [3,4]. This value tends to be underestimated due to developments in recent years. Primary aluminium production has shifted significantly in recent years, so that by 2020 most primary aluminium was produced in China [5,6]. At the same time, the share of coal-fired power plants in total electricity generation in China has increased, so that it is more than 60% between 2015 and 2020 [7]. Also not taken into account in such energy balances are various expenses such as the mining and transportation of bauxite as well as aluminium and its precursors. In addition to the high energy consumption, primary aluminium production has a strong impact on the environment and nature due to the mining of bauxite.

Content from this work may be used under the terms of the Creative Commons Attribution 3.0 license. Any further distribution of this work must maintain attribution to the author(s) and the title of the work, journal citation and DOI. Published under license by Materials Research Forum LLC.

One possibility for recycling old as well as new scrap is the secondary production process, which describes the conventional recycling strategy. Heavily contaminated scrap usually has to be freed from oils, greases and other impurities. The processed scrap is then fed into a melting furnace (melting temperature of aluminium is about T_m = 660 °C), melted down and subsequently cast into ingots. These ingots are usually processed into profiles or similar using further processes such as an extrusion process [2]. The amount of energy required for the conventional recycling process is significantly lower than the energy required for the primary manufacturing process. Nevertheless, primary aluminium must be included in the production process to some extent, which significantly increases the total energy requirement. If, in addition to the energy required to melt the aluminium, the effort required to dispose of the resulting salt slag is also included in an energy balance, the energy requirement is around 17.7 MJ/kg [8].

Despite the already significantly improved energy balance of the conventionally recycling strategy, there are extensive efforts to further optimize the aluminium recycling process. This is being done both from an energy point of view in the form of a further reduction in the amount of energy used and in an effort to avoid the creation of environmentally harmful salt slag. One way to reduce the amount of energy required is a lower processing temperature in the recycling process [9]. In case the aluminium scrap does not need to be heated to the melting temperature and can be processed at significantly lower temperatures, energy can be saved. Due to this lower processing temperature compared to the melting temperature, solid-state recycling processes are suitable here [10]. An example of such a process is the recycling of pre-compacted aluminium chips using a conventional extrusion process. Due to the fact that large quantities of alloy-pure and uniform aluminium chips are often available from the machining sector, more studies have been conducted in the field of recycling aluminium chips using solid-state recycling processes in recent years. Two advantages of this recycling approach compared to the conventional, melting-metallurgical recycling process of aluminium chips are the significantly lower amount of energy and the saving of material, which is otherwise disposed of in the form of oxides in the salt slag. Furthermore, solid-state recycling processes are usually a direct recycling process. This implies that the produced goods are not in the form of raw shapes such as ingots, but can be directly produced as user-specific geometry such as complex profiles [11]. The basis for achieving good properties comparable to conventionally manufactured products is a major degree of deformation of the parts to be recycled at high temperature at the same time. Only in this way the natural and very hard oxide layer on the aluminium can be destroyed and a high bonding strength between the individual particles be achieved [12]. Friction-induced solid state recycling processes include friction stir extrusion and friction stir consolidation [13]. The processing of aluminium chips with the friction stir extrusion process show that the temperature is a very strong influencing variable of the process forces as well as the properties of the recycled products [14]. Products with a full density and good mechanical properties can be produced, but the discontinuity is a limitation for the process [15].
Another solid-state process for recycling aluminium chips has recently been investigated at the Department of Forming and Machining Technology (LUF) at Paderborn University. Compared to the recycling process based on conventional extrusion, the friction-induced recycling process (FIRP) provides the advantage that profiles can be produced in unlimited lengths. In previous investigations, it was shown that a full profile with good mechanical properties of the wrought alloy EN AW-6060 could be produced in the stationary production phase of the friction-induced recycling process. Hardness measurements show a homogeneous distribution of properties over the entire cross-sectional area. The profiles produced show significant grain refinement within the microstructure compared to reference wires. Also for this recycling process a reduction of energy input could be achieved compared to secondary aluminium production [16,17].

The central motivation for the investigations presented here on the continuous and friction-induced recycling process is the investigation of the process parameters and influencing variables

necessary for solid state recycling. The friction induced recycling process is well suited for these parameter studies due to the steady state nature of the process. Within this stationary state, the key parameters of temperature, torque or extrusion pressure as well as the processed mass flow rate show constant characteristic values. A detailed analysis of the conditions required for the production of profiles is well possible in the steady state of the friction-induced process and is investigated in this publication as part of the determination of the microstructure properties correlation.

Processing Principle and Materials

The machine set up shown in Fig. 1, a) provides the basis for the investigations concerning the friction-induced recycling process described in the following. By using the here presented setup a wide variety of aluminium scrap, in terms of geometric size, can be processed. Therefore the material to be recycled is fed into the groove (6x7 mm) of the rotating wheel at a constant mass flow rate. The wheel is fixed on the output shaft of a powerful geared drive, which rotates at a constant rotational speed in the range between n = 6 - 11 rpm for the investigations described in this paper. A tool insert continuously reduces the cross-sectional area of the wheel groove by engaging in the groove of the wheel. This steadily compacts the aluminium chips, which initially have a very low bulk density. While the aluminium particles rotate within the wheel groove, they are compressed and plasticised, so that at the end the density of the aluminium is increased to ρ = 2.7 g/cm^3. Following the quarter turn, the entire cross-sectional area of the wheel is filled by a counterholder which deflects the material. The additional deformation of the deflection further breaks up the oxide layers of the material. Subsequently, the material is extruded through a shaping die in a manner analogous to extrusion.

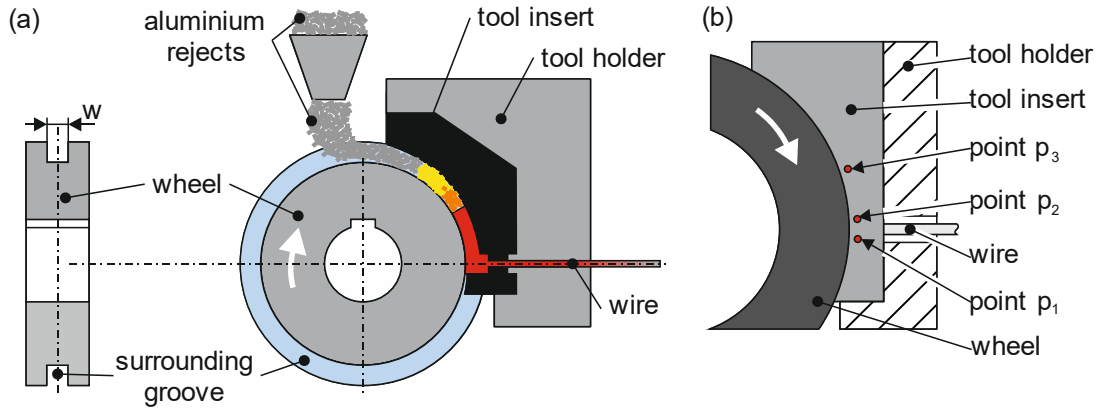

Fig. 1. Set up for the friction-induced recycling process. (a) Tool system. (b) Illustration of the temperature measuring points.

Central indicators of the friction-induced recycling process are the temperature as well as the torque applied by the gear motor (SIMOGEAR parallel shaft gear motor, Siemens AG). The torque is determined from an average value of the electrical power consumption of the frequency converter (SINAMICS G120, Siemens AG). The direct temperature measurement inside the extrusion channel to determine the true material temperature is very difficult. Instead, a tactile measuring principle is used to record the real temperature on the outside of the die insert at different measuring points depicted in Fig. 1, b). Type K thermocouples (G/G-24-KK-IEC, Therma Thermofühler GmbH) and an MX440A measuring amplifier (Hottinger Brüel & Kjaer GmbH) are used for this purpose. In validation tests it has been proven that this type of temperature measurement approximates the actual forming or extrusion temperature well. This could be demonstrated with the measurement of the temperature a few millimetres in front of the extrusion

channel as well as the exit temperature of the recycled wire, which corresponds to the temperature measured on the outside at points p_1 and p_2 in the stationary state.

Irrespective of the possibility of processing a wide variety of aluminium scrap, only aluminium chips are used for the investigations in this paper. The reason for this is the fact that these can be produced specifically under constant cutting conditions. This results in a constant chip size, which is necessary for setting a constant mass flow in the feed and thus also constant test conditions. The cutting conditions used for the production of the aluminium chips of the alloy EN AW-6060 (T66) as well as the resulting chip geometry are given in Table 1.

Table 1. Cutting conditions and resulting geometry of the chips used.

Machining parameters		Chip Size (Material EN AW-6060)	
Cutting speed	v_c = 1425 m/min	Raw Material	plate 300x200x20 mm
Feed	f = 0.2 mm	Chip length	$l_c \approx 1.9 \pm 0.12$ mm
Cutting depth	a_p = 2 mm	Chip width	$w_c \approx 1.5 \pm 0.1$ mm
Cutting width	a_e = 0.5 mm	Chip thickness	$t_c \approx 0.095 \pm 0.007$ mm

Results and Discussion

For a wide industrial application, the productivity of a process is an important decision parameter for the operational application in addition to the economic efficiency. The rotational speed of n = 6 rpm used in previous investigations results in a lower discharge and heating rate compared to conventional extrusion. This is to be improved in a first step by increasing the wheel rotational speed to n = 11 rpm in combination with a proportional increase in the filling rate. With the relationship described above, the discharge rate can be almost doubled. Fig. 2 shows the measured values of temperature and torque recorded in a test with n = 11 rpm. The torque is calculated from the electrical power consumption of the frequency inverter and represents an average value due to natural fluctuations. The three measuring points relevant for the temperature measurement are shown in Fig. 1, b) above. Points p_1 and p_2 are located below and above the extrusion channel, respectively. Measurement point p_3 is located further up on the tool, which can be seen as an explanation for the consistently lower temperatures compared to the other two measurement points.

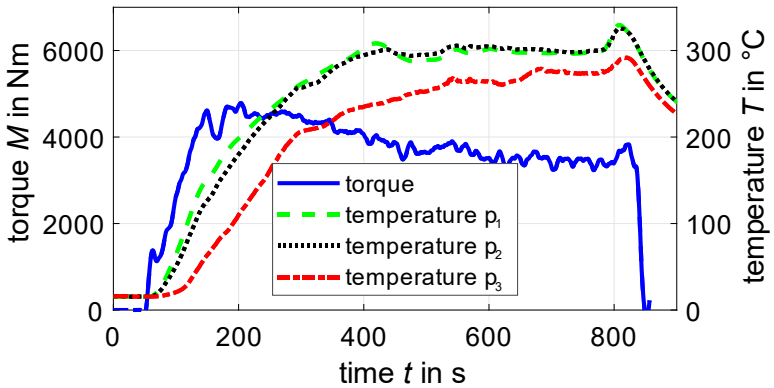

Fig. 2. Torque and tool/process temperatures for different measuring points.

At the beginning of the process (after approx. 45 seconds), the torque rises sharply when the gear motor is switched on and the chips are directly fed in, and initially remains at a high plateau. Analogous to the torque, the temperature readings also initially show a sharp increase. After a total time of approx. 435 seconds, a steady state is reached at nearly T = 300 °C with respect to the temperature values of measuring points p_1 and p_2. From the time the stationary process state is

reached the temperatures of these measuring points remain constant except for a slight increase when chip filling stops at the end of the process. With a delay of approx. 160 seconds, the torque also reaches a stationary state at $M = 3450$ Nm. In a direct comparison of the results presented here for the high rotational speed of $n = 11$ rpm compared to the previously published results with $n = 6$ rpm, there is a clear increase in the heating rate, so that the steady state is reached significantly earlier.

Temperature property correlation.

The aim of the investigations presented here is to describe the relationship between the mechanical strength and the temperature that prevails in the process. Due to the homogeneous temperature distribution within the die insert, the process temperature is equated with the temperature measured at the first or second point on the outside. To illustrate the influence of different rotational speeds (n = 6, 8, 10, 11 rpm) on the temperature balance as well as the mechanical properties, investigations and measurements have been carried out at different rotational speeds which shows macroscopic good properties of the recycled wires. For all four rotational speeds investigated, the process temperature is assigned to a specific location on the extruded wire by means of a time-dependent marker. This enables a precise analysis of the individual test points after the extrusion process to reveal the correlations between rotational speed, temperature and mechanical properties. The temperature was determined for all three rotational speeds at point p_1. Depending on the rotational speed and thus also the discharge rate, between 6 and 22 test points were recorded for each rotational speed. Even in the instationary process state for low temperatures < 200 °C, a homogeneous wire is produced with only minor inhomogeneities on the surface (see Fig. 3, a). Following the test, the wires were cut at the previously defined test points, embedded and subsequently subjected to a hardness test. The measured value of each test point represents the average of five individual measurements on the head surface (see Fig. 3, a) to counteract and compensate any uncertainties. Fig. 3, b shows these average values for the test points of all four rotational speeds (marked in colour) along with the temperature assigned to the respective point. For all four rotational speeds considered, the hardness decreases in the instationary start up phase as the temperature increases until the temperature of 270 °C is reached. In general, the original strength of the starting material is significantly reduced.

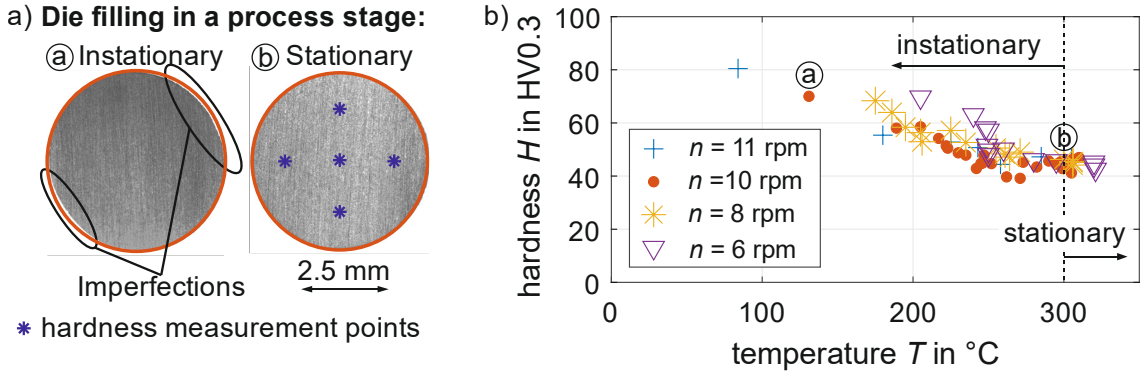

Fig. 3. Temperature-dependent development in, a) die filling, b) hardness as a function of temperature T and rotational speed n.

The mechanical hardness of the tubes used to machine the chips is about $H = 90$ HV 0.3 (in a T66 condition). The application of temperature in the extrusion process significantly reduces the strength or measured hardness due to recrystallisation. This reduction in the initial strength of the material due to the introduction of temperature has also been observed in comparable processes such as friction spinning. In the context of friction spinning, which also obtains the temperature from the friction between the forming tool and the workpiece, similar hardness values of between $H = 40$ - 50 HV 1 are obtained following the process [18].

Considering the temperature range above 270°C, which represents the steady state, it first becomes apparent that, due to the only slight temperature change, many measuring points show almost identical hardness values. This confirms the previously made assumption of constant properties within the steady state. Due to the fact that the stationary process state has been reached, no further heating will take place in the natural process. Regarding the influence of the rotational speed on the hardness, it can be summarised that in the stationary state of the temperature range considered the hardness is not influenced by the rotational speed. A check of the behaviour for temperatures above 310°C measured on the outside of the die must therefore be carried out in future investigations at higher rotational speeds, using modified tools or with the aid of heating cartridges.

One requirement for the use of products made from recycled materials is a consistent and reliable workpiece quality. In the friction-induced recycling process which is investigated in this paper, a steady state is established when a defined temperature level (for the above described trial with n = 11 rpm the stationary temperature is nearly 300°C) is reached. In the following, the extent to which the workpiece quality is consistent from the time the steady state is reached is analysed. The hardness distribution on the cross-sectional area of wire sections in the steady state of the friction-induced extrusion process of the high rotational speed of n = 11 rpm is analysed. Six wire sections from l = 2.5 m to l = 5 m were tested. It can be shown that the hardness values on the head surface vary only slightly around the respective mean value of the section. The standard deviation of the respective sections must therefore also be compared to the reference wire. The mean value of all 78 measurement points is H = 47.8 HV 0.3 with a standard deviation of SD = 2 HV 0.3. The consideration of the results of tensile tests also show a uniform average tensile strength of R_m = 155 MPa with a standard deviation of SD = 4.5 MPa. From these measurements, it can be concluded that friction-induced extrusion can be used to produce semi-finished products within the steady state that exhibit a homogeneous distribution of the mechanical property of hardness and tensile strength. The hardness and tensile strength of the recycled samples are comparable to the properties of semi-finished aluminium products of the alloy EN AW-6060 in the solution-annealed and softened T4 condition according to EN 755-2:2016. The softening can be attributed to the dynamic recovery and recrystallisation caused by temperature and deformation.

Microstructure Strength Correlation.

The decreasing strength of the recycled wires with increasing temperature will be explained in the following based on an analysis of the microstructure (grain size) on the cross-sectional and the longitudinal-sectional area surface of the wires. For this purpose, four sections produced at different temperatures, at the rotational speed of n = 10 rpm are embedded and electropolished for each area. The aim of this is to observe the microstructure and analyse the grain size. Fig. 4 shows the development of the microstructure and thus also of the grain size for four different test points, each at a different temperature.

The first test points (I) were generated at a temperature of T_1 ≈247°C and shows small, uniformly distributed grains with an average grain size of $d_{k,1} \approx 3.5$ µm on the cross-sectional and $d_{k,1} \approx 3.9$ µm on the longitudinal-sectional area. For the second as well as the third test point, the grain size increases with the temperature. This is valid for both the cross-sectional and the longitudinal-sectional area independent of smaller deviations between the two different areas. For the highest temperature considered of $T_4 \approx 310$°C, an average grain size of $d_{k,4} \approx 6{,}3$ µm on the cross-sectional and $d_{k,4} \approx 6{,}4$ µm on the longitudinal-sectional area can be measured. From these results, a clear progressive relationship between temperature and grain size can be determined.

The reduced hardness and growing grain size with increasing process temperature can be described by the microstructure restructuring due to recrystallisation in agreement with the Hall Petch relationship. In general, a dependence of the mechanical properties in terms of a hardening or softening can be made as a function on the grain size. This relationship is described by the Hall-

Petch equation. The yield strength or 0.2% yield point σ_y is determined on the basis of the material constant σ_0 which take the required stress for dislocation movement into account and a constant of yielding K as well as the average grain size d according to Eq. 1 [19,20].

$$\sigma_y = \sigma_0 + K \cdot d^{-1/2} \quad (1)$$

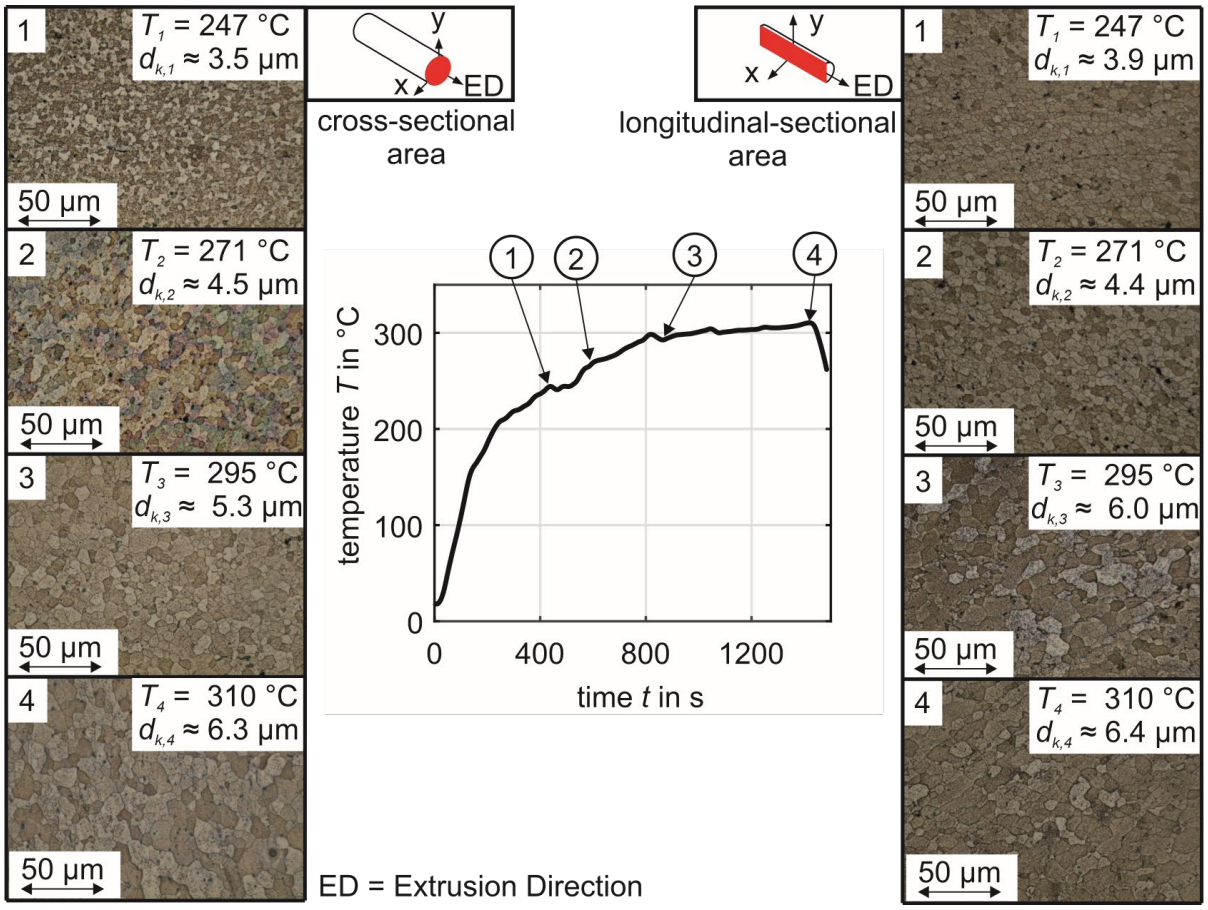

Fig. 4. Change in microstructure of wires produced at 10 rpm as a result of temperature changes measured on the outside of the tool.

As previously described, the grain size changes as a function of temperature in the friction-induced recycling process for both considered intersections. In order to verify the validity of the Hall-Petch relationship for this process, tensile tests of the individual sections are carried out. The results of the tensile tests in comparison to the temperature and the grain size are show in Table 2.

Table 2. Change in temperature, grain size, and yield strength.

Point of investigation	Temperature T in °C	Grain Size cross-sectional area d in µm	Grain Size longitudinal-section area d in µm	yield strength σ_y in MPa
1	247	3.5	3.9	104
2	271	4.5	4.4	98
3	295	5.3	6.0	95
4	310	6.3	6.4	93

Due to the steady increase in temperature, the tensile tests for the four points described above represent a temperature interval of ± 5°C around those used to determine the grain size. Each result of the yield strength shown in Figure 6 represents the average of two to four measurements (depending on availability). For the cross-sectional area, the constants are determined to be σ_0 = 59.8 MPa as well as K = 82 MPa µm$^{1/2}$ with a high coefficient of determination of R^2 = 0.988, and for the longitudinal-section area, the constants are determined to be σ_0 = 59.5 MPa as well as K = 85 MPa µm$^{1/2}$ with a coefficient of determination of R^2 = 0.9. In studies on the microstructural changes of equal channel angular pressing, a constant of K = 114.3 MPa µm$^{1/2}$ has been determined for the alloy EN AW-6060, which is also investigated in this paper. For the nearly pure EN AW-1100, a slightly lower constant of K = 105 MPa µm$^{1/2}$ is determined [20]. Other sources calculate K = 65 MPa µm$^{1/2}$ [21] or K = 70 MPa µm$^{1/2}$ [22] for the pure aluminium. The values investigated within the scope of this paper shows certain, but not too large deviations from the literature values. However, this can also be attributed to the smaller number of study points considered (n = 4). In general, it can be stated that both the results obtained from the experimental work in terms of yield strength and grain size correlate according to the Hall-Petch relationship and the strength mechanisms can be attributed to the change in grain sizes. A direct comparison of the friction-induced recycling process with similar forming processes for the production of semi-finished products shows that (when using the tool system of the friction-induced recycling process described here) a lower process temperature occurs compared to hot extrusion. This, coupled with the significantly shorter contact time of the process temperature in the recycling process, can be used as an explanation for the significantly smaller grain size of the recycled profiles compared to profiles produced with the hot extrusion process [23,24].

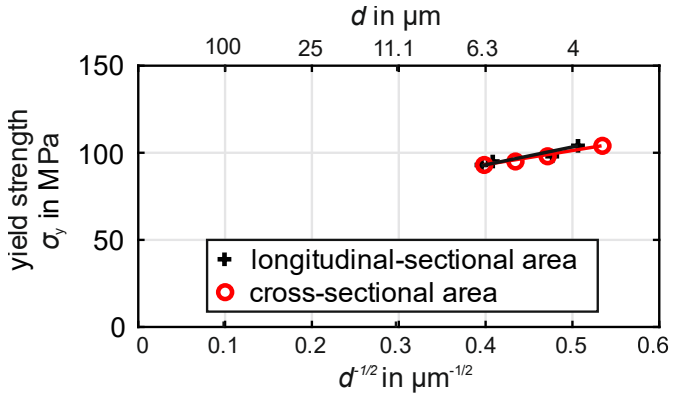

Fig. 6. Dependence of the mechanical strength (yield strength) on the grain size.

Summary
This paper presents further investigations on the energy-efficient and resource-saving friction-induced recycling process. Depending on the tool system used, a steady-state process condition is established after the heating phase, which was demonstrated by constant hardness values in the temperature range above 270°C. Further investigations also show a dependence of the microstructure in the form of the grain size as well as the strength in terms of the yield strength, which are modelled and represented using the Hall-Petch relationship. Considering the best practise in developing a resource and energy efficient recycling process the rotational speed of the wheel does not affect the hardness of the recycled profiles in the stationary production phase. Using higher rotational speeds can be useful to increase the output while recycling particles/ chips with a low density. First fundamental research shows the possibility of raising the processing temperature by increasing the extrusion channel length of the tooling system due to the increase in frictional surface considering the stationary production phase. These and further possibilities (e.g. modification in extrusion ratio) to affect the process temperature and mechanical properties of the products will be the aim of future investigations.

Acknowledgment
This research was funded by the state of Northrhine Westfalia via the Forschungskolleg ‘Leicht-Effizient-Mobil’ (LEM).

References
[1] BMU. Climate Action Report 2017 on the German Government's Climate Action Programme 2020, 2018.
[2] Q. Dai, J.C. Kelly, A. Burnham, A. Elgowainy, Updated Life-Cycle Analysis of Aluminum Production and Semi-Fabrication for the GREET Model. Energy Systems Division, 2015.
[3] E. Balomenos, D. Panias, I. Paspaliaris, Energy and Exergy Analysis of the Primary Aluminum Production Processes: A Review on Current and Future Sustainability, Miner. Process. Extr. Metall. Rev. 32 (2011) 69-89. http://doi.org/10.1080/08827508.2010.530721
[4] E. Balomenos, I. Gianopoulou, D. Panias, I. Paspaliaris, Efficient and Complete Exploitation of the Bauxite Residue (Red Mud) Produced in the Bayer Process, Proceedings of European Metallurgical Conference, 2011, pp. 745-757.
[5] R. Lumley, Fundamentals of aluminium metallurgy: Production, processing and applications, Woodhead Publishing, Oxford, 2011.
[6] G. Saevarsdottir, H. Kvande, B.J. Welch, Aluminum Production in the Times of Climate Change: The Global Challenge to Reduce the Carbon Footprint and Prevent Carbon Leakage, JOM-J. Min. Met. Mat. S. 72 (2020) 296-308. https://doi.org/10.1007/s11837-019-03918-6
[7] H. Zou, H. Du, D.C. Broadstock, J. Guo, Y. Gong, G. Mao, China's future energy mix and emissions reduction potential: a scenario analysis incorporating technological learning curves, J. Clean. Prod. 112 (2016) 1475-1485. https://doi.org/10.1016/j.jclepro.2015.08.012
[8] H.-G. Schwarz, Aluminum Production and Energy, in: Cutler J. Cleveland (Ed.), Encyclopedia of Energy, 2004, pp. 81-95.
[9] J.Z. Gronostajski, H. Marciniak, A. Matuszak, New methods of aluminium and aluminium-alloy chips recycling, J. Mater. Process. Technol. 106 (2000) 34-39. https://doi.org/10.1016/S0924-0136(00)00634-8
[10] B. Wan, W. Chen, T. Lu, F. Liu, Z. Jiang, M. Mao, Review of solid state recycling of aluminum chips, Resour. Conserv. Recycl. 125 (2017) 37-47. https://doi.org/10.1016/j.resconrec.2017.06.004
[11] T. Tokarski, Mechanical Properties of Solid-State Recycled 4xxx Aluminum Alloy Chips, J. Mater. Eng. Perform. 25 (2016) 3252-3259. https://doi.org/10.1007/s11665-016-2194-1

[12] A.E. Tekkaya, M. Schikorra, D. Becker, D. Biermann, N. Hammer, K. Pantke, Hot profile extrusion of AA-6060 aluminum chips, J. Mater. Process. Technol. 209 (2009) 3343-3350. https://doi.org/10.1016/j.jmatprotec.2008.07.047
[13] S. Shamsudin, M.A. Lajis, Z.W. Zhong, Solid-state recycling of light metals: A review, Adv. Mech. Eng. 8 (2016). http://doi.org/10.1177/1687814016661921
[14] M.E. Mehtedi, A. Forcellese, T. Mancia, M. Simoncini, S. Spigarelli, A new sustainable direct solid state recycling of AA1090 aluminum alloy chips by means of friction stir back extrusion process, Procedia CIRP 79 (2019) 638-643. https://doi.org/10.1016/j.procir.2019.02.062
[15] D. Baffari, G. Buffa, D. Campanella, L. Fratini, Design of continuous Friction Stir Extrusion machines for metal chip recycling: issues and difficulties, Procedia Manuf. 15 (2018) 280-286. https://doi.org/10.1016/j.promfg.2018.07.220
[16] T. Borgert, W. Homberg, Friction-Induced Recycling Process for User-Specific Semi-Finished Product Production, Metals 11 (2021) 663. https://doi.org/10.3390/met11040663
[17] T. Borgert, W. Homberg, Energy saving potentials of an efficient recycling process of different aluminum rejects, Energy Rep. 8 (2022) 399-404. https://doi.org/10.1016/j.egyr.2022.01.027
[18] B. Lossen, W. Homberg, Friction-Spinning - Influence of Tool and Machine Parameters on the Surface Texture, Key Eng. Mater. 651-653 (2015) 1109-1114. http://doi.org/10.4028/www.scientific.net/KEM.651-653.1109
[19] P. Luo, D.T. McDonald, W. Xu, S. Palanisamy, M.S. Dargusch, K. Xia, A modified Hall-Petch relationship in ultrafine-grained titanium recycled from chips by equal channel angular pressing, Scr. Mater. 66 (2012) 785-788. http://doi.org/10.1016%2Fj.scriptamat.2012.02.008
[20] T. Khelfa, M.A. Rekik, J.A. Muñoz-Bolaños, J.M. Cabrera-Marrero, M. Khitouni, Microstructure and strengthening mechanisms in an Al-Mg-Si alloy processed by equal channel angular pressing (ECAP), J. Adv. Manuf. Technol. 95 (2018) 1165-1177. https://doi.org/10.1007/s00170-017-1310-1
[21] J.D. Embury, D.J. Lloyd, T.R. Ramachandran, Strengthening Mechanisms in Aluminum Alloys, Treatise on materials science & technology, aluminum alloys-contemporary research and applications 31 (1989) 579-601.
[22] H.J. McQueen, The production and utility of recovered dislocation substructures, MTA 8 (1977) 807-824.
[23] D. Leśniak, P. Gromek, Estimation of Extrusion Welding Conditions for 6xxx Aluminum Alloys, Procedia Manuf. 47 (2020) 253-260. https://doi.org/10.1016/j.promfg.2020.04.213
[24] W.G. Frazier, J.C. Malas, E.A. Medina, S. Medeiros, S. Venugopal, W.M. Mullins, A. Chaudhary, R.D. Irwin, Application of control theory principles to optimization of grain size during hot extrusion, Mater. Sci. Technol. 14 (1998) 25-31. https://doi.org/10.1179/mst.1998.14.1.25

Materials Research Proceedings 28 (2023) 1967-1976 https://doi.org/10.21741/9781644902479-212

Sustainable tool technology: Wood-based forming tools

GEUEKE Michael[1,a *], STEINHEIMER Rainer[1,b], LUTZ Maximilian[2,c] and ENGEL Bernd[1,d]

[1]Forming Technology, Institute of Production Technologies, University of Siegen, 57076 Siegen, Germany

[2]International Production Engineering and Management, Institute of Production Technologies, University of Siegen, 57076 Siegen, Germany

[a]michael.geueke@uni-siegen.de, [b]rainer.steinheimer@uni-siegen.de, [c]Maximilian.Lutz@uni-siegen.de, [d]bernd.engel@uni-siegen.de

Keywords: Sheet Metal Forming, Sustainability, Wooden Tools, Flexibility, Mass Customization

Abstract. Conventional, dies are manufactured subtractive for sheet metal forming. Beside the forming process, high tooling costs, material exertion and energy consumption, the die production offers chances for economic improvements. Especially, individualization and mass customization for small batch series require sustainable low-cost tooling approaches, where sustainable advances through biologicalization may offer new possibilities. In this work, sheet metal forming tools are manufactured by laminated black locust dies to reduce the overall ecological impact. The deformation and wearing behavior of the wooden tools is investigated during a drawing operation for low batch size of an automotive conventional sheet material.

Introduction

Following the Kyoto Protocol, the Paris Agreement declared and signed by 197 nations clearly postulate the goal to limit the global human made temperature rise by 1.5°C [1]. To ensure this, more sustainable approaches in all areas (e.g., production, infrastructure, food) are required to reduce the manmade ecological impact. On the other hand, a paradigm change from economy of scale to flexibility and customization in any production and consumer industry continuously increasing the demand for highly individualized mass customization of small batch sizes [2]. To enable flexibility in metal forming under the geo-political restrictions, new approaches are required to reconcile both goals in an increased globalization and price competition [3].

Even though flexibility is intrinsic for generic forming tools (e.g., freeform bending), it may be increased via agile or smart production systems [4]. On the other hand, shape-related tools in forming applications (e.g., rotary-draw-bending, deep drawing) require more resources when aiming for mass customization and individualization, since there is typically just one tooling form for each desired part geometry. Shape-related tooling approaches produced by additive manufacturing can reduce the base material consumption for customized forming tools but result in high energy consumption during the additive tooling process. Whereas sheet metal forming processes are often layout for high batch volume production, an individualized low batch size mass customization does need to fit the economic restrictions of the production process [5]. Biologicalization may offer an alternative approach for higher flexibility in metal forming, particularly when aiming for small batch size production. Biologicalization has been defined as "*The use and integration of biological and bio-inspired principles, materials, functions, structures and resources for intelligent and sustainable manufacturing technologies and systems with the aim of achieving their full potential."[2].* When Potting et. al postulated the circular economy in 2017, they defined 9R-strategies to layout a more sustainable production scheme from linear to circular economy [6]. Within the 9R-strategies there are several approaches to reduce natural resource

Content from this work may be used under the terms of the Creative Commons Attribution 3.0 license. Any further distribution of this work must maintain attribution to the author(s) and the title of the work, journal citation and DOI. Published under license by Materials Research Forum LLC.

consumption and environmental pressure. When combining the 9R-strategies with biologicalization this reveals a potential for sustainable manufacturing technologies and systems.

Since there is no suitable and economically approved technique to ensure individualized and flexible small batch size production in deep drawing [7], further investigations have to be proceeded. This study reveals a biobased approach following alternative tooling approaches by additive manufacturing [5,6]. The performance of composite structures from black locust (robinia pseudoacacia) tools for sheet metal forming is evaluated experimentally based on the rubber pad forming process.

Literature Review

In sheet metal forming, deep drawing is a common used forming process, where blanks are peripheral restrained by blankholder units and radially drawn into a forming die (cavity) by a punch [10]. Deep drawing is a forming operation where material flow is allowed under the blankholder, aiming for constant material thickness, whereas stretch forming results in a thickness change [11,12]. Since both production methods typically aiming for mass size production, grey cast tooling molds with post-mill shaping are the conventional way of manufacturing [13]. The performance of drawing tools is mainly determined by the tool wear behaviour on highly stressed areas (radii, cavity inlets). Depending on the lot size, sheet material (hardness, thickness and strength), desired part surface quality, surface treatments and lubricants must be considered during tool design [14]. Rubber Pad forming (RPF), a specific deep drawing process, is widely used for automotive and aerospace applications, where one of the form-shaping tools is replaced by a rubber pad (Fig. 1). Advantages, compared to a conventional deep drawing process which consist at least of two complementary tools, can be stated in one flexible pad alignment for different shape geometries, high part surface quality, elimination in misalignment of tools, low tooling costs, no additional lubrication, avoidance of galling on the sheet metal and friction defined specific geometries [15,16]. Despite the benefits, a limited lifetime of the flexible pads, higher production cycle times and higher necessary press capacities due to the energy loss are the drawbacks of this technique [17]. RPF reveals economic and technological advantages for small batch size production [18], which makes it suitable when aiming for higher forming flexibility and mass customization. In Addition to this, the substitution of metal-based tooling materials through biologicalization may improve the ecological value of the process, when renewable tooling materials could be used for in a suitable process window.

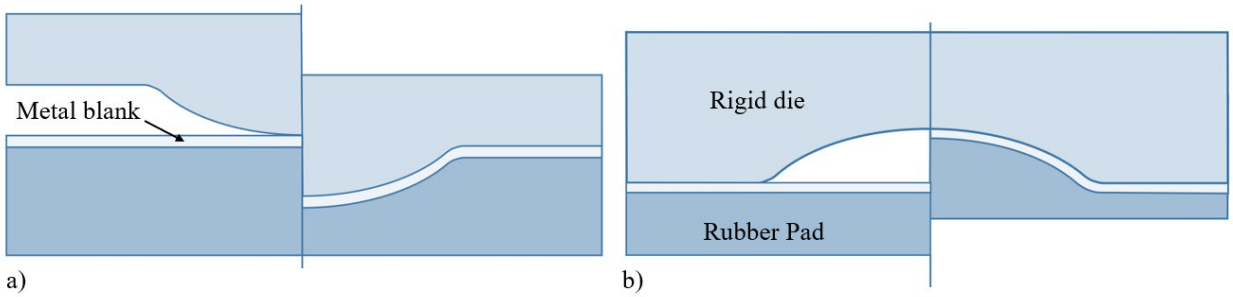

Fig. 1. Guerin process: Tool setup for (a) positive (male) and (b) negative (female) rubber pad forming.

Related Research

Higher product individualization, mass customization and changing consumer requirements regarding technical applications, lead to increasing derivatives in all production sectors. To ensure these demands without contravening geo-political restrictions, alternative approaches in

manufacturing are inevitable. Biologicalization and alternative equivalents are auspicious odds to cover the demands of the present production era.

Additive manufacturing (AM) as one of the major innovations in individualized mass customization and production offers a wide range of applications to substitute conventional manufacturing systems [7,19]. AM offers the opportunity to adapt optimized structures and to manufacture them precise without surplus material [20]. In manufacturing, AM was successfully implemented as tooling material e.g., sheet metal forming [8,9,21,22].

Along AM, biologicalization is a suitable mechanism to adapt nature based optimization and material range to sustainable manufacturing systems [2]. [23] studied the performance of wooden based tooling material for a deep drawing process in a feasibility study. The manufactured wooden based forming tools glued together of 4 mm black locust (BL) sheets. The investigated a good performance on low batch size (<500 parts) for radii greater 5 mm. [24] examined the performance of polymer and wood based tools for sheet metal forming for a batch of 500 parts each. The revealed an overall feasibility for radii of 7 mm with slightly higher deformation on the densified wood-based compared to the polymer tools.

Methodology

Preceding investigations.

The aim of the present study is the investigation of a potential substitution of conventional tooling materials for sheet metal forming applications through biologicalization. For comparison, similar process boundaries were applied as in the preceding studies [8,9], where the mechanical stability of fused deposition modeling (FDM) printed dies from polylactic acid (PLA) with solid and reduced infill was investigated in forming DC03 (0.7 mm) sheet metal parts in a rubber pad forming process featuring a polyurethane pad (shore hardness 40). Based on the previous work, the load collective of the drawing process was adopted for composite layered tools of BL.

Mechanical characterization of black locust.

Black locust is a hardwood that can be grown and harvested in nutrient-poor and dry locations, offering good mechanical properties compared to alternative wood or biobased materials. According to [25,26] black locust offers the highest mechanical properties for all native wood species. The mechanical characterization (tensile, compression, bending, hardness) was performed on a Zwick Roell Z250 universal testing machine i.e., for the following geometries, according to relevant standards DIN EN ISO 527-1, *DIN 52192* and DIN 52186 respectively (see. Fig. 2):

Fig. 2. Black locust test specimen for mechanical characterization.

The results are summarized in Table 1, next to data from relevant literature [27-30].

Table 1. Mechanical properties for black locust.

Tensile properties		**Characterization**	**LOMANN** [27]	**KOLMANN** [28]	**VORREITER** [29]	**WAGENFÜHR** [30]
Tensile strength parallel to fiber	[N/mm²]	153.14 (± 23.31)	88...136...184	98...145...181	145	88...136...184
Tensile strength perpendicular to fiber	[N/mm²]	7.59 (± 1.36)	—	4	4	4
Tensile modulus parallel to fiber	[N/mm²]	9325.95 (± 308.10)	—	—	—	—
Tensile modulus perpendicular to fiber	[N/mm²]	1394.06 (± 409.82)	—	—	—	—
Compression properties						
Compressive strength longitudinal	[N/mm²]	7.56 (± 2.01)	62...72...81	55...72...94	58	62...72...81
Compressive strength tangential	[N/mm²]	20.86 (± 3.63)	—	—	13	—
Compressive strength radial	[N/mm²]	28.02 (± 2.36)	—	19	13	—
Compressive modulus longitudinal	[N/mm²]	8720.43 (± 622.56)	—	—	—	—
Compressive modulus tangential	[N/mm²]	603.71 (± 28.03)	—	—	—	—
Compressive modulus radial	[N/mm²]	750.24 (± 48.18)	—	—	—	—
Bending properties						
Flexural strength tangential	[N/mm²]	141.54 (± 11.83)	103...136...169	147	118	103...136...169
Flexural strength radial	[N/mm²]	145.95 (± 14.04)				
Flexural modulus tangential	[N/mm²]	11107.98 (± 1327.36)	9000...11300...13500	8800...13300...16700	13300	9000...11300...13600
Flexural modulus radial	[N/mm²]	11334.11 (± 1198.52)				
Hardness properties						
Brinell Hardness longitudinal	[N/mm²]	79.15 (± 5.80)	—	73	78	67...78...88
Brinell hardness tangential	[N/mm²]	41.94 (± 4.95)	—	47	39	28...34...47
Brinell hardness radial	[N/mm²]	39.93 (± 3.38)	—			

Simulation of pristine and composite black locust specimen.

Following the mechanical characterization, the pristine longitudinal compression specimens were implemented in a simulation based on the Finite Element Method (FEM) in the Software LS Dyna. Based on the work of [31] two pre-defined material models were included for the simulation of BL specimen:

- MAT_143 (MAT_WOOD)
- MAT_058 (MAT_LAMINATED_COMPOSITE_FABRIC)

Implementing the base parameter gained from the mechanical testing both models were superimposed over the test curves of the BL samples (see Fig. 3). To estimate the performance of wooden based composite drawing tools from black locust, further numerical investigations were carried out. Assuming a deformable body for the forming dies an element stress analysis was performed, according to [9]. Even though the recent studies imply a deformable polymer die made from PLA, the volumetric analysis should reveal the performance of a deformable wooden composite structure from black locust. Since the RPF process applies the process force on the active tool (die) nearly lossless through the rubber pad, the stress distribution on a deformable body was assumed to be similar. From the analysis, the contour plot revealed the 3D element stress distribution through the die and emphasized the high stressed area along and into the radius inlet of the die cavity. Whereas the quantitative information is based on the PLA die, the qualitative outcome was assumed to be similar for the wooden composite die (see Fig. 4).

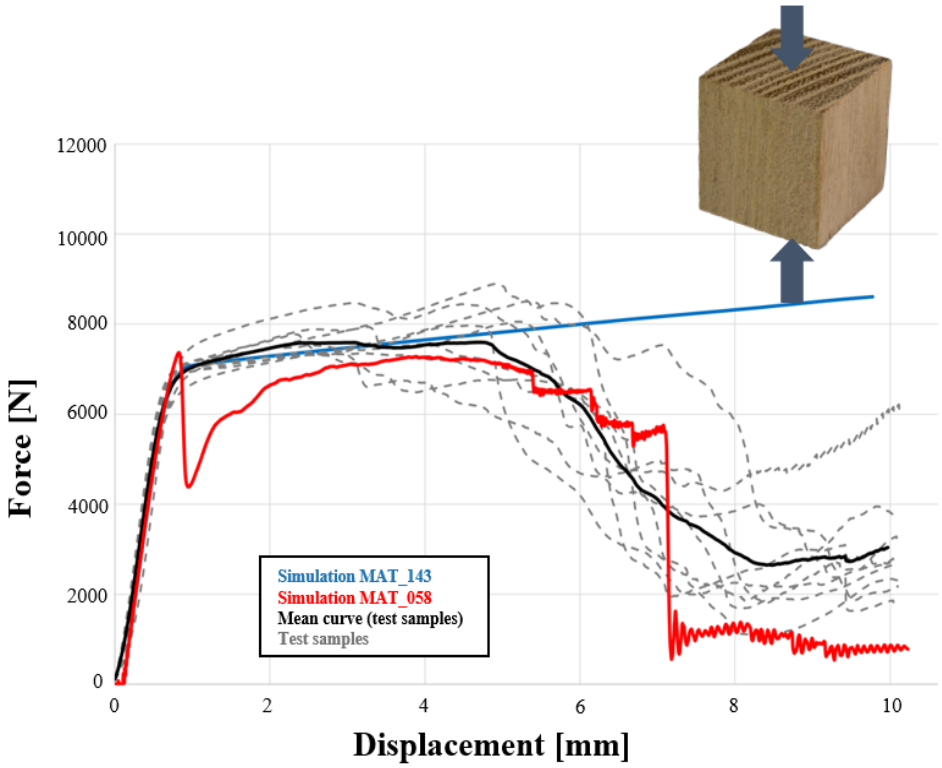

Fig. 4. Numerical validation with LS Dyna for longitudinal compression specimen for black locust.

From the stress contour plot gained from a linear static finite element simulation with ALTAIR Optistruct it is evident, that the drawing radius was heavily loaded while the cavity of the die faced minor contact forces except from the apex of the dome geometry. The load case, as maximum contact pressure over time, for the linear static finite element analysis was gathered from a forming simulation by PAM STAMP 2020.0. The hexahedron elements were discretized with a nominal

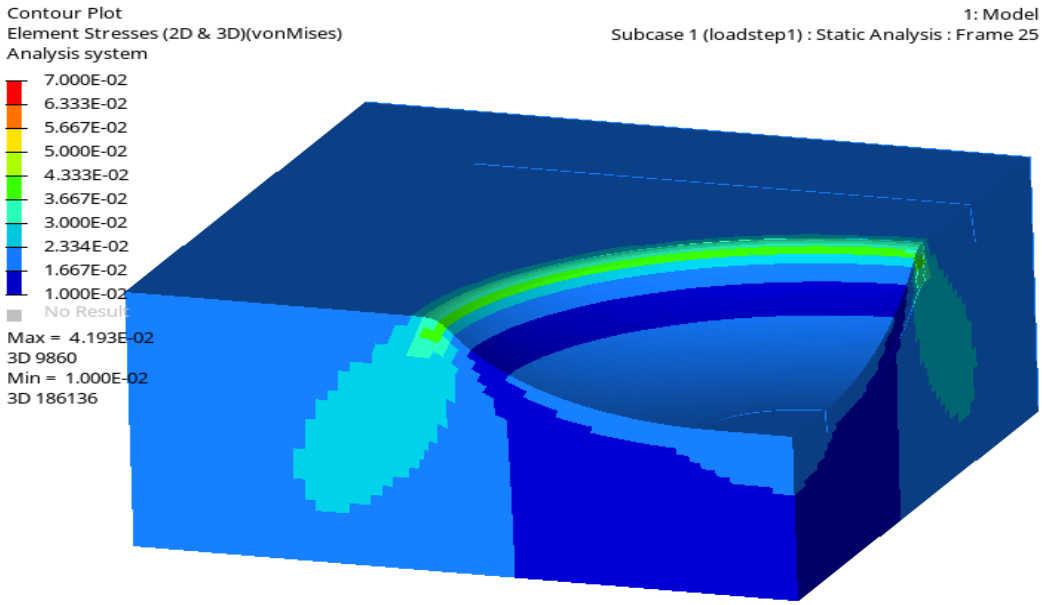

Fig. 3. Stress contour plot for deformable tool die.

size of 1.0 mm assuming an isotropic v. Mises material with young's modulus of 1.7 GPa. According to [9] the boundary conditions were displacements of the bottom surface of the die are constrained in surface normal direction.

Drawing results for wood-based forming tools manufactured of black locust.

Based on previous characterization and numerical analysis as well previous investigations from [8,9], two composite structures were rectangular aligned out of 3mm black locust sheets glued together with polyurethane (see Fig. 5), according to [23].

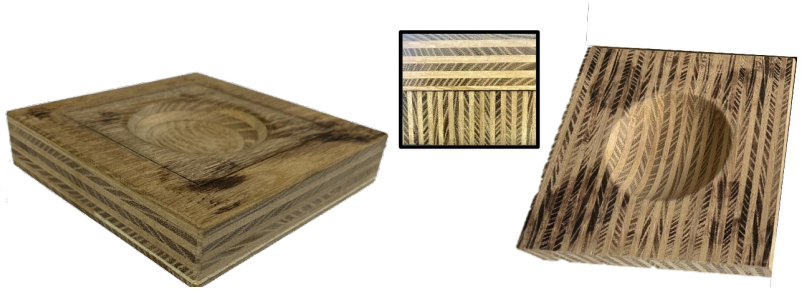

Fig. 5. Black locust composite drawing tools: horizontal (left), perpendicular (middle) and hybrid structure with 2mm sheet metal (right).

Solid black locust planks were cut into thin veneer sheets and sanded with coarse mesh (P80) on a surface sander prior to composite bonding. The bonding performed using a hydraulic veneer press without affecting or damaging the mechanical performance of the wood layers. The drawing dies included two composite (horizontal and perpendicular stacked) and, due to high process forces on the radii inlets (radius of 2.5 mm), two composite-hybrid structures (horizontal and perpendicular stacked each topped with a 2 mm sheet of tool steel grade 1.2312). All dies were operated on a uniaxial testing machine along with a 40-shore hardness polyurethane pad. For each die version, a batch of 64 parts from 0.7 mm DC04 sheet metal was drawn with 175 kN on the universal testing machine.

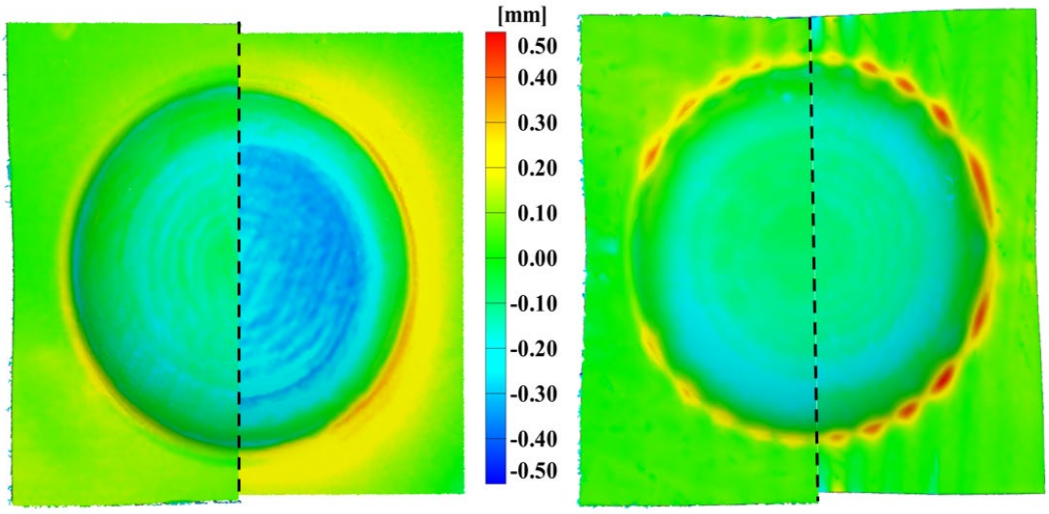

Fig. 5. Optical correlation for unused BL dies and the corresponding blank sheets of the first stroke (left half) and the 64th stroke (right half), for black locust horizontal (left application) and perpendicular (right application) composite die.

Due to permanent deformation of the wooden based forming tools, an optical analysis via optical surface scan was accomplished. Fig. 5 shows the spatial deviation for drawn sheet metal parts on wooden based forming tools (see. Fig., left and middle), where the left part shows the performance of the 1st and 64th part drawn on a black locust composite horizontal stacked and the right part shows the performance of the 1st and 64th part drawn on a black locust composite perpendicular stacked, respectively. The spatial deviation on the radii inlets correspond to the high stressed area in the contour plot (cf. Fig. 4).

Since Fig. 5 revealed qualitative differences of the forming behaviour between the first and 64th stroke for all drawn metal sheets, a comparison for the high stressed area along the radii inlet (cf. Fig. 4) was carried out to identify the drawing radius deviation of sheet metal parts on all BL dies (Fig. 6).

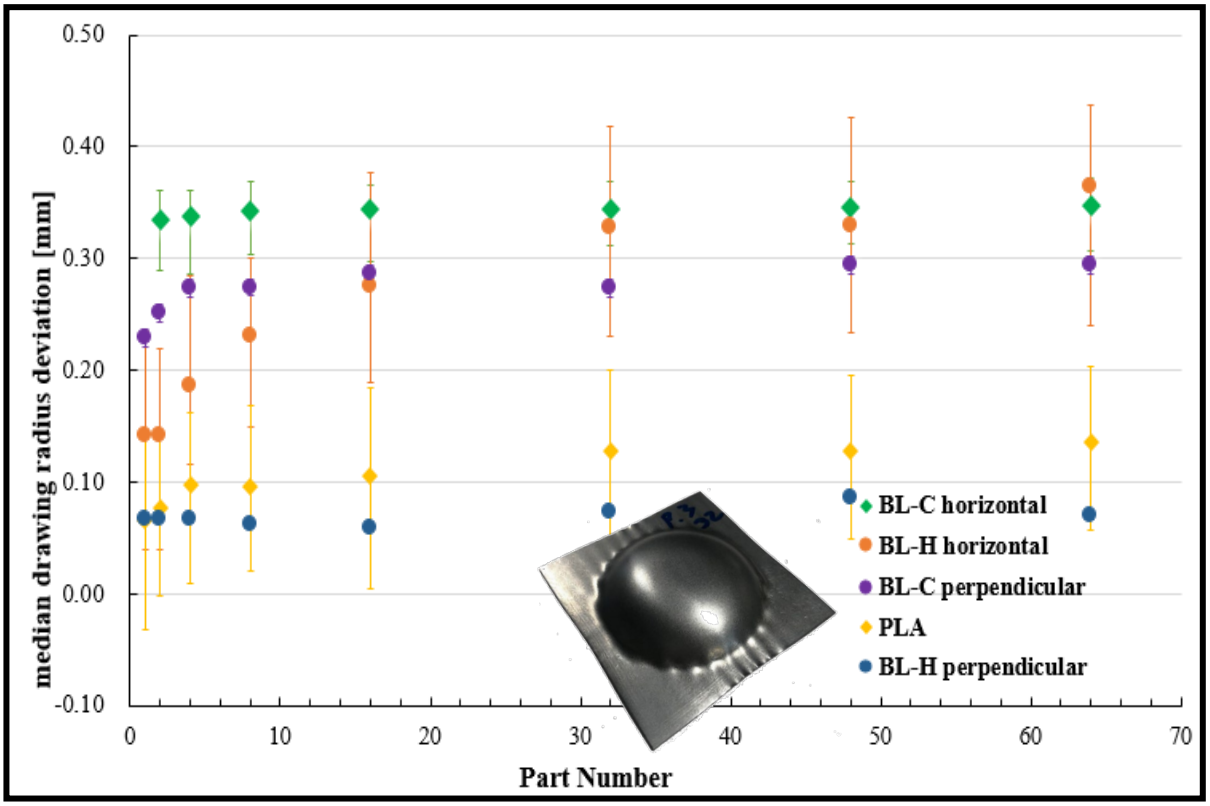

Fig. 6. Spatial deviation within the drawing radius for comparing the sheet metal parts produced by the BL-RPF process for different layouts. Statistical evaluation of a small batch series of metal parts indicates degressively increasing deviations from 0.09 mm (BL-H perpendicular) to 0.34 mm (BL-C horizontal).

Fig. 6 depicts the spatial drawing radii deviation up to 64 blank parts, drawn on BL dies with different stack layouts, showing the highest deviations on the BL-C horizontal die, whereas the hybrid BL-H perpendicular die reveals the lowest deviation. Along the batch size production, the deviation increased for all versions, which refers to the high contact stresses and the deformation behavior of the BL dies. Even though the metal parts drawn on the BL-H perpendicular die stabilize immediately after the first part, the remaining dies increased the radius deviation on the metal blanks roughly up to the 32nd part, which indicates a stabilizing character of BL dies in general, even without the hybrid components.

Summary
Biologicalization through wooden based forming tools offers chances to enhance flexibility and mass customization in sheet metal forming. While a solid and a topology optimized forming die manufactured by fused deposition modeling (FDM) successfully utilized for sheet metal forming in previous studies [8,9], in this study, the performance of the identical die geometry was investigated for different wooden based forming tools from black locust (robinia pseudoacacia). The wooden based tools are compared to a solid die from polylactic acid (PLA) regarding dimensional accuracy of formed sheet metal products. On each die variant, batches of 64 parts (steel grade DC04) are drawn in a rubber pad forming process and examined by optical correlation scans. The tests depict an overall comparable forming behavior of all die variants introduced to the process, while hybridization with tooling steel on the surface of the tooling dies lead to smaller drawing radius deviations on the cavity inlet. Slight permanent deformations are indicated along the drawing radii of all black locust forming tools caused by high contact stresses. Concluding, the wooden based forming tools revealed a suitable drawing performance for small batch size production. Future research should focus on high stressed areas of forming tools and appropriate replacement strategies via conventional metal inlays. In addition, further analysis of the deformation behaviour of wooden based tools could be conducted in numerical simulations as well as in forming tests to investigate the influence of local mechanical tool properties (e.g., local tool stiffness) on the product geometry.

Acknowledgements
The authors acknowledge the financial support by the Bundesministerium für Wirtschaft und Klimaschutz (BMWK) within the project ATLAS (grant number: 16TNW0003B). We acknowledge Jannik Stolz's contribution in providing the practical demonstrators.

References
[1] C.A. Horowitz, Paris Agreement, Int. Leg. Mater. 55 (2016) 740-755. https://doi.org/10.1017/S0020782900004253
[2] G. Byrne, D. Dimitrov, L. Monostori, R. Teti, F. van Houten, R. Wertheim, Biologicalisation: Biological transformation in manufacturing, CIRP J. Manuf. Sci. Technol. 21 (2018) 1-32. https://doi.org/10.1016/j.cirpj.2018.03.003
[3] G. Herrigel, Globalization and the German industrial production model, J. Labour Mark. Res. 48 (2015) 133-149. https://doi.org/10.1007/s12651-014-0170-5
[4] D.Y. Yang, M. Bambach, J. Cao, J.R. Duflou, P. Groche, T. Kuboki, A. Sterzing, A.E. Tekkaya, C.W. Lee, Flexibility in metal forming, CIRP Ann. 67 (2018) 743-765. https://doi.org/10.1016/j.cirp.2018.05.004
[5] H.A. ElMaraghy, Flexible and reconfigurable manufacturing systems paradigms, Int. J. Flex. Manuf. Syst. 17 (2005) 261-276. https://doi.org/10.1007/s10696-006-9028-7
[6] J. Potting, M.P. Hekkert, E. Worrell, A. Hanemaaijer, Circular Economy: Measuring innovation in the product chain, 2017.
[7] G. Schuh, G. Bergweiler, F. Fiedler, P. Bickendorf, C. Colag, A Review on Flexible Forming of Sheet Metal Parts, 2019 IEEE International Conference on Industrial Engineering and Engineering Management (IEEM), 2019, pp. 1221-1225. https://doi.org/10.1109/IEEM44572.2019.8978879
[8] P. Frohn-Sörensen, M. Geueke, T. Tuli, C. Kuhnhen, M. Manns, B. Engel, 3D printed prototyping tools for flexible sheet metal drawing, Int. J. Adv. Manuf. Technol. 115 (2021) 2623-2637. https://doi.org/10.1007/s00170-021-07312-y

[9] M. Geueke, P. Frohn-Sörensen, J. Reuter, N. Padavu, T. Reinicke, B. Engel, Structural optimization of additively manufactured polymer tools for flexible sheet metal forming, Procedia CIRP 104 (2021) 1345-1350. https://doi.org/10.1016/j.procir.2021.11.226
[10] T. Altan, A.E. Tekkaya, Sheet Metal Forming: Fundamentals, ASM International, 2012.
[11] H. Chalal, F. Abed-Meraim, Numerical Predictions of the Occurrence of Necking in Deep Drawing Processes, Met. - Open Access Metall. J. (2017) 20. https://doi.org/10.3390/met7110455
[12] Z. Marciniak, J.L. Duncan, S.J. Hu, 8 - Cylindrical deep drawing, in Mechanics of Sheet Metal Forming (Second Edition), Z. Marciniak, J.L. Duncan, S.J. Hu (Eds.), Oxford: Butterworth-Heinemann, 2002, pp. 117-128. https://doi.org/10.1016/B978-075065300-8/50011-X
[13] K. Siegert, B. Haller, Prototype Draw Dies for Sheet Metal Parts, SAE Trans. 107 (1998) 44-55.
[14] S.L. Semiatin, ASM Handbook, Volume 14B: Metalworking: Sheet Forming, Asm International, 2006.
[15] M. Tisza, Recent development trends in sheet metal forming, Int. J. Microstruct.. Mater. Prop. 8 (2013) 125-140. https://doi.org/10.1504/IJMMP.2013.052651
[16] E.L. Deladi, Static friction in rubber-metal contacts with application to rubber pad forming processes, University of Twente, Enschede, 2006.
[17] M. Ramezani, Z.M. Ripin, Rubber-Pad Forming Processes, 1st ed. Woodhead, 2012.
[18] P. Spoelstra, E. Djakow, W. Homberg, Rubber pad forming - Efficient approach for the manufacturing of complex structured sheet metal blanks for food industry, AIP Conf. Proceeding 1896 (2017) 080004. https://doi.org/10.1063/1.5008084
[19] C. Achillas, D. Tzetzis, M.O. Raimondo, Alternative production strategies based on the comparison of additive and traditional manufacturing technologies, Int. J. Prod. Res. 55 (2017) 3497-3509. https://doi.org/10.1080/00207543.2017.1282645
[20] C. Reintjes, J. Reuter, M. Hartisch, U. Lorenz, B. Engel, Towards CAD-Based Mathematical Optimization for Additive Manufacturing - Designing Forming Tools for Tool-Bound Bending, in Uncertainty in Mechanical Engineering, Cham, 2021, pp. 12-22. https://doi.org/10.1007/978-3-030-77256-7_2
[21] I. Durgun, Sheet metal forming using FDM rapid prototype tool, Rapid Prototyp. J. 21 (2015) 412-422. https://doi.org/10.1108/RPJ-01-2014-0003
[22] P. Frohn-Sörensen, M. Geueke, B. Engel, B. Loffler, P. Bickendorf, A. Asimi, G. Bergweiler, G. Schuth, Design for 3D Printed Tools: Mechanical Material Properties for Direct Polymer Additive Tooling, Polym. 14 (2022). https://doi.org/10.3390/polym14091694 https://doi.org/10.3390/polym14091694
[23] R. Kolleck, C. Koroschetz, G. Schickhofer, M. Augustin, Alternativer Werkstoff Holz spart Werkzeugkosten für die Blechumformung, Maschinenmarkt 38 (2008) 30-34.
[24] M. Pinto, A. Santos, P. Teixeira, P. Bolt, Study on the usability and robustness of polymer and wood materials for tooling in sheet metal forming, J. Mater. Process. Technol. 202 (2008) 47-53. https://doi.org/10.1016/j.jmatprotec.2007.08.082
[25] Das Holz der Robinie - Eigenschaften und Verwendung - LWF Wissen 84. https://www.lwf.bayern.de/forsttechnik-holz/holzverwendung/265497/index.php (accessed Dec. 01, 2022).
[26] D.W. Green, J.E. Winandy, D.E. Kretschmann, Mechanical properties of wood, Wood Handb. Wood Eng. Mater. Madison WI USDA For. Serv. For. Prod. Lab. 1999 Gen. Tech. Rep. FPL GTR-113 Pages 41-445, vol. 113, 1999. Available: https://www.fs.usda.gov/research/treesearch/7149
[27] U. Lohmann, Holz Handbuch, 7th ed. 2016.
[28] F. Kollmann, Technologie des Holzes und der Holzwerkstoffe, vol. 1, 1951.
[29] L. Vorreiter, Holztechnologisches Handbuch: Allgemeines, Holzkunde, Holzschutz und Holzvergütung. G. Fromme, 1949.

[30] R. Wagenführ, André Wagenführ, Holzatlas, 7th ed. 2021.
[31] G. Baumann, S. Hartmann, U. Müller, C. Kurzböck, F. Feist, Comparison of the two material models 58, 143 in LS Dyna for modelling solid birch wood, 2019.

Materials Research Proceedings 28 (2023) 1977-1986 https://doi.org/10.21741/9781644902479-213

Microstructure analysis of hybrid aluminum parts from recycled EN AW-6082 and EN AW-7075 chips

URSINUS Jonathan[1,a *], KOCH Alexander[2,b], BRUNOTTE Kai[1,c], WALTHER Frank[2,d] and BEHRENS Bernd-Arno[1,e]

[1]Institute of Metal Forming and Machines (IFUM), Leibniz University Hannover, An der Universität 2, 30823 Garbsen, Germany

[2]Chair of Materials Test Engineering (WPT), TU Dortmund University, Baroper Str. 303, 44227 Dortmund, Germany

[a]ursinus@ifum.uni-hannover.de, [b]alexander3.koch@tu-dortmund.de, [c]brunotte@ifum.uni-hannover.de, [d]frank.walther@tu-dortmund.de, [e]behrens@ifum.uni-hannover.de

Keywords: Aluminum, Recycling, Chips, FAST, Extrusion, Hybrid Materials

Abstract. In order to promote aluminum scrap recycling and reduce remelting losses, solid-state recycling processes are subject to increasing academic attention. These processes range from severe plastic deformation (SPD) to diffusion-based processes like field-assisted sintering (FAST). In this study, a FAST-based recycling route consisting of precompaction, FAST, and impact extrusion of dry machined EN AW-6082 and EN AW-7075 aluminum chips was used to create multi-material parts from different aluminum alloys. To examine the effect on the resulting part quality, two different hybrid material layouts were created during cold compaction of the chips. The subsequent sintering process took place in a field-assisted sintering (FAST) machine at 400°C and 500°C for a duration of 5 min under a pressure of 85 MPa, allowing for the analysis of inter-chip diffusion. These sintered blanks were then cold-formed by impact extrusion. Metallographic and computed tomography analyses as well as hardness measurements were performed for property evaluation before and after heat-treatment.

Introduction

Aluminum alloys are widely used for products in all industrial sectors and numerous applications. In line with global economic growth, the global production of primary aluminum increased by 20 % from 49 megatons in 2012 to 59 megatons in 2016 [1]. In 2019, this production increased to 66 megatons globally [2]. Combined with 33 megatons of recycled secondary aluminum, the global annual aluminum industry processes 100 megatons, with a strictly increasing tendency. Considering the high energy requirements for the production of primary aluminum of roughly 13 MWh/t [3,4], the use of aluminum scrap for the production of secondary aluminum offers great potential for energy savings, as it requires only 5 % (0.7 MWh/t) of the primary process' energy demands [5]. Consequently, the fraction of secondary aluminum in global production is increasing [6], however with significant regional differences in scrap return rates [7].

As with most metals, the production processes mainly include casting, forming and machining. Aluminum products are either cast directly after the metallurgical production of the alloy or it is processed into semi-finished products, e.g. bars or sheets. These are then later formed or machined into the desired product. Most processing steps involve material losses, due to flash formation, burn-off, chip production and other reasons. Generally, primary scrap (e.g. from casting) can be directly recycled. However, contaminations and the high specific surface of chips and fine flash lead to oxidation and metal losses between 5 and 20 wt.% during conventional melt-metallurgical recycling [8]. Therefore, the development of solid-state recycling (SSR) techniques promises

Content from this work may be used under the terms of the Creative Commons Attribution 3.0 license. Any further distribution of this work must maintain attribution to the author(s) and the title of the work, journal citation and DOI. Published under license by Materials Research Forum LLC.

advantages in material yield and energy consumption and may help to reduce material losses in a circular economy.

The origin of these SSR techniques dates back to 1945 when *Stern* received a patent on the recycling of aluminum scrap by hot extrusion [9]. Later, further investigation took place, while most research is younger than 20 years. *Gronostajski et al.* studied the extrusion of aluminum chips after ball milling and sintering [10] and the direct extrusion of the milled chips without sintering [11]. In both cases, nearly complete densification was achieved with tensile strengths of over 90 % of the base material reference [10,12]. The hot extrusion process was further studied by other researchers, focusing on bond formation [13], secondary extrusion [14], resulting material properties [15] and mathematical modelling [16]. These investigations share the general idea of applying pressure and temperature to the material during deformation and are part of a group of processes designated as severe plastic deformation (SPD) processes. The aim is to break up or disrupt the oxide layers covering the chips by applying pressure and deformation and thereby enable welding of the chip surfaces [17,18]. Other examples for SPD processes are equal channel angular pressure (ECAP) extrusion [19] or cyclic extrusion compression (CEC) [20]. With SPD processes, part geometry and deformation are determined by the process itself, with restricted process windows and therefore limited opportunity to consider part requirements.

An alternative approach involves the sintering of aluminum chips and a consolidation due to diffusion processes. While conventional die pressing and sintering requires milling of the chips into powder, pressure assisted sintering processes allow the direct processing of the chips after precompaction. Different authors were able to process aluminum chips by spark plasma sintering (SPS). *Paraskevas et al.* produced fully densified specimens from AA6061 and AA6082 chips by sintering at a temperature of 490°C and 200 MPa of axial pressure [21]. *Koch et al.* investigated the same alloy EN AW-6082 processed at different process parameters of 400°C and 40 MPa by field-assisted sintering technology (FAST). The sintered specimens were cold extruded and heat-treated (T6) to surpass the mechanical properties of the heat-treated reference [22]. A comparable pulsed electric current sintering (PECS) process was investigated on a smaller scale by *Cislo et al.*, using a Gleeble 3800 and a sintering temperature of about 450°C with a pressure of 64 MPa. The results showed an inhomogeneous microstructure and defective areas together with bonded parts [23]. While there are differences in the machinery used as well as in the application of the electrical current, the afore mentioned processes SPS, FAST and PECS share the same basic concept of directly heated pressure assisted sintering and are summarized using the term FAST [24]. They are in contrast to conventional hot pressing with indirect heating, which *Fogagnolo et al.* used for the recycling of AA6061 chips. These were sintered at a temperature of 500 °C and a pressure up to 700 MPa for 50 min. Nevertheless, the resulting microstructure required the authors to add hot extrusion as an additional consolidation process [25].

In summary, a variety of processes is proposed for SSR of aluminum chips. Especially FAST processes allow the consolidation of precompacted chips without major billet deformation. In this study, this aspect allows the production of hybrid specimens consisting of different aluminum alloys by recycling. This possibility is an inherent advantage compared to melt-metallurgical recycling and may help to improve part performance or to reduce the overall demand for high quality secondary alloys by a load-adapted component design. With forming operations, the sintered hybrid layout is deformed and adjusted to part requirements. At first, however, the general concept of layout creation and deformation is characterized and evaluated in the presented study. Furthermore, effects of material layout and sintering temperature on the resulting part geometry, defects and microstructure are investigated.

Experimental Setup

For the investigation, aluminum chips of the alloys EN AW-6082 and EN AW-7075 were used. The chips were produced by milling without the use of lubricant to eliminate the need for cleaning and its influence. The resulting chips' dimensions were measured manually and are given in Table 1 as mean values with standard deviation.

Table 1. Chip dimensions and apparent density.

Alloy	Length in mm	Width in mm	Height in mm	App. density in g/cm³
EN AW-6082	9.95 ± 1.80	1.01 ± 0.20	0.37 ± 0.05	0.25
EN AW-7075	6.42 ± 2.00	0.93 ± 0.07	0.18 ± 0.07	0.145

The chips were precompacted into briquettes using a manual hydraulic press with a pressure of 170 MPa. The precompacting step allowed different hybrid alloy layer designs:

(S) An axial layering consisting of three stacked briquettes with 30 g of chips each, 90 g in total. One briquette of EN AW-6082 was stacked between two briquettes of EN AW-7075.

(R) A radial layering created with the help of a specialized hollow punch tool. The inner core with a diameter of 15 mm consists of EN AW-7075 chips. For the outer material, EN AW-6082 chips were used.

All briquettes had an outer diameter of 35 mm. Fig. 1 shows a schematic of the cold compaction setup as well as the resulting hybrid layouts.

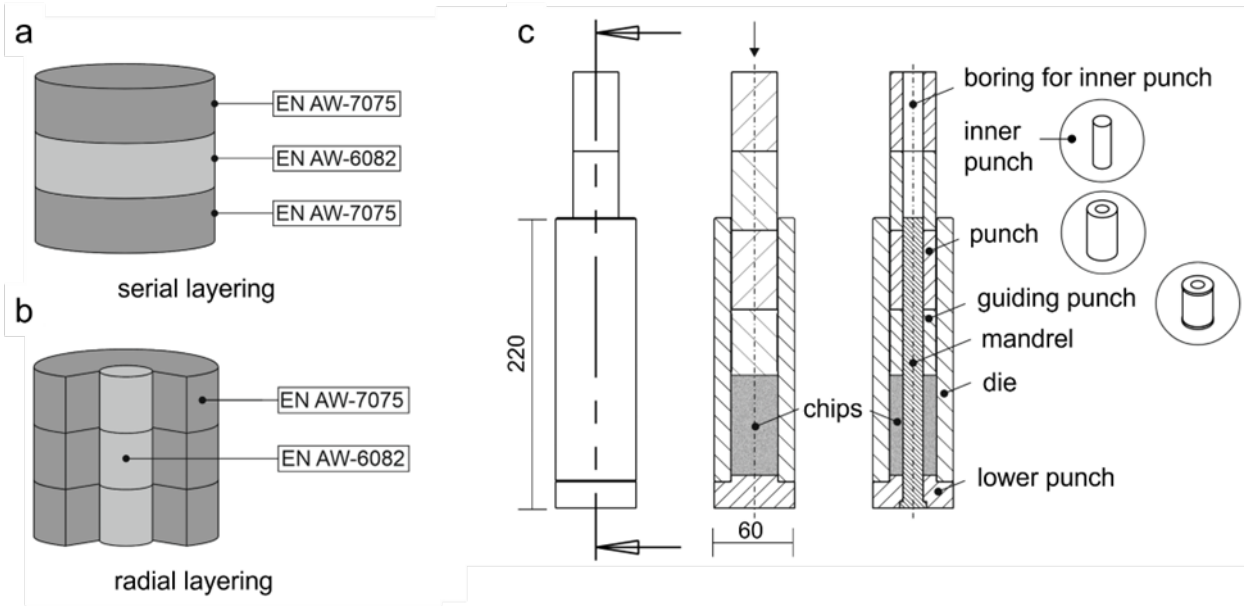

Fig. 1. Layout of the hybrid aluminum specimens, (a) axial layering strategy, (b) radial layering strategy and the used compaction tool (c).

After cold compaction, the three stacked briquettes were sintered using a Dr Fritsch DSP 507 FAST machine. The machine uses electrical current (DC) to directly heat the chip material by Joule heating. The temperature was measured by three thermocouples within the sintering die, with the highest value (generally TC 2) used for process power control. The tool setup with its components is depicted in Fig. 2.

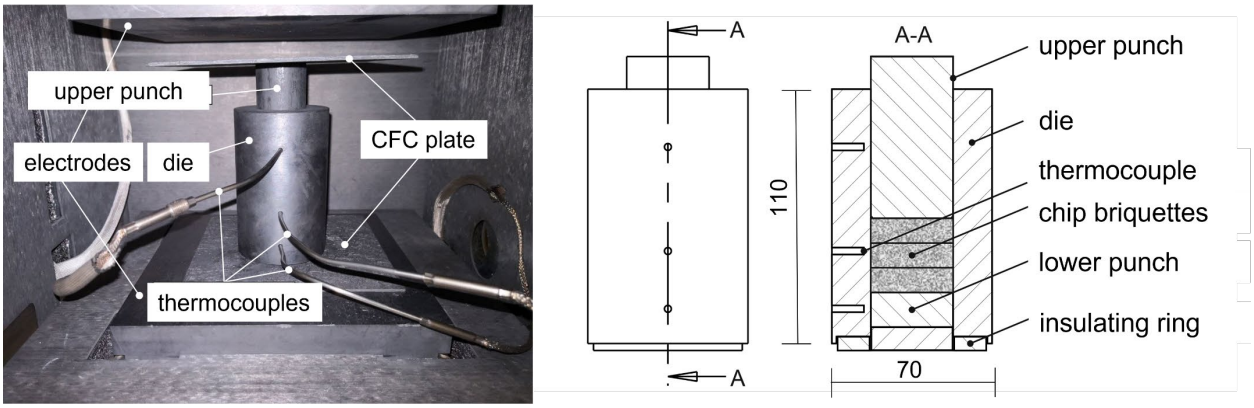

Fig. 2. Experimental setup of the field-assisted sintering process (left) and schematic representation of the sintering tool (right).

The hybrid layouts S and R were both sintered at two different temperatures of 400°C and 500°C for 5 mins resulting in 4 variants SL, SH, RL and RH. The sintering parameters given in Table 2 were based on previous experiments [22] and resulted all in above 99 % rel. density.

Table 2. Process variants.

Variant	Layout	Sintering temperature (°C)	Sintering time (s)	Sintering pressure (MPa)
SL	Serial	400	300	85
SH	Serial	500	300	85
RL	Radial	400	300	85
RH	Radial	500	300	85

After sintering, the specimens were air cooled and then analyzed using a Nikon XT H 160 computed tomography (CT) scanner. The scans were carried out using a current of 100 µA and an acceleration voltage of 150 kV resulting in a power of 15 W. By using a distance of 15 mm from the radiation source, a resolution of 40 µm could be achieved. The volume reconstructions were calculated with the help of Nikon CT Agent and analyzed with Volume Graphics VGStudioMax 2.2 software.

After performing the CT scans the specimens were formed using cold impact extrusion. Before extrusion the specimens were heated to 110°C and lubricated with LUBRODAL 24 W in a 1:2 solution with water. The resulting lubricant layer was dried for 24 h. The forming operation was carried out on a Weingarten PSR 160 screw press at room temperature. The diameter of the cylindrical specimens was reduced from 37 mm (including insertion tolerances for sintering and extrusion) to 16 mm, resulting in a mean plastic strain of $\varphi = 1.6$. The die shoulder angle was $2\alpha = 60°$ and the resulting extruded length was between 62 mm and 66 mm.

Subsequently, the specimens were scanned again by computed tomography. Furthermore, longitudinal sections were cut and investigated metallographically. Hardness measurements (HV 0.01) were performed within 5 mm of the interface in the centre of the shaft using a Shimadzu HMV-G automatic hardness testing device with a Vickers indenter and a force of 98.07 mN. EDX-line scans at the hybrid interface were performed on the SL and SH variants using Octane Elect Pro EDX detector by AMETEK Inc. in a Mira 3 SEM by Tescan. The cut specimens were then heat treated using a solution annealing temperature of 480°C. Water quenching cooled them rapidly to room temperature before cold aging. Finally, hardness measurements and metallographic examinations were repeated.

Results

The intermittent CT scans allowed the observation of the material distribution before and after cold extrusion. Combined with the metallographic analysis of the extruded specimens their deformation behavior and microstructural characteristic were investigated. The different alloy compositions cause transmissivity differences which allow the different materials to be distinguished. This results in EN AW-7075 material appearing brighter than EN AW-6082.

Before extrusion, the serial layouts SL and SH show a slight curvature of the axial interfaces in the CT images in Fig. 3. This is caused by friction forces acting on the outer diameter of the briquette stacks during sintering. As only the top punch moves in relation to the sintering die, this distortion, which is typical for one-sided compaction of powders, occurs.

After extrusion, the images show an elongation of the center of EN AW-6082 material into the surrounding EN AW-7075 material. This results in one half of the shaft being radially layered, however with a conical geometry of the interface. Consequently, the bonding surface between the two alloys was enlarged. The extruded SL specimen shows cracks at this interface near the extrusion shoulder, while for the SH-specimen no cracks could be observed.

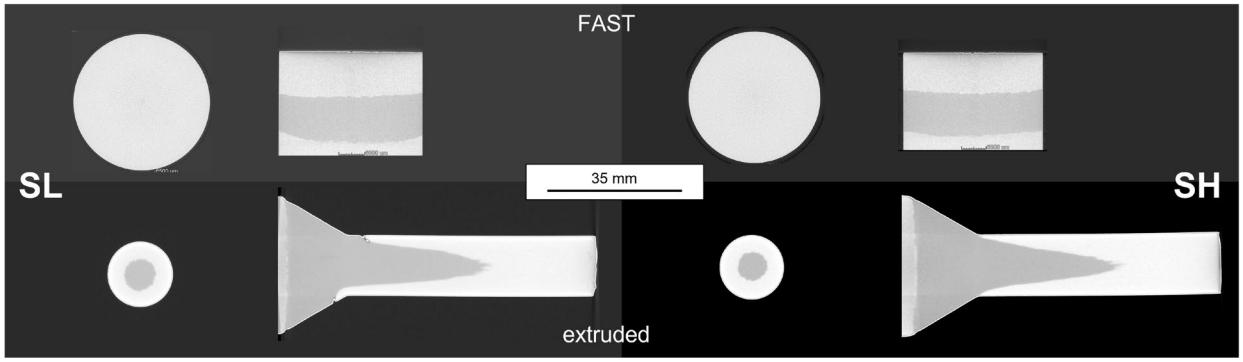

Fig. 3. CT imaging of the sintered (top) and extruded (bottom) serial specimens sintered at 400°C (left) and 500°C (right).

The radial layouts' material distribution before extrusion shows very limited deviation from the ideal concept, as can be seen in Fig. 4. There is no significant distortion of the interface during sintering and both alloys are still in coaxial arrangement. The extruded specimens exhibit a conical expansion of the softer EN AW-6082 material near the tip of the shaft, followed by a long section of uniform cross-section and material proportions. Both, the RL and RH specimens show cracks at the briquette interface at the tip of the extruded specimen. These are of reduced severity for the RH variant, which was sintered at higher temperature.

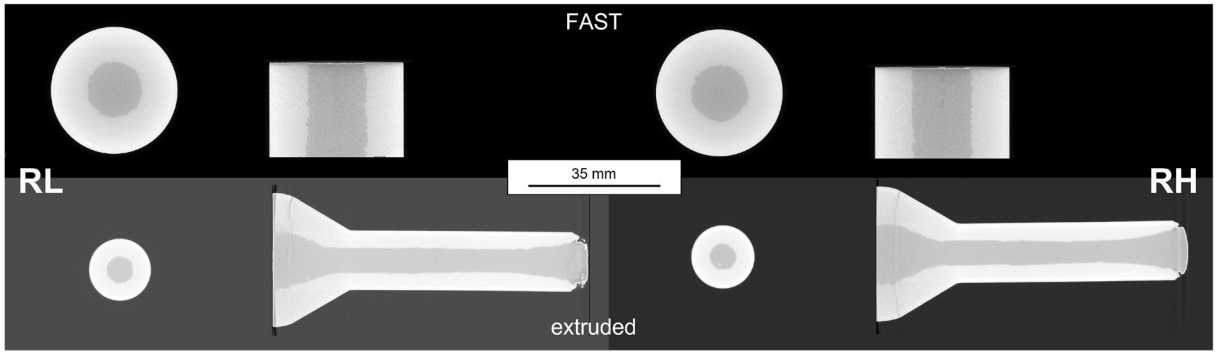

Fig. 4. CT imaging of the sintered (top) and extruded (bottom) radial specimens sintered at 400°C (left) and 500°C (right).

During the FAST process, changes in the microstructure occurred depending on the sintering temperature. After sintering at 400°C, the SL and RL variants showed a densified structure with some defects and the chip boundaries clearly visible as dark lines (see Fig. 5). The original sheared grain orientation is still prevalent within the individual chips of both alloys. By increasing the sintering temperature to 500°C for the SH and RH variant, the number of visible defects was significantly reduced and the former chip boundaries appear thinner. Additionally, grain growth and recrystallization can be observed for the EN AW-6082 material. At locations of thin or with missing chip boundary layer, grain recrystallization occurred across the interface, resulting in the visual disbanding of the dark oxide lines. In case of the EN AW-7075 material, the sheared microstructure of the chips remained visible within all four variants. After sintering at 500°C, the interface between both alloys shows signs of diffusion processes, indicated by a separation of the chip boundary oxide layer and the line of color change after etching.
Fig. 6a shows the results of the EDX line scans across the interface. The Al signal increases abruptly when crossing the interface of the SL specimen from EN AW-7075 to EN AW-6082, as the alloying element concentration drops. However, the graph for the SH specimen shows a gradual increase, confirming the metallographic observation of a pronounced diffusion zone. The microhardness results for the sintered conditions given in Fig. 6b show low values of 80 to 100 HV 0.01 for EN AW-7075 and 40 to 60 HV 0.01 for EN AW-6082 material. The values increase with increasing sintering temperature for both alloys.

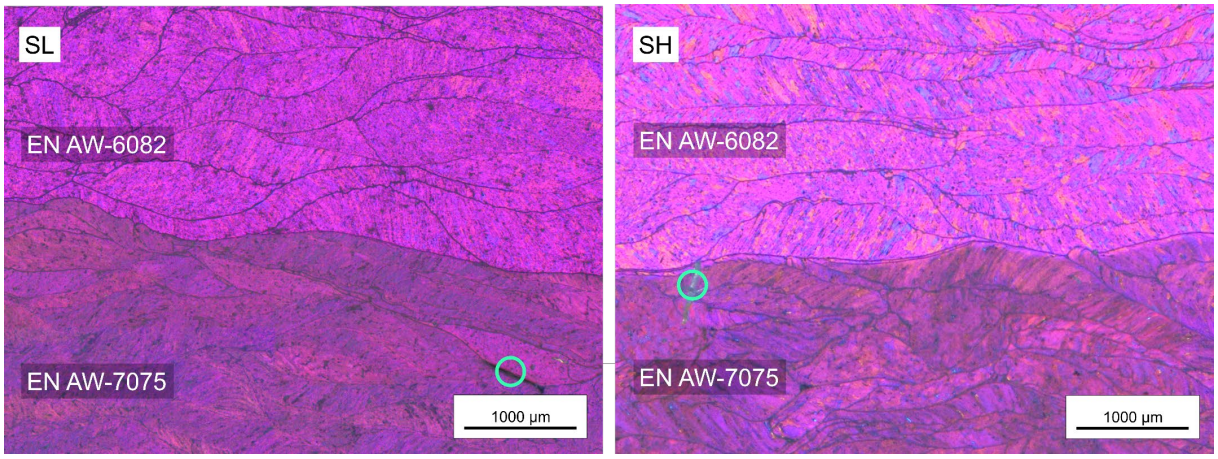

Fig. 5. Micrographs of the etched microstructure of the variants SL and SH in sintered condition. Defects are encircled in green.

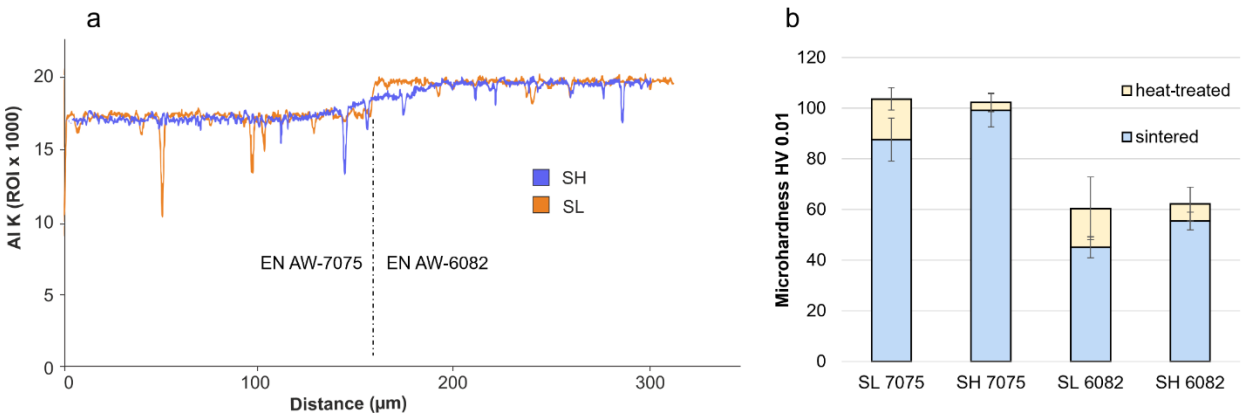

Fig. 6. Results of the EDX line scans (a) and the microhardness measurements (b) on the SL and SH variants.

After impact extrusion, the sintered microstructure is re-orientated in the direction of extrusion. Chips and chip boundary layers are stretched and elongated in the same direction (Fig. 7). This leads to the optical pronunciation of defects perpendicular to material extrusion, which were higher in number for the RL and SL variants than for RH and SH.

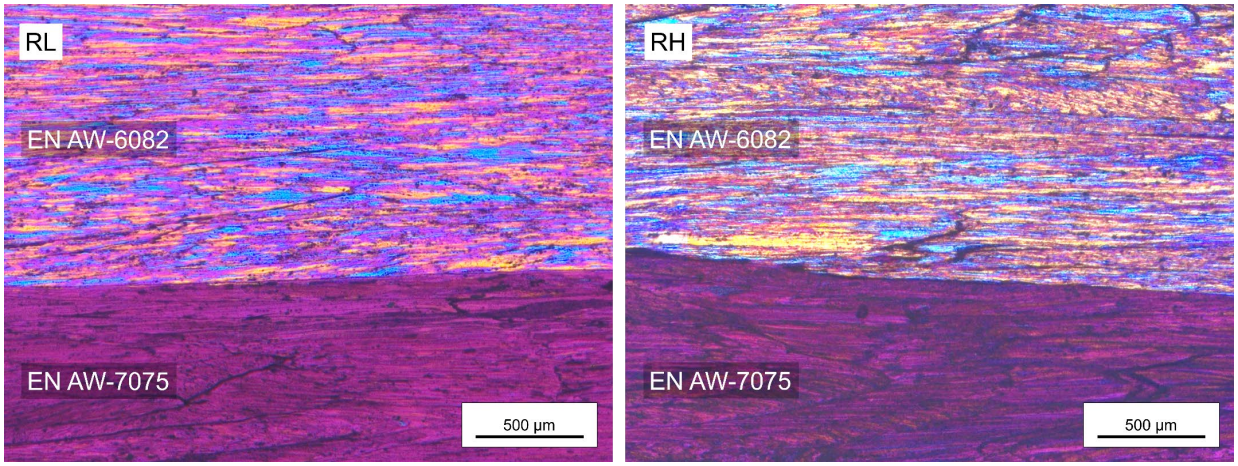

Fig. 7. Micrographs of the alloy interface of the radial variants RL and RH after extrusion.

After solution annealing and short cold aging, this deformed structure is recrystallized throughout the specimens. Fig. 8 shows metallographic images of the SH variant after the heat-treatment. While both alloys show coarse grains and few distinct chip boundaries, the material's orientation is still obvious in the EN AW-6082 and near the edge of the extruded shaft in the EN AW-7075 material. Furthermore, the interface shows a broad gradient in the etching/coloring, indicating growth of the diffusion zone. The results of the microhardness measurements in this heat-treated condition are given in Figure 6b. For both alloys, there is a significant increase in hardness over their respective low temperature variant in as-sintered condition. Compared to the values obtained from the SH variant, the hardness increase is smaller with only 4 HV 0.01 in case of EN AW-7075 and 7 HV in case of EN AW-6082 material.

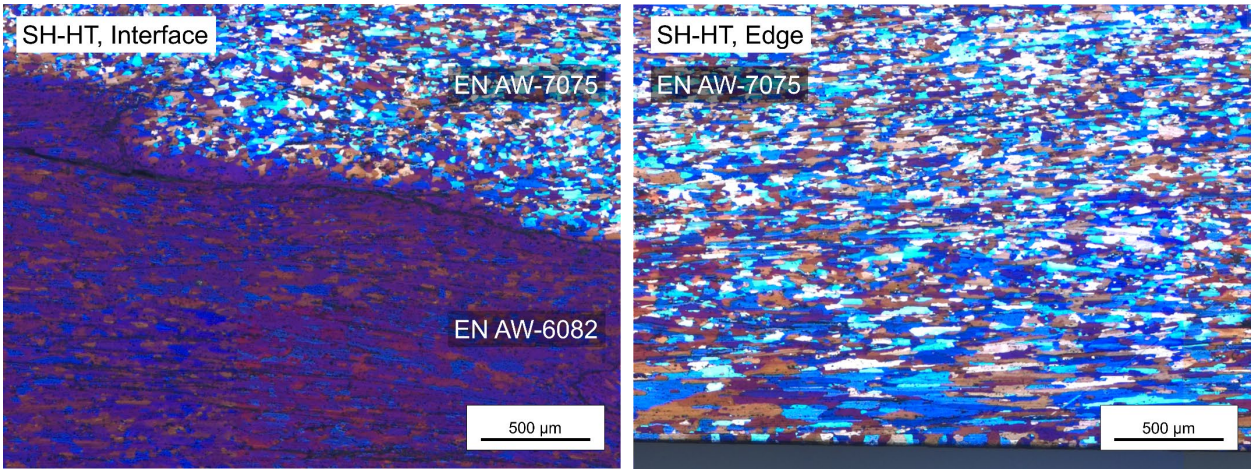

Fig. 8. Micrographs of the alloy interface of the edge of the part of the SH variant after extrusion and heat-treatment.

Discussion

The results indicate a significant influence of the sintering temperature on the diffusion processes across chip boundaries as well as on the microstructure within the individual aluminum chips. In previous work, tensile specimens were produced using the identical FAST process at 400°C for 5 min to recycle EN AW-6082 aluminum chips. After extrusion and T6 heat-treatment, the resulting tensile strength was comparable to the reference material in T6 condition at 379.8 MPa ultimate tensile strength and 354.7 MPa yield strength [22]. This indicates, that the presence of visible boundary layers between the chips may be tolerable for quasistatic properties. However, raising the sintering temperature to 500°C seems to activate diffusion mechanisms, which are not active or significantly reduced at 400°C. Due to the hybrid nature of the investigated specimens, this change could be observed in the material's response to etching and the EDX scans. Furthermore, recrystallization across the chip boundaries becomes more prevalent with higher temperature, effectively disrupting and dissolving the oxide layers. All defects, that were observed occurred in between chips. Hence, it may be assumed, that sintering at higher temperatures leads to increased formability and fatigue properties, because of fewer and smaller defects in the material.

The bond quality between the chips at the interface gains importance when creating hybrid parts form different alloys. These have different elastic and plastic material properties, which result in increased stresses on the interface during forming. This can be seen in Fig. 3 and 4 and is a challenge for all hybrid forming operations [26]. In the presented recycling process, defects were not reduced during cold impact extrusion, but deformed and elongated. Therefore, the FAST process needs to densify and consolidate the chips to a degree, which does not depend on further improvements through cold forming with low to medium plastic strains. Solution annealing after cold forming leads to complete recrystallization of the deformed microstructure after extrusion. The forming process still affects grain size and shape on the edge of the part. It is unclear whether this is due to increased local plastic strain or due to temperature gradients during annealing. In any case, the microstructure is reset to a condition with hardness similar to the as-sintered state and with a coarser and more homogeneous grain structure.

Finally, the presented recycling process allowed the production of hybrid parts with the potentially harder EN AW-7075 and the softer EN AW-6082 in two different layouts. The CT images indicate a nearly ideal macroscopic distribution of both alloys. However, metallography shows some curvature and localized interference of individual chips. The presented layouts were developed with potential application under torsional loads, using EN AW-7075 in the load-bearing outer area.

Summary

In summary, hybrid parts were successfully produced from aluminum chips of EN AW-6082 and EN AW-7075 alloys with a nearly defect-free structure. The geometry and distribution of both alloys within the billet after FAST and the final part after extrusion show little variance. Combined with reduced defect concentration and increased inter-chip diffusion due to increased sintering temperatures, promising results could be achieved. Using the presented process, the production of hybrid components directly from scrap material is feasible and can potentially be used to either compensate for inferior starting material with higher quality chips or to maximize part performance under certain loading conditions. Both aspects will be subject of further research.

Acknowledgements

The results presented were obtained in the project “Mechanism-based characterization and evaluation of the performance of resistively sintered semi-finished products based on recycled aluminum chips”, project no. 454199925. The authors thank the German Research Foundation (Deutsche Forschungsgemeinschaft, DFG) for their financial support.

References

[1] T.J. Brown, N.E. Idoine, E.R. Raycraft, R.A. Shaw, S.F. Hobbs, P. Everett, E.A. Deady, T. Bide, World Mineral Production 2012-16, Keyworth, Nottingham., 2018.

[2] Information on https://international-aluminium.org/resource/iai-material-flow-model-2021-update/

[3] R. Zhao, C. Nowicki, L. Gosselin, C. Duchesne, Energy and exergy inventory in aluminum smelter from a thermal integration point-of-view, Int. J. Energy Res. 40 (2016) 1321-1338. https://doi.org/10.1002/er.3508

[4] A. Gupta, B. Basu, Sustainable Primary Aluminium Production: Technology Status and Future Opportunities, Trans. Indian. Inst. Met. 72 (2019) 2135-2150. https://doi.org/10.1007/s12666-019-01699-9

[5] T.G. Gutowski, S. Sahni, J.M. Allwood, M.F. Ashby, E. Worrell, The energy required to produce materials: constraints on energy-intensity improvements, parameters of demand, Philos. Trans. A, Math. phys. eng. sci. 371 (2013) 20120003. https://doi.org/10.1098/rsta.2012.0003

[6] D. Brough, H. Jouhara, The aluminium industry: A review on state-of-the-art technologies, environmental impacts and possibilities for waste heat recovery, Int. J. Thermofluid. 1-2 (2020) 100007. https://doi.org/10.1016/j.ijft.2019.100007

[7] Information on https://www.umweltbundesamt.de/sites/default/files/medien/3521/dokumente/factsheet-aluminium_fi_barrierefrei.pdf

[8] Y. Xiao, M. Reuter, Recycling of distributed aluminium turning scrap, Miner. Eng. 15 (2002) 963-970. https://doi.org/10.1016/S0892-6875(02)00137-1

[9] M. Stern, U.S. Patent 2391,752 (1945).

[10] J. Gronostajski, A. Matuszak, The recycling of metals by plastic deformation: an example of recycling of aluminium and its alloys chips, J. Mater. Process. Technol. 92-93 (1999) 35-41. https://doi.org/10.1016/S0924-0136(99)00166-1

[11] J. Gronostajski, H. Marciniak, A. Matuszak, New methods of aluminium and aluminium-alloy chips recycling, J. Mater. Process. Technol. 106 (2000) 34-39. https://doi.org/10.1016/S0924-0136(00)00634-8

[12] J.Z. Gronostajski, J.W. Kaczmar, H. Marciniak, A. Matuszak, Direct recycling of aluminium chips into extruded products, J. Mater. Process. Technol. 64 (1997) 149-156. https://doi.org/10.1016/S0924-0136(96)02563-0

[13] V. Güley, A. Güzel, A. Jäger, N. Ben Khalifa, A.E. Tekkaya, W.Z. Misiolek, Effect of die design on the welding quality during solid state recycling of AA6060 chips by hot extrusion, Mater. Sci. Eng. A 574 (2013) 163-175. https://doi.org/10.1016/j.msea.2013.03.010

[14] M. Haase, A.E. Tekkaya, Cold extrusion of hot extruded aluminum chips, J. Mater. Process. Technol. 217 (2015) 356-367. https://doi.org/10.1016/j.jmatprotec.2014.11.028.
[15] M.I. Abd El Aal, M.A. Taha, A.I. Selmy, A.M. El-Gohry, H.S. Kim, Solid state recycling of aluminium AA6061 alloy chips by hot extrusion, Mater. Res. Express 6 (2019) 36525. https://doi.org/10.1088/2053-1591/aaf6e7
[16] B. Lela, J. Krolo, S. Jozić, Mathematical modeling of solid-state recycling of aluminum chips, Int. J. Adv. Manuf. Technol. 87 (2016) 1125-1133. https://doi.org/10.1007/s00170-016-8569-5
[17] N. Bay, Mechanisms Producing Metallic Bonds in Cold Welding, Weld. J. (1983) 137-142.
[18] D.R. Cooper, J.M. Allwood, The influence of deformation conditions in solid-state aluminium welding processes on the resulting weld strength, J. Mater. Process. Technol. 214 (2014) 2576-2592. https://doi.org/10.1016/j.jmatprotec.2014.04.018
[19] M. Haase, N. Ben Khalifa, A.E. Tekkaya, W.Z. Misiolek, Improving mechanical properties of chip-based aluminum extrudates by integrated extrusion and equal channel angular pressing (iECAP), Mater. Sci. Eng. A 539 (2012) 194-204. https://doi.org/10.1016/j.msea.2012.01.081
[20] J.R. Cui, W. Guo, H.J. Roven, Q.D. Wang, Y.J. Chen, T. Peng, Recycling of Aluminum Scrap by Severe Plastic Deformation.
[21] D. Paraskevas, K. Vanmeensel, J. Vleugels, W. Dewulf, Y. Deng, J.R. Duflou, Spark Plasma Sintering As a Solid-State Recycling Technique: The Case of Aluminum Alloy Scrap Consolidation, Mater. 7 (2014) 5664-5687. https://doi.org/10.3390/ma7085664
[22] A. Koch, M. Bonhage, M. Teschke, L. Luecker, B.-A. Behrens, F. Walther, Electrical resistance-based fatigue assessment and capability prediction of extrudates from recycled field-assisted sintered EN AW-6082 aluminium chips, Mater. Charact. 169 (2020) 110644. https://doi.org/10.1016/j.matchar.2020.110644
[23] C.N. Cislo, B. Kronthaler, B. Buchmayr, C. Weiß, Solid State Recycling of Aluminum Alloy Chips via Pulsed Electric Current Sintering, JMMP 4 (2020) 23. https://doi.org/10.3390/jmmp4010023
[24] R.H.R. Castro, K. van Benthem, Sintering: Mechanisms of convention nanodensification and field assisted processes, Springer, Berlin, New York, 2013.
[25] J. Fogagnolo, E. Ruiz-Navas, M. Simón, M. Martinez, Recycling of aluminium alloy and aluminium matrix composite chips by pressing and hot extrusion, J. Mater. Process. Technol. 143-144 (2003) 792-795. https://doi.org/10.1016/S0924-0136(03)00380-7
[26] B.A. Behrens, M. Bonhage, D. Bohr, D. Duran, Simulation Assisted Process Development for Tailored Forming, MSF 949 (2019) 101-111. https://doi.org/10.4028/www.scientific.net/MSF.949.101

Materials Research Proceedings 28 (2023) 1987-1996 https://doi.org/10.21741/9781644902479-214

Multi-criteria decision model of sustainable industrial production: A case study on 3D printed carbon PA

ANDREOZZI Marina[1,a], GENTILI Serena[1,b], MANCIA Tommaso[1,c *], SIMONCINI Michela[1,d] and VITA Alessio[1,e]

[1] Università Politecnica delle Marche, Via Brecce Bianche 12, 60123 Ancona, Italy

[a]m.andreozzi@pm.univpm.it, [b]s.gentili@pm.univpm.it, [c]t.mancia@pm.univpm.it, [d]m.simoncini@staff.univpm.it, [e]alessio.vita@staff.univpm.it

Keywords: Sustainability, Mechanical Properties, 3D Printing, Life Cycle Analysis

Abstract. In the Concurrent Engineering (CE) approach, several aspects of the life cycle of a product are considered at the same time during the design phase. This allows to respond more quickly to the market needs and improves the final products quality. However, with this approach, the design phase could result more time consuming and expensive and needs simple and easily applicable optimization models. For this reason, a new multi-criteria decision model is proposed in this paper. Additive manufacturing technologies for high performances polymers are gaining increasing interest as they are a valid option for the manufacturing of structural components. For these reasons, high performance 3D printed isogrid structures in short carbon fibers reinforced polyamide were selected as a case study. Production processes of as-printed and dried isogrid structures were carried out; mechanical characterization and environmental and cost analysis were performed on the considered scenarios. Following the proposed model, the results of the analyses were used to calculate a single value indicator for each product. In this way, it was possible to compare the different alternative and select the optimal solution.

Introduction

Nowadays, the development of increasingly complex industrial products, the increased competitiveness of companies, the need to reduce production times, and countless regulations and design standards are forcing engineers to develop high quality products that are as environmentally sustainable as possible and at the lowest cost, in order to be competitive in the global market.

In this context, Concurrent Engineering (CE) has become the foundation of modern engineering as it allows an optimal balance between cost and quality to be achieved. CE was born in the 1980s and represents a set of methodologies and tools that enable an integrated approach to product design and related manufacturing processes. The areas of product development that can be considered simultaneously during the design phase can cover all phases of the product life cycle, from conception to end-of-life. CE moves away from the traditional sequential approach in the execution of the design, process planning, production, and demanufacturing phases, and the individual activities are performed in parallel, so that the product can be evaluated over its entire life span, starting as early as the design phase [1,2].

CE is crucial when products of high complexity, with long development phases and the difficulty in predicting the impact of design decisions on next phases of the product life cycle is high; this is often coupled with the need to respond to a rapidly changing demand that inevitably requires shorter product life cycles.

It is obvious that, in such a complex context, the role of the engineer within companies is strongly oriented towards decision-making and the process of making decions in the short, medium or long term can determine the success or failure of production activities. Therefore, it's crucial to develop decision-making techniques that make decision-making more efficient and easier. The decision-making process starts with the identification of the problem and the objectives to be

Content from this work may be used under the terms of the Creative Commons Attribution 3.0 license. Any further distribution of this work must maintain attribution to the author(s) and the title of the work, journal citation and DOI. Published under license by Materials Research Forum LLC.

achieved, followed by the choice of decision criteria, their weights and the definition of a performance index to be maximised or minimised [3]. Consequently, to improve the performance index, alternative solutions must be developed, analysed and compared in order to choose the best alternative. It is also crucial that a mechanism of continuous implementation of the identified solutions is triggered through constant monitoring of the results achieved. The choice of criteria is not unique but depends on the specific case of application [4].

Traditionally, the decision criteria to be related to system performance are those represented in the production tetrahedron: time, cost, flexibility and quality. To these is added sustainability.

The concept of sustainability was first introduced in 1972, during the first United Nations Conference on the Environment, and, in 1987, within the so-called Brundtland Report, a sustainable model was defined as one that meets the needs of the present without compromising the ability of future generations to meet their own needs [5].

Environmental sustainability is becoming a cornerstone in industrial production and in general in any activity of modern society, thanks to the realisation that the planet's resources are not infinite but must be preserved, without waste, respecting ecosystems and biodiversity.

Thus, the need for environmental sustainability is linked to environmental protection, but in recent years, in addition to considering the ecological aspects, it has also been declined from an economic and social point of view.

There are qualitative evaluation criteria, such as checklists and guidelines, or methods capable of quantifying the environmental impacts of a system according to different impact categories; among these, Life Cycle Assessment (LCA) is the most widely used methodology. LCA quantifies environmental impacts, considering resource consumption and atmospheric emissions, and can be applied to the entire life cycle (from cradle to grave) [6-8].

In this context, a new mathematical model is proposed as a decision-making support for industrial applications that can be used as a product/process optimisation tool. The literature lacks a model capable of considering multiple decision criteria and simple to apply. Unlike the theoretical approaches present in the literature, this model has the possibility of being easily usable at an industrial level due to its mathematical simplicity and application. In fact, the novelty of this paper lies in the ease of application of in industrial context and the possibility of being adapted to specific cases (products/processes) in a short time.

In this regard, was examined the case of composite isogrid structures made by additive manufacturing processes [9]. The mechanical performances, the economic and environmental sustainability and production time of isogrids in different configurations (as-printed and dried) were evaluated. In addition, through the application of the theorised model, various scenarios were compared.

Materials and Methods

In a concurrent engineering perspective, it is crucial to develop quantitative models to consider multiple variables and criteria at the same time. Their ease in application is also required to be applied in an industrial context and help the design process.

The model here presented may include whichever factor the decision makers want to take into account as long as it can be evaluated in a quantitative way. Hence, it pairs well with procedures such as Life Cycle Assessment, flexibility and quality assessment tools that quantifies aspects of a process or a product that would be otherwise difficult to measure [6,10]. Moreover, the model can also consider traditional criteria such as cost (or Life Cycle Costing) and mechanical properties. It can be used to compare both products or industrial processes that have similar functions or yield to similar outputs. The mathematical model allows the comparison between different alternatives by calculating a performance index for each of them; the lower the index, the better the alternative. The index is calculated as sum of dimensionless parameters, each of which is the ratio between the criteria value for the considered system and that of the reference scenario.

An arbitrary number of parameters can be taken into account, depending on the design requirements; in this way, even complex decision problems can be easily solved. In addition, the model can be used to optimize a given process or a product by estimating the value of the performance index as key process parameters vary.

The general model is as follows:

$$I_i = p_i \frac{t_{0_i}}{t_{0_r}} + p_2 \frac{C_i}{C_r} + p_3 \frac{F_i}{F_r} + p_4 \frac{L_i}{L_r} + p_5 \frac{E_i}{E_r} + \cdots = \sum_j (p_j \frac{K_k}{K_r}) \quad (1)$$

where:

- I_i is the performance index for the i-th alternative
- p_j is the ponderation factor of the j-th decision criteria evaluated according to the company policies and the specific case study. Tools similar to a Weighted Decision Matrix can be employed to define p_i. The sum of al the ponderation factors is equal to 1.
- K_i and K_r are the quantitative values of the decision criteria for the i-th alternative and the reference system. They can be referred, for example, to the production time (t_{0i}, t_{0r}), product cost (C_i, C_r), mechanical performances, quality (L_i, L_r), system flexibility (F_i, F_r), environmental impacts (E_i, E_r), etc.

The reference scenario is used as a benchmark to evaluate the performances of the other systems and it is characterized by an Index I_r equal to 1. In the case of production systems, it can represent a traditional process previously used by the company or by a competitor and the production of a defined number of parts. If multiple options have to be compared and no previous system is known, the reference system can be chosen between one of these; then, if no alternative gets an index value lower than one, the reference scenario is also the best choice according to the considered criteria.

Evaluation of the decision criteria.

The value related to the environmental sustainability decision criteria can be calculated by means of the standardised methodology of Life Cycle Assessment. LCA is an iterative approach constituted by 4 phases defined by the ISO standard 14040 and 14044 [6,11]. It allows to quantify the environmental impacts of a product or a process according to several impact indicators (e.g. Global Warming Potential, damage to Human Health, ect.) and considering all the aspects of their life cycle. The standard procedure phases are: goal and scope definition, in which the focus of the analysis, the functional unit, the goal and the system boundaries are defined; Life Cycle Inventory, where the inputs and outputs of the system are identified and directly or indirectly quantified; Life Cycle Impact Assessment, in which the inputs and outputs are translated into potential environmental impacts according to selected indicators. Dedicated software are used to automatically carry out this phase; finally, the LCIA results are critically reviewed and criticalities and improvement possibilities are identified. E_i and E_r can be retrieved from the LCIA results by considering an impact indicator that is representative of the studied system. LCA can be paired with the Life Cycle Costing analysis, an economic tool used to evaluate the cost incurred by a functional unit throughout its life cycle. LCC can also be used to calculate the economic criteria indicator (C_i, C_r) of the performance index.

The production time expressed in seconds can be used as a decision criteria value; it can be directly measured during the production of the components or calculated by estimating the process time, the inspection time, the movement time and the queue time.

The reciprocal of the load at break of a component could be used as a decision criteria value related to the quality of the scenario. In this way, if the mechanical properties of the component increase, the value of the index of performance decreases. More in general, if a feature of the product or the process should be maximized, it is possible to use its reciprocal as a decision criteria value. Further criteria and assessment methodologies could be introduced in the model to respond to the designers requirements.

Ponderation decision matrix.

The design requirements that affect the production process can be translated into values depending on the evaluation that is associated with each aspect by the producer.

This type of evaluation has the function of assigning a value on a scale from 1 to 5 depending on the importance or weight that one wishes to assign to each factor that contributes to the generation of the performance index. The matrix thus generated, an example of which is shown in Table 1, is called Ponderation Decision Matrix (PDM) and allows values to be assigned for the calculation of the weighting factors p_i, shown in the previous section. The p_i calculation is done through the ratio of the value assigned to the specific parameter in the PDM, divided by the sum of the values assigned to all decision criteria.

Table 1. Ponderation Decision Matrix.

Decision Criteria	**Weight 1**	**Weight 2**	**Weight 3**	**Weight 4**	**Weight 5**	**p_i**
Mechanical Properties		**X**				2/14 = **0.14**
Environmental Sustainability				**X**		4/14 = **0.29**
Costs			**X**			3/14 = **0.21**
Production Time					**X**	5/14 = **0.36**
TOT	**0**	**2**	**3**	**4**	**5**	**1.00** / **14**

Case study: 3D printing of composite isogrid structure.

The case study analyzed in this work refers to an additive manufacturing production system for CFRP components. In particular, isogrid structures, generated by particular geometric configurations, have been realized through FFF technology and reported in Fig. 1.

The isogrid structures were designed by means of a CAD software by choosing rib width, rib thickness, cell height, global length and global width of 3, 8, 18, 106 and 80 mm, respectively, and then were exported as an .STL file for the creation of a .GCODE by the slicing software. The geometric construction parameters mentioned before are shown in Fig. 1.

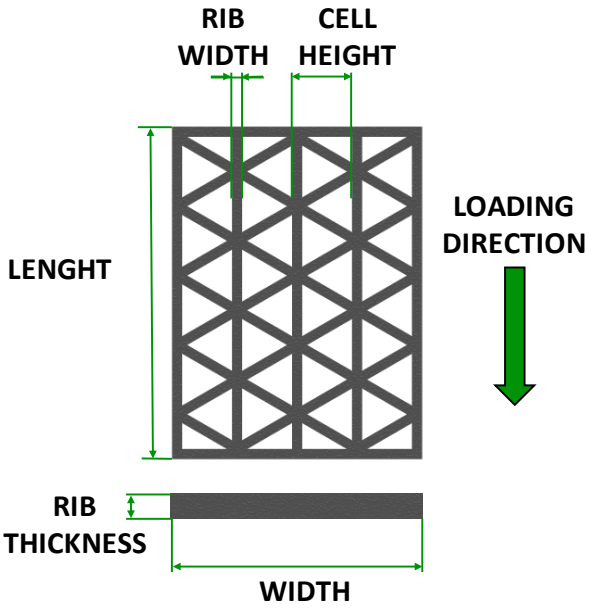

Fig. 1. Geometrical parameters of an isogrid structure.

The composite material used in this study, defined as Carbon PA, consists of a polyamide 6 reinforced with short (about 25 microns in length) carbon fibers at 20% in weight. According to the material datasheet, Carbon PA is characterized by an elastic modulus of 15.5 GPa and a ultimate tensile strength equal to 138 MPa, as also shown by authors in [9]. The material is supplied by Roboze S.P.A. in the form of a 1.75 mm diameter filament, suitable for processing through the Fused Filament Fabrication technique (FFF). The Roboze One+400 3D printer, equipped with FFF technology and supplied by Roboze Spa, was used for the additive manufacturing process, with the aim of realizing isogrid structures.

As the material is highly susceptible to moisture absorption, which causes a significant decrease in mechanical properties, Carbon PA was subjected to a drying process for about 4 h at the temperature of 120°C before the printing process. Moreover, during the printing phase, the material was maintained at 70°C in order to avoid moisture adsorption improving printing quality, reducing void formation. Main printing parameters for the realization of isogrid structures in CarbonPA through FFF technology are reported in Table 2.

Table 2. Main printing parameters.

Process Parameter	
Extruder Temperature	260°C
Bed Temperature	110°C
Infill Density	100%
Layer thickness	0.15 mm
Nozzle Diameter	0.4 mm
Nominal Printing Speed	50 mm/s
Infill Type	Linear
Raster angle	0°

With these process parameters, the effective printing time for the realization of each isogrid structure detected at the end of printing equals to 2.15 hours [7]. 3 on 6 printed isogrids were subjected to another drying process in the oven for 4 hours at 120°C to remove the moisture absorbed during and after printing, before being tested under compression load.

The mechanical performance of the as-printed and dried isogrid structures was calculated by subjecting them to compression tests with an MTS 810 universal testing machine under displacement control at a speed of 0.5 mm/min. The acquisition system connected to the machine's load cell made it possible to record the compressive load values associated with the relative displacement. The maximum load values in kN were then derived from each test.

Case study: Life Cycle Analyses.

The LCA methodology was employed to quantify the environmental impacts of the 3D printed isogrid structures. As for the mechanical test, two different scenarios were considered: the as printed isogrid structure (Scenario 1) and the one subjected to the drying process (Scenario 2). The goal of the study is to quantify and compare the impacts of the two scenarios with particular focus on the drying heat treatment of the printed structure. In fact, the LCA results are then to be used to calculate the multi objective performance index to determine whether or not the heat treatment represents a process improvement. Global Warming Potential (GWP, expressed in kg CO_2 eq) was selected as the environmental impact value of the performance index decision criteria. This impact indicator is widely used in literature LCA for production processes of composite parts and it is well representative of their environmental behaviour [12,13].

The functional unit is therefore defined as the 3D printing of a carbon fiber reinforced polyamide isogrid structure with defined dimensions (see paragraph 0). Considering the focus of the case study on the manufacturing process, a “cradle to gate” approach was used, and the following production phases were included: materials production (PA and short carbon fibers), transport, filament drying and temperature control during the printing, 3D printing process and isogrid post drying (only for Scenario 2). The use and End of Life phases were excluded from the analysis.

The Life Cycle Inventory phase is based on a previous work of the authors [14]. Primary data were retrieved from direct measurements during the production processes; this includes the energy consumptions of the machines and the weight of the components. Considering the composition of the filament defined in the datasheet (80% polyamide, 20% carbon fibers), the quantity of each constituent was calculated. Polyamide and electric energy impacts were retrieved from the Ecoinvent database while CF impacts were modelled according to Khalil et al [15]. Impacts related to the production of the machines used for the production and postprocessing were not included as their useful life is much longer than the time horizon considered in this study and they would have led to negligible contribution.

LCIA results were calculated by using the SimaPro software, equipped by default with the Ecoinvent commercial database. The environmental impacts analysis was paired with an economic assessment (LCC) that considered the same functional unit and the same scenarios. The cost associated with each structure was calculated considering all direct and depreciation costs and by considering appropriate allocation procedures.

Material cost was calculated considering the purchase price (120 €/kg) of the filament and the weight of the components (41.25 g). Energy costs were calculated considering the measured consumptions (1.366 kWh) and the cost per kWh. Machines depreciation was calculated considering their purchase price, their use time for the considered scenarios, their service life (expressed in hours) and their maintenance costs. Labour and design time were measured (0.3 h and 0.5 h respectively) and multiplied by the hourly staff cost (30 €/h for laboratory operator and 35€/h for designer) to evaluate personnel contribution to the total cost. Direct measurements of

time required for the production phases were also employed to calculate the total production time required for the two scenarios (4.45h for the first scenario and 6.55 h for the second one).

Results and Discussion

Fig. 2 shows the mean load vs. displacement curves of the dried and as-printed isogird structures tested under compressive load. It can be seen that there is a significant increase in performance when the material is subjected to a drying cycle prior to testing. The percentage increase in performance is equivalent to approximately 23%.

The average values of the maximum load measured for as-printed and dried isogrid structures are 13.08 kN and 16.08 kN, respectively.

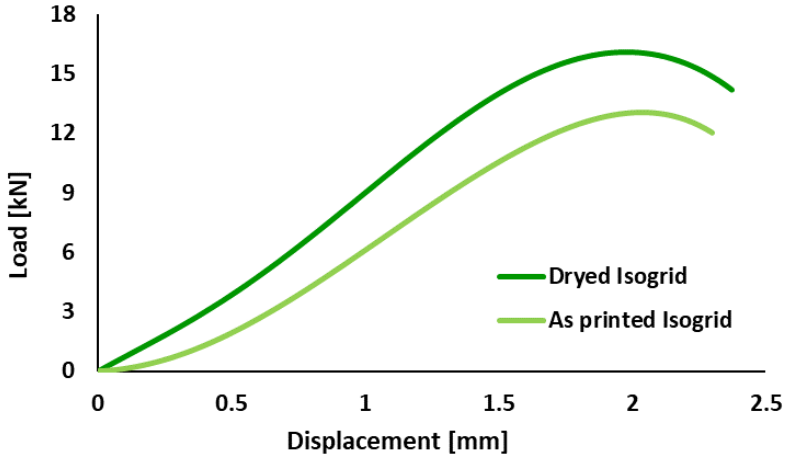

Fig. 2. Load vs. displacement curves of dried and as-printed isogrid structures.

Fig. 3 (a) presents the results of the LCA analysis in terms of Global Warming Potential. The two scenarios are the same with the exception of the structure drying process that is only present in Scenario 2. The as-printed isogrid structure showed environmental impacts about 20% lower than those of the heat treated parts (1.20 kg CO2 eq vs 1.46 kg CO2 eq). This is due to the electric energy production and consumption of the isogrid drying process.

Indeed, most of the production phases that include an electric energy consumption resulted in relevant environmental impacts; this also includes the filament initial drying (0.26 kg CO2 eq) and the filament temperature control during the printing phase (0.26 kg CO2 eq). This is due to the fact that the Italian energy mix is mainly composed of non-renewable sources. Improving the sustainability of the energy use could strongly reduce the overall impacts of the scenarios (e.g. by using renewable distributed energy sources).

The 3D printer has very low energy requirements for the stepper motors control and the nozzle heating and therefore resulted in low impact (0.05 kg CO2 eq). The most impactful phase is represented by the raw material (0.6 kg CO2 eq, between 41% and 50% of the total impacts, depending on the scenario); this is a common finding in many LCA literature studies focused on CFRP and it is attributed to the high-energy requirements of the matrixes and carbon fibers production.

Fig. 3 (b) reports the results of the economic assessment analysis for the two scenarios. As for the LCA, Scenario 2 is the best alternative with a total cost of 23.00 € while Scenario 1 has a total cost of 19.90€.

The main difference between the two scenarios is represented by the labour cost required in Scenario 2 for the post processing of the isogrid structure. Labor is also the most expensive cost item in both the alternatives. In 3D printing, labor is almost independent from the components

dimensions (and so the raw materials and machines use costs); hence, for small parts labor can be a major cost even if the process is highly automated.

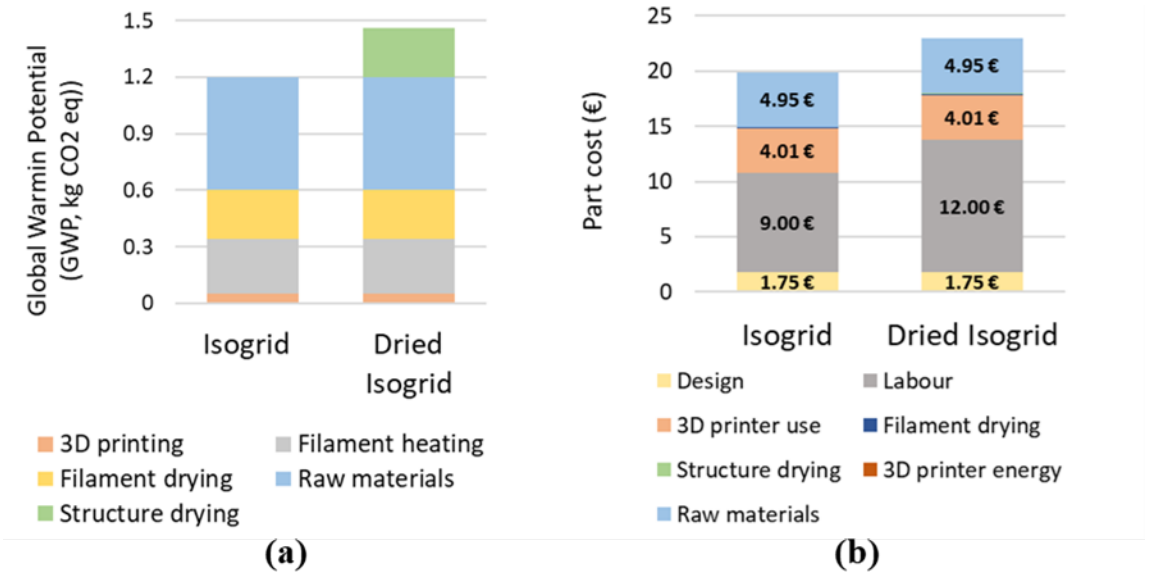

Fig. 3. LCA results in terms of GWP (a) and cost analysis results (b) for the two considered scenarios.

The depreciation costs of the oven for the heat treatment and the drying system are basically negligible due to their low purchase prices. Differently from the environmental assessment, the energy use has low relevance (about 1% of the total costs). Table 3 presents the production time of the different phases and the total manufacturing time of the two scenarios. The printing phase is the most time consuming, closely followed by the structure and filament drying. Overall, the post-printing heating treatment determines an increase in production time of about 50%.

Table 3. Production time for the two scenarios.

Production time		
Filament drying	2	h
Printing time	2.15	h
Printing setup	0.2	h
Part removal	0.1	h
Structure drying	2.1	h
Scenario 1	4.45	h
Scenario 2	6.55	h

Scenario 1 was selected as the reference scenario and the performance index of Scenario 2 was calculated accordingly. In line with the model, Scenario 1 index is equal to 1; Scenario 2 index is equal to 1.22 (Table 4), which means that it performed 22% worse than the baseline process according to the sum of decision criteria. The drying process allows to improve by 23% the decision criteria related to the mechanical properties. However, it lowers the performance of the system according to every other indicator, as it is time consuming, expensive and with high electrical energy requirement. The weight factors used for this case study are appropriate for low cost products with modest mechanical performances requirements (e.g. aesthetic components) and for which the sustainability is a major concern (e.g. for green labelled parts).

It is evident how the weight values are crucial for a correct use of the performance index and should be carefully identified in accordance with the company vision and the specific case study.

For example, considering the present case study, if the environmental sustainability criteria is not taken into account (weight factor equal to zero), the production time and cost relevance weight are lowered to 2 and 1 respectively, and the mechanical properties factor is set equal to 5, Scenario 2 becomes the best alternative with an index score equal to 0.98. That would be the case of structural components

This remarks the importance of a proper choice of the weighting factors and also the flexibility of the model. In fact, it can be a useful decision tool in almost every industrial sector for every set of decision criteria that the stakeholders wish to include in their evaluation process.

Table 4. Performance indexes for the two scenarios.

	Weight	Weighting factor	Scenario 1	Scenario 2
Mechanical properties	2	0.14	13.08 kN	16.08 kN
Environmental sustainability	4	0.29	1.2 kg CO2 eq	1.46 kg CO2 eq
Cost	3	0.21	19.9 €	23 €
Production time	5	0.36	4.55 h	6.55 h
Performance Index			1	1.22

Summary

In this paper, a new multi criteria decision model for industrial products and processes was proposed. The mathematical model provides a simple and effective tool to compare different alternatives and to select the best one according to several decision criteria. The tool can also be employed to optimize a base scenario by evaluating a multicriteria performance index as a function of defined variables.

The model was employed to compare “as printed” and “dried” 3D printed composite isogrid structure. Four different criteria were assessed: mechanical performances by means of compression tests, economic and environmental sustainability by means of LCA and LCC analyses and production times. The main results can be summarized as follows:

- On average, the drying process improves the compression resistance of the isogrid structures by 23% but it has negative effects for the other three decision criteria.
- The weighting factors can be calculated by means of the ponderation decision matrix considering the company vision and the analysed scenarios.
- The value of the performance index is strongly influenced by the weighting factors associated with each decision criteria. The best alternative can change depending on these factors and, therefore, on the company goals. For this reason, the model is suitable for a large variety of industrial components and decision criteria.

Future work could be focused on different applications of the proposed model to further validate it and to provide reference values for multicriteria decision processes.

References

[1] W.J.C. Verhagen, Concurrent Engineering in the 21st Century, 2015. https://doi.org/10.1007/978-3-319-13776-6

[2] K.M. Lopes, E. Zancul, Application of Set-Based Concurrent Engineering Principles in R&D Project Prioritization, Procedia CIRP 84 (2019) 49-54. https://doi.org/10.1016/J.PROCIR.2019.04.194

[3] M. Aruldoss, T.M. Lakshmi, V.P. Venkatesan, A Survey on Multi Criteria Decision Making Methods and Its Applications, Am. J. Inf. Syst. 1 (2013) 31-43. https://doi.org/10.12691/AJIS-1-1-5
[4] O.S. Vaidya, S. Kumar, Analytic hierarchy process: An overview of applications, Eur. J. Oper. Res. 169 (2006) 1-29. https://doi.org/10.1016/J.EJOR.2004.04.028
[5] A. Di Vaio, S. Hasan, R. Palladino, R. Hassan, The transition towards circular economy and waste within accounting and accountability models: a systematic literature review and conceptual framework, Environ. Dev. Sustain. (2022) 1-77. https://doi.org/10.1007/S10668-021-02078-5/TABLES/2
[6] International organization for standarization, Environmental Management - Life Cycle Assessment - Principles and Framework (ISO 14040:2006), Environ. Manag. Syst. Requir. 44 (2004).
[7] I. Bianchi, A. Forcellese, T. Mancia, M. Simoncini, A. Vita, Process parameters effect on environmental sustainability of composites FFF technology, Mater. Manuf. Process. 37 (2022) 591-601. https://doi.org/10.1080/10426914.2022.2049300
[8] D. Ross, V. Ferrero, B. DuPont, Exploring the Effectiveness of Providing Structured Design-for-the-Environment Strategies During Conceptual Design, J. Mech. Des. Trans. ASME. 144 (2022). https://doi.org/10.1115/1.4052513/1120545
[9] V. Di Pompeo, A. Forcellese, T. Mancia, M. Simoncini, A. Vita, Effect of Geometric Parameters and Moisture Content on the Mechanical Performances of 3D-Printed Isogrid Structures in Short Carbon Fiber-Reinforced Polyamide, J. Mater. Eng. Perform. 30 (2021) 5100-5107. https://doi.org/10.1007/s11665-021-05659-7
[10] K. Alexopoulos, N. Papakostas, D. Mourtzis, P. Gogos, G. Chryssolouris, Quantifying the flexibility of a manufacturing system by applying the transfer function, Int. J. Comput. Integr. Manuf. 20 (2007) 538-547. https://doi.org/10.1080/09511920600930046
[11] ISO-International Organization for Standardization, Environmental management - Life cycle assessment - Requirements and guidelines, ISO EN 14044, 2006.
[12] I. Bianchi, A. Forcellese, M. Simoncini, A. Vita, V. Castorani, M. Arganese, C. De Luca, Life cycle impact assessment of safety shoes toe caps realized with reclaimed composite materials, J. Clean. Prod. 347 (2022) 131321. https://doi.org/10.1016/J.JCLEPRO.2022.131321
[13] F. Meng, E.A. Olivetti, Y. Zhao, J.C. Chang, S.J. Pickering, J. McKechnie, Comparing Life Cycle Energy and Global Warming Potential of Carbon Fiber Composite Recycling Technologies and Waste Management Options, ACS Sustain. Chem. Eng. 6 (2018) 9854-9865. https://doi.org/10.1021/acssuschemeng.8b01026
[14] A. Forcellese, M. Marconi, M. Simoncini, A. Vita, Environmental and buckling performance analysis of 3D printed composite isogrid structures, Procedia CIRP. 98 (2021) 458-463. https://doi.org/10.1016/j.procir.2021.01.134
[15] Y.F. Khalil, Eco-efficient lightweight carbon-fiber reinforced polymer for environmentally greener commercial aviation industry, Sustain. Prod. Consum. 12 (2017) 16-26. https://doi.org/10.1016/j.spc.2017.05.004

Materials Research Proceedings 28 (2023) 1997-2004 https://doi.org/10.21741/9781644902479-215

Characterization of friction stir consolidated recycled billet by uniaxial compression tests with miniaturized cylindrical specimen

LATIF Abdul[1,a *], INGARAO Giuseppe[1,b], FRATINI Livan[1,c], HETZ Peter[2,d] and MERKLEIN Marion[2,e]

[1]University of Palermo, Viale delle Scienze, 90128 Palermo, Italy

[2]Institute of Manufacturing Technology, Friedrich-Alexander-Universität Erlangen-Nürnberg, Egerlandstraße 13, 91058 Erlangen, Germany

[a]abdul.latif@unipa.it, [b]giuseppe.ingarao@unia.it, [c]livan.fratini@unipa.it, [d]peter.hetz@fau.de, [e]marion.merklein@fau.de

Keywords: Aluminum Alloys, Recycling, Friction Stir Consolidation, Compression Test

Abstract. Friction stir consolidation (FSC) is a solid-state recycling method that directly converts machining scraps into semifinished billets. This process has been proven to be a more energy efficient and environmentally friendly technique compared to remelting based conventional recycling methods. During FSC, machining chips are transformed into a solid billet by the stirring action and friction heat of the rotating tool. Due to process mechanics, especially temperature gradient and strain rate, billets have shown different hardness values and grain size distribution across their sections. Therefore, in this research, miniaturized upsetting samples are extracted from the FSC billet. The purpose of minimizing the sample size is to get the local properties of a particular position. The intensive characterization was performed with future goals to find a more accurate numerical modelling and ultimately assign FSC billet to a potential industrial application.

Introduction

The current global demand for aluminum is 100 million tonnes per year [1]. The accelerating consumption, due to its growing application in lightweight transport, packaging, construction, and electronic industries, is putting immense pressure on industries to increase the production rate. However, per 1 ton of aluminum production from the primary source, 12-16 tons of greenhouse gas (GHG) are produced, which have severe adverse environmental impacts [2]. Besides, aluminum production from ores is also energy-intensive, leading to 13 Exa joules of energy consumption, and is therefore responsible for almost 1% of total global energy consumption [3].

Interestingly, aluminum is an infinitely recyclable material [3]. In Europe, almost 35 % of the aluminum demand is met by recycling aluminum scraps [4]. The conventional recycling route involves re-melting the metal, and thus it skips many of the complex steps of aluminum extraction from the primary source. Furthermore, recycling is highly energy efficient, requiring 5% of the energy compared to obtain aluminum from the primary bauxite source. Thus, recycling can shift aluminum's energy and carbon balance sustainability towards much greater sustainability.

The conventional recycling method has further limitations, especially during the recycling aluminum machining chips. The chip has a high surface-to-volume ratio and is highly oxidation prone, causing permanent material loss during the melting process. They cause adverse environmental impact, high cost, and significant permanent material loss [5]. Looking to the proportion, the machining scraps constitute almost 17% of the total scraps [6]. Therefore, the researchers turned to solid-state recycling (SSR) techniques. SSR are those methods that transform metal scraps directly into finished or semi-finished billet through mechanical means such as high pressure, friction, rotational speed, and force [7]. Recently, SSR processes have been analyzed as a potential alternative for recycling machining scraps.

Content from this work may be used under the terms of the Creative Commons Attribution 3.0 license. Any further distribution of this work must maintain attribution to the author(s) and the title of the work, journal citation and DOI. Published under license by Materials Research Forum LLC.

Various SRR methods have been introduced for recycling metal chips based on the process mechanics and properties of desired product [8-10]. In fact, by omitting the melting phase, permanent losses mainly due to oxidation are avoided. Duflou et al. [5] have proved that equal channel angular pressing and spark plasma sintering outperform conventional remelting-based routes from the environmental impact perspective. Baffari et al. [11] proved the energy efficiency of friction stir extrusion.

Recently FSC has proved to be one of the environment recycling techniques compared to conventional remelting [12]. This technology has attracted many researchers as it proved its potential beyond the concept of recycling toward upcycling method [13]. FSC has two main steps: compaction and consolidation. During compaction, chips or powder are pressed in a hollow die chamber by applying a specific load through a cylindrical tool. Then compacted materials are further pressed and stirred through the tool's downward force and rotational speed during the consolidation phase [14]. So far, researchers numerically modelled [15] FSC process, identified the key process parameters [12] and proved its environmental efficiency with respect to conventional remelting.

A typical FSC, due to process mechanics such as different temperatures and strain rate distribution, is characterized by variation in mechanical properties along the radial and longitudinal direction of the billet [13, 14]. Previously, this variation was validated by Vickers's hardness test and grain size distribution analysis [16]. It is also crucial to analyze the effect of process mechanics on other important properties such as mechanical strength, fracture strength, and ductility. These mechanical properties can be obtained through tensile tension or compression test. However, due to variation in properties across the FSC billet section, miniaturized samples were extracted from the billet section. Interestingly, the miniaturization of the sample leads to homogenization and thus gives details of local properties. The concept of miniaturized samples for upsetting test, previously implemented by Hetz et al. [17] for sheet metal, was applied to the FSC billet. The broader objective is to find a more accurate solution for the numerical modelling of the FSC process and find the potential industrial application.

Material and methods

Material and process set-up.

As-received material was a 20x20 mm squared bar of AA 2011-T3. The bar was reduced into chips by a milling operation. The machining scraps were kept submerged in acetone for 15 minutes for efficient cleaning. An input chip mass of 15g was loaded in the cylindrical die with a nominal diameter of 25.4 mm and compacted at 5 kN force through an H13 steel cylindrical tool with a 25 mm diameter. The die and pressing tool were integrated with ESAB-LEGIO (Fig. 1), a dedicated friction stir welding machine. The chips compaction was an important step in order to avoid spilling out chips during consolidation. Finally, chips were transformed into a cylindrical billet by applying the rotating tool at 1500 rpm and 20 kN load for a processing time of 30 seconds. The selected process parameters in the current investigation were based on previous studies [13,16] as promising conditions for manufacturing sound billet.

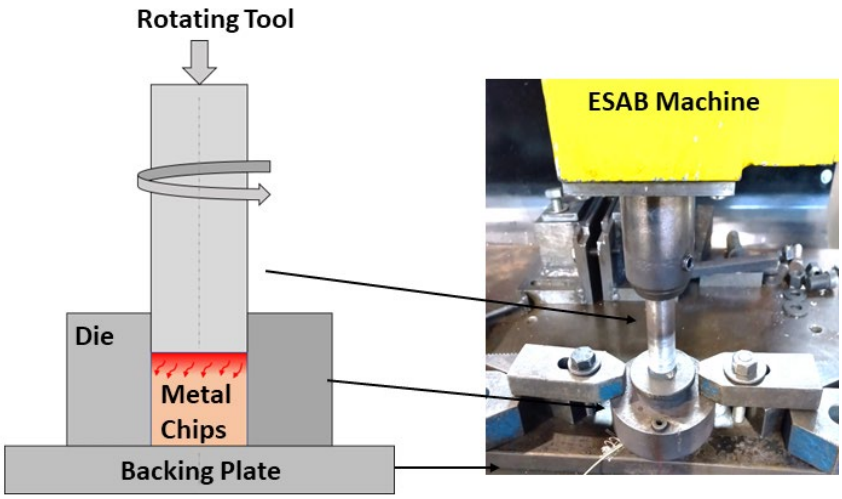

Fig. 1. Experimental setup of FSC.

Measured outputs.

After FSC consolidated step, the obtained billets had an average height and a diameter of 10 mm and 25 mm, respectively. First, the top and bottom surfaces of the FSC cylindrical billet were well polished to get a very flat surface. Then slices were cut (perpendicular to the cylindrical axis of the billet) from the top, middle, and bottom sections with a thickness of 1.5 mm and a diameter equal to the original billet diameter, as shown in Fig. 2 (right). From each disc slice, five miniaturized cylindrical upsetting samples were extracted that had a height (h) of 1.5 mm (slice thickness) and a diameter (d) of 1 mm through micro-EDM on an SX-200-HPM (Sarix SA). One sample (x1) was extracted from the center (r=0) and the remaining four samples (x2, x3, x4, and x5) were extracted at r=10 mm from the center of the billet. Upsetting tests were performed at a strain rate of 0.5%/s with upsetting sample dimensions given in Fig. 3. The height-to-diameter ratio (1.5) of the upsetting was selected based on the equation [17].

$$1 \leq \frac{h}{d} \leq 2 \tag{1}$$

According to this Eq. 1, a higher ratio exceeding the maximum limit leads to the buckling of the upsetting sample, which is considered a premature failure. On the other hand, a lower ratio emphasizes the effect of the frictional coefficient. Besides, Dionol ST V 1725-2 (MKU-Chemie GmbH) lubricant was applied to minimize friction.

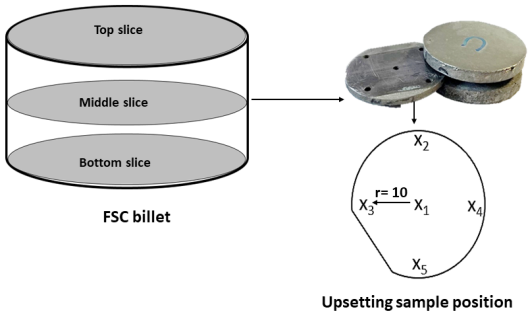

Fig. 2. Extraction of upsetting samples from FSC billet at different position.

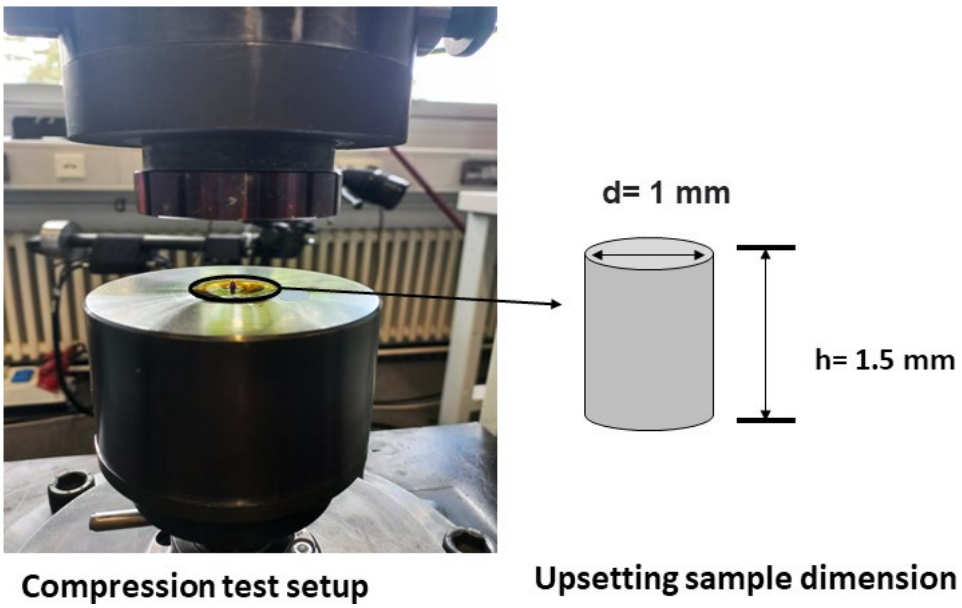

Fig. 3. Upsetting test and sample dimensions.

Results and Discussion

True-stress strain of FSC billet.

This section gives details information about the true strain-strain curves of the FSC 2011-T3 billet. It also provides evidence of how far true stress-strain graphs agree with the hardness distribution profile across the FSC billet section that the authors investigated in their previous research [13,16]. Further, a comparison was also made between the true stress-strain curve FSC recycled billet and as received AA 2011-T3 bar.

On the top slice (Fig.4), the central sample (x1) showed higher strength compared to the remaining upsetting samples (x2 to x5). The flow curves of the remaining four were found almost aligned with each other. The reason was samples x2 to x5 were extracted from the same height (top slice) and same radial distance (r=10 mm). Interestingly, the variation in properties is enabled by FSC process mechanics, i.e., different strain rate and temperature distributions across the billet section, as reported by Tang et al. [14]. Although, a detailed analysis has not been performed so far, it is quite clear that the die wall and back plate serve as heat sinks, reducing the temperature. Due to this, chips close to the die wall and back plate don't receive sufficient heat input and deformation to be fully recrystallized, but some bonding is, however, achieved.

Likewise, the top slice flow curves, almost the same trend was found for the middle slice. The central specimen showed higher strength than the other samples, with the exception that the x2 graph was not aligned with the x3, x4, and x5 curves. This deviation of the x2 graph was unexpected, as x2 was extracted from the same radial distance (r=10 mm) and the same height (middle slice). Therefore, this misalignment could be an error that occurred while manufacturing the samples.

For the bottom slice, almost uniform flow curves were found for all samples. It is well evident that the strength of the material varies both in the radial and longitudinal direction of the billet. Further, the top part of the billet shows higher strength than the bottom part, and along the radial direction the central part is stronger than the region near the external surface. Also, along the radial direction, the difference in true stress-strain curves between the samples at the center (x1) and the other samples (x2 to x5) is higher for the top slice, then difference diminishes at the middle slices, and finally, all curves are aligned with each other for the bottom slice. For better understanding,

the trend of true stress-strain curves is discussed in terms of hardness distribution in the following section.

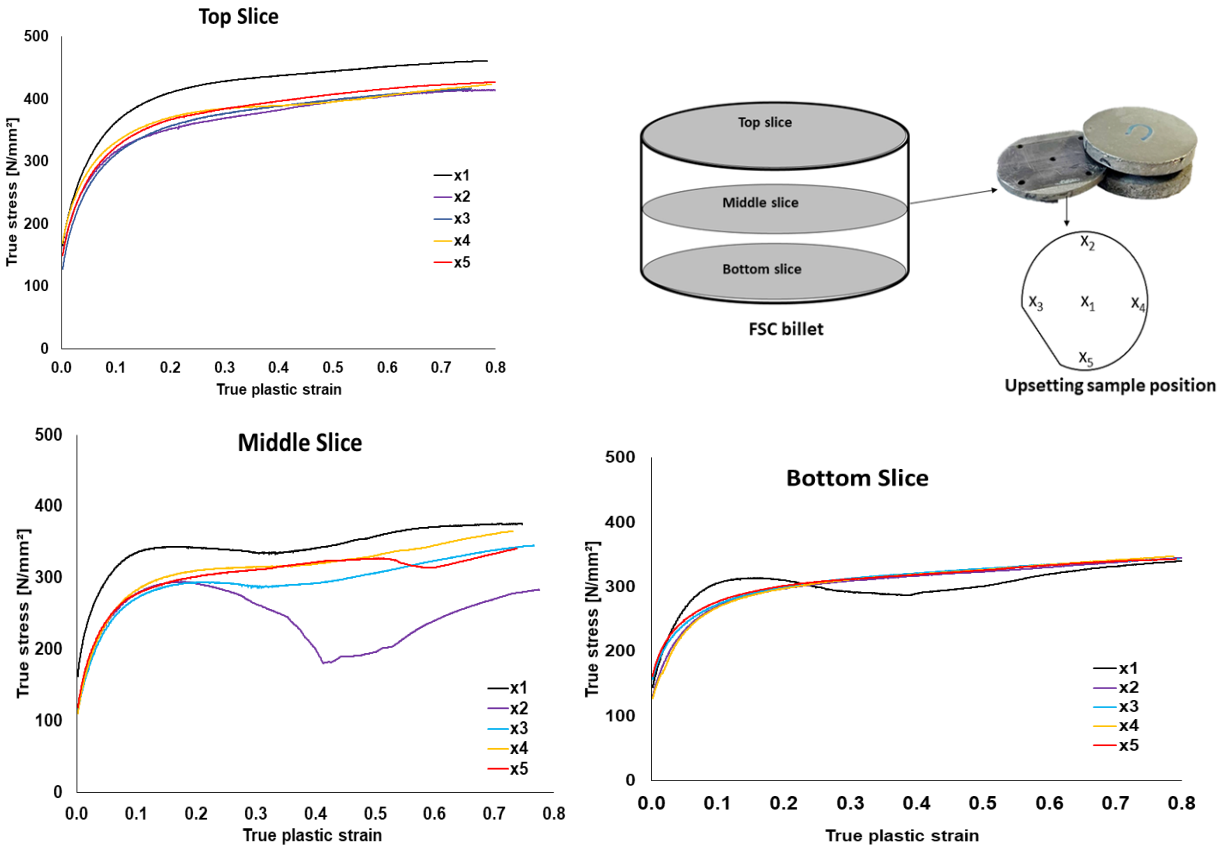

Fig. 4. True stress-strain curves for top, middle and bottom slices of FSC billet.

Comparison FSC billet true strain-strain and hardness trend.

Interestingly, the trend of true strain-strain profile was found very consistent with the hardness distribution trend. The hardness measurements were performed on the same material, AA 2011-T3, manufactured under the same process configuration as mentioned previous section. For hardness, a load of 49 N was applied for 15 seconds as dwell time.

As in Fig.5 (right side), on the top surface, the hardness value is higher, but variation in the radial direction is also very high. Similarly, in Fig.5 (left) the true stress-strain curves showed the material has good strength at the top (x1, x2, and x3), but the difference in material strength between x1 and x2/x3 is higher. It should be noted that x1 is an upsetting sample at the center (r=0), and x2 and x3 are at the left and right sides, respectively, of x1. Besides, x2 and x3 are at equidistance (r=10 mm) from x1.

Again in Fig.5 (right), the mid of the billet section shows a minor variation in hardness value along the radial direction. A similar relationship can be found for the flow curves of middle slice y1 and y2/y3 in Fig.5 (left).

For the bottom section, a lower but uniform hardness value can be noticed. Likewise, lower strengths but alignment of curves were noticed for the true stress-strain graphs of the bottom section (z1, z2, and z3).

It is quite clear that the true stress-strain curves followed the trend of hardness distribution. Overall, the central, and top zones show higher strength and higher hardness values in comparison

to the part near the external surface and bottom section, where relatively low hardness values were noticed.

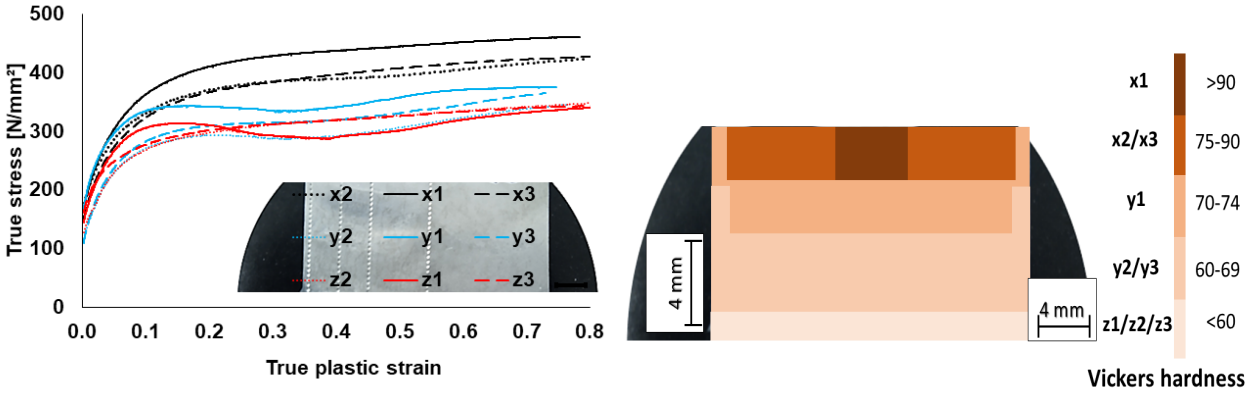

Fig. 5. Comparison between true stress-strain curves profiles and hardness distribution across FSC billet.

Comparison of true strain-strain profile of FSC billet and as-received material.

For the sake of better understanding, the true stress-strain curve of the as-received bar of AA 2011-T3 was compared with flow curves of specimens that were extracted from the center of the top (x1), middle (y1), and bottom (z1) slices of FSC billet section as shown in Fig. 6. Interestingly, the strength of the top layer of FSC billet was higher, middle slice's was comparable, and bottom slice strength was lower than as-received material. The variation in strength was previously also observed in the hardness profile. So, it is well evident that this phenomenon was enabled by FSC process mechanics [13,14, 16]. Dynamics recrystallization and full consolidation occur at the top surface, making the top surface superior to the as-received material.

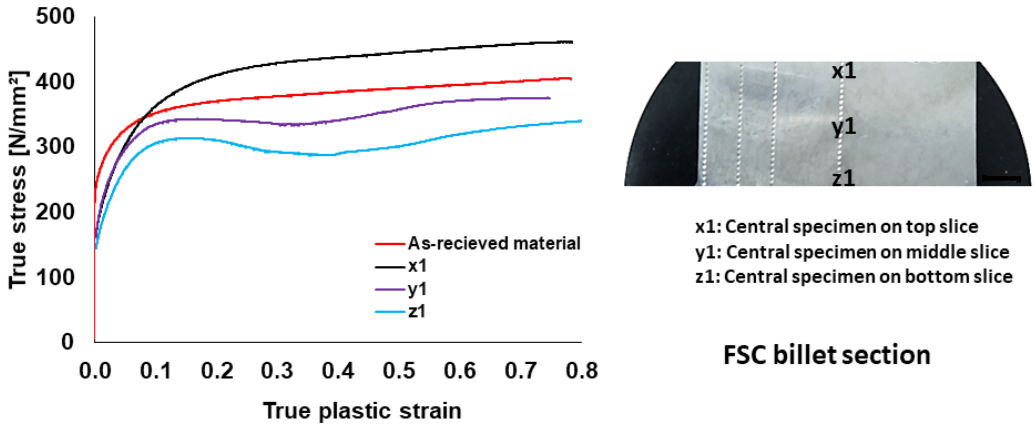

Fig. 6. Comparison of true stress-strain curve between as-received material and different section of FSC billet.

Summary

Based on the previous discussion, the following can be concluded.

1. The strength of FSC billet decreases both along billet advancing direction and radial direction.
2. The strength of top section is higher than strength of bottom section. Similarly, higher strength was found along the central part (r=0) compared to the strength of region near the external surface.
3. The flow curves were found in good agreement with the hardness trend across the billet section. It means that hardness is a good indicator for predicting FSC billet strength.

4. The region where the billet shows a higher hardness value also shows higher strength, and similar results were also valid for the zone of lower hardness value that showed lower strength.

It has been proved that the FSC process causes variations in the mechanical properties of the billet. The authors proved that multi-step FSC processes [16] implementation allows billet with more uniform mechanical and microstructural properties to be obtained. Further development will focus on the here presented characterization of multiple-step FSCed samples. The authors, in their previous studies [18], analyzed the performance of FSCed billets by conducting forging tests, and further developments are still in progress in terms of the double cup extrusion test. Also, an accurate numerical model will be developed in order to provide clarity on the process mechanics and to understand the actual factor causing the sample heterogeneity.

References

[1] Information on https://alucycle.international-aluminium.org/public-access/

[2] T.G. Gutowski, S. Sahni, J.M. Allwood, M.F. Ashby, E. Worrell, The energy required to produce materials: constraints on energy-intensity improvements, parameters of demand, Philos. Trans. Royal Soc. A: Math. Phys. Eng. Sci. 371 (2013) 20120003. https://doi.org/10.1098/rsta.2012.0003

[3] D. Raabe, D. Ponge, P.J. Uggowitzer, M. Roscher, M. Paolantonio, C. Liu, H. Antrekowitsch, E. Kozeschnik, D. Seidmann, B. Gault, F. De Geuser, A. Dechamps, C.R. Hutchinson, C. Liu, Z. Li, P. Prangnell, J. Robson, P. Shanthraj, S. Vakili, C.W. Sinclair, L. Bourgeois, S. Pogatcher, Making sustainable aluminum by recycling scrap: The science of "dirty" alloys, Progr. Mater. Sci. (2022) 100947. http://dx.doi.org/10.1016/j.pmatsci.2022.100947

[4] Information on https://www.iea.org/reports/material-efficiency-in-clean-energy-transitions

[5] J.R. Duflou, A.E. Tekkaya, M. Haase, T. Welo, K. Vanmeensel, K Kellens, W Dewulf, D. Paraskevas, Environmental assessment of solid state recycling routes for aluminium alloys: can solid state processes significantly reduce the environmental impact of aluminium recycling?. CIRP Annals 64 (2015) 37-40. https://doi.org/10.1016/j.cirp.2015.04.051

[6] U.M.J. Boin, M. Bertram. Melting standardized aluminum scrap: A mass balance model for Europe, JOM 57 (2005) 26-33. https://doi.org/10.1007/s11837-005-0164-4

[7] B. Wan, W. Chen, T. Lu, F. Liu, Z. Jiang, M. Mao, Review of solid state recycling of aluminum chips, Resources, Conservation and Recycling 125 (2017) 37-47. https://doi.org/10.1016/j.resconrec.2017.06.004

[8] M. Haase, N.B. Khalifa, A.E. Tekkaya, W.Z. Misiolek, Improving mechanical properties of chip-based aluminum extrudates by integrated extrusion and equal channel angular pressing (iECAP), Mater. Sci. Eng. A 539 (2012) 194-204. https://doi.org/10.1016/j.msea.2012.01.081

[9] F. Widerøe, T. Welo, Using contrast material techniques to determine metal flow in screw extrusion of aluminium, J. Mater. Process. Technol. 213 (2013) 1007-1018. http://doi.org/10.1016/j.jmatprotec.2012.11.013

[10] D. Paraskevas, S. Dadbakhsh, J. Vleugels, K Vanmeensel, W Dewulf, J Duflou, Solid state recycling of pure Mg and AZ31 Mg machining chips via spark plasma sintering, Mater. Des. 109 (2016) 520-529. http://doi.org/10.1016/j.matdes.2016.07.082

[11] D. Baffari, A.P. Reynolds, A. Masnata, L. Fratini, G. Ingarao, Friction stir extrusion to recycle aluminum alloys scraps: energy efficiency characterization, J. Manuf. Process. 43 (2019) 63-69. https://doi.org/10.1016/j.jmapro.2019.03.049

[12] G. Buffa, D. Baffari, G. Ingarao, L. Fratini, Uncovering technological and environmental potentials of aluminum alloy scraps recycling through friction stir consolidation, Int. J. Precis. Eng. Manuf.-Green Technol. 7 (2020) 955-964. https://doi.org/10.1007/s40684-019-00159-5

[13] A. Latif, G. Ingarao, L. Fratini, Multi-material based functionally graded billets manufacturing through friction stir consolidation of aluminium alloys chips, CIRP Annals 71 (2022) 261-264. https://doi.org/10.1016/j.cirp.2022.03.035

[14] W. Tang, A.P. Reynolds, Friction consolidation of aluminum chips, in: Friction Stir Welding and Processing VI., 2011, pp. 289-298. http://doi.org/10.1002/9781118062302.ch34
[15] D. Baffari, A.P. Reynolds, X. Li, L. Fratini Bonding prediction in friction stir consolidation of aluminum alloys: A preliminary study, in: AIP Conference Proceedings 1960 (2018) p. 050002, AIP Publishing LLC.
[16] A. Latif, G. Ingarao, M. Gucciardi, L. Fratini, A novel approach to enhance mechanical properties during recycling of aluminum alloy scrap through friction stir consolidation, Int. J. Adv. Manuf. Technol. 119 (2022) 1989-2005. https://doi.org/10.1007%2Fs00170-021-08346-y
[17] P. Hetz, M. Kraus, M. Merklein, Characterization of sheet metal components by using an upsetting test with miniaturized cylindrical specimen, CIRP Annals 71 (2022) 233-236. https://doi.org/10.1016/j.cirp.2022.03.010
[18] A. Latif, G. Ingarao, G. Buffa, L. Fratini, Forgeability characterization of multi-material based functionally graded materials manufactured through friction stir consolidation, in: IOP Conference Series: Mater. Sci. Eng. 1270 (2022) 012096. https://doi.org/10.1088/1757-899X/1270/1/012096

Materials Research Proceedings 28 (2023) 2005-2014 https://doi.org/10.21741/9781644902479-216

Innovative self-learning disturbance compensation for straightening processes

BATHELT Lukas[1,a *], DJAKOW Eugen[1,b], HENKE Christian[1,c] and TRÄCHTLER Ansgar[2,d]

[1]Fraunhofer IEM, Paderborn, Germany

[2]Heinz Nixdorf Institute, Paderborn, Germany

[a]lukas.bathelt@iem.fraunhofer.de, [b]eugen.djakow@iem.fraunhofer.de, [c]christian.henke@iem.fraunhofer.de, [d]ansgar.traechtler@hni.upb.de

Keywords: Mechatronic Straightening Machine, Self-Learning Disturbance Compensation, Punch-Bending Process

Abstract. To increase the sustainability of forming processes such as punch bending, homogenization of the processed semi-finished product is an essential step in the manufacturing process. High-strength wire materials are usually available as strip material before being further processed in a forming process. For storage and transport, the material is coiled onto coils and transported to the customer. During the coiling process, residual stresses and plastic deformation are introduced into the wire. Thus, the final product quality is also influenced by the geometry of the coil. Straightening machines are used in production lines to compensate for these. Once a straightening machine has been set up, the settings for the roll positions are usually not changed. As a result, there is no reaction to material fluctuations, which means that the components to be produced do not meet the dimensional accuracy requirements. This leads to an increase in the rejection rate in manufacturing processes. To reduce the rejection rate, it is necessary to enable dynamic and flexible infeed of the straightening rollers. In this context, an innovative control concept with disturbance compensation was developed for the straightening process. The disturbance compensation uses a disturbance model that predicts the change in bending curvature over the coil radius. With this prediction, the straightening machine can be adjusted specifically. The roller positions are adjusted by a subordinate position control. The additional feedback from measured geometric product properties from the following punching-bending process enables the straightening machine to be adjusted even in the case of unforeseen fluctuations in the material properties. In this way, it is possible to react to any material fluctuations as required. This novel, demand-oriented adjustment of the straightening machine is expected to result in a high increase in the efficiency of the production process and a reduction of the rejection rate.

Introduction

Semi-finished products made of high-strength flat wire are usually transported to the customer on coils and further processed in downstream processes such as punch-bending. Transport and storage on coils induce pre-curvatures and residual stresses in the semi-finished product, which fluctuate over the coil length during uncoiling. These fluctuations in the semi-finished product have a negative effect on component quality in the downstream processes. In order to compensate for the variable curvature of the incoming straightening material, straightening machines with a large number of straightening rolls are used [1].

To reduce the number of straightening rollers, the fluctuations of the material properties must be known, which is generally not the case. The fluctuations can only be identified with great effort and at the earliest in the straightening result [2]. In addition, online correction of the roller positions in the straightening process is necessary. The rollers of the currently used straightening machines

Content from this work may be used under the terms of the Creative Commons Attribution 3.0 license. Any further distribution of this work must maintain attribution to the author(s) and the title of the work, journal citation and DOI. Published under license by Materials Research Forum LLC.

are adjusted manually or by motor. After the initial positioning, however, the rollers usually remain in the same position during the entire production process for a coil. To keep the straightening result constant under these conditions, it is not possible to reduce the number of straightening rollers. With a high number of straightening rollers, the number of alternate bending operations and the accumulated deformation of the material due to the straightening process increase. This leads to a reduction in the strength properties of the material like yield strength, tensile strength, and elongation at fracture [3].

This paper presents an innovative straightening process in which the straightening roller positions are adjusted online. For this purpose, deterministic disturbance variables in the straightening process are estimated. During the straightening process, the straightening result is evaluated based on measurement data and, if necessary, adjustments of the roll positions are derived. The use of intelligent straightening processes offers great potential for making manufacturing processes more sustainable and resource-saving.

State of the Art

In recent years, several approaches have already been investigated to determine the appropriate roller setting for the straightening process. These approaches can be divided into two categories: These are, on the one hand, the numerical approaches, which use FE models to simulatively determine the roller settings. On the other hand, experimental approaches are investigated with the use of different measurement methods.

The numerical approaches are based on FE simulations and often require a high computational effort. An example of this is the work in [4, 5]. The aim is pursued to reduce the residual stresses in the straightened material. The used optimization algorithms rely on a high number of simulations. In [6], an approach is presented in which the settings of all bending triangles in a FE model are adjusted via a sub-routine. Here, the focus was placed on the analysis of the bending line in the straightening machine.

To reduce the simulation effort, a control loop was implemented in an FE simulation in [7]. Within the FE model, the position of the upper edge of the sheet metal at the end of the straightening process was used as the measured variable for determining the residual curvature. The position specification of the second last roller is used as the control variable.

This approach is also used in [2], where a concept for the automated adjustment of a five-roller straightening machine is presented. Based on a force measurement during the closing of the first bending triangle, the material parameters necessary to determine the roller positions are identified. Through a previously conducted simulative parameter study, the appropriate roller positions are known for a variety of different straightening material properties.

This work is continued in [8]. The main difference to [2] is its online capability. This makes it possible to detect changes in the yield strength and pre-curvature of the metal sheet and readjust the roller position accordingly. The disadvantage of these approaches is always a high simulation effort, and the data is only valid for one specific machine configuration.

In addition to numerical approaches, experimental approaches should also be mentioned. In [9], a way to set up a straightening machine for flat wire is presented. Via an offline curvature measurement, the pre-curvature is automatically detected, and possible roller configurations are suggested to the operator via an experimentally created database. A concept for controlling straightening machines during operation is developed in [10]. In order to adjust the position of the rollers, the curvature of the sheet metal is measured behind the straightening machine by distance sensors. An experimental validation of the concept was not carried out. Another concept for an online control is presented in [11]. In this work, the straightening rolls are also adjusted by a control algorithm based on a curvature measurement behind the straightening machine. The residual curvature is continuously determined with a specially developed curvature sensor. However, according to the authors, the curvature measurement is the weak point and does not provide reliable

results because the curvature is overlaid by other process forces. Another online approach is presented in [12]. Here, mechanical material properties of the material under study are estimated. However, straightened material is assumed for the estimation.

An approach to control a leveling process based on the magnetic properties is presented in [13]. The magnetic properties are investigated considering the Barkhausen effect in connection with the residual stresses present in the material. The authors noted that with this type of measurement, the residual stress distribution is not sufficiently accurate, so no implementation of the concept was made. In [14, 15 and 16] an innovative setup of a straightening system is presented, which has an eddy current measurement system. Its measurement results can be correlated to variable material properties.

As a conclusion of this chapter, on the one hand the listed works require either a high simulation effort or preliminary tests with a special test configuration of straightening machine and semi-finished product. On the other hand, the detection of state variables of the semi-finished product is not sufficiently robust to implement a dynamic roller adjustment for a good straightening result. However, these are the requirements for a robust and efficient straightening process in order to reduce the rejection rate in downstream processes. For the application of a process, a low simulation and parameterization effort as well as an efficient transferability to other wire types is desirable. A control approach should also ensure the adjustment of the straightening rollers in the process to be able to react to fluctuating wire properties. For this purpose, a robust and reliable measurement of state variables of the wire must be ensured. Based on these requirements, the control approach presented in this paper was developed.

System Description and Control Architecture

The dynamic adjustment of the straightening rollers during the manufacturing process is desirable in order to be able to react to fluctuating material properties of the semi-finished product. Particular focus is placed on the development of a robust and efficient method that does not require time-consuming or resource-intensive preliminary tests and is suitable for industrial use. To develop such an approach, this paper considers the system shown in Fig. 1

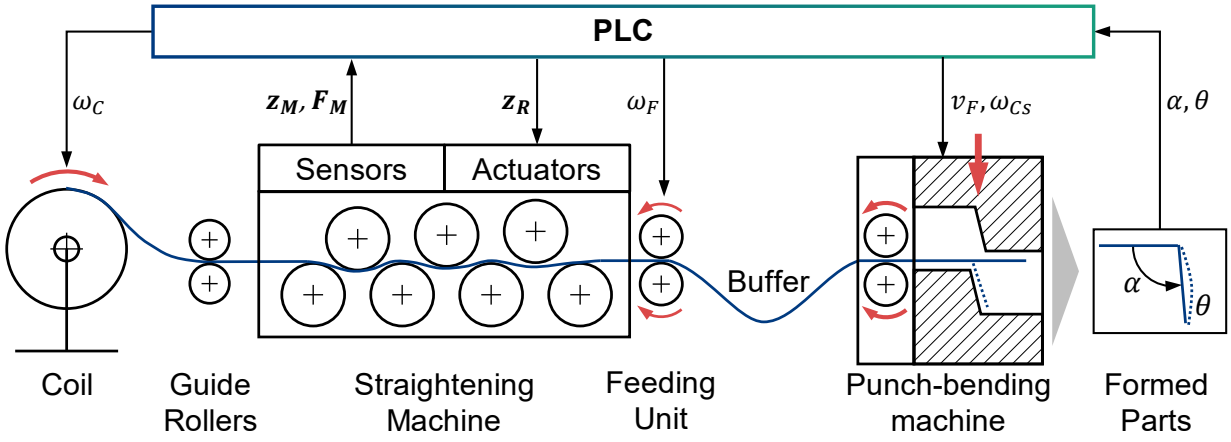

Fig. 1. Schematic representation of the entire manufacturing process.

Materials Research Proceedings 28 (2023) 2007-2016 https://doi.org/10.21741/9781644902479-216

The semi-finished product is uncoiled from a coil and fed to the straightening process via guide rollers. This is equipped with sensors to determine the roller positions $z_M = [z_{1,M}, z_{2,M}, z_{3,M}]^T$ and the straightening forces $F_M = [F_{1,M}, F_{2,M}, F_{3,M}]^T$ on these rollers. The semi-finished product is pulled through the straightening machine by a feeding unit. This is followed by a material buffer to make the transition from the continuous straightening process to the discontinuous punch-bending process. The punch-bending machine has a feeding unit and a punch unit. In this process, an L-shaped component is produced. The bending angle α and the straightness θ of the leg are recorded via a camera. A PLC controls all drives and processes the sensor data. The determining variables for the process speed are the coil speed ω_C upstream of the straightening machine, the feeding speed ω_F of the feeding unit downstream of the straightening machine, the feeding speed v_F at the punch-bending machine, and the cam disk speed ω_{CS} of the punch-bending machine.

The aim of the control approach presented here is the dynamic specification of the reference positions z_R for the straightening rollers. On the one hand, this should keep the quality of the straightening process reproducible at a high level. On the other hand, it should be possible to react to fluctuations in the material properties with a dynamic adjustment of the straightening rollers in the process. The fluctuations in the material properties are interpreted as disturbance variables and can be divided into two categories: deterministic and stochastic disturbance variables. In this approach, the change in pre-curvature over the coil radius is considered as a deterministic disturbance variable. Stochastic disturbances are, for example, width and thickness variations or the material composition.

Accordingly, the developed control approach is also divided into two parts. The feedforward control estimates and compensates for the change in pre-curvature with the aid of disturbance compensation. The feedback control is provided to correct the estimated roller positions in order to react to stochastic disturbances. The structure of the control approach is shown in Fig. 2 and is based on the two-degree-of-freedom structure (cf. [17]).

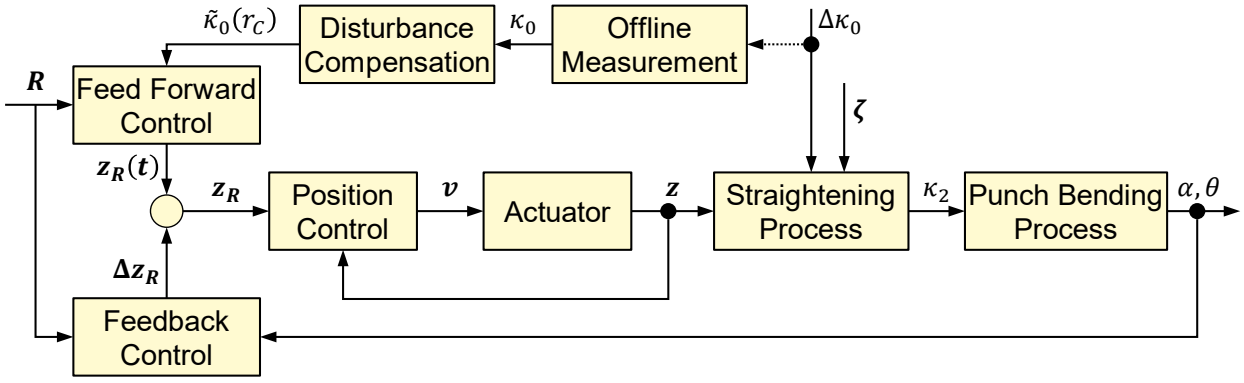

Fig. 2. Scheme of the control structure.

The vector R contains the setpoints for feedforward and feedback control:

$$R = [\kappa_{2,R},\ \alpha_R,\ \theta_R]^T \tag{1}$$

The variable $\kappa_{2,R}$ describes the reference value for the residual curvature of the flat wire behind the straightening machine. Corresponding, α_R and θ_R are the reference values for the characteristics of the component to be produced. Based on the reference specification, the feedforward control specifies a reference trajectory $z_R(t) = [z_{1,R}(t),\ z_{2,R}(t),\ z_{3,R}(t)]^T$ for the three movable straightening rollers. This is corrected by the closed loop control during the running

process by Δz_R, so that the final reference vector z_R is provided for the subordinate position control of the straightening rollers. These are controlled and act as manipulated variables on the flat wire in the first part of the controlled system, the forming process in the straightening machine. As deterministic disturbance variable, the change of the pre-curvature $\Delta\kappa_0$ influences the straightening process. The totality of all stochastic disturbances is summarized in the vector $\boldsymbol{\zeta}$. This includes, for example, variations in width, thickness, or material composition. With a residual curvature κ_2, the flat wire is fed to the punch-bending process, which represents the second part of the controlled system. In this, an L-shaped component is formed, which is characterized by the quantities α and θ (see Fig. 2). These quantities are measurable and can be fed to the control system as measured values.

The change of the pre-curvature $\Delta\kappa_0$ cannot be measured directly during the running process since it is overlaid by process-related tensile forces. This also applies to the residual curvature κ_2 behind the straightening machine. For this reason, only a measurement of the initial curvature κ_0 before starting the production process when inserting a new coil is possible via offline measurement. The initial curvature is fed to the disturbance model in the disturbance compensation. The disturbance compensation estimates the further variation of the curvature $\tilde{\kappa}_0$ over the coil radius r_C. In the feedforward control, a reference trajectory of the straightening roller positions as a function of time $z_R(t)$ is calculated. The exact operation of the disturbance compensation is presented in the following section. The algorithm of the feedback control is part of future work and will therefore not be considered further in detail.

Disturbance Compensation

After a flat wire has been produced in a rolling mill, it is coiled onto a coil for storage and transport purposes. The deformation of the wire on the coil does not immediately generate plastic deformation. Due to effects such as aging, hardening and also thermal influences a straightened coiled flat wire will again show curvature when it is uncoiled. With the right choice for the position of the straightening rollers, this pre-curvature can be compensated. However, the pre-curvature varies with the radius. The radius decreases continuously with the uncoiling of the flat wire and thus the pre-curvature of the wire increases (see Fig. 3 (a)). This requires a continuous adjustment of the straightening roller positions. To determine the roll positions, the pre-curvature must be known exactly. However, this cannot be measured continuously during the process, as this would require stopping the process and unraveling the wire. Therefore, the goal of the disturbance compensation is to estimate the pre-curvature $\tilde{\kappa}_0$ of the flat wire over the radius r_C.

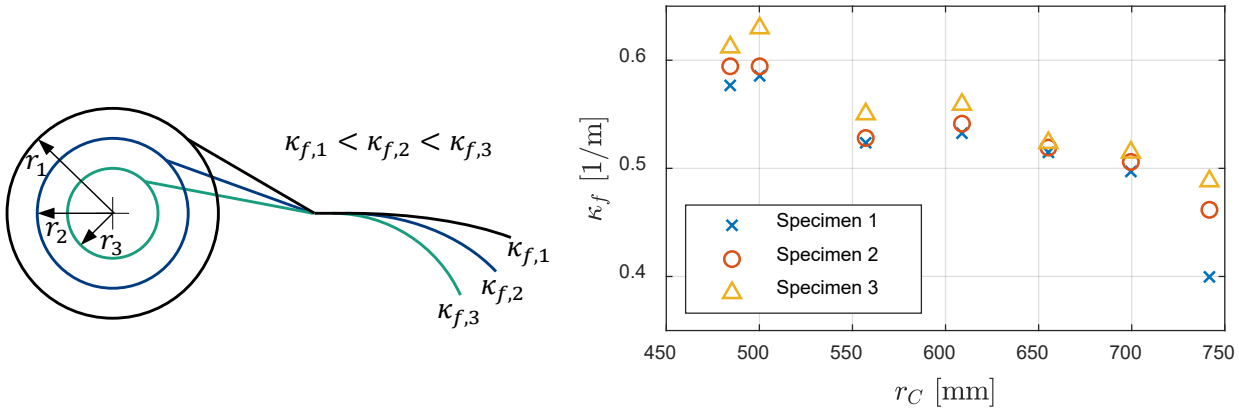

Fig. 3. Trajectory of the pre-curvature over the coil radius: (a) Schematic (left) and (b) measured (right).

Due to the mechanical material properties of steel, the wire springs back when it is uncoiled from the coil. This can be observed especially with wire made of high-strength spring steel. Thus, the curvature κ_f of the wire after uncoiling in the tension-free situation is not identical with the curvature κ_C of the wire in the forced position on the coil. To describe the dimension of this relationship, the springback ratio τ is defined:

$$\tau = \frac{\kappa_f}{\kappa_C} \tag{2}$$

The curvature κ_C during storage can be determined as the reciprocal of r_C. Thus, to calculate the spring-up ratio, it is necessary to measure the curvature of a wire segment in the tension-free state and to determine the coil radius on which the wire segment was stored. The springback ratio is an important parameter for the disturbance model, which will be presented in the following.

The change in pre-curvature during uncoiling a coil can only be measured destructively if specimens are taken from the different coil radii. The result of such an experiment is shown in Fig. 3 (b). The measurement shown was taken on a flat wire (material 1.4310) with a thickness of 0.5 mm and a width of 6.5 mm. The coil had an inner radius of 480 mm and an outer radius of 742 mm.

There is a wide range of factors that influence the trend. Both a fluctuating material composition and cross-section variations as well as the storage time and environmental influences such as temperature and air humidity during storage are to be mentioned here. Added to this are the tension conditions during coiling and the deformation history of the semi-finished product. Other influences such as anelasticity or hardening can be added. All these influencing factors are neither known nor individually measurable by the user who wants to process the semi-finished product into a product. For this reason, the disturbance model is initially kept intentionally simple. A linear relationship between the pre-curvature and the stock radius is assumed. Considering Fig. 3 (b), this is quite reasonable. Thus, the estimate $\tilde{\kappa}_0$ of the curvature over the coil radius r_C can be described with the disturbance model

$$\tilde{\kappa}_0(r_C) = m \cdot r_C + n \tag{3}$$

The parameters m and n describe the gradient and location of the linear function. On the one hand, this approach is particularly robust with respect to the large number of influencing factors and, on the other hand, it is straightforward to parameterize, which is advantageous in view of the limited data available when inserting a new coil. It is necessary to find at least two data points P_o at the outer and P_i at the inner of the coil, which give the information about the pre-curvature value and the corresponding coil radius.

The procedure for determining the two data points is shown in Fig. 4. The inner and outer coil radius $r_{C,i}$ and $r_{C,o}$ are geometrical parameters of the coil and therefore known. For the first data point P_o, the pre-curvature $\kappa_{0,o}$ can be measured using the offline measurement (see Fig. 2) after inserting a new coil. The pre-curvature $\kappa_{0,i}$ for the second data point P_i can only be measured when the coil has been completely uncoiled. Therefore, it is predicted using two sources of information. The first one is the springback ratio from Eq. 2. This can be calculated with the outer data point P_o. Assuming that the springback ratio is approximately constant over the coil radius, Eq. 2 can be transformed to κ_f and the pre-curvature at the coil inside can be predicted. The second source of data is a data base in which the curvature values of the previous coils are stored. Thus, the prediction $\tilde{\kappa}_{0,i,j}$ for the pre-curvature at the coil inside of the j-th coil can be calculated to:

$$\tilde{\kappa}_{0,i,j} = \varepsilon \cdot \tau_j \cdot r_{C,i} + (1 - \varepsilon) \cdot K_{0,i} \tag{4}$$

Here, ε indicates how much trust is placed in the estimation via the springback ratio. The value for ε can be set between 0 and 1. The closer ε is to 1, the more confidence is placed in the estimate of the springback ratio. $K_{0,i}$ indicates the moving average of the measured pre-curvature $\kappa_{0,i}$ of the previously processed coils:

$$K_{0,i} = \frac{1}{n}\sum_{k=1}^{n} \kappa_{0,i,(j-k)} \tag{5}$$

In it, n indicates the number of previously processed coils to be considered in the estimation. For the first coil, only the spring-back ratio is available for the estimation.

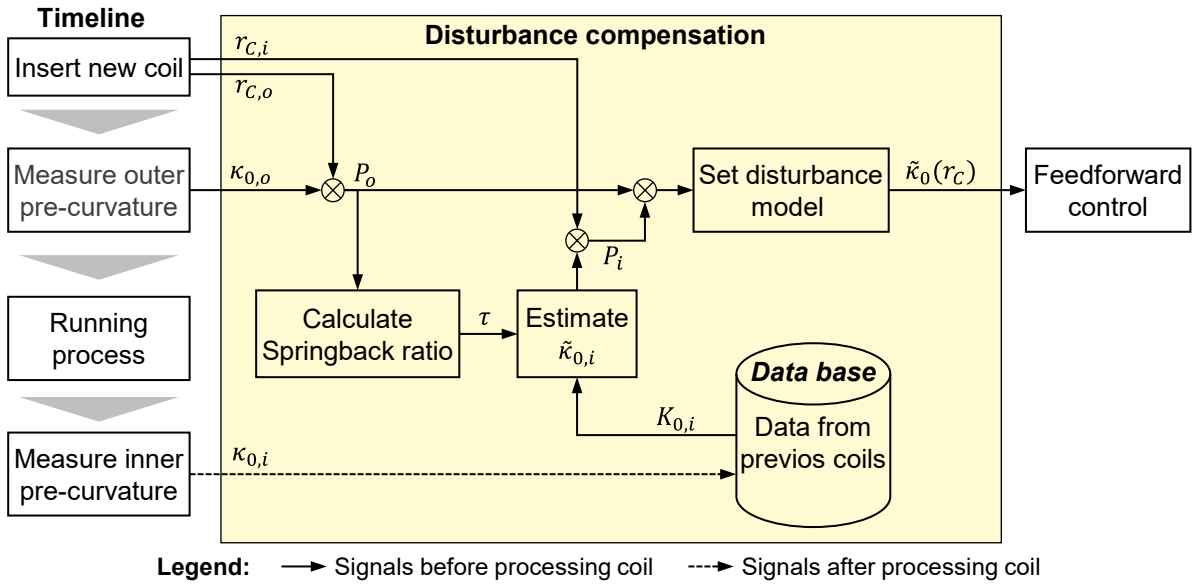

Fig. 4. Working principle of the disturbance compensation algorithm.

In the feedforward control, a nominal trajectory for the straightening rollers can now be determined based on a plant model of the straightening machine, so that the predicted pre-curvature trajectory is compensated over the radius. In combination with the process speed and the coil geometry, the feedforward control specifies a time-based reference trajectory for the positions of the straightening rollers.

This procedure takes into account the properties of the coil to be processed. At the same time, the material behavior on a coil is learned over several coils and the prediction is continuously improved. The more precise the prediction, the higher the straightening quality and the fewer straightening rollers have to be used. Thus, in addition to a high straightening quality, the number of straightening rollers is also reduced and thus the material is straightened more carefully and in line with requirements. As a result, the strength values are maintained and the overbending is reduced.

In order to show how the estimation algorithm works, it was carried out on three samples as an example. A flat wire made of the material 1.4310 and with the dimensions 6.5 mm x 0.5 mm (width and thickness) was considered. The coil had a diameter of 480 mm inside and 742 mm outside. The result is shown in Table 1. The measured pre-curvature $\kappa_{0,o}$ at the outer coil radius and the calculated springback ratio τ are listed in the second and third column. Subsequently, two estimates have been calculated. The first one is the estimate $\tilde{\kappa}_{0,i,1}$ calculated using only the springback ratio. The second estimate $\tilde{\kappa}_{0,i,2}$ was calculated using Eq. 4. For this purpose, $\varepsilon = 0.333$ was chosen. This means that the deflection ratio is trusted to be 33.3 % and the measured values of the previous

coils to be 66.7 %. The value was chosen because the estimate about the springback ratio on the first coil was a bit too high. This trend is confirmed on the other two specimens. Thus, for further coils, the trust ratio can be further adjusted in favor of the curvature values of previous coils. In the last column, the measurement of the pre-curvature $\kappa_{0,i}$ at the inner coil radius is shown for comparison.

Table 1. Result of the estimation algorithm ($\tilde{\boldsymbol{\kappa}}_{\mathbf{0},\boldsymbol{i},\mathbf{1}}$ corresponds to estimate only based on $\boldsymbol{\tau}$; $\tilde{\boldsymbol{\kappa}}_{\mathbf{0},\boldsymbol{i},\mathbf{2}}$ corresponds to the estimation according to equation 4 with $\boldsymbol{\varepsilon} = \mathbf{0.333}$).

#	$\kappa_{0,o}$ [1/m]	τ [-]	$\tilde{\kappa}_{0,i,1}$ [1/m]	$\tilde{\kappa}_{0,i,2}$ [1/m]	$\kappa_{0,i}$ [1/m]
Specimen 1	0.3996	0.2965	0.6177	-	0.5767
Specimen 2	0.4882	0.3622	0.7547	0.6360	0.5944
Specimen 3	0.4617	0.3426	0.7137	0.6282	0.6120

With these calculations, a trajectory for the straightening rollers can now be determined. In the case of specimen 3, the straightening machine would be set for a constant pre-curvature of 0.4882 1/m in a conventional straightening process. With the presented algorithm, a continuous change in pre-curvature from 0.4882 1/m to 0.6282 1/m is considered. This matches the actual change of the pre-curvature to 0.6120 1/m much better than assuming a constant progression. This shows the great advantage of the algorithm. With the estimation of the trajectory of the pre-curvature, the straightening rollers can be continuously adjusted during the running process. The small estimation error is acceptable in any case and is compensated by the feedback control. A static persistence of the straightening rollers in one position over the entire straightening process produces a considerably lower straightening quality and therefore requires a higher number of straightening rollers to compensate for this.

Summary

This paper presents a novel control concept for a manufacturing process consisting of a straightening machine and a punch-bending machine. The concept presented enables the straightening rollers to be readjusted during the manufacturing process. In this way, a novel possibility is created to be able to react to fluctuations in the material properties. Both deterministic and stochastic material fluctuations are addressed. With the help of the learning disturbance compensation, the deterministic change of the pre-curvature over the coil radius is estimated and compensated. Thus, over the entire manufacturing process, the estimation can be continuously improved, and the material behavior learned. Other stochastic material variations can be compensated via online measurement in the punch-bending process.

This method opens up completely new possibilities for an efficient and resource-saving manufacturing process. Compared to conventional levelers, the number of leveling rolls can be reduced. In addition, overbending can be avoided by straightening the semi-finished product as required, which preserves the strength properties of the material. This increases the sustainability of the forming processes in two key aspects: On the one hand, it is possible to react to material fluctuations and adjust the position of the straightening rollers. This leads to a reduction in the rejection rate of the manufacturing process. On the other hand, components can be designed slimmer and lighter by preserving the strength properties of high-strength steels. This results in a high potential for lightweight constructions with high strength steel. The combination of both aspects at the same time in one manufacturing process contributes significantly to a responsible and careful use of resources. At the present time, a potential of up to 8.5% in material savings is estimated. A detailed validation of this control concept is pending in the next research work.

Acknowledgement
The research project IFG 22114 N / P1565 "Development of an innovative straightening machine for three-dimensional straightening and forming" from the Research Association for steel Application (FOSTA), Düsseldorf, is supported by the Federal Ministry of Economic Affairs and Climate Action the German Federation of Industrial Research Associations (AiF) as part of the program for promoting industrial cooperative research (IGF) on the basis of a decision by the German Bundestag. The project is carried out at Fraunhofer IEM.

References
[1] M. Paech, Semi-automatic straightening technology, Wire 58 (2008) 40-46.
[2] M. Oligschläger, Modellbasierte Steuerung von Richtwalzanlagen mithilfe inverser Modellierung und schnell berechenbarer Metamodelle, Dissertation, RWTH Aachen, Aachen, 2015
[3] W. Guericke, Theoretische und experimentelle Untersuchungen der Kräfte und Drehmomente beim Richten von Walzgut auf Rollenrichtmaschinen, Magdeburg, T. H., F. f. Maschinenbau, Diss. v. 27. Jan. 1966 (Nicht f. d. Aust.), Magdeburg, 1966.
[4] A. Pernía, F.J. Martínez-de-Pisón, J. Ordieres, F. Alba, J. Blanco, Fine tuning straightening process using genetic algorithms and finite element methods, Ironmaking and Steelmaking 37 (2010) 119-125. https://doi.org/10.1179/030192309X12549935902301
[5] F.J. Martínez-de-Pisón, R. Lostado, A. Pernía, R. Fernández, Optimising tension levelling process by means of genetic algorithms and finite element method, Ironmaking and Steelmaking 38 (2011) 45-52. https://doi.org/10.1179/030192310X12700328926029
[6] R. Kaiser, T. Hatzenbichler, B. Buchmayr, T. Antretter, Simulation of the Roller Straightening Process with Respect to Residual Stresses and the Curvature Trend, Mater. Sci. Forum 768–769 (2013) 456-463. https://doi.org/10.4028/www.scientific.net/msf.768-769.456
[7] M. Oligschläger, G. Hirt, Implementation of Closed-loop Control Systems in Finite Element Simulations for Roller Leveling, Matériaux et techniques 100 (2012) 1-14.
[8] M. Grüber, Konzepte zur Steuerung des Richtwalzprozesses bei variierenden Richtguteigenschaften, Dissertation, RWTH Aachen, 2019.
[9] L. Bathelt, F. Bader, E. Djakow, C. Henke, A. Trächtler, W. Homberg, Innovative Assistance System for Setting up a Mechatronic Straightening Machine, Key Eng. Mater. 926 (2022) 2397-2405. https://doi.org/10.4028/p-vs07w9
[10] R. Haberland, G. Lauer, Sensorik für die geregelte Blechrichtmaschine, Bleche Rohe Profile 40 (1993) 599-601.
[11] B.-A. Behrens, R. Krimm, Automatisierung des Richtprozesses mit Hilfe einer computergestützten Regelung unter Berücksichtigung der Restkrümmung – Abschlussbericht, FWF, Frankfurt am Main, 2006.
[12] M. Paech, W. Van Raemdonck, Inline wire diagnosis, Wire J. Int. (2015) 92-97.
[13] D. Ashton, V. Deigelmann, M. Stolzenberg, B. Wolter, Closed loop automatic shape and residual stress control during levelling - Final report, Off. for Official Publ. of the European Communities, Vol. 22824, Luxembourg, 2007
[14] F. Bader, L. Bathelt, E. Djakow, W. Homberg, C. Henke, A. Trächtler, Self-optimized, Intelligent Open-Loop-Controlled Steel Strip Straightening Machine for Advanced Formability, in: G. Daehn, J. Cao, B. Kinsey, E. Tekkaya, A. Vivek, Y. Yoshida, (Eds.), Forming the Future. The Minerals, Metals and Materials Series, Springer, Cham, 2021. https://doi.org/10.1007/978-3-030-75381-8_1
[15] F. Bader, L. Bathelt, E. Djakow, W. Homberg, C. Henke, A. Trächtler, Innovative Measurement Of Stress Superposed Steel Strip For Straightening Machines, ESAFORM 2021, 24th International Conference on Material Forming, Liège, Belgique, 2021. https://doi.org/10.25518/esaform21.2382

[16] L. Bathelt, F. Bader, E. Djakow, C. Henke, A. Trächtler, W. Homberg, Mechatronische Richtapparate: Intelligente Richttechnik von hochfesten Flachdrähten, in: Fachtagung VDI MECHATRONIK 2022 , Darmstadt, 2022, pp. 19-24.
[17] O. Föllinger, Regelungstechnik: Einführung in die Methoden und ihre Anwendung, 13. überarbeitete Auflage 2022, VDE Verlag GMBH, Berlin, ISBN 978-3-8007-5518-9

Biodegradable polymers for cosmetic packaging: A technical and life cycle perspective

MIFSUD Sarah[1,a], REFALO Paul[1,b *] and ROCHMAN Arif[1,c]

[1]Department of Industrial and Manufacturing Engineering, Faculty of Engineering, University of Malta, Msida, MSD 2080 Malta

[a]sarah.mifsud@um.edu.mt, [b*]paul.refalo@um.edu.mt, [c]arif.rochman@um.edu.mt

Keywords: Biodegradable Polymers, Sustainable Packaging, Life Cycle Assessment

Abstract. The packaging industry is a significant contributor to the plastic pollution burdening our environment. One main issue with plastics is that they are designed to be durable, and so they persevere in the environment even after they have fulfilled their use. This study aims to analyse the potential benefits of switching to biodegradable and biobased polymers in the cosmetic packaging industry to lessen their environmental impact once disposed of. This assessment commenced with a sustainable material selection process to shortlist a set of viable biodegradable candidate materials (polylactic acid and wood plastic composites), for cosmetic compacts and then comparing them to acrylonitrile butadiene styrene as the benchmark material for this application. The functional, environmental and cost implications of such a change were quantified to validate the suitability of using biodegradable polymers. Functionally, polylactic acid and acrylonitrile butadiene styrene only passed the testing conducted making wood plastic composites an unviable option. wood plastic composites and polylactic acid were found to cost 40-53 per cent more than acrylonitrile butadiene styrene. In terms of the environmental impact, polylactic acid and wood plastic composites reduced the lifecycle impact by 18-30 per cent and the end-of-life impact by 26-42 per cent. The results obtained suggest great potential in shifting to such an alternative.

Introduction

People have become more aware of their impact on the environment, allowing sustainability to shape the way current businesses make long term decisions. This paradigm shift to sustainability is mainly brought about by consumer demand and legislation. Society demands that organisations become responsible corporate citizens and puts their money behind these demands. Therefore, businesses must shift to sustainable practices to remain competitive in today's market [1]. In the cosmetics industry, customers are seeking more eco-friendly products, this is substantiated by a projected natural and organic cosmetic market growth from €11.42 billion in 2021 to €17.35 billion by 2027 [2]. Moreover, fossil-based polymers are made from fossil fuels, a finite resource which is projected to run out by 2042 [3]. One benefit of using such materials is their relatively cheaper cost due to their popularity in the market. However, this will soon change, as the introduction of new regulations to cut down manufacturers' dependence on fossil fuels will lead to higher costs. In 2019, the global plastic production and incineration carbon footprint was estimated to be 850 Mt of CO_2. Such emissions could reach 1,340 Mt by 2030 and gradually increase to 2,800 Mt by 2050 [4]. By noting the accelerated growth of the bioplastic market, going from 2.11 million tonnes in 2018 to a projected 2.62 million tonnes in 2023, it is safe to assume that costs will be reduced as time progresses [5]. Therefore, it is imperative to explore alternative materials with lower carbon footprints throughout their whole life cycle.

A study conducted by Cinelli et al. commented on the unfeasibility of reusing or recycling cosmetic packages due to issues with post-use packaging collection and cleaning of residue contamination. Therefore, attaining a full circular economy proves to be challenging for the cosmetic packaging industry. They also commented on the vitality of considering the functional

Content from this work may be used under the terms of the Creative Commons Attribution 3.0 license. Any further distribution of this work must maintain attribution to the author(s) and the title of the work, journal citation and DOI. Published under license by Materials Research Forum LLC.

requirements of the cosmetic packaging when opting for a biodegradable alternative [6]. Various researchers discussed renewable materials such as PLA and WPC as being suitable candidates for cosmetic packaging due to their decent mechanical properties and affordable cost [7, 8]. Sebastião et al. took a Life Cycle Engineering cradle-to-grave approach to biodegradable material selection. When selecting a biodegradable polymer alternative, they evaluated each candidate material's environmental, financial, and functional benefits, correlating the three through a ternary diagram. Furthermore, by creating a Multi-Attribute Decision-Making process, Sebastião et al. could analyse the performance of the materials by correlating their mechanical properties with the product requirements. The environmental and economic effects were then defined using life cycle analysis (LCA) and life cycle costing methodologies. Finally, the suitability of biodegradable materials was determined, confirming that PLA was well suited for their application [9]. One limitation in this approach is the lack of consideration of biodegradability at EoL; moreover, a more detailed decision matrix would have corresponded to a more inclusive analysis.

After reviewing various literature in this field, the goals of this study were set to select and compare different biodegradable polymers suitable for the cosmetic packaging industry, from functional, environmental, and cost perspectives. Thus, concluding whether biodegradable materials are superior to fossil-based non-biodegradable materials in the cosmetic packaging industry.

Method and Materials

The method followed throughout this study is summarized in Fig. 1. The product definition was the first step in which the case study part for this assessment was selected by following the recommendations of the industrial partner of this study (Toly Products Ltd). The *infinity round compact* made from Acrylonitrile Butadiene Styrene (ABS) material, as seen in Fig. 2, was chosen having a production volume of 2 million compacts per year. In this assessment the term compact will be used to refer to the cosmetic packaging made up of the base and lid excluding any stainless-steel pins, mirrors or powder inserts.

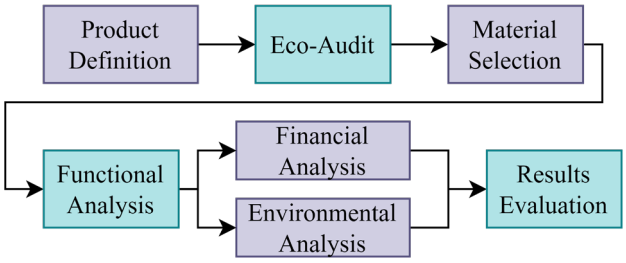

Fig. 1. Method Summary.

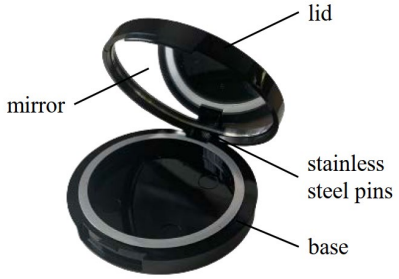

Fig. 2. Case Study Part.

Ansys Granta EduPack 2020 was used to conduct an 'eco-audit' on the case study part. This was used to establish the baseline energy and carbon footprints of the ABS compact at each life stage as shown in Fig. 3. This, together with the design requirements set by the industrial partner were used to create a translation table (Table 1) following the Ashby methodology [10]. By using the relative penalty function method, five materials were shortlisted: Polylactic acid (PLA), PLA with 30% natural fiber, PLA impact modified, Polyhydroxyalkanoates (PHA), Polycaprolactone (PCL) and wood plastic composites (WPC). The Ansys Granta EduPack synthesiser tool was used to create a material made of non-fibrous wood particles and PLA. This allowed for the inclusion of WPC in the assessment by incorporating it in the decision matrix constructed to rank the materials. The direct rating method was used to assign a unique weighting to each criterion in the decision matrix. Three main categories were highlighted and given equal importance: (i) *functional* (flexural strength, impact strength, density, and mould shrinkage), (ii) *financial* (cost), and (iii) *environmental* (biodegradability and carbon footprint). The ranking resulted in WPC placing first,

followed by the datum ABS and then PLA placing third. ABS HI121H, PLA 4043D and WPC Sulapac Universal grades were procured.

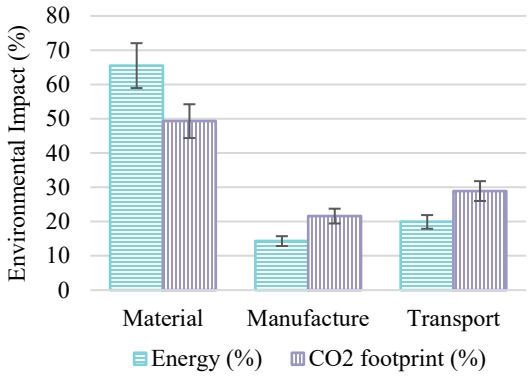

Fig. 3. Eco-Audit results for the Case Study Part.

Table 1. Material selection constraints and objectives.

Constraints	Geometrical: Radius; Thickness; Width Functional: 1. Must be biodegradable 2. Must be injection mouldable 3. Must support a flexural strength of F *[78MPa]* 4. The shrink rate must be like S *[0.4-0.7%]*
Objectives	1. Minimise Carbon Footprint 2. Minimise Embodied Energy 3. Maximise Impact Strength 4. Minimise Density 5. Minimise Cost

A thermal analysis using identiPol QA2 was performed on the materials to understand how their properties change with temperature. Three samples of ABS, PLA and WPC were run to build a database of these materials to be analysed by plotting Tan Delta and Stiffness vs Temperature plots. This equipment also allows the user to identify the contents of the tested material by running a quality index score test (QIS). Since WPC Sulapac Universal is a commercial material, this test was run to compare it to PLA due to an assumption that PLA was used as the biodegradable polymer matrix to which wood fibers were added. Therefore, ten samples of PLA were run through the identiPol QA2 to create a PLA reference dataset that could then be compared with WPC Sulapac Universal. Then, a score was generated between 0 and 10, 0 implying no match and 10 corresponding to a perfect match allowing the user to assume the composition of the material.

In terms of the quality analysis the standard procedure followed by the industrial partner to validate the compact's quality was adhered to. For the package integrity testing, an open-close cyclic test was performed, for which 400 open and close cycles were simulated. After 100 cycles, the compacts were checked to confirm whether the pins remained in the hinge. Furthermore, a drop test was performed on the compacts in which, five compacts were dropped with the compact base parallel and perpendicular to the ground from a height of one meter. The Mecmesin MultiTest 2.5dv force gauge was used to carry out the hinge break test, to determine the minimum force required to break the hinge, and a clip open test to determine the maximum force required to open the compacts' clip.

For the cost assessment the Part Cost Estimator tool available in Ansys Granta EduPack was used to allow for a cost comparison between the different materials. The tool required a series of cost and feature-related input data, from which it could estimate the manufacturing cost for one compact made from the different materials selected.

For the environmental assessment, a four step Life Cycle Assessment as shown in Fig. 4 (following ISO 14040:2006) using SimaPro 9.2 was used. Ecoinvent v3.3 was used for the inventory and impact assessment stages [11]. Furthermore, ReCiPe2016 (Hierarchist) was used as the impact assessment method to convert the life cycle inventories to a list of harmonised impact scores on a midpoint and endpoint level.

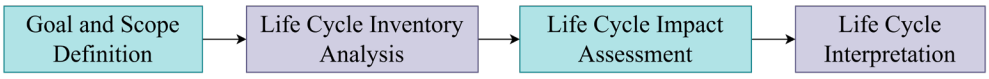

Fig. 4. LCA methodology.

The goals of the environmental LCA were as follows:

- Analyse and compare the impacts of the whole lifecycle of a PLA and WPC compact to those of an ABS compact.
- Compare the effects of different End-of-Life (EoL) scenarios i.e. (i) industrial composting, (ii) landfill, (iii) incineration, and (iv) recycling, for ABS, PLA and WPC compacts.

As for the scope of this assessment, the LCA was conducted for the base and lid of the compact, disregarding any pins and aluminium pans. Furthermore, a cradle-to-grave assessment was followed, neglecting the use and transportation phases. The use phase was ignored as the compact is a static object and thus consumes no energy or resources during its use phase. The transportation phase was also disregarded as it was assumed that similar routes would be followed by all three materials, thus having no significant influence on the overall environmental impact, given their relatively similar densities. Additionally, the functional unit, which is a quantified description of the system's performance was taken to be *2 million Infinity* Round Compacts. During the life cycle inventory assessment stage, the necessary inputs and outputs to evaluate the life cycle impacts of the compact were realised as highlighted in Table 2. The PLA and ABS readily available in SimaPro were selected for the raw material production phase. For WPC, the material was synthesised by first reviewing the material patent as in [12] and then relating this with the thermal analysis QIS test results. By noting that WPC Sulapac scored an 8 compared to PLA, it was assumed that it comprises 80% PLA and 20% wood fibers. As for the manufacturing phase, the injection moulding process was considered for all materials. For the EoL phase, landfilling, incineration, recycling, and industrial composting were considered. In Ecoinvent v3.3, there was no EoL scenario for industrial composting which was considered as an EoL scenario for the biodegradable polymers; thus, this was created by assuming that when the biodegradable compact is placed in an industrial composting facility, it transforms into carbon dioxide, water and humus as stated by NatureWorks in [13].

Table 2. Mass of raw material used per component.

Raw Material	Component	Volume (cm^3)	Density (g/cm^3)	Mass (g)
ABS	Lid	9.543	1.05	10.020
	Base	12.733		13.370
PLA	Lid	9.543	1.35	12.883
	Base	12.733		17.190
WPC	Lid	9.543	1.26	12.024
	Base	12.733		16.044

Following this, two assessments were conducted, (i) an EoL assessment and (ii) a Life Cycle assessment. For the latter, the EoL scenario considered was a mix of all scenarios. This was done as the probability of all the compacts ending up in the same waste disposal environment is highly unlikely as this depends on a series of factors such as the geographical location and product material. Therefore, the method adopted by Moretti et al. in [14] was implemented to model a complete life cycle of the compacts. For ABS, it was assumed that 30% was recycled, 39% was incinerated, and 31% was landfilled; for WPC and PLA, it was assumed that 15% was industrial composted, 15% was recycled, 39% was incinerated, and 31% was landfilled.

The results were interpreted by following the ReCiPe 2016 impact assessment method. This method follows a cause-and-effect pathway that allows for assessing the relationship between the inventories and their potential impacts. This addresses various environmental concerns at the midpoint level and then combines them into three endpoint categories, (in terms of damage to

Human Health, Ecosystems, and Resource Availability) allowing for a detailed and generalised assessment. The results obtained were then interpreted by first noting the impacts on the whole life cycle by switching from ABS to PLA and WPC, together with the effect of different EoL scenarios chosen. As highlighted in ISO 14040:2006, this phase must include the identification of significant issues highlighted throughout the assessment and an evaluation of the study itself [15]. This was done by first reviewing the life cycle inventory to confirm that the methods and data applied across the different materials were consistent and ensuring that long term emissions were considered in all scenarios.

Results and Discussion

Following the series of analyses conducted, the results were analysed to generate a comprehensive understanding of the impacts on the functional, cost and environmental factors when switching to PLA and WPC from ABS for the cosmetic compact case.

Thermal Analysis. From the Tan Delta vs Temperature graph shown in Fig. 5, the material's viscous to elastic response ratio was analysed. From the Tan Delta values at room temperature obtained, PLA registered the most significant Tan Delta value of 0.05 ± 0.01, followed closely by WPC at 0.03 ± 0.01 and then ABS at 0.02 ± 0.01. These values could imply that PLA has the relatively best energy absorption at room temperature. However, one must acknowledge that this is not related to the material's impact strength; thus, further functional testing is required to confirm such an assumption.

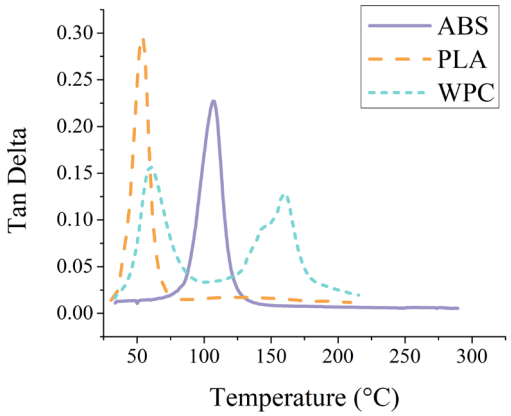

Fig. 5. Tan Delta vs. Temperature (˚C).

Furthermore, by noting the glass transition temperatures of the materials, ABS was the most thermally stable material, followed by PLA and WPC, which are relatively similar. The onset glass transition temperature for both PLA and WPC was initiated at approximately 40˚C, relatively close to room temperature. Therefore, when both compacts are used at temperatures above 40˚C (such as when the cosmetic compact is left in a car in summer), their structural integrity may not be upheld, and the compacts may warp or shrink depending on how excessive the temperatures are.

Table 3 summarises all thermal analysis results. ABS is an amorphous material, so no melting temperature was measured for this material. Furthermore, although PLA is a semicrystalline polymer, it behaved amorphously as no melting point was recorded. This is firstly due to its low crystallisation rate and secondly due to a relatively high cooling rate during the preparation of the testing samples. Therefore, the melting temperature of PLA listed in Table 3 was taken from its datasheet instead [16]. When comparing the WPC to PLA it was observed that the crystallisation rate increased for WPC, due to the presence of the wood particles, thus, resulting in a higher melting point.

Table 3. Thermal analysis results (Mean ± St. Deviation).

Material	Tan Delta at Room Temperature	Glass Transition Temperature (˚C)	Melting Temperature (˚C)
ABS	0.02 ± 0.01	108.50 ± 5.78	NA
PLA	0.05 ± 0.01	61.47 ± 2.25	145-160 [16]
WPC	0.03 ± 0.01	57.77 ± 1.85	187.77 ± 2.32

Quality Analysis. The results from the quality tests conducted were as seen in Fig. 6-9. Considering the overall performance of all three materials, PLA and ABS passed all tests, making PLA a viable biodegradable material for this case study part. WPC, on the other hand, while being visually attractive, was functionally inadequate. Throughout all the tests, the WPC compact was repeatedly failing from the hinge as a result of a low-quality weld line which was formed here, leading to the premature failure of the compact. It was assumed that the wood powder portion of WPC hindered the proper mixing of the two PLA melt flow fronts during injection moulding.

The injection moulded compacts were produced, having a relatively smooth surface finish. The PLA compact had a slight yellow tint which was not as attractive as the others. This may be improved by adding a colorant or master batch to cancel out the yellow tint. Furthermore, the PLA compact had visible streaks along the base, close to the injection point, as seen in Figure 6. These could be due to the low mobility of the polymer and could be avoided by increasing the melt temperature and back pressure during the injection moulding process as well as by adding a colorant. In all cases, there were no pronounced defects on the compact surfaces and all in all, they had a good surface finish.

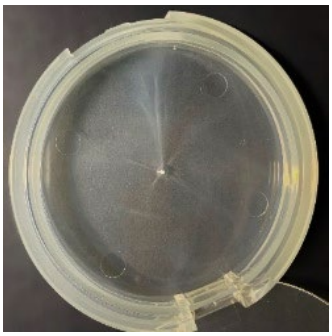

Fig. 6. Streaks along PLA base.

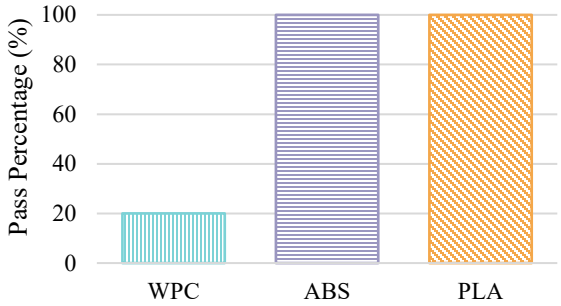

Fig. 7. Drop Test.

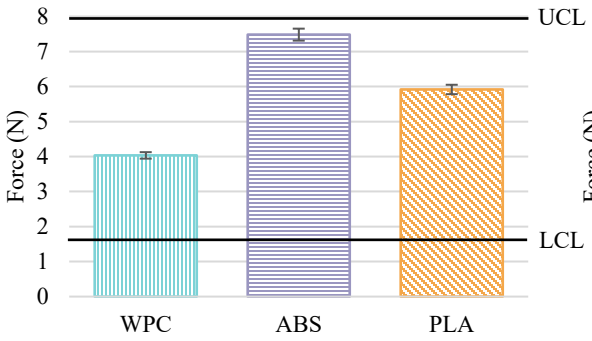

Fig. 8. Clip Opening Test (UCL = 8N, LCL =1.5N).

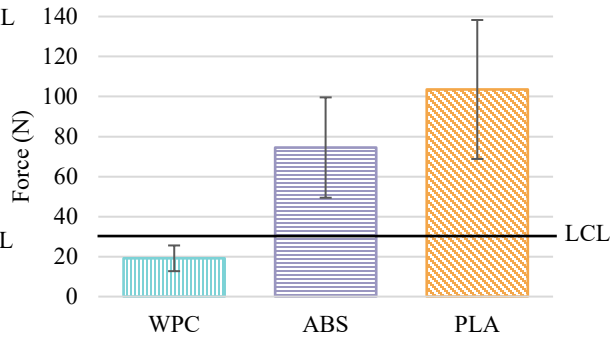

Fig. 9. Hinge Break Test (LCL = 26.5 N).

Cost Assessment. The cost per compact of ABS was €0.15, WPC was €0.21, and PLA was €0.23. The first observation was that biodegradable alternatives cost 40-53% more than ABS. This may be attributed to ABS's relatively more significant market presence. WPC and PLA compacts cost relatively alike, having only a 9% difference between them, which may seem minuscule, however, considering the yearly production of two million compacts, this difference will sum up to 40,000 EUR/yr. This distinction in price may be mainly attributed to the discrepancy in material cost rather than processing related costs.

Environmental Analysis. During the environmental assessment, three endpoint indicators were examined to obtain an understanding of the impact in terms of the effect on human health, resource availability and the ecosystem. To then generate a more in-depth assessment, the midpoint categories were used, allowing for a detailed understanding of the generated impact.

Life Cycle Assessment. After modelling the whole life cycle of the compacts, the relationship as seen in Fig. 10 was obtained by considering the total weighted impact of the three endpoint categories, which is the summation of the impact of the three endpoints. ABS had the overall highest environmental impact throughout its lifecycle. Opting for a WPC compact was found to correspond to a 35.2% reduction in life cycle environmental impact when compared to an ABS compact. Alternatively, opting for a PLA compact would lower the environmental impacts of the whole life cycle by 19.5%. During the material production phase, PLA generated the relatively most significant impact, 23.3% higher than that of ABS. WPC, however, generated relatively the same impact as ABS material production. Therefore, one may conclude that by increasing the content of wood powder in the PLA matrix for WPC, the impact during this life phase may be reduced. Moreover, for the manufacturing phase the biodegradable materials generated a more significant impact on the environment than ABS. The injection moulding of the PLA compact generated a 16.3% higher environmental impact than ABS, and WPC generated a 17.8% higher impact than ABS. This distinction corresponds to the relatively higher energy required and carbon footprint linked to the injection moulding of WPC and PLA [10].

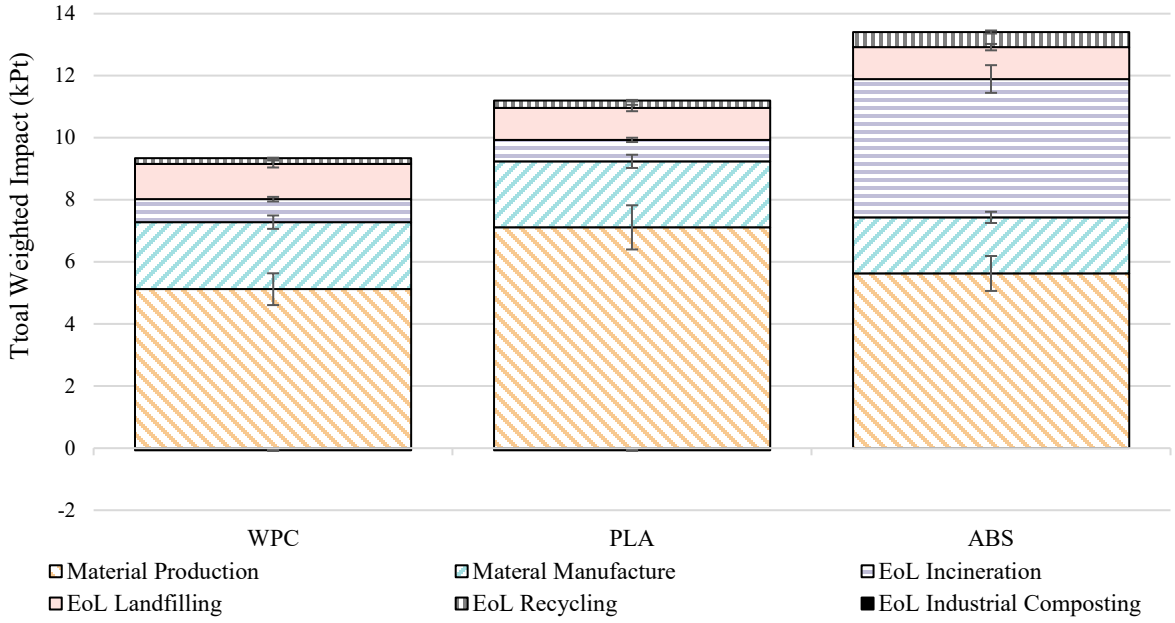

Fig. 10. Total weighted impact of the compact life cycle.

End-of-Life Assessment. In this assessment the EoL scenario was analysed by generating a total weighted impact score of the three endpoints as seen in Fig. 11. This allowed for the complete visualisation of the environmental impact of each EoL scenario.

If one were to assume that the compacts would be incinerated at EoL, opting for PLA would generate a 57.8% smaller environmental impact than ABS and WPC would generate a 78.4% smaller impact than ABS. This distinction could be linked to the carbon dioxide given off during incineration, corresponding to 314,000 kg CO_2 eq for ABS, which was found to be 62.2% more than PLA and 82.9% more than WPC. Additionally, ABS contributed to the emission of 49,600 kg CO_2 eq of methane, which was significantly much more than that of PLA and WPC.

In terms of recycling and landfilling the variation in the results is not as significant as with incineration. With recycling, opting for PLA would reduce the environmental impact by 15.6% and opting for WPC would reduce the impact by 36.3% than ABS. From a midpoint analysis, recycling ABS ranked relatively high, as a substantial amount of waste was being generated, which

in turn was ending up being incinerated. Furthermore, in terms of carbon dioxide emissions during recycling, ABS was found to emit 155,000 kg CO_2 eq, which was 37.5% higher than PLA and 76.2% higher than WPC.

When considering landfilling as an EoL option, PLA generated the most significant impact, while ABS and WPC had relatively the same overall impact. The 14.6% difference between PLA and WPC and the 20.1% difference between PLA and ABS may be attributed to the higher biogenic methane gas emissions of biodegradable materials when landfilled. When a biodegradable material is placed in a landfilling facility, it undergoes anaerobic digestion due to the lack of oxygen, resulting in the emission of excessive biogenic methane gas [17]. When landfilling WPC and PLA, more than 650 kg/year of biogenic methane gas would be given off than when landfilling ABS.

In terms of the industrial composting scenario, the impacts of both WPC and PLA were the lowest out of all other scenarios. The 32.3% difference in environmental impact between the two may be attributed to the 20% wood fibres considered in the WPC material. In fact, one common trend across all EoL scenarios is the relatively lower impact of WPC to PLA which is linked to the wood fibre in the PLA matrix. Therefore, it may be assumed that by increasing the wood content, the environmental impact may be reduced.

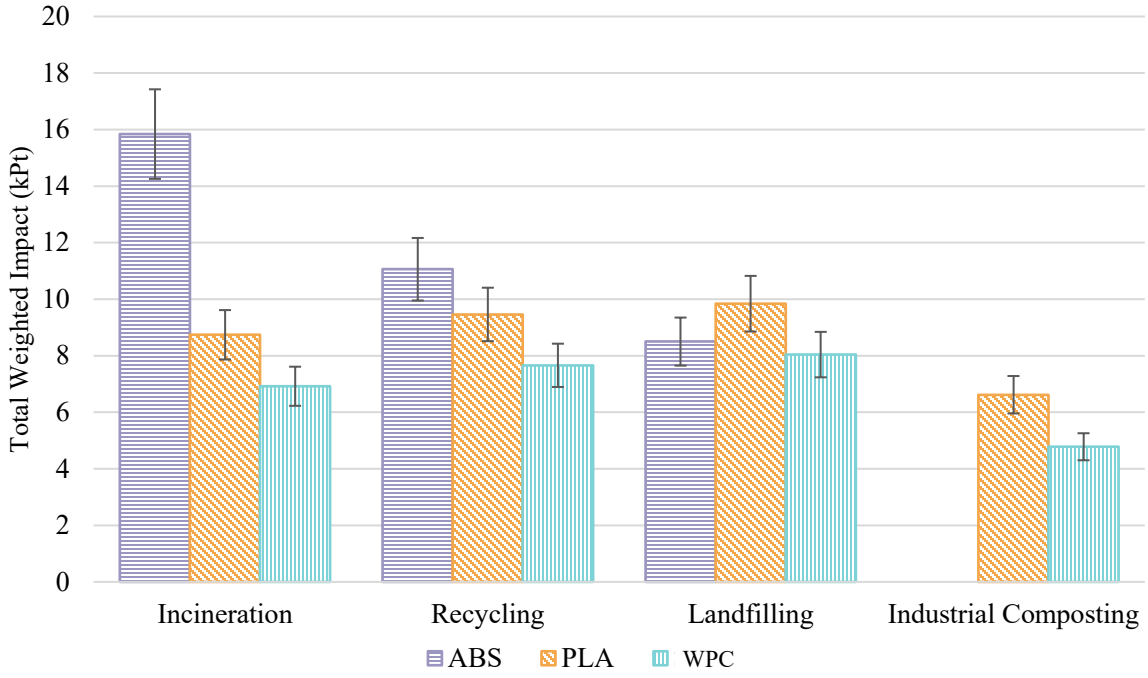

Summary

The target objectives of this study were met as the evaluation of using biodegradable materials in the cosmetic industry was made in terms of the functional, cost and environmental categories. Following this assessment, PLA was recommended as a viable biodegradable alternative to ABS, as it generated a 19.5% lower life cycle environmental impact to ABS and when considering the EoL scenarios for PLA, it generated a 57.8% lesser environmental impact during incineration which is the most likely EoL scenario for cosmetic packaging [6]. Furthermore, PLA was recommended as it passed all functional tests carried out at the industrial partner, at times performing better than ABS, the datum material of this study. The downside of using PLA is that it costs 53% more than ABS. However, this distinction is projected to decrease once biodegradable polymers establish themselves more on the polymer market. Also, by considering the ever-increasing costs of the fossil-based polymers, ABS may no longer be a viable option in the near

future. One must mention that WPC was not recommended as the biodegradable alternative to ABS simply because of its failure to pass the quality functional tests. Had WPC passed the hinge break test, and the drop tests it would have been a relatively better material than PLA in terms of both cost and environmental impact, and so should not be completely disregarded for its application in the cosmetics packaging industry. The results of WPC break test can significantly be improved simply by positioning the weld line away from the hinge area, which in turn can be accomplished by changing the position of the injection gate.

References

[1] J.D. Mittelstaedt, C.J. Shultz, W.E. Kilbourne, M. Peterson, Sustainability as Megatrend: Two Schools of Macromarketing Thought, J. Micromarket. 34 (2014). https://doi.org/10.1177/0276146713520551

[2] Global: natural and organic cosmetics revenue, Statista. Available: https://www.statista.com/forecasts/1264932/worldwide-revenue-natural-organic-cosmetics-market (accessed 01 December 2022).

[3] S. Shafiee, E. Topal, When will fossil fuel reserves be diminished?, Energy Policy 37 (2009) 181–189. https://doi.org/10.1016/j.enpol.2008.08.016

[4] I. Vanderreydt, A. Tenhunen, T. Rommens, L. F. Mortensen, I. Tange, Greenhouse gas emissions and natural capital implications of plastics (including biobased plastics), European Environment Agency, ETC/WMGE 2021/3.

[5] A. Morão, F. de Bie, Life Cycle Impact Assessment of Polylactic Acid (PLA) Produced from Sugarcane in Thailand, J. Polym. Environ. 27 (2019) 2523-2539. https://doi.org/10.1007/s10924-019-01525-9

[6] P. Cinelli, M.B. Coltelli, F. Signori, P. Morganti, A. Lazzeri, Cosmetic Packaging to Save the Environment: Future Perspectives, Cosmetics 6 (2019). https://doi.org/10.3390/cosmetics6020026

[7] A. Sahota, Sustainability: How the Cosmetics Industry Is Greening Up, New York, John Wiley & Sons, Incorporated, 2014, Available: http://ebookcentral.proquest.com/lib/ummt/detail.action?docID =1574356 (accessed 09 May 2022). https://doi.org/10.1002/9781118676516

[8] D. Friedrich, Success factors of Wood-Plastic Composites (WPC) as sustainable packaging material: A cross-sector expert study, Sustainable Prod. Consumpt. 30 (2022) 506-517. https://doi.org/10.1016/j.spc.2021.12.030

[9] J. Sebastiao, Application of Life Cycle Engineering in Material Selection: A case study on performance of Biodegradable Polymers in Injection Moulding, 2015.

[10] M.F. Ashby, Materials selection in mechanical design, 4th ed. Burlington, MA: Butterworth-Heinemann, 2011.

[11] SimaPro | LCA software for informed-change makers, SimaPro. https://simapro.com/ (accessed 18 March 2022).

[12] L. Kyllönen, S. Haimi, Novel materials for packaging, FI127576B, Sep. 14, 2018 Available: https://patents.google.com/patent/FI127576B/en, (accessed 10 March 2022).

[13] NatureWorks, Composting, Available: https://www.natureworksllc.com/What-isIngeo/Where-it-Goes/Composting (accessed 10 April 2022).

[14] C. Moretti et al., Cradle-to-grave life cycle assessment of single-use cups made from PLA, PP and PET, Resources, Conservation and Recycling 169 (2021) 105508. https://doi.org/10.1016/j.resconrec.2021.105508

[15] Life Cycle Interpretation - an overview, ScienceDirect Topics. Available: https://www.sciencedirect.com/topics/engineering/life-cycleinterpretation (accessed 15 April 2022).

[16] IngeoTM Biopolymer 4043D Technical Data Sheet, NatureWorks (accessed 10 April 2022).

[17] P.H.L. Nguyen, P. Kuruparan, C. Visvanathan, Anaerobic digestion of municipal solid waste as a treatment prior to landfill, Bioresource Technol. 98 (2007) 380-387. https://doi.org/10.1016/j.biortech.2005.12.018

Property-controlled forming

Materials Research Proceedings 28 (2023) 2027-2036 https://doi.org/10.21741/9781644902479-218

Analysis of tool heating in cold forging using thin-film sensors

GRÖTZINGER Karl C.[1,a *], SCHOTT Anna[2,b], REKOWSKI Martin[2,c], EHRBRECHT Bernd[3,d], HEHN Thorsten[3,e], GERASIMOV Dmitry[4,f] and LIEWALD Mathias [1,g]

[1]Institute for Metal Forming Technology, University of Stuttgart, Holzgartenstr. 17, 70174 Stuttgart, Germany

[2]Fraunhofer Institute for Surface Engineering and Thin Films IST, Bienroder Weg 54E, 38108 Braunschweig, Germany

[3]Hahn-Schickard, Wilhelm-Schickard-Str. 10, 78052 Villingen-Schwenningen, Germany

[4]Micas Simulations, Temple Court, 107 Oxford Road, Oxford, OX4 2ER, United Kingdom

[a]karl.groetzinger@ifu.uni-stuttgart.de, [b]anna.schott@ist.fraunhofer.de, [c]martin.rekowski@ist.fraunhofer.de, [d]Bernd.Ehrbrecht@Hahn-Schickard.de, [e]Thorsten.Hehn@Hahn-Schickard.de, [f]nick@qform3d.com, [g]mathias.liewald@ifu.uni-stuttgart.de

Keywords: Thin-Film Sensor, Cold Forging, Cyclic Simulation

Abstract. Data acquisition and data analysis to gain a better process understanding are one of the most promising trends in manufacturing technology. Especially in cold forging processes, data acquisition close to the deformation zone seems challenging due to the high surface pressure. Thus far, process parameters such as die temperature are mainly measured with state-of-the-art sensors, including standard thermocouples, which are integrated into the tooling system. The application of thin-film sensors has been tested in hot forging processes for local die temperature measurement. However, the process conditions regarding tribology and tool load in cold forging are even more difficult. In this contribution, the use of thin-film sensors, applied on a cold forging punch for cup backward extrusion, is subjected. The aim is to investigate the applicability of such thin-film sensors in cold forging with special emphasis on temperature measurement in cyclic forming processes. The thin-film sensor system and its manufacturing procedure by vacuum coating technology combined with microstructuring are described. With these thin-film sensors the cup backward cold extrusion of steel billets was investigated experimentally. Cyclic tool heating simulations with thermal parameter variations were performed as a reference to experimental results.

Introduction

Cold forging has a long and established history and is still one of the most cost- and energy-efficient technologies to produce metallic components on a large scale for fasteners industry and automotive drive train systems. Besides the high process productivity and the low energy consumption, the parts show increased yield strength as a consequence of strain hardening during cold forming. Scientific process investigations in cold forging technology are usually conducted under stationary conditions, neglecting effects such as cyclic tool heating, which is inevitably a part of industrial processes. Process instabilities can cause scrap and may lead to unplanned downtimes of the whole process. In recent times, process digitization and process monitoring became one of the most promising trends in manufacturing technology to identify such process instabilities [1]. One decisive parameter for both dimension of the forged component and the tribological system of the process is the thermal condition of the tooling system. Especially during

Content from this work may be used under the terms of the Creative Commons Attribution 3.0 license. Any further distribution of this work must maintain attribution to the author(s) and the title of the work, journal citation and DOI. Published under license by Materials Research Forum LLC.

transient ramp-up phase, temperature may increase a lot. To study the influence of tool heating on part dimensions, correct model boundaries are most important for a good prediction.
Fundamental investigations on elastic tool deformation considering both thermal expansion and mechanical compression were presented by Kuzman [2], who found a linear correlation between the normal pressure applied on a punch and its compression under different thermal conditions. The higher the temperature, the more the thermal expansion compensates the elastic compression of the punch due to mechanical loads. Numerical studies on die heating during process ramp-up in cold forging were shown by Qin et al. [3]. Tool heating was investigated with special emphasis on the characterization of ramp-up duration, until the die temperature reaches a steady state. Müller et al. [4] first investigated thoroughly the effect of temperature increase on friction conditions. In sliding friction tests could be shown, that a temperature increase ($\Delta T = 125$ K) during process ramp-up yields in friction coefficient decrease of up to 45 % for several lubricants such as molybdenum disulphide, polymer and soap. Furthermore, adhesion can be one limiting parameter under certain tribological loads and temperatures. Thus, it is important to be aware of the resulting temperature during the forming process close to the deformation zone - or even better, in the interface between tool and workpiece.

For the measurement of process data in the interface between two bodies, the use of thin-film sensors has been studied for different applications in manufacturing engineering [5]. A thin layer of a certain material featuring specific properties is applied on a surface layer, that insulates the sensory layer from the substrate material. Materials such as chromium are used to create thin-film sensors with a specific shape to allow measurement of the electrical resistance during changing external loads. Such sensors have been successfully applied in machining processes for temperature measurement of cutting inserts right on the rake face [6] as well as in grinding processes [7]. Novel application methods for the thin-film layer were studied in [8] and [9]. The application of thin-film thermocouples in surface textures of carbide tools was investigated in [10]. First applications in metal forming technology were shown in [11], where thin-film sensors were applied on hot forging tools to measure the die temperature in the interface between tool and workpiece during deformation. The wear resistance of the sensors, however, was limited.
In this publication, a first application example of thin-film sensors for temperature measurement on a punch surface in cup backward cold extrusion of steel cans is subjected. Especially the high tribological loads regarding normal pressure, sliding velocity, surface expansion and temperature prevailing in cold forging seem challenging for the application of such sensor systems. Wireless data acquisition is tested to gain real-time data during the experiments using an amplifier and data acquisition unit mounted to the press. The results show, that punch temperature profiles could be recorded, using the thin-film sensor system. Cyclic process simulations, considering the forming process itself, the ejection process and transfer time were performed using QForm UK 10.2.2 software. Parameter variations in cyclic simulations showed the main influencing factors during the die heating process within 250 forming cycles.

Experimental Setup and Process Simulation

System description.
For the investigation of the developed thin-film sensors in cold forging technology, a lab-scale cup backward extrusion process, consisting of a mechanical knuckle-joint press and a data acquisition system, was set up (see Fig. 1). The cup backward extrusion punch was chosen for the application of the thin-film sensors. An embedded system was connected to the press for data acquisition and transfer to a processing system via Bluetooth Low Energy (BLE). The thin-film layer system was designed according to the tribological loads applied to the tool surface, such as normal pressure, relative velocity, temperature and surface expansion, which were gained by numerical simulation. Data visualization and analysis was maintained by a data processing unit.

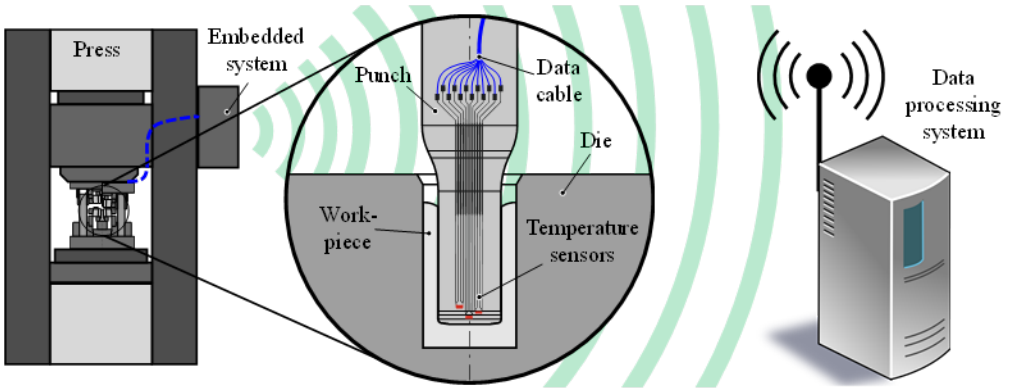

Fig. 1. Procedure for temperature measurement with thin-film sensors and data acquisition.

Thin-film sensor system.

The thin-film sensor system subjected here could be directly applied to the surface of a forging tool and consisted of three different functional layers. These layers were applied to the polished surface of the punch by means of physical vapor deposition (PVD) and plasma-enhanced chemical vapor deposition (PECVD) process. To realize sufficient electrical insulation in the required temperature range between the tool and the sensor structures, an aluminum oxide layer (Al_2O_3) was homogeneously deposited with a thickness of approx. 5 µm. An electrically conductive chromium layer with a thickness of 0.2 µm was chosen for the sensor layer. Due to the positive temperature coefficient (PTC) of chromium, the material was suitable as a temperature sensor, since an increasing temperature led to an increase in electrical resistance. The structuring of the metallic layer was achieved by a combination of photolithography and chemical wet etching. As shown in Fig. 2 a), a final layer of amorphous hydrogenated carbon (SICON®) was applied on top of the structured sensor layer for electrical insulation and wear resistance.

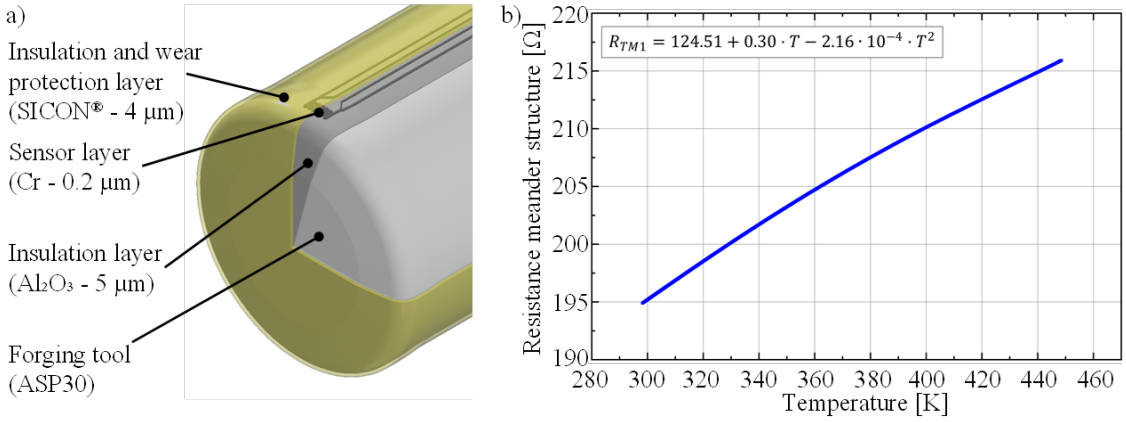

Fig. 2. a) Thin-film sensor on cold forging punch, b) temperature-resistance characterization.

The temperature sensors were conceived in a meandric design that enables a high spatial resolution of the measurement while keeping the sensor resistance in an optimal range for the measurement system. Due to the low resistance of the conductor paths, 4-wire sensing was used, enabling resistance measurements without an influence of the leads. To determine the characteristic curve for each sensor, the thermoresistive behavior was analyzed. For that purpose, the punch was heated up to 180°C in a furnace and cooled down to ambient temperature. A Pt100 reference sensor was positioned on the surface close to the sensor structure. As shown in Fig. 2 b), the dependence between resistance and temperature is approximately linear. To achieve higher accuracy, the measured values were fitted with a quadratic function.

Data acquisition system.

An embedded data acquisition unit was developed to collect the temperature data directly within the press in close distance to the sensory punch to suppress noise. The system is depicted in Fig. 3 a) featuring the sensory punch itself (1), the acquisition unit (2) and the data processing system (3).

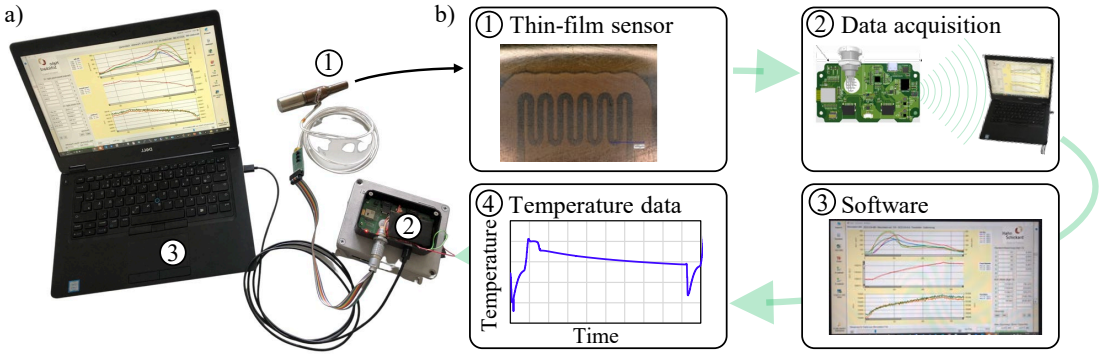

Fig. 3. a) Embedded data acquisition unit and b) process flow for temperature measurement.

The data acquisition process is shown in Fig. 3 b). A variation of the measured physical quantity, here punch temperature, led to a variation of the electrical resistance of the meandric thin-film sensor structure, which was measured by the data acquisition unit. This was achieved by sourcing a known current through the sensor and measuring the voltage drop across the sensor. To compensate the voltage drop over the wires, the sensor was connected with four wires. The known current in the range of 2 mA was flowing through two of them. The 4-point measurement method was used for the punch temperature sensor, as the sensor resistance was in the range of about 230 Ω. The main board included the power management unit, the USB- and BLE-interface for data exchange and the direct interface to the thin-film sensor via the analog frontend. To guarantee a good radio transmission, a polymer case surrounded the main board. Texas Instruments ADS131 analog to digital converter (ADC) was used within the embedded system. In the first stage, the embedded system sent raw digital data to a graphical user interface (GUI) running on a personal computer. The data was processed outside the embedded system. The digital value was transformed to the sensor resistance using the following Eq. 1.

$$R_{Sensor} = \frac{ADC_{value}}{ADC_{max}} \frac{U_{ref}}{I_{Sensor}} \quad (1)$$

where U_{ref} is the reference voltage of the ADC, I_{Sensor} is the known current trough the sensor, ADC_{value} is the measured ADC-Value of the ADC and ADC_{max} is the maximal ADC value of the ADC. Then, using the calibration curve of the sensor in Fig. 2 b), the resistance was transformed into the temperature signal.

Investigation of Tool Heating

Experimental investigations.

Cyclic tool heating was investigated experimentally based on an automated cold forging process. For the experiments, steel billets from DIN C15 (AISI 1015) were prepared by cropping and upsetting (d = 22.2 mm, l = 22.1 mm). A usual lubrication system, consisting of a phosphate conversion layer with soap lubricant (5 g/m^2) was applied to the billets. The cyclic cold forging experiments were performed on a mechanical knuckle joint press MAY MKN2-600/14 (F_{max} = 6,000 kN), equipped with a gripper automation system featuring 6.5 strokes per minute, see Fig. 4 a. Process subjected here was cup backward extrusion. The billet and a cross section of the cold extruded cup are shown in Fig. 4 b).

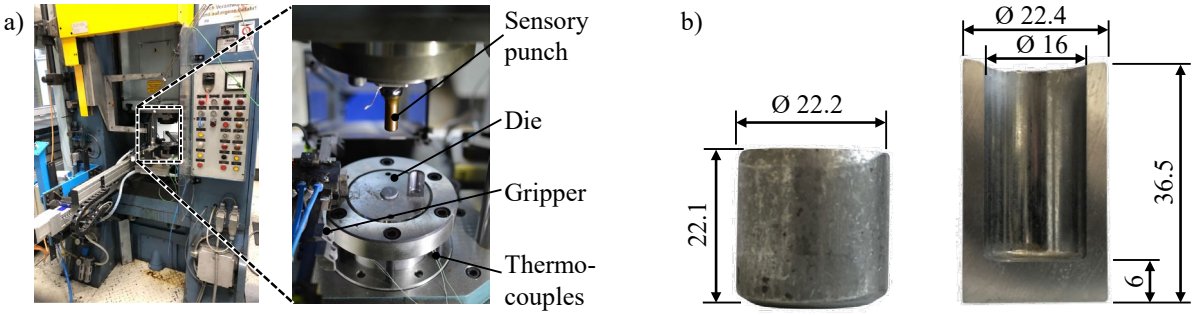

Fig. 4. Experimental setup for temperature measurement in punch and die during cyclic cold forging a) press and tool set, b) workpiece.

The average strain for this process was $\varepsilon_A = (d_a^2-d_i^2)/d_a^2 = 0.48$. During the experiments, process data such as ram stroke and punch load were recorded. As a central part of the investigation, thermal conditions of both die and punch were measured. For the application of thermocouples inside the forming die, a deep hole ($d = 0.9$ mm, $l/d = 50$) was manufactured by electrical discharge machining. The position and depth of the hole were chosen in such a way, that its ground was close to the inside die surface and close to the deformation zone during cup backward extrusion. The punch temperature acquisition was performed using the thin-film sensor and equipment described in 2.3 according to Fig. 2. The cyclic forging experiment was started at ambient temperature (28°C). A maximum of up to 250 cycles in one batch was performed with an average cycle time of 9.25 s.

Numerical investigations.

Punch diameter $d = 16$ mm was used to simulate the forming process of cups with an outer diameter $D = 22.4$ mm. Initial billet height was $h_0 = 22.1$ mm and final bottom height $h_1 = 6$ mm (see Fig. 4 b). Finite element code QForm UK 10.2.2 was used to create an axisymmetric process model with a plastic workpiece and rigid tools. Initial workpiece temperature was set to $T = 28$ °C and mixed friction model with a friction factor $m = 0.12$ and a friction coefficient $\mu = 0.05$ was used for contact definition between workpiece and tools. Decisive for the tool heating simulation were the heat transfer coefficients applied to the interface between the objects (see Fig. 5), such as heat transfer between workpiece and tools (including punch, ejector and die), heat transfer between die and compression ring / compression plates as well as heat transfer between die and environment, considering heat convection. Regarding the material properties, literature values for conductivity and heat capacity of M2 tool steel and AISI 1015 workpiece material were used. A full factorial design of experiments was set up for parameter identification according to the upper and lower limits depicted in Fig. 5. All parameter combinations were performed for 250 forming cycles. For analysis of the most suitable parameter combination, the temperature profiles of simulation variants and experiment were compared. The maximum temperature T_{max}, minimum temperature T_{min} and mean temperature $T_{mean} = (T_{max}+T_{min})/2$ were calculated for each cycle as shown in Fig. 5 b). For the simulated 250 forming cycles, an average value of the deviations in minimum, maximum and mean temperature between experiment and simulations was calculated for identification of the most suitable parameter set within the last third of the subjected number of strokes.

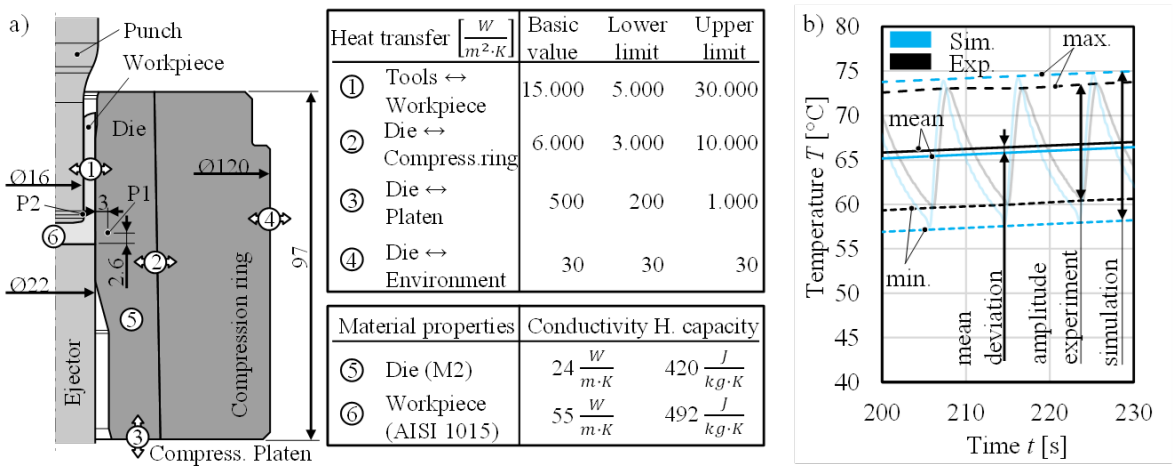

Heat transfer $\left[\frac{W}{m^2 \cdot K}\right]$	Basic value	Lower limit	Upper limit
① Tools ↔ Workpiece	15.000	5.000	30.000
② Die ↔ Compress.ring	6.000	3.000	10.000
③ Die ↔ Platen	500	200	1.000
④ Die ↔ Environment	30	30	30

Material properties	Conductivity	H. capacity
⑤ Die (M2)	$24 \frac{W}{m \cdot K}$	$420 \frac{J}{kg \cdot K}$
⑥ Workpiece (AISI 1015)	$55 \frac{W}{m \cdot K}$	$492 \frac{J}{kg \cdot K}$

Fig. 5. a) Simulation model for cyclic tool heating, b) analysis of heating curves.

Flow stress data for C15 steel was gained from compression tests at the Institute for Metal Forming Technology at the University of Stuttgart. The characterization tests were conducted on a thermomechanical testing system Gleeble 3800 C in a temperature range of 20°C ≤ T ≤ 200°C with strain rates of 0.1 s^{-1} ≤ $\dot{\varphi}$ ≤10 s^{-1}. Die and punch temperature were analyzed in the same area as measured by the thermocouples and the temperature meander, respectively (see Fig. 5 a). Using the cyclic heating simulation module in QForm UK 10.2.2, the whole process chain, consisting of forming operation, return stroke, ejection and transfer time, was modeled to gain representative results for thermal analysis. Mean cycle time in experiments was 9.25 s with a deviation of ± 0.6 %.

Results and Discussion

Experimental results.

The experimental investigations showed, that the embedded system and the wireless communication with the data processing system allowed to record the process data with a sampling rate of 60 Hz. For the punch temperature measurement, a maximum of 22 forming cycles were performed and for the die temperature measurement, 250 cycles were investigated. First surface scratches of the punch coating layer were detected in the area of the punch land after 22 cycles. The sensory structure considered here was not damaged, as it was located in the relief area of the punch. The experimental results for die heating (thermocouple at point P1, see Fig. 5 a) and punch heating (meander structure at point P2) are depicted in Fig. 6 for the second forming cycle of a continuous experiment. During forming process (1→2) with a duration of 1 s, heat was transferred to the tools and resulted in a die temperature increase. Due to the elastic compression of the punch, the measured resistance and thus the calculated temperature decreased in the first 0.2 s of the forming process. Possible reason for that behavior is a temporarily short-circuit between the sensory chromium layer and the punch substrate or the workpiece due to insufficient insulation under combined thermal and mechanical loads. As the heat transfer to the punch increased and the punch load decreased towards the end of the forming process, the calculated punch temperature significantly increased and reached its maximum. Elastic deformation of the workpiece as a consequence of residual stresses led to frictional heat and frictional forces during retraction of punch (2→3). This is why die temperature increased further, where the calculated punch temperature decreased due to the resulting axial and radial loads. During ejection process (3→4) and transfer time, both die and punch temperature decreased due to heat transfer to the surrounding objects and heat convection to the environment. For further analysis of the experimental punch heating profile, the areas with a significant influence of mechanical loads on the measured

resistance and temperature profile respectively, were neglected. Assuming, that the thin-film sensor measured the temperature without force influence only right after retraction of punch (2→3), a simplified linear segment between (A) and (B), as depicted in Fig. 6 a), was inserted. Due to the neglected thermal influence between (2→3), the temperature at point B was assumed as a lower bound estimation of the maximum cycle temperature.

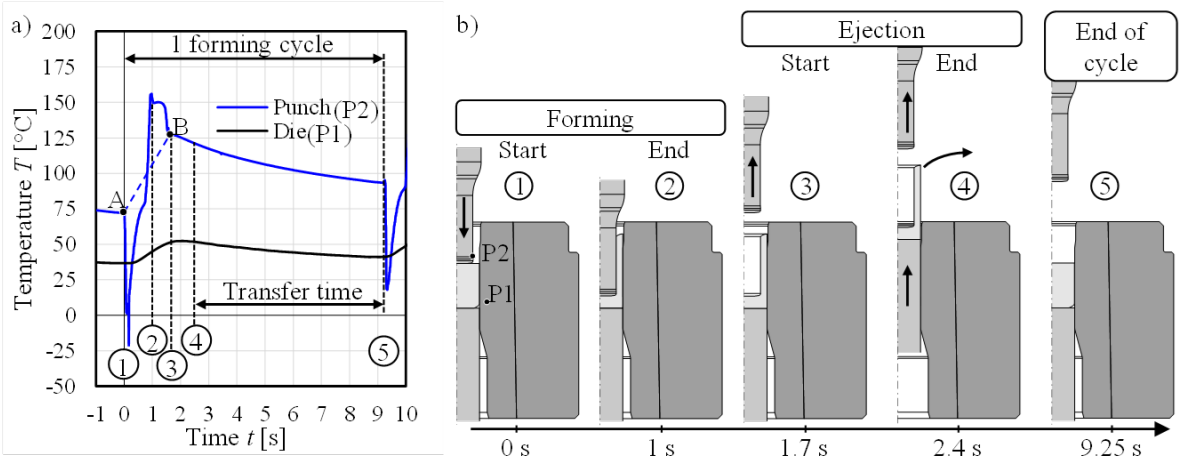

Fig. 6. a) Experimental tool heating profiles for one cycle; b) referring cold forging process.

The temperature profile for one forming cycle in Fig. 6 a) was extracted from a cyclic forming experiment depicted in Fig. 7. The diagram shows both punch and die heating during the first 22 forming cycles of the cold forging process. The punch temperature profile was simplified as described above by neglecting the influence of elastic punch deformation. Minimum, maximum and mean values of die and punch temperature profile were calculated as described in Fig. 5 b). Comparing the profiles after 22 strokes, the mean value of punch temperature is around 2.6 times higher than die temperature. The measurement position of punch temperature was close to the deformation zone, where frictional heat was generated.

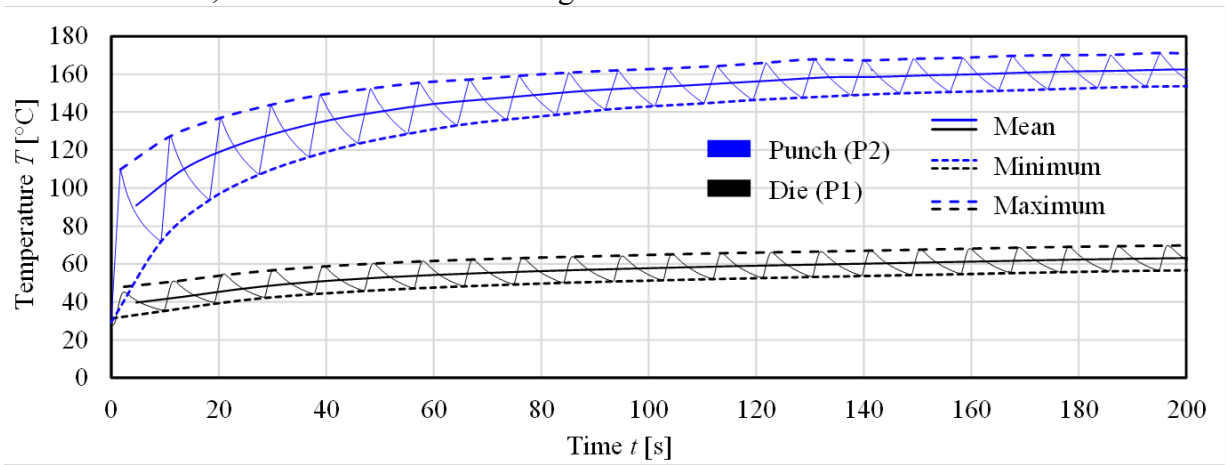

Fig. 7. Comparison of experimental punch and die heating profiles during 22 forming cycles.

While the die temperature amplitude showed a decrease of about 20 % within 22 strokes, the amplitude decrease in punch temperature was about 70 %. Starting from an initial temperature of 28°C, the punch temperature showed a significant increase within the first strokes and a significant decrease during transfer time, where heat convection to the environment was predominant. As the temperature was measured with the thin-film sensor on the punch surface, such effects were even more visible.

Simulation results.

The fitting between full-factorial numerical parameter variations and experiments was analyzed by means of the die heating profile. For each forming cycle, the difference in mean value and amplitude between simulation and experiment was calculated according to Fig. 5 b). For an overall comparison of the parameter variations, the average of both mean value difference and amplitude difference within the last third of the subjected 250 strokes (no. 166-250) was quantified. Fig. 8 shows the magnitudes of both parameters as relative values, referred to the experimental result, for all 27 parameter sets. The sampling of each parameter set, consisting of heat transfer coefficient between workpiece and tools (parameter 1), between die and compression ring (parameter 2) and between die and compression platen (parameter 3) according to Fig. 5 is given below the diagram. The results show, that parameters 1 and 3 were the most decisive for both mean value and amplitude deviation. An increase of the heat transfer coefficient between tool and workpiece decreased the mean value deviation, but in the same way led to a higher amplitude deviation. An increasing heat transfer between die and compression platens (parameter 3) yielded in decreasing mean values of the heating profiles. The thermal field within the die showed after 50 strokes temperatures in the interface between die and compression ring of about 60°C and in the lower area of the die, close to the compression plate, around 40°C. It can be assumed, that both parameters 2 and 3 showed low effect due to the limited die heating prevailing within 50 forming cycles. With increasing number of strokes, the thermal field propagates in the die, which is why the heat transfer between die and adjacent objects becomes more important as shown in Fig. 8.

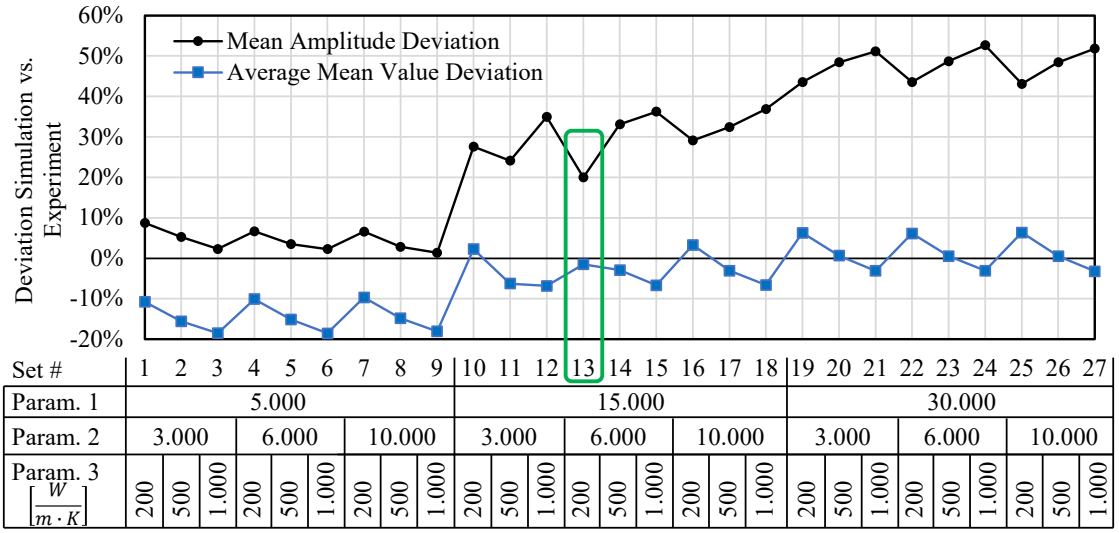

Set #	1	2	3	4	5	6	7	8	9	10	11	12	13	14	15	16	17	18	19	20	21	22	23	24	25	26	27
Param. 1	5.000									15.000									30.000								
Param. 2	3.000			6.000			10.000			3.000			6.000			10.000			3.000			6.000			10.000		
Param. 3 $\left[\frac{W}{m \cdot K}\right]$	200	500	1.000	200	500	1.000	200	500	1.000	200	500	1.000	200	500	1.000	200	500	1.000	200	500	1.000	200	500	1.000	200	500	1.000

Fig. 8. Deviation of cyclic die heating profiles between simulation and experiment as mean values for stroke no. 166-250 for a full factorial parameter study with 27 parameter sets.

For best fit between simulation and experimental results within the subjected strokes no. 166-250, the mean value deviation was the most important factor for the correct prediction of the heating profile. Parameter set no. 13, as highlighted in Fig. 8, was the most suitable for describing the experimental heating profile with a little mean value deviation (-1.5 %) in combination with an amplitude deviation of 20 %. The numerical die heating result for parameter set no. 13 is shown in Fig. 9 in comparison with the experimental results.

The simulation profile showed due to the little mean value difference a good agreement with the tendency of the experimental die heating profile, thus the amplitude difference was about 22 %. Parameter set no. 13 was used to track also the punch temperature profile as a reference to the experimental results for 22 forming cycles. The maximum value of the experimental punch heating profile was well represented by the cyclic simulation result, whereas the amplitude was

overestimated by two times in simulations. The large deviation in punch heating amplitude may arise from the assumptions described in Fig. 6 a). According to this, higher maximum temperature values of each stroke should appear considering the complex interaction between elastic and thermal deformation of the punch. Furthermore, the punch was modelled as a monolithic body, which does not include the thermal properties of the thin-film layer system on the punch surface.

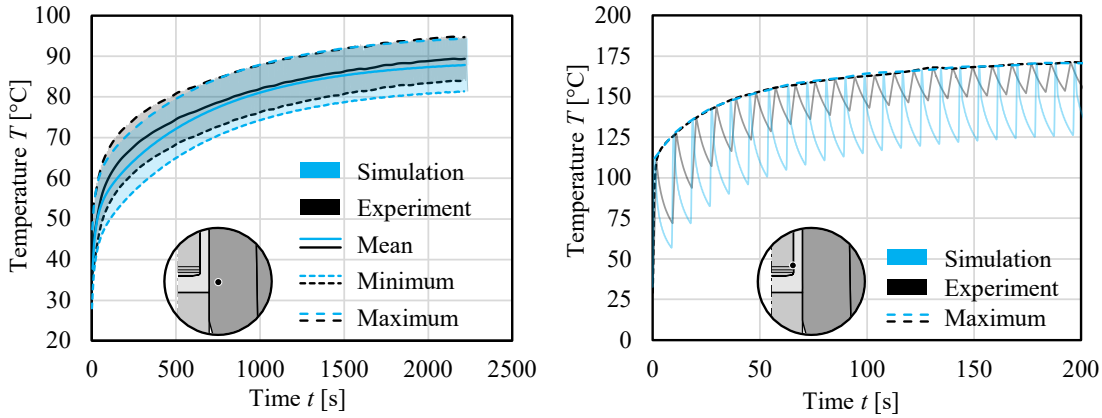

Fig. 9. Comparison of cyclic tool heating in simulation and experiment: a) die, b) punch.

Summary

In this contribution, the application of a thin-film sensor system on a cup backward extrusion punch in cold forging of C15 steel for temperature measurement close to the deformation zone was subjected. Punch heating during cold forging process was analyzed in experiments using the novel sensory structure in combination with the developed data acquisition unit featuring wireless data transfer. For calibration of simulation model, die temperature close to the deformation zone was measured with thermocouples inside the die. Numerical parameter variations were performed to gain suitable heat transfer coefficients for die heating and to use this data for punch heating simulation. The investigations showed, that the application of the thin-film sensor for temperature measurement on a cold forging punch close to the deformation zone is possible considering the prevailing tribological loads during 22 cyclic experiments. The developed embedded system allowed resistance measurement of the applied thin-film meander structure and wireless data transfer via Bluetooth Low Energy, where the actual punch temperature values were calculated based on calibration curves. The thin-film sensors for temperature measurement on the punch surface were due to the physics of the measuring principle force sensitive. A simplified punch temperature profile could be gained by neglecting the area of the process, where the punch was under mechanical load and thus yielded in a lower-bound estimation of the maximum temperature during deformation. The cup backward extrusion process could be modelled using the cyclic tool heating module in QForm UK 10.2.2 considering the whole process chain over a duration of 250 strokes. Parameter variations showed, that the heat transfer coefficients to adjacent objects, such as compression platens underneath the die, become more important for a correct prediction of the heating profile with increasing number of forming cycles. The analysis of mean amplitude deviation and average mean value deviation between measured and simulated die heating profile is a suitable method to find a best-fit parameter set. Using the most suitable parameter set of the die heating investigation also for the punch heating investigation yielded in an underestimation of the measured punch temperature profile, where maximum values were in good agreement.

In future investigations, the calibration of force influence on the measured resistance signal of the thin-film sensor should be considered for a precise estimation of the maximum temperatures during forming process. Furthermore, for both die and punch, more temperature measurement points should be investigated to make proof of the identified heat transfer parameters.

Acknowledgement
The research project was carried out in the framework of the industrial research program (IGF no. 21520 N). It was supported by the Federal Ministry for Economic Affairs and Climate Action (BMWK) through the AiF (German Federation of Industrial Research Associations eV). The authors would like to thank the IGF for the funding and the FSV and Hahn-Schickard for the support during the project period (Multisensorische Werkzeuge für die Kaltmassivumformung).

References
[1] M. Merklein, H. Hagenah, R. Schulte, 4.0 in metal forming - Questions and challenges, Procedia CIRP 79 (2019) 649-654. https://doi.org/10.1016/j.procir.2019.02.055
[2] K. Kuzman, Problems of accuracy control in cold forming, J. Mater. Process. Technol. 113 (2001) 10-15. https://doi.org/10.1016/S0924-0136(01)00688-4
[3] Y. Qin, R. Balendra, K. Chodnikiewicz, Method for the simulation of temperature stabilisation in the tools during multi-cycle cold-forging operations, J. Mater. Process. Technol. 107 (2000) 252-259. https://doi.org/10.1016/S0924-0136(00)00681-6
[4] C. Müller, J. Filzek, P. Groche, Temperaturentstehung und die tribologischen Folgen bei Produktionsbeginn der Kaltmassivumformung, Schmiede JOURNAL (2014) 28-32. Available: https://www.massivumformung.de/fileadmin/user_upload/6_Presse_und_Medien/Veroeffentlichungen/Schmiede-Journal/September_2014/Fachbeitrag_1.pdf
[5] A. Schott, Thin Film Sensor Systems for Use in Smart Production, Technologies for economic and functional lightweight design, Conference proceedings (2020), pp. 220-231. https://doi.org/10.1007/978-3-662-62924-6_19
[6] M. Plogmeyer, G. González, S. Biehl, V. Schulze, G. Brauer, Wear-resistive thin-film sensors on cutting tools for in-process temperature measurement, Procedia CIRP 101 (2020) 85-88. https://doi.org/10.1016/j.procir.2021.02.011
[7] G. Dumstorff, M. Sarma, M. Reimers, B. Kolkwitz, E. Brinksmeier, C. Heinzel, W. Lang, Steel integrated thin film sensors for characterizing grinding processes, Sensors and Actuators, A: Physical 242 (2016) 203-209. https://doi.org/10.1016/j.sna.2016.03.014
[8] Y.X. Cui, B.Y. Sun, W.Y. Ding, F.D. Sun, Development of multilayer composition thin film thermocouple cutting temperature sensor based on magnetron sputtering, Adv. Mater. Res. 69-70 (2009) 515-519. https://doi.org/10.4028/www.scientific.net/AMR.69-70.515
[9] A. Basti, T. Obikawa, J. Shinozuka, Tools with built-in thin film thermocouple sensors for monitoring cutting temperature, Int. J. Mach. Tool. Manuf. 47 (2007) 793-798. https://doi.org/10.1016/j.ijmachtools.2006.09.007
[10] J. Li, B. Tao, S. Huang, Z. Yin, Built-in thin film thermocouples in surface textures of cemented carbide tools for cutting temperature measurement, Sensors and Actuators, A: Physical 279 (2018) 663-670. https://doi.org/10.1016/j.sna.2018.07.017
[11] M. Plogmeyer, J. Kruse, M. Stonis, N. Paetsch, B.-A. Behrens, G. Brauer, Temperature measurement with thin film sensors during warm forging of steel, Microsyst. Technol. 27 (2021) 3841-3850. https://doi.org/10.1007/s00542-020-05179-9

Materials Research Proceedings 28 (2023) 2037-2048 https://doi.org/10.21741/9781644902479-219

Cryogenic reverse flow forming of AISI 304L

ARIAN Bahman[1,a *], HOMBERG Werner[1,b], ROZO VASQUEZ Julian[2,c], WALTHER Frank[2,d], KERSTING Lukas[3,e] and TRÄCHTLER Ansgar[3,f]

[1]Paderborn University, Forming and Machining Technology (LUF), Germany

[2]TU Dortmund University, Chair of Materials Test Engineering (WPT), Germany

[3]Fraunhofer Institute for Mechatronic Systems Design (IEM), Germany

[a]ba@luf.upb.de, [b]wh@luf.upb.de,[c]julian.rozo@tu-dortmund.de, [d]frank.walther@tu-dortmund.de, [e]lukas.kersting@iem.fraunhofer.de, [f]Ansgar.Traechtler@hni.uni-paderborn.de

Keywords: Reverse Flow Forming, Cryo Forming, α'-Martensite, Closed-Loop Control

Abstract. Workpiece property-control permits the application-oriented and time-efficient production of components. In reverse flow forming, for example, a control of the microstructure profile is not yet part of the state of the art, in contrast to the geometry control. This is, due to several reasons, particularly challenging when forming seamless tubes made of metastable austenitic stainless AISI 304L steel. Inducing mechanical and/or thermal energy can cause a phase transformation from austenite to martensite within this steel. The resulting α'-martensite has different mechanical and micromagnetic properties, which can be advantageous depending on the application. For purposes of local property control, the resulting α'-martensite content should be measured and controlled online during the forming process. This paper presents results from the usage of a custom developed cryo-system and different application strategies to use liquid nitrogen as a coolant for local enhancement of the forming-temperature depending α'-martensite content.

Introduction

With growing customer demands the requirements on materials, tools and processes within manufacturing companies are increasing accordingly [1]. Therefore, one of the main objectives of production and manufacturing technology is the reproducible production of (complex) defect-free components. The control of local workpiece properties (e.g. microstructure profile), satisfying customer needs while meeting requirements, has gained more and more importance. This still constitutes a challenge in reverse flow forming, since the process is affected by a large number of influencing factors e.g. tool and machine behavior, properties of the semi-finished product like eccentricity as well as the chemical composition and is therefore hard to predict [2]. A promising approach in this context is an according closed-loop process control. Extensive experimental investigations were carried out in regard to a better control of the α'-martensite content in austenitic stainless steel (AISI 304L) tubes during thermomechanical reverse flow forming. The focus of the investigations was the use of temperature as a control variable to influence local transformation behavior. Since cooling favors the phase transformation (austenite → α'-martensite) liquid nitrogen was applied through a custom developed cryogenic nozzle to maximize the cooling effect and therefore the α'-martensite formation. As part of the cryogenic reverse flow forming different process strategies (timing of cooling during the process) and different cooling strategies (varying cooling areas to produce axial and axial-angular graded α'-martensite areas) were investigated. Local property control e.g. wall thickness and α'-martensite offers an advantage in product labeling. This method can be utilized for a unique, invisible and novel product identification comparable to an invisible QR code. The local manipulation of the α'-martensite content, while maintaining the external dimensions, generates an individual and invisible microstructure profile, making the products tamper-proof. Previous and current work has shown, that two strategies can

Content from this work may be used under the terms of the Creative Commons Attribution 3.0 license. Any further distribution of this work must maintain attribution to the author(s) and the title of the work, journal citation and DOI. Published under license by Materials Research Forum LLC.

be differentiated to decouple the geometry and the product properties. The first strategy employs a multi-stage process that utilizes process parameters such as the feed rate and infeed, which has been demonstrated to be effective in earlier research. Our previous investigations have shown a correlation between the selection of these parameters and the α'-martensite content, while maintaining the external dimensions [3]. The second strategy is part of current work and involves thermomechanical forming, which locally affects the formation of α'-martensite in a single-stage process through the active manipulation of temperature (cooling/heating). To locally grade properties such as the α'-martensite content, it is necessary to differentiate between grading directions. One approach to improve the properties of the tube is through axial grading, where the martensite content is varied along the length of the tube. While previous research has shown success in this method [3], current efforts aim to enhance the technique by also controlling the α'-martensite content in the angular/circumferential direction. For this, rapid cooling methods or periodic/cyclic local cooling or heating must be implemented during the tube forming process, as the tubes need to reach varying temperature profiles in both the length and angular direction as they rotate. However, precise control of these properties remains a challenge and is yet to be established as a common practice. The ongoing research endeavors to develop new techniques and methods to overcome these challenges and achieve the desired level of local property control. The α'-martensite contents for local grading of the microstructure profile and the creation of an invisible labeling of the components must be distinctly detectable for the sensors to be used. The differences of the martensitic and non-martensitic ranges must be well above the measurement uncertainty of the measuring instrument. For these investigations the feritscope FMP30 from Helmut Fischer was used with a measuring accuracy of approx. ±1 %.

Principles and Material

Flow forming as an incremental process offers various advantages in terms of flexibility and efficiency [4]. Based on a defined wall thickness reduction within tubular components the process allows the production of parts with an excellent shape and dimensional accuracy as well as prime surface qualities [5]. Components that meet such high standards and offer the above-mentioned advantages can be used to produce, among others, components for the aerospace industry. Here, precision and lightweight play an essential role, which is covered by flow forming. Just to name a few application examples: drive shafts for jet engines and helicopters are flow formed components [6]. In principle, the rotating tube is set backlash-free on a rotating mandrel and is typically deformed by a multiple roller tool arrangement generating the necessary deformation forces for the wall thickness reduction. The roller tools can be moved in radial and axial direction, reducing the outer diameter of the tube and thus generating an elongation. In reverse flow forming, the material flows in the opposite direction to the roller tool movement [7], as demonstrated in Fig. 1. This process is the focus of this paper.

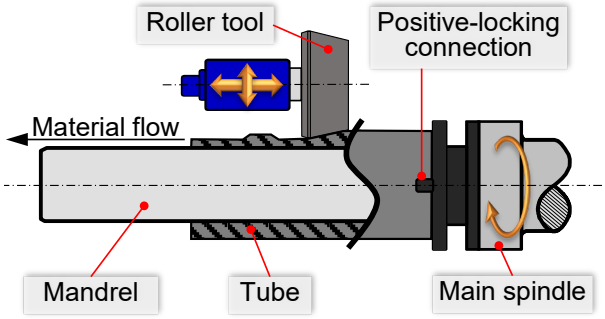

Fig. 1. Reverse flow forming principle.

The stainless steel AISI 304L (X2CrNi18-9, 1.4307), which is used as semi-finished material for the seamless tubes, is austenitic. Containing a metastable austenitic phase, a phase transformation from austenite to α'-martensite could occur strain- or temperature-induced [8]. The α'-martensite, nucleating at the intersections of the shear bands, has different mechanical and micromagnetic properties and can be detected offline (e.g. Feritscope) or online via micromagnetic sensor equipment (e.g. 3MA-II) like addressed in previous papers [9,10,11]. Besides the mentioned influencing factors, the α'-martensite formation is also dependent of the chemical composition and the austenite grain size of the semi-finished product [12,13]. Depending on the chemical composition of the material batch the potential for α'-martensite formation can significantly vary. The used material batch offers a qualitatively low potential for α'-martensite formation, since fractions of austenite stabilizing elements like nickel are relatively high [14]. Comparisons with different material batches show for the same process parameter combinations variations in resulting α'-martensite content between approx. 10 % and 85 %. This aspect again emphasizes the need for property control. For material batches with low potential for α'-martensite formation, more deformation and/or lower (cryogenic) forming temperatures must be achieved to reach similar α'-martensite contents. Since the semi-finished tubes with an outer diameter of 80 mm are seamless, they contain an eccentricity and therefore slight deviations from the nominal wall thickness of 4 mm.

Machine and Experimental Setup

All experiments were carried out on a PLB 400 spinning machine from Leifeld Metal Spinning GmbH (Ahlen, Germany) with a drive power of 11 kW and a maximum achievable spindle speed of 950 rpm. The hydraulically driven cross support equipped with two machining axes, was developed at LUF at Paderborn University and is capable of generating a maximum force of 35 kN on each of its axes (X/Y-axis). By default, the operating pressure of the external hydraulic system amounts 80 bar and can be increased up to 120 bar, when required. Additionally, a universal tool holder allows the attachment of a variety of tools or tool systems. For the investigations, a single-roller tool configuration was used to provide enough space for the sensor equipment, which will be applied for online-measurement purposes, which was presented in previous publications of the authors and is not the focus of this paper. The roller has an attack angle of $\alpha = 12°$, a transition radius of $R = 2$ mm and an exit angle of $\beta = 5°$. For the external dimensions, a rolling diameter of 155 mm and a roller width of 46.5 mm can be measured. In the process, a solid counter holder with two ball-bearing counter rollers is used to support the mandrel. A cryogenic cooling system was developed for the experiments and placed on the machine bed. It contains a liquid nitrogen tank, a flexible stainless steel tube for the liquid nitrogen, pneumatic tubes, a set of valves and a two-component cryogenic nozzle that bundles the liquid nitrogen and transports it with compressed air surrounding it. The cryogenic nozzle was mounted in a distance of 8 mm from the specimen, which was to be deformed. For temperature monitoring an infrared camera (Infratech VarioCam head HiRes 640) was used. Fig. 2 shows the machine and experimental setup.

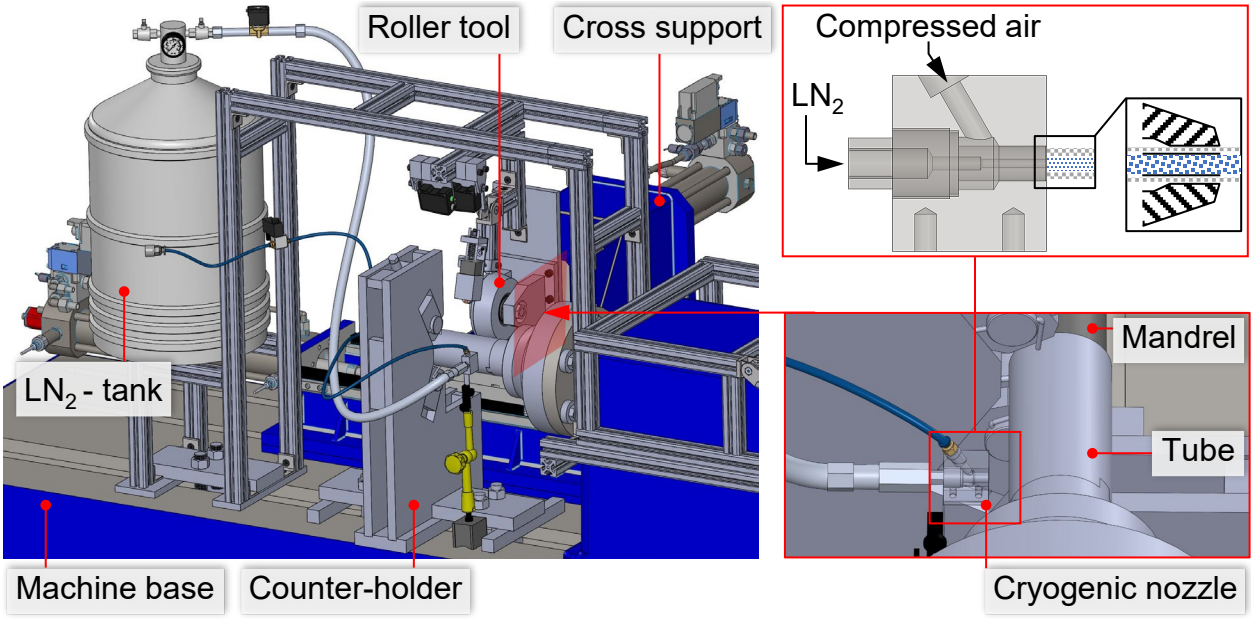

Fig. 2. Machine and experimental setup as 3D-model.

Experiments with three different cooling strategies were conducted. In the first experimental cooling strategy, the tube was rotated and simultaneously shock-cooled for a certain period of time prior to forming. Due to the stationary positioning of the cryogenic nozzle, this resulted in an axial section on the tube which was cooled down circumferentially (ring-shaped cooling prior to forming). The second experimental set-up was performed in analogy to the first strategy, with the difference that the shock cooling was conducted simultaneously to the flow forming (ring-shaped cooling while forming). In the third experimental set-up the aim was to create a spot that was shock-cooled before forming, which is why the rotation was switched off during the cooling of the component. (spot cooling prior to forming). For all three cooling strategies a radial infeed of 2 mm, a feed rate of 0.1 mm/s and a rotational speed of 5 rpm was selected. Fig. 3 shows the initial state of the specimens and the deformed specimens on which the cooled areas are highlighted in red.

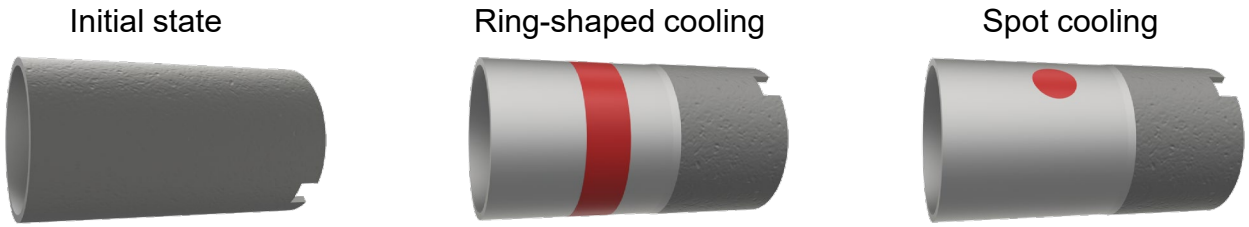

Fig. 3. Cryogenic deformed areas on specimens (highlighted in red).

Results and Discussion

For the first cooling strategy (ring-shaped cooling prior to forming) the tube, with an initial temperature of 16°C, was cooled down with the liquid nitrogen in the ring-shaped area for approx. 200 s to -8°C using a rotational speed of 5 rpm. Then the reverse flow forming process was initiated. The time span between the cooling of the tube and the deformation of the ring-shaped cooled area was approx. 115 s and the initial pressure of the liquid nitrogen tank was at 0.5 bar.

For the second cooling strategy (ring-shaped cooling while forming) the tube had an initial temperature of 17°C and was also cooled down to -8°C in the ring-shaped area using the liquid nitrogen. In this case, the forming process was started before cooling. Only after reaching the tube section to be cooled, the cooling was started and sustained for approx. 200 s, also at an initial

pressure of 0.5 bar. At a feed rate of 0.1 mm/s, an axial tube section of 20 mm was thus formed with active cooling. Fig. 4 shows the actual setup for the second cooling strategy.

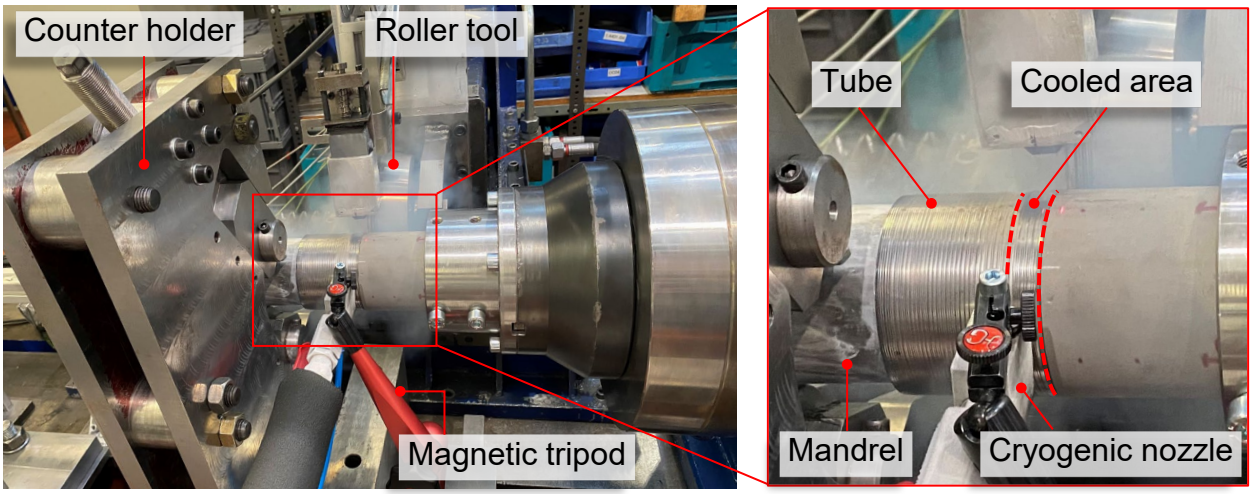

Fig. 4. Ring-shaped cooling while forming (second cooling strategy).

The third cooling strategy (spot cooling prior to forming) included a tube with an initial temperature of 15°C. After the reverse flow forming process was initiated prior to cooling, the axial feed and the rotation of the mandrel was switched off while forming was taking place. The system was switched off so that the area, in this case a circular spot, could be cooled down for approx. 130 s until the surface of the tube was frozen, again with a liquid nitrogen tank pressure of 0.5 bar. The infrared camera was not able to measure the temperature in the spot since it displayed a temperature of -273.15°C, which corresponds to absolute zero with 0 K. Then the cooling process was stopped and the reverse flow forming process was restarted to form the cooled spot as well as the rest of the tube. Here, the cooling process was not sustained while forming, since the rotation would again result in the cooling of a ring-shaped area. Fig. 5 shows the actual setup for the cooling strategy.

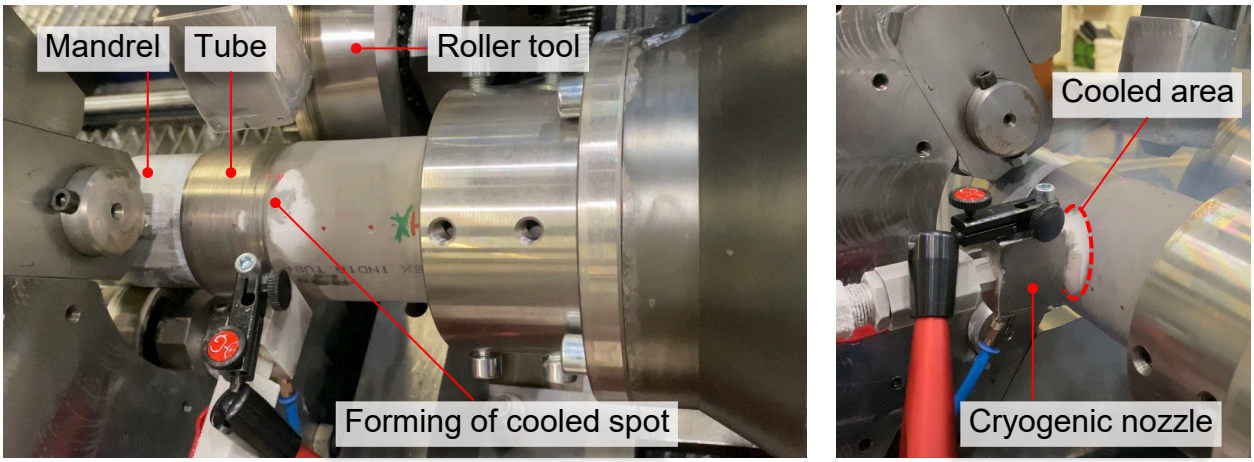

Fig. 5. Spot cooling prior to forming (experiment 3).

The resulting tubes were investigated through measurements with a Feritscope (FMP 30, Helmut Fischer) using the magnetic induction method, a micromagnetic sensor (3MA-II, Fraunhofer IZFP) based on magnetic Barkhausen noise (MBN) effect, eddy current analysis (Modulus r - 200 kHz) and hardness tests (HV3). The measurements were used to localize and

quantify the α'-martensite content, which correlates with the underlying measured variables such as the maximum amplitude of the MBN profile (Mmax) [15,16]. Fig. 6 shows the measurement results with the Feritscope, where cooled areas show higher α'-martensite contents. Four measuring circles with identical distances of 22 mm were used for the measurements. For this purpose, the measuring circles were divided into 30°-sections. The result for the second cooling strategy shows the highest α'-martensite content with a maximum of approx. 17 vol.-%, which is comparatively low due to the chemical composition of this specific material batch, which contains high proportions of austenite-stabilizing elements. This result can also be explained by the fact that the component was deformed during cooling and therefore could not warm up towards room temperature before deformation, in contrast to the first cooling strategy. Also, the coolant flow continuously dissipates the forming heat. In addition to measuring circle 2 where the cooling was mainly carried out, an increased α'-martensite content can be observed in measuring circle 1. This is due to the fact that this section adjacent to measuring circle 2 was also cooled during the cooling of measuring circle 2. Since there is little time between the cooling of measuring circle 2 and the forming of measuring circle 1, this result is also reasonable. The ups and downs for the α'-martensite measurement in the measuring circle 2 are due to pulsation of the liquid nitrogen. As a result of the evaporation of the liquid nitrogen, due to the comparatively warm hose, liquid nitrogen and a gas mixture alternately escape from the nozzle. This leads to inhomogeneous cooling of the rotating tube section. The first cooling strategy shows the same effect due to pulsation of the liquid nitrogen. The α'-martensite content is also lower than for cooling strategy 2, which is due to the time span between the cooling of and the deformation of the ring-shaped cooled area. For the cooling strategy 3 only one large peak for the α'-martensite content is visible, since only one spot was cooled down. An increase in α'-martensite content for areas close to the spot is due to thermal conduction to the adjacent area.

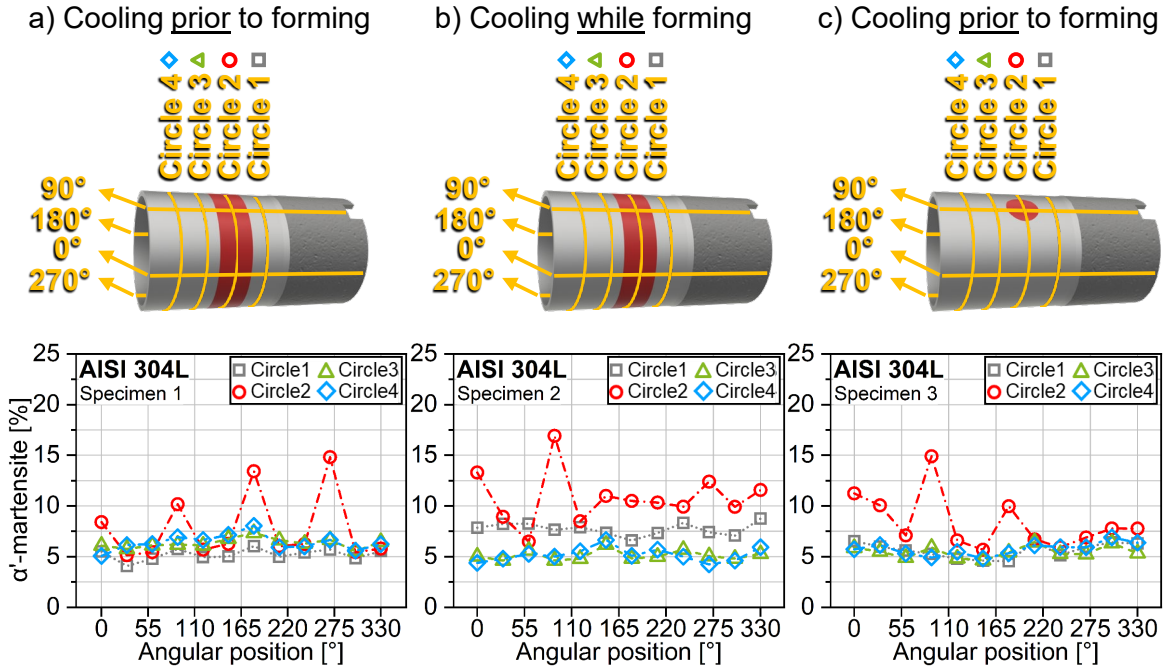

Fig. 6. Feritscope measurement results for the three applied cooling strategies.

The measurements with magnetic Barkhausen noise (MBN) effect performed with the 3MA-II, shown in Fig. 7, also display higher values for measuring circle 2, which is located in the cooled areas. Similar to the previous measurements with the Feritscope, areas adjacent to measuring circle 2 also have slightly higher values, as they have been co-cooled.

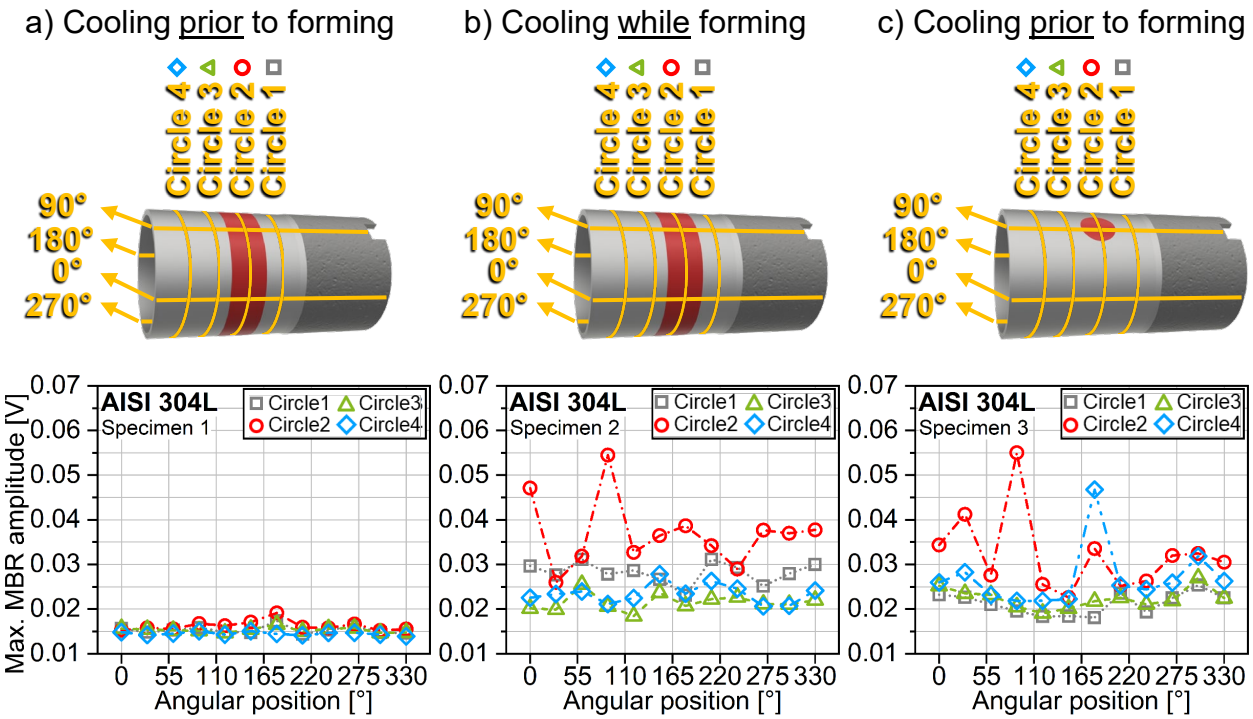

Fig. 7. 3MA-II measurement results for the three applied cooling strategies.

Other than expected, here the values for the measurements regarding cooling strategy 1 show low magnitudes for measuring circle 2. This might be due to the fact that the areas with martensitic microstructure might be smaller in terms of area than in cooling strategy 2, for example. However, it may also be caused by disturbance influences such as the incorrect alignment of the measuring head to the workpiece.

Eddy current analysis was used as a further non-destructive characterization technique. The changes of conductivity and permeability of the material due to the phase transformation from austenite into α'-martensite can be detected by means of the parameter "modulus r". This parameter is computed from real and imaginary parts of the impedance vector corresponding to each deformation state with respect to a point considered as the initial condition (unformed metastable austenite). The measurements, shown in Fig. 8, indicate a strong similarity to the measurements with the Feritscope. Here, the correlation of the measuring variable with the α'-martensite is also visible. The comparison of the measured α'-martensite contents with the Feritscope in Fig. 6 shows in cooling strategy 1 there are higher magnitudes for the parameter "modulus r" for lower α'-martensite contents, which could be due to a superposition of effects triggered by other variables influencing "modulus r".

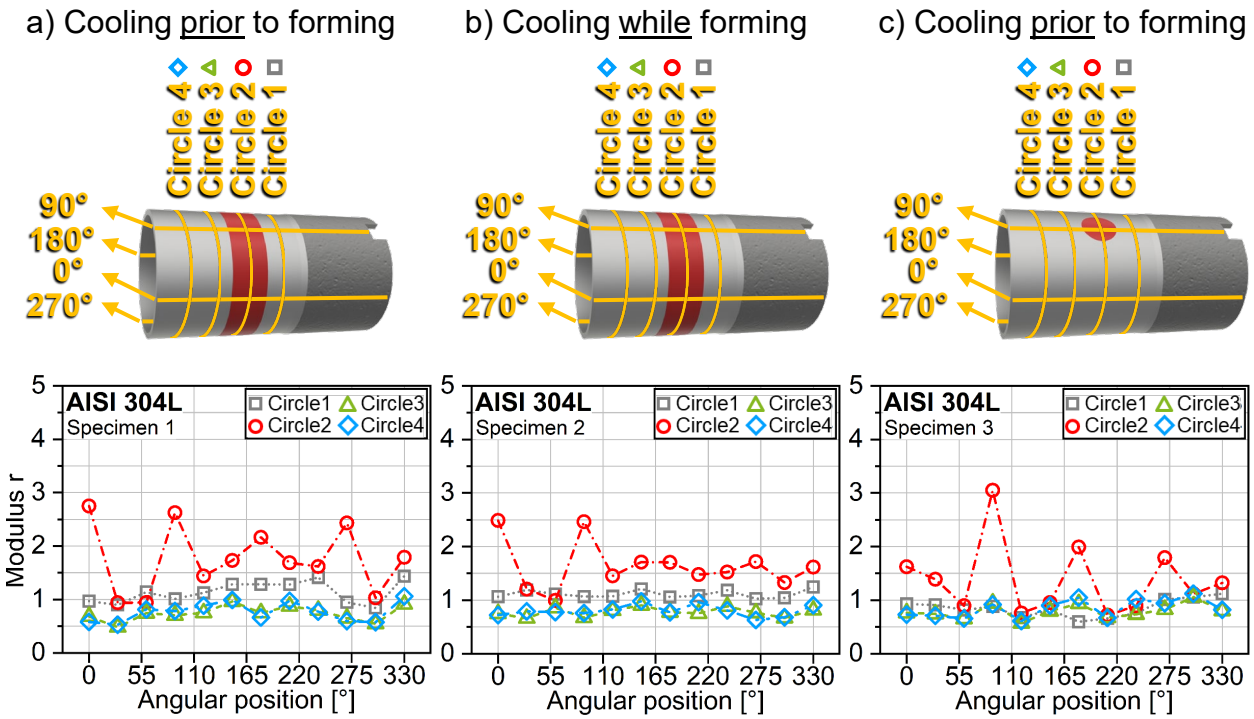

Fig. 8. Eddy current analysis for the three applied cooling strategies.

A comparison of the results from the hardness tests (HV3) in Fig. 9 show the same correlation with the α'-martensite content. The hardness increases with higher magnitudes of α'-martensite. As can be seen, for example, from the measurements for cooling strategy 3, the highest value for hardness results here, although the α'-martensite content is higher for cooling strategy 2 (compare Fig. 6). This is due to the influence by the work hardening, which can be quite different.

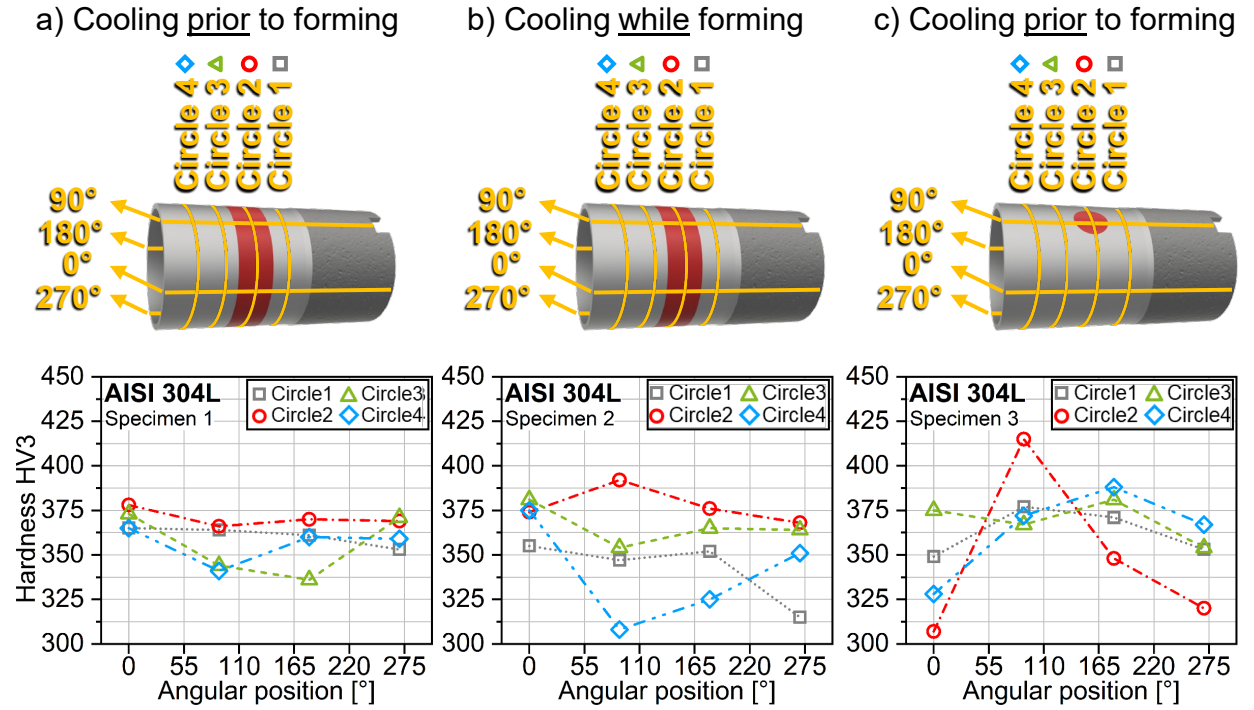

Fig. 9. Hardness tests (HV3) for the three applied cooling strategies.

Investigations of the wall thickness (compare Fig. 10) did not show any influence caused by the martensitic microstructure. The wall thickness increase in feed direction of the roller tool is caused due to material-pile-up in feed direction.

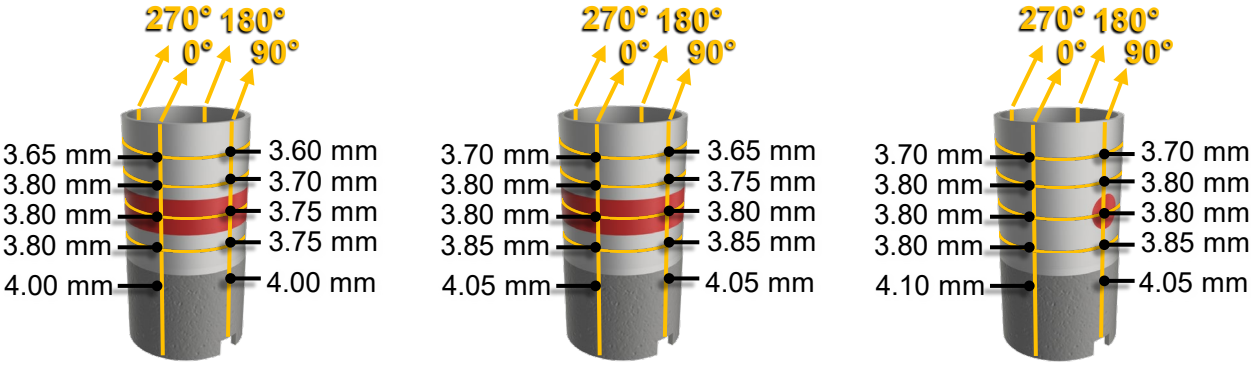

Fig. 10. Wall thicknesses resulting from the three applied cooling strategies.

The EBSD results in Fig. 11 show the microstructure of the cryogenic flow formed areas. The phase mappings display a qualitative distribution of austenite (blue) and α'-martensite (red) phases. The inverse pole figure (IPF) shows the grain orientation of the microstructure. The pictures of the areas deformed at room temperature conditions, indicate almost no transformation of the microstructure, which remains predominantly austenite (blue color in the phase mapping). This correlates well with the micromagnetic measurements on these areas, where almost no α'-martensite was detected. On the cryogenic flow formed area the dark lines in both pictures correspond to shear bands, which are a characteristic of the phase transformation during plastic deformation of metastable austenite. The intersection points of these shear bands are energetically favored nucleation points of the α'-martensite (red color in the phase mapping), which is shown on the red colored areas of the phase mapping.

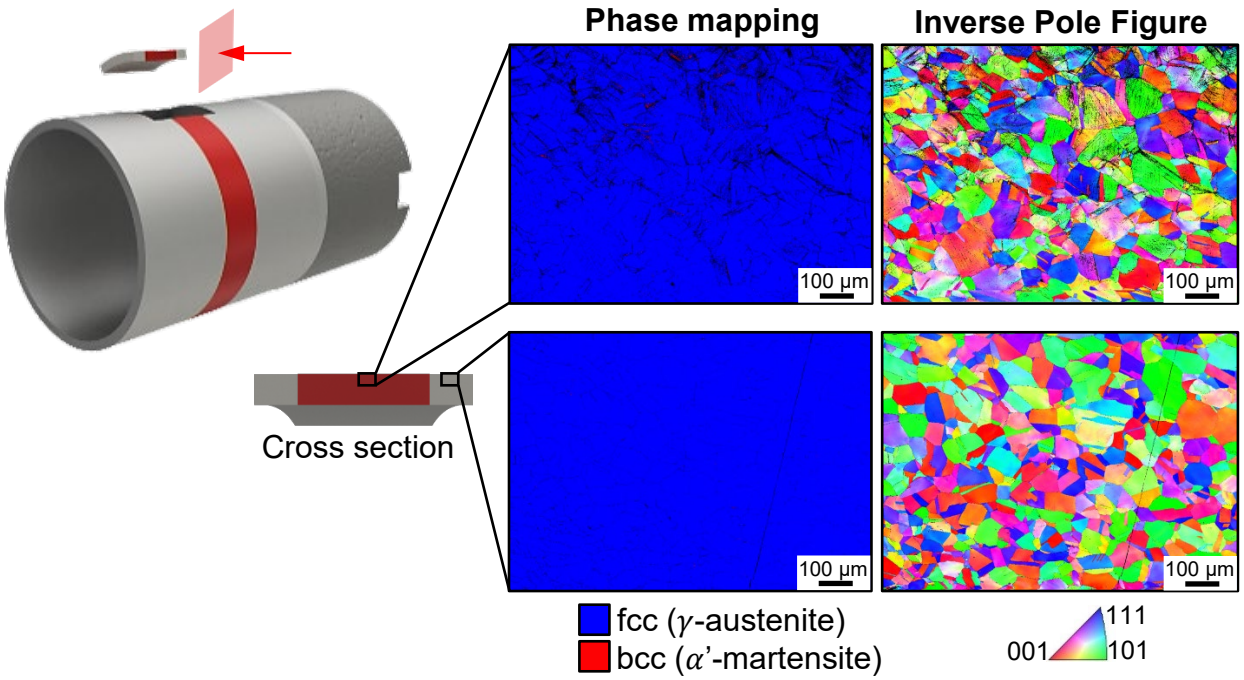

Fig. 11. EBSD results of the microstructure of the cryogenic flow formed area: phase mapping and inverse pole figure (IPF).

A higher quantity of shear bands and nucleation points of α'-martensite is present close to the outer surface, where the cryogenic deformation occurs. On the deeper areas, the deformation decreases which is evidenced in a lower quantity of shear bands and α'-martensite.

Summary

The results from the investigation show that the cryo system is useful for the invisible local enhancement of the α'-martensite content. The cryogenic nozzle is capable of focusing the liquid nitrogen surrounded by compressed air to form a cooling jet. As a result from the investigation of the different cooling strategies, cooling during forming was found to be the most effective method for maximizing the α'-martensite content. The investigations also show that the material batch of the tube used allows comparatively little α'-martensite formation due to its chemical composition, which contains high proportions of austenite-stabilizing elements. The investigations have also shown that automation of the cooling, i.e. inclusion of the cooling strategy in the process control, appears to be useful. Currently, to cool a spot, as with cooling strategy 3, both process stop and shock cooling were performed manually. In the future, the cryogenic system is to be further developed so that position-dependent (depending on the axial position of the roller tool) and angle-dependent (angular position of the tube to be formed) cooling is controlled automatically. This enables the automated production of so-called 2D-gradations (axially and angularly graded structures) similar to cooling strategy 3. For this purpose, an absolute encoder has been implemented within the forming machine, via which the angular position of the tube can also be incorporated into the control system. Furthermore, electromagnetic valves are currently being implemented in the control system in order to automate the release of the liquid nitrogen and the compressed air. The planned design of the cryogenic system is shown in Fig. 12.

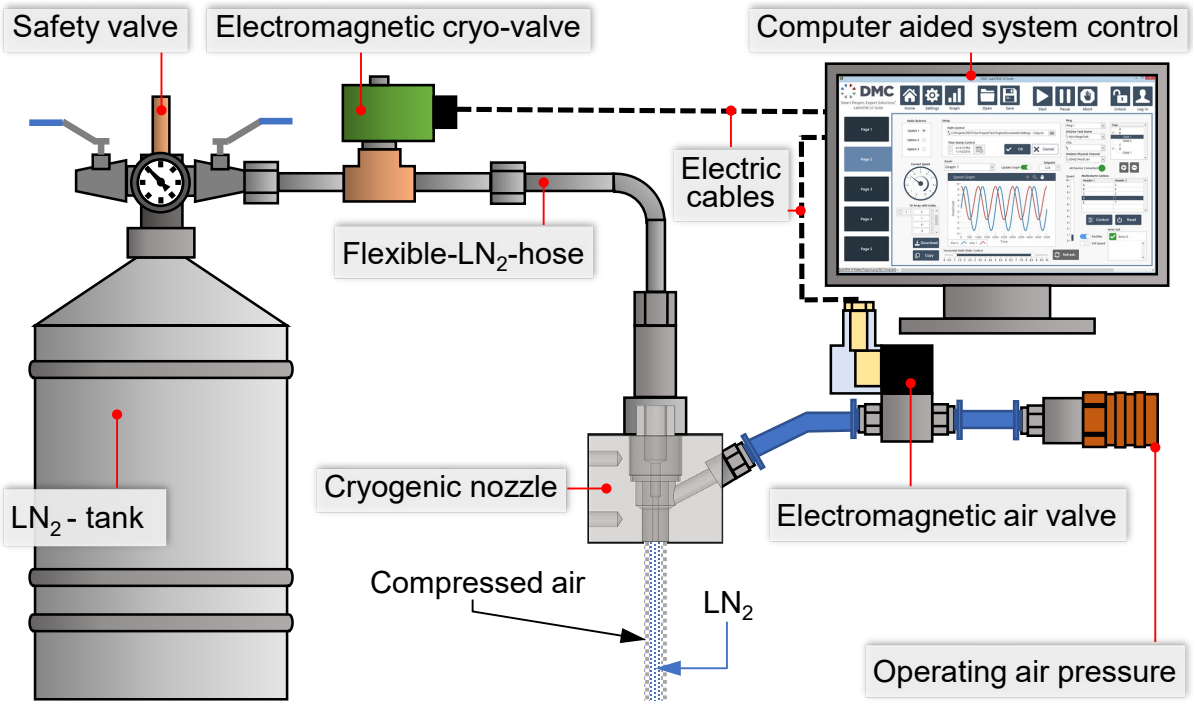

Fig. 12. Planned cryogenic system design.

With regard to thermomechanical forming, ongoing work is currently being conducted on an induction system which is to be used for purposely lowering the α'-martensite content locally through heating. In this way, for example, the co-cooling of adjacent tube sections can be prevented, which can improve the grading sharpness in the axial and angular direction. The

sharpness of local gradients in the grading process depends on various factors, including the geometry of the roller tool determining the contact area (e.g. transition radius and the attack angle of the roller), the achievable temperature differences in the areas being formed, the thermal conductivity of the material, the duration between cooling and forming. These factors, along with the constraints of the forming machine, such as achievable process parameters and actor dynamic, affect the formation of α' martensite and the distinction between different areas. Contact with warm tools and resulting process heat can decrease the temperature differences crucial for grading sharpness. These aspects are currently being investigated and will be quantified in future work.

Acknowledgment
The authors would like to thank the German Research Foundation (Deutsche Forschungsgemeinschaft, DFG) for their support of the depicted research within the priority program SPP 2183 "Property controlled deformation processes", through project no. 424335026 "Property control during spinning of metastable austenites". The authors further thank the German Research Foundation and the Ministry of Culture and Science of North Rhine-Westphalia (Ministerium für Kultur und Wissenschaft des Landes Nordrhein-Westfalen, MKWNRW) for funding of the Focused-Ion-Beam Scanning Electron Microscope (project no. 386509496) within the Major Research Instrumentation Program.

References
[1] D. Yang, M. Bambach, J. Cao, J. Duflou, P. Groche, T. Kuboki, A. Sterzing, A. Tekkaya, C. Lee, Flexibility in metal forming, CIRP Annals 67 (2018) 743-765. https://doi.org/10.1016/j.cirp.2018.05.004
[2] M.S. Mohebbi, A. Akbarzadeh, Experimental study and FEM analysis of redundant strains in flow forming of tubes, J. Mater. Process. Technol. 210 (2010) 389-395. https://doi.org/10.1016/j.jmatprotec.2009.09.028
[3] B. Arian, M. Riepold, J. Rozo Vasquez, W. Homberg, A. Trächtler, F. Walther, Forming of metastable austenitic stainless steel tubes with axially graded martensite content by flow-forming, ESAFORM 2021, Proceedings of the 24th International Conference on Material Forming, 2021.
[4] M. Runge, Spinning and Flow forming: spinning and flow forming technology, product design, equipment, control systems, Verlag Moderne Industrie, Landsberg/Lech, 1994.
[5] M. Sivanandini, S. Dhami, B. Pabla, Flow forming of tubes: A review, Int. J. Sci. Eng. Res. 3 (2012) 587-597.
[6] M. Riepold, B. Arian, J.V. Rozo, W. Homberg, F. Walther, A. Trächtler, Model approaches for closed-loop property control for flow forming, Adv. Industr. Manuf. Sci. 3 (2021). https://doi.org/10.1016/j.aime.2021.100057
[7] D. Marini, D. Cunningham, P. Xirouchakis, J. Corney, Flow forming: A review of research methodologies, prediction models and their applications, Int. J. Mech. Eng. Technol. 7 (2016) 285-315.
[8] A. Weidner, Deformation processes in TRIP/TWIP steels, Springer International Publishing, Cham, 2020.
[9] N. Gey, B. Petit, M. Humbert, Electron backscattered diffraction study of ε/α martensitic variants induced by plastic deformation in 304 stainless steel, Metall. Mater. Trans. A 36A (2005) 3291-3299. https://doi.org/10.1007/s11661-005-0003-9
[10] P. Haušild, V. Davydov, J. Drahokoupil, M. Landa, P. Pilvin, Characterization of strain-induced martensitic transformation in a metastable austenitic stainless steel, Mater. Des. 31 (2010) 1821-1827. https://doi.org/10.1016/j.matdes.2009.11.008
[11] B. Arian, W. Homberg, L. Kersting, A. Trächtler, J. Rozo Vasquez, F. Walther, Produktkennzeichnung durch lokal definierte Einstellung von ferromagnetischen Eigenschaften

beim Drückwalzen von metastabilen Stahlwerkstoffen, in: 36. Aachener Stahlkolloquium - Umformtechnik „Ideen Form Geben“, 2022, pp.333-347.
[12] T. Angel, Formation of martensite in austenitic stainless steels: Effects of deformation, temperature, and composition, J. Iron Steel Inst. 5 (1954) 165-174.
[13] S.K. Varma, J. Kalyanam, L. Murk, V. Srinivas, Effect of grain size on deformation-induced martensite formation in 304 and 316 stainless steels during room temperature tensile testing, J. Mater. Sci. Lett. 13 (1994) 107-111. https://doi.org/10.1007/BF00416816
[14] J. Biehler, H. Hoche, M. Oechsner, Nitriding behavior and corrosion properties of AISI 304L and 316L austenitic stainless steel with deformation-induced martensite, Surf. Coat. Technol. 324 (2017) 121-128. https://doi.org/10.1016/j.surfcoat.2017.05.059
[15] J. Talonen, P. Aspegren, H. Hänninen, Comparison of different methods for measuring strain induced α-martensite content in austenitic steels, Mater. Sci. Technol. 20 (2004) 1506-1512. https://doi.org/10.1179/026708304X4367
[16] M. Astudillo, M. Nicolás, J. Ruzzante, M. Gómez, G. Ferrari, L. Padovese, M. Pumarega, Correlation between martensitic phase transformation and magnetic Barkhausen noise of AISI 304 steel, Procedia Mater. Sci. 9 (2015) 435-443. https://doi.org/10.1016/j.mspro.2015.05.014

Materials Research Proceedings 28 (2023) 2049-2060 https://doi.org/10.21741/9781644902479-220

Control strategy for angular gradations by means of the flow forming process

KERSTING Lukas[1,a], ARIAN Bahman[2,b], ROZO VASQUEZ Julian[3,c], TRÄCHTLER Ansgar[1,4,d], HOMBERG Werner[2,e] and WALTHER Frank[3,f]

[1]Fraunhofer Institute for Mechatronic Systems Design (IEM), Paderborn, Germany

[2]Paderborn University, Forming and Machining Technology (LUF), Germany

[3]TU Dortmund University, Chair of Materials Test Engineering (WPT), Germany

[4]Heinz Nixdorf Institute (HNI), Paderborn University, Germany

[a]lukas.kersting@iem.fraunhofer.de, [b]ba@luf.uni-paderborn.de, [c]julian.rozo@tu-dortmund.de, [d]ansgar.traechtler@hni.uni-paderborn.de, [e]wh@luf.uni-paderborn.de, [f]frank.walther@tu-dortmund.de

Keywords: Flow Forming, Graded Structures, Control Strategy, Closed-Loop Property Control

Abstract. Climate change, rare resources and industrial transformation processes lead to a rising demand of multi-complex lightweight forming parts, especially in aerospace and automotive sectors. In these industries, flow forming is often used to produce cylindrical forming parts by reducing the wall thickness of tubular semifinished parts, e.g. for the production of hydraulic cylinders or gear shafts. The complexity and functionality of flow forming workpieces could be significantly increased by locally graded microstructure and geometry structures. This enables customized complex hardness distributions at wear surfaces or magnetic QR codes for a unique, tamper-proof product identification. The production of those complex, 2D (axial and angular) graded forming parts currently depicts a great challenge for the process and requires new solutions and strategies. Hence, this paper proposes a novel control strategy that includes online measurements from an absolute encoder to determine the angular workpiece position. Workpieces of AISI 304L stainless steel with 2D-graded structures are successfully manufactured using this new strategy and analyzed regarding the possible accuracy and resolution of the gradation. At this point, a dependency of the gradations on the sensor and actuator dynamics, accuracy and geometry could be noted. It is further evaluated how the control strategy could be extended by an observer-based closed-loop property control approach to enhance the accuracy of the suggested strategy.

Introduction

Current developments and transformation processes like climate change, the transition to electric vehicles and the rising scarcity of resources depict a great challenge for products as well as for production processes. Especially in the automotive, aerospace and railway industry, there is therefore a rising demand for high strength, lightweight forming parts [1]. Furthermore, product counterfeiting is a serious problem in several industrial fields. A locally graded microstructure distribution on the surface of a forming part could be a feasible new solution for both cases. This could be e.g. an invisible, magnetic QR code for unique product identification against counterfeiting or a locally restricted hardness distribution at wear surfaces that allows reducing the wall thickness of the components.

To produce those customized parts, there is a need of flexible forming processes that allow individual product shapes or product features by function integration in small batches. At this point, classical die based-forming processes like deep drawing are rather at a disadvantage since the product shape is defined by the product-specific tool design. Thus, incremental forming

Content from this work may be used under the terms of the Creative Commons Attribution 3.0 license. Any further distribution of this work must maintain attribution to the author(s) and the title of the work, journal citation and DOI. Published under license by Materials Research Forum LLC.

processes with mobile, universal tools like in the flow forming process are preferred in this case [2]. Flow forming is already used in the automotive and aerospace industry to produce cylindrical forming parts by reducing the wall thickness of tubular semifinished parts, e.g. for the production of hydraulic and pneumatic cylinders or gear shafts [3]. According to current knowledge, angular graded microstructure profiles have not yet been added to the products like an invisible QR code that represents additional functionality.

The process-integrated manufacturing of those novel graded parts requires special control strategies and information of the angular workpiece position during the whole process. For this purpose, a new control strategy is subsequently proposed in this paper that includes the sensor feedback of an absolute encoder to coordinate the actuator motion. Thus, it is possible to produce flow forming parts with locally restricted forming areas. These forming areas - in contrast to the workpiece area outside - incorporate a martensitic microstructure which is caused by deformation in terms of a strain-induced phase transformation. In the following, the special axial and angular restricted areas with a different microstructure are called 2D gradation. Each gradation produced by the proposed control strategy features a certain local accuracy which is further analyzed in this paper. Building on this, a closed-loop property control can be prospectively designed to enhance the accuracy of the gradations and simultaneously adjust geometric and material properties, so that the created QR code will be manufactured invisible.

Setup

Process and material.

This paper focusses on backward flow forming on a single roller flow forming machine. The investigations were performed with seamless tubes of stainless steel. The semifinished parts own a length of $L = 120$ mm, an outer diameter of $d_O = 80$ mm and a nominal wall thickness of $w = 4$ mm. The tubes are manufactured according DIN1127. Thus, the tubes feature an angular wall thickness eccentricity due to fabrication tolerances, with a deviation between maximum and minimum value of up to 15% [4]. The tube material is AISI 304L (X2CrNi18-9, 1.4307) which is a metastable austenitic stainless steel. By plastic deformation of this steel, a strain-induced phase transformation from austenite to α'-martensite can occur [5, 6] that influences the workpiece properties like the hardness and the micromagnetic properties. The process and material were already used in previous publications of the authors. Thus, it is referred to [7, 8] for additional information.

Machine and sensor concept.

The experiments were executed on a PLB 400 single roller spinning machine originally manufactured by Leifeld Metal Spinning GmbH (Ahlen, Germany) and later modified. The current setup is shown in Fig. 1 and was previously published in [7]. Here, the roller (entry angle $\alpha = 12°$, transition radius $R = 2$ mm, exit angle $\beta = 5°$) is mounted on a hydraulic actuated cross support that can be moved position-controlled in axial (x) and radial (y) direction for forming the workpiece. The specimen is positioned on a mandrel that is set into rotation by a spindle with an electric drive motor. The mandrel is also supported by two stationary rollers in opposite direction to the tool to compensate the high forming forces and to avoid mandrel deflection.

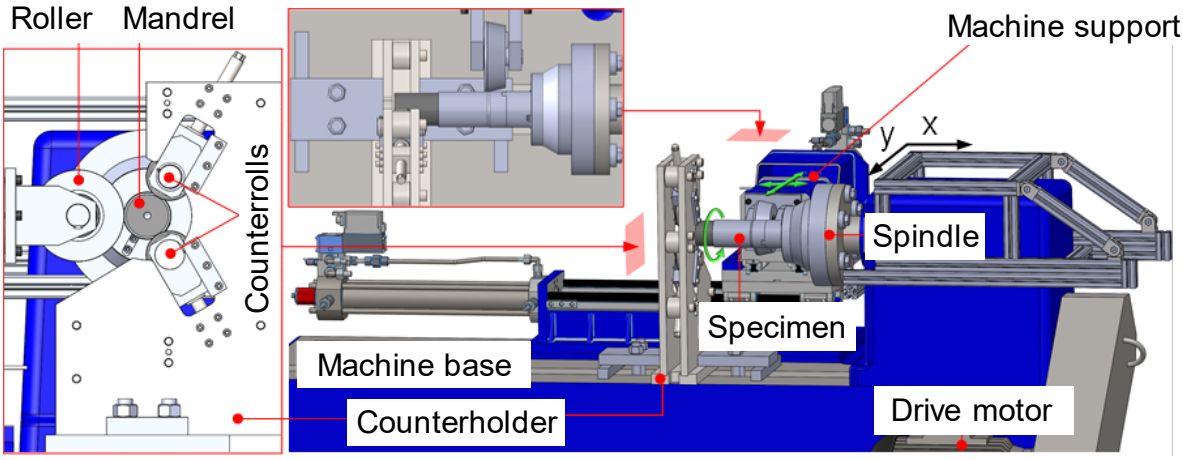

Fig. 1. Machine setup.

The machine setup includes an additional sensor system for angular gradations and property control purposes (see Fig. 2). An absolute encoder Hengstler Acuro AC58 is mounted at the end of the spindle shaft for the determination of the angular workpiece position and of the rotational speed. The sensor is specified with a resolution of 12 bit and 2048 incremental pulses in the single turn mode. The machine also contains a laser distance measuring system for measuring the resulting wall thickness reduction online during the forming process. Two laser sensors OM70 by Baumer Electric are connected to the machine support moving axially along the workpiece. One of the sensors points perpendicularly near of the forming zone with an angular offset of 90°, but no axial offset. The second sensor is positioned with an additional axial offset of 5 mm in front of the forming zone. While the first sensor is measuring the formed area, the latter measures the unformed. It is thus possible to calculate the resulting wall thickness reduction from the differential signal of both sensors. The sensor system also contains a micromagnetic 3MA-II sensor that is out of the focus of this paper (see [8] for additional information about the sensor concept).

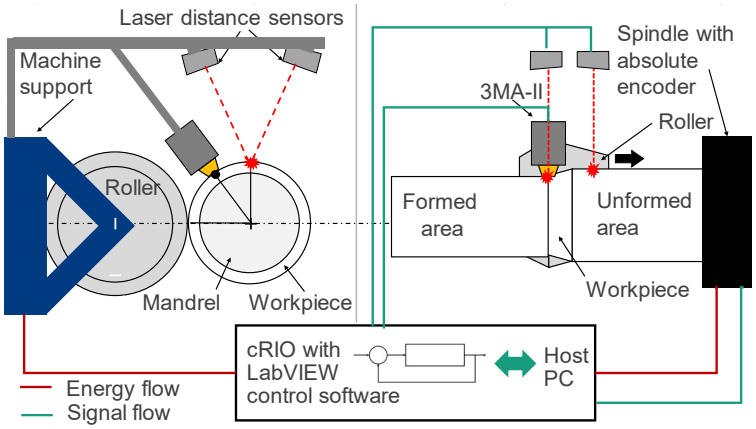

Fig. 2. Sensor concept (scheme).

Machine control architecture and control strategy.

The flow forming machine is equipped with a NI compactRIO real-time controller (cRIO 9035). On the controller, the overall machine control is executed including the position closed-loop control of the two hydraulic actuators and the control of the spindle motor. The additional sensor system is also connected to the cRIO controller (see [8] for further details). The absolute encoder transmits the measured rotational position and speed digitally using the BiSS-C protocol to a

special encoder module (SEA 9521) of the cRIO. The control on the cRIO is programmed in the LabVIEW development environment. It is a free programmable, CNC-orientated control software that was developed in [9] and [10] and extended in [8] for property control issues. In the control program, the toolpath is defined by

$$P = \begin{bmatrix} x_1 & y_1 & f_{x,1} & f_{y,1} & \theta_1 & n_1 \\ \vdots & \vdots & \vdots & \vdots & \vdots & \vdots \\ x_M & y_M & f_{x,M} & f_{y,M} & \theta_M & n_M \end{bmatrix} \quad (1)$$

Each row corresponds to a block of a conventional NC program. In each block, the desired final tool position in axial direction x and in radial direction y is defined, and in addition the feed in both directions for the tool movement (f_x and f_y) until reaching the specified final position. Those values act as an input to the internal position control of the machine support. The program is added in this paper by two additional columns for the rotational speed n and the desired angular position of the mandrel θ. Here, a transition to the next block (with new desired values for x_i, y_i, $f_{x,i}$ and $f_{y,i}$) is enforced when the measured value θ_{mes} amounts approximately θ_i. Since the absolute encoder delivers the measurement values with a certain accuracy and the rotation of the mandrel takes places continuously without stopping at θ_i, it is thus necessary to utilize a threshold value ε for defining the transition condition:

$$|\theta_{mes} - \theta_i| < \varepsilon \quad (2)$$

Procedure

Effective resolution of the absolute encoder within the control system.

For defining a suitable threshold value, the effective resolution of the absolute encoder within the setup is determined at first. It generally depends on the nominal resolution of the encoder itself and the signal sampling of the control system. For this purpose, the time signal of the absolute encoder is analyzed at different rotational speeds from 3 to 50 rpm. By comparing the measured angle values between two consecutive sample values, the effective angular resolution $\Delta\boldsymbol{\theta}$ is determined (see Fig. 3).

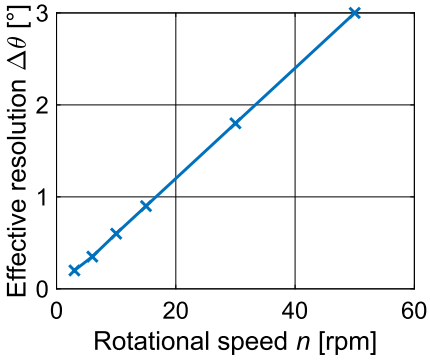

Fig. 3. Working principle of the forming control for angular parts.

The effective resolution $\Delta\theta$ significantly depends on the rotational speed n. It varies between 0.2° at the lowest speed and 3° at the highest. This effect is caused by the sampling time of the control system $t_{sample} = 0.01$ s. Since the nominal sensor resolution amounts $\Delta\theta_{nom} = \frac{360°}{2^{12}} = 0.088°$ and is much higher, the sampling effect is clearly dominating regarding the resolution. From the effective resolution, a suitable threshold value for the control can be defined since the threshold

should be greater (or equal at minimum) than the effect. In the worst case, the resolution is 3° in the experiments. Thus, the threshold value ε for the control is determined to ±3° in this paper.

Determination of the desired values (control strategy).

To produce axial and angular graded surface elements of 45°, 90° and 180° on the tube, an angle-dependent control strategy must be defined. In this paper, a rectangular strategy for the desired control values is proposed that alternates the actuator position in radial direction between a position near above the tube surface and a second position that corresponds to a desired infeed depth (see Fig. 4). The switching point of the desired value is

$$i \cdot \Delta\theta_{grad,des} \quad \text{for } i = 0 \ldots \frac{360°}{\Delta\theta_{grad,des}} \tag{3}$$

e.g. 0°, 90°, 270°, where $\Delta\theta_{grad,des}$ is the desired gradation angle. The sequence is repeated for several revolutions. Concurrently, an axial feed movement is defined. Thus, a gradation area occurs on the workpiece surface through the superposition of rotation and axial feed.

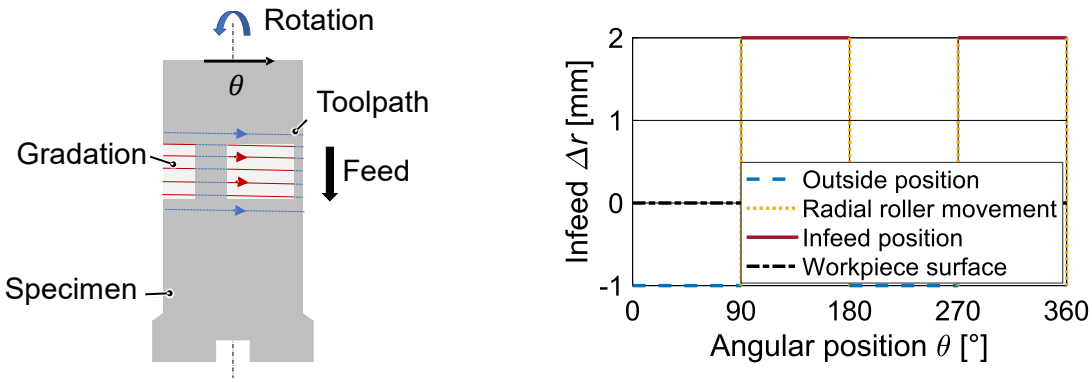

Fig. 4. Control strategy for 90°-gradations - desired actuator toolpath.

Experimental investigation by forming graded structures.

Two geometric gradation structures were investigated on specimens with the novel control strategy to validify the strategy and to analyze the accuracy of the produced gradations. Both specimens include three annular areas where gradations are placed. In the first area, a single gradation with $\Delta\theta_{grad,des} = 180°$ is placed, two 90°-gradations in the second and four 45°-gradations in the third (see Fig. 5).

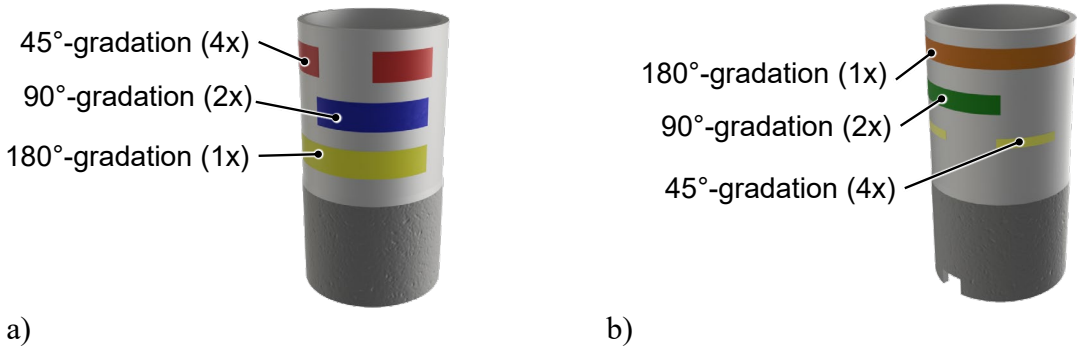

a) b)

Fig. 5. Specimen 1 (a) and specimen 2 (b) with graded structures.

Both specimens differ in the axial width of the gradations. In specimen 1, the axial width of each gradation is equal while the width is varying in specimen 2 by contrast. Here, the width is defined

by the number of rotations during the production of the specimen: 8 rotations for 180°-gradations, 4 rotations for 90°-gradations and 2 rotations for 45°-gradations. Thus, the width declines the shorter the gradation angle in this specimen.

Both experiments were performed with an axial feed of 0.1 mm/s according to former flow forming experiments of the authors in [7]. The rotational speed was defined by 5 rpm and the radial feed was set to 10 mm/s. The radial feed value f_y was determined after preliminary investigations (specimen type 3). Here, f_y was varied between 1 and 18 mm/s by a constant rotational speed of 5 rpm and a constant nominal gradation length (desired gradation angle) of 90°. This experiment was carried out without axial feed and only by performing a single rotation.

Results

Investigation on the radial feed.

At first, a specimen type 3 (produced with different radial feeds) was evaluated regarding the total length of the gradation. Since the gradations depict local areas with a reduced wall thickness and a gleaming, it was possible to evaluate the graded areas using a flexible measuring tape.

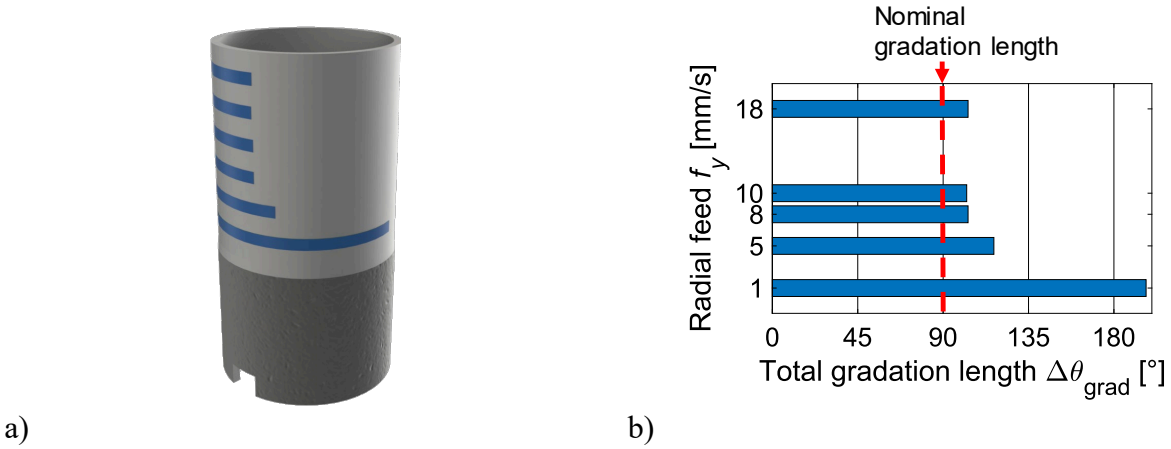

a) b)

Fig. 6. Influence of the radial feed/infeed velocity on the total angular gradation length: specimen (a) and results (b).

It can be seen from Fig. 6 that the total gradation length differs in every case from the desired nominal length of 90°, which is defined by the control. At a radial feed of 1 mm/s, the measured length amounts more than 180°. The total gradation length is significantly reduced by increasing the feed from 1 mm/s up to 8 mm/s. This is due to the shorter time the actuator takes until reaching the desired infeed position (see Fig. 8a). For infeed velocities of more than 8 mm/s, the total gradation length converges to approx. 103° despite of the faster actuator. This effect is probably caused by the contact area between roller and workpiece. Hence, the oversize of 13° cannot be compensated by a higher actuator dynamic. Additionally, a strong vibration occurs at the counter holder of the machine for radial feeds of more than 10 mm/s. The following experiments on different nominal gradation lengths are thus performed with a radial feed of 10 mm/s.

Local resolution and accuracy of the gradations.

Both specimens with different nominal gradation lengths (specimen 1 and 2) were analyzed regarding the gradation geometry and length. Hence, it is possible to exactly determine the resolution/accuracy of the gradations and to obtain a correlation between the resulting and nominal gradation length, which is the input to the control.

On specimen 2, the gradation width was also varied. Thus, there are gradations of a single rotation (single turn gradation) and of multiple rotations (multi turn gradation). A single turn gradation consists of three regions in axial and angular direction (see Fig. 7). In angular direction,

the gradation consists of three areas: a full width main area and two transition areas at the beginning and the end where the width increases or declines. Therefore, two different lengths of gradation could be distinguished: the inner length of the full width area and the total angular length of the gradation (full width area length + transition area length) that was already used as a measure in the preliminary investigation. The shape of the transition areas is mainly influenced by the roller geometry since the wall thickness is not constant in the axial direction of the whole gradation. There are two inclined surfaces in axial direction at the beginning and at the end of the gradation with a declining/increasing wall thickness. The inclined surfaces (entry and exit region) are caused by the entry and exit angle of the roller while the deepest point of the gradation corresponds to the nose region of the roller [11]. In the transition areas, the width of the entry and exit region decreases/increases to/from zero while the nose region exists on the whole length of the gradation.

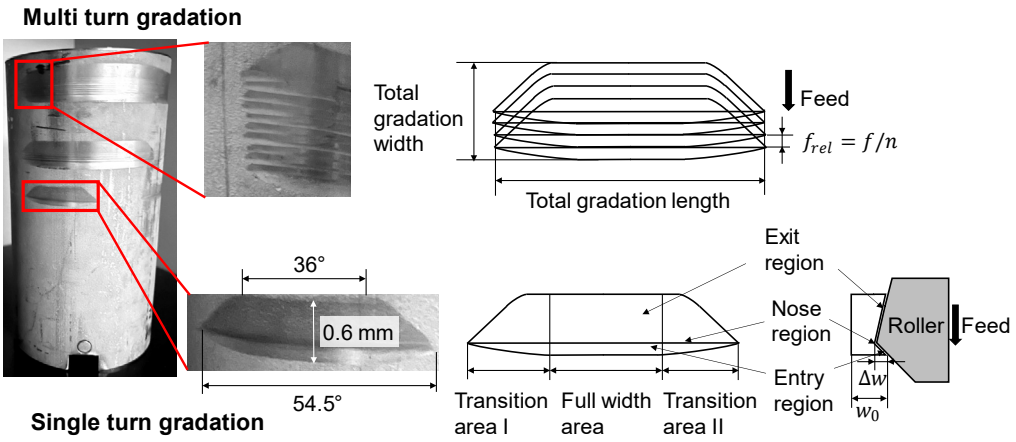

Fig. 7. Geometry of the gradations.

On the multi turn gradations (90° and 180°), the entry and exit region is rarely visible. This is due each multi turn gradation consists of a superposition of single turn gradations that are axially displaced by the related feed f_{rel} in axial direction. Through the axial feed, the entry and exit area are repeatedly shifted by the nose radius of the roller. The entry and exit region thus exist only on the two axial edges of the gradation. Hence, the full width area can only be measured at the edges while the length of the plan area inside the gradation corresponds to the total gradation length.
The results of the length measurement are summarized in Fig. 8b taking the example of specimen 2, but generally the results for specimen 1 are similar. In each case, the total angular gradation length exceeds the desired value of 45°, 90° or 180° (nominal gradation length) by approx. 15 – 25°, like in the results from the preliminary investigations. The precise value might vary between the gradations due to the accuracy of the switching condition (ε-condition, see section 2) up to ±3°. The full width area length amounts approximately 18° less than the total angular length of the gradation in every case. It can be seen that the mean value of the total angular length and the full width area length is approximately (with the accuracy of ±3°) equal to the nominal gradation length from the control. There are principally two reasons for the existence of the transition areas at the edges of the full width area: the actuator dynamics and the roller geometry. In case of the 90°-gradations, the actuator takes 2° until entering the workpiece surface and additional 7° until reaching the desired infeed of 2 mm (see Fig. 8a). Exactly 90° after starting the motion, the actuator is leaving the workpiece (with the same duration as entering but vice versa). This obviously leads to an angular displacement of the gradations of $2 \cdot 2°$ and to the elongation of the gradations due to the transition areas by $2 \cdot 9°$. Otherwise, it has been seen from the preliminary investigations that a higher actuator dynamic of more than $f_y = 10$ mm/s does not influence the total length of the gradations anymore. In this case, also the roller geometry in

circumferential direction leads to the transition area. This is due to the contact area between tube and roller that corresponds to an intersection of a cone (roller) and a cylinder (tube, see [11] for further information regarding the contact geometry).

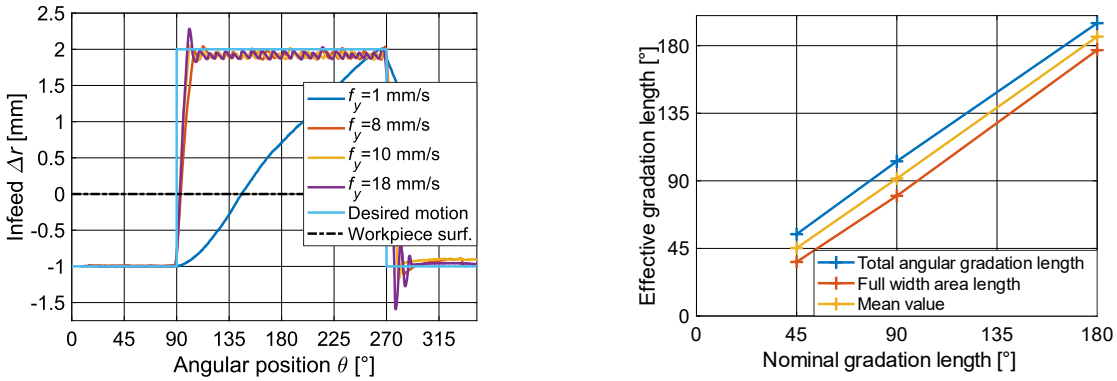

a) b)

Fig. 8. Influence of the radial feed/infeed velocity on the effective angular gradation length: a) measured actuator dynamics, b) measured gradation length.

By conclusion from the investigations on accuracy, the resulting gradation geometry is mainly influenced by the transition areas at the left and right edge of the gradation. Using the correlation from Fig. 8b, it could be possible to adjust the nominal gradation length in the control to receive a full width area length or total gradation length that matches to a desired value. But in every case, there will be a fuzziness of the gradation due to the physics of the actuator and roller geometry. In this context, also the minimal dimension of a gradation with the current machine setup (process parameter, controller, infeed, and roller geometry) can be derived. Here, the minimal angular length is 18° since the angular gradation length minimally amounts to the length of both transition areas. The minimal axial width corresponds to the width of a single turn gradation, namely the width of the entry, nose and exit region. In the experiment with an infeed of 2 mm, the minimal width amounts approximately 0.6 mm. Generally, it also depends on the wall thickness reduction since the contact area between roller and tube differs.

Wall thickness reduction of the gradations.

The gradations were also investigated regarding the resulting wall thickness reduction. Therefor, a caliper Kroeplin D4R50 (resolution: 0.05 mm) was used. The measured average wall thickness inside the gradations of specimen 1 amounts 3.74 mm, and in specimen 2 the wall thickness is 3.78 mm. The average initial wall thickness also differs between both specimens (3.95 mm for specimen 1 and 4.03 mm for specimen 2). The resulting wall thickness reduction is thus 0.21 mm (specimen 1) and 0.25 mm (specimen 2) which is nearly the same regarding the accuracy of the caliper. Hence, a deviation between the infeed of the roller (2 mm) and the thickness reduction is observed. This effect is essentially caused by undesired machine behavior, e.g. the flexibility of the support and the mandrel, and was already detected during previous investigations at the same machine (see [7] for example). The detailed results for each gradation are shown in Fig. 9. In angular direction, the wall thickness slightly differs between each gradation and moreover inside of them. This effect is caused by the eccentricity of the semifinished parts.

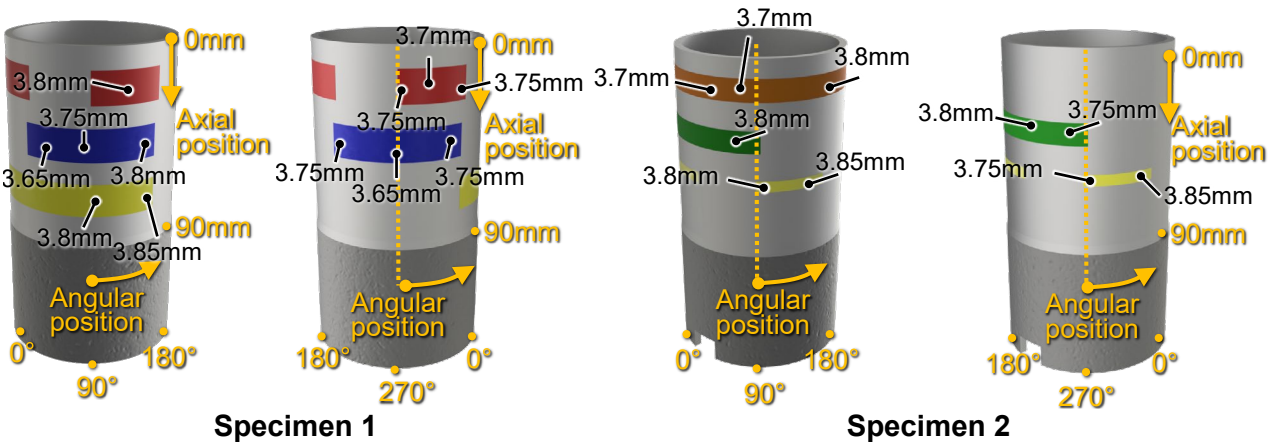

Fig. 9. Measured wall thickness inside the gradations.

α'-martensite formation inside the gradations.

A deformation-induced α'-martensite formation inside the gradations was expected due to metastable austenitic semifinished parts and the wall thickness reduction inside the gradations. For this purpose, the specimens were also analyzed by Feritscope FMP30 (Helmut Fischer GmbH, Sindelfingen, Germany) to detect the volume fraction of the α'-martensitic phase. The results (see Fig. 10) were measured at intervals of 5 mm in axial and 12° in angular direction.

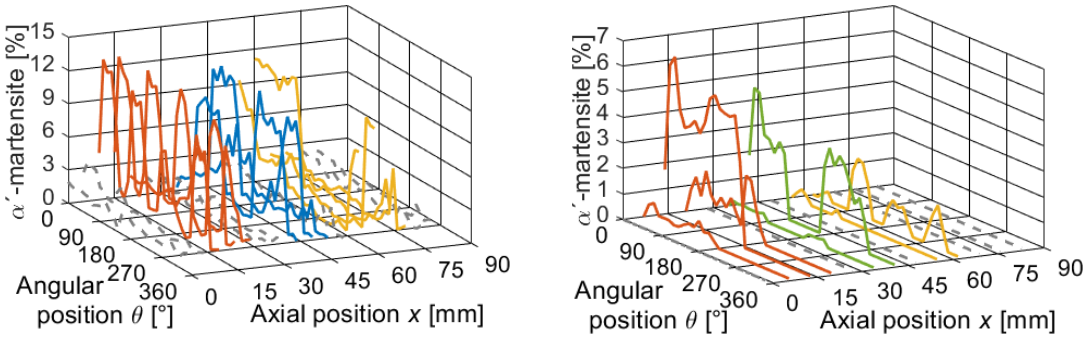

Fig. 10. Measured α'-martensite volume fraction of specimen 1 (left) and specimen 2 (right).

In each gradation of specimen 1, an α'-martensite volume fraction of approximately 11% was measured. In the non-deformed areas by contrast, the α'-martensite amounts less than 3%. Thus, a clearly graded α'-martensitic structure could be identified. On the axial edge of each gradation, the peak value of the α'-martensite measurement is on a lower level (e.g. 5% for the 90°-gradations). This effect could be influenced by the sensor spot that measures inside and outside the gradation at the edge. In angular direction, there is also a gradient of the measured amount of α'-martensite. At the beginning of the gradation (inside transition area I), the α'-martensite amount is lower than at the middle (full width area), where a maximum is reached, and decreases again until the gradation end (transition area II). This is because the contact conditions between tool and workpiece are optimal at the center. However, while forming the gradations, a forming force gradient is created over the material until the optimal contact conditions are reached (at the beginning) or released (at the end), which is reflected in the angular α'-martensite gradient.

Online measurements of the wall thickness reduction during forming.

Regarding a future use in a property control for 2D gradations, the measurements of the two laser distance sensors were also recorded during the production of the two specimens. Sensor 1 was placed on the same axial position as the forming tool, but with an angular displacement. Here,

the distances between the two sensors and the workpiece arise when the support starts infeeding at $t = 98.5$ s/$\varphi = 182°$ (see Fig. 11). Similarly, the distances decline with a distinct downshift at $t = 104.9$ s/$\varphi = 360°$ while the support moves back into the starting position. Both distance shifts are similar, so no wall thickness reduction is detected during the support motion. Wall thickness reduction is firstly measured with a temporal delay of 3.3 s to the actuator signal starting at $t = 101.8$ s/$\varphi = 275°$ and ending at $t = 108.2$ s/$\varphi = 90.5°$. This temporal delay is caused by the angular displacement between sensor and forming zone that amounts approximately 90°. The signal difference of both laser distance sensors amounts approximately 0.3 mm which corresponds roughly to the manually measured wall thickness reduction values.

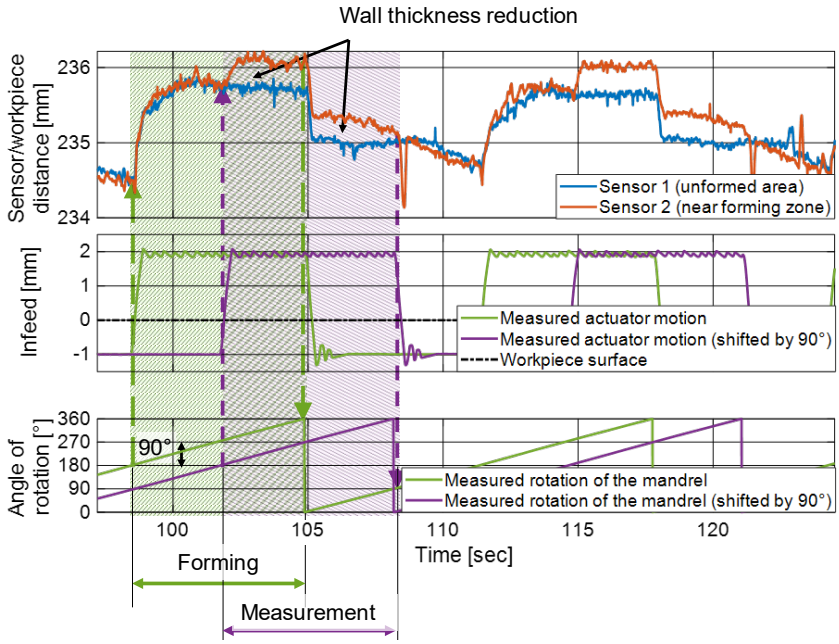

Fig. 11. Influence of the actuator movement and angular sensor displacement on the online wall thickness measurement (forming and measurement of the gradation).

Summary

In this paper, a novel control strategy for the flow forming process was presented. Here, flow forming was enabled to more complex, 2D (axial and angular) graded structures on the specimen surface like a QR code by integrating an absolute encoder into the control. This encoder-based control strategy was successfully validated by the experimental manufacturing of locally graded forming parts. The resolution and accuracy of these gradations in angular direction significantly depend on the actuator dynamics, namely the infeed velocity/feed in radial direction. Above a certain critical velocity, the effect of the actuator dynamic decreases. In this case, the imprint of the roller geometry on the specimen (contact area) becomes the dominating effect. The result is that the gradations own a greater total angular length than the actuator feeds in. In axial direction, the gradation edges were also influenced by the roller geometry. For this reason, a minimal gradation dimension of 0.6 mm in axial and of 18° in angular direction was concluded from the experiments. Thus, a required line thickness of 0.5 to 4 mm for a QR code could be almost realized. In angular direction, structures of 4° to 40° were required since multiple gradations should be circumferentially placed for a QR code. For this purpose, different roller geometries will be evaluated in further investigation to enhance the accuracy due a dependence on the roller radius is assumed. Besides the dimensional accuracy in angular and axial direction, the specimens were also investigated regarding the wall thickness reduction in radial direction. Here, a significant deviation between infeed and thickness reduction was noticed. Nevertheless, the wall thickness reduction

also leads to an α'-martensite formation and thus to a locally graded α'-martensite structure on the specimen. The resulting magnetic properties of the α'-martensite structure will be analyzed in future research.

The presented control strategy could be further extended by a closed-loop control of the wall thickness reduction to compensate the deviation of the reduction. Concurrently, it would be favorable to adjust the α'-martensite volume fraction by a closed-loop property control to a defined value (see Fig. 12).

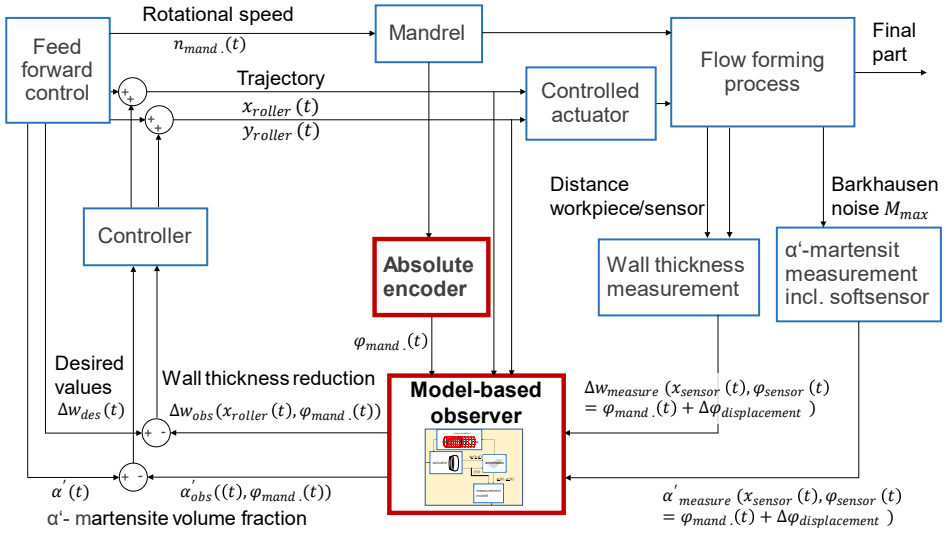

Fig. 12. Concept of a closed-loop property control structure with a model-based observer.

As seen from the measurements of the laser distance sensors, such a closed-loop control for 2D gradations is difficult since the forming result is detected with a spatial and temporal displacement. Therefore, it is not possible to simply compare the measured value to the desired. A possible solution to overcome this challenge is to include a model-based observer into the closed-loop control structure (see Fig. 12). The observer could allocate the measured values to the correct location within a model of the specimen surface and output the wall thickness and the α'-martensite fraction at the actual actuator position. Thus, it would be possible to correctly determine the control error and enhance the process accuracy by applying a closed-loop property control to the process.

Acknowledgement

The authors would like to thank the German Research Foundation (Deutsche Forschungsgemeinschaft, DFG) for their support of the depicted research within the priority program SPP 2183 "Property-controlled metal forming processes", through project no. 424335026 "Property control during spinning of metastable austenites".

References

[1] E. Tekkaya, N. Ben Khalifa, G. Grzancic, R. Hölker, Forming of lightweight metal components: need of new technologies, Procedia Eng. 81 (2014) 28-37. https://doi.org/10.1016/j.proeng.2014.09.125

[2] D. Yang, M. Bambach, J. Cao, J. Duflou, P. Groche, T. Kuboki, A. Sterzing, A. Tekkaya, C. Lee, Flexibility in metal forming, CIRP Annals 67 (2018) 743-765. https://doi.org/10.1016/j.cirp.2018.05.004

[3] P. Groche, Flow forming, in: The International Academy for Production Engineering et al. (eds.), CIRP Encyclopedia of Production Engineering, Springer, Berlin, Heidelberg, 2019. https://doi.org/10.1007/978-3-662-53120-4

[4] DIN Deutsches Institut für Normung (ed.), Nichtrostende Stahlrohre - Maße, Grenzabmaße und längenbezogene Masse, Beuth, Berlin, 1996.
[5] J. Talonen, P. Apegren, H. Hänninen, Comparison of different methods for measuring strain induced α-martensite content in austenitic steels, Mater. Sci. Technol. 20 (2004) 1506-1512. https://doi.org/10.1179/026708304X4367
[6] P. Haušild, V. Davydov, J. Drahokoupil, M. Landa, P. Pilvin, Characterization of strain-induced martensitic transformation in a metastable austenitic stainless steel, Mater. Des. 31 (2010) 1821-1827. https://doi.org/10.1016/j.matdes.2009.11.008.
[7] B. Arian, W. Homberg, L. Kersting, A. Trächtler, J. Rozo Vasquez, F. Walther, Produktkennzeichnung durch lokal definierte Einstellung von ferromagnetischen Eigenschaften beim Drückwalzen von metastabilen Stahlwerkstoffen, in: G. Hirt (Ed.), 36. Aachener Stahlkolloquium - Umformtechnik “Ideen Form geben“, Aachen, 2022, pp. 333-347.
[8] L. Kersting, B. Arian. J. Rozo Vasquez, A. Trächtler, W. Homberg, F. Walther, Innovative online measurement and modelling approach for property-controlled flow forming processes, Key Eng. Mater. 926 (2022) 862-874. https://doi.org/10.4028/p-yp2hj3
[9] D. Hornjak, Grundlegende Untersuchungen der Prozess- und Werkzeugparameter und ihre Wechselwirkungen für das thermo-mechanisch unterstützte inkrementelle Umformverfahren des Reib-Drückens, Doctoral Dissertation, Paderborn University, Shaker, Aachen, 2013.
[10] B. Lossen, Ein Beitrag zur Herstellung von hybriden Bauteilen mittels Reibdrücken, Doctoral Dissertation, Paderborn University, Shaker, Düren, 2019.
[11] M.J. Roy, D.M. Maijer, R.J. Klassen, J.T. Wood, E. Schost, Analytical solution of the tooling/workpiece contact interface shape during a flow forming operation, J. Mater. Process. Technol. 210 (2010) 1976-1985. https://doi.org/10.1016/j.jmatprotec.2010.07.011

Materials Research Proceedings 28 (2023) 2061-2070 https://doi.org/10.21741/9781644902479-221

Optimizing the microstructure in open-die forgings using reinforcement learning

REINISCH Niklas [1,a *],BAILLY David [1,b] and HIRT Gerhard[1,c]

[1]Institute of Metal Forming, RWTH Aachen University, Intzestraße 10, 52072 Aachen, Germany

[a]niklas.reinisch@ibf.rwth-aachen.de, [b]david.bailly@ibf.rwth-aachen.de, [c]gerhard.hirt@ibf.rwth-aachen.de

Keywords: Open-Die Forging, Reinforcement Learning, Process Optimization, Grain Size

Abstract. The open-die forging process can produce large workpieces with excellent material properties that can be used for heavy-duty applications like turbine shafts. The mechanical properties result from the microstructure, which in turn directly results from the process route. Since in open-die forging processes commonly hundreds of unique forming operations are carried out, numerous process routes lead to the same final geometry but produce different microstructures. This is why the prior design of an optimal pass schedule is essential to ensure good mechanical properties of open-die forgings. In the past reinforcement learning (RL) was already used to design optimized pass schedules for open-die forging that achieve the desired geometry, utilize the available press force, and reduce the number of passes. Furthermore, the design of a single pass schedule only took a few seconds which creates opportunities for the use of RL in control systems e.g. for the microstructure. This is why in this publication an existing RL algorithm is extended so that microstructure can be included in the optimization. Within this process, a microstructure model is integrated into the RL algorithm and the reward function (defines the goal of the training process) was extended in two steps to also rate the achieved average grain size continuously dependent on the temperature of the workpiece. In addition, the RL implementation was changed to ensure the production of the desired final geometry leading to a decrease in the complexity of the optimization problem. Thus, both an improvement of the designed pass schedules and a significant reduction of the training time of the RL algorithm was achieved.

Introduction

Open-die forging is a bulk metal forming process that offers the possibility to produce large mostly longitudinally oriented workpieces while removing casting defects from the component. This includes the closing of casting voids and the transformation of an unfavorable microstructure that can result from casting into a fine homogeneous one. Therefore, open-die forgings exhibit excellent mechanical properties and are often used for heavy duty applications like turbine shafts. During the forging process, the workpiece is incrementally formed using simple tools. Therefore, the final geometry of the component results from the sequence of forming operations, which can comprise up to several hundred individual strokes. This leads to an infinite number of different forging processes, which all result in the same final geometry, but can differ significantly in terms of the microstructure produced, the energy required, or the process duration.

To ensure efficient processes and high component quality in open-die forging targeted process design and, in the long term, process control are of great importance. An optimized process design, considering the microstructure produced, can be achieved e.g. via finite element (FE) simulations coupled with a microstructure model. Since FE simulations of open-die forging processes often require long computing times, a fast design or the control of forging processes is not possible using this approach. In the industry forging processes are until today often designed based on experience

Content from this work may be used under the terms of the Creative Commons Attribution 3.0 license. Any further distribution of this work must maintain attribution to the author(s) and the title of the work, journal citation and DOI. Published under license by Materials Research Forum LLC.

or using simple models describing e.g. the geometry development. In addition, commercial software to design pass schedules, such as the program "ForgeBase®" from SMS group GmbH [1] or "easy2forge" from Dr. Fister GmbH [2], are available. Although these programs can quickly design (in some instance optimum) pass schedules for various ingot geometries, considering e.g. plant boundaries, the microstructure generated is not yet included in the design. Overall, a need for new possibilities for rapid design of optimum pass schedules as well as targeted process control arises, whereby besides geometry further workpiece parameters such as grain size are included.

In this publication, a novel approach for the design of optimized open-die forging processes using the machine learning method reinforcement learning (RL) is presented. RL algorithms as well as deep reinforcement learning (DRL) approaches have been successfully applied in various manufacturing applications including metal forming for different process design and control tasks [3,4]. Gamal et al. [5] trained a deep deterministic policy gradient algorithm to control the roll gap in bar and wire hot rolling using real plant measurement data. Dornheim et al. [6] used a RL approach coupled to a FE-simulation of the process to optimize the blank holder force in sheet metal deep drawing. Scheiderer et al. [7] used a soft actor critic algorithm to design an optimal pass schedule for heavy plate rolling that produces a desired grain size.

Since RL algorithms learn and store general rules for optimal behavior in different situations, after a successful training process they can determine solutions for individual problems in a very short time. In addition, (deep) neural networks can be used to store the knowledge learned during the training process, which can map even highly nonlinear correlations that are often present in open-die forging e.g. due to the incremental forming. For this reason, a double deep q-learning (DDQL) algorithm for the optimized design of open-die forging processes was developed in [8]. The algorithm is capable of designing pass schedules that achieve the desired final geometry while making use of the available press force and reducing the number of passes. Since the design of one optimized pass schedule via RL took only 2-4 seconds, the potential of RL for process planning and control has already been demonstrated. Since microstructure has a great influence on the mechanical properties of a forging, in this publication, a microstructure model is incorporated into the existing DRL algorithm to enable consideration of the produced grain size in the design of optimized pass schedules for open-die forging.

Previous Reinforcement Learning in Open-Die Forging

The machine learning approach RL is similar to human trial-and-error learning [3]. In an industrial open-die forging plant, this learning procedure runs unconsciously. Both press and manipulator operators select process parameters such as height reduction or bite ratio on a daily basis, interacting with their environment the open-die forge. In addition, they receive subsequent feedback on the part quality, e.g. good part or scrap, and thus with time learn how different materials and workpiece geometries are forged optimally (cf. Fig. 1, left).

Throughout its training process, the RL algorithm implemented in [8] undergoes the same learning process. Here, a so-called RL agent (cf. Fig. 1, center) interacts with its environment by selecting actions that correspond to process parameters such as bite ratio or height reduction (cf. Fig 1, middle). In contrast to a plant operator, who learns directly from the real forging process, the RL agent uses a virtual forging environment (cf. Fig. 1, right). This incorporates fast process models that can calculate the change in key workpiece properties such as geometry [9], temperature [10], and equivalent strain (in the core fiber) [11] as well the process duration and press force. Since it is often necessary to design several thousands of pass schedules in a RL training process as well as analyzing them concerning the material and process properties achieved, using a real forging plant for training is not feasible. This is due to risks for operators and machines as well as considerable costs incurred from the material used, wear, and the occupancy of staff and plants.

The virtual forging environment uses the process parameters selected by the agent to adjust the current state of the workpiece, including its geometry, temperature, and equivalent strain (in core fiber). An evaluation of this action selection according to a so-called reward function follows. The reward function assigns a scalar reward to each process parameter selection of the algorithm considering the current ingot state and hence, defines the goal of the RL training process. Afterwards, the agent uses the rewards and the information on the state change to adapt its action selection rules stored in a neural network (cf. Fig 1).

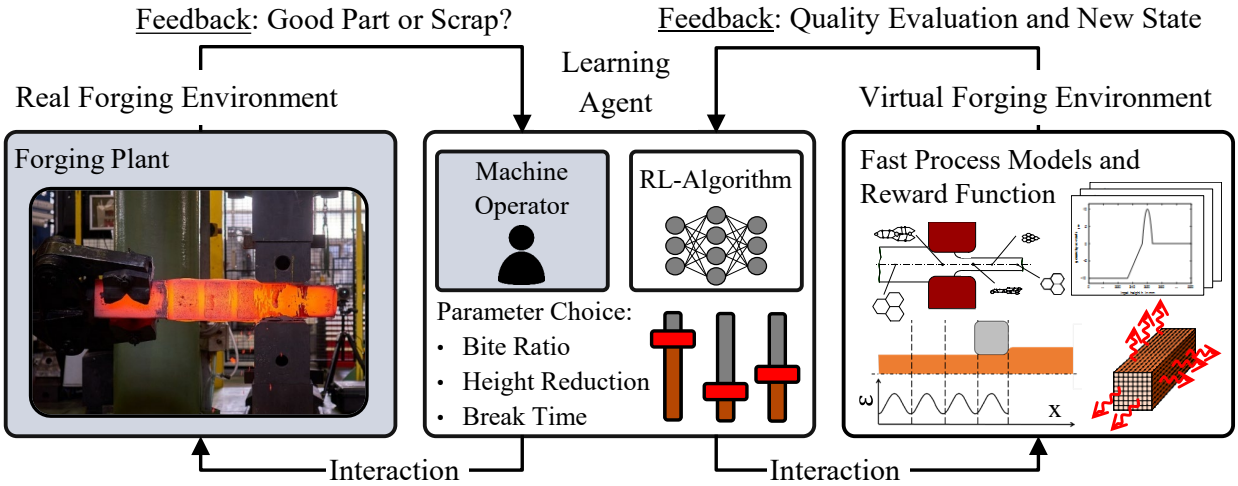

Fig. 1. Graphical representation of the trial-and-error learning procedure; left: human plant operator; right: RL algorithm.

In the given implementation, the RL agent learns how to design efficient forging processes. The goal includes not only to produce the desired final geometry but also to minimize the number of passes and to make the best possible use of the available press force. At the same time, process and plant limits such as the maximum force of the press are considered in the pass schedule design. For this reason, 80 % of the maximum press force is set as the nominal value, which, when adhered to, provides the maximum reward for the algorithm. In contrast, the reward function produces a penalty if the press force limit is exceeded. A detailed description of the implementation as well as the training process of the RL algorithm can be found in [8].

Description of the Use Case

To ensure good mechanical properties in open-die forged components while forging efficiently a targeted adjustment of the microstructure is essential. The RL algorithms presented throughout this publication are all trained to design pass schedules considering forging ingots made of 1.4301 steel (AISI 304), with a starting temperature of 1100°C and an initial grain size of 200 µm. The initial ingots have square initial cross-sections with edge lengths between 180 mm and 220 mm and are drawn out to final cross-sections with edge lengths between 100 mm and 140 mm. The initial length of the forging ingots is 500 mm. In the end, the trained RL algorithms should be able to give optimal pass schedules in seconds for various combinations of initial and final ingot geometries within the above-mentioned ranges. This would enable the use of RL-algorithms not only for fast offline design but also for online process adaption in order to control forging processes.

In a first step, the existing RL algorithm for efficient forging (no consideration of grain size) is trained without modifications. Afterwards, 400 different pass schedules with uniformly distributed combinations of initial and target geometry were designed using the RL agent. A semi-empirical microstructure model [12] was used to analyze the produced grain size along the core fiber of each pass schedule. This creates a comparative measure to rank the effectiveness of the later discussed

changes that account for grain size in the optimized pass schedule design. Fig. 2 shows the consolidated results using a heat map. Here, each box represents a pass schedule whose associated initial and target workpiece geometry can be read on the x and y axes, respectively. The coloration of the box represents the average austenitic grain size achieved in the core fiber of the workpiece at the end of the forging.

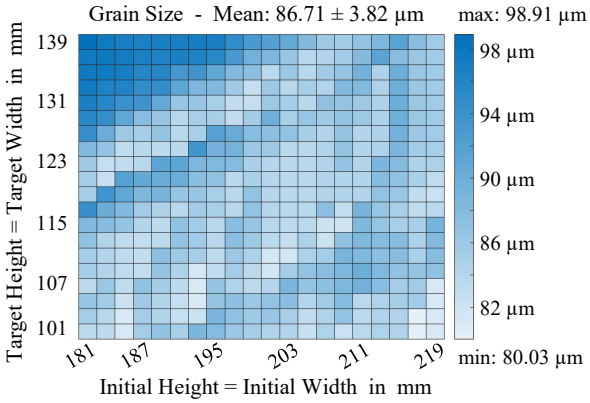

Fig. 2. Heatmap showing the produced average grain sizes of 400 different pass schedules designed by RL without a specific grain size reward.

The generated average grain sizes vary between 80.03 µm and 98.91 µm with a standard deviation of 3.82 µm. Averaged over the 400 pass schedules, the mean average grain size is 86.71 µm. Furthermore, averaged comparative values for the deviation from the target geometry (± 0.23 %), the average number of passes (6.15), and the utilization of the press force (± 5.02 %) are calculated and listed in Table 1.

Extension of the Previous RL Implementation

To enable the RL algorithm (cf. Fig. 1) to consider the production of a specific grain size in the process design, the existing implementation was extended in three steps. The first step consists of the implementation of a microstructure model developed by Karhausen et al [12] into the environment of the algorithm. The model uses semi-empirical equations to estimate recrystallization and grain growth, as well as a substructure modeling to determine the change in austenite grain size during forging. The model input is time-resolved data of temperature and equivalent strain along the core fiber that is already available in the environment of the RL algorithm.

In the second step, the previous reward function (cf. [8]) consisting of a weighted sum of the single rewards for force utilization and geometry, was complemented by an additional term R_{GS} to evaluate the generated mean austenitic grain size in the core fiber at the end of each process (cf. Fig. 3). As shown in Fig. 2, the mean average grain size produced by the previous algorithm was 86.71 ± 3.82 µm with a minimum grain size of 80.03 µm. To force the adapted RL agent to change its pass schedule design pattern for each combination of initial and target geometry, a target grain size of 70 µm, as well as a permissible maximum deviation of ± 10 µm, was chosen. This ensures that the new target grain size does not overlap with the previous grain size spectrum of the efficient forging use case (cf. Fig. 2).

To reflect this, a grain size reward function R_{GS} was designed, which is evaluated only once at the end of each pass schedule and hence, is referred to as a sparse reward. The reward R_{GS} divides into three characteristic sections depending on the mean grain size (cf. Fig. 3). The first section covers the permissible target grain size region of 70 ± 10 µm. Here, the reward increases parabolically and reaches its maximum at the exact target grain size. Outside the permissible grain size range, the reward drops linearly with increasing deviation from the target grain size in section two until it remains constant at its minimum in section three. This lower limit of the reward is called reward clipping. It prevents large gradients from occurring in the training process of the RL algorithm, which can increase the training stability.

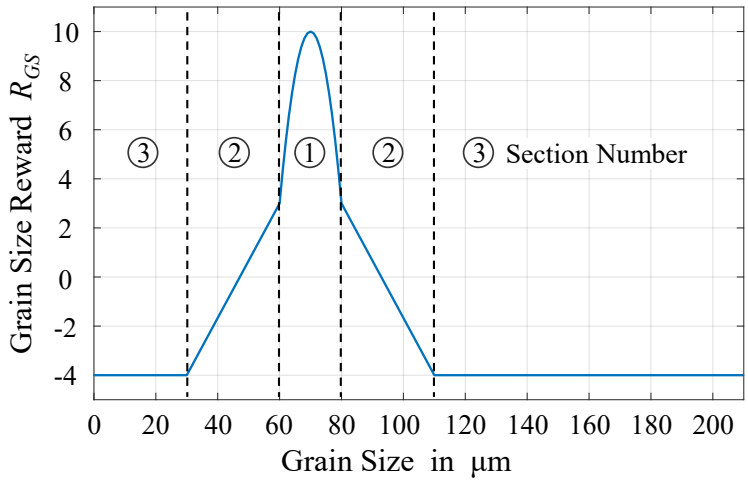

Fig. 3. Graphical representation of the sparse grain size reward R_{GS}.

Finally, the action selection of the algorithm, which previously consisted of height reduction (3% - 30%) and bite ratio (0.3 – 0.9), was extended by the selection of a break time between 0 and 120 seconds before every second pass. This enables the algorithm to influence the microstructure significantly more throughout the forming process. Now, depending on the current ingot state, the RL can e.g. lower the workpiece temperature by cooling or give material-physical processes such as static recrystallization or grain growth the necessary time to complete.

Training of the RL Algorithm – Sparse Grain Size Reward

After the RL algorithm was extended and the use case was defined, a new training process with 100,000 iterations was carried out. This corresponds to 100,000 designed pass schedules that are analyzed concerning their final workpiece properties by the environment using fast process models. The training process took about eight days on four cores of an Intel® Xeon® E5-2667 v3 processor with the algorithm successfully converging against high rewards.

To classify the quality of the generated pass schedules, again 400 different pass schedules were designed using the trained RL agent and then analyzed concerning their achieved grain sizes. Subsequently, averaging was used to generate comparable process parameters such as a mean number of passes or an averaged deviation from the target geometry. On average, the grain size over all 400 pass schedules is 70.99 ± 3.58 µm (cf. Fig. 4) and thus close to the desired target value of 70 µm. In comparison to the previous RL algorithm for efficient forging, the mean grain size decreased significantly throughout all 400 pass schedules (cf. Fig. 2) while the standard deviation remained almost the same. Moreover, nearly all processes produce a grain size within the permissible range between 60 µm and 80 µm. Only a small cluster of five pass schedules (cf. Fig. 4, red frame) exceeds the permissible maximum value of 80 µm with a maximum grain size of 82.05 µm for the combination of an initial height of 189 mm and a final height of 139 mm.

In addition to the new optimization goal of generating a defined grain size, the agent also successfully took into account the objectives for efficient open-die forging. The average number of passes was reduced to 5.9 while the designed pass schedules use the available press force well. This is underlined by a small average deviation of 6.1 % from the target press force, whereby the maximum press force is not exceeded in any pass schedule. In general, the designed pass schedules lead to the desired target geometry well resulting in an average deviation of 0.31% between generated and desired final height. Nevertheless, one of the 400 pass schedules (initial height = 213 mm and target height = 137 mm) failed on the permissible final height range (target height ± 1%) with a deviation of -1.02 % from the target geometry.

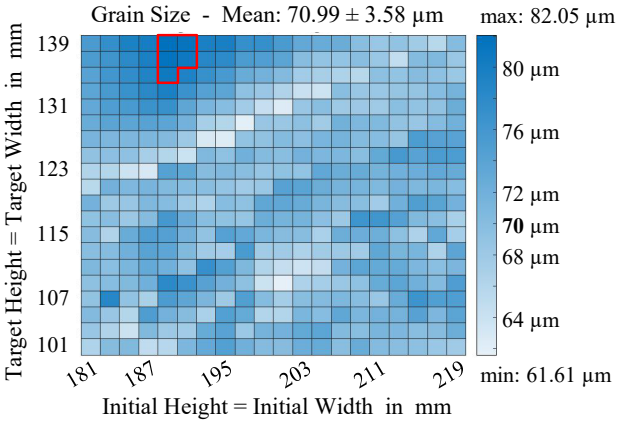

Fig. 4. Heatmap showing the produced average grain sizes of 400 different pass schedules designed by RL with a sparse grain size reward (cf. Fig. 3).

The pass schedules failing slightly on complying with the target grain size and target geometry ranges indicate that the algorithm might not have converged to its full extent yet. One reason for this slow and incomplete convergence could be the increased complexity of the optimization problem. Furthermore, an unclear formulation of the optimization goals within the reward function can result in bad convergence as well as the observed grain sizes outside of the desired range. A longer training process might improve the result quality but due to the already high training duration of several days, it is not a feasible solution. Instead of longer training durations, the following chapter aims at two different approaches to increase the efficiency of the training process: Reducing the complexity of the optimization problem and improving the reward function.

Reduction of Complexity

The first change to the implementation of the RL algorithm aims at reducing the complexity of the optimization problem to be solved. Until now, the algorithm has had to balance four optimization objectives (set final geometry, minimize number of passes, utilize press force, set grain size) and satisfy all of them simultaneously. So far, the final geometry resulted from the selected height reductions and bite ratios, considering the occurring spread. Since the desired final cross section is known upfront and fast process models can predict the geometry change during forging, from now on the desired final geometry is directly ensured in the implementation of the RL environment. As soon as the algorithm selects a combination of height reduction and bite ratio that causes the final height of the workpiece to fall below the desired final height, a correction of the last two passes happens. Here, the height reduction is inversely lowered by backwards calculation of the geometry model ensuring the exact production of the target geometry. The bite ratio and break time selected by the algorithm remain unchanged during this adjustment. This change to the implementation removes one of the four optimization objectives, so that the complexity of the optimization problem decreases significantly, which should lead to improved convergence in the training process. Since hereafter, the desired geometry is always produced perfectly, the associated reward calculated after the last pass is invalid and removed from the reward function.

Furthermore, a restriction of the number of actions selectable by the agent decreases the complexity even further. The discrete action choice of the used RL (double deep Q-learning) agent is based on the estimation of the value $Q(s,a)$ for all possible action choices a in the current state s. The Q value represents a measure of the total reward expected for the remaining process, which the agent tries to maximize. Therefore, the agent always chooses the actions with the highest Q-value, promising the highest total reward gained. So far, the RL agent can choose bite ratios between 0.3 and 0.9 in increments of 0.05, and height reductions between 3% and 30% in increments of 1%. In combination with break times, which the algorithm is allowed to choose between 0 s and 120 s in 30 s increments, 1820 combinations of action choices are possible in each state of the forging. Hence, before every action choice 1820 Q-values need to be calculated, leading to the conclusion that in the current implementation increasing discretization of actions leads to

slower action choices and hence to higher training durations. Furthermore, the algorithm must estimate the value *Q(s,a)* for all combinations of state *s* (state of the forging ingot) and action *a* (combination of process parameters) and store it in the neural network. This mapping becomes more difficult as the number of combinations increases. This is why the step size of the action choices bite ratio (0.3 : 0.05 : 0.9 → 0.3 : 0.1 : 0.9) and height reduction (3% : 1% : 30% → 3% : 3% : 30%) were reduced. Through this adjustment, the number of possible actions per state decreases from 1820 to 350 representing another significant reduction in complexity.

Adaption of the Reward Function

Besides the high complexity of the optimization problem, the design of the reward function can be a reason for the slow convergence behavior as well as the miss of the desired grain size range. The definition of the reward function is one of the most important issues in RL, because the reward function does not only influence the achieved result, here e.g. the quality of the generated pass schedules, but also the training process itself. A well-defined reward function contributes to accelerating the convergence of RL algorithms and leads to more stable training processes. It is known that compared to sparse rewards, continuous reward functions promote the convergence of RL algorithms and lead to better training results. In the present context of pass schedule design, a sparse reward corresponds to feedback that is given only once per pass schedule after the last pass, whereas a continuous reward is calculated after every second pass. The current reward function already includes continuous rewards for utilizing the available press force and for minimizing the number of passes, but producing a specific grain size is only rated sparsely (cf. Fig. 3). It is hardly possible to describe the microstructure evolution during open-die forging processes inversely due to the incremental forming and interaction of various material physical effects like recrystallization and grain growth. For this reason, there is no feasible benchmark for the continuous evaluation of the ingot state over the process to achieve a desired grain size at the end of the process.

To overcome this hurdle, a new temperature-dependent continuous reward of the grain size is introduced, which should help the algorithm to reliably achieve the desired final grain size across all combinations of initial and target geometry. This reward structure is based on the assumption that the algorithm can only influence the microstructure as long as the ingot is sufficiently hot. As the workpiece cools during forging, processes such as recrystallization and grain growth are increasingly restricted, and hence, the influence of the agent on the microstructure decreases. This insight enables the creation of a new reward function $R_{GS,C}$ for rating the grain size continuously throughout the pass schedule. A downward-opening parabola whose maximum occurs at the target grain size forms the basis of this function. As can be seen in Fig. 5, on the one hand, the minimum reward is lowered with falling temperatures. On the other hand, the parabola is unilaterally stretched in the direction of larger grain sizes with raising temperatures. Both effects described, apply linearly between 900°C and 1100°C and represent the decreasing influence on the grain size (cf. Fig. 5). Outside this temperature range the reward $R_{GS,C}$ remains constant. The new continuous grain size reward only complements the existing sparse grain size reward. Hence, at the end of a pass schedule still a grain size reward inspired by Fig. 3 is calculated. It is to be noted that $R_{GS,C}$ is deliberately defined as negative. The punishment granted for each pass indirectly represents the goal to also minimize the number of passes, since higher amounts of passes lead to more grain size evaluations resulting in a higher overall punishment.

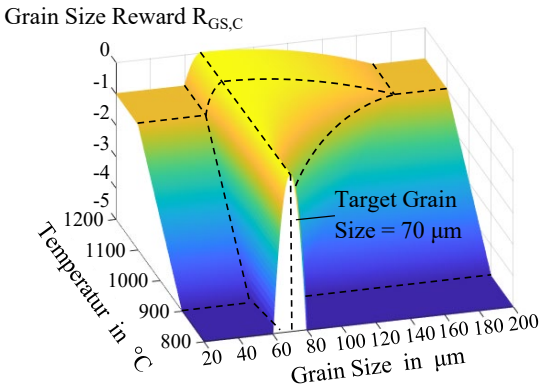

Fig. 5. Graphical representation of the continuous reward function for the grain size $R_{GS,C}$.

Retraining of the adapted RL algorithm – Continuous Grain Size Reward

To be able to assess the influence of the adjustments made, the adapted RL algorithm had to be retrained once again. This training process comprised 50,000 iterations that equal 50,000 designed and analyzed pass schedules, and took only 24 hours on four cores of an Intel® Xeon® E-2236 processor. Again, 400 different pass schedules were designed using the trained RL algorithm and the achieved mean austenitic grain sizes are summarized in Fig. 6.

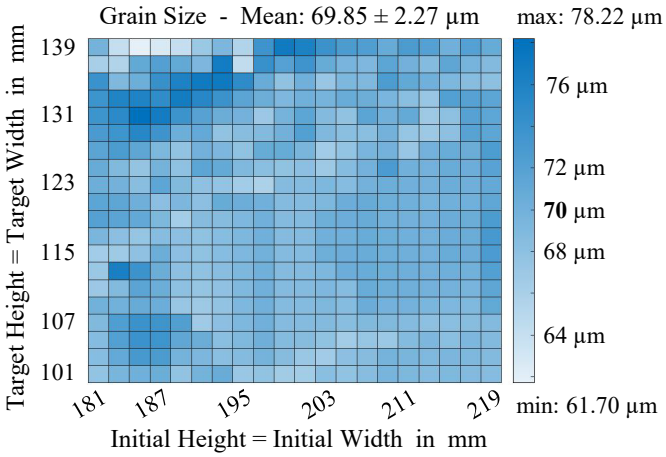

Fig. 6. Heatmap showing the produced average grain sizes of 400 different pass schedules designed by RL with a continuous grain size reward.

Averaged over all 400 pass schedules, the adapted RL algorithm produces a mean grain size of 69.85µm, which is very close to the target grain size of 70µm. The standard deviation results in 2.27µm while none of the 400 pass schedules produces a grain size outside the desired range. In addition, the algorithm continues to meet the goals of efficient open-die forging with an average number of passes of 5.55 and an average deviation of 5.5% between the predicted and nominal press force. At the same time, plant limits such as the maximum press force are observed in all pass schedules. Compared to the previous results from the RL algorithms with no and with sparse grain size rewards (cf. Table 1), a significant improvement in the quality of the designed forging processes was achieved.

Table 1. Summary of the pass schedule quality of all three RL algorithms.

RL algorithm	no GS reward	sparse GS reward	continuous GS reward
Average grain size [µm]	86.71 ± 3.82	70.99 ± 3.58	69.85 ± 2.27
Average number of passes	6.15	5.88	5.55
Avg. deviation nominal Force [%]	5.02	6.13	5.53
Avg. deviation from final height [%]	0.23	0.31	0

In general, the latest RL algorithm shows similar process design patterns compared to its predecessor with sparse grain size reward. Whenever possible, large height reductions are applied to reduce the number of passes. At the same time, break times and bite ratios are selected interdependently so that the press force is utilized well and the desired grain size is achieved. The greatest behavior change is present in the area in which the maximum permissible grain size of 80 µm was previously exceeded (see Fig. 4, red frame). Here, the adapted RL algorithm applies six passes instead of four while concentrating deformation in passes three and four. This leads to a different recrystallization timing, which shifts the final grain size into the desired range.

The significant improvement in the quality of the designed pass schedules, combined with the drastic reduction of the training duration from eight days to 24 hours, demonstrate the feasibility of RL for the design of optimized pass schedules in open-die forging with consideration of microstructure. After the training process, the design of one optimized pass schedule only takes about four seconds. This short calculation time enables the use of RL for the control of open-die forging processes when combined with a suitable process monitoring system (cf. [13]). If deviations from the target process route happen that would lead to e.g. an undesired change in final grain size, the monitoring system can detect those. Subsequently, a RL algorithm could be used to calculate a new optimized pass schedule in real time, starting from the intermediate state of the process and continuing to produce the desired final grain size. To achieve this, further changes to the RL algorithm are necessary, so that it can cope with sensor noise present in the real forging environment as well as a wider range of input states of the forging ingots.

Summary

In this publication, an existing RL algorithm for the design of efficient open-die forging processes was extended to successfully consider microstructure in the process design. In a first extension, a sparse grain size reward was introduced into the RL algorithm leading to an improved microstructure. The average grain size of 70.99 ± 3.58 µm was significantly closer to the target value of 70 µm compared to the original implementation (86.71 ± 3.82 µm). The goals of efficient open-die forging (produce target geometry, use available press force, reduce number of passes) were also met, although slightly worse than before (cf. Table 1). Since individual pass schedules still missed the desired range for the grain size as well as the target geometry, a new continuous reward structure depending on the ingot temperature was added in a second extension. Besides that, the complexity of the underlying optimization problem was reduced so that the RL algorithm is now able to design optimized pass schedules for all combinations of initial and target geometry. On average, the mean austenitic grain size after the forging resulted in 69.85 ± 2.27 µm while all designed pass schedules complied with the specified grain size limits. In addition, the adherence to the optimization objectives of efficient forging also improved, underlining the great potential of utilizing process knowledge for the improvement of reinforcement learning applications. Besides the raise of result quality the duration of the training process decreased from eight to one day and the design of individual optimized pass schedules still takes just a few seconds. This highlights not only the possibility to use RL for the fast design of optimized pass schedules, but also the potential to use RL for the control of open-die forging processes.

Outlook

In the future, forging experiments on the open-die forging press of the Institute of Metal Forming (IBF) as well as microstructure analysis are planned to validate the presented RL approach. In addition, after the extension, the algorithm is still able to design individual optimized pass schedules in a few seconds. This offers the potential to extend the RL algorithm from designing processes in advance to control open-die forgings with regard to microstructure. To achieve this, the RL has to be extended so that deviations from a nominal process, such as interruptions or varying initial temperatures, can be included in the training process and hence, be reacted to.

Acknowledgement.
This work was funded by the Deutsche Forschungsgemeinschaft (DFG, German Research Foundation) – 452539735.

References

[1] Information on https://www.sms-group.com/de-de/plants/open-die-forging-presses
[2] Information on https://easy2forge.com/
[3] A. Esteso, D. Peidro, J. Mula, M. Díaz-Madroñero, Reinforcement learning applied to production planning and control, Int. J. Prod. Res. (2022). https://doi.org/10.1080/00207543.2022.2104180
[4] C. Li, P. Zheng, Y. Yin, B. Wang, L. Wang, Deep reinforcement learning in smart manufacturing: A review and prospects, CIRP J. Manuf. Sci. Technol. 40 (2023) 75-101. http://doi.org/10.1016/j.cirpj.2022.11.003
[5] O. Gamal, M.I.P. Mohamed, C.G. Patel, H. Roth, Data-Driven Model-Free Intelligent Roll Gap Control of Bar and Wire Hot Rolling Process Using Reinforcement Learning, Int. J. Mech. Eng. Robot. Res. 10/7 (2021) 349-356.
[6] J. Dornheim, N. Link, P. Gumbsch, Model-free Adaptive Optimal Control of Episodic Fixed-horizon Manufacturing Processes Using Reinforcement Learning. Int. J. Control Autom. Syst. 18 (2020) 1593–1604
[7] C. Scheiderer, T. Thun, C. Idzik, A.F. Posada-Moreno, A. Krämer, J. Lohmar, G. Hirt, T. Meisen, Simulation-as-a-Service for Reinforcement Learning Applications by Example of Heavy Plate Rolling Processes, Procedia Manuf. 51 (2020) 897-903. https://doi.org/10.1016/j.promfg.2020.10.126
[8] N. Reinisch, F. Rudolph, S. Günther, D. Bailly, G. Hirt, Successful Pass Schedule Design in Open-Die Forging Using Double Deep Q-Learning, Processes 9 (2021) 1084. https://doi.org/10.3390/pr9071084
[9] A. Tomlinson, J.D. Stringer, Spread and elongation in flat tool forging, J. Iron Steel Inst. 193 (1959) 157-162.
[10] M. Wolfgarten, D. Rosenstock, F. Rudolph, G. Hirt, New approach for the optimization of pass-schedules in open-die forging, Int. J. Mater. Form. 12 (2019) 973-983. https://doi.org/10.1007/s12289-019-01471-w
[11] D. Recker, M. Franzke, G. Hirt, Fast models for online-optimization during open die forging, CIRP Annals – Manuf. Technol. 60 (2011) 295–298. http://doi.org/10.1016/j.cirp.2011.03.142
[12] K. Karhausen, R. Kopp, Model for integrated process and microstructure simulation in hot forming, Steel Res. 63 (1992) 247-256. https://doi.org/10.1002/srin.199200509
[13] F. Rudolph, M. Wolfgarten, V. Keray, G. Hirt, Optimization of Open-Die Forging Using Fast Models for Strain, Temperature, and Grain Size in the Context of an Assistance System, Forming the Future. The Minerals, Metals & Materials Series (2021) 1145-1159.

Materials Research Proceedings 28 (2023) 2071-2080 https://doi.org/10.21741/9781644902479-222

Monitoring of fluctuating material properties for optimizing sheet-metal forming processes: a systematic literature review

ORTJOHANN Lucia[1,a *], BECKER Marco[1,b], NIEMIETZ Philipp[1,c] and BERGS Thomas[1,2,d]

[1]Labratory for Machine Tools and Production Engineering (WZL) of RWTH Aachen University, Campus-Boulevard 30, 52074 Aachen

[2]Fraunhofer Institute for Production Technology IPT, Steinbachstr. 17, 52074 Aachen

[a]l.ortjohann@wzl.rwth-aachen.de, [b]m.becker@wzl.rwth-aachen.de, [c]p.niemietz@wzl.rwth-aachen.de, [d]t.bergs@wzl.rwth-aachen.de

Keywords: Sheet-Metal Forming, Material Properties, Property Monitoring, NDT

Abstract. Material properties can vary both along a sheet-metal coil and from coil to coil despite tight tolerances influencing the process stability of sheet-metal processes and the part quality, which leads to rejects and machine downtime [1]. This significantly affect the economic efficiency of the process. Monitoring fluctuations in material characteristics at regular intervals along sheet-metal coils is enabled directly by non-destructive testing (NDT) before the process offering conclusions on the material properties. Another material monitoring technique arises from monitoring process conditions of the upstream processes, e.g., cold rolling, leading indirectly to insights on material properties. In this work, a systematic literature review (SLR) [2] is conducted to investigate recent approaches for material monitoring and for the utilization of resulting material data for optimizing different sheet-metal forming processes. Existing approaches for different sheet-metal forming processes are critically appraised. Based on the SLR research gaps are revealed and research opportunities, e.g., arising from a potential transfer of existing solutions between different forming processes and recent advances in data-driven methods, are identified.

Introduction

Despite tight tolerances, variations in material properties along a sheet-metal coil or between different batches of the same material have been shown to occur during sheet-metal production [3]. These material fluctuations lead to defects such as burr formation or dishing behavior in shearing processes and to defects such as spring back in bending or forming operations [4]. Thus, fluctuating material properties result in rejects, robustness problems and downtime of sheet-metal forming processes. Typically, material properties are only measured at the beginning and at the end of coils. This makes it difficult to draw conclusions about the material quality in the event of defects.

With the rise of the digital transformation in manufacturing to the Industry 4.0 the concept of the Internet of Production is gaining more importance [5]. In an Internet of Production all process-characterizing information about a production process is available for the realization of real-time process control and decision support. In the case of material variation that means the information about the material properties along the coil needs to be available to achieve full transparency, to adapt the process to changes in material properties and in case of workpiece defects to provide data for effective troubleshooting.

One solution to this problem is to measure or monitor the material characteristics along the sheet-metal coil before the sheet-metal process with the help of non-destructive testing (NDT). Already in 1994, Engel et al. demonstrated the potentials of NDT for sheet-metal processes [6]. Nowadays NDT allows drawing direct conclusions about material properties, such as tensile

Content from this work may be used under the terms of the Creative Commons Attribution 3.0 license. Any further distribution of this work must maintain attribution to the author(s) and the title of the work, journal citation and DOI. Published under license by Materials Research Forum LLC.

strength or elongation at break, and can be performed inline at regular intervals along the coil as it is being processed [7].

Besides NDT, another approach to material monitoring arises from monitoring process conditions of the upstream processes of sheet-metal forming processes, e.g., hot rolling [8], leading indirectly to insights on material properties. The use of cross-process data fundamentally enables the identification of quality-relevant parameters in the process chain and thus, the optimization of the process itself or of the subsequent process in the process chain. The sharing of information along the process chain is one of the main goals of an Internet of Production.

Since a lot of research is already done in this field, this paper methodologically researches the approaches to handle fluctuating material properties for the usage in an Internet of Production. The two presented approaches of monitoring material properties along sheet-metal coils lead to following research questions:

RQ1. How can fluctuating material properties be directly measured by NDT?
RQ2. How can fluctuating material properties be indirectly measured by monitoring the upstream process?
RQ3. How is the knowledge of fluctuating material properties along the coil utilized to optimize sheet-metal processes?

To answer these questions a systematic literature review (SLR) is conducted. First, the research methodology is described in section 2 and after that in section 3,4 and 5 the research questions are discussed chronological based on the results of the SLR. In section 6, research gaps in the field of material monitoring are identified.

Research Methodology

The research methodology of the conducted SLR is based on the research methodology from Xiao and Watson [2]. It consists of three stages planning, conducting and reporting with different steps (Fig 1). The problem formulation is already described in section 1 in the form of three research questions.

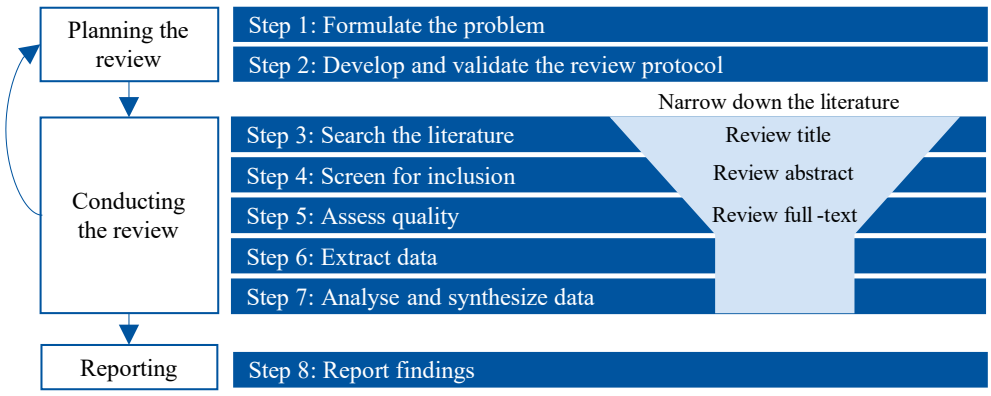

Fig. 1. Methodology of the SLR (adapted from [2]).

Based on these research questions, topics for keywords were selected (see Table 1). The first keyword topic focusses on “mechanical properties” and “material variations” ensuring that the retrieved literature contains these or synonyms of these terms. In addition, the literature search is intentionally limited to publications on sheet-metal forming, in particular, common sheet-metal forming or shearing technologies and the most important upstream processes for the production of sheet-metal coils. Here common sheet-metal forming processes were chosen. The last keyword topic focuses on different monitoring and utilization methods of known material properties based on the fact that known material characteristics are used for control or data-driven analysis.

Table 1. Keywords of the conducted SLR.

Material Properties		Sheet Metal Forming		Processes		Utilization
material variation **OR** material fluctuations **OR** material variability **OR** material scatter **OR** mechanical properties **OR** material properties **OR** steel strip properties **OR** sheet metal properties **OR** material characteristics **OR** material measurements	**AND**	sheet metal forming **OR** metal forming **OR** forming technology **OR** sheet metal separation **OR** strip steel **OR** steel sheets **OR** sheet metal **OR** sheet material **OR** steel strip **OR** cold rolled strip **OR** coil	**AND**	normal cutting **OR** shear cutting **OR** shearing **OR** blanking **OR** punching **OR** fine blanking **OR** fineblanking **OR**	**AND**	optimization **OR** monitoring **OR**
						NDE **OR** NDT **OR** non-destructive testing **OR** non-destructive evaluation **OR** non-destructive examination **OR** nondestructive testing **OR** nondestructive evaluation **OR** nondestructive examination **OR** eddy current **OR**
				stamping **OR** deep drawing **OR** car body part **OR** bending **OR**		closed loop control **OR** control materials **OR** feedback control **OR** feedforward control **OR** online control **OR** offline control **OR**
				levelling **OR** roller levelling **OR** roller leveler **OR** cold rolling **OR** hot rolling		machine learning **OR** AI **OR** digital transformation **OR** digital twin **OR** digitization **OR** digitalisation **OR** data based **OR** data driven **OR** decision support

With these keywords 355 publications were found in the database Scopus. Scopus only considers peer-reviewed papers, books, and conference papers. Duplicates and publications that were not in English or older than from the year 2000 were removed. Based on the research questions the publications were examined by their title and abstract. Then a backward/forward search was conducted. An overview of the conducted SLR is given in Fig. 2.

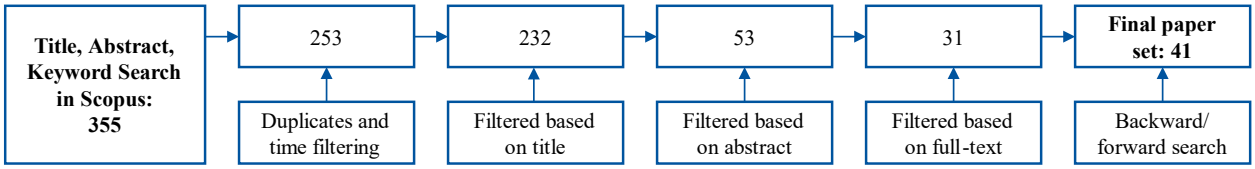

Fig. 2. Review process of the conducted SLR.

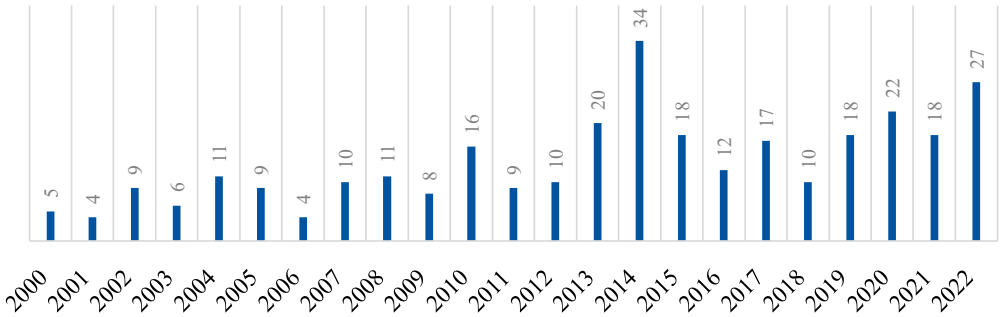

Fig. 3. Publication per year.

A first analysis of the publications per year shows that the topic of monitoring fluctuating material properties for optimizing sheet-metal forming processes became increasingly important until 2014 and after 2014 the importance remained, leading to the assumption that this topic is still relevant and will be relevant in the future.

To give a first overview of the results, Fig. 4 shows the number of publications found in the SLR after filtering for duplicates and time for different keyword topics displayed in the rows of column 3 of Table 1. It is evident that the topic of material variation is addressed primarily for the upstream processes, hot rolling, cold rolling, and roller levelling and for the sheet-metal forming processes stamping, deep drawing and bending. There are not many publications regarding sheet-metal separation processes.

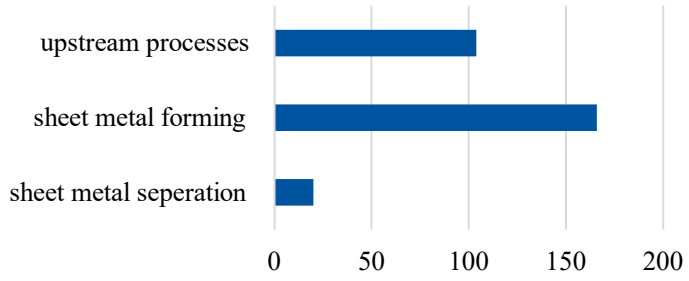

Fig. 4. Publication regarding different processes.

In the following three sections the research questions will be discussed based on the outcome of the SLR. A summary of the cited publications is given in Table 2.

Non-Destructive Testing in Sheet-Metal Forming (RQ1)

Non-destructive testing methods are suitable for measuring the material properties at regular intervals along the coil before the sheet-metal forming process. The operating principles of non-destructive testing methods include ultrasonic testing, X-ray examinations and electromagnetic methods. In sheet-metal forming, electromagnetic methods are commonly used because there is a correlation between the mechanical and electromagnetic properties of sheet-metal since the microstructure is influencing both. Several scientific publications study how signals from various electromagnetic sensors correlate with material properties.

For instance, Magnetic Barkhausen noise was used to measure hot-stamped high strength steel [9] and cold-rolled steel strips [10,11] in a lab setting. These measurements were used to predict different material properties, e.g., yield strength. Unterberg et al. distinguish whether material specimen were extracted from the start, the middle, or the end of a sheet-metal coil using a machine learning algorithm with magnetic Barkhausen noise as input data [12]. However, magnetic Barkhausen noise has not yet been used for inline monitoring.

Commonly used sensors for in-line measurements of sheet-metal material include, eddy current sensors (eddy current method), the 3MA sensor (micromagnetic, multiparametric microstructure and stress analysis), and the IMPOC sensor (magnetic inductive method). For each of these sensors, it has been shown that the sensor signals are related to the mechanical properties. Various publications report successfully using 3MA sensor for inline sheet-metal monitoring and predicting tensile strength, yield strength, residual stress, and hardness of the material along a coil with a regression based on 3MA data [13-15]. Heingärtner used multidimensional regression based on eddy current data to calculate the material parameters tensile strength, yield strength, uniform strain, and elongation at break in inline production [7]. Moreover, Lee et al. tested different machine learning algorithms to predict the yield stress and the uniform elongation based on 6 features of eddy current signals and achieved a high accuracy [16]. Zoesch et al. were able to detect cracks and thinning of material during deep drawing with two sensors (eddy current, 3MA) [17]. The IMPOC sensor was used to predict mechanical parameters such as tensile strength and yield strength [18] as well as to find uniformity in material properties along coils [19].

Indirect Measurements of Material Properties (RQ2)

The monitoring of processes that produce sheet-metal represents an alternative strategy to directly measuring the material in sheet-metal forming processes. The inline monitoring of sheet-metal producing processes not only facilitates the optimization of these processes itself, but also of downstream sheet-metal forming processes.

Table 2. Summary of the publication conducted in the SLR.

Research Question	Processes/Sensors	Literature
Fluctuating material properties	Sheet-metal forming in general	[1,3,4,20]
RQ1	Magnetic barkhausen noise	[9-12]
	Eddy current	[6,7,16,17]
	3MA	[13-15]
	IMPOC	[18,19]
RQ2	Hot rolling	[8,21-23]
	Cold rolling	[24]
	Roller levelling	[25-27]
	Stamping	[28]
RQ3	Stamping	[29-31]
	Deep drawing	[32-40]
	Bending	[41-43]

For the process of hot rolling, it was already shown in 2005 that it is possible to predict different mechanical properties such as yield strength of hot rolled steel coils based on data including process data such as coiling temperature and chemical factors with an artificial neural network. However, approximately 21% of the predicted yield strength values deviated more than ±15 MPA from the true value [23]. Chen and Fan showed in 2021 that based on the input data rolling temperature, curling temperature and the chemical composition of the material the material properties tensile strength, compression and elongation can be predicted by different regression models with an coefficient of determination of over 99% [8]. In [21] similar results were presented. In addition, electromagnetic monitoring was used in a hot strip mill to monitor the phase transformation and to extract the data of austenite transformation. Based on this data the hot rolling process was optimized in an offline control system [22]. Cuznar and Glavan investigated the data-driven optimization of the cold rolling process. The developed models enabled optimal cold rolling parametrization and real-time monitoring [24].

The roller levelling process was monitored by Nikula and Leiviskä using acceleration measurements. They utilized these measurements to predict the properties yield strength, width and thickness of the processed steel along the coil [27]. Magro et al. investigated an approach to predict the yield stress after the tension levelling process and to adapt the initial process parameters according to an analytical model [26]. Grüber and Hirt proposed a semi-analytical model that calculates the levelling force and determines in an inverse approach the material data [25].

In another approach, times series signals from force sensors of the stamping process as an upstream process are evaluated and used to predict the tensile strength, yield strength and elongation at break of the processed material [28].

Utilization of the Knowledge of Fluctuating Material Properties (RQ3)

Fluctuating material properties create uncertainties for downstream sheet-metal forming processes. These uncertainties influence the process stability, the process outcome and hence the product properties [20]. Thus, material fluctuations must be included in the process parameterization to increase the stability of the process or when adapting the process with different control strategies to optimize the process outcome.

For a stamping process, variations of material were measured with non-destructive testing and different motions for a servo-press were evaluated [29]. The data of this experiments were then evaluated using Bayesian logistic regression resulting in a model that determines motion profiles for a servo-press based on material characteristics [31]. Maretta and Di Lorenzo proposed a method were meta-models and Monte Carlo simulation were combined to analyze the influence of coil-to-

coil material variations on thinning and spring back to enhance the robustness of a stamping process [30].

A method for knowledge-based control of a deep drawing process was proposed by Fischer et al., combining feedforward control based on inline material measurements from an eddy current sensor and feedback control based on inline measurements of draw-in [36]. Another approach to minimize the influence of material variation by feedback control was presented by the same author [37]. Heingärtner et al. implemented an intelligent control system using numeric simulations and material data acquired by eddy current, process settings and draw-in measurements to optimize the manufacturing of kitchen sinks and tested it on a production site [38].

Endelt distinguishes between non-repetitive uncertainties and repetitive uncertainties in sheet-metal forming. While non-repetitive uncertainties are for example variance in sheet thickness and uneven lubrication. The repetitive uncertainties are for example changes in material properties, tool wear and tool temperature, which lead to process downtimes [33]. To handle these uncertainties Endelt and Danckert proposed a control strategy with an inner loop reducing the current draw-in error of the produced part and an outer loop based on a iterative learning control scheme handling the repetitive uncertainties and transfer information to optimize the draw-in flange from the produced part to the next part [35]. Endelt tested also a similar approach of iterative learning control algorithms on two benchmark problems [34]. Furthermore, Endelt develop the control strategy based on an inner loop and an outer loop further by adding numerical simulations to reduce the draw-in error [33]. A numerical study for a deep drawing process, where material fluctuations were included through a sensitivity analysis, and a proof of concept for a new control strategy by adapting the blank position was conducted by Briesenick et al. [32].

Based on various material data such as IMPOC signals and oil levels recorded in a stamping plant, van Stein implemented an anomaly detection algorithm in a car body stamping process to detect outliers in material properties along steel coils [39]. On the same press shop, Purr examined various data sources in a press shop from various measuring systems also IMPOC signals with the aim of detecting fluctuations in the process. The result shows that the material fluctuations have a strong influence on the quality of the car body components [40].

In bending, material variations lead to spring back and thus, control strategies have been developed. A summary of these strategies is given in [20]. In this systematic literature review the focus was on the fluctuations of material properties. In [41] the authors used finite element simulation to identify a spring back compensation strategy. It was shown that this compensation strategy is able to reduce spring back under varying material properties and sheet thickness. Lafon et al. modelled different uncertainties, especially material properties to find a robust optimization procedure for a draw bending process [42]. The effect of yield strength variation and part dislocation was studied by Waheed et al. to optimize bending force and residual stresses [43]. It was found that the yield strength has a major effect on bending force and residual stresses.

Identified Research Gaps

The SLR revealed existing scientific studies, which already apply different NDT methods to obtain insights about material properties at regular intervals along sheet-metal coils in-line at the shop floor. Nevertheless, only few studies investigate in-line monitoring of material properties in relation to the parametrization of sheet-metal forming processes and the outcoming part quality at industrial scale. The investigation of non-destructive material measurements along coils offers the quantification of influences originating from the material and enables profound data-driven evaluation based on a high amount of available data to realize decision support and real-time control. Furthermore, NDT has been used to predict material properties by using features of raw signals but further investigation of correlations between specific signal properties of the raw signals and specific material properties provide an opportunity to derive new insights into potentially underlying cause-and-effect relationships.

Although existing publications already report that knowledge of material properties was obtained by monitoring upstream processes, in particular hot rolling, cold rolling, roller levelling and stamping, it is at best used to optimize the same process but there is no publication using these insights to optimize the subsequent sheet-metal forming processes. Compared to NDT, the approach to monitoring upstream processes usually requires cross-company collaboration, which, combined with the heterogeneity of the different process data, further complicates this approach. However, research on other manufacturing technologies suggests, that a holistic optimization of process sequences not only offers economic but also ecological advantages [44]. A holistic approach in sheet-metal processing requires to overcome existing data silos and to share data across processes in the sense of an Internet of Production [45].

Another opportunity arises from the combination of the two material monitoring approaches to obtain larger data sets, facilitating the use of data-driven methods to adjust the sheet-metal process to ensure to enable a high-quality process outcome despite fluctuating material properties. Data-driven methods for process optimization and control in sheet metal processing offer the potential to learn complex, unknown interdependencies along process sequences. This leads not only to the optimization of the sheet metal forming process and the quality of the resulting part, but also to the adaptation of upstream processes to specified material requirements based on the previously established dependencies between varying material properties and process parameterization.

In addition, research is mainly limited to sheet metal forming processes, whereas the influence of material variations and a corresponding process optimization has not yet been investigated for sheet metal shearing processes. Hence, there is an opportunity to transfer the solutions presented from sheet metal forming to shearing processes.

Summary

A systematic literature review was conducted showing that there are two different approaches to monitoring fluctuating material properties along coils. It has been shown that non-destructive testing is used successfully inline to measure material properties. Moreover, various methods to monitor material properties in the upstreaming processes hot rolling, cold rolling, roller levelling and stamping were pointed out. The knowledge of material properties along a coil is already used to optimize stamping and deep drawing processes based on different control strategies and research considers fluctuating material properties to optimize different bending processes.

In addition, research gaps were identified: 1) The utilization of knowledge of material properties along coils in relation to the parametrization of sheet-metal forming processes and the outcoming part quality on an industrial scale needs to be investigated in more detail. 2) Further cross-process data exchange is required to research the optimization of downstream processes when fluctuations in material properties occur. 3) The investigation of material variations in sheet-metal shearing processes is still an open topic.

Acknowledgements

Funded by the Deutsche Forschungsgemeinschaft (DFG, German Research Foundation) under Germany's Excellence Strategy - EXC-2023 Internet of Production - 390621612.

References

[1] V. Sturm, Einfluss von Chargenschwankungen auf die Verarbeitungsgrenzen von Stahlwerkstoffen, Zugl.: Erlangen-Nürnberg, Univ., Techn. Fak., Meisenbach, Bamberg, 2013.

[2] Y. Xiao, M. Watson, Guidance on Conducting a Systematic Literature Review, J. Plann. Edu. Res. 39 (2019) 93-112. https://doi.org/10.1177/0739456X17723971

[3] D. Harsch, P. Fischer, B. Berisha, J Heingärtner, Y. Renkci, P. Hora, Considering fluctuations of material properties, stainless steel 1.4301, on manufacturability of kitchen sinks, IOP Conf. Ser.: Mater. Sci. Eng. 418 (2018) 12113. https://doi.org/10.1088/1757-899X/418/1/012113

[4] A. Kolhatkar, A. Pandey, Sheet Metal Tooling: Selective Review of Online Monitoring Trends, Int. J. Mech. Prod. Eng. Res. Develop. (IJMPERD) 9 (2019) 183-198.
[5] J. Pennekamp, R. Glebke, M. Henze, T. Meisen, C. Quix, R. Hai, L. Gleim, P. Niemietz, M. Rudack, S. Knape, Towards an Infrastructure Enabling the Internet of Production, 2019 IEEE International Conference on Industrial Cyber Physical Systems (ICPS), IEEE. (2019) pp. 31-37. https://doi.org/10.1109/ICPHYS.2019.8780276
[6] U. Engel, M. Schwind, S. Stancu, New Applications of Non-Destructive Testing in Metal Forming Technology, Proceedings of the Institution of Mechanical Engineers, Part B: J. Eng. Manuf. 208 (1994) 259-267. https://doi.org/10.1243/PIME_PROC_1994_208_087_02
[7] J. Heingärtner, M. Born et al., Online Acquisition of Mechanical Material Properties of Sheet Metal for the Reduction of Product Quality by Eddy Current, 10th European Conference on Non-Destructive Testing, Moscow, Russia, 2010.
[8] J. Chen, Z. Fan, An intelligent online detection approach based on big data for mechanical properties of hot-rolled strip, IJMIC 37 (2021) 106. https://doi.org/10.1504/IJMIC.2021.120210
[9] X. Luo, Y. Wang, L. Wang, J. Xie, Y. Zhang, Non-destructive Hardness Measurement of Hot-stamped High Strength Steel Sheets based on Magnetic Barkhausen Noise, Procedia Eng. 81 (2014) 1768-1773. https://doi.org/10.1016/j.proeng.2014.10.229
[10] H. Sheng, P. Wang, C. Tang, Predicting Mechanical Properties of Cold-Rolled Steel Strips Using Micro-Magnetic NDT Technologies, Materials, Basel, Switzerland, 15 (2022). https://doi.org/10.3390/ma15062151
[11] Y. Zhang, W. Liu, K. Li, P. Wang, C. Hang, Y. Chen, X. Han, W. Gao, Application of a back-propagation neural network for mechanical properties prediction of ferromagnetic materials by magnetic Barkhausen noise technique, Insight 61 (2019) 95-99. https://doi.org/10.1784/insi.2019.61.2.95
[12] M. Unterberg, P. Niemietz, D. Trauth, k. Wehrle, T. Bergs, In-situ material classification in sheet-metal blanking using deep convolutional neural networks, Prod. Eng. Res. Devel. 13 (2019) 743-749. https://doi.org/10.1007/s11740-019-00928-w
[13] G. Dobmann, I. Altpeter et al., Industrial applications of 3MA - Micromagnetic Multiparameter Microstructure and Stress Analysis, 5th Int. Conference Structural Integrity of Welded Structures, Timisora, Romani, 2008.
[14] F.J. Alamos, J.C. Gu et al., Evaluating the Reliability of a Nondestructive Evaluation (NDE) Tool to Measure the Incoming Sheet Mechanical Properties, in: G. Daehn, J. Cao, B. Kinsey, E. Tekkaya, A. Vivek, Y. Yoshida (Eds.), Forming the Future, Springer International Publishing, Cham, 2021, pp. 2573-2584.
[15] B. Wolter, Y. Gabi, C. Conrad, Nondestructive Testing with 3MA—An Overview of Principles and Applications, Appl. Sci. 9 (2019) 1068. https://doi.org/10.3390/app9061068
[16] K. Lee, C. Hong, E.H. Lee, W. Yang, Comparison of Artificial Intelligence Methods for Prediction of Mechanical Properties, IOP Conf. Ser.: Mater. Sci. Eng. 967 (2020) 12031. https://doi.org/10.1088/1757-899X/967/1/012031
[17] A. Zoesch, T. Wiener, M. Kuhl, Zero Defect Manufacturing: Detection of Cracks and Thinning of Material during Deep Drawing Processes, Procedia CIRP 33 (2015) 179-184. https://doi.org/10.1016/j.procir.2015.06.033
[18] K. Herrmann, M. Irle, IMPOC: an online material properties measurement system, in: Flat-Rolled Steel Processes: Advanced Technologies, 2009.
[19] G. Nastasi, C. Mocci et al., SOM-Based Analysis to Relate Non-uniformities in Magnetic Measurements to Hot Strip Mill Process Conditions, in: A. Esposito, M. Faudez-Zanuy, F.C. Morabito, E. Pasero (Eds.), Multidisciplinary Approaches to Neural Computing, Springer International Publishing, Cham, 2018, pp. 223-231.

[20] J.M. Allwood, S.R. Duncan, J. Cao, P. Groche, G. Hirt, B. Kinsey, T. Kuboki, M. Liewald, A. Sterzing, A.E. Tekkaya, Closed-loop control of product properties in metal forming, CIRP Annals 65 (2016) 573-596. https://doi.org/10.1016/j.cirp.2016.06.002
[21] X. He, X. Zhou, T. Tian, W. Li, Prediction of Mechanical Properties of Hot Rolled Strips With Generalized RBFNN and Composite Expectile Regression, IEEE Access 10 (2022) 106534-106542. https://doi.org/10.1109/ACCESS.2022.3212053
[22] A. Marmulev, L.M. Kaputkina, G. Herman, E.I. Poliak, Effects of Thermomechanical Processing on Uniformity of Microstructure and Properties of AHSS, MSF 783-786 (2014) 967-972. https://doi.org/10.4028/www.scientific.net/MSF.783-786.967
[23] A. Mukhopadhyay, A. Iqbal, Prediction of Mechanical Properties of Hot Rolled, Low-Carbon Steel Strips Using Artificial Neural Network, Mater. Manuf. Process. 20 (2005) 793-812. https://doi.org/10.1081/AMP-200055140
[24] K. Cuznar, M. Glavan, Optimization of cold rolling process recipes based on historical data, 2022 IEEE 21st Mediterranean Electrotechnical Conference (MELECON), IEEE (2022) 1-6.
[25] M. Grüber, G. Hirt, A semi-analytical model for inverse identification of cyclic material data from measured forces during roller levelling, Procedia Manuf. 29 (2019) 420-427. https://doi.org/10.1016/j.promfg.2019.02.157
[26] T. Magro, A. Ghiotti, S. Bruschi, A. Ferraiuolo, An artificial intelligence approach for the in-line evaluation of steels mechanical properties in rolling, Procedia CIRP 100 (2021) 193-198. https://doi.org/10.1016/j.procir.2021.05.054
[27] R.-P. Nikula, K. Leiviskä, Roller Leveler Monitoring Using Acceleration Measurements and Models for Steel Strip Properties, Machines 8 (2020) 43. https://doi.org/10.3390/machines8030043
[28] A. Schenek, M. Görz, M. Liewald, K. Riedmüller, Data-Driven Derivation of Sheet Metal Properties Gained from Punching Forces Using an Artificial Neural Network, Key Eng. Mater. 926 (2022) 2174-2182. https://doi.org/10.4028/p-41602a
[29] H. Kim, J.C. Gu, L. Zoller, Control of the servo-press in stamping considering the variation of the incoming material properties, IOP Conf. Ser.: Mater. Sci. Eng. 651 (2019) 12062. https://doi.org/10.1088/1757-899X/651/1/012062
[30] L. Marretta, R. Di Lorenzo, Influence of material properties variability on springback and thinning in sheet stamping processes: a stochastic analysis, Int. J. Adv. Manuf. Technol. 51 (2010) 117-134. https://doi.org/10.1007/s00170-010-2624-4
[31] N. Okuda, L. Mohr, H. Kim, A. Kitt, Profit-Driven Methodology for Servo Press Motion Selection under Material Variability, Appl. Sci. 11 (2021) 9530. https://doi.org/10.3390/app11209530
[32] D. Briesenick, M. Liewald, P. Cyron, Potentials of an adaptive blank positioning to control material and process fluctuations in deep drawing, IOP Conf. Ser.: Mater. Sci. Eng. 967 (2020) 12068. https://doi.org/10.1088/1757-899X/967/1/012068
[33] B. Endelt, Design strategy for optimal iterative learning control applied on a deep drawing process, Int. J. Adv. Manuf. Technol. 88 (2017). https://doi.org/10.1007/s00170-016-8501-z
[34] B. Endelt, Proposing a new iterative learning control algorithm based on a non-linear least square formulation - Minimising draw-in errors, J. Phys.: Conf. Ser. 896 (2017) 12036. https://doi.org/10.1088/1742-6596/896/1/012036
[35] B. Endelt, J. Danckert, Iterative Learning and Feedback Control Applied on a Deep Drawing Process, Int. J. Mater. Form. 3 (2010) 25-28. https://doi.org/10.1007/s12289-010-0698-z
[36] P. Fischer, D. Harsch, J. Heingärtner, Y. Renkci, P. Hora, A knowledge-based control system for the robust manufacturing of deep drawn parts, Procedia Eng. 207 (2017) 42-47. https://doi.org/10.1016/j.proeng.2017.10.735

[37] P. Fischer, J. Heingärtner, W. Aichholzer, D. Hortig, P. Hora, Feedback control in deep drawing based on experimental datasets, J. Phys.: Conf. Ser. 896 (2017) 12035. https://doi.org/10.1088/1742-6596%2F896%2F1%2F012035
[38] J. Heingärtner, P. Fischer, D. Harsch, Y. Renkci, P. Hora, Q-Guard - an intelligent process control system, J. Phys.: Conf. Ser. 896 (2017) 12032. https://doi.org/10.1088/1742-6596/896/1/012032
[39] B. van Stein, M. van Leeuwen et al., Towards Data Driven Process Control in Manufacturing Car Body Parts, 2016 International Conference on Computational Science and Computational Intelligence (CSCI), 2016.
[40] S. Purr, Datenerfassung für die Anwendung lernender Algorithmen bei der Herstellung von Blechformteilen, FAU Studien aus dem Maschinenbau 338, 2020.
[41] B. Engel, S. Kersten, P. Kopfer, Process-Controlled Forming Using an Intelligent Tool on a Servo Press, Key Eng. Mater. 622-623 (2014) 780-787. https://doi.org/10.4028/www.scientific.net/KEM.622-623.780
[42] P. Lafon, P.A. Adragna, V.D. Nguyen, Multi-objective optimization under uncertainty for sheet metal forming, MATEC Web Conf. 80 (2016) 10004. https://doi.org/10.1051/matecconf/20168010004
[43] R. Waheed, H.A. Saeed et al., Process Optimization of Bending SS 304L Sheets using Multi-Objective Genetic Algorithm and FEA, 2021 International Bhurban Conference on Applied Sciences and Technologies (IBCAST), IEEE, 2021, pp. 6-9.
[44] A. Beckers, T. Hommen, M.J.K. Kornely, E. Reuter, G. Grünert, L. Ortjohann, J. Jacob, P. Niemietz, S. Barth, T. Bergs, Digitalized manufacturing process sequences - foundations and analysis of the economic and ecological potential, CIRP J. Manuf. Sci. Technol. 39 (2022) 387-400. https://doi.org/10.1016/j.cirpj.2022.09.001
[45] P. Niemietz, J. Pennekamp, I. Kunze, D. Trauth, K. Wehrle, T. Bergs, Stamping Process Modelling in an Internet of Production, Procedia Manufacturing 49 (2020) 61-68. https://doi.org/10.1016/j.promfg.2020.06.012

Materials Research Proceedings 28 (2023) 2081-2090 https://doi.org/10.21741/9781644902479-223

Conception of a multivariable product property control for punch-hole-rolling

SPIES Daniel[1,a *], MOLITOR Dirk Alexander[1,b], DAMON James[2,c], KNOLL Maximilian[1,d], DIETRICH Stefan[2,e], SCHULZE Volker[2,f] and GROCHE Peter[1,g]

[1]Institute for Production Engineering and Forming Machines (PtU), Technical University Darmstadt, Germany

[2]Institute for Applied Materials (IAM), Karlsruhe Institute of Technology, Germany

[a*]daniel.spies@ptu.tu-darmstadt.de, [b]dirk.molitor@ptu.tu-darmstadt.de, [c]james.damon@kit.edu, [d]maximilian.knoll@ptu.tu-darmstadt.de, [e]stefan.dietrich@kit.edu, [f]volker.schulze@kit.edu, [g]peter.groche@ptu.tu-darmstadt.de

Keywords: Property Control, Forming, Punch-Hole-Rolling, Sheet-Bulk Metal Forming

Abstract. Process controls are getting increasingly more common in forming. Nevertheless, they are not suitable to achieve consistent quality when dealing with varying process disturbances. Differing properties of the raw material and other external influences like temperature variations and vibrations make it hard to achieve the tightly specified tolerances needed in today's production environment. Product property controls represent a solution for these difficulties and create the opportunity to integrate additional functionality into the product and the process. In this project, the implementation of a multivariable product property control is investigated using the example of a recently developed process, called punch-hole-rolling. It is targeted to control product properties such as the collar height and the hardness on the inner surface. It has been shown in previous publications that it is possible to control the collar height in 1.0338 by carefully choosing suitable process parameters. In recent works the possibility was presented to control the hardness by changing the same parameters, using the TRIP steel 1.4301. The publication at hand aims at proving the feasibility of the multivariable product property control by reviewing the previous results for 1.4301 and proving that it is possible to control the collar height and the hardness on the inside of the collar simultaneously. Further, a concept is presented for the implementation of such a control.

Introduction

In recent years resources have become increasingly scarce. In 2022, steel prices in northern Europe and especially Germany spiked at two times the rate it had, just three years ago [1,2]. Simultaneously, the price of energy has almost tripled in the same time period [1]. Furthermore, environmental protection is becoming increasingly more important as new legislation for example in Germany proves [3]. Reducing the material and energy consumption is an easy way to improve the human impact on nature. Given the current circumstances it is obvious that this also brings major economic benefits. Simply reducing the consumption is not an option in most industries, however, as this would lead directly to a proportionate reduction in production, which is neither economically viable nor desirable. Therefore, other solutions need to be found. One option is to switch from production processes which are less material and energy efficient to those that are more efficient. Here, forming processes have great advantages compared to cutting processes. They have a higher material utilization and use less energy on average [4]. Nevertheless, there are many products, which can not be produced by forming. Either the geometry cannot be formed or the products require tolerances, which cannot be produced by conventional forming processes. A

Content from this work may be used under the terms of the Creative Commons Attribution 3.0 license. Any further distribution of this work must maintain attribution to the author(s) and the title of the work, journal citation and DOI. Published under license by Materials Research Forum LLC.

great example for this type of products are bearing seats. Due to the great advantages of forming processes it is senseful to develop new processes to overcome these challenges. In the case of bearing seats, punch-hole-rolling is a proposed solution, which is a recently developed forming process that is presented in more detail in the following chapter. Another option to increase the resource efficiency of production processes is to reduce the proportion of parts that have to be scrapped. Fluctuations in the material can easily lead to product properties out of specification, especially in forming processes. Controls enable the compensation of disturbances, but conventional process controls in forming are not able to detect the specific deviations, and many conventional processes do not have the degrees of freedom to counteract them. In their work, Allwood et al. presented product property controls in combination with suitable processes as a solution for these problems [5]. With this technology it is also conceivable to control more than one property at a time and further enhance the advantages of forming processes.

Punch-hole-rolling.

Punch-hole-rolling is a process, which was recently developed at the Institute for Production Engineering and Forming Machines (PtU) at the Technical University of Darmstadt in cooperation with the Institute for Applied Materials (IAM) at the Karlsruhe Institute of Technology. It is a forming process which is best specified as sheet-bulk metal forming, according to the definition by Merklein et al. [6]. Additionally, the process is an incremental forming process. Knoll et al. classified the process as pressure forming due to the acting stresses and as a rolling process due to the main tooling used [7]. Punch-hole-rolling consists of two separate steps. The first step is the punching step in which the starting hole is generated. Unlike the name may suggest, the starting hole does not have to be punched. Previous tests showed that drilling is a suitable alternative. The two steps of the process also do not have to be performed directly after another. The second step is hole-rolling. In this step, the roller is inserted into the hole in the workpiece, which was created by the first operation. After that, the tool performs a spiral movement, in which the material of the sheet metal is pushed outwards and to the top and bottom. This movement enlarges the hole, simultaneously forming a collar on both faces of the metal sheet. Ideally both sides of the collar are mirrored copies of each other. In Fig. 1 the punch-hole-rolling process is pictured. On the left side of the figure, the process is shown from the top and the spiral movement of the roller is marked. On the right side of the figure, the process is shown from the front. The sectional view of the workpiece allows to see the forming of the collar. On the right-hand side of the workpiece the collar is pictured almost in the final stage, while the left-hand side shows it shortly after the process started.

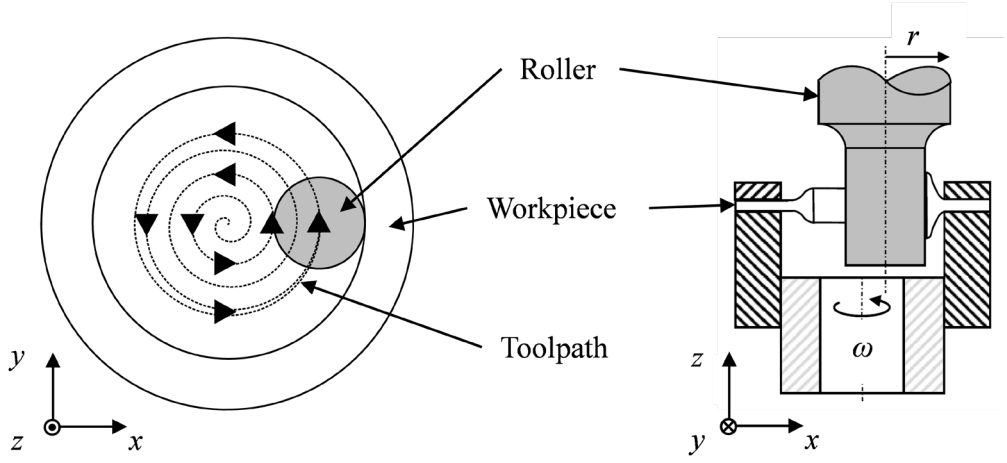

Fig, 1. Sketch of the punch-hole-rolling process, including the relevant process parameters [8].

The process can be influenced by changing the starting hole diameter in relation to the diameter of the finished product, the radial feed rate and the rotational speed. With these process parameters the two product properties of interest, collar height and hardness on the inner surface of the collar, can be influenced. The specific relations will be discussed in the subsequent chapters. In Fig. **2** the setup for performing the punch-hole-rolling process is shown. A conventional lathe is used for this purpose. Therefore, the sheet metal is mounted on the main spindle. The starting hole is drilled in this position with the tailstock. For rolling a tool, designed for this use, is fitted to the cross slide. The tool has a roller, which can freely rotate, additionally two sensors for measuring the process forces are integrated. A linear sensor from Burster is used to measure the radial movement. Due to the one-sided bearing of the roller in this setup, the process forces are limited significantly. Additionally, the deflection often leads to an asymmetrical collar. Therefore, a new tool is built [8]. Nevertheless, all tests for the publication at hand were performed with the setup on the conventional lathe.

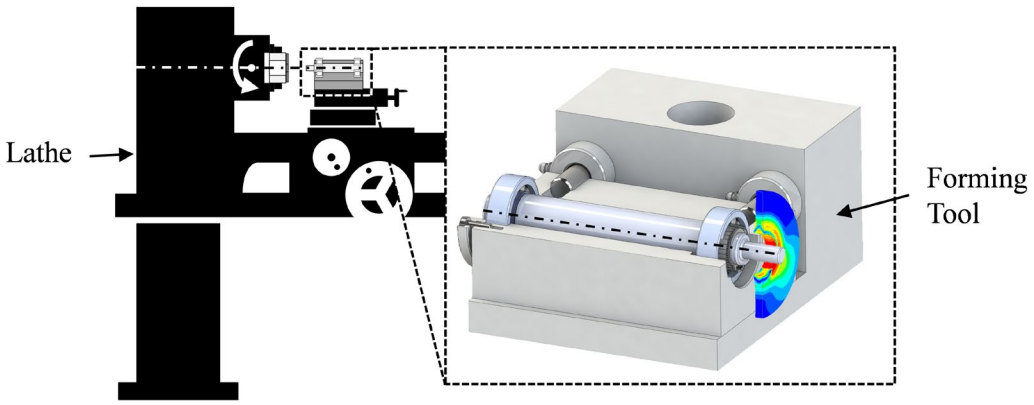

Fig. 2. Punch-hole-rolling setup on a conventional lathe cf. [7].

The final product of punch-hole-rolling is a hole with a collar on both sides of a metal sheet. Pure forming processes which produce similar geometries are collar forming and friction drilling. Compared to these two processes, punch-hole-rolling has three distinct advantages for the use case of forming bearing seats. Punch-hole-rolling produces a double-sided collar; Therefore, the bearing center and the sheet center can be aligned to enhance the force transfer from the bearing to the housing. Additionally, the incremental nature of the process allows for production of the small tolerances required for bearings. Furthermore, the process has multiple degrees of freedom, that can be used to control the material properties.

Characteristic of the Collar Height in Punch-Hole-Rolling

By varying the process parameters in punch-hole-rolling a few different product states can be produced. One of the product properties, that can be influenced is the height of the collar. The height depends strongly on the difference between the initial diameter and the final diameter of the hole in the product, but can be adjusted in a smaller range during the process.

Collar height in DC04.

In [7], tests were performed on DC04 to characterize the forming of the collar and, especially the development of the collar height in more detail. The collar height was found to increase approximately linearly with the change in radius. In [9], it was additionally found that changing the radial feed rate of the process leads to a change in the gradient of the graph. Thereby, a higher feed rate leads to a lower gradient and thus to a lower collar height. Furthermore, it was concluded, that the rotational speed does not influence the collar height in a significant way. In Fig. 3**,** three graphs are shown that highlight the different relations between the collar height and the various

process parameters. In each graph, the collar height is plotted over the radius of the hole. The x-axis starts on the starting hole radius, for which 4 mm is chosen in most tests. The y-axis begins at a collar height of 2 mm, which equals the thickness of the sheet metal. Each graph consists of many datapoints, measured on different test pieces, which are hole-rolled to various radii and measured offline. Therefore, steps in the graphs can occur due to variations in the process. On the left side of Fig. 3, the trends of collar height for three different rotational speeds and two different feed rates are depicted. As stated by Mühl et al., the difference in rotational speeds is insignificant compared to the change in feed rate. On the right side of Fig. 3, the trends of collar height for four different feed rates are shown. As can be seen in the first graph, and as stated before, it is clear that the feed rate influences the collar height in a significant way. Nevertheless, the maximum spread of the collar height is quite small with less than 2 mm for a 6 mm widened radius. By changing the starting hole diameter, the collar height can be adjusted in a wider range. For demonstration, a fifth trend is added of test pieces with a starting hole radius of 5 mm. The trend runs parallel to the one with the same feed rate but with a smaller starting hole.

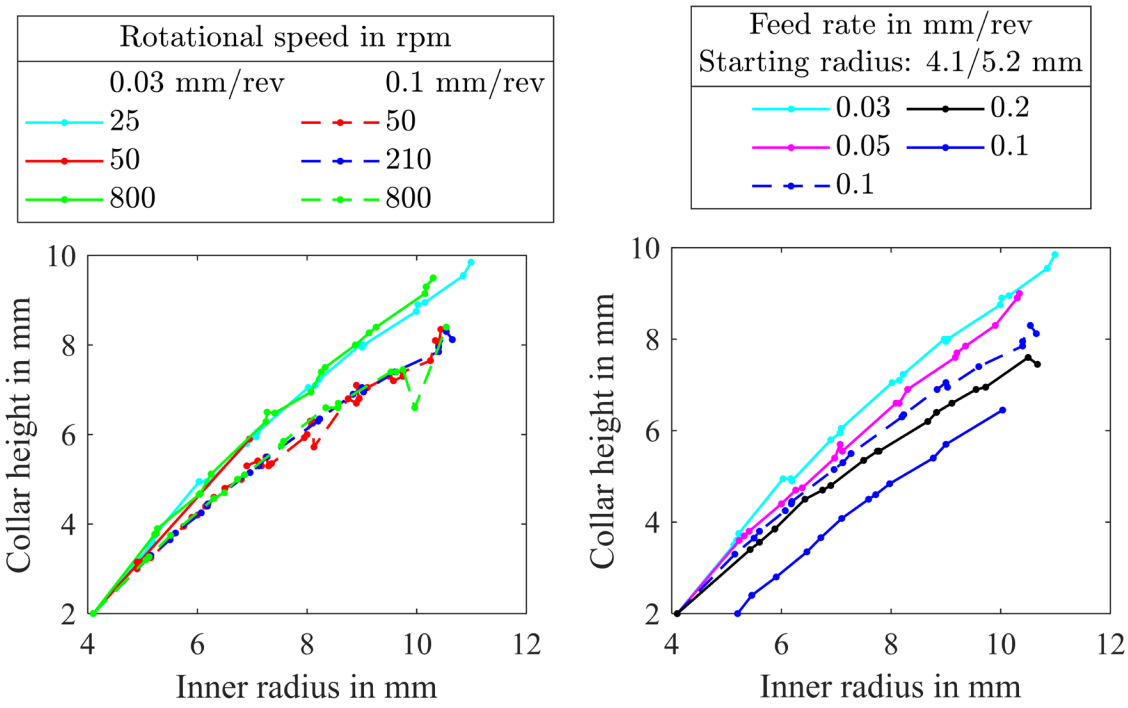

Fig. 3. Trend of the collar height over the inner radius in punch-hole-rolling in the material DC04 for varied process parameters left: for two different feed rates and three different rotational speeds each and right: for four different feed rates at rotational speeds between 25 and 210 rpm and for one varied starting diameter.

Collar height in 1.4301.

To identify the limits of the process and the current test setup, tests were also conducted with the stainless steel 1.4301. This steel has a significantly higher yield stress than the tested DC04. Additionally, this material is affected by the TRIP-effect, which is going to be used in the product property control. TRIP stands for transformation induced plasticity. The effect is the strain induced conversion to martensite. [10] Due to the higher hardness of martensite compared to the normal grain structure of the material, it is possible to change the hardness of the material in dependence of the martensite fraction. The influence of punch-hole-rolling on this product and material property will be discussed in more detail in the following chapter.

To evaluate the correlations between the process parameters and the collar height in 1.4301, the same tests as on DC04 are conducted. It is planned to determine if the same characteristics also can be seen in 1.4301. In Fig. 4, the trend for the collar height in 1.4301 is depicted. Due to the higher strain-hardening coefficient, the process force rises much faster than in DC04. Therefore, it is not possible to reach the same radii with the same force restriction. Additionally, a roller with a bigger diameter has to be used and the feed rate is highly restricted. As seen in Fig. 3, the feed rate has a significant influence on the collar height. Due to the limitations in choosing the process parameters, only a small variation can be achieved. In this case, feed rates of 0.03 mm/rev and 0.05 mm/rev are compared. Nevertheless, a similar trend as in DC04 can be observed. Even though the trend is noticeable, the difference between both parameters is quite small. To rule out measurement noise as a cause, another test is performed with 210 rpm instead of 25 rpm, which is expected not to differ significantly from the test with same feed rate. It can be observed that the trends for the two tests are quite similar and both show a significant difference to the test with the different feed rate. Therefore, it is assumed, that the collar height in 1.4301 has the same characteristics as in DC04. Nevertheless, it is necessary to conduct more tests with the planned, more advanced setup [8].

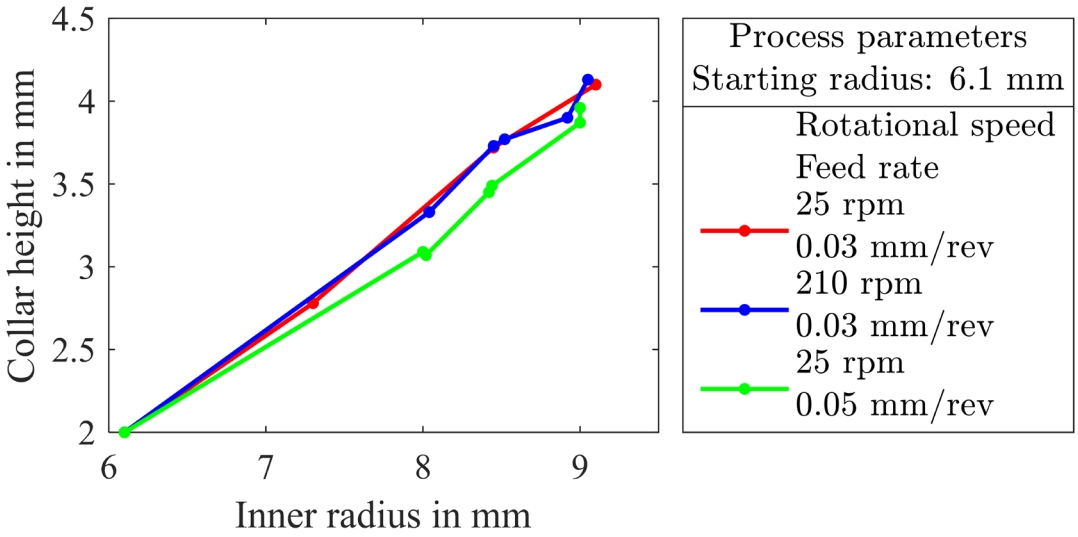

Fig. 4. Trend of the collar height over the inner radius in punch-hole-rolling in the material 1.4301 for varied process parameters.

Characteristic of the Hardness of the Inner Surface in Punch-Hole-Rolling

The second product property, which can be influenced by punch-hole-rolling is a non-geometric one. It is the hardness of the surface on the inside of the formed collar. The hardness is examined for two different materials with different effects for its hardening. The first is DC04, where the hardness increase was discovered and is explained by conventional cold hardening of the material due to the plastic deformation. In 1.4301, the TRIP effect leads to an increase in the martensite fraction and thus to a higher hardness of the material in general. Both characteristics are discussed in more detail in the following chapter.

Hardness in DC04.

In DC04, the hardening of the material due to punch-hole-rolling was measured for the first time. To determine the characteristics more closely in [9] specimens from the previous tests primarily concerning the collar height were examined in more detail. It was discovered that the hardness rises with increasing radius and thus deformation, but remains constant above a certain point. A correlation between the process parameters feed rate and rotational speed and hardness could not be observed. Therefore, the hardness in DC04 cannot be controlled with the punch-hole-

rolling process. It is suspected that the increase in hardness occurs due to cold hardening during the deformation of the material.

Hardness in 1.4301.

Due to the disadvantages with DC04, it is decided to use the stainless steel 1.4301 in future tests. As explained before, this steel is affected by the TRIP effect by which the grain structure of the material is transformed into martensite. This effect is strain induced. [10] In preliminary flat crush tests it was shown that the transformation depends on the plastic strain as well as the plastic strain rate. In punch-hole-rolling this leads to a dependence on all of the process parameters. The radial position of the roller in combination with the rotational speed determine the tangential speed between the roller and the material. In Fig. 5 the trend for the surface hardness over the inner radius is shown for two different sets of process parameters. To measure the hardness, the collar was cut and the slice embedded in epoxy. The hardness was measured by conventional means approximately 50 µm below the surface. It can be seen that the hardness generally increases with increasing inner radius and thus plastic strain. Additionally, the trend shows that the increase of hardness is reduced with higher forming rates. This also reflects the behavior observed in the preliminary tests and correlates with the lower measured martensite volume fractions of these samples.

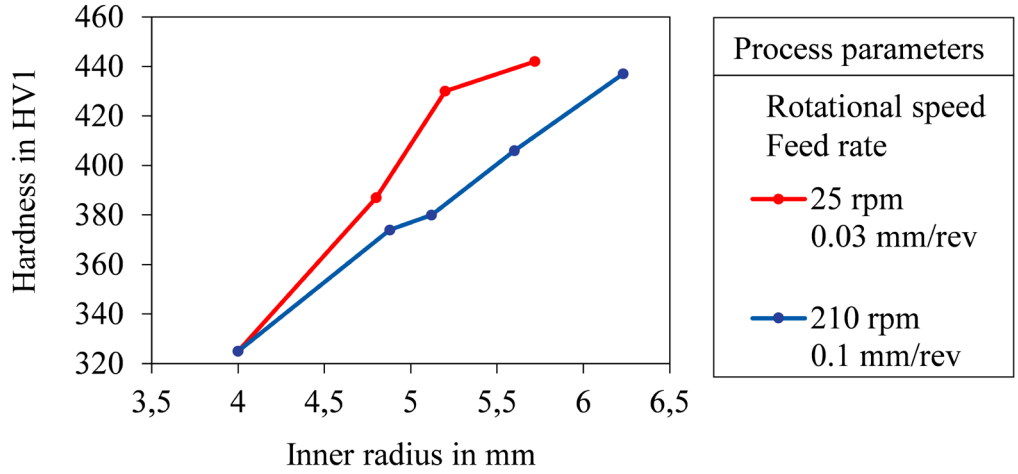

Fig. 5. Trend of surface hardness over the inner radius in punch-hole-rolling in the material 1.4301 for varied process parameters.

Barkhausen noise.

To be able to control the hardness of the material during the process, it is necessary to measure it first. This is especially challenging due to the needed real time capability of this sensor and the necessity to take the measurement without disturbing the forming process. As a suitable solution for this challenge, the Barkhausen noise analysis is identified. This analysis is based on the fact that in ferromagnetic materials the magnetic domains grow during magnetization and therefore the walls between the different domains are moved. Due to interactions of these domain walls with pinning sites such as material defects, sudden changes in the magnetization of the material occur. Measuring the magnetic flux density of the material during a cycle of magnetization and demagnetization results in the so called Barkhausen noise. Due to the interaction of the domain walls with the microstructure of the material the Barkhausen noise includes information about many different material properties. [11-14] In their paper, Mühl et al. showed that the hardness of the material after punch-hole-rolling can be correlated with the root mean square value of the Barkhausen noise signal. [9]. Furthermore Spies et al. have shown in their paper that this is also true for the amplitude of the signal and that it can also be correlated with the alpha martensite volume fraction and the plastic strain in 1.4301. Moreover, a concept was presented for the integration of the sensor into a future test rig. [8] All correlations were identified by taking offline

measurements and comparing them with the results of conventional measuring processes [8,9]. Using this data, the online Barkhausen noise measurements can be converted into the product properties of interest. All this taken together shows the theoretical feasibility of a magnetic Barkhausen noise sensor for the use in a process control for punch-hole-rolling.

Proof of the Feasibility of a Multivariable Product Property Control in Punch-Hole-Rolling

The previous chapters have shown, that the collar-height and hardness can be controlled individually in the material 1.4301. This includes proposing Barkhausen noise as a solution to the challenge of inline hardness measurements. The collar-height meanwhile could be measured by a 2D laser scanner. For a multivariable product property control it is nevertheless necessary to prove that this control can also be achieved simultaneously and independently from each other. Since the test setup is currently incapable of proving this experimentally, it is expedient to do so by a theoretical presentation of the proposed closed-loop control strategy instead. Therefore, the process is represented mathematically. In Equation 1 the dependencies of the product properties collar height and surface hardness are depicted. The height of the collar is dependent on the relative radius Δr and the feed rate $\dot{r}$. The starting radius is determined before the process starts, therefore it is not a variable that can be used. The product radius is demanded by the planned application. Therefore, the relative radius is also not variable. By solving the yet to be determined formula for the collar height for the feed rate, it is possible to determine the feed rate, necessary to achieve the desired collar height. The process is quite similar for the hardness, the only difference being that it also depends on the rotational speed. Due to the pre-determined feed rate the formula is solved for the necessary rotational speed.

$$\begin{bmatrix} h_{\mathrm{col}} \\ HV_{\mathrm{sur}} \end{bmatrix} = \begin{bmatrix} f_{\mathrm{hcol}}(\Delta r, \dot{r}) \\ f_{\mathrm{HVsur}}(\Delta r, \dot{r}, \omega) \end{bmatrix} \tag{1}$$

It is obvious that a poorly chosen start radius leads to not achievable numbers in the process parameters. Unachievable product properties will also lead to unrealistic process parameters. Therefore, the set of producible product parameters is finite. In addition, not all combinations of product properties can be reached, even though the properties can be simultaneously controlled in theory. To look into this in more detail, it is suitable to look at the properties that can be achieved with the given range for the forming parameters. Since the process varies a lot for different roller diameters and relative radii these will be defined for this example. The following numbers are valid for a roller diameter of 8 mm and a relative radius of 2 mm. The feed per revolution can be varied between 0.03 mm/rev and 2 mm/rev whilst the rotational speed can be varied between 25 rpm and 800 rpm. In Fig. 6, an approximation of the working area for this parameter set is shown. It should be noted that some of the depicted values are approximated an may change slightly with further research. Nevertheless, the diagram is suitable to get a quick overview. In the corners the extreme values of the possible parameter combinations are shown. The first number describes the rotational speed and the second one the feed per revolution. It can be noted that in the lower left corner two points correspond to another. This happens because the feed per revolution of 2 mm/rev is so high that no transformation to martensite is expected to occur even at the lowest rpm. The hardness of 300 HV1 matches the hardness of the base material. Due to cold hardening, this is nevertheless likely to increase to a limited extent.

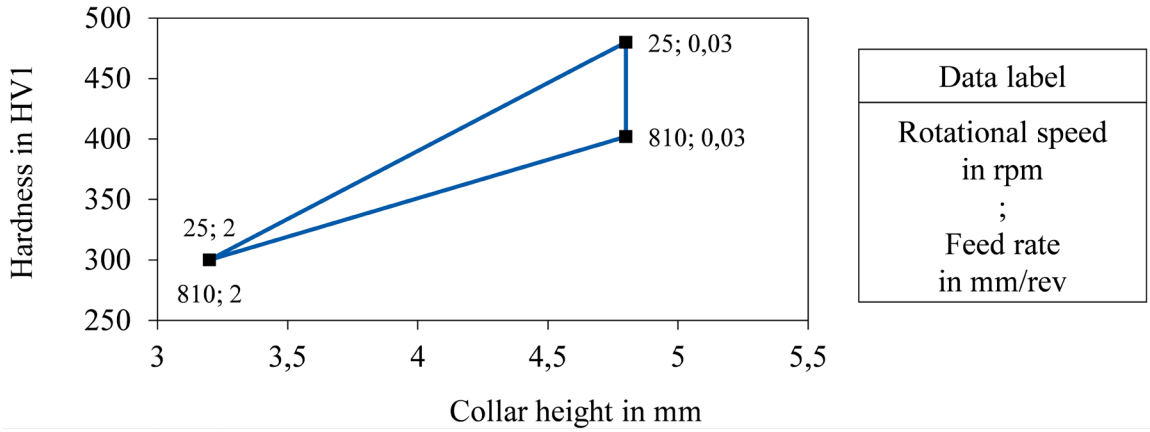

Fig. 6. Approximation of the achievable product properties, collar height and surface hardness for a given set of process parameters in the material 1.4301.

Concept for a Multivariable Product Property Control in Punch-Hole-Rolling

In order to control the process, the transfer behavior of the manipulated variables $\boldsymbol{u} = [\dot{r} \quad \omega]^T$ to the product properties to be controlled $\boldsymbol{x} = [h_{\mathrm{col}} \quad HV_{\mathrm{sur}}]^T$ is of essential importance. The relations described in Eq. 1 can be described using data-driven models of varying complexity. In this context, data-driven models have two elementary advantages. First, the complex relationships between manipulated and controlled variables do not need to be described by analytical models. Second, large parts of data-driven models are differentiable, which is especially useful for control engineering applications. If the functions f_{hcol} and f_{HVsur} presented in equation 1 are fitted via data-driven models and then derived with respect to the manipulated variables, formulas for the rates of change of the variables according to Eq. 2 follow.

$$\dot{\boldsymbol{x}} = \frac{\partial [f_{\mathrm{hcol}}(\boldsymbol{u}) \quad f_{\mathrm{HVsur}}(\boldsymbol{u})]}{\partial \boldsymbol{u}} \cdot \dot{\boldsymbol{u}} = \boldsymbol{J}(\boldsymbol{u}) \cdot \dot{\boldsymbol{u}} \tag{2}$$

The locally linearized inverse of the Jacobian matrix $\boldsymbol{J}(\boldsymbol{u})^{-1}$ can now be used to transform deviating-controlled variables $\boldsymbol{e}_x$ into velocity changes of the manipulated variables $\Delta\boldsymbol{u}$. Fig. 7 provides an overview of the proposed closed-loop control approach. The reference variable for the properties to be controlled is a time series whose final values are the final collar height and hardness. Deviations between the desired time series $\boldsymbol{x}_{\mathrm{des},t-1}$ and observed time series $\hat{\boldsymbol{x}}_{\mathrm{act},t-1}$ can be transformed into velocity changes of the manipulated variables $\Delta\boldsymbol{u}$ via the inverse Jacobian matrix $\boldsymbol{J}(\boldsymbol{u})^{-1}$ and carefully selected gain factors $k_{\mathrm{P},i}$ in the diagonal gain matrix $\boldsymbol{K}_{\mathrm{P}}$. The elements of the diagonal gain matrix thus weight the control deviations of the corresponding control variables x_i and lead to low control dynamics if chosen too low or to oscillations if chosen too high. These calculated velocity changes $\Delta\boldsymbol{u}$ can then be added to the manipulated variable $\boldsymbol{u}_{t-1}$ generated in the last cycle step of the control unit and lead to the manipulated variable $\boldsymbol{u}_t = \boldsymbol{u}_{t-1} + \Delta\boldsymbol{u}$ of the next cycle. In the punch hole rolling process, the implemented sensors are then used as input variables for an observer $\boldsymbol{f}_{\mathrm{obs}}$ that observes the product properties $\hat{\boldsymbol{x}}_{\mathrm{act}}$ from the sensor signals $\boldsymbol{s}$. In the observer, the correlations between recorded sensor signals and the controlled variables that have already been investigated in published papers (e.g. magnetic Barkhausen noise and hardness) are used to estimate the actual states of the controlled variables. [8, 9] These are then in turn used in the feedback loop of the control scheme to determine the control deviation.

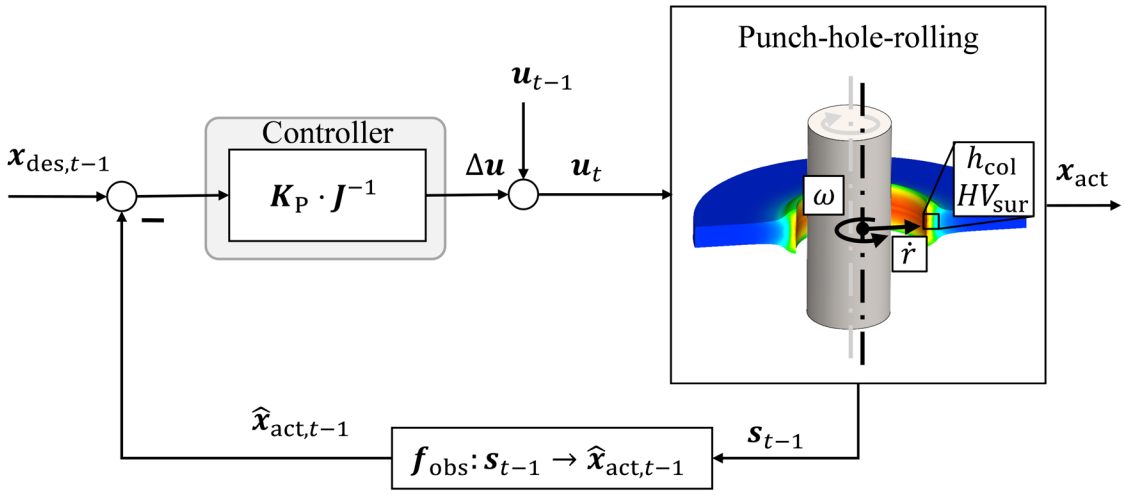

Fig. 7. Block Diagram of the proposed closed-loop control approach for punch-hole-rolling.

Summary

In this paper, the basic behavior of the material, formed by punch holing was presented. In particular, the changes of the product properties of interest, collar height and surface hardness on the inside of the collar during the process have been discussed. Subsequently, the possibility for a multivariable product property control in the punch-hole-rolling process was shown, supported by the data presented prior. Lastly, a concept for the control itself was established, considering the difficulty of controlling more than one property at a time, which are not completely independent of each other. It is planned to validate the theoretical possibility for the multivariable product property control presented in this paper in the near future by means of further tests. The upgraded test setup required for this is being built currently. It is also planned to implement the concept for the control scheme shown in the new test setup and to test and improve its suitability as well.

Acknowledgement

The authors would like to thank the German Research Foundation DFG for the support of the depicted research within the priority program ‘SPP2183’ through project no. ‘424334856‘.

References

[1] Statistisches Bundesamt (Destatis), Preise August 2022, Preise und Preisindizes für gewerbliche Produkte (Erzeugerpreise), Wiesbaden, 2022

[2] Statistisches Bundesamt (Destatis), Preise April 2019, Preise und Preisindizes für gewerbliche Produkte (Erzeugerpreise), Wiesbaden, 2019

[3] A. Weisgerber, K. Mindrup, K. Hilse, L. Köhler, L. Beutin, L. Badum, Beschlussempfehlung und Bericht, 19/30949, Bundesanzeiger Verlag GmbH, Köln, 2021.

[4] T. Hertan, Optimaler Energieeinsatz bei der Fertigung durch Massivumformung, Stuttgart, Universität Stuttgart, Institut für Umfonntechnik, 1989

[5] J. Allwood, S. Duncan, J. Cao, P. Groche, G. Hirt, B. Kinsey, T. Kuboki, M. Liewald, A. Sterzing, A. Tekkaya, Closed-loop control of product properties in metalforming, in: CIRP Annals – Manuf. Technol. 65 (2016) 573-596. https://doi.org/10.1016/j.cirp.2016.06.002

[6] M. Merklein, J.M. Allwood, B.-A. Behrens, A. Brosius, H. Hagenah, K. Kuzman, K. Mori, A.E. Tekkaya, A. Weckenmann, Bulk forming of sheet metal, in: CIRP Annals – Manuf. Technol. 61 (2012) 725-745. https://doi.org/10.1016/j.cirp.2012.05.007

[7] M. Knoll, F. Mühl, P. Groche, V. Schulze, Simulative basic investigation for a new forming process punch-hole-rolling, Procedia Manuf. 50 (2020) 503-509. https://doi.org/10.1016/j.promfg.2020.08.091
[8] D. Spies, F. Mühl, M. Knoll, S. Dietrich, P. Groche, V. Schulze, Integration of a magnetic Barkhausen noise sensor for the Product Property Control in a progressive press tool for punch-hole-rolling, in: 36. ASK Proceedings, 2022, pp. 445-454
[9] F. Mühl, M. Knoll, M. Khabou, S. Dietrich, P. Groche, V. Schulze, Soft sensor approach based on magnetic Barkhausen noise by means of the forming process punch-hole-rolling, Adv. Industr. Manuf. Eng. 2 (2021). http://doi.org/10.1016/j.aime.2021.100039
[10] T. Yoshihiro, I. Takeshi, Constitutive modeling of trip steel and its application to the improvement of mechanical properties, Int. J. Mech. Sci. 37 (1995) 1295-1305. https://doi.org/10.1016/0020-7403(95)00039-Z
[11] T. Le Manh, J.A.P Benitez, J.H.E. Hernandez, Lopez Hallen, J.M. (Eds.), Barkhausen Noise for Non-destructive Testing and Materials Characterization in Low Carbon Steels. in: Woodhead Publishing Series in Electronic and Optical Materials, 2020.
[12] H. Sakamoto, M. Okada, M. Homma, Theoretical analysis of barkhausen noise in carbon steels, IEEE Trans. Magnet. 23 (1987) 2236-2238. https://doi.org/10.1109/TMAG.1987.1065664
[13] R. Ranjan, D.C. Jiles, O. Buck, R.B. Thompson, Grain size measurement using magnetic and acoustic barkhausen noise, J. Appl. Phys. 61 (1987) 3199-3201. https://doi.org/10.1063/1.338900
[14] C. Gatelier-Rothea, J. Chicois, R. Fougeres, P. Fleischmann, Characterization of pure iron and (130p.p.m.) carbon–iron binary alloy by barkhausen noise measurements: study of the influence of stress and microstructure, Acta Mater. 46 (1998) 4873-4882. https://doi.org/10.1016/S1359-6454(98)00205-5

Materials Research Proceedings 28 (2023) 2091-2100 https://doi.org/10.21741/9781644902479-224

Experimental analysis on the influence of freeform bending on Barkhausen noise for steel tubes

MAIER Daniel[1, a*], SCANDOLA Lorenzo[1,b], WERNER Matthias[1,c], STEBNER Sophie[2,d], ISMAIL Ahmed[3,e], LOHMANN Boris[3,f], MÜNSTERMANN Sebastian[2,g], VOLK Wolfram[1,h] and LECHNER Philipp[1,i]

[1]Chair of Metal Forming and Casting, TUM School of Engineering and Design, Technical University of Munich, Germany

[2]Integrity of Materials and Structures, Department of Ferrous Metallurgy, RWTH Aachen University, Germany

[3]Chair of Automatic Control, TUM School of Engineering and Design, Technical University of Munich, Germany

[a]daniel.maier@tum.de, [b]lorenzo.scandola@utg.de, [c]matthias.werner@utg.de, [d]sophie.stebner@iehk.rwth-aachen.de, [e]a.ismail@tum.de, [f]lohmann@tum.de, [g]sebastian.muenstermann@iehk.rwth-aachen.de, [h]wolfram.volk@utg.de, [i]philipp.lechner@utg.de

Keywords: Freeform Bending, FEM, Barkhausen Noise, Softsensor, Closed-Loop Control

Abstract. Freeform bending with a movable die makes it possible to bend complex structures and seamless radii without changing the bending tools. Currently, most research focuses on minimizing the geometrical deviations without considering the mechanical properties of the bent tubes. A previous work showed, that the geometry can be decoupled from the mechanical properties with non-tangential bending [1]. The implementation of a soft sensor based on ultrasonic contact impedance measurements (UCI) of the property-controlled freeform bending has also been examined [2], as well as a structure for closed-loop control based on material properties [3]. The present work deals with a micro-magnetic sensor and Barkhausen noise (BHN) and investigates its suitability for the closed-loop control. For this purpose, different processing routes for freeform-bent steel tubes are experimentally investigated by their characteristic BHN. In addition to an existing simulation model, a data basis for the impact of freeform bending parameters is built to extend the existing model of a property-based closed-loop control.

Introduction

Freeform bending with a movable die is a forming technology that allows the bending of complex three-dimensional tube geometries without changing the bending die. The accuracy of the bending process depends on the tolerances and fluctuations in the mechanical properties as well as the tolerances of the process (e.g., friction, etc.). These disturbances significantly influence the bent part. In addition, inadequate knowledge of the mechanical properties before and after the bending process can lead to deviations in downstream processes. This leads to the conclusion, that there is a need for closed-loop control based on the mechanical properties of the tube, to reduce failures as well as scrap and to improve the quality of freeform-bent parts.

Non-tangential bending allows the decoupling of the geometry and mechanical properties [1]. In order to control the mechanical properties during the freeform bending process, a suitable measuring system must be available in addition to the intervention in the kinematics of the bending die. This paper provides an experimental analysis of the influence of freeform bending process parameters on BHN for steel tubes. Therefore, different states of the steel tubes (unbent, bent,

Content from this work may be used under the terms of the Creative Commons Attribution 3.0 license. Any further distribution of this work must maintain attribution to the author(s) and the title of the work, journal citation and DOI. Published under license by Materials Research Forum LLC.

unbent and annealed, annealed and bent) are measured with a micro-magnetic sensor and the BHN is analyzed. Furthermore, tubes formed with the new concept of non-tangential bending are under investigation. Ultimately, the results are compared to the numerical model to check the congruence between the numerical model and measurements on real bent tubes.

State of the Art

Freeform bending with a movable die is a process that has been investigated to a large extend. Most of the research focuses on improving the geometrical accuracy of the freeform-bent part, but only a few investigate the mechanical properties during the bending process. [4] showed that the manufacturing strategy of roll-formed tubes influences the material properties and the subsequent bending process. There have also been investigations that analyze the influence of different process parameters on the bending result in freeform bending using numerical simulations [5]. Numerical simulations are often used to get a better understanding of the freeform bending process. [6] showed two models for freeform bending with three and five degrees of freedom and a simulation model for rotary draw bending. Both round tubes and profiles were bent using these models. Another simulation model for freeform bending as the preform forming step of hydroforming was also investigated [7]. A simulation model is used to calculate the motion profile of the bending die to get better geometrical accuracy results while reducing scrap [8]. If only a 2D bending part is manufactured, the hole part can be described by the parameters radius and bending angle. In freeform bending there is a process-related, complex transition between straight tube segments and the area of constant curve curvature due to the particular motion profile of the bending die [9]. Accordingly, the specified bending radius is determined by means of regression only in the region of constant curve curvature [10]. The bending angle is calculated from the direction vectors of approximated straight lines at the beginning and end of the bent part. Automatic extraction of the bending line from discrete data and vice versa makes this analysis much faster and more efficient [11]. In terms of influencing factors, [12] conclude with numerical simulations and validation experiments that the yield strength affects the forming limit and wrinkling instability. The results also showed that friction and clamping pressure have a smaller impact on the forming limit compared to the axial propulsion speed and the gap between the tubes and bending die. The concept of [13] shows that a kinematic bending process can be controlled. A concept for both direct and indirect control of torque superposed spatial bending was presented in their work.

Different approaches are pursued to optimize the bending processes using the extended Kalman filter (EKF) in particular. On the one hand, it is used to predict the trajectory during freeform bending and thus to optimize the process and the process parameters [14]; on the other hand, the EKF is also used in the field of stress prediction and closed-loop control during freeform bending [1]. There have also been investigations into BHN measurements to analyze the residual stresses. BHN is affected by residual stresses to the same extent as it is by the microstructure, but a careful calibration process is necessary to get a good correlation between stresses and BHN [15]. BHN has also been installed in a broaching machine tool to conduct in-situ measurements during the orthogonal cutting process, and a correlation between the residual stress and the detected BHN signal was evaluated [16]. Another study showed that the reciprocal of the peak amplitude of the BHN has a linear relationship with the stresses [17]. Therefore, tensile tests with carburized SAE 9310 and 32CDV13 were applied. For low-frequency BHN measurements near the surface, it was shown that in case-carburized steel, the residual stresses change differently compared to the subsurface in response to the prior applied tensile or compressive stresses [18]. Although BHN has been the subject of numerous studies, the results are difficult to compare because most studies differ in terms of the material and samples used [19]. Therefore, it can be concluded that a better understanding of how different factors influence BHN is still needed.

As the state of the art indicates, BHN is suitable for measuring different specimens and a range of materials. In addition, it is also shown that freeform bending with its many degrees of freedom

is a suitable controllable process. Overall, the great need for closed-loop control based on the mechanical properties of the tube during freeform bending can clearly be seen.

Materials and Methods

This paper deals with the experimental analysis of the influence of residual stresses in the raw material on the geometry and BHN of freeform-bent steel tubes. The aim is to show that different stress states can be measured using a micro-magnetic sensor and analyzed using BHN. In addition, it will be shown that different stress states influence the resulting bent part. Due to the kinematic forming process and the associated many degrees of freedom, freeform bending with a movable die is particularly suitable for influencing the mechanical properties.

Freeform bending machine and tubular raw material. In this article, all experiments are performed using a 6-axis freeform bending machine with a movable die, built by J. Neu GmbH (Grünstadt). The machine has six degrees of freedom, of which three are translational and three are rotational. Fig. 1 shows the six degrees of freedom and all relevant parts of the freeform bending machine.

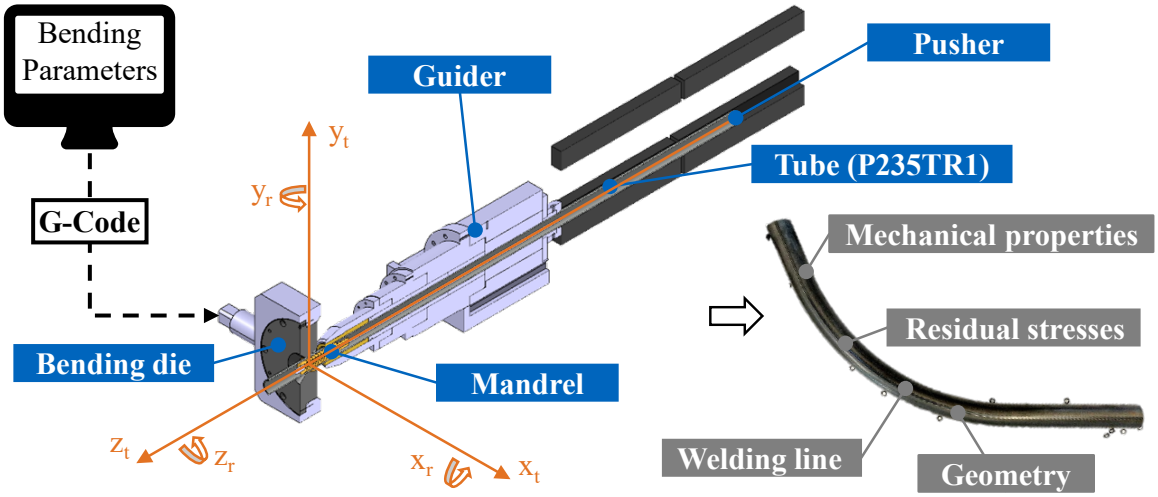

Fig. 1. Principal of freeform bending with movable die and the resulting bent part [1].

To produce a freeform-bent part, a round tube must first be inserted into the machine. The tube is then advanced along the z-axis at a constant speed. The tube is pushed over the bending mandrel and through the bending die. In addition to the feed, the die starts to move. The bending die can be deflected in the xy-plane and can rotate around all three axes (x-, y- and z-axis), performing the movements simultaneously. To bend a tube, as shown in Fig. **1**, the bending die is deflected and rotated to its maximum position, then stops and remains in the maximum deflected position until the bending angle is reached, and then returns to the starting position. This entire process occurs while the tube is being constantly advanced. The kinematic process can therefore be divided into three sections: the transition, the constant and return sections. For a more detailed understanding of the process, the authors refer to detailed studies of the freeform bending process [1-3, 7, 8].

For the experimental investigations in this paper, welded steel tubes made of P235 are used. The circular steel tubes have an outer diameter of 42.4 ± 0.5 mm, a thickness of 2.6 ± 0.3 mm and a length of 800 ± 2 mm with an evenly finished weld seam. The tubes are manufactured according to the international norms EN 10217-1 and EN 10219-1. The steel tubes have been used in other investigations and are already described in detail [1, 2, 20].

Analysis of bending geometry and Barkhausen noise signal. To analyze the geometry of the parts, a three-dimensional triangular surface mesh of the part is created by an optical measurement system with a handheld laser sensor. The bend angle is determined by fitting a cylinder at each

end of the tube and then measuring the angle between the two centerlines. To analyze the curvature, several sections are created along the longitudinal direction of the tube, and a circle is fitted through each section. The centers of all fitted circles are then connected, resulting in the centerline of the bent part. The curvature of the centerline is then calculated and evaluated. The curvature is divided into the same three sections as dictated by the kinematics of the bending tool (transition section, constant section and return section) and a non-bent section at the beginning and end of each tube.

To measure and analyze the BHN, a micro-magnetic sensor named *µmagnetic* in interaction with the software *Optimizer4D* from QASS GmbH (Wetter) is used. As BHN is a non-destructive testing method measurement method with high sampling rates, it is advantageous compared to other stress measurement methods, such as the hole drilling method. Since the BHN can be influenced by a gap between the sensor and workpiece, the sensor is placed directly on the tube to neglect this influence. To avoid short-circuiting or overdriving the BHN, a tape covers the sensor and, at the same time, minimizes the distance between the sensor and the tube. The sensor measures the inductive current, and the results are subsequently visualized using a Fourier transformation. The 3D landscape of the measurement signal consists of the axes frequency, time and amplitude. The process flow for the downstream signal processing of the BHN is shown in Fig. 2.

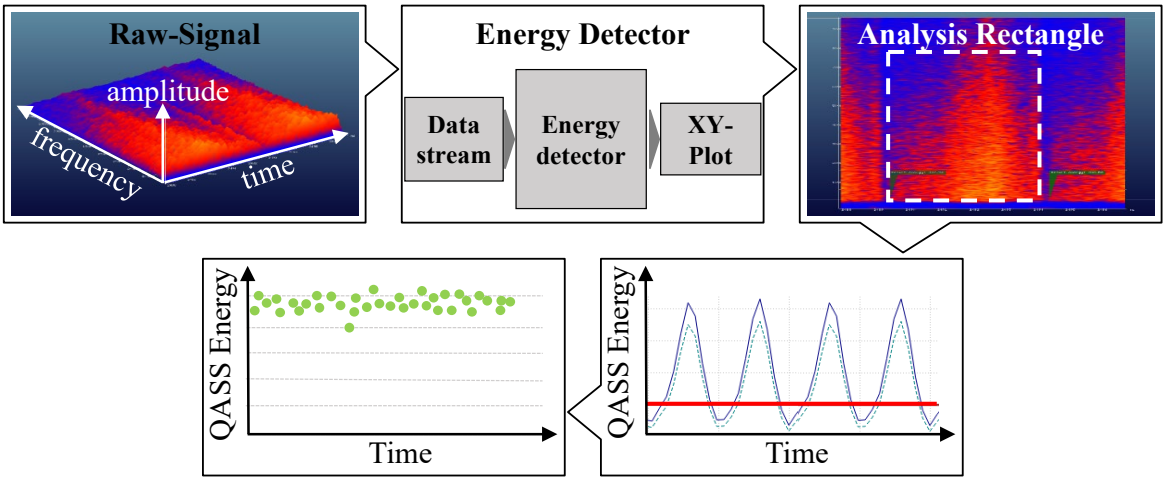

Fig. 2. Process flow for measuring and analyzing the MBH.

An analysis network with a so-called “energy detector” is used to analyze the Fourier-transformed BHN signal. It finds contiguous ranges of a certain minimum energy in a signal. The energy is calculated within a rectangular window (in time and frequency), which is successively shifted forward in time. Neighboring windows in which an energy threshold is exceeded are combined to form a pattern. This pattern is analyzed with respect to the mean value and standard deviation for each measurement point. To ensure a high penetration depth, an excitation frequency of 200 Hz and magnetizing voltage of 700 mV is set. At higher frequencies, the penetration depth is reduced. The *Optimizer4D* software offers an energy-related value in both the time and frequency axes, which is called QASS energy. This value cannot be expressed by the SI-unit system and is, therefore, given later on without a unit [16].

Strategy. The focus is on the influence of the stress state of the raw material in freeform bending and the suitability of the micro-magnetic sensor for inline measurement of property changes during freeform bending. Therefore, different conditions of the unbent tube are investigated, as well as freeform bending experiments with different starting conditions (see Fig. 3). With these experimental investigations and bending strategies, some research questions arise:

1. Can disturbances in the unbent raw material be measured with BHN and is there a difference compared to annealed raw material?
2. How does annealing influence freeform-bent tubes in terms of geometry and BHN?
3. Is it possible to measure a different BHN in non-tangential freeform-bent tubes?

This paper tries to find answers to these research questions by carrying out experimental investigations and micro-magnetic measurements on freeform-bent steel tubes.

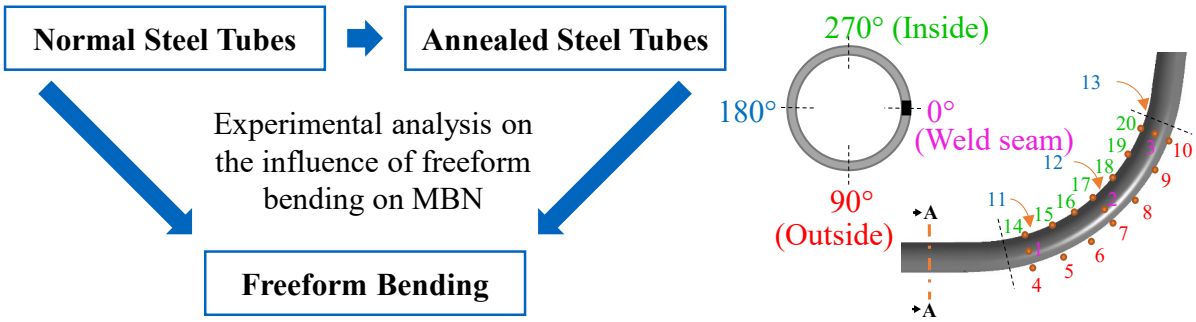

Fig. 3. Big picture and schematic depiction of measurement points on the unbent and bent part.

Experimental Investigations

This section describes the experimental investigations starting with residual stress annealing the unbent tubes, followed by the freeform bending process with a movable die, and the BHN measurement and analysis methods.

Residual stress annealing.

Residual stress annealing is used to minimize the residual stresses within the unbent tube. Table 1 shows the exact annealing parameters for the steel tubes made from P235. The annealing parameters were also part of other investigations with the same tubes [1].

Table 1. Residual stress annealing parameters for the experimental investigations.

Temperature	$T_0 \rightarrow$ 620 °C	620 °C	620 °C → T_0
Time	2 h	2 h	48 h

Fig. 4 shows the microstructure of the base material for normal and annealed tubes, based on the investigations of [1].

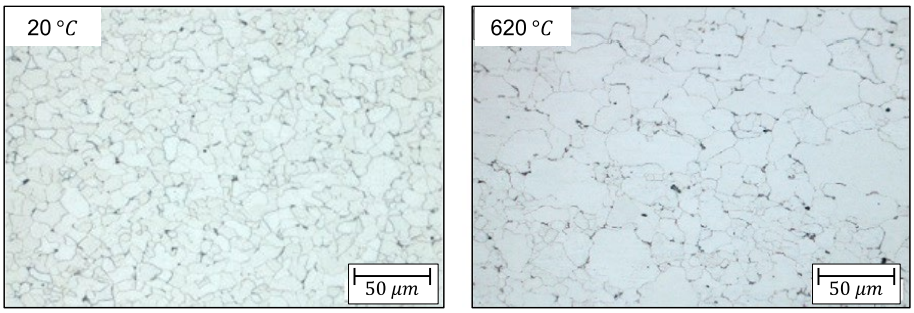

Fig. 4. Light microscopic image of the microstructure at x500 magnification Left: base material, Right: residual stress annealed [1].

Freeform bending and Barkhausen noise measurement. After the residual stress annealing, all tubes (normal and annealed) are bent with the freeform bending machine. Two different bending strategies are used. The first bending strategy includes five different part geometries (V01 - V05), where all result in a different curvature and bending angle. The second bending strategy includes seven different kinematics using the non-tangential bending technology [1]. This results in bent

parts with the same geometry but different residual stresses, according to [1]. The maximum deflection y_{max} and rotation φ_{max} of the bending die for all experiments are listed in Table 2.

Table 2. Freeform-bent parts with deflection and rotation of the bending die.

Name	**V01**	**V02**	**V03**	**V04**	**V05**		
y_{max}	5.85 mm	7.47 mm	9.85 mm	13.29 mm	18.15 mm		
φ_{max}	9.83 °	12.32 °	15.79 °	20.39 °	26.11 °		
Name	**A01**	**A02**	**A03**	**A04**	**A05**	**A06**	**A07**
y_{max}	9.00 mm	10.00 mm	10.00 mm	11.00 mm	11.00 mm	12.00 mm	12.00 mm
φ_{max}	22.00 °	16.00 °	20.00 °	13.00 °	14.00 °	12.00 °	13.00 °

The unbent (normal and annealed) and the bent tubes are measured at several measuring points with the micro-magnetic sensor; see Fig. 3. There are three measuring points on the sides of the tube, with one side corresponding to the weld seam (0°). On the inside (270°) and outside (90°), there are seven measuring points each since this is where the tube records the greatest possible deformation. Please note that all measurement points are on the constant section of the bent tube.

Results and Discussion

At the beginning, the unbent raw material and the annealed raw material are investigated by micro-magnetic measurements, and additionally, the influence of the annealing process on the geometrical dimensions of the unbent tubes is analyzed. Subsequently, the results of unbent tubes with and without prior annealing are described and discussed in terms of geometry and BHN. A distinction is made between tangentially and non-tangentially bent tubes for the bent components.

Unbent raw material.

There are two different conditions of the unbent material: normal and annealed. The annealing process has been carried out with the parameters shown in Table 1. Optical measurement technology was used to measure the surface of the tube and then evaluate the outer diameter (D_{Out}) and inner diameter (D_{In}). In addition, measurements were carried out with the micro-magnetic sensor at the positions shown in Fig. 3. The results are shown in Fig. 5.

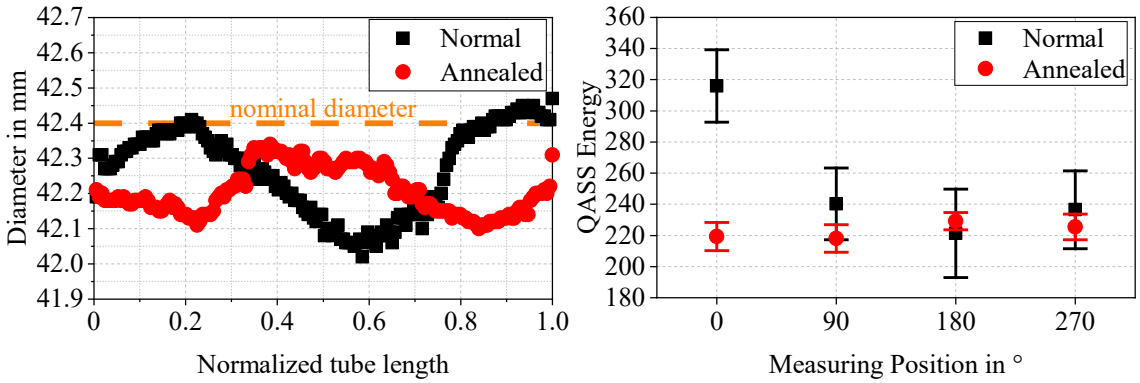

Fig. 5. Results for unbent tubes with and without residual stress annealing Left: Outer diameter, right: BHN.

For the outer diameter, it can be seen that all measurement points are within the desired tolerances (42.4±0.5 mm) for the normal and annealed tubes. The left side of Fig. 5 shows an example of a measured tube where the measuring points are distributed over the length. In addition, it appears that a trend reversal is occurring because of the annealing. At both ends, the normal tube

has a larger diameter than in the middle area, while the annealed tube shows the opposite trend. The deviation of the outer diameter is smaller after annealing compared to the normal material. The thickness of the material is within the tolerances (2.6±0.5 mm) for all measurement points. For geometrical tolerances, annealing has a positive impact due to the fact that the deviations become smaller.

On the right side of Fig. 5, the weld seam (0°) has a higher QASS energy level compared to the other measurement points for the normal tube. After annealing, the energy level of the weld seam decreases to approximately the same level as the other points. Because of the annealing process, the stresses throughout the tube were relieved, and the microstructure was affected. Fig. 4 shows significantly fewer grain boundaries in the annealed material, resulting in a lower QASS energy level. Overall, it can be stated that stress-relief annealing mainly affects the weld seam and results in a more homogeneous measurement signal with lower standard deviations.

Influence of bending process on BHN. Both unbent tube conditions (normal and annealed) are bent with the freeform bending machine and the exact same process parameters. The results are divided into the results for tangential bending (V01 - V05) and non-tangential bending (A01 - A07). The results are analyzed in comparison with numerical simulations based on a simulation model already described in [20].

In terms of geometry, it can be seen that the tubes made from the annealed material achieve higher constant curvature (equals smaller radii) than the non-annealed tubes, according to Fig. 6. This trend can be seen for all bent components V01 - V5 and A01 - A07. It can also be seen that for the non-tangential bent parts, approximately the same curvature results. This validates that constant curvature is possible for various non-tangential bending setups and builds the foundation for the following investigations. Since no differences were found in the geometric dimensions of the unbent annealed tube compared to the normal unbent tube, the differences in the curvature must be attributed either to the reduced stresses or the changed microstructure and the associated material properties after the annealing process.

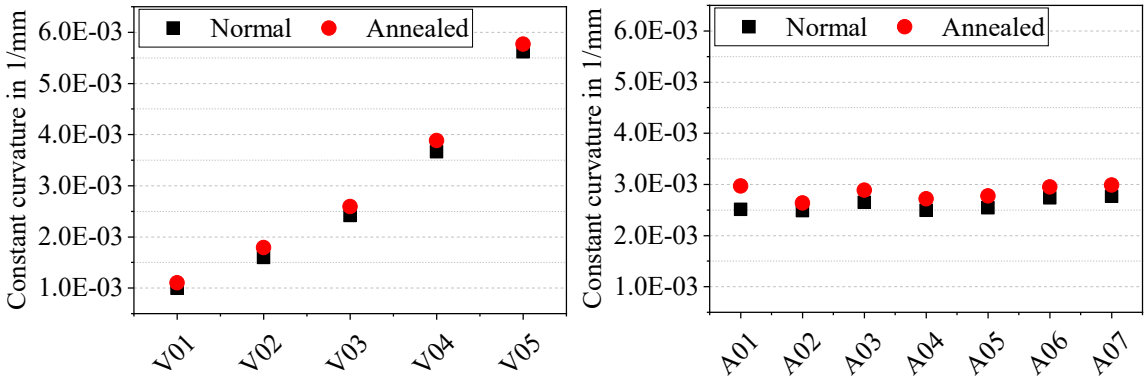

Fig. 6. Curvature of the freeform-bent parts made from normal and annealed straight tubes.

The results of the BHN analysis for the outside of the freeform-bent parts V01 - V05 and the non-tangential bent parts A01 - A07 with and without annealed raw material are shown in Fig. 7. The figure also shows the von Mises stresses determined by numerical simulations using the same measurement points as in the real bending investigations. In all tests and in the simulation, the results on the inside scatter strongly, which is why the evaluation concentrates only on the outside.

Fig. 7 shows that the BHN measurements for annealed tubes have greater fluctuations than the BHN results of normal tubes. A similar trend can be seen in the results of the annealed tubes and the simulation. With increasing curvature, the QASS energy level in the annealed tubes and the von Mises stresses determined in the simulation increase. This behavior is also to be expected due

to the bending process because the greatest strain occurs at the greatest curvature, which increases the stresses. The increase in the BHN can be explained by the fact that predominantly tensile stresses are expected on the outside of the bent tube, and these stresses increase the intensity of the BHN. Compressive stresses, on the other hand, reduce the intensity of the BHN. Only test V03 does not fit well with this trend. In contrast, this trend cannot be seen in the normal tubes. Here it seems like the QASS energy level decreases with increasing curvature. This allows the assumption that the stresses induced in the base material run counter to the stresses introduced by the freeform bending process. The fact that the results of the simulation fit better to the annealed tubes than to the normal tubes is because in the simulation, bending is done with a tube where the initial stress state is zero. The annealing reduces the stresses, and therefore the simulation corresponds more to these experiments.

In the following section, the results of non-tangential bending are examined in more detail. The quintessence of non-tangential bending is the introduction of different stress states at constant geometry. If we look at Fig. 7 together with Fig. 6, we can see exactly this relationship. Significant differences can be seen in both the simulations and the measured freeform-bent parts. On the outside, for example, the highest QASS energy level (A03) is more than 10% higher than the lowest (A01). In contrast to the previous results, a similar trend for the non-tangentially bent components can be seen between normally bent tubes and the simulation. The annealed tubes also fit with this trend, except for the outlier at A03. In the context of the BHN, the results show that as stresses decrease, the BHN also decreases, and as stresses increase, the BHN increases. Based on the results shown, it can be said that the sensor used and the BHN are suitable for measuring different stresses during freeform bending. However, in order to be able to use the sensor in a property-based control loop, a correlation of the BHN with the real stresses in the bent part must still be created. In addition, the magnetization parameters must be further refined in order to determine the various influences on freeform bending as much as possible, even in an inline measurement.

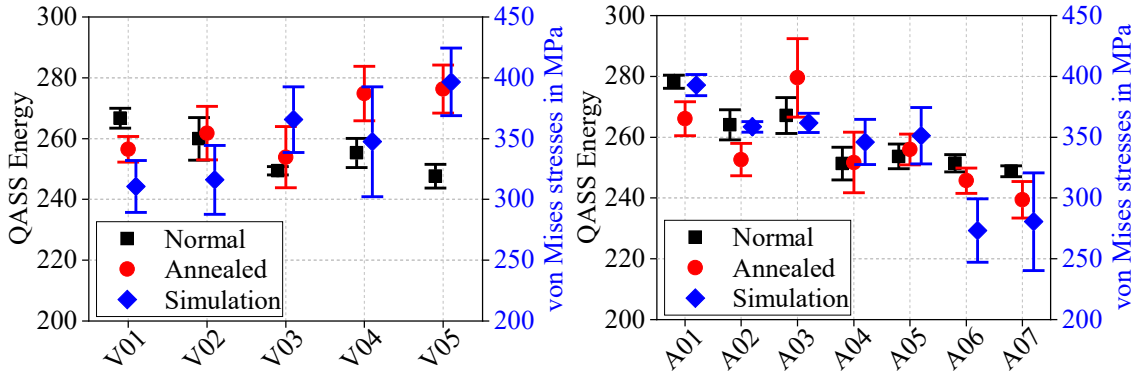

Fig. 7. Resulting BHN on the outside of freeform-bent tubes in comparison to von Mises stresses determined in numerical simulations. Left: tangential bending, right: non-tangential bending.

Summary

In the present work, the influence of different initial conditions in the tubes during freeform bending on the geometry and BHN was investigated. For this purpose, a series of tests were carried out with annealed and non-annealed tubes, which were then measured and evaluated with the micro-magnetic sensor. In addition, the results were compared with the results from the simulation. The following findings can be noted in relation to the research questions defined at the beginning of the study:

- Different QASS energy levels were found in the circumferential direction of the tube, with the weld seam significantly above the base material. The energy levels of the base material were all within a certain scatter band, which is reduced by annealing.

- In terms of geometry, it was found that the annealed tubes lead to smaller radii compared to non-annealed raw material. In terms of BHN, the annealed tubes showed better accordance with the simulation result and the presented theory.
- In non-tangential bending, it is possible to decouple the mechanical properties from the geometry. The differences in the non-tangentially bent tubes could be measured with BHN, showing a similar trend in the normal and annealed results as in the simulations.
- The micro-magnetic sensor can measure differences in freeform-bent parts, and the results are in good accordance with the simulation model. With these results, it can be said that the sensor can be used to measure BHN quickly and use the results in order to control the freeform bending process based on its properties.

For future work the parameters of the micro-magnetic sensor need to be optimized for the given steel tubes in order to measure more accurately. In addition, a correlation between the BHN and residual stresses is necessary to get a better understanding of the process and to control the bending process.

Acknowledgement
This work was supported by the German research foundation (DFG) under grant number [424334318].

References
[1] D. Maier, S. Stebner, A. Ismail, M. Dölz, B. Lohmann, S. Münstermann, W. Volk, The influence of freeform bending process parameters on residual stresses for steel tubes, Adv. Industr. Manuf. Eng. 2 (2021) 100047. https://doi.org/10.1016/j.aime.2021.100047
[2] S.C. Stebner, D. Maier, A. Ismail, S. Balyan, M. Dölz, B. Lohmann, W. Volk, S. Münstermann, A System Identification and Implementation of a Soft Sensor for Freeform Bending, Mater. 14 (2021) 4549. https://doi.org/10.3390/ma14164549
[3] A. Ismail, D. Maier, S. Stebner, W. Volk, S. Münstermann, B. Lohmann, A Structure for the Control of Geometry and Properties of a Freeform Bending Process, IFAC-PapersOnLine 54 (2021) 115-120. https://doi.org/10.1016/j.ifacol.2021.10.060
[4] N. Beulich, R. Mertens, J. Spoerer, W. Volk, Influence of tube rollforming on material properties and subsequent bending processes, Forming Technology Forum, 2019.
[5] N. Beulich, J. Spoerer, W. Volk, Sensitivity analysis of process and tube parameters in free-bending processes, IOP Conf. Ser.: Mater. Sci. Eng. 651 (2019) 12031. https://doi.org/10.1088/1757-899X/651/1/012031
[6] P. Gantner, D.K. Harrison, A.K. de Silva, H. Bauer, The Development of a Simulation Model and the Determination of the Die Control Data for the Free-Bending Technique, Proceedings of the Institution of Mechanical Engineers, Part B: J. Eng. Manuf. 221 (2007) 163-171. https://doi.org/10.1243/09544054JEM642
[7] N. Beulich, P. Craighero, W. Volk, FEA Simulation of Free-Bending - a Preforming Step in the Hydroforming Process Chain, J. Phys.: Conf. Ser. 896 (2017) 12063. https://doi.org/10.1088/1742-6596/896/1/012063
[8] M.K. Werner, D. Maier, L. Scandola, W. Volk, Motion profile calculation for freeform bending with moveable die based on tool parameters, ESAFORM 2021, 2021. https://doi.org/10.25518/esaform21.1879
[9] S. Groth, B. Engel, K. Langhammer, Algorithm for the quantitative description of freeform bend tubes produced by the three-roll-push-bending process, Prod. Eng. Res. Devel. 12 (2018) 517-524. https://doi.org/10.1007/s11740-018-0795-2
[10] N. Chernov, Circular and Linear Regression: Fitting circles and lines by least squares. [S.l.]: CRC PRESS, 2020.

[11] L. Scandola, D. Maier, M. Konrad Werner, C. Hartmann, W. Volk, Automatic Extraction and Conversion of the Bending Line from Parametric and Discrete Data for the Free-Form Bending Process, in The Minerals, Metals & Materials Series, NUMISHEET 2022, K. Inal, J. Levesque, M. Worswick, C. Butcher (Eds.), Cham: Springer International Publishing, 2022, pp. 813-826.
[12] W. Wei, H. Wang, H. Xiong, X. Cheng, J. Tao, X. Guo, Research on influencing factors and laws of free-bending forming limit of tube, Int. J. Adv. Manuf. Technol. 106 (2020) 1421-1430. https://doi.org/10.1007/s00170-019-04692-0
[13] D. Staupendahl, S. Chatti, A.E. Tekkaya, Closed-loop control concept for kinematic 3D-profile bending, in Nantes, France, 2016, p. 150002.
[14] J. Wu, B. Liang, J. Yang, Trajectory prediction of three-dimensional forming tube based on Kalman filter, Int. J. Adv. Manuf. Technol. 121 (2022) 5235-5254. https://doi.org/10.1007/s00170-022-09521-5
[15] S. Schuster, L. Dertinger, D. Dapprich, J. Gibmeier, Application of magnetic Barkhausen noise for residual stress analysis - Consideration of the microstructure, Mater. Test. 60 (2018) 545-552. https://doi.org/10.3139/120.111186
[16] K. Shimosaka, T. Bergs, D. Schraknepper, S. Münstermann, M. Meurer, In-situ Evaluation of Surface Integrity Modifications by means of Barkhausen Noise Measurement, Procedia CIRP 102 (2021) 465-470. https://doi.org/10.1016/j.procir.2021.09.079
[17] L. Mierczak, D.C. Jiles, G. Fantoni, A New Method for Evaluation of Mechanical Stress Using the Reciprocal Amplitude of Magnetic Barkhausen Noise, IEEE Trans. Magn. 47 (2011) 459-465. https://doi.org/10.1109/TMAG.2010.2091418
[18] V. Moorthy, B.A. Shaw, S. Day, Evaluation of applied and residual stresses in case-carburised En36 steel subjected to bending using the magnetic Barkhausen emission technique, Acta Mater. 52 (2004) 1927-1936. https://doi.org/10.1016/j.actamat.2003.12.034
[19] S. Santa-aho, A. Laitinen, A. Sorsa, M. Vippola, Barkhausen Noise Probes and Modelling: A Review, J. Nondestruct. Eval. 38 (2019). https://doi.org/10.1007/s10921-019-0636-z
[20] S.C. Stebner, D. Maier, A. Ismail, M. Dölz, B. Lohman, W. Volk, S. Münstermann, Extension of a Simulation Model of the Freeform Bending Process as Part of a Soft Sensor for a Property Control, Key Eng. Mater. 926 (2022) 2137-2145. https://doi.org/10.4028/p-d17700

Materials Research Proceedings 28 (2023) 2101-2113 https://doi.org/10.21741/9781644902479-225

Fine blanking of pre-hardened high manganese steel to investigate the sheared surface hardening and part quality

SCHWEINSHAUPT Frank[1,a *], VOIGTS Herman[1,b], HERRIG Tim[1,c] and BERGS Thomas[1,2,d]

[1]Laboratory for Machine Tools and Production Engineering (WZL) of RWTH Aachen University, Campus-Boulevard 30, 52074 Aachen, Germany

[2]Fraunhofer Institute for Production Technology IPT, Steinbachstraße 17, 52074 Aachen, Germany

[a]f.schweinshaupt@wzl.rwth-aachen.de, [b]H.Voigts@wzl.rwth-aachen.de, [c]T.Herrig@wzl.rwth-aachen.de, [d]t.bergs@wzl.rwth-aachen.de

Keywords: Fine Blanking, High Manganese Steel, Strain Hardening, Twinning Induced Plasticity, Die Roll, Sheared Part Quality

Abstract. Fine blanking is a highly productive process for manufacturing of high accuracy sheet metal parts with functional surfaces. The specific process characteristic leads to high forming in the shear zone and an associated strain hardening of the sheared functional surfaces. Utilization of the process-immanent sheared surface hardening can reduce time and resources of downstream heat treatment processes such as case hardening. High Manganese Steels (HMnS) are characterized by a high strain hardening capacity due to the deformation mechanisms of twinning and transformation induced plasticity occurring during forming. As a result of high tensile strengths, HMnS are suitable as lightweight materials, but often exhibit a relatively low yield strength in terms of structural design features. One approach for increasing the strength values without changing the alloy design is a forming-induced strain hardening of the semi-finished sheet metal by means of upsetting. Therefore, this paper deals with an experimental investigation of the influence of pre-hardening on the blanked part properties during fine blanking of HMnS X40MnCrAlV19-2 LY (1.7401). For this purpose, sheet blanks were strain hardened by means of flat coining and subsequently fine blanked with an analog geometry representing tribologically stressed functional surfaces. Relevant functional surfaces were then analyzed by means of microhardness measurements with regard to the sheared surface hardening as well as characterized in terms of the quality-determining attributes die roll and clean-shear area. Due to the deformation mechanism of twinning, fine blanking of pre-hardened HMnS resulted in a combination of process-immanent high sheared surface hardening and increased yield strength with simultaneous optimal functional surface quality.

Introduction

The intrinsically driven economic resource efficiency [1] as well as the reduction of ecologically harmful emissions [2] force a continuous optimization of product development and the necessary manufacturing processes in the sheet metal processing industry. Particularly in the development of dynamically moving sheet metal workpieces, this results in the implementation of consistent lightweight design strategies for saving raw materials and emissions through lightweight material, shape and concept design [3]. Fine blanking is a process for the series production of geometrically complex sheet metal workpieces with high dimensional and shape accuracy combined with optimum material utilization [4]. Due to the high accuracy and quality of the sheared surface, fine blanking is a near-net-shape technology, e.g. for the manufacturing of gears or sprockets [5]. Process characteristics of fine blanking (cf. Fig. 1b and c) are three independently acting process forces (blanking, counter and vee-ring force), a small relative die clearance, a wedge-shaped vee-

Content from this work may be used under the terms of the Creative Commons Attribution 3.0 license. Any further distribution of this work must maintain attribution to the author(s) and the title of the work, journal citation and DOI. Published under license by Materials Research Forum LLC.

ring as well as die edges prepared with a chamfer or radius [6]. During the shearing process, the vee-ring and counter force induce a high hydrostatic pressure in the shear zone [7]. The embossing of the vee-ring, the die edge preparation as well as a small die clearance favor the formation of additional compressive stresses [8]. The resulting superimposed compressive stress generates a plastic flow in the shear zone over the entire blanking path, which prevents tensile stresses and results in a smooth and tear-free sheared surface of high quality [9]. The load-bearing capacity of sheared functional surfaces is reduced by a die roll (cf. Fig. 1c), which is completely formed after 20 to 30% of the blanking path [10]. A large number of scientific studies have already investigated the factors influencing the clean-shear area and die roll during fine blanking and have shown comparable tendencies regarding the influence of process (e.g. vee-ring force), tool (e.g. die clearance) and workpiece parameters (e.g. material properties) [7].

In terms of process mechanics, a small die clearance with increasing blanking velocity from 10 to 70 mm/s causes a significant temperature increase of the shear zone during plastic flow as well as an increase of the blanking force [11]. The plastic flow of the sheet material in the shear zone basically leads to high deformation in the area in front of the die edge, which results in a significant increase in the dislocation density and thus in strain hardening of the sheared surface [12]. This process-immanent hardening in the near-surface area of fine blanked functional surfaces offers the potential to substitute a downstream heat treatment by using sheet materials with high strengths and strain hardening properties [8]. Regarding the use of lightweight materials, High Strength Steels (HSS) such as micro-alloyed fine grain steel S700MC (1.8974) are increasingly used for fine blanking [13]. However, as increasing strength is accompanied by a lower forming capacity [14], HSS are only suitable to a limited extent for forming sheet metal workpieces with spatially complex geometry. High Manganese Steels (HMnS) exhibit a superior combination of high strength and high formability [15] and thus offer the potential to address both lightweight material and shape design in sheet metal workpieces. HMnS are classified with a manganese content higher than 15 wt.% and characterized by a high strain hardening capacity during plastic deformation [16]. Forming of HMnS thus leads to a high strain hardening of the plasticized area, which is a result of the occurring secondary deformation mechanisms Twinning Induced Plasticity (TWIP) and Transformation Induced Plasticity (TRIP). With unchanging alloy design, the activation of different deformation mechanisms and thus the influence on the hardening behavior depends on the temperature [17], stress state [18] and strain rate [19]. The alloy design of a HMnS influences the magnitude of the stacking fault energy (SFE), which is used as a parameter to adjust the secondary deformation mechanism [16]. This enables the design of a specific deformation mechanism at a given temperature based on thermodynamic calculations of the SFE [20]. Despite the high strain hardening capacity, HMnS often exhibit low yield strength due to the soft austenitic matrix [17].

However, in order to exploit a lightweight and forming potential based on deformation mechanisms in fine blanking of HMnS, fundamental investigations are still lacking. Investigations on fine blanked sprockets made of non-alloy structural steel S275JR (SS400) have shown that these exhibit a higher wear resistance due to the sheared surface hardening than conventionally manufactured and heat-treated sprockets made of non-alloy quenched and tempered steel C50 (S50C) [21]. As a result of increased residual compressive stresses, fine blanked gears made of micro-alloyed fine grain steel S355MC (1.0976) showed a comparably high tooth root bending strength to low-alloy, heat-treated case-hardening steels [22]. Fine blanking of higher-strength Dual Phase (DP) steels DP600 [23] as well as DP780 and DP980 [24] offers potential for substitution of downstream heat treatment due to the strain hardening behavior, but also resulted in poor sheared surface quality with a tear-off height of more than 50% of the sheet thickness. Investigations on fine blanking of TRIP steel also revealed large tear-off heights of 40% of the sheet thickness at the sheared surfaces [25]. In a study on fine blanking of flat coined case-

hardening steel 16MnCr5 (1.7131), the die roll formation was reduced due to a forming-induced increase in the strength values [26].
In fine blanking of conventional steels, the sheared surface hardening has a positive effect on the behavior of tribologically stressed functional surfaces and thus shows potential for substituting heat treatment. The high deformation in the area in front of the die edge provides an ideal condition for utilizing the combination of high strain hardening and high formability during fine blanking of HMnS. Pre-hardening of the sheet material by means of upsetting represents a possible approach for influencing the strength values of HMnS. In order to achieve a combination of increased yield strength and high sheared surface hardening, fine blanking of pre-hardened HMnS was investigated in the present work. For this purpose, sheet metal blanks with various height reductions have been flat coined and fine blanked with a part geometry representing tribologically stressed functional surfaces. Depending on the part geometry, an analysis of the strain hardening as well as quality-determining attributes was then carried out.

Experimental Setup for Fine Blanking of Pre-Hardened HMnS

To investigate the influence of pre-hardened HMnS on the sheared part properties during fine blanking, sheet blanks made of hot-rolled X40MnCrAlV19-2 LY (1.7401) with the dimensions given in Fig. 1a were used. In order to evaluate the potential of mechanism-induced sheared surface hardening, additional sheet blanks of micro-alloyed fine grain steel S700MC (1.8974) have been fine blanked. Table 1 shows the yield strength $R_{\mathrm{p0.2}}$, ultimate tensile strength R_{m}, uniform elongation A_{G}, elongation at fracture A and initial hardness for the sheet materials.

Table 1. Characteristic values of the mechanical properties valid for room temperature T = 22°C

Material	$R_{\mathrm{p0.2}}$ [MPa]	R_{m} [MPa]	A_{G} [%]	A [%]	Initial hardness [HV0.1]
HMnS	407	843	50	A_{50} = 55	202 ±4
S700MC	780	865	9.5	A_{80} = 19.1	296 ±5

Fig. 1a and b show the schematic setup for fine blanking of pre-hardened HMnS. The pre-hardening of the sheet blanks was carried out in a tool for flat coining with two parallel ground upset plates. The tool-side adjustment of the height reductions Δs_i was carried out using spacers adapted to the target sheet thickness of s = 4.6 mm. In order to investigate two different pre-hardening stages of HMnS, sheet blanks have been surface ground on both sides to the initial sheet thicknesses $s_{\mathrm{I}i}$ specified in Fig. 1a. As a reference for the sheared part analysis, sheet blanks from both HMnS and S700MC were additionally surface ground to the target sheet thickness of s = 4.6 mm.

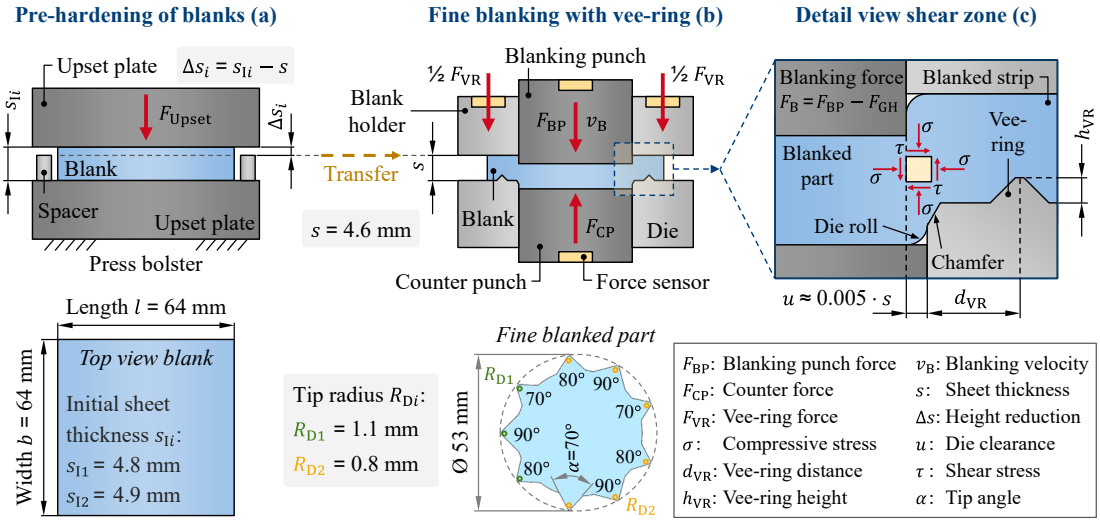

Fig. 1. Setup for pre-hardening (a) with subsequent fine blanking (b) and a detailed view of the shear zone (c).

Flat coining was carried out on a *Schuler HPX 400* hydraulic press with a ram velocity of 5 mm/s. After measuring the upset sheet blanks regarding the height reduction, the fine blanking tests were conducted on a servomechanical fine blanking press *Feintool XFT 2500 speed*. Fine blanking was performed with a modular designed single part producing tool (one part per stroke), which is instrumented with piezoelectric force sensors to measure the process forces. The sheared part geometry consisting of convex form elements with different tip angles α and tip radii R_{Di} represents an analogy application case for tribologically stressed functional surfaces. Acute angles with small radii are challenging (high difficulty level D) in terms of blanked part quality as well as punch edge load. To categorize the difficulty level, classification tables dependent on the sheet thickness and sheared part geometry (e.g. angles) are used according to [8], where $D = 1$ represents the lowest difficulty. The major geometric quantities of the sheared part are shown in Fig. 1b. The blanking punch and die were manufactured from *Böhler S390* powder metallurgical high speed steel with a hardness of 65 HRC and provided with the *Platit FeinAl* coating (AlCrN-based nanolayer coating) tailored to fine blanking. *Holifa VP1150/200* chlorine-free lubricant was used for the flat coining and fine blanking experiments. The process and tool parameters used for fine blanking are specified in Table 2.

Table 2. Process and tool parameters used for fine blanking.

Blanking velocity v_B	45 mm/s	**Die chamfer angle**	35°
Vee-ring force F_{VR}	620 kN	**Die chamfer height**	0.3 mm
Counter force F_{CP}	170 kN	**Vee-ring distance d_{VR}**	2.5 mm
Die clearance u	20 µm	**Vee-ring height h_{VR}**	0.7 mm

In order to investigate the mechanical properties and to evaluate the hardening behavior, tensile tests of the HMnS used were conducted at the *Steel Institute IEHK* according to DIN EN ISO 6892. The tensile tests were carried out at different temperatures using a *ZwickRoell Z250* tensile testing machine with a temperature chamber. The strain was measured in an open loop using *Zwick multiXtens*. Dynamic tensile tests were conducted at a strain rate of 10 /s using a servohydraulic 20kN *Roell-Amsler* high-speed (18m/s) tensile testing machine. The force was measured by a piezo

electric load cell and combined with strain gauges on the sample heads to obtain a smoothed signal [27]. The initial dimensions of the samples used had a thickness of 2mm, length of 15mm and width of 6mm. The analysis of the sheared surface hardening was carried out in dependence of the part geometry using the three convex form elements with the tip radius R_{D1} = 1.1 mm (Fig. 2a). For this purpose, samples at the corresponding tip angles α were separated out for each blanked part investigated in such a way that the separation line A-A is aligned normally to the functional surface. After metallographic preparation, microhardness measurements were conducted according to the scheme shown in Fig. 2.

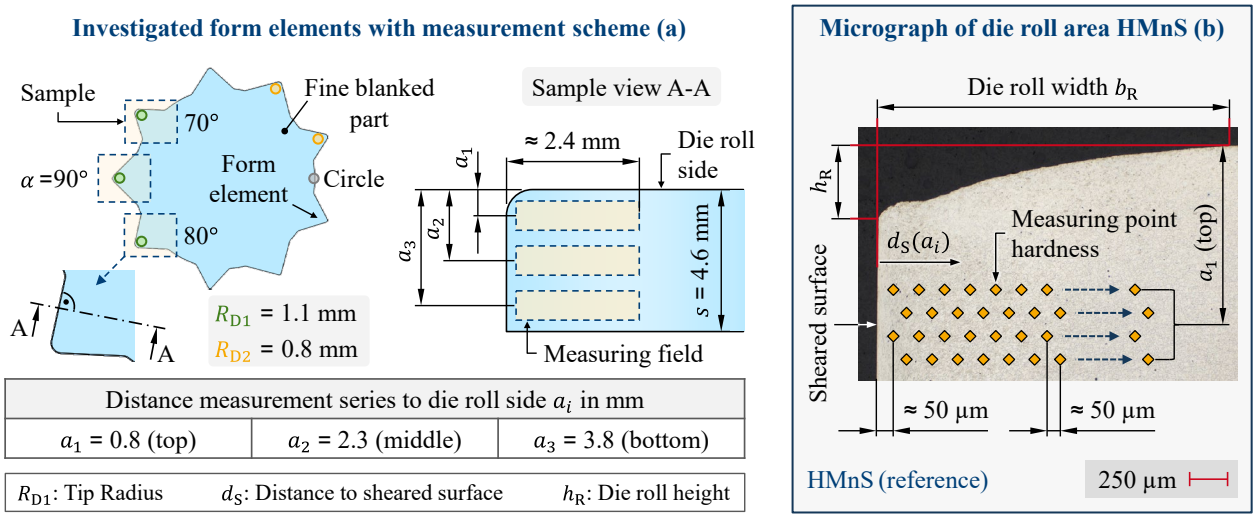

Fig. 2. Investigated form elements with measurement scheme (a) and a micrograph of the die roll area (b).

Since the sheared surface hardening depends on the blanking path, three measuring fields were investigated based on the distance to the die roll side a_i. Fig. 2b exemplarily shows a micrograph of the die roll area of HMnS at the position circle with the pattern of hardness indentations, which have horizontally as well as vertically an indentation distance of 100 µm to each other. The high strain hardening directly below the sheared surface enables the hardness measurement to start at a distance of 50 µm from it. To increase the resolution of the hardness profile, an associated series of measurements was carried out with an offset of half an indentation distance. In order to enable a smoothing of the hardness values by means of averaging, two of these patterns were measured for each measuring field. The microhardness measurements were done using a *Fischer* microhardness measuring system *Fischerscope HM2000* according to the force-indentation depth method with a holding time of 10 s. In this case, the Vickers hardness *HV* is determined by converting the plastic part of the universal hardness HU_{pl} based on DIN 50359-1 into HV_{pl}. In order to evaluate the quality-determining attributes of fine blanking, the die roll was measured and the functional surfaces were investigated regarding tear-off. To determine the die roll, the fine-blanked parts were polygonized using a *GOM ATOS Core 3D* scanner and a software-based target-actual comparison was conducted using a CAD model by means of *GOM Inspect Suite*. For this purpose, the height differences at the form elements marked with colored circles in Fig. 2a were measured in a 2D plot using sectional planes with an equidistant step size of 2.5 µm and evaluated script-based. For the investigation of the tear-off height, images of the functional surfaces were taken based on light optical microscopy (LOM) using a *Keyence VHX-5000* digital microscope and evaluated graphically. For each analyzed state regarding the pre-hardening of the HMnS as well as the additionally considered HSS S700MC, respectively two blanked parts were evaluated

and averaged for the hardness results. All other analysis results presented are based on the averaging of five blanked parts in each case.

Results Analysis

To evaluate the strain hardening behavior, Fig. 3a shows the calculated SFE of the investigated HMnS as a function of the temperature as well as the ranges of assumed secondary deformation mechanisms. The SFE was calculated based on a thermodynamic model using the chemical composition of X40MnCrAlV19-2 LY at a grain size of 30 µm [20]. Generally, a SFE below 18 to 20mJ/m^2 enables a TRIP effect and a higher SFE up to about 50mJ/m^2 results in a TWIP effect. [28]. Above an SFE of 45 to 50mJ/m^2, twinning is drastically reduced and dislocation slip (SLIP) is the preferred activated deformation mechanism [16]. For the HMnS investigated, the TWIP effect is assumed to occur in a temperature range of approx. -20 to 140°C.

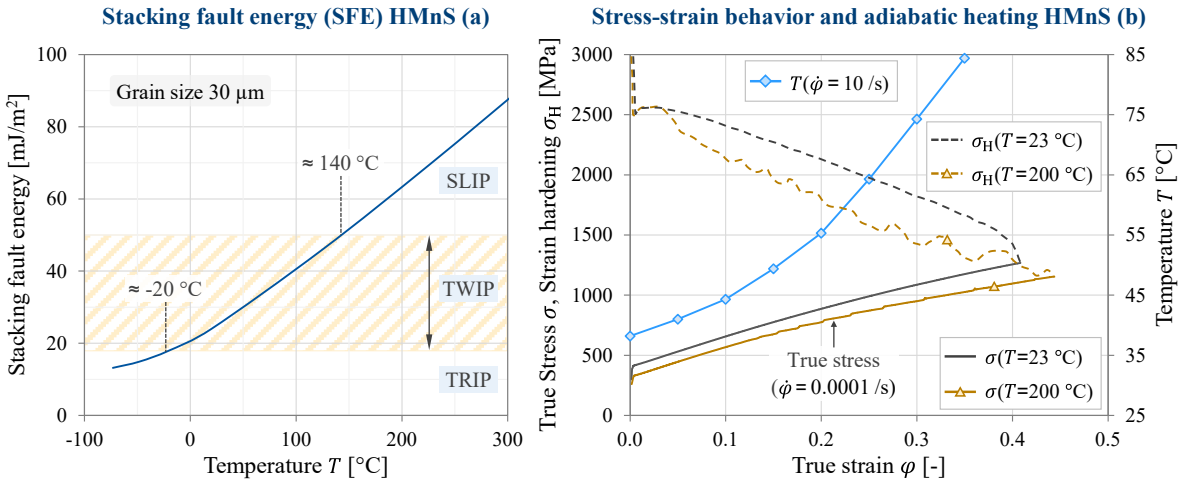

Fig. 3. Calculated SFE (a) and stress-strain behaviour (quasi-static) as well as adiabatic heating (dynamic) (b).

Fig. 3b shows the strain hardening behavior of HMnS based on true stress-strain and strain hardening curves determined from the tensile tests. The true stress-strain curves were determined for a temperature of 23 and 200°C with a strain rate of $\dot{\varphi}$ = 0.0001 /s. The corresponding strain hardening curves shown (dashed lines) result from the derivation of the respective stress-strain curves. An increase in temperature leads to a reduced flow stress in the stress-strain progression. Likewise, the corresponding strain hardening curve is significantly reduced with increasing temperature from a true strain of approx. $\varphi \approx 0.04$. Since the elastic strain of the tool elements in the force flow and the true strain of the sheet material in the shear zone are superimposed during fine blanking, the exact determination of the strain rate is challenging. Neglecting the elastic tool strain, the strain rate with regard to the investigated process parameters is about 10 /s during the shearing process. Fig. 3b additionally shows the temperature rise due to adiabatic heating measured by thermography during the dynamic tensile test for a strain rate of $\dot{\varphi}$ = 10 /s up to a true strain of $\varphi \approx 0.35$. The rising adiabatic heating as well as the reduction in strain hardening at higher temperature during the tensile tests indicate an increase in SFE (Fig. 3a) and thus an influence on the strain hardening behavior due to shearing of HMnS.

Based on the respective initial sheet thickness s_{1i}, the height reductions Δs_i were measured to determine the relative height reduction $\Delta h = \Delta s_i / s_{1i}$ of the upset sheet blanks. For the first pre-hardening stage, a height reduction Δs_1 = 0.2 mm with a deviation of ±0.012 mm was obtained, which corresponds to a relative height reduction of $\Delta h \approx 4.2\%$. With a deviation ±0.015 mm for Δs_2 = 0.3 mm, the relative height reduction for the second pre-hardening stage is $\Delta h \approx 6.1\%$. To

evaluate the process behavior during the shearing process, Fig. 4a shows the blanking force progression of the HMnS in the reference state (Δh = 0%) compared to HSS S700MC and exemplarily the specified vee-ring and counter force. Due to the sensor arrangement (cf. Fig. 1b), the blanking force F_B is determined by subtracting the counter force F_{CP} from the blanking punch force F_{BP}. In the fine blanking press used, the counter and vee-ring force are applied hydraulically and exhibit a subsiding oscillating curve over the shearing phase resulting from the closed loop control behavior. Both force curves are slightly above the set values after transient oscillation, but during the shearing phase the underlying settings are obtained on average.

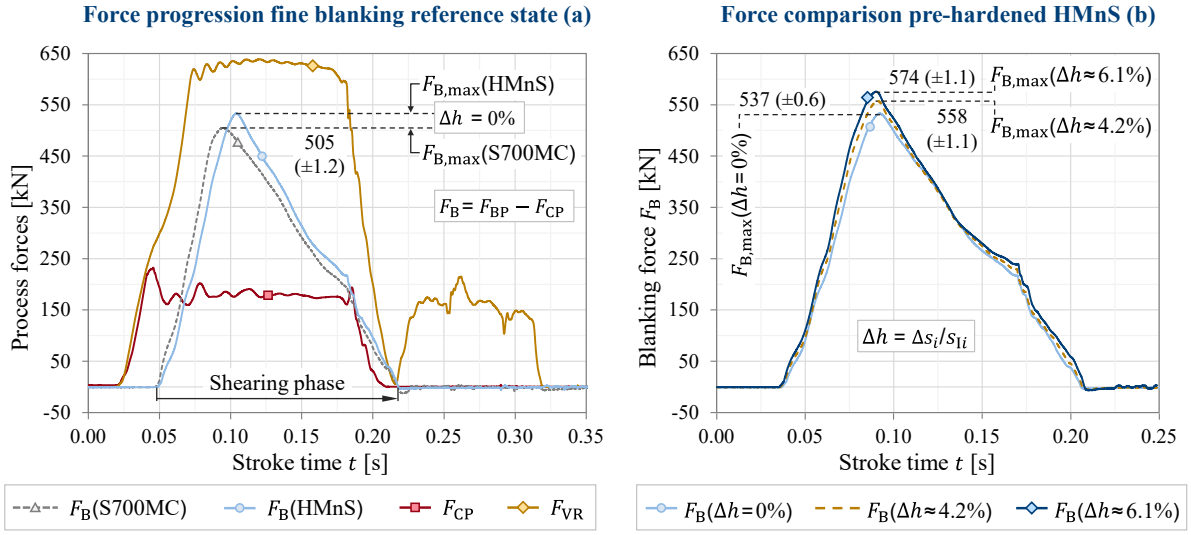

Fig. 4. Fine blanking forces of the reference state (a) and blanking force comparison of pre-hardened HMnS (b).

Despite almost equally high tensile strength compared to the HSS S700MC, an increased maximum blanking force $F_{B,max}$ of approx. 32 kN is observed for the reference state of the HMnS (Fig. 4a) due to the high hardening capacity. The slightly less steep increase in blanking force in the shearing phase is due to the forming behavior of HMnS reflected in the yield strength $R_{p0.2}$. In contrast, the comparison of pre-hardening stages shown in Fig. 4b indicates a more rapidly rising blanking force with increasing relative height reduction Δh, which can be explained by an increase of the yield strength. For the first pre-hardening stage (Δh = 4.2%), the maximum blanking force increases by 21 kN and for the second (Δh = 6.1%) by 37 kN compared to the reference state of HMnS. With less than 0.3%, the standard deviations of the maximum blanking force given in parentheses are to be considered as neglectable.

Fig. 5a shows the sheared surface hardening for fine blanked HMnS in the reference state (Δh = 0%) as well as for HSS S700MC with respect to the functional surface α = 80° for the measuring fields (cf. Fig. 2a) top (a_1) and bottom (a_3). As expected, the hardness values in the near-surface area ($d_S \leq 0.5$ mm) increase related to the die roll side with increasing blanking path (top to bottom). Due to the high strain hardening capacity, the HMnS is characterized in the near-surface area by a pronounced sheared surface hardening with an enormous hardness increase. Directly below the sheared surface, the hardness values of HMnS are approx. 140 HV higher than the values of S700MC for the top as well as the bottom measuring field. The plotted work hardening depth of the respective materials indicates the distance from the sheared surface where the bulk hardness is reached on average regarding the measuring field middle. With a value of about $d_S \approx 1.6$ mm, the HMnS in the reference state (Δh = 0%) achieves a work hardening depth more than twice as large as that of the micro-alloyed fine grain steel. According to DIN EN ISO

18203, the hardness value for determining the case hardening depth CHD is defined as 550 HV, and for determining the surface hardening depth SHD, limiting hardness values are specified based on the minimum surface hardness. For the measuring field bottom, the achieved sheared surface hardening of HMnS is accordingly comparable with a case hardening depth of CHD ≈ 0.15 mm and for a surface hardness ($d_S \approx 0$ mm) of 630 HV with a surface hardening depth of SHD ≈ 0.25 mm.

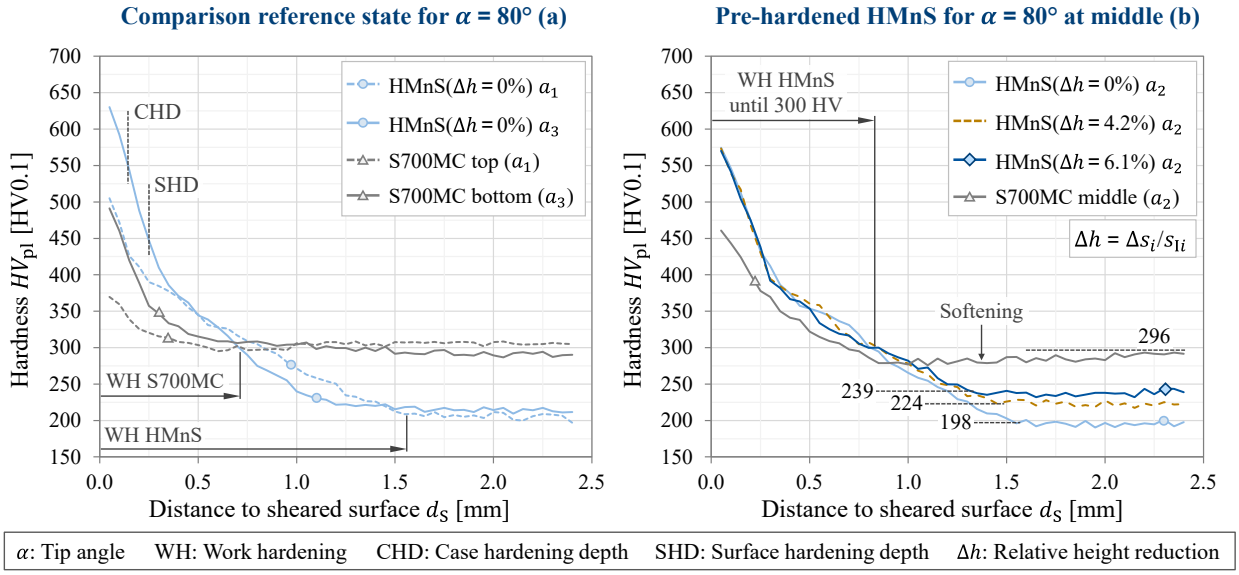

Fig. 5. Sheared surface hardening for tip angle α = 80° regarding the reference state (a) and pre-hardening (b).

Fig. 5b shows the hardening of the fine blanked functional surface α = 80° depending on the relative height reduction Δh carried out for pre-hardening of the HMnS in comparison to the HSS S700MC for the measuring field middle (a_2). The pre-hardening of the HMnS has no influence on the profile and the height of the sheared surface hardening in the near-surface area, but causes an increase in the bulk hardness, of which the averaged value is given for each hardness profile shown. The first pre-hardening stage (Δh = 4.2%) increases the bulk hardness by an average of 26 HV and the second (Δh = 6.1%) by an average of 43 HV, which in each case also suggests an increase in the yield strength. Compared to the measuring field middle, the hardness values for the reference state of the HMnS in the field bottom (Fig. 5a) are above the determined bulk hardness (~198 HV) after reaching the work hardening depth ($d_S \geq 1.6$ mm). One possible reason that the hardness values are on average 14 HV higher than the bulk hardness is a strain hardening due to the induced compressive stresses of the vee-ring and counter force at least in the area of the sheet surface close to the shear zone. The hardness profile for the S700MC in the measuring field middle (Fig. 5b) shows a slight softening with values about 20 HV lower than the bulk hardness (~296 HV) in the range of $d_S \approx 0.8$ to 2.2 mm. With increasing pre-hardening Δh, the achievable work hardening depth of the HMnS decreases (Fig. 5b). Based on a bulk hardness of 300 HV, a work hardening depth of at least $d_S \approx 0.8$ mm is to be expected for the measuring field middle with increasing pre-hardening of the HMnS.

The tip angle of the convex form elements also has no influence on the profile and height of the sheared surface hardening with respect to the investigated tip radius R_{D1} = 1.1 mm. Fig. 6a exemplarily shows the hardness profiles for pre-hardened HMnS (Δh = 6.1%) and S700MC for the measuring field middle (a_2) depending on the tip angle α. The achieved work hardening depth of the second pre-hardening stage of HMnS is about $d_S \approx 1.3$ mm. Regarding a comparison to case

and surface hardening, for the measuring field middle the hardening depths are CHD ≈ 0.1 mm and SHD ≈ 0.2 mm (surface hardness 570 HV). For all determined hardness profiles, the scatter of the averaged hardness values lies within a range of ±6.4 HV.

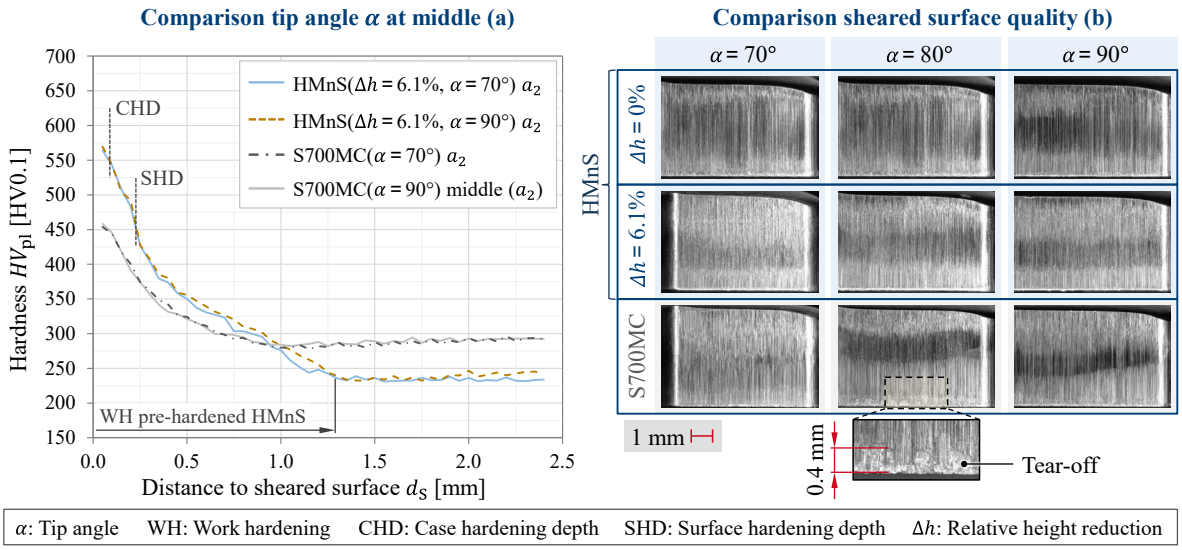

Fig. 6. Sheared surface hardening regarding the tip angle (a) and quality of the functional sheared surfaces (b).

The quality of the investigated functional surfaces is shown in Fig. 6b based on the LOM images for the reference state and the second pre-hardening stage of the HMnS compared to the HSS S700MC. Independent of the investigated tip angle α as well as the relative height reduction Δh, the fine blanked HMnS is characterized by a high sheared surface quality without tears and with tear-off heights below 0.05 mm. The micro-alloyed fine grain steel exhibits a comparably high sheared surface quality with minor tear-off heights of about 0.2 mm at α = 70° and 80° and a tear-off height of 0.4 mm at α = 90°.

For the analysis of the die roll formation, two tip angles with smaller tip radius (R_{D2} = 0.8 mm) were considered in addition to the form elements marked with R_{D1} in Fig. 2a. Fig. 7a shows the characteristics of the investigated fine blanked part and the sectional planes used to measure the die roll. The sectional planes are collinear to the respective angle bisector of the investigated tip angle α. In order to quantify the influence of pre-hardening on die roll formation during fine blanking of HMnS, relative reference values have been formed based on the values of the determined heights and widths. The relative die roll height difference Δh_{PH} indicates the relative reduction between the reference state (Δh = 0%) and the second pre-hardening stage (Δh = 6.1%) of the HMnS and is based on the minimal die roll height difference $\Delta h_{R,min}$ in each case for considering the variation range. The minimal die roll height difference was determined using the standard deviations calculated for the respective worst case (cf. Fig. 7b). The determination of the relative die roll width difference Δb_{PH} regarding the pre-hardening is based on an analogous approach to Δh_{PH}. The evaluation of the HMnS compared to the micro-alloyed fine grain steel is carried out on the basis of the relative die roll height difference Δh_{MF} as well as width difference Δb_{MF}. These reference values indicate the relative difference between the reference state of the HMnS and the HSS S700MC and were determined analogously to the procedure described before. The results of the die roll analysis are shown in Fig. 7b in dependence of the investigated form elements. The pre-hardening of the HMnS results in a reduction of the die roll at all form elements, which rises with increasing relative height reduction Δh. For the HMnS, the second pre-hardening stage results in reductions of about Δh_{PH} ≈ 7 to 11% in terms of the die roll height and about

$\Delta b_{PH} \approx 7$ to 14% in terms of the die roll width. Compared to the HSS S700MC, a larger die roll is formed for the reference state of the HMnS, which is characterized by approx. $\Delta h_{MF} \approx 30$ to 56% higher die roll heights and between $\Delta b_{MF} \approx 50$ to 60% higher die roll widths. For the second pre-hardening stage of HMnS, the relative difference values to S700MC are consequently lower.

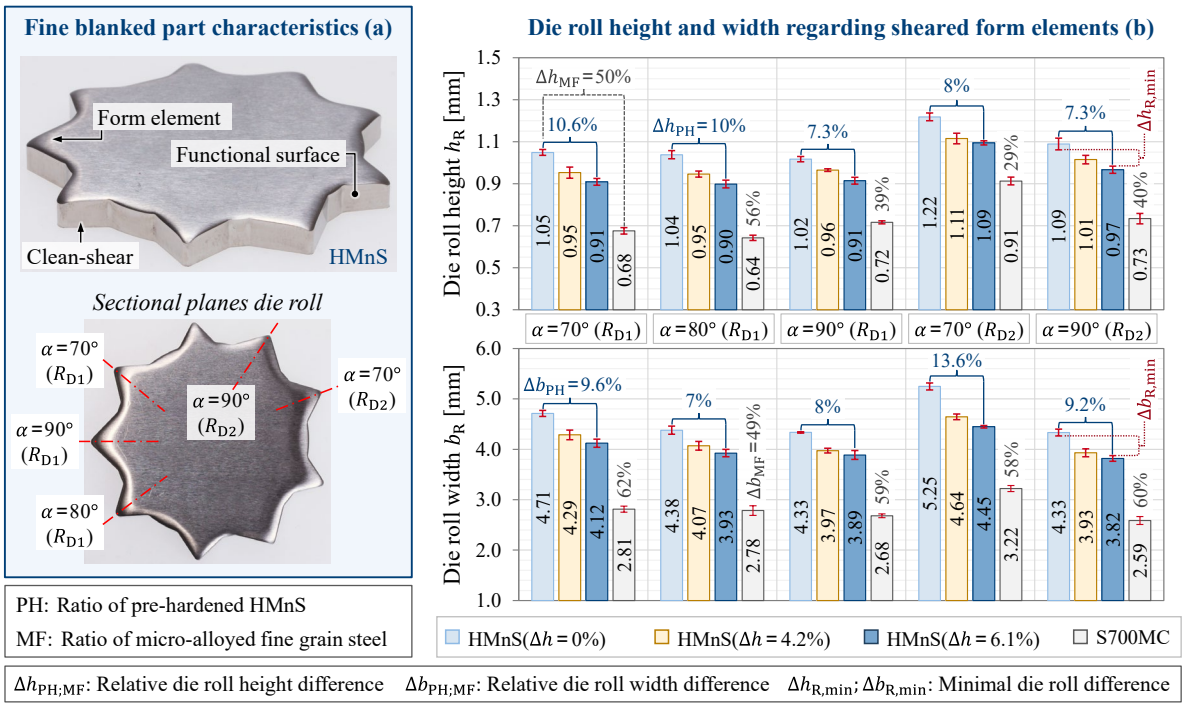

Fig. 7. Characteristics of the investigated fine blanked part (a) and comparison of die roll height width (b).

Regarding the comparison of related relative height reductions Δh of the HMnS, no influence of the tip angle α on the die roll height is observed in terms of the larger tip radius R_{D1} (Fig. 7b). In contrast, a slightly decreasing trend with increasing tip angle is detectable for the die roll width. With respect to the smaller tip radius R_{D2}, the comparison of the relative height reductions for HMnS shows a significant increase in die roll heights and widths with decreasing tip angle. For the S700MC, a comparable behavior to the HMnS is observed for both tip radii with regard to the influence of the tip angle on the die roll height and width.

Discussion and Conclusion on Fine Blanking of Pre-Hardened HMnS

The influence of pre-hardened HMnS X40MnCrAlV19-2 LY on the sheared surface hardening as well as the quality determining attributes during fine blanking was investigated. The process-immanent sheared surface hardening is described in the literature with a positive influence on the wear resistance as well as on the dynamic strengths of tribologically stressed functional surfaces and thus offers the potential to substitute a subsequent heat treatment after fine blanking. The investigated HMnS showed a good formability with high strain hardening during fine blanking, but with regard to the use as lightweight material also exhibits a low yield strength in relation to the tensile strength. In order to increase the strength values, HMnS sheet blanks were pre-hardened by means of flat coining and subsequently fine blanked with an analog geometry representing tribologically stressed functional surfaces (form elements). With almost the same tensile strength compared to the additionally fine blanked HSS S700MC, the hardening properties of HMnS lead to an increase in the maximum blanking force of 6.3% for the reference state and 13.7% for the second pre-hardening stage. Increased blanking forces cause especially at a high difficulty level D increased tool loads during fine blanking due to locally high stresses [24] and require the use of

appropriate tool materials regarding a sufficiently high tool life [13]. Compared to the reference state, the relative height reduction of the second pre-hardening stage (Δh = 6.1%) led to a steeper rise of the blanking force progression as well as to a 6.9% increase of the maximum blanking force. Forming-induced strain hardening generally results in an increase in yield as well as tensile strength due to dislocation accumulation and increased dislocation density [9]. This is reflected in the blanking force progression of the second pre-hardening stage of the HMnS, so that an increase in the strengths as well as in the yield strength ratio $R_{\mathrm{p0.2}}/R_{\mathrm{m}}$ can be assumed. The higher strength was also evident in a 20.7% increase in the bulk hardness for the second pre-hardening stage.
Based on the deformation mechanisms, the high strain hardening capacity of HMnS caused an enormous increase in hardness in the near-surface area ($d_S \leq 0.5$ mm) of the functional surfaces compared with HSS S700MC. Directly below the sheared surface, the hardness values increased with increasing blanking path from 500 HV (top) to 630 HV (bottom). Due to the process characteristics of fine blanking, the high deformation of the sheet material in the area in front of the die edge leads to heat dissipation. Based on results in the literature for shearing with a small die clearance [11], a temperature increase in the range of 170 to 210 °C is to be expected with increasing blanking path for the sheet thickness and blanking velocity investigated in this work. The tensile tests of HMnS showed a reduction of the strain hardening curve with a temperature increase in the quasi-static case and a significant increase in adiabatic heating with increasing true strain in the dynamic case. Regarding the calculated SFE of HMnS, the TWIP effect is assumed to be the dominant deformation mechanism for the high hardness increase of the sheared surface. However, due to the superposition of high true strain and high temperature rise with increasing blanking path, an influence on the strain hardening behavior in the shear zone as a result of reduced twinning cannot be excluded.

In terms of tribologically stressed functional surfaces, a non-uniform hardness distribution due to the hardening increase depending on the blanking path represents a disadvantage. One possibility to compensate for this hardness gradient is a strain hardening of the die roll side by means of a subsequent forming operation after fine blanking [8]. The pre-hardening state as well as the tip angle of the form elements had no influence on the hardness values in the near-surface area at the respective investigated position of the functional surface. An influence of local stresses due to the geometry of convex form elements on the sheared surface hardening is therefore not determinable. Based on the comparison to case and surface hardening, limit values of the achievable work hardening depth have been determined for the HMnS used as well as the process parameters applied, which allows a first evaluation of potential applications. Compared to the large tear-off heights during fine blanking of DP and TRIP steels described in previous studies, the investigated functional surfaces showed a high quality despite pre-hardening of the HMnS. The higher die roll of the form elements in comparison to S700MC is due to the lower yield strength ratio of HMnS [9]. The observed die roll reduction with increasing pre-hardening of the HMnS confirms the results of previous works [26].
The investigation on fine blanking of pre-hardened HMnS has shown that a combination of process-immanent high sheared surface hardening and increased yield strength with simultaneous optimal functional surface quality is achievable. Based on an appropriate adaptation of the heat treatment and the rolling process in semi-finished HMnS production [17], there is thus the potential to realize sufficiently high basic strengths with high sheared surface hardening for the implementation of lightweight design strategies by exploiting the deformation mechanisms during fine blanking. In summary, the following conclusions are to be derived:

1. Forming-induced pre-hardening in combination with fine blanking allows a targeted global or local increase in strength and thus an influence on the sheared part properties. The pre-hardening of the investigated HMnS increased the basic strength and reduced the die roll.

2. The superposition of high deformation and compressive stress in the shear zone enables an activation of the deformation mechanisms during fine blanking of HMnS. Compared to HSS S700MC, the investigated HMnS was characterized by a significantly increased sheared surface hardening due to the TWIP effect.
3. The achieved sheared surface hardness in the near-surface area was neither dependent on the pre-hardening state nor on the geometry of the sheared part. Due to the good formability of the investigated HMnS, the fine blanked functional surfaces showed a high sheared surface quality despite pre-hardening.
4. Semi-finished HMnS production designed for fine blanking offers the potential to realize application-specific sheared part properties in terms of high functional surface hardness, quality and basic strength by exploiting the deformation mechanisms.

Acknowledgement
The Authors would like to thank *thyssenkrupp Hohenlimburg GmbH* for providing the sheet materials investigated and the *Steel Institute IEHK of RWTH Aachen University* for characterizing the high manganese steel as well as supporting the interpretation of the results.

References
[1] K. Salonitis, P. Ball, Energy Efficient Manufacturing from Machine Tools to Manufacturing Systems, Procedia CIRP 7 (2013) 634-639. https://doi.org/10.1016/j.procir.2013.06.045
[2] L. Cabernard, S. Pfister, S. Hellweg, Improved sustainability assessment of the G20's supply chains of materials, fuels, and food, Environ. Res. Lett. 17 (2022) 34027. https://doi.org/10.1088/1748-9326/ac52c7
[3] S. Rosenthal, F. Maaß, M. Kamaliev, M. Hahn, S. Gies, A.E. Tekkaya, Lightweight in Automotive Components by Forming Technology, Automot. Innov. 3 (2020) 195-209. https://doi.org/10.1007/s42154-020-00103-3
[4] M. Kolbe, Stamping Practice, Springer Fachmedien Wiesbaden, Wiesbaden, 2022.
[5] K. Gupta, N.K. Jain, R. Laubscher, Advances in Gear Manufacturing, in: K. Gupta et al. (Eds.), Advanced Gear Manufacturing and Finishing, Elsevier, 2017, pp. 67-125.
[6] W. Volk, J. Stahl, Shear Cutting, in: T.I.A.f. Produ, L. Laperrière, G. Reinhart (Eds.), CIRP Encyclopedia of Production Engineering, Springer, Berlin, Heidelberg, 2015, pp. 1-9.
[7] U. Aravind, U. Chakkingal, P. Venugopal, A Review of Fine Blanking: Influence of Die Design and Process Parameters on Edge Quality, J. Mater. Eng. Perform. 30 (2021) 1-32. https://doi.org/10.1007/s11665-020-05339-y
[8] R.-A. Schmidt, Cold forming and Fineblanking, Carl Hanser Verlag, Munich, 2007.
[9] F. Klocke, Manufacturing Processes 4: Forming, Springer, Berlin, Heidelberg, 2013.
[10] N. Hatanaka, K. Yamaguchi, N. Takakura, Finite element simulation of the shearing mechanism in the blanking of sheet metal, J. Mater. Process. Technol. 139 (2003) 64-70. https://doi.org/10.1016/S0924-0136(03)00183-3
[11] P. Demmel, In-situ Temperaturmessung beim Scherschneiden. Dissertation, Munich, 2014.
[12] H. Hoffmann, Handbuch Umformen, Hanser Verlag, München, 2012.
[13] H. Voigts, T. Bergs, Investigation of Failure Mechanisms of Cemented Carbide Fine Blanking Punches by Means of Process Forces and Acoustic Emission, in: G. Daehn et al. (Eds.), Forming the Future, Springer International Publishing, Cham, 2021, pp. 1173-1187.
[14] S. Walzer, M. Liewald, Novel approach to decrease sheet thinning during sheet metal forming by using embossing technique, Procedia Manuf. 50 (2020) 795-799. https://doi.org/10.1016/j.promfg.2020.08.143
[15] C. Busch, A. Hatscher, M. Otto, S. Huinink, M. Vucetic, C. Bonk, A. Bouguecha, B.-A. Behrens, Properties and Application of High-manganese TWIP-steels in Sheet Metal Forming, Procedia Eng. 81 (2014) 939-944. https://doi.org/10.1016/j.proeng.2014.10.121

[16] B.C. de Cooman, Y. Estrin, S.K. Kim, Twinning-induced plasticity (TWIP) steels, Acta Mater. 142 (2018) 283-362. https://doi.org/10.1016/j.actamat.2017.06.046
[17] S. Wesselmecking, M. Haupt, Y. Ma, W. Song, G. Hirt, W. Bleck, Mechanism-controlled thermomechanical treatment of high manganese steels, Mater. Sci. Eng. A 828 (2021) 142056. https://doi.org/10.1016/j.msea.2021.142056
[18] A.M. Beese, D. Mohr, Effect of stress triaxiality and Lode angle on the kinetics of strain-induced austenite-to-martensite transformation, Acta Mater. 59 (2011) 2589-2600. https://doi.org/10.1016/j.actamat.2010.12.040
[19] S. Sun, A. Zhao, Q. Wu, Effect of strain rate on the work-hardening rate in high-Mn steel, Mater. Sci. Technol. 33 (2017) 1306-1311. https://doi.org/10.1080/02670836.2017.1288690
[20] A. Saeed-Akbari, J. Imlau, U. Prahl, W. Bleck, Derivation and Variation in Composition-Dependent Stacking Fault Energy Maps Based on Subregular Solution Model in High-Manganese Steels, Metall. Mater. Trans. A 40 (2009) 3076-3090. https://doi.org/10.1007/s11661-009-0050-8
[21] S. Thipprakmas, Improving wear resistance of sprocket parts using a fine-blanking process, Wear 271 (2011) 2396-2401. https://doi.org/10.1016/j.wear.2010.12.015
[22] D. Müller, J. Stahl, A. Nürnberger, R. Golle, T. Tobie, W. Volk, K. Stahl, Shear cutting induced residual stresses in involute gears and resulting tooth root bending strength of a fineblanked gear, Arch. Appl. Mech. 91 (2021) 3679-3692. https://doi.org/10.1007/s00419-021-01915-3
[23] P.J. Zhao, Z.H. Chen, C.F. Dong, Experimental and numerical analysis of micromechanical damage for DP600 steel in fine-blanking process, J. Mater. Process. Technol. 236 (2016) 16-25. https://doi.org/10.1016/j.jmatprotec.2016.05.002
[24] M.D. Gram, R.H. Wagoner, Fineblanking of high strength steels: Control of material properties for tool life, J. Mater. Process. Technol. 211 (2011) 717-728. https://doi.org/10.1016/j.jmatprotec.2010.12.005
[25] E. Spišák, J. Majerníková, E. Spišáková, The Influence of Punch-Die Clearance on Blanked Edge Quality in Fine Blanking of Automotive Sheets, MSF 818 (2015) 264-267. https://doi.org/10.4028/www.scientific.net/MSF.818.264
[26] F. Schweinshaupt, T. Herrig, T. Bergs, Investigation of Combined Flat Coining and Fine Blanking of 16MnCr5 to Influence the Die Roll Formation, in: B.-A. Behrens et al. (Eds.), Production at the Leading Edge of Technology, Springer International Publishing, Cham, 2022, pp. 112-121. https://doi.org/10.1007/978-3-030-78424-9_13
[27] W. Bleck, I. Schael, Determination of crash-relevant material parameters by dynamic tensile tests, Steel Res. 71 (2000) 173-178. https://doi.org/10.1002/srin.200005709
[28] W. Bleck, New insights into the properties of high-manganese steel, Int. J. Miner. Metall. Mater. 28 (2021) 782-796. https://doi.org/10.1007/s12613-020-2166-1

Materials Research Proceedings 28 (2023) 2115-2125 https://doi.org/10.21741/9781644902479-226

Modeling and control of tribological properties for subsequent forming process in skin-pass rolling

LI Xinyang[1,a *], SCHULTE Christopher[2,b], ZHU Runyu[1,c *], ABEL Dirk[2,d] and HIRT Gerhard[1,e]

[1]Institute of Metal Forming (IBF), RWTH Aachen University, Intzestraße 10, 52072 Aachen, Germany

[2]Institute of Automatic Control (IRT), RWTH Aachen University, Campus-Boulevard 30, 52074 Aachen, Germany

[a]Xinyang.Li@ibf.rwth-aachen.de, [b]C.Schulte@irt.rwth-aachen.de, [c]rzhu@rwth-aachen.de, [d]D.Abel@irt.rwth-aachen.de, [e]Gerhard.Hirt@ibf.rwth-aachen.de

Keywords: Skin-Pass Rolling, Friction Model, Property-Controlled Forming

Abstract. The surface roughness including average roughness (Ra) and peak number (RPc) after skin-pass rolling influences the strip's product properties, such as its friction coefficient in the subsequent sheet metal forming process. In order to both ensure an optimal tribological behavior and fulfill the process requirements of the following forming steps, predefined roughness combinations of Ra and RPc should be attained in skin-pass rolling. In this work, a preliminary friction model relating friction and combination of Ra and RPc is determined using flat die drawing tests for DC04 steel. The model is validated by deep drawing tests and embedded in a roughness control system for skin-pass rolling. To show a proof of concept for independent control of tribological properties from strip thickness, a simulation framework is implemented in Matlab/Simulink. The results indicate that the friction coefficient can be controlled between 0.0924 and 0.1003 for the considered test scenario (which is) characterized by a normal pressure of 75kN and a relative speed of 10mm/s.

Introduction and State of the Art

In modern industry, skin-pass rolling is used to adjust the strip's surface roughness by imprinting the work rolls' textured surface. Since skin-pass rolling is mostly the last rolling pass after conventional cold rolling, it influences the subsequent processes decisively by controlling the strip's surface quality. In accordance, correlations between the strip's roughness including average roughness (Ra) and peak number (RPc), and its tribological properties, i.e the friction coefficient, have been reported [1]. In sheet metal forming processes like deep drawing, friction is usually required to generate the necessary forming force and control the movement of the sheet within the dies [2]. At the same time, the friction coefficient significantly affects the springback, failure, minimal sheet thickness as well as the deviation of sheet thickness of the workpiece [3,4]. Under defined lubrication and deformation conditions, the sheet formability and cracking tendency also largely depends on the surface finish [5]. Hence, in skin-pass rolling a certain surface roughness shall be achieved in accordance with the subsequent forming condition for optimal tribological behavior to fulfill process requirements and avoid forming defects in the next process.

The friction coefficient primarily depends on the surface roughness, relative speed, normal pressure, and lubrication between the contact surfaces [2]. A common model is given by the Stribeck curve, which relates dynamic viscosity of the lubricants, relative speed, and normal pressure [6]. Three lubrication regimes can be identified from the Stribeck curve: boundary, mixed, and hydrodynamic lubrication, as shown in Fig. 1 (left). In the first two lubrication regimes asperity contact exists while in the third lubrication regime asperity contact can be neglected. Thus, there

Content from this work may be used under the terms of the Creative Commons Attribution 3.0 license. Any further distribution of this work must maintain attribution to the author(s) and the title of the work, journal citation and DOI. Published under license by Materials Research Forum LLC.

is less wear regarding both contact surfaces for high Hersey numbers. It can also be observed that the friction coefficient is relatively higher in boundary lubrication and the initial stage of mixed lubrication. Noteworthy, there is no clear boundary of the three lubrication regimes. Since in sheet metal forming the friction is required and avoiding the wear between sheet and tool is not the primary objective, only friction with limited amount of lubricant, i.e. boundary and mixed lubrication, is considered in this work.

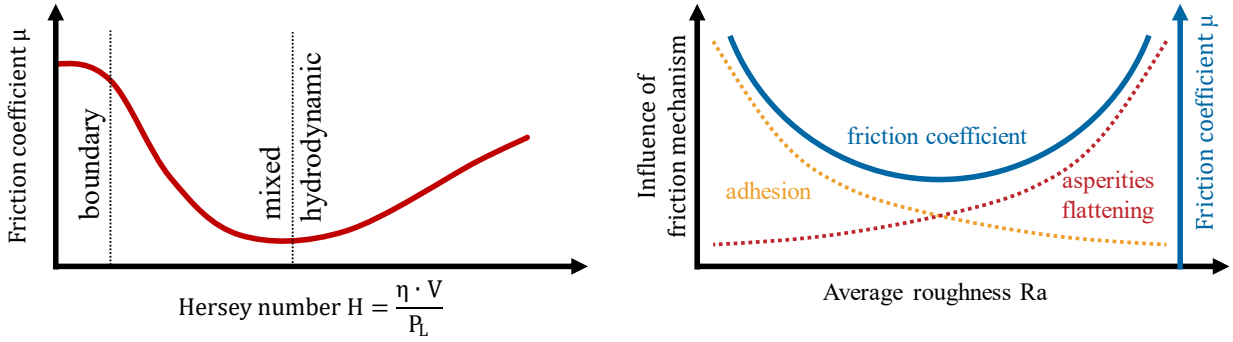

Fig. 1. Stribeck curve with the lubricant's dynamic viscosity η, relative speed V, and normal load per length PL (left); two mechanisms of influence of Ra on friction coefficient (right) [7] .

According to Stribeck curve the friction coefficient μ increases with lower relative speeds, higher normal pressures, and lower lubricant's viscosity in regions of boundary and mixed lubrication. However, some works [7,8] also show that a higher normal pressure causes lower friction in some pressure ranges and processes. The influence of surface roughness on friction has also been extensively studied in recent decades. Emmens et al. utilized flat die drawing tests and rotation friction tests to study the effect of surface roughness on friction for a deep drawing process with steel and aluminum [1,9]. Stribeck curves of specimens were determined for a surface roughness range from 0.1 µm to 3.08 µm. The result for steel indicates that a higher surface roughness regarding the maximal peak height (Rpm) causes a higher friction coefficient [1]. Here, the parameter Rpm is proportionally related to Ra. For aluminum the surface roughness shows a different influence on friction depending on the applied normal pressure. In case of lower normal pressure, the surface roughness has the same influence as for steel: higher Ra leads to a higher friction coefficient. However, when applying higher normal pressures, the friction coefficient drops slightly at first and then rises with a increasing Ra [9]. In another study, Zhou et al. investigated the influence of surface roughness on the friction coefficient by using a tribometer with a tool which moves reciprocally on the steel specimen surface[10]. The reciprocating frequencies were 2 Hz, 4 Hz, and 6 Hz and the specimen surface roughness (Ra) varied from 0.02 µm to 0.5 mm. The result reveals that below a testing frequency of 2 Hz a higher surface roughness causes a higher friction coefficient. For higher testing frequencies (4 and 6 Hz) the friction coefficient decreases at first and then increases again with increasing surface roughness. This non-linear behavior of the influence of roughness on friction coefficient (first decreasing and then increasing) is also observed by Lee [11] in flat die drawing tests and by Wihlborg [12] in bending under tension tests. This phenomenon can be explained as the interaction of two mechanisms, i.e., the adhesion between contacting asperities and the flattening of asperities, cf. Fig. 1 (right) [7]. With relatively lower surface roughness, the adhesion effect dominates while increasing roughness reduces the real area of contact and offers more lubricant pockets, therefore, friction coefficient decreases. With relatively higher surface roughness, the flattening effect dominates and asperities tend to be flattened by the normal load during the contact, which introduces more resistance for slide, and thus results in higher friction coefficient [7,13]. Because the decoupling of Ra and RPc is difficult in most roughening processes such as normal skin-pass

rolling, shot-blast texturing (SBT), or electric discharged texturing (EDT), there is only limited amount of works focusing on the influence of RPc on friction coefficient. In fact, both positive and negative correlations between RPc and the friction coefficient can be observed under different test conditions [14,15]. According to the aforementioned works, the effect of surface roughness on friction depends on test types, and multitude of different processes and lubrication conditions in different ranges of roughness. Due to this complexity, the type of friction test and its condition should be chosen carefully in accordance with the considered forming process.

In order to produce strips with a defined surface roughness in skin-pass rolling, the surface roughness of work rolls or the transfer ratio during imprinting should be adjusted. Because of the time and cost inefficiency of producing and changing rolls with different surface roughness, frequent change of work rolls should be avoided. Therefore, the adjustment of strip's surface roughness is usually achieved by changing the roughness transfer ratio, which is influenced by several process parameters. Kijima et al. [16,17] found that the peak pressure within the roll gap and work roll radius influence the roughness transfer ratio: Higher rolling forces lead to better roughness transfer as the peak pressure in the roll gap is higher, and a greater roll radius is favorable for roughness transfer due to higher peak pressure. The work of Çolak et al. [18] shows that in dry and lubricated condition higher rolling speeds and higher thickness reductions increase the rolling force and thus the transfer ratio. Furthermore, according to industrial practice lower strip tension in skin-pass rolling causes higher imprinting [19]. This effect was also investigated in preliminary work by Li et al. [20] and validated using multi-scale finite element (FE) simulations. Along with a higher thickness reduction, decreased strip tension causes higher average roll pressure and consequently increases the transfer ratio. The potential of changing the strip's surface roughness by varying strip tension was indicated in this work as well. The aforementioned process parameters, especially thickness reduction and strip tension, can be employed during skin-pass rolling for controlling the transfer ratio and adjusting the product's surface roughness, thus enabling automatic control.

Conventionally, a tandem rolling mill is used to control strip roughness during skin-pass rolling. It uses an allocation of the total height reduction between the two rolling stands to independently control the strip roughness from the strip thickness. Li et al. [21] used a tandem rolling mill together with a heuristic model to control the resulting strip roughness. The heuristic model employed here describes the correlation between the tactile measurement of the strip roughness with the process force, roll roughness, and roll radius. Overall, a roughness of (0.42 ± 0.05) µm could be ensured for 65 % of the material, in contrast to 15% in the uncontrolled case. The heuristic model of Bozhkov et al. [22] predicts the resulting strip roughness based on the average contact stress, roll radius and material strength. Here, experimental validation demonstrated that there was an average deviation between measured and predicted strip roughness of 7% with varying strip roughnesses between 1 µm and 2.5 µm over 170 km of strip.

Utilizing the strip tension to manipulate the imprinting represents an alternative method, first validated in [23]. The independent control of strip roughness and strip thickness with the use of strip tension has the advantage that no additional height reduction is necessary. However, it has the disadvantage that strip tensions of up to 40 % of the material yield strength are necessary to obtain a sufficiently large process window [23]. In preliminary work, the strip tension could be used together with the manipulation of the roll gap to vary the roughness of the strip by 0.3 µm with a height reduction of 5% and an initial strip thickness of 1 mm. However, due to the high measurement noise of the roughness measurement and the insufficiently high strip tension, this should only be considered as a proof-of-concept [23].

So far there is no publication on the process control of skin-pass rolling with regard to the strip's friction coefficient. As a preliminary trial, the task of this work is at first the determination of the friction coefficient of steel specimens with different surface roughness under test conditions, which

resemble a subsequent deep drawing process. The result is utilized to model the influence of Ra and RPc on the friction coefficient. The second task is including this friction model into a control system for skin-pass rolling with roughness control to ensure production of strips with desired tribological properties that meet the requirements of the subsequent forming process. A Matlab simulation framework is implemented based on process models validated in previous work. In particular, a model for predicting the rolling force according to Bland & Ford (1948) [24], a function for modeling the progressive roll stand deflection [25], and a heuristic function describing the imprinting of the rough work rolls are used [23]. Moreover, using the strip tension and tandem rolling as actuators, the two aforementioned concepts for roughness control in skin-pass rolling are combined in order to obtain the largest possible variation range of roughness and friction coefficient. A typical rolling test is presented in which the desired tribological property is varied while keeping a constant strip geometry.

Materials and Flat Die Drawing Test

In this study two steels, DC01 and DC04 are used. DC04 is primarily considered in the friction model and the considered deep drawing process. However, our DC04 strip is too narrow for the flat die drawing machine, and the amount of the wider DC04 plates we have is limited. Due to this geometric restriction, a similar material, DC01 is applied in friction tests. The result is compared to some additional friction tests with DC04 plate specimens to ensure the substitutability of DC01 for DC04 results.

The surface of test strips is treated by SBT to create different surface roughness. Roller leveling is used afterwards to ensure the flatness of specimens. The surface roughness Ra and RPc were measured using a mobile roughness measuring tool MarSurf PS1 by Mahr GmbH in accordance with DIN 4287. The Ra and RPc of the specimens are listed in Table 1. Note that #1 is not treated by SBT and as a result, shows both the lowest Ra and RPc values while in other specimens (#2 to #5) RPc decreases with a higher Ra.

Table 1. Specimens and parameters used in flat die drawing test.

Specimen	Material	Geometry [mm^3]	Ra [µm]	RPc [1/cm]	Normal pressure P [MPa]	Drawing speed V [mm/s]
#1	DC01	1*10*1000	1.02	66	10, 25, 50, 75	10
#2			1.55	171		
#3			2.14	146		
#4			2.96	125		
#5			3.46	105		5, 10, 50
#1-V	DC04	1*32*1000	1.04	72	50	10
#3-V			2.03	152		

As illustrated in Fig. 2, the friction parameter is determined using flat die drawing test with Tribometer 5000 by Raziol Zibulla & Sohn GmbH. The tool with a size of 200mm2 is made of steel 1.2379 with hardness of HRC 63. The DC01 specimens are tested with normal pressures of 10MPa, 25MPa, 50MPa, and 75MPa with a drawing speed of 10 mm/s to determine the influence of Ra, RPc, and normal pressure, see Table 1. For specimen #5 extra tests with varied drawing speeds of 5mm/s and 50mm/s are conducted to investigate according correlations. The tests with DC04 specimens (#1-V and #3-V) with a normal pressure of 50MPa and a drawing speed of 10mm/s are used as a comparison to the respective tests with DC01 (#1 and #3) to ensure that the result of DC01 can be generalized for DC04. The lubricant WISURA LS 710 by Fuchs Lubricants

Germany GmbH is applied while the lubrication condition for all tests in this work is controlled using a laboratory lubrication system by Raziol Zibulla & Sohn GmbH with a nozzle opening value of 35, nozzle height of 35mm, and oil pressure of 3 bar. Every test is repeated 4 times with fresh specimen. The results are then averaged for the subsequent analysis.

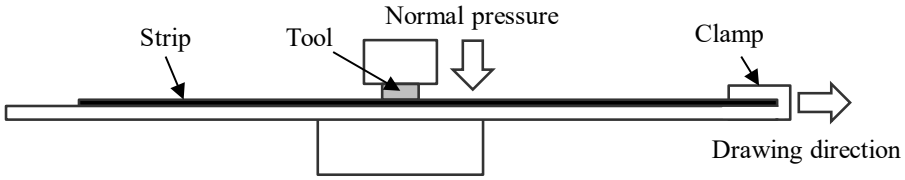

Fig. 2. Flat die drawing test.

The result of flat die drawing test for DC01 is depicted in Fig. 3. The influence of normal pressure P can be observed in Fig. 3 (left): Under this test condition a higher normal pressure causes a lower friction coefficient, which is also noticed in other works [7,8]. Because of the totally different Ra and RPc combinations of specimens the influences of Ra and RPc on friction coefficient are difficult to separate from each other, see Fig. 3 (middle, right). However, it can still be noticed that a descending tendency exists with higher Ra and lower RPc, if #1 is neglected due to the irregularity of its Ra and RPc combination. This influence of Ra can be explained with the domination of the adhesion mechanism: higher Ra decreases the real contact area, and thus, the friction coefficient [7,13]. Moreover, higher RPc results in narrower peaks and valleys on the contact surface, which then deforms easier due to the flattening effect [7]. Accordingly, the real contact area increases, the volume of lubricant pockets decreases and consequently higher friction coefficients result. It is also visible that the effect of Ra and RPc is more obvious with higher normal pressures: The maximal difference of friction coefficient at a normal pressure of 10 MPa is 0.0106, while the maximal difference of friction coefficient with a normal pressure of 75 MPa is 0.0231. This result of flat die drawing test is also plotted in 3D space, see Fig. 4 (left). Here, the different combinations of Ra and RPc of the specimens can be clearly identified.

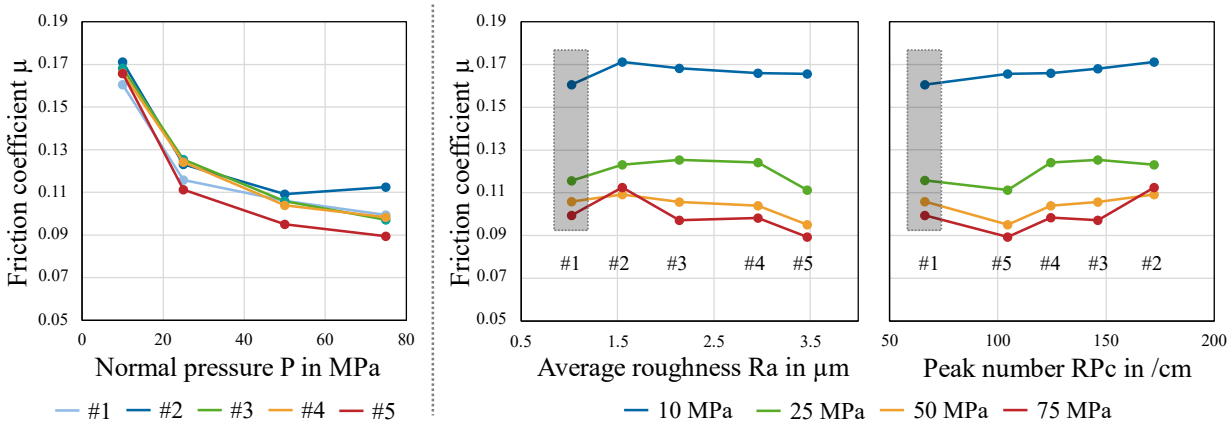

Fig. 3. Results of flat die drawing tests for DC01. The evolution of friction coefficient is illustrated over normal pressure P (left), average roughness Ra (middle), and peak number RPc (right).

Drawing speed is varied for test series #5 while a normal pressure of 50 MPa is applied. Fig. 4 (right) shows the minor influence of the drawing speed on friction under this test condition: Higher relative speeds lead to slightly lower friction coefficients, which is also observed in the Stribeck curve.

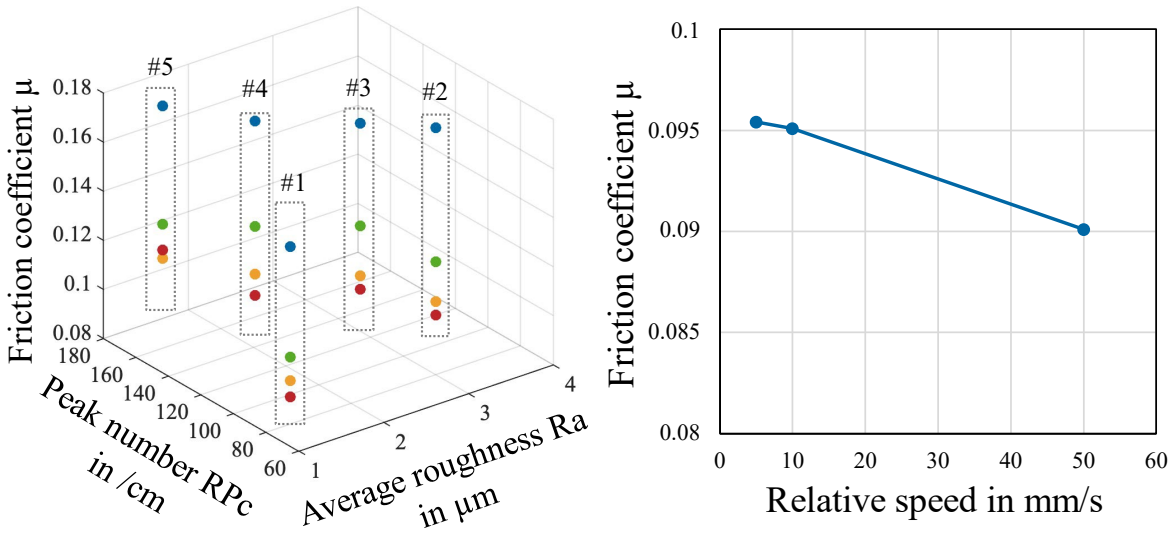

Fig. 4. Result of flat die drawing test for DC01 in 3D space (left); Influence of relative speed on friction coefficient (right).

Comparing the friction coefficients derived for DC04 and DC01, only small deviations are apparent, see Table 2. This result can also be supported by the similarity of the two steels' chemical compositions and mechanical properties. Therefore, the results obtained for DC01 can also be generalized for DC04, given the same test conditions.

Table 2. Comparison of the results of DC04 and DC01.

Specimen	Normal pressure P [MPa]	Drawing speed V [mm/s]	Friction coefficient μ[-]		Deviation [%]
			DC04	DC01	
#1-V (DC04) and #1 (DC01)	50	10	0.1058	0.1060	- 0.19
#3-V (DC04) and #3 (DC01)			0.1067	0.1057	0.95

Modeling of the Friction Coefficient

Based on the results of the flat strip drawing tests, a preliminary friction model considering the influence of normal pressure P, average roughness Ra, peak number RPc, and relative speed V is fitted using flat surfaces for different normal stresses, as shown in Fig. 5 (left). Accordingly, the friction coefficient μ is calculated as:

$$\mu = f(\mathrm{Ra}, \mathrm{RPc}, \mathrm{P}, \mathrm{V}) = (\mathrm{a} + \mathrm{b} * \mathrm{Ra} + \mathrm{c} * \mathrm{RPc}) * \mathrm{d} \quad (1)$$

where [b]= /µm and [c]=cm, and a and d are dimensionless. These fitting parameters a, b, c, and d mapping the normal pressure, Ra, RPc, and relative speed respectively. These fitting parameters are given by:

$$a = 1.987 * P^{-1.549} + 0.09679 \quad (2)$$

$$b = -0.0003376 * P^{0.763} + 0.001973 \quad (3)$$

$$c = 4.426 * 10^{-5} * P^3 - 5.358 * 10^{-8} * P^2 + 1.751 * 10^{-6} * P + 9.141 * 10^{-5} \quad (4)$$

$$d = 1 - 0.001038 * (V - 10) \quad (5)$$

with [Ra]= µm, [RPc]=/cm, [P]=MPa and [V]=mm/s. As extrapolation strategy, parameters b and c are fixed if the normal pressure is outside the measured data, i.e., lower than 10MPa and higher than 75MPa.

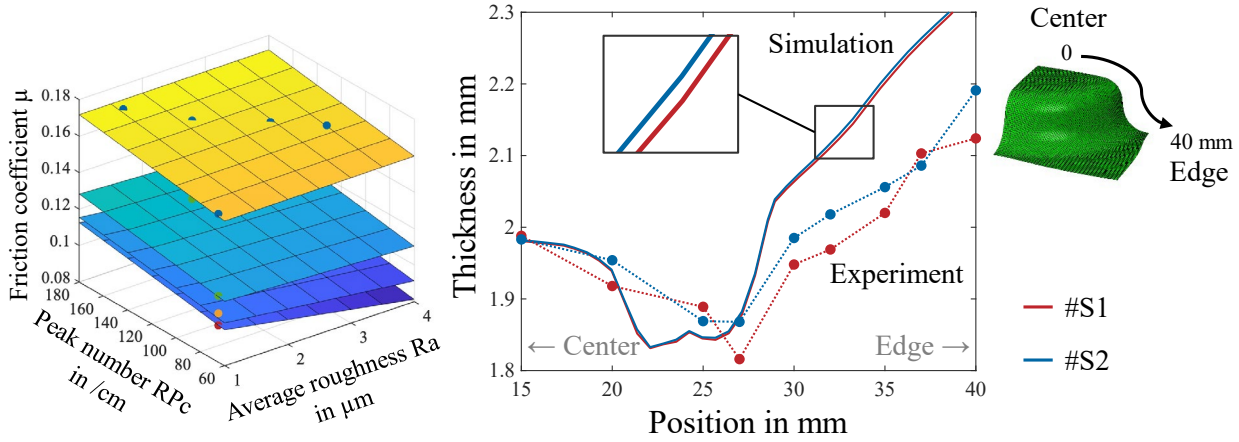

Fig. 5. Fitted friction model (left); Validation of the friction model (right).

With a maximal deviation of -5.77% the friction model shows a good agreement with the measured data and is sufficient to describe the friction behavior under the given conditions, see Table 3.

Table 3. Deviation of the fitted model from the measured data recorded at V = 10 mm/s.

Specimen	Deviation [%]			
	10 MPa	25 MPa	50 MPa	75 MPa
#1	-0.36	0.14	-5.43	-5.77
#2	0.04	2.68	2.99	3.62
#3	0.16	2.02	1.66	4.92
#4	1.57	4.13	1.86	3.78
#5	0.82	4.24	3.00	0.11

The friction model is also implemented in FE simulations using the user-subroutine FRIC_COEF with continuum shell elements in Abaqus/Standard 6.14. The results are validated with deep drawing (cupping) tests with tool speed of 5 mm/s, blankholder force of 60 kN, drawing depth of 15 mm, and punch diameter of 50 mm. As shown in Table 4 two DC04 plates with different surfaces are employed for validation. The corresponding experiment is conducted on a deep drawing press by Lauffer GmbH. After the experiment the thickness along the center line is measured using a thickness gauge by Mitutoyo with a precision of 0.01mm.

These measured thickness profiles are compared with the ones obtained from the simulation and presented in Fig. 5 (right). The results of simulation and experiment show the same tendency: from center to edge the thickness reduces at first, which is induced by large deformation in radial direction near the cup corner. Then the thickness increases significantly, which is caused by tangential material flow on the side and flange. On the edge of the specimens, the thickness of #S2 is higher than the thickness of #S1 due to the different initial surface roughnesses, which can also be observed in the simulation. The maximum relative deviations of #S1 and #S2 between simulation and experiment are 8.61% and 8.54%, respectively. This is due to the flattening of surface asperities on the edge, which is visible after the deep drawing experiments (see Fig. 6 left) and is not considered in the friction model. Another reason of this deviation is that the maximal normal stress in this deep drawing process is notably higher than for the flat die drawing tests.

Especially near the cup corner high normal stress is observed and it can cause poor extrapolation, cf. Fig. 6 (right). Moreover, the substitutability of the results of DC04 and DC01 can also be affected by the high normal stress. In addition, measurement errors stemming from the thickness gauge should also be considered.

Table 4. Specimens for deep drawing tests with their initial roughness.

Specimen	Material	Geometry [mm^3]	Ra [µm]	RPc [/cm]
#S1	DC04	2*80*80	2.92	130
#S2			4.44	99

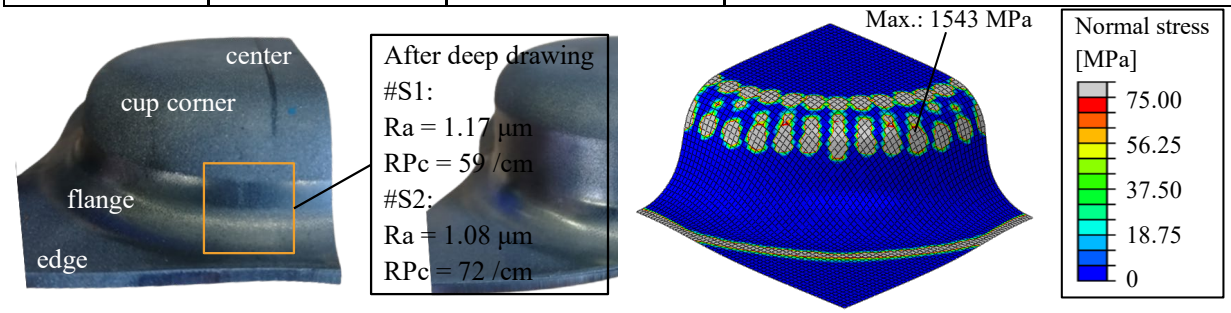

Fig. 6. Flattening of surface asperities after experiments (left); normal stress distribution in deep drawing (right).

Automatic Control of the Friction Coefficient

To show a proof of concept for independent control of tribological properties and strip thickness, a simulation framework is implemented in Matlab/Simulink. A tandem rolling mill with a quarto rolling stand with flat work rolls and a duo rolling stand with EDT work rolls with a Ra of 3 µm and RPc of 78 1/cm are modeled. In order to enlarge the process window, the control system is combining the roll gap actuation of a tandem rolling mill with the strip tension in the incoming and outgoing strip t_0 and t_2, respectively. The strip tension between the stands t_1 is kept constant in order to avoid cross-coupling of the two roll gaps. In order to keep the number of manipulated variables small, the strip tension at the entrance was set equal to the strip tension at the exit. This simplification had no negative impact on the possible process window of the control, since both actuators share a positive correlation with the friction coefficient.

The presented friction model as well as a cold rolling, roll stand deflection and imprinting model from prior work are embedded into the model-based optimal control system with a sampling time of 5 ms and a rolling speed of 100 m/s. The material under consideration is DC04 steel and a rolling speed of 50 m/min is selected, so that actuator speeds are well within in their respective admissible sets. Lubrication is neglected and the simulated process variables are superimposed by process and measurement noise according to a real tandem rolling mill from Bühler Redex GmbH with modified measurement setup [26]. The strip tension can be varied in the simulation between 150 N and 3000 N.

The simulative results are presented in Fig. 7. The actuator values are shown in the two lower diagrams. The roll gap heights of the two roll stands are shown at the bottom left and the strip tensions are shown at the bottom right. The diagram at the top left shows the initial strip thickness h_0, the strip thickness between the two roll stands h_1 and the strip thickness at the exit h_2 along its reference $h_{2,des}$. It can be seen that the outgoing strip thickness tracks the constant reference of 0.93 mm with minimal error (root mean squared error of 1.1 µm), despite of incoming strip thicknesses h_0 of (1 ± 0.008) mm, which reflects actual material tolerances present in DC04 steel. The measured and desired friction coefficient µ are shown in the diagram at the top right. Reference values between 0.093 and 0.101 are specified in 0.001 steps. The controller attains the

desired friction coefficients μ with exception of coefficients over 0.1 which prove infeasible due to the constraints on the strip tension and the minimal contact requirement of the second roll stand.

The feasible process window (friction coefficient as a function of the selected strip thickness h_2) for an exemplary sheet metal forming process with a normal pressure of 75kN, relative speed of 10 mm/s, and controlled lubrication condition is shown in Fig.8. Here, the maximum and minimum adjustable friction coefficient are shown as two enveloping lines. By increasing the total height reduction, the maximum of the friction coefficient can be significantly increased. For a height reduction of 7%, a friction coefficient between 0.0924 and 0.1003 can be set in the demonstrated process, which corresponds to a variation of 8.6%. Extending the actuators' working range would also increase the feasible process window.

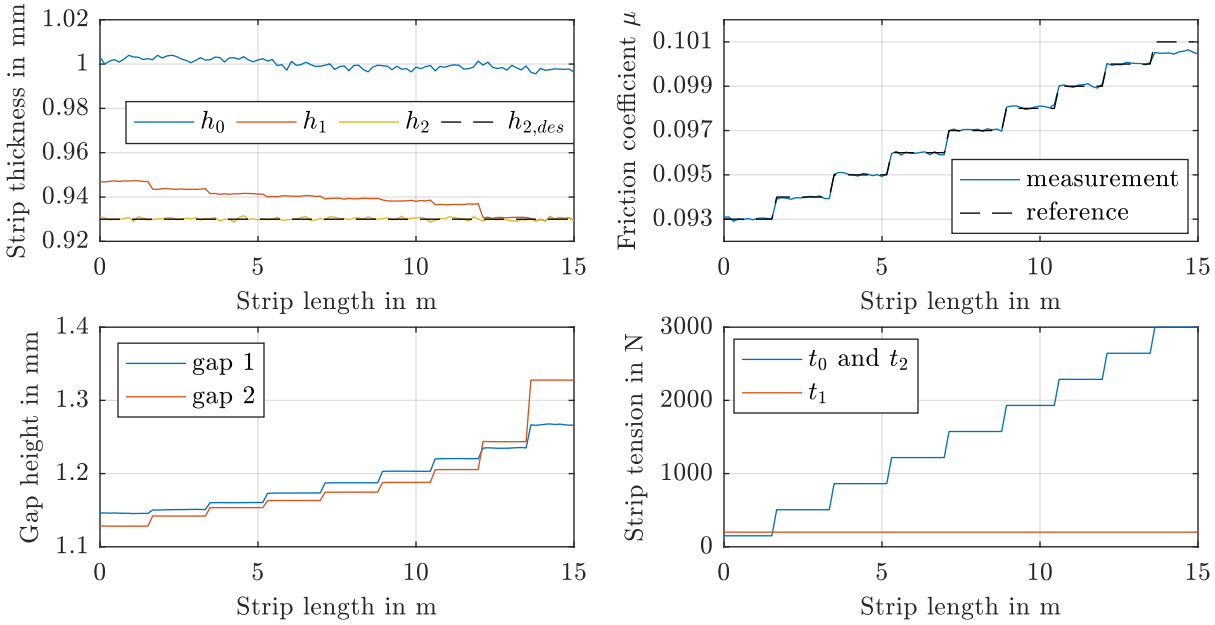

Fig. 7. Simulative results of independent control of strip thickness and friction coefficient μ.

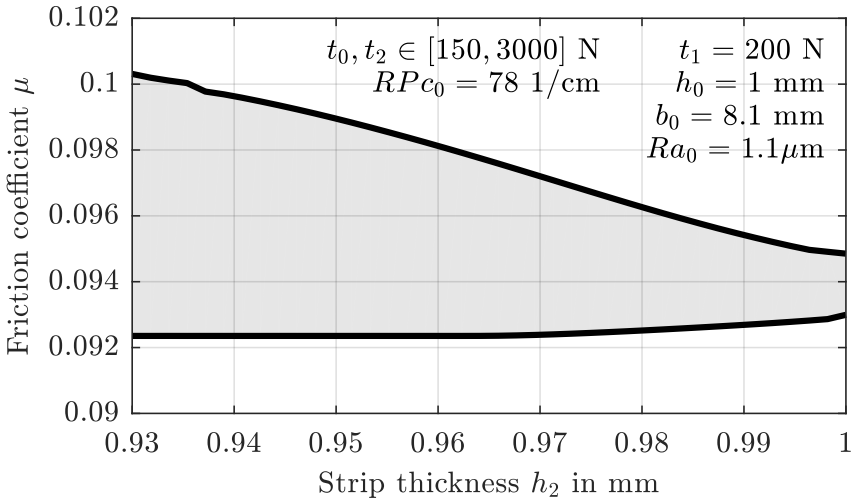

Fig. 8. Simulative evaluation of the realizable process window for DC04.

Summary

In this work, the influence of Ra and RPc on the friction coefficient of the considered deep drawing process is investigated in experiments and simulations. The results show that a higher Ra and lower RPc decrease the friction coefficient under the given conditions. Based on this result a preliminary friction model considering the influence of Ra, RPc, normal pressure, and relative speed is proposed. The model is validated qualitatively using deep drawing tests.

The friction model is embedded into a simulated control system for skin-pass rolling. The simulations suggest that the system is capable to control the surface roughness to optimize the tribological property of friction for the subsequent forming process while decoupling a predefined strip geometry

In future work, a more precise friction model should be determined by obtaining more measured data with higher normal stress and considering the asperity flattening during sheet metal forming. In addition, a validation of the simulation results should be performed to evaluate the transferability of the friction model derived from SBT surfaces to skin-pass rolling surfaces. Furthermore, the required roll surface per roll stand that extends the process window of control could be investigated, particularly with regard to the peak number.

References

[1] W. Emmens, The influence of surface roughness on friction, in: Proceedings of the 15th Congress of International Deep Drawing Research Group (IDDRG), 1988; pp. 63-70.

[2] W.C. Emmens, Tribology of flat contacts and its application in deep drawing, PhD Thesis, University of Twente, Enschede, 1997.

[3] I. Gil, J. Mendiguren, L. Galdos, E. Mugarra, E.S. de Argandoña, Influence of the pressure dependent coefficient of friction on deep drawing springback predictions, Tribol. Int. 103 (2016) 266-273. https://doi.org/10.1016/j.triboint.2016.07.004

[4] B. Wang, L. Fu, J. Zhou, M. Huang, Effect of friction coefficient in deep drawing of AA6111 sheet at elevated temperatures, Trans. Nonferrous Metal. Soc. China 25 (2015) 2342-2351. http://doi.org/10.1016/S1003-6326(15)63849-3

[5] J. Staeves, Beurteilung der Topografie von Blechen im Hinblick auf die Reibung bei der Umformung, Shaker Aachen, Germany: 1998.

[6] Q.J. Wang, Y.-W. Chung, Encyclopedia of tribology; Springer, 2013.

[7] T. Trzepieciński, R. Fejkiel, On the influence of deformation of deep drawing quality steel sheet on surface topography and friction, Tribol. Int. 115 (2017) 78-88. https://doi.org/10.1016/j.triboint.2017.05.007

[8] A. Azushima, K. Igarashi, K. Imai, Proposal of a new simulation method by means of tribometer controlled by computer for sheet metal forming and evaluation of tribological properties of lubricant for aluminum alloy sheet--tribology in sheet metal forming, II. J. Japan Soc. Technol. Plast. (Japan) 38 (1997) 73-78.

[9] W.C. Emmens, J. Bottema, Friction of aluminium in deep drawing, in: Proceedings of the IDDRG Congress, 1998, 52.

[10] Y. Zhou, H. Zhu, W. Zhang, X. Zuo, Y. Li, J. Yang, Influence of surface roughness on the friction property of textured surface, Adv. Mech. Eng. (2015) 7. https://doi.org/10.1177/1687814014568500

[11] B. Lee, Y. Keum, R. Wagoner, Modeling of the friction caused by lubrication and surface roughness in sheet metal forming, J. Mater. Process. Technol. 130 (2002) 60-63. https://doi.org/10.1016/S0924-0136(02)00784-7

[12] A. Wihlborg, L. Gunnarsson, A frictional study of uncoated EBT steel sheets in a bending under tension friction test, Wear 237 (2000) 129-136. https://doi.org/10.1016/S0043-1648(99)00319-1
[13] J. Hol, V.T. Meinders, M.B. de Rooij, A.H. van den Boogaard, Multi-scale friction modeling for sheet metal forming: The boundary lubrication regime, Tribol. Int. 81 (2015) 112-128. http://doi.org/10.1016/j.triboint.2014.07.015
[14] R. Calvo, R. D'Amato, E. Gómez, A. Ruggiero, Experimental analysis of the surface roughness in the coefficient of friction test, Procedia Manuf. 41 (2019) 153-160. https://doi.org/10.1016/j.promfg.2019.07.041
[15] B. Maas, M. Bretschneider, T. Routschek, M. Radszat, B. Hildebrandt, Range and Varieties of a single Surface Structure Technology for Sheet Steel–within and beyond the standard Roughness and Peak Count Values, in: Proceedings of the International Conference on Steels in Cars and Trucks, Braunschweig, 2014.
[16] H. Kijima, Influence of roll radius on contact condition and material deformation in skin-pass rolling of steel strip, J. Mater. Process. Technol. 213 (2013) 1764-1771. http://doi.org/10.1016/j.jmatprotec.2013.04.011
[17] H. Kijima, Influence of roll radius on roughness transfer in skin-pass rolling of steel strip, J. Mater. Process. Technol. 214 (2014) 1111-1119. http://doi.org/10.1016/j.jmatprotec.2013.12.019
[18] B. Çolak, N. Kurgan, An experimental investigation into roughness transfer in skin-pass rolling of steel strips, Int. J. Adv. Manuf. Technol. 96 (2018) 3321-3330. https://doi.org/10.1007/s00170-018-1691-9
[19] O. Wiklund, F. Sandberg, J. Lenard, Modelling and control of temper rolling and skin pass rolling, Metal Forming Science and Practice (2002) 313-343.
[20] X. Li, C. Schulte, D. Abel, M. Teller, G. Hirt, J. Lohmar, Modeling and exploiting the strip tension influence on surface imprinting during temper rolling of cold-rolled steel, Adv. Industr. Manuf. Eng. 3 (2021) 100045. https://doi.org/10.1016/j.aime.2021.100045
[21] R. Li, Q. Zhang, X. Zhang, M. Yu, B. Wang, Control method for steel strip roughness in two-stand temper mill rolling, Chinese J. Mech. Eng. 28 (2015) 573-579. https://doi.org/10.3901/CJME.2015.0310.027
[22] A. Bozhkov, D. Kovalev, M. Orekhov, S. Degtev, V. Chereshnev, Controlling the surface roughness of cold-rolled strip. Part 1, Steel in Translation 47 (2017) 691-694. https://doi.org/10.3103/S0967091217100023
[23] C. Schulte, X. Li, D. Abel, G. Hirt, Model-based Control of the Strip Roughness in Cold Rolling, IFAC-PapersOnLine 54 (2021) 109-114. Model-based Control of the Strip Roughness in Cold Rolling, IFAC-PapersOnLine 54 (2021) 109-114
[24] D. Bland, H. Ford, The calculation of roll force and torque in cold strip rolling with tensions, Proceedings of the Institution of Mechanical Engineers 159 (1948) 144-163.
[25] C. Schulte, X. Li, D. Abel, G. Hirt, High Precision Thickness Control in a Cold Rolling Mill using a Non-Linear Roll Stand Deflection Model, in: Proceedings of the 2021 European Control Conference (ECC), 2021, 1907-1912.
[26] S. Stockert, M. Wehr, J. Lohmar, G. Hirt, D. Abel, Improving the thickness accuracy of cold rolled narrow strip by piezoelectric roll gap control at high rolling speed, CIRP Annals 67 (2018) 313-316. https://doi.org/10.1016/j.cirp.2018.04.107

Keyword Index

3D Anisotropic Plasticity 1203
3D Printing 49,207,1719,1809,1987
3D Scanning 523
6016-T4 1491
6082 Al Alloy 1015
6XXX 477
7075 Aluminum Alloy 419
7075 787

AA6016 705
Abdominal Wall Hernia Repair 277
Additive Manufacturing (AM) 13,41,85, 169,179,207,339,111,119, 199,919, 969,1235,1255,132311861, 1939
Adhesion 139
Adiabatic Heating 675
Age Hardening 1015
Air Bending 695
AISI 4140 1029
Al/GNP Composites 455
ALE Approach 543
AlSi7Mg 75
Aluminium 6060 825
Aluminium Alloy 189,487,477, 847,855,997,1997
Aluminium 445,455,515,787, 9591091,1957,1977
Aluminum Extrusion 437,467
Aluminum-Matrix Composites (AMCs) 199
Analysis of Variance (ANOVA) 1369
Analytical Model 657
Anisotropic Magnets 505
Anisotropic Material 1387
Anisotropic Plasticity 1131
Annular Flow 1917
Arcan Test 1131
Artificial Intelligence 1265
Artificial Neural Network 385,1067
ASP 2030 1235
Asymmetric Rolling 847
Automated Fiber Placement 1897
Automated Layup 367
Automotive 891

Back-End Defect 543
Barkhausen Noise 2091
Bead Geometry 119
Benchmark 1491
Bend Shape 695
Bending 1683
Biaxial NCF 285
Biaxial Stress 779
Biaxial Tensile Test Simulation 1463
Biaxial Tube Expansion Test 779
Biax-NCF 331
Biocomposite 1809,1879
Biodegradable Polymers 2015
Biomechanics 1341
Biopolymers 169
Bipolar Plates 1531
Buckles 375
Bulge Test 855
Burnishing 31,1223,1341
Butterfly Specimen 737

CAE Methods 943
Calibration Procedure 159
Calibration 1397
Carbon Coated Tool 1775
Carbon Fiber Composites 1799
Carbon Fiber 293,1789,1861
Carbon Nanotube 111,1789
Carbon-Supersaturation 869

Casting Modulus 1175
CBS 239
Cemented Carbide 1213,1765
Ceramic Foams 1331
Cermet 129
CFRP 347
CFRPs 1683
Chevron Cracking 445
Chip Formation 1235
Chip Morphology 1285
Chips 1977
Circular Economy 1947
Clamped Surfaces 761
Classification 1265
Clinching 1059
Closed-Loop Control 2037,2091
Closed-Loop Property Control 2049
CMSG Theory 1453
Coarse Meshing 1583
Coating 583
Cocuring 305
Coefficient of Friction 1765
Cogging 621
Cohesive Zone Modelling 1443
Cohesive Zones 717
Cold Forging 495,929,2027
Cold Spray 49,305
Cold-Drawing 429
Compaction Behaviour 259
Composite Forming 293,385
Composite Material 85,399,407
Composites 57,219,455,1729,
1789,1819,1841,1861
Composites Materials 313
Compressibility 1689
Compression Molding 249,1871
Compression Test 1997
Computational Fluid Dynamics 1541
Computational Homogenization 1621
Consolidation Processes 85
Constitutive Model Calibration 1193
Constitutive Model 357,1143,1387
Constrained Friction Processing 1739
Constrained Optimization 1143
Contact Heating 959
Contact Length 1347
Contact Zone 657
Contamination 879
Continuous Reinforced Fiber 85
Contour of Plastic Work 779
Control Strategy 2049
Cooling Bed 1611
Cooling Channels 533
Copper Extrusion 523
CP800 737
Crack Formation 611
Crack Prevention 1059
Cracks 629
Critical Neck Thickness 1059
Cross Law 1917
Cross-Loading 747
Cruciform Sample 1463
Crush Core Forming 399
Cryo Forming 2037
Cryogenic Cooling 1357
Cryogenic Machining 1285
Crystal Plasticity Model 1417
Crystal Plasticity 179,553,1443,1471
Crystallization 139
Crystallographic Texture 799
Cutting Force 1295,1313
Cutting Tool 1265
Cyclic Simulation 2027

Damage Reduction 611
Damage 727,787,1435

Damping 1851
Deconsolidation 85
Deep Drawing Modelling 1491
Deep Drawing Tools 21
Deep Drawing 219,977,997,
Deep Rolling 987
Deformable Tools 1481
Deformation Field 657
Design of Experiments (DOE) 1521
Diamond-Like Carbon 583
DIC 1193,1887
Die Roll 2101
Die Technology 1799
Dies 533
Difficult-To-Cut Material 1747
Digital Image Correlation (DIC) 817, 695,1131
Digital Twin (DT) 1521
Dimensional Accuracy 937
Direct Energy Deposition (DED) 199
Direct Metal Laser Sintering 65
Direct-Vacuum-Casting (DVC) 199
Disc Milling 455
Disk Rolling 657
Dissimilar 1091
Divided Punch 1059
DP Steel 1631
DP800 705
Drag Finishing 1673
Draping 339
Dry EDM 1663
Dual Phase Steel 727,951,1407,1443
Ductile Damage Criterion 1463
Ductile Damage Modelling 1379
Ductile Damage to Fracture Transition 1603
Ductile Fracture 807,1593
Dynamic Behavior Model 649
Dynamic Deformation 839
Dynamic Recrystallisation 1559

EBSD Technique 437
ECM 1781
EDM 1663,1781
Effective Parameters 1759
Effective Properties 1621
Elastoplasticity 1143,1193
Electrical Discharge Drilling (EDD) 1747
Electrical Steel 1101
Electrically-Assisted Forming 997
Electro Discharge Machining 1663
Electrochemical Machining 1653,1759
Electrochemical Polishing 1673
Electromagnetic Stirring 1541
Electron Beam Melting 1939
Embossing 951
Energy Analysis 1947
Energy and Resource Efficiency 1929
Energy Director 1819
Energy Efficiency 1957
Engineering Plastics 1799
Epoxy Matrix 1871
Experimental Analysis 49
Experimental Characterization 331
Experimental-Numerical Procedure 737
Extrusion 455,477,505,533, 929,1809,1977

Fabrics/Textiles 331
FAST 1977
FDM 13,1879
FE Analysis 1697
FEA 219,683
FEM Simulation 347,639
FEM 239,477,543,667,787,855,2091
FFF 169
Fiber Content 249

Fiber Metal Laminates 977
Fiber Orientation 321
Fibers Reinforced Composite (FRC) 321
Fiber Placement 367
Fibre Metal Laminates 259
Field-Assisted-Sintering 1213
Filament Winding 347
Filament 1879
Fine Blanking 869,909,2101
Fine Grains 1739
Finite Element Analysis 899,1047
Finite Element Method (FEM) 159,487, 1037,1453,1503,1531,1551, 1593,1711,1759
Finite Element 231,1435
Fishtail 629
Flat-Knitting 239
Flax 1809
FLC 855
Flexibility 969,1967
Flexible Roll Forming 1047
Flour Waste 1879
Flow Curve Prediction 1503
Flow Forming of CuZn30 1021
Flow Forming Process 807
Flow Forming 1015,1029,2049,1929
Fluid-Structure Interaction 977
Flute Grinding 1213
FML 219
Foaming 1427
FORGE NxT® 1521
Forging Die 573
Forging 869
Form Variable Handling 1083
Formability 747,771,833
Forming Limit Diagram 705
Forming Optimisation 1155
Forming Processes 1603
Forming 231,259,339,919,2081
Fracture Characterisation 1407
Fracture Locus 807
Freeform Bending 2091
Friction Coefficient 1907
Friction Extrusion 487,515
Friction Model 2115
Friction Stir Consolidation 1997
Friction Stir Welding 1067
Friction Welding 591
Friction, Wear 891
Friction-Induced 1957
Friction-Spinning 1929
FSI 219
FSW, T-Joint 1091
Full Forward Impact Extrusion 445
Full-Field Measurements 1203
Full-Field Modelling 683
Function Integrated Handling 1083
Fused Filament Fabrication (FFF) 93,139
Fusion Welding 1711

Galling Free 869
Galling 891
Gapping 375
Gas Cylinder Forming 1929
Gears 495,1799
Genetic Algorithm 407,1175
Goldak’s Heat Source Parameters 159
Graded Grinding Wheels 1213
Graded Structures 2049
Grain Size 2061
Graphene 455
Graphite Nanoplatelets 1851
Green Ceramics 1245
Green Compaction 1799

Hammer Forging 675
Hardening of Aluminium Alloys 771

Hardness 129
Heat Transfer Coefficient 1175
Heat Transfer 139,1897
Heat Treatment 445,1029,1295
Heating Technology 959
Heterogeneous Test Evaluation 1131
Heterogeneous Tests 1121
High Manganese Steel 2101
High Strain Rate 1379
High Strength Steel 755,951
High-Manganese Steel 839
High-Speed Steel Punch 869
Hole Expansion Test 1369
Hot and Warm Forming 771
Hot Deformation 505
Hot Die Forging, Wear 583
Hot Extrusion 419
Hot Forging 591,675,1357
Hot Forming 639,959
Hot Isostatic Pressing 129,1427
Hot Press Forming 267
Hot Process 667
Hot Rolling 601
Hot Stamping 833,937
Hot Strip Rolling 1631
HS6-5-3-8 1235
HSS 1235
Human Machine Interface 1643
Hybrid Manufacturing 1245
Hybrid Materials 1977
Hybrid Parts 919
Hybrid Processes 1781
Hybrid SPD 825
Hyperelastic 285,357

Image Processing 101
Impregnation 1683
In Situ Solid Lubrication 869
Inconel 625 Alloy 1663
Incremental Bulk Forming 1583
Incremental Forming 657,1929
Incremental Shape Rolling 1047
Incremental Sheet Forming 1697
Incremental Sheet Metal Forming 1037
Indirect Training 1143
Industrial Robot 367
Infiltration 219
Infrared Camera 1897
Infusion Simulation 313
Ingot-to-Billet Conversion Process 621
Injection Gate Location 321
Injection Molding 207,321,1565
In-Plane Pull-Out 375
In-Situ Hybridization 977
Interfacial Bonding 139
Interior Liquid Channel 3
Interlocking 1101
Intermediate Rate Testing 675
Internal Variables 1631
Interpolation 1551
Invariant-Based 357
Inverse Identification 1131,1167
Inverse Methods 1203
Ironing Force Prediction 1491
Ironing Stage 1481

Jet-ECM 1643
JMAK 667
JMAK-Type Models 683
Johnson-Cook Model 1313
Joining Zone 591
Joining 1111

Knitted Textiles 277
KPIs 1121

Lamination Stacks 1101
Lankford Value 711
Large Rapid Deformation 1887
Large Strain Flow Curve 1167
Laser Engraving 1703
Laser Heat Treatment 855
Laser Line 101
Laser Metal Deposition 21,101
Laser Powder Bed Fusion 41,129
Laser Sintering 111
Laser Welding 1829
Laser Wire 119
LCA Sustainability 1947
Lead-Free Brass Alloy 1303
Lead-Free Brass 1357
Life Cycle Analysis 1987
Life Cycle Assessment 2015
Lightweight Design 249
Linear Stress Path 779
Liquid Nitrogen 533
Load Path 943
Loading Trajectory 943
Local Properties 149
Local Tensile Tests 717
Low-Cost Tooling 969
Low-Temperature Annealing 429
LPBF 189,1235
LPBF-Process 149
Lubricant Additive 879
Lüders Bands 1511
Machine Learning 57,321,385,1155, 1193,1417,
Machining 1265,1357,1683,1939
Machining, Cold Spray 1729
Macroscopic Plasticity 799
Magnesium Alloy 259,711
Mass Customization 1967
Material Behavior 1131
Material Characterization 3,1379
Material Failure 787
Material Flow 1091
Material Model Selection 1369
Material Modeling 1075,1759
Material Properties 2071
Material Removal 1673
Mean-Field Modelling 683
Mechanical Behavior 847
Mechanical Properties 85,455,675, 1879,1987
Mechanical Recycling 1683
Mechanical Test 779
Mechatronic Straightening Machine 2005
Medium Manganese Steel 833
Mesh Size Dependency 1511
Meshing 1583
Meso-Scale Model 285
Mesoscopic Defects 375
Metal Casting 1175,1729
Metal Foams 49
Metal Forming 495,563,799,899,1503
Metal Fused Filament Fabrication 3
Metal Matrix Composites (MMC) 1689
Metallization 305
Metallurgy Industry 1541
Metals 1323
Metal-Spinning 1929
Mg Alloy 1739
Microchannel 937
Microforming 825
Micro-Hole 1747
Micromachining 1323
Micro-Milling 1255
Micro-Stamping 1531
Microstructure Evolution 1631
Microstructure 65,189,477,129,675, 8391357,1427,1559
Mild Steel Sheet 779

Mild Temperature Forming 755
Milling 1245,1331
MK Method 705
MMC Fracture Model 1407
MMFC2 705
Modeling 13,189
Monitoring 1265
Monte Carlo and RSM Methods 1275
Monte Carlo Method 1551,1575
Multiaxial Coupling 357
Multifunctional Composites 1871
Multi-Material-System 1111
Multi-Objective Optimization 601
Multiphysics Simulation 1653
Multi-Step Industrial Forging 683

Nanocomposites 1851
Nanosecond Pulsed Laser 1703
NDT 2071
Neural Networks 57,1143
NiTi Alloys 429
NiTi Shape Memory Alloy 1275
Nitriding 583
Nonlinear Behavior 1887
Nonlinear Stress Path 779
Non-Proportional Load Paths 747
NSF (Near Solidus Forming) 1521
Numerical Analysis 523,1481,1711
Numerical Investigation 573
Numerical Modelling 717
Numerical Simulation 139,1369,1907

On-Demand 239
Online Measurement 573
Onset of Yielding 747
Open-Die Forging 2061
Optical Absorption 111
Optical Properties 1829
Optimization Methods 649
Optimization 1275
Orthogonal Cutting 1235
Orthogonal Turning 1313
Orthotropic Design 231
Osseointegration 1255
Out-of-Autoclave Molding 1789

Parameter Calibration 1417
Partial Cooling 591,1083
Particles 879
PEEK 1285
Pellet Additive Manufacturing 1245
Permeability 407
PET 93
Phase Change 1223
Phase Field Fracture 1593
Phase Field 1603
Phase Transformation 139
Photogrammetry 293
PINNs 1621
PLA 1879
Plane-Strain-Compression-Test 149
Plastic Anisotropic Models 1491
Plastic Die Deformation 523
Ply-Ply Adhesion 267
Polishing 1673
Polycarbonate 1907
Polycrystalline Model 799
Polymer Matrix Composites 305
Polymeric Materials 1719
Polymerization Kinetics 313
Polymers 1697
Polynomial Chaos Expansion 1183
Polypropylene 393
Porosity 1861
Porthole Dies 437
Post-Treatment 1861

Powder Consolidation 515
Powder Metallurgy 1799
Powder Pressing 1689
Powder-Metallurgical Steel 987
Pr/NdFeB 505
Precursors 49
Pre-Joined Hybrid Semi-Finished Parts 717
Prepregs 367, 393
Press Hardening 833
Pressure Vessel 347,1929
Process Analysis 1781
Process Development 249
Process Map 41
Process Monitoring 101
Process Optimization 2061
Process Simulation 219,487
Process Variability 1067
Process Variations 1575
Production Technology 495
Property Control 2081
Property Monitoring 2071
Property-Controlled Forming 2115
Pseudo-Plastic 1917
Pultrusion 393
Punch-Bending Process 2005
Punch-Hole-Rolling 2081
PyRolL 1575

QForm Extrusion 543
Quality Control 3
Quality Prediction 1565

Radial-Axial Ring Rolling 629
Random Cellular Automata 1559
Rapid Prototyping 207
Rapid Tooling 207
Reactive Resin 313
Recrystallisation 477,621,667
Recrystallization of CuZn30 1021
Recycling 1957,1977,1997
Reinforcement Learning 601,2061
Reinforcements 339
Research Equipment 1719
Residual Stress 987,1295
Resin Infusion 305,407
Reverse Flow Forming 2037
Rigid-Soft-Structures 339
Robotic Layup 367
Roll Forming 787
Rolling Simulation 1575
Room-Temperature Cup Drawing 711
Rotary Swaging 899
Roughness 1255,1841,1939

SAE304 Steel 1703
Sandwich Structures 399
Screw Press 649
Selective Laser Melting 31
Self-Learning Disturbance Compensation 2005
Self-Piercing Riveting 1111
Semicrystalline Polymer 139
Semi-Solid Processing 75
Sensing Properties 429
Sensitivity Study 649
Severe Plastic Deformation 553
Shape Memory Effect 93
Shape Recovery 93
Shear Strength 1819,1841
Sheared Part Quality 2101
Shearing 1007
Sheath-Core 1809
Sheet Forming 1075
Sheet Metal Forming 1131,1481,1967
Sheet Metal Lamination 21

Sheet Metal Remanufacturing 1947
Sheet Metal 943,1121
Sheet-Bulk Metal Forming 929,2081
Sheet-Metal Forming 2071
Shell Element 1037
Simulation 31,239,495,621,1223
Single Lap Shear Test 1829
Sinking Electrical Discharge Machining 1765
Sinter-Forging 1799
Size Effect 179,1453,1471
Skin Contamination 543
Skin 1091
Skin-Pass Rolling 2115
Sobol's Indices 1183
Softsensor 2091
Solid-State Materials Processing 487
Solid-State Processing 515,1739
Soundproofing 1719
Springback 755
Square Cup 1183
Stainless Steel 621,937
Steel Bars 1611
Steel 695
STL Generation 169
Stochastic Model 1631
Strain Distribution 695
Strain Gradient Plasticity 1453
Strain Gradient 1511
Strain Hardening 1015,2101
Strain Localization 1511
Strain Rate Field 657
Strengthal 65
Stress Superposition 611
Stress Triaxiality Dependency 1387
Stress-Based Diagram 761
Stretch Drawing 727
Stretch Flangeability 1007
Stretch Forming 943
Stringer 1091
Strong Form Meshless Method 1611
Super Duplex Stainless Steel 629
Supportless Manufacturing 3
Surface Characterization 1323
Surface Finish 1285,1295
Surface Integrity 987,1303,1341
Surface Quality 563,1331,1775
Surface Roughness 31,899,1673
Surface Topography 1245,1703
Surrogate Modelling 385
Surrogate 1155
Sustainability 1967,1987
Sustainable Manufacturing 1939
Sustainable Packaging 2015
Synthetic Images 1131
Synthetic Meshes 277

t/d Ratio Influence 1471
Tailor Welded Blanks 1075
Tailored Fibre Placement 231
Tailored Forming 591,1083
Tapes 393
Tapping 1303
Target Function 649
Temperature Monitoring 573
Temperature 839
Tensile Test 951
Textile Structure 339
Textile 339
Thermal Biaxial Tensile Test 1397
Thermal Conductivity 65
Thermal Diffusion 1819
Thermal History 189
Thermal Spray 57,1729
Thermal-Electrical Expansion 111
Thermoforming 385,1907

Thermography 1565
Thermo-Mechanical History 467
Thermomechanical Testing 675
Thermo-Mechanics 1611,1621
Thermoplastic Matrix Composites (TPC) 267
Thermoplastic 293,393,1829
Thermo-Viscoplastic Model 1397
Thickness Distribution 1907
Thickness Prediction 1491
Thickness Strain 711
Thin Foil 1531
Thin-Film Sensor 2027
Threading 1303
Ti Alloy 1427
Ti64β 1347
Ti-6Al-4V 675,1255
Titanium Grade 2 1663
Titanium 869,1091
Tool Design 573
Tool Life 583
Tool Steel Punch 869
Tool Steel 41
Tool Technology 959
Tool Wear 1331,1347
Toolpath Strategy 1697
Topological Optimization 533
Torsion Test 1167
Total Strain 695
Trabecular Bone 169
Tribological Testing 879
Tribology in Manufacturing 419
Tribology 891,909
Trimming 611
T-SIM® 1907
Tube Bending 969
Tube Rolling 639
Tubular Products 817
Tungsten Carbide 129
Turning 1265,1939
Twining-Induced Hardening 1223
Twinning Induced Plasticity 2101
Twinning 711,839
TWIP 839
Twist Extrusion 553

U-Channel 1037
UD-NCF 331
UFG Metals 825
Ultra-High Strength Steel Sheets 1007
Ultrasonic Burnishing 1775
Ultrasonic Tests 1427
Ultrasonic Welding 1819,1841,1851
Uncertainty 1183
Unidirectional 293
Unit Cell 285,1435

Vacuum Forming Process 1887
Validation 293
Variable Geometries 1155
Variable Thickness 399
V-Bending 755
VDOE 629
Velocity Field 657,1917
Versatile Joining 1111
Viscous Dissipation 1917
Vitrimer 1871
Voce Material Model 1503

Warm Forming 909
Welding 1551
Wire Arc Additive Manufacturing (WAAM) 159
Wire Drawing Process 563
Wire-Feed Additive Manufacturing 75
Wooden Tools 1967

Work Hardening 467
Woven Fabric 375
Wrinkling Limit 761
Wrinkling 1047

XCT 277

Yield Function 779
Yield Point Phenomenon 1511
Young’s Modulus 1427

Zinc Coatings 891
ZnMgAl Coating 817

α’-Martensite 2037

About the Editors

Lukasz Madej is a full professor and the head of the Industrial Digitalization and Multiscale Modelling Division at the Faculty of Metal Engineering and Industrial Computer Science at AGH University. His research focuses on the development of modern numerical solutions for the industry and, in particular full-field multiscale modelling models for materials science. He is a member of various scientific organizations, e.g., Polish Association of Computational Mechanics and Polish Materials Science Society. In 2022 he was elected as a Fellow of the CIRP - The International Academy for Production Engineering. Since 2020 he is also a member of the Board of Directors of the ESAFORM. At the same time, he is editor-in-chief of Computer Methods in Materials Science journal and a member of editorial boards in various academic journals, e.g., Steel Research International, International Journal of Material Forming, Journal of Materials Processing Technology or Production Engineering - Research and Development. He is the author and co-author of more than 250 published works, including 5 books. Besides scientific activities, he is also active in the Polish Forging Association, where he holds the position of vice president and in the EUROFORGE as an Executive Board member. More information can be found at the following website: http://home.agh.edu.pl/~lmadej

Mateusz Sitko is an assistant professor at the Faculty of Metal Engineering and Industrial Computer Science at AGH University. His research focuses on the development of multiscale models for microstructure evolution dedicated to high-performance computing environments and the incorporation of virtual and augmented reality tools into industrial applications. He is a member of various scientific organizations, e.g., Polish Association of Computational Mechanics, Polish Forging Association or ESAFORM. At the same time, he is the assistant editor of Computer Methods in Materials Science journal. He is the author and co-author of one book chapter and 35 journal articles. More information is available at the following website: http://home.agh.edu.pl/~msitko/en/

Konrad Perzynski is an assistant professor at the Faculty of Metal Engineering and Industrial Computer Science at AGH University. His research focuses on the numerical modelling of a wide range of industrial processes, including the development of full-field multiscale models for materials science. He is also involved in the modelling and analysis of thin film nanostructures. He is a member of several scientific organizations, e.g., Polish Association of Computational Mechanics or ESAFORM. He is also a core group member of the ECCOMAS Young Investigators committee. At the same time, he is the assistant editor of Computer Methods in Materials Science journal. He is the author and co-author of more than 70 journal articles. More information can be found at the following website: https://home.agh.edu.pl/~kperzyns/